

SPRINGER
REFERENCE

Dan Gabriel Cacuci
Editor

Handbook of Nuclear Engineering

Nuclear Engineering
Fundamentals

 Springer

Handbook of Nuclear Engineering

Dan Gabriel Cacuci (Ed.)

Handbook of Nuclear Engineering

With 1498 Figures and 393 Tables

Volume I

Nuclear Engineering Fundamentals

Professor Dan Gabriel Cacuci

Institute for Nuclear Technology and Reactor Safety
Karlsruher Institut für Technologie (KIT)
Gotthard-Franz-Str. 9
76131 Karlsruhe
Germany

Library of Congress Control Number: 2010927884

ISBN: 978-0-387-98130-7

This publication is available also as:

Electronic publication under ISBN 978-0-387-98149-9 and

Print and electronic bundle under ISBN 978-0-387-98150-5

© Springer Science+Business Media LLC 2010

All rights reserved. This work may not be translated or copied in whole or in part without the written permission of the publisher (Springer Science+Business Media, LLC., 233 Spring Street, New York, NY 10013, USA), except for brief excerpts in connection with reviews or scholarly analysis. Use in connection with any form of information storage and retrieval, electronic adaptation, computer software, or by similar or dissimilar methodology now known or hereafter developed is forbidden.

The use in this publication of trade names, trademarks, service marks, and similar terms, even if they are not identified as such, is not to be taken as an expression of opinion as to whether or not they are subject to proprietary rights.

Springer is part of Springer Science+Business Media

springer.com

Printed on acid-free paper

Preface

A new Handbook of Nuclear Engineering is indeed a rare event, although the engineering sciences – and especially nuclear engineering – have progressed immensely during the fifty-two years that have passed since the publication of the first handbook of this kind. Even if the basic principles of nuclear engineering have remained unchanged for decades, it is compelling to note that the professional practice in this sector has enjoyed great progress during this period.

Professor Dan Cacuci has embarked on an ambitious task: to edit a new Handbook of Nuclear Engineering, aiming at making it as all encompassing as possible. He successfully carried out this huge task in a very short time span, bringing together specialists of the highest international reputation.

Primordially, nuclear engineering draws its roots from the nuclear sciences, a field founded on the most fundamental advances in the physics of the 20th century. This is an exacting field conceptually, demanding knowledge not only of the intimate structure of matter, but also of the mathematical formalisms that represent this structure. A field that is, regrettably, increasingly more neglected in the general education.

At the same time, nuclear engineering is also about engineering at the highest level of exigency for harnessing the extremely high power density in nuclear systems, intertwined with the absolute necessity to control and operate these systems in conditions of maximum safety and economic feasibility.

Last but not least – and this is probably the source of its unique characteristics – nuclear engineering is anchored in time, in its own history, first and foremost, and especially in the extent of time over which the responsibility of nuclear engineers must last – from designing, constructing and operating reactors to the management of the ultimate destination of decommissioned reactor plants.

These exceptional stakes are becoming critical now – at a time when the “third-generation” of nuclear engineers needs to be educated, a generation which is to succeed the “master-builders”, who themselves had, in turn, succeeded the “pioneers”. This third-generation of nuclear engineers is already being called upon to fulfill a new demand – that of integrating all of the knowledge produced by its predecessors in the quest for meeting an increasing demand for energy production under enhanced safety requirements and optimal economic conditions.

Energy is a major stake of the 21th century. Humanity will imperatively need to manage the sustainable production, transportation, and applications of energy. Nuclear power will inevitably play a decisive role in this quest.

Needs for energy, needs for competences, needs for education and training, needs for reference books in nuclear engineering: I do make the wish that the present work would contribute its share towards satisfying these needs, enlightening the young generations to which we are passing on great responsibilities. In view of the contents of this Handbook, covering widely

and deeply the vast field of nuclear engineering, and the outstanding quality of this coverage – guaranteed by the worldwide reputation of the authors – I have no doubt that this wish will come true.

Laurent Turpin

August 2010

Director

National Institute for Nuclear Science and Technology (INSTN)

Commissariat à l'Énergie Atomique (CEA)

Centre CEA de Saclay

91191 Gif-sur-Yvette Cedex

France

About the Editor



Dan Gabriel Cacuci

Institute for Nuclear Technology and Reactor Safety
Karlsruher Institut für Technologie (KIT)
Gotthard-Franz-Str. 9
76131 Karlsruhe
Germany

Dan Gabriel Cacuci has received his Ph.D. degree in applied physics and nuclear engineering from Columbia University, New York, in 1978. His career has bridged activities in the academia and multidisciplinary national research centers. His teaching and research experience as a full professor at leading academic institutions includes appointments (tenured, part-time, visiting, or adjunct) at the University of Tennessee (1983–1988), University of California at Santa Barbara (1988–1990), University of Illinois at Urbana-Champaign (1990–1993), University of Virginia (1993–2000), University of Michigan (1995–2000), University of California at Berkeley (2001–2006), Royal Institute of Technology Stockholm (2003), the French National Institute for Nuclear Sciences and Technologies in Paris (since 2006), and the University of Karlsruhe (since 1992). Professor Cacuci has also served as a group leader and section head at Oak Ridge National Laboratory (1976–1988), Institute Director at the Nuclear Research Center Karlsruhe in Germany (1993–2004), and acted as Scientific Director of the Nuclear Energy Directorate, Commissariat à l’Energie Atomique, France (2005–2009).

Professor Cacuci’s scientific expertise encompasses several areas in nuclear engineering (reactor multi-physics, dynamics, safety and reliability), predictive best-estimate analysis of large-scale physical and engineering systems, and large-scale scientific computations. He has authored 3 books, 7 book chapters, and over 180 peer-reviewed articles.

Since 1984, Professor Cacuci has been the Editor of “Nuclear Science and Engineering –The Research Journal of the American Nuclear Society” (ANS). He is a member of the European Academy of Arts and Sciences, Honorary Member of the Romanian Academy, ANS Fellow, and has received many awards, including four titles of Doctor Honoris Causa, the Alexander von Humboldt Prize for Senior Scholars (Germany), the E. O. Lawrence Award and Gold Medal (US DOE), the Eugene P. Wigner Reactor Physics Award (ANS), and the Glenn Seaborg Medal (ANS). Professor Cacuci has served on numerous international committees, was founding coordinator of the EURATOM-Integrated Project NURESIM (European Platform for Nuclear Reactor Simulation, 2004–2008), and founding coordinator (2004–2007) of the Coordinated Action for establishing a Sustainable Nuclear Fission Technology Platform (SNF-TP) in Europe.



Table of Contents

Preface	v
About the Editor	vii
Contributors	xiii
Biographies of Contributors	xxi
Introduction	li

Volume 1 Nuclear Engineering Fundamentals

1 Neutron Cross Section Measurements	1
<i>Robert C. Block · Yaron Danon · Frank Gunsing · Robert C. Haight</i>	
2 Evaluated Nuclear Data	83
<i>Pavel Obložinský · Michal Herman · Said F. Mughabghab</i>	
3 Neutron Slowing Down and Thermalization	189
<i>Robert E. MacFarlane</i>	
4 Nuclear Data Preparation	279
<i>Dermott E. Cullen</i>	
5 General Principles of Neutron Transport	427
<i>Anil K. Prinja · Edward W. Larsen</i>	
6 Nuclear Materials and Irradiation Effects	543
<i>Clément Lemaignan</i>	
7 Mathematics for Nuclear Engineering	643
<i>Dan Gabriel Cacuci · Mihaela Ionescu-Bujor</i>	

Volume 2 Reactor Design

8 Multigroup Neutron Transport and Diffusion Computations	751
<i>Alain Hébert</i>	
9 Lattice Physics Computations	913
<i>Dave Knott · Akio Yamamoto</i>	
10 Core Isotopic Depletion and Fuel Management	1241
<i>Paul J. Turinsky</i>	

11	Radiation Shielding and Radiological Protection	1313
	<i>J. Kenneth Shultis · Richard E. Faw</i>	

12	High Performance Computing in Nuclear Engineering	1449
	<i>Christophe Calvin · David Nowak</i>	

Volume 3 Reactor Analysis

13	Analysis of Reactor Fuel Rod Behavior	1519
	<i>Paul Van Uffelen · Rudy J.M. Konings · Carlo Vitanza · James Tulenko</i>	

14	Noise Techniques in Nuclear Systems	1629
	<i>Imre Pázsit · Christophe Demazière</i>	

15	Deterministic and Probabilistic Safety Analysis	1739
	<i>Mohammad Modarres · Inn Seock Kim</i>	

16	Multiphase Flows: Compressible Multi-Hydrodynamics	1813
	<i>Daniel Lhuillier · Meng-Sing Liou · Theo G. Theofanous</i>	

17	Sensitivity and Uncertainty Analysis, Data Assimilation, and Predictive Best-Estimate Model Calibration	1913
	<i>Dan Gabriel Cacuci · Mihaela Ionescu-Bujor</i>	

18	Reactor Physics Experiments on Zero Power Reactors	2053
	<i>Gilles Bignan · Philippe Fougeras · Patrick Blaise · Jean-Pascal Hudelot · Frédéric Mellier</i>	

Volume 4 Reactors of Generations III and IV

19	Pressurized LWRs and HWRs in the Republic of Korea	2185
	<i>Nam Zin Cho · Han Gon Kim</i>	

20	VVER-Type Reactors of Russian Design	2249
	<i>Sergei B. Ryzhov · Victor A. Mokhov · Mikhail P. Nikitenko · George G. Bessalov · Alexander K. Podshibyakin · Dmitry A. Anufriev · Janos Gadó · Ulrich Rohde</i>	

21	Sodium Fast Reactor Design: Fuels, Neutronics, Thermal-Hydraulics, Structural Mechanics and Safety	2321
	<i>Jacques Rouault · P. Chellapandi · Baldev Raj · Philippe Dufour · Christian Latge · Laurent Paret · Pierre Lo Pinto · Gilles H. Rodriguez · Guy-Marie Gautier · Gian-Luigi Fiorini · Michel Pelletier · Dominique Gosset · Stéphane Bourganel · Gerard Mignot · Frédéric Varaine · Bernard Valentin · Patrick Masoni · Philippe Martin · Jean-Claude Queval · Daniel Broc · Nicolas Devictor</i>	

22	Gas-Cooled Reactors	2711
	<i>Bertrand Barré</i>	

23	Lead-Cooled Fast Reactor (LFR) Design: Safety, Neutronics, Thermal Hydraulics, Structural Mechanics, Fuel, Core, and Plant Design	2749
	<i>Luciano Cinotti · Craig F. Smith · Carlo Artioli · Giacomo Grasso · Giovanni Corsini</i>	
24	GEM* STAR: The Alternative Reactor Technology Comprising Graphite, Molten Salt, and Accelerators	2841
	<i>Charles D. Bowman · R. Bruce Vogelaar · Edward G. Bilpuch · Calvin R. Howell · Anton P. Tonchev · Werner Tornow · R.L. Walter</i>	
 Volume 5 Fuel Cycles, Decommissioning, Waste Disposal and Safeguards		
25	Front End of the Fuel Cycle	2895
	<i>Bertrand Barré</i>	
26	Transuranium Elements in the Nuclear Fuel Cycle	2935
	<i>Thomas Fanghänel · Jean-Paul Glatz · Rudy J.M. Konings · Vincenzo V. Rondinella · Joe Somers</i>	
27	Decommissioning of Nuclear Plants	2999
	<i>Maurizio Cumo</i>	
28	The Scientific Basis of Nuclear Waste Management	3253
	<i>Bernard Bonin</i>	
29	Proliferation Resistance and Safeguards	3421
	<i>Scott F. DeMuth</i>	
Index.....		3539



Contributors

Dmitry A. Anufriev

OKB "GIDROPRESS"
Joint Stock Company
State Atomic Energy Corporation "Rosatom"
Podolsk
Moscow Region
Russia

Carlo Artioli

Italian National Agency for
New Technologies, Energy and Sustainable
Economic Development
v. Martiri di Monte Sole 4
Bologna
ITALY
carlo.artioli@enea.it

Robert Bari

Brookhaven National Laboratory
Upton
NY 11973-5000
USA
bari@bnl.gov

Bertrand Barré

7 rue des Blanchisseurs
92370 INSTN
Chaville
France
bcbarre@wanadoo.fr

Charles G. Bathke

Los Alamos National Laboratory
Los Alamos
NM 87545
USA
bathke@lanl.gov

George G. Bessalov

OKB "GIDROPRESS"
Joint Stock Company
State Atomic Energy Corporation "Rosatom"
Podolsk

Moscow Region
Russia

Gilles Bignan

French Atomic Energy Commission
Reactor Studies Department
Cadarache Research Center
Saint Paul Lez Durance
France
gilles.bignan@cea.fr

Edward G. Bilpuch

Triangle Universities Nuclear Laboratory
Duke University
Durham
NC 27708
USA

Patrick Blaise

French Atomic Energy Commission
Reactor Studies Department
Cadarache Research Center
Saint Paul Lez Durance
France
patrick.blaise@cea.fr

Robert C. Block

Gaertner LINAC Laboratory
Mechanical, Aerospace & Nuclear
Engineering Department
Rensselaer Polytechnic Institute
Troy, NY 12180-3590
USA
blockr@rpi.edu

Bernard Bonin

Commissariat à l'Énergie Atomique
France
Nuclear Energy Directorate
CEA Saclay
Gif-sur-Yvette Cedex
France
Bernard.Bonin@cea.fr

Stéphane Bourganel

CEA Saclay
Centre d'Etudes Nucléaires de Saclay
91191 Gif-sur-Yvette
France
stephane.bourganel@cea.fr

Charles D. Bowman

ADNA Corporation
1045 Los Pueblos
Los Alamos
NM 87544
USA
cbowman@cybermesa.com

Brian Boyer

Los Alamos National Laboratory
Los Alamos
NM 87545
USA
bboyer@lanl.gov

Daniel Broc

French Atomic Energy Commission (CEA)
Saint Paul Lez Durance
France
daniel.broc@cea.fr

Thomas Burr

Los Alamos National Laboratory
Los Alamos
NM 87545
USA
tburr@lanl.gov

Dan Gabriel Cacuci

Institute for Nuclear Technology and
Reactor Safety
Karlsruher Institut für Technologie (KIT)
Karlsruhe
Germany
dan.cacuci@kit.edu

Christophe Calvin

CEA/DEN/DANS/DM2S CEA Saclay
91191 Gif-sur-Yvette
France
christophe.calvin@cea.fr

P. Chellapandi

Indira Gandhi Center for Atomic Research
Tamilnadu
India
pcp@igcar.gov.in

Nam Zin Cho

Department of Nuclear and
Quantum Engineering
Korea Advanced Institute of
Science and Technology
Daejeon
Korea
nzcho@kaist.ac.kr

Luciano Cinotti

MERIVUS srl
V. Orazio 10
Roma
ITALY
luciano.cinotti@gmail.com

Giovanni Corsini

Giovanni.Corsini@tele2.it

Dermott E. Cullen

Lawrence Livermore National Laboratory
Livermore
CA 94550
USA
redcullen1@comcast.net

Maurizio L. Cumo

University of Rome
Corso Vittorio Emanuele II
244 Rome 186
Rome
Italy
maurizio.cumo@uniroma1.it

Yaron Danon

Rensselaer Polytechnic Institute
Troy
NY
USA

Christophe Demazière

Department of Nuclear Engineering
Chalmers University of Technology
Göteborg
Sweden

Scott F. DeMuth

Los Alamos National Laboratory
Los Alamos
NM 87545
USA
scott.demuth44@comcast.net

Nicolas Devictor

French Atomic Energy Commission (CEA)
Saint Paul Lez Durance
France
nicolas.devictor@cea.fr

Philippe Dufour

Chargé de mission RNA-Na
CEA/DEN/CAD/DER/SESI
French Atomic Energy Commission (CEA)
Saint Paul Lez Durance
France
philippe.dufour@cea.fr

Michael Ehinger

Oak Ridge National Laboratory
Oak Ridge
TN 37830-8026
USA
ehingermh@ornl.gov

Thomas Fanghänel

European Commission
Joint Research Centre
Institute for Transuranium Elements
Karlsruhe
Germany
thomas.fanghaenel@ec.europa.eu

Richard E. Faw

Department of Mechanical and
Nuclear Engineering
Kansas State University
Manhattan

KS 66506

USA
fawre@triad.rr.com

Gian-Luigi Fiorini

French Atomic Energy Commission (CEA)
Saint Paul Lez Durance
France
gian-luigi.fiorini@cea.fr

Philippe Fougeras

French Atomic Energy Commission (CEA)
Reactor Studies Department
Cadarache Research Center
Saint Paul Lez Durance
France
philippe.fougeras@cea.fr

János Gadó

KfKI, Atomic Energy Research
Institute of the Hungarian
Academy of Sciences
Budapest
Hungary
Joint Stock Company
State Atomic Energy Corporation
"Rosatom"
Podolsk
Moscow Region
Russia
goolo@sunseru.kfki.hu

Guy-Marie Gautier

French Atomic Energy Commission (CEA)
Saint Paul Lez Durance
France
guy-marie.gautier@cea.fr

Jean-Paul Glatz

European Commission
Joint Research Centre
Institute for Transuranium Elements
Karlsruhe
Germany
jean-paul.glatz@ec.europa.eu

Dominique Gosset

French Atomic Energy Commission (CEA)
Saint Paul Lez Durance
France
dominique.gosset@cea.fr

Giacomo Grasso

Italian National Agency for
New Technologies
Energy and Sustainable
Economic Development
v. Martiri di Monte Sole 4
Bologna
ITALY
giacomo.grasso@enea.it

Frank Gunsing

CEA Saclay - Irfu
France
frank.gunsing@cea.fr

Robert C. Haight

Los Alamos National Laboratory
Los Alamos
NM 87545
USA

Alain Hébert

Institut de Génie Nucléaire
École Polytechnique de Montréal
Montréal
Québec
Canada
alain.hebert@polymtl.ca

Magnus Hedberg

Institute for Transuranium Elements
Karlsruhe
Germany
Magnus.HEDBERG@ec.europa.eu

Michal Herman

National Nuclear Data Center
Brookhaven National Laboratory
Upton
NY 11973-5000
USA
mwherman@bnl.gov

Calvin R. Howell

Triangle Universities Nuclear Laboratory
Duke University
Durham
NC 27708
USA

John Howell

Department of Mechanical Engineering,
Systems and Control
University of Glasgow
Glasgow G128QQ
UK
j.howell@mech.gla.ac.uk

Jean-Pascal Hudelot

French Atomic Energy Commission (CEA)
Reactor Studies Department
Cadarache Research Center
Saint Paul Lez Durance
France
jean-pascal.hudelot@cea.fr

Mihaela Ionescu-Bujor

Fusion Program
Karlsruher Institut für Technologie (KIT)
Karlsruhe
Germany
mihaela.ionescu-bujor@kit.edu

Frédérique Jasserand

CEA Saclay
Gif-Sur-Yvette
France

Han Gon Kim

Advanced Plant Development Office
Korea Hydro and Nuclear Power Co., Ltd
Daejeon
Korea
kimhangon@khnp.co.kr

Inn Seock Kim

ISSA Technology, Inc.
21318 Seneca Crossing Drive
Germantown
MD 20876
USA
innseockkim@gmail.com

Dave Knott

Studs vik Scandpower Inc.
Wilmington
NC
USA
Dave.Knott@studsvik.com

Rudy J.M. Konings

European Commission
Joint Research Centre
Institute for Transuranium Elements
Karlsruhe
Germany
rudy.konings@ec.europa.eu

Edward W. Larsen

Department of Nuclear Engineering
and Radiological Sciences
University of Michigan
Ann Arbor
MI
USA
edlarsen@umich.edu

Christian Latge

French Atomic Energy Commission (CEA)
Saint Paul Lez Durance
France
christian.latge@cea.fr

Clément Lemaignan

CEA-INSTN and CEA-DEN
Grenoble
France
clement.lemaignan@cea.fr

Daniel Lhuillier

Institut Jean le Rond d'Alembert
CNRS and University Paris 6
Paris
France
daniel.lhuillier@upmc.fr

Meng-Sing Liou

NASA Glenn Research Center
Cleveland, OH
USA
meng-sing.liou@nasa.gov

Pierre Lo Pinto

French Atomic Energy Commission (CEA)
Saint Paul Lez Durance
France
pierre.lopinto@cea.fr

Klaus Lützenkirchen

Institute for Transuranium Elements
Karlsruhe
Germany
Klaus-Richard.Luetzenkirchen@
ec.europa.eu

Robert E. MacFarlane

Nuclear and Particle Physics, Astrophysics
and Cosmology
Theoretical Division
Los Alamos National Laboratory
Los Alamos
NM 87544
USA
ryxm@lanl.gov

Philippe Martin

French Atomic Energy Commission (CEA)
Saint Paul Lez Durance
France
philippe.martin@drncad.cea.fr

Patrick Masoni

French Atomic Energy Commission (CEA)
Saint Paul Lez Durance
France
patrick.masoni@cea.fr

Klaus Mayer

Institute for Transuranium Elements
Karlsruhe
Germany
Klaus.Mayer@ec.europa.eu

Frédéric Mellier

French Atomic Energy Commission (CEA)
Reactor Studies Department
Cadarache Research Center
Saint Paul Lez Durance
France

Gerard Mignot

French Atomic Energy Commission (CEA)
Saint Paul Lez Durance
France
gerard.mignot@cea.fr

Mohammad Modarres

Department of Mechanical Engineering
University of Maryland
Martin Hall
College Park
MD 20742
USA
modarres@umd.edu

Victor A. Mokhov

OKB "GIDROPRESS"
Joint Stock Company
State Atomic Energy Corporation "Rosatom"
Podolsk
Moscow Region
Russia

Said F. Mughabghab

National Nuclear Data Center
Brookhaven National Laboratory
Upton
NY 11973-5000
USA
mugabgab@bnl.gov

Mikhail P. Nikitenko

OKB "GIDROPRESS"
Joint Stock Company
State Atomic Energy Corporation "Rosatom"
Podolsk
Moscow Region
Russia

David Nowak

Mathematics and Computer Science
Division Argonne National Laboratory
9700 South Cass Avenue
Argonne
IL 60439-4844
USA
nowak@mcs.anl.gov

Pavel Obložinský

National Nuclear Data Center
Brookhaven National Laboratory
Upton
NY 11973-5000
USA
oblozinsky@bnl.gov

Laurent Paret

French Atomic Energy Commission (CEA)
Saint Paul Lez Durance
France
laurent.paret@cea.fr

Imre Pázsit

Department of Nuclear Engineering
Chalmers University of Technology
Göteborg
Sweden
Department of Nuclear Engineering
and Radiological Sciences
University of Michigan
Ann Arbor
Michigan
USA
imre@chalmers.se

Michel Pelletier

French Atomic Energy Commission (CEA)
Saint Paul Lez Durance
France
michel.pelletier@cea.fr

Alexander K. Podshibiyakin

OKB "GIDROPRESS"
Joint Stock Company
State Atomic Energy Corporation "Rosatom"
Podolsk
Moscow Region
Russia

Anil K. Prinja

Chemical and Nuclear Engineering
Department
University of New Mexico
Albuquerque
NM
USA
prinja@unm.edu

Jean-Claude Queval

French Atomic Energy Commission (CEA)
Saint Paul Lez Durance
France
jean-claude.queval@cea.fr

Baldev Raj

Indira Gandhi Center for Atomic Research
Tamilnadu
India
dir@igcar.gov.in

Gilles H. Rodriguez

French Atomic Energy Commission (CEA)
Saint Paul Lez Durance
France
gilles.rodriquez@cea.fr

Ulrich Rohde

Institute of Safety Research
Research Center Dresden-Rossendorf
Germany
u.rohde@fzd.de

Vincenzo V. Rondinella

European Commission
Joint Research Centre
Institute for Transuranium Elements
Karlsruhe
Germany

Jacques Rouault

French Atomic Energy Commission (CEA)
Saint Paul Lez Durance
France
jacques.rouault@cea.fr

Sergei B. Ryzhov

OKB "GIDROPRESS"
Joint Stock Company
State Atomic Energy Corporation "Rosatom"
Podolsk
Moscow Region
Russia

Mark Schanfein

Idaho National Laboratory
Idaho Falls
ID 83415
USA
Mark.Schanfein@inl.gov

J. Kenneth Shultis

Department of Mechanical and
Nuclear Engineering
Kansas State University
Manhattan

KS 66506
USA
jks@ksu.edu

Craig F. Smith

Naval Postgraduate School
1 University Circle
Monterey
CA
USA
cfsmith@nps.edu

Joe Somers

European Commission
Joint Research Centre
Institute for Transuranium Elements
Karlsruhe
Germany

Ugo Spezia

SOGIN SpA
Roma
Italy

Rebecca Stevens

Los Alamos National Laboratory
Los Alamos
NM 87544
USA
rstevens@lanl.gov

Theo G. Theofanous

Department of Chemical Engineering
Department of Mechanical Engineering
Center for Risk Studies and Safety
University of California
Santa Barbara
CA
USA
theo@theofanous.net;
theo@engineering.ucsb.edu

Anton P. Tonchev

Triangle Universities Nuclear Laboratory
Duke University
Durham
NC 27708
USA

Werner Tornow

Triangle Universities Nuclear Laboratory
Duke University
Durham
NC 27708
USA

Ivo Tripputi

NEA Working Party on Decommissioning
and Dismantling (WPDD)
SOGIN SpA
Roma
Italy
tripputi@sogin.it

James Tulenko

202 Nuclear Science Center
University of Florida
Gainesville
FL
USA
tulenko@ufl.edu

Paul J. Turinsky

Department of Nuclear Engineering
North Carolina State University
Raleigh
NC
USA
turinsky@ncsu.edu

Paul Van Uffelen

European Commission
Joint Research Centre
Institute for Transuranium Elements
Karlsruhe
Germany
paul.van-uffelen@ec.europa.eu

Bernard Valentin

French Atomic Energy Commission (CEA)
Saint Paul Lez Durance
France
bernard.valentin@cea.fr

Frédéric Varaine

French Atomic Energy Commission (CEA)
Saint Paul Lez Durance
France
frederic.varaine@cea.fr

Carlo Vitanza

OECD Halden Reactor Project
Halden
Norway
Carlo.Vitanza@hrp.no

R. Bruce Vogelaar

Virginia Tech
Blacksburg
VA 24061
USA

Richard Wallace

Los Alamos National Laboratory
Los Alamos
NM 87544
USA
rwallace@lanl.gov

Maria Wallenius

Institute for Transuranium Elements
Karlsruhe
Germany
Maria-S.Wallenius@ec.europa.eu

R.L. Walter

Triangle Universities Nuclear Laboratory
Duke University
Durham
NC 27708
USA

Akio Yamamoto

Graduate School of Engineering
Nagoya University
Nagoya
Japan
a-yamamoto@nucl.nagoya-u.ac.jp

Biographies of Contributors

Dmitry A. Anufriev

Dmitry A. Anufriev was born on June 28, 1946, in Krivandino, Moscow region. He graduated in 1969 as an engineer in thermal physics from the Moscow Power Engineering University. Since 1969, he has worked at OKB “GIDROPRESS” in positions of increasing responsibilities, as head of group, and deputy head of the department. His professional interests are focused on VVER-1000 reactor plant design development, elaboration of the schemes and processes of reactor plant operation, protection and control system operation algorithms, and safety analyses.

Carlo Artioli

Dr. Ing. Carlo Artioli, received his degree in nuclear engineering (*summa cum laude*) at the University of Bologna, Italy, in 1975. He joined the former CNEN (Nuclear Energy National Committee) where he worked as core designer for fast reactors. He took part in the European activities for the harmonization of nuclear codes and in the programs for Plutonium management and Minor Actinides reduction. Currently serving as researcher for the Italian National Agency for New Technologies, Energy and Sustainable Economic Development (ENEA, former CNEN) in Bologna, he has been core design leader for the ADS EFIT within the European IP EUROTRANS and core neutronic design for the ELSY reactor, as well as in charge of definition and designing of the DEMO LFR in the Italian program. Also, he is professor of Neutronic Design of the Reactor in the Postgraduate Master on Advanced Nuclear Systems in the Bologna University. He is author of several papers; mainly about new concepts related to LFR and lead coolant ADS, in international conferences.

Robert Bari

Dr. Robert Bari has over 35 years of experience in the field of nuclear energy. He is a senior physicist and a senior advisor at Brookhaven National Laboratory and has directed numerous studies of advanced nuclear energy concepts involving subjects such as nuclear energy technology performance, safety, nonproliferation, economics, and waste management. He has lectured widely on nuclear technology and has published more than 100 papers. For over 25 years, Dr. Bari has served at various levels of management at Brookhaven National Laboratory and has directed numerous programs for the US Department of Energy and the US Nuclear Regulatory Commission. Dr. Bari is currently international cochairman of the working group that has developed a comprehensive methodology for evaluation of proliferation resistance and physical protection of new nuclear energy concepts proposed within the multinational Generation IV International Forum. He has served on the Board of Directors of the American Nuclear Society, and is the past president of the International Association for Probabilistic Safety Assessment and Management. He has served as an adjunct faculty member and advisor to several major universities in the field of nuclear technology and received his doctorate in physics from Brandeis University (1970) and his bachelor's degree in physics from Rutgers University (1965).

Bertrand Barré

Bertrand Barré is the scientific advisor to the Chairperson of the AREVA group. He is also professor emeritus of nuclear engineering at the Institut National des Sciences et Techniques Nucléaires, INSTN. From 1994 to 1999, he was the head of the Nuclear Reactor Directorate of the French Atomic Energy commission, CEA, and from 1999 to 2002, he was Vice-president in charge of R&D in COGEMA (now AREVA NC).

Past President of the European Nuclear Society (ENS) and of the International Nuclear Societies Council (INSC), Past chairman of the Standing Advisory Group on Nuclear Energy of the IAEA, Bertrand Barré has just left the Chair of the International Nuclear Energy Academy (INEA). His recent publications include *Nuclear Power, understanding the future* (with P.R. Bauquis – Hirlé, 2007. *Atlas des énergies – Autrement 2007. Les 100 mots du nucléaire* – PUF 2009. His personal Web site (French/English) is www.bertrandbarre.com.

Charles G. Bathke

Dr. Charles G. Bathke is a staff member in the D-5 “International and Nuclear Systems Engineering” group at Los Alamos National Laboratory (LANL). His knowledge of the nuclear fuel cycle derives from his past work on Accelerator Transmutation of Waste (ATW) and its successor the US Advanced Fuel Cycle Initiative (AFCI), where he developed the Nuclear Fuel Cycle Simulation (NFCSim) code that is used to simulate the civilian nuclear fuel cycle from cradle (mining) to grave (waste repository). In the course of his career, he has performed systems analyses of reactors based upon various magnetic fusion confinement schemes, proton accelerators used to generate tritium, electron accelerators used for X-ray radiography, and terrorist-induced biological events. For the past three years, his research interests have gravitated to the nonproliferation arena, where he has been analyzing the material attractiveness of nuclear materials associated with reprocessing. He received his Ph.D. in Nuclear Engineering from the University of Illinois in 1976, followed by a postdoc at the Princeton Plasma Physics Laboratory. He has been at LANL since 1978.

Georgy G. Bessalov

Georgy G. Bessalov was born on September 27, 1931, in Skopin, Ryazan region. He was graduated in 1955 as a mechanical engineer from Moscow Power Engineer University. Since 1955 he held the following positions at OKB “GIDROPRESS”: engineer, head of group, and head of department. Reactor plant design development, commissioning tests at NPPs with VVER-440, and safety analyses are his professional interests.

At present, he is a leading engineer on reactor plants with VVER-440 reactors.

Gilles Bignan

Gilles Bignan earned his Ph.D. in nuclear physics and instrumentation from the Caen University of Sciences (1989) and the degree of Engineer in nuclear energy from the Institute of nuclear sciences in Caen. He started his career at CEA in the development of nuclear measurement devices for various applications (online power estimation of a power reactor, fuel monitoring for safety-criticality risk assessment, and nuclear material control for Safeguards). Since 2000, he is working in the Research Reactor field for neutron physics and Safety test and he is currently involved in the new International Material Testing Reactor Project called Jules

Horowitz Reactor as the User Facility Manager. He is an expert for the IAEA in the field of research reactors.

Edward G. Bilpuch

Edward G. Bilpuch is a Henry W. Newson professor of Physics at Duke University. He did his undergraduate studies at the University North Carolina at Chapel Hill and earned a Ph.D. degree in physics from University of North Carolina at Chapel Hill in 1956. He began his career at Duke in 1956 as a research associate, subsequently was appointed to the faculty, and was promoted to professor in 1971. He was director of the Triangle Universities Nuclear Laboratory from 1978 through 1992, and named Henry W. Nelson professor of Physics in 1987.

Professor Bilpuch perfected high-resolution techniques in nuclear physics using linear accelerators. These endeavors culminated in an experiment that set new standards for measurements of properties of atomic nuclei.

Professor Bilpuch has authored or coauthored 122 articles published in professional journals and has given many seminars in the USA and throughout the world. He has directed or codirected over 40 Ph.D. graduate students associated with the nuclear laboratory. He was a guest professor at the University of Frankfurt, Germany, 1972 and 1973, and at Fudan University of Shanghai, China, 1983 and 1985. He was the recipient of a Senior US Scientist Humboldt Award in Germany in 1983. In 1986, he was named an honorary professor at Fudan University and in 1988 he was the recipient of the Distinguished Alumnus Award from the University of North Carolina in Chapel Hill. In 1992, he was awarded an honorary doctorate by Frankfurt University in Germany.

Patrick Blaise

Patrick Blaise, Ph.D., is an industrial engineer in Nuclear Energy from Brussels, and got his Ph.D. in reactor physics from Marseille University in 1996. He was involved in designing and conducting experimental programs in the EOLE critical Facility in Cadarache from 1997 to 2007, mainly in the frame of 100% MOX LWRs, and responsible for international collaborations in experimental reactor physics. Since 2007, he is a senior expert in Reactor Physics Experimental programs. He is currently in charge of code qualification for Advanced LWRs at the section for reactor physics and cycle at Cadarache.

Robert C. Block

Dr. Robert C. Block is professor emeritus of Nuclear Engineering at Rensselaer Polytechnic Institute (RPI). During his 40-year career at RPI, he served as Director of the Gaertner LINAC Laboratory, Chairman of the Department of Nuclear Engineering and Engineering Physics, and Associate Dean of Engineering. Before joining RPI, he was a staff member at the Oak Ridge National Laboratory. He has had sabbaticals at the AERE Laboratory at Harwell, UK; the Kyoto University Research Reactor Laboratory in Kumatori, Japan; and the Sandia National Laboratory. He is currently employed by the Knolls Atomic Power Laboratory and is a consultant to national laboratories and industry.

Dr. Block has served on numerous advisory committees and has almost 300 publications in journals and conference proceedings to his credit. He was awarded the ANS Seaborg Medal in

2005 from the American Nuclear Society, the Glenn Murphy Award in 1991 from the American Society for Engineering Education, and the William H. Wiley Distinguished Faculty Award in 1995 from RPI.

Bernard Bonin

Dr. Bernard Bonin has a background in fundamental research in high energy physics and materials physics. Between 1996 and 2000, he was head of a Service of Research and Studies on Nuclear Waste, within CEA's Institute for Nuclear Protection and Safety. His studies then aimed at obtaining an overall view of the scientific basis for nuclear waste management, with special interest in the migration of radioactive contaminants in the underground environment. In 2000, he was appointed assistant to the Director of Research and Development in COGEMA, in charge of the organization of the R&D on the front end of the nuclear fuel cycle, and on future nuclear energy systems. He received the Areva Innovation Award in 2002 for the development of a radon detection system. Since 2003, he is Deputy Scientific Director in the Nuclear Energy Division of the Commissariat à l'Énergie Atomique and professor at the French Institute for Nuclear Sciences and Techniques.

Stéphane Bourganel

An engineer and researcher at CEA/Saclay, Stéphane Bourganel earned a Ph.D. from the INPG School in Grenoble, France and contributes to R&D in the field of the PWR lifetime. He is involved in design and analysis of experiments dedicated to decay heat issues. He worked on the first fluence calculations for the fourth reactor generation lifetime. Furthermore, he takes part, as a teacher, in training course on the Monte Carlo computer code TRIPOLI-4.

Charles Daniel Bowman

Dr. Charles Daniel Bowman was awarded a Ph.D. from Duke University in 1961 in neutron physics. He led the development of world-class accelerator-based neutron sources and their application to basic and applied science at Lawrence Livermore National Laboratory, the National Institute of Science and Technology, and the Los Alamos National Laboratory. In 1970, he became a Fellow of the American Physical Society; in 1982, he was awarded the U S Department of Commerce Silver Medal; and in 1993, he was honored as a Fellow of the Los Alamos National Laboratory.

In 1993, Dr. Bowman became Project leader for the Los Alamos Accelerator-Driven Transmutation Technology (ADTT) program. When the US-funded International Science and Technology Center (ISTC) was formed in Moscow in 1993, Dr. Bowman also led Project 17 of the ISTC, which employed about 500 Russian scientists on the ADTT concept. In 1997, he organized ADNA Corporation (Accelerator-Driven Neutron Applications) to pursue the application of accelerator sources of neutrons in nuclear energy culminating in GEM*STAR.

Christophe Calvin

Christophe Calvin is leading a laboratory in the Nuclear Energy Division of the French Atomic Commission (CEA) in charge of the development of reactor physics simulation codes. He

received a Ph.D. in applied mathematics and parallel computing and worked, at CEA Grenoble, in a CFD code development team in charge of the code parallelization. He has also led the development of a new generation of reactor physics simulation code at CEA Saclay. He currently has an expert position in HPC at CEA Nuclear Energy Division, participating to international collaboration with European research institutes and with Japan academic laboratories and institutes in reactor physics simulation and high-performance computing. He has published more than 10 papers in international conferences or journals on scientific code architecture, parallel algorithms, and scientific code parallelization.

P. Chellapandi

An outstanding scientist of repute, P. Chellapandi is the director of Safety Group and associate director of Nuclear Engineering Group. He joined the Indira Gandhi Centre for Atomic Research, Kalpakkam, (IGCAR) in 1979. Since then, he has been working on the design and development of 500 MWe prototype fast breeder reactor (PFBR), over a wide spectrum of design, namely, conceptualization, development of sophisticated computer codes, detailed analysis, design validation, preparation of preliminary safety analysis reports, execution of R&D activities involving national academic institutions, and R&D establishments in the country. He is also the convener of a task force, which is coordinating for the manufacture and erection of reactor assembly components. He earned his B.E. (Hons.) in Mechanical Engineering from Madras University in 1978 securing the first rank, and M.Tech. in Engineering Mechanics (Gold Medalist with CGPA 10), and Ph.D. in Applied Mechanics from IIT Madras. He is a professor at the Homi Bhabha National Institute, and adjunct professor of PSG college, Coimbatore, and Sathyabama University, Chennai. He has guided more than 50 postgraduate students and published about 460 papers in journals, national and international conferences. He is a Fellow of Indian National Academy of Engineering.

Nam Zin Cho

Prof. Nam Zin Cho received his B.S. in nuclear engineering from Seoul National University and Ph.D. in nuclear engineering from University of California at Berkeley. He worked at Science Applications, Inc. in Palo Alto from 1980 to 1982, and at Brookhaven National Laboratory in Long Island from 1983 to 1987. In 1987, he joined the faculty at Korea Advanced Institute of Science and Technology (KAIST) in Korea, where he is mostly involved in teaching and research in reactor physics and neutron transport computation.

He is Fellow of American Nuclear Society and Associate Editor of Nuclear Science and Engineering. He was the Technical Program Chair for the PHYSOR 2002, a series of the ANS topical meetings on reactor physics, held in Seoul, Korea. From 2003 to 2006, he served as Commissioner of the Atomic Energy Commission of the Republic of Korea. From 2007 to 2008, he was President of Korean Nuclear Society.

Luciano Cinotti

Luciano Cinotti has been student at the Scuola Superiore degli Studi Universitari e Perfezionamento S. Anna, the renowned School linked to the University of Pisa, Italy, where he received his Dr. Ing. degree in 1975. He has served 5 years in France in the French-Italian Ansaldo-Novatome

team in charge of the development of the large sodium-cooled fast reactors. After returning to Italy, he has led the Ansaldo Nucleare activities for the improved European fast reactor (EFR) and the innovative reactors PIUS and PRISM, while conceiving ISIS, a full-passive reactor for the combined generation of electricity and heat. He has been responsible of the department of Nuclear Technology of Ansaldo Nuclear Division till 2006 and has been the coordinator of the ELSY STREP in the proposal preparation phase. He is currently involved in the development and promotion of the LFR and Euratom Representative and is the chairman in the GIF LFR Provisional Steering Committee. He is author of several papers on new reactors published in learned journals.

Giovanni Corsini

Giovanni Corsini received his degree of Dott. Ing. in chemical engineering in 1970 at the University of Pisa. After 10 years as a chemical project engineer in Foster Wheeler Italy, he joined Ansaldo in 1981, where he has gained experience in the field of pressurized heavy water reactors and in the field of fast reactors (SPX1 and particularly EFR, where he has been coleader of the decay heat removal subsystem). Subsequently, he has participated in the ECC-funded TACIS project for the safety improvement of the Russian VVER 430-type Novovoronezh and Kola power plants.

He worked in the Ansaldo team for the design of the experimental accelerator-driven system (XADS), in particular for issues relevant to corrosion protection in LBE. While continuing the participation in the ADS field, and in the European ELSY project, since 2002 he also worked as project engineer of the Intermediate Cooling Loop of Heat Removal System and the Cover Gas System of Megapie. At the end 2008, he left Ansaldo Nucleare but continues to work as an independent professional in the field of lead technology.

Dermott E. Cullen

Dermott E. Cullen earned his Ph.D. in nuclear engineering from Columbia University, New York City, in 1967. From 1967 through 1972, he worked at Brookhaven National Laboratory, Long Island, New York as a nuclear physicist. From 1972 through 1979, he worked at Lawrence Livermore National Laboratory, Livermore, California. From 1979 through 1987, he worked at the Nuclear Data Section, International Atomic Energy Agency, Vienna, Austria. From 1987 through 2009, he worked at Lawrence Livermore National Laboratory, Livermore, California. He is now retired and lives in Livermore, California. He has more than 40 years of experience with nuclear and atomic data, involving its preparation and use in particle transport calculations. He is the author of over 200 papers on this subject, as can be seen in his online resume located at <http://home.comcast.net/~redcullen1/RESUME.pdf>

Maurizio Luigi Cumo

Full professor of nuclear plants in the University of Rome Sapienza since 1976, Maurizio Luigi Cumo was engaged in experimental and theoretical research in the field of thermofluidynamics of nuclear plants systems and components in the ENEA Research Centre, Casaccia. He has published 10 books and over 200 scientific publications. Furthermore, he was engaged in nuclear safety researches as president of the Italian SOGIN Company for Nuclear Installations Decommissioning and chairman of the International Scientific Council of the Nuclear Energy Directorate of the French Commissariat à l'Énergie Atomique. He is a member of the Italian

Academy of Sciences, said of the forty, and of the European Academy of Sciences and Arts, leading as president the Italian Society for the Advancement of Sciences.

Yaron Danon

Dr. Yaron Danon is a professor in the department of Mechanical Aerospace and Nuclear Engineering at Rensselaer Polytechnic Institute (RPI) in Troy, New York. He is also the director of the Gaerttner Electron Linear Accelerator (LINAC) Laboratory at RPI. Dr. Danon is a member of the US Cross Section Evaluation Working Group and chairman of the Measurements Committee. He is also a member of the Nuclear Data Advisory Group (NDAG), which advises the US Nuclear Criticality Safety Program (NCSF) on issues relating to nuclear data. Dr. Danon has over 120 publications in archived journals and conference proceedings.

Christophe Demazière

Christophe Demazière (Ph.D. in reactor physics, Chalmers University of Technology, Sweden, 2002; Engineering degree, Hautes Etudes d'Ingénieur, France, 1996) is an associate professor in the department of Nuclear Engineering, Chalmers University of Technology, Gothenburg, Sweden, lecturing in nuclear reactor physics (reactor physics and nuclear thermal-hydraulics) and nuclear reactor modeling (deterministic methods). He is a member of the American Nuclear Society (Reactor Physics Division, Mathematics and Computation Division, Thermal Hydraulics Division, Education and Training Division) and of the Swedish Nuclear Society.

His research interests include pressurized water reactor and boiling water reactor physics, reactor dynamics applied to both critical and subcritical systems, power reactor noise and noise diagnostics, signal processing and data analysis (linear, nonlinear, wavelet, and fractal analysis), nuclear reactor modeling and calculations, (including coupled neutronics/thermal-hydraulics), and computational methods applied to nuclear reactor modeling.

Scott DeMuth

Dr. Scott DeMuth has a Ph.D. in chemical engineering and has been a staff member at Los Alamos National Laboratory for the past 20 years. Prior to Los Alamos, he was a research engineer at Oak Ridge National Laboratory for 10 years. His specialty is nuclear materials processing and safeguards. He has worked for research and development in all areas of the nuclear fuel cycle, including uranium enrichment, fuel fabrication, thermal and fast reactors, fuel reprocessing, and waste management. Currently he is on assignment in Washington, DC working for the US Department of Energy's Office of International Regimes and Agreements (NA-243).

Nicolas Devictor

After receiving a Ph.D. in applied mathematics, Nicolas Devictor worked from 1997 to 2007 on structural reliability, probabilistic safety assessment, and risk management. He is one of the editors of *Uncertainty in Industrial Practice – A Guide to Quantitative Uncertainty Management*, published by Wiley in 2008. He was in charge of the coordination of the project "Safety and Reliability of the facility," a transversal project in support of the sodium fast reactor and gas-cooled fast reactor, and served as the CEA-representative in the Working Group RISK of OECD/NEA. From 2007 to 2009, Nicolas Devictor was head of the laboratory in charge of the preconceptual

design of sodium fast-cooled reactors, and related safety analysis. Since 2010, Nicolas Devictor has been project manager for the R&D led by CEA team in support to SFR and Astrid project.

Philippe Dufour

After graduating from “Ecole Centrale de Paris,” Dufour joined CEA (Commissariat à l’Energie Atomique) in 1974. The beginning of his career was devoted to thermal-hydraulical studies for the Superphenix fast reactor. Subsequently, he was involved in other fields such as, neutronics, safety, development of computer codes, economy, and optimization, for various reactor types. From 1998 to 2007, Philippe Dufour was head of the laboratory in charge of the preconceptual design of sodium fast-cooled reactors, and related safety analysis. He is currently project advisor at the Department for Reactor Studies at Cadarache (DEN/DER/SESI).

Mike Ehinger

Mike Ehinger has worked in the areas of safeguards and nuclear nonproliferation for 40 years. He is currently at Oak Ridge National Laboratory as a senior program development manager working principally in the area of International Safeguards. From 1999 to 2006, he worked at the International Atomic Energy Agency (IAEA) in Vienna on the development, installation, and implementation of equipment and procedures for IAEA inspections at the Rokkasho Reprocessing Plant in Japan. Prior to going to Vienna, he was manager of safeguards programs at Oak Ridge. While at Oak Ridge, the Russian Material, Protection, Control and Accounting (MPC&A) program was among his responsibilities and he actively participated in the tasks related to the Russian fuel reprocessing sites Mayak and Tomsk. He was also involved with the US and Russian HEU down-blend program serving as a monitor at enrichment facilities. He has broad international experience having participated in activities at many reprocessing facilities throughout the world including England, France, and India. Prior to joining Oak Ridge in 1983, he was a senior nuclear material control engineer at the Barnwell Reprocessing Plant where he installed the Nuclear Material Accountancy system and demonstrated its capabilities to US and international regulatory, development, and operating organizations. From 1968 to 1974, he was the accountability supervisor during the operating years of the West Valley Reprocessing Plant. During this period, he hosted the very first IAEA inspection at a reprocessing facility.

Thomas Fanghänel

Prof. Dr. Thomas Fanghänel currently serves as the director of the Institute for Transuranium Elements (ITU), which is one of the seven institutes of the European Commission’s Joint Research Centre located in Karlsruhe, Germany. It is ITU’s mission to provide the scientific foundation for the protection of the European citizen against risks associated with the handling and storage of highly radioactive elements. Research is focused on (1) basic actinide science and applications, (2) safety of conventional and advanced nuclear fuel cycle including spent fuel disposal, and (3) safeguards and nuclear forensics.

Since 2002, he is professor of Radiochemistry at the Ruprecht-Karls-University Heidelberg. Prof. Fanghänel has degrees in Chemistry (Diplomchemiker), a Ph.D. and Habilitation in Inorganic and Physical Chemistry from the Technical University Bergakademie Freiberg. Before he was appointed as the director of ITU, he had been director of the Institute for Nuclear Waste

Disposal (INE) of the former Forschungszentrum Karlsruhe (now Karlsruhe Institute of Technology, KIT), director of the Institute of Radiochemistry, Forschungszentrum Rossendorf, and professor of Radiochemistry at the University of Dresden. He has more than 25 years of research experience with special expertise in Actinide chemistry and long-term safety of nuclear waste disposal. Since 2003, he is a member of the Reactor Safety Commission of the German Federal Ministry for the Environment, Nature Conservation, and Nuclear Safety.

Richard E. Faw

Richard E. Faw, born in rural Ohio, was educated at the University of Cincinnati (B.S., Chemical Engineering, 1959) and at the University of Minnesota (Ph.D., Chemical Engineering, 1962). In 1962, he joined the nuclear engineering faculty at Kansas State University, where he served until 2000. Appointments at the university include department head, 1972–1977, director of the Radiation Shielding Laboratory, 1968–1980, and director of the Nuclear Reactor Laboratory, 1976–1996. He is licensed by the Nuclear Regulatory Commission as a senior reactor operator and by Kansas and Ohio as a professional engineer. He is a Fellow of the American Nuclear Society and recipient of university awards for teaching and research. Dr. Faw is author or coauthor of four textbooks on radiation shielding and radiological assessment. Two of these books are in second editions.

Temporary assignments include service in the US Army Combat Developments Command from 1963 to 1965, and research appointments at Argonne National Laboratory (1975), UKAEA Culham Laboratory (1977–1983), and Oak Ridge National Laboratory (1990). Research and teaching interests include radiation shielding and dosimetry, boiling heat transfer, and nuclear reactor accident analysis. Dr. Faw was employed part time with Black & Veatch in ABWR plant design from 1998 to 2004 and with GE-Hitachi in ESBWR safety analysis from 2006 to 2009. Dr. Faw now makes his home in Winston-Salem, North Carolina.

Gian Luigi Fiorini

Gian Luigi Fiorini graduated in nuclear engineering (Pisa, Italy 1975) and joined the CEA in 1979. His professional experience spans 30 years of activities related to the definition, the realization, and the management of experimental and theoretical activities concerning the operation and the safety of fission reactors. Since the beginning, until the 1980s he worked essentially on the sodium LMFBR. Since 15 years, he has been engaged within the innovation program at CEA addressing all the nuclear technologies, including ADS and ITER. He is a former member of the Gen IV Roadmap Integration Team, and currently serves as a “Chargé de Mission Generation IV” at the CEA Department for Reactor Studies (DEN/DER/SESI). Strongly involved within the Gen IV Initiative implementation, he was member of the “Gen IV Sodium Fast Reactor (SFR) Steering committee,” cochairman of the SFR Design & Safety Management board and of the Gen IV Expert Group. He is currently cochairman of the “Gen IV Risk & Safety Working Group,” and member of the French Advisory Group on Safety (GCFS – AREVA, CEA, EDF).

Philippe Fougeras

Philippe Fougeras received his Ph.D. in reactor physics from the Orsay Faculty of Science in 1992. He started his career at CEA as physicist in the code validation team for Pu recycling in light water reactors (LWRs). He was in charge of the EOLE Critical Facility from 1996 to 2000,

covering the MISTRAL program, and was head of the Experimental Programs Laboratory of the CEA Cadarache from 2000 to 2007, supervising programs on EOLE, MINERVE, and MASURCA facilities, also involved in international collaborations and development of new experimental techniques. He is currently deputy head of the section for reactor physics and fuel cycles at Cadarache.

János Gadó

Dr. János Gadó is director of the KFKI Atomic Energy Research Institute, Budapest, since 1990. The institute belongs to the Hungarian Academy of Sciences. Dr. Gadó graduated at the Roland Eötvös University, Budapest, as a physicist (1969). He started to work in the field of reactor physics, and later he moved to the area of nuclear safety. He was project manager of various projects related to the safety of the Paks NPP, and represents Hungary on several international committees and projects. Dr. Gadó became Doctor of the Academy in 1999. He was awarded various medals and prizes.

Guy-Marie Gautier

Guy-Marie Gautier graduated in 1977 from “Ecole Nationale Supérieure d’Electricité et de Mécanique de Nancy,” and has over 25 years experience on the management of experimental facilities and the definition of operating points for sodium fast reactor (SFR) and pressurized water reactor (PWR). Since 1994, Mr. Gautier has been involved in the definition of the French Atomic Commission (CEA) Innovative Program. He was the coordinator of the innovative activities of the safeguard systems of PWRs, and he was in charge of the definition of the design options of innovative concepts, especially of PWR and now for SFR, including economic assessment studies.

Jean-Paul Glatz

Jean-Paul Glatz received his Ph.D. in analytical and radiochemistry, and has been working since 1981 at the European Commission’s Joint Research Center (JRC) Institute for Transuranium Elements (ITU), in Karlsruhe, in various research fields. From 1998 to 2008, he was head of the “Hot Cells” department at ITU responsible for all postirradiation examination work on irradiated fuel and other highly active materials, related to the safety of nuclear fuel, spent fuel characterization in view of storage and partitioning and transmutation (P&T). Since 2007, he has been head of the “Nuclear Chemistry” department, responsible for projects on chemical characterization of irradiated fuel and other highly radioactive materials. The corresponding projects include reprocessing studies, the behavior of spent nuclear fuel under repository conditions, and the behavior of radionuclides in the environment and the use of short-lived alpha-nuclides for cancer therapy.

Dominique Gosset

After receiving a Ph.D. in 1985 in the Yves Quéré’s Irradiated Solids Laboratory, Dominique Gosset joined the Absorber Materials Laboratory in CEA. This laboratory was in charge of fundamental and project studies on the absorber materials to be used in PWR (Ag–In–Cd alloy, hafnium compounds) and mainly in FBRs (boron carbide, moderators) and was a support unit for development laboratories in CEA, including international collaborations (Russia, Japan,

and the USA). D. Gosset was especially involved in structural and microstructural analysis of the materials (microscopy, X-ray diffraction), development of new materials and concepts and postirradiation examinations. In the 1990s, his main interests shifted toward fundamental analysis of the behavior of nuclear ceramics under irradiation, focused on microstructure evolutions (e.g., phase transformation in Zirconia and in spinels), through a close collaboration with a CNRS-Ecole Centrale Paris laboratory. More recently, part of his fields of interest come back to the carbides (ZrC, SiC), as potential materials for Gen-IV reactors. He authored or coauthored over 50 referred papers and patents.

Giacomo Grasso

Giacomo Grasso received his MS degree in nuclear engineering (*summa cum laude*) from the University of Bologna, Italy, in 2006. Subsequently, he received his Ph.D. in nuclear reactor physics at the Nuclear Engineering Laboratory (LIN) of Montecuccolino, Department of Energy and Nuclear Engineering and of Environmental Control (DIENCA), University of Bologna, in 2010. He currently serves as researcher in the Italian National Agency for New Technologies, Energy, and Sustainable Economic Development (ENEA) in Bologna, Italy. He worked on the modeling of neutron transport in nuclear reactors, Generation IV nuclear reactor design, computational methods for particle transport, plasma physics and complex system dynamics, and nuclear fuel cycle scenarios. He participated in the ELSY project as a neutronics core designer, and also participated in several European projects for fuel cycle scenario studies. He has authored 20 technical papers and articles in international conferences and journals.

Frank Gunsing

Dr. Frank Gunsing is a research team leader in the Nuclear Data Measurements Group of the Nuclear Physics Division (Irfu/SPhN) at the “Commissariat à l’Energie Atomique et aux Energies Alternatives” (CEA) in Saclay, France. Following his Ph.D. degree in nuclear physics from Delft University in the Netherlands in 1995, he worked at the IRMM in Belgium and joined the French CEA in 1996. He obtained the Habilitation to Direct Research from the University of Paris VII in 2005. He is interested in nuclear data and measurement techniques for applications in nuclear technology, astrophysics, and nuclear structure. He is involved in experimental work among others at the IRMM in Geel and at the n_TOF facility at CERN. He is active in European Framework research programs and serves on several scientific advisory committees.

Robert C. Haight

Dr. Robert C. Haight is a research team leader in the Neutron and Nuclear Science Group of the Los Alamos Neutron Science Center (LANSCE). Following his Ph.D. degree in nuclear physics from Princeton University, he entered experimental neutron physics 40 years ago and has held various positions at Los Alamos and at the Lawrence Livermore National Laboratory. He has used neutron sources based on cyclotrons, Van de Graaff accelerators, intense 14-MeV neutron generators with rotating tritium targets, and the spallation neutron sources at LANSCE. He has concentrated on charged-particle production in neutron-induced reactions, fission neutron spectra, and the physics of polarized neutrons. He is interested in applications of nuclear techniques and nuclear data to defense, medicine, space, and fission and fusion energy. He is a Fellow of the American Physical Society.

Alain Hébert

Alain Hébert has been a professor of the Institut de Génie Nucléaire at École Polytechnique de Montréal since 1981. From 1995 to 2001, he worked at the Commissariat à l'Énergie Atomique, located in Saclay, France. During this period, he led the development team of the APOLLO2 lattice code, an important component of the Science™ and Arcadia™ packages at Areva. Back in Montréal, he participated in the development of the DRAGON lattice and TRIVAC reactor codes, both available as *Open Source* software.

Alain Hébert is the author of *Applied Reactor Physics* (2009), a reference textbook in the domain. He is also a contributing author in more than 43 full papers and 67 conference papers, published between 1981 and now.

Magnus Hedberg

Magnus Hedberg is a project manager for one of the European Commissions Safeguards actions; “Nuclear and Trace analysis for Safeguards Purposes (NTAS).” His special interest is in particle analysis for nuclear Safeguards purposes. Hedberg was previously, for a period of 7 years, the unit head for a mass spectrometry group at the International Atomic Energy Agency laboratories in Austria. Hedberg is originally from Sweden where he earned a M.Sc. degree in electrical engineering at the technical faculty of Lund University in 1987.

Michal Herman

Michal Herman earned his M.S. in nuclear physics from the University of Warsaw, Warsaw in 1973, Ph.D. in nuclear physics from the Institute of Nuclear Research in Warsaw, Warsaw in 1980. His scientific carrier is dedicated to low-energy nuclear reactions, and is best known for contributions to multistep compound reaction theory. He is the main developer of the nuclear reaction model code EMPIRE widely used as nuclear reaction data evaluation tool.

He worked as a research scientist in the Institute of Nuclear Physics Research, Warsaw in 1973–1984, research scientist in ENEA, Bologna in 1985–1996; nuclear data physicist in the Nuclear Data Section, IAEA Vienna in 1997–2002; in 2003, he joined the National Nuclear Data Center at BNL. In January 2010, he took over US nuclear data leadership as the head of the National Nuclear Data Center and chair of the Cross Section Evaluation Working Group.

Calvin R. Howell

Calvin R. Howell received his B.S. degree from Davidson College in 1978 and obtained his Ph.D. degree from Duke University in 1984. He is a professor of physics at Duke University and the director of the Triangle Universities Nuclear Laboratory. He holds adjunct professorships in the Medical Physics Program at Duke University and in the physics department at North Carolina Central University. He is a Fellow of the American Physical Society (APS). His research includes the study of fundamental properties of nuclear systems, plant physiology using radioisotopes, and applications of nuclear physics in the areas of national security, nuclear energy, and medicine. He has coauthored more than 110 articles in scientific journals and has held visiting scientist positions at Los Alamos National Laboratory, the Stanford Linear Accelerator Center, and Jefferson Laboratory. Since joining the faculty at Duke University in 1985, he has served as faculty coordinator for the Carolina Ohio Science Education Network, as the faculty coordinator for the Mellon Minority Undergraduate Fellowship Program, and as the academic coordinator for the Summer Medical and Dental Education Program at the Duke

University Medical Center. Professor Howell has served the physics community extensively as a Nuclear Physics Program Director at the National Science Foundation (NSF), as a member of the Department of Energy (DOE)/NSF Nuclear Science Advisory Committee, as a member of the Executive Committee of the Division of Nuclear Physics of the APS, as chair of the Executive Committee of the Southeastern Section of the APS, as chair of the APS Committee on Minorities, and as a member of numerous NSF and DOE review and planning panels.

John Howell

Dr. John Howell has been with the Faculty of Engineering, University of Glasgow in the UK since 1984. Prior to this position, he was with the Control and Instrumentation Division of the United Kingdom Atomic Energy Authority. He started his career as a control and dynamics engineer with responsibilities for the assessment, design, and development of control and measurement systems for the UK's prototype fast reactor and associated reprocessing plant, which were located at Dounreay. Dynamic modeling was a core component of these activities. His research focus over the past 20 years has been on the evaluation of monitoring data collected from process plants, in general. The emphasis has been on isolation and diagnosis. Although his roots are very much in model-based reasoning, he has also researched into approaches including ICA, rule-based reasoning, and signed-graph analysis. He has contributed to the development of a number of solution monitoring systems for the IAEA.

Jean-Pascal Hudelot

Jean-Pascal Hudelot received his Ph.D. in reactor physics from the Grenoble Faculty of Science (1998). He started his career at CEA as a physicist in the development of innovative neutron and gamma measurement techniques on experimental facilities. He was in charge of the MINERVE Facility from 1998 to 2006, covering the OSMOSE, HTC, VALMONT, and OCEAN programs, and was also involved in international collaborations. He is now head of the Nuclear Project Laboratory at CEA Cadarache, supervising the development, validation and qualification of neutronics, and photonics calculation tools for experimental and irradiation reactors, including JHR, OSIRIS, CABRI.

Mihaela Ionescu-Bujor

Mihaela Ionescu-Bujor received her Dr.-Ing. degree from the Institute for Nuclear Technology and Reactor Safety, Faculty of Mechanical Engineering, University of Karlsruhe, Germany, in 2000, with the grade of "Excellent with Distinction." For 5 years prior to her doctoral degree, she was a staff researcher at Siemens AG, KWU, Erlangen, working in the reactor physics and thermal-hydraulics section. During 2000–2003, she served as group leader for sensitivity and uncertainty analysis in the Institute for Reactor Safety at Forschungszentrum Karlsruhe (FZK), performing original research on and supervising the implementation of the adjoint sensitivity analysis procedure (ASAP) into various large-scale multi-physics computational code systems. Typical systems included the development of the coupled two-fluid and heat structure adjoint models for the reactor safety code system RELAP5/MOD3.2, and sensitivity and uncertainty analysis of dynamic reliability of large-scale systems modeled by Markov chains. During 2003–2006, she served as a task force leader in the FUSION Program at FZK, providing management and scientific leadership for the design and construction of the Helium Loop Karlsruhe (HELOKA) facility at FZK. Since 2006, Dr. Ionescu-Bujor has been program manager at

the Karlsruhe Institute of Technology/Forschungszentrum Karlsruhe (KIT/FZK), responsible for planning KIT/FZK fusion projects, including scheduling, resource allocation, cost control, budget management, and quality management.

Dr. Ionescu-Bujor has extensive expertise in sensitivity and uncertainty analysis of large-scale systems; consistent assimilation of experimental and computational data for obtaining best estimate results with reduced uncertainties, reliability analysis, numerical methods for multi-physics (thermal-hydraulics, structural, neutronics) code systems, and computer software. Dr. Ionescu-Bujor has coauthored 2 books, 2 book chapters, and over 40 peer-reviewed articles.

Frédéric Jasserand

Frédéric Jasserand is an engineer at CEA in the radioprotection field, performing shielding studies, including dosimetry studies for fabrication and recycling facilities, and the conception of transport casks.

Han Gon Kim

Dr. Han Gon Kim received his B.S. in nuclear engineering from Seoul National University and Ph.D. in nuclear engineering from Korea Advanced Institute of Science and Technology (KAIST). In 1997, he became a member of Korea Hydro & Nuclear Power Co., Ltd. (KHNP) as a senior researcher, where he is actively involved in research and development in nuclear reactor thermal hydraulics. From 2005 until now, he is a team leader being responsible for design of nuclear steam supply system (NSSS) of advanced nuclear power plants. He is a member of Korea Nuclear Society.

Inn Seock Kim

Inn Seock Kim received his Ph.D. from the University of Maryland in the area of process diagnostics for large technological systems such as nuclear power plants, and his work in this area has been acknowledged by many organizations, including the Halden Reactor Project of the OECD and the Korea Atomic Energy Research Institute. Dr. Kim served on the scientific staff of Brookhaven National Laboratory from 1988 through 1995, and also used to teach many courses related to reliability engineering and probabilistic analysis of systems safety while serving on the Nuclear Engineering faculty of Hanyang University in Seoul, Republic of Korea.

Inn Seock Kim is particularly interested in helping secure safety in both operating and future nuclear power plants. He has been involved in research activities for enhancing decision-making infrastructure, licensing framework, and regulatory effectiveness by use of both deterministic and risk-informed methodologies. He has consulted to numerous organizations throughout the world, such as the US Nuclear Regulatory Commission, Swiss nuclear regulatory body, Spanish nuclear regulator, European Space Agency, and Korean nuclear institutions including Korea Institute of Nuclear Safety. He recently founded International System Safety Analysis (ISSA) Technology, Inc., in Maryland, which specializes in probabilistic safety assessment and applications, accident management, instrumentation and controls, and human factors analysis.

Dave Knott

Dave Knott received his Ph.D. in nuclear engineering, from the Pennsylvania State University in 1991, for development of the lattice physics code KRAM to model the detailed depletion

of Gadolinium isotopes from boiling water reactor (BWR) fuel designs. He has also received a Master of Computer Science from Cleveland State University in 2002. His career includes employment at the Perry Nuclear Power Plant (1985–1987, in-core analysis); Studsvik of America, Inc. (1991–1998, development of the lattice physics code CASMO-4); First Energy Nuclear Operating Company (1998–2004, creation of the core design and physics support group at the Perry Nuclear Power Plant); Global Nuclear Fuels (General Electric, 2004–2007, development of the lattice physics code LANCER02); Studsvik Scandpower, Inc., (2007–Present, development of the safety-related software MARLA for optimizing fuel movement during refueling outages and during dry storage cask loading campaigns). In his current position as a senior nuclear engineer at Studsvik Scandpower, Inc., in Wilmington, North Carolina, he has focused on developing software for improving capacity factors at boiling water reactors (BWRs) and pressurized water reactors (PWRs). He has served as a research adjunct associate professor of nuclear engineering, University of Cincinnati, 2003–2007. He has also served as a visiting scholar in nuclear engineering, Ohio State University, 2004, and an external advisor, Ph.D. thesis committee, Pennsylvania State University, 2006.

Rudy J. M. Konings

Rudy J. M. Konings received his Ph.D. in chemistry from the University of Amsterdam in 1990, working since 1985 for ECN, the Energy Research Centre of the Netherlands, on various topics related to nuclear fuel, such as fission product chemistry and transmutation. In 1998, he became the manager of the product group Fuels, Actinides and Isotopes at the Nuclear Research and consultancy Group (NRG), a partnership firm created by the merger nuclear activities of ECN and KEMA. A year later, he left NRG for a position at the European Commission's Joint Research Centre (JRC), Institute for Transuranium Elements (ITU). There he continued working on nuclear fuels, with a strong interest in thermodynamic studies. Since 2006, he is head of the Materials Research department of ITU, focusing on scientific research in support of the development of safe advanced fuel. Rudy Konings was appointed editor of *Journal of Nuclear Materials* in 2009.

Edward W. Larsen

Edward W. Larsen is a professor in the department of Nuclear Engineering and Radiological Sciences at the University of Michigan. In 1971, he obtained a Ph.D. in Mathematics from Rensselaer Polytechnic Institute and joined the faculty of the Department of Mathematics at New York University. In 1976, he became an associate professor in the Department of Mathematics at the University of Delaware. In 1977, he joined the Transport Theory Group at Los Alamos National Laboratory, and in 1986, he became a professor in the Department of Nuclear Engineering and Radiological Sciences at the University of Michigan.

Professor Larsen's research involves the development of advanced mathematical algorithms for solving particle transport problems. His work has included neutron transport methods for nuclear reactor applications, thermal radiation transport methods, and charged particle transport methods for medical physics applications. His research has helped extend the theory and simulation of neutral and charged particle transport processes through, for example, the development of improved discretization methods for deterministic transport calculations, improved acceleration methods for speeding up the iterative convergence of deterministic calculations, and new hybrid Monte Carlo-deterministic algorithms.

Professor Larsen is a Fellow of the American Nuclear Society (ANS). For his contributions to nuclear engineering, he received the US Department of Energy E.O. Lawrence Award (1994), the ANS Arthur Holly Compton Award (1996), and the ANS Eugene P. Wigner Reactor Physicist Award (2009).

Christian Latge

Christian Latge received his doctorate in chemical engineering, and engaged in R&D related to sodium fast reactor technology and SuperPhenix start-up at CEA, in 1983. During the period 1988–1995, he was involved in the thermonuclear project ITER for the design of tritium systems. From 1990 to 1996, he was head of Laboratory “Process Studies and consultancy” for nuclear reactor technologies. During 1996–2001, he served as the director of the Sodium School, while during 2000–2003, he was head of service for Process studies for Decontamination and Nuclear Waste Conditioning. Since 2003, he has been a research director at CEA, serving also as project director (2003–2012) of the International Project Megapie (Spallation target for waste transmutation). In addition, he currently serves as professor and International Expert in liquid metal technologies, involved in various European projects, including education and training.

Clément Lemaignan

Clément Lemaignan is a research director at CEA and professor at INSTN on nuclear metallurgy, physics of fracture and material science. Prof. Lemaignan holds 4 patents, and has authored 3 books, 6 review book chapters, and over 80 peer-reviewed articles. He has been editor for the Journal of Nuclear Materials for more than 15 years. He is an officer of the Palmes Académiques and has received many other distinctions.

Daniel Lhuillier

Daniel Lhuillier is a senior researcher with the French National Center for Scientific Research (CNRS). After graduating from the Ecole Normale Supérieure, he obtained a Ph.D. in physics from the University Pierre and Marie Curie (Paris, France). He began his research work at the Laboratory of Aerodynamics (Orsay, France), then moved to the Laboratory for Modeling in Mechanics and is presently a member of the Institute Jean le Rond d'Alembert (IJLRA) of the University Pierre and Marie Curie. Dr Lhuillier is a specialist of thermo-mechanics of continuous media, with applications to superfluid helium, polymer solutions, suspensions of particles, two-phase mixtures, and granular materials. He received the bronze medal of CNRS and the E.A. Brun prize of the French Academy of Sciences.

Meng-Sing Liou

Meng-Sing Liou is a senior technologist of NASA Glenn Research Center. He received B.S. in mechanical engineering from National Cheng Kung University, Taiwan and Ph.D. in aerospace engineering from the University of Michigan. His research interest has been centered about computational fluid dynamics, including development of numerical algorithms and applications to topical areas of high-speed aerodynamics, air-breathing propulsion, and multiphase flows. Multidisciplinary design optimization for aeronautical systems is another interest currently. Dr. Liou has received several major NASA awards, including Abe Silverstein Medal (2006), Exceptional Achievement Medal (2004), and Exceptional Scientific Achievement Medal (1992).

Pierre Lo Pinto

Pierre Lo Pinto is a senior engineer with over 25 years experience in the area of nuclear safety and fast neutron reactor system. He worked on analyzing fast sodium reactors (Phenix, Superphenix, etc.), and coordinated international collaborations (Japan, Russia, etc.) on several innovative design or safety studies in particular in the fields of SFR (e.g., ECRA, CAPRA). More recently, he has been in charge of designing innovative SFR concepts at CEA, and safety-related topics, and is involved as a CEA representative in the SMFR (small modular fast reactor) project involving ANL, CEA, and JAEA.

Klaus Lützenkirchen

Since 2002, Dr. Klaus Lützenkirchen has been head of the Nuclear Safeguards and Security Department of the European Commission's Joint Research Centre Institute for Transuranium Elements in Karlsruhe, Germany. His activities are focused on nuclear forensics, nuclear safeguards, and nonproliferation. He has previously worked at GSI (Gesellschaft für Schwerionenforschung) in Darmstadt, Germany, at the Weizmann Institute in Rehovot, Israel, as an assistant professor at the University of Mainz, and as professor of nuclear chemistry at the University of Strasbourg, France. He holds a doctorate in nuclear chemistry from the University of Mainz, Germany.

Robert E. MacFarlane

Robert E. MacFarlane has received his Ph.D. from the Carnegie Institute of Technology in 1967 and then joined the Physics Division at Los Alamos National Laboratory, where he did experimental studies of the lattice dynamics of bismuth and antimony with inelastic neutron scattering. When that program shut down, he moved to the Theoretical Division to work on nuclear data. There he led the development of the NJOY nuclear data processing system and worked on the production of data libraries for a wide range of applications, such as fast reactors, thermal reactors, fusion systems, accelerator systems, weapons, and cold-neutron facilities. During this period, he also had several administrative positions, including a number of years as group leader, he managed the group's network of workstations on the side, and he provided his group with an early presence on the World Wide Web. MacFarlane was also active in the Cross Section Evaluation Working Group (CSEWG), which manages the US-evaluated nuclear data files (ENDF/B). He was involved in the ENDF/B-V, VI, and VII libraries. He worked on the development of a number of formats, including the ENDF-6 structure, energy-angle distributions, charged-particle representations, atomic data, and thermal scattering data. He was heavily involved in data testing for the various ENDF/B versions, and he also participated in the evaluation effort. Some significant components of this were his work on (1) improving the performance of ENDF/B for fast critical assemblies, including Godiva, Jezebel, and Bigten; (2) energy balance issues for heating and damage; (3) thermal neutron scattering data for important moderators. MacFarlane officially retired in 2005, but remains active by continuing to work part time.

Philippe Martin

Philippe Martin has received his degree of Doctor Engineer in 1972, and has spent his professional career (1973–2008) at the Atomic Energy Commission (CEA), France. He served as head of the Components and Structures Design Laboratory and a member of the French Committee

for rules to be applied to Fast Reactors Design (1986–1993); head of the life extension Project of the Phénix reactor (1993–1997); senior expert (1995–1999); head of the Innovative reactors & systems Section (1997–2000); head of the Simulation of fuel behavior Section (2000–2002); deputy head of the Fuel Department in charge of development of fuels for fourth-generation reactors; and CEA's representative to the Gen-IV SFR Project arrangement negotiation (2002–2006). He is a member of the GEN IV Sodium Fast Reactors Steering Committee of GENIV International Organization (2006–2007) and contributor to CEA's Nuclear Energy Division SFR program. Since 2008, he has served as an engineer-consultant for the Nuclear Energy Division of CEA.

Patrick Masoni

Patrick Masoni is an engineer at CEA specializing in thermo-mechanical analysis of structures. During 1981–1984, he analyzed the thermomechanical static behavior of the cores of the French fast breeder reactors Phenix and Superphenix. During 1984–1995, he performed theoretical and experimental dynamic mechanical studies of light water reactor (LWR) fuel pins and fuel assemblies, and the mechanical behavior of the Phenix reactor core (vibrations, shocks, and seismic calculations). Since 1995, he has performed theoretical and experimental thermomechanical studies regarding the behavior of fuel pins for future (Gen-IV) reactors (GFR and SFR), and also assessed the static thermomechanical behavior of existing French fast breeder reactors.

Klaus Mayer

Dr. Klaus Mayer obtained his Ph.D. in 1987 in the field of radiochemistry and analytical chemistry from the University of Karlsruhe, Germany. He then worked for 2 years at the Institute for Transuranium Elements (ITU) as postdoctoral researcher. In 1990, he started working with the European Commission at IRMM Geel (Belgium) on actinide isotopic reference materials, high accuracy mass spectrometric measurements of U, Pu, and Th, the organization of an external quality control program for nuclear material measurements, and the coordination of support activities to the Euratom safeguards office and to the IAEA. In 1996, he moved to ITU Karlsruhe (Germany) for working on the development and application of analytical methods for nuclear safeguards purposes. He is chair of the ESARDA (European Safeguards Research and Development Association) Working Group on Destructive Analysis. Currently, he is in charge of ITU's activities on combating illicit trafficking and nuclear forensics, and is cochairman of the Nuclear Smuggling International Technical Working Group (ITWG).

Frederic Mellier

Frederic Mellier is a research engineer at CEA. He started his career participating to neutron physic studies for SUPERPHENIX before moving toward activities in support of PHENIX operating and irradiation program. He was in charge of the development and maintenance of the PHENIX core management tools and was involved in experiments for absorber rod reactivity worth measurements. He joined the MASURCA facility in 2002 as the person responsible for experimental programs. He coordinated the MUSE-4 program (funded by the European Commission within the framework of the fifth EURATOM/FP) and is now involved in the GUINEVERE project (sixth FP), both programs aiming at studying the reactivity measurement issue in subcritical systems driven by an external source.

Gerard Mignot

Gerard Mignot obtained his Ph.D. in 1994 at the Aix-Marseille University, option energy science. He joined CEA as an engineer, working on thermal-hydraulics with applications on different nuclear reactor types: sodium fast reactor, pressurized water reactor, and high temperature reactor. From 2003 to 2006, he was in charge of studies on light water reactor innovative fuels and systems in the service of innovative reactor studies in Cadarache. In 2007, he changed fields and coordinated core design studies for the future sodium-cooled fast reactor. Since 2008, he serves as a project manager in the Reactor Studies Department, in charge of the core and reactor design for sodium fast reactor within the CEA SFR program.

Mohammad Modarres

Mohammad Modarres is a University of Maryland distinguished scholar–teacher, a professor and director of Nuclear Engineering, and director of Reliability Engineering at the University of Maryland; he is also a Fellow of the American Nuclear Society. He received his Ph.D. in nuclear engineering from MIT in 1980 and M.S. in mechanical engineering also from MIT.

Professor Modarres' research areas are probabilistic risk assessment, uncertainty analysis, and physics of failure degradation modeling. He has served as a consultant to several governmental agencies, private organizations, and national laboratories in areas related to probabilistic risk assessment. Professor Modarres has authored or coauthored over 250 papers in archival journals and proceedings of conferences, 3 books, 1 handbook, 4 edited books, and 5 book chapters in various areas of risk and reliability engineering.

Dr. Modarres' interests in energy technologies are in the next-generation nuclear reactors and nuclear fuel cycle safety, risk assessment, and management. These areas include research to advance probabilistic risk and safety assessment techniques and applications to complex energy technologies and addressing possible safety issues of the next generation of nuclear power designs in the context of the current combined risk-informed and traditional defense-in-depth regulatory paradigm. His research focuses on understanding safety and regulatory implications of the advanced nuclear reactors. Prof. Modarres is also performing research on the following areas: (1) technology-neutral nuclear power plant regulation; (2) hazard assessment of fire in advanced nuclear power plants; (3) fatigue and corrosion-based degradation assessment of reactor vessels and piping of advanced nuclear power plants using probabilistic modeling based on physics of failure with characterization of uncertainties; (4) best estimate thermal-hydraulic analyses of reactor transients using probabilistic methods to account for variability and uncertainties; and (5) risk and performance-based maintenance techniques for monitoring and assessing nuclear plant system health.

Victor A. Mokhov

Dr. Victor A. Mokhov was born on February 25, 1957, in Sverdlovsk. In 1980, he graduated as a mechanical engineer from the Bauman Moscow State Technical University and joined OKB "GIDROPRESS" as an engineer. His career progressed through the positions of design engineer, deputy head of department, and head of department. He is currently the chief designer of OKB "GIDROPRESS," and is an honored designer of the Russian Federation. His professional interests include the following: reactor plant design, accident analysis, probabilistic safety analysis, and the development of thermal-hydraulic codes for reactor plant transient analyses.

Said Mughabghab

Dr. Said Mughabghab received his M.S. in nuclear physics from the American University of Beirut, Beirut in 1959, followed by Ph.D. in nuclear physics from the University of Pennsylvania, Philadelphia in 1964. He dedicated his scientific carrier to physics of nuclear reactions in the low-energy region, and is best known for numerous contributions to physics of neutron resonances and reaction mechanisms. He has gained worldwide reputation as key author of compendia of neutron resonance parameters and thermal cross sections commonly known as BNL-325, its fifth edition published as *Atlas of Neutron Resonances* in 2006. He has been a research scientist in the National Nuclear Data Center at Brookhaven National Laboratory since 1963, involved in neutron physics research, high-flux beam reactor experiments, neutron resonances, neutron radiative capture and nuclear level densities, compilation of neutron resonance parameters and thermal cross sections. From 1987 to 1993, he worked in the BNL Reactor System Division with J. Powell on the Space Nuclear Thermal Propulsion program to determine the feasibility of using a small reactor for nuclear rocket propulsion for possible future mission to Mars.

Mikhail P. Nikitenko

Dr. Mikhail P. Nikitenko was born on July 1, 1947, in Mariinsk, Khabarovsk region, and graduated as a physical engineer from the Tomsk Polytechnical University, in 1971. He joined OKB "GIDROPRESS" as an engineer in 1971, and became head of group, and head of department. Currently he is the deputy chief designer of OKB "GIDROPRESS," and is an honored designer of the Russian Federation. His professional interests include reactor plant design development, safety analysis, and reactor process analysis.

David Nowak

David Nowak graduated from Rensselaer Polytechnic Institute with a B.S. degree in physics and from the University of Chicago with a Ph.D. in theoretical physics. His current position at Argonne National Laboratory involves working with the Department of Energy to develop a modeling and simulation effort in support of a revitalized nuclear enterprise in the USA.

Prior to Argonne, Dr. Nowak held a series of senior management positions at Lawrence Livermore National Laboratory (LLNL) which included a broad spectrum of highly visible national security responsibilities. Until June 2005, he was deputy associate director for Defense and Nuclear Technologies. He was a founding member of and the first LLNL Program Leader for the Department of Energy's Accelerated Strategic Computing Initiative (ASCI) Program. He led the team that developed the acquisition strategy that culminated in the 100-Teraflops Purple system and the 360-Teraflops Blue Gene system. He was one of the principals developing and executing the ASCI University Alliance Program. Dr. Nowak served as advisor to the Assistant Secretary for Defense Programs in the Department of Energy. Currently, Dr. Nowak splits his time between Chicago and Paris.

Pavel Obložinský

Pavel Obložinský received his M.S. in nuclear physics from the Czech Technical University, Prague, in 1967, and his Ph.D. in nuclear physics from the Slovak Academy of Sciences, Bratislava, in 1973. His scientific carrier has been dedicated to low-energy nuclear reactions,

focusing on studies of neutron-induced reactions. He is best known for numerous contributions to pre-equilibrium nuclear reaction theory and nuclear reaction data evaluation projects. Dr. Obložinský held positions as head of Nuclear Physics Department, Slovak Academy of Sciences, Bratislava (1973–1980); deputy head of Nuclear Data Section of the International Atomic Energy Agency, Vienna (1993–1999); head of the National Nuclear Data Center, Brookhaven National Laboratory (2002–2009); chair of the US Nuclear Data Program (2002–2009); chair of the US Cross Section Evaluation Working Group (CSEWG) (2001–2009). He was responsible for the release of the US-evaluated nuclear data library ENDF/B-VII.0 in 2006.

Laurent Paret

Laurent Paret graduated from the Département Génie mécanique, Université de Technologie de Compiègne, in 1996. After working at AREVA NC as the engineer in charge of deployment of a software to manage MOX fuel fabrication, he joined the CEA, in 1999, to work on MOX-fuels fabrication for experimental irradiations. Since 2001, he has been performing fuels studies for Gen-IV reactors (GFR and SFR). Currently, he is project manager in charge of the sodium fast reactor (SFR) fuels development.

Imre Pázsit

Imre Pázsit (M.Sc., 1971; Ph.D., 1975, Budapest, Hungary) is professor and chair of the Department of Nuclear Engineering, Chalmers University of Technology, Göteborg, Sweden. Former employments include the Central Research Institute for Physics, Budapest (1975–1983) and the nuclear research center Studsvik, Nyköping, Sweden (1983–1991). Imre Pázsit is a Fellow of the American Nuclear Society (2006), and a member of the Executive Committee on the Mathematics and Computation Division of ANS. He is a member of the Royal Swedish Academy of Engineering Sciences (2008) and a working member of the Royal Academy of Arts and Sciences in Göteborg (2005). Since 2009, he has also been an adjunct professor in the Department of Nuclear Engineering and Radiological Sciences of the University of Michigan, Ann Arbor, USA. Between 2000 and 2008 he was the head of the Section for Mathematical Physics of the Swedish Physical Society.

His research interests include the following: fluctuations in neutron transport; atomic collision cascades and fusion plasmas; reactor dynamics; neutron noise analysis applied to reactor diagnostics and nondestructive analysis in nuclear safeguards; transport theory of neutral and charged particles; intelligent computing methods such as artificial neural networks and wavelet analysis; diagnostics of two-phase flow and fusion plasma; positron annihilation spectroscopy and positron transport. He coauthored with L. Pál a book entitled *Neutron Fluctuations – a Treatise on the Physics of Branching Processes*, Elsevier Science Ltd., 2008. He has published over 160 articles in international journals; several book chapters, numerous reports, conference proceedings, popular science booklets, and articles. He is a member of the Editorial Board of the *Annals of Nuclear Energy*, the *International Journal of Nuclear Science and Technology*, and the *Nuclear Technology and Radiation Protection Journal*.

Michel Pelletier

Michel Pelletier received his Ph.D. from the University of Paris IX (Orsay), in materials sciences, in 1981, and joined CEA, Cadarache working in experimental fuel studies (definition of irradiation, PIE, and synthesis). During 1991–2000, he was a member of the SFR fuel-safety

working group (CABRI program). A senior expert since 1996, he is also lecturer at the “Institut National des Sciences et Techniques Nucléaires” and at the School of plutonium (Cadarache), specializing in the modeling and design of reactor fuel behavior.

Alexander K. Podshibyakin

Dr. Alexander K. Podshibyakin was born on June 30, 1938, in Podolsk, Moscow region, and graduated as an engineer in thermal physics from the Moscow Power Engineering University, in 1965. He joined OKB “GIDROPRESS,” and progressed through a sequence of positions of increased responsibility: leading engineer, head of department, first deputy chief designer of OKB “GIDROPRESS.” Currently, he is the chief specialist on VVER NSSS, and is an honored designer of the Russian Federation. His professional interests include the following: reactor plant design development, analytical and theoretical studies, elaboration of the schemes and processes of reactor plant operation, commissioning tests at NPPs, safety analyses.

Anil K. Prinja

Anil K. Prinja is a professor and associate chair in the Department of Chemical and Nuclear Engineering at the University of New Mexico (UNM), USA. He obtained his B.Sc. (“1st Class Honors,” 1976) and Ph.D. (1980) in nuclear engineering from Queen Mary College, University of London, UK, and held a research staff appointment at the University of California, Los Angeles (UCLA), before joining UNM in 1987. He has since held visiting professor’s appointments at Chalmers University, Sweden, and at UCLA, and has an ongoing affiliate appointment at Los Alamos National Laboratory, USA.

Professor Prinja’s research interests include development of efficient solution techniques for stochastic and deterministic computation of high-energy charged particle transport, formulating models for radiation transport in random media, application of stochastic methods to uncertainty quantification in radiation transport, and investigating neutron branching processes in multiplying media. Professor Prinja is a Fellow of the American Nuclear Society. From 1995 to 2005, he was the associate editor of *Annals of Nuclear Energy* and presently serves on the Editorial Boards of *Transport Theory and Statistical Physics*, and *Annals of Nuclear Energy*.

Jean Claude Queval

Jean Claude Queval, born in 1950, graduated as an aerospace engineer in 1972, has a very extensive experience in dynamic and seismic behavior of equipment and structures, for 30 years. He is in charge of the experimental part of the EMSI Laboratory at CEA Saclay. He is the author of many papers in R&D and seismic qualification tests, fluid-structure interaction computation, and fuel assembly modeling.

Baldev Raj

Dr. Baldev Raj (born in 1947; B.E., Ph.D., D.Sc.) holds memberships in the International Nuclear Energy Academy, German National Academy of Sciences; he is a Fellow of the Third World Academy of Sciences, and Fellow of all Engineering and Science Academies in India. He is a distinguished scientist and director, Indira Gandhi Centre for Atomic Research, Kalpakkam, Tamil Nadu. His specializations include materials characterization, testing and evaluation using nondestructive evaluation methodologies, materials development and performance assessment

and technology management. He has more than 750 publications in leading refereed journals and books. He has coauthored 12 books and coedited 32 books and special journal volumes. He has 5 Indian Standards and 18 patents to his credit. He is editor-in-chief of two series of books: one related to NDE Science and Technology and another related to Metallurgy and Material Science. He is on the editorial boards of national and international journals. He is the member of many national and international committees and commissions. He has been invited to deliver plenary and panel speeches in the most eminent international forums and more than 50 occasions in 30 countries. He has won many national and international awards and honors. He has a passion for teaching, communications, and mentoring. His other interests include science and technology of cultural heritage and theosophy.

Ulrich Rohde

Ulrich Rohde studied physics at the University of Minsk (Byelorussia), obtaining a master's degree in 1976. During 1976–1998, he worked as a research scientist in the Central Institute for Nuclear Research in Rossendorf near Dresden, the later Forschungszentrum Dresden-Rossendorf (FZD). In June 1987, he obtained a doctorate in physics in the field of two-phase flow modeling and boiling water reactor (BWR) stability analysis. Since 1998, he has been the head of the Safety Analysis Department of the Institute of Safety Research of the FZD, performing research in reactor dynamics, thermal hydraulics, and fluid dynamics.

Dr. Rohde gained particular experience in reactor dynamics and safety analysis of VVER-type reactors. He contributed to the development and validation of the Rossendorf reactor dynamics code DYN3D, which was initially designed for VVER type reactors, and is currently used as a transient-analysis tool in most of the countries with operating VVER reactors; the code is a part of the European software platform NURSIM. He has participated on scientific and management level in several international projects on safety analyses and validation of coupled neutronics/thermal hydraulics codes for VVER. From 1992 until 2009, he was a member of the Scientific Council of Atomic Energy Research (AER), an international association on reactor safety and reactor safety of VVER.

Gilles H. Rodriguez

Gilles H. Rodriguez (Engineer, chemistry, University of Lyon, France, 1990; Master of Science in chemical and process engineering, Polytechnic University of Toulouse, France, 1991) is a senior expert engineer at CEA/CADARACHE (French Atomic Energy Commission/Cadarache center). He is working on Generation-IV Fast Reactor research program. His areas of expertise are fast reactor technology, liquid metal processes, and process engineering. Since 2007, he has been a project leader of sodium technology and components, within the CEA SFR project organization, and is representing CEA/France on the GEN IV SFR Project Management Board (component design and balance of plant).

Vincenzo V. Rondinella

Vincenzo V. Rondinella has received his Ph.D. in materials sciences from Rutgers University, New Jersey. Currently, he is the head of the Hot Cells (HC) department at the Institute of Transuranium Elements (ITU), the European Commission's Joint Research Centre (JRC) located in Karlsruhe, Germany. The HC department performs postirradiation examinations on light water reactor (LWR) and advanced reactor fuels and cladding materials, focusing

on properties and behavior related to various stages of the nuclear fuel cycle, including fuel behavior in-pile, effects associated with different irradiation history (burn up, temperature, power, etc.) and behavior/evolution during storage and disposal. Dr. Rondinella's main areas of interest include the following: radiation damage, properties of high burn up nuclear fuels, mechanical properties of the fuel rod system (fuel + cladding/coatings), and the development and characterization of advanced fuels for new reactors.

Jacques Rouault

Jacques Rouault graduated in 1976 from Ecole Centrale de Paris, and joined CEA (Commissariat à l'Énergie Atomique) in 1980. He spent most of his career in the field of fast reactors. He was successively involved in the field of fast reactor fuel behavior (postirradiation examinations, modeling). From 1993 to 1996, he was the CAPRA project manager (Feasibility studies of a fast reactor optimized to burn Pu) in the context of a large international collaboration. From 1996 to 2000, he managed the Section of fuel development (FBR, PWR), covering postirradiation examinations, code development, experimental irradiation in Phénix and other reactors, and the material program for Minor Actinides transmutation. From 2001 to 2007, he directed the Section of Innovative Systems Study mainly focusing on GEN IV system design. Since 2007, he has responsibilities in the CEA Gen-IV program management with emphasis on the sodium fast reactor.

Sergei B. Ryzhov

Dr. Sergei B. Ryzhov was born on November 18, 1959, in Chekhov, Moscow region. He was graduated in 1982 as a mechanical engineer, from the Bauman Moscow State Technical University, and joined OKB "GIDROPRESS" as an engineer. Since then, he progressed through appointments as design engineer, head of group, head of department, and chief designer. Currently, he is the director-general designer of OKB "GIDROPRESS," and has been designated an honored designer of the Russian Federation. His professional interests include the following: reactor plant design development, and participation in research and experimental activities.

Mark Schanfein

Mark Schanfein joined Idaho National Laboratory (INL) in September 2008 as their senior nonproliferation advisor, after a 20-year career at Los Alamos National Laboratory (LANL). His current focus is on leveraging INL technology, facilities, and nuclear material to build an international safeguards program. He has over 30 years of experience in international and domestic safeguards. This includes his 20 years at Los Alamos National Laboratory where he most recently served as the program manager for Nonproliferation and Security Technology, a portfolio that included international and domestic safeguards and security. He also spent 10 years at the LANL Plutonium Facility as the team leader for all NDA measurements at this facility, and the Chemistry and Material Research facility, totalling over 100 instruments. He has over 8 years of experience working at the International Atomic Energy Agency, where he served 4 years as a safeguards inspector and inspection group leader covering inspections on a diverse set of facilities, and another 4 years as the unit head for Unattended Monitoring Systems.

J. Kenneth Shultis

J. Kenneth Shultis, born in Toronto, Canada, graduated from the University of Toronto with a BA.Sc. degree in engineering physics (1964). He gained his M.S. (1965) and Ph.D. (1968) degrees in nuclear science and engineering from the University of Michigan. After a postdoctoral year at the Mathematics Institute of the University of Groningen, the Netherlands, he joined the Nuclear Engineering faculty at Kansas State University in 1969 where he presently holds the Black and Veatch Distinguished Professorship. He teaches and conducts research in radiation transport, radiation shielding, reactor physics, numerical analysis, particle combustion, remote sensing, and utility energy and economic analyses. He is a Fellow of the American Nuclear Society, and has received many awards for his teaching and research. Dr. Shultis is the author or coauthor of six textbooks on radiation shielding, radiological assessment, nuclear science and technology, and Monte Carlo methods. He has written over 200 research papers and reports, and served as a consultant to many private and governmental organizations.

Craig F. Smith

Dr. Craig F. Smith earned his B.S. degree in engineering (*summa cum laude*) at the University of California, Los Angeles (UCLA) in 1971 and his Ph.D. in nuclear science and engineering, also at UCLA, in 1975. He is a Fellow of the American Nuclear Society (ANS) and of the American Association for the Advancement of Science (AAAS). He is currently serving on assignment as the Lawrence Livermore National Laboratory (LLNL) chair professor of Physics at the Naval Postgraduate School (NPS) in Monterey. He also serves as adjunct faculty at the Monterey Institute of International Studies.

In addition to his faculty role, Dr. Smith leads research efforts in nuclear energy technology at LLNL. He is the US member of the Generation IV International Forum (GIF) Provisional System Steering Committee on lead-cooled fast reactors, and has worked internationally in research related to nuclear energy technology, radiation detection, and automated systems. He has authored more than 50 technical papers and articles and 4 books, including the recently published *Connections: Patterns of Discovery*, (Wiley, 2008).

Joe Somers

Joe Somers hails from Dublin, Ireland, where he completed a chemistry degree at Trinity College Dublin in 1981. Thereafter, he concluded a Ph.D. on surface chemistry (1986), before joining the Fritz Haber Institut der Max Planck Gesellschaft in Berlin. There, his investigations centered on the use of UV and soft X-ray photoelectron and absorption spectroscopy at the synchrotron radiation source BESSY for the elucidation of geometric and electronic structure of adsorbates on metal and semiconductor surfaces.

In 1990, he joined the scientific staff of the European Commission's Joint Research Centre at the Institute for Transuranium Elements (JRC-ITU) in Karlsruhe, initially investigating the agglomeration of airborne particles using very high intensity ultra sonic waves. For the last 15 years, his research interests have concentrated on the development and testing of ceramic materials for nuclear fuel applications. This research has covered a wide variety of nuclear fuels (UO₂, MOX, Minor actinide fuels) for a variety of reactor systems (LWR, HTR, SFR, GFR, ADS), and has been performed through institutional and international programs. In addition, the local structure of actinide-bearing compounds and its evolution due to irradiation damage

has been a subject of particular interest. Currently, he is head of the Nuclear Fuels department at the JRC-ITU.

Ugo Spezia

Ugo Spezia has a master's degree in nuclear engineering, and has been active in the Italian nuclear industry since 1981, working on the Italian Unified Nuclear Project. Since 1999, he has been the secretary-general of the Italian Nuclear Association (AIN), advisor of the Italian Nuclear Regulatory Agency (ANPA), and, since 2003, technical manager of the Italian Nuclear Plant Management Company (SOGIN), the state-owned company charged of the Italian nuclear plant decommissioning. Since 2009, he has been technical manager of the SOGIN Safety Project Control. He is author of several publications on nuclear energy and nuclear technology and coauthor of the book *Nuclear Plant Decommissioning* (2002).

Theofanis G. Theofanous

Theofanis (Theo) G. Theofanous is professor in the Chemical Engineering and Mechanical Engineering Departments at UCSB, and founding director of the Center for Risk Studies and Safety (CRSS). He is a graduate of the National Technical University of Athens, Greece, and holds a Ph.D. from the University of Minnesota, both in chemical engineering. Prior to coming to UCSB in 1985, he taught at Purdue's Chemical Engineering and Nuclear Engineering Departments, where he was also the founding director of the Nuclear Reactor Safety Laboratory.

Professor Theofanous has worked on the physics and computation of multiphase flows and on methodologies for addressing uncertainties in risk management; he championed a key-physics-based approach to addressing complexity as a basis for decision making; and he brought applications to completion on important safety issues in both the chemical and nuclear industries, and as of recently in the domain of National Defense. He is consulted extensively, and internationally, for industrial and governmental organizations, and served on a number of National Research Council Panels, including the one that assessed the safety of the Nation's Research and Production (Defense, Nuclear) Reactors in the aftermath of the Chernobyl accident. His practical credits include the following: the Risk Oriented Accident Analysis Methodology (ROAAM), the In-Vessel Retention (IVR) design concept for PWRs, and the Basemat-Internal Melt Arrest and Coolability (BiMAC) device for BWRs and large PWRs.

He is a member of the National Academy of Engineering, a fellow of the American Nuclear Society, and was awarded an honorary doctorate from the University of Lappeenranta in Finland. In 1997, he received the E. O. Lawrence Medal from the US Department of Energy for his work on managing risks of severe accidents in nuclear power reactors.

Anton Tonchev

Anton Tonchev is an assistant research professor at Duke University. He received his Ph.D. degree in 1995 from the Joint Institute for Nuclear Research, Dubna, Russia. His main area of research is nuclear structure and nuclear astrophysics, in particular the study of the nuclear dipole response and the different low-energy modes of excitation. These low-energy modes of excitation address important issues such as how protons and neutrons arrange themselves

in neutron-rich nuclei under electric dipole absorption. His other research interests include nuclear forensics and neutron science related to national security.

Werner Tornow

Werner Tornow is a nuclear physics experimentalist who received his doctorate in 1972 from the University of Tuebingen, Germany. He is a full professor at Duke University and served as director of the Triangle Universities Nuclear Laboratory from 1996 to 2006. His expertise is in neutron-induced reactions ranging from few-body systems to heavy nuclei. More recently, he has also been involved in photon-induced reaction studies, and in neutrino physics and double-beta decay searches.

Ivo Tripputi

Ivo Tripputi is a nuclear engineer who is in the nuclear industry for more than 35 years. He played several roles in the engineering department of ENEL for the development of new reactor projects for the Italian utility. Later he was involved in the development of utility requirements for advanced plants in USA and in Europe with leading roles. Recently he was decommissioning manager for all Italian nuclear fuel cycle plants and manager for R&D, innovation and special projects. He has been IAEA expert for development of safety guides and on special assistance projects in various parts of the world. He is currently chair of the Working Party for Decommissioning and Dismantling of OECD/NEA.

James S. Tulenko

James S. Tulenko is emeritus professor in the Department of Nuclear and Radiological Engineering at the University of Florida (UF) in Gainesville, Florida and served as chairman of the Department for 16 years (1986–2001). He currently is the director of the Laboratory for Development of Advanced Nuclear Fuels and Materials at UF. Prior to his academic career, Professor Tulenko spent 23 years in the nuclear industry as manager, Nuclear Fuel Engineering at Babcock and Wilcox; manager of Physics at Nuclear Materials and Equipment Corp; and manager, Nuclear Development at United Nuclear Corporation.

Professor Tulenko has numerous fields of interest in the nuclear area, most of which involve nuclear fuel and the nuclear fuel cycle. He was presented with the Silver Anniversary Award of the American Nuclear Society (ANS) for his contributions to the nuclear fuel cycle in the Society's first 25 years. He received the Mishma Award of the ANS in recognition of his many contributions to nuclear material research. He also received the Arthur Holly Compton Award for his contributions to nuclear science and technology, and the Glenn Murphy Award of the American Society for Engineering Education for his outstanding contributions to engineering education. Elected a Fellow of the ANS for his contributions to the nuclear fuel cycle, Professor Tulenko is a past president of the ANS, having served from 2004 to 2005.

Paul J. Turinsky

Paul J. Turinsky is a professor of Nuclear Engineering at North Carolina State University, where he also services as coordinator of the Interdisciplinary Graduate Program on Computational Engineering and Sciences, and university representative to and chair of the Battelle Energy Alliance Nuclear University Collaborators, which is associated with the operation of Idaho

National Laboratory. His area of expertise is computational reactor physics, with a focus on nuclear fuel management optimization, space-time kinetics, sensitivity/uncertainty analysis, and adaptive core simulation. He is a Fellow of the American Nuclear Society and recipient of numerous awards including the Glenn Murphy Award (ASEE), E. O. Lawrence Award in Nuclear Energy (US Department of Energy), Eugene P. Wigner Reactor Physics Award (ANS), and Arthur Holly Compton Award (ANS). He serves on several advisory committees and retains an active consulting practice supporting industry and government.

Bernard Valentin

Bernard Valentin graduated with a master's degree in heat transfer from National Institute of Nuclear Science and Technic (INSTN), and joined CEA in 1983. He has worked on modeling and computations related to safety of SFR, particularly on PHENIX and SPXI reactors. He is now a specialist of SFR core and subassembly cooling, developing the ELOGE platform for design and thermo-hydraulics computations of such cores and subassemblies.

Paul Van Uffelen

Paul Van Uffelen studied nuclear engineering in Belgium and in France. He obtained his Ph.D. in the field of nuclear engineering at the University of Liège. Since he started his research career at the Belgian nuclear research centre (SCKCEN) in 1994, Paul has been involved in research for light water reactor (LWR) fuel, more precisely in the field of fission gas behavior and heat transfer. During 1996–1997, he was a visiting scientist at the OECD Halden Reactor Project in Norway, where he worked under the supervision of Carlo Vitanza and Wolfgang Wiesnack on in-pile experiments. Since 2002, Paul is leading the modeling team at the Materials Research department of the European Commission's Joint Research Centre (JRC), Institute for Transuranium Elements. His present research activities cover modeling of LWR fuel under normal operating and design basis accident conditions, as well as advanced fuel behavior modeling by means of the TRANSURANUS fuel performance code.

Frédéric Varaine

Frédéric Varaine has over 15 years experience in the area of nuclear physics and core design for fast reactor. He was involved in the restart of SUPER-PHENIX in 1994, having performed core physics calculation, safety, and neutronics tests. Subsequently he became responsible for irradiations studies performed in the PHENIX reactor for the transmutation demonstration. From 2000 to 2006, he was a project manager for transmutation studies under the 1991 French law on the management of radioactive waste. Since 2002, he has been a group leader of the core design laboratory, which is conducting all neutronics studies for reactor design of Generation-IV systems and especially gas and sodium fast reactor. He participates in several collaborative projects on SFR with Japan, India, the USA, Russia, and China.

Carlo Vitanza

Carlo Vitanza graduated in nuclear physics at the University of Milan, Italy, in 1971. Until 1975, he worked in a nuclear fuel company in Italy. He then moved to the OECD Halden Reactor Project, Norway, where he worked for 24 years, dealing primarily with the large nuclear fuel program carried out through the Halden reactor experiments. During 1989–1999, he was the director of the Halden research establishment.

In 1999, he moved to the OECD Nuclear Energy Agency (NEA) in Paris, France, where among others he was in charge of the international research projects conducted under the OECD sponsorship in the nuclear safety area. During his stay at the OECD-NEA 1999–2009 he initiated a number of such international projects, mainly in the area of thermal-hydraulics, severe accidents, and fuel safety. In 2009, he returned at Halden, where he is currently responsible for new development and marketing.

R. Bruce Vogelaar

Dr. R. Bruce Vogelaar received his Ph.D. in accelerator-based nuclear astrophysics from the California Institute of Technology in 1989, and then became head of cyclotron operations at Princeton University, where he later joined their faculty as an assistant professor. He subsequently moved to Virginia Tech in 1998 becoming a professor with research in fundamental weak-interaction physics, using ultracold neutrons at the Los Alamos National Laboratory and very large neutrino detectors at the INFN underground laboratory in Gran Sasso, Italy. He led a team to advance Kimballton as a potential national underground facility, and is currently the founding director of the Kimballton Underground Research Facility in addition to leading an active National Science Foundation (NSF)-funded research group.

Dr. Vogelaar encouraged and participated in some of the earliest neutron transport experiments underlying the foundations of GEM*STAR and conducted GEM*STAR's most recent neutron transport and fuel burn-up studies using the code MNCPIX.

Richard Wallace

Dr. Richard Wallace has a Ph.D. in nuclear astrophysics from the University of California. He has 28 years experience in nuclear weapons analysis, nuclear materials use and protection, nuclear safeguards systems, and technical program management. Currently, he is a group leader for the N-4 Safeguards Systems Group at Los Alamos National Laboratory (LANL), overseeing a staff of experts in advanced safeguards systems development, nonproliferation policy analysis, international engagement activities related to the nuclear fuel cycle and safeguards, and IAEA activities related to developing potential proliferation indicators. From 2002 to 2005, Dr. Wallace was a senior analyst with the International Atomic Energy Agency (IAEA) in Vienna, Austria, working to collect, evaluate and analyze open source and proprietary information to identify and assess indicators of potential clandestine nuclear weapons activities. He shared in the 2005 Nobel Peace Prize that was awarded to the IAEA. From 1995 to 2001, he was a project leader for the US–Russian Nuclear Materials Protection, Control, and Accounting program at LANL and acting program manager for Russian Nonproliferation Programs. In 1995, he provided technical advice to Department of Energy (DOE) during negotiations for the Comprehensive Test Ban Treaty. From 1981 to 2004, he was involved in nuclear weapons physics simulation modeling.

R. L. Walter

Prof. R. L. Walter is a full professor in the department of Nuclear Physics at Duke University, and conducted most of his research at the Triangle University Nuclear Laboratory (TUNL) in Durham, North Carolina. He is an international leader in polarization in nuclear physics, and has supervised over 30 Ph.D. students, performing theses (mostly) on this subject. His studies

include the production of polarized charged particles and neutrons, and the use of such particle beams in studies of nuclear structure.

Akio Yamamoto

Dr. Akio Yamamoto received his Ph.D. in energy science at Kyoto University, in 1998, for his work on loading pattern optimization methods for light water reactors (LWRs). During 1989–2003, he was in charge of in-core fuel management and related methodology development for commercial LWRs at Nuclear Fuel Industries, Ltd., Japan. Currently, he is an associate professor in the Graduate School of Engineering, Nagoya University, Japan. His research is focusing on the development of advanced nuclear design methods for current and Gen-IV reactors, large-scale simulations using parallel/distributed computing, in-core fuel optimizations, education of reactor physics and energy policy/strategies. He is a member of both the Atomic Energy Society of Japan (AESJ) and American Nuclear Society (ANS).

Introduction

In 1958, when nuclear engineering was at the dawn of becoming an international profession, McGraw-Hill Book Company published the first *Nuclear Engineering Handbook*, edited by Harold Etherington. It contained 14 chapters, contributed by 70 specialists, all from the USA, spanning 1,872 pages, and served, for decades, as the reference book for nuclear engineers worldwide. Following the role model provided by that pioneering work, but surpassing it considerably in depth and extent, the present *Handbook of Nuclear Engineering* comprises 29 chapters in 5 volumes, spanning over 3,600 pages. The Editor is very grateful to the 100 international experts who contributed to turning this handbook, in a very short time, from a paper project into a comprehensive and inspiring reference work, at a time when the field of nuclear engineering and technology appears to be at the dawn of a worldwide renaissance, after some 2 decades of stagnation and even decline, in some countries.

Each of the five volumes of this handbook is devoted to a representative segment of the field of nuclear engineering and technology, as indicated by their respective titles. They commence with a presentation of the fundamental sciences underlying nuclear engineering and move successively on to reactor design and analysis, fuel cycles, decommissioning, waste disposal, and safeguards of nuclear materials. As a whole, the handbook strives, of course, to cover all of the representative aspects of this field. The five volumes of this handbook are:

Volume 1, entitled *Nuclear Engineering Fundamentals*, comprising Chaps. 1 through 7

Volume 2, entitled *Reactor Design*, comprising Chaps. 8 through 12

Volume 3, entitled *Reactor Analysis*, comprising Chaps. 13 through 18

Volume 4, entitled *Reactors of Generations III and IV*, comprising Chaps. 19 through 24

Volume 5, entitled *Fuel Cycles, Decommissioning, Waste Disposal and Safeguards*, comprising Chaps. 25 through 29

Each chapter strives to be self-contained, covering the current state-of-the-art and open issues in the respective area of nuclear science and engineering. An expert reader could go directly to the chapter of interest. Graduate students, on the other hand, may wish to consult the chapters in the first volume, since knowledge of the contents of those chapters will greatly facilitate the understanding of the material presented in the subsequent chapters/volumes. To assist the reader, the remainder of this *Introduction* briefly summarizes the contents of the handbook's chapters.

Chapter 1, entitled *Neutron Cross Section Measurements*, gives an overview of neutron-induced cross-section measurements, both past and present. Neutron cross sections are the key quantities required to calculate neutron reactions (e.g., in reactors, shields, nuclear explosions, detectors, stars). This chapter presents the principal characteristics of time-of-flight and mono-energetic fast neutron facilities and explains the physics of typical neutron cross sections and their measurements. In particular, the chapter provides an overview of the *R*-matrix formalism, which is the fundamental theory for describing resonance reactions. The chapter ends with a brief overview of the current libraries of evaluated cross sections, mentioning not only the major general purpose libraries, e.g., the ENDF (USA evaluated nuclear data library), the JEFF (European joint evaluated fission and fusion library), the JENDL (Japanese evaluated nuclear data library), the CENDL (Chinese evaluated nuclear data library), and the BROND

(Russian evaluated neutron reaction data library) but also the most important special purpose and derived libraries.

Chapter 2, entitled *Evaluated Nuclear Data*, describes the status of evaluated nuclear data for nuclear technology applications. The chapter commences with a presentation of the evaluation procedures for neutron-induced reactions, focusing on incident energies from thermal energy up to 20 MeV, although higher energies are also mentioned. The status of evaluated neutron data for actinides is discussed next, followed by paradigm examples of neutron-evaluated cross-section data for coolants/moderators, structural materials, and fission products. Neutron covariance data characterizing uncertainties and correlations are presented next, highlighting the procedures for validating evaluated data libraries against integral benchmark experiments. Additional information of importance for nuclear technology, including fission yields, thermal neutron scattering, and decay data is also presented. The chapter concludes with a brief introduction to current web retrieval systems, which allow easy access to a vast amount of up-to-date evaluated data for nuclear engineering and technology, including the latest versions of the major libraries ENDF/B-VII.0, JEFF-3.1, and JENDL-3.3.

Chapter 3 is entitled *Neutron Slowing Down and Thermalization* and presents the theory underlying the generation of thermal cross sections, concentrating on the phonon expansion method. Paradigm examples are given for graphite, water, heavy water, and zirconium hydride. The graphite example demonstrates incoherent inelastic scattering and coherent elastic scattering for crystalline solids. The water example demonstrates incoherent inelastic scattering for liquids with diffusive translations. Heavy water adds a treatment for intermolecular coherence. Zirconium hydride shows the effects of the “Einstein oscillations” of the hydrogen atoms in a cage of zirconium atoms, and it also demonstrates incoherent elastic scattering. Steady-state slowing down is illustrated for typical cross-section data, highlighting slowing down by elastic scattering, inelastic scattering, and resonance cross sections in the narrow resonance approximation. Intermediate resonance self-shielding effects are introduced using the NJOY flux calculator and the WIMS implementation. The effects of time and space on slowing down are demonstrated using Monte Carlo simulations. Neutron thermalization is modeled first by using Monte Carlo simulations of several systems, followed by modeling using multigroup discrete-ordinates and collision-probability methods. The chapter also demonstrates size effects in thermalization and concludes by reviewing open issues that warrant further theoretical and experimental investigations.

Chapter 4, entitled *Nuclear Data Preparation*, focuses on data-processing codes that translate and manipulate the evaluated cross-section and other nuclear data (e.g., photon interactions, thermal-scattering laws) from the universally used ENDF/B format to a variety of formats used by individual particle transport and diffusion code systems for various applications. Data processing codes prepare nuclear data for use in continuous energy Monte Carlo codes as well as in multigroup Monte Carlo and deterministic codes. The main tasks performed by data processing codes are the reconstruction of energy-dependent cross sections from resonance parameters and Doppler broadening to a variety of temperatures encountered in practical systems. The chapter underscores the importance of the multiband method for enhancing the accuracy of reactor criticality and shielding computations.

Chapter 5 is entitled *General Principles of Neutron Transport* and highlights the theory underlying the forward and the adjoint transport equations as well as the scaled transport and neutron precursor equations. In particular, the chapter includes a discussion of the lack of smoothness of the angular flux in multidimensional geometries, which impacts negative numerical simulations. The chapter also presents the derivation of the time-dependent

integral transport equation as well as derivations of the transport equation in specialized one-dimensional (1D), two-dimensional, and three-dimensional geometries. Since the exact transport equation cannot be solved for large-scale reactor physics applications, various approximations have been developed in time, in parallel with the development of computational resources. The chapter also features, in a more rigorous manner than hitherto presented in the literature, derivations of the transport equation's approximate forms used for practical applications, highlighting: (1) an asymptotic derivation of the point kinetics equation, (2) an asymptotic derivation of the multigroup P_1 and diffusion equations, (3) derivation of the spherical harmonics (P_N) and simplified spherical harmonic (SP_N) approximations, and (4) an asymptotic derivation of the point kinetics equations. Computational neutron transport methods are also discussed briefly, underscoring the salient features of the most popular deterministic methods, Monte Carlo methods, and hybrid Monte Carlo/deterministic methods.

Chapter 6 is entitled *Nuclear Materials and Irradiation Effects* and highlights the physical transformations induced in materials by neutron irradiation. Irradiation damage is caused by (n, α) reactions, as well as by elastic interactions of neutrons with atoms, leading to displacement cascades and generation of point defects. In turn, the migration and clustering of point defects induce major changes in microstructures. The physical mechanisms leading to irradiation hardening, reduction of ductility, swelling, and irradiation creep and growth are described in detail for the alloys (e.g., structural and stainless steels, aluminum, zirconium, and vanadium alloys) and ceramics used not only in operating reactors but also envisaged for use in future fission and fusion reactors. The chapter also describes water radiolysis and changes in electrical properties of insulating ceramics.

Chapter 7, entitled *Mathematics for Nuclear Engineering*, summarizes the main mathematical concepts and tools customarily used in nuclear science and engineering, thus facilitating the understanding of the mathematical derivations in the other chapters of the handbook. The material presented in this chapter highlights the following topics: vectors and vector spaces, matrices and matrix methods, linear operators and their adjoints in finite and infinite dimensional vector spaces, differential calculus in vector spaces, optimization, least squares estimation, special functions of mathematical physics, integral transforms, and probability theory.

Chapter 8, entitled *Multigroup Neutron Transport and Diffusion Computations*, reviews the traditional methods for solving the steady-state transport equation, including the spherical harmonics expansion method, the collision probability method, the discrete ordinates method, and the method of characteristics. The chapter also highlights the most popular discretization methods for solving the neutron diffusion equation numerically.

Chapter 9 is entitled *Lattice Physics Computations* and presents a detailed description of the elements that comprise a so-called "lattice physics code." Lattice physics codes analyze axial segments of fuel assemblies, referred to as "lattices," to determine the detailed spatial and spectral distribution of neutrons and photons within and across the segment. The major components of a lattice physics code include a corresponding cross-section library, and various modules for performing computations in the cross sections' resonance region, fine-mesh transport calculations within the heterogeneous lattice geometry, and burnup computations. The flux distribution obtained from lattice computations is used to condense and homogenize the cross-section data into the structure needed for coarser-level "nodal" codes, in which each lattice is treated as a "node." The nodal codes are used to model the coupled neutronics and thermal-hydraulics behavior of the entire reactor core during steady-state and transient operation.

Chapter 10 is entitled *Core Isotopic Depletion and Fuel Management*. It commences by discussing numerical methods for solving the Bateman equation, which models the transient behavior of the isotopes (fissile, fertile, burnable poison, and fission products) produced during reactor operation. After introducing the concepts of breeding, conversion, and transmutation, the chapter discusses out-of-core and in-core nuclear fuel management, emphasizing fuel management for light water reactors (LWRs). Out-of-core fuel management aims at optimizing decisions regarding: (1) fuel cycle length; (2) stretch-out operations; and (3) feed fuel number, fissile enrichment, burnable poison loading, and partially burnt fuel to be reinserted, for each cycle in the planning horizon. On the other hand, in-core fuel management requires decisions for determining the loading pattern, control rod program, lattice design, and assembly design. The chapter continues with a brief review of in-core fuel management decisions for heavy water reactors, very high temperature gas-cooled reactors, and advanced recycle reactors. The mathematical optimization techniques and the tools for accomplishing the computations which are required to support decision making in nuclear fuel management are discussed with a view toward further enhancing the capabilities in these areas. The chapter concludes by summarizing the current state of fuel depletion and management capabilities, while discussing the avenues for further progress in these areas.

Chapter 11, entitled *Radiation Shielding and Radiological Protection*, deals with shielding against gamma rays and neutrons with energies up to 10 MeV, while assessing the health effects from exposure to such radiation. The chapter commences by describing the features of radiation sources and fields, including the mathematical modeling of the energy and directional dependence of the radiation intensity. The interaction of neutrons and gamma rays with matter is presented next, highlighting the computation of various types of radiation doses stemming from radiation intensity and target characteristics. This discussion leads to a detailed description of photon radiation attenuation and neutron shielding calculations, as well as corresponding dose evaluations. The chapter presents the basic concepts of buildup factors and point-kernel methodology for photon attenuation computations, as well as the established concepts and computational methods for designing shielding against fast, intermediate, and thermal energy neutrons. The chapter also highlights the special cases of albedo, skyshine, and streaming dose calculations and concludes with a discussion of shielding materials, radiological assessments, and risk calculations.

Chapter 12 is entitled *High Performance Computing in Nuclear Engineering* and comprises an introduction to high-performance computer and processor architectures, highlighting the current parallelism models. The chapter then presents the key concepts and requirements for designing parallel programs. This presentation is followed by presentations of paradigm applications of high-performance computing in reactor physics, nuclear material sciences, and thermal-hydraulic nuclear engineering. The chapter concludes with a discussion of open issues and possible paths forward in this rapidly developing field.

Chapter 13, entitled *Analysis of Reactor Fuel Rod Behavior*, focuses on the behavior of light water reactor (LWR) fuel rods. Following a presentation of the main properties of fuel and cladding materials, this chapter systematically describes the thermal and mechanical behavior under irradiation as well as the behavior of the fission gas produced in the fuel. The chapter also highlights the typical phenomena and issues of interest for the design and licensing of LWR fuels, namely: the high burnup structure, pellet-cladding interaction, pellet-coolant interaction, loss-of-coolant accidents (LOCA), and reactivity-initiated accidents (RIA).

Chapter 14 is entitled *Noise Techniques in Nuclear Systems* and deals with neutron fluctuations in nuclear systems. Such neutron fluctuations, called “neutron noise,” provide valuable

information regarding the behavior of the reactor system. This chapter focuses on the concepts and methodologies for extracting nonintrusive information from neutron noise, aiming at the detection, identification, and quantification of potential operational anomalies, at the earliest possible stage.

Chapter 15 is entitled *Deterministic and Probabilistic Safety Analysis* and highlights the evolution of deterministic and probabilistic safety analyses, which play a crucial role for assuring public health and safety in the peaceful uses of nuclear power. The chapter commences with a review of the origins of nuclear power safety analysis, comprising both deterministic and probabilistic methods. Deterministic approaches, including the defense-in-depth and safety margin concepts, provide methodologies for quantifying deterministically uncertainties associated with the adequacy of safety features. The chapter also discusses in detail probabilistic safety assessment methods and their uses in nuclear power safety analysis and safety-related decision making, reflecting the maturing and widening applications of such methods.

Chapter 16, entitled *Multiphase Flows: Compressible Multi-Hydrodynamics*, presents a conceptual framework for modeling three-dimensional multiphase flows in terms of a local disperse system description (bubbles/drops in a continuous liquid/vapor phase). This framework is based on a new, “hybrid” effective-field method (EFM) that incorporates features of a statistical approach and reveals more clearly the nature of phase interactions at the individual particle scale. The resulting multiphase flow formulation is amenable to numerical simulations based on the direct solution of the Navier–Stokes equations resolved at the particle scale. The basic constitutive treatment concerns pseudo-turbulent fluctuations of the continuous phase, and the resulting systems of equations are fully closed and hyperbolic (and hence directly usable for computations) even in their non-dissipative form, except for a non-hyperbolic corridor around the transonic region. The results thus obtained are discussed in relation to formulations that form the basis of current numerical tools (codes) employed in nuclear reactor design and safety analyses (mostly addressing bubbly flows) as well as the formulations found in other contexts. The numerical implementation of this new mathematical formulation emphasizes flow compressibility, focusing on capturing shocks and contact discontinuities robustly, for all flow speeds and at arbitrarily high spatial resolutions. A key role is played by “upwinding,” applied within the context of a scheme that emphasizes conservative discretization, extending thereby the ideas underlying the Advection Upstream Splitting Method to compressible multi-hydrodynamics (including the EFM).

Chapter 17 is entitled *Sensitivity and Uncertainty Analysis, Data Assimilation, and Predictive Best-Estimate Model Calibration*. This chapter provides the theoretical and practical means of dealing with the discrepancies between experimental and computational results and is therefore of paramount importance for validating the design tools used in all aspects of nuclear engineering. Such discrepancies motivate the activities of model verification, validation, and predictive estimation. The chapter presents the modern statistical and deterministic methods for computing response sensitivities to model parameters, highlighting, in particular, the adjoint sensitivity analysis procedure (ASAP) for nonlinear large-scale systems with feedback. Response sensitivities to parameters and the corresponding uncertainties are the fundamental ingredients for *predictive estimation (PE)*, which aims at providing a probabilistic description of possible future outcomes based on all recognized errors and uncertainties. The key *PE* activity is *model calibration*, which uses *data assimilation* procedures for integrating computational and experimental data in order to update (calibrate or adjust) the values of selected parameters (such as cross sections and correlations) and responses (such as temperatures, pressures, reaction rates, or effective multiplication factors) in the simulation model. This chapter also presents a

state-of-the-art mathematical framework for time-dependent data assimilation and model calibration, using sensitivities and covariance matrices together with the maximum entropy principle and information theory to construct a prior distribution that encompasses all the available information (including correlated parameters and responses), while minimizing (in the sense of quadratic loss) the introduction of spurious information. When the experimental information is consistent with computational results, the posterior probability density function yields reduced best-estimate uncertainties for the best-estimate model parameters and responses. Open issues (e.g., explicit treatment of modeling errors, reducing the computational burden, treating non-Gaussian distributions) are addressed in the concluding section of this chapter.

Chapter 18 presents *Reactor Physics Experiments on Zero Power Reactors*, performed in the EOLE, MINERVE, and MASURCA Zero Power Reactors (ZPRs), operated by the Commissariat à l’Energie Atomique (CEA), France. The experimental programs in these ZPRs have long played a crucial role in the validation of neutron physics codes and nuclear data by reducing the uncertainties of the experimental databases. These ZPRs also provide accurate data regarding: (1) innovative materials for reactor (fuels, absorbers, coolants, and moderators); (2) new reactor concepts (advanced BWRs, sodium and gas-cooled Generation-IV reactors, as well as hybrid systems, involving a subcritical reactor coupled to an external accelerator); (3) plutonium and waste management (involving heavy nuclides and long-lived fission products); (4) transmutation of long-lived nuclides; and (5) data for the new materials testing reactor “Jules Horowitz,” currently under construction in Cadarache.

Chapter 19 is entitled *Pressurized LWRs and HWRs in the Republic of Korea*. It describes Korean experiences and accomplishments in the design, operation, and construction of two Generation-III pressurized light water reactor (LWR) plants (OPR1000 and APR1400, respectively), which are currently in service and/or under construction in the Republic of Korea. The chapter also presents the Korean experience regarding the pressurized heavy water reactors (CANDUs) built and operated in the Republic of Korea.

Chapter 20, entitled *VVER-Type Reactors of Russian Design*, describes the design and technical layout of the Russian VVER-440 and VVER-1000 reactor plants. VVER reactors are a special design of pressurized water reactors, featuring a hexagonal geometry for the fuel assemblies, with fuel rods arranged in a triangular grid. The cladding for the fuel rods is manufactured from a zirconium–niobium alloy. The large-sized equipment can be advantageously transported by railway to enable a complete manufacturing process under factory conditions, but this design feature imposes a limit on the outer diameter of the reactor pressure vessel. The design of the horizontal steam generators with a tube sheet in the form of two cylindrical heads is also original. Reactors with the designations RP V-392, V-412, and V-428 are Generation-III reactors. Comprehensive sections are devoted to the primary circuit systems and equipment, reactor coolant system, reactor core, main circulation pumps, pressurizer, steam generators, chemical and volume control systems, and secondary circuit components (main steam line system, main feedwater system, turbine, generator, and moisture separator reheater), for both VVER-440 and VVER-1000 reactor plants.

Chapter 21 is comprehensively entitled *Sodium Fast Reactor Design: Fuels, Neutronics, Thermal-Hydraulics, Structural Mechanics and Safety*. The chapter highlights the fundamental motivations for building a fast reactor system: effective utilization of uranium resources through the judicious exploitation (transmuting, converting, or breeding) of fertile material and a sustainable closed fuel cycle, permitting a flexible management of actinides to minimize high-level

waste and reduce the burden on deep geological storages. These advantages had been envisaged as early as in 1946 by Enrico Fermi, who demonstrated the breeding principle and stated: “The people who will develop SFR technology will lead the world in the future.” The chapter provides a comprehensive review of the development of sodium fast reactors (SFR) in the USA, Russia, France, the UK, Germany, Italy, Belgium, the Netherlands, Japan, India, China, and Korea, highlighting the motivation and challenge underlying the two basic design choices, namely “pool design” and “loop design.” The objectives, scope, and levels of the “defense in depth” safety principles are emphasized, aiming at the “practical elimination” of initiating events and sequences leading to hypothetical severe plant conditions. The considerations underlying the choice of materials (for fuel, structures, absorbers, shielding) are presented in depth, since these are paramount for optimizing the reactor core design (including geometrical parameters, neutronics, thermal-hydraulics, structural mechanics, reactivity effects) and performance objectives. The chapter also underscores several important specific issues regarding the design and analysis of the mechanical integrity of the reactor (comprising thermal striping, stratification, seismic-induced forces, fluid–structure interactions, buckling of thin shells). Design basis and design extension conditions, including residual risks, are analyzed for typical anticipated transients without scram. The vast French licensing experience with the Phenix, SPX-1, SPX-2 sodium-cooled fast reactors is discussed with a view toward innovations, leading to enhanced safety of future innovative SFR designs. The chapter concludes with presentations of the ongoing SFR activities in France and India.

Chapter 22 is entitled *Gas-Cooled Reactors* and presents the main features of reactors that use a gas (carbon dioxide or helium) as the primary fluid for cooling the core. The oldest reactors of this type were the British Magnox and the French natural uranium graphite gas (NUGG) reactors, which used carbon dioxide as coolant in graphite-moderated cores fueled with natural uranium. The availability of low-enriched uranium fuel allowed the British to develop the advanced gas-cooled reactor as a successor to the Magnox reactor. In a world progressively dominated by the water-cooled reactors, mostly PWR and BWR, helium remained under consideration as coolant for the prismatic and pebble-bed high-temperature reactors (HTR) moderated with graphite. Both of these HTRs use a very innovative fuel element – the coated particle. As recalled in this chapter, the same type of fuel was also used in the NERVA US-program, which aimed at developing nuclear propulsion for rockets. Helium cooling is also used for two envisaged Generation-IV concepts, namely the very high temperature reactor (VHTR) system aimed at both electricity generation and hydrogen production and the gas-cooled fast-neutrons reactor (GFR).

Chapter 23 is entitled *Lead-Cooled Fast Reactor (LFR) Design: Safety, Neutronics, Thermal Hydraulics, Structural Mechanics, Fuel, Core, and Plant Design*. The lead-cooled fast reactor (LFR) has both a long history and a currency of innovation. Early work on such reactors, dating back to the 1950s, was devoted to submarine propulsion, as Russian scientists pioneered the development of reactors cooled by heavy liquid metals (HLM). More recently, there has been substantial interest in both critical and subcritical reactors cooled by lead (Pb) or lead–bismuth eutectic (LBE), not only in Russia (BREST-300, SVBR-75) but also in Europe, Asia, and the USA. This chapter reviews the historical development of the LFR and provides detailed descriptions of the current initiatives to design LFRs for various missions. Currently, the leading designs are for: (1) accelerator-driven subcritical (ADS) systems for nuclear materials management, (2) small modular systems for deployment in remote locations, and (3) central station plants for integration into developed power grids. The chapter describes: design criteria and

system specifications; specific LFR features regarding neutronics, coolant properties, and material compatibility issues; core and reactor plant design; and considerations related to the balance of plant and plant layout for Generation-IV LFR and HLM-cooled ADS concepts (SSTAR, ELSY, MYRRHA, EFIT).

Chapter 24 is entitled *GEM*STAR: The Alternative Reactor Technology Comprising Graphite, Molten Salt, and Accelerators*, and it illustrates conceptually the possible benefits of implementing supplementary neutrons from accelerators in a futuristic reactor concept called GEM*STAR (Green Energy Multiplier*Subcritical Technology for Alternative Reactors) by its authors. This chapter does not aim at providing a complete history of molten salt, graphite, and accelerator technologies but rather a description of how these elements of nuclear power development might be integrated to address the main barriers that constrain the full deployment of today's nuclear power technology. The basis for the GEM*STAR concept is a subcritical (initial multiplication factor = 0.99) thermal-spectrum reactor, operating with a continuous flow of molten salt fuel in a graphite matrix. If sufficient external neutrons are available, GEM*STAR may operate with natural uranium and un-reprocessed LWR spent fuel, recycling its own fuel several times without needing external reprocessing.

Chapter 25 is entitled *Front End of the Fuel Cycle* and describes the complete set of industrial operations needed to produce a functional fuel element ready to be loaded in a nuclear reactor. This chapter commences by providing data concerning the element uranium (its abundance and relevant properties) and continues by describing the uranium exploration, mining, concentration, and site rehabilitation processes. Light water reactors, which constitute the vast majority of currently operating and under-construction nuclear reactors, must use uranium enriched in the isotope U-235. The enrichment process requires that uranium be converted into a gaseous compound. The enriched uranium is subsequently fabricated into solid ceramic pellets and assembled into leak tight metallic pins, which are, in turn, assembled to form the fresh fuel element. The chapter also provides valuable information on mixed uranium-plutonium oxide (MOX) fuel assemblies for recycling plutonium in LWR as well as basic data on plutonium and thorium. The chapter also provides an explanation of the fascinating Oklo Phenomenon, which occurred almost two billion years ago in a particular uranium deposit in Gabon.

Chapter 26 is entitled *Transuranium Elements in the Nuclear Fuel Cycle*. The transuranium elements neptunium, plutonium, americium, and curium are produced from actinides through neutron capture processes and therefore arise mostly as by-products of fuel irradiation during the operation of a nuclear reactor. The nuclear properties of transuranium (TRU) elements significantly affect the nuclear fuel cycle, largely determining the requirements and procedures for handling, storing, reprocessing, and disposing the spent fuel and high-level waste. Socio-economical and political considerations have so far prevented the establishment of a standard, universally accepted route for the treatment of TRU-elements. In particular, it is still a matter of political debate if plutonium is waste or a resource for the production of energy. This chapter provides an overview of past and current experiences and perspectives regarding the recovery and incorporation of TRU-elements in fuels and targets for advanced nuclear fuel cycles, as well as the disposal of TRU-elements as the main components of high-level nuclear waste. In particular, this chapter highlights the main properties of TRU fuels, the specific requirements for their fabrication, their irradiation behavior, and their impact on the back end of the fuel cycle. For the latter, a major issue is the development of options for reprocessing and separation of TRU-elements from spent fuel, in order to make these elements available for further treatment. The chapter also discusses the effects on long-term storage and final disposal caused by the presence of TRU-elements in irradiated fuel and high-level nuclear waste. At this time,

the final destination for TRU-elements continues to remain an open issue, as various countries pursue a diversified set of options. The comprehensive understanding of the worldwide knowledge and experience presented in this chapter provides an essential basis for developing viable, safe, and technologically effective options for the treatment of TRU-elements, which, in turn, are crucial for ensuring that nuclear energy remains a key component in a sustainable mix of energy production.

Chapter 27 is entitled *Decommissioning of Nuclear Plants* and covers all aspects related to the closure of the operating life of nuclear plants, providing a description of all activities and tools involved in the decision-making and operative processes of decommissioning. The main stages involved in the decommissioning process include the termination of operations, the withdrawal of the nuclear reactor plant from service, and the transformation of the plant into an out-of-service state without radiological risks. In some cases, decommissioning leads to the complete removal of the plant from its original site. Nuclear plant decommissioning comprises a complex, long, and highly specialized spectrum of activities including technological tools, industrial safety, environmental impact minimization, licensing, safety analysis, structural analysis, short- and long-term planning, calculation of cash flow and financing, waste disposal, and spent fuel strategy. All of these activities must be performed in a cost-effective manner, assigning top priority to the health and safety of the workers on site as well as the public and the environment. In some countries, decommissioning is actually called “deconstruction,” because it resembles, in many respects, the construction activity. Unlike the construction activities, though, decommissioning also deals with partially activated and contaminated structures. The chapter draws technical information from the direct experience of nuclear operators as well as from the results produced by working groups, special studies, comparisons of technologies, and recommendations from the OECD-NEA, IAEA, US-NRC, and the European Commission.

Chapter 28 is entitled *The Scientific Basis of Nuclear Waste Management* and provides the scientific concepts and data underlying the management of the highly radioactive waste produced at various stages of the nuclear fuel cycle. In a context in which science and technology interact strongly with social and economical issues, the scientific basis for high-level radioactive waste management continues to evolve. Within a closed fuel cycle, the management of high-level waste, from its production to its final destination, appears as a chain, whose links are treatment, recycling, conditioning, storage, and disposal. When the fuel cycle remains open, the first two links (treatment and recycling) are absent. The chapter commences by describing the origin, nature, volume, and flux of nuclear waste, while briefly presenting various management options. Waste conditioning is addressed next, emphasizing the elaboration and long-term behavior of two important conditioning matrices: cement-like materials and glass. Since some countries consider spent fuel to be “waste” that must therefore be conditioned as such, the chapter devotes a special section to this controversial issue. The chapter also describes in detail the design and properties of installations for interim storage of long-lived waste, since such installations are already operational in several countries that exploit nuclear power plants. Since the definition of “ultimate waste” varies from country to country due to socioeconomical issues, the means and ways for the disposal of such waste in deep geological repositories is not universally resolved, even though the basic scientific concepts and technological issues involved are largely known. Therefore, this chapter also emphasizes the mechanisms, models, and orders of magnitude of the main physical and chemical phenomena that govern the long-term evolution of various types of possible geological repositories for high-level radioactive ultimate waste. The chapter concludes with a short description of the methodology used for evaluating the safety of radioactive waste disposal installations.

Chapter 29 is entitled *Proliferation Resistance and Safeguards* and presents the status of the international activities regarding these very complex issues. As is well known, the Nuclear Nonproliferation Treaty (NNPT or NPT) is the primary cornerstone of international efforts to prevent the proliferation of nuclear weapons. Currently, 189 countries are party to the treaty, with only four sovereign states abstaining: India, Israel, Pakistan, and North Korea. The NPT is broadly interpreted to comprise three pillars: nonproliferation, disarmament, and the right to the peaceful use of nuclear technology. This chapter addresses each of these NPT-pillars and commences by analyzing the significance of the Strategic Arms Reduction Treaty (START), which was signed between the USA and the former Soviet Union on 31 July 1991. This treaty, considered by many to be the largest and most complex arms control treaty in history, has led to a significant reduction in the number of deployed warheads for both the USA and Soviet Union. Furthermore, the US and Russian presidents signed a preliminary agreement on 6 July 2009 to reduce further the number of active nuclear weapons to between 1,500 and 1,675 by 2012. Although these treaties have been the backbone of joint US and Russian efforts toward nuclear disarmament, they have not addressed the discontinuation of weapons-grade fissile material production and disposition of excess weapons-grade materials. The current situation is that the USA, France, and the UK have ceased the production of weapons-grade materials. In 1997, the USA and Russia signed the Plutonium Production Reactor Agreement to cease the production of plutonium for weapons production. Although Russia still operates nuclear reactors used previously for production of weapons material, to generate heat and electricity, it does not reprocess the spent fuel correspondingly, and plans to decommission these reactors. While India and Pakistan apparently are still producing weapons-grade material, unsubstantiated reports indicate that China has also instituted a moratorium on production, while Israel's position is unclear. In September 2000, the USA and Russia, each formally agreed to transform 34 metric tons of excess military plutonium into a more proliferation-resistant form over the course of 20 years, by irradiating it in nuclear power reactors. Currently, Russia favors irradiation in a new generation of fast reactors yet to be developed, and the USA favors irradiation in their existing commercial LWR fleet. Additionally, a joint program has been developed by the USA and Russia to disposition excess highly enriched uranium (HEU) by blending it with natural uranium to produce low enriched uranium (LEU) for commercial power reactor fuel. This chapter presents a broad overview of experimental and statistical methods and tools for assessing nonproliferation compliance at declared facilities. In the broader nonproliferation context, monitoring for undeclared activities involves many difficult additional statistical issues. The chapter concludes by presenting a paradigm example of validating a safeguard design for the detection of abrupt diversion.

Although this handbook represents the most comprehensive snapshot of the current state of nuclear engineering and technology worldwide, several topics were not treated comprehensively as they could have been, due to scheduling constraints. Thus, the Editor believes that full stand-alone chapters would be warranted for presenting in adequate detail topics such as: Monte Carlo and variational methods for reactor physics and shielding computations, reactor dynamics and control, nuclear instrumentation, corrosion under irradiation, life extension of Generation-II LWRs, advanced supercritical water reactors, and research and materials testing reactors. The next edition of this handbook envisages a comprehensive exposition of these and related topics, along with updates of the topics covered in the present 29 chapters.

The Editor commenced work on this handbook in the fall of 2007, while serving as the Scientific Director of the Nuclear Energy Directorate of the Commissariat à l'Énergie Atomique (CEA), France. The extensive yet focused work required during 2010 to finalize this handbook

has been greatly facilitated by the support of Mr. Laurent Turpin, Director of the National Institute for Nuclear Science and Technology (INSTN) at CEA, and the Editor wishes to express his heartfelt appreciation for this support. The Editor also wishes to acknowledge with distinctive pleasure the very cordial and efficient collaboration with the publication team of Springer-Verlag, led by Mr. Alex Green (Editorial Director for Engineering) in the USA. The Editor also wishes to express special thanks to Dr. Sylvia Blago, Lydia Mueller, and Simone Giesler, for their particularly dedicated professional and very friendly collaboration in weekly interactions over the almost 3 years dedicated to this handbook project.

Dan G. Cacuci
Institute for Nuclear Technology and Reactor Safety
Karlsruhe Institute for Technology
Germany

1 Neutron Cross Section Measurements

Robert C. Block¹ · Yaron Danon¹ · Frank Gunsing² · Robert C. Haight³

¹Rensselaer Polytechnic Institute, Troy (NY), USA

²CEA Saclay - Irfu, France

³Los Alamos National Laboratory, Los Alamos (NM), USA

1	<i>Introduction</i>	3
2	<i>History</i>	4
3	<i>Currently Active Laboratories</i>	6
3.1	Time-of-Flight Laboratories	6
3.1.1	The Gaertner LINAC Laboratory	8
3.1.2	The Los Alamos Neutron Science Center	11
3.1.3	The ORELA Laboratory at Oak Ridge National Laboratory	12
3.1.4	GELINA at the JRC-IRMM in Geel	13
3.1.5	The n_TOF Facility at CERN	16
3.1.6	The IREN Facility at Dubna	19
3.1.7	The PNF Laboratory at Pohang	20
3.1.8	Electron Linac at Kyoto University Research Reactor Institute, KURRI	21
3.2	Monoenergetic Fast Neutron Facilities	24
3.2.1	Neutron Energies Below 1 MeV	24
3.2.2	Neutron Energies in the MeV Region	27
3.2.3	Neutron Energies Near 14 MeV	31
3.2.4	Neutron Energies Above 30 MeV	33
4	<i>Neutron Cross Sections</i>	35
4.1	Introduction	35
4.2	Total Cross Section	39
4.3	Partial Cross Section	41
4.4	Resonance Cross Section	42
4.5	High Energy Cross Section	43
5	<i>Cross Section Measurements</i>	44
5.1	Thermal Energy Region	46
5.1.1	Thermal Flux Averaged Cross Section	46
5.2	Resonance Energy Region	47
5.3	Unresolved Resonance and Continuum Energy Region	49
5.4	The Neutron Time of Flight Method	51
5.4.1	Neutron Density and Flux Distributions at Thermal Energies	52
5.5	Surrogate Reactions	53

5.6	Cross Section Standards	57
6	<i>Nuclear Resonances and the R-Matrix Formalism</i>	57
6.1	Introduction	57
6.1.1	Channel Representation	59
6.1.2	The Wave Function in the External Region	61
6.1.3	The Collision Matrix U	63
6.1.4	The Relation Between the Cross Sections and the Collision Matrix U	63
6.1.5	The Wave Function in the Internal Region	65
6.1.6	The Relation Between the R-Matrix and the Collision Matrix U	67
6.2	Approximations of the R-Matrix	69
6.2.1	The Breit–Wigner Single Level Approximation	70
6.2.2	The Breit–Wigner Multi Level Approximation	70
6.2.3	The Reich–Moore Approximation	71
6.3	Average Cross Sections	72
7	<i>Concluding Remarks</i>	74
	<i>References</i>	74

Abstract: This chapter gives an overview of neutron-induced cross section measurements, both past and present. A selection of the principal characteristics of time-of-flight and monoenergetic fast neutron facilities is given together with several examples of measurements. The physics of typical neutron cross sections and their measurements are explained in detail. Finally an overview of the R -matrix formalism, which is at the basis of resonance reactions, is given. The many references provide a starting point for the interested reader.

1 Introduction

When a beam of particles impinges upon a nucleus, the ratio of the reaction rate (in units of s^{-1}) to the incident flux (in units of $\text{cm}^{-2}\text{s}^{-1}$) is defined as the “cross section” (in units of cm^2 or barn with $1 \text{ barn} = 10^{-24} \text{ cm}^2$). The cross section is thus a measure of the strength of a reaction.

Neutron cross sections are the key quantities required to calculate neutron reactions taking place in reactors, shields, transmuters, nuclear explosions, detectors, stars, etc. Neutron cross sections have been measured over the past 70 years and techniques are being continually developed to improve the accuracy and completeness of neutron cross section data for both stable and radioactive nuclei. As new reactors, neutron sources, waste transmutation devices, and medical applications emerge, there is need for improved neutron cross section measurements.

There is an ongoing major international effort to provide a complete-as-possible compilation of evaluated cross section data for nuclear calculations. Major evaluation compilations are ENDF (USA evaluated nuclear data library) (Chadwick et al. 2006), JEFF (European joint evaluated fission and fusion library) (Koning et al. 2006), JENDL (Japanese evaluated nuclear data library) (Shibata et al. 2002), CENDL (Chinese evaluated nuclear data library) (Ge Zhigang et al. 2008), and BROND (Russian evaluated neutron reaction data library) (Ignatyuk and Fursov 2008). Since evaluated data can be no better than the measurements upon which they are based, thus there is an ongoing need for better measurements. In addition experimental compilations like references Mughabghab (2006), Sukhoruchkin et al. (1998) or the international database EXFOR (previously also known as CSISRS) Zerkin et al. and available on the websites <http://www.nds.iaea.org/exfor>, <http://www.nea.fr/html/dbdata/x4>, <http://www.nndc.bnl.gov/>.

It is a difficult task to review such a large effort as neutron cross section measurements without committing errors of commission or omission. If we erroneously reported on your laboratory and/or its publications, we apologize in advance as it was never our intent to be in error. Also, if we either left you out of our summaries or did not give as much attention to your contributions as you deem we should have, again we apologize with the excuse that it was impossible to present all the work that has been and is now going on. We admit that we presented many details from the laboratories that the authors are working with – this was only because the authors are more familiar with these works and does not imply that they are superior to other laboratory efforts. Finally, we did not include any “figure-of-merit” listings that were so popular in the past when comparing neutron sources. In retrospect, these figures-of-merit frequently wound up making one’s own neutron source look superior to another’s, whereas the total merit of a neutron source can never be summarized by a single number. It is the total impact of the cross sections measured, the number of published articles and conference proceedings, the impact on the field, etc. that need to be taken into account in evaluating a neutron source. To paraphrase British Prime Minister Benjamin Disraeli’s famous statement “There are lies, damned lies and figures-of-merit.” (“There are lies, damned lies and statistics” is attributed to Prime

Minister Benjamin Disraeli in the nineteenth century. Mark Twain again made it famous in the twentieth century. Wikipedia: http://en.wikipedia.org/wiki/Lies,_damned_lies,_and_statistics (2009).

2 History

The neutron was discovered by Chadwick in 1932 from the interaction of alpha particles incident on beryllium or boron (Chadwick 1932). Neutrons were soon recognized as excellent particles to probe nuclei since their lack of charge enabled them to readily penetrate deeply into matter and into the charged nucleus. Fermi and coworkers used neutrons generated from natural alpha sources to study nuclear reactions over a large range of nuclei and found that the strength of interaction varied greatly from nucleus to nucleus and that in many cases the interaction can be enhanced by moderating the neutron energy with hydrogen (Amaldi and Fermi 1936). Ultimately the neutron was discovered to produce fission in uranium and this led to the major effort in the 1940s to produce nuclear reactors and weapons. The design of these neutron devices critically depended on neutron cross section data from thermal to tens of MeV energy and major laboratories in the US and Europe were set up to make these measurements.


In the 1930s and 1940s cross section measurements utilized the neutrons from accelerators and early reactors. Activation with and without Cd covering and reactivity measurements using devices such as the pile oscillator provided thermal-spectrum-averaged cross sections. Crystal spectrometers, neutron velocity selectors, and neutron choppers using the time-of-flight (TOF) method provided sufficient energy resolution to measure resonance energy cross sections typically up to ~ 100 eV. In the 1950s positive ion accelerators utilized nuclear reactions to produce monoenergetic neutron beams and these provided cross section data from the keV to MeV energy range. Pulsed accelerators for electrons and protons were used to produce intense bursts of neutrons which enhanced the TOF measurements well beyond what fast choppers could provide. Even nuclear explosions were used to provide a very intense pulse of neutrons for time-of-flight experiments.

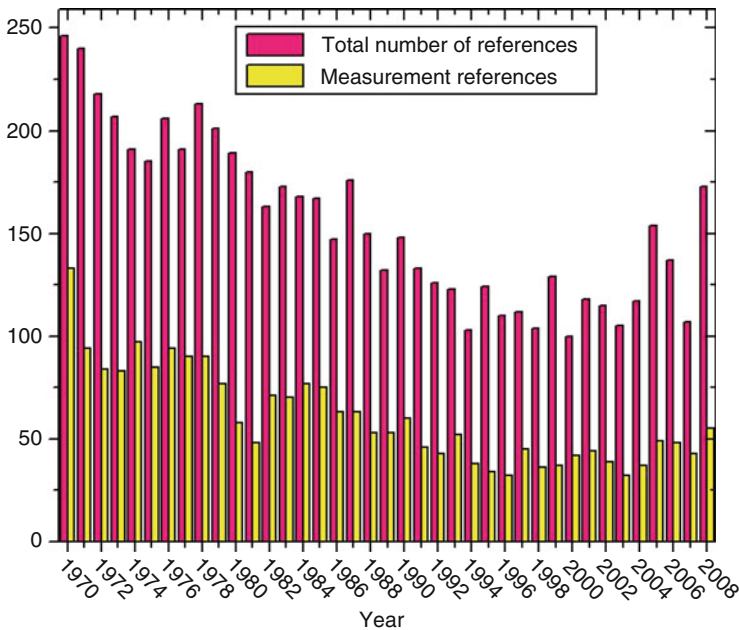
Since the 1970s cross sections were mainly obtained either by pulsed accelerator TOF methods (Ray and Good 1972) or neutrons derived from positive-ion-induced nuclear reactions. In the 1970s and 1980s neutron cross section measurement laboratories were set up in USA, Europe, and Japan. TOF measurements were carried out at the General Atomics Corporation (Orphan et al. 1969), Oak Ridge National Laboratory linac (Dabbs 1979) and Van de Graaff (Good et al. 1958), Rensselaer Polytechnic Institute (Hockenbury et al. 1969), the Lawrence Livermore National Laboratory (LLNL) linac (Behrens et al. 1982) and D-T source (Hansen et al. 1973), the LLNL cyclograff (Davis 1989), National Bureau of Standards (Carlson et al. 1983), the linacs at Harwell (Firk et al. 1963), Saclay (Blons 1973), and Geel (Kohler et al. 1985) the Karlsruhe cyclotron (Cierjacks et al. 1968) and Van de Graaff (Wisshak and Kappeler 1978, 1979), the Frascati Neutron Generator (Pillon et al. 1995), the pulsed reactor at Dubna (Frank and Pacher 1983), Kyoto University Research Reactor Institute (Fujita 1986) and the linac of the Japan Atomic Energy Research Institute at Tokai Mura (Asami 1973). Light-ion-based accelerator measurements were made at Los Alamos National Laboratory (Woods et al. 1974), Duke University (Farrell and Pineo 1968), Ohio University (Finlay et al. 1982), Lowell University (Kegel 1989), Argonne National Laboratory (Dudey et al. 1970), Bruyères-le-Châtel (Joly et al.


1978), the Forschungszentrum Jülich (Qaim et al. 1984; Grallert et al. 1993), Research Institute National Defence, Stockholm (Nystrom et al. 1971), the Institute of Physics and Power Engineering at Obninsk 14 MeV source (Lychagin et al. 1987), and pulsed Van de Graaff (Kononov et al. 1982; Kononov et al. 1987; Kornilov and Kagalenko 1995; Zhuravlev et al. 2007) and the DT source of Kossuth University at Debrecen, Hungary (Biro et al. 1975).

Recently the pulsed spallation sources at Los Alamos (Lisowski and Schoenberg 2006) and CERN (Borcea et al. 2003) have been utilized for TOF cross section measurements where their intense neutron pulses are well suited for both high resolution and high neutron intensity measurements. The high energy protons that produce these neutrons enables measurements up to 100s of MeV. Other initiatives concern the time-of-flight facility nELBE at the Forschungszentrum in Dresden-Rossendorf (Klug et al. 2007), the neutron source FRANZ at the Stern Gerlach Zentrum in Frankfurt (Petrich et al. 2008) and the neutron source JPARC at the Japan Atomic Energy Research Institute in Tokai (Futakawa et al. 2009) and in the future at SPIRAL2 at GANIL in Caen (Fadil and Rannou 2008).

The above list of laboratories is not exhaustive but the references will provide a good starting point for the interested reader.

Neutron cross section measurements increased rapidly into the 1950s and 1960s as many laboratories were set up throughout the world for these measurements. This activity peaked in the 1960s but decreased from 1970 to today, as shown in  Fig. 1. The upper bar graph



 **Figure 1**

The plot labeled “Total number of references” shows the total number of references published per year pertaining to neutron cross sections; these publications refer to both evaluation and experiments. The plot labeled “Measurement references” are for publications which contain information on neutron cross section measurements

is a plot of the number of journal references per year pertaining to neutron cross sections while the lower bar graph is a plot of the number which pertain to measurements of neutron cross sections. This plot was obtained by using the Engineering Village search program <http://www.engineeringvillage2.org>, Elsevier, Inc. (2009). Here we see that from 1970 to 2000 the “activity” in this field dropped by about a factor of two. This drop reflects the decrease in the funding in this field with the corresponding decrease in the number of laboratories working in this area. From 2000 to 2008 the activity increased $\approx 25\%$ and, with the renewed interest in new power reactors, it is predicted that this rate will continue to rise in the next decade or so.

3 Currently Active Laboratories

3.1 Time-of-Flight Laboratories

Major laboratories for time-of-flight cross section measurements are located in the USA, Europe, and Asia. All of these facilities utilize accelerators for electrons or protons to produce intense pulses of neutrons and typically have long flight paths to obtain good energy resolution. A non-exhaustive summary of these facilities is listed in [Table 1](#).

The three major laboratories in USA are the Gaertner LINAC Laboratory at Rensselaer Polytechnic Institute (RPI), the LANSCE Laboratory at Los Alamos National Laboratory and the ORELA Laboratory at Oak Ridge National Laboratory. The ORELA and Gaertner facilities utilize an electron linear accelerator while the LANSCE facility uses a high-energy proton linear accelerator. In Europe the GELINA facility of the Joint Research Center IRMM in Belgium has a long record of measurements. The new facility IREN in Russia is under construction but operational and has replaced the pulsed reactor IBR-30. The facility nELBE in Dresden-Rossendorf is a relatively new facility. The neutron source n_TOF at CERN, Geneva, is operational since 2001. For Asia we include PNF at PAL in Pohang, Korea, and KURRI in Kumatori, Japan. Also the neutron source MLF-NNRI at J-PARC has been put in operation.

Many of these laboratories have several flight paths such that several experiments can be set up and acquire data without interfering with each other.

The table lists the particle, its energy and the target used to generate the neutrons. Beam parameters like pulse width, beam power, and repetition rate are also given as well as the range of flight paths available. Finally the number of neutrons produced per pulse is given. Other parameters like the average current (beam power divided by the particle acceleration voltage, equivalent to its energy in eV), the pulse charge (average current divided by the frequency) or the number of neutrons per second (neutrons per pulse times frequency) are sometimes given in other facility descriptions, for example, in Koehler (2001); Lisowski and Schoenberg (2006); Klug et al. (2007). They can be easily derived from the listed parameters.

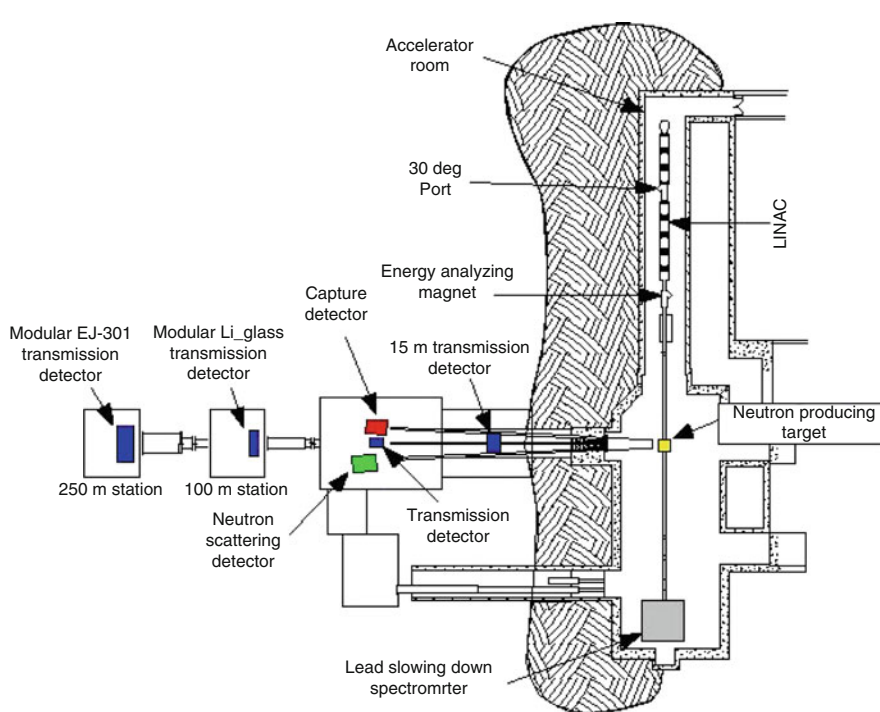
[Table 1](#) does not contain information about resolution components due to the target-moderator system. Neutron time-of-flight resolution reflects the distribution of the measured neutron time-of-flight for a given neutron energy. Its origin has several components, like the pulse width, the moderator geometry, and the detector used. This distribution known as the resolution function is usually highly non-Gaussian and changes with neutron energy. In the following some of the facilities are described in more detail.

Table 1
Parameters of several neutron time-of-flight facilities. For the new facilities parameters still may improve

Facility	Location	Particle	Beam energy (MeV)	Neutron target	Pulse width (ns)	Beam power (kW)	Pulse frequency (Hz)	Flight path lengths (m)	Neutron production (n/pulse)
RPI	RPI, Troy, USA	e-	60	Ta	5	0.6	500	15-250	3.6×10^9
		e-	60	Ta	5,000	>10	300	15, 25	4.8×10^{11}
ORELA	ORNL, Oak Ridge, USA	e-	180	Ta	2-30	60	12-1,000	9-200	1×10^{12}
GELINA	EC-JRC-IRMM, Geel, Belgium	e-	100	U	1	10	40-800	5-400	4.3×10^{10}
nELBE	FZD, Rossendorf, Germany	e-	40	L-Pb	0.01	40	500,000	4	5.4×10^7
IREN	JINR, Dubna, Russia	e-	30	W	100	0.42	50	10-750	7.7×10^{10}
PNF	PAL, Pohang, Korea	e-	75	Ta	2,000	0.09	12	11	1.7×10^{10}
KURRI	Kumatori Japan	e-	46	Ta	2	0.046	300	10, 13, 24	2×10^9
		e-	30	Ta	4,000	6	100	10, 13, 24	8×10^{10}
LANSCE-MLNSC	LANL, Los Alamos, USA	p	800	W	135	80	20	7-60	7×10^{14}
LANSCE-WNR	LANL, Los Alamos, USA	p	800	W	0.2	1.44	13,900	8-90	8×10^9
n_TOF	CERN, Geneva, Switzerland	p	20,000	Pb	6	10	0.4	185	2×10^{15}
MLF-NINRI	J-PARC, Tokai, Japan	p	3,000	Hg	1,000	1,000	25	30	1.2×10^{17}

3.1.1 The Gaerttner LINAC Laboratory

The Gaerttner LINAC Laboratory started its operation in December of 1961 and is since used for research and teaching at Rensselaer Polytechnic Institute (RPI). The laboratory and LINAC were designed and built in order to perform time-of-flight (TOF) measurements in the neutron energy range from thermal to 20 MeV. As such, it is a pulsed L band electron LINAC capable of delivering up to 100 MeV electrons at a repetition rate of up to 500 Hz and a pulse width that can vary from 5 ns to 5 μ s with up to 10 kW of average electron beam power.

The facility is equipped with several flight paths ranging from 15 to 250 m which enables measurements in a broad energy range and high energy resolution. In addition, it is equipped with a lead slowing-down spectrometer (LSDS) which provides a high neutron flux utilized for fission and (n, α) cross section measurements of small samples (< μ g) or samples with small cross sections (< μ b). A layout of the facility is shown in  Fig. 2.

Neutrons are produced by interaction of the electrons with a water- (or air-) cooled tantalum target which produces a high Bremsstrahlung flux that interacts with the tantalum to produce neutrons with an evaporation energy spectrum. Different neutron targets were constructed to produce tailored flux shapes for the different experiments (Danon et al. 1995; Overberg et al. 1999).

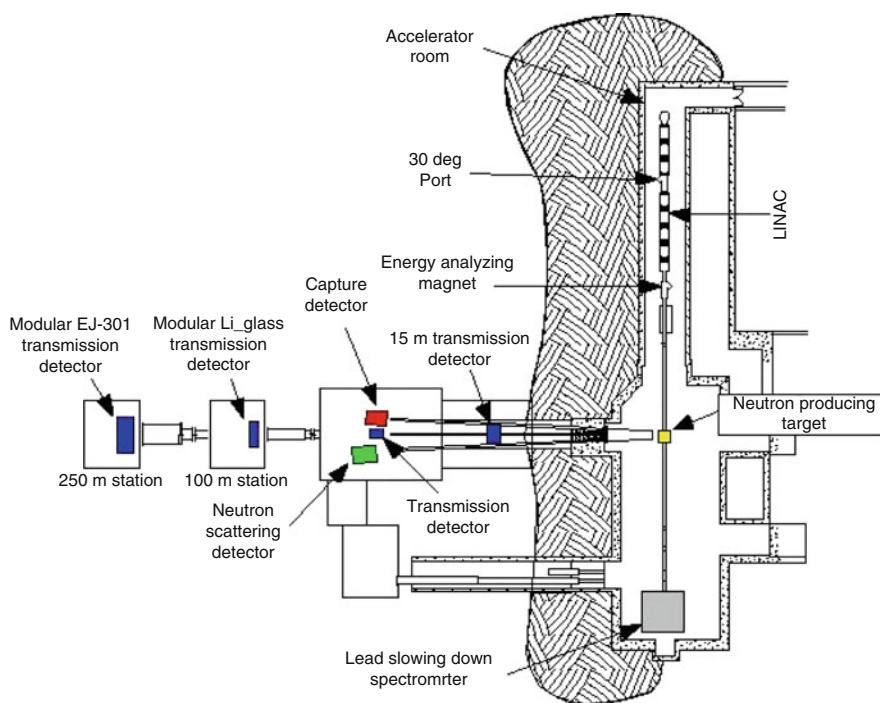
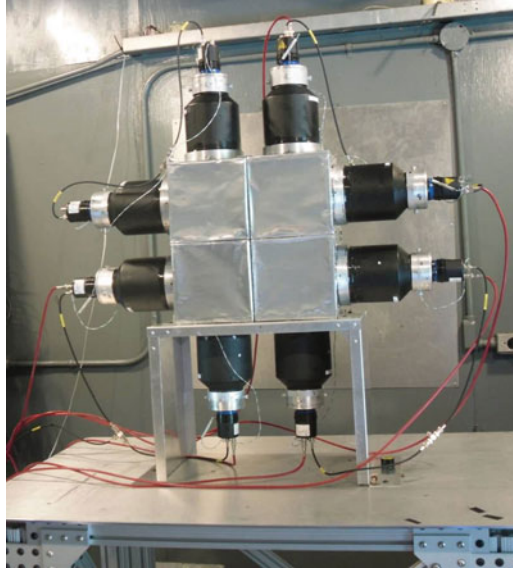


 Figure 2

Layout of the RPI LINAC and beam ports and detectors



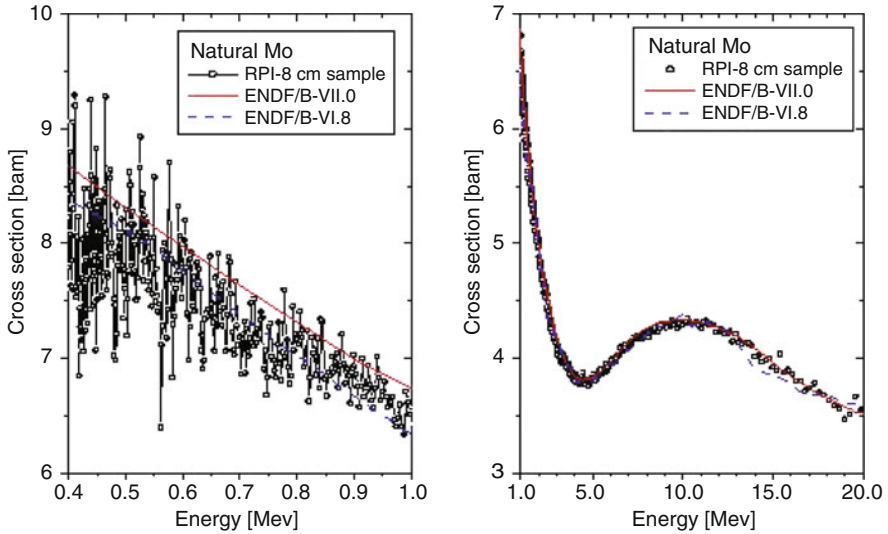
■ Figure 3

A picture of a modular neutron detector for neutron transmission measurement at a TOF path length of 100 m

For transmission measurements in the neutron energy range from thermal to a few hundreds of keV, ^6Li -glass detectors are utilized (Barry 2003) at flight paths of 15, 25, 31, and 100 m. At the 100 m flight station, a modular ^6Li -glass detector shown in [Fig. 3](#) was installed to enable high energy resolution transmission measurements. In order to improve the detector resolution the design employs photomultipliers outside the neutron beam which reduces neutron scattering back to the ^6Li -glass. For measurements of neutrons with energies above 0.4 MeV a modular liquid scintillator is utilized at 100 m or 250 m flight path (Rapp et al. 2009). An example of Mo total cross section data measured with the liquid scintillator detector positioned at 100 m is shown in [Fig. 4](#).

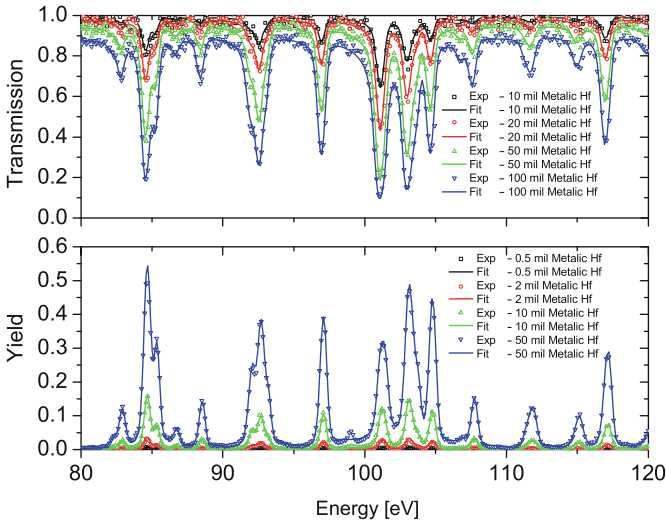
A 16-section NaI multiplicity detector (Block et al. 1988) is used on one of the flight paths at about 25 m. Capture, scattering, and fission data are obtained as a function of the total energy deposited in the detector and the number of NaI segments which detect each event. Scattering events are detected from neutron interactions with a ceramic $^{10}\text{B}_4\text{C}$ liner surrounding the sample. The 477 keV gammas from ^{10}B ($n, \alpha\gamma$) interactions are used to provide a distinct signature of neutron scattering into the liner. [Figure 5](#) shows an example of natural Hf capture and transmission data obtained with this detector and a ^6Li -glass detector at 25 m (Trbovich et al. 2009).

A fast-neutron scattering detector system was installed at a 30 m flight path. The system includes eight liquid scintillator detectors surrounding a sample with a digital data acquisition system capable of pulse shape analysis to separate neutron from gamma events and has 1 ns TOF resolution (Saglione et al. 2006). Measurements with this system serve as benchmark data to qualify cross section libraries by simulation of the whole experimental setup (Saglione et al. 2009).



■ Figure 4

Transmission of 8 cm natural Mo sample and evaluated data. Left – showing cross section structure at the low energy range. Right – showing the high energy range




■ Figure 5

An example of ^{nat}Hf transmission (*top*) and capture (*lower*) data measured, respectively, with the ^6Li -glass and multiplicity detectors (Trbovich et al. 2009). Note that the results of four transmission and four capture measurements have been simultaneously fitted with one set of resonance parameters

A lead slowing-down spectrometer driven by the LINAC provides a neutron flux intensity which is about 3 orders of magnitude higher than a TOF experiment with a flight path producing an equivalent energy-time relation (5.6 m). The resolution of the spectrometer is about 35% (FWHM) in the energy range from 1 eV to 20 keV. Measurements with the LSDS include fission cross sections of small samples (< 1 μg) for actinides such as ^{254}Es , ^{250}Cf and ^{245}Cm (Danon et al. 1991). Recently the LSDS was used for neutron energy dependent fission fragment spectroscopy and demonstrated the method for ^{235}U and ^{239}Pu samples (Romano et al. 2008). In addition methods were developed for (n,α) and (n,p) measurement of samples with small cross sections and the (n,α) cross section of $^{147,149}\text{Sm}$ isotopes were successfully measured.

The large target room and flexibility of the facility were used to develop methods for high accuracy transmission measurements using an iron filtered beam (Danon et al. 2009a), and neutron resonance scattering to provide benchmark data for scattering kernel development (Danon et al. 2009b).

3.1.2 The Los Alamos Neutron Science Center

The Los Alamos Neutron Science Center (LANSCE) at the Los Alamos National Laboratory features three separate neutron sources that are used for nuclear data measurements. All are driven by 800 MeV protons from a linear accelerator, which bombard tungsten targets of different designs. The resulting spallation spectrum of neutrons is similar to a fission neutron spectrum with a high energy tail that extends in principle to 800 MeV and, in practice, has been used up to 600 MeV. This spectrum can be moderated to lower neutron energies by water or liquid hydrogen moderators (Lujan Neutron Scattering Center (MLNSC) facility), taken directly (WNR facility), or slowly moderated by an assembly of pure lead (lead slowing-down spectrometer). The beam lines and detector stations are shown in  Fig. 6.

The Lujan facility at LANSCE (LANSCE-MLNSC) provides white sources of neutrons based on a moderated spallation source (Mocko et al. 2008). The 800 MeV proton beam from the linac, which is several hundred microseconds long, is compressed by a proton storage ring into a 135 ns (FWHM) bunch and then is directed to a two-stage tungsten target. Spallation neutrons are moderated by water or liquid hydrogen moderators. The target-moderator-reflector system (TMRS) includes neutron reflectors to increase the neutron flux in the flight paths. The repetition rate of the source is 20 Hz with 3.7×10^{13} protons per burst, making approximately 1.4×10^{16} neutrons per second. Of the 16 flight paths, 3 are used for nuclear reaction experiments including neutron capture, fission, and fundamental neutron properties. The neutron energies span the range of cold neutrons (a few milli-electron volts) to several hundred keV. The detector for advanced neutron capture experiments (DANCE) is a nearly 4π highly-segmented calorimeter of BaF₂ scintillators with very high efficiency that permits neutron capture cross section measurements on samples of 1 mg or less (Jandel et al. 2008). Fission experiments are carried out on another flight path with parallel-plate ionization chambers.

The Weapons Neutron Research (LANSCE-WNR) facility is based on micropulses from the linear accelerator providing bunched 800 MeV proton bursts on a bare tungsten target. The macrostructure of the proton beam consists of trains of micropulses, approximately 625 μs long, with a macropulse frequency of 40 Hz. Internal to the macropulse are micropulses of up to 8×10^8 protons with spacings adjustable in units of 180 ns. Common micropulse spacings are 1.8 and 3.6 μs. The proton micropulse width is approximately 0.2 ns and therefore allows

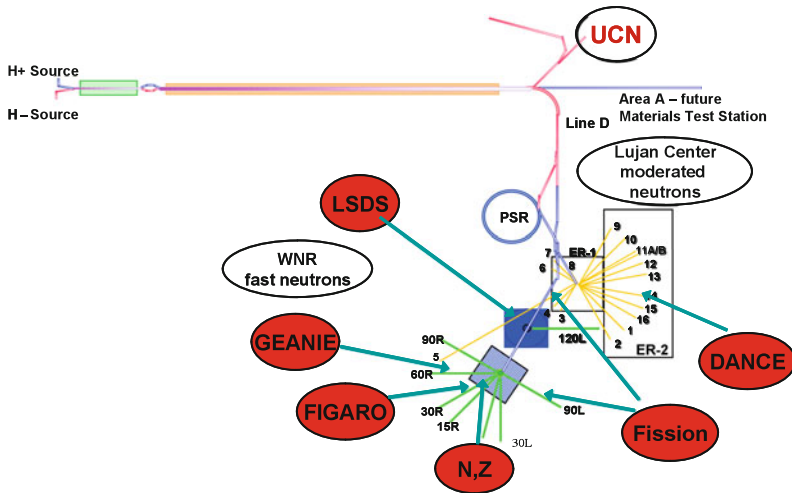


Figure 6

The beam lines and detector stations at the Los Alamos LANSCE facility

high-energy experiments with excellent timing. The unmoderated spallation neutrons are collimated in six flight paths with production angles from 15° to 90° . Experimental stations at flight paths of 8–90 m are set up for high-resolution gamma-ray detection (GEANIE array with 26 HPGe detectors), neutron emission (FIGARO array with 20 liquid scintillation neutron detectors), charged-particle emission (NZ with four charged-particle telescopes), medium-energy few-nucleon research, long-flight path experiments, industrial irradiations of electronic components (ICEHOUSE), and fission cross section measurements. A representative measurement is shown in Fig. 7 for the ratio of the ^{237}Np to ^{235}U fission cross sections. Detailed information on the beams and research is given on the LANSCE web site and references (Tovesson et al. 2009; Bernstein et al. 2002; Rochman et al. 2004).

A lead slowing-down spectrometer is used for high neutron flux experiments. It is driven by the proton beam, either the micropulse beam usually used at WNR or the beam from the proton storage ring. The beam hits a tungsten target at the center of a 20-ton cube of pure lead, 1.2 m on a side. Materials and detectors are placed in channels in the cube and are subjected to very large fluxes of neutrons for cross section measurements as functions of neutron energy. The reaction rate is measured as a function of time, which can be converted into average neutron energy in the range 0.1 eV–100 keV. The conversion is equivalent to a time-of-flight experiment with a flight path of 6.2 m. The trade-off for this approach is that the energy resolution is only about 30% (FWHM) in $\Delta E/E$ (Rochman et al. 2005). With the very large neutron flux, cross sections have been measured with samples less than 10 ng.

3.1.3 The ORELA Laboratory at Oak Ridge National Laboratory

The Oak Ridge electron linear accelerator (ORELA) is a high power, high resolution, and highly versatile white neutron source (Dabbs 1979). Over the course of the last 30 years, ORELA

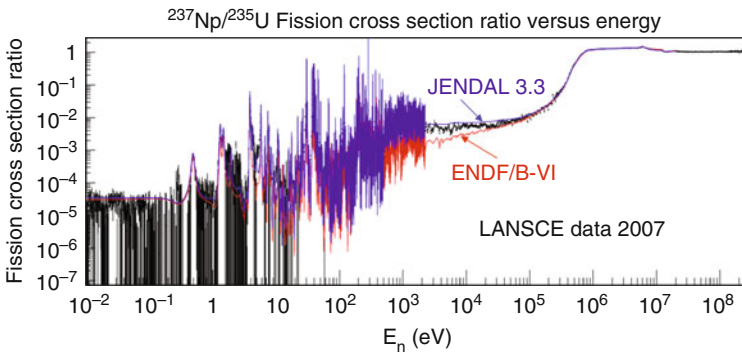


Figure 7

Ratio of fission cross section for ^{237}Np to that of ^{235}U over 10 orders of magnitude in neutron energy from data taken at LANSCCE (Tovesson and Hill 2007, 2008). The experimental values are compared with data in the JENDL3.3 and ENDF/B-VI libraries and were used to improve the data for ^{237}Np in the new ENDF/B-VII library

experiments have contributed the majority of neutron nuclear data that are used for applied and basic nuclear physics programs around the world such as nuclear criticality safety, nuclear reactor physics, neutron shielding, nuclear medicine, and nuclear astrophysics.

ORELA consists of a 180 MeV electron linear accelerator, neutron producing targets, underground and evacuated flight tubes, sophisticated detectors, and data acquisition systems. Simultaneous measurements are possible at 18 detector stations on 10 separate flight paths at distances between 9 and 200 m from the neutron source. An artist's view of the laboratory is shown in [Fig. 8](#).

Neutron capture, (n,γ) , measurements routinely are performed using a pair of deuterated benzene scintillation detectors on flight path 7 at the 40-m station. Improvement in this apparatus over the last few years has resulted in substantially reduced background from scattered neutrons and ORELA measurements with this new system have demonstrated that previous (n,γ) cross-sections are in error, sometimes substantially, due to this effect (see [Fig. 9](#)).

Total cross section measurements can be performed with an NE-110 plastic (above 100 keV) or ^6Li glass (below 100 keV) scintillator. The sample can be cooled to 10 K to significantly improve the resolution of closely spaced resonances by reducing the Doppler broadening as shown in [Fig. 10](#). Fission measurements have been performed using a variety of ionization chambers, such as a small hemispherical ion chamber for high alpha-activity rejection.

A new type of detector, called a compensated ion chamber, was pioneered at ORELA and made possible the first measurements of (n,α) cross sections on intermediate- to heavy-mass nuclides at astrophysical relevant energies. These data demonstrated that the latest nuclear models used to calculate astrophysical (α,γ) and (α,p) reaction rates for explosive nucleosynthesis studies are in need of serious revision.

3.1.4 GELINA at the JRC-IRMM in Geel

The neutron time-of-flight facility GELINA (Geel Linear Electron Accelerator) of the European Commission's Joint Research Center IRMM in Geel, Belgium, has been operational for more

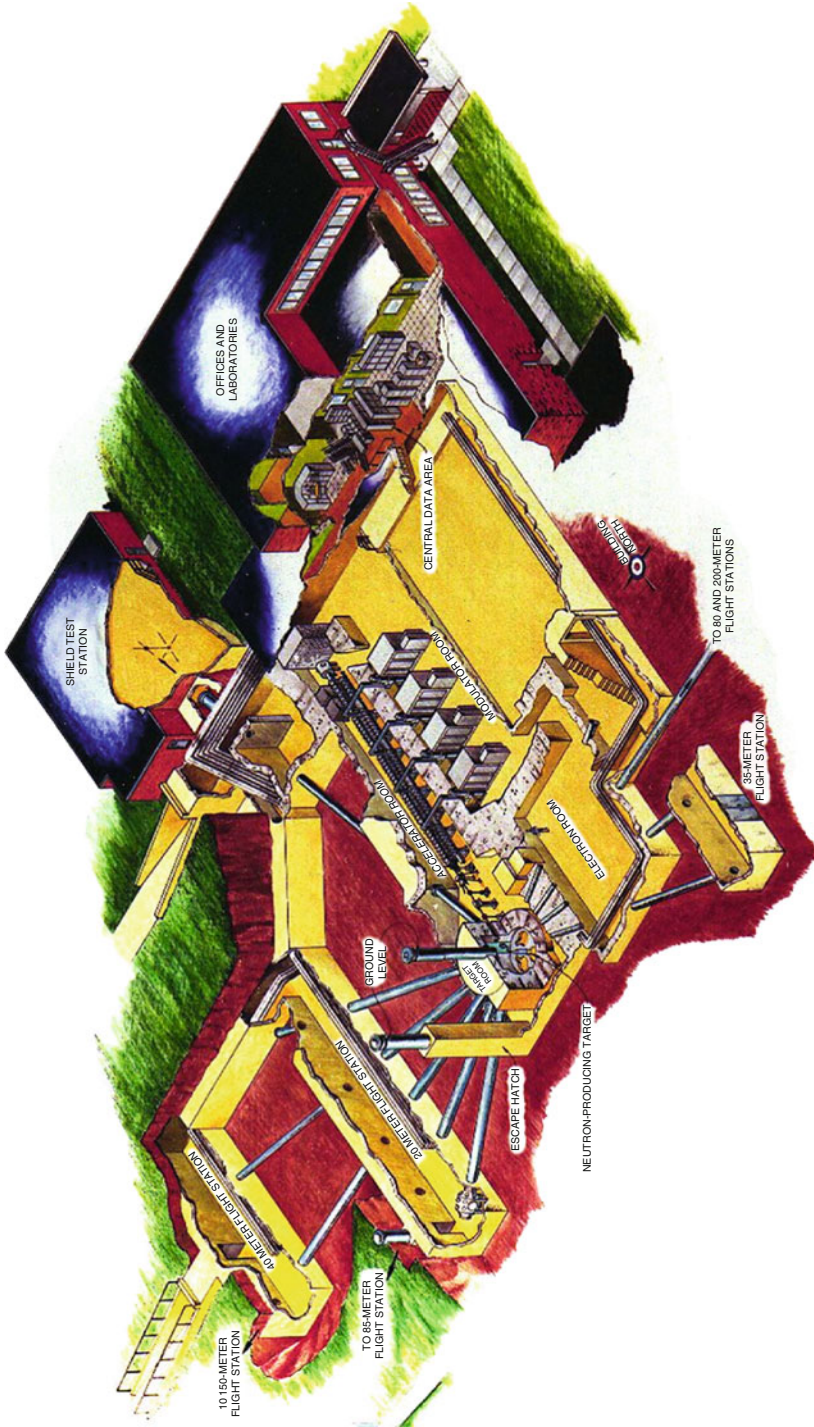


Figure 8
Cutaway view of ORELA showing linac, cylindrical target room, and flight paths

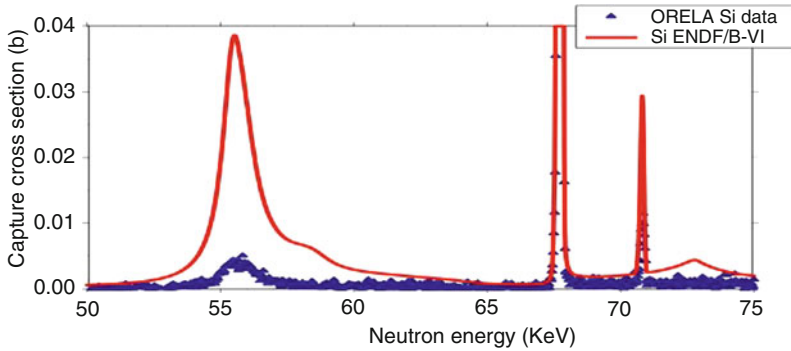


Figure 9

Comparison of the ENDF/B-VI and recent ORELA ^{28}Si capture cross section from 50 to 75 keV (Guber et al. 2005). Due to the neutron sensitivity of the experimental set up the previous $^{28}\text{Si}(n,\gamma)$ experiments (on which ENDF/B-VI is based) seriously overestimated the capture cross section

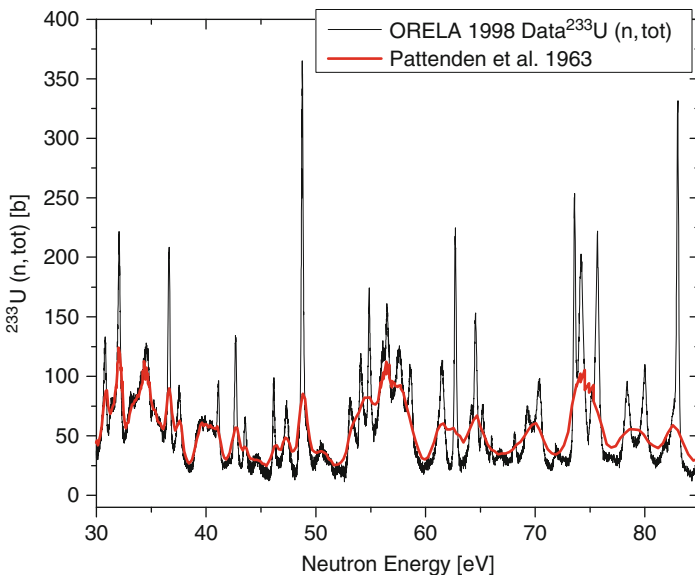


Figure 10

Comparison of recent ORELA measurements with previous ^{233}U total cross sections. Using a cryogenically cooled sample significantly improved the resolution

than 30 years. Neutron-induced reaction data have been measured for a variety of applications related to nuclear technology and nuclear science.

The facility is based on an electron LINAC providing a pulsed electron beam of 100 MeV average energy and a typical power of 10 kW, impinging on a rotating uranium target cooled by a flow of mercury. Typical operation frequencies range from 40 to 800 Hz. The initial electron burst, consisting of a train of micropulses with energies from 70 to 140 MeV, is compressed by a

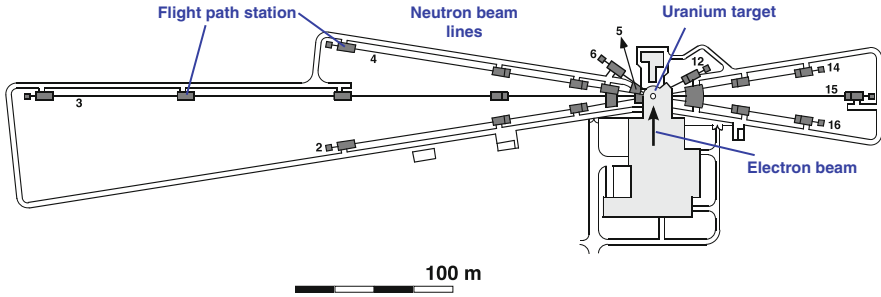


Figure 11
A schematic view of the neutron beam lines of GELINA

post-acceleration 360° bending magnet system to a bunch of less than 1 ns FWHM, preserving the average current. The Bremsstrahlung induced in the uranium target by the electron beam produces neutrons by (γ, n) and (γ, f) reactions. The neutron distribution emitted by the uranium target has a typical fission-evaporation spectrum peaked at around 1 MeV with a small intensity of low-energy neutrons.

Two moderators consisting of slabs of 4 cm thick water canned in beryllium are placed under and above the uranium target. They modify this fast spectrum to a partial moderated spectrum containing a Maxwellian peak at thermal energies and an approximate $1/E$ energy dependence at higher energies. At 800 Hz the average neutron production rate at the source is 3.4×10^{13} neutrons/s.

Twelve neutron flight paths leading to experimental stations at distances from 5 to 400 m depart from the neutron source under angles which are multiples of 9° , as is shown in [Fig. 11](#). Each flight path can be shielded either from the uranium neutron production target or from the water moderators by 30 cm long shadow bars consisting of lead and copper, in order to obtain a fast or moderated neutron spectrum. More details on the facility can be found, for example, in Tronc et al. (1985) and Flaska et al. (2004).

The experimental stations are equipped with measurement setups for neutron capture with Ge, BGO, or low neutron-sensitive C_6D_6 detectors in combination with the weighting function technique (Borella et al. 2007a; Schut et al. 2008), for transmission experiments using ${}^6\text{Li}$ -glass detectors (Kopecky and Brusegan 2006, Borella et al. 2007b), for fission measurements with dedicated fission chambers (Wagemans et al. 2008), and for $(n, xn\gamma)$ measurements HPGe detectors (Mihailescu et al. 2008) and other experiments.

In [Fig. 12](#) an example of a neutron capture and transmission experiment on an enriched ${}^{206}\text{Pb}$ sample is shown in the left panel. The capture yield shows the measured yield, the background contribution, and the measured scattered neutron contribution. The transmission factor and a zoom on the 66 keV s -wave resonance are shown in the right panel. Resonance parameters were obtained by a simultaneous analysis of the capture and transmission data (Borella et al. 2007b).

3.1.5 The n_TOF Facility at CERN

The construction and commissioning of the neutron time-of-flight facility at CERN, Switzerland, after an initial proposal (Rubbia et al. 1998), was finished in 2001 when the facility became operational.

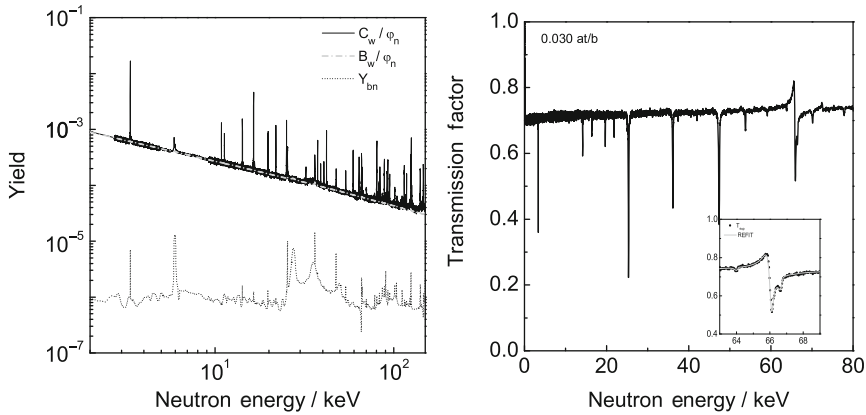


Figure 12

The neutron capture yield spectrum of ^{206}Pb (left panel), together with the transmission factor (right panel), both measured at GELINA (Data are from Borella et al. 2007b)

The facility uses a 6 ns wide, 20 GeV/c proton beam with up to 7×10^{12} protons per pulse hitting a lead target, yielding about 300 neutrons per incident proton. A water slab surrounding the target serves as coolant and as moderator. At present a single flight path is available with an experimental station located at 185 m. A 1.5 T sweeping magnet is placed at a distance of 145 m from the spallation target to remove residual charged particles. One collimator with an inner diameter of 11 cm is placed at 135 m while a second collimator with a variable diameter of either 1.8 cm or 8 cm is situated at 175 m from the production target. The main elements of the neutron beam line are shown in Fig. 13. The repetition period of the proton pulses from CERN's PS accelerator is a multiple of 1.2 s, which allows to cover the energy range down to subthermal energies without overlapping of slow neutrons in subsequent cycles. A full description of the characteristics and performances of the facility is described elsewhere (Abbondanno et al. 2003). The facility is mainly used for capture and fission measurements. The energy distribution of the incident neutron flux is continuously measured during the experiments with an in-beam neutron flux detector (Marrone et al. 2004). The spatial distribution has been obtained with a MicroMegas-based detector (Pancin et al. 2004). The developed data acquisition system

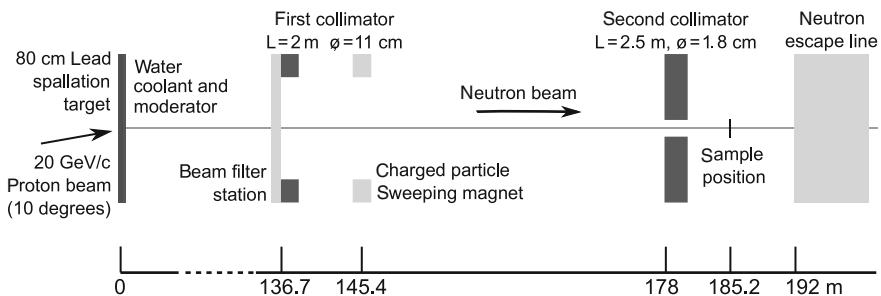


Figure 13



A schematic view of the neutron beam line of n_{TOF} at CERN

(Abbondanno et al. 2005) uses sampling of the detector signals in order to extract the deposited energy and the time of flight.

In-house developed deuterated benzene C_6D_6 gamma-ray detectors contained in a cylindrical low mass carbon fibre housing (Plag et al. 2003) have been used for neutron capture measurements. Samples are kept in position by a carbon fiber sample changer. The low neutron capture cross sections of both carbon and deuterium assure a low contribution to the background from sample scattered neutrons. Since this detector does not measure the full gamma-ray cascade following neutron capture, it requires the use of weighting functions to reconstruct the neutron capture yield (Abbondanno et al. 2004; Borella et al. 2007a). Although the detection efficiency for a single detector is only about 3% for a 1 MeV gamma-ray, due to the gamma-ray multiplicity after neutron capture, in the order of 3–4 for medium and high mass nuclei, the efficiency to detect capture event is roughly 20% for the set of two detectors.

A second neutron capture detection system consists of a 4π 100% efficiency total absorption capture detector, made up of 40 BaF_2 crystals contained in ^{10}B loaded carbon fiber capsules, coupled to XP4512B photomultipliers equipped with (for this purpose) especially designed voltage dividers. Samples are surrounded by a $C_{12}H_{20}O_4(^6Li)_2$ neutron absorber which moderates and absorbs sample scattered neutrons.

Fission experiments have been performed with two different detector systems. Two fission ionization chambers (FIC) use deposits of fissile isotopes on 100 μm thick aluminum foils. The FIC-0 detector was used for the low activity samples while the FIC-1 detector was used for the samples with higher activity (Calviani et al. 2008, 2009).

As an example the $^{233}U(n,f)$ cross section measured at n_TOF with the FIC detector is shown (Calviani et al. 2009) in  Fig. 14. In  Fig. 15 the neutron capture spectrum of ^{232}Th measured with the optimized C_6D_6 gamma-ray detectors is shown (n_TOF Collaboration 2009).

The second type of fission detector is based on parallel plate avalanche counters (PPACs), developed with target deposits on 1.5 μm thin mylar or 2 μm aluminum foils, allowing to detect the two fission fragments in coincidence (Paradela et al. 2009).

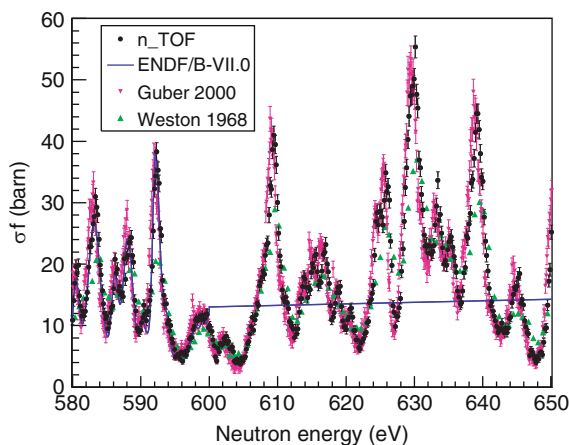
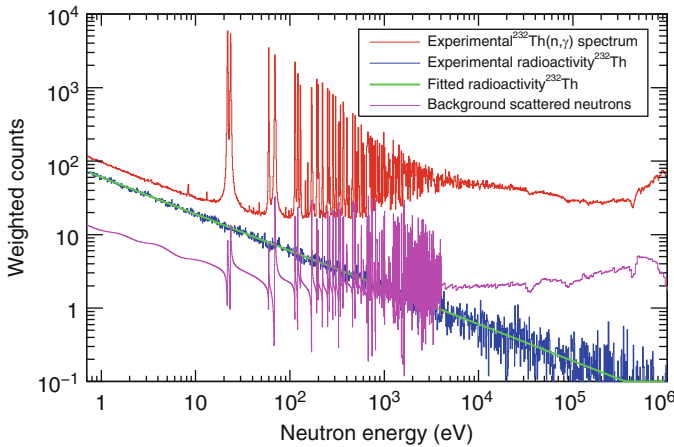


 Figure 14

Part of the measured $^{233}U(n,f)$ cross section at n_TOF at CERN (Data from Calviani et al. 2009)



■ Figure 15

The count rate spectrum of the $^{232}\text{Th}(n,\gamma)$ reaction and the calculated background contribution from sample scattered neutrons. For comparison also the contribution of the natural radioactivity of ^{232}Th is shown (Data are from n_TOF Collaboration 2009)

The facility has been operating from 2000 to 2004 (phase-I) with neutron capture and fission measurements and was upgraded in 2008 with a new spallation target (phase-II). Future plans include the construction of a short flight path (phase-III).

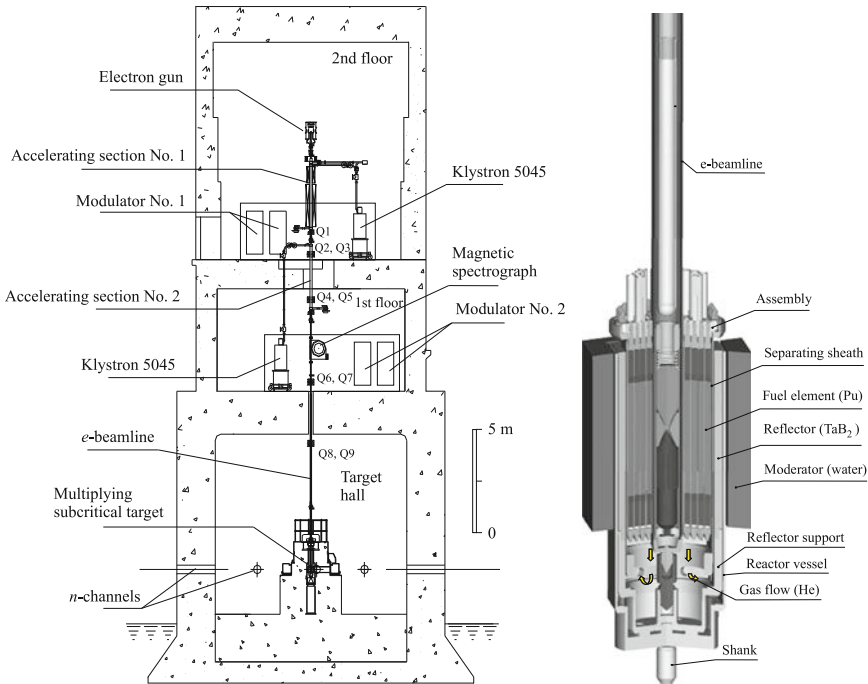
3.1.6 The IREN Facility at Dubna

The pulsed neutron source research complex IREN is a new facility which will be realized in several stages. Eventually, the facility will comprise a 200 MeV electron linac delivering 10 kW beam power, and impinging on a tungsten electron-neutron converter located in the center of a subcritical neutron multiplying target. This target will consist of about 24 kg of highly enriched (more than 95% ^{239}Pu) metallic plutonium, resulting in a neutron yield of 10^{15} n/s and a pulse width of 600 ns.

These are target values that will be achieved gradually. By the middle of 2009 a 30 MeV electron linac together with a non-multiplying tungsten target had been put in operation, making the installation ready in the first stage for high resolution neutron spectroscopy experiments in the energy range up to several 100s of keV. Planned experiments are foreseen in the field of nuclear astrophysics, nuclear data, nuclear structure and fundamental symmetries, as well as neutron and gamma activation analysis and medical radioactive isotope production. The neutron source parameters of this first stage have been included in ► Table 1.

The neutron source has replaced the phased-out facility IBR-30, which was also an accelerator-driven subcritical assembly. IREN uses the existing flight path infrastructure of eight neutron beams with lengths from 10 to 1,000 m. In ► Fig. 16 a schematic view of the future subcritical core is shown.

An example of a measurement of the first stage is the $^{181}\text{Ta}(n,\gamma)$ reaction with both the IBR-30 and IREN neutron source, shown in ► Fig. 17, measured with a six times 351 segmented liquid scintillator detector located at the 60 m flight path.



■ Figure 16

A schematic view of the IREN facility (left panel) and its subcritical core (right panel) (Figure from Ananiev et al. 2005)

3.1.7 The PNF Laboratory at Pohang

The Pohang neutron facility (PNF) (Kim et al. 2002; Wang et al. 2008) consists of a 100 MeV electron linac, a water-cooled Ta target, and an 11-m long TOF path which has recently been set up in Pohang, Korea. The maximum electron energy for TOF measurements is 75 MeV, and the measured peak beam currents at the entrance of the first accelerating structure and at the end of linac are 100 and 50 mA, respectively. The duration of electron beam pulses are 1–2 μ s, and the pulse repetition rate is 12 Hz. The measured energy spread is $\pm 1\%$ at its minimum. The energy spread is reduced when optimizing the RF phase of the RF-gun and the magnetic field strength of the alpha magnet.

The neutron target is water cooled and composed of ten 4.9-cm diameter Ta disks with different thickness and a total Ta thickness of 7.4 cm. This target is set at the center of a cylindrical water moderator contained in an aluminum cylinder with a diameter of 30 cm and a height of 30 cm. The distributions of neutrons with and without water moderator are described elsewhere. The photoneutrons produced in the giant dipole resonance region consist of a large number of evaporated neutrons and a small fraction of directly emitted neutrons, which dominate at higher energies. The MCNP calculated neutron yield per kW of beam power for electron energies above 60 MeV at the Ta target is 1.91×10^{12} n/s (Nguyen et al. 2006), which is consistent with the calculated value based on Swanson's formula, $1.21 \times 10^{11} Z^{0.66}$, where Z is the atomic

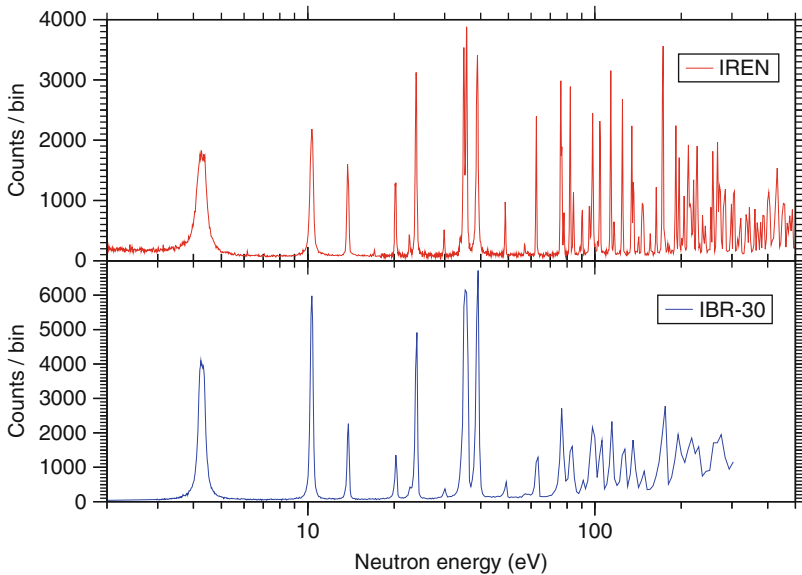


Figure 17

Example of a measurement of the $^{181}\text{Ta}(n,\gamma)$ neutron capture reaction performed during the commissioning phase in 2009 with a six times 35 l segmented liquid scintillator detector located at the 60 m flight path using both the IBR-30 (lower panel) and IREN (upper panel) neutron source (Data from Belikov et al. 2010)

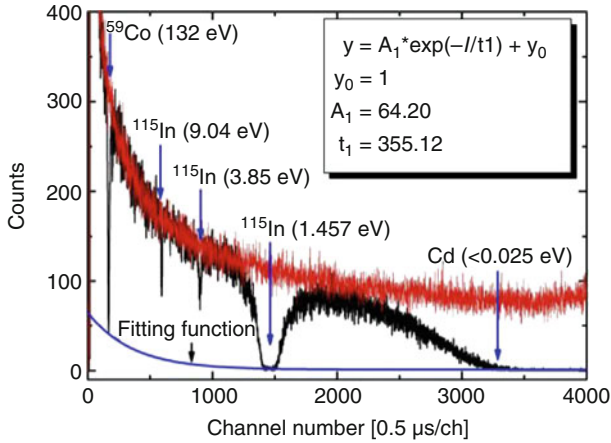
number of the target material. The total neutron yield per kW of beam power is measured to be $(2.30 \pm 0.28) \times 10^{12}$ n/s by using the multiple-foil activation technique.

Neutron flight tubes are constructed of stainless steel and placed perpendicularly to the electron beam. The collimation system is mainly composed of H_3BO_3 , Pb, and Fe collimators. Transmission measurements are made with a $^6\text{Li-ZnS}(\text{Ag})$ scintillator (BC702) with a diameter of 12.5 cm and a thickness of 1.6 cm . A typical TOF spectrum is shown in Fig. 18 where the upper curve is with no sample in the beam and the black curve has Co, In and Cd in the beam to determine the background at strong resonances.

A large volume bismuth germanate ($\text{Bi}_4\text{Ge}_3\text{O}_{12}$; BGO) detector is under construction for the measurement of neutron capture cross sections. This detector is an assembly of BGO bricks and will have a total volume of 2.25 l .

3.1.8 Electron Linac at Kyoto University Research Reactor Institute, KURRI

The electron linear accelerator (KURRI-LINAC) at the Kyoto University Research Institute in Kumatori, Japan, was installed in 1965 as a 23 MeV machine and subsequently upgraded to 46 MeV . The accelerator operates at L-band ($1,300\text{ MHz}$) and provides electron pulse widths from 2 ns to $4\text{ }\mu\text{s}$. The research covers a wide range of neutron measurements using the TOF

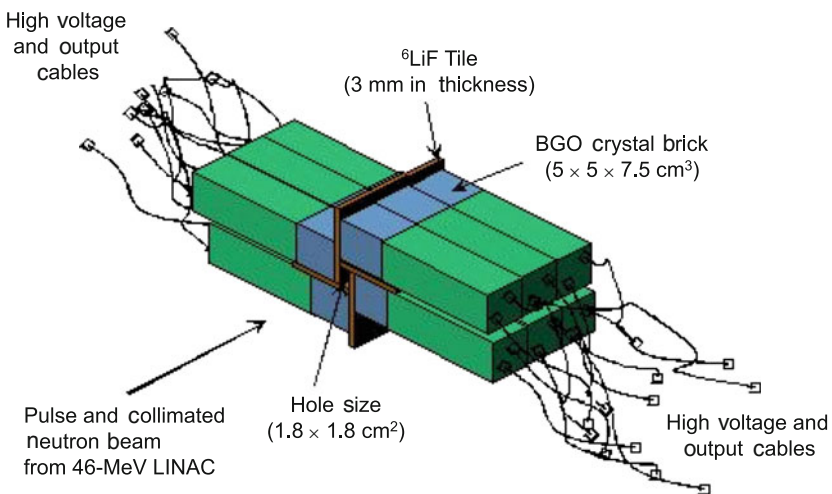


■ Figure 18

Background level determination with Co, In, and Cd samples in the beam at Pohang. The background was determined by fitting to the counts at the blacked-out resonances produced by these samples

method. Currently two flight paths are used for TOF experiments with detector stations at 10.0, 12.7, and 24.2 m. In particular, neutron capture measurements are made with a 4π total absorption BGO spectrometer, another BGO detector, a C_6D_6 liquid scintillation detector and a 4π Ge spectrometer (on loan from JAEA) (Kobayashi et al. 2002; Shcherbakov et al. 2005; Kobayashi et al. 2004; Hori et al. 2008).

► Figure 19 shows the BGO total absorption spectrometer where 12 blocks of BGO surround a ${}^6\text{LiF}$ shielded capture sample and ► Fig. 20 shows a measurement of the ${}^{127}\text{I}$ capture



■ Figure 19

The BGO total absorption spectrometer for neutron capture measurements at the Kyoto linac

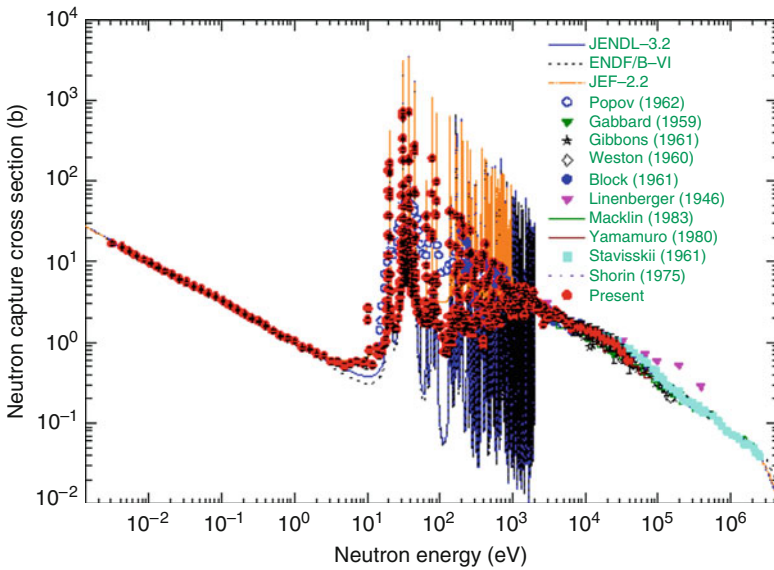


Figure 20

Capture cross section of ^{127}I measured at the Kyoto linac (Hori 2009 private communication)

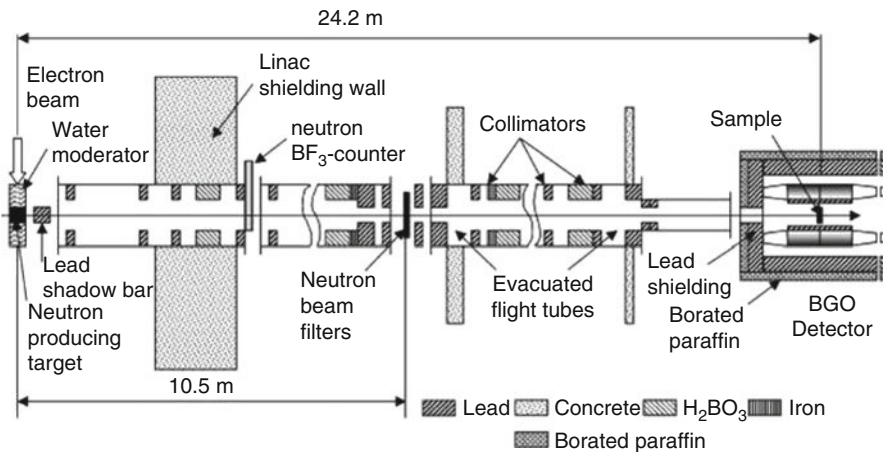
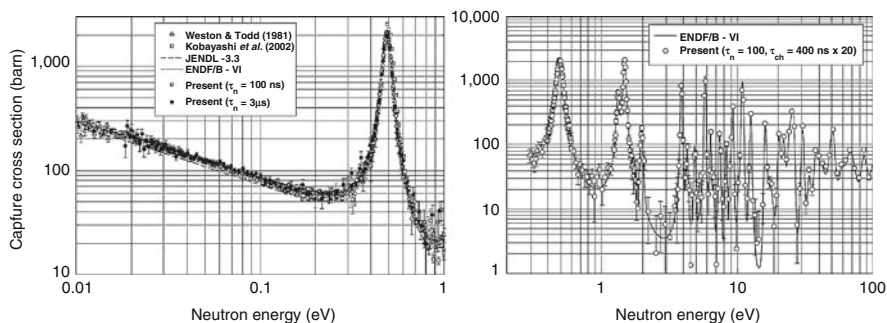


Figure 21

Experimental arrangement for a BGO detector capture cross section measurement at the 24.2 m flight station at the Kyoto linac

cross section obtained with this detector. In Fig. 21 the geometry is shown used for the ^{237}Np capture cross section measurement and Fig. 22 shows the results of this measurement.

A lead slowing-down spectrometer is also installed at KURRI to facilitate fission cross section measurements of small samples.



■ Figure 22

²³⁷Np capture cross section below 1 eV (left panel) and above 1 eV (right panel). “Present data” are from the Kyoto linac

3.2 Monoenergetic Fast Neutron Facilities

Cross section measurements in the energy range 10 keV to many MeV are frequently carried out with light-ion-induced nuclear reactions that lead to monoenergetic or quasi-monoenergetic neutrons. Typically, a source reaction is chosen to produce neutrons of one energy (with a small energy spread), and these neutrons can either be continuous in time or pulsed. For the latter type of source, TOF techniques can be used to reject parasitic neutrons of other energies. TOF is also commonly used in neutron scattering and neutron-emission measurements where the energy of the outgoing neutron is determined by the flight time from the sample to the detector. Data on the neutron source reactions are available from the International Atomic Energy Agency (IAEA) (Drosg 2005).

Many low energy accelerator facilities have produced monoenergetic neutron cross section data over the past 70 years. Although several of these facilities are no longer operational, some are still very productive. Facilities that specialize in TOF measurements typically have special capabilities including pulsed beams with time spreads approaching 1 ns and flexible pulse spacing. Most facilities feature relatively high beam currents in order to produce usable neutron fluxes, neutron-production targets that can withstand the high beam current, gas production targets with pressures of several atmospheres of ²H₂ or ³H₂, ⁷Li, ⁹Be targets, and experimental areas that have low-mass floors and large target rooms to minimize room back-scattering into the sample or the detectors. The available accelerator beams and beam energies determine the range of neutron energies. Unique detector capabilities at certain facilities give them a special status. Here, we give examples of facilities that are optimized for monoenergetic measurements with neutrons in the 10s and 100s of keV range, others in the range 1–26 MeV, specialized 14-MeV neutron facilities, and sources that produce neutrons in the 20–200 MeV range. A selection of monoenergetic neutron source facilities is given in [Table 2](#). Examples are given of measurements performed in this wide energy range.

3.2.1 Neutron Energies Below 1 MeV

Neutron capture reactions have been studied extensively in the keV region at the Van de Graaff laboratories at the Forschungszentrum Karlsruhe (FZK) and in Japan at the Tokyo Institute of

■ Table 2

Table of monoenergetic or quasi-monoenergetic neutron sources

Laboratory	Location	Accelerator	Particle ^a	Beam Energy ^b (max)	Common Reaction	Neutron Energies (typical)
Tokyo Inst. of Techn.	Tokyo, Japan	3 MV Pelletron	p	3 MeV	⁷ Li(p,n)	5 keV–1 MeV
JAEA	Tokai, Japan	4 MV Pelletron	p	4 MeV	⁷ Li(p,n) ² H(d,n) ³ H(d,n)	5 keV–20 MeV
FZK ^c	Karlsruhe, Germany	3.7 MV Van de Graaff	p	3.7 MeV	⁷ Li(p,n)	1 keV–1.5 MeV
Univ. Frankfurt	Frankfurt, Germany	RFQ/DTL ^d	p	2.1 MeV	⁷ Li(p,n)	1–500 keV
U. Mass Lowell	Lowell (MA), USA	5.5 MV Van de Graaff	p	5.5 MeV	⁷ Li(p,n)	5 keV–1 MeV
Tohoku Univ.	Sendai, Japan	4.5 MV Dynamitron	p, d	4.5 MeV	³ H(d,n) ¹⁵ N(d,n)	14–18 MeV 11 MeV
Ohio Univ.	Athens (OH), USA	4.5 MV Tandem VdG	p, d	9 MeV	² H(d,n) ³ H(d,n)	3–11, 15–26 MeV
IRMM	Geel Belgium	7 MV Van de Graaff	p, d	7 MeV	³ H(p,n) ² H(d,n) ³ H(d,n)	0.5–21 MeV
TUNL	Durham (NC), USA	10 MV Tandem VdG	p, d	20 MeV	² H(d,n)	2–20 MeV
PTB	Braunschweig, Germany	Cyclotron	p d	19 MeV 13.5 MeV	⁹ Be(p,n) ² H(d,n)	4–18 MeV
CIAE	Beijing, China	13 MV Van de Graaff	d	26 MeV	³ H(p,n) ² H(d,n) ³ H(d,n)	26 MeV
Osaka - OCTAVIAN	Osaka, Japan	Electrostatic	d	245 keV	³ H(d,n)	14 MeV
JAEA- FNS	Tokai-Mura, Japan	Electrostatic	d	350 keV	³ H(d,n)	14 MeV
CIAE	Beijing, China	Cockroft-Walton	d	600 keV	³ H(d,n)	14 MeV
Tohoku Univ. CYRIC	Sendai, Japan	Cyclotron	p	70 MeV	⁶ Li(p,n) ⁷ Li(p,n)	20–70 MeV
Louvain	Lovain, Belgium	Cyclotron	p	65 MeV	⁷ Li(p,n)	20–65 MeV
JAEA-TIARA	Tokai-Mura, Japan	Cyclotron	p	90 MeV	⁷ Li(p,n)	40–90 MeV
TSL-Uppsala	Uppsala, Sweden	S-Cyclotron	p	200 MeV	⁷ Li(p,n)	50–196 MeV
iThemba	Faure, South Africa	S-Cyclotron	p	230 MeV	⁹ Be(p,xn)	70–160 MeV

^a particles: proton (p), deuteron (d)

^b Max beam energy for nuclear data measurements

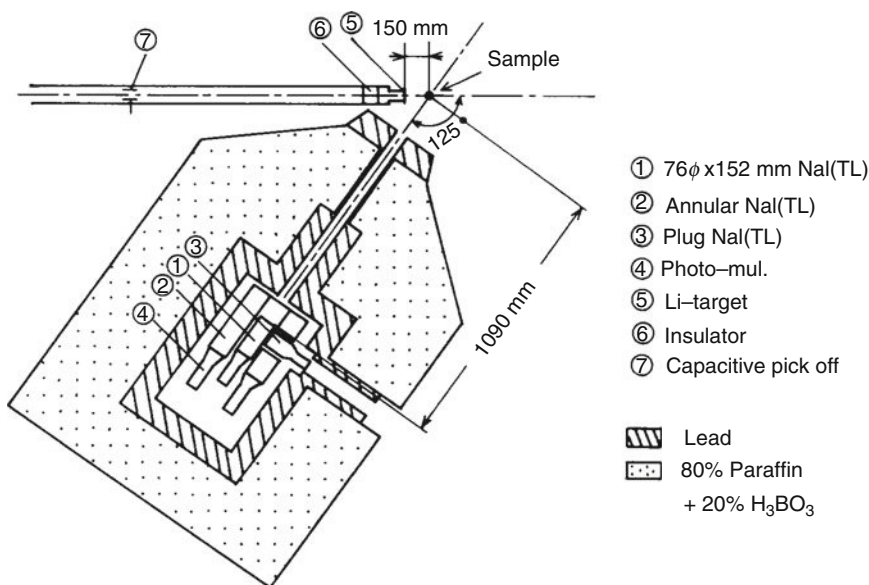
^c recently shut down, included here for recent data and technique

^d Radio-frequency quadrupole (RFQ), Drift tube linac (DTL)

Technology and the Japan Atomic Energy Agency laboratory in Tokai. All of these facilities use the ${}^7\text{Li}(p,n)$ reaction with proton beams in the 1.8–4 MeV range to produce monoenergetic neutrons in the range 1 keV–2 MeV. Pulsed beams of ≈ 1 ns width can be used with TOF techniques to separate neutrons from gamma rays produced at the source. Although the FZK facility is no longer operational, an upgraded facility at the Goethe University, Frankfurt, Germany, is expected to begin operation soon with neutron fluxes increased by 2–3 orders of magnitude relative to the FZK flux.

Neutron capture is detected by a single, well-shielded NaI(Tl) gamma-ray detector at Tokyo, (Igashira et al. 1986), (● Fig. 23) and by a 4π calorimeter of BaF₂ crystal scintillators at Karlsruhe (● Fig. 24) (Wisshak et al. 1990). The former is used to measure discrete high energy gamma rays whereas the latter detects the full energy of the gamma-ray cascade, which is the Q -value of the capture plus the incident neutron energy in the center of mass, a specificity that can help distinguish capture in the sample from background captures in other materials. TOF techniques can be used to deduce the capture cross section or capture-to-fission ratio as a function of neutron energy, for example, (Beer and Kappeler 1979) and (Wisshak et al. 2004).

For activation experiments, a neutron continuum spectrum approximating a Maxwellian spectrum with $kT \approx 25$ keV can be produced with the ${}^7\text{Li}(p,n)$ reaction with 1.911 MeV protons on a stopping lithium target (Beer and Kappeler 1980). This approach has been used in favorable cases to measure the neutron capture cross section for radioactive isotopes such as ${}^{155}\text{Eu}$ (Jaag and Kappeler 1995). This particular temperature for the Maxwellian is of importance in understanding s -process nucleosynthesis in stars.



■ Figure 23

Typical experimental arrangement used in keV-neutron capture gamma-ray measurements at the Tokyo Institute of Technology (Igashira et al. 1986)

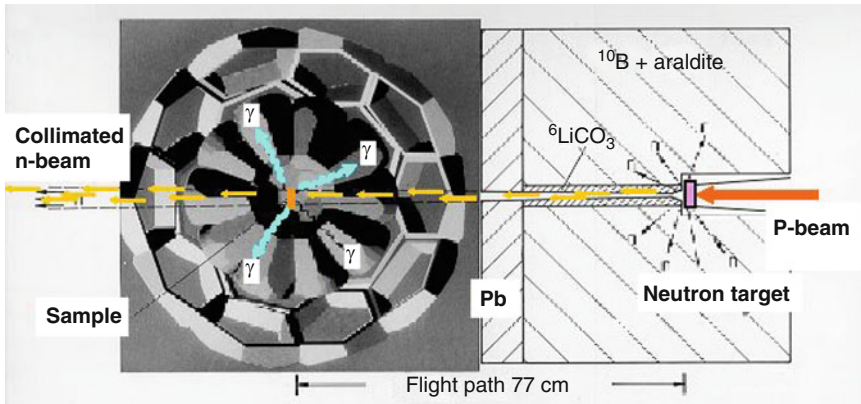


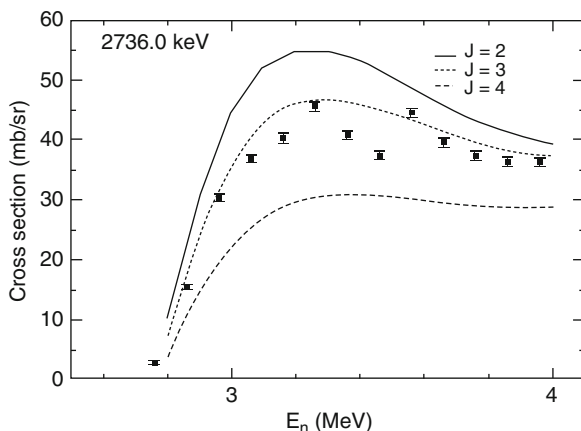
Figure 24

Calorimetric array of BaF_2 scintillators at Karlsruhe covering close to the full 4π solid angle. Neutrons produced by the ${}^7\text{Li}(p,n)$ reaction are incident on a sample in the middle of the array and the cascade of gamma rays following neutron capture is detected by the scintillators (Wisshak et al. 1990)

3.2.2 Neutron Energies in the MeV Region

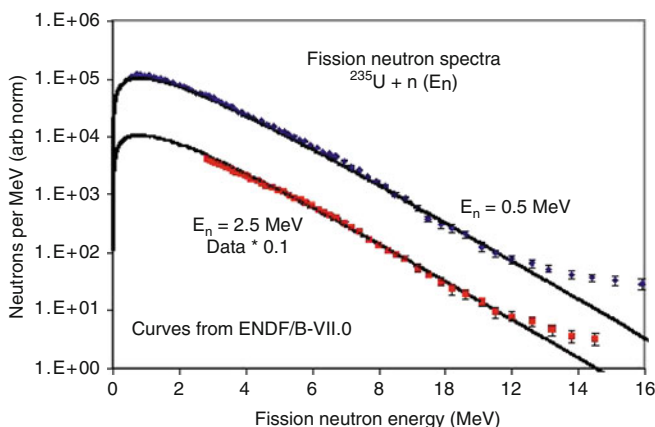
At the University of Kentucky, a vertical electrostatic accelerator, extensively rebuilt from its original Van de Graaff accelerator, provides beams of protons, deuterons, ${}^3\text{He}$ ions, and ${}^4\text{He}$ ions from 0.5 to 7 MeV. Neutron fluxes are provided by the ${}^3\text{H}(p,n){}^3\text{He}$ reaction from 0.5 to 5 MeV, by the ${}^7\text{Li}(p,n){}^7\text{Be}$ reaction from 0.05 keV to 0.5 MeV, by the ${}^2\text{H}(d,n){}^3\text{He}$ reaction from 5 to 9.5 MeV, and from 15 to 20 MeV by the ${}^3\text{H}(d,n){}^4\text{He}$ reaction. The Van de Graaff accelerator terminal provides continuous beams, those pulsed to 10 ns, and pulsed and bunched beams of 1 ns burst width at a repetition rate of 1.875 MHz. Almost all neutron-induced reactions have been done with ≈ 1 ns pulsed and bunched beams. For neutron-detection experiments, a post-acceleration buncher provides sub-nanosecond pulses. Most neutron experiments take place in a “neutron hall,” with a thin metal floor above a pit of 1.5 m depth, and an area $9.7\text{ m} \times 9.7\text{ m}$. Shielded detectors for pulsed-beam neutron detection are used for TOF detection with flight paths up to 4 m. Gamma-ray detection usually uses shorter flight paths of about 1.2 m. Gamma-ray detection is available with HPGe detectors, actively shielded with BGO annulus detectors. The whole assembly is housed in a large shield. A variety of liquid scintillation neutron detectors is available with diameters of 5.1 cm or 11.4 cm and thickness from 1.2 to 12.5 cm. Four large HPGe detectors are housed in a coincidence array (KEGS) for gamma-gamma correlation experiments. An example of inelastic scattering cross section data is shown in Fig. 25 where the excitation of specific levels as a function of incident neutron energy was determined by detecting their gamma-ray decay (Lesher et al. 2007). Analysis of the Doppler shift of the gamma rays gives information on the lifetimes of the states.

Another single-end Van de Graaff used for neutron research is at the University of Massachusetts Lowell Radiation Laboratory. A typical neutron source is produced by the ${}^7\text{Li}(p,n)$ reaction with a tightly bunched proton beam with a maximum energy of 5.5 MeV. Neutron emission is measured with this facility, an example being the spectrum of neutrons emitted



■ Figure 25

Data for the level at 2735.98 keV in ^{96}Mo are compared with statistical model calculations for three different spin possibilities. These data are from the University of Kentucky. The best fit for this level is $J = 3$ (Leshner et al. 2007)



■ Figure 26

Fission neutron spectral shapes for $^{235}\text{U}(n,f)$ at two different incident energies. The data are from University of Massachusetts at Lowell (Staples et al. 1995) and are compared with the shapes evaluated in ENDF/B-VII

in the fission of actinides. ➤ Figure 26 gives a result for the neutron emission spectra from neutron-induced fission of ^{235}U (Staples et al. 1995).

In the European Union, high intensity quasi mono-energetic neutron sources are produced at the Institute for Reference Materials and Measurements (IRMM) at Geel, Belgium, by a vertical 7 MV Van de Graaff accelerator with either continuous or pulsed ion beams (Reimer et al. 2009; Semkova and Plompen 2007). The installation has two pulsing systems: (1) a fast beam pulsing generating a minimum ion beam pulse width of 2 ns and pulse repetition rates of 2.5, 1.25 or 0.625 MHz, and (2) a slow pulsing system giving a minimum pulsing width of 10 μs at an

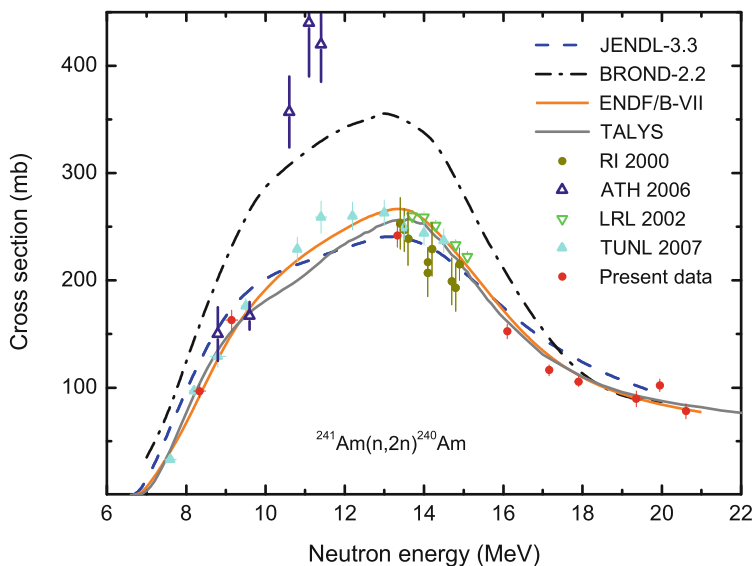


Figure 27

Cross sections for the $^{241}\text{Am}(n,2n)^{240}\text{Am}$ reaction with recent data from the VdG Geel (from Sage et al. 2009)

adjustable frequency up to 5 kHz. Neutron fields that have well-defined energies are produced by the nuclear reactions $^7\text{Li}(p,n)$, $^3\text{H}(p,n)$, $^2\text{H}(d,n)$ or $^3\text{H}(d,n)$ giving neutrons within the energy regions 0.3 to 10.0 MeV and 14.5 to 24 MeV. This facility houses six experimental set-ups in two large laboratory halls. In addition to TOF experiments, many neutron activation experiments have been carried out. An example of activation cross section results is shown in Fig. 27 for the $^{241}\text{Am}(n,2n)^{240}\text{Am}$ reaction (Sage et al. 2009).

At Ohio University, a high current tandem Van de Graaff accelerator with a terminal voltage up to 4.5 MV accelerates hydrogen ions to 9.0 MeV and other ions to higher energies. Beams of protons, deuterons, ^3He , ^4He , ^6Li , ^7Li , ^9Be , ^{10}B , ^{11}B , ^{12}C , and ^{13}C are produced. A central focus of the laboratory is neutron physics, and a pulsing and bunching system is available to produce beams of about 1 ns width for protons and deuterons, and 2.5–4 ns width for Li through O. A particularly important piece of experimental equipment is a “beam swinger,” which allows the beam incident on a target to be rotated through a range of angles (Finlay et al. 1982). One flight path with length of 4 to 30 m is used with the swinger to investigate neutron scattering from 0° to 160° . The laboratory is equipped with gas cell target assemblies that can be used with $^2\text{H}_2$ or $^3\text{H}_2$ gas. Solid targets containing tritium are also available. Efficiency calibrations of neutron detectors can be carried out with a ^{252}Cf source or with previously measured spectra from deuteron bombardment of stopping targets of B or Al (Massey et al. 1998; Di Lullo et al. 2008). This facility (Fig. 28) has been used for neutron elastic and inelastic scattering studies. An example of the angular distribution of elastic scattering of neutrons is shown in Fig. 29. The data from this facility have greatly improved the understanding of the neutron-nucleus optical model.

Somewhat higher neutron energies are provided by the Triangle Universities’ 10 MV FN tandem Van de Graaff accelerator at Duke University. It is equipped with a variety of ion sources,

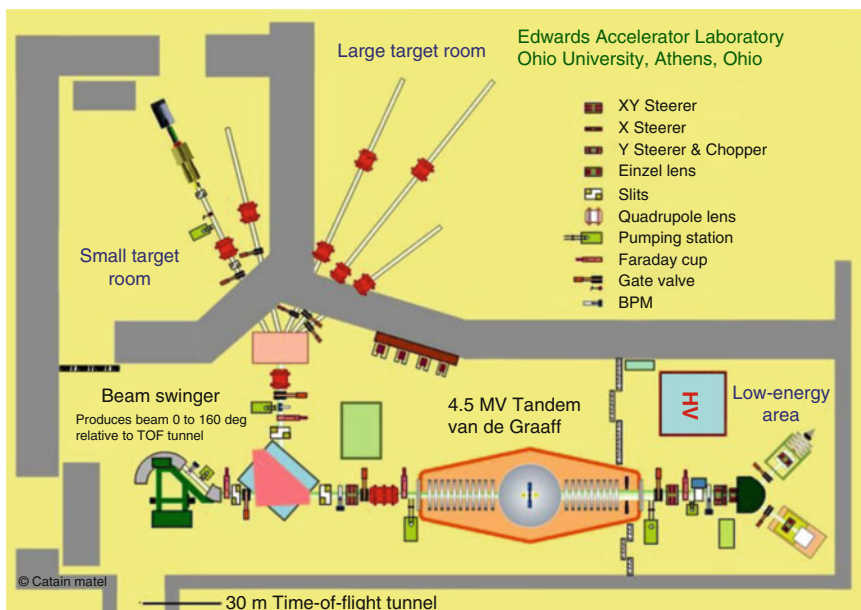


Figure 28

Schematic layout of the Ohio University Tandem Van de Graaff facility showing the accelerator, the beam swinger, the 30-m time-of-flight tunnel and other beam lines

beam lines, and target stations. The associated polarized ion source is the most intense source of dc polarized H^+ and D^+ ions in the world. Unpolarized beams of protons and deuterons are available from a direct-extraction negative-ion source. These beams are being used in a wide range of nuclear reaction studies including few-body reactions, radiative capture, and polarized neutron induced reactions. An example of neutron scattering from ${}^6\text{Li}$ is given in [Fig. 30](#) (Hogue et al. 1979).

At the Physikalisch-Technische Bundesanstalt (PTB) standards laboratory in Braunschweig, Germany, a cyclotron is used to produce standard neutron fields and to make basic cross section measurements of activation and differential scattering. High current beams of protons up to 19 MeV, deuteron beams up to 13.5 MeV and alpha particles up to 28 MeV are produced here. This very well characterized facility is unique in that the cyclotron is moved around the scattering sample in order to change the set of scattering angles ([Fig. 31](#)) (Mannhart and Schmidt 2002; Schmidt 2008).

A high-energy tandem Van de Graaff with a terminal voltage up to 13 MV is used at the Chinese Institute of Atomic Energy in Beijing, China. A multi-detector array of liquid scintillators detects the scattered neutrons. Another approach, the so-called “abnormal” TOF spectrometer is used to overcome difficulties of source breakup neutron interference in the ${}^2\text{H}(d,n)$ reaction in the 8–13 MeV region (Schmidt et al. 2005). In the latter, the neutrons are collimated to a narrow beam and the scattering sample is placed approximately 2 m from the source. Detectors for the scattered neutrons are located 50–100 cm from the sample. In this method, neutron emission from the sample can be studied down to 1 MeV in the emitted neutron energies.

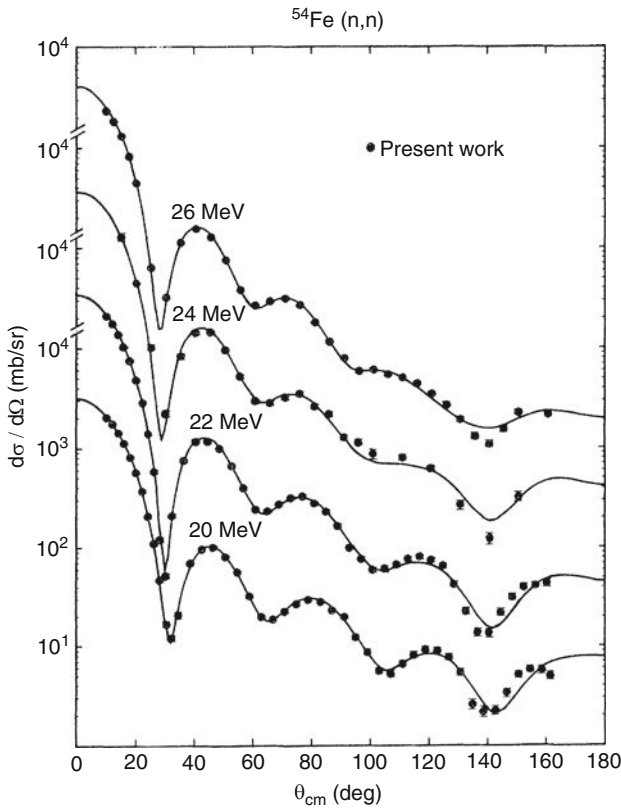


Figure 29

Elastic differential cross section for neutron scattering from ^{54}Fe at three incident energies taken at Ohio University compared with phenomenological optical model fits (Mellema et al. 1983)

3.2.3 Neutron Energies Near 14 MeV

A special neutron energy is 14 MeV, where neutrons can be produced with high intensity by the $^3\text{H}(d,n)^4\text{He}$ reaction which has a large cross section near the wide resonance just above 100 keV and which is, therefore, accessible to low energy deuteron accelerators. This 14 MeV source reaction (also called a D-T source reaction for deuterons plus tritons) is also the most favorable for fusion energy, and therefore data at this energy are very important for those applications. Many laboratories, both small and large, have used 14 MeV neutrons for cross section measurements. An example is the Octavian facility at Osaka University and one type of measurement made there is neutron emission spectra and angular distributions (Fig. 32). Other types of measurements made at laboratories of this type are neutron activation (of importance to waste disposal for fusion reactors), hydrogen and helium production (important for radiation damage of structural materials), standard cross section measurements, and integral tests of neutron transport, such as the pulsed sphere measurements carried out at several laboratories (Hansen et al. 1980).

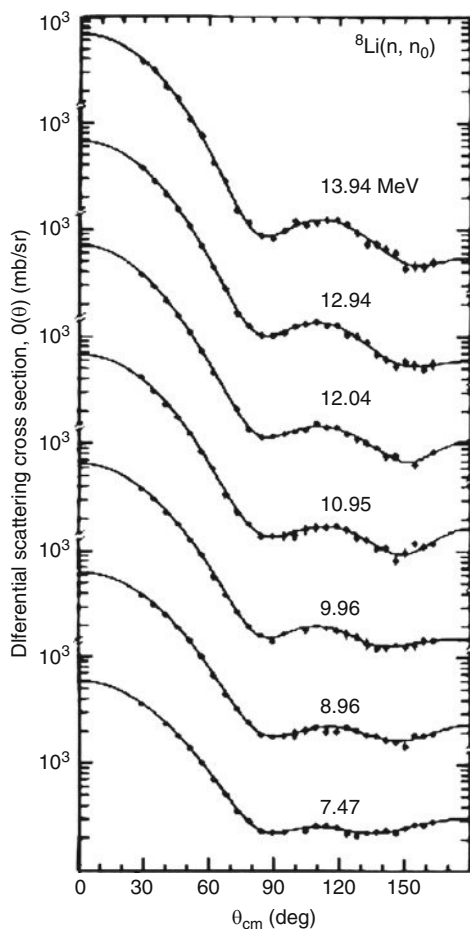


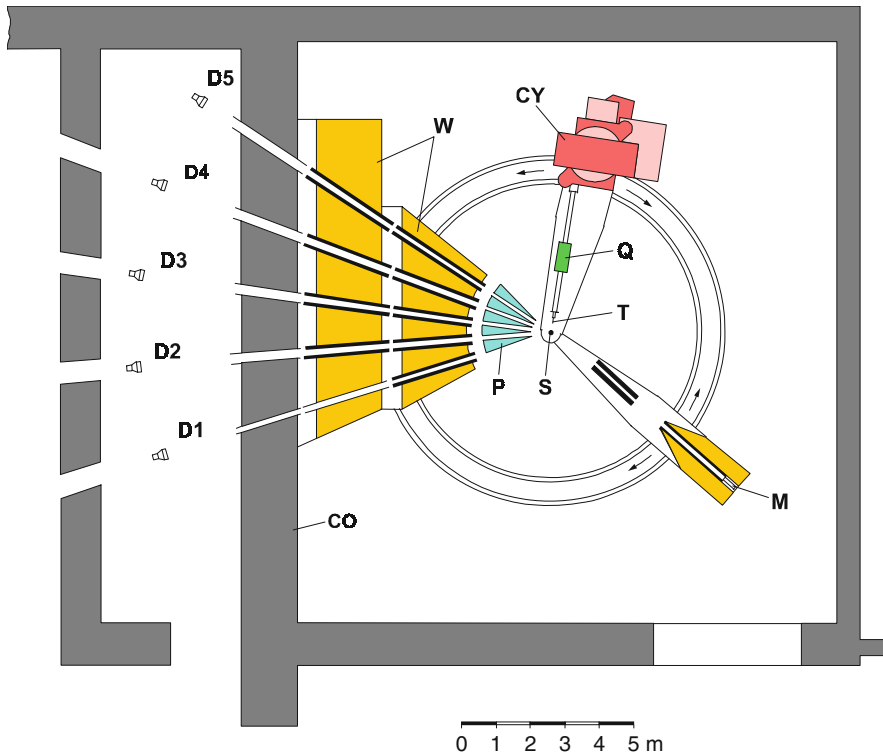
Figure 30

Angular distribution of elastic scattering of neutrons from ${}^6\text{Li}$ (Hogue et al. 1979). The data are from the Triangle Universities Nuclear Laboratory

For much higher neutron-production rates, rotating tritium-loaded targets are used to handle beam currents on the order of 10s or even 100 mA. Present facilities at the Japan Atomic Energy Agency (fast neutron source – FNS) can produce 14-MeV neutron fluxes well in excess of 10^{12} n/cm²/s for samples close to the source.

With a source of very high intensity, neutrons can be collimated in very narrow beams, sometimes called “pencil beams,” and still retain enough intensity for cross section measurements. The advantages of this approach are described in Kondo et al. (2006).

One special technique, referred to as “neutron-tagging” or “associated-particle” technique, is particularly appropriate for D-T neutron sources when the number of neutrons incident on a sample needs to be known precisely. The reaction at low incident neutron energy produces an alpha particle in addition to the neutron, and the two are correlated in angle by two-body kinematics. The alpha particle is usually detected at a back angle and the direction of the associated



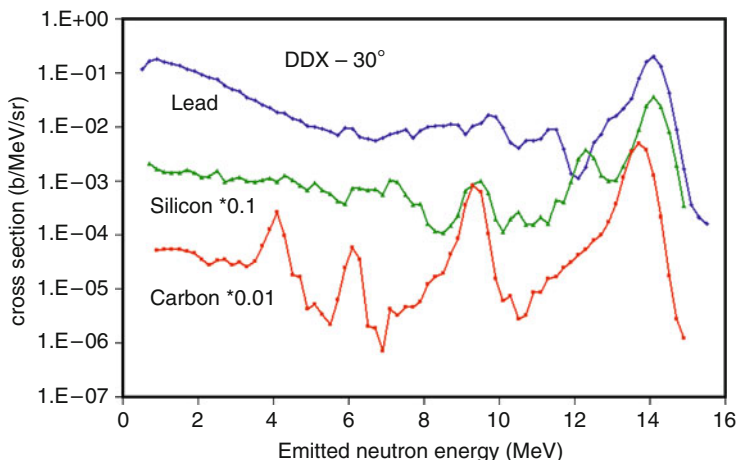
■ Figure 31

Cyclotron and time-of-flight paths for neutron scattering experiments at PTB. Note that the cyclotron can be moved to change the set of scattering angles

neutron is known exactly, to within the angular resolution of the alpha particle detector. This technique is used to measure cross sections without the need to refer to another, so-called “standard,” reaction cross section. This technique is not limited to the D-T reaction and 14 MeV neutrons but other reactions, such as ${}^2\text{H}(d,n){}^3\text{He}$ also provide an associated charged particle in addition to the neutron. This technique is not used much at present due to the improvements in “standard” cross sections, but it is still very useful when very precise neutron detector calibrations or absolute cross section measurements are desired.

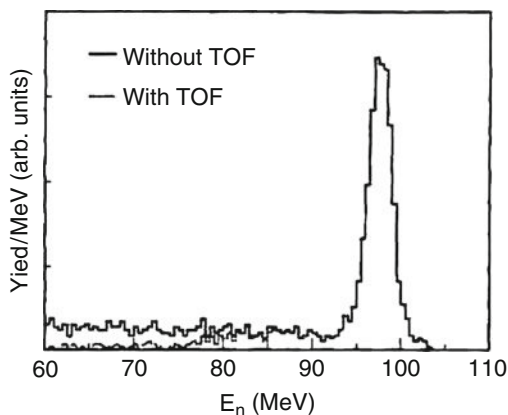
3.2.4 Neutron Energies Above 30 MeV

The Svedberg Laboratory (TSL) (Klug et al. 2002) at Uppsala, Sweden, is a good example of a laboratory using neutrons in the 10s of MeV region and higher. It consists of a cyclotron that can accelerate protons up to 180 MeV, deuterons up to 96 MeV, alpha particles up to 200 MeV and all the way up to ${}^{129}\text{Xe}$ to 1240 MeV. ● Figure 33 shows the neutron energy distribution for a quasi-monoenergetic peak around 96 MeV obtained from the ${}^7\text{Li}(p,n){}^7\text{Be}$ reaction. Approximately, half of the neutrons generated are in the peak. The low energy tail can be removed in the data analysis by TOF techniques.



■ Figure 32

Neutron emission spectra at 30° from 14.1 MeV neutron bombardment of carbon (data times 0.01), silicon (data times 0.1), and lead measured at Osaka (Takahashi et al. 1988). The data are expressed as double-differential cross sections. Elastically scattered neutrons are in the peaks near 14 MeV. Inelastic scattering to resolved levels in carbon with excitation energy of 4.43 MeV is observed with an emitted neutron energy of about 9 MeV. Other resolved states are seen in carbon and silicon, and to some extent in lead



■ Figure 33

The quasi-monoenergetic 96 MeV neutron beam distribution at the The Svedberg Laboratory (TSL) at Uppsala, Sweden, obtained from the ${}^7\text{Li}(p,n){}^7\text{Be}$ reaction. The upper histogram is for all the neutrons generated. For the lower histogram, time of flight was used to reduce the low energy tail. Approximately half of the neutrons are contained in the peak

Other facilities for neutrons in this energy range include the CYCLONE cyclotron (protons to 75 MeV, high mass particles up to Xe) at Louvain-la-Neuve, Belgium (Jongen and Ryckewaert 1976), the TIARA cyclotron ($K = 110$ AVF) at the JAEA Laboratory at Tokai-Mura, Japan (Baba et al. 2002; Ibaraki et al. 2000), the AVF cyclotron (90 MeV protons, 65 MeV deuterons and higher masses) at Tohoku University, Japan (Baba 2005), and the cyclotrons at the iThemba Laboratory for accelerator based sciences (LABS) at Faure, South Africa (up to 230 MeV protons) (<http://www.tlabs.ac.za>).

4 Neutron Cross Sections

4.1 Introduction

In the interaction between neutrons and nuclei, the kinetic energy of the neutron determines the nature of the interaction. A characteristic quantity is the reduced de Broglie wave length $\lambda = \hbar/2\pi$ of the neutron-nucleus center-of-mass system, defined by

$$\lambda = \sqrt{\frac{\hbar^2}{2mE}} \quad (1)$$

where m is the reduced mass, E the kinetic energy in the center of mass frame, and $\hbar = h/2\pi$ is the reduced Planck constant. If the nucleus has a mass A times that of the neutron m_n , then

$$m = \frac{A}{A+1} \times m_n. \quad (2)$$

At very low neutron energies, typically in the meV range and below, this wave length has a size of the order of the spacing between the nuclei in their material, for example, a crystalline structure. The neutron then does not see individual nuclei but interacts by scattering from the crystalline structure. Since this is a wave phenomenon one does not refer to the neutron kinetic energy, but rather to the neutron wavelength. This technique is commonly used in neutron diffraction.

In the energy range between roughly 1 meV and 10 MeV, the wave length varies from the distance between the atoms to the size of a single nucleon, therefore covering approximately the same order of magnitude as the size of the nucleus. Since the electrically neutral neutron has no Coulomb barrier to overcome, and has a negligible interaction with the electrons in matter, it can directly penetrate the atomic nucleus and interact with it.

For these energies, reactions often go through the formation of a compound nucleus. The compound nucleus model was introduced by Bohr (1936) to explain the observed resonances in neutron-nucleus reactions.

In this theory the formation of the compound nucleus is decoupled from its decay, such that the reaction cross section $\sigma_{n,x}$ can be factored into the product of the cross section for forming the compound nucleus, σ_c , times the probability of decay via reaction x as shown in the equation

$$\sigma_{n,x} = \sigma_c \frac{\Gamma_x}{\Gamma}. \quad (3)$$

Here Γ_x/Γ , the probability of decay via reaction x , is expressed as the partial width Γ_x divided by the total width Γ (of the resonance). In this picture, the neutron binding energy which becomes

available to the compound nucleus is rearranged among all nucleons, and gives rise to a complex configuration corresponding to a well-defined nuclear state with an energy, spin, and parity. Within Fermi's description of excitations of particle-hole configurations, such a state would correspond to an extremely complicated configuration of a many particle, many hole state.

At the high excitation energies above the neutron binding energies, for most nuclei the nuclear system is extremely complex and no nuclear model is capable of predicting the position and other properties of these excited states. For a heavy nucleus the level density in this region near the neutron binding energy is very high. A neighboring eigenstate can be excited by only a small change in excitation energy and may have a completely different wave function. This is a manifestation of what is also called chaotic behavior. Due to extreme configuration mixing, the nucleus in this regime above the neutron binding energy has a statistical behavior. This is expressed by the assumption that the matrix elements, relating nuclear states, have a random character, governed by a Gaussian distribution with zero mean. This statistical model of the compound nucleus is referred to as the Gaussian orthogonal ensemble (GOE) (Lynn 1968; Mehta 1960; Haq et al. 1982; Bohigas et al. 1984; Mehta 1991).

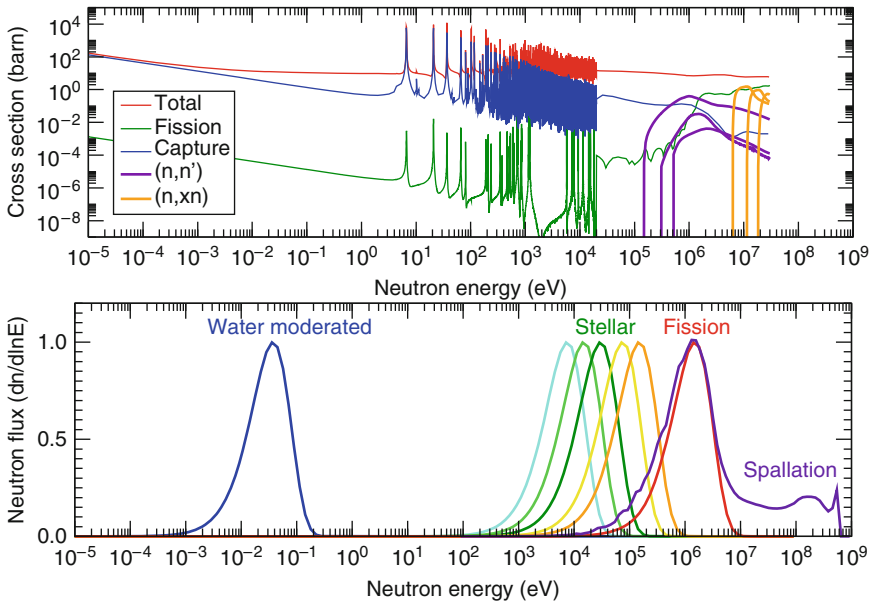
The statistical model has direct consequences on the observables of the reaction cross sections. The channel widths are proportional to the square of the matrix elements and have, therefore, a chi-squared distribution with one degree of freedom, also called the Porter-Thomas distribution (Porter and Thomas 1956). The observed gamma width of a resonance is the sum of many, for heavy nuclei, several tens of thousand, individual gamma widths, and each of these widths varies over the resonances according to a Porter-Thomas distribution. Therefore, the total radiation width for many heavy nuclei is of a similar order of magnitude. Observed fission widths correspond to a relatively small number of fission channels, at maximum three or four. The resulting distribution can be approximated by an effective chi-squared distribution with a small, fractional number of degrees of freedom.

With increasing excitation energy the Γ widths of the states start to overlap and the resulting cross sections become smooth. The properties of the eigenstates, like the decay widths, fluctuating from one state to another, become apparent as values averaged over many resonances. These average values now can be predicted by nuclear models, parameterized with average properties. Measured average cross sections can therefore finetune the parametrization of these models.

At even higher excitation energies, many more decay channels open up. Some reaction cross sections may only be accessible by nuclear model calculations.

► *Figure 34* shows some typical neutron-induced cross sections for the nucleus ^{238}U . In addition to the total, capture, and fission cross sections showing resolved resonances up to several keV, some threshold reactions are also shown. The cross sections for inelastic scattering leaving the nucleus in the first, second, and third excited state are shown, as well as three (n,xn) reactions with $x = 2, 3, 4$.

In the same ► *Fig. 34* typical neutron spectra are shown in the energy range from 10^{-5} to 10^9 eV. The energy region around a few tens of meV is called the thermal region and is of importance in reactor physics where the water moderated neutrons are in thermal equilibrium with the water and have Maxwell-Boltzmann distributed velocities peaked at an equivalent kinetic energy of $kT = 25.3$ meV. A different energy distribution is found for neutrons in certain stars where the synthesis of the isotopes heavier than about $A = 60$ takes place (Wallerstein et al. 1997). The neutrons are present as a hot gas and also have a Maxwellian kinetic energy distribution in the figure shown for temperatures with kT ranging from 5 to 100 keV in Asymptotic Giant Branch stars. The velocities of neutrons from ^{235}U thermal neutron-induced fission follow in good agreement a Maxwell-Boltzmann energy distribution, peaked at about 1 MeV as



■ Figure 34

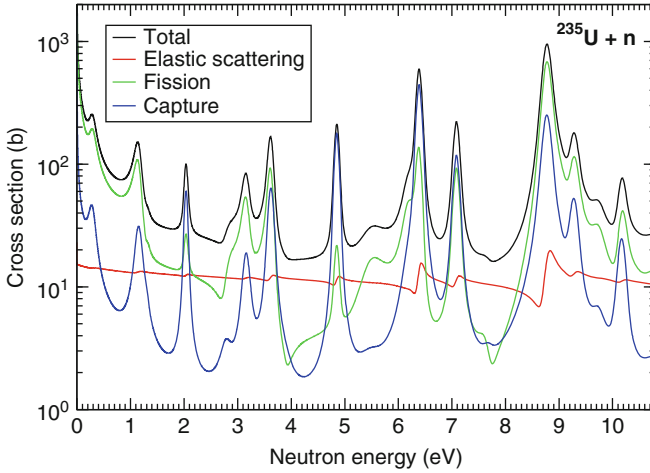
Typical neutron-induced cross sections (upper panel) here for the nucleus ^{238}U over an energy range from 10^{-5} to 10^9 eV, together with on the same scale some typical neutron energy distributions (lower panel), from fully moderated neutrons, stellar spectra at several temperatures, fission neutrons, and a typical spallation spectrum (also see text)

shown in ► Fig. 34. A typical spallation neutron spectrum in an accelerator-driven subcritical system, in this case MEGAPIE at PSI in Switzerland (Panebianco et al. 2009), is shown as well.

But at excitation energies just above the neutron binding energy, usually just a few decay channels are open. In ► Fig. 35 the cross sections for $^{235}\text{U} + n$ are shown for incident neutrons up to 11 eV. Only the capture, elastic scattering, and fission channels are open for these energies. The eigenstates are visible as resonances at the same energy in each of the cross sections.

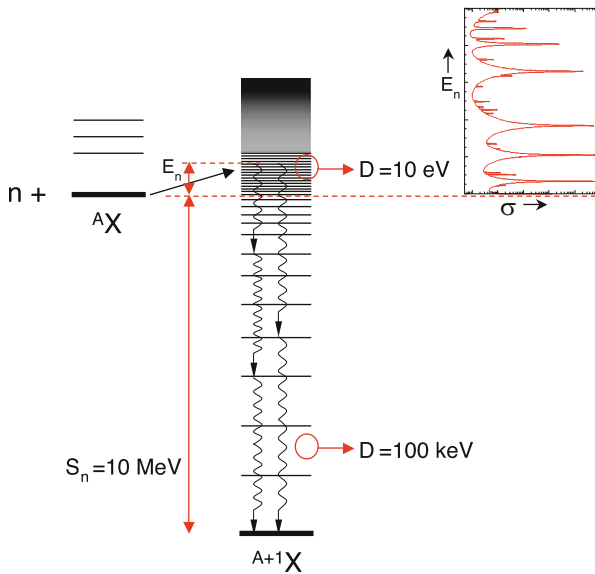
Since these states are not bound, the compound nucleus decays eventually through the emission of a gamma ray(s), a neutron, a charged particle, or the scission into mostly two fission fragments. The way of decay and the decay probability of the compound nucleus are considered to be independent from the way the compound nucleus was formed, but respecting conservation of energy and angular momentum. The decay probability through a decay channel c with width Γ_c is the branching ratio Γ_c/Γ (3). At low energy (in non-fissile nuclei) such a channel corresponds mainly to the emission of gamma rays or a neutron.

Typical widths Γ of measured resonances are in the order of electron volts. According to Heisenberg's uncertainty principle, the corresponding life time of the compound nucleus is in the order of $\tau = \hbar/\Gamma \approx 10^{-15}$ s, several orders of magnitude larger than the typical time needed by a neutron to cross a nucleus without interaction. In ► Fig. 36 a picture of the compound nucleus reaction is sketched. After the formation of the highly excited state by an incident neutron, the compound nucleus can decay by emission of gamma radiation, which is called radiative neutron capture, or by emission of a neutron, which is elastic scattering. If the kinetic energy



■ Figure 35

The neutron capture, elastic, and fission cross section for ^{235}U up to 11 eV, showing the resonance structure



■ Figure 36

Schematic view of the formation and decay of a compound nucleus with the orders of magnitude of the level spacing and neutron separation energy for a heavy mass nucleus. The resonances observed in the reaction cross section correspond to the excitation of nuclear levels

of the neutron is high enough, threshold reactions are possible, like inelastic scattering, leaving the target nucleus in an excited state.

Heavier nuclei are fissionable since the nuclear potential energy becomes lower than that of the ground state at large deformation. If the nucleus has an excitation energy higher than the barrier height, the nucleus can fission. This may be the case when a compound nucleus is formed, even with a neutron with nearly zero kinetic energy. But also when the compound nucleus is in a state below the fission barrier height, fission can occur through tunneling (subthreshold fission). If the nucleus in its ground state fissions, we speak of spontaneous fission.

In direct reactions, the opposite reaction mechanism to compound nucleus reactions, the incident neutron interacts directly with one or a few nucleons without forming a compound nucleus. The time scale of direct reactions is of the order of 10^{-22} s, a much shorter time than for compound-nucleus resonance reactions. Direct reactions become important for the heavier nuclei at neutron energies higher than about 10 MeV where the de Broglie wavelength of the neutron becomes comparable to the size of nucleons. But also at lower neutron energies, mainly for light A or closed shell nuclei, direct reactions may contribute significantly to the total cross section.

The width of an isolated resonance in a reaction cross section has in good approximation a Breit–Wigner shape (Breit and Wigner 1936), which is the typical shape for any quantum-mechanical state with a finite lifetime. This can be derived from the time dependence of the wave function $\Psi(t)$ of a non-stationary state with an energy E_0 and a lifetime τ . The time dependence of this wave function is


$$\Psi(t) = \Psi(0)e^{-iE_0t/\hbar} e^{-t/2\tau} \quad (4)$$

is observed as an exponential decay in time, like for example the familiar decay of the activity of a radioactive source. The squared absolute value of the Fourier transform of $\Psi(t)$, and defining $\Gamma = \hbar/\tau$ gives the energy distribution $P(E)$ having the Breit–Wigner form

$$P(E) \propto \frac{\Gamma}{(E - E_0)^2 + \Gamma^2/4} \quad (5)$$

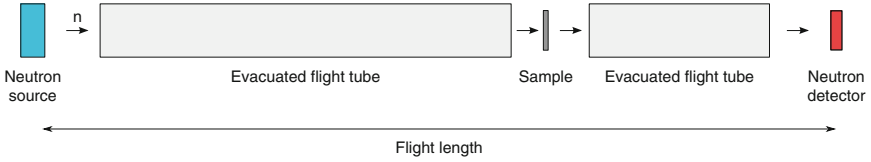
This Breit–Wigner form is present in the formulas for resonance cross sections. Also the more exact R -matrix expressions result in Breit–Wigner shapes in the limiting cases.

4.2 Total Cross Section

In principle, the “simplest” cross section to measure is the total cross section using the transmission method.  *Figure 37* shows a typical transmission method setup where a neutron beam impinges on a detector and a sample of the nuclei of interest is cycled in and out of the beam. The neutron transmission T is given by

$$T = \frac{\text{sample in counting rate}}{\text{sample out counting rate}} = e^{-N\sigma_t} \quad (6)$$

where N is the areal sample thickness (in units of atoms/barn) and σ_t is the neutron total cross section (in units of barns, where 1 barn equals 10^{-24} cm²). It should be noted that this measurement does not require accurate knowledge of the neutron flux or the detector efficiency. It



■ Figure 37

The principle of the transmission experiment setup. The neutron detector is located far from the sample in order to detect only neutrons that have not undergone an interaction in the sample (sample in position). The neutron flux incident on the sample is measured by removing the sample from the beam (sample out position)

only requires a neutron source that is constant in time or one that can be normalized for equal numbers of neutrons for the sample-in and sample-out runs.

Atoms inside the target are in thermal motion so that the measured total cross section σ_t in (6) is actually a Doppler broadened cross section. Thus, the transmission at neutron energy E is

$$T(E) = \exp\left(-N \int \sigma_t(E') P_E(E', t) dE'\right) \quad (7)$$

where $T(E)$ is the transmission at incident neutron energy E ; $P_E(E', t)$ is the probability, the result of thermal motion of the target atoms at temperature t , that the interaction takes place with energy E' ; and the integral is over all energies. The integral is called the Doppler-broadened total cross section $\sigma_{\Delta, t}$.

For some materials like metals, the free gas model (Lamb 1939) with an effective temperature T describes in good approximation Doppler broadening by a Gaussian with a standard deviation

$$\sigma_D = \sqrt{\frac{Mm}{(M+m)^2} 2kTE} \simeq \sqrt{\frac{2kTE}{A}} \quad (8)$$

with M the mass of the target nucleus, m that of the incident neutron, and A the atomic number, close to M/m for medium and heavy nuclei. Note that in the literature we often see the Doppler width Δ_D defined as $\Delta_D = \sqrt{2}\sigma_D$. For other materials, like poly-atomic crystalline lattices, a more complicated description is sometimes needed (Meister 1994; Naberejnev et al. 1999; Dagan 2008). The Doppler broadening effect is symmetric and will, therefore, not result in an apparent shift of the resonance energy.

In most measurements the incident neutrons are not at energy E but rather have a distribution of energy about E . Thus, the measured transmission T_m at energy E and temperature t is

$$\begin{aligned} T_m(E, t) &= \int R(E, E'') T(E'') dE'' \\ &= \int R(E, E'') \exp\left(-N \int \sigma_t(E') P_{E''}(E', t) dE'\right) dE'' \end{aligned} \quad (9)$$

where $R(E, E'')$ is the resolution function and is the probability that at nominal energy E the neutron has energy E'' . Both integrals are taken over all energies.

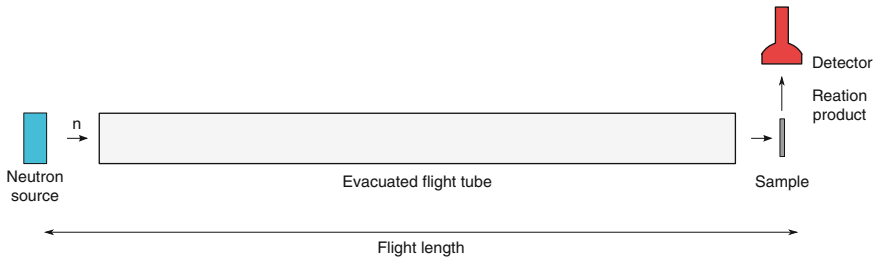


Figure 38

The principle of the reaction experiment setup. The detector for the reaction products may be in the beam together with the sample, for example, for (n,f) or (n,α) experiments, or outside the beam, like for capture or scattering reactions. The off-beam detector can be close to 4π configuration or cover a smaller solid angle

4.3 Partial Cross Section

The total cross section is the sum of all the partial cross sections such as scattering cross section, capture cross section, fission cross section, etc. A typical partial cross section experiment is shown in Fig. 38 where a beam of neutrons is incident upon a sample and the reactions of interest are observed in a detector. The yield for reaction x is defined as

$$Y_x = \frac{\text{number of } x\text{-reactions}}{\text{number of incident neutrons}} \quad (10)$$

Note that Y_x is the number of occurred reactions, not the number of detected reactions which depend largely on experimental factors as the detector efficiency and the solid angle covered. The primary yield Y_p is defined as the yield for first interactions. It is defined as the ratio of the reaction to total cross section σ_x/σ_t times the fraction of neutrons $(1 - T)$ inducing a reaction. Therefore,

$$Y_{x,p} = [1 - T] \frac{\sigma_x}{\sigma_t} = [1 - e^{-N\sigma_t}] \frac{\sigma_x}{\sigma_t} \quad (11)$$

where σ_x is the partial cross section. For simplicity, Doppler effects and resolution broadening are ignored in (11). The term within the brackets is the fraction of the incident beam, which interacts in the sample and the ratio of cross sections is the fraction of interactions which are of type x .

In addition to the primary yield there is multiple scattering in the sample which produces additional x reactions in the sample. Thus, the total yield Y_x is

$$Y_x = Y_{x,p} + Y_{x,m} \quad (12)$$

where $Y_{x,m}$ is the result of multiple scattering and subsequent reactions of type x in the sample.

For thin samples where $N\sigma_t \ll 1$, multiple scattering becomes negligible and $Y_{x,p}$ can be expanded as

$$Y_x = [1 - 1 + N\sigma_t - (N\sigma_t)^2/2! + (N\sigma_t)^3/3! + \dots] \frac{\sigma_x}{\sigma_t} \approx N\sigma_x \quad (13)$$

or

$$\sigma_x \approx \frac{Y_x}{N} \quad (14)$$

Thus, for thin samples the partial cross section is equal to the partial yield divided by the areal sample thickness.

For fission measurements, the sample can be very thin and the detector counts the fission reactions. For this case, the measured partial cross section of type x is merely the resolution broadened cross section. Applying both Doppler and resolution broadening, one obtains for thin samples the measured cross section at nominal energy E and temperature t

$$\sigma_m(E, t) = \int R(E, E'') \left[\int \sigma_x(E') P_{E''}(E', t) dE' \right] dE'' \quad (15)$$

4.4 Resonance Cross Section

Neutron cross sections exhibit many resonances in the energy region above thermal energies. The cross section of an isolated resonance can be described by the single-level Breit-Wigner formula. At low energies where the neutron has zero orbital angular momentum (s -wave), the partial reaction cross section of an isolated s -wave resonance is given by

$$\sigma_x(E) = \pi \lambda^2 g \frac{\Gamma_n \Gamma_x}{(E - E_0)^2 + (\Gamma/2)^2} \quad (16)$$

where E is the neutron energy (in the center of mass system), λ is the reduced neutron wavelength, g is the statistical weight factor, Γ_n is the neutron width, Γ_x is the reaction width, Γ is the total width (full width at half maximum), and E_0 is the neutron energy at the peak of the resonance. The statistical weight factor g is given by

$$g = \frac{2J + 1}{2(2I + 1)} \quad (17)$$

where J is the total angular momentum (resonance spin) of the compound nucleus and I is the total angular momentum (spin) of the target nucleus. The neutron width Γ_n is energy dependent and can be represented by

$$\Gamma_n(E) = \Gamma_n(E_0) \sqrt{\frac{E_0}{E}} \quad (18)$$

Equation (16) can be transformed by dividing numerator and denominator by $(\Gamma/2)^2$ and by introducing the peak cross section at resonance to become

$$\sigma_x(E) = \sigma_0 \frac{\Gamma_x}{\Gamma} \sqrt{\frac{E_0}{E}} \left(\frac{1}{1 + y^2} \right) \quad (19)$$

where the peak cross section σ_0 is given by

$$\sigma_0 = 4\pi \lambda_0^2 g \frac{\Gamma_n(E_0)}{\Gamma} \quad (20)$$

$\Gamma_n(E_0)$ is the neutron width at the resonance energy, λ_0 is the reduced neutron wavelength at E_0 , and y is given by

$$y = \frac{E - E_0}{\Gamma/2} \quad (21)$$

The total cross section is the sum of the scattering cross section and the sum of all the partial cross sections. The total cross section for an isolated s -wave resonance is

$$\begin{aligned} \sigma_t(E) &= \pi\lambda^2 g \frac{\Gamma_n\Gamma + 4\Gamma_n(E - E_0)R/\lambda}{(E - E_0)^2 + (\Gamma/2)^2} + 4\pi R^2 \\ &= \sigma_0 \sqrt{\frac{E_0}{E}} \left(\frac{1}{1 + y^2} \right) + \sigma_0 \sqrt{\frac{E_0}{E}} \left(\frac{y}{1 + y^2} \right) \frac{2R}{\lambda} + 4\pi R^2 \end{aligned} \quad (22)$$

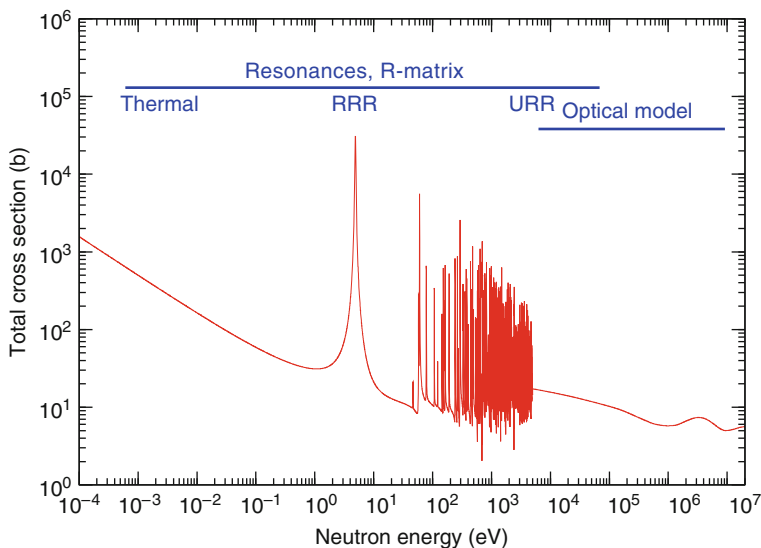
where the last term is the potential scattering cross section and R is the potential scattering radius. The second term represents the resonance-potential interference and, in some cases, leads to almost zero total cross section.

Thus, the neutron cross section of an isolated resonance can be calculated from a set of parameters termed “resonance parameters.” These parameters are the resonance energy E_0 , total width Γ , neutron width Γ_n , reaction width(s) Γ_x , total angular momentum J , target nucleus spin I , and the orbital angular momentum of the neutron. For non-fissile resonances the only reaction width is the radiative width Γ_γ . From these parameters and the Debye temperature of the target nucleus the Doppler-broadened cross section can be calculated.

To account for nearby or overlapping resonances the Breit–Wigner formula is no longer valid and an R -matrix formalism, explained in more detail in [Sect. 6](#), is used to calculate the neutron cross sections. However, the same resonance parameters are used for these calculations. Thus, the measured transmission and/or partial cross sections which include the effects of Doppler broadening and resolution broadening can still be interpreted in terms of these resonance parameters. Originally, the Breit–Wigner formalism was used to fit the measured transmission and partial cross sections to obtain these parameters. Today, there are two major codes, REFIT (Moxon and Brisland 1991) and SAMMY (Larson 2006) based on the R -matrix formalism, which can extract resonance parameters from the measured data. These programs calculate the Doppler-broadened cross section, apply resolution broadening to simulate the observed transmission and partial yield data, and then determine the resonance parameters that provide the best fit to all of the measured data. It is these parameters that are used to calculate neutron cross sections for reactor and other applications.

4.5 High Energy Cross Section

With increasing neutron energy the average spacing between levels $\langle D \rangle$ decreases (the result of level density $\rho(E)$ increasing with energy) while the average resonance width $\langle \Gamma \rangle$ increases. In the energy region where $\langle \Gamma \rangle$ is comparable to $\langle D \rangle$ the cross section exhibits structure caused by unresolved clusters of partially overlapping resonances. This is a very difficult region to express analytically, so statistical representations based on average parameters are typically used in neutronic calculations. At higher energies where $\langle \Gamma \rangle$ is much larger than $\langle D \rangle$, the cross section is in a continuum region and is typically represented by optical and collective model expressions based on a Hauser–Feshbach description with width fluctuation corrections (see also [Sect. 6.3](#)).



■ Figure 39

The ENDF/B-VII.0 evaluated total cross section of ^{197}Au

5 Cross Section Measurements

Cross sections of interest to nuclear engineering cover the range from subthermal energies in the millielectron volts to tens of millions of electron volts. A typical example of a cross section is shown in [Fig. 39](#) where the ENDF/B evaluated total cross section of Au is plotted (Chadwick et al. 2006). For convenience this large energy span can be divided into four energy ranges: thermal, resolved resonance, unresolved resonance and continuum energy regions. In this figure the thermal region extends up to ~ 0.1 eV and the resolved resonance region falls between approximately 0.1 eV and 4.8 keV. Note that above 4.8 keV the cross section is represented as a smooth curve.

However, immediately above 4.8 keV the cross section is still dominated by resonance structure but is considered “unresolved.” This structure is considered unresolved because the experimental resolutions could not resolve individual resonances and/or, even if the experimental resolution were “perfect” and truly resolved all the structure in the cross section, the resonances partially overlap and cannot be clearly distinguished from each other. Even though this unresolved resonance region is represented in the evaluation as a smooth average cross section, the cross section fluctuations about the average result in fluctuations in self-shielding and must be taken into account in neutronic calculations in this energy region. In the MeV energy region the Au resonances have overlapped to the extent that the cross section is now a smooth continuum and here, we only see very wide optical diffraction peaks in the cross section above ~ 1 MeV; this is the continuum energy region.

The boundaries between the different regions, thermal, resolved resonances, unresolved resonances, and continuum, are different for each nucleus and depend on the level density of the

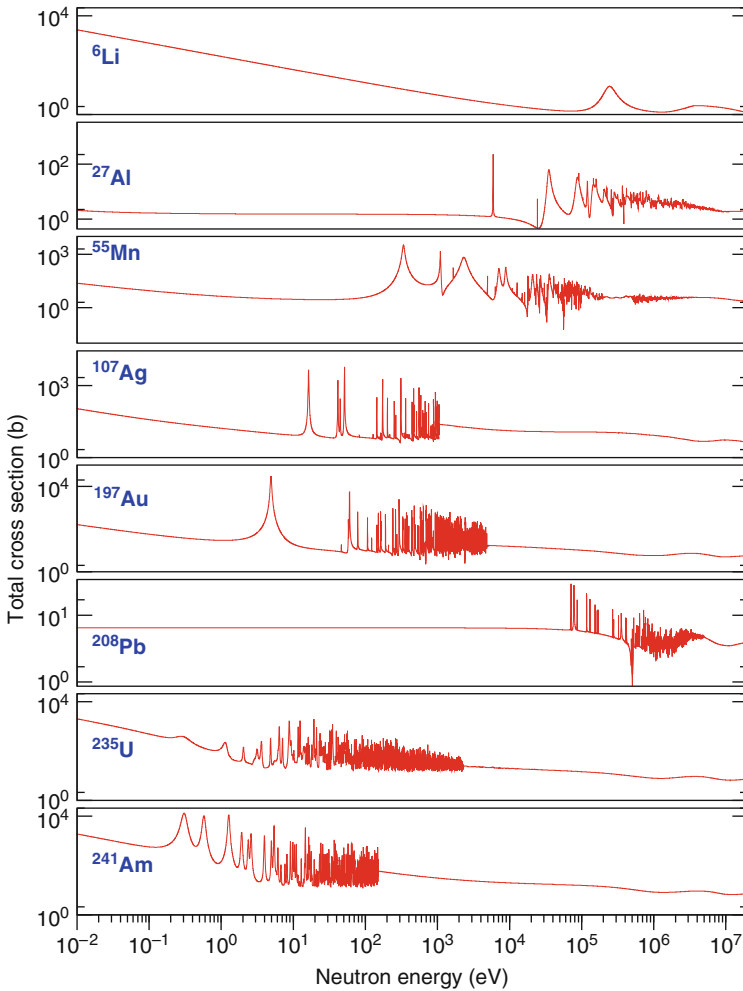


Figure 40

The neutron total cross section of several nuclei showing large differences in the resonance spacings

compound nucleus. In fact, resolved neutron resonances are an important source to obtain level density information.

In [Fig. 40](#) the neutron-induced total cross section is shown for several nuclei of increasing mass. Since the level density increases with mass, resonances are more closely spaced for heavier nuclei. But near a double closed shell nucleus like ${}^{208}\text{Pb}$, the level density is much lower, and we observe a much higher level spacing. Also nuclei with neighboring masses may show large differences in the level density due to shell effects.

As a result of the different structure in each of these energy regions, the cross section measurement techniques in each region can be quite different. These techniques are reviewed below.

5.1 Thermal Energy Region

This region typically extends from a fraction of an eV down into the meV region. The cross section here is equal to the sum of the scattering cross section and the absorption cross section. The absorption cross section typically varies as $1/v$ where v is the velocity of the neutron. This can be seen from (19) and (22), where at low energies the cross sections are proportional to $1/\sqrt{E}$ (or $1/v$); this is also seen in the low energy ^{197}Au total cross section shown in [Fig. 39](#). Some “famous” absorption cross sections at 0.0253 eV, which corresponds to the maximum at 2,200 m/s in the Maxwell–Boltzmann distribution of the neutron velocities at a temperature of 293.6 K, are 3,840 barns for the (n, α) reaction in ^{10}B , 25,200 barns for the (n, γ) reaction in $^{\text{nat}}\text{Cd}$, and 585 barns for the (n,f) reaction in ^{235}U . The scattering cross section can be more complex as solid state effects take place. Neutrons can undergo Bragg scattering by any crystalline material present, undergo paramagnetic scattering with the target nuclei and neutrons can be up-scattered or down-scattered in energy from the thermal motion of the nuclei they interact with.

Thermal reactors have been used for many of the early absorption cross section measurements. Samples of the material of interest were placed inside the thermal spectrum where the induced radioactivity in the samples or the change in reactivity of the reactor were interpreted in terms of the sample absorption cross section. Reactors were used to provide monoenergetic neutron beams using crystal spectrometers or velocity selectors for cross section measurements. Fast choppers were used to produce pulses of neutrons for TOF measurements. More recently, bent tubes have been used to provide extremely pure neutron beams in the millielectron volt range for precise sub-thermal cross section measurements.

For the past 30 years the energy-dependent cross sections in the thermal region have been measured predominantly by TOF techniques using pulsed accelerators. This technique provides good resolution well into the resolved resonance region so that in a single measurement, both thermal and resonance regions data can be obtained. Since the thermal absorption cross sections of most materials is the result of the tails of resonances, the accelerator time-of-flight method provides data over the whole energy region which contributes to the thermal cross section.

An example of a measurement of the total cross in the thermal region is shown in [Fig. 41](#) for ^{165}Ho (Danon et al. 1998). The TOF transmission method was used for the RPI measurement. A paramagnetic scattering cross section of 28.3 barns at 0.0253 eV was calculated for ^{165}Ho and this had to be accounted for in analyzing ^{165}Ho for both thermal absorption cross section and total cross section.

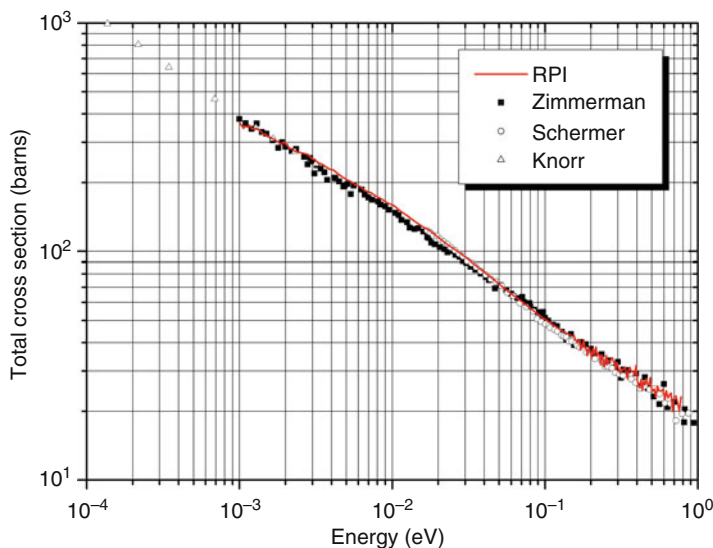
5.1.1 Thermal Flux Averaged Cross Section

The flux averaged cross section $\bar{\sigma} = \int \sigma(E)\phi_E(E)dE$ of a reaction is a useful quantity for irradiation experiments. If the cross section has a smooth shape of the form

$$\sigma(E) = \left(\frac{E}{E_r}\right)^\alpha \sigma_r \quad (23)$$

where σ_r is the cross section at energy E_r , then we can calculate the flux averaged cross section as

$$\bar{\sigma} = \frac{\int \sigma(E)\phi(E)dE}{\int \phi(E)dE} = \left(\frac{kT}{E_r}\right)^\alpha \sigma_r \Gamma(\alpha + 2) \quad (24)$$



■ **Figure 41**
Total cross section of ^{165}Ho in the thermal energy region

where $\Gamma(x)$ is here the gamma function. This is particularly useful at low, thermal energies where the cross section has a $1/v$ shape, so $\sigma(E_n) \propto E_n^{-1/2}$, that is, $\alpha = -1/2$. The flux averaged cross section becomes then

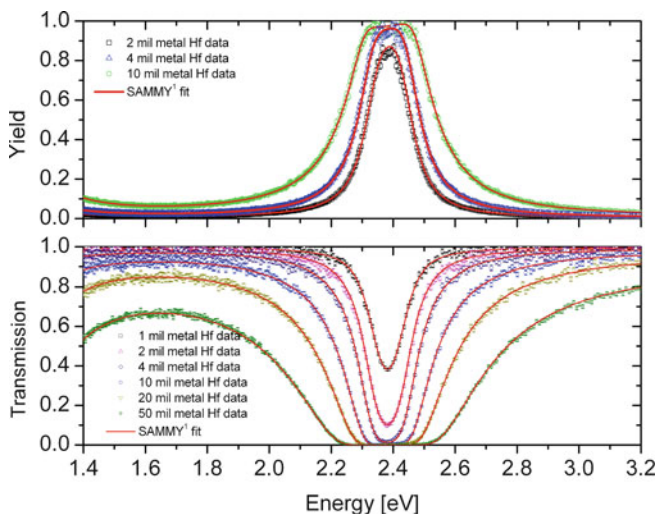
$$\bar{\sigma} = \sqrt{\frac{\pi}{4}} \sqrt{\frac{E_r}{kT}} \sigma_r \quad (25)$$

In this case we often choose E_r such that we have the cross section at $v = 2,200$ m/s, that is, at $E_r = 24.3$ meV.

5.2 Resonance Energy Region

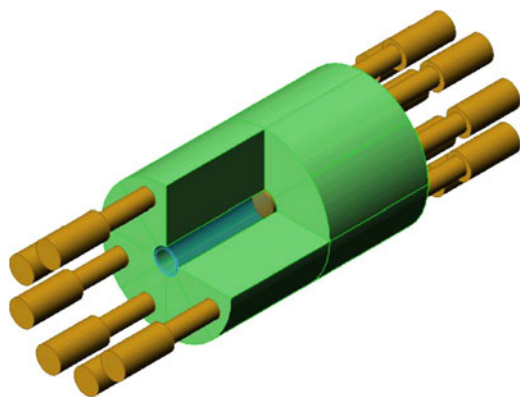
This is the region in which resonances can be resolved by the technique being used for the measurement. This energy typically spans an energy region from ~ 1 eV to several MeV for light nuclei like Be and C, into the 100s of keV for the structural materials like Fe and Ni, into the keV region for rare earth nuclei like Ho or Gd and into the 100s of eV to keV region for heavy nuclei like U. It is in the resonance region where the TOF measurements at pulsed accelerators have made the major contributions.

Each resonance represents an excited state in the compound nucleus formed by the incident neutron. The focus of these measurements is the extraction of resonance parameters both for understanding the underlying science of nuclear levels and for the practical need of being able to calculate cross sections at any operating temperature (such as in a reactor). Typical resonance parameters are the resonance energy E_0 , resonance spin J , orbital angular momentum of the incoming neutron ℓ , resonance total width Γ , the always present neutron width Γ_n , and, if applicable, other, partial widths like the radiative width Γ_γ or the fission width Γ_f .



■ Figure 42

Capture yield and transmission of metallic Hf samples near the 2.39 eV resonance in ^{177}Hf



■ Figure 43

Cutaway view of the 16-section NaI multiplicity detector. A capture sample is placed in the center of the detector and the neutron beam is collimated along the detector axis

An example of data from a TOF measurement optimized to measure resonance parameters is shown in [▶ Fig. 42](#). These data were obtained from low energy capture and transmission measurements at the Rensselaer Polytechnic Institute LINAC with elemental Hf (Trbovich et al. 2009). A high-efficiency calorimeter-type detector was used for the capture measurements and is shown in [▶ Fig. 43](#). A ^6Li glass scintillator detector was used for the transmission measurements. Here, both transmission and capture measurements were performed on many sample thicknesses, and the Bayesian-based SAMMY code (Larson 2006) was used to obtain a single set of parameters to fit all the data. In this region the resonances are reasonably well separated

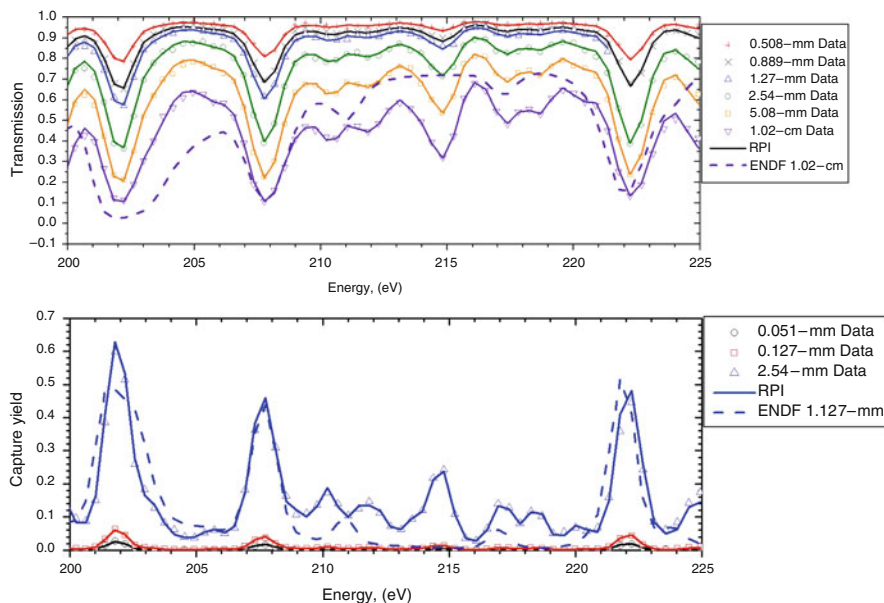


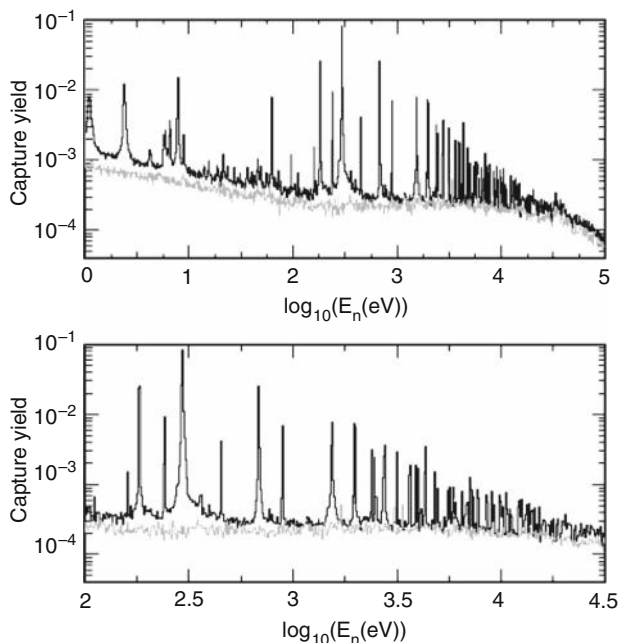
Figure 44
Transmission and capture yield from multiple samples of elemental Gd

and it is relatively easy to obtain a good fit. In the example of a higher-energy measurement, as shown in [Fig. 44](#) for elemental Gd (Leinweber et al. 2006), the resonances are beginning to overlap and it is more difficult to make the fit. Eventually, the resonances overlap so much that it becomes very difficult to resolve them from each other. In this case better TOF resolution and/or the use of separated isotopes can extend the energy range for clearer separation of resonances and ultimate determination of resonance parameters.

[Figure 45](#) shows an example of a capture measurement of isotopically-enriched ^{91}Zr at the n_TOF facility at CERN (Tagliente et al. 2008). This measurement spans the energy range from 1 eV to 100 keV and shows the transition from clearly separated ^{91}Zr resonances at lower energies to the keV region where the resonances are only partially resolved. These data were taken with a C_6D_6 scintillator detector that was designed with minimum absorbing material to reduce its sensitivity to neutrons scattered by the capture sample. Resonance parameters were determined up to 26 keV; above this energy the fluctuations in the yield clearly show the effects of unresolved resonances.

5.3 Unresolved Resonance and Continuum Energy Region

An example of the change from the unresolved to continuum energy region is shown by the recently measured (at RPI) total cross section of elemental Zr above 0.3 MeV shown in [Fig. 46](#). Here, we clearly see the effects of unresolved resonance structure up to ~ 3 MeV. Above ~ 3 MeV are seen the effect of nuclear optical structure with a very broad peak near 9 MeV;



■ Figure 45

Capture yield (black) and background (gray) of ^{91}Zr between 1 eV and 100 keV measured at n_TOF (Tagliente et al. 2008)

this is clearly in the continuum energy region. This type of structure below 3 MeV can be interpreted in terms of the fluctuations in the observed cross section; an excellent example of this type of analysis has been applied to total cross section measurements of ^{31}P , ^{32}S , ^{39}K , ^{51}V , ^{56}Fe , and ^{59}Co between 0.75 and 11.3 MeV (Abfalterer et al. 2000) to obtain average level densities and resonance widths as a function of excitation energy.

To represent the cross section in the unresolved resonance region for neutronic applications, two distinct approaches have been successful: ladders of pseudo resonances and probability lookup tables. Both of these approaches select resonances stochastically from a level spacing and a level strength distribution, which are based on the average spacings and strengths extrapolated from the resolved resonance region. In the ladder case a set of parameters is stochastically selected over a given energy range and a pseudo cross section is calculated from these parameters. The pseudo cross section is then used in neutronic calculations over this energy range. In the probability lookup case a pseudo cross is calculated over a given energy range and the probability distribution of a given value of cross section is determined over this energy range. For neutronic calculations, the probability of a given cross section is stochastically sampled from the probability distribution.

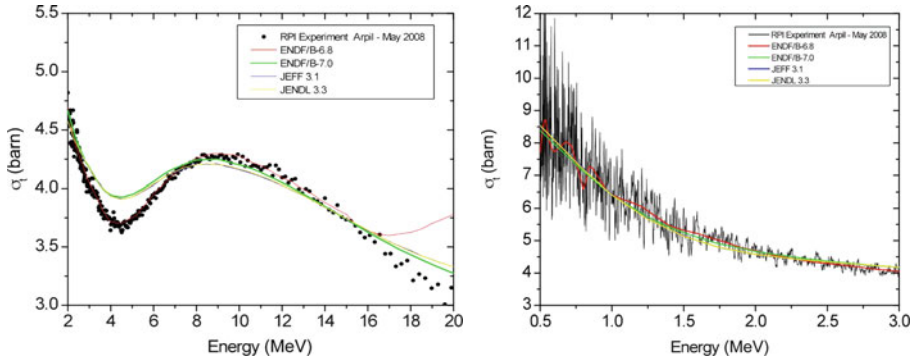


Figure 46

The measured and evaluated total cross section of ${}^{\text{nat}}\text{Zr}$ from 0.5 to 20 MeV

5.4 The Neutron Time of Flight Method

The principle of neutron time of flight measurements is based on the pulsed neutron source which produces at a time t_0 neutrons in a wide energy range. For reaction measurements a sample is put in the neutron beam at a well know distance L and the reactions are observed with a detector. The detection of the reaction determines the time of arrival t_n of the neutron at the sample and therefore its velocity $v = (t_n - t_0)/L$, which gives the kinetic energy of the neutron. The idea is illustrated in [Fig. 47](#).

Accelerator-based pulsed white neutron sources are in general either electron-based sources where the neutrons are produced via Bremsstrahlung on a high Z target, or proton-based sources where the neutrons are produced by spallation on a target of heavy nuclei.

The neutrons created by the pulsed source travel along the flight path with length L during a time t before possibly undergoing a reaction in a capture, scattering or fission setup, or before getting detected in a transmission experiment (see [Fig. 37](#)). The neutron kinetic energy is determined relativistically from the neutron velocity $v = L/t$ and momentum $p = mv$ as

$$E_n = E_{tot} - mc^2 = \sqrt{c^2 p^2 + m^2 c^4} - mc^2 = mc^2(\gamma - 1) \quad (26)$$

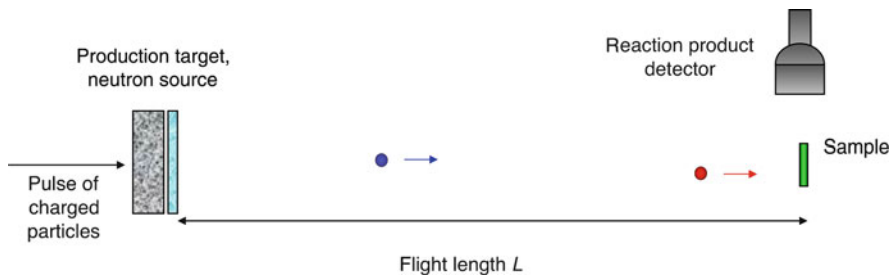


Figure 47

The principle of the neutron time-of-flight method

with $\gamma = (1 - v^2/c^2)^{-1/2}$ and where c is the speed of light. For low energies where $v \ll c$ and therefore $\gamma \rightarrow 1$, the relativistic expression can be conveniently written as a series expansion of γ

$$\gamma = 1 + \frac{1}{2} \frac{v^2}{c^2} + \frac{3}{8} \left(\frac{v^2}{c^2} \right)^2 + \frac{5}{16} \left(\frac{v^2}{c^2} \right)^3 + O\left(\frac{v^2}{c^2} \right)^4 \quad (27)$$

For resolved resonances the first two terms of the series expansion of the relativistic expression are usually sufficient, which results in the classical definition of kinetic energy

$$E_n \approx \frac{1}{2} m v^2 = \alpha^2 \frac{L^2}{t^2}. \quad (28)$$

Taking the definition of the speed of light $c = 299,792,458$ m/s and taking $m = 939.6$ MeV/ c^2 for the neutron mass, we get $\alpha = 72.3 \mu\text{s}\sqrt{\text{eV}/\text{m}}$ when using units eV, m, and μs for E_n , L , and t respectively.

See also, for example, Foderaro (1971), Krane (1987), Knoll (2000), and Reuss (2008) for a wider discussion on neutron physics and associated instrumentation.

5.4.1 Neutron Density and Flux Distributions at Thermal Energies

Fully thermalized neutrons behave like an ideal gas and can, therefore, be described in good approximation by Maxwell–Boltzmann statistics. The neutron density, that is, the number of neutrons per unit of volume, has a Maxwell–Boltzmann velocity distribution $n_v(v)$ of the form

$$n_v(v) = 4\pi \left(\frac{m}{2\pi kT} \right)^{3/2} v^2 \exp\left(-\frac{mv^2}{2kT} \right) \quad (29)$$

where k is the Boltzmann constant, m the neutron mass, and T the temperature.

This distribution shows a maximum at $v = \sqrt{2kT/m}$ corresponding to a kinetic energy of $E_{\text{max}} = kT$. For a velocity of 2,200 m/s, used as a reference for thermal neutrons, this gives $E_{\text{max}} = 25.3$ meV, $\lambda = 0.18$ nm, and $T = mv^2/2k = 293.6$ K, which is practically room temperature.

From the velocity distribution $n_v(v)$ we can obtain the distribution $n_E(E)$ of the kinetic energy E , the distribution $n_t(t)$ of the time-of-flight t , and the distribution $n_\lambda(\lambda)$ of the wavelength λ using the relations

$$n_v(v)dv = n_E(E)dE = n_t(t)dt = n_\lambda(\lambda)d\lambda \quad (30)$$

where dv , dE , dt , and $d\lambda$ are obtained from taking the derivatives of the expressions

$$E = \frac{1}{2} m v^2 = \frac{1}{2} m \frac{L^2}{t^2} \quad (31)$$

and

$$\lambda = \frac{h}{mv} = \frac{ht}{mL} \quad (32)$$

One is often interested in the distribution of the neutron flux. The velocity distribution of the neutron flux $\varphi_v(v)$ is related to $n_v(v)$ as

$$\varphi_v(v) = C_v \times v \times n_v(v) \quad (33)$$

where C_v is the appropriate normalization constant to normalize the integral to unity $\int \varphi_v(v) dv = 1$ ($C_v = \sqrt{8kT/(\pi m)}$ in this case). In a similar way as in (30) the kinetic energy, time-of-flight, and wavelength distributions of the neutron flux can be obtained using

$$\varphi_v(v)dv = \varphi_E(E)dE = \varphi_t(t)dt = \varphi_\lambda(\lambda)d\lambda \quad (34)$$

Applying this and by introducing the characteristic variables

$$v_T = \sqrt{\frac{2kT}{m}} \quad (35)$$

$$E_T = kT \quad (36)$$

$$t_T = L\sqrt{\frac{m}{2kT}} \quad (37)$$

$$\lambda_T = \sqrt{\frac{h^2}{2mkT}} \quad (38)$$

we obtain the expressions for the neutron density and neutron flux distributions as given in **Table 3**. This table is similar to the one in (Molnar 2004). Here, we also add the time-of-flight distributions which are analogous to the wavelength distributions with the characteristic variables.

Note from the equivalent maximum values that the energy distribution of the flux has a maximum at $E = E_T = kT$ and that the time-of-flight distribution, which is typically measured at a TOF facility, shows the maximum at flight time which corresponds to an energy of $E = (5/2)kT$. So a room temperature water moderated neutron source with a thermal peak of 25 meV has a peak in a time-of-flight spectrum at 63 meV.

5.5 Surrogate Reactions

A different approach to study neutron-induced reactions in some cases is to use surrogate reactions. This technique, developed by Cramer and Britt (1970) uses light charged particles, typically, but not only deuterons, tritons, ^3He or α particles, to form a compound nucleus by a few-nucleon transfer reaction. The target nucleus and charged particle is selected in such a way that the same compound nucleus is formed as in the neutron-induced reaction. In this way, the decay of the compound nucleus for a particular decay channel can be measured. The formation of the compound nucleus for the neutron-induced reaction has to be calculated using optical model calculations. The reactions are usually described using Hauser–Feshbach calculations, which in some energy ranges can be done in the Weisskopf–Ewing approximation where spin and orbital angular momentum are ignored (Weisskopf and Ewing 1940; Ait-Tahar and Hodgson 1987).

Table 3

Neutron density and flux distributions for Maxwell–Boltzmann distributed neutrons at temperature T , as a function of velocity v , energy E , wavelength λ , and time-of-flight t

Distribution	Most probable value	Equivalent in E_T	Mean value
$n_v(v) = \frac{4}{\sqrt{\pi}} \frac{v^2}{v_T^3} e^{-\frac{v^2}{v_T^2}}$	$v_{\max} = v_T$	E_T	$\langle v \rangle = \frac{2}{\sqrt{\pi}} v_T$
$n_E(E) = \frac{2}{\sqrt{\pi}} \sqrt{\frac{E}{E_T^3}} e^{-\frac{E}{E_T}}$	$E_{\max} = \frac{1}{2} E_T$	$\frac{1}{2} E_T$	$\langle E \rangle = \frac{3}{2} E_T$
$n_t(t) = \frac{4}{\sqrt{\pi}} \frac{t_T^3}{t^4} e^{-\frac{t_T^2}{t^2}}$	$t_{\max} = \frac{1}{\sqrt{2}} t_T$	E_T	$\langle t \rangle = \frac{2}{\sqrt{\pi}} t_T$
$n_\lambda(\lambda) = \frac{4}{\sqrt{\pi}} \frac{\lambda_T^3}{\lambda^4} e^{-\frac{\lambda_T^2}{\lambda^2}}$	$\lambda_{\max} = \frac{1}{\sqrt{2}} \lambda_T$	E_T	$\langle \lambda \rangle = \frac{2}{\sqrt{\pi}} \lambda_T$
$\varphi_v(v) = 2 \frac{v^3}{v_T^4} e^{-\frac{v^2}{v_T^2}}$	$v_{\max} = \sqrt{\frac{3}{2}} v_T$	$\frac{3}{2} E_T$	$\langle \varphi_v \rangle = \sqrt{\frac{3}{2}} v_T$
$\varphi_E(E) = \frac{E}{E_T^2} e^{-\frac{E}{E_T}}$	$E_{\max} = E_T$	E_T	$\langle \varphi_E \rangle = 2 E_T$
$\varphi_t(t) = 2 \frac{t_T^4}{t^5} e^{-\frac{t_T^2}{t^2}}$	$t_{\max} = \sqrt{\frac{2}{5}} t_T$	$\frac{5}{2} E_T$	$\langle \varphi_t \rangle = \frac{\sqrt{\pi}}{2} t_T$
$\varphi_\lambda(\lambda) = 2 \frac{\lambda_T^4}{\lambda^5} e^{-\frac{\lambda_T^2}{\lambda^2}}$	$\lambda_{\max} = \sqrt{\frac{2}{5}} \lambda_T$	$\frac{5}{2} E_T$	$\langle \varphi_\lambda \rangle = \frac{\sqrt{\pi}}{2} \lambda_T$

The method has gained renewed interest by several recent measurements, especially for fission and capture reactions. In [Table 4](#) a few examples of surrogate reactions and their equivalent neutron-induced reaction, are given.

Because of the different involved spins and orbital momenta, in some cases a different spin-parity distribution may influence the decay probabilities if the same compound nucleus has been formed by a neutron or by a charged particle. This effect can often be neglected (Younes and Britt 2003; Escher and Dietrich 2006). More details and references may be found in refs (Petit et al. 2004; Plettner et al. 2005; Boyer et al. 2006; Lyles et al. 2007; Hatarik et al. 2009).

In [Fig. 48](#) the surrogate reaction $^{232}\text{Th}(^3\text{He},\text{p})^{234}\text{Pa}^*$ is shown. From the measured gamma decay the $^{233}\text{Pa}(n,\gamma)$ cross section is derived and compared to evaluated data (Boyer et al. 2006).

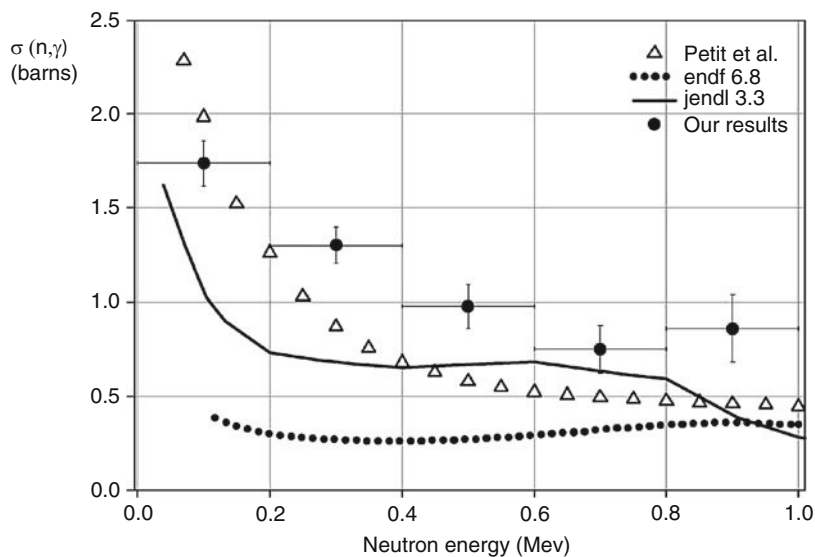
The surrogate ratio $^{234}\text{U}(\alpha,\alpha'f)/^{236}\text{U}(\alpha,\alpha'f)$ is shown in [Fig. 49](#). These reactions are well above their thresholds and are in a range where the Weisskopf-Ewing approximation to a Hauser-Feshbach calculation is expected to represent the reactions rather well.

The comparison of the known $^{235}\text{U}(n,\gamma)$ and (n,f) cross section ratio as evaluated in ENDF/B-VII to that measured in the surrogate reactions $^{235}\text{U}(d,\text{p}\gamma)$ and $^{235}\text{U}(d,\text{p fission})$

■ Table 4

Some examples of surrogate reactions for actinides and their equivalent neutron induced reaction, where the asterisk denotes a compound nucleus

Neutron induced reaction	Surrogate reaction
$^{235}\text{U} + n \rightarrow ^{236}\text{U}^*$	$^{234}\text{U}(t,p)^{236}\text{U}^*$
$^{235}\text{U} + n \rightarrow ^{236}\text{U}^*$	$^{235}\text{U}(d,p\gamma)^{236}\text{U}^*$
$^{235}\text{U} + n \rightarrow ^{236}\text{U}^*$	$^{236}\text{U}(\alpha,\alpha')^{236}\text{U}^*$
$^{233}\text{Pa} + n \rightarrow ^{234}\text{Pa}^*$	$^{232}\text{Th}(^3\text{He},p)^{234}\text{Pa}^*$
$^{241}\text{Am} + n \rightarrow ^{242}\text{Am}^*$	$^{243}\text{Am}(^3\text{He},\alpha)^{242}\text{Am}^*$
$^{243}\text{Cm} + n \rightarrow ^{244}\text{Cm}^*$	$^{243}\text{Am}(^3\text{He},d)^{244}\text{Cm}^*$

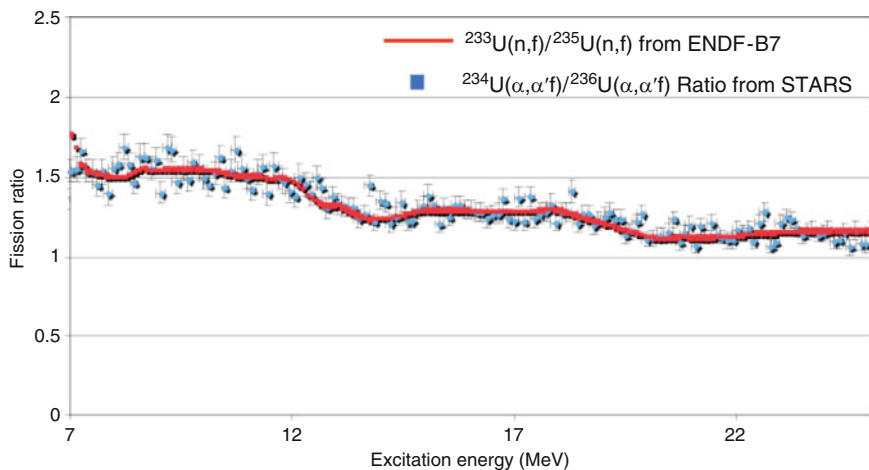


■ Figure 48

The $^{233}\text{Pa}(n,\gamma)$ cross section measured with the surrogate reaction $^{232}\text{Th}(^3\text{He},p)^{234}\text{Pa}^*$ (Data are from Boyer et al. 2006)

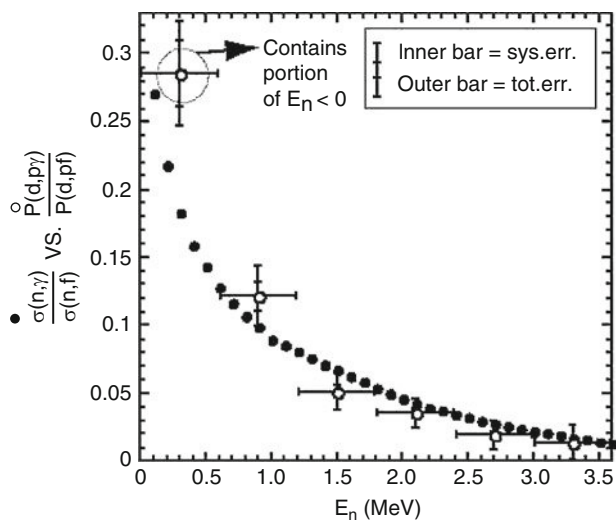
(Allmond et al. 2009) is shown in [Fig. 50](#). This comparison shows the data obtained in surrogate reactions at equivalent low incident neutron energies.

In [Fig. 51](#) the $^{236}\text{U}(n,f)$ cross section as determined by the surrogate ratio method is compared with values from the ENDF/B-VII evaluated data (Lyles et al. 2007). This comparison shows that the surrogate method does well for fission cross sections a few MeV above threshold.



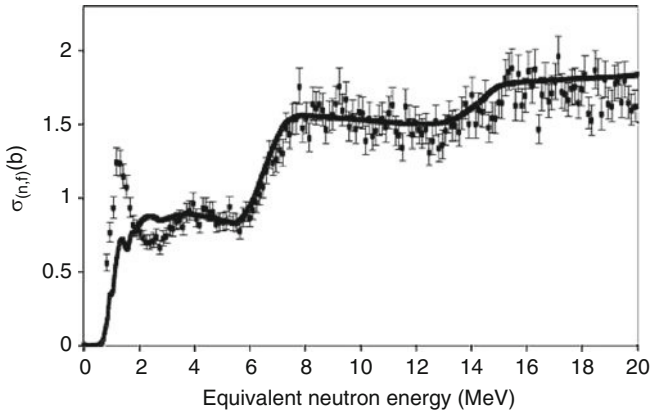
■ Figure 49

Results of the surrogate ratio $^{234}\text{U}(\alpha,\alpha'f)/^{236}\text{U}(\alpha,\alpha'f)$ compared to the ENDF-BVII ratio of $^{233}\text{U}(n,f)/^{235}\text{U}(n,f)$ (Burke et al. 2008)



■ Figure 50

Comparison of the known $^{235}\text{U}(n,\gamma)$ and (n,f) cross section ratio as evaluated in ENDF/B-VII to that measured in the surrogate reactions, $^{235}\text{U}(d,p\gamma)$ and $^{235}\text{U}(d,p$ fission) (Allmond et al. 2009)



■ Figure 51

The $^{236}\text{U}(n,f)$ cross section as determined by the surrogate ratio method (Lyles et al. 2007) is compared with values from the ENDF/B-VII evaluated data

5.6 Cross Section Standards

Many cross sections are measured relative to well understood, well measured, “standard” cross sections (Carlson et al. 2009). If the standard is measured along with the reaction of interest, then there is no need to measure the neutron flux. The particular reactions that are considered standards have been agreed to internationally and the standards data are maintained by the Nuclear Data Section of the International Atomic Energy (<http://www.nds.org/standards/>). Standards data include scattering, capture, and fission cross sections. In addition, for activation, there is the International Reactor Dosimetry File with recommended cross sections (not officially “standards”) (http://www-pub.iaea.org/MTCD/publications/TRS452_web.pdf).

6 Nuclear Resonances and the *R*-Matrix Formalism

6.1 Introduction

If the wave functions of the nuclear system before and after the reaction were known, one could calculate the cross section with the usual concepts of reaction theory. While the incoming waves are known, the reaction modifies the outgoing wave functions in a generally unknown way.

The idea behind the *R*-matrix formalism is to use the wave function of the nuclear system of two particles when they are so close that they form a compound nucleus. Although the wave function of the compound nucleus is extremely complicated, one can expand it in its eigenstates. Matching, then, the incoming and outgoing waves to the internal wave function provides a way to describe the cross section of the reaction in terms of the properties of the eigenstates of the compound nucleus. These properties are basically the energy, spin, parity, and a set of partial widths related to the widths of the decay modes of the compound nucleus.

This method of describing a reaction cross section using only the properties of nuclear excitation levels, is at the same time also the most important limitation. No information of the forces inside the nucleus is needed or can be extracted. The nucleus is treated as a black box of which the properties of the eigenstates have to be measured in order to describe the cross sections.


The binary nuclear reactions proceeding from one system of two particles to another system of two particles can be described with the general R -matrix theory. Not only in neutron-induced reactions, but also in other cases, such a reaction goes often through the formation of a compound nucleus X^* .



The R -matrix formalism does not only apply to compound nucleus reactions. Both direct and indirect reactions can be described with it. The inclusion of the Coulomb interaction allows us to use it also for charged particle reactions. But the theory is applicable only in a general way for binary reactions, which is appropriate for neutron-induced reactions up to energies of several tens of MeV.

In a very general way, the cross section of a two-body nuclear reaction could be calculated if the nuclear wave functions were known. The wave functions could be calculated by solving the Schrödinger equation for the nuclear system. This requires that the nuclear potential is known. When the two particles are far away, the interaction can be considered absent for neutral particles or to be the Coulomb interaction for charged particles. In these cases it is indeed possible to calculate the wave functions.

When the two particles are so close to each other that a nuclear reaction takes place, the potential of the interaction is extremely complicated. For certain energy ranges and reactions this potential can still be approximated or calculated (Bauge et al. 2001) and the wave functions and cross sections can be calculated. In other cases however, and especially in the resolved resonance region, the complexity of the reacting system does not allow this.

The first step is to consider that the reaction process can be split up geometrically into two regions for each channel where a channel is the precise constellation of particles and their spins. If the separation is smaller than the channel radius a_c , all nucleons involved in the reaction are close to each other and form a compound nucleus. Although the wave function of the compound nucleus is extremely complicated, it can be expanded as a linear combination of its eigenstates without solving explicitly the Schrödinger equation of the system. In the external region, at distances larger than a_c , the potential is zero for neutral particles or is the Coulomb interaction for charged particles and the Schrödinger equation of the system can be solved. The properties of the eigenstates of the compound nucleus are included in the R -matrix. Equating the values and derivatives of the wave functions at the boundary of the internal and external region assures a smooth wave function and the cross sections can be calculated as is illustrated in  Fig. 52. The exact internal wave function is not needed, only the values and derivatives at the nuclear surface.

In the following we describe in more detail the R -matrix formalism which links the properties of the nuclear states to the cross sections. The cross section in the thermal energy region is also described by the R -matrix formalism. Reaction cross sections at thermal energy are the sum of the contributions of all nuclear states, that is, the resonances but also the bound states, sometimes referred to as “negative energy” resonances. Other reaction formalisms have been used in the past, like the K -matrix formalism (Payne and Schlessinger 1970) still in use for particle physics (Shyam and Scholten 2008), but for neutron-induced resonance reactions the

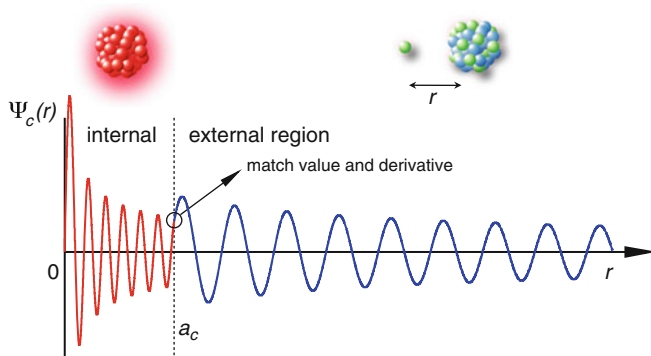


Figure 52

Schematic view of the wave function of a channel as a function of the separation distance r . The wave function in the internal region $r < a_c$ is an expansion of the eigenstates of the compound nucleus. The full internal ($r < a_c$) wave function is not needed, only the value and derivative at $r = a_c$ where it matches the known external ($r > a_c$) wave function which is related to the Bessel functions

R -matrix formalism, and in particular one of its approximations, is nowadays the preferred formalism.

The R -matrix formalism was first introduced by Wigner and Eisenbud (1947). A most extensive and detailed overview has been given by Lane and Thomas (1958) and by Lynn (1968). Recently Fröhner (2000) summarized the R -matrix formalism together with other useful considerations on nuclear data evaluation. Other related references of interest can be found elsewhere (Humblet and Rosenfeld 1961; Vogt 1962; Schmittroth and Tobocman 1971; Foderaro 1971; Adler 1972; Feshbach 1991; Luk'yanov and Yaneva 1997; Brune 2002). A brief outline of the formalism will be given in order to understand its basic principles.

6.1.1 Channel Representation

It is customary to use the concept of channels in the description of nuclear reactions, which will be limited to two particle reactions in the following. The entrance channel c consists of a particular initial constellation of particles and all the quantum numbers necessary to describe the corresponding partial wave function. The type of the two particles α_1 and α_2 , with their spins I_{α_1} and I_{α_2} , and their states of internal excitation are denoted by α . Four quantum numbers are needed to include the spins of the particles in a channel. The most appropriate combination is the orbital angular momentum ℓ , the channel spin j , which is the combined spin of the two particles

$$\mathbf{j} = \mathbf{I}_{\alpha_1} + \mathbf{I}_{\alpha_2}, \quad (40)$$

the total angular momentum J

$$\mathbf{J} = \mathbf{j} + \boldsymbol{\ell} \quad (41)$$

and its projection on the z -axis m_j . So the entrance channel c can be designated by the set

$$c = \{\alpha, \ell, j, J, m_j\} \quad (42)$$

Similarly, the exit channel is given by

$$c' = \{\alpha', \ell', j', J', m_j'\} \quad (43)$$

The reaction $\alpha \rightarrow \alpha'$ may go through the formation of a compound nucleus, like often the case with neutron-induced reactions. The reaction can then be written as $\alpha \rightarrow A^* \rightarrow \alpha'$. The spin and parity are of course conserved in all stages of the reaction and the compound nucleus has its defined spin J and parity π . The conservation of spin and parity puts restrictions on the entrance channels that are open to form the compound nucleus or the exit channels open for the decay of the compound nucleus. For neutrons and protons the intrinsic spin is $1/2$ and the intrinsic parity is positive. Conservation of angular momentum gives the vector addition:

$$\mathbf{J} = \mathbf{I}_{\alpha_1} + \mathbf{I}_{\alpha_2} + \boldsymbol{\ell} = \mathbf{I}_{\alpha'_1} + \mathbf{I}_{\alpha'_2} + \boldsymbol{\ell}' \quad (44)$$

and conservation of parity gives, using $+1$ for positive and -1 for negative parity:

$$\pi = \pi_{I_{\alpha_1}} \times \pi_{I_{\alpha_2}} \times (-1)^\ell = \pi_{I_{\alpha'_1}} \times \pi_{I_{\alpha'_2}} \times (-1)^{\ell'} \quad (45)$$

The conservation of angular momentum has important consequences for cross section calculations based on channels. The total number of possible combinations to sum the spins and orbital momentum is $(2I_{\alpha_1} + 1)(2I_{\alpha_2} + 1)(2\ell + 1)$. Only $2J + 1$ orientations of them add up to J . For this reason in expressions for cross sections of the formation of a compound nucleus level with spin J for a given ℓ the statistical factor $g(J)$

$$g(J) = \frac{2J + 1}{(2I_{\alpha_1} + 1)(2I_{\alpha_2} + 1)} \quad (46)$$

is taken into account.

The boundary $r = a_c$ is the limit between the internal region, where all the nucleons interact, and the external region where the incident and target particles do not have a nuclear interaction, other than possibly a Coulomb interaction. Although there is no sharp limit, in practice the channel radius a_c can be taken just slightly larger than the radius $R' = R_0 A^{1/3}$ of a spherical nuclear volume with $A = A_{\alpha_1} + A_{\alpha_2}$ nucleons, and where for R_0 usually the value 1.35 fm is used. This scattering radius can be used as a first approximation of the low-energy potential scattering cross section σ_{pot} with the relation

$$\sigma_{\text{pot}} = 4\pi R'^2 \quad (47)$$

Experimental values of R' show larger structures around the smooth curve $R' = R_0 A^{1/3}$, which can be well described with optical model calculations. In evaluated nuclear libraries, the channel radius a_c can be defined to have either the numerical value of a possibly energy-dependent scattering radius R' , or an energy-independent, mass-dependent channel radius given by

$$a_c = 0.8 + 1.23A^{1/3} \text{ fm} \quad (48)$$

where A' is the ratio of the isotope mass to the mass of the neutron. The channel is defined in the center of mass and the reduced mass of the particles is

$$m_c = m_\alpha = \frac{m_{\alpha_1} m_{\alpha_2}}{m_{\alpha_1} + m_{\alpha_2}} \quad (49)$$

and the wave number k , related to the de Broglie wavelength λ , is

$$k_c = k_\alpha = \frac{1}{\lambda_c} = \sqrt{\frac{2m_\alpha E_\alpha}{\hbar^2}} \quad (50)$$

and the relative velocity is

$$v_c = v_\alpha = \hbar k_c / m_c \quad (51)$$

The dimensionless distance ρ_c is used to indicate the distance r_c in measures of de Broglie wavelengths.

$$\rho_c = \rho_\alpha = k_c r_c \quad (52)$$

6.1.2 The Wave Function in the External Region

The system of the two particles interacting through a central potential $V(r)$ can be described by the Schrödinger equation of the motion of the reduced mass particle. Also, using spherical coordinates, the solution $\psi(r, \theta, \phi)$ can, in case of a central potential, be separated in a radial and an angular part

$$\psi(r, \theta, \phi) = R(r)\Theta(\theta)\Phi(\phi) \quad (53)$$

The radial part $R(r)$ although still depends on the nonnegative integer solutions $\ell(\ell + 1)$ of $\Theta(\theta)$. The integers appearing in the solution of $\Phi(\phi)$ are $m_\ell = 0, \pm 1, \pm 2, \dots, \pm \ell$. The solutions of the angular part $\Theta(\theta)\Phi(\phi)$ do not depend on the central potential and are the spherical harmonics $Y_{m_\ell}^\ell(\theta, \phi)$. Only the solution $R(r)$ of the radial part depends on the potential $V(r)$. The radial Schrödinger equation

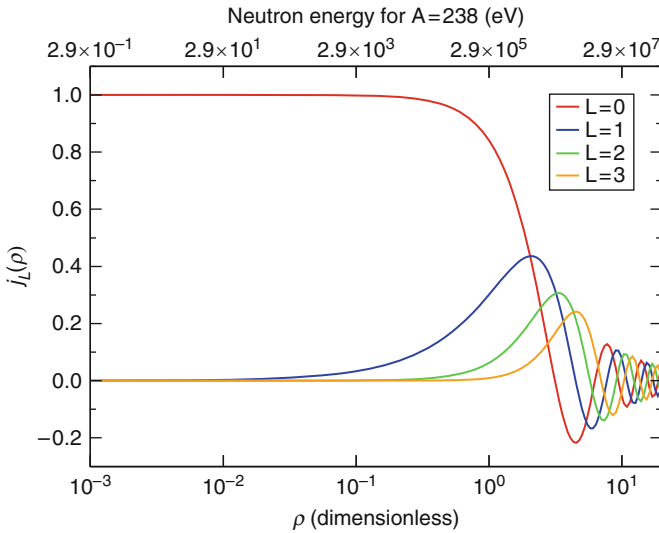
$$\left[\frac{d^2}{dr^2} - \frac{\ell(\ell + 1)}{r^2} - \frac{2m_c}{\hbar^2} (V(r) - E) \right] R(r) = 0 \quad (54)$$

can be solved for the case of the Coulomb potential $V(r) = -Z_{\alpha_1} Z_{\alpha_2} e^2 / (4\pi\epsilon_0 r)$. The general solution is a linear combination of regular and irregular Coulomb wave functions. In the special case that $V(r) = 0$, such as for neutrons, (54), after a rearrangement in dimensionless form, is called the spherical Bessel equation. The solution consists of a linear combination of spherical Bessel functions of the first type $j_\ell(\rho)$, and of the second type $n_\ell(\rho)$ (or Neumann functions). Two linearly independent complex combinations of j_ℓ and n_ℓ are known as spherical Bessel functions of the third type (or Hankel functions) $h_\ell^+(\rho)$ and $h_\ell^-(\rho)$ (Abramowitz 1965; Zwillinger 2003). These are functions of the dimensionless parameter $\rho = kr$. Although $n_\ell(\rho) \rightarrow -\infty$ for $r \rightarrow 0$, this irregular solution should be included because we only need this

■ Table 5

The spherical Bessel functions and the incoming and outgoing waves from equations (55) and (56). Derived quantities are given in ► Table 6

ℓ	j_ℓ	n_ℓ	$O_\ell = I_\ell^*$
0	$\frac{\sin \rho}{\rho}$	$-\frac{\cos \rho}{\rho}$	$e^{i\rho}$
1	$\frac{\sin \rho}{\rho^2} - \frac{\cos \rho}{\rho}$	$-\frac{\cos \rho}{\rho^2} - \frac{\sin \rho}{\rho}$	$e^{i\rho} \left(\frac{1}{\rho} - i \right)$
ℓ	$(-1)^\ell \rho^\ell \left(\frac{1}{\rho} \frac{d}{d\rho} \right)^\ell \frac{\sin \rho}{\rho}$	$-(-1)^\ell \rho^\ell \left(\frac{1}{\rho} \frac{d}{d\rho} \right)^\ell \frac{\cos \rho}{\rho}$	



■ Figure 53

The Bessel function $j_\ell(\rho)$ for $\ell = 0, 1, 2, 3$ is shown as a function of ρ and as a function of equivalent energy for a nucleus with mass $A = 238$

solution in the external region $r > a_c$. The appropriate solution for a channel c is a linear combination of waves corresponding to incoming $I_c(r)$ and outgoing $O_c(r)$ waves for a free particle, $R(r) = R_\ell(r) = y_\ell I_\ell(r) + x_\ell O_\ell(r)$, with

$$I_c(r) = I_\ell(r) = -iph_\ell^-(\rho) = -i\rho(j_\ell(\rho) - in_\ell(\rho)) \quad (55)$$

and

$$O_c(r) = O_\ell(r) = -iph_\ell^+(\rho) = i\rho(j_\ell(\rho) + in_\ell(\rho)) \quad (56)$$

The functions $j_\ell(\rho)$ and $n_\ell(\rho)$ together with $O_\ell(\rho)$ are given in ► Table 5. In ► Fig. 53 the function $j_\ell(\rho)$ is shown as a function of ρ and as a function of equivalent energy for a nucleus with mass $A = 238$.

6.1.3 The Collision Matrix U

The total wave function Ψ in the external region can be expressed as the superposition of all incoming and outgoing partial waves \mathcal{I}_c and \mathcal{O}_c , with amplitudes y_c and x_c , and summed over all possible channels c .

$$\Psi = \sum_c y_c \mathcal{I}_c + \sum_{c'} x_{c'} \mathcal{O}_{c'} \quad (57)$$

The complete wave functions in the channel, \mathcal{I}_c and \mathcal{O}_c , contain the radial parts I_c and O_c , but also the angular part of relative motion $Y_{m_\ell}^\ell$, as well as the internal wave functions of the particles and the channel spin, combined in φ_c , and are written as

$$\mathcal{I}_c = I_c r^{-1} \varphi_c i^\ell Y_{m_\ell}^\ell(\theta, \phi) / \sqrt{v_c} \quad (58)$$

and

$$\mathcal{O}_c = O_c r^{-1} \varphi_c i^\ell Y_{m_\ell}^\ell(\theta, \phi) / \sqrt{v_c} \quad (59)$$

The factor $1/\sqrt{v_c}$ normalizes the waves to unit flux. The physical process of the reaction will result in a modification of the outgoing waves. In the reaction, the coefficients x_c of the outgoing waves, depending on the details of the reaction which are observable in the cross section, have to be determined with respect to the coefficients of the incoming waves y_c . The collision matrix $U_{cc'}$ is now defined as the relation between the coefficients of the incoming and outgoing waves:

$$x_{c'} \equiv - \sum_c U_{c'c} y_c \quad (60)$$

All the physics of the reaction is contained in the elements of the collision matrix. The collision matrix has two important properties. From the conservation of probability flux in the reaction it follows that the collision matrix is unitary, which means that its complex conjugate equals its reciprocal, $\mathbf{U}^* = \mathbf{U}^{-1}$ or

$$\sum_c U_{cc'}^* U_{cc''} = \delta_{c'c''} \quad (61)$$

The second property follows from time reversal conservation and implies that the collision matrix is symmetric, $U_{cc'} = U_{c'c}$.

Finally, we can express the total wave function of (57) in terms of the collision matrix:

$$\Psi = \sum_c y_c \left(\mathcal{I}_c - \sum_{c'} U_{cc'} \mathcal{O}_{c'} \right) \quad (62)$$

which is a linear combination of the wave functions for each channel c , consisting of an ingoing wave and the modified outgoing waves summed over all channels c' .

6.1.4 The Relation Between the Cross Sections and the Collision Matrix U

The relation between reaction cross sections and wave functions, describing a probability, is based on the conservation of probability density. The probability density of an incident plain

wave, which is the flux of particles \mathbf{j}_φ is given by the quantum mechanical expression

$$\mathbf{j}_\varphi = \frac{\hbar}{2mi} (\psi^* \nabla \psi - \psi \nabla \psi^*) \quad (63)$$

The connection with the cross section is best illustrated by considering a flux of incident particles j_{inc} , represented by a plain wave ψ_{inc} , which can be expanded in a series of partial radial waves, scattering elastically at a point $r = 0$ because of an unknown physical process. The scattered wave, originating at $r = 0$ is a radial wave ψ_{sc} and far from the scattering center at a distance r in a solid angle element $d\Omega$ the current of scattered particles across the surface $r^2 d\Omega$ is j_{sc} . The total wave $\psi = \psi_{\text{inc}} + \psi_{\text{sc}}$ is a solution of the Schrödinger equation for this system. The cross section of this reaction, which is a differential cross section, is defined as

$$d\sigma = \frac{j_{\text{sc}}}{j_{\text{inc}}} r^2 d\Omega \quad (64)$$

Integrating over $d\Omega$ gives the total scattering cross section. If elastic scattering were the only process to occur, the total current of ingoing particles equals that of the outgoing particles. Any reaction, defined as any other process than elastic scattering, means that there is a difference in the absolute values of the ingoing and outgoing current.

In the more general description of channels the total wave function is (62). Elastic scattering means here that the entrance and exit channel are the same. A change of channel in the outgoing wave is considered as a reaction. With a similar approach, including the expansion of the incoming plane wave into an infinite sum of partial waves ℓ , and using the full description of the channel wave functions, the angular differential cross section for the reaction $\alpha \rightarrow \alpha'$ has been worked out by Blatt and Biedenharn (1952). For zero Coulomb interaction the expression is

$$\frac{d\sigma}{d\Omega} = \frac{1}{2j+1} \lambda^2 \sum_{\ell=0}^{\infty} B_\ell(c, c') P_\ell(\cos \theta) \quad (65)$$

The coefficients $B_\ell(c, c')$ are rather complicated factors and contain the collision matrix elements $U_{cc'}$ and relations containing Clebsch–Gordan coefficients for the spin bookkeeping, eliminating most of the terms in the infinite sum over ℓ .

The cross section for an interaction from channel c to channel c' is then

$$\sigma_{cc'} = \pi \lambda_c^2 |\delta_{c'c} - U_{c'c}|^2 \quad (66)$$

If the interaction occurs without a change in the channel c then the process is called elastic scattering. The cross section is, putting $c' = c$

$$\sigma_{cc} = \pi \lambda_c^2 |1 - U_{cc}|^2 \quad (67)$$

and the cross section for a channel reaction, i.e. any interaction which is not elastic scattering, is obtained by summing (66) over all c' except c

$$\sigma_{cr} = \pi \lambda_c^2 (1 - |U_{cc}|^2) \quad (68)$$

and the total cross section is obtained by summing all channels c'

$$\sigma_{c,T} = \sigma_c = 2\pi \lambda_c^2 (1 - \text{Re } U_{cc}) \quad (69)$$

In practice, channel to channel cross sections are not useful. One would like to have the cross sections of $\alpha \rightarrow \alpha'$ for the component of total angular momentum J . The total reaction cross section is obtained by integrating (65) over the full solid angle to obtain the total cross section for the component of total angular momentum J

$$\sigma_{\alpha\alpha'}(J) = \pi\lambda_\alpha^2 g(J) \sum_{j,j',\ell,\ell'} |\delta_{jj'\ell\ell'} - U_{j\ell,j'\ell'}|^2 \quad (70)$$

and the total cross section by summing over all α'

$$\sigma_{\alpha,T}(J) = 2\pi\lambda_\alpha^2 g(J) \sum_{j,\ell} (1 - \text{Re } U_{j\ell,j\ell}) \quad (71)$$

6.1.5 The Wave Function in the Internal Region

The complete wave function Ψ can be described as the product of the function of relative motion and the channel-spin function, giving the internal states of the particles α_1 and α_2 and their combined spin. From the function of relative motion the radial part $R(r)$ is separated and the remaining part is combined with the channel-spin function to give the channel surface function φ_c

$$\Psi = \sum_c \varphi_c R_c(a_c). \quad (72)$$

The surface functions φ_c have the property of orthonormality over the surface S_c given by $r = a_c$. This will be exploited to expand certain quantities in terms of surface functions. It follows immediately that

$$R_c(a_c) = \int \varphi_c^* \Psi dS_c. \quad (73)$$

The integration over a surface, instead of integrating over a volume, is particularly useful in deriving the R -matrix relation using Green's theorem, expressing a volume integral in a surface integral.

At the channel surface $r = a_c$ the radial wave function for the internal and external region should match. The value V_c and derivative D_c are defined with a normalization constant as

$$\begin{aligned} V_c &= \sqrt{\frac{\hbar^2}{2m_c a_c}} u_c(a_c) \\ &= \sqrt{\frac{\hbar^2}{2m_c a_c}} \int \varphi_c^* \Psi dS_c \end{aligned} \quad (74)$$

and

$$\begin{aligned} D_c &= \sqrt{\frac{\hbar^2}{2m_c a_c}} a_c \left(\frac{du_c}{dr} \right)_{r=a_c} \\ &= \sqrt{\frac{\hbar^2}{2m_c a_c}} \int \varphi_c^* \nabla_n (r\Psi) dS_c \\ &= V_c + \sqrt{\frac{\hbar^2}{2m_c a_c}} a_c \int \varphi_c^* dS_c \end{aligned} \quad (75)$$

In the internal region the wave function cannot be calculated readily by solving the Schrödinger equation since the nuclear potential is in general very complicated and the nucleus has many interacting nucleons. But the wave function can be expressed as an expansion in eigenfunctions X_λ and eigenvalues E_λ

$$\Psi = \sum_{\lambda} A_{\lambda} X_{\lambda} \quad (76)$$

and the coefficients A_λ can be expressed as

$$A_{\lambda} = \int X_{\lambda}^* \Psi d\tau \quad (77)$$

where the integration goes over the volume $d\tau$ of the internal region given by $r < a_c$.

The values and derivatives on the surface $r = a_c$ are defined, analog to (74) and (75), as

$$\gamma_{\lambda c} = \sqrt{\frac{\hbar^2}{2m_c a_c}} \int \varphi_c^* X_{\lambda} dS_c \quad (78)$$

and

$$\delta_{\lambda c} = \gamma_{\lambda c} + \sqrt{\frac{\hbar^2}{2m_c a_c}} a_c \int \varphi_c^* \nabla_n(X_{\lambda}) dS_c. \quad (79)$$

The boundary conditions to be satisfied on the channel surface are taken identical for all λ

$$B_c = \delta_{\lambda c} / \gamma_{\lambda c}. \quad (80)$$

Applying Green's theorem to (77) gives

$$\begin{aligned} A_{\lambda} &= \int X_{\lambda}^* \Psi d\tau \\ &= (E_{\lambda} - E)^{-1} \frac{\hbar^2}{2m_c} \int (X_{\lambda}^* \nabla_n(\Psi) - \Psi \nabla_n(X_{\lambda}^*)) dS_c \\ &= (E_{\lambda} - E)^{-1} \sum_c (D_c - B_c V_c) \gamma_{\lambda c} \end{aligned} \quad (81)$$

using (74), (75), (78), (79), and (80). The expression (76) for the wavefunction can now be written as

$$\Psi = \sum_c \left[\sum_{\lambda} \frac{X_{\lambda} \gamma_{\lambda c}}{E_{\lambda} - E} \right] (D_c - B_c V_c). \quad (82)$$

By multiplying each side of (82) by $\varphi_{c'}$, integrating over the surface $r = a_c$ and using (78) one obtains

$$V_{c'} = \sum_c R_{cc'} (D_c - B_c V_c) \quad (83)$$

with

$$R_{cc'} = \sum_{\lambda} \frac{\gamma_{\lambda c} \gamma_{\lambda c'}}{E_{\lambda} - E}. \quad (84)$$

The quantity $R_{cc'}$ is the R -matrix and contains the properties E_{λ} and $\gamma_{\lambda c}$ of the eigenstates λ . The boundary constant B_c can be chosen freely.

6.1.6 The Relation Between the R -Matrix and the Collision Matrix \mathbf{U}

The values and derivatives of the internal wave function are given by the R -matrix relation (83). The external wave function is given by (62) and is known except for the boundary conditions. The boundary condition is that both the internal and external wave functions have the same value and radial derivative at $r = a_c$ in order to have a smooth transition. By matching these conditions and after considerable rearrangements, the collision matrix $U_{cc'}$ can be given explicitly as a function of the R -matrix in matrix notation by

$$\mathbf{U} = \Omega \mathbf{P}^{1/2} [1 - \mathbf{R}(\mathbf{L} - \mathbf{B})]^{-1} [1 - \mathbf{R}(\mathbf{L}^* - \mathbf{B})] \mathbf{P}^{-1/2} \Omega. \quad (85)$$

The introduced complex matrix \mathbf{L} is given by

$$L_c = S_c + iP_c = \left(\frac{\rho}{O_c} \frac{dO_c}{d\rho} \right)_{r=a_c} \quad (86)$$

where real matrices S_c is called the shift factor and P_c the penetrability factor. The matrix Ω_c is

$$\Omega_c = \left(\frac{I_c}{O_c} \right)_{r=a_c} \quad (87)$$

which can be reduced for neutral particles, using (55) and (56), to

$$\Omega_c = \exp(-i\phi_c) \quad (88)$$

from which ϕ_c follows

$$\phi_c = \arg O_c(a_c) = \arctan \left(\frac{\text{Im } O_c}{\text{Re } O_c} \right) = \arctan \left(-\frac{j_\ell(\rho)}{n_\ell(\rho)} \right) \quad (89)$$

All matrices in (85) are diagonal matrices except \mathbf{U} and \mathbf{R} . A table of P_ℓ , S_ℓ , and ϕ_ℓ is given in [Table 6](#). They are directly related to the solution of the Schrödinger equation in the external region, which are the spherical Bessel and Neumann functions $j_\ell(\rho)$ and $n_\ell(\rho)$ for neutral particles, and can be derived from the quantities listed in [Table 5](#).

Table 6

The penetrability P_ℓ , the level shift S_ℓ and the hard-sphere phase shift ϕ_ℓ for reaction channels without Coulomb interaction, as a function of $\rho = ka_c$. These parameters are derived from the quantities in [Table 5](#)

ℓ	P_ℓ	S_ℓ	ϕ_ℓ
0	ρ	0	ρ
1	$\rho^3/(1 + \rho^2)$	$-1/(1 + \rho^2)$	$\rho - \arctan \rho$
ℓ	$\frac{\rho^2 P_{\ell-1}}{(\ell - S_{\ell-1})^2 + P_{\ell-1}^2}$	$\frac{\rho^2 (\ell - S_{\ell-1})}{(\ell - S_{\ell-1})^2 + P_{\ell-1}^2} - \ell$	$\phi_{\ell-1} - \arctan \frac{P_{\ell-1}}{\ell - S_{\ell-1}}$

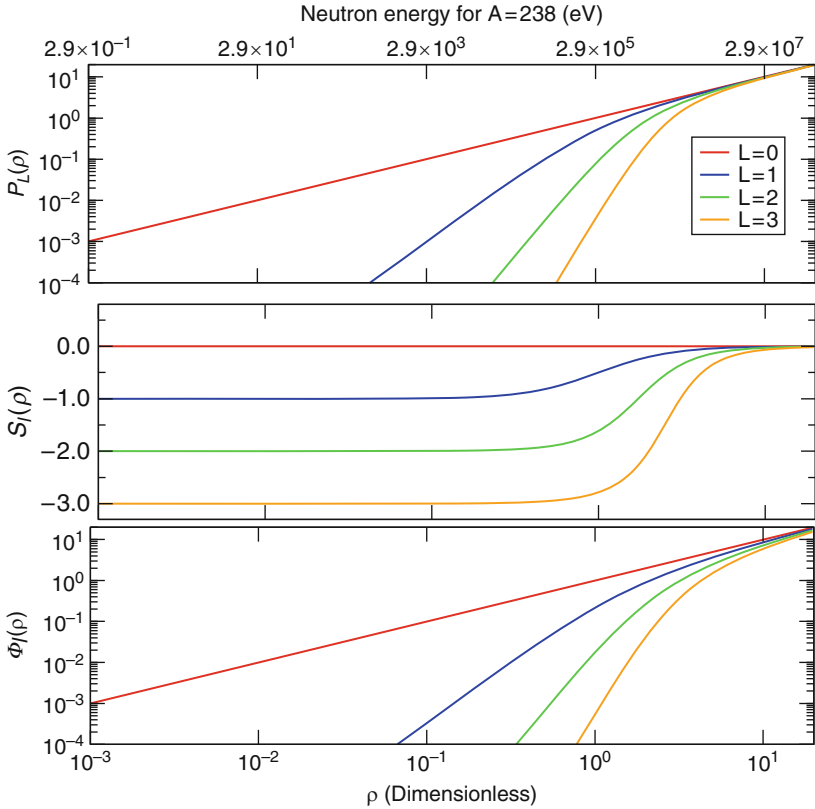


Figure 54

The functions $P_\ell(\rho)$, $S_\ell(\rho)$, and $\phi_\ell(\rho)$ for $\ell = 0, 1, 2, 3$ shown as a function of ρ and as a function of equivalent energy for a nucleus with mass $A = 238$

If the boundary conditions B_c , defined by (80), are real, then the $\delta_{\lambda c}$ and the $\gamma_{\lambda c}$ are real and hence \mathbf{R} is real. In addition \mathbf{R} is symmetrical. A common choice is to take

$$B_c = S_c \quad (90)$$

which eliminates the shift factor for s -waves, but introduces an energy dependence. The choice $B_c = -\ell$ has also been proposed (Fröhner 2000). At low energy this is equivalent as can be seen in Fig. 54, where P_ℓ , S_ℓ and ϕ_ℓ are plotted as a function of ρ and as a function of equivalent energy for a nucleus with mass $A = 238$.

So (85) defines the collision matrix in terms of the parameters of the R -matrix, $\gamma_{\lambda c}$ and E_λ , representing the physical process of the reaction, and the quantities P_c , S_c , ϕ_c , describing the known incoming and outgoing waves I_c and O_c , outside a sphere with radius a_c . The values B_c determine the boundary conditions at the matching point of the internal and external region, and are free to be chosen. The unknowns of the R -matrix, $\gamma_{\lambda c}$ and E_λ , need to be determined in order to know the U -matrix and subsequently the cross sections.

6.2 Approximations of the R -Matrix

Several approximations of the R -matrix have been developed in the past in order to overcome the complications of inverting the matrix

$$[1 - \mathbf{R}(\mathbf{L} - \mathbf{B})]^{-1}$$

appearing in (85). Except in the case where only one or two channels are involved, the inversion is in general impossible without additional assumptions. The problem can be put in terms of the inversion of a level matrix \mathbf{A} of which the elements refer to the properties of the levels λ of the system. The problem of inverting a matrix concerning all channels is now put in a problem of inverting a matrix concerning levels.

The level matrix $A_{\lambda\mu}$ is introduced by putting the following form

$$([1 - \mathbf{R}(\mathbf{L} - \mathbf{B})]^{-1})_{cc'} = \delta_{cc'} + \sum_{\lambda\mu} \gamma_{\lambda c} \gamma_{\mu c'} (L_{c'} - B_{c'}) A_{\lambda\mu} \quad (91)$$

from which the elements of the inverse of \mathbf{A} are

$$\begin{aligned} (\mathbf{A}^{-1})_{\lambda\mu} &= (E_\lambda - E) \delta_{\lambda\mu} - \sum_c \gamma_{\lambda c} \gamma_{\mu c} (L_c - B_c) \\ &= (E_\lambda - E) \delta_{\lambda\mu} - \Delta_{\lambda\mu} - \frac{1}{2} i \Gamma_{\lambda\mu} \end{aligned} \quad (92)$$

with the quantities $\Delta_{\lambda\mu}$ and $\Gamma_{\lambda\mu}$ defined by

$$\Delta_{\lambda\mu} = \sum_c (S_c - B_c) \gamma_{\lambda c} \gamma_{\mu c} \quad (93)$$

and

$$\Gamma_{\lambda\mu} = 2 \sum_c P_c \gamma_{\lambda c} \gamma_{\mu c} \quad (94)$$

Now the collision matrix from (85) can be expressed in terms of \mathbf{A}

$$U_{cc'} = \Omega_c \Omega_{c'} \left(\delta_{cc'} + 2i \sqrt{P_c P_{c'}} \sum_{\lambda\mu} A_{\lambda\mu} \gamma_{\lambda c} \gamma_{\mu c'} \right) \quad (95)$$

Additional approximations have been formulated in order to simplify this expression. The most illustrative is the Breit and Wigner single level (SLBW) approximation where only one level is considered. It can be extended to several, independent levels, which is the Breit and Wigner multi level (MLBW) approximation. The formalism of Reich and Moore (1958) neglects only the off-diagonal contributions of the photon channels, which is an accurate approximation for medium and heavy nuclei. It takes into account the interference between levels and reduces to the SLBW approximation in the limit of a single level. These three formalisms will be described in some more detail. Other formalisms exist of which we mention here the formalisms of Kapur and Peierls (1938), Wigner and Eisenbud (1947), Adler (1972), Hwang (1973), and more recently Luk'yanov and Yaneva (1997).

6.2.1 The Breit–Wigner Single Level Approximation

The expression (92) can be simplified if only a single level is present. In that case the matrix contains only a single element. Therefore,

$$(\mathbf{A}^{-1})_{\lambda\mu} = A^{-1} = E_\lambda - E + \Delta_\lambda - i\Gamma_\lambda/2 \quad (96)$$

with

$$\Delta_\lambda = \Delta_{\lambda\lambda} = -\sum_c (S_c - B_c)\gamma_{\lambda c}^2 \quad (97)$$

and

$$\Gamma_\lambda = \Gamma_{\lambda\lambda} = \sum_c \Gamma_{\lambda c} = \sum_c 2P_c\gamma_{\lambda c}^2 \quad (98)$$

Substituting these expressions in (95) gives the collision matrix

$$U_{cc'} = e^{-i(\phi_c + \phi_{c'})} \left(\delta_{cc'} + \frac{i\sqrt{\Gamma_{\lambda c}\Gamma_{\lambda c'}}}{E_\lambda + \Delta_\lambda - E - i\Gamma_\lambda/2} \right) \quad (99)$$

From the collision matrix the cross sections can be calculated. For the total cross section this results in

$$\sigma_c = \pi\lambda_c^2 g_c \left(4 \sin^2 \phi_c + \frac{\Gamma_\lambda \Gamma_{\lambda c} \cos 2\phi_c + 2(E - E_\lambda - \Delta_\lambda) \Gamma_{\lambda c} \sin 2\phi_c}{(E - E_\lambda - \Delta_\lambda)^2 + \Gamma_\lambda^2/4} \right) \quad (100)$$

The first part of the total cross section is the potential scattering or hard sphere scattering cross section $\sigma_p = 4\pi\lambda_c^2 g_c \sin^2 \phi_c$. It is associated with the elastic scattering of the incoming neutron from the potential of the nucleus without forming a compound state. The term with the factor $\sin 2\phi_c$ is the interference of the potential scattering and the resonant elastic scattering through formation of a compound nucleus. Finally, the term with $\cos 2\phi_c$ describes the resonance cross sections of the channels.

In a more practical case, we can see what the cross sections becomes for a neutron entrance channel $c = n$. We assume that the only open channels are elastic scattering and neutron capture, $\Gamma_\lambda = \Gamma = \Gamma_n + \Gamma_\gamma$.

A series expansion of the trigonometric factors gives for $\ell = 0$ at low energy in good approximation $\sin \phi_c = \rho = ka_c$ and $\sin \phi_c = 0$ for $\ell > 0$. The cosine term can be approximated by $\cos \phi_c = 1$ for all ℓ .

In the same way, the reaction cross section is

$$\sigma_{cc'} = \pi\lambda_c^2 g_c \frac{\Gamma_{\lambda c}\Gamma_{\lambda c'}}{(E - E_\lambda - \Delta_\lambda)^2 + \Gamma_\lambda^2/4} \quad (101)$$

and the shift Δ_λ results from the boundary condition.

6.2.2 The Breit–Wigner Multi Level Approximation

Several resonances can be taken into account as a sum of Breit and Wigner single level cross sections. This is the most simple treatment of cross sections of many resonances. It neglects any possible interference between channels and levels (resonances).

The Breit and Wigner multi level (BWML) approach uses a sum over the levels in the collision matrix. In the inverse of the level matrix \mathbf{A} all off-diagonal elements $A_{\lambda}^{-1}\mu$ are neglected, which means neglecting all interference terms between channels, but not between levels.

$$(\mathbf{A}^{-1})_{\lambda\mu} = (E_{\lambda} - E + \Delta_{\lambda} - i\Gamma_{\lambda}/2)\delta_{\lambda\mu} \quad (102)$$

$$U_{cc'} = e^{-i(\phi_c + \phi_{c'})} \left(\delta_{cc'} + \sum_{\lambda} \frac{i\sqrt{\Gamma_{\lambda c}\Gamma_{\lambda c'}}}{E_{\lambda} + \Delta_{\lambda} - E - i\Gamma_{\lambda}/2} \right) \quad (103)$$

6.2.3 The Reich–Moore Approximation

In the approximation of Reich and Moore (1958) it is assumed that the amplitudes $\gamma_{\lambda c}$ are uncorrelated and have a Gaussian distribution with zero mean. This is a consequence of the chaotic behavior of the compound nucleus, except for the very light nuclei. This is known as the Gaussian orthogonal ensemble (Lynn 1968; Mehta 1960, 1991).

In medium and heavy nuclei, the number of photon channels is very large. And since the amplitudes are supposed to have a random distribution with zero mean, the expectation value of the product of two amplitudes is zero for $\lambda \neq \mu$, that is, $\langle \gamma_{\lambda c}\gamma_{\mu c} \rangle = \gamma_{\lambda c}^2\delta_{\lambda\mu}$. Summing over the photon channels gives

$$\sum_{c \in \text{photon}} \gamma_{\lambda c}\gamma_{\mu c} = \sum_{c \in \text{photon}} \gamma_{\lambda c}^2\delta_{\lambda\mu} = \Gamma_{\lambda\gamma}\delta_{\lambda\mu} \quad (104)$$

Therefore, the general expression for \mathbf{A}^{-1} , (92), can be simplified for the photon channels and becomes

$$\begin{aligned} (\mathbf{A}^{-1})_{\lambda\mu} &= (E_{\lambda} - E)\delta_{\lambda\mu} - \sum_{c \in \text{photon}} \gamma_{\lambda c}\gamma_{\mu c}(L_c - B_c) - \sum_{c \in \text{photon}} \gamma_{\lambda c}\gamma_{\mu c}(L_c - B_c) \\ &= (E_{\lambda} - E)\delta_{\lambda\mu} - \Gamma_{\lambda\gamma}(L_c - B_c)\delta_{\lambda\mu} - \sum_{c \in \text{photon}} \gamma_{\lambda c}\gamma_{\mu c}(L_c - B_c) \\ &= (E_{\lambda} - E + \Delta_{\lambda} - i\Gamma_{\lambda\gamma}/2)\delta_{\lambda\mu} - \sum_{c \in \text{photon}} \gamma_{\lambda c}\gamma_{\mu c}(L_c - B_c) \end{aligned} \quad (105)$$

Comparing this to (92), the approximation may be written as a reduced R -matrix in the sense that the photon channels are excluded and the eigenvalue E_{λ} is replaced by $E_{\lambda} - i\Gamma_{\lambda\gamma}/2$. This Reich–Moore R -matrix is

$$R_{cc'} = \sum_{\lambda} \frac{\gamma_{\lambda c}\gamma_{\lambda c'}}{E_{\lambda} - E - i\Gamma_{\lambda\gamma}/2} \quad c \notin \text{photon} \quad (106)$$

The number of energy levels, which may be over hundreds of thousands in heavy nuclei, determines the number of possible photon decay channels. Excluding them reduces largely the number of channels and, therefore, the matrix inversion needed in the relation between the R -matrix and the cross sections. In the often occurring case at low energy that only the elastic scattering and neutron capture channels are open, the number of channels in the R -matrix is one, namely, that of the neutron channel, the photon channels being excluded explicitly. The

total radiation width is present however in the denominator of (106). The R -matrix becomes in this case an R -function of which the inversion is trivial. Including other channels, like one or two fission channels, keeps the number of channels low and makes the inversion still feasible. This approximation of the general R -matrix is the most accurate one used.

6.3 Average Cross Sections

At higher energies the widths of the resonances overlap and the cross sections appear smooth and with a slow variation with energy. The total and scattering cross sections without sharply separated or observed resonances can be adequately described by representing the particle-nucleus interaction by a complex potential. This optical potential, so called because mathematically analogous to the scattering and absorption of light in a medium (cloudy crystal ball), results in the partial scattering or absorption of the beam. The solution of the Schrödinger equation, usually numerically, with a given potential gives the wave functions from which the cross sections can be obtained (Fernbach et al. 1949). Much progress has been made since in the theoretical development and parametrization of a suitable optical model potentials, see for example Camarda et al. (1989), Leeb and Wilmsen (2000), Bauge et al. (2001), Dietrich et al. (2003), Capote et al. (2005) and Quesada et al. (2007).

By making averages over resonances, the energy averaged collision matrix $\overline{U_{cc}}$ can be related to the energy-averaged cross sections $\overline{\sigma}$. The development of a given shape of the optical model potential results in a value for $\overline{U_{cc}}$. From the usual R -matrix expressions we can formulate a number of cross sections as follows. By analogy to (67) the average scattering cross section $\overline{\sigma_{cc}}$ can be written as

$$\overline{\sigma_{cc}} = \pi \lambda_c^2 g_c \overline{|1 - U_{cc}|^2} \quad (107)$$

which can be split up into an average shape elastic scattering cross section

$$\overline{\sigma_{cc}^{se}} = \pi \lambda_c^2 g_c \overline{|1 - \overline{U_{cc}}|^2} \quad (108)$$

associated with potential scattering, and an average compound elastic scattering cross section due to resonance scattering

$$\overline{\sigma_{cc}^{ce}} = \pi \lambda_c^2 g_c \left(\overline{|U_{cc}|^2} - |\overline{U_{cc}}|^2 \right) \quad (109)$$

and after (68) the average reaction cross section $\overline{\sigma_{cr}}$, corresponding to all nonelastic partial cross sections, as

$$\overline{\sigma_{cr}} = \pi \lambda_c^2 g_c (1 - |\overline{U_{cc}}|^2) \quad (110)$$

and following (69) the average total cross section $\overline{\sigma_{c,T}}$ can be written as

$$\overline{\sigma_{c,T}} = 2\pi \lambda_c^2 g_c (1 - \text{Re } \overline{U_{cc}}). \quad (111)$$

The sum of the average compound elastic scattering cross section $\overline{\sigma_{cc}^{ce}}$ and the average reaction cross section $\overline{\sigma_{cr}}$ can be considered as the cross section for the formation of the compound nucleus $\overline{\sigma_c}$, and can be written as

$$\begin{aligned} \overline{\sigma_c} &= \overline{\sigma_{cc}^{ce}} + \overline{\sigma_{cr}} = \pi \lambda_c^2 g_c \left(\overline{|U_{cc}|^2} - |\overline{U_{cc}}|^2 + 1 - |\overline{U_{cc}}|^2 \right) \\ &= \pi \lambda_c^2 g_c (1 - |\overline{U_{cc}}|^2) \end{aligned} \quad (112)$$

Then the sum of this compound nucleus formation cross section $\overline{\sigma_c}$ and the average shape elastic scattering cross section $\overline{\sigma_{cc}^{se}}$ equals the total cross section $\overline{\sigma_{c,T}}$, which can be checked by

$$\begin{aligned}\overline{\sigma_c} + \overline{\sigma_{cc}^{se}} &= \pi\lambda_c^2 g_c (1 - |\overline{U_{cc}}|^2 + |1 - \overline{U_{cc}}|^2) \\ &= \pi\lambda_c^2 g_c (1 - |\overline{U_{cc}}|^2 + 1 - 2 \operatorname{Re} \overline{U_{cc}} + |\overline{U_{cc}}|^2) = \overline{\sigma_{c,T}}\end{aligned}\quad (113)$$

From the above expressions, only the total, shape elastic, and compound nucleus formation cross sections $\overline{\sigma_{c,T}}$, $\overline{\sigma_{cc}^{se}}$, and $\overline{\sigma_c}$ contain the elements $\overline{U_{cc}}$, calculated by optical model, without other terms like $|\overline{U_{cc}}|^2$ which cannot be extracted from optical model calculations. For a direct comparison with experimental data, only the calculated average total cross section (111) can be used in a general way. The shape elastic scattering cross section cannot be distinguished from the compound elastic scattering. The calculated compound nucleus formation cross section (112) is also not directly observable, but can be used in combination with measured decay channels, like in the surrogate measurements.

Finally, the average cross section for a single reaction $\overline{\sigma_{cc'}}$ is

$$\overline{\sigma_{cc'}} = \pi\lambda_c^2 g_c |\overline{\delta_{cc'} - U_{cc'}}|^2 \quad (114)$$

which contains the nearly impossible averaging over $|U_{cc'}|^2$.

When we introduce the transmission coefficient

$$T_c = 1 - |\overline{U_{cc}}|^2 \quad (115)$$

the compound nucleus formation cross section (unaveraged) can be written as

$$\sigma_c = \pi\lambda_c^2 g_c T_c \quad (116)$$

Using the usual concepts in nuclear reaction theory (reciprocity, time-reversal invariance), the probability of decay through channel c' as $T_{c'}/\sum T_i$ the cross section for the reaction $c \rightarrow c'$ is then

$$\sigma_{cc'} = \pi\lambda_c^2 g_c T_c \frac{T_{c'}}{\sum T_i} \quad (117)$$

where the sum runs over all possible channels. Averaging over a small energy interval with many resonances, taking into account shape elastic scattering in addition to compound reactions and redefining T_c as

$$T_c = 1 - |\overline{U_{cc}}|^2 \quad (118)$$

results in the Hauser–Feshbach formula (see also Hauser and Feshbach 1952; Feshbach et al. 1954; Hodgson 1971; Moldauer 1975b,a 1976, 1980; Fröhner 2000; Sirakov et al. 2008 for more details)

$$\overline{\sigma_{cc'}} = \overline{\sigma_{cc}^{se}} \delta_{cc'} + \pi\lambda_c^2 g_c \frac{T_c T_{c'}}{\sum T_i} W_{cc'} \quad (119)$$

where the factor $W_{cc'}$ is factor that includes elastic enhancement and a correction for width fluctuations, which can be written as (see for example Moldauer 1976)

$$W_{cc'} = \left(\frac{\overline{\Gamma_c \Gamma_{c'}}}{\Gamma} \right) \frac{\overline{\Gamma}}{\overline{\Gamma_c \Gamma_{c'}}} \quad (120)$$

The width fluctuations can be calculated most accurately using the GOE triple integral (Verbaarschot et al. 1985; Verbaarschot 1986), but also with simpler approximations.

The transmission coefficients for particle channels are given by (118). Two other channels exist which are the photon and fission channels. Their transmission coefficients, related to the average widths and level spacing, are defined as

$$T_\gamma = 2\pi \frac{\overline{\Gamma}_\gamma}{D} \quad (121)$$

and

$$T_f = 2\pi \frac{\overline{\Gamma}_f}{D} \quad (122)$$

Dedicated modelizations on photon strength functions, level densities, and fission models, are used for the photon and fission transmission coefficients, but are beyond the scope of this overview. Good starting points for further reading are the user guides of specialized computer codes like EMPIRE (Herman et al. 2007), TALYS (Koning et al. 2007), and others.

7 Concluding Remarks

The importance of neutron-induced reaction data is evident in a wide variety of research fields, ranging from stellar nucleosynthesis and nuclear structure to applications of nuclear technology. The present chapter has sketched out an impression of neutron cross section measurements at time-of-flight facilities and at monoenergetic fast neutron sources. The principal measurement techniques have been summarized. Also details on the *R*-matrix formalism linking measurable nuclear properties to useable nuclear cross sections have been presented.

Many details were intentionally omitted but the provided references should form a good starting point for the interested reader.

References

- Abbondanno U et al (2003) CERN n_TOF facility: performance report. Tech. Rep. ERNSL-2002-053 ECT
- Abbondanno U et al (2004) New experimental validation of the pulse height weighting technique for capture cross-section measurements. Nucl Instrum Methods Phys Res Sect A 521(2–3):454–467
- Abbondanno U et al (2005) The data acquisition system of the neutron time-of-flight facility n_TOF at CERN. Nucl Instrum Methods Phys Res Sect A 538(1–3):692
- Abfalterer WP, Finlay RW, Grimes SM (2000) Level widths and level densities of nuclei in the $32 \leq A \leq 60$ mass region inferred from fluctuation analysis of total neutron cross sections. Phys Rev C 62(6):064312
- Abramowitz M (1965) Handbook of mathematical functions with formulas, graphs, and mathematical table. Dover Publications, New York
- Adler DB, Adler FT (1972) Uniqueness of *R*-matrix parameters in the analysis of low-energy neutron cross sections of fissile nuclei. Phys Rev C 6:986–1001
- Ait-Tahar S, Hodgson PE (1987) Weisskopf-Ewing calculations – neutron-induced reactions. J Phys G 13(7):945–956
- Allmond JM, Bernstein LA, Beausang CW et al (2009) Relative U-235(n,γ) and (n,f) cross sections from U-235(d,p γ) and (d,pf). Phys Rev C 79(5):054610
- Amaldi E, Fermi E (1936) On the absorption and the diffusion of slow neutrons. Phys Rev 50: 899

- Ananiev VD et al (2005) Intense resonance neutron source (IREN) – new pulsed source for nuclear physical and applied investigations. Phys Elementary Part At Nuclei (PEPAN) 126: 11–18
- Asami A (1973) JAERI new linac. J At Energy Soc Jpn 15:37–42
- Baba M (2005) Experimental studies on particle and radionuclide production cross sections for tens of MeV neutrons and protons. AIP 769: 884–889
- Baba M, Ibaraki M, Miura T et al (2002) Experiments on neutron scattering and fission neutron spectra. J Nucl Sci Technol 1(suppl. 2): 204–209
- Barry DP (2003) Neodymium neutron transmission and capture measurements and development of a new transmission detector. PhD thesis, Rensselaer Polytechnic Institute
- Bauge E, Delaroche JP, Giro M (2001) Lane-consistent, semimicroscopic nucleon-nucleus optical model. Phys Rev C 63:024607
- Beer H, Kappeler F (1979) Capture-to-fission ratio of U-235 in the neutron energy-range from 10 to 500 keV. Phys Rev C 20(1):201–211
- Beer H, Kappeler F (1980) Neutron-capture cross-sections on Ba-138, Ce-140, Ce-142, Lu-175, Lu-176, and Ta-181 at 30 keV – prerequisite for investigation of the Lu-176 cosmic clock. Phys Rev C 21(2):534–544
- Behrens JW, Browne JC, Ables E (1982) Measurement of the neutron-induced fission cross-section of Th-232 relative to U-235 from 0.7 to 30 MeV. Nucl Sci Eng 81(4):512–519
- Belikov OV et al (2010) Physical start-up of the first stage of IREN facility. J Phys Conference Series 205:012053
- Bernstein LA et al (2002) Pu-239(n,2n) Pu-238 cross section deduced using a combination of experiment and theory. Phys Rev C 65(2): 021601
- Biro T, Sudar S, Miligy, Z, Dezso Z, and Csikai, J (1975) Investigations of (n,t) cross sections at 14.7 MeV. J Inorg Nucl Chem 37(7–8):1583–1585.
- Blatt JM, Biedenharn LC (1952) The angular distribution of scattering and reaction cross sections. Rev Mod Phys 24(4):258–272
- Block RC, Marano PJ, Drindak NJ et al (1988) A multiplicity detector for accurate low-energy neutron capture measurements. In: Proceedings of the international conference on nuclear data for science and technology, Mito, p 383
- Blons J (1973) High-resolution measurements of neutron-induced fission cross-sections for U-233 U-235 Pu-239 and Pu-241 below 30 keV. Nucl Sci Eng 51(2):130–147
- Bohigas O, Giannoni MJ, Schmit C (1984) Characterization of chaotic quantum spectra and universality of level fluctuation laws. Phys Rev Lett 52: 1–4
- Bohr N (1936) Neutron capture and nuclear constitution. Nature 137:344
- Borcea C et al (2003) Results from the commissioning of the n_TOF spallation neutron source at CERN. Nucl Instrum Methods Phys Res Sect A 51:524–537
- Borella A, Aerts G, Günsing F et al (2007a) The use of C₆D₆ detectors for neutron induced capture cross-section measurements in the resonance region. Nucl Instrum Methods Phys Res Sect A 577(3):626–640
- Borella A, Günsing F, Moxon M et al (2007b) High-resolution neutron transmission and capture measurements of the nucleus Pb-206. Phys Rev C 76(1):014605
- Boyer S, Dassie D, Wilson JN et al (2006) Determination of the 233Pa(n,γ) capture cross section up to neutron energies of 1 MeV using the transfer reaction 232Th(3He,p)234Pa*. Nucl Phys A 775(3–4):175–187
- Breit G, Wigner EP (1936) Capture of slow neutrons. Phys Rev 49(7):519–581
- Burke JT, Bernstein LA, Scielzo ND et al (2008) Surrogate Reactions in the Actinide Region, AIP Conference Proceedings 1005:96–100
- Calviani M, Cennini P, Karadimos D et al (2008) A fast ionization chamber for fission cross-section measurements at n_TOF. Nucl Instrum Methods Phys Res Sect A 594(2):220–227
- Calviani M, Praena J, Abbondanno U et al (2009) High-accuracy 233U(n,f) cross-section measurement at the white-neutron source n_TOF from near-thermal to 1 MeV neutron energy. Phys Rev C 80(4):044604
- Camarda HS, Dietrich FS, Phillips TW (1989) Microscopic optical-model calculations of neutron total cross-sections and cross-section differences. Phys Rev C 39(5):1725–1729
- Capote R, Soukhovitskii ES, Quesada JM et al (2005) Is a global coupled-channel dispersive optical model potential for actinides feasible? Phys Rev C 72(6):064610
- Carlson AD, Behrens JW (1983) Measurement of the ²³⁵U(n,f) cross section from 0.3 to 3.0 MeV using the NBS electron linac, Proceedings of the International Conference on Nuclear Data for Science and Technology, 6–10 Sept. 1982, Antwerp, Belgium, ed. K. H. Bockhoff, (Dordrecht, Netherlands; Reidel, 1983) pp. 456–459
- Carlson AD et al (2009) International evaluation of neutron cross section standards. Nucl Data Sheets 110(12):3215–3324

- Chadwick J (1932) Possible existence of a neutron. *Nature* 129:312
- Chadwick MB et al (2006). ENDF/B-VII.0: Next generation evaluated nuclear data library for nuclear science and technology. ENDF data can be accessed at the National Nuclear Data Center at Brookhaven National Laboratory [www.nndc.bnl.gov]. *Nucl Data Sheets* 107(12):2931-3059
- Cierjacks S, Duelli B, Forti P et al (1968) Fast neutron time-of-flight spectrometer used with the karlsruhe isochronous cyclotron. *Rev Sci Instrum* 39(9):1279-1288
- Cramer JD, Britt HC (1970) Neutron fission cross sections for Th-231, Th-233, U-235, U-237, U-239, Pu-241, and Pu-243 from 0.5 to 2.25 MeV using (t, pf) reactions. *Nucl Sci Eng* 41(2):177
- Dabbs JWT (1979) Neutron cross section measurements at ORELA. In: *Nuclear cross sections for technology proceedings of the international conference on nuclear cross sections for technology*, Knoxville, p 929
- Dagan R (2008) On the angular distribution of the ideal gas scattering kernel. *Ann Nucl Energy* 35:1109-1116
- Danon Y, Slovacek RE, Block RC et al (1991) Fission cross-section measurements of Cm-247, Es-254, and Cf-250 from 0.1eV to 80 keV. *Nucl Sci Eng* 109(4):341-349
- Danon Y, Block RC, Slovacek RE (1995) Design and construction of a thermal-neutron target for the RPI linac. *Nucl Instrum Methods Phys Res Sect A* 352(3):596-603
- Danon Y, Werner CJ, Youk G et al (1998) Neutron total cross-section measurements and resonance parameter analysis of holmium, thulium, and erbium from 0.001 to 20 eV. *Nucl Sci Eng* 128(1):61-69
- Danon Y, Block RC, Rapp MJ et al (2009a) Beryllium and graphite high-accuracy total cross-section measurements in the energy range from 24 to 900 keV. *Nucl Sci Eng* 161(3):321-330
- Danon Y, Liu E, Barry D et al (2009b) Benchmark experiment of neutron resonance scattering models in Monte Carlo codes. *International Conference on Mathematics, Computational Methods & Reactor Physics (M&C 2009)* Saratoga Springs, New York, May 3-7, 2009, on CD-ROM, American Nuclear Society, LaGrange Park, IL (2009).
- Davis JC (1989) The LLNL multi-user tandem laboratory. *Nucl Instrum Methods B* 40-41(Part 2):705-708
- Di Lullo AR, Massey TN, Grimes SM et al (2008) A fission chamber measurement of the B-nat(d,n) cross section for use in neutron detector calibration. *Nucl Sci Eng* 159(3):346-350
- Dietrich FS, Anderson JD, Bauer RW et al (2003) Importance of isovector effects in reproducing neutron total cross section differences in the W isotopes. *Phys Rev C* 67(4):044606
- Drosg M (2005) Drog-2000, codes and database for 59 neutron source reactions, Tech. Rep. IAEA report IAEA-NDS-87, Rev. 9 (May 2005). <http://www.nds.iaea.org/drosg2000.html>.
- Dudey ND, Heinrich RR, Madson AA (1970) Reaction cross sections of Rb-85(n,gamma)Rb-86m, Rb-87(n,gamma)Rb-88, and Y-89(n,gamma)Y-90m between 0.16 MeV and 1.5 MeV. *J Nucl Energy* 24(4):181
- Elsevier, Inc. Engineering village (2009). <http://www.engineeringvillage2.org>
- Escher JE, Dietrich FS (2006) Determining (n, f) cross sections for actinide nuclei indirectly: examination of the surrogate ratio method. *Phys Rev C* 74(5):054601
- Fadil M, Rannou B (2008) About the production rates and the activation of the uranium carbide target for SPIRAL2. *Nucl Instrum Methods B* 266 (19-20):4318-4321
- Farrell JA and Pineo WFE (1968) Neutron cross sections of ${}^6\text{Li}$ in the kilovolt region. In: *Proceedings of the conference on neutron cross sections and technology*. NBS Special Publication 299(1):153-158
- Fernbach S, Serber R, Taylor TB (1949) The scattering of high energy neutrons by nuclei. *Phys Rev* 75(9):1352-1355
- Feshbach H, Porter CE, Weisskopf VF (1954) Model for nuclear reactions with neutrons. *Phys Rev* 96(2):448-464
- Finlay RW, Brient CE, Carter DE et al (1982) The Ohio-University beam swinger facility. *Nucl Instrum Methods Phys Res* 198(2-3):197-206
- Firk F, Whittaker J, Bowey E et al (1963) A nanosecond neutron time-of-flight system for the Harwell 30 MeV electron linac. *Nucl Instrum Methods* 23:141-146
- Flaska M, Borella A, Lathouwers D et al (2004) Modeling of the GELINA neutron target using coupled electron-photon-neutron transport with the MCNP4C3 code. *Nucl Instrum Methods Phys Sect A* 531(3):392-406
- Foderaro A (1971) *The elements of neutron interaction theory*. MIT Press, Cambridge
- Frank IM, Pacher P (1983) 1st experience on the high-intensity pulsed reactor IBR-2. *Physica B* 120(1-3):37-44

- Fröhner F (2000) Evaluation and analysis of nuclear resonance data. Tech. Rep. JEFF Report 18, OECD/NEA
- Fujita Y (1986) Neutron TOF spectrometer at KURRI electron linac. In: Proceedings of the 1985 seminar on nuclear data (JAERI-M-86-080), Kyoto, p 334-337
- Futakawa M, Haga K, Wakui T et al (2009) Development of the HP target in the J-PARC neutron source. Nucl Instrum Methods A 600(1): 18-21
- Ge Zhigang et al (2008) The updated version of the Chinese Evaluated Nuclear Data Library (CENDL-3.1) and China nuclear data evaluation activities. In: Proceedings of the international conference on nuclear data for science and technology ND2007, EDP Sciences, 07570
- Good WM, Neiler JH, Gibbons JH (1958) Neutron total cross sections in the keV region by fast time-of-flight measurements. Phys Rev 109(3):926-933
- Grallert A, Csikai J, Qaim SM et al (1993) Recommended target materials for d-d neutron sources. Nucl Instrum Methods Phys Res Sect A 334(1):154-159
- Guber KH et al (2005) New neutron cross-section measurements at ORELA for improved nuclear data calculations. In: Haight RC, Chadwick MB, Kawano T, Talou P (eds) International conference on nuclear data for science and technology, AIP, vol 769, Santa Fe, p 1706
- Gunsing F, n_TOF Collaboration et al (2009) Measurement of the $^{232}\text{Th}(n,\gamma)$ resonance reaction at the n_TOF facility at CERN, unpublished
- Hansen LF, Anderson JD, Brown PS et al (1973) Measurements and calculations of neutron-spectra from iron bombarded with 14-MeV neutrons. Nucl Sci Eng 51(3):278-295
- Hansen LF, Wong C, Komoto TT et al (1980) Measurements and calculations of the neutron emission-spectra from materials used in fusion-fission reactors. Nucl Technol 51(1): 70-77
- Haq RU, Pandey A, Bohigas O (1982) Fluctuations properties of nuclear energy levels: do theory and experiment agree? Phys Rev Lett 48(6): 1086-1089
- Hatarik R, Bernstein LA, Burke JT et al (2009) Using (d,p gamma) as a surrogate reaction for (n,gamma) AIP Conference Proceedings (2009) Vol.1090, p. 445-449
- Hauser W, Feshbach H (1952) The inelastic scattering of neutrons. Phys Rev 87(2):366-373
- Herman M, Capote R, Carlson BV et al (2007) EMPIRE: Nuclear reaction model code system for data evaluation. Nucl Data Sheets 108(12):2655-2715
- Hockenbury RW, Bartolome ZM, Tatarczuk JR et al (1969) Neutron radiative capture in Na, Al, Fe, and Ni from 1 to 200 keV. Phys Rev 178(4): 1746-1769
- Hodgson PE (1971) Nuclear reactions and nuclear structure. Clarendon Press, Oxford
- Hogue HH, Vonbehren PL, Glasgow DW et al (1979) Elastic and inelastic-scattering of 7-MeV to 14-MeV neutrons from Li-6 and Li-7. Nucl Sci Eng 69(1):22-29
- Hori J et al (2008) Neutron capture cross section measurement on ^{243}Am with a 4π Ge spectrometer. In: Proceedings of the 2008 symposium on nuclear data, Tokai, pp. 20-21
- Humblet J, Rosenfeld L (1961) Theory of nuclear reactions: I. resonant states and collision matrix. Nucl Phys 26(4):529-578
- Hwang RN (1973) Efficient methods for treatment of resonance cross-sections. Nucl Sci Eng 52(2):157-175
- Ibaraki M, Baba M, Miura T et al (2000) Experimental method for neutron elastic scattering cross-section measurement in 40-90 MeV region at TIARA. Nucl Instrum Methods Phys Res Sect A 446(3):536-544
- Igashira M, Kitazawa H, Yamamuro N (1986) A heavy shield for the gamma-ray detector used in fast-neutron experiments. Nucl Instrum Methods Phys Res Sect A 245(2-3): 432-437
- Ignatyuk AV, Fursov BI (2008) The latest BROND-3 developments. In: Proceedings of the international conference on nuclear data for science and technology ND2007, EDP Sciences, 07641
- Jaag S, Kappeler F (1995) Stellar (n,gamma) cross-section of the unstable isotope Eu-155. Phys Rev C 51(6):3465-3471
- Jandel M et al (2008) Neutron capture cross section of Am-241. Phys Rev C 78(3):034 609
- Joly S, Voignier J, Grenier G et al (1978) Measurement of fast-neutron capture cross-sections using a NaI spectrometer. Nucl Instrum Methods 153(2-3):493-501
- Jongen Y, Ryckewaert G (1976) Heavy-ion acceleration at CYCLONE (Belgium). IEEE Trans Nucl Sci 23(2):987-990
- Kapur PL, Peierls RE (1938) Dispersion formula for nuclear reactions. Proc R Soc A166:277-295
- Kegel GHR (1989) Fast-neutron generation with a type Cn Van De graaff accelerator. Nucl Instrum Methods Phys Res Sect B 40-1:1165-1168

- Kim GN et al (2002) Measurement of photoneutron spectrum at Pohang neutron facility. *Nucl Instrum Methods Phys Res Sect A* 485(3): 458–467
- Klug J et al (2002) SCANDAL – a facility for elastic neutron scattering studies in the 50–130 MeV range. *Nucl Instrum Methods Phys Res Sect A* 489(1–3):282–303
- Klug J, Altstadt E, Beckert C et al (2007) Development of a neutron time-of-flight source at the ELBE accelerator. *Nucl Instrum Methods Phys Res Sect A* 577(3):641–653
- Knoll G (2000) Radiation detection & measurement. John Wiley & Sons, New York
- Kobayashi K, Lee S, Yamamoto S et al (2002) Measurement of neutron capture cross section of Np-237 by linac time-of-flight method and with linac-driven lead slowing-down spectrometer. *J Nucl Sci Technol* 39(2):111–119
- Kobayashi K, Lee S, Yamamoto S (2004) Neutron capture cross-section measurement of Tc-99 by linac time-of-flight method and the resonance analysis. *Nucl Sci Eng* 146(2):209–220
- Koehler PE (2001) Comparison of white neutron sources for nuclear astrophysics experiments using very small samples. *Nucl Instrum Methods A* 460:352–361
- Kohler R, Mewissen L, Poortmans F et al (1985) High-resolution neutron resonance spectroscopy. *AIP Conf Proc* 124:306–307
- Kondo K, Murata I, Ochiai K et al (2006) Charged-particle spectrometry using a pencil-beam DT neutron source for double-differential cross-section measurement. *Nucl Instrum Methods Phys Res Sect A* 568(2):723–733
- Koning A et al (2006) The JEFF-31 nuclear data library, JEFF report 21. Tech. rep., JEFF data can be accessed at the OECD Nuclear Energy Agency
- Koning AJ, Hilaire S, Duijvestijn M (2007) TALYS a nuclear reaction program. Tech. rep.
- Kononov VN et al (1982) Fast-neutron radiative-capture cross-sections and d-wave strength functions. Proceedings of the 4th international symposium on capture gamma-ray spectroscopy and related topics, London, pp 518–519
- Kononov VN, Poletaev ED, Timokhov VM et al (1987) Fast-neutron radiative-capture cross-sections and transmissions for tungsten isotopes. *Sov J Nucl Phys* 46(1):33–34
- Kopecky S, Brusegan A (2006) The total neutron cross section of Ni-61. *Nucl Phys A* 773(3–4): 173–186
- Kornilov NV, Kagalenko AB (1995) Inelastic neutron-scattering by U-235 and U-238 nuclei. *Nucl Sci Eng* 120(1):55–64
- Krane K (1987) Introductory nuclear physics. John Wiley & Sons, New York
- Lamb WE (1939) Capture of neutrons by atoms in a crystal. *Phys Rev* 55(2):190–197
- Lane AM, Thomas RG (1958) R-matrix theory of nuclear reactions. *Rev Mod Phys* 30(2): 257–353
- Larson NM (2006) Updated users' guide for SAMMY: Multilevel R-matrix fits to neutron data using Bayes' equations. SAMMY, computer code Report ORNL/TM-9179/R7, Oak Ridge National Laboratory
- Leeb H, Wilmsen S (2000) Violation of pseudospin symmetry in nucleon-nucleus scattering: Exact relations. *Phys Rev C* 62(2):024602
- Leinweber G, Barry DP, Trbovich MJ et al (2006) Neutron capture and total cross-section measurements and resonance parameters of gadolinium. *Nucl Sci Eng* 154(3):261–279
- Leshner SR, McKay CJ, Mynk M et al (2007) Low-spin structure of Mo96 studied with the (n, n'γ) reaction. *Phys Rev C* 75(3):034318
- Lisowski PW, Schoenberg KF (2006) The Los Alamos neutron science center. *Nucl Instrum Methods Phys Res sect A* 562(2):910–914
- Luk'yanov AA, Yaneva NB (1997) Multilevel parametrization of resonance neutron cross sections. *Phys Part Nucl* 28:331–347
- Lychagin AA, Simakov SP, Devkin BV et al (1987) Study of the Fe(n, n' γ) reaction with 14.1-MeV neutrons. *Sov J Nucl Phys* 45(5): 761–766
- Lyles BF, Bernstein LA, Burke JT et al (2007) Absolute and relative surrogate measurements of the U-236(n,f) cross section as probe of angular momentum effects. *Phys Rev C* 76(1):014606
- Lynn JE (1968) The theory of neutron resonance reactions, Clarendon Press, Oxford
- Mannhart W, Schmidt D (2002) Measurement of the ²⁸Si(n,p), ²⁹Si(n,p) and ³⁰Si(n,α) cross sections between 6.9 and 14.0 MeV. *J Nucl Sci Technol* 1:218–221
- Mannhart W, Schmidt D (2005) Measurement of neutron reaction sections between 8 and 14 MeV. *AIP* 769:609–612
- Marrone S et al (2004) A low background neutron flux monitor for the n_TOF facility at CERN. *Nucl Instrum Methods Phys Res Sect A* 517 (1–3):389
- Massey TN, Al-Quraishi S, Brient CE et al (1998) A measurement of the Al-27 (d,n) spectrum for use in neutron detector calibration. *Nucl Sci Eng* 129(2):175–179
- Mehta ML (1960) On the statistical properties of the level-spacings in nuclear spectra. *Nucl Phys* 18:395

- Mehta ML (1991) Random matrices. Academic, Boston
- Meister A (1994) Calculations on lattice vibration effects in the doppler broadening of the 0.18 eV Cd neutron resonance cross section. Tech. Rep. CE/R/VG/78/94, JRC-IRMM
- Mellema S, Finlay RW, Dietrich FS et al (1983) Microscopic and conventional optical-model analysis of fast-neutron scattering from Fe-54, Fe-56. *Phys Rev C* 28(6):2267–2277
- Mihailescu LC, Borcea C, Koning AJ et al (2008) High resolution measurement of neutron inelastic scattering and (n,2n) cross-sections for Bi-209. *Nucl Phys A* 799:1–29
- Mocko M, Muhrer G, Tovesson F (2008) Advantages and limitations of nuclear physics experiments at an ISIS-class spallation neutron source. *Nucl Instrum Methods Phys Res Sect A* 589(3): 455–464
- Moldauer PA (1975b) Why Hauser-Feshbach formula works. *Phys Rev C* 11(2):426–436
- Moldauer PA (1975a) Direct reaction effects on compound cross-sections. *Phys Rev C* 12(3): 744–756
- Moldauer PA (1976) Evaluation of fluctuation enhancement factor. *Phys Rev C* 14(2): 764–766
- Moldauer PA (1980) Statistics and the average cross-section. *Nucl Phys A* 344(2):185–195
- Molnar G (2004) Handbook of prompt gamma activation analysis. Springer, Berlin
- Moxon MC, Brisland JB (1991) REFIT, a least squares fitting program for resonance analysis of neutron transmission and capture data computer code. Tech. rep., United Kingdom Atomic Energy Authority
- Mughabghab SF (2006) Atlas of neutron resonances. Elsevier Science, Amsterdam
- Naberejnev DG, Mounier C, Sanchez R (1999) The influence of crystalline binding on resonant absorption and reaction rates. *Nucl Sci Eng* 131:220
- Nguyen VD et al (2006) Measurements of neutron and photon distributions by using an activation technique at the Pohang neutron facility. *J Korean Phys Soc* 48(3):382–389
- Nuclear data standards for nuclear measurements (1991) NEANDC/INDC standards file. Tech. Rep. NEANDC-311. <http://www.nds.iaea.org/standards/>
- Nystrom G, Bergqvist I, Lundberg B (1971) Neutron-capture cross-sections in F, Mg, Al, Si, P and S from 20 to 80 keV. *Phys Scr* 4(3):95
- Orphan V, Hoot C, Carlson A et al (1969) A facility for measuring cross sections of (n,xgamma) reactions using an electron linac. *Nucl Instrum Methods* 73(1):1–12
- Overberg ME, Moretti BE, Slovacek RE et al (1999) Photoneutron target development for the RPI linear accelerator. *Nucl Instrum Methods Phys Res Sect A* 438(2–3):253–264
- Pancin J et al (2004) Measurement of the n_TOF beam profile with a micromegas detector. *Nucl Instrum Methods Phys Res Sect A* 524(1–3):102
- Panebianco S, Berg K, David JC et al (2009) Neutronic characterization of the MEGAPIE target. *Ann Nucl Energy* 36(3):350–354
- Paradela C et al (2009) Neutron induced fission cross section of ²³⁴U and ²³⁷Np measured at the n_TOF facility. unpublished
- Payne GL, Schlessinger L (1970) Properties of the K-matrix in nuclear-reaction theory. *Phys Rev C* 2(5):1648–1653
- Petit M et al (2004) Determination of the ²³³Pa reaction cross section from 0.5 to 10 MeV neutron energy using the transfer reaction ²³²Th(³He, p)²³⁴Pa. *Nucl Phys A* 735:345–371
- Petrich D, Neil M, Kappeler F et al (2008) A neutron production target for FRANZ. *Nucl Instrum Methods A* 596(3):269–275
- Pillon M, Angelone M, Martone M, Rado V (1995) Characterization of the source neutrons produced by the Frascati neutron generator. *Fus Eng Des* 28:683–688
- Plag R et al (2003) An optimized C₆D₆ detector for studies of resonance-dominated (n,γ) cross-sections. *Nucl Instrum Methods Phys Res Sect A* 496:425
- Plettner C, Ai H, Beausang CW et al (2005) Estimation of (n,f) cross sections by measuring reaction probability ratios. *Phys Rev C* 71(5):051602
- Porter CE, Thomas RG (1956) Fluctuations of nuclear reaction widths. *Phys Rev* 104(2):483–491
- Qaim SM, Wolffe R, Rahman MM et al (1984) Measurement of (n,p) and (n,α) reaction cross-sections on some isotopes of nickel in the energy region of 5 to 10 MeV using a deuterium gas-target at a compact cyclotron. *Nucl Sci Eng* 88(2):143–153
- Quesada JM, Capote R, Soukhovitskii ES et al (2007) Approximate Lane consistency of the dispersive coupled-channels potential for actinides. *Phys Rev C* 76(5):057602
- Rapp M, Danon Y, Block RC et al (2009) High energy neutron time of flight measurements of carbon and beryllium samples at the RPI linac. In: Society AN (ed) International conference on mathematics, computational methods & reactor physics 2009, Saratoga Springs
- Ray ER, Good WM (1972) Experimental neutron resonance spectroscopy, Academic, New

- York, chap. Pulsed Accelerator Time-of-Flight Spectrometers
- Reich CW, Moore MS (1958) Multilevel formula for the fission process. *Phys Rev* 111(3):929–933
- Reimer P, Koning AJ, Plompen AJM et al (2009) Neutron induced reaction cross sections for the radioactive target nucleus Tc-99. *Nucl Phys A* 815:1–17
- Reuss P (2008) Neutron physics. EDP Sciences, Oakland
- Rochman D, Haight RC, O'Donnell JM et al (2004) Neutron-induced reaction studies at FIGARO using a spallation source. *Nucl Instrum Methods Phys Res Sect A* 523(1–2):102–115
- Rochman D et al (2005) Characteristics of a lead slowing-down spectrometer coupled to the LANSCE accelerator. *Nucl Instrum Methods Phys Res Sect A* 550(1–2):397–413
- Romano C, Danon Y, Block R et al (2008) Measurements of fission fragment properties using RPI's lead slowing-down spectrometer. In: Bersillon, O, Gunging, F, Bauge, E, Jacqmin, R, Leray, S (eds), Proceedings of the international conference on nuclear data for science and technology, Nice, France, EDP Sciences Vol. 1, pp. 371–374
- Rubbia C et al (1998) A high resolution spallation driven facility at the CERN-PS to measure neutron cross sections in the interval from 1eV to 250 MeV. Tech. Rep. CERN/LHC/98–02, CERN
- Sage C, Semkova V, Bouland O et al (2009) High resolution measurements of the $^{241}\text{Am}(n,2n)$ reaction cross section. unpublished
- Saglione FJ III, Danon Y, Block R (2006) Digital data acquisition system for time of flight neutron beam measurements. In: The American Nuclear Society's 14th Biennial Topical Meeting of the Radiation Protection and Shielding Division, Carlsbad, p 368
- Saglione F, Danon Y, Block R et al (2009) High energy neutron scattering benchmark of Monte Carlo computations. In: International conference on mathematics, computational methods & reactor physics (M&C 2009), Saratoga Springs
- Schmidt D (2008) Determination of neutron scattering cross sections with high precision at PTB in the energy region 8 to 14 MeV. *Nucl Sci Eng* 160:349–362
- Schmidt D, Zhou ZY, Ruan XC et al (2005) Application of non-monoenergetic sources in fast neutron scattering measurements. *Nucl Instrum Methods Phys Res Sect A* 545(3):658–682
- Schmittroth F, Tobocman W (1971) Comparison of the R -matrix nuclear reaction theories. *Phys Rev C* 3:1010–1019
- Schut PAC, Kockelmann W, Postma H et al (2008) Neutron resonance capture and neutron diffraction analysis of roman bronze water taps. *J Radioanal Nucl Chem* 278(1):151–164
- Semkova V, Plompen AJM (2007) Neutron-induced dosimetry reaction cross-section measurements from the threshold up to 20 MeV. *Radiat Prot Dosimetry* 126(1–4):126–129
- Shcherbakov O, Furutaka K, Nakamura S et al (2005) Measurement of neutron capture cross section of Np-237 from 0.02 to 100 eV. *J Nucl Sci Technol* 42(2):135–144
- Shibata K et al (2002) Japanese evaluated nuclear data library version 3 revision-3: JENDL-3.3. *J Nucl Sci Technol* 39(11):1125–1136
- Shyam R, Scholten O (2008) Photoproduction of eta mesons within a coupled-channels K -matrix approach. *Phys Rev C* 78(6):065201
- Sirakov I, Capote R, Gunging F et al (2008) An ENDF-6 compatible evaluation for neutron induced reactions of Th-232 in the unresolved resonance region. *Ann Nucl Energy* 35(7):1223–1231
- Staples P, Egan JJ, Kegel GHR et al (1995) Prompt fission neutron energy-spectra induced by fast-neutrons. *Nucl Phys A* 591(1):41–60
- Sukhoruchkin SI, Soroko ZN, Deriglazov VV (1998) Low energy neutron physics, tables of neutron resonance parameters, vol 1/16B. Springer, Landolt-Börnstein, Berlin
- Tagliente G et al (2008) Experimental study of the $\text{Zr-91}(n, \gamma)$ reaction up to 26 keV. *Phys Rev C* 78(4):045804
- Takahashi A, Ichimura E, Sasaki Y et al (1988) Measurement of double differential neutron emission cross-sections for incident neutrons of 14-MeV. *J Nucl Sci Technol* 25(3):215–232
- Tovesson F, Hill TS (2007) Neutron induced fission cross section of Np-237 from 100 keV to 200 MeV. *Phys Rev C* 75(3):034610
- Tovesson F, Hill TS (2008) Subthreshold fission cross section of ^{237}Np . *Nucl Sci Eng* 159:94
- Tovesson F, Hill TS, Mocko M et al (2009) Neutron induced fission of Pu-240 , Pu-242 from 1eV to 200 MeV. *Phys Rev C* 79(1):014613
- Trbovich MJ, Barry DP, Slovacek RE et al (2009) Hafnium resonance parameter analysis using neutron capture and transmission experiments. *Nucl Sci Eng* 161(3):303–320
- Tronc D, Salome JM, Bockhoff KH (1985) A new pulse-compression system for intense relativistic electron-beams. *Nucl Instrum Methods Phys Res Sect A* 228(2–3):217–227
- Verbaarschot JJM (1986) Investigation of the formula for the average of two S -matrix elements in compound nucleus reactions. *Ann Phys* 168(2):368–386

- Verbaarschot JJM, Weidenmuller HA, Zirnbauer MR (1985) Grassmann integration in stochastic quantum physics – the case of compound nucleus scattering. *Phys Rep Rev Sect Phys Lett* 129(6):367–438
- Vogt E (1962) Theory of low energy nuclear reactions. *Rev Mod Phys* 34(4):723–747
- Wagemans C, De Smet L, Vermote S et al (2008) Measurement of the U-236(n, f) cross section in the neutron energy range from 0.5 eV up to 25 keV. *Nucl Sci Eng* 160(2):200–206
- Wallerstein G et al (1997) Synthesis of the elements in stars: forty years of progress. *Rev Mod Phys* 69:995
- Wang T et al (2008) Measurement of the total neutron cross-section and resonance parameters of molybdenum using pulsed neutrons generated by an electron linac. *Nucl Instrum Methods Phys Res Sect B* 266(4):561–569
- Weisskopf VF, Ewing DH (1940) On the yield of nuclear reactions with heavy elements. *Phys Rev* 57(6):472–485; erratum 57(10):935
- Wigner EP, Eisenbud L (1947) Higher angular momenta and long range interaction in resonance reactions. *Phys Rev* 72(1):29–41
- Wisshak K, Guber K, Kappeler F et al (1990) The Karlsruhe 4- π barium fluoride detector. *Nucl Instrum Methods Phys Res Sect A* 292(3):595–618
- Wisshak K, Kappeler F (1978) Neutron-capture cross-section ratios of Pu-240, Pu-242, U-238, and Au-197 in energy-range from 10 to 90 keV. *Nucl Sci Eng* 66(3):363–377
- Wisshak K, Kappeler F (1979) Neutron-capture cross-section ratios of Pu-240 and Pu-242 versus Au-197 in the energy-range from 50 to 250 keV. *Nucl Sci Eng* 69(1):39–46
- Wisshak K, Voss F, Arlandini C et al (2004) Stellar neutron capture on Ta-180m. I. cross section measurement between 10 keV and 100 keV. *Phys Rev C* 69(5):055801
- Woods R, Mckibben JL, Henkel RL (1974) Los-Alamos 3-stage Van de Graaff facility. *Nucl Instrum Methods* 122(1–2):81–97
- Younes W, Britt HC (2003) Neutron-induced fission cross sections simulated from (t,pf) results. *Phys Rev C* 67(2):024610
- Zerkin VV, McLane V, Herman MW et al (2005) EXFOR-CINDA-ENDF: migration of databases to give higher-quality nuclear data services. *AIP Conf Proc* 769(1): 586
- Zhuravlev BV, Demenkov VG, Lychagin AA et al (2007) A measuring complex for time-of-flight spectrometry of fast neutrons. *Instrum Exp Tech* 50(6):730–736
- Zwillinger D (2003) CRC standard mathematical tables and formulae. CRC Press, Boca Raton



2 Evaluated Nuclear Data

Pavel Obložinský · Michal Herman · Said F. Mughabghab

National Nuclear Data Center, Brookhaven National Laboratory,

Upton, NY, USA

oblozinsky@bnl.gov

mwherman@bnl.gov

mugabgab@bnl.gov

1	<i>Evaluation Methodology for Neutron Data</i>	86
1.1	Basic Ingredients	87
1.2	Thermal and Resolved Resonance Region	89
1.2.1	Thermal Energy Region	89
1.2.2	Westcott Factors and Resonance Integrals	92
1.2.3	Resolved Resonance Energy Region	92
1.3	Unresolved Resonance Region	95
1.4	Fast Neutron Region	97
1.4.1	Optical Model and Direct Reactions	97
1.4.2	Compound Nucleus Decay	98
1.4.3	Width Fluctuation Correction	100
1.4.4	Preequilibrium Models	100
1.4.5	Light Nuclei	101
1.5	Fission	101
1.5.1	Fission Modeling	102
1.5.2	Prompt Fission Neutron Spectra	104
1.5.3	Peculiarities of Fission Cross Section Evaluation	106
2	<i>Neutron Data for Actinides</i>	106
2.1	²³⁵ U Evaluation	106
2.1.1	²³⁵ U, Unresolved Resonance Region	106
2.1.2	²³⁵ U, Fast Neutron Region	107
2.2	²³⁸ U Evaluation	110
2.2.1	²³⁸ U, Resolved and Unresolved Resonance Region	110
2.2.2	²³⁸ U, Fast Neutron Region	111
2.3	²³⁹ Pu Evaluation	115
2.3.1	²³⁹ Pu, Resonance Region	115
2.3.2	²³⁹ Pu, Fast Neutron Region	115
2.4	²³² Th Evaluation	118
2.5	Minor Actinides	119
2.5.1	²³³ U Evaluation	119
2.5.2	^{232,234,236,237,239,240,241} U Evaluations	120
2.6	Thermal Constants	121
2.7	Nubars	121

2.8	Delayed Neutrons	122
2.8.1	Fission-Product Delayed Neutrons	122
2.8.2	^{235}U Thermal $\bar{\nu}_d$	124
2.9	Fission Energy Release	126
2.9.1	Nuclear Heating	126
3	<i>Neutron Data for Other Materials</i>	128
3.1	Light Nuclei	128
3.2	Structural Materials	129
3.2.1	Evaluations of Major Structural Materials	130
3.2.2	New Evaluations for ENDF/B-VII.0	130
3.3	Fission Products	131
3.3.1	Priority Fission Products	131
3.3.2	Complete Isotopic Chains	131
3.3.3	Specific Case of ^{90}Zr	132
3.3.4	Remaining Fission Products	134
4	<i>Covariances for Neutron Data</i>	134
4.1	Evaluation Methodology	135
4.1.1	Resonance Region	136
4.1.2	Fast Neutron Region	137
4.2	Sample Case: Gd	139
4.3	Major Actinides	140
4.3.1	$^{233,235,238}\text{U}$ Covariances	141
4.3.2	^{239}Pu Covariances	141
4.3.3	^{232}Th Covariances	142
4.4	Covariance Libraries	143
4.4.1	Low-Fidelity Covariance Library	144
4.4.2	SCALE-6 Covariance Library	145
4.4.3	AFCI Covariance Library	145
5	<i>Validation of Neutron Data</i>	146
5.1	Criticality Testing	146
5.2	Fast U and Pu Benchmarks	148
5.3	Thermal U and Pu Benchmarks	151
5.3.1	^{235}U Solution Benchmarks	151
5.3.2	U Fuel Rod Benchmarks	153
5.3.3	Pu Solution and MOX Benchmarks	155
5.4	Conclusions from Criticality Testing	156
5.5	Delayed Neutron Testing, β_{eff}	157
5.6	Reaction Rates in Critical Assemblies	157
5.7	Shielding and Pulsed-Sphere Testing	159
5.8	Testing of Thermal Values and Resonance Integrals	161
6	<i>Other Nuclear Data of Interest</i>	162
6.1	Fission Yields	162
6.2	Thermal Neutron Scattering	163
6.2.1	H_2O and D_2O	163
6.2.2	O in UO_2 and U in UO_2	164

6.2.3	H in ZrH	164
6.2.4	Other Modified Materials	164
6.3	Decay Data	165
6.3.1	Decay Heat Calculations	166
7	<i>Evaluated Nuclear Data Libraries</i>	167
7.1	Overview of Libraries	168
7.1.1	General Purpose Libraries	168
7.1.2	Special Purpose Libraries	168
7.1.3	Derived Libraries	170
7.2	ENDF-6 Format	170
7.3	ENDF/B-VII.0 (USA, 2006)	176
7.3.1	Overview of the ENDF/B-VII.0 Library	176
7.3.2	Processing and Data Verification	178
7.4	JEFF-3.1 (Europe, 2005)	179
7.5	JENDL-3.3 (Japan, 2002)	179
7.6	Web Access to Nuclear Data	180
	<i>References</i>	181

Abstract: This chapter describes the current status of evaluated nuclear data for nuclear technology applications. We start with evaluation procedures for neutron-induced reactions focusing on incident energies from the thermal energy up to 20 MeV, though higher energies are also mentioned. This is followed by examining the status of evaluated neutron data for actinides that play a dominant role in most of the applications, followed by coolants/moderators, structural materials, and fission products. We then discuss neutron covariance data that characterize uncertainties and correlations. We explain how modern nuclear evaluated data libraries are validated against an extensive set of integral benchmark experiments. Afterward, we briefly examine other data of importance for nuclear technology, including fission yields, thermal neutron scattering, and decay data. A description of three major evaluated nuclear data libraries is provided, including the latest version of the US library ENDF/B-VII.0, European JEFF-3.1, and Japanese JENDL-3.3. A brief introduction is made to current web retrieval systems that allow easy access to a vast amount of up-to-date evaluated nuclear data for nuclear technology applications.

1 Evaluation Methodology for Neutron Data

The evaluated (recommended) neutron cross-section data represent the backbone of data needed for nuclear technology applications. The incident energies of interest cover an extremely broad energy range of 13 orders of magnitude. Thus, for fission and fusion reactor systems one needs neutrons from 10^{-5} to $2 \times 10^{+7}$ eV (20 MeV), to be extended up to about 200 MeV for accelerator-driven systems. If higher incident energies are needed, one resorts to on-fly calculations (not covered here) rather than to evaluated nuclear data libraries.

Such a large range of incident neutron energies represents an enormous challenge for developers of evaluated nuclear data libraries. This is coupled to another challenge that stems from the fact that nuclear technology applications need data for about 400 atomic nuclei, covering the atomic mass range of $A = 1-250$, from hydrogen to the actinides.

There is no simple way to describe the physics of neutrons interacting with atomic nuclei throughout this vast range of energies and different types of nuclei. Rather, nuclear physics uses different approaches and many different models to describe underlying physics. The role of experimental data in the evaluation process is absolutely crucial, with the understanding that measured data must be combined with physics-based models to fill in the gaps and to gain confidence in the judgment as to what is the best reflection of nature.

The goals for the evaluations are to comply as closely as possible with experimental microscopic (differential) data, and at the same time to accurately match results from simple benchmark (integral) experiments. The evaluation is a complex process, requiring a detailed knowledge of nuclear reaction physics, experimental databases, nuclear modeling, considerable experience, and attention to details. Once the whole set of isotopes (materials) is evaluated and a library is assembled, a validation of the entire library is performed against hundreds of benchmark experiments.

The description of evaluation methodology given below reflects the state-of-the-art methods used in the development of the latest US-evaluated data library, ENDF/B-VII.0. This library, released in December 2006, is described in detail in the extensive paper by Chadwick et al. (2006). The evaluated data are stored in the internationally adopted ENDF-6 format (Herman and Trkov 2009).

1.1 Basic Ingredients

Basic ingredients of the evaluation process for neutron cross-section data include the EXFOR database of microscopic experimental data, *Atlas of Neutron Resonances*, and nuclear reaction model codes. Consequently, the evaluation methodology consists of three parts:

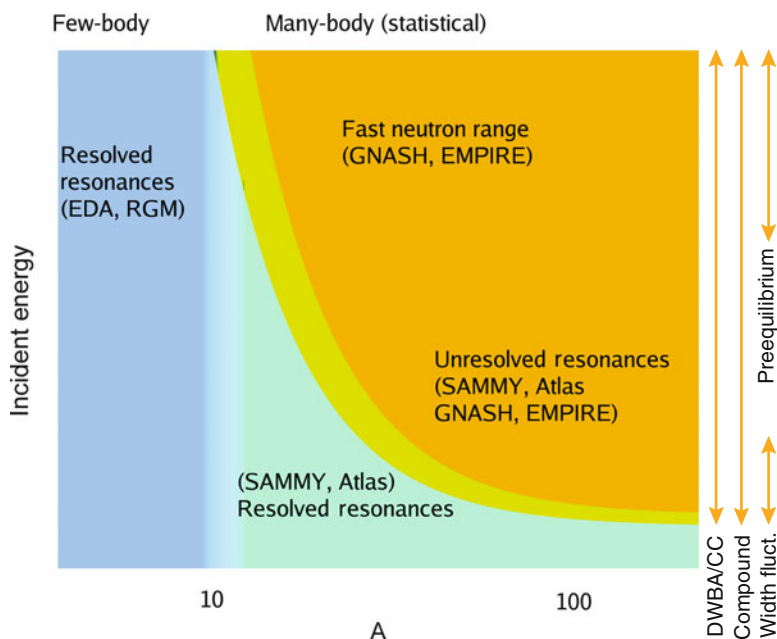
- Careful analysis of microscopic experimental data. (“Microscopic” is the term used by nuclear data physicists to describe properties of individual nuclei and their interactions, which should be distinguished from properties of large-scale ensembles of nuclei. Thus, microscopic cross section is the interaction probability of one neutron incident on a single target nucleus.)
- The low energy region (thermal energy, resolved resonances, and unresolved resonances) is treated by methods developed to analyze neutron resonances.
- The fast neutron region is evaluated using methods based on nuclear reaction model calculations and experimental data.

Nuclear theory and modeling has played a central role in developing complete cross-section evaluations, by which we mean representations that cover all incident projectile energies, outgoing particle and photon energies, as well as angular distributions. Nuclear reaction theory codes provide a powerful tool to interpolate and extrapolate from the measured data, and naturally incorporate constraints such as unitarity, and energy and momentum conservation. A number of reaction physics codes have been developed that support this work:

- Statistical, preequilibrium, direct, and fission models, for use in modeling medium and heavy nucleus reactions, notably Los Alamos National Laboratory (LANL) code GNASH (Young and Arthur, 1977; Young et al., 1992, 1998) and code EMPIRE (Brookhaven National Laboratory, Herman et al., 2005b, 2007), often used in conjunction with coupled-channels optical model code ECIS (CEA Saclay, Raynal, 1994).
- R-matrix codes for light nucleus reactions, and for lower incident energy reactions on heavier targets, notably the Los Alamos code energy-dependent analysis (EDA) (Hale, 1992) and the Oak Ridge code SAMMY (Larson, 2006).
- Atlas code system (Oh et al., 2000) for analyzing neutron resonances in terms of multilevel Breit–Wigner (MLBW) formalism by Mughabghab at Brookhaven to produce a comprehensive evaluation of resonance parameters, thermal cross sections, and average resonance parameters for the *Atlas of Neutron Resonances* (Mughabghab, 2006).

➤ *Figure 1* qualitatively summarizes nuclear reaction models and related codes as used in the ENDF/B-VII.0 evaluations for various combinations of mass number and incident energy. In light nuclei, the excited states are generally sparse and well isolated. This feature necessitates the use of special few-body techniques that are feasible due to a limited number of nucleons in the system. We have used the explicit R-matrix theory, implemented in the Los Alamos code EDA, for evaluations of nuclides up to the atomic mass $A \approx 10$ (with a few exceptions). This approach, although formally strict, relies on experimental input. In ➤ *Fig. 1* the few-body regime is depicted as a vertical rectangle at the left of the picture. Note, that in this case the same methodology is applied throughout the whole energy range.

Increasing the number of nucleons in the target makes usage of few-body models impractical. On the other hand, the large number of excited states facilitates approaches that,



■ Figure 1

Schematic representation depicting the use of various evaluation techniques and related codes (in brackets) depending on target mass and incident energy. Arrows to the right of the figure indicate major reaction mechanisms in the fast neutron region and their energy range of applicability

to a certain extent, are built upon statistical assumptions. This “statistical regime” appears in [Fig. 1](#) to the right of $A \sim 10$. We have to deal with three distinct energy regions for these nuclei:

- Resolved resonance region (including thermal neutrons)
- Unresolved resonance region (URR)
- Fast neutron region

Since the density of neutron resonances increases with A , the upper limit of the resolved resonance region decreases when moving to heavier nuclei. A neighboring region is known as the URR in which overlapping resonances usually produce quite smooth cross sections. Each of these three regions needs different techniques and different reaction modeling.

Except for very light nuclei, there is no theory capable of predicting individual resonances. Therefore, realistic evaluations require experimental data for neutron resonances. In ENDF/B-VII.0, the Reich–Moore approach derived from the R-matrix theory, as implemented in the Oak Ridge code SAMMY, was utilized for the important actinides. For about 150 fission product nuclei, the MLBW formalism and statistical methods from the *Atlas of Neutron Resonances* (Mughabghab, 2006) were used at BNL.

The URR is a transitional region that could be treated with the methods from the resolved region as well as in the terms of the models used in the fast neutron region.

The fast neutron region involves a whole suite of nuclear reaction models with a strong statistical component resulting from the averaging over many resonances. The Hauser–Feshbach

formulation of the compound nucleus is a key model for any evaluation in the fast neutron region, although in the low energy range it must be corrected to account for the width fluctuation effects. At incident energies above some 10 MeV, preequilibrium emission has to be taken into account and one implements a variety of semiclassical and quantum-mechanical models.

While most of the nuclear reaction models used for the evaluations are predominantly phenomenological, their usage involves a huge number of input parameters. The development of the ENDF/B-VII.0 library largely benefited from the reference input parameter library (RIPL) (Ignatyuk et al., 1998; Young et al., 2005; Capote et al., 2009), an international project coordinated by the International Atomic Energy Agency (IAEA), Vienna.

1.2 Thermal and Resolved Resonance Region

Usually, the first step in neutron resonance evaluation is to inspect the well-known compendium of data produced over the years by Mughabghab, BNL, traditionally known as BNL-325. Its fifth and latest edition has been published in 2006 as *Atlas of Neutron Resonances: Resonance Parameters and Thermal Cross Sections* (Mughabghab, 2006), representing a considerable update to the 1981 (Mughabghab et al., 1981) and 1984 editions (Mughabghab, 1984). Often, one is satisfied with these data and adopts them as they are. Indeed, these latest thermal values and resonance parameters provided a basis for more than 150 new evaluations included in ENDF/B-VII.0. In many other cases, however, one performs additional evaluation by applying sophisticated R-matrix analysis to most recent experiments using the Oak Ridge code SAMMY (Larson, 2006).

1.2.1 Thermal Energy Region

Accurate knowledge of the thermal neutron capture and fission cross sections are of paramount importance for many applications and considerable experimental as well as evaluation effort was expended in obtaining precise and consistent constants at a neutron energy of 0.0253 eV (velocity $v_0 = 2,200$ m/s). The parameters under consideration are the absorption (σ_{abs}), radiative capture (σ_γ) and fission (σ_f) cross sections, the neutron yield data ($\bar{\nu}$, η), as well as Westcott factors g_w . Some of these quantities are interrelated as

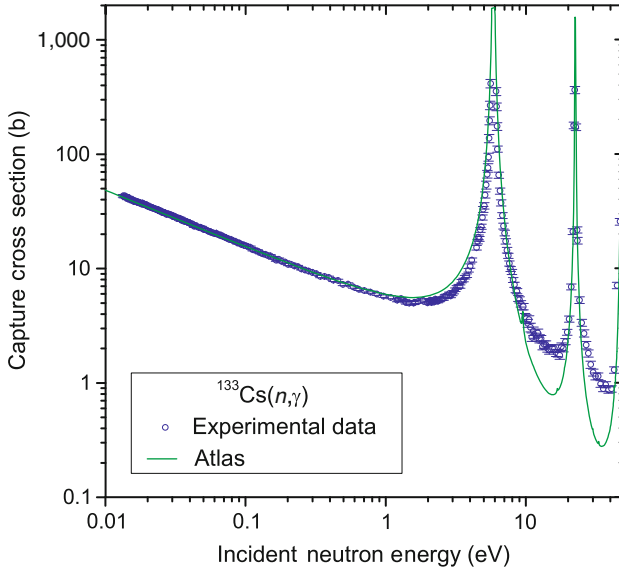
$$\eta = \bar{\nu} \frac{\sigma_f}{\sigma_{\text{abs}}} = \frac{\bar{\nu}}{1 + \alpha}, \quad (1)$$

where $\bar{\nu} = \bar{\nu}_p + \bar{\nu}_d$ is the average number of neutrons emitted per neutron-induced fission obtained by the sum of prompt and delayed values,

$$\sigma_{\text{abs}} = \sigma_\gamma + \sigma_f \quad \text{and} \quad \alpha = \frac{\sigma_\gamma}{\sigma_f}. \quad (2)$$

When the scattering cross section (σ_s) is known, the absorption cross section can be determined absolutely to a high degree of accuracy from a measurement of the total cross section as $\sigma_{\text{abs}} = \sigma_{\text{tot}} - \sigma_s$.

The capture cross section for a single resonance is usually represented by the Breit-Wigner formalism. (“Capture” is the short-hand term used by nuclear physicists to describe



■ Figure 2

Neutron capture cross sections for ^{133}Cs in the thermal and resolved resonance energy region computed from Atlas are compared with experimental data. The calculated cross section is Doppler-broadened to 300 K; the experimental resolution is not included. Two bound levels were invoked in order to fit the thermal constants

radiative capture, i.e., (n, γ) cross sections. This differs from what nuclear engineers might consider “capture,” which is given by the sum of neutron removal cross sections, i.e., $(n, \gamma) + (n, p) + (n, \alpha) + \dots$. In the case of several s-wave resonances, the thermal capture cross section at $E = 0.0253$ eV is given by

$$\sigma_{\gamma}(E) = \frac{2.608 \times 10^6}{\sqrt{E}} \left(\frac{A+1}{A} \right)^2 \sum_j \frac{g_j \Gamma_{nj}^0 \Gamma_{\gamma j}}{\Gamma_j^2 + 4(E - E_{0j})^2}. \quad (3)$$

In this relation, Γ_{nj} , $\Gamma_{\gamma j}$, and Γ_j are the neutron scattering, radiative, and total width of the resonance j , respectively; E_{0j} is the resonance energy, A is the atomic mass number of the target nucleus, and g_j is the statistical spin weight factor defined as

$$g_j = \frac{2J+1}{2(2I+1)}, \quad (4)$$

where J is the resonance spin and I is the target nucleus spin. As an example, ► Fig. 2 shows the evaluated capture cross sections for ^{133}Cs in the thermal along with the low-energy resonance region compared with the available experimental data.

Similarly, the fission cross section can be described as a sum over positive and negative energy resonance contributions. In the framework of the Breit–Wigner formalism, the fission cross section can be obtained from

$$\sigma_f(E) = \frac{2.608 \times 10^6}{\sqrt{E}} \left(\frac{A+1}{A} \right)^2 \sum_j \frac{g_l \Gamma_{nj}^0 \Gamma_{fj}}{\Gamma_j^2 + 4(E - E_{0j})^2}, \quad (5)$$

where

$$\Gamma_j(E) = \Gamma_{nj}(E) + \Gamma_{\gamma j} + \Gamma_{fj}. \quad (6)$$

The formalism for neutron elastic scattering is more complicated. Thus, the elastic cross section for a single resonance can be expressed by the sum of three terms

$$\sigma_n(E) = 4\pi \frac{2I+1}{k^2} \sin^2 \phi_l + \pi \frac{g_l}{k^2} \frac{\Gamma_n \Gamma \cos(2\phi_l) + 2(E - E_0) \Gamma_n \sin(2\phi_l)}{(E - E_0)^2 + \frac{1}{4} \Gamma^2}, \quad (7)$$

where k is the neutron wave number, ϕ_l are the phase shifts determined by k , and the potential scattering radius R' . The first term describes potential scattering, σ_{pot} , which is nearly constant as a function of energy. The second term stands for the symmetric resonance cross section. The third term, containing $2(E - E_0) \Gamma_n \sin(2\phi_l)$ in the numerator, describes interference between potential (hard-sphere) and resonance scattering, which is negative at $E < E_0$ and positive at $E > E_0$. Note that Eq. (7) does not include resonance–resonance interference term.

In order to obtain the thermal scattering cross section, one should resort to an extended version of the above expression, such as provided by the MLBW formalism. We note that in the low-energy approximation simplified expressions can be obtained, including that for potential scattering

$$\sigma_{\text{pot}} \approx 4\pi R'^2. \quad (8)$$

The neutron scattering can also be expressed in terms of spin-dependent free nuclear scattering lengths, a_+ and a_- , associated with spin states $I + 1/2$ and $I - 1/2$, as

$$a_{\pm} = R' + \sum_j \frac{\lambda_j \Gamma_{nj}}{2(E - E_{0j}) - i\Gamma_j}, \quad (9)$$

where $\lambda_j = 1/k$ is de Broglie's wavelength divided by 2π . We note that a_{\pm} contain imaginary components and the summation is carried out over all s-wave resonances with the same spin.

The total coherent scattering length for nonzero spin target nuclei is then the sum of the spin-dependent coherent scattering widths, a_+ and a_- , weighted by the spin statistical factor, $g_+ = (I + 1)/(2I + 1)$ and $g_- = I/(2I + 1)$,

$$a = g_+ a_+ + g_- a_-. \quad (10)$$

The total scattering cross section can then be expressed as

$$\sigma_s = 4\pi (g_+ a_+^2 + g_- a_-^2). \quad (11)$$

If the results of the calculated cross sections do not agree with measurements within the uncertainty limits, then one or two negative energy (bound) levels are invoked.

The potential scattering length or radius, R' , is an important parameter, which is required in the calculation of scattering and total cross sections. It can be expressed as

$$R' = R(1 - R^\infty), \quad (12)$$

where R is the channel or interaction radius, and R^∞ is related to the distant s-wave resonance contribution. We note that R' can be determined to a high degree of accuracy from the measured coherent scattering amplitude by (9) when the resonance data are complete.

1.2.2 Westcott Factors and Resonance Integrals

In general, in the thermal energy region, capture cross sections follow the $1/v$ law, where v is the neutron velocity. Deviations from this behavior are due to the proximity of the first resonance to the thermal energy of 0.0253 eV, notable examples being ^{113}Cd , ^{149}Sm , and ^{155}Gd . Westcott factors, ideally equal to unity, can be used as a suitable measure of the validity of this law. They are defined as the ratio of the Maxwellian averaged cross section, σ , to the thermal cross section, σ_0 ,

$$g_w = \frac{\sigma}{\sigma_0} = \frac{1}{v_0 \sigma_0} \int_0^\infty \frac{1}{\pi^{1/2}} \frac{v^3}{v_T^3} e^{-v^2/v_T^2} \sigma(v) dv, \quad (13)$$

where $v_0 = 2,200$ m/s and v_T is the most probable velocity for Maxwellian spectrum at temperature T .

Resonance integrals represent useful quantities that characterize cross sections in the thermal and resonance region. For a particular reaction $\sigma_x(E)$, such as total, elastic scattering, capture, and fission ($x = \text{tot}, s, \gamma, f$), in a $1/E$ spectrum these are defined as

$$I_x = \int_{0.5 \text{ eV}}^\infty \sigma_x(E) \frac{dE}{E}, \quad (14)$$

where the low energy is determined by the cadmium cutoff energy usually set to 0.5 eV, while the upper energy is sometimes set to 100 keV (JEFF3, 2005). It is important to note that both the thermal energies and resonances contribute to the resonance integrals.

Often Westcott factors and resonance integrals are readily available in tabulated form, an example being JEFF-3.1 library (JEFF3, 2005). They can also be conveniently obtained from the web using retrieval systems such as Sigma (Pritychenko and Sonzogni, 2008) developed and maintained by the National Nuclear Data Center (NNDC) at Brookhaven.

1.2.3 Resolved Resonance Energy Region

Neutron time-of-flight techniques that employ accelerator facilities as neutron sources are used to perform high-resolution cross-section measurements in the resonance region. Then, the measured data are analyzed by a state-of-the-art tool such as SAMMY (Larson, 2006). This code combines multichannel multilevel R-matrix formalism with corrections for experimental conditions to fit experimental data using generalized least-squares fitting procedures.

Resolved resonances are described by the R-matrix collision theory, which is exact, and the resulting formalism is fairly transparent, though the expressions look rather formidable. In practical applications, several approximations are widely used. The most precise is Reich–Moore followed by the MLBW, while the least precise is single-level Breit–Wigner (SLBW). In ENDF/B-VII.0 library, Reich–Moore is mostly used for actinides, MLBW is adopted for majority of other materials, while SLBW was essentially abandoned and its use is restricted to the URR.

R-matrix channels are characterized by the two particles with spin i and I , the orbital angular momentum l , the channel spin s (where $s = i \pm I$), and the total spin J (where $\vec{J} = \vec{s} + \vec{I}$) and parity π . Those channels having the same J and π (the only two quantum numbers that are conserved) are collected in the same spin group. Resonances (which appear generally as peaks in the cross sections) are assigned to particular spin groups depending on their individual characteristics; initial assignments may be changed as knowledge is gained during the evaluation process. The goal of the evaluation is to determine those values for the resonance energy (peak position), channel widths, and spin for each of the resonances that provide the best fit to the measured data.

In general, partial cross sections can be obtained from a collision matrix U_{ab} , which connects entrance channels a with exit channels b . The formalism, applied to neutron reactions, implies $a = n$ and

$$\sigma_{nb} = \frac{\pi}{k^2} g_J |\delta_{nb} - U_{nb}|^2, \quad (15)$$

where k is the neutron wave number and δ_{nb} is the Kronecker delta symbol. These partial cross sections must be summed over the appropriate entrance and exit channels to yield observable cross sections. The statistical factor g_J is the probability of getting the correct angular momentum J from the spins of collision partners, and π/k^2 relates probability and cross section.

In the Reich–Moore formalism as implemented in ENDF-6, the only reactions requiring explicit channel definitions are total, elastic scattering and fission; capture is obtained by subtraction (although it is possible to obtain it directly from the collision matrix elements). Neutron channels are labeled by quantum numbers, l , s , and J .

The channel spin s is the vector sum of the target spin I and the neutron spin $i = 1/2$, and takes on the range of values $|I - 1/2|$ to $I + 1/2$. The total angular momentum J is the vector sum of l and s , and runs from $|l - s|$ to $l + s$. The fission channels $f1$ and $f2$ do not correspond to individual two-body fission product breakup, but to Bohr-channels in deformation space, which is why two are adequate for describing many neutron-induced fission cross sections.

If one sums over all incident channels n and exit channels b , and invokes unitarity, the resulting total cross section can be expressed in terms of the diagonal matrix elements as

$$\sigma_{\text{tot}}(E) = \frac{2\pi}{k^2} \sum_{lsJ} \sum_{l's'J'} g_J \text{Re}[1 - U_{lsJ,l's'J'}]. \quad (16)$$

The elastic cross section is obtained by summing the incident neutron channels over all possible lsJ values and the exit neutron channels over those quantities $l's'J'$ that have the same ranges as lsJ . The conservation of total angular momentum requires that $J' = J$; usually additional, simplifying conservation rules are imposed, namely, $l' = l$ and $s' = s$. The sixfold summation then reduces to the familiar form

$$\sigma_{nn}(E) = \frac{2\pi}{k^2} \sum_{lsj} g_J |1 - U_{lsj,lsj}|^2. \quad (17)$$

The absorption (nonelastic) cross section is obtained by subtraction

$$\sigma_{\text{abs}}(E) = \sigma_{\text{tot}}(E) - \sigma_{nn}(E). \quad (18)$$

Fission is obtained from the collision matrix by summing (15) over all incident lsj values and over the two exit fission channels, $b = f1$ and $b = f2$,

$$\sigma_f(E) = \frac{2\pi}{k^2} \sum_{lsj} g_J \left(|U_{nf1}^{lsj}|^2 + |U_{nf2}^{lsj}|^2 \right). \quad (19)$$

The level-matrix form of the collision matrix is given as

$$U_{nb}^J = e^{-i(\phi_n + \phi_b)} \left\{ 2[(1 - K)^{-1}]_{nb} - \delta_{nb} \right\}, \quad (20)$$

where

$$(1 - K)_{nb}^{-1} = \delta_{nb} - \frac{i}{2} \sum_r \frac{\Gamma_{nr}^{1/2} \Gamma_{br}^{1/2}}{E_r - E - i \Gamma_{\gamma r} / 2}. \quad (21)$$

Here, ϕ_b is zero for fission, $\phi_n = \phi_l$, and the summation is over those resonances r that have partial widths in both of the channels n and b ; E_r is the resonance energy; $\Gamma_{\gamma r}$ is the “eliminated” radiation width; Γ_{nr} and Γ_{br} are the partial widths for the r th resonance in channels n and b .

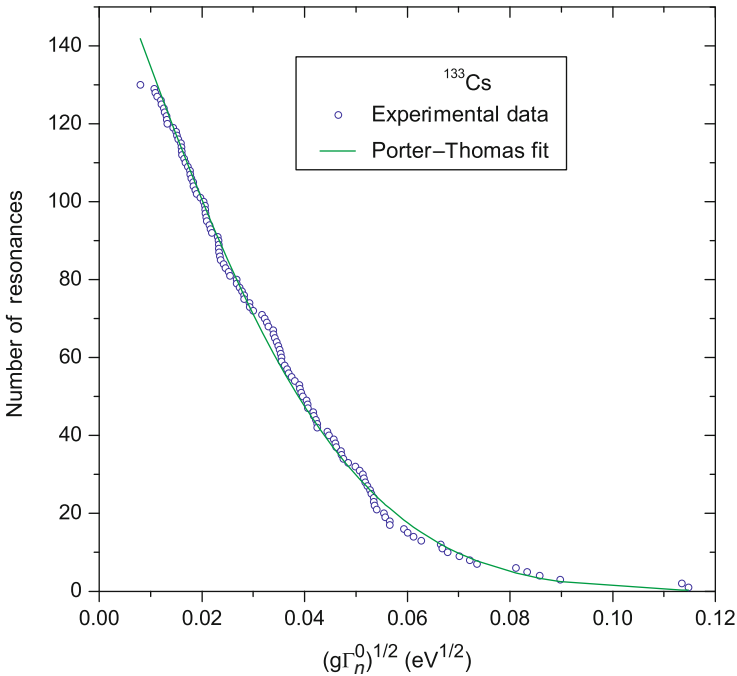
The shift factor has been set equal to zero in the above equations ($E_r' \rightarrow E_r$); hence they are strictly correct only for s-wave resonances. Originally, the ENDF Reich–Moore format was used for low-energy resonances in fissile materials, which are s-waves. However, it is believed that the “no-shift” formulae can be safely applied to higher l -values also, since the difference in shape between a shifted resonance and one that is not shifted at the same energy has no practical significance.

One of the tasks of the evaluator is to assign the orbital momentum, l , for resonances where this has not been done experimentally. In the *Atlas of Neutron Resonances* this was done by the Bayesian approach that assigns these values probabilistically. The first investigators to apply Bayes’ conditional probability for the determination of parities of ^{238}U resonances were Bollinger and Thomas (1968). Subsequently, Perkins and Gyullassy (1972) and Oh et al. (2000) extensively applied this procedure in the evaluation of resonance parameters.

For a resonance with a neutron width weighted by the spin statistical factor, $g_J \Gamma_n$, the probability that this resonance is p-wave is given according to Bayes’ theorem of conditional probability by

$$P(p|g_J \Gamma_n) = \left(1 + \frac{P(g_J \Gamma_n | s) \langle D_1 \rangle}{P(g_J \Gamma_n | p) \langle D_0 \rangle} \right)^{-1}, \quad (22)$$

where $\langle D_1 \rangle / \langle D_0 \rangle$ are the level-spacing ratio, and $P(g_J \Gamma_n | s)$ is the probability that the neutron width is $g_J \Gamma_n$ if the resonance is s-wave and similarly for p-waves. The Bayesian equation can be solved by taking into account the Porter and Thomas (1956) distribution and taking into account $(2J + 1)$ degeneration of nuclear levels.



■ Figure 3

Porter–Thomas distribution of reduced neutron widths, $g\Gamma_n^0$, for s-wave resonances of ^{133}Cs in the energy region below 3,400 eV

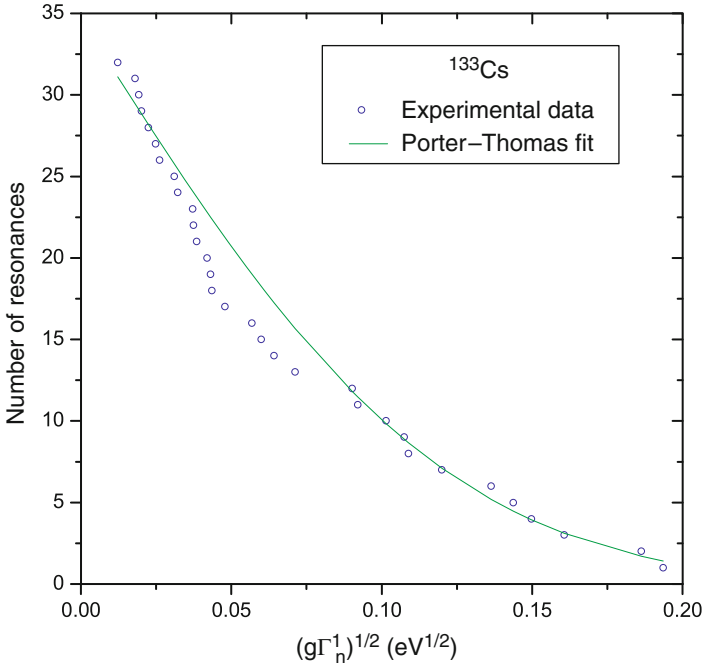
► Figures 3 and ► 4 illustrate the Porter–Thomas analysis as applied to the s- and p-wave resonances of ^{133}Cs . From this procedure also the average level spacings and strength functions for the s- and p-waves are determined, see (26) and (27).

1.3 Unresolved Resonance Region

In the URR, the situation is different than in the resolved resonance energy region. The experimental resolution is larger than the width of the resonances and individual resonance parameters can no more be extracted from cross-section fitting. The formalism used for cross-section treatment in URR is therefore based on average values of physical quantities obtained in the resolved resonance range. The values for statistical quantities are determined from the resolved energy region and used as starting values for the unresolved evaluation.

The theoretical basis for URR description is the Lane–Lynn approach (Lane and Lynn, 1957), which for capture gives

$$\langle \sigma_Y \rangle = \sum_{Jl} \langle \sigma_Y \rangle_{Jl} = \frac{2\pi^2}{k^2} \sum_{Jl} \langle \Gamma_Y \rangle_l S_l V_l E_n^{1/2} g_J \frac{F(\alpha_{Jl})}{\langle \Gamma_J \rangle}, \quad (23)$$



■ Figure 4

Porter-Thomas distribution of reduced neutron widths, $g\Gamma_n^1$, for p-wave resonances of ^{133}Cs in the energy region below 387 eV where the p-wave resonances are detected

where the averaged quantities are given in brackets $\langle \rangle$, V_l is the penetrability factor divided by kR ; $F(\alpha_{jl})$ is the fluctuation factor, α_{jl} being the ratio of mean radiative and neutron widths; summation is carried over partial waves l and spins J .

The URR is treated within the SLBW formalism, which requires the following parameters: the average level spacing, D_l , the strength functions, S_l , the average radiative widths, $\Gamma_{\gamma l}$, and R' . After the determination of l values for all resonances, the reduced neutron widths are analyzed in terms of the Porter-Thomas distribution (Porter and Thomas, 1956) if the number of measured resonances is large enough for a statistical sample.

Instead of working with the Porter-Thomas distribution, it is often much simpler to analyze the resonance parameter data with the cumulative Porter-Thomas distribution. Since resonances with small neutron widths are usually missed in measurements, it is necessary to exclude resonances whose reduced widths are smaller than a certain magnitude. By setting a cutoff value, that is, a minimum magnitude of reduced neutron width, the effect of missed small resonances on the resulting average parameters is reduced significantly. The result is

$$N(y) = N_r(1 - \text{erf}(y)), \quad (24)$$

where erf is the error function, N_r is the corrected total number of resonances, and $N(y)$ is the total number of resonances with reduced neutron width larger than a specified value y ,

$$y = \left(\Gamma_n^l / 2 \left\langle \Gamma_n^l \right\rangle \right)^{1/2}, \quad (25)$$

where Γ_n^l is the reduced neutron width for orbital angular momentum l and $\langle \Gamma_n^l \rangle$ is its average value. The two parameters N_r and $\langle g\Gamma_n^l \rangle$ are determined through the fitting procedure.

The resulting average level spacing D_l and neutron strength function S_l in a determined energy interval ΔE are then calculated by

$$D_l = \frac{\Delta E}{N_r - 1}, \quad (26)$$

$$S_l = \frac{\langle g\Gamma_n^l \rangle}{(2l + 1)D_l}. \quad (27)$$

The average radiative widths of neutron resonances are determined from measurements in the resolved energy region by calculating the weighted as well as unweighted values. For nuclei with unmeasured radiative widths, the systematics of s-, p-, and d-wave radiative widths as a function of atomic mass number are used (Mughabghab, 2006).

► *Figure 5* shows the evaluated capture cross sections in the unresolved energy resonance region, compared with the available experimental data for ^{133}Cs . The URR is extended up to the first excited level, which is 90 keV for ^{133}Cs . At higher energies (fast neutrons), the evaluations were done by the code EMPIRE. We note an excellent match of cross sections in the boundary of the two energy regions.

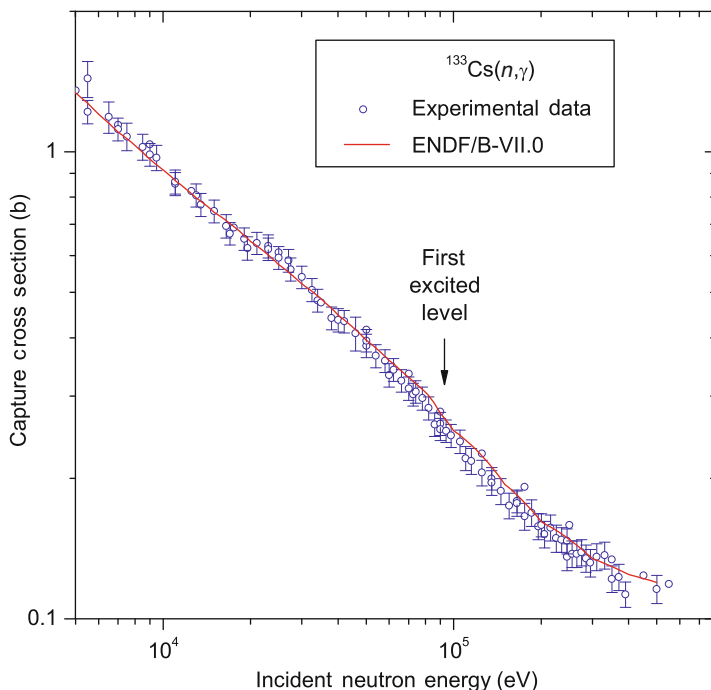
We note that in the code SAMMY, the unresolved resonance formalism is based on the methodology adopted by the statistical model code FITACS developed by Fröhner (1982). Values of the average parameters are found from fitting the calculated cross sections to experimental cross sections. The set of parameters that best reproduces the data cannot be reported directly to ENDF/B because the ENDF-6 format uses a less rigorous SLBW representation. SAMMY/FITACS parameters must therefore be converted into average widths before insertion into ENDF/B library.

1.4 Fast Neutron Region

Fast neutron region is defined as incident energies above the URR (materials with $Z > 42$) or above resolved resonances that vary between hundreds keV–MeV for light nuclei and eV–keV for actinides. The upper end of the fast neutron region is in general 20 MeV, though in about 10% cases in ENDF/B-VII.0 this has been extended to 150–200 MeV. In this energy range, several distinct nuclear reaction models are used to describe the interaction of fast neutrons with atomic nuclei.

1.4.1 Optical Model and Direct Reactions

Spherical optical model is usually used to calculate transmission coefficients for all ejectiles involved in a reaction. In the case of spherical nuclei, the same calculations also determined



■ Figure 5

Neutron capture cross section for ^{133}Cs in the unresolved resonance energy region extended up to the first excited level. The evaluation at higher energies was performed by EMPIRE. Evaluation adopted by ENDF/B-VII.0 is compared with experimental data

reaction (absorption) cross sections. For deformed nuclei, the incident channel is treated in terms of coupled-channels rather than the spherical optical model. In the latter case, proper coupling also provided cross sections for inelastic scattering to collective levels and related angular distributions of scattered neutrons. In certain cases we also included direct scattering to the collective levels embedded in the continuum. Generally, we chose optical model potentials from a vast selection available in the RIPL library (Capote et al., 2009), but in the course of ENDF/B-VII.0 development the original RIPL potentials were often adjusted to improve agreement with recent experimental data or to match the cross section obtained in the unresolved resonance evaluation, and in some cases totally new potentials were constructed.

1.4.2 Compound Nucleus Decay

The statistical model provides the basic underpinning for the whole evaluation procedure. The decay of the compound nucleus (CN) is modeled by the Hauser-Feshbach equations, using transmission coefficients and level densities to represent the relative probabilities of decay in the various open channels.

Schematically, the cross section for a reaction (a, b) that proceeds through the compound nucleus mechanism can be written as

$$\sigma_{a,b} = \sigma_a \frac{\Gamma_b}{\sum_c \Gamma_c}. \quad (28)$$

The summation over compound nucleus spin J and parity π , and integration over excitation energy E is implicit in (28). The decay width Γ_c is given by

$$\Gamma_c = \frac{1}{2\pi\rho_{CN}(E)} \sum_{c'} \int_0^{E-B_c} \rho_c(E') T_c(E - B_c - E') dE', \quad (29)$$

where B_c is the binding energy of particle c in the compound nucleus, ρ is the level density, and $T_c(\epsilon)$ stands for the transmission coefficient for particle c having channel energy $\epsilon = E - B_c - E'$. Again, for simplicity, we drop explicit reference to the spin and parity in (29) and the summation extends over all open channels c' . For low incident energies, (28) needs to be corrected for width fluctuation corrections. Since the evaluations extend at least up to 20 MeV, sequential multiparticle emission had to be included in the Hauser–Feshbach calculations, which in practice implies an energy convolution of multiple integrals of the type of (29).

In order to account for the competition between γ -emission and emission of particles along the deexcitation chain, our calculations always involve a full modeling of the γ -cascade that conserves angular momentum. The formalism for γ -rays transitions is based on the giant dipole resonance (GDR) model known as the Brink–Axel hypothesis (Alex, 1962; Brink, 1955, unpublished). GDR parameters are taken from the experimental compilation and/or systematics contained in the RIPL library. We note, that our calculations account for GDR splitting due to nuclear deformation. In GNASH, the γ -ray transmission coefficients are obtained from the γ -ray strength function formalism of Kopecky and Uhl (1990). EMPIRE allows for a suite of γ -ray strength functions. Typically, we used Mughabghab and Dunford’s prescription known as GFL (Mughabghab and Dunford, 2000) or Plujko’s modified Lorentzian referred to as MLO1 (Plujko and Herman, 2006). In both codes, the γ -ray strength functions can be, and often are, normalized to experimental information on $2\pi\Gamma_\gamma/D_0$ or adjusted to reproduce capture cross sections.

Nuclear level densities along with optical model transmission coefficients are the two most important ingredients of the statistical model. In GNASH, the description of the level densities in the continuum follows the Ignatyuk form of the Gilbert–Cameron formalism, including a washing out of shell effects with increasing excitation energy. Most of the evaluations performed with EMPIRE employed level densities that are specific to the EMPIRE code. The formalism uses the superfluid model below a critical excitation energy and the Fermi gas model at energies above it. Collective enhancements due to nuclear vibration and rotation are taken into account in the nonadiabatic approximation, that is, they are washed out when excitation energy increases. Differently from other formulations, EMPIRE-specific level densities explicitly account for the rotation-induced deformation of the nucleus and determine spin distributions by subtracting rotational energy from the energy available for intrinsic excitations.

1.4.3 Width Fluctuation Correction

At low incident energies, the statistical approximation that entrance and exit channels are independent (Bohr independence hypothesis) is not valid anymore due to correlations between entrance and exit channels. The Hauser–Feshbach equations have to be modified in order to include the so-called width fluctuation correction factors accounting for the coupling between the incident and outgoing waves in the elastic channel.

The GNASH code does not calculate these correction factors but rather imports them as the result from an auxiliary code (usually COMNUC, Dunford, 1971, which uses the Moldauer model). EMPIRE, by default, uses internal implementation of the HRTW approach (Hofmann et al., 1975) that can be summarized with the following equation:

$$\sigma_{ab}^{HRTW} = V_a V_b \left(\sum_c V_c \right)^{-1} [1 + \delta_{ab} (W_a - 1)]. \quad (30)$$

This formula is, essentially, equivalent to the Hauser–Feshbach expression (28) but the elastic channel is enhanced by the factor W_a . In (30) the quantities V_c replace optical model transmission coefficients that appear in the original Hauser–Feshbach formula.

1.4.4 Preequilibrium Models

The probability that a system composed of an incident neutron and a target nucleus decays before thermal equilibrium is attained becomes significant at incident energies above 10 MeV. In any preequilibrium model, the excited nuclear system (composite nucleus) follows a series of ever more complicated configurations, where more and more particle-hole (p-h) states are excited. In each stage, a possible emission of a particle competes with the creation of an intrinsic particle-hole pair that brings the system toward the equilibrium stage. Particle emission from the early stages is characterized by a harder spectrum and forward peaked angular distributions.

The exciton model is a semiclassical formulation of the preequilibrium emission that is used in GNASH and EMPIRE. The core of the model is the so-called master-equation that governs time dependence of occupation probabilities, P_n , for various p-h stages

$$\hbar \frac{dP_n}{dt} = \sum_m \Lambda_{n,m} P_m - \Gamma_n P_n, \quad (31)$$

where the total decay width of the stage n is given in terms of the partial transition widths $\Lambda_{l,n}$ and partial width $\Gamma_{e,n}$ for the emission of particle e by

$$\Gamma_n = \sum_l \Lambda_{l,n} + \sum_e \Gamma_{e,n}. \quad (32)$$

Due to the two-body nature of the nuclear force, intrinsic transitions occur only between neighboring stages, and the transition matrix Λ is tri-diagonal, the off-diagonal terms accounting for backward and forward transitions.

In GNASH, the preequilibrium phase is addressed through the semiclassical exciton model in combination with the Kalbach angular-distribution systematics (Kalbach, 1988). These systematics provide a reasonably reliable representation of the experimental database.

EMPIRE implements a suite of preequilibrium codes including two versions of the exciton model (PCROSS and DEGAS, Běták and Obložinský, 1993), and the Monte-Carlo approach DDHMS (Blann, 1996; Blann and Chadwick, 1998, 2000) in addition to the quantum-mechanical multistep direct (MSD) and multistep compound models.

A new Monte Carlo preequilibrium model allows unlimited emission of preequilibrium neutrons and protons, and is therefore well suited for the study of high-energy reactions up to a few hundreds of MeV. The model of choice in EMPIRE is the statistical MSD theory of preequilibrium scattering to the continuum originally proposed by Tamura, Udagawa, and Lenske (TUL) (Tamura et al., 1982). The evolution of the projectile-target system from small to large energy losses in the open channel space is described in the MSD theory with a combination of direct reaction (DR), microscopic nuclear structure, and statistical methods.

The modeling of multistep compound (MSC) processes in EMPIRE follows the approach of Nishioka et al. (NVWY) (1986). The formal structure of the NVWY formula resembles the matrix representation of the master-equation typical for classical preequilibrium models. However, the NVWY formalism is strictly derived from basic principles. Microscopic quantities that constitute ingredients of the NVWY formula were linked to the macroscopic, experimentally known, quantities in Herman et al. (1992), which was an essential step allowing for practical application of the theory.

1.4.5 Light Nuclei

In the case of light nuclei (from hydrogen to oxygen, $A = 1-18$, which mostly serve as coolants and moderators), the statistical approach cannot be applied and the above methodology should be replaced by the R-matrix approach. In the USA, this approach is pursued by Los Alamos and virtually all light nuclei evaluations in ENDF/B-VII.0 were performed by the EDA code developed over the years by Hale (1992, 2008), which is based on R-matrix formalism in its most general form.

R-matrix theory is a general framework for describing nuclear reactions that are particularly well suited for including resonances. It is the mathematically rigorous phenomenological description of what is actually seen in an experiment. This is not a model of neutron–nucleus interaction, rather it parametrizes measurements in terms of observable quantities. This theory properly describes multichannel nuclear reactions and builds in all the fundamental conservation laws, symmetries, and analytic properties of nuclear interactions. The experimental cross-section data from all relevant reactions, including neutron and charged particles, are taken into account and fitted simultaneously. This allows obtaining a single set of multichannel, multilevel R-matrix parameters that describe all the desired neutron-induced cross sections for light nucleus under consideration.

1.5 Fission


Nuclear fission remains the most complex topic in applied nuclear physics. Since its discovery, it has remained an active field of research, and from the evaluation point of view it poses one of the most difficult problems.

1.5.1 Fission Modeling

The status of fission modeling and related parametrization relevant to evaluation is summarized in the extensive paper dedicated to the RIPL by Capote et al. (2009). The main concepts of nuclear fission theory are based essentially on the liquid-drop model (Bohr and Wheeler, 1939; Frenkel, 1939). According to this model, when a nucleus is being deformed, the competition between the surface tension of a nuclear liquid drop and the Coulomb repulsion related to the nuclear charge leads to the formation of an energy barrier, which prevents spontaneous decay of the nucleus by fission. The penetrability of this barrier depends on its height and width and is a dominant factor in determining the fission cross section. Decrease in height and/or width results in an exponential increase in barrier penetrability, which leads to increased fission.

For most of the practical calculations, one-dimensional fission barrier is considered. The present knowledge indicates that the pre-actinides have single-hump barriers, while the actinides have double- or triple-humped barriers. Usually, the barriers are parametrized as a function of the deformation (β) by inverted parabolas,

$$B_i(\beta) = B_{fi} - \frac{1}{2}\mu\hbar^2\omega_i^2(\beta - \beta_i)^2, \quad i = 1, N, \quad (33)$$

where N is the number of humps, the energies B_{fi} represent maxima of the deformation potential, β_i are the deformations corresponding to these maxima (saddle points), the harmonic oscillator frequencies ω_i define the curvature of the parabolas, and μ is the inertial mass parameter approximated usually by a semiempirical expression.  Figure 6 illustrates the relationship among the above-mentioned quantities in a typical case of a double-humped fission barrier ($N=2$). The quasi-stationary states in the second well (the class II states) are also depicted in the plot.

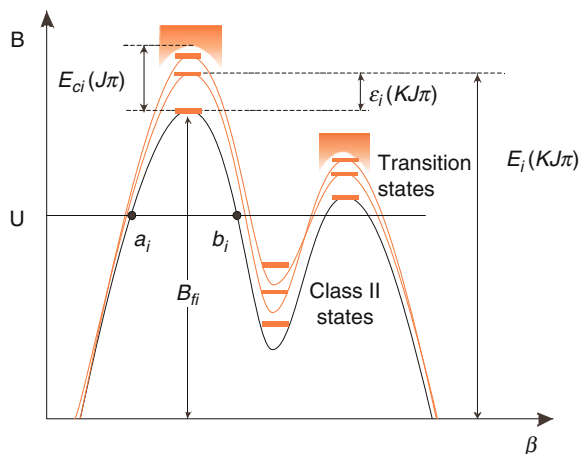



 Figure 6

Energy of a double-humped fission barrier in function of the deformation β along with associated barrier parameters: B_{fi} is the height of the fundamental fission barrier i ; $\epsilon_i(KJ\pi)$ is the energy of the transition state i ; $E_{ci}(J\pi)$ is the cutoff energy, above which the continuum starts for a barrier i . Fission barriers associated with each discrete transition state are shown


Above each barrier hump there is a spectrum of excited levels commonly referred to as transition states. Close to the top of the hump these levels are well separated and can be treated individually while at higher excitation energies (above E_{ci}) the concept of level densities must be invoked, as indicated in  Fig. 6 with the shaded regions. The discrete transition states for all barriers i ($i = 1, 2$ for a double-humped barrier) are obtained by building rotational levels on top of vibrational or non-collective levels that serve as a base (bandheads). They are characterized by a set of quantum numbers (angular momentum J , parity π , and angular momentum projection on the nuclear symmetry axis K) with the excitation energies

$$E_i(KJ\pi) = B_{fi} + \epsilon_i(KJ\pi) = B_{fi} + \epsilon_i(K\pi) + \frac{\hbar^2}{2\mathcal{I}_i} [J(J+1) - K(K+1)], \quad (34)$$

where $\epsilon_i(K\pi)$ are the bandhead energies and $\hbar^2/2\mathcal{I}_i$ are the inertial parameters. A parabolic barrier with height $E_i(KJ\pi)$ and curvature $\hbar\omega_i$ is associated with each transition state.

The transmission coefficients through each hump are expressed in first-order approximation in terms of the momentum integrals for the humps

$$K_i(U) = \pm \left| \int_{a_i}^{b_i} \sqrt{2\mu[U - B_{fi}(\beta)]/\hbar^2} d\beta \right|, \quad i = 1, 2, \quad (35)$$

where a_i and b_i are the points indicated in  Fig. 6 and U is the excitation energy in the fissioning nucleus. The + sign is taken when the excitation energy U is lower than the hump under consideration and the - sign when it is higher. In the case of a single parabolic barrier, (35) yields the well-known Hill–Wheeler transmission coefficient (Bjornholm and Lynn, 1980a)

$$T_i^{HW}(U) = \frac{1}{1 + \exp[-(2\pi/\hbar\omega_i)(U - B_{fi})]}. \quad (36)$$

The total fission transmission coefficient for a given excitation energy U , spin J , and parity π is determined by summing the penetrabilities through barriers associated with all allowed transition levels, that is,

$$T_i(UJ\pi) = \sum_{K \leq J} T_i(UK\pi) + \int_{E_{ci}}^{\infty} \frac{\rho_i(\epsilon J\pi) d\epsilon}{1 + \exp[-\frac{2\pi}{\hbar}\omega_i(U - B_{fi} - \epsilon)]}. \quad (37)$$

The sum runs over all the discrete transition levels having the same spin J and parity π as those of the decaying compound nucleus, and the integration runs over the continuum of the transition levels described by the level densities $\rho_i(\epsilon J\pi)$. Usually the wells are considered deep enough so that the transmission coefficient can be averaged over the intermediate structures. For a double-humped barrier the fission coefficient becomes

$$T_f(UJ\pi) = \frac{T_1(UJ\pi)T_2(UJ\pi)}{T_1(UJ\pi) + T_2(UJ\pi) + T_{\gamma_{II}}(UJ\pi)}, \quad (38)$$

where T_1 and T_2 are the penetrabilities of the inner and the outer humps, respectively, calculated according to (37), and $T_{\gamma_{II}}$ is the probability for gamma decay in the second well.

Finally, the relation used in the statistical model for the fission cross section is

$$\sigma_{a,f}(E) = \sum_{J\pi} \sigma_a(EJ\pi)P_f(EJ\pi), \quad (39)$$


where $\sigma_a(EJ\pi)$ is the population of the fissioning nucleus in the state $EJ\pi$, and $P_f(EJ\pi)$ represents the fission probability computed for a specific representation of fission barrier. The fission probability is usually defined as the ratio of the fission coefficient T_f to the sum of all the transmission coefficients including the competing channels $\sum_d T_d$,

$$P_f(EJ\pi) = \frac{T_f(EJ\pi)}{T_f(EJ\pi) + \sum_d T_d(EJ\pi)}. \quad (40)$$

Similar definitions apply for other decay probabilities.


In GNASH, fission probabilities are calculated from the quantum-mechanical transmission coefficient through a simple double-humped fission barrier, using uncoupled oscillators for the representation of the barriers. The barrier penetrabilities are computed using the Hill–Wheeler formula for inverted parabolas. An additional parameter is used to account for level density enhancement due to asymmetry at saddle points (Young et al., 1998).

Version 2.19 (Lodi) of the EMPIRE code introduced an advanced fission formalism that is applicable to multi-chance fission induced by light particles and photons. It uses an optical model for fission, that is, allows for an absorption through the imaginary potential in the second well, to calculate transmission through coupled single-, double-, and triple-humped fission barriers. Such calculations can start from sub-barrier excitation energies. In the case of a double-humped barrier, the expression is generalized to account for multimodal fission. For light actinides, a triple-humped fission barrier with a shallow tertiary well, which accommodates undamped vibrational states, is employed. This fission model can provide a good description of experimental data, including gross vibrational resonant structure at sub-barrier energies.

As an example of the complexity of the fission channel modeling in EMPIRE, we show ^{232}Th fission cross sections in  Fig. 7. Fine details can be seen in the insert, revealing complex resonance-like structure of fission in the threshold energy region. These fine details are fully described by the model, with the caveat that the fission model parametrization was obtained from careful fits to data.

1.5.2 Prompt Fission Neutron Spectra

One of the most intriguing aspects of evaluation of actinides are prompt neutron fission spectra. The Los Alamos (Madland–Nix) model of the prompt fission neutron spectrum and average prompt neutron multiplicity is based upon classical nuclear evaporation theory and utilizes an isospin-dependent optical potential for the inverse process of compound nucleus formation in neutron-rich fission fragments (Madland and Nix, 1982). This model, in its exact energy-dependent formulation, has been used to calculate the prompt fission neutron spectrum matrix for the $n + ^{235}\text{U}$, $n + ^{238}\text{U}$, and $n + ^{239}\text{Pu}$ systems, and these appear in ENDF/B-VII.0 with the tabulated distribution (LF=1) law.

 Figure 8 shows the average prompt fission neutron emission energy as a function of incident energy for $^{235,238}\text{U}$ and ^{239}Pu for both the new ENDF/B-VII.0 evaluations and the old ENDF/B-VI evaluations.

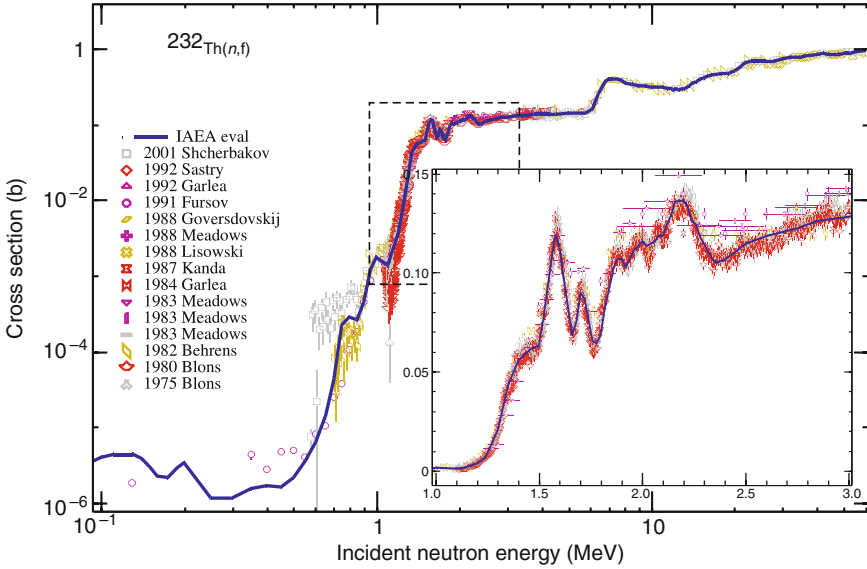


Figure 7

Neutron-induced fission cross section on ^{232}Th compared with experimental data from EXFOR. Insert shows fine details of the resonance-like structure of these fission cross sections

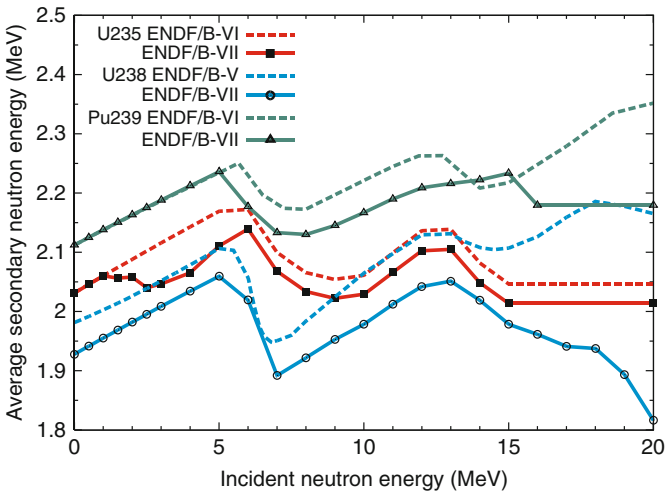



Figure 8

First moments (average energies) of $^{235,238}\text{U}$ and ^{239}Pu prompt fission neutron spectra from ENDF/B-VII.0 calculated with the Los Alamos model (Madland and Nix, 1982) in comparison with those of ENDF/B-VI

1.5.3 Peculiarities of Fission Cross Section Evaluation

It is notoriously difficult to describe and parametrize the fission process. In particular, fission is extremely sensitive to fission barriers that are very difficult to predict and their actual values depend on other parameters such as nuclear level densities.

In view of this, in most cases fission cross sections are directly adopted from experiments. Then, the modeling is performed and used to evaluate all other reaction channels. This is the approach applied for years by Los Alamos, using the code GNASH. Most recently it has been used in the unprecedented evaluation of a complete set of ten uranium isotopes $^{232,233,234,235,236,237,238,239,240,241}\text{U}$ as well as ^{239}Pu by Young et al. (2007), from keV energies to 30 MeV. These evaluations can be seen as the core of the ENDF/B-VII.0 library, with more details provided in the subsequent part of this chapter.

Recent advances in fission modeling, gradually implemented into the codes such as EMPIRE, allow cautious bypassing traditional mantra of using purely experimental data for fission cross-section evaluations. An example would be ^{232}Th evaluation adopted by ENDF/B-VII.0. In that evaluation, the fission channel was based on modeling with parametrization derived from fits to data, see  Fig. 7.

2 Neutron Data for Actinides

In general, actinides are the most important materials (isotopes) in most of the nuclear technology applications. The “big three” actinides, ^{235}U , ^{238}U , and ^{239}Pu , usually play the dominant role. These three plus ^{232}Th constitute the major actinides; the remaining about 15 actinides including other isotopes of U and Pu as well as Np, Am, and Cm fall into the category of minor actinides.

It should be emphasized that major actinides are evaluated extremely carefully and attention paid to details is exceptionally high. The nuclear data community spent considerable amount of time on these evaluations (Young et al., 2007). What is shown below is a glimpse on progress made between 2001 release of the US library ENDF/B-VII.8 and 2006 release of the ENDF/B-VII.0 library (Chadwick et al., 2006).

2.1 ^{235}U Evaluation

The ENDF/B-VII.0 evaluation in the URR was performed by ORNL. This was complemented with the evaluation in the fast neutron region performed by LANL. The remaining data were taken over from ENDF/B-VI.8.

2.1.1 ^{235}U , Unresolved Resonance Region

The SAMMY code has been used to perform the unresolved resonance evaluation of the ^{235}U cross sections from 2.25 up to 25 keV (Leal et al., 2004). SAMMY generates average resonance parameters based on a statistical model analysis of the experimental average cross sections. The primary use of the average resonance parameters is to reproduce the fluctuations in the cross sections for the purposes of energy self-shielding calculations.

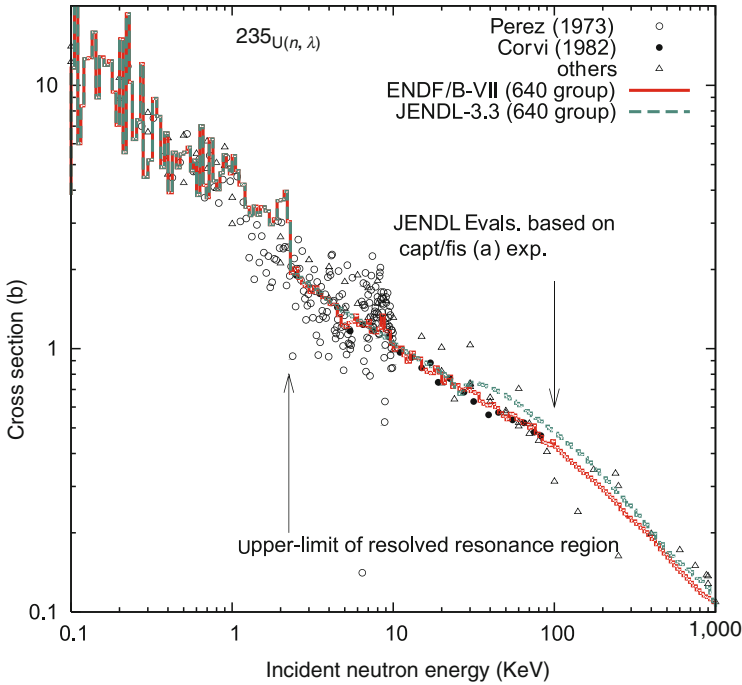


Figure 9
 Evaluated $^{235}\text{U}(n, \gamma)$ capture cross section compared with data and with the JENDL-3.3 evaluation

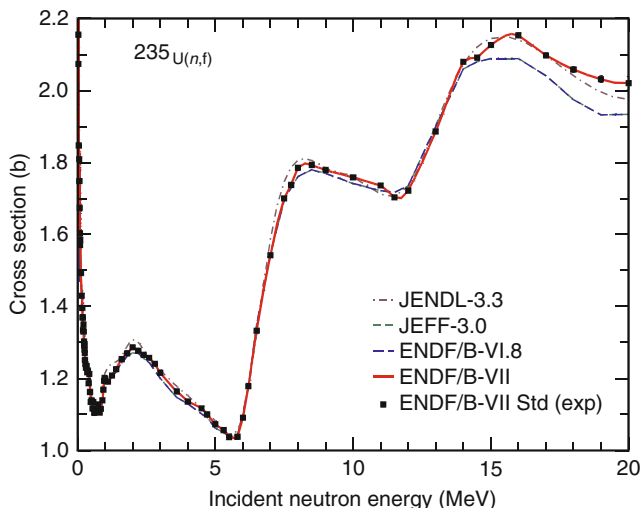
A good representation of the average cross section was achieved with the new evaluation as shown for the ^{235}U radiative capture in Fig. 9.

The thermal $\bar{\nu}$ value for ^{235}U , which was taken over from ENDF/B-VI.8, is $\bar{\nu} = 2.4367$. This value is slightly higher than that from the neutron standards, 2.4355, but within experimental uncertainties in order to optimize agreement with the critical assembly benchmarks.

2.1.2 ^{235}U , Fast Neutron Region

The new ^{235}U evaluation builds upon the previous ENDF/B-VI.8 file, with a number of improvements from Los Alamos. They include improved fission cross sections from the new standards, prompt $\bar{\nu}$ based on a covariance analysis of experimental data, $(n, 2n)$, $(n, 3n)$ cross sections based on new data, new prompt fission spectra taken from Madland, new delayed neutron time-dependent data, and improved inelastic scattering at 14 MeV and below.

The previous ^{235}U ENDF/B-VI.8 evaluation has performed reasonably well in integral validation tests based on simulations of critical assemblies. The principal deficiency the ENDF/B-VII.0 developers wanted to remove was an underprediction of reactivity. For instance, the calculated k_{eff} for Godiva, a fast critical assembly based upon highly enriched uranium (HEU) in a spherical configuration, was 0.9966, compared to experiment of 1.0000.



■ Figure 10

Evaluated fission cross section compared with measured data, as represented by a covariance analysis of experimental data (referred to as ENDF/B-VII.0 Standard). Our new evaluation follows the Standard evaluation of the experimental data. Other evaluations from joint evaluated fission and fusion (JEFF) and JENDL are also shown

The ^{235}U fission cross section is shown in [Fig. 10](#), with comparison to the previous ENDF/B-VI.8 evaluation, and to the latest joint evaluated fission and fusion (JEFF) and JENDL evaluations. This new result comes from the recent international standards project, and the evaluation follows the statistical analysis of the measured data. This evaluation is 0.5–1.5% higher than the previous ENDF/B-VI Standard in the 1–5 MeV region, and significantly higher above 15 MeV. The impact of the higher fission cross section in the fast region (a few MeV) is particularly important, having the effect of increasing the criticality of fast systems.

The Nuclear Energy Agency (NEA Paris) project studied the fission prompt neutron spectrum for ^{235}U . The final report (Weigmann et al., 2003) noted that significant uncertainties still exist in the prompt spectrum at thermal energies. Because of this uncertainty, adopted were Madland's new data for all energies except thermal, where the previous ENDF/B-VI evaluation was preserved.

In [Fig. 11](#), we show the prompt fission neutron emission spectrum, compared with measurements by Boykov et al. (1991) for 2.9 MeV neutrons on ^{235}U and plotted as a ratio to the $\sigma_c = \text{constant}$ approximation to the Los Alamos model (Madland and Nix, 1982). It is evident that the present ENDF/B-VII.0 agrees better with the data by Boykov et al.

The new $^{235}\text{U}(n, 2n)$ cross section comes from a GNASH code theory prediction, baselined against the measured data. A comparison with experimental data, and with ENDF/B-VI.8, JEFF-3.0, and JENDL-3.3 is given in [Fig. 12](#).

The previous ^{235}U evaluation was known to poorly model Livermore pulsed sphere data that measure the downscattering of 14 MeV neutrons, in the region corresponding to inelastic scattering (the 2–4 MeV excitation energy region in ^{235}U). The angle-integrated spectrum for

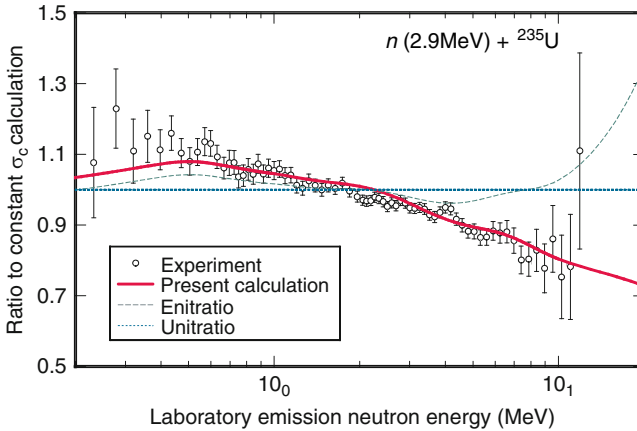


Figure 11

Prompt fission spectrum for 2.9 MeV neutrons incident on ^{235}U shown as a ratio to the $\sigma_c = \text{constant}$ approximation to the Los Alamos model. The data are from Boykov et al. (1991)

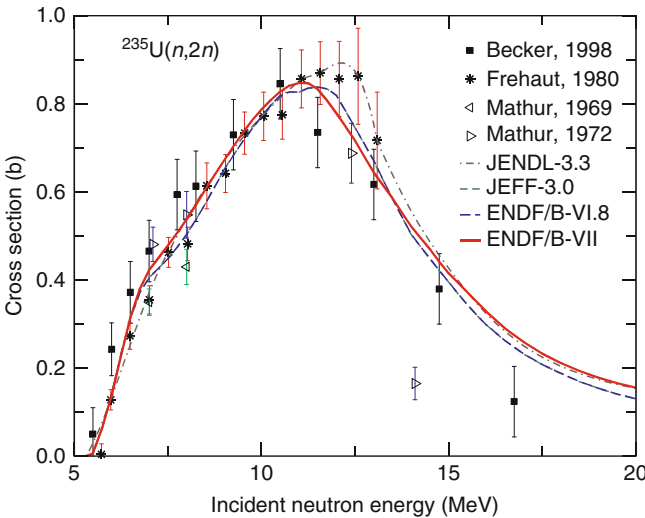
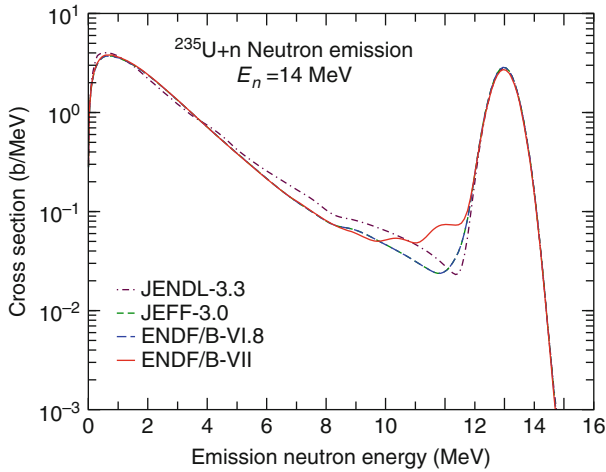


Figure 12

Evaluated $^{235}\text{U}(n,2n)$ cross section compared with data and with previous evaluations

14 MeV is shown in Fig. 13, and the oscillatory structure between 9 and 13 MeV emission energy is due to the new inelastic scattering to collective states. This is the first time that pre-equilibrium and DWBA mechanisms for inelastic scattering have been included high into the continuum for evaluated actinide databases. In ENDF/B-VII.0, this approach was followed for $^{233,235,236,238}\text{U}$, ^{239}Pu , ^{232}Th , and $^{231,233}\text{Pa}$.



■ Figure 13

Evaluated $^{235}\text{U}(n, xn)$ neutron production energy-spectrum compared with previous evaluations. No measured data exist, though our calculations were guided by measured data for ^{238}U

2.2 ^{238}U Evaluation

In natural uranium, ^{238}U is the dominant isotope, with 99.27% abundance and a half-life of 4.468×10^7 years. Although it is fast fissioner, not suitable for thermal systems, its high abundance stipulates that it must be evaluated very carefully.

2.2.1 ^{238}U , Resolved and Unresolved Resonance Region

Numerous criticality studies, involving low-enriched thermal benchmarks demonstrated a systematic k_{eff} underprediction of about -0.5% (-500 pcm) or more with ENDF/B-VI.8. International activity was formed to solve this problem. First, the ^{238}U capture cross sections were investigated using specific integral experiments sensitive to the capture resonance integrals:

- Correlation between k_{eff} and ^{238}U capture fraction
- Measurements of ^{238}U spectral indices and effective capture resonance integral
- Postirradiation experiments that measure the ^{239}Pu isotopic ratio as a function of burn-up

These tests (Courcelle, 2004) supported a slight reduction of the effective resonance integral between 0.5 and 1%. A new analysis of the ^{238}U cross section in the resolved-resonance range was performed at ORNL in collaboration with the CEA (Derrien et al., 2004). The SAMMY (Larson, 2006) analysis of the lowest s-wave resonances below 102 eV led to resonance parameters slightly different from those of ENDF/B-VI.8 as shown in [Table 1](#).

The $^{238}\text{U}(n, \gamma)$ thermal cross section, recently recommended by Trkov et al. (2005), $\sigma_0 = 2.683 \pm 0.012b$, was adopted. The scattering cross section at thermal energy was also

■ Table 1

Resonance parameters of the ^{238}U s-wave resonances in ENDF/B-VII.0 and ENDF/B-VI.8

Energy (eV)	ENDF/B-VII.0 $R' = 9.48$ fm		ENDF/B-VI.8 $R' = 9.42$ fm	
	Γ_γ (MeV)	Γ_n (MeV)	Γ_γ (MeV)	Γ_n (MeV)
6.673	23.00	1.476	23.00	1.493
20.87	22.86	10.09	22.91	10.26
36.68	23.00	33.55	22.89	34.13
66.03	23.31	24.18	23.36	24.60
80.75	23.39	1.874	23.00	1.865
102.56	24.08	70.77	23.40	71.70

Although the differences look small, they have a positive impact on performance

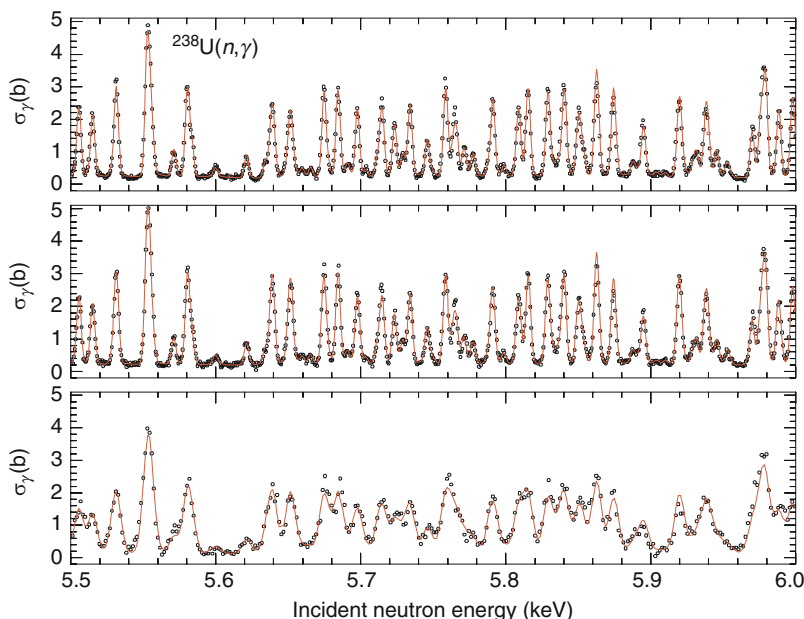
revisited and the effective scattering radius R_{eff} as well as the parameters of the external levels have been carefully assessed.

► *Figure 14* shows an example of the SAMMY fit of capture measurements in the keV energy range. As suggested by integral experiments, this new evaluation proposes a slight decrease of the effective capture resonance integral by about 0.6%, compared to ENDF/B-VI.8. One expected consequence of this new evaluation is an increase of the calculated multiplication factor for low-enriched lattices from about 0.1 to 0.15% (100–150 pcm), depending on the moderation ratio. The combination of the new LANL ^{238}U inelastic data in the fast neutron region with the ORNL resonance parameter set gave a satisfactory correction of the reactivity underprediction.

2.2.2 ^{238}U , Fast Neutron Region

The new ENDF/B-VII.0 evaluation is based upon evaluations of experimental data and use of GNASH and ECIS nuclear model calculations to predict cross sections and spectra. Prior to the present work, there were some long-standing deficiencies, as evident in critical assembly integral data testing. First, there was the reflector bias – the phenomenon whereby fast critical assemblies showed a reactivity swing in the calculated k_{eff} in going from a bare critical assembly (e.g., Godiva (HEU) or Jezebel (^{239}Pu)) to ^{238}U -reflected critical assembly (e.g., Flattop-25, or Flattop-Pu), whereas measurements showed $k_{\text{eff}} = 1$ for both assemblies.

Second, thermal critical assemblies involving ^{238}U have showed a calculated under-reactivity for ENDF/B-VI.8. Third, some intermediate energy critical assemblies involving large quantities of ^{238}U , such as Big-10, were modeled very poorly using ENDF/B-VI.8 data. The nuclear data improvements made for ENDF/B-VII.0 largely removed these deficiencies. Similar methods in the fast neutron region applied at the CEA/Bruyères-le-Châtel lead to similar improvements in the JEFF-3.1 library (López Jiménez et al., 2004).



■ Figure 14

Experimental capture data on ^{238}U (one sample measured by De Saussure and two samples by Macklin) compared to the results of the SAMMY fit in the range 5.5–6.0 keV

The fission cross section was taken from the new recommendations of the IAEA Standards group, based on a Bayesian analysis of measured data. As can be seen in [Fig. 15](#), the fission cross section differs from the previous ENDF/B-VI.8 cross section in some important ways, being $\approx 1.5\%$ larger in the 2–4 MeV region, and 1–5% larger in the 14–20 MeV region. Above 14 MeV, the principal reason for the change is newer and more precise measurements from various laboratories, which were not available for ENDF/B-VI.

The prompt fission spectrum in ENDF/B-VII.0 for ^{238}U came from a new analysis by Madland using the Los Alamos model. The average energies are compared with Los Alamos model predictions in [Fig. 16](#), and the agreement with experimental data is seen to be good.

Nuclear reaction modeling with the GNASH and ECIS codes played an important role for improving the treatment of inelastic scattering to discrete levels and to the continuum. This work impacts both the scattering in the fast region, as well as at 14 MeV and below. In the former case – inelastic scattering in the fast (a few MeV) region – our improved data for inelastic scattering result in significant improvements in the critical assembly validation tests, not just for fast critical assemblies, but also for more moderated and thermal assemblies (the LEU-COMPTHERM series).

An example of the secondary neutron emission spectrum at 6.1 MeV incident energy on ^{238}U is shown in [Fig. 17](#) for an emission angle of 45° . It is evident that the new ENDF/B-VII.0 evaluation provides a much more accurate representation of the secondary spectrum, and its angular distribution, than the earlier ENDF/B-VI.8 evaluation.

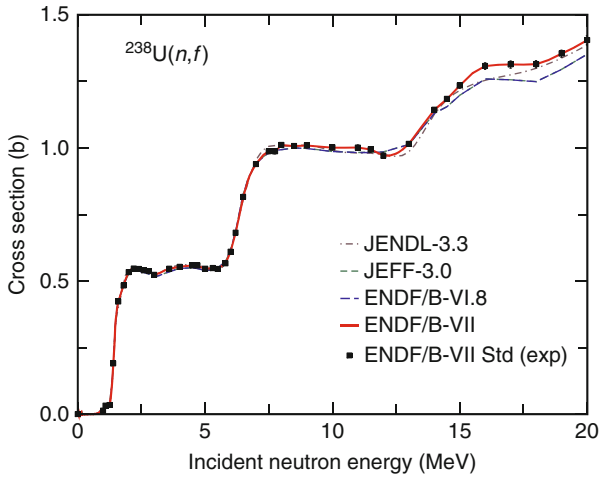


Figure 15 Evaluated ^{238}U fission cross section based on a covariance analysis of the experimental data from the Standards project (labeled Std)

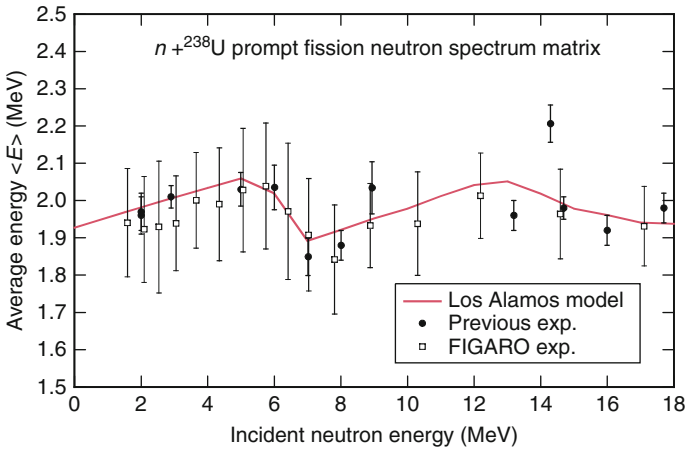
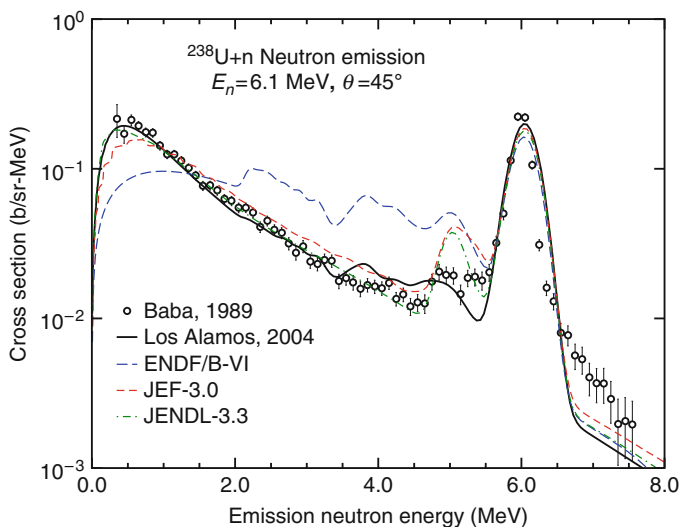


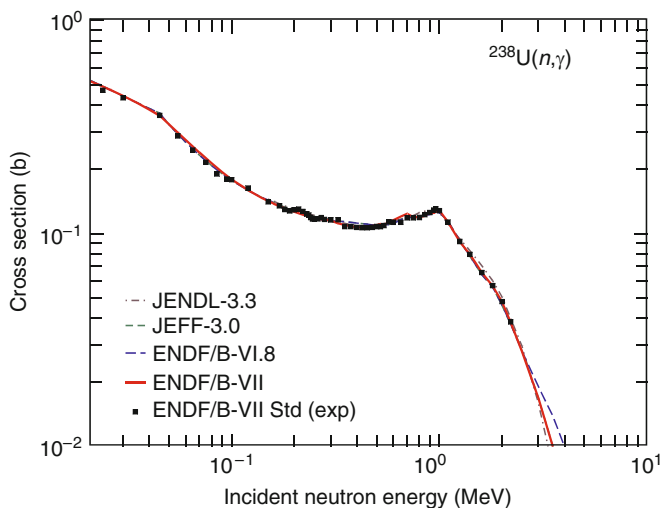
Figure 16 First moment (average energies) of the $n+^{238}\text{U}$ prompt fission neutron spectrum matrix calculated with the Los Alamos model shown together with those extracted from earlier experiments and the more recent CEA/Los Alamos FIGARO measurements (Ethvignot et al., 2003)

Our evaluated neutron capture cross section is shown in [Fig. 18](#), and is compared with the result from the Standards project (which represents a Bayesian analysis of a large amount of experimental data). It should be noted that in the 10s–100s keV region, the evaluated cross section lies below the bulk of the measurements that one might find in the CSISRS (EXFOR) experimental database. This is intentional and represents the conclusions of evaluators who



■ Figure 17

Evaluated $^{238}\text{U}(n, xn)$ neutron production energy-spectrum, compared with data, and with different evaluations



■ Figure 18

Evaluated $^{238}\text{U}(n, \gamma)$ neutron capture cross section, compared with data (labeled Std), and with previous evaluations. The standards evaluation resulted in uncertainties less than 3% over the $E_n = 10^{-4}$ –2.2 MeV region

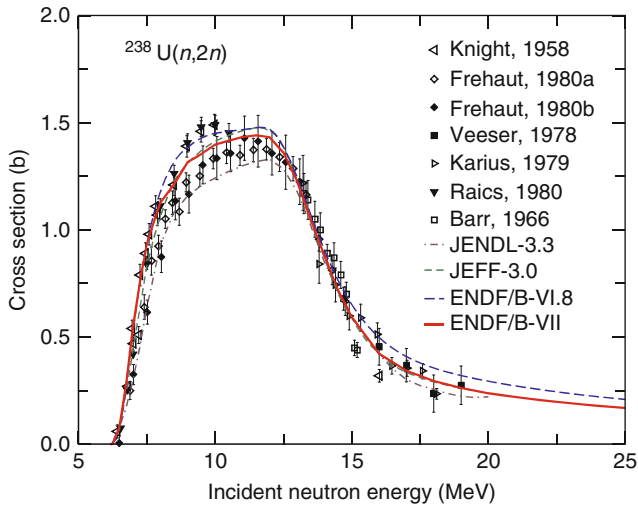


Figure 19
Evaluated $^{238}\text{U}(n,2n)$ cross section compared with data and with previous evaluations

have studied the various measurements and concluded that the lower measurements are most accurate. See, for instance, the NEA WPEC Subgroup-4 report (Kanda and Baba, 1999).

The neutron capture cross section of ^{238}U can be tested in an integral way by comparing the production of ^{239}U in a critical assembly for various neutron spectra in different critical assemblies, ranging from soft spectra to hard spectra. The results show that the evaluation reproduces integral capture rates reasonably well.

Like radiative capture, cross sections such as $(n,2n)$ and $(n,3n)$ are also important for production–depletion studies of uranium isotope inventories and transmutation. Our new evaluation of the $(n,2n)$ cross section is shown in Fig. 19 and is compared with ENDF/B-VI.8 and with measured data.

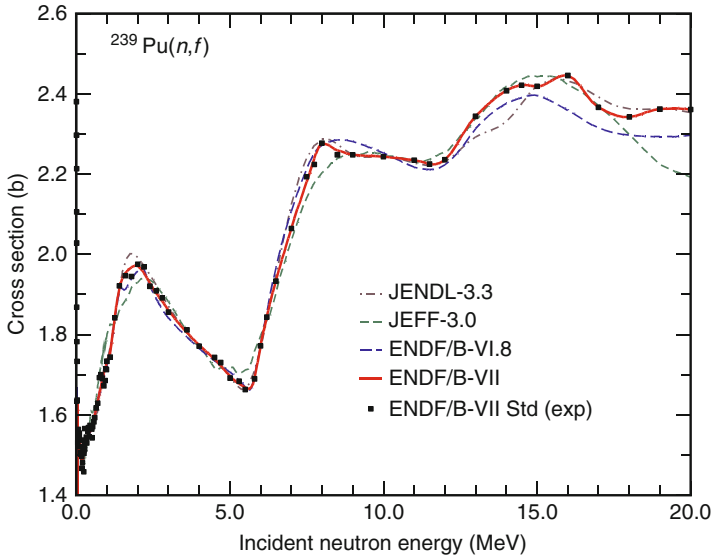
2.3 ^{239}Pu Evaluation

2.3.1 ^{239}Pu , Resonance Region

The evaluation by Derrien and Nakagawa of the resonance region was taken over from the ENDF/B-VI.8 library without any change.

2.3.2 ^{239}Pu , Fast Neutron Region

The upgrades made to the ^{239}Pu evaluation included improved description of $^{239}\text{Pu}(n,2n)$, adoption of fission cross section from Standards, new analysis of the prompt fission spectrum,



■ Figure 20

Evaluated ^{239}Pu fission cross section compared with measured data, as represented by a covariance analysis of experimental data (referred to as ENDF/B-VII.0 Standard). The new evaluation follows the Standard evaluation of the experimental data. Other evaluations from JEFF and JENDL are also shown

new delayed neutron time-dependent data, $\bar{\nu}$ modifications, and improved inelastic scattering at 14 MeV and below.

The earlier ^{239}Pu ENDF/B-VI.8 evaluation exhibited an under-reactivity, with the simulated Jezebel k_{eff} being ≈ 0.997 . The new evaluation is more reactive, mainly because of the higher fission cross section in the fast region, with $k_{\text{eff}} \approx 1.000$.

The new fission cross section is shown in [Fig. 20](#) and is compared with the older ENDF/B-VI.8 evaluation. Because the earlier ^{235}U ENDF/B-VI.8 standard fission cross section was too low in the fast neutron energy region, and has now been increased in ENDF/B-VII.0, this leads to an increased ^{239}Pu fission cross section in this energy region too, since the plutonium fission cross section is strongly dependent on $^{239}\text{Pu}/^{235}\text{U}$ fission ratio measurements.

The prompt fission neutron spectrum, as a function of incident neutron energy, was reevaluated using the Madland–Nix approach. An example of the prompt fission spectrum is shown in [Fig. 21](#), for 1.5 MeV neutrons incident on ^{239}Pu , compared with the data by Staples et al. (1995).

The new $(n, 2n)$ cross section was based upon a Livermore–Los Alamos collaboration, involving GEANIE gamma-ray measurements of the prompt gamma rays in ^{238}Pu , together with GNASH code theory predictions of unmeasured contributions to the cross section. Prior to this work, precision activation measurements had been made near 14 MeV by Loughheed et al. (2001). Other measurements based on measuring the two secondary neutrons were thought to be problematic and were therefore discounted in the evaluation ([Fig. 22](#)).

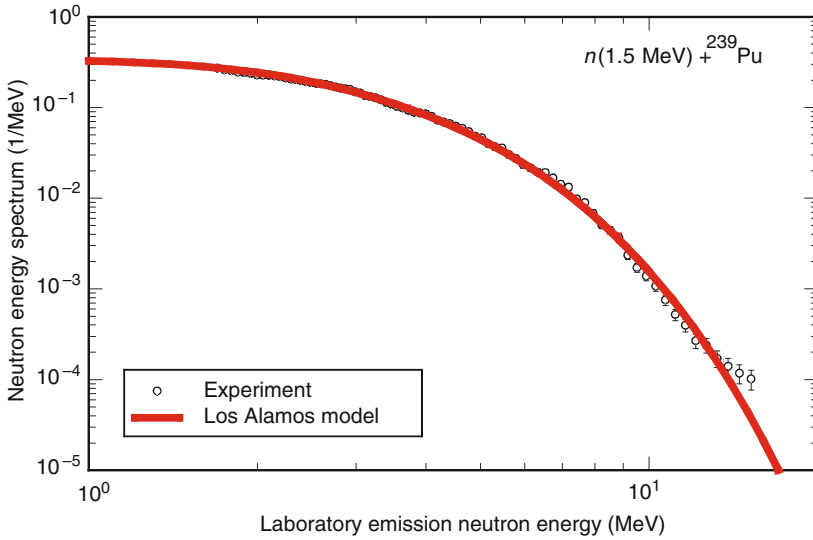


Figure 21 Prompt fission neutron spectrum for 1.5 MeV neutrons incident on ^{239}Pu . The data of Staples et al. (1995) are shown together with the least-squares adjustment to the Los Alamos model

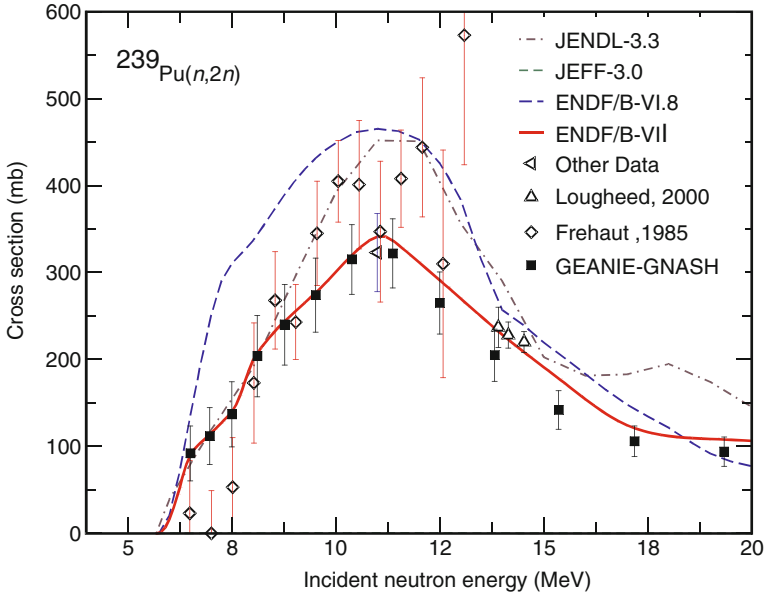
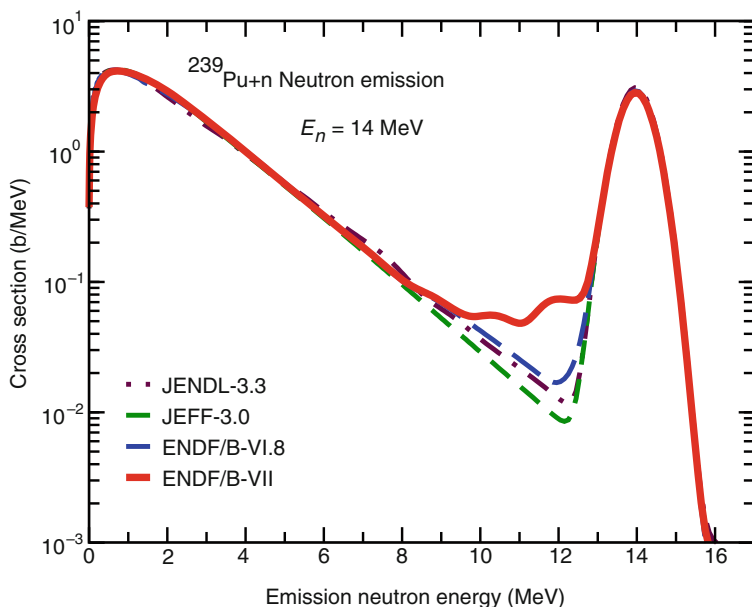


Figure 22 Evaluated $^{239}\text{Pu}(n,2n)$ cross section compared with data, and with previous evaluations. The evaluation was based upon the GEANIE-GNASH data and the Loughheed et al. 14 MeV data (Loughheed et al., 2001). The ENDF/B-VII.0 evaluation (red line) is also referred to as the “GEANIE-project” evaluation



■ **Figure 23**

Evaluated $^{239}\text{Pu}(n, xn)$ neutron production energy-spectrum compared with previous evaluations. No fundamental experimental data exist for this reaction, although Livermore pulsed data for transmission do exist

As was the case for ^{235}U , the previous ^{239}Pu evaluation did not include enough inelastic scattering into the continuum for 14 MeV neutron energy and below, leading to poor performance in simulations of Livermore pulsed spheres in the 2–4 MeV excitation energy region. We inferred collective excitation strength from DR analyses of ^{238}U data by Baba et al. and assumed similar strengths for ^{239}Pu . ➤ *Figure 23* shows the new angle-integrated neutron spectrum data compared to the ENDF/B-VI.8 evaluation (no measurements exist). This procedure led to a much improved MCNP modeling of the pulsed-sphere data.


2.4 ^{232}Th Evaluation

Recent developments in innovative fuel cycle concepts and accelerator-driven systems for the transmutation of nuclear waste have created a new interest in nuclear data for light actinides, with fission being crucially important for the design of new reactor systems. Additionally, there is strong scientific interest in the “thorium anomaly” (Bjornholm and Lynn, 1980b), which implies that in the thorium region the second-order shell effects split the outer fission barrier giving the so-called triple-humped structure.

The evaluation of ^{232}Th was completed in 2006 (Trkov, 2003, 2006). The resonance parameters were obtained by Leal and Derrien (2006) from a sequential Bayes analysis with the SAMMY code of the experimental database including Olsen neutron transmission at

ORELA (Olsen and Ingle, 1981), not yet published capture data by Schillebeeckx (GELINA), and Gusing (n-TOF) in the energy range 1–4 keV. Unresolved resonance parameters (4–100 keV) were derived by Sirakov et al. (2006, ^{232}Th : evaluation of the average resonance parameters and their covariances in the URR from 4 to 100 keV, private communication).

Evaluation in the fast energy region (Capote et al. 2006, evaluation of fast neutron-induced reactions on ^{232}Th and $^{231,233}\text{Pa}$ up to 60 MeV, private communication) was fully based on nuclear model calculations using the EMPIRE-2.19 code (Herman et al., 2005a,b; Sin et al., 2004). A crucial point was the selection of the proper coupled-channel optical model potential. The direct interaction cross sections and transmission coefficients for the incident channel on ^{232}Th were obtained from the dispersive coupled-channel potential of Soukhovitskii et al. (2005) (RIPL 608). Hauser–Feshbach (Hauser and Feshbach, 1952) and HRTW (Hofmann et al., 1975) versions of the statistical model were used for the compound nucleus cross section calculations. Both approaches include fission decay probabilities deduced in the optical model for fission (Sin et al., 2006) and account for the multiple-particle emission and the full γ -ray cascade.

A new model to describe fission on light actinides, which takes into account transmission through a triple-humped fission barrier with absorption, was developed (Sin et al., 2006) and applied for the first time to fission cross section evaluations. This formalism is capable of interpreting complex structure in the light actinide fission cross section in a wide energy range. The agreement with experimental fission cross sections is impressive as can be seen in  Fig. 7 discussed earlier. The complex resonance structure in the first-chance neutron-induced fission cross section of ^{232}Th has been very well reproduced. Prompt fission neutron spectra and $\bar{\nu}$ values were calculated using a new PFNS module of the EMPIRE code. The calculated $\bar{\nu}$ values were normalized to BROND-3 values (Ignatyuk et al., 2006), which are based on an extensive experimental database and contain covariance information.

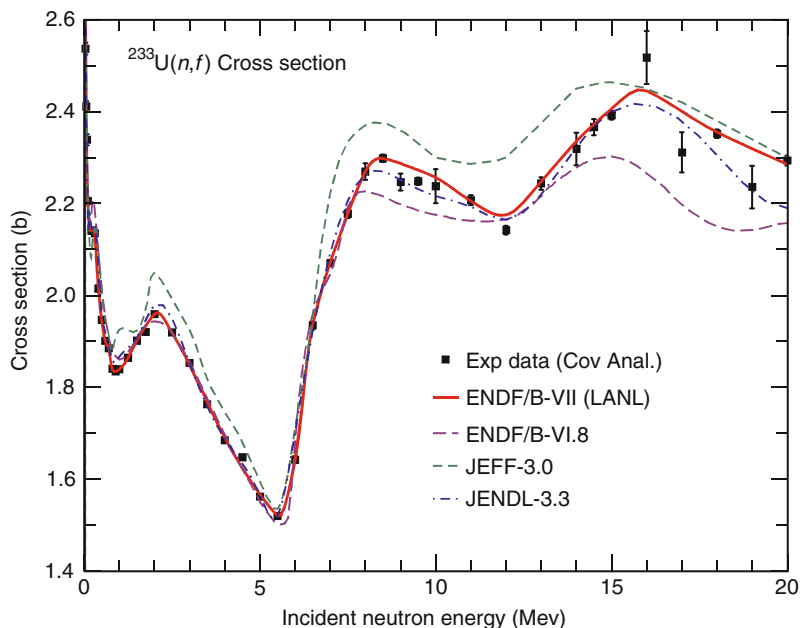
The EMPIRE calculations were merged with the resonance data, including resonance covariance file and the delayed neutron data from the BROND-3 file (Ignatyuk et al., 2006). Since the evaluation extends up to 60 MeV, exclusive spectra are only given for the first three emissions, such as $(n, 3n)$ and $(n, 2np)$, while all the remaining channels are lumped into $MT = 5$. The validation of the thorium file was carried out by Trkov and Capote (2006), showing improvement over previous evaluations.

2.5 Minor Actinides

Minor actinides are defined broadly as fissionable nuclei beyond the four major actinides. They include minor isotopes of U and Pu as well as isotopes of Np, Am, and Cm and ultimately also all heavier actinides. For example, advanced reactor systems are interested in 15 minor actinides, $^{233,234,236}\text{U}$, $^{238,240,241,242}\text{Pu}$, ^{237}Np , $^{241,242m,243}\text{Am}$, and $^{242,243,244,245}\text{Cm}$.

2.5.1 ^{233}U Evaluation

The latest evaluation for ^{233}U (Young et al., 2007) was specifically performed for ENDF/B-VII.0 library. The fission cross section is taken from a covariance statistical analysis of all experimental data, including $^{233}\text{U}/^{235}\text{U}$ fission ratio measurements converted using the ENDF/B-VII.0



■ Figure 24

Evaluated fission cross section that follows the measured data (shown as a covariance analysis of the experimental data). Other evaluations from JEFF and JENDL are also included

standard ^{235}U cross section, as shown in ► Fig. 24. The somewhat higher ^{233}U fission cross section in the fission spectrum region produces better agreement with fast critical benchmark experiments.

2.5.2 $^{232,234,236,237,239,240,241}\text{U}$ Evaluations

These evaluations were done by the well-established Los Alamos group led by Young et al. (2007). Depending upon the isotope, varying amounts of measured data are available. In some cases, the experimental database is extremely sparse. For example, for ^{237}U , there are no direct measurements of the fission cross section at monoenergetic incident neutron energies, and there are no capture measurements. However, for ^{237}U and ^{239}U , indirect information does exist on the fission cross section in the few-MeV region, using surrogate (t,p) “Decay Ratio” (DR) experiments from Los Alamos, which have recently been reanalyzed by Younes and Britt (2003) at Livermore and from a more recent Lawrence Livermore National Laboratory (LLNL) experiment by Bernstein et al. (Plettner et al., 2005). These data allow an assessment of the equivalent neutron-induced fission cross section, and Younes and Britt have shown that such surrogate approaches can be accurate to better than 15%.

In the case of ^{237}U , a measurement has been made of the fission cross section in a fast fission spectrum within a Flattop (fast) critical assembly, at two locations – the center region and the tamper region (where the spectrum is softer). This kind of measurement also provides indirect information on the fission cross section.

Table 2

Thermal (0.0253 eV) constants obtained from the standards evaluation, g_w^f and g_w^{abs} are the Westcott factors

Quantity	²³³ U	²³⁵ U	²³⁹ Pu	²⁴¹ Pu
σ_{nf} (b)	531.22 ± 0.25% (531.22)	584.33 ± 0.17% (585.09)	750.00 ± 0.24% (747.40)	1013.96 ± 0.65% (1011.85)
σ_{ny} (b)	45.56 ± 1.50% (45.24)	99.40 ± 0.72% (98.69)	271.50 ± 0.79% (270.33)	361.79 ± 1.37% (363.05)
σ_{nn} (b)	12.11 ± 5.48% (12.15)	14.087 ± 1.56% (15.08)	7.800 ± 12.30% (7.975)	12.13 ± 21.50% (11.24)
g_w^f	0.9956 ± 0.14% (0.9966)	0.9773 ± 0.08% (0.9764)	1.0554 ± 0.20% (1.0542)	1.0454 ± 0.53% (1.046)
g_w^{abs}	0.9996 ± 0.11% (0.9994)	0.9788 ± 0.08% (0.9785)	1.0780 ± 0.22% (1.0782)	1.0440 ± 0.19% (1.042)
$\bar{\nu}_{tot}$	2.497 ± 0.14% (2.497)	2.4355 ± 0.09% (2.4367)	2.8836 ± 0.16% (2.8789)	2.9479 ± 0.18% (2.9453)

The neutron sublibrary values are given in brackets. The nubar obtained from the standards evaluation process for ²⁵²Cf is $\bar{\nu}_{tot} = 3.7692 \pm 0.125\%$, comprised of $\bar{\nu}_p = 3.7606$ and $\bar{\nu}_d = 0.0086$. In ENDF/B-VI.8, $\bar{\nu}_{tot}$ was 3.7676, comprised of $\bar{\nu}_p = 3.759$ and $\bar{\nu}_d = 0.0086$

2.6 Thermal Constants

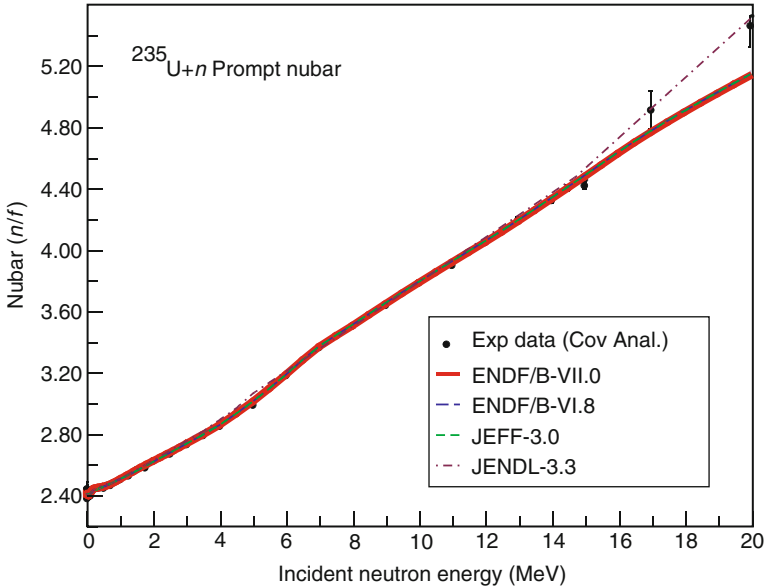
It is useful to summarize the thermal constants in the ENDF/B-VII.0 neutron sublibrary for important materials and compare them with the values given in the neutron cross section standards sublibrary. This is done in [Table 2](#). One can see that there are differences between the two sublibraries, though these are generally very small and within ≈ 0.5 standard deviation. The only item shown in this table that is considered a standard is the thermal ²³⁵U(*n, f*) cross section.

2.7 Nubars

The average number of neutrons per fission, also known as fission neutron multiplicity, represent quantities of exceptional importance. These quantities are evaluated with utmost care and high precision of data has been achieved. The total nubar (denoted as $\bar{\nu}$ or $\bar{\nu}_{tot}$) is obtained as a sum of prompt and delayed nubars,

$$\bar{\nu}_{tot} = \bar{\nu}_p + \bar{\nu}_d \tag{41}$$

For ²³⁵U, the energy dependence of the prompt $\bar{\nu}_p$ is shown in [Fig. 25](#). This new ENDF/B-VII.0 evaluation follows covariance analysis of the experimental data, generally within uncertainties, and includes renormalization of the measured values to the latest standard value for ²⁵²Cf.



■ Figure 25

Evaluated ^{235}U prompt fission neutron multiplicity, $\bar{\nu}_p$, compared with measured data, as represented by a covariance analysis of experimental data. Other evaluations from JEFF (Europe) and JENDL (Japan) are also shown

For ^{238}U , the energy dependence of prompt fission neutron multiplicity, the ENDF/B-VII.0 data are identical to ENDF/B-VI, except the energy range was extended from 20 to 30 MeV. The ENDF/B-VI data are based on an evaluation by Frehaut (2000). For the results and comparison see [▶ Fig. 26](#).

The ^{239}Pu evaluated prompt fission nubar is shown in [▶ Fig. 27](#), compared with statistical covariance analysis of all measured data (again re-normalized to the latest californium standard). In the fast region, our evaluation follows the upper uncertainty bars of the statistical analysis of the experimental data, allowing us to optimize the integral performance in criticality benchmarks for the fast Jezebel ^{239}Pu spherical assembly.

2.8 Delayed Neutrons

Delayed neutrons originate from the radioactive decay of nuclei produced in fission and hence they are different for each fissioning system.

2.8.1 Fission-Product Delayed Neutrons

Delayed neutrons, also referred to as temporal fission-product delayed neutrons, are stored in ENDF-6 formatted files as MF=1, MT=455. Related experiments typically report data as a series

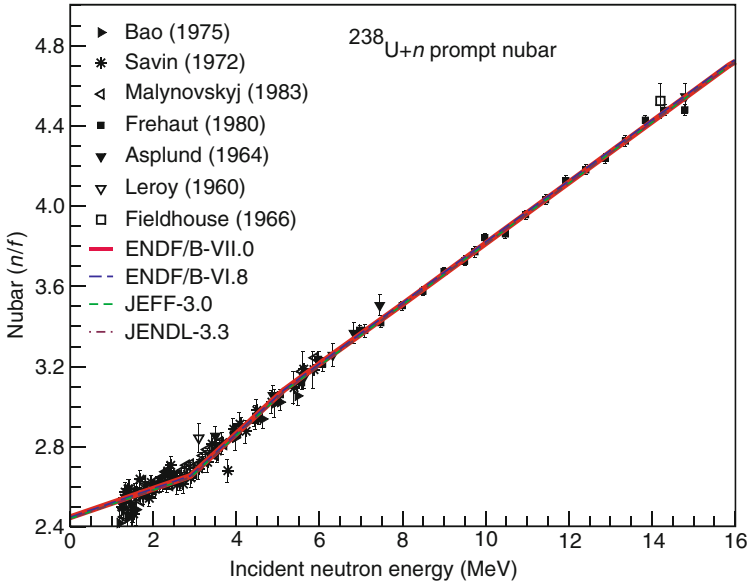


Figure 26
 Evaluated ^{238}U prompt fission neutron multiplicity based on a covariance analysis of the experimental data

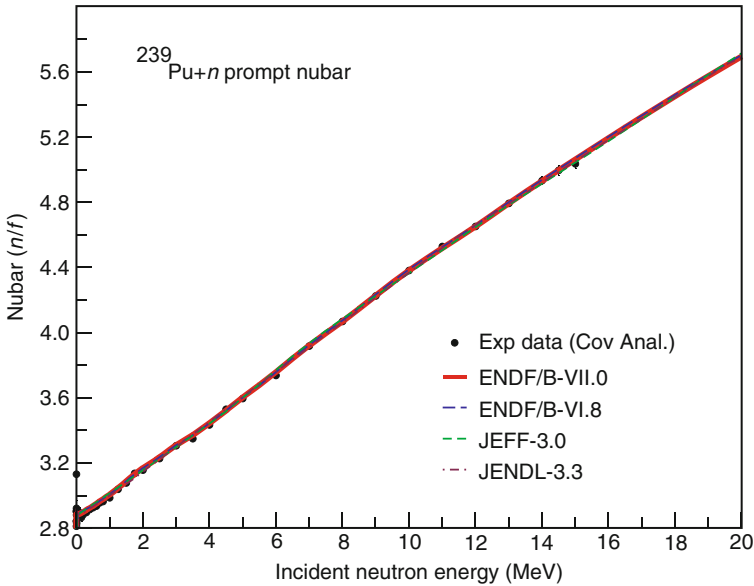


Figure 27
 Evaluated ^{239}Pu prompt fission neutron multiplicity, $\bar{\nu}_p$, compared with measured data, as represented by a covariance analysis of experimental data. Other evaluations from JEFF and JENDL are also shown


of exponential terms. An experiment includes measurements characteristically made for a set of irradiation, cooling, and counting periods. Integrally detected delayed neutrons, adjusted for efficiencies and assigned uncertainties, are fit for maximum likelihood with an exponential series.

The most common function used has been a series of six exponential terms emulating the sum of contributions of six uncoupled delayed-neutron precursors or precursor groups of differing time constants – hence the use of “six-group fits” in common parlance. This series is generally given in terms of $\bar{\nu}_d$ – the total number of delayed neutrons per fission – times the normalized sum of six exponential terms giving the temporal production at time t following a fission event.

The delayed neutron yields in ENDF/B-VII.0 were carried over from ENDF/B-VI.8, with the exception of the modifications to ^{235}U thermal $\bar{\nu}_d$ as described in the next subsection. Therefore, these yields are based on experimental data. The six-group parameters describing the time dependence of the delayed neutrons are discussed in more detail below. But we note that an explicit incident energy dependence is not given in the ENDF file as was also the case in the previous ENDF/B-VI.8 evaluation. The six-group values in the ENDF file correspond to fast neutron incident energies.

CINDER’90 calculations of a single fission pulse were replaced with a series of calculations for a variety of irradiation periods followed by decay times to 800 s, defining delayed neutron production in terms of irradiation and cooling times improving fits at very short and very long cooling times (Wilson and England, 2002). Subsequent improvements in P_n and half-life data were obtained using evaluated measured data of Pfeiffer et al. (2002) and NUBASE2003 (Audi et al., 2003). Use of the earlier systematics of Kratz and Herrmann was then replaced by results obtained with our own model.

A new CINDER’90 data library, including all delayed neutron data developed, now includes 534 delayed neutron precursors, with 477 precursors in the fission-product range $65 < A < 173$. Use of the fission product yields (FPY) data (England and Rider, 1993) results in the production of 281–440 of these precursors yielded in the 60 fission systems. These data have been used to produce new temporal delayed neutron fits for all 60 fission systems. Fits for some systems are included in this release of ENDF/B-VII.0; spectra, where present, are taken from the ENDF/B-VI.8 files using the new group abundances.

For illustration, in  Fig. 28 we show delayed neutron fraction emitted as function of the time following a ^{235}U thermal fission pulse. As shown in the inset, differences between ENDF/B-VII.0 and the other evaluations are smaller than 20% for times larger than 1 s.

2.8.2 ^{235}U Thermal $\bar{\nu}_d$

When Keepin (1965) measured delayed nubar ($\bar{\nu}_d$) for ^{235}U , he found a difference between thermal and fast values: 0.0158 ± 0.0005 and 0.0165 ± 0.0005 , respectively. Since second-chance fission was above the energy of his measurements, he assumed it was an experimental error, and recommended the cleaner fast data for kinetics applications, including thermal. This posed a problem for thermal reactor designers: use the more accurate fast value, or the more relevant thermal data. Mostly, they opted for the latter.

Experiments continued to send mixed signals. Conant and Palmedo (1971) and Tuttle (1975) supported a difference between fast and thermal values, and thermal reactor kinetics

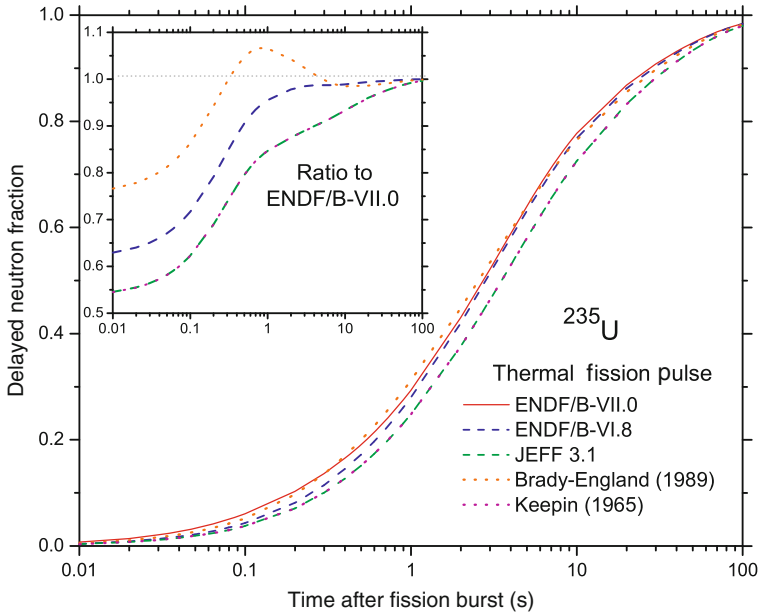


Figure 28

Delayed neutron fraction as a function of time following a ^{235}U thermal fission pulse for ENDF/B-VII.0, ENDF/B-VI.8, JEFF 3.1, Brady and England (1989), and Keepin (1965). The inset shows the ratio of the delayed neutron fractions for the other evaluations to the ENDF/B-VII.0

calculations failed to show a problem with the lower value. Fast measurements and summation calculations tended to raise the 0.0167 value even higher.

Two recent developments provided a plausible resolution to this problem:

1. Fission theory allowed an energy-variation of delayed nuclide in the resonance region (Ohsawa and Oyama, 1999; Ohsawa and Hamsch, 2004). The change in ^{235}U delayed nuclide is a series of small dips, one at each resonance, but for engineering purposes, only the average value over the thermal region is important. As the energy increases, the fluctuations decrease and the value approaches the higher fast value.
2. Analysis of beta-effective measurements supported the view that thermal delayed nuclide is about 5% lower than the fast value (Nakajima, 2001; Sakurai and Okajima, 2002; van der Marck, 2005).

The ENDF/B-VII.0 ^{235}U delayed nuclide file is not a reevaluation of the data, but a minimum adjustment to ENDF/B-VI, which reflects current usage and recognizes the thermal-fast difference. An appropriate time to revisit this issue will be when the ANS-19.9 Standard is finalized. The delayed value at thermal energy ($\bar{\nu}_d = 0.01585$) was taken from JENDL-3.3. It then ramps linearly to 0.0167 at 50 keV. JENDL ramps to 0.0162, but 0.0167 minimizes the change to ENDF/B-VI. Above 50 keV, the ENDF/B-VI data are unchanged. To avoid disturbing thermal criticality benchmark results, which depend on total nuclide, the thermal prompt value was changed to keep total nuclide the same, $\bar{\nu}_{\text{tot}} = 2.42000-2.42085$.

2.9 Fission Energy Release

The ENDF/B-VII.0 library includes new information for the energy released in fission for the major actinides, $^{235,238}\text{U}$ and ^{239}Pu . A recent study by Madland (2006) found a new representation for the prompt fission product energy $E_{FR}(e_{\text{inc}})$, prompt neutron energy $E_{NP}(e_{\text{inc}})$, and prompt photon energy $E_{GP}(e_{\text{inc}})$ functions. Their sum, the average total prompt fission energy deposition, is given by

$$\langle E_d(e_{\text{inc}}) \rangle = E_{FR}(e_{\text{inc}}) + E_{NP}(e_{\text{inc}}) + E_{GP}(e_{\text{inc}}). \quad (42)$$

This expression is based upon published experimental measurements and application of the Los Alamos model (Madland and Nix, 1982), and it shows that, to first order, these quantities can be represented by linear or quadratic polynomials in the incident neutron energy e_{inc} ,

$$E_i(e_{\text{inc}}) = c_0 + c_1 e_{\text{inc}} + c_2 e_{\text{inc}}^2, \quad (43)$$

where E_i is one of E_{FR} , E_{NP} , or E_{GP} .

The recommended coefficients for $^{235,238}\text{U}$ and ^{239}Pu are provided in [Table 3](#). The average total prompt energy deposition $\langle E_d \rangle$ obtained using these coefficients in (42) and (43) is shown in [Fig. 29](#). Madland's recommended c_0 values for E_{FR} have been adopted in the new ENDF/B-VII.0 files for $^{235,238}\text{U}$ and ^{239}Pu .

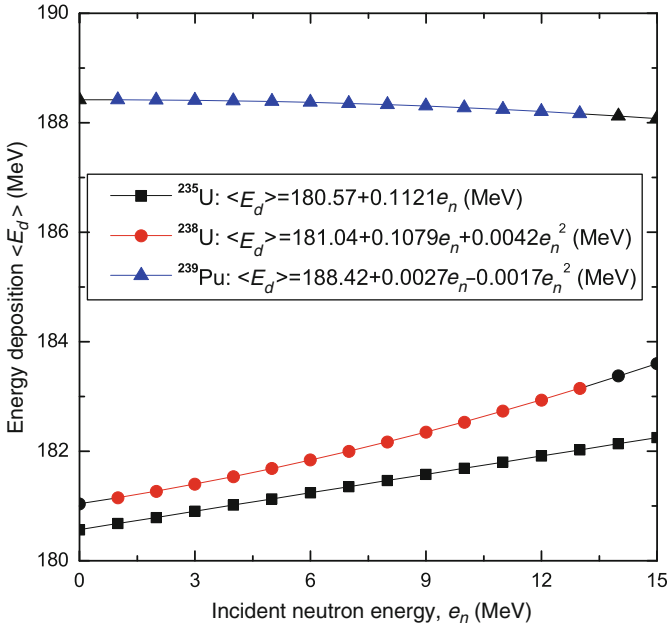
2.9.1 Nuclear Heating

Nuclear heating is an important quantity in any nuclear system. It is a topic that should be explored in relation to the energy release presented above and its handling by the processing code NJOY. In general, heating as a function of energy, $H(e_{\text{inc}})$, may be given in terms of kinetic

Table 3
Madland's recommended energy release polynomial coefficients, in MeV

Nuclide	Parameter	c_0	c_1	c_2
^{235}U	E_{FR}	169.13	-0.2660	0.0
	E_{NP}	4.838	+0.3004	0.0
	E_{GP}	6.600	+0.0777	0.0
^{238}U	E_{FR}	169.8	-0.3230	0.004206
	E_{NP}	4.558	+0.3070	0.0
	E_{GP}	6.6800	+0.1239	0.0
^{239}Pu	E_{FR}	175.55	-0.4566	0.0
	E_{NP}	6.128	0.3428	0.0
	E_{GP}	6.741	+0.1165	-0.0017

See (43) for explanation



■ Figure 29

Average total prompt fission energy deposition as a function of the incident neutron energy. See (42) for explanation

energy released in materials (KERMA) coefficients (the International Commission on Radiation Units and Measurements in its document ICRU-63 (ICRU, 2000) recommends using the name “KERMA coefficient” instead of “KERMA factor”), $k_{ij}(e_{\text{inc}})$, as

$$H(e_{\text{inc}}) = \sum_i \sum_j \rho_i k_{ij}(e_{\text{inc}}) \Phi(e_{\text{inc}}), \quad (44)$$

where ρ_i is the number density of the i th material, $k_{ij}(e_{\text{inc}})$ is the KERMA coefficient for the i th material and j th reaction at energy e_{inc} , and $\Phi(e_{\text{inc}})$ is the scalar flux. A rigorous calculation of the KERMA coefficient for each reaction requires knowledge of the total kinetic energy carried away by all secondary particles following that reaction, data that frequently are not available in evaluated files. An alternative technique, known as the energy balance method (Muir, 1976), is used by NJOY. KERMA coefficient calculations by this method require knowledge of the incident particle energy, the reaction Q -value, and other terms.

The prompt fission reaction Q -value required for prompt fission KERMA including the energy-dependent prompt fission Q -value can be calculated as

$$Q(e_{\text{inc}}) = E_R - 8.07 \times 10^6 [\bar{v}(e_{\text{inc}}) - \bar{v}(0)] + 0.307 e_{\text{inc}} - E_B - E_{GD}, \quad (45)$$

where E_R is the total energy minus neutron energy, E_B is the total energy released by delayed betas, and E_{GD} is the total energy of delayed photons.

■ **Table 4**

Prompt fission Q-values in MeV obtained with ENDF/B-VII.0 data^a

Nuclide	Incident energy e_{inc}	ENDF/B VII.0	Madland	NJOY (old)	NJOY (45)
²³⁵ U	0.0253 eV	180.65	180.57	180.65	180.65
	1.0 MeV	180.19	179.68	179.84	180.19
	14.0 MeV	169.07	168.14	164.24	169.14
²³⁸ U	0.0253 eV	181.28	181.04	181.30	181.30
	1.0 MeV	181.02	180.15	180.68	181.03
	14.0 MeV	169.59	169.37	164.86	169.76
²³⁹ Pu	0.0253 eV	188.38	188.42	189.37	188.37
	1.0 MeV	187.58	187.42	187.24	187.59
	14.0 MeV	175.98	174.12	171.10	176.00

^a Given for the sum of prompt fission products, prompt neutrons, and prompt gammas
To get total energy deposition, add the incident energy to total Q-values tabulated here

Results based upon new ENDF/B-VII.0 are shown in [Table 4](#). We note that the prompt fission Q-value calculated with the traditional ENDF formulas are now in much better agreement with Madland's calculations.

3 Neutron Data for Other Materials

In addition to actinides, there are three other categories of materials of interest for nuclear technology applications. These are light nuclei that often serve as moderators and coolants, structural materials, and fission products.

3.1 Light Nuclei

Several light-element evaluations were contributed to ENDF/B-VII.0, based on R-matrix analysis done at Los Alamos using the EDA code. Among the neutron-induced evaluations were those for ¹H, ³H, ⁶Li, ⁹Be, and ¹⁰B. For the light-element standards, R-matrix results for ⁶Li(*n*, α) and ¹⁰B(*n*, α) were contributed to the standards process, which combined the results of two different R-matrix analyses with ratio data using generalized least-squares. Differences persisted between the two R-matrix analyses even with the same data sets that are not completely understood, but probably are related to different treatments of systematic errors in the experimental data.

Below we summarize upgrades that have been made for ENDF/B-VII.0. Where no changes have been made compared to ENDF/B-VI.8 (e.g., for *n* + ²H), we do not discuss reactions on these isotopes.

¹H: The hydrogen evaluation came from an analysis of the *N* – *N* system that includes data for *p* + *p* and *n* + *p* scattering, as well as data for the reaction ¹H(*n*, γ)²H in the forward (capture) and reverse (photodisintegration) directions. The R-matrix parametrization, which is

completely relativistic, uses charge-independent constraints to relate the data in the $p+p$ system to those in the $n+p$ system. It also uses a new treatment of photon channels in R-matrix theory that is more consistent with identifying the vector potential with a photon “wavefunction.”

In the last stages of the analysis, the thermal capture cross section was forced to a value of 332.0 mb (as in ENDF/B-VI.8), rather than the “best” experimental value of 332.6 ± 0.7 mb (Cokinos and Melkonian, 1977), since criticality data testing of aqueous thermal systems showed a slight preference for the lower value. Also, the latest measurement (Schoen et al., 2003) of the coherent $n+p$ scattering length was used, resulting in close agreement with that value, and with an earlier measurement of the thermal scattering cross section (Houk, 1971), but not with a later, more precise value (Dilg, 1975).

This analysis also improved a problem with the $n+p$ angular distribution in ENDF/B-VI.8 near 14 MeV by including new measurements (Boukharaba et al., 2002; Buerkle and Mertens, 1997) and making corrections to some of the earlier data that had strongly influenced the previous evaluation.

^3H : The $n+^3\text{H}$ evaluation resulted from a charge-symmetric reflection of the parameters from a $p+^3\text{He}$ analysis that was done some time ago. This prediction (Hale et al., 1990) resulted in good agreement with $n+t$ scattering lengths and total cross sections that were newly measured at the time, and which gave a substantially higher total cross section at low energies than did the ENDF/B-VI evaluation. At higher energies, the differences were not so large, and the angular distributions also remained similar to those of the earlier evaluation.

^9Be : The $n+^9\text{Be}$ evaluation was based on a preliminary analysis of the ^{10}Be system that did a single-channel fit only to the total cross section data at energies up to about 14 MeV. A more complete analysis should take into account the multichannel partitioning of the total cross section, especially into the $(n, 2n)$ channels. An adequate representation of these multibody final states will probably require changes in the EDA code. For ENDF/B-VII.0, the elastic (and total) cross section was modified to utilize the new EDA analysis, which accurately parametrizes the measured total elastic data, while the previous ENDF/B-VI.8 angular distributions were carried over.

Data testing of the file (including only the changes in the total cross sections) appeared to give better results for beryllium-reflecting assemblies, and so it was decided to include this preliminary version in the ENDF/B-VII.0 release.

^{16}O : The evaluated cross section of the $^{16}\text{O}(n, \alpha_0)$ reaction in the laboratory neutron energy region between 2.4 and 8.9 MeV was reduced by 32% at LANL. The $^{16}\text{O}(n, \alpha)$ cross section was changed accordingly and the elastic cross sections were adjusted to conserve unitarity. This reduction was based upon more recent measurements. We note that this led to a small increase in the calculated criticality of LCT assemblies.

3.2 Structural Materials

Structural materials play a prominent role in nuclear applications and hence neutron reaction data are evaluated very carefully.

In the ENDF/B-VII.0, the main evaluation effort was concentrated on the major actinides and the fission products ($Z = 31-68$) that together cover more than half of the ENDF/B-VII.0 neutron sublibrary. Outside of these two groups, only few materials were fully or partially evaluated for ENDF/B-VII.0, as described below.

3.2.1 Evaluations of Major Structural Materials

Structural materials fall into a category of priority materials in all major evaluated data libraries. The list is dominated by Cr, Fe, and Ni, the most important isotopes being major structural materials ^{52}Cr (natural abundance 83.8%), ^{56}Fe (91.7%), and ^{58}Ni (68.1%), followed by less abundant isotopes $^{50,53}\text{Cr}$, $^{54,57}\text{Fe}$, ^{60}Ni , etc.

In the USA, considerable attention to evaluations of structural materials has been devoted in the past. These evaluations have been performed by the highly experienced team at ORNL up to 20 MeV in the 1980s, in particular in reference to the celebrated ENDF/B-V library. We note that ORNL supplied complete evaluations in the entire energy range, combining the capabilities in the thermal and resonance region (code SAMMY) with the then advanced nuclear reaction modeling code TNG in the fast neutron region. An example would be the 1986 update for iron by Fu et al. (1986). Since then, virtually no updates below 20 MeV have been made. In view of the data need for accelerator driven systems in the 1990s, the evaluations of structural materials have been extended to 150 MeV by Los Alamos and incorporated into the ENDF/B-VI library. Then, these have been adopted without any change by the latest version of the ENDF/B-VII.0 library, which was released in 2006.

3.2.2 New Evaluations for ENDF/B-VII.0

^{nat}V : Cross sections for the (n, np) reaction were revised at BNL (Rochman et al., 2006) by adjusting the EMPIRE-2.19 calculations to reproduce two indirect measurements by Grimes et al. (1978) and Kokoo et al. (1999) at 14.1 and 14.7 MeV, respectively. This resulted in the substantial reduction (about 350 mb at the maximum) of the (n, np) cross section. Similarly, the (n, t) reaction was revised to reproduce experimental results of Woelfle et al. (1990). The inelastic scattering to the continuum was adjusted accordingly to preserve the original total cross section.

$^{191,193}\text{Ir}$: These are two entirely new evaluations performed jointly by T-16 (LANL) and the NNDC (BNL) in view of recent GEANIE data on γ -rays following neutron irradiation. The resolved and unresolved resonance parameters are based on the analysis presented in Mughabghab (2006). New GNASH model calculations were performed for the γ -rays measured by the GEANIE detector, and related (n, xn) reactions cross sections were deduced (Kawano et al., 2006). We also include an evaluation of the $^{193}\text{Ir}(n, n')$ reaction to the isomer. The remaining cross sections and energy-angle correlated spectra were calculated with the EMPIRE code. The results were validated against integral reaction rates.

^{208}Pb : A new T-16 (LANL) analysis with the GNASH code was performed over the incident neutron energy range from 1.0 to 30.0 MeV. The Koning–Delaroche optical model potential (Koning and Delaroche, 2003) from the RIPL-2 database was used to calculate neutron and proton transmission coefficients for calculations of the cross sections. Minor adjustments were made to several inelastic cross sections to improve agreement with experimental data. Additionally, continuum cross sections and energy-angle correlated spectra were obtained from the GNASH calculations for (n, n') , (n, p) , (n, d) , (n, t) , and (n, α) reactions. Elastic scattering angular distributions were also calculated with the Koning–Delaroche potential and incorporated in the evaluation at neutron energies below 30 MeV.

This new ^{208}Pb evaluation led to a significant improvement in the lead-reflected critical assembly data. This is especially true for fast assemblies, but some problems remained for thermal assemblies.

3.3 Fission Products

Fission products represent the largest category of nuclei (materials) in the evaluated nuclear data libraries. Defined broadly as materials with $Z = 31\text{--}68$, in the latest US library ENDF/B-VII.0 they supply 219 nuclei. We follow this definition with the understanding that it covers also several other important materials such as structural Mo and Zr, and absorbers Cd and Gd.

Many fission product evaluations in ENDF/B had not been revised for nearly 30–35 years. Not surprisingly an analysis performed by Wright (ORNL) and MacFarlane (LANL) in 2000 revealed considerable deficiencies in ENDF/B-VI (Wright and MacFarlane, 2000).

In this situation, fission product evaluations in ENDF/B-VI.8 were completely abandoned and ENDF/B-VII.0 adopted new or recently developed evaluations. For a set of 74 materials, including 19 materials considered to be of priority, entirely new evaluations were performed using the Atlas-EMPIRE evaluation procedure (Herman et al., 2007) including those by Kim et al. (2006, 2008). For the remaining 145 materials, evaluations were adopted from the recently developed International Fission Product Library of Neutron Cross Section Evaluations completed in December 2005 and described in the 2009 report (Obložinský et al., 2009b).

3.3.1 Priority Fission Products

New evaluations were performed for materials considered to be priority fission products. The list includes 19 materials,

- ^{95}Mo , ^{99}Tc , ^{101}Ru , ^{103}Rh , ^{105}Pd , ^{109}Ag , ^{131}Xe , ^{133}Cs , ^{141}Pr , ^{153}Eu , $^{143,145}\text{Nd}$, $^{147,149,150,151,152}\text{Sm}$, $^{155,157}\text{Gd}$.

This selection (Oh et al., 2000) was based on the analysis by DeHart, ORNL, which was performed in 1995 (DeHart, 1995). It was motivated by the need to improve existing evaluations for materials of importance for a number of applications, including criticality safety, burn-up credit for spent fuel transportation, disposal criticality analysis, and design of advanced fuels.

3.3.2 Complete Isotopic Chains

As a part of modern approach to evaluation, complete isotopic chains were evaluated for several fission products, including Ge, Nd, Sm, Gd, and Dy.

A simultaneous evaluation of the complete isotopic chain for a given element became possible thanks to tremendous progress in the development of evaluation tools in recent years. This includes highly integrated evaluation code systems such as EMPIRE, coupled to experimental database EXFOR and to the library of input parameters RIPL. Complete isotopic chains for Ge,

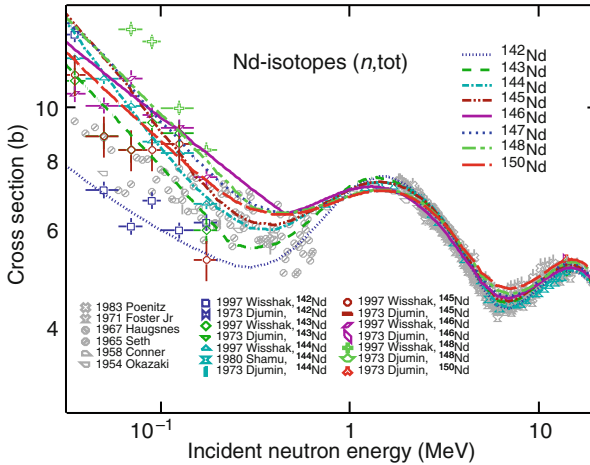


Figure 30

Total cross sections for Nd isotopes. Note the consistency among different isotopes resulting from the simultaneous evaluation of the full chain of neodymium isotopes

Nd, Sm, Gd, and Dy, totaling 37 materials were evaluated for ENDF/B-VII.0. As an example, we discuss isotopes of Nd.

A set of neodymium evaluations include two priority fission products, $^{143,145}\text{Nd}$, another five stable isotopes, and the radioactive ^{147}Nd . Neodymium is one of the most reactive rare-earth metals. It is important in nuclear reactor engineering as a fission product that absorbs neutrons in a reactor core. A new evaluation was performed by Kim et al. (2008). In Fig. 30, we show total neutron cross sections of all Nd isotopes in comparison with available data measured on isotopic samples as well as on elemental samples.

Of special interest to radiochemical applications is the radioactive ^{147}Nd for which no data exist in the fast neutron region. A good fit to available data on other stable isotopes gives confidence that predictions for ^{147}Nd cross sections are sound. This is illustrated in Figs. 31 and 32 where we show $(n, 2n)$ and neutron capture cross sections, respectively, for all Nd isotopes.

3.3.3 Specific Case of ^{90}Zr

Zirconium is an important material for nuclear reactors since, owing to its corrosion-resistance and low absorption cross section for thermal neutrons, it is used in fuel rods cladding. Benchmark testing performed at Bettis and KAPL showed an undesirable drop in the reactivity when the beta version of ENDF/B-VII.0 was used. Taking into account the importance of zirconium in reactor calculations, BNL undertook an entirely new evaluation of the fast neutron region in ^{90}Zr using the EMPIRE code. A good description of the total cross section of ^{90}Zr confirmed the higher elastic scattering cross section, see Fig. 33. The new file met expectations when validated against integral measurements at KAPL.

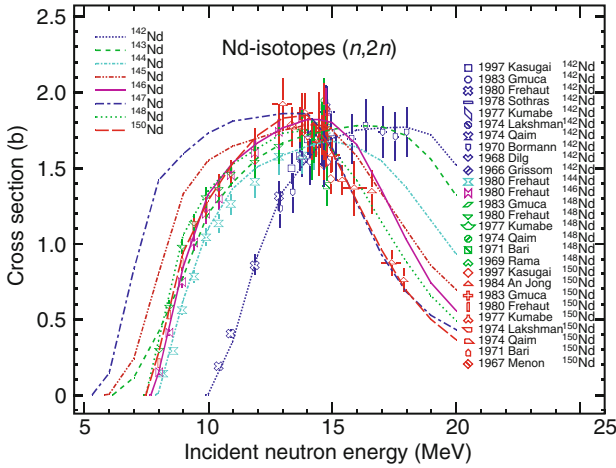


Figure 31 $(n,2n)$ cross sections for Nd isotopes. Good fit to the available data justifies prediction of cross sections for the radioactive ^{147}Nd

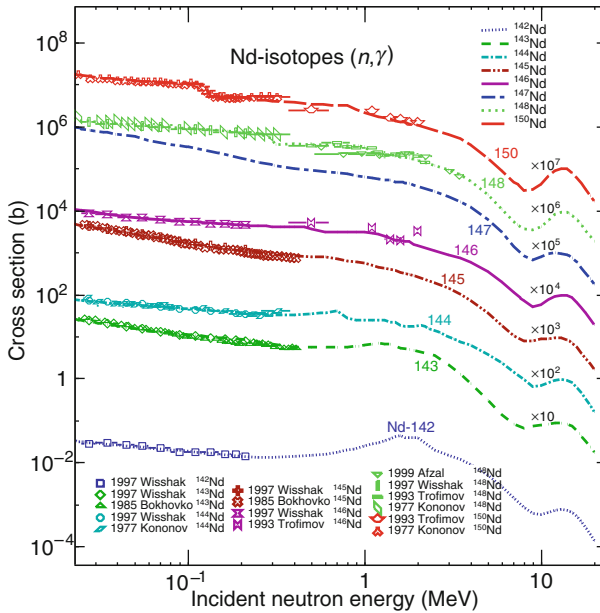
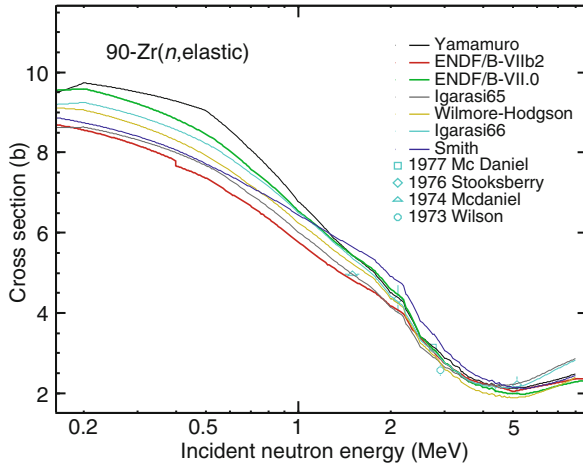


Figure 32 Neutron capture cross sections for Nd isotopes. Good fit to the available data endorses prediction of cross sections for the radioactive ^{147}Nd



■ Figure 33

Comparison of ^{90}Zr elastic cross sections calculated with various optical model potentials. The preliminary ENDF/B-VII evaluation (denoted ENDF/B-VIIb2) yields the lowest cross sections. The ENDF/B-VII.0 evaluation is considerably higher as suggested by the integral experiments

3.3.4 Remaining Fission Products

Recognizing a need to modernize the fission product evaluations, an international project was conducted during 2001–2005 to select the best evaluations from the available evaluated nuclear data libraries. Evaluated nuclear data libraries of five major efforts were considered, namely, the USA (ENDF/B-VI.8 and preliminary ENDF/B-VII), Japan (JENDL-3.3, released in 2002), Europe (JEFF-3.0, released in 2000), Russia (BROND-2.2, released in 1992), and China (CENDL-3.0, made available for this project in 2001).

As a result, the International Fission Product Library of Neutron Cross Section Evaluations (IFPL) was created for 219 materials (Obložinský et al., 2009b). Afterward, IFPL was adopted in full by the ENDF/B-VII.0 library, see 📍 Table 5 for a summary.

4 Covariances for Neutron Data

A covariance matrix specifies uncertainties and usually energy–energy correlations of data (cross sections, $\bar{\nu}$, etc.) that are required to assess uncertainties of design and operational parameters in nuclear technology applications. Covariances are obtained from the analysis of experimental data and they are stored as variances and correlations in the basic nuclear data libraries.

Early procedures for generating nuclear data covariances were widely discussed in the 1970s and 1980s (Smith, 1991). Accordingly, many of the presently existing covariance data were developed about 30 years ago for the ENDF/B-V library (Kinsey, 1979; Magurno et al., 1982). This earlier activity languished during the 1990s due to limited interest by users and constrained resources.

■ **Table 5**
Summary of 219 fission product evaluations included in the ENDF/B-VII.0 library

Library (data source)	Full file	Resonance region	Fast region
ENDF/B-VI.8, released in 2001	1	3	13
New evals for ENDF/B-VII.0	74	74	–
JEFF-3.1, released in 2005	1	–	–
JENDL-3.3, released in 2002	47	7	56
CENDL-3.0, released in 2001	11	–	15
BROND-2.2, released in 1992	1	–	–
Total number of materials	135	84	84

Full files were taken over from single libraries (data sources) for 135 materials; the remaining 84 files were put together from two different data sources

■ **Table 6**
Summary of methods used for the ENDF/B-VII.0 covariance evaluations

Energy region	Evaluation method	Material
Resolved resonances	Direct SAMMY	^{232}Th
	Retroactive SAMMY	$^{152,153,154,155,156,157,158,160}\text{Gd}$
	Atlas-KALMAN	^{89}Y , ^{99}Tc , $^{191,193}\text{Ir}$
Unresolved resonances	Experimental	^{232}Th
	Atlas-KALMAN	^{99}Tc , ^{193}Ir
	EMPIRE-KALMAN	$^{152,153,154,155,156,157,158,160}\text{Gd}$, ^{89}Y , ^{191}Ir
Fast neutrons	EMPIRE-KALMAN	$^{152,153,154,155,156,157,158,160}\text{Gd}$, ^{89}Y , ^{99}Tc , $^{191,193}\text{Ir}$
	EMPIRE-GANDR	^{232}Th

Distinguished are three energy regions: resolved resonances, unresolved resonances, and fast neutron region

More recently, intensive interest in the design of a new generation of nuclear power reactors, as well as in criticality safety and national security applications has stimulated a revival in the demand for covariances as demonstrated at the major Covariance Workshop held in 2008 (Obložinský, 2008).

4.1 Evaluation Methodology

New covariance data in the ENDF/B-VII.0 neutron sublibrary were produced for 13 materials using the evaluation techniques summarized in [Table 6](#).

4.1.1 Resonance Region

Covariances in the resonance region can be produced by three different methods. The most sophisticated approach is based on the code SAMMY (Larson, 2006), which uses generalized least-squares fits to experimental data. The intermediate Atlas method propagates resonance parameter uncertainties (Mughabghab, 2006) to cross-section covariances. The simplest and most transparent method uses uncertainties of thermal cross sections and resonance integrals as estimate of covariances (Williams, 2004).

SAMMY Covariance Method

This method is normally applied to actual experimental data as the integral part of simultaneous evaluation of both resonance parameters and their covariances (files MF2 and MF32 in ENDF-6 format terminology, Herman and Trkov, 2009). However, out of practical necessity an alternative retroactive procedure is often used. One proceeds in three steps:

First, one either starts with actual experimental data or these are artificially (“retroactively”) generated using R-matrix theory and known resonance parameters. In the latter case, usually transmission, capture, and fission is calculated assuming realistic experimental conditions. Then, realistic statistical uncertainties are assigned to each data point, and realistic values are assumed for data-reduction parameters such as normalization and background.

Afterward, initial covariance matrix is established. Let D represent the experimental data and V the covariance matrix for experimental/retroactive data. Values for V (both on- and off-diagonal elements) are derived from the statistical uncertainties of the individual data points, v_i , and from the uncertainties of the data-reduction parameters, in the usual fashion

$$V_{ij} = v_i \delta_{ij} + \sum_k g_{ik} \Delta^2 r_k g_{jk}. \quad (46)$$

In this equation, $\Delta^2 r_k$ represents the uncertainty on the k th data-reduction parameter r_k , and g_{ik} is the partial derivative of the cross section at energy E_i with respect to r_k . Then, the covariance matrix V_{ij} describes all the known experimental uncertainties.

Finally, the generalized least-squares equations are used to determine the set of resonance parameters, P' , and associated resonance parameter covariance matrix, M' , that fit these data. If P is the original set of resonance parameters (for which we wish to determine the covariance matrix), and T is the theoretical curve generated from those parameters, then, in matrix notation, the least-squares equations are

$$P' = P + M + G^t V^{-1} (D - T) \quad \text{and} \quad M' = (G^t V^{-1} G)^{-1}. \quad (47)$$

Here, G is the set of partial derivatives of the theoretical values T with respect to the resonance parameters P ; G is sometimes called the sensitivity matrix.

The solutions of (47) provide the new parameter values P' and the associated resonance parameter covariance matrix M' , fitting all directly measured/retroactive data simultaneously and using the full off-diagonal data covariance matrix for each data set.

Atlas Covariance Method

This method combines the wealth of data given in the *Atlas of Neutron Resonances* (Mughabghab, 2006) with the filtering code KALMAN (Kawano et al., 1999; Kosako and Yanano, 1999). Atlas

provides values and uncertainties for neutron resonance parameters and also integral quantities such as capture thermal cross sections, resonance integrals, and 30-keV Maxwellian averages. The procedure consists of two major steps:

- One starts with the resonance parameters and their uncertainties and uses MLBW formalism to compute cross sections along with their sensitivities.
- Uncertainties of resonance parameters are propagated to cross sections with the code KALMAN. Uncertainties of thermal values are obtained by suitable adjustment of resonance parameter uncertainties, if necessary, inferring anticorrelation with bound (negative energy) resonances.

An alternative approach would be to take resonance parameter uncertainties, put them into file MF32, and leave the job of propagation of these uncertainties into cross-section covariances to well-established processing codes.

Low-Fidelity Covariance Method

This simple, yet extremely transparent and useful method, provides an estimate of covariance data using known uncertainties of thermal cross sections and integral quantities. It was proposed by Williams (2004) and later used extensively in the “Low-fidelity Covariance Project” by ANL-BNL-LANL-ORNL collaboration that was completed in 2008 (Little et al., 2008).

4.1.2 Fast Neutron Region

EMPIRE-KALMAN Covariance Method

EMPIRE-KALMAN methodology can serve as an example of recently developed covariance methods in the fast neutron region. The KALMAN filter techniques are based on minimum variance estimation and naturally combine covariances of model parameters, of experimental data, and of cross sections. This universality is a major advantage of the method.

The key ingredient of the method is the sensitivity matrix, which represents complex nuclear reaction calculations. If we denote the combination of nuclear reaction models as an operator \hat{M} that transforms the vector of model parameters \mathbf{p} into a vector of cross sections $\sigma(\mathbf{p})$ for a specific reaction channel, then the sensitivity matrix \mathbf{S} can be interpreted as the linear term in the expansion of the operator \hat{M} ,

$$\hat{M}\mathbf{p} = \sigma(\mathbf{p})$$

and

$$\hat{M}(\mathbf{p} + \delta\mathbf{p}) = \sigma(\mathbf{p}) + \mathbf{S}\delta\mathbf{p} + \dots, \quad (48)$$

where \hat{M} is the operator rather than a matrix. In practice, the elements $s_{i,j}$ of the sensitivity matrix are calculated numerically as partial derivatives of the cross sections σ at the energy E_i with respect to the parameter p_j ,

$$s_{i,j} = \frac{\partial\sigma(E_i, \mathbf{p})}{\partial p_j}. \quad (49)$$

In case of covariance determination, the initial values of the parameters, \mathbf{p}_0 , are already optimized, that is, when used in the model calculations they provide the evaluated cross sections.

Their covariance matrix \mathbf{P}_0 is assumed to be diagonal while the uncertainties of the parameters are estimated using systematics, independent measurements, or educated guesses. The model-based covariance matrix (prior) for the cross sections, \mathbf{C}_0 , can be obtained through a simple error propagation formula,

$$\mathbf{C}_0 = \mathbf{S}\mathbf{P}_0\mathbf{S}^T, \quad (50)$$

where superscript T indicates a transposed matrix.

The experimental data, if available, are included through a sequential update of the parameter vector \mathbf{p} and the related covariance matrix \mathbf{P} as

$$\mathbf{p}_{n+1} = \mathbf{p}_n + \mathbf{P}_n\mathbf{S}^T\mathbf{Q}_{n+1}(\sigma_{n+1}^{\text{exp}} - \sigma(\mathbf{p}_n)), \quad (51)$$

$$\mathbf{P}_{n+1} = \mathbf{P}_n - \mathbf{P}_n\mathbf{S}^T\mathbf{Q}_{n+1}\mathbf{S}\mathbf{P}_n.$$

Here,

$$\mathbf{Q}_{n+1} = (\mathbf{C}_n + \mathbf{C}_{n+1}^{\text{exp}})^{-1}, \quad (52)$$

where $n = 0, 1, 2, \dots$ and $n + 1$ denotes update related to the sequential inclusion of the $(n + 1)$ th experimental data set. In particular, the subscript 1 $\equiv 0 + 1$ denotes updating model prior ($n = 0$) with the first experiment. Vector \mathbf{p}_{n+1} contains the improved values of the parameters starting from the vector \mathbf{p}_n , and \mathbf{P}_{n+1} is the updated covariance matrix of the parameters \mathbf{p}_{n+1} . The $\mathbf{C}_{n+1}^{\text{exp}}$ is the cross-section covariance matrix for the $(n + 1)$ th experiment. The updated (posterior) covariance matrix for the cross sections is obtained by replacing \mathbf{P}_0 with \mathbf{P}_{n+1} in (50),

$$\mathbf{C}_{n+1} = \mathbf{S}\mathbf{P}_{n+1}\mathbf{S}^T. \quad (53)$$

The updating procedure described above is often called Bayesian, although (50)–(53) can be derived without any reference to the Bayes theorem as shown in Muir (1989).

The experimental covariance matrix, $\mathbf{C}_n^{\text{exp}}$, is usually non-diagonal, due to the correlations among various energy points E_i . Assuming that systematic experimental uncertainties are fully correlated, the matrix elements are expressed through the statistical, $\Delta^{\text{sta}}\sigma_n^{\text{exp}}$, and systematic, $\Delta^{\text{sys}}\sigma_n^{\text{exp}}$, experimental uncertainties. This yields

$$c_n^{\text{exp}}(i, i) = (\Delta^{\text{sta}}\sigma_n^{\text{exp}}(E_i))^2 + (\Delta^{\text{sta}}\sigma_n^{\text{exp}}(E_i))^2 \quad (54)$$

and, for $i \neq k$,

$$c_n^{\text{exp}}(i, k) = \Delta^{\text{sys}}\sigma_n^{\text{exp}}(E_i) \times \Delta^{\text{sys}}\sigma_n^{\text{exp}}(E_k). \quad (55)$$

The quality and consistency of the evaluated cross sections can be assessed by scalar quantity

$$\chi^2 = \sum_{n=1}^N (\sigma_n^{\text{exp}} - \sigma(\mathbf{p}_N))^T (\mathbf{C}_n^{\text{exp}})^{-1} (\sigma_n^{\text{exp}} - \sigma(\mathbf{p}_N)), \quad (56)$$

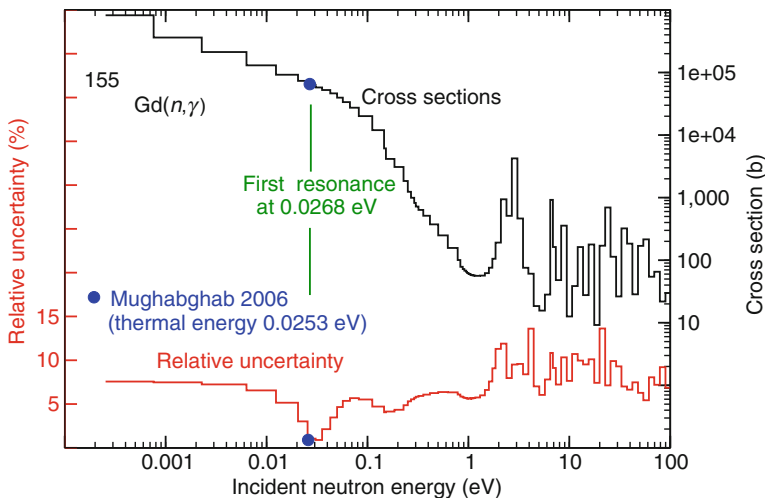
where \mathbf{p}_N is the final set of model parameters corresponding to the inclusion of N experiments. A value of χ^2 per degree of freedom exceeding unity indicates underestimation of the evaluated uncertainties. It is a fairly common practice to multiply such uncertainties by a square root of χ^2 per degree of freedom to address this issue.

4.2 Sample Case: Gd

Covariance evaluation of Gd isotopes was produced as a sample case for ENDF/B-VII.0. There are seven stable Gd isotopes, $^{152,154,155,156,157,158,160}\text{Gd}$ and the radioactive ^{153}Gd . All covariances were produced by SAMMY retroactive method in the resolved resonance region and EMPIRE-KALMAN at higher energies.

► *Figure 34* shows uncertainties for ^{155}Gd capture cross sections at low energies. The thermal cross section and its uncertainty in the *Atlas of Neutron Resonances* (Mughabghab, 2006) are very well reproduced. The particular feature that ^{155}Gd shares with ^{157}Gd is a very close vicinity of the first positive resonance to the thermal energy. Therefore, the thermal cross section is determined by the first resonance rather than $1/v$ dependence typical for other nuclei.

► *Figure 34* also demonstrates anti-correlation between uncertainties and cross sections in the resonance region. The highest uncertainties are being found between the resonances, that is, at dips of cross sections. This feature is clearly visible although it is, to some extent, obscured by the groupwise representation that lumps close resonances together.



■ **Figure 34**

Relative uncertainties for $^{155}\text{Gd}(n, \gamma)$ obtained with the retroactive SAMMY method plotted along with the cross sections to show anti-correlation between the two quantities. The experimental cross section (60,900 b) and its uncertainty (0.82%) at the thermal energy (Mughabghab, 2006) are well reproduced

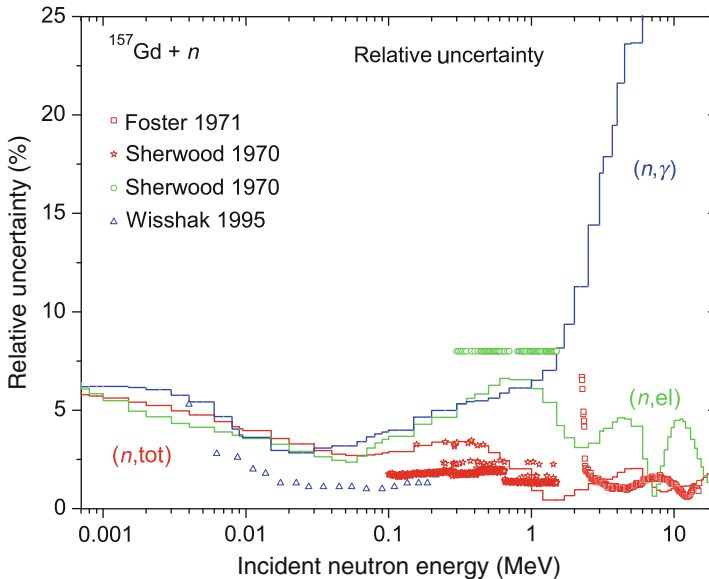


Figure 35

Relative uncertainties in the unresolved resonance and fast neutron range for the total, elastic and capture cross sections on ^{157}Gd obtained with the EMPIRE-KALMAN method

The covariances for the unresolved resonance and fast neutron regions were produced with the EMPIRE-KALMAN method. In [Fig. 35](#) we show relative uncertainties for $^{157}\text{Gd}(n,\text{tot})$, $^{157}\text{Gd}(n,\text{elastic})$, and $^{157}\text{Gd}(n,\gamma)$ cross sections for incident neutron energies above 1 keV. [Figure 36](#) shows the correlation matrix for the $^{157}\text{Gd}(n,\gamma)$ cross section. This matrix reveals complicated structures with strong correlations aligned within a relatively narrow band along the diagonal.

4.3 Major Actinides

Covariances for major actinides play a crucial role in many applications. There was insufficient time to complete new covariance evaluations for these important actinides prior to the release of the ENDF/B-VII.0 library in 2006. This work was completed in 2008, but it has not yet been officially approved by Cross Section Evaluation Working Group (CSEWG) (status at the end of 2009).

One of the issues that has been resolved was conversion of huge multimillion line long resonance parameter covariance matrices (MF32 files) into cross-section covariances (MF33 files). Such a conversion reduced the size of the files considerably, though the ^{235}U and ^{239}Pu covariance files still remain very large (about 50 and 30 MB, respectively).

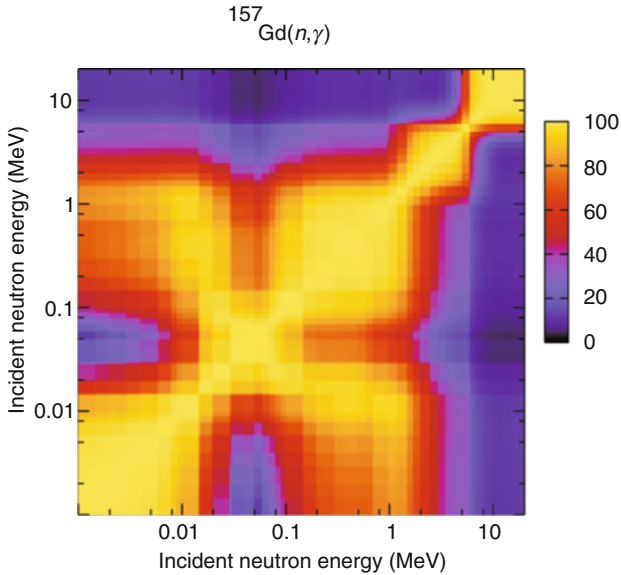


Figure 36

Correlation matrix for the $^{157}\text{Gd}(n,\gamma)$ neutron capture cross sections in the fast neutron region obtained with the EMPIRE-KALMAN method

4.3.1 $^{233,235,238}\text{U}$ Covariances

The evaluation of $^{233,235,238}\text{U}$ covariances was performed by ORNL-LANL collaboration. ORNL covered the resonance region and LANL supplied covariances in the fast neutron region.

Due to the huge size of the resonance parameter covariances (MF32), the files were converted into cross-section covariances (MF33). Still, the size of the largest ^{235}U file is considerable, in excess of 52 MB.

The preliminary version of these evaluations are available in the recently reestablished ENDF/A library, which contains candidate evaluations for the next release of ENDF/B-VII library. It is expected that all these files will be included into ENDF/B-VII.1 release. As an example of these evaluations, $^{235}\text{U}(n, f)$ covariances are shown in [Fig. 37](#), see also discussion later in this chapter under the advanced fuel cycle initiative (AFCI) covariance library.

4.3.2 ^{239}Pu Covariances

The evaluation of ^{239}Pu covariances was also performed by ORNL-LANL collaboration. ORNL covered the resonance region and LANL supplied covariances in the fast neutron region.

The file was also converted into cross-section covariances (MF33), its reduced size is 32 MB. The preliminary version of this evaluation is available in the ENDF/A library and it is expected that the file will be included into ENDF/B-VII.1 release.

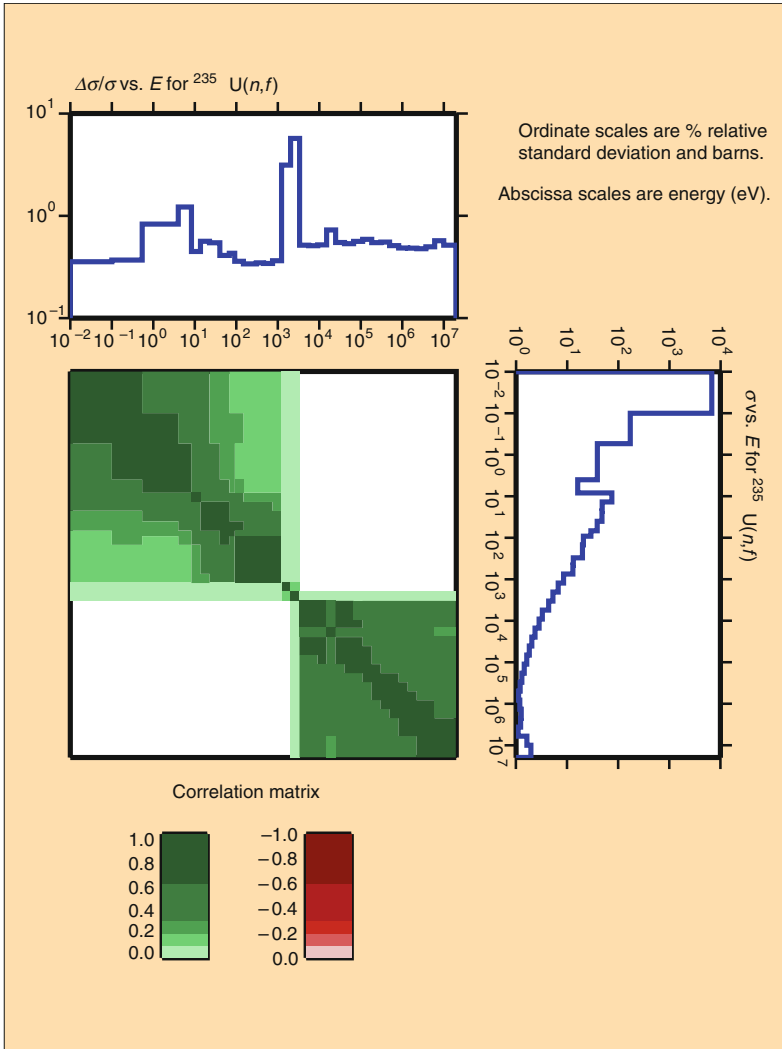
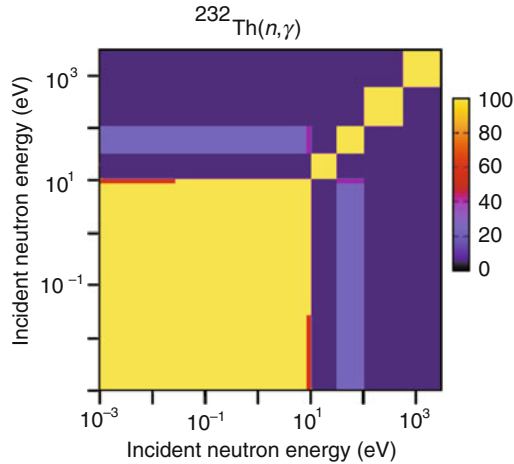


Figure 37

Covariances for $^{235}\text{U}(n, f)$ taken from ENDF/A (November 2009), which collects candidate evaluations for the next release of ENDF/B-VII. Data are given in 33-energy group representation adopted by the advanced fuel cycle initiative (AFCI) covariance library: *top* – cross-section uncertainties, *right* – cross sections, *middle* – energy–energy correlations

4.3.3 ^{232}Th Covariances

The covariance evaluation for ^{232}Th includes the resolved resonance, unresolved resonance, and the fast neutron regions as well as $\bar{\nu}$. In the resolved resonance region, a Reich–Moore evaluation was performed (Derrien et al., 2006) in the energy range up to 4 keV using the code



■ Figure 38

Correlation matrix for ^{232}Th neutron radiative capture cross sections in the thermal and resolved resonance region

SAMMY. The correlation matrix for the radiative capture cross section is shown in [Fig. 38](#). In the URR, the experimental method was used (Sirakov et al. 2006, ^{232}Th : evaluation of the average resonance parameters and their covariances in the URR from 4 to 100 keV, private communication).

Cross-section covariance data in the fast neutron region were generated by the Monte Carlo technique (Smith, 2004) using the EMPIRE code. In the Monte Carlo approach, a large collection of nuclear parameter sets (normally more than 1,000) is generated by randomly varying these parameters with respect to chosen central values. These parameter sets are then used to calculate a corresponding large collection of nuclear model derived values for selected physical quantities, such as cross sections and angular distributions. These results are subjected to a statistical analysis to generate covariance information. The GANDR code system (Trkov, 2005) updates these nuclear model covariance results by merging them with the uncertainty information for available experimental data using the generalized least-squares technique.

Covariances for $\bar{\nu}$ were obtained from the unpublished evaluation performed by Ignatyuk (Obninsk) for the Russian library BROND-3 (this library has not been released yet). This evaluation was based on the analysis of experimental data.

4.4 Covariance Libraries

Despite the fact that only a limited amount of covariance evaluations have been produced to date (end of 2009), three covariance libraries were created in the USA as briefly described below. It should be understood that each of these libraries represents an approximate solution and has, therefore, inherent limitation. This stems from the fact that the development of quality covariances is a formidable task that requires considerable resources. This challenge should

be addressed by future releases of major evaluated libraries. Accordingly, it is expected that covariances will be part of the next release of the ENDF/B-VII library.

4.4.1 Low-Fidelity Covariance Library

The development of this library was funded by the US Nuclear Criticality Safety Program. The library provides the first complete, yet simple, estimate of neutron covariances for 387 materials listed in ENDF/B-VII.0; for details see Little et al. (2008). Covariances cover main reaction channels, elastic scattering, inelastic scattering, radiative capture, and fission (cross sections and nubar) over the energy range from 10^{-5} eV to 20 MeV. Various approximations were utilized depending on the mass of the target, the neutron energy range, and the neutron reaction. The resulting covariances are not an official part of ENDF/B-VII.0, but they are available for testing in nuclear applications.

In general, at low energies simple estimates were made following the approach proposed by Williams (2004). In the thermal region, defined by the cutoff energy 0.5 eV, experimental uncertainties of thermal cross sections were uniformly adopted. In the epithermal region, from 0.5 eV to 5 keV, the uncertainties of resonance integrals were used and uniformly applied. This led to simple and often reasonable estimates of cross section uncertainties. An example is shown in [Fig. 39](#).

In the fast neutron region, the model-based estimates of covariances were produced for 307 materials from ^{19}F to ^{209}Bi (Pigni et al., 2009). To this end, EMPIRE code was employed

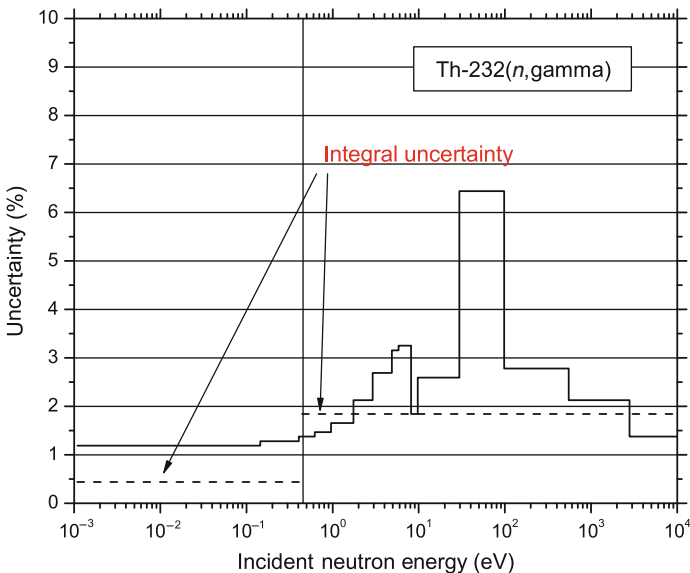


Figure 39

Low-fidelity uncertainties for $^{232}\text{Th}(n, \gamma)$ cross sections, labeled as integral quantities, are compared with ENDF/B-VII.0 values

■ **Table 7**

Sources of covariance data in the SCALE-6 covariance library

Source	Material
ENDF/B-VII.0	$^{152,158,160}\text{Gd}$, ^{232}Th , ^{99}Tc , $^{191,193}\text{Ir}$
ENDF/A	$^{233,235,238}\text{U}$, ^{239}Pu
ENDF/B-VI.8	^{23}Na , $^{28,29,30}\text{Si}$, ^{45}Sc , ^{51}V , $^{50,52,53,54}\text{Cr}$, ^{55}Mn , $^{54,56,57,58}\text{Fe}$, $^{58,60,61,62,64}\text{Ni}$, $^{63,65}\text{Cu}$, ^{89}Y , ^{93}Nb , <i>nat</i> In , $^{185,187}\text{Re}$, ^{197}Au , $^{206,207,208}\text{Pb}$, ^{209}Bi , ^{241}Am
JENDL-3.3	$^{240,241}\text{Pu}$
LANL new	^1H , ^6Li , ^{10}B
Low-fidelity	About 200 materials, mostly fission products and minor actinides

and parametrization from the latest version of the RIPL library (Capote et al., 2009) was adopted along with global estimates of related model parameters. Parameter uncertainties were propagated into cross-section uncertainties.

Light nuclei, $A < 19$, were treated differently. Recent R-matrix evaluations were adopted for three materials; for the remaining materials, simple estimates were supplied by looking into experimental data in the entire energy region.

Actinides in the fast neutron region were again treated differently. Latest full scale evaluations by ORNL-LANL were used for major actinides, while simple model-based estimates using EMPIRE were used for minor actinides.

4.4.2 SCALE-6 Covariance Library

This is the covariance library included in the well-known ORNL reactor licensing code SCALE (2000). The library was produced by selecting covariances from a variety of sources as summarized in [▶ Table 7](#) (Williams and Rearden, 2008).

It should be noted that inherent limitation of selecting covariances from various sources is inconsistency with basic cross sections, which may or may not be negligible.

4.4.3 AFCI Covariance Library

This library was developed for AFCI funded by the US DOE Nuclear Energy. It should be suitable for nuclear data adjustment needed for fast reactor applications, such as advanced burner reactor (ABR). The list of materials contains 110 materials, including

- Twelve light nuclei
- Seventy-eight structural materials and fission products
- Twenty actinides

Covariances are produced by BNL-LANL collaboration (Obložinský et al., 2009a). Major reaction channels are covered and covariance data are supplied in 33-energy group representation.

It is important to note that these covariances are tested by highly experienced reactor users in Argonne and Idaho National Laboratory.

It is expected that a fairly robust version of the AFCI covariance library will be available by the end of 2010. Then, it should serve as the basis for producing ENDF-6 formatted files suitable for inclusion into the next release of ENDF/B-VII. We note that whenever possible, AFCI library adopts new covariance evaluations produced for ENDF/B-VII. As an example, we refer the reader to [► Fig. 37](#) where we have shown covariances for $^{235}\text{U}(n, f)$ in AFCI 33-energy group representation.

5 Validation of Neutron Data

Integral data testing of evaluated cross sections plays an essential role for validation purposes. The importance is twofold: First, since many of the integral experiments are very well understood (especially the critical assembly experiments), they provide a strong test of the accuracy of the underlying nuclear data used to model the assemblies, and can point to deficiencies that need to be resolved. Second, such integral data testing can be viewed as a form of “acceptance testing” prior to these data being used in various applications. Many applications, ranging from reactor technologies to defense applications, have a high standard required of a nuclear database before it is adopted for use. Critical assemblies, while involving many different nuclear reaction processes, can still be thought of as “single-effect” phenomena that probe the neutronics and nuclear data (but not other phenomena), and therefore an important acceptance test is that a sophisticated radiation transport simulation of the assembly should reproduce the measured k_{eff} to a high degree.

Of necessity, the testing of an evaluated data library must be performed after the evaluation process. Ideally though, this testing is not performed as an afterthought, but more as an integral part of the evaluation process. It has been demonstrated many times that a close link between the data evaluators and the data users can provide valuable feedback to the evaluation process – quantifying the sensitivity of performance parameters to specific changes in nuclear data.

We note that ENDF/B-VII.0 benchmarking was largely facilitated by the fact that for the first time benchmark model descriptions were available from the International Criticality Safety Benchmark Evaluation Project (ICSBEP) handbook. This criticality safety handbook contains benchmark descriptions of almost 4,000 critical assembly configurations (compared to the tens of benchmark descriptions contained in the ENDF-202 Benchmark Specifications used previously). Furthermore, this rich collection of benchmark descriptions spans the range of fuel types, compositions, spectra, geometries, etc. However, an additional feature of these benchmarks is the evaluation of the benchmark uncertainties, that is, estimates of the total experimental uncertainties combined with any additional modeling uncertainties (Briggs et al., 2004). As a result, the most diverse and robust aspect of the ENDF/B-VII.0 validation effort was the analysis of hundreds of criticality configurations compared with their benchmark eigenvalues and uncertainties.

5.1 Criticality Testing

In reference to ENDF/B-VII.0, C/E values for k_{eff} (for the sake of clarity we use the term “C/E value for k_{eff} ” rather than the term “normalized eigenvalue;” here, C/E stands for the ratio of

■ Table 8

The number of benchmarks per main International Criticality Safety Benchmark Evaluation Project (ICSBEP) category for compound, metal, and solution systems with thermal, intermediate, fast, and mixed neutron spectrum used in ENDF/B-VII.0 validation (van der Marck, 2006)

	COMP				MET				SOL	
	Ther	Inter	Fast	Mix	Ther	Inter	Fast	Mix	ther	Total
Low-enriched U	257				1				49	307
Intermediate-enriched U	6	4					16			26
High-enriched U		6		1	41	5	66	5	87	211
Mixed	34		1				4		10	49
Low-energy Pu		1				1	7	6	105	120
²³³ U	8						4		5	17
Total	305	11	1	1	42	6	97	11	256	730

calculated to experimental values, and k_{eff} means the effective multiplication factor defined as the ratio of the average number of neutrons produced to the average number of neutrons absorbed per unit time) have been calculated for hundreds of critical benchmarks using continuous energy Monte Carlo programs including MCNP (versions 4c3 or 5), RCP01, RACER, and VIM. These calculations generally use benchmark models derived from the ICSBEP Handbook. Benchmark evaluations in this handbook are revised and extended on an annual basis. Unless otherwise noted, benchmark models derived from the 2004 or 2005 editions of the handbook were used in the calculations described below.

Since the C/E values for k_{eff} have all been obtained using continuous energy Monte Carlo calculations there is a stochastic uncertainty associated with each C/E value for k_{eff} . The magnitude of this uncertainty is very small, typically less than 25 pcm (0.025%, pcm is derived from Italian “per cento mille,” meaning per hundred thousands; it is a unit of reactivity, where 1 pcm = 0.00001 $\Delta k/k$, i.e., 100 pcm is a 0.1% discrepancy).

A paper by van der Marck (2006) presents independent European data testing of ENDF/B-VII.0, using MCNP4c3 with data processed by NJOY, and also shows extensive neutron transmission benchmark comparisons. ▶ Table 8 provides a summary of 730 benchmark criticality experiments that were simulated and compared with measurements.

▶ Table 9 summarizes the average value of C/E-1 (the average deviation of Calculation/Experiment from unity) for these benchmarks. We show for comparison in *italics* the values for the previous ENDF/B-VI.8. While it is important to study the individual benchmark results for a more thorough understanding, it is still very useful to observe the overall averaged behavior shown in ▶ Table 9:

- The low-enriched U (LEU) compound benchmarks are modeled much more accurately (owing to improved ²³⁸U, as well as ¹⁶O and ¹H).
- The intermediate-enriched U (IEU) benchmarks are modeled more accurately.
- The Pu and HEU fast benchmarks are modeled more accurately.

■ Table 9

The average value of C/E –1 in pcm (100 pcm = 0.1%) for ENDF/B-VII.0 per main ICSBEP benchmark category

	COMP				MET				SOL
	Ther	Inter	Fast	Mix	Ther	Inter	Fast	Mix	ther
LEU	17				–41				123
	–452				–270				<i>107</i>
IEU	103	219					182		
	–299	–238					712		
HEU		1,744		104	–51	88	147	812	108
		1,442		–273	–411	–42	186	462	142
MIX	428		110				193		–254
	377		978				69		–257
PU		1,110				4,565	229	936	620
		967				4,654	375	745	531
²³³ U	146						–364 ^a		66
	–380						–338		–292

^aThis becomes –64 pcm versus –254 pcm if we restrict ourselves to the well-understood UMF-001 and UMF-006 assemblies Shown in *italics* are the values for the ENDF/B-VI.8 library

- The ²³³U thermal benchmarks are modeled more accurately. Although the ²³³U fast benchmarks simulations appear to have become worse, this is perhaps more due to deficiencies in modeling of beryllium for two of the assemblies studied – for bare ²³³U (Jezebel-23 and Flattop-23) the new ENDF/B-VII.0 are clearly much better.
- Lower energy Pu (PU) benchmarks were modeled poorly in ENDF/B-VI.8 and continue to be modeled poorly in the new library.

5.2 Fast U and Pu Benchmarks

Fast U and Pu benchmarks were given considerable attention in the validation of the ENDF/B-VII.0 library. Shown below are selected examples for several benchmark categories.

Bare, and ²³⁸U reflected, assemblies: A large number of well-known Los Alamos fast benchmark experiments have been incorporated into the ICSBEP Handbook and are routinely calculated to test new cross-section data. Unmoderated enriched ²³⁵U benchmarks include Godiva (HEU-MET-FAST-001 or HMF1) (“HEU-MET-FAST-001” is the identifier assigned in the ICSBEP Handbook for this assembly. It is comprised of four parts which, respectively, classify the assembly by fissile materials (PU, HEU, LEU), fuel form (METal, SOLution, COMpound), and energy-spectrum (FAST, INTERmediate, THERMal, or MIXED) and benchmark

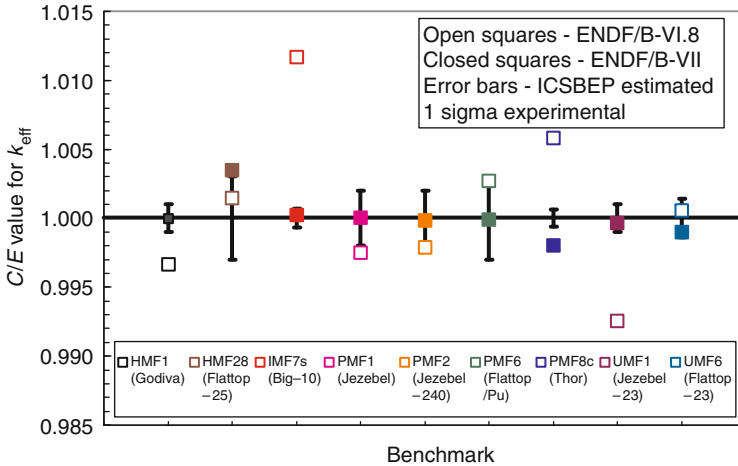


Figure 40

Los Alamos National Laboratory (LANL) highly enriched uranium (HEU), Pu and ^{233}U unmoderated benchmark C/E values for k_{eff} calculated with ENDF/B-VI.8 and ENDF/B-VII.0 cross-section data

number (-NNN). It is also common to use a shorthand form for this identifier, such as HMF1 for HEU-MET-FAST-001), Flattop-25, and Big-10 assemblies.

Results of MCNP5 k_{eff} calculations with ENDF/B-VI.8 and ENDF/B-VII.0 cross sections for this suite of benchmarks are displayed in [Fig. 40](#). The improved accuracy in calculated k_{eff} for these systems with the new ENDF/B-VII.0 cross sections is readily apparent.

Assemblies with various reflectors: A number of additional HEU benchmarks, either bare or with one of a variety of reflector materials including water, polyethylene, aluminum, steel, lead, and uranium have also been calculated with MCNP5 and both ENDF/B-VI.8 and ENDF/B-VII.0 cross sections. The calculated values for k_{eff} are illustrated in [Fig. 41](#). Once again, significant improvement in the calculated k_{eff} is observed with the ENDF/B-VII.0 cross sections.

Pb-reflected assemblies: Two reflector elements of particular historical interest are lead and beryllium. Often there are multiple evaluations that contain similar materials, in particular the same core with differing reflectors, thereby facilitating testing of cross-section data for individual reflector materials. Such is the situation for lead, displayed in [Fig. 42](#), with calculated k_{eff} for a variety of benchmarks.

The significant improvements in these lead-reflected calculated k_{eff} reflects improvements made in the new ENDF/B-VII.0 ^{208}Pb evaluation, which was based on modern calculational methods together with careful attention to accurately predicting cross-section measurements, and by adopting the JEFF-3.1 evaluations for $^{204,206,207}\text{Pb}$, which (together with the JEFF-3.1 file for ^{208}Pb) have reduced this bias by a similar amount in JEFF-3.1 benchmarking.

The situation is not so clear for thermally moderated systems (LCT) as shown in [Fig. 42](#). This figure also shows the k_{eff} calculations for the HMF57 benchmark, which consists of either a spherical or cylindrical HEU core with a lead reflector. In any event, the C/E values for k_{eff} are significantly different from unity in most cases regardless of cross-section data set.

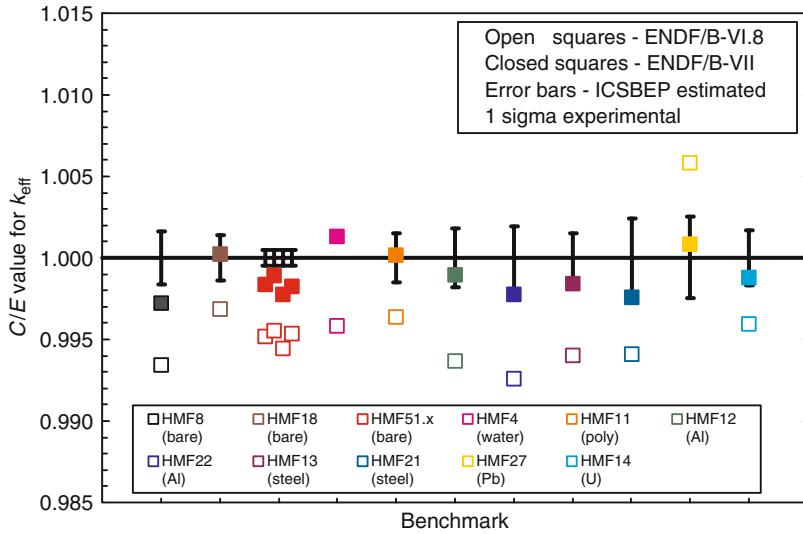


Figure 41

HEU-MET-FAST benchmark C/E values for k_{eff} calculated with ENDF/B-VI.8 and ENDF/B-VII.0 cross-section data

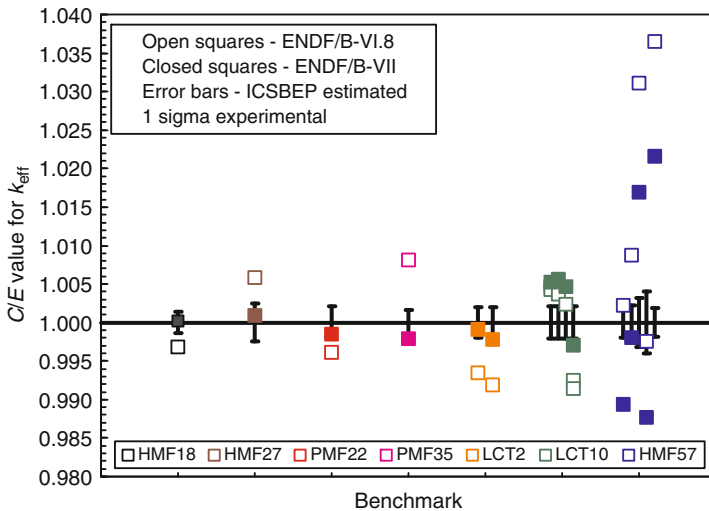


Figure 42

Bare and lead-reflected C/E values for k_{eff} calculated with ENDF/B-VI.8 and ENDF/B-VII.0 cross-section data for several HMF, PMF, and LCT benchmarks

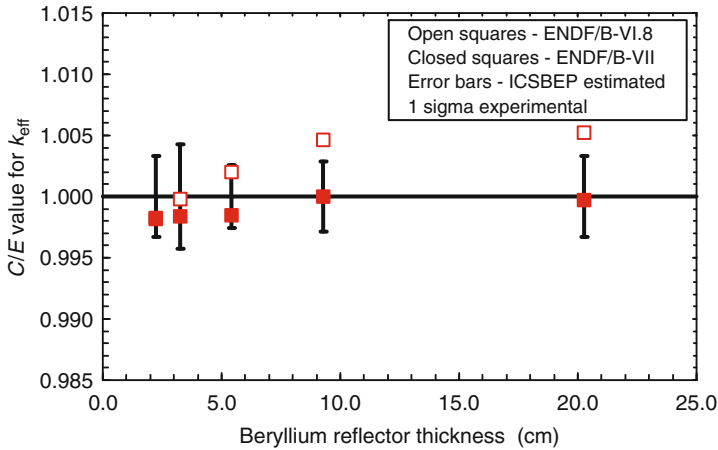


Figure 43

HEU-MET-FAST-058 benchmark C/E values for k_{eff} with ENDF/B-VI.8 and ENDF/B-VII.0 cross-section data as a function of the beryllium reflector thickness

Be-reflected assemblies: C/E values for k_{eff} of beryllium-reflected benchmarks are shown in ► Figs. 43 and ► 44. These comparisons are useful to assess the changes made in the ^9Be cross sections for ENDF/B-VII.0.

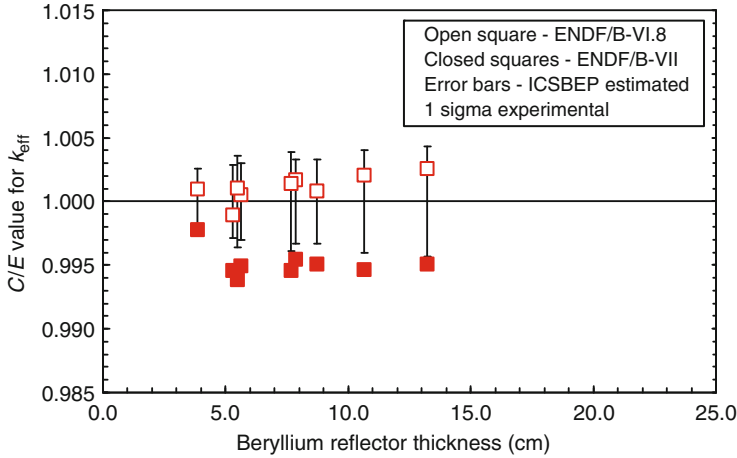
Zero power reactor assemblies: The k_{eff} calculations by the code VIM for a suite of 26 Argonne zero power reactor (ZPR) or zero power physics reactor (ZPPR) benchmarks are presented in ► Fig. 45. These benchmarks come from various areas of the ICSBEP Handbook. These benchmarks exhibit large variation in calculated k_{eff} , with the smallest k_{eff} being biased several tenths of a percent below unity while the maximum positive C/E k_{eff} bias is in excess of 3%. Calculated k_{eff} with ENDF/B-VII.0 cross sections are generally an improvement over those obtained with ENDF/B-VI.8, but significant deviations from unity remain.

5.3 Thermal U and Pu Benchmarks

Thermal benchmarks are of considerable interest to reactor applications. Shown below are selected examples for ^{235}U solution benchmarks, fuel rod U benchmarks, and Pu solution, as well as MOX benchmarks.

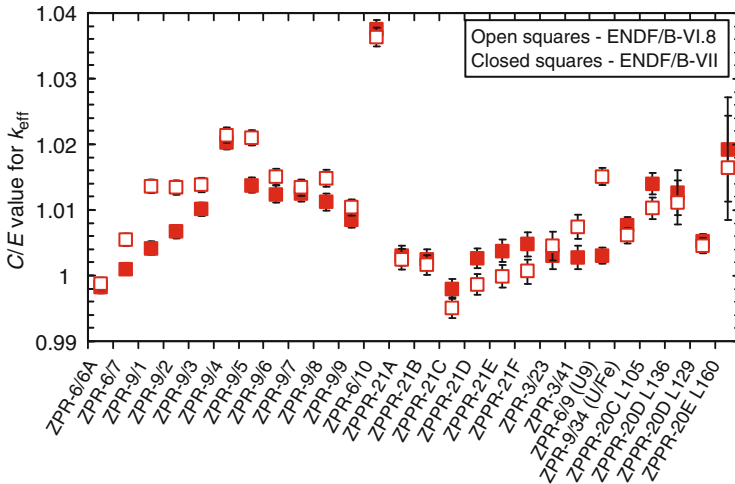
5.3.1 ^{235}U Solution Benchmarks

Thermal, highly enriched ^{235}U homogeneous solution benchmarks were used to test the accuracy of low energy ENDF/B cross-section data sets for many years. The new ENDF/B-VII.0 library, like the old ENDF/B-VI.8 library, performs well for these assemblies. C/E values for k_{eff} have been calculated for a suite of critical assemblies from 14 HEU-SOL-THERM (HST)



■ Figure 44

HEU-MET-FAST-066 benchmark C/E values for k_{eff} for ENDF/B-VI.8 and ENDF/B-VII.0 cross-section data as a function of the beryllium reflector thickness. The poorer agreement using ENDF/B-VII.0 appears to be in contradiction to the results shown in [Fig. 43](#)



■ Figure 45

C/E values for k_{eff} for 26 zero power reactor (ZPR) and zero power physics reactor (ZPPR) benchmarks from Argonne. The ENDF/B-VII results are for the beta2 version, but one does not expect significant changes for ENDF/B-VII.0

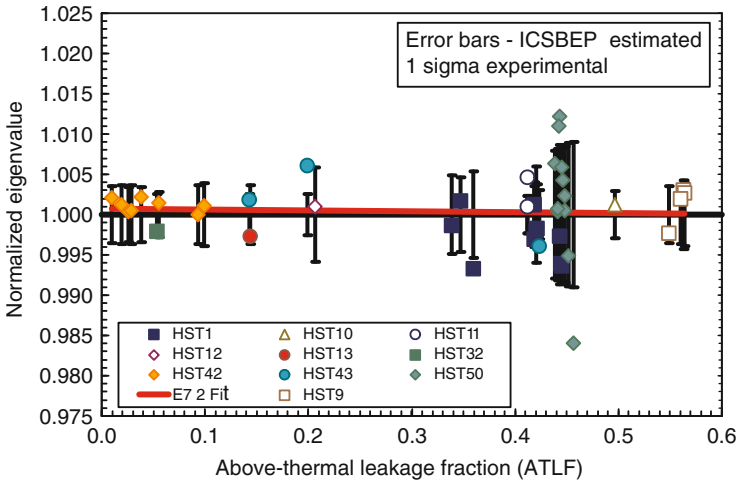


Figure 46

HEU-SOL-THERM (HST) benchmark C/E values for k_{eff} with ENDF/B-VII.0 cross sections

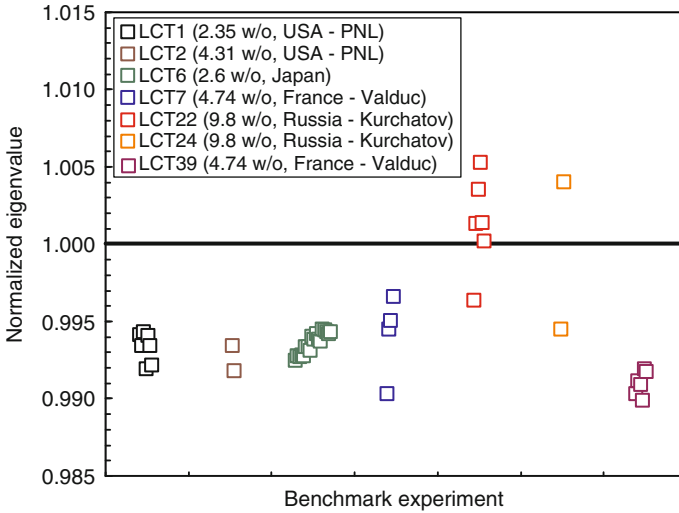
or LEU-SOL-THERM (LST) benchmark evaluations. These benchmarks have most commonly been correlated versus above-thermal leakage fraction (ATLF), for example, $k_{\text{calc}}(\text{ATLF}) = b_0 + b_1 \cdot \text{ATLF}$, where ATLF is the net leakage out of the solution of neutrons whose energies exceed 0.625 eV. Smaller systems with large ATLF test the higher energy cross sections, the ^{235}U fission spectrum, elastic scattering angular distributions, and, for reflected systems, the slowing down and reflection of above-thermal neutrons back into the fissile solution.

An important goal in developing the new ENDF/B-VII.0 library was to improve the data files while at the same time retain the good performance seen with ENDF/B-VI.8 (in the homogeneous solution benchmark category). As shown in Fig. 46, this goal has been attained. This result is nontrivial, since we have made changes in the ENDF/B-VII.0 library for ^{16}O (the n, α cross section was significantly reduced) and for hydrogen (a new standard cross section, as well as an updated scattering kernel).

5.3.2 U Fuel Rod Benchmarks

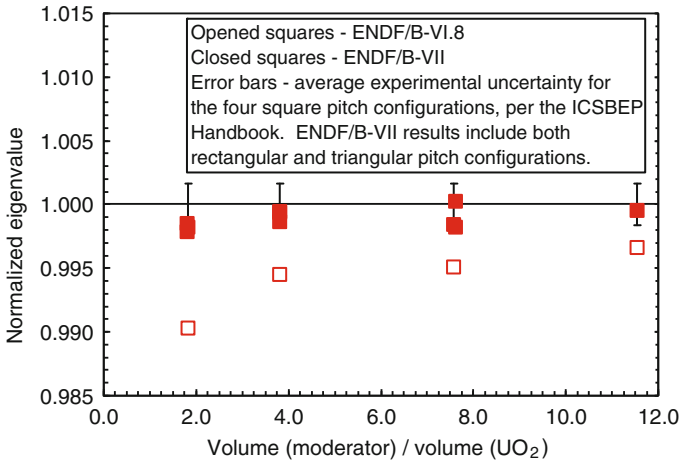
The ^{238}U cross-section data in ENDF/B-VII.0 have led to major improvements in the ability to accurately calculate thermal LEU benchmark C/E values for k_{eff} . Calculated C/E for k_{eff} for arrays of low-enriched UO_2 fuel rods have historically been biased with previous data libraries including ENDF/B-VI.8, frequently falling 500–1,000 pcm below unity. These C/E values have also varied systematically when correlated against parameters such as rod pitch, average fission energy, unit cell H/U ratio, or ^{238}U absorption fraction. Some of these characteristics are illustrated in Figs. 47 and 48, which illustrate calculated k_{eff} obtained with MCNP5 and either ENDF/B-VI.8 and/or ENDF/B-VII.0 cross sections.

Results using the new ENDF/B-VII.0 cross sections are significantly more accurate as shown in Fig. 48, which illustrates calculated k_{eff} for the LCT7 benchmark with both ENDF/B-VI.8



■ Figure 47

LEU-COMP-THERM benchmark C/E values for k_{eff} with the old ENDF/B-VI.8 cross sections



■ Figure 48

LEU-COMP-THERM-007 benchmark C/E values for k_{eff} for the ENDF/B-VI.8 and ENDF/B-VII.0 cross sections

and ENDF/B-VII.0 cross sections. The ENDF/B-VI.8 C/E for k_{eff} trend and bias have both been eliminated with the ENDF/B-VII.0 cross-section data set.

A summary of all water moderator and reflected LCT k_{eff} reveals that previously identified deficiencies have been largely eliminated. A total of 58 LEU-COMP-THERM benchmarks have

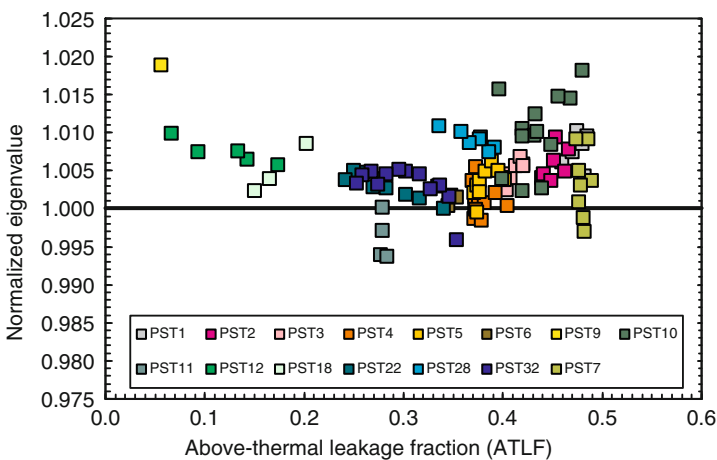
been calculated with the ENDF/B-VII.0 cross-section data set. The average calculated k_{eff} is 1.0000 with a population standard deviation of 0.0025. This standard deviation represents a significant decrease over that obtained with ENDF/B-VI.8 cross sections and is further evidence for the reduction or elimination in C/E k_{eff} trends, such as versus H/U ratio (► Fig. 48), with the ENDF/B-VII.0 cross sections.

The ENDF/B-VII.0 cross section changes that are responsible for the improved C/E k_{eff} are due primarily to (1) ORNL and CEA ^{238}U revisions in the resonance range for ^{238}U , and (2) the new Los Alamos analysis of ^{238}U inelastic scattering in the fast region. The contribution to the increased calculated criticality of these two revisions are of about the same magnitude. Two additional cross section changes also contributed to increase the calculated k_{eff} of these assemblies: the reduced $^{16}\text{O}(n, \alpha)$ cross section, and a revised scattering kernel for hydrogen bound in water.

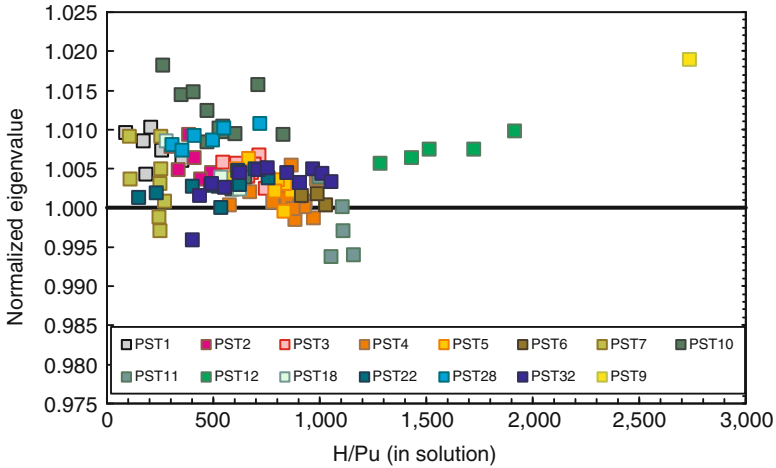
5.3.3 Pu Solution and MOX Benchmarks

While excellent calculated k_{eff} results continue to be obtained for thermal uranium solution critical assemblies, the same cannot be said for plutonium solution (PU-SOL-THERM, or PST) assemblies. MCNP5 C/E values for k_{eff} , calculated with ENDF/B-VII.0 cross sections are plotted versus ATLF and versus H/Pu ratio in ► Figs. 49 and ► 50, respectively. There are obvious variations in these C/E values for k_{eff} when plotted versus ATLF or H/Pu ratio, but it is not obvious what changes in the plutonium cross-section evaluation that could also be supported by the underlying microscopic experimental cross-section data would mitigate these trends.

The results for a MOX benchmark, six critical configurations from MIX-COMP-THERM-002, show less variation than the solutions, possibly because there are fewer of them. The fuel pins contain 2 wt.% MOX, and the plutonium contains 8% ^{240}Pu . The benchmarks include a



► Figure 49
PU-SOL-THERM (PST) benchmark C/E values for k_{eff} with ENDF/B-VII.0 cross sections as a function of the above-thermal leakage fraction (ATLF)



■ Figure 50

PST benchmark C/E values for k_{eff} with ENDF/B-VII.0 cross sections as a function of the H/Pu ratio

highly (several hundred ppm) borated case and a slightly (a few ppm) borated case for each of the three lattice pitches. The highly borated cases contain many more fuel pins than the slightly borated cases and exhibit a small positive bias, but all three fall within a band of about a quarter of a percent in reactivity.

5.4 Conclusions from Criticality Testing

Hundreds of criticality benchmarks from the ICSBEP Handbook have been calculated to test the accuracy of the ENDF/B-VII.0 cross-section library. Significant improvement in C/E values for k_{eff} has been observed in many cases, including bare and reflected fast uranium and plutonium systems and in particular for arrays of low-enriched fuel rod lattices. The C/E values for k_{eff} for bare HEU and Pu assemblies are larger compared to those obtained with ENDF/B-VI.8 data, and now agree very well with the measurements. The reflector bias for the ^{238}U reflected Flattop assemblies has been largely eliminated.

Furthermore, major improvements have been obtained in the calculations for intermediate energy assemblies such as Big-10 and, to a lesser extent, the Argonne ZPR assemblies. Homogeneous uranium solution systems have been calculated accurately with the last several versions of ENDF/B-VI cross sections, and these accurate results are retained with the ENDF/B-VII.0 cross-section library. Many fast-reflected systems are more accurately calculated with the ENDF/B-VII.0 cross-section library, but disturbing discrepancies remain, particularly in lead- and beryllium-reflected systems (although certain reflector-bias improvements were obtained using the new data for these isotopes).

A significant accomplishment has been excellent C/E for k_{eff} for the LCT assemblies, where the historical underprediction of criticality has been removed. This advance has come from improved ^{238}U evaluation (both in the resonance region and in the fast region), together with

revisions to the $^{16}\text{O}(n, \alpha)$ cross section and the hydrogen bound in water scattering kernel. Plutonium solution systems are not calculated as well as uranium solutions, with C/E values for k_{eff} typically being several tenths of a percent greater than unity. There is a 1.5% spread in these C/E values for k_{eff} , but there does not appear to be a trend as a function of ^{239}Pu abundance. Although advances have been made at Los Alamos to the ^{239}Pu cross sections in the fast region, there has been no recent work on ^{239}Pu at lower energies. Clearly such efforts are needed in the future. The performance of the new ENDF/B-VII.0 evaluations for ^{233}U and ^{232}Th is much improved in both fast and thermal critical assemblies; an analysis of the Np-U composite fast benchmark suggests important improvements have been made in ^{237}Np fission cross-section evaluation.

5.5 Delayed Neutron Testing, β_{eff}

Delayed neutron data can be tested against measurements of the effective delayed neutron fraction β_{eff} in critical configurations. Unlike the situation for k_{eff} , only a handful of measurements of β_{eff} have been reported in the open literature with sufficiently detailed information. In van der Marck (2006), more than twenty measurements are listed, including two thermal spectrum cores and five fast spectrum cores:

TCA: A light water-moderated low-enriched UO_2 core in the Tank-type Critical Assembly (Nakajima, 2001).

IPEN/MB-01: A core consisting of 28×26 UO_2 (4.3% enriched) fuel rods inside a light water-filled tank (dos Santos et al., 2004).

Masurca: Measurements of β_{eff} by several international groups in two unmoderated cores in Masurca (R2 had ~30% enriched uranium, ZONA2 had both plutonium and depleted uranium), surrounded by a 50–50% UO_2 -Na mixture blanket and by steel shielding (Okajima et al., 2002).

FCA: Measurements of β_{eff} in three unmoderated cores in the Fast Critical Assembly (HEU; plutonium and natural uranium; plutonium), surrounded by two blanket regions, one with depleted uranium oxide and sodium, the other with only depleted uranium metal (Okajima et al., 2002).

The calculation of β_{eff} for these systems was done using a version of MCNP-4C3 with an extra option added to it as described in Klein Meulekamp and van der Marck (2006). This method was used earlier to test delayed neutron data from JEFF-3.1 and JENDL-3.3 (van der Marck et al., 2004). The results based on ENDF/B-VII.0 are given in [Table 10](#), as well as the results based on those other libraries. One can see that the calculated β_{eff} now agrees better with experiment as compared to the old ENDF/B-VI.8 (specially for the more thermal systems).

5.6 Reaction Rates in Critical Assemblies

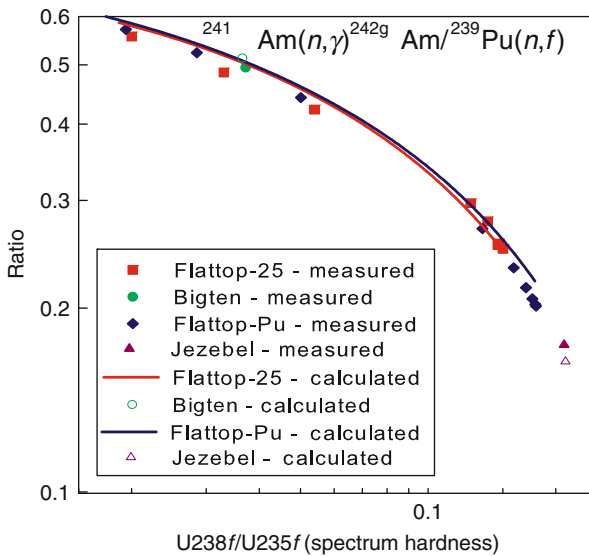
Many different critical assemblies have been developed over the years: Godiva is a bare sphere of HEU; Jezebel is a bare sphere of plutonium; Jezebel 23 is a bare sphere of ^{233}U . The Flattop experiments involved spherical cores of HEU or plutonium surrounded by ^{238}U reflector material to make the composite systems critical. These different systems all produce neutron spectra within them that are “fast,” that is, the neutrons are predominantly of energies in the 100 keV to

■ Table 10

C/E values for β_{eff} of several critical systems, using ENDF/B-VII.0 and other libraries

System	C/E β_{eff}			
	ENDF/B-VII.0	ENDF/B-VI.8	JEFF-3.1	JENDL-3.3
TCA	0.998 ± 0.002	1.053 ± 0.011	1.029 ± 0.002	0.987 ± 0.012
IPEN/MB-01	1.008 ± 0.005	1.054 ± 0.005	1.040 ± 0.005	1.019 ± 0.005
Masurca R2	1.012 ± 0.009	1.035 ± 0.009	1.011 ± 0.009	1.018 ± 0.010
Masurca ZONA2	0.973 ± 0.013	0.983 ± 0.015	1.021 ± 0.013	0.994 ± 0.014
FCA XIX-1	0.987 ± 0.010	1.005 ± 0.011	1.010 ± 0.010	0.985 ± 0.011
FCA XIX-2	1.010 ± 0.013	1.003 ± 0.014	1.054 ± 0.013	1.022 ± 0.013
FCA XIX-3	0.981 ± 0.017	1.016 ± 0.016	0.997 ± 0.016	0.996 ± 0.016

The uncertainties in the C/E values are statistical uncertainties from the calculations only



■ Figure 51

The integral ^{241}Am neutron capture rate (divided by the ^{239}Pu fission rate) as a function of spectral index for different critical assembly locations. In this case, the measurements, which detect the ^{242}Cm , are divided by 0.84 to account for the fraction of ^{242g}Am that beta decays to ^{242}Cm

few MeV region, but the exact spectra vary from system to system. The neutron spectrum gets softer as one moves out from the center of the assembly, thereby giving additional information about the quality of the cross-section data in different energy regimes.

Neutron capture of ^{241}Am is shown in  Fig. 51 for different critical assembly spectra. We see good agreement between the calculations and the measurements, except that for the

hardest-spectrum system (Jezebel) the measurement appears to be underpredicted by up to 6%. This tells us that the ^{241}Am capture cross section to the ground state may be too low in the current evaluation in the $\approx 0.5\text{--}1$ MeV region.

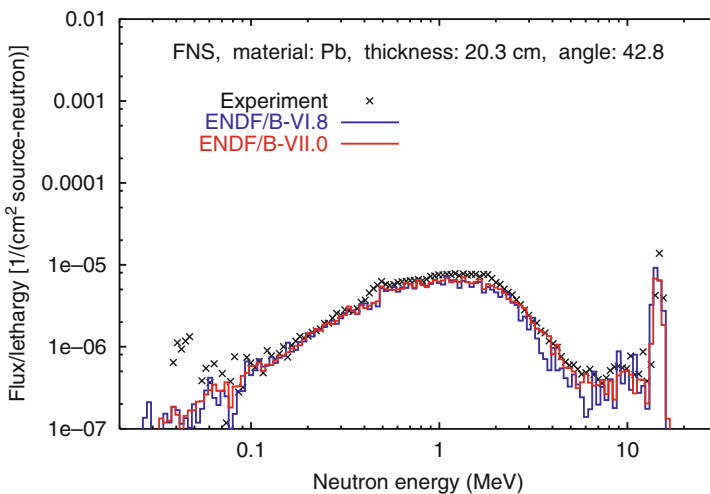
5.7 Shielding and Pulsed-Sphere Testing

In a paper (van der Marck, 2006), Steven van der Marck presents extensive data testing results for neutron transmission (shielding) benchmarks. We show some illustrative examples from that paper, focusing on validation benchmarks that test 14 MeV evaluations that have changed between ENDF/B-VI.8 and ENDF/B-VII.0 (e.g., $^{235,238}\text{U}$, ^{239}Pu , Pb, Li, and Be). These comparisons test the accuracy of the secondary emission spectra of neutrons following nuclear reactions.

► [Figure 52](#) shows an example from the above paper for the fusion neutronics source (FNS) benchmark corresponding to 14 MeV neutrons transmitted through 20 cm lead at an angle of 42.8° . The agreement between simulation and the FNS data is seen to be good, it shows an improvement on the earlier ENDF/B-VI.8 data and provides support for the accuracy of the new ^{208}Pb evaluation.

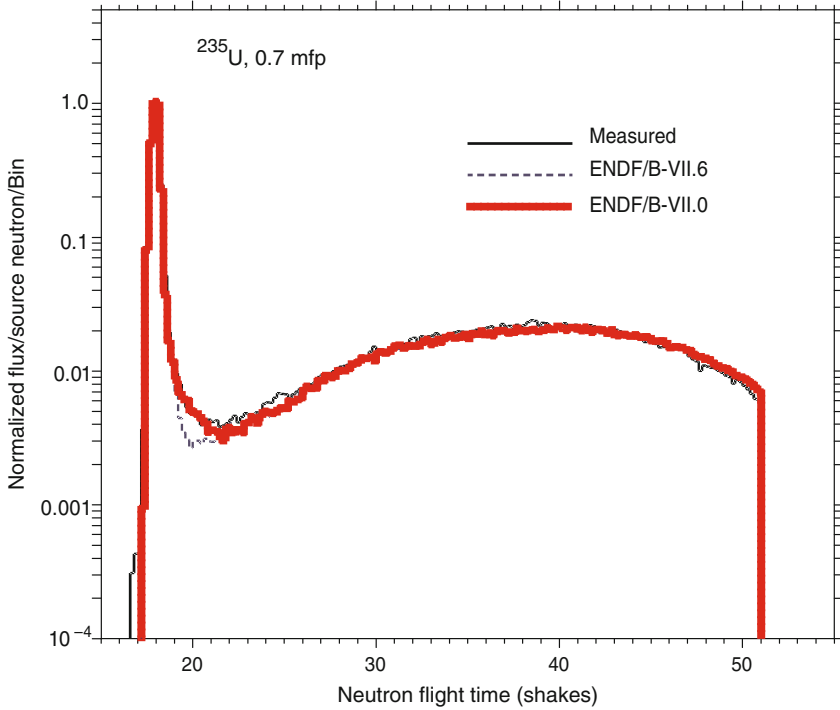
Numerous high-energy pulsed-sphere experiments (Wong et al., 1972; Webster et al., 1976) have been performed in which small, medium, and large spheres of 32 different materials were pulsed with a burst of high-energy (14 MeV) neutrons at LLNL's insulated core transformer (ICT) accelerator facility. Measured time-dependent neutron fluxes at collimated detectors located at a distance of 7–10 m provide a benchmark by which various neutron transport codes and cross-section libraries may be evaluated.

The results can be seen in ► [Fig. 53](#). The peak on the left-hand side corresponds to the transmission of the 14 MeV source neutrons; the broad peak further right (lower energies) corresponds to the neutrons created through compound nucleus and fission mechanisms.



■ **Figure 52**

Simulation of 14 MeV neutron transmission through 20 cm Pb at 42.8° (van der Marck, 2006)



■ Figure 53

Comparison of the simulated results using ENDF/B-VI.6 and ENDF/B-VII.0 data for the 0.7 mfp ^{235}U sphere. The experiment used a NE-213 detector biased at 1.6 MeV and located 9.455 m along the 26° flightpath. See the footnote for the definition of shake. Note the improved simulation predictions in the minimum region ($E_n \approx 8\text{--}12$ MeV), where preequilibrium and direct inelastic scattering are present

Numerous improvements (Marchetti and Hedstrom, 1998; Frankle, 2004a,b; Bucholz and Frankle, 2002) to the simulations have been made since the early implementations of these benchmarks. Simulations were performed by comparing the measured data with calculated results using ENDF/B-VI.6 or ENDF/B-VII.0 data with MCNP for the smallest spheres of ^{235}U , ^{238}U , and ^{239}Pu . With improvements in the modeling of the pulsed sphere experiments, problems with down-scattering from 14-MeV to the 8–12 MeV energy region had been noted especially for ^{235}U and ^{239}Pu . Recent efforts by LANL to improve the evaluated data for inelastic scattering at these higher incident neutron energies have been incorporated into the ENDF/B-VII.0 evaluations.

As shown in ► Fig. 53, the ENDF/B-VII.0 library improves the treatment of inelastic scattering for ^{235}U and ^{239}Pu showing much better agreement with the measured data. The improvements in modeling these integral transmission data experiments in the minimum region around 20 shakes (a shake is an informal unit of time used in nuclear science, 10^{-8} s; the word comes from the expression “two shakes of a lamb’s tail” to mean a very short time

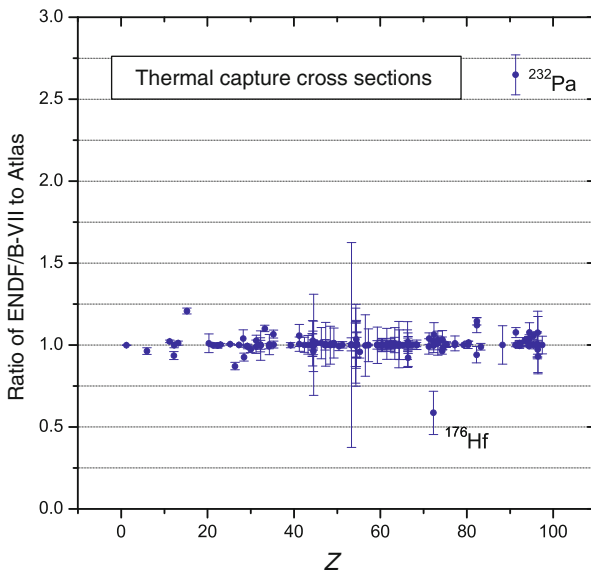
interval) can be directly related to the cross-section improvements in the fundamental data for an incident energy of 14 and 8–12 MeV emission energies, (see [▶ Fig. 23](#)).

5.8 Testing of Thermal Values and Resonance Integrals

Important quantities at low neutron energies are thermal capture cross sections and capture resonance integrals. These quantities can be extracted from the ENDF/B-VII.0 files and compared with the data in the recently published *Atlas of Neutron Resonances* (Mughabghab, 2006).

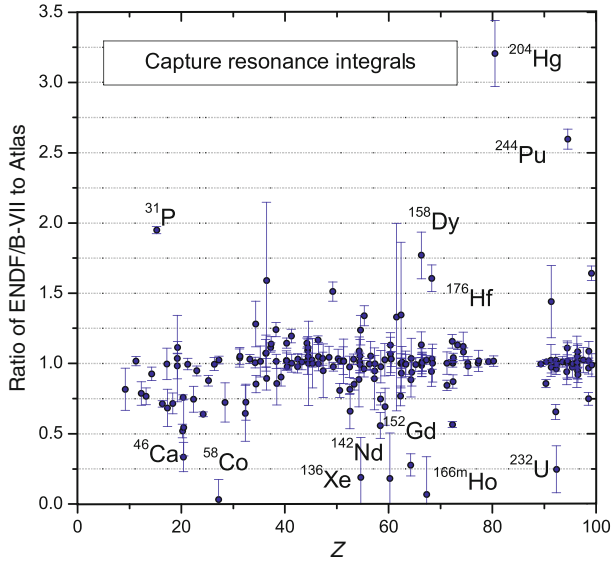
Ratios of capture cross sections at thermal energies are shown in [▶ Fig. 54](#). Overall, there is a fairly good agreement between the values in ENDF/B-VII.0 and the Atlas, although in several instances there are notable discrepancies. The thermal region in ^{232}Pa was revised for ENDF/B-VII.0 by Wright (ORNL) leading to the thermal capture nearly 3 times bigger than the one reported in the Atlas. The origin of this discrepancy is not clear and should be addressed in the future.

Ratios for capture resonances integrals can be seen in [▶ Fig. 55](#). Several comments should be made. Resonance integrals for ^{136}Xe , ^{142}Nd , ^{152}Gd , and ^{232}U : these ratios deviate from unity since there are inconsistencies between resonance parameters and resonance integral measurements reported in Mughabghab (2006) and the evaluators adopted resonance parameters rather than the experimental integrals. In the extreme case of ^{166m}Ho , the experiment is deemed doubtful due to the cadmium cutoff because of the low energy resonance at 0.274 eV. In ^{158}Dy , the resolved resonance range is very limited (up to 86 eV) and extrapolation of the URR to such low energies might not be reliable (in particular, the exact position of the lower boundary might play



■ Figure 54

Thermal neutron capture cross sections in ENDF/B-VII.0 compared to the *Atlas of Neutron Resonances* (Mughabghab, 2006)



■ Figure 55

Neutron capture resonance integrals in ENDF/B-VII.0 compared to the *Atlas of Neutron Resonances* (Mughabghab, 2006)

a significant role). The remaining outliers (^{31}P , ^{46}Ca , ^{58}Co , ^{176}Hf , ^{204}Hg , ^{244}Pu) are real discrepancies. These are old evaluations that will have to be updated in future releases of the ENDF/B library.

6 Other Nuclear Data of Interest

Other evaluated nuclear data of interest to nuclear technology applications, primarily to fission reactor applications, are fission yields (also termed FPY), thermal neutron scattering, and radioactive decay data.

6.1 Fission Yields

The fission yields from the 1989 LANL evaluation by England and Rides (1992) were adopted by ENDF/B-VII.0. In this evaluation, fission yield measurements reported in the literature and calculated charge distributions were used to produce a recommended set of yields for the fission products. Independent yields were taken from a calculated charge distribution model. A Gaussian charge distribution was calculated by using the most probable charge and Gaussian width. The weighted average experimental independent yields, the weighted average experimental cumulative yields, the weighted average experimental cumulative yields, and the calculated cumulative yields were combined statistically to form a recommended value.

There are two fission product yield sublibraries in ENDF/B-VII.0. Both of them have been taken over from ENDF/B-VII.8 without any change:

- The neutron-induced fission yields sublibrary contains data for 31 actinides. Incident neutron interacts with the target material that undergoes fission, which gives rise to extensive number of fission products. There are 31 such target materials, from ^{227}Th to ^{255}Fm ; neutron incident energies include the thermal energy of 0.0253 eV, 500 keV, and 14 MeV. While for some materials, such as ^{235}U , fission yields are given for all three energies, for many other materials, yields are given only for one or two energies.
- Spontaneous fission yields sublibrary contains nine materials, ^{238}U , $^{244,246,248}\text{Cm}$, $^{250,252}\text{Cf}$, ^{253}Es , and $^{243,256}\text{Fm}$. Each of these material undergoes spontaneous fission, which again gives rise to an extensive set of fission products.

Fission yields can be conveniently retrieved and plotted by Sigma web interface (Pritychenko and Sonzogni, 2008), which was developed and continues to be maintained by the NNDC, BNL.

6.2 Thermal Neutron Scattering

In ENDF/B-VII.0, this sublibrary contains 20 evaluations. As described below, seven were reevaluated or updated due to the combined efforts of MacFarlane, Los Alamos, and by Mattes and Keinert, IKE Stuttgart (Mattes and Keinert, 2005). The remaining evaluations were taken over from the ENDF/B-VI.8 library.

New thermal neutron scattering evaluations were generated by the LEAPR module of the NJOY code (MacFarlane, 1994). The physical model has been improved over the one used at General Atomics in 1969 to produce the original ENDF/B-III evaluations (Koppel and Houston, 1978). The alpha and beta grids have been extended to allow for larger incident energies and to properly represent the features of $S(\alpha, \beta)$ for the various integrations required. The physical constants have been updated for ENDF/B-VII.0 to match the current hydrogen and oxygen evaluations. The changes include additional alpha and beta points, interpolating the rotational energy distributions and translational energies onto the new temperature grid, and slightly reducing the rotational energies to improve the energy region between 0.01 and 0.1 eV.

6.2.1 H_2O and D_2O

H_2O : This evaluation was generated by Mattes and Keinert (2005). Water is represented by freely moving H_2O molecule clusters with some temperature dependence to the clustering effect. Each molecule can undergo torsional harmonic oscillations (hindered rotations) with a broad spectrum of distributed modes. The excitation spectra were improved over the older ENDF model, and they are given with a temperature variation. In addition, there are two internal modes of vibration at 205 and 436 meV. The stretching mode was reduced from the older ENDF value of 480 meV to account for the liquid state. Scattering by the oxygen atoms is not included in the tabulated scattering law data. It should be taken into account by adding the scattering for free oxygen of mass 16.

We note that the new H_2O thermal scattering kernel in ENDF/B-VII.0 led to a slight increase in calculated criticality of LEU-COMP-THERM critical assemblies.

D₂O: This was based on the IKE-IAEA-JEFF-3.1 evaluation done by Mattes and Keinert (2005). Changes made for ENDF/B-VII include using a more ENDF-like temperature grid and an extension of the α and β grids to improve results for higher incident energies.

6.2.2 O in UO₂ and U in UO₂

Uranium dioxide has a structure similar to fluoride, CaF₂. A lattice dynamical model was developed by Dolling, Cowley, and Woods to fit dispersion curve measurements. In addition to short-range core-core forces, the model includes shell-core, shell-shell, and long-range Coulomb interactions. Weighted frequency distributions were calculated from a dynamical matrix based on this model. The O in UO₂ part is kept separate from the U in O₂ part, and one-fourth of the coherent elastic cross section from the original General Atomics evaluation was included. The various constants were updated to agree with the ENDF/B-VII.0 evaluation of oxygen.

6.2.3 H in ZrH

The lattice dynamics of ZrH were computed from a central force model. The slightly tetragonal lattice of ZrH₂ was approximated by a face-centered cubic lattice. Four force constants (μ , γ , ν , and δ) were introduced describing, respectively, the interaction of a zirconium atom with its nearest neighbors (8 H atoms) and its next nearest neighbors (12 Zr atoms), and the interaction of a hydrogen atom with its next nearest neighbors (6 H atoms) and its third nearest atoms (12 H atoms). Eigenvalues and eigenvectors of the dynamical matrix were calculated and a phonon frequency spectrum was obtained by means of a root sampling technique. Weighted frequency spectra for hydrogen in ZrH were then obtained by appropriate use of the dynamical matrix eigenvectors. The final values of the four force constants were obtained by fitting both specific heat and neutron data. The position of an optical peak observed by neutron scattering techniques to be centered roughly around 0.14 eV determines the constant μ , while the overall width and shape of this peak determine ν and δ , respectively. Existing neutron data are not sufficiently precise to confirm the structure predicted in the optical peak by the central force model. Specific heat data were used to determine the force constant γ , which primarily determines the upper limit on the phonon energies associated with acoustic modes.

6.2.4 Other Modified Materials

Liquid methane at 100 K used the model of Agrawal and Yip as implemented by Picton, modified to include a diffusive component. Solid methane at 22 K used the model of Picton based on the spectrum of Harker and Brugger. Liquid para and ortho hydrogen at 20 K were computed with LEAPR. The scattering law is based on the model of Keinert and Sax (1987), which includes spin correlations from the Young and Koppel (1964) model, diffusion and local hindered motions from an effective translational scattering law based on a frequency distribution, and intermolecular coherence after Vineyard (1957).

Data for aluminum are provided for temperatures of 20, 80, 293.6, 400, 600, and 800 K using frequency distribution of Stedman et al. (1967). ^{56}Fe was modeled using iron frequency distribution of Brockhouse et al. (1967).

6.3 Decay Data

The decay data part of the ENDF/B-VII.0 library was produced by Sonzogni (NNDC, BNL) in 2006. This new sublibrary contains 3,838 materials and is mostly derived from the Evaluated Nuclear Structure Data File (ENSDF, 2006) and the 2005 edition of the *Nuclear Wallet Cards* (Tuli, 2005). Each material corresponds to the ground state or an isomeric level of a given nucleus. The library provides information for stable and unstable nuclei, from the neutron to ^{283}Rg ($Z = 111$).

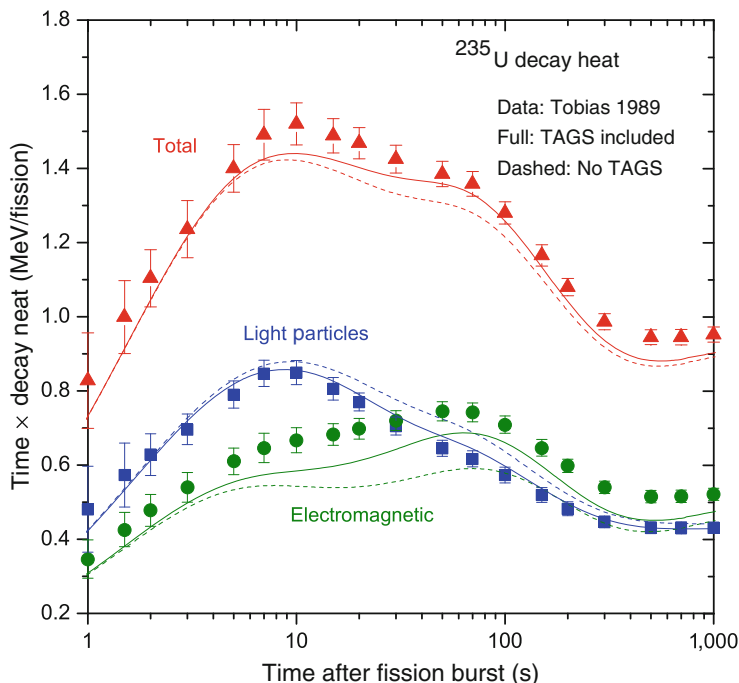
For sections of the library corresponding to unstable levels, the half-life, decay modes, and energy released during the decay is presented. For stable levels, the only information given is the spin and parity of the level. The energy released can be given with varying degrees of detail. The most basic information includes mean electromagnetic energy (EEM), mean light particle energy (ELP), and mean heavy particle energy (EHP).

For materials whose decay scheme is well known, that is, satisfying that the sum of the average energies for each radiation type is very close to the effective Q -value, the ENSDF database was used and discrete radiation information was provided. In contrast, for materials with unknown or poorly known decay schemes, the Nuclear Wallet Cards database was used. In this case, a simple rule was used to obtain the mean energies. If for instance the level in question undergoes beta decay, it was assumed that EEM and ELP corresponds each to a third of decay Q -value, while the neutrinos take the remaining third. For β -delayed particle emission, it was assumed that the neutrinos carried away a quarter of the available energy and that leptons, baryons, and photons took a quarter each.

The measurement of decay characteristics of fission products becomes increasingly difficult as the fission products are further from the valley of stability. Typically, as the β -decay Q -value increases, more weak gamma rays are produced, which are difficult to place or simply escape detection. To address this issue, a series of measurements using a ^{252}Cf source and a total absorption gamma spectrometer (TAGS) were performed at INL, Idaho (Greenwood et al., 1997). Using these data, EEM and ELP values were obtained for 48 materials, which can improve the decay heat predicting power of the library (Hagura et al., 2006). To obtain the EEM and ELP values from TAGS experiments, the evaluator followed the prescription developed by Hagura et al. (2006), where it is assumed that the decay from excited levels proceeds only by gamma emission, that is, conversion electrons are neglected. As a result, the EEM values is really an upper limit and the ELP a lower one. The effect of electron conversion is expected to be small, less than 10% of EEM. The use of TAGS data in decay data libraries is one of the issues under study by WPEC Subgroup 25 (Yoshida et al., 2006).

Additionally, the following features were included:

- Internal conversion coefficients were calculated for all gamma rays of known multipolarity using the code BRICC (Band et al., 2002).
- For ^{36}Cl , ^{59}Fe , ^{99}Tc , ^{129}I , and ^{137}Cs average β -energies for second forbidden nonunique transitions were calculated using the code SPEBETA (Cassette, 1992).



■ Figure 56

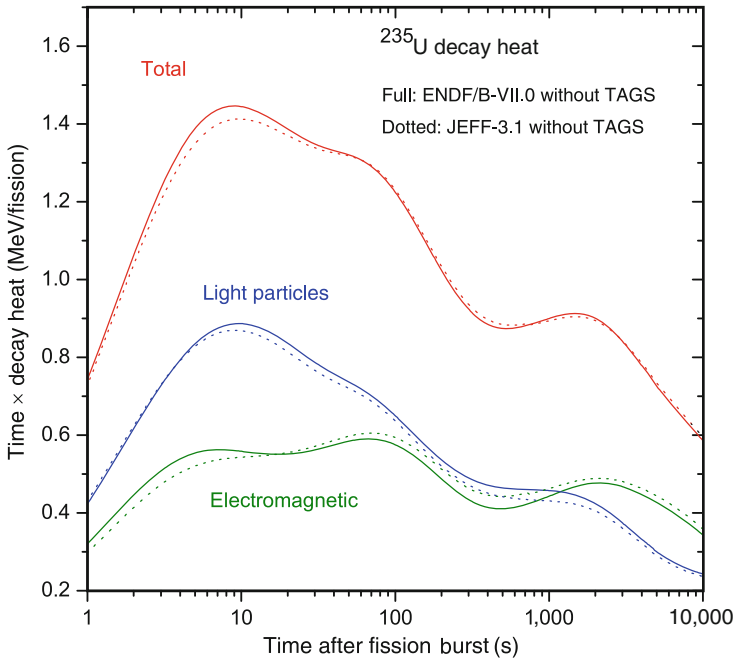
Decay heat per fission for a ^{235}U sample as a function of time. Shown is the total decay heat and its two components (light particles, electromagnetic)

- Theoretical β -decay half-lives and β -delayed neutron emission probabilities (P_n) using the Kratz–Hermann systematics (Pfeiffer et al., 2002) were used for some neutron-rich nuclides that were produced in the fission of ^{235}U and ^{239}Pu with limited experimental $T_{1/2}$ or P_n information.

6.3.1 Decay Heat Calculations

A plot of the decay heat following a fission event of ^{235}U can be seen in [Fig. 56](#). The total decay heat is separated into two components, electromagnetic and light particles. The former includes gamma and X-rays, while the latter includes electrons from β -decay as well conversion and Auger electrons. A heavy particle component, including neutrons and alphas is negligible. The data come from the 1989 compilation of Tobias and Mills (1989, private communication). The effect of the TAGS data is clearly visible. Without including it, many unmeasured weak gamma rays would be missing due to incomplete decay schemes, resulting in artificially high values of electron and neutrino mean energies as well as artificially low values of mean gamma energies.

The JEFF-3.1 decay data library was released in 2005 (correction to TAGS not yet introduced) and shares a similar spirit and scope with the ENDF/B-VII.0 decay data library. One



■ Figure 57

Decay heat per fission for a ^{235}U sample as a function of time using the ENDF/B-VII.0 and the JEFF-3.1 decay data without total absorption gamma spectrometer (TAGS) data

possible way of comparing both libraries would be to plot decay heats without TAGS data for ^{235}U . This is shown in [Fig. 57](#) and, as expected, both libraries give very similar results under this condition.

7 Evaluated Nuclear Data Libraries

There are numerous evaluated nuclear data libraries available from various nuclear data centers. National interests and different applications are the two principal factors causing this variety. Countries with strong nuclear programs, such as the USA, the European Union, Japan, Russia, and China, develop their own general purpose libraries to maintain evaluation expertise and ensure technological independence.

On the other hand, various applications of nuclear technology require special purpose libraries that satisfy particular needs of a given application. These derived libraries add another class to that mentioned above. One should also take into account various versions (releases) of the major libraries. Frequent sharing of evaluations among different libraries, often with some modifications, makes this picture even more complicated.

7.1 Overview of Libraries

A brief overview of evaluated nuclear data libraries should assist users to make the right choice for their application. It should be understood that there is internal dynamics in data development. Therefore, users should always consult webpages of the most prominent data centers to make sure that the library they are interested in is the latest version available.

7.1.1 General Purpose Libraries

General purpose libraries are not limited to any specific application and they are meant to satisfy a broad class of users. In practice, though, they often started as libraries for reactor applications.

Evaluations in a general purpose library are usually most complete in terms of physical quantities and nuclear reactions. They have to be suitable for transport calculations and as such have to fulfill quite strict requirements regarding completeness and consistency. Thus, neutron evaluations have to cover thermal, resolved, and unresolved resonance as well as fast neutron ranges extending at least up to 20 MeV, contain all major reaction channels, provide cross sections and possibly angular distributions, energy-angle correlated cross sections, and photon production data. Internal consistency implies that individual cross sections must sum up to the total cross section and the integrals of emission spectra correspond to the respective reaction cross sections.

Typically, the general purpose libraries are extensively validated against integral measurements. Sometimes, results of these integral measurements are incorporated into a library. This procedure introduces implicit correlations between various reactions and materials causing such a library to become an entity rather than a simple collection of individual evaluations.

Major general purpose libraries are maintained by the following countries:

1. USA – ENDF/B-VII.0, released in 2006; new version is expected in 2011.
2. Europe – JEFF-3.1, released in 2005; new version is expected in 2010.
3. Japan – JENDL-3.3, released in 2002; JENDL-4 is expected in 2010.
4. Russia – BROND-2.2, released in 1992; BROND-3 has not been completed yet, it is partly available in the selected evaluations of ROSFOND, which was released in 2008.
5. China – CENDL-2, released in 1991; CENDL-3 was developed but not internationally released; development of CENDL-4 is underway.

Over the first decade of the twenty-first century three evaluated data libraries (ENDF/B, JEFF, and JENDL) have been continuously updated and improved. These libraries will be briefly summarized later in this section.

7.1.2 Special Purpose Libraries

The special purpose libraries address particular exigencies of certain applications. Typical examples of such libraries are:

- International Reactor Dosimetry File, IRDF (Griffin and Paviotti-Corcuera, [2003](#))
- European Activation File, EAF (Forrest et al., [2007](#))
- Standards neutron cross section library (Carlson et al., [2009](#)), and
- Fusion Evaluated Nuclear Data Library, FENDL (Lopez Aldama and Trkov, [2004](#))

Evaluations in these libraries are not as comprehensive as those in the general purpose libraries but excel in certain features that would be impractical or too costly to be implemented in the general purpose files.

For example, activation library does not have to cover the full energy range, does not require spectra and angular distributions but does need to provide cross sections for the reactions leading to the radioactive products. Often, these are metastable states that are rarely considered in the general purpose libraries. There is no internal consistency requirement, but the amount of materials in the activation library is usually far larger than in the general purpose libraries.

The dosimetry libraries are similar to the activation ones but cover very limited number of well-known reactions that are used for the determination of neutron spectra. Cross-section covariances are critical for spectra deconvolution and are mandatory in dosimetry libraries.

On top of this pyramid are libraries of standards that include cross sections and covariances for an even smaller number of reactions that are known to a very high accuracy. The evaluation of standards is particularly thorough and is predominantly based on a detailed analysis of precise experimental data. Since standards are used as reference in many measurements they are a potential source of correlations among seemingly independent experiments. Therefore, cross-correlations among standards cross sections are required in the standards library. These libraries provide by far most accurate and reliable data but their coverage is very fragmentary.

Another type of special purpose libraries are those that are created as a selection of evaluations from various major libraries to better serve particular application. The prominent example is FENDL (Lopez Aldama and Trkov, 2004), the international library compiled under auspices of the IAEA in support of the fusion program.

Some examples of special purpose libraries are:

- IRDF-2002: The International Reactor Dosimetry File (Griffin and Paviotti-Corcuera, 2003) is a standardized, updated, and benchmarked evaluated cross section library of neutron dosimetry reactions with uncertainty information for use in lifetime management assessments of nuclear power reactors and other neutron metrology applications such as boron neutron capture therapy, therapeutic use of medical isotopes, nuclear physics measurements, and reactor safety applications. It contains damage cross sections, decay data, standard spectra, and dosimetry cross sections in ENDF-6 pointwise and groupwise representation. The development of IRDF-2002 was coordinated by IAEA during 2001–2004.
- INDL/TSL: An improved set of thermal neutron scattering law data prepared for ten elements/compounds in 2004–2006 by Mattes and Keinert under auspices of the IAEA.
- IAEA-Standards, 2006: The most respected international library of neutron cross-section standards (Carlson et al., 2009). It contains data for nine reactions including covariances. The library relies on a very careful evaluation of the selected set of most precise and reliable experiments. ENDF/B-VII.0 adjusted its neutron sublibrary to these cross sections and the whole set is available in its standards sublibrary.
- EAF-2003: The European Activation File (Forrest et al., 2003) is the most extensive library of neutron activation cross sections. It contains 12 617 excitation functions on 774 different targets from ^1H to ^{257}Fm stored in the extended ENDF-6 format (EAF format). The ENDF-6 formatted version is included as JEFF-3.1/A sublibrary in the general purpose library JEFF-3.1.
- EAF-2007: An extension of the European Activation File to proton- and deuteron-induced reactions (Forrest et al., 2007) in addition to the traditional neutron-induced data (Forrest et al., 2003). The deuteron-induced library contains 66,864 reactions, while the proton-induced

library contains 67,925 reactions. The library makes extensive use of model calculations with the TALYS code (Koning et al., 2004).

JENDL/AC-2008: The JENDL Actinoid File 2008 is a consistent set of new evaluations for 79 actinides ($89 \leq Z \leq 100$) released in 2008 with the intention of being included in JENDL-4.

MINSK: The library of original evaluations for 17 actinides developed by Maslov et al. (Minsk, Belarus) between 1995 and 2003. It contains data for isotopes of Th, Pa, U, Np, Pu, Am, and Cm.

MENDL-2: The neutron reaction data library for nuclear activation and transmutation at intermediate energies developed by Shubin et al. (IPPE Obninsk) around 1995–1998. It contains production cross sections for the formation of radioactive product nuclides for incident neutrons with energies up to 100 MeV. The 505 nuclides included cover the range from ^{26}Al to ^{210}Po with half-lives larger than one day.

ENDF/HE-VI: The high-energy library developed by S. Perlstein (BNL) and T. Fukahori (JAERI) in the 1990s containing neutron and proton data for ^{12}C , ^{56}Fe , ^{208}Pb , and ^{209}Bi up to 1,000 MeV.

7.1.3 Derived Libraries

Derived libraries are obtained from the libraries discussed above by processing them with a dedicated computer code such as NJOY (MacFarlane and Muir, 1994). In most cases, this processing is carried out to reconstruct cross sections in the resonance region, perform their Doppler broadening at a given temperature (pointwise representation), and to provide averages over certain energy intervals (groupwise representation). Derived libraries are generally needed for transport calculations (e.g., ACE libraries used in the Monte Carlo MCNP code (X5-MCNP-Team, 2003)).

The derived libraries may also be adjusted to reproduce particular set of integral experiments. In most cases, such adjustment is performed on the groupwise library and targets very well-defined applications such as sodium cooled fast reactors. The performance of the adjusted library is superior when it is used for the intended application but it might be poor for other applications. This is a consequence of the selection of integral experiments and adoption of energy-group structure that are tailored for the intended application.

7.2 ENDF-6 Format

Use of the ENDF-6 format is common for most of the evaluated nuclear data libraries. Only some of the activation and derived libraries deviate from this standard. Otherwise, all major libraries are using ENDF-6 format that has been accepted internationally. This unification had a great impact on the worldwide cooperation, greatly facilitated by exchanging files between the national libraries and easy comparison of the data.

The ENDF format has been developed by the CSEWG and it is maintained by the NNDC. The work started in 1966, the first version was released in 1968, and then in 1970, 1972, 1975, 1979, and 1990 along with the subsequent releases of the US ENDF library. The current

version, ENDF-6 (Herman and Trkov, 2009), has been used for both the ENDF/B-VI and ENDF/B-VII library implying that a new version of the format has not been developed for the ENDF/B-VII. We note that to differentiate it from the library that is denoted with Roman numerals (say, ENDF/B-VI), the ENDF format is always denoted with the Arabic numeral (ENDF-6).

For historic reasons, the ENDF-6 format uses 80-character records conforming to the old-fashioned versions of FORTRAN. It is organized in a strict hierarchical structure. Any library is a collection of material evaluations from a recognized evaluation group. It is divided into sublibraries that distinguish between different incident particles and types of data, namely, neutron induced-reactions, proton-induced reactions, thermal scattering data, fission yields, decay data, etc. The sublibraries contain the data for different materials identified by MAT numbers. Each material evaluation contains data blocks referred to as “Files” and denoted with MF numbers.

File 1: MF=1 is the descriptive part of the numerical file with details of evaluation, it also contains $\bar{\nu}$ values.

File 2: MF=2 contains neutron resonance parameters. Neither thermal constants, nor cross sections in the resonance region are provided, these are reconstructed from resonance parameters by processing codes.


File 3: MF=3 contains cross sections. The minimum required energy range for neutron reactions is from the threshold or from $10^{4.55}$ eV up to 20 MeV, but higher energies are allowed. There is a section for each important reaction or sum of reactions. The reaction MT-numbers for these sections are chosen based on the emitted particles.

Files 4–6: Energy and angle distributions for emitted neutrons and other particles or nuclei. File 4 is used for simple two-body reactions (elastic, discrete inelastic). Files 4 and 5 are used for simple continuum reactions, which are nearly isotropic and emit only one important particle. File 6 is used for more complex reactions that require energy-angle correlation that are important for heating or damage, or that have several important products that must be tallied.

Files 8–10: If any of the reaction products are radioactive, they should be described further in File 8. This file indicates how the production cross section is to be determined (from Files 3, 6, 9, or 10) and gives minimal information on the further decay of the product. Additional decay information can be retrieved from the decay data sublibrary when required. Branching ratios (or relative yields) for the production of different isomeric states of a radionuclide may be given in File 9. Alternatively, radionuclide isomer-production cross sections can be given in File 10.

Files 12–15: For compatibility with earlier versions, photon production and photon distributions can be described using File 12 (photon production yields), File 13 (photon production cross sections), File 14 (photon angular distributions), and File 15 (photon energy distributions). File 12 is preferred over File 13 when strong resonances are present (capture, fission).

Files 30–40: Covariance data are given in Files 30–40, with $\bar{\nu}$ covariances in File 31, resonance parameter covariances in File 32, and cross-section covariances in File 33.

A concise list of basic definitions and constants used in the ENDF-6 format is given in  [Table 11](#). For a detailed description we refer to the extensive manual (Herman and Trkov, 2009).

■ Table 11

ENDF-6 format: Selected definitions and constants. See Herman and Trkov (2009) for more details

File	Section	Quantity
MF=1		General information
MF=1	MT=451	Description of the evaluation
	MT=452	Average number of neutrons per fission, $\bar{\nu}$ ($\bar{\nu} = \bar{\nu}_d + \bar{\nu}_p$)
	MT=455	Average number of delayed neutrons per fission, $\bar{\nu}_d$
	MT=456	Average number of prompt neutrons per fission, $\bar{\nu}_p$
	MT=458	Energy release in fission for incident neutrons
	MT=460	β -Delayed photon spectra
MF=2		Resonance parameters
MF=2	MT=151	Resolved resonance parameters, flag LRU=1
	MT=151	Unresolved resonance parameters, flag LRU=2
MF=3		Reaction cross sections
MF=3	MT=1	Total cross sections
	MT=2	Elastic cross sections
	MT=4	Sum of all inelastic cross sections
	MT=5	Sum of cross sections for all reaction channels not given explicitly under other MT numbers
	MT=16	$(n,2n)$ cross sections
	MT=17	$(n,3n)$ cross sections
	MT=18	(n,xf) total fission cross sections
	MT=19	(n,f) first chance fission cross sections
	MT=20	(n,nf) second chance fission cross sections
	MT=21	$(n,2nf)$ third chance fission cross sections
	MT=22	$(n,n'\alpha)$ cross sections
	MT=28	$(n,n'p)$ cross sections
	MT=51	(n,n') cross sections (inelastic scattering to the 1 st excited level)
	MT=52	(n,n'_2) cross sections (inelastic scattering to the 2 nd excited level)
	MT=91	(n,n'_{cont}) cross sections (inelastic scattering to continuum)
	MT=102	(n,γ) cross sections
	MT=103	(n,p) cross sections
MT=105	(n,t) cross sections	
MT=107	(n,α) cross sections	

Table 11 (continued)

File	Section	Quantity
	MT=601	(n,p_1) cross sections for the (n,p) reaction leaving residual nucleus in the 1 st excited level
	MT=600	(n,p_0) cross sections for the (n,p) reaction leaving residual nucleus in the ground state
	MT=801	(n,α_1) cross sections for the (n,α) reaction leaving residual nucleus in the 1 st excited level
MF=4		Angular distributions of emitted particles expressed as normalized probability distributions
MF=4	MT=2	Angular distributions for elastic scattering
	MT=51	Angular distributions for inelastic scattering to the 1 st excited level
MF=5		Energy distributions (spectra) of emitted particles expressed as normalized probability distributions
MF=5	MT=16	Spectra of emitted neutrons, photons, and recoils for the $(n,2n)$ reaction (neutron spectra contain both cascading neutrons)
MF=6		Energy-angle distributions of emitted particles (for a given reaction should contain subsections for all reaction products including γ 's and recoils)
MF=6	MT=5	Energy-angle distributions of products for all reactions lumped into MT=5 (reactions are identified by the residual nuclei)
	MT=91	Energy-angle distributions of continuum neutrons (only those neutrons that were not followed by any other particle emission are counted)
	MT=28	Energy-angle distributions of neutrons, protons, residual nuclei, and photons emitted in the $(n,n'p)$ reaction
MF=7		Thermal neutron scattering on moderating materials
MF=7	MT=2	Elastic thermal neutron scattering
	MT=4	Inelastic thermal neutron scattering
MF=8		Decay data and fission-product yields
MF=8	MT=454	Independent fission product yields
	MT=459	Cumulative fission product yields
	MT=457	Radioactive decay data
MF=9		Multiplicities for production of radioactive nuclei (activation/isomeric cross sections expressed as a fraction of the respective cross sections in MF=3)

■ Table 11 (continued)

File	Section	Quantity
MF=10		Absolute cross sections for production of radioactive nuclei (similar to MF=9 but without reference to MF=3)
MF=12		Multiplicities for photon production and branching ratios for γ transitions between discrete levels (respective cross sections in MF=3 must be used for absolute values)
MF=13		Absolute photon spectra and photon production cross sections (similar to MF=12 but without reference to MF=3)
MF=14		Angular distributions for discrete and continuum photons
MF=15		Energy spectra for continuum photons (normalized distributions to be multiplied by the respective cross sections in MF=3)
MF=23		Electromagnetic interaction cross sections (such as total, coherent and incoherent (Compton) elastic scattering for photons and elastic scattering, brehm- sstrahlung and ionization for electrons)
MF=23	MT=501	Total cross section for incident photons
	MT=502	Photon coherent scattering cross section
	MT=516	Pair production cross section
	MT=522	Photoelectric absorption cross section
	MT=527	Electro-atomic brehmsstrahlung cross section
MF=26		Spectra and angular distributions of photons and electrons emitted in inter-action of photons or electrons with atoms
MF=27		Atomic form factors or scattering functions for angular distribution of photons
MF=28		Atomic relaxation data (emission of X-rays and electrons from ionized atoms)
MF=31		Covariances for nubar ($\bar{\nu}$)
MF=32		Covariances for resonance parameters
MF=33		Covariances for cross sections
MF=33	MT=1	Covariances for total cross sections
	MT=2	Covariances for elastic cross sections
	MT=851–870	Covariances for cross sections of lumped channels
MF=34		Covariances for angular distributions of emitted particles
MF=35		Covariances for energy spectra of emitted particles
MF=40		Covariances for activation cross sections

■ Table 11 (continued)

NLIB	Library	Full name
0	ENDF/B	US Evaluated Nuclear Data File
1	ENDF/A	US Evaluated Nuclear Data File for preliminary or incomplete evaluations
2	JEFF	Joint European Evaluated File
3	EFF	European Fusion File (now in JEFF)
4	ENDF/HE	US High Energy File
5	CENDL	Chinese Evaluated Nuclear Data Library
6	JENDL	Japanese Evaluated Nuclear Data Library
21	IFPL	NEA International Fission Product Library
33	FENDL	IAEA Fusion Evaluated Nuclear Data Library
34	IRDF	IAEA International Reactor Dosimetry File
37	FENDL/A	FENDL Activation File
41	BROND	Russian Biblioteka (library) of Recommended Neutron Data
Symbol	Definition	Recommended value
m_n	neutron mass	1.008 664 916 amu
m_e	electron mass	$5.485 799 110 \times 10^{-4}$ amu
m_p	proton mass	1.007 276 467 amu
m_d	deuteron mass	2.013 553 213 amu
m_t	triton mass	3.015 500 713 amu
m_h	^3He mass	3.014 932 244 amu
m_α	α -particle mass	4.001 506 179 amu
amu	atomic mass unit	$931.494 013 \times 10^6$ eV
e	elementary charge	$1.602 176 462 \times 10^{-19}$ C
h	Planck's constant	$4.135 667 27 \times 10^{-15}$ eV s
$h/2\pi$	Planck's const./ 2π	$6.582 118 89 \times 10^{-16}$ eV s
k	Boltzmann's constant	$8.617 342 \times 10^{-5}$ eV/K
c	Speed of light	299 792 458 m/s
N_A	Avogadro's number	$6.022 141 99 \times 10^{23}$ 1/mol

■ **Table 12**

Major releases of the ENDF/B library of the USA. The library is maintained by the Cross Section Evaluation Working Group (CSEWG), established in 1966

ENDF/B	I	II	III	IV	V	VI	VII
Year	1968	1970	1972	1974	1978	1990	2006

7.3 ENDF/B-VII.0 (USA, 2006)

The ENDF/B-VII.0 library, released by the US CSEWG in December 2006, contains data primarily for reactions with incident neutrons, protons, and photons on almost 400 isotopes, based on experimental data and theory predictions. The new library plays an important role in nuclear technology applications, including transport simulations supporting national security, nonproliferation, advanced reactor and fuel cycle concepts, criticality safety, fusion, medicine, space applications, nuclear astrophysics, and nuclear physics facility design.

Major releases of the US ENDF/B library are summarized in ▶ [Table 12](#). After an initial 2-year release cycle, CSEWG moved to ever longer release cycles. Recent releases occurred at widely spaced intervals: ENDF/B-V was released in 1978, ENDF/B-VI in 1990, followed by this ENDF/B-VII.0 release in 2006. However, interim releases have occurred more frequently and ENDF/B-VI had upgrades embodied in eight releases, the last one occurring in October 2001 and referred to as ENDF/B-VI.8 (CSEWG-Collaboration, [2001](#)).

7.3.1 Overview of the ENDF/B-VII.0 Library

The ENDF/B-VII.0 library contains 14 sublibraries, summarized in ▶ [Table 13](#), according to the identification number NSUB. The number of materials (isotopes or elements) are given for both the new (VII.0) and previous (VI.8) versions of the ENDF/B library. Although the ENDF/B library is widely known for evaluated neutron cross sections, it also contains a considerable amount of non-neutron data.

Out of the total of 14 sublibraries, there are two new sublibraries; seven sublibraries were considerably updated and extended, and the remaining five sublibraries were taken over from ENDF/B-VI.8 without any change:

1. The photonuclear sublibrary is new; it contains evaluated cross sections for 163 materials (all isotopes) mostly up to 140 MeV. The sublibrary has been supplied by LANL and it is largely based on the IAEA-coordinated collaboration completed in 2000 (Chadwick et al., [2000](#)).
2. The photo-atomic sublibrary has been taken over from ENDF/B-VI.8. It contains data for photons from 10 eV up to 100 GeV interacting with atoms for 100 materials (all elements). The sublibrary has been supplied by LLNL.
3. The decay data sublibrary has been completely reevaluated and considerably extended by the NNDC, BNL.
4. The spontaneous fission yields were taken over from ENDF/B-VI.8. The data were supplied by LANL.

■ Table 13

Contents of the ENDF/B-VII.0 library, with ENDF/B-VI.8 shown for comparison

No.	NSUB	Sublibrary name	Short name	ENDF/B- VII.0 materials	ENDF/B-VI.8 materials
1	0	Photonuclear	g	163	–
2	3	Photo-atomic	Photo	100	100
3	4	Radioactive decay	Decay	3,838	979
4	5	Spontaneous fission yields	s/fpy	9	9
5	6	Atomic relaxation	ard	100	100
6	10	Neutron	n	393	328
7	11	Neutron fission yields	n/fpy	31	31
8	12	Thermal scattering	tsl	20	15
9	19	Standards	Std	8	8
10	113	Electro-atomic	e	100	100
11	10010	Proton	p	48	35
12	10020	Deuteron	d	5	2
13	10030	Triton	t	3	1
14	20030	³ He	he3	2	1

NSUB stands for the sublibrary number, given in the last two columns are the number of materials (isotopes or elements)

- The atomic relaxation sublibrary was taken over from ENDF/B-VI.8. It contains data for 100 materials (all elements) supplied by LLNL.
- The neutron reaction sublibrary represents the heart of the ENDF/B-VII.0 library. The sublibrary has been considerably updated and extended; it contains 393 materials, including 390 isotopic evaluations and 3 elemental ones (C, V, and Zn). These evaluations can be considered to be complete (the only exception is ²⁵³Es that contains (*n*, γ) dosimetry cross sections) since they contain data needed in neutronics calculations. Important improvements were made to the actinides by LANL, often in collaboration with ORNL. Evaluations in the fission product range ($Z = 31\text{--}68$) have been entirely changed. Of the 393 materials, about two-thirds of the evaluations are based upon recent important contributions from US evaluators. The remaining evaluations were adopted from other sources (mostly the JENDL-3.3 library). LLNL provided β -delayed γ -ray data for ²³⁵U and ²³⁹Pu for the first time in ENDF/B.
- Neutron fission yields were taken over from ENDF/B-VI.8. The data were supplied by LANL.
- The thermal neutron scattering sublibrary contains thermal scattering-law data, largely supplied by LANL, with several important updates and extensions (Mattes and Keinert, 2005).
- The neutron cross-section standards sublibrary is new. Although standards traditionally constituted part of the ENDF/B library, in the past these data were stored on a tape. As the

concept of tapes has been abandoned in ENDF/B-VII.0, the new sublibrary (short name *std*, sublibrary number NSUB = 19) has been introduced. Out of eight standards materials, six were newly evaluated, while the $^3\text{He}(n,p)$ and $^{nat}\text{C}(n,n)$ standards were taken over from ENDF/B-VI.8. The standard cross sections were adopted by the neutron reaction sublibrary except for the thermal cross section for $^{235}\text{U}(n,f)$ where a slight difference occurs to satisfy thermal data testing. These new evaluations come from the international collaboration coordinated by the IAEA (Carlson et al., 2009).

10. The electro-atomic sublibrary was taken over from ENDF/B-VI.8. It contains data for 100 materials (all elements) supplied by LLNL.
11. The proton-induced reactions were supplied by LANL, the data being mostly up to 150 MeV. There are several updates and several new evaluations.
12. The deuteron-induced reactions were supplied by LANL. This sublibrary contains five evaluations.
13. The triton-induced reactions were supplied by LANL. This sublibrary contains three evaluations.
14. Reactions induced with ^3He were supplied by LANL. This sublibrary contains two evaluations.

7.3.2 Processing and Data Verification

The ENDF/B-VII.0 library was issued in its basic format defined by the ENDF-6 Formats Manual (Herman and Trkov, 2009). For practical applications, the library must be processed so that basic data are converted into formats suitable as input for applied codes such as the Monte Carlo transport code, MCNP, and the reactor licensing code, SCALE (SCALE, 2000). Recommended processing codes:

- Los Alamos code NJOY-99 (MacFarlane and Muir 1994; MacFarlane and Kahler, 2009, “NJOY-99.304”, www.t2.lanl.gov/codes/njoy99/index.html (5 october 2009), to be obtained from RSICC (RSICC, 2009) or NEA Data Bank (2009), with patches available at the LANL T-2 webpage (2009).
- Two codes are available for processing of covariance data, ERRORJ (Kosako, 2001) – since recently a part of the NJOY package, and PUFF (Wiarda and Dunn, 2006) – a module of the Oak Ridge processing code AMPX (Dunn and Greene, 2002).

Data verification was performed by the NNDC, BNL:

- Checking the library by ENDF-6 utility codes (CHECKR, FIZCON, PSYCHE) (Dunford, 2005) for possible formatting problems and inconsistencies in physics.
- Processing of photonuclear, neutron, thermal scattering, and proton sublibraries by NJOY-99 to ensure that a processed library suitable for neutronics calculations can be produced.
- Use of the processed files by the Monte Carlo codes MCNP (X5-MCNP-Team, 2003) and MCNPX (2006) in simple neutronics test to ensure that neutronics calculations can be performed.
- Processing of covariance data to ensure that multigroup data for applied calculations can be produced.

Data validation is a complex process described earlier in this chapter. CSEWG used continuous energy Monte Carlo transport codes and validation focused on the neutron reaction and thermal neutron scattering sublibraries. These are the best validated sublibraries. The neutron standards sublibrary contains a special category of data where the highest quality was achieved. The photonuclear sublibrary was subject to partial validation, and the decay data sublibrary went through some limited testing. The remaining nine sublibraries were not included in the ENDF/B-VII.0 validation process.

7.4 JEFF-3.1 (Europe, 2005)

The JEFF project is a collaborative effort among the European member countries of the NEA Data Bank. The initial objective was to improve performance for existing reactors and fuel cycles. More recently, the goal is to provide users with a more extensive set of data for a wider range of applications, including innovative reactor concept (Gen-IV), transmutation of radioactive waste, fusion, and medical applications. These data include neutron- and proton-induced reactions, radioactive decay, fission yields, thermal scattering law, and photo-atomic interactions.

The JEFF-3.1 version of the library was released in May 2005, for summary description see JEFF Report 19 (JEFF3, 2005). The library combines the efforts of the JEFF and EFF/EAF (European Fusion File/European Activation File) working groups. The neutron general purpose sublibrary contains 381 materials from ^1H to ^{255}Fm . The activation sublibrary is based on the EAF-2003 and contains cross sections for neutron reactions on 774 targets; radioactive decay sublibrary contains three 852 isotopes of which only 226 are stable; proton sublibrary covers 26 materials from ^{40}Ca to ^{209}Bi ; thermal scattering law sublibrary includes nine materials; neutron-induced-fission-yield sublibrary covers 19 isotopes from ^{232}Th to ^{245}Cm , and spontaneous-fission-yield sublibrary contains $^{242,244}\text{Cm}$ and ^{252}Cf .

The JEFF-3.0 library was upgraded mainly because of underprediction of the reactivity for LEU systems relevant to light water reactors. The reactivity issue was linked to the ^{238}U cross sections and the improved evaluation was assembled as a result of the broad international effort. Transport calculations proved that the predictions of this reactivity was appreciably improved.

New evaluations or major revisions were performed for Ti isotopes (IRK Vienna); Ca, Sc, Fe, Ge, Pb, and Bi isotopes (NRG Petten); ^{103}Rh , $^{127,129}\text{I}$, and Hf isotopes; and $^{236,237,238}\text{U}$ and ^{214}Am (CEA). For other isotopes, more recent evaluations from other libraries were adopted. Revised thermal scattering data have been produced for all important moderator and structural materials.

The JEFF project put considerable effort to validation of the library, which was done particularly carefully from the point of view of nuclear reactor applications. The overall performance of the library is excellent.

7.5 JENDL-3.3 (Japan, 2002)

JENDL-3.3 is the Japanese evaluated library that was released in 2002, see the summary paper by Shibata et al. (2002b). The library is largely based on evaluations that originated in Japan, thus representing probably the most extensive source of independent evaluations, just after the US effort.

The objective of the JENDL effort is to supply Japanese evaluated data for fast breeder reactors, thermal reactors, fusion neutronics, and shielding calculations, as well as other applications. The JENDL-3.3 library contains data for 337 materials, from 10^{-5} to 20 MeV. Major issues in the previous version of the library, JENDL-3.2, were addressed: overestimation of criticality values for thermal fission reactors was improved by the modification of fission cross sections and fission neutron spectra for ^{235}U ; incorrect energy distributions of secondary neutrons from important heavy materials were replaced by the statistical model results; inconsistency between elemental and isotopic evaluations were removed for medium-heavy nuclides.

JENDL-3.3 also contains covariances for 20 most important materials. Of them, 16 materials have been originally developed for JENDL-3.2 covariance file, made available in March 2002 (Shibata et al., 2002a), and adopted shortly afterward with minor modifications by JENDL-3.3. Three additional materials were produced for JENDL-3.3, while the dosimetry material ^{55}Mn was taken over. The list of resulting 20 materials includes actinides, structural materials, and light nuclides, which are of interest primarily for fast reactor applications:

- ^1H , $^{10,11}\text{B}$, ^{16}O , ^{23}Na , ^{48}Ti , V, ^{52}Cr , ^{55}Mn , ^{56}Fe , ^{59}Co , $^{58,60}\text{Ni}$, ^{90}Zr , $^{233,235,238}\text{U}$, $^{239,240,241}\text{Pu}$.

A new version of the library, JENDL-4, is under development, with a release expected in 2010.

7.6 Web Access to Nuclear Data

Several major webpages offer evaluated nuclear data. These are regularly maintained by the four well-established data centers:

1. NNDC, USA, www.nndc.bnl.gov
2. IAEA, Nuclear Data Section (IAEA-NDS), Vienna, www.nds.iaea.org
3. Nuclear Energy Agency, Data Bank (NEA-DB), Paris, www.nea.fr/html/dbdata
4. Nuclear Data Center, Japan Atomic Energy Agency (NDC-JAEA), Japan, wwwndc.tokai-sc.jaea.go.jp

The NNDC has probably the largest portfolio of data with web retrieval capabilities, including both nuclear structure (ENSDF, NuDat, Chart of Nuclides) and nuclear reactions (EXFOR, ENDF, Sigma).

For the readers of the present Handbook of most interest would be *Sigma* nuclear reaction retrieval and plotting system, which was developed by the NNDC to satisfy needs of both professional users and those without knowledge of complex ENDF-6 formatting system. Sigma uses the latest web technologies to provide browsing and search tools as well as interactive graphics. It can be easily accessed at www.nndc.bnl.gov/sigma and includes the following capabilities:

1. Retrieval, browsing, search
2. Plotting
 - Cross sections
 - Angular distributions, energy spectra
 - Covariances (MF33)
 - Fission yields
3. Computations (ratios, integrals, weighting)

4. Thermal values and resonance integrals

Sigma offers data from the following nuclear reaction libraries:

- ENDF/B-VII.0 (USA, 2006)
- JEFF-3.1 (Europe, 2005)
- JENDL-3.3 (Japan, 2002)
- ROSFOND (Russia, 2008)
- ENDF/B-VI.8 (USA, 2001)
- ENDF/A (USA, selected files only)
- EXFOR (NRDC network, experimental data, latest version)

The IAEA Nuclear Data Service (Vienna) offers major nuclear reaction data libraries as well as a number of smaller libraries and specialized results of the IAEA-coordinated data projects. Its signature nuclear reaction retrieval system is *ENDF*, which is also offered by the NNDC as an alternative to Sigma.

The NEA Data Bank (Paris) data services are more restricted, focusing on nuclear reaction data and nuclear reaction computer codes. Its signature nuclear reaction data retrieval and plotting system is Java-based *JANIS*.

The Nuclear Data Center of the Japan Atomic Energy Agency (Tokaimura) offers data services with the focus on data included in the Japanese Evaluated Nuclear Data Library, JENDL.

Acknowledgments

It would not have been possible to write this chapter without results produced by the dedicated work of numerous scientists and colleagues over years, both in the USA and abroad. We are particularly grateful to members of CSEWG and many other colleagues who contributed to ENDF/B-VII.0 and other nuclear data libraries. We owe special thanks to the authors of the “Big Paper” on ENDF/B-VII.0 (Chadwick et al., 2006), which supplied most of the figures and served as the basis for preparing this chapter.

References

- | | |
|--|---|
| <p>Audi G, Bersillon O, Blachot J, Wapstra A (2003) The NUBASE evaluation of nuclear and decay properties. <i>Nucl Phys A</i> 729:3</p> <p>Axel P (1962) Electric dipole ground state transition width strength function and 7 MeV photon interaction. <i>Phys Rev</i> 126:671</p> <p>Band I, Trzhaskovskaya M, Nestor C Jr, Tikkanen P, Raman S (2002) Dirac-Fock internal conversion coefficients. <i>At Data Nucl Data Tables</i> 81:1</p> <p>Běťák E, Obložinský P (1993) Code PEGAS: pre-equilibrium exciton model with spin conservation and gamma emission. Technical report INDC(SLK)-001, IAEA/Slovak Academy of Sciences (Note: DEGAS is an extended version of the code PEGAS using two-parameteric p-h level densities.)</p> | <p>Bjornholm S, Lynn J (1980a) The double-humped fission barrier. <i>Rev Mod Phys</i> 52:725–931</p> <p>Bjornholm S, Lynn JE (1980b) The double-humped fission barrier. <i>Rev Mod Phys</i> 52:725</p> <p>Blann M (1996) New precompound decay model. <i>Phys Rev C</i> 54:1341</p> <p>Blann M, Chadwick MB (1998) New precompound model: angular distributions. <i>Phys Rev C</i> 57:233</p> <p>Blann M, Chadwick MB (2000) Precompound Monte-Carlo model for cluster induced reactions. <i>Phys Rev C</i> 6203:4604</p> <p>Bohr N, Wheeler J (1939) The mechanism of nuclear fission. <i>Phys Rev</i> 56:426–450</p> <p>Bollinger LM, Thomas GE (1968) p-Wave resonances of ^{238}U. <i>Phys Rev</i> 171:1293</p> |
|--|---|

- Boukharaba N et al (2002) Measurement of the n-p elastic scattering angular distribution at $E_n = 10$ MeV. *Phys Rev C* 65:014004
- Boykov G et al (1991) Prompt neutron fission spectra of ^{235}U . *Sov J Nucl Phys* 53:392
- Brady M, England T (1989) Delayed neutron data and group parameters for 43 fissioning systems. *Nucl Sci Eng* 103:129–149
- Briggs JB et al (2004) International handbook of evaluated criticality safety benchmark experiments. Technical report NEA/NSC/DOC(95) 04/I, Nuclear Energy Agency, Paris, France
- Brockhouse BN, Abou-Helal HE, Hallman ED (1967) Lattice vibrations in iron at 296°K. *Solid State Commun* 5:211
- Bucholz J, Frankle S (2002) Improving the LLNL pulsed-sphere experiments database and MCNP models. *Trans Am Nucl Soc* 86:433–435
- Buerkle W, Mertens G (1997) Measurement of the neutron-proton differential cross section at 14.1 MeV. *Few Body Syst* 22:11
- Capote R, Herman M, Obložinský P et al (2009) RIPL – reference input parameter library for calculation of nuclear reactions and nuclear data evaluations. *Nucl Data Sheets* 110:3107
- Carlson A, Pronyaev V, Smith D et al (2009) International evaluation of neutron cross section standards. *Nucl Data Sheets* 110:3215–3325
- Cassette P (1992) SPEBETA programme de calcul du spectre en energie des electros emis par des radionucleides emetterus beta. Technical report CEA, Technical Note LPRI/92/307/J, CEA Saclay
- Chadwick M, Obložinský P, Blokhin A et al (2000) Handbook on photonuclear data for applications: cross-sections and spectra. Technical report IAEA-TECDOC-1178, International Atomic Energy Agency
- Chadwick M, Obložinský P, Herman M, Greene N, McKnight R, Smith D, Young P, MacFarlane R, Hale G, Frankle S, Kahler A, Kawano T, Little R, Madland D, Moller P, Mosteller R, Page P, Talou P, Trelue H, White M, Wilson W, Arcilla R, Dunford C, Mughabghab S, Pritychenko B, Rochman D, Sonzogni A, Lubitz C, Trumbull T, Weinman J, Brown D, Cullen D, Heinrichs D, McNabb D, Derrien H, Dunn M, Larson N, Leal L, Carlson A, Block R, Briggs J, Cheng E, Huria H, Zerkle M, Kozier K, Courcelle A, Pronyaev V, van der Marck S (2006) ENDF/B-VII.0: next generation evaluated nuclear data library for nuclear science and technology. *Nucl Data Sheets* 107(12):2931–3118
- Cokinos D, Melkonian E (1977) Measurement of the 2200 m/sec neutron-proton capture cross section. *Phys Rev C* 15:1636
- Conant J, Palmedo P (1971) Delayed neutron data. *Nucl Sci Eng* 44:173
- Courcelle A (2004) First conclusions of the WPEC Subgroup-22. In: Haight R, Chadwick M, Kawano T, Talou P (eds) Proceedings of the international conference on nuclear data for science and technology, American Institute of Physics, New York, Santa Fe, Sept 26–Oct 1, 2004, pp 462–467
- CSEWG-Collaboration (2001) Evaluated nuclear data file ENDF/B-VI.8. <http://www.nndc.bnl.gov/endlf>, Mar 5, 2010
- DeHart MD (1995) Sensitivity and parametric evaluations of significant aspects of burnup credit for PWR spent fuel packages. Technical report ORNL/TM-12973, ORNL
- Derrien H, Courcelle A, Leal L, Larson NM, Santamarina A (2004) Evaluation of ^{238}U resonance parameters from 0 to 20 keV. In: Haight R, Chadwick M, Kawano T, Talou P (eds) Proceedings of the international conference on nuclear data for science and technology, American Institute of Physics, New York, Santa Fe, Sept 26–Oct 1, 2004, pp 276–281
- Derrien H, Leal LC, Larson NM (2006) Evaluation of ^{232}Th neutron resonance parameters in the energy range 0 to 4 keV. Technical report ORNL/TM-2006/53, ORNL
- Dilg W (1975) Measurement of the neutron-proton total cross section at 132 eV. *Phys Rev C* 11:103
- dos Santos A, Diniz R, Fanaro L, Jerez R, de Andrade e Silva G, Yamaguchi M (2004) The experimental determination of the effective delayed neutron parameters of the IPEN/MB-01 reactor. In: PHYSOR, Chicago, April 25–29
- Dunford C (1971) Compound nuclear analysis programs COMNUC and CASCADE. Technical report T1-707-130-013, Atomics International
- Dunford C (2005) ENDF utility codes, version 7.02. <http://www.nndc.bnl.gov/nndcscr/endlf/endlf-util-7.02/>, Dec 15, 2006
- Dunn M, Greene N (2002) AMPX-2002: a cross section processing system for generating nuclear data for criticality safety applications. Technical report, Transactions of the American Nuclear Society, ORNL
- England T, Rider B (1992) Evaluation and compilation of fission product yields. Technical report ENDF-349, Los Alamos National Laboratory, Los Alamos
- England T, Rider B (1993) Nuclear modeling of the $^{239}\text{Pu}(n, xn)$ excitation function. Technical report LA-UR-94-3106 ENDF-349, Los Alamos National Laboratory, Los Alamos

- ENSDF (2006) ENSDF, Evaluated Nuclear Structure Data File. <http://www.nndc.bnl.gov/ensdf>, 15 Dec 2006
- Ethvignot T et al (2003) Prompt-fission-neutron average energy for $^{238}\text{U}(n, f)$ from threshold to 200 MeV. *Phys Lett B* 575:221
- Forrest R, Kopecky J, Sublet J-C (2003) The European activation file: EAF-2003 cross section library. Technical report FUS 486, United Kingdom AEA
- Forrest R, Kopecky J, Sublet J-C (2007) The European activation file: EAF-2007 neutron-induced cross section library. Technical report FUS 435, United Kingdom AEA
- Frankle S (2004a) Possible impact of additional collimators on the LLNL pulsed-sphere experiments. Technical report X-5:SCF-04-001 and LA-UR-05-5877, Los Alamos National Laboratory, Los Alamos
- Frankle S (2004b) LLNL pulsed-sphere measurements and detector response functions. Technical report X-5:SCF-04-004 and LA-UR-05-5878, Los Alamos National Laboratory, Los Alamos
- Frehaut J (2000) Coherent evaluation of nu-bar (prompt) for $^{235,238}\text{U}$ and ^{239}Pu . Technical report JEFDOC-17, NEA, JEFF Project
- Frenkel Y (1939) On the splitting of heavy nuclei by slow neutrons. *Phys Rev* 55:987-987
- Fröhner F, Goel B, Fischer U (1982) FITACS computer code. Technical report ANL-83-4, Kernforschungszentrum Karlsruhe, p 116 (Note: Presented at Specialists' Meeting on Fast Neutron Capture Cross Sections, ANL.)
- Fu C, Hetrick D (1986) Update of ENDF/B-V Mod-3 iron: neutron-producing reaction cross sections and energy-angle correlations. ORNL/TM-9964, ENDF-341, ORNL
- Greenwood R, Helmer R, Putnam M, Watts K (1997) Measurement of β -decay intensity distributions of several fission-product isotopes using a total absorption γ -ray spectrometer. *Nucl Instr Meth Phys Res A* 390:95
- Griffin PJ, Paviotti-Corcuera R (2003) Summary report of the final technical meeting on international reactor dosimetry file: IRDF-2002. Technical report INDC(NDS)-448, IAEA, Vienna, Austria
- Grimes S et al (1978) Charged particle-producing reactions of 15-MeV neutrons on ^{51}V and ^{93}Nb . *Phys Rev C* 17:508
- Hagura N, Yoshida T, Tachibana T (2006) Reconsideration of the theoretical supplementation of decay data in fission-product decay heat summation calculations. *J Nucl Sci Technol* 43:497-504
- Hale GM (1992) Use of R-matrix methods in light element evaluations. In: Dunford C (ed) *Proceedings of the international symposium on nuclear data evaluation methodology*, Brookhaven National Laboratory, World Scientific, Singapore, pp 306-314
- Hale G (2008) Covariances from light-element R-matrix analyses. *Nucl Data Sheets* 109:2812
- Hale GM et al (1990) Neutron-triton cross sections and scattering lengths obtained from $p\text{-}^3\text{He}$ scattering. *Phys Rev C* 42:438
- Hauser W, Feshbach H (1952) The inelastic scattering of neutrons. *Phys Rev* 87:366-373
- Herman M, Trkov A (2009) ENDF-6 formats manual: data formats and procedures for the evaluated nuclear data file ENDF/B-VI and ENDF/B-VII. Technical report BNL-90365-2009, Brookhaven National Laboratory
- Herman M, Reffo G, Weidenmüller HA (1992) Multistep-compound contribution to precompound reaction cross section. *Nucl Phys A* 536:124
- Herman M, Obložinský P, Capote R, Sin M, Trkov A, Ventura A, Zerkin V (2005a) Recent developments of the nuclear reaction model code EMPIRE. In: Haight R, Chadwick M, Kawano T, Talou P (eds) *Proceedings of the international conference on nuclear data for science and technology*, American Institute of Physics, New York, Santa Fe, Sept 26-Oct 1, 2004, p 1184
- Herman M, Capote R, Carlson B, Obložinský P, Sin M, Trkov A, Zerkin V (2005b) EMPIRE nuclear reaction model code, version 2.19 (Lodi). <http://www.nndc.bnl.gov/empire219/>, Dec 15, 2006
- Herman M, Capote R, Carlson B, Obložinský P, Sin M, Trkov A, Wienke H, Zerkin V (2007) EMPIRE: nuclear reaction model code system for data evaluation. *Nucl Data Sheets* 108(12):2655-2715
- Hofmann HM, Richert J, Tepel JW, Weidenmüller HA (1975) Direct reactions and Hauser-Feshbach theory. *Ann Phys* 90:403
- Houk TL (1971) Neutron-proton scattering cross section at a few electron volts and charge independence. *Phys Rev C* 3:1886
- ICRU (2000) ICRU-Report-63. In: *Nuclear data for neutron and proton radiotherapy and for radiation protection*, International Communications on Radiation Units and Measurements, Bethesda
- Ignatyuk A, Obložinský P, Chadwick M et al (1998) *Handbook for calculations of nuclear reaction data: reference input parameter library (RIPL-1)*. Technical report TECDOC-1034, IAEA, Vienna
- Ignatyuk A, Lunev V, Shubin Y, Gai E, Titarenko N (2006) Evaluation of $n + ^{232}\text{Th}$ cross sections for the energy range up to 150 MeV. Provided

- to the IAEA CRP on Th-U cycle, see Report INDC(NDS)-0494, pp 8–12
- JEFF3 (2005) The JEFF-3.0 nuclear data library. Technical report JEFF Report 19, OECD Nuclear Energy Agency
- Kalbach C (1988) Systematics of continuum angular distributions: extensions to higher energies. *Phys Rev C* 37:2350–2370
- Kanda Y, Baba M (1999) WPEC-SG4 report: ^{238}U capture and inelastic cross sections. Technical report NEA/WPEC-4, NEA, Paris
- Kawano T, Ohsawa T, Shibata K, Nakashima H (1999) Evaluation of covariance for fission neutron spectra. Technical report 99-009, JAERI
- Kawano T et al (2006) Production of isomers by neutron-induced inelastic scattering on ^{193}Ir and influence of spin distribution in the preequilibrium process. *Nucl Instr Meth* 562:774
- Keepin GR (1965) *Physics of neutron kinetics*. Addison-Wesley, New York
- Keinert J, Sax J (1987) Investigation of neutron scattering dynamics in liquid hydrogen and deuterium for cold neutron sources. *Kerntechnik* 51:19
- Kim H-I, Lee Y-O, Herman M, Mughabghab SF, Obložinský P, Rochman D (2006) Evaluation of neutron induced reactions for 32 fission products. Technical report BNL-77775-2007-IR, Brookhaven National Laboratory
- Kim H-I, Herman M, Mughabghab SF, Obložinský P, Rochman D, Lee Y-O (2008) Evaluation of neutron cross sections for a complete set of Nd isotopes. *Nucl Sci Eng* 160:168
- Kinsey R (1979) ENDF-201: ENDF/B summary documentation. Technical report BNL-NCS-17541, National Nuclear Data Center, BNL (Note: 3rd Edition, ENDF/B-V Library.)
- Klein Meulekamp R, van der Marck S (2006) Re-evaluation of the effective delayed neutron fraction measured by the substitution technique for a light water moderated low-enriched uranium core. *Nucl Sci Eng* 152:142–148
- Kokoo O, Murata I, Takahashi A (1999) Measurements of double-differential cross sections of charged-particle emission reactions for several structural elements of fusion power reactors by 14.1-MeV incident neutrons. *Nucl Sci Eng* 132:16
- Koning AJ, Delaroche JP (2003) Local and global nucleon optical models from 1 keV to 200 MeV. *Nucl Phys A* 713:231
- Koning A, Hilaire S, Duijvestijn M (2004) TALYS: comprehensive nuclear reaction modeling. In: Haight R, Chadwick M, Kawano T, Talou P (eds) *Proceedings of the international conference on nuclear data for science and technology*, American Institute of Physics, New York, Santa Fe, Sept 26–Oct 1, 2004, pp 1154–1159
- Kopecky J, Uhl M (1990) Test of gamma-ray strength functions in nuclear-reaction model-calculations. *Phys Rev C* 41:1941–1955
- Koppel J, Houston D (1978) Reference manual for ENDF thermal neutron scattering data, report GA-8774 revised and reissued as ENDF-269 by the National Nuclear Data Center, General Atomic, July 1978
- Kosako K (2001) Covariance data processing code: ERRORJ. In: Katakura J (ed) *The specialists' meeting of reactor group constants*, JAERI, Tokai, Japan, 22–23 February 2001, JAERI-Conf 2001-009, p 30
- Kosako K, Yanano N (1999) Preparation of a covariance processing system for the evaluated nuclear data file, JENDL. Technical report JNC TJ-9440, 99-003, JAERI
- Lane A, Lynn, J (1957) Fast neutron capture below 1 MeV: the cross sections for ^{238}U and ^{232}Th . *Proc Phys Soc (London) A* 70:557
- LANL (2009) Webpage, T-2 Information Service, Los Alamos National Laboratory, Los Alamos. <http://www.t2.lanl.gov>, Dec 15, 2009
- Larson NM (2006) Updated users' guide for SAMMY: multilevel R-matrix fits to neutron data using Bayes' equations. Technical report ORNL/TM-9179/R7, Document ENDF-364, ORNL
- Leal L, Derrien H (2006) Evaluation of the resonance parameters for ^{232}Th in the energy range 0 to 4 keV. Technical report, ORNL
- Leal LC, Derrien H, Larson NM, Courcelle A (2004) An unresolved resonance evaluation for ^{235}U . In: *PHYSOR conference*, Chicago, 25–29 April 2004
- Little R, Kawano T, Hale G et al (2008) Low-fidelity covariance project. *Nucl Data Sheets* 109:2828
- Lopez Aldama D, Trkov A (2004) FENDL-2.1 update of an evaluated nuclear data library for fusion applications. Technical report INDC(NDS)-467, IAEA, Vienna, Austria
- López Jiménez M, Morillon B, Romain P (2004) Overview of recent Bruyères-le-Châtel actinide evaluations. In: Haight R, Chadwick M, Kawano T, Talou P (eds) *Proceedings of the international conference on nuclear data for science and technology*, American Institute of Physics, New York, Santa Fe, Sept 26–Oct 1, 2004, pp 314–316
- Lougheed RW et al (2001) ^{239}Pu and ^{241}Am (n,2n) cross section measurements near 14 MeV. Technical report UCRL-ID-145592, Lawrence Livermore National Laboratory
- MacFarlane RE (1994) New thermal neutron scattering files for ENDF/B-VI release 2. Technical

- report LA-12639-MS (1994), Los Alamos National Laboratory, Los Alamos
- MacFarlane RE, Muir DW (1994) The NJOY nuclear data processing system, version 91. Technical report LA-12740-M, Los Alamos National Laboratory, Los Alamos
- MacFarlane RE, Kahler AC (2009) NJOY-99.304, www.t2.lanl.gov/codes/njoy99/index.html (5 October 2009)
- Madland D (2006) Total prompt energy release in the neutron-induced fission of ^{235}U , ^{238}U , and ^{239}Pu . Nucl Phys A 772:113
- Madland DG, Nix JR (1982) New calculation of prompt fission neutron-spectra and average prompt neutron multiplicities. Nucl Sci Eng 81:213–271
- Magurno B, Kinsey R, Scheffel F (1982) Guidebook for the ENDF/B-V nuclear data files. Technical report EPRI NP-2510, BNL-NCS-31451, ENDF-328, Brookhaven National Laboratory and Electric Power Research Institute
- Marchetti A, Hedstrom G (1998) New Monte Carlo simulations of the LLNL pulsed-sphere experiments. Technical report UCRL-ID-131461, Lawrence Livermore National Laboratory
- Mattes M, Keinert J (2005) Thermal neutron scattering data for the moderator materials H_2O , D_2O , and ZrH_2 in ENDF-6 format and as ACE library for MCNP(X) codes. Report INDC(NDS)-0470, IAEA
- MCNPX (2006) MCNPX transport code for charged particles. <http://www.mcnp.x.lanl.gov>
- Mughabghab SF (1984) Neutron cross sections: Z=61–100, vol 1B. Academic, New York
- Mughabghab SF (2006) Atlas of neutron resonances: thermal cross sections and resonance parameters. Elsevier, Amsterdam
- Mughabghab SF, Dunford CL (2000) A dipole-quadrupole interaction term in E1 photon transitions. Phys Lett B 487:155
- Mughabghab SF, Divadeenam M, Holden NE (1981) Neutron cross sections: Z=1–60, vol 1A. Academic, New York
- Muir D (1976) Gamma rays, Q-values and kerma factors. Technical report LA-6258-MS, Los Alamos National Laboratory, Los Alamos
- Muir DW (1989) Evaluation of correlated data using partitioned least squares: a minimum-variance derivation. Nucl Sci Eng 101:88–93
- Nakajima K (2001) Re-evaluation of the effective delayed neutron fraction measured by the substitution technique for a light water moderated low-enriched uranium core. J Nucl Sci Technol 38:1120–1125
- NEA (2009) Webpage, Nuclear Energy Agency Data Bank. <http://www.nea.fr/html/databank/>
- Nishioka H, Verbaarschot JJM, Weidenmüller HA, Yoshida S (1986) Statistical theory of precompound reactions: multistep compound process. Ann Phys 172:67
- Obložinský P (ed) (2008) Workshop on neutron cross section covariances. In: Nuclear data sheets, vol 109, Port Jefferson, 24–28 June 2008, pp 2725–2922
- Obložinský P, Mattoon C, Herman M, Mughabghab S, Pigni M, Talou P, Hale G, Kahler A, Kawano T, Little R, Young P (2009a) Progress on nuclear data covariances: AFCI-1.2 covariance library. Technical report unpublished, Brookhaven National Laboratory and Los Alamos National Laboratory
- Obložinský P et al (2009b) Evaluated data library for the bulk of fission products. Technical report NEA/WPEC-23, OECD Nuclear Energy Agency, Paris
- Oh S, Chang J, Mughabghab SF (2000) Neutron cross section evaluations of fission products below the fast neutron region. Technical report BNL-NCS-67469, Brookhaven National Laboratory
- Ohsawa T, Hamsch F-J (2004) An interpretation of energy-dependence of delayed neutron yields in the resonance region for ^{235}U and ^{239}Pu . Nucl Sci Eng 148:50
- Ohsawa T, Oyama T (1999) Possible fluctuations in delayed neutron yields in the resonance region of U-235. In: Katakura J (ed) Proceedings of the specialists' meeting on delayed neutron nuclear data, JAERI, American Institute of Physics, Tokaimura, Japan, p 43
- Okajima S, Sakurai T, Lebrat J, Averlant V, Martini M (2002) Summary on international benchmark experiments for effective delayed neutron fraction. Prog Nucl Energy 41:285–301
- Olsen D, Ingle R (1981) Measurement of neutron transmission spectra through ^{232}Th from 8 MeV to 4 keV. Report ORNL/TM-7661(ENDF-307), ORNL
- Perkins ST, Gyulassy GE (1972) An integrated system for production of neutronics and photonics calculational constants, vol 12. Technical report UCRL-50400, University of California
- Pfeiffer B, Kratz K-L, Moller P (2002) Status of delayed-neutron data: half-lives and neutron emission probabilities. Prog Nucl Energy 41: 39–69
- Pigni M, Herman M, Obložinský P (2009) Extensive set of cross section covariance estimates in the fast neutron region. Nucl Sci Eng 162: 25–40
- Plettner C, Ai H, Beausang CW et al (2005) Estimation of (n,f) cross sections by measuring reaction probability ratios. Phys Rev C 71(5):051602

- Plujko V, Herman M (2006) Handbook for calculations of nuclear reaction data, RIPL-2, ch. 7: gamma-ray strength functions. No. TECDOC-1506, IAEA, Vienna, p 120
- Porter CE, Thomas RG (1956) Fluctuations of nuclear reaction widths. *Phys Rev* 104:483–491
- Pritychenko B, Sonzogni A (2008) Sigma: web retrieval interface for nuclear reaction data. *Nucl Data Sheets* 109:2822
- Raynal J (1994) Notes on ECIS. CEA-N-2772, Commissariat à l'Énergie Atomique
- Rochman D, Herman M, Obložinský P (2006) New evaluation of $^{51}\text{V}(n, np+pn)$ and (n, t) cross sections for the ENDF/B-VII library. *Fusion Eng Des* 81:2109–2113
- RSICC (2009) Webpage, Radiation Safety Information Computational Center. <http://www-rsicc.ornl.gov>
- Sakurai T, Okajima S (2002) Adjustment of delayed neutron yields in JENDL-3.2. *J Nucl Sci Technol* 39:19–30
- SCALE (2000) SCALE: a modular code system for performing standardized computer analysis for licensing evaluation. NUREG/CR-0200, Rev. 6 (ORNL/NUREG/CSD-2/R6), vols I, II, and III, May 2000 (Available from the Radiation Safety Information Computational Center at ORNL as CCC-545.)
- Schoen K et al (2003) Precision neutron interferometric measurements and updated evaluations of the n-p and n-d coherent neutron scattering lengths. *Phys Rev C* 67:044005
- Shibata K, Hasegawa A, Iwamoto O et al (2002a) JENDL-3.2 covariance file. *J Nucl Sci Technol* (2):40–43
- Shibata K, Kawano T, Nakagawa T et al (2002b) Japanese evaluated nuclear data library version 3 revision-3: JENDL-3.3. *J Nucl Sci Technol* 39:1125–1136
- Sin M, Capote R, Herman M, Obložinský P, Ventura A, Trkov A (2004) Improvement of the fission channel in the EMPIRE code. In: Haight R, Chadwick M, Kawano T, Talou P (eds) Proceedings of the international conference on nuclear data for science and technology, American Institute of Physics, New York, Santa Fe, Sept 26–Oct 1, 2004, p 1249
- Sin M, Capote R, Ventura A, Herman M, Obložinský P (2006) Fission of light actinides: $^{232}\text{Th}(n,f)$ and $^{231}\text{Pa}(n,f)$ reactions. *Phys Rev C* 74(1): 014608
- Smith DL (1991) Probability, statistics, and data uncertainties in nuclear science and technology. American Nuclear Society, LaGrange Park
- Smith D (2004) Covariance matrices for nuclear cross sections derived from nuclear model calculations. Report ANL/NDM-159 November, Argonne National Laboratory
- Soukhovitskii ES, Capote R, Quesada JM, Chiba S (2005) Dispersive coupled-channel analysis of nucleon scattering from ^{232}Th up to 200 MeV. *Phys Rev C* 72:024604
- Staples P et al (1995) Prompt fission neutron energy spectra induced by fast neutrons. *Nucl Phys A* 591:41–60
- Stedman R, Almqvist L, Nilsson G (1967) Phonon-frequency distributions and heat capacities of aluminum and lead. *Phys Rev* 162:549–557
- Tamura T, Udagawa T, Lenske H (1982) Multistep direct reaction analysis of continuum spectra in reactions induced by light ions. *Phys Rev C* 26:379
- Trkov A (2003) 2nd IAEA research co-ordination meeting on evaluated nuclear data for thorium-uranium fuel cycle. Technical report INDC(NDS)-447, IAEA, Vienna
- Trkov A (2005) Summary report of a technical meeting on covariances of nuclear reaction data: GANDR project. INDC(NDS)-471, IAEA, Vienna
- Trkov A (2006) Evaluated nuclear data for Th-U fuel cycle summary report of the third research coordination meeting. Technical report INDC(NDS)-494, IAEA, Vienna
- Trkov A, Capote R (2006) Validation of ^{232}Th evaluated nuclear data through benchmark experiments. In: Proceedings of the international conference on nuclear energy for new Europe 2006, Portorož, Slovenia, 18–21 Sept 2006
- Trkov A et al (2005) Revisiting the ^{238}U thermal capture cross-section and gamma emission probabilities from ^{239}Np decay. *Nucl Sci Eng* 150:336–348
- Tuli J (2005) Nuclear wallet cards. Electronic version. <http://www.nndc.bnl.gov/wallet>
- Tuttle R (1975) Delayed neutron data. *Nucl Sci Eng* 56:37
- van der Marck S (2005) Benchmarking ENDF/B-VII beta1. CSEWG 2005 meeting report. <http://www.nndc.bnl.gov/csewg/>. Dec 15, 2006
- van der Marck SC (2006) Benchmarking ENDF/B-VII.0. *Nucl Data Sheets* 107:3061–3118
- van der Marck S, Klein Meulekamp R, Hogenbirk A, Koning A (2004) Benchmark results for delayed neutron data, AIP Conf. Proc. 769. American Institute of Physics, New York, Santa Fe, Sept 26–Oct 1, 2004, pp 531–534
- Vineyard GH (1957) Frequency factors and isotope effects in solid state rate processes. *J Phys Chem Solids* 3(1–2):121–127
- Webster W et al (1976) Measurements of the neutron emission spectra from spheres of N, O, W,

- U-235, U-238, and Pu-239, pulsed by 14 MeV neutrons. Technical report UCID-17332
- Weigmann H, Hamsch J, Mannhart W, Baba M, Tingjin L, Kornilov N, Madland D, Staples P (2003) Fission neutron spectra of ^{235}U . Report NEA/WPEC-9, OECD
- Wiarda D, Dunn M (2006) PUFF-IV: code system to generate multigroup covariance matrices from ENDF/B-VI uncertainty files. Radiation Safety Information Computational Center (RSICC) Code Package PSR-534, ORNL
- Williams M (2004) Generation of approximate covariance data. ORNL memo, August 2004
- Williams M, Rearden B (2008) SCALE-6 sensitivity/uncertainty methods and covariance data. Nucl Data Sheets 109:2797
- Wilson W, England T (2002) Delayed neutron study using ENDF/B-VI basic nuclear data. Prog Nucl Energy 41:71–107
- Woelfle R et al (1990) Neutron activation cross section measurements. Radiochimica Acta 50:5
- Wong C et al (1972) Livermore pulsed sphere program: program summary through July 1971. Technical report UCRL-51144, Rev I, and Addendum (1973), Lawrence Livermore National Laboratory
- Wright RQ, MacFarlane RE (2000) Review of ENDF/B-VI fission-product cross sections. Technical report ORNL/TM-13723, ORNL, Oak Ridge
- X5-MCNP-Team (2003) MCNP – a general Monte Carlo N-particle transport code, version 5, volume I: overview and theory. Technical report LA-UR-03-1987, Los Alamos National Laboratory
- Yoshida T et al (2006) Validation of fission product decay data for decay heat calculations. WPEC Subgroup-25. <http://www.nea.fr/html/science/projects/SG25>, Dec 15 2006
- Younes W, Britt HC (2003) Neutron-induced fission cross sections simulated from (t,pf) results. Phys Rev C 67(2):024610
- Young PG, Arthur ED (1977) GNASH: a pre-equilibrium statistical nuclear model code for calculations of cross sections and emission spectra. Technical report LA-6947, Los Alamos National Laboratory, Los Alamos
- Young JA, Koppel JU (1964) Slow neutron scattering by molecular hydrogen and deuterium. Phys Rev 135:A603–A611
- Young PG, Arthur ED, Chadwick MB (1992) Comprehensive nuclear model calculations: introduction to the theory and use of the GNASH code. Technical report LA-12343-MS, Los Alamos National Laboratory, Los Alamos
- Young PG, Arthur ED, Chadwick MB (1998) Comprehensive nuclear model calculations: theory and use of the GNASH code. In: Gandini A, Reffo G (eds) Proceedings of the IAEA workshop on nuclear reaction data and nuclear reactors, World Scientific Publishing, Singapore, April 15–May 17 1998, pp 227–404
- Young P, Herman M, Obložinský P et al (2005) Handbook for calculations of nuclear reaction data: reference input parameter Library-2. TECDOC-1506, IAEA, Vienna
- Young P, Chadwick M, MacFarlane R, Talou P, Kawano T, Madland D, Wilson W, Wilkerson C (2007) Evaluation of neutron reactions for ENDF/B-VII: $^{232-241}\text{U}$ and ^{239}Pu . Nucl Data Sheets 108(12):2589–2654



3 Neutron Slowing Down and Thermalization

Robert E. MacFarlane

Nuclear and Particle Physics, Astrophysics and Cosmology,

Theoretical Division, Los Alamos National Laboratory,

Los Alamos, NM, USA

ryxm@lanl.gov

1	<i>Thermal Neutron Scattering</i>	191
1.1	Introduction	191
1.2	Chemical Binding	191
1.3	Coherent and Incoherent Scattering	192
1.4	The Quantum Mechanical Scattering Function	193
1.5	The Intermediate Scattering Function	193
1.6	Detailed Balance	194
1.7	The Scattering Law	194
1.8	The Phonon Expansion	196
1.9	The Short Collision Time Approximation	197
1.10	Diffusive Translations	198
1.11	Discrete Oscillators	199
1.12	Incoherent Elastic Scattering	200
1.13	Coherent Elastic Scattering	200
1.14	Example of Thermal Scattering in Graphite	202
1.15	Example of Thermal Scattering in Water	205
1.16	Example for Thermal Scattering in Heavy Water	212
1.17	Example for Thermal Scattering in Zirconium Hydride	216
1.18	Using the ENDF/B Thermal Scattering Evaluations	216
2	<i>Neutron Thermalization</i>	221
2.1	Introduction	221
2.2	Monte Carlo Simulations of Neutron Thermalization	221
2.3	Discrete Ordinates Methods	226
2.3.1	S_N Theory	227
2.3.2	Transport Corrections	228
2.3.3	Fission Source	229
2.3.4	The Eigenvalue Iteration	230
2.3.5	S_N Data Requirements	231
2.3.6	Example for HST42-5	231
2.3.7	Preparing S_N Cross-Section Data	233
2.3.8	Example for an Infinite Pin-Cell Lattice	234
2.3.9	Monte Carlo vs. Multigroup	235
2.4	Collision Probability Methods	235

2.5	Size Effects in Thermalization	236
3	<i>Steady-State Slowing Down</i>	238
3.1	Introduction	238
3.2	Slowing-Down Cross Sections	238
3.3	Spectra for Elastic Downscatter	241
3.4	Spectra for Inelastic Downscatter	243
3.5	Resonance Cross Sections	245
3.5.1	Single-Level Breit–Wigner Representation	245
3.5.2	Multi-Level Breit–Wigner Representation	247
3.5.3	Reich–Moore Representation	249
3.5.4	Reich–Moore-Limited Representation	250
3.5.5	Angular Distributions	252
3.5.6	Resonance Reconstruction and Doppler Broadening	253
3.5.7	Thermal Constants	253
3.6	Resonance Slowing Down	253
3.7	Flux Calculations	257
3.8	Intermediate Resonance Self-Shielding	259
3.9	Unresolved Resonance Range Methods	262
4	<i>Time and Space in Slowing Down</i>	266
4.1	Introduction	266
4.2	Time Dependence of the Energy Spectrum	266
4.3	Time Dependence of the Spatial Distribution	268
4.4	Eigenvalues and Eigenfunctions	271
4.5	Analytic Age Theory	272
5	<i>Concluding Remarks and Outlook</i>	274
	<i>References</i>	276

Abstract: The theory behind the generation of thermal cross sections is presented, concentrating on the phonon expansion method. Examples are given for graphite, water, heavy water, and zirconium hydride. The graphite example demonstrates incoherent inelastic scattering and coherent elastic scattering for crystalline solids. The water example demonstrates incoherent inelastic scattering for liquids with diffusive translations. Heavy water adds a treatment for intermolecular coherence. Zirconium hydride shows the effects of the “Einstein oscillations” of the hydrogen atoms in a cage of zirconium atoms, and it also demonstrates incoherent elastic scattering. Neutron thermalization is introduced using Monte Carlo simulations of several systems, followed by multigroup discrete-ordinates and collision-probability methods. Size effects in thermalization are demonstrated. Steady-state slowing down is discussed by illustrating typical cross-section data, and showing slowing down by elastic scattering, inelastic scattering, and resonance cross sections in the narrow resonance approximation. Intermediate resonance self-shielding effects are introduced using the NJOY flux calculator and the WIMS implementation. The effects of time and space on slowing down are demonstrated using Monte Carlo simulations, and the theoretical basis is summarized.

1 Thermal Neutron Scattering

1.1 Introduction

At high energies, the wavelengths of neutrons are small, and it is reasonable to treat scattering as classical collisions between particles. At thermal energies, however, the wavelengths of neutrons approach the size of molecules and the spacing of crystalline lattices. Scattering becomes a quantum mechanical problem. The theory for this was worked out in the late 1950s and is described in detail by Williams (1966). This theory was reduced to practice for the US Evaluated Nuclear Data File (ENDF) in the 1960s, mainly by researchers at General Atomic (Koppel and Houston 1978). This theoretical basis remains largely valid today except for the improvements in scope and detail allowed by modern computing machines (MacFarlane 1994; Mattes and Keinert 2005).

In this section, we will summarize the theoretical basis for the thermal scattering evaluations in ENDF/B-VII (Tuli et al. 2006), and show examples for graphite, water, heavy water, and zirconium hydride as they are currently given in ENDF format (Herman 2005).

1.2 Chemical Binding

The simplest system of targets is a free gas of protons moving in thermal equilibrium with a temperature T . From basic statistical mechanics, the energies of these protons will be given by the Maxwell–Boltzmann distribution

$$M(E) = e^{-E/kT} \quad (1)$$

where k is Boltzmann’s constant. These protons are free to recoil, so a neutron can lose energy by colliding with a proton, but because the protons are moving, the neutron can also gain energy in a scattering event. It is assumed that the density of neutrons is small with respect to the density of scatterers; thus, the distribution of neutron energies does not affect the thermal distribution

of the scatterers. In this one case, the thermal scattering can be obtained by both quantum and classical methods.

Now if we bind the protons into a free gas of water molecules, the scattering process gets more interesting. Collisions of a neutron with a water molecule can result in a gain or loss of energy by reducing or increasing the velocity of the molecule (translational modes), and they can interact to make the molecule slow down or speed up its rotations (rotational modes) or vibrations (vibrational modes). The thermal energy kT for the gas of water molecules is divided among the various possible translational, rotational, and vibrational modes according to their characteristic energies by the Maxwell–Boltzmann distribution. The chemical binding of the proton into the water molecule reduces its ability to change the energy of the neutron upon scattering.

Now, to get more realistic, we condense this gas of water molecules into a liquid. The vibrational modes are not changed very much by this condensation. The rotational modes become hindered rotations. You can visualize little V-shaped molecules moving back and forth like torsional oscillators. The translational modes act like the diffusion of clusters of molecules with some internal order moving through a matrix of other clusters. All of these modes are considered to be quantized. The good quantum numbers are energy and momentum, and the energies of the modes are distributed according to the Maxwell–Boltzmann distribution. The good quantum numbers for the incident and scattered neutron are also energy and momentum (or wave vector). When the neutron scatters in the liquid, it changes its energy and momentum. The difference is associated with a change in the energy and momentum of various modes of excitation in the liquid.

In a solid, the possible modes of excitation are various wave-like vibrations of the crystal lattice. In quantum language, these excitations are called “phonons.” Phonons are characterized by particular energies and momenta (or wave vectors). The equilibrium distribution of phonon energies is described by the Maxwell–Boltzmann distribution. When a neutron scatters through a crystalline lattice, it can exchange energy and momentum by creating or annihilating phonons in such a way as to conserve energy and momentum. This can lead to a change of energy and direction (wave vector) for the neutron. There is another thing that can happen. Because the neutron can be characterized as a wave, it can scatter from the lattice in the same way that light scatters from a diffraction grating. This is called “coherent elastic scattering,” and it results in a change of direction for the neutron with no change in energy.

1.3 Coherent and Incoherent Scattering

When the neutron wave impinges on the crystalline lattice, there is a secondary wave produced from each scattering center. If the resulting waves are “coherent,” they can combine constructively and destructively to produce maxima and minima in various directions. This is similar to the behavior of a diffraction grating for light. For a material of randomly ordered crystallites, this would result in rings of neutron intensity in the forward direction. However, the diffraction can also be “incoherent.” A primary example of this is scattering from bound protons. Protons have spin, like the neutron, and the spins can be randomly arranged in a hydrogenous scatter. This randomness breaks the coherence and destroys the diffraction pattern. Inelastic scattering also tends to reduce the coherence in the scattering, and we normally assume that inelastic thermal scattering can be treated as incoherent. In general, hydrogenous materials

scatter incoherently. Nuclei with spin zero (many important materials) scatter coherently for elastic scattering (no energy change), but incoherently for inelastic scattering.

1.4 The Quantum Mechanical Scattering Function

This process has been analyzed in terms of a position and time correlation function. Let $G(\mathbf{r}, t)$ be the probability that a particle will be at the origin at time $t = 0$ and at position \mathbf{r} at time t (s for “self” particle). Using the incoherent approximation and assuming a liquid or a powdered crystalline material, the scattering function can be written as

$$\sigma_{inc}(E \rightarrow E', \mu) = (a_{inc}^2 + a_{coh}^2) \frac{k'}{k} \int d\mathbf{r} \int dt e^{i(\kappa \cdot \mathbf{r} - \varepsilon t/\hbar)} G_s(\mathbf{r}, t), \quad (2)$$

where E and E' are the incident and secondary energies, μ is the cosine of the scattering angle, a_{inc} and a_{coh} are the characteristic scattering lengths for the material, k and k' are the incident and outgoing wave numbers (momenta), κ is the change in wave vector in scattering, and ε is the energy transfer in scattering.

1.5 The Intermediate Scattering Function

This expression is often written in terms of the “intermediate scattering function” χ , or

$$\sigma_{inc}(E \rightarrow E', \mu) = (a_{inc}^2 + a_{coh}^2) \frac{k'}{k} \int dt e^{i\varepsilon t/\hbar} \chi_s(\kappa, t), \quad (3)$$

where the coherent scattering is treated with the incoherent approximation. For most of the cases of interest in thermal scattering, it turns out that χ takes on a Gaussian form in momentum transfer κ

$$\chi(\kappa, t) = e^{-\gamma(t)}, \quad (4)$$

where

$$\gamma(t) = \kappa^2 \int_{-\infty}^{\infty} P(\varepsilon) (1 - e^{-i\varepsilon t/\hbar}) e^{-\varepsilon/2kT} d\varepsilon, \quad (5)$$

and where

$$P(\varepsilon) = \frac{\rho(\varepsilon)}{2\varepsilon \sinh(\varepsilon/2kt)}. \quad (6)$$

The quantity $\rho(\varepsilon)$ is the energy spectrum of excitations in the system. In this context, the Gaussian approximation is basically equivalent to treating the internal excitations of the system as quantized harmonic oscillators. The excitation energy spectrum is often written as $\rho(\omega)$, with $\varepsilon = \hbar\omega$ and called a “frequency distribution.”

1.6 Detailed Balance

The thermal scattering cross section must obey a very important property called the condition of “detailed balance” or “reciprocity.” From very basic principles like time reversal invariance, it can be shown that for thermal equilibrium, the down-scattering must be balanced by the up-scattering. Thus,

$$EM(E, T)\sigma(E \rightarrow E', \mu) = E'M(E', T)\sigma(E' \rightarrow E, \mu). \quad (7)$$

This condition guarantees that the thermal neutron flux spectrum in an infinite non-absorbing medium at temperature T will take on a Maxwell–Boltzmann flux shape appropriate to the temperature T ; that is, the flux shape will be

$$\phi(E) = Ee^{-E/kT}. \quad (8)$$

Absorption and leakage from the medium can modify the spectrum from this ideal shape.

1.7 The Scattering Law

It has proved to be convenient to write the thermal neutron scattering cross section in terms of the “scattering law.” First, the momentum transfer and the energy transfer are written in terms of two new variables

$$\alpha = \frac{\hbar^2 \kappa^2}{kT} = \frac{E' + E - 2\mu\sqrt{E'E}}{AkT}, \quad (9)$$

and

$$\beta = \frac{\varepsilon}{kT} = \frac{E' - E}{kT}, \quad (10)$$

where A is the ratio of the target mass to the neutron mass. Then we write

$$\sigma_{inc}(E \rightarrow E', \mu) = \frac{\sigma_b}{2kT} \sqrt{\frac{E'}{E}} \hat{S}(\alpha, \beta), \quad (11)$$

where $\sigma_b = 4\pi(a_{coh}^2 + a_{inc}^2)$ is the characteristic bound scattering cross section for the material. Note that all the nuclear terms involving the cross section, the incident wave, and the scattered wave have been separated from the chemical-binding effects, all of which have been consolidated in \hat{S} . Specifically, \hat{S} does not depend on incident energy E or the scattered energy E' , but only on the amount of energy transferred between the scattered neutron and the material. This will be true as long as the atomic motions are small enough for the oscillations to remain harmonic. Anharmonicity and actual disruption of molecules or displacements of atoms from their normal lattice positions could eventually cause this theory to break down for large energy transfers at high incident energies.

Using this form of the incoherent scattering cross section and the principle of detail balance, we see that

$$\hat{S}(\alpha, \beta) = e^\beta \hat{S}(\alpha, -\beta). \quad (12)$$

The scattering law must also obey two so-called moments theorems or sum rules: the zeroth moment theorem or sum rule

$$\int \hat{S}(\alpha, \beta) d\beta = 1, \quad (13)$$

and the first moment theorem or sum rule

$$\int \hat{S}(\alpha, \beta) \beta d\beta = -\alpha. \quad (14)$$

The latter guarantees that the thermal cross section will approach the correct limit at high incident energies, namely, the free cross section σ_f , where

$$\sigma_b = \left(\frac{A+1}{A} \right)^2 \sigma_f. \quad (15)$$

In practice, the symmetric form of the scattering law is often used

$$S(\alpha, \beta) = e^{\beta/2} \hat{S}(\alpha, \beta). \quad (16)$$

Then, the detail balance condition becomes

$$S(\alpha, \beta) = S(\alpha, -\beta), \quad (17)$$

and the scattering law is symmetric in β (energy transfer). Thermal neutron scattering laws in ENDF format are normally given in terms of S , but this can lead to numerical difficulties. The asymmetric \hat{S} function can be represented by normal numbers (say 10^{-8} to 1) for all β . But the symmetric S can be smaller than \hat{S} by factors like $e^{-\beta/2} \approx e^{-80} \approx 10^{-35}$. Processing codes have to be careful to allow for this huge range of values. The problem can be even more difficult for cold moderators where numbers ranging from 1 to 10^{-99} can be required in evaluated data files.

As discussed above, the chemical binding for protons in water can be decomposed into translational, rotational, and vibrational modes. More formally, we can write

$$\rho(\varepsilon) = \sum_i w_i \rho_i(\varepsilon), \quad (18)$$

where the following possibilities are allowed

$$\rho_j(\beta) = \delta(\beta_j) \quad \text{discrete oscillator} \quad (19)$$

$$\rho_j(\beta) = \rho_s(\beta) \quad \text{solid-type spectrum} \quad (20)$$

$$\rho_j(\beta) = \rho_t(\beta) \quad \text{translational spectrum} \quad (21)$$

The solid-type spectrum must vary as ε^2 , as ε goes to zero, and it must integrate to w_s , the weight for the solid-type law. The translational spectrum is sometimes represented as a free gas for liquids, but more realistically, it can be represented using a diffusion-type spectrum represented with the approximation of Egelstaff and Schofield that will be discussed later. In either case, the spectrum must integrate to w_t , the translational weight. The sum of all the partial weights must equal 1. This partition of the energy distribution leads to a recursive formula for the scattering law:

$$\hat{S}(\alpha, \beta) = \hat{S}^{(K)}(\alpha, \beta), \quad (22)$$

where

$$\hat{S}^{(J)}(\alpha, \beta) = \int \hat{S}_J(\alpha, \beta') \hat{S}^{(J-1)}(\alpha, \beta - \beta') d\beta'. \quad (23)$$

As an example of the use of this recursive procedure, consider a case where the desired frequency spectrum is a combination of ρ_s and two discrete oscillators. First, calculate $\hat{S}^{(1)} = \hat{S}_1$ using ρ_s . Then calculate \hat{S}_2 using $\rho(\beta_1)$, the distribution for the first discrete oscillator, and convolve \hat{S}_2 with $\hat{S}^{(1)}$ to obtain $\hat{S}^{(2)}$, the composite scattering law for the first two partial distributions. Repeat the process with the second discrete oscillator to obtain $\hat{S}^{(3)}$, which is equal to $\hat{S}(\alpha, \beta)$ for the full distribution.

One simple example of the translational component of the scattering law represents the free gas with a weight of w_t :

$$\hat{S}(\alpha, -\beta) = \frac{1}{\sqrt{4\pi w_t \alpha}} \exp\left[-\frac{(w_t \alpha - \beta)^2}{4w_t \alpha}\right], \quad (24)$$

and

$$\hat{S}_t(\alpha, \beta) = e^{-\beta} \hat{S}_t(\alpha, -\beta), \quad (25)$$

with β positive. Note that for large α and β , the main contribution to this comes from the region $w_t \alpha \approx \beta$. The shape is a Gaussian, and as α and β increase (high incident energies), the Gaussian gradually goes over to a delta function, and we recover the normal classical elastic scattering behavior.

A number of approximate methods and full-up computer methods have been used over the years to compute the scattering law for realistic cases. Notable among these was the GASKET method, (Koppel et al. 1967) which was used by General Atomic to prepare the initial ENDF/B thermal scattering evaluations. Here we will limit our discussion to the phonon expansion method as implemented in the LEAPR module of the NJOY Nuclear Data Processing System (MacFarlane and Muir 1994), which has been used to prepare the more recent thermal scattering evaluations available in modern neutron cross-section compilations. LEAPR is a descendent of the British codes LEAP and ADDELTA (Butland 1973).

1.8 The Phonon Expansion

Consider first $\gamma_s(t)$, the Gaussian function for solid-type excitation spectra. Expanding the time-dependent part of the exponential gives

$$e^{-\gamma_s(t)} = -\alpha \lambda_s \sum_{n=0}^{\infty} \frac{1}{n!} \left[\alpha \int_{-\infty}^{\infty} P_s(\beta) e^{-\beta/2} e^{-i\beta t} d\beta \right]^n, \quad (26)$$

where λ_s is the Debye–Waller coefficient

$$\lambda_s = \int_{-\infty}^{\infty} P_s(\beta) e^{-\beta/2} d\beta. \quad (27)$$

The scattering law becomes

$$\hat{S}_s(\alpha, \beta) = e^{-\alpha\lambda_s} \sum_{n=0}^{\infty} \frac{1}{n!} \alpha^n \times \frac{1}{2\pi} \int_{-\infty}^{\infty} e^{i\beta t} \left[\int_{-\infty}^{\infty} P_s(\beta') e^{-\beta'/2} e^{-i\beta' t} d\beta' \right]^n dt. \quad (28)$$

For convenience, define the quantity in the second line of this equation to be $\lambda_s^n \mathcal{T}_n(\beta)$. Then clearly,

$$\hat{S}_s(\alpha, \beta) = e^{-\alpha\lambda_s} \sum_{n=0}^{\infty} \frac{1}{n!} [\alpha\lambda_s]^n \mathcal{T}_n(\beta), \quad (29)$$

where

$$\mathcal{T}_0(\beta) = \frac{1}{2\pi} \int_{-\infty}^{\infty} e^{i\beta t} dt = \delta(\beta), \quad (30)$$

and

$$\mathcal{T}_1(\beta) = \int_{-\infty}^{\infty} \frac{P_s(\beta') e^{-\beta'/2}}{\lambda_s} \left\{ \frac{1}{2\pi} \int_{-\infty}^{\infty} e^{i(\beta-\beta')t} dt \right\} d\beta' = \frac{P_s(\beta) e^{-\beta/2}}{\lambda_s}. \quad (31)$$

In general,

$$\mathcal{T}_n(\beta) = \int_{-\infty}^{\infty} \mathcal{T}_1(\beta') \mathcal{T}_{n-1}(\beta-\beta') d\beta'. \quad (32)$$

The \mathcal{T} functions obey the relationship $\mathcal{T}_n(\beta) = e^{-\beta} \mathcal{T}_n(-\beta)$. In addition, each of the \mathcal{T}_n functions obeys the following normalization condition:

$$\int_{-\infty}^{\infty} \mathcal{T}_n(\beta) d\beta = 1. \quad (33)$$

In LEAPR, the \mathcal{T} functions are computed up to some specified maximum value, typically 100, and these results are used to compute $\hat{S}(\alpha, \beta)$. What does the phonon expansion mean physically? Consider a neutron scattering in water. If the energy loss of the neutron is large, there is no way that energy can be absorbed by only kicking the mass 18 molecule into additional motion. That would violate conservation of momentum. But it is possible to transfer part of the energy to translations and the rest to exciting rotations and vibrations. In other words, a multiplicity of phonons is excited. For small energy changes in scattering, only a few phonons may be required, but large transfers may require up to 100. For water in equilibrium at temperature T , intermolecular collisions will excite a spectrum of these 100 different modes in accordance with their characteristic energies following the Maxwell–Boltzmann distribution. This very complicated target motion can then deliver energy and momentum to a slow neutron, thus scattering it up to higher energies. It is assumed that the changes in the occupation of target modes caused by the neutrons are very small when compared to the thermal excitation of the target modes – this linearizes the scattering problem.

1.9 The Short Collision Time Approximation

Very large energy transfers may even require more than 100 phonons to be created or annihilated. In this case, a limiting form of the phonon expansion is available called the short collision time (SCT) approximation, which can be written

$$\hat{S}_s(\alpha, -\beta) = \frac{1}{\sqrt{4\pi w_s \alpha \bar{T}_s / T}} \exp \left[-\frac{(w_s \alpha - \beta)^2}{w_s \alpha \bar{T}_s / T} \right], \quad (34)$$

and

$$\hat{S}_s(\alpha, \beta) = e^{-\beta} \hat{S}_s(\alpha, -\beta), \quad (35)$$

where β is positive and where the effective temperature is given by

$$\bar{T}_s = \frac{T}{2w_s} \int_{-\infty}^{\infty} \beta^2 P_s(\beta) e^{-\beta} d\beta. \quad (36)$$

As above, w_s is the weight for the solid-type spectrum. The effective temperature can be substantially higher than the ambient temperature; for example, the effective temperature is about 1,370 K at room temperature for hydrogen bound in water.

1.10 Diffusive Translations

As discussed above, translational effects in liquids like water are often represented using a diffusion term. The “effective width model” of Egelstaff and Schofield provides a tractable approximation for the diffusive motion:

$$\hat{S}_t(\alpha, \beta) = \frac{2c w_t \alpha}{\pi} e^{2c^2 w_t \alpha - \beta/2} \frac{\sqrt{c^2 + 0.25}}{\sqrt{\beta^2 + 4c^2 w_t^2 \alpha^2}} K_1 \left\{ \sqrt{c^2 + 0.25} \sqrt{\beta^2 + 4c^2 w_t^2 \alpha^2} \right\}, \quad (37)$$

and

$$\rho(\beta) = w_t \frac{4c}{\pi \beta} \sqrt{c^2 + 0.25} \sinh(\beta/2) K_1 \left\{ \sqrt{c^2 + 0.25} \beta \right\}. \quad (38)$$

In these equations, $K_1(x)$ is a modified Bessel function of the second kind, and the translational weight w_t and the diffusion constant c are chosen to try to represent experiment. The scattering law for a combination of solid-type modes and diffusion can be computed as follows:

$$\hat{S}(\alpha, \beta) = \hat{S}_t(\alpha, \beta) e^{-\alpha \lambda_s} + \int_{-\infty}^{\infty} \hat{S}_t(\alpha, \beta') \hat{S}_s(\alpha, \beta - \beta') d\beta'. \quad (39)$$

The first term in this equation comes from the delta function in (37), the “zero phonon” term, which is not included in the normal calculation of \hat{S} . The effective temperature for a combination of solid-type and diffusive modes is given by

$$\bar{T}_s = \frac{w_t T + w_s \bar{T}_s}{w_t + w_s}. \quad (40)$$

The “effective width” refers to the width of the pseudo-elastic peak seen in neutron scattering experiments. Crudely speaking, one can think of clusters of water molecules with some internal order diffusing through a matrix of other clusters. Larger clusters are harder to set into motion

with neutron collisions, and the translational effects on neutron scattering are reduced from the free molecule value. Although this diffusive model helps to achieve better agreement with experiment at modest thermal energies, it leaves something to be desired at very low thermal energies. However, because of the effects of detail balance, the actual value of the cross section at the lowest neutron energies has little effect on the shape of the equilibrium flux, so this failure of the diffusive effect has normally been accepted. Some experiments seem to show that there is a distribution of cluster sizes in real liquids, and taking better account of this distribution might improve the agreement with experiment.

1.11 Discrete Oscillators

Polyatomic molecules normally support a number of vibrational modes that can be represented as discrete oscillators. The distribution function for one oscillator is given by $w_i \delta(\beta_i)$, where w_i is the fractional weight for mode i , and β_i is the energy-transfer parameter computed from the mode's vibrational frequency. The corresponding scattering law is given by

$$\begin{aligned}\hat{S}_i(\alpha, \beta) &= e^{-\alpha\lambda_i} \sum_{n=-\infty}^{\infty} \delta(\beta - n\beta_i) I_n \left[\frac{\alpha w_i}{\beta_i \sinh(\beta_i/2)} \right] e^{-n\beta_i/2} \\ &= \sum_{n=-\infty}^{\infty} A_{in}(\alpha) \delta(\beta - n\beta_i),\end{aligned}\quad (41)$$

where

$$\lambda_i = w_i \frac{\coth(\beta_i/2)}{\beta_i}.$$
 (42)

The combination of a solid-type mode (s) with discrete oscillators (1) and (2) would give

$$\hat{S}^{(0)}(\alpha, \beta) = \hat{S}_s(\alpha, \beta),$$
 (43)

$$\begin{aligned}\hat{S}^{(1)}(\alpha, \beta) &= \int_{-\infty}^{\infty} \hat{S}_1(\alpha, \beta') \hat{S}^{(0)}(\alpha, \beta - \beta') d\beta' \\ &= \sum_{n=-\infty}^{\infty} A_{1n}(\alpha) \hat{S}^{(0)}(\alpha, \beta - n\beta_1),\end{aligned}\quad (44)$$

$$\begin{aligned}\hat{S}^{(2)}(\alpha, \beta) &= \int_{-\infty}^{\infty} \hat{S}_2(\alpha, \beta') \hat{S}^{(1)}(\alpha, \beta - \beta') d\beta' \\ &= \sum_{m=-\infty}^{\infty} A_{2m}(\alpha) \sum_{n=-\infty}^{\infty} A_{1n}(\alpha) \hat{S}^{(0)}(\alpha, \beta - n\beta_1 - m\beta_2).\end{aligned}\quad (45)$$

and so on through $\hat{S}_3(\alpha, \beta)$, $\hat{S}^{(4)}(\alpha, \beta)$, etc., until all the discrete oscillators have been included. The Debye-Waller λ for the combined modes is computed using

$$\lambda = \lambda_s + \sum_{i=1}^N \lambda_i.$$
 (46)

The effective temperature for the combined modes is given by

$$\bar{T}_s = w_t T + w_s \bar{T}_s + \sum_{i=1}^N w_i \frac{\beta_i}{2} \coth\left(\frac{\beta_i}{2}\right) T.$$
 (47)

1.12 Incoherent Elastic Scattering

In hydrogenous solids (such as polyethylene), there is an elastic (no energy loss) component of scattering arising from the zero-phonon term of the phonon expansion. This is called the “incoherent elastic” term. Clearly,

$$S_{\text{iel}}(\alpha, \beta) = e^{-\alpha\lambda} \delta(\beta). \quad (48)$$

The corresponding differential scattering cross section is

$$\sigma(E, \mu) = \frac{\sigma_b}{2} e^{-2WE(1-\mu)}, \quad (49)$$

and the integrated cross section is

$$\sigma(E) = \frac{\sigma_b}{2} \left\{ \frac{1 - e^{-4WE}}{2WE} \right\}. \quad (50)$$

In these equations, the Debye–Waller coefficient is given by

$$W = \frac{\lambda}{AkT}, \quad (51)$$

where λ is computed from the input frequency spectrum as modified by the presence of discrete oscillators (if any) any as shown above.

1.13 Coherent Elastic Scattering

In solids consisting of coherent scatterers (e.g., graphite) the zero-phonon term leads to interference scattering from the various planes of atoms of the crystals making up the solid. Once again, there is no energy loss. The neutrons only change direction. This is called “coherent elastic scattering.” The differential scattering cross section is given by

$$\sigma_{\text{coh}}(E, \mu) = \frac{\sigma_c}{E} \sum_{E_i < E} f_i e^{-4WE_i} \delta(\mu - \mu_i), \quad (52)$$

where

$$\mu_i = 1 - E_i/E, \quad (53)$$

and the integrated cross section is given by

$$\sigma_{\text{coh}} = \frac{\sigma_c}{E} \sum_{E_i < E} f_i e^{-4WE_i}. \quad (54)$$

In these equations, σ_c is the effective bound coherent scattering cross section for the material, W is the effective Debye–Waller coefficient, E_i are the so-called Bragg Edges, and the f_i are related to the crystallographic structure factors.

It can be seen from (52) that the cross section is zero below the first Bragg edge (typically about 2–5 meV). It then jumps sharply to a value determined by f_i and the Debye–Waller term. At higher energies, the cross section drops off as $1/E$ until $E = E_2$. It then takes another jump and continues falling off like $1/E$. The sizes of the jumps gradually become smaller, and at high energies, there is nothing left but an asymptotic $1/E$ decrease (typically above 1–2 eV).

The calculation of the E_i and f_i depends on a knowledge of the crystal structure of the scattering material. The Bragg edges are given by

$$E_i = \frac{\hbar^2 \tau_i^2}{8m}, \quad (55)$$

where τ_i is the length of the vectors of one particular “shell” of the reciprocal lattice, and m is the neutron mass. The f_i factors for a material containing a single atomic species are given by

$$f_i = \frac{2\pi\hbar^2}{4mNV} \sum_{\tau_i} |F(\tau)|^2, \quad (56)$$

where the sum extends over all reciprocal lattice vectors of the given length, and the crystallographic structure factor is given by

$$|F(\tau)|^2 = \left| \sum_{j=1}^N e^{i2\pi\phi_j} \right|^2, \quad (57)$$

where N is the number of atoms in the unit cell, $\phi_j = \vec{\tau} \cdot \vec{\rho}_j$ are the phases for the atoms, and the $\vec{\rho}_j$ are their positions. The situation is a little more difficult for a material with more than one atomic species, such as BeO, and an approximation has to be made for the effective Debye–Waller factor for the cell.

As an example of this process, consider graphite. It has an hexagonal lattice described by the constants a and c . The reciprocal lattice vector lengths are given by

$$\left(\frac{\tau}{2\pi} \right)^2 = \frac{4}{3a^2} (\ell_1^2 + \ell_2^2 + \ell_1\ell_2) + \frac{1}{c^2} \ell_3^2, \quad (58)$$

where ℓ_1, ℓ_2 , and ℓ_3 run over all the positive and negative integers, including zero. The volume of the unit cell is

$$V = \sqrt{3}a_2c/2. \quad (59)$$

For graphite, there are four atoms in the unit cell at positions (Wyckoff 1963)

$$(0, 0, 0), \left(-\frac{1}{3}, \frac{1}{3}, 0 \right), \left(-\frac{2}{3}, -\frac{1}{3}, \frac{1}{2} \right), \left(-\frac{1}{3}, \frac{1}{3}, \frac{1}{2} \right).$$

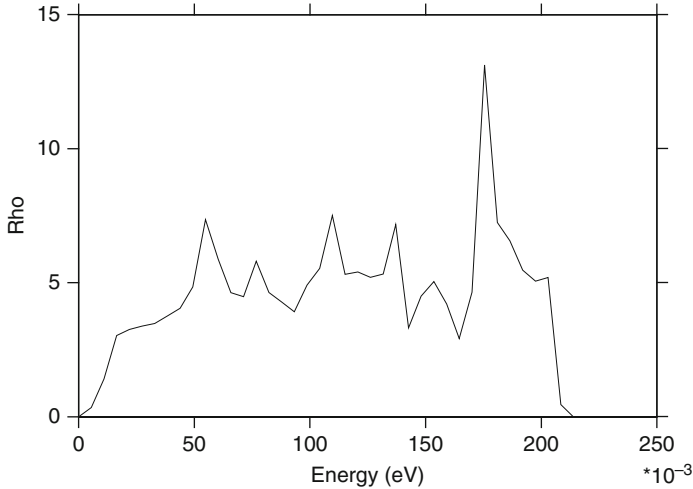
These positions give the following phases:

$$\phi_1 = 0, \quad (60)$$

$$\phi_2 = (-\ell_1 + \ell_2)/3, \quad (61)$$

$$\phi_3 = -(2/3)\ell_1 - (1/3)\ell_2 + (1/2)\ell_3, \quad (62)$$

$$\phi_4 = -(1/3)\ell_1 + (1/3)\ell_2 + (1/2)\ell_3. \quad (63)$$



■ Figure 1
The phonon frequency spectrum $\rho(\epsilon)$ used for graphite

The form factor for graphite becomes

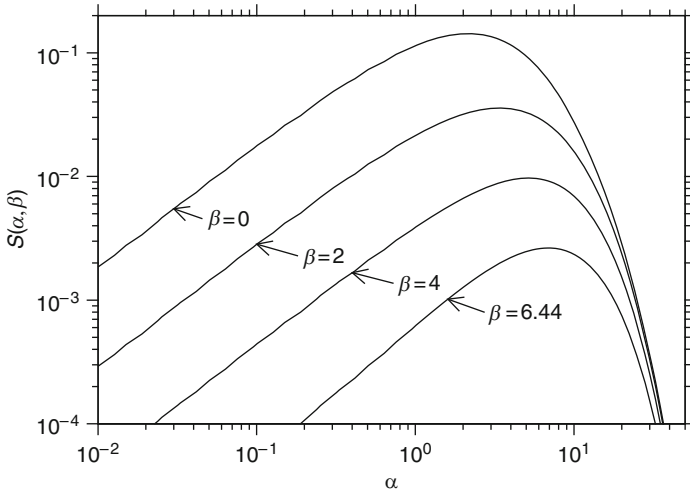
$$|F|^2 = \begin{cases} 6 + 10 \cos[2\pi(\ell_1 - \ell_2)/3] & \ell_3 \text{ even} \\ 4 \sin^2[\pi(\ell_1 - \ell_2)/3] & \ell_3 \text{ odd} \end{cases} \quad (64)$$

Similar methods can be used to obtain the lattice vectors and structure factors for the HCP structure (beryllium), the FCC structure (aluminum), or the BCC structure (iron). These options are built into the LEAPR module of the NJOY processing system.

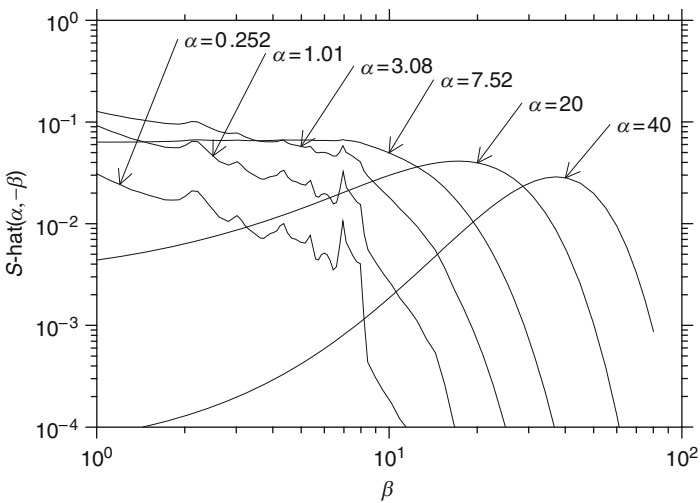
1.14 Example of Thermal Scattering in Graphite

As an example of the application of the theory presented above, we consider graphite, the moderator used in the very first critical reactor. To obtain the phonon excitation spectrum, the binding in graphite is modeled using four force constants: a nearest neighbor central force that binds the hexagonal planes together, a bond-bending force in an hexagonal plane, a bond-stretching force between nearest neighbors in the plane, and a restoring force against bending of the hexagonal plane. These force constants are then used to compute the phonon energies in various directions in the crystal, the “phonon dispersion curves.” These results are analyzed to get the phonon density of states; that is, the number of phonons that can exist with energies in a given range. The phonon excitation curve used for the ENDF/B-VII evaluation of thermal scattering in graphite is shown in [Fig. 1](#). Note the ϵ^2 dependence at low energy transfers.

This frequency spectrum can be used with the phonon expansion method to generate the \hat{S} scattering law using NJOY’s LEAPR module. Some results are shown in [Figs. 2](#) and [3](#).



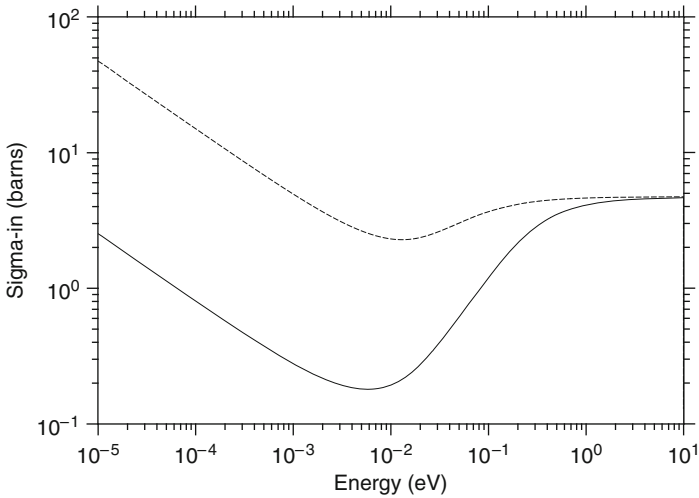
■ **Figure 2**
 $\hat{S}(\alpha, \beta)$ vs. α for several values of β in graphite at 293.6 K



■ **Figure 3**
 $\hat{S}(\alpha, \beta)$ vs. β for several values of α in graphite at 293.6 K. Note how the shape approaches a smooth Gaussian as α increases

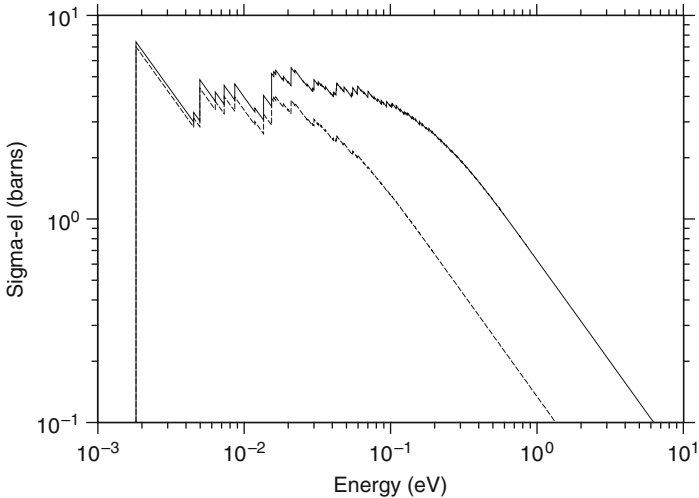
Note that as α increases, the curves get smoother and begin to look like Gaussians, as predicted by the SCT extension to the phonon expansion.

In [Fig. 4](#), we show the incoherent part of the inelastic scattering from graphite at two temperatures, and in [Fig. 5](#), we show the coherent elastic contribution to the cross section displaying the low-energy cutoff and the Bragg edges.



■ Figure 4

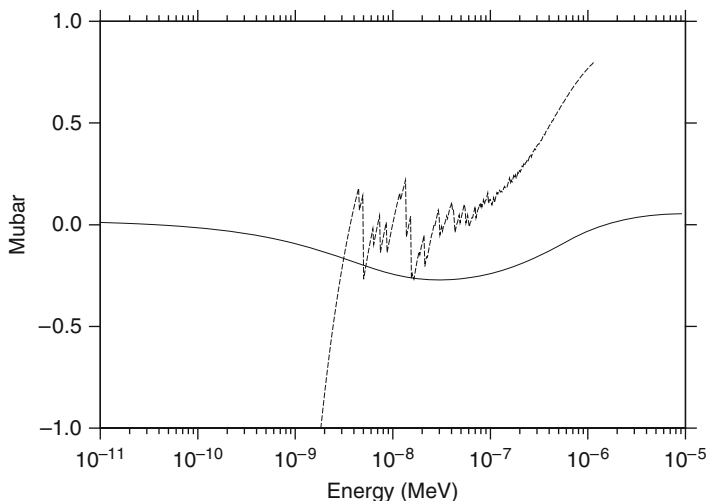
Incoherent inelastic cross section of graphite at 293.6 K (solid curve) and 1,600 K (dashed curve). Note how the cross section approaches the free-atom value at high incident energies



■ Figure 5

Coherent elastic cross section of graphite at 293.6 K (solid curve) and 1,600 K (dashed curve) showing the Bragg edges and the asymptotic $1/E$ decrease at high energies

There are also thermal effects on the angular distributions for scattering. ➤ [Figure 6](#) shows the average cosine for scattering for both coherent elastic and incoherent inelastic scattering. Note how the scattering cosine for elastic scattering varies from a backward direction at the Bragg edge toward the forward direction as the energy increases above the edge. The inelastic $\bar{\mu}$ is less than the normal high-energy value of 0.05556.



■ **Figure 6**
Average scattering cosine for inelastic (solid curve) and elastic (dashed curve) in graphite at room temperature

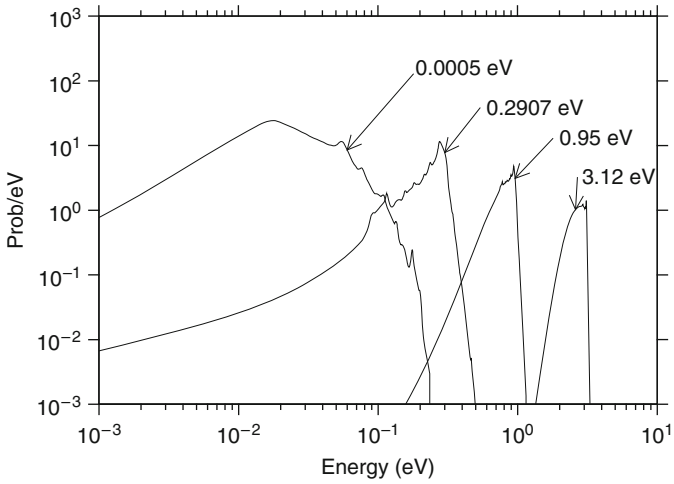
In [Fig. 7](#), we show the neutron emission curves for the incoherent inelastic component of the scattering at room temperature (293.6 K) featuring the low-energy range. For the low-energy incident neutrons, these curves show upscatter structure with peaks coming from the excitation peaks in the graphite phonon spectrum that are excited at thermal equilibrium at room temperature. For the higher incident energies, the emission spectra show features in the downscatter resulting from exciting phonons corresponding to the peaks in the phonon spectrum. At the highest incident energy, the scattering begins to look more and more like the rectangle-shaped characteristic of high-energy elastic scattering.

Finally, [Fig. 8](#) gives a perspective view of the energy distribution for inelastic scattering in graphite at room temperature.

1.15 Example of Thermal Scattering in Water

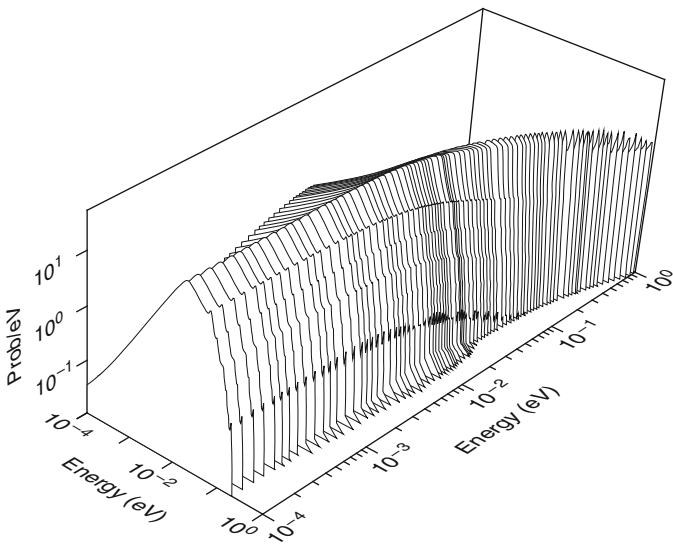
The current ENDF/B-VII evaluation for the thermal scattering law for H bound in H_2O is based on recent work done under IAEA auspices (Mattes and Keinert 2005) with some slight modifications. It is assumed that scattering from the oxygen atom can be treated as a free gas of mass 16. The hydrogen binding has a component describing hindered rotations of the water molecules using the phonon frequency distribution shown in [Fig. 9](#) with a weight of 0.4904. The translational modes are treated as the diffusion of water clusters through the liquid with a weight of 0.0192. Finally, there are two discrete oscillator frequencies with energies of 0.205 and 0.436 eV and weights of 0.16347 and 0.326933, respectively.

The scattering law computed from this model using the LEAPR module of NJOY is shown in the next few figures. In [Fig. 10](#), the peak at low α and β comes from the diffusive translations.



■ Figure 7

Spectra from thermal inelastic scattering for graphite at room temperature showing several incident energies



■ Figure 8

Perspective view of the spectra from thermal scattering on graphite at 293.6 K

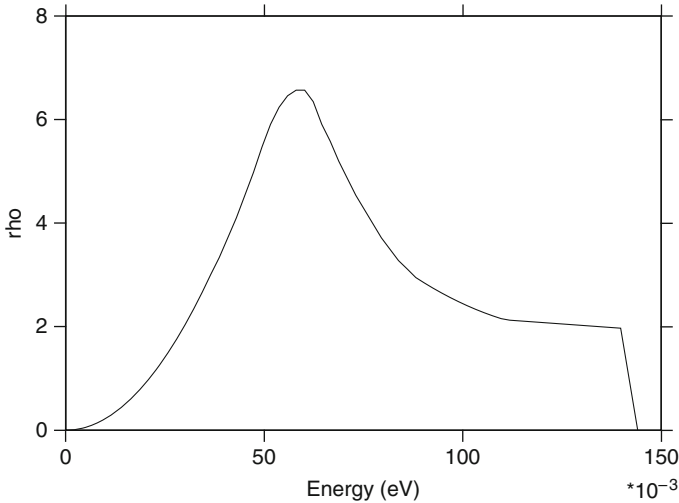


Figure 9
The phonon frequency spectrum $\rho(\epsilon)$ used for H in H_2O

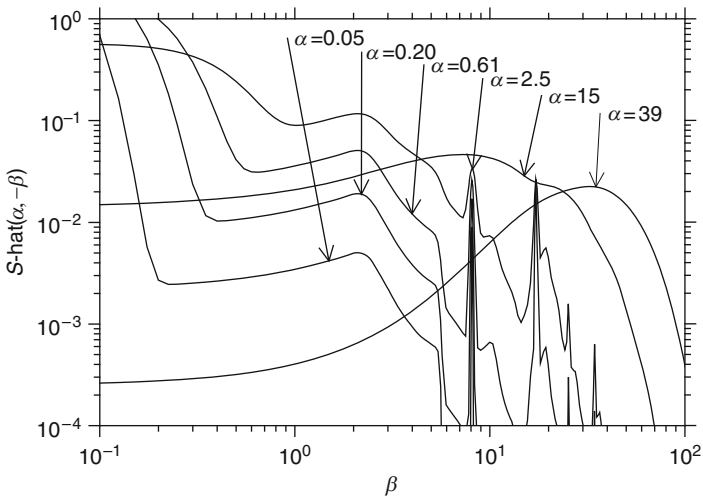


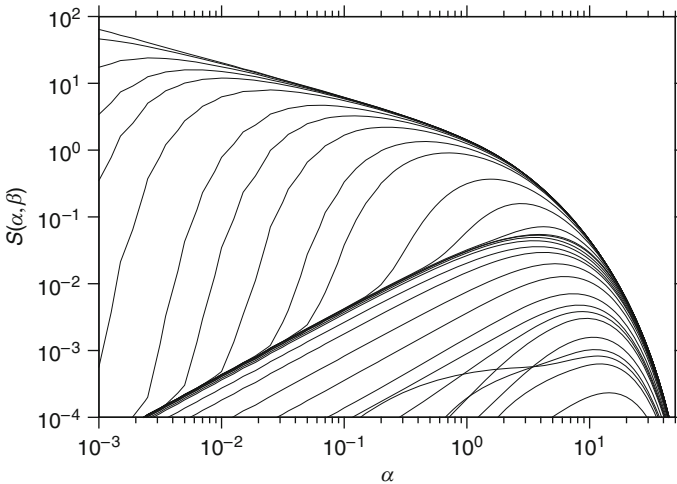
Figure 10
 $\hat{S}(\alpha, -\beta)$ for H in H_2O at room temperature plotted versus β for various values of α

For high α , the curves begin to take on the Gaussian shape predicted by the SCT approximation. In between, the peaks in the curves come from the effects of the discrete oscillators.

As discussed above, there are peaks at the main oscillator energies and at various “harmonics,” that is, sums and differences of multiples of the basic energies. Table 1 shows the oscillator energies possible for $\alpha = 1$.

■ **Table 1**
Discrete oscillator β values and weights for $\alpha = 1$ for H in H₂O

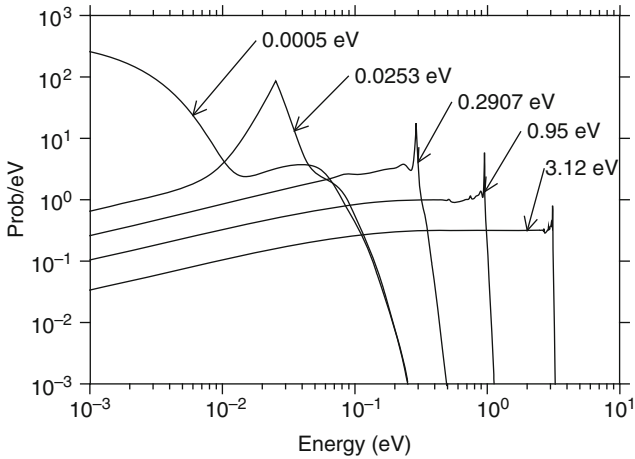
Beta	Weight
0.0000	9.6160E-01
-8.1026	1.9405E-02
-17.2328	1.8243E-02
-25.3353	3.6814E-04
-16.2051	1.9580E-04
-34.4655	1.7304E-04
8.1026	5.8752E-06
-33.4379	3.7146E-06
-42.5680	4.4920E-06
-24.3077	1.3171E-06
-51.6983	1.0943E-06



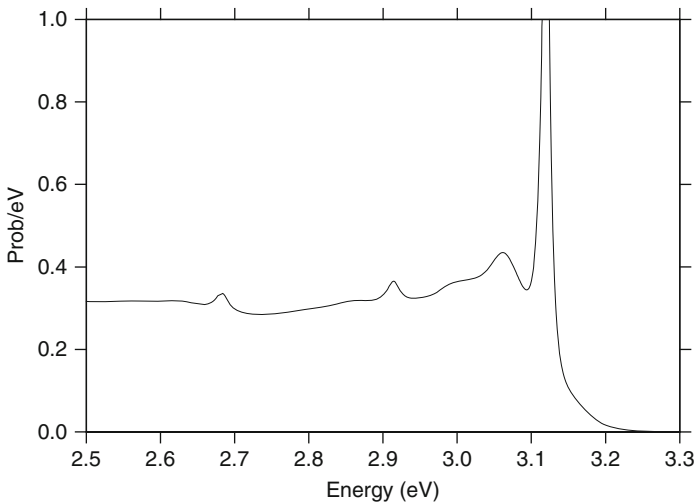
■ **Figure 11**
 $\hat{S}(\alpha, -\beta)$ vs. α for a number of β values

In **Fig. 11** the high-energy cutoff of the energy distribution for the rotational modes is visible, as well as the effect of the discrete oscillators. Note the singularity at low α and β where the slope changes sign. This is an effect characteristic of the translational modes in liquids.

The neutron emission spectra for incoherent inelastic scattering that results from processing this scattering law is shown in **Fig. 12** for several incident energies. For very low incident energies, the neutron gains energy from the rotational modes excited at thermal equilibrium.



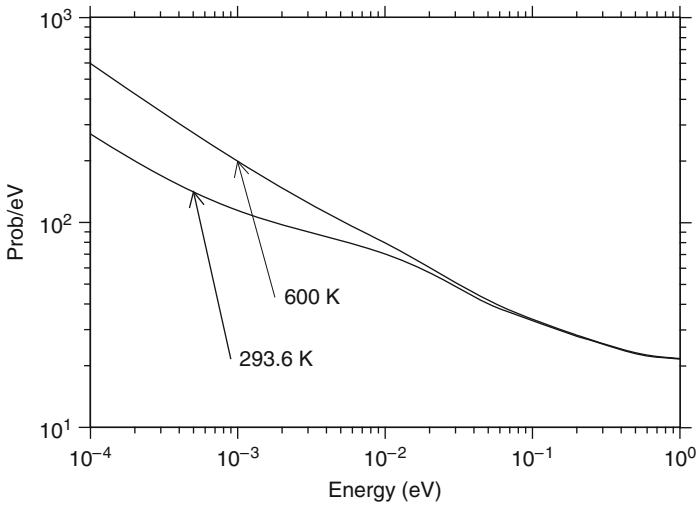
■ **Figure 12**
Incoherent inelastic spectra for several incident energies for H in H₂O



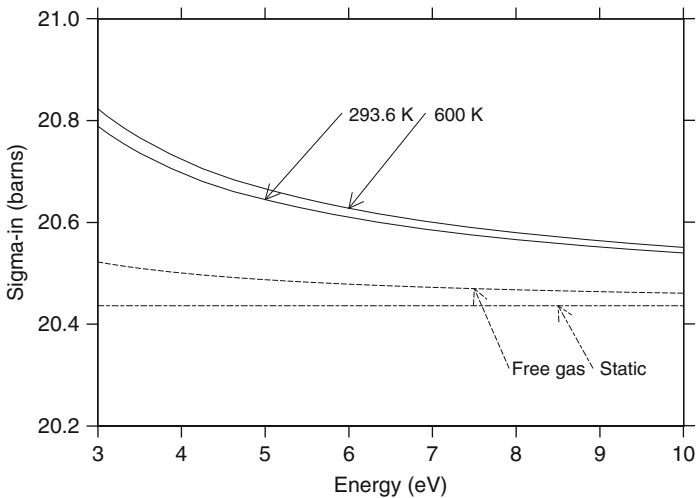
■ **Figure 13**
Detailed view of a neutron emission spectrum for inelastic scattering for H in H₂O

For higher energies, it is more probable that the neutron will lose energy, and the effects of exciting translational, rotational, and vibrational modes are visible. The downscatter behavior is shown in more detail in [▶ Fig. 13](#). The sharp peak at $E' = E$ is the quasi-elastic peak coming from the diffusive translations. The next lower hump is from rotational modes, and the other peaks are from vibrational modes.

The integrated cross section is shown in [▶ Figs. 14](#) and [▶ 15](#) for two temperatures. As the incident energy increases, the cross section begins to approach the free-atom value, as predicted



■ Figure 14
The incoherent inelastic cross section for H in H₂O at two temperatures

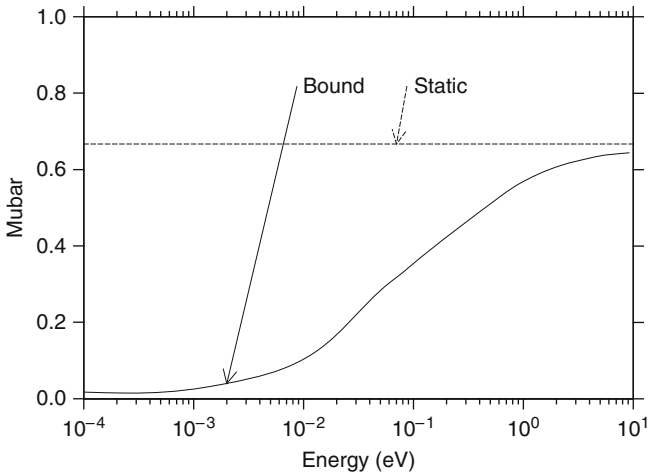


■ Figure 15
The incoherent inelastic cross section for H in H₂O for higher incident energies showing the static limit (scattering from atoms at rest) and the free-gas cross section

by the theory. In practice, multigroup codes would normally change from the thermal value to the target-at-rest value at some particular break-point energy chosen so that error caused by the additional discontinuity at that energy group was not too significant. Monte Carlo codes normally change from the thermal cross section to the free-gas cross section at some break-point

■ **Table 2**
Effective temperatures for the short collision time approximation for H in H₂O

Temp. (K)	Eff. Temp. (K)
293.6	1,269
350	1,276
400	1,289
450	1,305
500	1,324
550	1,344
600	1,367
800	1,473



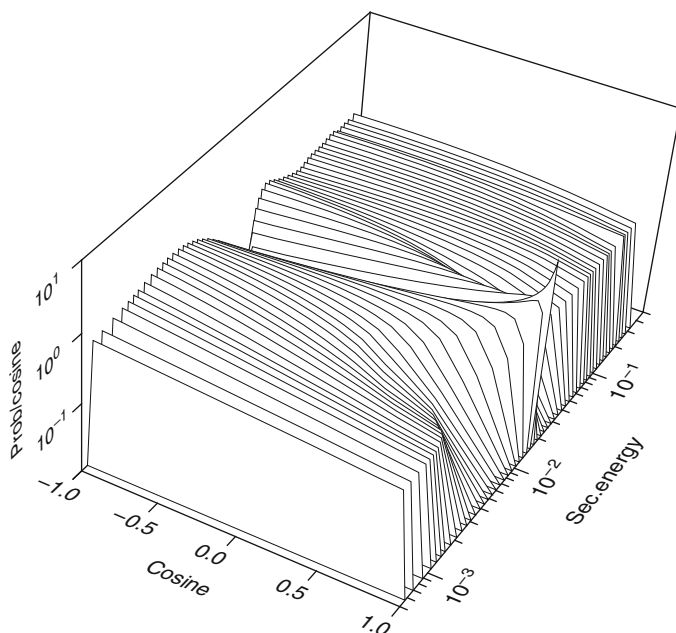
■ **Figure 16**

The average scattering cosine for H in H₂O compared to the static value for scattering from atoms at rest. The effect of the binding of H in H₂O is to make the scattering more isotropic at thermal energies

energy. There again, it is hoped that the break-point can be made high enough to minimize the adverse effects of the discontinuity.

Another approach that has been used in practice is to shift from the thermal cross section to an SCT cross section, that is, a free-gas cross section at a higher temperature than the ambient value. ➤ [Table 2](#) shows the effective SCT temperatures for H in H₂O. This approach gives a fairly good integrated cross section versus energy above the thermal cutoff of the scattering law calculation, and it gives a good downscatter spectrum, but the upscatter is too large.

The angular behavior of thermal scattering is also of interest. For H bound in H₂O, the hydrogen atom is not as free to recoil as the free atom. This makes it look like it has a higher effective mass, and it causes the scattering to be more isotropic on the average. See ➤ [Fig. 16](#).



■ Figure 17
A perspective view of an angle-energy distribution for H in H₂O

However, as ► Fig. 17 demonstrates, there are still interesting anisotropies seen, especially near $E' = E$, where translational effects are important. ► Figure 18 shows a perspective view of the thermal scattering for H in H₂O.

As the description of the evaluation for H in H₂O demonstrates, ENDF scattering law data are not obtained directly from experimental measurement. That would require more complete differential data than are currently available. Instead, they are modeled based on various kinds of input data ranging from neutron scattering measurements to optical results. The model results are then compared to the available experimental data to see how good a job was done with the evaluation. Examples of the comparison of the modeled thermal cross section for water with experiment are shown in ► Figs. 19 and ► 20. Additional comparisons with differential data are shown in the report on the IAEA evaluation (Mattes and Keinert 2005). The results are fairly good, except around 300–400 meV and below 1 meV. The problem at the lowest energies comes from the failure of the diffusive model. As discussed above, because of the principle of detailed balance, the value of the cross section in this region does not have much influence on the computed flux in a water-moderated system. Therefore, this discrepancy can be accepted for nuclear engineering calculations.

1.16 Example for Thermal Scattering in Heavy Water

The structure of heavy water is similar to that of water, except that the weights on the ends of the arms of the vee are twice as heavy. This shifts the scale of the rotational and vibrational modes.

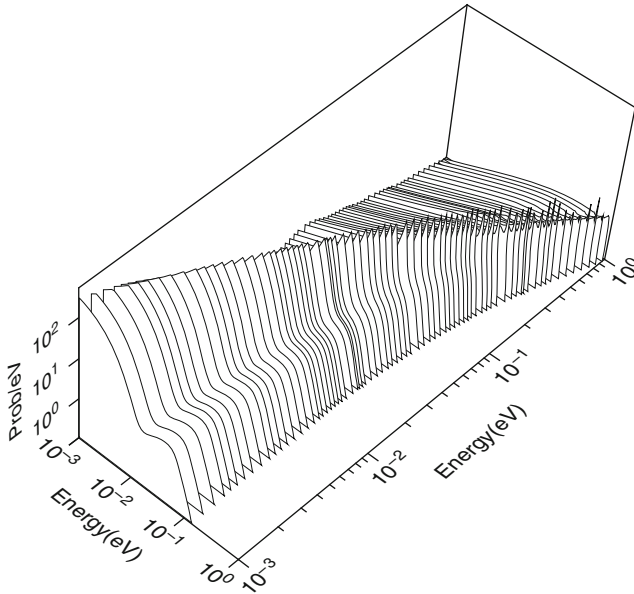


Figure 18

A perspective view of the isotropic part of the incoherent inelastic scattering from H in H₂O. The variations in the size of the quasi-elastic peak are artifacts of the plotting program

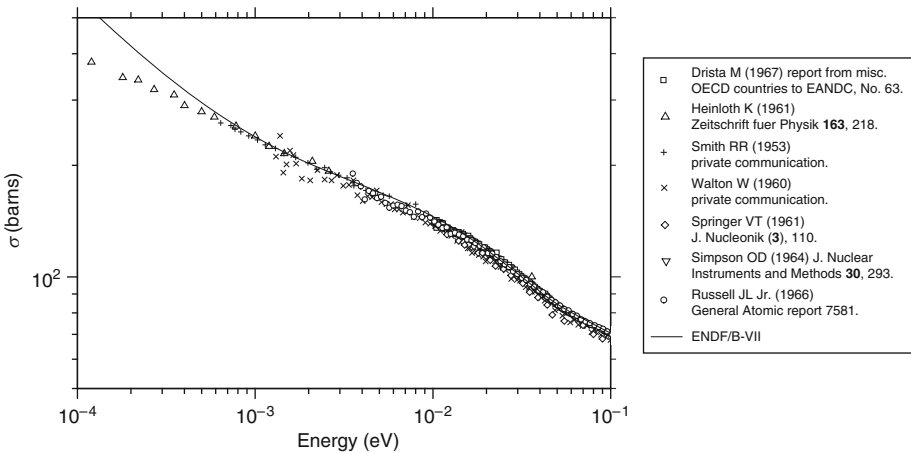


Figure 19

Comparison of the ENDF/B-VII thermal cross section for water at lower incident energies with experimental results for the CSISRS compilation at the the National Nuclear Data Center of the Brookhaven National Laboratory

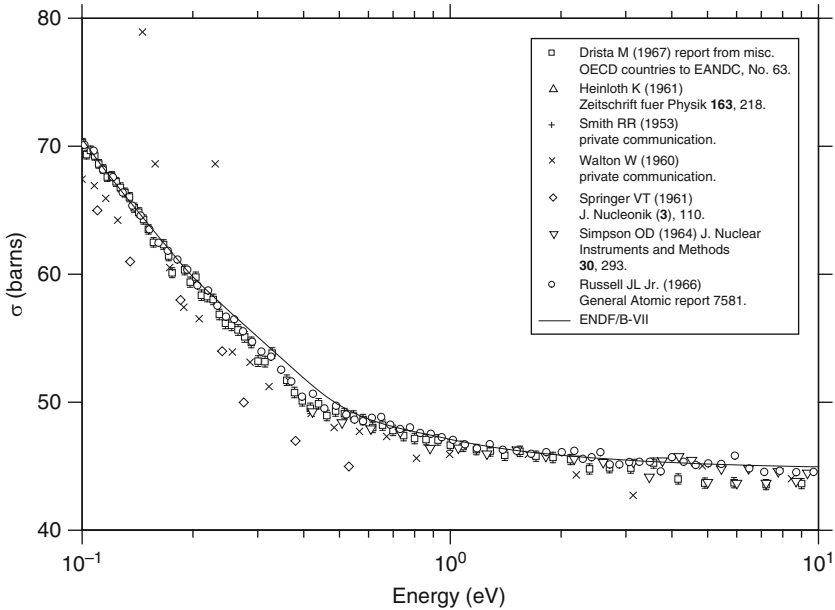


Figure 20

Comparison of the ENDF/B-VII thermal cross section for water at higher incident energies with experimental results for the CSISRS compilation at the the National Nuclear Data Center of the Brookhaven National Laboratory

The work of Mattes and Keinert (2005) resulted in the temperature-dependent frequency distribution shown in Fig. 21. The two oscillator frequencies are 0.145 and 0.338 eV (they were 0.205 and 0.48 for water – the scaling is the square root of the mass ratio)).

The new feature illustrated by this example is intermolecular coherence. As discussed above, the random orientation of proton spins in water allows us to use an incoherent approximation for the calculation. But the spin of the deuterons in D_2O is zero and this simplification does not apply. Even though heavy water is a liquid, there is still some persistent structure. There tends to be certain characteristic values of the spacing between the molecules, and this is sufficient to preserve some degree of coherence in the scattering. This effect is made more objective by using a “static structure factor,” such as the ones shown in Fig. 22. These were generated assuming a hard core for small distances and a Lennard-Jones potential for larger distances. The scattering function is then computed using the Skold approximation (Skold 1967):

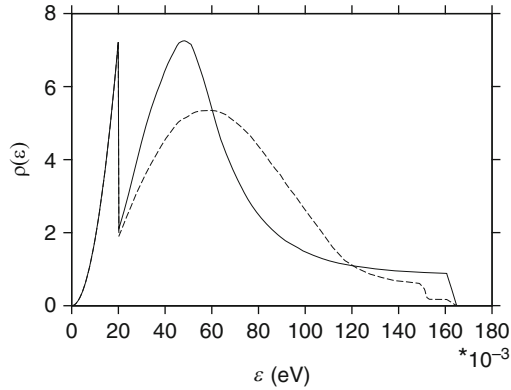
$$S(\alpha, \beta) = (1 - f) S^{inc}(\alpha, \beta) + f s^{inc}(\alpha', \beta) S(\kappa), \quad (65)$$

where

$$f = \frac{\sigma^{coh}}{\sigma^{inc} + \sigma^{coh}}, \quad (66)$$

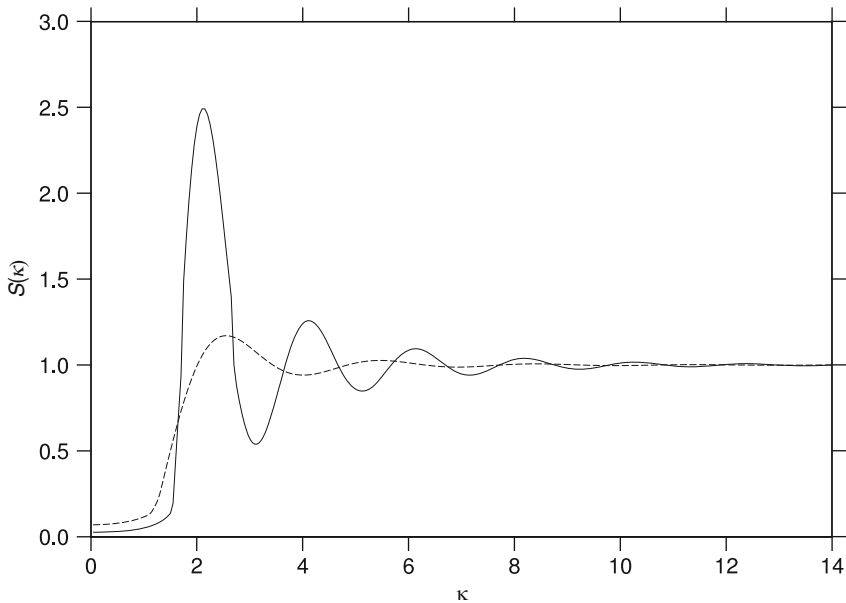
and

$$\alpha' = \frac{\alpha}{S(\kappa)}. \quad (67)$$



■ Figure 21

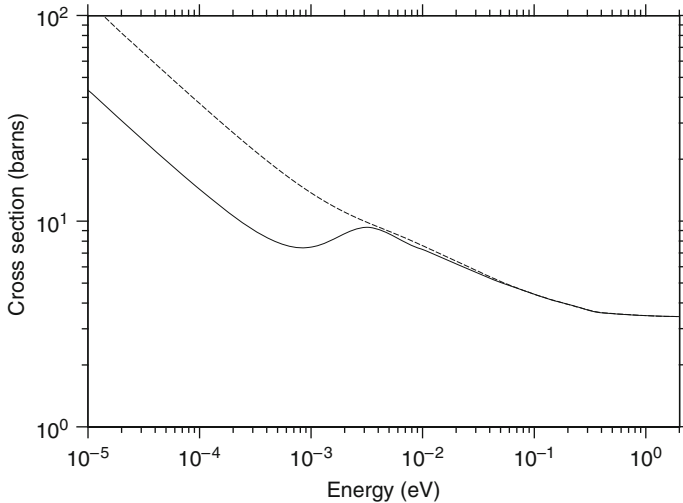
Frequency distribution for D in heavy water. The solid line is for a temperature of 293.6 K, and the dashed line is for a temperature of 600 K



■ Figure 22

Static structure factor for D in heavy water. The solid curve is for a temperature of 293.6 K, and the dashed curve is for a temperature of 600 K

The static structure factor for room temperature shows strong structure, but as the temperature increases, the correlations in spacing get smoothed out and the coherence is suppressed. This is evident in the computed cross sections shown in [Fig. 23](#). The dip below 3 meV in the room temperature curve comes from the coherence – it has basically disappeared at 600 K. The curve at the higher temperature looks more like the water cross section.



■ Figure 23

Incoherent inelastic scattering for D in D_2O . The solid curve is for a temperature of 293.6 K, and the dashed curve is for a temperature of 600 K

➤ [Figure 24](#) compares the calculated cross section with experimental data for heavy water extracted from the CSISRS compilation at the NNDC. The match is not perfect, but it is clear that the new evaluation partially accounts for the dip below 2 meV due to intramolecular coherence.

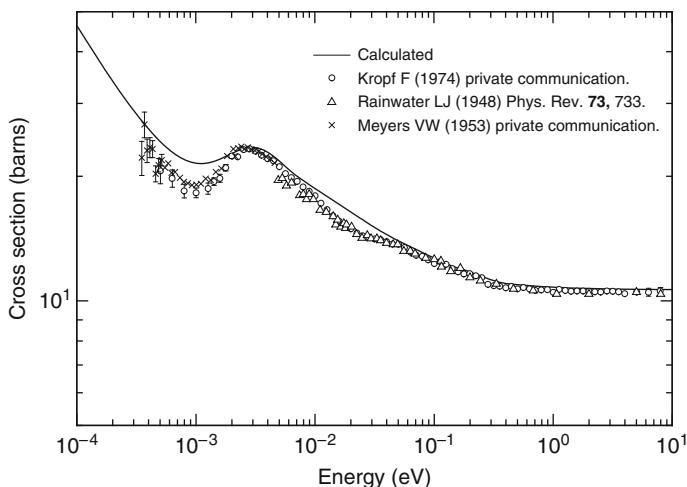
1.17 Example for Thermal Scattering in Zirconium Hydride

Zirconium hydride, ZrH_x , has variable stoichiometry with x near 2. Therefore, it is necessary to treat it as two separate materials, namely, H bound in ZrH , and Zr bound in ZrH . We will only consider the first of those here. The ENDF/B-VII evaluation follows the GA model (Koppel and Houston 1978) with a few small changes. It used a force-constant model to generate the frequency distribution. Because there are two atoms in the unit cell, there are both low-energy acoustic modes and high-energy optical modes. These two parts of the distribution are shown separately in ➤ [Figs. 25](#) and ➤ [26](#).

The optical modes form an isolated peak near 0.14 eV. This comes about because the hydrogen atoms sit in a cage of surrounding zirconium atoms (the variable stoichiometry results from some of these cages being occupied and some being empty). The cage provides a potential well for the hydrogen atom to vibrate in. In quantum language, this is an “Einstein oscillator,” and the spectrum of evenly spaced states in this well lead to interesting oscillations in $S(\alpha, \beta)$, the integrated cross section (➤ [Fig. 27](#)), and the spectra of emitted neutrons (➤ [Fig. 29](#)). ➤ [Figure 28](#) shows the incoherent elastic cross section.

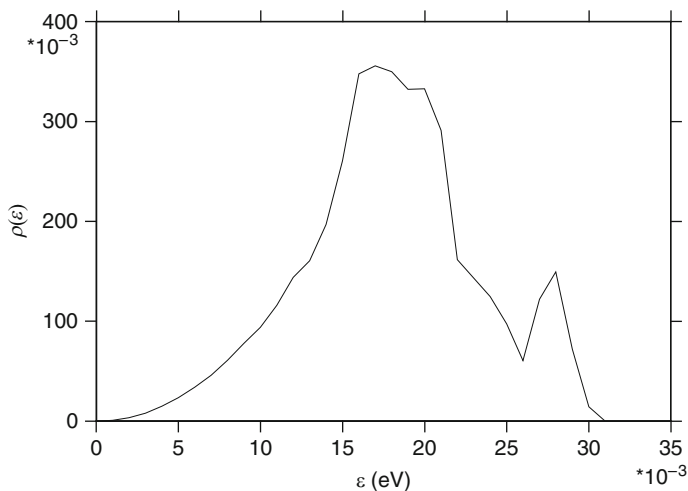
1.18 Using the ENDF/B Thermal Scattering Evaluations

➤ [Table 3](#) gives a summary of the thermal scattering evaluations available in ENDF/B-VII.



■ Figure 24

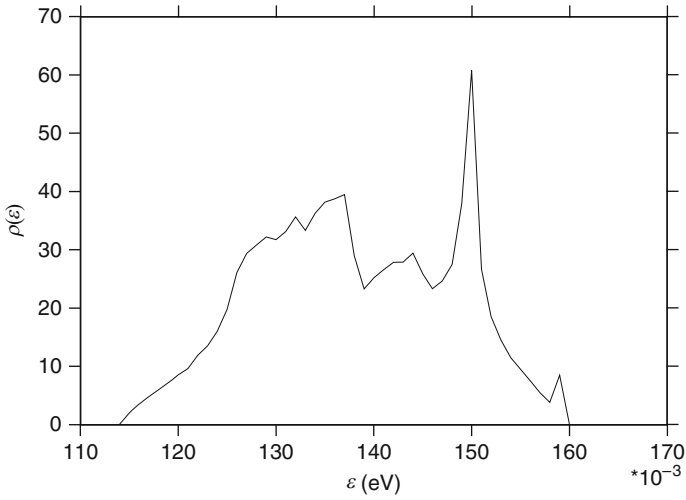
Comparison of the calculated cross section for heavy water to experiment. The dip due to coherence below 2 meV is partially accounted for by the evaluation. The experimental data are from the CSISRS compilation maintained by the NNDC at BNL. See the compilation for the references



■ Figure 25

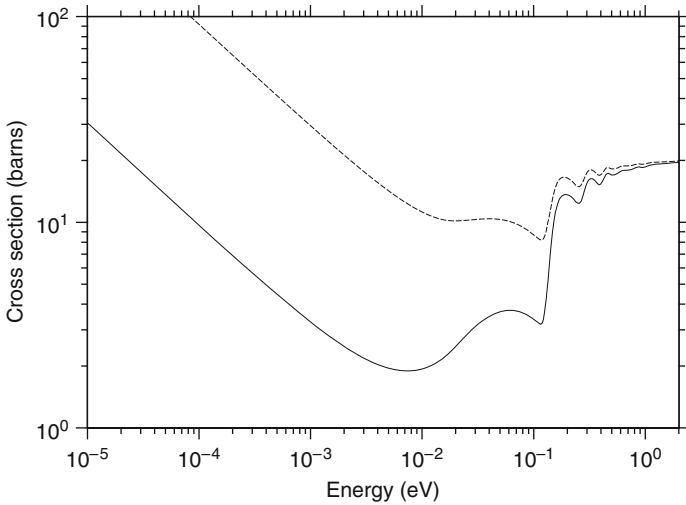
Frequency distribution for H in ZrH for the acoustic modes

Note the “Secondary scatterer” column. For H in H₂O, the evaluation only describes the H scattering. The effect of oxygen is to be added on using free-gas scattering. On the other hand, the benzene evaluation (C₆H₆) includes both C and H scattering. Care must be taken to not add on free C scattering in the thermal range.



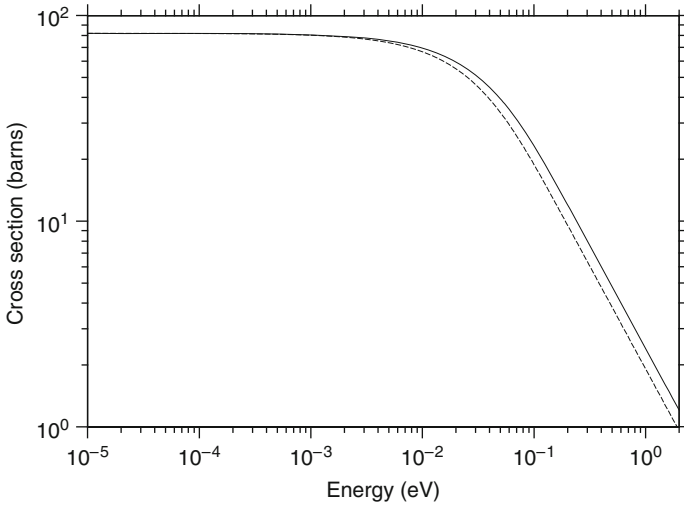
■ Figure 26

Frequency distribution for H in ZrH for the optical modes. The function is zero from the top of the acoustic modes to the start of the optical modes



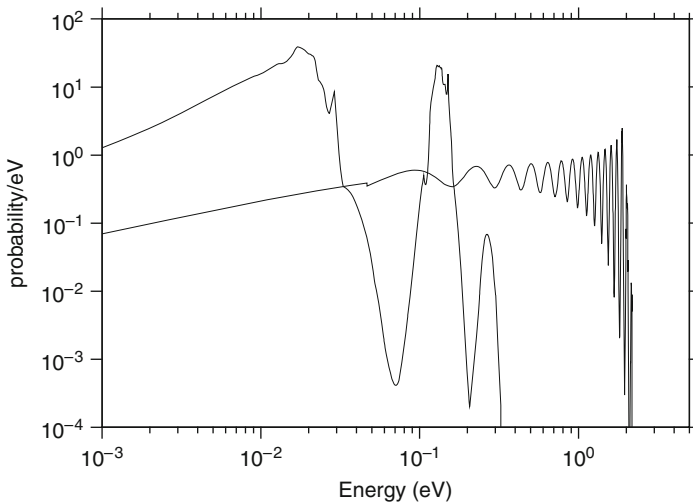
■ Figure 27

Incoherent inelastic scattering cross section for H in ZrH. The solid curve is for a temperature of 293.6 K, and the dashed curve is for a temperature of 600 K



■ Figure 28

Incoherent elastic scattering cross section for H in ZrH. The solid curve is for a temperature of 293.6 K, and the dashed curve is for a temperature of 600 K



■ Figure 29

Neutron emission spectra for incoherent inelastic scattering from H in ZrH at energies of 0.001 and 2.0 eV. The effect of the Einstein oscillator is seen as peaks in the upscatter for the low-energy curve and as strong oscillations in the downscatter for the high-energy curve

■ **Table 3**

Summary of the thermal scattering evaluations available in ENDF/B-VII

Evaluation name	Secondary scatterer	Material number	Temperatures (K)
H in H ₂ O	Free O	1	293.6, 350, 400, 450, 500, 550, 600, 650, 800
H in CH ₂	Free C	37	296, 350
Benzene	None	40	296, 350, 400, 450, 500, 600, 800, 1,000
H in ZrH	None	7	296, 400, 500, 600, 700, 800, 1,000, 1,200
D in D ₂ O	Free O	11	293.6, 350, 400, 450, 500, 550, 600, 650
Be in metal	None	26	296, 400, 500, 600, 700, 800, 1,000, 1,200
Be in BeO	None	27	293.6, 400, 500, 600, 700, 800, 1,000, 1,200
Graphite	None	31	296, 400, 500, 600, 700, 1,000, 1,200, 1,600, 2,000
O in BeO	None	28	293.6, 400, 500, 600, 700, 800, 1,000, 1,200
O in UO ₂	None	75	296, 400, 500, 600, 700, 800, 1,000, 1,200
Al in metal	None	45	20, 80, 293.6, 400, 600, 800
Fe in metal	None	56	20, 80, 293.6, 400, 600, 800
Zr in ZrH	None	58	296, 400, 500, 600, 700, 800, 1,000, 1,200
U in UO ₂	None	76	293.6, 400, 500, 600, 700, 800, 1,000, 1,200
Para H ₂	None	2	20
Ortho H ₂	None	3	20
Para D ₂	None	12	19
Ortho D ₂	None	13	19
Liquid CH ₄	None	33	100
Solid CH ₄	None	34	22

A number of these evaluations were prepared for use at neutron scattering centers where moderators are cooled down to make long wavelength neutrons. They are not needed for reactor calculations.

The ENDF/B thermal scattering evaluations are not ready to be used directly in practical reactor calculations. They have to be converted into cross sections in appropriate formats by a nuclear data processing code such as NJOY (MacFarlane and Muir 1994). In NJOY, this is done using the THERMR module. It reads in an ENDF thermal scattering evaluation and produces cross sections versus energy and scattering distributions giving incident energy, secondary energy, probability, and a set of discrete emission cosines for incoherent inelastic scattering. For crystalline coherent scattering, it just produces a cross section with Bragg edges. The angular distribution can be deduced from that in subsequent codes. For incoherent elastic scattering, it produces a cross section and a set of emission cosines. The output from the THERMR module can be passed to GROUPT to be formatted for multigroup codes or to ACER to be formatted for the MCNP continuous energy Monte Carlo code.

2 Neutron Thermalization

2.1 Introduction

In nuclear reactors, neutrons are born at million electron-volts (MeV) energies, and they slow down (are “moderated”) by elastic and inelastic collisions with the materials in the reactor until they reach the thermal range below a few electron-volts (eV). In this range, in addition to losing energy in collisions, they can also gain energy by collisions with atoms and molecules in thermal motion. After some time, the distribution of the neutrons will come into equilibrium with the thermal motion of the atoms or molecules of the material and show a Maxwellian-like shape. Fission reactions caused by this distribution of neutrons will lead to the production of more neutrons at high energies, continuing the thermalization process. In addition to causing fission, the thermal neutrons can suffer absorption losses, and neutrons can be lost by leaking out of the system. These absorptions and leakages can affect the shape of the equilibrium neutron spectrum.

In this section, we will consider the process of neutron thermalization in the region below a few eV, how to compute the equilibrium neutron spectrum, and the various influences on the shape of the equilibrium spectrum. We will first demonstrate this by direct Monte Carlo simulation of the thermalization process, and then move on to methods based on solving the transport equation for thermal neutrons (the Boltzmann equation) using multigroup techniques.

2.2 Monte Carlo Simulations of Neutron Thermalization

The Monte Carlo method is based on following the histories of many particles using a random selection of the reactions that the neutrons go through between their production in a fission event, and their eventual death by absorption or leakage from the system. There are a number of Monte Carlo codes available that perform well for thermal neutrons. The examples in this section use MCNP (2003).

As a first example, let us consider a cylindrical steel tank partly filled with a solution of highly enriched uranium nitrate in water. This particular case is called HIGH-ENRICHED-SOLUTION-THERMAL-42-5 (or shortly HST42-5) in the International Criticality System Benchmark Experiment Program (ICSBEP) handbook (Briggs et al. 2004). Using cross sections from ENDF/B-VII (Tuli et al. 2006) and running this assembly for 50 million histories gives a predicted multiplication k_{eff} of 1.00019 with an estimated standard deviation of 0.00004 as compared to an experimental prediction of 1.0000 ± 0.0034 .

What this means is that the production rate of neutrons by fission is almost exactly balanced by the loss rate of neutrons to absorption and leakage from the system, or

$$k_{\text{eff}} = \frac{\bar{\nu}\sigma_f\phi}{(\sigma_f + \sigma_{n\gamma})\phi + L}, \quad (68)$$

where these quantities stand for integrals over energy and space, $\bar{\nu}$ is the number of neutrons produced per fission, σ_f is the fission cross section, $\sigma_{n\gamma}$ is the capture cross section, L is the leakage rate from the system, and ϕ is the neutron flux. In practice, this equation is a little too simple. The reactions $(n, 2n)$ and $(n, 3n)$ also produce neutron multiplication, and there are also other less-common reactions that produce neutron multiplication. MCNP and many of

the multigroup transport codes handle this by reducing the absorption to compensate for the increased production

$$k_{\text{eff}} = \frac{\bar{\nu}\sigma_f\phi}{(\sigma_f + \sigma_{n\gamma} - \sigma_{n2n} - 2\sigma_{n3n})\phi + L}. \quad (69)$$

MCNP normalizes itself so that the denominator of this equation is one. Some other transport codes use the full production in the numerator, getting

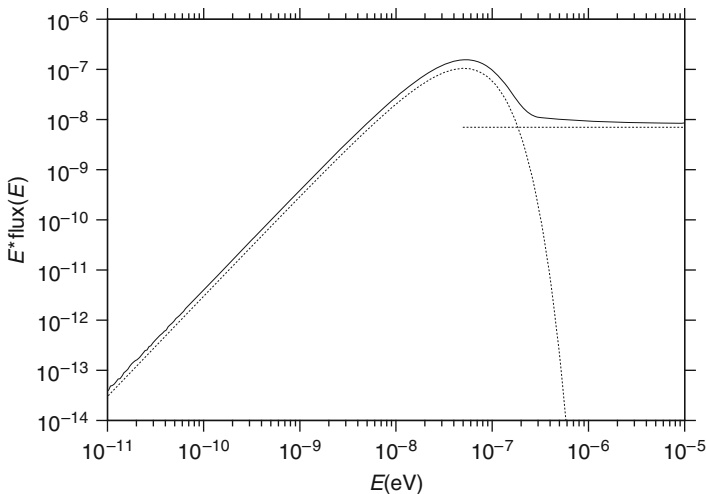
$$k_{\text{eff}} = \frac{(\bar{\nu} + 2\sigma_{n2n} + 3\sigma_{n3n})\phi}{(\sigma_f + \sigma_{n\gamma} + \sigma_{n2n} + \sigma_{n3n})\phi + L}. \quad (70)$$

These two different definitions are equivalent when k_{eff} is not too far from unity.

The MCNP result for the HST42-5 case gives $L = 0.032446$; therefore, the leakage is fairly small for this case. It is strongly thermalized. **►** *Figure 30* shows the computed flux (solid curve) compared to a Maxwellian at room temperature and the effective contribution due to slowing down from higher energies (dotted curves). The numbers plotted in this figure are the hits in MCNP tally bins defined logarithmically with 50 bins per decade; therefore, they are proportional to “flux per unit lethargy.” The term “lethargy” is often used in reactor physics. It is defined as

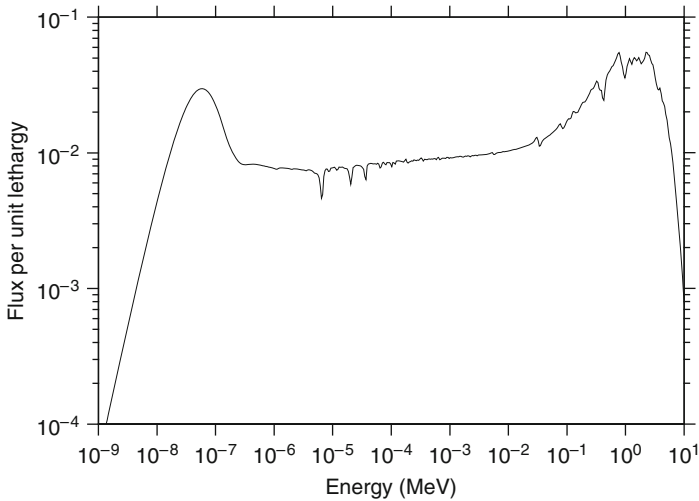
$$\text{lethargy} = \exp\left[\frac{10 \text{ MeV}}{E}\right]. \quad (71)$$

It increases as the neutron slows down. The flux per unit lethargy is equivalent to $E * \phi(E)$. Because the epithermal slowing down in a system like this gives a shape close to $1/E$, the flux per unit lethargy plots are approximately flat in the epithermal region.



■ *Figure 30*

Calculated flux for the HST42-5 critical assembly (solid curve). The dotted curves show the theoretical Maxwellian flux and nominal $1/E$ source due to slowing down from higher energies



■ **Figure 31**
 Calculated flux for the LCT6-6 critical assembly. The average over the lattice region is shown

For a more realistic example, we consider the assembly called LCT6-6. This one has a 19×19 square lattice of 2.6%-enriched uranium oxide rods with aluminum cladding placed in a tank of water. The water outside the lattice acts as a reflector. The calculated k_{eff} using ENDF/B-VII cross sections is 1.00047 ± 0.00010 as compared to the evaluated model k_{eff} of 1.0000 ± 0.0020 .

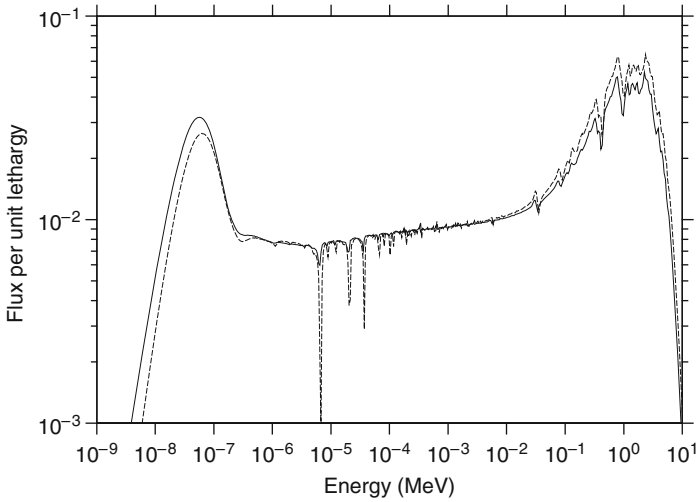
► **Figure 31** shows the flux in the lattice region (not including the water reflector).

The region around each fuel rod can be defined as a “cell,” where each square cell contains a fuel pin, the aluminum cladding, and the associated water. With MCNP, we can calculate (or “tally”) the flux in the fuel pin and the flux in the associated water separately as averages over the entire lattice. The result is shown in ► **Fig. 32**. At high energies, the flux in the pin is higher than the flux in the water because of the fission neutron source there. At the middle energies, we see strong dips in the fuel flux from absorption resonances, but the water flux is smoother. The $1/E$ shape we saw in the previous example is modified somewhat because of the losses to absorption in the fuel. At thermal energies, we see typical Maxwellian flux shapes from thermalization, but the thermal flux in the fuel is depressed because of the absorption by capture and fission.

► **Figure 33** shows an expanded view of the thermal region. The solid line is the water flux, and the dotted lines are the theoretical Maxwellian and slowing-down shapes. It is clear that the water flux matches the expected Maxwellian shape quite well. However, the fuel flux (dashed curve) has been depressed by the absorption from capture and fission, and its shape is been “hardened” somewhat.

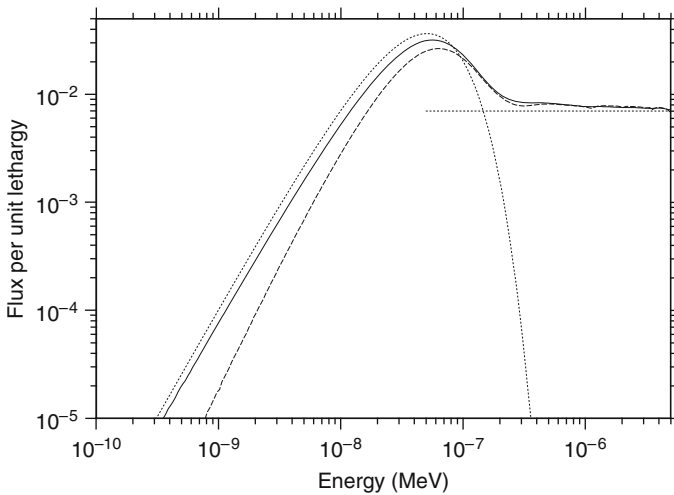
► **Figure 34** shows an expanded view of the resonance region. The slowing down in the water shows a slightly harder shape than $1/E$ because of the losses to absorption in the fuel, and also because some effect of the strong absorption resonances in the fuel shows up as dips in the water flux. The absorption dips in the fuel are very large and lead to the “self-shielding” effects that will be discussed below.

In order to get a better idea of the details of thermalization in a lattice like LCT6-6, we consider an infinite lattice of LCT6 pin cells. With MCNP, this is represented as a single pin



■ Figure 32

Calculated flux for the LCT6-6 critical assembly showing water flux (solid) and fuel flux (dashed)

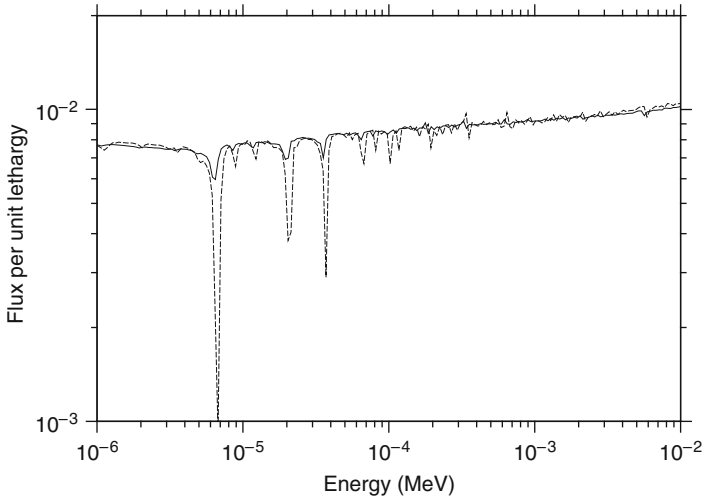


■ Figure 33

Expanded view of the thermal region flux for the LCT6-6 critical assembly showing water flux (solid), fuel flux (dashed), and the theoretical Maxwellian and slowing down shapes (dotted)

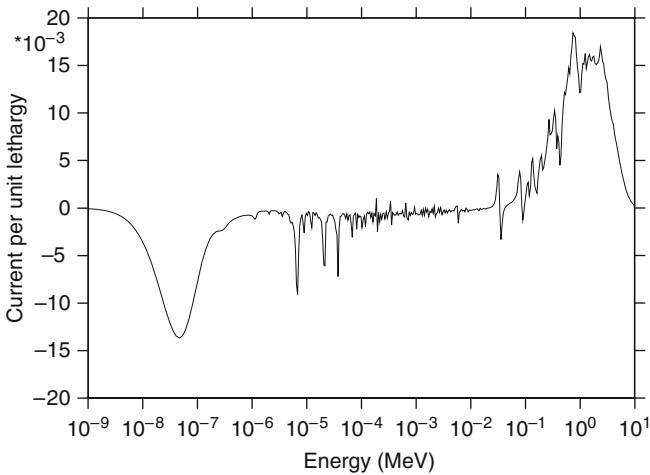
of fuel and clad surrounded by water in a square cross section with reflecting surfaces and extended vertically with reflecting ends. Of course, without the leakage, this cell is supercritical with $k_{\infty} = 1.37577$.

➤ *Figure 35* shows the net current out of the pin (actually at the surface of the clad) into the water moderator. Note that the current is positive at high energies where the fission neutron



■ Figure 34

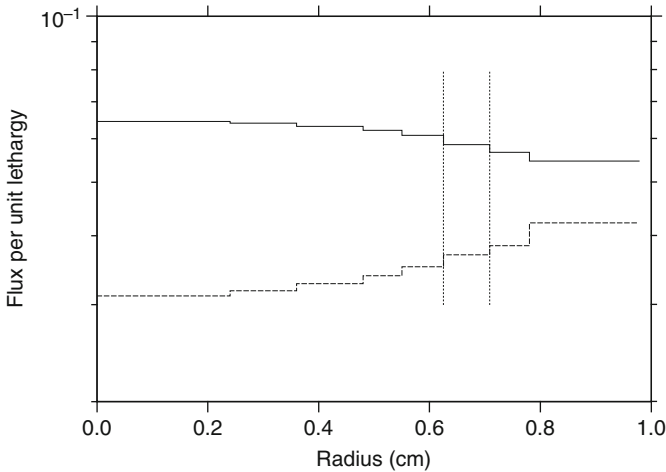
Expanded view of the resonance region flux for the LCT6-6 critical assembly. The solid curve shows the flux in the cell water, and the dashed curve shows the flux in the fuel pin



■ Figure 35

Net current out of pin into water for an infinite lattice of LCT6 pin cells showing fission neutrons entering the water at high energies, slowing down, and reentering the pin at low energies

are born. Many of the fission neutrons are leaking from the fuel pin into the moderator. They then slow down quickly to thermal energies and reenter the fuel pin (negative current) to cause new fissions or to be killed by capture. In the epithermal range, there are occasional negative dips in the current where neutrons are being drawn out of the moderator by strong absorption



■ Figure 36

Flux vs. radius in the fission peak around 2 MeV (solid) and the thermal dip around 0.05 eV (dashed). The vertical dotted lines show the location of the clad

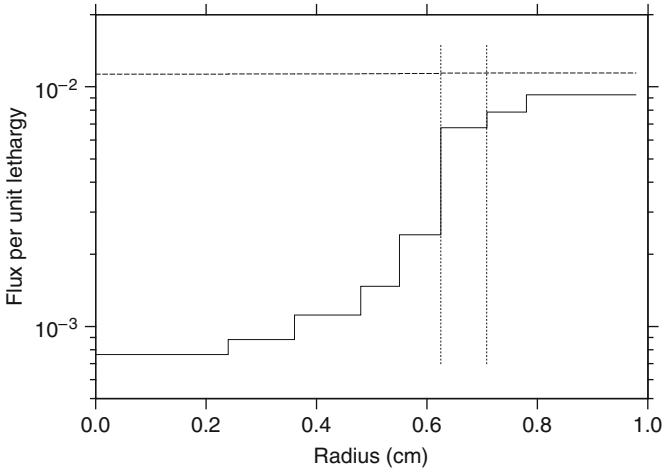
resonances in the fuel (especially around 6.7 eV). At higher energies, you can see the effects of the aluminum and oxygen resonances.

► *Figure 36* shows the radial shape of the flux in the fission peak around 2 MeV and in the thermal dip around 0.05 eV. The fission source is slightly peaked in the center and decreases as you move out into the moderator due to the leakage into the moderator. The thermal shape is depressed in the center of the pin due to absorption from fission and capture. More dramatically, ► *Fig. 37* shows the strong depression in the center of the pin due to absorption in the 6.7 eV capture resonance of U-238. The mean free path of the neutrons near the center of the resonance is very small, and they do not penetrate very far into the pin. Only a small fraction of the U-238 in the pin actually contributes to the absorption, and this is the real source of the dip in the flux seen in ► *Fig. 34*. The U-238 in the center of the pin is “self-shielded” from the neutrons in the moderator. Energy self-shielding and spatial self-shielding are seen to closely related.

This example helps to explain why a heterogeneous arrangement of fuel pins in a moderator is used in thermal reactors. Having the neutrons slow down in a moderator outside the fuel pins allows most of the neutrons to avoid being absorbed in the strong resonances of U-238, thereby allowing them to reach thermal energies where they can continue the fission chain reaction. The HST42 example could reach criticality using a homogeneous arrangement for fuel and moderator because the fuel was highly enriched in U-235, making the U-238 absorptions less of a problem. The LCT6 fuel is a low-enriched material (2.6% U-235) and U-238 absorption must be well managed to design an effective reactor.

2.3 Discrete Ordinates Methods

The examples above used simulations of the real physical process going on during thermalization, following the neutron as it bounced around the assembly losing and gaining energy until



■ Figure 37

Flux vs. radius in the 6.7 eV resonance (solid) and below the resonance at 3 eV (dashed). The vertical dotted lines show the location of the clad

it came into equilibrium and was lost by absorption or escape from the system. An alternate approach is to solve the Boltzmann transport equation, which describes the balance of neutrons in a region of space and energy. There are a number of highly developed computer codes that solve this equation using the multigroup “discrete ordinates,” or S_N , method. An example of this is PARTISN (Alcouffe et al. 2005) from Los Alamos.

2.3.1 S_N Theory

The S_N transport codes solve the equation (Bell and Glasstone 1970)

$$\mu \frac{\partial}{\partial x} \phi_g(\mu, x) + \sigma_g^{S_N}(x) \phi_g(\mu, x) = \sum_{\ell=0}^N P_\ell(\mu) \sum_{g'} \sigma_{\ell g \leftarrow g'}^{S_N}(x) \phi_{lg'} + S_g(\mu, x), \quad (72)$$

where one-dimensional plane geometry has been used for simplicity, μ is the scattering cosine, x is position, $\phi(\mu, x)$ is the angular flux for group g , ϕ_{lg} is the Legendre flux for group g , $P_\ell(\mu)$ is a Legendre polynomial, and $S_g(\mu, x)$ is the external and fission source into group g . The cross sections in (72) must be defined to make ϕ_g as close as possible to the solution of the Boltzmann equation. As shown in the reference, the multigroup Boltzmann equation can be written in the P_N form:

$$\mu \frac{\partial}{\partial x} \psi_g(\mu, x) + \sum_{\ell=0}^N P_\ell(\mu) \sigma_{\ell g}^{P_N}(x) \psi_{\ell g} = \sum_{\ell=0}^N P_\ell(\mu) \sum_{g'} \sigma_{\ell g \leftarrow g'}^{P_N}(x) \psi_{\ell g'} + S_g(\mu, x), \quad (73)$$

where the P_N cross sections are given by the following group averages:

$$\sigma_{\ell t g}^{P_N} = \frac{\int_g \sigma_t(E) W_\ell(E) dE}{\int_g W_\ell(E) dE}, \quad (74)$$

and

$$\sigma_{\ell g \leftarrow g'}^{P_N} = \frac{\int_{g'} dE' \int_g dE \sigma_\ell(E' \rightarrow E) W_\ell(E')}{\int_{g'} dE' W_\ell(E')}. \quad (75)$$

In these formulas, $\sigma_t(E)$ and $\sigma_\ell(E' \rightarrow E)$ are the basic energy-dependent total and scattering cross sections, and $W_\ell(E)$ is a weighting flux that should be chosen to be as similar to ψ as possible.

So “there’s the rub.” To solve for the unknown flux, we have to have a good estimate of the flux to start with! This is not a serious problem for thermalization. As we saw in [Fig. 30](#), the thermalized flux is well represented by a Maxwellian flux shape with a $1/E$ slowing-down contribution. This will almost always be the case for a practical thermal reactor. To keep good neutron economy, it is important not to lose too many neutrons to unproductive leakage or capture, which tends to preserve the well-thermalized flux shape shown in the picture. We can use the Maxwellian flux shape with a slowing-down contribution for the weighting function $W_\ell(E)$. It is still necessary to divide the thermal range into a number of energy groups to account for deviations from the simple Maxwell plus slowing-down shape, such as the hardening seen in [Fig. 33](#), and especially around the break between the two functions or where strong resonances may occur (e.g., the 1 eV resonance of Pu-240). The venerable THERMOS-LASER structure used 35 groups between 0.00253 and 1.855 eV with velocity spacing over most of the range and extra coverage around 1 eV. The widely used WIMS structure uses 42 thermal groups between 10^{-5} and 4 eV. Because of the increased capabilities of modern computers, many newer systems use even more thermal groups.

2.3.2 Transport Corrections

When (73) is compared with (72), it is evident that the S_N equations require

$$\sigma_{\ell g \leftarrow g'}^{S_N} = \sigma_{\ell g \leftarrow g'}^{P_N} \quad \text{for } g' \neq g, \quad (76)$$

and

$$\sigma_{\ell g \leftarrow g}^{S_N} = \sigma_{\ell g \leftarrow g}^{P_N} - \sigma_{\ell t g}^{P_N} + \sigma_g^{S_N}, \quad (77)$$

where $\sigma_g^{S_N}$ is not determined. The choice of $\sigma_g^{S_N}$ gives rise to a “transport approximation” and various recipes are in use. It is convenient to write

$$\sigma_{\ell g \leftarrow g}^{S_N} = \sigma_{\ell g \leftarrow g}^{P_N} - \left(\sigma_{\ell t g}^{P_N} - \sigma_{o t g}^{P_N} \right) - \Delta_g^N, \quad (78)$$

and

$$\sigma_g^{S_N} = \sigma_{o t g}^{P_N} - \Delta_g^N. \quad (79)$$

The term in parentheses corrects for the anisotropy in the total reaction rate term of the Boltzmann equation, and Δ_g^N can be chosen to minimize the effects of truncating the Legendre expansion at $\ell = N$. Some recipes for doing this follow:

Consistent-P approximation:

$$\Delta_g^N = 0, \quad (80)$$

Inconsistent-P approximation:

$$\Delta_g^N = \sigma_{otg}^{P_N} - \sigma_{N+1,tg}^{P_N}, \quad (81)$$

Diagonal transport approximation:

$$\Delta_g^N = \sigma_{otg}^{P_N} - \sigma_{N+1,tg}^{P_N} + \sigma_{N+1,g \leftarrow g}^{P_N}, \quad (82)$$

Bell–Hansen–Sandmeier (BHS) or extended transport approximation:

$$\Delta_g^N = \sigma_{otg}^{P_N} - \sigma_{N+1,tg}^{P_N} + \sum_{g'} \sigma_{N+1,g' \leftarrow g}^{P_N}, \quad (83)$$

and

Inflow transport approximation:

$$\Delta_g^N = \sigma_{otg}^{P_N} - \sigma_{N+1,tg}^{P_N} + \frac{\sum_{g'} \sigma_{N+1,g \leftarrow g'}^{P_N} \phi_{N+1,g'}}{\phi_{N+1,g}}. \quad (84)$$

The first two approximations are most appropriate when the scattering orders above N are small. The inconsistent option removes most of the delta-function of forward scattering introduced by the correction for the anisotropy in the total scattering rate and should normally be more convergent than the consistent option. For libraries produced with an ℓ -independent flux guess and in the absence of self-shielding, the difference between “consistent” and “inconsistent” vanishes.

The diagonal and BHS recipes make an attempt to correct for anisotropy in the scattering matrix and are especially effective for the forward-peaked scattering normally seen for high neutron energies. The BHS form is most often used, but the diagonal option can be substituted when BHS produces negative values, which is often the case in the thermal range.

The inflow recipe makes the $N+1$ term of the P_N expansion vanish, but it requires a good knowledge of the $N+1$ flux moment from some previous calculation. Inflow reduces to BHS for systems in equilibrium by detail balance (i.e., the thermal region). The diffusion approximation obtained using the inflow formula is equivalent to a P_1 transport solution.

These corrections require data from the $(N+1)$ -th Legendre moments of the cross sections to prepare a corrected N -table set.

2.3.3 Fission Source

The source of fission neutrons into a group is given by

$$S_g = \sum_{g'} \sigma_{fg \leftarrow g'} \phi_{0g'}, \quad (85)$$

where $\sigma_{fg \leftarrow g'}$ is the fission matrix computed from the energy-dependent fission spectra given in the ENDF-format evaluation. However, most existing transport codes do not use this matrix form because the upscatter is expensive to handle and a reasonably accurate alternative exists. Except for relatively high neutron energies, the spectrum of fission neutrons is only weakly dependent on initial energy. Therefore, the fission source can be written as

$$S_g = \chi_g \sum_{g'} \bar{v}_{g'} \sigma_{fg'} \phi_{0g'}, \quad (86)$$

where \bar{v}_g is the fission neutron yield, σ_{fg} is the fission cross sections, and χ_g is the average fission spectrum, which can be defined by

$$\chi_g = \frac{\sum_{g'} \sigma_{fg \leftarrow g'} \phi_{0g'}}{\sum_{g'} \bar{v}_{g'} \sigma_{fg'} \phi_{0g'}}, \quad (87)$$

where the fission neutron production rate can also be written as

$$\sum_{g'} \bar{v}_{g'} \sigma_{fg'} \phi_{0g'} = \sum_g \sum_{g'} \sigma_{fg \leftarrow g'} \phi_{0g'}. \quad (88)$$

Clearly, χ_g as given by (87) depends on the flux in the system of interest. The dependence is weak except for high incident energies, and a rough guess for ϕ_{0g} usually gives an accurate spectrum. When this is not the case, a sequence of calculations can be made, using the flux from each step to improve the χ_g for the next step.

The matrix as described above represents the prompt part of fission only. Steady-state (SS) fission is obtained using two auxiliary pieces of data: delayed \bar{v} and delayed χ . Therefore,

$$\bar{v}_{g'}^{SS} \sigma_{fg'} = \sum_g \sigma_{fg \leftarrow g'} + \bar{v}_{g'}^D \sigma_{fg'}, \quad (89)$$

and

$$\chi_g^{SS} = \frac{\sum_{g'} \sigma_{fg \leftarrow g'} \phi_{0g'} + \chi_g^D \sum_{g'} \bar{v}_{g'}^D \sigma_{fg'} \phi_{0g'}}{\sum_g \sum_{g'} \sigma_{fg \leftarrow g'} \phi_{0g'} + \sum_{g'} \bar{v}_{g'}^D \sigma_{fg'} \phi_{0g'}}. \quad (90)$$

2.3.4 The Eigenvalue Iteration

In order to solve (72), it is converted into an eigenvalue problem by multiplying the fission source term by a factor k . Starting with an initial estimate for k (such as $k = 1$), the flux is computed. This is called the “inner iteration.” This flux is then used to compute a new value for k , and a new flux is computed. This is called the “outer iteration.” It is continued until a sufficiently converged value for k is obtained. The outer iteration is needed to adjust the fission source and the thermal upscatter source. Referring back to the discussion of (69) and (70), we see that this method produces the value of k_{eff} defined for fission productions.

2.3.5 S_N Data Requirements

The data required for an S_N flux solution using (72) have been shown to be


$$\sigma_g, \sigma_{\ell g \leftarrow g'}, \bar{v}_g \sigma_{fg}, \text{ and } \chi_g,$$

where the superscript S_N has been omitted for simplicity. The S_N codes also traditionally use a particle-balance cross section (often loosely called “absorption”) defined by

$$\sigma_{ag} = \sigma_g - \sum_{g'} \sigma_{0g' \leftarrow g}. \quad (91)$$

This quantity can also be computed by adding all the absorption reactions [(n, γ), fission, (n, p), (n, α), etc.] and subtracting ($n, 2n$), twice ($n, 3n$), and so on. The two methods are formally equivalent, except that small numerical differences due to cross-section processing lead to unreasonable values for σ_{ag} , as computed from (91), when σ_{ag} is small in relation to σ_g . In such cases, σ_{ag} can be replaced by the value from the direct calculation, and the σ_g position of the transport table is adjusted accordingly. Note that σ_{ag} can be negative if more particles are produced by (n, xn) reactions than are absorbed. Note that σ_a is the quantity that appears in the denominator of the fission-based definition for k_{eff} (see (69)).


When the flux calculation is complete, it is often necessary to compute some response such as heating, radiation damage, gas production, photon production, or dose to tissue. Therefore, S_N codes allow for reading several response-function edit cross sections, σ_{Eg} .

The original S_N codes read χ as a special array, and the cross sections were arranged into “transport tables” by “position” as shown in  Table 4. Note that the positions containing scattering data give all the source groups that scatter into the same final or “sink” group. Even the newer codes retain many features of this structure. We call this “DTF format” in honor of the pioneering discrete ordinates code (Lathrop 1965).

A transport table like this is required for each group, Legendre order, and material. The tables may be “material-ordered” or “group-ordered.” Material ordering is the natural result of preparing a library from evaluated nuclear data. The tables are written onto a library with the outermost loop being material, then Legendre order, and then group as the inner loop. However, group ordering is the way the cross sections are needed in the codes. The S_N equations are solved by sweeping down from group 1 to the lower energy groups, so cross sections for all materials and orders are needed for each group in sequence. The library is ordered with group as the outermost loop, then Legendre order, and then material.

2.3.6 Example for HST42-5

An S_N model for HST42-5 can be constructed using two-dimensional r - z geometry, including the vessel and the solution level inside the vessel. Effective cross sections can be constructed (see below) including the appropriate thermal scattering data for H in H_2O and self-shielded cross sections in the resonance range. When PARTISN is used to run the problem, it finds a k_{eff} value of 0.99979 as compared to 1.00019 from MCNP, which is satisfactory agreement. This calculation was done with 187 groups; P_3 , S_{16} , 55 radial intervals; and 115 axial intervals.

 Figure 38 shows the flux at an energy of 0.05 eV (or $2kT$, the maximum of the flux per

■ **Table 4**
Transport table terminology

Position	Contents for Group g
1	} σ_{Eg} Response edits
:	
NED	
.....
NED+1	σ_{ag}
NED+2	$\bar{v}_g \sigma_{fg}$ Standard edits
NED+3	σ_g
.....
NED+4	} $\sigma_{g \leftarrow g'}$ Upscatter ($g' > g$)
:	
NED+NUP+3	
.....
NED+NUP+4	$\sigma_{g \leftarrow g'}$ In-group ($g' = g$)
.....
NED+NUP+5	} $\sigma_{g \leftarrow g'}$ Downscatter ($g' < g$)
:	
NTABL	

NED = number of extra response edits ($NED \geq 0$)

NUP = maximum number of upscatter groups ($0 \leq NUP \leq NGROUP$)

NTABL = table length ($NED + 4 + NUP \leq NTABL \leq NED + 4 + NUP + NGROUP$)

NGROUP = number of energy groups

IPTOT = $NED + 3$ = position of total cross section

unit lethargy) vs. the radial coordinate r and the axial coordinate z . The cosine shape of the axial distribution is typical; it is called the “fundamental mode” shape. ➤ *Figure 39* shows a view of the HST42-5 flux per unit lethargy vs. energy and radius at the axial midpoint of the solution region. Just as for the MCNP result shown in ➤ *Fig. 31*, we see the fission source at high energies, the $1/E$ slowing down region, and the thermal peak at low energies.

➤ *Table 5* compares the reaction-rate balances for PARTISN and MCNP. At this point, it might be well to remind ourselves that a k calculation does not determine the actual values of the flux or reaction rates; a reactor can be critical at a wide range of operating power values. The normalization in a table like this is arbitrary. The default normalization for both PARTISN and MCNP is to make the effective loss rate (i.e., the denominator of (69)) equal to one. The entry “ (n, xn) ” in the table is the amount subtracted from capture + fission to get the effective absorption. Specifically, it is $(n, 2n) + 2(n, 3n) + \dots$. As a counterexample, the TART Monte Carlo code (Cullen 2005) normalizes itself so that the total production $v\sigma_f + 2(n, 2n) + 3(n, 3n) + \dots$ is one (see the numerator of (70)).

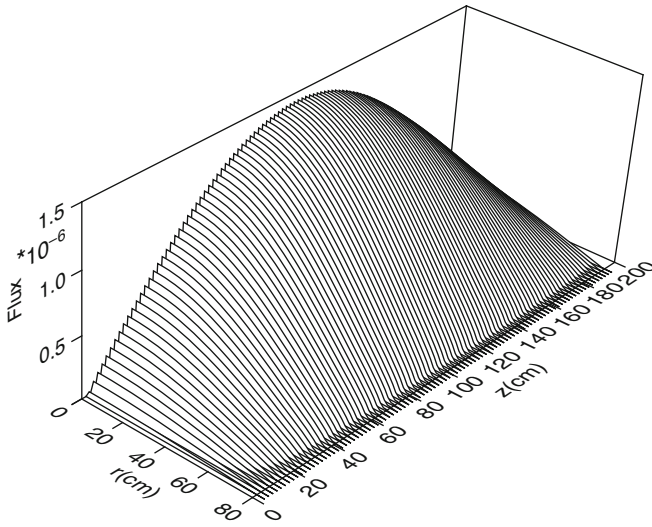


Figure 38
Flux for HST042-5 vs. r and z at 0.05 eV as computed by S_N methods

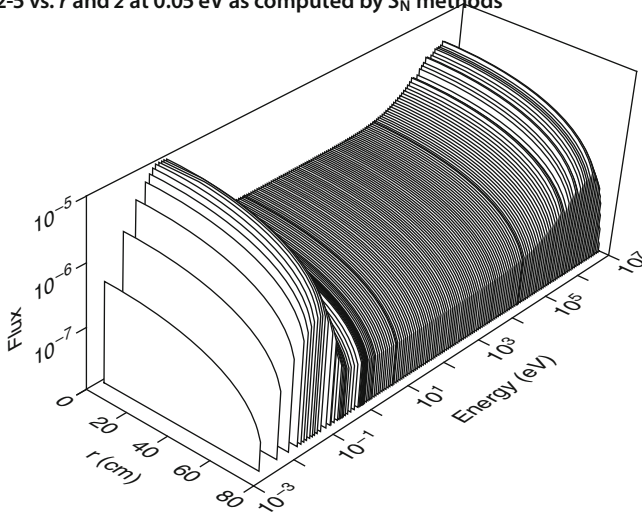


Figure 39
Flux per unit lethargy for HST42-5 vs. energy and radius at the axial midpoint as computed by S_N methods

2.3.7 Preparing S_N Cross-Section Data

Normal multigroup cross-section data need some extra processing to be used for a calculation like this HST42-5 example. The microscopic cross sections need to be assembled into macroscopic cross sections that include the shielding effects on the resonance features of the actinides

■ **Table 5**
Reaction balances for HST42-5

Reaction rate	PARTISN	MCNP
$\nu\sigma_f$	0.99979	
Leakage	0.032556	0.032446
Absorption	0.96744	0.96753
Losses	1.00000	0.99998
Fission		0.41039
$(n,\chi n)$		0.00001

in the solution. In addition, the normal low-energy scattering cross section for H-1 has to be modified to include the H in H₂O thermal scattering, and the other materials need to be modified to include thermal free-gas scattering. One way to do this additional processing is with the TRANSX code (MacFarlane 1992). TRANSX works with multigroup libraries produced by NJOY in MATXS format. The libraries provide tables of self-shielded microscopic cross sections vs. background cross section and temperature (more on these kinds of self-shielded cross sections will be found below). TRANSX determines the background cross section using the mixture and geometry information provided by the user and interpolates for the effective cross sections. The libraries contain normal target-at-rest down scatter at low energies, and they also contain tables of the bound and free thermal-scattering cross sections with upscatter. TRANSX will replace the target-at-rest values with the proper thermal data as specified by the user. The code will also prepare the fission source in the χ and $\nu\sigma_f$ representation, using a user-supplied weighting flux to get the good χ vector. This feature can be used to iterate for an improved χ for cases where the library weighting function does not match the computed flux very well. This problem is common for fast critical assemblies. Other features provided by TRANSX include group collapse, cell homogenization, coupled sets, adjoint cross sections, and data for the multigroup mode of MCNP. Output can be prepared in formats adaptable to a number of popular multigroup transport codes.


2.3.8 Example for an Infinite Pin-Cell Lattice

With S_N codes, the normal way to simulate an infinite pin-cell lattice is to convert the square cells with reflective boundaries into cylindrical shells with white boundary conditions. This allows us to use a one-dimensional calculation. That runs very fast with PARTISN, giving $k_\infty = 1.38158$ (as compared to the MCNP value of 1.37577). The result of that calculation is region fluxes for 187 groups in the fuel, clad, and moderator. These fluxes can be used in a second TRANSX run to perform a cell homogenization and group collapse. A simplified result of such a calculation is shown in ► [Table 6](#). These macroscopic effective cross sections can then be used in a large-scale calculation for the entire reactor using transport, diffusion, or collision-probability methods.


The TRANSX self-shielding calculation for the infinite lattice also included a Dancoff correction. When a neutron escapes from the fuel pin in a lattice, there is a possibility that it will reach another fuel pin before scattering from the moderator material. In that case, it would be as

■ **Table 6**
Two-group macroscopic cross sections for a pin cell in an infinite lattice

Reaction	Group 1 3.92 eV–20 MeV $\sigma \text{ cm}^{-1}$	Group 2 1e-5 eV–3.92 eV $\sigma \text{ cm}^{-1}$
nf	1.4509-3	2.1708-2
ng	6.3808-4	1.8059-2
abs	2.2180-3	3.9767-2
nusigf	4.0130-3	5.2894-2
Total	2.1677-1	4.5865-1

if it did not escape from the fuel pin at all. There is a reduction in the effective escape probability. TRANSX handles that effect with several possible Dancoff correction options, for example, pins in a square lattice. Another improvement to this calculation is possible using PARTISN. It is possible to simulate the cosine “fundamental mode” axial shape seen in  Fig. 38 by imposing a “buckling.” This simulates axial leakage from the top and bottom of the lattice of cells, leaving the effective radius or x - y extent of the entire core large (zero leakage).

2.3.9 Monte Carlo vs. Multigroup

From these examples, we can begin to appreciate the different advantages and disadvantages of the Monte Carlo and multigroup methods. The Monte Carlo method uses good physics for slowing down and resonance reactions, and it allows for a very complete geometry representation. However, it is a statistical calculation, and it is not so good for looking at small differences or for getting smooth detailed distributions like those shown in  Fig. 38. The Monte Carlo calculations are also relatively expensive. On the other hand, the multigroup methods are relatively fast, and they are useful for looking for the effects of small differences in materials or geometry. They are good for getting smooth distributions of things like flux or nuclear heating over the geometry. However, they work best for simple geometries (requiring some approximation of the actual arrangements). The self-shielding effects from the resonances are not handled as accurately as with Monte Carlo.

In the end, it has been the speed advantages of the multigroup methods that have kept them prominent in reactor core calculations. This is especially important when time-dependent fuel burnup and fission-product accumulation are considered – in these cases many time steps are required, making the Monte Carlo approach even more expensive.

2.4 Collision Probability Methods

Collision probability methods are based on the integral form of the transport equation. As used above, the transport equation was of integro-differential form. As shown in Bell and Glasstone (1970), standard mathematical methods can be used to convert that form of the equation

into integral form. For our purposes, let us limit ourselves to the time-independent case with isotropic scattering and source. Then

$$\phi(\mathbf{r}, E) = \int \frac{\exp[-\tau(E, \mathbf{r}' \rightarrow \mathbf{r})]}{4\pi|\mathbf{r} - \mathbf{r}'|^2} \times \left[\int \sigma(\mathbf{r}', E \rightarrow E) \phi(\mathbf{r}', E') dE' + Q(\mathbf{r}', E) \right] dV', \quad (92)$$

where $\tau(E, \mathbf{r}' \rightarrow \mathbf{r})$ is the optical path length from \mathbf{r}' to \mathbf{r} (i.e., the number of mean free paths, or the integral of $\sigma(\mathbf{r}, E)$ along the path from \mathbf{r}' to \mathbf{r}). Clearly, the quantity in square brackets is the source into energy E and volume element dV' around \mathbf{r}' due to scattering from other energies and external contributions. The factor in the first line is the attenuation of that while traveling from \mathbf{r}' to \mathbf{r} . In practice, the energy range is divided into a number of energy groups within which the cross section can be taken as constant, and the geometry is divided into a number of subregions in which the flux and source can be taken as constant. The result is

$$\phi_{g,i} = \frac{1}{V_i \sigma_{g,i}} \sum_j V_j P_{g,j \rightarrow i} \left[\sum_{g'} \sigma_{g' \rightarrow g,j} \phi_{g',j} + Q_{g,j} \right], \quad (93)$$

where $P_{g,j \rightarrow i}$ is the probability that a neutron born in group g and subregion j will suffer its next collision in subregion i . This is the collision probability matrix

$$P_{g,j \rightarrow i} = \frac{\sigma_{g,i}}{V_j} \int_{V_i} \int_{V_j} \frac{\exp[-\tau(E_g, \mathbf{r}' \rightarrow \mathbf{r})]}{4\pi|\mathbf{r} - \mathbf{r}'|^2} dV dV'. \quad (94)$$

The limitation to isotropic scattering can be alleviated by using a transport correction similar to the ones described above in connection with the S_N method.

Collision probability methods have been widely used for core physics calculations. An early example was the THERMOS code (Honek 1961), which could compute CP matrices for plate and pin-cell geometries in the thermal region. For a pin cell, the fuel, clad, and moderator regions were subdivided into a number of parts in order to handle the spatial self-shielding well. The resulting flux was then used to homogenize the cell and collapse to a coarser group structure. These numbers could then be used by simpler methods, such as diffusion, to complete the calculation for the whole reactor.

In comparing CP and S_N methods, we see that the CP approach can handle very complex geometries, while the S_N method works best when it can work with simpler geometries, such as slab, sphere, or cylindrical r - z . However, the CP methods couples every cell in the calculation to every other cell. With N subregions and G groups, the problem grows like $N^2 G$. This makes the CP method impractical for representing a reactor in all its awful detail. However, it has been used for quite complex fuel bundles in the past. To handle larger problems, it makes sense to use the CP method on a fuel element or cluster, homogenize, and collapse. Then another CP calculation can be made using the effective fuel element cross sections for the core region and modeling the radial and axial components as a CP matrix.

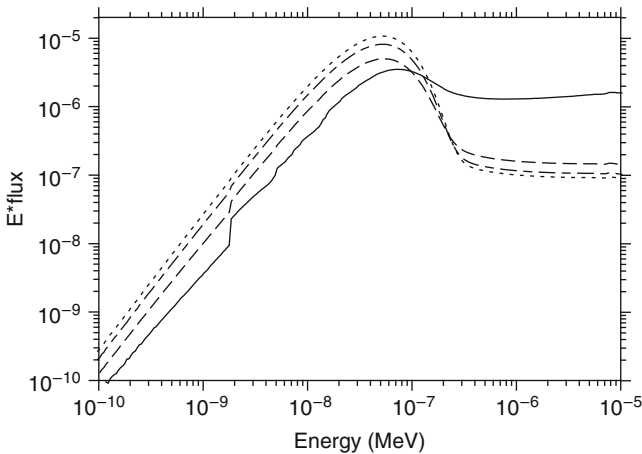
2.5 Size Effects in Thermalization

Full thermalization requires multiple collisions between the neutrons and the material to bring the neutrons into equilibrium at the temperature of the material. This implies that the system

■ **Table 7**

Mean free paths near 1 meV (10^{-3} eV) for several moderators

Moderator material	Mean free path near 1 meV
Water	0.045 cm
Heavy water	0.5 cm
Graphite	25 cm



■ **Figure 40**

Effect of size on thermalization in graphite. The flux in spheres with radii of 30, 90, 150, and 250 cm are shown (some curves were shifted vertically for clarity)

must be large with respect to the mean free path of the neutrons in the material. ➤ [Table 7](#) shows the mean free paths at energies around 1 meV (10^{-9} MeV) for three common moderators.

➤ [Figure 40](#) shows fluxes computed using MCNP for spheres of graphite of various sizes. At a radius of 250 cm, the flux is nearly thermalized, showing the typical Maxwellian shape. However, for a radius of 30 cm, the flux shows features coming from the cross-section shape. The Bragg edges previously seen in ➤ [Fig. 5](#) are evident.

It is apparent that systems with sizes of ten mean free paths or more will produce a Maxwellian flux shape independent of the details of the shape of the scattering cross section. This is a consequence of the detail balance as discussed in ➤ [Sect. 1.6](#). It is also the reasoning behind the statement at the end of ➤ [Sect. 1.15](#) claiming that the problem that theory has in matching the experimental cross section below 1 meV (see ➤ [Fig. 19](#)) is not too important in practice. The part of any capture or fission reaction rate that comes from the millivolt region will not depend on the detailed shape of the scattering cross section there.

In heavy water, the ENDF/B-VII evaluation shows a dip in the scattering cross section below about 3 meV coming from intermolecular coherence (see ➤ [Fig. 23](#)). This effect was not included in earlier ENDF/B versions. The original GA evaluators (Koppel and Houston 1978)


said, "... integral quantities like the thermal neutron spectra can actually be predicted quite accurately with an incoherent model." This is born out by MCNP calculations of the flux in spheres of heavy water, which show a Maxwellian shape at low energies even at relatively small sizes. The effect of the coherence dip is not visible.

3 Steady-State Slowing Down

3.1 Introduction



If a nuclear assembly is driven by a steady-state source, the neutrons will slow down and become thermalized. In this section, we will summarize the elastic and inelastic cross sections that are responsible for the slowing down, study the spectra of the downscattered neutrons, and discuss how resonance structure affects slowing down.

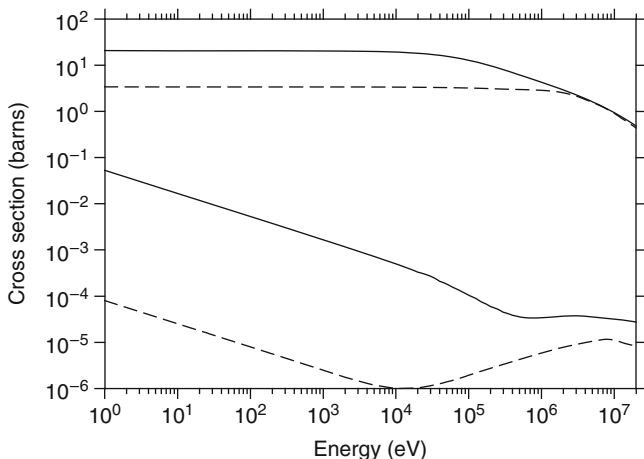
3.2 Slowing-Down Cross Sections

The important materials for neutron slowing down are the ones that occur in large concentrations in nuclear systems. We will concentrate on H-1, H-2, O-16, C-nat, and U-238 in this section. The simplest materials are H-1 and H-2. They only support elastic scattering and (n, γ) capture.  [Figure 41](#) shows those cross sections as obtained from the tabulated data in the ENDF/B-VII evaluations for the two isotopes. The elastic cross sections for both materials are basically constant over much of their energy range, and the capture cross sections are small with a $1/v$ energy dependence (mostly). This makes materials containing H-1 or H-2 very useful as neutron moderators. The angular distributions in the center-of-mass (CM) system are nearly isotropic for the lower energies, gradually becoming somewhat backwardly peaked at the higher energies. In the ENDF/B-VII file for H-1, the angular distribution in the CM is represented using an expansion in Legendre polynomials

$$f(E, \omega) = \sum_{\ell} \frac{2\ell + 1}{2} a_{\ell}(E) P_{\ell}(\omega), \quad (95)$$

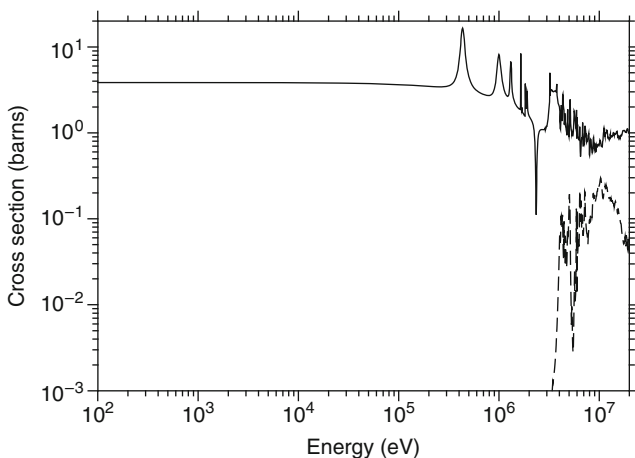
where ω is the scattering cosine in the CM system and ℓ is the Legendre order varying from zero to some stated maximum. The angular distribution for H-2 is given as a set of tabulations of $f(E, \omega)$ vs. ω . The center-of-mass motion causes the angular distributions in the laboratory system to be forward-peaked. At the lower energies, the average cosine for elastic scattering goes like $2/3A$, where A is the ratio of the scatterer mass to the neutron mass. Thus, the nominal $\bar{\mu}$ is 0.667 for H-1 and 0.334 for H-2. Here, we use the symbol μ for the scattering cosine in the laboratory system.

For O-16, the elastic cross section has the additional complication of resonant behavior at the higher energies, as shown in  [Fig. 42](#). The (n, γ) capture cross section for O-16 is extremely small, and it is not plotted in the figure. However, at higher energies, an (n, α) channel opens, and this absorption cross section, although small, does have some effect on criticality in water systems. O-16 also has the additional complication of inelastic scattering, as shown in  [Fig. 43](#). Only the first four inelastic levels are shown. The deep dip in the elastic scattering is a cross-section "window." This kind of feature can lead to additional leakage because the mean free path



■ Figure 41

Elastic and capture cross sections for H-1 (solid) and H-2 (dashed) from ENDF/B-VII

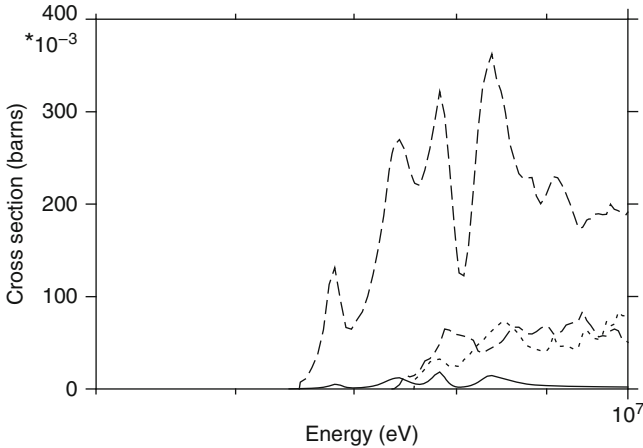


■ Figure 42

Elastic (solid) and (n, α) (dashed) cross sections for O-16 from ENDF/B-VII

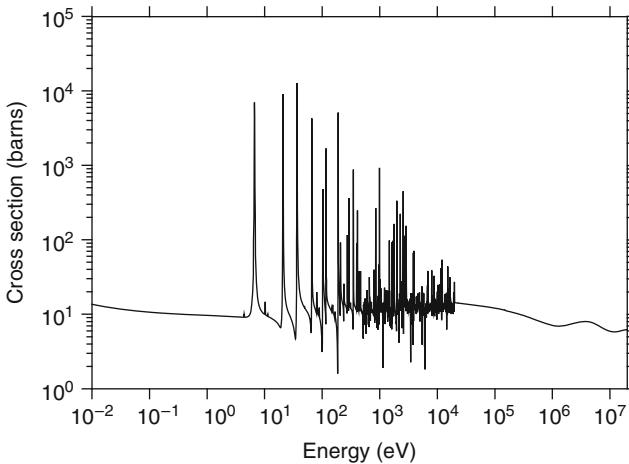
is very large in the window. The CM angular distribution for elastic scattering is fairly isotropic up to the 10 keV region. Because of the higher atomic mass, the laboratory scattering angular distribution is fairly isotropic with a $\bar{\mu}$ of 0.042.

The total cross section for U-238 is shown in [Fig. 44](#). For heavy materials like this, the resonance behavior becomes pronounced. The range from 10^{-5} eV to 20 keV is the “resolved resonance region” (RRR), the range from 20 to 149 keV is the “unresolved resonance region” (URR), and the range above 149 keV is the “fast region.”



■ Figure 43

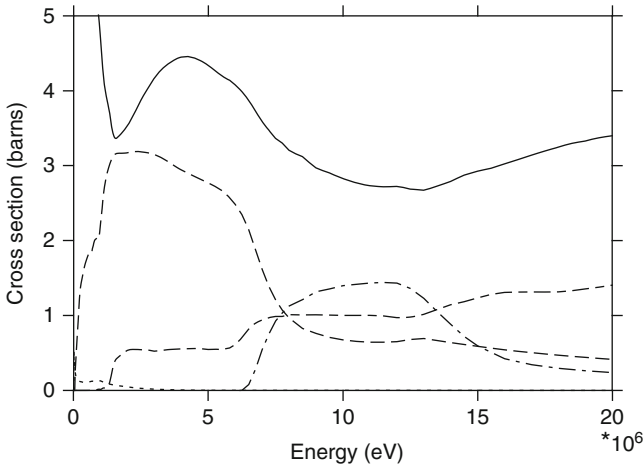
The first four levels of inelastic scattering for O-16 from ENDF/B-VII (in increasing order of excitation energy, solid, dash, chain-dash, dotted)



■ Figure 44

The total cross section of U-238 at room temperature

➤ Figure 45 shows the cross sections for U-238 in the fast range. (The $(n, 3n)$ reaction, which is open above 11.33 MeV, was omitted.) The inelastic reaction includes 40 discrete inelastic channels and a continuum inelastic channel. Note that U-238 is a threshold fissioner – there is only a small amount of subthreshold fission below the effective threshold near 800 keV. Also note that the (n, γ) capture cross section is very small in this range. The angular distributions for elastic scattering are given using the Legendre representation, and they show significant



■ Figure 45

The fast region for U-238 showing elastic (solid), inelastic (dashed), fission (chain-dash), $(n, 2n)$ (chain-dot), and (n, γ) capture (dotted)

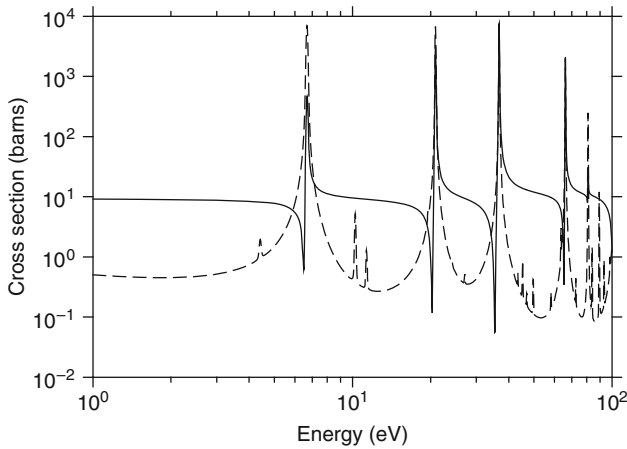
structure. This structure has proved to be important for getting the proper leakage out of uranium bodies in critical assembly benchmarks. The angular distributions for the discrete inelastic levels are also given using the Legendre representation and show significant structure. The continuum inelastic and $(n, 2n)$ reactions are represented as coupled energy-angle distributions. An angular distribution specification is given for each $E \rightarrow E'$ scattering. At lower energies, these distributions are fairly isotropic. The excited compound system resulting from the initial collision has had time to come to equilibrium; thus, the emitted neutron has “forgotten” the direction of the incident neutron. At higher energies, we begin to see preequilibrium emissions, and the angular distributions become more and more forward peaked.

In the unresolved resonance region, a tabulated cross section is given to represent the average behavior. However, there are resonance effects there that lead to self-shielding of the cross sections. This will be discussed in more detail below. The resonance effects are described by giving average parameters and distribution rules for the unresolved resonances. The average parameters include spacing and resonance widths. These data can be used to produce self-shielded cross sections for multigroup methods or probability tables for Monte Carlo methods.

The resolved resonance region can be extremely complex. 🔍 Figure 46 shows the elastic and capture cross sections between 1 and 100 eV. The 6.7 eV capture resonance is very important for thermal reactors. We have already seen its effect in 🔍 Fig. 34.

3.3 Spectra for Elastic Downscatter

Because the neutron wavelength is very small at the higher energies, neutron elastic scattering can be treated by classical “billiard ball” kinematics. If ω is the cosine of the scattering angle in



■ Figure 46

The elastic (solid) and capture (dashed) cross sections of U-238 for room temperature at the lower end of the resolved resonance range

the CM system, E is the incident energy, and A is the ratio of the target mass to the neutron mass, the secondary energy E' and laboratory scattering cosine μ are given by

$$E' = \frac{E}{(A+1)^2} (A^2 + 1 + 2A\omega), \quad (96)$$

and

$$\mu = \frac{1 + A\omega}{\sqrt{A^2 + 1 + 2A\omega}}. \quad (97)$$

Clearly, the maximum fractional energy change in elastic scattering (commonly called α) occurs when $\omega = -1$ and is given by

$$\alpha = \left[\frac{A-1}{A+1} \right]^2. \quad (98)$$

For H-1 with $A = 0.9991673$, α is almost zero, and a neutron can lose almost all of its energy in an elastic scattering event. If the CM scattering distribution is isotropic, the energy distribution for elastically scattered neutrons is given by

$$f(E, E') = \frac{1}{(1-\alpha)E}, \quad (99)$$

for E' between αE and E , and zero otherwise. We can simulate the behavior of elastic downscatter by running MCNP on a “broomstick.” We take a very long, very thin cylinder of a material, start neutrons into one end, and look at the spectrum of neutrons escaping from the surface integrated over all angles. Because the cylinder is very thin, these neutrons will have undergone only one scattering event, and the distribution we see will be just $\sigma(E \rightarrow E') = \sigma(E)f(E, E')$.

► Figure 47 shows an example of elastic downscatter spectra for D_2O . At the lowest energy, we see the rectangular shapes predicted by (99) with the effects of both H-2 and O-16 visible. The rectangle for O-16 is narrower than that for H-2 because of its larger mass (larger A). For the higher incident energies, the effects of anisotropy in the scattering cross section show up.

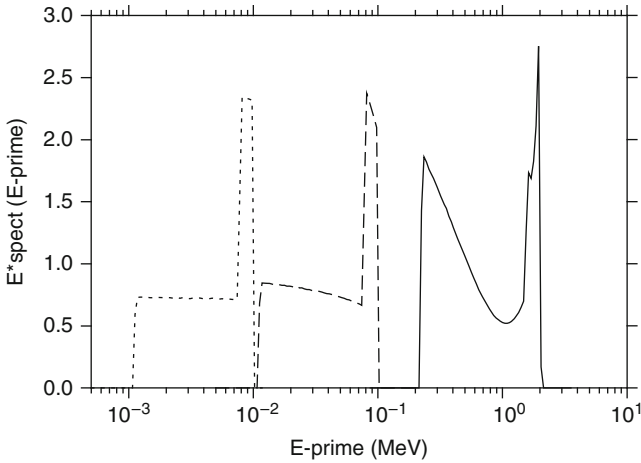


Figure 47
Elastic slowing-down spectra for D_2O at 0.01, 0.10, and 2 MeV

3.4 Spectra for Inelastic Downscatter

At high incident energies, inelastic neutron scattering becomes possible. For the lighter isotopes, the first inelastic threshold is in the million electron volts range, but for heavy isotopes, it can come down to tens of kiloelectron volts or lower. We can extend the kinematics formulas to include inelastic scattering (and even charged-particle emission) as follows:

$$E' = \frac{A'E}{(A+1)^2} (\beta^2 + 1 + 2\beta\omega), \quad (100)$$

and

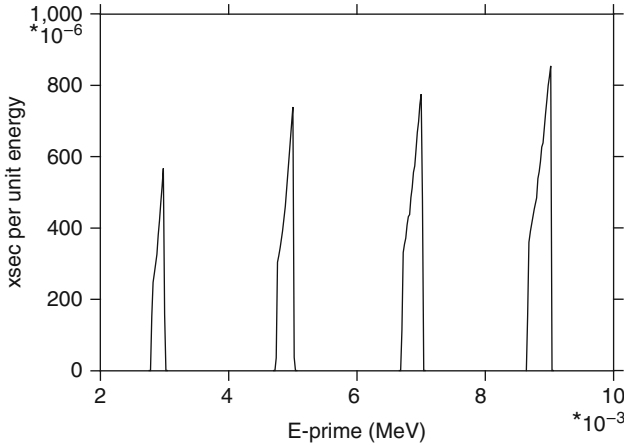
$$\mu = \frac{1 + \beta\omega}{\sqrt{\beta^2 + 1 + 2\beta\omega}}, \quad (101)$$

where

$$\beta = \left(\frac{A(A+1-A')}{A'} \left[1 + \frac{A+1}{A} \frac{Q}{E} \right] \right)^{1/2}. \quad (102)$$

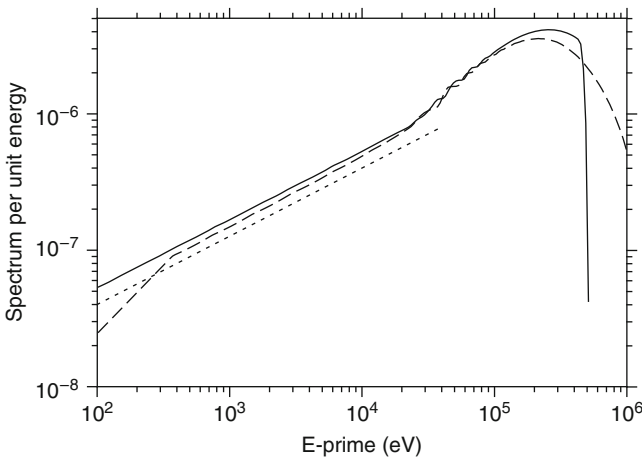
The quantity A' is the ratio of mass of the emitted particle to the mass of the incident particle; thus it is equal to one for neutron inelastic scattering. The quantity $(A+1)(-Q)/A$ is the threshold energy for the inelastic level with excitation energy Q . The quantity β acts sort of like an effective mass ratio. When E is close to the inelastic threshold, β is small, and a scattered neutron can lose a large part of its energy, just as elastic scattering from a light target can cause the neutron to lose a large part of its energy. ▶ [Figure 48](#) illustrates this for U-238 just above the threshold for the first inelastic level at 45.09 keV.

As the neutron energy increases in the inelastic region, the levels get closer and closer together. At some point, it becomes reasonable to treat them continuously. ◀ [Figure 49](#) shows the continuum inelastic spectra for incident energies near 1.25 and 3 MeV. The dotted line shows



■ Figure 48

Inelastic slowing-down spectra for the first inelastic level for U-238 at incident energies of 0.048, 0.050, 0.052 and 0.054 MeV. The threshold for this level is 0.04509 MeV



■ Figure 49

Inelastic slowing-down spectra for the continuum inelastic reaction for U-238 at incident energies of 1.25 and 3 MeV. The dotted line goes as \sqrt{E}

the expected shape for low energies, namely \sqrt{E} . From theory, we expect that the low-energy shape for the CM distribution will go as $\sqrt{E_{CM}}$. The Jacobian for transforming from the CM to the laboratory frame is $\sqrt{E_{lab}/E_{CM}}$, so both the CM and the lab distributions must take on the \sqrt{E} shape.

Actual ENDF/B evaluations often use fairly coarse histogram representations for curves like this (they come from nuclear model calculations). We have smoothed the low-energy \sqrt{E} shape of these curves for this plot.

3.5 Resonance Cross Sections

In the ENDF format (Herman 2005), resolved resonance range cross sections are represented using resonance parameters based on four different methodologies: Single-Level Breit–Wigner (SLBW), Multi-Level Breit–Wigner (MLBW), Reich–Moore (RM), and Reich–Moore Limited (RML). Additional representations were used in the past, but they are no longer represented in the ENDF/B-VII library (Tuli et al. 2006).

3.5.1 Single-Level Breit–Wigner Representation

The SLBW resonance shapes are given by

$$\sigma_n = \sigma_p + \sum_{\ell} \sum_r \sigma_{mr} \left\{ \left[\cos 2\phi_{\ell} - \left(1 - \frac{\Gamma_{nr}}{\Gamma_r} \right) \right] \psi(\theta, x) + \sin 2\phi_{\ell} \chi(\theta, x) \right\}, \quad (103)$$

$$\sigma_f = \sum_{\ell} \sum_r \sigma_{mr} \frac{\Gamma_{fr}}{\Gamma_r} \psi(\theta, x), \quad (104)$$

$$\sigma_{\gamma} = \sum_{\ell} \sum_r \sigma_{mr} \frac{\Gamma_{\gamma r}}{\Gamma_r} \psi(\theta, x), \quad (105)$$

and

$$\sigma_p = \sum_{\ell} \frac{4\pi}{k^2} (2\ell + 1) \sin^2 \theta_{\ell}, \quad (106)$$

where σ_n , σ_f , σ_{γ} , and σ_p are the neutron (elastic), fission, radiative capture, and potential scattering components of the cross section arising from the given resonances. There can be “background” cross sections given that must be added to these values to account for competitive reactions such as inelastic scattering or to correct for the inadequacies of the single-level representation with regard to multilevel effects or missed resonances. The sums extend over all the ℓ values and all the resolved resonances r with a particular value of ℓ . Each resonance is characterized by its total, neutron, fission, and capture widths (Γ , Γ_n , Γ_f , Γ_{γ}), by its J value (AJ in the file), and by its maximum value σ_{mr}/Γ_r

$$\sigma_{mr} = \frac{4\pi}{k^2} g_J \frac{\Gamma_{nr}}{\Gamma_r}, \quad (107)$$

where g_J is the spin statistical factor

$$g_J = \frac{2J + 1}{4I + 2}, \quad (108)$$

and I is the target spin, and k is the neutron wave number, which depends on incident energy E and the atomic weight ratio to the neutron for the isotope A as follows:

$$k = (2.196771 \times 10^{-3}) \frac{A}{A + 1} \sqrt{E}. \quad (109)$$

There are two different characteristic lengths that appear in the ENDF resonance formulas: first, there is the “scattering radius” \hat{a} , and second, there is the “channel radius” a , which is given by

$$a = 0.123 A^{1/3} + 0.08. \quad (110)$$

In some cases, a is set equal to \hat{a} in calculating penetrabilities and shift factors (see below). The neutron width in the equations for the SLBW cross sections is energy-dependent due to the penetration factors P_ℓ ; that is,

$$\Gamma_{nr}(E) = \frac{P_\ell(E) \Gamma_{nr}}{P_\ell(|E_r|)}, \quad (111)$$

where

$$P_0 = \rho, \quad (112)$$

$$P_1 = \frac{\rho^3}{1 + \rho^2}, \quad (113)$$

$$P_2 = \frac{\rho^5}{9 + 3\rho^2 + \rho^4}, \quad (114)$$

$$P_3 = \frac{\rho^7}{225 + 45\rho^2 + 6\rho^4 + \rho^6}, \quad (115)$$

and

$$P_4 = \frac{\rho^9}{11025 + 1575\rho^2 + 135\rho^4 + 10\rho^6 + \rho^8}, \quad (116)$$

where E_r is the resonance energy and $\rho = ka$ depends on the channel radius or the scattering radius. The phase shifts are given by

$$\phi_0 = \hat{\rho}, \quad (117)$$

$$\phi_1 = \hat{\rho} - \tan^{-1} \hat{\rho}, \quad (118)$$

$$\phi_2 = \hat{\rho} - \tan^{-1} \frac{3\hat{\rho}}{3 - \hat{\rho}^2}, \quad (119)$$

$$\phi_3 = \hat{\rho} - \tan^{-1} \frac{15\hat{\rho} - \hat{\rho}^2}{15 - 6\hat{\rho}^2}, \quad (120)$$

and

$$\phi_4 = \hat{\rho} - \tan^{-1} \frac{105\hat{\rho} - 10\hat{\rho}^3}{105 - 45\hat{\rho}^2 + \hat{\rho}^4}, \quad (121)$$

where $\hat{\rho} = k\hat{a}$ depends on the scattering radius. The final components of the cross section are the actual line shape functions ψ and χ . At zero temperature,

$$\psi = \frac{1}{1 + x^2}, \quad (122)$$

$$\chi = \frac{x}{1 + x^2}, \quad (123)$$

$$x = \frac{2(E - E'_r)}{\Gamma_r}, \quad (124)$$

and

$$E'_r = E_r + \frac{S_\ell(|E_r|) - S_\ell(E)}{2(P_\ell(|E_r|))} \Gamma_{nr}(|E_r|), \quad (125)$$

in terms of the shift factors

$$S_0 = 0, \quad (126)$$

$$S_1 = -\frac{1}{1 + \rho^2}, \quad (127)$$

$$S_2 = -\frac{18 + 3\rho^2}{9 + 3\rho^2 + \rho^4}, \quad (128)$$

$$S_3 = -\frac{675 + 90\rho^2 + 6\rho^4}{225 + 45\rho^2 + 6\rho^4 + \rho^6}, \quad (129)$$

and

$$S_4 = -\frac{44100 + 4725\rho^2 + 270\rho^4 + 10\rho^6}{11025 + 1575\rho^2 + 135\rho^4 + 10\rho^6 + \rho^8}. \quad (130)$$

To go to higher temperatures, define

$$\theta = \frac{\Gamma_r}{\sqrt{\frac{4kTE}{A}}}, \quad (131)$$

where k is the Boltzmann constant and T is the absolute temperature. The line shapes ψ and χ are now given by

$$\psi = \frac{\sqrt{\pi}}{2} \theta \operatorname{Re} W\left(\frac{\theta x}{2}, \frac{\theta}{2}\right), \quad (132)$$

and

$$\chi = \frac{\sqrt{\pi}}{2} \theta \operatorname{Im} W\left(\frac{\theta x}{2}, \frac{\theta}{2}\right), \quad (133)$$

in terms of the complex probability function.

$$W(x, y) = e^{-z^2} \operatorname{erfc}(-iz) = \frac{i}{\pi} \int_{-\infty}^{\infty} \frac{e^{-t^2}}{z - t} dt, \quad (134)$$

where $z = x + iy$. The $\psi\chi$ method is not as accurate as kernel broadening (see below) because the backgrounds (which are sometimes quite complex) are not broadened, and terms important for energies less than about $16kT/A$ are neglected; however, the $\psi\chi$ method is less expensive than kernel broadening.

The SLBW formalism is deprecated for new evaluations, and there are only a few holdovers remaining in ENDF/B-VII. It has the problem of sometimes producing negative cross sections from the χ interference term. However, it is the basis for the unresolved range methodology, and it is still important to understand it.

3.5.2 Multi-Level Breit-Wigner Representation

The MLBW representation is formulated as follows:

$$\sigma_n(E) = \frac{\pi}{k^2} \sum_{\ell} \sum_{s=|I-\frac{1}{2}|}^{I+\frac{1}{2}} \sum_{J=|I-s|}^{I+s} g_J \left| 1 - U_{nn}^{\ell s J}(E) \right|^2, \quad (135)$$

with

$$U_{nn}^{\ell J}(E) = e^{2i\phi_\ell} - \sum_r \frac{i\Gamma_{nr}}{E_r' - E - i\Gamma_r/2}, \quad (136)$$

where the other symbols are the same as those used above. Expanding the complex operations gives

$$\begin{aligned} \sigma_n(E) = \frac{\pi}{k^2} \sum_\ell \sum_{s=|I-\frac{1}{2}|}^{I+\frac{1}{2}} \sum_{J=|I-s|}^{I+s} g_J \left\{ \left(1 - \cos 2\phi_\ell - \sum_r \frac{\Gamma_{nr}}{\Gamma_r} \frac{2}{1+x_r^2} \right)^2 \right. \\ \left. + \left(\sin 2\phi_\ell + \sum_r \frac{\Gamma_{nr}}{\Gamma_r} \frac{2x_r}{1+x_r^2} \right)^2 \right\}, \end{aligned} \quad (137)$$

where the sums over r are limited to resonances in spin sequence ℓ that have the specified value of s and J . Unfortunately, the s dependence of Γ is not known. The file contains only $\Gamma_J = \Gamma_{s_1 J} + \Gamma_{s_2 J}$. It is assumed that the Γ_J can be used for one of the two values of s , and zero is used for the other. Of course, it is important to include both channel-spin terms in the potential scattering. Therefore, the equation is written in the following form:

$$\begin{aligned} \sigma_n(E) = \frac{\pi}{k^2} \sum_\ell \left[\sum_J g_J \left\{ \left(1 - \cos 2\phi_\ell - \sum_r \frac{\Gamma_{nr}}{\Gamma_r} \frac{2}{1+x_r^2} \right)^2 \right. \right. \\ \left. \left. + \left(\sin 2\phi_\ell + \sum_r \frac{\Gamma_{nr}}{\Gamma_r} \frac{2x_r}{1+x_r^2} \right)^2 \right\} + 2D_\ell(1 - \cos 2\phi_\ell) \right], \end{aligned} \quad (138)$$

where the summation over J now runs from

$$\left| |I - \ell| - \frac{1}{2} \right| \rightarrow I + \ell + \frac{1}{2}, \quad (139)$$

and D_ℓ gives the additional contribution to the statistical weight resulting from duplicate J values not included in the new J sum; namely,

$$D_\ell = \sum_{s=|I-\frac{1}{2}|}^{I+\frac{1}{2}} \sum_{J=|I-s|}^{I+s} g_J - \sum_{J=||I-\ell|-\frac{1}{2}|}^{I+\ell+\frac{1}{2}} g_J \quad (140)$$

$$= (2\ell + 1) - \sum_{J=||I-\ell|-\frac{1}{2}|}^{I+\ell+\frac{1}{2}} g_J. \quad (141)$$

A case where this correction would appear is the $\ell = 1$ term for a spin-1 nuclide. There will be $5J$ values: $1/2$, $3/2$, and $5/2$ for channel spin $3/2$; and $1/2$ and $3/2$ for channel spin $1/2$. All five contribute to the potential scattering, but the file will only include resonances for the first three.

The fission and capture cross sections are the same as for the single-level option.

The $\psi\chi$ Doppler-broadening cannot be used with this formulation of the MLBW representation.

However, there is an alternate formulation that can be used with $\psi\chi$ broadening:

$$\begin{aligned} \sigma_n = \sigma_p + \sum_{\ell} \sum_r \sigma_{mr} \left\{ \left[\cos 2\phi_{\ell} - \left(1 - \frac{\Gamma_{nr}}{\Gamma_r} \right) + \frac{G_{r\ell}}{\Gamma_{nr}} \right] \psi(\theta, x) \right. \\ \left. + \left(\sin 2\phi_{\ell} + \frac{H_{r\ell}}{\Gamma_{nr}} \right) \chi(\theta, x) \right\}, \end{aligned} \quad (142)$$

where

$$G_{r\ell} = \frac{1}{2} \sum_{\substack{r' \neq r \\ J_{r'} \neq J_r}} \Gamma_{nr} \Gamma_{nr'} \frac{\Gamma_r + \Gamma_{r'}}{(E_r - E_{r'})^2 + (\Gamma_r + \Gamma_{r'})^2/4}, \quad (143)$$

and

$$H_{r\ell} = \sum_{\substack{r' \neq r \\ J_{r'} \neq J_r}} \Gamma_{nr} \Gamma_{nr'} \frac{E_r - E_{r'}}{(E_r - E_{r'})^2 + (\Gamma_r + \Gamma_{r'})^2/4}. \quad (144)$$

Nominally, this method is slower than the previous one because it contains a double sum over resonances at each energy. However, it turns out that G and H are slowly varying functions of energy, and the calculation can be accelerated by computing them at just a subset of the energies and getting intermediate values by interpolation. It is important to use a large number of r' values on each side of r .

The GH method works well at higher energies when compared to the more accurate kernel broadening method (more on this below). However, in the electron volts range and below, it compares more poorly with kernel broadening. Since the accelerated GH method is only marginally faster than kernel broadening, it probably should not be used at the lower energies for cases where the details of elastic scattering are important. This still leaves it useful for materials like fission products where absorption is the most important factor.

The MLBW representation does not produce the negative cross sections that plague the SLBW method. However, it is more expensive to use. It is used extensively for mid-mass isotopes (such as fission products) in the ENDF/B-VII library.

3.5.3 Reich–Moore Representation

The RM representation is a multilevel formulation with two fission channels; hence, it is useful for both structural and fissionable materials. (The name “Reich” is pronounced like “rich” by the co-originator of this method.) The cross sections are given by

$$\sigma_t = \frac{2\pi}{k^2} \sum_{\ell} \sum_J g_J \left\{ (1 - \text{Re } U_{nm}^{\ell J}) + 2d_{\ell J} [1 - \cos(2\phi_{\ell})] \right\}, \quad (145)$$

$$\sigma_n = \frac{\pi}{k^2} \sum_{\ell} \sum_J g_J \left\{ |1 - U_{nn}^{\ell J}|^2 + 2d_{\ell J} [1 - \cos(2\phi_{\ell})] \right\}, \quad (146)$$

$$\sigma_f = \frac{4\pi}{k^2} \sum_{\ell} \sum_J g_J \sum_c |\mathcal{I}_{nc}^{\ell J}|^2, \quad (147)$$

and

$$\sigma_y = \sigma_t - \sigma_n - \sigma_f, \quad (148)$$

where \mathcal{I}_{nc} is an element of the inverse of the complex R-matrix and

$$U_{nn}^{\ell J} = e^{2i\phi_\ell} [2\mathcal{I}_{nn} - 1]. \quad (149)$$

The elements of the R-matrix are given by

$$R_{nc}^{\ell J} = \delta_{nc} - \frac{i}{2} \sum_r \frac{\Gamma_{nr}^{1/2} \Gamma_{cr}^{1/2}}{E_r - E - \frac{i}{2} \Gamma_{\gamma r}}. \quad (150)$$

In these equations, “c” stands for the fission channel, “r” indexes the resonances belonging to spin sequence (ℓ, J) , and the other symbols have the same meanings as for SLBW or MLBW. Of course, when fission is not present, σ_f can be ignored. The R-matrix reduces to an R-function, and the matrix inversion normally required to get \mathcal{I}_{nn} reduces to a simple inversion of a complex number.

As in the MLBW case, the summation over J runs from

$$\left| |I - \ell| - \frac{1}{2} \right| \rightarrow I + \ell + \frac{1}{2}. \quad (151)$$

The term $d_{\ell J}$ in the expressions for the total and elastic cross sections is used to account for the possibility of an additional contribution to the potential scattering cross section from the second channel spin. There is unity if there is a second J value equal to J , and zero otherwise. This is just a slightly different approach for making the correction discussed in connection with (141). Returning to the $I = 1, \ell = 1$ example given above, d will be one for $J = 1/2$ and $J = 3/2$, and it will be zero for $J = 5/2$.

The RM representation is used for many of the most important isotopes in ENDF/B-VII, because it is very true to the underlying physics, resulting in good fits to experimental data. For fissile materials, its ability to handle two fission channels provides a better representation of the effects of the double-humped fission barriers seen for isotopes like U-235.

3.5.4 Reich–Moore-Limited Representation

The new RML representation is a more general multilevel and multichannel formulation. In addition to the normal elastic, fission, and capture reactions, it allows for inelastic scattering and Coulomb reactions. Furthermore, it allows resonance angular distributions to be calculated. The RML processing in NJOY is based on the SAMMY code (Larson 2008).

The quantities that are conserved during neutron scattering and reactions are the total angular momentum J and its associated parity π , and the RML format lumps all the channels with a given $J\pi$ into a “spin group.” In each spin group, the reaction channels are defined by $c = (\alpha, \ell, s, J)$, where α stands for the particle pair (masses, charges, spins, parities, and Q-value), ℓ is the orbital angular momentum with associated parity $(-1)^\ell$, and s is the channel spin (the vector sum of the spins of the two particles of the pair). The ℓ and s values must vector sum to $J\pi$ for the spin group. The channels are divided into incident channels and exit channels. Here, the important input channel is defined by the particle pair neutron + target. There can be several such incident channels in a given spin group. The exit channel particle pair defines

the reaction taking place. If the exit channel is the same as the incident channel, the reaction is elastic scattering. There can be several exit channels that contribute to a given reaction.

The R-matrix in the RM “eliminated width” approximation for a given spin group is given by

$$R_{cc'} = \sum_{\lambda} \frac{\gamma_{\lambda c} \gamma_{\lambda c'}}{E_{\lambda} - E - i\Gamma_{\lambda\gamma}/2} + R_c^b \delta_{cc'}, \quad (152)$$

where c and c' are incident and exit channel indexes, λ is the resonance index for resonances in this spin group, E_{λ} is a resonance energy, $\gamma_{\lambda c}$ is a resonance amplitude, and $\Gamma_{\lambda\gamma}$ is the “eliminated width,” which normally includes all of the radiation width (capture). The channel indexes run over the “particle channels” only, which does not include capture. The quantity R_c^b is the “background R-matrix.”

In order to calculate the contribution of this spin group to the cross sections, we first compute the following quantity:

$$X_{cc'} = P_c^{1/2} L_c^{-1} \sum_{c''} Y_{cc''}^{-1} R_{c''c'} P_{c'}^{1/2}, \quad (153)$$

where

$$Y_{cc''} = L_c^{-1} \delta_{cc''} - R_{cc''}, \quad (154)$$

and

$$L_c = S_c - B_c + iP_c. \quad (155)$$

Here, the P_c and S_c are penetrability and shift factors, and the B_c are boundary constants. The cross sections can now be written down in terms of the $X_{cc'}$. For elastic scattering

$$\sigma_{\text{elastic}} = \frac{4\pi}{k_{\alpha}^2} \sum_{J\pi} \left[\sin^2 \phi_c (1 - 2X_{cc}^i) - X_{cc}^r \sin(2\phi_c) + \sum_{c'} |X_{cc'}|^2 \right], \quad (156)$$

where $X_{cc'}^r$ is the real part of $X_{cc'}$, $X_{cc'}^i$ is the imaginary part, ϕ_c is the phase shift, the sum over $J\pi$ is a sum over spin groups, the sum over c is limited to incident channels in the spin group with particle pair α equal to neutron + target, and the sum over c' is limited to exit channels in the spin group with particle pair α . Similarly, the capture cross section becomes

$$\sigma_{\text{capture}} = \frac{4\pi}{k_{\alpha}^2} \sum_{J\pi} \sum_c g_{J\alpha} \sum_{c'} \left[X_{cc}^i - \sum_{c'} |X_{cc'}|^2 \right], \quad (157)$$

where the sum over $J\pi$ is a sum over spin groups, the sum over c is a sum over incident channels in the spin group with particle pair α equal to neutron + target, and the sum over c' includes all channels in the spin group. The cross sections for other reactions (if present) are given by

$$\sigma_{\text{reaction}} = \frac{4\pi}{k_{\alpha}^2} \sum_{J\pi} g_{J\alpha} \sum_c \left[X_{cc}^i - \sum_{c'} |X_{cc'}|^2 \right], \quad (158)$$

where the sum over c is limited to channels in the spin group $J\pi$ with particle pair α equal to neutron + target, and the sum over c' is limited to channels in the spin group with particle pair α' . The reaction is defined by $\alpha \rightarrow \alpha'$. This is one of the strengths of the RML representation. The reaction cross sections can include multiple inelastic levels with full resonance behavior. They

can also include cross sections for outgoing charged particles, such as (n, α) cross sections, with full resonance behavior. The total cross section can be computed by summing up its parts.


For non-Coulomb channels, the penetrabilities P , shift factors S , and phase shift ϕ are the same as those given for the SLBW representation. They are a little more complicated for Coulomb channels. See the SAMMY reference for more details.

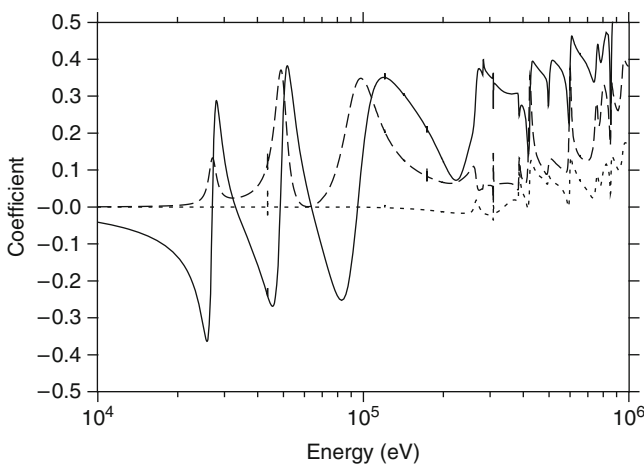
The RML representation is new to the ENDF format and is not represented by any cases in ENDF/B-VII. There are experimental evaluations for F-19 and Cl-37 available. However, the RML approach provides a very faithful representation of resonance physics, and it should see increasing use in the future. NJOY is currently able to process RML evaluations using coding adapted from SAMMY.


3.5.5 Angular Distributions

One of the physics advances available when using the RML format is the calculation of angular distributions from the resonance parameters. A Legendre representation is used:

$$\frac{d\sigma_{\alpha\alpha'}}{d\Omega_{\text{CM}}} = \sum_L B_{L\alpha\alpha'}(E) P_L(\cos \beta), \quad (159)$$


where the subscript $\alpha\alpha'$ indicates the cross section as defined by the particle pairs, P_L is the Legendre polynomial of order L , and β is the angle of the outgoing particle with respect to the incoming neutron in the CM system. The coefficients $B_{L\alpha\alpha'}(E)$ are given by a complicated six-level summation that we will omit from this text.  [Figure 50](#) shows the first few Legendre coefficients for the elastic scattering cross sections as computed by NJOY from the experimental evaluation for F-19.




 **Figure 50**

Legendre coefficients of the angular distribution for elastic scattering in F-19 using the RML resonance representation (P_1 solid, P_2 dashed, P_3 dotted)


3.5.6 Resonance Reconstruction and Doppler Broadening

In practice, the formulas presented in the preceding paragraphs must be used to generate cross section vs. energy tables – this is called “resonance reconstruction.” There are a number of computer codes available that carry out this reconstruction. The examples in this chapter were generated using the RECONR module of NJOY (MacFarlane and Muir 1994). Another system that provides resonance reconstruction and Doppler broadening is PREPRO (Cullen 2007). Most commonly, the resonances are reconstructed at 0 K, and they are Doppler broadened to the required temperatures. For this chapter, we used the BROADR module of NJOY. The methods for resonance reconstruction and Doppler broadening are described in detail in Volume I,  Chap. 4.

3.5.7 Thermal Constants

In thermal-reactor work, people make very effective use of a few standard thermal constants to characterize nuclear cross sections. These parameters include the cross sections at the standard thermal value of 0.0253 eV (2,200 m/s), the integrals of the cross sections against a Maxwellian distribution for 0.0253 eV, the g-factors (which express the deviation of the cross section from $1/v$; namely, $2/\sqrt{\pi}$ times the ratio of the Maxwellian integral to the corresponding thermal cross section), η , α , and $K1$. Here, η is the Maxwellian-weighted average of $(\bar{v}\sigma_f)/(\sigma_f + \sigma_c)$, α is the average of σ_c/σ_f , and $K1$ is the average of $(\bar{v} - 1)\sigma_f - \sigma_c$. These quantities are routinely calculated by NJOY when it does Doppler broadening to the temperature corresponding to 0.0253 eV (293.6 K).  [Table 8](#) shows values for three important nuclides from ENDF/B-VII.

3.6 Resonance Slowing Down

Continuous-energy Monte Carlo codes like MCNP (2003) simulate the physics of the slowing-down process. The cross-section tables are used to randomly select the reaction channel following a collision. If elastic scattering is selected, the angular distribution is used to randomly select an emission cosine to get a new particle direction, and this cosine is used to compute the energy of the scattered neutron. This process is very faithful to the physics for some materials and energy ranges, but in practice there are two problems. First, at low energies the motion of the target nuclei corresponding to the temperature of the material becomes important. The Doppler broadening method described in Volume I,  Chap. 4 preserves the total reaction rate for the neutron at energy E averaged over all angles, but it does not produce a correct shape for the energy spectrum of the scattered neutrons. Current codes use the Doppler-broadened cross section with the target-at-rest downscatter spectrum given by (99). Second, the detailed variation of the angular distribution as the energy through a resonance is often not available in current data libraries. Average angular distributions over a range of resonances are more commonly provided.

Multigroup methods for calculating neutron slowing down require average cross sections like those defined in (74) and (75). The problem is coming up with good estimates for the neutron flux shape inside the group $W(E)$. One approach to this is based on B_0 theory. Using

■ Table 8

Thermal constants for three important resonance nuclides from ENDF/B-VII

Thermal constant	U-238	U-235	Pu-239
Thermal fission xsec	1.6808E-5	5.8490E+2	7.4769E+2
Thermal fission nubar	2.4921E+0	2.4367E+0	2.8789E+0
Thermal capture xsec	2.6848E+0	9.8665E+1	2.7066E+2
Thermal capture integral	2.3852E+0	8.6639E+1	2.7461E+2
Thermal capture g-factor	1.0025E+0	9.9098E-1	1.1448E+0
Capture resonance integral	2.7559E+2	1.4043E+2	1.8144E+2
Thermal fission integral	1.4921E-5	5.0605E+2	6.9863E+2
Thermal fission g-factor	1.0017E+0	9.7628E-1	1.0544E+0
Thermal alpha integral	1.5998E+5	1.6828E-1	4.0784E-1
Thermal eta integral	1.5578E-5	2.0859E+0	2.0474E+0
Thermal K1 integral	-2.3852E+0	6.4040E+2	1.0370E+3
Equivalent K1	-2.6916E+0	7.2262E+2	1.1701E+3
Fission resonance integral	2.6916E+0	2.7596E+2	3.0260E+2

one-dimensional slab geometry for simplicity, the Boltzmann transport equation can be written in the form

$$\mu \frac{\partial}{\partial x} \phi(E, \mu, x) + \Sigma(E, x) \phi(E, \mu, x) = \int_E^\infty \Sigma_s(E' \rightarrow E, \mu' \rightarrow \mu, x) \phi(E', \mu', x) + S(E, \mu, x), \quad (160)$$

where we are now using the symbol Σ for the macroscopic cross sections. Next, we assume that the flux and the source can be separated into spatial- and energy-angle parts

$$\phi(E, \mu, x) = \phi(E, \mu) e^{iBx}, \quad (161)$$

and

$$S(E, \mu, x) = S(E, \mu) e^{iBx}. \quad (162)$$

This assumption certainly is not valid over the entire energy range, but it may be reasonable for the energy range of one group. To get an idea of the physical meaning of this, consider a critical slab. The B parameter is positive, and the real part of the flux has a cosine shape across the slab with its zeros a bit outside of the slab. Here $1/B$ becomes a measure of the thickness of the system. For a slab with a source on one face, B is imaginary, and the flux decreases exponentially as you move through the slab.

After inserting the separated flux and source into the Boltzmann equation, expanding the flux using Legendre polynomials, and assuming that the scattering cross section is isotropic, we

get the B_0 equations:

$$\Sigma(E)\phi_\ell(E) = A_{0\ell} \int_E^\infty \Sigma_s(E' \rightarrow E)\phi_0(E') + S_0(E), \quad (163)$$

where the A coefficients that we need are given by

$$A_{00} = \frac{\tanh^{-1}y}{y}, \quad (164)$$

and

$$A_{01} = \frac{A_{00} - 1}{y}, \quad (165)$$

where

$$y = \frac{iB}{\Sigma(E)}. \quad (166)$$

Note that small y indicates that the system is large with respect to the mean free path of the neutrons. This leads us to our next approximation. If the system is very large, we can take the limit of small y , getting $A_{00} = 1$ and $A_{01} = y/3$. The P_0 and P_1 (current) components of the flux become

$$\phi_0(E) = \frac{1}{\Sigma(E)} \left[\int_E^\infty \Sigma_s(E' \rightarrow E)\phi(E') + S_0(E) \right], \quad (167)$$

and

$$\phi_1(E) = \frac{B}{3\Sigma(E)^2} \left[\int_E^\infty \Sigma_s(E' \rightarrow E)\phi(E') + S_0(E) \right]. \quad (168)$$

We can now make another important approximation, the “narrow resonance approximation” (NR). If the resonances near E are narrow with respect to the downscatter predicted by Σ_s , the contributions to the bracketed term in (167) and (168) will come from energies well above the resonances near E and will not contain any structure correlated with those resonances. Therefore, we can replace the bracketed term with a smooth function $C(E)$, such as $1/E$. Let us assume that the material consists of a resonance isotope mixed with a moderator material that has a constant cross section. Then the weighting function for the group cross sections becomes

$$W_\ell(E) = \frac{C(E)}{[\sigma_0 + \sigma_t(E)]^{\ell+1}}, \quad (169)$$

where σ_t is the microscopic total cross section for the absorber nuclide the “background cross section” σ_0 represents the effect of the other isotopes in the material. As an example, the multigroup total cross section for isotope i and group g becomes

$$\sigma_{tg}^i = \frac{\int_g \frac{\sigma_t^i(E)C(E)}{\sigma_{0g}^i + \sigma_t^i(E)} dE}{\int_g \frac{C(E)}{\sigma_{0g}^i + \sigma_t^i(E)} dE}. \quad (170)$$

Physically, the term $\sigma_t^i(E)$ in the denominators puts a dip in the weighting flux that corresponds to the resonance peak in the cross section in the numerator. The size of this dip is controlled by

σ_{0g}^i . When the background cross section is large with respect to the heights of the resonances, the dips are very small. This is called “infinite dilution,” because it corresponds to the case of a solution of the absorber and the moderator with very small amounts of the absorber. When the background cross section is smaller, there can be a significant dip in the weighting flux. This dip then cancels out a part of the effect of the resonance in the numerator – the resonance is “self-shielded.” This approach is often called the “Bondarenko Method” after the Russian scientist who originally put it into practice (Bondarenko 1964). For a mixture of materials, the background cross section for isotope i is given by

$$\sigma_{0g}^i = \frac{1}{\rho_i} \sum_{j \neq i} \rho_j \sigma_{tg}^j. \quad (171)$$

This formula makes sense for homogeneous systems, but when heterogeneity effects are important, the background cross-section method can be extended as follows. In an infinite system of two regions (fuel and moderator), the neutron balance equations are

$$V_f \sigma_f \phi_f = (1 - P_f) V_f S_f + P_m V_m S_m, \quad (172)$$

and

$$V_m \sigma_m \phi_m = P_f V_f S_f + (1 - P_m) V_m S_m, \quad (173)$$

where V_f and V_m are the region volumes, σ_f and σ_m are the corresponding total macroscopic cross sections, S_f and S_m are the sources per unit volume in each region, P_f is the probability that a neutron born in the fuel will suffer its next collision in the moderator, and P_m is the probability that a neutron born in the moderator will suffer its next collision in the fuel. We then apply the reciprocity theorem,

$$V_f \sigma_f P_f = V_m \sigma_m P_m, \quad (174)$$

and the Wigner rational approximation to the fuel escape probability,

$$P_f = \frac{\sigma_e}{\sigma_e + \sigma_f}, \quad (175)$$

where σ_e is a slowly varying function of energy called the escape cross section, to obtain an equation for the fuel flux in the form

$$(\sigma_f + \sigma_e) \phi_f = \frac{\sigma_e S_m}{\sigma_m} + S_f. \quad (176)$$

In the limit where the resonances are narrow with respect to both fuel and moderator scattering, the source terms S_f and S_m take on their asymptotic forms of σ_p/E and σ_m/E , respectively, and this equation becomes equivalent to the Bondarenko model quoted above with

$$\sigma_0^f = \frac{\sigma_e}{\rho_f}, \quad (177)$$

and

$$C(E) = \frac{\sigma_e + \sigma_p}{\rho_f E}. \quad (178)$$

Note that a large escape cross section (a sample that is small relative to the average distance to collision), corresponds to infinite dilution as discussed above. To illustrate the general case, consider a neutron traveling through a lump of uranium oxide with an energy close to a resonance energy. If the neutron scatters from an oxygen nucleus, it will lose enough energy so that it can no longer react with the uranium resonance. Similarly, if the neutron escapes from the lump, it can no longer react with the uranium resonance. The processes of moderator scattering and escape are equivalent in some way. Comparing (177) with (171) gives an “equivalence principle” that says that a lump of particular dimensions and a mixture of particular composition will have the same self-shielded cross sections when the narrow resonance approximation is valid. The effects of material mixing and escape can simply be added to obtain the effective σ_0 for a lump containing admixed moderator material. Therefore, (171) is extended to read

$$\sigma_{0g}^i = \frac{1}{\rho_i} \left\{ \sigma_e + \sum_{j \neq i} \rho_j \sigma_{i0g}^j (\sigma_{0g}^j, T) \right\}, \quad (179)$$

where the escape cross section for simple convex objects (such as plates, spheres, or cylinders) is given by $(4V/S)^{-1}$, where V and S are the volume and surface area of the object, respectively. The quantity $4V/S$ is often called the “mean chord length” $\bar{\ell}$. For example, the mean chord length for a sphere is equal to the radius, the mean chord length for a cylinder is equal to twice its radius, and the mean chord length for a slab is twice its thickness. Many codes that use the background cross-section method modify the escape cross section as defined above to correct for errors in the Wigner rational approximation (“Bell factor,” “Levine factor”), or to correct for the interaction between different lumps in the moderating region (“Dancoff correction”). These enhancements will not be discussed here. Note that a thin slab is equivalent to a dilute solution – they both will have infinitely dilute cross sections.

3.7 Flux Calculations

This narrow-resonance approach is quite useful for practical fast reactor problems. However, for nuclear systems sensitive to energies from 1 to 500 eV, there are many broad- and intermediate-width resonances that cannot be self-shielded with sufficient accuracy using the Bondarenko approach. The GROUPE module of NJOY contains a flux calculator that can give some insight for such problems.

Consider an infinite homogeneous mixture of two materials and assume isotropic scattering in the center-of-mass system. The integral slowing-down equation becomes

$$\sigma(E) \phi(E) = \int_E^{E/\alpha_1} \frac{\sigma_{s1}(E')}{(1-\alpha_1)E'} \phi(E') dE' + \int_E^{E/\alpha_2} \frac{\sigma_{s2}(E')}{(1-\alpha_2)E'} \phi(E') dE'. \quad (180)$$

Furthermore, assume that material 1 is a pure scatterer with constant cross section and transform to the σ_0 representation. The integral equation becomes

$$[\sigma_0 + \sigma_{t2}(E)] \phi(E) = \int_E^{E/\alpha_1} \frac{\sigma_0}{(1-\alpha_1)E'} \phi(E') dE' + \int_E^{E/\alpha_2} \frac{\sigma_{s2}(E')}{(1-\alpha_2)E'} \phi(E') dE'. \quad (181)$$

Finally, assume that the moderator (material 1) is light enough so that all the resonances of material 2 are narrow with respect to scattering from material 1. This allows the first integral

to be approximated by its asymptotic form $1/E$. More generally, the integral is assumed to be a smooth function of E given by $C(E)$. In this way, material 1 can represent a mixture of other materials just as in the Bondarenko method. Fission source and thermal upscatter effects can also be lumped in $C(E)$. The integral equation has now been reduced to

$$[\sigma_0 + \sigma_t(E)] \phi(E) = C(E) \sigma_0 + \int_E^{E/\alpha} \frac{\sigma_s(E')}{(1-\alpha)E'} \phi(E') dE'. \quad (182)$$

This is the simplest problem that can be solved using the flux calculator. The results still depend on the single parameter σ_0 , and they can be used easily by codes that accept Bondarenko cross sections.

For heterogeneous problems, when the narrow-resonance approximation fails, both S_f and S_m in (176) will show resonance features. To proceed further with the solution of this equation, it is necessary to eliminate the moderator flux that is implicit in S_m . As a sample case, consider a fuel pin immersed in a large region of water. The fission neutrons appear at high energies, escape from the pin, slow down in the moderator (giving a $1/E$ flux), and are absorbed by the resonances in the pin. In this limit, any dips in the moderator flux caused by resonances in the fuel are small. On the other hand, in a closely packed lattice, the flux in the moderator is very similar to the flux in the fuel, and resonance dips in the moderator flux become very evident. Intermediate cases can be approximated (MacFarlane 1980) by assuming

$$\phi_m = (1 - \beta) C(E) + \beta \phi_f, \quad (183)$$

where β is a heterogeneity parameter given by

$$\beta = \frac{V_f \sigma_e}{V_m \sigma_m}, \quad (184)$$

Note that $\beta \rightarrow 0$ gives the isolated rod limit and $\beta \rightarrow 1$ gives the close-packed lattice limit. This substitution reduces the calculation of the fuel flux to

$$(\sigma_f + \sigma_e) \phi_f = (1 - \beta) C(E) \sigma_e + S_\beta, \quad (185)$$

where S_β is the source term corresponding to a homogeneous mixture of the fuel isotopes with the isotopes from the moderator region changed by the factor $\beta \sigma_e / \sigma_m$. If the fuel and moderator each consisted of a single isotope and for isotropic scattering in the center-of-mass system, the integral equation would become

$$\begin{aligned} [\sigma_0 + \sigma_t(E)] \phi_f(E) &= (1 - \beta) C(E) \sigma_0 + \int_E^{E/\alpha_m} \frac{\beta \sigma_0}{(1 - \alpha_m) E'} \phi_f(E') dE' \\ &+ \int_E^{E/\alpha_f} \frac{\sigma_{sf}(E')}{(1 - \alpha_f) E'} \phi_f(E') dE', \end{aligned} \quad (186)$$

where σ_0 is σ_e divided by the fuel density (units are barns/atom), α_m and α_f are the maximum fractional energy change in scattering for the two isotopes, and $\sigma_{sf}(E')$ is the fuel-scattering cross section.

This result has a form parallel to that of (182), but the solution depends on the two parameters β and σ_0 . For any given data set, β must be chosen in advance. This might not be difficult if

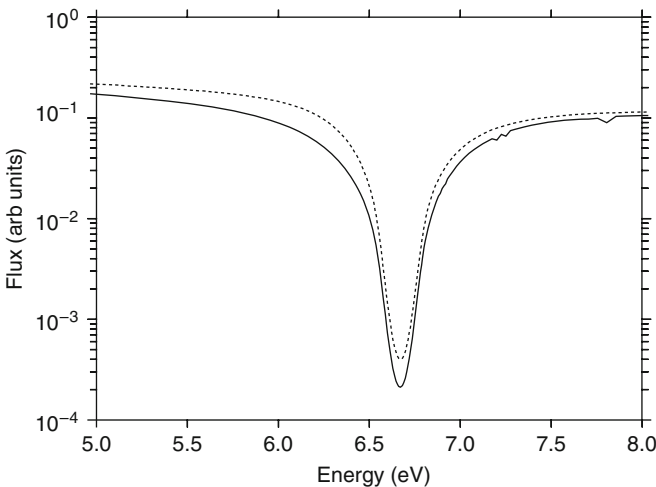
the data are to be used for one particular system, such as pressurized water reactors. The routine also has the capability to include one more moderator integral with a different α value and a constant cross section. The full equation is

$$\begin{aligned}
 [\sigma_0 + \sigma_t(E)] \phi_f(E) = & (1 - \beta) C(E) \sigma_0 + \int_E^{E/\alpha_3} \frac{\beta(1 - \gamma)(\sigma_0 - \sigma_{am})}{(1 - \alpha_3)E'} \phi_f(E') dE' \\
 & + \int_E^{E/\alpha_2} \frac{\sigma_{am} + \beta\gamma(\sigma_0 - \sigma_{am})}{(1 - \alpha_2)E'} \phi_f(E') dE' \\
 & + \int_E^{E/\alpha_f} \frac{\sigma_{sf}(E')}{(1 - \alpha_f)E'} \phi_f(E') dE', \quad (187)
 \end{aligned}$$

where σ_{am} is the cross section of the admixed moderator (with energy loss α_2), and γ is the fraction of the admixed moderator that is mixed with the external moderator (which has energy loss α_3). This allows calculations with H₂O as the moderator and an oxide as the fuel. The flux calculator can thus obtain quite realistic flux shapes for a variety of fuel, admixed moderator, and external moderator combinations. An example comparing the Bondarenko flux with a more realistic computed flux is given in [▶ Fig. 51](#).

3.8 Intermediate Resonance Self-Shielding

In this section, we will describe how the reactor-physics code WIMS (Askew et al. 1966) treats the problem of self-shielding for intermediate resonances. First, we refer back to (167). If the



■ Figure 51

A comparison of the Bondarenko flux model (dashed) with a realistic computed flux (solid) for a U-238 oxide pin in water in the region of the 6.7 eV resonance

energy lost by the downscatter represented by the integral is small with respect to the width of a resonance, the integral can be replaced by $\Sigma_s(E)\phi(E)$, and the equation becomes

$$[\Sigma(E) - \Sigma_s(E)]\phi(E) = S_0(E). \quad (188)$$

The weighting flux would become

$$W_0(E) = \frac{C(E)}{\sigma_0 + \sigma_a(E)}, \quad (189)$$

where σ_a is the absorption cross section. This is called the “wide resonance” (WR) or the “narrow resonance infinite mass” (NRIM) approximation. For resonances with widths intermediate to the NR and WR limits, we can change the formulas for the weighting flux and background cross section for for isotope i to

$$W_{0g}^i(E) = \frac{C(E)}{\sigma_{Pg}^i + \sigma_{ag}^i}, \quad (190)$$

and

$$\sigma_{Pg}^i = \frac{1}{\rho_i} \left\{ \sigma_\epsilon + \sum_j \rho_j \lambda_g^j \sigma_{Pg}^j \right\}. \quad (191)$$

Note that the sum is now over all j , and we have used the potential scattering cross section rather than the total cross section (which neglects the effect of scattering resonances on the weighting flux). If $\lambda_g^i = 1$, we get back the narrow resonance result because σ_p^i adds to σ_{ag}^i to return the total cross section (still neglecting resonance scattering). For $\lambda_g^i = 0$, we get the WR result. With intermediate values of λ , we get the “intermediate resonance” (IR) approximation. The equivalence principle is the same as for narrow resonances; namely, all systems with the same value of IR σ_{Pg}^i will have the same self-shielded cross sections for that isotope and group.

WIMS takes the additional step of expressing the self-shielding data in terms of “resonance integrals,” instead of using the self-shielded cross sections produced by GROUPE. That is,

$$\sigma_x(\sigma_0) = \frac{\sigma_p I_x(\sigma_p)}{\sigma_p - I_a(\sigma_p)}, \quad (192)$$

and

$$I_x(\sigma_p) = \frac{\sigma_p \sigma_x(\sigma_0)}{\sigma_p + \sigma_a(\sigma_0)}, \quad (193)$$

where $\sigma_x(\sigma_0)$ is a normal cross section as produced by the GROUPE module of NJOY, and x can stand for capture, fission, or nu-fission.

In order to clarify the meaning of this pair of equations, consider a homogeneous mixture of U-238 and hydrogen with concentrations such that there are 50 barns of hydrogen scattering per atom of uranium. The GROUPE flux calculator can be used to solve for the flux in this mixture, and GROUPE can then calculate the corresponding absorption cross section for U-238. Assuming that $\lambda = 0.1$ and $\sigma_p = 10$ for the uranium, the numbers being appropriate for WIMS group 25, we get $\sigma_p = 51$. This value of σ_p goes into the the WIMS library along with the corresponding I_a .

At some later time, a WIMS user runs a problem for a homogeneous mixture of U-238 and hydrogen that matches these specifications. WIMS will compute a value of σ_p of 51.0, interpolate in the table of resonance integrals, and compute a new absorption cross section that is exactly equal to the accurate computed result from the original GROUPE flux-calculator run.

This argument can be extended to more complex systems. For example, the assembly calculated using the flux calculator could represent an enriched uranium-oxide fuel pin of a size typical of a user's reactor system with a water moderator. The computed absorption cross section is converted to a resonance integral and stored with the computed value of σ_p . In any later calculation that happens to mimic the same composition and geometry, WIMS will return the accurate calculated absorption cross section. Equivalence theory, with all its approximations, is only used to interpolate and extrapolate around these calculated values. This is a powerful approach, because it allows a user to optimize the library in order to obtain very accurate results for a limited range of systems without having to modify the methods used in the lattice-physics code.

Let us call the homogeneous uranium-hydrogen case discussed above "case 0." Now, consider a homogeneous mixture of U-238, oxygen, and hydrogen. Arrange the ratio of the number densities to the uranium density such that there is 1 barn/atom of oxygen scattering and 50 barn/atom of hydrogen scattering. Carry out an accurate flux calculation for the mixture, and call the result "case 1." Also do an accurate flux calculation with only hydrogen, but at a density corresponding to 51 barns/atom. Call this result "case 2." The IR lambda value for oxygen is then given by

$$\lambda = \frac{\sigma_a(1) - \sigma_a(0)}{\sigma_a(2) - \sigma_a(0)}. \quad (194)$$

Note that λ will be 1 if the oxygen and hydrogen have exactly the same effect on the absorption cross section. In practice, $\lambda = 0.91$ for WIMS group 27 (which contains the large 6.7 eV resonance of U-238), and $\lambda = 1$ for all the other resonance groups. That is, all the resonances above the 6.7 eV resonance are effectively narrow with respect to oxygen scattering.

This process can be continued for additional admixed materials from each important range of atomic mass. The result is the table of λ_{gi} values needed as WIMSR input.

What are the implications of this discussion? The foremost is the observation that the lambda values for the isotopes are a function of the composition of the mixture that was used for the base calculation. To make the effect of this clear, let us consider two different types of cells:

1. A homogeneous mixture of U-238 and hydrogen
2. A homogeneous mixture of U-235 and hydrogen

A look at the pointwise cross sections in group 27 shows very different pictures for the two uranium isotopes. The U-238 cross section has one large, fairly wide resonance at 6.7 eV, and the U-235 cross section has several narrower resonances scattered across the group. If the lambda values are computed for these two different situations, the results in [Table 9](#) are obtained.

It is clear that the energy dependence of the two lambda sets is quite different. This is because of the difference in the resonance structure between U-238 and U-235. Clearly, the one resonance in group 27 in U-238 is effectively wider than the group of resonances in group 27 for U-235. Group 26 has essentially no resonance character for U-238, which reverses the sense of the difference. In groups 24 and 25, the U-238 resonances become more narrow, while the U-238 resonances stay fairly wide. Finally, in group 23, the U-238 resonances begin to get narrower.

These results imply that completely different sets of λ values should be used for different fuel/moderator systems, such as U-238/water, U-235/water, or U-238/graphite. In practice, this is rarely done.

■ Table 9

IR λ values for several resonance groups and two different reactor systems

WIMS group	$\lambda(U)$ U-238@50b	$\lambda(O)$ U-238@50b	$\lambda(U)$ U-235@200b	$\lambda(O)$ U-235@200b
27	0.035	0.91	0.20	1.00
26	0.50	1.00	0.38	1.00
25	0.092	1.00	0.44	1.00
24	0.090	1.00	0.55	1.00
23	0.29	1.00	0.46	1.00

3.9 Unresolved Resonance Range Methods

In the unresolved resonance range, there are still significant fluctuations in the cross sections, but we do not know exactly where they are. However, it is possible to evaluate the average properties of the unresolved resonances. The ENDF format provides the average spacing \bar{D} and the average widths for the elastic, capture, fission, and competitive reactions ($\bar{\Gamma}_n$, $\bar{\Gamma}_\gamma$, $\bar{\Gamma}_f$, and $\bar{\Gamma}_x$). All of these can depend on E , J , and ℓ . The resonance spacing is normally assumed to be distributed with the Wigner distribution, and the resonance widths are distributed with chi-square distributions with degrees of freedom μ_n , μ_γ , μ_f , and μ_x , for the elastic, capture, fission, and competitive widths, respectively. These quantities are also functions of E , J , and ℓ .

The infinitely dilute cross sections in the unresolved resonance region can be computed using these parameters in the SLBW method.

$$\sigma_n(E) = \sigma_p + \frac{2\pi^2}{k^2} \sum_{\ell, J} \frac{g_J}{D} \left[\bar{\Gamma}_n^2 R_n - 2\bar{\Gamma}_n \sin^2 \phi_\ell \right], \quad (195)$$

$$\sigma_x(E) = \frac{2\pi^2}{k^2} \sum_{\ell, J} \frac{g_J}{D} \bar{\Gamma}_n \bar{\Gamma}_x R_x \quad (196)$$

and

$$\sigma_p = \frac{4\pi}{k^2} \sum_{\ell} (2\ell + 1) \sin^2 \phi_\ell, \quad (197)$$

where σ_p is the potential scattering cross section, the \sin^2 term is the interference correction, x stands for either fission or capture, $\bar{\Gamma}_i$ and \bar{D} are the appropriate average widths and spacing for the ℓ, J spin sequence, and R_i is the fluctuation integral for the reaction and sequence. These integrals are simply the averages taken over the chi-square distributions specified in the file; for example,

$$\bar{\Gamma}_n \bar{\Gamma}_f R_i = \left\langle \frac{\Gamma_n \Gamma_f}{\Gamma} \right\rangle$$

$$\begin{aligned}
&= \int dx_n P_\mu(x_n) \int dx_f P_\nu(x_f) \int dx_c P_\lambda(x_c) \\
&\quad \times \frac{\Gamma_n(x_n) \Gamma_f(x_f)}{\Gamma_n(x_n) + \Gamma_f(x_f) + \Gamma_\gamma + \Gamma_c(x_c)}, \tag{198}
\end{aligned}$$

where $P_\mu(x)$ is the chi-square distribution for μ degrees of freedom. The integrals are evaluated with the quadrature scheme developed by R. Hwang for the MC²-2 code (Henryson et al. 1976) giving

$$R_f = \sum_i W_i^\mu \sum_j W_j^\nu \sum_k W_k^\lambda \frac{Q_i^\mu Q_j^\nu}{\bar{\Gamma}_n Q_i^\mu + \bar{\Gamma}_f Q_j^\nu + \Gamma_\gamma + \bar{\Gamma}_c Q_k^\lambda}. \tag{199}$$

The W_i^μ and Q_i^μ are the appropriate quadrature weights and values for μ degrees of freedom, and Γ_γ is assumed to be constant (many degrees of freedom). The competitive width $\bar{\Gamma}_c$ is assumed to affect the fluctuations, but a corresponding cross section is not computed (we will discuss this in more detail below).

It should be noted that the reduced average neutron width Γ_n^0 is given in the evaluations, and

$$\bar{\Gamma}_n = \Gamma_n^0 \sqrt{E} V_\ell(E), \tag{200}$$

where the penetrabilities for the unresolved region are defined as

$$V_0 = 1, \tag{201}$$

$$V_1 = \frac{\rho^2}{1 + \rho^2}, \tag{202}$$

and

$$V_2 = \frac{\rho^4}{\rho + 3\rho^2 + \rho^4}. \tag{203}$$

Other parameters are defined as for SLBW.

In practice, this simple unresolved resonance representation can not always fit the experimental data with sufficient accuracy. For actinide fission, the double-humped fission barriers seen there lead to “secondary structure” in the cross sections that are not included in the simple theory. In addition, if the break from the resolved range to the unresolved range is not high enough, there can be semi-resolved resonances or clusters of resonances underlying the resonances that do not act like the simple theory predicts. Because of this, the ENDF format has an option to provide evaluated experimental values directly for the infinitely dilute unresolved resonance range cross sections (examples are U-235 and U-238). In these cases, the simple unresolved resonance theory is only used to calculate self-shielding (see below). In other cases, the parameters of the theory are adjusted to try to give reasonable agreement to experiment, even for the features that are not consistent with the simple theory (e.g., Pu-239). Both the infinitely dilute cross section and the self-shielding are computed using the simple theory. Both of these procedures leave much to be desired. However, the self-shielding effects of the unresolved energy range are quite small for thermal reactor systems and modest for fast reactor system; therefore, fairly large uncertainties can be accepted in the unresolved resonance range without serious impact on normal calculations. Work is underway in the nuclear-data community to improve this situation.

There are two methods in common use for calculating self-shielding effects in the unresolved resonance range. For multigroup codes, tables of self-shielded cross sections using the Bondarenko method are normally provided. For continuous-energy Monte Carlo codes like MCNP, probability tables are normally used. The PURR module of NJOY can be used to generate both types of data. This method is based on generating “ladders” of resonances using the statistical properties of the unresolved range. One ladder can be generated appropriate for an energy E by randomly selecting a starting resonance energy for one ℓ, J sequence, and also randomly selecting a set of widths for that resonance using the appropriate average widths and chi-square distribution functions. We can then select the next higher resonance energy by sampling from the Wigner distribution for resonance spacings, and we can choose a new set of widths for that resonance. The process is continued until we have a long ladder of resonances for that ℓ, J . We then repeat the process for the other ℓ, J sequences, each such sequence being uncorrelated in positions from the others. With this ladder of resonance parameters in place, PURR randomly samples energy values and computes the cross sections at those energy using the SLBW method. This random sampling is consistent with the narrow resonance approximation in which neutrons arrive without a knowledge of the local resonance structure. These cross sections can be used in formulas like (170) to obtain statistical estimates for the self-shielded cross sections to be used in multigroup codes. They can also be used to obtain a probability distribution function for the total cross section. This is done by accumulating the “hits” in a set of predefined total cross-section bins. This can be used to determine the probability that the total cross section will present a value in that bin’s range and the average total cross section for that range. At the same time, conditional averages can be accumulated for the elastic, capture, and fission reactions. A conditional average is the average value for the reaction over a bin when the associated total cross also falls in that bin. Once all the cross section samples have been processed for the ladder, a new ladder is constructed, and the entire process is repeated. A typical calculation uses 20 bins and 32 ladders. The structure of a probability table for one energy is shown in ► [Table 10](#). In MCNP, a random number is used with the cumulative probability to select a bin, and the resulting cross sections are returned to characterize the collision. Intermediate incident energies are obtained by interpolation.

■ **Table 10**
Contents of an unresolved resonance range probability table

Lowest bin bound
Upper bin bound for N bins
Partial probability for N bins
Cumulative probability for N bins
Average total σ for N bins
Average elastic σ for N bins
Average fission σ for N bins
Average capture σ for N bins

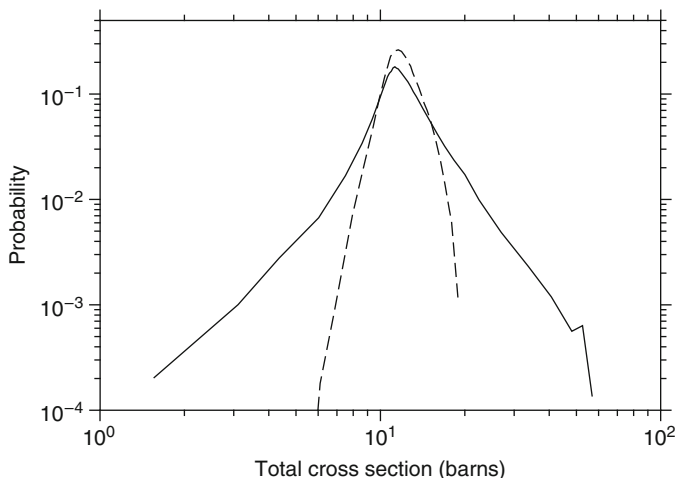


Figure 52

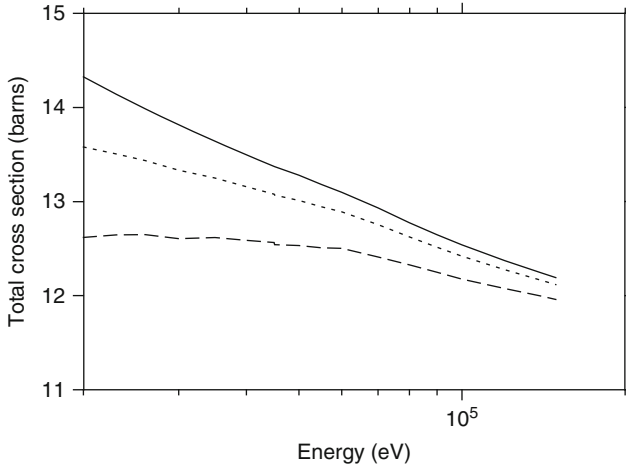
The probability distribution for the total cross section at 20 keV (solid) and 140 keV (dashed) in the unresolved resonance range of U-238

The probability table can be used to generate a picture of the probability distribution for the total cross section as shown in [Fig. 52](#). This example is for U-238. It demonstrates how the fluctuations get smaller as energy increases, which means that the self-shielding effect also gets smaller. The probability table can also be used to generate Bondarenko self-shielded cross sections as follows:

$$\sigma_x(E) = \frac{\sum_i \frac{P_i(E)\sigma_{xi}(E)}{\sigma_0 + \sigma_{ti}(E)}}{\sum_i \frac{P_i(E)}{\sigma_0 + \sigma_{ti}}}, \quad (204)$$

where x is t , n , f , or γ . An example of the self-shielded total cross section for the unresolved resonance range of U-238 is shown in [Fig. 53](#). In practice, a σ_0 value of about 30 is characteristic of an oxide reactor pin, and one of 1 is appropriate for a very fast system with large amounts of U-238.

In U-238, the threshold for the (n, n_1) inelastic level is 45.09125 keV, well within the unresolved resonance range. The threshold for (n, n_2) is 149.0288 keV, which is the upper limit of the unresolved resonance range. In this energy range, inelastic scattering competes with elastic scattering and capture – this is the origin of the “competitive width” mentioned above. In the current ENDF procedures, we are instructed to use the unshielded value of the inelastic cross section as given in the evaluation when constructing the cross section libraries. However, theory predicts that the inelastic cross section should have resonance fluctuations in this energy range just as the other channels do. Adding this self-shielding effect would affect the inelastic slowing down, and the nuclear data community is working to understand the effects of this. One processing system currently attempts to include this inelastic self-shielding effect (Sublet et al. 2006).



■ Figure 53

Self-shielded unresolved resonance range total cross section for U-238 at σ_0 values of infinity (solid), 30 (dotted), and 1 barn (dashed)

4 Time and Space in Slowing Down

4.1 Introduction

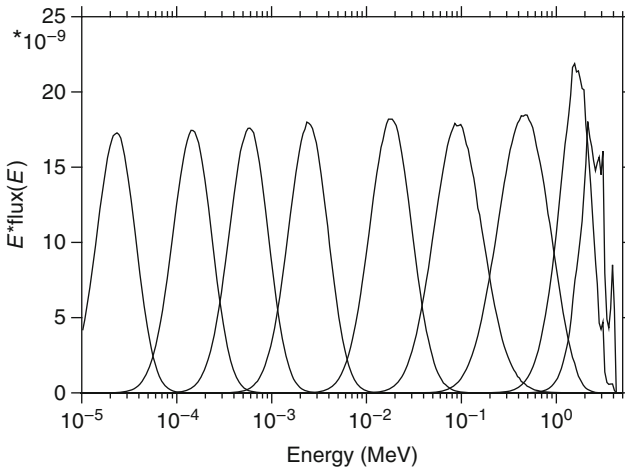
For most reactor-physics applications, the equilibrium slowing down and thermalization discussed above is sufficient. However, to get a more complete understanding of the process, it is useful to consider time dependence. The MCNP Monte Carlo code can be used to do time-dependent simulations; for example, what is the behavior of a pulse of neutrons introduced at time zero and position zero as time increases and the neutron flux spreads out from the origin. This is a problem that was analyzed in the past using eigenvalue–eigenfunction theory or age theory.

4.2 Time Dependence of the Energy Spectrum

In this section, we introduce a pulse of neutrons at some initial energy at the center of a large sphere of a material and watch the evolution of the energy spectrum averaged over the entire assembly as a function of time. The first example is for graphite. The initial energy is taken to be 4 MeV to avoid the inelastic levels. The time-dependent flux contours are shown in [Fig. 54](#). At early times, there are complex transients resulting from the delta-function source interacting with the discontinuous slowing-down kernel. But as time increases, the flux peaks smooth out into Gaussian shapes that slow down with time with little change in shape. Note that the natural time unit for MCNP is the shake (10^{-8} s).

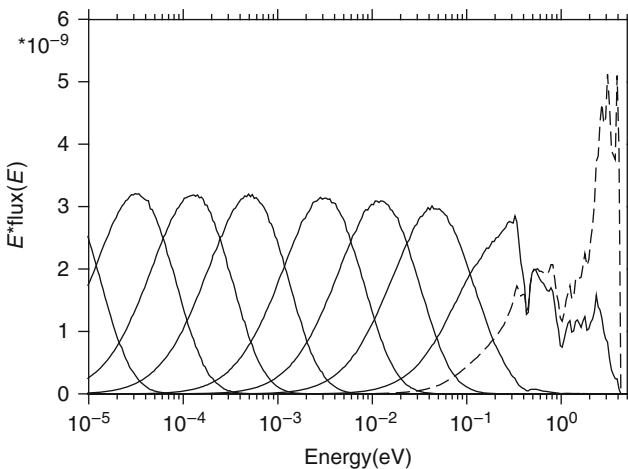
If we do the same thing for heavy water, we get similar results (see [▶ Fig. 55](#)). Note that the slowing down is faster for heavy water than it was for carbon, and the pulses shapes are slightly broader.

This behavior of neutron pulses in large systems is the basis for the experimental technique called the “lead slowing-down spectrometer.” Theory says that for large A , the width of the pulse (the dispersion) should vary as $1/\sqrt{A}$. [▶ Figure 56](#) shows the slowing-down behavior in a very



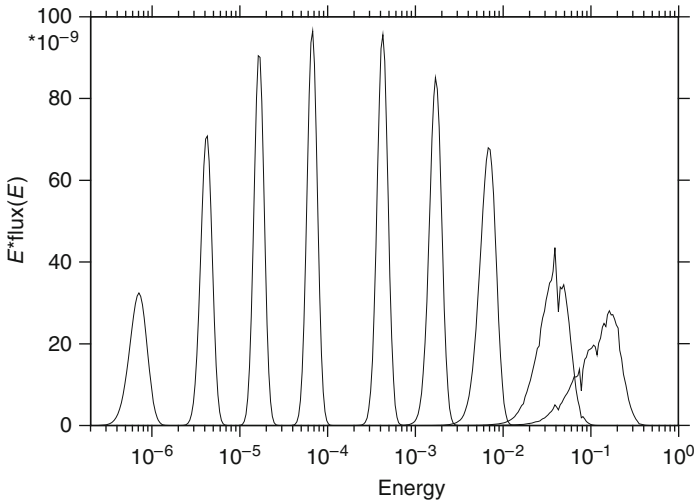
■ Figure 54

Neutron spectra for slowing down in carbon. The curves are for 10% time bins around times of 1, 2, 5, 10, 20, 50, 100, 200, and 500 shakes (one shake is 10^{-8} s)



■ Figure 55

Neutron spectra for slowing down in heavy water. The curves are for 10% time bins around times of 1, 2, 5, 10, 20, 50, 100, 200, and 500 shakes (one shake is 10^{-8} s)



■ **Figure 56**

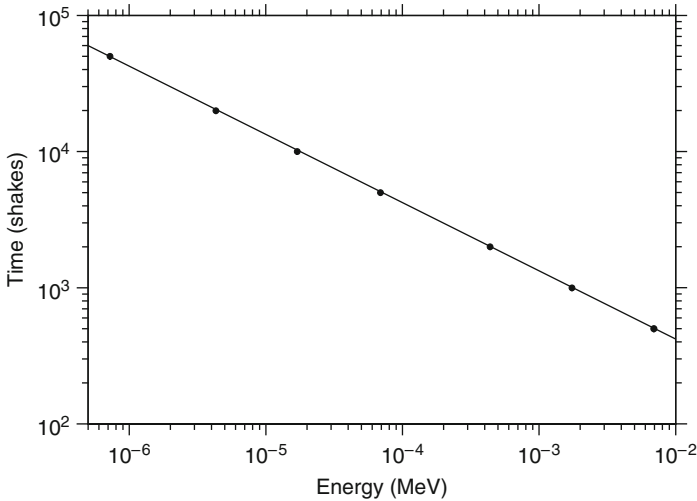
Neutron spectra for slowing down from a point source at 14 MeV in a large lead sphere. The curves correspond to 10% time bins around times of 50, 100, 200, 500, 1,000, 2,000, 5,000, 10,000, and 20,000 shakes (one shake is 10^{-8} s)

large sphere of lead. Note that the pulses are narrower than they were for the lighter materials and that the slowing down is much slower. If you put a sample inside the block of lead, you can observe its response to different energies by observing it at different times. Theory says that the time for a given energy should vary like $1/v$. ➤ [Figure 57](#) shows that the calculation shown in ➤ [Fig. 56](#) obeys this prediction.

A classical experiment is the measurement of “slowing down time.” A pulse is introduced at high energies, and the time required to excite a known resonance in a sample is measured. We can simulate that using MCNP. The definition of “high energy” is ambiguous, but neutrons slow down very quickly near the source energy from inelastic scattering, so the effect of using different starting energies is not too serious. Looking at ➤ [Fig. 57](#), we can pick off the time associated with an energy of 1 eV and call that the slowing-down time. ➤ [Table 11](#) shows results for several materials from ENDF/B-VII.

4.3 Time Dependence of the Spatial Distribution

To look at the spatial distribution of slowing down, we start a pulse of 1 MeV neutrons in the center of a large sphere of graphite and watch how the integrated flux spreads out with time. See ➤ [Fig. 58](#). This was an MCNP calculation using five million source particles. At early times, the distribution is still close to the origin, but as time increases it gradually gets broader. The neutrons act like they are diffusing outward. The outward diffusive current is strong at early times because of the large gradient in the flux. As the central flux is depleted, it gets smaller and flatter, and the outward current gets smaller. As a result, the central flux does not decrease as fast as time increases.



■ Figure 57

Time vs. peak energy for slowing down in lead (points). The solid curve is the theoretical $1/v$ dependence

■ Table 11

Slowing down time for several materials from ENDF/B-VII

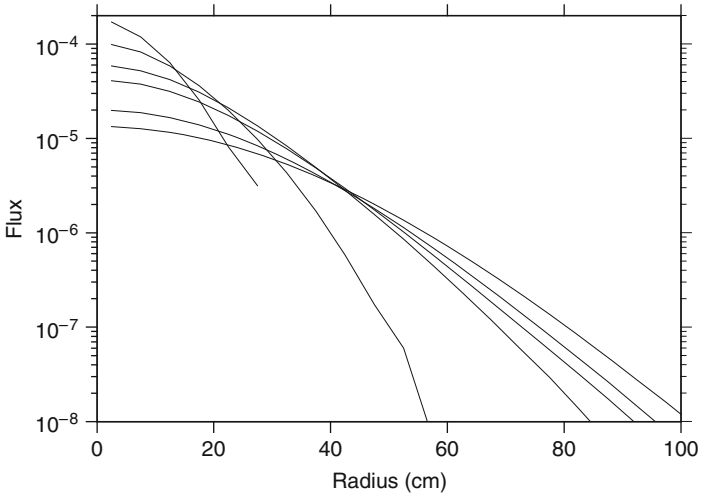
Material	Slowing-down time (μs)
Heavy water	11.5
Carbon	24.0
Sodium	200
Lead	425

At long times, the flux shape will approach the “fundamental mode” shape. For a spherical geometry, the shape would be

$$\frac{1}{r} \sin\left(\frac{\pi r}{\hat{R}}\right), \quad (205)$$

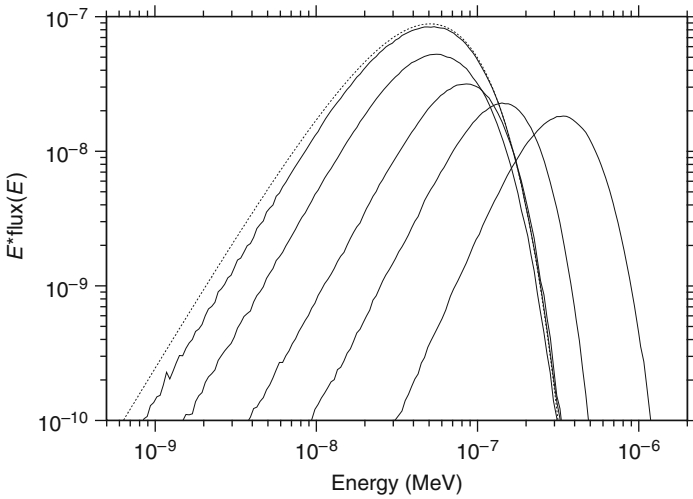
where \hat{R} is the extrapolated endpoint radius just outside of the real radius R . For spheres that are large with respect to the mean free path, \hat{R} will be close to R . What does “long times” mean?

➤ Figure 59 shows the final stages of the thermalization of the neutron pulse. The dotted line is the theoretical Maxwellian shape for an infinite medium with no absorption. It is clear that the computed flux in this graphite sphere is approaching the theoretical limit after about 1,000 μs . As we saw in ➤ Table 11, the slowing down time to 1 eV for carbon is about 24 μs . The thermalization time is seen to be much larger than that. This is a consequence of the chemical binding of the carbon atoms in the graphite and the presence of upscatter. After about 1,000 μs ,



■ Figure 58

Spatial dependence of slowing down in carbon. The curves are for 10% time bins around times of 1, 2, 5, 10, 100, and 1,000 shakes (one shake is 10^{-8} s)



■ Figure 59

Final thermalization of a pulse in a graphite sphere. The solid curves are for 10% time bins around times of 5,000, 10,000, 20,000, 50,000, and 100,000 shakes (one shake is 10^{-8} s). The dotted curve is a Maxwellian thermal spectrum

the spatial flux shape in the graphite sphere should have reached the fundamental mode shape shown in the equation above.

4.4 Eigenvalues and Eigenfunctions

One theoretical approach to time-dependent slowing down and thermalization makes use of eigenvalues and eigenfunctions. In the diffusion approximation, the transport equation for a homogeneous medium with an isotropic source at energy E_0 and time $t = 0$ can be written as

$$\begin{aligned} \frac{1}{v} \frac{\partial \phi(E, \mathbf{r}, t)}{\partial t} + \Sigma_a(E) \phi(E, \mathbf{r}, t) - D(E) \nabla^2 \phi(E, \mathbf{r}, t) \\ = \mathbf{S}_0 \phi(E, \mathbf{r}, t) + \delta(E - E_0) \delta(t) Q(\mathbf{r}), \end{aligned} \quad (206)$$

where $Q(\mathbf{r})$ is the shape of the source, $D(E)$ is the diffusion coefficient, Σ_a is the macroscopic absorption cross section, and the scattering operator is given by

$$\mathbf{S}_0 \phi(E) = \int_0^\infty \Sigma(E' \rightarrow E) \phi(E') dE' - \Sigma_s(E) \phi(E), \quad (207)$$

where $\Sigma(E' \rightarrow E)$ is the differential scattering cross section, and $\Sigma_s(E)$ is the integrated scattering cross section. Following the scheme described in (Williams 1966). We first separate out the spatial part by writing

$$\phi(E, \mathbf{r}, t) = \sum_n \phi_n(E, t) F_n(\mathbf{r}). \quad (208)$$

The F_n are given by a Helmholtz equation

$$\nabla^2 F_n(\mathbf{r}) + B_n^2 F_n(\mathbf{r}) = 0. \quad (209)$$

subject to appropriate boundary conditions at the edge of the system. The B_n^2 are spatial eigenvalues with associated spatial eigenfunctions F_n . We will give an example below. The ϕ_n are solutions of

$$\begin{aligned} \frac{1}{v} \frac{\partial \phi_n(E, t)}{\partial t} + \Sigma_a(E) \phi_n(E, t) - D(E) B_n^2 \phi_n(E, t) \\ = \mathbf{S}_0 \phi_n(E, t) + \delta(E - E_0) \delta(t) Q_n, \end{aligned} \quad (210)$$

where

$$Q_n = \int d\mathbf{r} Q(\mathbf{r}) F_n(\mathbf{r}). \quad (211)$$

We next assume that the flux can be divided into energy and time factors as follows:

$$\phi_n(E, t) = \phi_n(E) e^{-\lambda_n t}. \quad (212)$$

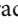
The equation for the ϕ_n becomes

$$\left[-\frac{\lambda_n}{v} + D(E) B_n^2 \right] \phi_n(E) = \mathbf{S}_0 \phi_n(E) + \delta(E - E_0) \delta(t) Q_n. \quad (213)$$

The homogeneous part of this provides another eigenvalue problem

$$\mathbf{S}_0 \phi_n(E) = \left[-\frac{\lambda_n}{v} + D(E)B_n^2 \right] \phi_n(E). \quad (214)$$

The eigenvalues of this equation (square brackets) correlate the spatial eigenvalues B_n^2 with the time-decay eigenvalues λ_n .

In principle, this eigenvalue problem can be attacked by expanding ϕ_n and Q_n using an appropriate set of orthonormal basis functions and solving for the eigenvalues and expansion coefficients. In practice, this is rather difficult in general. As we saw from  Fig. 59, the temporal eigenfunction corresponding to λ_0 would have to be similar to the Maxwellian distribution $M(E)$, and higher eigenfunctions would have to represent the faster decaying Gaussian peaks from the slowing-down process. Similarly, the spatial eigenfunction corresponding to B_0^2 would be the fundamental mode shape, and the higher modes would correspond to higher values of λ_n and would decay away faster. The eigenvalue–eigenfunction approach is useful in understanding how the temporal and spatial modes behave, but Monte Carlo and multigroup methods are much more useful in practice.

As an example of the spatial eigenfunctions, consider the simple slab reactor of thickness T . A good set of basis functions is

$$\psi_n(x) = \begin{cases} \cos \frac{n\pi x}{\hat{T}}, & n = 1, 3, 5, \dots \\ \sin \frac{n\pi x}{\hat{T}}, & n = 2, 4, 6, \dots, \end{cases} \quad (215)$$

and the corresponding eigenvalues are

$$B_n^2 = \left(\frac{n\pi}{\hat{T}} \right)^2, \quad n = 1, 2, 3, \dots \quad (216)$$

All these eigenfunctions are zero at the extrapolated half widths of the slab $-\hat{T}/2$ and $+\hat{T}/2$. The ψ_1 function is the fundamental mode, and it is nonzero over the entire slab. The ψ_2 function is asymmetric with a zero at the midpoint of the slab. The ψ_3 function is symmetric with two zeros. If one imagines starting with an initial source that is off center, the flux soon after the initial pulse would also be off center and would be represented by a Fourier series containing sine terms that reflects that. But these higher modes will have larger λ values and decay away faster than the lower modes. The spatial flux will gradually become smoother, and by the time that full thermalization is obtained, only the fundamental mode will remain.

4.5 Analytic Age Theory

To understand age theory and other “continuous slowing down” methods, it is useful to write the P_1 approximation to the transport equation in terms of the lethargy

$$\frac{\partial \phi_1(x, u)}{\partial x} + \Sigma_t(x, u) \phi_0(x, u) = \int \Sigma_s(x, u' \rightarrow u) \phi_0(x, u') du' + Q_0(x, u) \quad (217)$$

$$\frac{\partial \phi_0(x, u)}{\partial x} + \Sigma_t(x, u) \phi_1(x, u) = 3 \int \Sigma_s(x, u' \rightarrow u) \phi_1(x, u') du' + 3Q_1(x, u). \quad (218)$$

If A is not too small, in the energy range where elastic scattering dominates, and if the absorption is not too large, the collision density $\Sigma_s \phi_0$ tends to be slowly varying. It is reasonable to make Taylor expansions of the P_0 and P_1 collision densities, keeping two terms for the first and one for the second. Making the following definitions

$$\int \Sigma_s(x, u' \rightarrow u) du' = \Sigma_s(x, u), \quad (219)$$

$$\int (u - u') \Sigma_s(x, u' \rightarrow u) du' = \xi(u) \Sigma_s(x, u), \quad (220)$$

and

$$\int \Sigma_1(x, u' \rightarrow u) du' = \bar{\mu}(u) \Sigma_s(x, u), \quad (221)$$

the P_1 equations become

$$\frac{\partial \phi_1}{\partial x} + (\Sigma_t - \Sigma_s) \phi_0 = \frac{\partial}{\partial u} (\xi \Sigma_s \phi_0) + Q_0 \quad (222)$$

$$\frac{\partial \phi_0}{\partial x} + 3(\Sigma_t - \bar{\mu} \Sigma_s) \phi_1 = 3Q_1. \quad (223)$$

Taking $Q_1 = 0$, the second equation gives “Fick’s Law,”

$$\psi_1 = -\frac{1}{3(\Sigma_t - \bar{\mu} \Sigma_s)} \frac{\partial \phi_0}{\partial x} = -D \frac{\partial \phi_0}{\partial x}, \quad (224)$$

where D is the diffusion coefficient. Putting this into the first of the P_1 equations gives the “age-diffusion equation”

$$-\frac{\partial}{\partial x} \left(D \frac{\partial \phi_0}{\partial x} \right) + (\Sigma_t - \Sigma_s) \phi_0 = \frac{\partial}{\partial u} (\xi \Sigma_s \phi_0) + Q_0. \quad (225)$$

The quantity ξ is the average increase in lethargy for a neutron–nucleus collision, and $\bar{\mu}$ is the average cosine for scattering. For isotropic CM scattering in a single material, these two quantities take on the simple values

$$\xi = 1 + \frac{\alpha \ln \alpha}{1 - \alpha} \quad (226)$$

$$\bar{\mu} = \frac{2}{3A}. \quad (227)$$

The quantity $\xi \Sigma_s \phi_0$ is called the “slowing-down density” and is usually denoted by $q(x, u)$. If $Q_0 = 0$ and there is no absorption ($\Sigma_t = \Sigma_s$), the age-diffusion equation is reduced to

$$\frac{\partial^2 q(x, u)}{\partial x^2} = \frac{\partial q}{\partial \tau}, \quad (228)$$

where τ is called the Fermi age,

$$\tau(u) = \int_0^u \frac{D}{\xi \Sigma_s} du'. \quad (229)$$

This is the “Fermi age equation” in plane geometry. Note that τ has the dimensions of square centimeters, strange for an “age.” It is really something like the square of the mean distance to a collision.

An interesting variation on age theory comes about if we write the time-dependent and space-independent version for a pulsed source in the form

$$\frac{1}{v} \frac{\partial \phi(u, t)}{\partial t} = -\frac{\partial}{\partial u} [\xi \Sigma_s \phi(u, t)] + \delta(u) \delta(t). \quad (230)$$

This equation can be solved using a Laplace transform, giving

$$\xi \Sigma_s(u) \phi(u, t) = \delta \left(t - \int_0^u \frac{1}{v' \xi \Sigma_s(u')} du' \right), \quad (231)$$

that is, the pulse retains its original shape and slows down with time. We saw this behavior in [▶ Fig. 56](#).

Age theory is mostly of historical significance in these days of fast computers. It does not work for hydrogen, and it is weak for other light moderators, like heavy water and beryllium. There are other slightly more complicated continuous slowing-down models, such as the Selengut–Goertzel and Greuling–Goertzel methods, that have found some usefulness in fast-reactor analysis.

5 Concluding Remarks and Outlook

This chapter opened with a discussion on how to generate scattering cross sections in the thermal range with the $S(\alpha, \beta, T)$ representation. Experience has shown that this approach works well for calculating water–uranium critical systems (Tuli et al. 2006). However, [▶ Figs. 19](#) and [▶ Figure 20](#) suggest that further improvements for H in H_2O are possible, especially for the diffusive representation at low neutron energies. The region from 0.2 to 0.5 eV is also of concern. Some correspondents have been concerned about the effects of the break between the $S(\alpha, \beta, T)$ representation at low energies and the epithermal treatment above. The discontinuity at the breakpoint looks nonphysical. Current methods use breakpoints all the way from 0.625 to 10 eV. It is not clear whether the $S(\alpha, \beta, T)$ representation works for energies as high as 10 eV. At some point, anharmonic effects should begin to show up. At higher energies, bond breaking and atomic displacements could even occur. The current experimental data are not good enough to resolve these questions. Additional high-accuracy differential and integrated experimental data could drive improvements for the water scattering data.


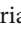
[▶ Figure 24](#) showed some improvement in matching experimental data for heavy water coming from the treatment of intermolecular interference, but there are still problems around 1 meV and in the region from 0.01 to 0.05 eV that suggest that further physics improvements are needed. There may also be problems with the temperature dependence of the interference effect coming from the static structure factor ([▶ Fig. 22](#)). There are only a few good heavy-water critical assemblies available for test calculations, so the confidence we have for water–uranium systems is not available for heavy-water systems.

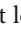
A shortage of reliable critical experiments also exists for other moderator materials, including beryllium and graphite.

A key problem with the $S(\alpha, \beta, T)$ approach is that it only works for materials for which the free-scattering cross section is constant. This condition is well satisfied for the light materials like water, heavy water, and graphite. However, it certainly breaks down for uranium oxide. New methods would be required to extend the thermal-scattering treatment for U-238 to 10 eV, spanning the important 6.7 eV resonance. Some work has been done on this in recent years, but it has not been reduced to common practice as yet.

Finally, from time to time, people have expressed the desire for $S(\alpha, \beta, T)$ data for additional materials. These evaluations are fairly difficult, and there are few people with experience in the field. Progress is slow.

The second section discussed thermalization. There are several computer code systems available that treat this well, as demonstrated by the good results obtained for many thermal critical assemblies during ENDF/B-VII data testing (Tuli et al. 2006). The Monte Carlo approach works best here because of its good treatments of the complex geometry features of many of the critical experiments.

The third section discussed steady-state slowing down. At higher energies and for lighter isotopes, both Monte Carlo and S_N methods are capable of calculating slowing down well. The limitations come from the nuclear data. As we saw from  Fig. 47, the slowing-down spectra are sensitive to the angular distributions. These are not always as good as we would like for current evaluations. During the development of the ENDF/B-VII data for U-238, good improvement in matching critical-experiment data for both lattice experiments and fast-reflected criticals was obtained, and part of this improvement came from using the best current nuclear models for the elastic angular distributions. The agreement between calculation and experiment is not that good for fast-reflected critical assemblies with other reflectors (lead, iron, nickel, and copper). This suggests that the angular distributions for scattering could be improved for other materials, resulting in better slowing-down calculations. If there are resonances in the higher energy part of the slowing-down range, a more complete representation of the change in the angular distributions across the resonances, such as the variations shown in  Fig. 50, could be helpful. This would require more extensive use of the RML resonance representation and enhancements in data-processing and transport codes to make use of these data.

Another data issue for slowing down comes from the representation of continuum scattering reactions, such as (n, n'_c) and $(n, 2n)$. These data are often obtained from nuclear model calculations, which normally produce histogram representations of the scattering. In current evaluations, these histogram representations are often fairly coarse and do not do a good job of simulating the \sqrt{E} dependence of these distributions at low energies. See  Fig. 49. This histogram issue also comes up for low-energy delayed-neutron spectra.

For the heavier isotopes, the slowing down eventually passes into the unresolved resonance range where reactions are treated statistically. Here, the cross sections are treated to include the temperature, but the downscatter shapes are not. Some correspondents have questioned the reliance on the Single-Level Breit-Wigner representation currently used. A multilevel treatment of scattering might be needed. A more complicated resonance representation might be necessary to handle the secondary structure coming from the double-humped fission barriers. In most current methods, self-shielding effects are omitted for the slowing down from inelastic scattering in the unresolved range.

In the resolved resonance range for the heavier isotopes, Doppler broadening of the resonances becomes important. We currently handle that well for the integrated cross sections, but the downscatter shapes are taken from the target-at-rest representation. In addition, we do not normally treat the angular distributions for resonance scattering in detail. The technical

problems with properly Doppler-broadening scattering distributions and angular distribution are very difficult. The current methods work reasonably well for most reactor problems. Resolved resonance self-shielding is handled in good detail by the continuous-energy Monte Carlo codes, but with less accuracy by codes that depend on multigroup self-shielding factors.

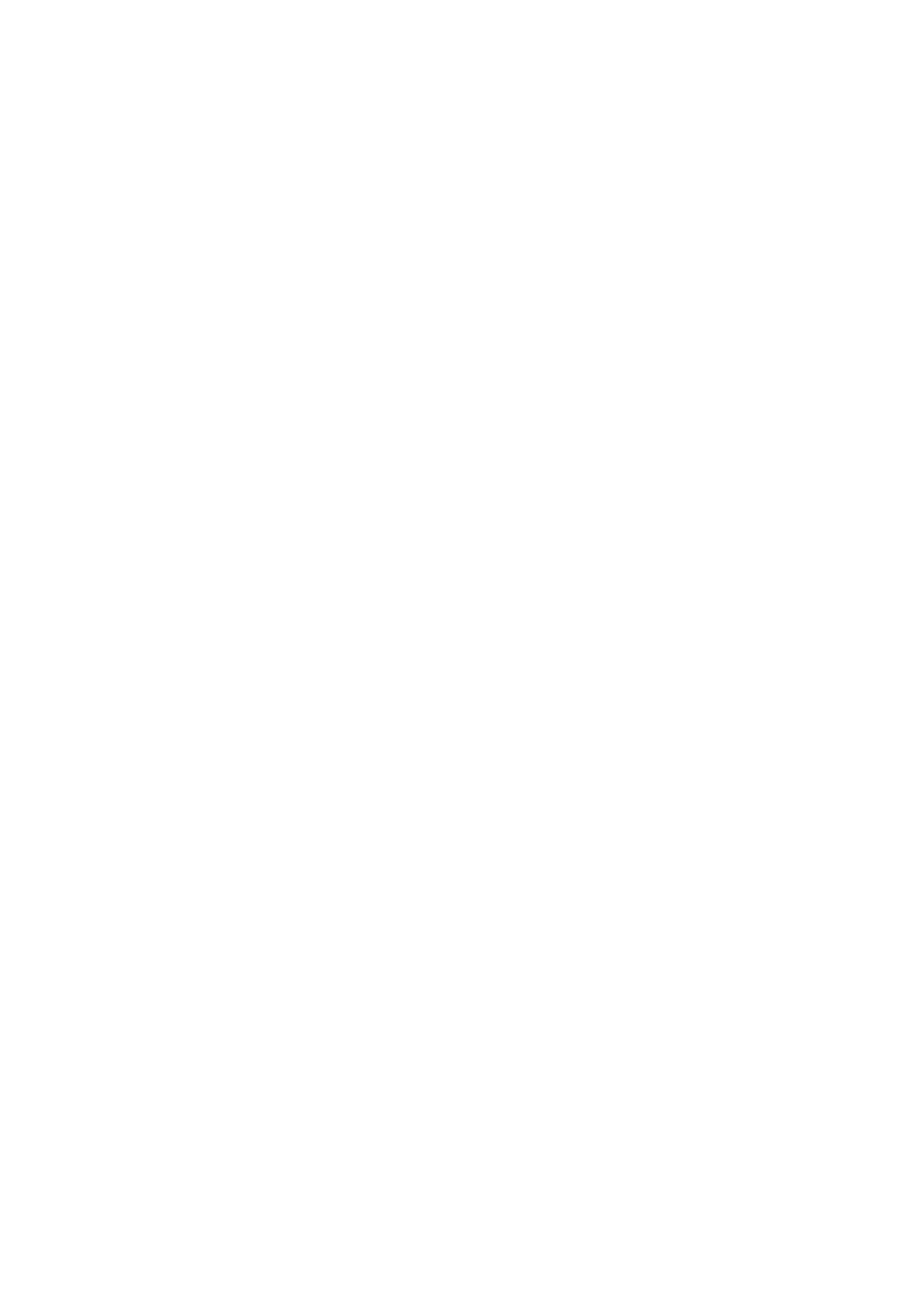
The discussion of time-dependent slowing down concentrated on providing some understanding of the effects using Monte Carlo examples. The theoretical methods presented help to provide some of this understanding, but they are of mostly historical interest. They are not really used for modern reactor calculations.

In summary, the data and methods used to describe neutron slowing down and thermalization are in fairly good shape for reactor calculations, but there are improvements that we can look forward to in future years.

References

- Alcouffe RE, Baker RS, Dahl JA, Turner SA, Ward RC (Rev. May 2005) PARTISN: a time-dependent, parallel neutron particle transport code system, Los Alamos National Laboratory report LA-UR-05-3925.
- Askew JR, Fayes FJ, Kemshell PB (1966) A general description of the lattice code WIMS. *J Brit Nucl Energy Soc* 5:564.
- Bell GI, Glasstone S (1970) *Nuclear reactor theory*. Van Nostrand Reinhold Company, New York
- Bondarenko II (ed) (1964) *Group constants for nuclear reactor calculations*. Consultants Bureau, New York.
- Briggs JB et al (2004) *International handbook of evaluated criticality safety benchmark experiments*. Tech. Rep. NEA/NSC/DOC(95)04/I, Nuclear Energy Agency, Paris
- Butland AT (1973) LEAP and ADDEL, a users guide to two complementary codes on the ICL-470 for calculating the scattering law from a phonon frequency function. Atomic Energy Establishment Winfrith report AEEW-M-1200
- Cullen DE (November 2005) TART 2005: a coupled neutron-photon 3-D, time dependent, combinatorial geometry monte carlo transport code. Lawrence Livermore National Laboratory report UCRL-SM-218009
- Cullen DE (2007) PREPRO 2007: 2007 ENDF/B pre-processing codes. IAEA-NDS-39, Rev. 13. Nuclear Data Section, International Atomic Energy Agency, Vienna
- Herman M, (ed) (2005) *Data Formats and Procedures for the Evaluated Nuclear Data File ENDF/B-VI and ENDF/B-VII*, Brookhaven National Laboratory report BNL-NCS-44945-05-Rev (ENDF-102)
- Henryson H II, Toppel BJ, Stenberg CG (1976) MC2-2: a code to calculate fast neutron spectra and multigroup cross sections. Argonne National Laboratory report ANL-8144 (ENDF-239)
- Honek H (1961) THERMOS, a thermalization transport theory code for reactor lattice calculations. Brookhaven National Laboratory report 5826
- Koppel JU, Houston DH (July 1978) Reference manual for ENDF thermal neutron scattering data. General Atomic report GA-8774 revised and reissued as ENDF-269 by the National Nuclear Data Center at the Brookhaven National Laboratory
- Koppel JU, Triplett JR, Naliboff YD (March 1967) GASKET: a unified code for thermal neutron scattering. General Atomics report GA-7417 (Rev.)
- Larson NM (October 2008) Updated Users' guide for SAMMY: multilevel R-matrix fits to neutron data using Bayes' equations. Oak Ridge National Laboratory report ORNL/TM-9179/R8
- Lathrop, KD (November 1965) DTF-IV, a FORTRAN program for solving the multigroup transport equation with anisotropic scattering. Los Alamos Scientific Laboratory report LA-3373
- MacFarlane RE (September 1980) ENDF/B-IV and -V Cross sections for thermal power reactor analysis. In: *Proceedings international conference of nuclear cross sections for technology*, Knoxville, October 22-26, 1979, National Bureau of Standards Publication 594
- MacFarlane RE (July 1992) TRANSX2: a code for interfacing MATXS cross-section libraries to nuclear transport codes. Los Alamos National Laboratory report LA-12312-MS

- MacFarlane RE (March 1994) New thermal neutron scattering files for ENDF/B-VI release 2. Los Alamos National Laboratory report LA-12639-MS
- MacFarlane RE, Muir DW (1994) The NJOY nuclear data processing system, version 91, Los Alamos National Laboratory report LA-12740-M
- Mattes M, Keinert J (2005) Thermal neutron scattering data for the moderator materials H₂O, D₂O and ZrHx in ENDF-6 format and as ACE library for MCNP(X) codes. International Nuclear Data Committee report INDC(NDS)-0470, April 2005.
- X-5 Monte Carlo Team (2003) MCNP—A General Monte Carlo N-Particle Transport Code, Version 5, Los Alamos National Laboratory report LA-UR-03-1987 (April 2003)
- Skold K (1967) Small energy transfer scattering of cold neutrons from liquid argon. *Phys Rev Lett* 19:1023
- Sublet J-Ch, Ribon P, Coste-Delcalaux M (2006) CALENDF-2005: user manual. CEA report CEA-R-6131
- Tuli JK, Oblizinsky P, Herman M (eds) (December 2006) Special issue on evaluated nuclear data file ENDF/B-VII.0. *Nucl Dat Sheets* 107(12):2931–3060
- Williams MMR (1966) *The slowing down and thermalization of neutrons*. North-Holland Publishing Company/Wiley, Amsterdam/New York
- Wycoff RWG (1963) *Crystal Structures*. Wiley, New York/London



4 Nuclear Data Preparation

Dermott E. Cullen

Lawrence Livermore National Laboratory, Livermore, CA,

USA

redcullen1@comcast.net

1	<i>Overview</i>	282
1.1	Introduction.....	282
1.2	The ENDF/B Format.....	284
1.2.1	ENDF/B Tables and Interpolation.....	285
1.3	The Importance of Nuclear Data-Processing Codes.....	287
1.4	First-Order Approximations: Space, Energy, and Time.....	287
1.5	Basic Equations.....	287
1.6	Species of Particles.....	289
1.7	Evaluated Data.....	290
1.7.1	Neutron-Interaction Data.....	291
1.7.2	Neutron-Induced Photon Production.....	293
1.7.3	Photon Interaction Data.....	295
1.8	Approximate Methods.....	297
1.8.1	Monte Carlo Versus Deterministic Codes.....	297
1.8.2	Continuous Energy.....	298
1.8.3	Multigroup.....	302
1.9	Summary.....	303
2	<i>Reconstruction of Energy-Dependent Cross Sections</i>	303
2.1	Introduction.....	303
2.2	Representation of Cross Sections.....	303
2.3	Tabulated Cross Sections.....	304
2.3.1	Linearized Cross Sections.....	306
2.4	Reconstructing the Contribution of Resonances.....	312
2.4.1	The Resolved-Resonance Region.....	312
2.4.2	Unresolved-Resonance Region.....	316
2.4.3	Adding Resonance and Background Cross Sections.....	317
2.4.4	Output Format.....	318
3	<i>Doppler Broadening</i>	319
3.1	Introduction.....	319
3.1.1	What Causes Doppler Broadening?.....	319
3.2	The Doppler-Broadening Equation.....	321
3.2.1	Mathematical Interpretation.....	326
3.3	Methods of Solution.....	330
3.3.1	Kernel Broadening.....	331
3.3.2	Tabulated Broadened Cross Sections.....	333
3.3.3	TEMPO and Psi-Chi Methods.....	336

3.3.4	Mathematical Comparisons	340
3.4	Numerical Results	343
3.4.1	Low Energies	343
3.4.2	Resonance Region	348
3.4.3	High Energies	350
4	<i>Self-Shielding</i>	352
4.1	Introduction	352
4.2	Narrow, Intermediate, and Wide Resonances	355
4.2.1	Narrow Resonances	356
4.2.2	Wide Resonances	356
4.2.3	Intermediate Resonances	357
4.3	Cross-section Dependence of Flux	358
4.4	Computation of Multigroup Cross Sections	359
4.4.1	Tabulated Cross Sections	361
4.4.2	Linearly Interpolable Data	361
4.4.3	Solution	364
4.4.4	Direct Integration	369
4.5	Comparison of Results	373
5	<i>Transfer Matrix</i>	374
5.1	Introduction	374
5.2	Solution	377
5.2.1	Uncorrelated Distributions	378
5.2.2	Angular Distributions	378
5.2.3	Energy Distributions	381
5.2.4	Correlated Distributions	383
5.2.5	Solution of the Inner Integral	387
5.2.6	Thermal-Scattering Law Data: $S(\alpha, \beta)$	388
6	<i>Group Collapse</i>	388
6.1	Introduction	388
6.2	Noncoincident-Group Boundaries	390
7	<i>The Multiband Method</i>	393
7.1	Introduction	393
7.2	Multiband Equations	397
7.3	Multiband Parameters	399
7.4	Solution for Band Parameters	402
7.4.1	Analytical Solution for Two Bands	403
7.4.2	Generalization to N Bands	405
7.4.3	How Many Bands are Required?	406
7.5	Transfer Matrix	408
7.6	Boundary Condition	410
7.7	Example Results	411
7.7.1	Theoretical Cases	411
7.7.2	Bramblett-Czirr Plate Measurements	415
7.7.3	Criticality Calculations	416
7.7.4	Shielding Calculations	418

7.7.5	Fusion Reactor Blanket	420
7.8	Conclusions	420
	<i>References</i>	422

Abstract: Today, new evaluated data are almost always prepared in the now universally accepted ENDF/B format. Between the originally evaluated data as coded in the ENDF/B format and our particle transport codes, which actually use the evaluated data, are the often overlooked data-processing codes. These data-processing codes translate and manipulate the data from the single universal ENDF/B format to a variety of formats used by our individual particle transport codes, that is, in contrast to our universally accepted evaluated data format, ENDF/B, as yet there is no universally accepted format used by all of our application codes.

This chapter covers in detail the work done by our data-processing codes to prepare the evaluated data for use in our applications: this includes reconstructing energy-dependent cross sections from resonance parameters, Doppler broadening to a variety of temperatures encountered in real systems, defining data for use in both continuous energy Monte Carlo codes, as well as multigroup Monte Carlo and deterministic methods codes.

In this chapter, both WHAT needs to be done by our data-processing codes and WHY have been defined; also, the overall perspective of a general plan, “The Big Picture,” for the historical and current development of the methods used over the last half century as well as today, has been given.

The importance that processing code verification projects have played over the past decades as well as today has been stressed here. It should be remembered that computer codes have always been very complicated, and it is almost impossible to verify the results calculated by any one code without any comparison with one or more other independently developed codes. A classic mistake is to assume that checking the results will impede progress, whereas in fact experience has shown that taking the time to verify results can actually in the long run lead to savings in time and major improvements in the reliability of our codes.

1 Overview

1.1 Introduction

The chapter on Nuclear Data Preparation for the CRC Handbook of Nuclear Reactors Calculations (Cullen 1986) was written by me in 1986; the present chapter is an update of this earlier work. When this earlier work was reread now, what was surprising is that even after 20 years only a very little has changed. Most of the methods described here are the same that we used back then. The big differences between the Nuclear Data Preparation then and now are mostly due to the enormous advances that have occurred in computer size and power since then. This now allows us to routinely do things in a few minutes that 20 years ago took us days or weeks or was simply not feasible at all. Closely related are the advances in nuclear model codes, which have resulted in current nuclear data that are much more detailed, and advances in particle transport codes that are capable of using this much more detailed data. Standing as an interface between the evaluators and their evaluations, on the one hand, and the transport codes, on the other hand, are our nuclear data-processing codes; these data-processing codes have also made great strides to take advantage of the enormous increase in computer size and power, and to accommodate changes in modern evaluations and their use in our transport codes. In order to document the historical development of the methods that we use today, references to the methods as they were originally developed have been retained;

these are references: Weinberg and Wigner (1958), Glasstone and Edlund (1962), Kinsey (1970), Howerton et al. (1975, 1978), Igarasi et al. (1969), Pope (1973), Goel and Krieg (1975), Kolesave and Nikolaev (1977), Garber and Brewster (1975), Plechaty et al. (1978a,b), Alder et al. (1963), Cashwell et al. (1972), Lichtenstein et al. (1979), Plechaty and Kimlinger (1971), Emmett (1975), Engle (1967), Mynatt et al. (1973), Lathrop and Brinkley (1970), Hardie and Little (1969), Fowler et al. (1971), Cullen (1974, 1976, 1977a,b, 1978a,b, 1979a–c, 1980a–c), Cashwell and Everett (1959), Seamon (1981), Cullen et al. (1973, 1975, 1976, 1978, 1980, 1982a,b), Garber and Kinsey (1967), Ozer (1973), MacFarlane et al. (1982), Weisbin et al. (1974, 1976), Rieffe et al. (1981), Panini (1973), Vertes (1981), Pope et al. (in press), Greene et al. (1976), Lamb (1939), Wigner and Wilkins (1944), Meghreblian and Holmes (1960), Friedman (1961), Breit and Wigner (1936), Gregson and James (1965), Hutchins et al. (1973), Green and Pitterle (1968), Patrick (1982), Mughabghab et al. (1981), Gyulassy et al. (1972), Jeans (1948), Toppel (1971), Joanou et al. (1961), Goldstein and Cohen (1962), Goldstein (1972, 1975), Abramowitz and Stegun (1965), Doyas et al. (1971), Lathrop (1965), Bondarenko et al. (1964), Shakespeare (1982), Weisbin and LaBauve (1973), Zijp et al. (1981), Konshin (1981), Ganesan (1981), Ganesan et al. (1982), Perez et al. (1981), Buchholz (1980), Westfall (1978), MacFarlane and Boicourt (1975), Perkins (1982), Greene (1973), Hong and Shultis (1982), Nikolaev and Phillipov (1963), Stewart (1964), Levitt (1972), Cullen and Pomraning (1980), Plechaty and Kimlinger (in press), Graves-Morris (1973), Askew et al. (1966), Bremblett and Czirr (1969), Czirr and Bramblett (1967), Lewis and Soran (1978), Plechaty (1977), and updated references starting with Cullen (1986) have also been added by me. It is hoped that this allows us to preserve the historical record, and much of this chapter presents details of methods used in today's data-processing codes, ll in particular the ENDF/B preprocessing codes – PREPRO (Cullen 2007a–c) and NJOY (MacFarlane and Muir 1994), as they exist today. (Note that the SIGMA1 convention of extending cross sections outside of their tabulated range as $1/V$ differs from the original convention of extending them as constant. The $1/V$ convention is an improvement based upon accumulated years of experience using the SIGMA1 method; This result indicates that to minimize the error in the contribution from any given energy, such as a resonance peak energy, E_R , the Doppler width should be defined at $\sqrt{E_0} = 1/2 (\sqrt{E_R} + \sqrt{E})$, not simply ER ; The Joint Evaluated File (JEF), to be distributed by the NEA-Data Bank, Saclay, on behalf of the contributing OECD countries.)

This *Handbook of Nuclear Energy* will present a variety of methods that are currently used to solve nuclear fission-related problems, with emphasis on reactor core problems. The solution of these problems involves describing the transport of neutrons, photons, and charged particles through matter and the interaction of these “particles” with matter. Throughout the following discussion, for simplicity, neutrons, photons, and charged particles will collectively be referred to as particles.

In this handbook, there will be a great deal of discussion concerning solution of the linearized Boltzmann equation in order to determine the distribution of particles or flux in space, direction, energy, and time. For time-dependent problems, we may also have to solve a related system of equations to describe the change in composition of the medium, due to burn-up and radioactive decay. Throughout this discussion, it is important to remember that generally the determination of the distribution of particles or flux is a means to an end, rather than an end itself. That is to say, generally, what we are interested in describing is some effect caused by the interaction of the particles with the medium through which they are transported. For example, in reactor core calculations, we are interested in determining the reaction rates for

individual reactions and leakage from the core. These may in turn be used to determine a variety of quantities or properties, including

1. The *static and dynamic multiplication factor* of the system, which will allow us to determine whether or not the system is statically stable (i.e., is critical) and whether or not the system is dynamically stable (e.g., has a negative Doppler coefficient).
2. The *energy deposition rate*, which will allow us to determine the amount of power generated and the temperature distribution throughout the system. This information can be used to determine how much power a reactor can safely generate and temperature-dependent effects within the reactor.
3. The *rate of disappearance or build-up of materials* within the reactor, which will allow us to determine the time-dependent composition of the system. This information can be used to establish a fuel management program and will allow us to determine the radiation damage to the reactor, e.g., gas production, atom displacement, etc.

Any number of examples of such kind may be given. The important point to understand is that none of these quantities can be defined directly in terms of the distribution of particles, such as the neutron flux; so it is not sufficient to merely solve the linearized Boltzmann equation to define the flux. Again, let us stress that knowing the flux distribution is merely a means to an end. All the effects we are really interested in depend on nuclear data. Even if one could somehow exactly calculate the distribution of particles or flux, without any adequate nuclear data, it would still not be possible to determine the effects that we are really interested in. The second point is that in discussing the nuclear data we must consider not only the data that are used directly to determine the distribution of particles, but also the data that are then subsequently used in conjunction with the determined distribution of particles or flux to define the quantities that we are really interested in, e.g., energy deposition, gas production, and many other quantities as explained later in this chapter. The third point is that throughout this book many methods and approximations will be introduced; and in all cases, these methods and approximations will attempt to conserve some basic properties of the Boltzmann equation. However, since we are interested in effects, as opposed to determining the particle distributions alone, we will attempt to conserve reactions, rather than flux or cross section. In principle, reactions are a physical observable that we can directly relate to what is happening in any system.

1.2 The ENDF/B Format

As of the mid-1960s there were many nuclear data libraries; basically, each laboratory had its own data library, in its own format, for its own computer codes. Each library was designed to get the “best” answers using the laboratories’ own computer codes, for the specific applications that each laboratory was interested in. This often required nonphysical “fixes” or fits to force agreement between computer code results and the laboratory’s finished applications.

By the mid-1960s an effort had begun to establish a nuclear data library, containing evaluated data based solely on the “best” available differential measurements and nuclear model calculations. It was hoped that one common library of data could be universally adopted for use throughout the world. Unfortunately, this goal has not been achieved yet. Even today we have a variety of nuclear data libraries, to name a few: ENDF/B-VII in the United States, JEF in the European Community, JENDL in Japan, CENDL in China, and BROND in Russia.

Even over 40 years after the start of the ENDF/B project we still have significant differences between the important evaluations in these various data libraries; these differences are often based on valid, scientifically based judgments that one set of measured data or one nuclear model calculation is better than another; unfortunately, the differences can also be based on national “pride and prejudice”; simply, the human nature that we cannot seem to avoid.

Even though the ENDF/B effort has not led to a common set of evaluated nuclear data, it has led to a common universally accepted format for the data; e.g., all the nuclear data libraries mentioned earlier: ENDF/B-VII, JEF, JENDL, CENDL, and BROAD have all adopted the ENDF/B format, which is now in its sixth version and is named ENDF/B-6 (Kinsey 1970; Rose and Dunford 1990). This common format is a great step forward, because it allows us to more easily compare data from the various libraries, and has also greatly reduced the effort on the nuclear data-processing codes. Compared to the earlier situation wherein each laboratory had to develop its own codes to process its own nuclear data, in its own computer-based format, today there are only a few nuclear data-processing code systems that service the needs of the entire international nuclear community.

As today the ENDF/B-6 format is universally used, it simplifies the writing of this chapter; because the focus can be on this single format and the few nuclear data-processing code systems that are used today are being focused. The latest ENDF/B-VII.0 data (Oblozinsky et al. 2006), which are now freely available online (Cullen 2007a–c), are also scrutinized.

1.2.1 ENDF/B Tables and Interpolation

Most of the nuclear data contained in the ENDF/B system are in the form of tabulated values with an interpolation law defining how to interpolate between the tabulated values. Since we are interested in the integral results, these interpolation laws are very important in order to uniquely define our nuclear data at all energies; and not just the energies at which the data are tabulated. The interpolation laws allowed in ENDF/B include histogram, linear or log in the x and y dimensions (five basic interpolation laws), and additional laws for special cases such as charged-particle thresholds.

These interpolation laws are very useful during the evaluation process; e.g., low-energy capture and fission cross sections tend to vary as $1/V$, which can be exactly defined using log–log interpolation. Similarly, spectra often have analytical forms such as \sqrt{E} at low energy and exponential at high energy, which can be defined exactly using nonlinear interpolation laws. For these reasons, we would like to maintain these quite general interpolation laws for use during evaluation and presentation of original evaluations in the ENDF/B format.

But these interpolation laws present problems when we want to use the evaluated data in the ENDF/B format. The most obvious problem is that the sum (redundant) cross sections, such as the total, cannot be exactly defined using any of the ENDF/B interpolation laws, except linear–linear. Less obvious is that although the nonlinear interpolation laws can be used to analytically define integrals of the data, these integrals are often numerically unstable in ways that are difficult to detect, and can cause errors in our calculated results.

Soon after my work got started at Brookhaven National Laboratory in 1967, over 40 years ago, it was realized that the interpolation laws defined for use with ENDF/B were a great advantage to allow evaluators to use analytical shapes for cross sections and secondary-particle

distributions. For example, at low energies both capture and fission cross sections are $1/V$ in shape, which can be exactly defined using log-log interpolation; similarly, at low energy many secondary-neutron distributions tend to vary as \sqrt{E} , which can also be defined using log-log interpolation.

However, at the same time, the flexibility of these interpolation laws has a disadvantage when these evaluations are used in applications. The most obvious disadvantage being that it can cause inconsistency in the cross sections. Subsequently, we will see an example wherein the tabulated total cross section is not the sum of its parts, solely because of the use, or in this case, misuse, of nonlinear interpolation.

To allow for both the advantages to evaluators and avoid problems during the use of the evaluations, it was realized that the solution was to provide computer codes to allow the evaluated data in the ENDF/B format to be converted from their original nonlinear-tabulated form to linearly interpolable tabulated form, to within any accuracy needed for use in applications; these codes could be used by evaluators to insure that their evaluations are consistent, and also by evaluated data users to insure that whether or not the original evaluator data are consistent, what they use in their applications are consistent.

To meet this need, a series of codes were worked out and they are all included in the ENDF/B Pre-processing codes: PREPRO (Cullen 1980a–c, 2007a–c): (1) LINEAR, to convert tabulated data to linearly interpolable form, (2) RECENT, to reconstruct linearly interpolable cross sections from resonance parameters, (3) SIGMA1, the sigma1 method to Doppler-broaden linearly interpolable cross sections was invented by me, (4) FIXUP, to define the redundant cross sections, such as total, by summation. These codes were required to make linearly interpolable cross sections available to ENDF/B-formatted evaluations. To complete the definition of cross sections, the multiband method was developed by me to handle the unresolved-resonance region. Finally to handle secondary distributions, (5) LEGEND, to linearize angular distributions, and (6) SPECTRA, to linearize energy distributions were added. As these codes were made available they were adopted by MINX (Weisbin et al. 1976), and then inherited by MINX's successor NJOY (MacFarlane et al. 1982; MacFarlane and Muir 1994); thus we now have several code systems that use this linearized data concept.

Initially, there was a great deal of resistance to the idea of replacing an “exact” cross section, such as $1/V$ at low energy by a linearized “approximation.” But eventually, data users accepted the idea as they realized that it was needed for them to be able to have consistent data for use in their applications. Today, nobody seems to question this approach, and it is widely used in our nuclear data-processing codes and our neutron transport codes. This linearizing is now such an integral part of our codes that much of this chapter is devoted to how it is used to reconstruct cross sections from resonance parameters, to Doppler-broaden cross sections, and to calculate multigroup constants.

Development of these codes has taken many years to complete; but today, we have complete systems that are freely available to data users, which include the PREPRO (Cullen 2007a–c) and NJOY (MacFarlane and Muir 1994). Much of this chapter is designed to document what these codes do, and of at least equal importance, why they do it. As successful as these efforts have been we must accept the fact that it is time to pass the torch to the next generation of nuclear data-processing code designers, wherein we will change from our traditional FORTRAN codes to a new generation of C and other language computer codes. Hopefully, this chapter will help make this transition a smooth one by allowing the new generation to understand not only what we did, but also why.

1.3 The Importance of Nuclear Data-Processing Codes

It is now common practice for transport code users to define the transport codes and nuclear data they are using, as when we say we used MCNP (Cashwell et al. 1972; X-5 Monte Carlo Team 2003) and the ENDF/B-VII.0 nuclear data (Oblozinsky et al. 2006; Cullen 2007a–c). This ignores a very important step, namely the nuclear data-processing code; this is what we call the overlooked, but often limiting factor. For example, in addition to telling users that we used MCNP and ENDF/B-VII.0, it is important for users to know that we used the NJOY data-processing system (MacFarlane and Muir 1994), and also know what versions of MCNP and NJOY were used. Only then would we be able to describe how our calculations were done.

Our recent studies (Cullen et al. 2006, 2007a–c) demonstrate that our transport codes are now very accurate, and many of the remaining limitations in the accuracy of our solutions can be traced not to transport, or even the nuclear data, but rather to approximations introduced by our data-processing codes. This suggests that rather than being the overlooked factor, more emphasis should be placed on improving the accuracy and reliability of our nuclear data-processing codes. In this chapter, we will attempt to clearly define the approximations that are being introduced by our data-processing codes.

1.4 First-Order Approximations: Space, Energy, and Time

Even today, with all the available computer size and speed it is still not possible for us to exactly solve the linearized Boltzmann equation. Today's methods still include approximations needed to allow us to solve our problems within sufficient accuracy and in a timely manner to meet our programmatic needs. The most obvious, first-order approximations, is that we do not attempt to define solutions on a continuous spatial and energy basis. Instead, we try to accurately define “average” values; averaged over spatial zones, over-energy groups, and sometimes over time intervals. In terms of our applications wherein we are interested in physical observables, if we can accurately define averages these are usually good enough to meet our programmatic needs. Beyond these first-order approximations, there are other approximations that are related to the accuracy of our nuclear data, and how accurately our nuclear data can be processed into a form that it can be used by our transport codes; this includes multigroup cross sections and group-to-group transfer matrices, which are also averaged over energy ranges and spatial zones and time intervals.

1.5 Basic Equations

In this handbook, we will be discussing how to solve the linearized Boltzmann equation, which in its energy- and time-dependent form can be written as (1),

$$\begin{aligned} \frac{1}{v} \frac{\partial}{\partial t} N(r, \Omega, E, t) + \vec{\Omega} \cdot \vec{\nabla} N(r, \Omega, E, t) + \Sigma_t(r, E, t) N(r, \Omega, E, t) \\ = \frac{1}{4\pi} \int_0^\infty dE' \int_{\Omega'} d\Omega' \Sigma(r, E' \rightarrow E, \Omega' \rightarrow \Omega) N(r, \Omega', E', t) + S(r, \Omega, E, t), \end{aligned} \quad (1)$$

where

$N(r, \Omega, E, t)$ neutron flux per unit volume, energy, and solid angle at time t .

v is the neutron speed (not, velocity).

$\Sigma_t(r, E, t)$ total macroscopic cross section at location r and time t for a particle of energy E .

Generally, the macroscopic cross sections will be spatially dependent since different materials will be used at different positions (e.g., core vs. shield) and time dependent because of burn-up.

$\Sigma(r, E' \rightarrow E, \Omega' \rightarrow \Omega)$ differential cross section, describing the transfer of particles with initial coordinates E', Ω' before the interaction to E, Ω after the interaction. Written in this form, it includes the effect of all possible processes, e.g., scatter, fission, ($n, 2n$), etc.

$S(r, \Omega, E, t)$ flux-independent neutron source.

The differential cross section can be written in terms of the contributions from the individual reactions in the form

$$\Sigma(r, E' \rightarrow E, \Omega' \rightarrow \Omega) = \sum_k M_k(E') \Sigma_k(r, E') P_k(E' \rightarrow E, \Omega' \rightarrow \Omega), \quad (2)$$

where the summation is over reactions k , e.g., $k =$ elastic, fission, etc., and

$M_k(E')$ Multiplicity or average number of secondary neutrons, e.g., 1 for elastic, 2 for ($n, 2n$), and $\nu(E')$ for fission.

$\Sigma_k(r, E')$ Reaction cross section for process k .

$P_k(E' \rightarrow E, \Omega' \rightarrow \Omega)$ Probability distribution for process k , describing the transfer of particles with initial coordinates E', Ω' before the interaction to E, Ω after the interaction. This is a normalized distribution which is equal to unity when integrated over all final E, Ω .

For the linearized Boltzmann as written previously, everything is assumed to happen instantaneously at time t , at a given spatial location r . If we consider delayed neutrons, the equation is further complicated by an additional integral over all earlier times t' ; for simplicity, this complication will not be included in the following equations.

If we are to consider the changes in composition due to burn-up and/or radioactive decay, we must consider the coupled set of equations describing the changes in the composition for each constituent material $N_j(r, t)$ as a function of position and time.

$$\frac{dA_j(r, t)}{dt} = -[R_j(r, t) + \lambda_j]A_j(r, t) + \sum_{j'} [R_{j'}(r, t)\alpha(j' \rightarrow j) + \beta(j' \rightarrow j)]A_{j'}(r, t)$$

and

$$R_j(r, t) = \int_0^{\infty} dE \sigma_j(E) N_0(r, E, t), \quad (3)$$

where

$A_j(r, t)$ Atoms of nuclide j

λ_j Decay constant of nuclide j

$\sigma_j(E)$ Microscopic cross section of nuclide j

$\alpha(j' \rightarrow j)$ Probability that an interaction with a nuclide j' atom will create a nuclide j atom

- $\beta(j' \rightarrow j)$ Probability that a decay of a nuclide j' atom will create a nuclide j atom
 $N_0(r, E, t)$ Scalar neutron flux (integrated over direction Ω)
 $R_j(r, t)$ Reaction rate of nuclide j at (r, t)

1.6 Species of Particles

Within a fission reactor, each fission event results in the release of approximately 190–200 MeV of energy. This energy is distributed approximately as follows (2),

Kinetic energy of fission production	162 MeV
Beta decay energy	5
Gamma decay energy	5
Neutrino energy	11
Fission neutron energy	6
Instantaneous gamma ray energy	6
Total	195 MeV

In addition to the energy released in fission, energy is also released because of exoergic reactions, such as (n, p) . Finally, the energy of the neutron as it slows down is distributed to other species of particles because of photon production from inelastic scatter and nuclear recoil due to scatter.

Since energy within the reactor core is distributed between neutrons, photons, and charged particles, in principle, there will be similar equations for each species and these equations will be coupled, since one species of particles can produce particles of a different species, e.g., photon production due to neutron capture, and photonuclear neutrons due to photon interactions. However, as applied to nuclear-fission reactor cores, the only transport calculations that will be considered here will be transport of neutrons and photons.

The mean-free path of fission products and charged particles is short enough that they may be considered to come to rest and deposit their energy at the point at which they are “created” or emitted by a nucleus, and their transport need not be considered at all. Although the transport of charged particles be ignored, the production of charged particles will be considered, as it is important to consider the production of hydrogen and helium gas due to proton, deuteron, triton, He₃, and alpha emission. The production of such gases can be determined directly from a known (previously calculated) distribution of neutrons, since evaluated data libraries now contain hydrogen- and helium-production cross sections (Kinsey 1970; Rose and Dunford 1990). Similarly, effects such as heat production (KERMA) and displacement production (DPA) can be calculated. From a known neutron distribution and production cross section, the production of gas of type x can be simply calculated from


$$\frac{dG_x(r, t)}{dt} = \int_0^\infty dE \Sigma_x(r, E, t) N_0(r, E, t), \quad (4)$$

where

- $\frac{dG_x(r, t)}{dt}$ Production rate of gas of type x
 $\Sigma_x(r, E, t)$ Macroscopic production cross section of gas x
 $N_0(r, E, t)$ Scalar flux (integrated over direction Ω)

The transport of photons is important in reactor core calculations. Since photons tend to transport longer distances than neutrons, the photons tend to have a smoothing influence on energy deposition, by depositing their energy over a wider spatial region. In principle, neutron production due to photon interaction (photonuclear reactions) should also be considered; there are a number of situations wherein such production is important, e.g., systems containing appreciable quantities of beryllium. However, coupling of the neutron and photon transport equations in this way complicates the solution of the equations and for reactor core calculations, it is generally judged as “not to be worth the effort.” Therefore, the only coupling that we will consider may be photon production due to neutron interactions. With this assumption, the neutron transport equation may be solved independently; the then known neutron distribution may be used to define a neutron-induced photon source, and the photon transport equation may then in turn be solved. Therefore, the cross sections that we must consider include the following five categories:

1. Neutron interaction
2. Neutron-induced photon production
3. Photon interaction
4. Gas (charged particle) production due to neutron interaction
5. “Effect” production, such as heat (MERMA) and displacement (DPA)

Of these five categories, gas and “effect” production can be calculated using a known (previously calculated) neutron distribution and production cross sections, as in (4). Since it is completely analogous to our treatment of multigroup cross sections presented later in this chapter, it will not be explicitly considered further in this chapter. Another type of data that must be considered is thermal-scattering law data; this data is briefly discussed here and more extensively in  Chap. 3 on slowing down and thermalization.

Of the remaining three categories, since the emphasis of this handbook is on nuclear power and fission reactor core calculations, major emphasis will be placed on the treatment of neutron interactions. Much of the treatment of photon interaction and production is very similar to the treatment of neutron interactions and secondary-neutron energy distributions. Therefore, photon interaction and production will only be mentioned when its treatment differs from that required for neutron interactions.

1.7 Evaluated Data

In order to solve (1), obviously we need to know the total cross section and the cross section, and multiplicity and secondary energy–angle distributions for each reaction. In order to solve (3), we need to know the cross sections for individual reactions, half-lives, and probability of production of nuclides due to interaction or absorption of other nuclides. Of the data required to solve (3), only the cross sections need to be processed prior to use; half-lives and production probabilities are basic nuclear data that may be used directly in applications. The treatment of cross sections for use in (3) is completely analogous to the treatment of cross sections for use in (1); and as such, (3) will not be explicitly considered further in this chapter.

At the present time, there is no single unified theory of nuclear cross sections that will allow us to predict all nuclear cross sections. Therefore, the presently available cross sections are obtained by combining the results of differential and integral experimental measurements with the results of nuclear model calculations, to define the evaluated cross sections that are

used in reactor calculations. The presently available, evaluated nuclear data libraries contain almost all the data that we require, and in the following sections, we will briefly review the representations that are used in these data libraries. Examples of data that may not be explicitly present in the evaluated libraries and may require the use of additional models is the calculation of KERMA and DPA; these additional models will be covered elsewhere in this handbook.

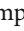
1.7.1 Neutron-Interaction Data




Cross Sections

Evaluations represent the total, elastic, capture, and fission cross sections in the form of resonance parameters plus a tabulated-background cross section (Kinsey 1970; Rose and Dunford 1990). The most general representation at successively higher energies is

1. Tabulated cross sections at low energy.
2. Resolved-resonance parameters plus a tabulated background cross section.
3. Unresolved-resonance parameters plus a tabulated background cross section.
4. Tabulated cross sections at higher energies.

The cross sections for all other reactions are represented in tabular form, e.g., inelastic, ($n, 2n$), etc. Since in order to use cross sections they must be defined at all energies, all tabulated cross sections also have an interpolation law associated with them, in order to uniquely define the cross sections at all energies between the energies at which the cross sections are tabulated.

The major difficulty in processing the neutron-interaction data for later use in applications is that modern evaluations contain a great deal of resonance structure, which makes it very difficult to accurately define the combination of resonances and background cross sections. For example,  [Fig. 1](#) illustrates the ENDF/B-VII.0 (Cullen 2007a–c), U238 elastic cross section, at 0 and 300 K, which has been reconstructed from resonance and background combinations; and in the case of 300 K data, Doppler broadened, in order to obtain the energy-dependent cross section in tabulated form (Cullen 2007a–c). Here, just this one elastic cross section requires between 250,000 energy points (at 0 K) and 50,000 (at 300 K). The sheer size of these data tables can cause a problem during not only during data processing, but also during subsequent use in applications.

 [Figure 1](#) shows some interesting details that we should mention. First at the top of the figure, we can see that the resolved-resonance region extends from 10^{-5} eV up to 20 keV, and above this the unresolved-resonance region extends from 20 keV up to 149 keV. Note the resonance structure in the resolved-resonance region that abruptly changes to the smooth cross section in the unresolved-resonance region; this is because for this figure in the unresolved-resonance region we only plot the infinitely dilute cross section (explained later). Note also the effect of temperature, with the 300 K temperature cross section being much smoother than the 0 K data, in the resolved-resonance region.  [Figure 2](#) for the 1–2 keV energy range, shows the effect of Doppler broadening in better details. Finally, note the range of the cross section that extends over many orders of magnitude, in very narrow energy ranges; this makes the sampling of this data with accuracy, very difficult. For example, if we randomly sample an energy in the energy range of  [Fig. 2](#), we can see that in most cases we will completely miss the resonances and select the smooth potential cross section between resonances.

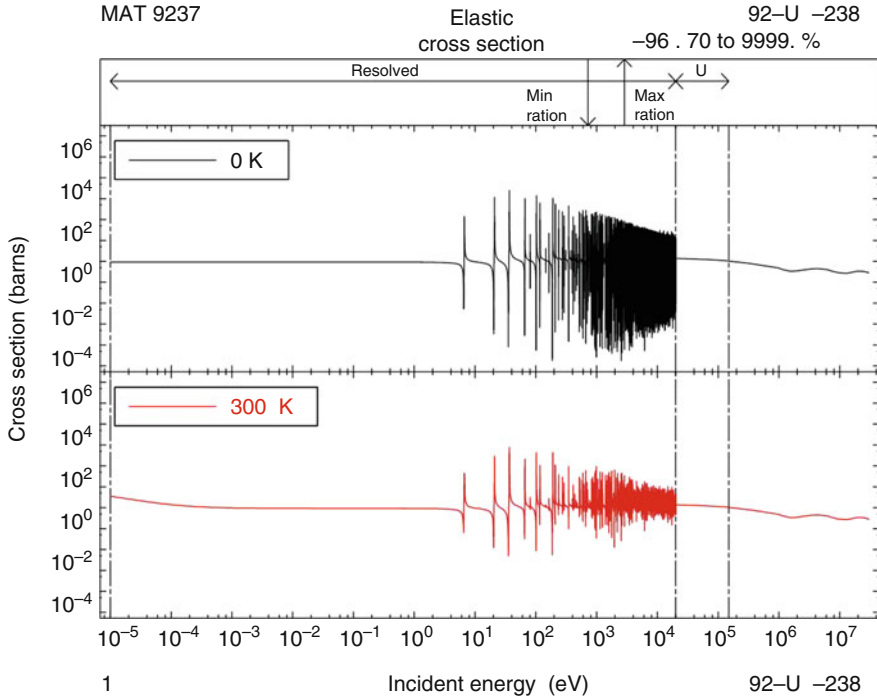


Figure 1
U238 elastic cross section, entire energy range

Secondary-Neutron Distributions

The secondary-neutron distributions are represented in one of several available forms depending on whether the secondary energy and scattering angle are considered to be correlated or uncorrelated. For two body reactions, such as elastic and inelastic scattering, the scattering angle and secondary energy are exactly correlated. In order to describe such reactions, the angular distribution is specified and the corresponding secondary energy can be uniquely calculated by considering conservation of energy and momentum. In this case, the angular distribution may be given in either tabulated or Legendre coefficient form and is given in the center-of-mass system. Figure 3 illustrates elastic angular distributions for ENDF/B-VII.0 (Oblozinsky et al. 2006; Cullen 2007a–c), which were reconstructed from Legendre coefficients using the LEGEND code (Cullen 2007a–c).

For uncorrelated reactions, both angular and energy distributions of secondary neutrons are specified and the final distribution is the product of these two distributions. In this case, the angular distribution must be given in the laboratory system. The most common representation for such reactions in current evaluations is to specify the angular distribution as isotropic.

Figure 4 illustrates some fission spectra for ENDF/B-VII.0 (Oblozinsky et al. 2006; Cullen 2007a–c), which are given as uncorrelated data, with tabulated energy spectra and isotopic angular distributions. From this figure, we can see that the fission spectra between 0 and 5 MeV incident neutron energy are very smoothly varying with incident neutron energy.

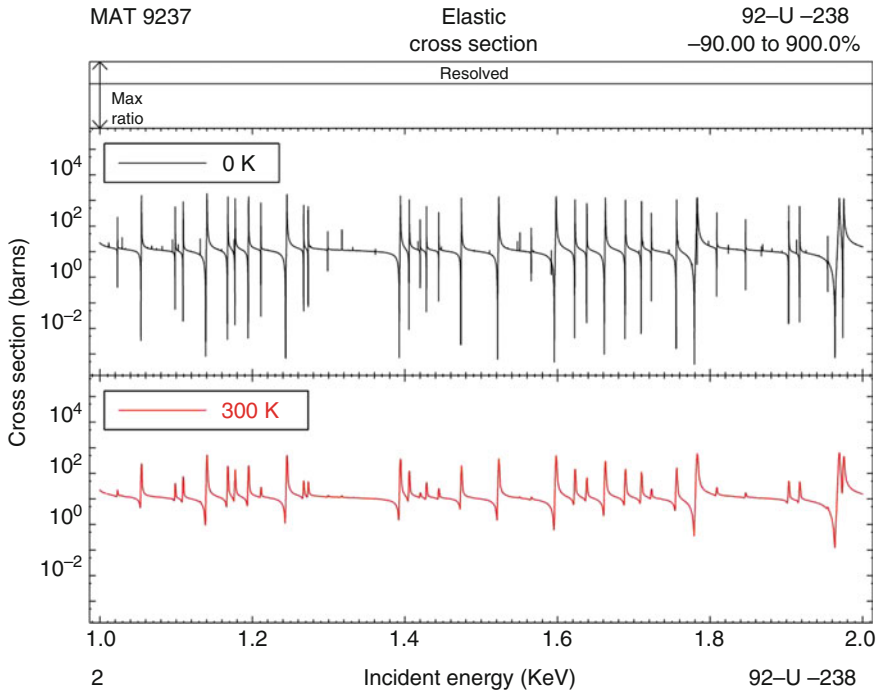


Figure 2
U238 elastic cross section, 1–2 keV energy range

Finally we have correlated energy–angle distributions, which are correlated, but not exactly correlated. In this case, we have distributions that are defined as functions of both secondary energy and direction; defined by specifying either the energy spectra at a given set of directions, or the angular distributions at a given set of secondary energies. Recent evaluations are using correlated energy–angle distributions more and more, indicating the improved ability of our nuclear model codes to accurately calculate such distributions. Figure 5 illustrates some (n, n') continuum spectra for ENDF/B-VII.0 (Oblozinsky et al. 2006; Cullen 2007a–c) that are given as correlated energy–angle distributions, which were reconstructed as energy spectra for viewing using the SIXPAK code (Cullen 2007a–c). These correlated energy–angle distributions were created using a nuclear model code that outputs results as histograms, rather than as continuous in energy. These histogram steps are typically keV wide and at high energy; these are more than adequate, but we can see that at low energy these histograms result in unrealistic “steps” in the distributions; our transport codes are already dealing with this problem (Cullen et al. 2007a–c).

1.7.2 Neutron-Induced Photon Production

Photon production is complicated because in general it will be composed of both discrete and continuum photons; and in addition, there may also be a time-dependent component wherein

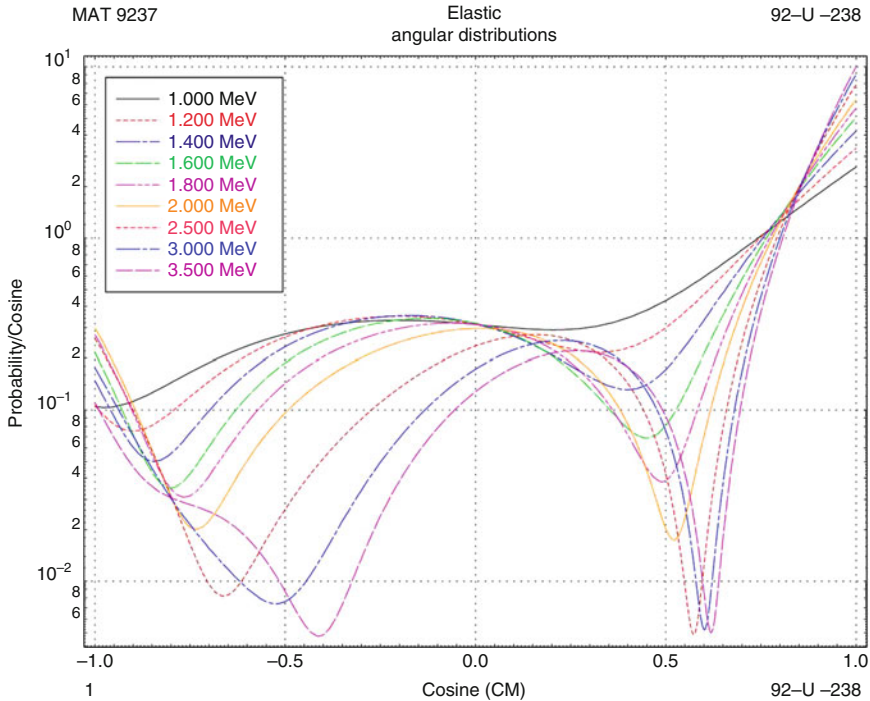
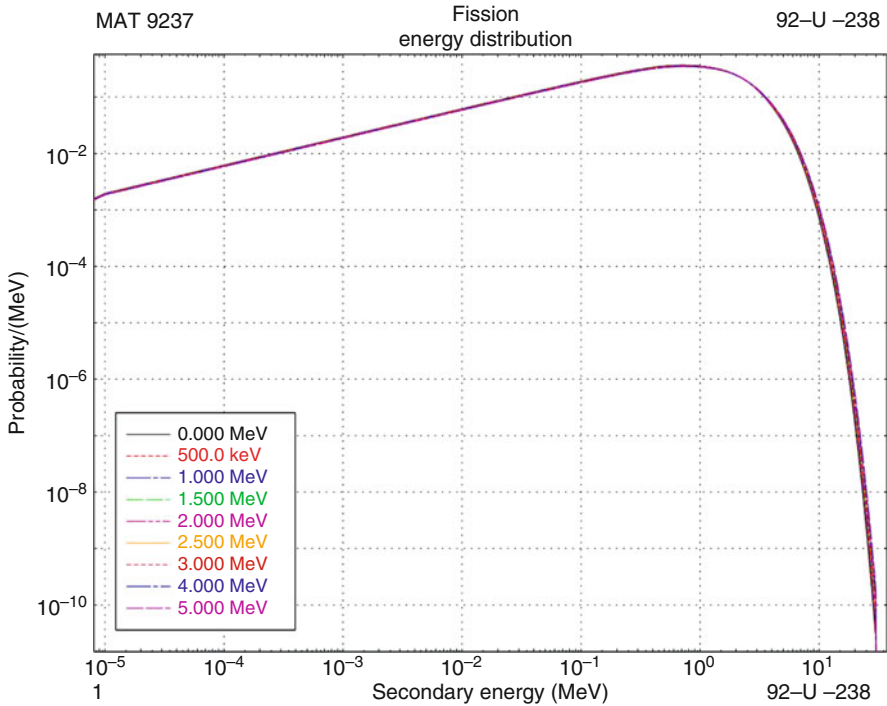


Figure 3
U238 elastic angular distributions, 1–3.5 MeV energy range

some photons are not produced instantaneously at the time of the neutron collision. Discrete photons may be represented in a number of different forms (Kinsey 1970; Rose and Dunford 1990). In one form, the cross section for a given reaction and the resulting transition probability array, between levels, are given. In a second form, one may specify the multiplicity (average number of photons) and cross section for the production of each discrete photon. Both these representations require knowledge of the neutron cross section that induced the reaction. Alternatively, one may simply specify a photon-production cross section for each discrete photon and the continuum.

The distribution of neutron-induced photon production is represented in a form similar to the distribution of secondary neutrons. For discrete photons, energy and angle are exactly correlated and only the angular distribution of photons is specified. For continuum photons, both angular- and energy distribution of photons must be specified. In most current evaluations, the angular distribution of photon production is isotropic, which greatly simplifies the calculation and use of photon-production data (► Fig. 6).

Nuclear data users should be warned that many current evaluations do not include neutron-induced photon-production data. For example, the ENDF/B-VII.0 library (Oblozinsky et al. 2006; Cullen 2007a–c) contains 393 evaluations (isotopes and elemental) and only about half of these include neutron-induced photon production; the fraction is even lower in older data libraries. Almost none of the current evaluations include capture-gamma ray lines, which are

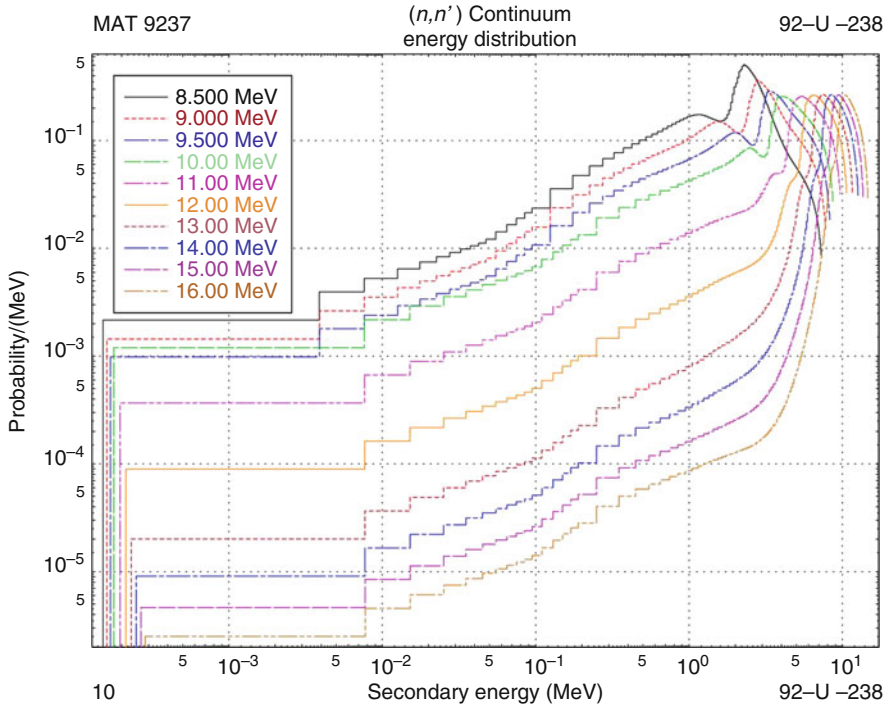


■ **Figure 4**
U238 elastic fission spectra, 0–5 MeV energy range

unique to each isotope. A second warning is that when the neutron-induced photon production is included, energy conservation can be a problem; this can be so severe that photons carry off more energy than is available in a reaction.

1.7.3 Photon Interaction Data

The ENDF/B-VII.0 photon-interaction data is based entirely on the Livermore Evaluated Photon Data Library (EPDL) (Cullen et al. 1997). For those interested in fluorescence and/or electron transport, there are also two other libraries included in ENDF/B-VII.0: The Evaluated Atomic Data Library (EADL) (Cullen et al. 1991a,b) and the Evaluated Electron Data Library (EEDL) (Cullen et al. 1991a,b); these libraries are of little interest for reactor core calculations and as such will not be discussed further in this chapter. The EPDL library included elemental data for all $Z = 1-100$. Photon-interaction cross sections are given in a tabulated form with an interpolation law specified between tabulated points. Compared to neutron cross sections, photon-interaction cross sections are relatively smooth and do not create any special processing problems. For uranium, photon-interaction cross sections are shown in [Fig. 7](#).



■ **Figure 5**
 U238 (n, n') continuum spectra, 8.5–16 MeV energy range

In principle, the angular distribution of secondary photons could be specified in the same form as is used for neutrons. However, in the case of photons, a more natural representation is to use a combination of analytical forms and a correction factor: for coherent scattering, this correction factor is named the form factor; and for incoherent scattering, it is named the scattering function. At high energies, the Klein–Nishina formula is an excellent means of describing incoherent scattering; and at low energies, the coherent distribution assumes the simple form $(1 + \mu^2)$, where μ is the scattering cosine. At other energies, these analytical forms are modified by the form factor (coherent scatter) and scattering function (incoherent scatter), as shown in [Fig. 8](#).

Generally, when compared with neutrons, the processing of photon cross sections are rather straightforward and present little or no difficulty. However, processing the angular distributions of secondary photons can be difficult for two reasons. First, although analytical forms and correction factors are a convenient means to represent angular distributions, Legendre coefficients or tabulated angular distributions are more convenient for use in many applications. Second, the angular distributions can be very anisotropic and difficult to adequately represent in transport calculations, e.g., in S_n calculations, many Legendre coefficients are required to accurately represent the angular distributions. An alternative method of using these correction factors is defined in (Cullen 1995).

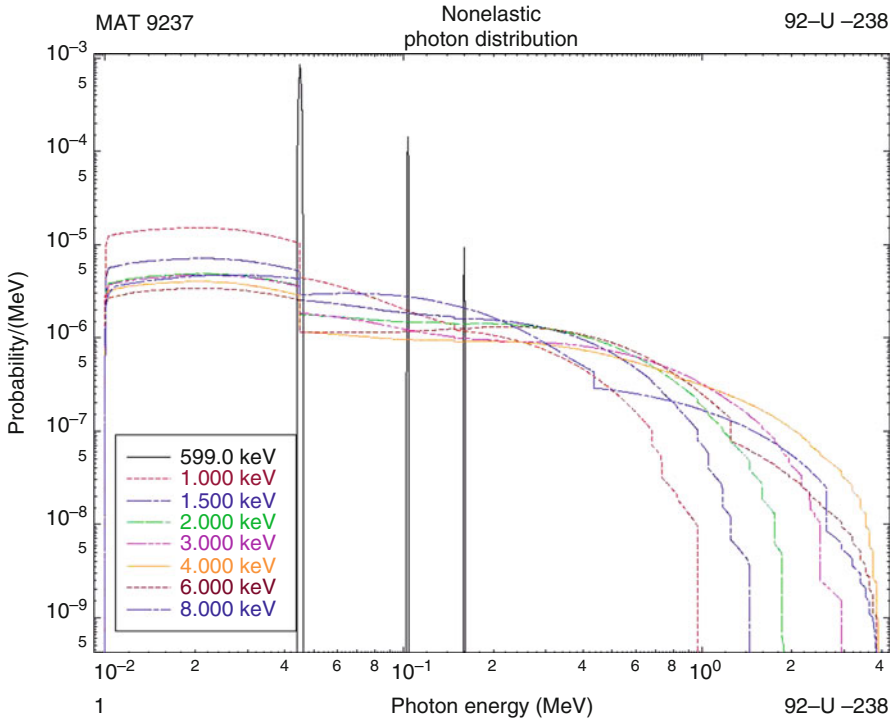


Figure 6
U238 (n, n') nonelastic photon emission spectra

1.8 Approximate Methods

Unfortunately, an exact solution to Boltzmann equation (1) is still beyond our capabilities, even with the most modern and powerful computers that we have today, and we must introduce certain simplifying assumptions before attempting a solution. Once we consider introducing simplifying assumptions, we find that there are a variety of them that can be used, each of which leads to a different method of solving the pertinent equations. For example, several well-known methods include Monte Carlo, discrete ordinates (S_n), and diffusion. Even within each of these methods there are still further subdivisions, such as continuous energy or multigroup Monte Carlo. Unfortunately, the data requirements and methods of cross-section preparation depend on the method that will subsequently be used to solve the Boltzmann equation or an approximation to it.

1.8.1 Monte Carlo Versus Deterministic Codes

There are two basic approaches to using cross sections: continuous energy and multigroup. Generally, continuous energy particles and cross sections are used in Monte Carlo calculations as eight (8) codes, such as the code used in a recent code comparison (Cullen et al. 2007a-c), in the

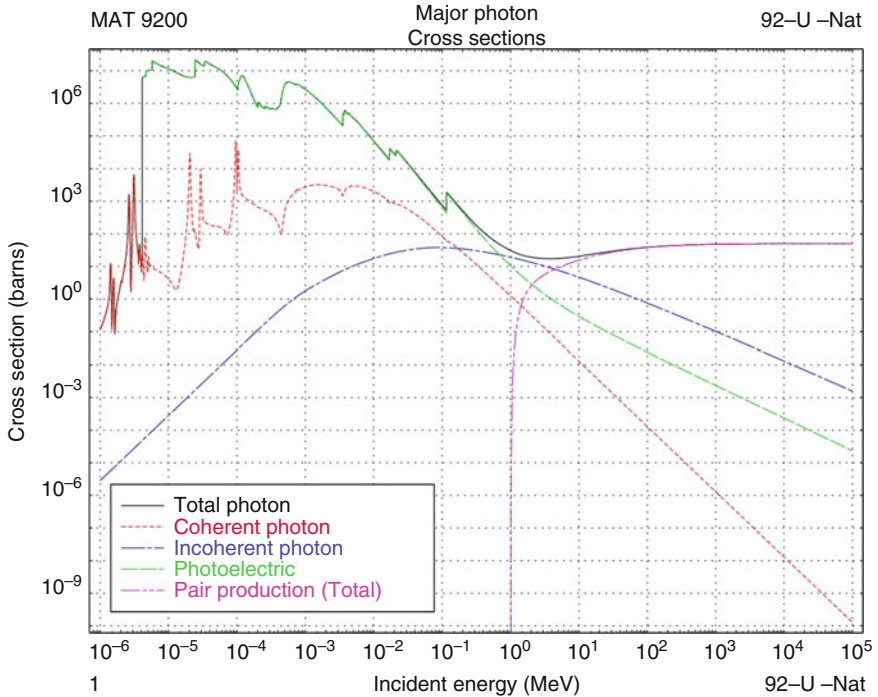


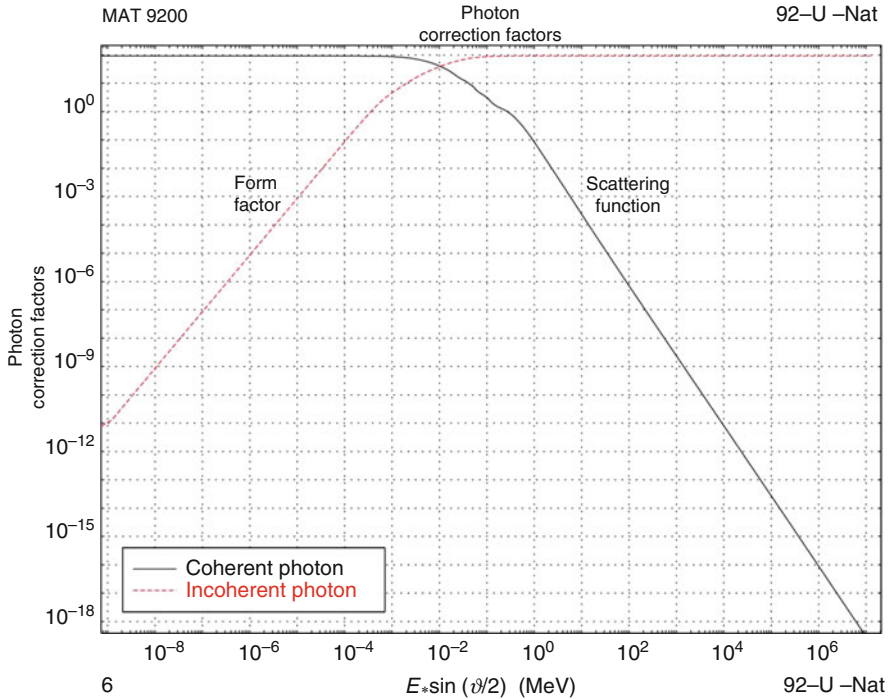
Figure 7
Uranium photon-interaction cross sections

following alphabetical order: COG, CE-KENO, MCNP, MERCURY, MONK, TRIPOLI, TART, and VIM. However, there are also Monte Carlo codes such as TART (Cullen 2005), which uses continuous energy particles and can use either continuous energy or multigroup cross sections, and even Monte Carlo codes such as MORSE (Emmett 1975) which uses multigroup particles and cross sections. Multigroup particles and cross sections are used in discrete ordinates codes, such as ANISN (Engle 1967), DOT (Mynatt et al. 1973), TWOTRAN (Lathrop and Brinkley 1970), and PARTISN (Ray et al. 2005) and diffusion codes such as 1DX (Hardie and Little 1969) and CITATION (Fowler et al. 1971). We will consider each of these approaches in turn.

1.8.2 Continuous Energy

Cross Sections

In this section, we will discuss continuous-energy cross sections and secondary-neutron distributions as used in Monte Carlo codes. The main difficulties in processing cross sections for use in these codes are reconstruction of energy-dependent cross sections and Doppler broadening, in order to account for temperature dependent effects. Each of these topics requires extensive discussion and is covered in detail in the later sections of this chapter.



■ **Figure 8**
Uranium form factor and scattering function

Another problem is how to define the cross sections in the unresolved-resonance energy region. In the unresolved-resonance region, modern evaluations do not uniquely define energy-dependent cross sections; they only define the distribution of resonance widths and spacing (Kinsey 1970; Rose and Dunford 1990), from which it is possible to uniquely define average properties. One of three approaches may be used in the unresolved-resonance region:

1. *Use group-average cross sections* processing of data into this form is discussed later in this chapter under self-shielding.
2. *Statistically select a ladder of resonances* from the distribution of resonance widths and spacings. The ladder of resonances can be either used to calculate energy-dependent cross sections, for direct use in transport codes or can be processed further into the form of cross-section probability tables (Levitt 1972), for later use in Monte Carlo calculations. This approach essentially eliminates the unresolved region or at least allows it to be treated in a manner similar to the resolved-resonance region, as will be discussed later in this chapter under reconstruction and Doppler broadening.
3. *Statistically include the distribution of cross sections* by attempting to simultaneously reproduce both shielded and unshielded conditions. This approach will be described later in this chapter under the multiband method (Cullen 1972, 1974, 1977a,b, 1978a,b).

Angular Distributions

In order to describe the angular distribution of secondary neutrons, the normalized angular distributions are converted into the form of either a continuous integral distribution or equally probable angular bins. For example, given a tabulated, linearly interpolable angular distribution for one reaction,

$$1 = \int_{-1}^{+1} p(E, \mu') d\mu', \quad (5)$$

where μ' is the cosine of the scattering angle.

We can define a continuous cumulative angular distribution

$$P(E, \mu) = \int_{-1}^{\mu} p(E, \mu') d\mu'.$$

Starting from a given tabulated, linearly interpolable angular distribution, the continuous cumulative angular distribution will be quadratically interpolable; and in order to reproduce the differential distribution $p(E, \mu)$, it is very important that quadratic interpolation be used, e.g., assuming the cumulative distribution as linearly interpolable is equivalent to assuming the differential distribution as a constant between tabulated values, similar to the equally probable bins described later. Following this procedure makes sampling very accurate, but it can be expensive too.

An alternative is N equally probable angular bins, where one solves for cosines μ_k such that

$$\frac{k}{N} = \int_{-1}^{\mu_k} p(E, \mu') d\mu', \quad k = 1, 2, \dots, N. \quad (6)$$

Within each bin, the distribution is then assumed to be constant. Following this procedure makes sampling very fast.

Within a Monte Carlo code, either of these representations can be randomly sampled. Each of these representations has its advantages and disadvantages. The continuous cumulative angular distribution has the advantage of being very accurate, but it has the disadvantage that it can be time consuming to sample. The equally probable angular bins have the advantage of being very fast to sample, but it has the disadvantage of being less accurate, and details of the angular distribution may be lost. When many equally probable bins are used, we expect the results using either approximation to yield similar results.

In the evaluated data, angular distributions are given at a set of incident neutron energies; again, we show an example of U238 elastic angular distributions.

One problem that either method has is how to accurately interpolate in incident energy between incident neutron energies at which angular distributions are tabulated. For example, from the previous figures we can see how the interference minima and maxima shift with incident neutron energy. Obviously, to interpolate between say 3 and 3.5 MeV incident neutron energy, we would introduce an error if we interpolate the earlier-shown differential angular distributions orthogonally, along lines of constant cosine; and yet, many codes do exactly this, and this is what ENDF-102 specifies for the evaluated data (Kinsey 1970; Rose and Dunford 1990). It is much more accurate to interpolate the cumulative angular distribution; the shifting minima and maxima are better modeled as continuously shifting with the cumulative integrals.

Energy Distributions

For uncorrelated distributions, the secondary-energy distribution must also be sampled. This can be done directly using the functional forms available in evaluations, such as Maxwellian, exponential, etc. Alternatively, this can be done using a technique that is completely analogous to the treatment of angular distributions described earlier.

If this is done, using the cumulative distribution can be very expensive, as it may require many tabulated secondary-energy points to represent each tabulated spectrum. When using equally probable bins, extreme care must be taken in order to avoid distorting the secondary-energy distributions, as illustrated in [Fig. 9](#).

Unlike the angular distributions that extend over the cosine interval $(-1, +1)$ alone, the secondary-energy distributions in principle can extend over the entire range of possible secondary energies, up to $(0, \infty)$, and over many decades in value. The histogram representation of secondary-energy distributions can result in very wide energy bins in low-probability energy ranges. This is particularly a problem if it occurs at the low- and high-energy limit of the distributions. For example, starting from a Maxwellian or Watt distribution (Kinsey 1970; Rose and Dunford 1990) to represent the spectrum of fission neutrons, using 32 equally probable bins, can result in the highest energy bin extending from only several MeV to the upper-energy limit of the evaluation, e.g., 20 MeV. Using more bins cannot solve this problem because in this case even using 1024 bins can result in the highest energy bin extending from near 9 to 10 MeV,

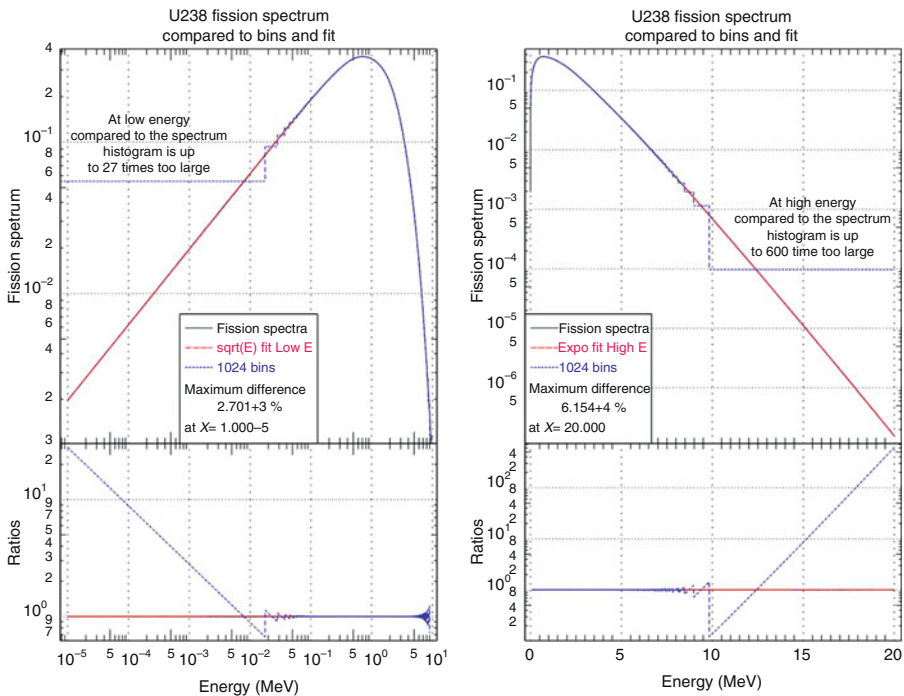





Figure 9
U238 fission spectrum compared to bins and fit

up to 20 MeV, as shown in  Fig. 9. This uniform distribution over this energy range may be compared to the exponential decrease with energy predicted by the Maxwellian or Watt distribution to realize how much this representation can distort the actual distribution; e.g., in  Fig. 9 the last bin from about 9–20 MeV overestimates the extreme high-energy spectrum by a factor of over 60 (6,000%). An alternative treatment of energy distributions is to sample an analytical expression in low-probability energy ranges. For example, at low energy most energy distributions will vary as \sqrt{E} in E , and at high energy as $\text{Exp}[-A \cdot E]$ or $E \cdot \text{Exp}[-A \cdot E]$. This figure illustrates the results for a U238 fission spectrum, where we have shown 1,024 equally probable bins, as well as a low-energy \sqrt{E} fit and a high energy $E \cdot \text{Exp}[-A \cdot E]$ fit. Note how poorly the equally probable bins agree with the fission spectrum in the low-probability energy ranges at low and high energy. In contrast, the analytical extensions show an excellent agreement with the fission spectrum. This illustrates that equally probable bins, for speed of sampling, can be combined with analytical extension to produce accurate results over the entire secondary-energy range of spectra.

As in the case of angular distributions, one also has the problem of how to accurately interpolate in incident energy, between the energies at which the energy spectra are tabulated. Here, it is also much more accurate to interpolate the cumulative energy distribution; the shifting minima and maxima are better modeled as continuously shifting with the cumulative integrals.

1.8.3 Multigroup

By examining  Fig. 1 it is easy to see that modern evaluations require an enormous number of data points to represent cross sections in energy-dependent form. This makes it very difficult and expensive to use cross sections in continuous energy form. An alternative is to average (1) over adjacent energy intervals to obtain the equation

$$\begin{aligned} & \frac{1}{v} \frac{\partial}{\partial t} N_g(r, \Omega, t) + \vec{\Omega} \cdot \vec{\nabla} N_g(r, \Omega, t) + \Sigma_t g(r, t) N_g(r, \Omega, t) \\ & = \frac{1}{4\pi} \sum_{g'} \int_{\Omega'} d\Omega T(g', g' - > g; \Omega' - > \Omega) N_{g'}(r, \Omega', t) + S_g(r, \Omega, t), \end{aligned} \quad (7)$$

where

$$\begin{aligned} N_g(r, \Omega, t) &= \int_{E'_g}^{E'_{g+1}} N(r, \Omega, E', t) dE', \\ \Sigma_t g(r, t) N_g(r, \Omega, t) &= \int_{E'_g}^{E'_{g+1}} \Sigma_t(r, E', t) N(r, \Omega, E', t) dE', \\ T(g', g' - > g; \Omega' - > \Omega) N_{g'}(r, \Omega', t) \\ &= \int_{E_g}^{E_{g+1}} dE \int_{E_{g'}}^{E'_{g+1}} dE' \Sigma(r, E' - > E, \Omega' - > \Omega) N(r, \Omega', E', t). \end{aligned} \quad (8)$$

Since in general we are really interested in effects caused by the distribution of neutrons and these effects depend on integral or average values of the distributions alone, if we can accurately solve these equations, then the solution is usually adequate to meet our needs, that is,

it is not necessary to determine the continuous energy-dependent distribution of neutrons. The processing of cross sections for use in these equations requires a discussion of the subject of self-shielding. In addition, the group-to-group transfer matrix must also be defined. Finally, the concept of group collapse is important. All these points are addressed in the following sections of this chapter.

The multigroup approach has a number of basic drawbacks that are difficult to eliminate by using more groups. An alternative approach to improve the multigroup approach is presented later in this chapter under the multiband method.

1.9 Summary

The preceding sections have described what nuclear data are required to be processed before they can be used in transport calculations. The following sections will describe how the data are actually processed, which include (1) reconstruction of energy-dependent cross sections from resonance parameters and (2) Doppler broadening. These two sections are required in order to obtain energy-dependent cross sections for use in Monte Carlo neutron transport codes; they also serve as a source of data in order to obtain cross sections for use in multigroup codes. In order to meet the needs of multigroup codes, we will consider (3) self-shielding, (4) the group-to-group transfer matrix, and (5) group collapse. Finally, because of the limitations of the multigroup method we will consider improvements under (6) the multiband method. By the conclusion of this chapter, we will be ready to proceed to the following chapters of this handbook, which will consider actual applications.

2 Reconstruction of Energy-Dependent Cross Sections

2.1 Introduction

Modern evaluated libraries may be divided into two separate classes depending on how cross sections are represented. One class of libraries represents cross sections using resonance parameters directly in the evaluated files, which includes ENDF/B, JEF, JENDL, CENDL, and BROND. The other class of libraries represents cross sections in tabulated form with a defined interpolation law between tabulated points, which include KEDAK, UKNDL, and ENDL. Even though the latter class of libraries does not use resonance parameters directly in the evaluated files, it does use resonance parameters in order to derive its tabulated cross sections. Therefore, by the time cross sections are ready to be used in any given application, virtually all modern evaluations have the problem of reconstructing or at least defining the resonance contribution to the cross section. In a later section on self-shielding, the problem of defining the resonance contribution in an integral sense will be addressed. Here we will address the problem of calculating energy-dependent cross sections alone.

2.2 Representation of Cross Sections

Current evaluations represent cross sections as a combination of tabulated cross sections and resonance parameters. The most general representation is

1. Tabulated cross sections at low (thermal) energy.
2. At higher energies, resolved-resonance parameters plus possibly a background section in the “the resolved-resonance region.”
3. Above the resolved-resonance region, unresolved-resonance parameters plus a background cross section in “the unresolved-resonance region.”
4. At still higher energies, tabulated cross sections extending up to the upper-energy limit of the evaluation.

We must consider how to combine these tabulated cross sections and resonance parameters in order to obtain energy-dependent cross sections spanning the entire energy range of interest. In order to do this in the following sections, we will first address the problem of how to simplify the representation of tabulated cross sections and then how to treat the resonance contribution.

2.3 Tabulated Cross Sections

In order to be used in transport calculations, cross sections must be uniquely defined at all energies. In tabular form, this is accomplished by representing the cross section as a series of (energy, cross section) tabulated points and an interpolation law between tabulated points. It is important to understand that since we are interested in integral effects we must define our data at ALL energies, not just at the energies where they are tabulated.

Some libraries use only one interpolation law to define cross sections, e.g., ENDL and SOKRATOR always assume that between tabulated points the cross section may be defined by linear interpolation in energy and cross section, whereas KEDAK and UKNDL assume logarithmic interpolation. The ENDF/B, JEF, and JENDL libraries use the ENDF/B format, which allows cross sections to be represented over different energy ranges by up to five different types of interpolation laws, such as

1. Constant cross section between tabulated energies (constant or histogram).
2. Linear variation in cross section and energy (linear-linear).
3. Linear variation in cross section, log variation in energy (linear-log).
4. Log variation in cross section, linear variation in energy (log-linear).
5. Log variation in cross section and energy (log-log).

In addition, there are interpolation laws to handle special situations, such as charged particle thresholds.

Some of these interpolation laws are extremely useful during the evaluation process as they lend themselves to accurately and simply represent some cross-section shapes, e.g., a $1/V$ cross section can be exactly represented using log-log interpolation. Even though these interpolation laws are convenient to use, care must be exercised as they can introduce inconsistencies during the evaluation process and can result in a nonunique representation of the cross section during later use in applications.

As long as the cross sections for each reaction are represented separately and there are no redundant cross sections (i.e., no sums of reactions), these five interpolation laws described earlier may be used in any combination to represent the cross sections for each reaction. However, formats such as ENDF/B do normally include redundant cross sections, e.g., the total cross section, total inelastic cross section, etc. This presents a problem, since if two different reactions are evaluated using different interpolation laws over the same energy range, generally the sum

of these reactions cannot be exactly represented by any of the five interpolation laws, with the following exceptions,

1. Constant + constant can be represented as constant.
2. Constant + linear can be represented as linear.
3. Linear + linear can be represented as linear.

There are no other legal combinations of interpolation laws. In particular, if one reaction uses any of the log-interpolation laws, it cannot be added together with any other reaction to yield a sum which can be exactly represented by any of the five interpolation laws. For example, at low energy the elastic cross section may be constant and the capture cross section may be $1/V$. If we use the constant interpolation law to represent the elastic and log-log to represent the capture, we may be able to represent each of these two reactions by tabulated points at 10^{-2} and 100 eV and their interpolation laws between these two tabulated points. However, the total cross section, which is the sum of the elastic and capture, cannot be represented by tabulated points at 10^{-2} and 100 eV and any of the allowable five interpolation laws.

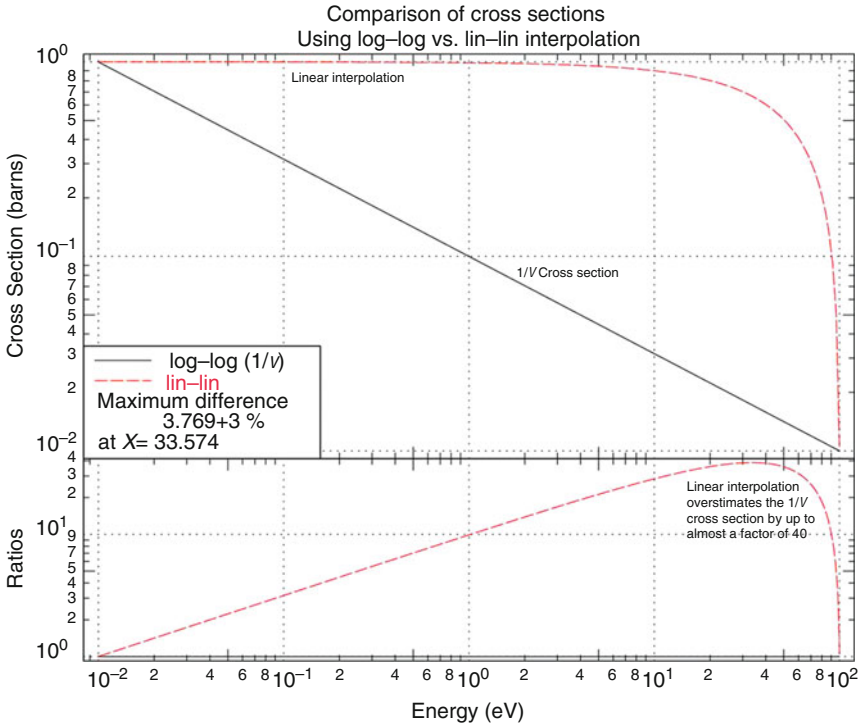
How much difference does it make if in the previous example we use one interpolation law or the other to represent the total cross section? More generally, is it important to worry about interpolation laws at all? Obviously, at the tabulated energies we obtain the same cross section regardless of how we interpolate between values. What are the consequences if we simply ignore the interpolation law specified by the evaluator and assume linear-linear variation between tabulated points?

◆ *Figure 10* presents a comparison between a $1/V$ cross section and linear-linear variation for a cross section tabulated at 10^{-2} and 100 eV, as in the case of the capture cross section in the above example. From this example, it is easy to see that the difference between interpolated values using different interpolation laws can be enormous. In this case, the energy-dependent values differ by up to almost a factor of 40 (4,000%), and the average value of the cross section using linear-linear interpolation over this energy range is over five times higher than the average obtained assuming $1/V$ (log-log) variation. We can agree that such large errors are not acceptable in our applications; we need a unique interpretation of our nuclear data to avoid such errors.

This is by no means merely a theoretical example; with currently available libraries, such as ENDF/B-VII (Oblozinsky et al. 2006; Cullen 2007a-c), when one calculates even broadly energy-dependent quantities, such as resonance integrals, it is found that for many evaluations the total resonance integral is not equal to the sum of the parts. By examining the evaluations it can be seen that these differences are due to the inconsistencies in the cross sections due to the use of log interpolation.

From the preceding discussion, it may be seen that the availability of a variety of interpolation laws to represent cross sections is very convenient during the evaluation process; however, interpolation laws may introduce inconsistencies into the final evaluation. In addition, when the cross sections are actually used in applications, log interpolation laws can cause difficulties because

1. In order to make cross sections consistent, it may be necessary to ignore one or more cross sections. For example, one may ignore the tabulated total cross section and always define the total cross section as the sum of all other reactions. Alternatively, based on our experimental knowledge of cross sections, one could claim that the total is better known than the elastic, and one could also define the elastic as the total minus of all other reactions. The fact that



■ Figure 10

Example of interpolation error

there is more than one possible way to interpret an evaluation, in order to make an evaluation that uses log interpolation consistent, means that the results obtained using the evaluation may not be unique.

2. Failure to recognize the inconsistency due to interpolation laws may result in inconsistencies during a transport calculation. For example, if the total cross section is more than the sum of its parts, the difference between the total and sum of its parts can be mathematically equivalent to additional neutron disappearance. Alternatively, if the total is less than the sum of its parts, the difference can be equivalent to additional neutron multiplication. In a Monte Carlo calculation, such inconsistencies can cause a computer code to simply get confused, resulting in unreliable answers.
3. Even though it is possible to express the group integrals of cross sections using log interpolation in an analytical form, the resulting expressions when applied to use on a computer can be extremely numerically unstable, in very subtle ways that are difficult to analyze.

2.3.1 Linearized Cross Sections

For all the reasons mentioned, here we will introduce an algorithm that allows one to start from an evaluation in which any combination of the five interpolation laws described earlier are used

and reduce all cross sections to linearly interpolable form. The first question to ask is whether or not it is always possible to reduce cross sections which use any one of the five interpolation laws, between two tabulated points, to linearly interpolable form.

The constant interpolation (law 1) represents the cross section as constant (histogram), equal to the tabulated value of the cross section at one energy, for all energies between the tabulated energy and the next higher tabulated energy. This constant interpolation law can be exactly reduced to linearly interpolable form by replacing each original (energy, cross section) pair by two final (energy, cross section) pairs, one at the lower and another at the upper limit of the energy interval, with the cross section for both final pairs equal to the cross section of the original pair. For example, starting from tabulated cross sections with constant (histogram) interpolation,

$E1$ A
 $E2$ B
 $E3$ C, etc.

This table can be exactly reduced to the linearly interpolable form,

$E1$ A
 $E2$ A
 $E2$ B
 $E3$ B
 $E3$ C, etc.

Tables using law 2 are already linearly interpolable and need not be considered.

Tables obeying interpolation laws 3, 4, or 5 can be reduced to linearly interpolable form by using an interval-halving technique. Each interval is divided in half, until the value at the middle of each interval can be approximated to within some acceptable accuracy by linear interpolation between the ends of the interval. In this process, the midpoint of an interval is defined in a linear sense $(E_K + E_{K+1})/2$ for interpolation law 4 (linear E) and in a logarithmic sense $(E_K E_{K+1})^{1/2}$ for interpolation laws 3 or 5 (log E).

The convergence of the interval-halving technique can be demonstrated for these three cases by considering the difference between values obtained using linear interpolation and the exact values obtained using the given interpolation law. In terms of the interval endpoints (X_K, Y_K) and (X_{K+1}, Y_{K+1}) , the interpolation laws are

$$\begin{aligned} Y(2) &= Y_K + A_K(X - X_K); & A_K &= (Y_{K+1} - Y_K)/(X_{K+1} - X_K), \\ Y(3) &= Y_K + B_K \log(X/X_K); & B_K &= (Y_{K+1} - Y_K)/\log(X_{K+1}/X_K), \\ \log Y(4) &= \log Y_K + C_K(X - X_K); & C_K &= \log(Y_{K+1}/Y_K)/(X_{K+1} - X_K), \\ \log Y(5) &= \log Y_K + D_K \log(X/X_K); & D_K &= \log(Y_{K+1}/Y_K)/\log(X_{K+1}/X_K). \end{aligned} \quad (9)$$

Here (2), (3), (4), and (5) refer to the interpolation laws 2 through 5.

The differences between each interpolation law and linear interpolation are

$$\begin{aligned} \delta 3 &= Y(2) - Y(3) = A_K(X - X_K) - B_K \log(X/X_K), \\ \delta 4 &= Y(2) - Y(4) = A_K(X - X_K) + Y_K[1 - \exp(C_K(X - X_K))], \\ \delta 5 &= Y(2) - Y(5) = A_K(X - X_K) + Y_K \left[1 - \left(\frac{X}{X_K} \right)^{D_K} \right] \end{aligned} \quad (10)$$

We differentiate with respect to X to define

$$\begin{aligned}\frac{d\delta 3}{dX} &= A_K - \frac{Bk}{X}, \\ \frac{d\delta 4}{dX} &= A_K - C_K Y_K \exp [C_K (X - X_K)], \\ \frac{d\delta 5}{dX} &= A_K - \frac{Dk Y_K}{Xk} \left(\frac{X}{Xk} \right)^{Dk-1}.\end{aligned}\quad (11)$$

The points of maximum difference are found by setting these expressions equal to zero, as

$$\begin{aligned}X(3)_{\max} &= \frac{Bk}{A_K}, \\ X(4)_{\max} &= X_K + \frac{1}{C_K} \log \left(\frac{A_K}{Xk Y_K} \right), \\ X(5)_{\max} &= X_K \left(\frac{A_K Xk}{Dk Y_K} \right)^{1/[Dk-1]}.\end{aligned}\quad (12)$$

An important point to note is that in each case there is only one point of maximum difference. This means that during interval halving a straight line drawn between the ends of the interval will always lie either above or below the exact curve, thus preventing false convergence (see false convergence later in this chapter). This property is a result of the variation in X and Y , being either linear or log in each dimension; this is not true for other interpolation laws, such as quadratic or spline; in these cases, convergence cannot be proven.

The maximum differences are

$$\begin{aligned}\delta 3 &= B_K - A_K X_K - B_K \log \left(\frac{Bk}{A_K Xk} \right), \\ \delta 4 &= Y_K \left[1 - \frac{A_K}{C_K Y_K} \right] + \frac{A_K}{C_K} \log \left(\frac{A_K}{C_K Y_K} \right), \\ \delta 5 &= Y_K \left[1 - \left(\frac{1}{Xk} \right)^{Dk} \left(\frac{A_K Xk}{Dk Y_K} \right)^{Dk/(Dk-1)} \right] + A_K X_K \left[\left(\frac{A_K Xk}{Dk Y_K} \right)^{1/(Dk-1)} - 1 \right].\end{aligned}\quad (13)$$

By expanding these expressions and studying their convergence as the length of the interval decreases (i.e., $E_K \geq E_{K+1}$), it can be shown that all the above maximum differences approach zero as fast as $(E_{K+1} - E_K)$, except for three trivial cases. Thus, any algorithm for subdividing intervals will yield data points between which linear interpolation is satisfactory. The three cases in which the maximum error does not approach zero as fast as $(E_{K+1} - E_K)$ are the following:

1. $E_{K+1} = E_K$, $Y_{K+1} \neq Y_K$, a cross-section discontinuity that can be treated as a histogram.
2. $Y_{K+1} = Y_K$, a constant cross section that is already linear interpolable.
3. $D_K = 0$ or 1 , the cross section is already constant ($D_K = 0$) or linear ($D_K = 1$).

The subdivision at points given by (12) could be used instead of interval halving; both algorithms yield roughly the same number of final energy points. However, comparison of the two algorithms indicates that interval halving is simpler and faster.

More General Interpolation Laws

It is important to understand that although the interval-halving technique converges and allows all cross sections which initially use any of the ENDF/B interpolation laws to be reduced to

linearly interpolable form, it is not a general method of reducing an arbitrary function $f(X)$ to linearly interpolable form. An example of a case that does not converge is $f(X) = X^2$, for X between 0 and 1.

Over the decades since the start of the ENDF/B effort, other more general interpolation laws have been proposed, but they have been rejected, because they do not lend themselves to controlled convergence. An example is a cubic spline, which today is widely used in many scientific applications, but it is difficult to control. In the case of ALL, the current ENDF/B interpolation laws – the tabulated data points at the two ends of each interval (X_K , Y_K) and (X_{K+1} , Y_{K+1}) are the extrema of $Y(X)$, that is, for all values of X between X_K and X_{K+1} , the function $Y(X)$ is bound between Y_K and Y_{K+1} . This is an important point because it allows us to use the mean value theorem to bound integrals, to within any accuracy that we require. This may not be true for other interpolation laws; and in particular, it is certainly not true for cubic splines. This is an important point to understand as it affects our ability to accurately define the integral quantities that we are interested in.

Effect in Integral Quantities

If we start from any exactly known cross section subject to any of the five ENDF/B interpolation laws, we can construct an approximate cross section that can be linearly interpolated. In addition, we can guarantee that the approximate cross section is within some acceptable error of the exact cross section at ALL energies, that is,

$$(1 - \varepsilon) \sigma_{\text{exact}}(E) \leq \sigma_{\text{approx}}(E) \leq (1 + \varepsilon) \sigma_{\text{exact}}(E) \quad (14)$$

for all E .

When we multiply by some weighting spectrum and integrate, we find

$$(1 - \varepsilon) \int_{E_1}^{E_2} \sigma_{\text{exact}}(E) \Phi(E) dE \leq \int_{E_1}^{E_2} \sigma_{\text{approx}}(E) \Phi(E) dE \leq (1 + \varepsilon) \int_{E_1}^{E_2} \sigma_{\text{exact}}(E) \Phi(E) dE. \quad (15)$$

Similarly, if we integrate a weighted reciprocal cross section we find

$$\frac{1}{(1 - \varepsilon)} \int_{E_1}^{E_2} \frac{\Phi(E)}{\sigma_{\text{exact}}(E)} dE \leq \int_{E_1}^{E_2} \frac{\Phi(E)}{\sigma_{\text{approx}}(E)} dE \leq \frac{1}{(1 + \varepsilon)} \int_{E_1}^{E_2} \frac{\Phi(E)}{\sigma_{\text{exact}}(E)} dE. \quad (16)$$

Therefore, the integral quantities of the earlier mentioned form using linearly interpolable cross sections are always guaranteed to be within ε of the exact integrals (because of cross cancellation of errors during integration the results are generally much closer than ε).

Summary of Linearizing

In the preceding section, an algorithm that allows cross sections to be reduced to linearly interpolable form has been presented. This algorithm is only of practical use if the number of data points in the resulting linearized evaluation is comparable to the number of points in the original (nonlinear) evaluation. Application of this algorithm to entire ENDF/B libraries (IV, V, VI, and VII), by linearizing each library to within 0.1% accuracy, demonstrates that in some

evaluations the resulting number of points can be slightly less or more than the original evaluation, but for each library taken as a whole, the total number of data points in the linearized library is actually slightly less than in the original library. Therefore, linearizing all cross sections is practical in the sense that it significantly increases neither the size of the resulting library nor the number of data points that must be used in the later calculations.

As mentioned earlier, this process of linearizing data can be used by evaluators to guarantee the consistency of their cross sections by performing their evaluations using the convenience of the ENDF/B interpolation laws (i.e., exact $1/V$ capture and fission at low energy). After the evaluation is complete, but before distribution, it is recommended that evaluators always convert all cross sections to linearly interpolable form and define all sum cross sections (such as total) consistently by performing the additions in the linearly interpolable form. Finally, the evaluator can present the final evaluation in a linearly interpolable form for use in applications. Program LINEAR (Cullen 2007a–c) is freely available online to linearize cross sections in the ENDF/B format.

Unfortunately, evaluators do not always understand the importance of doing this. Let us take a simple example of a current evaluation to illustrate the effect that this can have on the consistency of an evaluation; consider an actual current evaluation, 1-H-1 from ENDF/B-VII.0 (Oblozinsky et al. 2006; Cullen 2007a–c). At low energy, the only possible reactions are elastic scatter, which is almost constant and uses interpolation law 2 (lin–lin), and capture, which is $1/V$ and uses interpolation law 5 (log–log). Both are good logical choices for these individual reactions. But evaluators introduced an error by assuming that the total cross section, which is the sum of elastic and capture, can be “accurately” defined using interpolation law 5 (log–log); unfortunately, there is no ENDF/B interpolation law that can exactly represent the sum of a constant and $1/V$ cross section; indeed, the only interpolation law that can be used to represent redundant cross sections, such as total, is law 2, linear (lin–lin) interpolation. What this means is that the total defined by the evaluator is not actually equal to the sum of its parts over the entire energy range. ➤ *Figure 11* illustrates that this seemingly trivial oversight introduces an inconsistency in the 1-H-1 ENDF/B-VII.0 data of over 0.5% in the total cross section. In this figure, we see “loops” showing that at the energy points where the cross sections are tabulated, the given total is equal to the sum of its parts; but between these energies, the inconsistent interpolation laws introduce an error. Note that the error is always on only one side of the original data, so that any errors in integrals based on this data will be maximized; this can be seen if one calculated the resonance integrals from the originally evaluated data, not only in this case but also for many current evaluations.

Most evaluated data users would be shocked if told that such a trivial oversight could have such a relatively large effect on one of the best-known cross sections (1-H-1), but unfortunately that is the reality of the currently available evaluator data. This is but one trivial example of how misuse of ENDF/B interpolation laws can introduce inconsistencies in the evaluated data that can lead to a nonunique interpretation of the data. For example, in this case, when people actually use this data, they will either end up with inconsistent results (the total is not the sum of its parts) or have to make a decision as to how to make them consistent, such as ignoring the given total, linearizing all cross sections, and then adding them up to define a consistent total (what we recommended), or use some other procedure, such as assuming that the elastic is least well known and define it as the difference between the total and capture (sounds reasonable, but leads to strange results).

This confusion could have been easily avoided if the evaluator had understood the importance and limitations of ENDF/B cross-section representation, and made the cross consistent by

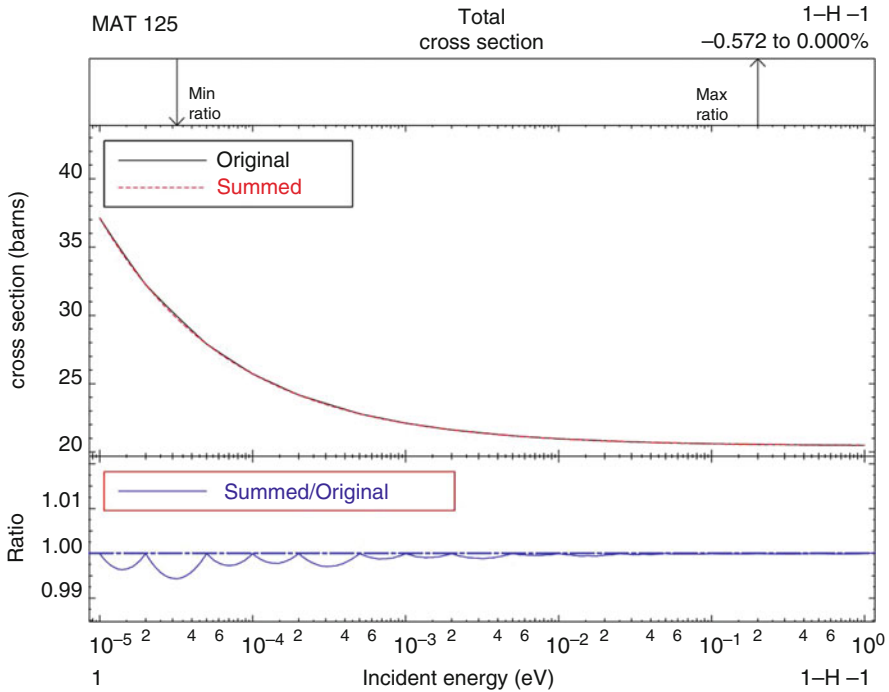


Figure 11
Example of interpolation error in 1-H-1 data

linearizing them, and then consistently defining the total by summing the linearized elastic and capture. Only after this has been done should the evaluation be considered finished and ready for distribution. Program FIXUP (Cullen 2007a–c) is freely available online to make consistent cross sections in the ENDF/B format.

As this example illustrates, evaluations do not always contain consistent data, so users are forced to make the data consistent before using it. This process of linearizing data can be used by data users to simplify their processing codes by linearizing all cross sections and defining redundant cross sections (such as total) by summation, as a first step in their data processing. Then all subsequent codes for resonance reconstruction, Doppler broadening, and group averaging can be greatly simplified and made more numerically stable by assuming that all cross sections are in a linearly interpolable form. This is the approach built into a number of currently available nuclear data-processing codes (Cullen 2007a–c; MacFarlane and Muir 1994).

The bottom line is that we strongly recommend that the distributed evaluated data NEVER use nonlinear ENDF/B interpolation laws, because this always leads to inconsistencies in the cross sections. Evaluators are certainly free to take advantage of nonlinear interpolation (e.g., $1/V$ capture and fission at low energy), during the evaluation process. But before distributing any evaluation, ALL cross sections should be linearizing, and redundant cross sections (such as total) be defining by summation. This is the only way that evaluators can be sure that their data

are uniquely defined and interpreted for use in applications. Any evaluation in which the cross sections are not linearly interpolable should come with the warning: CAVEAT EMPTOR!!!!

2.4 Reconstructing the Contribution of Resonances

There are now a number of programs available to reconstruct energy-dependent cross sections from a combination of resonance parameters and tabulated cross sections. In principle, the procedures used by all these codes are equivalent and yield equivalent results. In practice, in a comparison of the cross sections generated by these programs, large differences were found (Cullen et al. 1985, 1988). Here we will concentrate on pointing out those areas that require care if accurate cross sections are to be obtained.

In the resolved-resonance region, the ENDF/B format allows the following types of parameters:

1. Breit–Wigner single-level parameters
2. Breit–Wigner multilevel parameters
3. Reich–Moore parameters
4. Adler–Adler parameters
5. General R-matrix parameters
6. Hybrid R-function parameters

In the unresolved region, the ENDF/B format allows the following types of parameters:

1. Constant, or energy-independent, parameters
2. Energy-dependent fission width, all other widths constant
3. All widths energy dependent

All the pertinent equations for these resolved and unresolved representations are presented in ENDF-102, the formats and convention manual (Kinsey 1970; Rose and Dunford 1990), and will not be reproduced here. The important point that we will focus on here is not the exact equations, but rather the procedures that are used to accurately calculate energy-dependent cross sections from these parameters. Since these are different in the resolved and unresolved energy ranges, we will consider each region separately.

2.4.1 The Resolved-Resonance Region

In principle, the approach for reconstructing energy-dependent cross sections is quite straightforward. There are three basic approaches that are used. In one approach, starting from the peak of a resonance, the total width of the resonance is used to define a grid of energy points located as multiples of the total width on either side of the peak of the resonance. In the second approach, starting from the peaks of two adjacent resonances, the intervening energy interval is subdivided, using the interval-halving technique, described in the preceding section, until the cross section is linearly interpolable over each of the resulting energy intervals. The third approach combines the first two approaches. In the third approach, the total width of two adjacent resonances is first used to subdivide the intervening energy between the two resonances into a number of subintervals; the length of each subinterval is determined by the total width of

the nearest resonance. Each subinterval is then subdivided using the interval-halving technique, until the cross section is linearly interpolable over each resulting energy interval.

In principle, if performed to high precision using many data points all three approaches will yield identical results. Each approach offers advantages and disadvantages. The first approach is the most economical since it does not involve any iteration; however, this approach does not attempt to guarantee the accuracy of the resulting cross section to within any given criteria. The second approach is mechanically the simplest since it only involves selecting two resonance peak energies and applying the interval-halving technique; however, this approach can lead to false convergence (as described later) and for widely spaced and narrow resonances, the convergence between resonances can be quite slow. The third approach, while more complicated than the second, can actually be much more economical to use. The reason for this is that the third approach uses the fact that in any iterative procedure convergence can be accelerated by starting as close to the solution as possible. By defining subintervals, as multiples of the total width around each resonance, the third approach does not begin iterating until it has already roughly defined the shape of each resonance. In contrast, the second method does not use any initial information concerning the shape of the two adjacent resonances, and as such can iterate for a considerable period of time before achieving convergence.

The third approach, being the most general, will be described in detail in the following section. Reference will be made to the other two approaches for comparison purposes when appropriate to illustrate where care must be exercised in order to insure their accuracy.

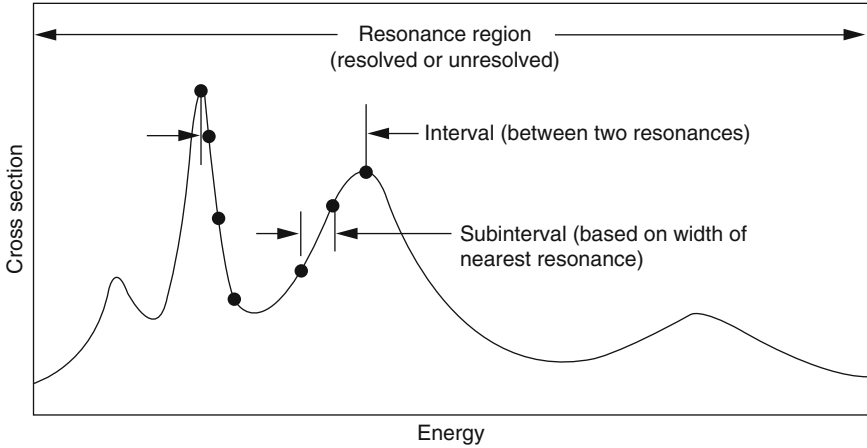
Subdivision into Intervals

In the ENDF/B format within each evaluation, resolved-resonance parameters are given for each isotope that contributes to the evaluation; each evaluation can be for a single isotope or for an elemental mixture of isotopes. For each isotope, resolved parameters are given for each L state (i.e., s, p, d wave). First, the resolved resonance for all isotopes and L states are sorted into ascending energy order, and each interval is defined as extending from the peak of one resonance to the peak of the next resonance. Up to this point, the approach is similar to the second method, the difference being that at this point the second method begins iterating. The third method subdivides intervals into subintervals.

Subdivision into Subintervals

Starting at each end of an interval and using the total width of the resonance at that end, subinterval boundaries are placed as multiples of the total width from the peak of the resonance, e.g., 1, 2, 4, 6, 10, 20, 40, 60, and 100 half-widths from the end or until the midway point between two resonances is reached. “Midway” is here defined as equidistant from the ends of the interval measured in half-widths of the resonance at each end of the interval. ➤ [Figure 12](#) illustrates this process.

With this algorithm, the interval between two narrow, widely spaced resonances is divided into many subintervals, while the interval between two wide, closely spaced resonances is divided into only a few subintervals. From ➤ [Fig. 12](#), the starting point for iteration using the third method can be visualized as the shape obtained by drawing a straight line between the dots (ends of subintervals). This may be compared with the starting point using the second method, which is a straight line between the peaks of the two resonances. From this comparison, it is easy to see why the third method generally converges much faster than the second. The shape



■ **Figure 12**
Subdivision of a resonance region into intervals and subintervals

obtained by drawing a straight line between the dots may be visualized as the shape obtained using the first method, since in the first method there is no subsequent iteration or subdivision.

Subinterval Halving

Each subinterval is further subdivided using the iterative interval-halving technique, until the cross section can be approximated by linear interpolation between successive energy points. Because of the similarity between the calculations for total, elastic, capture, and fission, the most economical approach is to calculate all four simultaneously, using the same energy grid and continue to subdivide until all four have converged.

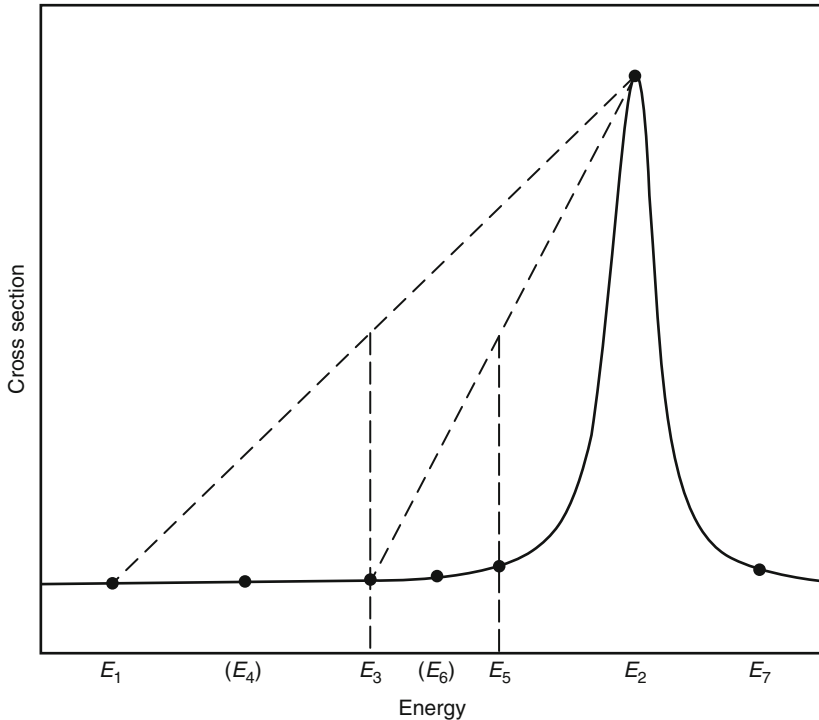
The interval-halving technique begins at the lower end of the energy range of interest and proceeds as follows (see the ► [Fig. 13](#)). Consider the two successive energy points, $E1$ and $E2$. Tentatively define the energy point $E3$, halfway between $E1$ and $E2$, and calculate the total, elastic, capture, and fission cross sections at each of these three points. The point at $E3$ need not be kept and the interval between $E1$ and $E2$ need not be further subdivided if any of the following criteria are met:

1. All four cross sections can be approximated at the midpoint $E3$ by linear interpolation from the ends of the interval to within an allowable fractional uncertainty ϵ_{\max} . Calculate the exact cross section $\sigma_k(E1)$, $\sigma_k(E2)$, and $\sigma_k(E3)$, for $k = 1, 2, 3$, and 4 (where the indices refer to the four reactions) and the approximate cross section at the midpoint by linear interpolation

$$\sigma_k^*(E3) = \frac{1}{2} [\sigma_k(E2) + \sigma_k(E1)]. \quad (17)$$


The convergence criterion is met if for all reactions, k ,

$$|\sigma_k(E3) - \sigma_k^*(E3)| \leq \epsilon_{\max} |\sigma_k(E3)|. \quad (18)$$



■ **Figure 13**
Iteration to convergence

2. The absolute value of all four cross sections at both ends of the interval is less than some minimum cross section of interest, e.g., less than 10^{-10} barns. The cross section may be positive or negative, but convergence is assumed if the cross section at both ends of the interval is closer to zero than the minimum cross section. This prevents needlessly homing in on the energy at which the cross section goes from positive to negative; cross sections are probabilities, so physically they cannot be really negative, but unfortunately negative values occasionally arise for elastic-scattering cross sections that have been reconstructed from single-level Breit–Wigner parameters.
3. The reconstructed cross sections are to be the output in the ENDF/B format, and $E3$ is closer to $E1$ than the energy resolution of the format. For example, if an interval extends from 123.456813 to 123.457294, both energies would be equal to 1.23457E+2 in the six-digit format and are thus indistinguishable. Today, modern codes such as RECENT (Cullen 2007a–c) minimize this problem by outputting energies to 9-digit accuracy, e.g., if output is in F rather than E format, we can distinguish between 123.456813 and 123.457294, in the ENDF/B format, and this would not be considered as convergence.

If one or more of these criteria are met, the point $E3$ is dropped, and the next higher subinterval ($E2$ – $E7$ in  Fig. 13) is subdivided. If not the point $E3$ is included, and the convergence tests are applied again to the point $E4$, the midway between $E1$ and $E3$. This procedure is continued until the entire energy range of interest has been treated.

False Convergence

False convergence of the interval-halving method may be most easily explained by an example. If we attempt to calculate $\sin(x)$ from 0 to 2π by starting at the end points 0 and 2π , we will find that as soon as we subdivide, the first time our iteration will converge since $\sin(x)$ is exactly zero at $x = 0, \pi,$ and 2π , and we would reach the ridiculous conclusion that $\sin(x)$ is everywhere exactly zero. In order to insure that the interval-halving technique converges to the correct answer, it is important to first divide the interval of interest into subintervals in each of which the function is either concave or convex. For example, in the $\sin(x)$ example, it is sufficient to start with the subintervals $x = 0$ to π and $x = \pi$ to 2π in order to obtain convergence; however, convergence can be accelerated by starting with smaller subintervals that better approximate the shape of $\sin(x)$ before beginning interval halving.

For a single isolated resonance, the cross section within one half-width of the peak of the resonance is convex, and it is concave for all energies further from the peak of the resonance. Therefore, a straight line (as used in linear interpolation) drawn from the peak of the resonance to points more than one half-width from the peak may pass through the exact shape of the resonance at some point. This may cause false convergence of the interval-halving technique, as the value calculated by linear interpolation to the midpoint of the interval may be quite close to the exact value calculated at the midpoint of the interval. For example, linear interpolation from the peak of the resonance to a point two half-widths from the resonance may indicate that the shape of the resonance can be accurately approximated by the straight line between the two points. If this result is believed, the integral contribution of the resonance (i.e., the area under the curve) will be drastically underestimated. The third method described above prevents this problem, since the iteration is only performed within subintervals, and subintervals have been defined to isolate the convex and concave energy ranges of each resonance in different subintervals. Therefore, during iteration a straight line drawn between the ends of any subinterval will always lie either above or below the exact value and cannot lead to false convergence.

Resonance Energies

In all the aforementioned methods, we have merely used the term “resonance energy.” In order to insure the accuracy of the methods described here, it is important that the “resonance energy” be defined as the observed peak energy of the resonance, so that the division starts from the actual peak of the resonance and does not miss a peak. For the data in the ENDF/B format, the convention (see ENDF-102, appendix D) is that all resonance energies are observed peak energies, and there is no problem with the methods described here. In some other neutron-data libraries, the resonance energies are eigenvalues of the nucleus. For s-wave resonances, the two correspond, but for p, d, etc., wave resonances, the two differ by the shift factor (again see ENDF-102, appendix D). Since these resonances can be quite narrow, failure to use the observed peaks to define the ends of intervals for subdivision can cause narrow p- and d-wave resonances which would otherwise be missed.

2.4.2 Unresolved-Resonance Region

In the unresolved-resonance region, the unresolved-resonance parameters do not uniquely define the energy-dependent cross section; they only define the probability distribution of the cross sections at each energy region, from which only averaged cross sections can be

derived. Therefore, in principle, the discussion of the unresolved-resonance region should be covered later in this chapter, under self-shielding. However, for convenience during reconstruction of the energy-dependent cross section, many codes will also calculate the infinitely dilute cross section in the unresolved-resonance region. Generally, this is a simpler calculation than that involved in calculating the cross sections in the resolved-resonance-energy region; the cross sections are generally smooth and have simple variations between the tabulated values.

The main source of differences in calculating the cross sections in the unresolved-resonance region is due to interpolation. The ENDF/B convention (ENDF-102, page 2.20) is that cross sections should be calculated at the energy points at which unresolved parameters are given, and in order to define the cross section at other energies the cross section, not the parameters, should be interpolated. Although ENDF-102 asks evaluators to use a “dense enough” energy grid to insure that either interpolation of parameters or cross sections yield essentially identical answers, evaluators often do not follow these guidelines, e.g., comparisons for some ENDF/B-V-evaluated data show 18% differences between the cross sections obtained by interpolating parameters versus cross sections. These differences are not due to errors in individual processing codes, but are rather due to the ambiguity in the ENDF/B conventions, because “dense enough” is not quantitatively defined for either evaluators or processing-code designers. If a code designer assumes that an evaluator knows best and has provided parameters on a “dense enough” energy grid, the results will be quite different from those obtained by assuming that the parameters are not given on a “dense enough” energy grid and that they must first be interpolated to a “dense enough” grid using parameter interpolation. Although these two approaches lead to quite different answers, both seem to be justified under ENDF/B conventions as long as “dense enough” is not uniquely defined. This is but one example of where ENDF/B conventions can lead to ambiguity in interpreting the data.

2.4.3 Adding Resonance and Background Cross Sections

Once the resonance contribution has been calculated, it must be added to the background cross section to define the actual energy-dependent cross section; background or correction cross sections are used most often with single-level, Breit–Wigner resonance parameters, to correct for limitations in the single-level resonance model. Since the resonance contribution has been calculated to be linearly interpolable, if the background cross section is also linearly interpolable, as pointed out earlier, the two can be added together to obtain a linearly interpolable cross section. An additional consideration is that the ENDF/B formats and convention (Kinsey 1970; Rose and Dunford 1990) define how to reconstruct 0 K cross sections; so that once reconstructed these can only be added to a 0 K background cross section. Therefore, the necessary constraints on the background cross section to allow it to be added to the resonance contribution are that it has to be defined at 0 K temperature and be linearly interpolable.

However, if the background cross section is not linearly interpolable, the two cannot be added together to obtain a cross section that can be represented by any of the ENDF/B interpolation laws. Failure to recognize this fact can lead to large errors in the cross section. For example, if the resonance contribution and background are added together and given as an output using the interpolation law of the background, in many cases, ENDF/B evaluations define the background to be zero over the entire resolved-resonance region and represented by the constant

interpolation law. In this case, even though the background makes zero contribution, the combined cross section will be described as constant (a series of histograms) between tabulated values, instead of the original linearly interpolable form in which the resonance contribution was calculated. Therefore, before reconstructing the resonance contribution, all background cross sections should be converted to linearly interpolable form. Note that this is in agreement with my earlier recommendation that ALL ENDF/B-formatted cross sections be linearized before distribution.

All the ENDF/B-resonance equations define the cross sections at 0 K temperature. Therefore, another case in which the resonance contribution and background cannot be immediately added together is if the background cross section is not defined at 0 K temperature. In this case, the resonance contribution can be Doppler broadened to the temperature of the background, and the two can then be added together. Program LINEAR (Cullen 2007a–c) is designed to allow cross sections to be converted to linearly interpolable form; program RECENT (Cullen 2007a–c) can then be used to reconstruct the resonance contribution and added to the background cross section to define the complete cross sections; if necessary, program SIGMA1 (Cullen 2007a–c) can be used to Doppler-broaden cross sections to any required temperature(s).

2.4.4 Output Format

If after reconstruction the cross sections are stored in a binary form, the full accuracy of the reconstructed cross sections will be preserved. However, if they are written in character form, significant errors can be introduced if care is not taken. For example, if the cross sections are written in the ENDF/B character format, limiting floating point numbers to 11 columns, the number of digits normally used to represent energies is not sufficient to accurately represent the shape of narrow resonances, particularly for heavy even–even isotopes such as Th232, U238, and Pu240. Truncation of energies can cause narrow resonances to either disappear or appear to be much wider than they really are.

As part of a cross-section processing-code verification study (Cullen et al. 1985, 1988), the ENDF/B-VI dosimetry library was used to calculate energy-dependent cross sections to within 0.1% accuracy, and three different forms were used as output in the ENDF/B format representing the energies to 5 – (1.2345E + 3), 6 – (1.23456 + 3), and 9 – (1234.56789) digit accuracy. The results showed that the cross sections with energies to five-digit accuracy differed from the nine-digit output by up to 72%. The six-digit results differed from the nine-digit results by up to 6%. Therefore, even integral results are affected unless care is used to accurately represent the data, particularly the energies associated with cross sections reconstructed from narrow resonances. It is important to understand that since in the above example within the computer memory the cross sections in all three cases are calculated to exactly the same 0.1% accuracy and were identical, the above-quoted differences are due solely to truncation of the energy during output to the 11-column ENDF/B, floating-point number format.

At present, two different approaches have been introduced to prevent this truncation problem. In one approach by recognizing that the exponent associated with the energy is always one digit, the ENDF/B E11.4 format or energies can be extended to present energies to seven digits, e.g., 1234.56789 can be made output as 1.234568 + 3. In the second approach, it is recognized that for energies between 10^{-3} eV and 100 MeV, the energy can be written to more than six digits of accuracy, simply to writing the energy in F, rather than E format, e.g., 1234.56789 can be made

output as 1234.56789. For energies below 10^{-3} eV and above 100 MeV, the normal six-digit output is used; since there are no narrow resonances in these energy ranges, this does not present any serious limitation to the algorithm.

A word of WARNING: output such as 1.234568 + 3, used by some codes to add an additional digit of accuracy to the output by dropping the “E” or “D” preceding the exponent, is compatible and can be read by FORTRAN codes, but it is not compatible for use with C codes; indeed, C codes will read this without indicating any error, and incorrectly interpret the data, in ways that differ from one computer to another. For this reason, this output form without the “E” or “D” is no longer used as the PREPRO codes (Cullen 2007a–c), and all PREPRO output is now C compatible, such as all the ENDF/B-VII.0 data is now available online (Cullen 2007a–c).

3 Doppler Broadening

3.1 Introduction

In the following section, the concept of Doppler broadening is introduced. The physical phenomenon that causes Doppler broadening is described with emphasis on the effect that we expect broadening to have a variety of commonly encountered cross-section shapes. Next, the methods commonly used to calculate Doppler-broadened cross sections are presented, including an explicit description of the approximations introduced by each method and how these approximations limit the range of applicability of each method. Throughout this section, numerous references are made to computer codes that actually use these methods. Hopefully, by the end of this section, users will be able to decide which of the available methods is most applicable to their applications and will be aware of which computer codes are available for use.

The following discussion will be limited to the effect of Doppler broadening due to the so-called free atoms. We will not discuss thermal-scattering law data, which includes binding effects such as vibration and rotation of crystals; this topic will be covered in another chapter of this handbook.

Since the primary intent of this handbook is for use in fission-reactor core calculations, emphasis will be placed on the role that Doppler broadening plays for broadening of neutron-induced cross sections at fission-reactor temperatures, particularly in the resonance region. However, for generality, reference will also be made to fusion and astrophysics applications, involving neutron- and charged particle-induced cross sections.

3.1.1 What Causes Doppler Broadening?

Let me first cover the most important point to understand: free-atom cross sections are not temperature dependent. That is, the cross sections for the same relative speed between a projectile (neutron) and a target atom are independent of temperature. Note that this is not true for thermal-scattering law data, wherein temperature will affect binding; that is one reason that thermal-scattering law data are not covered here.

Although the cross section in the relative frame of reference is not temperature dependent, the Boltzmann equation that we solve using our transport codes is expressed in the laboratory frame of reference, rather than in the relative frame between the neutron and target nuclei. It is because we want to perform our calculations in the laboratory frame of reference that requires us to define our cross sections in this frame of reference, and it is solely due to our necessity to transform data from the relative to laboratory frame of reference that forces us to include Doppler broadening of cross sections.

The cross section or probability of a neutron interacting with any given nucleus depends on the relative speed between the neutron and the nucleus. In neutron transport, usually neutron energy rather than speed is used, and evaluated data libraries present cross sections and resonance parameter as a function of neutron energy, wherein the neutron energy is measured relative to stationary target nuclei. However, the transport equation describes neutrons in the laboratory frame of reference, and, therefore, in order to solve this equation, we must define cross sections in the same frame of reference. If all the nuclei in a medium were stationary (the so-called “cold” medium), then the energy of the neutron in the laboratory system would be exactly equal to the energy measured, relative to the nuclei in the medium, that is, in this case, the relative and lab frames of references coincide. In this case, the evaluated data as presented in evaluated libraries are exactly what we need for use in the transport equation. However, in any real case, the nuclei in a medium will have a distribution of kinetic energies and will be moving about in a random manner. In this case, for any given neutron energy in the laboratory system, there will not be one unique neutron energy, measured relative to the distribution of randomly moving nuclei, rather there will be an entire spectrum of relative energies.

Visualize a neutron with laboratory energy corresponding to the peak energy of a resonance, incident upon a medium in which the nuclei are moving about due to thermal agitation. Since the nuclei are moving about, there is a probability that the nucleus that the neutron actually interacts with is moving either toward or away from the neutron before the collision; this would cause the relative energy of the neutron to either increase or decrease, respectively. Since we assumed that the neutron was incident with a laboratory energy corresponding to the peak of the resonance, if the relative energy is lower or higher than this value, the cross section that the neutron actually encounters will be lower than the peak value. Of course, there is also a probability that the neutron will interact with a nuclei such that its relative energy is identical to the peak of the resonance. We must consider not only a single neutron interacting with one nuclei, but rather the average due to an ensemble of neutrons interacting with the ensemble of nuclei within the medium. It is easy to see that in the case of this example if we consider neutrons incident with a laboratory energy corresponding to the peak of a resonance, the average cross section that they encounter will actually be less than the cross section corresponding to the peak of the resonance. Therefore, when the nuclei are moving about due to thermal agitation, the cross section that a neutron of a given laboratory energy encounters will be different from the cold (0 K) cross sections.

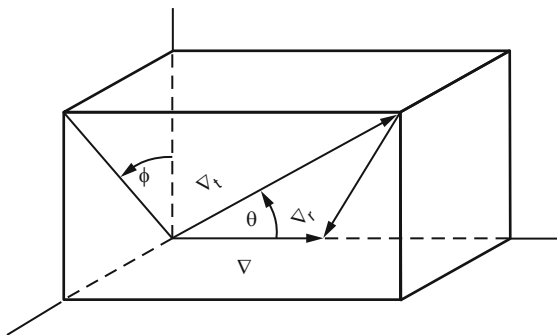
To further complicate the situation, when the bulk temperature of the medium changes, the kinetic energy of the nuclei in the medium changes, which changes the distribution of relative speeds, or energy, between a neutron of a given laboratory energy and the nuclei in the medium. Therefore, we should expect the effects that we see to depend upon the temperature of the medium. If we are to solve our transport equation in the laboratory system, we must somehow reduce this complicated situation to define a single “equivalent” laboratory frame-of-reference cross section.

In what sense should our cross section in the laboratory frame-of-reference be “equivalent” to what is happening in the relative frame-of-reference? What we are interested in conserving is what we can observe in either frame of reference. We cannot observe neutrons, flux, or barns directly. We can only observe when neutrons interact with the medium; in other words, we can only observe reactions. Therefore, we will define our laboratory frame-of-reference cross sections in order to assure that the number of reactions per unit time will be the same in either system. In the following discussion, this laboratory frame-of-reference cross section will simply be referred to as the Doppler-broadened cross section.

3.2 The Doppler-Broadening Equation

► **Figure 14** illustrates the physical significance of the following terms.

m	Projectile mass (e.g., neutron, proton, alpha)
\bar{V}	Projectile velocity
V	$ \bar{V} $ = Projectile speed
E	$1/2mV^2$ = Projectile energy
M	Target nuclei mass
\bar{V}_T	Target velocity
V_T	$ \bar{V}_T $ = Target speed
E_T	$1/2MV_T^2$ = Target energy
A	M/m = Atomic weight ration (target mass/projectile mass)
\bar{V}_r	$\bar{V} - \bar{V}_T$ = Relative velocity
V_r	$ \bar{V}_r $ = Relative speed
E_r	$1/2mV_r^2$ = Relative energy of the projectile
$\sigma(V, 0)$	Cold (0 K) cross section
$\sigma(V, T)$	Doppler-broadened cross section at temperature T
$R(V, T)$	$V\sigma(V, T)$ = Reaction rate (per unit time and particle)
$P(\bar{V}_T)d\bar{V}_T$	Normalized target-nuclei velocity distribution



► **Figure 14**
Coordinates for interaction of neutron and nucleus

Although the following derivation is expressed in terms of neutrons, it is equally applicable to any particle incident with nonrelativistic energy.

As mentioned above, we will define our Doppler-broadened cross section in order to conserve the reaction rate observed in either system. In a medium in which the nuclei are stationary (0 K temperature), the relative speed (V_R) between a monoenergetic beam of neutrons and the target nuclei is merely the speed of the neutrons (V). In such a medium in order to conserve reactions, the cross section is simply defined as the ratio of reactions to flux, or per incident neutron,

$$\begin{aligned} \text{Lab reactions} &= \text{Relative reactions} \\ V\sigma(V, 0) &= V_r\sigma(V_r, 0) = R(V, 0). \end{aligned}$$

Since in this case the speed of the neutron is equal to the relative speed, we obtain a simple identity. In terms of conserving reaction rate, we need not be concerned with the point $V = V_r = 0$, since it does not contribute to the reaction rate.

In any real medium at a temperature above absolute zero, the target nuclei are in thermal agitation and possess a distribution of velocities. Here, the relative speed (V_R) between a monoenergetic beam of neutrons incident upon the medium and the nuclei within the medium will also be distributed. In such a medium, we must still define our laboratory cross section to agree with the observed reaction rate. However, because the cross section is determined by the relative speed, as opposed to the laboratory speed of the neutron, the Doppler-broadened cross section will not generally be the same as the cold cross section. The observed reaction rate per unit neutron will be

$$\begin{aligned} \text{Lab reactions} &= \text{Relative reactions} \\ R(V, T) = V\sigma(V, T) &= \int_{[V_r:V_r>0]} R(V_r, 0) p(\bar{V}_T) d\bar{V}_T \\ &= \int_{[V_r:V_r>0]} V_r\sigma(V_r, 0) p(\bar{V}_T) d\bar{V}_T. \end{aligned} \quad (19)$$

Since $p(\bar{V}_T) d\bar{V}_T$ is a normalized distribution, it is obvious from this equation that if the reaction rate $V_r\sigma(V_r, 0)$ is constant, the broadened cross section $V\sigma(V, T)$ will also be constant, independent of temperature, regardless of the model, $p(\bar{V}_T) d\bar{V}_T$, used to describe the thermal motion of the target nuclei. That is, to say, a $1/V$ cross section will be independent of temperature. It has been demonstrated elsewhere that a $1/V$ cross section is the only cross-section shape that is independent of temperature. Therefore, in all other cases, we must consider Doppler broadening, as we expect the laboratory cross section to be temperature dependent.

From our earlier discussion of physically what causes Doppler broadening, it is easy to understand why a $1/V$ cross section is independent of temperature. In this case, if we have a neutron with speed V that interacts with a nucleus such that the relative speed is V_r , the reaction rate observed will be exactly the same regardless of the value of V_r ; the reaction rate will be exactly the same as if the interaction had occurred with a relative speed V , independent of the velocity distribution of the target nuclei. This is not true even for simple cross-section shapes, such as a constant cross section; since in this case, if the relative speed V_r is larger than V , the observed reaction rate will be larger, and it will conversely be lower if V_r is smaller than V .

It will be shown later in this work that these two effects of larger and smaller values of V_r do not quite balance out, and a cold constant cross section is temperature dependent.

In order to derive the Doppler-broadening equation, it will be assumed that the velocity distribution of the target nuclei is isotropic, when

$$p(\bar{V}_T) d\bar{V}_T = \frac{1}{4\pi} P(V_T) dV_T d\mu d\phi, \quad (20)$$

where $\mu = \cos(\theta)$ and the form of $P(V_T)$ depends on the specific model of the thermal distribution of nuclei. Upon integrating over $d\phi$, (19) becomes

$$V\sigma(V, T) = \frac{1}{2} \int_{-1}^{+1} d\mu \int_{[V_i; V_r > 0]} V_r \sigma(V_r, 0) p(V_T) dV_T. \quad (21)$$

From the  Fig. 14, we have


$$\frac{1}{2} m V_r^2 = \frac{1}{2} m [V^2 - 2\mu V_T V + V_T^2]. \quad (22)$$

The Jacobian transformation is

$$d\mu = \frac{V_r dV_r}{V V_t}, \quad (23)$$

and the Doppler-broadening equation for a general isotropic thermal distribution of target nuclei is

$$V\sigma(V, T) = \frac{1}{2V} \int_0^\infty [V_r \sigma(V_r, 0)] V_r dV_r \int_{|V-V_r|}^{|V+V_r|} P(V_t) \frac{dV_t}{V_t}. \quad (24)$$

The limits of integration are illustrated in  Fig. 15, which shows the area of integration in the (V_r, V_t) plane. For any given thermal distribution $P(V_t)$, the inner integral may be evaluated to define the Doppler-broadened cross section in terms of a singly dimensioned integral over the relative speed V_r .

Usually, the Maxwell gas model is used to represent the thermal distribution of nuclei in the medium. Although this model is not exact, Lamb (Lamb 1939) has demonstrated that many materials of interest in reactor calculations can be treated as an ideal monatomic gas at an effective temperature. This model improves with increasing temperature where crystalline effects become progressively less important.

For the Maxwell gas model, the distribution of nuclei speed is assumed to be

$$P(V_t) dV_t = \frac{4}{\sqrt{\pi}} \beta^{3/2} V_t^2 \exp[-\beta V_t^2] dV_t : \beta = \frac{m}{2KT}, \quad (25)$$

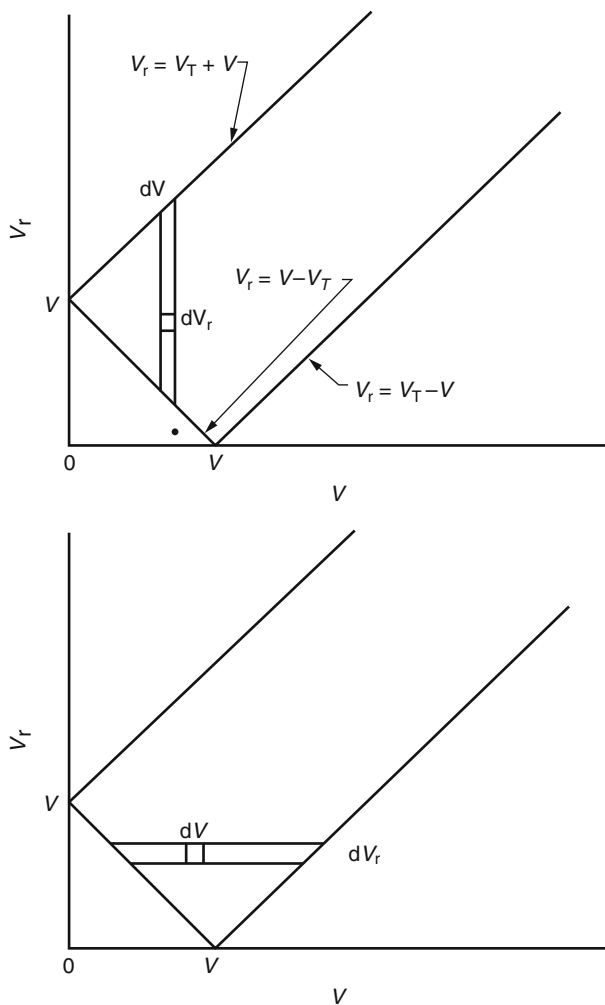


Figure 15
Region of Integration

where K is Boltzmann's constant. By assuming this form for $P(V_t)$ in (24), after evaluating the inner integral, the well-known Doppler-broadening equation is obtained, in terms of speed, as

$$\begin{aligned}
 V\sigma(V, T) = & \frac{1}{V} \left(\frac{\beta}{\pi} \right)^{1/2} \int_0^{\infty} [V_r \sigma(V_r, 0)] V_r dV_r \\
 & \times \{ \text{Exp}[-\beta(V - V_r)^2] - \text{Exp}[-\beta(V + V_r)^2] \}
 \end{aligned} \quad (26)$$

or in terms of energy, as

$$\begin{aligned} \sqrt{E}\sigma(E, T) &= \frac{1}{2} \left(\frac{\alpha}{\pi E} \right)^{1/2} \int_0^{\infty} [\sqrt{E_r}\sigma(E_r, 0)] dE_r \\ &\times \left\{ \text{Exp} \left[-\alpha(\sqrt{E} + \sqrt{E_r})^2 \right] - \text{Exp} \left[-\alpha(\sqrt{E} - \sqrt{E_r})^2 \right] \right\}, \end{aligned} \quad (27)$$

where

$$\alpha = \frac{2\beta}{m} = \frac{A}{KT} : A = \frac{M}{m}.$$

This Doppler-broadening equation can be generalized by recognizing that not only can it be used to broaden cross sections from 0 K to a higher temperature, but it can also be used to broaden cross sections from any temperature T_1 to any higher temperature T_2 (Meghreblian and Holmes 1960). For example, it is possible to start from experimentally measured data at room temperature (293.6 K) and Doppler broaden it to 600 K to obtain cross sections, which in turn can be used to broaden from 600 to 1,000 K. The generalized equation are identical to the above equations with the temperatures 0 and T replaced by T_1 and T_2 , as

$$\begin{aligned} V\sigma(V, T_2) &= \frac{1}{V} \left(\frac{\beta}{\pi} \right)^{1/2} \int_0^{\infty} [V_r\sigma(V_r, T_1)] V_r dV_r \\ &\times \left\{ \text{Exp} \left[-\beta(V - V_r)^2 \right] - \text{Exp} \left[-\beta(V + V_r)^2 \right] \right\}, \end{aligned} \quad (28)$$

where

$$\begin{aligned} \beta &= \frac{m}{2K(T_2 - T_1)}, \\ \sqrt{E}\sigma(E, T_2) &= \frac{1}{2} \left(\frac{\alpha}{\pi E} \right)^{1/2} \int_0^{\infty} [\sqrt{E_r}\sigma(E_r, T_1)] dE_r \\ &\times \left\{ \text{Exp} \left[-\alpha(\sqrt{E} + \sqrt{E_r})^2 \right] - \text{Exp} \left[-\alpha(\sqrt{E} - \sqrt{E_r})^2 \right] \right\}, \end{aligned} \quad (29)$$

where

$$\alpha = \frac{A}{K(T_2 - T_1)}.$$

It is important to recognize that in these equations the V_r and E_r associated with the T_1 cross sections $\sigma(V_r, T_1)$ is merely the laboratory speed or energy of the neutron and not the relative or center of mass energy of the neutron. Therefore, starting from cross sections at 0 K, where the relative energy E is identical to the laboratory energy of the neutron, the Doppler-broadened equation can be used to calculate Doppler-broadened cross section versus the laboratory energy of the neutron for a temperature T_1 . This data are then exactly in the form that can be used in turn to broaden the data from T_1 to any higher temperature T_2 . This is a well-known property of the Doppler-broadening equation that allows cross sections to be bootstrapped from one temperature to the next higher temperature; this can result in a major decrease in the computer time required, comparing to always starting at 0 K to create cross sections at a series of higher temperatures.

3.2.1 Mathematical Interpretation

In terms of reaction rate, (28) can be written in the form

$$VR(V, T2) = \left[\frac{1}{4\pi\tau} \right]^{1/2} \int_0^\infty V_r R(V_r, T1) dV_r \times \{ \text{Exp}[-(V - V_r)^2/4\tau] - \text{Exp}[-(V + V_r)^2/4\tau] \},$$

where

$$\tau = \frac{k(T2 - T1)}{2M}, \quad (30)$$

which by differentiating can be shown to be mathematically analogous to the diffusion equation (age diffusion for neutrons or heat conduction) equation in an infinite, homogenous, spherically symmetric system. In this analogy, the normal independent variables of space and time in the neutron or heat-diffusion equation are equivalent in the Doppler-broadening equation to the independent variables, neutron speed, and temperature of the medium. Similarly, the normal-dependent variable neutron flux or temperature is analogous to the dependent-variable reaction rate in the Doppler-broadening equation. The differential form of the Doppler-broadening equation is

$$\nabla^2 R(V, \tau) = \frac{\partial}{\partial \tau} R(V, \tau), \quad (31)$$

where ∇^2 is the Lapacian operator in spherical coordinates

$$\nabla^2 = \frac{1}{V} \frac{\partial}{\partial V^2} [VR(V, \tau)],$$

and the “initial” condition is that $R(V, \tau_1)$ is known for some initial value of $\tau = \tau_1$.

The main reason for demonstrating at this point that the Doppler-broadening equation is simply the diffusion equation is not because this is a simple or convenient starting point to solve the Doppler-broadening equation; indeed, trying to solve the differential form of this equation can lead to many numerical difficulties when applied to neutron cross sections. The main reason is to improve our understanding of the Doppler-broadening process and to be able to simply predict what will happen to a cross section under Doppler broadening to successively higher temperatures by analogy to what happens to a temperature distribution at successively later times when we solve the diffusion equation.

Two well-known properties of the diffusion equation are its smoothing and conservation properties. As is well known, in the diffusion equation, the effect of increasing the independent variable τ (e.g., time in the heat-conduction equation, temperature in the Doppler-broadening equation) is to “smooth” the dependent variable (e.g., temperature in the heat-conduction equation, reaction rate in the Doppler-broadening equation). Therefore, starting from any initial reaction-rate distribution $R(V, 0)$, as the temperature is increased, the reaction rate $R(V, \tau)$ will become smoother, and will asymptotically approach a constant or uniform distribution throughout all V space. The second important property of the diffusion equation is that if the initial condition $R(V, 0)$ can be integrated over all V space, the quantity $R(V, \tau)$ integrated over all space will be conserved, independent of τ .

For an infinite, spherical symmetric system, these two properties of the diffusion equation may be written in the following form:

1. *Asymptotic value*

$$\text{Lim} \overline{R(\tau)} = \text{Lim} \frac{4\pi \int_0^{V_{\max}} V^2 R(V, 0) dV}{4\pi \int_0^{V_{\max}} V^2 dV}, \quad (32)$$

where $\tau \rightarrow \infty$, $V_{\max} \rightarrow \infty$, independent of V .

2. *Conserved integral*

$$I = \text{Lim} 4\pi \int_0^{V_{\max}} V^2 R(V, 0) dV, \quad (33)$$

where $V_{\max} \rightarrow \infty$, independent of τ .

By comparing (32) and (33), we can see that if the integral, I , is finite, the reaction rate $R(V, \tau)$ will asymptotically approach zero for increasing τ . That is to say, starting from a reaction rate whose integral over all velocity space, (33), is finite, the integral will be conserved for all τ ; when, due to Doppler broadening the finite integral I is uniformly distributed over the infinite velocity space, (32), the average value of the reaction rate will obviously be zero.

From the differential form of the Doppler-broadening equation, (31), the natural dependent variable is the reaction rate $R(V, \tau)$, and it is this variable which becomes smooth and is conserved. It is important to note that without introducing additional approximations, it is not possible to derive a diffusion equation involving the cross section, rather than the reaction rate. Similarly, there is no conservation law which involves the cross section. In particular, the so-called “area under the curve” of the cross section is not conserved, and variations of this area as a function of temperature can be quite large. It is a common error in many textbooks to state that the “area under the curve” is conserved; it is not stressed enough in these textbooks that this is in general not true, and only becomes true after a variety of approximations are introduced in the Doppler-broadening model.

A corollary to the smoothing property of the diffusion equation in a spherically symmetric system is that the reaction rate must be constant at the origin, as

$$\text{Lim} \frac{\partial}{\partial V} [R(V, \tau)] = 0; \text{ all } \tau > 0 \quad (34)$$

where $V \rightarrow 0$, or equivalently, $\text{Lim} R(V, \tau) = \text{constant}$, where $V \rightarrow 0$.

Therefore, for all temperatures greater than 0 K, since the low-energy limit of the reaction rate must be constant, the low-energy limit of all cross sections must be $1/V$. At exactly 0 K, the initial condition $R(V, 0)$ can contradict this condition.

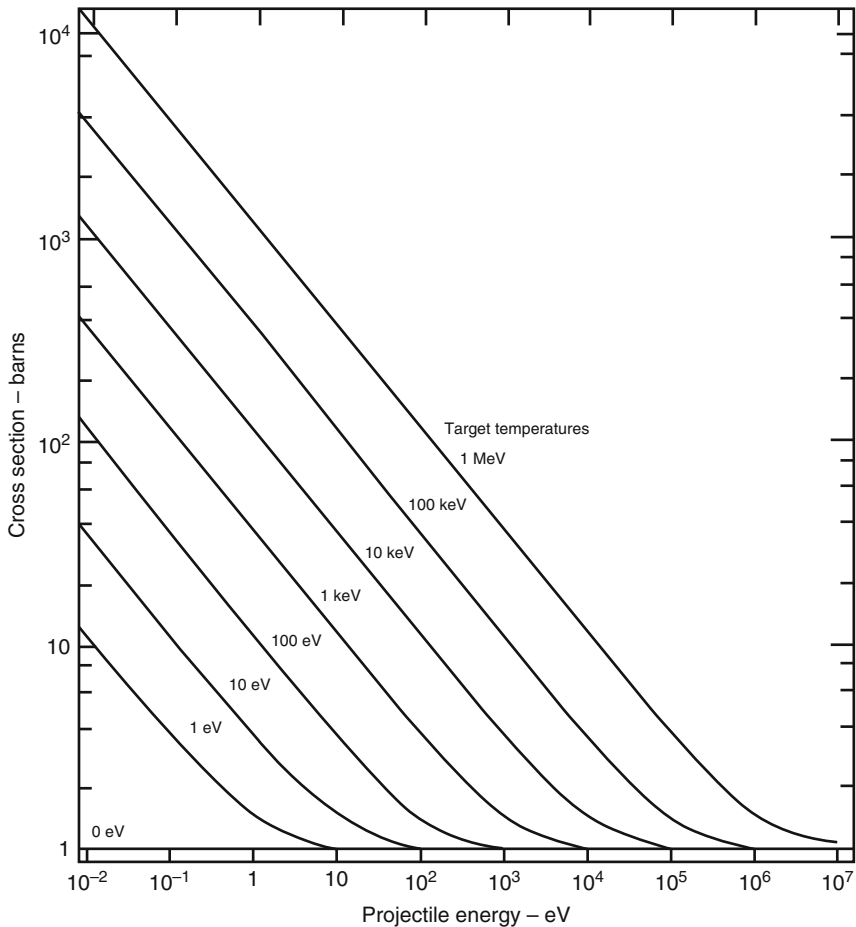
With this as background, we can now use these smoothing and conservation properties to simply predict the effect of Doppler broadening. We will consider the following four cases:

1. $R(V, 0) = C$ ($1/V$ cross section): Since the reaction rate is already smooth, Doppler broadening will not have any effect, that is, a $1/V$ cross section is independent of temperature. Since

this is the only case in which the reaction rate is constant, it is easy to understand why this is the only case where the cross section is independent of temperature. This is an important actual case, since most low-energy capture and fission cross sections tend to be $1/V$ in shape.

2. $R(V, 0) = CV$ (*constant cross section*): Since the reaction rate is initially minimum at the origin ($V = 0$), as the temperature increases the reaction rate will attempt to become uniform by increasing to higher and higher values in the vicinity of the origin (● Fig. 16).

Since the integral of the reaction rate is highly divergent (see (23)), the reaction rate will continue to rise toward infinity. In terms of cross section, since the low-energy limit must be $1/V$, at successively higher temperature, this $1/V$ behavior will extend to higher and higher neutron energies as illustrated in the above figure. The fact that a constant cross section is temperature dependent is often overlooked and yet the change due to broadening can be



■ Figure 16

Doppler broadening of initially constant cross section

quite large. For example, by Doppler broadening the hydrogen elastic cross section, which at 0 K is constant at low energy, we find that even at room temperature the cross section at thermal energy (0.0253 eV) is 30 barns as opposed to the cold 0 K value of 20 barns (a difference of 50%). This is an important actual case, as most low-energy elastic cross sections tend to be constant in shape.

3. $R(V, 0) = C \delta(V - V_0)$ – a Dirac delta function: For a Dirac delta function the reaction rate will be

$$VR(V, \tau) = C \left(\frac{1}{4\pi} \right)^{1/2} V_0 \{ \text{Exp} [-(V - V_0)^2 / 4\tau] - \text{Exp} [-(V + V_0)^2 / 4\tau] \}. \quad (35)$$

By examining the low- V limit, it can be demonstrated that the constant low-energy reaction rate ($1/V$ cross section) is still obtained. Since the integral of the reaction rate over all velocity space is finite (see (32)), the reaction rate will asymptotically approach zero for increasing τ . This case is of interest because it approximates the behavior of any resonance that is very narrow when compared with the width of the Gaussian shape of the kernel in the Doppler-broadening equation (see (30)). This case illustrates that such resonances when Doppler broadened, regardless of the details of their shape, will assume a Gaussian shape characteristic, solely of the temperature of medium, and have a magnitude consistent with the conservation of the reaction rate.

4. *A simple Briet–Wigner line shape:*

(a) *Capture and fission resonance*

$$\sigma(E, 0) = \left(\frac{E_0}{E} \right)^{1/2} (\Gamma/2) A / [(\Gamma/2)^2 + (E - E_0)^2]$$

and

$$R(V, 0) = V_0 (\Gamma'/2) A / [(\Gamma'/2)^2 + (V^2 - V_0^2)^2]. \quad (36)$$

(b) *Elastic resonance*

$$\sigma(E, 0) = (\Gamma/2) A / [(\Gamma/2)^2 + (E - E_0)^2]$$

and

$$R(V, 0) = V (\Gamma'/2) A / [(\Gamma'/2)^2 + (V^2 - V_0^2)^2].$$

(c) *Elastic interference*

$$\begin{aligned} \sigma(E, 0) &= B(E - E_0) / [(\Gamma/2)^2 + (E - E_0)^2] \\ R(V, 0) &= VB'(V^2 - V_0^2) / [(\Gamma'/2)^2 + (V^2 - V_0^2)^2]. \end{aligned}$$

By examining the integral of these reaction rates over all velocity space (33), it can be demonstrated that in all cases the average value (32) will asymptotically approach zero for increasing τ .

However, of the three, only the capture and fission resonance has a finite integral over all velocity space, while the other two have $\log(V)$ and V^2 divergence, respectively. The relative strength of these three forms indicates that the capture and fission will dissipate the fastest, and the elastic interference will be the most persistent. This is in marked contrast to the prediction of ψ - χ (Greene et al. 1976; Hutchins et al. 1973; Green and Pitterle 1968), and other approximate Doppler-broadening methods, in which the elastic interference rapidly dissipates because of its asymmetric form.

3.3 Methods of Solution

With the preceding sections as background on Doppler broadening and the effect that it has on different cross-section shapes, we will now proceed to examine the various methods that are used to actually solve the Doppler-broadening equation. Today, there are basically two approaches to solving the Doppler-broadening equation. One approach starts from tabulated cross sections or reaction rates as a function of energy and solves the equation directly; this approach is referred to as a kernel broadening and is typified by SIGMA1 (Cullen 1979a-c), TEMPO (Gregson and James 1965), and SIGAR (Pope et al. in press). The second approach starts from resonance parameters and by introducing certain approximations, obtains an expression for the broadened cross section in terms of easily tabulated and calculated functions; this is the so-called ψ - χ (Greene et al. 1976; Hutchins et al. 1973; Green and Pitterle 1968) method. Each of these methods has its own advantages and disadvantages.

The advantage of the kernel-broadening approach is that it can be applied to any cross sections that are either initially in tabulated form or can be reduced to tabulated form (see Reconstruction of Energy-Dependent Cross Sections), and it can be used to accurately calculate broadened cross sections at any energy and temperature. Since all modern evaluations can be reduced to tabulated form, the kernel approach is a general approach that can be applied to any cross section. The major disadvantage of the kernel-broadening approach is that relative to the ψ - χ method it can be quite expensive in terms of computer time.

The advantage of the ψ - χ method is that it is relatively inexpensive and for many reactor applications, it is sufficiently accurate of calculating broadened cross sections. The major disadvantage of the ψ - χ method is that it can only be applied to evaluations in which the cross sections are represented by single-level, Breit-Wigner resonances or Adler-Adler parameters. There are other restrictions on the ψ - χ method regarding the energy range and resonance spacing wherein the method may be applied accurately, which will be discussed later in this chapter.

Both these approaches have their place in reactor calculations and are somewhat complementary in the sense that there are a variety of applications where one approach is more applicable than the other. For example, in the situation in which an evaluated library will be processed to a few standard temperatures (Cullen 2007a-c) and then used for a large number of subsequent reactor calculations, it may be worth the initial investment of computer time to use the kernel method in order to guarantee the general utility and accuracy of the broadened cross sections. However, survey calculations involving a large number of temperatures and calculations that must be performed quickly and cheaply can best be done using the ψ - χ method. In order to assist the reader in deciding which of these methods is most appropriate for any application, each method will be examined.

3.3.1 Kernel Broadening

The SIGMA1 (Cullen 1973, 1979a–c) method that has been invented by me assumes that the cross section is given as a table of cross sections versus incident neutron energy, with linear interpolation in cross section and energy between tabulated values; this form was assumed for compatibility with the representation of cross sections in the ENDF/B format. The SIGAR (Pope et al. in press) method is similar except that it assumes that the reaction rate, rather than the cross section, is tabulated and linearly interpolable. With either of these assumptions, the Doppler-broadening equation can be solved exactly without any further approximations. Therefore, these two methods are quite general and do not include any energy or temperature restrictions and are equally applicable to neutron or charged-particle cross sections.

Returning to the well-known Doppler-broadening equations (28) and (29), and substituting

$$Y^2 = \alpha E = \beta V^2$$

and

$$X^2 = \alpha E_r = \beta V_r^2,$$

the Doppler-broadening equation assumes the form

$$\sigma(Y, T2) = \frac{1}{Y^2} \left(\frac{1}{\pi} \right)^{1/2} \int_0^{\infty} X^2 \sigma(X, T1) dX \{ \text{Exp}[-(X-Y)^2] - \text{Exp}[-(X+Y)^2] \}. \quad (37)$$

The following development can be simplified by defining

$$\sigma * (Y, T2) = \frac{1}{Y^2} \left(\frac{1}{\pi} \right)^{1/2} \int_0^{\infty} X^2 \sigma(X, T1) \text{Exp}[-(X-Y)^2] dX, \quad (38)$$

and noting that the Doppler-broadened cross section is

$$\sigma(Y, T2) = \sigma * (Y, T2) - \sigma * (-Y, T2). \quad (39)$$

The SIGMA1 method assumes that the cross section is given as a table of cross sections versus energy and linear interpolation between tabulated values

$$\begin{aligned} \sigma(E, T1) &= \left[\frac{E - E_k}{E_{k+1} - E_k} \right] \sigma_{k+1} + \left[\frac{E_{k+1} - E}{E_{k+1} - E_k} \right] \sigma_k \\ &= A_k + B_k E; \quad E \in (E_k, E_{k+1}), \end{aligned} \quad (40)$$

which is equivalent to

$$\sigma(X, T1) = A_k + C_k X^2; \quad X \in (X_k, X_{k+1}). \quad (41)$$

Since tabulated cross sections only span a finite-energy range (e.g., 10^{-5} eV to 20 MeV), the cross section is extended outside of their tabulated energy range as $1/V$ (e.g., a constant reaction rate). With this assumed form for the cross section, (38) becomes

$$\sigma * (Y, T2) = \frac{1}{Y^2} \left(\frac{1}{\pi} \right)^{1/2} \sum_k \int_0^{\infty} X^2 [A_k + C_k X^2] \text{Exp}[-(X-Y)^2] dX. \quad (42)$$

Changing variables, let $Z = X - Y$ and collecting terms in powers of Z ,

$$\sigma * (Y, T2) = \frac{1}{Y^2} \left(\frac{1}{\pi} \right)^{1/2} \sum_k \int_0^\infty F_k(Z) \text{Exp}[-Z^2] dZ$$

and

$$F_k(Z) = C_k Z^4 + 4C_k Y Z^3 + (A_k + 6C_k Y^2) Z^2 + (2A_k Y + 4C_k Y^3) Z + (A_k Y^2 + C_k Y^4). \quad (43)$$

Similarly, the SIGAR method assumes that the reaction rate is tabulated and linearly interpolable between tabulated values

$$X\sigma(X, T1) = D_k + F_k X^2; \quad X \in (X_k, X_{k+1}). \quad (44)$$

Substituting this expression into (38), changing variables to $Z = X - Y$, and collecting terms in powers of Z , we obtain

$$\sigma * (Y, T2) = \frac{1}{Y^2} \left(\frac{1}{\pi} \right)^{1/2} \sum_k \int_0^\infty G_k(Z) \text{Exp}[-Z^2] dZ$$

and

$$G_k(Z) = F_k Z^3 + 2F_k Y Z^2 + (D_k + 2F_k Y^2) Z + (D_k Y + F_k Y^3). \quad (45)$$

Either the SIGMA1 (43) or the SIGAR (45) can be defined exactly in terms of the family of function,

$$H^n(a, b) = F^n(a) - F^n(b); \quad n = 0, 1, 2, 3, 4$$

and

$$F^n(a) = 2 \left(\frac{1}{\pi} \right)^{1/2} \int_0^a Z^n \text{Exp}[-Z^2] dZ. \quad (46)$$

These functions can easily be shown to satisfy the recursion relationship

$$F^n(a) = \frac{n-1}{2} F^{n-2}(a) - \left(\frac{1}{\pi} \right)^{1/2} a^{n-1} \text{Exp}[-a^2] + \left(\frac{1}{\pi} \right)^{1/2} \delta_{n,1}. \quad (47)$$

By explicitly evaluating (46) for $n = 0$ and 1 and then applying the recursion relationship, the required functions are

$$\begin{aligned} F0(a) &= \text{ERF}(a), \\ F1(a) &= \left(\frac{1}{\pi} \right)^{1/2} [1 - \text{Exp}(-a^2)], \\ F2(a) &= \frac{1}{2} \text{ERF}(a) - a \left(\frac{1}{\pi} \right)^{1/2} \text{Exp}(-a^2), \\ F3(a) &= \left(\frac{1}{\pi} \right)^{1/2} [1 - (1 + a^2) \text{Exp}(-a^2)], \\ F4(a) &= \frac{3}{4} \text{ERF}(a) - \left(\frac{1}{\pi} \right)^{1/2} \left[\frac{3a}{2} + a^3 \right] \text{Exp}(-a^2). \end{aligned} \quad (48)$$

With the definition of these functions, the algorithm describing the SIGMA1 and SIGAR methods to calculate Doppler-broadened cross sections at any arbitrary energy is complete. For additional considerations regarding how to optimize and stabilize this algorithm as actually implemented in computer codes (Cullen 1973) and (Cullen 2007a–c), see the documentation for these codes.

3.3.2 Tabulated Broadened Cross Sections

The preceding algorithms describe how to calculate the broadened cross section at any given energy, but they do not specify how to choose the energies at which to calculate the broadened cross sections. In order to address this question, the SIGMA1 and SIGAR methods use different approaches.

The SIGMA1 program is one of a series of computer programs that are intended to insure that their calculated output cross sections are in a tabulated form with linear interpolation between tabulated values. This convention was adopted because of the existence of a variety of programs that produce multigroup data or use continuous-energy cross sections in applications (e.g., Monte Carlo), starting from tabulated, linearly interpolable cross sections. Therefore, with this convention, output from each of the series of codes, of which SIGMA1 is one, can be used directly as input to many other codes.

Although the SIGMA1 Doppler-broadening algorithm described above allows the cross section to be calculated at any given energy, it does not guarantee that the broadened cross section is linearly interpolable between any two given energies. Even though the cross sections that SIGMA1 uses as input are linearly interpolable, the same energy grid cannot be used for the broadened cross section. The reason is that from the preceding discussion we know that the reaction rate, not the cross section, will become smoother under Doppler broadening. However, “smoothing” occurs on an average basis, and not necessarily at all energies. For example, visualize a series of narrow, widely spaced resonances. At low temperature, much of the energy between resonances will be smooth or even constant and does not require many energy points to describe the energy dependence. But with increasing temperature, the resonance will “smooth,” becoming broader, and the wings of the resonances will extend into the formally constant cross-section energy range between resonances, requiring more points to describe the energy dependence.

At higher energies where the dominant structure in the cross section is due to resonances, the distinction between the reaction rate and cross section is not that important. However, at lower energies, where the cold cross section may be smooth, the distinction is extremely important. For example, the “cold” (0 K) hydrogen-elastic cross section is approximately 20 barns from 10^{-5} eV up to 1 keV; see (Cullen 2007a–c). Although two tabulated energy points (at 10^{-5} eV and 1 keV) and linear interpolation between these points can be used to represent the 0 K elastic cross sections over this energy range and to calculate the broadened cross section at 10^{-5} eV and 1 keV, the broadened cross section is certainly not linearly interpolable between these two energy points. Enormous errors would result if subsequent processing or application programs used such data and assumed linear dependence. For example, in the case of hydrogen at room temperature, the actual broadened cross section at thermal energy, 0.0253 eV, is roughly 30 barns. The room-temperature cross section at 10^{-5} eV is roughly 1140 barns, and the cross section at 1 keV is about 20 barns. Linearly interpolating between the two

values at 10^{-5} eV and 1 keV predicts a thermal cross section of essentially 1140 barns, when compared with the actual broadened value of 30 barns. Therefore, in this simple example, the error introduced by using the input-energy grid structure for the output cross sections and assuming linear interpolation leads to an error of a factor of almost 40 (4,000%) in the hydrogen-thermal cross section.

The SIGMA1 method uses the smoothing properties of the Doppler-broadening process and the fact that the cold cross section that it uses are linearly interpolable in order to define an energy grid for the broadened cross section. Doppler broadening is a “smoothing” process, but it is the reaction rate and not the cross section, which is smoothed. Therefore, if the energy grid that is used to represent the unbroadened (cold) reaction is sufficiently dense, as a starting point, the smoother Doppler-broadened reaction rate can be adequately represented using the same energy grid. At higher energies ($AE \gg KT$), this smoothing process applies equally well to the cross section. However, at lower energies, although the reaction rate is becoming smoother, the same may not be true of the cross section because the two differ by a factor of $1/V$ [$R(V, T) = V\sigma(V, T)$]. To insure that this low-energy $1/V$ tail does not prevent the cross section from being linearly interpolable, it is sufficient to choose an energy grid for the broadened data that is merely the energy grid for the unbroadened data supplemented by an additional set of energy points. These additional points are selected such that between any two energy points of the broadened energy grid the difference between linear interpolation and $1/V$ variation in the section is always lesser than some allowable error, e.g., 0.1%. Once this starting energy grid is defined, the SIGMA1 method then uses the interval-halving technique described earlier to iterate to convergence to within any user-defined accuracy.

This can be done easily as it is very simple to replace a $1/V$ cross section by a linearly interpolable table of cross sections, where linearly interpolable cross sections are everywhere within any given allowable uncertainty of the $1/V$ cross section. For example, consider two possible representations of a cross section: $1/V$ and tabulated, linearly interpolable, with the additional condition that the tabulated cross sections agree exactly with the $1/V$ at the energies at which it is tabulated and also that successive energies are multiples of one another, as

$$\sigma(V) = \frac{1}{V}, V \in (V_1, V_2)$$

and

$$\sigma(V) = \frac{1}{V_1} - \frac{(V^2 - V_1^2)}{V_1^3 S(S+1)}, V_2 = SV_1. \quad (49)$$

The fractional difference between these two representations and the variation at this point are

$$V_{\max} = V_1 \left[\frac{1}{3} (1+S+S^2) \right]^{1/2}$$

and

$$\varepsilon(V_{\max}) = 1 - \left(\frac{2}{3} \right) \left(\frac{2}{3} \right)^{1/2} \frac{(1+S+S^2)^{1/2}}{S(S+1)}.$$

Note that $\epsilon(V_{\max})$ is independent of V , and depends only on the spacing, S , between points. This demonstrates that it is possible to represent $1/V$ variation by linear variation in energy to within any allowable error ϵ , simply by ensuring that the energies for successive tabulated values are within S^2E of one another, independent of E .

➤ *Table 1* illustrates the typical factor S required for any allowable tolerance ϵ , for ϵ in the range from 0.1 to 1.0%. This table also shows the number of energy points that would be required to space points S^2E apart between 10^{-5} eV and 20 MeV. For example, an allowable uncertainty of 0.5% would require only 124 energy points or roughly 10 per energy decade.

Therefore, in order to insure that the Doppler-broadened cross sections are linearly interpolable in cross section and energy, it is sufficient to start from the same energy points that are used to represent the cold (0 K) cross sections; and to supplement this grid in any interval where the points are more widely spaced than S^2E , where S depends on the allowable uncertainty (➤ *Table 1*). Relative to the number of points normally encountered in current evaluations (Oblozinsky et al. 2006; Cullen 2007a–c), this procedure introduces only a modest increase in the total number of points, and, as such, this procedure is an economically practical method of ensuring that the broadened cross sections are linearly interpolable over their entire energy range. Once this starting energy grid is defined, the SIGMA1 method then uses the interval-halving technique described earlier to iterate to convergence to within any user-defined accuracy. The SIGMA1 method of generating linearly interpolable Doppler-broadened cross sections has now been completely described.

The SIGAR (Pope et al. in press) method uses a different approach to selection of the energy grid. Unlike SIGMA1 which starts from linearly interpolable cross sections, SIGAR starts from resonance parameters and defines two separate energy grids: the first grid for the cold (0 K) cross sections, based on the natural width of each resonance, and the second grid for the broadened cross sections, based on the broadened width of each resonance. Rather than attempting to insure that the reaction rate in either of these grids is linearly interpolable the SIGAR method simply selects energy points which are a multiple of widths on either side of each resonance. Preliminary comparisons of SIGMA1 and SIGAR results indicate that they yield results which closely agree.

■ **Table 1**

Linear approximation to $1/V$

Tolerance	Factor	Points
0.001	1.0530	276
0.002	1.0757	195
0.003	1.0935	160
0.004	1.1087	139
0.005	1.1223	124
0.006	1.1347	114
0.007	1.1463	105
0.008	1.1571	99
0.009	1.1674	93
0.010	1.1772	88

3.3.3 TEMPO and Psi-Chi Methods

The Doppler-broadening equation (30) is the starting point for many approximate methods of calculating Doppler-broadened cross sections. Among these methods is the TEMPO method (Gregson and James 1965) that calculates Doppler-broadened cross sections starting from tabulated linearly interpolable reaction rates (similar to SIGAR) and the psi-chi method (Greene et al. 1976; Hutchins et al. 1973; Green and Pitterle 1968), which calculated broadened cross sections directly from resonance parameters.

Both the TEMPO and psi-chi methods introduce certain approximations before proceeding to solve the Doppler-broadening equation (30). The validity of these approximations is based on the strongly convergent properties of the exponentials in the Doppler-broadening kernel. The Gaussian character of these exponentials indicates that in order for the cross section at an energy E_R to make a nontrivial contribution to the integral, it must be close to E .

To better understand the validity of the approximations introduced by these approximate methods, we should briefly examine the Doppler-broadening equation (19), in this case, explicitly including the normalization of the distribution of target nuclei, $p(\bar{V}_T) d\bar{V}_T$, as

Lab reactions = Relative reactions, that is

$$R(V, T) = V\sigma(V, T) = \frac{\int_{[V_i; V_r > 0]} V_r \sigma(V_r, 0) p(\bar{V}_T) d\bar{V}_T}{\int_{[V_i; V_r > 0]} p(\bar{V}_T) d\bar{V}_T}.$$

The denominator in this equation defining the normalization of $p(\bar{V}_T) d\bar{V}_T$ is only implicit in the form of the Doppler-broadening equation that is normally used. We will see that following approximations take the liberty of “changing,” $p(\bar{V}_T) d\bar{V}_T$, without considering that this is a normalized distribution.

The approximations introduced are as follows:

In the Doppler-broadening kernel, the second exponential can be ignored when compared with the first as

$$\begin{aligned} & \text{Exp} \left[-\alpha \left(\sqrt{E_R} - \sqrt{E} \right)^2 \right] - \text{Exp} \left[-\alpha \left(\sqrt{E_R} + \sqrt{E} \right)^2 \right] \\ &= \text{Exp} \left[-\alpha \left(\sqrt{E_R} - \sqrt{E} \right)^2 \right] \left[1 - \text{Exp} \left(-4\alpha \sqrt{EE_R} \right) \right] \\ &\approx \text{Exp} \left[-\alpha \left(\sqrt{E_R} - \sqrt{E} \right)^2 \right]. \end{aligned} \quad (50)$$

In this form, it may be seen that this approximation is valid for large $\alpha\sqrt{EE_R}$ ($\sim AE/KT$). If applied at lower energies, ignoring the second exponential will overestimate the broadened kernel (it ignores a negative term), and will result in larger Doppler-broadened reaction rates (and therefore, cross sections) than would be obtained using the exact kernel.

The major contribution to the remaining integral comes from a narrow range of E_R either close to E or close to some other energy E_0 (usually the peak of a resonance). This assumption allows $\sqrt{E_R}$ to be expanded in a Taylor series of about E or E_0 . An equivalent form that better lends itself to analysis can be obtained simply by adding and subtracting terms to find

$$\alpha \left(\sqrt{E_R} - \sqrt{E} \right)^2 = \frac{\alpha}{4E} (E_R - E)^2 - \frac{\alpha}{4E} \left(\sqrt{E_R} - \sqrt{E} \right)^2 \left[\left(\sqrt{E_R} - \sqrt{E} \right) \left(\sqrt{E_R} - 3\sqrt{E} \right) \right] \quad (51)$$

or

$$\alpha \left(\sqrt{E_R} - \sqrt{E} \right)^2 = \frac{\alpha}{4E} (E_R - E)^2 - \frac{\alpha}{4E} \left(\sqrt{E_R} - \sqrt{E} \right)^2 \times \left[\left(\sqrt{E_R} - \sqrt{E} \right) \left(\sqrt{E_R} + 3\sqrt{E} \right) + 4(E - E_0) \right]. \quad (52)$$

Defining the Doppler width, evaluated at any arbitrary energy E_A (either E_R or E_0),

$$\Delta_A = 2 \left(\frac{E_A}{\alpha} \right)^{1/2} = \left(\frac{4KTE_A}{A} \right)^{1/2}, \quad T = T_2 - T_1. \quad (53)$$

And ignoring higher-order terms, it is found that

$$\alpha \left(\sqrt{E_R} - \sqrt{E} \right)^2 \approx \left[\frac{E_R - E}{\Delta_A} \right]^2. \quad (54)$$

By examining (55) and (58), we can see that in both cases the magnitude of the error introduced by this assumption increases with decreasing energy. The error in both equations is asymmetric about the point $\sqrt{E_R} = \sqrt{E}$ or $\sqrt{E_R} = 2\sqrt{E_0} - \sqrt{E}$, respectively. Relative to this point of asymmetry, for fixed E and E_0 , the variation in the error as a function of E_R is identical in both cases.

For various values of αE , **Table 2** illustrates the error introduced into the Doppler-broadening kernel by this approximation. For $\alpha E = 10^6$ and higher energies, the error introduced by this assumption is less than 1% over the entire range of the table. For example, since αE is simply AE/KT , for U238 at room temperature ($KT = 0.0253$ eV), $AE/KT = 10^6$ corresponds to roughly 100 eV. Since $\alpha E_R = \alpha E = 1$, the second exponential in the Doppler-broadening equation (30) is about 0.01 and less for higher energies; it is obvious that of the two approximations introduced so far, the second is the more restrictive in terms of limiting the validity of the approximation to higher energies. From **Table 2**, we can see that the error introduced by this approximation is asymmetric. Therefore, for fairly symmetric reaction rates, such as constant or near the peak of a resonance, this asymmetry of the error causes first-order cancellations of the errors and helps to provide better results than one would expect from **Table 2**. However, for asymmetric reaction rates, such as on the sides of resonances, or near as minimum elastic interference, the errors reinforce and cause worse results.

The psi-chi method introduces a third approximation by extending the lower limit of the integration from 0 to $-\infty$, assuming that the contribution to the integral from the interval $(-\infty, 0)$ is negligible. Generally, this assumption is less restrictive than the second assumption, and as such is consistent with the second assumption introduced above.

Introducing these approximations allows the Doppler-broadening equation (30) to be reduced to the form

$$\sqrt{E}\sigma(E, T_2) = \frac{1}{\Delta\sqrt{\pi}} \int_a^{\infty} \sqrt{E_R}\sigma(E_R, T_1) \text{Exp} \left\{ - \left[\frac{(E_R - E)}{\Delta} \right]^2 \right\} dE_R, \quad (55)$$

where

$$\begin{aligned} a &= 0 - \text{TEMPO} \\ &= -\infty - \text{psi-chi.} \end{aligned}$$

Table 2
Error Introduced by Doppler width

$\frac{\alpha}{4E} (E - E_r)^2$	$\alpha E = 10^2$			$\alpha E = 10^3$			$\alpha E = 10^4$			$\alpha E = 10^5$		
	Approximate	αE_r	Error	Exact	αE_r	Error	Exact	αE_r	Error	Exact	αE_r	Error
4.0	0.0183	60.00	-194.7	0.0062	873.51	-31.6	0.0139	9600.00	-8.6	0.0169	98735.09	-2.6
3.0	0.0498	65.36	-95.3	0.0255	890.46	-19.3	0.0417	9653.59	-5.5	0.0472	98904.56	-1.7
2.0	0.1353	71.72	-41.3	0.0958	910.56	-9.9	0.1231	9717.16	-2.9	0.1315	99105.57	-0.9
1.0	0.3679	80.00	-12.1	0.3281	936.75	-3.3	0.3560	9800.00	-1.0	0.3642	99367.54	-0.3
0	1.0000	100.00	0	1.0000	1000.00	0	1.0000	0	0	1.0000	100000.00	0
1.0	0.3679	120.00	8.5	0.4021	1063.25	3.0	0.3792	0200.00	1.0	0.3715	100632.46	0.3
2.0	0.1353	128.28	21.4	0.1722	1089.44	8.1	0.1473	0282.84	2.7	0.1391	100894.43	0.9
3.0	0.0498	134.64	34.9	0.0764	1109.54	14.3	0.0581	0346.41	5.0	0.0524	101095.45	1.6
4.0	0.0183	140.00	47.4	0.0348	1126.49	20.9	0.0232	0400.00	7.5	0.0198	101264.91	2.5

Note: Error = 100% × (exact-approximate)/exact

$$\text{Exact} = \exp \left[-\alpha \left(\sqrt{E} - \sqrt{E_r} \right)^2 \right]$$

$$\text{Approximate} = \exp \left[-\frac{\alpha}{4E} (E - E_r)^2 \right]$$

Note that the approximations introduced result in the “weighting function” (the equivalent of $p(\bar{V}_T)d\bar{V}_T$) that is unnormalized.

At this point, the TEMPO and psi-chi method separate by assuming different forms for the reaction rate (or cross section). The psi-chi method assumes that the 0 K cross sections are composed of a series of single-level, Breit–Wigner resonances, each of the form,

Capture and fission

$$\sigma(E_R, 0) = \left(\frac{E_0}{E_R}\right)^{1/2} \frac{(\Gamma/2)A}{(\Gamma/2)^2 + (E_R - E_0)^2}.$$

Elastic

$$\sigma(E_R, 0) = \frac{(\Gamma/2)B}{(\Gamma/2)^2 + (E_R - E_0)^2} \frac{C(E_R - E_0)}{(\Gamma/2)^2 + (E_R - E_0)^2}, \quad (56)$$

where E = Laboratory energy, E_R = relative energy, E_0 = resonance energy, and Γ = resonance total width. By evaluating the Doppler width at the resonance energy $\Delta = (4KTE_0/A)^{1/2}$ and assuming $(E_0/E_R)^{1/2} \approx 1$ and by changing variables

$$\begin{aligned} \xi_R &= \frac{\Gamma}{\Delta} = \Gamma \left(\frac{A}{4KTE_0}\right)^{1/2}, \\ X &= 2(E_0 - E_R)/\Gamma, \\ Y &= 2(E - E_R)/\Gamma, \end{aligned} \quad (57)$$

the Doppler-broadening equation can be written in the form

Capture and fission $\sigma(E, T) = \left(\frac{2}{\Gamma}\right) \left(\frac{E_R}{E}\right)^{1/2} A \Psi(X, \xi_R)$.

$$\text{Elastic } \sigma(E, T) = \left(\frac{2}{\Gamma}\right) [B\Psi(X, \xi_R) + C\chi(X, \xi_R)], \quad (58)$$

where the psi Ψ and chi χ functions are defined by

$$\Psi(X, \xi_R) = \left(\frac{\xi_R}{2}\right) \left(\frac{1}{\pi}\right)^{1/2} \int_{-\infty}^{+\infty} \text{Exp} \left\{ - \left[\frac{(X - Y)}{2} \xi_R \right]^2 \right\} \frac{dY}{Y^2 + 1}$$

and

$$\chi(X, \xi_R) = \left(\frac{\xi_R}{2}\right) \left(\frac{1}{\pi}\right)^{1/2} \int_{-\infty}^{+\infty} \text{Exp} \left\{ - \left[\frac{(X - Y)}{2} \xi_R \right]^2 \right\} \frac{YdY}{Y^2 + 1}. \quad (59)$$

In addition to the approximations explicitly introduced to accomplish the transition from (59)–(63), there is an additional assumption concerning the energy dependence of Γ , A , B , and C . Although these are fairly complicated functions of incident neutron energy, they are usually slowly varying functions of energy. The psi-chi method only broadens the simple Breit–Wigner line shape and maintains the energy dependence of Γ , A , B , and C by writing the final equations in the form,

$$\sigma(E, T) = \left(\frac{2}{\Gamma(E)}\right) \left(\frac{E_R}{E}\right)^{1/2} A(E) \Psi(X, \xi_R)$$

and

$$\sigma(E, T) = \left(\frac{2}{\Gamma(E)} \right) [B(E) \Psi(X, \xi_R) + C(E) \chi(X, \xi_R)]. \quad (60)$$

Historically, the psi-chi method has been the most heavily used for Doppler calculations as the method is both relatively inexpensive to use and fairly accurate for many reactor calculations. However, more and more evaluations are representing cross sections in terms of not just single-level parameters, but rather in terms of either single-level parameters plus a background cross section (which includes resonant structure), other resonance formalisms, or directly in terms of tabulated cross sections. For these evaluations, the user is forced to either use other methods (e.g., SIGMA1, SIGAR, or TEMPO) or introduce additional approximations in order to justify using the psi-chi method.

The TEMPO method proceeds from (59) by assuming that the cold (0 K) reaction rate $\sqrt{E_R} \sigma(E_R, T1)$ is a tabulated function with linear variation in energy between tabulated values. By introducing this assumption, the approximate Doppler-broadening equation (59) can be written as

$$R(E, T2) = \sqrt{E} \sigma(E, T2) = \frac{1}{\Delta \sqrt{\pi}} \sum_k \int_{E_k}^{E_{k+1}} [P_k + Q_k E_R] \text{Exp} \left\{ - \left[(E_R - E) / \Delta \right]^2 \right\} dE_R. \quad (61)$$

By changing variables to $x = (E_R - E) / \Delta$, (65) can immediately be analytically integrated to yield

$$R(E, T2) = \sqrt{E} \sigma(E, T2) = \frac{1}{2} \sum_k \left\{ [P_k + Q_k E] [\text{ERF}(x_{k+1}) - \text{ERF}(x_k)] + \Delta \left(\frac{1}{\pi} \right)^{1/2} [\text{Exp}(-x_k^2) - \text{Exp}(-x_{k+1}^2)] \right\}. \quad (62)$$

The TEMPO method has the same limitations as the psi-chi method, in that it can only be applied to those energy ranges where αE is large when compared with unity. However, compared with the psi-chi method, the TEMPO method has the advantage that by reconstructing the 0 K reaction rate in a linearly interpolable form (e.g., from resonance parameters plus background cross sections) it can be used to Doppler broaden virtually any currently available evaluation of cross sections. However, the TEMPO method does not have any significant advantage when compared with the more accurate and less-restrictive SIGMA1 and SIGAR methods.

3.3.4 Mathematical Comparisons

The derivation of the various methods that are commonly used to Doppler broaden is now complete. However, it is interesting to proceed further to compare the results that the various approximations used to derive each method have on the resulting equations. The intent here is to improve the reader's understanding of the Doppler-broadening process and the effect of the various approximations, as opposed to proposing an alternative method to solving the Doppler-broadening equation.

It has already been demonstrated in this work that the Doppler-broadening equation, (29) and (30), is equivalent to solving the diffusion equation in an infinite spherically symmetric

velocity space. It is interesting to note that the approximate equation used by the psi-chi and the TEMPO method is also a diffusion equation. In fact, all the Doppler-broadening methods discussed in this work can be shown to satisfy the integral equation

$$F(X, \tau) = \left(\frac{1}{4\pi\tau} \right)^{1/2} \int_{-\infty}^{+\infty} F(X', 0) \text{Exp} \left[-(X - X')^2 / 4\tau \right] dX', \quad (63)$$

or the equivalent differential equation and initial condition,

$$\begin{aligned} \frac{\partial^2 F}{\partial X^2}(X, \tau) &= \frac{\partial F}{\partial \tau}(X, \tau), \\ F(X, 0) &= q(X); \quad q(X) \text{ given.} \end{aligned} \quad (64)$$

The only difference between the various methods is the physical interpretation of $F(X, \tau)$, X , τ , and the initial condition. **► Table 3** summarizes the interpretation of these parameters for each of the methods discussed in this work.

As pointed out earlier, the differential form of the Doppler-broadening equation as applied to neutron cross sections is difficult to solve numerically, but it is of great use in examining the effect of each approximation introduced to derive the psi-chi and TEMPO methods. Specifically, starting from the exact differential equation (32) and changing variables to those used in the other methods, e.g., change from speed to energy and from $VR(V, \tau)$ to $R(E, \tau)$ or $\sigma(E, \tau)$, leads to the equations

TEMPO or psi-chi capture/fission:

$$\frac{A}{KE} \frac{\partial}{\partial t} R(E, t) \frac{\partial^2}{\partial E^2} R(E, t) \frac{3}{2E} \frac{\partial}{\partial E} R(E, t) \quad (65)$$

► **Table 3**

Interpretation of diffusion equation parameters

Method	x	t	$f(x, t)$	Initial conditions		Conservation
Exact	V	$\frac{kT}{2M}$	$VR(V, t)$	$(-\infty, \infty)$	$VR(V , 0)$	$4\pi \int_0^{+\infty} R(V, t) V^2 dV$
TEMPO	E	$\frac{kTE_0}{A}$	$R(E, t)$	$(0, \infty)$	$R(E, 0)$	None (see applications)
				$(-\infty, 0)$	0	
Psi-chi capture or fission	E	$\frac{kTE_0}{A}$	$R(E, t)$	$(0, \infty)$	$R(E, 0)$	$\int_{-\infty}^{+\infty} R(E, t) dE$
				$(-\infty, 0)$ extend	$R(E, 0)$	
Psi-chi elastic	E	$\frac{kTE_0}{A}$	$\sigma(E, t)$	$(0, \infty)$	$\sigma(E, 0)$	$\int_{-\infty}^{+\infty} \sigma(E, t) dE$
				$(-\infty, 0)$ extend	$\sigma(E, 0)$	

and

$$\text{Psi-chi elastic : } \frac{A}{KE} \frac{\partial}{\partial t} \sigma(E, t) = \frac{\partial^2}{\partial E^2} \sigma(E, t) + \frac{5}{2E} \frac{\partial}{\partial E} \sigma(E, t) + \frac{1}{2E^2} \sigma(E, t). \quad (66)$$

These two equations are exactly equivalent to the Doppler-broadening equations (29) and (30). Besides the initial conditions, the only difference between the SIGMA1 and SIGAR and the approximate psi-chi and TEMPO methods is that the approximate methods only include the first term on the right-hand side of equations (69) and (70). As such, the approximate equations are only valid wherein the other trailing terms are small when compared with the first term.


How were these terms eliminated during the derivation of the psi-chi and TEMPO methods? The first derivative term was eliminated by expansion of the exponential argument; and in the case of elastic scatter, the cross-section term was eliminated by assuming $(E_0/E_R) \approx 1$. Ignoring the second exponential and extending the lower limit of integration change the initial conditions, but not the differential equation.

The net effect of ignoring these trailing terms is to convert from the exact diffusion equation using speed in a spherical system, to using energy in a planar system, in which either the reaction rate or cross section will become “smoother” under Doppler broadening. Earlier, it was pointed out that the approximations introduced in order to derive the psi-chi and TEMPO methods limit then to “large” E . From the mathematical comparisons, here we see that this is equivalent to saying that far from the origin (i.e., at large E), a spherical system may be approximated as linear. For example, on the surface of the earth many physical problems may be accurately approximated by assuming that we live on a plane surface. Similarly, the approximate methods introduced here can be quite accurate when restricted to their ranges of applicability.

The introduction of the approximations that allow us to convert from speed to energy space is also the genesis of the conservation of the “area under the curve.” To reiterate, this is NOT a property of the exact Doppler-broadening equation, but rather a consequence of the approximations introduced to obtain the approximate broadening equation. Therefore, the concept of conservation of “area under the curve” must be restricted to those energy ranges where the approximations are valid. In particular, it must not be extended to low energies, e.g., CAVEAT EMPYTOR in resonance-integral calculations.

The only cases where it is exactly valid to ignore the trailing terms on (65) and (66) are

1. In (65) for a constant reaction rate ($1/V$ cross section) and
2. In (66) for a cross section of the highly unlikely form $(E/E_0)^{-1/5}$.

In other cases, the $1/E$ and $1/E^2$ dependence of the trailing terms are used as justification to apply the approximate methods at higher energies. However, from (65) and (66), it can be seen that even at high energy the values and the first derivatives should also be considered. As e.g.,  Table 4 lists the 0 K values and derivatives for a simple Breit–Wigner resonance of the terms that appear in (66). In addition, the value of these terms at the peak inflection point, $E_R = E_0 \pm (\Gamma/2)$, where the second derivative is zero and the distant energy $E_R \gg E_0$, are also listed. From this table, three points that are obvious are as follows:

1. Close to the peak of the resonance, the trailing terms can be ignored if the half-width is much smaller than the energy, that is, $(\Gamma/2) \ll E$.
2. By definition, at the inflection point, where the second derivative is zero, the trailing terms cannot be ignored.

■ **Table 4**
Breit–Wigner resonances and parameters

		Peak	Inflection	Distant
$\frac{1}{2E} \sigma(E, 0)$	$\frac{1}{2E^2} \frac{(\Gamma/2)^2}{(\Gamma/2)^2 + (E - E_R)^2}$	$\frac{1}{2E^2}$	$\frac{1}{2E_1^2(4/3)}$	$\frac{(\Gamma/2)^2}{2E^4}$
$\frac{1}{2E} \frac{\partial \sigma}{\partial E}(E, 0)$	$-\frac{(E - E_R)/(\Gamma/2)^2}{E[(\Gamma/2)^2 + (E - E_R)^2]^2}$	0	$\pm \frac{(1/3)^{1/2}}{E_1(4/3)^2}$	$\pm \frac{(\Gamma/2)^2}{E^4}$
$\frac{\partial^2}{\partial E^2} \sigma(E, 0)$	$\frac{(\Gamma/2)^2 [6(E - E_R)^2 - 2(\Gamma/2)^2]}{[(\Gamma/2)^2 + (E - E_R)^2]^3}$	$-\frac{1}{(\Gamma/2)^2}$	0	$\frac{6(\Gamma/2)^2}{E^4}$

3. At distant energies, the contribution from all three terms is comparable magnitude and the trailing terms cannot be ignored.

These results may be summarized by stating that the psi–chi and TEMPO methods applied at a single-level Breit–Wigner resonance at higher energy (e.g., $AE \gg KT$) will yield accurate results close to the peak of the resonance. However, caution is advised in applying these methods to calculate the broadened cross sections far from the peak of the resonance, e.g., heavy even–even nuclei, such as Th232, U238, and Pu240, in which the ratio of the mean-level spacing to total width is very large (~ 500).

3.4 Numerical Results

In the preceding sections, the approximations introduced to obtain the approximate Doppler-broadening equation (55) were quantitatively explained to restrict the range of applicability of the psi–chi and TEMPO methods to the energy range where $AE/KT \gg 1$. In this section, we will first quantitatively examine the effect of these approximations when applied to low energy. Next, examples will be presented in order to illustrate the effect of Doppler broadening at higher energies in the resonance region. Finally, an example will be presented to illustrate the effect that the very high temperatures, such as those occur in fusion plasmas, have on cross sections.

3.4.1 Low Energies

It can be seen that for light isotopes the low-energy limit of the various reactions at 0 K is either constant or $1/V$. Usually, such behavior extends into the keV energy range so that the following analysis is valid even for CTR core temperatures. Since the low-energy limit of a single-level Breit–Wigner resonance is also either constant (elastic) or $1/V$ (capture and fission), in principle the following also applies to the low-energy tails of such resonances. However, in practice only materials with a large atomic weight (i.e., large A) have resonances at lower energies, and in such materials, the effects that are described as follows occur only at extremely low energies.

In order to examine the effect of Doppler broadening at lower energies and the approximations introduced in the psi-chi and TEMPO methods, we will define two functions:

$$F(\pm X) = \frac{1}{X^2} \left(\frac{1}{\pi}\right)^{1/2} \int_0^{\infty} Y^2 \sigma(Y, T) \text{Exp}[-(Y \mp X)^2] dY$$

and

$$G(\pm X) = \frac{1}{X^2} \left(\frac{1}{\pi}\right)^{1/2} \int_0^{\infty} Y^2 \sigma(Y, T) \text{Exp}\left[-\left(\frac{Y^2 \mp X^2}{2X}\right)^2\right] dY.$$

In terms of these two functions, the various methods described here correspond to

$F(X) - F(-X)$ Exact SIGMA1 and SIGAR,

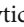


$F(X)$ Ignore second exponential,

$F(X) + F(-X)$ Ignore second exponential and extend integral from ∞ to $-\infty$,

$G(X) - G(-X)$ Expand argument of exponential,

$G(X)$ Expand argument and ignore second exponential (TEMPO),

$G(X) + G(-X)$ Expand argument, ignore second exponential, and extend integral from ∞ to $-\infty$.

For a cross section that, at 0 K, is either constant or $1/V$ cross section, these functions can be easily evaluated analytically. For comparison purposes,  Fig. 17 presents graphical results and  Tables 5 and  6 tabular results.

The $1/V$ results illustrate that of the six possible combinations examined here, only the exact and psi-chi methods reproduce a $1/V$ -cross section independent of temperature. Since a $1/V$ cross section is a constant reaction rate integrated over the target nuclei velocity

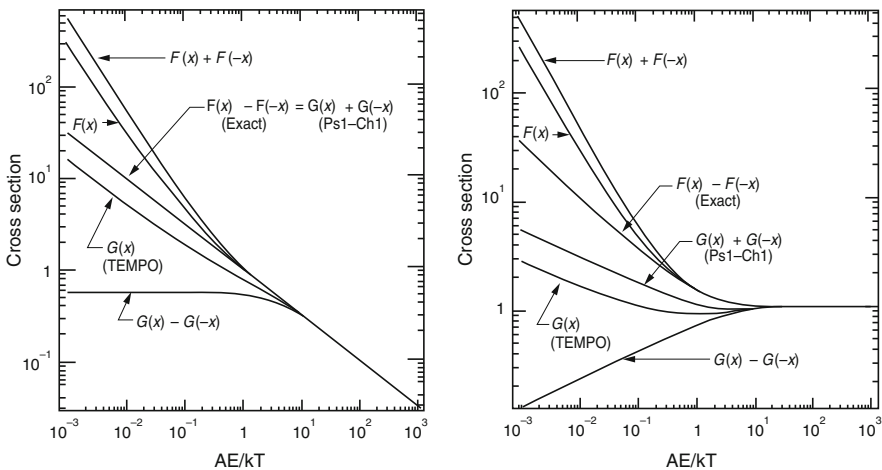


 Figure 17

Effect of Doppler broadening on $1/V$ and constant cross section

Table 5
Doppler broadened 0 K 1/V cross section

AE/KT	$(F+) - (F-)$	$(F+)$	$(F+) + (F-)$	$(G+) - (G-)$	$(G+)$	$(G+) + (G-)$
10,000.000	1.000E - 02	1.000E - 02	1.000E - 02	1.000E - 02	1.000E - 02	1.000E - 02
8,000.000	1.118E - 02	1.118E - 02	1.118E - 02	1.118E - 02	1.118E - 02	1.118E - 02
6,000.000	1.291E - 02	1.291E - 02	1.291E - 02	1.291E - 02	1.291E - 02	1.291E - 02
4,000.000	1.581E - 02	1.581E - 02	1.581E - 02	1.581E - 02	1.581E - 02	1.581E - 02
2,000.000	2.236E - 02	2.236E - 02	2.236E - 02	2.236E - 02	2.236E - 02	2.236E - 02
1,000.000	3.162E - 02	3.162E - 02	3.162E - 02	3.162E - 02	3.162E - 02	3.162E - 02
800.000	3.536E - 02	3.536E - 02	3.536E - 02	3.536E - 02	3.536E - 02	3.536E - 02
600.000	4.082E - 02	4.082E - 02	4.082E - 02	4.082E - 02	4.082E - 02	4.082E - 02
400.000	5.000E - 02	5.000E - 02	5.000E - 02	5.000E - 02	5.000E - 02	5.000E - 02
200.000	7.071E - 02	7.071E - 02	7.071E - 02	7.071E - 02	7.071E - 02	7.071E - 02
100.000	1.000E - 01	1.000E - 01	1.000E - 01	1.000E - 01	1.000E - 01	1.000E - 01
80.000	1.118E - 01	1.118E - 01	1.118E - 01	1.118E - 01	1.118E - 01	1.118E - 01
60.000	1.291E - 01	1.291E - 01	1.291E - 01	1.291E - 01	1.291E - 01	1.291E - 01
40.000	1.581E - 01	1.581E - 01	1.581E - 01	1.581E - 01	1.581E - 01	1.581E - 01
20.000	2.236E - 01	2.236E - 01	2.236E - 01	2.233E - 01	2.234E - 01	2.236E - 01
10.000	3.162E - 01	3.162E - 01	3.162E - 01	3.082E - 01	3.122E - 01	3.162E - 01
8.000	3.536E - 01	3.536E - 01	3.536E - 01	3.375E - 01	3.455E - 01	3.535E - 01
6.000	4.082E - 01	4.083E - 01	4.083E - 01	3.743E - 01	3.913E - 01	4.082E - 01
4.000	5.000E - 01	5.001E - 01	5.002E - 01	4.214E - 01	4.607E - 01	5.000E - 01
2.000	7.071E - 01	7.101E - 01	7.131E - 01	4.827E - 01	5.949E - 01	7.071E - 01
1.000	1.000E + 00	1.025E + 00	1.050E + 00	5.205E - 01	7.602E - 01	1.000E + 00
0.800	1.118E + 00	1.161E + 00	1.205E + 00	5.287E - 01	8.234E - 01	1.118E + 00
0.600	1.291E + 00	1.373E + 00	1.454E + 00	5.372E - 01	9.141E - 01	1.291E + 00
0.400	1.581E + 00	1.760E + 00	1.940E + 00	5.459E - 01	1.064E + 00	1.581E + 00
0.200	2.236E + 00	2.802E + 00	3.367E + 00	5.549E - 01	1.395E + 00	2.236E + 00
0.100	3.162E + 00	4.680E + 00	6.197E + 00	5.595E - 01	1.861E + 00	3.162E + 00
0.080	3.536E + 00	5.572E + 00	7.609E + 00	5.605E - 01	2.048E + 00	3.535E + 00
0.060	4.082E + 00	7.022E + 00	9.962E + 00	5.614E - 01	2.322E + 00	4.082E + 00
0.040	5.000E + 00	9.832E + 00	1.466E + 01	5.623E - 01	2.781E + 00	5.000E + 00
0.020	7.071E + 00	1.792E + 01	2.877E + 01	5.633E - 01	3.817E + 00	7.071E + 00
0.010	1.000E + 01	3.349E + 01	5.698E + 01	5.637E + 01	5.282E + 00	1.000E + 01
0.008	1.118E + 01	4.113E + 01	7.109E + 01	5.638E + 01	5.872E + 00	1.118E + 01
0.006	1.291E + 01	5.375E + 01	9.459E + 01	5.639E - 01	6.737E + 00	1.291E + 01

▣ Table 5 (continued)

AE/KT	$(F_+) - (F_-)$	(F_+)	$(F_+) + (F_-)$	$(G_+) - (G_-)$	(G_+)	$(G_+) + (G_-)$
0.004	1.581E + 01	7.871E + 01	1.416E + 02	5.640E - 01	8.188E + 00	1.581E + 01
0.002	2.236E + 01	1.525E + 02	2.827E + 02	5.641E - 01	1.146E + 01	2.236E + 01
0.001	3.162E + 01	2.982E + 02	5.647E + 02	5.641E - 01	1.609E + 01	3.162E + 01

▣ Table 6

Doppler broadened 0 K constant cross section

AE/KT	$(F_+) - (F_-)$	(F_+)	$(F_+) + (F_-)$	$(G_+) - (G_-)$	(G_+)	$(G_+) + (G_-)$
10,000.000	1.000E + 00	1.000E + 00	1.000E + 00	1.000E + 00	1.000E + 00	1.000E + 00
8,000.000	1.000E + 00	1.000E + 00	1.000E + 00	1.000E + 00	1.000E + 00	1.000E + 00
6,000.000	1.000E + 00	1.000E + 00	1.000E + 00	1.000E + 00	1.000E + 00	1.000E + 00
4,000.000	1.000E + 00	1.000E + 00	1.000E + 00	9.999E - 01	9.999E - 01	9.999E - 01
2,000.000	1.000E + 00	1.000E + 00	1.000E + 00	9.999E - 01	9.999E - 01	9.999E - 01
1,000.000	1.001E + 00	1.001E + 00	1.001E + 00	9.997E - 01	9.997E - 01	9.997E - 01
800.000	1.001E + 00	1.001E + 00	1.001E + 00	9.997E - 01	9.997E - 01	9.997E - 01
600.000	1.001E + 00	1.001E + 00	1.001E + 00	9.996E - 01	9.996E - 01	9.996E - 01
400.000	1.001E + 00	1.001E + 00	1.001E + 00	9.994E - 01	9.994E - 01	9.994E - 01
200.000	1.002E + 00	1.002E + 00	1.002E + 00	9.987E - 01	9.987E - 01	9.987E - 01
100.000	1.005E + 00	1.005E + 00	1.005E + 00	9.975E - 01	9.975E - 01	9.975E - 01
80.000	1.006E + 00	1.006E + 00	1.006E + 00	9.968E - 01	9.968E - 01	9.968E - 01
60.000	1.008E + 01	1.008E + 00	1.008E + 00	9.957E - 01	9.957E - 01	9.957E - 01
40.000	1.012E + 00	1.012E + 00	1.012E + 00	9.934E - 01	9.934E - 01	9.934E - 01
20.000	1.025E + 00	1.025E + 00	1.025E + 00	9.856E - 01	9.858E - 01	9.860E - 01
10.000	1.050E + 00	1.050E + 00	1.050E + 00	9.635E - 01	9.679E - 01	9.724E - 01
8.000	1.062E + 00	1.062E + 00	1.062E + 00	9.505E - 01	9.593E - 01	9.681E - 01
6.000	1.083E + 00	1.083E + 00	1.083E + 00	9.284E - 01	9.465E - 01	9.646E - 01
4.000	1.125E + 00	1.125E + 00	1.125E + 00	8.872E - 01	9.273E - 01	9.674E - 01
2.000	1.247E + 00	1.249E + 00	1.250E + 00	7.964E - 01	9.006E - 01	1.005E + 00
1.000	1.472E + 00	1.486E + 00	1.500E + 00	6.949E - 01	8.938E - 01	1.093E + 00
0.800	1.574E + 00	1.599E + 00	1.625E + 00	6.623E - 01	8.973E - 01	1.132E + 00
0.600	1.732E + 00	1.783E + 00	1.833E + 00	6.212E - 01	9.062E - 01	1.191E + 00
0.400	2.013E + 00	2.132E + 00	2.250E + 00	5.658E - 01	9.276E - 01	1.289E + 00
0.200	2.688E + 00	3.094E + 00	3.500E + 00	4.797E - 01	9.889E - 01	1.498E + 00
0.100	3.686E + 00	4.843E + 00	6.000E + 00	4.050E - 01	1.083E + 00	1.760E + 00

Table 6 (continued)

AE/KT	(F+) - (F-)	(F+)	(F+) + (F-)	(G+) - (G-)	(G+)	(G+) + (G-)
0.080	4.095E + 00	5.672E + 00	7.250E + 00	3.833E - 01	1.120E + 00	1.857E + 00
0.060	4.698E + 00	7.016E + 00	9.333E + 00	3.570E - 01	1.174E + 00	1.990E + 00
0.040	5.717E + 00	9.608E + 00	1.350E + 01	3.229E - 01	1.260E + 00	2.197E + 00
0.020	8.032E + 00	1.702E + 01	2.600E + 01	2.717E - 01	1.439E + 00	2.606E + 00
0.010	1.132E + 01	3.116E + 01	5.100E + 01	2.286E - 01	1.662E + 00	3.096E + 00
0.008	1.265E + 01	3.807E + 01	6.350E + 01	2.162E - 01	1.744E + 00	3.273E + 00
0.006	1.460E + 01	4.946E + 01	8.433E + 01	2.012E - 01	1.858E + 00	3.516E + 00
0.004	1.787E + 01	7.193E + 01	1.260E + 02	1.818E - 01	2.036E + 00	3.890E + 00
0.002	2.525E + 01	1.381E + 02	2.510E + 02	1.529E - 01	2.389E + 00	4.625E + 00
0.001	3.569E + 01	2.683E + 02	5.010E + 02	1.286E - 01	2.814E + 00	5.499E + 00

distribution (19), this illustrates that the other combinations are not properly normalized. It should always be remembered that implied in the Doppler-broadening equations is a normalizing target nuclei velocity distribution as a denominator to the equations

$$R(x,t) = \frac{\int R(x',0) M(V) dV}{\int M(V) dV},$$

such that when $R(x',0) = C$ (a 1/cross section), this reduced to an identity

$$R(x,t) = C = C \frac{\int M(V) dV}{\int M(V) dV}.$$

So that in this case, $R(x,t)$ is independent of temperature.

Any approximation introduced into the numerator of the equation should also be introduced into the implied denominator. In the case of the psi-chi method, the combination of approximations does conserve this normalization, whereas in the TEMPO equations it does not; and the lower energy TEMPO results converge to only one-half of the exact value. If the TEMPO method is renormalized by $[1 + \text{ERF}(X)]/2$, it will yield the correct $1/V$ behavior and will also agree well with the psi-chi results for a constant cross section (described later). As actually implemented in computer codes, in contrast to the equations presented in the TEMPO report (Gregson and James 1965), this normalization problem has been eliminated by renormalizing as described here.

The results for the constant cross section case illustrates that for a reaction rate that is increasing with energy, that is $R(V,0) = V$, the approximations introduced cause the psi-chi and TEMPO methods to underestimate the low-energy cross sections. This result is expected from (65) and (66), since in this case in (37) the derivative of the reaction rate is a positive constant; and in (66), although the derivative of the cross section is zero the value of the cross section is positive and ignoring these terms underestimate the then effect of broadening.

From \blacktriangleright Fig. 17 we can see that expanding the exponential is the most restrictive of the approximations since $G(x)$ deviates from the exact solution at a higher energy than $F(x)$. From \blacktriangleright Tables 5 and \blacktriangleright 6, it can be seen that expanding the argument of the first exponential and keeping the correct second exponential $G(x) - F(-x)$, can lead to negative cross sections.

From \blacktriangleright Fig. 17, we can see that for the two cases considered here the results presented by the various methods are virtually indistinguishable from one another for $AE/KT > 100$. For example, at room temperature (i.e., $KT = 0.0253$ eV) for hydrogen ($A = 1$), the approximate methods should only be applied for $E > 2.5$ eV.

3.4.2 Resonance Region

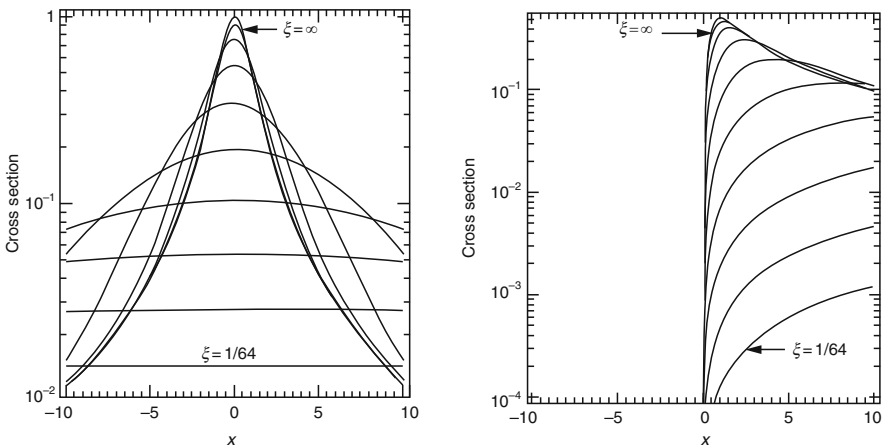
At higher energies, in the resonance region, the psi-chi method can be an accurate and economical means of defining broadened cross sections, particularly close to the peak of a resonance. In order to illustrate the effect of broadening in the resonance region, \blacktriangleright Figs. 18 and \blacktriangleright 19 illustrate the psi and chi functions, respectively. The psi and chi functions, (59), are particularly convenient and economical to use as they are only a function of two variables

1. The distance from the peak of the resonance, measured in half-widths

$$X = 2(E - E_0)/\Gamma \quad \text{and}$$

2. The ratio of the total width to Doppler widths

$$\Delta_A = \Gamma (A/4KTE_A)^{1/2}.$$



\blacksquare Figure 18
Psi and chi functions

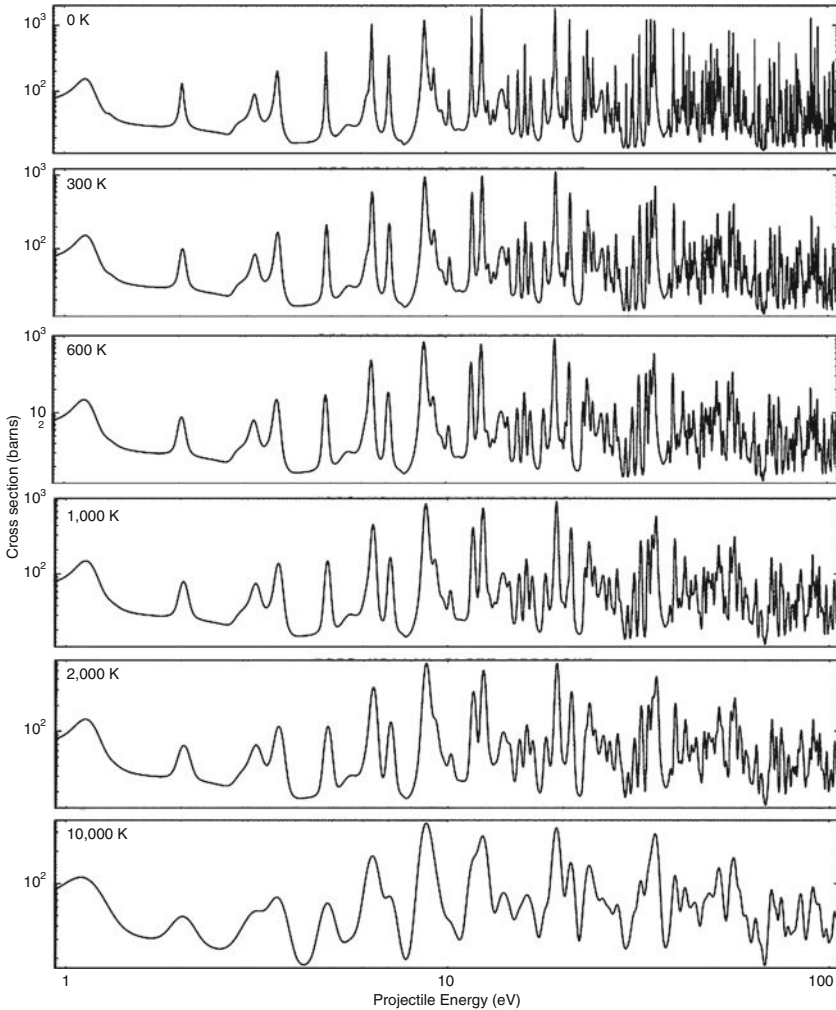


Figure 19
U235 Total, 0 to 10,000 K temperature

Figure 18 illustrates the psi and chi functions for a range of $\xi = \infty, 4, 2, 1, 1/2 \dots 1/64$. For successively smaller ξ (higher T), the resonance broadens (psi) and the interference dissipates (chi).

Figure 19 illustrates the effect of Doppler broadening the U235 total cross section for temperatures between 0 and 10,000 K. In the resolved-resonance region, the difference between the broadened cross sections obtained by each of the methods described here can differ for two reasons: (1) the approximations introduced to obtain the approximate Doppler-broadening equation (55) and (2) the cross section may not be described by a series of single-level, Breit–Wigner resonances.

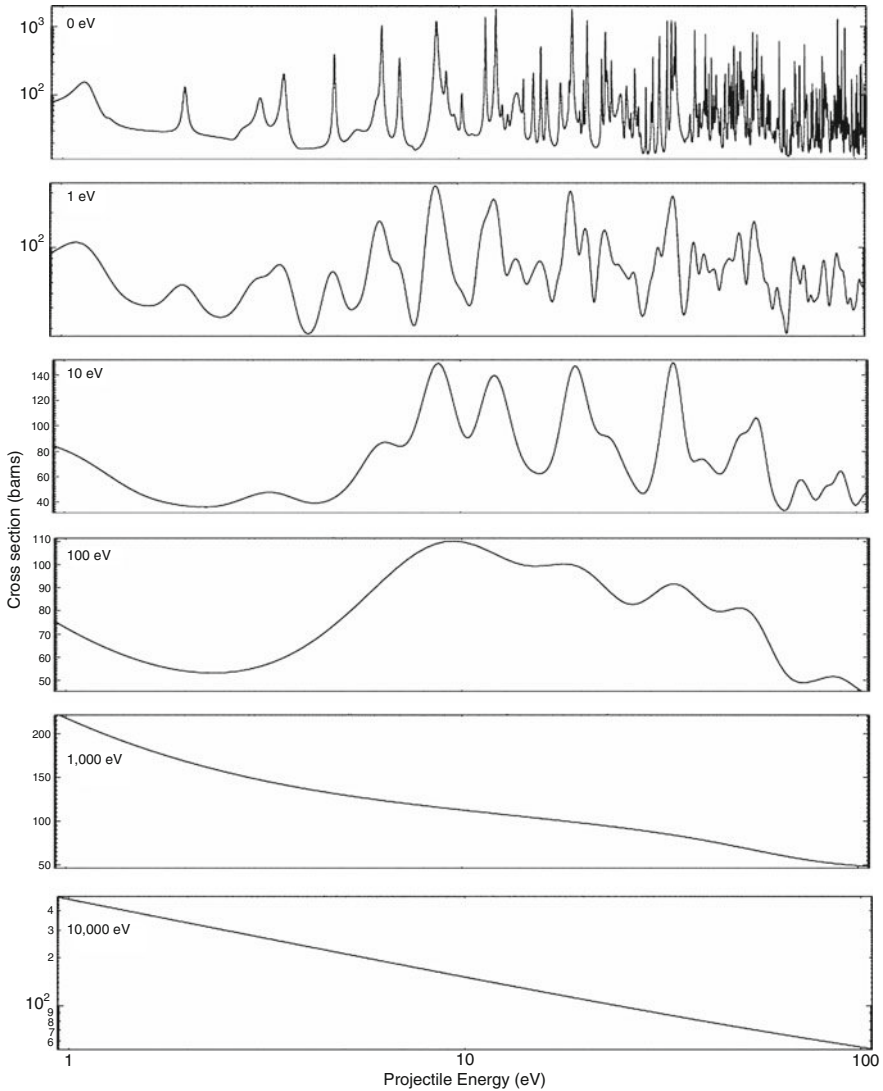
The approximations introduced will limit the accuracy of the psi–chi and TEMPO methods to high energies, as described in the preceding sections, but also limits these methods to calculate cross sections close to the peak of resonances. For example, for isotopes with wide overlapping resonances, such as U235- and Pu239 s-wave resonances, we expect the psi–chi and TEMPO methods to be accurate methods of calculating cross sections both near the peaks of resonances and at energies between the resonances. This is because the cross section between resonances will be dominated by the contributions from neighboring resonances, which are never more than a few half-widths distant. Although the contribution of distant resonances may not be calculated accurately, their actual contribution to the cross section will be so small as to not affect the accuracy of the overall result.

In contrast for heavy even–even nuclei with narrow, widely spaced resonances, such as Th232, U238, and Pu240, on average resonances are about 500 half-widths apart. In this case, the cross section between resonances can be dominated by a single nearest resonance, in which mid-way between resonances is 250 half-widths away; on average, the next nearest resonance will be 750 half-widths away. For the elastic cross section, this presents no calculational problems, since far from the nearest resonance the resonance contribution will become small when compared with the potential scattering and the broadened cross section will simply reduce to the potential-scattering cross section. However, the Doppler-broadened capture and fission cross sections between resonances will be defined solely in terms of the contribution from the nearest resonance, or resonances, which can be many half-widths distant. In this case, the approximations introduced by the psi–chi and TEMPO methods can introduce large errors.

3.4.3 High Energies

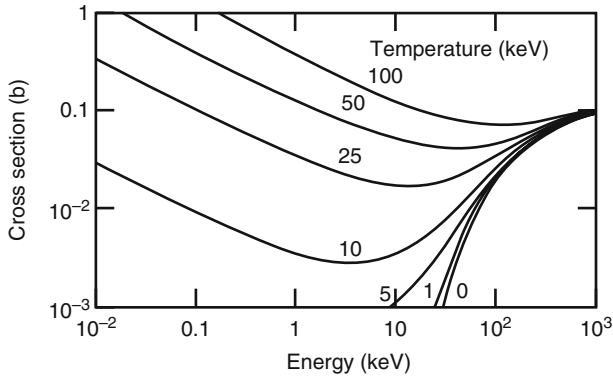
At energies higher than the resolved-resonance region, in the unresolved-resonance region, it is still important to consider Doppler broadening. However, in this energy range evaluations do not uniquely define a set of resonance energies and widths; rather, the evaluations define distributions of resonance spacings and widths. Therefore, it is not possible to discuss calculating energy-dependent cross sections directly from the data given in evaluations. In this energy range, two approaches are possible to define Doppler-broadened cross sections: (1) the distribution of resonance widths and spacings may be sampled to obtain a ladder of resonances. Once a ladder is chosen, any of the methods described here may be used to broaden the cross sections and (2) the distribution of resonance widths and spacings is used directly to define temperature-dependent, self-shielded, group-averaged cross sections; this approach will be described later in this chapter under self-shielding.

At still higher energies above the unresolved-resonance region, usually the resonance structure overlaps, the cold (0 K) cross section becomes smooth, and Doppler broadening has little or no effect on neutron-induced cross sections. Therefore, generally for fission-reactor core application, Doppler broadening need not be considered in this energy range. However, for completeness in this section on Doppler broadening, it will be mentioned and illustrated that for fusion plasma and astrophysics, temperature effects on cross sections can be important even at high energies. The reason is the enormously high temperatures that are encountered in plasmas and astrophysics. For example, in a plasma temperature is usually described in energy units, using KT ($T = 293.6$ is equivalent to $KT = 0.0253$ eV), and temperatures in the keV range are required for plasma ignition, to cause any significant fusion. The enormity of these temperatures



■ **Figure 20**
U235 total, 0–10,000 eV temperature

can be appreciated by first examining ► *Fig. 19* which illustrates broadening with temperatures up to 10,000 K, which is roughly an order of magnitude higher than what would be encountered in a fission reactor, and then realize that in forms of temperatures expressed in energy 12,000 K is approximately only 1 eV. For comparison, ► *Fig. 20* illustrates the effect of broadening to plasma-like temperatures; note the eventual $1/V$ shape of the cross section at very high energy, corresponding to smoothing of the reaction rate.



■ Figure 21
 (D, D) cross section 0–100 keV temperature

One important effect on the equivalent laboratory frame of reference cross section that must be considered at plasma-like temperatures is that for threshold reactions even projectiles with laboratory energies below the threshold may interact with a target nuclei whose motion may combine with that of the projectile to produce a relative energy above the threshold and make the reaction energetically possible. The result of this phenomenon is to make the effective-laboratory threshold energy for any reaction decrease to a lower energy as the temperature of the medium is increased. As the temperature of the medium approaches the energy of the threshold, there is essentially no longer a laboratory frame of reference threshold, since in this case there is an appreciable cross section or probability of a thermal projectile resulting in a relative energy that lies above the reaction threshold. 📌 Figure 21 illustrates the effect of temperature on the (D, D) fusion cross section for temperatures between 0 and 100 keV. In principle, a similar phenomenon occurs to threshold reactions in fission-reactor cores. However, in practice, the temperatures encountered in fission systems are so low when compared with the threshold energies that the effect is negligible and can be ignored, e.g., for fission reactors we need not consider Doppler broadening of inelastic cross sections.

4 Self-Shielding

4.1 Introduction

Since the neutron flux at any energy E is merely the total distance traveled per unit time by all neutrons of energy E , it is not surprising that increasing the cross section, which decreases the average distance that neutrons travel between collisions, lead to a decrease in the neutron flux. This phenomenon is referred to as self-shielding, since in terms of resonances it is the increase in cross section itself that depresses, or shields the resonance, from the flux.

By considering certain limiting cases, it is easy to see the effect that self-shielding has on the neutron flux. First, consider a uniform source in a totally absorbing infinite medium. In this case, the Boltzmann equation reduces to

$$\Sigma_T(E) \Phi_0(E) = S_0(E). \quad (67)$$

Obviously by dividing both sides of this equation by the total cross section, we find that the scalar flux will vary inversely to the total cross section.

Next consider a monoenergetic source in a totally scattering infinite medium. In this case, the Boltzmann equation at energies below the source energy reduces to


$$\Sigma_T(E) \Phi_0(E) = \frac{1}{1-\alpha} \int_E^{E/\alpha} \Sigma_T(E') \Phi_0(E') \frac{dE'}{E'}. \quad (68)$$

It is easy to demonstrate by substitution that the solution to this equation is simply

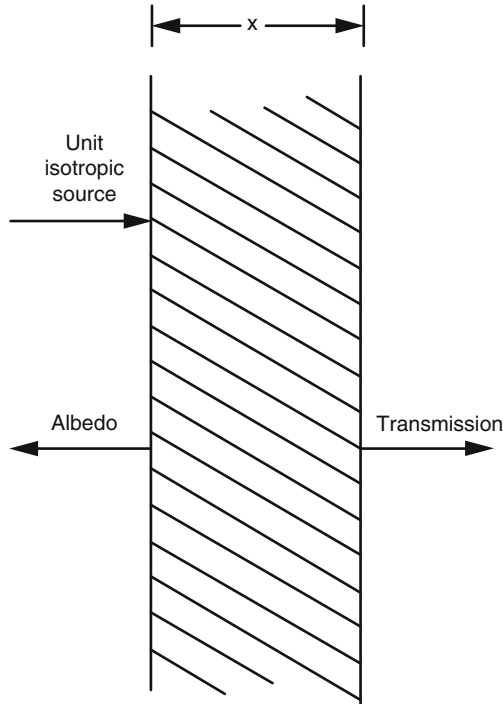
$$\Phi_0(E) = \frac{C}{E \Sigma_T(E)}, \quad (69)$$

where the constant C only depends upon the source strength. Therefore, we again see that the flux varies inversely to the total cross section.

Since both the extremes of total absorption and total scattering lead to the same simple inverse relationship between flux and total cross section, it is tempting to consider the possibility that this relationship always exists between flux and cross section. Unfortunately, such is not the case and the effects of self-shielding are much more complicated than this.

In order to illustrate the complexity of self-shielding, consider a slab of material with a source of neutrons incident upon it, from the left, as shown in  Fig. 22.

At the left-hand-side boundary of this slab for directions oriented into the slab, the flux is simply equal to the source, and as such the flux is not self-shielded; in terms of cause and effect, since the source has not yet “seen” or interacted with the material in the slab, it could not possibly be self-shielded. However, if we look at the neutrons which are transmitted through the slab, we will see depressions in the flux corresponding to peaks in the total cross section. If we change the thickness of the slab, the magnitude of the flux depressions will also change. This illustrates that self-shielding is a spatially dependent phenomena (since it is different at the left- and right-hand sides of the slab), which also depends on geometry (since varying the slab thickness will vary the amount of flux depression or self-shielding). This spatial dependence is widely known, but what is often overlooked is that self-shielding is also a direction-dependent phenomena. For example, the albedo from the left-hand side of the slab in our example will also show depressions at energies corresponding to peaks in the total cross section. The incident flux at the left-hand boundary is merely equal to the incident source and is not self-shielded, but the albedo is, obviously the amount of self-shielding, depending on direction. This would imply, e.g., that S_n programs (Engle 1967; Mynatt et al. 1973; Lathrop and Brinkley 1970), should use different self-shielded cross sections along each ray; to my knowledge, this is never done.



■ **Figure 22**
Finite thickness slab geometry

Somehow we must try to combine all these effects in order to obtain an adequate description of the self-shielded flux, or usually the Legendre moments of the flux, in order to use it as a weighting function to obtain the required group-averaged data for use in the multigroup equations. For example, in the case of our slab, at the left-hand boundary, in order to define the self-shielding of the scalar flux, we must somehow combine the unshielded incident source with the self-shielded albedo to define an equivalent average, self-shielding factor. However, this average will also depend upon the source, since if in our slab problem there was also a source incident on the right boundary of the slab it would change the balance between the incident source and the leakage at the left boundary, thereby changing the average self-shielding of the flux.

This may seem to be an impossible task to define a self-shielding factor that is a function of geometry, space, direction, source, energy, and possibly time (the latter of which we have not even discussed). However, what is actually done in reactor calculations is to use the results of certain limiting cases (such as the absorption and scattering problems that we discussed earlier) and various approximations so that in each spatial region it is possible to define one single self-shielding factor for the scalar flux, and possibly scalar current, which can be applied as an average for the entire region, e.g., one form within a fuel rod and another within the surrounding moderator.

4.2 Narrow, Intermediate, and Wide Resonances

In this chapter, we only describe self-shielding alone as it effects the generation of application-independent, multigroup libraries. Other chapters of this handbook will consider more details as they relate to specific applications and classes of calculations, in particular the energy ranges in which these models are valid.

Since the most pronounced effects of self-shielding occur when the neutron cross section rapidly changes as a function of energy, it is natural to examine the effect that resonances have on the neutron flux. Therefore, we will consider the case of neutrons produced by fission, slowing down in a mixture of a heavy resonant material (such as a fuel), and a light material (such as a moderator). For simplicity, in the following discussion, these two materials will be referred to as the absorber and the moderator. In an infinite medium, we can write the Boltzmann equation in the following form

$$[\Sigma_T(E) + \Sigma_0(E)] \Phi_0(E) = R_0(E),$$

where

$$R_0(E) = \frac{1}{1 - \alpha} \int_E^{E/\alpha} \Sigma_s(E') \Phi_0(E') \frac{dE'}{E'} + \frac{1}{1 - \alpha_m} \int_E^{E/\alpha_m} \Sigma_m(E') \Phi_0(E') \frac{dE'}{E'}, \quad (70)$$

in which,

- $\Phi_0(E)$ Scalar flux,
- $R_0(E)$ Secondary distribution of elastically scattered neutrons,
- $\Sigma_T(E)$ Total cross section of the absorber,
- $\Sigma_0(E)$ Total cross section of the moderator,
- $\Sigma_s(E)$ Scattering cross section of the absorber, and
- $\Sigma_m(E)$ Scattering cross section of the moderator.

To the first order, spatially dependent effects may be included in the equations by adding a buckling factor, as in the B_n method (Joanou et al. 1961). Inclusion of a buckling term will merely have the effect of adding a term $DB^2 \Phi_0(E)$ to the left-hand side of (70). Therefore, the following discussion may be generalized to consider the first-order spatial corrections by considering $\Sigma_0(E)$ as the sum of the moderator total cross section plus the buckling term DB^2 to account for spatially dependent leakage.

Each of the methods used to obtain an approximate solution to this equation proceeds by assuming a different form for the secondary distribution of neutrons. In all approximations that will be discussed later, the range of secondary energies to which neutrons can scatter from the moderator atom will be considered to be large when compared with the width of the resonance. In this case, the effect of scattering from the wide range of initial energies E' will be to produce a smooth distribution of scattered neutron at E , that is,

$$\frac{1}{1 - \alpha_m} \int_E^{E/\alpha_m} \Sigma_m(E') \Phi_0(E') \frac{dE'}{E'} \approx \frac{1}{E} \langle \Sigma_m \Phi_0 \rangle. \quad (71)$$

In particular, there will be no correlation between the value of the absorber cross section at E and the arrival of scattered neutrons from higher energies E' .

4.2.1 Narrow Resonances

In the narrow-resonance (NR) approximation, it is assumed that the resonances are also narrow when compared with the range of secondary energies to which neutrons can scatter from an absorber atom, in which case (70) reduces to

$$[\Sigma_T(E) + \Sigma_0(E)] \Phi_0(E) \approx \frac{1}{E} [\langle \Sigma_s \Phi_0 \rangle + \langle \Sigma_m \Phi_0 \rangle]. \quad (72)$$

This relationship simply predicts that the flux will vary inversely as the total cross section of the mixture. Since generally the total cross section of a moderator is much smoother than that of heavy absorber materials, over-energy ranges comparable to the width of an energy group, it may be considered to be independent of energy, $\Sigma_0(E) \approx \Sigma_0$, and in the NR approximation, the predicted form of the flux is

$$\Phi_0(E) \propto \frac{1}{E [\Sigma_T(E) + \Sigma_0]}. \quad (73)$$

Different mixtures of fuel (absorber) and moderator may be considered simply by different values of Σ_0 . First-order geometric corrections may also be included by the addition of DB^2 to Σ_0 .

The ratio of moderator to fuel cross sections may be anywhere between zero (pure fuel, no moderator) to infinity (pure moderator, infinitely dilute fuel). Therefore, the NR predicts a flux that will be maximally self-shielded for pure fuel; in which case, the flux will vary inversely to the total cross section of the fuel and the energy as

$$\Phi_0(E) \propto \frac{1}{E \Sigma_T(E)} : \Sigma_0 = 0. \quad (74)$$

Conversely for the case wherein the fuel is infinitely dilute, the flux will not be self-shielded as

$$\Phi_0(E) \propto \frac{1}{E} : \Sigma_0 \gg \Sigma_T(E), \Sigma_0 \text{ constant}. \quad (75)$$

Since the NR approximation depends only on the details of the absorber cross section, it leads itself to development of application-independent, multigroup libraries (MacFarlane et al. 1982; MacFarlane and Muir 1994).

4.2.2 Wide Resonances

In the wide-resonance (WR) or wide-resonance, infinite absorber (WRIA) approximation, the resonance is assumed to be wide when compared with the range of secondary energies that can be reached by scattering from the absorber atom. In this case, the absorber is treated as infinitely heavy (not as the name WRIA seems to imply, infinitely absorbing), and neutron slowing down occurs only because of scattering from moderator atoms. In this case, the scatter from an absorber atom merely leads to the emission of a scattered neutron at the incident

energy, that is,

$$\frac{1}{1-\alpha} \int_E^{E/\alpha} \Sigma_S(E') \Phi_0(E') \frac{dE'}{E'} \approx \Sigma_S(E) \Phi_0(E). \quad (76)$$

In this case, (70) becomes

$$[\Sigma_T(E) + \Sigma_0(E)] \Phi_0(E) = \Sigma_S(E) \Phi_0(E) + \frac{1}{E} \langle \Sigma_m \Phi_0 \rangle, \quad (77)$$

or upon subtracting the absorber elastic scattering from both sides of this equation,

$$\begin{aligned} [\Sigma_A(E) + \Sigma_0(E)] \Phi_0(E) &= \frac{1}{E} \langle \Sigma_m \Phi_0 \rangle \\ \Sigma_A(E) &\text{ - absorber absorption cross section.} \end{aligned} \quad (78)$$

Again recognizing that over-energy ranges comparable to the width of an energy group, the moderator cross section, will be much smoother than the absorber cross section, and that as such they may be treated as a constant, the wide resonance infinite absorber (WRIA) approximation predicts a flux of the form as

$$\Phi_0(E) \propto \frac{1}{E [\Sigma_A(E) + \Sigma_0]}. \quad (79)$$

As in the case of the NR approximation, the ratio of cross sections may be anywhere from zero to infinity, and the WR approximation predicts a maximum self-shielding for a pure fuel (absorber) and no self-shielding for an infinitely dilute fuel.

4.2.3 Intermediate Resonances

When we compare the maximum energy loss in the elastic scattering for a variety of materials to the widths of resonances in these materials, it is obvious that all resonances do not neatly fall into any one of these two categories of NRs or WRs. In reality, resonances span the entire range of widths from narrow to intermediate to wide (Mughabghab et al. 1981; Gyulassy et al. 1972).

The intermediate-resonance (IR) approximation (Goldstein and Cohen 1962; Goldstein 1972, 1975), was developed in order to treat the entire range of resonances. Since the original development of this method, it has been greatly extended to handle complex geometric situations. In this chapter, only the basic IR approximation will be presented. In the basic IR approximation, the secondary-energy distribution of neutrons elastically scattered by an absorber atom is assumed to be described by a linear combination of the distributions obtained from the NR and WR approximations as

$$\frac{1}{1-\alpha} \int_E^{E/\alpha} \Sigma_S(E') \Phi_0(E') \frac{dE'}{E'} \approx \left\{ \lambda \frac{\langle \Sigma_S \Phi_0 \rangle}{E} + (1-\lambda) \Sigma_S(E) \Phi_0(E) \right\}. \quad (80)$$

Substituting this expression into (70) for the absorber scattering, using (71) to describe the moderating scattering and solving for the scalar flux, it is found that

$$\Phi_0(E) \propto \frac{1}{E} \left\{ \frac{\langle \Sigma_m \Phi_0 \rangle + \lambda \langle \Sigma_s \Phi_0 \rangle}{\Sigma_A(E) + \lambda \Sigma_s(E) + \Sigma_0} \right\}. \quad (81)$$

The NR and WR approximations may be easily recognized to correspond to the limits of λ equal to unity (narrow) or zero (wide), respectively; in most cases, λ is different for each resonance and lies in the range, zero to unity.

In the chapter on unit-cell calculations, these three models of NR, IRs, and WRs will be discussed in more detail. Here, the important point to be observed is that each of these three models leads to a scalar flux which can be expressed as the product of two terms: an energy-dependent spectrum $M(E)$ (in this case $1/E$) and a self-shielding factor $W_0(\Sigma)$ that explicitly depends on the cross sections alone. It should be noted that this result is not restricted to resonances alone, as we obtained similar results for pure absorption, (67) and pure scattering, and (69) cases considered earlier. Therefore, in the following sections, to describe the scalar flux we will use a model that is a product of two independent terms.

4.3 Cross-Section Dependence of Flux

We now have a model that can be used to describe the scalar flux. However, generally we need to describe the Legendre moments of the angular flux, e.g., scalar flux, scalar current, etc. Here, we will examine a simple model to predict the cross-section dependence of any Legendre moment of the flux.

In the resonance region, the neutron energy is low enough that we may consider scattering to be isotropic. In plane geometry, we may write the Boltzmann equation in the form

$$\mu \frac{\partial \Phi}{\partial z}(z, \mu, E) + \Sigma_T(E) \Phi(z, \mu, E) = \frac{1}{4\pi} R_0(z, E). \quad (82)$$

Introducing the assumption

$$\Phi(z, \mu, E) = \Phi_v(\mu, E) \text{Exp}[-z/\nu]$$

and

$$R_0(z, E) = R_{0v}(E) \text{Exp}[-z/\nu] \quad (83)$$

leads to the equation

$$[\nu \Sigma_T(E) - \mu] \Phi_v(\mu, E) = \frac{\nu}{4\pi} R_{0v}(E). \quad (84)$$

Any Legendre moment of the flux may be determined by dividing by $[\nu \Sigma_T(E) - \mu]$, multiplying by $P_n(\mu)$, and integrating over the angular range $\bar{\Omega}$, to find

$$\Phi_{vn}(E) = \nu Q_n(\nu \Sigma_T(E)) R_{0v}(E), \quad (85)$$

where Q_n is merely the Legendre function of the second kind (Abramowitz and Stegun 1965) as

$$Q_n(X) = \frac{1}{2} \int_{-1}^{+1} \frac{P_n(\mu) d\mu}{X - \mu}. \quad (86)$$

From the discussion in the preceding section, the NR approximation predicts that the energy of $R_0(z, E)$ will simply be proportional to $1/E$. Therefore, (85) again gives us a result wherein any Legendre moment of the flux may be expressed as the product of two terms: one that explicitly depends on energy alone and the other that explicitly depends on cross section alone.

In order to determine the cross-section dependence of each Legendre moment, we need to look only at the definition of the Legendre functions of the second kind (Abramowitz and Stegun 1965) as

$$Q_n(X) = \frac{1}{2} \left(\frac{1}{X}\right)^{n+1} \sum_{m=0}^{\infty} \left(\frac{1}{X}\right)^{2m} \frac{(n+2m)!(n+m)!}{m!(2n+2m+1)!}. \quad (87)$$

Therefore, any Legendre moment of the flux can be written in the form

$$\Phi_{vn}(E) \propto \frac{\nu}{E [\nu \Sigma_T(E)]^{n+1}} \left\{ 1 + C_{2n} \left(\frac{1}{\nu \Sigma_T(E)}\right)^2 + C_{4n} \left(\frac{1}{\nu \Sigma_T(E)}\right)^4 \right\} + \dots \quad (88)$$

In particular, as we approach the infinite medium case ν approaches infinity (no spatial dependence), and the Legendre moments approach

$$\Phi_{vn}(E) \rightarrow \frac{1}{E [\Sigma_T(E)]^{n+1}}. \quad (89)$$

This limit agrees with the NR approximation result that we obtained earlier for the scalar flux ($n = 0$) where we found a $1/\Sigma_T(E)$ dependence. However, this result can now be used to define other moments of the flux, such as the current ($n = 1$) which is predicted to be self-shielded by $1/\Sigma_T^2(E)$. From (88), we also obtain the result that for finite media the self-shielding will also depend on higher moments of the cross sections.

4.4 Computation of Multigroup Cross Sections

Now that we have a model to describe the energy and cross-section dependence of the moments of the flux, we can return to evaluation of the multigroup cross sections. The general definition of the multigroup cross section, weighted by moments of the flux, is,

$$\langle \Sigma_{Rn} \rangle_g = \frac{\int_{E_g}^{E_{g+1}} \Sigma_R(E) \Phi_n(E) dE}{\int_{E_g}^{E_{g+1}} \Phi_n(E) dE}, \quad (90)$$

where $\Sigma_R(E)$ is the cross section for any reaction R , e.g., $R =$ total, elastic, capture, etc., and $\Phi_n(E)$ is the n th Legendre moment of the flux, e.g., $0 =$ scalar flux and $1 =$ scalar current. In our

model, each component of the flux will be defined as the product of two independent terms: the energy-dependent weighting spectrum $M_n(E)$ and the cross-section-dependent, self-shielding factor $W_n(\Sigma_T)$.

In principle, the spectrum is different for each Legendre moment of the flux, and some computer codes are capable of using different spectrum for each component (Weisbin et al. 1976; Doyas et al. 1971). However, in practice most codes use only a single weighting function (MacFarlane et al. 1982; MacFarlane and Muir 1994; Weisbin et al. 1976; Rieffe et al. 1981; Panini 1973; Vertes 1981), and (Pope et al. in press). In such codes, the effect of different spectrum may be examined by making a series of computer runs, one for each spectrum. In the following development, we will discuss the use of an energy-dependent spectrum, which the reader may interpret to be the same for all moments or different for each moment of the flux.

The result of the NR, IR, and WR approximations is that the self-shielding factor for the scalar flux will vary inversely with cross sections, either the total cross of the mixture, the sum of the absorber absorption and moderator total cross section, or a linear combination of the two. Then we saw that, in general, the NR approximation for the higher Legendre moments of the flux will depend on higher reciprocal powers of the total cross section of the mixture. In the following section, we will use the results of the NR approximation to illustrate how to compute self-shielded cross sections. This approach will highlight the computational problems involved and can easily be extended to include IR and WR effects. Therefore, we will assume a weighting function of the form

$$\frac{M(E)}{[\Sigma_T(E) + \Sigma_0]^k} : k = 0, 1, 2, \dots, \quad (91)$$

where

$M(E)$ Energy-dependent spectrum, e.g., Maxwellian, $1/E$, fission, and fusion spectrum at progressively higher energy.

$\Sigma_T(E)$ Total cross section of the material of interest

Σ_0 Total cross section of all other constituents of the mixture (possibly including DB^2 or equivalent to escape cross section for spatial effects).

k Integer for different Legendre moments

0 = no self-shielding

1 = self-shielded scalar flux




2 = self-shielded scalar current

In order to consider different atom ratios of absorber and moderator, all values of Σ_0 between zero (no moderator, pure absorber) and infinity (infinitely dilute absorber) will be considered. Note that the limit as Σ_0 approaching infinity corresponds to the no self-shielding, or $k = 0$, for each moment of the flux.

This model corresponds to the Bondarenko model of self-shielding (Bondarenko et al. 1964), and is widely used in a number of cross-section-processing codes. The most commonly used procedure is to create application-independent libraries of self-shielded cross sections for a variety of values of Σ_0 , usually powers of 10, e.g., 0, 10, 100, 1,000, etc. (Bondarenko et al. 1964). Once calculated at fixed values of Σ_0 , the tables of self-shielded cross sections are interpolated to define the self-shielded cross section at any other value of Σ_0 .

For any reaction R and group g , we must calculate the self-shielded, group-averaged cross section as

$$\langle \Sigma_{Rk}(\Sigma_0) \rangle_g = \frac{\int_{E_g}^{E_{g+1}} \frac{\Sigma_R(E) M(E) dE}{[\Sigma_T(E) + \Sigma_0]^k}}{\int_{E_g}^{E_{g+1}} \frac{M(E) dE}{[\Sigma_T(E) + \Sigma_0]^k}}. \quad (92)$$

Before considering how to perform this calculation, the first question to be asked is – Is all of this complexity necessary, or is this merely a “much ado about nothing”? (Shakespeare 1982). How much does self-shielding actually affect cross sections? In order to answer this question,  Fig. 23 illustrates the Th232-unshielded, 175 group ENDL cross sections (Plechaty et al. 1978a,b), and  Fig. 24 illustrates the Th232 self-shielding factors, which are merely the ratio of the shielded to unshielded cross section. If self-shielding has little or no effect, we would expect the ratio of shielded to unshielded cross sections to be close to unity. However, from  Fig. 24 in the resonance region, the ratio is drastically different from unity and, in the worst case, has a value of only 0.02. This corresponds to a change between unshielded and shielded cross sections of a factor of 50 (5,000%) in the Th232 capture cross section. By examining results for a variety of materials (Plechaty et al. 1978a,b), we can see that the effect of self-shielding is very important for virtually any material that has a resonant structure (Howerton et al. 1978; Garber and Brewster 1975; Cullen et al. 1976).

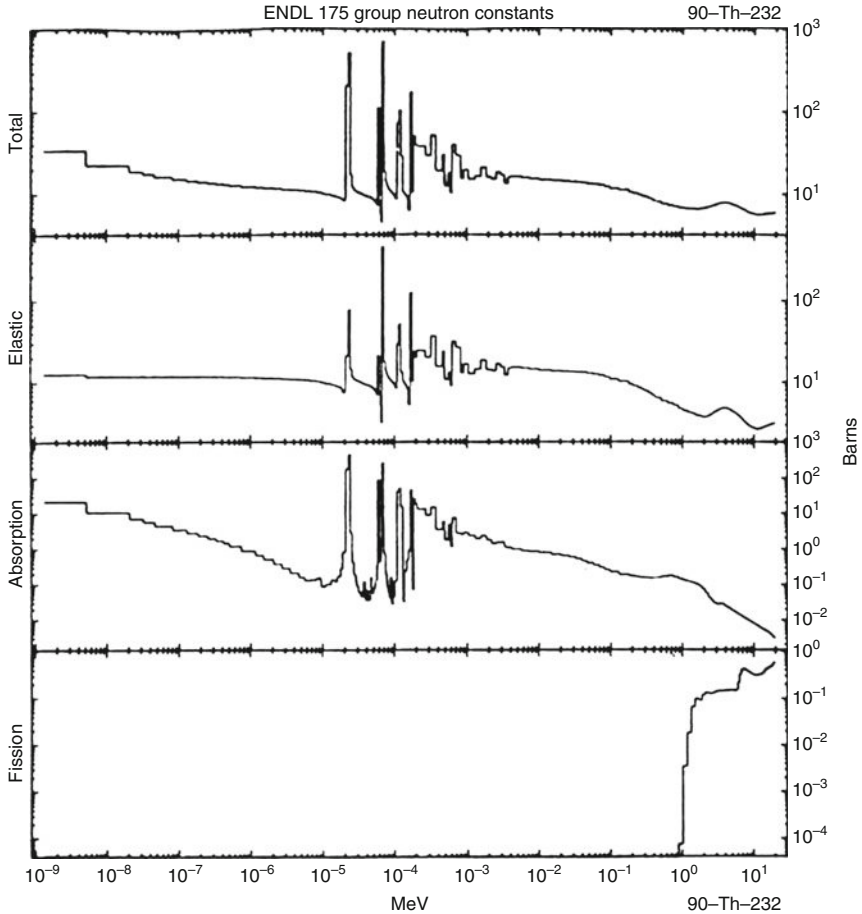
4.4.1 Tabulated Cross Sections

In order to calculate self-shielded cross sections, we will first consider the case in which the required cross sections $\Sigma_R(E)$ and $\Sigma_T(E)$ are each given in a tabulated form with an interpolation law between tabulated values. In this case, the methods used in the preceding section on Doppler broadening may be used to prepare tabulated cross sections at one or more temperatures; and in this section, we need not explicitly consider Doppler broadening, that is, the cross sections that we discuss later may be at any temperature.

The energy-dependent weighting spectrum $M(E)$ is chosen to agree with some system of interest: a common choice is a combination of Maxwellian, $1/E$, fission, and fusion spectra at successively higher energies (Cullen 1980a–c). If a large number of groups is used, the resulting group averages become insensitive to the selection of the energy-dependent weighting spectrum, and it is acceptable to use a constant or flat-weighting spectrum within each group to create a truly application-independent library (Plechaty et al. 1978a,b; Weisbin and LaBauve 1973). Such a library can be used as an economical starting point to group collapse, using a specific weighting spectrum in order to obtain a library that is tailored to a specific application (Cullen 1979a–c).

4.4.2 Linearly Interpolable Data

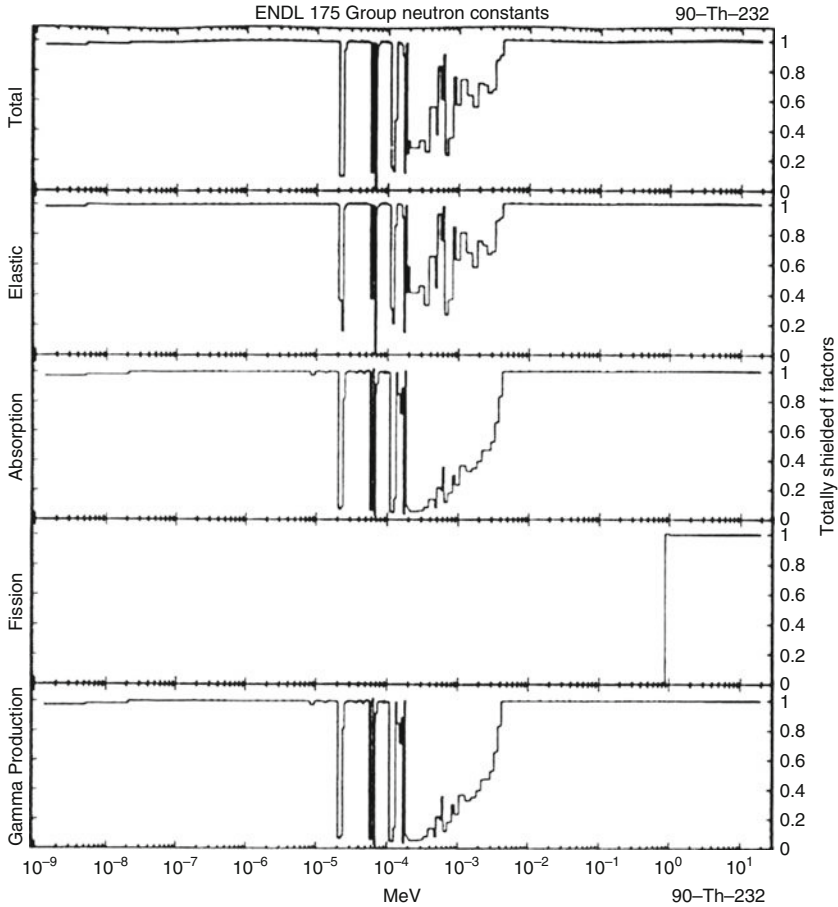
In principle, it is possible to use any one of a number of analytical forms for the weighting spectrum $M(E)$ (e.g., Maxwellian, $1/E$, fission, and fusion spectra at successively higher energies)



■ **Figure 23**
Th232, 175-group unshielded cross sections

and tabulated cross sections, using any combination of linear or log interpolation in energy or cross section, to define the required group-averaged cross sections in terms of analytical integrals. However, in practice, as applied to use on a digital computer, this general approach is extremely error prone, because the resulting equations can be extremely numerically unstable and can lead to large errors in extremely subtle ways that are difficult to detect.

Therefore, in this section, an approach that is completely numerically stable, yields answers that are always within any allowable uncertainty ε of the exact answer, and requires the fewest possible integrals and stability conditions to analyze and program will be presented. The approach is quite simple: prepare the energy-dependent spectrum and all cross sections in a tabular form with linear interpolation in energy and cross section between tabulated values. In the preceding section on reconstruction of cross sections, it was pointed out that it is possible



■ **Figure 24**
Th232-, 175-group totally shielded f -factors

to economically replace all the cross sections in a library, such as ENDF/B (Cullen 2007a–c), which can use any combination of log and linear interpolation in energy and cross section, by a table of cross sections with linear interpolation in energy and cross section between tabulated values, such that the resulting linearly interpolable cross sections are everywhere within some allowed uncertainty ε of the original cross section. That is to say, if the original cross sections are $\Sigma_n(E)$ and the linearized cross sections are $\bar{\Sigma}(E)$, we have the relationship

$$(1 - \varepsilon)\Sigma_n(E) \leq \bar{\Sigma}(E) \leq (1 + \varepsilon)\Sigma_n(E), \quad (93)$$

not just at the energy points where these cross sections are tabulated alone, but at all energies itself.

Since the energy-dependent weighting spectrum is inherently positive, the preceding section on the reconstruction of cross sections applies equally well to converting the weighting

spectrum from its functional form $M(E)$ (e.g., Maxwellian, $1/E$, fission, and fusion spectra at successively higher energies) to a tabulated linearly interpolable form, such that if $M(E)$ is the original weighting spectrum and $\bar{M}(E)$ the tabulated approximation, at all energies E , then

$$(1 - \varepsilon)M(E) \leq \bar{M}(E) \leq (1 + \varepsilon)M(E). \quad (94)$$

Generally, the size of the resulting linearized spectrum tabulations, when compared with the size of the tabulations of modern evaluations, is very small; and as such, this approach is an economical and practical means of treating the weighting spectrum.

The important point to realize is that once we have all the required data in a linearly interpolable form, we will be able to express our group averages in terms of only one function (the natural logo and we can use the error bounds on our linear data to guarantee the accuracy of our resulting integrals. As long as our spectrum and cross sections are not negative (they are be zero or positive), we have bounds that the approximate integral using the linearized data

$$\bar{F} = \int_{E_g}^{E_{g+1}} \frac{\bar{\Sigma}_R(E) \bar{M}(E) dE}{[\bar{\Sigma}_T(E) + \Sigma_0]^k} \quad (95)$$

and the exact integral using the original data

$$F = \int_{E_g}^{E_{g+1}} \frac{\Sigma_R(E) M(E) dE}{[\Sigma_T(E) + \Sigma_0]^k} \quad (96)$$

are related through

$$\frac{(1 - \varepsilon_R)(1 - \varepsilon_M)}{(1 + \varepsilon_T)^k} F \leq \bar{F} \leq \frac{(1 + \varepsilon_R)(1 + \varepsilon_M)}{(1 - \varepsilon_T)^k} F, \quad (97)$$

and therefore, we can guarantee the accuracy of the resulting integrals. For example, if all data are reconstructed to within an accuracy of 0.1%, all of the resulting, scale flux ($k = 1$)-weighted integrals are guaranteed to be accurate to within 0.3% (approximately $\varepsilon_R + \varepsilon_M + \varepsilon_T$). Furthermore, since the uncertainty in the spectrum and the total cross section appear in both numerator and denominator of the definition of the group-averaged cross section, (92), when we use the ratio to define the actual group-averaged cross section, there is a strong tendency for cancellation of errors and to obtain results that are accurate to well within the accuracy to which the cross section $\Sigma_R(E)$ was linearized.

4.4.3 Solution

Once the spectrum and cross sections are represented in a linearly interpolable form, the integrals required to define the group-averaged cross sections for any group g can be expressed in terms of a sum of integrals; each integral over an energy interval that lies within the group and within which all of the tabulated data are linearly interpolable. For example, if we wish to integrate from 5 to 35 eV and the cross sections are tabulated at 5, 15, 25, and 35 eV, and the

spectrum is tabulated at 0, 10, 20, 30, and 40 eV, the required integral can be expressed in terms of the sum of integrals over the energy ranges 5–10, 10–15, 15–20, 20–25, 25–30, and 30–35; note that within each of these six energy intervals, the spectrum and cross sections are both linearly interpolable. Therefore, we can write the required integral in the form

$$\int_{E_g}^{E_{g+1}} \frac{\Sigma_R(E) M(E) dE}{[\Sigma_T(E) + \Sigma_0]^k} = \sum_j \int_{E_j}^{E_{j+1}} \frac{\Sigma_R(E) M(E) dE}{[\Sigma_T(E) + \Sigma_0]^k}, \quad (98)$$

where within each energy interval, E_j to E_{j+1} , each of the three functions, $\Sigma_R(E)$, $M(E)$, $\Sigma_T(E)$ is linearly interpolable, and as such can be written in the form

$$F(E) = \frac{(E - E_j)}{(E_{j+1} - E_j)} F_{j+1} + \frac{(E_{j+1} - E)}{(E_{j+1} - E_j)} F_j, \quad (99)$$

where F_j and F_{j+1} are the tabulated values of $F(E)$ at the energies E_j and E_{j+1} , respectively.

This form can be inserted for $\Sigma_R(E)$, $M(E)$, $\Sigma_T(E)$ and the resulting equation evaluated in terms of energy. However, even this seemingly simple equation involving linear interpolable functions can lead to numerical instability, particularly for cross sections in the resonance region, unless extreme care is used to evaluate this equation.

It is better to transform the integral over the energy range E_j to E_{j+1} into an integral in the “normal form” over the interval -1 to $+1$, by changing variables to

$$Z = 2 \left[\frac{E - (E_j + E_{j+1})/2}{(E_{j+1} - E_j)} \right]$$

and

$$dZ = \frac{2dE}{(E_{j+1} - E_j)}. \quad (100)$$

In terms of this new variable, each of the three functions can be written in the form

$$\begin{aligned} F(Z) &= \left(\frac{1}{2}\right) (1 + Z) F_{j+1} + \left(\frac{1}{2}\right) (1 - Z) F_j \\ &= \left(\frac{1}{2}\right) (F_{j+1} + F_j) + \left(\frac{1}{2}\right) (F_{j+1} - F_j) Z. \end{aligned} \quad (101)$$

If we define the average value over the interval E_j to E_{j+1} , then

$$\langle F \rangle_j = \left(\frac{1}{2}\right) (F_{j+1} + F_j). \quad (102)$$

And the relative change in the function

$$\Delta_j = \frac{(F_{j+1} - F_j)}{(F_{j+1} + F_j)}. \quad (103)$$

Each function can be written in the form

$$F(Z) = \langle F \rangle_j [1 + \Delta_j Z]. \quad (104)$$

And the integral becomes

$$\sum_j \frac{(E_{j+1} - E_j)}{2} \frac{\langle \Sigma_R \rangle_j \langle M \rangle}{\langle \Sigma_T^* \rangle_j^k} \int_{-1}^{+1} \frac{[1 + \Delta_R Z][1 + \Delta_M Z]}{[1 + \Delta_T^* Z]^k}, \quad (105)$$

where Σ_T^* is merely the total cross section of the mixture, that is, $\Sigma_T(E) + \Sigma_0$; and Δ_T^* is the corresponding relative change in the total mixture.

In this normal form, the integral has the following important properties:

1. Energy has been completely removed from the integral; it only spears as $(E_{j+1} - E_j)$ outside the integral. Therefore, points of discontinuity (i.e., points where $E_j = E_{j+1}$, but $F_j \neq F_{j+1}$) do not lead to numerical instability because of the infinite derivatives in the cross section. In particular, energy intervals of zero length, $E_j = E_{j+1}$, will automatically make zero contribution to the integral.
2. The only variable terms that appear in the integral are tabulated values of Σ_R , M , Σ_M . Therefore, as long as the tabulated values are finite and the total cross section is positive, the value obtained for the integral will be numerically stable and well defined.
3. If any function is constant over an interval (i.e., $F_j = F_{j+1}$), its contribution to the integral automatically reduces to its average value, (102), without any further differences or cross cancellation in the definition of the integral; this further improves numerical stability.
4. For any positive function F , the average value $(F_{j+1} + F_j)/2$ will always be greater than the change $(F_{j+1} - F_j)/2$. Therefore, the effect of the constant term in the definition of each function in the normal form, (104), will be dominant, further improving the numerical stability.

The required integrals can be written as

$$\sum_j \frac{(E_{j+1} - E_j)}{2} \frac{\langle \Sigma_R \rangle_j \langle M \rangle}{\langle \Sigma_T^* \rangle_j^k} [F_k^0(\Delta_T) + (\Delta_R + \Delta_M) F_k^1(\Delta_T) + \Delta_R \Delta_M F_k^2(\Delta_T)], \quad (106)$$

where

$$F_k^L(\Delta_T) = \int_{-1}^{+1} \frac{Z^L dZ}{[1 + \Delta_T Z]^k}. \quad (107)$$

This family of functions, $F_k^L(\Delta_T)$, can be shown to satisfy recursion relations that allow functions of higher values of L and k to be expressed in terms of functions with lower values of L and k . These functions are particularly easy to accurately compute since for fixed L and k they are only a function of a single variable Δ_T and they can be expressed in terms of functions that are no more complicated than a natural log. \blacktriangleright [Table 7](#) presents expressions for a number of functions $F_k^L(\Delta_T) : L = 0, 1, 2, k = 0, 1, 2, 3$.

Even to evaluate these relatively simple functions $F_k^L(\Delta_T)$ requires care if we are to obtain numerically stable results. By inspection of (105) and (107) when $\Delta_T = 0$, we obtain a particularly simple result which is independent of k . Since $\Delta_T = 0$ corresponds to a constant total cross section over the energy interval E_j to E_{j+1} , this is what we would expect, namely, the integral reduces to the averaging of the product of the cross section Σ_R and the spectrum M to obtain,

$$\frac{\langle \Sigma_R \rangle_j \langle M \rangle}{\langle \Sigma_T^* \rangle_j^k} \left[1 + \frac{1}{3} \Delta_R \Delta_M \right]. \quad (108)$$

In order to obtain this result and have a numerically stable algorithm, care must be exercised as Δ_T approaches zero. For example, from \blacklozenge Table 7 we can see that

$$F_1^0(\Delta) = \frac{1}{\Delta} \text{Log} \left[\frac{1+\Delta}{1-\Delta} \right]. \quad (109)$$

\blacksquare Table 7

Function form for $F_k^L(\Delta_T)$

J	N	Integral $F_N^L(\delta)$	Expansion for small
0	0	2	-
0	1	$\frac{1}{\delta} \ln \left(\frac{1+\delta}{1-\delta} \right)$	$2 \left(1 + \frac{1}{3} \delta^2 + \frac{1}{5} \delta^4 + \frac{1}{7} \delta^6 \right)$
0	2	$\frac{2}{1-\delta^2}$	-
0	3	$\frac{2}{(1-\delta^2)^2}$	-
1	0	0	-
1	1	$\frac{1}{\delta} \left[2 - \frac{1}{\delta} \ln \left(\frac{1+\delta}{1-\delta} \right) \right]$	$-2\delta \left(\frac{1}{3} + \frac{1}{5} \delta^2 + \frac{1}{7} \delta^4 + \frac{1}{9} \delta^6 \right)$
1	2	$\frac{1}{\delta} \left[\frac{1}{\delta} \ln \left(\frac{1+\delta}{1-\delta} \right) - \frac{2}{1-\delta^2} \right]$	$\frac{4\delta}{1-\delta^2} \left(\frac{1}{3} + \frac{1}{15} \delta^2 + \frac{1}{35} \delta^4 + \frac{1}{63} \delta^6 \right)$
1	3	$-\frac{2\delta}{(1-\delta^2)^2}$	-
2	0	$\frac{2}{3}$	-
2	1	$\frac{1}{\delta^2} \left[\frac{1}{\delta} \ln \left(\frac{1+\delta}{1-\delta} \right) - 2 \right]$	$2 \left(\frac{1}{3} + \frac{1}{5} \delta^2 + \frac{1}{7} \delta^4 + \frac{1}{9} \delta^6 \right)$
2	2	$\frac{2}{\delta^2} \left[\frac{2-\delta^2}{1-\delta^2} - \frac{1}{\delta} \ln \left(\frac{1+\delta}{1-\delta} \right) \right]$	$\frac{2}{1-\delta^2} \left(\frac{1}{3} + \frac{4}{15} \delta^2 + \frac{4}{35} \delta^4 + \frac{4}{63} \delta^6 \right)$
2	3	$\frac{1}{\delta^2} \left[\frac{1}{\delta} \ln \left(\frac{1+\delta}{1-\delta} \right) - \frac{2-4\delta^2}{(1-\delta^2)^2} \right]$	$\frac{2}{(1-\delta^2)^2} \left(\frac{1}{3} + \frac{8}{35} \delta^2 + \frac{8}{105} \delta^4 + \frac{8}{315} \delta^6 \right)$

However, as Δ approaches zero, this assumes the indeterminate form of zero divided by zero. This is nonsense since the zero- Δ limit of $F_1^0(\Delta)$, (107), merely corresponds to uniformly integrating from -1 to $+1$, to obtain a result of 2. This indeterminate form can be avoided by expanding the natural log in the definition of this family of functions, (see [Table 7](#)) and examining the small- Δ limit. For example, in the case of $F_1^0(\Delta)$, following this procedure, we find the completely stable for small Δ as

$$F_1^0(\Delta) = 2 \left[1 + \frac{1}{3}\Delta^2 + \frac{1}{5}\Delta^4 + \frac{1}{7}\Delta^6 + \frac{1}{9}\Delta^8 \right] + \dots \quad (110)$$

For all those functions that involve natural logarithms, [Table 7](#) also presents numerically stable forms for small Δ . In each of these expressions, the first term is of order unity and the expansion is truncated at order Δ^8 . Therefore for $|\Delta| \leq 10^{-2}$, these expressions will be accurate to approximately 16 digits; and for larger values of Δ , the analytical expressions in terms of natural logarithms can be used without encountering any numerical instability. The combination of the analytical expressions plus the expansion for small Δ can therefore be used in a combination to define all of the required functions in a completely stable manner to the maximum accuracy available on today's computers. Since the required function $F_k^L(\Delta_T)$ is a function of a continuous variable Δ , no other limiting cases need to be considered. In [Table 7e](#), for convenience, the notation, $\Delta = \delta$, has been used.

The definition of the group-averaged cross section, (25), actually involves the ratio of two integrals, and so far, we have only discussed how to evaluate the numerator. However, evaluation of the denominator is completely analogous to the evaluation of the numerator by simply setting $\Sigma_R(E)$ as equal to unity.

One last word of caution concerning evaluation of the self-shielded total cross section. If we use the notation,

$$\left\langle \frac{\Sigma_T}{(\Sigma_T + \Sigma_0)^k} \right\rangle = \int_{E_g}^{E_{g+1}} \frac{\Sigma_R(E) M(E) dE}{[\Sigma_T(E) + \Sigma_0]^k} \quad (111)$$

It is tempting to rewrite this equation in the form,

$$\begin{aligned} \left\langle \frac{\Sigma_T}{(\Sigma_T + \Sigma_0)^k} \right\rangle &= \left\langle \frac{(\Sigma_T + \Sigma_0)}{(\Sigma_T + \Sigma_0)^k} \right\rangle - \left\langle \frac{\Sigma_0}{(\Sigma_T + \Sigma_0)^k} \right\rangle \\ &= \left\langle \frac{1}{(\Sigma_T + \Sigma_0)^{k-1}} \right\rangle - \Sigma_0 \left\langle \frac{1}{(\Sigma_T + \Sigma_0)^k} \right\rangle. \end{aligned} \quad (112)$$

Since these two integrals correspond to the denominators required to define the averages of other reactions $\Sigma_R(E)$, this would appear to be an efficient approach to follow; if the average of any other reaction is evaluated, the average of the total can be evaluated without computing any additional integrals. Here, for large values of Σ_0 , this is an unstable approach to calculating the average total cross section, as it will be defined by a small difference between two large numbers.

The above mentioned algorithms that have been described for the Bondarenko (Bondarenko et al. 1964) or NR approximation are easily extended to handle the IR approximation,

simply by using a differently tabulated, linearly interpolable cross section in the denominator of the self-shielding factor. Those algorithms have been implemented for use with ENDF/B-formatted cross sections (MacFarlane et al. 1982; MacFarlane and Muir 1994; Weisbin et al. 1976; Cullen 1980a–c).

The amount of detail required to insure the numerical stability of even this simple approach to calculating average cross sections, using only linearly interpolable data, may seem extensive, but it is minor when compared with what would have to be done in order to obtain numerical stability if one attempts to use analytical spectra and cross sections that may be log or linearly interpolable in either cross section or energy. The number of special limiting cases that must be considered using the latter approach is enormous and many of these limiting cases occur in extremely subtle situations that are difficult to detect and analyze. Therefore, the latter approach is not recommended. Indeed, in closing this section, it is fair to say that the simplicity and stability of the methods we use to define self-shielded multigroup cross sections by first LINEARIZING EVERYTHING, is an excellent example of why in this chapter so much emphasis is placed on linearizing nuclear data; the payback comes when we use the simplified data in our applications.

4.4.4 Direct Integration

So far we have discussed calculating group-averaged cross sections starting from tabulated energy-dependent cross sections. There are a number of other approaches that either start from resonance parameters in the resolved-resonance region or distributions of resonance parameters in the unresolved-resonance region, and calculate group averages directly without an intermediate step of creating energy-dependent, tabulated cross section data files.

One class of computer programs will start from resonance parameters and use the psi-chi method (Greene et al. 1976) to define broadened cross sections in the resolved-resonance region. Beyond this point, there are two approaches to defining averages. In one approach, the psi-chi representation of the cross section is used to calculate cross sections at specific energy points, and an iterative procedure is used to subdivide the energy intervals and calculate average values until convergence is achieved in the integrals (Rieffe et al. 1981). Although physically this approach differs from that described earlier, logically it reduces to the same algorithms, the major difference being the use of psi-chi rather than the more accurate SIGMA1 of broadening. At the end, the averages are calculated by integrating between energy points at which the cross sections are calculated; the cross sections are simply not tabulated in advance. In a comparison of cold (0 K), unshielded fine-group constants calculated directly from resonance parameters (Rieffe et al. 1981), to those calculated from tabulated cross sections (Cullen 1980a–c), the results were found to be in good agreement (Cullen et al. 1985, 1988); we would expect this result since the psi-chi method is fairly accurate to define cross sections near the peaks of resonances. But large differences are found when self-shielded cross sections were compared.

In a second approach, the psi-chi representation in the resolved-resonance region is used to calculate integrals directly, without recourse to first-defining energy-dependent cross sections. If we examine our definition of average cross section, (92), and consider the cold (0 K) cross section for some reaction R , $\Sigma_R(E)$, and the total cross section, $\Sigma_T(E)$, each to be composed of

a series of single-level resonances, then the Doppler-broadened cross section will be composed of a series of psi and chi functions as

$$\Sigma_R(E) = \sum_j A_{Rj}(E) \Psi(\xi_j, X_j)$$

and

$$\Sigma_T(E) = \Sigma_p(E) + \sum_j \{A_{Tj}(E) \Psi(\xi_j, X_j) + B_{Tj}(E) \chi(\xi_j, X_j)\}, \quad (113)$$

where $\Sigma_p(E)$ is the potential-scattering cross section, and the summation is over all resonances. For simplicity, in the following, the chi function will not be written explicitly; this is merely for simplicity, but it is consistent with the treatment used by many codes, which ignores the effect of elastic interference on the total cross section when describing the self-shielding factor.

Using this representation for the cross section, the group-averaged cross section can be defined as

$$\frac{\sum_j A_{Rj}(E) \int_{E_g}^{E_{g+1}} \frac{\Psi(\xi_j, X_j) dE}{\left[\sum_{j'} A_{Tj'}(E) \Psi(\xi_{j'}, X_{j'}) + \Sigma_p + \Sigma_0 \right]^k}}{\int_{E_g}^{E_{g+1}} \frac{dE}{\left[\sum_{j'} A_{Tj'}(E) \Psi(\xi_{j'}, X_{j'}) + \Sigma_p + \Sigma_0 \right]^k}}. \quad (114)$$

Usually, this expression is only calculated for $k = 1$ (scalar flux weighting) and only this case will be described below. The main difficulty that is encountered when one tries to define these integrals is due to the summation of resonances in the denominator, used to define the total cross section. If the resonances are well separated, then in the neighborhood of any single resonance, the total cross section may be considered to be given by the contribution from that one resonance, plus a smooth contribution from distant resonances,

$$\sum_{j'} A_{Tj'}(E) \Psi(\xi_{j'}, X_{j'}) + \Sigma_p + \Sigma_0 \approx A_{Tm}(E) \Psi(\xi_m, X_m) + \Sigma_p^* + \Sigma_0, \quad (115)$$

where E is close to the peak of the m th resonance, and Σ_p^* is the contribution of the potential-scattering cross section plus a smooth contribution from distant resonances.

In this approximation, the average cross section can be written in the form of the contribution from each resonance as,

$$\sum_j A_{Rj}(E) \frac{\int_{E_g}^{E_{g+1}} \frac{\Psi(\xi_j, X_j) dE}{\Psi(\xi_j, X_j) + \beta_j}}{\int_{E_g}^{E_{g+1}} \frac{dE}{\Psi(\xi_j, X_j) + \beta_j}}, \quad (116)$$

where

$$\beta_j = \frac{\Sigma_p^* + \Sigma_0}{A_{Tj}}. \quad (117)$$

If the resonance is narrow when compared with the width of the group, it may be considered to lie totally within the group. When we change variables from E to X ,

$$X = 2(E - E_j) / \Gamma_{Tj}, \quad (118)$$

where E_j and Γ_{Tj} are the energy and total width of the j th resonance, the resulting integrals will extend for $(-\infty, +\infty)$. However, since the psi function is a symmetric function of X and appears in both numerator and denominator, we can define the functions as

$$J(\beta, \xi) = \int_0^{\infty} \frac{\Psi(\xi, X) dX}{\Psi(\xi, X) + \beta}$$

and

$$K(\beta, \xi) = \int_0^{\infty} \frac{dX}{\Psi(\xi, X) + \beta}. \quad (119)$$

And our group-averaged cross section can be written in the form

$$\sum_j A_{Rj}(E) \frac{J(\beta_j, \xi_j)}{K(\beta_j, \xi_j)}. \quad (120)$$

We have arrived at a definition of the group-averaged cross section, but there are a number of approximations that have been introduced to reach this point. Let us briefly review these approximations and examine how appropriate they are

1. The psi-chi method is used to describe the Doppler-broadened cross sections. The range of applicability of this method has been discussed in the section under Doppler broadening and will not be discussed further here.
2. We ignore the elastic interference in describing the self-shielding function. This is usually valid since the resonances are either widely spaced and the interference minima occur in an energy range where resonance-reaction cross sections are low and will not make an appreciable contribution to the group integral, or the resonances overlap in energy and the interference minima will not have a noted effect on the total cross section.
3. We assume that the resonances are isolated (widely spaced) and the local cross section can be approximated as the contribution from a single local resonance plus a smooth contribution from other resonances. At first glance, this might appear to be an extremely restrictive assumption. However, in practice, it works surprisingly well if implemented properly. Even when resonances are partially or extremely overlapped allowing for different sequences of resonances, some narrow and some wide, the local flux will be dominated by each resonance in turn; and this approximation works quite well if the contribution of all resonances other

than the local resonance are properly included. If we define the average contribution to the total cross section of all resonances except the local resonance, then

$$\langle \Sigma \rangle_j = \sum_{j' \neq j} A_{Tj'}(E) \frac{J(\beta_j, \xi_j)}{K(\beta_j, \xi_j)}. \quad (121)$$

This can be added to the potential cross section Σ_p in order to define the contribution of all other resonances to define Σ_p^* , for use in the definition of the group average. This is an iterative procedure as when we begin to solve these equations we would not know what the contribution of all other resonances would be and we would have to use some initial guess for each $\langle \Sigma \rangle_j$, solve our equations to obtain an improved approximation for $\langle \Sigma \rangle_j$, and then repeat the calculations until we obtain convergence. With this approach, the method works quite well to describe the relative self-shielding in the vicinity of each resonance.

4. We assume that resonances are locally totally within the group, i.e., many half-widths from either group boundary. This would appear to be a very restrictive assumption. However, it should be remembered that in developing this model of self-shielding we are using the NR approximation.

For the important wide resonances, such as that occur at low energies in U235 and Pu239, this approximation is quite poor. However, these resonances are not NRs, and this self-shielding model is inappropriate. The self-shielding of such resonances can best be treated by solving the actual slowing-down (58) in the neighborhood of these resonances, to determine a good approximation to the flux, and to then use this flux as a weighting function to calculate the self-shielded group-averaged cross sections.

The last case to consider is calculation of self-shielded, group-averaged cross sections in the unresolved-resonance region. In the unresolved-resonance-region evaluated data (Kinsey 1970; Rose and Dunford 1990), a unique sequence of resonances need not be defined, as only the average level widths and spacings are only given. Associated with this data are models that represent the level widths as distributed according to a chi-squared distribution with a given number of degrees of freedom (Konshin 1981), and the level spacings as distributed according to a Wigner distribution (Konshin 1981).

In this case, if we again use the psi-chi method to represent the Doppler-broadened cross section and ignore the elastic interference, we arrive at an equation similar to (114). However, instead of a summation over a sequence of discrete resonances, as in (114), our summation will be replaced by a weighted (according to their distribution) integral over the distribution of resonance widths and spacings. In order to evaluate these expressions, the integrals will be replaced by quadratures to obtain a weighted sum over contributions from resonances of different widths and spacings. Once this approximation has been introduced, we obtain an expression that is completely analogous to (114), for the series of resonances in the resolved-resonance region; the only difference is that here our sum is not over true resonances, but merely a contribution from each portion of our distribution of widths and spacings.

If we now introduce the assumptions that we introduced earlier in order to solve (114) in the resolved-resonance region, we obtain a completely analogous solution to that obtained in the resolved-resonance region (120). However, in introducing these assumptions it is found that the summations are simplified because when we introduce the “local”-resonance assumption, we find that the quadrature over resonance spacing merely reduces to multiplying the contribution of each resonance sequence (Mughabghab et al. 1981; Gyulassy et al. 1972), by the

reciprocal of the level spacing for that sequence. Physically, this makes sense as it merely states that for isolated resonances if the spacing between resonances decreases by a factor of two, in any given energy interval, we will then have twice as many resonances, each will be shielded independently (as isolated), and the group-averaged cross section over this energy interval will be as twice as large. As actually applied with all the assumptions introduced to obtain and solve (120), the level spacing will affect the calculation of the nonlocal resonances, $\langle \Sigma \rangle_j$, (121), and the iterative procedure used to determine the final, group-averaged, self-shielded cross section in the unresolved-resonance region.

The above discussion presents an overview of procedures used to define self-shielded cross sections. Considerations concerning resonance overlap (overlap for resonances for the same isotope, sequence of resonances: same isotope, sequence–sequence; isotope–isotope), and ranges of applicability for specific applications will be presented elsewhere in this handbook.

4.5 Comparison of Results

There are many more sophisticated methods of calculating self-shielded cross sections for specific applications of transport models (Vertes 1981; Green and Pitterle 1968; Toppel 1971); however, at this point, we will digress in order to examine how accurate our methods are. In order to do this, we will compare the cross sections calculated by the various methods presented in this section. Presumably, consistent with our model of self-shielding, we should obtain the most accurate results by calculating self-shielded cross sections directly from tabulated results data, as this approach uses the fewest approximations. We will consider two cases, the resolved and the unresolved-resonance regions. Ganesan reported (Ganesan 1982), that starting from ENDF/B data, by comparing the results obtained by preparing linearly interpolable data and group averaging it (Cullen 1980a–c), to his results obtained by direct integration in the resolved-resonance region (Ganesan et al. 1981), he obtained differences of up to a factor of two, that is, 100% differences.

In order to define unresolved parameters, the usual methods used (Mughabghab et al. 1981; Gyulassy et al. 1972), involve extrapolation of the observed, average-resonance widths and spacing from the resolved energy range into the unresolved energy range. When this is done, we would expect the group-averaged cross sections calculated from resolved-resonance parameters near the upper-energy limit of the resolved-resonance region to be similar to the group-averaged cross sections calculated from unresolved-resonance parameters near the lower-energy limit of the unresolved-resonance region. Perez (Perez et al. 1981) used resolved-resonance parameters to calculate tabulated cross sections and then group averaged this data to define averages in the resolved-resonance region. Next he used unresolved-resonance parameters to calculate group averages in the unresolved-resonance region. For two groups, one on either side of the resolved–unresolved-resonance-region boundary, he found differences in excess of 30%.

These results indicate that there is an inconsistency in the models that are used to calculate self-shielded cross sections; as yet, the source of this inconsistency is not yet fully understood. Until it is understood, we must assume that the errors introduced by these self-shielding models are of the order of those quoted above, based on the results of Ganesan and Perez.

Naturally, the differences reported by Ganesan and Perez may not lead to differences of the same magnitude in specific macroscopic calculated quantities (e.g., K-eff), when these cross

sections are used in transport calculations of any specific application. This is particularly true of quantities, such as K -eff, that are more sensitive to ratios than to absolute cross sections. However, it should be realized that quantities, such as reaction rates, can be directly affected by uncertainties in cross sections.

5 Transfer Matrix

5.1 Introduction

Consider the definition of the group-to-group transfer

$$\int_{E'_g}^{E'_{g+1}} dE' \int_{\Omega'} d\Omega' \Phi(\Omega', E') \int_{E_g}^{E_{g+1}} dE \Sigma(\Omega' \rightarrow \Omega, E' \rightarrow E). \quad (122)$$

One of the difficulties associated with this definition is that we must define the probability of scattering from an initial direction Ω' and energy E' to the final direction Ω and energy E . However, the evaluated data are presented not in terms of fixed spatial directions, but rather in terms of the scattering angle, or, cosine. This is because we assume that a medium is homogeneous and isotropic, so that the scattering can only be a function of the angle between the initial and final directions, Ω' and Ω . The cosine of this scattering angle, μ_s , in terms of the initial and final directions can be written in the form (Meghreblian and Holmes 1960)

$$\mu_s = \Omega' \cdot \Omega = \mu' \mu + \sqrt{1 - \mu'^2} \sqrt{1 - \mu^2} \cos(\psi' - \psi), \quad (123)$$

and in general,

$$\Sigma(\Omega' \rightarrow \Omega, E' \rightarrow E) = \Sigma(\mu_s, E' \rightarrow E). \quad (124)$$

In order to convert this into a function of initial and final directions, we will expand the distribution in a series of Legendre polynomials

$$\Sigma(\mu_s, E' \rightarrow E) = \sum_{n=0}^{\infty} \frac{2n+1}{2} \Sigma_n(E' \rightarrow E) P_n(\mu_s), \quad (125)$$

where

$$\Sigma_n(E' \rightarrow E) = \int_{-1}^{+1} d\mu_s P_n(\mu) \Sigma(\mu_s, E' \rightarrow E), \quad (126)$$

and use the relationship,

$$P_n(\mu_s) = \sum_{m=-n}^n Y_n^m(\Omega') Y_n^m(\Omega). \quad (127)$$

Substituting this expression into (122), we obtain

$$\sum_{n=0}^{\infty} \frac{2n+1}{2} \sum_{m=-n}^n Y_n^m(\Omega) \int_{E'_g}^{E'_{g+1}} dE' \int_{\Omega'} d\Omega' Y_n^m(\Omega') \Phi(\Omega', E') \int_{E_g}^{E_{g+1}} dE \Sigma_s(E' \rightarrow E). \quad (128)$$

Upon defining the spherical harmonic moment of the flux, as

$$\Phi_n^m(E') = \int_{\Omega'} Y_n^m(\Omega') \Phi(\Omega', E') d\Omega', \quad (129)$$

we obtain the expression

$$\sum_{n=0}^{\infty} \frac{2n+1}{2} \sum_{m=-n}^n Y_n^m(\Omega) \int_{E'_g}^{E'_{g+1}} dE' \Phi_n^m(E') \int_{E_g}^{E_{g+1}} dE \Sigma_s(E' \rightarrow E) \quad (130)$$

which expresses the transfer to the final direction Ω , in terms of the spherical harmonics moments of the flux.

In the azimuthally symmetric system, (130) can be simplified by integrating over the azimuthal angle; in this case, all the terms will be zero except those with $m = 0$, and we find

$$\sum_{n=0}^{\infty} \frac{2n+1}{2} P_n(\mu) \int_{E'_g}^{E'_{g+1}} dE' \Phi_n(E') \int_{E_g}^{E_{g+1}} dE \Sigma_s(E' \rightarrow E), \quad (131)$$

where

$$\Phi_n(E') = \int_{-1}^{+1} P_n(\mu) \Phi(\mu, E') d\mu \quad (132)$$

is a Legendre moment of the flux. From either of these equations, we can define the Legendre moment of the transfer

$$\sum_{n=0}^{\infty} \frac{2n+1}{2} \sum_{m=-n}^n Y_n^m(\Omega') \Phi_{ng'}^m \Sigma_{g' \rightarrow g}^n, \quad (133)$$

where

$$\Phi_{ng'}^m \Sigma_{g' \rightarrow g}^n = \int_{E'_g}^{E'_{g+1}} dE' \Phi_n^m(E') \int_{E_g}^{E_{g+1}} dE \Sigma_n(E \rightarrow E'). \quad (134)$$

In the absence of additional information, it will be assumed that the energy dependence will be the same for all spherical harmonic moments of the flux with the same n , but any m . With this assumption, we can generate geometry-independent moments of the transfer matrix. In any given application, these moments can be used to reconstruct the transfer in one dimension

(Engle 1967), as in (131); or in two or three dimensions (Mynatt et al. 1973; Lathrop and Brinkley 1970; Ray et al. 2005), as in (130). In the S_n method, a quadrature is used to reconstruct the required Legendre or spherical harmonic moments of the flux.

In order to understand the implications of (130), we will consider two cases: uncorrelated and correlated. For uncorrelated distributions, the distribution will be expressed as the product of an angular distribution in the laboratory system and an energy distribution, as

$$\Sigma(\mu_s, E' \rightarrow E) = \Sigma(E', \mu_s) g(E' \rightarrow E), \quad (135)$$

and generally, the angular distribution is either isotropic or can be expressed by a low-order Legendre expansion, as

$$\Sigma(E', \mu_s) = \sum_{l=0}^L \frac{2l+1}{2} \Sigma_l(E') P_l(\mu_s). \quad (136)$$

In this case, from (136), we find

$$\begin{aligned} \Sigma_n(E' \rightarrow E) &= \Sigma_n(E') g(E' \rightarrow E) : n \leq L \\ &= 0 : n > L \end{aligned} \quad (137)$$

and the infinite series implied by (130) and (131) is truncated at the same order as the order of the Legendre expansion of the uncorrelated angle distribution.

For the correlated distribution, the distribution will be expressed as the product of an angular distribution, in the laboratory or center of mass, and a Dirac delta function that expresses the exact correlation between scattering angle and initial and final energies, as

$$\Sigma(\mu_s, E' \rightarrow E) = \Sigma(E', \mu_s) \delta[\mu_s - \mu(E, E')]. \quad (138)$$

In this case, from (126) we find,

$$\Sigma(\mu_s, E' \rightarrow E) = \Sigma[E', \mu(E, E')] P_n[\mu(E, E')]. \quad (139)$$

Therefore, the infinite series in (130) and (131) is not truncated, since all the Legendre coefficients will be nonzero. That is to say, even a correlated distribution that is isotropic in the laboratory system will lead to an infinite number of terms in the transfer matrix. This is an important effect that is sometimes overlooked; even at low energies in heavy materials where the scattering is essentially isotropic, the transfer matrix will contain nonisotropic terms due to the correlation between scattering cosine and initial and final energies. The importance, or magnitude, of these terms depends on the material involved and the group structure used. For groups that are wide (few groups) when compared with the maximum energy loss in elastic scattering, these non-isotropic terms tend to be very small. However, for very narrow groups (many groups), which tend to accentuate the transfer between specific initial and final directions, these terms can be large and important.

5.2 Solution

The n th moment of the flux may be written as in (134)

$$\int_{E'_g}^{E'_{g+1}} dE' \Phi_n(E') \int_{E_g}^{E_{g+1}} dE \Sigma_n(E \rightarrow E), \quad (140)$$

or by using (126) to define the n th Legendre moment of the distribution

$$\int_{E'_g}^{E'_{g+1}} dE' \Phi_n(E') \int_{E_g}^{E_{g+1}} dE \int_{-1}^{+1} d\mu_s P_n(\mu) \Sigma(\mu_s, E' \rightarrow E). \quad (141)$$

The latter form is how it is normally expressed as the starting point in order to evaluate these terms.

Since cross section is a probability and therefore inherently positive, all the integrals that we have considered in the preceding sections have been expressed as the sum of positive terms, and, if properly written and evaluated, led to numerically stable algorithms. Physically, all the terms in the above equation should be positive, except for the Legendre polynomials, $P_n(\mu_s)$. The presence of this polynomial makes the accurate evaluation of this equation very difficult, as we expect cross cancellation between negative and positive contributions to the integral. Therefore, extreme care must be exercised in order to express this integral in a form that is numerically stable.

Before proceeding to solve this equation, we will first express the secondary-energy-angle distribution in the form that it is represented in evaluated libraries (Kinsey 1970; Rose and Dunford 1990), where each reaction is represented in the form

$$\Sigma(\mu_s, E' \rightarrow E) = m(E') \Sigma_s(E') p(E', \mu_s) g(\mu_s, E' \rightarrow E), \quad (142)$$

where

$m(E')$ Multiplicity for the reaction, e.g., 1 for elastic, inelastic; 2 for $(n, 2n)$; $\nu(E')$ for fission.

In evaluated libraries, this is either given explicitly as in the case of $\nu(E')$, or implied by the reaction (elastic).

$\Sigma(E')$ Cross section for the reaction.

$p(E', \mu_s)$ Angular distribution, which is a function of the incident energy. For correlated distributions, it is usually given in the center-of-mass system. Uncorrelated distributions are given in the laboratory system. Either may be given in terms of Legendre coefficients or tabulated values.

$g(\mu_s, E' \rightarrow E)$ Energy distribution: For correlated distributions, this is an implied Dirac delta function, which expresses the exact correlation between scattering cosine and initial and final energies. For uncorrelated distributions, it is the actual secondary-energy distribution, independent of μ_s .

Uncorrelated and correlated distributions will each be discussed as follows.

5.2.1 Uncorrelated Distributions

Let us consider the uncorrelated case first. In this case the secondary distribution is expressed as the product of two independent distributions, one in angle and another in energy, and each is normalized to unity when integrated over secondary-angle or -energy, respectively,

$$p(\mu_s, E' \rightarrow E) = p(E', \mu_s) g(E' \rightarrow E). \quad (143)$$

5.2.2 Angular Distributions

The angular distribution will be given in the laboratory system in terms of Legendre coefficients or tabulated values. In either case, we may immediately perform the integral over angle in (141), as

$$\int_{-1}^{+1} d\mu_s P_n(\mu_s) p(E', \mu_s). \quad (144)$$

For the angular distribution given in terms of Legendre coefficients,

$$p(E', \mu_s) = \sum_{l=0}^{\infty} \frac{2l+1}{2} p_l(E') P_l(\mu_s). \quad (145)$$

The integral in (144) immediately reduces to the n th laboratory Legendre coefficient of the angular distribution as

$$p_n(E') = \int_{-1}^{+1} d\mu_s P_n(\mu_s) p(E', \mu_s). \quad (146)$$

For the angular distribution given in tabular form, we can reduce it to be linearly interpolable by LEGEND (Cullen 2007a-c), as

$$p(E', \mu_s) = \frac{(\mu - \mu_k) p_{k+1}(E') + (\mu_{k+1} - \mu) p_k(E')}{\mu_{k+1} - \mu_k} : \mu \in (\mu_k, \mu_{k+1}), \quad (147)$$

where $p_k(E')$ and $p_{k+1}(E')$ are the values of the angular distribution tabulated at μ_k and μ_{k+1} , respectively. In this case, the integral becomes

$$\sum_k \int_{\mu_k}^{\mu_{k+1}} d\mu_s P_n(\mu_s) \left\{ \frac{(\mu - \mu_k) p_{k+1}(E') + (\mu_{k+1} - \mu) p_k(E')}{\mu_{k+1} - \mu_k} \right\}. \quad (148)$$

Once this expression is evaluated, we will obtain the equivalent of the n th laboratory Legendre coefficient $p_n(E')$ of the tabulated distribution. Since the Legendre polynomial $P_n(\mu_s)$ is merely an n th-order polynomial, we could write this expression as a sum of powers of μ_s and then integrate. However, the resulting expression can be numerically unstable. In order to

obtain a numerically stable expression, we will introduce a change of variable to convert the above expression into an integral in a formal form over the interval $(-1, +1)$, as

$$\begin{aligned}
 Z &= \frac{2\mu - (\mu_{k+1} + \mu_k)}{\mu_{k+1} - \mu_k}, \\
 \mu &= \langle \mu \rangle_k [1 + \Delta_k Z], \\
 \langle \mu \rangle_k &= \frac{1}{2} (\mu_{k+1} + \mu_k), \\
 \Delta_k &= \frac{1}{2} \left(\frac{\mu_{k+1} - \mu_k}{\mu_{k+1} + \mu_k} \right), \\
 d\mu &= \langle \mu \rangle_k \Delta_k dZ = \frac{1}{2} (\mu_{k+1} - \mu_k) dZ;
 \end{aligned} \tag{149}$$

the tabulated angular distribution takes the form

$$\begin{aligned}
 f(Z) &= \langle f \rangle_k [1 + \delta_k Z], \\
 \langle f \rangle_k &= \frac{1}{2} (f_{k+1} + f_k), \\
 \delta_k &= \frac{1}{2} \left(\frac{f_{k+1} - f_k}{f_{k+1} + f_k} \right);
 \end{aligned} \tag{150}$$

and the integral becomes

$$\frac{1}{2} \sum_k (\mu_{k+1} - \mu_k) \langle f \rangle_k \int_{k-1}^{+1} dZ P_n [\langle \mu \rangle_k (1 + \Delta_k Z)] [1 + \delta_k Z]. \tag{151}$$

In most transport calculations, this expression is normally only evaluated for a small number of n values, typically three for P_3 scattering. Therefore, the evaluation of this expression will be presented here for the first four terms (P_0 through P_3) for illustrative purposes; this procedure can easily be extended to any required order of n . From the definition of the Legendre polynomials, we get

$$\begin{aligned}
 P_0 &= 1, \\
 P_1 &= \langle \mu \rangle_k [1 + \Delta_k Z], \\
 P_2 &= \frac{3}{2} \langle \mu \rangle_k^2 [1 + \Delta_k Z]^2 - \frac{1}{2}, \\
 P_3 &= \frac{5}{2} \langle \mu \rangle_k^3 [1 + \Delta_k Z]^3 - \frac{3}{2} \langle \mu \rangle_k [1 + \Delta_k Z].
 \end{aligned} \tag{152}$$

We obtain an expression for the integral in terms of a sum of powers of Z , but since the integral is over the normal interval $(-1, +1)$ we will only obtain nonzero contributions from the even

powers of Z . Using our expression for the Legendre polynomials, we can easily evaluate

$$\begin{aligned} & \frac{1}{2} \int_{-1}^{+1} dZ P_n[< \mu >_k (1 + \Delta_k Z)] [1 + \delta_k Z], & (153) \\ n = 0 : 1, \\ n = 1 : & < \mu >_k \left[1 + \frac{1}{3} \Delta_k \delta_k \right], \\ n = 2 : & \frac{3}{2} < \mu >_k^2 \left[1 + \frac{1}{3} (\Delta_k^2 + 2\Delta_k \delta_k) - \frac{1}{2} \right], \\ n = 3 : & \frac{5}{2} < \mu >_k^3 \left[1 + (\Delta_k^2 + \Delta_k \delta_k) + \frac{1}{5} \Delta_k^3 \delta_k \right] - \frac{3}{2} < \mu >_k \left[1 + \frac{1}{3} \Delta_k \delta_k \right]. & (154) \end{aligned}$$

Expressed in this form, we can see that for any angular distribution that is tabulated on a very fine cosine grid (i.e., very small Δ_k), the integral reduces to a sum of terms, each of which is just the width of the cosine interval times, the average value of the tabulated angular distribution times, the Legendre polynomial evaluated at the middle of the cosine interval,

$$\sum_k (\mu_{k+1} - \mu_k) < f >_k P_n[< \mu >_k]. \quad (155)$$

This form is much more numerically stable than the integrating (148) in terms of powers of the cosine, but it is still not an optimum algorithm as generally there will still be a cross section of positive and negative terms, since the Legendre polynomial will be positive and negative over different cosines ranges.

Stability can be further enhanced by using the parity property of the Legendre polynomials, as

$$P_n(-\mu) = (-1)^n P_n(\mu), \quad (156)$$

and rewriting the expression for the n th Legendre coefficient, (144), in the form

$$\int_0^{+1} d\mu_s P_n(\mu_s) [p(E', \mu_s) + (-1)^n p(E', -\mu_s)], \quad (157)$$

and tabulating

$$p * (E', \mu_s) = p(E', \mu_s) + (-1)^n p(E', -\mu_s) : \mu_s \in (0, 1). \quad (158)$$

One can use the procedures presented above to evaluate this integral. Note that in this form for any symmetric angular distribution, all the odd Legendre coefficients automatically reduce to zero without taking any differences other than those explicitly already included in (158).

5.2.3 Energy Distributions

Having calculated the n th Legendre coefficient of the angular distribution, the group-to-group transfer matrix can be written in the form

$$\Phi_{ng'} \Sigma_{g' \rightarrow g}^n = \int_{E_{g'}}^{E_{g'+1}} dE' m(E') \Sigma(E') p_n(E') \Phi_n(E') \int_{E_g}^{E_{g+1}} dE g(E' \rightarrow E). \quad (159)$$

We note that the integral over the secondary-energy distribution is independent of n ; this is a consequence of our assumption that the angular and energy distributions are uncorrelated.

In order to proceed further, we must examine the representations of the secondary-energy distribution that are used in the evaluated data libraries (Kinsey 1970; Rose and Dunford 1990). These include

1. *An arbitrary tabulated function* – for a series of incident energies, E' , the secondary distribution is tabulated as a function of the secondary energy, E .
2. *General evaporation spectrum (Maxwellian)*

$$g(E' \rightarrow E) = g(E/\theta(E')), \quad (160)$$

where $\theta(E')$ is tabulated as a function of the incident energy E' , and $g(X)$ is tabulated as a function of $X : X = E/\theta(E')$.

3. *Simple fission spectrum (Maxwellian)*

$$\begin{aligned} g(E' \rightarrow E) &= \frac{\sqrt{E}}{I} \text{Exp}[-E/\theta(E')], \\ I &= \theta^{3/2} \left[\frac{\sqrt{\pi}}{2} \text{ERF}(\sqrt{X}) - \sqrt{X} \text{Exp}(-X) \right], \\ X &= (E' - U)/\theta. \end{aligned} \quad (161)$$

While θ is tabulated as a function of the incident energy E' , U is a constant introduced to define the upper limit of the secondary-energy distribution: $0 \leq E \leq E' - U$.

4. *Evaporation spectrum*

$$\begin{aligned} g(E' \rightarrow E) &= \frac{E}{I} \text{Exp}[-E/\theta(E')], \\ I &= \theta^2 [1 - (1 + X) \text{Exp}(-X)], \\ X &= (E' - U)/\theta. \end{aligned} \quad (162)$$

θ is tabulated as a function of the incident energy E' . U is a constant introduced to define the upper limit of the secondary-energy distribution: $0 \leq E \leq E' - U$.

5. Energy-dependent Watt spectrum

$$\begin{aligned}
 g(E' \rightarrow E) &= \frac{1}{I} \text{Exp}[-E/a] \sinh[\sqrt{bE}], \\
 I &= \frac{1}{2} \sqrt{\frac{\pi a^2 b}{4}} \text{Exp}\left[\frac{ab}{4}\right] \left[\text{ERF}(\sqrt{X} - \sqrt{C}) + \text{ERF}(\sqrt{X} + \sqrt{C}) \right] - a \text{Exp}[-X \sinh(D)], \\
 X &= (E' - U)/\theta, \\
 C &= ab/4, \\
 D &= \sqrt{b(E' - U)}.
 \end{aligned} \tag{163}$$

While a and b are tabulated as a function of incident energy E' , U is a constant introduced to define the upper limit of the secondary-energy distribution:

$$0 \leq E \leq E' - U.$$

Any of these representations may be integrated over the secondary energy, E , in order to reduce (141) to a singly dimensioned integral over the initial energy distribution

$$\Phi_{ng'} \Sigma_{g' \rightarrow g}^n = \int_{E_{g'}}^{E_{g'+1}} dE' m(E') \Sigma(E') p_n(E') \Phi_n(E') g(E' \rightarrow g), \tag{164}$$

where

$$g(E' \rightarrow g) = \int_{E_g}^{E_{g+1}} dE g(E' \rightarrow E). \tag{165}$$

For the tabulated forms of $g(E' \rightarrow E)$ described above, the transformation to the normal interval $(-1, +1)$ should be used to improve numerical stability of the resulting integrals. The analytical expressions for the integral of $g(E' \rightarrow E)$ in (165) will be similar in form to the “ I ” in (161) through (163), only evaluated at E_g and E_{g+1} . In order to insure numerical stability, care must be exercised in evaluating these analytical expressions, particularly for small-energy intervals (fine-energy groups) wherein round-off problems may error.

The major difficulty in evaluating (164) is the dependence of $g(E' \rightarrow g)$ on the initial energy E' ; all the other terms can be reduced to linearly interpolable form and integrated using the procedures described earlier under self-shielding. Fortunately, even though in principle any of the forms described above for $g(E' \rightarrow E)$ can be used, in practice usually the secondary-energy distribution is either independent of initial energy, or at least has coefficients that vary slowly with energy. When the secondary-energy distribution is independent of initial energy, (159) and (164) just become the product of an integral over initial energy, which can be solved in a manner analogous to the procedures introduced earlier under self-shielding, and the integral of $g(E' \rightarrow E)$ over secondary-energy equation (165). When the secondary-energy distribution is dependent on the initial energy, the slow variation of its coefficients may be used to divide the integral into a series of integrals in each of which $g(E' \rightarrow E)$ may be considered to be linearly variable, or even constant. Therefore, here we will only illustrate the result that is obtained

using an arbitrary tabulated, energy distribution. We assume that for each initial energy E' , the angular distribution is given in linearly interpolable form by LEGEND (Cullen 2007a–c), as a function of secondary energy; using our normalized coordinates, this can be written in the form

$$\begin{aligned} g(E' \rightarrow E) &= \langle g(E') \rangle_k [1 + \delta_k Z] : E \in (E_k, E_{k+1}), \\ Z &= \frac{2E - (E_k + E_{k+1})}{E_{k+1} - E_k}, \\ \langle g(E') \rangle_k &= \frac{1}{2} [g_{k+1}(E') + g_k(E')], \\ \delta_k(E') &= \frac{1}{2} \left[\frac{g_{k+1}(E') - g_k(E')}{g_{k+1}(E') + g_k(E')} \right]. \end{aligned} \quad (166)$$

If we further assume that the energy distribution is also a linearly interpolable function of the incident energy, E' , we obtain an analogous expression for

$$\langle g(E') \rangle_k = g_{k'k} [1 + \delta_{k'k} Z'] : E' \in (E'_k, E'_{k+1}). \quad (167)$$

Integrating (166) over those energy integrals that lie within the energy range (E_g, E_{g+1}) yields

$$g(E' \rightarrow g) = \int_{E_g}^{E_{g+1}} dE g(E' \rightarrow E) = \sum_k (E_{k+1} - E_k) \langle g(E') \rangle_k, \quad (168)$$

which states that since $g(E' \rightarrow E)$ depends on the secondary energy, integrating this distribution over each secondary-energy interval that lies in the range (E_g, E_{g+1}) , simply contributes the width of each energy interval times the average value of g within the energy interval; it does not depend on the detailed-energy dependence within each secondary-energy interval.

From (167) and (168), we now have an expression for $g(E' \rightarrow E)$ as a linearly interpolable function of E' . All the terms in (161) can be reduced to a similar form, and the procedure described under self-shielding can be used to evaluate the resulting expression. Of the terms in (161), all are inherently positive except the Legendre coefficient $p_n(E')$. If $p_n(E')$ does not change sign within the energy interval (E'_g, E'_{g+1}) , the resulting integral will be numerically stable; if it does change sign, cross cancellation may introduce round-off problems.

5.2.4 Correlated Distributions

In the case of correlated distributions, the secondary distribution is expressed as the product of the angular distribution and a Dirac delta function expressing the exact correlation between scattering angle and initial and final energies, as

$$p(\mu_s, E' \rightarrow E) = p(E', \mu_s) \delta[\mu_s - S(E, E')]. \quad (169)$$

For example, for neutron inelastic scattering,

$$\mu_s = S(E, E') = \frac{1}{2} \left(\frac{E'}{E} \right)^{1/2} \left[(A+1) \left(\frac{E}{E'} \right) - (A-1) + \frac{AQ}{E} \right],$$

and for photon Compton scattering,

$$\mu_s = S(E, E') = 1 - \frac{\beta}{E} + \frac{\beta}{E'},$$

where β is the energy equivalent of the electron rest mass, m_0c^2 (roughly 0.51 MeV). For correlated distributions, the angular distribution may be given in Legendre coefficient or tabulated form and is usually in the center of mass system.

Since correlated distributions occur in two-body interactions alone with defined Q-values (e.g., elastic and discrete, inelastic neutron scattering, or Compton photon scattering), it may be assumed that the multiplicity in (142) is always unity for such interactions and need not be explicitly written in the following equations.

The presence of the Dirac delta function reduces the number of the dimensions of the integral in (141) from three to two. At present, there are a variety of methods in use to solve this equation, and they are worth reviewing.

Most of the methods presently in use write (141) in the form

$$\int_{E_{g'}}^{E_{g'+1}} dE' \Sigma(E') \Phi_n(E') F_n(E'), \quad (170)$$

where

$$F_n(E') = \int_{-1}^{+1} \mu_s P_n(\mu_s) \int_{E_g}^{E_{g+1}} dE p(E', \mu_s) \delta[\mu - S(E, E')]. \quad (171)$$

This may be written in terms of a singly dimensioned integral over the cosine in either of the laboratory system

$$F_n(E') = \int_{\mu_{\min}}^{\mu_{\max}} p(E', \mu_s) P_n(\mu_s) d\mu_s, \quad (172)$$

or the center-of-mass system,

$$F_n(E') = \int_{\eta_{\min}}^{\eta_{\max}} p(E', \eta_s) P_n(\mu_s) d\eta_s, \quad (173)$$

or a mix of the above two systems,

$$F_n(E') = \int_{\mu_{\min}}^{\mu_{\max}} p(E', \eta_s) P_n(\mu_s) \left| \frac{d\eta_s}{d\mu_s} \right| d\mu_s. \quad (174)$$

In these equations, the cosine limits are a function of the incident energy E' and correspond to the minimum and maximum scattering cosines that will permit a particle with an initial energy E' to end up with a secondary energy between E_g and E_{g+1} .

By assuming that the angular distribution is given in terms of a Legendre expansion in the laboratory system,

$$p(E', \mu_s) = \sum_{l=0}^L \frac{2l+1}{2} P_l(E') P_l(\mu_s). \quad (175)$$

Equation (172) can be written in the form

$$F_n(E') = \sum_{l=0}^L \frac{2l+1}{2} P_l(E') Y_l^n(E'), \quad (176)$$

where

$$Y_l^n(E') = \int_{\mu_{\min}}^{\mu_{\max}} P_l(\mu_s) P_n(\mu_s) d\mu_s. \quad (177)$$

This is the approach developed by Weisbin et al. (1974), and used in the MINX code (Weisbin et al. 1976).

By assuming that the angular distribution is given in terms of a Legendre expansion in the center-of-mass system

$$p(E', \eta_s) = \sum_{l=0}^L \frac{2l+1}{2} \tilde{p}(E') P_l(\eta_s), \quad (178)$$

One obtains a similar expression with

$$\tilde{Y}_l^n(E') = \int_{\mu_{\min}}^{\mu_{\max}} P_l(\eta_s) P_n(\mu_s) \left| \frac{d\eta_s}{d\mu_s} \right| d\mu_s \quad (179)$$

and

$$F_n(E') = \sum_{l=0}^L \frac{2l+1}{2} \tilde{p}_l(E') \tilde{Y}_l^n(E'). \quad (180)$$

This is the approach developed by Buchholz (1980), and used in the ROLAIDS code (Westfall 1978).

If the integration in (177) is performed over the center-of-mass cosine, rather than the laboratory cosine, then

$$\tilde{Y}_l^n(E') = \int_{\eta_{\min}}^{\eta_{\max}} P_l(\eta_s) P_n(\mu_s) d\eta_s. \quad (181)$$

Then, $F_n(E')$ corresponds to the “feed function” introduced by MacFarlane and Boicourt (MacFarlane and Boicourt 1975), and used in the NJOY code (MacFarlane et al. 1982; MacFarlane and Muir 1994).

Starting from a tabulated, linearly interpolable distribution in the center-of-mass system, this feed function can be written in the form

$$F_n(E') = \sum_k \int_{\eta_{k \min}}^{\eta_{k \max}} f_k(\eta_s) P_n(\mu_s) d\eta_s, \quad (182)$$

$$F_n(E') = \sum_k \int_{\mu_{k \min}}^{\mu_{k \max}} f_k(\eta_s) P_n(\mu_s) \left| \frac{d\eta_{ss}}{d\mu_s} \right| d\mu_s, \quad (183)$$

where $f_k(\eta_s)$ is the tabulated angular distribution that is linearly interpolable in η between η_k and η_{k+1} , and the cosine limits correspond to those portions of the cosine intervals that lie within the contribution cosine range as η_{\min} and η_{\max} or μ_{\min} and μ_{\max} , respectively. Equation (183) corresponds to the approach developed by Perkins and Giles (Graves-Morris 1973) and used in the CLYDE code (Doyas et al. 1971).

All the above approaches save the integration over the initial energy for last. In some of the above approaches, the so-called “feed function” can be defined in an analytical form, notably the Bucholz formulation for the Legendre coefficient representation in the center-of-mass system and the Perkins–Giles formulation for the tabulated representation in the center-of-mass system. Since the angular distributions are smoother in the center-of-mass system, the use of this system is the most appropriate in which to represent the data and the Bucholz’s and Perkins–Giles’s analytical results are the most important to consider.

An alternative approach to all the methods considered above is to save the integration over cosine for last and to write (141) in the form

$$\int_{-1}^{+1} d\mu_s P(\mu_s) \Sigma_{g' \rightarrow g}^n(\mu_s), \quad (184)$$

where

$$\begin{aligned} \Sigma_{g' \rightarrow g}^n(\mu_s) &= \int_{E_{g'}}^{E_{g'+1}} dE' \Sigma(E') \Phi_n(E') \int_{E_g}^{E_{g+1}} dE p(\mu_s, E' \rightarrow E) \\ &= \int_{E_{g'}}^{E_{g'+1}} dE' \Sigma(E') \Phi_n(E') p(E' \eta_s) \left| \frac{d\eta_s}{d\mu_s} \right|. \end{aligned} \quad (185)$$

This is the approach developed by Greene (1973), and used in the AMPX code (Greene et al. 1976). After solving for the group-to-group transfer due to scatter through a given cosine, AMPX uses a Gaussian quadrature to solve (184). Hong and Shultis (Hong and Shultis 1982), have shown that this approach can be greatly improved in terms of efficiency and accuracy by dividing the range of the final integral into a number of subranges, such that $\Sigma_{g' \rightarrow g}(\mu_s)$ is smooth within each subrange.

It is impossible to thoroughly cover all these methods in this chapter. However, because of the analytical results obtained by Bucholz and Perkins–Giles, their methods will be presented for illustration purposes. Once the definition of the transfer matrix is reduced to a singly dimensioned integral, the methods introduced earlier under self-shielding can be used to evaluate it. Therefore, here we need to consider only the inner integral.

5.2.5 Solution of the Inner Integral

Both Bucholz and Perkins–Giles recognized the advantage of expressing the inner integral in terms of an angular distribution in the center-of-mass system, but performing the integration over the laboratory cosine. In this form, the inner integral can be written as

$$F_n(E') = \int_{\mu_{\min}}^{\mu_{\max}} p(E', \eta) P_n(\mu) \left| \frac{d\eta}{d\mu} \right| d\mu. \quad (186)$$

For neutrons elastically scattering from a nucleus of weight A times the neutron mass, the relationship between the center-of-mass and laboratory cosine is

$$\eta = \frac{1}{A} [\mu^2 - 1 + \mu r] : r = (a^2 + \mu^2)^{1/2} : a = A^2 - 1. \quad (187)$$

By differentiating, we find

$$\frac{d\eta}{d\mu} = \frac{1}{A} \left[2\mu + r + \frac{\mu^2}{r} \right]. \quad (188)$$

Therefore, (186) can be written in a form that involves μ alone,


$$F_n(E') = \frac{1}{A} \int_{\mu_{\min}}^{\mu_{\max}} p \left[E', \frac{1}{A} (\mu^2 - 1 + \mu r) \right] P_n(\mu) \left[2\mu + r + \frac{\mu^2}{r} \right] d\mu. \quad (189)$$

At this point, Bucholz assumes that the angular distribution can be written in terms of a Legendre expansion in the center-of-mass cosine, and Perkins–Giles assume that it can be written in terms of a tabulated distribution that is linearly interpolable in cosine. The result of either of these assumptions is that since the Legendre polynomials can be written in terms of powers of μ , the resulting integral can be defined exactly in terms of the family of functions,

$$\begin{aligned} f_n(X) &= \int X^n dX, \\ g_n(X) &= \int X^n r dX, \\ h_n(X) &= \int \frac{X^n}{r} dX. \end{aligned} \quad (190)$$

These functions satisfy a number of convenient recursion relationships and can be defined in terms of analytical functions (Perkins 1982). Perkins–Giles (Perkins 1982) present results for a general two-body problem, and their results can be used to extend the results presented by Bucholz (1980), for elastic scattering, to handle inelastic scattering. After solving this inner integral, the solution of the final singly dimensioned integral is rather straightforward and as mentioned earlier, it can be evaluated using the techniques described earlier under self-shielding.

5.2.6 Thermal-Scattering Law Data: $S(\alpha, \beta)$

The thermal-scattering law data $S(\alpha, \beta)$ is covered in  Chap. 3 on slowing down and thermalization.

6 Group Collapse

6.1 Introduction

The preceding sections describe how to calculate multigroup sections and transfer matrices. An efficient approach to utilizing multigroup cross sections is to generate fine-group, multigroup data directly from the evaluated data in an application-independent form and to group collapse the fine-group data for use in any specific application (MacFarlane et al. 1982, Weisbin et al. 1976; Cullen 1979a–c; MacFarlane and Muir 1994).

The selection of both fine and collapsed group boundaries should consider “important” threshold regions and prominent WRs. Since what is “important” depends on the specific application, guidelines will not be provided in this chapter; this point is only mentioned here to impress on the reader the importance of selecting an appropriate set of groups to meet the needs of individual applications.

Recalling the definition of the multigroup cross section and transfer matrix,

$$\langle \Sigma_R \rangle_g = \frac{\int_{E_g}^{E_{g+1}} \Sigma_R(E) \Phi(E) dE}{\int_{E_g}^{E_{g+1}} \Phi(E) dE}, \quad (191)$$

$$T_{Rg' \rightarrow g} = \frac{\int_{E_g}^{E_{g+1}} dE \int_{E_{g'}}^{E_{g'+1}} dE' T_R(E' \rightarrow E) \Phi(E')}{\int_{E_{g'}}^{E_{g'+1}} \Phi(E') dE'}, \quad (192)$$

where,

$\Sigma_R(E)$ Cross section for any reaction R (R = total, elastic, capture, etc.),

$\Phi(E)$ Energy-dependent weighting spectrum, e.g., scalar flux,

$T_R(E' \rightarrow E)$ Reaction R , transfer function from source energy E' to sink energy E ,

g', g Source- and sink-group indices, respectively,

$(E_g, E_{g'+1})$ Energy range of source group,

(E_g, E_{g+1}) Energy range of sink group,

$\langle \Sigma_R \rangle_g$ Group-averaged cross section for reaction R in group g ,

$T_{Rg' \rightarrow g}$ Group-averaged transfer matrix for reaction R describing the transfer from source group g' to sink group g ,

In group collapsing, instead of performing the integrals in (191) and (192), we would like to define our group averages for one group structure in terms of known-group averages for

another, more detailed or finer, group structure. In order to accomplish this, we may partition the ranges of the integrals in (191) and (192) into a collection of subintervals as follows:

$$\langle \Sigma_R \rangle_g = \frac{\sum_j \int_{E_j^*}^{E_{j+1}^*} \Sigma_R(E) \Phi(E) dE}{\sum_j \int_{E_j^*}^{E_{j+1}^*} \Phi(E) dE}, \quad (193)$$

$$T_{Rg' \rightarrow g} = \frac{\sum_j \sum_{j'} \int_{E_j^*}^{E_{j+1}^*} dE \int_{E_{j'}^*}^{E_{j'+1}^*} dE' T_R(E' \rightarrow E) \Phi(E')}{\sum_{j'} \int_{E_{j'}^*}^{E_{j'+1}^*} \Phi(E') dE'}. \quad (194)$$

j', j Source- and sink-group indices for our fine-group structure.

$(E_{j'}^*, E_{j'+1}^*)$ That portion of the energy range of the source-fine group that lies within the energy range of the source-coarse group.

(E_j^*, E_{j+1}^*) That portion of the energy range of the sink-fine group that lies within the energy range of the sink-coarse group.

The summation over j and j' extends over those fine groups which either partially or totally overlap the energy range of the coarse groups g' and g . The energy range of fine group j will overlap the energy range of coarse group g if $E_{j+1} \geq E_g$ and $E_j \leq E_{g+1}$. That is to say, the energy ranges will overlap if the upper-energy limit of the fine group is greater than the lower limit of the coarse group and the lower limit of the fine group is less than the upper-energy limit of the coarse group. Given that fine group j does overlap coarse group g , the range and fraction of overlap are given by

$$E_j^* = \max(E_j, E_g),$$

$$E_{j+1}^* = \min(E_{j+1}, E_{g+1}), \quad (195)$$


$$P_j = \frac{E_{j+1}^* - E_j^*}{E_{j+1} - E_j}. \quad (196)$$

If we treat the fine-group data as exact histograms in source- and sink energy, we may rewrite the group-collapse equations in the forms

$$\langle \Sigma_R \rangle_g = \frac{\sum_j P_j < \Sigma_R >_j I_j(\Phi)}{\sum_j P_j I_j(\Phi)}, \quad (197)$$

$$T_{Rg' \rightarrow g} = \frac{\sum_j \sum_{j'} P_j P_{j'} T_{Rj' \rightarrow j} I_{j'}(\Phi)}{\sum_{j'} P_{j'} I_{j'}(\Phi)}, \quad (198)$$

5.2.6 Thermal-Scattering Law Data: $S(\alpha, \beta)$

The thermal-scattering law data $S(\alpha, \beta)$ is covered in  Chap. 3 on slowing down and thermalization.

6 Group Collapse

6.1 Introduction

The preceding sections describe how to calculate multigroup sections and transfer matrices. An efficient approach to utilizing multigroup cross sections is to generate fine-group, multigroup data directly from the evaluated data in an application-independent form and to group collapse the fine-group data for use in any specific application (MacFarlane et al. 1982, Weisbin et al. 1976; Cullen 1979a–c; MacFarlane and Muir 1994).

The selection of both fine and collapsed group boundaries should consider “important” threshold regions and prominent WRs. Since what is “important” depends on the specific application, guidelines will not be provided in this chapter; this point is only mentioned here to impress on the reader the importance of selecting an appropriate set of groups to meet the needs of individual applications.

Recalling the definition of the multigroup cross section and transfer matrix,

$$\langle \Sigma_R \rangle_g = \frac{\int_{E_g}^{E_{g+1}} \Sigma_R(E) \Phi(E) dE}{\int_{E_g}^{E_{g+1}} \Phi(E) dE}, \quad (191)$$

$$T_{Rg' \rightarrow g} = \frac{\int_{E_g}^{E_{g+1}} dE \int_{E_{g'}}^{E_{g'+1}} dE' T_R(E' \rightarrow E) \Phi(E')}{\int_{E_{g'}}^{E_{g'+1}} \Phi(E') dE'}, \quad (192)$$

where,

$\Sigma_R(E)$ Cross section for any reaction R (R = total, elastic, capture, etc.),

$\Phi(E)$ Energy-dependent weighting spectrum, e.g., scalar flux,

$T_R(E' \rightarrow E)$ Reaction R , transfer function from source energy E' to sink energy E ,

g', g Source- and sink-group indices, respectively,

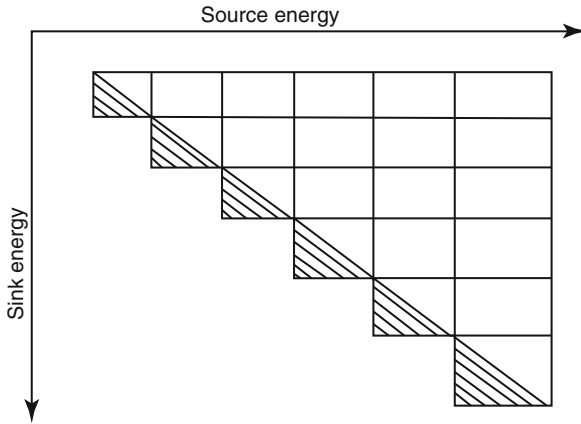
$(E_g, E_{g'+1})$ Energy range of source group,

(E_g, E_{g+1}) Energy range of sink group,

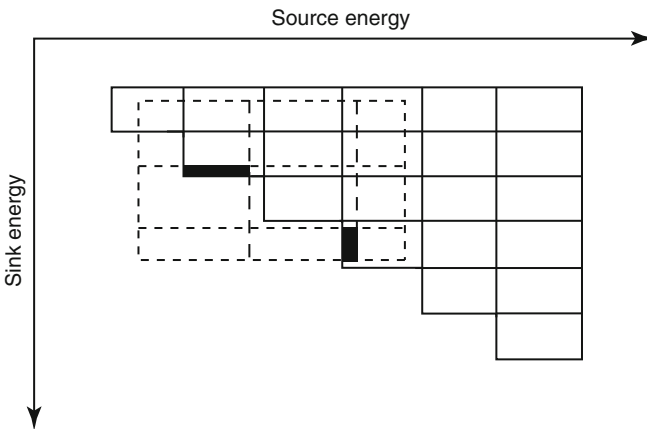
$\langle \Sigma_R \rangle_g$ Group-averaged cross section for reaction R in group g ,

$T_{Rg' \rightarrow g}$ Group-averaged transfer matrix for reaction R describing the transfer from source group g' to sink group g ,

In group collapsing, instead of performing the integrals in (191) and (192), we would like to define our group averages for one group structure in terms of known-group averages for



■ Figure 25
Comparison of exact- and six-group transfer



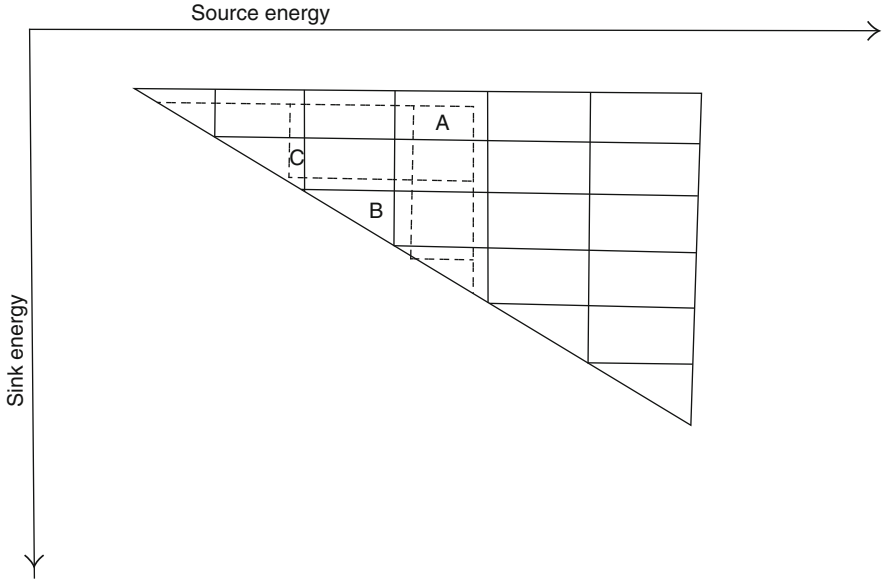
■ Figure 26
Comparison of six- and three-group transfer

Off-diagonal initial elements represent a rectangular area in (source, sink) energy space given by

$$(E_{j+1} - E_j)(E_{j'+1} - E_{j'}). \quad (200)$$

On diagonal initial elements represent a triangular area in (source, sink) energy space given by

$$\frac{1}{2}(E_{j+1} - E_j)^2. \quad (201)$$



■ Figure 27

Comparison of six- and three-group downscattering transfer

The contribution of an off-diagonal initial element to any final element is a rectangular area in (source, sink) energy space given by

$$(E_{j+1}^* - E_j^*)(E_{j'+1}^* - E_{j'}^*). \quad (202)$$

See ► Fig. 27 and (195) for a definition of E_j^* , etc.

Therefore, assuming the initial element to be uniformly distributed over its rectangular area $(E_{j+1} - E_j)(E_{j'+1} - E_{j'})$, its contribution to the final group will be the magnitude of the initial element times the ratio of the overlap area to the total area of the initial element,

$$P_j P_{j'} T_{j' \rightarrow j} = \frac{(E_{j+1}^* - E_j^*)(E_{j'+1}^* - E_{j'}^*)}{(E_{j+1} - E_j)(E_{j'+1} - E_{j'})} T_{j' \rightarrow j}, \quad (203)$$

which is identical to the contribution for a general transfer matrix.

The contribution of an on-diagonal initial element to an off-diagonal final element is a triangular area in (source, sink) energy space given by

$$\frac{1}{2} (E_{j+1}^* - E_j^*)^2. \quad (204)$$

See ► Fig. 25, area B, and (195) for a definition of E_j^* , etc.

Again assuming that the initial element to be uniformly distributed over its triangular area $1/2(E_{j+1} - E_j)^2$, its contribution to the final group will be the magnitude of the initial element


times the ratio of overlap area to the total area of the initial element,

$$P_j P_j T_{j \rightarrow j} = \frac{\frac{1}{2} (E_{j+1}^* - E_j^*)^2}{\frac{1}{2} (E_{j+1} - E_j)^2}. \quad (205)$$

The factors of 1/2 cancel, and we again obtain an expression which is identical to that obtained for a general transfer matrix.


The contribution of an on-diagonal initial element to an off-diagonal final element is a rectangular area in (source, sink) energy space given by

$$(E_{j+1}^* - E_j^*) (E_{j'+1}^* - E_{j'}^*). \quad (206)$$

See  [Fig. 25](#), area C, and (195) for a definition of E_j^* , etc. Again assuming that the initial element to be uniformly distributed over its triangular area $1/2(E_{j+1} - E_j)^2$, its contribution to the final group will be the magnitude of the initial element times the ratio of the square overlap area to the triangular total area of the initial element,

$$2P_j P_j T_{j \rightarrow j} = \frac{(E_{j+1}^* - E_j^*)^2}{\frac{1}{2} (E_{j+1} - E_j)^2}, \quad (207)$$

which is twice the contribution for a general transfer matrix.

This doubling of weight may be understood by examining  [Fig. 25](#). If we assume that the initial transfer element $T_{2 \rightarrow 2}$ is uniformly distributed over the upper triangular area $1/2(E_3 - E_2)^2$ alone, then the fraction of the area occupied by area C will be twice as large as if we had assumed a uniform distribution over the square area $(E_3 - E_2)^2$. Therefore, the fraction of the initial transfer element $T_{2 \rightarrow 2}$ contributing to the final element will be twice as large in this case.

From the above discussion, it may be seen that interpreting a transfer matrix as the only downscattering will eliminate upscattering, and otherwise, only effect the contribution of any diagonal elements to off-diagonal elements. To reiterate, group collapse is not recommended unless the coarse-group boundaries are a subset of the fine-group boundaries. However, if this condition is not met, the above procedures will at least prevent misinterpreting downscattering transfer matrices.

7 The Multiband Method

7.1 Introduction

From the preceding section on self-shielding, it can be seen that self-shielding is a fairly complicated process that involves a large number of approximations before one can obtain self-shielded cross sections for use in multigroup calculations. One particularly restrictive approximation is the use of a single set of self-shielded cross sections for the entire volumes of a problem; since from our earlier discussions, we know that the self-shielded cross section can actually be a continuous varying function of space and direction. For example, if we consider a piece of

Th232, which will be used to breed U233, at the surface for neutrons incident upon Th232, we would expect the cross section to be the unshielded values, see ref. (Plechaty et al. 1978a,b) and [Fig. 23](#). Deep inside the Th232, we would expect the cross sections to be heavily self-shielded. From our earlier discussion, we know that the self-shielded Th232-capture cross section would be much smaller than its unshielded value, with up to a factor of 50 (5,000%) difference between the two ([Fig. 24](#)). Therefore, in this case, even if we can somehow define a single, spatially averaged, self-shielded cross section which will allow us to correctly calculate the spatial dependence of the flux within the Th232, if we then use the correctly calculated flux and the spatially averaged self-shielded cross section, we will underestimate the capture near the surface and overestimate it deep within the Th232. An example of the magnitude of the resulting differences will be given later in this section.

There is an alternative approach that can be used to avoid the problems encountered when one tried to calculate self-shielded cross sections. In the preceding section on self-shielding, we found that in numerous limiting situations the self-shielded flux can be approximated by the product of an energy-dependent term (the energy-dependent spectrum) times a cross-section-dependent term (the self-shielding factor). We found this result for a purely absorbing or scattering medium as well as in the case of NRs, IRs, and WRs. The main difficulty in applying this knowledge is that the self-shielding factor can be strongly spatially and directionally dependent and must be approximated or guessed in advance, in order to calculate self-shielded cross sections for use in the actual multigroup transport calculation. From our earlier discussion we can see that a poor guess can lead to totally incorrect self-shielded cross sections and even if we do manage to obtain a good “average” cross section for a zone, it can lead to large errors if it is used to calculate reaction rates at specific space points within the zone. This latter point can effect burn-up, isotope production, energy deposition and therefore temperature, etc.

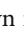
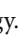
There are two approaches than can be used to avoid the problem of self-shielding. Since the self-shielding factors that we have found depend on the variation of the total cross section within the group, one approach is to use enough groups such that the variation in the total cross section within any group is small. This approach is not really very practical, since for modern evaluations (Garber and Brewster 1975; Cullen et al. 1976), an enormous number of groups would be required; essentially each group would have to be narrow when compared with the width of any resonance. Therefore, this approach is similar to and has no advantage over using continuous energy-dependent rather than multigroup cross sections. In addition, this approach is not practical in the unresolved-resonance region, since in this region evaluations do not provide enough information to allow the energy to be finely subdivided enough to ever uniquely define the resonance structure in the cross section.


The second approach recognizes that the objective of finely dividing the energy range into more groups is merely to arrive at the point where the variation in the cross section in each group is small, that is, to reduce the range of the total cross section within each group. If this is the objective and it cannot be attained by dividing the energy range into more energy groups, why not at some point stop the division and address the problem directly by dividing each energy group into a number of total cross section ranges. Since our discussion on self-shielding points out that the self-shielded flux depends strongly on the total cross section, it makes sense to group together those neutrons that interact with similar total cross sections.


In multigroup transport or diffusion, Nikolaev and Phillipov (1963) for neutrons, and Stewart (1964) for photons, originated the idea of characterizing the neutrons or photons within each group by the value of the total cross section with which they interact. The underlying idea of their approaches is to make full use of the predictions of various limiting transport problems,

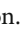
some of which have been discussed earlier in this work. Levitt (1972) independently developed his probability table method, which is equivalent to Nikolaev's subgroup method (Nikolaev and Phillipov 1963), when applied to Monte Carlo in the unresolved-resonance region. I have combined the aspects of Nikolaev's, Stewart's, and Levitt's work with Goldstein's work on IRs (Goldstein 1962, 1972, 1975), in order to develop the multiband method (Cullen 1974, 1977a,b; Cullen and Pomraning 1980), which can be applied to neutrons or photons, in any energy range, using Monte Carlo (Plechaty and Kimlinger 1971; Cullen 2005), deterministic transport, S_n , and diffusion.


In the normal multigroup method, one can attempt to improve the transport model by using more energy groups. This is accomplished by further subdividing each energy group. Within each energy group, all neutrons interact with the same cross section. In the multiband method, each group is further subdivided, not into smaller energy intervals, but rather into total cross section ranges. The resulting equations allow the neutrons within each group to interact with more than one total cross section. More importantly, instead of the multigroup approach where one has to approximate or guess how the flux varies as a function of cross section, in the multiband method the cross section dependent on the flux is actually calculated, and even starting from spatially and directionally independent multiband cross sections, the equivalent multigroup cross section can be spatially and directionally continuously variable.

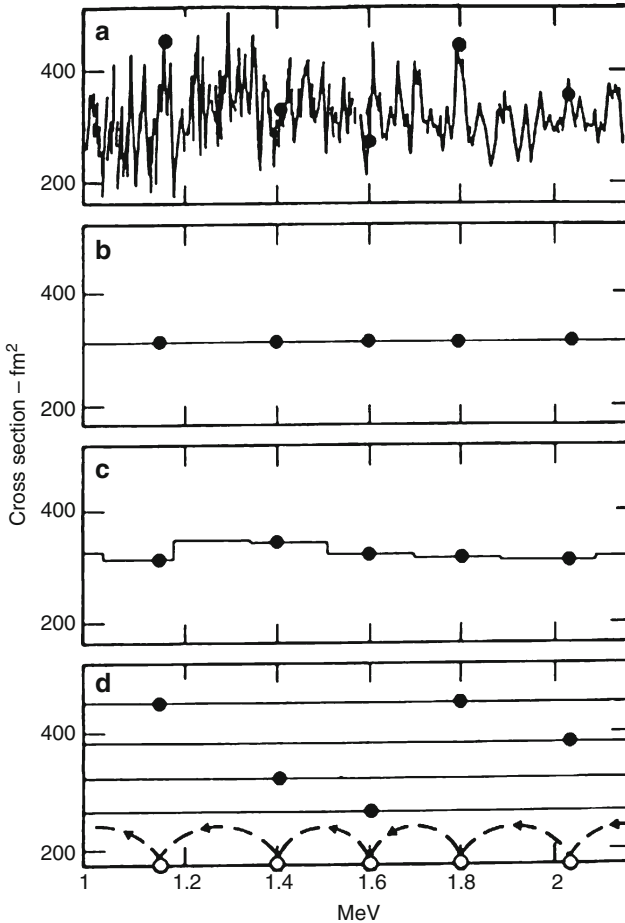
To illustrate how the multiband method differs from other methods consider the schematic of neutron transport shown in  Fig. 28. Here, we are interested in calculating the neutron flux, which at each energy is equal to the path length per unit volume and time traveled by the neutrons at that energy.  Figure 28 illustrates a neutron slowing down due to elastic scattering in the 2.2–1.0 MeV neutron energy range. The neutron loses energy in a series of collisions indicated by dots and connected by the looping dashed line at the bottom of the figure. In the time between collisions the neutron moves in space and thereby, contributes to the flux.

 Figure 28a shows the detailed total cross section variation over this energy range of nickel (Howerton 1978) that exhibits a rapidly varying cross section. The cross sections are quite different following each collision, and therefore on the average the contribution of neutrons to the flux (the distance traveled by the neutrons) varies for different energies.

 Figure 28b shows how a 26-group cross section (Bondarenko et al. 1964), continuous energy calculation handles this situation. Since in this group structure the energy range from 1.0 to 2.2 MeV all lies within the same group, a single multigroup cross section applies to all energies within the group, and therefore on the average the contribution of a neutron to the flux tends to be the same at all energies within this group.

The conventional approach to improving this multigroup approximation is to divide the energy range into narrower segments so that the average cross section more closely approximates the true cross section.  Figure 28c illustrates the effect of using 176 groups (Plechaty et al. 1978a,b), instead of 26 groups. Because of the narrow peaks and valleys in the cross section in this case, each of the new groups in this energy range has about the same average cross section as the single group in the 26-group case. As a result the flux calculated in this energy interval with the 175-group calculation is hardly any improvement over that calculated using 26 groups. This illustrates that increasing the number of groups does not necessarily improve the results of a multigroup calculation.

 Fig. 28d, the total cross section is divided into four total cross



■ **Figure 28**
Schematic comparison of methods

section ranges, or bands, and an average total in each band cross section range is defined in each band. Following each collision, neutrons are allowed to interact not with only one cross section, as in the multigroup method, but rather they may statistically interact with any one of the four cross sections. If the statistical probabilities of interacting with each of these four cross section bands are properly defined, this model can simulate the variations in the cross section and flux, as illustrated in [Fig. 28d](#).

The multigroup approach may have limitations due to self-shielding, but it has the advantage that it has been widely investigated and used, and at present there are a large number of computer codes that may be used to solve the multigroup equations. Realizing this, the multiband method was designed to utilize these available multigroup codes and to introduce the multiband method only by modifying the input “multigroup” data and by making minor internal modifications to the multigroup code itself.

7.2 Multiband Equations

Starting from the time-independent linearized neutron, Boltzmann equation

$$\begin{aligned} \Omega * \nabla N(r, \Omega, E) + \Sigma_t(r, E)N(r, \Omega, E) &= R(r, \Omega, E), \\ R(r, \Omega, E) &= \frac{1}{4\pi} \int_0^\infty dE' \int_{\Omega'} d\Omega' \Sigma(r, E' \rightarrow E, \Omega' \rightarrow \Omega) N(r, \Omega', E'). \end{aligned} \quad (208)$$

The multigroup equations are obtained from (208) by integrating over adjacent energy intervals extending from E_g to E_{g+1} (Weinberg and Wigner 1958; Glasstone and Edlund 1962). This yields the coupled set of equations

$$\Omega * \nabla N_g(r, \Omega) + \Sigma_{tg}(r)N_g(r, \Omega) = R_g(r, \Omega), \quad (209)$$

where N_g , $\Sigma_{tg}N_g$, and R_g are defined by integration over energy, e.g.,

$$N_g(r, \Omega) = \int_{E_g}^{E_{g+1}} N(r, \Omega, E) dE. \quad (210)$$

And R_g describes the contribution of all other groups and directions to group g and direction Ω ,

$$R_g(r, \Omega) = \frac{1}{4\pi} \sum_{g'} \int_0^\infty dE' \int_{\Omega'} d\Omega' \Sigma(r, g' \rightarrow g, \Omega' \rightarrow \Omega) N_g(r, \Omega'). \quad (211)$$

The multiband equations are obtained in a similar manner, however, in order to select specific total cross section ranges, (208) is first multiplied by the weighting function,

$$\delta[\Sigma_t(E) - \Sigma_t^*]. \quad (212)$$

And then integrated over both an energy group and a total cross section range, with respect to Σ_t . The result is a coupled set of equations

$$\Omega * \nabla N_{gB}(r, \Omega) + \Sigma_{tgB}(r)N_{gB}(r, \Omega) = R_{gB}(r, \Omega), \quad (213)$$

where N_{gB} , $\Sigma_{tgB}N_{gB}$, and R_{gB} are defined by integration over energy and total cross section range, e.g.,

$$N_{gB}(r, \Omega) = \int_{\Sigma_{tgB}}^{\Sigma_{tgB+1}} d\Sigma_t^* \int_{E_g}^{E_{g+1}} N(r, \Omega, E) \delta[\Sigma_t(E) - \Sigma_t^*] dE. \quad (214)$$

Physically, the effect of the delta function is to only select those energy intervals in the group where the total cross section is between Σ_{tgB} and Σ_{tgB+1} . ► Figures 29 and ► 30 illustrate the procedure involved in dividing an energy range (E_g, E_{g+1}) into four total cross section bands. In

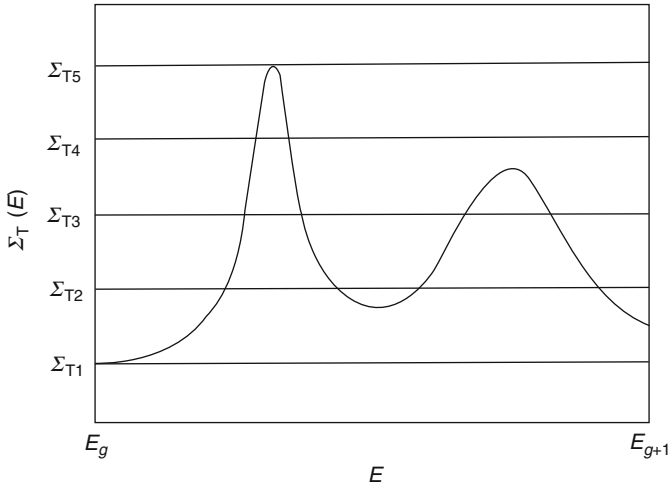


Figure 29
Total cross section showing four cross sections bands

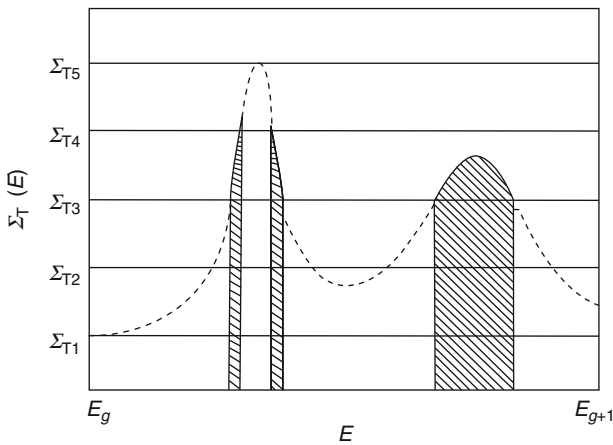


Figure 30
Total cross section contribution of third band

► Fig. 29 the total cross section is divided into four cross section ranges (bands). ► Figure 30 illustrates the effect of multiplying (208) by the Dirac delta function in total cross section, (212) and integrating over the energy range of the group and the third cross section band. Only those energy ranges in which the total cross section is between Σ_{T3} and Σ_{T4} contribute to the integral.

It is important to note that the multiband equations (213) and the multigroup equations (209) are identical in form and differ only in the magnitude of the cross sections, Σ_{igB} and Σ_{ig} , and the transfer into the group, band (R_{gB}) or group (R_g). Therefore, in principle once

these parameters are defined, the multiband equations can be solved by an existing multigroup computer code, such as MBANISN (MultiBand ANISN), a variant of ANISN (Engle 1967).

If the multigroup and multiband equations are so similar, why is there an advantage to the multiband equations? In either approach, we must approximate or guess the energy and cross section dependence of the flux in order to calculate the group or group, band parameters before performing the transport calculation. However, just as in the multiband method where we only need to specify the form of the flux within each group, (210), in the multiband method we only need to specify the form of the flux within each group, band (214). Since each group, band spans only a portion of the total cross section range, its variation within each group, band is smaller than within each group and our results are less sensitive to the approximation used to represent the self-shielding within each group, band. Indeed viewed in combination the set of group, band fluxes N_{gB} for the bands within each energy group defines the spatially and directionally dependent self-shielding factor. Therefore, the solution of the multiband equations allows for spatially and directionally dependent group self-shielding, even if the group, band cross sections are spatially independent.

Once the multiband equations have been solved to define the neutron flux and reaction rates in each group, band of a group, from definitions, (210) and (214), the equivalent multigroup quantities can be defined simply by summing over the bands in each group; e.g., the group flux is

$$N_g(r, \Omega) = \sum_B N_{gB}(r, \Omega). \quad (215a)$$

One important characteristic of the multiband method is that by defining the equivalent multigroup cross section in the normal way, as the ratio of reactions to flux, we find

$$\Sigma_{tg}(r, \Omega) = \frac{\sum_B \Sigma_{tgB} N_{gB}(r, \Omega)}{\sum_B N_{gB}(r, \Omega)}. \quad (215b)$$

We can see that even starting from spatially and directionally independent, multiband cross section Σ_{tgB} , the equivalent multiband cross sections defined by (215b) may be spatially and directionally dependent due to the variation of the neutron flux within each cross section band; i.e., we obtain spatially and directionally dependent self-shielding.

7.3 Multiband Parameters

The practicality of using the multiband method depends on the number of cross section bands required within each group. For example, if a large number of bands are required in each group, the method may not be a practical alternative to merely subdividing the energy range into many more energy groups. Fortunately, such is not the case and in all cases only a few bands per group are required; usually, only two and never more than four; this is shown next.

The direct use of (214) to define multigroup, band parameters would be complicated and expensive. However, there is a simple procedure that may be used to derive the required multiband parameters from the existing group's self-shielded data libraries (MacFarlane et al. 1982; MacFarlane and Muir 1994; Weisbin et al. 1976; Greene et al. 1976; Cullen 1980a–c). In order to illustrate this, first it is shown that the normal definition of multigroup cross sections in

terms of integrals over energy can be exactly transformed into an integral over total cross section. This point is not surprising, since it merely shows that one can either integrate over the energy interval in the Riemann sense or over the total cross section range in the Lebesgue sense. This exercise is important because it introduces the concept of a band weight or cross section probability.

Considering the normal definition of a multigroup cross section for reaction R (R = total, elastic, capture, etc.) in group g .

$$\Sigma_{Rg} = \frac{\int_{E_g}^{E_{g+1}} \Sigma_R(E) \Phi(E) dE}{\int_E^{E_{g+1}} \Phi(E) dE}. \quad (216)$$

If we introduce the approximate form for the flux that we calculated earlier, namely the product of an energy-dependent spectrum times a cross-section-dependent self-shielding factor, we can rewrite the definition of our multigroup cross section in the form,

$$\Sigma_{Rg} = \frac{\int_{E_g}^{E_{g+1}} \Sigma_R(E) M(E) W[\Sigma_T(E)] dE}{\int_E^{E_{g+1}} M(E) W_T[\Sigma(E)] dE} \quad (217)$$

or equivalently,

$$\Sigma_{Rg} = \frac{\int_{E_g}^{E_{g+1}} dE \int_{\Sigma_T^*} d\Sigma_T^* \delta[\Sigma_T^* - \Sigma_T(E)] \Sigma_R(E) M(E) W(\Sigma_T^*)}{\int_{E_g}^{E_{g+1}} dE \int_{\Sigma_T^*} d\Sigma_T^* \delta[\Sigma_T^* - \Sigma_T(E)] M(E) W(\Sigma_T^*)}. \quad (218)$$

Equations (217) and (218) are equivalent in the sense that if the integration over Σ_T^* in (218) is performed first, we merely obtain (217). However, if the integration over E is performed first, we obtain the equivalent equation

$$\Sigma_{Rg} = \frac{\int d\Sigma_T^* \Sigma_R(\Sigma_T^*) W(\Sigma_T^*) P(\Sigma_T^*)}{\int d\Sigma_T^* W(\Sigma_T^*) P(\Sigma_T^*)}, \quad (219)$$

where we have defined

$$P(\Sigma_T^*) = \frac{\int_{E_g}^{E_{g+1}} dE \delta[\Sigma_T^* - \Sigma_T(E)] M(E)}{\int_{E_g}^{E_{g+1}} dEM(E)}, \quad (220)$$

$$\Sigma_R(\Sigma_T^*) P(\Sigma_T^*) = \int_{E_g}^{E_{g+1}} dE \delta[\Sigma_T^* - \Sigma_T(E)] \Sigma_R(E) M(E). \quad (221)$$

Equations (220) and (221) define the total cross section probability density $P(\Sigma_T^*)$ and the cross section for reaction R as a function of the total cross section $\Sigma_R(\Sigma_T^*)$. $P(\Sigma_T^*) d\Sigma_T^*$ is merely the normalized probability of the total cross section within $d\Sigma_T^*$ of Σ_T^* within the energy interval (E_g, E_{g+1}) .





The transformation from the normal definition of multigroup cross sections, (216) as an integral over energy to (219) in terms of an integral over cross section does not really require the assumption of a separable flux; this assumption has been introduced here merely to simplify the definitions in (220) and (221) and the two forms (energy or cross section integral) are exactly equivalent.

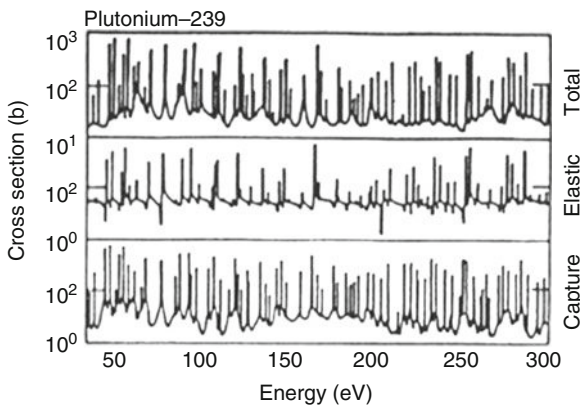
If one uses a self-shielding model that characterizes the flux as only depending on the total cross section within each group (e.g., NR or Bondarenko model), there are obvious advantages of using the cross-section-dependent form to define group-averaged cross sections. This may be illustrated by considering the relative difficulty of evaluating the same integral in the energy

$$\int_{E_g}^{E_{g+1}} \frac{dE}{E[\Sigma_T(E) + \Sigma_0]} \quad (222)$$

or in terms of the cross section

$$\int_{\Sigma_{T \min}}^{\Sigma_{T \max}} \frac{d\Sigma_T^* P(\Sigma_T^*)}{[\Sigma_T^* + \Sigma_0]} = \int_0^1 \frac{dP}{[\Sigma_T^*(P) + \Sigma_0]}, \quad (223)$$

where in this example $P(\Sigma_T^*)$ is given by (220) with $M(E)$ equal to $1/E$.  Figures 31 and  32 illustrate the Pu239 total cross section between 40 and 300 eV in the energy and cross section probability planes, respectively. From  Fig. 31 it is obvious that for fixed Σ_0 in the energy plane, $\Sigma_T(E) + \Sigma_0$ is a rapidly varying function of energy, which in this case is represented by thousands of tabulated data points. In contrast to  Fig. 32, for fixed Σ_0 in the



 **Figure 31**
Pu239 Neutron-Interaction cross section versus energy

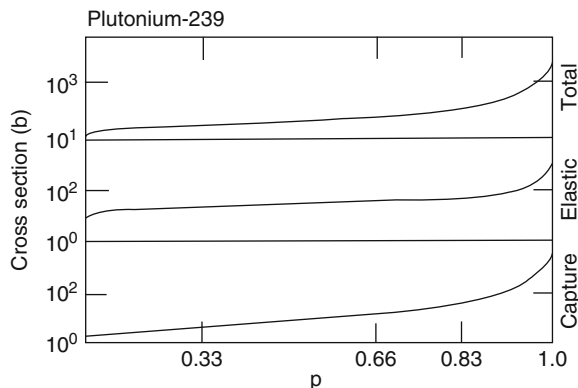


Figure 32
Pu239 Neutron-Interaction cross section versus probability

cross section probability plane $\Sigma_T(P) + \Sigma_0$ is a simple monotonically increasing function of P . Therefore, once the total cross section probability density is known, integrals in the cross section versus probability plane may be performed very efficiently for a variety of self-shielding factors $W(\Sigma_T^*)$ in (219). Another advantage of using the cross section versus probability is the increased insight that is obtained by allowing one to examine the importance of certain cross section ranges as shown in [Fig. 32](#), instead of having to deal with hundreds of minima and maxima, as shown in [Fig. 31](#).

In order to define the multiband parameters, the exact definition of the multigroup section, (219), as an integral over the total cross section, is replaced by a quadrature

$$\Sigma_{Rg} = \frac{\int d\Sigma_T^* \Sigma_R(\Sigma_T^*) W(\Sigma_T^*) P(\Sigma_T^*)}{\int d\Sigma_T^* W(\Sigma_T^*) P(\Sigma_T^*)} = \frac{\sum_B \Sigma_{RB} W(\Sigma_{TB}) P_B}{\sum_B W(\Sigma_{TB}) P_B}. \quad (224)$$

This is obviously equivalent to assuming that the cross section probability density $P(\Sigma_T^*)$ is given by a series of Dirac delta functions

$$P(\Sigma_T^*) = \sum_B P_B \delta[\Sigma_T^* - \Sigma_{TB}]. \quad (225)$$

Once the band weights P_B and cross sections Σ_{RB} are known, (224) may be used to define the multigroup, self-shielded cross section Σ_{Rg} , using any self-shielding model $W(\Sigma_{TB})$.

However, we use the reverse procedure. If we know a set of group-averaged cross sections, obtained using a variety of different weighting functions, $W(\Sigma_{TB})$, (224) may be solved to determine the required weights P_B and cross sections Σ_{RB} .

7.4 Solution for Band Parameters

Since we know the forms that we expect the self-shielded moments of the flux to assume in a number of widely applicable cases, we define our quadrature to insure that in these cases,

we obtain exactly the correct self-shielded cross sections. For example, if we have a standard, self-shielded multigroup library for each group, material, and reaction, we will have a variety of self-shielded cross sections, each corresponding to using a different self-shielding factor in the form,

$$W(\Sigma_T) = \frac{1}{[\Sigma_T + \Sigma_0]^k}; \quad \text{for various } k \text{ and } \Sigma_0 \quad (226)$$

as described in the preceding section on self-shielding. Since from this library we know the self-shielded cross sections (the equivalent of Σ_{Rg} in (224) corresponding to each self-shielding factor (the equivalent of $W(\Sigma_{TB})$ in (224)) as defined by (226), we can use this information to solve the system of equations (224) to define our multiband weights, P_B , and cross sections, Σ_{RB} , for each band.

7.4.1 Analytical Solution for Two Bands

In order to illustrate this procedure, consider the simplest possible case of using two bands; in this case we have four unknowns, the two-band weights P_1 and P_2 , and the two-band cross sections Σ_{R1} and Σ_{R2} , for each reaction R . Assume that from a normal, multigroup-processing code calculation we have calculated the unshielded cross section ($W(\Sigma_T) = 1$), the totally shielded flux weighted cross section ($W(\Sigma_T) = 1/\Sigma_T$) and the totally shielded current weighted cross section ($W(\Sigma_T) = 1/\Sigma_T^2$), which we donate by $\langle \Sigma_0 \rangle$, $\langle \Sigma_1 \rangle$, $\langle \Sigma_2 \rangle$, respectively. Then for the total cross section ($\Sigma_R = \Sigma_T$), the four equations sufficient to uniquely calculate our two-band parameters are obtained by realizing that our quadrature must be normalized

$$P_1 + P_2 = 1 \quad (227)$$

and by inserting each of the three weighting functions into (224) and equating the resulting equations to three known, precalculated self-shielded cross sections

$$\begin{aligned} \langle \Sigma_0 \rangle &= \frac{\Sigma_{T1}P_1 + \Sigma_{T2}P_2}{P_1 + P_2}; & (W(\Sigma_T) = 1), \\ \langle \Sigma_1 \rangle &= \frac{P_1 + P_2}{\frac{P_1}{\Sigma_{T1}} + \frac{P_2}{\Sigma_{T2}}}; & (W(\Sigma_T) = 1/\Sigma_T), \\ \langle \Sigma_2 \rangle &= \frac{\frac{P_1}{\Sigma_{T1}} + \frac{P_2}{\Sigma_{T2}}}{\frac{P_1}{\Sigma_{T1}^2} + \frac{P_2}{\Sigma_{T2}^2}}; & (W(\Sigma_T) = 1/\Sigma_T^2). \end{aligned} \quad (228)$$

We obtain a set of four nonlinear equations in four unknowns. Unfortunately, the solution to this set of equations is not unique. For example, the two bands are indistinguishable, so that if we obtain one solution for this system of equations, we can obtain a second solution merely by exchanging the weights and cross sections for the two bands. The solution does not become unique until we introduce an ordering into the parameters, such that $\Sigma_{T1} \leq \Sigma_{T2}$. This leads us to believe that the two-band parameters are related to the roots of a quadratic equation, which

are also not unique without an ordering. Therefore, we make the standard change of variables used to solve a quadratic equation,

$$\begin{aligned} P_1 &= \frac{1}{2} + \delta; & \Sigma_{T1} &= \frac{1}{X_1} = \frac{1}{A+B}, \\ P_2 &= \frac{1}{2} - \delta; & \Sigma_{T2} &= \frac{1}{X_2} = \frac{1}{A-B}. \end{aligned} \quad (229)$$

This change of variables immediately satisfies (227) and the remaining three equations are easily solved to find

$$\begin{aligned} \delta &= \frac{1 - A < \Sigma_1 >}{2B < \Sigma_1 >}, \\ A &= \frac{1}{2 < \Sigma_2 >} \left[\frac{< \Sigma_0 > - < \Sigma_2 >}{< \Sigma_0 > - < \Sigma_1 >} \right], \\ B^2 &= \frac{1}{< \Sigma_0 >} [1 - 2A + < \Sigma_0 > A^2]. \end{aligned} \quad (230)$$

As expected there are two possible equations for B , corresponding to the positive and negative roots of B^2 (230). This is the result of the nonuniqueness of the solution without an ordering. From the definitions of Σ_{T1} , Σ_{T2} and δ in terms of A and B (229), we can see that choosing the positive or negative root of B^2 merely corresponds to the same solution with the two bands interchanged. In order to obtain a unique solution we always define B to be positive, which from (229) corresponds to introducing the ordering $\Sigma_{T1} \leq \Sigma_{T2}$.

The above algorithm always produces physically acceptable parameters (positive band weights and cross sections) as long as $< \Sigma_0 > \geq < \Sigma_1 > \geq < \Sigma_2 >$. It can be demonstrated (Cullen et al. 1978) that the only time when the three of these are equal is when the total cross section is independent of energy across the group (i.e., the total is constant); in all other cases this inequality is true. When the total cross section is constant, the two bands become indistinguishable and only one band is required in the group (i.e., the normal multigroup equation).

Once the two-band parameters for the total cross section are known, from (229) and (230), for each other reaction R (R = elastic, capture), we may return to (224). For this two-band example for each reaction there are two unknowns, the two-band cross sections Σ_{R1} and Σ_{R2} . If from the normal multigroup library for each reaction we know the unshielded cross section ($W(\Sigma_T) = 1$), and the totally shielded flux weighted cross section ($W(\Sigma_T) = 1/\Sigma_T$) then we can use (224) to obtain two equations for each reaction R

$$\begin{aligned} < \Sigma_0 >_R &= \frac{\Sigma_{R1}P_1 + \Sigma_{R2}P_2}{P_1 + P_2}; & (W(\Sigma_T) = 1), \\ < \Sigma_1 >_R &= \frac{\Sigma_{R1}P_1 + \Sigma_{R2}P_2}{\frac{\Sigma_{T1}}{P_1} + \frac{\Sigma_{T2}}{P_2}}; & (W(\Sigma_T) = 1/\Sigma_T). \end{aligned} \quad (231)$$

Since from the total cross section definitions, (229) and (230), we know P_1 , P_2 , Σ_{T1} and Σ_{T2} , we may solve these two linear equations to define the unknowns Σ_{R1} and Σ_{R2} . In order to solve

these two equations, it is convenient to introduce the change of variables,

$$\begin{aligned}\Sigma_{R1} &= \langle \Sigma_0 \rangle_R - \frac{C}{P_1}, \\ \Sigma_{R2} &= \langle \Sigma_0 \rangle_R + \frac{C}{P_2}.\end{aligned}\quad (232)$$

This change of variables immediately satisfies the first equation, and the second can be solved to find

$$C = [\langle \Sigma_0 \rangle_R - \langle \Sigma_1 \rangle_R] \left[\frac{\frac{P_1}{\Sigma_{T1}} + \frac{P_2}{\Sigma_{T2}}}{1 - \frac{1}{\Sigma_{T1}} - \frac{1}{\Sigma_{T2}}} \right] = [\langle \Sigma_0 \rangle_R - \langle \Sigma_1 \rangle_R] \frac{1}{2B}.\quad (233)$$

Again, the only case when this equation cannot be used is identical to the case mentioned earlier for the total cross section, namely when the total cross section is constant across the entire group. In this case only one band is used in each group and the definition of the cross section for each reaction R reduces to its normal multigroup unshielded average $\langle \Sigma_0 \rangle_R$.

From (232) and (233) we can see that for any reaction where the unshielded and shielded cross sections $\langle \Sigma_0 \rangle_R$ and $\langle \Sigma_1 \rangle_R$ are equal, we find $C = 0$, and the two-band cross sections are the same in both bands and equal to their normal unshielded multigroup average. This will be the case for reactions that do not include resonant structure. Therefore, normally in using the multiband method (Plechaty and Kimlinger 1971; Cullen 1977a,b, 1980a–c, 2005; Otter et al. 1972), is to calculate multiband parameters for total, elastic, capture, and fission, and to use the normal, multigroup-unshielded, cross section for all other reactions. Although other reactions do have variations (Howerton et al. 1978; Garber and Brewster 1975), for the number of groups regularly used in multiband calculations (Plechaty and Kimlinger 1971; Cullen 2005), their self-shielding is negligible and can be ignored.

Once these two-band parameters have been defined, they may be used in transport calculations and they correctly reproduce the limiting cases of unshielded and totally shielded flux. For example, again consider a piece of Th232 in which we use two-band spatially and directionally independent parameters. In this case the combination of the two bands at the boundary for directions oriented into the Th232 produces the correct equivalent of the unshielded-group-averaged cross section. However, deep within the Th232 the flux in the band with a larger cross section is suppressed, relative to the other band, and the equivalent, group-averaged cross sections approach their self-shielded value, that is, we are reproducing continuously varying spatially dependent self-shielding. If we consider the albedo from the surface the flux in the larger cross section band will be suppressed, relative to the other band, which will result in self-shielding, that is, we are reproducing directionally dependent self-shielding, with the flux incident on the slab unshielded, and at exactly the same spatial point, the albedo from the slab is self-shielded.

7.4.2 Generalization to N Bands

The procedures introduced earlier to define two-band parameters may be generalized to define the band parameters for any number of bands per group. In general, (224) is a system of coupled,

nonlinear algebraic equations. Given a set of self-shielded cross sections, this system must be solved for the band cross sections Σ_{RB} and Σ_{TB} and band weights P_B .

This is a classic moments problem: for $\Sigma_0 = 0$ and various values of N , it is the Hausdorff moments problem (Graves-Morris 1973), while for $N = 1$ and various values of Σ_0 it is the Stieltjes–Hilbert moments problem (Graves-Morris 1973). Both of these problems have been widely studied, and only pertinent results are given here.

First take $R = \text{total}$. In this case, for N bands we have $2N$ unknowns: they are P_B and Σ_{TB} , for $B = 1, 2, \dots, N$. Given $2N$ values of the self-shielded total cross sections (defined for $2N$ different combinations of Σ_0 and N), the system of equations (224) can be solved uniquely for P_B and Σ_{TB} . Given more than $2N$ values of the self-shielded cross section, the system can be solved in some “best fit” sense (e.g., least squares or min-max),

Once the P_B and Σ_{TB} are known, the system of equations (224) is linear in the N unknowns Σ_{RB} for $R = \text{elastic, capture, fission}$; given N or more values of the self-shielded cross section for reaction R , the system is easy to solve uniquely or in some “best fit” sense.

7.4.3 How Many Bands are Required?

If the multiband approach is to be a practical alternative to the multigroup method in all energy ranges, it must be demonstrated that only a few bands are needed to correctly reproduce the self-shielding effects that we expect to encounter in a wide variety of applications; clearly if several hundred bands were required in each energy group, the method would not be economically feasible. In a wide variety of applications, we have seen that the neutron scalar flux is of the form

$$\frac{1}{[\Sigma_T(E) + \Sigma_0]^N} \text{ with } \Sigma_0 \geq 0 \text{ and } N = 1.$$

If we allow for all transport situations, so that Σ_0 can have any value between 0 and ∞ , how many bands are required to reproduce the entire self-shielding curve within some acceptable uncertainty? In order to answer this question, program GROUPIE (Cullen 1980a–c, 2007a–c), calculates the self-shielded cross section in each group for a large number of values of Σ_0 between 0 and ∞ (the ∞ limit corresponds to calculating the unshielded $N = 0$ value). Using 23 values of Σ_0 (0 and ∞ and multiples of the unshielded cross section between 2^{-10} and 2^{+10} , a range of over 1 million variation in Σ_0) GROUPIE finds the minimum number of bands such that for all 23 values of Σ_0 ,

$$\left| \langle \Sigma_T(\Sigma_0, N) \rangle - \frac{\sum_B \frac{\Sigma_{TB} P_B}{\Sigma_{TB} + \Sigma_0}}{\sum_B \frac{P_B}{\Sigma_{TB} + \Sigma_0}} \right| \leq \epsilon_{\max} \langle \Sigma_T(\Sigma_0, N) \rangle. \quad (234)$$

► **Table 8** presents the results for the entire ENDL library (Howerton et al. 1978) using the TART-175-group structure (Plechaty et al. 1978a,b). This table shows that the entire curve of self-shielded total cross sections can be reproduced within 0.1% accuracy for every material in the library with two or three (or occasionally four) bands. These results indicate that the multiband method can be used in all energy groups and will be both accurate and economical to use.

Table 8

Percent error in multiband fit of self-shielded total cross sections

Target	1 band ^a	2 bands	3 bands	4 bands	Target	1 band	2 bands	3 bands	4 bands
0-n-1	0.29	0.00			63-Eu-nat	132.52	0.71	0.01	
1-H-1	0.16	0.00			64-Gd-nat	456.50	2.25	0.05	
1-H-2	0.04	0.00			67-Ho-165	1825.96	6.73	0.43	0.02
1-H-3	0.03	0.00			73-Ta-181	1807.27	13.12	0.59	0.04
2-He-3	3.70	0.00			74-W-nat	2316.44	8.43	0.66	0.03
2-He-4	1.75	0.00			75-Re-185	1261.69	6.92	0.38	0.02
3-Li-6	8.97	0.01			75-Re-187	2104.84	9.00	0.37	0.06
3-Li-7	14.79	0.02			78-Pt-nat	260.57	2.36	0.05	
4-Be-7	4.01	0.00			79-Au-197	466.87	4.30	0.10	
4-Be-9	8.13	0.00			82-Pb-nat	4.15	0.01		
5-B-10	3.70	0.00			90-Th-231	8.18	0.01		
5-B-11	5.11	0.00			90-Th-232	5658.84	14.09	0.89	0.10
6-C-12	6.00	0.01			90-Th-233	3.69	0.00		
7-N-14	10.83	0.01			92-U-233	152.01	1.22	0.01	
8-O-16	73.31	0.40	0.00		92-U-234	3.42	0.00		
9-F-19	116.98	0.68	0.01		92-U-235	236.94	1.47	0.03	
11-Na-23	66.86	0.48	0.00		92-U-236	2818.67	5.44	0.15	0.01
12-Mg-nat	44.33	0.16	0.00		92-U-237	3.62	0.00		
13-Al-27	68.93	2.32	0.09		92-U-238	2990.51	8.23	0.44	0.03
14-Si-nat	174.90	0.77	0.01		92-U-239	18.42	0.04		
15-P-31	17.46	0.06			92-U-240	1.44	0.00		
16-S-32	32.72	0.28	0.00		93-Np-237	798.30	7.65	0.25	0.02
17-Cl-nat	89.16	0.93	0.02		94-Pu-238	1615.13	8.50	0.41	0.02
18-Ar-nat	17.11	0.01			94-Pu-239	623.01	3.57	0.08	
19-K-nat	165.07	1.53	0.07		94-Pu-240	6892.58	10.65	0.58	0.07
20-Ca-nat	89.78	0.54	0.01		94-Pu-241	87.37	0.18	0.00	
22-Ti-nat	314.87	3.04	0.11	0.00	94-Pu-242	2678.86	7.73	0.51	0.07
23-V-51	686.72	4.28	0.13	0.01	94-Pu-243	487.05	2.89	0.08	
24-Cr-nat	131.70	0.92	0.01		95-Am-241	322.40	2.01	0.07	
25-Mn-55	1155.01	2.89	0.11	0.01	95-Am-242	61.96	0.25	0.00	
26-Fe-nat	77.36	0.89	0.02		95-Am-243	532.32	2.61	0.06	
27-Co-59	225.18	3.02	0.10		96-Cm-242	991.85	6.06	0.30	0.01
28-Ni-nat	185.98	0.91	0.01		96-Cm-243	128.77	0.90	0.01	

■ Table 8 (continued)

Target	1 band ^a	2 bands	3 bands	4 bands	Target	1 band	2 bands	3 bands	4 bands
28-Ni-58	190.58	1.18	0.01		96-Cm-244	1273.68	7.30	0.48	0.02
29-Cu-nat	19.90	0.06			96-Cm-245	132.99	0.95	0.01	
31-Ga-nat	43.36	0.12	0.00		96-Cm-246	669.11	3.46	0.13	0.00
40-Zr-nat	161.08	2.95	0.07		96-Cm-247	341.71	2.32	0.06	
41-Nb-93	274.08	3.91	0.10		96-Cm-248	847.79	5.41	0.15	0.01
42-Mo-nat	80.95	0.26	0.00		97-Bk-249	946.69	3.65	0.12	0.01
47-Ag-107	829.74	5.97	0.16	0.01	98-Cf-249	263.58	1.48	0.04	
47-Ag-109	1723.35	8.80	0.31	0.02	98-Cf-250	499.59	2.09	0.10	
48-Cd-nat	63.37	0.47	0.01		98-Cf-251	102.48	0.44	0.01	
50-Sn-nat	94.49	0.43	0.00		98-Cf-252	986.71	4.79	0.16	0.01
56-Ba-138	21.23	0.04			Fission product	4.23	0.00		

^a1 band = unshielded multigroup cross sections.

7.5 Transfer Matrix

So far we have only discussed how to calculate multiband cross sections. However, in order to actually complete the analogy to the multigroup equations and to be able to perform multiband calculations, we must also define the transfer matrix between one (group, band) and another (group, band). In the subgroup method (Nikolaev and Phillipov 1963), and probability table method (Levitt 1972), the NR approximation is used to define the transfer matrix. Specifically, if a neutron scatters at some initial energy E' to some final energy E , the probability of the final energy E lying in any given energy interval (E_G, E_{G+1}) is independent of the cross section at both the initial energy E' and the final energy E . Therefore, we expect the probability of scattering from a band in any initial group to any final group to be the same for all bands in the initial group. The NR approximation is used only to describe the distribution of scattered neutrons between the bands in the final group. Specifically, the NR approximation is that the energy range over which neutrons scatter is wide when compared with the WR and as such the probability of scattering to any final band is independent of the initial band and only depends upon the probability of the final cross-section band, that is, it only depends on the weight of the final band.

Starting from the normal elastic multigroup transfer matrix in the form

$$T_{G' \rightarrow G} = \langle \Sigma_{\text{elastic}} \rangle_{G'} P_{G' \rightarrow G}. \quad (235)$$

Since the probability of scattering to any final group is independent of the initial- and final-group sections, we expect the transfer from any initial (group, band) to any final group to merely depend on the initial (group, band) elastic cross section and exactly the same group-to-group

transfer probability as occurs in the normal, multigroup transfer matrix,

$$T_{B'G' \rightarrow G} = \langle \Sigma_{\text{elastic}} \rangle_{B'G'} P_{G' \rightarrow G}. \quad (236)$$

This is a general result for any scattering model.

The NR model, used by the subgroup (Nikolaev and Phillipov 1963), and probability table methods (Levitt 1972), is equivalent to distributing all the neutrons scattered into group G among the bands in group G only according to the weight of each band in group G

$$T_{B'G' \rightarrow BG} = P_B \langle \Sigma_{\text{elastic}} \rangle_{B'G'} P_{G' \rightarrow G}. \quad (237)$$

Comparison of this multigroup, band-transfer matrix to the normal, multigroup transfer matrix, (235), illustrates that the former can be derived from the latter as

$$T_{B'G' \rightarrow BG} = P_B \frac{\langle \Sigma_{\text{elastic}} \rangle_{B'G'}}{\langle \Sigma_{\text{elastic}} \rangle_{G'}} T_{G' \rightarrow G}. \quad (238)$$

The multiband method extends the range of validity of this approximation by using the IR approximation (Cullen 1977). The basic IR approximation, described earlier in this chapter, is a linear combination of the NR and WR approximations. As pointed out earlier, the NR approximation is equivalent to assuming no correlation between the initial and final cross sections. Since the WR approximation assuming no slowing down due to the absorber, scattered neutrons will have a secondary energy equal to their initial energy and as such there will be an exact correlation between the initial and final cross sections. That is to say in the WR approximation elastic scatter from the absorber may change the direction of the neutron, but it will stay in the same group, that is, for a WR scattering from the absorber leads to

$$T_{B'G' \rightarrow BG} = \langle \Sigma_{\text{elastic}} \rangle_{B'G'} \delta_{B'B} \delta_{G'G}. \quad (239)$$

The IR approximation is equivalent to using the NR approximation to describe the scatter from one initial group to any other final group (use (237) and (238)). However, for the in-group scatter, the transfer matrix will be

$$T_{B'G' \rightarrow BG} = [\lambda P_B + (1 - \lambda) \delta_{B'B}] \langle \Sigma_{\text{elastic}} \rangle_{B'G'} P_{G' \rightarrow G}. \quad (240)$$

This equation states that elastic scatter happens in (group, band) $B'G'$ with cross section $\langle \Sigma_{\text{elastic}} \rangle_{B'G'}$ and of those that collide, a fraction $P_{G' \rightarrow G}$ remains within the energy range of the group G' . Of this fraction that stays in group G' , λ are randomly distributed among the bands in the group (NR approximation), according to the weight of each band P_B , and the remaining $(1 - \lambda)$ remain in the same band they were in prior to the collision (WR approximation).

The only new parameter introduced here is λ , which is slightly different from Goldstein's IR treatment, wherein each resonance has a λ associated with it. Here, we use λ in the sense of a group-averaged value. However, even these group-averaged λ are available in multigroup libraries (MacFarlane et al. 1982; Askew et al. 1966). Therefore, as in the case of multiband weights and cross sections, we can use an existing multigroup library containing

group-to-group transfer matrices in order to derive the multi (group, band) transfer matrix. Therefore, all the required multiband parameters can be derived from existing self-shielded multigroup data libraries.

7.6 Boundary Condition

As in the case of multigroup transport, the multiband method must guarantee continuity of the group-averaged angular flux across all boundaries, indeed in the absence of concentrated sources it must guarantee continuity at all points. In addition, the multiband method must exactly correlate cross sections for the same material encountered in two different spatial zones. Continuity of the group angular flux is guaranteed in the multiband method if the sum of group, band fluxes (i.e., the group flux) is the same on both sides of each boundary surface, e.g.,

$$\sum_B \Phi_{BG}(-\vec{s}, \Omega) = \sum_B \Phi_{BG}(+\vec{s}, \Omega), \quad (241)$$

where $\Phi_{BG}(-\vec{s}, \Omega)$ and $\Phi_{BG}(+\vec{s}, \Omega)$ are the (group, band) fluxes on either side of the boundary surface \vec{s} .

In Monte Carlo calculations (Plechaty and Kimlinger 1971; Cullen 2005), the fact that the cross section in each material is uncorrelated means that following a scatter, multiband parameters may be selected independently for each material in the zone, and if the neutron then transports without collision to another zone, if any new materials are encountered, multiband parameters may be selected independently for each of them. The fact that cross sections for the same material in two different zones are exactly correlated means that once a material has been encountered in any other zone, the multiband parameters selected when the material was first encountered MUST be used to describe the material in the new zone. In Monte Carlo, this is easily achieved (Plechaty and Kimlinger 1971; Cullen 2005) by keeping a list of materials encountered by the neutron between collisions, and multiband parameters are selected only once for each material; the list is re-initialized when a collision occurs.

In deterministic methods, it is possible to maintain this exact boundary condition as in Nikolaev's so-called "all the way" method (Nikolaev and Phillipov 1963) where each material is treated as having N -bands independent from other materials. However, for any realistic problem, this can lead to an enormous number of bands per group, negating the advantage of the multiband method. For example, for a problem involving 10 materials each with two bands per group, there will be $2^{10} = 1,024$ bands per group of the transport problem.

An alternative approach is to use an approximate boundary condition which works quite well for many problems. The correct condition of continuity of the group, band flux within each material zone will be used. The approximate condition is used at the boundary between zones containing different materials. At this boundary the correct condition will be continuity of the group flux and the cross sections on the two sides of the boundary will be uncorrelated.

The fact that the cross section in any two materials is uncorrelated means that the group flux crossing a material boundary should be distributed into the bands in the next region according to the probability of each band. That is, if we define the group flux for all directions $\vec{\Omega}$ oriented from the region on the $-\vec{s}$ side of the boundary to the region on the $+\vec{s}$ side of a boundary surface \vec{s} ,

$$\Phi_G(-\vec{s}, \vec{\Omega}) = \sum_B \Phi_{BG}(-\vec{s}, \vec{\Omega}) \quad (242)$$

this flux should be distributed across the boundary into the bands in the $+\vec{s}$ region according to the weight of each band in the $+\vec{s}$ region

$$\Phi_{BG}(+\vec{s}, \vec{\Omega}) = P_{BG}^+ \Phi_G(-\vec{s}, \vec{\Omega}), \quad (243)$$

where P_{BG}^+ is the weight of each band on the $+\vec{s}$ side of the boundary.


This boundary condition is approximate because it ignores the correlation that exists between the cross sections for the same material in adjacent or nearby zones. For instance, if there is U238 in zone A and the neutron transports without collision from zone A, through adjacent zone B, and into another zone C which also contains U238, this boundary condition ignores the correlation between the U238 cross sections in zones A and C. However, in many practical cases in which there is an intervening zone, if it is optically thick (over a few mean-free paths), the probability of transiting the intervening zone without collision is small and the correlation can be ignored. An example of this situation is a collection of fuel pins, each surrounded by moderator.

7.7 Example Results

7.7.1 Theoretical Cases

In order to illustrate the effect of the multiband method, let us first consider two theoretical problems: first a totally absorbing medium and next a totally scattering medium. First consider a totally absorbing planar half space with a source incident from the left, so that our flux at $x = 0$ is given by


$$\Phi(0, E, \mu) = S(E, \mu). \quad (244)$$


The exact solution to this problem is exponential attenuation independently at each energy. For our example we consider $S(E, \mu)$ to be independent of energy, incident perpendicular to the surface, and normalized to one “particle” incident per unit time and area, as shown in  Fig. 33.

$$\Phi(0, E, \mu) = S(E, \mu) = \delta(\mu - 1)$$

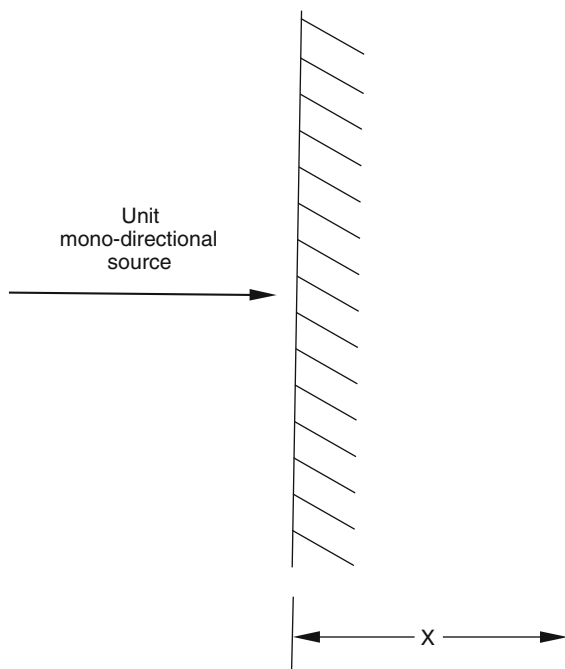
For this source the contribution of any energy to the flux at any point x depends only on the total cross section $\Sigma_T(E)$. This cross section is assumed to have a simple linear variation across the energy range of interest, with,

$$\Sigma_T(E_G) = 10; \quad \Sigma_T(E_{G+1}) = 0.1 \quad (245)$$

It should be emphasized that the group-averaged flux over this energy interval will be the same for any cross section which has the same cross section probability density as that corresponding to (245). For example, the solution for each of the total cross section variations shown in  Fig. 34 will be identical.

 Figure 35 illustrates the results of an exact calculation compared to using unshielded, totally shielded, and two-band cross sections for the flux

$$\Phi_0(x) = \int_{E_G}^{E_{G+1}} \text{Exp}[-\Sigma_T(E)x] dE. \quad (246)$$



■ Figure 33
Absorbing half-space geometry

And the absorption rate

$$R_0(x) = \int_{E_G}^{E_{G=1}} \Sigma_T(E) \text{Exp}[-\Sigma_T(E)x] dE. \quad (247)$$

From ► Fig. 35 we can see that using unshielded cross sections causes the flux to rapidly deviate from the exact solution. The solution obtained using shielded cross sections stays closer to the exact solution flux deeper into the medium, but eventually it too deviates from the exact solution. By comparison, the two-band solution approximates the exact solution quite well over the entire range of x shown in ► Fig. 35.

From ► Fig. 35 we can see one of the problems associated with using normal-group, self-shielded cross sections. At $x = 0$ by taking the ratio of (247) and (246) we can see that the exact group-averaged cross section is the unshielded average. The use of self-shielded cross sections allows the flux to penetrate further into the slab, as shown in ► Fig. 35, by reducing the cross section and therefore the reaction rate. In the case presented here, the effect of using self-shielded cross sections is to lower the absorption rate by a factor of 2 at the point of highest reaction rate, $x = 0$.

In this example we are being somewhat unfair by comparing the multiband method to using unshielded or totally shielded cross sections, since in this example the multiband method was

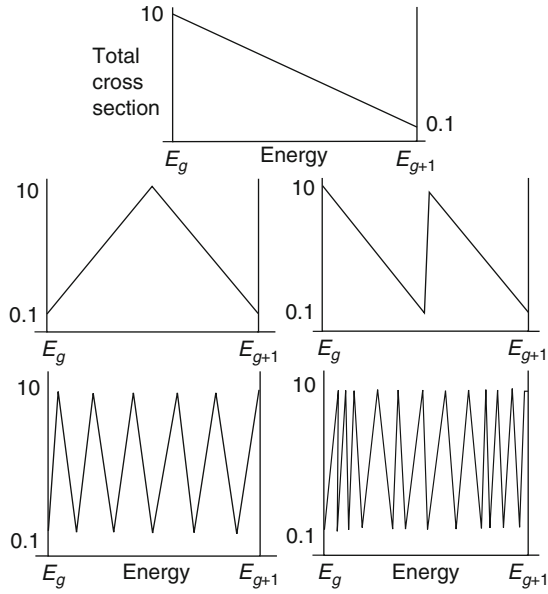


Figure 34
Cross sections that ALL yield the same answer

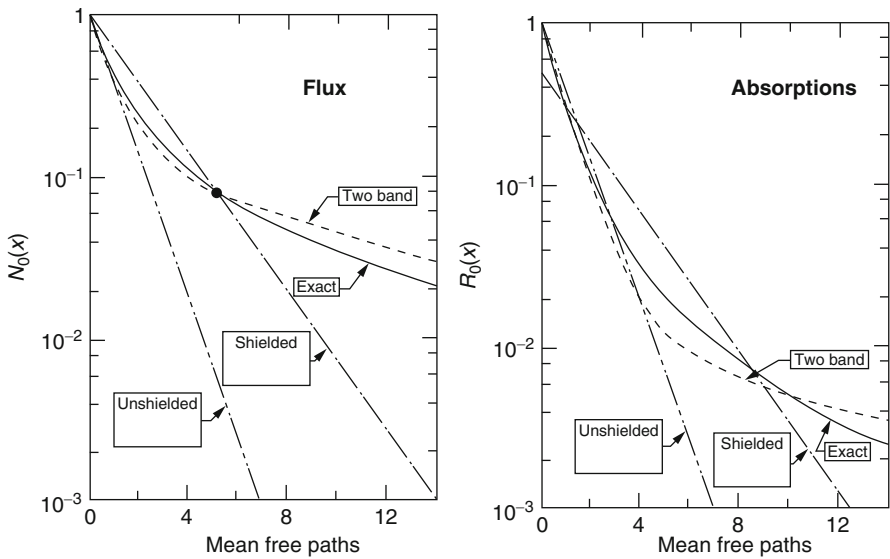
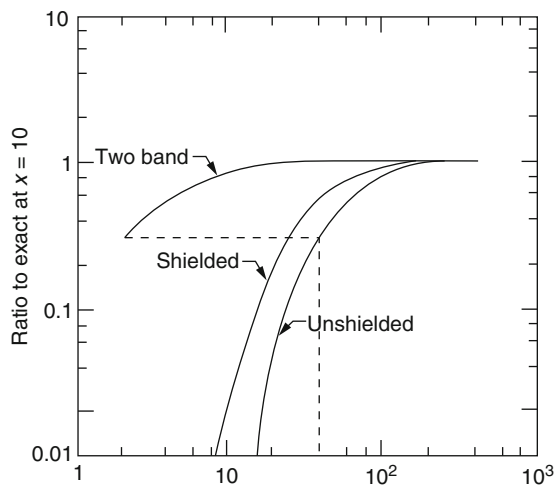


Figure 35
Scalar flux and absorptions for totally absorbing half-space

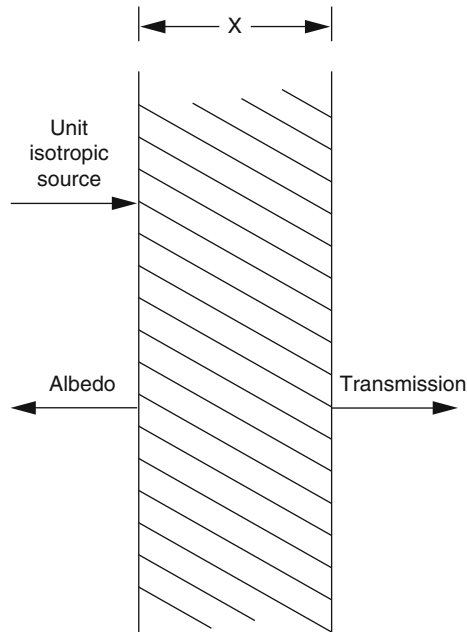
illustrated using two bands, which involved solving two equations, while using unshielded or shielded cross sections only involved solving one equation. Furthermore, none of the methods exactly reproduce the exact answer. It is reasonable to inquire as to what happens if we subdivide the energy interval E_G to E_{G+1} into successively more groups. For a fair comparison, we compare a 10-group, 2-band solution to 20-group multigroup solutions. **►** *Figure 36* illustrates the results obtained for each method by using progressively more groups. In this figure, for each method, the ratio of the approximate method to the exact solution at $x = 10$ is plotted versus the number of equations used. From **►** *Fig. 36* we can see that in order to obtain a solution using group unshielded or shielded cross sections to the same accuracy as a two-band solution, one needs an order of magnitude more equations. In particular, the dotted line in this figure shows that a two-group, two-band solution is comparable in accuracy to 25 groups with shielded cross sections or 40 groups with unshielded cross sections. This is a characteristic that the two-band solution exhibits in many applications: the two-band method can be very accurate using only a few groups.

In the opposite extreme to the case just considered, we may investigate what happens in a purely scattering medium. In this case, we consider a steady-state problem with an isotropic source incident upon a slab of isotropically scattering material of thickness X , as shown schematically in **►** *Fig. 37*. Since there is no absorption, the incident radiation will either be reflected or transmitted. **►** *Figure 38* presents results obtained for the transmission and albedo as the slab thickness is varied between 0.01 and 1,000 shielded mean-free paths. For this example the shielded total cross section is assumed to be 0.1 times the unshielded total cross section. What we expect is that for optically thin slabs the solution will be that corresponding to the use of unshielded cross sections, and for thick slabs it will be that corresponding to the use of shielded cross sections. **►** *Figure 38* clearly illustrates an important characteristic of the multiband method; it smoothly varies between the correct unshielded and shielded limiting cases.



■ *Figure 36*

Comparison of multiband and multigroup number versus equations



■ **Figure 37**
Scattering finite slab geometry

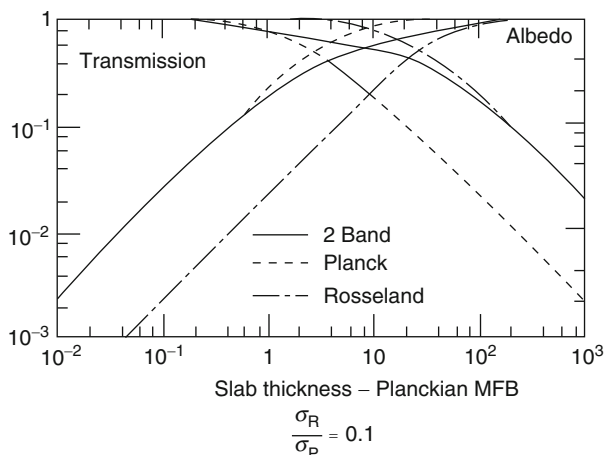
That is to say one spatially independent set of multiband parameters, in this case only two bands, may be used to reproduce geometrically dependent results, such as that occur when exactly the same material is used in small or large volumes.

The above examples illustrate some of the properties of the multiband method when applied to theoretical problems. Let us now see how well the multiband method performs when used in actual transport calculations. In the following examples only two bands per group were used. Even so the improvement over normal multigroup calculations is striking.

7.7.2 Bramblett–Czirr Plate Measurements

In the Bramblett–Czirr plate measurements (Bramblett and Czirr 1968; Czirr and Bramblett 1967), the fission rate was measured in fission chambers behind the plates of various thicknesses of U235 or Pu239, because of a $1/E$ spectrum incident on the plate. Because of a combination of geometry and timing, this measurement is equivalent to measuring the fission rate due to the uncollided flux.

Because of the many maxima and minima in the U235 and Pu239 cross sections (Howerton et al. 1978; Garber and Brewster 1975), this measurement has always been difficult to reproduce in a transport calculation without an extremely detailed representation of energy dependence of the cross section. In particular, multigroup calculations, even with a very large number of groups, fail to reproduce the measured results.



■ **Figure 38**
Scattering slab results

When one uses a given transport method to simulate this experiment, uncertainties in the results are introduced due to both uncertainties in the evaluated data (Howerton et al. 1975), as well as the uncertainty introduced due to the transport model used. In order to determine the uncertainty introduced by the transport model, we compare (Cullen 1978a,b),

1. An analytical calculation of the fission rate due to the uncollided (i.e., exponentially attenuated) flux using the energy-dependent ENDL cross sections (Howerton et al. 1975).
2. A 175-group, two-band calculation (Plechaty and Kimlinger 1971; Cullen 2005).
3. A 175-group calculation (Plechaty and Kimlinger 1971; Cullen 2005).
4. A 2020-group calculation (Plechaty and Kimlinger 1971; Cullen 2005).

The result of this calculation (Cullen 1978a,b) clearly illustrates that the two-band calculation accurately reproduces the analytical calculation. The 175-group calculation, on the other hand, differs from the analytical results in some energy ranges by over 40%. The 2020-group calculation is a definite improvement compared to the 175-group calculation, but it is not as accurate as the two-band, 175-group calculation. These results indicate that if the multiband method is used to analyze these measurements, any differences between the calculated results and the measurement will be only due to the uncertainties in the evaluated data and the experiment itself. Therefore, the multiband calculated results may be used to validate evaluated data. The multi-group approach, however, introduces significant calculational errors, which make its results difficult to rely on.

7.7.3 Criticality Calculations

Results have been reported (Lewis and Soran 1978), comparing the critical radius of a sphere of uranium hydride (UH₃) as a function of enrichment in U235, using four different transport

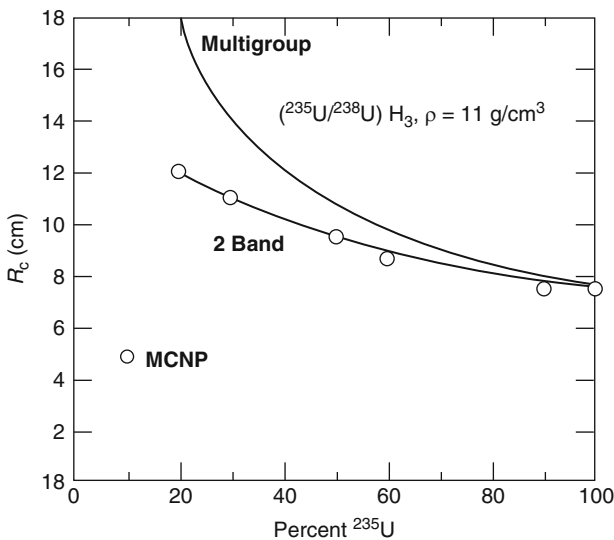
models. All four models used continuous energy Monte Carlo to describe the neutrons and they differ only in the treatment of the cross sections. The four models were

1. Continuous energy-dependent cross sections: MCNP (Cashwell et al. 1972; X-5 Monte Carlo Team 2003).
2. Two band, 175-group cross sections: TART (Plechaty and Kimlinger 1971; Cullen 2005).
3. 175-group cross sections: TART (Plechaty and Kimlinger 1971; Cullen 2005).
4. 2020-group cross sections: TART (Plechaty and Kimlinger 1971; Cullen 2005).

► *Figure 39* presents the results obtained for the first three of these models. The results illustrate that the multiband method results agree with the continuous energy cross section results over the entire range of U235 enrichment. By contrast, the 175-group results significantly overpredict the critical radius of the sphere. The 2020-group results are an improvement compared to the 175-group results, but they do not agree with the continuous energy cross section results as the multiband results do.

Similar results have been obtained for homogenous mixtures of enriched uranium and water (Lewis and Soran 1978), as a function of the hydrogen to uranium atom fraction. ► *Table 9* presents the results obtained using three methods: (1) 2 band, 175 group, (2) 175 groups, and (3) 2020 groups. The reactivity (K-eff) results indicate that, as in the previous problem, the 175 group calculation underpredicts the reactivity. Using 2020 groups improves results, but even 2020 groups are insufficient to represent the NRs in U238.

► *Table 9* also presents the median energy of neutrons that induce fission as calculated by each of the three methods; this helps to explain the differences that we see in reactivity. Since the uranium cross sections have a more resonant structure, whereas the hydrogen cross sections



■ **Figure 39**
Critical radius of sphere of uranium hydride versus enrichment

■ **Table 9**

Reactivity (K-eff) and median fission energy for uranium/water sphere

Method	Hydrogen/ ²³⁸ U ratio		
	3/1	10/1	30/1
Calculated reactivity ^a			
175 groups	0.901	0.859	0.866
2020 groups	0.950	0.978	0.993
175 groups, 2 bands	0.957	0.989	0.996
Calculated median energy of neutrons inducing fission, eV			
175 groups	12,600	113.2	0.364
2020 groups	7,700	56.6	0.244
175 groups, 2 bands	7,250	54.3	0.244

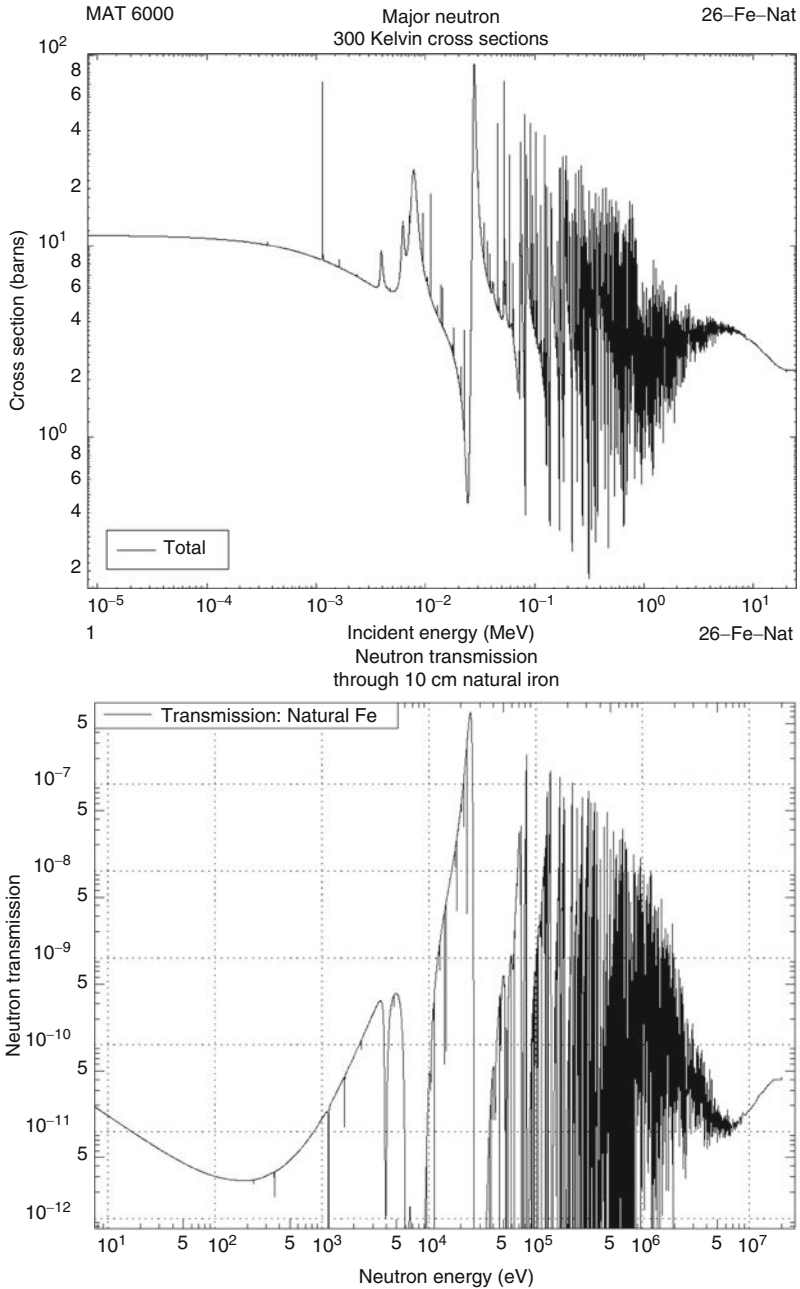
^aAll reactivity values are ± 0.003 .

are relatively smooth, self-shielding will reduce the effective, group-averaged cross sections, but not the hydrogen cross section. The net effect is to make the hydrogen more effective in slowing down neutrons, thereby shifting the neutron spectrum to lower energies where the fission cross section is higher, resulting in an increase in reactivity.

The preceding two problems illustrate the importance of self-shielding in the eV to low keV neutron energy range, i.e., the resonance region. Self-shielding is also important at higher energies, up into the MeV energy range. We illustrate this by considering the reactivity of a fast nickel reflected critical assembly, where experimentally K-eff = 1.0. TART-175 group calculations (Plechaty and Kimlinger 1971; Cullen 2005) have always overpredicted the reactivity of this type of system; for a typical system the TART calculated K-eff = 1.018. A multiband calculation (Cullen 1978a,b) of the same system yields a lower and more acceptable answer of K-eff = 1.004. This decrease may be understood by examining the nickel cross sections. Nickel has a resonance structure well into the MeV energy range. Self-shielding of these resonances lowers the effective nickel cross section and increases the depth that neutrons will penetrate into the nickel reflector, which thereby reduces the reflectivity of the nickel reflector back into the core. The net effect is a decrease in the reactivity of the system.

7.7.4 Shielding Calculations

As an illustration of a shielding problem a number of computer codes were used to calculate the uncollided transmission through an iron slab 30.4 cm (1 foot) thick due to an incident spectrum of neutrons from $1/E$ sources, 10 eV to 20 MeV. ➤ *Figure 40* illustrates the natural iron total cross sections. ➤ *Figure 40* illustrates the uncollided flux transmitted through the first 10m cm of iron. The many minima and maxima in the transmission indicate how difficult it would be to calculate this experiment using the multigroup method. ➤ *Table 10* compares the results obtained using various computational models. The analytical solution is simply the



■ Figure 40

(a) Energy-dependent total cross section for natural Fe. (b) Energy spectrum of uncollided flux transmitted through 10 cm of iron

■ **Table 10**

Uncollided transmission of neutrons through 30.4 cm (1 foot) of iron

Method	Transmission (%)	Ratio to analytic
Analytic	0.486	1.0
MCNP	0.478	1.02
TART, 2 bands, 175 groups	0.463	1.05
TART, 175 groups	0.065	7.48
TART, 2020 groups	0.430	1.13

uncollided, exponentially attenuated flux at each energy, and is obtained using all the details of the energy-dependent cross section. The MCNP Monte Carlo code (Cashwell et al. 1972; X-5 Monte Carlo Team 2003) is in excellent agreement with the analytical solution, as is the multi-band solution (2 band, 175 groups) (Plechaty and Kimlinger 1971; Cullen 2005). By contrast, the 175-group solution is a factor of 7 lower than the analytical solution. Even when we increase the number of groups to 2020 the agreement is still not as good as with the 2-band, 175-group method.

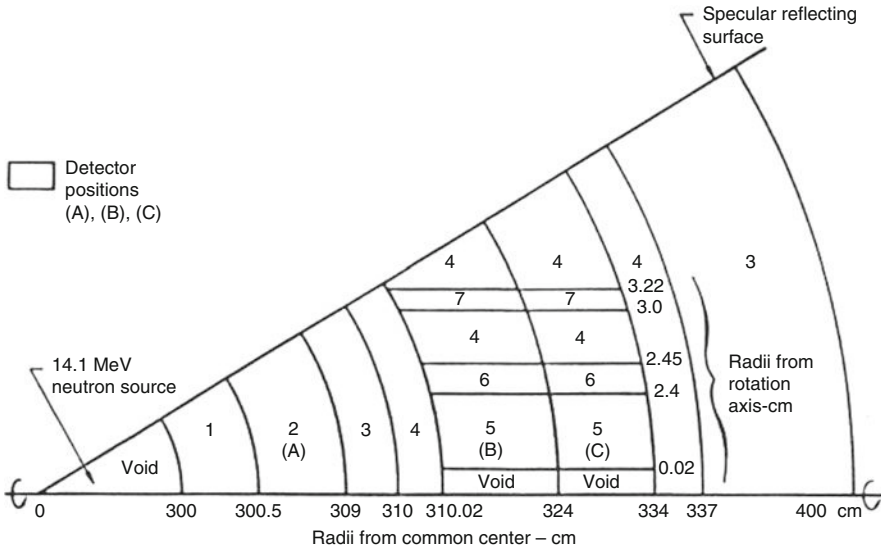
7.7.5 Fusion Reactor Blanket

➤ *Figure 41* illustrates a geometrically complicated fusion reactor blanket. The multiband and multigroup methods were used to calculate the fission rate observed at three fission detector positions, per 14.12 MeV source neutron, at the center of the assembly. For detectors located successively further from the source the multigroup results deviate more from the multiband results, up to a difference of 43% at the detector position labeled C in ➤ *Fig. 41*.

In this case the self-shielding has two important effects: it increases both the neutron's penetration depth and the moderation due to the light materials. The net result is more fission at greater distances from the source, than that predicted by the multigroup method.

7.8 Conclusions

Comparison of the calculational results obtained using a variety of cross section treatments (i.e., continuous energy, multiband, and multigroup) and a variety of problems indicate that the multiband results agree well with the results obtained using continuous energy cross sections. In particular, it should be noted that the multiband results were in better agreement with the continuous energy results, than were the results obtained using over an order of



■ **Figure 41**
Geometrically complex fusion source system

magnitude more energy groups (i.e., 2 band, 175 groups, versus 2020 groups). All these results were obtained using a simple two-band per-group calculation and spatially independent, unshielded multiband parameters. Further improvements in the multiband method are easy to achieve using more bands per group (Cullen 1980a–c). However, agreement with the Bondarenko self-shielding model (Bondarenko et al. 1964) can be obtained usually with two or three and in no case more than four bands per group (🔗 [Table 8](#)).

Acknowledgments

The author thanks Robert E. MacFarlane (LANL) for the cooperation he has shared for decades in comparing nuclear data processing (NJOY versus PREPRO) and use of nuclear data in applications (MCNP versus TART). The author thanks Andrej Trkov (Jozef Stefan Institute, Ljubljana, Slovenia), S. Ganesan (BARC, India), and Ivan Sirakov (Geel, Belgium), who have significantly contributed to improving the PREPRO nuclear data processing codes. The author also thanks Ernest F. Plechaty, the original author of TART, who retired many years ago, but who has nonetheless unselfishly continued to contribute ideas and constructive criticism of TART and its use. Last, but certainly not the least, the author thanks Prof. Herbert Goldstein (Columbia University), who taught him everything he knows about this subject.

References

- Abramowitz M, Stegun IA (1965) Handbook of mathematical functions with formulas, graphs, and mathematical tables. U.S. National Bureau of Standards, Washington
- Alder B et al (1963) Methods in computational physics. Academic, New York
- Askew JR et al (1966). J Br Nucl Energy Soc 5:504
- Bondarenko II et al (1964) Group constants for nuclear reactor calculations. Consultants Bureau, New York
- Breit G, Wigner EP (1936) Phys Rev 49:519
- Bremblett RL, Czirr JB (1969) Nucl Sci Eng 35:350
- Bucholz JA (1980) Nucl Sci Eng 74:163
- Cashwell ED, Everett CJ (1959) A practical manual on the Monte Carlo method for random walk problems. Pergamon Press, New York
- Cashwell ED et al (1972) MCNP: a neutron Monte Carlo code. LA-4751, Los Alamos Scientific Laboratory, Los Alamos
- Cullen DE (1973) Nucl Sci Eng 52:498, and exact Doppler broadening of tabulated cross sections. Nucl Sci Eng 60:199 (1975)
- Cullen DE (1974) Application of the probability table method to multi-group calculations. Nucl Sci Eng 56:387–400
- Cullen DE (1976) Nucl Sci Eng 60:199
- Cullen DE (1977a) Calculation of probability table parameters to include intermediate resonance self-shielding, UCRL-79762. Lawrence Livermore National Laboratory
- Cullen DE (1977b) Calculation of probability table parameters to include intermediate resonance self-shielding Lawrence Livermore Laboratory Report UCRL-79761, San Francisco, December 1977
- Cullen DE (1978a) Multiband calculations of neutron and photo transport, UCRL-52000-78-10, vol 25. Lawrence Livermore National Laboratory, Livermore
- Cullen DE (1978b) Multi-band parameters and Bondarenko self-shielded cross sections derived from the ENDL library. Lawrence Livermore Laboratory Report UCRL-50400, vol 20, 1978
- Cullen DE (1979a) DOWNER (version 79–1): group collapse cross sections and transfer matrices, UCRL-50400, vol 127, part F. Lawrence Livermore National Laboratory
- Cullen DE (1979b) Program SIGMA1 (version 79–1): Doppler broaden evaluated cross sections in the evaluated nuclear data file/version B (ENDF/B) format, UCRL-50400, vol 17, part B. Lawrence Livermore National Laboratory, Livermore
- Cullen DE (1979c) Program SIGMAL (version 79–1): Doppler broaden evaluated cross sections in the Livermore evaluated nuclear data library (ENDL) format, UCRL-50400, vol 21, part C. Lawrence Livermore National Laboratory, Livermore
- Cullen DE (1980a) Program LINEAR (Version 79–1): linearize data in the evaluated nuclear data file/version B (ENDF/B) format, vol 17, part A. UCRL-50400, Lawrence Livermore National Laboratory, Livermore
- Cullen DE (1980b) Program RECENT (version 79–1): reconstruction of energy dependent neutron cross sections from resonance parameters in the ENDF/B format, UCRL-50400, vol 17, part C. Lawrence Livermore National Laboratory, Livermore
- Cullen DE (1980c) Program, GROUPIE (version 79–1): Calculation of Bondarenko self-shielded cross sections and multiband parameters from data in the ENDF/B format, UCRL-50400, vol 17, part D. Lawrence Livermore National Laboratory, Livermore
- Cullen DE (1986) Nuclear cross section processing. In: Ronen Y (ed) Handbook of nuclear reactor calculation, vol I. CRC Press, Inc., Boca Raton
- Cullen DE (1995) A simple model of photon transport. Lawrence Livermore National Laboratory, UCRL-JC-118254, Rev. 1, Sept. 1994; Nucl. Instrum Meth: Phys Res B 101: 499–510
- Cullen DE (2005), TART 2005: A coupled neutron-photon 3-D, time dependent, combinatorial geometry Monte Carlo transport code. Lawrence Livermore National Laboratory, UCRL-SM-218009, November 22, 2005
- Cullen DE (2007a) POINT 2007: A temperature dependent ENDF/B-VII.0 data cross section library. Lawrence Livermore National Laboratory, UCRL-TR-228089, online at <http://www-nds.iaea.org/point2007>
- Cullen DE (2007b) PREPRO 2007: 2007 ENDF/B pre-processing codes, IAEA-NDS-39, Rev. 13, Nuclear data section. International Atomic Energy Agency, Vienna, Austria
- Cullen DE (2007c) Application of the probability table method of multi-group calculations, BNL-17000, and BNL-50387 (ENDF-187), Brookhaven, New York
- Cullen DE, Pomraning JRJ (1980) Quant Spectrosc Radiat Transf 24–97

- Cullen DE et al (1975) Tabular cross section generation and utilization techniques. In: Proc. nuclear cross sections and technology conference, National Bureau of Standards, Washington
- Cullen DE et al (1976) Major neutron induced interactions: graphical experimental data, UCRL-50400, vol 7, parts A and B, and supplemental neutron induced interactions: graphical experimental data, UCRL-50400, vol 8, parts A and B. Lawrence Livermore National Laboratory, Livermore
- Cullen DE et al (1978) Cross section probability tables in multigroup transport calculations. In: Proc. radiation shielding information center (RSIC) seminar-workshop, Oak Ridge National Laboratory, Oak Ridge
- Cullen DE, Howerton RJ, Plechaty EF (1980) Nucl Sci Eng 74:140
- Cullen DE et al (1982a) The international reactor dosimetry file (PRDF-82), IAEA-NDS-41 and 48. International Atomic Energy Agency, Vienna
- Cullen DE et al (1982b) Verification of nuclear cross section processing codes, INDC(NDC)-134. International Atomic Energy Agency, Vienna
- Cullen DE et al (1985) Report on the IAEA cross section processing code verification project, IAEA, Vienna, INDC(NDS)-170, May 1985
- Cullen DE et al (1988) The accuracy of processed nuclear data. Nucl Sci Eng 99:172-181
- Cullen DE et al (1991a) Tables and graphs of atomic subshell and relaxation data derived from the LLNL evaluated atomic data library (EADL), $Z = 1-100$, UCRL-50400, vol 30, Lawrence Livermore National Laboratory, October 1991
- Cullen DE et al (1991b) Tables and graphs of electron interaction cross 10 eV to 100 GeV derived from the LLNL evaluated electron data library (EEDL), $Z = 1-100$, Lawrence Livermore National Laboratory, UCRL-50400, vol 31, November 1991
- Cullen DE et al (1997) EPDL97: The evaluated photon data library, '97 version, Lawrence Livermore National Laboratory, UCRL-50400, vol 6, Rev. 5, September 1997
- Cullen DE et al (2006) How accurately can we calculate neutrons slowing down in water? Lawrence Livermore National Laboratory, UCRL-TR-220605, April 1, 2006
- Cullen DE et al (2007a) Criticality calculations using LANL and LLNL neutron transport codes. Lawrence Livermore National Laboratory, UCRL-TR-237333, November 2007
- Cullen DE et al (2007b) ENDF/B-VI.0 data testing for three fast critical assemblies. Lawrence Livermore National Laboratory, UCRL-TR-233310, June 2007
- Czurr JB, Bramblett RL (1967) Nucl Sci Eng 28:62
- Doyas RJ et al (1971) CLYDE: A code for the production of calculational constants for nuclear data, UCRL-50400, vol 5. Lawrence Livermore National Laboratory
- Emmett MB (1975) The MORSE Monte Carlo radiation transport system. ORNL-4972, Oak Ridge National Laboratory, Oak Ridge, see also Fraley SK (1976) User's guide to MORSE-SOC. ORNL-CSD-7, Oak Ridge National Laboratory, Oak Ridge
- Engle WW Jr (1967) A User's manual for ANISN: A one dimensional discrete ordinate transport code with anisotropic scattering. K-1693, Computing Technology Center, Union Carbide Corporation, Oak Ridge
- Fowler TB et al (1971) Nuclear reactor core analysis code citation. ORNL-TM-2496, Rev. 2, Oak Ridge National Laboratory, Oak Ridge
- Friedman B (1961) Principles and techniques of applied mathematics, vol 293. Wiley, New York
- Ganesan S (1982) Private communication
- Ganesan S et al (1981) Development of a new fast reactor processing code RHAMBA at RRC, Workshop on nuclear data evaluation, processing and testing, Kalpakkam, India, INDC(IND)-30, International Atomic Energy Agency, Vienna
- Garber DI, Brewster C (1975) ENDF/B cross sections. BNL-17100 (ENDF-200), 2nd edn. Brookhaven National Laboratory, Upton
- Garber DI, Kinsey RR (1967) Neutron cross sections, vol 2, curves, 3rd edn. BNL-325, Brookhaven National Laboratory, Upton
- Glasstone S, Edlund MC (1962) The elements of nuclear reactor theory. Van Nostrand, Princeton
- Goel B, Krieg B (1975) Status of the nuclear data library KEDAK-3, KFK-2234. Kernforschungszentrum, Karlsruhe
- Goldstein R (1972) Nucl Sci Eng 48:248
- Goldstein R (1975) Trans Am Nucl Soc 21:493
- Goldstein R, Cohen ER (1962) Nucl Sci Eng 13:132
- Graves-Morris PR (ed) (1973) Pade approximants and their applications. Academic, New York
- Green DM, Pitterle TA (1968) ETOE: A program for ENDF/B to MC2 data conversion. APDA-219 (ENDF-120), Atomic Power Development Associates, Inc
- Greene NM (1973) Trans Am Nucl Soc 17:549
- Greene NM et al (1976) AMPX: a modular code system for generating coupled multigroup neutron-gamma libraries from ENDF/B. ORNL-TM-3706, Oak Ridge National Laboratory, Oak Ridge
- Gregson K, James MF (1965) TEMPO - a general Doppler broadening program for neutron cross

- sections. AEEW-M518, Atomic Energy Establishment, Winfrith, England, UK; the TEMPO results presented here were obtained using Equations 1 through 6 of AEEW-M518; James MF (1975) Private communications, has pointed out that the limits of integration used in the TEMPO code are correctly programmed to be $(-\infty, +\infty)$
- Gyulassy M et al (1972) Analysis of resolved neutron resonance parameters, m UCRL-50400, vol 12. Lawrence Livermore National Laboratory
- Hardie RW, Little WW (1969) IDX: A one dimensional diffusion code for generating effective nuclear cross sections. BNWL-954, Hanford, Wash
- Hong KJ, Shultz JK (1982) Nucl Sci Eng 80:570
- Howerton RJ et al (1975) Evaluation techniques and documentation of specific evaluations of the LLL evaluated nuclear data library (ENDL). UCRL-50400, vol 15. Lawrence Livermore National Laboratory, Livermore
- Howerton RJ et al (1978) The LLL evaluated nuclear data library (ENDL): graphs of cross sections from the library. UCRL-50400, vol 15, part B, rev. 1. Lawrence Livermore National Laboratory, Livermore
- Hutchins BA et al (1973) ENDRUN-II: A computer code to generate a generalized multigroup data file from ENDF/B, GEAP-13704 (ENDF-145). General Electric Company, Sunnyvale
- Igarasi S et al (1969) Japanese evaluated nuclear data library, version 1, JENDL-1, JAERI-1261, INDC(JAP)-45. Japanese Atomic Energy Research Institute, Tokai-Mura, Japan
- Jeans J (1948) An introduction to the kinetic theory of gases, 1st edn. Cambridge University Press, London
- Joanou GD et al (1961) GAM-I: a consistent P1 multigroup code of the calculation of the fast neutron spectrum and multigroup constants. GA-1950, General Atomic, La Jolla
- Kinsey R (1970) Data formats and procedures for the evaluated nuclear data file. ENDF, BNL-NCS-50496, ENDF-102, 2nd edn. Brookhaven National Laboratory, Upton
- Kolesave VE, Nikolaev MN (1977) Sokrator manual: Format of the recommended nuclear data library for reactor calculations. INDC(CCP)-97, International Atomic Energy Agency, Vienna
- Konshin VA (1981) Application of the nuclear theory to the computation of neutron cross sections for actinide isotopes. In: Nuclear theory for applications, IAEA-SMR-68/I, International Atomic Energy Agency, Vienna
- Lamb WE (1939) Phys Rev 55:130
- Lathrop KD (1965) DTF-IV: a FORTRAN program for solving the multigroup transport equation with anisotropic scattering. LA-3373, Los Alamos Scientific Laboratory, Los Alamos, NM
- Lathrop KD, Brinkley FW (1970) Theory and use of the general geometry TWOTRAN program. LA-4432, Los Alamos Scientific Laboratory, Los Alamos
- Levitt LB (1972) Nucl Sci Eng 49:450
- Lewis FH, Soran PD (1978) Nucl Sci Eng 68:116
- Lichtenstein H et al (1979) The SAM-CE Monte Carlo system for radiation transport and criticality calculations in complex configurations (revision 7.0). EPRL-CCM-8, Electric Power Research Institute, Palo Alto
- MacFarlane RE, Boicourt RM (1975) Trans Am Nucl Soc 33:720
- MacFarlane RE, Muir DW (1994) The NJOY nuclear data processing system, version 91. Los Alamos National Laboratory Report LA-12740-M, October 1994 is still the latest official manual
- MacFarlane RE et al (1982) The NJOY nuclear data processing system, LA-9303-M (ENDF-324). Los Alamos National Laboratory, Los Alamos, NM
- Meghreblian RV, Holmes DK (1960) Reactor analysis, vol 137. McGraw-Hill, New York
- Mughabghab SF, Divadeenam M, Holden NE (1981) Neutron cross sections, vol I, Neutron resonance parameters and thermal cross sections. Academic, New York
- Mynatt FR et al (1973) The DOT-III two dimensional discrete ordinate transport code. ORNL-TM-4280, Oak Ridge National Laboratory, Oak Ridge
- Nikoleav MN, Phillipov VV (1963) Atom Energy 15:493
- Oblozinsky P et al (2006) ENDF/B-VII.0: next generation evaluated nuclear data library for nuclear science and technology, Nuclear data sheets, vol 107, pp 2931-3060
- Otter JM et al (1972) U3R - a code to calculate unresolved resonance cross section probability tables. AI-AEC-13024, Atomics International, San Diego
- Ozer O (1973) RESEND: a program to preprocess ENDF/B materials with resonance parameters into a pointwise form. BNL-17134, Brookhaven National Laboratory, Upton
- Panini G.C (1973) FOURACES - a programme for producing group averaged cross sections from different files, TR/FI(73)16. Comitato Nazionale Energia Nucleare, Bologna
- Patrick BH (1982) Private communication.
- Perez RB et al (1981) Trans Am Nucl Soc 39:883
- Perkins ST (1982) Nucl Sci Eng 80; Perkins ST, Giles PC Nucl Sci Eng 80:579

- Plechaty EF (1977) Monte Carlo criticality calculations of hydrogen moderated uranium systems using the probability table method and multigroup cross section representations, UCID-17455. Lawrence Livermore National Laboratory
- Plechaty EF, Kimlinger JR (1971) TART Monte Carlo transport code. UCIR-522, Lawrence Livermore National Laboratory, Livermore
- Plechaty EF, Kimlinger JR (in press) ALICE multiband Monte Carlo neutron transport code. Lawrence Livermore National Laboratory, Livermore
- Plechaty EF et al (1978a) Tables and graphs of photon interaction cross sections from 0.1keV to 100 MeV, derived the LLL evaluated nuclear data library. UCRL-50400, vol 6, rev. 2. Lawrence Livermore National Laboratory, Livermore
- Plechaty EF et al (1978b) Tabular and graphical presentation of 175 neutron group constants derived from the LLL evaluated neutron data library (ENDL), UCRL-50400, vol 16. Lawrence Livermore National Laboratory, Livermore
- Pope AL (1973) Current edition of the main tape NDL-1 of the UK nuclear data library. AEEW-1208. UK Atomic Energy Establishment, Winfrith
- Pope AL et al (in press) User's guide for SIGAR7: A FORTRAN programme for calculating resonance cross sections with Doppler broadening, UK. Atomic Energy Establishment, Winfrith
- Ray EA et al (2005) PARTISN: a time-dependent, parallel neutral particle transport code system. Los Alamos National Laboratory, LA-UR-05-3925, May 2005
- Rieffe HC et al (1981) ENTOSAN: a program for the calculation of fine group cross section values for ENDF/B data. Netherlands Energy Research Foundation, Petten
- Rose PF, Dunford CL (eds) (1990) ENDF-102: data formats and procedures for the evaluated nuclear data file, ENDF-6. Brookhaven National Laboratory Report, BNL-NCS-44945
- Seamon RE (1981) Private Communication, Los Alamos Scientific Laboratory, Los Alamos
- Shakespeare W (1982) Private communication
- Stewart JCJ (1964) Quant. Spectrosc Radiat Transf 4 :723
- Toppel B.J (1971) The new multigroup cross section code MC2-II. In: Proc. Conf. new developments of reactor mathematics and applications, CONF-710302, Idaho Falls, Idaho; see also Henryson H II et al (1976) MC2-II: a code to calculate fast neutron spectra and multigroup cross sections, ANL-8144 (ENDF-239). Argonne National Laboratory, Argonne
- Vertes P (1981) FEDGROUP-3: A program system for processing evaluated nuclear data in ENDF/B, KEDAK or UKNDL formats to constants to be used in reactor physics calculations, KFK2-1981-34, Central Research Institute for Physics, Budapest
- Weinberg AM, Wigner EP (1958) The physical theory of neutron chain reactors, University of Chicago Press, Chicago
- Weisbin CR, LaBaue RJ (1973) Specifications of Generally useful multigroup structure for neutron transport. LA-5277MS, Los Alamos Scientific Laboratory, Los Alamos
- Weisbin CR et al (1974) Nucl Sci Eng 55:329
- Weisbin CR et al (1976) MINX: A multigroup interpretation of nuclear X-sections, from ENDF/B, LA-6486-MS (ENDF-237). Los Alamos National Laboratory, Los Alamos
- Westfall RM (1978) Theory and validation of ROLAIDS: AMPX module for treating resonance shielding in multigroup geometries. Oak Ridge National Laboratory, Oak Ridge
- Wigner EP, Wilkins JE Jr (1944) Effect of the temperature of the moderator on the velocity distribution of neutrons with numerical calculation for H as the moderator, AECD-2275. Clinton Laboratory (now Oak Ridge National Laboratory), Oak Ridge
- X-5 Monte Carlo Team (2003) MCNP - a general Monte Carlo N-particle transport code, version 5, vol I: Overview and theory. Los Alamos National Laboratory Report LA-UR-03-1987, April 24, 2003
- Zijp WL et al (1981) Comparison of two fine group cross section libraries resulting from the ENDF/B-VI dosimetry library, ECN-97. Netherlands Energy Research Foundation, Petten



5 General Principles of Neutron Transport

Anil K. Prinja¹ · Edward W. Larsen²

¹Chemical and Nuclear Engineering Department,
University of New Mexico, Albuquerque, NM, USA
prinja@unm.edu

²Department of Nuclear Engineering and Radiological
Sciences, University of Michigan, Ann Arbor, MI, USA
edlarsen@umich.edu

1	<i>Introduction</i>	430
2	<i>Derivation of the Neutron Transport (Linear Boltzmann) Equation</i>	431
2.1	Independent Variables	432
2.2	The Basic Physics of Neutron Transport	434
2.3	The Angular Neutron Density and Angular Flux	440
2.4	Internal and Boundary Sources	444
2.5	The Time-Dependent Equations of Neutron Transport	445
2.6	Time-Dependent Neutron Transport Without Delayed Neutrons	450
2.7	The Steady-State Neutron Transport Equation	451
2.8	<i>k</i> -Eigenvalue Problems	452
2.9	The Monoenergetic Neutron Transport Equation	452
2.10	Mathematical Issues	454
2.10.1	Existence, Uniqueness, and Nonnegativity of Transport Solutions	455
2.10.2	The <i>n</i> th Collided Fluxes	456
2.10.3	Smoothness of the Angular Flux	457
2.11	Generalizations of the Neutron Transport Equation	460
2.11.1	Reflecting Boundaries	460
2.11.2	Periodic Boundaries	461
2.11.3	Anisotropic Sources	461
2.11.4	Coupled Neutron/Photon Transport	461
2.11.5	Temperature-Dependent Cross Sections	462
2.11.6	Advection and Diffusion of Fission Products	462
2.12	Limitations of the Neutron Transport Equation	462
2.13	Discussion	464
3	<i>The Transport Equation in Special Geometries</i>	464
3.1	3-D Cartesian Geometry	465
3.2	1-D Planar Geometry	467
3.3	2-D (X,Y)-Geometry	469
3.4	1-D Spherical Geometry	471

3.5	3-D (r, ϑ, z) -Geometry	473
3.6	2-D (r, z) -Geometry	477
3.7	1-D Cylindrical Geometry	477
3.8	Discussion	478
4	<i>Integral Equation for Neutron Transport</i>	479
4.1	Integral Equation for the Angular Flux	479
4.2	The Integral Equation for the Scalar Flux	484
4.3	Discussion	485
5	<i>The Adjoint Neutron Transport Equation</i>	485
5.1	Definitions	486
5.2	Illustrative Example	487
5.3	The Adjoint Transport Equation	490
5.4	Adjoint Flux as an Importance Function	494
5.4.1	Source-Detector Problems	495
5.5	Green's Functions	497
5.6	Discussion	499
6	<i>The Multigroup and One-Speed Neutron Transport Equations</i>	500
6.1	The Continuous-Energy Problem	500
6.2	The Multigroup Transport Equations	500
6.3	The Within-Group and One-Group Transport Equations	505
6.4	Discussion	506
7	<i>The Age and Wigner Approximations</i>	507
7.1	The Infinite-Medium Neutron Spectrum Equation	507
7.2	The "Conservative" Form of the Neutron Transport Equation	509
7.3	The Age Approximation	512
7.4	The Wigner Approximation	513
7.5	Discussion	517
8	<i>The Diffusion Approximation</i>	518
8.1	Derivation of the Diffusion Equation	518
8.2	Homogenized Diffusion Theory	522
8.3	Spherical Harmonic (P_N) and Simplified Spherical Harmonic (SP_N) Approximations	523
8.4	Discussion	523
9	<i>The Point Kinetics Approximation</i>	524
9.1	Preliminaries	524
9.2	The Scaled Transport and Neutron Precursor Equations	526
9.3	Asymptotic Derivation of the Point Kinetics Equations	527
9.4	Discussion	531
10	<i>Computational Neutron Transport</i>	532
10.1	Monte Carlo Methods	533
10.2	Deterministic Methods	534

10.3	Hybrid Monte Carlo/Deterministic Methods	538
10.4	Discussion	540
II	<i>Concluding Remarks</i>	540
	<i>References</i>	540

Abstract: This chapter describes the basic theory underlying the neutron transport equation and the principal approximations used in this equation's applications to reactor physics. In addition to presenting detailed classical derivations of various forms of the transport equation, we discuss several important topics in a more rigorous manner than is found in typical derivations. For instance, we include (i) a discussion of the lack of smoothness of the angular flux in multi-dimensional geometries (this has a negative impact on numerical simulations); (ii) derivations of the transport equation in specialized 1-D, 2-D, and 3-D geometries; (iii) a derivation of the time-dependent integral transport equation; (iv) an asymptotic derivation of the point kinetic equation; and (v) an asymptotic derivation of the multigroup P_1 and diffusion equations. The basic approach taken by the authors in this chapter is theoretical, in the hope that this will complement more intuitive presentations of related topics found in other chapters of this handbook.

1 Introduction

A central problem in the design and analysis of nuclear reactors is the accurate and detailed prediction of the space, angle, energy, and time-dependence of neutron and photon distributions in all components of the reactor. Neutrons are responsible for propagating the chain reaction and releasing energy through fission, but neutrons and photons, through fission, capture, scattering, and excitation/ionization interactions, also induce a thermal-mechanical response in the reactor core and, moreover, cause degradation of structural components, fuel rods, and the control system, through radiation damage, depletion, and fission product poison buildup. These consequences, in turn, affect the distribution of the radiation field itself through several feedback mechanisms. A synergistic description of all nuclear and nonnuclear processes is therefore essential for the economic development and safe operation of nuclear power plants, and driving much of this challenge is the need to have an appropriate mathematical and computational framework for adequately characterizing the neutron and photon distributions.

The transport of neutral radiation, including but not restricted to neutrons and photons, through matter is extremely well described by the transport equation, a linear version of Boltzmann's celebrated equation originally developed within the framework of the kinetic theory of gases (for this reason, the transport equation is sometimes also referred to as the linear Boltzmann equation). This equation is an integrodifferential equation having (generally) seven independent variables, whose solution is not smooth, and which can only be solved exactly for the simplest of problems. Essentially, all neutron transport problems of practical interest must be solved either approximately or numerically.

In this chapter, we present the basic theory underlying the neutron transport equation, and we describe some of this equation's principal approximations. In [▶ Sect. 2](#), we derive the transport equation and discuss some of its general properties. In [▶ Sect. 3](#), we discuss problems with special spatial symmetries, which enable the transport equation to be formulated using fewer independent variables; these formulations are at the heart of all practical 1-D and 2-D computer simulations of neutron transport. In [▶ Sect. 4](#), we discuss the integral form of the transport equation, which, under certain conditions, is advantageous for computer simulations. In [▶ Sect. 5](#), we describe the adjoint transport equation and some of its applications. [▶ Sect. 6](#) describes the standard multigroup approximation to the energy variable, along with the one-speed transport equation. [▶ Sect. 7](#) develops the Age and Wigner approximations, which enable certain neutron slowing-down problems to be solved analytically. [▶ Sect. 8](#) is

devoted to the diffusion approximation, the most important approximate form of the transport equation for nuclear reactor core problems. ➤ Sect. 9 describes the point kinetics approximation, which is used for time-dependent simulations of nuclear reactors. ➤ Sect. 10 provides a brief discussion of numerical methods for simulating neutron and photon transport problems, and we close ➤ Chap. 5 with some concluding remarks in ➤ Sect. 11.

We have consciously adopted a somewhat theoretical approach to this chapter of the handbook, but we have strived for an exposition that presents advanced material in a pedagogical manner that will hopefully appeal both to the novice and to the expert in the field of neutron transport. We include detailed, self-contained presentations of classical material, such as the derivation of the forward and adjoint integrodifferential equations and the forward integral equation, but also, in several of the sections in this chapter, we present material that is either not commonly found in standard texts, or represents a different and more rigorous theoretical approach than standard approaches to the topics under discussion. For instance, ➤ Sect. 2 includes a discussion of the (lack of) smoothness of the angular flux in multidimensional problems; this negatively affects the accuracy of numerical solutions of multidimensional transport problems. Also, ➤ Sect. 3 on the different forms of the Boltzmann equation for 1-D, 2-D, and 3-D geometries is exceptionally important in practice, but this material is not found in standard texts. ➤ Sect. 9 presents a new asymptotic derivation of the point kinetics equation; formerly, this equation has been derived by ad hoc, or at best by variational approaches. Also, ➤ Sect. 7 derives the standard Age and Wigner approximations without introducing the lethargy variable, and ➤ Sect. 8 on the diffusion approximation attempts to put some rigor into the standard P_1 approximation that leads to the multigroup form of this approximation.

Overall, we have attempted to cover significant material in a way that makes use of theoretical approaches that have been developed in recent years, but that has not found its way yet into standard texts. We hope that this will make the chapter more interesting, and that it will provide a more fundamental approach to basic material that may be presented more intuitively in other chapters of this handbook.

2 Derivation of the Neutron Transport (Linear Boltzmann) Equation

Neutron transport is the process in which neutrons propagate through the atoms in a physical system. This includes the *streaming* of neutrons from one collision site (an atomic nucleus) to the next, the *scattering* of neutrons off nuclei, the *capture* of neutrons by nuclei, and the initiation by neutrons of *fission events*, in which a nucleus splits and two or more neutrons are emitted. In this chapter, we develop the mathematical equations that describe the neutron transport process. We begin by defining the necessary independent variables. Then we (i) outline the relevant physics, (ii) define the relevant unknowns (angular flux, precursor densities – for problems with delayed neutrons), and (iii) derive the appropriate mathematical equations for these unknowns. (Our derivation is patterned closely on previous derivations in classic texts [Bell and Glasstone 1970; Case and Zweifel 1967; Henry 1975; Weinberg and Wigner 1958].) Finally, we discuss conditions under which the transport equation is valid and some properties of its solution.

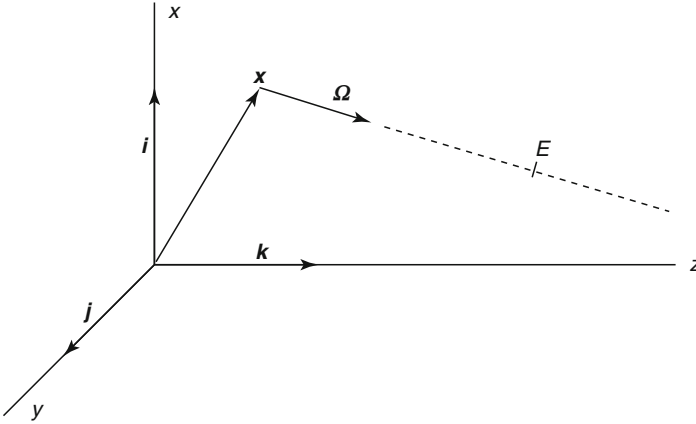


Figure 1

The spatial (x), direction-of-flight or angular (Ω), and energy (E) variables

2.1 Independent Variables

To characterize a general 3-D neutron transport process, *seven* independent variables are required: three components of the position vector \mathbf{x} , two angles to specify the unit vector Ω denoting the direction of flight, the kinetic energy E , and time t . These variables enable one to specify the population of neutrons (i) at an arbitrary point \mathbf{x} in the system, (ii) traveling in an arbitrary direction of flight Ω , (iii) with any energy E , and (iv) at any time t (Fig. 1).

In steady-state problems, the time variable is extraneous, and in problems with spatial symmetries (discussed in Sect. 3), fewer spatial and/or angular variables are required.

To derive the 3-D transport equation, it is convenient to use the familiar Cartesian coordinates, defined in the usual manner by:

$$\mathbf{x} = x\mathbf{i} + y\mathbf{j} + z\mathbf{k}, \quad (1)$$

where \mathbf{i} , \mathbf{j} , and \mathbf{k} are mutually orthogonal unit vectors.

The direction-of-flight vector Ω , a unit vector ($|\Omega| = 1$), is specified using a *polar angle* θ , defined relative to the z -axis, and an *azimuthal angle* ω , defined relative to the x -axis (Fig. 2). In terms of the *direction cosines* projected onto the three Cartesian axes, we have:

$$\Omega = \Omega_x\mathbf{i} + \Omega_y\mathbf{j} + \Omega_z\mathbf{k}, \quad (2a)$$

where:

$$\Omega_x = l_3 = \sqrt{1 - \mu^2} \cos \omega, \quad (2b)$$

$$\Omega_y = l_4 = \sqrt{1 - \mu^2} \sin \omega, \quad (2c)$$

$$\Omega_z = l_1 = \mu. \quad (2d)$$

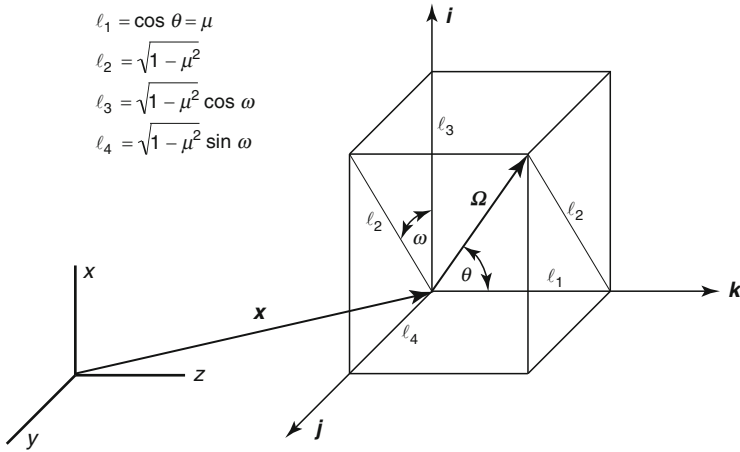


Figure 2
The polar angle θ and azimuthal angle ω

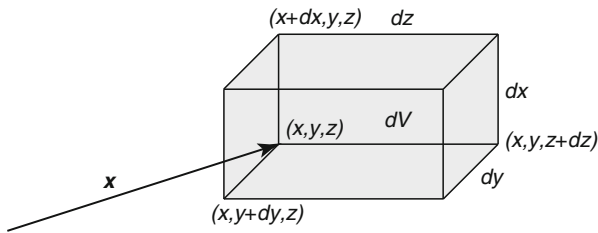


Figure 3
Incremental volume dV

If we independently displace the spatial variables x , y , and z by incremental (very small) amounts dx , dy , and dz , the spatial variable \mathbf{x} will sweep out an incremental hexahedral volume $dV = dx dy dz$ about \mathbf{x} (see \blacktriangleright Fig. 3).

Similarly, if we independently displace the angular variables μ and ω by incremental amounts $d\mu$ and $d\omega$, then the unit vector Ω will sweep out an incremental, rectangular, dimensionless *element of area* or *solid angle* $d\Omega = ds dl$ on the unit sphere (see \blacktriangleright Fig. 4).

\blacktriangleright Figure 4 shows that $ds = d\omega \sqrt{1 - \mu^2}$, and \blacktriangleright Fig. 5, drawn in the plane generated by Ω and \mathbf{k} , shows that $dl = d\mu / \sqrt{1 - \mu^2}$. Thus, $d\Omega$ is given by:

$$d\Omega = ds dl = \left(d\omega \sqrt{1 - \mu^2} \right) \left(\frac{d\mu}{\sqrt{1 - \mu^2}} \right) = d\mu d\omega. \tag{3}$$

For example, the surface area of the entire unit sphere is then:

$$\text{Area} = \int_{4\pi} d\Omega = \int_0^{2\pi} \int_{-1}^1 d\mu d\omega = 4\pi,$$

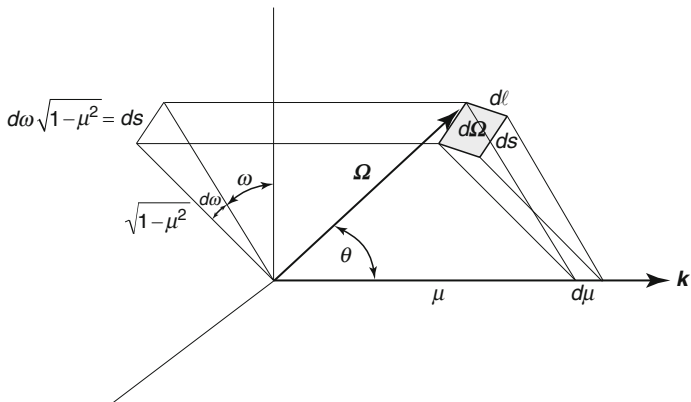


Figure 4
Solid angle $d\Omega$

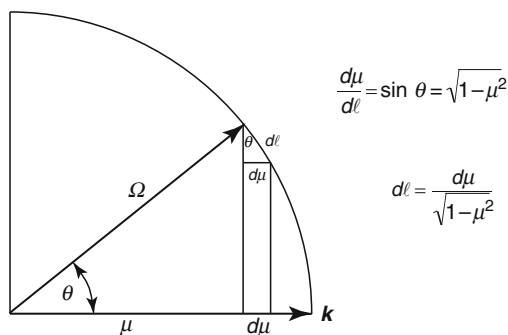


Figure 5
Relationship between $d\mu$ and $d\ell$

where integration over the unit sphere is denoted by:

$$\int_{4\pi} f(\Omega) d\Omega = \int_0^{2\pi} \int_{-1}^1 f(\Omega) d\mu d\omega = \int_0^{2\pi} \int_{-1}^1 f(\mu, \omega) d\mu d\omega.$$

2.2 The Basic Physics of Neutron Transport

Let us consider a neutron, streaming with direction Ω and energy E inside a material with known physical properties. As the neutron travels an incremental distance ds , there is an incremental probability dp that the neutron will interact with a nucleus. To determine the

relationship between dp and ds , let us consider the neutron to be normally incident, at an arbitrary point, on a target of area A and incremental thickness ds (see [Fig. 6](#)).

We assume that the *microscopic cross-sectional area of a target nucleus* $\sigma(E)$ (cm^2) and the *number density of target nuclei* N (cm^{-3}) are known. The *neutron's-eye-view* of the target is depicted in [Fig. 7](#).

If the target is sufficiently thin that one target nucleus does not shield another, then the probability of a collision is:

$$\begin{aligned} dp &= \frac{\text{total area of nuclei}}{\text{area of target}} \\ &= \frac{n\sigma}{A}, \end{aligned} \quad (4)$$

where $n = NdV = N(Ads)$ = the number of nuclei in the target. [Equation \(4\)](#) gives:

$$dp = \frac{N(Ads)\sigma}{A} = (N\sigma)ds.$$

Therefore, dp is proportional to ds :

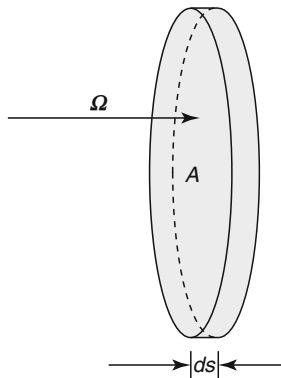


Figure 6
Incrementally thin neutron target

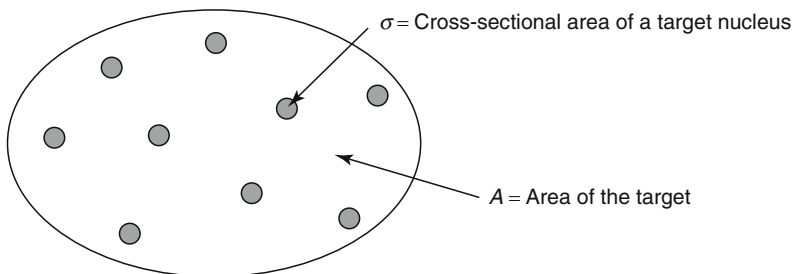


Figure 7
Neutron's-eye-view of the target

$$dp = \Sigma_t(E) ds, \quad (5a)$$

where the “constant” of proportionality is:

$$\Sigma_t(E) = N\sigma(E) = \text{total macroscopic cross section} \quad (\text{cm}^{-1}). \quad (5b)$$

When a neutron collides with a nucleus, it is captured with probability $p_\gamma(E)$, scatters with probability $p_s(E)$, or initiates a fission event with probability $p_f(E)$. (We ignore other possible, but generally rare, events such as (n, α) , (n, p) , and $(n, 2n)$.) Then:

$$p_\gamma(E) + p_s(E) + p_f(E) = 1. \quad (6)$$

With $r = (\gamma, s, f)$, the probabilities also define the *macroscopic cross sections* $\Sigma_r(E)$, such that:

$$\Sigma_r(E) ds = \Sigma_t(E) ds p_r(E) \quad (7)$$

is the probability that a neutron with energy E , while traveling a distance ds , will experience a collision of type r . The total macroscopic cross section then satisfies:

$$\Sigma_t(E) = \Sigma_\gamma(E) + \Sigma_s(E) + \Sigma_f(E). \quad (8)$$

If the neutron is captured, it is considered to be removed from the system. If the neutron (with direction Ω and energy E) scatters, it emerges from the scattering event with a new direction Ω' and energy E' . We assume that the distribution of post-collision directions Ω' and energies E' is known and can be expressed as:

$$p(\Omega \cdot \Omega', E \rightarrow E') d\Omega' dE' = \text{probability that the scattered neutron} \\ \text{has direction in } d\Omega' \text{ about } \Omega' \text{ and} \\ \text{energy in } dE' \text{ about } E'. \quad (9)$$

In writing p as $p(\Omega \cdot \Omega', E \rightarrow E')$, we indicate that scattering in media with randomly distributed scattering centers (nuclei) is *rotationally invariant*. That is, the probability that a neutron will scatter from direction Ω to direction Ω' depends only on the *scattering angle* θ_0 between Ω and Ω' (or, on the cosine of this angle, $\mu_0 = \cos \theta_0 = \Omega \cdot \Omega'$). Thus, all scattered directions of flight Ω' on the cone of equal scattering angle are equally probable (► Fig. 8).

The distribution function for elastic s -wave neutron scattering, which is isotropic in the center-of-mass frame, can be shown from kinematics (Duderstadt and Hamilton 1976) to be given by:

$$p(\Omega \cdot \Omega', E \rightarrow E') = p_0(E \rightarrow E') \frac{\delta[\Omega \cdot \Omega' - \mu_0(E \rightarrow E')]}{2\pi}. \quad (10a)$$

Here, $p_0(E \rightarrow E')$ is a histogram distribution function for outgoing energies E' :

$$p_0(E \rightarrow E') = \begin{cases} \frac{1}{(1-\alpha)E} & \text{if } \alpha E < E' < E, \\ 0 & \text{otherwise,} \end{cases} \quad (10b)$$

where:

$$\alpha = \left(\frac{A-1}{A+1} \right)^2, \tag{10c}$$

and A is the nucleus-to-neutron mass ratio ($A \geq 1$). Also, δ is the familiar delta-function, and $\mu_0(E \rightarrow E')$ is the scattering cosine for a neutron, initially with energy E , that elastically scatters into energy E' :

$$\mu_0(E \rightarrow E') = \left(\frac{A+1}{2} \right) \sqrt{\frac{E'}{E}} - \left(\frac{A-1}{2} \right) \sqrt{\frac{E}{E'}}. \tag{10d}$$

Thus, the outgoing neutron energy E' is random and *uniformly distributed* between αE and E . Once E' is known, the scattering cosine $\mu_s(E \rightarrow E')$ is uniquely specified by (10d), but the scattering azimuthal angle ω' is random and uniformly distributed on $0 \leq \omega' < 2\pi$. As depicted in **Fig. 9**, the minimum neutron energy loss is associated with the minimal change in direction of the neutron (“forward” scattering, $\mu_s = +1$), while the maximum neutron energy loss is associated with the maximum change in direction of the neutron (“backward” scattering, $\mu_s = -1$).

We now define the *macroscopic differential scattering cross section* as:

$$\Sigma_s(\Omega \cdot \Omega', E \rightarrow E') = \Sigma_s(E) p(\Omega \cdot \Omega', E \rightarrow E'), \tag{11}$$

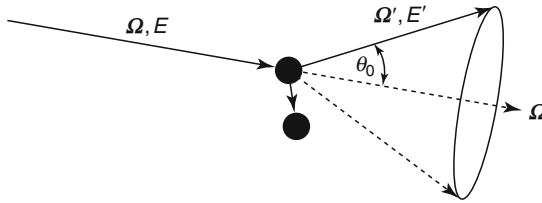


Figure 8
Scattering angle θ_0

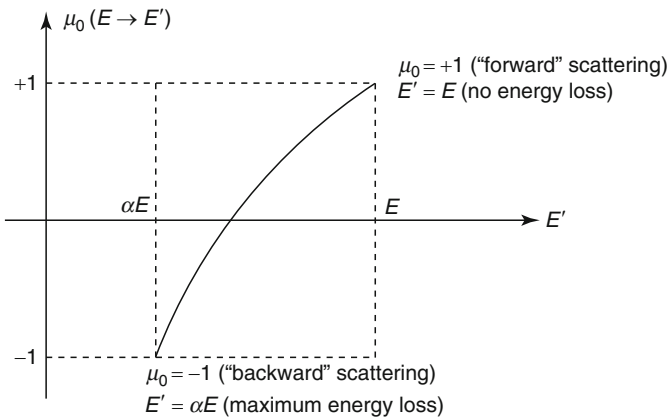


Figure 9
Scattering cosine as a function of the outgoing energy E'

which has dimension $\text{cm}^{-1} \text{MeV}^{-1}$. Then:

$$\Sigma_s(\mathbf{\Omega} \cdot \mathbf{\Omega}', E \rightarrow E') ds d\Omega' dE' = \text{probability that a neutron, with direction } \mathbf{\Omega} \text{ and energy } E \text{ and traveling a distance } ds, \text{ will scatter into } d\Omega' \text{ about } \mathbf{\Omega}' \text{ and } dE' \text{ about } E'. \quad (12)$$

Equations (9)–11 imply:

$$\int_0^\infty \int_{4\pi} p(\mathbf{\Omega} \cdot \mathbf{\Omega}', E \rightarrow E') d\Omega' dE' = 1, \quad (13a)$$

$$\int_0^\infty \int_{4\pi} \Sigma_s(\mathbf{\Omega} \cdot \mathbf{\Omega}', E \rightarrow E') d\Omega' dE' = \Sigma_s(E). \quad (13b)$$

If a neutron with energy E initiates a fission event, the target nucleus splits into two smaller *daughter nuclei*, and on the average, $\nu(E)$ neutrons are released. Of this number, $\nu(E)[1 - \beta(E)]$ are *prompt* (emitted within 10^{-15} s of the fission event) and $\nu(E)\beta(E)$ are *delayed* (emitted roughly 0.1–60 s after the fission event). Thus, the *delayed neutron fraction* $\beta(E)$ is the probability that a fission neutron, created by a neutron with energy E , is delayed ($\beta \approx 0.01$). Delayed fission neutrons are created from the radioactive decay of unstable daughter nuclei, which can be produced during fission events.

Prompt fission neutrons are born at the location of the fission event, their initial direction of flight is *isotropic* (uniformly distributed on the unit sphere), and their initial energy is consistent with the *prompt fission spectrum* $\chi_p(E')$, defined by:

$$\chi_p(E') dE' = \text{the probability that a prompt fission neutron has energy in } dE' \text{ about } E'. \quad (14a)$$

This definition implies:

$$\int_0^\infty \chi_p(E) dE = 1. \quad (14b)$$

The unstable daughter nuclei are often grouped into six *precursor groups*, each with its own *radioactive decay constant* λ_j , *delayed fraction* $\beta_j(E)$, and *delayed neutron fission spectrum* $\chi_j(E)$, where $1 \leq j \leq 6$. The functions $\beta_j(E)$ satisfy:

$$\sum_{j=1}^6 \beta_j(E) = \beta(E). \quad (15)$$

To conclude this discussion, we introduce the notion of the neutron *mean free path*. Let us consider a large number (N_0) of neutrons, all emitted in the same direction of flight, with the same energy E , and from the same spatial point within a large homogeneous region. Each neutron travels along the same flight path within the system and eventually undergoes a collision with a nucleus. Let $N(s, E)$ be the number of neutrons that penetrate to depth s without experiencing a collision. Clearly, $N(s, E)$ is a decreasing function of s , starting with the initial value

$N(0, E) = N_0$. For $s > 0$ and an incremental distance $ds > 0$, the number of neutron–nucleus collisions between s and $s + ds$ is given by:

$$\begin{aligned} N(s, E) - N(s + ds, E) &\approx N(s, E) - \left(N(s, E) + ds \frac{\partial N}{\partial s}(s, E) \right) \\ &= - ds \frac{\partial N}{\partial s}(s, E). \end{aligned} \quad (16)$$

Dividing by $N(s, E)$ and noting that the left side becomes the probability that a neutron will have a collision while traveling a distance ds , we have from (5a):

$$\frac{1}{N(s, E)} \left(- \frac{\partial N}{\partial s}(s, E) ds \right) = \Sigma_t(E) ds.$$

This relationship can be rearranged to yield the differential equation:

$$\frac{\partial N}{\partial s}(s, E) + \Sigma_t(E)N(s, E) = 0, \quad N(0, E) = N_0,$$

which has the solution:

$$N(s, E) = N_0 e^{-\Sigma_t(E)s}. \quad (17)$$

Next, defining $P(s, E)ds$ as the probability that an uncollided neutron will collide with a nucleus between s and $s + ds$, we have:

$$\begin{aligned} P(s, E)ds &= \frac{\text{the number of collisions between } s \text{ and } s + ds}{\text{the initial number of neutrons (at } s = 0)} \\ &= \frac{1}{N_0} \left(- \frac{\partial N}{\partial s}(s, E) ds \right) \quad (\text{by [16]}) \\ &= \Sigma_t(E) e^{-\Sigma_t(E)s} ds \quad (\text{by [17]}). \end{aligned}$$

Thus,

$$P(s, E) = \Sigma_t(E) e^{-\Sigma_t(E)s}. \quad (18a)$$

We note that P satisfies the normalization $\int_0^\infty P(s, E)ds = \int_0^\infty \Sigma_t(E) e^{-\Sigma_t(E)s} ds = 1$, which simply states that in an infinite medium, a neutron must collide somewhere.

The probability density $P(s, E)$ can be used to obtain the mean distance-to-collision, or the *mean free path*:

$$\lambda(E) = \int_0^\infty s P(s, E) ds = \frac{1}{\Sigma_t(E)}. \quad (18b)$$

Thus, the mean free path of a neutron with energy E is equal to the inverse of the macroscopic total cross section at that energy.

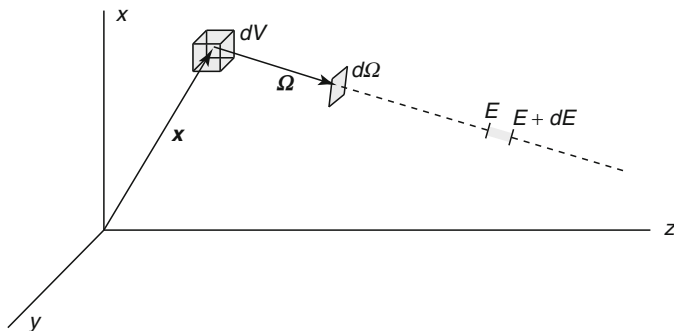


Figure 10
 dV about \mathbf{x} , $d\Omega$ about Ω , and dE about E

2.3 The Angular Neutron Density and Angular Flux

We now define the physical quantities needed to describe the neutron population. We consider all neutrons that, at time t , (i) are geometrically located in a volume increment dV about a point \mathbf{x} , (ii) travel within a solid angle $d\Omega$ about the direction Ω , and (iii) have energies between E and $E + dE$ (see Fig. 10). The *angular neutron density* $N(\mathbf{x}, \Omega, E, t)$, a function of (generally) seven independent variables, is defined by:

$$N(\mathbf{x}, \Omega, E, t) dV d\Omega dE = \text{the number of neutrons in } dV d\Omega dE \\ \text{about } (\mathbf{x}, \Omega, E) \text{ at time } t. \quad (19)$$

This definition implies that the value of N is independent of the increments dV , $d\Omega$, and dE . Also, N is a *phase space density*; it has the dimensions $\text{cm}^{-3} \text{MeV}^{-1}$.

Knowledge of $N(\mathbf{x}, \Omega, E, t)$ enables one to calculate the number of neutrons that exist in any “volume” of 6-D phase space (\mathbf{x}, Ω, E) at any time t . For example, for any $E_1 < E_2$ and any subregion R of the physical system V , we have:

$$\int_{E_1}^{E_2} \int_{4\pi} \int_R N(\mathbf{x}, \Omega, E, t) dV d\Omega dE = n(t) = \text{the number of neutrons in } R, \\ \text{with energies between } E_1 \text{ and } E_2, \text{ at time } t.$$

Next, let us consider a planar surface area element dS , located at any point \mathbf{x} in V , with a unit normal vector \mathbf{n} (Fig. 11). We consider neutrons located near \mathbf{x} , traveling in directions in $d\Omega$ about Ω , with energies in dE about E , at time t . What is the *rate* (number per second) at which these neutrons flow through dS at time t ?

In the plane generated by Ω and \mathbf{n} , and with $v =$ neutron speed $= \sqrt{2E/m}$, we consider a volume dV obtained by sweeping dS a distance $ds = vdt$ along the direction of flight Ω (Fig. 12):

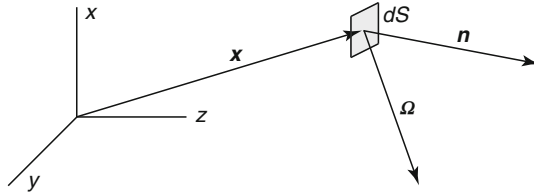


Figure 11
Neutron flow through dS

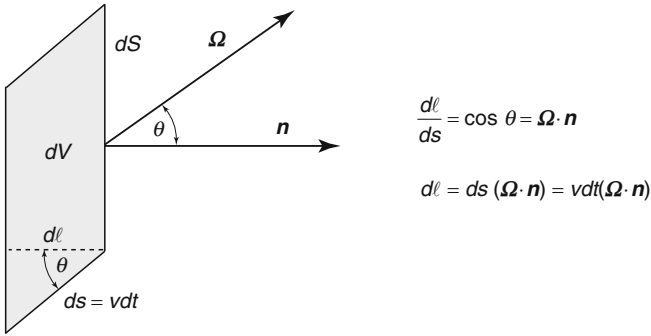


Figure 12
Volume increment dV

In time increment dt , neutrons travel the distance $ds = vdt$. Thus, in time dt , among all neutrons traveling in $d\Omega$ about Ω and dE about E , only those physically located in the incremental volume dV will flow through dS .

The volume of dV is:

$$dV = (dS)(d\ell) = dS(vdt)(\Omega \cdot \mathbf{n}).$$

Thus, the number of neutrons located within $dVd\Omega dE$ about (\mathbf{x}, Ω, E) is:

$$NdVd\Omega dE = NdS(vdt)(\Omega \cdot \mathbf{n})d\Omega dE = [(\Omega \cdot \mathbf{n})vN]dSd\Omega dE dt,$$

and this is the number of neutrons traveling in $d\Omega dE$ about (Ω, E) that pass through dS during time dt about t . Dividing by dt , we obtain:

$$(\Omega \cdot \mathbf{n})vN(\mathbf{x}, \Omega, E, t)dSd\Omega dE = \text{the rate (number per second) at which neutrons, traveling in } d\Omega dE \text{ about } (\Omega, E), \text{ flow through } dS \text{ at time } t. \tag{20}$$

Each incremental surface dS has two normal vectors, \mathbf{n} and $-\mathbf{n}$. The choice of \mathbf{n} determines “positive” and “negative” directions of flow through dS . A positive (negative) rate indicates flow through dS in the hemisphere of directions $\Omega \cdot \mathbf{n} > 0$ ($\Omega \cdot \mathbf{n} < 0$). (see Fig. 13).

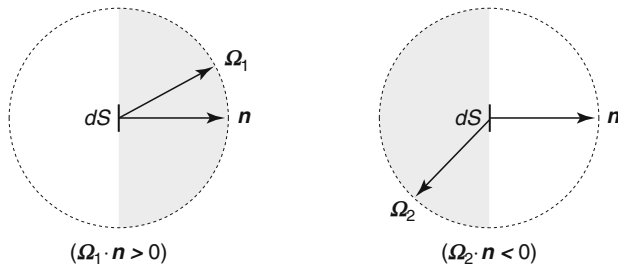


Figure 13

“Positive” and “negative” directions of neutron flow through dS

The *angular flux* (or *fluence rate*) $\psi(\mathbf{x}, \boldsymbol{\Omega}, E, t)$ is defined by:

$$\psi(\mathbf{x}, \boldsymbol{\Omega}, E, t) = vN(\mathbf{x}, \boldsymbol{\Omega}, E, t), \quad (21)$$

where $v = \sqrt{2E/m}$ is the neutron speed. The dimensions of ψ are $\text{cm}^{-2} \text{MeV}^{-1} \text{s}^{-1}$. A physical interpretation for ψ is obtained by considering neutrons in $dVd\boldsymbol{\Omega}dE$ about $(\mathbf{x}, \boldsymbol{\Omega}, E)$ at time t . During a time increment dt about t ,

$$\begin{aligned} \psi dVd\boldsymbol{\Omega}dEdt &= v(NdVd\boldsymbol{\Omega}dE)dt \\ &= (vdt)(NdVd\boldsymbol{\Omega}dE) \\ &= [\text{distance (path length) traveled by one neutron in time } dt] \\ &\quad \times [\text{number of neutrons in } dVd\boldsymbol{\Omega}dE \text{ about } (\mathbf{x}, \boldsymbol{\Omega}, E)] \\ &= \text{total path length traveled by neutrons, in } dVd\boldsymbol{\Omega}dE \\ &\quad \text{about } (\mathbf{x}, \boldsymbol{\Omega}, E), \text{ during time increment } dt \text{ about } t. \end{aligned}$$

Dividing by dt , we obtain the following *volume-based interpretation* for ψ :

$$\psi(\mathbf{x}, \boldsymbol{\Omega}, E, t)dVd\boldsymbol{\Omega}dE = \text{rate at which path length is generated by neutrons in } dVd\boldsymbol{\Omega}dE \text{ about } (\mathbf{x}, \boldsymbol{\Omega}, E) \text{ at time } t. \quad (22)$$

(Hence, ψ is sometimes called the *path length density*.) Also, (20) implies the following *surface-based interpretation* for ψ :

$$|\boldsymbol{\Omega} \cdot \mathbf{n}|\psi(\mathbf{x}, \boldsymbol{\Omega}, E, t)dSd\boldsymbol{\Omega}dE = \text{the absolute rate at which neutrons, traveling in } d\boldsymbol{\Omega}dE \text{ about } (\boldsymbol{\Omega}, E), \text{ flow through } dS \text{ at time } t. \quad (23)$$

If the surface increment dS is perpendicular to the direction of neutron travel (i.e., if $\mathbf{n} = \boldsymbol{\Omega}$) (Fig. 14), then (23) reduces to:

$$\psi(\mathbf{x}, \boldsymbol{\Omega}, E, t)dSd\boldsymbol{\Omega}dE = \text{the absolute rate at which neutrons, traveling in } d\boldsymbol{\Omega}dE \text{ about } (\boldsymbol{\Omega}, E), \text{ flow through a surface increment } dS \text{ perpendicular to } \boldsymbol{\Omega} \text{ at time } t. \quad (24)$$

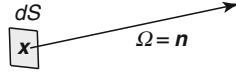


Figure 14

Neutron flow through dS in the direction $\Omega = n$

Equation (22) defines ψ in terms of a volume element dV , while (23) and (24) define ψ in terms of a surface element dS . Both interpretations are useful.

For example, if R is a subregion of V and \mathbf{n} is the unit outer normal vector on ∂R , then (23) implies:

$$\begin{aligned} J_R^+(t) &\equiv \int_0^\infty \int_{\partial R} \int_{\Omega \cdot \mathbf{n} > 0} \Omega \cdot \mathbf{n} \psi(\mathbf{x}, \Omega, E, t) d\Omega dS dE \\ &= \text{the rate at which neutrons flow (leak) out of } R \text{ at time } t, \end{aligned} \quad (25a)$$

$$\begin{aligned} J_R^-(t) &\equiv \int_0^\infty \int_{\partial R} \int_{\Omega \cdot \mathbf{n} < 0} |\Omega \cdot \mathbf{n}| \psi(\mathbf{x}, \Omega, E, t) d\Omega dS dE \\ &= \text{the rate at which neutrons flow into } R \text{ at time } t. \end{aligned} \quad (25b)$$

Therefore,

$$\begin{aligned} J_R(t) &\equiv J_R^+(t) - J_R^-(t) \\ &= \int_0^\infty \int_{\partial R} \int_{4\pi} (\Omega \cdot \mathbf{n}) \psi(\mathbf{x}, \Omega, E, t) d\Omega dS dE \\ &= \text{the net rate at which neutrons flow (leak) out of } R \text{ at time } t. \end{aligned} \quad (26)$$

Using the *divergence theorem*,

$$\int_{\partial R} \mathbf{n} f(\mathbf{x}) dS = \int_R \nabla f(\mathbf{x}) dV, \quad (27)$$

we obtain from (26) the equivalent result:

$$\begin{aligned} J_R(t) &= J_R^+(t) - J_R^-(t) \\ &= \int_0^\infty \int_R \int_{4\pi} (\Omega \cdot \nabla) \psi(\mathbf{x}, \Omega, E, t) d\Omega dV dE \\ &= \text{the net rate at which neutrons flow (leak) out of } R \text{ at time } t. \end{aligned} \quad (28)$$

Thus, the “surface” definition (23) of ψ can be used to determine the rates at which neutrons flow across surfaces. (Equations (25) also hold for surfaces that are not closed, i.e., that do not enclose a volume.)

The “volume” definition (22) of ψ is useful because the number of collisions with nuclei that neutrons experience in an incremental time interval is proportional to the incremental distance that the neutrons travel during that time interval. Thus, *the rate at which neutrons interact with nuclei in a volume is proportional to the rate at which the neutrons generate path length in the volume*. The constants of proportionality are the macroscopic cross sections.

In addition to the neutron angular flux $\psi(\mathbf{x}, \boldsymbol{\Omega}, E, t)$, the *precursor densities* $C_j(\mathbf{x}, t)$ for the six delayed neutron precursor groups are also required. For $1 \leq j \leq 6$ and for an incremental volume dV about \mathbf{x} , these are defined by:

$$C_j(\mathbf{x}, t)dV = \begin{array}{l} \text{the number of group-}j \text{ precursor nuclei} \\ \text{in } dV \text{ about } \mathbf{x} \text{ at time } t. \end{array} \quad (29)$$

Each precursor nucleus will eventually decay and emit one delayed neutron. Thus, the rate at which group- j precursor nuclei experience radioactive decay equals the rate at which delayed neutrons are emitted by these nuclei.

2.4 Internal and Boundary Sources

In addition to the physical data described above, neutron sources must be prescribed. These exist in two categories: *internal sources* and *boundary sources*.

An internal neutron source $Q(\mathbf{x}, E, t)$, generally produced by radioactive decay, is located inside the physical system V and is usually *isotropic* (in radioactive decay, neutrons are emitted in all directions $\boldsymbol{\Omega}$ with equal probability). Q is defined by:

$$\frac{Q(\mathbf{x}, E, t)}{4\pi}dVd\boldsymbol{\Omega}dE = \begin{array}{l} \text{the incremental rate at which neutrons} \\ \text{are produced in } dVd\boldsymbol{\Omega}dE \text{ about } (\mathbf{x}, \boldsymbol{\Omega}, E) \\ \text{from an internal source, at time } t. \end{array} \quad (30a)$$

This definition implies that the numerical value of Q is independent of dV , $d\boldsymbol{\Omega}$, and dE . The factor 4π is included so that integration of (30a) over the unit sphere gives the following equivalent (for an isotropic source) definition:

$$Q(\mathbf{x}, E, t)dVdE = \begin{array}{l} \text{the incremental rate at which neutrons are} \\ \text{isotropically introduced into } dVdE \text{ about } (\mathbf{x}, E) \\ \text{from an internal source, at time } t. \end{array} \quad (30b)$$

$Q(\mathbf{x}, E, t)$ must be specified for all points \mathbf{x} in V , all energies E , and all times after the initial time.

Boundary sources are specified neutron fluxes that enter the physical system V through its outer boundary ∂V . V is usually assumed to be convex; then neutrons leaking out of V cannot reenter through ∂V . The boundary angular flux $\psi^b(\mathbf{x}, \boldsymbol{\Omega}, E, t)$ is an external source, independent of the flux within the system, which must be specified for: (i) all points on the outer boundary of the system ($\mathbf{x} \in \partial V$), (ii) all directions of flight pointing into the system ($\boldsymbol{\Omega} \cdot \mathbf{n} < 0$, where \mathbf{n} is the unit outer normal vector at $\mathbf{x} \in \partial V$), (iii) all energies, and (iv) all times after the initial time. The angular flux is required to satisfy:

$$\psi(\mathbf{x}, \boldsymbol{\Omega}, E, t) = \psi^b(\mathbf{x}, \boldsymbol{\Omega}, E, t), \quad \mathbf{x} \in \partial V, \quad \boldsymbol{\Omega} \cdot \mathbf{n} < 0, \quad 0 < E < \infty, \quad 0 < t. \quad (31)$$

If $\psi^b = 0$, ∂V is called a *vacuum boundary* (► Fig. 15).

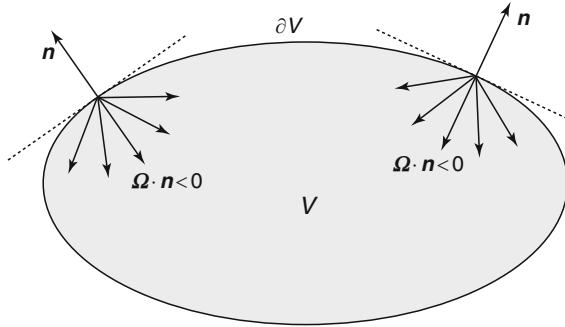


Figure 15
Incident directions of flight on ∂V

The internal and boundary neutron sources are specified and independent of the neutron distribution within V . Generally, neutron transport problems are *driven* by these known sources, which generate the “original” neutrons in the problem. After neutrons are introduced into V by the internal or boundary sources, they “transport” within V according to the physical processes of streaming, absorption, scattering, and fission, discussed above.

In nuclear reactor problems, the term *fission source* describes the neutrons that are produced by fission events in V . This “source” directly depends on ψ and must be calculated. Likewise, the *scattering source* of neutrons emitted from scattering events also directly depends on ψ and must be calculated. (Thus, the term “source” sometimes describes a quantity that depends on ψ .) However, to repeat, the *internal* and *boundary* sources are independent of ψ and must be specified.

2.5 The Time-Dependent Equations of Neutron Transport

Next, we derive seven mathematical equations that determine the neutron angular flux $\psi(\mathbf{x}, \boldsymbol{\Omega}, E, t)$ and the six neutron precursor densities $C_j(\mathbf{x}, t)$. Each of these seven equations is a *conservation equation* – each is based on the simple physical concept that the rate of change (of neutrons and precursor densities within increments of phase space) equals the rate of gain minus the rate of loss.

We first consider the incremental population of neutrons within $dVd\Omega dE$ about $(\mathbf{x}, \boldsymbol{\Omega}, E)$ at time t . By (19), the number of these neutrons is:

$$dN = N(\mathbf{x}, \boldsymbol{\Omega}, E, t) dVd\Omega dE = \frac{1}{v} \psi(\mathbf{x}, \boldsymbol{\Omega}, E, t) dVd\Omega dE.$$

Thus, the time rate of change of dN is:

$$\begin{aligned} \frac{\partial N}{\partial t} &= \frac{1}{v} \frac{\partial \psi}{\partial t}(\mathbf{x}, \boldsymbol{\Omega}, E, t) dVd\Omega dE \\ &= (\text{rate of gain}) - (\text{rate of loss}). \end{aligned} \tag{32a}$$

From our discussion of neutron physics, we have:

$$\begin{aligned} \text{Rate of loss} &= (\text{collision rate} + \text{net leakage rate}) \\ &\text{in } dVd\Omega dE \text{ about } (\mathbf{x}, \boldsymbol{\Omega}, E) \text{ at time } t, \end{aligned} \quad (32b)$$

and:

$$\begin{aligned} \text{Rate of gain} &= (\text{in-scattering rate} + \text{prompt fission rate} + \text{delayed fission rate} \\ &+ \text{source rate}) \text{ in } dVd\Omega dE \text{ about } (\mathbf{x}, \boldsymbol{\Omega}, E) \text{ at time } t. \end{aligned} \quad (32c)$$

First, we consider the “loss” terms in (32a) and (32b). From (5a) and (19) we have, using $v = ds/dt$, for neutrons in $dVd\Omega dE$ about $(\mathbf{x}, \boldsymbol{\Omega}, E)$:

$$\begin{aligned} \Sigma_t(E)\psi(\mathbf{x}, \boldsymbol{\Omega}, E, t)dVd\Omega dE &= \Sigma_t(E) \frac{ds}{dt} N(\mathbf{x}, \boldsymbol{\Omega}, E, t) dVd\Omega dE \\ &= \frac{1}{dt} [\Sigma_t(E) ds] [N(\mathbf{x}, \boldsymbol{\Omega}, E, t) dVd\Omega dE] \\ &= \frac{1}{dt} \left[\begin{array}{l} \text{the probability that a (single) neutron with energy } E \\ \text{will undergo a collision in time interval } dt \end{array} \right] \\ &\quad \times \left[\begin{array}{l} \text{the number of neutrons in } dVd\Omega dE \text{ about} \\ (\mathbf{x}, \boldsymbol{\Omega}, E, t) \text{ at time } t \end{array} \right] \\ &= \frac{1}{dt} \left[\begin{array}{l} \text{the number of collisions in } dVd\Omega dE \text{ about } (\mathbf{x}, \boldsymbol{\Omega}, E) \\ \text{in time interval } dt \text{ about } t \end{array} \right] \\ &= \text{Collision rate (in [32b])}. \end{aligned} \quad (33a)$$

Also, in (28), we let R shrink to an incremental volume dV and directly get:

$$\boldsymbol{\Omega} \cdot \nabla \psi(\mathbf{x}, \boldsymbol{\Omega}, E, t) dVd\Omega dE = \text{Net leakage rate (in [32b])}. \quad (33b)$$

Introducing (33) into (32b), we obtain:

$$\text{Rate of loss} = [\Sigma_t(E)\psi(\mathbf{x}, \boldsymbol{\Omega}, E, t) + \boldsymbol{\Omega} \cdot \nabla \psi(\mathbf{x}, \boldsymbol{\Omega}, E, t)] dVd\Omega dE. \quad (34)$$

The derivation of (33b) relies on the use of the divergence theorem (27) to convert a surface integral into a volume integral. A more physically intuitive understanding of (33b) can be obtained by considering dV to be a special cylindrical volume. Specifically, let us consider neutrons in $dVd\Omega dE$ about $(\mathbf{x}, \boldsymbol{\Omega}, E)$, where dV is an incremental cylindrical volume of length ds and cross-sectional area dA , centered at \mathbf{x} and oriented in the direction $\boldsymbol{\Omega}$, as depicted in

► Fig. 16.

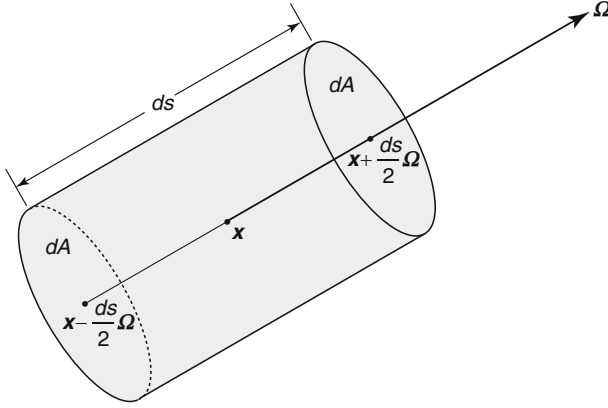


Figure 16
 Cylindrical incremental volume dV

Then $dV = dsdA$, and neutrons in $d\Omega dE$ about (Ω, E) flow into dV through the surface dA at $\mathbf{x} - (ds/2)\Omega$, and flow out of dV through the surface dA at $\mathbf{x} + (ds/2)\Omega$. Hence, by (24), we have:

$$\begin{aligned}
 & \text{Net rate at which neutrons in } d\Omega dE \text{ about } (\Omega, E) \text{ leak out of } dV \\
 &= \left[\psi \left(\mathbf{x} + \frac{ds}{2} \Omega, E \right) - \psi \left(\mathbf{x} - \frac{ds}{2} \Omega, E \right) \right] dA d\Omega dE \\
 &= \left[\frac{\psi \left(\mathbf{x} + \frac{ds}{2} \Omega, E \right) - \psi \left(\mathbf{x} - \frac{ds}{2} \Omega, E \right)}{ds} \right] dV d\Omega dE \\
 &= [\Omega \cdot \nabla \psi(\mathbf{x}, \Omega, E)] dV d\Omega dE. \tag{35}
 \end{aligned}$$

Next, we consider the “gain” terms in (32a) and (32c). From (12) and (19), we have for neutrons in $dV d\Omega' dE'$ about $(\mathbf{x}, \Omega', E')$:

$$\begin{aligned}
 & \Sigma_s(\Omega' \cdot \Omega, E' \rightarrow E) \psi(\mathbf{x}, \Omega', E', t) dV d\Omega' dE' d\Omega dE \\
 &= \Sigma_s(\Omega' \cdot \Omega, E' \rightarrow E) \frac{ds}{dt} N(\mathbf{x}, \Omega', E', t) dV d\Omega' dE' d\Omega dE \\
 &= \frac{1}{dt} [N(\mathbf{x}, \Omega', E', t) dV d\Omega' dE'] [\Sigma_s(\Omega' \cdot \Omega, E' \rightarrow E) ds d\Omega dE] \\
 &= \frac{1}{dt} \left[\text{the number of neutrons in } dV d\Omega' dE' \text{ about } (\mathbf{x}, \Omega', E') \text{ at time } t \right] \\
 &\quad \times \left[\text{the probability that one of these neutrons will scatter into} \right. \\
 &\quad \left. d\Omega dE \text{ about } (\Omega, E) \text{ during time interval } dt \right] \\
 &= \frac{1}{dt} \left[\text{the number of neutrons in } dV \text{ about } \mathbf{x} \text{ that scatter from} \right. \\
 &\quad \left. d\Omega' dE' \text{ about } (\Omega', E') \text{ into } d\Omega dE \text{ about } (\Omega, E) \right. \\
 &\quad \left. \text{during time interval } dt \text{ about } t \right]
 \end{aligned}$$

= the rate at which neutrons in dV about \mathbf{x} scatter from $d\Omega'dE'$
 = the rate at which neutrons in dV about \mathbf{x} scatter from $d\Omega'dE'$
 about (Ω', E') into $d\Omega dE$ about (Ω, E) at time t .

Integrating this expression over all initial directions Ω' and energies E' , we obtain:

$$\left[\int_0^\infty \int_{4\pi} \Sigma_s(\Omega' \cdot \Omega, E' \rightarrow E) \psi(\mathbf{x}, \Omega', E', t) d\Omega' dE' \right] dV d\Omega dE$$

= the rate at which neutrons in dV about \mathbf{x} scatter
 into $d\Omega dE$ about (Ω, E) at time t
 = In-scattering rate (in [32c]).

(36a)

Similarly, the rate at which prompt fission neutrons are produced in $dV d\Omega' dE'$ about $(\mathbf{x}, \Omega', E')$ is given by:

$$[1 - \beta(E')] v(E') \Sigma_f(E') \psi(\mathbf{x}, \Omega', E', t) dV d\Omega' dE'.$$

Integrating this expression over all initial directions Ω' and energies E' , and multiplying by $[\chi_p(E)/4\pi] d\Omega dE$, we obtain:

$$\left[\frac{\chi_p(E)}{4\pi} \int_0^\infty \int_{4\pi} [1 - \beta(E')] v(E') \Sigma_f(E') \psi(\mathbf{x}, \Omega', E', t) d\Omega' dE' \right] dV d\Omega dE$$

= the rate at which prompt fission neutrons are
 produced in $dV d\Omega dE$ about (\mathbf{x}, Ω, E) at time t .

(36b)

Also,

$$\sum_{j=1}^6 \frac{\chi_j(E)}{4\pi} \lambda_j C_j(\mathbf{x}, t) dV d\Omega dE = \text{the rate at which delayed neutrons}$$

are emitted into $dV d\Omega dE$
 about (\mathbf{x}, Ω, E) at time t .

(36c)

Finally, by (30a), we have:

$$\frac{Q(\mathbf{x}, E, t)}{4\pi} dV d\Omega dE = \text{source rate (in [32c])}.$$
(37)

Introducing (36) and (37) into (32c), we obtain:

$$\begin{aligned} \text{Rate of gain} = & \left[\int_0^\infty \int_{4\pi} \Sigma_s(\Omega' \cdot \Omega, E' \rightarrow E) \psi(\mathbf{x}, \Omega', E', t) d\Omega' dE' \right. \\ & + \frac{\chi_p(E)}{4\pi} \int_0^\infty \int_{4\pi} [1 - \beta(E')] v \Sigma_f(E') \psi(\mathbf{x}, \Omega', E', t) d\Omega' dE' \\ & \left. + \frac{1}{4\pi} \sum_{j=1}^6 \chi_j(E) \lambda_j C_j(\mathbf{x}, t) + \frac{1}{4\pi} Q(\mathbf{x}, E, t) \right] dV d\Omega dE. \end{aligned}$$
(38)

Introducing the rate of loss terms (34) and the rate of gain terms (38) into the general conservation equation (32a), we get:

$$\begin{aligned} \frac{1}{v} \frac{\partial \psi}{\partial t} dV d\Omega dE = & \left[\int_0^\infty \int_{4\pi} \Sigma_s \psi d\Omega' dE' + \frac{\chi_p}{4\pi} \int_0^\infty \int_{4\pi} [1 - \beta] v \Sigma_f \psi d\Omega' dE' \right. \\ & \left. + \frac{1}{4\pi} \sum_{j=1}^6 \chi_j \lambda_j C_j + \frac{1}{4\pi} Q \right] dV d\Omega dE - \left[\Sigma_t \psi + \boldsymbol{\Omega} \cdot \nabla \psi \right] dV d\Omega dE. \end{aligned}$$

Dividing by $dV d\Omega dE$ and rearranging, we obtain the following first-order *integro-differential* equation:

$$\begin{aligned} \frac{1}{v} \frac{\partial \psi}{\partial t}(\mathbf{x}, \boldsymbol{\Omega}, E, t) + \boldsymbol{\Omega} \cdot \nabla \psi(\mathbf{x}, \boldsymbol{\Omega}, E, t) + \Sigma_t(E) \psi(\mathbf{x}, \boldsymbol{\Omega}, E, t) \\ = \int_0^\infty \int_{4\pi} \Sigma_s(\boldsymbol{\Omega}' \cdot \boldsymbol{\Omega}, E' \rightarrow E) \psi(\mathbf{x}, \boldsymbol{\Omega}', E', t) d\Omega' dE' \\ + \frac{\chi_p(E)}{4\pi} \int_0^\infty \int_{4\pi} [1 - \beta(E')] v \Sigma_f(E') \psi(\mathbf{x}, \boldsymbol{\Omega}', E', t) d\Omega' dE' \\ + \frac{1}{4\pi} \sum_{j=1}^6 \chi_j(E) \lambda_j C_j(\mathbf{x}, t) + \frac{1}{4\pi} Q(\mathbf{x}, E, t). \end{aligned} \quad (39)$$

This is the *time-dependent neutron transport equation (with delayed neutron precursors)*, also called the *linear Boltzmann equation*. The derivation of this equation shows that each of its terms describes a specific physical process that causes a gain or loss of neutrons in each increment of phase space.

We must also derive an equation for each precursor density. The time rate of change of the species- j precursor density may be expressed as:

$$\begin{aligned} \frac{\partial C_j}{\partial t}(\mathbf{x}, t) dV = & \text{the rate of change of the number of group-}j \\ & \text{precursor nuclei in } dV \text{ about } \mathbf{x} \text{ at time } t \\ = & (\text{Rate of gain}) - (\text{rate of loss}). \end{aligned} \quad (40)$$

The rate of loss (due to decay) of these precursors is given by:

$$\begin{aligned} \lambda_j C_j(\mathbf{x}, t) dV = & \text{the rate at which group-}j \text{ precursor nuclei undergo} \\ & \text{radioactive decay in } dV \text{ about } \mathbf{x} \text{ at time } t. \end{aligned} \quad (41)$$

On the other hand,

$$\begin{aligned} \beta_j(E') v \Sigma_f(E') \psi(\mathbf{x}, \boldsymbol{\Omega}', E', t) dV d\Omega' dE' \\ = & \text{the rate at which group-}j \text{ precursor nuclei are produced} \\ & \text{by neutrons in } dV d\Omega' dE' \text{ about } (\mathbf{x}, \boldsymbol{\Omega}', E') \text{ at time } t. \end{aligned}$$

Integrating over Ω' and E' , we get the total rate of gain of the group- j precursor nuclei:

$$\left[\int_0^\infty \int_{4\pi} \beta_j(E') v \Sigma_f(E') \psi(\mathbf{x}, \Omega', E', t) d\Omega' dE' \right] dV$$

= the rate at which group- j precursor nuclei
are produced in dV about \mathbf{x} at time t .

(42)

After some rearrangement, (40–42) give for $1 \leq j \leq 6$ the following equations for the precursor densities:

$$\frac{\partial C_j}{\partial t}(\mathbf{x}, t) + \lambda_j C_j(\mathbf{x}, t) = \int_0^\infty \int_{4\pi} \beta_j(E') v \Sigma_f(E') \psi(\mathbf{x}, \Omega', E', t) d\Omega' dE'. \quad (43)$$

As with the transport equation, each term in these equations describes a physical process that causes a gain or loss of group- j neutron precursor nuclei.

Equation (43) must be solved jointly with the neutron transport equation (39). In addition, ψ must satisfy the boundary condition:

$$\psi(\mathbf{x}, \Omega, E, t) = \psi^b(\mathbf{x}, \Omega, E, t), \quad \mathbf{x} \in \partial V, \quad \Omega \cdot \mathbf{n} < 0, \quad 0 < E < \infty, \quad 0 < t, \quad (44)$$

and ψ and C_j must satisfy the initial conditions:

$$\psi(\mathbf{x}, \Omega, E, 0) = \psi^i(\mathbf{x}, \Omega, E), \quad \mathbf{x} \in V, \quad \Omega \in 4\pi, \quad 0 < E < \infty, \quad (45a)$$

$$C_j(\mathbf{x}, 0) = C_j^i(\mathbf{x}), \quad \mathbf{x} \in V, \quad (45b)$$

where ψ^b , ψ^i , and C_j^i are specified.

In full generality, the neutron angular flux $\psi(\mathbf{x}, \Omega, E, t)$ and the precursor densities $C_j(\mathbf{x}, t)$ are obtained by solving (39) and (43), subject to the boundary condition stated in (44) and the initial conditions stated in (45). The subject of *nuclear reactor kinetics* is based on this system of equations.

2.6 Time-Dependent Neutron Transport Without Delayed Neutrons

In some time-dependent problems, the relatively small value of β (≈ 0.01) justifies the neglect of the delayed neutron terms. In such problems one can set $\beta_j = C_j = 0$ in (39). The resulting single transport equation for ψ :

$$\begin{aligned} & \frac{1}{v} \frac{\partial \psi}{\partial t}(\mathbf{x}, \Omega, E, t) + \Omega \cdot \nabla \psi(\mathbf{x}, \Omega, E, t) + \Sigma_t(E) \psi(\mathbf{x}, \Omega, E, t) \\ &= \int_0^\infty \int_{4\pi} \Sigma_s(\Omega' \cdot \Omega, E' \rightarrow E) \psi(\mathbf{x}, \Omega', E', t) d\Omega' dE' \\ &+ \frac{\chi_p(E)}{4\pi} \int_0^\infty \int_{4\pi} v \Sigma_f(E') \psi(\mathbf{x}, \Omega', E', t) d\Omega' dE' + \frac{1}{4\pi} Q(\mathbf{x}, E, t), \end{aligned} \quad (46a)$$

is solved subject to the boundary condition (44) and initial condition (45a):

$$\psi(\mathbf{x}, \boldsymbol{\Omega}, E, t) = \psi^b(\mathbf{x}, \boldsymbol{\Omega}, E, t), \quad \mathbf{x} \in \partial V, \quad \boldsymbol{\Omega} \cdot \mathbf{n} < 0, \quad 0 < E < \infty, \quad 0 < t, \quad (46b)$$

$$\psi(\mathbf{x}, \boldsymbol{\Omega}, E, 0) = \psi^i(\mathbf{x}, \boldsymbol{\Omega}, E), \quad \mathbf{x} \in V, \quad \boldsymbol{\Omega} \in 4\pi, \quad 0 < E < \infty. \quad (46c)$$

2.7 The Steady-State Neutron Transport Equation

In steady-state problems, the precursor densities can be eliminated to obtain a single equation for ψ . Setting $\partial C_j / \partial t = 0$, in (43), we get:

$$\lambda_j C_j(\mathbf{x}) = \int_0^\infty \int_{4\pi} \beta_j(E') \nu \Sigma_f(E') \psi(\mathbf{x}, \boldsymbol{\Omega}', E') d\Omega' dE',$$

and introducing these expressions into the steady-state equation (39), we obtain:

$$\begin{aligned} & \boldsymbol{\Omega} \cdot \nabla \psi(\mathbf{x}, \boldsymbol{\Omega}, E) + \Sigma_t(E) \psi(\mathbf{x}, \boldsymbol{\Omega}, E) \\ &= \int_0^\infty \int_{4\pi} \Sigma_s(\boldsymbol{\Omega}' \cdot \boldsymbol{\Omega}, E' \rightarrow E) \psi(\mathbf{x}, \boldsymbol{\Omega}', E') d\Omega' dE' \\ &+ \frac{\chi_p(E)}{4\pi} \int_0^\infty \int_{4\pi} [1 - \beta(E')] \nu \Sigma_f(E') \psi(\mathbf{x}, \boldsymbol{\Omega}', E') d\Omega' dE' \\ &+ \frac{1}{4\pi} \sum_{j=1}^6 \chi_j(E) \int_0^\infty \int_{4\pi} \beta_j(E') \nu \Sigma_f(E') \psi(\mathbf{x}, \boldsymbol{\Omega}', E') d\Omega' dE' + \frac{1}{4\pi} Q(\mathbf{x}, E). \end{aligned} \quad (47)$$

Since $\beta = \sum \beta_j \approx 0.01$, it is often acceptable to set $\beta_j = 0$. In this case, (47) simplifies to:

$$\begin{aligned} & \boldsymbol{\Omega} \cdot \nabla \psi(\mathbf{x}, \boldsymbol{\Omega}, E) + \Sigma_t(E) \psi(\mathbf{x}, \boldsymbol{\Omega}, E) \\ &= \int_0^\infty \int_{4\pi} \Sigma_s(\boldsymbol{\Omega}' \cdot \boldsymbol{\Omega}, E' \rightarrow E) \psi(\mathbf{x}, \boldsymbol{\Omega}', E') d\Omega' dE' \\ &+ \frac{\chi_p(E)}{4\pi} \int_0^\infty \int_{4\pi} \nu \Sigma_f(E') \psi(\mathbf{x}, \boldsymbol{\Omega}', E') d\Omega' dE' \\ &+ \frac{1}{4\pi} Q(\mathbf{x}, E), \quad \mathbf{x} \in V, \quad \boldsymbol{\Omega} \in 4\pi, \quad 0 < E < \infty. \end{aligned} \quad (48a)$$

The first term on the right side of this equation is often called the *scattering source*. The second term is the *fission source*; this is isotropic and *separable* in space and energy – it is the product of a (known) function of energy and an (unknown) function only of space. (This separable form of the fission source is useful in developing strategies to solve [48a].) The third term is the specified *internal source*.

Equation (48a) must be solved subject to the steady-state boundary condition:

$$\psi(\mathbf{x}, \boldsymbol{\Omega}, E) = \psi^b(\mathbf{x}, \boldsymbol{\Omega}, E), \quad \mathbf{x} \in \partial V, \quad \boldsymbol{\Omega} \cdot \mathbf{n} < 0, \quad 0 < E < \infty, \quad (48b)$$

which is obtained from (44). As before, if the specified incident boundary flux $\psi^b = 0$, then ∂V is called a *vacuum boundary*.

2.8 k -Eigenvalue Problems

In steady-state reactor calculations, one often sees the following version of (48) in which the inhomogeneous source Q and the boundary source ψ^b are set to zero, and the fission source is modified by a constant factor $1/k$:

$$\begin{aligned} \Omega \cdot \nabla \psi(\mathbf{x}, \Omega, E) + \Sigma_t(E)\psi(\mathbf{x}, \Omega, E) &= \int_0^\infty \int_{4\pi} \Sigma_s(\Omega' \cdot \Omega, E' \rightarrow E)\psi(\mathbf{x}, \Omega', E') d\Omega' dE' \\ &+ \frac{\chi_p(E)}{4\pi k} \int_0^\infty \int_{4\pi} \nu \Sigma_f(E')\psi(\mathbf{x}, \Omega', E') d\Omega' dE', \\ \mathbf{x} \in V, \quad \Omega \in 4\pi, \quad 0 < E < \infty, & \quad (49a) \\ \psi(\mathbf{x}, \Omega, E) = 0, \quad \mathbf{x} \in \partial V, \quad \Omega \cdot \mathbf{n} < 0, \quad 0 < E < \infty. & \quad (49b) \end{aligned}$$

These equations always have the zero solution: $\psi = 0$. The goal is to find the *largest* value of k such that a nonzero solution ψ exists. This k is called the *criticality* (or *criticality eigenvalue*) of the system V ; the corresponding ψ is called the *eigenfunction* or *fundamental mode*.

If a system V has a fissile region, then it can be shown that the criticality eigenvalue k always exists, and the corresponding eigenfunction ψ is unique (up to a multiplicative constant) and positive. (If V has no fissile region, then we adopt the convention that $k = 0$.)

The motivation for defining k in the above manner is as follows. In any system V with fission, neutrons are lost due to capture and leakage, and are produced by fission. If the production of neutrons due to fission exactly balances the loss of neutrons due to capture and leakage, then a nonzero, steady-state neutron flux is possible. (This concept underlies a steady-state power reactor.) By adjusting the magnitude of the fission source through the eigenvalue k , one can make this exact balance occur. If $k < 1$, the fission source must be increased for a steady-state solution to exist; this implies that capture and leakage dominate fission, and the reactor is *subcritical*. If $k > 1$, the fission source must be decreased for a steady-state solution to exist; this implies that fission dominates capture and leakage, and the reactor is *supercritical*. If $k = 1$, capture and leakage exactly balance fission, and the reactor is *critical*. The calculation of k for differing reactor configurations is one of the most important and ubiquitous calculations in the design and operation of nuclear reactors.

In some problems (in particular, the field of reactor kinetics), the criticality k is replaced by the *reactivity* ρ , defined by

$$\frac{1}{k} = 1 - \rho. \quad (50)$$

A reactor is subcritical if $\rho < 0$, critical if $\rho = 0$, and supercritical if $\rho > 0$.

2.9 The Monoenergetic Neutron Transport Equation

A common simplifying assumption is to ignore energy dependence altogether, giving the so-called *one-speed* or *monoenergetic* form of the transport equation. Despite an apparently drastic approximation of the physics, this equation has been, and continues to be, the subject of much investigation, for several reasons. Under certain circumstances, the absence of the energy variable promotes a rigorous mathematical analysis of the transport equation, in

particular the establishment of existence, uniqueness, and completeness theorems for elementary solutions of the transport equation. Also, in special geometries, it is sometimes possible to construct analytic solutions to the one-speed transport equation. These solutions serve as benchmarks against which approximation methods and numerical solution techniques can be evaluated, and they provide insight into the nature of the transport process. In addition, in the widely used *multigroup* treatment of the energy variable in numerical work, the group-wise equations for the group-averaged angular fluxes are of one-speed form. Neutron transfers into a given energy group from all other groups appear only as sources in that group. Thus, methods developed for the solution of the one-speed transport equation can be applicable even when the energy variable is retained.

The monoenergetic transport equation can be derived from first principles, as we did above for the energy-dependent case, but with the one-speed assumption introduced at the outset. Alternatively, the energy-dependent transport equation (48a), in the steady-state case, can be manipulated to obtain the same result. We do this next.

The restriction of (48a) to single-energy neutrons requires the following assumptions:

1. The angular deflection of neutrons during scattering occurs without energy loss. In this case the differential cross section given in (11) can be expressed as:

$$\Sigma_s(\boldsymbol{\Omega} \cdot \boldsymbol{\Omega}', E \rightarrow E') = \Sigma_s(E', \boldsymbol{\Omega} \cdot \boldsymbol{\Omega}') \delta(E' - E). \quad (51a)$$

2. The internal and boundary sources are monoenergetic at some characteristic energy E_0 :

$$Q(\mathbf{x}, E) = Q(\mathbf{x}) \delta(E - E_0), \quad (51b)$$

$$\psi^b(\mathbf{x}, \boldsymbol{\Omega}, E) = \psi^b(\mathbf{x}, \boldsymbol{\Omega}) \delta(E - E_0). \quad (51c)$$

3. All fission neutrons are born at the characteristic energy E_0 :

$$\chi_p(E) = \delta(E - E_0). \quad (51d)$$

Then, since all neutrons are “born” with energy E_0 and cannot change their energy through scattering, the angular flux must contain only neutrons with energy E_0 :

$$\psi(\mathbf{x}, \boldsymbol{\Omega}, E) = \psi(\mathbf{x}, \boldsymbol{\Omega}) \delta(E - E_0). \quad (52)$$

Introducing (51–52) into (48a), we find that $\psi(\mathbf{x}, \boldsymbol{\Omega})$ satisfies the following energy-independent equation:

$$\begin{aligned} \boldsymbol{\Omega} \cdot \nabla \psi(\mathbf{x}, \boldsymbol{\Omega}) + \Sigma_t(E_0) \psi(\mathbf{x}, \boldsymbol{\Omega}) &= \int_{4\pi} \Sigma_s(E_0, \boldsymbol{\Omega}' \cdot \boldsymbol{\Omega}) \psi(\mathbf{x}, \boldsymbol{\Omega}') d\Omega' \\ &+ \frac{\nu \Sigma_f(E_0)}{4\pi} \int_{4\pi} \psi(\mathbf{x}, \boldsymbol{\Omega}') d\Omega' + \frac{Q(\mathbf{x})}{4\pi}, \quad \mathbf{x} \in V, \quad \boldsymbol{\Omega} \in 4\pi, \end{aligned} \quad (53)$$

with boundary condition:

$$\psi(\mathbf{x}, \boldsymbol{\Omega}) = \psi^b(\mathbf{x}, \boldsymbol{\Omega}), \quad \mathbf{x} \in \partial V, \quad \boldsymbol{\Omega} \cdot \mathbf{n} < 0. \quad (54)$$

The energy variable appears here only as a parameter, serving to fix the numerical values of the scattering, fission, and total cross section.

Further simplification ensues when scattering is isotropic in the laboratory frame, for then the differential cross section in (53) can be written as:

$$\Sigma_s(E_0, \boldsymbol{\Omega}' \cdot \boldsymbol{\Omega}) \equiv \Sigma_s(E_0) p(E_0, \boldsymbol{\Omega}' \cdot \boldsymbol{\Omega}) = \frac{\Sigma_s(E_0)}{4\pi}, \quad (55)$$

and (53) becomes:

$$\boldsymbol{\Omega} \cdot \nabla \psi(\mathbf{x}, \boldsymbol{\Omega}) + \Sigma_t \psi(\mathbf{x}, \boldsymbol{\Omega}) = \frac{(\Sigma_s + \nu \Sigma_f)}{4\pi} \int_{4\pi} \psi(\mathbf{x}, \boldsymbol{\Omega}') d\Omega' + \frac{Q(\mathbf{x})}{4\pi}. \quad (56)$$

Finally, when the system is *homogeneous* (the cross sections are independent of \mathbf{x}) and the dimensionless *optical depth* variable is introduced:

$$\boldsymbol{\tau} = \mathbf{x} \Sigma_t, \quad (57)$$

then distance becomes measured in units of mean free paths and (56) assumes the following simpler form:

$$\boldsymbol{\Omega} \cdot \nabla \psi(\boldsymbol{\tau}, \boldsymbol{\Omega}) + \psi(\boldsymbol{\tau}, \boldsymbol{\Omega}) = \frac{c}{4\pi} \int_{4\pi} \psi(\boldsymbol{\tau}, \boldsymbol{\Omega}') d\Omega' + \frac{Q_0(\boldsymbol{\tau})}{4\pi}. \quad (58)$$

Here, $Q_0 = Q/\Sigma_t$ and c is the *mean number of secondary neutrons produced per collision*:

$$c = \frac{(\Sigma_s + \nu \Sigma_f)}{\Sigma_t}. \quad (59)$$

If $\nu \sigma_f = 0$, then $c = \Sigma_s/\Sigma_t$ is also called the *scattering ratio*.

Monoenergetic eigenvalue problems can be formulated by setting $\psi^b = 0$ in (54), $Q = 0$ in (56), and letting c be the eigenvalue. The k -eigenvalue is then given in terms of this eigenvalue, or *critical value of c* , by:

$$k = \frac{\nu \Sigma_f}{c \Sigma_t - \Sigma_s}.$$

2.10 Mathematical Issues

Next, we briefly discuss some fundamental (mathematical) questions. Specifically:

1. Do solutions $\psi(\mathbf{x}, \boldsymbol{\Omega}, E, t)$ and $C_j(\mathbf{x}, \boldsymbol{\Omega}, t)$ of the neutron transport equations exist?
2. Are the solutions unique?
3. Are the solutions nonnegative (as they should be, physically)?
4. What can be said about the *smoothness* of these solutions?

In our discussion of these questions, we make a few basic and practically relevant assumptions: the physical system V is specified and finite and has at most a finite number of subregions, each having its own material cross sections. (The cross sections are histogram functions of \mathbf{x} .) The prescribed internal source, the prescribed incident boundary fluxes, and the prescribed

neutron flux and precursor densities at the initial time ($t = 0$) are all specified and nonnegative. The eigenvalue k of V has been calculated (see ● sect. 2.5.4), and V is either subcritical ($0 \leq k < 1$), critical ($k = 1$), or supercritical ($k > 1$). In the following, we attempt to state the basic results with a minimum of mathematical detail.

2.10.1 Existence, Uniqueness, and Nonnegativity of Transport Solutions

Briefly, each time-dependent neutron transport problem, with or without precursor densities, *always* has a unique nonnegative solution. Steady-state neutron transport problems (in which precursor densities are neglected) do not always have a unique nonnegative solution, but when they do not, there is a physical explanation. (A classic theoretical discussion of the existence of solutions of time-dependent transport problems is given in Case and Zweifel (1967).)

To discuss the connection between solutions of time-dependent and steady-state neutron transport problems, we consider time-dependent and steady-state problems without precursor densities in which the internal source and the prescribed incident boundary fluxes are nonnegative and independent of t . We then have:

1. If V is subcritical ($k < 1$), the time-dependent neutron flux limits as $t \rightarrow \infty$ to a steady-state neutron flux, which is the (unique, nonnegative) solution of the steady-state neutron transport problem.
2. If V is critical ($k = 1$) and the internal source and prescribed incident boundary fluxes are *nonzero*, the time-dependent neutron flux grows linearly in t as $t \rightarrow \infty$. In this situation, no limiting ($t \rightarrow \infty$) steady-state solution of the time-dependent problem exists, and no solution of the corresponding steady-state neutron transport problem exists.

However, if the internal source and prescribed incident boundary fluxes are *zero*, then the time-dependent neutron flux limits as $t \rightarrow \infty$ to a steady-state neutron flux of the form:

$$\psi(\mathbf{x}, \Omega, E, t) \approx C\Psi(\mathbf{x}, \Omega, E) \quad \text{for } t \approx \infty, \quad (60)$$

where Ψ is the k -eigenfunction for the critical system and C is a constant that depends on the initial condition ψ^i of the time-dependent problem. In this situation, the steady-state neutron transport problem has an infinite number of solutions, all given by (60), with the constant C arbitrary.

3. If V is supercritical ($k > 1$), the time-dependent neutron flux grows exponentially in t as $t \rightarrow \infty$. If the internal source and prescribed incident boundary fluxes are nonzero, the corresponding steady-state neutron transport problem either has a unique nonpositive solution, or no solution exists.

If the internal source and prescribed incident boundary fluxes are *zero*, then the steady-state neutron transport problem will either have the solution $\psi = 0$, or an infinite number of solutions of the form of (60), where Ψ is now some other (than the $k = 1$) eigenfunction of the system; this eigenfunction is nonpositive (nonphysical).

In all cases, a unique, positive solution of the time-dependent neutron transport problem exists. Also, a positive solution of the steady-state neutron transport problem exists if and only if the solution of a corresponding time-dependent problem has a steady-state limit as $t \rightarrow \infty$; and if the steady-state limit of the time-dependent problem does exist, it *is* a solution of the steady-state problem. Some of these issues are discussed in Case and Zweifel (1967).

2.10.2 The n th Collided Fluxes

The solution of source-driven neutron transport problems can be written in an advantageous way. To illustrate, let us consider the following monoenergetic steady-state problem with isotropic scattering:

$$\boldsymbol{\Omega} \cdot \nabla \psi(\mathbf{x}, \boldsymbol{\Omega}) + \Sigma_t(\mathbf{x})\psi(\mathbf{x}, \boldsymbol{\Omega}) = \frac{\Sigma_s(\mathbf{x})}{4\pi} \int_{4\pi} \psi(\mathbf{x}, \boldsymbol{\Omega}') d\boldsymbol{\Omega}' + \frac{Q(\mathbf{x})}{4\pi}, \quad \mathbf{x} \in V, \quad |\boldsymbol{\Omega}| = 1, \quad (61a)$$

$$\psi(\mathbf{x}, \boldsymbol{\Omega}) = \psi^b(\mathbf{x}, \boldsymbol{\Omega}), \quad \mathbf{x} \in \partial V, \quad \boldsymbol{\Omega} \cdot \mathbf{n} < 0. \quad (61b)$$

If we define the following problem for $\psi_0(\mathbf{x}, \boldsymbol{\Omega})$:

$$\boldsymbol{\Omega} \cdot \nabla \psi_0(\mathbf{x}, \boldsymbol{\Omega}) + \Sigma_t(\mathbf{x})\psi_0(\mathbf{x}, \boldsymbol{\Omega}) = \frac{Q(\mathbf{x})}{4\pi}, \quad \mathbf{x} \in V, \quad |\boldsymbol{\Omega}| = 1, \quad (62a)$$

$$\psi_0(\mathbf{x}, \boldsymbol{\Omega}) = \psi^b(\mathbf{x}, \boldsymbol{\Omega}), \quad \mathbf{x} \in \partial V, \quad \boldsymbol{\Omega} \cdot \mathbf{n} < 0, \quad (62b)$$

and for $1 \leq n < \infty$ the following problems for $\psi_n(\mathbf{x}, \boldsymbol{\Omega})$:

$$\boldsymbol{\Omega} \cdot \nabla \psi_n(\mathbf{x}, \boldsymbol{\Omega}) + \Sigma_t(\mathbf{x})\psi_n(\mathbf{x}, \boldsymbol{\Omega}) = \frac{\Sigma_s(\mathbf{x})}{4\pi} \int_{4\pi} \psi_{n-1}(\mathbf{x}, \boldsymbol{\Omega}') d\boldsymbol{\Omega}', \quad \mathbf{x} \in V, \quad |\boldsymbol{\Omega}| = 1, \quad (63a)$$

$$\psi_n(\mathbf{x}, \boldsymbol{\Omega}) = 0, \quad \mathbf{x} \in \partial V, \quad \boldsymbol{\Omega} \cdot \mathbf{n} < 0, \quad (63b)$$

then it is possible to interpret each ψ_n as a particular “component” of ψ .

First, in (62) for ψ_0 , neutrons are *created* by the same internal and boundary sources and have the same mean free path as in (61); but when the neutrons in (62) experience a collision, they *die*. Thus, $\psi_0(\mathbf{x}, \boldsymbol{\Omega})$ describes the *uncollided* neutrons in problem (61) – the neutrons in V that have just been born and have yet to experience a collision in V or leak out of V .

Equation (63) for $n = 1$ have as their sole source the uncollided neutrons that scatter; when these (once-scattered) neutrons experience a collision, they die. Thus, $\psi_1(\mathbf{x}, \boldsymbol{\Omega})$ describes the *once-collided* neutron flux in problem (61) – the flux due to neutrons in V that have experienced exactly one scattering event and have yet to experience a second collision in V or leak out of V .

By continuing in this manner, we have for all $n \geq 0$,

$$\begin{aligned} \psi_n(\mathbf{x}, \boldsymbol{\Omega}) &= \text{the } n\text{th collided neutron flux} \\ &= \text{the flux due to neutrons in } V \text{ that have experienced} \\ &\quad \text{exactly } n \text{ scattering events in } V. \end{aligned} \quad (64)$$

Also, if (62) and (63) are summed over $0 \leq n < \infty$, it is easily seen that $\sum \psi_n$ satisfies (61) for ψ . Thus, the solution ψ of (61) can be written:

$$\psi(\mathbf{x}, \boldsymbol{\Omega}) = \sum_{n=0}^{\infty} \psi_n(\mathbf{x}, \boldsymbol{\Omega}). \quad (65)$$

Therefore: at any instant in time, the neutron population consists of “newly born” neutrons, which have experienced only a few collisions (and have scattered in each), with “older” neutrons,

which have experienced many collisions (and have also scattered in each). Moreover, (62) and (63) show how to explicitly calculate, for each n , the flux of neutrons that have experienced exactly n collisions.

This view of neutron transport problems has practical benefits. For example, numerical methods for solving (61) are usually based on the *source iteration* algorithm, in which, effectively, (62) and (63) are solved recursively and the results added, as in (65). Source iteration converges rapidly for small, leaky systems, or systems with significant capture cross sections; here neutrons are unlikely to have long lives, so $\psi_n \rightarrow 0$ quickly. However, source iteration converges slowly for “diffusive” problems, which are many mean free paths in width (having small leakage rates) and scattering-dominated (having small neutron capture rates). For diffusive problems, neutrons can have long lives, so $\psi_n \rightarrow 0$ slowly.

A second benefit of (61–65) occurs in solving problems with localized or point sources. Here, $\psi_0(\mathbf{x}, \Omega)$ [and to a lesser extent $\psi_1(\mathbf{x}, \Omega)$] are strongly varying functions of \mathbf{x} and Ω and are difficult to model numerically. A common strategy is to calculate the uncollided flux ψ_0 analytically and then calculate the collided fluxes ψ_n for $n \geq 1$ numerically. (In recent work, both ψ_0 and ψ_1 have been calculated analytically and the remaining ψ_n are calculated numerically.) This approach makes use of the fact that for point source problems, ψ_0 (and ψ_1) do not have to be treated by numerical methods that are likely to cause large errors.

A third practical benefit of (61–65) occurs in assessing the smoothness of solutions of (61). We briefly discuss this next and refer to Kellog (1974) for a more complete discussion.

2.10.3 Smoothness of the Angular Flux

This often poorly understood topic, dealing with the continuity and differentiability properties of the angular flux, has major implications in the accuracy of approximation schemes and numerical methods for simulating transport problems. It is not possible to discuss this subject fully here; instead we give some illustrative examples. (See Kellog (1974) for a more thorough discussion.) The basic facts are as follows:

1. Solutions of planar-geometry transport problems with vacuum boundaries and finite isotropic internal sources are *smooth* (continuous with continuous first derivatives) functions of x and μ , except at outer boundaries and material interfaces between regions with different cross sections and internal sources. At such interfaces, ψ is (i) continuous in x with a discontinuous first derivative, and (ii) discontinuous in μ at $\mu = 0$. This *boundary-layer* behavior occurs only at the interface between different material regions, and at the outer boundary of the system.
2. Angular flux solutions of multidimensional transport problems with vacuum boundaries exhibit the same boundary-layer behavior as described above at material interfaces and the outer boundary of the system. However, because of geometrical effects, multidimensional angular fluxes also lack smoothness away from boundary layers. Generally, multidimensional transport solutions are continuous functions of \mathbf{x} and Ω but have discontinuous first derivatives. Occasionally, these solutions can even be discontinuous. Thus, multidimensional transport solutions are inherently not “smooth”; they lack even one continuous derivative in \mathbf{x} and Ω . The lack of smoothness of the transport solution is an impediment to the calculation of accurate numerical solutions of multidimensional neutron transport problems.

3. Solutions of problems with nonzero but smooth prescribed incident boundary fluxes have the same smoothness properties as described above. However, if the incident boundary fluxes are not smooth, then the uncollided flux component of ψ can be nonsmooth throughout V . For example, an incident monodirectional (delta function) beam of neutrons on ∂V creates a delta function component of ψ that propagates entirely through V .

To illustrate the lack of smoothness for multidimensional problems (item 2 above), let us consider an infinite ($-\infty < x, y, z < \infty$) purely absorbing ($\Sigma_s = 0$) system with constant total cross section $\Sigma_t = \Sigma_\gamma$, driven by an isotropic, spatially histogram internal source:

$$Q(x, y) = \begin{cases} Q_0, & |x| < X, \quad |y| < Y, \\ 0, & \text{otherwise.} \end{cases} \quad (66)$$

Because of the lack of z -dependence in the geometry and sources, the angular flux ψ is independent of z . The neutron transport equation (see [56] and [2]) is:


$$\sqrt{1-\mu^2} \left(\cos \omega \frac{\partial \psi}{\partial x} + \sin \omega \frac{\partial \psi}{\partial y} \right) + \Sigma_t \psi(x, y, \mu, \omega) = \frac{Q(x, y)}{4\pi}. \quad (67)$$

Also, $\psi \rightarrow 0$ as $|x| \rightarrow \infty$ and $|y| \rightarrow \infty$.

The analytic solution, obtained by integrating (67) along the characteristic curve (the *flight path* of neutrons) $x(s) = x - s \cos \omega$, $y(s) = y - s \sin \omega$ for $0 < s < \infty$, can be written:

$$\psi(x, y, \mu, \omega) = \frac{1}{4\pi\sqrt{1-\mu^2}} \int_0^\infty Q(x - s \cos \omega, y - s \sin \omega) e^{-(\Sigma_t s / \sqrt{1-\mu^2})} ds. \quad (68)$$

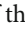
If the point (x, y) is outside the source region (which we henceforth assume) and the flight path does not intersect the source region, then $\psi = 0$.

If the flight path intersects the boundary of the source region, it does so for two values of s : $s_0(x, y, \omega) \leq s_1(x, y, \omega)$, as shown in  Fig. 17. In this situation, we obtain explicitly from (68) and (66):

$$\begin{aligned} \psi(x, y, \mu, \omega) &= \frac{1}{\sqrt{1-\mu^2}} \int_{s_0}^{s_1} \frac{Q_0}{4\pi} e^{-(\Sigma_t s / \sqrt{1-\mu^2})} ds \\ &= \frac{Q_0}{4\pi\Sigma_t} \left(e^{-(\Sigma_t s_0(x, y, \omega) / \sqrt{1-\mu^2})} - e^{-(\Sigma_t s_1(x, y, \omega) / \sqrt{1-\mu^2})} \right). \end{aligned} \quad (69)$$

This result can be extended to all points (x, y) outside the source region and all ω by simply defining $s_0 = s_1$ when the flight path does not intersect the source region.

For fixed x, y , and ω , it is evident that $\psi(x, y, \mu, \omega)$ is continuous and infinitely differentiable in the variable μ , with $\psi \rightarrow 0$ as $\mu \rightarrow \pm 1$.

Also, s_0 and s_1 are continuous and infinitely differentiable for most values of x, y , and ω . However, for each spatial point (x, y) , there are generally four azimuthal angles ω for which the flight path passes through a corner of the source region (see  Fig. 18). At one or two of these phase space points, $s_1(x, y, \omega)$ is a continuous function of x, y , and ω , but it has discontinuous first derivatives with respect to all three of these variables! Likewise, at zero or one of these phase space points, $s_0(x, y, \omega)$ is a continuous function of x, y , and ω , but it has discontinuous first derivatives with respect to all three of these variables. At all four of these phase space points,

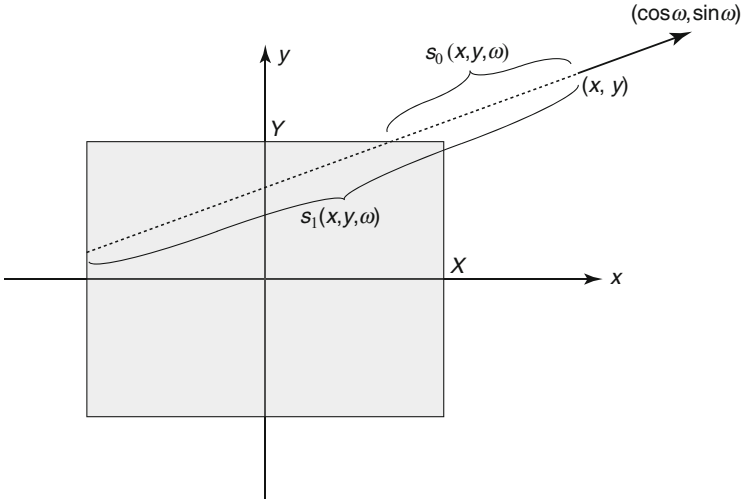


Figure 17
 $s_0(x, y, \omega)$ and $s_1(x, y, \omega)$

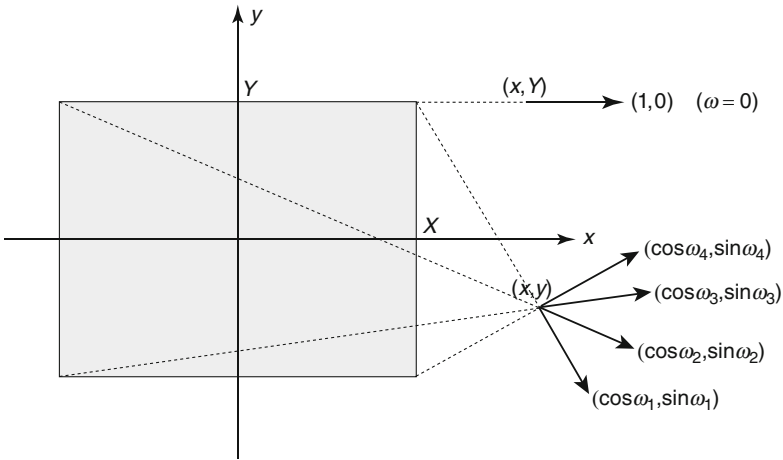


Figure 18
 $s_1(x, y, \omega)$ is not smooth at the indicated values of ω

$\psi(x, y, \mu, \omega)$ is a continuous function of x , y , and ω , but it has discontinuous first derivatives with respect to all three of these variables.

A more extreme situation occurs when the point (x, y) lies on a plane generated by an outer edge of the source region, and when the flight path traces along this outer edge of the source region. For example, from (68) we get for $x > X$, $y = Y$, $\omega = 0$, and any $\epsilon > 0$ (see Fig. 18):

$$\psi(x, Y + \epsilon, \mu, 0) = 0, \tag{70a}$$

$$\psi(x, Y - \epsilon, \mu, 0) = \frac{Q_0}{4\pi\Sigma_t} \left(e^{-\Sigma_t(x-X)/\sqrt{1-\mu^2}} - e^{-\Sigma_t(x+X)/\sqrt{1-\mu^2}} \right). \tag{70b}$$

This implies that at the phase space point $(x, y, \mu, \omega) = (x, Y, \mu, 0)$, ψ is a discontinuous function of y . (And, a discontinuous function of ω .)

This simple problem applies to the uncollided angular flux in any source-driven problem. In general, when the flight path $\mathbf{x} - s\boldsymbol{\Omega}$ passes through a “corner” of a source region, $\psi(\mathbf{x}, \boldsymbol{\Omega}, E)$ is continuous with a discontinuous derivative (with respect to x , y , or ω). When the flight path passes through a corner of a material region that does not contain a source, ψ has a weaker singularity (a continuous first derivative but a discontinuous second derivative). And, as we showed above, when the flight path traces along the planar edge of a source region, ψ is discontinuous. For problems with scattering, the statements in this paragraph hold for each n th collided flux ψ_n , and for ψ itself. For problems driven by boundary sources, similar results also follow.

In general, for multidimensional, multiregion problems, ψ is generally a function with weak smoothness properties (Kellogg 1974). This basic fact has not stopped practitioners from employing numerical methods that require the exact solution to be smoother than it actually is to achieve the theoretically optimal accuracy. However, the lack of smoothness of ψ negatively affects the accuracy and convergence rates of the resulting numerical solutions. For example, methods that would be second-order accurate if the solution is unrealistically smooth exhibit convergence rates that are less than second order when applied to realistic problems (Duo and Azmy 2007; Larsen 1982). (However, numerical experiments also show that certain integrals of the flux actually do converge with second-order accuracy (Larsen 1982).) The topic of the lack of smoothness of the angular flux and how this affects multidimensional numerical simulations is only qualitatively understood.

2.11 Generalizations of the Neutron Transport Equation

For simplicity, the transport equations and boundary conditions discussed above have not been written in the most general possible form. Here, we briefly describe some common generalizations.

2.11.1 Reflecting Boundaries

For physical systems V that possess a planar *symmetry boundary*, an equivalent transport problem can be formulated on a subregion of V using *symmetry* or *reflecting* boundary conditions. For example, the planar-geometry system $-Z \leq z \leq Z$ has a symmetry boundary at $z = 0$ if (i) the cross sections and internal source are even functions of z , e.g., $\Sigma_t(z, E) = \Sigma(-z, E)$, and (ii) the prescribed incident fluxes at $z = -Z$ and Z satisfy $\psi^b(-Z, \mu, E) = \psi^b(Z, -\mu, E)$ for $0 \leq \mu \leq 1$. In this case, symmetry considerations show that the angular flux must satisfy:

$$\psi(z, \mu, E) = \psi(-z, -\mu, E), \quad -Z < z < Z, \quad -1 \leq \mu \leq 1, \quad 0 < E < \infty. \quad (71a)$$

Here, one can formulate an equivalent planar-geometry transport problem on the half-system $0 \leq z \leq Z$. The transport equation on this half-system and the boundary condition at $z = Z$ are the same as before. The new *symmetry* or *reflecting* boundary condition at $z = 0$, obtained by setting $z = 0$ in (71a), is:

$$\psi(0, \mu, E) = \psi(0, -\mu, E), \quad 0 \leq \mu \leq 1, \quad 0 < E < \infty. \quad (71b)$$

If the transport problem on the half-system is solved, then the angular flux over the full system is obtained from (71a).

This strategy enables computer simulations to be performed more efficiently. In 1-D problems with a symmetry boundary, the savings is a factor of 2; in 2-D problems with two symmetry boundaries, the savings is a factor of 4; and in 3-D problems with three symmetry boundaries, the savings is a factor of 8.

2.11.2 Periodic Boundaries

Similarly, if a physical system is infinite with a *periodic* or *lattice* structure, and the angular flux itself is spatially periodic, then for obvious reasons it becomes imperative to formulate an equivalent problem on a single cell of the lattice. For example, if an infinite 1-D planar system $-\infty < z < \infty$ has spatially periodic cross sections and internal sources, e.g., $\Sigma_t(z) = \Sigma_t(z + Z)$, and if there are no sources at $z = \pm\infty$, then the angular flux is spatially periodic:


$$\psi(z, \mu, E) = \psi(z + Z, \mu, E). \quad (72a)$$

In this case, an equivalent transport problem can be formulated on a single cell $0 \leq z \leq Z$ with *periodic* boundary conditions obtained from (72a):

$$\psi(0, \mu, E) = \psi(Z, \mu, E), \quad -1 \leq \mu \leq 1, \quad 0 < E < \infty. \quad (72b)$$

If the transport problem on the single cell is solved, then the angular flux over the full system can be obtained from (72a).

2.11.3 Anisotropic Sources

Physically, internal neutron sources due to radioactive decay or spontaneous fission are isotropic – all directions of flight are equally probable. However, it is sometimes necessary to consider anisotropic internal sources $Q(\mathbf{x}, \boldsymbol{\Omega}, E)$ – for example, in calculating certain Green's functions, or in multigroup calculations, when including the source of neutrons that anisotropically scatter into a given energy group with the internal source for that group. (This latter topic will be discussed in detail in  sect. 6.3). Overall, there is no mathematical reason why the internal neutron sources must be assumed to be isotropic; if appropriate, these sources can be taken to be anisotropic.

2.11.4 Coupled Neutron/Photon Transport

In reactor core calculations, the calculation of reaction rates relies on the determination of the neutron fluxes. However, in reactor shielding calculations, the calculation of dose rates relies on both the neutron fluxes and gamma-ray (photon) fluxes. The photons, which are produced by neutron absorption and inelastic neutron scattering, are more deeply penetrating than neutrons; the dose to humans on the far side of a reactor shield is due mostly to the transmitted

photons. To account for the photon transport in the shield, two coupled transport equations are formulated: one for the neutrons and one for the photons. When these are approximated using the multigroup approximation (discussed in [sect. 6](#)), the resulting two sets of multigroup equations can be merged into a single system of multigroup equations, with some groups describing neutrons and other groups describing photons.

2.11.5 Temperature-Dependent Cross Sections

Our derivation of the neutron transport equation ignores changes that occur in the macroscopic cross sections when temperature changes in the core occur due to an increase or decrease in the neutron flux (with a corresponding increase or decrease in reactor power). This approximation is generally valid when the reactor operates near a steady-state mode, but not when the reactor experiences significant transients in the neutron fluxes. To account for this, (i) an additional equation must be formulated yielding the temperature within the reactor $T(\mathbf{x}, t)$ as a function of space and time, with a source that depends on the reactor power, and (ii) the macroscopic cross sections in the reactor must be expressed as functions of $T(\mathbf{x}, t)$. The resulting equations are *nonlinear*: the neutron flux affects the temperature, which affects the macroscopic cross sections, which affects the flux. This is an extremely important topic in the fields of reactor kinetics and reactor safety.

2.11.6 Advection and Diffusion of Fission Products

Our derivation of the transport equation also ignores the spatial diffusion of fission products; delayed neutrons are assumed to be emitted at the site of the primary fission event. This is an excellent approximation for solid fuel reactors, but not when significant fuel motion is possible, as occurs, for instance, in liquid fuel reactors. The spatial motion of fission products can be accommodated by adding suitable advection or diffusion terms in the equations for the precursor densities. Then, in addition to the delayed emission in time, the delayed neutrons are emitted nonlocally in space.

2.12 Limitations of the Neutron Transport Equation

The neutron transport equation provides an extremely accurate description of the phase space neutron density in a nuclear reactor. In conjunction with appropriately formatted neutron–nucleus interaction data, this equation underlies the methods and codes used in the design of all existing nuclear reactors. However, the derivation of the transport equation has inherent approximations that limit the validity of the equation. Some of these approximations can be relaxed without significantly altering the mathematical structure of the equation. Other approximations are more fundamental and can only be relaxed at the expense of a much more complicated mathematical description. Some of the significant assumptions underlying the neutron transport equation are delineated below.

1. *The neutron is a point, structureless particle whose free motion between interactions can be described by classical mechanics.* Neutron properties requiring a quantum mechanical

description, such as spin and polarization, are assumed to influence only the interaction cross sections which, for the purpose of transport theory, are regarded as given. While the neutron phase space can be expanded to include internal states like spin and polarization, such effects are unimportant in most applications of neutron transport, but especially in reactor physics.

2. *The interaction centers, where neutrons collide with nuclei, are assumed to be randomly located with a Poisson distribution in the host medium, and collisions between neutrons and nuclei are well-defined isolated two-body interactions. Moreover, the probability of interaction with the target nuclei is assumed to depend only on the instantaneous state of the neutron and not on its prior interaction history.* In other words, the transport process is assumed to be *Markovian*, a statement that is encapsulated in the expression for the collision probability:

$$p(s)ds = \Sigma_t(\vec{x}, E, t)ds.$$

That is, the probability of an interaction in an incremental distance ds is proportional to ds and depends only on the neutron's current position and energy at the time of collision. The rate constant for the transition of state is just the macroscopic cross section. Also, the probability that the neutron can suffer more than one collision in ds is $o(ds)$, i.e., is negligible compared to ds . Corrections for non-Markovian effects have not been found necessary in the numerous applications of neutron transport theory. However, this may not be true in applications involving other types of particles. An example is low energy (\sim keV or less) atomic collision phenomena in solids, where isolated two-body collisions cannot be defined.

3. *The neutron transport equation, as derived in this section, describes the "expected" or "mean" neutron population in a medium.* Because of the statistical nature of neutron interactions and of the number of neutrons released per fission, the actual neutron number fluctuates about this mean value. However, the magnitude of the fluctuations depends on the population size. In power reactors, where the neutron number may be $\sim 10^{15}$, the deviation of the neutron population from the mean is small and the neutron transport equation for the expected density provides an accurate description of the transport process. However, for small neutron populations, such as encountered at start up in the presence of a weak source, the instantaneous neutron density will differ significantly and randomly from the mean density. This is because fission chains from a weak source are well separated, and some fission chains die prematurely, while others propagate for unusually long times. Therefore, a sufficiently strong overlap of chains does not occur for fluctuations to cancel out and a mean density to become established. Thus, although the neutron transport equation yields the correct mean neutron density, this is an incomplete characterization of the actual neutron population. Under these circumstances, a fully stochastic description of the neutron population is necessary. A generalization of the theory to explicitly account for stochastic effects in neutron transport is beyond the scope of this chapter but has been presented by Bell (1965).
4. *The neutron transport equation is a linear equation in which the macroscopic cross sections do not directly depend on the neutron density.* Two assumptions are necessary to ensure this independence:
 - (a) *Neutron-neutron collisions are negligible.* In nuclear reactor applications, this is an excellent approximation because the density of target nuclei (10^{22} nuclei per cm^3) greatly exceeds the neutron density ($<10^{15}$ neutrons per cm^3). In applications where interactions between moving particles is important, such as in the kinetic theory of gases, the collision operator becomes nonlinear and the appropriate transport equation becomes

the original (nonlinear) Boltzmann equation, which includes binary collisions between the particles.

- (b) *The neutron reaction rate density is sufficiently small so as to not appreciably modify the isotopic makeup of the host medium, except during very long timescales.* This is also an excellent approximation in nuclear reactor applications. Since changes in material properties due to fuel burnup (density, thermal conductivity, poison accumulation, etc.) occur over much longer timescales than the timescale over which the neutron distribution relaxes, these effects can be treated by performing static transport calculations over various snapshots of the medium.

2.13 Discussion

We have (i) described the basic physical processes that underlie neutron transport, (ii) derived the mathematical equations that describe this process for time-dependent and steady-state nuclear reactor calculations, (iii) discussed some basic properties of the solutions of these equations, and (iv) discussed the conditions of validity of the equation. The neutron transport and precursor density equations form the basis for practical neutron (and photon) transport calculations in nuclear reactors and shields.

3 The Transport Equation in Special Geometries

Phase space for general neutron transport problems is 7-D: there are three spatial dimensions, two angular (*direction-of-flight*) dimensions, one energy dimension, and one temporal dimension. This is problematic for calculating deterministic numerical solutions of realistic problems; if each of the seven independent variables is discretized on a grid with a modest 10^2 cells, the resulting discrete problem will have 10^{14} unknowns! Problems of this magnitude will be beyond the capacity of the world's largest and fastest supercomputers for many years to come.

To formulate practical methods for solving realistic neutron transport problems, the size of phase space must be reduced as much as possible. For 3-D problems that have special space-angle symmetries, this can be done by reducing the number of spatial (and possibly angular) independent variables. In particular, one can formulate and solve a mathematically equivalent neutron transport equation with fewer than three independent spatial variables and possibly one rather than two angular variables. These special geometries are extremely important; for many years it was only possible to obtain practical numerical solutions of spatially 1-D and 2-D transport problems. In recent years, 3-D codes for practical problems have become available, but they are so costly to run that the great majority of neutron transport simulations remain 1-D and 2-D.

In the remainder of this chapter, we discuss the most important special geometries for which the transport equation can be formulated using one or two independent spatial variables. In each situation, we describe the geometry and derive the appropriate form of the transport equation.

To begin, we define a general 3-D problem for steady-state, monoenergetic, anisotropically scattering neutron transport in a prescribed convex spatial region V . This problem is driven by an internal isotropic source $Q(\mathbf{x})$, which is prescribed for all points \mathbf{x} in V , and an incident

flux $\psi^b(\mathbf{x}, \boldsymbol{\Omega})$, which is prescribed for all points \mathbf{x} on the outer boundary ∂V of V and for all incident directions of flight $\boldsymbol{\Omega}$ at \mathbf{x} . The three restrictions of this problem: (i) steady-state, (ii) no fission, and (iii) monoenergetic transport, are made for simplicity only and can easily be relaxed. The problem is:

$$\boldsymbol{\Omega} \cdot \nabla \psi(\mathbf{x}, \boldsymbol{\Omega}) + \Sigma_t(\mathbf{x})\psi(\mathbf{x}, \boldsymbol{\Omega}) = \int_{4\pi} \Sigma_s(\mathbf{x}, \boldsymbol{\Omega} \cdot \boldsymbol{\Omega}')\psi(\mathbf{x}, \boldsymbol{\Omega}')d\Omega' + \frac{Q(\mathbf{x})}{4\pi}, \quad \mathbf{x} \in V, \quad \boldsymbol{\Omega} \in 4\pi, \quad (73a)$$

$$\psi(\mathbf{x}, \boldsymbol{\Omega}) = \psi^b(\mathbf{x}, \boldsymbol{\Omega}), \quad \mathbf{x} \in \partial V, \quad \boldsymbol{\Omega} \cdot \mathbf{n} < 0. \quad (73b)$$

In the various geometries considered below, two terms in (73a) will change form: the *leakage* term $\boldsymbol{\Omega} \cdot \nabla \psi$ on the left side, and the *scattering integral* $\int \Sigma_s \psi d\Omega'$ on the right side.

To begin, we formulate the above problem using standard 3-D Cartesian spatial variables and spherical harmonic functions to expand the scattering integral. Then, we describe the problem for two simpler Cartesian geometries: (1-D) planar geometry and (2-D) x, y -geometry. After this, we formulate the transport problem in the following *curvilinear* geometries: 1-D spherical geometry, 3-D (r, ϑ, z) -geometry, 2-D (r, z) -geometry, and 1-D cylindrical geometry. The 2-D (r, z) - and 1-D cylindrical-geometry transport equations are special cases of the 3-D (r, ϑ, z) -geometry equation. The most widely used geometries in practical 2-D applications are (x, y) and (r, z) .

3.1 3-D Cartesian Geometry

For a standard 3-D Cartesian (x, y, z) -coordinate system (► Fig. 19) with $\theta =$ polar angle, $\omega =$ azimuthal angle, and $\mu = \cos \theta =$ polar cosine, we have:

$$\mathbf{x} = x\mathbf{i} + y\mathbf{j} + z\mathbf{k}, \quad (74a)$$

$$\begin{aligned} \boldsymbol{\Omega} &= \Omega_x\mathbf{i} + \Omega_y\mathbf{j} + \Omega_z\mathbf{k} \\ &= \sqrt{1 - \mu^2} (\cos \omega \mathbf{i} + \sin \omega \mathbf{j}) + \mu\mathbf{k}, \end{aligned} \quad (74b)$$

$$\mu = \cos \theta, \quad (74c)$$

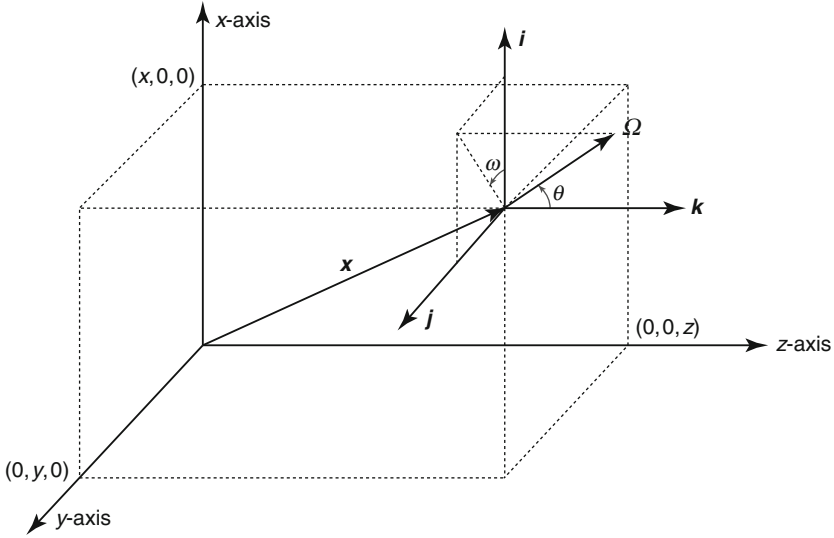
$$d\boldsymbol{\Omega} = d\mu d\omega. \quad (74d)$$

In this geometry,

$$\psi(\mathbf{x}, \boldsymbol{\Omega}) = \Psi(x, y, z, \mu, \omega), \quad (75)$$

and the leakage term in the transport equation can be written:

$$\begin{aligned} \boldsymbol{\Omega} \cdot \nabla \psi(\mathbf{x}, \boldsymbol{\Omega}) &= \left(\Omega_x \frac{\partial}{\partial x} + \Omega_y \frac{\partial}{\partial y} + \Omega_z \frac{\partial}{\partial z} \right) \Psi(x, y, z, \mu, \omega) \\ &= \left[\sqrt{1 - \mu^2} \left(\cos \omega \frac{\partial}{\partial x} + \sin \omega \frac{\partial}{\partial y} \right) + \mu \frac{\partial}{\partial z} \right] \Psi(x, y, z, \mu, \omega). \end{aligned} \quad (76)$$



■ Figure 19
3-D Cartesian geometry

Thus, the leakage operator depends explicitly on all the spatial and angular variables. (*Note:* In this discussion, ψ denotes the angular flux as a *general* function of space \mathbf{x} and direction Ω ; Ψ denotes the angular flux as a function of angular and direction variables that correspond to *specific* coordinate systems.)

To express the scattering integral, we use the fact that scattering is rotationally invariant. Thus, the differential scattering cross section is a function of the scattering cosine $\mu_0 = \Omega \cdot \Omega'$ and can be written as a Legendre polynomial expansion:

$$\Sigma_s(\mathbf{x}, \Omega \cdot \Omega') = \sum_{n=0}^N \frac{2n+1}{4\pi} \Sigma_{s,n}(\mathbf{x}) P_n(\Omega \cdot \Omega'), \quad (77)$$

where $P_n(\mu_0)$ is the n th Legendre polynomial (Duderstadt and Hamilton 1976). The order N of this expansion is generally infinite, but in applications the series is truncated and N is taken to be finite. If $N = 0$ (or 1), scattering is said to be *isotropic* (or *linearly anisotropic*).

The Legendre polynomials satisfy the *addition theorem*:

$$P_n(\Omega \cdot \Omega') = \frac{4\pi}{2n+1} \sum_{m=-n}^n Y_{n,m}(\Omega) Y_{n,m}^*(\Omega'), \quad (78)$$

where for $0 \leq |m| \leq n < \infty$, $Y_{n,m}(\Omega)$ is a *spherical harmonic* function:

$$Y_{n,m}(\Omega) = Y_{n,m}(\mu, \omega) = a_{n,m} P_n^{(|m|)}(\mu) e^{im\omega}, \quad (79a)$$

$$P_n^{l|m|}(\mu) = (1 - \mu^2)^{|m|/2} \left(\frac{d}{d\mu} \right)^{|m|} P_n(\mu)$$

= Associated Legendre function, (79b)

$$a_{n,m} = (-1)^{(m+|m|)/2} \left[\frac{2n+1}{4\pi} \frac{(n-|m|)!}{(n+|m|)!} \right]^{1/2}. \quad (79c)$$

Here * denotes complex conjugate, and $0! = 1$.

Introducing (78) into (77), we obtain:

$$\Sigma_s(\mathbf{x}, \boldsymbol{\Omega} \cdot \boldsymbol{\Omega}') = \sum_{n=0}^N \sum_{m=-n}^n \Sigma_{s,n}(\mathbf{x}) Y_{n,m}(\boldsymbol{\Omega}) Y_{n,m}^*(\boldsymbol{\Omega}'). \quad (80)$$

Thus, the scattering integral in (73a) can be written:

$$\int_{4\pi} \Sigma_s(\mathbf{x}, \boldsymbol{\Omega} \cdot \boldsymbol{\Omega}') \psi(\mathbf{x}, \boldsymbol{\Omega}') d\boldsymbol{\Omega}'$$

$$= \sum_{n=0}^N \sum_{m=-n}^n \Sigma_{s,n}(\mathbf{x}) Y_{n,m}(\mu, \omega) \int_{-1}^1 \int_0^{2\pi} Y_{n,m}^*(\mu', \omega') \Psi(x, y, z, \mu', \omega') d\omega' d\mu'. \quad (81)$$

Introducing (76) and (81) into (73a), we obtain the following 3-D Cartesian-geometry transport equation:

$$\left[\sqrt{1 - \mu^2} \left(\cos \omega \frac{\partial}{\partial x} + \sin \omega \frac{\partial}{\partial y} \right) + \mu \frac{\partial}{\partial z} \right] \psi(\mathbf{x}, \boldsymbol{\Omega}) + \Sigma_t(\mathbf{x}) \psi(\mathbf{x}, \boldsymbol{\Omega})$$

$$= \sum_{n=0}^N \sum_{m=-n}^n \Sigma_{s,n}(\mathbf{x}) Y_{n,m}(\boldsymbol{\Omega}) \int_{4\pi} Y_{n,m}^*(\boldsymbol{\Omega}') \psi(\mathbf{x}, \boldsymbol{\Omega}') d\boldsymbol{\Omega}' + \frac{Q(\mathbf{x})}{4\pi}. \quad (82)$$

In (82), the shorthand notations of (75) and (79a) have been used. Equation (82) holds for all spatial points $\mathbf{x} \in V$ and all unit vectors $\boldsymbol{\Omega}$ ($-1 \leq \mu \leq 1$ and $0 \leq \omega < 2\pi$). To determine ψ , (82) must be solved subject to the boundary condition expressed in (73b).

3.2 1-D Planar Geometry

In problems with 1-D planar symmetry,

1. The physical system is a planar “slab” consisting of spatial points (x, y, z) with $-\infty < x, y < \infty$ and $0 < z < Z$. Thus, the system is infinite in the (*transverse*) x - and y -directions and finite or possibly infinite in the (*depth*) z -direction.
2. The cross sections, isotropic internal source, and prescribed incident boundary fluxes are independent of the transverse variables x and y .

Because the problem geometry and neutron sources are independent of x and y , the angular flux itself is independent of x and y :

$$\psi(\mathbf{x}, \boldsymbol{\Omega}) = \Psi(z, \boldsymbol{\Omega}) = \Psi(z, \mu, \omega). \quad (83a)$$

In these circumstances, (82) immediately reduces to:

$$\mu \frac{\partial \Psi}{\partial z}(z, \Omega) + \Sigma_t(z) \Psi(z, \Omega) = \sum_{n=0}^N \sum_{m=-n}^n \Sigma_{s,n}(z) Y_{n,m}(\Omega) \int_{4\pi} Y_{n,m}^*(\Omega') \Psi(z, \Omega') d\Omega' + \frac{Q(z)}{4\pi}, \quad 0 < z < Z, \quad \Omega \in 4\pi. \quad (83b)$$

The boundary conditions prescribe the incident angular fluxes on the left and right edges of the slab:

$$\Psi(0, \mu, \omega) = \psi^b(\mu, \omega), \quad 0 < \mu \leq 1, \quad 0 \leq \omega < 2\pi, \quad (83c)$$

$$\Psi(Z, \mu, \omega) = \psi^b(\mu, \omega), \quad -1 \leq \mu < 0, \quad 0 \leq \omega < 2\pi. \quad (83d)$$

Equations (83) describe planar-geometry neutron transport *without azimuthal symmetry*.

The azimuthal angle can be eliminated by integrating the equations over $0 \leq \omega < 2\pi$. If we define the *azimuthally integrated angular flux*:

$$\Psi(z, \mu) = \int_0^{2\pi} \Psi(z, \mu, \omega) d\omega, \quad (84)$$

then upon integration over ω , (83b) yields:

$$\begin{aligned} \mu \frac{\partial \Psi}{\partial z}(z, \mu) + \Sigma_t(z) \Psi(z, \mu) &= \sum_{n=0}^N \sum_{m=-n}^n \Sigma_{s,n}(z) \left(\int_0^{2\pi} Y_{n,m}(\Omega) d\omega \right) \int_{4\pi} Y_{n,m}^*(\Omega') \Psi(z, \Omega') d\Omega' \\ &+ \frac{Q(z)}{2}, \quad 0 < z < Z, \quad -1 \leq \mu \leq 1. \end{aligned} \quad (85a)$$

However, (79) imply:

$$\int_0^{2\pi} Y_{n,m}(\Omega) d\omega = 2\pi \delta_{m,0} \left(\frac{2n+1}{4\pi} \right)^{1/2} P_n(\mu), \quad (85b)$$

and:

$$\begin{aligned} \int_{4\pi} Y_{n,0}^*(\Omega') \Psi(z, \Omega') d\Omega' &= \int_{-1}^1 \int_0^{2\pi} \left(\frac{2n+1}{4\pi} \right)^{1/2} P_n(\mu') \Psi(z, \mu', \omega') d\omega' d\mu' \\ &= \left(\frac{2n+1}{4\pi} \right)^{1/2} \int_{-1}^1 P_n(\mu') \Psi(z, \mu') d\mu'. \end{aligned} \quad (85c)$$

Introducing these results into (85a), we obtain the following simpler equation for $\Psi(z, \mu)$:

$$\begin{aligned} \mu \frac{\partial \Psi}{\partial z}(z, \mu) + \Sigma_t(z) \Psi(z, \mu) &= \sum_{n=0}^N \left(\frac{2n+1}{2} \right) \Sigma_{s,n}(z) P_n(\mu) \int_{-1}^1 P_n(\mu') \Psi(z, \mu') d\mu' \\ &+ \frac{Q(z)}{2}, \quad 0 < z < Z, \quad -1 \leq \mu \leq 1. \end{aligned} \quad (86a)$$

Also, integrating the boundary conditions (83c) and (83d) over ω , we obtain:

$$\Psi(0, \mu) = \psi^b(\mu) = \int_0^{2\pi} \psi^b(\mu, \omega) d\omega, \quad 0 < \mu \leq 1, \tag{86b}$$

$$\Psi(Z, \mu) = \psi^b(\mu) = \int_0^{2\pi} \psi^b(\mu, \omega) d\omega, \quad -1 \leq \mu < 0. \tag{86c}$$

Equation (86a) describe azimuthally integrated planar-geometry neutron transport.

To determine $\Psi(z, \mu)$, (86) must be solved. By (84), this solution is the azimuthally integrated angular flux of the original problem.

3.3 2-D (X,Y)-Geometry

In problems with 2-D (x, y) -symmetry (🔗 Fig. 20),

1. The physical system is an infinite “cylinder,” consisting of spatial points (x, y, z) with $(x, y) \in D$ (a convex region in the (x, y) -plane) and $-\infty < z < \infty$.
2. The cross sections, isotropic internal source, and prescribed incident boundary fluxes are independent of z .
3. The prescribed incident boundary fluxes are even functions of $\mu = \boldsymbol{\Omega} \cdot \mathbf{k}$:

$$\psi^b(x, y, \boldsymbol{\Omega}) = \psi^b(x, y, \boldsymbol{\Omega}_r), \quad (x, y) \in \partial D, \quad \boldsymbol{\Omega} \cdot \mathbf{n} < 0, \tag{87a}$$

where:

$$\begin{aligned} \boldsymbol{\Omega} &= \sqrt{1 - \mu^2} \cos \omega \mathbf{i} + \sqrt{1 - \mu^2} \sin \omega \mathbf{j} + \mu \mathbf{k} \\ &= \eta \mathbf{i} + \xi \mathbf{j} + \mu \mathbf{k}, \end{aligned} \tag{87b}$$

$$\begin{aligned} \boldsymbol{\Omega}_r &= \eta \mathbf{i} + \xi \mathbf{j} - \mu \mathbf{k}, \\ &= \text{Reflection of } \boldsymbol{\Omega} \text{ across the } (x, y)\text{-plane.} \end{aligned} \tag{87c}$$

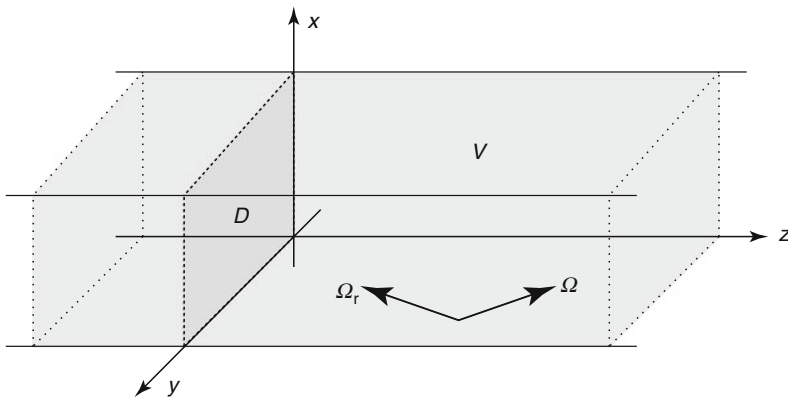


Figure 20
2-D (x, y) -geometry

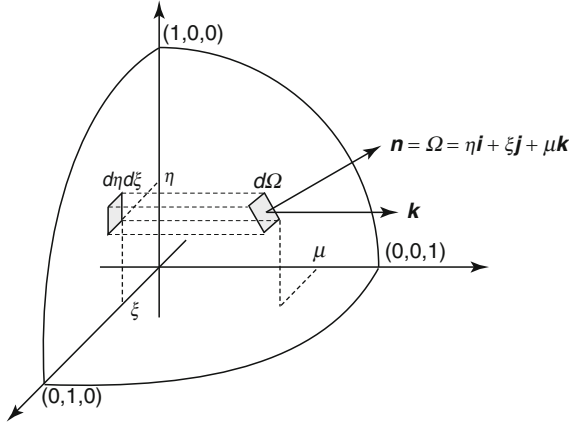


Figure 21
 $d\eta d\xi$ and $d\Omega$

Because the problem geometry is independent of z and the neutron sources are even functions of μ , the neutron angular is also independent of z and an even function of μ : $\psi(\mathbf{x}, \Omega) = \Psi(x, y, \mu, \omega) = \Psi(x, y, -\mu, \omega)$.

If we define:

$$\eta = \Omega_x = \sqrt{1 - \mu^2} \cos \omega, \quad (88a)$$

$$\xi = \Omega_y = \sqrt{1 - \mu^2} \sin \omega, \quad (88b)$$

then $|\Omega| = 1$ implies that for each value of η and ξ , there are two values of μ : $\mu^\pm = \pm\sqrt{1 - \eta^2 - \xi^2}$. Thus, if a function $f(\Omega)$ is an even function of μ , i.e., if for each η and ξ it has the same value at μ^+ and μ^- , then we can write:

$$f(\Omega) = g(\eta, \xi), \quad \eta^2 + \xi^2 \leq 1. \quad (89)$$

Also, from Fig. 21, we have:

$$d\Omega = \left(\frac{d\Omega}{d\eta d\xi} \right) d\eta d\xi = \frac{1}{|\mathbf{n} \cdot \mathbf{k}|} d\eta d\xi = \frac{d\eta d\xi}{|\mu|} = \frac{d\eta d\xi}{\sqrt{1 - \eta^2 - \xi^2}},$$

which implies:

$$\int_{4\pi} f(\Omega) d\Omega = 2 \int_{\eta^2 + \xi^2 \leq 1} \frac{g(\eta, \xi)}{\sqrt{1 - \eta^2 - \xi^2}} d\eta d\xi. \quad (90)$$

(The factor 2 occurs because the integral over $\eta^2 + \xi^2 \leq 1$ accounts for integration over only one hemisphere.)

From the above considerations, we can write:

$$\psi(\mathbf{x}, \boldsymbol{\Omega}) = \frac{1}{2} \Psi(x, y, \eta, \xi). \quad (91)$$

Using (91) and (88) in (76), we immediately get:

$$\boldsymbol{\Omega} \cdot \nabla \psi(\mathbf{x}, \boldsymbol{\Omega}) = \frac{1}{2} \left(\eta \frac{\partial}{\partial x} + \xi \frac{\partial}{\partial y} \right) \Psi(x, y, \eta, \xi). \quad (92)$$

Also, the spherical harmonic functions $Y_{n,m}(\boldsymbol{\Omega}) = Y_{n,m}(\mu, \omega)$ are even functions of μ for $n + m = \text{even}$, and odd functions of μ for $n + m = \text{odd}$ (see [79]). Therefore,

$$\begin{aligned} \int_{4\pi} Y_{n,m}^*(\boldsymbol{\Omega}') \psi(\mathbf{x}, \boldsymbol{\Omega}') d\Omega' &= \frac{1 + (-1)^{n+m}}{2} \int_{4\pi} Y_{n,m}^*(\boldsymbol{\Omega}') \psi(\mathbf{x}, \boldsymbol{\Omega}') d\Omega' \\ &= \frac{1 + (-1)^{n+m}}{2} \int_{(\eta')^2 + (\xi')^2 \leq 1} \frac{Y_{n,m}^*(\eta', \xi') \Psi(x, y, \eta', \xi')}{\sqrt{1 - (\eta')^2 - (\xi')^2}} d\eta' d\xi'. \end{aligned} \quad (93)$$

Introducing (92) and (93) into (82), we obtain the following (x, y) -geometry neutron transport equation:

$$\begin{aligned} \left(\eta \frac{\partial}{\partial x} + \xi \frac{\partial}{\partial y} \right) \Psi(x, y, \eta, \xi) + \Sigma_t(x, y) \Psi(x, y, \eta, \xi) \\ = \sum_{n=0}^{\infty} \sum_{m=-n}^n [1 + (-1)^{n+m}] \Sigma_{s,n}(x, y) Y_{n,m}(\eta, \xi) \\ \times \int_{(\eta')^2 + (\xi')^2 \leq 1} \frac{Y_{n,m}^*(\eta', \xi') \Psi(x, y, \eta', \xi')}{\sqrt{1 - (\eta')^2 - (\xi')^2}} d\eta' d\xi' \\ + \frac{Q(x, y)}{2\pi}, \quad (x, y) \in D, \quad \eta^2 + \xi^2 \leq 1. \end{aligned} \quad (94)$$

The (x, y) -geometry boundary condition prescribes the incident neutron flux for spatial points $(x, y) \in \partial D$ and for inward-pointing directions of flight $\boldsymbol{\Omega}$:

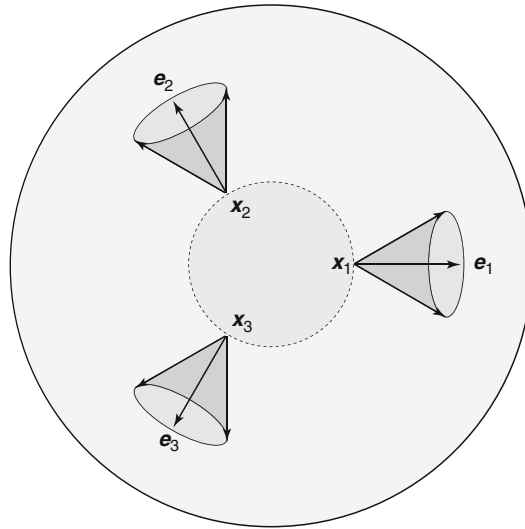
$$\begin{aligned} \Psi(x, y, \eta, \xi) = \Psi^b(x, y, \eta, \xi) = 2\Psi^b(x, y, \eta, \xi, \mu^+), \\ (x, y) \in \partial D, \quad (\eta \mathbf{i} + \xi \mathbf{j}) \cdot \mathbf{n} < 0. \end{aligned} \quad (95)$$

To determine $\Psi(x, y, \eta, \xi)$, (94) must be solved subject to the boundary conditions equation (95). The angular flux is then given by (91).

3.4 1-D Spherical Geometry

In problems with 1-D spherical symmetry (► Fig. 22),

The physical system is a sphere of radius R . (In the following, we take the center of the sphere to be the origin of the Cartesian coordinate system.)



■ Figure 22

1-D spherical symmetry. The angular flux is constant for: (i) spatial points \mathbf{x} equally distant from the center of the sphere and (ii) directions of flight Ω that make an equal angle with $\mathbf{e} = \mathbf{x}/r$

The cross sections and internal source are functions only of the radial variable

$$r = (x^2 + y^2 + z^2)^{1/2}. \quad (96)$$

For spatial points on the surface of the sphere ($|\mathbf{x}| = r = R$) and for inward-pointing directions of flight ($\Omega \cdot \mathbf{x} < 0$), the incident boundary fluxes are functions only of:

$$\begin{aligned} \mu &= \Omega \cdot (\mathbf{x}/r) \\ &= \text{Cosine of the angle between the direction of flight } \Omega \\ &\quad \text{and the radially outward direction } \mathbf{e} = \mathbf{x}/r. \end{aligned} \quad (97)$$

In these circumstances, the angular flux should be a function only of r and μ :

$$\psi(\mathbf{x}, \Omega) = \frac{1}{2\pi} \Psi(r, \mu). \quad (98)$$

[The factor 2π is included so that, as in planar geometry,

$$\int_{4\pi} \psi(\mathbf{x}, \Omega) d\Omega = \int_{-1}^1 \Psi(r, \mu) d\mu.] \quad (99)$$

Equation (98) implies:

$$\Omega \cdot \nabla \psi(\mathbf{x}, \Omega) = \frac{1}{2\pi} \left(\frac{\partial \Psi}{\partial r} \Omega \cdot \nabla r + \frac{\partial \Psi}{\partial \mu} \Omega \cdot \nabla \mu \right),$$

where, using (96) and (97), we have:

$$\begin{aligned}\boldsymbol{\Omega} \cdot \nabla r &= \left(\Omega_x \frac{\partial}{\partial x} + \Omega_y \frac{\partial}{\partial y} + \Omega_z \frac{\partial}{\partial z} \right) r = \Omega_x \frac{x}{r} + \Omega_y \frac{y}{r} + \Omega_z \frac{z}{r} = \mu, \\ \boldsymbol{\Omega} \cdot \nabla \mu &= \left(\Omega_x \frac{\partial}{\partial x} + \Omega_y \frac{\partial}{\partial y} + \Omega_z \frac{\partial}{\partial z} \right) \left(\frac{\Omega_x x + \Omega_y y + \Omega_z z}{r} \right) = \dots = \frac{1 - \mu^2}{r}.\end{aligned}$$

Therefore,

$$\boldsymbol{\Omega} \cdot \nabla \Psi(\mathbf{x}, \boldsymbol{\Omega}) = \frac{1}{2\pi} \left(\mu \frac{\partial}{\partial r} + \frac{1 - \mu^2}{r} \frac{\partial}{\partial \mu} \right) \Psi(r, \mu). \quad (100)$$

Also, defining the polar cosine μ locally (at each point) by (97) and letting ω be any consistently defined azimuthal angle, it is evident that Ψ is independent of ω . Thus, (85b) and (85c) hold, with $\Sigma_{s,n}(z)$ and $\Psi(z, \mu)$ replaced by $\Sigma_{s,n}(r)$ and $\Psi(r, \mu)$. Using this and (100) in (83b), we obtain the following 1-D spherical-geometry transport equation:


$$\begin{aligned}& \left(\mu \frac{\partial}{\partial r} + \frac{1 - \mu^2}{r} \frac{\partial}{\partial \mu} \right) \Psi(r, \mu) + \Sigma_t(r) \Psi(r, \mu) \\ &= \sum_{n=0}^{\infty} \left(\frac{2n+1}{2} \right) \Sigma_{s,n}(r) P_n(\mu) \int_{-1}^1 P_n(\mu') \Psi(r, \mu') d\mu' + \frac{Q(r)}{2}, \\ & 0 \leq r \leq R, \quad -1 \leq \mu \leq 1.\end{aligned} \quad (101)$$

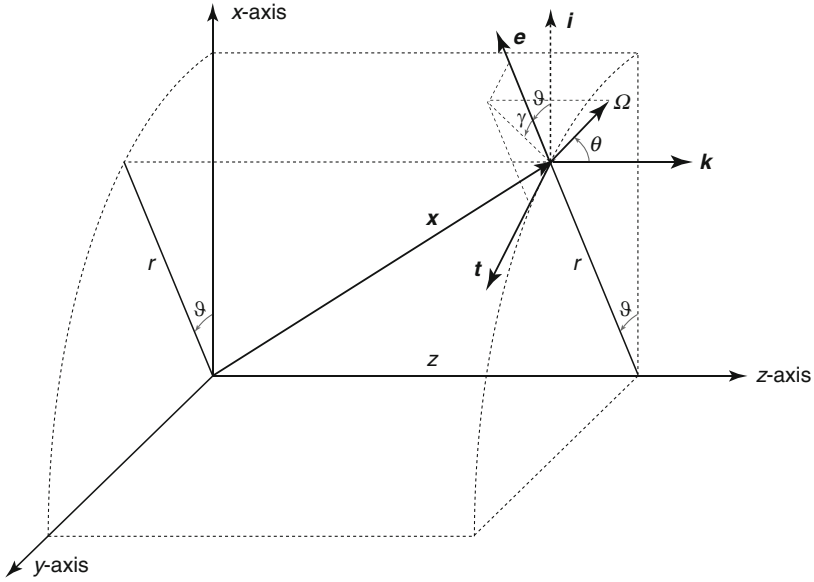
The spherical-geometry boundary condition prescribes the incident fluxes on the outer boundary of the sphere:

$$\Psi(R, \mu) = \Psi^b(\mu) = 2\pi \psi^b(R, \mu), \quad -1 \leq \mu < 0. \quad (102)$$

To determine $\Psi(r, \mu)$, (101) must be solved subject to the boundary condition (102). The angular flux is then given by (98).

3.5 3-D (r, ϑ, z) -Geometry

To derive the 2-D (r, z) and the 1-D cylindrical transport equations, we first derive the 3-D transport equation expressed in terms of cylindrical variables: the *radial spatial variable* $r = \sqrt{x^2 + y^2}$ and the *azimuthal spatial angle* $\vartheta = \tan^{-1}(y/x)$. We also replace the azimuthal directional angle ω by the angular deflection γ from the spatial azimuthal angle ϑ . γ ranges over $-\pi \leq \gamma \leq \pi$. Directions satisfying $|\gamma| < \pi/2$ are *outgoing* and describe flow away from $r = 0$. Directions satisfying $|\gamma| > \pi/2$ are *incoming* and describe flow toward $r = 0$. The spatial variable z and the polar cosine μ retain their Cartesian geometry interpretations (see  Fig. 23).



■ **Figure 23**
3-D (r, ϑ, z) variables

The Cartesian spatial variables x and y , and the azimuthal angular variable ω are expressed in terms of the *curvilinear* variables r and ϑ , and the azimuthal angular variable γ by:

$$x = r \cos \vartheta, \quad (103a)$$

$$y = r \sin \vartheta, \quad (103b)$$

$$\omega = \vartheta + \gamma. \quad (103c)$$

Then, defining the unit vectors (see [Fig. 23](#)):

$$\mathbf{e} = \frac{x}{r} \mathbf{i} + \frac{y}{r} \mathbf{j} = \cos \vartheta \mathbf{i} + \sin \vartheta \mathbf{j}, \quad (104a)$$

$$\mathbf{t} = -\frac{y}{r} \mathbf{i} + \frac{x}{r} \mathbf{j} = -\sin \vartheta \mathbf{i} + \cos \vartheta \mathbf{j}, \quad (104b)$$

we have:

$$\tilde{\mathbf{x}} = r\mathbf{e} + z\mathbf{k}, \quad (105a)$$

$$\tilde{\Omega} = \sqrt{1 - \mu^2} (\cos \gamma \mathbf{e} + \sin \gamma \mathbf{t}) + \mu \mathbf{k}, \quad (105b)$$

$$d\tilde{\Omega} = d\mu d\gamma = d\mu d\omega = d\Omega. \quad (105c)$$

(A tilde signifies that $\tilde{\mathbf{x}}$ is expressed in terms of r , ϑ , and z rather than x , y , and z , and that $\tilde{\mathbf{\Omega}}$ is expressed in terms of γ and μ rather than ω and μ . We note that $\tilde{\mathbf{x}} = \mathbf{x}$ and $\tilde{\mathbf{\Omega}} = \mathbf{\Omega}$.) The angular flux is now expressed in terms of the new variables:

$$\begin{aligned}\psi(\mathbf{x}, \mathbf{\Omega}) &= \psi(x, y, z, \mu, \omega) = \psi(r \cos \vartheta, r \sin \vartheta, z, \mu, \vartheta + \gamma) \\ &\equiv \Psi(r, \vartheta, z, \mu, \gamma) = \Psi(\tilde{\mathbf{x}}, \tilde{\mathbf{\Omega}}).\end{aligned}\quad (106)$$

The following identities can easily be shown:

$$\mathbf{\Omega} \cdot \nabla r = \cos \gamma \sqrt{1 - \mu^2}, \quad (107a)$$

$$\mathbf{\Omega} \cdot \nabla \vartheta = \frac{\sin \gamma}{r} \sqrt{1 - \mu^2}, \quad (107b)$$

$$\mathbf{\Omega} \cdot \nabla z = \mu, \quad (107c)$$

$$\mathbf{\Omega} \cdot \nabla \mu = 0, \quad (107d)$$

$$\mathbf{\Omega} \cdot \nabla \gamma = -\frac{\sin \gamma}{r} \sqrt{1 - \mu^2}. \quad (107e)$$

Equations (106) and (107) then give:

$$\mathbf{\Omega} \cdot \nabla \psi = \mu \frac{\partial \Psi}{\partial z} + \cos \gamma \sqrt{1 - \mu^2} \frac{\partial \Psi}{\partial r} + \frac{\sin \gamma}{r} \sqrt{1 - \mu^2} \left(\frac{\partial \Psi}{\partial \vartheta} - \frac{\partial \Psi}{\partial \gamma} \right). \quad (108)$$

We also have the identity:

$$\begin{aligned}\mu_0 &= \mathbf{\Omega} \cdot \mathbf{\Omega}' = \sqrt{1 - \mu^2} \sqrt{1 - (\mu')^2} (\cos \omega \cos \omega' + \sin \omega \sin \omega') + \mu \mu' \\ &= \sqrt{1 - \mu^2} \sqrt{1 - (\mu')^2} \cos(\omega - \omega') + \mu \mu' \\ &= \sqrt{1 - \mu^2} \sqrt{1 - (\mu')^2} \cos(\gamma - \gamma') + \mu \mu' \\ &= \sqrt{1 - \mu^2} \sqrt{1 - (\mu')^2} (\cos \gamma \cos \gamma' + \sin \gamma \sin \gamma') + \mu \mu' \\ &= \tilde{\mathbf{\Omega}} \cdot \tilde{\mathbf{\Omega}}' = \tilde{\mu}_0.\end{aligned}\quad (109)$$

We may define:

$$\begin{aligned}\Sigma_t(\mathbf{x}) &= \Sigma_t(x, y, z) = \Sigma_t(r \cos \vartheta, r \sin \vartheta, z) \\ &\equiv \tilde{\Sigma}_t(r, \vartheta, z) = \tilde{\Sigma}_t(\tilde{\mathbf{x}}),\end{aligned}\quad (110a)$$

$$\begin{aligned}\Sigma_s(\mathbf{x}, \mu_0) &= \Sigma_s(x, y, z, \mu_0) = \Sigma_s(r \cos \vartheta, r \sin \vartheta, z, \mu_0) \\ &\equiv \tilde{\Sigma}_s(r, \vartheta, z, \tilde{\mu}_0) = \tilde{\Sigma}_s(\tilde{\mathbf{x}}, \tilde{\mu}_0),\end{aligned}\quad (110b)$$

$$\begin{aligned}Q(\mathbf{x}) &= Q(x, y, z) = Q(r \cos \vartheta, r \sin \vartheta, z) \\ &\equiv \tilde{Q}(r, \vartheta, z) = \tilde{Q}(\tilde{\mathbf{x}}).\end{aligned}\quad (110c)$$

From (81), the scattering integral becomes:

$$\begin{aligned}&\int_{4\pi} \Sigma_s(\mathbf{x}, \mathbf{\Omega} \cdot \mathbf{\Omega}') \psi(\mathbf{x}, \mathbf{\Omega}') d\Omega' \\ &= \sum_{n=0}^N \sum_{m=-n}^n \tilde{\Sigma}_{s,n}(\tilde{\mathbf{x}}) Y_{n,m}(\mu, \gamma) \int_{-1}^1 \int_{-\pi}^{\pi} Y_{n,m}^*(\mu', \gamma') \Psi(r, \vartheta, z, \mu', \gamma') d\gamma' d\mu'.\end{aligned}\quad (111)$$

Using (109) and (111) in (73a), we obtain the following (r, ϑ, z) -geometry transport equation:

$$\begin{aligned} & \sqrt{1-\mu^2} \left[\cos \gamma \frac{\partial \Psi}{\partial r}(\tilde{\mathbf{x}}, \tilde{\Omega}) + \frac{\sin \gamma}{r} \left(\frac{\partial \Psi}{\partial \vartheta}(\tilde{\mathbf{x}}, \tilde{\Omega}) - \frac{\partial \Psi}{\partial \gamma}(\tilde{\mathbf{x}}, \tilde{\Omega}) \right) \right] + \mu \frac{\partial \Psi}{\partial z}(\tilde{\mathbf{x}}, \tilde{\Omega}) + \tilde{\Sigma}_t(\tilde{\mathbf{x}}) \Psi(\tilde{\mathbf{x}}, \tilde{\Omega}) \\ & = \sum_{n=0}^N \sum_{m=-n}^n \tilde{\Sigma}_{s,n}(\tilde{\mathbf{x}}) Y_{n,m}(\tilde{\Omega}) \int_{4\pi} Y_{n,m}^*(\tilde{\Omega}') \Psi(r, \vartheta, z, \tilde{\Omega}') d\tilde{\Omega}' + \frac{\tilde{Q}(\tilde{\mathbf{x}})}{4\pi}. \end{aligned} \quad (112a)$$

This equation describes 3-D neutron transport in, e.g., a finite cylindrical system of radius R and length Z . The spatial and angular variables then vary over:

$$0 < r \leq R, \quad -\pi \leq \vartheta \leq \pi, \quad 0 \leq z \leq Z, \quad -1 \leq \mu \leq 1, \quad -\pi \leq \gamma \leq \pi. \quad (112b)$$

In addition to (112), we must prescribe the incident angular flux on the outer boundary of the cylinder. First, on the outer “cylindrical” surface, we have:

$$\Psi(R, \vartheta, z, \mu, \gamma) = \Psi^b(\vartheta, z, \mu, \gamma), \quad 0 \leq z \leq Z, \quad -\pi \leq \vartheta \leq \pi, \quad -1 \leq \mu \leq 1, \quad |\gamma| > \frac{\pi}{2}. \quad (113a)$$

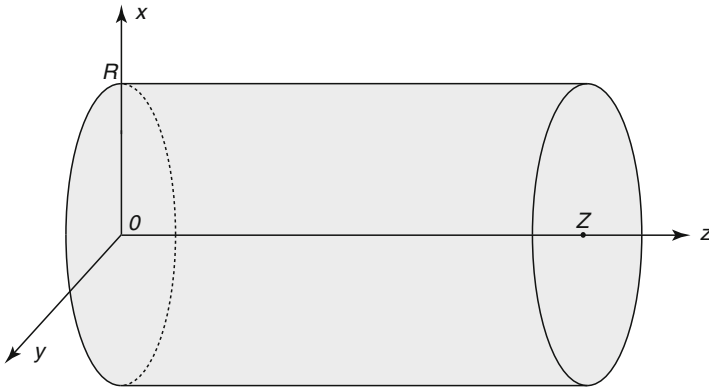
At the circular “cap” at $z = 0$, we have:


$$\Psi(r, \vartheta, 0, \mu, \gamma) = \Psi^b(r, \vartheta, \mu, \gamma), \quad 0 < r \leq R, \quad -\pi \leq \vartheta \leq \pi, \quad 0 < \mu \leq 1, \quad -\pi \leq \gamma \leq \pi. \quad (113b)$$

At the other circular “cap” at $z = Z$, we have:

$$\Psi(r, \vartheta, Z, \mu, \gamma) = \Psi^b(r, \vartheta, \mu, \gamma), \quad 0 < r \leq R, \quad -\pi \leq \vartheta \leq \pi, \quad -1 \leq \mu < 0, \quad -\pi \leq \gamma \leq \pi. \quad (113c)$$


Equations (112) and (113) describe 3-D neutron transport in the finite cylindrical system depicted in  Fig. 24.



 **Figure 24**
Finite cylindrical system

3.6 2-D (r, z)-Geometry

In problems with 2-D (r, z)-symmetry,

1. The physical system is typically a finite cylinder consisting of spatial points (r, ϑ, z) with $0 \leq r \leq R$, $-\pi \leq \vartheta \leq \pi$, and $0 \leq z \leq Z$ (see  Fig. 24).
2. The cross sections, internal isotropic source, and prescribed boundary conditions are independent of ϑ .
3. The prescribed incident boundary conditions are arbitrary functions of z, μ , and γ .

Thus, the system is symmetric through rotations of the spatial azimuthal angle ϑ (about the z -axis). The neutron angular flux will also have this symmetry, i.e., will be independent of ϑ :

$$\psi(\mathbf{x}, \boldsymbol{\Omega}) = \Psi(r, z, \mu, \gamma). \quad (114)$$

The (r, z)-geometry transport equation (and boundary conditions) can be obtained as a special case of the (r, ϑ, z)-geometry transport equations in which all quantities are independent of ϑ . Equations (112) and (113) yield:

$$\begin{aligned} \mu \frac{\partial \Psi}{\partial z}(r, z, \tilde{\boldsymbol{\Omega}}) + \sqrt{1 - \mu^2} \left(\cos \gamma \frac{\partial \Psi}{\partial r}(r, z, \tilde{\boldsymbol{\Omega}}) - \frac{\sin \gamma}{r} \frac{\partial \Psi}{\partial \gamma}(r, z, \tilde{\boldsymbol{\Omega}}) \right) + \tilde{\Sigma}_t(r, z) \Psi(r, z, \tilde{\boldsymbol{\Omega}}) \\ = \int_{4\pi} \tilde{\Sigma}_s(r, z, \tilde{\boldsymbol{\Omega}} \cdot \tilde{\boldsymbol{\Omega}}') \Psi(r, z, \tilde{\boldsymbol{\Omega}}') d\tilde{\boldsymbol{\Omega}}' + \frac{\tilde{Q}(r, z)}{4\pi}, \quad 0 < r \leq R, \quad 0 \leq z \leq Z, \\ -1 \leq \mu \leq 1, \quad -\pi \leq \gamma \leq \pi, \end{aligned} \quad (115)$$

and:

$$\Psi(R, z, \mu, \gamma) = \Psi^b(z, \mu, \gamma), \quad 0 \leq z \leq Z, \quad -1 \leq \mu \leq 1, \quad |\gamma| > \frac{\pi}{2}, \quad (116a)$$

$$\Psi(r, 0, \mu, \gamma) = \Psi^b(r, \mu, \gamma), \quad 0 < r \leq R, \quad 0 < \mu \leq 1, \quad -\pi \leq \gamma \leq \pi, \quad (116b)$$

$$\Psi(r, Z, \mu, \gamma) = \Psi^b(r, \mu, \gamma), \quad 0 < r \leq R, \quad -1 \leq \mu < 0, \quad -\pi \leq \gamma \leq \pi. \quad (116c)$$

The scattering integral in (115) can be written as in (111) or (112).

Equations (115) and (116) describe neutron transport in a finite cylindrical system with rotational symmetry.

3.7 1-D Cylindrical Geometry

In problems with 1-D cylindrical symmetry,

1. The physical system is an infinite cylinder consisting of spatial points (r, ϑ, z) with $0 \leq r \leq R$, $-\pi \leq \vartheta \leq \pi$, and $-\infty < z < \infty$.
2. The cross sections, internal isotropic source, and prescribed boundary conditions are independent of ϑ and z .
3. The prescribed incident boundary conditions are arbitrary functions of μ and γ .

Because the system is independent of ϑ and z , the neutron flux will also be independent of these variables:

$$\psi(\mathbf{x}, \boldsymbol{\Omega}) = \Psi(r, \mu, \gamma) = \Psi(r, \tilde{\boldsymbol{\Omega}}). \quad (117)$$

The 1-D cylindrical-geometry transport equation (and boundary conditions) is a special case of the (r, z) -geometry transport equations in which all quantities are independent of z . Equations (115) and (116) yield:

$$\begin{aligned} & \sqrt{1 - \mu^2} \left(\cos \gamma \frac{\partial \Psi}{\partial r}(r, \tilde{\boldsymbol{\Omega}}) - \frac{\sin \gamma}{r} \frac{\partial \Psi}{\partial \gamma}(r, \tilde{\boldsymbol{\Omega}}) \right) + \tilde{\Sigma}_t(r) \Psi(r, \tilde{\boldsymbol{\Omega}}) \\ &= \int_{4\pi} \tilde{\Sigma}_s(r, \tilde{\boldsymbol{\Omega}} \cdot \tilde{\boldsymbol{\Omega}}') \Psi(r, \tilde{\boldsymbol{\Omega}}') d\tilde{\boldsymbol{\Omega}}' + \frac{\tilde{Q}(r)}{4\pi}, \quad 0 < r \leq R, \quad -1 \leq \mu \leq 1, \quad -\pi \leq \gamma \leq \pi, \end{aligned} \quad (118)$$

and:

$$\Psi(R, \mu, \gamma) = \Psi^b(\mu, \gamma), \quad -1 \leq \mu \leq 1, \quad |\gamma| > \frac{\pi}{2}. \quad (119)$$

The scattering integral in (118) can be written as in (111) or (112).

Equations (118) and (119) describe neutron transport in an infinite cylindrical system with rotational symmetry and no axial (z -) dependence. The equations have one spatial variable (r) and two angular variables (μ and γ). In contrast, the 1-D planar and 1-D spherical-geometry transport equations have one spatial variable and only one angular variable.

3.8 Discussion

We have derived several forms of the neutron transport equation for 3-D problems in which geometric symmetries cause the angular flux to depend on fewer than three independent spatial variables. This has been done only for the most widely used 2-D geometries: (x, y) and (r, z) . Less important 2-D geometries, which are not treated here, are the two 2-D spherical geometries, cylindrical (ϑ, z) -geometry, and 2-D *helical* geometry (Larsen 2007). Also, we have not treated 3-D spherical geometry.

In the preceding derivations, we assumed for simplicity monoenergetic transport, no time-dependence, and no fission. However, it is straightforward to include these extra features.

We also assumed that in each geometry, the prescribed internal source Q is isotropic. This can immediately be relaxed to allow an internal anisotropic source whose spatial and angular dependences are the same as those allowed for the angular flux. For instance, in 1-D spherical geometry the angular flux is a function of r and μ , and one can include an internal anisotropic source, which is also a function of r and μ . Such sources arise naturally in multigroup problems, in which all the group angular fluxes have the same space-angle symmetry, and thus the source of neutrons that scatter into each group also share this symmetry.

In our derivations, we have not always stated the most general possible allowed geometric form of the spatial region V . For example, in 1-D spherical geometry, the physical system V was assumed to be the interior of a sphere of radius R . However, R could also be the *exterior* of a sphere of radius R , or, more generally, a *shell* consisting of points (r, ϑ, z) satisfying $R_0 \leq r \leq R_1$.

In these new cases, boundary conditions that prescribe the incident flux must be imposed on *all* physical boundaries.

Also, *reflecting* boundary conditions can be used along planes of geometric symmetry, and *periodic* boundary conditions are used to model one cell of an infinite periodic lattice. These and other types of boundary conditions are often employed in applications.

In all curvilinear geometries, the angular variables are expressed locally in space and change their value continuously as neutrons stream along flight paths. This gives rise to *angular derivative* terms in the neutron transport equation that significantly complicate the derivation of accurate numerical solutions (Lewis and Miller 1984). For example, the 1-D spherical-geometry transport equation (101) contains partial derivatives with respect to both r and μ . Mathematically, this leakage operator is a 2-D partial differential operator. Nonetheless, the historical tradition in the nuclear engineering community is to count only the spatial variables when describing a transport operator as 1-D, 2-D, or 3-D. Thus, the spherical-geometry transport equation is *called* a 1-D transport equation, even though it has partial derivatives with respect to two independent variables.

4 Integral Equation for Neutron Transport

In this section, we derive the integral form of the transport equation (Bell and Glasstone 1970; Case and Zweifel 1967; Williams 1971), an alternate but equivalent description of the transport process embodied in the integrodifferential form that we have been discussing thus far. The integral transport equation can be derived using first flight kernels to relate the angular flux in an element of phase space to the neutron emission rate due to fixed, scattering, and fission sources everywhere in the medium, and to sources on the boundary. Here, though, we proceed directly from the differential part of the integrodifferential transport equation by noting that it is formally a linear first-order partial differential operator that can be inverted using standard techniques. The result is not an explicit solution for the angular flux, because the right side of the equation contains the scattering and fission sources, but is an alternate form of the Boltzmann equation, which has the form of an integral equation.

4.1 Integral Equation for the Angular Flux

We begin by compactly expressing the time- and energy-dependent general-geometry transport equation (46a) as:

$$\frac{1}{v} \frac{\partial \psi}{\partial t}(\mathbf{x}, \boldsymbol{\Omega}, E, t) + \boldsymbol{\Omega} \cdot \nabla \psi(\mathbf{x}, \boldsymbol{\Omega}, E, t) + \Sigma_t(\mathbf{x}, E, t) \psi(\mathbf{x}, \boldsymbol{\Omega}, E, t) = Q(\mathbf{x}, \boldsymbol{\Omega}, E, t), \quad \mathbf{x} \in V, \quad (120a)$$

with the boundary condition (44) and initial condition (45a):

$$\psi(\mathbf{x}, \boldsymbol{\Omega}, E, t) = \psi^b(\mathbf{x}, \boldsymbol{\Omega}, E, t), \quad \mathbf{x} \in \partial V, \quad \boldsymbol{\Omega} \cdot \mathbf{n} < 0, \quad 0 < E < \infty, \quad 0 < t, \quad (120b)$$

$$\psi(\mathbf{x}, \boldsymbol{\Omega}, E, 0) = \psi^i(\mathbf{x}, \boldsymbol{\Omega}, E), \quad \mathbf{x} \in V, \quad \boldsymbol{\Omega} \in 4\pi, \quad 0 < E < \infty. \quad (120c)$$

The source Q in (120a), now including neutrons arising from inscatter and fission, is given by:

$$Q(\mathbf{x}, \boldsymbol{\Omega}, E, t) = \int_0^\infty \int_{4\pi} \Sigma_s(\boldsymbol{\Omega}' \cdot \boldsymbol{\Omega}, E' \rightarrow E) \psi(\mathbf{x}, \boldsymbol{\Omega}', E', t) d\Omega' dE' \\ + \frac{\chi_p(E)}{4\pi} \int_0^\infty \int_{4\pi} \nu \Sigma_f(E') \psi(\mathbf{x}, \boldsymbol{\Omega}', E', t) d\Omega' dE' + \frac{1}{4\pi} Q(\mathbf{x}, E, t). \quad (121)$$

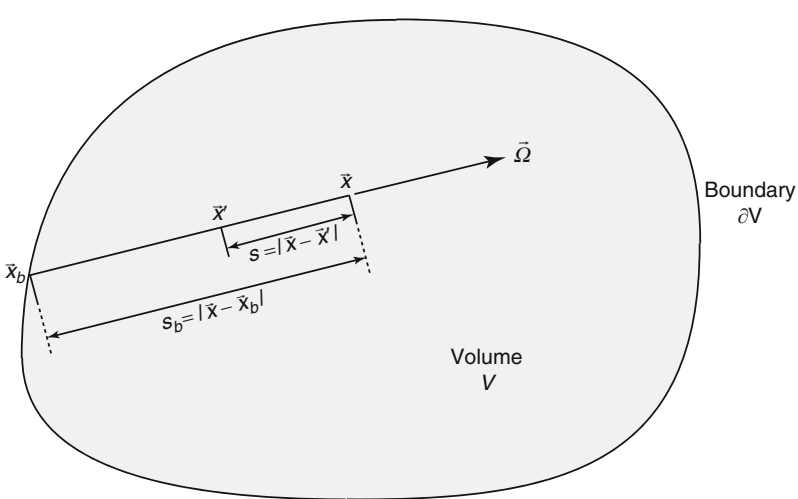
We ignore for the moment the fact that this source depends on the unknown angular flux and view (120) as a transport equation in a purely absorbing medium with a distributed source, and we seek an exact solution for the angular flux. To proceed in the general case, it is convenient to incorporate the initial condition as a source in the transport equation. Equation (120a) then reads:

$$\frac{1}{v} \frac{\partial \psi}{\partial t}(\mathbf{x}, \boldsymbol{\Omega}, E, t) + \boldsymbol{\Omega} \cdot \nabla \psi(\mathbf{x}, \boldsymbol{\Omega}, E, t) + \Sigma_t(\mathbf{x}, E, t) \psi(\mathbf{x}, \boldsymbol{\Omega}, E, t) = \widehat{Q}(\mathbf{x}, \boldsymbol{\Omega}, E, t), \quad \mathbf{x} \in V, \quad (122)$$

where:

$$\widehat{Q}(\mathbf{x}, \boldsymbol{\Omega}, E, t) = Q(\mathbf{x}, \boldsymbol{\Omega}, E, t) + \frac{1}{v} \delta(t) \psi^i(\mathbf{x}, \boldsymbol{\Omega}, E), \quad (123)$$

where $\widehat{Q}(\mathbf{x}, E, \boldsymbol{\Omega}, t) = \psi(\mathbf{x}, \boldsymbol{\Omega}, E, t) = 0$ for $t < 0$. The boundary condition remains as given by (120b).

We consider a point $\mathbf{x}' \in V$ that lies a distance s from $\mathbf{x} \in V$ along the direction $-\boldsymbol{\Omega}$, which intersects the boundary ∂V at a point \mathbf{x}_b , as shown in  Fig. 25:

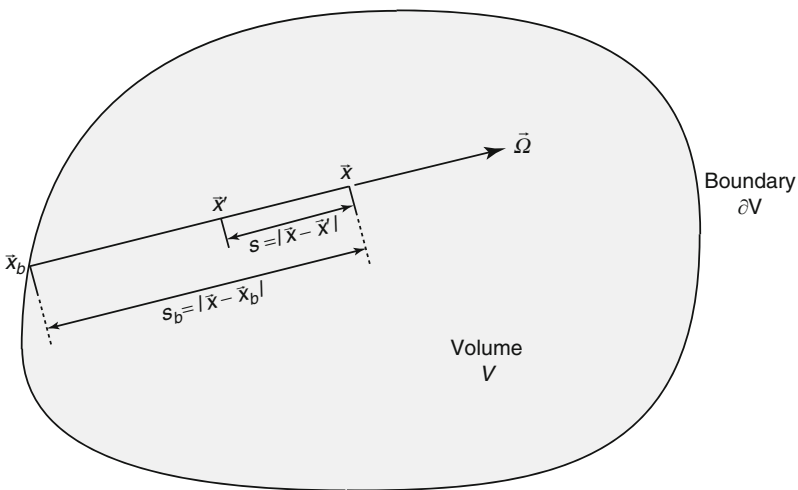


 Figure 25

Coordinates for the integral transport equation

Straightforward vector addition gives:

$$\mathbf{x}' = \mathbf{x} - s\boldsymbol{\Omega}, \quad (124a)$$

$$\mathbf{x}_b = \mathbf{x} - s_b\boldsymbol{\Omega}, \quad (124b)$$

where s_b is the distance from \mathbf{x} to the boundary along the direction $-\boldsymbol{\Omega}$. Similarly, if t is the time at which the neutron traveling along $\boldsymbol{\Omega}$ is found at position \mathbf{x} , then the neutron passed through position \mathbf{x}' at the earlier time t' given by:

$$t' = t - \frac{s}{v}. \quad (125)$$

We now write (122) with respect to the independent variables $(\mathbf{x}', \boldsymbol{\Omega}, E, t')$:

$$\frac{1}{v} \frac{\partial \psi}{\partial t'}(\mathbf{x}', \boldsymbol{\Omega}, E, t') + \boldsymbol{\Omega} \cdot \nabla \psi(\mathbf{x}', \boldsymbol{\Omega}, E, t') + \Sigma_t(\mathbf{x}', E, t') \psi(\mathbf{x}', \boldsymbol{\Omega}, E, t') = \widehat{Q}(\mathbf{x}', \boldsymbol{\Omega}, E, t'), \quad \mathbf{x}' \in V, \quad (126)$$

where ∇ now operates on \mathbf{x}' , and we consider the derivative of the angular flux with respect to s :

$$\begin{aligned} -\frac{d}{ds} \psi(\mathbf{x}', \boldsymbol{\Omega}, E, t') &= -\frac{d}{ds} \psi\left(\mathbf{x} - s\boldsymbol{\Omega}, \boldsymbol{\Omega}, E, t - \frac{s}{v}\right) \\ &= -\left[\frac{\partial t'}{\partial s} \frac{\partial \psi}{\partial t'} + \frac{\partial \mathbf{x}'}{\partial s} \cdot \nabla \psi \right] \\ &= -\left[\frac{\partial \left(t - \frac{s}{v}\right)}{\partial s} \frac{\partial \psi}{\partial t'} + \frac{\partial (\mathbf{x} - s\boldsymbol{\Omega})}{\partial s} \cdot \nabla \psi \right] \\ &= \frac{1}{v} \frac{\partial \psi}{\partial t'} + \boldsymbol{\Omega} \cdot \nabla \psi. \end{aligned} \quad (127)$$

Thus, the streaming operator in (126) is the total derivative or directional derivative along the path of the neutron. We can then rewrite (126) as:

$$\begin{aligned} -\frac{d\psi}{ds}\left(\mathbf{x} - s\boldsymbol{\Omega}, \boldsymbol{\Omega}, E, t - \frac{s}{v}\right) + \Sigma_t\left(\mathbf{x} - s\boldsymbol{\Omega}, E, t - \frac{s}{v}\right) \psi\left(\mathbf{x} - s\boldsymbol{\Omega}, \boldsymbol{\Omega}, E, t - \frac{s}{v}\right) \\ = \widehat{Q}\left(\mathbf{x} - s\boldsymbol{\Omega}, \boldsymbol{\Omega}, E, t - \frac{s}{v}\right), \quad 0 \leq s \leq s_b, \end{aligned} \quad (128)$$

where:

$$\widehat{Q}\left(\mathbf{x} - s\boldsymbol{\Omega}, \boldsymbol{\Omega}, E, t - \frac{s}{v}\right) = Q\left(\mathbf{x} - s\boldsymbol{\Omega}, \boldsymbol{\Omega}, E, t - \frac{s}{v}\right) + \frac{1}{v} \delta\left(t - \frac{s}{v}\right) \psi^i(\mathbf{x} - s\boldsymbol{\Omega}, \boldsymbol{\Omega}, E). \quad (129)$$

Equation (128) is a first-order ordinary differential equation in s , which can be solved using the integrating factor method. Multiplying (128) by the integrating factor:

$$\exp\left[-\int_0^s \Sigma_t\left(\mathbf{x} - s''\boldsymbol{\Omega}, E, t - \frac{s''}{v}\right) ds''\right]$$

and manipulating the resulting equation in the usual way gives:

$$\begin{aligned} & \frac{d}{ds} \left[\exp \left(- \int_0^s \Sigma_t \left(\mathbf{x} - s'' \boldsymbol{\Omega}, E, t - \frac{s''}{v} \right) ds'' \right) \psi \left(\mathbf{x} - s \boldsymbol{\Omega}, \boldsymbol{\Omega}, E, t - \frac{s}{v} \right) \right] \\ & = -\widehat{Q} \left(\mathbf{x} - s \boldsymbol{\Omega}, \boldsymbol{\Omega}, E, t - \frac{s}{v} \right) \exp \left[- \int_0^s \Sigma_t \left(\mathbf{x} - s'' \boldsymbol{\Omega}, E, t - \frac{s''}{v} \right) ds'' \right]. \end{aligned} \quad (130)$$

Integrating (130) between 0 and s and reorganizing terms yields, after a bit of algebra:

$$\begin{aligned} \psi(\mathbf{x}, \boldsymbol{\Omega}, E, t) &= \exp \left(- \int_0^s \Sigma_t \left(\mathbf{x} - s'' \boldsymbol{\Omega}, E, t - \frac{s''}{v} \right) ds'' \right) \psi \left(\mathbf{x} - s \boldsymbol{\Omega}, \boldsymbol{\Omega}, E, t - \frac{s}{v} \right) \\ &+ \int_0^s \widehat{Q} \left(\mathbf{x} - s' \boldsymbol{\Omega}, \boldsymbol{\Omega}, E, t - \frac{s'}{v} \right) \exp \left[- \int_0^{s'} \Sigma_t \left(\mathbf{x} - s'' \boldsymbol{\Omega}, E, t - \frac{s''}{v} \right) ds'' \right] ds'. \end{aligned} \quad (131)$$

Evaluating (131) at the boundary point $s = s_b$ and noting that:

$$\begin{aligned} \psi \left(\mathbf{x} - s_b \boldsymbol{\Omega}, \boldsymbol{\Omega}, E, t - \frac{s_b}{v} \right) &= \psi \left(\mathbf{x}_b, \boldsymbol{\Omega}, E, t - \frac{s_b}{v} \right), \\ &= \psi^b \left(\mathbf{x}_b, \boldsymbol{\Omega}, E, t - \frac{s_b}{v} \right) U(\nu t - s_b), \end{aligned} \quad (132)$$

where $U(\cdot)$ is the Heaviside unit step function, we obtain:

$$\begin{aligned} \psi(\mathbf{x}, \boldsymbol{\Omega}, E, t) &= \exp \left(- \int_0^{s_b} \Sigma_t \left(\mathbf{x} - s'' \boldsymbol{\Omega}, E, t - \frac{s''}{v} \right) ds'' \right) \psi^b \left(\mathbf{x}_b, \boldsymbol{\Omega}, E, t - \frac{s_b}{v} \right) U(\nu t - s_b) \\ &+ \int_0^{s_b} \widehat{Q} \left(\mathbf{x} - s' \boldsymbol{\Omega}, \boldsymbol{\Omega}, E, t - \frac{s'}{v} \right) \exp \left[- \int_0^{s'} \Sigma_t \left(\mathbf{x} - s'' \boldsymbol{\Omega}, E, t - \frac{s''}{v} \right) ds'' \right] ds'. \end{aligned} \quad (133)$$

The Heaviside function $U(\nu t - s_b)$ in (133) accounts for the finite neutron speed; a source neutron originating at the boundary and traveling at speed ν cannot stream a distance s_b to arrive at position \mathbf{x} at time t if $\nu t < s_b$.

Next, we note that the integral over s' in (133) for the initial condition part of the source \widehat{Q} can be explicitly carried out to give:

$$\begin{aligned} & \int_0^{s_b} \frac{1}{v} \delta \left(t - \frac{s'}{v} \right) \psi^i(\mathbf{x} - s' \boldsymbol{\Omega}, \boldsymbol{\Omega}, E) \exp \left[- \int_0^{s'} \Sigma_t \left(\mathbf{x} - s'' \boldsymbol{\Omega}, E, t - \frac{s''}{v} \right) ds'' \right] ds' \\ &= \psi^i(\mathbf{x} - \nu t \boldsymbol{\Omega}, \boldsymbol{\Omega}, E) \exp \left[- \int_0^{\nu t} \Sigma_t \left(\mathbf{x} - s'' \boldsymbol{\Omega}, E, t - \frac{s''}{v} \right) ds'' \right] U(s_b - \nu t), \end{aligned} \quad (134)$$

where well-known properties of the delta function have been used. Isolating this term in (133) and noting from (124a) and (124b) that:

$$s_b = |\mathbf{x} - \mathbf{x}_b|, \quad (135)$$

we obtain:

$$\begin{aligned}
 \psi(\mathbf{x}, \boldsymbol{\Omega}, E, t) &= \psi^b\left(\mathbf{x}_b, \boldsymbol{\Omega}, E, t - \frac{|\mathbf{x} - \mathbf{x}_b|}{v}\right) \exp\left(-\int_0^{|\mathbf{x} - \mathbf{x}_b|} \Sigma_t\left(\mathbf{x} - s''\boldsymbol{\Omega}, E, t - \frac{s''}{v}\right) ds''\right) \\
 &\times U(vt - |\mathbf{x} - \mathbf{x}_b|) + \psi^i(\mathbf{x} - vt\boldsymbol{\Omega}, \boldsymbol{\Omega}, E) \exp\left(-\int_0^{vt} \Sigma_t\left(\mathbf{x} - s''\boldsymbol{\Omega}, E, t - \frac{s''}{v}\right) ds''\right) \\
 &\times U(|\mathbf{x} - \mathbf{x}_b| - vt) + \int_0^{|\mathbf{x} - \mathbf{x}_b|} Q\left(\mathbf{x} - s'\boldsymbol{\Omega}, \boldsymbol{\Omega}, E, t - \frac{s'}{v}\right) \\
 &\times \exp\left(-\int_0^{s'} \Sigma_t\left(\mathbf{x} - s''\boldsymbol{\Omega}, E, t - \frac{s''}{v}\right) ds''\right) ds'. \tag{136}
 \end{aligned}$$

To obtain the final result, we transform the line integral in the last term in (136) to a volume integral. To effect this transformation, we first introduce an angular direction variable $\boldsymbol{\Omega}'$ and express this term as:

$$\begin{aligned}
 &\int_{4\pi} \int_0^{|\mathbf{x} - \mathbf{x}_b|} \delta(\boldsymbol{\Omega} - \boldsymbol{\Omega}') Q\left(\mathbf{x} - s'\boldsymbol{\Omega}', \boldsymbol{\Omega}', E, t - \frac{s'}{v}\right) \\
 &\times \exp\left(-\int_0^{s'} \Sigma_t\left(\mathbf{x} - s''\boldsymbol{\Omega}', E, t - \frac{s''}{v}\right) ds''\right) ds' d\boldsymbol{\Omega}'. \tag{137}
 \end{aligned}$$

Defining the intermediate position vector:

$$\mathbf{x}' = \mathbf{x} - s'\boldsymbol{\Omega}', \tag{138}$$

we note that an elementary volume about \mathbf{x}' can be written as:

$$dV' = (s' d\theta')(s' \sin \theta' d\phi') ds' = s'^2 ds' \sin \theta' d\theta' d\phi' = s'^2 ds' d\boldsymbol{\Omega}'. \tag{139}$$

Further, noting from (138) that $s' = |\mathbf{x} - \mathbf{x}'|$, (139) yields:

$$ds' d\boldsymbol{\Omega}' = \frac{dV'}{s'^2} = \frac{dV'}{|\mathbf{x} - \mathbf{x}'|^2}. \tag{140}$$

Introducing these results into (136), we obtain:

$$\begin{aligned}
 \psi(\mathbf{x}, \boldsymbol{\Omega}, E, t) &= \psi^b\left(\mathbf{x}_b, \boldsymbol{\Omega}, E, t - \frac{|\mathbf{x} - \mathbf{x}_b|}{v}\right) \exp\left(-\int_0^{|\mathbf{x} - \mathbf{x}_b|} \Sigma_t\left(\mathbf{x} - s''\boldsymbol{\Omega}, E, t - \frac{s''}{v}\right) ds''\right) \\
 &\times U(vt - |\mathbf{x} - \mathbf{x}_b|) + \psi^i(\mathbf{x} - vt\boldsymbol{\Omega}, \boldsymbol{\Omega}, E) \exp\left(-\int_0^{vt} \Sigma_t\left(\mathbf{x} - s''\boldsymbol{\Omega}, E, t - \frac{s''}{v}\right) ds''\right) \\
 &\times U(|\mathbf{x} - \mathbf{x}_b| - vt) + \int_V Q\left(\mathbf{x}', \boldsymbol{\Omega}', E, t - \frac{|\mathbf{x} - \mathbf{x}'|}{v}\right) \\
 &\times \frac{\exp\left[-\int_0^{|\mathbf{x} - \mathbf{x}'|} \Sigma_t\left(\mathbf{x} - s''\boldsymbol{\Omega}', E, t - \frac{s''}{v}\right) ds''\right]}{|\mathbf{x} - \mathbf{x}'|^2} \delta(\boldsymbol{\Omega} - \boldsymbol{\Omega}') dV', \tag{141}
 \end{aligned}$$

where we have noted that the integration domain $[0, s_b] \times [0, \pi] \times [0, 2\pi]$ is just the volume V of the medium.

Equation (141), with the source given by (121), represents the most general form of the integral transport equation for the angular flux. It is valid for an arbitrary boundary source, initial condition, and fixed source. Although complicated in appearance, the terms in this equation each have a simple physical interpretation. To see this, we first note that the integral:

$$\tau(\mathbf{x}, \mathbf{x}', \boldsymbol{\Omega}, E, t) = \int_0^{|\mathbf{x}-\mathbf{x}'|} \Sigma_t \left(\mathbf{x} - s''\boldsymbol{\Omega}, E, t - \frac{s''}{v} \right) ds'', \quad (142)$$

is the *optical distance* (the number of mean free paths) that a neutron with energy E experiences while traveling from \mathbf{x}' (at time $t' = t - |\mathbf{x} - \mathbf{x}'|/v$) to \mathbf{x} (at time t) in the direction of flight $\boldsymbol{\Omega} = (\mathbf{x} - \mathbf{x}')/|\mathbf{x} - \mathbf{x}'|$. The exponential factor $\exp[-\tau(\dots)]$ appearing in (141) is the probability that a neutron will not suffer a collision over this distance, while $\exp[-\tau(\dots)]/|\mathbf{x} - \mathbf{x}'|^2$ is the free flight kernel that additionally accounts for geometric spreading of a point source of neutrons. Thus, the first term in (141) describes the contribution to the angular flux at $(\mathbf{x}, \boldsymbol{\Omega}, E, t)$ from neutrons that originated at the boundary \mathbf{x}_b with energy E and direction $\boldsymbol{\Omega}$ at an earlier time $|\mathbf{x} - \mathbf{x}_b|/v$ and arrive at \mathbf{x} without suffering any collisions. The second term describes neutrons from the initial distribution with energy E and direction $\boldsymbol{\Omega}$ that are initially located at $\mathbf{x} - v t \boldsymbol{\Omega}$ and experience no collisions during the subsequent time interval t while streaming to \mathbf{x} . The third term accounts for source neutrons, as well as neutrons born in scattering and fission collisions with energy E and direction $\boldsymbol{\Omega}$ over the entire medium at an earlier time $|\mathbf{x} - \mathbf{x}_b|/v$ that subsequently arrive at \mathbf{x} unattenuated.

4.2 The Integral Equation for the Scalar Flux

The complexity of the integral equation is greatly reduced, and its utility greatly enhanced, when scattering is isotropic and a steady state is assumed. Under these conditions, (141) can be reduced without approximation to an integral equation for the scalar flux. To show this, we observe that the source Q given by (121) becomes independent of $\boldsymbol{\Omega}$ and simplifies to:

$$\begin{aligned} Q(\mathbf{x}, \boldsymbol{\Omega}, E) &= \frac{1}{4\pi} \int_0^\infty \Sigma_s(E' \rightarrow E) \phi(\mathbf{x}, E') dE' \\ &+ \frac{\chi_p(E)}{4\pi} \int_0^\infty v \Sigma_f(E') \phi(\mathbf{x}, E') dE' + \frac{1}{4\pi} Q(\mathbf{x}, E). \end{aligned} \quad (143)$$

Further, assuming a free surface condition, i.e., $\psi^b = 0$ and a homogeneous medium, the integral equation (141) becomes:

$$\psi(\mathbf{x}, \boldsymbol{\Omega}, E) = \int_V \frac{\exp(-\Sigma_t(E)|\mathbf{x} - \mathbf{x}'|)}{|\mathbf{x} - \mathbf{x}'|^2} Q(\mathbf{x}', E) \delta(\boldsymbol{\Omega} - \boldsymbol{\Omega}') dV'. \quad (144)$$

Integrating (144) over $\boldsymbol{\Omega}$ and substituting (143) into (144), we obtain the final result:

$$\begin{aligned} \phi(\mathbf{x}, E) &= \int_V \frac{\exp(-\Sigma_t(E)|\mathbf{x} - \mathbf{x}'|)}{4\pi|\mathbf{x} - \mathbf{x}'|^2} \int_0^\infty dE' [\Sigma_s(E' \rightarrow E) + \chi_p(E)v\Sigma_f(E')] \\ &\times \phi(\mathbf{x}', E') dV' + \int_V \frac{\exp(-\Sigma_t(E)|\mathbf{x} - \mathbf{x}'|)}{4\pi|\mathbf{x} - \mathbf{x}'|^2} Q(\mathbf{x}', E) dV'. \end{aligned} \quad (145)$$

This form of the integral equation, which has the scalar flux as the unknown, is known as *Peierls' equation*. Although stated above for a homogeneous medium with a free surface, it is apparent from the foregoing that Peierls' equation can be modified to account for boundary sources and material inhomogeneities.

4.3 Discussion

Peierls' equation is used in reactor physics for computing collision and escape probabilities in the context of fuel assembly homogenization. *Peierls' equation* has the advantage that the angular part of the flux is exactly treated, so that quadrature approximations of angular integrals are not necessary in numerical work. Moreover, boundary conditions are explicitly incorporated into the equation and therefore are not affected by numerical schemes devised to approximate the integral operator. However, unlike the integrodifferential transport equation, the integral equation is spatially nonlocal, which makes it less efficient for numerical solution.

At a more mathematical level, the integral equation is used in establishing the existence and uniqueness of solutions to the integrodifferential equation and, when expressed in terms of the collision density, in establishing rigorous results for convergence of the Monte Carlo method. Finally, we note that (145) can be reduced to the familiar forms of Peierls' equation appropriate in slab, spherically symmetric, and cylindrically symmetric geometries by suitable reductions of the free flight kernel.

5 The Adjoint Neutron Transport Equation

The transport operator is *non-self-adjoint*, and in many circumstances it is useful to formulate and solve the *adjoint transport equation*. This “dual” description is a powerful and enriching feature of the theory of linear operators and has been effectively exploited in reactor physics and neutron transport theory (Bell and Glasstone 1970; Case and Zweifel 1967; Henry 1975; Weinberg and Wigner 1958). Moreover, although the adjoint flux is a mathematical artifice, it can be interpreted physically as an “importance function” that quantifies the relative contribution of neutrons to a desired physical quantity (Lewins 1965). Adjoint formulations underlie the development of perturbation theory and variational methods (Bell and Glasstone 1970; Lewins 1968; Pomraning 1967a,b; Stacey 1974), sensitivity and uncertainty analysis (Cacuci 2003), and play a prominent role in the construction of a priori error estimates in the deterministic numerical solution of the transport equation. Also, neutron importance maps generated from the adjoint flux can be used to develop efficient variance reduction techniques that can result in dramatic improvements in the efficiency of Monte Carlo simulation methods (Van Ripper et al. 1997). Finally, in criticality problems, the adjoint fundamental eigenfunction is pivotal in developing a rigorous basis for reduced-order models, such as the point kinetics equations.

In this section, we derive the equation that is the mathematical adjoint of the general integrodifferential transport equation given by (46). For reasons that will become apparent below, we refer to the latter as the *forward transport equation*. We show how adjoint boundary and initial conditions can be assigned that are consistent with the importance interpretation of the adjoint angular flux, and we close with a presentation on forward and adjoint Green's functions.

A rigorous development of the theory of adjoint operators would rely heavily on techniques from functional analysis, a level of abstraction that is beyond the scope of this book. Instead, we adopt a more pedestrian approach that relies on explicit construction and emphasizes physical interpretation over mathematical rigor.

5.1 Definitions

We begin by defining the inner product, also known as the scalar product, of two real functions u and w of the phase space and time coordinates (\vec{x}, Ω, E, t) as:

$$\langle u, w \rangle = \int_0^T \int_0^\infty \int_R \int_{4\pi} u(\vec{x}, \Omega, E, t) w(\vec{x}, \Omega, E, t) d\Omega dV dE dt. \quad (146)$$

The integration domain is the phase space covering the volume of the body, the surface of the unit sphere, an allowable range of energies, and a time span which in principle can be infinite. The restriction to real functions is not unreasonable, since the functions encountered in neutronics applications, such as cross sections, sources, neutron number, angular flux, neutron importance, etc., are real and have well-defined physical interpretations. Moreover, the operators that act on these functions are also real. Smoothness and continuity of all functions and sufficient orders of their derivatives is tacitly assumed, and all mathematical operations employed are assumed to be valid. Useful properties of the inner product that follow, and which will be applied repeatedly in the ensuing, include symmetry, linearity, and homogeneity. These properties are encapsulated in the following statements:

$$\langle u, w \rangle = \langle w, u \rangle, \quad (147)$$

$$\langle \alpha_1 u_1 + \alpha_2 u_2, \alpha_3 w \rangle = \alpha_1 \alpha_3 \langle u_1, w \rangle + \alpha_2 \alpha_3 \langle u_2, w \rangle, \quad (148)$$

where α_1 , α_2 , and α_3 are real scalars. These properties of the inner product must be modified if the functions of interest are not real.

Given a linear operator \mathcal{L} , which may be differential, integral, or integro-differential, two real functions u and w , and an inner product, the *adjoint* of this operator, denoted by \mathcal{L}^\dagger , is defined by the inner-product identity:

$$\langle w, \mathcal{L}u \rangle = \langle u, \mathcal{L}^\dagger w \rangle. \quad (149)$$

Besides serving as a formal definition of an adjoint operator, this identity also defines an algorithm for the explicit construction of \mathcal{L}^\dagger . In this context, it is understood that all necessary elementary operations from calculus (differentiation rules, integration by parts, switching orders of integration, manipulating dummy variables) are applied until the function u stands freely under the inner product while w is acted upon by an operator. The latter operator is the adjoint operator. If \mathcal{L} is either entirely or partially differential in form, boundary terms will arise during this process, and these must be dealt with to complete the adjoint formulation. Strictly

speaking, \mathcal{L}^\dagger without regard to the boundary terms is referred to as the *formal adjoint* of \mathcal{L} , and the identity equation (149) is more precisely expressed as:

$$\langle w, \mathcal{L}u \rangle = P[u, w] + \langle u, \mathcal{L}^\dagger w \rangle, \quad (150)$$

where P denotes a boundary functional, also known as the bilinear concomitant. When $\mathcal{L}^\dagger = \mathcal{L}$, we say that the operator \mathcal{L} is *formally self-adjoint*. As we shall be treating all boundary terms explicitly, we drop the qualifying “formal” and, in what follows, simply refer to \mathcal{L}^\dagger as the adjoint operator.

5.2 Illustrative Example

Before proceeding with the derivation of the adjoint of the transport operator, it is instructive to apply the process to a 1-D second-order differential operator. Although this is done here for illustrative purposes, it is worth pointing out that the diffusion approximation to the transport equation and heavy gas models in neutron thermalization are described by second-order differential operators in spatial and energy variables, respectively. Thus, let us consider \mathcal{L} to be defined by:

$$\mathcal{L}u = a_2(x) \frac{d^2 u(x)}{dx^2} + a_1(x) \frac{du(x)}{dx} + a_0(x)u(x); \quad x \in [a, b], \quad (151)$$

with the inner product:

$$\langle u, w \rangle = \int_a^b u(x)w(x)dx. \quad (152)$$

Suitable boundary conditions on $u(x)$ are presumed prescribed at $x = a$ and $x = b$, and the coefficients a_0 , a_1 , and a_2 are specified functions of x . Proceeding, we multiply (151) by another function $w(x)$ and integrate over the domain of x . Noting the linearity of the inner product, the resulting expression may be written as a sum of inner products of w with the individual components of \mathcal{L} :

$$\begin{aligned} \langle w, \mathcal{L}u \rangle &= \langle w, \mathcal{L}_2 u \rangle + \langle w, \mathcal{L}_1 u \rangle + \langle w, \mathcal{L}_0 u \rangle \\ &= \int_a^b w(x) a_2(x) \frac{d^2 u(x)}{dx^2} dx + \int_a^b w(x) a_1(x) \frac{du(x)}{dx} dx \\ &\quad + \int_a^b w(x) a_0(x) u(x) dx. \end{aligned} \quad (153)$$

We consider each term independently and manipulate the integrands such that $u(x)$ is free-standing. Beginning with the last term on the right, we note that since multiplication is a commutative operation, we can write simply:

$$\begin{aligned} \langle w, \mathcal{L}_0 u \rangle &= \int_a^b w(x) a_0(x) u(x) dx \\ &= \int_a^b u(x) a_0(x) w(x) dx \\ &= \langle u, \mathcal{L}_0^\dagger w \rangle \equiv \langle u, \mathcal{L}_0 w \rangle. \end{aligned} \quad (154a)$$

This shows that the operation of multiplication is self-adjoint. Next, we consider the term involving the first derivative of u and integrate by parts:

$$\begin{aligned}
 \langle w, \mathcal{L}_1 u \rangle &= \int_a^b w(x) a_1(x) \frac{du(x)}{dx} dx \\
 &= \left[w(x) a_1(x) u(x) \right]_a^b - \int_a^b u(x) \frac{d}{dx} [a_1(x) w(x)] dx \\
 &= \left[w(x) a_1(x) u(x) \right]_a^b + \int_a^b u(x) \left\{ -\frac{d}{dx} [a_1(x) w(x)] \right\} dx \\
 &= \left[w(x) a_1(x) u(x) \right]_a^b + \langle u, \mathcal{L}_1^\dagger w \rangle.
 \end{aligned} \tag{154b}$$

This shows that a first-order differential operator is non-self-adjoint. However, when $a_1 = \text{constant}$, i.e., when \mathcal{L}_1 is a pure first derivative, we have the simple relationship $\mathcal{L}_1^\dagger = -\mathcal{L}_1$. We consider finally the term involving the second derivative of u and integrate by parts twice:

$$\begin{aligned}
 \langle w, \mathcal{L}_2 u \rangle &= \int_a^b w(x) a_2(x) \frac{d^2 u(x)}{dx^2} dx \\
 &= \left[w(x) a_2(x) \frac{du(x)}{dx} \right]_a^b - \int_a^b \frac{du(x)}{dx} \frac{d}{dx} [a_2(x) w(x)] dx \\
 &= \left[w(x) a_2(x) \frac{du(x)}{dx} - u(x) \frac{d}{dx} [a_2(x) w(x)] \right]_a^b + \int_a^b u(x) \frac{d^2}{dx^2} [a_2(x) w(x)] dx \\
 &= \left[w(x) a_2(x) \frac{du(x)}{dx} - u(x) \frac{d}{dx} [a_2(x) w(x)] \right]_a^b + \langle u, \mathcal{L}_2^\dagger w \rangle.
 \end{aligned} \tag{154c}$$

This shows that, in general, a second-order differential operator is non-self-adjoint. However, there are two circumstances under which \mathcal{L}_2 is self-adjoint: (i) when $a_2 = \text{constant}$, i.e., when \mathcal{L}_2 is a pure second derivative, and (ii) when the second-order differential operator appears in the symmetric form:

$$\mathcal{L}_2 u = \frac{d}{dx} \left[a_2(x) \frac{du(x)}{dx} \right]. \tag{155}$$

Combining (154) and inserting them into (153), we obtain for the adjoint of a general second-order ordinary differential operator:

$$\mathcal{L}^\dagger w = \frac{d^2}{dx^2} [a_2(x) w(x)] - \frac{d}{dx} [a_1(x) w(x)] + a_0(x) w(x); \quad x \in [a, b]. \tag{156}$$

We remark that although the operator defined by (151) is non-self-adjoint, it is well known and readily verified that any second-order differential operator can be converted into the self-adjoint form:

$$\mathcal{L} u = \frac{d}{dx} \left[p(x) \frac{du(x)}{dx} \right] + r(x) u(x), \tag{157}$$

by a suitable transformation of the coefficients. To complete this illustration, it is necessary to comment on the boundary functional associated with \mathcal{L} , which is given by:

$$P[u, w] = \left[w(x) a_2(x) \frac{du(x)}{dx} - u(x) \left(\frac{d}{dx} [a_2(x)w(x)] - a_1(x)w(x) \right) \right]_a^b. \quad (158)$$

Since u represents a physical quantity (such as the neutron scalar flux, chemical concentration, or temperature) that satisfies a well-posed mathematical model, a sufficient number of boundary conditions are presumably available. In the above example, these may take the form of u and/or its first derivative being specified at one or the other boundary $x = a$ and $x = b$. However, the adjoint function w is an arbitrary function (assumed sufficiently smooth) with no apparent physical attribute on which to base the assignment of boundary conditions. It will be shown below that a consistent set of boundary conditions can be obtained by requiring the boundary functional $P[u, w]$ to vanish. Thus, in the above example, if u satisfies:

$$u(a) = 0, \quad (159a)$$

$$u(b) = 0, \quad (159b)$$

then, $P[u, w]$ will vanish if:

$$w(a) = 0, \quad (160a)$$

$$w(b) = 0. \quad (160b)$$

On the other hand, if u satisfies:

$$\left. \frac{du}{dx} \right|_a = 0, \quad (161a)$$

$$\left. \frac{du}{dx} \right|_b = 0, \quad (161b)$$

then for $P[u, w]$ to vanish, w must satisfy the mixed boundary conditions:

$$\left. \frac{d}{dx} [a_2(x)w(x)] \right|_a - a_1(a)w(a) = 0, \quad (162a)$$

$$\left. \frac{d}{dx} [a_2(x)w(x)] \right|_b - a_1(b)w(b) = 0. \quad (162b)$$

Similarly, mixed boundary conditions on u , i.e., a linear combination of (159a, 159b) and (161a, 161b), yield mixed boundary conditions on w . Inhomogeneous boundary conditions and inhomogeneous terms (sources) can also be accommodated, as is demonstrated below for the adjoint neutron transport equation. Finally, if the operator is self-adjoint and the boundary conditions for u and w are identical, the problem is said to be self-adjoint, otherwise it is non-self-adjoint.

We close by remarking that the adjoints of 2-D and 3-D second-order differential operators can be similarly derived, employing Green's identities in lieu of integration by parts.

5.3 The Adjoint Transport Equation

We now apply the procedure developed above to derive the adjoint of the time-dependent forward transport equation, which we recall from (46) is:

$$\begin{aligned} & \frac{1}{v} \frac{\partial \psi}{\partial t}(\mathbf{x}, \boldsymbol{\Omega}, E, t) + \boldsymbol{\Omega} \cdot \nabla \psi(\mathbf{x}, \boldsymbol{\Omega}, E, t) + \Sigma_t(E) \psi(\mathbf{x}, \boldsymbol{\Omega}, E, t) \\ &= \int_0^\infty \int_{4\pi} \Sigma_s(\boldsymbol{\Omega}' \cdot \boldsymbol{\Omega}, E' \rightarrow E) \psi(\mathbf{x}, \boldsymbol{\Omega}', E', t) d\boldsymbol{\Omega}' dE' \\ &+ \frac{\chi_p(E)}{4\pi} \int_0^\infty \int_{4\pi} v \Sigma_f(E') \psi(\mathbf{x}, \boldsymbol{\Omega}', E', t) d\boldsymbol{\Omega}' dE' + \frac{1}{4\pi} Q(\mathbf{x}, E, t), \end{aligned} \quad (163a)$$

subject to the boundary condition and initial conditions:

$$\psi(\mathbf{x}, \boldsymbol{\Omega}, E, t) = \psi^b(\mathbf{x}, \boldsymbol{\Omega}, E, t), \quad \mathbf{x} \in \partial V, \quad \boldsymbol{\Omega} \cdot \mathbf{n} < 0, \quad 0 < E < \infty, \quad 0 < t < T, \quad (163b)$$

$$\psi(\mathbf{x}, \boldsymbol{\Omega}, E, 0) = \psi^i(\mathbf{x}, \boldsymbol{\Omega}, E), \quad \mathbf{x} \in V, \quad \boldsymbol{\Omega} \in 4\pi, \quad 0 < E < \infty. \quad (163c)$$

It is convenient to express (163a) in the compact form:

$$\mathcal{L}\psi = \mathcal{L}_t\psi + \mathcal{L}_l\psi + \mathcal{L}_r\psi - \mathcal{L}_s\psi - \mathcal{L}_f\psi = Q, \quad (164)$$

where components of \mathcal{L} symbolically describe time evolution, free streaming or leakage, removal (outscatter and absorption), inscatter, and fission operators, respectively, and Q is the fixed source. Proceeding as outlined earlier, we take the inner product of an auxiliary function $\psi^\dagger(\mathbf{x}, \boldsymbol{\Omega}, E, t)$ with $\mathcal{L}\psi$ and define the adjoint operator \mathcal{L}^\dagger through the inner-product identity:

$$\langle \psi^\dagger, \mathcal{L}\psi \rangle = P[\psi, \psi^\dagger] + \langle \psi, \mathcal{L}^\dagger \psi^\dagger \rangle, \quad (165)$$

where we have explicitly noted that boundary terms arise from the differential components of the transport operator. Inserting (164) into (165) and noting the linearity of \mathcal{L} , we can write:

$$\langle \psi^\dagger, \mathcal{L}\psi \rangle = \langle \psi, \mathcal{L}_t^\dagger \psi^\dagger \rangle + \langle \psi, \mathcal{L}_l^\dagger \psi^\dagger \rangle + \langle \psi, \mathcal{L}_r^\dagger \psi^\dagger \rangle - \langle \psi, \mathcal{L}_s^\dagger \psi^\dagger \rangle - \langle \psi, \mathcal{L}_f^\dagger \psi^\dagger \rangle. \quad (166)$$

We begin our treatment with the simplest term, namely, the removal term:

$$\begin{aligned} \langle \psi^\dagger, \mathcal{L}_r\psi \rangle &= \int_0^T dt \int_0^\infty dE \int_{4\pi} d\boldsymbol{\Omega} \int_V dV \psi^\dagger(\mathbf{x}, \boldsymbol{\Omega}, E, t) \Sigma_t(E) \psi(\mathbf{x}, \boldsymbol{\Omega}, E, t) \\ &= \int_0^T dt \int_0^\infty dE \int_{4\pi} d\boldsymbol{\Omega} \int_V dV \psi(\mathbf{x}, \boldsymbol{\Omega}, E, t) \Sigma_t(E) \psi^\dagger(\mathbf{x}, \boldsymbol{\Omega}, E, t) \\ &= \langle \psi, \mathcal{L}_r^\dagger \psi^\dagger \rangle = \langle \psi, \mathcal{L}_r \psi^\dagger \rangle. \end{aligned} \quad (167a)$$

Thus, the removal term is trivially self-adjoint. Next, we consider the time evolution term and integrate by parts:

$$\begin{aligned}
 \langle \psi^\dagger, \mathcal{L}_t \psi \rangle &= \int_0^\infty dE \int_{4\pi} d\Omega \int_V dV \int_0^T dt \psi^\dagger(\mathbf{x}, \boldsymbol{\Omega}, E, t) \frac{1}{v} \frac{\partial \psi}{\partial t}(\mathbf{x}, \boldsymbol{\Omega}, E, t) \\
 &= \int_0^\infty dE \int_{4\pi} d\Omega \int_V dV \left[\frac{1}{v} \psi^\dagger(\mathbf{x}, \boldsymbol{\Omega}, E, t) \psi(\mathbf{x}, \boldsymbol{\Omega}, E, t) \right]_0^T \\
 &\quad + \int_0^T dt \int_0^\infty dE \int_{4\pi} d\Omega \int_V dV \psi^\dagger(\mathbf{x}, \boldsymbol{\Omega}, E, t) \left[-\frac{1}{v} \frac{\partial \psi^\dagger}{\partial t}(\mathbf{x}, \boldsymbol{\Omega}, E, t) \right] \\
 &= P_t[\psi, \psi^\dagger] + \langle \psi, \mathcal{L}_t^\dagger \psi^\dagger \rangle. \tag{167b}
 \end{aligned}$$

The boundary functional P_t denotes a restricted inner product, wherein the time variable is constrained to take its initial and final values only. Being a first-order differential operator, the time evolution operator is non-self-adjoint. Proceeding likewise for the streaming operator, we first note the vector identity:

$$\psi^\dagger \mathcal{L}_l \psi = \psi^\dagger \boldsymbol{\Omega} \cdot \nabla \psi = \nabla \cdot (\boldsymbol{\Omega} \psi \psi^\dagger) - \psi \boldsymbol{\Omega} \cdot \nabla \psi^\dagger$$

and apply the divergence theorem to get:

$$\begin{aligned}
 \langle \psi^\dagger, \mathcal{L}_l \psi \rangle &= \int_0^T dt \int_0^\infty dE \int_{4\pi} d\Omega \int_V dV \left[\nabla \cdot (\boldsymbol{\Omega} \psi \psi^\dagger) - \psi \boldsymbol{\Omega} \cdot \nabla \psi^\dagger \right] \\
 &= \int_0^T dt \int_0^\infty dE \int_{4\pi} d\Omega \int_{\partial V} dA \mathbf{n} \cdot \boldsymbol{\Omega} \psi(\mathbf{x}, \boldsymbol{\Omega}, E, t) \psi^\dagger(\mathbf{x}, \boldsymbol{\Omega}, E, t) \\
 &\quad + \int_0^T dt \int_0^\infty dE \int_{4\pi} d\Omega \int_V dV \psi(\mathbf{x}, \boldsymbol{\Omega}, E, t) \left[-\boldsymbol{\Omega} \cdot \nabla \psi^\dagger \right] \\
 &= P_l[\psi, \psi^\dagger] + \langle \psi, \mathcal{L}_l^\dagger \psi^\dagger \rangle. \tag{167c}
 \end{aligned}$$

The boundary functional P_l denotes a restricted inner product, wherein the spatial variable is constrained to lie on the surface of the body. We observe that the streaming operator is also non-self-adjoint.

We consider now the adjoint of the inscatter operator, which is an integral operator. The significance of this is that boundary terms will not arise. Thus:

$$\begin{aligned}
 \langle \psi^\dagger, \mathcal{L}_s \psi \rangle &= \int_0^T dt \int_V dV \int_0^\infty dE \int_{4\pi} d\Omega \\
 &\quad \psi^\dagger(\mathbf{x}, \boldsymbol{\Omega}, E, t) \int_0^\infty dE' \int_{4\pi} d\Omega' \Sigma_s(\boldsymbol{\Omega}' \cdot \boldsymbol{\Omega}, E' \rightarrow E) \psi(\mathbf{x}, \boldsymbol{\Omega}', E', t) \\
 &= \int_0^T dt \int_V dV \int_0^\infty dE' \int_{4\pi} d\Omega' \\
 &\quad \int_0^\infty dE \int_{4\pi} d\Omega \psi^\dagger(\mathbf{x}, \boldsymbol{\Omega}, E, t) \Sigma_s(\boldsymbol{\Omega}' \cdot \boldsymbol{\Omega}, E' \rightarrow E) \psi(\mathbf{x}, \boldsymbol{\Omega}', E', t)
 \end{aligned}$$

$$\begin{aligned}
&= \int_0^T dt \int_V dV \int_0^\infty dE \int_{4\pi} d\Omega \\
&\quad \int_0^\infty dE' \int_{4\pi} d\Omega' \psi(\mathbf{x}, \boldsymbol{\Omega}, E, t) \Sigma_s(\boldsymbol{\Omega} \cdot \boldsymbol{\Omega}', E \rightarrow E') \psi^\dagger(\mathbf{x}, \boldsymbol{\Omega}', E', t) \\
&= \int_0^T dt \int_V dV \int_0^\infty dE \int_{4\pi} d\Omega \\
&\quad \psi(\mathbf{x}, \boldsymbol{\Omega}, E, t) \int_0^\infty dE' \int_{4\pi} d\Omega' \Sigma_s(\boldsymbol{\Omega} \cdot \boldsymbol{\Omega}', E \rightarrow E') \psi^\dagger(\mathbf{x}, \boldsymbol{\Omega}', E', t) \\
&= \langle \psi, \mathcal{L}_s^\dagger \psi^\dagger \rangle, \tag{167d}
\end{aligned}$$

where in the first step, the orders of integration for the pre- and post-collision energies were switched, as were the corresponding directions, and in the second step, the dummy variables for pre- and post-collision energies were interchanged, as were those of the corresponding directions. We notice that the adjoint of the inscatter operator is obtained simply by reversing the orders of the pre- and post-collision arguments in the scattering kernel. Since scattering is rotationally symmetric, this affects only the energy loss part of the kernel. In other words, the scattering operator for coherent scattering (i.e., scattering without energy loss) is self-adjoint.

Manipulating the fission operator in the same manner as the scattering operator, we get:

$$\begin{aligned}
\langle \psi^\dagger, \mathcal{L}_f \psi \rangle &= \int_0^T dt \int_V dV \int_0^\infty dE \int_{4\pi} d\Omega \\
&\quad \psi^\dagger(\mathbf{x}, \boldsymbol{\Omega}, E, t) \frac{\chi_p(E)}{4\pi} \int_0^\infty dE' \int_{4\pi} d\Omega' \nu \Sigma_f(E') \psi(\mathbf{x}, \boldsymbol{\Omega}', E', t) \\
&= \int_0^T dt \int_V dV \int_0^\infty dE' \int_{4\pi} d\Omega' \\
&\quad \int_0^\infty dE \int_{4\pi} d\Omega \frac{\chi_p(E)}{4\pi} \psi^\dagger(\mathbf{x}, \boldsymbol{\Omega}, E, t) \nu \Sigma_f(E') \psi(\mathbf{x}, \boldsymbol{\Omega}', E', t) \\
&= \int_0^T dt \int_V dV \int_0^\infty dE \int_{4\pi} d\Omega \\
&\quad \int_0^\infty dE' \int_{4\pi} d\Omega' \frac{\chi_p(E')}{4\pi} \psi(\mathbf{x}, \boldsymbol{\Omega}, E, t) \nu \Sigma_f(E) \psi^\dagger(\mathbf{x}, \boldsymbol{\Omega}', E', t) \\
&= \int_0^T dt \int_V dV \int_0^\infty dE \int_{4\pi} d\Omega \\
&\quad \psi(\mathbf{x}, \boldsymbol{\Omega}, E, t) \nu \Sigma_f(E) \int_0^\infty dE' \int_{4\pi} d\Omega' \frac{\chi_p(E')}{4\pi} \psi^\dagger(\mathbf{x}, \boldsymbol{\Omega}', E', t) \\
&= \langle \psi, \mathcal{L}_f^\dagger \psi^\dagger \rangle. \tag{167e}
\end{aligned}$$

The fission operator is non-self-adjoint with respect to the energy variable, the angular distribution being isotropic. It becomes self-adjoint when the fission cross section is energy independent and all fission neutrons are born with the same energy, i.e., in the one-speed approximation.

Finally, substituting (167a–167e) into (166) yields:

$$\langle \psi^\dagger, \mathcal{L} \psi \rangle = P_t [\psi, \psi^\dagger] + P_l [\psi, \psi^\dagger] + \langle \psi, \mathcal{L}^\dagger \psi^\dagger \rangle, \tag{168}$$

and thus for the adjoint transport operator:

$$\begin{aligned} \mathcal{L}^\dagger \psi^\dagger = & -\frac{1}{v} \frac{\partial \psi^\dagger}{\partial t}(\mathbf{x}, \boldsymbol{\Omega}, E, t) - \boldsymbol{\Omega} \cdot \nabla \psi^\dagger(\mathbf{x}, \boldsymbol{\Omega}, E, t) + \Sigma_t(E) \psi^\dagger(\mathbf{x}, \boldsymbol{\Omega}, E, t) \\ & - \int_0^\infty \int_{4\pi} \Sigma_s(\boldsymbol{\Omega} \cdot \boldsymbol{\Omega}', E \rightarrow E') \psi^\dagger(\mathbf{x}, \boldsymbol{\Omega}', E', t) d\Omega' dE' \\ & - v \Sigma_f(E) \int_0^\infty \int_{4\pi} \frac{\chi_p(E')}{4\pi} \psi^\dagger(\mathbf{x}, \boldsymbol{\Omega}', E', t) d\Omega' dE'. \end{aligned} \quad (169)$$

Although $\psi^\dagger(\mathbf{x}, \boldsymbol{\Omega}, E, t)$ is referred to as the *adjoint angular flux*, the physical interpretation of this quantity (hence its units) can only be established when it is related to some functional of the forward angular flux $\psi(\mathbf{x}, \boldsymbol{\Omega}, E, t)$, which, moreover, will dictate the choice of the adjoint source and adjoint boundary-initial conditions. This will be demonstrated shortly below, but first we make some general observations on the adjoint transport process.

An adjoint problem is defined such that the adjoint angular flux $\psi^\dagger(\mathbf{x}, \boldsymbol{\Omega}, E, t)$ is a solution of the following adjoint transport equation:

$$\begin{aligned} & -\frac{1}{v} \frac{\partial \psi^\dagger}{\partial t}(\mathbf{x}, \boldsymbol{\Omega}, E, t) - \boldsymbol{\Omega} \cdot \nabla \psi^\dagger(\mathbf{x}, \boldsymbol{\Omega}, E, t) + \Sigma_t(E) \psi^\dagger(\mathbf{x}, \boldsymbol{\Omega}, E, t) \\ & = \int_0^\infty \int_{4\pi} \Sigma_s(\boldsymbol{\Omega} \cdot \boldsymbol{\Omega}', E \rightarrow E') \psi^\dagger(\mathbf{x}, \boldsymbol{\Omega}', E', t) d\Omega' dE' \\ & \quad + v \Sigma_f(E) \int_0^\infty \int_{4\pi} \frac{\chi_p(E')}{4\pi} \psi^\dagger(\mathbf{x}, \boldsymbol{\Omega}', E', t) d\Omega' dE' + Q^\dagger(\mathbf{x}, \boldsymbol{\Omega}, E, t), \end{aligned} \quad (170)$$

for a given source adjoint Q^\dagger and given adjoint boundary and initial conditions. The adjoint flux represents the flow of pseudo-particles, or adjoint particles (sometimes also referred to as “adjunctons”), which, like neutrons, are created, destroyed, and redistributed in phase space. However, the adjoint transport process is fundamentally different. Adjoint particles:

- Are born in the medium distributed in phase space according to the adjoint source, but beginning at some *final* or *terminal* time
- Stream in *reverse* time to earlier times and travel in *reverse* directions
- *Gain* energy in scattering collisions, but the inscattering and outscattering terms do not balance when integrated over all energies and directions, i.e., the energy-dependent adjoint scattering operator is *nonconservative*
- Are isotropically emitted in fission reactions, but the energy-dependence of the adjoint fission cross section is proportional to the neutron fission spectrum while the energy spectrum of the resulting adjoint fission particles is proportional to the neutron fission cross section.

In other words, the adjoint equation is a *backward* transport equation, the adjoint angular flux satisfying a final or terminal condition in time instead of an initial condition, and a boundary condition which is specified for outgoing directions instead of incoming directions. To emphasize this distinction between the two approaches, the neutron transport equation is referred to as a *forward* transport equation.

Like the forward transport equation, the adjoint transport equation has a unique solution for subcritical systems with fixed sources, while adjoint k -eigenvalue and adjoint α -eigenvalue problems can be defined for multiplying systems. For both types of eigenvalue problems, it can

be shown that the adjoint fundamental mode is positive and the dominant adjoint eigenvalue is identical to the dominant eigenvalue of the forward problem.

5.4 Adjoint Flux as an Importance Function

Adjoint transport problems lead to a natural physical interpretation of the adjoint flux and, under certain circumstances, an adjoint formulation results in a more efficient solution to a physical problem than the traditional forward approach. We demonstrate this next.

Expressing the forward and adjoint problems in condensed notation as:

$$\mathcal{L}\psi = Q, \quad (171)$$

$$\mathcal{L}^\dagger \psi^\dagger = Q^\dagger, \quad (172)$$

and then subtracting the inner product of ψ with (172) from the inner-product of ψ^\dagger with (171), we obtain:

$$\langle \psi^\dagger, \mathcal{L}\psi \rangle - \langle \psi, \mathcal{L}^\dagger \psi^\dagger \rangle = \langle \psi^\dagger, Q \rangle - \langle \psi, Q^\dagger \rangle. \quad (173)$$

Noting the definition of the adjoint operator as expressed by the inner product identity equation (168), the left-hand side of (173) can be simplified to obtain:

$$P_t [\psi, \psi^\dagger] + P_l [\psi, \psi^\dagger] = \langle \psi^\dagger, Q \rangle - \langle \psi, Q^\dagger \rangle, \quad (174)$$

where P_t is given by:

$$\begin{aligned} P_t [\psi, \psi^\dagger] &= \int_0^\infty dE \int_{4\pi} d\Omega \int_V dV \frac{1}{v} \psi^\dagger(\mathbf{x}, \boldsymbol{\Omega}, E, T) \psi(\mathbf{x}, \boldsymbol{\Omega}, E, T) \\ &\quad - \int_0^\infty dE \int_{4\pi} d\Omega \int_V dV \frac{1}{v} \psi^\dagger(\mathbf{x}, \boldsymbol{\Omega}, E, 0) \psi(\mathbf{x}, \boldsymbol{\Omega}, E, 0), \end{aligned} \quad (175)$$

and P_l by:

$$\begin{aligned} P_l [\psi, \psi^\dagger] &= \int_0^T dt \int_0^\infty dE \int_{4\pi} d\Omega \int_{\partial V} dA \mathbf{n} \cdot \boldsymbol{\Omega} \psi(\mathbf{x}, \boldsymbol{\Omega}, E, t) \psi^\dagger(\mathbf{x}, \boldsymbol{\Omega}, E, t) \\ &= \int_0^T dt \int_0^\infty dE \int_{\mathbf{n} \cdot \boldsymbol{\Omega} > 0} d\Omega \int_{\partial V} dA \mathbf{n} \cdot \boldsymbol{\Omega} \psi(\mathbf{x}, \boldsymbol{\Omega}, E, t) \psi^\dagger(\mathbf{x}, \boldsymbol{\Omega}, E, t) \\ &\quad - \int_0^T dt \int_0^\infty dE \int_{\mathbf{n} \cdot \boldsymbol{\Omega} < 0} d\Omega \int_{\partial V} dA |\mathbf{n} \cdot \boldsymbol{\Omega}| \psi(\mathbf{x}, \boldsymbol{\Omega}, E, t) \psi^\dagger(\mathbf{x}, \boldsymbol{\Omega}, E, t). \end{aligned} \quad (176)$$

The identity expressed by (174) is a key result in the adjoint-space formulation of transport problems. It relates functionals of the forward and adjoint angular fluxes at initial and final times and along incoming and outgoing directions at the surface of the body to the functionals of these fluxes in the interior of the body with fixed sources. This *generalized reciprocity relationship* enables transport problems to be posed using either forward or adjoint descriptions, provides a physical interpretation of the adjoint flux, and imposes consistent adjoint boundary and terminal conditions. While the class of such problems is wide, we highlight here so-called source-detector problems for subcritical systems at steady state, for which the adjoint formulation is extensively employed.

5.4.1 Source-Detector Problems

A classic forward problem is to determine a desired linear functional of the steady-state flux for a given interior source distribution and a free surface boundary condition. That is, we are interested in the solution of the forward transport equation:

$$\mathcal{L}\psi = Q, \quad (177a)$$

$$\psi = 0, \quad \mathbf{x} \in \partial V, \quad \boldsymbol{\Omega} \cdot \mathbf{n} < 0, \quad 0 < E < \infty, \quad (177b)$$

which is used to compute the functional:

$$\langle f, \psi \rangle = \int_0^\infty dE \int_{4\pi} d\Omega \int_R dV f(\mathbf{x}, \boldsymbol{\Omega}, E) \psi(\mathbf{x}, \boldsymbol{\Omega}, E), \quad (178)$$

where R is a subregion in the body and $f(\mathbf{x}, \boldsymbol{\Omega}, E)$ is a real function that makes the above functional a useful physical quantity. For instance, if it is desired to know the response of a detector to the local neutron flux, then f would be equated with the detector cross section $\Sigma_d(E)$, and subregion R would be the detector volume. If the detector is localized at some point \mathbf{x}_0 so that:

$$f(\mathbf{x}, \boldsymbol{\Omega}, E) = \Sigma_d(E) \delta(\mathbf{x} - \mathbf{x}_0), \quad (179)$$

then the desired functional gives the reaction rate at this point:

$$\begin{aligned} \langle f, \psi \rangle &= \int_0^\infty dE \int_{4\pi} d\Omega \Sigma_d(E) \psi(\mathbf{x}_0, \boldsymbol{\Omega}, E) \\ &= \int_0^\infty dE \Sigma_d(E) \phi(\mathbf{x}_0, E), \end{aligned} \quad (180)$$

where ϕ is the scalar flux at the detector. By choosing f appropriately, the functional can be generalized to yield energy and/or angle-dependent responses.

Since we are dealing with time-independent situations, the reciprocity condition, (174), reduces, upon substituting the vacuum boundary condition (177b), to:

$$\langle \psi^\dagger, Q \rangle - \langle \psi, Q^\dagger \rangle = \int_0^\infty dE \int_{n \cdot \boldsymbol{\Omega} > 0} d\Omega \int_{\partial V} dA \mathbf{n} \cdot \boldsymbol{\Omega} \psi(\mathbf{x}, \boldsymbol{\Omega}, E) \psi^\dagger(\mathbf{x}, \boldsymbol{\Omega}, E), \quad (181)$$

where the right-hand side contains the outward-directed forward and adjoint angular fluxes at the boundary. If now Q^\dagger is identified with f , a permissible operation because of the arbitrariness of the adjoint source, and moreover if we require the outward-directed adjoint flux at the boundary to vanish, (181) reduces to the particularly simple form:

$$\langle f, \psi \rangle = \langle \psi^\dagger, Q \rangle. \quad (182)$$

This result states that the desired functional of the forward flux can alternatively be obtained as the inner product of the adjoint flux with the physical source, where the adjoint flux now solves the *specific* adjoint transport problem:

$$\mathcal{L}^\dagger \psi^\dagger = f, \quad (183a)$$

$$\psi^\dagger = 0, \quad \mathbf{x} \in \partial V, \quad \boldsymbol{\Omega} \cdot \mathbf{n} > 0, \quad 0 < E < \infty. \quad (183b)$$

The significance of this adjoint formulation of a detector response is twofold. First, it will be observed that the adjoint problem given by (183a,b) is independent of the source Q in the forward problem. Thus, if a detector response is desired for multiple different sources, an adjoint computation would be more efficient than a forward computation. The latter would require multiple solutions of the forward transport equation, one for each source, followed by evaluation of the inner product $\langle f, \psi \rangle$ for each such solution. The adjoint approach, on the other hand, necessitates obtaining a single solution to the adjoint transport equation, followed by evaluation of the inner product $\langle \psi^\dagger, Q \rangle$ for each source. This is computationally far less laborious than solving the forward problem for each different source. If multiple generalized responses are of interest for the same forward source, the forward computation is preferred for precisely the same reasons.

Second, let us assume that the forward source corresponds to one particle injected into the system locally in phase space, at a specified point \mathbf{x}_0 , direction of flight $\boldsymbol{\Omega}_0$, and energy E_0 :

$$Q(\mathbf{x}, \boldsymbol{\Omega}, E) = \delta(\mathbf{x} - \mathbf{x}_0) \delta(\boldsymbol{\Omega} - \boldsymbol{\Omega}_0) \delta(E - E_0). \quad (184)$$

Then, from (182), the resulting detector response is given by:

$$\langle f, \psi \rangle = \psi^\dagger(\mathbf{x}_0, \boldsymbol{\Omega}_0, E_0). \quad (185)$$

This result indicates that the detector response is equal to the adjoint flux at the point of injection of the neutron. Thus, the adjoint flux is a direct measure of the *importance* of a locally injected neutron to the response of a detector. For this reason, the adjoint flux is commonly referred to as the *importance function*. Moreover, the boundary (and terminal) conditions assigned to the adjoint flux become physically reasonable and consistent with this notion of importance. For instance, in the above problem, a neutron leaving the body at the boundary cannot contribute to the detector response, and hence its importance is *zero*.

For external detector locations, measuring the importance of outgoing neutrons, the adjoint boundary conditions require modification. In this case, we take $Q^\dagger = 0$ and by way of illustration, consider a monodirectional and monoenergetic incident beam condition for the forward problem:

$$\psi(\mathbf{x}, \boldsymbol{\Omega}, E) = \delta(\mathbf{x} - \mathbf{x}_b) \delta(\boldsymbol{\Omega} - \boldsymbol{\Omega}_b) \delta(E - E_b), \quad \mathbf{x} \in \partial V, \quad \boldsymbol{\Omega} \cdot \mathbf{n} < 0, \quad 0 < E < \infty, \quad (186)$$

where \mathbf{x}_b is the point on the boundary at which the beam of neutrons of energy E_b is incident along direction $\boldsymbol{\Omega}_b$. Note that since \mathbf{x} is restricted to lie on the boundary, the delta function

$\delta(\mathbf{x} - \mathbf{x}_b)$ is 2-D. This then gives a source normalization of one incident particle per second. The reciprocity relationship equation (174) reduces in this case to:

$$\begin{aligned} \int_0^\infty dE \int_{\mathbf{n} \cdot \boldsymbol{\Omega} > 0} d\Omega \int_{\partial V} dA \mathbf{n} \cdot \boldsymbol{\Omega} \psi(\mathbf{x}, \boldsymbol{\Omega}, E) \psi^\dagger(\mathbf{x}, \boldsymbol{\Omega}, E) \\ = |\mathbf{n} \cdot \boldsymbol{\Omega}_b| \psi^\dagger(\mathbf{x}_b, \boldsymbol{\Omega}_b, E_b), \quad \boldsymbol{\Omega}_b \cdot \mathbf{n} < 0. \end{aligned} \quad (187)$$

If the desired quantity is the total leakage from the body, we may assign:

$$\psi^\dagger(\mathbf{x}, \boldsymbol{\Omega}, E) = 1, \quad \mathbf{x} \in \partial V, \quad \boldsymbol{\Omega} \cdot \mathbf{n} > 0, \quad 0 < E < \infty, \quad (188)$$

and (187) then becomes:

$$\begin{aligned} J^+ &= \int_0^\infty dE \int_{\mathbf{n} \cdot \boldsymbol{\Omega} > 0} d\Omega \int_{\partial V} dA \mathbf{n} \cdot \boldsymbol{\Omega} \psi(\mathbf{x}, \boldsymbol{\Omega}, E) \\ &= |\mathbf{n} \cdot \boldsymbol{\Omega}_b| \psi^\dagger(\mathbf{x}_b, \boldsymbol{\Omega}_b, E_b), \quad \boldsymbol{\Omega}_b \cdot \mathbf{n} < 0. \end{aligned} \quad (189)$$

Thus, the total leakage from a body, given a monodirectional and monoenergetic incident beam, can be obtained by solving the homogeneous adjoint transport equation with unit outgoing adjoint flux at the boundary. In this case, the importance to the detector of neutrons *exiting* the medium will be the highest of any other group of neutrons. Since the forward problem involves singular functions at the boundary while the adjoint problem does not, numerical solution of the adjoint transport equation will be more efficient. With an appropriate choice of adjoint boundary condition in (187), it is evident that adjoint space formulation of surface energy spectra and/or angular distributions can be realized, with and without interior sources. This analysis can be further extended to show that the adjoint flux in a critical system measures the importance of a neutron injected at a particular phase space location in sustaining the fundamental mode.

From the considerations of this section, we observe that the adjoint problem cannot be considered independently of the forward problem. The identification of the adjoint source and assignment of adjoint boundary (and terminal) conditions makes the adjoint formulation (forward-) problem dependent. However, regardless of the application, the adjoint flux can always be imbued with an “importance” attribute, thereby rendering it a physically meaningful quantity.

5.5 Green's Functions

Finally, we consider a particularly interesting special case of the generalized reciprocity relationship given by (174). Let the forward and adjoint sources be completely localized in phase space and in time:

$$Q(\mathbf{x}, \boldsymbol{\Omega}, E, t) = \delta(\mathbf{x} - \mathbf{x}_0) \delta(\boldsymbol{\Omega} - \boldsymbol{\Omega}_0) \delta(E - E_0) \delta(t - t_0), \quad (190a)$$

$$Q^\dagger(\mathbf{x}, \boldsymbol{\Omega}, E, t) = \delta(\mathbf{x} - \mathbf{x}_1) \delta(\boldsymbol{\Omega} - \boldsymbol{\Omega}_1) \delta(E - E_1) \delta(t - t_1). \quad (190b)$$

The resulting solutions of the forward and adjoint transport equations with homogeneous boundary and initial/terminal conditions are the forward and adjoint volume Green's functions and are denoted by:

$$\psi(\mathbf{x}, \boldsymbol{\Omega}, E, t) \equiv G(\mathbf{x}, \boldsymbol{\Omega}, E, t; \mathbf{x}_0, \boldsymbol{\Omega}_0, E_0, t_0), \quad (191a)$$

$$\psi^\dagger(\mathbf{x}, \boldsymbol{\Omega}, E, t) \equiv G^\dagger(\mathbf{x}, \boldsymbol{\Omega}, E, t; \mathbf{x}_b, \boldsymbol{\Omega}_b, E_b, t_b). \quad (191b)$$

For these sources, the reciprocity condition equation (174) reduces to:

$$\langle G^\dagger, Q \rangle = \langle G, Q^\dagger \rangle, \quad (192)$$

which, upon inserting (190a) and (190b) then yields the result:

$$G^\dagger(\mathbf{x}_0, \boldsymbol{\Omega}_0, E_0, t_0; \mathbf{x}_1, \boldsymbol{\Omega}_1, E_1, t_1) = G(\mathbf{x}_1, \boldsymbol{\Omega}_1, E_1, t_1; \mathbf{x}_0, \boldsymbol{\Omega}_0, E_0, t_0), \quad (193)$$

where from causality we require that $t_1 > t_0$. The right-hand side of the above equation is the neutron angular flux at the phase space point $(\mathbf{x}_1, \boldsymbol{\Omega}_1, E_1)$ at time t_1 , known as the field variables, resulting from the injection of a neutron at another phase space point $(\mathbf{x}_0, \boldsymbol{\Omega}_0, E_0)$ at an earlier time t_0 , known as the source variables. Equation (193) shows that this is identical to the angular flux for the adjoint problem but with the source and field variables reversed. A similar relationship involving surface Green's functions may be derived by imposing an incident beam on the boundary:

$$\begin{aligned} \psi(\mathbf{x}, \boldsymbol{\Omega}, E, t) &= \delta(\mathbf{x} - \mathbf{x}_0) \delta(\boldsymbol{\Omega} - \boldsymbol{\Omega}_0) \delta(E - E_0) \delta(t - t_0), \\ &\mathbf{x} \in \partial V, \quad \boldsymbol{\Omega} \cdot \mathbf{n} < 0, \quad 0 < E < \infty, \end{aligned} \quad (194a)$$

$$\begin{aligned} \psi^\dagger(\mathbf{x}, \boldsymbol{\Omega}, E, t) &= \delta(\mathbf{x} - \mathbf{x}_1) \delta(\boldsymbol{\Omega} - \boldsymbol{\Omega}_1) \delta(E - E_1) \delta(t - t_1), \\ &\mathbf{x} \in \partial V, \quad \boldsymbol{\Omega} \cdot \mathbf{n} > 0, \quad 0 < E < \infty, \end{aligned} \quad (194b)$$

where \mathbf{x}_0 and \mathbf{x}_1 are two arbitrary points on boundary, and the source normalization is one particle (neutron and adjunction) per second. Substituting these into (174) we obtain:

$$|\mathbf{n} \cdot \boldsymbol{\Omega}_0| G^\dagger(\mathbf{x}_0, \boldsymbol{\Omega}_0, E_0, t_0; \mathbf{x}_1, \boldsymbol{\Omega}_1, E_1, t_1) = |\mathbf{n} \cdot \boldsymbol{\Omega}_1| G(\mathbf{x}_1, \boldsymbol{\Omega}_1, E_1, t_1; \mathbf{x}_0, \boldsymbol{\Omega}_0, E_0, t_0), \quad (195)$$

subject to the causality constraint $t_1 > t_0$ and where again homogeneous initial and terminal conditions have been assumed.

These reciprocity relationships can be used to construct the angular flux for a distributed source from the corresponding Green's function. Let us consider a localized adjoint interior source, for which the adjoint angular flux is just the adjoint Green's function G^\dagger , and a distributed forward source, for which the solution is the forward angular flux ψ . The reciprocity condition for this problem reads:

$$\langle G^\dagger, Q \rangle = \langle \psi, Q^\dagger \rangle, \quad (196)$$

or, more explicitly:

$$\begin{aligned} \psi(\mathbf{x}, \boldsymbol{\Omega}, E, t) &= \int_0^t dt' \int_V dV' \int_0^\infty dE' \int_{4\pi} d\Omega' Q(\mathbf{x}', \boldsymbol{\Omega}', E', t') G^\dagger(\mathbf{x}', \boldsymbol{\Omega}', E', t'; \mathbf{x}, \boldsymbol{\Omega}, E, t). \end{aligned} \quad (197)$$

Recalling (193), the adjoint Green's function in (197) can be replaced by the forward Green's function but with field and source variables reversed, to finally obtain:

$$\begin{aligned} \psi(\mathbf{x}, \boldsymbol{\Omega}, E, t) &= \int_0^t dt' \int_V dV' \int_0^\infty dE' \int_{4\pi} d\Omega' Q(\mathbf{x}', \boldsymbol{\Omega}', E', t') G(\mathbf{x}, \boldsymbol{\Omega}, E, t; \mathbf{x}', \boldsymbol{\Omega}', E', t'). \end{aligned} \quad (198)$$

This result is a statement of the *superposition principle* for linear systems: the angular flux corresponding to a distributed source can be obtained by a superposition of angular fluxes for elementary sources. It is a direct consequence of the linearity of the transport operator.

5.6 Discussion

We have seen that neutron transport problems can be mathematically modeled using either a forward or an adjoint formulation. The adjoint operator is commonly derived using an inner-product identity, and the adjoint formulation always inherits physical relevance that is unique to the forward problem. The interpretation of the adjoint flux as an importance function makes it possible to derive the adjoint transport equation from first principles, using balance arguments akin to those employed in the derivation of the forward equation (Bell and Glasstone 1970; Henry 1975; Lewins 1965). For certain applications, adjoint formulations have clear computational advantages over forward formulations, while for other applications the reverse is true. Forward and adjoint functions taken collectively provide a means of generating highly accurate approximate solutions at reduced cost, as exemplified by their use in variational methods, perturbation theory, and Monte Carlo simulations.

The derivations and results of this section simplify considerably for neutron transport in the one-speed approximation. Under these conditions, the scattering and fission operators become self-adjoint, leaving only the time evolution and streaming operators as non-self-adjoint. However, upon reflecting the direction and time variables, i.e., setting $\boldsymbol{\Omega} \rightarrow -\boldsymbol{\Omega}$ and $t \rightarrow -t$, the one-speed adjoint transport equation becomes identical to the forward transport equation. The distinction between the two formulations then stems purely from the respective sources and boundary and initial/terminal conditions, but for criticality problems in particular, this consequence obviates the need to independently solve the adjoint transport equation – the adjoint angular flux is obtained by simply reflecting the direction variable in the forward angular flux. Moreover, in a critical system, where sources are absent and homogeneous boundary conditions are imposed, the adjoint scalar flux is identical to the forward scalar flux.

Finally, we remark that under certain restrictive conditions, a hybrid forward–backward formulation can be developed to describe linear transport processes. Although this approach has not found utility in reactor physics or neutron transport applications, it is nevertheless widely used in the theory of radiation damage and atomic sputtering (Prinja 1989; Sigmund 1969; Williams 1979).

6 The Multigroup and One-Speed Neutron Transport Equations

The *multigroup* approximation to the neutron transport equation is almost universally used to discretize the continuous-energy variable E (Duderstadt and Hamilton 1976; Henry 1975; Lewis and Miller 1993). The structure of the resulting multigroup transport equations is closely related to that of the original transport equation, the difference being that the energy variable is discrete rather than continuous. (Thus, integrals over E are replaced by sums over *energy groups*.) Several important identities of the original continuous-energy scattering operator are preserved in the multigroup approximation. Here, we derive the multigroup transport equations and discuss some of their properties.

6.1 The Continuous-Energy Problem

We consider a general, steady-state, 3-D neutron transport equation:

$$\begin{aligned} & \Omega \cdot \nabla \psi(\mathbf{x}, \Omega, E) + \Sigma_t(\mathbf{x}, E) \psi(\mathbf{x}, \Omega, E) \\ &= \int_0^\infty \int_{4\pi} \Sigma_s(\mathbf{x}, \Omega' \cdot \Omega, E' \rightarrow E) \psi(\mathbf{x}, \Omega', E') d\Omega' dE' \\ &+ \frac{\chi(\mathbf{x}, E)}{4\pi} \int_0^\infty \int_{4\pi} \nu \Sigma_f(\mathbf{x}, E') \psi(\mathbf{x}, \Omega', E') d\Omega' dE' \\ &+ \frac{1}{4\pi} Q(\mathbf{x}, E), \quad \mathbf{x} \in V, \quad \Omega \in 4\pi, \quad 0 < E < \infty, \end{aligned} \quad (199a)$$

with the boundary condition:

$$\psi(\mathbf{x}, \Omega, E) = \psi^b(\mathbf{x}, \Omega, E), \quad \mathbf{x} \in \partial V, \quad \Omega \cdot \mathbf{n} < 0, \quad 0 < E < \infty. \quad (199b)$$

The cross sections and fission spectrum in these equations satisfy the usual identities (see [8], [13b], [14b], and [77]):

$$\Sigma_t(E) = \Sigma_s(E) + \Sigma_y(E) + \Sigma_f(E), \quad (200a)$$

$$\Sigma_s(E) = \int_0^\infty \int_{4\pi} \Sigma_s(\Omega \cdot \Omega', E \rightarrow E') d\Omega' dE' \quad (200b)$$

$$\int_0^\infty \chi(E) dE = 1, \quad (200c)$$

$$\Sigma_s(\Omega' \cdot \Omega, E' \rightarrow E) = \sum_{n=0}^N \frac{2n+1}{4\pi} \Sigma_{s,n}(E' \rightarrow E) P_n(\Omega' \cdot \Omega). \quad (200d)$$

6.2 The Multigroup Transport Equations

The multigroup approximation requires that a finite number G of energy bins or *groups* be chosen:

$$E_{min} = E_G < E_{G-1} < \cdots < E_g < E_{g-1} < \cdots < E_2 < E_1 = E_{max},$$

with E_{min} sufficiently small that neutrons with energies less than E_{min} are negligible, and with E_{max} sufficiently large that neutrons with energies greater than E_{max} are negligible. The energy range $E_g \leq E < E_{g-1}$ is the g th *energy group*. It is customary to order the energy groups with

the group index g increasing as the energies decrease. Then the slowing down of fast fission neutrons occurs through energy groups with increasing indices.

For each $1 \leq g \leq G$, we define:

$$\begin{aligned}\psi_g(\mathbf{x}, \boldsymbol{\Omega}) &= \int_{E_g}^{E_{g-1}} \psi(\mathbf{x}, \boldsymbol{\Omega}, E) dE \\ &= \text{Angular flux for group } g,\end{aligned}\quad (201a)$$

$$\begin{aligned}\chi_g(\mathbf{x}) &= \int_{E_g}^{E_{g-1}} \chi(\mathbf{x}, E) dE \\ &= \text{Multigroup fission spectrum for group } g,\end{aligned}\quad (201b)$$

$$\begin{aligned}Q_g(\mathbf{x}) &= \int_{E_g}^{E_{g-1}} Q(\mathbf{x}, E) dE \\ &= \text{Internal multigroup source to group } g.\end{aligned}\quad (201c)$$

Because these quantities are integrals over energy groups, the group fluxes have dimensions $\text{cm}^{-2} \text{s}^{-1}$, the multigroup fission spectrum is dimensionless, and the multigroup sources have dimensions $\text{cm}^{-3} \text{s}^{-1}$. Also, by the preceding definitions and (200c), the multigroup fission spectrum automatically satisfies:

$$\sum_{g=1}^G \chi_g(\mathbf{x}) = \sum_{g=1}^G \int_{E_g}^{E_{g-1}} \chi(\mathbf{x}, E) dE = \int_{E_{min}}^{E_{max}} \chi(\mathbf{x}, E) dE = 1. \quad (202)$$

To proceed, we integrate (199a) over the g th energy group, obtaining:

$$\begin{aligned}\boldsymbol{\Omega} \cdot \nabla \psi_g(\mathbf{x}, \boldsymbol{\Omega}) + \int_{E_g}^{E_{g-1}} \Sigma_t(\mathbf{x}, E) \psi(\mathbf{x}, \boldsymbol{\Omega}, E) dE \\ = \sum_{g'=1}^G \int_{E_g}^{E_{g-1}} \int_{E_{g'}}^{E_{g'-1}} \int_{4\pi} \Sigma_s(\mathbf{x}, E' \rightarrow E, \boldsymbol{\Omega}' \cdot \boldsymbol{\Omega}) \psi(\mathbf{x}, \boldsymbol{\Omega}', E') d\Omega' dE' dE \\ + \frac{\chi_g(\mathbf{x})}{4\pi} \sum_{g'=1}^G \int_{E_{g'}}^{E_{g'-1}} \int_{4\pi} \nu \Sigma_f(\mathbf{x}, E') \psi(\mathbf{x}, \boldsymbol{\Omega}', E') d\Omega' dE' + \frac{Q_g(\mathbf{x})}{4\pi}.\end{aligned}\quad (203)$$

Equivalently,

$$\begin{aligned}\boldsymbol{\Omega} \cdot \nabla \psi_g(\mathbf{x}, \boldsymbol{\Omega}) + \left[\frac{\int_{E_g}^{E_{g-1}} \Sigma_t(\mathbf{x}, E) \psi(\mathbf{x}, \boldsymbol{\Omega}, E) dE}{\int_{E_g}^{E_{g-1}} \psi(\mathbf{x}, \boldsymbol{\Omega}, E) dE} \right] \psi_g(\mathbf{x}, \boldsymbol{\Omega}) \\ = \sum_{g'=1}^G \int_{4\pi} \left[\frac{\int_{E_g}^{E_{g-1}} \int_{E_{g'}}^{E_{g'-1}} \Sigma_s(\mathbf{x}, E' \rightarrow E, \boldsymbol{\Omega}' \cdot \boldsymbol{\Omega}) \psi(\mathbf{x}, \boldsymbol{\Omega}', E') dE' dE}{\int_{E_{g'}}^{E_{g'-1}} \psi(\mathbf{x}, \boldsymbol{\Omega}', E') dE'} \right] \psi_{g'}(\mathbf{x}, \boldsymbol{\Omega}') d\Omega' \\ + \frac{\chi_g(\mathbf{x})}{4\pi} \sum_{g'=1}^G \int_{4\pi} \left[\frac{\int_{E_{g'}}^{E_{g'-1}} \nu \Sigma_f(\mathbf{x}, E') \psi(\mathbf{x}, \boldsymbol{\Omega}', E') dE'}{\int_{E_{g'}}^{E_{g'-1}} \psi(\mathbf{x}, \boldsymbol{\Omega}', E') dE'} \right] \psi_{g'}(\mathbf{x}, \boldsymbol{\Omega}') d\Omega' \\ + \frac{Q_g(\mathbf{x})}{4\pi},\end{aligned}\quad (204)$$

or:

$$\begin{aligned} \boldsymbol{\Omega} \cdot \nabla \psi_g(\mathbf{x}, \boldsymbol{\Omega}) + \hat{\Sigma}_{t,g}(\mathbf{x}, \boldsymbol{\Omega}) \psi_g(\mathbf{x}, \boldsymbol{\Omega}) &= \sum_{g'=1}^G \int_{4\pi} \hat{\Sigma}_{s,g' \rightarrow g}(\mathbf{x}, \boldsymbol{\Omega}', \boldsymbol{\Omega}) \psi_{g'}(\mathbf{x}, \boldsymbol{\Omega}') d\Omega' \\ &+ \frac{\chi_g(\mathbf{x})}{4\pi} \sum_{g'=1}^G \int_{4\pi} \hat{\nu} \hat{\Sigma}_{f,g}(\mathbf{x}, \boldsymbol{\Omega}') \psi_{g'}(\mathbf{x}, \boldsymbol{\Omega}') d\Omega' + \frac{Q_g(\mathbf{x})}{4\pi}, \end{aligned} \quad (205)$$

where:

$$\hat{\Sigma}_{t,g}(\mathbf{x}, \boldsymbol{\Omega}) = \left[\frac{\int_{E_g}^{E_{g-1}} \Sigma_t(\mathbf{x}, E) \psi(\mathbf{x}, \boldsymbol{\Omega}, E) dE}{\int_{E_g}^{E_{g-1}} \psi(\mathbf{x}, \boldsymbol{\Omega}, E) dE} \right], \quad (206a)$$

$$\hat{\Sigma}_{s,g' \rightarrow g}(\mathbf{x}, \boldsymbol{\Omega}', \boldsymbol{\Omega}) = \left[\frac{\int_{E_g}^{E_{g-1}} \int_{E_{g'}}^{E_{g'-1}} \Sigma_s(\mathbf{x}, E' \rightarrow E, \boldsymbol{\Omega}' \cdot \boldsymbol{\Omega}) \psi(\mathbf{x}, \boldsymbol{\Omega}', E') dE' dE}{\int_{E_{g'}}^{E_{g'-1}} \psi(\mathbf{x}, \boldsymbol{\Omega}', E') dE'} \right], \quad (206b)$$

$$\hat{\nu} \hat{\Sigma}_{f,g}(\mathbf{x}, \boldsymbol{\Omega}') = \left[\frac{\int_{E_{g'}}^{E_{g'-1}} \nu \Sigma_f(\mathbf{x}, E') \psi(\mathbf{x}, \boldsymbol{\Omega}', E') dE'}{\int_{E_{g'}}^{E_{g'-1}} \psi(\mathbf{x}, \boldsymbol{\Omega}', E') dE'} \right]. \quad (206c)$$

Exact boundary conditions can be obtained by integrating (199b) over the energy groups:

$$\psi_g(\mathbf{x}, \boldsymbol{\Omega}) = \psi_g^b(\mathbf{x}, \boldsymbol{\Omega}) = \int_{E_g}^{E_{g-1}} \psi^b(\mathbf{x}, \boldsymbol{\Omega}, E) dE, \quad \mathbf{x} \in V, \quad \boldsymbol{\Omega} \cdot \mathbf{n} < 0. \quad (207)$$

Equations (205–207) are an exact system of equations for the group fluxes. If the hatted coefficients in (205) were known, then (205) and (207) would, in the absence of spatial and angular discretizations, yield the exact group fluxes. However, by (206), the hatted coefficients depend on the solution of the continuous-energy problem and are not known.

In the multigroup approximation, an approximation for ψ is specified and introduced into the right sides of (206). The resulting approximate *multigroup cross sections* are then used in (205).

Specifically, in each of the bracketed terms in (206), we introduce the approximation:

$$\psi(\mathbf{x}, \boldsymbol{\Omega}, E) \approx \Psi(\mathbf{x}, E) f(\mathbf{x}, \boldsymbol{\Omega}), \quad (208)$$

where $\Psi(\mathbf{x}, E)$ is a specified *neutron spectrum*. The function $f(\mathbf{x}, \boldsymbol{\Omega})$ cancels out of each numerator and denominator, and (206) yield the *multigroup cross sections*:

$$\Sigma_{t,g}(\mathbf{x}) = \left[\frac{\int_{E_g}^{E_{g-1}} \Sigma_t(\mathbf{x}, E) \Psi(\mathbf{x}, E) dE}{\int_{E_g}^{E_{g-1}} \Psi(\mathbf{x}, E) dE} \right], \quad (209a)$$

$$\Sigma_{s,g' \rightarrow g}(\mathbf{x}, \boldsymbol{\Omega}' \cdot \boldsymbol{\Omega}) = \left[\frac{\int_{E_g}^{E_{g-1}} \int_{E_{g'}}^{E_{g'-1}} \Sigma_s(\mathbf{x}, E' \rightarrow E, \boldsymbol{\Omega}' \cdot \boldsymbol{\Omega}) \Psi(\mathbf{x}, E') dE' dE}{\int_{E_{g'}}^{E_{g'-1}} \Psi(\mathbf{x}, E') dE'} \right], \quad (209b)$$

$$v\Sigma_{f,g}(\mathbf{x}) = \left[\frac{\int_{E_{g'}}^{E_{g'-1}} v\Sigma_f(\mathbf{x}, E')\Psi(\mathbf{x}, E')dE'}{\int_{E_{g'}}^{E_{g'-1}} \Psi(\mathbf{x}, E)dE'} \right]. \quad (209c)$$

Introducing these expressions into (205), we obtain the *multigroup transport equations* (Duderstadt and Hamilton 1976; Henry 1975; Lewis and Miller 1993):

$$\begin{aligned} \boldsymbol{\Omega} \cdot \nabla \psi_g(\mathbf{x}, \boldsymbol{\Omega}) + \Sigma_{t,g}(\mathbf{x})\psi_g(\mathbf{x}, \boldsymbol{\Omega}) &= \sum_{g'=1}^G \int_{4\pi} \Sigma_{s,g' \rightarrow g}(\mathbf{x}, \boldsymbol{\Omega}' \cdot \boldsymbol{\Omega})\psi_{g'}(\mathbf{x}, \boldsymbol{\Omega}')d\Omega' \\ &+ \frac{\chi_g(\mathbf{x})}{4\pi} \sum_{g'=1}^G \int_{4\pi} v\hat{\Sigma}_{f,g}(\mathbf{x})\psi_{g'}(\mathbf{x}, \boldsymbol{\Omega}')d\Omega' + \frac{Q_g(\mathbf{x})}{4\pi}, \quad \mathbf{x} \in V, \quad \boldsymbol{\Omega} \in 4\pi, \quad 1 \leq g \leq G. \end{aligned} \quad (210)$$

The multigroup fluxes $\psi_g(\mathbf{x}, \boldsymbol{\Omega})$ are obtained by solving these equations with the *multigroup boundary conditions* (207).

To complete the multigroup approximation, the multigroup capture, fission, and scattering cross sections are defined analogous to (209):

$$\Sigma_{\gamma,g}(\mathbf{x}) = \left[\frac{\int_{E_g}^{E_{g-1}} \Sigma_{\gamma}(\mathbf{x}, E)\Psi(\mathbf{x}, E)dE}{\int_{E_g}^{E_{g-1}} \Psi(\mathbf{x}, E)dE} \right], \quad (211a)$$

$$\Sigma_{f,g}(\mathbf{x}) = \left[\frac{\int_{E_g}^{E_{g-1}} \Sigma_f(\mathbf{x}, E)\Psi(\mathbf{x}, E)dE}{\int_{E_g}^{E_{g-1}} \Psi(\mathbf{x}, E)dE} \right], \quad (211b)$$

$$\Sigma_{s,n,g' \rightarrow g}(\mathbf{x}) = \left[\frac{\int_{E_g}^{E_{g-1}} \int_{E_{g'}}^{E_{g'-1}} \Sigma_{s,n}(\mathbf{x}, E' \rightarrow E)\Psi(\mathbf{x}, E')dE'dE}{\int_{E_{g'}}^{E_{g'-1}} \Psi(\mathbf{x}, E')dE'} \right]. \quad (211c)$$

Then by (209), (211), and (200a), the following identities hold for all g and g' :

$$\begin{aligned} \Sigma_{t,g}(\mathbf{x}) &= \frac{\int_{E_g}^{E_{g-1}} [\Sigma_s(\mathbf{x}, E) + \Sigma_{\gamma}(\mathbf{x}, E) + \Sigma_f(\mathbf{x}, E)]\Psi(\mathbf{x}, E)dE}{\int_{E_g}^{E_{g-1}} \Psi(\mathbf{x}, E)dE} \\ &= \Sigma_{s,g}(\mathbf{x}) + \Sigma_{\gamma,g}(\mathbf{x}) + \Sigma_{f,g}(\mathbf{x}), \end{aligned} \quad (212a)$$

$$\begin{aligned} \Sigma_{s,g' \rightarrow g}(\mathbf{x}, \boldsymbol{\Omega}' \cdot \boldsymbol{\Omega}) &= \frac{\int_{E_g}^{E_{g-1}} \int_{E_{g'}}^{E_{g'-1}} \left[\sum_{n=0}^N \frac{2n+1}{4\pi} \Sigma_{s,n}(E' \rightarrow E) P_n(\boldsymbol{\Omega}' \cdot \boldsymbol{\Omega}) \right] \Psi(\mathbf{x}, E')dE'dE}{\int_{E_{g'}}^{E_{g'-1}} \Psi(\mathbf{x}, E')dE'} \\ &= \sum_{n=0}^N \frac{2n+1}{4\pi} \Sigma_{s,n,g' \rightarrow g} P_n(\boldsymbol{\Omega}' \cdot \boldsymbol{\Omega}), \end{aligned} \quad (212b)$$

and:

$$\begin{aligned}
 \sum_{g'=1}^G \int_{4\pi} \Sigma_{s,g \rightarrow g'}(\mathbf{x}, \boldsymbol{\Omega}' \cdot \boldsymbol{\Omega}) d\boldsymbol{\Omega}' &= \sum_{g'=1}^G \int_{4\pi} \left[\sum_{n=0}^N \frac{2n+1}{4\pi} \Sigma_{s,n,g \rightarrow g'}(\mathbf{x}) P_n(\boldsymbol{\Omega}' \cdot \boldsymbol{\Omega}) \right] d\boldsymbol{\Omega}' \\
 &= \sum_{g'=1}^G \left[\sum_{n=0}^N \frac{2n+1}{4\pi} \Sigma_{s,n,g \rightarrow g'}(\mathbf{x}) \int_{4\pi} P_n(\boldsymbol{\Omega}' \cdot \boldsymbol{\Omega}) d\boldsymbol{\Omega}' \right] \\
 &= \sum_{g'=1}^G \left[\sum_{n=0}^N \frac{2n+1}{4\pi} \Sigma_{s,n,g \rightarrow g'}(\mathbf{x}) 4\pi \delta_{n,0} \right] \\
 &= \sum_{g'=1}^G \Sigma_{s,0,g \rightarrow g'}(\mathbf{x}) \\
 &= \sum_{g'=1}^G \left[\frac{\int_{E_g^{g'-1}}^{E_g} \int_{E_g}^{E_{g-1}} \Sigma_{s,0}(\mathbf{x}, E' \rightarrow E) \Psi(\mathbf{x}, E') dE' dE}{\int_{E_g}^{E_{g-1}} \Psi(\mathbf{x}, E') dE'} \right] \\
 &= \frac{\int_{E_{min}}^{E_{max}} \left[\int_{E_g}^{E_{g-1}} \Sigma_{s,0}(\mathbf{x}, E' \rightarrow E) \Psi(\mathbf{x}, E') dE' \right] dE}{\int_{E_g}^{E_{g-1}} \Psi(\mathbf{x}, E') dE'} \\
 &= \frac{\int_{E_g}^{E_{g-1}} \Sigma_s(\mathbf{x}, E') \Psi(\mathbf{x}, E') dE'}{\int_{E_g}^{E_{g-1}} \Psi(\mathbf{x}, E') dE'} \\
 &= \Sigma_{s,g}(\mathbf{x}). \tag{212c}
 \end{aligned}$$

Equations (202) and (212) hold for any choice of $\Psi(\mathbf{x}, E)$; they are the multigroup analog of the continuous-energy identities (200). These identities have the following significance: (i) Equations (200a) and (212a) guarantee that the multigroup transport equations describe the same types of physical reactions between neutrons and nuclei as the continuous-energy transport equations. (ii) Equations (200b) and (212c) guarantee that the continuous-energy and multigroup scattering operators are *conservative* – they neither create nor destroy neutrons. (These operators only rearrange neutrons in $(\boldsymbol{\Omega}, E)$ -space.) (iii) Equations (200c) and (201b) guarantee that the continuous-energy and multigroup fission spectra satisfy the same normalization. (iv) Equations (200d) and (212b) guarantee that the continuous-energy and multigroup differential scattering cross sections satisfy the same type of Legendre polynomial expansions.

We have noted that the structure of the multigroup transport equations is similar to that of the continuous-energy transport equation, the difference being that in the multigroup equations, the energy variable is discrete rather than continuous. From the above derivation, the only error in the multigroup equations occurs in replacing the “exact” multigroup cross sections (206) by the approximate multigroup cross sections (209). This replacement is exact in three hypothetical situations:

1. *The continuous-energy angular flux $\psi(\mathbf{x}, \boldsymbol{\Omega}, E)$ has the form of (208) and Ψ is known.* Unfortunately, (208) requires the angular flux to have the same energy spectrum for each direction of flight and the same direction-dependence for each energy. This occurs for an infinite homogeneous spatial medium where ψ is isotropic, but it does not generally occur otherwise.
2. *The continuous-energy cross sections are histograms in E and E' on the specified energy grid.* In this situation, the multigroup cross sections are independent of Ψ and equal to the

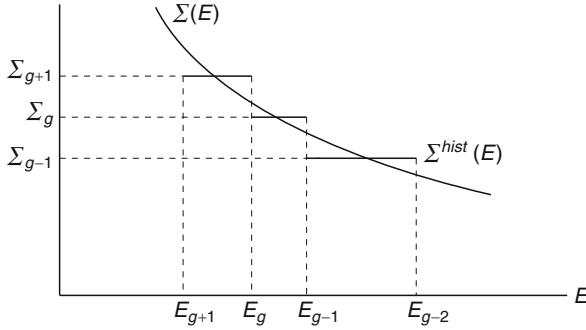


Figure 26
Continuous-energy histogram cross sections

continuous-energy cross sections within each group (see [Fig. 26](#)). Unfortunately, physical cross sections lack this simple histogram energy-dependence.

3. *The number of energy groups G becomes very large and the group widths $\Delta E_g = E_{g-1} - E_g$ become small.* In this limiting case, the multigroup cross sections become independent of Ψ and equal to the continuous-energy cross section evaluated at E_g (and $E_{g'}$).

Thus, the multigroup neutron transport equations are rarely exact for realistic neutron transport problems.

Nonetheless, item 2 in the preceding list suggests a useful way to interpret the multigroup transport equations: *they exactly represent a continuous-energy transport problem with cross sections that are histograms in energy.* If a multigroup approximation for a continuous-energy transport problem is developed, then the multigroup approximation yields the exact group fluxes for the continuous-energy transport problem whose (continuous-energy) cross sections $\Sigma^{hist}(E)$ are equal to the multigroup cross sections on each energy group:

$$\Sigma^{hist}(E) = \Sigma_g, \quad E_g \leq E < E_{g-1}, \quad 1 \leq g \leq G.$$

Effectively, then, the multigroup approximation is an approximation to the continuous-energy cross sections. If the physical continuous-energy cross sections are approximated by histograms in energy, then the multigroup approximation will yield the exact group fluxes for the approximate problem with histogram cross sections.

This discussion makes it plausible that as the number of energy groups increases and the energy group widths decrease, the error in the multigroup approximation should decrease. In fact, this is seen in practice.

6.3 The Within-Group and One-Group Transport Equations

For each g , (210) can be written:

$$\begin{aligned} \Omega \cdot \nabla \psi_g(\mathbf{x}, \Omega) + \Sigma_{t,g}(\mathbf{x}) \psi_g(\mathbf{x}, \Omega) &= \int_{4\pi} \Sigma_{s,g \rightarrow g}(\mathbf{x}, \Omega' \cdot \Omega) \psi_g(\mathbf{x}, \Omega') d\Omega' \\ &+ \frac{\chi_g(\mathbf{x})}{4\pi} \int_{4\pi} \nu \hat{\Sigma}_{f,g}(\mathbf{x}) \psi_g(\mathbf{x}, \Omega') d\Omega' + S_g(\mathbf{x}, \Omega), \end{aligned} \quad (213a)$$

where:

$$S_g(\mathbf{x}, \boldsymbol{\Omega}) = \frac{Q_g(\mathbf{x})}{4\pi} + \sum_{g' \neq g} \int_{4\pi} \Sigma_{s, g' \rightarrow g}(\mathbf{x}, \boldsymbol{\Omega}' \cdot \boldsymbol{\Omega}) \psi_{g'}(\mathbf{x}, \boldsymbol{\Omega}') d\Omega' + \frac{\lambda_g(\mathbf{x})}{4\pi} \sum_{g' \neq g} \int_{4\pi} v \hat{\Sigma}_{f, g}(\mathbf{x}) \psi_{g'}(\mathbf{x}, \boldsymbol{\Omega}') d\Omega'. \quad (213b)$$

Equation (213a) is the *within-group* transport equation; it has the form of a monoenergetic transport equation, with an anisotropic *group-to-group source* S_g representing (i) the internal neutron source, (ii) the scattering source from groups g' to g , and (iii) the fission source from groups g' to g .

Equations (213) suggest an iterative strategy for solving multigroup transport problems. Specifically, estimates of $\psi_{g'}$ could be introduced into (213b) to obtain estimates of S_g . Then (213a) could be solved to obtain new estimates of ψ_g , and the process could be repeated. Variations on this idea are used in practical simulations (Lewis and Miller 1993).

6.4 Discussion

For obvious reasons, a practical goal is to make the number of energy groups G as small as possible and yet achieve sufficient accuracy. For this reason, great care is often taken in the derivation of the neutron spectrum $\Psi(\mathbf{x}, E)$ used to calculate multigroup cross sections. We cannot discuss here the various procedures used to calculate Ψ . However, we do note that different physical circumstances can lead to very different values of G .

For example, in light water reactor cores, where (208) is often a valid approximation, satisfactory numerical results can often be achieved with only $G = 2$ energy groups, group 1 representing the fast neutrons and group 2 representing the thermal neutrons. However, in shielding problems, where the neutron spectrum changes radically (and continuously) from one side of the shield to the other, often $G > 100$ energy groups are required to achieve accurate results.

A fundamental limitation with the conventional multigroup approximation presented here is the assumption (208) that at each spatial point, the energy spectrum is independent of direction $\boldsymbol{\Omega}$. This assumption is not valid at material interfaces between two materials with different capture cross sections. (If the material to the left of an interface has absorption resonances at different energies than the material to the right of the interface, then near the resonance, the neutrons traveling to the right will have an energy spectrum associated with the material on the left of the interface, and the neutrons traveling to the left will have a different energy spectrum associated with the material on the right of the interface.) At present, if highly accurate results are desired near material interfaces, the only option is to use a large number of energy groups G .

Another issue is that because neutron cross sections $\Sigma(E)$ can be extraordinarily complicated functions of E , the angular flux $\psi(\mathbf{x}, \boldsymbol{\Omega}, E)$ will also be a complicated function of E . In such cases, it is, as a practical matter, impossible to choose an energy group structure fine enough to “resolve” all the energy-dependent peaks and valleys of Σ and ψ . Hence, the calculation of suitable multigroup cross sections (i.e., the calculation of suitable neutron spectra to be used in [209] and [211]) becomes a problem-dependent, time-consuming, and yet essential

task. Because of this, the multigroup approximation is, although relatively simple to formulate, difficult to implement in detail for practical problems.

7 The Age and Wigner Approximations

In the classic Age and Wigner approximations to the neutron transport equation, the neutron scattering operator is approximated either directly (in the Age approximation) or indirectly (in the Wigner approximation) by a first-order differential operator (Larsen and Ahrens 2001; Weinberg and Wigner 1958). The resulting approximate equations are easier to solve numerically, and in certain problems, they can be solved analytically.

Conventional derivations of the Age and Wigner approximations from the infinite-medium neutron spectrum equation make use of a transformation of the equation from the energy variable E to the *lethargy* variable $u = \ln(E_0/E)$, where $E_0 \geq$ maximum neutron energy. After this transformation is made, the Age and Wigner approximations are derived, and then the results are converted back to E . (These derivations do not explain why the transformation from E to u is made to facilitate the approximations.) Here, the Age and Wigner approximations are derived directly from the scattering operator expressed in terms of E ; we do not first transform the infinite-medium neutron spectrum equation from E to u . Thus, the derivations given here have a certain pedagogical advantage: they do not involve the lethargy variable.

However, after deriving the Age and Wigner approximations, we briefly discuss why the use of the lethargy variable has a certain practical advantage in the calculation of multigroup cross sections.

7.1 The Infinite-Medium Neutron Spectrum Equation

We consider the eigenvalue problem defined by (49), with the elastic differential scattering cross section defined by (10) and (11). (Equations (10) are valid for *epithermal* energies $E \gg kT =$ the mean thermal energy of the nuclei.) Integrating (49a) over Ω and defining

$$\phi(\mathbf{x}, E) = \int_{4\pi} \psi(\mathbf{x}, \Omega, E) d\Omega = \text{scalar flux}, \quad (214a)$$

$$\mathbf{J}(\mathbf{x}, E) = \int_{4\pi} \Omega \psi(\mathbf{x}, \Omega, E) d\Omega = \text{neutron current}, \quad (214b)$$

we obtain:

$$\nabla \cdot \mathbf{J}(\mathbf{x}, E) + \Sigma_t(E)\phi(\mathbf{x}, E) = \int_E^{E/\alpha} \frac{\Sigma_s(E')\phi(\mathbf{x}, E')}{(1-\alpha)E'} dE' + \frac{\chi_p(E)}{k} \int_0^\infty \nu \Sigma_f(E')\phi(\mathbf{x}, E') dE',$$

where:

$$\alpha = \left(\frac{A-1}{A+1} \right)^2.$$

For an infinite homogeneous medium, ϕ and \mathbf{J} are independent of \mathbf{x} , and the previous equation can be written:

$$\Sigma_t(E)\phi(E) = \int_E^{E/\alpha} \frac{\Sigma_s(E')\phi(E')}{(1-\alpha)E'} dE' + Q(E), \quad (215a)$$

or:

$$\Sigma_a(E)\phi(E) = \mathcal{L}\phi(E) + Q(E), \quad (215b)$$

where $Q(E)$ is the fission source and \mathcal{L} is the *elastic neutron scattering operator*:

$$Q(E) = \frac{\chi_p(E)}{k} \int_0^\infty v\Sigma_f(E')\phi(E')dE', \quad (215c)$$

$$\mathcal{L}\phi(E) = \int_E^{E/\alpha} \frac{\Sigma_s(E')\phi(E')}{(1-\alpha)E'}dE' - \Sigma_s(E)\phi(E). \quad (215d)$$

In the following, we assume that $Q(E) = C\chi_p(E)$, where the constant C is given.

For $A = 1$ (epithermal elastic neutron scattering off hydrogen nuclei), $\alpha = 0$ and (215) become:

$$\Sigma_t(E)\phi(E) = \int_E^\infty \frac{\Sigma_s(E')\phi(E')}{E'}dE' + Q(E). \quad (216)$$

This equation can be solved analytically. Differentiating it with respect to E , we get:

$$\frac{d}{dE} [\Sigma_t(E)\phi(E) - Q(E)] = -\frac{\Sigma_t(E)\phi(E)}{E}, \quad (217)$$

which is an easily solved first-order ordinary differential equation. Assuming $Q(E) = \phi(E) = 0$ for $E \geq E_0$, we obtain the analytic solution:

$$\phi(E) = \frac{1}{\Sigma_t(E)} \left[Q(E) + \int_E^{E_0} Q(E') \frac{\Sigma_s(E')}{\Sigma_t(E')E'} e^{\int_E^{E'} \frac{\Sigma_s(E'')}{\Sigma_t(E'')} \frac{dE''}{E''}} dE' \right]. \quad (218)$$

However,

$$\int_E^{E'} \frac{\Sigma_s(E'')}{\Sigma_t(E'')} \frac{dE''}{E''} = \int_E^{E'} \frac{\Sigma_t(E'') - \Sigma_a(E'')}{\Sigma_t(E'')} \frac{dE''}{E''} = \left(\ln \frac{E'}{E} \right) - \int_E^{E'} \frac{\Sigma_a(E'')}{\Sigma_t(E'')} \frac{dE''}{E''},$$

so (218) can be written in the equivalent and more common form:

$$\phi(E) = \frac{1}{\Sigma_t(E)} \left[Q(E) + \frac{1}{E} \int_E^{E_0} Q(E') \frac{\Sigma_s(E')}{\Sigma_t(E')} e^{-\int_E^{E'} \frac{\Sigma_a(E'')}{\Sigma_t(E'')} \frac{dE''}{E''}} dE' \right]. \quad (219)$$

Unfortunately, for $A > 1$, it is not possible to perform these operations and solve (215). Thus, for $A > 1$, it is desirable to *accurately approximate* (215) in a form similar to (217), i.e., as an explicitly solvable first-order ordinary differential equation. Accomplishing this is the task at hand.

Before proceeding, we note that for any constant C ,

$$\mathcal{L} \left[\frac{C}{E\Sigma_s(E)} \right] = \int_E^{E/\alpha} \frac{C}{(1-\alpha)(E')^2} dE' - \frac{C}{E} = 0. \quad (220)$$

Thus, for $\Sigma_a(E) = 0$ and $Q(E) = 0$,

$$\phi_{eq}(E) = \frac{C}{E\Sigma_s(E)} \quad (221)$$

is an *equilibrium solution* of (215a). For intervals of energy in which $\Sigma_a(E) = 0$ and $Q(E) = 0$, $\phi(E)$ is very well approximated by (221), with a suitably defined C .

Also, for any $\phi(E)$, we have

$$\begin{aligned} \int_0^\infty \mathcal{L}\phi(E)dE &= \int_0^\infty \int_E^{E/\alpha} \frac{\Sigma_s(E')\phi(E')}{(1-\alpha)E'} dE' dE - \int_0^\infty \Sigma_s(E)\phi(E)dE \\ &= \int_{E'=0}^\infty \left(\int_{E=\alpha E'}^{E'} dE \right) \frac{\Sigma_s(E')\phi(E')}{(1-\alpha)E'} dE' - \int_0^\infty \Sigma_s(E)\phi(E)dE = 0. \end{aligned} \quad (222)$$

This equation states that scattering is *conservative*: the rate at which neutrons enter scattering events equals the rate at which neutrons exit scattering events.

In the following, we require any acceptable approximation of \mathcal{L} to satisfy (220) and (222). Thus, an approximate scattering operator should preserve the equilibrium solution $\phi_{eq}(E)$, and it should be conservative. (In fact, we will demand more, but we state these first two conditions here.)


7.2 The “Conservative” Form of the Neutron Transport Equation

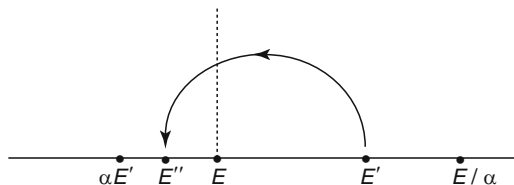
The out-scattering (integral) operator in (215a) contains the differential scattering cross section:

$$\Sigma_s(E' \rightarrow E'') = \begin{cases} \frac{\Sigma_s(E')}{(1-\alpha)E'}, & E'' < E' < E''/\alpha \\ 0, & \text{otherwise.} \end{cases} \quad (223)$$

Using this, it is possible to determine the *slowing-down density* $F(E)$, defined by:

$$F(E) = \text{the rate per unit volume at which neutrons slow down from energies } (E') \text{ greater than } E \text{ to energies } (E'') \text{ less than } E. \quad (224)$$

As depicted in  Fig. 27, a neutron with energy E' in the interval $E < E' < E/\alpha$ can directly scatter into an energy $E'' < E$ only if E'' is in the interval $\alpha E' < E'' < E$.



■ **Figure 27**

Scattering from $E' > E$ to $E'' < E$

From (223), we have

$\Sigma_s(E' \rightarrow E'')\phi(E')dE'dE''$ = the rate per unit volume at which neutrons scatter from the interval $(E', E' + dE')$ to the interval $(E'', E'' + dE'')$.

Integrating this expression over $\alpha E' < E'' < E$ and then over $E < E' < E/\alpha$, and using the definition (224), we obtain:

$$F(E) = \int_{E'=E}^{E/\alpha} \int_{E''=\alpha E'}^E \frac{\Sigma_s(E')\phi(E')}{(1-\alpha)E'} dE'' dE' = \int_{E'=E}^{E/\alpha} \frac{E - \alpha E'}{(1-\alpha)E'} \Sigma_s(E')\phi(E') dE'. \quad (225)$$

Differentiating $F(E)$, we get:

$$\begin{aligned} \frac{dF}{dE}(E) &= \int_E^{E/\alpha} \frac{\Sigma_s(E')\phi(E')}{(1-\alpha)E'} dE' - \Sigma_s(E)\phi(E) \\ &= \mathcal{L}\phi(E). \end{aligned} \quad (226)$$

Therefore, the infinite-medium spectrum equation (215b) can be written in the advantageous *conservative* form:

$$\Sigma_a(E)\phi(E) = \frac{dF}{dE}(E) + Q(E), \quad (227a)$$

where:

$$F(E) = \frac{1}{1-\alpha} \int_{E'=E}^{E/\alpha} \frac{E - \alpha E'}{E'} \Sigma_s(E')\phi(E') dE'. \quad (227b)$$

To illustrate the utility of (227), let us consider for any mass number $A \geq 1$ a purely scattering problem [$\Sigma_a(E) = 0$] with $Q(E) > 0$ only for $E_1 < E < E_0$ (► Fig. 28). Then, operating on (227a) by $\int_E^{E_0} (\cdot) dE'$, we obtain for $E < E_1$:

$$F(E) = \int_{E_1}^{E_0} Q(E') dE' = \text{constant (independent of } E). \quad (228a)$$

However, since $\Sigma_a(E) = 0$ and $Q(E) = 0$ for $E < E_1$, then for $E \ll E_1$, $\phi_A(E)$ is very well-represented by (221):

$$\phi_A(E) \approx \frac{C}{E\Sigma_s(E)}, \quad (228b)$$

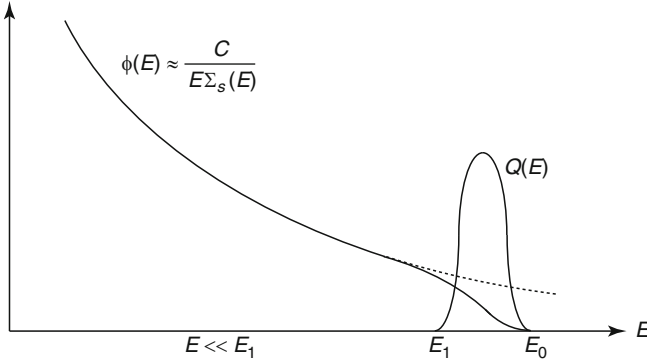


Figure 28
Purely scattering problem with $\Sigma_a(E) = 0$

where the constant C is undetermined. Assuming $E \ll E_1$, and introducing (228a) into the left side of (227b) and (228b) into the right side of (227b), we obtain

$$\begin{aligned} \int_{E_1}^{E_0} Q(E) dE &\approx \frac{1}{1-\alpha} \int_{E'=E}^{E/\alpha} \frac{E-\alpha E'}{E'} \left(\frac{C}{E'}\right) dE' \\ &= \frac{C}{1-\alpha} \int_{E'=E}^{E/\alpha} \frac{E-\alpha E'}{(E')^2} dE' = C\xi, \end{aligned} \tag{228c}$$

where (see Fig. 29):

$$\begin{aligned} \xi &= 1 + \frac{\alpha \ln \alpha}{1-\alpha} \\ &= \begin{cases} 1, & \alpha = 0 \quad (A = 1) \\ \frac{1-\alpha}{2} + O(1-\alpha)^2, & \alpha \approx 1 \quad (A \gg 1). \end{cases} \end{aligned} \tag{229}$$

Solving (228c) for C and introducing this expression into (228b), we obtain:

$$\phi_A(E) \approx \frac{1}{E\Sigma_s(E)} \left[\frac{1}{\xi} \int_{E_1}^{E_0} Q(E') dE' \right]. \tag{230}$$

Equation (230) is essentially exact for all α and for all $E < E_1$. We note that since $\xi = 1$ for $A = 1$ (see [229]), then (230) agrees with (219) for $A = 1$ and $\Sigma_a(E) = 0$.

As the mass number A of the scattering nuclei increases, α increases, so ξ decreases, and so $\phi(E)$ in (230) increases. Physically, this happens because for larger A , neutrons on the average lose less energy per collision, i.e., the slowing-down process becomes less efficient. Thus, neutrons increasingly “pile up” as they slow down. The constant ξ in (229) and (230) exactly calibrates this “piling-up” effect for the purely scattering problems considered above:

$$\frac{\phi_A(E)}{\phi_1(E)} = \frac{1}{\xi}, \quad E < E_1, \tag{231}$$

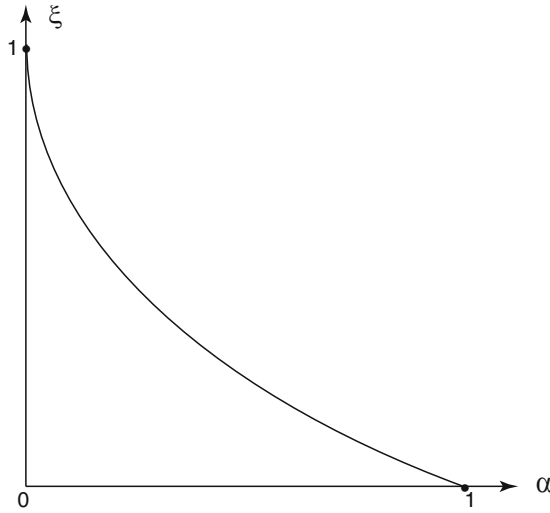


Figure 29
 ξ versus α

7.3 The Age Approximation

In (227), let us consider $A \gg 1$. Then

$$\alpha = \left(\frac{A-1}{A+1} \right)^2 = 1 - \frac{4}{A} + O\left(\frac{1}{A^2}\right), \quad (232)$$

so the width of the interval of integration in (225) is $O(1/A)$. (This implies $F(E) = O(1/A)$.) We approximate (225) as:

$$\begin{aligned} F(E) &= \int_{E'=E}^{E/\alpha} \frac{E - \alpha E'}{(1 - \alpha)(E')^2} [E' \Sigma_s(E') \phi(E')] dE' \\ &= \int_{E'=E}^{E/\alpha} \frac{E - \alpha E'}{(1 - \alpha)(E')^2} [E \Sigma_s(E) \phi(E) + O(E' - E)] dE' \\ &= \xi E \Sigma_s(E) \phi(E) + O\left(\frac{1}{A^2}\right). \end{aligned} \quad (233)$$

(The remainder term is $O(1/A^2)$ because $E' - E = O(1/A)$ and the interval of integration is $O(1/A)$.)

Introducing (233) into (227a) and ignoring the $O(1/A^2)$ terms, we obtain the following *Age Approximation* to the infinite-medium neutron spectrum equation:

$$\Sigma_a(E) \phi(E) = \xi \frac{d}{dE} E \Sigma_s(E) \phi(E) + Q(E). \quad (234)$$

(For electron transport problems, this result is called the *continuous slowing down* (CSD) approximation.) Equation (234) contains the basic approximation:

$$\mathcal{L}_A \phi(E) = \xi \frac{d}{dE} E \Sigma_s(E) \phi(E), \quad (235)$$

which satisfies (220) and (222), provided only that $E \Sigma_s(E) \phi(E)$ vanishes at $E = 0$ and ∞ .

The Age equation has $O(1/A^2)$ error for $A \gg 1$, so at this point its validity for small mass numbers A is unclear. For all A , (234), applied to the purely scattering problem discussed above yields the solution defined by (230) for all $E < E_1$. This shows that the Age approximation is valid for *some* problems for all A .

Equation (234) can be solved in closed form, yielding:

$$\phi(E) = \frac{1}{\xi E \Sigma_s(E)} \int_E^{E_0} e^{-\frac{1}{\xi} \int_E^{E'} \frac{\Sigma_a(E'')}{E'' \Sigma_s(E'')} dE''} Q(E') dE'. \quad (236)$$

For $A = 1$ ($\xi = 1$), this result reduces to the exact $A = 1$ solution given in (219) only if $E < E_1$ and $\Sigma_a(E) = 0$. Thus, the Age approximation is generally not accurate unless $A \gg 1$, $E < E_1$, and $\Sigma_a(E) \ll \Sigma_s(E)$.

A more accurate approximation, derived by Wigner, has the desirable features of the Age approximation *and* the additional desirable properties that it is exact for $A = 1$ and is generally much more accurate than the Age approximation. We discuss this next.

7.4 The Wigner Approximation

For $A \gg 1$, (234) holds with $O(1/A^2)$ error. Adding $\Sigma_s(E) \phi(E)$ to both sides of this equation and using $\xi = O(1/A)$, we obtain:

$$\begin{aligned} \Sigma_t(E) \phi(E) &= \left[\Sigma_s(E) \phi(E) + \xi \frac{d}{dE} E \Sigma_s(E) \phi(E) \right] + Q(E) + O\left(\frac{1}{A^2}\right) \\ &= \frac{1}{E} \left(I + \xi E \frac{d}{dE} \right) E \Sigma_s(E) \phi(E) + Q(E) + O\left(\frac{1}{A^2}\right) \\ &= \frac{1}{E} \left(I - \xi E \frac{d}{dE} \right)^{-1} E \Sigma_s(E) \phi(E) + Q(E) + O\left(\frac{1}{A^2}\right). \end{aligned} \quad (237)$$

Ignoring the $O(1/A^2)$ terms, we obtain the basic form of the *Wigner approximation* to the infinite-medium neutron spectrum equation:

$$\Sigma_t(E) \phi(E) = \frac{1}{E} \left(I - \xi E \frac{d}{dE} \right)^{-1} E \Sigma_s(E) \phi(E) + Q(E). \quad (238a)$$

The first term on the right side:

$$H_W(E) = \frac{1}{E} \left(I - \xi E \frac{d}{dE} \right)^{-1} E \Sigma_s(E) \phi(E) \quad (238b)$$

satisfies the first-order ordinary differential equation:

$$\left(I - \xi E \frac{d}{dE}\right) E H_W(E) = E \Sigma_s(E) \phi(E),$$

or:

$$H_W(E) - \xi \frac{d}{dE} E H_W(E) = \Sigma_s(E) \phi(E).$$

The solution of this equation is:

$$H_W(E) = \frac{1}{\xi E} \int_E^\infty \left(\frac{E}{E'}\right)^{1/\xi} \Sigma_s(E') \phi(E') dE'. \quad (238c)$$

Introducing (238c) into (238a), we get:

$$\Sigma_t(E) \phi(E) = \frac{1}{\xi E} \int_E^\infty \left(\frac{E}{E'}\right)^{1/\xi} \Sigma_s(E') \phi(E') dE' + Q(E). \quad (238d)$$

Thus, unlike the Age approximation, the Wigner approximation approximates the scattering integral by an actual integral, $H_W(E)$. For $A \gg 1$, $H_W(E)$ is an $O(1/A^2)$ approximation to the exact scattering integral in (215b):

$$H(E) = \frac{1}{1 - \alpha} \int_E^{E/\alpha} \frac{\Sigma_s(E') \phi(E')}{E'} dE'. \quad (239)$$

However, for $A = 1$, $\alpha = 0$ and $\xi = 1$, so $H_W(E) = H(E)$, and Wigner's approximation is exact!

Also, the Wigner approximation to the scattering operator \mathcal{L} :

$$\begin{aligned} \mathcal{L}_W \phi(E) &= \left[\frac{1}{E} \left(I - \xi E \frac{d}{dE} \right)^{-1} E - I \right] \Sigma_s(E) \phi(E) \\ &= \frac{1}{E} \left[\left(I - \xi E \frac{d}{dE} \right)^{-1} - I \right] E \Sigma_s(E) \phi(E) \end{aligned} \quad (240)$$

can be written in two equivalent forms:

$$\begin{aligned} \mathcal{L}_W \phi(E) &= \frac{1}{E} \left(I - \xi E \frac{d}{dE} \right)^{-1} \left[I - \left(I - \xi E \frac{d}{dE} \right) \right] E \Sigma_s(E) \phi(E) \\ &= \frac{\xi}{E} \left(I - \xi E \frac{d}{dE} \right)^{-1} E \frac{d}{dE} E \Sigma_s(E) \phi(E), \end{aligned} \quad (241)$$

and:

$$\begin{aligned} \mathcal{L}_W \phi(E) &= \frac{1}{E} \left[I - \left(I - \xi E \frac{d}{dE} \right) \right] \left(I - \xi E \frac{d}{dE} \right)^{-1} E \Sigma_s(E) \phi(E) \\ &= \xi \frac{d}{dE} \left(I - \xi E \frac{d}{dE} \right)^{-1} E \Sigma_s(E) \phi(E). \end{aligned} \quad (242)$$

Equation (241) shows that \mathcal{L}_W preserves $\phi_{eq}(E)$, and (242) shows that \mathcal{L}_W is conservative. Wigner's equation (238) can also be written:

$$\left(I - \xi E \frac{d}{dE}\right) E [\Sigma_t(E)\phi(E) - Q(E)] = E \Sigma_s(E)\phi(E),$$

or:

$$\Sigma_t(E)\phi(E) - Q(E) - \xi \frac{d}{dE} E [\Sigma_t(E)\phi(E) - Q(E)] = \Sigma_s(E)\phi(E)$$

or:

$$\Sigma_a(E)\phi(E) = \xi \frac{d}{dE} E [\Sigma_t(E)\phi(E) - Q(E)] + Q(E). \quad (243)$$

Solving this first-order ordinary differential equation with $\phi(E_0) = 0$, we obtain:

$$\phi_W(E) = \frac{1}{\Sigma_t(E)} \left[Q(E) + \frac{1}{\xi E} \int_E^{E_0} e^{-\frac{1}{\xi} \int_E^{E'} \frac{\Sigma_a(E'')}{E'' \Sigma_t(E'')} dE''} \frac{\Sigma_s(E')}{\Sigma_t(E')} Q(E') dE' \right]. \quad (244)$$

This result is exact for $A = 1$ and has $O(1/A^2)$ error for $A \gg 1$.

If we consider a monoenergetic source:

$$Q(E) = Q_0 \delta(E - E_0),$$

then for $E < E_0$, (244) can be written as the product of four factors:

$$\phi_W(E) = \left[\frac{Q_0}{\xi E \Sigma_s(E)} \right] \left[\frac{\Sigma_s(E_0)}{\Sigma_t(E_0)} \right] \left[e^{-\frac{1}{\xi} \int_E^{E_0} \frac{\Sigma_a(E')}{E' \Sigma_t(E')} dE'} \right] \left[\frac{\Sigma_s(E)}{\Sigma_t(E)} \right], \quad (245)$$

each of which has a straightforward physical interpretation.

The first factor is the equilibrium solution for a problem emitting Q_0 neutrons per cm^3 per s with $\Sigma_a(E) = 0$:

$$\phi_{eq}(E) = \frac{Q_0}{\xi E \Sigma_s(E)}. \quad (246a)$$

If $\Sigma_a(E) = 0$, the remaining three factors on the right side of (245) all equal unity, and then $\phi_W(E) = \phi_{eq}(E)$. The three terms suppress $\phi_W(E)$ in ways that account for absorption.

The second factor is the *scattering ratio at energy E_0* :

$$c(E_0) = \frac{\Sigma_s(E_0)}{\Sigma_t(E_0)} = \text{the probability that a (source) neutron with energy } E_0 \text{ will not be absorbed.} \quad (246b)$$

This factor is necessary because only the source neutrons (all of which are born at energy E_0) that scatter can contribute to $\phi(E)$. Effectively, the product

$$q_0 = Q_0 \frac{\Sigma_s(E_0)}{\Sigma_t(E_0)}$$

is a *reduced source rate*, which accounts for source neutrons born at E_0 that are immediately absorbed and hence do not slow down.

The third factor on the right side of (245) is the *resonance escape probability*:

$$p(E_0 \rightarrow E) = e^{-\frac{1}{\xi} \int_E^{E_0} \frac{\Sigma_a(E')}{E' \Sigma_t(E')} dE'}$$

= the probability that a neutron will not be absorbed
while slowing down from E_0 to E . (246c)

The fourth factor is the scattering ratio $c(E)$, to account for the suppression of $\phi(E)$ due to absorption at energy E .

Equation (245) is therefore not only an accurate result, but it has an intuitive physical interpretation. (The expression for the resonance escape probability in (245) is especially accurate and useful.) We now turn to providing a general sketch of $\phi_W(E)$.

For heavy nuclei, $\Sigma_a(E)$ often consists of narrow, isolated absorption resonances, while $\Sigma_s(E)$ is relatively constant (see \blacktriangleright Fig. 30). In this situation, $c(E)$ has the form depicted in \blacktriangleright Fig. 31, and $p(E_0 \rightarrow E)$ has the form depicted in \blacktriangleright Fig. 32. Combining these, the product $\phi(E)$ expressed in (245) has the form depicted in \blacktriangleright Fig. 33.

Hence, as neutrons slow down through each absorption resonance, $\phi_W(E)$ experiences a narrow “dip” within the resonance and returns to a new equilibrium solution below the resonance (the amplitude is reduced because of neutrons that are absorbed within the resonance).

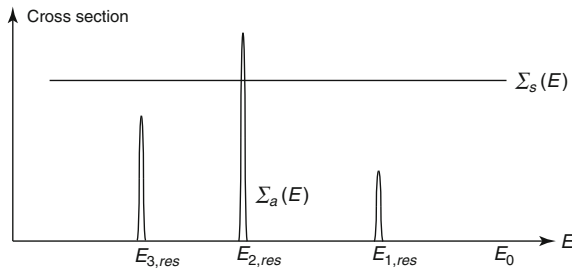


Figure 30
 $\Sigma_a(E)$ and $\Sigma_s(E)$

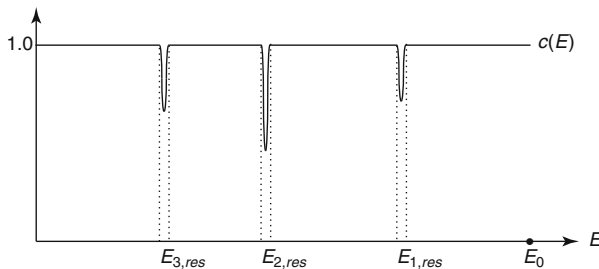


Figure 31
 $c(E)$

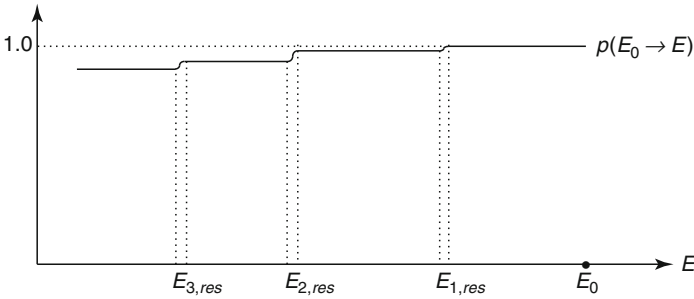


Figure 32
 $\rho(E_0 \rightarrow E)$

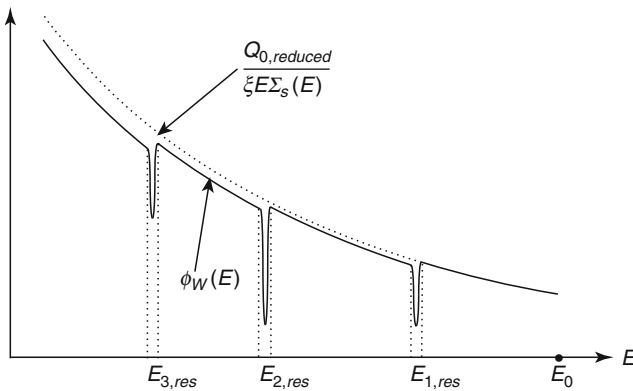


Figure 33
 $\phi_W(E)$

The above Wigner depiction of $\phi(E)$ is surprisingly accurate. The simpler Age depiction of $\phi(E)$ is usually less accurate, unless $\Sigma_a(E) \ll \Sigma_s(E)$.

7.5 Discussion

We have derived the *Age* (or CSD) approximation (234), and the *Wigner* approximation (243) of the infinite-medium neutron spectrum equation (215a). The Age and Wigner approximations both:

1. Are conservative.
2. Preserve the equilibrium solution $\phi_{eq}(E)$.
3. Are $O(1/A^2)$ asymptotic approximations to the spectrum equation for $A \gg 1$.
4. Yield for $E < E_1$ the solution (230) of the purely scattering problem.

However, the Wigner approximation is generally more accurate than the Age approximation, for the following reasons:

1. The Wigner approximation $H_W(E)$ of the out-scattering integral $H(E)$ is itself an integral [see (238c) and (239)], and $H_W(E) = H(E)$ for $A = 1$.
2. Because the Wigner approximation is exact for $A = 1$ and highly accurate for $A \gg 1$, it is also quite accurate for intermediate values of A .

Therefore, the Wigner approximation is quite accurate for all values of A , whereas the simpler Age approximation is generally only accurate for $A \gg 1$.

8 The Diffusion Approximation

Because of its relative simplicity and range of applicability, the diffusion approximation to the Boltzmann transport equation is widely used for reactor core simulations. However, the diffusion approximation has several subtleties, and even today there are issues in its use that are not fully understood.

Here we derive the approximate diffusion equation for a 1-D planar-geometry problem, using a simplified version of asymptotic derivations that have been published during the past 35 years (Habetler and Matkowsky 1975; Larsen 1980; Larsen and Keller 1974; Larsen et al. 1996; Papanicolaou 1975). The choice of 1-D planar geometry enables us to perform the derivation with the Legendre polynomials, rather than the more complex spherical harmonic functions, which are necessary for 2-D, and 3-D problems. However, the basic underlying issues in 1-D, 2-D, and 3-D geometries are the same.

8.1 Derivation of the Diffusion Equation

We consider the energy-dependent, planar-geometry Boltzmann transport equation with anisotropic scattering:

$$\begin{aligned} & \mu \frac{\partial \psi}{\partial x}(x, \mu, E) + \Sigma_t(x, E)\psi(x, \mu, E) \\ &= \sum_{m=0}^{\infty} \frac{2m+1}{2} P_m(\mu) \int_0^{\infty} \int_{-1}^1 P_m(\mu') \Sigma_{s,m}(x, E' \rightarrow E) \psi(x, \mu', E') d\mu' dE' \\ &+ \frac{Q(x, E)}{2}, \end{aligned} \quad (247a)$$

on the system $0 \leq x \leq X$, with boundary conditions:

$$\psi(0, \mu, E) = \psi(0, -\mu, E), \quad 0 < \mu \leq 1, \quad (247b)$$

$$\psi(X, \mu, E) = \psi^b(\mu, E), \quad -1 \leq \mu < 0. \quad (247c)$$

(Equation [247b] is a reflection or symmetry boundary condition; [247c] specifies the incident flux $\psi^b(\mu, E)$ on the right boundary of the system.)

To initiate the derivation of the diffusion approximation to (247), let us first consider (247a) for an *infinite homogeneous* medium having no spatial dependence:

$$\Sigma_t(E)\psi(\mu, E) = \sum_{m=0}^{\infty} \frac{2m+1}{2} P_m(\mu) \int_0^{\infty} \int_{-1}^1 P_m(\mu') \Sigma_{s,m}(E' \rightarrow E) \psi(\mu', E') d\mu' dE' + \frac{Q(E)}{2}. \quad (248)$$

To represent the exact solution of (248), we operate on this equation by $\int_{-1}^1 P_n(\mu)(\cdot) d\mu$. Defining the n th Legendre moment of the angular flux as:

$$\int_{-1}^1 P_n(\mu) \psi(\mu, E) d\mu = \phi_n(E),$$

and using:

$$\int_{-1}^1 P_n(\mu) P_m(\mu) d\mu = \delta_{m,n},$$

we obtain the system of equations:

$$\Sigma_t(E)\phi_n(E) = \int_0^{\infty} \Sigma_{s,n}(E' \rightarrow E) \phi_n(E') dE' + Q(E)\delta_{n,0}, \quad 0 \leq n. \quad (249)$$

Hence, for $n \geq 1$, $\phi_n(E) = 0$, and:

$$\psi(\mu, E) = \sum_{n=0}^{\infty} \frac{2n+1}{2} P_n(\mu) \phi_n(E) = \frac{1}{2} \phi_0(E), \quad (250)$$

where $\phi_0(E)$ satisfies (249) with $n = 0$. Equations (248–250) show that *for an infinite, spatially uniform problem with an isotropic source, the angular flux is independent of both space (x) and angle (μ).*

We now return to (247) and assume that the spatial derivative in ψ is *small* in comparison to the other terms. (Physically, the net leakage rate from a spatial increment dx is assumed to be small in comparison to the collision rate and scattering rates in dx .) To analytically describe this, we write (247a) as:

$$\begin{aligned} \epsilon \mu \frac{\partial \psi}{\partial x}(x, \mu, E) + \Sigma_t(x, E) \psi(x, \mu, E) \\ = \sum_{m=0}^{\infty} \frac{2m+1}{2} P_m(\mu) \int_0^{\infty} \int_{-1}^1 P_m(\mu') \Sigma_{s,m}(x, E' \rightarrow E) \psi(x, \mu', E') d\mu' dE' \\ + \frac{Q(x, E)}{2}, \end{aligned} \quad (251)$$

where ϵ is a small dimensionless parameter, indicating that the leakage term is small. (At the conclusion of this analysis, we set $\epsilon = 1$.)

Because ψ has a weak spatial dependence, we anticipate that ψ should also have a weak angular dependence. (As the spatial derivative of ψ limits to zero, ψ should become isotropic.) Consistent with this expectation, we show that the solution of (251) has the Legendre polynomial expansion:

$$\psi(x, \mu, E) = \sum_{m=0}^{\infty} \frac{2m+1}{2} \epsilon^m P_m(\mu) \phi_m(x, E), \quad (252)$$

where $\phi_n(E) = O(1)$ for all n . (In (252), the m th Legendre moment of $\psi(x, \mu, E)$ is $\varepsilon^m \phi_m(x, E)$.)

Introducing (252) into (251), using the identity:

$$\mu P_m(\mu) = \frac{m+1}{2m+1} P_{m+1}(\mu) + \frac{m}{2m+1} P_{m-1}(\mu),$$

and operating by $\int_{-1}^1 P_n(\mu)(\cdot) d\mu$, we obtain for all $n \geq 0$:

$$\begin{aligned} \frac{n}{2n+1} \frac{\partial \phi_{n-1}}{\partial x}(x, E) + \varepsilon^2 \frac{n+1}{2n+1} \frac{\partial \phi_{n+1}}{\partial x}(x, E) + \Sigma_t(x, E) \phi_n(x, E) \\ = \int_0^\infty \Sigma_{s,n}(x, E' \rightarrow E) \phi_n(x, E') dE' + \delta_{n,0} Q(x, E). \end{aligned} \quad (253)$$

These equations are consistent with the assumption in (252) that $\phi_n(x, E) = O(1)$, and thus that the n th Legendre moment of ψ is $O(\varepsilon^n)$.

Specifically, (253) with $n = 0$ and $n = 1$ yields:

$$\varepsilon^2 \frac{\partial \phi_1}{\partial x}(x, E) + \Sigma_t(x, E) \phi_0(x, E) = \int_0^\infty \Sigma_{s,0}(x, E' \rightarrow E) \phi_0(x, E') dE' + Q(x, E), \quad (254a)$$

$$\frac{1}{3} \frac{\partial \phi_0}{\partial x}(x, E) + \frac{2\varepsilon^2}{3} \frac{\partial \phi_2}{\partial x}(x, E) + \Sigma_t(x, E) \phi_1(x, E) = \int_0^\infty \Sigma_{s,1}(x, E' \rightarrow E) \phi_1(x, E') dE'. \quad (254b)$$

To derive the diffusion equation, we make the following two approximations to (254b):

1. We set:

$$\varepsilon^2 \frac{\partial \phi_2}{\partial x}(x, E) \approx 0. \quad (255a)$$

(This introduces an error of $O(\varepsilon^2)$ in the equations for ϕ_0 and ϕ_1 .)

2. We introduce the approximation:

$$\Sigma_{s,1}(E' \rightarrow E) \approx \Sigma_{s,1}(x, E') \delta(E' - E), \quad (255b)$$

where:

$$\Sigma_{s,1}(x, E') = \int_0^\infty \Sigma_{s,1}(E' \rightarrow E) dE. \quad (256)$$

(This creates an error of undetermined order with respect to ε . However, the following integral is preserved:

$$\int_0^\infty [\Sigma_{s,1}(x, E' \rightarrow E)] dE = \int_0^\infty [\Sigma_{s,1}(x, E') \delta(E' - E)] dE = \Sigma_{s,1}(x, E'),$$

and thus the integral of the right side of (254) over E is preserved.)

Making these two approximations, (254b) becomes:

$$\frac{1}{3} \frac{\partial \phi_0}{\partial x}(x, E) + \Sigma_t(x, E) \phi_1(x, E) = \Sigma_{s,1}(x, E) \phi_1(x, E). \quad (257)$$

If we now define:

$$\Sigma_{tr}(x, E) = \Sigma_t(x, E) - \Sigma_{s,1}(x, E) = \text{transport cross section}, \quad (258a)$$

then (257) yields *Fick's Law*:

$$\phi_1(x, E) = -\frac{1}{3\Sigma_{tr}(x, E)} \frac{\partial \phi_0}{\partial x}(x, E). \quad (258b)$$

Introducing (258a) into (254a), we obtain the following *energy-dependent diffusion equation*:

$$-\varepsilon^2 \frac{\partial}{\partial x} \frac{1}{3\Sigma_{tr}(x, E)} \frac{\partial \phi_0}{\partial x}(x, E) + \Sigma_t(x, E) \phi_0(x, E) = \int_0^\infty \Sigma_{s,0}(x, E' \rightarrow E) \phi_n(x, E') dE' + Q(x, E). \quad (259)$$

Also, from (252) and (258), we have the following representation of ψ :

$$\psi(x, \mu, E) = \frac{1}{2} \phi_0(x, E) - \frac{\varepsilon \mu}{2\Sigma_{tr}(x, E)} \frac{\partial \phi_0}{\partial x}(x, E) + O(\varepsilon^2). \quad (260)$$

Ignoring the $O(\varepsilon^2)$ component of ψ , we see that the transport reflection boundary condition (247b) at $x = 0$ is satisfied by (260) if:

$$\frac{\partial \phi_0}{\partial x}(0, E) = 0. \quad (261)$$

This is the diffusion *reflection* or *symmetry* boundary condition.

However, since ϕ_0 is independent of μ , the transport boundary condition at $x = X$:

$$\begin{aligned} \psi^b(X, \mu) &= \psi(X, \mu) \\ &= \frac{1}{2} \phi_0(X, E) - \frac{\varepsilon \mu}{2\Sigma_{tr}(X, E)} \frac{\partial \phi_0}{\partial x}(X, E), \quad -1 \leq \mu < 0 \end{aligned}$$

cannot generally be satisfied. Operating on both sides of this equation by $\int_{-1}^0 w(|\mu|)(\cdot) d\mu$, where $w(\mu)$ is any positive function, which for convenience is normalized by $\int_0^1 w(\mu) d\mu = 1$, we obtain:

$$2 \int_{-1}^0 w(|\mu|) \psi^b(\mu, E) d\mu = \phi_0(X, E) + \frac{\varepsilon}{\Sigma_{tr}(X, E)} \left(\int_0^1 \mu w(\mu) d\mu \right) \frac{\partial \phi_0}{\partial x}(X, E), \quad (262)$$

and this boundary condition *can* be used to determine ϕ_0 . However, it is not clear how to choose $w(\mu)$.

A common, physically based choice of $w(\mu)$ is:

$$w(\mu) = 2\mu, \quad (263a)$$

which yields the *Marshak boundary condition*:

$$4J^-(X) = \phi_0(X, E) + \frac{2\varepsilon}{3\Sigma_{tr}(X, E)} \frac{\partial \phi_0}{\partial x}(X, E), \quad (263b)$$

where:

$$\begin{aligned} J^-(X) &= \int_{-1}^0 |\mu| \psi^b(\mu, E) d\mu \\ &= \text{incident partial current at } x = X. \end{aligned} \quad (263c)$$

This boundary condition preserves the rate at which neutrons enter the system on its incident-flux boundary.

A more accurate diffusion boundary condition can be obtained by appealing to transport theory, or to a variational analysis, which yields the following approximation to $w(\mu)$:

$$w(\mu) = \mu + \frac{3}{2}\mu^2. \quad (264a)$$

This yields:

$$2 \int_{-1}^0 w(|\mu|) \psi^b(\mu, E) d\mu = \phi_0(X, E) + \frac{17\varepsilon}{24\Sigma_{tr}(X, E)} \frac{\partial \phi_0}{\partial x}(X, E). \quad (264b)$$

Setting $\varepsilon = 1$ in (259–263), we obtain the standard energy-dependent diffusion equation with Marshak boundary conditions. If the boundary condition (263) is replaced by (264), one obtains a more accurate result.

The diffusion solution is accurate for transport problems in which the angular flux ψ has a weak space-dependence (its spatial derivatives are small). In this case, ψ also has a weak angle-dependence (is nearly isotropic). In the diffusion equations (259), (261), and (262) the angular variable is entirely eliminated. The constraint that ψ must have weak spatial and angular dependences is often valid in reactor cores, but not in shields. For this reason, the diffusion approximation, or variants thereof, are generally used to simulate neutron transport in nuclear reactor cores, but not in shields.

8.2 Homogenized Diffusion Theory

The “variants” of diffusion theory mentioned in the previous paragraph refer to other approximations used in practical reactor core simulations. In many problems, an extra step is included that is difficult to justify theoretically: each reactor assembly in a core is *homogenized*, i.e., approximated by a fictitious homogeneous system in which the homogenized cross sections are defined to preserve certain features of the original heterogeneous system. Then, the diffusion approximation is applied to the homogenized system.

The homogenization process is not unique because different quantities can be preserved, and there has been considerable debate about the proper manner in which homogenization should be done (Benoist 1964; Dorning 2003; Gelbard 1974; Larsen and Hughes 1980). Different definitions work acceptably for different applications, but no one definition seems to work best for all (or even most) applications. As a consequence, the optimal definition of homogenized diffusion coefficients remains an unsolved problem.

8.3 Spherical Harmonic (P_N) and Simplified Spherical Harmonic (SP_N) Approximations

The diffusion approximation is the simplest useful approximation that has been derived from (251) and (252). Other higher-order in angle approximations can also be derived.

In particular, the 1-D P_N approximation (for N odd and ≥ 3) can be derived from (251) and (252) by calculating the first $N + 1$ Legendre moments of (251) and using (252) with $\phi_n = 0$ for $n > N$ to truncate the series. The resulting equations are closely related to diffusion equations; for one-group problems, they can be written exactly as a coupled system of $(N + 1)/2$ diffusion equations. Unfortunately, this relatively simple form of the P_N equations does not hold for 2-D and 3-D problems. The greater complexity of the P_N equations for 2-D and 3-D geometries has been a significant factor to their relative unpopularity.

A different class of approximations, which are less accurate but simpler than the P_N approximations, and more accurate than the diffusion approximation, has been developed; this is the so-called *simplified spherical harmonic* (SP_N) equations, originally proposed by Gelbard (1960, 1961, 1962). The 1-D SP_N equations are identical to the diffusion form of the 1-D P_N equations described in the previous paragraph. The multidimensional SP_N equations can be formally derived from the 1-D P_N or SP_N equations by replacing, in each equation, the 1-D diffusion operator by the multidimensional diffusion operator:

$$\frac{d}{dx}D(x)\frac{d\phi}{dx}(x) \rightarrow \nabla \cdot D(\mathbf{x})\nabla\phi(\mathbf{x}).$$

(More mathematically rigorous derivations of the SP_N equations, using asymptotic and variational analyses, have been developed [Brantley and Larsen 2000; Larsen et al. 1996; Tomašević and Larsen 1996].) The multidimensional SP_N equations have the relatively simple form of coupled multidimensional diffusion equations, and they become equivalent to the P_N equations in 1-D.

Because of their diffusion form, the SP_N equations can be implemented in a multigroup diffusion code without significantly restructuring the code. In certain practical problems, the low-order SP_3 equations have been shown to capture “more than 80%” of the transport effects that are not present in the diffusion (P_1) solution (Gamino 1989, 1991). Generally, the SP_N equations are useful for problems in which the diffusion solution is a reasonable, but not sufficiently accurate, approximation to the transport solution. However, the SP_N equations are not always accurate for problems in which the diffusion solution is a poor approximation.

8.4 Discussion

The diffusion equation is used almost universally as an approximation to the Boltzmann transport equation for reactor core simulations, after the core has been suitably “homogenized.” The principal advantage of the diffusion approximation is that the angular variable Ω is eliminated, thereby greatly reducing the amount of work and the expense necessary to solve the approximate problem. However, the diffusion solution has limited accuracy, and the proper definition of homogenized diffusion coefficients remains an open question.

9 The Point Kinetics Approximation

The point kinetics equations (PKEs) are a classic approximation of the time-dependent neutron transport and precursor density equations (Bell and Glasstone 1970; Henry 1975; Hetrick 1993; Lewis and Miller 1993; Ott 1985). For a *critical* system, the (i) neutron transport and precursor and (ii) PKEs both have steady-state solutions. For systems that are *nearly critical* and have solutions that *vary slowly* in t , the solutions of the PKEs can accurately approximate the corresponding solutions of the time-dependent transport and precursor density equations. Also, the PKEs are much simpler than the transport and precursor density equations and can be solved much more efficiently. For these reasons, the PKEs are widely used in time-dependent reactor simulations and stability studies. Previously, the PKEs have been derived by *variational approximations*; here they are derived from the full transport and neutron precursor equations, using an asymptotic analysis that is related to the analyses used in [Sect. 8](#) to derive the diffusion approximation.

9.1 Preliminaries

We begin by restating the general time-dependent transport problem with neutron precursors for a system V with vacuum boundary conditions and no internal source. The problem consists of the time-dependent transport equation for the angular flux $\psi(\mathbf{x}, \boldsymbol{\Omega}, E, t)$:

$$\begin{aligned} & \frac{1}{v} \frac{\partial \psi}{\partial t}(\mathbf{x}, \boldsymbol{\Omega}, E, t) + \boldsymbol{\Omega} \cdot \nabla \psi(\mathbf{x}, \boldsymbol{\Omega}, E, t) + \Sigma_t(\mathbf{x}, E, t) \psi(\mathbf{x}, \boldsymbol{\Omega}, E, t) \\ &= \int_0^\infty \int_{4\pi} \Sigma_s(\mathbf{x}, \boldsymbol{\Omega}' \cdot \boldsymbol{\Omega}, E' \rightarrow E, t) \psi(\mathbf{x}, \boldsymbol{\Omega}', E', t) d\boldsymbol{\Omega}' dE' \\ &+ \frac{\chi_p(\mathbf{x}, E, t)}{4\pi} \int_0^\infty \int_{4\pi} [1 - \beta(\mathbf{x}, E', t)] v \Sigma_f(\mathbf{x}, E', t) \psi(\mathbf{x}, \boldsymbol{\Omega}', E', t) d\boldsymbol{\Omega}' dE' \\ &+ \frac{1}{4\pi} \sum_{j=1}^6 \chi_j(\mathbf{x}, E, t) \lambda_j C_j(\mathbf{x}, t), \quad \mathbf{x} \in V, \quad \boldsymbol{\Omega} \in 4\pi, \quad 0 < E < \infty, \quad 0 < t, \end{aligned} \quad (265)$$

the time-dependent equations for the neutron precursor densities $C_j(\mathbf{x}, t)$:

$$\begin{aligned} & \frac{\partial C_j}{\partial t}(\mathbf{x}, t) + \lambda_j C_j(\mathbf{x}, t) \\ &= \int_0^\infty \int_{4\pi} \beta_j(\mathbf{x}, E', t) v \Sigma_f(\mathbf{x}, E', t) \psi(\mathbf{x}, \boldsymbol{\Omega}', E', t) d\boldsymbol{\Omega}' dE', \quad \mathbf{x} \in V, \quad 0 < t, \quad 1 \leq j \leq 6, \end{aligned} \quad (266)$$

the specified initial conditions for ψ and C_j :

$$\psi(\mathbf{x}, \boldsymbol{\Omega}, E, 0) = \psi^i(\mathbf{x}, \boldsymbol{\Omega}, E), \quad \mathbf{x} \in V, \quad \boldsymbol{\Omega} \in 4\pi, \quad 0 < E < \infty, \quad (267a)$$

$$C_j(\mathbf{x}, 0) = C_j^i(\mathbf{x}), \quad \mathbf{x} \in V, \quad 1 \leq j \leq 6, \quad (267b)$$

and the vacuum boundary condition for ψ :

$$\psi(\mathbf{x}, \boldsymbol{\Omega}, E, t) = 0, \quad \mathbf{x} \in \partial V, \quad \boldsymbol{\Omega} \cdot \mathbf{n} < 0, \quad 0 < E < \infty, \quad 0 < t. \quad (267c)$$

Also, β and β_j satisfy:

$$\beta(\mathbf{x}, E, t) = \sum_{n=1}^6 \beta_j(\mathbf{x}, E, t). \quad (268)$$

Equations (265) and (266) explicitly allow space- and time-dependence of all cross sections to account for the time-dependent movement of control rods within the core. However, we do not (for simplicity) include a nonlinear temperature-dependence of the cross sections, and we assume that the cross sections are specified for $t \geq 0$.

Because the cross sections are known for $t > 0$, it is in principle possible to calculate the reactivity $\rho(t)$ and the corresponding forward eigenfunction $\Psi(\mathbf{x}, \boldsymbol{\Omega}, E, t)$ for $t > 0$. These are defined by the familiar eigenvalue problem:

$$\begin{aligned} & \boldsymbol{\Omega} \cdot \nabla \Psi(\mathbf{x}, \boldsymbol{\Omega}, E, t) + \Sigma_t(\mathbf{x}, E, t) \Psi(\mathbf{x}, \boldsymbol{\Omega}, E, t) \\ &= \int_0^\infty \int_{4\pi} \Sigma_s(\mathbf{x}, \boldsymbol{\Omega}' \cdot \boldsymbol{\Omega}, E' \rightarrow E, t) \Psi(\mathbf{x}, \boldsymbol{\Omega}', E', t) d\Omega' dE' \\ &+ [1 - \rho(t)] \frac{\chi_p(\mathbf{x}, E, t)}{4\pi} \int_0^\infty \int_{4\pi} \nu \Sigma_f(\mathbf{x}, E', t) \Psi(\mathbf{x}, \boldsymbol{\Omega}', E', t) d\Omega' dE', \\ & \mathbf{x} \in V, \quad \boldsymbol{\Omega} \in 4\pi, \quad 0 < E < \infty, \end{aligned} \quad (269a)$$

$$\Psi(\mathbf{x}, \boldsymbol{\Omega}, E, t) = 0, \quad \mathbf{x} \in \partial V, \quad \boldsymbol{\Omega} \cdot \mathbf{n} < 0, \quad 0 < E < \infty. \quad (269b)$$

In these equations, t appears only as a parameter, and we normalize the eigenfunction Ψ by:

$$\int \int_0^\infty \int_{4\pi} \frac{1}{\nu} \Psi(\mathbf{x}, \boldsymbol{\Omega}, E, t) d\Omega dE dV = 1. \quad (269c)$$

Equations (269a) and (269b) have no external sources, and the eigenvalue $\rho(t)$ must be determined so that a positive solution Ψ exists. If $\rho(t) < 0$, the fission term in (269a) is increased by the factor $[1 - \rho(t)]$ to produce a steady-state solution, so the system is *subcritical*. If $\rho(t) > 0$, the fission term is reduced by the factor $[1 - \rho(t)]$ to produce a steady-state solution, so the system is *supercritical*. If $\rho(t) = 0$, then no adjustment to the fission term is made, and the system is *critical*.

The time-dependent cross sections, the reactivity $\rho(t)$, the forward eigenfunction $\Psi(\mathbf{x}, \boldsymbol{\Omega}, E, t)$, and the adjoint eigenfunction $\Psi^\dagger(\mathbf{x}, \boldsymbol{\Omega}, E, t)$ (of the problem which is adjoint to [269]) all explicitly occur in the asymptotic analysis. In the following, we assume that all of these quantities are known. (Then the forward and adjoint scalar fluxes $\Phi(\mathbf{x}, E, t) = \int_{4\pi} \Psi(\mathbf{x}, \boldsymbol{\Omega}, E, t) d\Omega$ and $\Phi^\dagger(\mathbf{x}, E, t) = \int_{4\pi} \Psi^\dagger(\mathbf{x}, \boldsymbol{\Omega}, E, t) d\Omega$ are also known.) The asymptotic analysis determines time-dependent equations for ψ and C_j having coefficients that

are expressed in terms of the time-dependent cross sections $\Sigma(\mathbf{x}, E, t)$, reactivity $\rho(t)$, and eigenfunctions $\Psi(\mathbf{x}, \Omega, E, t)$ and $\Psi^\dagger(\mathbf{x}, \Omega, E, t)$.

9.2 The Scaled Transport and Neutron Precursor Equations

Next, we make physical assumptions that are consistent with the basic overall requirement that the system V be *nearly critical* and *slowly varying in time*.

- The reactivity $\rho(t)$ is small. (The system is *nearly critical* for all $t > 0$.)
- β_j and β are small. In practice, this assumption is valid; β is dimensionless and ≈ 0.01 .
- If t is measured on the timescale for precursor decay (e.g., in seconds), then the mean neutron speed is large. In practice, this assumption is valid.
- Since the mean neutron speed is large and $\psi = vN$, then ψ is large.
- All specified time-dependent quantities in (265–266) vary on the same slow timescale (seconds) on which the neutron precursors decay.

To express these conditions mathematically, we introduce a small positive dimensionless parameter ε and define:

$$\rho(t) = \varepsilon \hat{\rho}(t), \quad (270a)$$

$$\beta_j(\mathbf{x}, E, t) = \varepsilon \hat{\beta}_j(\mathbf{x}, E, t) \quad \text{and} \quad \beta(\mathbf{x}, E, t) = \varepsilon \hat{\beta}(\mathbf{x}, E, t), \quad (270b)$$

$$v = \frac{\hat{v}}{\varepsilon}, \quad (270c)$$

$$\psi(\mathbf{x}, \Omega, E, t) = \frac{\hat{\psi}(\mathbf{x}, \Omega, E, t)}{\varepsilon}, \quad (270d)$$

$$\psi^i(\mathbf{x}, \Omega, E, t) = \frac{\hat{\psi}^i(\mathbf{x}, \Omega, E, t)}{\varepsilon}. \quad (270e)$$

In these equations, all the hatted quantities are assumed to be $O(1)$.

Introducing (270) into (265–268), we obtain:

$$\begin{aligned} & \frac{1}{\hat{v}} \frac{\partial \hat{\psi}}{\partial t}(\mathbf{x}, \Omega, E, t) + \frac{1}{\varepsilon} \Omega \cdot \nabla \hat{\psi}(\mathbf{x}, \Omega, E, t) + \frac{1}{\varepsilon} \Sigma_t(\mathbf{x}, E, t) \hat{\psi}(\mathbf{x}, \Omega, E, t) \\ &= \frac{1}{\varepsilon} \int_0^\infty \int_{4\pi} \Sigma_s(\mathbf{x}, \Omega' \cdot \Omega, E' \rightarrow E, t) \hat{\psi}(\mathbf{x}, \Omega', E', t) d\Omega' dE' \\ & \quad + \frac{\chi_p(\mathbf{x}, E, t)}{4\pi\varepsilon} \int_0^\infty \int_{4\pi} [1 - \rho(t) + \varepsilon \hat{\rho}(t) - \varepsilon \hat{\beta}(\mathbf{x}, E', t)] \\ & \quad \times v \Sigma_f(\mathbf{x}, E', t) \hat{\psi}(\mathbf{x}, \Omega', E', t) d\Omega' dE' \\ & \quad + \frac{1}{4\pi} \sum_{j=1}^6 \chi_j(\mathbf{x}, E, t) \lambda_j C_j(\mathbf{x}, t) + \frac{Q(\mathbf{x}, E, t)}{4\pi}, \end{aligned} \quad (271a)$$

$$\frac{\partial C_j}{\partial t}(\mathbf{x}, t) + \lambda_j C_j(\mathbf{x}, t) = \int_0^\infty \int_{4\pi} \hat{\beta}_j(\mathbf{x}, E', t) v \Sigma_f(\mathbf{x}, E', t) \hat{\psi}(\mathbf{x}, \Omega', E', t) d\Omega' dE', \quad (271b)$$

where the expression $-\rho(t) + \varepsilon \hat{\rho}(t) = 0$ has been included in the integrand of the prompt fission term in (271a) so that the small reactivity $\rho(t) = \varepsilon \hat{\rho}(t)$ occurs in the scaled equations to leading order. We also have the boundary and initial conditions:

$$\hat{\psi}(\mathbf{x}, \boldsymbol{\Omega}, E, t) = 0, \quad \mathbf{x} \in \partial V, \quad \boldsymbol{\Omega} \cdot \mathbf{n} < 0, \quad 0 < E < \infty, \quad 0 < t, \quad (272)$$

$$\hat{\psi}(\mathbf{x}, \boldsymbol{\Omega}, E, 0) = \hat{\psi}^i(\mathbf{x}, \boldsymbol{\Omega}, E), \quad \mathbf{x} \in V, \quad \boldsymbol{\Omega} \in 4\pi, \quad 0 < E < \infty, \quad (273a)$$

$$C_j(\mathbf{x}, 0) = C_j^i(\mathbf{x}), \quad \mathbf{x} \in V, \quad (273b)$$

and:

$$\hat{\beta}(\mathbf{x}, E, t) = \sum_{j=1}^6 \hat{\beta}_j(\mathbf{x}, E, t). \quad (274)$$

The scaled equations (271–274) for $\hat{\psi}$ and C_j are equivalent to the original equations (265–268) for ψ and C_j ; no approximations have yet been made.

9.3 Asymptotic Derivation of the Point Kinetics Equations

To proceed, we introduce the *ansatz*:

$$\hat{\psi}(\mathbf{x}, \boldsymbol{\Omega}, E, t) = \sum_{n=0}^{\infty} \varepsilon^n \hat{\psi}_n(\mathbf{x}, \boldsymbol{\Omega}, E, t), \quad (275a)$$

$$C_j(\mathbf{x}, t) = \sum_{n=0}^{\infty} \varepsilon^n C_{j,n}(\mathbf{x}, t), \quad (275b)$$

into (271–273) and equate the coefficients of different powers of ε . The sole $O(\varepsilon^{-1})$ equation is:

$$\begin{aligned} & \boldsymbol{\Omega} \cdot \nabla \hat{\psi}_0(\mathbf{x}, \boldsymbol{\Omega}, E, t) + \Sigma_t(\mathbf{x}, E, t) \hat{\psi}_0(\mathbf{x}, \boldsymbol{\Omega}, E, t) \\ & - \int_0^{\infty} \int_{4\pi} \Sigma_s(\mathbf{x}, \boldsymbol{\Omega}' \cdot \boldsymbol{\Omega}, E' \rightarrow E, t) \hat{\psi}_0(\mathbf{x}, \boldsymbol{\Omega}', E', t) d\boldsymbol{\Omega}' dE' \\ & - [1 - \rho(t)] \frac{\chi_p(\mathbf{x}, E, t)}{4\pi} \int_0^{\infty} \int_{4\pi} \nu \Sigma_f(\mathbf{x}, E', t) \hat{\psi}_0(\mathbf{x}, \boldsymbol{\Omega}', E', t) d\boldsymbol{\Omega}' dE' = 0, \end{aligned} \quad (276)$$

with the vacuum boundary condition for $\hat{\psi}_0$. By (269), the general solution of these equations is:

$$\hat{\psi}_0(\mathbf{x}, \boldsymbol{\Omega}, E, t) = \Psi(\mathbf{x}, \boldsymbol{\Omega}, E, t) N_0(t), \quad (277)$$

where $N_0(t)$ is, at this point, undetermined. We note that by (269c),

$$\int_V \int_0^{\infty} \int_{4\pi} \frac{1}{v} \hat{\psi}_0(\mathbf{x}, \boldsymbol{\Omega}, E, t) d\boldsymbol{\Omega} dE dV = N_0(t), \quad (278a)$$

so:

$$N_0(t) = \text{the number of neutrons in } V \text{ at time } t. \quad (278b)$$

Next, we introduce (277) for $\hat{\psi}_0$ into the $O(1)$ components of (271) and obtain the following equations for $\hat{\psi}_1$ and $C_{j,0}$:

$$\begin{aligned}
 & \Omega \cdot \nabla \hat{\psi}_1(\mathbf{x}, \Omega, E, t) + \Sigma_t(\mathbf{x}, E, t) \hat{\psi}_1(\mathbf{x}, \Omega, E, t) \\
 & - \int_0^\infty \int_{4\pi} \Sigma_s(\mathbf{x}, \Omega' \cdot \Omega, E' \rightarrow E, t) \hat{\psi}_1(\mathbf{x}, \Omega', E', t) d\Omega' dE' \\
 & - [1 - \rho(t)] \frac{\chi_p(\mathbf{x}, E, t)}{4\pi} \int_0^\infty \int_{4\pi} \nu \Sigma_f(\mathbf{x}, E', t) \hat{\psi}_1(\mathbf{x}, \Omega', E', t) d\Omega' dE' \\
 & = -\frac{1}{v} \frac{\partial}{\partial t} \Psi(\mathbf{x}, \Omega, E, t) N_0(t) \\
 & + \frac{\chi_p(\mathbf{x}, E, t)}{4\pi} \int_0^\infty [\hat{\rho}(t) - \hat{\beta}(\mathbf{x}, E', t)] \nu \Sigma_f(\mathbf{x}, E', t) \Phi(\mathbf{x}, E', t) dE' N_0(t) \\
 & + \frac{1}{4\pi} \sum_{j=1}^6 \chi_j(\mathbf{x}, E, t) \lambda_j C_{j,0}(\mathbf{x}, t) + \frac{Q(\mathbf{x}, E, t)}{4\pi}, \tag{279}
 \end{aligned}$$

$$\frac{\partial C_{j,0}}{\partial t}(\mathbf{x}, t) + \lambda_j C_{j,0}(\mathbf{x}, t) = \left(\int_0^\infty \hat{\beta}_j(\mathbf{x}, E', t) \nu \Sigma_f(\mathbf{x}, E', t) \Phi(\mathbf{x}, E', t) dE' \right) N_0(t). \tag{280}$$

The operator on the left side of (279) is the same as the operator on the left side of (276). Operating on both sides of (279) by:

$$\int \int_0^\infty \int_{4\pi} \Psi^\dagger(\mathbf{x}, \Omega, E, t) (\cdot) d\Omega dE dV,$$

the left side vanishes, and we obtain the *solvability condition*:

$$\begin{aligned}
 0 & = - \int \int_0^\infty \int_{4\pi} \Psi^\dagger \frac{1}{v} \frac{\partial}{\partial t} \Psi N_0(t) d\Omega dE dV \\
 & + \frac{\hat{\rho}(t)}{4\pi} \int \left(\int_0^\infty \Phi^\dagger \chi_p dE \right) \left(\int_0^\infty \nu \Sigma_f \Phi dE \right) dV N_0(t) \\
 & - \frac{1}{4\pi} \int \left(\int_0^\infty \Phi^\dagger \chi_p dE \right) \left(\int_0^\infty \hat{\beta} \nu \Sigma_f \Phi dE \right) dV N_0(t) \\
 & + \sum_j \frac{\lambda_j}{4\pi} \int \int_0^\infty \Phi^\dagger C_{j,0} \chi_j dE dV + \frac{1}{4\pi} \int \int_0^\infty \Phi^\dagger Q dE dV. \tag{281}
 \end{aligned}$$

To simplify this result, we define the functions:

$$\theta(t) = \frac{\int \int_0^\infty \int_{4\pi} \Psi^\dagger \frac{1}{v} \frac{d\Psi}{dt} d\Omega dE dV}{\int \int_0^\infty \int_{4\pi} \Psi^\dagger \frac{1}{v} \Psi d\Omega dE dV}, \tag{282a}$$

$$\frac{1}{\Lambda(t)} = \frac{\int \left(\int_0^\infty \Phi^\dagger \chi_p dE \right) \left(\int_0^\infty \nu \Sigma_f \Phi dE' \right) dV}{4\pi \int \int_0^\infty \int_{4\pi} \Psi^\dagger \frac{1}{v} \Psi d\Omega dE dV}, \tag{282b}$$

$$\hat{\beta}(t) = \frac{\int \left(\int_0^\infty \Phi^\dagger \chi_p dE \right) \left(\int_0^\infty \hat{\beta} \nu \Sigma_f \Phi dE' \right) dV}{\int \left(\int_0^\infty \Phi^\dagger \chi_p dE \right) \left(\int_0^\infty \nu \Sigma_f \Phi dE' \right) dV}, \tag{282c}$$

$$c_j(t) = \frac{\int \int_0^\infty \Phi^\dagger C_{j,0} \chi_j dE dV}{4\pi \int \int_0^\infty \int_{4\pi} \Psi^\dagger \frac{1}{v} \Psi d\Omega dE dV}, \tag{282d}$$

$$q(t) = \frac{\int \int_0^\infty \Phi^\dagger Q dE dV}{4\pi \int \int_0^\infty \int_{4\pi} \Psi^\dagger \frac{1}{v} \Psi d\Omega dE dV}; \quad (282e)$$

then (281) becomes:

$$\frac{dN_0}{dt}(t) + \theta(t)N_0(t) = \frac{\hat{\rho}(t) - \hat{\beta}(t)}{\Lambda(t)} N_0(t) + \sum_j \lambda_j c_j(t) + q(t). \quad (283)$$

To obtain equations for $c_j(t)$, we analytically solve (280) for $C_{j,0}(\mathbf{x}, t)$, obtaining:

$$C_{j,0}(\mathbf{x}, t) = C_j^i(\mathbf{x}) e^{-\lambda_j t} + \int_0^t e^{-\lambda_j(t-t')} \left(\int_0^\infty \hat{\beta}_j v \Sigma_f \Phi dE' \right) N_0(t') dt'.$$

Then we operate on this result by:

$$\frac{1}{4\pi \int \int_0^\infty \int_{4\pi} \Psi^\dagger \frac{1}{v} \Psi d\Omega dE dV} \int \int_0^\infty \Phi^\dagger \chi_j [\cdot] dE dV$$

and use the definition (282d) to obtain:

$$c_j(t) = c_j^i e^{-\lambda_j t} + \frac{\int \left(\int_0^\infty \Phi^\dagger \chi_j dE \right) \left[\int_0^t e^{-\lambda_j(t-t')} \left(\int_0^\infty \hat{\beta}_j v \Sigma_f \Phi dE' \right) N_0(t') dt' \right] dV}{4\pi \int \int_0^\infty \int_{4\pi} \Psi^\dagger \frac{1}{v} \Psi d\Omega dE dV}. \quad (284)$$

Equations (283) and (284) define $N_0(t)$ and $c_j(t)$ for $t > 0$.

Next, we convert these results back to the original unscaled (unhatted) variables. This is done by using (270) to systematically replace all scaled (hatted) quantities in (277) and (282–284) by unscaled (unhatted) quantities. Defining $N(t) = N_0(t)/\varepsilon$ and omitting the straightforward details, we obtain for $t > 0$:

$$\psi(\mathbf{x}, \Omega, E, t) \approx \Psi(\mathbf{x}, \Omega, E, t) N(t), \quad (285)$$

where $N(t)$ satisfies the equations:

$$\frac{dN}{dt}(t) + \theta(t)N(t) = \frac{\rho(t) - \beta(t)}{\Lambda(t)} N(t) + \sum_{j=1}^6 \lambda_j c_j(t) + q(t), \quad (286)$$

and:

$$c_j(t) = c_j^i e^{-\lambda_j t} + \frac{\int \left(\int_0^\infty \Phi^\dagger \chi_j dE \right) \left[\int_0^t e^{-\lambda_j(t-t')} \left(\int_0^\infty \beta_j v \Sigma_f \Phi dE' \right) N(t') dt' \right] dV}{4\pi \int \int_0^\infty \int_{4\pi} \Psi^\dagger \frac{1}{v} \Psi d\Omega dE dV}, \quad (287)$$

where:

$$\beta(t) = \frac{\int \left(\int_0^\infty \Phi^\dagger \chi_p dE \right) \left(\int_0^\infty \beta v \Sigma_f \Phi dE \right) dV}{\int \left(\int_0^\infty \Phi^\dagger \chi_p dE \right) \left(\int_0^\infty v \Sigma_f \Phi dE \right) dV}. \quad (288)$$

Also, (267), (285), and (282d) yield the following initial conditions for $N(t)$ and $c_j(t)$:

$$N(0) = \int \int_0^\infty \int_{4\pi} \frac{1}{v} \psi^i(\mathbf{x}, \boldsymbol{\Omega}, E) d\boldsymbol{\Omega} dE dV, \quad (289)$$

$$c_j(0) = c_j^i = \frac{\int \int_0^\infty \Phi^\dagger(\mathbf{x}, E, 0) C_j^i(\mathbf{x}) \chi(\mathbf{x}, E, 0) dE dV}{4\pi \int \int_0^\infty \int_{4\pi} \Psi^\dagger(\mathbf{x}, \boldsymbol{\Omega}, E, 0) \frac{1}{v} \Psi(\mathbf{x}, \boldsymbol{\Omega}, E, 0) d\boldsymbol{\Omega} dE dV}. \quad (290)$$

To obtain the standard PKEs, it is necessary to make two further assumptions. The first assumption is:

$$\frac{\partial}{\partial t} \left(\frac{\int_0^\infty \Phi^\dagger \chi_j dE}{\int \int_0^\infty \int_{4\pi} \Psi^\dagger \frac{1}{v} \Psi d\boldsymbol{\Omega} dE dV} \right) \approx 0. \quad (291)$$

Then (287) can be written:

$$c_j(t) = c_j^i e^{-\lambda_j t} + \int_0^t e^{-\lambda_j(t-t')} \frac{\beta_j(t')}{\Lambda(t')} N(t') dt', \quad (292)$$

where:

$$\beta_j(t) = \frac{\int \left(\int_0^\infty \Phi^\dagger \chi_p dE \right) \left(\int_0^\infty \beta_j v \Sigma_f \Phi dE \right) dV}{\int \left(\int_0^\infty \Phi^\dagger \chi_p dE \right) \left(\int_0^\infty v \Sigma_f \Phi dE \right) dV}. \quad (293)$$

The second assumption is:

$$\theta(t) = \frac{\int \int_0^\infty \int_{4\pi} \Psi^\dagger \frac{1}{v} \frac{d\Psi}{dt} d\boldsymbol{\Omega} dE dV}{\int \int_0^\infty \int_{4\pi} \Psi^\dagger \frac{1}{v} \Psi d\boldsymbol{\Omega} dE dV} \approx 0. \quad (294)$$

If (291) and (294) both hold, then (286) and (292) reduce to the standard PKEs:

$$\frac{dN}{dt}(t) = \frac{\rho(t) - \beta(t)}{\Lambda(t)} N(t) + \sum_{j=1}^6 \lambda_j c_j(t) + q(t), \quad (295a)$$

$$\frac{dc_j}{dt}(t) + \lambda_j c_j(t) = \frac{\beta_j(t)}{\Lambda(t)} N(t), \quad 1 \leq j \leq 6. \quad (295b)$$

Also, from (274), (288), and (293), we have:

$$\beta(t) = \sum_{n=1}^6 \beta_j(t). \quad (296)$$

Thus, the neutron angular flux $\psi(\mathbf{x}, \boldsymbol{\Omega}, E, t)$ is asymptotically given by (285), where $N(t)$ is obtained by solving the PKEs (295) and (296), with initial conditions given by (289) and (290). Because of the very specific angular and energy dependence of the asymptotic solution (285), this solution cannot generally satisfy the arbitrary initial conditions specified in (267). This deficiency can be overcome by including an *initial-layer* solution, which describes the rapid transition from the general initial conditions for ψ and C_j to the near-equilibrium solution that forms the basis of the PKEs. The asymptotic initial-layer analysis is not presented here because this analysis has no effect on the PKEs.

9.4 Discussion

For a fissile system that is nearly critical and slowly varying, in the sense described by the scalings in (270), we have shown that the time-dependent angular flux is described asymptotically by (285–290). Furthermore, if (291) and (294) hold, then the approximating equations simplify to the standard PKEs (295), (296).

The PKEs have been obtained previously using derivations that are tantamount to variational approximations. In these earlier derivations, $\Psi(\mathbf{x}, \boldsymbol{\Omega}, E, t)$ is called the *shape function* and is not necessarily an eigenfunction; it is chosen. Also, $\Psi^\dagger(\mathbf{x}, \boldsymbol{\Omega}, E, t)$ is called the *weight function*; it too is not necessarily an (adjoint) eigenfunction and is chosen. The subsequent derivations lead to equations of the form of (285) and (295), but with the coefficients in these equations usually defined differently than in (282) and (288). In particular, in the asymptotic analysis presented here, $\rho(t)$ is the true reactivity of the system at time t , as defined by the eigenvalue problem (269). In other formulations, $\rho(t)$ is not always the true reactivity. The analysis presented here suggests that these earlier formulations of the PKEs may not represent asymptotic approximations of the time-dependent transport equations. However, the asymptotic result derived here is potentially more expensive to implement because $\rho(t)$, $\Psi(\mathbf{x}, \boldsymbol{\Omega}, E, t)$, and $\Psi^\dagger(\mathbf{x}, \boldsymbol{\Omega}, E, t)$ must be calculated by solving eigenvalue problems for each time t . (This point is discussed further below.) It is possible that by using a less sophisticated approximation to Ψ and ρ , one can reduce the cost of the calculation and still obtain acceptably accurate results.

In previous derivations of the PKEs, the shape and weight functions are often assumed to be independent of time (at least, for specified time intervals). If this were true in the asymptotic analysis, and if the time-dependent variations of the system occur only in non-fissile regions, then (291) and (294) would be valid. This situation can effectively occur if, for a critical reactor, control rods are *very slowly and slightly* moved in or out, thereby making the reactor slightly subcritical or supercritical. Then the temporal changes in $\Psi(\mathbf{x}, \boldsymbol{\Omega}, E, t)$ and $\Psi^\dagger(\mathbf{x}, \boldsymbol{\Omega}, E, t)$ would be very small and, effectively, $\theta(t) = 0$, $\Lambda(t) = \Lambda = \text{constant}$, and $\beta_j(t) = \beta_j = \text{constant}$.

Also, we note that by suitably altering the normalization (269c) on Ψ , then by (277) and (278), $N(t) =$ the power output of the reactor at time t .

The asymptotic analysis shows that the neutron flux can be predicted by means of PKEs that depend on time-dependent knowledge of the cross sections, the reactivity, and the forward and adjoint eigenfunctions. Although it is not practical to calculate ρ , Ψ , and Ψ^\dagger *continuously* for all $t > 0$, it is possible to calculate these quantities at discrete times, e.g., $t_n = n\Delta t$, and to evaluate $\rho(t)$ and the time-dependent parameters in (288) by linearly interpolating between t_n and t_{n+1} . By doing this, the asymptotic result obtained here could be the basis of a realistic point kinetics model.

Other asymptotic expansions that lead to results of the form of the PKEs are possible. For example, in the analysis presented here, the reactivity ρ of the system is calculated by neglecting the delayed neutrons (see [269]). By including a steady-state term in (269) to account for the different energy spectrum of the delayed neutrons, a different and possibly more accurate expression for ρ might be obtained. Also, a more sophisticated asymptotic analysis could include temperature-dependent cross sections, with an extra equation relating the temperature $T(\mathbf{x}, t)$ within the reactor as a function of the neutron flux. In addition, an asymptotic derivation of the PKEs can be based on the α -eigenvalues and eigenfunctions of the transport

equation (Lewis and Miller 1984), rather than the k -eigenvalues and eigenfunctions. (Such a derivation would actually be more natural, because the α -eigenvalues are associated with the time-behavior of the system.) However, none of these generalizations can be discussed further here.

10 Computational Neutron Transport

Analytic solutions of the Boltzmann transport equation can be obtained only for the simplest problems. For realistic, multidimensional, energy-dependent problems, it is necessary to calculate numerical solutions as accurately and efficiently as possible. This can be an extremely daunting task. Research on computational methods for the Boltzmann transport equation has been actively pursued from the 1950s up to the present (Adams and Larsen 2002; Carlson and Lathrop 1968; Carter and Cashwell 1975; Haghighat and Wagner 2003; Kalos and Whitlock 1986; Larsen 1992; Larsen and Morel 2009; Lewis and Miller 1993; Lux and Koblinger 1991; Marchuk and Lebedev 1981; Sanchez and McCormick 1982; Spanier and Gelbard 2008; X-5 Monte Carlo Team 2003). During this time, the speed and memory of computers has increased by many orders of magnitude. Nonetheless, it has been argued that the gains in efficiency of simulations of particle transport problems, due to improvements in computational algorithms, exceeds the gains due to improvements in computer hardware. Here, we give a brief overview of the major advances in computational neutron transport algorithms. For details, we refer the reader to previous publications.

The history of computational transport methods is basically the history of two fundamentally different approaches, commonly called *stochastic* and *deterministic*. Stochastic (or *Monte Carlo*) methods are based on a probabilistic interpretation of the transport process. In this approach, the random *histories* of individual particles are calculated using pseudorandom number sequences and the results are averaged over a large number of histories. Stochastic methods have no need of a Boltzmann transport equation; they rely only on the detailed physics of interactions between individual neutrons and nuclei. Deterministic methods instead are based on (i) discretizing the Boltzmann transport equation in each of its independent variables, resulting in a (typically very large) algebraic system of equations, and then (ii) solving this algebraic system.

For the past 50 years, Monte Carlo and deterministic algorithms have been developed independently. The two approaches were viewed as being incompatible, and two basically disjoint technical communities evolved to develop codes for them. Major technical advances for one type of method (e.g., acceleration techniques for deterministic methods, variance reduction techniques for Monte Carlo methods) had no impact on the other method. Except for specialized applications, the two methods were not implemented in the same (production) computer code. Monte Carlo and deterministic methods became viewed as complementary: one approach was advantageous for certain problems, the other advantageous for different problems. Because of their complementarity, both methods have survived and matured.

However, during the past 10 years, it has become fairly widely understood that *hybrid* methods – which combine aspects of both Monte Carlo and deterministic methods – can be used to enhance the strengths and overcome the weaknesses of the individual approaches. Although hybrid methods are in the early stages of their development and implementation, they have already demonstrated that they can yield major improvements in efficiency and accuracy for difficult problems. It now appears that hybrid methods represent a promising third

approach, offering a way to significantly improve the efficiency and ease of simulations for difficult practical particle transport problems.

In the following, we discuss the general issues associated with deterministic, stochastic, and hybrid particle transport methodologies.

10.1 Monte Carlo Methods

In the physical process of *particle transport*, typically a *very* large number of particles undergo random and independent histories. Each element of an individual particle's history (distance to collision, probability of scattering, post-scattering energy, and direction of flight) has a specific probability distribution function. Because of this, the collective behavior of the particle population is predictable, with a small statistical noise that decreases as the number of particles $N \rightarrow \infty$.

Stochastic or *Monte Carlo* methods model this process by applying the known distribution functions to simulate the random histories of N_{MC} fictitious *Monte Carlo particles*, and averaging the results over the histories (Carter and Cashwell 1975; Kalos and Whitlock 1986; Lux and Koblinger 1991; Spanier and Gelbard 2008; X-5 Monte Carlo Team 2003). However, because the number of simulated particles [$N_{MC} \approx O(10^7)$] is usually much smaller than the number of physical particles [$N \approx O(10^{15})$], Monte Carlo simulations usually have orders of magnitude more statistical noise than the actual physical process. This is a significant issue when Monte Carlo methods are used to estimate *rare events*, such as the response rate in a detector located far from a source.

Nonetheless, Monte Carlo methods have certain basic advantages. If the geometry of the system and its cross sections are known, then the results of the Monte Carlo simulation contain only statistical errors. By processing a sufficient number of Monte Carlo particles, it is possible to reduce the probable statistical error below any specified level.

According to the *central limit theorem*, for any Monte Carlo simulation, the statistical error in the estimation of a given quantity is, with probability 0.68, bounded by:

$$\text{Statistical error} \leq \frac{\sigma}{\sqrt{N_{MC}}}, \quad (297)$$

where σ (the *standard deviation*) is specific to the given problem and the quantity estimated, and (297) holds only for N_{MC} sufficiently large. The positive feature of (297) is that as N_{MC} increases, the statistical error will, with high probability, also decrease. The negative feature is that the rate of decrease of the statistical error is slow. For instance, (297) shows that to decrease the statistical error by a factor of 10, it is necessary to increase N_{MC} (and hence the computational expense) by a factor of 100.

Monte Carlo methods are widely used because of their relative ease of implementation, their ability to treat complex geometries with great fidelity, and their ability to solve problems accurately with cross-sectional data that can have extremely complex energy-dependence. However, Monte Carlo simulations can be costly, both to set up and to run.

In particular, when attempting to calculate a rare event, such as a detector response far from a source, such a small fraction of the physical particles participate in this event that the number of Monte Carlo particles that create a “score” is *very* small – and the resulting statistical error is unacceptably large. In this situation, the “rules” of the Monte Carlo “game” can be

altered so that Monte Carlo particles are “encouraged” to travel from the source to the detector region. The result is that the desired response is estimated with smaller statistical error and computational effort. In effect, the Monte Carlo process is changed so that the estimate of the response is preserved, but the standard deviation in this estimate (the constant σ in [297]) is reduced.

To accomplish this alteration of the Monte Carlo process, the code user must input a (generally) large number of *biasing parameters* that successfully “encourage” Monte Carlo particles to migrate from the source to the specified detector region. These parameters are strongly problem-dependent, and generating them can be a slow and laborious task. For difficult problems, a lengthy process of trial and error may be necessary, and there is no guarantee that at the end of this process, the code user will have been successful.

Another difficulty with Monte Carlo simulations is that they operate most efficiently when calculating limited information, such as a single detector response. If several detector responses are desired, and the detectors are located far from the source and far from each other, then often the best solution is to run several different Monte Carlo simulations, each with its own specially defined set of biasing parameters.

Thus, while Monte Carlo codes are widely used, running these codes efficiently is problematic for complex problems. In these situations, Monte Carlo codes are not a “black box” into which a user can simply specify the problem, press the “start” button, and expect reliable answer in a short time. *In addition to specifying the physical problem, the user must also specify the problem-dependent biasing parameters*, and this can be a formidable task.

Historically, research on Monte Carlo methods has focused on new approaches that show hope of alleviating the major difficulties associated with the method. For example, different biasing methods to encourage Monte Carlo particles to travel toward specified detector regions have been developed and tested. Also, methods have been developed to obtain, via the Monte Carlo process itself, the biasing parameters for difficult problems. In addition, sophisticated statistical methods have been developed to analyze Monte Carlo simulations and better determine the magnitude of the statistical errors. (For example, obtaining accurate estimates of the standard deviation σ , and hence of the true statistical error, can be problematic, particularly for eigenvalue problems.)

During the past 50 years, many significant advances in Monte Carlo techniques have been developed and implemented in large-scale codes. However, the difficulties described above remain significant obstacles to running these codes optimally.

10.2 Deterministic Methods

Because the particle transport process is governed by specified probability distribution functions, the Boltzmann transport equation exists for predicting the *mean* or *average* flux of particles at each location in phase space. *Deterministic*, or *discrete-ordinates*, or S_N methods are based on discretizing the Boltzmann equation in each of its independent variables, and solving the resulting (typically very large) system of algebraic equations (Adams and Larsen 2002; Carlson and Lathrop 1968; Larsen 1992; Larsen and Morel 2009; Lewis and Miller 1993; Marchuk and Lebedev 1986; Sanchez and McCormick 1982).

Because the Boltzmann equation depends on its independent variables in significantly different ways, different methods have been developed for their discretization.

For time-dependent problems, the most common method for discretizing the time variable t is the *implicit*, or *backward Euler* method. Other methods are possible and have been tested, but the implicit method is the most widely used because of its simplicity and robustness.

Of all the independent variables in the transport equation, the energy variable E is the most problematic. The reason for this is that typically, the material cross sections, and hence the particle flux itself, have an extraordinarily complex energy-dependence. If the simple rule of thumb is followed that an energy grid should be chosen for which the solution varies in energy from one grid point to the next by no more than about 15%, then for typical problems, *millions* of grid points in E would be required. This constraint would render the solution of typical problems to be outside the range of possibility.

However, the *multigroup* method (discussed previously in [▶ Sect. 6](#)) has been developed to deal with this difficulty, and because of its success, it is almost universally used. This method requires the user to carefully specify a set of *multigroup* cross sections, whose values are determined by calculating integrals over E of the flux and the flux times the cross section. The optimal specification of a multigroup cross section depends on the given problem. From the user standpoint, determining accurate problem-dependent multigroup cross sections is the most challenging and time-consuming aspect of deterministic calculations.

The angular, or direction-of-flight variable Ω is generally discretized in one of two ways: *discrete-ordinates*, or *collocation* (or S_N) methods, and *spherical harmonic* (or P_N) methods. S_N methods are more commonly used because the structure of the resulting discrete equations is more closely linked to the innate physical interpretation of particle transport. (In Cartesian geometries, S_N methods can be interpreted as ones in which particles travel only in a finite, specified set of directions Ω_m .) However, S_N and P_N methods have characteristic errors. In particular, S_N methods have *ray effects*, which are most apparent in problems with strong absorption and localized sources. For problems whose solutions have a strong direction-dependence, such as neutron streaming through a voided channel, it is necessary to use a very high-order angular quadrature set. P_N methods also have angular truncation errors, but of a different nature. Like S_N methods, P_N methods cannot easily describe an angular flux with a complicated direction-dependence. Also, the P_N equations have a form and structure that are more difficult (than the S_N equations) to interpret in terms of the physics of particle transport.

The spatial variable x has probably been subjected to a greater variety of discretization methods than any other independent variable in the Boltzmann transport equation. In the early years, relatively simple *finite difference* (diamond difference and weighted diamond difference) methods were favored. Later, more sophisticated *finite element*, *nodal*, *characteristic*, and *corner balance* methods were introduced (Larsen and Morel 2009). Each of these types of methods tends to have its own advantages and disadvantages (Azmy 1992; Duo and Azmy 2007). For example, finite difference and (to a certain extent) nodal methods are relatively easy to implement on Cartesian (orthogonal, or box-like) spatial grids, while finite element, characteristic, and corner balance methods are better adapted to non-Cartesian (*triangular*, *tetrahedral*, or *unstructured*) spatial grids.

Cartesian grids were favored in early computer codes; but more recently, non-Cartesian grids have been employed, to better enable the spatial grid to fit the curved or non-right-angular surfaces occurring on material boundaries in many realistic applications.

A major issue in discretizing the spatial variable is the number of unknowns that must be calculated (and stored) per spatial cell. Methods that require a minimum amount of storage are generally less accurate on a specified grid, but the storage demand of particle transport problems is so high that in many problems, the simpler methods are preferred.

Another issue in spatial discretizations concerns accuracy in optically thick, scattering-dominated (*diffusive*) regions. For example, in electron and thermal radiation transport problems, the cross sections (or *opacities*) can be so high that it is not possible, due to computer storage limitations, to solve problems using a spatial grid in which the spatial cell widths are on the order of a mean free path or less. (In many neutron transport problems, spatial cell widths are chosen to be fractions of mean free paths.) Some discretization methods are significantly more accurate than others for problems in which the spatial grid is not optically thin; these methods tend to have a greater number of unknowns per cell (Adams et al. 1998; Adams 2001; Larsen 1992; Larsen and Morel 2009).

In practical neutron/photon transport problems, the total number of unknowns can be extraordinarily large. To estimate this number, let us consider a steady-state, 3-D, multigroup S_N problem.

The number G of energy groups can range from $G = 2$ for special light water reactor core problems to $G = 200$ for difficult shielding problems.

The number M of directions of flight in a typical 3-D S_N calculation varies, depending on the nature and order of the quadrature set. The 3-D S_N level-symmetric quadrature sets have $M = N(N + 2)$ directions. Thus, the commonly used S_4 and S_8 level-symmetric quadrature sets have 24 and 80 directions of flight, respectively.

The number of spatial cells can also vary. It is not atypical for a Cartesian spatial grid to have each independent variable (x , y , and z) defined on a grid of 100 points. Thus, the number I of discrete values of x is 100, and the same is true for $J =$ the number of discrete values of y and $K =$ the number of discrete values of z .


Thus, if we consider “typical” values $G = 20$, $M = 50$, and $I = J = K = 100$, then the total number N_{tot} of unknowns is

$$N_{\text{tot}} = G \times M \times I \times J \times K = 10^9.$$

This extremely large number (and in many problems the number is much higher) is a direct consequence of the fact that steady-state 3-D transport problems require a 6-D phase space.

To minimize the number of unknowns, computer codes have been written for 3-D problems with 1-D or 2-D spatial symmetry. This reduces the number of independent spatial variables from 3 to 2 or 1, and it possibly reduces the number of angular variables from 2 to 1. The problems that can be accurately treated by 1-D or 2-D codes are geometrically constrained but, fortunately, many important applications can be adequately represented by a 1-D or 2-D geometric model.


In addition to the issue of storing and processing the unknowns in the discretized Boltzmann equation, there is the fact that a linear algebraic system of equations with $N \approx 10^9$ equations and unknowns cannot be solved by direct matrix inversion. For most practical problems, it is necessary to use *iterative methods* to calculate solutions.

The simplest iteration strategy is based on *sweeping*, which itself is based on the observation that with standard discretization schemes, problems with no scattering or fission can be solved directly and noniteratively by *marching* through the spatial grid in the direction of particle flow. (Different directions of flow can require a different direction of marching, or sweeping.) The angular flux solution of such a problem is termed the *uncollided flux*; it consists of all particles that have not experienced a collision. (When a particle does experience a collision, it is absorbed. See  Subsect. 2.10.12.)

For problems with scattering, the *source iteration* strategy consists of performing sweeps and iterating on the scattering source. If the first sweep is performed with the scattering source

estimated to be zero, then at the end of the first sweep, the estimated angular flux is the uncollided flux. If this (uncollided) flux is used to estimate the scattering source and a second sweep is performed, then at the end of the second sweep, the estimated angular flux is the sum of the uncollided and the *once-collided* fluxes. At the end of N sweeps, the estimated angular flux $\psi^{(N)}$ is:

$$\psi^{(N)} = \sum_{n=0}^N \psi_n, \quad (298)$$

where ψ_n is the angular flux of particles that have scattered exactly n times. (See  Subject. 2.10.12.)

If a physical system is small and “leaky,” or has significant absorption, then particles will generally have short histories, and the series (298) will converge rapidly. However, if a problem has a subregion which is many mean free paths thick and dominated by scattering (rather than capture), then particles in that subregion will have long histories, and the series (298) will converge slowly. In the former case, the source iteration strategy converges rapidly, but in the latter case, source iteration converges slowly (Carlson and Lathrop 1968; Larsen and Morel 2009).

To speed up the convergence of source iterations for problems with optically thick, scattering-dominated subregions, *iterative acceleration* strategies have been devised. The earliest of these was the *Chebyshev acceleration*, a technique based on concepts from matrix algebra. This method worked to a limited extent, but it was not sufficiently efficient for many problems.

Later, the *rebalance* method was developed and used widely for a number of years. This method operates by calculating and applying, at the end of each sweep, *rebalance factors* on a fine or coarse space-energy grid. The rebalance method tends to become unstable when used on a fine space-energy grid, and to become stable but inefficient when used on a very coarse grid. The optimal (intermediate) grid is problem-dependent and must be found by trial and error. Even when the optimal grid is found, the resulting method is often not as efficient as desired (Adams and Larsen 2002).

Later still, *diffusion synthetic acceleration* (DSA) was developed to speed up the convergence of source iterations. DSA is based on the following concept. At the end of a transport sweep, an exact transport equation is derived for the iteration error (the difference between the latest iterate and the converged solution). This equation is just as difficult to solve as the original transport equation for the angular flux. In DSA, this *exact transport equation for the iteration error* is replaced by an *approximate diffusion equation for the iterative error*; the diffusion equation is solved; and the diffusion estimate of the iterative error is combined with the most recent estimate of the flux to obtain an updated and much more accurate estimate of the angular flux (Adams and Larsen 2002; Alcouffe 1977).

In practice, DSA is highly efficient for optically thin spatial grids. Unfortunately, unless great care is taken in the discretization of the diffusion part of the algorithm, it can become inefficient or unstable for optically thick spatial grids (Adams and Larsen 2002; Azmy 1998).

More recently, *Krylov methods* have been used, often in conjunction with DSA. Although Krylov methods require significant extra storage, they can be remarkably effective at stabilizing and speeding up the iterative convergence of methods based on source iterations, or on DSA (Adams and Larsen 2002; Faber and Mantueffel 1989).

All the work cited above describes advances in the basic mathematical algorithms for solving transport problems. Other equally important work has taken advantage of changes in computer architecture, i.e., on the details of how computers process arithmetic for large-scale problems

(Baker and Koch 1998). This type of research is becoming increasingly important as computers are becoming increasingly parallel in nature.

Historically, the research on S_N methods has tended to focus on (i) advanced discretization methods in space, angle, energy, and time, and (ii) advanced iterative methods that converge the iterative solution more rapidly and efficiently. In the past 50 years, major advances in all these areas have been made. The discretization and iteration schemes used in many advanced simulation codes today have little resemblance to the methods used 50 years ago.

However, a fundamental difficulty remains at the heart of deterministic calculations: the costly and time-consuming task of obtaining adequate multigroup cross sections for a specified difficult problem. This aspect of deterministic simulations remains the most significant obstacle to obtaining useful, accurate deterministic solutions of practical transport problems in a reliable, efficient, and user-friendly manner.

10.3 Hybrid Monte Carlo/Deterministic Methods

In the last 10–15 years, it has become understood that the most challenging aspect of difficult Monte Carlo simulations – the determination of problem-dependent biasing parameters – can be done efficiently by a deterministic simulation.

Specifically, for source-detector problems, the biasing parameters can be obtained by (i) solving an adjoint problem in which the detector response function is the source, as discussed in [▶ Sect. 5](#), and (ii) processing the resulting adjoint scalar or angular fluxes. The original “hybrid” concept is to use a deterministic code to perform this task (Chucas and Grimstone 1994; Haghghat and Wagner 2003; Smith and Wagner 2005; Van Riper et al. 1997).

The advantages to this procedure are that (i) it removes from the code user the burdensome task of calculating the biasing parameters, and (ii) the resulting computer-generated biasing parameters are usually much more efficient at reducing the Monte Carlo variance than the biasing parameters obtained by human trial and error (Smith and Wagner 2005).

The principal disadvantage is that two separate codes (Monte Carlo and deterministic) must be set up to run the same geometric problem, and the results of the deterministic code must be processed, formatted properly, and then input to the Monte Carlo code. This process can be unwieldy unless a suitable investment has been made in the computing infrastructure, enabling the process to occur automatically.

Most public particle transport codes are either Monte Carlo or deterministic, but a small number of user-friendly hybrid codes are now available. For example, the hybrid code MCBEND (Chucas and Grimstone 1994) uses a multigroup diffusion solver to determine weight windows for Monte Carlo simulation. Also, the recent SCALE 6.0 package from Oak Ridge National Laboratory contains software that enables, with one geometric input deck, deterministically generated multigroup S_N solutions to be calculated, turned into weight windows, and then used in Monte Carlo simulations (Haghghat and Wagner 2003; Smith and Wagner 2005).

The type of problem for which deterministic methods have been most widely used to derive biasing parameters for Monte Carlo simulations is the classic source-detector problem – in which particles are born in a source, and a single detector response, in a possibly distant detector, is desired. The biasing parameters for this problem “encourage” Monte Carlo particles to migrate from the source to the specified detector region in such a way that estimates of the desired response have a significantly reduced variance. The biasing parameters can be obtained by solving an adjoint transport problem. In the resulting *nonanalog* Monte Carlo simulations

of source-detector problems, Monte Carlo particles are discouraged from migrating to regions far from the detector. Consequently, estimates of reaction rates at these locations generally have larger variances than before.

One of the features of deterministic calculations is that at the end of a simulation, estimates of the flux are inherently available at *all* points in the 6-D phase space. For the reasons discussed in the previous paragraph, this *global* information is generally not considered to be available in a useful sense from Monte Carlo simulations.

However, recent work has shown that if weight windows are properly defined using information from both adjoint *and* forward calculations, then Monte Carlo particles are “encouraged” to become distributed throughout the system in a manner that is much more uniform than the distribution of physical particles. In this case, accurate (low-variance) estimates of reaction rates throughout a physical system can be obtained from a *single* Monte Carlo calculation (Becker and Larsen 2009; Cooper and Larsen 2001; Wagner et al. 2007, 2009).

To date, the term “hybrid” has implied a method in which a deterministic simulation is used to assist – through the calculation of biasing parameters – a Monte Carlo simulation. However, deterministic and Monte Carlo techniques can be merged in different advantageous ways. For example, it has been demonstrated that for source-detector problems, an adjoint calculation can be used to *actively* modify the physical scattering process, so that Monte Carlo particles are encouraged to scatter into directions and energies that will bring them from regions of low importance to regions of greater importance (Turner and Larsen 1997). This *local importance function transform* method requires a greater amount of computation per particle history. However, for optically thick, deep-penetration source-detector problems, the method can be significantly more efficient than a standard weight window. It has also been shown that for problems with high scattering ratios, hybrid methods based on variational principles can yield estimates of reaction rates and eigenvalues that are significantly more efficient than standard estimates (Densmore and Larsen 2004). In addition, recent work on the *functional Monte Carlo* method has shown that even more accurate estimates of eigenvalues and eigenfunctions can be obtained by a hybrid method in which the Monte Carlo simulation is *not* used to obtain estimates of the flux, but rather to obtain estimates of certain *nonlinear functionals*, which are then used to obtain estimates of the flux (Larsen and Yang 2008).

Is there a class of hybrid methods for which Monte Carlo can be used to directly assist the accurate calculation of deterministic solutions? Possibly, the answer to this question is *yes*. As discussed previously, the principal difficulty with deterministic methods is the laborious calculation of multigroup cross sections. If continuous-energy Monte Carlo simulations could be efficiently run, to automatically determine (problem-dependent) multigroup cross sections, then this would be a way in which Monte Carlo simulations could significantly influence deterministic solutions. Promising work in this area has recently been reported (Wolters et al. 2009; Yang and Larsen 2009).

If such methods can be developed, then it is possible to imagine a future particle transport code, containing both Monte Carlo and deterministic modules, in which the Monte Carlo module “supplies” multigroup cross sections to the deterministic module, and the deterministic module “supplies” biasing parameters to the Monte Carlo module. (It might be necessary to perform these tasks iteratively.) One would then have a particle transport code that is much closer to a “black box” than present-day transport codes; it would require the user to input neither the biasing parameters for Monte Carlo simulations, nor the multigroup cross sections for deterministic simulations; it would determine these quantities automatically, and more accurately.

In principle, a code containing these features could make effective use of future advances in Monte Carlo, deterministic, and hybrid methods. Such a hybrid code does not exist today, but it is a distinctly logical possibility, given the thrust of past and current research in computational particle transport methods and the practical difficulties experienced by current-day code users.

10.4 Discussion

During the past 50 years, computational methods for performing neutron and coupled neutron/photon simulations have been an active and vibrant area of research in the nuclear engineering community. Major advances in algorithms for Monte Carlo and deterministic simulations have been made. There is little doubt that, due to the increasing demands on increased realism in simulations, research will continue on different fronts to improve the accuracy and efficiency of these simulations. Also, hybrid methods may become a distinct third approach, which would have its own class of difficult problems for which it is best suited.

11 Concluding Remarks

This concludes the chapter on *general principles of neutron transport*. The theory and methods discussed here apply to photon as well as neutron transport, although photon transport is of practical interest mainly in radiation shields. Important topics could not be presented, including (for example) (i) a discussion on variational methods, which are heavily dependent on the adjoint transport equation discussed in [Sect. 5](#); (ii) a more complete discussion on homogenized diffusion theory, which is used in most practical reactor core simulations; and (iii) a detailed exposition of computational methods for neutron and photon transport. Nonetheless, the authors hope that the material presented in this chapter, and the references provided below, will give the reader a useful foundation for more applied techniques described in other chapters of this handbook, and elsewhere.

References

- Adams ML (2001) Discontinuous finite element transport solutions in thick diffusive problems. *Nucl Sci Eng* 137:298
- Adams ML, Larsen EW (2002) Fast iterative methods for discrete-ordinates particle transport calculations. *Prog Nucl Energy* 40:3 [Review article]
- Adams ML, Wareing TA, Walters WF (1998) Characteristic methods in thick diffusive problems. *Nucl Sci Eng* 130:18
- Alcouffe RE (1977) Diffusion synthetic acceleration methods for the diamond-differenced discrete-ordinates equations. *Nucl Sci Eng* 64:344
- Azmy YY (1992) Arbitrarily high order characteristic methods for solving the neutron transport equation. *Ann Nucl Energy* 19:593
- Azmy YY (1998) Impossibility of unconditional stability and robustness of diffusive acceleration schemes. In: Proceedings of the ANS topical meeting on radiation protection and shielding, Nashville, 19–23 April 1998, vol 1, p 480
- Baker RS, Koch KR (1998) An SN algorithm for the massively parallel CM-200 computer. *Nucl Sci Eng* 128:312
- Becker TL, Larsen EW (2009) The application of weight windows to “global” Monte Carlo problems. In: Proceedings of the 2009 international conference on advances in mathematics, computational methods, and reactor physics, Saratoga Springs, New York 3–7 May 2009

- Bell GI (1965) On the stochastic theory of neutron transport. *Nucl Sci Eng* 21:390
- Bell GI, Glasstone S (1970) *Nuclear reactor theory*. Van Nostrand Reinhold, New York
- Benoist P (1964) Théorie du coefficient de diffusion des neutrons dans un réseau comportant des cavités. CEA-R2278, Centre d'Etudes Nucléaires – Saclay
- Brantley PS, Larsen EW (2000) The simplified P3 approximation. *Nucl Sci Eng* 134:1
- Cacuci DG (2003) *Sensitivity and uncertainty analysis: theory*. Chapman & Hall/CRC Press, Boca Raton
- Carlson BG, Lathrop KD (1968) Transport theory – the method of discrete ordinates. In: Greenspan H, Kelber CN, Okrent D (eds) *Computing methods in reactor physics*. Gordon & Breach, New York
- Carter LL, Cashwell ED (1975) Particle transport simulation with the Monte Carlo method. TID-26607, National Technical Information Service, U.S. Department of Commerce
- Case KM, Zweifel PF (1967) *Linear transport theory*. Addison-Wesley, Reading
- Chucas SJ, Grimstone MJ (1994) The accelerated techniques used in the Monte Carlo code MCBEND. In: *Proceedings of the eighth international conference on radiation shielding*, Arlington, 24–28 April 1994, vol 2, p 1126
- Cooper MA, Larsen EW (2001) Automated weight windows for global Monte Carlo deep penetration neutron transport calculations. *Nucl Sci Eng* 137:1
- Densmore JD, Larsen EW (2004) Variational variance reduction for Monte Carlo eigenvalue and eigenfunction problems. *Nucl Sci Eng* 146:121
- Dorning JJ (2003) Homogenized multigroup and energy-dependent diffusion equations as asymptotic approximations to the Boltzmann equation. *Trans Am Nucl Soc* 89:313
- Duderstadt J, Hamilton L (1976) *Nuclear reactor analysis*. Wiley, New York
- Duo JI, Azmy YY (2007) Error comparison of diamond difference, nodal, and characteristic methods for solving multidimensional transport problems with the discrete ordinates approximation. *Nucl Sci Eng* 156:139
- Faber V, Mantueffel TA (1989) A look at transport theory from the viewpoint of linear algebra. In: Nelson P et al (eds) *Transport theory, invariant imbedding, and integral equations (Lecture notes in pure and applied mathematics)*, vol 115. Marcel Dekker, New York, p 37
- Gamino RG (1989) Simplified PL nodal transport applied to two-dimensional deep penetration problems. *Trans Am Nucl Soc* 59:149
- Gamino RG (1991) 3-dimensional nodal transport using the simplified PL method. In: *Proceedings of the ANS M&C conference on advances in mathematics, computations, and reactor physics*, Pittsburgh, 29 April–2 May 1991, vol 2, section 7.1
- Gelbard EM (1960) Application of spherical harmonics methods to reactor problems. WAPDBT-20, Bettis Atomic Power Laboratory
- Gelbard EM (1961) Simplified spherical harmonics equations and their use in shielding problems. WAPD-T-1182, Bettis Atomic Power Laboratory
- Gelbard EM (1962) Applications of the simplified spherical harmonics equations in spherical geometry. WAPD-TM-294, Bettis Atomic Power Laboratory
- Gelbard EM (1974) Anisotropic neutron diffusion in lattices of the zero-power plutonium reactor experiments. *Nucl Sci Eng* 54:327
- Habetler GJ, Matkowsky BJ (1975) Uniform asymptotic expansions in transport theory with small mean free paths, and the diffusion approximation. *J Math Phys* 16:846
- Haghighat A, Wagner J (2003) Monte Carlo variance reduction with deterministic importance functions. *Prog Nucl Energy* 42:25 [Review article]
- Henry AF (1975) *Nuclear-reactor analysis*. MIT Press, Cambridge
- Hetrick DO (1993) *Dynamics of nuclear reactors*. American Nuclear Society, La Grange Park
- Kalos MH, Whitlock PA (1986) *Monte Carlo methods*. Wiley, New York
- Kellog RB (1974) First derivatives of solutions of the plane neutron transport equation. Technical Note BN-783, Institute for Fluid Dynamics and Applied Mathematics, University of Maryland
- Larsen EW (1980) Diffusion theory as an asymptotic limit of transport theory for nearly critical systems with small mean free paths. *Ann Nucl Energy* 7:249 [Review article]
- Larsen EW (1982) Spatial convergence properties of the diamond-difference method in X,Y geometry. *Nucl Sci Eng* 80:710
- Larsen EW (1992) The asymptotic diffusion limit of discretized transport problems. *Nucl Sci Eng* 112:336 [Review article]
- Larsen EW (2007) The description of particle transport problems with helical symmetry. *Nucl Sci Eng* 156:68
- Larsen EW, Ahrens C (2001) The Greuling-Goertzel and Wigner approximations in the theory of neutron slowing down. *Ann Nucl Energy* 28:1809
- Larsen EW, Hughes RP (1980) Homogenized diffusion approximations to the neutron transport equation. *Nucl Sci Eng* 73:274

- Larsen EW, Keller JB (1974) Asymptotic solution of neutron transport problems for small mean free paths. *J Math Phys* 15:75
- Larsen EW, Morel JE (2009) Advances in discrete-ordinates methodology. In: Azmy YY, Sartori E (eds) *Nuclear computational science: a century in review*. Springer, Berlin [Review article]
- Larsen EW, Yang J (2008) A “functional Monte Carlo” method for k-eigenvalue problems. *Nucl Sci Eng* 159:107
- Larsen EW, Morel JE, McGhee JM (1996) Asymptotic derivation of the multigroup P1 and simplified PN equations with anisotropic scattering. *Nucl Sci Eng* 123:328
- Lewins J (1965) *Importance: the adjoint function*. Pergamon, Oxford
- Lewins J (1968) Developments in perturbation theory. *Adv Nucl Sci Technol* 4:309
- Lewis EE, Miller WF (1993) *Computational methods of neutron transport*. American Nuclear Society, LaGrange Park. Originally published by Wiley-Interscience, New York (1984)
- Lux I, Koblinger L (1991) *Monte Carlo particle transport methods: neutron and photon calculations*. CRC Press, Boca Raton
- Marchuk GI, Lebedev VI (1986) *Numerical methods in the theory of neutron transport*. Harwood, London. Originally published in Russian by Isdatel'stvo Atomizdat, Moscow (1981)
- Ott KO (1985) *Nuclear reactor dynamics*. American Nuclear Society, La Grange Park
- Papanicolaou GC (1975) Asymptotic analysis of transport processes. *Bull Am Math Soc* 81:330
- Pomraning GC (1967a) A derivation of variational principles for inhomogeneous equations. *Nucl Sci Eng* 29:220
- Pomraning GC (1967b) Variational principle for eigenvalue equations. *J Math Phys* 8:149
- Prinja AK (1989) Forward-backward transport theories of ion-solid interactions: variational approach. *Phys Rev B* 39:8858
- Sanchez R, McCormick NJ (1982) A review of neutron transport approximations. *Nucl Sci Eng* 80:481 [Review article]
- Sigmund P (1969) Theory of sputtering. I. Sputtering yield of amorphous and polycrystalline targets. *Phys Rev* 184:383
- Smith HP, Wagner JC (2005) A case study in manual and automated Monte Carlo variance reduction with a deep penetration reactor shielding problem. *Nucl Sci Eng* 149:23
- Spanier J, Gelbard E (2008) *Monte Carlo principles and neutron transport problems*. Dover, New York. Originally published by Addison-Wesley, Reading (1969)
- Stacey WM (1974) *Variational methods in nuclear reactor physics*. Academic, New York
- Tomašević DI, Larsen EW (1996) The simplified P2 approximation. *Nucl Sci Eng* 122:309
- Turner SA, Larsen EW (1997) Automatic variance reduction for 3-D Monte Carlo simulations by the local importance function transform – Part I: Analysis. *Nucl Sci Eng* 127:22; Part II: Numerical results. *Nucl Sci Eng* 127:36
- Van Riper KA, Urbatsch TJ, Soran PD, Parsons DK, Morel JE, McKinney GW, Lee SR, Crotzer LA, Brinkley FW, Anderson JW, Alcouffe RE (1997) AVATAR – automatic variance reduction in Monte Carlo calculations. In: *Proceedings of the ANS M&C international conference on mathematical methods and supercomputing in nuclear applications*, Saratoga Springs, New York, 6–10 October 1997, American Nuclear Society, vol 1, p 661
- Wagner JC, Blakeman ED, Peplow DE (2007) Forward-weighted CADIS method for global variance reduction. *Trans Am Nucl Soc* 97:630
- Wagner JC, Blakeman ED, Peplow DE (2009) Forward-weighted CADIS method for variance reduction of Monte Carlo calculations of distributions and multiple localized quantities. In: *Proceedings of the 2009 international conference on advances in mathematics, computational methods, and reactor physics*, Saratoga Springs, New York, 3–7 May 2009
- Weinberg AM, Wigner EP (1958) *The physical theory of neutron chain reactors*. University of Chicago Press, Chicago, pp 314–316
- Williams MMR (1971) *Mathematical methods in particle transport theory*. Butterworth, London
- Williams MMR (1979) The role of the Boltzmann equations in radiation damage calculations. *Prog Nucl Energy* 3:1
- Wolters ER, Larsen EW, Martin WR (2009) A hybrid Monte Carlo-S2 method for preserving neutron transport effects. In: *Proceedings of the 2009 international conference on advances in mathematics, computational methods, and reactor physics*, Saratoga Springs, New York, 3–7 May 2009
- X-5 Monte Carlo Team (2003) MCNP – a general Monte Carlo N-particle transport code, Version 5. Los Alamos National Laboratory, LA-UR-03-1987 (Revised October 2005)
- Yang J, Larsen EW (2009) Application of the “functional Monte Carlo” method to estimate continuous energy k-eigenvalues and eigenfunctions. In: *Proceedings of the 2009 international conference on advances in mathematics, computational methods, and reactor physics*, Saratoga Springs, New York, 3–7 May 2009

6 Nuclear Materials and Irradiation Effects

Clément Lemaignan

CEA-INSTN and CEA-DEN, Grenoble, France

clement.lemaignan@cea.fr

1	<i>Introduction</i>	545
1.1	Definition of Nuclear Materials	545
1.2	Radiation Fluxes in Nuclear Reactors	546
2	<i>Radiation Damage</i>	548
2.1	Irradiation Damage by Neutrons	548
2.1.1	Inelastic Interactions: Chemical Changes	548
2.1.2	Elastic Interactions by Neutrons	550
2.1.3	Damage Cross Section	554
2.1.4	Computation of Damage for Power Reactors	555
2.1.5	Time Evolution of the Point Defects	557
2.2	Effects on Microstructure and Engineering Properties	560
2.2.1	PD Clustering, Dislocation Loop, and Cavities	562
2.2.2	Segregations, Phase Transformations, and Amorphization	563
2.2.3	Computational Techniques for Nuclear Material Science	566
2.2.4	Impact of Irradiation on Engineering Design Properties	569
2.3	Irradiation Damage in Ceramics	576
2.3.1	General Aspects	576
2.3.2	Irradiation Damage	577
2.3.3	Changes in Microstructure	579
2.3.4	Change in Properties	580
2.4	Irradiation Damage by Photons and Electrons	582
2.4.1	Radiation-Induced Conductivity in Ceramics	582
2.4.2	Radiolysis: Water and Polymers	583
3	<i>Impact of Irradiation Damage on Structural Material Behavior</i>	589
3.1	Ferritic Steels (LWR Pressure Vessel)	589
3.1.1	General Aspects	589
3.1.2	Microstructural Aspects	590
3.1.3	Pressure Vessel Steel Embrittlement	591
3.2	Austenitic Stainless Steels (LWR Internals)	598
3.2.1	Changes in Microstructure and Mechanical Properties	598
3.2.2	Radiation-Induced Segregation	600
4	<i>Reactor Core Materials</i>	602
4.1	Stainless Steels in SFR	602
4.1.1	Changes in Microstructure	602

4.1.2	Swelling	603
4.1.3	Irradiation Hardening and Irradiation Creep	611
4.1.4	Development of Low Swelling Alloys	614
4.2	Zirconium Alloys in Water Reactors	616
4.2.1	Zirconium Alloys: Zircaloy and Zr-Nb	616
4.2.2	Dislocation Loops: Growth and Irradiation Creep	619
4.2.3	Postirradiation Plastic Behavior	621
4.2.4	Corrosion Behavior and Effects of Irradiation on Corrosion	622
4.2.5	Interaction with Fission Products I-SCC and PCI Failure	625
4.3	Carbon and Graphite	626
4.3.1	Nuclear Graphite	626
4.3.2	Behavior Under Irradiation	627
4.3.3	Creep and Wigner Effect	628
4.3.4	Corrosion	629
5	<i>Fusion Reactor Materials</i>	629
5.1	Specific Environment of the Fusion Reactors	629
5.2	Plasma Facing and High Heat Flux Components	630
5.3	First Wall and the Blanket Structures	630
5.4	Blankets and Tritium Breeding Materials	631
6	<i>Corrosion in Nuclear Environments</i>	631
7	<i>Prospects</i>	632
	<i>References</i>	635

Abstract: Two types of materials are selected by the nuclear industry to be used in nuclear reactors: either materials having specific nuclear properties, or standard engineering alloys corresponding to the thermomechanical loadings and environment.

The first class corresponds to the fuels neutron absorbing isotopes or alloys of low neutron capture cross sections. These atomic properties do not preclude the chemical state of the species, and the best chemical state could be selected (e.g., B, a neutron absorber, can be used in water solution as boric acid or as refractory carbide: B₄C). The second class corresponds to alloys, such as structural steels, stainless steels (SS), aluminum alloys, etc. Few specific alloys have been developed for particular applications, such as Zr alloys in water reactors or vanadium alloys in fusion devices.

All these materials have to support the environment of a nuclear reactor. In addition to standard engineering constrains (mechanical loadings, corrosion, high temperatures, etc.), the irradiation itself induces major changes in structure, properties, and behavior of all the materials.

Irradiation damage includes chemical changes induced by irradiation, with the specificity of in situ He formation, by (n, α) reactions, promoting swelling. However, the major mechanism of irradiation damage is mostly due to elastic interaction of neutrons with the atoms, leading to displacement cascades and generation of point defects (PD). The migration and clustering of these PD induce major changes in microstructure with corresponding changes in behavior.

Irradiation hardening, reduction of ductility, irradiation creep and growth, and swelling are described in detail in their physical mechanisms and their specific characteristics for the alloys and ceramics for current use and of future interest. Other irradiation effects such as radiolysis on water, or changes in electrical properties of insulating ceramics are also described.

After a generic description of the physics of the transformations induced in the microstructures by irradiation, the phenomena of major concern are presented for the different components of various reactors. The corresponding conditions are analyzed for various types of experimental reactors, power reactors (thermal and breeder), and fusion devices.

1 Introduction

1.1 Definition of Nuclear Materials

The aim of this chapter is to provide the reader with a comprehensive view of the materials aspects of the nuclear reactor design and operations. Indeed, nuclear reactors require the selection of materials having good or outstanding engineering properties, in very specific environments (temperatures, irradiation, time scales, etc.). In addition, the neutron physics of the reactors leads to the selection of alloys having specific properties with respect to interaction with neutrons (interaction cross sections). Last, the irradiation itself induces transformations in the alloys, with evolutions of the microstructures and changes in mechanical and engineering properties. The field of nuclear materials covers therefore two different domains:

- The effect of irradiation on materials, whatever the type of materials, as long as they are exposed to an irradiation field. This will include the physics of irradiation damage, the

changes induced in microstructure and their effects on the properties. The alloys concerned are standard alloys used for their properties in numerous industrial environments.

- Other materials of concern are those of specific physical properties, namely the nuclear properties. Most of them are the materials used in the cores of the reactors. The first class includes the species corresponding to the fissile materials (U, Pu, etc.) and to the neutron absorbers (Cd, In, B, etc.) used to produce and control the nuclear chain reaction. The second class covers the materials selected for their low interactions with neutrons and having good engineering properties (Zr alloys, or moderators such as graphite, etc.). These materials are also subject to irradiation-induced transformation and property changes.

1.2 Radiation Fluxes in Nuclear Reactors

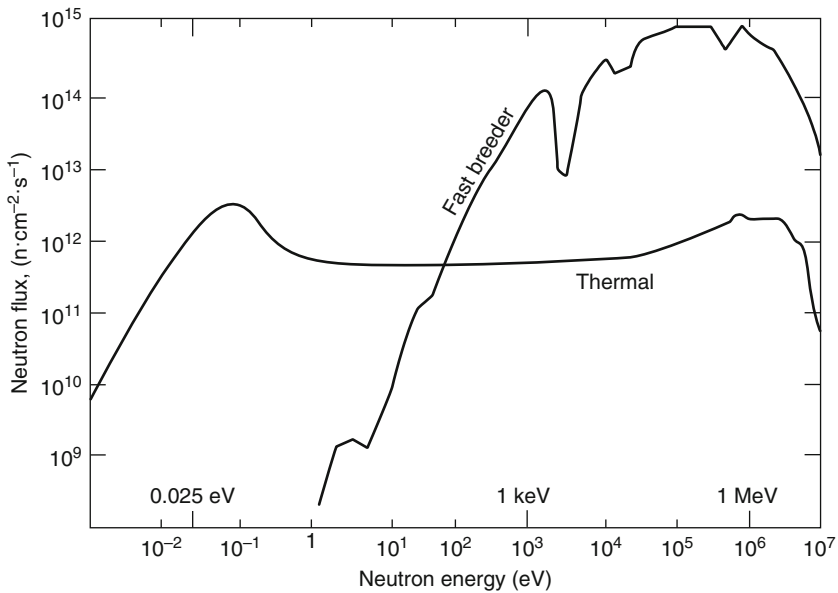
In the nuclear reactors, various types of irradiation fluxes can be observed, whose nature, spectra, and intensity can vary over large extends. The previous [▶ Chap. 1](#), [▶ 5–11](#) describe in detail the computation procedures used to obtain a full description of them. Indeed the neutron, electron and photon spectra are location, time, and reactor type dependent. In this section, typical values of the irradiation fluxes will be given, with special emphasis on areas where their effects will be significant for the behavior of the materials.

In fission reactors, the neutrons produced during fission have high energies, typically a few MeV. In fast neutron reactors, the neutrons are maintained in this energy range, and their spectra in the core have very low contributions at low energies. However, due to the low fission cross sections in the high energy range, very high neutron fluxes are required for their operation.

In the core of the thermal reactors, the energies of the neutrons are reduced by series of elastic interactions with light, nonabsorbing elements, i.e., the moderator. The result is a much higher contribution of the low energy neutrons, and lower fast neutron intensity. Typical spectra of neutron energies are given in [▶ Fig. 1](#). Maximal values of fast neutrons flux ($E > 1$ MeV) are roughly 5×10^{16} and $6 \times 10^{19} \text{ n} \cdot \text{m}^{-2} \cdot \text{s}^{-1}$, for thermal and fast neutron reactors, respectively.

In the very specific case of the future fusion reactors, the fission products have very different characteristics. The neutrons, produced in the D-T reaction with an energy of 14.1 MeV, escape from the plasma without interaction and interact with the walls and structural materials by various processes, while the α 's, in spite of their high energies, due to their charged nature, are trapped by the magnetic field and will not interact immediately with the walls of the vacuum vessel. They will only interact with the surface of the divertor, at much lower energies after having heated the plasma. Due to the unusual processes relevant to the fusion reactor irradiation damage mechanisms, corresponding to extreme conditions of the mechanisms described in fission reactors, they will be described in [▶ Sect. 5](#).

The neutrons fluxes and energy spectra depend on the location where they are analyzed. In fast reactors, the flux gradient is high and neutron doses are very different within the core. The surrounding structures, such as the containment vessel, are far apart and therefore almost free of irradiation damage. In thermal reactors, the flux in-core is roughly constant, but the pressure vessel is close to the core and despite the gradient at the periphery of the core, radiation damage is observed in the internals and in the pressure vessels. Therefore any analysis of the effects of irradiation should consider the exact neutron history and characteristics, at the location of the material considered.



■ **Figure 1**
Neutron flux spectra in fission reactors (fast breeder and LWR)

For the different mechanisms of modification of the behavior of the materials under irradiation, the parameters to be considered may not be the same. Thus, irradiation can be considered at two different time scales. Instantaneously, the parameter is the neutron flux (Φ), expressed in units of $\text{n} \cdot \text{m}^{-2} \cdot \text{s}^{-1}$. The time integral is called the fluence (Φt , units: $\text{n} \cdot \text{m}^{-2}$). These two parameters act differently and the same fluence, obtained with different fluxes over different time spans, can lead to very different irradiation effects. Similarly, the flux itself can control specific behaviors, such as irradiation creep or transport properties.

As it will be detailed in the following section, the major contribution to irradiation damage is due to the high energy part of the neutron spectrum. This is the reason why the neutron fluxes are usually described by their high energy parts. The link between neutron flux and damage integrates all the mechanisms of damage formation and specific procedures have to be used to reduce the whole spectrum to a reduced neutron flux of a given energy. This will be detailed in

➤ [Sect. 2.1.4.](#)

In addition to the neutrons, other irradiation fields have to be considered.

- High energy photons are released by nuclei during the fission process, by decay of fission products or other neutron inelastic interactions. Created with well-defined energies, their energy distribution is degraded by successive Compton interactions, leading to a continuous in-core spectrum of γ photons. The fractional contribution of the γ photons to the total energy release is about 6–7%, with a wide energy range (0–2 MeV).
- The electron flux is induced either by β^- decay or by Compton interactions of the γ photons. The major part of the β^- decay electrons is released within the fuel and, due to the low range of the corresponding electrons, remains localized inside the fuel elements. The Compton

electrons and photoelectrons are produced everywhere in the core and around. They are formed by the natural degradation processes of the photons interacting with matter. The β^- decay mechanism produces in addition a neutrino that has a too low interaction cross section with matter to be of concern. The neutrino flux will therefore not be considered further in this chapter.

- The last irradiation flux to be considered is formed by the heavy ions. They are created either directly during fission, where the fission fragments will have energies of 100–70 MeV, respectively for the light and heavy recoils. Having recoil ranges shorter than 10 μm , they remain within the fuel, and induce damage localized only in the fuel material. Other energetic heavy ions are the α and associated recoil atom, during any (n, α) reaction.

2 Radiation Damage

2.1 Irradiation Damage by Neutrons

The interaction of a neutron with the atoms occurs only with the nucleus. Two different mechanism may occur: either inelastic interaction, where the neutron reacts with the nucleus, producing nuclear interaction (capture, (n, α) , fission or any other reactions, etc.) or elastic interaction where the neutron hits the nucleus and transfers to it only part of its momentum and kinetic energy.

All these processes are characterized by the interaction cross section, σ , describing the probability of interaction for each process. This quantity is dependent of the exact process considered, of the nature of the target (chemical and isotopic state) and of the energy of the impacting neutron. The reaction rate is thus given in the following equation:

$$N_i = N_v \sigma(E) \varphi_n(E) \quad (1)$$

where N_i is the number of interactions occurring per unit volume and unit time, N_v is the number of atoms that could interact in the unit volume, $\sigma(E)$ is the interaction cross section, and $\varphi_n(E)$ is the neutron flux at the energy range considered.

2.1.1 Inelastic Interactions: Chemical Changes

Inelastic interactions are either positively searched for operation of the reactor, such as neutron absorption for reactivity control, fission for energy generation, or are suffered for their contribution for chemical changes, damage, etc.

Except the case of the (n, α) reactions that concerns almost all the chemical species at high neutron energies, the changes in chemistry induced by the inelastic interactions are limited to very specific cases. A few of them will be presented in this section, for illustration purposes.

- Control rods and absorbers.

The absorbers are designed with a specific constrain of high neutron trapping efficiency. This means a high capture cross section in the energy range concerned. B, In, Cd are the major absorber materials used in fission reactors. These species are used either as compounds (B_4C) or as alloys (AIC, for silver-indium-cadmium). For safety reasons, the control rods, that contain

the absorbing materials, are partly inserted in the core and their extremities are thus subject to a significant neutron flux. Therefore, captures occur, in consistency with the aim of these devices.

- AIC in PWR

In the case of AIC PWR control rods, the change in chemistry induced by such captures is a matter of concern. An AIC control rod consists of a stainless steel tube filled with an Ag-In-Cd alloy. The initial composition is typically the following: Ag 80, Cd 5, In 15 (w %). It corresponds to a single phase fcc solid solution.

The different neutron capture reaction mechanisms induce large changes in composition, with decrease in Ag and In, increase in Cd and formation of a new component: Sn, shifting, after a few years in reactor, to typical compositions such as Ag 72, Cd 8–10, In 10–12, Sn 2–5 (w %). The quaternary phase diagram of these alloys forecasts a phase change from the dense fcc structure, for high Ag content, to an hexagonal close packed (hcp) structure of lower density (Bourgouin et al. 1999). The corresponding swelling induces hoop stresses in the SS cladding, leading to stress corrosion cracking (SCC), leaking absorber rod, and corrosive interaction of the coolant with the absorber alloy.

- B₄C in thermal and fast reactors.

Boron is a very efficient neutron absorber, with a thermal neutron absorption cross section larger than 1,000 barns, decreasing with the energy of the incident neutron down below 0.5 barn for 1 MeV neutrons. The principal reaction is described as $^{10}\text{B}(n, \alpha)^7\text{Li}$ and produces an He atom and releases 2.8 MeV of energy. The generation of He bubbles in B₄C reduces its thermal conductivity and induces matrix swelling. High temperatures and He supersaturation drives the release of He out of this material. At low temperatures, He in solid solution induces internal lattice strains (Simeone et al. 1999), and at higher temperatures, He precipitates as elongated bubbles, inducing swelling (Stoto et al. 1990).

- Other specific cases

In material testing pool reactors, the structural parts are often made out of Al-alloys of 5xxx type, where Mg in solid solution enhances mechanical strength and corrosion resistance. Under thermal neutron irradiation, an (n, γ) reaction occurs on Al, leading to in-situ formation of Si (up to a few % for long irradiations). This change in chemistry shifts the alloy to the 6xxx class, where the mechanical strength is obtained by small Mg₂Si precipitates. An irradiation hardening is therefore observed, whose origin lies in the chemically induced change in microstructure (Farrell 1981).

The (n, α) reactions are common with fast neutrons. They have very high importance, as they continuously dope the alloys with He. Their consequences will be considered in the section devoted to stainless steels and swelling (➤ 4.1.2). In the case of materials for fusion reactors, the high energy of the neutrons leads to high cross section of these reactions and therefore very high He creation for the same irradiation damage. It should however be remembered that more complex He production mechanisms can be obtained: in thermal reactors, and in the outer part of the breeders, a double reaction occurs on Ni, with high cross section for thermal and epithermal neutrons: A first capture $^{58}\text{Ni}(n, \gamma)^{59}\text{Ni}$, is followed by the $^{59}\text{Ni}(n, \alpha)^{56}\text{Fe}$ reaction, and formation of an atom of helium.

In the case of tungsten, considered for specific fusion applications, the high capture cross sections on the different isotopes of this element, lead to significant chemical changes: After 2.5 years of exposure, up to 25% of the W is transformed in Os and Re, inducing a structural change in the alloy, with formation of a brittle σ phase (Forty et al. 1994).

2.1.2 Elastic Interactions by Neutrons

Although chemical changes induced by irradiation can affect the behavior of alloys, the main mechanisms of irradiation damage are connected to the displacement of atoms following an interaction with fast neutrons. The aim of the following sections is to describe the physical phenomena controlling the ballistic irradiation effects.

- Energy transfer, displacement cross sections

In this case, there is no modification of the structure of the nucleus, but part of the kinetic energy of the neutron is transferred to the target atom, according to (2):

$$E_T = 4E_n \cos^2 \theta \frac{m_n \cdot m_T}{(m_n + m_T)^2} \quad (2)$$

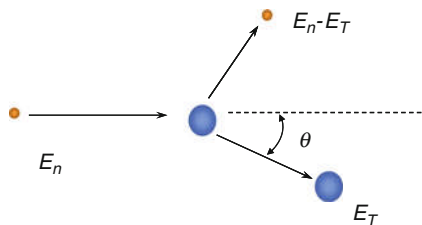
where E_T is the energy transferred to the target, m_n and m_T are the masses of the neutron and of the target atom, E_n is the kinetic energy of the neutron before impact, and θ is the scattering angle expressed in the centre of mass coordinates (► Fig. 2). The ratio between the maximum transferred energy and E_n is often called the energy transfer parameter, Λ . The mean value of the transferred energy, for all the different scattering angles, is roughly equal to half of the maximal value.

The transfer of energy induces different consequences, depending on its relative value. It has to be compared to a critical value required for atomic displacement out of the crystal lattice site.

For low values of the energy transferred, the target atom cannot leave its position in the crystal. The increase in kinetic energy only increases its vibration amplitude within the lattice site. The impact is thus only a source of local vibrations, a phonon, i.e., nothing but a local source of heat that will diffuse in the alloy, by propagation of the phonons.

If the energy transferred is larger than a critical value, called the displacement energy E_d , which is for common metals close to 20–40 eV, the target atom can escape from its lattice site.

The displacement energies were measured experimentally on different alloys using electron irradiation at various accelerating voltage. The minimum transferred energy above which a change in physical property can be observed (usually electric resistivity) gives the displacement energy, E_d . It was found that E_d varies with species, and crystallographic orientation (Urban and Yoshida 1981). Since the computation of irradiation damage is scaled with the displacement energy, it is highly recommended to use the standard values listed in ASTM standard E 521 for



■ Figure 2

Schematics of an elastic interaction between a neutron and a target atom (center of mass frame)

a unified computation of the irradiation damage (ASTM Standards E-521-96 2003), whatever the irradiation mechanism (neutron, electron, or heavy ions).

Following the impact and energy transfer to the target atom, different phenomena occur:

- For a low transferred energy (a few E_d), it will not disturb the other atoms from their sites and only loses energy along its path, to stop as an interstitial when its energy is too low for further motion. At the end of the process, the final damage is the combination of a vacancy, the former location of the atom, and an interstitial, which is not necessarily the initial atom hit. This pair of point defects is called a Frenkel pair. Typically, this is what will occur during high-energy electron irradiation, where the transferred energies are of the order of a few tens of eV.
- For high values of the energy transferred, the target atom, called now the primary knocked-on atom (pka), interacts with the other atoms of the alloy along its track. For each interaction, it transfers on the average half its current energy on the secondary target, as they have equal masses. Each of them will similarly interact with other atoms and a cascade of interactions occurs. The result is a large number of atoms displaced (up to a few hundreds), in a “displacement cascade.” After a few picoseconds, the highly damaged area restructures itself, leaving a few isolated, surviving PD and clusters of PD.

Overall, the irradiation by neutrons results in a continuous creation of point defects, and heat, in the bulk of the alloys. These PDs cannot increase in concentration without limits. The PD can recombine, migrate, agglomerate as large clusters of PD or disappear on various sinks such as free surfaces, grain boundaries, or dislocations.

A good knowledge of the radiation damage requires therefore an accurate description of the various quantities involved in these processes. In the following sections, the probability of interaction (cross sections), the displacement energies E_d , the PD energies and mobilities, the cascade configurations, and the strengths of the sinks where they can disappear will be described in detail for generic alloys. These data will be used to describe the formation of the resultant microstructures (dislocation loop formation, precipitation, phase instability, etc.), by combination of all the processes involved in radiation damage. Then it will be possible to illustrate the consequences for the properties of the alloys and their modified behavior under and after irradiation.

- Vacancy and interstitials, Frenkel pairs

The net result of the displacement of atoms in a crystallized material is the formation of a pair of opposite defects, the vacancy, and the interstitial.

Compared to the interstitial, the vacancy has a low formation energy (typically $E_{f-v} \sim 0.7\text{--}1.2$ eV) and a high migration energy ($E_{m-v} \sim 0.8\text{--}1.5$ eV). Due to the low formation energy of the vacancies, a low concentration of vacancies is thermally obtained at high temperature (around $10^{-3}\text{--}10^{-4}$ near the melting temperatures). Around a vacancy, the surrounding atoms only slightly relax their positions, and the relaxation volume of a vacancy is only a small fraction of the atomic volume. Their migration energies restrict their mobilities to the high temperature domains ($T > 1/3 \cdot T/T_m$).

The insertion of an interstitial atom in the lattice requires large displacements of the surrounding atoms. It has therefore a high formation energy (typically $E_{f-i} \sim 3\text{--}4$ eV). Being more than an extra atom inserted in a disturbed site within the packed atoms of the crystal, the atomistic geometry of the interstitial consists usually in a pair of atoms sharing the same lattice site, in a highly crowded configuration. Often the two atoms form a dumbbell along specific

crystallographic directions (e.g., $\langle 100 \rangle$ in fcc or $\langle 110 \rangle$ dumbbells in bcc Fe) or extended defects such as $\langle 111 \rangle$ crowdion in non magnetic bcc crystals. One atom of this pair can easily jump to any next lattice site, forming a similar configuration with another atom, leading to the migration of the defect. Therefore the interstitials are observed to be highly mobile and usually can migrate well below room temperature ($E_{m-i} \sim 0.05\text{--}0.3\text{ eV}$). The relaxation volume of the interstitial is usually of the order of the atomic volume or larger.

For low transferred energies, the target atom cannot induce significant displacement of the surrounding atoms to remove them from their own lattice sites. It moves only slightly away from its position, transferring part of its energy to the atoms hit along its track, until it cannot migrate anymore, where it forms the interstitial defect. If the final distance between the vacancy and the interstitial is too low, the configuration of the pair of PD's is elastically unstable and the two opposite PD's recombine instantaneously, and the two defects disappear, releasing their energies as a phonon diffusing in the lattice. The volume in which two opposite PD's elastically recombine is called the recombination volume. The size of the recombination volume is in the range of 100–150 atomic volumes. It has been measured by the observation of a saturation of PD concentration during low temperature irradiations, and confirmed by molecular dynamics (MD) computations.

If the distance between the initial location of the target atom, now the vacancy, and the stopping site of the interstitial is high enough, the result is the creation of a stable pair of correlated opposite defects, the Frenkel pair.

- Displacement cascades

For typical fast neutrons, energies transferred to the pka atom of structural materials are in the range of a few tens of keV. For these kinetic energies, the pka has very high interaction cross sections with any atoms along its track. Since the atoms knocked by the pka have similar masses as the pka, and according to (2), the energy of the pka is, on average, shared between the target atom and the pka. The two interacting atoms usually will repeat the interaction process with surrounding atoms, leading to a cascade of displacements. The process is repeated unless the transferred energy is lower than the displacement energy.

Simple partition of the kinetic energy between all the interacting atoms leads to the number of atoms displaced in a cascade as proposed by Norgett et al. (1975). According to this modeling, the number of atoms displaced in a cascade is simply:

$$N_{\text{NRT}} = 0.8 \cdot \frac{E_{\text{pka}}}{E_d} \quad (3)$$

Typical values amount for a few hundreds of displaced atoms in a cascade. Following a given irradiation, the fraction of atoms hit by neutron to form pka multiplied by this value of N_{NRT} gives the irradiation damage, in term of displacement per atoms (dpa_{NRT}).

$$\text{dpa}_{\text{NRT}} = \frac{\rho \cdot N}{M_a} \cdot \sigma \cdot \phi \cdot \frac{E_n}{E_d} \cdot \frac{1.6 \cdot (m_T + m_n)}{(m_T \cdot m_n)^2} \quad (4)$$

where ρ is the specific mass of the alloy, N is the Avogadro's number, M_a is the atomic mass of the alloy, σ is the diffusion cross section at the energy considered, ϕ is the neutron flux, E_n is the kinetic energy of the incident neutron, E_t is the mass of the target atom, m_T and m_n are the masses of the target atom and the neutron, respectively.

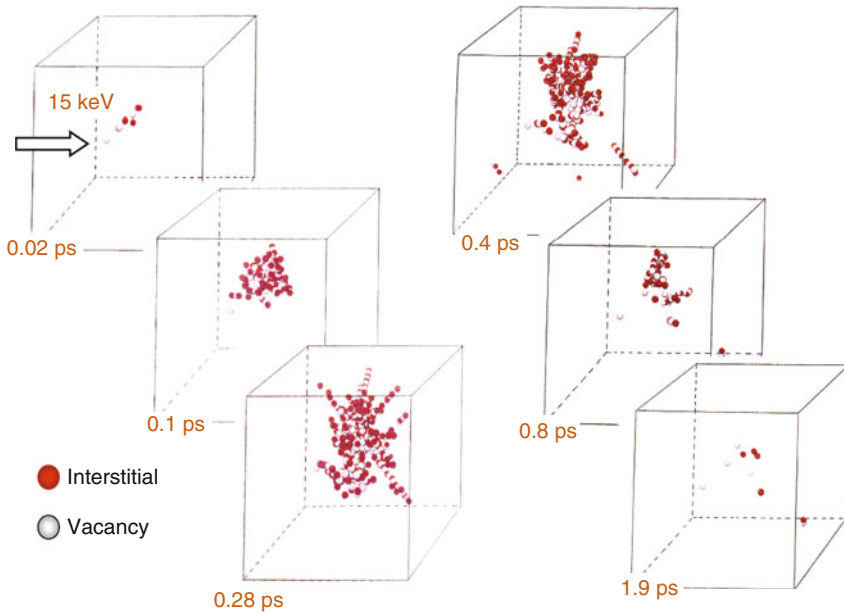


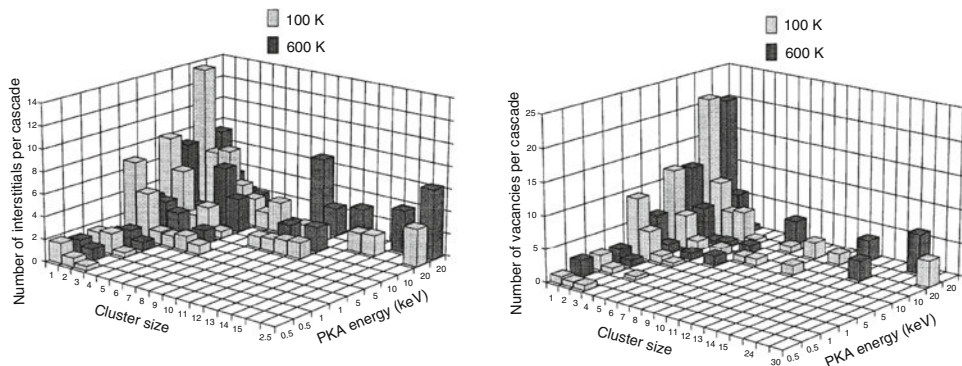
Figure 3

Time evolution of a displacement cascade in Fe (15 keV) (Molecular dynamics simulation, after Souidi et al. 2001)

Advanced description of the behavior of a cascade is obtained using molecular dynamics computations (Bacon et al. 1995). These computations allow deriving important features of the cascades (e.g., see Fig. 3):

- The life of a cascade is short. The development period (ballistic phase), at the end of which all the atoms have kinetic energies similar to the thermal energy last 0.2–0.8 ps, depending of the pka energy. Within 5–10 ps, the highly damaged area recovers and, due to the locally very high density of PD, most of them recombine, and a very low number of isolated PD survive to the cascade.
- For low energy cascades, significant spatial extension of the cascade can be observed, induced by focusing sequences, while at high energies, the cascades have a tendency to split into a few sub-cascades slightly separated, that behave independently (Voskoboinikov et al. 2008).
- The efficiency of the cascade, i.e., the number of free defects normalized to the displaced atoms, decreases with the energy of the pka. For most of the alloys a simple relationship exists between the energy of the cascade and the number of Frenkel pairs N_F . The ratio between the number of atom displaced (N_{NRT}) to the number of remaining defects is the cascade efficiency. Typical values are in the range of 0.1–0.15. It is observed to decrease with cascade energy (Bacon et al. 1995; Voskoboinikov et al. 2008; Gao et al. 2008). A simple relationship exists between the number of Frenkel pairs and the energy of the pka:

$$N_F = A \cdot (E_{pka})^m \quad (5)$$



■ Figure 4

Size of the PD clusters in Zr cascades as computed for cascades of different pka energies in Zr (From Gao et al. 2001)

- The values of A and m have been obtained for various metals (Bacon et al. 1995).
- At the end of high energy cascades, clusters of PD of the same types may be formed, such as small interstitial or vacancy loops, stacking fault tetrahedra in fcc, etc. The higher the energy of the cascade, the higher the fraction of surviving PD's trapped in such clusters (Bacon et al. 1995; Gao et al. 2001).
 - Of course, the results of MD computations are dependent of the interatomic potentials chosen, but the tendency of the physical phenomena remains qualitatively similar using different potentials (Becquart et al. 2000). For alloys the results remain similar, but special phenomena, such as preferential species for the PD, can be observed (Malerba et al. 2004).

As an example, the size distributions of PD in Zr after various cascades are plotted in **Fig. 4**. Large clusters of the two types, either interstitials or vacancies were observed. A difference is noticeable between the two types of PD. In the case of vacancies, the number of surviving vacancies as individual or di-vacancies is high, and the number of vacancy clusters low. The reverse was obtained for the interstitials.

A major consequence, clearly seen in **Fig. 4**, is that the number of surviving isolated defects is not the same for the two types of PD. Isolated and free vacancies are released by the cascades in much higher number. This effect is known as the *production bias* that has to be considered when solving the rate equations in the mean-field approach of PD evolution described latter (8) (Woo and Singh 1995).

The number of remaining point defects and clusters of interstitials or vacancies are the initial conditions for the thermal evolution of the alloys under irradiation. Indeed, for a larger time scale than the evolution of the cascade, the point defects will migrate and recombine, cluster or annihilate on various sinks. Major changes in the microstructure will result, inducing modification of the properties, as will be described below.

2.1.3 Damage Cross Section

The irradiation damage is often expressed in the form of fast neutron fluence ($n \cdot m^{-2}$) and an indication of the “fast” neutron energy limit, or with the effective damage in dpa. The conversion

factor will vary according to the exact neutron physics of each reactor, i.e., according to the exact neutron energy spectra. In water reactors, a rough conversion factor between fast dose and displacement damage corresponds to 1 dpa being induced by a fluence of $5 \times 10^{24} \text{ n} \cdot \text{m}^{-2}$ ($E > 1 \text{ MeV}$) for Zr. In fast reactors, the different spectrum and the use of SS leads to 1 dpa $\sim 2 \times 10^{25} \text{ n} \cdot \text{m}^{-2}$ ($E > 0.1 \text{ MeV}$) on Fe atoms.


Therefore a detailed conversion procedure is required to compare irradiations performed in different reactors. Indeed, the impact of irradiation on various properties can be determined by testing materials in different reactors (e.g., LWR power plants, material testing reactors or fast breeders for high fluence irradiations). In addition, basic irradiation studies are often performed using electron or heavy ion irradiations and the results obtained have to be compared with the reactor irradiations.

The irradiation damage is mainly obtained by elastic interaction between fast neutrons and the atoms of the alloy. Indeed, the low energy neutrons (below a few hundred eV) do not transfer enough energy to induce atomic displacement. However, nuclear interactions can occur of (n, γ) , (n, α) , (n, n') or $(n, 2n)$ types, the later being significant only at high energies. The contribution of these reactions, and their decay followers, has to be computed with consideration of the detailed neutron energy spectrum of each reactor, if not each location inside the reactor (Greenwood and Garner 2004). The irradiation damage is thus computed considering all these processes inducing displacements. The rate of formation of displaced atoms is simply equal to the expansion of the previous equations (4) to the full energy range of the neutrons:

$$R_d = N \int_{E_d/\Lambda}^{\infty} \varphi(E_n) dE_n \int_{E_d}^{\Lambda E_n} \sigma_n(E_n, T) v(T) dT \quad (6)$$


where N is the number of atoms per unit volume, Λ is the energy transfer parameter defined in (2), and the other terms described earlier. The second integral allows defining the displacement cross section, σ_d .

$$\sigma_d(E_n) = \int_{E_d}^{\Lambda E_n} \sigma_n(E_n, T) v(T) dT \quad (7)$$

This displacement cross section has been determined for several chemical species using the nuclear data tables ENDF-BV. It is available for most of the components of structural materials (Greenwood and Smither 1985). As an example, it is given for Zr in  Fig. 5.

The rate of irradiation damage is the integral of the product of this displacement cross section by the neutron flux for each energy of the neutrons. Since different reactors have different neutron spectra, the ratio between damage formation rate and neutron flux varies accordingly (Piercy 1969; Greenwood 1994). Care should be taken to the fact that $\sigma_d(E_n)$ includes also a hidden parameter, the displacement energy E_d . The recommended value is 40 eV, but basic studies have sometimes used the other values, like the minimal E_d for detection of irradiation damage (25 eV) (Pecheur 1993; de Carlan 1996).

2.1.4 Computation of Damage for Power Reactors

Since it is impossible to describe the full spectrum of neutrons for each irradiation ( Fig. 1), it is common to characterize the neutron flux (or fluence) only by its fast neutron contribution, since it is responsible for most of the collision damage. This simplified approach induces a bias due to the definition of the “fast” neutron. In fast neutron reactors, a cut-off value of $E > 0.1 \text{ MeV}$ is

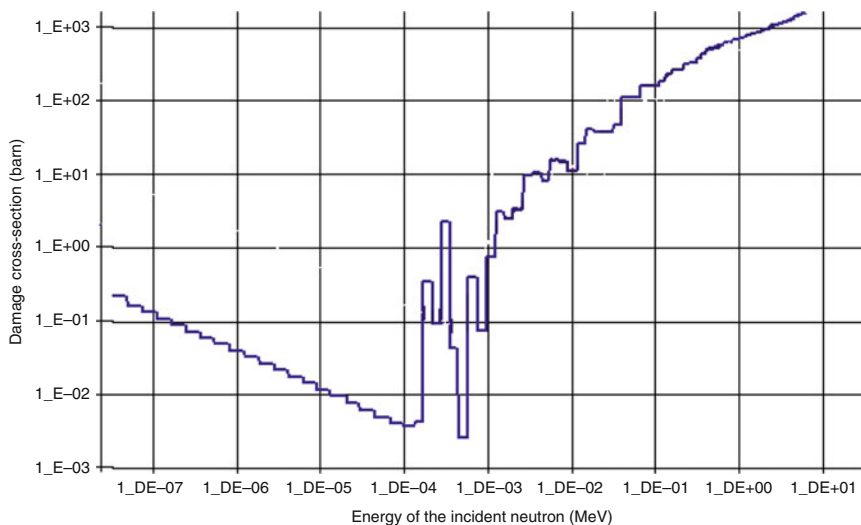


Figure 5
Displacement cross section $\sigma_d(E_n)$ for Zr, with $E_d = 40$ eV

usual, while $E > 1$ MeV is commonly preferred in LWR. Other limits have also been historically used (0.85 MeV).

Computation of the damage requires an accurate knowledge of the neutron flux history and spectra at the exact location where the damage is to be computed. This is the aim of neutron physics codes and dosimetry survey. In addition the damage cross section is to be known, as described in the preceding section. A standard procedure has been developed for pressure vessel of LWR and should be used for intercomparisons of tests of different origins (ASTM Standards E-693-01 2007). For other components, a similar procedure is recommended.

Selecting such a limit for the fast neutrons does not mean that only these neutrons are considered for damage, but is just a way to scale the flux intensity. Decreasing the energy limit for the fast neutrons value increases the flux considered, but does not change the damage. Therefore irradiations to the same fluences, but expressed as $E > 1$ MeV and $E > 0.1$ MeV correspond to different damages, the later being smaller, by a factor of about 2 (Table 1).

In old publications, a special unit can be found: nv or nvt. It stands for number (of neutrons per unit volume), velocity, and time. The product of n neutrons (in number-cm⁻³) by the velocity (cm · s⁻¹) is indeed similar to a flux (cm⁻² · s⁻¹). Once multiplied by the time, a flux integral (fluence) is obtained. The velocity of the neutrons is obtained from their kinetic energies ($1/2 mv^2$). Similar problems occurred for the selection of the mean energy of the fast neutrons. In the early days, the French scientists used also a special dose index: the dpa_F, with an equivalence of $1 \text{ dpa}_F \approx 0.77 \text{ dpa}_{\text{NRT}}$ in stainless steel claddings.

For the fuel cladding materials (Zr alloys in water reactors, and stainless steels in fast liquid metal reactors), the irradiation is also often expressed using a quantity related to the fuel irradiation: the fuel burn-up (BU). It is expressed in term of energy produced by unit mass of fuel (MW · d · t⁻¹). The correspondence between BU and dpa is much more reactor dependent than the flux – dpa ratio, due to the major contribution of the thermal neutrons to the fission. A fair

■ **Table 1**
Neutron fluences ($n \cdot m^{-2}$) for 1 dpa in various reactors

Type of reactor	Atom	$E > 0.1$	$E > 1 \text{ MeV}$
LWR pressure vessel	Fe		7×10^{24}
PWR BWR (steam 40%)	Zr	1.3×10^{25}	6.4×10^{24}
Na fast reactor	Fe Cr	$\approx 2.2 \times 10^{25}$	
HT GCR	Si C	0.8×10^{25}	

conversion factor is: 1 dpa in Zr is obtained in the cladding for a BU of about $4\text{--}5 \text{ GW} \cdot \text{d} \cdot \text{t}^{-1} \text{U}$ in a LWR. In Na-cooled SFR, 1 dpa is obtained for a fluence of $2 \times 10^{25} \text{ n} \cdot \text{m}^{-2}$, for which a typical BU would be $1 \text{ GW} \cdot \text{d} \cdot \text{t}^{-1} \text{ox}$ corresponding to a fraction of fissioned atoms of 0.1 FIMA (fissions per initial metal atom).

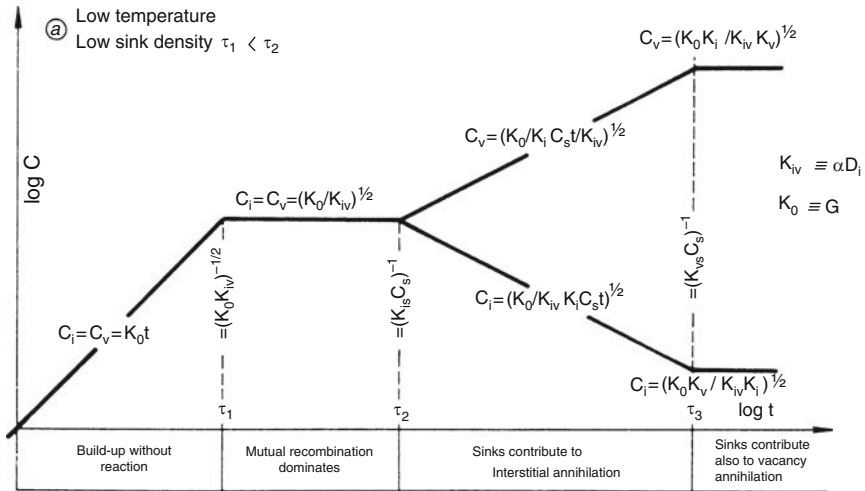
2.1.5 Time Evolution of the Point Defects

In power reactors, the continuous irradiation induces a steady state creation rate of PD's resulting from the final evolution of the cascades. The remaining defects form either isolated defects or small cluster of interstitials or vacancies. Since these two types of PD's are mobile, their migration occurs under thermal activation. The interstitial are highly mobile and their migration occurs well below room temperature, while the vacancies diffuse more slowly and their mobility is activated at higher temperatures (250–600 K). The computation of the time evolution of these defects requires the knowledge of their migration kinetics and of all their interactions with all the microstructure singularities on which they could disappear or interact (other PD's or different atoms, small PD clusters, dislocations, any interfaces, etc.).

The isolated point defects can migrate anywhere in the alloy and interact with any other crystal defects: An interstitial diffusing to the recombination volume of a vacancy will annihilate there, but they can also merge with other interstitials and form clusters of interstitials, acting as nuclei for interstitial dislocation loops, and similarly for vacancies. In addition, for intermetallic compounds, exchange of species can occur when an interstitial atom falls in the vacancy site of another chemical specie (anti-site). This leads to chemical disorder, a driving force for phase changes, including amorphous transformation.

Clustering of interstitials leads necessarily to planar dislocation loops, while vacancies can produce 2D and 3D defects (i.e., dislocation loops and cavities). The later induce material swelling. When the dislocations present in the alloy act as sinks for interstitials and vacancies, the trapping of PD's on dislocations results in the climb of these dislocations, inducing locally some irreversible strain. If the directions of the strain induced by climbs are not isotropic, this results in a macroscopic strain. When the anisotropy is induced by applied stresses, irradiation creep occurs. In the absence of applied stress, but for anisotropic materials having a crystallographic texture, growth can be observed (e.g., Zr or U alloys, etc).

The classical approach to model PD evolution under irradiation is to solve the kinetics equations for their interaction with the extended defects (Sizmann 1978). A set to two coupled equations is obtained, in which, for each species (vacancies or interstitials), the concentration



■ Figure 6

Evolution of PD population with irradiation time (From Stoller and Mansur 1990)

evolution is controlled the balance between PD generation by irradiation, G , and their disappearance either mutually with the opposite type of defect, or on any kind of sinks. Each sink can be assigned its own strength leading to a kinetic coefficient k . The set of equations obtained is the following:

$$\begin{aligned} \frac{\partial c_v}{\partial t} &= G_v - R_{iv} D_i c_i c_v - \sum_j k_{j,v} D_v c_v + \sum_j k_{j,v} D_v c_{vj}^e \\ \frac{\partial c_i}{\partial t} &= G_i - R_{iv} D_i c_i c_v - \sum_j k_{j,i} D_i c_i \end{aligned} \quad (8)$$

For the vacancies, a thermal release from the dislocations and free surfaces has also to be considered: $\sum_j k_{j,v} D_v c_{vj}^e$. This contribution to the vacancy concentration is important only for high temperature irradiations. However, this term is of high importance for PD annealing occurring during post irradiation heat treatments, since then the thermal vacancies are the only PD's responsible for atom mobility in the absence of irradiation.

The solution of this system of coupled differential equations gives a description of the evolution of the PD with time, but it assumes that the sink concentration (i.e., the dislocations and loops) remains constant. The steady state solution of this system gives a concentration of vacancies in the range of $c_v \approx 10^{-5}$ and, as expected, a much lower value for the interstitials: $c_i \approx 10^{-10}$ for a Zr cladding in a typical LWR (Stoller and Mansur 1990). Typical asymptotic solutions are sketched in ► Fig. 6.

PD Clustering

The trapping of a PD by loops or cavities results in a net change in their sizes. The change in loop or cavity size is an important feature of the microstructural change induced by irradiation

(dislocation density for loop growth and swelling for cavities). Therefore an accurate modeling of their evolution is important to forecast the evolution of the microstructure, and as a consequence, of the properties. The change in size is due to the net flux of PD that will increase or decrease their sizes. For instance, for a cavity the trapping of a vacancy is an increase in cavity size, while an interstitial trapped by the cavity decreases its volume. Detailed procedure of such modeling is given below for the loop size evolution. For the cavities, the impact of He atoms (generated by (n, α) reactions) enhancing the nucleation of cavities (Mansur and Coghlan 1983) is detailed in a specific section devoted to swelling (4.1.2).

The size evolution of a single loop, considered isolated in an infinite medium surrounded by a given concentration of interstitials and vacancies, can be computed by methods based upon the balance of fluxes at the sink formed by the dislocation (Mansur 1994). The interaction energy between PD's and the dislocation loops is found to be decreasing with the loop size. However, it is suggested that the loop sink strength (i.e., the efficiency of PD trapping, function of loop size, density, orientation, etc.), which controls the size evolution rate through the $k_{j,i}$ and $k_{j,v}$ factors, is increasing strongly for the large ones, due to the increased density of dislocation lines. In addition, the sink strength depends of the type of PD considered. The loop growth is therefore expected to be dependent on the size and type of the loops. For interstitial loops, the net flux of PD's leads to a limited growth for small loops and early saturation, while for vacancy loops, a more continuous growth is expected (Bullough et al. 1979). The calculated loop growth rate is forecasted to be proportional to the root of the irradiation time $(\varphi \cdot t) \approx 0.5$, corresponding well to the observations in high voltage TEM (HV-TEM) on Ni (Yoo and Stiegler 1978).

For the extended defects, such as dislocation loops, interacting with each other via the fluxes of PD's, the computation of their concentrations and size distributions has to be done using another method: the cluster dynamics approach, in which the rate of growth and shrinkage of each loop is analyzed by condensation and emission of individual PD. The modeling is based on an extension of the equations (8), with the reactions of the PD analyzed on all the loops of different sizes. This leads to a much larger system of equations, since all the dislocation loop types and sizes have to be considered individually. The change in concentration of interstitial loops of size n is due to the balance in the growth of the loops of size $n - 1$ by absorption of an interstitial, the shrinkage of the loops of size $n + 1$ by absorption of a vacancy, and the disappearance of a loop of size n by the two former processes. The symmetric mechanisms hold for the vacancy loops:

$$\begin{aligned} \frac{dc_{n,i}}{dt} &= \beta_{n-1,i}^i D_i c_i c_{n-1,i} + \beta_{n+1,i}^v D_v c_v c_{n+1,i} - (\beta_{n,i}^v D_v c_v + \beta_{n,i}^i D_i c_i) c_{n,i} \\ \frac{dc_{n,v}}{dt} &= \beta_{n-1,v}^v D_v c_v c_{n-1,v} + \beta_{n+1,v}^i D_i c_i c_{n+1,v} - (\beta_{n,v}^v D_v c_v + \beta_{n,i}^i D_i c_i) c_{n,v} \end{aligned} \quad (9)$$

Due to the computing limitations induced by such large systems (more than a few hundred classes of loop sizes), the system of discrete sizes is transformed in a continuous distribution for the largest loops considered (Hardouin Duparc et al. 2002). One of the critical aspects of this approach is to obtain a good description of the kinetic coefficients $\beta_{n,PD}^{PD}$. In the case of Zr, a choice of suitable parameters for the evaluation of the β 's, permitted an explanation of the simultaneous stability of the two types of loops (interstitial and vacancy types) (Dubinko et al. 2006).

2.2 Effects on Microstructure and Engineering Properties

Physical Properties

During the irradiation the creation and the evolution of the PD's induce changes in the microstructure at various scales: PD concentrations are increased (mainly vacancies, but also interstitials while at lower concentrations), clustering of PD leads to formation of dislocations loops that may interact during their growth, leading to a dense dislocation network, cavities will induce swelling, segregations occur by flux coupling of alloying elements and PD diffusing to the sinks. These changes in microstructure induce significant evolution of the properties of the alloys under irradiation.

The effect of PD concentration on physical properties is very limited and can be measured only on electrical resistivity ρ_e at low temperatures. Indeed the PD act as diffusing centers for the electrons and the increase in electric resistivity is directly proportional to their concentration. The resistivity is indeed easily measured and the accuracy in resistivity changes allow to measure concentrations of Frenkel pairs as low as 10^{-10} in pure metals. In the early days of irradiation experiments, the changes in ρ_e were used to measure accurately the displacement energy, observing the minimum accelerating voltage during electron irradiation to induce measurable damage at low temperature (4–20 K). In addition, during recovery, the temperature evolution of ρ_e allows to measure the migration energies of these PD or their interaction energies with alloying elements or impurities (Balluffi 1978; Kraut et al. 1971; Takaki et al. 1983; Dimitrov et al. 1976; Neely 1970).

The other physical properties, such as specific mass, modulus of elasticity, or thermal expansion coefficient are not affected significantly by PD concentrations.

Diffusion Under Irradiation

Since the diffusion is the displacement of atoms from one lattice site to another one, any mechanism of atom displacement has to be considered to contribute to diffusion. Under irradiation at low temperature, the diffusion is enhanced and can be faster than thermal diffusion by several orders of magnitude (● Fig. 7). The mechanisms to be considered are the following:

- At very low temperature, the PD, whatever the type, are immobile and cannot contribute in any manner to the migration of the atoms. However the mixing occurring inside the cascades induces a diffusion mechanism (ballistic diffusion). The corresponding diffusion coefficient is proportional to the irradiation flux and is strictly temperature independent. This is for instance the regime of ion beam mixing in compounds (Averback 1986). Then the ballistic diffusion coefficient is roughly given by the following expression:

$$D_{\text{ball}} \text{ (m}^2 \cdot \text{s}^{-1}\text{)} \approx 10^{-17 \text{ to } -16} k_0 \quad (10)$$

where k_0 is the Frenkel pair production rate expressed as fractional lattice sites per seconds ($\text{dpa} \cdot \text{s}^{-1}$) (Macht et al. 1981).

- At intermediate temperatures and irradiation fluxes, two specific regimes exist in which the migration of PD's created by irradiation is thermally controlled (Sizmann 1978):
 - When the sink density is low (i.e., the PD concentration is controlled by their recombination kinetics), the vacancy and interstitial concentrations, obtained from equations (8) are given as:

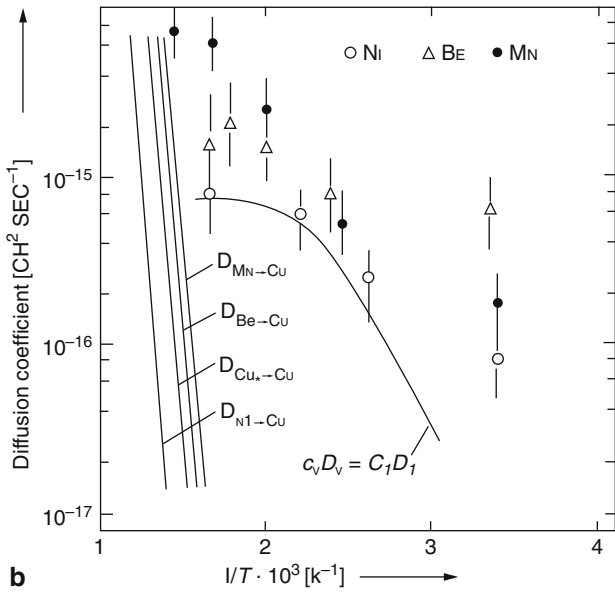
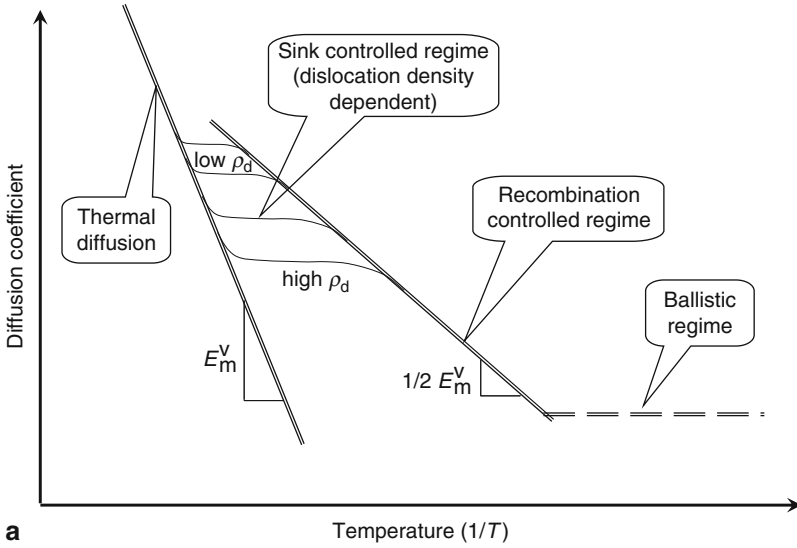


Figure 7

(a) The different regimes of diffusion under irradiation. (b) Radiation-induced diffusion of dilute elements in Cu (From Wollenberger 1994)

$c_v = \sqrt{\frac{\Omega G k_i}{2\pi r_r k_v D_v}}$ and $c_i = \sqrt{\frac{\Omega G k_v}{2\pi r_r k_i D_i^2}}$ where Ω is the atomic volume and r_r the recombination volume. Since the diffusion coefficient D is the sum of the two diffusion mechanisms induced by vacancy and interstitial mobilities, it can be expressed as: $D = c_i D_i + c_v D_v$ and the diffusion coefficient reduces to $D_{irr} = \beta \sqrt{\Omega G D_v / 2\pi r_r}$, where β is the function of the relative sink efficiency for vacancies and interstitials. As a consequence of D_{irr} being proportional to the root of the thermal diffusion of vacancies, the apparent activation energy for irradiation diffusion in this regime is equal to half the activation energy for the thermal diffusion.

- For high sink densities (i.e., the PD concentration is controlled by the dislocation density), the vacancy and interstitial concentrations, obtained from equations (8) are simply: $c_v = G/k_v D_v$ and $c_i = G/k_i D_i$. The diffusion coefficient reduces to $D_{irr} = G/k_v$, and the diffusion in this regime is then proportional to the irradiation flux and decreases with increasing dislocation density.
- At high temperatures and low irradiation intensity, the concentration of PD due to irradiation is small compared to the thermal equilibrium concentration of vacancies and the thermal diffusion regime is dominant. The corresponding diffusion coefficients are the standard thermal diffusion coefficients.

The enhanced diffusion under irradiation impacts all the transport controlled phenomena, such as the kinetics of phase transformation (dissolution or precipitation) and creep.

2.2.1 PD Clustering, Dislocation Loop, and Cavities

The migration and clustering of PD induce various evolutions of the microstructures under irradiation.

- The nucleation and growth of dislocation loops by clustering of PD leads to a microstructure specific to irradiated materials. Typical geometries of the loops are usually fine in size (3–20 nm) and of high volume density ($10^{21-23} \text{ m}^{-3}$) (► Fig. 8). Depending of the crystallography of the alloys, the loops may have different habit planes, and in fcc alloys with low stacking fault energies, stacking fault tetrahedra can be observed. During their growth, the dislocation loops may interact within each other, resulting in a new dislocation network, whose structure tends to stabilize with characteristics independent of the initial microstructure. This new dislocation structure affects strongly the mechanical properties, as described latter. In the case of anisotropic distribution of the loops (due to applied stress or textured materials), permanent strain can be induced (irradiation creep and growth).
- The normal clustering of vacancies would lead to planar defects, i.e., dislocation loops, due to the energy balance between separated and gathered PD's: During the clustering of vacancies as a loop or a cavity, the formation energy of the vacancies is recovered, but either a dislocation line or a free surface is created, requiring their respective formation energies. The balance is in favor of the loop formation in standard cases. In the case of gas present in the alloys (e.g., produced in situ by (n,α) reactions), gas atoms enhance the nucleation of cavities and the clustering of vacancies leads to the formation of 3D defects, i.e., cavities,



■ Figure 8

Observation of fine dislocation loops in neutron irradiated 304 stainless steel (From Pokor et al. 2004a)

inducing swelling. Such cavities can be observed in oxygen doped copper irradiated with Cu^+ ions (► Fig. 9). The swelling induce changes of the geometry of the component, of the specific mass. It has an impact on mechanical strength and induces a reduction in ductility.

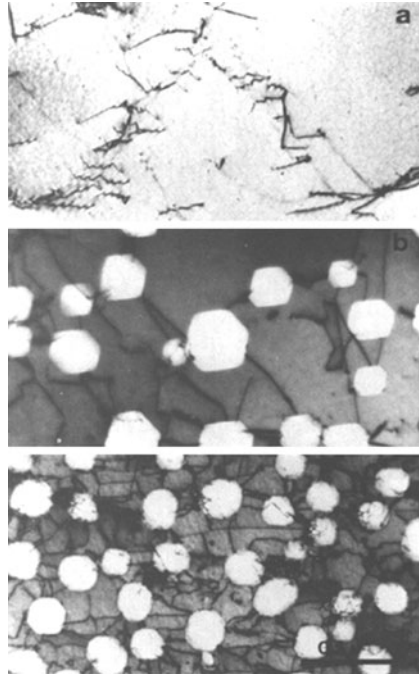
2.2.2 Segregations, Phase Transformations, and Amorphization

Solute Transport and Segregations

In addition to the development of the dislocation network or cavities, the migration of PD's occurring under irradiation has direct impacts on the microstructure, either by forced ballistic mixing, or by the coupling of alloying element and PD fluxes. Radiation-induced segregations (RIS), shifts in phase diagram boundaries, occurrence of new phases, or amorphous transformation can be observed (Russell 1984).

Radiation-induced segregations are due to the coupling of PD fluxes with alloying elements or impurities. The diffusion of PD's results in a net flux of PD's to their sinks, where they disappear. If an interaction exists between a vacancy and a solute, the migration of the vacancy drags the solute in its motion, inducing segregation to the sink. This phenomenon can occur at different scales and on different sinks:

- Free surfaces are perfect sinks for any PD and such transport of solute can be observed on thin samples, such as TEM foils. Following HV-TEM (or heavy ion) irradiation, the free



■ Figure 9

Formation of cavities in Cu irradiated at 500°C with 500 keV Cu ions at $3 \times 10^{-3} \text{ dpa} \cdot \text{s}^{-1}$; oxygen content 30, 70, and 110 ppm (From Glowinski and Fiche 1976)

surfaces of the sample can be enriched of one element, to a large range of concentrations, leading to segregation or, in limit cases to surface precipitations.

- Grain boundaries are strong sinks present in the bulk of large samples. The same mechanisms can induce similar effects and large changes in GB composition have been observed. Such radiation-induced segregations are often combined with a sister phenomenon: the *inverse Kirkendall effect*: The jump of a vacancy from one site to the next one requires the migration of an atom counterpart in the opposite direction. In a solution, the fastest species will be the one the most frequently involved. Thus the flux of vacancies from the bulk of the grains to the GB induces an opposite flux of fast diffusing species from the GB to the bulk. The net result is a depletion of this element at the GB. In stainless steels, for a specific temperature range, the two processes induce an increase of Si and Ni by the former process and a decrease of Cr and Fe by the later. The impact is a lower resistance of the GB to corrosion (see ► 3.2.2).
- Inside the grains, and therefore at a finer scale, similar phenomena occurs with the line sinks formed by the dislocations. The disappearance of the PD in the dislocations results in their climb. But, in addition, in the case of coupling the PD and solute migration, segregation at dislocations can be observed. A very specific phenomenon can be induced when the recombination rate of the PD's is solute concentration dependent. The diffusion of the PD's to the areas of high recombination rate drags simultaneously the solute to this location,

increasing its concentration and thus the local recombination rate. Then a patterning of solute distribution, up to precipitation in the extreme cases, can be observed for specific alloys and temperatures under irradiation (Enrique and Bellon 2000).

The phenomena described above are radiation-induced phenomena that have to be distinguished from radiation-enhanced phenomena. In particular higher diffusion coefficients are observed under irradiation and the kinetics of structure changes due to complex temperature histories may be increased by irradiation. For instance, in two phase alloys, in the case of an increase of solute content at high temperatures, the kinetics of solute depletion in the major phase, or of solute precipitation, can be much faster than thermal recovery. This is for instance the case of (Cu-Mn-Ni) precipitates in pressure vessel steels, for which these elements were homogenized in the temper heat treatment, and the operating temperature is too low of thermal reprecipitation. In a similar way, a very fine precipitation of Nb in Zr-Nb alloys is observed after long irradiations in fuel claddings or pressure tubes. These precipitates could only be observed with thermal treatments of much longer durations.

Phase Diagrams Under Irradiation

With respect to phase diagrams, the classical thermodynamics states that the equilibrium of a system is obtained as the best compromise for the minimal stored internal energy and lowest ordering. This is obtained by minimizing the Helmholtz free energy. To fulfill this condition, the system explores the space of possible configurations by individual changes of atom locations. This is possible due to the Maxwell distribution of the atom energies ($\sim eV$). This allows thermally activated statistical changes in atom locations.

Under irradiation new conditions arise: The system is not anymore isolated, as it receives a continuous flow of energy from the irradiating particles, the concentration of PD is clearly out of thermal equilibrium and the large impulse transferred to the hit atoms allows the exploration of configurations of very different energies ($\sim keV$), giving access to metastable configurations that would never have been obtained thermally. Therefore, a strict treatment of a system under irradiation cannot be performed solely using classical thermodynamics. Indeed the ballistic jumps occur in parallel with the thermally activated ones. Based on the consideration of these two different contributions (thermal and ballistic), specific potentials can be proposed, whose minima allow a description of the state of the system under irradiation (Martin and Bellon 1997).

For a rough approximation of the effect of irradiation on a system, the relative values of the thermal and irradiation diffusion coefficients (D_{th}/D_{irr}) allows to define the effective temperature T_{eff} that gives the shift in temperature to be applied to the equilibrium phase diagrams (Martin 1984). Under generic conditions, a system under irradiation behaves as if it would be at the effective temperature:

$$T_{eff} = T \left(1 + \frac{D_{irr}}{D_{th}} \right). \quad (11)$$

This equation allows rationalizing numerous results of irradiation. At high temperatures, and not too high irradiation flux, the thermal diffusion, large compared to the irradiation contribution, drives the system and the irradiation effects are surpassed by the thermal ones: The system behaves as if it would be without irradiation. For low temperatures and high enough irradiation fluxes, the effective temperature increases drastically and, for instance, in two phase

alloys will tend to disordered state or liquid like, i.e., amorphous. This approach can only be used as a “rule of thumb” in order to explain or forecast structures, but in numerous cases the predications are surprisingly accurate.

Extensive reviews of the phase changes under irradiation are available and different behaviors have been reported (Russell 1984).

- At low temperatures, the irradiation can induce the jump of atoms out of the precipitates by ballistic mixing, at a rate larger than the reformation of the precipitate. A homogeneous structure is finally obtained with a ballistic re-resolution of the fine precipitates.
- Phase boundaries are shifted leading to higher solubility under high irradiation fluxes.
- Unexpected phases can be observed, thermally unexpected.
- Lastly amorphous transformation can be observed, usually in compounds.

The amorphous transformation under irradiation has been first observed on U_6Fe precipitates in metallic U matrix, that itself remained crystalline (Bloch 1962). This first observation raised the importance of the disorder build-up as the driving force for the amorphous transformation. The amorphous transformation is easily obtained in compounds and especially in ionic ones (► Sect. 2.3). The basic mechanisms of the amorphous transformations are still only partly understood and deserve further investigation.

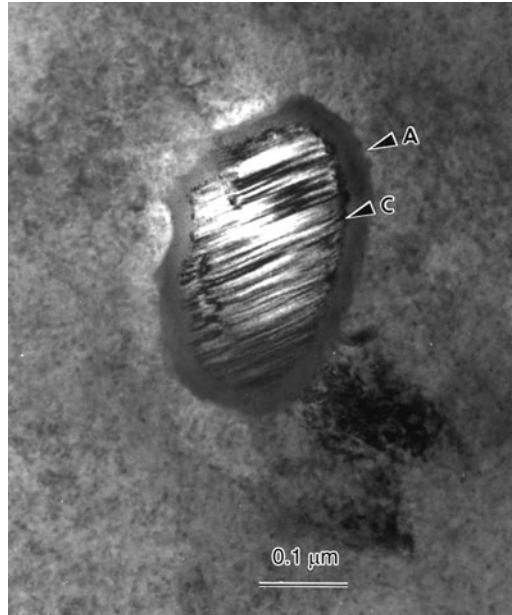
A minimal irradiation dose is required for amorphous transformation. The irradiation dose for amorphous transformation decreases at low temperatures, but a limit is observed above which amorphous transformation cannot be observed anymore. This dose is crystallographic structure dependent and large differences can be observed on similar compounds.

It can occur locally at the cascade location and, as the irradiation proceeds, covers all the material, or start at an interface and grow to the bulk of the grain or precipitate. ► Figure 10 gives an example of an amorphous transformation occurring in a $Zr(Fe,Cr)_2$ precipitate embedded in a Zr matrix (Motta et al. 1991). An amorphous layer is observed that grows at constant speed (about $10\text{ nm} \cdot \text{dpa}^{-1}$) and absorbs the crystalline core (Motta and Lemaignan 1992). The consequences of this amorphous transformation on the chemical evolution (release of Fe to the matrix), corrosion behavior and accelerated growth will be described in the Zr section (► 4.2.4).

2.2.3 Computational Techniques for Nuclear Material Science

The development of computer simulations of physical phenomena is increasing in any scientific field. Material sciences do not avoid this tendency, with significant success. In the specific case of nuclear materials, the cost, difficulties, and durations of experiments on irradiated materials increase the interest of such developments. In addition the importance of phenomena occurring at atomic scales (e.g., PD creation and mobilities, intra cascade behavior, or clustering) requires reaching descriptions of the phenomena at these scales. Therefore a large volume of R&D has been devoted to the area of computational materials science focused in nuclear materials and irradiation effects.

Although typical results provided by these techniques are presented throughout this entire chapter, this section intends to describe the basics of the different procedures used in these computations. Starting at the cohesion of atoms, using quantum physics approaches, they scale up to the collective strain behavior of a cluster of grains under applied stresses.



■ Figure 10

Amorphous transformation of a $\text{Zr}(\text{Fe}, \text{Cr})_2$ precipitate induced by neutron irradiation (From Motta et al. 1991)

First Principle (Ab Initio)

The basis of the ab-initio techniques is to solve the Schrödinger's equation on a given number of atoms. The inputs are simply limited to the location of the nuclei, assumed to be immobile, and their charges. The computation of the orbitals leads to the energy of the systems, for this geometry. The changes in energy with changes in geometry allow computing the interatomic potentials. Since any geometry can be assumed, such as different crystallographic phases or the presence of PD (vacancies, interstitials, or different atoms), the most stable phase can be predicted, as well as the formation energies of the different PD. Relaxation of the initial structure is required in order to obtain the real configuration and not to maintain the initial geometry assumed for the structure. Migration energies can be obtained by forcing the migration of one atom from a site to a new one.

Unfortunately the Schrödinger's equation cannot be solved analytically and the exact numerical solutions would require computation resources far behind the capabilities available in a foreseeable future. Therefore approximations are required to simplify the computation:

- Only the valence electrons are taken into account to solve the equation, i.e., the core electrons are treated as producing potentials only, being approximated by their fundamental state.
- The interactions of the electrons between each other are treated using the density functional theory (DFT) (Kohn and Sham 1965). This theory states that the energy of a system of electrons is a functional of the electronic density only. This approximation does not allow the consideration of the contribution of motion correlations and energy exchanges between electrons in the computation of the energy. Improved accuracy is obtained with a fine description

of the electron density (local density approximation – LDA) or by considerations of the gradient in electron density (generalized gradient approximation – GGA).

Various codes are now available for such computations (SIESTA, WASP, etc.). Their use requires a good skill in interpreting the results, especially in the case of transition metals, of magnetic materials or ionic compounds. However they provide data of high values for the knowledge of PD energy and migration. A typical result can be given by the computation of migration energies of various interstitial clusters in Fe that perfectly match the experimental peaks observed during thermal recovery of pure Fe irradiated at low temperature (Fu et al. 2005).

Molecular Dynamics

The molecular dynamic simulation computes the trajectories of a large set of atoms maintained in a given volume, and interacting between each others according to interatomic potentials. The system of equations to be solved is simply the equation of motion for each atom:

$$m_i \frac{\partial^2 r_i}{\partial t^2} = \frac{\partial U(r_{i,j})}{\partial r_i}, \quad i = 1, \dots, N \quad (12)$$

where m_i is the mass of the atom, r_i is its position in space, and $U(r_{i,j})$ is the potential energy function.

The critical point is the description of the interatomic potential $U(r_{i,j})$. Usually empirical pair potentials are used, that describes the interaction as a simple function of the interatomic distance. The parameters describing the potentials are tuned to the bulk properties, such as crystallographic data, elastic constants or other specific properties. In the case of computations aiming at irradiation effect simulations, care should be taken for a good description of the repulsive part of the potential, as it contribute strongly to the behavior of interstitials, and is poorly assessed from bulk properties.

The MD techniques have been used very early for a detailed understanding of the damage evolution in cascades, or displacement energies for low energy impacts. Among the first uses of the MD computations, descriptions of cascades have been undertaken (Gibson et al. 1960). They were initially limited to very low pka energies (a few 100 eV), but have continuously been increased in number of atoms and pka energies. The current computations consider very large sets of atoms (several millions) allowing the study of large cascades induced by the high energy pka's produced by fast neutrons (Bacon et al. 2000). The time evolution of the cascades gives information on the number and states of the surviving PD after thermal recovery of the cascade (Fig. 3). The required computation times restricts analyzing the dynamic behavior for only a few 10^{-12} s. at most. In order to compute the average number of surviving PD during irradiation, a large number of computations have to be performed for various pka energies, impact orientations and temperatures (Fig. 4). These results are used as input for the kinetic evolution of the PD (8) (Osetsyky et al. 2002).

The MD techniques have been used to analyze the dynamic behavior of dislocations, either alone in perfect crystals, to compute the friction stresses versus temperature, mechanisms of Peierls friction during glide, or interaction of a gliding dislocation with a cluster of PD's, such as dislocation loop or stacking fault tetrahedra (Rodney and Martin 2000).

Monte Carlo

The Monte-Carlo method is used when a statistical description of the phenomena is sufficient and there is no specific requirement for a deterministic approach. For the simulation of microstructure evolution, a set of configurations is generated as input and its evolution is analyzed with time, considering the probability of change from one configuration to the next one. A random number generator is used to test if the transition should occur, according to its probability of occurrence. The latter is obtained from the knowledge of the energies of the configurations. For instance, the jumps of an atom from one site to the next vacancy has a probability of occurrence of $\exp(-\Delta H/kT)$ and a frequency of attack given by the Debye frequency. The knowledge of the activation energies for each process of configuration changes is therefore the most critical point.

Among the phenomena studied with the MC methods, significant success have been obtained on the migration of PD, diffusion, clustering of PD and solute atoms (Vincent et al. 2008), including GB segregation (Soisson 2006), swelling, or growth (► Fig. 11).

2.2.4 Impact of Irradiation on Engineering Design Properties

Irradiation effects on the engineering properties of materials have been considered and observed since the early days of the nuclear industry. Changes in geometry (due to swelling or growth), increase in yield strength and reduction in ductility, or irradiation enhanced creep are the most frequent changes reported. The aim of this section is to give a general overview of the mechanisms involved in these processes.

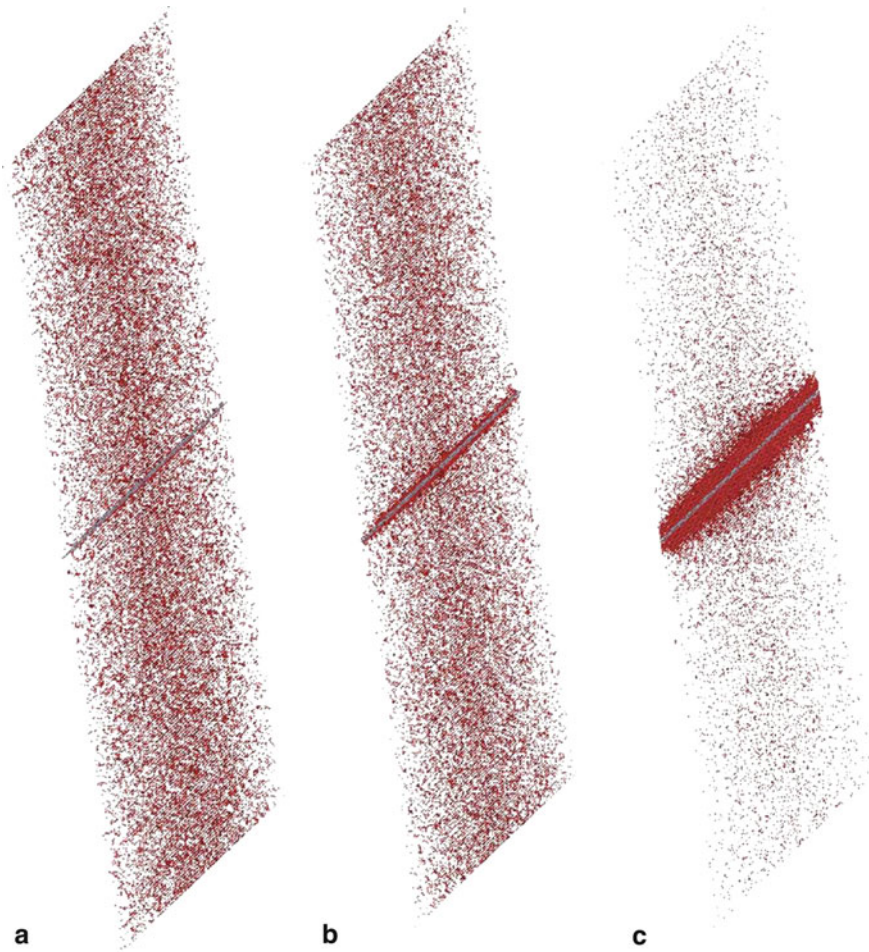
Thermoelastic Properties

Irradiation has not observable impact on the elastic properties, except the special case of swelling, where the presence of cavities or bubbles reduces the stiffness of the materials in proportion to the reduction of solid fraction. For fractional volume of cavities below 15%, the reduction of equivalent Young modulus can be expressed as (Kachanov 1993):

$$E(\pi) = E_0 (1 - k\pi) \quad (13)$$

where π is the porosity and k is a coefficient function of pore sizes and shapes. For $\pi < 0.15$ and spherical cavities, typical values of k would be: $k \sim 2-2.5$. Since the heat flow in a thermal gradient corresponds to the same type of continuous behavior under a constant potential, a similar degradation of the heat conductivity λ_{th} with porosity is expected and is observed (Cunningham and Peddicord 1981). These irradiation effects induce mandatory corrections for design considerations in the case of the high heat flows found in fuel pellets and claddings.

The thermal expansion coefficients are not affected by irradiation, for the same reason as the absence of effect on the modulus of elasticity: both quantities relate to collective interatomic behaviors induced by the curvature of the interatomic potential. Even if the irradiation has induced numerous PD's and changes the microstructure, as described above, their densities are far too small to affect the mean interatomic distances and therefore E or ν .



■ Figure 11
Monte Carlo simulation of the grain boundary segregation in an A-B alloy at different irradiation damage (From Soisson 2006)

Radiation Hardening and Plastic Behavior

The buildup of isolated PD's in the crystals due to the irradiation has limited impact on mechanical strength, and concerns only pure metals at low temperature. Indeed such sort-range obstacles induce only local interactions with the dislocations, and their pinning strength is reduced by thermal activation. However PD hardening has been observed on Al and Cu single crystal irradiated with high energy electrons and tested below 30 K. The irradiation conditions allowed only PD's to be created and no clustering occurred. The increase in yield strength has been found to increase proportionally as the square-root of electron irradiation dose and was attributed to the presence of the interstitials (Ono et al. 1968). This increase in yield strength, only due to high concentration of isolated PD, remains of limited impact for engineering aspects. The major effects in mechanical properties to be considered are restricted to

the effects induced by the changes in microstructure resulting from PD clustering, as described below.

The basic mechanisms of radiation hardening are related to the formation of various types of PD clusters that act as pinning centers for the dislocations. The consequence is an increase in yield strength with irradiation dose.

Following the classical dislocation theory, any crystallographic defect along the glide plane of a dislocation induces a force to the dislocation, reducing its mobility. The increase in shear strength is given by the following relationship:

$$\Delta\tau = \frac{\alpha\mu b}{L} \quad (14)$$

where μ is the shear modulus of the crystal, b is the Burgers vector of the dislocation, and L is the average distance between obstacles along the gliding plane. α is defined as the strength of the obstacle, always lower than 1, but with actual value depending of the obstacle types, as discussed later.

In the case of the typical obstacles obtained after irradiation, i.e., dislocation loops, the separation distance between the obstacles can be deduced from the loop diameter d , and loop density ρ_L : $L = (d\rho_L)^{1/2}$. In the case of a forest of dislocation of density ρ_\perp , this expression reduces to $L = (\rho_\perp)^{1/2}$.

Expressed in engineering terms of yield strength, the irradiation-induced microstructure defects are the sums of all the hardening due to all the types of PD clusters and larger defects.

In the case of small loops and small clusters, the increase in yield strength is thus given by the following relation:

$$\Delta\sigma_Y = M\alpha\mu b(d\rho_L)^{1/2} \quad (15)$$

and in the case of a dislocation forest:

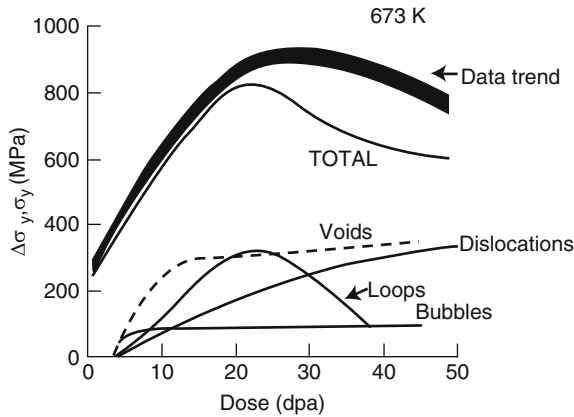
$$\Delta\sigma_Y = M\alpha\mu b(\rho_\perp)^{1/2} \quad (16)$$

In these expressions M is the so-called Taylor factor that links the shear strength on a given glide plane of a single crystal τ , to the yield strength of polycrystals ($M \approx 3$ for alloys of interest (Lucas 1993)).

The strengths of each type of PD clusters differ according mostly to their sizes. For large voids or precipitates, the strength α is close to 1 and there are considered as strong obstacles. Medium strength obstacles correspond to Frank loops in fcc alloys or fine loops in bcc and dispersion phases ($\alpha \approx 0.3-0.4$), while dislocations and very small loops and clusters are considered as weak barriers for the dislocations ($\alpha \approx 0.12-0.22$).

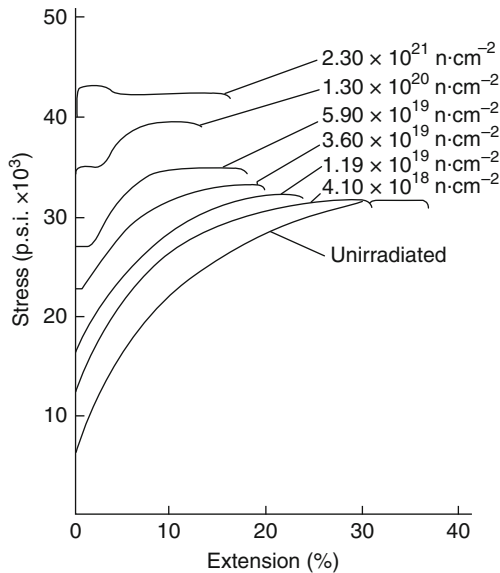
Knowing the distribution of the PD clusters obtained after irradiation the contribution of all these clusters to the reduction of mobility of the dislocations can be computed. An increase in yield strength can be explained, and the results follow, at least qualitatively, the actual behavior of the alloys after irradiation. Typical example of such analysis can be found in [Fig. 12](#).

In addition to the increase in strength, large changes in plastic behavior are often observed. The strain hardening is drastically reduced, the plastic deformation is more localized and the uniform and total ductility are reduced ([Fig. 13](#)). This behavior is explained by the different behavior of the dislocations during plastic strain for unirradiated and irradiated materials. For the former, the interaction of dislocations with obstacles (other dislocations, precipitates, etc.)



■ Figure 12

Computed contribution of the different mechanisms to radiation hardening in austenitic SS irradiated at 673 K (From Lucas 1993)



■ Figure 13

Irradiation hardening of pure Cu under fast neutron irradiation (From Makin 1967)

leads to the multiplication of dislocations, and therefore to a general trend in strain hardening, and large uniform elongation, up to necking. In the case of irradiated materials, however, the interaction of the dislocations with the irradiation-induced obstacles (loops, clusters of PD's, etc.) can lead to the annihilation of these defects. The obstacles responsible of the radiation hardening are therefore removed in the areas of plastic deformation and easy, localized plastic deformation is observed (➤ Fig. 14).

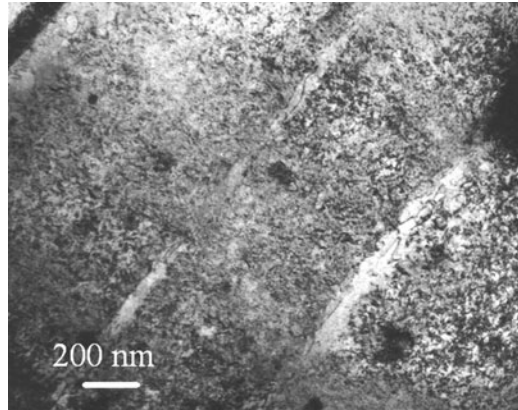


Figure 14

Channeling on Zry4 strained at RT after neutron irradiation in a PWR (From Regnard et al. 2002)

A reduction of the value of the hardening exponent is observed (it can reduce to almost 0) inducing a drastic reduction in uniform ductility. However, such reduction of uniform elongation does not correspond to an embrittlement. The local strain in the areas of localized deformation remains very high and the engineering strain reduction is only due to the drastic reduction of the volume concerned by plastic strain. Strains larger than unity have indeed been reported in the location of intense dislocation glide, such as the channels.

Various mechanisms of interactions between radiation defects and gliding dislocations have been proposed for the elimination of these loops. The general trend is an inclusion of the loops in the gliding dislocations, resulting in a jog, or a drag of the loops along its gliding cylinder, out of its initial position (Lucas 1993). Molecular dynamics computations have confirmed the physical processes and inclusion of interstitial loops in gliding dislocations have been simulated (Rodney and Martin 2000).

On a larger scale, discrete dislocation dynamics allowed simulating the pinning of dislocations by irradiation-induced clusters of defects, subsequent unpinning as defects are absorbed by the dislocations, and cross-slip of the latter as the stress is again increased. Loop free channels were also obtained, the width of which remaining limited by the interaction among opposing dislocation dipole segments and the remaining defect clusters (Diaz de la Rubia et al. 2000).

Embrittlement and Reduction in Ductility

In addition to the reduction of uniform ductility described above, which is due to the intrinsic plastic strain behavior of the irradiated materials, specific mechanisms of embrittlement can be observed in irradiated materials.

One major concern with respect to the irradiation embrittlement relates to the case of bcc materials (e.g., structural steels such as pressure vessel steels or vanadium alloys considered for specific components of fusion reactors). For this crystallographic structure a transition exists in fracture behavior, between brittle at low temperature, governed by cleavage, and ductile fracture with plastic strain and dimple fracture at higher temperatures. The competition of the two

mechanisms occurs at a given temperature, for which cleavage is easier than plastic deformation. Indeed, in bcc crystals, the plastic strain mechanisms are highly thermoactivated and the stress level for plastic strain increases strongly as the temperature is reduced or the strain rate is increased. The cleavage stress however remains practically independent of the temperature. The transition is referred as the ductile–brittle transition temperature (DBTT). It is measured by the simple Charpy test or more advanced techniques such as the fracture toughness curve (K_{IC}) or the Pellini drop weight test (RT_{NDT}).

Any process by which the stress required to activate plastic strain is increased enhances the tendency for easier cleavage compared to ductile plastic deformation. The formation of various types of PD clusters induced by irradiation is one way of increasing the yield strength of the alloys. This results in a shift in the DBTT to higher temperatures, known as radiation embrittlement. In the case of typical pressure vessel steels, for light water reactors, this shift is of the order of 0.6 K for each MPa of increase in yield strength. Shifts as high as 150–250 K can be observed for steels prone to radiation embrittlement. Such major changes in mechanical properties have to be strictly controlled and monitored in industrial reactors, and this phenomenon remains a major source of concern for the designers and operators. Therefore a detailed description of this phenomenon and the procedures used to deal with will be given in [3.1.3](#).

For the fcc crystallographic structures, not concerned by the DBTT, irradiation embrittlement can be observed. The main origins of this complex phenomenon, are due to the production of He by (n, α) reactions, and to the swelling (see [4.1.2](#)), or to channel deformation mechanisms. In austenitic SS, large reductions in ductility are observed, whose values are strongly dependent on irradiation and testing temperatures.

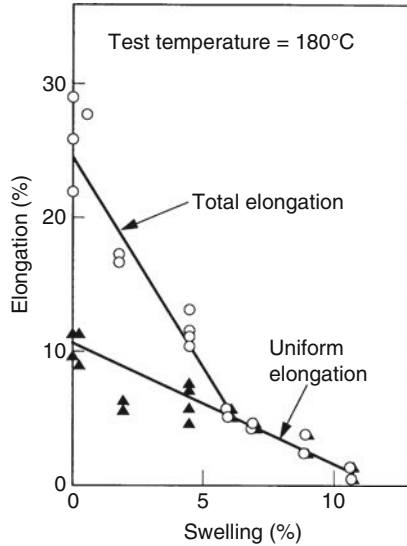
For irradiation and testing near 350–400°C, channel fracture is reported, where the planar transgranular fracture occurs along glide planes. These planes are the former loop free channels described in the previous section (Hamilton et al. 1987).

For alloys irradiated at the maximum swelling rates (420–470°C), the reduction in ductility is directly correlated to the swelling. Above 6% swelling, the uniform and total ductility's are equal, i.e., the ruptures occur without reduction of area. Above 10% swelling, the ductility cannot be measured anymore and the fracture is brittle ([Fig. 15](#)) (Fissolo et al. 1990). Numerous cases of brittle failure have been reported during handling in hot cells, for highly swelled steel (above 15%) (Neustroev and Garner 2009). The loss of ductility is clearly linked to the cavities formed during swelling that act as nucleation centers for the dimples of the locally ductile fracture. Some effects of segregation of Ni on the surface or the cavities, inducing a local formation of brittle martensite has also been observed and could contribute to the irradiation embrittlement (Hamilton et al. 1987).

Irradiation Creep

Under nonhydrostatic stress, at moderate temperature, a specific creep phenomenon is observed under irradiation. The irradiation creep rate can be much larger than for thermal creep and has to be considered in detail for operation design. The mechanism of creep rate increase under irradiation is not directly due to an increase in diffusion or vacancy concentrations, but to the impact of the anisotropic flux of interstitials on dislocations, where they disappear, inducing their climb.

The stress-induced preferred absorption mechanism of irradiation creep has been proposed and improved continuously (Mansur 1979). In the early approaches, the basic mechanism is the change in bias induced on the edge dislocations with respect to their orientation with respect



■ Figure 15

Correlation between loss of ductility and swelling in various 316 Ti SS irradiated in the Phénix SFR (From Fissolo et al. 1990)

to applied tensile or compressive stress. The differences in interaction energies between an interstitial and two edge dislocations, parallel and perpendicular to the applied stress, is proportional to the magnitude of this stress. Considering the balance in the fluxes of interstitials and vacancies to these dislocations, a climb velocity can be computed, which, averaged over all the dislocations, leads to a macroscopic deformation rate:

$$\dot{\epsilon}_{\text{SIPA}} = \alpha c_i D_i Z_{0i} \frac{\sigma}{\mu \Delta \Omega_i} \rho_{\perp} \quad (17)$$

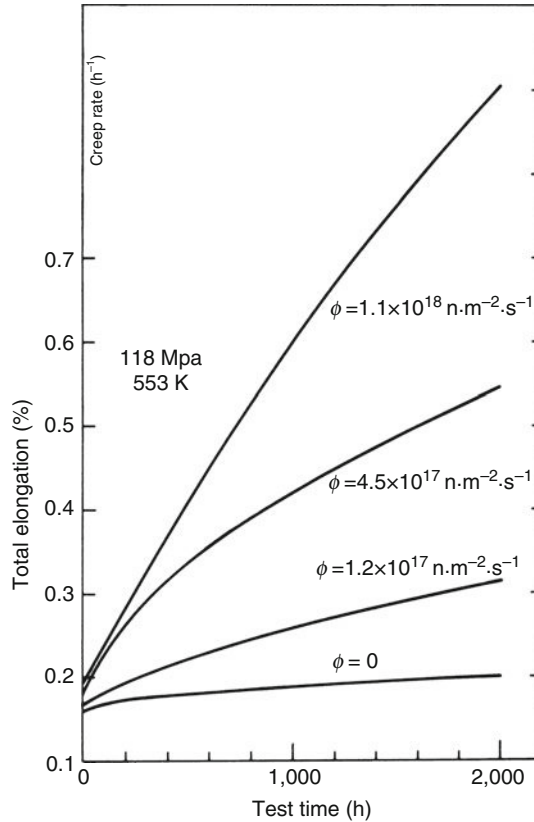
where α is a geometrical factor, c_i is the flux of the interstitials, D_i is proportional to the irradiation flux ϕ , and $\Delta \Omega_i$ is the elastic distortion induced by an interstitial. This expression can be reduced to a simple linear relation between strain rate, applied stress, and irradiation flux:

$$\dot{\epsilon}_{\text{SIPA}} = K_1 \sigma \rho_{\perp} \phi \quad (18)$$

An example of irradiation creep on Zry cladding pressurized capsules irradiated in a test reactor is given in ► Fig. 16. A clear linear dependency of the creep rate with the flux intensity can be observed.

In the case of formation of cavities and swelling, the biases at cavity surfaces and dislocations allow a net difference between interstitial and vacancy fluxes to the dislocations, inducing their climb. They can then be unpinned from the obstacles and glide along the slip plane, under shear component of the stresses (Matthews and Finnis 1988). This “climb and glide” type of irradiation creep has many variants, but all reduce to similar simple expressions:

$$\dot{\epsilon}_{\text{CG}} = K_1 \sigma^2 \rho_{\perp}^{1/2} \phi \quad (19)$$



■ Figure 16

Irradiation creep of CW Zry2 at different neutron fluxes showing the linear dependence of strain rate with flux (118 MPa, 553 K) (From Fidleris 1988)

The stress and dislocation density dependency of the creep rates of these two mechanisms are different. However both are temperature independent and, compared to the thermal creep, have a low sensitivity to the applied stress (exponent between 1 and 2). Therefore irradiation creep is mostly observed at low temperatures and low stresses. At higher temperatures and stresses, the thermal creep out pass the irradiation creep rates.

2.3 Irradiation Damage in Ceramics

2.3.1 General Aspects

The reactor components are mostly made out of metallic alloys. However ceramics are also present and their behavior under irradiation should be analyzed. The different types of materials to be considered is increasing as new reactor designs appear. The most important ceramic to consider is the fuel itself: UO_2 , mixed oxide and other compounds such as carbides or nitrides.

Important from the neutron physics point of view, the absorbents, such as pellets of boron carbide (B_4C), are also ceramics used for the nuclear reaction control. For these specific materials, a strong contribution of the chemical changes (fission products, He production by (n, α) reactions, etc.) impacts the behavior under irradiation.

A renewal of the interest of the ceramics as structural materials for nuclear application is linked to the development of new designs for power reactors operated at high temperatures, to the concern with end of cycle (waste management, storage, and recycling) and to the R&D connected to fusion devices: High-temperature reactors use silicon carbide (SiC) for fuel particle claddings and the fusion devices require insulators or transparent windows, such as alumina or silica, or tritium breeding ceramics, such as Li_4SiO_4 or variants. The selection of the waste immobilization matrixes is still an open matter, but natural or advanced ceramics are strongly considered and their long term stability under self irradiation remains a critical criterion (Weber et al. 1998).

Most of the engineering properties of these materials are described in detail in the relevant chapters of this Handbook of Nuclear Engineering (➤ Chaps. 6, ➤ 7, ➤ 10, ➤ 19, ➤ 21, ➤ 22 and ➤ 24). However common mechanisms control their behavior under irradiation and their generic aspects deserve to be described in details, due to a few specificities compared to metallic alloys.

Indeed sharp differences exist between ceramics and metallic alloys that affect strongly the mechanisms of irradiation damage build-up and recovery:

- The type of interatomic bonding: ceramic materials exhibit either ionic or covalent bonds, or any mixture of them. A consequence is that their valence electrons are strongly localized (they behave as insulators) and, due to the absence of free electrons, any electronic damage is hardly recoverable and may remain as a local charge defect, a configuration nonexistent in alloys. Therefore ionizing irradiations could induce damage, either as local charge defect or by atomic displacement induced by these local charge defects.
- Ceramics are usually compounds of several chemical species, each with each own charge state (cations and anions). Their crystallography may be complex, due to the balance between Coulomb interactions and geometrical packing. Thus, the crystals may be considered as compact (e.g., MgO), open or complex. Indeed, the conservation of stoichiometry may require that possible positions are not occupied (e.g., 1/3 of the octahedral Al sites in Al_2O_3 are empty). Such crystallographic constraints affect the displacement mechanisms or point defect configuration (e.g., very high energy of any antisite) (Pells 1994a). In addition, if the bindings have significant covalent contributions, their directionality has to be taken into account.

2.3.2 Irradiation Damage

Ionization mechanisms, described below, may induce atom displacement in specific materials such as alkali halides or silicon oxide (Hobbs et al. 1994). Radiolytically induced displacements are obtained when an anion is ionized and recombines with another anion to build a molecule such as Cl_2 (in NaCl) or O_2 (in SiO_2), occupying the site of one former anion (H center) or forming a peroxy linkage $-O-O-$ between Si atoms, leaving an empty O site (E' center), charged with one or two electrons. Such recombination's, energetically more favorable than the charge mismatch at lattice location, are very efficient in these materials. They lead to migration of atoms, without transfer of momentum to the nuclei.

■ **Table 2**

Displacement energies for various oxides {computed values, questionable}

Compound	UO ₂	Al ₂ O ₃	ZrSiO ₄	La ₂ Zr ₂ O ₇	MgO	MgAl ₂ O ₄
E_{d-O} (eV)	20	65	38	38 and 68 (2 # sites)	60	60
E_{d-M} (eV)	40–59	20	90(Zr) 92(Si)	150(La) 188(Zr)	53	20–30
References	Weber et al. (1998) and MacEwen et al. (1984)	Weber et al. (1998) and Pells (1994)	Meis (2001)	Chartier et al. (2003)	Weber et al. (1998) and Wilks (1968)	Weber et al. (1998) and Summers et al. (1980)

Due to this process, measurements of the displacement energies in these materials are difficult: Indeed, during electron irradiation, a displacement may be induced by electron–electron interaction, inducing ionization and activating the process described above, while the momentum transfer to the nucleus remains below the displacement energy (Zinkle and Kinoshita 1997).

Displacement energies are often very different for the different ionic species. No general rules can be given and the highest E_d can correspond to any ion. ▶ **Table 2** summarizes typical displacement energies for ionic compounds. The crystallographic structure explains at least qualitatively this behavior: The presence of an empty site in the vicinity of the displaced ion allows easy migration and reduces its displacement energy. For instance, Al ions in Al₂O₃ have an occupancy of 2/3 of the sites and the corresponding displacement energy ($E_{d-Al} = 20$ eV) is low compared to 65 eV for O. However in the fluorite structure of UO₂, the occupancy of the octahedral sites of U is only 1/2, but the O ions are easier to displace: $E_{d-O} = 20$ eV for O in UO₂ and 53 for U (Meis and Chartier 2005).

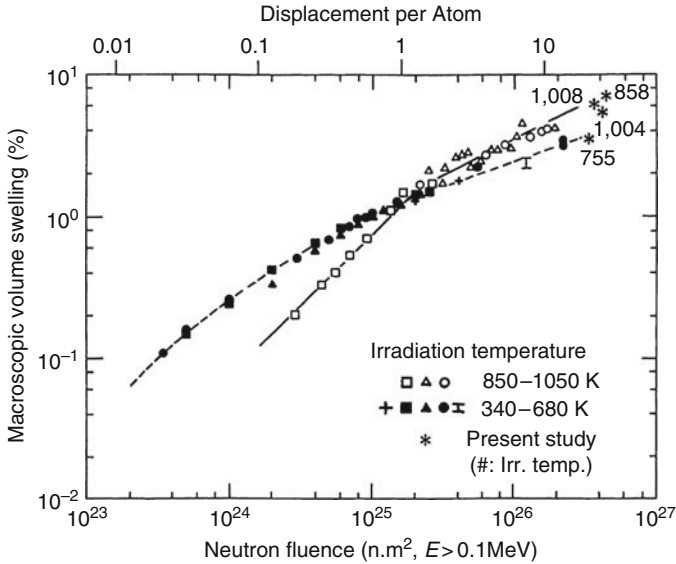
Due to the largely different displacement energies of the different ions, electron irradiations can be performed at accelerating voltages allowing the displacement of only one given type of ions. Then, large unbalance in point defect production occurs, with Frenkel pairs of only one species, and then the PD production does not respect the stoichiometry. Due to the fact that all these PD have the same charge, they cannot cluster to form loops, unless Coulomb interactions induce migration of the ions of opposite charges in order to maintain electroneutrality. Then dislocation loops of large Burgers vectors, requiring the migration of both the cations and the anions, can be observed, even if the ballistic displacements occurred only for one type of ions (Stathopoulos and Pells 1983).

For high energy transfers and development of cascades, an even formation of PD of the different species is roughly obtained. However, contrarily to metals and alloys, the recombination of a vacancy and an interstitial is not possible for PD's of different natures. The Coulomb energy of such antisite would be much larger than the elastic energy of a PD and the balance is in favor of either molecular interactions, as described above with clusters of atoms in metallic state and O₂ molecules in gaseous phase, or major recombination and Coulomb-induced displacement of ions, with loop formation. However their nucleation is very difficult, due to their large Burgers vectors required to avoid space charges (Pells 1994b).

2.3.3 Changes in Microstructure

Macroscopic behaviors induced by irradiation damage in ceramics are very different according to the crystallography and properties of the different compounds:

- A few compounds appear to be very resistant to any irradiation damage. Spinel (MgAl_2O_4), for instance, appears to be very resistant to irradiation, and only scarce complex dislocations have been observed after high temperatures irradiation at high doses (Hobbs et al. 1994). Swellings reported for spinel, if any, remain within the measurements scatters (Konings et al. 1998).
- No visible, or very limited, damage induced by point defects (dislocation loops or cavities) can be observed in specific compounds, such as UO_2 or B_4C , when irradiated in conditions preventing nuclear reactions (e^- or ion irradiations). Under neutron irradiation, their evolution is due to the production of high quantities of insoluble fission gases (Xe, Kr, or He). In UO_2 , the high mobility of O^{2-} ions allows easy recombination of O Frenkel defects, improving the resistance to irradiation damage. Irradiation of CeO_2 , a similar structure without nuclear reaction revealed only a low density of dislocation loops (Konings et al. 1998). In B_4C , the PD are assumed to be too mobile, even at low temperature, to allow nucleation of clusters (Stoto et al. 1985), and the damage observed is only due to the clustering of He atoms as helium bubbles, that tend to exhibit a disc morphology with the plane of the discs parallel to (111) (Jostsons et al. 1973). Strong lattice strain fields ($\epsilon > 5 \times 10^{-3}$) around the lenticular bubbles evidenced a high internal pressure, above 5 GPa (Stoto et al. 1990). The high density of these lenticular bubbles induces swelling as high as 15% for He atom creation above 10^{28} m^{-3} . The high strain field associated with these pressurized bubbles can be released by thermal annealings above 1,400°C (Simeone et al. 1999), but the swelling, and the microcracking induced remains a matter of concern for long term operation of B_4C control rods in FBR.
- Dislocation loops may be observed on several ceramics, with very different densities according to irradiation conditions. The ability to develop dislocation loops is correlated to the complexity of the crystalline structure: size of the Burgers vector, atomic packing dependency of the stacking fault energy, mobility of the different types of PD's (Hobbs et al. 1994), etc. Loops are easily observed in MgO after any type of irradiation, without any dimensional change. Grain boundaries are assumed to be efficient sinks for PD, impeding swelling (Pells 1994a). For Al_2O_3 , the behavior is slightly more complex. Loops are also observed at low doses, but swelling is observed at high doses (Pells 1994b). The lattice parameter measured in the dislocation sink regime shows an expansion in the c -axis, induced by the clustering of interstitials along the basal planes. Since the usual processing of alumina does not induce any crystallographic texture, this anisotropic behavior does not induce growth. However the anisotropic grain dilation leads to extensive grain boundary separation, due to strain incompatibility between adjacent grains (Hobbs et al. 1994). Above ~ 0.3 dpa, at 950 K, voids nucleate randomly and act as sinks for vacancies. They tend to order as planar arrays of cavities along the c -planes above 10 dpa. Swelling larger than 5% can be observed above 5 dpa (🔍 Fig. 17). As for alloys, swelling is restricted to a narrow temperature range. For zircon (ZrSiO_4), swelling up to 15–20% has been reported in Pu doped materials and in natural minerals, and has been shown to be induced by α self-irradiation when He content is above 1,000 appm (Weber et al. 1998).



■ Figure 17

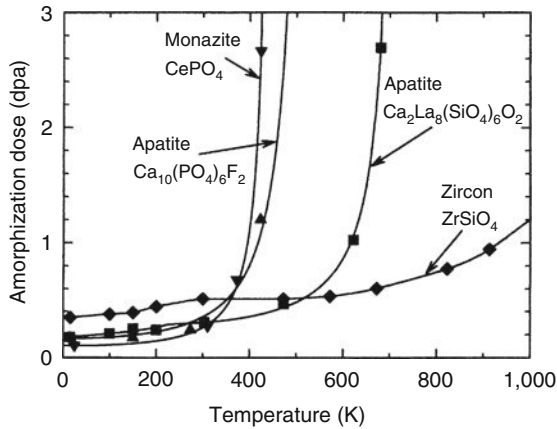
Macroscopic volume swelling of alumina as a function of neutron fluence (From Pells 1994; updated by Yano et al. 2000)

- Amorphous transformation is frequent in ceramics irradiated at temperatures low enough to avoid thermal recovery. Usually easier amorphization occurs in materials where recovery is difficult. This corresponds to a balance between PD formation and migration energies (Chartier et al. 2003). Analyzed in detail for silica, zircon, and several materials of potential interest for waste immobilization, different mechanisms of amorphous transformation have been identified:
 - Progressive accumulation of PD's and homogeneous transformation
 - Interface controlled reaction, leading to linear dose dependence
 - Cascade overlaps (a process occurring in zircon)
 - In-cascade amorphization (apatite)

Each process has its own dose dependence, and they have been indeed identified. Typical values of the dose for full amorphous transformations are in the range of fractions of dpa to a few dpa (► Fig. 18). In the case of silica (quartz SiO_2), the amorphous transformation leads to vitreous silica, with an increase in specific volume of 14% corresponding exactly to the change in density between the vitreous and crystallized forms of SiO_2 (Weber et al. 1998).

2.3.4 Change in Properties

In additions to the changes in geometry described above, important physical properties are affected by the irradiation. The heat conductivity is usually degraded after irradiation due to a combination of PD's (or nuclear reaction products) acting as diffusing centers for the phonons



■ Figure 18

Temperature dependence of amorphization for several compound irradiated with 1.5 MeV Kr⁺ ions (From Weber et al. 1998)

(e.g., alumina (Pells 1994b)) or to the presence of cavities or bubbles acting as thermal barriers for heat flow (e.g., B₄C (Stoto et al. 1990)). Mechanical property measurements in ceramics are too much procedure dependent in such brittle materials for quantitative reliable measurements. The general trends of hardening and reduction of fracture strength with dose are even questionable (Pells 1994b).

A change in electrical conductivity after irradiation has been observed in pure aluminum oxide (Al₂O₃), after a few 10⁻⁵ – 10⁻³ dpa, depending of dose rate, when the irradiation is performed under a strong electrical field (~10⁵ V · m⁻¹) (Hodgson 1994). The effect called “radiation-induced electrical degradation” (RIED) has been observed in different oxide ceramics as a large and permanent increase in the electrical conductivity of ceramics, only if they have been irradiated under a large electric field applied (Hobbs et al. 1994). RIED is clearly observed in many other ceramics, and appears to be frequent in doped materials. This phenomenon differs from of radiation-induced conductivity (RIC) phenomenon (described in the next section), in that the increase in RIED conductivity persists after the radiation is stopped.

The RIED phenomenon has been studied by many research groups, with extreme variability in the results, therefore it remains controversial. For the single case of alumina, minor changes in purity allowed to report conductivity after irradiation (10⁻³ – 10⁻¹ dpa under an electric field of 1–5 × 10⁵ V · m⁻¹) varying from no measurable changes to an increase in conductivity up to 10⁻⁴ S · m⁻¹ (Zinkle et al. 1997). The discrepancies in the results reflect the lack of understanding of the phenomenon. Differences in chemistry of the materials, irradiation conditions and sample geometries have been claimed to rationalize the different behavior observed. No common agreement can be found with respect to this phenomenon. The absence of any sound understanding of RIED rises questions with respect to the capability to forecast the behavior of such insulators for fusion device applications (Hodgson 2002).

Various explanations for the occurrence of RIED have been proposed, and seem applicable to specific cases, but should be considered with caution, as no common behavior can be considered (Kinoshita and Zinkle 1996). They are linked to the following phenomena:

- Formation of colloids under irradiation, with small metallic precipitates, that would enhance the electronic conductivity
- Electron fast diffusion along various dislocations, whose cores would have high local charge defects
- Large electric fields around PD's, allowing dielectric breakdown
- Space charge induced by PD clustering and internal microcracking providing short circuits on the bulk of the materials

2.4 Irradiation Damage by Photons and Electrons


2.4.1 Radiation-Induced Conductivity in Ceramics

The irradiation of insulators such as ceramics or polymers by electrons or γ photons has a strong impact on the electrical conductivity of these materials. The RIC occurs due to the transfer of valence electrons to the conduction band. Under γ (or e^- , H^+ , etc.) irradiations, the interaction of the irradiation particles with electrons results in the formation of electron-hole pairs. The free electron, whose typical lifetimes are of the order of $10^{-11} - 10^{-9}$ s, can migrate under the applied electrical field and allows charge migration, i.e., a significant conductivity is observed (Hobbs et al. 1994). Due to the short lifetime of the electrons freed by the photons and to their absence without irradiation, the conductivity observed occurs immediately under γ irradiation and stops as soon as the irradiation is stopped.

This electronic conductivity σ_e is a direct function of the γ irradiation intensity R , according to the simple relation:

$$\sigma_e = KR^\delta \quad (20)$$

The value of the exponent δ depends slightly on temperature or irradiation intensity, but remains close to unity, in the range of temperatures of industrial interest (500–900 K). The effect of temperature is due the thermal untrapping of the electrons from shallow and deeper traps. Indeed, local point defects trap electrons by changing their charge state (e.g., in Cr-doped Al_2O_3 : $Cr^{3+} + e^- \Rightarrow Cr^{2+}$).

The RIC coefficient K is in the range of $K \sim 10^{-10 \pm 1} S \cdot s \cdot Gy^{-1} \cdot m^{-1}$, and is reduced in the presence of point defects (i.e., in the case of chemically doped or neutron irradiated materials (Klaffky et al. 1980; White et al. 1998)). Typical values of RIC for pure oxide ceramics are given in  Fig. 19. Recent measurements on other types of oxide ceramics gave the same orders of magnitude for various irradiation modes (Tanaka et al. 2006).

The physics of the RIC explains this simple relationship: The formation of each electron-hole pair requires an energy of the order of twice the gap energy. Since all the insulators have gap energies in the same range, around 10 eV, the rate of electron-hole formation by γ irradiation is similar in different materials for the same energy deposition rate, leading to similar RIC. However the trapping of holes, and to a lesser extend of electrons, by various point defects reduces their mobilities, and therefore the induced electron mobility, for materials of low purity or for pure materials after irradiation. In these cases, a reduction of the K factor by up to two orders of magnitude can be observed (Klaffky et al. 1980).

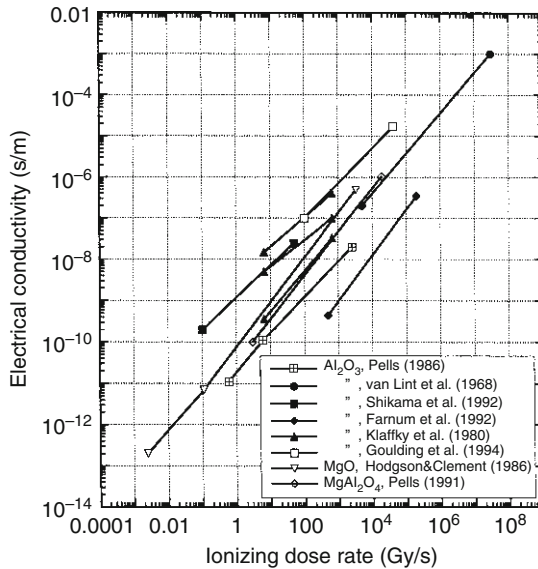


Figure 19

RIC behavior of pure oxides γ and e^- irradiated at RT (From Hobbs et al. 1994)

2.4.2 Radiolysis: Water and Polymers

The chemical evolution of water under irradiation is of uppermost importance for various engineering aspects of the nuclear equipments (stability, chemical potentials of oxidizing species, corrosion, etc.). The irradiation effects on water solutions and polymers have therefore been studied in detail since the earliest days of the nuclear science (Curie and Debiere 1901). Known as “radiolysis,” the chemical evolution of these covalent compounds is now well understood. Phenomenological descriptions of the chemical evolution were available in the 1980s and detailed description at picosecond and atomic scales are now widely accepted (LaVerne 2000).

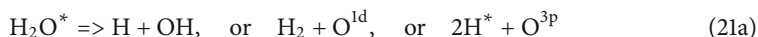
The interaction of ionizing particles, such as phonons, electrons or heavy ions, on matter is mostly controlled by the reactions on electrons. Due to the local role of the electrons for the atomic binding of covalent molecules, this type of irradiations induces major damages in these compounds at the molecular scales. Radiolysis consists in series of processes by which covalent molecules are perturbed by ionizing irradiation particles and evolve chemically afterwards, leading to a new chemistry under irradiation.

Radiolysis occurs in numerous environments: water as coolant and/or moderator in power reactors, water in cements and bitumen for wastes, polymers for instrumentation and insulators, chemical solutions in the reprocessing plants, not forgetting the complex molecules of the living organisms (DNA, proteins, etc.). Limiting the analysis to the cases of the nuclear energy cycle, the physical processes and their consequences on industrial aspects will be described.

Mechanisms of Radiolysis

The most frequent interaction of a high energy photon with an electron is the Compton process, by which part of the energy of the photon is transferred to the electron, leading usually to its ejection from its orbital (ionization: $\text{H}_2\text{O}^+ + e^-$). The Compton electron, ejected from the molecule by this reaction, will induce similar reactions in other remote locations along its track. For the rare case of energy transfer too low for ionization, only mechanical excitation of the molecule occurs (H_2O^*). This first step of interaction, controlled by physical processes, is fast ($\sim 10^{-15}$ s) and leaves the water molecule in a very unstable state. The energy deposition in the molecule by this process is in the range of 50–80 eV. In metals, the availability of replacement electrons captured from the conduction band reservoir allows almost instantaneous easy reconfiguration of the core orbitals and the damage ends up as heat. In covalent molecules, the electronic defect induces major evolution of the molecule:

In the case of the water molecule, the first step is the reconfiguration of the constituents in metastable free radicals. It forms the physicochemical step ($\sim 10^{-12}$ s). This occurs very locally, at the location of the primary interaction and ionizations or excitations, and these species are therefore very heterogeneously created, in so-called “spurs” along the track of the incident electrons:



These free radicals, formed in the spurs, react very fast with the surrounding water molecules and their diffusion trend to homogenize the distribution of these species. They are called the “primary species” (e^- , H, OH, H_3O^+ , OH^- , H_2 , H_2O_2) and include two stable molecules (H_2 and H_2O_2). The “solvated electron” is a thermalized electron surrounded by a cluster of water molecules, due to their polar nature. This heterogeneous chemistry step of the radiolysis ends within 10^{-6} s and the result is an homogenous distribution of the primary species in the water (Swiatla-Wojcik and Buxton 1995).

For neutron irradiation, the damage induced by the incident neutron is restricted to momentum transfer to nuclei, mostly on the H atoms of the water molecule. The mechanisms of water molecule destruction are therefore different but the final results are similar, and the primary species formed are the same, but with different fractions (► Table 3).

The quantity of primary species generated is simply a linear function of the energy released in the water by the irradiation. The generation rates of each species (G) give the amount of

■ Table 3
Radiolytic yields in water at room temperature

Radiation	LET (keV/μm)	H_2O	H_2	e^-_{aq}	H	H_3O^+	OH	H_2O_2	HO_2
$\beta\gamma$	0.25–0.6	–9.63	0.45	2.66	0.55	2.76	2.67	0.72	0.01
α	130–220	–2.77	1.30	0.06	0.21	0.06	0.24	0.99	0.22
Neutrons	40	–3.19	0.88	0.93	0.50	0.93	1.09	0.99	0.04

Source: From Burns and Moore (1976); Elliot et al. (1993)

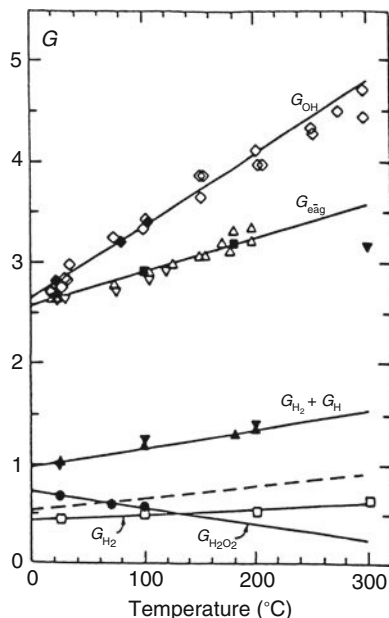


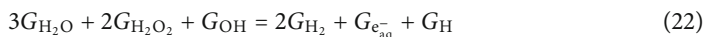
Figure 20

Effect of temperature on the radiolysis yields for γ irradiation of water (From Elliot et al. 1993)

atomic or molecular species formed for each 100 eV released in the water. Table 3 gives the recommended values of the G 's at room temperature.

The G values depend slightly on pH, but the reported variations remain questionable (Fer-radini and Jay-Gerin 2000). The G 's depend more on temperature (Elliot et al. 1993; Sunaryo et al. 1995a) and on the linear density of energy deposition rate (LET) of the particle inducing radiolysis (LaVerne 2000). These effects are due to the diffusion kinetics within the spurs and to the linear density of spurs along the track of the particle, respectively. Indeed at high temperature, the radicals escape easily from the spurs to the surrounding water and, for high LET, the spurs are closer and a higher fraction of the free radicals reacts within the closely located spurs before diffusing in the surrounding water to form the primary species (LaVerne and Pim-blott 1993). The evolution of G 's with temperature for γ irradiation in pure water is plotted in Fig. 20.

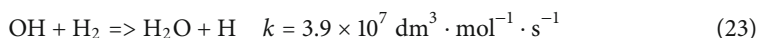
The G values are measured using various techniques, and therefore the G 's may come from different experiments or irradiation conditions. It is important to recall that the formation of the primary species results from the decomposition of water molecules and therefore that species and charges cannot be created ex-nihilo. The relation (22) between G 's expresses the corresponding conservations in terms of equal quantities of oxidizing and reducing species formed by radiolysis:



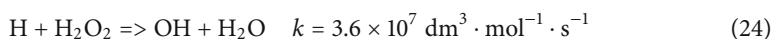
The primary species, obtained by the processes described above within a few microseconds after the interaction, form the initial condition for homogenous chemical evolution of the

species. Numerous chemical reactions can occur in solution: About 30 chemical reactions are known for the pure water and many others for water solutions of technical or scientific interest. All of them have very large ranges of kinetics.

Among them a few are of high importance for long term radiochemical evolution under steady state irradiation. For pure water, the main reactions leading to a steady state concentration of radiolytic species is known as the Allen chain: The radiolytic molecular H_2 reacts with the very oxidizing radical OH:



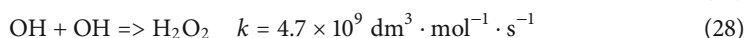
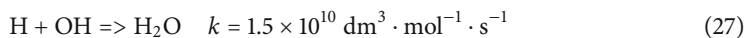
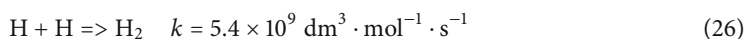
and the H radical recombines with hydrogen peroxide:



The summation of the these two reactions corresponds to the recombination of the two molecular species as two water molecules:



For the radicals, specific reactions control their consumption:



However, for a detailed knowledge of the chemical evolution at small time or space scales, or with varying irradiation conditions (e.g., coolant water circulating in- and out-of-core in the primary circuit), all the equations, with they specific kinetic constants have to be considered. In the case of solution containing specific additions, such as Li, B, or metallic ions in the reactor coolant or mineral species for the mineral water surrounding nuclear waste in storage, the contribution of reactions involving the corresponding species could affect strongly the radiolytic yields (G 's) and the final chemistry under irradiation (Cai et al. 2001; Pastina et al. 1999).

As shown in the equations described above, each chemical species could be involved in different reactions, being either the reactant or the product of the reactions. Thus the chemical evolution of the water under irradiation is obtained solving a set of 30–50 coupled differentials equations (Buxton et al. 1995). In order to solve them, various dedicated softwares have been developed, such as MAKSIMA-CHEMIST (Carver et al. 1979), FACSIMILE (Chance et al. 1977) or CHEMSIMUL (Kirkegaard et al. 2007), with similar efficiencies in computing the chemical evolution of water and solutions under irradiation.

Under continuous irradiation, the chemical evolution of water under irradiation reaches a steady state within a minute and is strongly dependent of the initial conditions. For pure water, large amount of oxidizing species are obtained. These conditions correspond to the case of BWR chemistry, for which additives, such as H_2 , cannot be maintained in water. On the other hand, since H_2 can act as catalyzer for recombination of the oxidizing species OH and H_2O_2 (reactions 23–24), small additions of H_2 in water solutions would enhance their recombination.

► *Figure 21* gives two illustrations of the radiolytic evolution of chemistry of water at 250°C under a dose rate of 450 Gy · h⁻¹ (Sunaryo et al. 1995b). The addition of H_2 clearly dims the oxidizing conditions induced by the radiolysis within a minute.

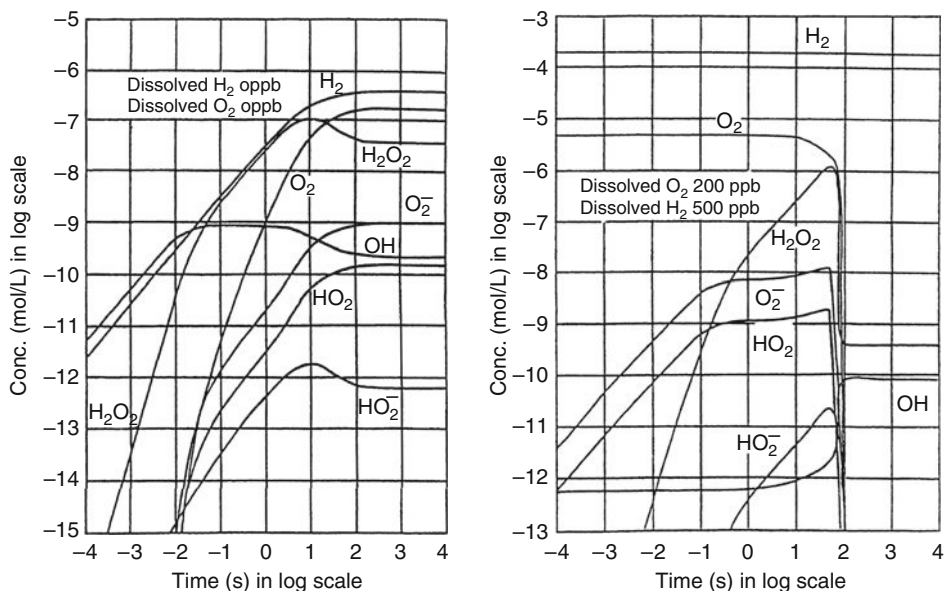


Figure 21

Effect of H₂ addition on the radiolysis of pure water (γ irradiation at 250°C, dose rate 0.125 Gy · s⁻¹) (From Sunaryo et al. 1995b; IAEA 1993)

Table 4

Typical values of the different contributions of energy deposition rates in a PWR

Origin of the radiolysis	W · g ⁻¹	Gy · h ⁻¹	eV · g ⁻¹ · s ⁻¹
β - γ	1.45	5.2 × 10 ⁶	9 × 10 ¹⁸
Neutrons	4.85	1.7 × 10 ⁷	3 × 10 ¹⁹
¹⁰ B(n, α) ⁷ Li (at 850 ppm B)	3.2	1.2 × 10 ⁷	2 × 10 ¹⁹

Source: From Christensen (1994)

Technological Impact of Water Radiolysis for the Nuclear industry

For water power reactors, the chemistry of the coolant depends of the type of reactor. In PWR, the single liquid phase of the coolant allows additions, such as boric acid for reactivity control, lithium hydroxide for pH adjustment and H₂ for mitigation of radiolysis. In BWR, the continuous escape of volatile species in the steam inhibits simple control of the chemistry.

In PWR the chemical additives induce several contribution to the radiolysis to be considered, induced by photons, fast neutrons and alpha from boron. Typical values of their contributions are given in Table 4: The H₂ dissolved enhances the recombination of oxidizing species, and, in addition, allows the recombination of initial O₂ dissolved in water. Therefore the primary coolant in PWR exhibits a rather strong reducing character. Recommended concentrations of H₂ in PWR primary coolant are in the range of 2.2–4.5 ppm (25–50 cm³ · STP · kg⁻¹).

In BWR, the energy deposition induced by the (n, α) reactions does not exist due to the absence of boron in the coolant. In addition, due to the absence of H_2 dissolved in the coolant, the radiolysis enhances the oxidizing character of the water (Yeh et al. 1995), leading to frequent problems of stress corrosion cracking of stainless steel pipings in different locations of the primary circuit (● Sect. 3.2), or to faster corrosion of Zr alloys (Burns and Moore 1976). The mitigation procedure is to introduce continuously H_2 in the feed water. This delicate procedure, known as “Hydrogen Water Chemistry (HWC)” has been implemented with success in various BWR plants (Burns and Moore 1976; Wada et al. 1999).

For wastes stored after the irradiation, the β, γ decay of the fission products of the fuel releases enough energy to induce radiolysis in its surrounding environment. Although this radiolysis occurs with kinetics and temperatures very different from reactor cores, it still induces sufficient consequences to be considered for design and during operations:

- Radiolysis impacts the technical aspects of transport of irradiated fuel in wet casks, due to the build-up of internal pressure of hydrogen (Bonin et al. 2000; Huang 1996).
- The reprocessing of spent nuclear fuel involves the use of extractants and diluents (solvent) for separation of the reusable actinides from the unwanted fission products. The most widely used processes employ tributyl phosphate (TBP) diluted with normal-paraffin hydrocarbon. Long-term irradiation of the solvent induces very complex radiolytic chemical reactions, reducing extraction efficiency. A review of the mechanisms of the degradations of the solvent system and the consequences for operations of the reprocessing plants can be found in (Tahraoui and Morris 1995).
- For long-term disposal (concrete in geological pits), the radiolytic phenomena are complicated by the interactions of the radiolytic primary species with the ions and complexes dissolved from the components of the cements in the pores (Bouniol and Bjergbakke 2008).

Radiolysis in Polymers

The polymers such as alkanes, or other chains of higher complexities such as PMMA, epoxy, etc., up to DNA, are also sensitive to γ irradiation and suffer radiolysis. However, the reactions that could occur following the interaction with a photon are much more complex than for the simple water molecule.

For instance, in alkanes, among the possibilities, interatomic bond failure leads to frequent C–H scissions, but also to fewer C–C ruptures. Free H^\bullet atoms can react with each other, forming H_2 molecules or many other volatile hydrocarbons or simple molecules, such as CH_4 , CO , CO_2 , depending on the species building the chain of the polymer, etc. The gas release corresponds to an internal formation of molecular gases within the polymer. The thermal reptation of the chains may allow the pending $R-C^\bullet-R$ radicals to encounter and to rebuilt links, leading to cross-links and formation of reticulated polymers of much higher strength (Ungar 1981). This phenomenon is in particular activated for the production of heat shrinkable polymers. A typical dose would be for polyethylene films an electron irradiation of about 200 kGy (Drobny 2003). The G values for the reactions described above are given in ► Table 5 for polyethylene.

The release of H_2 and other gaseous species due to radiolysis are also responsible for swelling of the bitumen used in the early days for waste conditioning, leading to the formation of foams (Phillips et al. 1984). Additions of cobalt sulphide (CoS) can be used to fix the hydrogen released and thus to avoid spills out of the storage tanks (Pichon et al. 2007).

Polymers having less localized electrons, such as chains of aromatic monomers, have electrons loosely localized and therefore available for recovery of the bonds after the excitation.

■ Table 5

Radiolysis yield for the different primary processes observed in polyethylene under γ irradiation

Process	H ₂ release	Cross link	Chain break
G values	4.1	2	1.8

They are therefore less prone to radiation damage (Tavlet et al. 1998). Based on this approach, specific polymers have been developed for use in satellites, where the long duration irradiations with high energy cosmic ions induce significant irradiation damage to the polymers selected for the structural parts (Dole 1991).

3 Impact of Irradiation Damage on Structural Material Behavior

3.1 Ferritic Steels (LWR Pressure Vessel)

3.1.1 General Aspects

The reactor pressure vessel (RPV) steels used in LWR are variants of standard Mn, Mo, Ni structural steels used in chemical industry for intermediate temperatures, with good strength and creep resistance up to 400°C: ASTM A 508 Cl. 3 in the USA, similar alloys in other major nuclear countries (16 MND5 in France, 20 MnMoNi in FRG, or 15Kh2NMFA in Russia). The pressure vessel fabrication includes forging, welding, and the standard quench and temper heat treatment of ferritic steels. The microstructure is a tempered bainite that satisfies the code requirement of yield strength above 300 MPa and UTS above 500 MPa at 350°C.


Due to the size and load supported by the pressure vessel, a critical property of the steel used is its capability to resist to crack propagation and brittle fracture. Therefore strict requirements are mandatory with respect to the fracture toughness and the DBTT. Indeed in ferritic steels, a transition exist between the low temperature behavior, where cleavage is easy and fracture occurs with low energy dissipation and the high temperature, where easy plastic deformation accommodates the stress singularity at the crack tips, increasing the fracture toughness.

The later point is a matter of concern for the pressure vessels. Indeed they surround the cores and are therefore slightly irradiated. The irradiation damage is in the range of 0.1 dpa at the end of the design life. Due to irradiation hardening obtained at this dose, the DBTT is shifted to higher temperatures. This phenomenon is called the irradiation embrittlement, and requires a good knowledge of the mechanisms, of the kinetics of DBTT shift and a rigorous surveillance program of the actual behavior of the steel (Odette 2001).

3.1.2 Microstructural Aspects

The hardening of ferritic steels, and the shift in DBTT, has been studied since the beginning of LWR development (Steele 1966; Hunter and Williams 1971). The irradiation effect is increasing with irradiation dose, with a strong tendency for saturation, usually expressed by a fluence dependency to the 1/2 power roughly. It is strongly influenced by irradiation temperature: the lower the irradiation temperature, the higher the embrittlement.

It has been early recognized that the main mechanism inducing irradiation hardening and embrittlement was connected to the Cu content (Ficher and Buswell 1987). Although the content of Cu in the pressure vessel steels is normally low, few early vessel steels have rather high content ($(\text{Cu}) > 0.3\%$). The solubility of Cu in bcc α -Fe is very small: Substitutional solid solution of copper in the iron matrix is saturated at about 0.3% at $\sim 600^\circ\text{C}$, but decreases strongly at lower temperatures, down to below 0.01% at $\sim 290^\circ\text{C}$. Thus, during the final tempering heat treatment all the Cu present in the alloy forms a solid solution within the α matrix, but this later is supersaturated at operating temperatures. During the decades of operation, the mobility of atoms, enhanced by the high concentration of vacancies occurring under irradiation, allows the migration of Cu atoms to form clusters (Odette 1985). For high Cu content, irradiation-enhanced precipitation of Cu occurs, while, at low Cu content, an irradiation-induced segregation of Cu atoms on PD clusters is observed. Such clusters or precipitates can clearly be imaged using atomic microprobe (Auger et al. 1985). The cascades are considered to act a nucleation sites for the formation of these clusters (Radiguet et al. 2007). Although they do not precipitate as a second phase (the Cu clusters remain with a bcc structure (Radiguet et al. 2007)), they act as barriers for the gliding dislocations (Auger et al. 2000). Significant increase in yield strength is thus obtained, which has for consequence a correlated increase in DBTT.

The actual pressure vessel steels are more complex steels than simple model binary Fe-Cu alloys used to understand the physical mechanisms of irradiation effects. The complex chemistry of the reactor steels leads to various types of clusters, containing other species such as Mn, Ni, Si, P (Odette 2001; Auger et al. 2000; Miller and Russell 2007). These clusters have average diameters in the range of 1.5–3 nm and densities of $N = 10^{23-24} \text{ m}^{-3}$, depending of irradiation time and temperatures (Odette and Lucas 1998). Phosphorus is also found to segregate at dislocations and grain boundaries, as it can be observed in  Fig. 22.

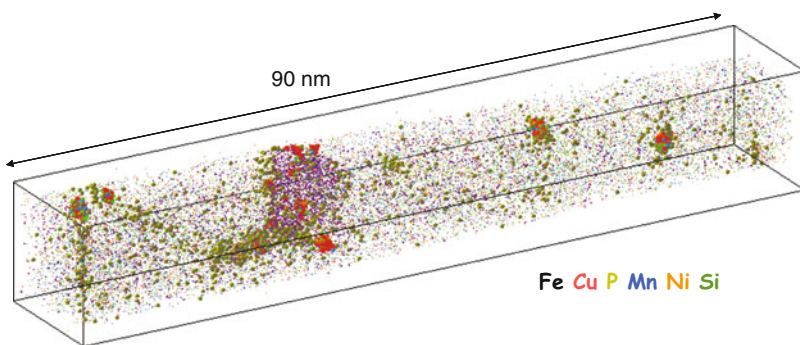


 Figure 22

Complex cluster in a pressure vessel steel after irradiation (From Auger et al. 2000)

These clusters interact with the dislocations and, reducing their mobility, increase the yield strength of the alloys. At engineering temperatures, the stress required on a dislocation to glide along its slip plane is controlled by the distance between pinning centers. For obstacles of spherical shapes, the yield strength is given by the Orowan expression:

$$\sigma_y = \beta \mu b (Nd)^{1/2} \quad (29)$$

where β is an efficiency parameter of the obstacle (~ 0.1 – 0.2 for the clusters), μ is the shear modulus, b is the Burgers vector of the dislocation, N is the volume density of clusters, and d is their mean diameters. The observed cluster sizes and densities, induce hardening in the range of 200–300 MPa.

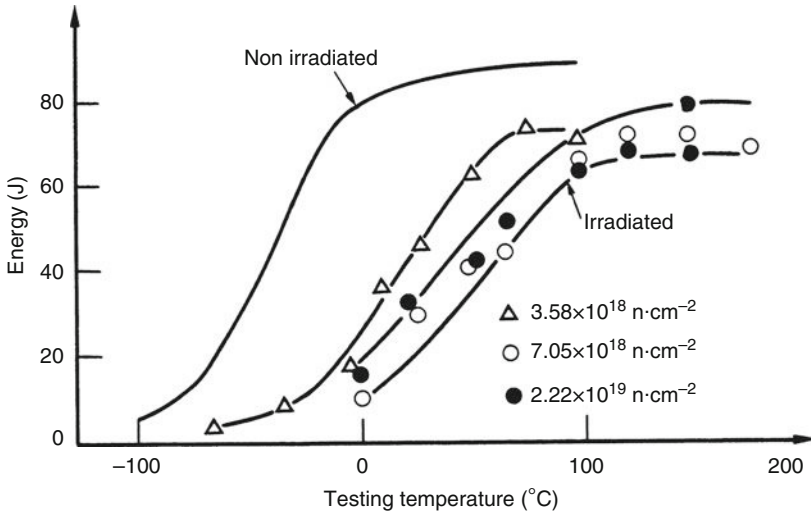
Since the solubility and the mobility of the atoms clustered increase with temperature, annealing heat treatments can be performed on pressure vessels after that an irradiation has induced embrittlement not acceptable for further safe operation. These heat treatments induce a mixture of resolution of Cu and Cu cluster coarsening, reducing the density of dislocation pinning defects and therefore the irradiation hardening (Odette 2001).

Early US PWR and Russian VVER are reactors for which such heat treatments have been studied and, for a few of them, realized. Various studies have shown that the recovery can reach 80% following 160 h at 460°C, for steels in which the major process of embrittlement is due to Cu cluster formation (Odette 2001; Miller et al. 2006). The effect of this recovery treatment is to activate the coarsening of the Cu clusters, reducing their density and strengthening effect. In the case of Ni richer alloys, such as the one selected for the VVER 1000, the Ni-Mn-Cu clusters appear to be more stable and require a higher temperature for full recovery of the toughness (Kryukov et al. 1998).

3.1.3 Pressure Vessel Steel Embrittlement

The effect of irradiation hardening is an increase in the DBTT. This temperature is measured using the standard Charpy test, easy to perform since it uses samples of small size ($10 \times 10 \times 55$ mm). The energy absorbed during the impact of such a notched sample is plotted versus sample temperature. The transition occurs in pressure vessel steels over a temperature range of (50–100°C). At low temperature, the fracture occurs without significant plastic strain, by separation of {100} crystallographic planes. The fracture surface exhibits cleavage planes on each grains and no deformation of the sample. At higher temperature, plastic strain occurred at a strain rate compatible with loading rate, and the fracture surface consists of ductile dimples. The dimples are highly deformed and the high impact energy corresponds to the energy dissipated in plastic strain.

The competition between the two behaviors controls the DBTT: The stress level to induce cleavage is weakly temperature dependent, while the plastic strain is thermally activated and easier at higher temperatures. At a given temperature, the tendency for cleavage or plastic strain is therefore affected by any mechanisms of strengthening. The clusters described above interact with dislocations and increase the strength, inducing irradiation embrittlement. The balance between cleavage cracking and plastic deformation is such that, for typical RPV steels, an increase in yield strength of 1 MPa increases the DBTT by 0.5–0.7°C. On a physical point of view, the effect of irradiation is a strengthening, but for practical purposes, the DBTT shift is



■ **Figure 23**

Shift in Charpy curve of a PWR pressure vessel steel with irradiation dose

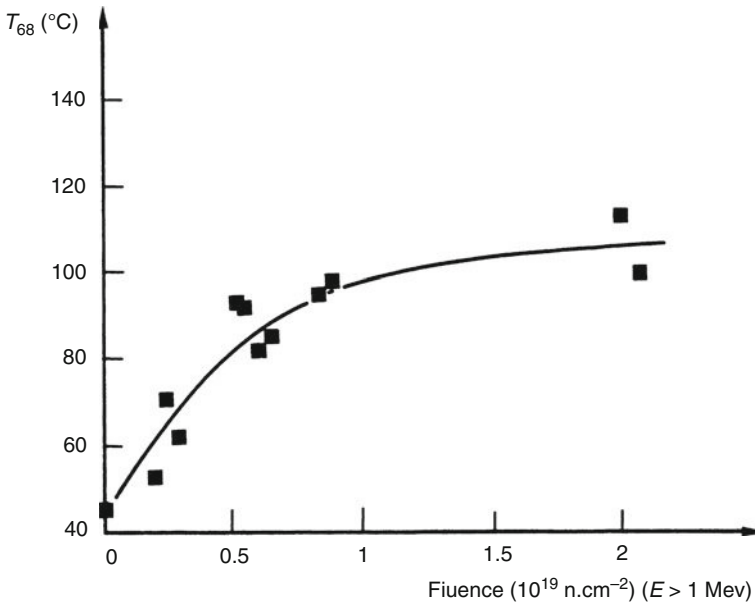
considered. However, the increase in yield strength is the critical aim of the physical modeling of the irradiation embrittlement.

The transition temperature is often chosen as the temperature for a given absorbed energy, corresponding roughly to half of the upper shelf energy, whose exact value may vary according to specific engineering standards (e.g., 41 J, 68 J, or $70 \text{ J} \cdot \text{cm}^{-2}$). Due to the expected shift in DBTT, the initial DBTT has to occur at low temperatures. This is usually obtained by the request of minimal Charpy values at low temperatures (ASME code: 41 J at 4.4°C ; RCCM code: 56 J at 0°C , etc.).

Following fast neutron irradiation, a shift is observed. For RPV steels prone to irradiation embrittlement, it has been observed to be as high as 200°C for standard irradiation histories. In [▶ Fig. 23](#), the main physical phenomena of irradiation embrittlement can be observed: The Charpy transition curve moves to higher temperatures, the super shelf energy is lowered and the shift in DBTT is not linear with irradiation dose, but seems to saturate. Indeed, the two highest irradiation doses induce only marginal embrittlement, compared to the lowest irradiation, while the ratio of the different doses are 1/2/7. Saturation of the RPV steel embrittlement is presented in more detail in [▶ Fig. 24](#).

Very large international irradiation programs have been undertaken along the development of the nuclear power industry. PWR, and to a lesser extent BWR, pressure vessels are concerned by the irradiation embrittlement. Among the main parameters controlling the irradiation embrittlement, chemistry and dose were easily identified.

- As described previously, the Cu atoms cluster under irradiation, as well as other minor elements in solid solution. Therefore the chemical composition is considered for embrittlement forecast. The alloying elements considered in the embrittlement formulae, are Cu and Ni. The interaction of Ni in Cu clusters, leads to a synergistic effect: the embrittlement contribution



■ Figure 24

Saturation of the DBTT shift with irradiation dose

of Ni or Cu is only increased for high Cu or Ni content, respectively. For the impurities, P is known to play a detrimental role.

- The sub-linear dose effect of the irradiation embrittlement is due to many factors. One is linked to the completeness of the clustering of Cu in solid solution, leading to depletion of Cu from the matrix. The coarsening phenomenon that has to follow is too slow to induce significant recovery of the mechanical properties. For design and operation, this saturation is usually expressed by a dependency of the DBTT shift with irradiation dose such as ΔT^n , with $n \sim 0.3-0.5$.
- Various equations are available for the change in transition temperature that include irradiation temperature, neutron flux and fluence, steel composition and nature (plate, forgings, welds, etc.). Safety regulations vary with countries, but the differences are minor and international comparisons of the different rules showed a very high consistency of the different laws (Steele 1993). As a typical example, the “high irradiation formula” used by EDF is the following for the PWRs designed by AREVA:

$$\Delta RT_{\text{NDT}} = 8 + \{24 + 1537 (P-0.008) + 238 (Cu-0.08) + 191Ni^2Cu\} (F/10^{19})^{0.35} \quad (30)$$

It is valid only for irradiation temperatures between 275°C and 300°C , fluences between 10^{18} and $10^{19} \text{ n}\cdot\text{cm}^{-2}$ and for P and Cu contents above 0.008% and 0.08% respectively (Rupa et al. 2006). The actual shifts in DBTT are found to remain below the values expected from these expressions.

Fracture Mechanics


In order to be able to design the pressure vessel, or to analyze its ability to support high stresses in the presence of a defect, the knowledge of the irradiation embrittlement, as measured by the Charpy test is not sufficient. Fracture mechanics concepts have to be used. They have been developed with the aim of describing the stress singularity in the vicinity of a crack tip, and to characterize the capability of the material to support this singularity. At the tip of any crack under external loadings, a stress singularity exists: At a point P in the vicinity of the crack tip, the stress state can be expressed by the following equation:

$$\sigma_{loc}(r, \theta) = \frac{K_I}{\sqrt{2\pi r}} \cdot f(\theta) \quad \left| \begin{array}{c} \square P \\ \text{---} r \text{---} \\ \text{---} \theta \text{---} \\ \text{---} a \text{---} \end{array} \right. \quad (31a)$$

$$K_I = \sigma \sqrt{\pi a} \quad (31b)$$

where K_I is the so-called the stress intensity factor. The local stress distribution $\sigma_{loc}(r, \theta)$ is fully described by the knowledge of K_I . This quantity includes the geometry of the crack of size a , and the macroscopic stress state that would have existed without the crack (σ). In the case of single ribbon crack of width $2a$ in an infinite medium, the value of the stress intensity factor is given in (31b). For actual cases of more complex geometries, either at the surface or internal cracks, several atlases or design rules exist for accurate computations of the value of K_I . For a rough estimate of the stress intensity factor, (31b) can be used for any crack geometry.

For a given material, the presence of a crack does not mean that failure will be obtained, whatever the stress level. Actually, any material can sustain the stress singularity induced by a crack, as long as the corresponding K_I remains below a critical value. The fracture toughness of a material, K_{IC} , is the critical value of K_I for which unstable crack propagation occurs. For brittle ceramics or glasses, the value of K_{IC} is in the range of 0.5–2 MPa · m^{1/2}. For metallic alloys, thanks to the plastic strain at the crack tip that accommodates the stress singularity, much higher values of K_{IC} are observed, in the range of up to 50–200 MPa · m^{1/2}. In the case of structural steels, including RPV steels, the values of K_{IC} follow the trend observed for Charpy, and a transition is observed: low values at low temperatures and transition up to a tough plateau.

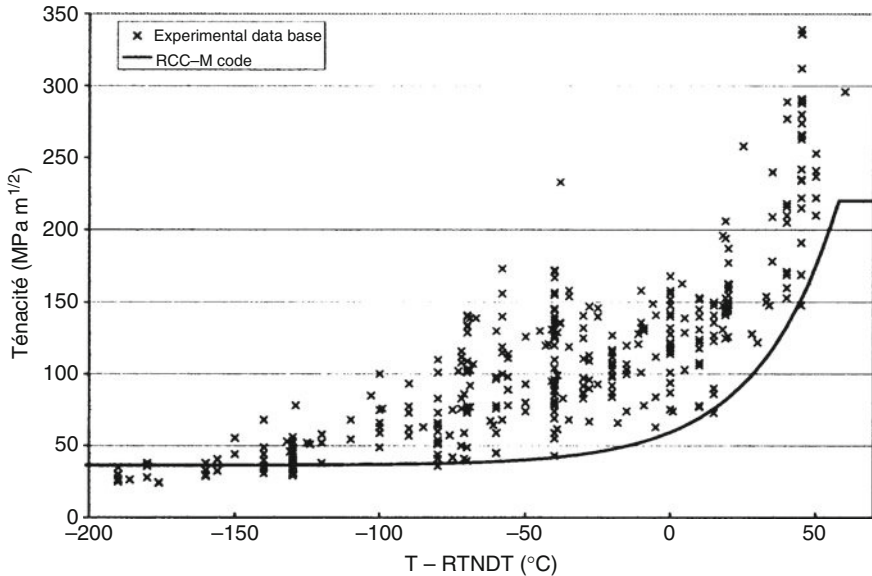
For all the RPV steels, the temperature dependence of the K_{IC} is described by the same equation, normalized to a reference temperature, whose value is connected to the Charpy DBTT. This “Master Curve” is described by (32). Its determination recognizes the physical nature of the scatter in the results (see  Fig. 25) (ASTM Standards E-1921-97 1998):

$$K_{IC}(T) = 36.5 + 3.1 \exp[0.036(T - RT_{NDT} + 55.5)] \text{ MPa} \cdot \text{m}^{1/2} \quad (32)$$

$$K_{IC \text{ max}} = 220 \text{ MPa} \cdot \text{m}^{1/2}$$

Before irradiation the reference temperature of nil ductility transition RT_{NDT} , is measured on extra-lengths of the pressure vessel forgings, out of which coupons are machined. The value of RT_{NDT} is determined by the combination of two tests, the Pellini crack arrest temperature test and the Charpy curves:

- The crack arrest drop weight test consists of impacting a large sample of steel (16 mm thick) with heavy hammer. At the external surface of the sample, a crack starter is obtained by machining a notch on a weld embrittled by P doping. Tests at various temperatures, in 5°C



■ Figure 25

Experimental international data base for actual toughness of RPV steels, as a function of temperature, scaled to RT_{NDT} (From Rupa et al. 2006)

steps, allow to determine the nil ductility temperature (NDT) above which a crack cannot propagate in the material.

- It is also required to determine the temperature TCV for which three Charpy tests have an impact energy above $86 \text{ J} \cdot \text{cm}^{-2}$ and a lateral expansion of the sample larger than 0.9 mm.
- Then the RT_{NDT} is given by $RT_{NDT} = \min \{NDT, (TCV-33)\}$. Its knowledge gives the temperature evolution of the K_{IC} of the steel, as plotted in ► Fig. 25.

The temperature shift induced by irradiation on RT_{NDT} is assessed using equations such as (30). During the operation life of the power plant, the irradiation embrittlement is also controlled on coupons, machined out of extra-lengths of the RPV steel and irradiated inside the pressure vessel itself. The irradiation is performed on special holding stages, closer to the core than the pressure vessel, allowing an anticipation factor of about 3. This surveillance program allows comparing the actual shift in DBTT with the anticipated one. This shift in DBTT measured with the Charpy specimens is applied to the RT_{NDT} and thus the value of K_{IC} for the irradiated materials is known at any temperature.

For safety aspects, an important point is to obtain a detailed knowledge of the exact irradiation dose received by the vessel at any location, and to forecast its behavior in the design life. In addition to advanced neutron physics computations, flux integrators are positioned in the boxes containing the surveillance program steel samples. These neutron detectors are used to benchmark the neutron physics computations and give confidence in the irradiation doses forecasted in any location of the pressure vessels.

Once the K_{IC} is known at any location and time of the RPV, nondestructive examination (NDE) techniques, usually ultrasonic testing, are used to detect any defect in the pressure vessel, to characterize their exact shapes and to monitor their potential evolution of geometry with

time. The mechanical (and thermomechanical) loadings are used to deduce the values of K_I at all the crack tips, for any configuration (normal operations, accidental conditions, etc.). The values of K_I should always remain below the K_{IC} at the dose and temperature studied. This requirement impacts, for instance, the pressure/temperature route for the starting procedures of the plant (Ahlf et al. 1989).

Master Curve and New Issues

As described above the DBTT is controlled by the balance between cleavage and plastic flow at a given temperature. The mechanism of cleavage crack initiation has an intrinsic stochastic behavior. Indeed, whatever the physical process of crack initiation (cracking of MnS inclusions or carbides, pile-up of dislocations at grain boundaries, etc.), the exact conditions that trigger the initial cleavage crack formation are changing with the location of concern (exact position and geometry of the inclusions, grain size, relative orientations of the grains, etc.). Therefore, the transition temperature data obtained from Charpy or K_{IC} samples exhibit a large scatter (e.g., [Figs. 23](#) and [25](#)), that is intrinsic to the transition and not due to any experimental inaccuracy.

In order to take into account this physical scatter, statistical approaches have been developed, that include the distribution of the data in their analysis. The two major models assume that the sample will fail when initiation has occurred:

- Considering that the probability of cracking of inclusions or carbides is proportional to the plastic local strain in the plastic zone ahead of the crack tip (whose size is K_I dependent), Wallin obtained a fracture probability given by

$$P_f = 1 - \exp \left[-\frac{B}{B_0} \left\{ \frac{K_I - K_{\min}}{K_I - K_{\min}} \right\}^4 \right] \quad (33)$$

where B_0 and K_0 are normalization constants and K_{\min} is the lowest K value for cleavage, typically $20 \text{ MPa} \cdot \text{m}^{1/2}$ (Wallin 1993).

- Using a weakest link behavior for cleavage fracture, described with a Weibull distribution function, Beremin and Pineau obtained a failure probability of similar form:

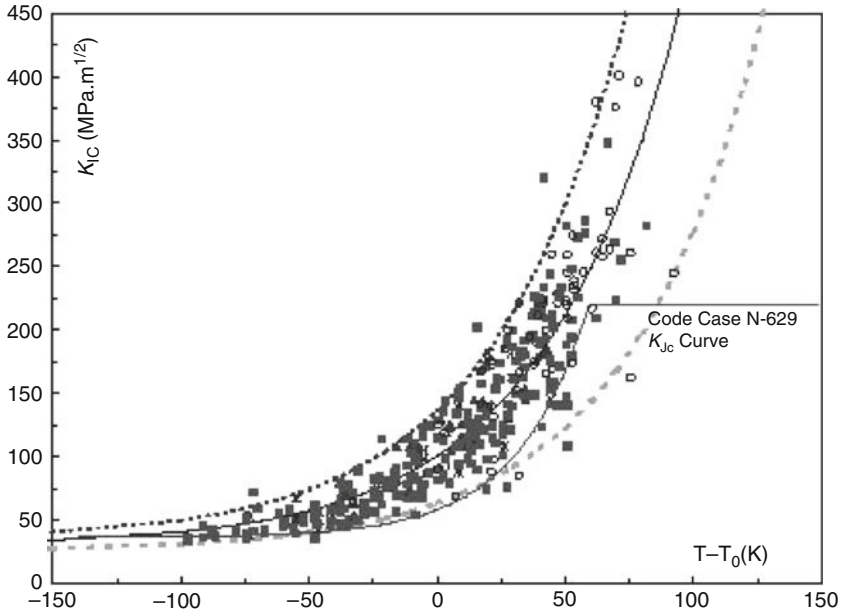
$$P_f = 1 - \exp - \frac{K_{IC}^4 B \sigma_Y^{m-4} C_m}{V_u \sigma_u^m} \quad (34)$$

where m is the Weibull modulus, V_u is an arbitrary unit volume, σ_u is the average cleavage strength of that unit volume, σ_Y is the yield strength, and B is the thickness of the specimen (Pineau 2006).

It is interesting to remark that both models lead to very similar failure probabilities, while deduced from different analysis. Combined with the exponential shape of the K_{IC} vs. temperature curves for RPV steels (32), a general equation expressing the probability of failure (X) at given K_I and temperature can be obtained:

$$K_I(X) = 20 + \left[\ln \frac{1}{1-X} \right]^{1/4} \{11 + 77 \exp [0.019 (T - T_0)]\} \quad (35)$$

where T_0 is the temperature at which $K_I(0.5) = 100 \text{ MPa} \cdot \text{m}^{1/2}$.



■ Figure 26

K_{IC} data with Master Curves (5%, median and 95% bounds) and comparison with the standard K_{IC} analysis (From Yoon et al. 2001)

This equation is the basis of the “Master Curve” analysis. A standard procedure has been developed and is under extensive use for statistical analysis of the RPV steel toughness and radiation embrittlement (ASTM Standards 1998). Since the shape of the $K_{IC}(T)$ curve is not affected by the irradiation, but only translated to higher temperatures, the behavior of irradiated steel can be measured directly on small CT specimens provided by the surveillance programs, by scaling the above equation with experimental data (► Fig. 26). Details of this procedure to implement the Master Curve testing for the RPV steels has been provided by the IAEA (2005).

The value of K_{IC} is affected by all the thermomechanical history of the material studied. Among the different impacts, the plastic deformation and strain hardening induces major changes in mechanical properties. In the specific conditions of the presence of a crack, tensile stresses applied induce a plastic zone ahead of the crack tip that increases locally the strength. Therefore, higher toughness could be expected. An important question is therefore related to the effect of prestressing, at temperatures high enough to avoid brittle failure, on further loading at lower temperature. This phenomenon, known as warm prestress (WPS) corresponds to the case where high K_I is applied at high temperature T_1 , where K_{IC} is high $K_I(T_1) < K_{IC}(T_1)$, before testing at lower temperature T_2 . If the WPS is high enough, large improvement in K_{IC} are commonly observed and the new $K_{IC}(T_2)$ value is above the value of the loading at T_1 (Wallin 2003). Inclusion of this beneficial behavior that improves the pressure vessel integrity would require to record all the pressure-temperature histories of the reactors and to consider K_{IC} as a function of the full history of the component.

Similarly, the behavior of a crack initiated in a cold part and propagating in a warmer area could lead to crack arrest due to the large increase in K_{IC} with temperature. Conditions such as pressurized thermal shocks (PTS) are leading to possible crack arrest and should be analyzed accordingly (Bass et al. 2005).

3.2 Austenitic Stainless Steels (LWR Internals)

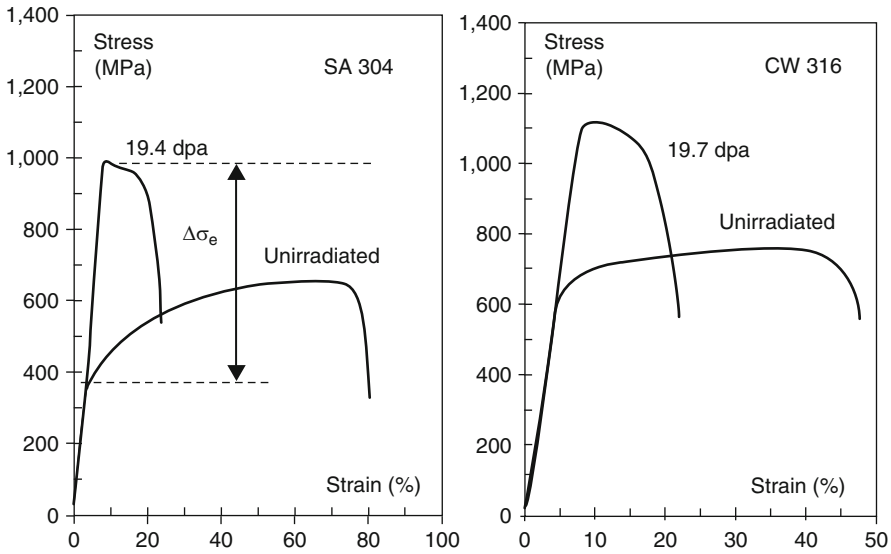
The use of austenitic SS in water-cooled nuclear reactor corresponds to their excellent resistance to corrosion in hot water and steam and for their good mechanical properties at the operating temperatures. The uniform corrosion behavior of these steels is excellent and no problems have been identified with that respect. However, for components very close to the core subject to high irradiation doses, such as the baffle, large changes have been observed on the dislocation microstructure, increasing the yield strength and reducing the uniform ductility. In addition, radiation-induced changes in chemistry are observed at the grain boundaries. These segregations are responsible for enhancing intergranular stress corrosion cracking. The aim of this section is to provide information on the mechanisms and consequences of these phenomena.

3.2.1 Changes in Microstructure and Mechanical Properties

In light water reactors, large components are located close to the core. Usually made out of austenitic stainless steels (SA 304 or CW 316), they are exposed to high neutron fluxes. For instance the high exposure points in the baffle of a PWR receive up to $2 \text{ dpa} \cdot \text{y}^{-1}$. Since these components are designed for the life of the reactor, doses larger than 80 dpa could be expected.

TEM examination of samples machined out of components from actual reactors, as well as tests samples irradiated in various MTR in the temperature range of 300–360°C, allowed a good description of the changes induced by the irradiation: After neutron irradiation, the initial dislocation network present in CW materials is completely removed. The mechanisms of this annealing of the initial dislocation structure appear to be due to dislocation climb by trapping of interstitials and mutual annihilation. A new dislocation microstructure is observed, consisting of small dislocation loops of Frank type (interstitial faulted loops on $\{111\}$ planes with $1/3 \langle 111 \rangle$ Burgers vectors). Their size is small, increasing slowly with dose, to saturate around 5–10 nm for 5–10 dpa, depending on the exact irradiation conditions. Their density is high: $1\text{--}5 \times 10^{22} \text{ m}^{-3}$. Very rare cavities were only observed in the most irradiated and hottest locations (Pokor et al. 2004a).

This high density of Frank loops induced a large increase in mechanical properties. For the two materials used, the yield strength and the UTS are increased, and the total ductility is reduced. The uniform ductility may even vanish (► Fig. 27). Above 10–20 dpa, saturation occurs: the yield strength and UTS become close to 900–1,000 MPa and no further changes are observed up to 100 dpa (Pokor et al. 2004b). The increase in yield strength can be described and modeled to be due to the interactions of the gliding dislocations with the Frank loops,



■ Figure 27

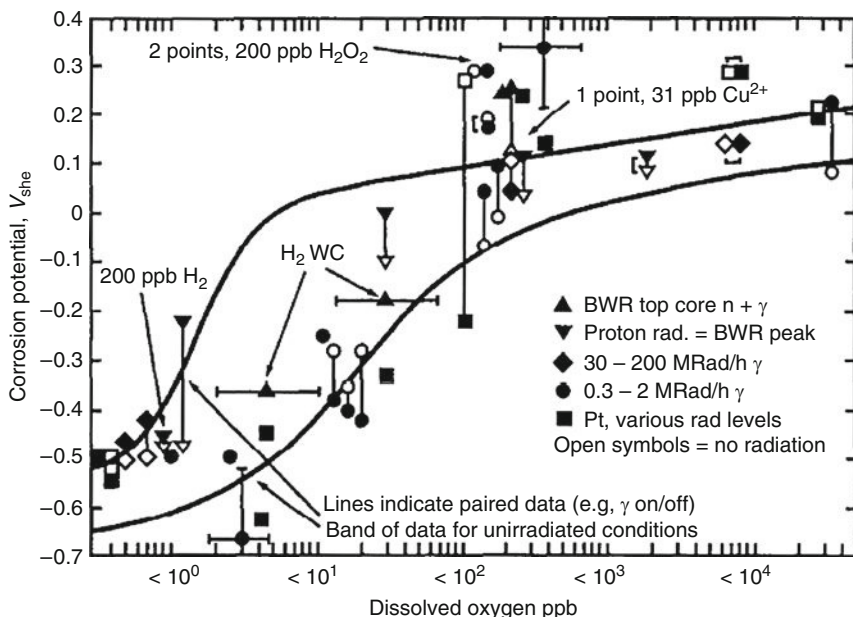
Engineering stress–strain curves for the SA 304L and CW 316 steels irradiated in BOR-60 reactor at 320°C and 20 dpa (From Pokor et al. 2004b)

while the reduction in uniform ductility corresponds to the clearing of the loops by the gliding dislocations and to the development of channels.

Irradiation-Assisted Stress Corrosion Cracking

Intergranular irradiation-assisted stress corrosion cracking (IASCC) has been observed since the use of austenitic SS stressed under irradiation in LWR (Scott 1994): 304 SS fuel cladding stressed by fuel swelling, bolts and springs under service loadings, etc. The conditions for such cracking are a minimum irradiation dose ($\phi > 5 \times 10^{24} \text{ n} \cdot \text{m}^{-2}$, $E > 1 \text{ MeV}$ or 0.7 dpa in BWR and slightly higher in PWR $\phi > 1\text{--}2 \times 10^{25} \text{ n} \cdot \text{m}^{-2}$), a corrosive water environment (e.g., high O_2 content induced by radiolysis in BWR, leading to a high electrical conductivity of the water $\sigma_{\text{elec}} > 2\text{--}5 \times 10^{-5} \text{ S} \cdot \text{m}^{-1}$), and usually a stressed material (service load or material swelling). Tensile tests of materials exhibiting IASCC, performed in hot cells after irradiation showed ductile failure with dimples fractures, confirming the absence of mechanical embrittlement, but a tendency to intergranular cracking in weakly corrosive environments.

The effect of irradiation on water chemistry has been described in 2.4.2. In the case of BWR environments, the high oxygen content cannot be reduced by the recombination enhanced by hydrogen additions. The corrosion potential is therefore increased to levels of easy corrosion. Moreover, the irradiation itself increases the corrosion potential by about 200 mV (Fig. 28). Many cases of enhanced corrosion of various pipes, welds, or bolts located outside irradiated areas are due to these changes in water chemistry. Grain boundaries sensitized to localized corrosion, due to carbide precipitation, and reduced chromium content in the matrix, at the grain boundaries during heat treatments were found to develop intergranular cracking when exposed to such conditions.



■ Figure 28

Effect of irradiation on the corrosion potential of 304 SS versus oxygen content (From Andersen 1996)

3.2.2 Radiation-Induced Segregation

Under neutron irradiation, the PD's surviving from the cascades migrate and disappear on various sinks. Among them grain boundaries are important ones, as phenomena such as coupled diffusion fluxes induce transport of specific species to and from the grain boundaries (GB).

The RIS phenomenon has been observed in austenitic SS under specific conditions. It occurs in ranges of temperatures and irradiation fluxes such that thermal emission of vacancies is too low to avoid thermal recovery of any segregation and re-homogenization, and high enough to activate their mobility and to avoid recombination of Frenkel pairs in the bulk of the grains. Unfortunately these conditions are best fulfilled in typical LWR environments and very narrow band of high segregations at GB's are observed.

During their migration from the bulk of the grains to the GB's, interstitials can interact with alloying elements, inducing a net flux of such species to the GB's. This is specifically the case for the atoms considered to be present in solution as interstitials, such as Si or P, and to a lesser extent S. These elements are dragged by the interstitials as they move to the GB's. Enrichments by factors of 3 and 10 for Si and P respectively have been observed. The impact of these enrichments on corrosion resistance seems however to be limited (Andersen 1996). For sulfur, impurity levels maintained below 20 ppm appear beneficial for the resistance to IASCC (Chung and Shack 2006).

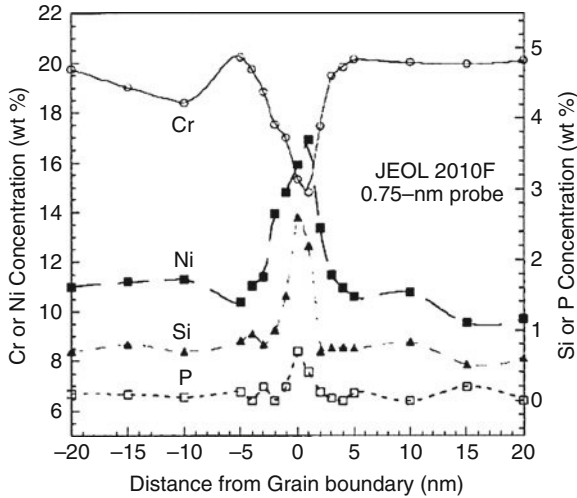


Figure 29

Typical composition profile across the grain boundary of a 304 SS after irradiation (From Bruemmer et al. 1999)

On the other hand, the migration of vacancies requires a flux of atoms in the opposite direction. The backwards migration atoms are those exhibiting the fastest diffusion rates. This mechanism, known as “inverse Kirkendall effect” induces a depletion from the GB’s of such species. The local Cr and Fe concentrations are decreased, while Ni is increased, due to the conservation of lattice sites (➤ Fig. 29). Since the chromium content is the major parameter of corrosion resistance in SS, the local decrease induced, below the level required for good corrosion resistance, allow GB corrosion and crack propagation along the GB’s.

The reduction of Cr content at the GB’s is clearly not due to the formation of carbides, but is an intrinsic behavior under irradiation. Mitigation of this phenomenon using stabilized SS by additions of Ti or Nb (SS 321 or 347) would be irrelevant. However, additions of large substitutional atoms, such as Zr or Hf, are promising solutions by reduction of the vacancy mobility (Fournier et al. 2003).

Other radiation-induced phenomena are also considered as possibly affecting the intergranular corrosion resistance of SS. Among them the followings have been demonstrated to affect the cracking tendency:

- Increase of yield strength due to the formation of clusters of PD and He build up inducing He embrittlement (Scott 1994).
- Localized strain with formation of channels. The channel glide induces very high localized strains, near the GB, that can enhance dissolution at GB, when a crack is growing in the corresponding area (Was and Busby 2005).
- Enhanced increase in corrosion potential under irradiation due to confined radiolysis and chemistry (Urquidi-Macdonald et al. 2007).

4 Reactor Core Materials

4.1 Stainless Steels in SFR

In the sodium-cooled fast reactors, the structural components to be considered are metallic parts of the fuel assemblies: The fuel assembly wrapper (also called duct) and the fuel cladding tubes. The later is a critical component since its aim is to ensure the structural integrity of the fuel and the confinement of the radioactive fuel and fission products. Therefore the mechanical behavior during the entire life of the fuel has to remain good enough to inhibit any cladding failure. Indeed in case of cladding failure in Na-cooled reactor, the Na flows inside the fuel pin by capillarity and reacts with the fuel and the fission products, to form loose sodium (-cesium) urano-plutonates of generic compositions $\text{Na}_3(\text{U, Pu})\text{O}_4$. The high volume expansion and swelling character of this reaction induces tensile stresses on the cladding adjacent to the initial defect, inducing its propagation and major degradation of the entire fuel pin, with dispersion of fuel power in the coolant. Therefore very severe requirements have been set up for the design of these components. The selection criteria include the followings:

- Good mechanical properties (i.e., strength, creep resistance, geometrical stability, etc.) in the temperature range of consideration (400–700°C)
- Compatibility with the coolant (Na) and with the fuel and the fission products.
- Capability to support high fast neutron flux and fluences: The next generation of SFR has a target irradiation dose of 200 dpa for the fuel cladding.
- In order to improve the neutron efficiency of these reactors, a low capture cross section of the alloys for a fast neutron spectrum. This constrain induces a tendency to reduce Ni and Mo contents in austenitic SS, but does not support Zr as in LWR, since its capture cross section for fast neutrons is not lower than the components in SS.

The good behavior of the austenitic SS under these conditions has induced the selection of the 316 CW as the first material for these components. The discovery of microstructure evolution and significant swelling above 50 dpa, described in the next sections, has been a major driving force for understanding the mechanism of these microstructure and geometrical evolutions and for R&D aiming at developing low swelling alloys.

4.1.1 Changes in Microstructure

The austenitic stainless steels are stable in fcc structure at room temperature by addition of austenite stabilizing elements such as Ni, Mn, etc. Depending on the concentration of such elements, the stability of this phase may be limited and, following a solution anneal treatment, long thermal treatments at moderate temperature could induce phase evolution of the alloy, such as bcc phase formation or intermetallic compound precipitation.

In reactor, irradiation-enhanced or -induced precipitations have been observed in these steels (Russell 1984; Brager and Garner 1982). Among the various transformations observed, the most important are the followings:

- Precipitation of carbides: $(\text{Cr, Fe})_{23}\text{C}_6$ whose precipitation is retarded under irradiation, while the precipitation of $(\text{Cr, Ni, Si})_6\text{C}$ is irradiation enhanced, or $(\text{Ti, Nb})\text{C}$ in stabilized alloys.

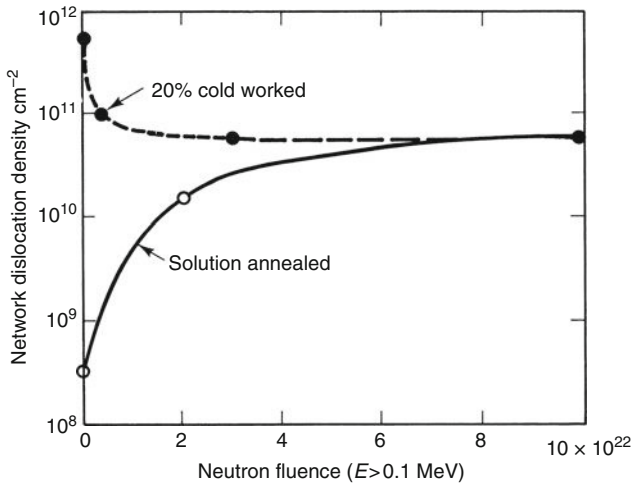


Figure 30

Saturation of dislocation density in both SA and 20%CW 316 SS under irradiation at 500°C (From Brager et al. 1977)

- Precipitation of specific phases due to composition changes. Due to the segregations induced by irradiation at grain boundaries (3.2.2), chemical evolutions at the GB's consist of reduction of Cr and increase in Ni and Si. This induces the formation of γ' or G phases of composition $\text{Ni}_3(\text{Ti},\text{Si})$ and $(\text{Ti}, \text{Nb}, \text{Mn})_6\text{Ni}_{16}\text{Si}_7$. Formation of ferrite has also been observed in 321 SS.

After processing, the SS components have very large differences in dislocation densities. The solution annealed alloys are completely recrystallized and have low dislocation densities, while the cold worked materials have been strained usually around 20% and their dislocation densities are in the range of $10^{15-16} \text{ m}^{-2}$. Under irradiation the initial dislocation structure is completely modified and above 20 dpa stabilizes around $6 \pm 2 \times 10^{14} \text{ m}^{-2}$, whatever the initial conditions of irradiation temperature, neutron flux, and spectrum, within the normal range of SFR conditions (Fig. 30) (Brager et al. 1977).

The presence of these precipitates and the evolution of the dislocation network impact the PD evolution under irradiation. Indeed the dislocation density and the presence of incoherent interfaces around the precipitates control the strength of the sinks for the PD, and the bias. Higher strength of the dislocations in favor of the interstitials induces, as described earlier, higher concentrations of vacancies, compared to interstitials. As a consequence, the clustering of the vacancies induces swelling, a phenomenon of major concern for the SFR. It is described in the next section.

4.1.2 Swelling

- General aspects:

The early designs of the fuel elements for sodium-cooled fast neutron reactors selected austenitic stainless steels as reference materials for the cladding and structural parts such as

the assembly ducts. As soon the first stainless steels components were examined after significant fast neutron exposure, an isotropic expansion of the alloy due to the formation of internal microscopic cavities has been evidenced. This swelling phenomenon became then a matter of critical concern, since it affects directly the geometry and the performance of the core. While He was suspected to play a role, it was noticed very early that the amount of He created by the (n,α) reactions is not sufficient to explain the size and density of the cavities observed by TEM, and that He only acts in the nucleation process of the cavities where the vacancies cluster (Cawthorne and Fulton 1967).

A large amount of international work has been performed on the subject of swelling of austenitic stainless steels, with the aim of understanding the physical phenomena involved in order to control and reduce the swelling behavior of the alloys. Following two decades of irradiations, simulation experiments and modeling, a fair understanding of the mechanisms and of the role of the parameters is now commonly accepted (Lucas 1993; Zinkle et al. 1993; Mansur 1993; Garner 1994).

The swelling is observed as a homogenous decrease of the density of the alloy, leading to an increase of the dimensions of the component under consideration. The swelling occurs after a minimum incubation time, is only significant in a given temperature range and is strongly dependent of the metallurgical state of the alloy (composition, microstructure, thermomechanical treatment, etc.). The mechanism of swelling is linked to the clustering of vacancies in 3D cavities, whose nucleation is enhanced by supersaturation of He created by (n,α) reactions. After the nucleation process, under steady state operation, the swelling usually reaches a rate close to $1\% \text{ dpa}^{-1}$.

- Microstructural mechanisms

The concentrations of PD's described in (8) are mainly controlled by the mechanisms of PD disappearance, either by recombination or by annihilation on sinks. The relative efficiency of these mechanisms is controlled by PD mobility, which is temperature dependent, and is also controlled by the density and strength of the sinks.

As many interstitials are created as the vacancies, but an unbalance exists for the annihilation efficiency of the DP on sinks. Indeed the interstitials have a higher elastic interaction with the dislocations and annihilate faster on them than vacancies. The net result is an increase in vacancy concentration, and a higher probability for the vacancy to cluster together. They can form clusters of 2D or 3D geometries (loops or cavities). Nucleation energy barrier considerations show that vacancies should cluster as loops and cannot nucleate cavities. This is indeed what is observed in alloys whose isotopic composition avoids formation of He during irradiation.

In austenitic stainless steels, the high Ni content allows in-situ formation of He by (n,α) reactions at measurable levels. As it would be expected for a rare gas, He is almost insoluble in metallic alloys and tends to precipitate, at a geometrical scale controlled by diffusion kinetics. He atoms, either located as interstitials or linked to vacancies, can migrate slowly, to form mixed clusters of He atoms and vacancies. These clusters of He atoms can then be considered as nanometric bubbles. Helium bubble nucleation occurs either homogeneously or heterogeneously. However, the low diffusion coefficient of He in fcc stainless steels does not allow long range diffusion of He for large bubble nucleation, and most of the nuclei are formed homogeneously, except in the case of very high density of heterogeneous nucleation centers (fine numerous precipitates or interfaces, etc.).

The nucleation of these He bubbles requires a minimal driving force, i.e., a minimal supersaturation of He, therefore it occurs only after a minimal dose of irradiation. Then nuclei of a few hundreds of He atoms form, with typical nucleus volume densities of $10^{21-24} \text{ m}^{-3}$. The formation of these nuclei does not affect appreciably the volume of the alloy and is not directly linked to the swelling itself. The importance of He generation is highlighted in future fusion reactor materials for which interaction of 14.1 MeV neutrons with steel components have much higher cross sections for the (n, α) reactions.

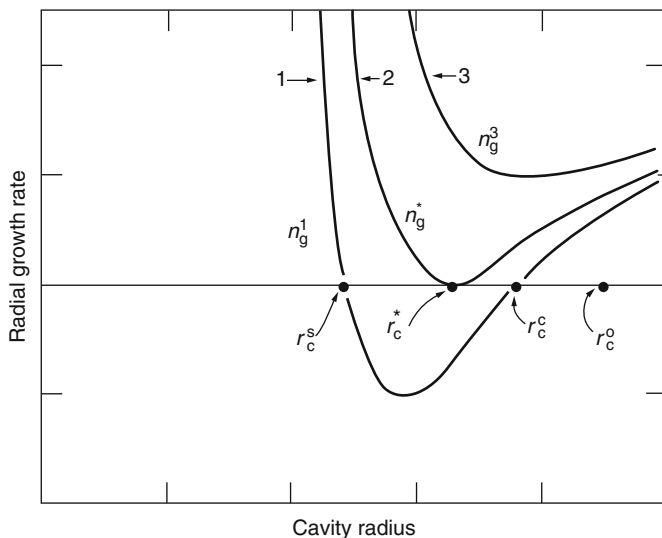
Following the formation of these He bubbles, the major concern, with respect to swelling, is related to their size/composition history. The size evolution of such nuclei is controlled by the balance between vacancy trapping, which will increase the size of the cavity, and the trapping of interstitials or thermal emission of vacancies, reducing it. Helium atoms can only be trapped by the cavities and cannot return to the matrix. If the evolution of the PD concentration is such that vacancies and interstitials are in equal concentration, the trapping at equal rates of the two types of PD lives the nuclei at their original sizes and no swelling occurs.

Detail analysis of the driving forces and trapping efficiency shows that a critical radius exists (or equivalently a critical number of He atoms clustered), function of irradiation conditions and microstructure, above which the cavity becomes unstable and grows by trapping of vacancies (Mansur 1993). The analysis of the size distribution of the cavities and bubbles in irradiated SS confirm a bimodal distribution of bubbles/cavities (Zinkle et al. 1993; Mansur 1993). Some bubbles are very small and contain mainly He atoms, their radii remaining below the critical radius for growth. They form the population of stable bubbles, emitting vacancies faster than trapping them, and therefore unable to grow. Above the critical radius, i.e., for a high enough number of trapped He atoms, vacancy absorption rate overcomes emission and these bubbles can grow as cavities at a rate controlled by the balanced flux of vacancies – interstitials to their surfaces (► Fig. 31).

For this growth to occur, annihilation of vacancy on cavities should be dominant. This requires a regime of balance strength of the annihilation sites (dislocation and voids). Indeed the PD's disappear by recombination or annihilation on sinks. The parameter controlling the relative rate of the two processes is the ratio of the efficiency of PD capture on the dislocations and on the cavities, Q . It is related to the density of these sinks:

$$Q = \frac{L}{4\pi r_c N_c} \quad (36)$$

where L is the total dislocation length, and r_c and N_c are the radius and total number of cavities. Large Q means that the PD's annihilate on dislocations, because there are very few cavities, low Q means that the PD's annihilate on cavities for the reverse reason. For these two cases, the vacancies and the interstitials disappear at the same rates and there is no swelling. In the case of equivalent importance of the sinks, the PD's annihilate on the two types of sinks; but a bias occurs: The interaction of interstitials with dislocations is higher than for the vacancies and the interstitials annihilate more frequently on dislocations, i.e., vacancies annihilate more on cavities, allowing the cavities to grow (Brailsford and Bullough 1972; Lee and Mansur 1990).

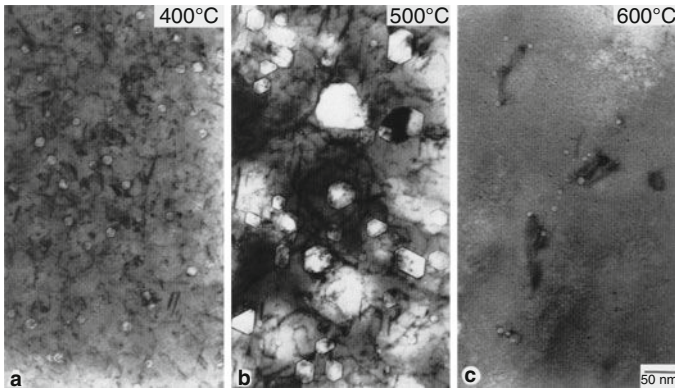


■ Figure 31

Calculated growth rate of cavities containing increasing numbers of He atoms (curves 1, 2, 3). For a critical number of He atoms and a critical size, the cavity grows unstable, below it shrinks. For gas contents below n_g^* , there are two roots, r_c^s , and r_c^c (curve 1). Above n_g^* , the cavity exhibits positive growth rate at all sizes (curve 3). r_c^0 is the critical radius for no gas (From Mansur 1993)

This approach explains, at least qualitatively, the results observed on irradiated alloys:

- At low temperature, swelling is not observed. The reason is a too low migration rate of the vacancies. Being not mobile, they cannot migrate and disappear only by recombination with interstitials diffusing randomly in the matrix. This is the recombination regime.
- Reduction of swelling (by delay of the onset of swelling) is obtained in cold worked materials in which the dislocation density are 6–8 orders of magnitude larger than in solution annealed alloys. This leads to a very high Q parameter (Zinkle et al. 1993).
- Similarly, delay for swelling is obtained by numerous and very fine precipitates such as M_2P , that can act as nucleation sites for He bubbles and allow a high density of such bubbles (Mansur 1993; Dubuisson et al. 1992). They act as traps for both types of PD and the corresponding low Q delays swelling occurrence.
- Once the He bubbles have passed their critical radii, their growth rates are maximal for Q values close to 1 and the swelling rates observed are almost constant and proportional to the dose rate (Garner 1994). Therefore the only way to avoid swelling is to delay as much as possible the dose for unstable cavity growth.
- At high temperatures the swelling disappears, due to the thermal emission of vacancies from the cavities. This occurs when vacancy formation can just be thermally activated.
- Although early observations raised the hope of some saturation in swelling, detailed reexamination of the data confirmed a continuous swelling rate once the incubation period has been reached (Garner and Black 2000). Swelling above 55% have even been observed in standard austenitic stainless steel ducts irradiated in BOR 60 up to 67 dpa



■ Figure 32

Influence of the temperature on cavity structure and void swelling of 15–15 Ti SA austenitic steel neutron irradiated to 11–13 dpa with a high He generation rate (From Maziasz 1993)

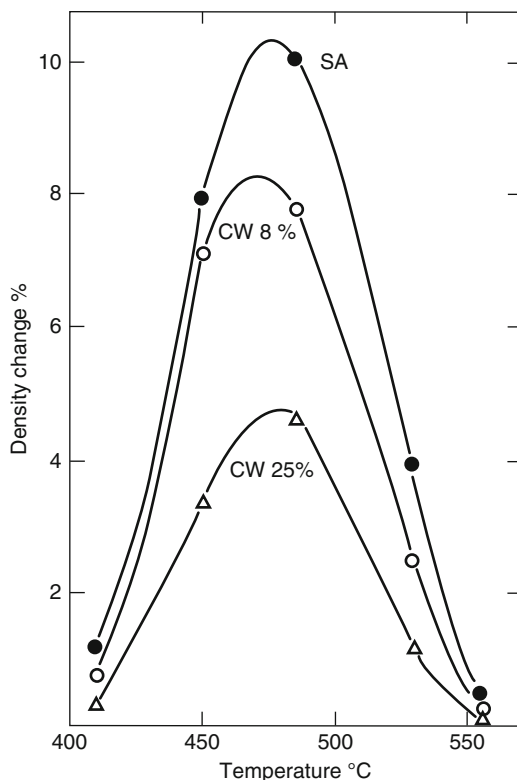
(Neustroev and Garner 2008). For high swelling values, in addition to the expected degradation of mechanical properties, all the physical properties (E , ν , ρ_{elec} , λ_{th} , etc.) are affected (Balachov et al. 2004).

- Parameters controlling swelling:

The crystal structure is known to affect the swelling behavior: after the onset of swelling, a constant swelling rate of about $1\% \times \text{dpa}^{-1}$ is observed in austenitic steels. In ferritic steels (e.g., Fe-Cr alloys), the nucleation of swelling occurs late and the swelling rate is lower (probably $< 0.1\% \times \text{dpa}^{-1}$) (Gelles 1995). Lower swelling rates were observed for more complex alloys leading to ferritic/martensitic structures, probably at the onset of swelling (Odette 1988). This behavior is not intrinsic to the bcc structure (V or Mo alloys do swell), and various reasons for this resistance swelling are proposed: the lower He generation rate, due to low Ni content, the more open bcc structure exhibits higher diffusion coefficients, the crystallographic structure of the dislocations in bcc could induce a lower bias for interstitial capture, PD trapping by solute atoms such as carbon and the very fine microstructure of martensitic steels, where the high density of lath boundaries may act as sinks for PD's (Little 1993). Hcp alloys (Zr, Ti, Mg, Zn, etc.) do not exhibit swelling, but only formation of dislocation loops, responsible for growth (dimension change at constant volume, see ► 4.2.2) (Griffiths 1993).

The temperature controls the swelling behavior for reasons explained earlier. Roughly, swelling is only observed in metallic alloys for reduce temperature in the range of $0.3 < T/T_f > 0.65$. Unfortunately, this temperature range corresponds, for industrial steels, to the design temperatures of fast reactor cores. It is observed that the maximal swelling is observed in SFR in the upper part of the fuel assemblies, slightly above mid-core plane, corresponding to the best combination of neutron flux and temperature. The influence of temperature on swelling is clearly evidenced on ► Fig. 32. The possibility of very limited swelling of internals in PWR operating at much lower temperatures is still an open question (Garner and Toloczko 1997; Garner and Makenas 2006).

The metallurgical state of the alloy is an important controlling parameter of the swelling behavior. Almost any feature of the microstructure may affect the evolution of the PD created



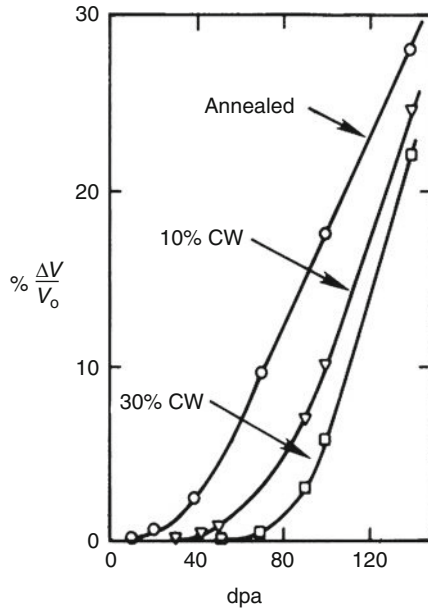
■ Figure 33

Influence of cold work and temperature on swelling of 316 austenitic stainless steel irradiated in SFR (From Dupouy et al. 1978)

during irradiation. Dislocations, interfaces, grain boundaries or free surfaces, including cavities, act as sinks for the PD.

The effect of cold work in reducing the swelling has been clearly evidenced very early and the advantage of high strength, due to strain hardened structure, and low swelling lead to the use of cold worked alloys very early. ➤ Figures 33 and ➤ 34 illustrate the strong effect of cold work. However, this effect is only effective for the incubation phase (Garner 1993; Dupouy et al. 1978). Actually, the irradiation induces changes in the microstructure, modifying the initial dislocation arrangements and inducing a new dislocation network, whose density is almost independent of the initial structure (Zinkle et al. 1993). This is the reason why the post incubation swelling rate is independent from the initial microstructure (Garner 1994).

The chemical compositions of the alloys have been naturally considered as variables for swelling control. From the standard composition of 304 and 316 austenitic stainless steels, variants have been considered, with changes in the major alloying elements (Cr, Ni, Mo, etc.) and minor additions (Ti, Si, C, P, etc.). The effect of variations in chemistry is rather complex and only limited generic rules can be extracted from the large amount of experimental data's

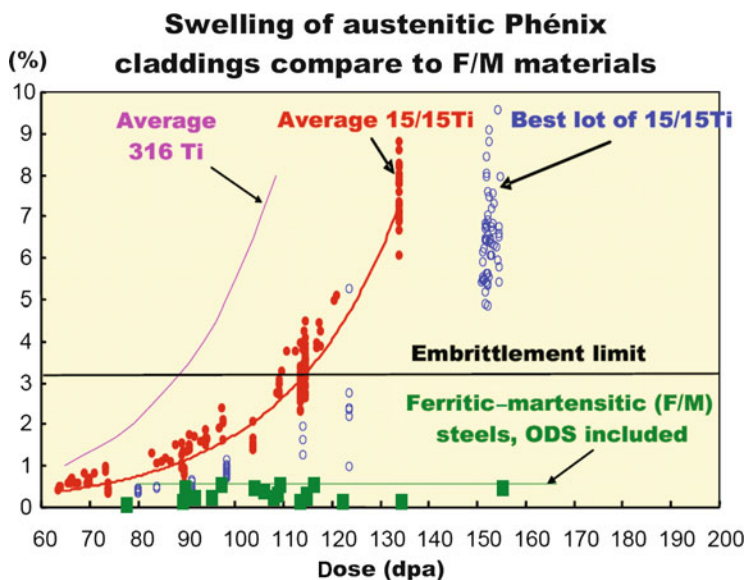


■ Figure 34

Influence of cold work on swelling of 15-15 austenitic stainless steel irradiated at 650°C with 1 MeV Cr ions (From Garner 1993)

(Garner 1994). The chemical changes affect only the incubation dose and not the steady state swelling rate.

- The major impact is obtained with Ni: increasing the Ni content reduces drastically the swelling. Initially observed with ion irradiation, the effect is confirmed under neutron irradiation. Ni contents in the range of 30–50% correspond to the most efficient alloys, but an increase to 15–20% appears to be enough for industrial applications, when other additions are considered (Seran et al. 1992).
- Chromium has exactly the reverse effect: the swelling rate is increased with Cr content. However Cr content has to remain high enough for corrosion resistance. The effect of Ni and Cr contents are not fully explained, the changes in diffusion coefficients associated with the composition shifts are too low to explain such reduction in swelling (Rothman et al. 1980). The change in stacking fault energy with composition may affect the interaction energy between interstitials and dislocations, reducing their bias.
- Molybdenum, a usual component of 316 SS, induces a complex behavior: it reduces weakly the swelling at low temperatures, but increases it at high temperatures.
- Titanium is usually added in these alloys for stabilization by precipitation of TiC instead of chromium carbides. Due to the interactions of C with Ti, the states of these elements (solid solution or carbides) vary with temperature and change their role as sinks for PD's. Ti increases swelling at low temperatures (420–470°C), while it reduce it in the higher range (530–630°C) and the reverse occurs for C.



■ Figure 35

Influence composition and structure on swelling of stainless steel irradiated in the Phénix fast reactor (From Seran et al. 1992)

- Silicon and phosphorus show a swelling increase at low concentrations, but then reduce swelling. Si has to be above 0.5% to be efficient in reducing swelling, and P above 0.05%. For these two minor additions, the state of the component is very important (in solid solution, or as precipitates). The mechanisms involved in their effects on swelling associate PD interactions with the atoms in solute solution, or the efficiency of precipitate matrix interfaces as sinks for PD's and highly dense heterogeneous nucleation sites for He bubbles (Zinkle et al. 1993; Dubuisson et al. 1992). By increasing the number of cavities for He precipitation, the number of He atoms in each bubble is reduced and a higher dose is required for them to reach the critical radii (Mansur 1993).

The dose rate controls the concentration of PD's, and therefore their ability to recombine and to inhibit cavity nucleation. At high dose rate the peak swelling is observed at higher temperatures. This can be observed with ion irradiation, having very high rates compared to reactor irradiations. Two orders in magnitude increase in dose rate, correspond to a shift in peak swelling temperature of 100 K (Mansur 1993; Westmoreland et al. 1975). Similarly, the high dose rate gradient characteristic of SFR cores allows the reveal the effect of dose rates on swelling: The highest dose rates reduce the onset of swelling (Seran and Dupouy 1982).

The saturation of swelling that has been reported at high neutron doses has been reanalyzed and appears now to be due to an artifact due to dose measurements or bias in extrapolations (Garner et al. 2000).

The slow industrial evolution of SS composition allowed the introduction of high Ni alloys with specific additions, such as Ti, Si, P, or other less publicized. The historical evolution of the performance of SS claddings for the French SFR program is shown in Fig. 35. The reactors of

the next generation (GEN-IV) will require very low swellings at very high doses, and the choice will be between advanced high Ni austenitic steels or ferritic/martensitic steels.

4.1.3 Irradiation Hardening and Irradiation Creep

Irradiation Hardening

During irradiation, the change in dislocation microstructure is the main mechanism inducing hardening or softening. For solution annealed or cold worked materials, which initial dislocation densities differ by several orders of magnitude, the dislocation densities stabilizes after a moderate irradiation (15–25 dpa) at a dislocation density of $3 \times 10^{14-15} \text{ m}^{-2}$ whatever the initial state, but with a tendency for lower dislocation densities at higher irradiation temperatures (Garner 1994). The same behavior has been confirmed under different types of irradiation (Mazey et al. 1971; Azam et al. 1973).

Since the mechanical strength is controlled by the pinning efficiency of the obstacles for dislocation glide, the change in dislocation microstructure induces a similar change in mechanical properties. Indeed, the strength of cavities as pinning centers for the dislocations is much lower than the dislocation of the forest and can be forgiven. For SA alloys, the low initial dislocation density is largely exceeded by the dislocation network formed during the growth and interaction of the dislocation loops generated by irradiation. This leads to a large radiation hardening and the yield strength is observed to increase with dose to reach a saturation value close to 900 MPa after about 15–20 dpa at 370°C. For higher irradiation temperatures, an in-situ recovery of the dislocation network allows a reduction in yield strength (Fish and Holmes 1973; Garner et al. 1981).

For cold worked material, the initial dense dislocation network is completely restructured during irradiation and a new steady state dislocation network forms, rather similar to the one observed for saturation of SA alloys. This leads to some irradiation softening and the strength of the two types of microstructures (SA and CW) exhibit similar properties at high doses (Garner et al. 1981) (► Figs. 36 and ► 37).

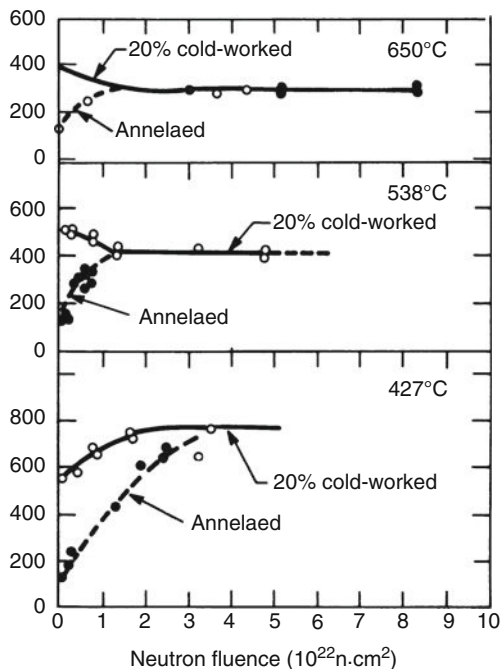
An expected correlation can be verified between the dislocation loop density (or the dislocation network density) and the mechanical properties (yield strength), corresponding to the standard strengthening by a geometrical density of obstacles on dislocation motion (Yoshida et al. 1991; Brager et al. 1984).

$$\Delta\sigma = \alpha \cdot \mu \cdot \vec{b} \cdot (\rho_d)^{1/2} \quad (37)$$

This confirms the major role of the dislocations on mechanical properties.

In addition to the strengthening induced by the dislocations, different other mechanisms affect the mechanical properties:

- Due to the saturation in dislocation density at high doses, strain hardening does not occur anymore, (some strain softening could even occur) and the result is a localized strain and very low uniform elongation, leading to low ductility of engineering concern (Crawford et al. 2007; Fissolo et al. 1994).
- Cavities responsible for swelling act as nucleation centers for dimples in the ductile fracture process, therefore high swelling induces a very low ductility. The consequence is a restriction



■ Figure 36

Convergence of the yield strength at high doses for cold worked and SA 316 SS under fast neutron irradiation (From Garner et al. 1981)

in total swelling below 6% (Hamilton et al. 1967). At 10% swelling, the steel does not exhibit any ductility anymore. For these conditions, the fracture appearance is transgranular, with planar zones, corresponding to “channel fracture,” perpendicular to the tensile axis. These areas are not cleavage surfaces, but planes of intense dislocation channeling where the cavities are completely flattened and merge by localized intense shear (see [Fig. 15](#)) (Garner 1994; Fissolo et al. 1994).

- The He precipitated or segregated at grain boundaries induces an embrittlement and grain boundaries separation is observed for high temperature creep testing.

Irradiation Creep

Irradiation creep of the steels used for cladding and assembly ducts is a complex process to study, due to the difficulties in performing creep experiments in material testing reactors and due to the interaction between creep and swelling. In the ranges of temperatures, stresses and dose rates relevant to actual fuel assembly components, the stress-induced preferential absorption (SIPA) mechanism is responsible for the majority of the strain among the different irradiation creep mechanisms that could be considered (Matthews and Finnis 1988; Garner 1994). Other minor components of strain at the beginning of the loading (primary creep), due to the evolution of the dislocation microstructure or to strain associated with radiation-induced precipitation, will not be described here.

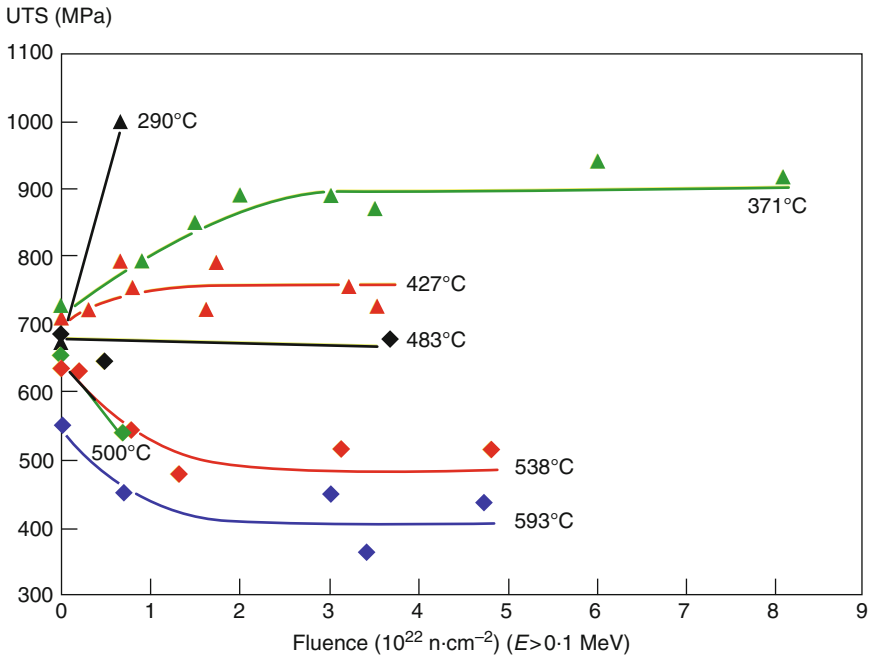


Figure 37

Effect of temperature on the variation of mechanical properties of 316 cold worked austenitic SS under irradiation (From Garner et al. 1981)

The SIPA considers that the elastic interaction of interstitials with dislocations is modified by the applied stress and that this anisotropic contribution leads to preferential annihilation of the interstitials on dislocations whose climb induces strain in the direction of applied tensile stress. In a similar way to annihilation of vacancies on cavities for swelling, it states that SIPA creep occurs when interstitials disappear on dislocations, i.e., when the dislocation density is high and recombination mechanisms low. Therefore irradiation creep occurs faster on high dislocation density materials such as cold worked materials or only after a given irradiation for the development of a dense network of dislocations (Bullough and Willis 1975). The creep rate of SIPA irradiation creep is derived to be proportional to the dislocation density and to the flux of PD's arriving to the dislocations, itself proportional to the PD generation rate G (38).

$$\dot{\epsilon}_{\text{SIPA}} = C \frac{\sigma}{\mu} \rho_{\text{disl}} G F(\eta) \quad (38)$$

where μ is the shear modulus, and $F(\eta)$ a quantity expressing the balance of recombination and thermal emission of the defect population.

This irradiation-induced SIPA creep is temperature independent. The reason is that it is controlled by interstitial mobility, a process of very low activation energy. This has been confirmed by careful measurements of temperature dependence of irradiation creep. It was indeed found

an activation energy of irradiation creep corresponding to 0.13 eV in austenitic SS (Wassilew et al. 1987). The increase in irradiation creep with higher dislocation density ρ_{disl} has been confirmed in a large number of observations, as well as the linear dependence with fast neutron flux (Garner 1994). Since the density of dislocations has a tendency to stabilize around $10^{14-15} \text{ m}^{-2}$ after a few dpa, the creep rate appears to be only dependent of irradiation dose and is imply expressed as:

$$\dot{\epsilon} = B_0 \sigma G \quad (39)$$

where B_0 has been measured close to $10^{-6} \text{ MPa}^{-1} \cdot \text{dpa}^{-1}$ in austenitic SS and to $0.5 \times 10^{-6} \text{ MPa}^{-1} \cdot \text{dpa}^{-1}$ in ferritic SS (Garner 1994; Seran et al. 1992).

The occurrence of swelling affects the irradiation creep and very strong correlation has been found between creep rate increase and swelling. Thus a more accurate description of the irradiation creep equation should include the swelling rate:

$$\dot{\epsilon} = \sigma (B_0 G + D \dot{S}) \quad (40)$$

where \dot{S} is the instantaneous swelling rate. In the French analysis, the coefficient D is replaced by α , which is applied to the total swelling rate. D is in the close to $0.5 \times 10^{-2} \text{ MPa}^{-1}$ and is the same for austenitic and ferritic SS (Seran et al. 1992).

The reason for an increase in creep rate when swelling starts is linked to the behavior of the interstitials. As described above, the swelling is induced by higher vacancy trapping at cavities, due to preferential annihilation of the interstitials on dislocations. Then the bias of interstitials on the dislocations enhances the climb of the dislocations and, as matter of consequence, the strain by SIPA creep (Woo and Garner 1992).

It is usually difficult to predict the creep of fuel pin cladding only based upon the swelling and creep behavior obtained with simple irradiation tests. This is due to a major difference in stress history between creep or swelling experiments and fuel pin: In a pressurized capsule the stress state remains constant during all the experiment, while the internal pressure of a fuel pin increases as the burn-up and fission gas release increases. In the former case, creep starts before swelling, while in fuel pins, swelling can appear before significant creep strain (Seran et al. 1990; Garner et al. 1987). In addition, at high doses, the creep rate has a tendency for reduction in strain rate, and can even vanish, adding a degree of complexity in the modeling of the actual behavior (Garner et al. 1987).

4.1.4 Development of Low Swelling Alloys

During the decades of operation of fast reactors, a large number of variants of austenitic steels have been tested in order to reduce the swelling rates. Advanced alloys, with high Ni content and various additives (Ti, P, etc.) have shown promising behaviors. Alloys for cladding in such reactors are available for doses close to 150 dpa. However the design of advanced fast reactors of GEN IV will require much lower swelling due to geometrical requirements induced by their advanced neutron physics.

The ferritic steels were observed to be highly resistant to swelling in the rare experiments performed with these alloys. The bcc structure of these steels cannot be the main reason for

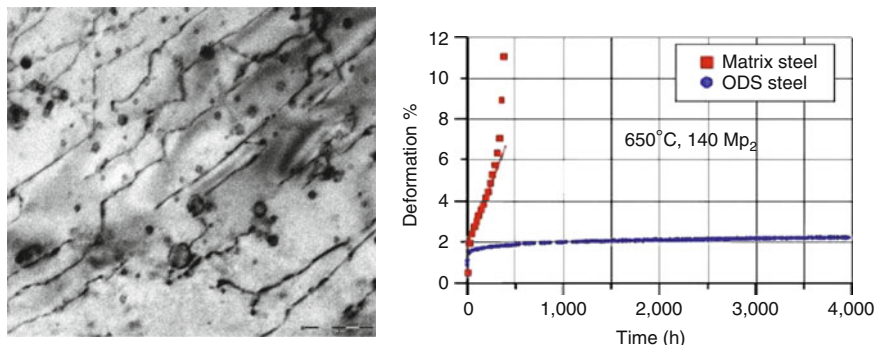


Figure 38

Microstructure of ODS steels, with yttria dispersions and corresponding increase in creep resistance. The pinning of the dislocations by the dispersoids leads to a drastic increase in creep resistance (From Yamamoto et al. 2007)

such a behavior. Indeed, V or Mo alloys do exhibit swelling. Early measurements of ferritic steel swelling reported low swelling rates, close to $0.05\% \text{ dpa}^{-1}$. However voids were observed at higher doses (Gelles 1995). A detailed survey of all the data related to swelling of steels lead to the conclusion that the ferritic steels exhibit roughly the same behavior as the austenitic ones. They have usually a much longer incubation period, strongly Cr content dependant. The shortest incubation (100 dpa) are obtained with 8–10% Cr, while 15% Cr leads to a delay in the onset of swelling above 170 dpa. However, after the incubation dose is reached, the swelling rates are similar, but smaller than the fcc steels, i.e., close to $0.2\% \text{ dpa}^{-1}$, and possibly higher (Garner et al. 2000).

Whatever their swelling resistance, the high Cr ferritic steels will be susceptible to radiation embrittlement, i.e., increase in DBTT with dose. This drawback, currently not analyzed in detail, would be a matter of concern for the handling of the fuel after irradiation.

For fast Na-cooled reactors, the high core temperatures require a cladding material of high resistance to creep. Due to the large thermal activation of the deformation mechanisms in bcc steels, their creep resistance at operating temperatures would not fulfill the design requirements.

For specific applications, these ferritic steels have been strengthened by dispersion of non-soluble oxides such as Y, Ti, or Mg oxides (ODS steels), a structure obtained by mechanical alloying followed by high temperature and high isostatic pressure sintering. They show a very high creep resistance (► Fig. 38). The high PD sink density induced by the very fine structure of the oxide dispersoids is expected to reduce the swelling rates. Preliminary tests are promising (Yamamoto et al. 2007). This microstructure of the ODS, preliminarily proposed for ferritic steels has been proposed as a possible route for improvement of austenitic steels (Rowcliffe 2009). Among the problems to be solved, the high dose stability of these oxide dispersoids appears to remain an open question. Indeed while the oxide particles inserted by mechanical alloying are fully insoluble and therefore highly stable, with no dissolution and coarsening at high temperature, the ballistic mixing can induce diffusion of the components of these particles back into the matrix (Monnet et al. 2004).

4.2 Zirconium Alloys in Water Reactors

Zirconium has been selected for LWR early in the history of the nuclear industry. In the process of selecting new structural alloys for water reactors, zirconium and its alloys were chosen because of the conjunction of the following properties: low thermal neutron capture cross section, high resistance to corrosion in high temperature water and relatively high mechanical strength.

4.2.1 Zirconium Alloys: Zircaloy and Zr-Nb

In the usual ore (zircon: ZrSiO_4) zirconium is commonly found associated with its lower row counterpart in the periodic table, hafnium, at a concentration of 1.5–2.5%. Due the high thermal neutron capture cross section of Hf ($\sigma = 105 \pm 5$ barns), it has to be removed from Zr for nuclear applications.

The processing of Zr alloy industrial components is rather difficult because of the high reactivity of the metal with oxygen. The first step is to transform the zircon into ZrCl_4 , through a carbo-chlorination process. After, Zr and Hf are separated using a vapor phase distillation, at 350°C . Zr metal is obtained by the reduction of ZrCl_4 in gaseous form by liquid magnesium, giving the sponge cake. This is the base product for alloy ingot preparation. Sponge fragments are compacted with the alloying elements – O (in the form of ZrO_2), Sn, Fe, Cr, Ni, and Nb – to the desired composition. It is melted in a consumable electrode vacuum furnace, three to four times.

Industrial use of Zr alloys requires either tube- or plate-shaped material. The first step in mechanical processing is forging or hot rolling in the β phase, at a temperature close to $1,050^\circ\text{C}$, or lower in the $\alpha + \beta$ range. Hot extrusion followed by one cold reduction step is used to obtain tube shells or TREX (tube reduced extrusions), while hot rolling is used for flat products. Further reduction in size is obtained by cold rolling either on pilgrim-rolling or flat mills. Low temperature ($500\text{--}700^\circ\text{C}$) annealings are performed between the steps.

Industrial Alloys

Pure zirconium crystallizes at ambient temperatures in the hcp system, with a c/a ratio of 1.593 (α phase). Lattice parameters are $a = 0.323$ nm and $c = 0.515$ nm. The β bcc phase appears above 865°C for pure Zr.

The zirconium alloys in use today for nuclear applications are limited in number: The alloys are based upon the two systems giving significant solid solutions: Zr-Sn: the Zircaloy's series and Zr-Nb either 1% or 2.5% (► [Table 6](#)).

Oxygen is clearly an alloying element. It induces an increase in the yield strength by solution strengthening: a typical addition of 1,200 ppm oxygen addition increases the yield strength by 180 MPa at room temperature, compared to O-free Zr.

Tin, at a concentration of 1.2–1.7%, was originally added to increase the corrosion resistance, especially by mitigating the deleterious effects of nitrogen. It increases the creep resistance of the alloys. There is a modern tendency to reduce its content.

Iron, Chromium, and Nickel, at their usual concentrations (below 0.5% total content), are fully soluble in the β phase. In the α phase their solubility is very low: about 120 ppm for

■ **Table 6**

ASTM specifications for Zr and Zr alloys in nuclear industry

Alloy	Sn (%)	Nb (%)	O (ppm)	Fe (%)	Cr (%)	Ni (%)
Zry 2	1.2-1.7		1,200–1,400	0.07–0.20	0.05–0.15	0.03–0.08
Zry 4	1.2-1.7		1,200–1,400	0.18–0.24	0.07–0.13	
Zr-1Nb		1	1,200–1,400			
Zr-2.5Nb		2.4–2.8	1,200–1,400			

Fe and 200 ppm for Cr at the maximum solubility temperature. In the Zircaloy's, they form intermetallic compounds: $Zr_2(Ni, Fe)$ and $Zr(Cr, Fe)_2$.

Niobium (columbium) is a β stabilizer. A monotectoid transformation occurs at about 620°C and around 18.5 at % Nb. By water quenching from the β or upper $\alpha + \beta$ regions, the β Nb-rich grains transform by martensitic decomposition into an α' supersaturated hcp phase; subsequent heat treatment below the monotectoid temperature leads to the precipitation of β' Nb precipitates at twin boundaries of α' needles.

Microstructure

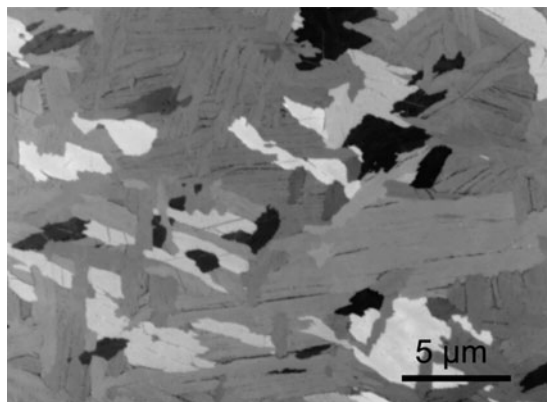
After ingot melting, the thermomechanical processing commonly used for industrial alloys is the following:

- Hot forging in the β range (1,000–1,050°C)
- Water quenching from the homogeneous β phase (above 1,000°C)
- Intermediate temperature (upper α) forging and rolling, or extrusion for tubes
- A series of cold temperature rolling steps followed by intermediate anneals under vacuum

Homogenization in the β phase leads to the complete dissolution of all the second phase particles, but induces significant grain growth. During the water quench, the β grains transform into α needles by bainitic transformation according to the cooling rates of the large ingots involved. The β -eutectoid elements are repelled by the transformation front and precipitate at the boundaries of those needles. This β quench is a reference state for further processing (► *Fig. 39*). The cold working steps and intermediate anneals allow further control of the precipitate size whose size distribution is critical for corrosion control.

In Zr-1%Nb alloys used for cladding material, such as E110 or M5[®], the α -Zr structure is close to fully recrystallized after the final anneal at 580°C. The structure of the tubes reveals finely dispersed β -Nb precipitates along boundaries of α -Zr grains and in the matrix, but the α -Zr phase itself is supersaturated in Nb and an irradiation-induced precipitation occurs, which is considered to be the origin of the improvement of corrosion resistance after irradiation of these alloys.

Advanced multicomponent alloys are under development. Based on Zry, Zirlo[®] or E635, the multicomponent Zr 1%Nb 0.7-1.3%Sn 0.2-0.6 %Fe alloys, proposed as cladding and pressure tube material, are claimed to exhibit a higher corrosion resistance than the Zircaloy's in specific



■ Figure 39

Microstructure of a β -quenched Zr alloy. The four orientations of the α grains come from the same former β grain (polarized light)

environments. This is caused by the availability of intermetallic particles containing Zr, Nb, Fe in the form of $Zr(Nb, Fe)_2$ or $(Zr, Nb)_4Fe_2$ types.

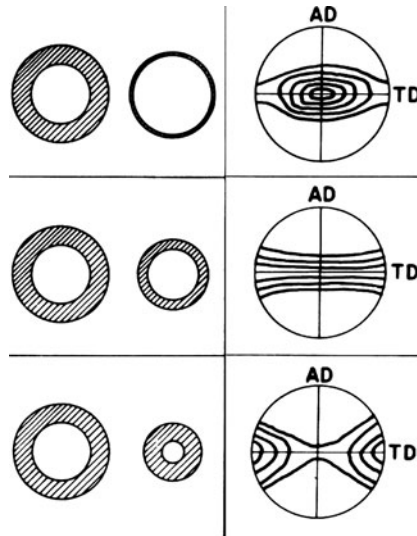
Deformation Processing and Textures

The room temperature deformation mechanisms of the hexagonal Zr follow two main mechanisms, depending on the relative orientations of the grains in the stress field. Plastic deformation of Zr alloys is obtained either by dislocation slip, mostly with glide on prism planes or by twinning during cold rolling. At higher deformations and temperatures, $(c+a)$ -type slip is activated on pyramidal planes.

At the large strains obtained during mechanical processing, steady state interactions occur between the twinning and slip systems that tend to align the basal planes parallel to the direction of the main deformation. For cold-rolled materials (sheets or tubes), the crystallographic textures are such that the majority of the grains have their c -axis tilted $30\text{--}40^\circ$ away from the normal of the sheet, or of the tube surface, towards the tangential direction, as can be seen in the $\langle 0001 \rangle$ pole figure sketched in ► Fig. 40. During tube rolling, the spread of the texture can be reduced by action on the ratio of the thickness to diameter reduction (Q factor): a reduction in thickness higher than the reduction in diameter gives a more radial texture, i.e., a texture with the $\langle c \rangle$ poles closer to the radial direction.

Mechanical Properties

At room temperature, in the annealed state, pure, oxygen-free Zr, has a low yield strength of 150 MPa. This yield strength can be increased by solution strengthening, using alloying elements of high solubility: Oxygen, tin, and niobium. As a result, the Zircaloy's have minimal yield strengths in the range of 250–300 MPa and the Zr 2.5%-Nb alloy of 300 MPa. Additional strength is obtained by cold working, with yield strength above 400–450 MPa. In order to restore ductility without drastic reduction in strength, a final stress-relief heat treatment is often



■ **Figure 40**
Effect of the Q ratio on the crystallographic texture of Zr alloy tubes (From Cook et al. 1991)

performed. Finally, the texture itself can increase the material strength by changing the Schmid factor for slip or twinning.

4.2.2 Dislocation Loops: Growth and Irradiation Creep

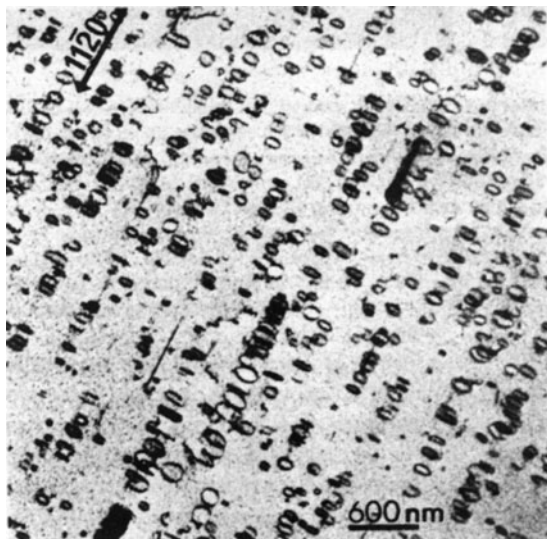
Irradiation Effects in the Zr Matrix

Contrary to the behavior of stainless steel, Zircaloy does not exhibit significant void formation under neutron irradiation. Dislocation loops developing under irradiation are mostly $\langle a \rangle$ type $1/3 \langle 11\bar{2}0 \rangle$ loops, as shown in ► [Fig. 41](#). Both vacancy and interstitial loops have been reported, in roughly comparable proportions (Northwood 2005; Griffiths et al. 1983). This is an unusual feature of microstructural development under irradiation specific to Zr and its alloys, as compared to cubic metals and other hcp metals, where only one type of loop usually grows.

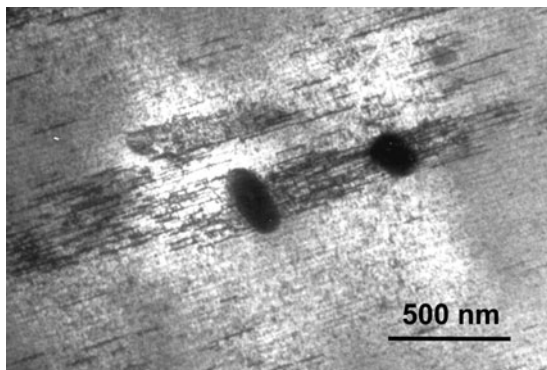
After neutron irradiation to around $3 \times 10^{25} \text{ n} \cdot \text{m}^{-2}$ at temperatures between 560 K and 773 K, $\langle c \rangle$ -component dislocations start to develop in annealed Zircaloy-2. They are located on the basal plane, are vacancy in character and have a $1/6 \langle 20\bar{2}3 \rangle$ Burgers vector. Some of those $\langle c \rangle$ -type loops are shown developing near dissolving amorphous precipitates (see ► [Fig. 42](#)). They have been linked to the occurrence of breakaway growth.

Irradiation Effects on Second Phases

An important effects of irradiation on Zr alloys is the crystalline to amorphous transformation (amorphization) observed in the intermetallic precipitates $\text{Zr}(\text{Cr}, \text{Fe})_2$ and $\text{Zr}_2(\text{Ni}, \text{Fe})$ (see ► [Fig. 10](#)). At 350 K, both types of precipitates are completely amorphous after very low



■ Figure 41
Alignment of $\langle a \rangle$ loops in Zircaloy irradiated at a low dose (From Northwood 2005)



■ Figure 42
 $\langle c \rangle$ -type dislocation loops in the vicinity of an amorphous precipitate (From de Carlan 1996)

fluences (0.5–1 dpa). At the higher temperature range, the $Zr_2(Ni,Fe)$ precipitates are completely crystalline, while the $Zr(Cr,Fe)_2$ precipitates are partially amorphous having developed a “duplex” structure, consisting of an amorphous layer that starts at the precipitate–matrix interface, and gradually moves into the precipitate until the precipitate is completely amorphous (Griffiths 1988). Amorphization is associated with a depletion of iron from the amorphous layer into the Zr matrix, while the Cr concentration in the precipitate remains constant.

Irradiation Growth

Irradiation growth refers to the dimensional changes at constant volume of an unstressed material under irradiation. Irradiation growth is due to the partitioning of interstitials and vacancies to different sinks that are not isotropically distributed in the material: cold-work- or irradiation-induced dislocations and grain boundaries of different orientations.

For Zr single crystals, irradiation growth consists of an expansion along the $\langle a \rangle$ direction, and corresponding contraction along the $\langle c \rangle$ axis. In polycrystalline materials the situation is more complex, since grain boundaries can act as biased sinks for point defects, so that grain shape and orientation play also a role (Fidleris 1988).

The fabrication process of Zr alloy components induces a crystallographic texture: For Zircaloy cladding tubes, prism planes are preferentially aligned perpendicular to the axial (longitudinal) direction. Thus, irradiation growth causes the axial length to increase and the cladding thickness to diminish. Irradiation growth is influenced by microstructural variables such as amount of cold work, residual stresses and alloying additions, as well as by irradiation variables such as flux and temperature. In addition to “normal growth,” after a fluence of about $3 \times 10^{25} \text{ n} \cdot \text{m}^{-2}$ a “breakaway phenomenon” is observed, which has been linked to the development of $\langle c \rangle$ component dislocations (► Fig. 42) (Griffiths et al. 1989; Christien and Barbu 2009).

Irradiation Creep

Irradiation creep refers to the steady deformation rate observed under external stresses experienced by materials under irradiation. A large amount of creep tests has been performed in materials test reactors, as well as in detailed examinations of structural material behavior of power reactors. For practical purposes and for typical ranges of operating parameters, the thermal and irradiation creep strains may be added and described accurately with a simple equation of the form:

$$\dot{\epsilon} = A\sigma^n \cdot \exp\left(\frac{-Q}{kT}\right) + B\sigma^m \phi^n \quad (41)$$

where the effect of flux, stress, and temperature can be separated. The standard values of those exponents are $m = 0.6\text{--}1$ and n near $2\text{--}4$. The activation energy, Q , is low, in the range of $0.05\text{--}0.16 \text{ eV} \cdot \text{at}^{-1}$. It is thought that irradiation creep deformation occurs by dislocation climb and glide, the climb being controlled by the stress-modified absorption of point defects at dislocations (Ribis et al. 2009; Gilbon et al. 2005; Causey 1981). According to the so-called SIPA mechanism, dislocations that have their Burgers vectors parallel to the applied stress preferentially annihilate interstitials better than vacancies, leading to dimensional changes due to the dislocation climb itself and to the subsequent dislocation glide. In addition, migration anisotropy of interstitials in an applied stress field has to be taken into account.

4.2.3 Postirradiation Plastic Behavior

Due to the high concentration of PD clusters produced by neutron irradiation (point defects and dislocation loops), dislocation slip is inhibited and thus the yield strength increases after irradiation. This effect is rapidly saturated at fluences which vary with irradiation temperatures. For power reactors, the increase of the yield strength or UTS saturates above

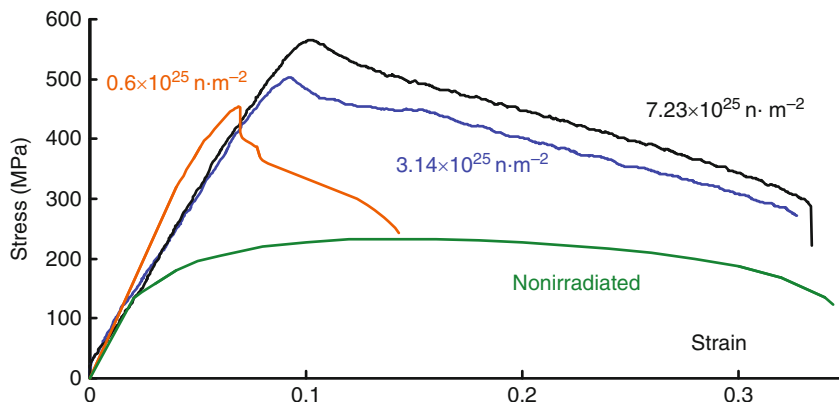


Figure 43
Effect of irradiation on the mechanical properties of Zry4 (From Regnard et al. 2002)

about $5 \times 10^{24-25} \text{ n} \cdot \text{m}^{-2}$. This saturation value is the same for both SR and RX Zircaloy's: The increased density of dislocation loops increases the critical shear stress for dislocation glide. Since the increase in loop concentration under neutron irradiation saturates rapidly due to overlap of their influence volumes, the increase in yield strength saturates as well.

This increase in yield strength is associated with a reduction in ductility, affecting both the uniform elongation (through a reduction of the strain hardening exponent), and the total elongation, decreasing from about 20% to a few % (► Fig. 43) (Adamson and Bell 1985; Adamson 2000).

The reduction in strain hardening exponent can lead to a strain softening behavior after irradiation. The high density of dislocation loops in the prismatic planes inhibits the mobility of the gliding dislocations along these planes and a basal slip is activated. The interaction between the loops and these gliding dislocations, of identical Burgers' vector, leads to the annealing of the loops (Carpenter 1976; Onimus et al. 2004). The result is the formation of loop free channels along which easy basal slip is obtained (see ► Fig. 14).

4.2.4 Corrosion Behavior and Effects of Irradiation on Corrosion

General Corrosion Behavior

Zr alloys are highly resistant to corrosion in common media and are used for that reason in the chemical industry. Those alloys are however not immune to oxidation and in the high temperature water environment found in a power reactors (water at 280–340°C and 10–15 MPa), corrosion is a critical design parameter for the fuel rods and other components.

In the early stages of oxidation in such environments, a thin compact black oxide film develops that is protective and inhibits further oxidation. The kinetics of this first corrosion step follows a power law, usually described by a thermally activated power law:

$$\varepsilon_{\text{ZrO}_2} = k_c t^n \exp\left(\frac{-Q}{kT}\right) \quad (42)$$

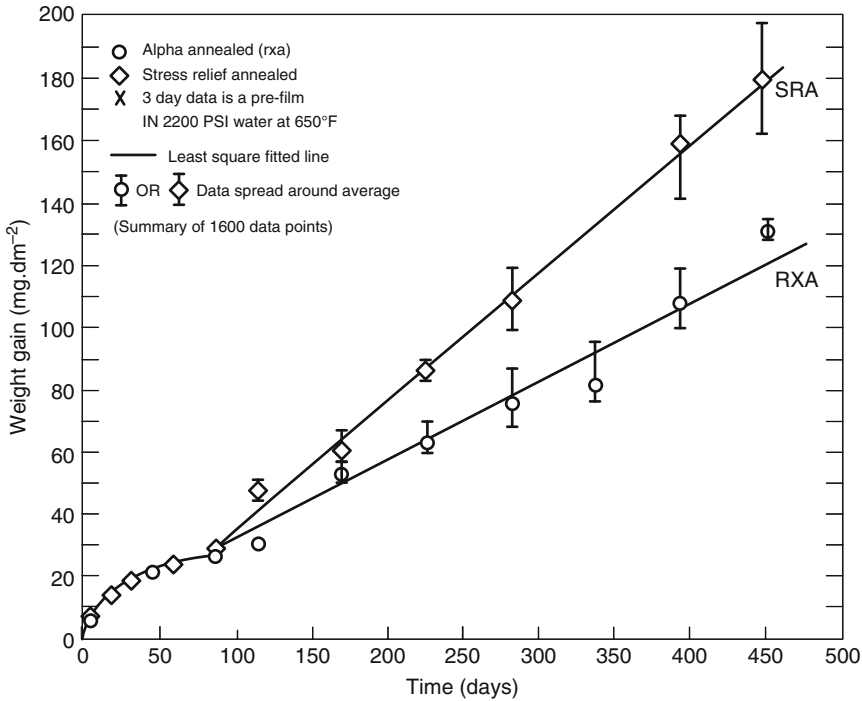
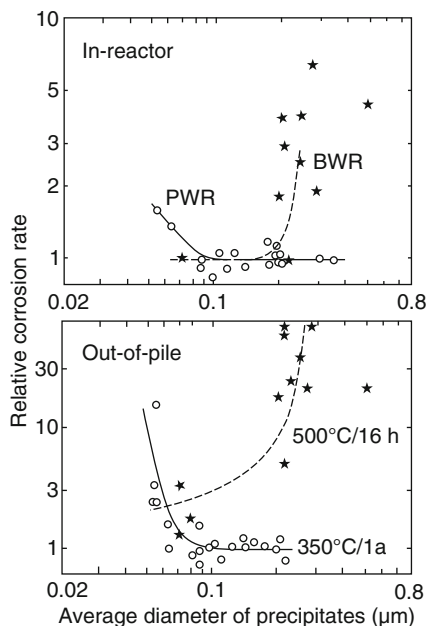


Figure 44

Corrosion kinetics of Zry, showing the transition at about $2\ \mu\text{m}$ (From Cheng et al. 1994)

The activation energy of $1.35\ \text{eV}\cdot\text{at}^{-1}$, for corrosion in the dense oxide regime, is equivalent to activation of the diffusion of oxygen in zirconia. Oxygen is indeed considered to diffuse from the free surface of the oxide as O^{-2} , by a vacancy mechanism through the zirconia layer along the grain boundaries, and to react with the zirconium at the matrix–oxide interface (Cox et al. 2008).

The inner dense layer of zirconia is rich in the tetragonal allotropic form, a phase normally stable at high pressure and temperature. The swelling induced by oxidation (Pilling–Bedworth ratio of 1.56) leads to the build-up of compressive stresses that stabilize this high pressure phase (Bouvier et al. 2002). As the oxidation proceeds, the compressive stresses in the oxide layer cannot be counterbalanced by the tensile stresses in the metallic substrate and plastic yield in the metal limits the compression in the oxide. The tetragonal phase becomes unstable and the oxide transforms to the monoclinic form. In connection with this transformation, a very fine interconnected porosity develops and allows the oxidizing water to access closer to the corrosion interface (Parise et al. 1998; Petigny et al. 2000). Once this transformation has occurred, only a portion of the oxide layer remains protective. The corrosion kinetics is therefore now controlled by diffusion of oxygen through the dense protective oxide layer only. Since the thickness of this layer remains constant, in the range of $1\ \mu\text{m}$, the corrosion rate is constant after this transition (Fig. 44).



■ Figure 45

Impact of precipitate size and environment on the corrosion kinetics of Zry (From Garzarolli et al. 1994)

In this dense oxide layer the structure of the zirconia, which controls the post-transition corrosion kinetics, is complex and still under discussion. Starting from the metal–oxide interface, a very thin layer of questionable amorphous oxide has been reported under particular conditions, a few nm in thickness. It is followed by a zone of very small zirconia crystallites, 10–20 nm, that become larger in diameter and columnar in shape further into the oxide layer. For thick oxide layers, in excess of 100 μm , the oxide may spall-out.

The intermetallic precipitates are known to remain unoxidized in the dense oxide layer. During their oxidation, they are supposed to act as Fe reservoirs, improving the protective behavior of the zirconia layer. Such behavior would explain the impact of precipitate size on corrosion behavior (► Fig. 45) (Iltis et al. 1995; Pecheur et al. 1994).

In BWR's, nodular corrosion has been a design limiting phenomenon. Several mechanisms have been proposed for the nucleation of those nodules, leading to various possible sites for nodule nucleation: metallic matrix grain boundaries, local rupture of the continuous dense oxide at an early stage of growth, local variations in composition and precipitates densities or crystallographic orientation of clusters of grains (Kruger et al. 1992).

For the Zr-Nb alloys, the corrosion behavior is slightly different, with a less pronounced transition and a beneficial effect of irradiation. Indeed the corrosion kinetics seems to be more controlled by surface reaction kinetics than by the migration of O^{2-} through the Zr layer. Under irradiation, the Nb that was left in supersaturation after the final heat treatments can precipitate by an irradiation-enhanced mechanism. Indeed the kinetics of thermal precipitation is very

low, but the faster diffusion under irradiation allows an acceleration of diffusion and precipitation. The microstructure obtained has a better corrosion resistance (Jeong et al. 2003). Thus in opposite of the Zry's, Zr-Nb alloys usually exhibit an improvement in corrosion resistance after irradiation (Lin and Woo 2000; Doriot et al. 2005).

Hydrogen Pick-Up

During oxidation of Zr alloy, H is released according to:



The reduction of the water molecules at the coolant-oxide interface releases hydrogen as radicals H^+ . Most of them recombine creating hydrogen molecules that escape through the pore and dissolve into the coolant. A limited amount (5–40% of the H formed) can ingress in the oxide, migrate through to the metallic matrix and then react with Zr for the formation of hydrides.

A consequence of the H pick-up is the hydride embrittlement. The high concentration of H dissolved in the Zr alloy after corrosion can exceed the solubility in temperature, but H will always precipitate at room temperature. Indeed, the solubility of H in Zr alloys is strongly temperature dependent. Higher than 200 ppm at operating temperature, it is below 1 ppm at room temperature. During cooling, H precipitates as fine platelets of hydrides Zr $\text{H}_{1.6}$. This phase is brittle at low temperatures and high H concentrations can lead to a brittle behavior during fuel maneuvering or other low temperature operations (Singh et al. 2004; Bertolino et al. 2003).

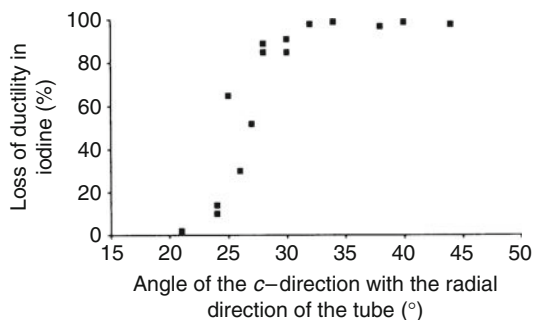
4.2.5 Interaction with Fission Products I-SCC and PCI Failure

Pellet cladding Interaction (PCI) is a mode of water reactor fuel rod failure that has been observed after fast power transients. Early observations of PCI on BWR's was rapidly analyzed as a mechanical interaction between the cladding and the expanding UO_2 pellet, associated with chemical interaction of some fission products with the Zircaloy cladding (Cox 1990). A combined contribution of stresses induced by fuel pellet expansion due to linear heat generation rate (LHGR) increase and the presence of an active corrosion agent, the iodine, created in the fuel rod as a fission product, induces failure by stress corrosion cracking (SCC).

Fuel rods of various design and irradiation histories were tested in irradiation devices of test reactors. The maximum power allowable for a fuel rod of BU above $20 \text{ GW} \cdot \text{d} \cdot \text{t}^{-1}$, is in the range of $40\text{--}47 \text{ kW} \cdot \text{m}^{-1}$.

In fuel rods, the closure of the internal gap due to cladding creep-down requires in PWR's and BWR's a year or two. Once the gap is closed, any change in pellet dimension is transferred to the cladding. For a power change from 20 to $40 \text{ kW} \cdot \text{m}^{-1}$, the increase in temperatures induces a thermal expansion of about 0.5%, high enough to induce stresses close to or above the yield strength in the cladding. In the presence of iodine, SCC is expected to occur. Indeed iodine, as well as the other halogens, is known to induce such failure mechanisms in Zr and Ti alloys (Fournier et al. 2009; Fregonese et al. 2000; Sidky 1998).

The fracture surfaces are transgranular and consist mostly of large pseudo-cleavage areas along the basal planes, interconnected by fluted walls in which plastic deformation is evident. Thus the relative orientation of the basal plane with respect to the applied tensile stresses is



■ **Figure 46**
Effect of texture on I-SCC (From Schuster et al. 1993)

critical, and the effect of the texture on I-SCC is remarkable (Haddad and Dorado 1994). Constant stress and fracture mechanics tests have indeed shown that when the c -type planes tend to be aligned with the macroscopic crack surface, the susceptibility to SCC increases (Schuster et al. 1993). For cladding tubes, where the tensile stresses are the hoop stresses due to the pellet expansion, the best texture corresponds to a maximum intensity of the c direction in the radial direction (🔍 Fig. 46).

A simple solution to the PCI problem is to reduce the power change rates. Specific procedures have been implemented with success, but the drawback is a loss of power availability. For practical purposes, remedies have been found and tested to avoid PCI-type failures. For BWR's "barrier" fuel rods contain an internal layer of pure recrystallized Zr that is coextruded with the trex and is cold rolled with the base Zircaloy metal to obtain a perfect metallurgical bond.

4.3 Carbon and Graphite

4.3.1 Nuclear Graphite

The physical properties of carbon are of interest for nuclear reactors: Its atomic mass (12) and very low capture cross section (3.3×10^{-3} barn) make it a fairly good candidate for moderation. In addition, its very high temperature behavior (sublimation temperature $\sim 2,500$ K, melting around 4,700 K) allows the use of graphite for high temperature applications. Therefore graphite is used in thermal neutron reactors as moderators or structural components (UNGG, AGR, HTR, RBMK, etc.).

Graphite is the stable form of carbon. It crystallizes in a hexagonal P 63/mmc system, consisting in parallel planes of strongly bound carbon atoms in hexagonal patterns. Within the plane the bounds are covalent hybridized sp^2 links, while between planes interatomic interaction are weaker, similar to Van der Waals bounds. Therefore the graphite crystals exhibit a very high degree of anisotropy (Wang and Zheng 2007): For the thermoelastic properties, a stiff behavior is observed in plane and a soft behavior perpendicular to the hexagonal planes. For instance the interatomic distance is 0.142 nm in the basal plane, while these planes are 0.323 nm apart. The modulus of elasticity is near 1,060 GPa in plane and only 36 GPa perpendicular.

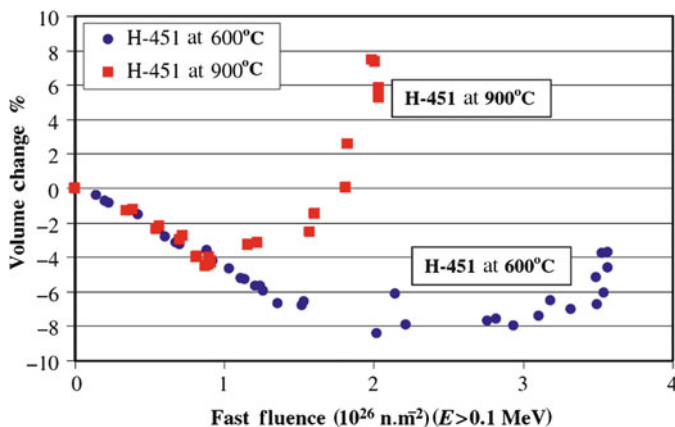
Similarly, the thermal expansion coefficient is $-1.1 \times 10^{-6} \text{ K}^{-1}$ in plane and $26 \times 10^{-6} \text{ K}^{-1}$ perpendicular. Due to the delocalized electrons within the hexagonal planes, thermal and electrical conductivities are also much larger in plane and strongly anisotropic, with differences as large as a factor of 200. Therefore the properties of industrial materials will highly depend on the crystallographic texture of the material. The consequence is that the processing routes will allow, at least partly, controlling and reducing the anisotropy.

The source of graphite for the fabrication of nuclear reactor components is restricted to a synthetic processing obtained by transformation of coke obtained from petroleum or gilsonite heated at 1,300–1,400°C. This gives a high purity for the raw material, compared to natural graphite that would not be suitable for nuclear applications. Specifically sulfur, boron, cobalt, and other neutron absorber have to be strictly controlled (Eu, Gd, Li, etc.). Blended with pitch, the coke is extruded for green shapes, before sintering and cooking at 800°C. The final product is obtained after graphitization obtained during a long treatment at very high temperature (several weeks at 2,800°C). During this process, most of the volatile impurities are removed, the crystal structure is closer to the ideal graphite structure and the density is increased. It remains however low compared to the ideal crystallographic density ($\rho_{\text{ind.}} \sim 1.7\text{--}1.8 \text{ kg} \cdot \text{dm}^{-3}$ and $\rho_{\text{theo.}} \sim 2.26 \text{ kg} \cdot \text{dm}^{-3}$) providing evidence of a sizable remaining porosity.

4.3.2 Behavior Under Irradiation

Under irradiation, damage by atom displacement occurs once the momentum transferred to the pka is above the displacement energy ($E_d \sim 30 \text{ eV}$; Iwata and Nihira 1971). The formation and migration energies of the PD have been evaluated by various means in graphite: The formation energies are high due to the covalent contribution of the bounds in the vicinity of the PD ($E_{\text{fv}} \sim 7.8 \text{ eV}$ and $E_{\text{fi}} 5.5\text{--}7 \text{ eV}$), leading to a high energy of the Frankel pairs ($E_{\text{FrankP}} \sim 14 \text{ eV}$). The interstitials are located between the hexagonal planes that are apart enough to avoid large strains for insertion and they are rather mobiles with migration energies reported between 0.1 and 1.4 eV (Telling et al. 2003). The reason for such large range of values, seems to be connected to the stability of complex clusters of these interstitial (Latham et al. 2008). The development of these clusters of interstitials between the basal planes induces the formation of interstitial dislocation loops and therefore deformations under irradiation in textured materials. For single crystals at low temperatures ($T_{\text{irr}} < 200^\circ\text{C}$), dilations are observed perpendicular to the basal planes, saturating at values as large as 25–30% for doses $> 10^{25} \text{ n} \cdot \text{m}^{-2}$ ($E > 50 \text{ keV}$), while smaller but continuous decrease in the basal directions are observed (Marsden 1995).

Similar to the growth in its mechanism, the irradiation-induced deformation of graphite begins however with a general reduction in dimension parallel and perpendicular to the processing direction, due to a reduction of the processing porosity, followed by an increase in the perpendicular direction above a dose of $1.5\text{--}2 \times 10^{26} \text{ n} \cdot \text{m}^{-2}$ ($E > 50 \text{ keV}$). Reduction in volume by 5% can be observed, followed by swelling up to 5% (► Fig. 47). The actual values are temperature and processing history dependent. For fabrication conditions leading to isotropic textures, reduced irradiation-induced strains and swelling can be obtained (Burchell and Snead 2007). These changes are associated with an increase in elastic stiffness, roughly a factor 2 for irradiation at 500°C, but lower at higher temperatures (50% increase for irradiation at 1,100–1,200°C).



■ Figure 47

Irradiation-induced volume changes for a nuclear graphite at two irradiation temperatures (From Burchell and Snead 2007)

4.3.3 Creep and Wigner Effect

Graphite is known to creep under irradiation. Two contributions on the creep strain are considered and the general equation for graphite creep is the sum of a steady state creep rate, proportional to the irradiation flux, and a transient creep, that has been found to be thermally recoverable (44)

$$\varepsilon_{\text{creep}} = \frac{\sigma}{E_0} \left[\alpha \varphi + \left(1 - e^{-\beta \varphi} \right) \right], \quad (44)$$

where α and β are parameters dependent of the type of graphite (processing) and of the temperature. Typical values of the coefficients for standard irradiation temperatures (150–650°C) are $\alpha \sim 0.20$, $\beta \sim 4$ when the fluence is expressed in $10^{24} \text{ n} \cdot \text{m}^{-2}$ EDN (equivalent DIDO nickel: $\phi \text{ EDN} \sim 0.9 \phi (E > 1 \text{ MeV})$) (Marsden 1995). The irradiation creep could induce deformations equivalent to several times the initial elastic strain.

A minimum creep rate is observed at intermediate temperatures (400–500°C) and the effect of crystallographic texture on the elastic stiffness induces a correlation between creep strain and thermal expansion, both varying in opposite directions (Davies and Bradford 2008).

An important effect of irradiation in graphite is known as the Wigner effect. It corresponds to the increase in concentration in PD and increase of internal energy induced by the build-up of this irradiation damage, and to the kinetics of the release of the corresponding energy during heat treatments: For irradiation below 200°C, any further heat treatment performed 50°C above the irradiation temperature will enhance the mobility of the PD's, allowing their recombination and the release of the corresponding energy of the Frankel pairs. Accumulations of internal energy by formation of PD's higher than $2,600 \text{ J} \cdot \text{g}^{-1}$ have been recorded. Would this energy be released adiabatically, a temperature rise of more than 1,500 K could be reached (Simmons 1965). To avoid such phenomenon to occur, with potential dramatic consequences, scheduled

thermal recoveries of the irradiated structures are programmed along the life of the reactors operating at low temperatures. Careful monitoring of the process is mandatory to avoid uncontrolled evolution of this recovery process. Such unwanted event occurred however in Windscale (UK) in 1957, leading to important release of radioactive materials in the environment (Garland and Wakeford 2007).

4.3.4 Corrosion

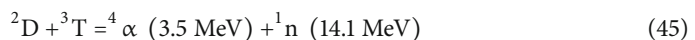
Graphite cannot be considered as an inert material in the reactor environment: CO₂, used as coolant in the corresponding reactors, can react with graphite. In HTR and variants using He as coolant, the impurities present in the cooling gas (traces of H₂O, CO₂, H₂, etc.) will also interact with graphite, leading to its corrosion. In addition, uncontrolled contaminations of the coolant by air or cooling water have to be considered during safety analysis.

The kinetics of graphite corrosion depends on its structure and on the temperature (Zherdev et al. 1992; Kelly 1985). Below 500–600°C, the step controlling process is the chemical interaction between the gaseous molecule and the graphite at any free surface. At higher temperature, and up to 1,000°C, the diffusion of gaseous species within the pores of the graphite controls the kinetics. Internal oxidation can then occur with homogeneous degradation of the properties of the component. Above 1,000°C, any gaseous oxidant will react with the carbon atoms of the graphite, and the kinetics of the reaction is only controlled by the supply of oxidant to the surface of component. Then only the external surface reacts and the component shrinks in size by external ablation.

5 Fusion Reactor Materials

5.1 Specific Environment of the Fusion Reactors

For any foreseeable future, the fusion reaction to be considered in any power fusion plants will operate with deuterium and tritium, according to the nuclear reaction:



This equation states the origins of the constraints and difficulties that the fusion reactor environment will apply to the materials. These are due to the production of tritium, and to the presence of high energy neutrons. Due to their high energy, in addition to the irradiation damage described earlier, fusion neutrons induce nuclear reactions at much higher rates than in fission reactors, inducing He and H doping, as well as large changes in composition due to transmutations. This would be the case for tungsten, changing from pure W to a W-Os-Re alloy, with more than 15% of alloying elements after 5 years of 14 MeV neutron irradiation, or Cu to Cu-Ni-Zr, Ta to Ta-W, or V to V-Cr-Ti.

The kinetic energy required for the deuterium and tritium nuclei to interact in a fusion reaction has to be higher than the Columbian repulsive energy. This is obtained within the hot plasma magnetically confined in a device called “Tokomak.” The main components of concern are the plasma facing and high heat flux components, the ³T breeding blanket, the first wall and the blanket structural parts, not forgetting all the numerous diagnostics and electromagnetic control devices.

Since for decades the R&D on fusion was mostly focused on the physical aspects (plasma behavior: heating and stability, superconducting coils, etc.) and performed on devices running far less than 100 h a year, the impact on materials remained limited and irradiation damage and long term behavior of the materials were not limiting. Material aspects have been matters of major research only recently. A consequence is that numerous design options are still open and the selection of alloys, or the class of alloys to develop, for the various components of a fusion device or a common agreement within the scientific community is still under intense international debate and cooperation (Baluc et al. 2007).

5.2 Plasma Facing and High Heat Flux Components

Depending of the location within the reactor, the interaction with the plasma and the heat flux is a strong engineering challenge. The interaction with ions escaping from the plasma leads to surface irradiation damage and sputtering, a phenomenon by which atoms of the surfaces are released when a high energy ion track is crossing the surface (Davis and Haasz 1997). In addition these elements receive a heat flux in the range of $0.5\text{--}10\text{ MW} \cdot \text{m}^{-2}$. For the highest heat fluxes, corresponding to the plasma limiters during incidental conditions, highly conducting alloys are considered, based on Cu, doped with different additions to increase the mechanical strength in temperature (Davis and Kalinin 1998).

5.3 First Wall and the Blanket Structures

For the structural components, such as the first wall and the blanket structures, the high heat and fast neutron fluxes, austenitic SS are considered due to the large data base on their behaviors. If the fast neutrons will induce a displacement damage similar to what obtained in FBR (a few hundred dpa), the high contribution of (n,α) and (n,p) reactions would significantly increase the tendency to swelling. Indeed, for a commercial fusion reactor, He and H production in these alloys could reach 6,000 and 20,000 appm respectively. The ratio of the He production to the irradiation damage is therefore more than 100-fold higher than for fission neutron irradiation, and the simulation of this high He production ratio required specific irradiation devices (Ishino 1996). Since He clusters act as nuclei for cavity nucleation (see ► 4.1.2), a higher tendency to swelling (lower incubation doses) should be expected.

Alloys for long-term development could include ferritic–martensitic steels, vanadium alloys, or SiC/SiC composites. Indeed, a potential interest of the fusion reactors is the lack of radioactive wastes produced by the fuel. Therefore, low or reduced activation materials would be of high interest to confirm fusion as a “clean” energy source.

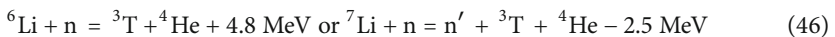
- Low activation ferritic–martensitic steels should exhibit a low swelling rate and satisfactory high temperature strength. Variant of the standard 9Cr-1Mo alloy (EM10), such as Eurofer 97 or F82H, where Mo has been replaced by W and with minor additions of V and Ta, have shown promising behaviors (Schaaf et al. 2009). ODS variants of these alloys are considered for improvements in creep behavior and reduced swelling tendency.
- Vanadium has a low activation tendency, with short decay and can be used as base metal for low activation structural alloys. Combined with Cr and Ti, as main alloying elements, V-4Cr-4Ti alloys have been developed, with compositions and structures optimized for low

irradiation embrittlement and high creep resistance. In these alloys, minor interstitial elements such as C, O, or N affect significantly the mechanical and structural behavior and their content should sharply be controlled (Kurtz et al. 2004).

- SiC–SiC fiber composites are considered for structural components of the divertor. The low activation of both Si and C, as well as the high temperature potential, would be of interest for the high thermal flux of the divertor. However the sputtering allows C and Si atoms to react with the plasma, forming methane and other hydrocarbons, which can condense in cold spots of the device, trapping H isotopes, including tritium. In case of vacuum vessel leakage, these molecules would oxidize, releasing tritiated water in the environment. The radiological consequences of such process would probably limit the potential use of C or SiC in the future fusion reactors (Rubel 2004).

5.4 Blankets and Tritium Breeding Materials

Since the fusion reaction requires tritium at a rate of about 300 g per day in a standard power plant, the fusion reactor has to produce it at the same rate as it is consumed. This is performed using nuclear reactions by high energy neutrons on Li, according to the reactions:



Due to the unavoidable neutron leakage, the continuous production of tritium at the rate it is burned requires a neutron multiplication procedure. This is obtained, with 14.1 MeV neutrons interacting with Pb or Be, for which a (n,2n) reaction occurs with significant cross section for the fusion neutrons (2 and 0.5 mbarn, respectively for 14.1 MeV neutrons).

Different design options are under consideration for the blankets, either using molten salts (Flibe, i.e., Li_2BeF_4), liquid Li–Pb alloys, or porous ceramics, swept by H_2 and He to extract tritium (Ihli et al. 2009). The radiological constraints associated with tritium handling requires an extraction–purification procedure absolutely leak proof. This technological requirement has to be achieved with consideration of the diffusion of tritium through all the high temperature metallic alloys.

6 Corrosion in Nuclear Environments

In addition to the classical corrosion phenomena observed in any industrial environment, the irradiation affects the corrosion performance of the alloys in many ways:

- Change in the corrosiveness of the environment. As described in [2.4.2](#), radiolysis in the coolant water increases the oxidizing power of the coolant. The impact is drastically evidenced in BWR's, in which numerous cracking of SS components have been reported.
- Formation of new species by nuclear reactions. For instance in fuel elements the fission products can react with the cladding. The process can be either SCC, inducing failure of the Zr alloys due to iodine, or uniform corrosion by a blend of fission products in FBR fuel pins (fuel-cladding chemical interaction) (Götzmann 1979).
- Operation of materials under chemical environment not found in other industries: primary coolant chemistry, liquid metal at high temperatures, etc.

In BWR's, the oxidizing coolant enhances the intergranular corrosion observed in sensitized SS. Numerous failures have been reported in shroud supports, control rod drives, recirculation pipes, etc. To mitigate the SCC mechanisms, actions in the three terms of SCC have been taken: Reduction of residual stresses by heat treatments after welding, grinding, or forming; reduction of sensibility of the alloys by high temperature heat treatments for solution annealing and reduction of the aggressiveness of the environment by additions (Zn injection in noble water chemistry or H₂ injection in HWC). In these environments, the crack propagation rate of SCC, is stress intensity factor dependent and can be expressed as

$$\frac{da}{dt} = 2 \times 10^{-11} K_I^2 \quad (47)$$

where da/dt is obtained in $m \cdot s^{-1}$ for K_I in $MPa \cdot m^{1/2}$.

In PWR's, corrosion in steel is of lower concern for the internals but has been a problem for the steam generators (SG). Initially made of alloy 600, the SG's have been damaged a rate much higher than anticipated by design. Intergranular cracking has been observed on the inner side of the U-bend tubes. This was induced by long incubation period of the SCC in this alloy of low Cr content.

On the secondary coolant side, environment in favor of SCC developed in various locations: denting on tube plates, inducing stresses by oxide swelling or at tube ends where the crevice configurations allowed sludge's rich in magnetite and silica to form, inducing the development of complex corrosive chemistries (NaOH, KOH, S-bearing species, carbonates, and degradation products of the resins, etc.). Design and material changes of the tube plates suppressed the denting and special procedures for swaging of the SG tubes to the tube support plate allowed to reduce the residual stresses; regular sludge lance cleaning helped in controlling the local chemistry and high Cr content alloys were used to design SG of extended operational life.

More impressive, corrosion problems induced by various leaks of primary water occurred in PWR's. The primary coolant contains boric acid: Due to leaks near the welds or due to cracking of control rod vessel penetration nozzles by SCC, primary water went in contact with the structural steel, inducing classical uniform corrosion by concentrated boric acid solution (Beznau-1, Switzerland, 1971; D. Besse, Ohio 1998–2002, etc.). Major corrosion occurred, leading to mandatory changes of the pressure vessel closing heads in numerous power plants (<http://www.nrc.gov/reactors/operating/ops-experience/vessel-head-degradation.html>). Other cases of corrosion can be found in dedicated reports. They also concern the nonnuclear parts of the plants.

7 Prospects

As in any industry, the performances of the materials used in the nuclear reactors are of uppermost importance for a sustainable operation and confidence. With that respect, the industrial operation of nuclear plants adds very severe conditions, compared to the other industrial fields. In addition to the irradiation, which is very specific to this industry and cannot be avoided to test any new alloy, the nuclear industry has two other specificities: First, due to long decay of some of the radioactive materials produced by irradiation, the behavior of the materials has to be analyzed at time scales far behind common practices; second, the dramatic consequences of potential failure requires a level of reliability only shared with the aerospace industry.

The phenomena of irradiation damage and irradiation-induced changes in behaviors are fairly well understood, at least qualitatively, and in many cases quantitatively. If the actual behaviors of alloys are not always predictable from theory, the large body of experimental testing and industrial feedback is sound enough for a safe design and operation of the industrial units.

However the material science is a science of complexity. Any industrial alloy contains 10–15 species and the microstructures, for a given composition, can be very different according to processing histories. The behavior itself is also depending of the thermomechanical loadings and of the irradiation histories. Bifurcations in behavior have been observed and care should be taken in fast screening tests. The experimental testing of these materials is becoming unfortunately more and more difficult and expensive, due to regulatory restrictions and reduced availability of material testing reactors and hot cells. In addition, irradiations cannot always be accelerated without loss of confidences. Therefore the nuclear material R&D has long experiment and testing cycles. Typically 10 years are required between the melting of a new alloy, its irradiation, analysis in hot cells, detailed results and their interpretations of the improvement of the leading composition, and a new cycle.

Therefore the current development of computational material science is a major opportunity for in depth understanding and forecasting of the mechanisms of irradiation damage under irradiation. In that direction multiscale modeling is particularly suited to nuclear materials. The scientific community of nuclear materials has already started to include these tools in their standard research methodologies. Improvements in the computations capabilities should allow extending these results, obtained on model alloys, to complex industrial alloys. One expectation would be to propose, using these techniques, nuclear grade variants of the alloys used in nonnuclear industry or to improve the ones already known, for a better behavior or extended design life. The current international reactivation of the nuclear projects is expecting important progresses in materials for more efficient and reliable plants that would require such efficient approaches.

List of Acronyms

AIC	Silver-indium-cadmium alloy for control rods
CW	Cold worked
DBTT	Ductile–brittle transition temperature
FBR	Fast breeder reactor
FIMA	Fission per initial metallic atom
GB	Grain boundary
HWC	Hydrogen water chemistry
IASCC	Irradiation-assisted stress corrosion cracking
LET	Linear energy deposition rate (radiolysis)
LHGR	Linear heat generation rate (fuel rod power)
LWR	Light water reactor
MD	Molecular dynamics
MTR	Material testing reactor
NDE	Nondestructive examination

PCI	Pellet cladding interaction
PD	Point defect
pka	Primary knock-on atom
RIC	Radiation-induced conductivity
RIED	Radiation-induced electrical degradation
RIS	Radiation-induced segregation
RPV	Reactor pressure vessel
RT_{NDT}	Reference temperature for nil ductility transition
SCC	Stress corrosion cracking
SFR	Sodium-cooled fast neutron reactor
SG	Steam generator
SIPA	Stress-induced preferential absorption (creep)
SS	Stainless steel
TREX	Tube-reduced extrusions (Zr fuel cladding processing)
WPS	Warm pre-stress

Appendix

Industrial Steels for Reactor Design

► *Tables A1–A3* are given for general information and orders of magnitudes. The compositions given correspond to the standard values. For design, actual values of composition and mechanical properties have to be verified and to fulfill the requirements of the classical design codes, such as ASME or RCCM, and be approved by the regulatory bodies having domestic authority.

■ **Table A1**
Pressure vessel steels

	C	Si	Mn	Ni	Mo
A508 Cl 3	0.2	0.2	1.3	0.6	0.3
16MND5	0.15	0.2	1.3	0.6	
A533 B	0.15	0.2–0.4	1.25	0.4–0.7	0.5

■ **Table A2**
Stainless steels for internals and pipings

	C	Si	Mn	Ni	Cr	Mo
SA 304	0.02	0.5	1.8	10	18	
CW 316	0.05	0.5	1.2	12	18	2.5
321	0.08	1	2	9–12	17–19	Ti
CF8M	0.08 max.	1.5 max.	1.5	9–12	18–21	2–3

■ Table A3

Stainless steels for steam generator tubes

Alloy	C	Fe	Si	Mn	Ni	Cr	Other
600	0.1	8	0.2	1.8	72	15.5	
690	0.05	7–11	0.5	0.5	58–60	27–30	
800	<0.1	40			30–35		Al: 0.5, Ti: 0.5

References

- Adamson, RB (2000) Effects of neutron irradiation on microstructure and properties of Zircaloy. ASTM-STP 1354:15–31
- Adamson, RB, Bell WL (1985) Effect of neutron irradiation and oxygen content on the microstructure and mechanical properties of Zry. In: *Microstructure and mechanical behaviour of materials*, Xian, China, EMAS, Warley, UK, Internal Symposiums, vol 1, pp 237–246
- Ahlf J et al (1989) The consideration of irradiation embrittlement of RPV steels in German licensing rules as compared to recent results of irradiation experiments. *Nucl Eng Des* 112:155–164
- Andersen, PL (1996), Irradiation-assisted stress-corrosion-cracking. In: Jones RH (ed) *Stress corrosion cracking – materials performance and evaluation*. ASM International, Materials Park, ISBN: 9780871704412, pp 181–210
- ASTM Standards E-1921-97 (1998) Standard test method for determination of reference temperature T_0 for ferritic steels in the transition range
- ASTM Standards E-521-96 (2003) Standard practice for neutron radiation damage simulation by charged-particle irradiation
- ASTM Standards E-693-01 (2007) Standard practice for characterizing neutron exposures in iron and low alloy steels in terms of displacements per atom (DPA)
- Auger P et al (1995) APFIM investigation of clustering in neutron-irradiated Fe-Cu alloys and pressure vessel steels. *J Nucl Mater* 225:225–230
- Auger P et al (2000) Synthesis of atom probe experiments on irradiation-induced solute segregation in French ferritic pressure vessel steels. *J Nucl Mater* 280:331–344
- Averback RS (1986) Fundamental aspects of ion beam mixing. *Nucl Inst Meth B* 15:675–687
- Azam N, Le Naour L, Delaplace J (1973) Evolution de la densité de dislocations dans des aciers austénitiques du type 316 L irradiés par des ions Ni⁺ de moyenne énergie. *J Nucl Mater* 49:197–208
- Bacon DJ et al (1995) Computer simulation of defect production by displacement cascades in metals. *Nucl Inst Meth B* 102:37–46
- Bacon DJ, Gao F, Osetsyky Y (2000) The primary damage state in fcc, bcc and hcp metals as seen in molecular dynamics simulations. *J Nucl Mater* 276:1–12
- Balachov II et al (2004) Influence of radiation-induced voids and bubbles on physical properties of austenitic structural alloys. *J Nucl Mater* 329–333:617–620
- Balluffi RW (1978) Vacancy defect mobilities and binding energies obtained from annealing studies. *J Nucl Mater* 69–70:240–263
- Baluc N et al (2007) Status of R&D activities on materials for fusion power reactors. *Nucl Fusion* 47:S696–S717
- Bass BR, Williams PT, Pugh CE (2005) An updated correlation for crack-arrest fracture toughness for nuclear reactor pressure vessel steels. *Int J Pressure Vessels Piping* 82:489–495
- Becquart CS et al (2000) Influence of the interatomic potentials on molecular dynamics simulations of displacement cascades. *J Nucl Mater* 280:73–85
- Bertolino G, Meyer G, Perez Ipina J (2003) Effects of hydrogen content and temperature on fracture toughness of Zircaloy-4. *J Nucl Mater* 320:272–279
- Bloch J (1962) Effet de l'irradiation par les neutrons sur les alliages uranium-fer a faible teneur en fer. *J Nucl Mater* 6:203–212
- Bonin B, Colin M, Dutfoy A (2000) Pressure building during the early stages of gas production in a radioactive waste repository. *J Nucl Mater* 281:1–14
- Bouniol P, Bjergbakke E (2008) A comprehensive model to describe radiolytic processes in cement medium. *J Nucl Mater* 372:1–15
- Bourgouin J et al (1999) The behaviour of control rod absorber under irradiation. *J Nucl Mater* 275:296–304

- Bouvier P, Godlewski J, Lucazeau G (2002) A Raman study of the nanocrystallite size effect on the pressure-temperature phase diagram of zirconia grown by zirconium-based alloys oxidation. *J Nucl Mater* 300:118-126
- Brager HR, Garner FA (1982) Influence of neutron spectra on the radiation-induced evolution of AISI 316. *J Nucl Mater* 108-109:347-358
- Brager HR, Garner FA, Gilbert ER, Flinn JE, Wolfer WG (1977) Radiation effects in breeder reactor structural materials, Scottsdale, AZ, pp 727-755
- Brager HR, Blackburn LD, Greenslade DL (1984) The dependence on displacement rate of radiation-induced changes in microstructure and tensile properties of AISI 304 and 316. *J Nucl Mater* 122:332-337
- Brailsford AD, Bullough R (1972) The rate theory of swelling due to void growth in irradiated metals. *J Nucl Mater* 44:121-135
- Bruemmer SM et al (1999) Radiation-induced material changes and susceptibility to intergranular failure of light-water-reactor core internals. *J Nucl Mater* 274:299-314
- Bullough R, Willis JR (1975) The stress-induced point defect-dislocation interaction and its relevance to irradiation creep. *Phil Mag* 31:855-861
- Bullough R, Hayns MR, Woo CH (1979) The sink strength of dislocation loops and their growth in irradiated materials. *J Nucl Mater* 84: 93-100
- Burchell TD, Snead LL (2007) The effect of neutron irradiation damage on the properties of grade NBG-10 graphite. *J Nucl Mater* 371:18-27
- Burns WG, Moore PB (1976) Water radiolysis and its effect upon in-reactor Zircaloy corrosion. *Radiat Effects Defects Solids* 30:233-242
- Buxton GV, Mulazzani QG, Ross AB (1995) Critical review of rate constants for reactions of transients from metal ions and metal complexes in aqueous solution. *J Phys Chem Ref Data* 24: 1055-1349
- Cai Z et al (2001) Radiolysis of bicarbonate and carbonate aqueous solutions: product analysis and simulation of radiolytic processes. *Nucl Tech* 136:231-240
- de Carlan Y et al (1996) Influence of iron in the nucleation of $\langle c \rangle$ component dislocation loops in irradiated Zircaloy-4. *ASTM-STP* 1295:638-653
- Carpenter GJC (1976) Dislocation channelling by prism slip in hcp metals. *Scr Metall* 10:411-413
- Carver MB, Hanley DV, Chaplin KR (1979) MAKSIMA-CHEMIST: a program for mass action kinetics simulation by automatic chemical equation manipulation and integration using stiff techniques. *AECL-6413*
- Causey AR (1981) Anisotropy of irradiation creep of Zr-2.5wt%Nb and Zircaloy-2 alloys. *J Nucl Mater* 98:313-321
- Cawthorne C, Fulton EJ (1967) Voids in irradiated stainless steel. *Nature* 216:575-576
- Chance EM et al (1977) FACSIMILE: a computer program for flow and chemistry simulation, and general initial value problems. *AERE-R* 8775
- Chartier A et al (2003) Atomistic modeling of displacement cascades in $\text{La}_2\text{Zr}_2\text{O}_7$ pyrochlore. *Phys Rev B* 67:174102-1-13
- Cheng B, Kruger RM, Adamson RB (1994) Corrosion behaviour of irradiated Zircaloy. *ASTM-STP* 1245:400-418
- Christensen H (1994) Remodelling of the oxidant species during radiolysis of high-temperature water in a pressurized water reactor. *Nucl Tech* 109:373-382
- Christien F, Barbu A (2009) Cluster dynamics modelling of irradiation growth of zirconium single crystals. *J Nucl Mater* 393:153-161
- Chung HM, Shack WJ (2006) Irradiation-assisted stress corrosion cracking behavior of austenitic stainless steels applicable to LWR core internals. *NUREG/CR-6892 ANL-04/10*
- Cook CS et al (1991) Texture control in Zy tubing through processing. *ASTM-STP* 1132:80-95
- Cox B (1990) Pellet-clad interaction (PCI) failures of zirconium alloy fuel cladding - a review. *J Nucl Mater* 172:249-292
- Cox B et al (1998) Waterside corrosion of zirconium alloys in nuclear power plants. *IAEA TECDOC-996*, pp 1-331
- Crawford DC, Porter DL, Hayes SL (2007) Fuels for sodium-cooled fast reactors: US perspective. *J Nucl Mater* 371:202-231
- Cunningham ME, Peddicord KL (1981) Heat conduction in spheres packed in an infinite regular cubical array. *Int J Heat Mass Transfer* 24: 1081-1088
- Curie P, Debierne A (1901) Sur la radio-activité induite et les gaz activés par le radium. *Compt Rend Ac Sci Fr* 132:768-770
- Davis JW, Haasz AA (1997) Impurity release from low-Z materials under light particle bombardment. *J Nucl Mater* 241-243:37-51
- Davis JW, Kalinin GM (1998) Material properties and design requirements for copper alloys used in ITER. *J Nucl Mater* 258-263:323-328
- Davies MA, Bradford M (2008): A revised description of graphite irradiation induced creep. *J Nucl Mater* 381:39-45
- Diaz de la Rubia T et al (2000) Multiscale modelling of plastic flow localization in irradiated materials. *Nature* 406:871-874

- Dimitrov O et al (1976) Comparison of the effects of Mg and Ga additions on defect production and recovery in aluminium, neutron-irradiated at 4.6 K. *Radiat Effects Defects Solids* 30:135–146
- Dole M (1991) The radiation chemistry of polymer composites. *Int J Radiat Appl Instrum Part C Radiat Phys Chem* 37:65–70
- Doriot S et al (2005) Microstructural stability of M5 alloy irradiated up to high neutron fluences. *J ASTM Int* 2:175–201
- Drobny G (2003) *Radiation technology for polymers*. CRC Press LLC, Boca Raton, ISBN 978-1587161087
- Dubinko VI et al (2006) Modelling of the simultaneous evolution of vacancy and interstitial loops in hcp metals under irradiation. *ASTM-STP* 1467:157–174
- Dubuisson P et al (1992) The effect of phosphorus on the radiation-induced microstructure of stabilized austenitic stainless steels. *ASTM-STP* 1125:995–1014
- Dupouy JM, Lehmann J, Boutard JL (1978): Swelling and microstructure of neutron-irradiated cold worked 316 stainless steels. In: *Reactor materials science, Alushta, USSR*, pp 280–293
- Elliot AJ, Chenier MP, Ouellette DC (1993) Temperature dependence of g values for H_2O and D_2O irradiated with low linear energy transfer radiation. *J Chem Soc Faraday Trans* 89:1193–1197
- Enrique RIA, Bellon, P (2000): Compositional patterning in systems driven by competing dynamics of different length scale. *Phys Rev Lett* 84:2885–2888
- Farrell K (1981) Microstructure and tensile properties of heavily irradiated 5052-0 aluminum alloy. *J Nucl Mater* 97:33–43
- Ferradini C, Jay-Gerin JP (2000) The effect of pH on water radiolysis: a still open question – a minireview. *Res Chem Intermed* 26:549–565
- Ficher SB, Buswell JT (1987) A model for PWR pressure vessel embrittlement. *Int J Press Vessels Piping* 27:91–135
- Fidleris V (1988) The irradiation creep and growth phenomena. *J Nucl Mater* 159:22–42
- Fish RL, Holmes JJ (1973) Tensile properties of annealed type 316 stainless steel after EBR-II irradiation. *J Nucl Mater* 46:113–120
- Fissolo A et al (1990) Influence of swelling on irradiated Ti modified 316 embrittlement. *ASTM-STP* 1046:700–713
- Fissolo A et al (1994) Tensile properties of neutron irradiated 316Ti and 15-15Ti steels. *ASTM-STP* 1175:646–663
- Forty CBA, Butterworth GJ, Sublet J-C (1994) Burnup of some refractory metals in a fusion neutron spectrum. *J Nucl Mater* 212–215:640–643
- Fournier L et al (2003) The influence of oversized solute additions on radiation-induced changes and postirradiation intergranular stress corrosion cracking behavior in high-purity 316 stainless steels. *J Nucl Mater* 321:192–209
- Fournier L et al (2009) Proton irradiation effect on microstructure, strain localization and iodine-induced stress corrosion cracking in Zircaloy-4. *J Nucl Mater* 384:38–47
- Fregonese M et al (2000) Failure mechanisms of irradiated Zr alloys related to PCI: activated slip systems, localized strain and iodine-induced stress corrosion cracking. *ASTM-STP* 1354:377–398
- Fu C et al (2005) Multiscale modelling of defect kinetics in irradiated iron. *Nat Mater* 4:68–74
- Gao F et al (2001) Temperature-dependence of defect creation and clustering by displacement cascades in α -zirconium. *J Nucl Mater* 294:288–298
- Garland JA, Wakeford R (2007) Atmospheric emissions from the Windscale accident of October 1957. *Atmos Environ* 41:3904–3920
- Garner FA (1993) Evolution of microstructure in face-centred cubic metals during irradiation. *J Nucl Mater* 205:98–117
- Garner FA (1994) Irradiation performance of cladding and structural steels in liquid metal reactors. In: Frost B (ed) *Nuclear materials (10-A)*. VCH, Weinheim, ISBN: 0-89573-698-5, pp 419–543
- Garner FA, Black CA (2000) The question of saturation of voids swelling in Fe-Cr-Ni austenitic alloys. *ASTM-STP* 1366:767–777
- Garner FA, Makenas BJ (2006) Recent experimental results on neutron-induced void swelling of AISI 304 stainless steel concerning its interactive dependence on temperature and displacement rate. In: *Contribution of materials investigations to improve the safety and performance of LWRs*, Fontevraud Royal Abbey, France, SFEN, Paris, pp 625–636
- Garner FA, Toloczko MB (1997) Irradiation creep and void swelling of austenitic stainless steels at low displacement rates in light water energy systems. *J Nucl Mater* 251:252–261
- Garner FA et al (1981) The microstructural origins of yield strength changes in aisi 316 during fission or fusion irradiation. *J Nucl Mater* 103–104:803–807
- Garner FA, Porter DL, Makenas BJ (1987) A third stage of irradiation creep involving its cessation at high neutron exposures. *J Nucl Mater* 148:279–287
- Garner FA, Toloczko MB, Sencer BH (2000) Comparison of swelling and irradiation creep behavior of fcc-austenitic and bcc-ferritic/martensitic

- alloys at high neutron exposure. *J Nucl Mater* 276:123–142
- Garzarolli F, Schumann R, Steinberg E (1994) Corrosion optimized Zircaloy for BWR fuel elements. *ASTM-STP* 1245:709–723
- Gelles DS (1995) Void swelling in binary Fe-Cr alloys at 200 dpa. *J Nucl Mater* 225:163–174
- Gibson JB et al (1960) Dynamics of radiation damage. *Phys Rev* 120:1229–1253
- Gilbon D et al (2005) Irradiation creep and growth behavior, and microstructural evolution of advanced Zr-base alloys. *ASTM-STP* 1354: 51–73
- Glowinski LD, Fiche C (1976) Etude de la formation des cavités d'irradiation dans le cuivre III-irradiation aux ions cuivre de 500 keV – effet des gaz implantés. *J Nucl Mater* 61:29–40
- Götzmann O (1979) A thermodynamic model for the attack behaviour in stainless steel clad oxide fuel pins. *J Nucl Mater* 84:39–54
- Greenwood LR (1994) Neutron interactions and atomic recoil spectra. *J Nucl Mater* 216:29–44
- Greenwood LR, Garner FA (2004) Impact of transmutation issues on interpretation of data obtained from fast reactor irradiation experiments. *J Nucl Mater* 329–333:1147–1150
- Greenwood LR, Smither R (1985) SPECTER: neutron damage calculations for materials irradiations. *ANL/FPP/TM-197*
- Griffiths M (1988) A review of microstructure evolution in zirconium alloys during irradiation. *J Nucl Mater* 159:190–218
- Griffiths M (1993) Evolution of microstructure in hcp metals during irradiation. *J Nucl Mater* 205: 225–241
- Griffiths M, Loretto MH, Smallman RE (1983) Electron damage in zirconium: I. Defect structure and loop character. *J Nucl Mater* 115:313–322
- Griffiths M, Gilbert RW, Fidleris V (1989) Accelerated irradiation growth on zirconium alloys. *ASTM-STP* 1023:658–677
- International Atomic Energy Agency (2005) Guidelines for application of the master curve approach to reactor pressure vessel integrity in nuclear plants. Technical report series no. 429
- Haddad RE, Dorado AO (1994) Grain-to grain study of the mechanisms of crack propagation during iodine stress corrosion cracking of Zircaloy-4. *ASTM-STP* 1245:559–575
- Hamilton ML et al (1987) Mechanical properties and fracture behavior of 20% cold-worked 316 stainless steel irradiated to very high exposures. *ASTM-STP* 956:245–270
- Hardouin Duparc A et al (2002) Microstructure modelling of ferritic alloys under high flux 1 MeV electron irradiations. *J Nucl Mater* 302:143–155
- Hobbs LW et al (1994) Radiation effects in ceramics. *J Nucl Mater* 216:291–321
- Hodgson ER (1994) The paramount importance of dose rate in RIED effect experiments. *J Nucl Mater* 212–215:1123–1127
- Hodgson ER (2002) Challenges for insulating materials in fusion applications. *Nucl Inst Meth B* 191:744–751
<http://www.nrc.gov/reactors/operating/ops-experience/vessel-head-degradation.html>
- Huang FH (1996) Container materials in environments of corroded spent nuclear fuel. *J Nucl Mater* 231:74–82
- Hunter CW, Williams JA (1971) Fracture and tensile behavior of neutron-irradiated A533-B pressure vessel steel. *Nucl Eng Des* 17:131–148
- IAEA (1993) Corrosion of zirconium in nuclear power plants. *TECDOC-684*
- Ihli T, Basu T et al (2009) Review of blanket designs for advanced fusion reactors. *Fusion Eng Des* 83:912–919
- Iltis X, Lefebvre F, Lemaignan C (1995) Microstructural study of oxide layers formed on Zircaloy-4 in autoclave and in reactor part II: impact of the chemical evolution of intermetallic precipitates on their zirconia environment. *J Nucl Mater* 224:121–130
- Ishino S (1996) Implications of fundamental radiation damage studies in the research and development of materials for a fusion reactor. *J Nucl Mater* 239:24–33
- Iwata T, Nihira, T (1971) Atomic displacements by electron irradiation in pyrolytic graphite. *J Phys Soc Jpn* 31:1761–1783
- Jeong YH et al (2003) Influence of Nb concentration in the α -matrix on the corrosion behavior of Zr-xNb binary alloys. *J Nucl Mater* 323: 72–80
- Jostons A et al (1973) Defect structure of neutron irradiated boron carbide. *J Nucl Mater* 49: 136–150
- Kachanov M (1993) On the effective moduli of solids with cavities and cracks. *Int J Fract* 59:R17–R21
- Kelly BT (1985) The radiolytic corrosion of advanced gas-cooled reactor graphite. *Prog Nucl Energy* 16:73–96
- Kinoshita C, Zinkle SJ (1996) Potential and limitations of ceramics in terms of structural and electrical integrity in fusion environments. *J Nucl Mater* 233–237:100–110
- Kirkegaard P, Bjergbakke E, Olsen J (2007): CHEM-SIMUL: a chemical kinetics software package, <http://www.risoe.dk/jta/chemsimul/>
- Klaffky RW et al (1980) Radiation-induced conductivity of Al_2O_3 : experiment and theory. *Phys Rev B* 21:3610–3634

- Kohn W, Sham LJ (1965) Self-consistent equations including exchange and correlation effects. *Phys Rev* 140:A1133
- Konings RJM et al (1998) The influence of neutron irradiation on the microstructure of Al_2O_3 , MgAl_2O_4 , $\text{Y}_3\text{Al}_5\text{O}_{12}$ and CeO_2 . *J Nucl Mater* 254:135–142
- Kraut A, Dworschak F, Wollenberger H (1971) Analysis of point defect states in copper. III. Interaction between copper interstitials and impurities. *Phys Stat Sol (b)* 44:805–812
- Kruger RM, Adamson RB, Brenner SS (1992) Effects of microchemistry and precipitate size on nodular corrosion resistance of Zircaloy-2. *J Nucl Mater* 189:193–200
- Kryukov AM, Nikolaev Y, Nikolaeva AV (1998) Behavior of mechanical properties of nickel-alloyed reactor pressure vessel steel under neutron irradiation and post-irradiation annealing. *Nucl Eng Des* 186:353–359
- Kurtz RJ et al (2004) Recent progress on development of vanadium alloys for fusion. *J Nucl Mater* 329–333:47–55
- Latham CD et al (2008) The di-interstitial in graphite. *J Phys Condens Matter* 20:395220.1–.8
- LaVerne JA (2000) Track effects of heavy ions in liquid water. *Radiat Res* 153:487–496
- LaVerne JA, Pimblott, SM (1993) Diffusion-kinetic modeling of the electron radiolysis of water at elevated temperatures. *J Phys Chem* 97: 3291–3297
- Lee EH, Mansur LK (1990) Unified theoretical analysis of experimental swelling data for irradiated austenitic and ferritic/martensitic alloys. *Met Trans A* 21A:1021–1035
- Lin YP, Woo OT (2000) Oxidation of β -Zr and related phases in Zr-Nb alloys: an electron microscopy investigation. *J Nucl Mater* 277: 11–27
- Little EA (1993) Microstructural evolution in irradiated ferritic–martensitic steels: transitions to high dose behaviour. *J Nucl Mater* 206: 324–334
- Lucas GE (1993) The evolution of mechanical property change in irradiated austenitic stainless steels. *J Nucl Mater* 206:287–305
- MacEwen SR et al (1984) Point defect production and annihilation in neutron-irradiated zirconium. *J Nucl Mater* 123:1036–1040
- Macht M-P, Naundorf V, Wollenberger H (1981) Diffusion of alloy components under simulation irradiation. *J Nucl Mater* 104:1487–1491
- Makin MJ (1967) Radiation damage in face centered cubic metals and alloys. In: Shelly WF (ed) *Radiation effects*. Gordon and Breach Science, New York, pp 627–669
- Malerba L et al (2004) Molecular dynamics simulation of displacement cascades in Fe-Cr alloys. *J Nucl Mater* 329–333:1156–1160
- Mansur LK (1979) Irradiation creep by climb-enabled glide of dislocations resulting from preferred absorption of point defects. *Phil Mag A* 39: 497–506
- Mansur LK (1993) Theory of transitions in dose dependence of radiation effects in structural alloys. *J Nucl Mater* 206:306–323
- Mansur LK (1994) Theory and experimental background on dimensional changes in irradiated alloys. *J Nucl Mater* 216:97–123
- Mansur LK, Coghlan WA (1983) Mechanisms of helium interaction with radiation effects in metals and alloys: A review. *J Nucl Mater* 119: 1–25
- Marsden BJ (1995) Irradiation damage in graphite. IAEA-TECDOC 901-XA9642900, pp 17–46
- Martin G (1984) Phase stability under irradiation: ballistic effects. *Phys Rev B* 30:1424–1436
- Martin G, Bellon P (1997) Driven alloys. *Sol State Phys* 50:189–331
- Matthews JR, Finnis MW (1988) Irradiation creep models – an overview. *J Nucl Mater* 159: 257–285
- Mazey DJ, Hudson JA, Nelson RS (1971) The dose dependence of void swelling in A.I.S.I. 316 stainless steel during 20 MeV C^{++} irradiation at 525°C. *J Nucl Mater* 41: 257–273
- Maziasz PJ (1993) Overview of microstructural evolution in neutron-irradiated austenitic stainless steels. *J Nucl Mater* 205:118–145
- Meis C (2001) Computational study of plutonium–neodymium fluorobriholite $\text{Ca}_9\text{Nd}_{0.5}\text{Pu}_{0.5}(\text{SiO}_4)(\text{PO}_4)_5\text{F}_2$ thermodynamic properties and threshold displacement energies. *J Nucl Mater* 289:167–176
- Meis C, Chartier A (2005) Calculation of the threshold displacement energies in UO_2 using ionic potentials. *J Nucl Mater* 341:25–30
- Miller MK, Russell KF (2007) Embrittlement of RPV steels: an atom probe tomography perspective. *J Nucl Mater* 371:145–160
- Miller MK et al (2006) The effects of irradiation, annealing and reirradiation on RPV steels. *J Nucl Mater* 351:216–222
- Monnet I et al (2004) Microstructural investigation of the stability under irradiation of oxide dispersion strengthened ferritic steels. *J Nucl Mater* 335:311–321
- Motta AT, Lemaignan C (1992) A ballistic mixing model for the amorphization of precipitates in Zircaloy under neutron irradiation. *J Nucl Mater* 195:277–285

- Motta AT, Lefebvre F, Lemaignan C (1991): Amorphisation of precipitates in Zircaloy under neutron and charged particle irradiation. *ASTM-STP 1132:718–739*
- Neely HH (1970) Damage rate and recovery measurements on zirconium after electron irradiation at low temperatures. *Radiat Effects 3:189–201*
- Neustroev VS, Garner FA (2008) Very high swelling and embrittlement observed in a Fe-18Cr-10Ni-Ti hexagonal fuel wrapper irradiated in the BOR-60 fast reactor. *J Nucl Mater 378:327–332*
- Neustroev VS, Garner FA (2009) Severe embrittlement of neutron irradiated austenitic steels arising from high void swelling. *J Nucl Mater 386–388:157–160*
- Norgett MJ, Robinson MT, Torrens IM (1975) A proposed method of calculating displacement dose rates. *Nucl Eng Des 33:50–54*
- Northwood DO (2005) Irradiation damage in zirconium and its alloys. *Atom Energy Rev 15: 547–610*
- Odette GR (1983) On the dominant mechanism of irradiation embrittlement of reactor pressure vessel steels. *Scr Metall 17:183–1188*
- Odette GR (1988) On mechanisms controlling swelling in ferritic and martensitic alloys. *J Nucl Mater 155–157:921–927*
- Odette GR (2001) Nuclear reactors: pressure vessel steels. In: Buschow KHJ, Cahn RW, Flemings MC, Ilshchner B, Kramer EJ, Mahajan S, Veyssi re P (eds), *Encyclopedia of materials: Science and technology*. Elsevier, Oxford, ISBN: 0-08-0431526, pp 6369–6376
- Odette GR, Lucas GE (1998) Recent progress in understanding reactor pressure vessel steel embrittlement. *Radiat Effects Defects Solids 144:189–231*
- Onimus F et al (2004) A statistical TEM investigation of dislocation channelling mechanism in neutron irradiated zirconium alloys. *J Nucl Mater 328:165–179*
- Ono K, Mifune T, Meshii M (1968) Yield stress increase in electron irradiated copper. *Phil Mag 17:235–240*
- Osetsky Y et al (2002) Atomistic study of the generation, interaction, accumulation and annihilation of cascade-induced defect clusters. *J Nucl Mater 307–311:852–861*
- Parise M, Sicardy O, Cailletaud G (1998) Modelling of the mechanical behavior of the metal-oxide system during Zr alloy oxidation. *J Nucl Mater 256:35–46*
- Pastina B, Isabey J, Hickel B (1999) The influence of water chemistry on the radiolysis of the primary coolant water in pressurized water reactors. *J Nucl Mater 264:309–318*
- Pecheur D et al (1993) Effect of irradiation on the precipitate stability in Zr alloys. *J Nucl Mater 205:445–451*
- Pecheur D et al (1994) Oxidation of Inter metallic precipitates in Zircaloy 4: impact of irradiation. *ASTM STP 1245:687–708*
- Pells GP (1994a) Radiation effects in ceramic insulators. In: *Microstructure of irradiated materials*, Boston, MA, MRS Symp. Proc., vol 373, pp 275–285
- Pells GP (1994b) Radiation damage effects in alumina. *J Am Ceram Soc 77:368–377*
- Petigny N et al (2000) In situ XRD analysis of the oxide layers formed by oxidation at 743 K on Zircaloy 4 and Zr-1Nb-O. *J Nucl Mater 280: 318–330*
- Phillips DC et al (1984) The radiation swelling of bitumens and bitumenised wastes. *J Nucl Mater 125:202–218*
- Pichon C et al (2007) Effect of cobalt hydroxosulphide on organic material radiolysis. *J Nucl Mater 362:502–509*
- Piercy GR (1969) The effect of the fast neutron spectrum on the rate and distribution of damage in zirconium. *J Nucl Mater 29:267–284*
- Pineau A (2006) Development of the local approach to fracture over the past 25-years: theory and applications. *Int J Fract 138:139–166*
- Pokor C et al (2004a) Irradiation damage in 304 and 316 stainless steels: experimental investigation and modeling. Part I: evolution of the microstructure. *J Nucl Mater 326:19–29*
- Pokor C et al (2004b) Irradiation damage in 304 and 316 stainless steels: experimental investigation and modeling. Part II: irradiation induced hardening. *J Nucl Mater 326: 30–37*
- Radiguet B, Barbu A, Pareige P (2007) Understanding of copper precipitation under electron or ion irradiations in FeCu 0.1wt% ferritic alloy by combination of experiments and modelling. *J Nucl Mater 360:104–117*
- Regnard C et al (2002) Activated slip systems and localized straining of irradiated alloys in circumferential loadings. *ASTM-STP 1423:384–399*
- Ribis J et al (2009) Creep behavior of irradiated zirconium alloys, an experimental approach and a micromechanical modelling. *ASTM-STP 1505:674–689*
- Rodney D, Martin G (2000) Dislocation pinning by glissile interstitial loops in a nickel crystal: a molecular-dynamics study. *Phys Rev B 61:8714–8725*
- Rothman SJ, Nowicki LJ, Murch GE (1980) Self diffusion in austenitic Fe-Cr-Ni alloys. *J Phys F Met Phys 10:383–398*

- Rowcliffe AF (2009) Perspectives on radiation effects in nickel-base alloys for applications in advanced reactors. *J Nucl Mater*, 292:341–352
- Rubel M (2004) Fusion reactor materials and components: issues related to radioactivity and radiation-induced effects. *Fusion Sci Technol* 45:467–474
- Rupa N, Churier-Bossennec H, Bezdikian G (2006) Materials and NDE aspects in the RPV operating condition behaviour. In: Contribution of materials investigations to improve the safety and performance of LWRs, Fontevraud, France, SFEN, Paris, France, pp 715–729
- Russell KC (1984) Phase stability under irradiation. *Prog Mater Sci* 28:229–434
- Schaaf BVD et al (2009) High dose, up to 80 dpa, mechanical properties of Eurofer 97. *J Nucl Mater* 386–388:236–240
- Schuster I, Lemaignan C, Joseph J (1993) Influence of irradiation on iodine induced stress corrosion cracking behaviour of Zircaloy4. *SMIRT-12*. C03-2, pp 45–50
- Scott P (1994) A review of irradiation assisted stress corrosion cracking. *J Nucl Mater* 211:101–122
- Seran J, Dupouy JM (1982) The swelling of solution annealed 316 cladding in Rapsodie and Phénix. *ASTM-STP* 782:5–16
- Seran J et al (1990) The swelling behavior of Ti stabilized steels used as structural materials of fissile subassemblies in Phénix. *ASTM-STP* 1046: 739–752
- Seran J et al (1992) Behavior under neutron irradiation of the 15-15Ti and EMI0 steels used as standard materials of the Phénix fuel subassembly. *ASTM-STP* 1125:1209–1233
- Sidky PS (1998) Iodine stress corrosion cracking of Zircaloy reactor cladding: iodine chemistry (a review). *J Nucl Mater* 256:1–17
- Simeone D et al (1999) Study of B_4C microstructure evolution under neutron irradiation by x-ray diffraction profiles analysis. *J Nucl Mater* 264:295–308
- Simmons JHW (1965) Radiation damage in graphite. Pergamon Press, Oxford
- Singh RN et al (2004) Stress-reorientation of hydrides and hydride embrittlement of Zr-2.5 wt% Nb pressure tube alloy. *J Nucl Mater* 325:26–33
- Sizmann R (1978) The effect of radiation upon diffusion in metals. *J Nucl Mater* 69–70:386–412
- Soisson F (2006) Kinetic Monte Carlo simulations of radiation induced segregation and precipitation. *J Nucl Mater* 349:235–250
- Souidi A et al (2001) Atomic displacement cascade distributions in iron. *J Nucl Mater* 295: 179–188
- Stathopoulos AY, Pells GP (1983) Damage in the cation sublattice of Al_2O_3 irradiated in an HVEM. *Phil Mag A* 47:381–394
- Steele LE (1966) Radiation embrittlement of reactor pressure vessel steels. *Nucl Eng Des* 3:287–298
- Steele LE (1993) Radiation embrittlement of nuclear reactor pressure vessel steels: an international review. *ASTM-STP* 1170, Philadelphia, ISBN 0-8031-1478-8
- Stoller RE, Mansur LK (1990) The influence of displacement rate on damage accumulation during the point defect transient in irradiated materials. In: International conference on radiation material science, Alushta (USSR), pp 52–67
- Stoto T, Zuppiroli L, Pelissier J (1985) Absence of defect clusters in electron irradiated boron carbide. *Radiat Effects Defects Solids* 90:161–170
- Stoto T et al (1990) Swelling and microcracking of boron carbide subjected to fast neutron irradiations. *J Appl Phys* 68:3198–3206
- Summers GP et al (1980) Radiation damage in $MgAl_2O_4$. *Phys Rev B* 21:2578–2584
- Sunaryo G et al (1995a) Radiolysis of water at elevated temperatures – II. Irradiation with γ -rays and fast neutrons up to 250°C. *Radiat Phys Chem* 45:131–139
- Sunaryo G, Katsumura Y, Ishigure K (1995b): Radiolysis of water at elevated temperatures – III. Simulation of radiolytic products at 25 and 250°C under the irradiation with γ -rays and fast neutrons. *Radiat Phys Chem* 45:703–714
- Swiatla-Wojcik D, Buxton GV (1995) Modeling of radiation spur processes in water at temperatures up to 300°C. *J Phys Chem* 99:11464–11471
- Tahraoui A, Morris JH (1995) Decomposition of Solvent extraction media during nuclear reprocessing: literature review. *Sep Sci Technol* 30: 2603–2630
- Takaki S et al (1983) The resistivity recovery of high purity and carbon doped iron following low temperature electron irradiation. *Radiat Effects Defects Solids* 79:87–122
- Tanaka T et al (2006) Comparison of electrical properties of ceramic insulators under gamma ray and ion irradiation. *Fusion Eng Des* 81:1027–1031
- Tavlet M, Fontaine A, Schönbacher H (1998) Compilation of radiation damage test data, II, CERN, Geneva
- Telling RH et al (2003) Wigner defects bridge the graphite gap. *Nat Mater* 2:333–337
- Ungar G (1981) Radiation effects in polyethylene and *n*-alkanes. *J Mat Sci* 16:2635–2656
- Urban K, Yoshida N (1981) The threshold energy for atom displacement in irradiated copper studied by high-voltage electron microscopy. *Phil Mag A* 44:1193–1212

- Urquidi-Macdonald M, Pitt, J, Macdonald, DD (2007) The impact of radiolytic yield on the calculated ECP in PWR primary coolant circuits. *J Nucl Mater* 362:1–13
- Vincent E et al (2008) Precipitation of the FeCu system: a critical review of atomic kinetic Monte Carlo simulations. *J Nucl Mater* 373:387–401
- Voskoboinikov RE, Osetsky Y, Bacon DJ (2008) Computer simulation of primary damage creation in displacement cascades in copper. I. Defect creation and cluster statistics. *J Nucl Mater* 377: 385–395
- Wada Y et al (1999) Empirical understanding of the dependency of hydrogen water chemistry effectiveness on BWR designs. *J Nucl Sci Technol* 36:169–178
- Wallin K (1993) Irradiation damage effects on the fracture toughness transition curve shape for reactor pressure vessel steels. *Int J Pressure Vessels Piping* 55:61–79
- Wallin K (2003) Master Curve implementation of the warm pre-stress effect. *Eng Fract Mech* 70: 2587–2602
- Wang LF, Zheng QS (2007) Extreme anisotropy of graphite and single-walled carbon nanotube bundles. *Appl Phys Lett* 90:153113
- Was GS, Busby JT (2005) Role of irradiated microstructure and microchemistry in irradiation-assisted stress corrosion cracking. *Phil Mag* 85:443–465
- Wassilew C, Ehrlich K, Bergmann HJ (1987): Analysis of the in-reactor creep and rupture life behavior of stabilized austenitic stainless steels and the nickel-base alloy Hastelloy-X. *ASTM-STP* 956:30–53
- Weber WJ et al (1998) Radiation effects in crystalline ceramics for immobilisation of high level nuclear waste and plutonium. *J Mater Res* 13:1434–1484
- Westmoreland JE et al (1975) Dose rate effects in nickel-ion-irradiated nickel. *Radiat Effects Defects Solids* 26:1–16
- White DP et al (1998) In situ measurement of radiation induced conductivity in oxide insulators during neutron irradiation. *J Appl Phys* 83: 1924–1930
- Wilks RS (1968) Neutron-induced damage in BeO, Al₂O₃ and MgO – a review. *J Nucl Mater* 26: 137–173
- Wollenberger H (1994) Phase transformations under irradiation. *J Nucl Mater* 216:63–77
- Woo CH, Garner FA (1992) A SIPA-based theory of irradiation creep in the low swelling rate regime. *J Nucl Mater* 191–194:1309–1312
- Woo CH, Singh BN (1992) Production bias due to clustering of point defects in irradiation-induced cascades. *Phil Mag A* 65:889–912
- Yamamoto T et al (2007) The transport and fate of helium in nanostructured ferritic alloys at fusion relevant He/dpa ratios and dpa rates. *J Nucl Mater* 367–370:399–410
- Yano T et al (2000) Neutron irradiation damage in aluminum oxide and nitride ceramics up to a fluence of 4.2×10^{26} n/m². *J Nucl Mater* 283–287:947–951
- Yeh T-K, McDonald DD, Motta AT (1995) Modeling water chemistry, electrochemical potential and crack growth rate in the boiling water reactor heat transport circuit – I: The DAMAGE PREDICTOR algorithm. *Nucl Sci Eng* 121:468–482
- Yoo MH, Stiegler JO (1978) Point defect interactions and growth of dislocation loops. *J Nucl Mater* 69–70:813–815
- Yoon KK et al (2001) Japanese fracture toughness data analysis using Master Curve method. In: ASME pressure vessel and piping, Atlanta, GA, ASME
- Yoshida N et al (1991) Microstructure-tensile property correlation of 316 SS in low-dose neutron irradiations. *J Nucl Mater* 179–181:1078–1082
- Zherdev FF et al (1992) The effect of neutron irradiation on the reactor graphite corrosion kinetics. *J Nucl Mater* 189:333–342
- Zinkle SJ, Kinoshita C (1997) Defect production in ceramics. *J Nucl Mater* 251:200–217
- Zinkle SJ, Maziasz PJ, Stoller RE (1993) Dose dependence of the microstructural evolution in neutron-irradiated austenitic stainless steel. *J Nucl Mater* 206:266–286
- Zinkle SJ, Hodgson ER, Shikama T (1997) Summary of the 9th IEA workshop on radiation effects in ceramic insulators. ORNL/L-6068, pp 1–9

7 Mathematics for Nuclear Engineering

Dan Gabriel Cacuci¹ · Mihaela Ionescu-Bujor²

¹Institute for Nuclear Technology and Reactor Safety,
Karlsruher Institut für Technologie (KIT), Karlsruhe, Germany
dan.cacuci@kit.edu

²Fusion Program, Karlsruher Institut für Technologie (KIT),
Karlsruhe, Germany

1	<i>Finite-Dimensional Vector Spaces</i>	645
1.1	Vectors: Definitions and Operations	645
1.2	Matrices: Basic Definitions and Properties	649
2	<i>Elements of Functional Analysis</i>	663
2.1	Operators in Vector Spaces	663
2.2	Differential Calculus	675
3	<i>Special Functions</i>	682
3.1	The Gamma Function: $\Gamma(z)$	682
3.2	The Beta Function	684
3.3	The ψ Function	685
3.4	The Generalized Zeta and Riemann's Zeta Functions	686
3.5	Bernoulli's Numbers and Polynomials	687
4	<i>Bessel Functions</i>	688
4.1	Bessel Functions of General Order	688
4.2	Modified Bessel Functions of General Order	688
4.3	Bessel Functions of Integer Order	689
4.4	Modified Bessel Functions of Integer Order	690
4.5	Spherical Bessel Functions	690
4.6	Miscellaneous Formulas	691
4.7	Zeros of Bessel Functions	691
4.8	Fourier-Bessel and Dini Series	693
4.9	Asymptotic Expansions	694
4.10	Integrals	695
4.11	Additional Theorems and Related Series	697
5	<i>Associated Legendre Functions</i>	697
5.1	Differential Equation	697
5.2	Asymptotic Series for Large Values of $ v $	699
5.3	Recursion Relations	700
5.4	Spherical Functions (Associated Legendre Functions with Integral Indices)	701
6	<i>Orthogonal Polynomials</i>	704

6.1	Legendre Polynomials: $P_n(z)$	705
6.2	Gegenbauer Polynomials: $C_n^\lambda(t)$	708
6.3	Chebyshev Polynomials $T_n(x)$ and $U_n(x)$	709
6.4	Hermite Polynomials $H_n(x)$	710
6.5	Laguerre Polynomials	712
7	<i>Probability Theory and Statistical Estimation</i>	714
7.1	Introduction	714
7.2	Multivariate Probability Distributions	720
7.3	Expectations and Moments	723
7.4	Variance, Standard Deviation, Covariance, and Correlation	725
7.5	Commonly Encountered Probability Distributions	732
7.6	Central Limit Theorem	740
7.7	Statistical Estimation	741
7.8	Stationary Random Sequence and White Noise	746
8	<i>Fourier Transforms</i>	746
8.1	Fourier Transforms of Continuous Functions	746
8.2	Properties of Fourier Transform	747
8.3	Fourier Transform of Discrete Functions	747
8.4	Fourier Series	747
	<i>Bibliography</i>	749

Abstract: This chapter intends to provide a ready reference to mathematical concepts and tools customarily used in nuclear science and engineering, thus facilitating the reading of the other chapters in this handbook. The material presented in this chapter addresses the mathematical requisites at the graduate level in nuclear engineering, summarizing the following topics: vectors and vector spaces, matrices and matrix methods, linear operators and their adjoints in finite and infinite dimensional vector spaces, differential calculus in vector spaces, optimization, least squares estimation, special functions of mathematical physics, integral transforms, and probability theory. A list of suggested textbooks, covering many of the details omitted in this chapter, is provided in the Bibliography Section.

1 Finite-Dimensional Vector Spaces

1.1 Vectors: Definitions and Operations

A *number field* \mathcal{F} is defined as an arbitrary collection of numbers within which the four operations of addition, subtraction, multiplication, and division by a nonzero number can always be carried out. Examples of number fields are the set of all integer numbers, the set of all rational numbers, the set of all real numbers, and the set of all complex numbers.

Vectors: Let \mathbb{R} denote the set of all *real* numbers. A *real row vector* \mathbf{x} is an ordered m -tuple of real numbers (x_1, x_2, \dots, x_m) arranged in a row $\mathbf{x} = (x_1, x_2, \dots, x_m)$. The term x_i is called the i^{th} -*component* or the *coordinate* (with respect to the standard coordinate system) of the row vector \mathbf{x} of *size* or *order* or *dimension* m . The *column vector* $\mathbf{x} = (x_1, x_2, \dots, x_m)^T$ is obtained by transposing a row vector; in this context, “ T ” denotes transposition. By convention, the vectors considered in this chapter are column vectors (unless specified otherwise), and \mathbb{R}^m denotes the *set of all m -dimensional real column vectors*. The *null* or *zero* vector is the vector with all components zero, and is denoted by $\mathbf{0}$. A *real scalar* is defined as a real vector having just one component. Similarly, \mathbb{C} denotes the set of all *complex* numbers, and \mathbb{C}^m denotes the set of all complex vectors of size m .

Operations on vectors: Consider the vectors $\mathbf{x} = (x_1, x_2, \dots, x_m)^T$, $\mathbf{y} = (y_1, y_2, \dots, y_m)^T$ and $\mathbf{z} = (z_1, z_2, \dots, z_m)^T$, together with the real scalars a , b , and c . The component-wise *sum* or *addition* of vectors is defined as $\mathbf{z} = \mathbf{x} + \mathbf{y}$, where $z_i = x_i + y_i$ for $i = 1, \dots, m$. The *vector difference* is also defined similarly. The *scalar multiplication* of a vector \mathbf{x} by a real number a is defined as $\mathbf{z} = a\mathbf{x}$, where $z_i = ax_i$, for $i = 1, \dots, m$.

Linear vector space: A *set* or a *collection*, \mathcal{V} , of real vectors of size m is called a (*linear*) *vector space* if the following conditions are fulfilled:

- (a) $\mathbf{x} + \mathbf{y} \in \mathcal{V}$ whenever $\mathbf{x}, \mathbf{y} \in \mathcal{V}$; \mathcal{V} is *closed* under addition.
- (b) $(\mathbf{x} + \mathbf{y}) + \mathbf{z} = \mathbf{x} + (\mathbf{y} + \mathbf{z})$; addition is *associative*.
- (c) $\mathbf{x} + \mathbf{y} = \mathbf{y} + \mathbf{x}$; addition is *commutative*.
- (d) \mathcal{V} contains the null vector $\mathbf{0}$ and $\mathbf{x} + \mathbf{0} = \mathbf{0} + \mathbf{x} = \mathbf{x}$.
- (e) For every \mathbf{x} , there is a *unique* \mathbf{y} in \mathcal{V} such that $\mathbf{x} + \mathbf{y} = \mathbf{y} + \mathbf{x} = \mathbf{0}$; \mathbf{y} is called the (*additive*) *inverse* of \mathbf{x} and is denoted by $-\mathbf{x}$.
- (f) $a\mathbf{x}$ is in \mathcal{V} if \mathbf{x} is in \mathcal{V} ; \mathcal{V} is closed under *scalar* multiplication.
- (g) $a(b\mathbf{x}) = (ab)\mathbf{x}$, for all $\mathbf{x} \in \mathcal{V}$, and $a, b \in \mathbb{R}$.
- (h) $1(\mathbf{x}) = \mathbf{x}$, where 1 is the real number 1, for all $\mathbf{x} \in \mathcal{V}$.
- (i) $a(\mathbf{x} + \mathbf{y}) = a\mathbf{x} + a\mathbf{y}$; *distributivity*.
- (j) $(a + b)\mathbf{x} = a\mathbf{x} + b\mathbf{x}$; *distributivity*.

The space \mathcal{V} is called a complex vector space if the scalar field is the set of all complex numbers, \mathbb{C} , or a real vector space if the scalar field is the set of all real numbers, \mathbb{R} . The members \mathbf{x} , \mathbf{y} , and \mathbf{z} of \mathcal{V} are called points, elements, or vectors depending on the respective context. If there exists a positive integer n such that \mathcal{V} contains n , but not $n + 1$ linearly independent vectors, then \mathcal{V} is said to be *finite dimensional* with dimension n ; \mathcal{V} is *infinite dimensional* if and only if (iff) it is not finite dimensional. The *finite-dimensional vector space of dimension n* is denoted by \mathbb{R}^n , for every $n \geq 1$. The finite set \mathcal{S} of vectors in an n -dimensional space \mathcal{V} is called a *basis* of \mathcal{V} iff \mathcal{S} is linearly independent, and each element of \mathcal{V} may be written as $\sum_1^n \alpha_j \mathbf{x}_j$ for some $\alpha_1, \dots, \alpha_n \in \mathbb{C}$ and $\mathbf{x}_1, \dots, \mathbf{x}_n \in \mathcal{S}$. An infinite-dimensional space is obtained by generalizing \mathbb{R}^n or \mathbb{C}^n , and taking infinite sequences $\mathbf{x} = (\mathbf{x}_n)$ as the elements of the space. This space is known as a *sequence space* and is usually denoted by ℓ .

For an infinite sequence $\mathbf{x} = \{x_0, x_1, x_2, \dots\}$, such that $\sum_{i=0}^{\infty} x_i^2 < \infty$, the sequence \mathbf{x} is called *square summable*. The set of all square summable sequences is denoted by l_2 , and constitutes a vector space under component-wise addition and scalar multiplication.

Consider that \mathcal{S} is a subset of \mathcal{V} , and define its complement \mathcal{V}/\mathcal{S} as the set of all elements in \mathcal{V} that do not belong to \mathcal{S} . Next, define a new subset $\bar{\mathcal{S}} \subset \mathcal{V}$, called the closure of \mathcal{S} , by requiring that $\mathbf{x} \in \bar{\mathcal{S}}$ iff there is a sequence of (not necessarily distinct) points of \mathcal{S} converging to \mathbf{x} . The set \mathcal{S} is called closed iff $\mathcal{S} = \bar{\mathcal{S}}$. A subset \mathcal{S} of \mathcal{V} is said to be open iff its complement \mathcal{V}/\mathcal{S} is closed. If $\mathcal{S}_1 \subset \mathcal{S}_2 \subset \mathcal{V}$, then \mathcal{S}_1 is said to be *open* in \mathcal{S}_2 iff it is the intersection of an open set with \mathcal{S}_2 . A *neighborhood* of a point is any set that contains an open set that itself contains the point. A point \mathbf{x} is an *interior point* of $\mathcal{S} \subset \mathcal{V}$ iff there is a neighborhood of \mathbf{x} contained in \mathcal{S} . The *interior* \mathcal{S}° of \mathcal{S} is the set of interior points of \mathcal{S} (and is open). A point \mathbf{x} is a *boundary point* of \mathcal{S} iff every neighborhood of \mathbf{x} contains points of both \mathcal{S} and its complement \mathcal{V}/\mathcal{S} . The *boundary* $\partial\mathcal{S}$ of \mathcal{S} is the set of boundary points of \mathcal{S} .

Inner Product: The *inner* or *scalar* product of two vectors \mathbf{x} and \mathbf{y} in \mathbb{R}^m , denoted by $\langle \mathbf{x}, \mathbf{y} \rangle$ and/or $\mathbf{x}^T \mathbf{y}$, is defined as

$$\langle \mathbf{x}, \mathbf{y} \rangle = \mathbf{x}^T \mathbf{y} = \sum_{i=1}^m x_i y_i = \sum_{i=1}^m y_i x_i = \mathbf{y}^T \mathbf{x} = \langle \mathbf{y}, \mathbf{x} \rangle$$

and satisfies the following properties:

- Positive definite:* $\langle \mathbf{x}, \mathbf{y} \rangle > 0$ if $\mathbf{x} \neq \mathbf{0}$; $\langle \mathbf{x}, \mathbf{y} \rangle = 0$ if and only if $\mathbf{x} = \mathbf{0}$.
- Commutative:* $\langle \mathbf{x}, \mathbf{y} \rangle = \langle \mathbf{y}, \mathbf{x} \rangle$.
- Additive:* $\langle \mathbf{x} + \mathbf{y}, \mathbf{z} \rangle = \langle \mathbf{x}, \mathbf{z} \rangle + \langle \mathbf{y}, \mathbf{z} \rangle$.
- Homogeneous:* $\langle a\mathbf{x}, \mathbf{y} \rangle = a \langle \mathbf{x}, \mathbf{y} \rangle = \langle \mathbf{x}, a\mathbf{y} \rangle$.

If $\langle \mathbf{x}, \mathbf{z} \rangle = \langle \mathbf{y}, \mathbf{z} \rangle$ for \mathbf{x} , \mathbf{y} , \mathbf{z} in \mathbb{R}^m , then $\mathbf{x} = \mathbf{y}$. When \mathbf{x} and \mathbf{y} are *complex vectors*, then the inner product is defined as $\langle \mathbf{x}, \mathbf{y} \rangle = \sum_{i=1}^m x_i \bar{y}_i$ where \bar{y}_i is the complex conjugate of y_i .

Outer Product: The *outer product* of \mathbf{x} and \mathbf{y} in \mathbb{R}^m is denoted by $\mathbf{x}\mathbf{y}^T$ and is defined as the $m \times m$ matrix

$$\begin{aligned} \mathbf{x}\mathbf{y}^T &= \begin{pmatrix} x_1 \\ x_2 \\ \dots \\ x_m \end{pmatrix} (y_1, y_2, \dots, y_m) = [\mathbf{x}y_1, \mathbf{x}y_2, \dots, \mathbf{x}y_m] = \begin{bmatrix} x_1\mathbf{y}^T \\ x_2\mathbf{y}^T \\ \dots \\ x_m\mathbf{y}^T \end{bmatrix} \\ &= \begin{bmatrix} x_1y_1 & x_1y_2 & \dots & x_1y_m \\ x_2y_1 & x_2y_2 & \dots & x_2y_m \\ \vdots & \vdots & \vdots & \vdots \\ x_my_1 & x_my_2 & \dots & x_my_m \end{bmatrix}. \end{aligned}$$

Norm: The *norm* of a vector $\mathbf{x} \in \mathbb{R}^m$, denoted by $\|\mathbf{x}\|$, is a nonnegative real scalar that indicates the size or the length of the vector \mathbf{x} , and satisfies the following properties:

1. *Positive definite:* $\|\mathbf{x}\| > 0$ if $\mathbf{x} \neq \mathbf{0}$; $\|\mathbf{x}\| = 0$ if $\mathbf{x} = \mathbf{0}$.
2. *Homogeneous:* $\|a\mathbf{x}\| = |a| \|\mathbf{x}\|$.
3. *Triangle inequality:* $\|\mathbf{x} + \mathbf{y}\| \leq \|\mathbf{x}\| + \|\mathbf{y}\|$.

A vector space \mathcal{V} endowed with a norm as defined above is called a *normed* vector space. For finite dimensional spaces, the most frequently used vector norm is the *Hölder* or ℓ_p -*norm*, defined as

$$\|\mathbf{x}\|_p = \left(\sum_{i=1}^n |x_i|^p \right)^{1/p}, \quad p > 0.$$

The most frequently used norms are

- (a) *Euclidian or 2-norm* $\|\mathbf{x}\|_2 = \sqrt{\sum_{i=1}^n |x_i|^2}$; note that $\|\mathbf{x}\|_2^2 = \langle \mathbf{x}, \mathbf{x} \rangle = \mathbf{x}^T \mathbf{x}$.
- (b) *Manhattan or 1-norm* $\|\mathbf{x}\|_1 = \sum_{i=1}^m |x_i|$.
- (c) *Chebyshev or ∞ -norm* $\|\mathbf{x}\|_\infty = \max_i |x_i|$.
- (d) *Energy norm* $\|\mathbf{x}\|_A = \langle \mathbf{x}, A\mathbf{x} \rangle^{1/2} = (\mathbf{x}^T A \mathbf{x})^{1/2}$, where $A \in \mathfrak{R}^{m \times m}$ is a *real, symmetric and positive definite* matrix.

Note that the 2-norm satisfies the *parallelogram identity*

$$\|\mathbf{x} + \mathbf{y}\|_2^2 + \|\mathbf{x} - \mathbf{y}\|_2^2 = 2(\|\mathbf{x}\|_2^2 + \|\mathbf{y}\|_2^2).$$

If the length of a vector \mathbf{x} is finite in one norm and is also finite in another norm, the two norms are said to be *equivalent*. The 2-norm, 1-norm, and ∞ -norm are all equivalent, and are related through the following inequalities: $\|\mathbf{x}\|_2 \leq \|\mathbf{x}\|_1 \leq \sqrt{n} \|\mathbf{x}\|_2$; $\|\mathbf{x}\|_\infty \leq \|\mathbf{x}\|_2 \leq \sqrt{n} \|\mathbf{x}\|_\infty$; $\|\mathbf{x}\|_\infty \leq \|\mathbf{x}\|_1 \leq n \|\mathbf{x}\|_\infty$.

The *distance* between two vectors \mathbf{x} and \mathbf{y} , denoted by $d(\mathbf{x}, \mathbf{y})$, is defined as $d(\mathbf{x}, \mathbf{y}) = \|\mathbf{x} - \mathbf{y}\|$. In particular, the \mathbb{R}^n -space endowed with the 2-norm is called the *finite-dimensional Euclidean space*. The *unit vector*, $\hat{\mathbf{x}}$, in the direction of \mathbf{x} , $\mathbf{x} \in \mathbb{R}^m$, is given by $\hat{\mathbf{x}} = \mathbf{x} / \|\mathbf{x}\|_2 = (\hat{x}_1, \hat{x}_2, \dots, \hat{x}_m)^T$, where the components \hat{x}_i are called the *direction cosines* (the cosine of the angle made by the vector \mathbf{x} with respect to the i^{th} -coordinate axis, for $i = 1, \dots, m$). If p and q are such that $1/p + 1/q = 1$, then the *Minkowski inequality* $\mathbf{x}^T \mathbf{y} \leq \|\mathbf{x}\|_p \|\mathbf{y}\|_q$ holds; The special case $p = q = 2$ is called the *Cauchy-Schwartz inequality*:

$$\langle \mathbf{x}, \mathbf{y} \rangle = \mathbf{x}^T \mathbf{y} = \|\mathbf{x}\|_2 \|\mathbf{y}\|_2 \cos \theta \leq \|\mathbf{x}\|_2 \|\mathbf{y}\|_2; \quad \theta \text{ is the angle between } \mathbf{x} \text{ and } \mathbf{y}.$$

Assuming that the basic operations – *add, subtract, multiply, divide* and *compare*, take an equal amount of time that is taken as the unit of time, the number of *floating point operations (FLOP)* for the various vector operations are as follows: vector sum/difference (m FLOPs); scalar times a vector (m FLOPs); inner product ($2m-1$ FLOPs); outer product (m^2 FLOPs); 2-norm squared ($2m-1$ FLOPs).

Orthogonality: two vectors \mathbf{x} and \mathbf{y} are called *orthogonal*, and denoted as $\mathbf{x} \perp \mathbf{y}$, if their inner product is zero:

$$\mathbf{x} \perp \mathbf{y} \text{ if } \langle \mathbf{x}, \mathbf{y} \rangle = \mathbf{x}^T \mathbf{y} = 0.$$

In a set of n vectors, $\mathcal{S} = \{\mathbf{x}_1, \mathbf{x}_2, \dots, \mathbf{x}_n\}$, $\mathbf{x}_i \in \mathbb{R}^m$, the respective vectors are called *mutually orthogonal* if they are pairwise orthogonal, i. e.,

$$\langle \mathbf{x}_i, \mathbf{x}_j \rangle = \mathbf{x}_i^T \mathbf{x}_j = \begin{cases} 0, & \text{for } i \neq j, \\ \|\mathbf{x}_i\|_2, & \text{for } i = j. \end{cases}$$

If the vectors in \mathcal{S} are also normalized to have unit length, then \mathcal{S} is called an *orthonormal* set.

Conjugacy Two vectors \mathbf{x} and \mathbf{y} in \mathbb{R}^m are called *A-conjugate* if $\langle \mathbf{x}, \mathbf{A}\mathbf{y} \rangle = \mathbf{x}^T \mathbf{A}\mathbf{y} = 0$, where $\mathbf{A} \in \mathbb{R}^{m \times m}$ is a *symmetric positive definite matrix*. Similarly, a set of n vectors, $\mathcal{S} = \{\mathbf{x}_1, \mathbf{x}_2, \dots, \mathbf{x}_n\}$, $\mathbf{x}_i \in \mathbb{R}^m$, is called *A-conjugate* if

$$\langle \mathbf{x}_i, \mathbf{A}\mathbf{x}_j \rangle = \begin{cases} 0, & \text{for } i \neq j, \\ \mathbf{x}_i^T \mathbf{A}\mathbf{x}_i = \|\mathbf{x}_i\|_A^2, & \text{for } i = j. \end{cases}$$

Linear combination: The vector \mathbf{y} , defined as $\mathbf{y} = a_1\mathbf{x}_1 + a_2\mathbf{x}_2 + \dots + a_n\mathbf{x}_n$, where $\mathbf{x}_i = (x_{i1}, x_{i2}, \dots, x_{im})^T$ are vectors in a set $\mathcal{S} = \{\mathbf{x}_1, \mathbf{x}_2, \dots, \mathbf{x}_n\}$, $\mathbf{x}_i \in \mathbb{R}^m$, and where a_1, a_2, \dots, a_n denote scalars, is called a *linear combination* of vectors in \mathcal{S} . If this linear combination is zero when *not all* the scalars a_i are zero, then the vectors in \mathcal{S} are said to be *linearly dependent*. On the other hand, if \mathbf{y} is zero only when all the scalars a_i are zero, then the vectors in \mathcal{S} are called *linearly independent*.

Span and subspace: The *span* of a set $\mathcal{S} = \{\mathbf{x}_1, \mathbf{x}_2, \dots, \mathbf{x}_n\}$, $\mathbf{x}_i \in \mathbb{R}^m$, denotes the set of all linear combination of vectors in \mathcal{S} , i.e., $\text{Span}(\mathcal{S}) = \{\mathbf{y} | \mathbf{y} = \sum_{i=1}^n a_i \mathbf{x}_i, a_i \in \mathbb{R}^m\}$. $\text{Span}(\mathcal{S})$ is a linear vector space (generated by vectors in \mathcal{S}) called the *subspace* of \mathbb{R}^m , i.e., $\text{Span}(\mathcal{S}) \subseteq \mathbb{R}^m$. The null vector $\mathbf{0}$ belongs to $\text{Span}(\mathcal{S})$; furthermore, the set $\{\mathbf{0}\}$, consisting of all null vector, is also a subspace of \mathbb{R}^m , called the *trivial subspace*.

Basis and dimension: Consider that \mathcal{V} is a vector space and \mathcal{S} is a subset of linearly independent vectors in \mathcal{V} . If every vector in \mathcal{V} can be uniquely expressed as a linear combination of those in \mathcal{S} , then \mathcal{S} is called a *basis* for \mathcal{V} . The number of linearly independent vectors in \mathcal{S} is called the *dimension* of \mathcal{V} , denoted by $\text{Dim}(\mathcal{V})$. If the vectors of \mathcal{S} are orthogonal (orthonormal), then \mathcal{S} is called an orthogonal (orthonormal) *basis* for \mathcal{V} .

Standard unit vectors and basis: the set $\mathcal{S} = \{\mathbf{e}_1, \mathbf{e}_2, \dots, \mathbf{e}_m\}$, where $\mathbf{e}_i = (0, 0, \dots, 1, 0, \dots, 0)^T \in \mathbb{R}^m$ is a vector with 1 as its i^{th} -element, is called the *standard basis* for \mathbb{R}^m ; the vector \mathbf{e}_i is called the *standard unit vector* for \mathbb{R}^m . Any vector $\mathbf{x} = (x_1, x_2, \dots, x_m)^T$ in \mathbb{R}^m can be written as $\mathbf{x} = \{x_1\mathbf{e}_1, x_2\mathbf{e}_2, \dots, x_m\mathbf{e}_m\}$; the scalar x_i is called the i^{th} -coordinate of \mathbf{x} .

Direct sum and orthogonal complement: Consider two vector spaces, \mathcal{V}_1 and \mathcal{V}_2 . If every vector in \mathcal{V}_1 is also a vector in \mathcal{V}_2 , but *not* vice versa, then \mathcal{V}_1 is called the *proper subspace* of \mathcal{V}_2 , and is denoted by $\mathcal{V}_1 \subset \mathcal{V}_2$. The following relation holds: $\text{Dim}(\mathcal{V}_1 \cup \mathcal{V}_2) = \text{Dim}(\mathcal{V}_1) + \text{Dim}(\mathcal{V}_2) - \text{Dim}(\mathcal{V}_1 \cap \mathcal{V}_2)$. Consider now that $\mathcal{S} \subset \mathcal{V}$ is a subspace of a vector space \mathcal{V} . The set \mathcal{S}^\perp of all vectors in \mathcal{V} that are orthogonal to those in \mathcal{S} is called the *orthogonal complement* of \mathcal{S} in \mathcal{V} . The following relation holds: $\mathcal{V} = \mathcal{S} \oplus \mathcal{S}^\perp$, an operation called the *direct sum* of \mathcal{S} and \mathcal{S}^\perp . Note that $\mathcal{S} \cap \mathcal{S}^\perp = \{\mathbf{0}\}$ and $\text{Dim}(\mathcal{V}) = \text{Dim}(\mathcal{S}) + \text{Dim}(\mathcal{S}^\perp)$.

Completion theorem: Consider that $\mathcal{S}_1 = \{\mathbf{x}_1, \mathbf{x}_2, \dots, \mathbf{x}_n\}$ is a set of n linearly independent vectors in a vector space \mathcal{V} of dimension $m, n < m$. Then there exists a set $\mathcal{S}_2 = \{\mathbf{y}_1, \mathbf{y}_2, \dots, \mathbf{y}_{m-n}\}$ of linearly independent vectors (distinct from \mathcal{S}_1), such that $\mathcal{S} = \{\mathbf{x}_1, \mathbf{x}_2, \dots, \mathbf{x}_n, \mathbf{y}_1, \mathbf{y}_2, \dots, \mathbf{y}_{m-n}\}$ is a set of m linearly independent vector that constitutes a basis for \mathcal{V} .

Projection of a vector: Consider a *unit vector* $\mathbf{h} \in \mathbb{R}^m$ together with an arbitrary vector $\mathbf{z} \in \mathbb{R}^m$; the vector $(\mathbf{z}^T \mathbf{h}) \mathbf{h}$ is the representation of \mathbf{z} in the direction \mathbf{h} and is called the *projection of \mathbf{z} onto \mathbf{h}* . The inner product $\mathbf{z}^T \mathbf{h}$ is called the magnitude of the projection of \mathbf{z} onto the direction of \mathbf{h} . Consider next that \mathcal{S} is a subspace of a vector space \mathcal{V} . For any vector $\mathbf{z} \in \mathcal{V}$, the norm $\|\mathbf{z} - \mathbf{z}^*\|_2$, with $\mathbf{z}^* \in \mathcal{S}$, is minimized exactly when the vector $(\mathbf{z} - \mathbf{z}^*)$ is orthogonal to \mathcal{S} . Such a vector \mathbf{z}^* is called the *orthogonal projection* of \mathbf{z} onto \mathcal{S} .

Bessel's inequality and Parseval's identity: Consider that $\mathcal{S} = \{\mathbf{h}_1, \mathbf{h}_2, \dots, \mathbf{h}_n\}$ is an orthonormal set of vectors in \mathbb{R}^m . The vector $\mathbf{z}^* = (\mathbf{z}^T \mathbf{h}_1) \mathbf{h}_1 + (\mathbf{z}^T \mathbf{h}_2) \mathbf{h}_2 + \dots + (\mathbf{z}^T \mathbf{h}_n) \mathbf{h}_n$ is called the projection of the vector $\mathbf{z} \in \mathbb{R}^m$ onto \mathcal{S} . The vector $(\mathbf{z} - \mathbf{z}^*)$ is *orthogonal* to \mathcal{S} , and *Bessel's inequality* $\sum_{i=1}^n (\mathbf{z}^T \mathbf{h}_i)^2 \leq \|\mathbf{z}\|^2$ holds. If the orthonormal set \mathcal{S} is such that $\sum_{i=1}^n (\mathbf{z}^T \mathbf{h}_i)^2 = \|\mathbf{z}\|^2$, then \mathcal{S} is called a *complete orthonormal set*, and this relation is called *Parseval's identity*.

Fourier expansion: The representation of a vector $\mathbf{z} \in \mathbb{R}^m$ in the form

$$\mathbf{z} = \sum_{i=1}^m (\mathbf{z}^T \mathbf{h}_i) \mathbf{h}_i,$$

where $\mathcal{S} = \{\mathbf{h}_1, \mathbf{h}_2, \dots, \mathbf{h}_m\}$ is any complete orthonormal basis, is called the *Fourier expansion* of \mathbf{z} ; the inner products $(\mathbf{z}^T \mathbf{h}_i)$ are called the *Fourier coefficients*. The right-side of the above representation is called the *spectral expansion* of \mathbf{z} . Parseval's identity indicates that the total energy in any representation remains unchanged when \mathcal{S} is a complete orthonormal basis.

1.2 Matrices: Basic Definitions and Properties

A *number field* \mathcal{F} is defined as an arbitrary collection of numbers within which the four operations of addition, subtraction, multiplication, and division by a nonzero number can always be carried out. Examples of number fields are the set of all integer numbers, the set of all rational numbers, the set of all real numbers, and the set of all complex numbers.

A rectangular array of numbers of the field \mathcal{F} , composed of m rows and n columns

$$\mathbf{A} = \begin{pmatrix} a_{11} & a_{12} \cdots a_{1n} \\ a_{21} & a_{22} \cdots a_{2n} \\ \dots & \dots \\ a_{m1} & a_{m2} \cdots a_{mn} \end{pmatrix}$$

is called a *rectangular matrix* of dimension $m \times n$. The numbers $a_{ij}, (i = 1, 2, \dots, m; j = 1, 2, \dots, n)$; are called the elements of \mathbf{A} . The set of all real $m \times n$ matrices is denoted by $\mathbb{R}^{m \times n}$. When $m = n$, the matrix \mathbf{A} is called square and the number m , equal to n , is called the order of \mathbf{A} . The *null* or *zero* matrix has all of its elements zero. The order of the subscripts is important in the double-subscript notation for the elements a_{ij} : the first subscript, i , denotes the row, while the second subscript, j , denotes the column containing the given element. The set of elements $(a_{11}, a_{22}, \dots, a_{mm})$ is called the *principal or main diagonal* of \mathbf{A} . Diagonals parallel to this principal diagonal and *above* (*below*) the main diagonal are called *super* (*sub*) diagonals. Often, the notation for the matrix defined above is abbreviated as

$$\mathbf{A} = (a_{ij}), (i = 1, 2, \dots, m, j = 1, 2, \dots, n),$$

or simply \mathbf{A} , when its elements and dimensions are understood from context.

A *column matrix* is a rectangular matrix consisting of a single column,

$$\begin{pmatrix} x_1 \\ x_2 \\ \dots \\ x_n \end{pmatrix},$$

while a *row matrix* is a rectangular matrix consisting of a single row,

$$(a_1, a_2, \dots, a_n).$$

A *diagonal matrix*, \mathbf{D} , is a square matrix with zero off-diagonal elements: $a_{ij} = 0$, for $i \neq j$. Note that the diagonal elements $a_{ii} = d_i$ may (or may not) be different from 0. Note also that $\mathbf{D} = (d_i \delta_{ik})$, where (δ_{ik}) is the Kronecker symbol,

$$\delta_{ik} = \begin{cases} 1, & i = k, \\ 0, & i \neq k. \end{cases}$$

A *unit (or identity) matrix*, \mathbf{I} , is a diagonal matrix with $a_{ii} = 1$, for all i , i.e., $\mathbf{I} = (\delta_{ik})$. A *zero matrix*, $\mathbf{0}$, is a matrix with all its elements zero. A *lower triangular matrix* is a matrix with elements $a_{ij} = 0$, for $i < j$, while an *upper triangular matrix* is a matrix with elements $a_{ij} = 0$, for $i > j$. Two matrices \mathbf{A} and \mathbf{B} are said to be equal if their corresponding elements are equal, i.e., if $a_{ij} = b_{ij}$, for all $i = 1, \dots, m$ and $j = 1, \dots, n$. The *transpose* \mathbf{A}^T of a matrix $\mathbf{A} = (a_{ik})$, ($i = 1, 2, \dots, m; k = 1, 2, \dots, n$), is defined as $\mathbf{A}^T = (a_{ki})$, ($i = 1, 2, \dots, m; k = 1, 2, \dots, n$). The following properties of the operation of transposition are often encountered in applications: $(\mathbf{A} + \mathbf{B})^T = \mathbf{A}^T + \mathbf{B}^T$, $(a\mathbf{A})^T = a\mathbf{A}^T$, $(\mathbf{AB})^T = \mathbf{B}^T \mathbf{A}^T$. A square matrix \mathbf{S} that coincides with its transpose, i.e., $a_{ij} = a_{ji}$, for all i, j , is called a *symmetric matrix*. A *skew-symmetric matrix* is a matrix with elements $a_{ij} = -a_{ji}$, for all i, j . A *hermitian matrix* is a matrix with elements $a_{ij} = \bar{a}_{ji}$, for all i, j ; here, the overbar denotes complex conjugation. This definition implies that the diagonal elements of a hermitian matrix are real. A *skew-hermitian matrix* is a matrix with elements $a_{ij} = -\bar{a}_{ji}$, for all i, j ; this definition indicates that the diagonal elements of a skew-hermitian matrix are purely imaginary.

Linear transformation: If m quantities y_1, y_2, \dots, y_m have linear and homogeneous expressions in terms of n other quantities x_1, x_2, \dots, x_n such that

$$\left. \begin{aligned} y_1 &= a_{11}x_1 + a_{12}x_2 + \dots + a_{1n}x_n \\ y_2 &= a_{21}x_1 + a_{22}x_2 + \dots + a_{2n}x_n \\ &\dots\dots\dots \\ y_m &= a_{m1}x_1 + a_{m2}x_2 + \dots + a_{mn}x_n \end{aligned} \right\},$$

then the transformation of the quantities x_1, x_2, \dots, x_n into the quantities y_1, y_2, \dots, y_m by means of the above formulas is called a *linear transformation*. The coefficients of the above transformation form the rectangular matrix of dimension $m \times n$. Note that this linear transformation determines the corresponding matrix uniquely, and vice versa.

Operations on matrices: The basic operations on matrices are: *addition (summation)* of matrices, *scalar multiplication of a matrix by a number*, and *multiplication* of matrices. Thus,

the *sum/difference* of two rectangular matrices $\mathbf{A} = (a_{ik})$ and $\mathbf{B} = (b_{ik})$, both of dimension $m \times n$, is the matrix $\mathbf{C} = (c_{ik})$, of the same dimension, whose elements are

$$\mathbf{C} = \mathbf{A} \pm \mathbf{B}, \text{ with } c_{ik} = a_{ik} \pm b_{ik}, (i = 1, \dots, m, \text{ and } k = 1, \dots, n).$$

The matrix addition of arbitrary rectangular matrices of equal dimensions is commutative and associative: $\mathbf{A} + \mathbf{B} = \mathbf{B} + \mathbf{A}$, and $(\mathbf{A} + \mathbf{B}) + \mathbf{C} = \mathbf{A} + (\mathbf{B} + \mathbf{C})$.

The *scalar multiplication* of a matrix $\mathbf{A} = (a_{ik})$ by a number β of \mathcal{F} is the matrix $\mathbf{C} = (c_{ik})$ such that

$$\mathbf{C} = \beta \mathbf{A}, \text{ with } c_{ik} = \beta a_{ik}, (i = 1, \dots, m, \text{ and } k = 1, \dots, n).$$

The *matrix-vector product* is defined as $\mathbf{A}\mathbf{x} = \mathbf{y}$, where the i^{th} -element of \mathbf{y} is defined to be the *inner product* of the i^{th} -row of \mathbf{A} with \mathbf{x} , i.e., $y_i = \sum_{j=1}^n a_{ij}x_j$ for $1 \leq i \leq m$.

The **matrix-matrix product** $\mathbf{C} = \mathbf{A}\mathbf{B} \in \mathbb{R}^{m \times r}$ of two matrices, $\mathbf{A} \in \mathbb{R}^{m \times n}$ and $\mathbf{B} \in \mathbb{R}^{n \times r}$, can be defined in three equivalent ways, as follows

1. *Inner product*: The element c_{ij} is the *inner product* of the i^{th} row of \mathbf{A} , and j^{th} column of \mathbf{B} :

$$c_{ij} = \sum_{k=1}^n a_{ik}b_{kj}, \quad 1 \leq i \leq m, \quad 1 \leq j \leq r.$$

2. *Scalar times a vector*: The j^{th} -column c_{*j} of \mathbf{C} is the *linear combination of the columns of \mathbf{A}* , using the elements of the j^{th} -column of \mathbf{B} as the coefficients:

$$c_{*j} = \sum_{i=1}^n a_{*j}b_{ij}, \quad 1 \leq j \leq r.$$

3. *Outer product*: The product matrix \mathbf{C} can also be expressed as the sum of n *outer product* matrices obtained by the j^{th} -column of \mathbf{A} and j^{th} -row of \mathbf{B} as

$$\mathbf{C} = \sum_{j=1}^n a_{*j}b_{j*}.$$

The above operations satisfy the following properties:

- (a) $\mathbf{A} + \mathbf{B} = \mathbf{B} + \mathbf{A}$
- (b) $p\mathbf{A} = \mathbf{A}p$
- (c) $\mathbf{A}\mathbf{B} \neq \mathbf{B}\mathbf{A}$; in the special case when $\mathbf{A}\mathbf{B} = \mathbf{B}\mathbf{A}$, the matrices \mathbf{A} and \mathbf{B} are called *permutable* or *commuting*
- (d) $\mathbf{A}(\mathbf{x} + \mathbf{y}) = \mathbf{A}\mathbf{x} + \mathbf{A}\mathbf{y}$
- (e) $(\mathbf{A} + \mathbf{B})\mathbf{C} = \mathbf{A}\mathbf{C} + \mathbf{B}\mathbf{C}$
- (f) $(p + q)\mathbf{A} = p\mathbf{A} + q\mathbf{A}$
- (g) $(\mathbf{A}\mathbf{B})\mathbf{C} = \mathbf{A}(\mathbf{B}\mathbf{C})$
- (h) $\mathbf{A} + (-\mathbf{A}) = \mathbf{0}$
- (i) $p(\mathbf{A} + \mathbf{B}) = p\mathbf{A} + p\mathbf{B}$

Power of a square matrix: the p^{th} -power of a matrix $A = (a_{ik})$ is defined as

$$A^p = \underbrace{AA \cdots A}_p, \quad (p = 1, 2, \dots); \quad \text{with } A^0 \equiv I.$$

Since matrix multiplication is associative, it follows that $A^p A^q = A^{p+q}$, for p and q arbitrary nonnegative integers. A square matrix A is called *nilpotent* iff there is an integer p such that $A^p = 0$. The smallest such integer p is called the *index of nilpotence*.

Consider now a polynomial $f(t)$ with coefficients in the field \mathcal{F} , namely $f(t) = \alpha_0 t^m + \alpha_1 t^{m-1} + \cdots + \alpha_m$. Then a *polynomial, $f(A)$, in a matrix A* , is defined to be the matrix

$$f(A) = \alpha_0 A^m + \alpha_1 A^{m-1} + \cdots + \alpha_m I.$$

Determinant of a square matrix: The *determinant* of a square matrix A is a scalar quantity, denoted by $\det A$ or $|A|$, and is given by

$$|A| = \sum_{j_1, j_2, \dots, j_n} p(j_1, j_2, \dots, j_n) a_{1j_1} a_{2j_2} \cdots a_{nj_n},$$

where $p(j_1, j_2, \dots, j_n)$ is a permutation equal to ± 1 , written in general as $p(j_1, j_2, \dots, j_n) = \text{sign} \prod_{1 \leq s < r \leq n} (j_r - j_s)$. The determinant can also be written in the alternative forms

$$|A| = \sum_{j=1}^n a_{ij} C_{ij}, \quad i = \text{constant}, \quad \text{or} \quad |A| = \sum_{i=1}^n a_{ij} C_{ij}, \quad j = \text{constant},$$

where C_{ij} is called the *cofactor* of the element a_{ij} . Note also that $C_{ij} = (-1)^{i+j} M_{ij}$, where M_{ij} , called the *minor*, is the determinant of the submatrix obtained from the matrix A by deleting the i^{th} row and j^{th} column. When the rows and columns deleted from A have the same indices, the resulting submatrix is located symmetrically with respect to the main diagonal of A , and the corresponding minor is called the *principal minor* of A . The minor

$$\begin{vmatrix} a_{11} & \cdots & a_{1r} \\ \vdots & & \vdots \\ a_{r1} & \cdots & a_{rr} \end{vmatrix}$$

is called the *leading principal minor* of A of order r .

Commonly used properties of determinants are as follows:

1. $|A| = |A^T|$.
2. If any column or row of A is multiplied by a scalar α , then the determinant of the new matrix becomes $\alpha |A|$.
3. If any column or row of A is zero, then $|A| = 0$.
4. If two rows or columns of A are interchanged, then the determinant of the new matrix has the same absolute value but opposite sign to the original determinant.
5. If two rows or columns in A are identical, then $|A| = 0$.
6. If a matrix A has elements $a_{sj} = c_{sj} + b_{sj}$, for all $j = 1, 2, \dots, n$, then the determinant of A is equal to the sum of two determinants such that the first determinant is obtained by

replacing a_{sj} in \mathbf{A} by c_{sj} for all $j = 1, 2, \dots, n$, while the second determinant is obtained by replacing a_{sj} in \mathbf{A} by b_{sj} for all $j = 1, \dots, n$.

7. $|\mathbf{AB}| = |\mathbf{A}||\mathbf{B}|$.
8. The sum of the product of the elements of a row by the cofactors of another row is equal to zero, i.e., $\sum_{j=1}^n a_{ij}C_{kj} = 0$, for all $i \neq k$.
9. The determinant of a matrix \mathbf{A} does not change if the elements of any row are multiplied by a constant and then added to another row.
10. The derivative $(d|\mathbf{A}(\lambda)|/d\lambda)$, of a determinant $|\mathbf{A}(\lambda)| = \sum_{j_1, \dots, j_n} p(j_1, \dots, j_n) a_{1j_1}(\lambda) \dots a_{nj_n}(\lambda)$, with respect to a parameter λ , is obtained as the sum of the determinants obtained by differentiating the rows of \mathbf{A} with respect to λ one at a time, i.e.,

$$\begin{aligned} \frac{d}{d\lambda} |\mathbf{A}| &= \sum_{j_1, \dots, j_n} p(j_1, \dots, j_n) \frac{da_{1j_1}(\lambda)}{d\lambda} a_{2j_2}(\lambda) \dots a_{nj_n}(\lambda) \\ &+ \sum_{j_1, \dots, j_n} p(j_1, \dots, j_n) a_{1j_1}(\lambda) \frac{da_{2j_2}(\lambda)}{d\lambda} \dots a_{nj_n}(\lambda) \\ &+ \dots + \sum_{j_1, \dots, j_n} p(j_1, \dots, j_n) a_{1j_1}(\lambda) \dots a_{n-1j_{n-1}}(\lambda) \frac{da_{nj_n}(\lambda)}{d\lambda}. \end{aligned}$$

Rank of a matrix $\mathbf{A} \in \mathbb{R}^{m \times n}$: The number of *linearly independent columns (rows)* of \mathbf{A} is called the *column (row) rank* of \mathbf{A} . Thus, the column (row) rank of \mathbf{A} is less than or equal to n (m). For any given matrix \mathbf{A} , its column and row ranks are always equal; this common integer value is called the *rank* of \mathbf{A} , and is denoted by $\text{Rank}(\mathbf{A})$, i.e.,

$$0 \leq \text{Rank}(\mathbf{A}) \leq \min\{m, n\}.$$

If $\text{Rank}(\mathbf{A}) = \min\{m, n\}$, then \mathbf{A} is called a matrix of *full rank*, otherwise it is called *rank-deficient*. Several important properties of rank are:

$$\begin{aligned} \text{Rank}(\mathbf{A}^T) &= \text{Rank}(\mathbf{A}), \\ \text{Rank}(\mathbf{A} + \mathbf{B}) &\leq \text{Rank}(\mathbf{A}) + \text{Rank}(\mathbf{B}), \\ \text{Rank}(\mathbf{A} - \mathbf{B}) &\geq |\text{Rank}(\mathbf{A}) - \text{Rank}(\mathbf{B})|. \end{aligned}$$

If $\mathbf{A} \in \mathbb{R}^{m \times n}$ and $\mathbf{B} \in \mathbb{R}^{n \times r}$, then $\text{Rank}(\mathbf{AB}) \leq \min\{\text{Rank}(\mathbf{A}), \text{Rank}(\mathbf{B})\}$. In particular, if $\mathbf{x}, \mathbf{y} \in \mathbb{R}^m$, then their outer product matrix has $\text{Rank}(\mathbf{xy}^T) = 1$.

Singular/nonsingular matrix: A square matrix $\mathbf{A} \in \mathbb{R}^{n \times n}$ is called *nonsingular* if (i) $\det(\mathbf{A}) \neq 0$, or, (equivalently), if (ii) all columns (rows) of \mathbf{A} are linearly independent, or if (iii) $\text{Rank}(\mathbf{A}) = n$. Otherwise, \mathbf{A} is called *singular* (e.g., if $|\mathbf{A}| = 0$).

Consider the linear transformation

$$y_i = \sum_{k=1}^n a_{ik}x_k, \quad (i = 1, 2, \dots, n),$$

with $\mathbf{A} = (a_{ik})$ being nonsingular, i.e., $|\mathbf{A}| \neq 0$. Regarding the above system as equations for x_1, x_2, \dots, x_n , and solving them in terms of y_1, y_2, \dots, y_n , yields:

$$x_i = \frac{1}{|\mathbf{A}|} \begin{vmatrix} a_{11} \dots a_{1,i-1} & y_1 & a_{1,i+1} \dots a_{1n} \\ a_{21} \dots a_{2,i-1} & y_2 & a_{2,i+1} \dots a_{2n} \\ \dots & \dots & \dots \\ a_{n1} \dots a_{n,i-1} & y_n & a_{n,i+1} \dots a_{nn} \end{vmatrix} \equiv \sum_{k=1}^n a_{ik}^{(-1)} y_k \quad (i = 1, 2, \dots, n).$$

The transformation yielding the quantities x_i in terms of the quantities y_k is the “inverse” of the transformation for the quantities y_i . The coefficient matrix

$$\mathbf{A}^{-1} = \left(a_{ik}^{(-1)} \right) \text{ with } a_{ik}^{(-1)} = \frac{A_{ki}}{|\mathbf{A}|}, \quad (i, k = 1, 2, \dots, n),$$

is called the *inverse matrix* of \mathbf{A} , and A_{ki} is the algebraic complement (the cofactor) of the elements a_{ki} ($i, k = 1, 2, \dots, n$) in the determinant $|\mathbf{A}|$.

The composite transformation of the transformations for \mathbf{x} and \mathbf{y} , in either order, gives the identity transformation $\mathbf{A}\mathbf{A}^{-1} = \mathbf{A}^{-1}\mathbf{A} = \mathbf{I}$. Note that the matrix equations $\mathbf{A}\mathbf{X} = \mathbf{I}$ and $\mathbf{X}\mathbf{A} = \mathbf{I}$, $|\mathbf{A}| \neq 0$ admit only the solution $\mathbf{X} = \mathbf{A}^{-1}$. Note also that $|\mathbf{A}^{-1}| = 1/|\mathbf{A}|$, $(\mathbf{A}\mathbf{B})^{-1} = \mathbf{B}^{-1}\mathbf{A}^{-1}$, and $(\mathbf{A}^{-1})^T = (\mathbf{A}^T)^{-1}$.

Trace of a matrix: the *trace* of $\mathbf{A} \in \mathbb{R}^{m \times m}$, denoted by $\text{tr}(\mathbf{A})$, is a scalar defined by the sum of the diagonal elements of \mathbf{A} :

$$\text{tr}(\mathbf{A}) = \sum_{i=1}^m a_{ii}.$$

Notable properties of $\text{tr}(\mathbf{A})$ are:

$$\begin{aligned} \text{tr}(\mathbf{A}) &= \text{tr}(\mathbf{A}^T), \quad \text{tr}(\mathbf{A} + \mathbf{B}) = \text{tr}(\mathbf{A}) + \text{tr}(\mathbf{B}), \quad \text{tr}(\alpha\mathbf{A}) = \alpha \text{tr}(\mathbf{A}), \\ \text{tr}(\mathbf{A}\mathbf{B}) &= \text{tr}(\mathbf{B}\mathbf{A}), \quad \text{tr}(\mathbf{A}\mathbf{B}\mathbf{C}) = \text{tr}(\mathbf{B}\mathbf{C}\mathbf{A}) = \text{tr}(\mathbf{C}\mathbf{A}\mathbf{B}), \quad \text{tr}(\mathbf{A}^{-1}\mathbf{B}\mathbf{A}) = \text{tr}(\mathbf{B}). \end{aligned}$$

Useful identities: Adding an outer-product matrix $\mathbf{c}\mathbf{d}^T$, where $\mathbf{c}, \mathbf{d} \in \mathbb{R}^m$, to a non-singular matrix \mathbf{A} is called the *rank-one perturbation*. In the following identities, the matrices \mathbf{A} and \mathbf{B} are considered to be invertible, and $\mathbf{C} \in \mathbb{R}^{m \times k}$ and $\mathbf{D} \in \mathbb{R}^{m \times k}$ are matrices of rank k :

$$\begin{aligned} (\mathbf{I}_m + \mathbf{c}\mathbf{d}^T)^{-1} &= \mathbf{I}_m - \frac{\mathbf{c}\mathbf{d}^T}{1 + \mathbf{d}^T\mathbf{c}}, \\ (\mathbf{A} + \mathbf{c}\mathbf{d}^T)^{-1} &= \mathbf{A}^{-1} - \frac{\mathbf{A}^{-1}\mathbf{c}\mathbf{d}^T\mathbf{A}^{-1}}{1 + \mathbf{d}^T\mathbf{A}^{-1}\mathbf{c}} \quad (\text{Sherman-Morrison formula}), \\ (\mathbf{A} + \mathbf{C}\mathbf{D}^T)^{-1} &= \mathbf{A}^{-1} - \mathbf{A}^{-1}\mathbf{C}[\mathbf{I}_k + \mathbf{D}^T\mathbf{A}^{-1}\mathbf{C}]^{-1}\mathbf{D}^T\mathbf{A}^{-1} \quad (\text{Woodbury's extension}), \\ (\mathbf{A} + \mathbf{C}\mathbf{B}\mathbf{D}^T)^{-1} &= \mathbf{A}^{-1} - \mathbf{A}^{-1}\mathbf{C}[\mathbf{B}^{-1} + \mathbf{D}^T\mathbf{A}^{-1}\mathbf{C}]^{-1}\mathbf{D}^T\mathbf{A}^{-1}, \\ [\mathbf{A}^T\mathbf{B}^{-1}\mathbf{A} + \mathbf{D}^{-1}]\mathbf{A}^T\mathbf{B}^{-1} &= \mathbf{D}\mathbf{A}^T[\mathbf{B} + \mathbf{A}\mathbf{D}\mathbf{A}^T]^{-1}. \end{aligned}$$

Moore-Penrose generalized inverse: The matrix $\mathbf{A}^+ \in \mathbb{R}^{n \times m}$ is called the *Moore-Penrose inverse* of the matrix $\mathbf{A} \in \mathbb{R}^{m \times n}$ if the following four conditions hold:

1. $\mathbf{A}\mathbf{A}^+\mathbf{A} = \mathbf{A}$.
2. $\mathbf{A}^+\mathbf{A}\mathbf{A}^+ = \mathbf{A}^+$.
3. $(\mathbf{A}^+\mathbf{A})^T = \mathbf{A}^+\mathbf{A}$, ($\mathbf{A}^+\mathbf{A}$ is a symmetric matrix).
4. $(\mathbf{A}\mathbf{A}^+)^T = \mathbf{A}\mathbf{A}^+$, ($\mathbf{A}\mathbf{A}^+$ is a symmetric matrix).

The symmetric matrix $\mathbf{A}\mathbf{A}^+ \in \mathbb{R}^{m \times m}$ represents the orthogonal projection onto the subspace spanned by the columns of \mathbf{A} , which is called the *range space* of \mathbf{A} , and is denoted as $R(\mathbf{A})$.

Similarly, the symmetric matrix $\mathbf{A}^+\mathbf{A} \in \mathbb{R}^{n \times n}$ represents the orthogonal projection on to the subspace spanned by the rows of \mathbf{A} , which is called the range space of \mathbf{A}^T , and is denoted as $R(\mathbf{A}^T)$. When $\mathbf{A} \in \mathbb{R}^{m \times m}$ is non-singular, then $\mathbf{A}^+ = \mathbf{A}^{-1}$ and $\mathbf{A}\mathbf{A}^{-1} = \mathbf{A}^{-1}\mathbf{A} = \mathbf{I}_m$.

Range and null space of a matrix: Consider two vector spaces $\mathcal{V} \subseteq \mathbb{R}^n$ and $\mathcal{W} \subseteq \mathbb{R}^m$ and a matrix $\mathbf{A} \in \mathbb{R}^{m \times n}$, $\mathbf{A} : \mathcal{V} \rightarrow \mathcal{W}$. The range of \mathbf{A} , also known as *column space* of \mathbf{A} , is usually denoted by $R(\mathbf{A})$, and is defined as

$$R(\mathbf{A}) = \{ \mathbf{y} \in \mathbb{R}^m \mid \mathbf{y} = \mathbf{A}\mathbf{x} \text{ for all } \mathbf{x} \in \mathcal{V} \} \subseteq \mathcal{W}$$

is the set of linear combinations of the columns of \mathbf{A} . That is, $R(\mathbf{A})$ is the linear vector space generated by the columns of \mathbf{A} and, hence, is called the *image* of \mathcal{V} under \mathbf{A} or (simply as) the *image space* of \mathbf{A} . The range of \mathbf{A}^T , defined as

$$R(\mathbf{A}^T) = \{ \mathbf{x} \in \mathbb{R}^n \mid \mathbf{x} = \mathbf{A}^T \mathbf{y} \text{ for all } \mathbf{y} \in \mathbb{R}^m \} \subseteq \mathcal{V}$$

is also called the *row space* of \mathbf{A} . The *null space* of \mathbf{A} , denoted by $N(\mathbf{A})$, is defined as

$$N(\mathbf{A}) = \{ \mathbf{x} \in \mathbb{R}^n \mid \mathbf{A}\mathbf{x} = \mathbf{0} \} \subseteq \mathcal{V}.$$

Thus, $N(\mathbf{A})$ consists of all solutions to the homogeneous systems $\mathbf{A}\mathbf{x} = \mathbf{0}$, and is also called the *kernel* of \mathbf{A} . It can be verified that $N(\mathbf{A})$ is a vector space. The null space of \mathbf{A}^T is defined as

$$N(\mathbf{A}^T) = \{ \mathbf{y} \in \mathbb{R}^m \mid \mathbf{A}^T \mathbf{y} = \mathbf{0} \} \subseteq \mathcal{W}.$$

The following relations hold between the four vector spaces $R(\mathbf{A})$, $R(\mathbf{A}^T)$, $N(\mathbf{A})$; and $N(\mathbf{A}^T)$; associated with a matrix $\mathbf{A} \in \mathbb{R}^{m \times n}$.

1. The null space of \mathbf{A} is orthogonal to the range space of \mathbf{A}^T : $N(\mathbf{A}) = R^\perp(\mathbf{A}^T)$; similarly, $N(\mathbf{A}^T) = R^\perp(\mathbf{A})$.
2. When \mathbf{A} is a square symmetric matrix, then $R(\mathbf{A}) = R(\mathbf{A}^T)$, $N(\mathbf{A}) = N(\mathbf{A}^T)$, and $N(\mathbf{A}) = R^\perp(\mathbf{A}^T)$.
3. $\text{Dim}[R(\mathbf{A})] = \text{Rank}(\mathbf{A}) = \text{Dim}[R(\mathbf{A}^T)]$.
4. $\text{Dim}[N(\mathbf{A})] = n - r$, where $r = \text{Rank}(\mathbf{A})$, is called the *nullity* of \mathbf{A} ;
5. $\text{Dim}[R(\mathbf{A})] + \text{Dim}[N(\mathbf{A})] = n$, for all $\mathbf{A} \in \mathbb{R}^{m \times n}$.
6. $\text{Dim}[N(\mathbf{A})] = 0$ when \mathbf{A} is square and non-singular.
7. $\text{Dim}[N(\mathbf{A}^T)] = m - r$.

In many applications, it is convenient to use matrices that are partitioned into rectangular parts, or “cells” or “blocks.” An arbitrary rectangular matrix $\mathbf{A} = (a_{ik})$ ($i = 1, 2, \dots, m; k = 1, 2, \dots, n$) can be partitioned into rectangular blocks by means of horizontal and vertical lines, as follows:

$$\mathbf{A} = \begin{pmatrix} \mathbf{A}_{11} & \mathbf{A}_{12} & \cdots & \mathbf{A}_{1t} \\ \mathbf{A}_{21} & \mathbf{A}_{22} & \cdots & \mathbf{A}_{2t} \\ \cdots & \cdots & \cdots & \cdots \\ \mathbf{A}_{s1} & \mathbf{A}_{s2} & \cdots & \mathbf{A}_{st} \end{pmatrix} \begin{matrix} \} & m_1 \\ \} & m_2 \\ & \vdots \\ \} & m_s \end{matrix}.$$

$n_1 \qquad n_2 \qquad n_t$

The matrix A above is said to be *partitioned* into $s \times t$ blocks (or *cells*) $A_{\alpha\beta}$ of dimensions $m_\alpha \times n_\beta$ ($\alpha = 1, 2, \dots, s$; $\beta = 1, 2, \dots, t$), or that it is represented in the form of a *partitioned*, or *blocked*, matrix. By analogy with the customary notation for matrices, the matrix A is written as $A = (A_{\alpha\beta})$, ($\alpha = 1, 2, \dots, s$; $\beta = 1, 2, \dots, t$). When $s = t$, then A is a square block matrix, denoted as $A = (A_{\alpha\beta})_s^s$, or simply $A = (A_{\alpha\beta})$, when the meaning of s is clear from the context. Operations on partitioned matrices are performed using the same formal rules as used for matrices that have scalar elements instead of blocks. For example, the operation of addition of two rectangular matrices $A = (A_{\alpha\beta})$, $B = (B_{\alpha\beta})$, ($\alpha = 1, 2, \dots, s$; $\beta = 1, 2, \dots, t$) becomes $A + B = (A_{\alpha\beta} + B_{\alpha\beta})$.

For block-multiplication of two rectangular matrices A and B , the length of the rows of the first factor A must be the same as the height of the columns of the second factor B , and the partitioning into blocks must ensure that the horizontal dimensions in the first factor are the same as the corresponding vertical dimensions in the second:

$$A = \left(\begin{array}{ccc} \overbrace{A_{11}}^{n_1} & \overbrace{A_{12}}^{n_2} & \cdots & \overbrace{A_{1t}}^{n_t} \\ \overbrace{A_{21}}^{n_1} & \overbrace{A_{22}}^{n_2} & \cdots & \overbrace{A_{2t}}^{n_t} \\ \cdots & \cdots & \cdots & \cdots \\ \overbrace{A_{s1}}^{n_1} & \overbrace{A_{s2}}^{n_2} & \cdots & \overbrace{A_{st}}^{n_t} \end{array} \right) \left. \begin{array}{l} \} \\ \} \\ \vdots \\ \} \end{array} \right\} \begin{array}{l} m_1 \\ m_2 \\ \vdots \\ m_s \end{array}, \quad B = \left(\begin{array}{ccc} \overbrace{B_{11}}^{p_1} & \overbrace{B_{12}}^{p_2} & \cdots & \overbrace{B_{1u}}^{p_u} \\ \overbrace{B_{21}}^{p_1} & \overbrace{B_{22}}^{p_2} & \cdots & \overbrace{B_{2u}}^{p_u} \\ \cdots & \cdots & \cdots & \cdots \\ \overbrace{B_{t1}}^{p_1} & \overbrace{B_{t2}}^{p_2} & \cdots & \overbrace{B_{tu}}^{p_u} \end{array} \right) \left. \begin{array}{l} \} \\ \} \\ \vdots \\ \} \end{array} \right\} \begin{array}{l} n_1 \\ n_2 \\ \vdots \\ n_t \end{array}.$$

The operation of block-multiplication can then be written in the customary form, namely:

$$AB = C = (C_{\alpha\beta}), \quad \text{where} \quad C_{\alpha\beta} = \sum_{\delta=1}^t A_{\alpha\delta} B_{\delta\beta} \quad \left(\begin{array}{l} \alpha = 1, 2, \dots, s \\ \beta = 1, 2, \dots, u \end{array} \right).$$

When A is a *quasi-diagonal* matrix (with $s = t$ and $A_{\alpha\beta} = 0$ when $\alpha \neq \beta$), then the above equation reduces to $C_{\alpha\beta} = A_{\alpha\alpha} B_{\alpha\beta}$, ($\alpha = 1, 2, \dots, s$; $\beta = 1, 2, \dots, u$). Similarly, when B is a quasi-diagonal matrix (with $t = u$ and $B_{\alpha\beta} = 0$ for $\alpha \neq \beta$), then the above equation becomes $C_{\alpha\beta} = A_{\alpha\beta} B_{\beta\beta}$. The partitioned matrix from the above equation is called *upper (lower) quasi-triangular* if $s = t$ and $A_{\alpha\beta} = 0$ for $\alpha > \beta$ ($\alpha < \beta$). A quasi-diagonal matrix is a special case of a quasi-triangular matrix. Note that the product of two upper (lower) quasi-triangular matrices is itself an upper (lower) quasi-triangular matrix. Furthermore, the determinant of a quasi-triangular matrix (or, in particular, a quasi-diagonal matrix) is equal to the product of the determinant of the diagonal cells:

$$|A| = |A_{11}| |A_{22}| \cdots |A_{ss}|.$$

Consider that the block A_{11} of the partitioned matrix A is square and nonsingular ($|A_{11}| \neq 0$). The block A_{21} can be eliminated by multiplying the first row of A on the left by $-A_{\alpha 1} A_{11}^{-1}$ ($\alpha = 2, \dots, s$) and adding the result to the α th row of A . If the matrix $A_{22}^{(1)}$ is square and nonsingular, the process can be continued. This procedure is called Gauss elimination for block-matrices, and provides a method for computing the determinant of a partitioned matrix:

$$|A| = |B_1| = |A_{11}| \left| \begin{array}{c} A_{22}^{(1)} \cdots A_{2t}^{(1)} \\ \cdots \cdots \cdots \\ A_{s2}^{(1)} \cdots A_{st}^{(1)} \end{array} \right|.$$

The above formula reduces the computation of the determinant $|A|$, consisting of $s \times t$ blocks, to the computation of a determinant of lower order, consisting of $(s-1) \times (t-1)$ blocks.

If $A_{22}^{(1)}$ is a square matrix and $|A_{22}^{(1)}| \neq 0$, then this determinant of $(s - 1)(t - 1)$ blocks can again be subjected to the same procedure as above. As a particular example, consider a determinant Δ partitioned into four blocks, namely: $\Delta = \begin{vmatrix} A & B \\ C & D \end{vmatrix}$, where A and D are square matrices, with $|A| \neq 0$. Multiplying the first row on the left by CA^{-1} and subtracting it from the second row yields

$$\Delta = \begin{vmatrix} A & B \\ \mathbf{0} & D - CA^{-1}B \end{vmatrix} = |A| |D - CA^{-1}B|.$$

On the other hand, if $|D| \neq 0$, then the Gauss elimination procedure can be applied to the second row of Δ , leading to

$$\Delta = \begin{vmatrix} A - BD^{-1}C & \mathbf{0} \\ C & D \end{vmatrix} = |A - BD^{-1}C| |D|.$$

In the special case in which all four matrices, A , B , C , and D , are square matrices of order n , then these equations become $\Delta = |AD - ACA^{-1}B|$, when $|A| \neq 0$ or $\Delta = |AD - BD^{-1}CD|$, when $|D| \neq 0$, respectively. These results are known as the *formulas of Schur*, and they reduce the computation of a determinant of order $2n$ to the computation of a determinant of order n .

Two matrices A and B connected by the relation $B = T^{-1}AT$, where T is a nonsingular matrix, are called *similar*, and have the following three properties: *reflexivity* (a matrix A is always similar to itself); *symmetry* (if A is similar to B , then B is similar to A); and *transitivity* (if A is similar to B , and B is similar to C , then A is similar to C). Two similar matrices have equal determinants, since $|B| = |T|^{-1}|A||T| = |A|$. However, the equality $|B| = |A|$ is only a necessary but not a sufficient condition for the matrices A and B to be similar.

Under certain conditions, it is possible to define *elementary functions of a matrix A*, just as one defines functions of a scalar. The matrix functions most commonly encountered in practical applications are:

$$\begin{aligned} e^A &= I + A + \frac{A^2}{2!} + \dots, & \sin A &= A - \frac{A^3}{3!} + \frac{A^5}{5!} - \dots, \\ \cos A &= I - \frac{A^2}{2!} + \frac{A^4}{4!} - \dots, \\ \sinh A &= A + \frac{A^3}{3!} + \frac{A^5}{5!} + \dots, & \cosh A &= I + \frac{A^2}{2!} + \frac{A^4}{4!} + \dots, \\ \tan A &= (\cos A)^{-1} \sin A, & \tanh A &= (\cosh A)^{-1} \sinh A, \\ \log(I + A) &= A - \frac{A^2}{2} + \frac{A^3}{3} - \dots, & (I - A)^{-1} &= I + A + A^2 + \dots \end{aligned}$$

Bilinear form: The scalar-valued function $f_A(\mathbf{x}, \mathbf{y}) : \mathbb{R}^m \times \mathbb{R}^n \rightarrow \mathbb{R}$ of two vectors defined by:

$$f_A = \mathbf{x}^T A \mathbf{y},$$

where $\mathbf{A} \in \mathbb{R}^{m \times n}$ and $\mathbf{x} \in \mathbb{R}^m$ and $\mathbf{y} \in \mathbb{R}^n$ is called a *bilinear form*, since the components of the vectors \mathbf{x} and \mathbf{y} appear in their first degree in $f_A(\mathbf{x}, \mathbf{y})$. In particular, when $\mathbf{A} \in \mathbb{R}^{m \times m}$ and $\mathbf{x} \in \mathbb{R}^m$, the scalar-valued function $Q_A: \mathbb{R}^m \rightarrow \mathbb{R}$ defined as

$$Q_A(\mathbf{x}) = \mathbf{x}^T \mathbf{A} \mathbf{x}$$

is a second-degree multivariate polynomial in the elements of \mathbf{x} , called a *quadratic form*.

Positive/negative definite matrix: A real symmetric matrix $\mathbf{A} \in \mathbb{R}^{m \times m}$ is said to be *positive definite* if

$$\mathbf{x}^T \mathbf{A} \mathbf{x} \begin{cases} > 0, & \text{if } \mathbf{x} \neq 0, \\ = 0, & \text{exactly when } \mathbf{x} = 0. \end{cases}$$

A real symmetric matrix \mathbf{A} is said to be *positive semi-definite* if $\mathbf{x}^T \mathbf{A} \mathbf{x} \geq 0$ for all $\mathbf{x} \in \mathbb{R}^m$. A real symmetric matrix \mathbf{A} is said to be *negative definite* and *negative semi-definite*, if the above properties hold with the inequalities reversed. The matrix \mathbf{A} is said to be *indefinite* if $\mathbf{x}^T \mathbf{A} \mathbf{x} \geq 0$ for some $\mathbf{x} \in \mathbb{R}^m$ and < 0 for some other values of \mathbf{x} . The diagonal elements, the principal minors of all orders and the determinant of a positive definite matrix are all positive. If \mathbf{A} is positive definite then the inverse matrix \mathbf{A}^{-1} is also positive definite. If \mathbf{A} is positive definite and \mathbf{B} is non-singular, then $(\mathbf{B}^{-1})^T \mathbf{A} \mathbf{B}^{-1}$ is positive definite. The eigenvalues of a real-symmetric and positive definite matrix are all real and positive, and those of a positive semi-definite matrix are real and non-negative. If \mathbf{A} is a symmetric and positive definite, then there exists an orthogonal matrix \mathbf{Q} such that $\mathbf{Q}^T \mathbf{A} \mathbf{Q} = \mathbf{\Lambda} = \text{Diag}(\lambda_1, \lambda_2, \dots, \lambda_m)$ where $\lambda_i > 0$ are the eigenvalues of \mathbf{A} and the columns of \mathbf{Q} are the corresponding orthonormal set of eigenvectors, furthermore, the relation $\mathbf{Q}^T \mathbf{A} \mathbf{Q} = \mathbf{\Lambda}$ implies the decomposition

$$\mathbf{A} = \mathbf{Q} \mathbf{\Lambda} \mathbf{Q}^T = \mathbf{Q} \mathbf{\Lambda}^{1/2} \mathbf{\Lambda}^{1/2} \mathbf{Q}^T = (\mathbf{Q} \mathbf{\Lambda}^{1/2}) (\mathbf{Q} \mathbf{\Lambda}^{1/2})^T = \mathbf{C} \mathbf{C}^T.$$

Diagonally dominant matrix: A square matrix $\mathbf{A} \in \mathbb{R}^{m \times m}$ is said to be *diagonally dominant* if

$$|a_{ii}| \geq \sum_{j \neq i} |a_{ij}|$$

and *strictly diagonally dominant* if strict inequality holds for all $i = 1, 2, \dots, m$. It can be shown that a diagonally dominant matrix is non-singular.

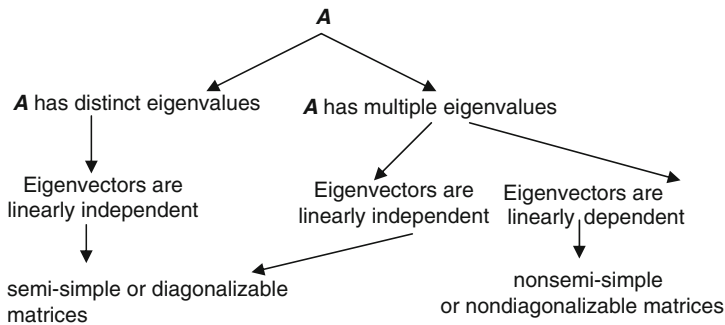
Orthogonal matrix: A matrix $\mathbf{Q} \in \mathbb{R}^{m \times m}$ is called an *orthogonal* matrix, if $\mathbf{Q}^{-1} = \mathbf{Q}^T$, i.e., $\mathbf{Q}^T \mathbf{Q} = \mathbf{Q} \mathbf{Q}^T = \mathbf{I}_m$. An orthogonal matrix \mathbf{Q} has the following properties:

- \mathbf{Q} is non-singular.
- The columns (rows) of $\mathbf{Q} \in \mathbb{R}^{m \times m}$ form a complete orthonormal basis for \mathbb{R}^m .
- $\det(\mathbf{Q}^T \mathbf{A} \mathbf{Q}) = \det(\mathbf{A})$.
- If $\mathbf{x} \in \mathbb{R}^m$, then the Euclidean norm $\|\mathbf{x}\|_2 = \|\mathbf{Q} \mathbf{x}\|_2$ is *invariant* under an orthogonal transformation; hence, orthogonal transformations are called *isometric* transformations, and represent a rigid body rotations.
- If \mathbf{Q}_1 and \mathbf{Q}_2 are orthogonal, then $\mathbf{Q}_1 \mathbf{Q}_2$ is also an orthogonal matrix.

Permutation matrix: The matrix $\mathbf{P} = [\mathbf{p}_{ij}] \in \mathbb{R}^{m \times m}$ is a *permutation* matrix if $\mathbf{p}_{ij} \in \{0, 1\}$ and there is only one 1 in each row and in each column. Some important properties of permutation matrices are as follows.

and $\text{tr}(\mathbf{A}) = m_1\lambda_1 + m_2\lambda_2 + \dots + m_k\lambda_k$, where m_i , is the *algebraic multiplicity* of λ_i . Similar matrices have the same set of eigenvalues; thus, if (λ, \mathbf{x}) is an eigen-pair of $\mathbf{B}^{-1}\mathbf{A}\mathbf{B}$, then $(\lambda, \mathbf{B}\mathbf{x})$ is the corresponding pair for \mathbf{A} .

In general, the characteristic equation admits three kinds of eigenvalues: (1) distinct eigenvalues with corresponding linearly independent eigenvectors, (2) multiple eigenvalues with corresponding linearly independent eigenvectors, and (3) multiple eigenvalues with linearly dependent eigenvectors. The first two kinds are called *semi-simple* eigenvalues and the last ones are called *nonsemi-simple* eigenvalues. The diagram below shows all possibilities for a matrix \mathbf{A} .



Solution of linear systems: Given $\mathbf{A} \in \mathbb{R}^{m \times n}$ and $\mathbf{b} \in \mathbb{R}^m$, the problem of finding the vector $\mathbf{x} \in \mathbb{R}^n$ such that $\mathbf{A}\mathbf{x} = \mathbf{b}$ requires the solution of a set of m equations in n unknowns for determining the components of \mathbf{x} . If the vector $\mathbf{b} \in R(\mathbf{A})$, then \mathbf{b} must be expressible as a linear combination of the columns of \mathbf{A} and the coefficients of this linear combination constitutes the components of the vector \mathbf{x} we are seeking. In this case, the linear system $\mathbf{A}\mathbf{x} = \mathbf{b}$ is called a *consistent* system. If \mathbf{b} does *not* belong to $R(\mathbf{A})$, then there does *not* exist a vector $\mathbf{x} \in \mathbb{R}^n$ such that $\mathbf{A}\mathbf{x} = \mathbf{b}$ and in this case it is termed as an *inconsistent* system. When the vector $\mathbf{b} = 0$, the linear system $\mathbf{A}\mathbf{x} = 0$ is called a *homogeneous system*; otherwise, it is known as a *non-homogeneous system*. Recall that $\text{Rank}(\mathbf{A}) \leq \min(m, n)$. If $\text{Rank}(\mathbf{A}) = \min(m, n)$, then the linear system is said to be of *full rank*; otherwise, it is called *rank deficient*. If m , the *number of equations*, is equal to n , the *number of variables*, the $\mathbf{A}\mathbf{x} = \mathbf{b}$ it is called a *determined* system; if $m > n$, it is called an *over-determined* system, and if $m < n$, it is called an *under-determined* system. Combining these various attributes (consistent/inconsistent, homogeneous/non-homogeneous, full-rank/rank-deficient, and determined/over or under-determined) yields the following cases:

- If $m = n$, and \mathbf{A} is of full rank, the system is always consistent and the solution exists and is unique. If $\mathbf{b} \neq 0$, then $\mathbf{x} = \mathbf{A}^{-1}\mathbf{b}$ and if $\mathbf{b} = 0$, $\mathbf{x} = 0$ is the only solution.
- If $m > n$, the system is over-determined. The unique solution is given by $\mathbf{x} = \mathbf{A}^+\mathbf{b}$ where \mathbf{A}^+ is the Moore–Penrose inverse of \mathbf{A} . In the special case when \mathbf{A} is of full rank, this generalized inverse is given by $\mathbf{A}^+ = (\mathbf{A}^T\mathbf{A})^{-1}\mathbf{A}^T$.
- If $m < n$, the system is under-determined. The unique solution is given by $\mathbf{x} = \mathbf{A}^+\mathbf{b}$, where \mathbf{A}^+ is the Moore–Penrose inverse. In the special case when \mathbf{A} is of full rank, this generalized inverse is given by $\mathbf{A}^+ = \mathbf{A}^T(\mathbf{A}\mathbf{A}^T)^{-1}$.

A matrix A has a generalized inverse A^i , iff $AA^iA = A$, where $A^i = P \begin{bmatrix} I_\rho & U \\ V & W \end{bmatrix} R$, where:

(1) ρ is the rank of A , (2) P and R are selected such that $RAP = \begin{bmatrix} I_\rho & 0 \\ 0 & 0 \end{bmatrix}$, and (3) U , V , and W are arbitrary matrices. The generalized inverse A^i is used to solve a set of linear simultaneous equations $Ax = b$, where A is of order (m, n) . The solution is given by $x = A^i b$, or, equivalently,

$$x = A^i b + (I - A^i A) z,$$

where z is an arbitrary vector (which accounts for U , V , and W), and A^t is the part of A^i that does not depend on U , V , and W . In general, A^t is obtained from A^i by setting U , V , and W to

zero, or, equivalently, by partitioning P and R in the form $P = [P_1 : P_2]$, $R = \begin{bmatrix} R_1 \\ \dots \\ R_2 \end{bmatrix}$, where P_1 and R_1 are respectively of order (n, ρ) and (ρ, m) , so that $A^t = P_1 R_1$.

Symmetric matrices play a prominent role in several nuclear engineering fields, including numerical simulations, model validation, data assimilation for best-estimate parameter calibration, uncertainty analysis, and predictive estimation. In particular, covariance matrices are symmetric and also positive-definite. Several important properties of eigenvectors and eigenvalues of a *symmetric matrix* $A \in \mathbb{R}^{m \times m}$ are summarized in the following:

- (a) The number of non-zero eigenvalues of $A = \text{Rank}(A)$.
- (a) The eigenvalues of A are real and orthogonal.
- (c) $AP = PA$, where $P = [x_1, x_2, \dots, x_m]$ denotes the orthonormal matrix of the m eigenvectors of A , and $\Lambda = \text{Diag}(\lambda_1, \lambda_2, \dots, \lambda_n)$ denotes the diagonal matrix of the eigenvalues of A .
- (d) Spectral decomposition: Since P is orthogonal, it follows that

$$A = PAP^T = [x_1, x_2, \dots, x_m] \begin{bmatrix} \lambda_1 & & & \\ & \lambda_2 & & \\ & & \ddots & \\ & & & \lambda_m \end{bmatrix} \begin{bmatrix} x_1^T \\ x_2^T \\ \vdots \\ x_m^T \end{bmatrix} = \sum_{i=1}^m \lambda_i x_i x_i^T = \sum_{i=1}^m \lambda_i P_i,$$

where the *rank-one outer-product* matrices $P_i = x_i x_i^T$ are *orthogonal projection matrices* onto the $\text{Span}\{x_i\}$. The above expansion of A as the linear combination of the orthogonal projection matrices is called the *spectral decomposition* of A .

If $A \in \mathbb{R}^{m \times m}$ and $B \in \mathbb{R}^{m \times m}$ are two permutable symmetric matrices (i.e., $AB = BA$), then there exists a common orthogonal matrix P such that $AP = P\Lambda$ and $BP = P\Sigma$, where Λ and Σ are diagonal matrices of eigenvalues of A and B , respectively.

All eigenvalues of a *symmetric and positive (negative) definite matrix* $A \in \mathbb{R}^{m \times m}$ are positive (negative). The bilinear form $Q(x) = x^T Ax$ defines a *hyper-ellipsoid* in \mathbb{R}^m ; $Q(x) = x^T (P\Lambda P^T) x = (Px)^T \Lambda (Px)$, where $\Lambda = \text{Diag}(\lambda_1, \lambda_2, \dots, \lambda_n)$ and $P = [x_1, x_2, \dots, x_m]$. Therefore, if $x = P^T y$ or $Px = y$ (representing a rigid-body rotation of the standard coordinate system using the orthogonal matrix P), then $Q(x)$ is the hyper-ellipsoid whose m principal axes coincide with the m orthogonal eigenvectors of A and $1/\sqrt{\lambda_i}$ denotes the length of the semi-axis in the i^{th} principal direction, i.e., $Q(x) = Q(P^T y) = y^T \Lambda y = \sum_{i=1}^m \lambda_i y_i^2$.

Krylov Subspace: Let $\mathbf{y} \in \mathbb{R}^m$ be any vector. Then, there exists an eigenvector \mathbf{x} of \mathbf{A} that belongs to the vector space

$$K_A(\mathbf{A}, \mathbf{y}) = \{\mathbf{y}, \mathbf{A}\mathbf{y}, \mathbf{A}^2\mathbf{y}, \dots, \mathbf{A}^{r-1}\mathbf{y}\}$$

for some integer $r \geq 0$, called the *Krylov subspace*. Krylov subspaces are intimately related to matrix-polynomials, and are important in reduced-space computations and error estimation.

Rayleigh coefficient: For a symmetric matrix $\mathbf{A} \in \mathbb{R}^{n \times n}$, the quantity $r(\mathbf{x}) = \mathbf{x}^T \mathbf{A} \mathbf{x} / \mathbf{x}^T \mathbf{x}$ is called the *Rayleigh coefficient*. If $\mathbf{A} \in \mathbb{R}^{n \times n}$ and $\mathbf{B} \in \mathbb{R}^{n \times n}$ are two symmetric and positive definite matrices, and $\lambda \in \mathbb{R}$ and $\mathbf{x} \in \mathbb{R}^n$ are the *generalized eigenvalue* and *generalized eigenvector* of the pair (\mathbf{A}, \mathbf{B}) , i.e., $\mathbf{A}\mathbf{x} = \lambda\mathbf{B}\mathbf{x}$, then λ is given by Rayleigh coefficient $\lambda = r(\mathbf{x}) = \mathbf{x}^T \mathbf{A} \mathbf{x} / \mathbf{x}^T \mathbf{B} \mathbf{x}$. Furthermore, $r(\mathbf{x})$ minimizes the norm $g(\lambda) = \|(\mathbf{A} - \lambda\mathbf{B})\mathbf{x}\|_{\mathbf{B}^{-1}}^2$.

The **norm of a square matrix** \mathbf{A} , denoted by $\|\mathbf{A}\|$, is a nonnegative real scalar that satisfies the following relations:

1. $\|\mathbf{A}\| > 0$, if $\mathbf{A} \neq \mathbf{0}$ (nonnegative);
2. $\|\alpha\mathbf{A}\| = |\alpha| \|\mathbf{A}\|$, for any complex scalar α (homogeneous);
3. $\|\mathbf{A} + \mathbf{B}\| \leq \|\mathbf{A}\| + \|\mathbf{B}\|$, (triangle inequality);
4. $\|\mathbf{A}\mathbf{B}\| \leq \|\mathbf{A}\| \|\mathbf{B}\|$, (sub-multiplicative).

There are many matrix norms that satisfy the above relations. The most frequently used norm is the *matrix-Hölder norm induced by (or subordinate to) the Hölder vector norm*, defined as

$$\|\mathbf{A}\|_p \equiv \max_x \frac{\|\mathbf{A}\mathbf{x}\|_p}{\|\mathbf{x}\|_p}.$$

The most widely used matrix-Hölder norms are those obtained for the following values of p :

- (a) $p = 1$, the *maximum column sum matrix norm*, induced by the ℓ_1 vector norm:

$$\|\mathbf{A}\|_1 \equiv \max_x \frac{\|\mathbf{A}\mathbf{x}\|_1}{\|\mathbf{x}\|_1} = \max_j \sum_{i=1}^n |a_{ij}|.$$

- (b) $p = 2$, the *spectral norm*, induced by the ℓ_2 vector norm:

$$\|\mathbf{A}\|_2 \equiv \max_x \frac{\|\mathbf{A}\mathbf{x}\|_2}{\|\mathbf{x}\|_2} = \max_\lambda \{\sqrt{\lambda}\}, \text{ where } \lambda \text{ is an eigenvalue of } (\mathbf{A}^*)\mathbf{A}.$$

- (c) $p = \infty$, the *maximum row sum matrix norm*, induced by the ℓ_∞ vector norm:

$$\|\mathbf{A}\|_\infty \equiv \max_x \frac{\|\mathbf{A}\mathbf{x}\|_\infty}{\|\mathbf{x}\|_\infty} = \max_i \sum_{j=1}^n |a_{ij}|.$$

The *condition number* of a square matrix \mathbf{A} is a nonnegative real scalar defined in connection with the Hölder matrix and vector norms as

$$\gamma_p(\mathbf{A}) \equiv \max_{\mathbf{u}, \mathbf{v}} \frac{\|\mathbf{A}\mathbf{u}\|_p}{\|\mathbf{A}\mathbf{v}\|_p}, \|\mathbf{u}\|_p = \|\mathbf{v}\|_p = 1.$$

A geometrical interpretation of the condition number $\gamma_p(\mathbf{A})$ can be envisaged by considering that the surface $\|\mathbf{x}\| = 1$ is mapped by the linear transformation $\mathbf{y} = \mathbf{A}\mathbf{x}$ onto some surface S . Then, the condition number $\gamma_p(\mathbf{A})$ is the ratio of the largest to the smallest distances from the origin to points on S . This interpretation indicates that $\gamma_p(\mathbf{A}) \geq 1$, when \mathbf{A} is nonsingular, and $\gamma_p(\mathbf{A}) = \infty$, when \mathbf{A} is singular. Rearranging the above definition leads to $\gamma_p(\mathbf{A}) = |\mathbf{A}^{-1}| \|\mathbf{A}\|$, which implies that $\gamma_p(\mathbf{A})$ becomes large when $|\mathbf{A}|$ is small; in such cases, the matrix \mathbf{A} is called *ill-conditioned*. Ill-conditioning may be regarded as an approach towards singularity, a situation that causes considerable difficulties when solving linear simultaneous equations, since a small change in the coefficients of the equations causes a large displacement in the solution, leading to loss of solution accuracy due to the loss of significant figures during the computation.

Reduced singular value decomposition (SVD) of a rectangular matrix $\mathbf{A}^{m \times n}$ of full rank:

$$\mathbf{A} = \mathbf{U}\sqrt{\boldsymbol{\Lambda}}\mathbf{V}^T = [\mathbf{u}_1, \mathbf{u}_2, \dots, \mathbf{u}_n] \begin{bmatrix} \sqrt{\lambda_1} & 0 & \dots & 0 \\ 0 & \sqrt{\lambda_2} & \dots & 0 \\ \vdots & \vdots & \ddots & \vdots \\ 0 & 0 & \dots & \sqrt{\lambda_n} \end{bmatrix} \begin{bmatrix} \mathbf{v}_1^T \\ \mathbf{v}_2^T \\ \vdots \\ \mathbf{v}_n^T \end{bmatrix} = \sum_{i=1}^n \sqrt{\lambda_i} \mathbf{u}_i \mathbf{v}_i^T,$$

where

$$\begin{aligned} (\mathbf{A}^T \mathbf{A}) \mathbf{v}_i &= \lambda_i \mathbf{v}_i, & \mathbf{v}_i &\in \mathbb{R}^n, & \mathbf{V} &= [\mathbf{v}_1, \mathbf{v}_2, \dots, \mathbf{v}_n] \in \mathbb{R}^{m \times n}, \\ (\mathbf{A}\mathbf{A}^T) \mathbf{u}_i &= \lambda_i \mathbf{u}_i, & \mathbf{u}_i &\in \mathbb{R}^m, & \mathbf{U} &= [\mathbf{u}_1, \mathbf{u}_2, \dots, \mathbf{u}_n] \in \mathbb{R}^{m \times n}, \\ \mathbf{A} &= \text{Diag}[\lambda_1, \lambda_2, \dots, \lambda_n] \in \mathbb{R}^{n \times n}. \end{aligned}$$

The columns of \mathbf{U} and those of \mathbf{V} are called the *left* and the *right singular vectors* of \mathbf{A} , respectively, while $\sqrt{\lambda_i}$ are called the *singular values*; note that the outer product $\mathbf{u}_i \mathbf{v}_i^T$, is a *rank-one* matrix.

In the particular case when $\mathbf{A} \in \mathbb{R}^{n \times n}$ is symmetric, $\mathbf{A} = \mathbf{A}^T$, and $\mathbf{A}^T \mathbf{A} = \mathbf{A}\mathbf{A}^T = \mathbf{A}^2$, so that $\mathbf{u}_i = \mathbf{v}_i$, while λ_i is the eigenvalue of \mathbf{A}^2 , and $\sqrt{\lambda_i}$ that of \mathbf{A} . In this case, the expansion $\mathbf{U}\sqrt{\boldsymbol{\Lambda}}\mathbf{V}^T$ becomes $\mathbf{A} = \sum_{i=1}^n \sqrt{\lambda_i} \mathbf{u}_i \mathbf{u}_i^T$.

If $\mathbf{A}^{m \times n}$ is not of full rank, e.g., $\text{Rank}(\mathbf{A}) = r$, where $r < \min\{m, n\}$, then $\mathbf{A} = \mathbf{U}_1 \sqrt{\boldsymbol{\Sigma}_{11}} \mathbf{V}_1^T$, where \mathbf{U}_1 contains the first r columns of \mathbf{U} , $\boldsymbol{\Sigma}_{11} \in \mathbb{R}^{r \times r}$ is a diagonal matrix containing the r singular values, and $\mathbf{V}_1^T \in \mathbb{R}^{r \times n}$ contains the first r columns of \mathbf{A} .

2 Elements of Functional Analysis

2.1 Operators in Vector Spaces

A nonempty set \mathcal{V} is called a vector space if any pair of elements $f, g \in \mathcal{V}$ can be:

- (i) added together by an operation called addition to give an element $f + g$ in \mathcal{V} , such that, for any $f, g, h \in \mathcal{V}$, the following properties hold:

$$\begin{aligned} f + g &= g + f, \\ f + (g + h) &= (f + g) + h. \end{aligned}$$

There is a unique element 0 in \mathcal{V} such that $f + 0 = f$ for all $f \in \mathcal{V}$; For each $f \in \mathcal{V}$ there is a unique element $(-f)$ in \mathcal{V} such that $f + (-f) = 0$.

- (ii) Multiplied by any scalar α of a field \mathcal{F} to give an element αf in \mathcal{V} ; furthermore, for any scalars α, β , the following properties must hold:

$$\begin{aligned}\alpha(f + g) &= \alpha f + \alpha g, \\ (\alpha + \beta)f &= \alpha f + \beta f, \\ (\alpha\beta)f &= \alpha(\beta f), \\ 1 \times f &= f.\end{aligned}$$

The *norm* of a vector $f \in \mathcal{V}$, denoted by $\|f\|$, is a nonnegative real scalar that satisfies the following relations, for all $f, g \in \mathcal{V}$:

$$\begin{aligned}\|f\| &= 0 \text{ iff } f = 0, \\ \|\alpha f\| &= |\alpha| \|f\| \text{ for any scalar } \alpha, \\ \|f + g\| &\leq \|f\| + \|g\| \text{ (the triangle inequality)}.\end{aligned}$$

A vector space \mathcal{V} endowed with a norm as defined above is called a *normed vector space*; the notation $\|\bullet\|$ highlights the role of the norm as a generalization of the customary distance in \mathbb{R}^3 .

The infinite-dimensional space obtained by generalizing \mathbb{R}^n or \mathbb{C}^n , and taking infinite sequences $f = (f_n)$ as the elements of the space is known as a *sequence space* and is usually denoted by ℓ . In the *sequence space* ℓ_p , the quantity $\|\bullet\|_p$, defined as

$$\begin{aligned}\|f\|_p &= \left\{ \sum |f_n|^p \right\}^{1/p}, \quad (1 \leq p < \infty), \\ \|f\|_\infty &= \sup |f_n|\end{aligned}$$

is a norm on the subset of those f where $\|f\|_p$ is finite. Two numbers, p, q , with $1 \leq p, q \leq \infty$, are called *conjugate indices* iff $p^{-1} + q^{-1} = 1$; if $p = 1$, then $q = \infty$. When $1 \leq p \leq \infty$, and q is the conjugate index, the following inequalities hold for any $f, g \in \ell_p$ (infinite values being allowed):

$$\begin{aligned}\|fg\|_1 &\leq \|f\|_p \|g\|_q \text{ (Hölder's inequality)}, \\ \|f + g\|_p &\leq \|f\|_p + \|g\|_p \text{ (Minkowski's inequality)}.\end{aligned}$$

A complex valued function f , defined on $\Omega \in \mathbb{R}^n$, is called *continuous at the point* $x_0 \in \Omega$ iff for each $\varepsilon > 0$ there exists $\delta > 0$ such that $|f(x) - f(x_0)| < \varepsilon$ whenever $x \in \Omega$ and $|x - x_0| < \delta$. The function f is said to be *uniformly continuous* on Ω iff for each $\varepsilon > 0$ there exists a $\delta > 0$ such that $|f(x) - f(x_0)| < \varepsilon$, whenever $x, x_0 \in \Omega$ and $|x - x_0| < \delta$.

Thus, when Ω is the finite interval $[a, b]$, continuity at a or b is to be interpreted as continuity from the right or left, respectively. If f is continuous on $[a, b]$, then it is bounded, but f need not be bounded if it is continuous only on (a, b) . For functions of several variables, continuity in the sense of the above definition is sometimes referred to as “joint continuity” to distinguish it from “separate continuity;” the latter terminology means that the function is continuous in each variable in turn when the other variables are fixed. For example, if f is a function of two variables, separate continuity requires only that $f(x, \bullet)$ and $f(\bullet, y)$ should be continuous for

fixed x and y , respectively. (The notation $f(x, \bullet)$ indicates that x is fixed, and the function is regarded as a function of its second argument only.) Uniform continuity is in general stronger than continuity, since the same δ must serve for every $x_0 \in \Omega$, but if $\Omega \subset \mathbb{R}^n$ is closed and bounded, then these concepts are equivalent.

The vector space of bounded continuous complex valued functions defined on $\Omega \subset \mathbb{R}^n$ is denoted by $\mathcal{C}(\Omega)$. The space $\mathcal{C}(\Omega)$ may be normed in several ways. The sup norm $\|\bullet\|$, defined as

$$\|f\| = \sup_{x \in \Omega} |f(x)|,$$

is most often used in practical applications. Generalizations of $\mathcal{C}(\Omega)$ are often used for treating differential equations. Thus, $\mathcal{C}(\Omega, \mathbb{R}^m)$ denotes the normed vector space of \mathbb{R}^m -valued functions equipped with the sup norm

$$\|f\| = \max_{1 \leq j \leq m} \sup_{x \in \Omega} |f_j(x)|.$$

The vector space denoted by $\mathcal{C}^k(\Omega, \mathbb{R}^m)$ consists of all \mathbb{R}^m -valued functions defined on Ω such that all partial derivatives up to and including those of order $k > 0$ of all components are bounded and continuous. The vector space $\mathcal{C}^\infty(\Omega, \mathbb{R}^m)$ consists of functions in $\mathcal{C}^k(\Omega, \mathbb{R}^m)$ such that $\mathcal{C}^\infty(\Omega, \mathbb{R}^m) = \cap_{k=1}^\infty \mathcal{C}^k(\Omega, \mathbb{R}^m)$. The space $\mathcal{C}^k(\bar{\Omega}, \mathbb{R}^m)$ consists of those continuous functions defined on $\bar{\Omega}$ which on Ω have bounded and uniformly continuous partial derivatives up to and including those of order k . (For $n > 1$, this convention avoids difficulties with the definition of derivatives on $\partial\Omega$, which is not necessarily a smooth set.) It also follows that $\mathcal{C}^\infty(\bar{\Omega}, \mathbb{R}^m) = \cap_{k=1}^\infty \mathcal{C}^k(\bar{\Omega}, \mathbb{R}^m)$.

The spaces $\mathcal{C}_0^\infty(\Omega', \mathbb{R}^m)$, where $\Omega \subset \Omega' \subset \bar{\Omega}$, are used when it is convenient to exclude the boundary from consideration. These spaces consist of those functions in $\mathcal{C}^k(\Omega, \mathbb{R}^m)$ that have bounded support contained in the interior of Ω' . (Recall that the support of a function is the closure of the set on which the function is nonzero; the support may vary from function to function.)

For example, for the finite interval $[a, b]$, a function is in $\mathcal{C}^1([a, b])$ if and only if (iff) it has a continuous derivative on (a, b) and has left and right derivatives at b and a , respectively, which are the limits of the derivatives in the interior. Another possibility is to take $\Omega = (a, b)$ and to set

$$\|f\|_{\mathcal{C}^k} = \sum_{j=0}^k \sup_{x \in [a, b]} |f^{(j)}(x)|,$$

where $f^{(j)}$ denotes the j^{th} derivative of f . The above norm is often used as a basis for analysis in $\mathcal{C}^k(\bar{\Omega})$. Corresponding norms may be defined when Ω is a subset of \mathbb{R}^n for $n > 1$ by summing over the partial derivatives.

A comparison of the concept of “closeness” for two functions f and g in the sup norm and in $\|\bullet\|_1$ shows that the sup norm bounds the difference $|f(x) - g(x)|$ for every x , whereas $\|\bullet\|_1$ only restricts the average value of this difference. Convergence in sup norm is a very strong condition and implies convergence in $\|\bullet\|_1$; the converse implication is not true.

A sequence of functions (f_n) in a normed vector space \mathcal{V} is called a Cauchy sequence iff $\lim_{m, n \rightarrow \infty} \|f_n - f_m\| = 0$. A set \mathcal{S} in a normed vector space \mathcal{V} is said to be complete iff each

Cauchy sequence in \mathcal{S} converges to a point of \mathcal{S} . A complete normed vector space \mathcal{V} is usually called a *Banach space*.

An *inner product*, denoted by (\bullet, \bullet) , on a normed vector space \mathcal{V} is a complex (respectively, real) valued function on $\mathcal{V} \times \mathcal{V}$ such that for all $f, g, h \in \mathcal{V}$ and $\alpha \in \mathbb{C}$ (respectively, $\alpha \in \mathbb{R}$) the following properties hold:

1. $(f, f) \geq 0$; the equality $(f, f) = 0$ holds iff $f = 0$.
2. $(f, g + h) = (f, g) + (f, h)$.
3. $(f, g) = \overline{(g, f)}$, where the overbar denotes complex conjugation.
4. $(\alpha f, g) = \alpha (f, g)$.

Pre-Hilbert or inner product space: A space \mathcal{V} equipped with an inner product is called a *pre-Hilbert* or *inner product space*. If \mathcal{V} is a real vector space, and the inner product is real-valued, then the respective space is called a *real pre-Hilbert space*.

Hilbert space: A pre-Hilbert space that is *complete with respect to the norm* is called a *Hilbert space*, and is usually denoted as \mathcal{H} . The spaces \mathbb{R}^n and \mathbb{C}^n with the usual inner product are Hilbert spaces, and so is the infinite sequence space equipped with the inner product

$$(f, g) = \sum f_n \bar{g}_n,$$

where $f = (f_1, f_2, \dots)$, $g = (g_1, g_2, \dots)$.

A set \mathcal{K} of vectors in \mathcal{H} is said to be *complete* iff $(f, \varphi) = 0$ for all $\varphi \in \mathcal{K}$ implies that $f = 0$. A countable set $\mathcal{K} = \{\varphi_n\}_{n=1}^{\infty}$ is called *orthonormal* iff $(\varphi_n, \varphi_m) = \delta_{nm}$ for all $m, n \geq 1$. The numbers (f, φ_n) are called the *Fourier coefficients* of f (with respect to \mathcal{K}), and the *Fourier series* of f is the formal series $\sum_n (f, \varphi_n) \varphi_n$.

Orthonormal basis: An orthonormal set $\mathcal{K} = \{\varphi_n\}$ is called an *orthonormal basis* of \mathcal{H} iff every $f \in \mathcal{H}$ can be represented in the *Fourier series*

$$f = \sum_n (f, \varphi_n) \varphi_n.$$

A sequence of vectors $\mathbf{x}_1, \mathbf{x}_2, \dots$ is called *nondegenerate* if, for every p , the vectors $\mathbf{x}_1, \mathbf{x}_2, \dots, \mathbf{x}_p$ are linearly independent. A sequence of vectors is called *orthogonal* if any two vectors of the sequence are orthogonal; *orthogonalization* of a sequence of vectors is the process of replacing the sequence by an equivalent orthogonal sequence. Every nondegenerate sequence of vectors can be orthogonalized. The orthogonalization process leads to vectors that are uniquely determined to within scalar multiples.

Every finite-dimensional subspace \mathcal{S} (and, in particular, the entire space \mathbb{R} if it is finite-dimensional) has an orthonormal basis; in such a basis, the coordinates of a vector are equal to its projections onto the corresponding basis vectors:

$$\mathbf{x} = \sum_{i=1}^n (\mathbf{x}, \mathbf{e}_i) \mathbf{e}_i.$$

Consider that $\mathbf{x}_1, \mathbf{x}_2, \dots, \mathbf{x}_n$ and $\mathbf{x}'_1, \mathbf{x}'_2, \dots, \mathbf{x}'_n$ are the coordinates of the same vector \mathbf{x} in two different orthonormal bases $\mathbf{e}_1, \mathbf{e}_2, \dots, \mathbf{e}_n$ and $\mathbf{e}'_1, \mathbf{e}'_2, \dots, \mathbf{e}'_n$ of a unitary space \mathbb{R} . The transformation between the two coordinate systems is given by

$$\mathbf{x}_i = \sum_{k=1}^n u_{ik} \mathbf{x}'_k \quad (i = 1, 2, \dots, n),$$

where the coefficients $u_{1k}, u_{2k}, \dots, u_{nk}$ satisfy the relations

$$\sum_{i=1}^n u_{ik} \bar{u}_{il} = \delta_{kl} = \begin{cases} 1, & \text{for } k = l, \\ 0, & \text{for } k \neq l. \end{cases}$$

The above transformation is called *unitary* and the corresponding matrix $U = (u_{ik})$ is called a *unitary matrix*. Thus, in an n -dimensional unitary space the transition from one orthonormal basis to another is effected by a unitary coordinate transformation. In an n -dimensional Euclidean space, the transition from one orthonormal basis to another is effected by an *orthogonal* coordinate transformation, and the matrix underlying an orthogonal transformation is called an *orthogonal matrix*.

For example, orthogonalization of the sequence of powers $1, x, x^2, x^3, \dots$, using the inner product $(f, g) = \int_a^b f(x) g(x) \tau(x) dx$, where $\tau(x) \geq 0$ and $a \leq x \leq b$, yields sequences of orthogonal polynomials. For example, using $a = -1, b = 1$, and $\tau(x) = 1$ leads to the Legendre polynomials

$$P_0(x) = 1, P_m(x) = \frac{1}{2^m m!} \frac{d^m (x^2 - 1)^m}{dx^m} \quad (m = 1, 2, \dots).$$

On the other hand, using $a = -1, b = 1$, and $\tau(x) = 1/\sqrt{1 - x^2}$ leads to the Tchebyshev (Chebyshev) polynomials $T_n(x) = \cos(n \arccos x)/(2^{n-1})$. Furthermore, using $a = -\infty, b = +\infty$, and $\tau(x) = e^{-x^2}$ leads to the Hermite polynomials, and so on.

Consider an arbitrary vector \mathbf{x} , an orthonormal sequence of vectors $\mathbf{z}_1, \mathbf{z}_2, \dots, \mathbf{z}_p, \dots$, with $p = (1, 2, \dots)$; consider also the sequence $\xi_p \equiv (\mathbf{x}, \mathbf{z}_p)$. If the limit

$$\lim_{p \rightarrow \infty} \left(\|\mathbf{x}\| - \sum_{k=1}^p |\xi_k|^2 \right)^{1/2} = 0$$

holds, then the series $\sum_{k=1}^{\infty} \xi_k \mathbf{z}_k$ is said to converge in the mean (or with respect to the norm) to the vector \mathbf{x} , and the norm of \mathbf{x} is given by:

$$\|\mathbf{x}\| = |\mathbf{x}|^2 = \sum_{k=1}^{\infty} |\xi_k|^2.$$

If, for every vector \mathbf{x} of \mathbb{R} , the series $\sum_{k=1}^{\infty} \xi_k \mathbf{z}_k$ converges in the mean to \mathbf{x} , then the orthonormal sequence of vectors $\mathbf{z}_1, \mathbf{z}_2, \dots, \mathbf{z}_p, \dots$ is complete. In terms of such a complete orthonormal sequence \mathbf{z}_k , the scalar product of two vectors \mathbf{x} and \mathbf{y} in \mathbb{R} becomes

$$(\mathbf{x}, \mathbf{y}) = \sum_{k=1}^{\infty} \xi_k \bar{\eta}_k \quad (\xi_k = \langle \mathbf{x}, \mathbf{z}_k \rangle, \eta_k = \langle \mathbf{y}, \mathbf{z}_k \rangle, k = 1, 2, \dots).$$

As a further example, consider the space of all complex functions $f(t)$, where t is a real variable, that are piecewise continuous in the closed interval $[0, 2\pi]$, with the norm and the scalar product defined, respectively, as $\|f\| = \int_0^{2\pi} |f(t)|^2 dt$, and $(f, g) = \int_0^{2\pi} f(t) \bar{g}(t) dt$. Consider now the infinite sequence of orthogonal and complete functions $e^{ikt}/\sqrt{2\pi}$, ($k = 0, \pm 1, \pm 2, \dots$). Then, the *Fourier series* of $f(t)$, namely $\sum_{k=-\infty}^{\infty} f_k e^{ikt}$, with

Fourier coefficients $f_k = (\int_0^{2\pi} f(t) e^{-ikt} dt)/2\pi$, ($k = 0, \pm 1, \pm 2, \dots$), converges in the mean to $f(t)$ in the interval $[0, 2\pi]$. The condition of completeness for the function f is called Parseval's equality:

$$\int_0^{2\pi} f(t) \overline{g(t)} dt = \sum_{k=-\infty}^{+\infty} \frac{1}{2\pi} \int_0^{2\pi} f(t) e^{-ikt} dt \int_0^{2\pi} \overline{g(t)} e^{ikt} dt.$$

If $f(t)$ is a real function, then f_0 is real, and f_k and f_{-k} are conjugate complex numbers. Therefore, for a real function $f(t)$, the Fourier series becomes $f(t) = a_0/2 + \sum_{k=1}^{\infty} (a_k \cos kt + b_k \sin kt)$, where $a_k = (\int_0^{2\pi} f(t) \cos kt)/\pi$ and $b_k = (\int_0^{2\pi} f(t) \sin kt)/\pi$, for $k = 0, 1, 2, \dots$

The space \mathcal{L}_p (or $\mathcal{L}_p(X)$, if X needs emphasis) is defined to be the set of measurable functions f such that $\|f\|_p < \infty$, where

$$\|f\|_p = \left\{ \int |f|^p d\mu \right\}^{1/p}, \quad (1 \leq p < \infty),$$

$$\|f\|_\infty = \text{ess sup } |f|.$$

Frequently, X will be an interval of the real line with end points a and b , while μ will be the Lebesgue measure; in this case, the space will be denoted by $\mathcal{L}_p(a, b)$. Two functions f and g in $\mathcal{L}_p(X)$ are said to be equal iff $f = g$ almost everywhere. Thus, all functions in $\mathcal{L}_p(X)$ are finite almost everywhere. When $p = \infty$, then $\|f\|_\infty = \sup |f(x)|$, for f continuous and μ representing the Lebesgue measure. Thus, the continuous bounded functions with the sup norm form a closed subspace of \mathcal{L}_∞ . If a function f in \mathcal{L}_∞ is not continuous, the measure of the set for which $|f(x)| > \|f\|_\infty$ is zero. The space \mathcal{L}_p may be thought of as the continuous analogue of the sequence space, with integration replacing summation; for $p \geq 1$, \mathcal{L}_p is a Banach space under the norm $\|\bullet\|_p$. Furthermore, \mathcal{L}_p is separable if $1 \leq p < \infty$; in particular, \mathcal{L}_2 is a Hilbert space when equipped with the inner product $(f, g) = \int f \bar{g} d\mu$.

The set $\mathcal{D}(A)$ (sometimes denoted just by \mathcal{D} if there is only one mapping under consideration) is called the *domain* of a mapping A . For $f \in \mathcal{D}(A)$, the element Af is called the *image* of f . Likewise, the image $A(S)$ of a set $S \subset \mathcal{D}(A)$ is the set of the images of all the elements of S . In particular, the image of $\mathcal{D}(A)$ is called the *range* of A and is written as $\mathcal{R}(A)$. The *preimage* of a set $\mathcal{S}_1 \subset \mathcal{W}$ is the set $A^{-1}(\mathcal{S}_1) = \{f : f \in \mathcal{D}(A), Af \in \mathcal{S}_1\}$.

Operator, function, functional: The mapping A is called an *operator* or a *function* from \mathcal{V} into \mathcal{W} . The notation $A : \mathcal{S} \rightarrow \mathcal{W}$ indicates that A is an operator with domain \mathcal{S} and range in \mathcal{W} , or, equivalently, that A maps \mathcal{S} into \mathcal{W} . Note that an operator is always single-valued, in that it assigns exactly one element of its range to each element in its domain. Furthermore, although there is no strict distinction between "operator" and "function," it is customary to reserve "function" for the case when \mathcal{V} and \mathcal{W} are finite dimensional and to use "operator" otherwise. In view of its importance, one particular type of operator is given a name of its own: *the operator from \mathcal{V} into the field \mathcal{F} of scalars (real or complex) is called a functional.*

An operator A from \mathcal{V} into \mathcal{W} is called *injective* iff for each $g \in \mathcal{R}(A)$, there is exactly one $f \in \mathcal{D}(A)$ such that $Af = g$; A is called *surjective* iff $\mathcal{R}(A) = \mathcal{W}$, and A is called *bijective* iff it is both injective and surjective. The terms "one-to-one," "onto," "one-to-one and onto," respectively, are common alternatives in the literature. An operator A from \mathcal{V} into \mathcal{W} is *continuous at the point $f_0 \in \mathcal{D}(A)$* iff for each $\varepsilon > 0$, there is a $\delta > 0$ such that $\|Af - Af_0\| < \varepsilon$ if $f \in \mathcal{D}(A)$ and $\|f - f_0\| < \delta$; A is said to be *continuous* iff it is continuous at every point of $\mathcal{D}(A)$.

An operator L from \mathcal{V} into \mathcal{W} with domain $\mathcal{D}(L)$ is called *linear* iff $L(\alpha f + \beta g) = \alpha Lf + \beta Lg$ for all $\alpha, \beta \in \mathbb{C}$ (or $\alpha, \beta \in \mathbb{R}$, if \mathcal{V} and \mathcal{W} are real spaces), and all $f, g \in \mathcal{D}(L)$. A linear operator is the vector space analogue of a function in one dimension represented by a straight line through the origin, that is, a function $\varphi : \mathbb{R} \rightarrow \mathbb{R}$ where $\varphi(x) = \lambda x$ for some $\lambda \in \mathbb{R}$. In particular, the *identity* operator, denoted by I , is the operator from \mathcal{V} onto itself such that $If = f$ for all $f \in \mathbb{R}$.

A wide variety of equations may be written in the form $Lf = g$, with L a linear operator. For example, the simultaneous algebraic equations

$$\sum_{j=1}^n \alpha_{ij} f_j = g_i, \quad (i = 1, \dots, m),$$

define the operator L via the relation

$$(Lf)_i = \sum_{j=1}^n \alpha_{ij} f_j, \quad (i = 1, \dots, m).$$

In this case, $L : \mathbb{C}^n \rightarrow \mathbb{C}^m$ is a linear operator and the above equation can be written as $Lf = g$. Conversely, every linear operator $\mathbb{C}^n \rightarrow \mathbb{C}^m$ may be expressed in the above form by choosing bases for \mathbb{C}^n and \mathbb{C}^m . The above equations may also be put in matrix form, but note that there is a distinction between the matrix, which depends on the chosen basis, and the operator L , which does not.

As a further example, the Fredholm integral equation $f(x) - \int_0^1 k(x, y) f(y) dy = g(x)$, $0 \leq x \leq 1$, where k and g are given and f is the unknown function, can also be written in operator form as $f - Kf = g$, where K is a linear operator. Similarly, the differential equation $a_0 f''(x) + a_1 f'(x) + a_2 f(x) = g(x)$, $0 \leq x \leq 1$, where $a_0, a_1, a_2 \in \mathbb{C}$, and g is a given continuous function, can be written in the form $Lf = g$, with $L : \mathbb{C}^2([0, 1]) \rightarrow \mathbb{C}([0, 1])$ being a linear operator.

The operator equation $Lf = g$, where L is a linear operator from \mathcal{V} into \mathcal{W} with domain $\mathcal{D}(L)$, may or may not have a solution f for every $g \in \mathcal{R}(L)$, depending on the following possibilities:

- (i) L is *not injective*, in which case a reasonable interpretation of the inverse operator L^{-1} is not possible. The equation $Lf = g$ always has more than one solution if $g \in \mathcal{R}(L)$.
- (ii) L is *injective but not surjective*. In this case, the equation $Lf = g$ has exactly one solution if $g \in \mathcal{R}(L)$, but no solution otherwise. The inverse L^{-1} is the operator with domain $\mathcal{R}(L)$ and range $\mathcal{D}(L)$ defined by $f = L^{-1}g$. The set $\mathcal{N}(L) \subset \mathcal{D}(L)$ of solutions of the equation $Lf = 0$ is called the *null space* of L . Note that $\mathcal{N}(L)$ is a linear subspace, and $\mathcal{N}(L) = 0$ iff L is injective.
- (iii) L is *bijective*. In this case, L^{-1} is a linear operator with domain \mathcal{W} , and $Lf = g$ has exactly one solution for each $g \in \mathcal{W}$.

If a linear operator L from \mathcal{V} into \mathcal{W} is continuous at some point $f \in \mathcal{D}(L)$, then L is continuous everywhere. A linear operator L is *bounded* on $\mathcal{D}(L)$ iff there is a finite number m such that $\|Lf\| \leq m \|f\|$, with $f \in \mathcal{D}(L)$. If L is not bounded on $\mathcal{D}(L)$, it is said to be *unbounded*. The infimum of all constants m such that this inequality holds is denoted by $\|L\|$, and is called the operator norm of L . Note that $\|Lf\| \leq \|L\| \|f\|$; this relationship may be compared with the relation $|\varphi(x)| = |\lambda x| = |\lambda| |x|$ for a linear operator $\varphi(x) = \lambda x$, $\varphi : \mathbb{R} \rightarrow \mathbb{R}$. Since $|\lambda|$ is a measure of the gradient of φ , the norm of the operator L may therefore be thought of as its maximum gradient.

Suppose that L is a (possibly unbounded) linear operator from a Banach space \mathcal{B} into \mathcal{B} . The set $\rho(L)$ of complex numbers for which $(\lambda I - L)^{-1}$ belongs to the space of linear operators on \mathcal{B} is called the *resolvent set* of L . For $\lambda \in \rho(L)$, the operator $R(\lambda; L) \equiv (\lambda I - L)^{-1}$ is known as the *resolvent* of L . The complement $\sigma(L)$ in \mathcal{C} of $\rho(L)$ is the *spectrum* of L . A complex number λ is called an *eigenvalue* (*characteristic value*) of L iff the equation $\lambda f - Lf = 0$ has a nonzero solution. The corresponding nonzero solutions are called *eigenfunctions* (*characteristic functions*), and the linear subspace spanned by these is called the *eigenspace* (*characteristic space*) corresponding to λ . The set $\sigma_p(L)$ of eigenvalues is known as the *point spectrum* of L . The set consisting of those $\lambda \in \sigma(L)$ for which $(\lambda I - L)$ is injective and $R(\lambda I - L)$ is dense (respectively, not dense) in \mathcal{B} is called the *continuous spectrum* (respectively, the *residual spectrum*). Thus, $\lambda \in \rho(L)$ iff $\lambda I - L$ is bijective; in this case $\sigma(L)$ is the union of the point, continuous and residual spectra, which are disjoint sets. If \mathcal{B} is finite dimensional, then $\sigma(L) = \sigma_p(L)$.

Formal differential operators: The operator

$$l = \sum_{r=0}^n p_r(x) \left(\frac{d}{dx} \right)^r,$$

where p_r ($r = 0, 1, \dots, n$) are given functions on \mathbb{R} , is called a *formal ordinary differential operator* of order n . In a Hilbert space, it is convenient to refer loosely to any operator L obtained from l by setting $Lf = lf(x) = \sum_{r=0}^n p_r(x) f^{(r)}(x)$, for f in some specified domain, as a *differential operator*. For a general *partial differential equation* in n dimensions, the notational complexity can be reduced considerably by the use of multi-indices, which are defined as follows: a *multi-index* α is an n -tuple $(\alpha_1, \dots, \alpha_n)$ of nonnegative integers. It is also convenient to use the notation $|\alpha| = \alpha_1 + \dots + \alpha_n$ for a multi-index; even though this notation conflicts with the notation for the Euclidean distance \mathbb{R}^n , the meaning will always be clear from the context.

In the following, multi-indices will be denoted by α and β , and a point in \mathbb{R}^n will be denoted as $x = (x_1, \dots, x_n)$, with $x^\alpha = x_1^{\alpha_1} \dots x_n^{\alpha_n}$. The notation used for derivatives is $D_j = \partial/\partial x_j$ and $D^\alpha = D_1^{\alpha_1} \dots D_n^{\alpha_n}$. Consider that $p_{\alpha\beta} \neq 0$ are complex-valued variable coefficients such that $p_{\alpha\beta} \in C^\infty(\overline{\Omega})$, for multi-indices α and β , with $|\alpha| = |\beta| = m$. Consider, in addition, a function $\phi \in C^{2m}$; then, the *formal partial differential operator* l of order $2m$ is defined as

$$l\phi \equiv \sum_{|\alpha|, |\beta| \leq m} (-1)^{|\alpha|} D^\alpha (p_{\alpha\beta} D^\beta \phi).$$

The operator l_p , defined as

$$l_p\phi \equiv (-1)^m \sum_{|\alpha|=|\beta|=m} D^\alpha (p_{\alpha\beta} D^\beta \phi),$$

is called the *principal part* of the formal partial differential operator l .

Formal adjoint operator: Furthermore, the operator l^+ defined as

$$l^+\phi \equiv \sum_{|\alpha|, |\beta| \leq m} (-1)^{|\alpha|} D^\alpha (\overline{p_{\beta\alpha}} D^\beta \phi) \quad (\phi \in C^{2m})$$

is called the *formal adjoint* of l . Iff $l = l^+$, then l is called *formally self-adjoint*.

Define \mathcal{L}_p^{loc} to be the set of all functions that lie in $\mathcal{L}_p(\mathcal{S})$ for every set \mathcal{S} bounded and closed in \mathbb{R}^n . Then, a function f in \mathcal{L}_2^{loc} has a α^{th} weak derivative iff there exists a function $g \in \mathcal{L}_0^{loc}$ such that

$$\int_{\Omega} g\phi \, dx = (-1)^{|\alpha|} \int_{\Omega} f \cdot (D^{\alpha} \phi) \, dx$$

for all $\phi \in C_0^{\infty}$; the function g is called the α^{th} weak derivative of f , and we write $D^{\alpha} f = g$. Weak derivatives are unique in the context of \mathcal{L}_2 spaces, in the sense that if g_1 and g_2 are both weak α^{th} derivatives of f , then

$$\int_{\Omega} (g_1 - g_2) \phi \, dx = 0 \quad (\phi \in C_0^{\infty}),$$

which implies that $g_1 = g_2$ almost everywhere in Ω . The above relation also implies that if a function has an α^{th} derivative g in the ordinary sense in \mathcal{L}_2^{loc} , then g is the weak α^{th} derivative of f . The weak derivatives may be thought of as averaging out the discontinuities in f . Consequently, it is permissible to exchange the order of differentiation: $D_i D_j f = D_j D_i f$. In one dimension, a function has a weak first derivative iff it is absolutely continuous and has a first derivative in \mathcal{L}_2^{loc} . However, note that f may have an ordinary derivative almost everywhere without having a weak derivative. For example, if $f(x) = 1$ for $x > 0$ and $f(x) = 0$ for $x < 0$, then $\int_{-1}^1 f\phi' \, dx = \int_0^1 \phi' \, dx = -\phi(0)$, but f does not have a weak derivative since there is no $g \in \mathcal{L}_0^{loc}$ such that $\phi(0) = \int_{-1}^1 g\phi \, dx$ for all $\phi \in C_0^{\infty}$.

Sobolev spaces: The analysis of differential operators is carried out in special Hilbert spaces, called Sobolev spaces. The Sobolev space \mathcal{H}^m (or $\mathcal{H}^m(\Omega)$ if the domain requires emphasis) of order m , where m is a nonnegative integer, consists of the set of functions f such that for $0 \leq |\alpha| \leq m$, all the weak derivatives $D^{\alpha} f$ exist and are in \mathcal{L}_2 ; furthermore, \mathcal{H}^m is equipped with an inner product and a norm defined, respectively, as:

$$(f, g)_m = \sum_{|\alpha| \leq m} \int_{\Omega} D^{\alpha} f \cdot \overline{D^{\alpha} g} \, dx,$$

$$\|f\|_m^2 = (f, f)_m = \sum_{|\alpha| \leq m} \int_{\Omega} |D^{\alpha} f|^2 \, dx.$$

The above norm may be regarded as measuring the average value of the weak derivatives. Note that \mathcal{H}^m is a proper subset of the set of functions with m^{th} weak derivatives, since the derivatives $D^{\alpha} f$ are required to be in \mathcal{L}_2 , and not merely in \mathcal{L}_2^{loc} . The closure of C^{∞} in $\|\cdot\|_m$ is \mathcal{H}^m , and the closure in \mathcal{H}^m of C_0^{∞} is the Sobolev space \mathcal{H}_0^m , of order m . The following chains of inclusions hold for the higher order Sobolev spaces:

$$C^{\infty} \subset \dots \subset \mathcal{H}^{m+1} \subset \mathcal{H}^m \subset \dots \subset \mathcal{H}^0 = \mathcal{L}_2,$$

$$C_0^{\infty} \subset \dots \subset \mathcal{H}_0^{m+1} \subset \mathcal{H}_0^m \subset \dots \subset \mathcal{H}_0^0 = \mathcal{L}_2.$$

Bilinear form: The bilinear form, $B[f, \phi]$, associated with the formal differential operator l is defined for all functions $f, \phi \in \mathcal{H}_0^m$ as

$$B[f, \phi] = \sum_{|\alpha|, |\beta| \leq m} \left(p_{\alpha\beta} D^{\alpha} f, D^{\beta} \phi \right)_0.$$

Note that $B[f, \phi]$ is a bounded bilinear form on $\mathcal{H}_0^m \times \mathcal{H}_0^m$. The problem of finding $f \in \mathcal{H}_0^m$ such that $B[f, \phi] = (g, \phi)_0$ for all $\phi \in \mathcal{H}_0^m$ and $g \in \mathcal{L}_2$ is called the *generalized Dirichlet problem*.

Adjoint operators: The space of continuous linear functionals on a Banach space \mathcal{B} is called the *dual* of \mathcal{B} , and is denoted here by \mathcal{B}^+ . For a bounded linear operator $L : \mathcal{B} \rightarrow \mathcal{C}$, the relation

$$g^+(Lf) = L^+g^+(f),$$

required to hold for all $f \in \mathcal{B}$ and all $g^+ \in \mathcal{C}^+$, defines an operator L^+ from \mathcal{C}^+ into \mathcal{B}^+ , called the *adjoint* of L . For example, the adjoint of an integral operator of the form $Kf(x) = \int_0^1 k(x, y)f(y) dy$, for a continuous kernel $k : [0, 1] \times [0, 1] \rightarrow \mathbb{R}$, is the operator $K^+ : \mathcal{L}_\infty(0, 1) \rightarrow \mathcal{L}_\infty(0, 1)$ defined as $K^+g^+(y) = \int_0^1 k(x, y)g^+(x) dx$.

As the next example, consider the finite dimensional operator $L : \ell_1^{(n)} \rightarrow \ell_1^{(n)}$ corresponding to the matrix (α_{ij}) , namely

$$(Lf)_i = \sum_{j=1}^n \alpha_{ij}f_j, \quad (i = 1, \dots, n).$$

The corresponding adjoint operator, $L^+ : \ell_\infty^{(n)} \rightarrow \ell_\infty^{(n)}$, is represented by the transposed matrix $(\alpha_{ij})^T$, as can be seen by applying the definition of the adjoint operator:

$$g^+(Lf) = \sum_{i=1}^n (Lf)_i g_i^+ = \sum_{i=1}^n g_i^+ \sum_{j=1}^n \alpha_{ij}f_j = \sum_{j=1}^n f_j \sum_{i=1}^n \alpha_{ij}g_i^+ = (L^+g^+)(f).$$

Thus, even in finite dimensions, the adjoint operator depends on the norm of the space and has more significance than the algebraic “transpose.” For example, the relation $\|L\| = \|L^+\|$ will only hold if the dual space is correctly selected.

In an n -dimensional unitary space \mathbb{R} , the linear operator A^+ is called *adjoint* to the operator A iff, for any two vectors \mathbf{x}, \mathbf{y} of \mathbb{R} , the following relationship holds

$$(A\mathbf{x}, \mathbf{y}) = (\mathbf{x}, A^+\mathbf{y}).$$

In an orthonormal basis $\mathbf{e}_1, \mathbf{e}_2, \dots, \mathbf{e}_n$ in \mathbb{R} , the adjoint operator A^+ can be represented *uniquely* in the form

$$A^+\mathbf{y} = \sum_{k=1}^n \langle \mathbf{y}, A\mathbf{e}_k \rangle \mathbf{e}_k,$$

for any vector \mathbf{y} of \mathbb{R} . Consider that A is a linear operator in a unitary space and that $A = \|a_{ik}\|_i^n$ is the corresponding matrix that represents A in an orthonormal basis $\mathbf{e}_1, \mathbf{e}_2, \dots, \mathbf{e}_n$. Then, the matrix A^+ corresponding to the representation of the adjoint operator A^+ in the same basis is the complex conjugate of the transpose of A , i.e.,

$$A^+ = \overline{A}^T.$$

The matrix A^+ is called the *adjoint* of A . Thus, *in an orthonormal basis, adjoint matrices correspond to adjoint operators*. The adjoint operator has the following properties:

1. $(A^+)^+ = A$,
2. $(A + B)^+ = A^+ + B^+$,
3. $(\alpha A)^+ = \bar{\alpha}A^+$ (α a scalar),
4. $(AB)^+ = B^+A^+$,
5. If an arbitrary subspace \mathcal{S} of \mathbb{R} is invariant with respect to A , then the orthogonal complement \mathcal{T} of the subspace \mathcal{S} is invariant with respect to A^+ .

Two systems of vectors $\mathbf{x}_1, \mathbf{x}_2, \dots, \mathbf{x}_n$ and $\mathbf{y}_1, \mathbf{y}_2, \dots, \mathbf{y}_n$ are by definition *bi-orthogonal* if

$$\langle \mathbf{x}_i, \mathbf{y}_k \rangle = \delta_{ik}, (i, k = 1, 2, \dots, m),$$

where δ_{ik} is the Kronecker symbol.

If A is a linear operator of simple structure, then the adjoint operator A^+ is also of simple structure; therefore, complete systems of characteristic vectors $\mathbf{x}_1, \mathbf{x}_2, \dots, \mathbf{x}_n$ and $\mathbf{y}_1, \mathbf{y}_2, \dots, \mathbf{y}_n$ of A and A^+ , respectively, can be chosen such that they are bi-orthogonal:

$$A\mathbf{x}_i = \lambda_i\mathbf{x}_i, \quad A^+\mathbf{y}_i = \lambda_i\mathbf{y}_i, \quad \langle \mathbf{x}_i, \mathbf{y}_k \rangle = \delta_{ik}, (i, k = 1, 2, \dots, n).$$

Furthermore, if the operators A and A^+ have a common characteristic vector, then the corresponding characteristic values are complex conjugates. A linear operator A is called *normal* if it commutes with its adjoint:

$$AA^+ = A^+A.$$

A linear operator H is called *hermitian* if it is equal to its adjoint:

$$H^+ = H.$$

A linear operator U is called *unitary* if it is inverse to its adjoint:

$$UU^+ = I.$$

From the above definitions, it follows that (i) the product of two unitary operators is itself a unitary operator, (ii) the unit operator I is unitary, and (iii) the inverse of a unitary operator is also unitary. Therefore the set of all unitary operators forms a group, called the *unitary group*. Note that hermitian and unitary operators are special cases of a normal operator. Note also that a hermitian operator H is called *positive semidefinite* if the inequality $\langle H\mathbf{x}, \mathbf{x} \rangle \geq 0$ holds for every vector \mathbf{x} of \mathbb{R} ; H is called *positive definite* if the *strict* inequality $\langle H\mathbf{x}, \mathbf{x} \rangle > 0$ holds for every vector $\mathbf{x} \neq \mathbf{0}$ of \mathbb{R} .

Just as in the case of operators, a matrix is called *normal* if it commutes with its adjoint, *hermitian* if it is equal to its adjoint, and *unitary* if it is inverse to its adjoint. Thus, in an orthonormal basis, a normal (hermitian, unitary) operator corresponds to a normal (hermitian, unitary) matrix. Note that every characteristic vector of a normal operator A is a characteristic vector of the adjoint operator A^+ , i.e., if A is a normal operator, then A and A^+ have the same characteristic vectors. Furthermore, a linear operator is normal iff it has a complete orthonormal

system of characteristic vectors. If A is a normal operator, then each of the operators A and A^+ can be represented as a polynomial in the other; these two polynomials are determined by the characteristic values of A .

Hermitian and unitary operators can also be characterized in terms of their respective spectra. Thus, a linear operator is hermitian iff it has a complete orthonormal system of characteristic vectors with real characteristic values. Furthermore, a linear operator is unitary iff it has a complete orthonormal system of characteristic vectors with characteristic values of modulus 1. Consequently, a matrix A is normal iff it is unitarily similar to a diagonal matrix,

$$A = U \|\lambda_i \delta_{ik}\|_1^n U^{-1}, \quad U^+ = U^{-1}.$$

A matrix H is hermitian iff it is unitarily similar to a diagonal matrix with real diagonal elements:

$$H = U \|\lambda_i \delta_{ik}\|_1^n U^{-1}, \quad U^+ = U^{-1}, \quad \lambda_i = \bar{\lambda}_i, \quad (i = 1, 2, \dots, n).$$

Finally, a matrix U is unitary iff it is unitarily similar to a diagonal matrix with diagonal elements of modulus 1:

$$U = U_1 \|\lambda_i \delta_{ik}\|_1^n U_1^{-1}, \quad U_1^+ = U_1^{-1}, \quad |\lambda_i| = 1, \quad (i = 1, 2, \dots, n).$$

Note also that a hermitian operator is positive semidefinite (positive definite) iff all its characteristic values are nonnegative (positive).

In a Hilbert space \mathcal{H} , the relation $g^+(Lf) = L^+g^+(f)$ becomes

$$(Lf, g) = (f, L^+g),$$

for all f and $g \in \mathcal{H}$; thus, the above relation defines the bounded linear operator L^+ , called the (*Hilbert space*) *adjoint* of L . The *Riesz Representation Theorem* ensures that for every element g^+ of the dual \mathcal{H}^+ of a Hilbert space \mathcal{H} , there is a unique element g of \mathcal{H} such that $g^+(f) = (f, g)$ for all $f \in \mathcal{H}$. The equality $\|g^+\| = \|g\|$ also holds.

Self-adjoint operator: The class of bounded operators from a Hilbert space \mathcal{H} into itself is particularly important. Thus, if L is a linear operator on the Hilbert space \mathcal{H} , then L is said to be *self-adjoint* iff $L = L^+$. For example, for $\sum \sum |\alpha_{ij}|^2 < \infty$, the operator $L : \mathcal{L}_2 \rightarrow \mathcal{L}_2$ defined as $(Lf)_i = \sum_{j=1}^{\infty} \alpha_{ij} f_j$ is self-adjoint iff $\alpha_{ij} = \bar{\alpha}_{ji}$, ($i, j = 1, 2, \dots$), that is, iff the infinite matrix (α_{ij}) is *hermitian*, since $(L^+g)_j = \sum_{i=1}^{\infty} \bar{\alpha}_{ij} g_i$. The adjoint $L^+ : \mathcal{L}_2 \rightarrow \mathcal{L}_2$ is therefore represented by the conjugate transpose of the infinite matrix (α_{ij}) . As another example, the integral operator $Kf(x) = \int_0^1 k(x, y) f(y) dy$, $K : \mathcal{L}_2(0, 1) \rightarrow \mathcal{L}_2(0, 1)$ is bounded and is self-adjoint iff the kernel is, in the complex case, *hermitian*: $k(x, y) = \overline{k(y, x)}$, or, in the real case, *symmetric*: $k(x, y) = k(y, x)$.

Fredholm alternative theorem: The existence of solutions for operator equations involving linear compact operators is elucidated by the *Fredholm Alternative Theorem* (in a Hilbert space \mathcal{H}), which can be formulated as follows: consider that $L : \mathcal{H} \rightarrow \mathcal{H}$ is a linear compact operator, and consider the equation

$$(\lambda I - L)g = g, \quad g \in \mathcal{H}, \quad \lambda \neq 0.$$

Then, one of the following alternatives holds:

- (a) The homogeneous equation has only the zero solution; in this case, $\lambda \in \rho(L)$, where $\rho(L)$ denotes the *resolvent set* of L , implying thus that λ cannot be an eigenvalue of L . Furthermore, $(\lambda I - L)^{-1}$ is bounded, and the inhomogeneous equation has exactly one solution $f = (\lambda I - L)^{-1}g$, for each $g \in \mathcal{H}$.
- (b) The homogeneous equation has a nonzero solution; in this case, the inhomogeneous equation has a solution, necessarily nonunique, iff $\langle g, \varphi^+ \rangle = 0$, for every solution φ^+ of the adjoint equation $\lambda \varphi^+ = L^+ \varphi^+$, where L^+ denotes the operator adjoint to L , and $\langle \cdot, \cdot \rangle$ denotes the inner product in the respective Hilbert space \mathcal{H} .

Adjoint of an unbounded linear operator: Consider now that L denotes an *unbounded* linear operator from \mathcal{H} into \mathcal{H} , with domain $\mathcal{D}(L)$ dense in \mathcal{H} . Recall that the specification of a domain is an essential part of the definition of an unbounded operator. Define $\mathcal{D}(L^+)$ to be the set of elements g such that there is an h with $(Lf, g) = (f, h)$ for all $f \in \mathcal{D}(L)$. Let L^+ be the operator with domain $\mathcal{D}(L^+)$ and with $L^+g = h$ on $\mathcal{D}(L^+)$, or, equivalently, consider that L^+ satisfies the relation

$$(Lf, g) = (f, L^+g), \quad f \in \mathcal{D}(L), \quad g \in \mathcal{D}(L^+).$$

Then the operator L^+ is called the *adjoint* of L . Furthermore, a densely defined linear operator L from a Hilbert space into itself is called *self-adjoint* iff $L = L^+$. Note that necessarily $\mathcal{D}(L) = \mathcal{D}(L^+)$ for self-adjoint operators.

It is important to note that the operator theoretic concept of “adjoint” involves the boundary conditions in an essential manner, and is therefore a more comprehensive concept than the *formal adjoint operator*, which merely described the coefficients of a certain differential operator. To illustrate the difference between the (operator theoretic) adjoint of an unbounded operator and the underlying formal adjoint operator, consider the formal differential operator $l = id/dx$ on the interval $[0, 1]$, and consider the operator $Lf = if$. Furthermore, denote by \mathcal{A} the linear subspace of $\mathcal{H} = \mathcal{L}_2(0, 1)$ consisting of absolutely continuous functions with derivatives in $\mathcal{L}_2(0, 1)$. Suppose first that no boundary conditions are specified for L , so that $\mathcal{D}(L) = \mathcal{A}$; in this case, the proper adjoint boundary conditions are $\mathcal{D}(L^+) = \{g : g \in \mathcal{A}, g(0) = g(1) = 0\}$. On the other hand, suppose that the boundary conditions imposed on L are $\mathcal{D}(L) = \{f : f \in \mathcal{A}, f(0) = f(1) = 0\}$; in this case, the proper adjoint boundary conditions are $\mathcal{D}(L^+) = \mathcal{A}$. Note that L is not equal to L^+ , in either of these two examples, although l is “self-adjoint” in the sense of classical differential equation theory. To construct a self-adjoint operator from the formal operator $l = id/dx$ on $[0, 1]$, it is necessary to choose boundary conditions so as to ensure that $\mathcal{D}(L) = \mathcal{D}(L^+)$, implying that the proper domain is $\mathcal{D}(L) = \{f : f \in \mathcal{A}, f(1) = e^{i\theta}f(0), \theta \in \mathbb{R}\}$, which means that there are infinitely many self-adjoint operators based on the formal operator id/dx on the interval $[0, 1]$.

2.2 Differential Calculus

Gâteaux and Fréchet variations, differentials and derivatives: Consider that I is an open interval of the real line and \mathcal{V} is a normed real space. The *derivative* of a mapping (or operator) $\phi : I \rightarrow \mathcal{V}$ at $t_0 \in I$ is defined as $\lim_{t \rightarrow t_0} (\phi(t) - \phi(t_0))/(t - t_0)$ if this limit exists, and

is denoted by $\phi'(t_0)$. The limit is to be understood in the sense of the norm in \mathcal{V} , namely $\|(\phi(t) - \phi(t_0))/(t - t_0) - \phi'(t_0)\| \rightarrow 0$ as $t \rightarrow 0$. Consider next that \mathcal{V} and \mathcal{W} are normed real spaces and \mathcal{D} is an open subset of \mathcal{V} . Consider that $x_0 \in \mathcal{D}$, and h is a fixed nonzero element in \mathcal{V} . Since \mathcal{D} is open, there exists an interval $I = (-\tau, \tau)$ for some $\tau > 0$ such that if $t \in I$, then $x_0 + th \in \mathcal{D}$. If the mapping $\phi : I \rightarrow \mathcal{V}$ defined by $\phi(t) = F(x_0 + th)$ has a derivative at $t = 0$, then $\phi'(0)$ is called the *Gâteaux variation* of F at x_0 with increment h , and is denoted by $\delta F(x_0; h)$, i.e.,

$$\delta F(x_0; h) \equiv \left. \frac{d}{dt} F(x_0 + th) \right|_{t=0} = \lim_{t \rightarrow 0} \frac{1}{t} \{F(x_0 + th) - F(x_0)\}.$$

The above relation may be used to define $\delta F(x_0; h)$ when \mathcal{V} is any linear space, not necessarily normed. When $\delta F(x_0; h)$ exists, it is homogeneous in h of degree one, i.e., for each real number λ , $\delta F(x_0; \lambda h)$ exists and is equal to $\lambda \delta F(x_0; h)$. The Gâteaux variation is a generalization of the notion of the directional derivative in calculus and of the notion of the first variation arising in the calculus of variations. The existence of the Gâteaux variation at $x_0 \in \mathcal{D}$ provides a local approximation property in the following sense:

$$F(x_0 + h) - F(x_0) = \delta F(x_0; h) + r(x_0; h), \quad \text{where } \lim_{t \rightarrow 0} \frac{r(x_0; th)}{t} = 0.$$

The existence of $\delta F(x_0; h)$ implies the *directional continuity* of F at x_0 , i.e.,

$$\|F(x_0 + th) - F(x_0)\| \rightarrow 0 \text{ as } t \rightarrow 0 \text{ for fixed } h,$$

but does not imply that F is continuous at x_0 . This is equivalent to saying that, in general, the above limit does not hold uniformly with respect to h on the bounded set $\{h : \|h\| = 1\}$. Note also that the operator $h \rightarrow \delta F(x_0; h)$ is not necessarily linear or continuous in h .

If F and G have a Gâteaux variation at x_0 , then so does the operator $T = \alpha F + \beta G$, where α, β are real numbers, and the relation $\delta T(x_0; h) = \alpha \delta F(x_0; h) + \beta \delta G(x_0; h)$ holds. However, the chain rule for the differentiation of a composite function does not hold in general.

An operator F has a *Gâteaux differential* at x_0 if $\delta F(x_0; \bullet)$ is linear and continuous; in this case, $\delta F(x_0; \bullet)$ is denoted by $DF(x_0)$ and is called the *Gâteaux derivative*. The necessary and sufficient condition for $\delta F(x_0; h)$ to be linear and continuous in h is that F satisfies the following two relations:

- To each h , there corresponds $\delta(h)$ such that $|t| \leq \delta$ implies $\|F(x_0 + th) - F(x_0)\| \leq M \|th\|$, where M does not depend on h .
- $F(x_0 + th_1 + th_2) - F(x_0 + th_1) - F(x_0 + th_2) + F(x_0) = o(t)$.

Note that the chain rule does not necessarily hold for Gâteaux derivatives. Note also that if $\delta F(x_0; \bullet)$ is additive, then $\delta F(x_0; h)$ is directionally continuous in h , i.e.,

$$\lim_{\tau \rightarrow 0} \delta F(x_0; h + \tau k) = \delta F(x_0; h).$$

An operator $F : \mathcal{D} \rightarrow \mathcal{W}$, where \mathcal{D} is an open subset of \mathcal{V} and \mathcal{V} and \mathcal{W} are normed real linear spaces, is called *Fréchet differentiable* at $x_0 \in \mathcal{D}$ if there exists a continuous linear operator $L(x_0) : \mathcal{V} \rightarrow \mathcal{W}$ such that the following representation holds for every $h \in \mathcal{V}$ with $x_0 + h \in \mathcal{D}$:

$$F(x_0 + h) - F(x_0) = L(x_0)h + r(x_0; h), \quad \text{with } \lim_{h \rightarrow 0} \frac{\|r(x_0; h)\|}{\|h\|} = 0.$$

The unique operator $L(x_0)h$ in the above equation is called the *Fréchet differential* of F at x_0 and is usually denoted by $dF(x_0; h)$. The linear operator $F'(x_0) : \mathcal{V} \rightarrow \mathcal{W}$ defined by $h \rightarrow dF(x_0; h)$ is called the *Fréchet derivative* of F at x_0 , and $dF(x_0; h) = F'(x_0)h$.

The Fréchet differential has the usual properties of the classical differential of a function of one or several variables. In particular, the chain rule holds for $F \bullet G$ if F has a Fréchet differential and G has a Gâteaux differential. Note that the chain rule may not hold for $F \bullet G$ if F has a Gâteaux differential and G has a Fréchet differential. Fréchet differentiability of F at x_0 implies continuity of F at x_0 .

Consider an operator $F : \mathcal{V} \rightarrow \mathcal{W}$, where \mathcal{V} is an open subset of the product space $\mathcal{P} = \mathcal{E}_1 \times \dots \times \mathcal{E}_n$. The *Gâteaux partial differential* at $u \equiv (u_1, \dots, u_n)$ of F with respect to u_i is the bounded linear operator $D_i F(u_1, \dots, u_n; h_i) : \mathcal{E}_i \rightarrow \mathcal{W}$ defined such that the following relation holds:

$$F(u_1, \dots, u_{i-1}, u_i + h_i, u_{i+1}, \dots, u_n) - F(u_1, \dots, u_n) = D_i F(u_1, \dots, u_n; h_i) + R(u_1, \dots, u_n; h_i)$$

with $\lim_{t \rightarrow 0} R(u_1, \dots, u_n; th_i) / t = 0$.

The operator F is said to be *totally Gâteaux differentiable* at u_0 if F , considered as a mapping on $\mathcal{V} \subset \mathcal{P}$ into \mathcal{W} , is Gâteaux differentiable at u_0 . This means that

$$F(u_1 + h_1, \dots, u_n + h_n) - F(u_1, \dots, u_n) = L(u_1, \dots, u_n; h_1, \dots, h_n) + R(u_1, \dots, u_n; h_1, \dots, h_n),$$

where the total Gâteaux differential L is a continuous linear operator in $h = (h_1 \dots h_n)$ and where $\lim_{t \rightarrow 0} (t^{-1}) R(u_1, \dots, u_n; th_1, \dots, th_n) = 0$.

The *Fréchet partial differential* at (u_1, \dots, u_n) of F with respect to u_i is the bounded linear operator $d_i F(u_1, \dots, u_n; h_i)$ defined such that, for all $h_i \in \mathcal{E}_i$, with $(u_1, \dots, u_{i-1}, u_i + h_i, u_{i+1}, \dots, u_n) \in \mathcal{V}$, the following relation holds:

$$F(u_1, \dots, u_{i-1}, u_i + h_i, \dots, u_n) - F(u_1, \dots, u_n) = d_i F(u_1, \dots, u_n; h_i) + R(u_1, \dots, u_n; h_i),$$

where $\|R(u_1, \dots, u_n; h_i)\| / \|h_i\| \rightarrow 0$ as $h_i \rightarrow 0$.

The *total Fréchet differential* of F is denoted by $dF(u_1, \dots, u_n; h_1, \dots, h_n)$ and is defined as the linear mapping on $\mathcal{V} \subset \mathcal{E}_1 \times \dots \times \mathcal{E}_n$ into \mathcal{W} , which is continuous in $h = (h_1, \dots, h_n)$, such that the following relation holds:

$$\lim_{h \rightarrow 0} \frac{\|F(u_1 + h_1, \dots, u_n + h_n) - F(u_1, \dots, u_n) - dF(u_1, \dots, u_n; h_1, \dots, h_n)\|}{\|h_1\| + \dots + \|h_n\|} = 0.$$

An operator $F : \mathcal{V} \subset \mathcal{P} \rightarrow \mathcal{W}$ that is totally differentiable at (u_1, \dots, u_n) , is partially differentiable with respect to each variable, and its total differential is the sum of the differentials with respect to each of the variables. If F is totally differentiable at each point of \mathcal{V} , then a necessary and sufficient condition for $F' : \mathcal{V} \rightarrow L(\mathcal{E}_1 \times \dots \times \mathcal{E}_n; \mathcal{W})$ to be continuous is that the partial derivatives $F'_i : \mathcal{V} \rightarrow L(\mathcal{E}_i; \mathcal{W})$, $(i = 1, \dots, n)$, be continuous.

Higher order partial derivatives are defined by induction. Note, in particular, that if $F : \mathcal{V} \rightarrow \mathcal{W}$ is twice Fréchet (totally) differentiable at x_0 , then the second order partial derivatives $\partial^2 F(x_0) / \partial x_i \partial x_j \in L(\mathcal{E}_i, \mathcal{E}_j, \mathcal{W})$, ($i, j = 1, \dots, n$) exist, and

$$d^2 F(x_0; k_1, \dots, k_n; h_1, \dots, h_n) = \sum_{i,j=1}^n \frac{\partial^2 F(x_0)}{\partial x_i \partial x_j} k_i h_j.$$

Thus the second order derivative $F''(x_0)$ may be represented by the array $\{\partial^2 F(x_0) / \partial x_i \partial x_j; (i, j = 1, \dots, n)\}$. Note that $d^2 F(x_0; h, k)$ is symmetric in h and k ; consequently, the mixed partial derivatives are also symmetric, i.e.,

$$\frac{\partial^2 F(x_0)}{\partial x_i \partial x_j} = \frac{\partial^2 F(x_0)}{\partial x_j \partial x_i}, (i, j = 1, \dots, n).$$

If the operator $F : \mathcal{D} \rightarrow \mathcal{W}$ has a n th-variation on \mathcal{D} , $\delta^n F(x_0 + th; h)$, which is continuous in t on $[0, 1]$, then the following Taylor-expansion with integral remainder holds for $x_0, x_0 + h \in \mathcal{D}$:

$$F(x_0 + h) = F(x_0) + \delta F(x_0; h) + \frac{1}{2} \delta^2 F(x_0; h) + \dots + \frac{1}{(n-1)!} \delta^{n-1} F(x_0; h) + \int_0^1 \frac{(1-t)^{n-1}}{(n-1)!} \delta^n F(x_0 + th; h) dt.$$

Note that the above integral exists and is a Banach space-valued integral in the Riemann sense; note also that $\delta^k F(x_0; h) = \delta^k F(x_0; h_1, \dots, h_k)$ for $h_1 = \dots = h_k = h$. Furthermore, if an operator $F : \mathcal{D} \rightarrow \mathcal{W}$ has a n th-order Fréchet differential, and if the map $\varphi : [0, 1] \rightarrow F^{(n)}(x_0 + th)$ is bounded and its set of discontinuities is of measure zero, then the Taylor expansion becomes

$$F(x_0 + h) = F(x_0) + F'(x_0) h + \frac{1}{2} F''(x_0) h^2 + \dots + \frac{1}{(n-1)!} F^{(n-1)}(x_0) h^{n-1} + \int_0^1 \frac{(1-t)^{n-1}}{(n-1)!} F^{(n)}(x_0 + th) h^n dt.$$

In the above expansion, $F^{(k)}(x_0) h^k$ denotes the value of the k -linear operator $F^{(k)}$ at (h, \dots, h) . The relation between the various differentiation concepts for a nonlinear operator F is shown schematically below, where “uniform in h ” indicates the validity of the relation $\lim_{h \rightarrow 0} \|F(x+h) - F(x) - \delta F(x; h)\| / \|h\| = 0$:

$$\begin{array}{ccccc} \text{G-differential} & \xrightarrow{\text{uniform in } h} & \text{F-differential} & \xrightarrow{\text{linear in } h} & \text{F-derivative,} \\ \text{G-differential} & \xrightarrow{\text{linear in } h} & \text{G-derivative} & \xrightarrow{\text{uniform in } h} & \text{F-derivative.} \end{array}$$

Gradient and Hessian: If the scalar-valued function of a vector ϕ , $\phi : \mathbb{R}^n \rightarrow \mathbb{R}$, has continuous partial derivatives in the neighborhood of \mathbf{x} , then ϕ is differentiable at \mathbf{x} , and the *gradient* of ϕ , denoted by $\nabla \phi(\mathbf{x})$, is defined as:

$$\nabla \phi(\mathbf{x}) = \left(\frac{\partial \phi}{\partial x_1}, \frac{\partial \phi}{\partial x_2}, \dots, \frac{\partial \phi}{\partial x_n} \right)^T.$$

The *directional derivative of $\phi(\mathbf{x})$ of second order* with respect to two directions \mathbf{z} and \mathbf{w} , denoted by $\phi''(\mathbf{x}; \mathbf{z}, \mathbf{w})$, is defined as the directional derivative in the direction \mathbf{w} of the directional derivative in the direction \mathbf{z} of ϕ at the point \mathbf{x} , where \mathbf{z} and \mathbf{w} are two unit vectors in \mathbb{R}^n , and is given by the expression

$$\begin{aligned} \phi''(\mathbf{x}; \mathbf{z}, \mathbf{w}) &= \mathbf{w}^T \nabla \left(\mathbf{z}^T \nabla \phi(\mathbf{x}) \right) = \sum_{i=1}^n w_i \frac{\partial}{\partial x_i} \left(\sum_{j=1}^n z_j \frac{\partial \phi}{\partial x_j} \right) \\ &= \sum_{i=1}^n \sum_{j=1}^n w_i z_j \left(\frac{\partial^2 \phi}{\partial x_i \partial x_j} \right) = \mathbf{w}^T \left[\nabla^2 \phi(\mathbf{x}) \right] \mathbf{z} \\ \nabla^2 \phi(\mathbf{x}) &= \left[\frac{\partial^2 \phi}{\partial x_i \partial x_j} \right], \text{ for } 1 \leq i, j \leq n. \end{aligned}$$

The $n \times n$ symmetric matrix, $\nabla^2 \phi(\mathbf{x})$, of second partial derivatives of $\phi(\mathbf{x})$, is called the *Hessian* of $\phi(\mathbf{x})$. Note that $\phi''(\mathbf{x}; \mathbf{z}, \mathbf{w})$ is a bilinear form in \mathbf{z} and \mathbf{w} ; $\mathbf{z} = \mathbf{w}$, then $\phi''(\mathbf{x}; \mathbf{z}, \mathbf{w}) = \mathbf{z}^T \left[\nabla^2 \phi(\mathbf{x}) \right] \mathbf{z}$ is a quadratic form in \mathbf{z} .

Jacobian: Assuming that each component function $\phi_i(\mathbf{x})$, $1 \leq i \leq m$, $\mathbf{x} = (x_1, x_2, \dots, x_n)^T$, of a vector-valued function $\phi(\mathbf{x}) = (\phi_1(\mathbf{x}), \phi_2(\mathbf{x}), \dots, \phi_m(\mathbf{x}))^T$, $\phi: \mathbb{R}^n \rightarrow \mathbb{R}^m$ satisfies the conditions for the existence of directional derivatives in the direction of a unit vector $\mathbf{z} \in \mathbb{R}^n$, the directional derivative $\phi'(\mathbf{x}; \mathbf{z})$ of $\phi(\mathbf{x})$ in the direction \mathbf{z} is a *column vector* defined by $\phi'(\mathbf{x}; \mathbf{z}) = (\phi'_1(\mathbf{x}; \mathbf{z}), \phi'_2(\mathbf{x}; \mathbf{z}), \dots, \phi'_m(\mathbf{x}; \mathbf{z}))^T$. Since each $\phi_i: \mathbb{R}^n \rightarrow \mathbb{R}$, it follows that

$$\phi'(\mathbf{x}; \mathbf{z}) = \begin{pmatrix} \mathbf{z}^T \nabla \phi_1(\mathbf{x}) \\ \mathbf{z}^T \nabla \phi_2(\mathbf{x}) \\ \vdots \\ \mathbf{z}^T \nabla \phi_m(\mathbf{x}) \end{pmatrix} = \begin{pmatrix} \frac{\partial \phi_1}{\partial x_1} & \frac{\partial \phi_1}{\partial x_2} & \dots & \frac{\partial \phi_1}{\partial x_n} \\ \frac{\partial \phi_2}{\partial x_1} & \frac{\partial \phi_2}{\partial x_2} & \dots & \frac{\partial \phi_2}{\partial x_n} \\ \vdots & \vdots & \ddots & \vdots \\ \frac{\partial \phi_m}{\partial x_1} & \frac{\partial \phi_m}{\partial x_2} & \dots & \frac{\partial \phi_m}{\partial x_n} \end{pmatrix} \begin{pmatrix} z_1 \\ z_2 \\ \vdots \\ z_n \end{pmatrix} = \mathbf{D}_\phi(\mathbf{x}) \mathbf{z}.$$

The $m \times n$ matrix $\mathbf{D}_\phi(\mathbf{x}) = \left[\frac{\partial \phi_i}{\partial x_j} \right]$, $1 \leq i \leq m$; $1 \leq j \leq n$, is called the *Jacobian* of $\phi(\mathbf{x})$. In particular, when $m = 1$, $\mathbf{D}_\phi(\mathbf{x}) = \left[\nabla \phi(\mathbf{x}) \right]^T$, is the transpose of the gradient of $\phi(\mathbf{x})$.

The second-order directional derivative of $\phi(\mathbf{x}) = (\phi_1(\mathbf{x}), \phi_2(\mathbf{x}), \dots, \phi_m(\mathbf{x}))^T$ in the directions of two unit vectors \mathbf{z} and \mathbf{w} in \mathbb{R}^n , denoted by $\phi''(\mathbf{x}; \mathbf{z}, \mathbf{w})$ or, interchangeably, $\mathbf{D}_\phi^2(\mathbf{x}; \mathbf{z}, \mathbf{w})$, is defined as the directional derivative in the direction \mathbf{w} of the vector-valued function $\phi'(\mathbf{x}; \mathbf{z})$. This gives

$$\phi''(\mathbf{x}; \mathbf{z}, \mathbf{w}) = \begin{pmatrix} \mathbf{w}^T \nabla \phi'_1(\mathbf{x}; \mathbf{z}) \\ \mathbf{w}^T \nabla \phi'_2(\mathbf{x}; \mathbf{z}) \\ \vdots \\ \mathbf{w}^T \nabla \phi'_m(\mathbf{x}; \mathbf{z}) \end{pmatrix} = \begin{pmatrix} \mathbf{w}^T \nabla^2 \phi_1(\mathbf{x}) \mathbf{z} \\ \mathbf{w}^T \nabla^2 \phi_2(\mathbf{x}) \mathbf{z} \\ \vdots \\ \mathbf{w}^T \nabla^2 \phi_m(\mathbf{x}) \mathbf{z} \end{pmatrix} \triangleq \mathbf{D}_\phi^2(\mathbf{x}; \mathbf{z}, \mathbf{w})$$

In particular, when $\mathbf{w} = \mathbf{z}$, then $\phi''(\mathbf{x}; \mathbf{z}, \mathbf{z}) = \mathbf{D}_\phi^2(\mathbf{x}; \mathbf{z})$.

Second order Taylor series: The second order Taylor series of a scalar-valued function of a vector $\phi : \mathbb{R}^n \rightarrow \mathbb{R}$ in C_2 , for any $\mathbf{y} \in \mathbb{R}^n$, such that $\|\mathbf{y}\|$ is small, can be written as

$$\phi(\mathbf{x} + \mathbf{y}) \approx \phi(\mathbf{x}) + \langle \mathbf{y}, \nabla \phi(\mathbf{x}) \rangle + \frac{1}{2} \langle \mathbf{y}, \nabla^2 \phi(\mathbf{x}) \mathbf{y} \rangle.$$

Similarly, the second order Taylor series of a vector-valued function of a vector $\phi : \mathbb{R}^n \rightarrow \mathbb{R}^m$, with each component of ϕ in C_2 , can be written for any $\mathbf{y} \in \mathbb{R}^n$, such that $\|\mathbf{y}\|$ is small, in the form

$$\phi(\mathbf{x} + \mathbf{y}) \approx \phi(\mathbf{x}) + \mathbf{D}_\phi(\mathbf{x}) \mathbf{y} + \frac{1}{2} \mathbf{D}_\phi^2(\mathbf{x}; \mathbf{y}).$$

First and second variations: For a vector-valued function $\phi(\mathbf{x}) = (\phi_1(\mathbf{x}), \phi_2(\mathbf{x}), \dots, \phi_m(\mathbf{x}))^T$, $\phi : \mathbb{R}^n \rightarrow \mathbb{R}^m$ and $\mathbf{x} \in \mathbb{R}^n$, the *first variation* $\delta\phi(\mathbf{x})$ is a vector given by

$$\delta\phi = \begin{pmatrix} \delta\phi_1 \\ \delta\phi_2 \\ \vdots \\ \delta\phi_m \end{pmatrix} = \begin{pmatrix} \langle \delta\mathbf{x}, \nabla\phi_1(\mathbf{x}) \rangle \\ \langle \delta\mathbf{x}, \nabla\phi_2(\mathbf{x}) \rangle \\ \vdots \\ \langle \delta\mathbf{x}, \nabla\phi_m(\mathbf{x}) \rangle \end{pmatrix} = \mathbf{D}_\phi(\mathbf{x}) \delta\mathbf{x},$$

where $\mathbf{D}_\phi \in \mathbb{R}^{m \times n}$ is the Jacobian of ϕ . Similarly, the *second variation* of ϕ is given by

$$\delta^2\phi(\mathbf{x}) = \delta[\delta\phi(\mathbf{x})] = \begin{pmatrix} \delta[\delta\phi_1(\mathbf{x})] \\ \delta[\delta\phi_2(\mathbf{x})] \\ \vdots \\ \delta[\delta\phi_m(\mathbf{x})] \end{pmatrix} = \begin{pmatrix} \langle \delta\mathbf{x}, [\nabla^2\phi_1(\mathbf{x})] \delta(\mathbf{x}) \rangle \\ \langle \delta\mathbf{x}, [\nabla^2\phi_2(\mathbf{x})] \delta(\mathbf{x}) \rangle \\ \vdots \\ \langle \delta\mathbf{x}, [\nabla^2\phi_m(\mathbf{x})] \delta(\mathbf{x}) \rangle \end{pmatrix} = \|\delta\mathbf{x}\|^2 \mathbf{D}_\phi^2(\mathbf{x}; \mathbf{z})$$

First derivative of a matrix-valued function of a scalar: Consider a matrix $\mathbf{F}(\mathbf{x}) = [F_{ij}(\mathbf{x})] \in \mathbb{R}^{n \times n}$ of functions $F_{ij} : \mathbb{R} \rightarrow \mathbb{R}$, $1 \leq i, j \leq n$, $\mathbf{x} \in \mathbb{R}$; the derivative is given by

$$\frac{d\mathbf{F}(\mathbf{x})}{d\mathbf{x}} = \left[\frac{dF_{ij}(\mathbf{x})}{d\mathbf{x}} \right].$$

First derivative of a scalar-valued function of a matrix: Consider that $F : \mathbb{R}^{n \times n} \rightarrow \mathbb{R}$ is a scalar-valued function of the elements of a matrix $\mathbf{X} = [x_{ij}] \in \mathbb{R}^{n \times n}$. Examples of such functions include the trace and determinant of matrices. The derivative of F with respect to the matrix \mathbf{X} denoted by $\partial F / \partial \mathbf{X}$ is a matrix given by

$$\frac{\partial F}{\partial \mathbf{X}} = \left[\frac{\partial F}{\partial x_{ij}} \right].$$

First derivative of the trace of a matrix-valued function of a matrix: Consider the trace, $\text{tr}[\mathbf{F}(\mathbf{X})] = \sum_{i=1}^n F_{ii}(\mathbf{X})$, of $\mathbf{F}(\mathbf{X}) = [F_{ij}(\mathbf{X})]$, $\mathbf{F} : \mathbb{R}^{n \times n} \rightarrow \mathbb{R}^{n \times n}$, $\mathbf{X} \in \mathbb{R}^{n \times n}$ and $F_{ij} : \mathbb{R}^{n \times n} \rightarrow \mathbb{R}$. Then,

$$\frac{\partial \text{tr}[\mathbf{F}(\mathbf{X})]}{\partial \mathbf{X}} = \frac{\partial}{\partial \mathbf{X}} \left[\sum_{i=1}^n F_{ii}(\mathbf{X}) \right] = \sum_{i=1}^n \frac{\partial F_{ii}(\mathbf{X})}{\partial \mathbf{X}}$$

Taking into account that $\text{tr}(\mathbf{A}) = \text{tr}(\mathbf{A}^T)$ and $\text{tr}(\mathbf{AB}) = \text{tr}(\mathbf{BA})$, some particular cases which are often encountered in practice are listed below:

$$\begin{aligned} \frac{\partial \text{tr}(\mathbf{AX})}{\partial \mathbf{X}} &= \mathbf{A}^T = \frac{\partial \text{tr}(\mathbf{XA})}{\partial \mathbf{X}} = \frac{\partial \text{tr}(\mathbf{A}^T \mathbf{X}^T)}{\partial \mathbf{X}} = \frac{\partial \text{tr}(\mathbf{X}^T \mathbf{A}^T)}{\partial \mathbf{X}}, \\ \frac{\partial \text{tr}(\mathbf{A}^T \mathbf{X})}{\partial \mathbf{X}} &= \mathbf{A} = \frac{\partial \text{tr}(\mathbf{XA}^T)}{\partial \mathbf{X}} = \frac{\partial \text{tr}(\mathbf{AX}^T)}{\partial \mathbf{X}} = \frac{\partial \text{tr}(\mathbf{X}^T \mathbf{A})}{\partial \mathbf{X}}, \\ \frac{\partial \text{tr}(\mathbf{ABX})}{\partial \mathbf{X}} &= \mathbf{B}^T \mathbf{A}^T = \frac{\partial \text{tr}(\mathbf{XAB})}{\partial \mathbf{X}} = \frac{\partial \text{tr}(\mathbf{BXA})}{\partial \mathbf{X}}, \\ \frac{\partial \text{tr}(\mathbf{XAX}^T)}{\partial \mathbf{X}} &= 2\mathbf{XA}^T, \\ \frac{\partial \text{tr}(\mathbf{X}^T \mathbf{AX})}{\partial \mathbf{X}} &= 2\mathbf{AX} = \frac{\partial \text{tr}(\mathbf{XX}^T \mathbf{A})}{\partial \mathbf{X}} = \frac{\partial \text{tr}(\mathbf{AXX}^T)}{\partial \mathbf{X}} = \frac{\partial \text{tr}(\mathbf{X}^T \mathbf{A}^T \mathbf{X})}{\partial \mathbf{X}} \\ &= \frac{\partial \text{tr}(\mathbf{XX}^T \mathbf{A})}{\partial \mathbf{X}} = \frac{\partial \text{tr}(\mathbf{AXX}^T)}{\partial \mathbf{X}}. \end{aligned}$$

Optimization in a finite-dimensional vector space: One of the most important applications of gradients and Hessians of functions is in optimization problems. A function $\phi(\mathbf{x})$ is said to attain a *relative* or *local minimum* at $\mathbf{x} = \hat{\mathbf{x}}$ in a domain Ω , if the inequality

$$\phi(\hat{\mathbf{x}}) \leq \phi(\mathbf{x})$$

holds for all points \mathbf{x} in a sufficiently small neighborhood $N_\epsilon(\hat{\mathbf{x}}) = \{\mathbf{x} \mid \|\mathbf{x} - \hat{\mathbf{x}}\| < \epsilon\}$. If strict inequality $\phi(\hat{\mathbf{x}}) < \phi(\mathbf{x})$ holds for all $N_\epsilon(\hat{\mathbf{x}})$ except $\hat{\mathbf{x}}$, then $\hat{\mathbf{x}}$ is called a *strict local minimum*. If $\phi(\hat{\mathbf{x}}) \leq \phi(\mathbf{x})$ holds for all $\mathbf{x} \in \Omega$, then $\hat{\mathbf{x}}$ is called the *absolute* or *global minimum*. If strict inequality $\phi(\hat{\mathbf{x}}) < \phi(\mathbf{x})$ holds for all $\mathbf{x} \in \Omega$ except for $\hat{\mathbf{x}}$, then $\hat{\mathbf{x}}$ is the *strict global minimum*. A minimization problem involves finding the point (or set of points) in Ω where $\phi(\mathbf{x})$ attains minimum value. If Ω is a proper subset of \mathbb{R}^n , then the problem is called a *constrained minimization* problem, otherwise, when $\Omega = \mathbb{R}^n$, it is called an *unconstrained minimization* problem. The necessary and sufficient conditions for a real-valued functional $\phi(\mathbf{x}) : \Omega \rightarrow \mathbb{R}$ of a vector $\mathbf{x} = (x_1, x_2, \dots, x_n)^T$, where Ω denotes a subset of \mathbb{R}^n , to attain a minimum are obtained by expanding the functional in a Taylor series of the form

$$\Delta\phi(\mathbf{x}) = \phi(\mathbf{x} + \Delta\mathbf{x}) - \phi(\mathbf{x}) = (\Delta\mathbf{x})^T \nabla\phi(\mathbf{x}) + \frac{1}{2} (\Delta\mathbf{x})^T \nabla^2\phi(\mathbf{x}) \Delta\mathbf{x},$$

where the gradient $\nabla\phi(\mathbf{x})$ and the Hessian $\nabla^2\phi(\mathbf{x})$ are assumed to exist. Setting the gradient to zero and examining the Hessian leads to the following *necessary condition*: $\phi(\mathbf{x})$ attains a local minimum at $\hat{\mathbf{x}}$ if $\nabla\phi(\hat{\mathbf{x}}) = 0$ and $\nabla^2\phi(\hat{\mathbf{x}})$ is non-negative definite. The *sufficient condition* for $\phi(\mathbf{x})$ to attain a local minimum at $\hat{\mathbf{x}}$ is that $\nabla\phi(\hat{\mathbf{x}}) = 0$ and $\nabla^2\phi(\hat{\mathbf{x}})$ be positive definite.

Lagrange's method for minimization subject to equality constraints: When Ω is specified by a collection of k equality constraints of the form

$$f_i(\mathbf{x}) = 0, \quad 1 \leq i \leq k$$

where each $f_i(\mathbf{x})$ is twice differentiable, the constrained minimization of $\phi(\mathbf{x})$ can be transformed into an unconstrained minimization problem by using a vector $\lambda = (\lambda_1, \lambda_2, \dots, \lambda_k)^T$ of

Lagrange multipliers λ_i , to construct the Lagrangian functional

$$L(\mathbf{x}, \lambda) = \phi(\mathbf{x}) + \sum_{i=1}^k \lambda_i f_i(\mathbf{x}).$$

The arguments for the unconstrained case can now be applied to the above Lagrangian to obtain the following first-order necessary conditions

$$\begin{aligned} \nabla_{\mathbf{x}} L(\mathbf{x}, \lambda) &\equiv \nabla_{\mathbf{x}} \phi(\mathbf{x}) + \sum_{i=1}^k \lambda_i \nabla_{\mathbf{x}} f_i(\mathbf{x}) = 0, \\ \nabla_{\lambda} L(\mathbf{x}, \lambda) &= f_i(\mathbf{x}) = 0, \quad \text{for } 1 \leq i \leq k. \end{aligned}$$

The values of the $(n+k)$ variables at a relative minimum $\hat{\mathbf{x}}$ of $\phi(\mathbf{x})$ are obtained as the solution of the $(n+k)$ equations represented by $\nabla_{\mathbf{x}} L = 0$ and $\nabla_{\lambda} L = 0$. The equation $\nabla_{\lambda} L = 0$ ensures that the constraints are satisfied at the minimum, while $\nabla_{\mathbf{x}} L = 0$ implies that, at the minimum, $\nabla_{\mathbf{x}} \phi(\mathbf{x})$ is a linear combination of the gradient $\nabla_{\mathbf{x}} f_i(\mathbf{x})$ of the constraint function $f_i(\mathbf{x})$ for $1 \leq i \leq k$. In addition to the necessary conditions represented by the equations $\nabla_{\mathbf{x}} L = 0$ and $\nabla_{\lambda} L = 0$, the second-order sufficiency condition for a relative minimum \mathbf{x}^* of $\phi(\mathbf{x})$ under the equality constraints requires that the matrix

$$H(\mathbf{x}^*) \triangleq \nabla^2 \phi(\mathbf{x}^*) + \sum_{i=1}^k \lambda_i \nabla^2 f_i(\mathbf{x}^*)$$

be positive definite on the tangent plane to $f_i(\mathbf{x})$ at \mathbf{x}^* , i.e., $\mathbf{y}G(\mathbf{x}^*)\mathbf{y} > 0$ for any $\mathbf{y} \neq \mathbf{0}$ and $\mathbf{y} \in \{\mathbf{y} | \mathbf{y}^T \nabla f_i(\mathbf{x}^*) = 0, 1 \leq i \leq k\}$, comprising all vectors \mathbf{y} that are orthogonal to $\nabla f_i(\mathbf{x})$, $1 \leq i \leq k$.

3 Special Functions

3.1 The Gamma Function: $\Gamma(z)$

Definition: The gamma function $\Gamma(z)$ can be defined by one of the following expressions:

$$\begin{aligned} \Gamma(z) &= \int_0^{\infty} e^{-t} t^{z-1} dt = \int_0^1 (\log 1/t)^{z-1} dt, \quad \text{Re } z > 0, \\ \Gamma(z) &= \lim_{n \rightarrow \infty} \frac{n! n^z}{z(z+1)\cdots(z+n)} = \lim_{n \rightarrow \infty} \frac{n^z}{z(1+z)(1+\frac{1}{2}z)\cdots(1+z/n)} \\ &= z^{-1} \prod_{n=1}^{\infty} \left[(1+1/n)^z (1+z/n)^{-1} \right], \\ 1/\Gamma(z) &= z e^{\gamma z} \prod_{n=1}^{\infty} \left[(1+z/n) e^{-z/n} \right], \\ \gamma &= \lim_{m \rightarrow \infty} \left(\sum_{n=1}^m 1/n - \log m \right) = 0.5772156649\dots \end{aligned}$$

In the above expression, $\gamma = 0.5772156649\dots$ is Euler's constant. Note that $\Gamma(z)$ has simple poles at $z = -n$, ($n = 0, 1, 2, \dots$), with residues $(-1)^n/n!$.

Functional relations: The basic relation satisfied by the Gamma Function is $\Gamma(1+z) = z\Gamma(z)$. Other relations often used in practice, in which n is a positive integer, are:

$$\begin{aligned} \Gamma(z) \Gamma(-z) &= -\pi z^{-1} \csc(\pi z), & \Gamma(z) \Gamma(1-z) &= \pi \csc(\pi z), \\ \Gamma(1/2+z) \Gamma(1/2-z) &= \pi \sec(\pi z), \\ \frac{\Gamma(n+z) \Gamma(n-z)}{[(n-1)!]^2} &= \frac{\pi z}{\sin(\pi z)} \prod_{m=1}^{n-1} (1 - z^2/m^2), \quad n = 1, 2, 3, \dots, \\ \frac{\Gamma(n+1/2+z) \Gamma(n+1/2-z)}{[\Gamma(n+1/2)]^2} &= \frac{1}{\cos(\pi z)} \prod_{m=1}^n \left[1 - \frac{4z^2}{(2m-1)^2} \right], \quad n = 1, 2, 3, \dots, \\ \Gamma(z+n) &= z(z+1)(z+2)\dots(z+n-1)\Gamma(z), & \Gamma(n+1) &= 1 \cdot 2 \cdot 3 \dots n = n!, \\ \Gamma(z)/\Gamma(z-n) &= (z-1)(z-2)\dots(z-n) = (-1)^n \Gamma(-z+n+1)/\Gamma(-z+1), \\ \Gamma(-z+n)/\Gamma(-z) &= (-1)^n z(z-1)\dots(z-n+1) = (-1)^n \Gamma(z+1)/\Gamma(z-n+1). \end{aligned}$$

Particular values: $\Gamma(1) = \int_0^\infty e^{-t} dt = 1$; $\Gamma(1/2) = 2 \int_0^\infty e^{-v^2} dv = \sqrt{\pi}$.

The multiplication formula of Gauss:

$$\prod_{r=0}^{m-1} \Gamma(z+r/m) = (2\pi)^{\frac{1}{2}(m-1)} m^{\frac{1}{2}-mz} \Gamma(mz), \quad m = 2, 3, 4, \dots$$

Particular case, $m = 2$ (Legendre's formula):

$$\Gamma(2z) = 2^{2z-1} \pi^{-1/2} \Gamma(z) \Gamma(z+1/2).$$

Note also the integrals:

$$\begin{aligned} \int_0^\infty e^{i\delta} t^{\alpha-1} e^{-st} dt &= \Gamma(\alpha) s^{-\alpha}, \quad \text{Re } \alpha > 0, -\left(\frac{1}{2}\pi + \delta\right) < \arg s < \frac{1}{2}\pi - \delta, \\ \int_0^\infty t^{\alpha-1} e^{-ct \cos \beta} \cos(ct \sin \beta) dt &= \Gamma(\alpha) c^{-\alpha} \cos(\alpha\beta), \\ c > 0, \quad \text{Re } \alpha > 0, -\frac{1}{2}\pi < \beta < \frac{1}{2}\pi, \\ \int_0^\infty t^{\alpha-1} e^{-ct \cos \beta} \sin(ct \sin \beta) dt &= \Gamma(\alpha) c^{-\alpha} \sin(\alpha\beta) \\ c > 0, \quad \text{Re } \alpha > -1, -\frac{1}{2}\pi < \beta < \frac{1}{2}\pi. \\ \int_0^\infty t^{\alpha-1} \cos(ct) dt &= c^{-\alpha} \Gamma(\alpha) \cos\left(\frac{1}{2}\pi\alpha\right), \quad 0 < \text{Re } \alpha < 1, \\ \int_0^\infty t^{\alpha-1} \sin(ct) dt &= c^{-\alpha} \Gamma(\alpha) \sin\left(\frac{1}{2}\pi\alpha\right), \quad -1 < \text{Re } \alpha < 1, \end{aligned}$$

$$\int_0^{\infty} \cos(at^p) dt = (p a^{1/p})^{-1} \Gamma(1/p) \cos[\pi(2p)^{-1}], \quad a > 0, p > 1,$$

$$\int_0^{\infty} \sin(at^p) dt = (p a^{1/p})^{-1} \Gamma(1/p) \sin[\pi(2p)^{-1}],$$

$$\int_x^{x+n} \log \Gamma(x) dx = x \log x + (x+1) \log(x+1) + \dots + (x+n-1) \log(x+n-1) \\ - nx - \frac{1}{2}n(n-1) + \frac{1}{2}n \log(2\pi), \quad n = 1, 2, 3, \dots,$$

$$\int_0^1 \log \Gamma(x) dx = \frac{1}{2} \log(2\pi),$$

$$\int_0^1 \log \Gamma(x) \sin(2\pi n x) dx = \frac{\gamma + \log(2\pi n)}{2\pi n},$$

$$\int_0^1 \log \Gamma(x) \cos(2\pi n x) dx = \frac{1}{4n}, \quad n = 1, 2, 3, \dots$$

Asymptotic expansions:

$$\Gamma(z) = e^{-z} e^{(z-(1/2)) \log z} (2\pi)^{\frac{1}{2}} \left[1 + \frac{z^{-1}}{12} + \frac{z^{-2}}{288} - \frac{139z^{-3}}{51840} - O(z^{-4}) \right],$$

$$|\arg z| < \pi,$$

$$\log \Gamma(z) = \left(z - \frac{1}{2}\right) \log z - z + \frac{1}{2} \log(2\pi) + \sum_{n=1}^m B_{2n} / [(2n-1)(2n)z^{2n-1}] \\ + O(z^{-2m-1}), \quad |\arg z| < \pi,$$

$$\log \Gamma(z) = \left(z - \frac{1}{2}\right) \log \left(z - \frac{1}{2}\right) - z - \frac{1}{2} + \frac{1}{2} \log(2\pi) \\ - \sum_{n=1}^{\infty} \frac{\zeta(2n, z)}{[2^{2n} 2n(2n+1)]}, \quad \operatorname{Re} z \geq -\frac{1}{2},$$

$$\log \Gamma(z + \alpha) = \left(z + \alpha - \frac{1}{2}\right) \log z - z + \frac{1}{2} \log(2\pi) + O(z^{-1}),$$

$$\frac{\Gamma(z + \alpha)}{\Gamma(z + \beta)} = z^{\alpha-\beta} \left[1 + \frac{1}{2} z^{-1} (\alpha - \beta)(\alpha + \beta - 1) + O(z^{-2}) \right],$$

$$\log \Gamma(z + \alpha) = \left(z + \alpha - \frac{1}{2}\right) \log z - z + \frac{1}{2} \log(2\pi) + \frac{B_2(\alpha)z^{-1}}{1 \cdot 2} \\ - \dots + \frac{(-1)^{n+1} B_{n+1}(\alpha)z^{-n}}{n(n+1)} + O(z^{-n-1}), \quad |\arg z| < \pi, n = 1, 2, 3, \dots,$$

$$\lim_{|z| \rightarrow \infty} e^{-\alpha \log z} \frac{\Gamma(z + \alpha)}{\Gamma(z)} = 1, \quad \lim_{|y| \rightarrow \infty} |\Gamma(x + iy)| e^{(1/2)\pi|y|} |y|^{\frac{1}{2}-x} = (2\pi)^{\frac{1}{2}}, \quad x, y \text{ real.}$$

3.2 The Beta Function

Definition: The beta function is defined by the integral

$$B(x, y) = \int_0^1 t^{x-1} (1-t)^{y-1} dt, \quad \operatorname{Re} x > 0, \operatorname{Re} y > 0.$$

Substituting $t = v/(1 + v)$ in the above definition yields the following equivalent relations:

$$B(x, y) = \int_0^\infty v^{x-1}(1 + v)^{-x-y} dv = \int_0^1 (v^{x-1} + v^{y-1})(1 + v)^{-x-y} dv, \\ \text{Re } x > 0, \text{ Re } y > 0.$$

The relation between beta and gamma functions is

$$B(x, y) = \frac{\Gamma(x)\Gamma(y)}{\Gamma(x + y)} = B(y, x), \\ B(x, y + 1) = (y/x)B(x + 1, y) = \left[\frac{y}{(x + y)} \right] B(x, y), \\ B(x, y)B(x + y, z) = B(y, z)B(y + z, x) = B(z, x)B(x + z, y), \\ B(x, y)B(x + y, z)B(x + y + z, u) = \frac{\Gamma(x)\Gamma(y)\Gamma(z)\Gamma(u)}{\Gamma(x + y + z + u)}, \\ \frac{1}{B(n, m)} = m \binom{n + m - 1}{n - 1} = n \binom{n + m - 1}{m - 1}, \quad n, m, \text{ positive integers.}$$

3.3 The ψ Function

The function $\psi(z)$ is the logarithmic derivative of the gamma function $\Gamma(z)$:

$$\psi(z) = \frac{d \log \Gamma(z)}{dz} = \frac{\Gamma'(z)}{\Gamma(z)}, \quad \text{or} \quad \log \Gamma(z) = \int_1^z \psi(z) dz.$$

The ψ function is meromorphic with simple poles at $z = 0, -1, -2, \dots$

$$\psi(z) = \lim_{n \rightarrow \infty} \left[\log n - \frac{1}{z} - \frac{1}{z + 1} - \frac{1}{z + 2} - \dots - \frac{1}{z + n} \right], \\ \psi(z) = -\gamma - (1/z) + \sum_{n=1}^\infty z/[n(z + n)] = -\gamma + (z - 1) \sum_{n=0}^\infty 1/[(n + 1)(z + n)], \\ \psi(z) = \log z - \sum_{n=0}^\infty \left\{ (n + z)^{-1} - \log \left[1 + \frac{1}{(n + z)} \right] \right\}, \\ \gamma = -\psi(1) = \sum_{n=1}^\infty [n^{-1} - \log(1 + n^{-1})] = - \int_0^\infty e^{-t} \log t dt.$$

Functional equations for $\psi(z)$:

$$\begin{aligned}\psi(z) &= \psi(1+z) - \frac{1}{z}, \quad \psi(z) - \psi(1-z) = -\pi \operatorname{ctn}(\pi z), \\ \psi\left(\frac{1}{2} + z\right) - \psi\left(\frac{1}{2} - z\right) &= \pi \tan(\pi z), \\ \psi(z) - \psi(-z) &= -\pi \operatorname{ctn}(\pi z) - 1/z, \quad \psi(1+z) - \psi(1-z) = z^{-1} - \pi \operatorname{ctn}(\pi z), \\ \psi(z+n) &= \frac{1}{z} + \frac{1}{z+1} + \cdots + \frac{1}{z+n-1} + \psi(z), \quad n = 1, 2, 3, \dots, \\ \psi(1+n) &= 1 + \frac{1}{2} + \frac{1}{3} + \cdots + \frac{1}{n} - \gamma, \\ \psi(mz) &= m^{-1} \sum_{r=0}^{m-1} \psi(z+r/m) + \log m. \\ \psi(z) &= -\gamma + \int_0^1 (1-t^{z-1})(1-t)^{-1} dt, \quad \operatorname{Re} z > 0.\end{aligned}$$

Asymptotic expansion: $\psi(z) = \log z - (2z)^{-1} - \sum_{n=1}^m B_{2n} z^{-2n} / (2n) + O(z^{-2m-2})$.

3.4 The Generalized Zeta and Riemann's Zeta Functions

Definition: The generalized zeta function is defined by the equation

$$\zeta(s, \nu) = \sum_{n=0}^{\infty} (\nu + n)^{-s}, \quad \operatorname{Re} s > 0, \nu \neq 0, -1, -2, \dots$$

Special case when $\nu = 1$: Riemann's zeta-function $\zeta(s)$:

$$\zeta(s) = \zeta(s, 1) = \Phi(1, s, 1) = \sum_{n=1}^{\infty} (1/n^s), \quad \operatorname{Re} s > 1.$$

Special case $s = -m$:

$$\zeta(-m, \nu) = -\frac{B_{m+1}(\nu)}{m+1}, \quad m = 0, 1, 2, \dots, \quad B_m(\nu) = \text{Bernoulli's polynomials.}$$

Functional equation:

$$\begin{aligned}\zeta(s, \nu) &= \zeta(s, m+\nu) + \sum_{n=0}^{m-1} (n+\nu)^{-s}, \quad m = 1, 2, 3, \dots, \\ \zeta(s) &= \frac{2\Gamma(1-s)}{(2\pi)^{1-s}} \sin(\pi s/2) \zeta(1-s), \quad \zeta(1-s) = (2\pi)^{-s} 2\Gamma(s) \cos(\pi s/2) \zeta(s).\end{aligned}$$

Particular values:

$$\begin{aligned}\zeta(0) &= -\frac{1}{2}, \quad \zeta'(0) = -\frac{1}{2} \log(2\pi), \quad \lim_{s \rightarrow 1} [\zeta(s) - 1/(s-1)] = -\psi(1) = \gamma, \\ \zeta(-2m) &= 0, \quad \zeta(2m) = (-1)^{m+1} (2\pi)^{2m} \frac{B_{2m}}{2(2m)!}, \quad m = 1, 2, 3, \dots, \\ \zeta[-(2m-1)] &= -\frac{B_{2m}}{2m}, \quad \zeta(-m) = -\frac{B_{m+1}}{m+1}, \quad m = 1, 2, 3, \dots\end{aligned}$$

Integrals:

$$\begin{aligned} \Gamma(s)\zeta(s) &= \int_0^\infty t^{s-1}(e^t - 1)^{-1} dt = 2^{s-1} \int_0^\infty e^{-t} t^{s-1} \operatorname{csch} t dt, \quad \operatorname{Re} s > 1, \\ (1 - 2^{1-s})\Gamma(s)\zeta(s) &= \int_0^\infty t^{s-1}(e^t + 1)^{-1} dt = 2^{s-1} \int_0^\infty e^{-t} t^{s-1} \operatorname{sech} t dt, \quad \operatorname{Re} s > 0, \\ 2\Gamma(s)(1 - 2^{-s})\zeta(s) &= \int_0^\infty t^{s-1} \operatorname{csch} t dt, \quad \operatorname{Re} s > 1. \end{aligned}$$

Asymptotic expansion of $\zeta(s, \nu)$ for large values of $|\nu|$ with $|\arg \nu| < \pi$:

$$\begin{aligned} \zeta(s, \nu) &= [1/\Gamma(s)] \left\{ \nu^{1-s} \Gamma(s-1) + \frac{1}{2} \nu^{-s} \Gamma(s) \right. \\ &\quad \left. + \sum_{n=1}^m B_{2n} \Gamma(s+2n-1) / [(2n)! \nu^{2n+s-1}] + O(\nu^{-2m-s-1}) \right\}, \quad \operatorname{Re} s > 1. \end{aligned}$$

3.5 Bernoulli's Numbers and Polynomials

Definition: The Bernoulli numbers B_n are defined as the coefficients in the expansion $z(e^z - 1)^{-1} = \sum_{n=0}^\infty B_n z^n / n!$ for $z < 2\pi$. The Bernoulli polynomials $B_n(x)$ are defined as the coefficients in the expansion $ze^{xz}(e^z - 1)^{-1} = \sum_{n=0}^\infty B_n(x) z^n / n!$ for $|z| < 2\pi$.

Functional relation:

$$\begin{aligned} B_n(x) &= x^n + \binom{n}{1} B_1 x^{n-1} + \dots + \binom{n}{n-1} B_{n-1} x + \binom{n}{n} \\ B_n &= \sum_{r=0}^n \binom{n}{r} B_r x^{n-r}, \\ B'_n(x) &= n B_{n-1}(x), \\ B_0(x+1) &= B_0(x), \quad B_1(x+1) - B_1(x) = 1, \quad B_n(x+1) - B_n(x) = nx^{n-1}, \\ &\quad n = 2, 3, 4, \dots, \\ \sum_{r=0}^n \binom{n}{r} B_r(x) &= B_n(x+1), \quad \sum_{r=0}^{n-1} \binom{n}{r} B_r(x) = nx^{n-1}, \quad n = 2, 3, 4, \dots \end{aligned}$$

Particular values:

$$\begin{aligned} B_0(x) &= 1, \quad B_1(x) = x - 1/2, \quad B_2(x) = x^2 - x + 1/6, \\ B_3(x) &= x^3 - 3/2x^2 + x/2, \quad B_4(x) = x^4 - 2x^3 + x^2 - 1/30, \\ B_n(0) &= B_n, \quad B_n(1) = B_n(0) = B_n \quad \text{for } n \geq 2. \end{aligned}$$

Integrals:

$$\begin{aligned} \int_x^y B_n(t) dt &= \frac{B_{n+1}(y) - B_{n+1}(x)}{n+1}, \quad \int_x^{x+1} B_n(t) dt = x^n, \\ \sum_{r=0}^{m-1} r^n &= \sum_{r=0}^{m-1} \int_r^{r+1} B_n(t) dt = \int_0^m B_n(t) dt = \frac{B_{n+1}(m) - B_{n+1}}{n+1}, \quad n = 2, 3, 4, \dots \end{aligned}$$

4 Bessel Functions

4.1 Bessel Functions of General Order

Bessel functions are solutions of Bessel's differential equation

$$\nabla_v w \equiv z^2 \frac{d^2 w}{dz^2} + z \frac{dw}{dz} + (z^2 - v^2)w = z \frac{d}{dz} \left(z \frac{dw}{dz} \right) + (z^2 - v^2)w = 0.$$

When v, z are unrestricted, the above differential equation has a regular singularity at $z = 0$ and an irregular singularity at $z = \infty$; all other points are ordinary points. In the neighborhood of a regular singularity, Bessel's equation admits the solutions $J_{-v}(z)$ and $J_v(z)$, respectively, defined as

$$J_v(z) = \sum_{m=0}^{\infty} (-1)^m \frac{\left(\frac{1}{2}z\right)^{2m+v}}{m! \Gamma(m+v+1)}.$$

The solution $J_v(z)$ is called the Bessel function of the first kind; z is the *variable* and v is the *order* of the Bessel function. The series $z^{-v} J_v(z)$ converges absolutely and uniformly in any bounded domain of z . The following linear combinations are also solutions of Bessel's equation:

$$\begin{aligned} Y_v(z) &= (\sin v\pi)^{-1} [J_v(z) \cos(v\pi) - J_{-v}(z)], \\ H_v^{(1)}(z) &= J_v(z) + iY_v(z) = [i \sin(v\pi)]^{-1} [J_{-v}(z) - J_v(z) e^{-iv\pi}], \\ H_v^{(2)}(z) &= J_v(z) - iY_v(z) = (i \sin v\pi)^{-1} [J_v(z) e^{iv\pi} - J_{-v}(z)]. \end{aligned}$$

The function Y_v is called the *Bessel function of the second kind* or *Neumann's function*, while $H_v^{(1)}$ and $H_v^{(2)}$ are the *Bessel functions of the third kind*, respectively; they are also called the *first and second Hankel functions*. In particular, J_v and Y_v are real if the order, v , is real and the variable z is positive. All four Bessel functions are single-valued in the z -plane cut along the negative real axis from 0 to $-\infty$. For a general v , they all have branch points at $z = 0$. The Bessel function of the first kind is an entire function of v ; for integer $v = n$, the Bessel functions of the second and third kind are also entire functions of $v = n$.

4.2 Modified Bessel Functions of General Order

Definition: Replacing z by iz yields the modified Bessel differential equation

$$z^2 \frac{d^2 w}{dz^2} + z \frac{dw}{dz} - (z^2 + v^2)w = 0.$$

When ν is not an integer, $J_\nu(iz)$ and $J_{-\nu}(iz)$ are two linearly independent solutions in the above equation. Customarily, however, the functions $I_\nu(z)$ and $I_{-\nu}(z)$ are used as two independent solutions, with $I_\nu(z)$ defined as

$$\begin{aligned} I_\nu(z) &= e^{-i\frac{\nu\pi}{2}} J_\nu\left(ze^{i\frac{\nu\pi}{2}}\right) = \sum_{m=0}^{\infty} \left(\frac{1}{2}z\right)^{2m+\nu} \Big/ [m!\Gamma(m+\nu+1)] \\ &= \frac{\left(\frac{1}{2}z\right)^\nu}{\Gamma(\nu+1)} {}_0F_1\left(\nu+1; \frac{1}{4}z^2\right) = \frac{\left(\frac{1}{2}z\right)^\nu e^{-z}}{\Gamma(\nu+1)} {}_1F_1\left(\nu+\frac{1}{2}; 2\nu+1; 2z\right) \\ &= 2^{-2\nu-\frac{1}{2}} z^{-\frac{1}{2}} M_{0,\nu}(2z)/\Gamma(\nu+1). \end{aligned}$$

The functions $I_\nu(z)$ and $I_{-\nu}(z)$ are called the *modified Bessel functions of the first kind*, and are real when ν is real and z is positive. The function $K_\nu(z)$, defined as

$$K_\nu(z) = \frac{1}{2}\pi(\sin \nu\pi)^{-1}[I_{-\nu}(z) - I_\nu(z)] = \left(\frac{1}{2}\frac{\pi}{z}\right)^{\frac{1}{2}} W_{0,\nu}(2z),$$

is also a solution of the modified Bessel equation, and is called a *Bessel function of the third kind* or *Bessel's function*. All Bessel functions are entire functions of ν . Note that $K_\nu(z)$ is real when ν is real and z is positive,

$$K_{-\nu}(z) = K_\nu(z) \quad \text{and} \quad K_\nu(z) = \frac{1}{2}i\pi e^{i\frac{\nu\pi}{2}} H_\nu^{(1)}\left(ze^{i\frac{\nu\pi}{2}}\right) = -\frac{1}{2}i\pi e^{-i\frac{\nu\pi}{2}} H_\nu^{(2)}\left(ze^{-i\frac{\nu\pi}{2}}\right).$$

Recurrence and differentiation formulas:

$$\begin{aligned} \left(\frac{d}{zdz}\right)^m [z^\nu I_\nu(z)] &= z^{\nu-m} I_{\nu-m}(z), \quad \left(\frac{d}{zdz}\right)^m [z^{-\nu} I_\nu(z)] = z^{-\nu-m} I_{\nu+m}(z), \\ \left(\frac{d}{zdz}\right)^m [z^\nu K_\nu(z)] &= (-1)^m z^{\nu-m} K_{\nu-m}(z), \\ \left(\frac{d}{zdz}\right)^m [z^{-\nu} K_\nu(z)] &= (-1)^m z^{-\nu-m} K_{\nu+m}(z), \\ I_{\nu-1}(z) - I_{\nu+1}(z) &= 2\nu z^{-1} I_\nu(z), \quad I_{\nu-1}(z) + I_{\nu+1}(z) = 2I'_\nu(z), \\ K_{\nu-1}(z) - K_{\nu+1}(z) &= -2\nu z^{-1} K_\nu(z), \quad K_{\nu-1}(z) + K_{\nu+1}(z) = -2K'_\nu(z). \end{aligned}$$

4.3 Bessel Functions of Integer Order

Definition: Bessel functions of the *first kind of integer order* are called *Bessel coefficients*, and are generated by the expansion of $\exp\left[\frac{1}{2}z(t-t^{-1})\right]$ in powers of t , i.e., $\exp\left[\frac{1}{2}z(t-t^{-1})\right] = \sum_{n=-\infty}^{\infty} t^n J_n(z)$, $J_{-n}(z) = (-1)^n J_n(z)$.

Note also that

$$Y_n(z) = \pi^{-1} \left[\frac{\partial J_\nu}{\partial \nu} - (-1)^n \frac{\partial J_{-\nu}}{\partial \nu} \right]_{\nu=n}, \quad Y_{-n}(z) = (-1)^n Y_n(z), \quad n = 1, 2, 3, \dots$$

4.4 Modified Bessel Functions of Integer Order

The modified Bessel functions of integer order are the functions $I_n(z)$ and $K_n(z)$, satisfying the relations

$$I_{-n}(z) = I_n(z), \quad K_n(z) = (-1)^n \frac{1}{2} \left[\frac{\partial I_{-v}}{\partial v} - \frac{\partial I_v}{\partial v} \right]_{v=n} \quad \text{for } n = 1, 2, 3, \dots$$

4.5 Spherical Bessel Functions

The Bessel functions and modified Bessel functions reduce to combinations of elementary functions when ν is half of an odd integer, i.e., $\nu = n + 1/2$ for $n = 0, 1, 2, \dots$. These functions often occur in connection with spherical waves, hence the name.

$$\begin{aligned} K_{n+(1/2)}(z) &= \left(\frac{\pi}{2z}\right)^{1/2} \frac{e^{-z}}{n!} \int_0^\infty e^{-t} (1+t/2z)^n t^n dt \\ &= \left(\frac{\pi}{2z}\right)^{1/2} e^{-z} \sum_{m=0}^n (2z)^{-m} \frac{\Gamma(n+m+1)}{m! \Gamma(n+1-m)}, \\ J_{n+(1/2)}(z) &= \left(\frac{1}{2}\pi z\right)^{-1/2} \left[\sin\left(z - \frac{n\pi}{2}\right) \sum_{m=0}^{\leq(1/2)n} (-1)^m \left(n + \frac{1}{2}, 2m\right) (2z)^{-2m} \right. \\ &\quad \left. + \cos\left(z - \frac{n\pi}{2}\right) \sum_{m=0}^{\leq(1/2)n-(1/2)} (-1)^m \left(n + \frac{1}{2}, 2m+1\right) (2z)^{-2m-1} \right], \\ Y_{n+1/2}(z) &= \left(\frac{\pi z}{2}\right)^{-1/2} \left[\sin\left(z - \frac{n\pi}{2}\right) \sum_{m=0}^{\leq(1/2)n-(1/2)} (-1)^m \left(n + \frac{1}{2}, 2m+1\right) (2z)^{-2m-1} \right. \\ &\quad \left. - \cos\left(z - \frac{n\pi}{2}\right) \sum_{m=0}^{\leq(1/2)n} (-1)^m \left(n + \frac{1}{2}, 2m\right) (2z)^{-2m} \right], \\ H_{n+(1/2)}^{(1)}(z) &= \left(\frac{\pi z}{2}\right)^{-1/2} i^{-n-1} e^{iz} \sum_{m=0}^n i^m \left(n + \frac{1}{2}, m\right) (2z)^{-m}, \\ H_{n+(1/2)}^{(2)}(z) &= \left(\frac{\pi z}{2}\right)^{-1/2} i^{n+1} e^{-iz} \sum_{m=0}^n (-i)^m \left(n + \frac{1}{2}, m\right) (2z)^{-m}, \\ J_{-n-(1/2)}(z) &= (-1)^{n+1} Y_{n+(1/2)}(z), \quad Y_{-n-(1/2)}(z) = (-1)^n J_{n+(1/2)}(z), \\ H_{-n-(1/2)}^{(1)}(z) &= i(-1)^n H_{n+(1/2)}^{(1)}(z), \quad H_{-n-(1/2)}^{(2)}(z) = -i(-1)^n H_{n+(1/2)}^{(2)}(z), \\ J_{1/2}(z) &= Y_{-1/2}(z) = \left(\frac{\pi z}{2}\right)^{-1/2} \sin z, \quad Y_{1/2}(z) = -J_{-1/2}(z) = -\left(\frac{\pi z}{2}\right)^{-1/2} \cos z, \\ I_{1/2}(z) &= \left(\frac{\pi z}{2}\right)^{-1/2} \sinh z, \\ H_{1/2}^{(1)}(z) &= -iH_{-1/2}^{(1)}(z) = -i\left(\frac{\pi z}{2}\right)^{-1/2} e^{iz}, \\ H_{1/2}^{(2)}(z) &= iH_{-1/2}^{(2)}(z) = i\left(\frac{\pi z}{2}\right)^{-1/2} e^{-iz}. \end{aligned}$$

4.6 Miscellaneous Formulas

Products of Bessel functions:

$$\Gamma(\nu + 1)J_\nu(\beta z)J_\mu(\alpha z) = \left(\frac{\alpha z}{2}\right)^\mu \left(\frac{\beta z}{2}\right)^\nu \sum_{m=0}^\infty \frac{(-1)^m \left(\frac{\alpha z}{2}\right)^{2m}}{m! \Gamma(\mu + m + 1)} {}_2F_1(-m, -\mu - m; \nu + 1; \beta^2 \alpha^{-2}).$$

When $\beta = \alpha$, the above formula becomes

$$\begin{aligned} J_\nu(z)J_\mu(z) &= \sum_{m=0}^\infty \frac{(-1)^m \left(\frac{z}{2}\right)^{\nu+\mu+2m} \Gamma(\nu + \mu + 2m + 1)}{m! \Gamma(\mu + m + 1) \Gamma(\nu + m + 1) \Gamma(\nu + \mu + m + 1)} \\ &= [\Gamma(\nu + 1) \Gamma(\mu + 1)]^{-1} \left(\frac{z}{2}\right)^{\nu+\mu} {}_2F_3\left(\frac{1}{2} + \frac{\nu}{2} + \frac{\mu}{2}, 1 + \frac{\nu}{2} + \frac{\mu}{2}; 1 + \nu, 1 + \mu, 1 + \nu + \mu; -z^2\right), \\ e^{\pm iz} J_\nu(z) &= \pi^{-1/2} (2z)^\nu \sum_{n=0}^\infty \frac{\Gamma(\nu + n + 1/2) (\pm 2iz)^n}{n! \Gamma(2\nu + n + 1)}, \\ \left(\frac{d}{zdz}\right)^m [z^\nu J_\nu(z)] &= z^{\nu-m} J_{\nu-m}(z), \quad m = 1, 2, 3, \dots, \\ \left(\frac{d}{zdz}\right)^m [z^{-\nu} J_\nu(z)] &= (-1)^m z^{-\nu-m} J_{\nu+m}(z), \quad m = 1, 2, 3, \dots, \\ J_{\nu-1}(z) + J_{\nu+1}(z) &= 2\nu z^{-1} J_\nu(z), \quad J_{\nu-1}(z) - J_{\nu+1}(z) = 2 \frac{dJ_\nu(z)}{dz}. \end{aligned}$$

Wronskians: The Wronskian of two solutions w_1 and w_2 of Bessel's equation is a constant multiple of $\exp[-\int z^{-1} dz]$; $W(w_1, w_2) \equiv w_1 w_2' - w_2 w_1' = Cz^{-1}$. The constant C can be computed from the first terms of the series expansions of the solutions involved. The most important cases are listed below.

$$\begin{aligned} W(J_\nu, J_{-\nu}) &= -2(\pi z)^{-1} \sin(\nu\pi), \quad W(J_\nu, Y_\nu) = 2(\pi z)^{-1}, \quad W(I_\nu, K_\nu) = -z^{-1}, \\ W\left(J_\nu, H_\nu^{(1),(2)}\right) &= \pm 2i(\pi z)^{-1}, \quad W\left(H_\nu^{(1)}, H_\nu^{(2)}\right) = -4i(\pi z)^{-1}, \\ W(I_\nu, I_{-\nu}) &= -2(\pi z)^{-1} \sin(\nu\pi) = I_\nu(z)I_{-\nu+1}(z) - I_{-\nu}(z)I_{\nu-1}(z), \\ J_\nu(z)J_{-\nu+1}(z) + J_{-\nu}(z)J_{\nu-1}(z) &= 2(\pi z)^{-1} \sin(\nu\pi), \\ J_\nu(z)Y_{\nu-1}(z) - Y_\nu(z)J_{\nu-1}(z) &= 2(\pi z)^{-1}, \quad K_{\nu+1}(z)I_\nu(z) + K_\nu(z)I_{\nu+1}(z) = z^{-1}, \\ H_\nu^{(1)}(z)H_{\nu-1}^{(2)}(z) - H_{\nu-1}^{(1)}(z)H_\nu^{(2)}(z) &= -4i(\pi z)^{-1}, \\ J_{\nu-1}(z)H_\nu^{(1)}(z) - J_\nu(z)H_{\nu-1}^{(1)}(z) &= 2(\pi iz)^{-1}, \\ J_\nu(z)H_{\nu-1}^{(2)}(z) - J_{\nu-1}(z)H_\nu^{(2)}(z) &= 2(\pi iz)^{-1}. \end{aligned}$$

4.7 Zeros of Bessel Functions

Bessel functions of the first kind: For real ν , $J_\nu(z)$ has an infinite number of real zeros. The zeros of $J_\nu(z)$ and $J'_\nu(z)$ are symmetric with respect to the axes of coordinates. If $\gamma_{\nu,1}, \gamma_{\nu,2}, \dots$ are the

positive zeros of $J_\nu(x)$ arranged in ascending order of magnitude, then

$$0 < \gamma_{\nu,1} < \gamma_{\nu+1,1} < \gamma_{\nu,2} < \gamma_{\nu+1,2} < \gamma_{\nu,3} < \dots, \quad \nu > -1.$$

Asymptotic formula for γ_ν : $\gamma_\nu = \nu + 1, 855, 757\nu^{1/3} + 103, 315\nu^{-1/3} + O(\nu^{-1})$.

When $\nu > -1$ and A, B, C, D are real numbers such that $AD - BC \neq 0$, then the positive zeros of $AJ_\nu(x) + BxJ'_\nu(x)$ and $CJ_\nu(x) + DxJ'_\nu(x)$ separate one another and no function of this type can have a repeated zero other than $x = 0$. When A and B are real and $\nu > -1$, the function $AJ_\nu(x) + BzJ'_\nu(z)$ has only real zeros except for two purely imaginary zeros when $A/B + \nu < 0$. For $\nu > 1$, the function $J_{-\nu}(z)$ has an infinity of real zeros and also $2[\nu]$ conjugate complex zeros, among them two pure imaginary zeros when $[\nu]$ is an odd integer.

The principal branch of the function

$$AJ_\nu(z) + BJ_{-\nu}(z), \quad (A, B, \text{ real}, B \neq 0, \nu > 0)$$

has $[\nu]$ complex zeros with a positive real part in case $[\nu]$ is even; when $[\nu]$ is odd, there exist $[\nu] - 1$ or $[\nu] + 1$ complex zeros with a positive real part accordingly $(A/B) > / < 0$. The function $J_\nu(z)$ and $J_{\nu+m}(z)$ ($m = 1, 2, 3, \dots$) have no common roots other than zero. For positive fixed real values of z , the zeros ν_n of $J_\nu(z)$ are real and simple functions of ν , asymptotically approaching negative integers. The graph of $J_\nu(x)$ for fixed $\nu > -1$ and variable $x \geq 0$ resembles the graph of a damped oscillation. The successive areas of "half-waves" above and below the axis $x \geq 0$ form a decreasing sequence. If γ_ν , γ'_ν , and γ''_ν denote the smallest positive zeros of $J_\nu(x)$, $J'_\nu(x)$, and $J''_\nu(x)$ respectively; then the following inequalities hold:

$$\begin{aligned} [\nu(\nu + 2)]^{1/2} < \gamma_\nu < [2(\nu + 1)(\nu + 3)]^{1/2}, \quad \nu > 0, \\ [\nu(\nu + 2)]^{1/2} < \gamma'_\nu < [2\nu(\nu + 1)]^{1/2}, \quad \nu > 0, \\ [\nu(\nu - 1)]^{1/2} < \gamma''_\nu < (\nu^2 - 1)^{1/2}, \quad \nu > 1. \end{aligned}$$

Bessel functions of the second kind: Thus $Y_{2n}(z)$ and $Y_{2n+1}(z)$ ($n = 0, 1, 2, \dots$) have $2n$ complex zeros in $|\arg z| \leq 1/2\pi$; $Y_\nu(z)$ has positive real zeros on the principal branch only if ν is rational but not an integer.

Bessel functions of the third kind: The function $H_\nu^{(1)}(z)$, $\nu \geq 0$, has no zeros in $0 \leq \arg z \leq \pi$. The zeros, for $\nu \geq 0$, of $H_\nu^{(1)}$ in $-\pi < \arg z < 0$ and those of $H_\nu^{(2)}$ in $0 < \arg z < \pi$ lie symmetrically with respect to the imaginary axis. There are no pure imaginary zeros except when $\nu = (2k - 1) + 1/2$ ($k = 1, 2, 3, \dots$) in which case there is one such zero. The total number of the zeros of $H_\nu^{(1),(2)}(z)$ on the principal branch is: 0 if $0 \leq \nu < 3/2$; $2k - 1$, if $\nu = (2k - 1) + 1/2$; and $2k$, if $(2k - 1) + 1/2 < \nu < 2k + 1/2$; for $k = 1, 2, 3, \dots$ furthermore, $H_\nu^{(1),(2)}(x)$ and $H_{\nu+m}^{(1),(2)}(x)$ have no common zeros when ν is real ≥ -1 and $m = 1, 2, 3, \dots$

Modified Bessel functions of the third kind: For $\nu \geq 0$, $K_\nu(z)$ has no zeros for which $|\arg z| \leq \pi/2$. The number of zeros in $|\arg z| < \pi$ is the even integer nearest to $\nu - 1/2$ unless $\nu - 1/2$ is an integer, in which case the number is $\nu - 1/2$. When $\nu + 1$ is positive real, and m a positive integer, $K_\nu(z)$ and $K_{\nu+m}(z)$ have no common zero.

4.8 Fourier-Bessel and Dini Series

Denoting two positive zeros of $J_\nu(x)$ by $x = \gamma_m$ and $x = \gamma_n$ (in this case all the zeros of $J_\nu(x)$ are real), the following orthogonal relation holds for $\nu > -1$:

$$\int_0^1 t J_\nu(\gamma_m t) J_\nu(\gamma_n t) dt = \begin{cases} 0, & n \neq m, \\ \frac{1}{2} [J_{\nu+1}(\gamma_m)]^2, & n = m. \end{cases}$$

Similarly, if λ_m and λ_n denote two positive zeros of the function $zJ'_\nu(z) + aJ_\nu(z)$, the following orthogonality relation holds for a given constant a and $\nu \geq -1/2$:

$$\int_0^1 t J_\nu(\lambda_m t) J_\nu(\lambda_n t) dt = \begin{cases} 0, & n \neq m, \\ \frac{1}{2} \lambda_m^{-2} \{ \lambda_m^2 [J'_\nu(\lambda_m)]^2 + (\lambda_m^2 - \nu^2) [J_\nu(\lambda_m)]^2 \}, & n = m. \end{cases}$$

Fourier-Bessel expansion: An arbitrary function $f(x)$ of a real variable x can be written as

$$f(x) = \sum_{m=1}^\infty a_m J_\nu(\gamma_m x), \quad \text{with } \frac{1}{2} [J_{\nu+1}(\gamma_m)]^2 a_m = \int_0^1 t f(t) J_\nu(\gamma_m t) dt,$$

where $\gamma_1, \gamma_2, \gamma_3, \dots$ are the positive zeros of the function $J_\nu(x)$ arranged in ascending order of magnitude.

Dini expansion: An arbitrary function $f(x)$ of a real variable x can be written as

$$f(x) = \sum_{m=1}^\infty b_m J_\nu(\lambda_m x),$$

with $\{ \lambda_m^2 [J'_\nu(\lambda_m)]^2 + (\lambda_m^2 - \nu^2) [J_\nu(\lambda_m)]^2 \} b_m = 2\lambda_m^2 \int_0^1 t J_\nu(\lambda_m t) f(t) dt$, where $\nu \geq -1/2$ and $\lambda_1, \lambda_2, \dots$ are the positive zeros of the function $zJ'_\nu(z) + aJ_\nu(z)$ arranged in ascending order of magnitude.

A function $f(x)$ defined for $a < x < b (a > 0)$ can be expanded in the series

$$f(x) = \sum_{m=1}^\infty a_m [J_\nu(\gamma_m x) Y_\nu(\gamma_m b) - Y_\nu(\gamma_m x) J_\nu(\gamma_m b)],$$

where $z = \gamma_m$ is the m th positive root of $J_\nu(az) Y_\nu(bz) - Y_\nu(az) J_\nu(bz) = 0$, and

$$\begin{aligned} & \{ [J_\nu(\gamma_m a)]^2 - [J_\nu(\gamma_m b)]^2 \} a_m \\ &= \frac{1}{2} \pi \gamma_m^2 [J_\nu(\gamma_m a)]^2 \int_a^b [J_\nu(\gamma_m t) Y_\nu(\gamma_m b) - Y_\nu(\gamma_m t) J_\nu(\gamma_m b)] t f(t) dt. \end{aligned}$$

4.9 Asymptotic Expansions

Asymptotic expansions for large variable:

$$\begin{aligned} \left(\frac{\pi z}{2}\right)^{\frac{1}{2}} J_\nu(z) &= \cos\left(z - \frac{\nu\pi}{2} - \pi\right) \left[\sum_{m=0}^{M-1} (-1)^m (v, 2m) (2z)^{-2m} + O(|z|^{-2M}) \right] \\ &\quad - \sin\left(z - \frac{\nu\pi}{2} - \frac{\pi}{4}\right) \left[\sum_{m=0}^{M-1} (-1)^m (v, 2m+1) (2z)^{-2m-1} \right. \\ &\quad \left. + O(|z|^{-2M-1}) \right], \quad -\pi < \arg z < \pi, \end{aligned}$$

$$\begin{aligned} \left(\frac{\pi z}{2}\right)^{\frac{1}{2}} Y_\nu(z) &= \sin\left(z - \frac{\nu\pi}{2} - \frac{\pi}{4}\right) \left[\sum_{m=0}^{M-1} (-1)^m (v, 2m) (2z)^{-2m} + O(|z|^{-2M}) \right] \\ &\quad \times \cos\left(z - \frac{\nu\pi}{2} - \frac{\pi}{4}\right) \left[\sum_{m=0}^{M-1} (-1)^m (v, 2m+1) (2z)^{-2m-1} \right. \\ &\quad \left. + O(|z|^{-2M-1}) \right], \quad -\pi < \arg z < \pi, \end{aligned}$$

$$\begin{aligned} (2\pi z)^{\frac{1}{2}} I_\nu(z) &= e^z \left[\sum_{m=0}^{M-1} (-1)^m (v, m) (2z)^{-m} + O(|z|^{-M}) \right] \\ &\quad + i e^{-z+iv\pi} \left[\sum_{m=0}^{M-1} (v, m) (2z)^{-m} + O(|z|^{-M}) \right], \\ &\quad -\pi/2 < \arg z < 3\pi/2, \end{aligned}$$

$$\begin{aligned} (2z)^{\frac{1}{2}} \pi^{\frac{3}{2}} [\cos(\pi\nu)]^{-1} I_\nu(z) &= \sum_{m=0}^{M-1} [e^z - i] (-1)^m e^{-i\pi\nu z} \Gamma\left(m + \frac{1}{2} - \nu\right) \Gamma\left(m + \frac{1}{2} + \nu\right) \\ &\quad \times (2z)^{-m} / m! + e^z O(|z|^{-M}), \quad 3\pi/2 < \arg z < \pi/2, \end{aligned}$$

$$\begin{aligned} K_\nu(z) &= \left(\frac{\pi}{2z}\right)^{\frac{1}{2}} e^{-z} \left[\sum_{m=0}^{M-1} (v, m) (2z)^{-m} + O(|z|^{-M}) \right], \\ &\quad -3\pi/2 < \arg z < 3\pi/2. \end{aligned}$$

The following notation has been used in the above formulas:

$$(v, m) = 2^{-2m} \frac{\{(4v^2 - 1)(4v^2 - 3^2) \cdots [4v^2 - (2m-1)^2]\}}{m!} = \frac{\Gamma\left(\frac{1}{2} + v + m\right)}{m! \Gamma\left(\frac{1}{2} + v - m\right)}.$$

Asymptotic expansions for large order:

$$\begin{aligned} 2\pi I_p(x) &= 2^{\frac{1}{2}} (p^2 + x^2)^{-\frac{1}{4}} \exp[(p^2 + x^2)^{\frac{1}{2}} - p \sinh^{-1}(p/x)] \\ &\quad \times \left[\sum_{m=0}^{M-1} (-2)^m a_m \Gamma\left(m + \frac{1}{2}\right) (p^2 + x^2)^{-\frac{1}{2}m} + O(x^{-M}) \right], \quad p, x > 0, \end{aligned}$$

$$\begin{aligned} K_p(x) &= 2^{-\frac{1}{2}} (p^2 + x^2)^{-\frac{1}{4}} \exp[-(p^2 + x^2)^{\frac{1}{2}} + p \sinh^{-1}(p/x)] \\ &\quad \times \left[\sum_{m=0}^{M-1} 2^m a_m \Gamma\left(m + \frac{1}{2}\right) (p^2 + x^2)^{-\frac{1}{2}m} + O(x^{-M}) \right], \quad p, x > 0. \end{aligned}$$

In the above formulas, the first few coefficients a_m are as follows:

$$\begin{aligned}
 a_0 &= 1, \quad a_1 = -\frac{1}{8} + \frac{5}{24} \left(1 + \frac{x^2}{p^2}\right)^{-1}, \quad a_2 = \frac{3}{128} - \frac{77}{576} \left(1 + \frac{x^2}{p^2}\right)^{-1} + \frac{385}{3,456} \left(1 + \frac{x^2}{p^2}\right)^{-2}, \\
 \pi H_p^{(1)}(x) &= 2^{\frac{1}{2}} (x^2 - p^2)^{-\frac{1}{4}} \exp[i(x^2 - p^2)^{\frac{1}{2}} + ip \sinh^{-1}(p/x)] \\
 &\quad \times e^{-i\frac{\pi}{2}(p+\frac{1}{2})} \left[\sum_{m=0}^{M-1} 2^m b_m \Gamma\left(m + \frac{1}{2}\right) (-i)^m (x^2 - p^2)^{-\frac{1}{2}m} + O(x^{-M}) \right], \quad x > p > 0, \\
 \pi H_p^{(1)}(x) &= -i2^{\frac{1}{2}} (p^2 - x^2)^{-\frac{1}{4}} \exp[-(p^2 - x^2)^{\frac{1}{2}} + p \cosh^{-1}(p/x)] \\
 &\quad \times \left[\sum_{m=0}^{M-1} (-1)^m 2^m b_m \Gamma\left(m + \frac{1}{2}\right) (p^2 - x^2)^{-m/2} + O(x^{-M}) \right], \quad p > x > 0, \\
 2\pi J_p(x) &= 2^{\frac{1}{2}} (p^2 - x^2)^{-\frac{1}{4}} \exp[(p^2 - x^2)^{\frac{1}{2}} - p \sinh^{-1}(p/x)] \\
 &\quad \times \left[\sum_{m=0}^{M-1} 2^m b_m \Gamma\left(m + \frac{1}{2}\right) (p^2 - x^2)^{-\frac{m}{2}} + O(x^{-M}) \right], \quad p > x > 0.
 \end{aligned}$$

In the above formulas, the first few coefficients b_m are as follows:

$$\begin{aligned}
 b_0 &= 1, \quad b_1 = \frac{1}{8} - \frac{5}{24} \left(1 - \frac{x^2}{p^2}\right)^{-1}, \quad b_2 = \frac{3}{128} - \frac{77}{576} \left(1 - \frac{x^2}{p^2}\right)^{-1} + \frac{385}{3,456} \left(1 - \frac{x^2}{p^2}\right)^{-2}, \\
 \pi H_p^{(1)}(x) &\sim -\frac{2}{3} \sum_{m=0}^{\infty} e^{2(m+1)\pi i/3} B_m(\varepsilon x) \sin\left[(m+1)\frac{\pi}{3}\right] \Gamma\left(m + \frac{1}{3}\right) \left(\frac{x}{6}\right)^{-(m+1)/3}, \\
 p &\approx x, \quad p, x > 0, \quad \varepsilon = 1 - \frac{p}{x}, \quad \varepsilon = o(x^{-2/3}).
 \end{aligned}$$

In the above formula, the first few coefficients $B_m(\varepsilon x)$ are as follows:

$$\begin{aligned}
 B_0(\varepsilon x) &= 1, \quad B_1(\varepsilon x) = \varepsilon x, \quad B_2(\varepsilon x) = \frac{1}{2}(\varepsilon x)^2 - \frac{1}{20}, \\
 B_3(\varepsilon x) &= \frac{1}{6}(\varepsilon x)^3 - \frac{1}{15}\varepsilon x, \quad B_4(\varepsilon x) = \frac{1}{24}(\varepsilon x)^4 - \frac{1}{24}(\varepsilon x)^2 + \frac{1}{280}, \\
 B_5(\varepsilon x) &= \frac{1}{120}(\varepsilon x)^5 - \frac{1}{60}(\varepsilon x)^3 + \frac{43}{8400}\varepsilon x.
 \end{aligned}$$

4.10 Integrals

$$\begin{aligned}
 \int z^{\nu+1} I_\nu(z) dz &= z^{\nu+1} I_{\nu+1}(z), \quad \int z^{-\nu+1} I_\nu(z) dz = z^{-\nu+1} I_{\nu-1}(z), \\
 \int z^{\nu+1} K_\nu(z) dz &= -z^{\nu+1} K_{\nu+1}(z), \quad \int z^{-\nu+1} K_\nu(z) dz = -z^{-\nu+1} K_{\nu-1}(z), \\
 \int z^\nu J_\nu(z) dz &= 2^{\nu-1} \pi^{\frac{1}{2}} \Gamma\left(\nu + \frac{1}{2}\right) z [J_\nu(z) \mathbf{H}_{\nu-1}(z) - \mathbf{H}_\nu(z) J_{\nu-1}(z)], \\
 \int z^\nu K_\nu(z) dz &= 2^{\nu-1} \pi^{\frac{1}{2}} \Gamma\left(\nu + \frac{1}{2}\right) z [K_\nu(z) \mathbf{L}_{\nu-1}(z) + \mathbf{L}_\nu(z) K_{\nu-1}(z)].
 \end{aligned}$$

The following integral relations are satisfied by any Bessel functions $w_\nu(z)$ and $W_\mu(z)$ of the first, second, or third kind, and order ν and/or μ , respectively:

$$\begin{aligned} \int \left[(\beta^2 - \alpha^2)z + \frac{\nu^2 - \mu^2}{z} \right] w_\nu(\alpha z) W_\mu(\beta z) dz &= z[\alpha W_\mu(\beta z) w'_\nu(\alpha z) - \beta w_\nu(\alpha z) W'_\mu(\beta z)] \\ &= \alpha z W_\mu(\beta z) w_{\nu-1}(\alpha z) - \beta z W_{\mu-1}(\beta z) w_\nu(\alpha z) + (\mu - \nu) W_\mu(\beta z) w_\nu(\alpha z), \\ \int z w_\nu(\alpha z) W_\nu(\beta z) dz &= z(\beta^2 - \alpha^2)^{-1} [\beta W_{\nu+1}(\beta z) w_\nu(\alpha z) - \alpha W_\nu(\beta z) w_{\nu+1}(\alpha z)], \\ \int z w_\nu(\alpha z) W_\nu(\alpha z) dz &= \frac{z^2}{4} [[2w_\nu(\alpha z) W_\nu(\alpha z) - w_{\nu+1}(\alpha z) W_{\nu-1}(\alpha z) \\ &\quad - w_{\nu-1}(\alpha z) W_{\nu+1}(\alpha z)], \\ \int z^{-1} w_\nu(\alpha z) W_\nu(\alpha z) dz &= (2\nu)^{-1} w_\nu(\alpha z) W_\nu(\alpha z) \\ &\quad + (2\nu)^{-1} \alpha z \left[w_{\nu+1}(\alpha z) \frac{\partial W_\nu(\alpha z)}{\partial \nu} - w_\nu(\alpha z) \frac{\partial W_{\nu+1}(\alpha z)}{\partial \nu} \right]. \end{aligned}$$

The following integrals are satisfied by any modified Bessel function of the first or second kind $v_\nu(z)$ and $V_\mu(z)$, of order ν and μ , respectively:

$$\begin{aligned} \int \left[(\beta^2 - \alpha^2)z + \frac{\mu^2 - \nu^2}{z} \right] v_\nu(\alpha z) V_\mu(\beta z) dz &= z[-\alpha V_\mu(\beta z) v'_\nu(\alpha z) + \beta v_\nu(\alpha z) V'_\mu(\beta z)], \\ \int z [v_\nu(\alpha z)]^2 dz &= -\frac{1}{2} z^2 \{ [v'_\nu(\alpha z)]^2 - [v_\nu(\alpha z)]^2 (1 + \alpha^{-2} z^{-2} \nu^{-2}) \}, \\ \int_0^\infty Y_{2\nu}(\alpha t) e^{-\gamma^2 t^2} dt &= -\frac{1}{2} \pi^{\frac{1}{2}} \gamma^{-1} \exp\left(-\frac{1}{8} \alpha^2 / \gamma^2\right) \\ &\quad \times \left[I_\nu\left(\frac{\alpha^2}{8\gamma^2}\right) \tan \nu\pi + \frac{1}{\pi} K_\nu\left(\frac{\alpha^2}{8\gamma^2}\right) \sec \nu\pi \right], \quad |\operatorname{Re} \nu| < \frac{1}{2}, \\ \int_0^\infty e^{-t} t^{-1} H_\nu^{(1)}\left(\frac{2x^2}{t}\right) dt &= 2K_\nu(2x) H_\nu^{(1)}(2x), \\ \int_0^\infty I_\nu(\alpha t) e^{-\gamma^2 t^2} dt &= \frac{1}{2} \pi^{\frac{1}{2}} \gamma^{-1} \exp\left(\frac{\alpha^2}{8\gamma^2}\right) I_{(1/2)\nu}\left(\frac{\alpha^2}{8\gamma^2}\right), \quad \operatorname{Re} \nu > -1, \operatorname{Re} \gamma^2 > 0, \\ \int_0^\infty t^{-1} J_\mu(\alpha t) \sin(bt) dt &= \begin{cases} \mu^{-1} \sin[\mu \sin^{-1}(b/a)], & b < a, \\ a^\mu \mu^{-1} \sin\left(\frac{\mu\pi}{2}\right) [b + (b^2 - a^2)^{\frac{1}{2}}]^{-\mu}, & b > a, \end{cases} \\ \operatorname{Re} \mu > -1, \\ \int_0^\infty t^{-1} J_\mu(\alpha t) \cos(bt) dt &= \begin{cases} \mu^{-1} \cos[\mu \sin^{-1}(b/a)], & b < a, \\ a^\mu \mu^{-1} \cos\left(\frac{\mu\pi}{2}\right) [b + (b^2 - a^2)^{\frac{1}{2}}]^{-\mu}, & b > a, \end{cases} \\ \operatorname{Re} \mu > 0, \\ \int_0^\infty J_\mu(\alpha t) \sin(bt) dt &= \begin{cases} (a^2 - b^2)^{-1/2} \sin[\mu \sin^{-1}(b/a)], & b < a, \\ a^\mu \cos\left(\frac{\mu\pi}{2}\right) (b^2 - a^2)^{-1/2} [b + (b^2 - a^2)^{1/2}]^{-\mu}, & b > a, \end{cases} \\ \operatorname{Re} \mu > -2, \end{aligned}$$

$$\int_0^\infty J_\mu(at) \cos(bt) dt = \begin{cases} (a^2 - b^2)^{-1/2} \cos[\mu \sin^{-1}(b/a)], & b < a, \\ -a^\mu \sin\left(\frac{\mu\pi}{2}\right) (a^2 - b^2)^{-1/2} [b + (b^2 - a^2)^{1/2}]^{-\mu}, & b > a, \end{cases}$$

$$\operatorname{Re} \mu > -1,$$

$$\frac{1}{2} \pi (v^2 - \mu^2) \int_0^\infty J_\mu(at) J_\nu(at) t^{-1} dt = \sin \frac{(v - \mu)\pi}{2}, \quad \operatorname{Re}(v + \mu) > 0,$$

$$\int_0^\infty J_\mu(at) J_\nu(at) t^{-(v+\mu)} dt = \frac{\pi^{1/2} \left(\frac{a}{2}\right)^{v+\mu} \Gamma(\mu + \nu)}{a \Gamma\left(\frac{1}{2} + v + \mu\right) \Gamma\left(\mu + \frac{1}{2}\right) \Gamma\left(\nu + \frac{1}{2}\right)}, \quad \operatorname{Re}(v + \mu) > 0,$$

$$\int_0^\infty J_\mu(at) J_\nu(bt) t^{\mu-v+1} dt = \begin{cases} \frac{2^{\mu-v+1}}{\Gamma(v - \mu)} a^\mu b^{-v} (b^2 - a^2)^{v-\mu-1}, & b > a, \\ 0, & b < a, \end{cases}$$

$$\operatorname{Re} v > \operatorname{Re} \mu > -1.$$

4.11 Additional Theorems and Related Series

$$J_0((z^2 + Z^2 - 2zZ \cos \phi)^{1/2}) = J_0(z)J_0(Z) + 2 \sum_{n=1}^\infty J_n(z)J_n(Z) \cos(n\phi),$$

$$\left(2z \sin \frac{\phi}{2}\right)^{-v} J_v\left(2z \sin \frac{\phi}{2}\right) = 2^v \Gamma(v) \sum_{n=0}^\infty (v+n) [z^{-v} J_{v+n}(z)]^2 C_n^v(\cos \phi),$$

$$v \neq 0, -1, -2, \dots,$$

$$J_0\left(2z \sin \frac{\phi}{2}\right) = [J_0(z)]^2 + 2 \sum_{n=1}^\infty [J_n(z)]^2 \cos(n\phi),$$

$$z^v e^{yz} = 2^v \Gamma(v) \sum_{n=0}^\infty (v+n) C_n^v(y) I_{v+n}(z),$$

$$\left(\frac{z}{2}\right)^{\mu-v} J_\nu(z) = \sum_{n=0}^\infty \frac{\Gamma(\mu+n)\Gamma(v+1-\mu)(\mu+2n)}{n! \Gamma(v+1-\mu-n)\Gamma(v+n+1)} J_{\mu+2n}(z),$$

$$J_\nu(z \sin \theta) = \left(\frac{\pi z}{2}\right)^{-\frac{1}{2}} (\sin \theta)^v \sum_{n=0}^\infty \frac{\left(v + \frac{1}{2} + 2n\right) \Gamma\left(n + \frac{1}{2}\right)}{\Gamma(n + v + 1)} \Gamma\left(v + \frac{1}{2}\right) \\ \times C_{2n}^{v+\frac{1}{2}}(\cos \theta) J_{v+\frac{1}{2}+2n}(z).$$

5 Associated Legendre Functions

5.1 Differential Equation

Definition: An associated Legendre function is a solution of the differential equation

$$(1 - z^2) \frac{d^2 u}{dz^2} - 2z \frac{du}{dz} + \left[v(v+1) - \frac{\mu^2}{1 - z^2} \right] u = 0,$$

in which z denotes an arbitrary complex variable, while ν and μ denote arbitrary complex constants unless the contrary is explicitly stated. The points $+1, -1, \infty$, are ordinary branch points (i.e., singular points) of the above equation. It is customary to use the following notations: the letter x ($x = \cos \varphi$, where φ is a real number) denotes a real variable that varies over the interval $[-1, +1]$. The symbols $P_\nu^\mu(z)$, $Q_\nu^\mu(z)$ customarily denote those solutions of the above equation which are single-valued and regular for $|z| < 1$; in particular, these are uniquely determined for $z = x$. The symbols $P_\nu^\mu(z)$, $Q_\nu^\mu(z)$ customarily denote those solutions which are single-valued and regular for $\text{Re} z > 1$. When these functions cannot be unrestrictedly extended without violating their single-valuedness, a cut along the real axis is made to the left of the point $z = 1$. The values of the functions $P_\nu^\mu(z)$ and $Q_\nu^\mu(z)$ on the upper and lower boundaries of that portion of the cut lying between the points -1 and $+1$ are denoted respectively by $P_\nu^\mu(x \pm i0)$, $Q_\nu^\mu(x \pm i0)$. The letters n and m denote natural numbers or zero, while the letters ν and μ denote arbitrary complex numbers. The upper index is omitted when it is equal to zero, i.e.,

$$P_\nu^0(z) = P_\nu(z), \quad Q_\nu^0(z) = Q_\nu(z), \quad P_\nu^0(z) = P_\nu(z), \quad P_\nu^0(z) = Q_\nu(z).$$

Associated Legendre (or spherical) functions of the first and second kinds $P_\nu^\mu(z)$ and $Q_\nu^\mu(z)$: These functions are defined as the two *linearly independent* solutions of the above differential equation, namely

$$P_\nu^\mu(z) = \frac{1}{\Gamma(1-\mu)} \left(\frac{z+1}{z-1}\right)^{\mu/2} F\left(-\nu, \nu+1; 1-\mu; \frac{1-z}{2}\right), \quad \arg \frac{z+1}{z-1} = 0, \quad z > 1, \text{ real},$$

$$Q_\nu^\mu(z) = \frac{e^{\mu\pi i} \Gamma(\nu+\mu+1) \Gamma(\frac{1}{2})}{2^{\nu+1} \Gamma(\nu+\frac{3}{2})} (z^2-1)^{\mu/2} z^{-\nu-\mu-1} \times F\left(\frac{\nu+\mu+2}{2}, \frac{\nu+\mu+1}{2}; \nu+\frac{3}{2}; \frac{1}{z^2}\right),$$

with $\arg(z^2-1) = 0$ when z is real and greater than 1; or $\arg z = 0$ when z is real and greater than zero. These functions are uniquely defined, respectively, in the intervals $|1-z| < 2$ and $|z| > 1$ with the portion of the real axis that lies between $-\infty$ and $+1$ excluded. They can be extended by means of hypergeometric series to the entire z -plane where the above-mentioned cut was made. These expressions for $P_\nu^\mu(z)$ and $Q_\nu^\mu(z)$ lose their meaning when $1-\mu$ and $\nu+\frac{3}{2}$ are non-positive integers, respectively. When $z = x = \cos \varphi$ is a real number lying on the interval $[-1, +1]$, the following functions are taken as the linearly independent solutions:

$$P_\nu^\mu(x) = \frac{1}{2} \left[e^{\frac{1}{2}\mu\pi i} P_\nu^\mu(\cos \varphi + i0) + e^{-\frac{1}{2}\mu\pi i} P_\nu^\mu(\cos \varphi - i0) \right]$$

$$= \frac{1}{\Gamma(1-\mu)} \left(\frac{1+x}{1-x}\right)^{\mu/2} F\left(-\nu, \nu+1; 1-\mu; \frac{1-x}{2}\right),$$

$$Q_\nu^\mu(x) = \frac{1}{2} e^{-\mu\pi i} \left[e^{-\frac{1}{2}\mu\pi i} Q_\nu^\mu(x+i0) + e^{\frac{1}{2}\mu\pi i} Q_\nu^\mu(x-i0) \right]$$

$$= \frac{\pi}{2 \sin \mu\pi} \left[P_\nu^\mu(x) \cos \mu\pi - \frac{\Gamma(\nu+\mu+1)}{\Gamma(\nu-\mu+1)} P_\nu^{-\mu}(x) \right].$$

When $\mu = \pm m$ is an integer, the last equation loses its meaning, so that $Q_\nu^\mu(x)$ is defined as follows:

$$Q_\nu^m(x) = \left(-1^m (1-x^2)^{m/2} \frac{d^m}{dx^m} Q_\nu(x) \right), \quad Q_\nu^{-m}(x) = (-1)^m \frac{\Gamma(\nu-m+1)}{\Gamma(\nu+m+1)} Q_\nu^m(x).$$

The functions $Q_v^\mu(z)$ are not defined when $\nu + \mu$ is equal to a negative integer. Therefore, the cases $\nu + \mu = -1, -2, -3, \dots$ are excluded in the above formulas.

The functions

$$P_v^{\pm\mu}(\pm z), \quad Q_v^{\pm\mu}(\pm z), \quad P_{-\nu-1}^{\pm\mu}(\pm z), \quad Q_{-\nu-1}^{\pm\mu}(\pm z)$$

are linearly independent solutions of the differential equation for $\nu + \mu \neq 0, \pm 1, \pm 2, \dots$

5.2 Asymptotic Series for Large Values of $|\nu|$

The series

$$P_v^\mu(\cos \varphi) = \frac{2}{\sqrt{\pi}} \Gamma(\nu + \mu + 1) \sum_{k=0}^{\infty} \frac{\Gamma(\mu + k + \frac{1}{2}) \cos[(\nu + k + \frac{1}{2})\varphi - \frac{\pi}{4}(2k + 1) + \frac{\mu\pi}{2}]}{\Gamma(\mu - k + \frac{1}{2}) k! \Gamma(\nu - k + \frac{3}{2}) (2 \sin \varphi)^{k + \frac{1}{2}}},$$

$$\nu + \mu \neq -1, -2, -3, \dots; \nu \neq -\frac{3}{2}, -\frac{5}{2}, -\frac{7}{2}, \dots; \text{for } \frac{\pi}{6} < \varphi < \frac{5\pi}{6},$$

$$Q_v^\mu(\cos \varphi) = \sqrt{\pi} \Gamma(\nu + \mu + 1) \sum_{k=0}^{\infty} (-1)^k \frac{\Gamma(\mu + k + \frac{1}{2}) \cos[(\nu + k + \frac{1}{2})\varphi + \frac{\pi}{4}(2k + 1) + \frac{\mu\pi}{2}]}{\Gamma(\mu - k + \frac{1}{2}) k! \Gamma(\nu - k + \frac{3}{2}) (2 \sin \varphi)^{k + \frac{1}{2}}},$$

$$\nu + \mu \neq -1, -2, -3, \dots; \nu \neq -\frac{3}{2}, \frac{5}{2}, -\frac{7}{2}, \dots; \text{for } \frac{\pi}{6} < \varphi < \frac{5\pi}{6}$$

are both convergent for complex and real values of ν and μ , such that $|\nu| \gg 1, |\nu| \gg |\mu|, |\arg \nu| < \pi$. In the remaining cases, they are asymptotic expansions for $\nu > 0, \mu > 0$, and $0 < \varepsilon \leq \varphi \leq \pi - \varepsilon$. Note also the following asymptotic series, which hold for $0 < \varepsilon \leq \varphi \leq \pi - \varepsilon, |\nu| \gg 1/\varepsilon$:

$$P_v^\mu(\cos \varphi) = \frac{2}{\sqrt{\pi}} \frac{\Gamma(\nu + \mu + 1)}{\Gamma(\nu + \frac{3}{2})} \frac{\cos[(\nu + \frac{1}{2})\varphi - \frac{\pi}{4} + \frac{\mu\pi}{2}]}{\sqrt{2 \sin \varphi}} \left[1 + O\left(\frac{1}{\nu}\right) \right],$$

$$\nu^{-\mu} P_v^\mu(\cos \varphi) = \sqrt{\frac{2}{\nu \pi \sin \varphi}} \cos\left[\left(\nu + \frac{1}{2}\right)\varphi - \frac{\pi}{4} + \frac{\mu\pi}{2}\right] + O\left(\frac{1}{\sqrt{\nu^3}}\right),$$

$$\nu^{-\mu} Q_v^\mu(\cos \varphi) = \sqrt{\frac{\pi}{2\nu \sin \varphi}} \cos\left[\left(\nu + \frac{1}{2}\right)\varphi + \frac{\pi}{4} + \frac{\mu\pi}{2}\right] + O\left(\frac{1}{\sqrt{\nu^3}}\right).$$

For small values of φ sufficiently close to 0 or π , such that $\nu\varphi$ or $\nu(\pi - \varphi)$ is much smaller than 1, the above asymptotic formulas become unsuitable, and should be replaced by the following asymptotic representation for $\mu \geq 0, \nu \gg 1$, where $\eta = (2\nu + 1) \sin \frac{\varphi}{2}$:

$$\left[\left(\nu + \frac{1}{2}\right) \cos \frac{\varphi}{2} \right]^\mu P_v^{-\mu}(\cos \varphi) = J_\mu(\eta) + \sin^2 \frac{\varphi}{2} \left[\frac{J_{\mu+1}(\eta)}{2\eta} - J_{\mu+2}(\eta) + \frac{\eta}{6} J_{\mu+3}(\eta) \right] + O\left(\sin^4 \frac{\varphi}{2}\right).$$

In particular, the above expansion indicates that $\lim_{\nu \rightarrow \infty} \nu^\mu P_v^{-\mu}(\cos x/\nu) = J_\mu(x)$.

5.3 Recursion Relations

Among the many known relations involving Legendre function, some of the most frequently used for a complex argument z are the following:

$$(z^2 - 1) \frac{dP_v^\mu(z)}{dz} = (v - \mu + 1)P_{v+1}^\mu(z) - (v + 1)zP_v^\mu(z),$$

$$(2v + 1)zP_v^\mu(z) = (v - \mu + 1)P_{v+1}^\mu(z) + (v + \mu)P_{v-1}^\mu(z),$$

$$P_v^{\mu+2}(z) + 2(\mu + 1) \frac{z}{\sqrt{z^2 - 1}} P_v^{\mu+1}(z) = (v - \mu)(v + \mu + 1)P_v^\mu(z),$$

$$P_{v+1}^\mu(z) - P_{v-1}^\mu(z) = (2v + 1)\sqrt{z^2 - 1}P_v^{\mu-1}(z), \quad P_{-v-1}^\mu(z) = P_v^\mu(z),$$

$$(z^2 - 1) \frac{dQ_v^\mu(z)}{dz} = (v - \mu + 1)Q_{v+1}^\mu(z) - (v + 1)zQ_v^\mu(z),$$

$$(2v + 1)zQ_v^\mu(z) = (v - \mu + 1)Q_{v+1}^\mu(z) + (v + \mu)zQ_{v-1}^\mu(z),$$

$$Q_v^{\mu+2}(z) + 2(\mu + 1) \frac{z}{\sqrt{z^2 - 1}} Q_v^{\mu+1}(z) = (v - \mu)(v + \mu + 1)Q_v^\mu(z),$$

$$Q_{v-1}^\mu(z) - Q_{v+1}^\mu(z) = -(2v + 1)\sqrt{z^2 - 1}Q_v^{\mu-1}(z),$$

$$e^{-\mu\pi i} Q_v^\mu(x \pm i0) = e^{\pm \frac{1}{2}\mu\pi i} \left[Q_v^\mu(x) \mp i \frac{\pi}{2} P_v^\mu(x) \right],$$

$$\frac{\partial P_v^{-\mu}(x)}{\partial v} = \frac{1}{\Gamma(\mu + 1)} \left(\frac{1-x}{1+x} \right)^{\frac{\mu}{2}} \sum_{n=1}^{\infty} \frac{(-v)(1-v)\dots(n-1-v)(v+1)(v+2)\dots(v+n)}{(\mu+1)(\mu+2)\dots(\mu+n)1 \cdot 2 \cdot \dots \cdot n} \\ \times [\psi(v+n+1) - \psi(v-n+1)] \left(\frac{1-x}{2} \right)^n \quad [v \neq 0, \pm 1, \pm 2, \dots; \operatorname{Re} \mu > -1],$$

$$\left[\frac{\partial P_v(\cos \varphi)}{\partial v} \right]_{v=0} = 2 \ln \cos \frac{\varphi}{2}, \quad \left[\frac{\partial P_v^{-1}(\cos \varphi)}{\partial v} \right]_{v=0} = -\operatorname{tg} \frac{\varphi}{2} - 2 \operatorname{ctg} \frac{\varphi}{2} \ln \cos \frac{\varphi}{2},$$

$$P_v^{-\mu}(x) \frac{dP_v^\mu(x)}{dx} - P_v^\mu(x) \frac{dP_v^{-\mu}(x)}{dx} = \frac{2 \sin \mu\pi}{\pi(1-x^2)},$$

$$P_v^\mu(x) \frac{dQ_v^\mu(x)}{dx} - Q_v^\mu(x) \frac{dP_v^\mu(x)}{dx} = \frac{2^{2\mu}}{1-x^2} \frac{\Gamma\left(\frac{v+\mu+1}{2}\right) \Gamma\left(\frac{v+\mu}{2}+1\right)}{\Gamma\left(\frac{v-\mu+1}{2}\right) \Gamma\left(\frac{v-\mu}{2}+1\right)},$$

$$P_v^\mu(0) = \frac{2^\mu \sqrt{\pi}}{\Gamma\left(\frac{v-\mu}{2}+1\right) \Gamma\left(\frac{-v-\mu+1}{2}\right)}, \quad \frac{dP_v^\mu(0)}{dx} = \frac{2^{\mu+1} \sin \frac{(v+\mu)\pi}{2} \Gamma\left(\frac{v+\mu}{2}+1\right)}{\sqrt{\pi} \Gamma\left(\frac{v-\mu+1}{2}\right)},$$

$$Q_v^\mu(0) = -2^{\mu-1} \sqrt{\pi} \sin \frac{(v+\mu)\pi}{2} \frac{\Gamma\left(\frac{v+\mu+1}{2}\right)}{\Gamma\left(\frac{v-\mu}{2}+1\right)},$$

$$\frac{dQ_v^\mu(0)}{dx} = 2^\mu \sqrt{\pi} \cos \frac{(v+\mu)\pi}{2} \frac{\Gamma\left(\frac{v+\mu}{2}+1\right)}{\Gamma\left(\frac{v-\mu+1}{2}\right)}.$$

5.4 Spherical Functions (Associated Legendre Functions with Integral Indices)

For real x and *integral* values of ν and μ , $|\nu| > |\mu|$, the Legendre differential equation has as solutions the functions $P_n^m(x)$ which are called *associated Legendre functions* (or *spherical functions*) of the first kind. The number n is called the *degree* and the number m is called the *order* of the function $P_n^m(x)$. The functions $\cos m\vartheta P_n^m(\cos \varphi)$, $\sin m\vartheta P_n^m(\cos \varphi)$, which depend on the angles φ and ϑ , are called *tesseral harmonics* for $m < n$ and *sectoral harmonics* for $m = n$. The sectoral harmonics are periodic with respect to the angles φ and ϑ , with periods π and 2π , respectively. These functions are single-valued and continuous everywhere on the surface of the unit sphere $x_1^2 + x_2^2 + x_3^2 = 1$ (where $x_1 = \sin \varphi \cos \vartheta$, $x_2 = \sin \varphi \sin \vartheta$, and $x_3 = \cos \varphi$), and are solutions of the differential equation

$$\frac{1}{\sin \varphi} \frac{\partial}{\partial \varphi} \left(\sin \varphi \frac{\partial Y}{\partial \varphi} \right) + \frac{1}{\sin^2 \varphi} \frac{\partial^2 Y}{\partial \vartheta^2} + n(n+1)Y = 0.$$

The expressions of the first few spherical functions are:

$$P_1^1(x) = -(1-x^2)^{\frac{1}{2}} = -\sin \varphi, \quad P_2^1(x) = -3(1-x^2)^{\frac{1}{2}}x = -\frac{3}{2}\sin 2\varphi,$$

$$P_2^2(x) = -3(1-x^2)^{\frac{1}{2}}x = -\frac{3}{2}\sin 2\varphi, \quad P_2^0(x) = 3(1-x^2) = \frac{3}{2}(1-\cos 2\varphi).$$

Orthogonality relations:

$$\int_{-1}^1 P_n^m(x)P_k^m(x) dx = \begin{cases} 0, & n \neq k, \\ \frac{2}{2n+1} \frac{(n+m)!}{(n-m)!}, & n = k, \end{cases}$$

$$\int_{-1}^1 P_\nu(x)P_\sigma(x) dx = \begin{cases} \frac{2\pi \sin \pi(\sigma - \nu) + 4 \sin(\pi\nu) \sin(\pi\sigma) [\psi(\nu+1) - \psi(\sigma+1)]}{\pi^2(\sigma - \nu)(\sigma + \nu + 1)}, & \sigma + \nu + 1 \neq 0, \\ \frac{\pi^2 - 2(\sin \pi\nu)^2 \psi'(\nu+1)}{\pi^2 \left(\nu + \frac{1}{2}\right)}, & \sigma = \nu, \end{cases}$$

$$\int_{-1}^1 Q_n^m(x)P_k^m(x) dx = (-1)^m \frac{1 - (-1)^{n+k} (n+m)!}{(k-n)(k+n+1)(n-m)!}.$$

Two functions $Y_{n_1}(\varphi, \vartheta)$ and $Z_{n_2}(\varphi, \vartheta)$, defined as

$$Y_{n_1}(\varphi, \vartheta) = a_0 P_{n_1}(\cos \varphi) + \sum_{m=1}^{n_1} (a_m \cos m\vartheta + b_m \sin m\vartheta) P_{n_1}^m(\cos \varphi),$$

$$Z_{n_2}(\varphi, \vartheta) = \alpha_0 P_{n_2}(\cos \varphi) + \sum_{m=1}^{n_2} (\alpha_m \cos m\vartheta + \beta_m \sin m\vartheta) P_{n_2}^m(\cos \varphi),$$

satisfy the following integral relations:

$$\int_0^{2\pi} d\vartheta \int_0^\pi \sin \varphi d\varphi Y_{n_1}(\varphi, \vartheta) Z_{n_2}(\varphi, \vartheta) = 0,$$

$$\int_0^{2\pi} d\vartheta \int_0^\pi \sin \varphi d\varphi Y_n(\varphi, \vartheta) P_n[\cos \varphi \cos \psi + \sin \varphi \sin \psi \cos(\vartheta - \theta)] = \frac{4\pi}{2n+1} Y_n(\psi, \theta).$$

The spherical functions satisfy the following important “addition” theorems:

$$(\cos \varphi + i \sin \varphi \cos \vartheta)^n = P_n(\cos \varphi) + 2 \sum_{m=1}^n (-1)^m \frac{n!}{(n+m)!} \cos m\vartheta P_n^m(\cos \varphi),$$

$$P_n(\cos \varphi_1 \cos \varphi_2 + \sin \varphi_1 \sin \varphi_2 \cos \Theta) = P_n(\cos \varphi_1) P_n(\cos \varphi_2) + 2 \sum_{m=1}^n \frac{(n-m)!}{(n+m)!} P_n^m(\cos \varphi_1) \\ \times P_n^m(\cos \varphi_2) \cos m\Theta,$$

$$\int_0^1 [P_v^{n-v}(x)]^2 \frac{dx}{1-x^2} = -\frac{n!}{2(n-v)\Gamma(1-n+2v)}, \quad n = 0, 1, 2, \dots, \operatorname{Re} v > n,$$

$$\int_{-1}^1 P_n^m(x) P_n^k(x) \frac{dx}{1-x^2} = 0, \quad 0 \leq m \leq n, 0 \leq k \leq n, m \neq k.$$

Legendre functions of the first and second kind $P_\nu(z)$ and $Q_\nu(z)$ are the two linearly independent solutions of the differential equation

$$\frac{d}{dz} \left[(1-z^2) \frac{du}{dz} \right] + \nu(\nu+1)u = 0,$$

where the parameter ν can be an arbitrary number and are expressed in terms of hypergeometric functions as follows:

$$P_\nu(z) = F\left(-\nu, \nu+1; 1; \frac{1-z}{2}\right),$$

$$Q_\nu(z) = \frac{\Gamma(\nu+1)\Gamma\left(\frac{1}{2}\right)}{2^{\nu+1}\Gamma\left(\nu+\frac{3}{2}\right)} z^{-\nu-1} F\left(\frac{\nu+2}{2}, \frac{\nu+1}{2}; \frac{2\nu+3}{2}; \frac{1}{z^2}\right).$$

When ν is not an integer, $\nu \neq 0, 1, 2, \dots$, the function $Q_\nu(z)$ has branch points at the points $z = \pm 1$ and $z = \infty$, while the function $P_\nu(z)$ has singularities at $z = -1$ and $z = \infty$. On the other hand, if $\nu = n = 0, 1, 2, \dots$, the function $Q_n(z)$ is single-valued for $|z| > 1$ and regular for $z = \infty$, while the function $P_\nu(z)$ becomes the *Legendre polynomial* $P_n(z)$. For $\nu = -n = -1, -2, \dots$, the relation $P_{-n-1}(z) = P_n(z)$ holds. The first few functions take on the following forms and special values:

$$Q_0(x) = \frac{1}{2} \ln \frac{1+x}{1-x} = \operatorname{Arth} x, \quad Q_1(x) = \frac{x}{2} \ln \frac{1+x}{1-x} - 1,$$

$$Q_2(x) = \frac{1}{4} (3x^2 - 1) \ln \frac{1+x}{1-x} - \frac{3}{2}x, \quad Q_3(x) = \frac{1}{4} (5x^3 - 3x) \ln \frac{1+x}{1-x} - \frac{5}{2}x^2 + \frac{2}{3},$$

$$\begin{aligned}
 P_\nu(1) &= 1, \quad P_\nu(0) = -\frac{1}{2} \frac{\sin \nu\pi}{\sqrt{\pi^3}} \Gamma\left(\frac{\nu+1}{2}\right) \Gamma\left(-\frac{\nu}{2}\right), \\
 Q_\nu(0) &= \frac{1}{4\sqrt{\pi}} (1 - \cos \nu\pi) \Gamma\left(\frac{\nu+1}{2}\right) \Gamma\left(-\frac{\nu}{2}\right), \\
 Q_\nu(x) &= \frac{\pi}{2 \sin \nu\pi} [\cos \nu\pi P_\nu(x) - P_\nu(-x)], \quad \nu \neq 0, \pm 1, \pm 2, \dots, \\
 Q_n(x) &= \frac{1}{2} P_n(x) \ln \frac{1+x}{1-x} - W_{n-1}(x),
 \end{aligned}$$

where $W_{-1}(x) \equiv 0$, and

$$W_{n-1}(x) = \sum_{k=0}^{2E(\frac{n-1}{2})} \frac{2(n-2k)-1}{(2k+1)(n-k)} P_{n-2k-1}(x) = \sum_{k=1}^n \frac{1}{k} P_{k-1}(x) P_{n-k}(x), \quad n = 0, 1, 2, \dots,$$

$$(z^2 - 1) \frac{dP_\nu(z)}{dz} = (\nu + 1)[P_{\nu+1}(z) - zP_\nu(z)], \quad (2\nu + 1)zP_\nu(z) = (\nu + 1)P_{\nu+1}(z) + \nu P_{\nu-1}(z),$$

$$(z^2 - 1) \frac{dQ_\nu(z)}{dz} = (\nu + 1)[Q_{\nu+1}(z) - zQ_\nu(z)], \quad (2\nu + 1)zQ_\nu(z) = (\nu + 1)Q_{\nu+1}(z) + \nu Q_{\nu-1}(z).$$

Integrals:

$$\int_{\cos \varphi}^1 P_\nu(x) dx = \sin \varphi P_\nu^{-1}(\cos \varphi),$$

$$\int_{-1}^1 P_\nu(x) Q_\sigma(x) dx = \begin{cases} \frac{1 - \cos \pi(\sigma - \nu) - 2\pi^{-1} \sin(\pi\nu) \cos(\pi\sigma) [\psi(\nu + 1) - \psi(\sigma + 1)]}{(\nu - \sigma)(\nu + \sigma + 1)}, & \text{Re } \nu > 0, \text{ Re } \sigma > 0, \sigma \neq \nu, \\ -\frac{\sin(2\nu\pi) \psi'(\nu + 1)}{\pi(2\nu + 1)}, & \text{Re } \nu > 0, \sigma = \nu, \end{cases}$$

$$\int_{-1}^1 Q_\nu(x) Q_\sigma(x) dx = \begin{cases} \frac{[\psi(\nu + 1) - \psi(\sigma + 1)][1 + \cos(\pi\sigma) \cos(\nu\pi)] - \frac{\pi}{2} \sin \pi(\nu - \sigma)}{(\sigma - \nu)(\sigma + \nu + 1)}, & \sigma + \nu + 1 \neq 0; \\ & \nu, \sigma \neq -1, -2, -3, \dots, \\ \frac{\frac{1}{2} \pi^2 - \psi'(\nu + 1)[1 + (\cos \nu\pi)^2]}{2\nu + 1}, & \nu = \sigma, \nu \neq -1, -2, -3, \dots \end{cases}$$

Notation: $C = \frac{\Gamma((1+\nu)/2)\Gamma(1+(\sigma/2))}{\Gamma((1+\sigma)/2)\Gamma(1+(\nu/2))}$; $[\text{Re } \nu > 0, \text{ Re } \sigma > 0]$

$$\int_0^1 P_\nu(x) P_\sigma(x) dx = \frac{C \sin \frac{\pi\sigma}{2} \cos \frac{\pi\nu}{2} - C^{-1} \sin \frac{\pi\nu}{2} \cos \frac{\pi\sigma}{2}}{\frac{1}{2} \pi(\sigma - \nu)(\sigma + \nu + 1)},$$

$$\int_0^1 Q_\nu(x)Q_\sigma(x) dx = \frac{\psi(\nu+1) - \psi(\sigma+1) - \frac{\pi}{2} \left[(C - C^{-1}) \sin \frac{\pi(\sigma+\nu)}{2} - (C + C^{-1}) \sin \frac{\pi(\sigma-\nu)}{2} \right]}{(\sigma-\nu)(\sigma+\nu+1)} \quad \begin{array}{l} \text{Re} \nu > 0, \\ \text{Re} \sigma > 0, \end{array}$$

$$\int_0^1 P_\nu(x)Q_\sigma(x) dx = \frac{A^{-1} \cos \frac{\pi(\nu-\sigma)}{2} - 1}{(\sigma-\nu)(\sigma+\nu+1)}, \quad \text{Re} \nu > 0, \text{Re} \sigma > 0,$$

$$\int_1^\infty P_\nu(x)Q_\sigma(x) dx = \frac{1}{(\sigma-\nu)(\sigma+\nu+1)}, \quad \text{Re}(\sigma-\nu) > 0, \text{Re}(\sigma+\nu) > -1,$$

$$\int_1^\infty Q_\nu(x)Q_\sigma(x) dx = \frac{\psi(\sigma+1) - \psi(\nu+1)}{(\sigma-\nu)(\sigma+\nu+1)}, \quad \text{Re}(\nu+\sigma) > -1, \sigma, \nu \neq -1, -2, -3, \dots,$$

$$\int_1^\infty Q_\nu(x) dx = \frac{1}{\nu(\nu+1)}, \quad \text{Re} \nu > 0.$$

6 Orthogonal Polynomials

General properties: Consider a nonnegative real function $w(x) \geq 0$ of a real variable x such that the integral $\int_a^b w(x) dx > 0$, with (a, b) a fixed interval on the x -axis. If the integral $\int_a^b x^n w(x) dx$ exists for $n = 0, 1, 2, \dots$ then there exists a *system of orthogonal polynomials* $p_n(x)$, $n = 0, 1, 2, \dots$, on the interval (a, b) with the weight function $w(x)$; this sequence is uniquely determined by the following conditions:

1. $p_n(x)$ is a polynomial of degree n and the coefficient of x^n in this polynomial is positive
2. The polynomials $p_0(x), p_1(x), \dots$ are orthonormal, i.e.,

$$\int_a^b p_n(x)p_m(x)w(x) dx = \begin{cases} 0, & \text{for } n \neq m, \\ 1, & \text{for } n = m. \end{cases}$$

Darboux-Christoffel formula: Denoting the coefficient of x^n in the polynomials $p_n(x)$ by q_n , the following summation formulas hold

$$\sum_{k=0}^n p_k(x)p_k(y) = \frac{q_n}{q_{n+1}} \frac{p_{n+1}(x)p_n(y) - p_n(x)p_{n+1}(y)}{x-y},$$

$$\sum_{k=0}^n [p_k(x)]^2 = \frac{q_n}{q_{n+1}} [p_n(x)p'_{n+1}(x) - p'_n(x)p_{n+1}(x)].$$

Recursion formula: Three consecutive orthogonal polynomials satisfy the recursion relation

$$p_n(x) = (A_n x + B_n)p_{n-1}(x) - C_n p_{n-2}(x), \quad A_n = \frac{q_n}{q_{n-1}}, \quad C_n = \frac{q_n q_{n-2}}{q_{n-1}^2}, \quad n = 2, 3, 4, \dots$$

Special systems of normalized orthogonal polynomials:

1. Normalized Legendre polynomials:

$$\left(n + \frac{1}{2}\right)^{\frac{1}{2}} P_n(x), \quad (a, b) \rightarrow (-1, +1), \quad \text{weight} : w(x) = 1.$$

2. Normalized Gegenbauer polynomials:

$$2^\lambda \Gamma(\lambda) \left[\frac{(n+\lambda)n!}{2\pi\Gamma(2\lambda+n)} \right]^{\frac{1}{2}} C_n^\lambda(x), \quad (a, b) \rightarrow (-1, +1), \quad w(x) = (1-x^2)^{\lambda-\frac{1}{2}}.$$

3. Normalized Chebyshev polynomials:

$$\sqrt{\frac{\varepsilon_n}{\pi}} T_n(x); \quad \varepsilon_0 = 1, \quad \varepsilon_n = 2; \quad \text{for } n = 1, 2, 3, \dots, \quad (a, b) \rightarrow (-1, +1), \quad w(x) = (1-x^2)^{-\frac{1}{2}}.$$

4. Normalized Hermite polynomials:

$$2^{-\frac{n}{2}} \pi^{-\frac{1}{4}} (n!)^{-\frac{1}{2}} H_n(x), \quad (a, b) \rightarrow (-\infty, +\infty), \quad w(x) = e^{-x^2}.$$

5. Normalized Jacobi polynomials:

$$\left[\frac{\Gamma(n+1)\Gamma(\alpha+\beta+1+n)(\alpha+\beta+1+2n)}{\Gamma(\alpha+1+n)\Gamma(\beta+1+n)2^{\alpha+\beta+1}} \right]^{\frac{1}{2}} P_n^{(\alpha, \beta)}(x), \quad (a, b) \rightarrow (-1, +1),$$

$$w(x) = (1-x)^\alpha (1+x)^\beta.$$

6. Normalized Laguerre polynomials:

$$\left[\frac{\Gamma(n+1)}{\Gamma(\alpha+n+1)} \right]^{\frac{1}{2}} L_n^\alpha(x), \quad (a, b) \rightarrow (0, +\infty), \quad w(x) = x^\alpha e^{-x}.$$

6.1 Legendre Polynomials: $P_n(z)$

The differential equation

$$(1-z^2) \frac{d^2 u}{dz^2} - 2z \frac{du}{dz} + n(n+1)u = 0$$

admits polynomial solutions if, and only if, n is an integer; these polynomial solutions are the *Legendre polynomials* $P_n(z)$, which are hence special types of associated Legendre functions of degree n , of the form

$$P_n(z) = \frac{1}{2^n n!} \frac{d^n}{dz^n} (z^2 - 1)^n.$$

Written as a function of $z = \cos \varphi$, the Legendre polynomials $P_n(z)$ take on the forms:

$$\begin{aligned} P_n(z) &= \frac{1}{2^n} \sum_{k=0}^{E(\frac{n}{2})} \frac{(-1)^k (2n-2k)!}{k!(n-k)!(n-2k)!} z^{n-2k} \\ &= \frac{(2n-1)!!}{n!} z^n F\left(-\frac{n}{2}, \frac{1-n}{2}; \frac{1}{2}-n; \frac{1}{z^2}\right) \\ &= \sum_{k=0}^n \frac{(-1)^k (n+k)!}{(n-k)!(k!)2^{2k+1}} [(1-z)^k + (-1)^n (1+z)^k], \\ P_n(\cos \varphi) &= \frac{(2n-1)!!}{2^n n!} \left(\cos n\varphi + \frac{1}{2} \frac{n}{2n-1} \cos(n-2)\varphi + \frac{1 \cdot 3}{1 \cdot 2} \frac{n(n-1)}{(2n-1)(2n-3)} \cos(n-4)\varphi \right. \\ &\quad \left. + \frac{1 \cdot 3 \cdot 5}{1 \cdot 2 \cdot 3} \frac{n(n-1)(n-2)}{(2n-1)(2n-3)(2n-5)} \cos(n-6)\varphi - \dots \right). \end{aligned}$$

Special cases:

$$\begin{aligned} P_0(x) &= 1, \quad P_1(x) = x = \cos \varphi, \quad P_2(x) = \frac{1}{2}(3x^2 - 1) = \frac{1}{4}(3 \cos 2\varphi + 1), \\ P_3(x) &= \frac{1}{2}(5x^3 - 3x) = \frac{1}{8}(5 \cos 3\varphi + 3 \cos \varphi), \\ P_4(x) &= \frac{1}{8}(35x^4 - 30x^2 + 3) = \frac{1}{64}(35 \cos 4\varphi + 20 \cos 2\varphi + 9), \\ P_5(x) &= \frac{1}{8}(63x^5 - 70x^3 + 15x) = \frac{1}{128}(63 \cos 5\varphi + 35 \cos 3\varphi + 30 \cos \varphi). \end{aligned}$$

The generating function:

$$\begin{aligned} \frac{1}{\sqrt{1-2tz+t^2}} &= \sum_{k=0}^{\infty} t^k P_k(z), \quad \text{for } [|t| < \min |z \pm \sqrt{z^2-1}|] \\ &= \sum_{k=0}^{\infty} \frac{1}{t^{k+1}} P_k(z), \quad \text{for } [|t| > \max |z \pm \sqrt{z^2-1}|]. \end{aligned}$$

Inequalities:

$$\begin{aligned} \text{For } x > 1: \quad & P_0(x) < P_1(x) < P_2(x) < \dots < P_n(x) < \dots, \\ \text{For } x > -1: \quad & P_0(x) + P_1(x) + \dots + P_n(x) > 0, \\ [P_n(\cos \varphi)]^2 &> \frac{\sin(2n+1)\varphi}{(2n+1)\sin \varphi}, \quad [0 < \varphi < \pi], \\ \sqrt{n \sin \varphi} |P_n(\cos \varphi)| &\leq 1, \quad |P_n(\cos \varphi)| \leq 1. \end{aligned}$$

Recurrence relations:

$$\begin{aligned} (n+1)P_{n+1}(z) - (2n+1)zP_n(z) + nP_{n-1}(z) &= 0, \\ (z^2-1) \frac{dP_n}{dz} &= n[zP_n(z) - P_{n-1}(z)] = \frac{n(n+1)}{2n+1} [P_{n+1}(z) - P_{n-1}(z)]. \end{aligned}$$

Summations and series:

$$\begin{aligned} \sum_{k=0}^n (2k+1)P_k(x)P_k(y) &= (n+1) \frac{P_n(x)P_{n+1}(y) - P_n(y)P_{n+1}(x)}{y-x}, \\ z^{2n} &= \frac{1}{2n+1}P_0(z) + \sum_{k=1}^{\infty} (4k+1) \frac{2n(2n-2)\dots(2n-2k+2)}{(2n+1)(2n+3)\dots(2n+2k+1)}P_{2k}(z), \\ z^{2n+1} &= \frac{3}{2n+3}P_1(z) + \sum_{k=1}^{\infty} (4k+3) \frac{2n(2n-2)\dots(2n-2k+2)}{(2n+3)(2n+5)\dots(2n+2k+3)}P_{2k+1}(z), \\ \sum_{n=1}^{\infty} \frac{1}{n}P_n(\cos \theta) &= \ln \frac{2tg \frac{\pi-\theta}{4}}{\sin \theta} = -\ln \sin \frac{\theta}{2} - \ln \left(1 + \sin \frac{\theta}{2}\right), \\ \sum_{n=1}^{\infty} \frac{1}{n+1}P_n(\cos \theta) &= \ln \frac{1 + \sin \frac{\theta}{2}}{\sin \frac{\theta}{2}} - 1. \end{aligned}$$

Integrals:

$$\begin{aligned} P_n(\cos \varphi) &= \frac{2}{\pi} \int_{\varphi}^{\pi} \frac{\sin \left(n + \frac{1}{2}\right) t}{\sqrt{2(\cos \varphi - \cos t)}} dt, \\ \int_{-1}^1 P_n(x)P_m(x) dx &= \frac{2}{2n+1} \delta_{mn}, \\ \int_0^1 P_n(x)P_m(x) dx &= \frac{1}{2n+1} [m = n] \\ &= 0 [n - m \text{ is even, } m \neq n] \\ &= \frac{(-1)^{\frac{1}{2}(m+n-1)} m!n!}{2^{m+n-1}(n-m)(n+m+1) \left[\left(\frac{n}{2}\right)! \left(\frac{m-1}{2}\right)!\right]^2} [n = \text{even, } m = \text{odd}], \\ \int_0^{2\pi} P_{2n}(\cos \varphi) d\varphi &= 2\pi \left[\binom{2n}{n} 2^{-2n}\right]^2, \\ \int_{-1}^1 x^m P_n(x) dx &= 0, \quad \text{for } m < n, \\ \int_{-1}^1 (1+x)^{m+n} P_m(x)P_n(x) dx &= \frac{2^{m+n+1} [(m+n)!]^4}{(m!n!)^2 (2m+2n+1)!}, \\ \int_{-1}^1 (1+x)^{m-n-1} P_m(x)P_n(x) dx &= 0, \quad m > n, \\ \int_{-1}^1 (1-x^2)^n P_{2m}(x) dx &= \frac{2n^2}{(n-m)(2m+2n+1)} \int_{-1}^1 (1-x^2)^{n-1} P_{2m}(x) dx \quad m < n, \\ \int_{-1}^1 \frac{1}{z-x} \{P_n(x)P_{n-1}(z) - P_{n-1}(x)P_n(z)\} dx &= -\frac{2}{n}, \\ \int_{-1}^x (x-t)^{-\frac{1}{2}} P_n(t) dt &= \left(n + \frac{1}{2}\right)^{-1} (1+x)^{-\frac{1}{2}} [T_n(x) + T_{n+1}(x)], \\ \int_x^1 (t-x)^{-\frac{1}{2}} P_n(t) dt &= \left(n + \frac{1}{2}\right)^{-1} (1-x)^{-\frac{1}{2}} [T_n(x) - T_{n+1}(x)]. \end{aligned}$$

In the following integrals, z belongs to the complex plane with a discontinuity along the interval from -1 to $+1$.

$$\int_{-1}^1 (z-x)^{-1} P_n(x) dx = 2Q_n(z), \quad \int_{-1}^1 x(z-x)^{-1} P_0(x) dx = 2Q_1(z),$$

$$\int_{-1}^1 x(z-x)^{-1} P_m(x) P_n(x) dx = 2zP_m(z)Q_n(z), \quad m < n,$$

$$\int_{-1}^1 x(z-x)^{-1} [P_n(x)]^2 dx = 2zP_n(z)Q_n(z) - \frac{2}{2n+1}.$$

6.2 Gegenbauer Polynomials: $C_n^\lambda(t)$

The *Gegenbauer polynomials* $C_n^\lambda(t)$ of degree n represent a *generalization of the Legendre polynomials*, being defined as the coefficients of α^n in the power-series expansion of the function

$$(1 - 2t\alpha + \alpha^2)^{-\lambda} = \sum_{n=0}^{\infty} C_n^\lambda(t) \alpha^n.$$

Recursion formulas:

$$(n+2)C_{n+2}^\lambda(t) = 2(\lambda+n+1)tC_{n+1}^\lambda(t) - (2\lambda+n)C_n^\lambda(t),$$

$$nC_n^\lambda(t) = 2\lambda[tC_{n-1}^{\lambda+1}(t) - C_{n-2}^{\lambda+1}(t)],$$

$$(2\lambda+n)C_n^\lambda(t) = 2\lambda[C_n^{\lambda+1}(t) - tC_{n-1}^{\lambda+1}(t)],$$

$$nC_n^\lambda(t) = (2\lambda+n-1)tC_{n-1}^\lambda(t) - 2\lambda(1-t^2)C_{n-2}^{\lambda-1}(t).$$

Summation theorem:

$$C_n^\lambda(\cos\psi \cos\vartheta + \sin\psi \sin\vartheta \cos\varphi)$$

$$= \frac{\Gamma(2\lambda-1)}{[\Gamma(\lambda)]^2} \sum_{k=0}^n \frac{2^{2k}(n-k)![\Gamma(\lambda+k)]^2}{\Gamma(2\lambda+n+k)} (2\lambda+2k-1) \sin^k\psi \sin^k\vartheta$$

$$\times C_{n-k}^{\lambda+k}(\cos\psi) C_{n-k}^{\lambda+k}(\cos\vartheta) C_k^{\lambda-\frac{1}{2}}(\cos\varphi), \quad \psi, \vartheta, \varphi \text{ real; } \lambda \neq \frac{1}{2},$$

$$\frac{d^k}{dt^k} C_n^\lambda(t) = 2^k \frac{\Gamma(\lambda+k)}{\Gamma(\lambda)} C_{n-k}^{\lambda+k}(t),$$

$$C_n^\lambda(t) = \frac{\Gamma(2\lambda+n)\Gamma(\lambda+\frac{1}{2})}{\Gamma(2\lambda)\Gamma(n+1)} \left\{ \frac{1}{4}(t^2-1) \right\}^{\frac{1}{4}-\frac{\lambda}{2}} P_{\lambda+n-\frac{1}{2}}^{\frac{1}{2}-\lambda}(t),$$

$$\lim_{\lambda \rightarrow 0} \Gamma(\lambda) C_n^\lambda(\cos\varphi) = \frac{2 \cos n\varphi}{n}, \quad \lim_{\lambda \rightarrow \infty} \lambda^{-\frac{n}{2}} C_n^{\frac{\lambda}{2}} \left(t \sqrt{\frac{2}{\lambda}} \right) = \frac{2^{-\frac{n}{2}}}{n!} H_n(t),$$

$$\lim_{\lambda \rightarrow \infty} \lambda^{-\frac{n}{2}} C_n^{\frac{\lambda}{2}} \left(t \sqrt{\frac{2}{\lambda}} \right) = \frac{2^{-\frac{n}{2}}}{n!} H_n(t).$$

Special cases:

$$C_n^1(\cos\varphi) = \frac{\sin(n+1)\varphi}{\sin\varphi}, \quad C_0^0(\cos\varphi) = 1, C_0^\lambda(t) \equiv 1, C_n^\lambda(1) = \binom{2\lambda+n-1}{n},$$

$$\int_{-1}^1 (1-x^2)^{\nu-\frac{1}{2}} C_n^\nu(x) dx = 0, \quad n > 0, \operatorname{Re} \nu > -\frac{1}{2},$$

$$\int_0^1 x^{n+2\rho} (1-x^2)^{\nu-\frac{1}{2}} C_n^\nu(x) dx = \frac{\Gamma(2\nu+n)\Gamma(2\rho+n+1)\Gamma\left(\nu+\frac{1}{2}\right)\Gamma\left(\rho+\frac{1}{2}\right)}{2^{n+1}\Gamma(2\nu)\Gamma(2\rho+1)n!\Gamma(n+\nu+\rho+1)}, \quad \operatorname{Re} \rho > -\frac{1}{2}, \operatorname{Re} \nu > -\frac{1}{2},$$

$$\int_{-1}^1 (1-x)^{\nu-\frac{1}{2}} (1+x)^\beta C_n^\nu(x) dx = \frac{2^{\beta+\nu+\frac{1}{2}}\Gamma(\beta+1)\Gamma\left(\nu+\frac{1}{2}\right)\Gamma(2\nu+n)\Gamma\left(\beta-\nu+\frac{3}{2}\right)}{n!\Gamma(2\nu)\Gamma\left(\beta-\nu-n+\frac{3}{2}\right)\Gamma\left(\beta+\nu+n+\frac{3}{2}\right)}, \quad \operatorname{Re} \beta > -1, \operatorname{Re} \nu > -\frac{1}{2},$$

$$\int_{-1}^1 (1-x^2)^{\nu-\frac{1}{2}} C_m^\nu(x) C_n^\nu(x) dx = \frac{\pi 2^{1-2\nu}\Gamma(2\nu+n)}{n!(n+\nu)[\Gamma(\nu)]^2} \delta_{mn}, \quad \operatorname{Re} \nu > -\frac{1}{2}.$$

6.3 Chebyshev Polynomials $T_n(x)$ and $U_n(x)$

Definition: The Chebyshev's polynomials of the first kind, $T_n(x)$, are defined as

$$T_n(x) = \cos(n \arccos x) = \frac{1}{2} \left[(x + i\sqrt{1-x^2})^n + (x - i\sqrt{1-x^2})^n \right]$$

$$= x^n - \binom{n}{2} x^{n-2} (1-x^2) + \binom{n}{4} x^{n-4} (1-x^2)^2 - \binom{n}{6} x^{n-6} (1-x^2)^3 + \dots.$$

The Chebyshev's polynomials of the second kind, $U_n(x)$, are defined as:

$$U_n(x) = \frac{\sin[(n+1) \arccos x]}{\sin[\arccos x]} = \frac{1}{2i\sqrt{1-x^2}} \left[(x + i\sqrt{1-x^2})^{n+1} - (x - i\sqrt{1-x^2})^{n+1} \right]$$

$$= \binom{n+1}{1} x^n - \binom{n+1}{3} x^{n-2} (1-x^2) + \binom{n+1}{5} x^{n-4} (1-x^2)^2 - \dots.$$

All zeros of $T_n(x)$ and $U_n(x)$ are real, simple, and lie within the interval $(-1, +1)$. Of all polynomials of degree n with leading coefficient equal to 1, the one that deviates the least from zero on the interval $[-1, +1]$ is the polynomial $2^{-n+1} T_n(x)$. The functions $T_n(x)$ and $\sqrt{1-x^2} U_{n-1}(x)$ are two linearly independent solutions of the differential equation

$$(1-x^2) \frac{d^2 y}{dx^2} - x \frac{dy}{dx} + n^2 y = 0.$$

Generating functions:

$$\frac{1-t^2}{1-2tx+t^2} = T_0(x) + 2 \sum_{k=1}^{\infty} T_k(x) t^k, \quad \frac{1}{1-2tx+t^2} = \sum_{k=0}^{\infty} U_k(x) t^k.$$

Recursion formulas:

$$T_{n+1}(x) - 2xT_n(x) + T_{n-1}(x) = 0, \quad U_{n+1}(x) - 2xU_n(x) + U_{n-1}(x) = 0,$$

$$T_n(x) = U_n(x) - xU_{n-1}(x), \quad (1-x^2)U_{n-1}(x) = xT_n(x) - T_{n+1}(x).$$

Special cases:

$$T_0(x) = 1, \quad T_1(x) = x, \quad T_2(x) = 2x^2 - 1, \quad T_3(x) = 4x^3 - 3x,$$

$$T_4(x) = 8x^4 - 8x^2 + 1, \quad T_5(x) = 16x^5 - 20x^3 + 5x,$$

$$U_0(x) = 1, \quad U_1(x) = 2x, \quad U_2(x) = 4x^2 - 1,$$

$$U_3(x) = 8x^3 - 4x, \quad U_4(x) = 16x^4 - 12x^2 + 1,$$

$$T_n(1) = 1, \quad T_n(-1) = (-1)^n, \quad T_{2n}(0) = (-1)^n, \quad T_{2n+1}(0) = 0,$$

$$U_{2n+1}(0) = 0, \quad U_{2n}(0) = (-1)^n.$$

Integrals:

$$\int_{-1}^1 T_n(x)T_m(x) \frac{dx}{\sqrt{1-x^2}} = \begin{cases} 0, & m \neq n, \\ \frac{\pi}{2}, & m = n \neq 0, \\ \pi, & m = n = 0, \end{cases}$$

$$\int_{-1}^1 \sqrt{1-x^2} U_n(x)U_m(x) dx = \begin{cases} 0, & m \neq n \text{ or } m = n = 0, \\ \frac{\pi}{2}, & m = n \neq 0, \end{cases}$$

$$\int_{-1}^1 [T_n(x)]^2 dx = 1 - (4n^2 - 1)^{-1},$$

$$\int_{-1}^1 U_n[x(1-y^2)^{\frac{1}{2}}(1-z^2)^{\frac{1}{2}} + yz] dx = \frac{2}{n+1} U_n(y)U_n(z), \quad |y| < 1, |z| < 1,$$

$$\int_{-1}^1 (1-x)^{-\frac{1}{2}}(1+x)^{m-n-\frac{3}{2}} T_m(x)T_n(x) dx = 0, \quad m > n,$$

$$\int_{-1}^1 (1-x)^{-\frac{1}{2}}(1+x)^{m+n-\frac{3}{2}} T_m(x)T_n(x) dx = \frac{\pi(2m+2n-2)!}{2^{m+n}(2m-1)!(2n-1)!}, \quad m+n \neq 0,$$

$$\int_{-1}^1 (1-x)^{\frac{1}{2}}(1+x)^{m+n+\frac{3}{2}} U_m(x)U_n(x) dx = \frac{\pi(2m+2n+2)!}{2^{m+n+2}(2m+1)!(2n+1)!},$$

$$\int_{-1}^1 (1-x)^{\frac{1}{2}}(1+x)^{m-n-\frac{1}{2}} U_m(x)U_n(x) dx = 0, \quad m > n.$$

6.4 Hermite Polynomials $H_n(x)$

Definition: The Hermite polynomials $H_n(x)$ are defined via the following expressions:

$$H_n(x) = (-1)^n e^{x^2} \frac{d^n}{dx^n} (e^{-x^2}), \quad H_n(x) = \frac{2^n}{\sqrt{\pi}} \int_{-\infty}^{\infty} (x+it)^n e^{-t^2} dt,$$

$$H_n(x) = 2^n x^n - 2^{n-1} \binom{n}{2} x^{n-2} + 2^{n-2} \cdot 1 \cdot 3 \cdot \binom{n}{4} x^{n-4} - 2^{n-3} \cdot 1 \cdot 3 \cdot 5 \cdot \binom{n}{6} x^{n-6} + \dots$$

The Hermite polynomials satisfy the differential equation

$$\frac{d^2 u_n}{dx^2} - 2x \frac{du_n}{dx} + 2n u_n = 0.$$

A second solution of this differential equation is provided by the functions:

$$u_{2n} = (-1)^n A x \Phi\left(\frac{1}{2} - n; \frac{3}{2}; x^2\right), \quad u_{2n+1} = (-1)^n B \Phi\left(-\frac{1}{2} - n; \frac{1}{2}; x^2\right),$$

$A, B = \text{const.}$

Recursion formulas:

$$\frac{dH_n(x)}{dx} = 2nH_{n-1}(x), \quad H_{n+1}(x) = 2xH_n(x) - 2nH_{n-1}(x).$$

Generating function: $\exp(-t^2 + 2tx) = \sum_{k=0}^{\infty} (t^k/k!)H_k(x)$.

Special cases:

$$H_0(x) = 1, \quad H_1(x) = 2x, \quad H_2(x) = 4x^2 - 2, \quad H_3(x) = 8x^3 - 12x,$$

$$H_4(x) = 16x^4 - 48x^2 + 12,$$

$$H_{2n}(0) = (-1)^n 2^n (2n-1)!!, \quad H_{2n+1}(0) = 0.$$

Inequalities:

$$|H_n(x)| \leq 2^{\frac{n}{2} - E(\frac{n}{2})} \frac{n!}{\left[E\left(\frac{n}{2}\right)\right]!} e^{2x\sqrt{E(\frac{n}{2})}} \quad [x > 0].$$

Asymptotic representation:

$$H_{2n}(x) = (-1)^n 2^n (2n-1)!! e^{\frac{x^2}{2}} \left[\cos(\sqrt{4n+1}x) + O\left(\frac{1}{\sqrt[4]{n}}\right) \right],$$

$$H_{2n+1}(x) = (-1)^n 2^{n+\frac{1}{2}} (2n-1)!! \sqrt{2n+1} e^{\frac{x^2}{2}} \left[\sin(\sqrt{4n+3}x) + O\left(\frac{1}{\sqrt[4]{n}}\right) \right].$$

Summation theorem:

$$\frac{\left(\sum_{k=1}^r a_k^2\right)^{\frac{n}{2}}}{n!} H_n\left(\frac{\sum_{k=1}^r a_k x_k}{\sqrt{\sum_{k=1}^r a_k^2}}\right) = \sum_{m_1+m_2+\dots+m_r=n} \prod_{k=1}^r \left\{ \frac{a_k^{m_k}}{m_k!} H_{m_k}(x_k) \right\}.$$

Integrals:

$$\int_{-\infty}^{\infty} e^{-x^2} H_m(x) H_n(x) dx = \begin{cases} 0, & m \neq n, \\ 2^n \cdot n! \sqrt{\pi}, & m = n, \end{cases}$$

$$\int_{-\infty}^{\infty} e^{-2x^2} H_m(x) H_n(x) dx = (-1)^{\frac{1}{2}(m+n)} 2^{\frac{m+n-1}{2}} \Gamma\left(\frac{m+n+1}{2}\right), \quad m+n \text{ is even,}$$

$$\int_{-\infty}^{\infty} e^{-x^2} H_m(ax) H_n(x) dx = 0, \quad m < n,$$

$$\int_0^x e^{-y^2} H_n(y) dy = H_{n-1}(0) - e^{-x^2} H_{n-1}(x),$$

$$\int_{-\infty}^{\infty} e^{-x^2} H_{2m}(xy) dx = \sqrt{\pi} \frac{(2m)!}{m!} (y^2 - 1)^m.$$

6.5 Laguerre Polynomials

Definition: The Laguerre polynomials $L_n^\alpha(x)$ are defined as

$$L_n^\alpha(x) = \frac{1}{n!} e^x x^{-\alpha} \frac{d^n}{dx^n} (e^{-x} x^{n+\alpha}) = \sum_{m=0}^n (-1)^m \binom{n+\alpha}{n-m} \frac{x^m}{m!}, \quad L_n^0(x) = L_n(x).$$

The Laguerre polynomials satisfy the differential equation

$$x \frac{d^2 u}{dx^2} + (\alpha - x + 1) \frac{du}{dx} + nu = 0.$$

Recursion formulas:

$$\frac{d}{dx} [L_n^\alpha(x) - L_{n+1}^\alpha(x)] = L_n^\alpha(x), \quad \frac{d}{dx} L_n^\alpha(x) = -L_{n-1}^{\alpha+1}(x),$$

$$x \frac{d}{dx} L_n^\alpha(x) = n L_n^\alpha(x) - (n + \alpha) L_{n-1}^\alpha(x) = (n + 1) L_{n+1}^\alpha(x) - (n + \alpha + 1 - x) L_n^\alpha(x),$$

$$x L_n^{\alpha+1}(x) = (n + \alpha + 1) L_n^\alpha(x) - (n + 1) L_{n+1}^\alpha(x) = (n + \alpha) L_{n-1}^\alpha(x) - (n - x) L_n^\alpha(x),$$

$$(n + 1) L_{n+1}^\alpha(x) - (2n + \alpha + 1 - x) L_n^\alpha(x) + (n + \alpha) L_{n-1}^\alpha(x) = 0, \quad n = 1, 2, \dots,$$

$$L_n^{\alpha-1}(x) = L_n^\alpha(x) - L_{n-1}^\alpha(x).$$

Connections with Hermite polynomials:

$$H_{2n}(x) = (-1)^n 2^{2n} n! L_n^{-\frac{1}{2}}(x^2), \quad H_{2n+1}(x) = (-1)^n 2^{2n+1} n! x L_n^{\frac{1}{2}}(x^2).$$

Special cases:

$$L_0^\alpha(x) = 1, \quad L_1^\alpha(x) = \alpha + 1 - x, \quad L_n^{-n}(x) = (-1)^n \frac{x^n}{n!}, \quad L_n^\alpha(0) = \binom{n+\alpha}{n},$$

$$L_1(x) = 1 - x, \quad L_2(x) = 1 - 2x + \frac{x^2}{2}.$$

Summations:

$$L_n^{\alpha_1+\alpha_2+\dots+\alpha_k+k-1}(x_1+x_2+\dots+x_k) = \sum_{(i_1+i_2+\dots+i_k=n)} L_{i_1}^{\alpha_1}(x_1)L_{i_2}^{\alpha_2}(x_2)\dots L_{i_k}^{\alpha_k}(x_k),$$

$$L_n^\alpha(x+y) = e^y \sum_{k=0}^\infty \frac{(-1)^k}{k!} y^k L_n^{\alpha+k}(x),$$

$$\sum_{m=0}^n \frac{m!}{\Gamma(m+\alpha+1)} L_m^\alpha(x)L_m^\alpha(y) = \frac{(n+1)!}{\Gamma(n+\alpha+1)(x-y)} [L_n^\alpha(x)L_{n+1}^\alpha(y) - L_{n+1}^\alpha(x)L_n^\alpha(y)],$$

$$\sum_{m=0}^n L_m^\alpha(x) = L_n^{\alpha+1}(x), \quad \sum_{m=0}^n L_m^\alpha(x)L_{n-m}^\beta(y) = L_n^{\alpha+\beta+1}(x+y),$$

$$(1-z)^{-\alpha-1} \exp \frac{xz}{z-1} = \sum_{n=0}^\infty L_n^\alpha(x)z^n, \quad |z| < 1,$$

$$e^{-xz}(1+z)^\alpha = \sum_{n=0}^\infty L_n^{\alpha-n}(x)z^n, \quad |z| < 1, \quad J_\alpha(2\sqrt{xz})e^z(xz)^{-\frac{1}{2}\alpha}$$

$$= \sum_{n=0}^\infty \frac{z^n}{\Gamma(n+\alpha+1)} L_n^\alpha(x), \quad \alpha > -1,$$

$$\sum_{n=0}^\infty n! \frac{L_n^\alpha(x)L_n^\alpha(y)z^n}{\Gamma(n+\alpha+1)} = \frac{(xyz)^{-\frac{1}{2}\alpha}}{1-z} \exp\left(-z\frac{x+y}{1-z}\right) I_\alpha\left(2\frac{\sqrt{xyz}}{1-z}\right), \quad |z| < 1,$$

$$\sum_{n=0}^\infty \frac{L_n^\alpha(x)}{n+1} = e^x x^{-\alpha} \Gamma(\alpha, x), \quad \alpha > -1, x > 0.$$

Asymptotic behavior:

$$L_n^\alpha(x) = \lim_{\beta \rightarrow \infty} P_n^{(\alpha, \beta)}\left(1 - \frac{2x}{\beta}\right), \quad \lim_{n \rightarrow \infty} \left[n^{-\alpha} L_n^\alpha\left(\frac{x}{n}\right)\right] = x^{-\frac{1}{2}\alpha} J_\alpha(2\sqrt{x}),$$

$$L_n^\alpha(x) = \frac{1}{\sqrt{\pi}} e^{\frac{1}{2}x} x^{-\frac{1}{2}\alpha - \frac{1}{4}} n^{\frac{1}{2}\alpha - \frac{1}{4}} \cos\left[2\sqrt{nx} - \frac{\alpha\pi}{2} - \frac{\pi}{4}\right] + O\left(n^{\frac{1}{2}\alpha - \frac{3}{4}}\right), \quad \text{Im } \alpha = 0, x > 0.$$

Integrals:

$$\int_0^t L_n^\alpha(x) dx = L_n^\alpha(t) - L_{n+1}^\alpha(t) - \binom{n+\alpha}{n} + \binom{n+1+\alpha}{n+1},$$

$$\int_0^t L_{n-1}^{\alpha+1}(x) dx = -L_n^\alpha(t) + \binom{n+\alpha}{n},$$

$$\int_0^t L_m(x)L_n(t-x) dx = L_{m+n}(t) - L_{m+n+1}(t),$$

$$\int_0^1 x^\alpha(1-x)^\beta L_m^\alpha(xy)L_n^\beta[(1-x)y] dx$$

$$= \frac{(m+n)!\Gamma(\alpha+m+1)\Gamma(\beta+n+1)}{m!n!\Gamma(\alpha+\beta+m+n+2)} L_{m+n}^{\alpha+\beta+1}(y), \quad \text{Re } \alpha > -1, \text{Re } \beta > -1,$$

$$\int_y^\infty e^{-x} L_n^\alpha(x) dx = e^{-y} [L_n^\alpha(y) - L_{n-1}^\alpha(y)],$$

$$\int_0^\infty e^{-bx} L_n(\lambda x) L_n(\mu x) dx = \frac{(b - \lambda - \mu)^n}{b^{n+1}} P_n \left[\frac{b^2 - (\lambda + \mu)b + 2\lambda\mu}{b(b - \lambda - \mu)} \right], \quad \operatorname{Re} b > 0,$$

$$\int_0^\infty e^{-x} x^\alpha L_n^\alpha(x) L_m^\alpha(x) dx = \begin{cases} 0, & m \neq n, \quad \operatorname{Re} \alpha > -1, \\ \frac{\Gamma(\alpha + n + 1)}{n!}, & m = n, \quad \operatorname{Re} \alpha > 0. \end{cases}$$

7 Probability Theory and Statistical Estimation

7.1 Introduction

Probability theory is a branch of mathematical sciences that provides a model for describing the process of observation. The need for probability theory arises from the fact that most observations of natural phenomena do not lead to uniquely predictable results. Probability theory provides the tools for dealing with actual variations in the outcome of realistic observations and measurements. The challenging pursuit to develop a theory of probability that is mathematically rigorous and describes many phenomena observable in nature has generated over the years notable disputes over conceptual and logical problems. Modern probability theory is based on postulates constructed from three axioms attributed to A. Kolmogorov, all of which are consistent with the notion of frequency of occurrence of events. The alternative approach, traceable to P. Laplace, is based on the concept that probability is simply a way of providing a numerical scale to quantify our reasonable beliefs about a situation which we do not know completely. This approach is consistent with Bayes' theorem, conditional probabilities, and inductive reasoning. Either approach to probability theory would completely describe a natural phenomenon if sufficient information were available to determine the underlying probability distribution exactly. In practice, though, such exact knowledge is seldom available, so that the features of the probability distribution underlying the physical phenomenon under consideration must be estimated. Such estimations form the study object of statistics, which is defined as the branch of mathematical sciences that uses the results of observations and measurements to estimate, in a mathematically well-defined manner, the essential features of probability distributions.

Both statistics and probability theory use certain generic terms for defining the objects or phenomena under study. A system is the object or phenomena under study. It represents the largest unit being considered. A system can refer to a nuclear reactor, corporation, chemical process, mechanical device, biological mechanism, society, economy, or any other conceivable object that is under study. The output or response of a system is a result that can be measured quantitatively or enumerated. The temperature of a nuclear reactor, the profit of a corporation, yield of a chemical process, torque of a motor, life span of an organism, and the inflation rate of an economy are all examples of system outputs. A model is a mathematical idealization that is used as an approximation to represent the output of a system. Models can be quite simple or highly complex; they can be expressed in terms of a single variable, many variables, or sets of nonlinear integro-differential equations. Regardless of its complexity, the model is an idealization of the system, so it cannot be exact; usually, the more complex the system is the less exact

the model becomes, particularly because the ability to solve exactly the highly complex mathematical expressions diminishes with increasing complexity. The dilemma facing the analyst is: the more the model is simplified, the easier it is to analyze but the less precise the results.

A statistical model comprises mathematical formulations that express the various outputs of a system in terms of probabilities. Usually, a statistical model is used when the output of the system cannot be expressed as a fixed function of the input variables. Statistical models are particularly useful for representing the behavior of a system based on a limited number of measurements, and for summarizing and/or analyzing a set of data obtained experimentally or numerically.

The group study to be measured or counted, or the conceptual entity for which predictions are to be made, is called *population*. A *parameter* of a model is a quantity that expresses a characteristic of the system; a parameter could be constant or variable. A sample is a subset of the population selected for study. An experiment is a sequence of a limited (or, occasionally, unlimited) number of trials. An event is an outcome of an experiment. The set of all events (i.e., the set that represents all outcomes of an experiment) is called the event space or sample space of the experiment; the respective events are also referred to as sample points.

In order to consider multiple events, the following basic ideas from set theory need to be recalled: if $(\mathcal{E}_1, \mathcal{E}_2, \dots, \mathcal{E}_k)$ denote any k events (sets) in an event space \mathcal{S} , then:

1. The event consisting of all sample points belonging to either \mathcal{E}_1 or \mathcal{E}_2, \dots , or \mathcal{E}_k is called the union of the events $(\mathcal{E}_1, \mathcal{E}_2, \dots, \mathcal{E}_k)$ and is denoted as $\cup_{i=1}^k \mathcal{E}_i$.
2. The event consisting of all sample points belonging to \mathcal{E}_1 and \mathcal{E}_2, \dots , and \mathcal{E}_k is called the intersection of the events $(\mathcal{E}_1, \mathcal{E}_2, \dots, \mathcal{E}_k)$ and is denoted as $\cap_{i=1}^k \mathcal{E}_i$.
3. The null event is the event \emptyset that contains no sample points; \emptyset is also termed the vacuous event, the empty event, i.e., the event that never occurs.
4. The universal event is the same as the entire sample space \mathcal{S} , i.e., it is the set of all sample points in the sample space.
5. If \mathcal{E} is any event, then the complement of \mathcal{E} , denoted as $\bar{\mathcal{E}}$, is the event consisting of all sample points in the sample space \mathcal{S} that do not belong to \mathcal{E} .
6. The event \mathcal{E}_1 is said to be a subevent of \mathcal{E}_2 , denoted as $\mathcal{E}_1 \subset \mathcal{E}_2$, if every sample point of \mathcal{E}_1 is also a sample point of \mathcal{E}_2 . If the relations $\mathcal{E}_2 \subset \mathcal{E}_1$ and $\mathcal{E}_1 \subset \mathcal{E}_2$ hold simultaneously, then \mathcal{E}_2 and \mathcal{E}_1 contain the same sample points, i.e., $\mathcal{E}_1 = \mathcal{E}_2$.
7. The event $\mathcal{E}_1 - \mathcal{E}_2$ is the set of all sample points that belong to \mathcal{E}_1 but not to \mathcal{E}_2 . Equivalently, $\mathcal{E}_1 - \mathcal{E}_2 = \mathcal{E}_1 \cap \bar{\mathcal{E}}_2$.
8. Two events \mathcal{E}_1 and \mathcal{E}_2 are said to be mutually exclusive if their intersection is the null event, i.e., if $\mathcal{E}_1 \cap \mathcal{E}_2 = \emptyset$.

The outcome of experiments and/or observations is described in terms of compound events, consisting of combinations of elementary events. In turn, the combinations of elementary events are analyzed in terms of k -tuples; a k -tuple is a collection of k quantities generated from elementary events in a space \mathcal{S} . If the position of every event in the k -tuple is unimportant, then the respective k -tuple is called unordered; otherwise, the respective k -tuple is called ordered (or an arrangement). Two k -tuples containing the same elementary events are called distinguishable if ordering is considered; otherwise, they are called undistinguishable.

In statistical, nuclear, or particle physics, it is useful to visualize k -tuples in terms of a collection of unique cells, which may or may not be occupied. Then, a k -tuple is equivalent to a k -fold specification of the occupancy of these cells. The k elements occupying these cells may or may not be distinct and multiple occupancy of cells may or may not be allowed. This way, for

example, the basis for the Maxwell–Boltzmann law of classical statistical physics is obtained by calculating the number, Z_{MB} , of ordered k -tuples that can be formed by selecting events (atoms or molecules) with replacements (i.e., the atoms or molecules are “distinguishable!”) from an event set (the classical gas) \mathcal{S} of finite size n ; this yields $Z_{MB} = n^k$. On the other hand, nonclassical particles such as fermions behave like indistinguishable particles that are forbidden (by Pauli’s exclusion principle) to multiply occupy a cell. The corresponding Fermi–Dirac statistics, obtained by calculating the number, Z_{FD} , of unordered k -tuples in which multiple occupancy of available states is forbidden, is given by $Z_{FD} = C_k^n = n!/[k!(n-k)!]$. The bosons are also nonclassical particles (i.e., they too are “indistinguishable”) but, in contradistinction to fermions, bosons favor multiple occupancies of available energy states. Counting, in this case, the total number, Z_{BE} , of unordered k -tuples with replacement and multiple occupancy of cells gives $Z_{BE} = C_k^{n+k-1}$.

When a process operates on an event space such that the individual outcomes of the observations cannot be controlled, the respective process is called a *random process* and the respective events are called *random events*. Although the exact outcome of any single random trial is unpredictable, a sample of random trials of reasonable size is expected to yield a pattern of outcomes. In other words, randomness implies lack of deterministic regularity but existence of statistical regularity. Thus, random phenomena must be distinguished from totally unpredictable phenomena, for which no pattern can be construed, even for exceedingly large samples. Observations of physical phenomena tend to fall somewhere between total unpredictability, at the one extreme, and statistically well-behaved processes, at the other extreme. For this reason, experimentalists must invest a considerable effort to identify and eliminate, as much as possible, statistically unpredictable effects (e.g., malfunctioning equipment), to perform experiments under controlled conditions conducive to generating statistically meaningful results.

The quantitative analysis of statistical models relies on concepts of probability theory. The basic concepts of probability theory can be introduced in several ways, ranging from the intuitive notion of *frequency* of occurrence to the *axiomatic* development initiated by A. Kolmogorov in 1933, including the *subjective inductive reasoning* ideas based on “degree of belief” as originally formulated by Laplace and Bayes. All three of these interpretations of probability are employed in nuclear science and engineering to take advantage of their respective strengths. From a mathematical point of view, however, the concepts of probability theory are optimally introduced by using Kolmogorov’s axiomatic approach, in which probability is postulated in terms of abstract functions operating on well-defined event spaces. This axiomatic approach avoids both the mathematical ambiguities inherent to the concept of relative frequencies and the pitfalls of inadvertently misusing the concept of inductive reasoning.

Thus, consider that \mathcal{S} is the sample space consisting of a certain number of events, the interpretation of which is left open for the moment. Assigned to each subset \mathcal{A} of \mathcal{S} , there exists a real number $P(\mathcal{A})$, called a probability, defined by the following three axioms (after A. Kolmogorov 1933):

AXIOM I (EXISTENCE): For every subset \mathcal{A} in \mathcal{S} , the respective probability exists and is nonnegative, i.e., $P(\mathcal{A}) \geq 0$.

AXIOM II (ADDITIVITY): For any two subsets \mathcal{A} and \mathcal{B} that are disjoint (i.e., $\mathcal{A} \cap \mathcal{B} = \emptyset$), the probability assigned to the union of \mathcal{A} and \mathcal{B} is the sum of the two corresponding probabilities, i.e., $P(\mathcal{A} \cup \mathcal{B}) = P(\mathcal{A}) + P(\mathcal{B})$.

AXIOM III (NORMALIZATION): The probability assigned to the entire sample space is one, i.e., $P(\mathcal{S}) = 1$; in other words, the certain event has unit probability.

Note that, the statements of the three axioms mentioned earlier are not entirely rigorous from the standpoint of pure mathematics, but suffice for the applications to nuclear engineering. Several useful properties of probabilities can be readily derived from the axiomatic definition introduced above:

$$\begin{aligned}
 P(\bar{\mathcal{A}}) &= 1 - P(\mathcal{A}), \text{ where } \bar{\mathcal{A}} \text{ is the complement of } \mathcal{A} \\
 P(\mathcal{A} \cup \bar{\mathcal{A}}) &= 1 \\
 0 &\leq P(\mathcal{A}) \leq 1 \\
 P(\emptyset) &= 0, \text{ but } P(\mathcal{A}) = 0 \text{ does NOT mean that } \mathcal{A} = \emptyset \\
 \text{If } \mathcal{A} &\subset \mathcal{B}, \text{ then } P(\mathcal{A}) \leq P(\mathcal{B}) \\
 P(\mathcal{A} \cup \mathcal{B}) &= P(\mathcal{A}) + P(\mathcal{B}) - P(\mathcal{A} \cap \mathcal{B})
 \end{aligned}$$

The last relation above is known as Poincaré’s theorem of probability addition. This theorem can be extended to any finite sequence of events $(\mathcal{E}_1, \mathcal{E}_2, \dots, \mathcal{E}_k)$ in a sample space \mathcal{S} , in which case it becomes

$$P\left(\bigcup_{i=1}^n \mathcal{E}_i\right) = \sum_{i=1}^n P(\mathcal{E}_i) - \sum_{i \neq j} P(\mathcal{E}_i \cap \mathcal{E}_j) + \sum_{i \neq j \neq k} P(\mathcal{E}_i \cap \mathcal{E}_j \cap \mathcal{E}_k) + \dots + (-1)^{n+1} P\left(\bigcap_{i=1}^n \mathcal{E}_i\right).$$

When the events $(\mathcal{E}_1, \mathcal{E}_2, \dots, \mathcal{E}_n)$ form a finite sequence of mutually exclusive events, the above expression reduces to

$$P\left(\bigcup_{i=1}^n \mathcal{E}_i\right) = \sum_{i=1}^n P(\mathcal{E}_i).$$

When extended to the infinite case $n \rightarrow \infty$, the above relation expresses one of the defining properties of the probability measure, which makes it possible to introduce the concept of probability function defined on an event space \mathcal{S} . Specifically, a function P is a probability function defined on \mathcal{S} if and only if it possesses the following properties:

$$\begin{aligned}
 P(\emptyset) &= 0, \quad \text{where } \emptyset \text{ is the null set,} \\
 P(\mathcal{S}) &= 1, \\
 0 &\leq P(\mathcal{E}) \leq 1, \quad \text{where } \mathcal{E} \text{ is any event in } \mathcal{S}, \\
 P\left(\bigcup_{i=1}^{\infty} \mathcal{E}_i\right) &= \sum_{i=1}^{\infty} P(\mathcal{E}_i),
 \end{aligned}$$

where $(\mathcal{E}_1, \mathcal{E}_2, \dots)$ is any sequence of mutually exclusive events in \mathcal{S} .

An additional concept of *conditional probability* is introduced in order to address conditions (implied or explicit) such as “What is the probability that event \mathcal{E}_2 occurs if it is known that event \mathcal{E}_1 has actually occurred?” The conditional probability $P(\mathcal{E}_2|\mathcal{E}_1)$ that event \mathcal{E}_2 occurs given the occurrence of \mathcal{E}_1 is defined as

$$P(\mathcal{E}_2|\mathcal{E}_1) \equiv \frac{P(\mathcal{E}_1 \cap \mathcal{E}_2)}{P(\mathcal{E}_1)}.$$

As can be seen from the definition introduced earlier, conditional probabilities also satisfy the axioms of probability. In particular, this definition implies that the usual probability

$P(\mathcal{E}_1)$ can itself be regarded as a conditional probability, because $P(\mathcal{E}_1) = P(\mathcal{E}_1|\mathcal{S})$ (i.e., $P(\mathcal{E}_1)$ is the conditional probability for \mathcal{E}_1 given \mathcal{S}). The definition of conditional probability can be extended to more than two events by partitioning the sample space \mathcal{S} into k mutually exclusive events $(\mathcal{E}_1, \mathcal{E}_2, \dots, \mathcal{E}_k)$, and by considering that $\mathcal{E} \subset \mathcal{S}$ is an arbitrary event in \mathcal{S} with $P(\mathcal{E}) > 0$. Then the probability that event \mathcal{E}_i occurs given the occurrence of \mathcal{E} , $P(\mathcal{E}_i|\mathcal{E})$ is expressed as

$$P(\mathcal{E}_i|\mathcal{E}) = \frac{P(\mathcal{E}|\mathcal{E}_i)P(\mathcal{E}_i)}{\sum_{j=1}^k P(\mathcal{E}|\mathcal{E}_j)P(\mathcal{E}_j)} \quad (i = 1, 2, \dots, k), \quad (\text{Bayes' theorem}),$$

where $P(\mathcal{E}|\mathcal{E}_i)$ denotes the probability that event \mathcal{E} occurs, given the occurrence of \mathcal{E}_i . The above relation is known as *Bayes' theorem*, and is of fundamental importance to practical applications of probability theory.

Two events, \mathcal{E}_1 and \mathcal{E}_2 , are *statistically independent* if $P(\mathcal{E}_2|\mathcal{E}_1) = P(\mathcal{E}_2)$. This means that the occurrence (or nonoccurrence) of \mathcal{E}_1 does not affect the occurrence of \mathcal{E}_2 . Note that, if \mathcal{E}_1 and \mathcal{E}_2 are statistically independent, then $P(\mathcal{E}_1\mathcal{E}_2) = P(\mathcal{E}_1)P(\mathcal{E}_2)$, $P(\mathcal{E}_1|\mathcal{E}_2) = P(\mathcal{E}_1)$, and also conversely.

The numerical representation of the elementary events \mathcal{E} in a set \mathcal{S} is accomplished by introducing a function, X , which operates on all events $\mathcal{E} \subset \mathcal{S}$ in such a way as to establish a particular correspondence between \mathcal{E} and the real number $x = X(\mathcal{E})$. The function X defined in this way is called a *random variable*. Note that, X itself is the random variable rather than the individual values $x = X(\mathcal{E})$, where X generates by operating on \mathcal{E} . Thus, although X has the characteristics of a “function” rather than those of a “variable,” the usual convention in probability theory and statistics is to call X a “random variable” rather than a “random function.” As is seen in the following section, there also exists “functions of random variables,” which may, or may not, be random themselves.

Random events $\mathcal{E} \subset \mathcal{S}$ that can be completely characterized by a single-dimensional random variable X are called single-variable events. The qualifier “single-dimensional” is omitted when it is apparent from the respective context. The concept of single-dimensional random variable, introduced to represent numerically a single-variable event, can be extended to a multi-variable event $\mathcal{E} \subset \mathcal{S}$. Thus, an n -variable event $\mathcal{E} \subset \mathcal{S}$ is represented numerically by establishing the correspondence $\mathbf{x} = \mathbf{X}(\mathcal{E})$, where $\mathbf{x} = (x_1, x_2, \dots, x_n)$ is a vector of real numbers and $\mathbf{X} = (X_1, X_2, \dots, X_n)$ is a multi-dimensional random variable (or random vector, for short) that takes on the specific values \mathbf{x} .

The dimensionality of a random number is defined by the dimensionality of the particular set of values $x = X(\mathcal{E})$, generated by the function X when operating on the events \mathcal{E} . By definition, *finite random variables* are those for which the set of values x obtainable from X operating on \mathcal{E} is in one-to-one correspondence with a finite set of integers. *Infinite discrete random variables* are those for which the set of values x obtainable from X operating on \mathcal{E} is in one-to-one correspondence with the infinite set of all integers. Unaccountable or *non-denumerable random variables* are those for which the set of values x obtainable from X operating on \mathcal{E} is in one-to-one correspondence with the infinite set of all real numbers.

The main interpretations of probability commonly encountered in data and model analysis are that of relative frequency (which is used, in particular, for assigning statistical errors to measurements) and that of subjective probability (which is used, in particular, to quantify systematic uncertainties). In data analysis, probability is more commonly interpreted as a limiting relative frequency. In this interpretation, the elements of the set \mathcal{S} correspond to the possible

outcomes of a measurement, assumed to be (at least hypothetically) repeatable. A subset \mathcal{E} of \mathcal{S} corresponds to the occurrence of any of the outcomes in the subset. Such a subset is called an event, which is said to occur if the outcome of a measurement is in the subset. A subset of \mathcal{S} consisting of only one element denotes an elementary outcome. The probability of an elementary outcome \mathcal{E} is defined as the fraction of times that \mathcal{E} occurs in the limit when the measurement is repeated many of times infinitely, namely:

$$P(\mathcal{E}) = \lim_{n \rightarrow \infty} \frac{\text{number of occurrences of outcome } \mathcal{E} \text{ in } n \text{ measurements}}{n}.$$

The probability for the occurrence of any one of several outcomes (i.e., for a nonelementary subset \mathcal{E}) is determined from the probabilities for individual elementary outcomes by using the addition rule provided by the axioms of probability. These individual probabilities correspond, in turn, to relative frequencies of occurrence. The relative frequency interpretation is consistent with the axioms of probability, because the fraction of occurrence is always greater than or equal to zero, the frequency of any outcome is the sum of the individual frequencies of the individual outcomes (as long as the set of individual outcomes is disjoint), and the measurement must, by definition, eventually yield some outcome (i.e., $P(\mathcal{S}) = 1$). Correspondingly, the conditional probability $P(\mathcal{E}_2|\mathcal{E}_1)$ represents the number of cases where both \mathcal{E}_2 and \mathcal{E}_1 occur divided by the number of cases in which \mathcal{E}_1 occurs, regardless of whether \mathcal{E}_2 occurs. In other words, $P(\mathcal{E}_2|\mathcal{E}_1)$ gives the frequency of \mathcal{E}_2 with the subset \mathcal{E}_1 taken as the sample space.

The concept of probability as a relative frequency becomes questionable when attempting to assign probabilities for very rare (or even uniquely occurring) phenomena (such as a core meltdown in a nuclear reactor). In such cases, probability must be considered as a mental construct to assist us in expressing a degree of belief, and the elements of the sample space are considered to correspond to hypotheses or propositions, i.e., statements that are either true or false; the sample space is often called the hypothesis space. This mental construct provides the premises of the so-called *subjective* or *Bayesian interpretation* of probability. In this interpretation, the probability associated with a cause or hypothesis \mathcal{A} is interpreted as a measure of degree of belief, namely:

$$P(\mathcal{A}) \equiv \text{a priori measure of the rational degree of belief} \\ \text{that } \mathcal{A} \text{ is the correct cause or hypothesis.}$$

The sample space \mathcal{S} must be constructed so that the elementary hypotheses are mutually exclusive, i.e., only one of them is true. A subset consisting of more than one hypothesis is true if any of the hypotheses in the subset is true. This means that the union of sets corresponds to the Boolean OR operation, while the intersection of sets corresponds to the Boolean AND operation. One of the hypotheses must necessarily be true, implying $P(\mathcal{S}) = 1$.

Since the statement “a measurement will yield a given outcome for a certain fraction of the time” can be regarded as a hypothesis, it follows that the framework of subjective probability includes the relative frequency interpretation. Furthermore, subjective probability can be associated with, for example, the value of an unknown constant; this association reflects one’s confidence that the value of the respective probability is contained within a certain fixed interval. This is in contrast with the frequency interpretation of probability, where the “probability for an unknown constant” is not meaningful, since it would be either zero or one, but one would not know which. For example, the mass of a physical quantity (e.g., neutron) may not be exactly known, but there is considerable evidence, in practice, that it lays between some upper and

lower limits of a given interval. In the frequency interpretation, the statement “the probability that the mass of the neutron lies within a given interval” is meaningless. By contrast, though, a subjective probability of 90% that the neutron mass is contained within the given interval is a meaningful reflection of one’s state of knowledge.

The use of subjective probability is closely related to Bayes’ theorem: in Bayesian statistics, the subset \mathcal{E}_2 appearing in the definition of conditional probability is interpreted as the hypothesis that “a certain theory is true,” while the subset \mathcal{E}_1 designates the hypothesis that “an experiment will yield a particular result (i.e., data).” In this interpretation, Bayes’ theorem takes on the form

$$P(\text{theory}|\text{data}) \propto P(\text{data}|\text{theory}) \cdot P(\text{theory}).$$

In the above expression of proportionality, $P(\text{theory})$ represents the prior probability that the theory is true, while the likelihood $P(\text{data}|\text{theory})$ expresses the probability of observing the data that were actually obtained under the assumption that the theory is true. The posterior probability, that the theory is correct after seeing the result of the experiment, is given by $P(\text{theory}|\text{data})$. Note that, the prior probability for the data, $P(\text{data})$, does not appear explicitly, so the above relation expresses a proportionality rather than an equality. Furthermore, Bayesian statistics provides no fundamental rule for assigning the prior probability to a theory. However, once a prior probability has been assigned, Bayesian statistics indicates how one’s degree of belief should change after obtaining additional information (e.g., experimental data).

7.2 Multivariate Probability Distributions

Consider that \mathcal{S} is a sample space in k -dimensions. As has been discussed in the previous section, if each random variable X_i ($i = 1, 2, \dots, k$) is a real-valued function defined on a domain \mathcal{N}_i (representing the i th dimension of \mathcal{S}), then (X_1, \dots, X_k) is a multivariate random variable or random vector. Furthermore, consider that each domain \mathcal{N}_i ($i = 1, 2, \dots, k$) is a discrete set, either finite or denumerably infinite (\mathcal{N}_i is usually the set of nonnegative integers or a subset thereof). Then, a probability function, $p(x_1, \dots, x_k)$, of the discrete random vector (X_1, \dots, X_k) is defined by requiring $p(x_1, \dots, x_k)$ to satisfy, for each value x_i taken on by X_i ($i = 1, 2, \dots, k$), the following properties:

1. $p(x_1, x_2, \dots, x_k) = P\{X_1 = x_1, X_2 = x_2, \dots, X_k = x_k\}$ and
2. $P\{\mathcal{A}\} = \sum_{(x_1, \dots, x_k) \in \mathcal{A}} p(x_1, \dots, x_k)$

for any subset \mathcal{A} of \mathcal{N} , where \mathcal{N} is the k -dimensional set whose i th component is \mathcal{N}_i ($i = 1, 2, \dots, k$) with $P\{\mathcal{N}\} = 1$.

Consider that \mathcal{A} is the set of all random vectors (X_1, \dots, X_k) such that $X_i \leq x_i$ ($i = 1, 2, \dots, k$). Then

$$P\{\mathcal{A}\} = P\{X_1 \leq x_1, X_2 \leq x_2, \dots, X_k \leq x_k\}$$

is called the cumulative distribution function (CDF) of (X_1, \dots, X_k) . The usual notation for the CDF of (X_1, \dots, X_k) is $F(x_1, \dots, x_k)$. Note that, the CDF is not a random variable; rather, it is a real numerical-valued function whose arguments represent compound events.

To define the probability density function (PDF) of a continuous random vector (X_1, \dots, X_k) , consider that (X_1, \dots, X_k) is a random vector whose i th component, X_i , is defined on the real line $(-\infty, \infty)$ or on a subset thereof. Suppose $p(x_1, \dots, x_k) > 0$ is a function such that for all $x_i \in [a_i, b_i]$ ($i = 1, 2, \dots, k$), the following properties hold:

1. $P\{a_1 < X_1 < b_1, \dots, a_k < X_k < b_k\} = \int_{a_k}^{b_k} \dots \int_{a_1}^{b_1} p(x_1, \dots, x_k) dx_1 \dots dx_k$ and if \mathcal{A} is any subset of k -dimensional intervals,
2. $P\{\mathcal{A}\} = \int_{(x_1, \dots, x_k) \in \mathcal{A}} \dots \int p(x_1, x_2, \dots, x_k) dx_1 dx_2 \dots dx_k$ then $p(x_1, \dots, x_k)$ is said to be a joint PDF of the continuous random vector (X_1, \dots, X_k) , if it is normalized to unity over its domain.

Consider that the set (x_1, \dots, x_k) represents a collection of random variables with a multivariate joint probability density $p(x_1, \dots, x_k) > 0$; then, the marginal probability density of x_i , denoted by $p_i(x_i)$, is defined as

$$p_i(x_i) = \int_{-\infty}^{\infty} dx_1 \dots \int_{-\infty}^{\infty} dx_{i-1} \int_{-\infty}^{\infty} dx_{i+1} \dots \int_{-\infty}^{\infty} p(x_1, x_2, \dots, x_k) dx_k.$$

Also, the conditional PDF $p(x_1, \dots, x_{i-1}, x_{i+1}, \dots, x_k | x_i)$ can be defined whenever $p_i(x_i) \neq 0$ by means of the expression

$$p(x_1, \dots, x_{i-1}, x_{i+1}, \dots, x_k | x_i) = p(x_1, \dots, x_k) / p_i(x_i).$$

The meaning of marginal and conditional probability can be illustrated by considering bivariate distributions. Thus, if (X, Y) is a discrete random vector whose joint probability function is $p(x, y)$, where X is defined over \mathcal{N}_1 and Y is defined over \mathcal{N}_2 , then the marginal probability distribution function (PDF) of X , $p_x(x)$, is defined as

$$p_x(x) = \sum_{y \in \mathcal{N}_2} p(x, y).$$

On the other hand, if (X, Y) is a continuous random vector whose joint PDF is $p(x, y)$, where X and Y are each defined over the domain $(-\infty, \infty)$, then the marginal PDF of X , $p_x(x)$, is defined by the integral

$$p_x(x) = \int_{-\infty}^{\infty} p(x, y) dy.$$

Consider that (X, Y) is a random vector (continuous or discrete) whose joint PDF is $p(x, y)$. The conditional PDF of y given $X = x$ (fixed), denoted by $h(y|x)$, is defined as

$$h(y|x) = \frac{p(x, y)}{p_x(x)},$$

where the domain of y may depend on x , and where $p_x(x)$ is the marginal PDF of X , with $p_x(x) > 0$.

Similarly, the conditional PDF, say $g(x|y)$, for x given y is

$$g(x|y) = \frac{p(x, y)}{p_y(y)} = \frac{p(x, y)}{\int p(x', y) dx'}.$$

Combining the last two definitions gives the following relationship between $g(x|y)$ and $h(y|x)$,

$$g(x|y) = \frac{h(y|x)p_x(x)}{p_y(y)},$$

which expresses *Bayes' theorem* for the case of continuous variables.

Consider that (X, Y) is a random vector whose joint PDF is $p(x, y)$. The random variables X and Y are called stochastically independent if and only if

$$p(x, y) = p_x(x)p_y(y)$$

over the entire domain of (X, Y) (i.e., for all x and y). From this definition and from Bayes' theorem, it follows that X and Y are independent iff $g(x|y) = p_x(x)$ over the entire domain of (X, Y) . Of course, this definition of stochastic independence can be generalized to random vectors.

For certain cases, the PDF of a function of random variables can be found by using integral transforms. In particular, Fourier transforms are well-suited for dealing with the PDF of sums of random variables, while Mellin transforms are well suited for dealing with PDF of products of random variables. For example, the PDF $f(z)$, of the sum $z = x + y$, where x and y are two independent random variables distributed according to $g(x)$ and $h(y)$, respectively, is obtained as

$$f(z) = \int_{-\infty}^{\infty} g(x)h(z-x) dx = \int_{-\infty}^{\infty} g(z-y)h(y) dy.$$

The function f in the above equation is actually the Fourier convolution of g and h , and is often written in the form $f = g \otimes h$.

On the other hand, the PDF, $f(z)$, of the product $z = xy$, where x and y are two random variables distributed according to $g(x)$ and $h(y)$, is given by

$$f(z) = \int_{-\infty}^{\infty} g(x)h(z/x) \frac{dx}{|x|} = \int_{-\infty}^{\infty} g(z/y)h(y) \frac{dy}{|y|},$$

where the second equivalent expression is obtained by reversing the order of integration. The function f defined above is actually the Mellin convolution of g and h , often written (also) in the convolution form $f = g \otimes h$. Taking the Mellin transform of the Mellin convolution of g and h , or taking the Fourier transform of the Fourier convolution of g and h , respectively, converts the respective convolution equations $f = g \otimes h$ into the respective products $\tilde{f} = \tilde{g} \cdot \tilde{h}$ of the transformed density functions. The actual PDF is subsequently obtained by finding the inverse transform of the respective \tilde{f} 's.

Consider that $\mathbf{x} = (x_1, \dots, x_n)$ and $\mathbf{y} = (y_1, \dots, y_n)$ are two distinct vector random variables that describe the same events. Consider, further, that the respective multivariate probability densities $p_x(\mathbf{x})$ and $p_y(\mathbf{y})$ are such that the mappings $y_i = y_i(x_1, \dots, x_n)$, ($i = 1, 2, \dots, n$), are continuous, one-to-one, and all partial derivatives $\partial y_i / \partial x_j$, ($i, j = 1, \dots, n$), exist. Then, the transformation from one PDF to the other is given by the relationship

$$p_y(\mathbf{y})|d\mathbf{y}| = p_x(\mathbf{x})|d\mathbf{x}| \quad \text{or} \quad p_x(\mathbf{x}) = |J|p_y(\mathbf{y}),$$

where $|J| \equiv \det |\partial y_i / \partial x_j|$, ($i, j = 1, \dots, n$), is the Jacobian of the respective transformation.

As an example of applying the above transformation, consider the linear transformation $\mathbf{y} = g(\mathbf{x}) = \mathbf{A}\mathbf{x} + \mathbf{b}$, where $\mathbf{A} \in \mathbb{R}^{n \times n}$ is non-singular, $\mathbf{b} \in \mathbb{R}^n$, and $\mathbf{x} \in \mathbb{R}^n$ is a normal random vector, $\mathbf{x} \sim N(\mu_x, \Sigma_x)$, i.e.,

$$p_x(\mathbf{x}) = \frac{1}{(2\pi)^{\frac{n}{2}} |\Sigma_x|^{\frac{1}{2}}} \exp[-(\mathbf{x} - \mu_x)^T \Sigma_x^{-1} (\mathbf{x} - \mu_x)].$$

It then follows that $|J| = |\mathbf{A}|$ and

$$\begin{aligned} p_y(\mathbf{y}) &= \frac{1}{|\mathbf{A}|} p_x(\mathbf{A}^{-1}(\mathbf{y} - \mathbf{b})) \\ &= \frac{1}{(2\pi)^{\frac{n}{2}} |\Sigma_x|^{\frac{1}{2}} |\mathbf{A}|} \exp[-[\mathbf{A}^{-1}(\mathbf{y} - \mathbf{b}) - \mu_x]^T \Sigma_x^{-1} [\mathbf{A}^{-1}(\mathbf{y} - \mathbf{b}) - \mu_x]]. \end{aligned}$$

The exponent above can be re-written as follows:

$$\begin{aligned} &[\mathbf{A}^{-1}(\mathbf{y} - \mathbf{b}) - \mu_x]^T \Sigma_x^{-1} [\mathbf{A}^{-1}(\mathbf{y} - \mathbf{b}) - \mu_x] \\ &= [\mathbf{A}^{-1}(\mathbf{y} - (\mathbf{A}\mu_x + \mathbf{b}))]^T \Sigma_x^{-1} [\mathbf{A}^{-1}(\mathbf{y} - (\mathbf{A}\mu_x + \mathbf{b}))] \\ &= (\mathbf{y} - \mu_y)^T \Sigma_y^{-1} (\mathbf{y} - \mu_y), \end{aligned}$$

where $\mu_y = \mathbf{A}\mu_x + \mathbf{b}$ and $\Sigma_y = \mathbf{A}\Sigma_x\mathbf{A}^T$. Since $|\Sigma_y| = |\mathbf{A}\Sigma_x\mathbf{A}^T| = |\mathbf{A}|^2 |\Sigma_x|$, it follows that $\mathbf{y} \sim N(\mathbf{A}\mu_x + \mathbf{b}, \mathbf{A}\Sigma_x\mathbf{A}^T)$, i.e.,

$$h(\mathbf{y}) = \frac{1}{(2\pi)^{\frac{n}{2}} |\Sigma_y|^{\frac{1}{2}}} \exp[-(\mathbf{y} - \mu_y)^T \Sigma_y^{-1} (\mathbf{y} - \mu_y)].$$

7.3 Expectations and Moments

Probabilities cannot be measured directly; they can be inferred from the results of observations or they can be postulated and (partially) verified through accumulated experience. In practice, though, certain random vectors tend to be more probable, so that most probability functions of practical interest tend to be localized. Therefore, the essential features regarding probability distributions of practical interest are measures of location and of dispersion. These measures are provided by the expectation and moments of the respective probability function. If the probability function is known, then these moments can be calculated directly through a process called statistical deduction. Otherwise, the respective moments must be estimated from experiments through a process called statistical inference.

Consider that $\mathbf{x} = (x_1, \dots, x_n)$ is a collection of random variables that represents the events in a space \mathcal{E} , and consider that S_x represents the n -dimensional space formed by all possible values of \mathbf{x} . The space S_x may encompass the entire range of real numbers (i.e., $-\infty < x_i < \infty$, $i = 1, \dots, n$) or a subset thereof. Furthermore, consider a real-valued function, $g(\mathbf{x})$, and a probability density, $p(\mathbf{x})$, both defined on S_x . Then, the expectation of $g(\mathbf{x})$, denoted as $E(g(\mathbf{x}))$, is defined as:

$$E(g(\mathbf{x})) \equiv \int_{S_x} g(\mathbf{x}) p(\mathbf{x}) d\mathbf{x}$$

if the condition of absolute convergence, $E(|g|) = \int_{\mathcal{S}_x} |g(\mathbf{x})| p(\mathbf{x}) d\mathbf{x} < \infty$ is satisfied. When x is discrete with the domain \mathcal{N} , the expectation of g is defined as

$$E(g(\mathbf{x})) = \sum_{\mathbf{x} \in \mathcal{N}} g(\mathbf{x}) p(\mathbf{x}), \quad \text{if } E(|g(\mathbf{x})|) < \infty.$$

In particular, the *moment of order k* about a point c is defined for a univariate probability function as

$$E((x - c)^k) \equiv \int_{\mathcal{S}_x} (x - c)^k p(x) dx,$$

where \mathcal{S}_x denotes the set of values of x for which $p(x)$ is defined, and the integral above is absolutely convergent. The zeroth-order moment is obtained by setting $k = 0$ in the above definition.

For a multivariate probability function, given a collection of n random-variables (x_1, \dots, x_n) and a set of constants (c_1, \dots, c_n) , the mixed moment of order k is defined as

$$E((x_1 - c_1)^{k_1}, \dots, (x_n - c_n)^{k_n}) \equiv \int_{\mathcal{S}_{x_1}} dx_1 \dots \int_{\mathcal{S}_{x_n}} dx_n (x_1 - c_1)^{k_1} \dots (x_n - c_n)^{k_n} p(x_1 \dots x_n).$$

The *zeroth-order moment* is obtained by setting $k_1 = \dots = k_n = 0$ (for multivariate probability) in the above definition. Since probability functions are required to be normalized, the zeroth moment is always equal to unity.

In particular, when $c = 0$ (for univariate probability) or when $c_1 = \dots = c_n = 0$ (for multivariate probability), the quantities defined as $\nu_k \equiv E(x^k)$, and, respectively, $\nu_{k_1 \dots k_n} \equiv E(x_1^{k_1} \dots x_n^{k_n})$ are called the *moments about the origin* (often also called *raw* or *crude moments*). If $\sum_{i=1, n} k_i = k$, then the moments of the form $\nu_{k_1 \dots k_n}$ are called the mixed raw moments of order k . For $k = 1$, these moments are called *mean values*, and are denoted as $m_o = \nu_1 = E(x)$ for univariate probability, and $m_{oi} \equiv \nu_{o \dots 1 \dots o} \equiv E(x_i)$, ($i = 1, \dots, n$), for multivariate probability, respectively. Note that, a “0” in the j th subscript position signifies that $k_j = 0$ for the particular raw moment in question, while a “1” in the i th subscript position indicates that $k_i = 1$ for the respective moment.

The moments about the mean or central moments are defined as $\mu_k \equiv E((x - m_o)^k)$, for univariate probability, and $\mu_{k_1 \dots k_n} \equiv E((x_1 - m_{o1})^{k_1} \dots (x_n - m_{on})^{k_n})$, for multivariate probability.

Furthermore, if $\sum_{i=1, n} k_i = k$, then the above moments are called the *mixed central moments* of order k . Note that the central moments vanish whenever one particular $k_i = 1$ and all other $k_j = 0$, i.e., $\mu_{o \dots 1 \dots o} = 0$. Note also that all even-power central moments of univariate probability functions (i.e., μ_k , for $k = \text{even}$) are nonnegative.

The central moments for $k = 2$ play very important roles in statistical theory and are therefore assigned special names. Thus, for univariate probability, the second moment, $\mu_2 \equiv E((x - m_o)^2)$, is called *variance* that is usually denoted as $\text{var}(x)$ or σ^2 . The positive square root of the variance is called the *standard deviation*, denoted as σ , and defined as

$$\sigma \equiv [\text{var}(x)]^{1/2} \equiv \mu_2^{1/2} \equiv [E((x - m_o)^2)]^{1/2}.$$

The terminology and notation used for univariate probability are also used for multivariate probability. In particular, the standard deviation of the i th component is defined as:

$$\mu_{o \dots 2 \dots o} \equiv \text{var}(x_i) \equiv \sigma_i^2 \equiv E((x_i - m_o)^2).$$

To simplify the notation, the subscripts accompanying the moments ν and μ for multivariate probability functions are usually dropped and alternative notation is used. For example, μ_{ii} is often employed to denote $\text{var}(x_i)$, and μ_{ij} signifies $E((x_i - m_{oi})(x_j - m_{oj}))$, ($i, j = 1, \dots, n$).

The raw and central moments are related to each other through the important relationship

$$\mu_k = \sum_{i=0}^k C_i^k (-1)^i \nu_{k-i} \nu_1^i \quad (k \geq 1),$$

where $C_i^k = k! / [(k-i)!i!]$ is the binomial coefficient. This formula is very useful for estimating central moments from sampling data, because, in practice, it is more convenient to estimate the raw moments directly from the data, and then derive the central moments by using the above equation.

7.4 Variance, Standard Deviation, Covariance, and Correlation

Since measurements never yield true values, it is necessary to introduce surrogate parameters to measure location and dispersion for the observed results. Practice indicates that location is best described by the mean value, while dispersion of observed results appears to be best described by the variance or standard deviation. In particular, the mean value can be interpreted as a locator of the center of gravity, whereas the variance is analogous to the moment of inertia (which linearly relates applied torque to induced angular acceleration in mechanics). Also very useful for the study of errors is the *Minimum Variance Theorem*, which states that: if c is a real constant and x is a random variable, then $\text{var}(x) \leq E((x - c)^2)$.

Henceforth, when we speak of *errors* in physical observations, they are to be interpreted as standard deviations. In short, errors are simply the measures of dispersion in the underlying probability functions that govern observational processes. The fractional relative error or coefficient of variation, f_x , is defined by $f_x = \sigma / |E(x)|$, when $E(x) \neq 0$. The reciprocal, $(1/f_x)$, is commonly called (particularly in engineering applications) the signal-to-noise ratio. Finally, the term percent error refers to the quantity $100 f_x$.

When the probability function is known and the respective mean and variance (or standard deviation) exist, they can be computed directly from their definitions. However, when the actual distribution is not known, it is considerably more difficult to interpret the knowledge of the mean and standard deviation in terms of confidence that they are representative of the distribution of measurements. The difficulty can be illustrated by considering a confidence indicator associated with the probability function p , $C_p(k\sigma)$, defined by means of the integral

$$C_p(k\sigma) \equiv \int_{m_o - k\sigma}^{m_o + k\sigma} p(x) dx,$$

where σ is the standard deviation and $k \geq 1$ is an integer. Since the probability density integrated over the entire underlying domain is normalized to unity, it follows that $C_p(k\sigma) < 1$ for all k . However, $C_p(k\sigma) \approx 1$ whenever $k \gg 1$. Thus, $C_p(k\sigma)$ can vary substantially in magnitude for different types of probability functions p , even for fixed values of σ and k . This result indicates that although the variance or standard deviation are useful parameters for measuring dispersion (error), knowledge of them alone does not provide an unambiguous measure of confidence

in a result, unless the probability family to which the distribution in question belongs is a priori known. Consequently, when an experiment involves several observational processes, each governed by a distinct law of probability, it is difficult to interpret overall errors (which consist of several components) in terms of confidence. However, the consequences are often mitigated in practice by a very important theorem of statistics, called the *central limit theorem*, which will be presented in the sequel.

For multivariate probability, the second-order central moments comprise not only the variances $\mu_{ii} = \text{var}(x_i) = E((x_i - m_{oi})^2)$, ($i = 1, \dots, n$), but also the moments $\mu_{ij} = E((x_i - m_{oi})(x_j - m_{oj}))$, ($i, j = 1, \dots, n$). These moments are called *covariances*, and the notation $\text{cov}(x_i, x_j) \equiv \mu_{ij}$ is often used. The collection of all second-order moments of a multivariate probability function involving n random variables forms an $n \times n$ matrix, denoted as \mathbf{V}_x , and called the variance-covariance matrix, or, simply, the covariance matrix. Since $\mu_{ij} = \mu_{ji}$ for all i and j , covariance matrices are symmetric.

Since covariance matrices are symmetric, an $n \times n$ matrix contains no more than $n + [n(n - 1/2)]$ distinct elements, comprising the off-diagonal covariances and the n variances along the diagonal. Often, therefore, only the diagonal and upper or lower triangular part of covariance and correlation matrices are listed in the literature. A formula often used in practical computations of covariances is obtained by rewriting the respective definition in the form

$$\text{cov}(x_i, x_j) = E(x_i x_j) - m_{oi} m_{oj}.$$

Note that, if any two random variables, x_i and x_j , in a collection of n random variables are independent, then $\text{cov}(x_i, x_j) = 0$. The converse of this statement is false, meaning that $\text{cov}(x_i, x_j) = 0$ does not necessarily imply that x_i and x_j are independent.

A very useful tool for practical applications is the so-called *scaling and translation theorem*, which states that if x_i and x_j are any two members of a collection of n random variables, then the following relations hold for the random variables $y_i = a_i x_i + b_i$ and $y_j = a_j x_j + b_j$:

$$\begin{aligned} E(y_i) &= a_i E(x_i) + b_i, & \text{var}(y_i) &= a_i^2 \text{var}(x_i), & (i = 1, \dots, n), \\ \text{cov}(y_i, y_j) &= a_i a_j \text{cov}(x_i, x_j), & (i, j = 1, \dots, n, i \neq j). \end{aligned}$$

The constants a_i and a_j are called *scaling* parameters, while the constants b_i and b_j are called *translation* parameters. The above relationships show that mean values are affected by both scaling and translation, while the variances and covariances are only affected by scaling. In particular, the above relationships can be used to establish the following theorem regarding the relationship between ordinary random variables x_i and their standard random variable counterparts $u_i = (x_i - m_{oi})/\sigma_i$, ($i = 1, \dots, n$): "the covariance matrix for the standard random variables $u_i = (x_i - m_{oi})/\sigma_i$ is the same as the correlation matrix for the random variables x_i ." In matrix form, if \mathbf{x} and \mathbf{y} are two random vectors of size n , and \mathbf{A} and \mathbf{B} are two $n \times n$ matrices, with $E(\mathbf{x}) = \boldsymbol{\mu}_x$ and $E(\mathbf{y}) = \boldsymbol{\mu}_y$, then

$$\begin{aligned} \text{Cov}(\mathbf{Ax}, \mathbf{By}) &= E[(\mathbf{Ax} - \mathbf{A}\boldsymbol{\mu}_x)(\mathbf{By} - \mathbf{B}\boldsymbol{\mu}_y)^T] = E[\mathbf{A}(\mathbf{x} - \boldsymbol{\mu}_x)(\mathbf{y} - \boldsymbol{\mu}_y)^T \mathbf{B}^T] \\ &= \mathbf{A}E[(\mathbf{x} - \boldsymbol{\mu}_x)(\mathbf{y} - \boldsymbol{\mu}_y)^T] \mathbf{B}^T = \mathbf{A} \text{Cov}(\mathbf{x}, \mathbf{y}) \mathbf{B}^T. \end{aligned}$$

When $\mu_{ii} > 0$, ($i = 1, \dots, n$), it is often convenient to use the quantities ρ_{ij} defined by the relationship

$$\rho_{ij} \equiv \mu_{ij} / (\mu_{ii} \mu_{jj})^{1/2}, \quad (i, j = 1, \dots, n),$$

and called *correlation coefficients* or, simply, *correlations*. The matrix obtained using the correlations, ρ_{ij} , is called the correlation matrix, and will be denoted as C_x .

Using the Cauchy–Schwartz inequality, it can be shown that the elements of V_x always satisfy the relationship

$$|\mu_{ij}| \leq (\mu_{ii}\mu_{jj})^{1/2} \quad (i, j = 1, n),$$

while the elements ρ_{ij} of the correlation matrix C_x satisfy the relationship

$$-1 \leq \rho_{ij} \leq 1.$$

In the context of covariance matrices, the Cauchy–Schwartz inequality provides an indicator of data consistency that is very useful to verify practical procedures for processing experimental information. Occasionally, practical procedures may generate covariance matrices with negative eigenvalues (thus violating the condition of positive-definitiveness), or with coefficients that would violate the Cauchy–Schwartz inequality; such matrices would, of course, be unsuitable for representing physical uncertainty. Although the mathematical definition of the variance only indicates that it must be nonnegative, the variance for physical quantities should in practice be positive, because it provides a mathematical basis for the representation of physical uncertainty. Since zero variance means no error, probability functions for which some of the random variables have zero variance are not realistic choices for the representation of physical phenomena, since such probability functions would indicate that some parameters were without error, which is never the case in practice. Furthermore, a situation where $\mu_{ii} < 0$ would imply an imaginary standard deviation (since $\sigma_i = \mu_{ii}^{1/2}$), which is clearly unrealistic. The reason for mentioning these points here is because, in practice, the elements of covariance matrices are very rarely obtained from direct evaluation of expectations, but are obtained by a variety of other methods, many of them ad hoc. Practical considerations also lead to the requirement that $|\rho_{ij}| < 1$, for $i \neq j$, but a presentation of the arguments underlying this requirement is beyond the purpose of this book. These and other constraints on covariance and correlation matrices lead to the conclusion that matrices which properly represent physical uncertainties are positive definite.

Denoting by $\Sigma \triangleq \text{diag}(\sigma_i)$, the diagonal matrix having the standard deviations σ_i on the main diagonal, it follows that the covariance matrix V_x and the correlation matrix C_x are related through the relation

$$C_x = \Sigma^{-1}V_x\Sigma^{-1}, \quad C_x = \text{Cor}(z), \quad \text{with } z = \Sigma^{-1}(x - \langle x \rangle).$$

The *conditional expectation* of x_1 given x_2 is defined as

$$E[x_1|x_2 = a] = \int_{-\infty}^{\infty} x_1 f(x_1, x_2 = a) dx_1.$$

As x_2 takes on different values in its domain, this conditional expectation will also take different values. Thus, the conditional expectation $E(x_1|x_2)$ is a function of the conditioning random variable, and hence is itself a random variable. Sometimes, the conditional expectation operator is distinguished by using the conditioning random variable as the subscript, thus

denoting $E(x_1|x_2)$ as $E_{x_2}(x_1)$. Note also that

$$\begin{aligned} E\{E_{x_2}(x_1)\} &= E\{E(x_1|x_2)\} = \int_{-\infty}^{\infty} \left[\int_{-\infty}^{\infty} x_1 f(x_1|x_2) dx_1 \right] f_2(x_2) dx_2 \\ &= \int_{-\infty}^{\infty} x_1 \left[\int_{-\infty}^{\infty} f(x_1|x_2) f_2(x_2) dx_2 \right] dx_1 \\ &= \int_{-\infty}^{\infty} x_1 f_1(x_1) dx_1 = E(x_1). \end{aligned}$$

Thus, the random variable $E_{x_2}(x_1)$ has the same expectation as x_1 ; the above relation is customarily called the *law of iterated expectations*. A useful particular result is the following: if $\mathbf{x} \in \mathbb{R}^n$ and $\mathbf{z} \in \mathbb{R}^m$ are jointly normal random vectors, with mean $\mathbf{m} = \begin{pmatrix} m_x \\ m_z \end{pmatrix}$ and covariance matrix $\Sigma = \begin{bmatrix} \Sigma_x & \Sigma_{xz} \\ \Sigma_{zx} & \Sigma_z \end{bmatrix}$, then the *conditional density* of $f(\mathbf{x}|\mathbf{z})$ of \mathbf{x} given \mathbf{z} is also normal with the *conditional mean* $\mu = E[\mathbf{x}|\mathbf{z}] = m_x + \Sigma_{xz}\Sigma_z^{-1}[\mathbf{z} - m_z]$ and the *conditional covariance* $\mathbf{A} = \text{Cov}(\mathbf{x}|\mathbf{z}) = \Sigma_x - \Sigma_{xz}\Sigma_z^{-1}\Sigma_{zx}$.

The determinant, $\det(\mathbf{V}_x)$, of the variance matrix is often referred to as the generalized variance, since it degenerates to a simple variance for univariate distributions. The probability distribution is called nondegenerate when $\det(\mathbf{V}_x) \neq 0$; when $\det(\mathbf{V}_x) = 0$, however, the distribution is called degenerate. Degeneracy is an indication that the information content of the set \mathbf{x} of random variable is less than rank n , or that the probability function is confined to a hyperspace of dimension lower than n . The determinant of a covariance matrix vanishes if there exist (one or more) linear relationships among the random variables of the set \mathbf{x} .

Since \mathbf{V}_x must be positive definite in order to provide a meaningful representation of uncertainty, it follows that $\det(\mathbf{V}_x) > 0$. Due to the properties of \mathbf{V}_x mentioned above, it also follows that

$$\det(\mathbf{V}_x) \leq \prod_{i=1,n} \text{var}(x_i) = \prod_{i=1,n} \sigma_i^2.$$

The equality in the above relation is reached only when \mathbf{V}_x is diagonal, i.e., when $\text{cov}(x_i, x_j) = 0$, ($i, j = 1, n, i \neq j$); in this case, $\det(\mathbf{V}_x)$ attains its maximum value, equal to the product of the respective variances. The determinant $\det(\mathbf{V}_x)$ is related to the determinant of the correlation matrix, $\det(\mathbf{C}_x)$, by the relationship

$$\det(\mathbf{V}_x) = \det(\mathbf{C}_x) \prod_{i=1,n} \sigma_i^2.$$

From above relations, it follows that $\det(\mathbf{C}_x) \leq 1$. It further follows that $\det(\mathbf{C}_x)$ attains its maximum value of unity only when $\text{cov}(x_i, x_j) = 0$, ($i, j = 1, n, i \neq j$). In practice, $\det(\mathbf{C}_x)$ is used as a measure of degeneracy of the multivariate probability function. In particular, the quantity $[\det(\mathbf{C}_x)]^{1/2}$ is called the scatter coefficient for the probability function. Note that $\det(\mathbf{C}_x) = 0$ when $\rho_{ij} = \rho_{ji} = 1$ for at least one pair (x_i, x_j) , with $i \neq j$.

Two random variables, x_i and x_j , with $i \neq j$, are called *fully-correlated* if $\text{cor}(x_i, x_j) = 1$; this situation arises if and only if the corresponding standard random variables u_i and u_j are identical, i.e., $u_i = u_j$. On the other hand, if $\text{cor}(x_i, x_j) = -1$, then x_i and x_j are *fully anti-correlated*, which can happen iff $u_i = -u_j$. Therefore, the statistical properties of fully correlated or fully anti-correlated random variables are identical, so that only one of them needs

to be considered, a fact reflected by the practice of referring to such random variables as being redundant.

In addition to covariance matrices, V_x , and their corresponding correlation matrices, C_x , a third matrix, called the *relative covariance matrix* or *fractional error matrix*, can also be defined when the elements of the covariance matrix satisfy the condition that $m_{oi} \neq 0$, ($i = 1, \dots, n$). This matrix is usually denoted as R_x and its elements $(R_x)_{ij} = \eta_{ij}$ are defined as $\eta_{ij} = \mu_{ij}/(m_{oi}m_{oj})$.

Moments of first and second order (i.e., means and covariance matrices) provide information regarding only the location and dispersion of probability distributions. Additional information on the nature of probability distributions is carried by the higher-order moments, although moments beyond fourth-order are seldom examined in practice. The nature of such information can be intuitively understood by considering the third- and fourth-order moments of univariate probability functions. For this purpose, it is the easiest to consider the respective reduced central moments, α_k , defined in terms of central moments and the standard deviation by the relationship $\alpha_k \equiv \mu_k/\sigma^k$. The reduced central moment α_3 is called the *skewness* of the probability distribution, because it measures quantitatively the departure of the probability distribution from symmetry (a symmetric distribution is characterized by the value $\alpha_3 = 0$). Thus, if $\alpha_3 < 0$, the distribution is skewed toward the left (i.e., it favors lower values of x relative to the mean), while $\alpha_3 > 0$ indicates a distribution skewed toward the right (i.e., it favors higher values of x relative to the mean). The reduced central moment α_4 measures the degree of sharpness in the peaking of a probability distribution and it is called *kurtosis*. Kurtosis is always nonnegative. The standard for comparison of kurtosis is the normal distribution (Gaussian) for which $\alpha_4 = 3$. Distributions with $\alpha_4 < 3$ are called *platykurtic* distributions. Those with $\alpha_4 = 3$ are called *mesokurtic* distributions. Finally, distributions with $\alpha_4 > 3$ are called *leptokurtic* distributions.

Very often in practice, the details of the distribution are unknown and only the mean and standard deviations can be estimated from the limited amount of information available. Even under such circumstances, it is still possible to make statements regarding confidence by relying on *Chebyshev's theorem*, which can be stated as follows. Consider that m_o and $\sigma > 0$ denote the mean value and standard deviation, respectively, of an otherwise unknown multivariate probability density p involving the random variable x . Furthermore, consider that P represents cumulative probability, C_p represents confidence, and $k \geq 1$ is a real constant (not necessarily an integer). Then, Chebyshev's theorem states that the following relationship holds:

$$C_p(k\sigma) = P(|x - m_o| \leq k\sigma) \geq 1 - (1/k^2).$$

Chebyshev's theorem is a weak law of statistics in that it provides an upper bound on the probability of a particular deviation ε . The actual probability of such a deviation (if the probability function were known in detail so that it could be precisely calculated) would always be smaller (implying greater confidence) than Chebyshev's limit. This important point is illustrated in [► Table 1](#), which presents probabilities for observing particular deviations, ε , from the mean when sampling from a normal distribution, and the corresponding bounds predicted by Chebyshev's theorem.

[► Table 1](#) clearly underscores the fact that normally distributed random variables are much more sharply localized with respect to the mean than indicated by Chebyshev's theorem.

■ **Table 1**
Probability of occurrence

Deviation σ	Normal distribution	Chebyshev's limit
$> \sigma$	< 0.3173	< 1.0
$> 2\sigma$	< 0.0455	< 0.25
$> 3\sigma$	< 0.00270	< 0.1111
$> 4\sigma$	< 0.0000634	< 0.0625
$> 5\sigma$	$< 5.73 \cdot 10^{-7}$	< 0.04
$> 6\sigma$	$< 2.0 \cdot 10^{-9}$	< 0.02778

The characteristic function $\phi_x(k)$ for a random variable x with PDF $p(x)$ is defined as the expectation value of e^{ikx} , namely

$$\phi_x(k) \equiv E(e^{ikx}) = \int_{-\infty}^{\infty} e^{ikx} p(x) dx.$$

The above definition is essentially the Fourier transform of the PDF; there is a one-to-one correspondence between the PDF and the characteristic function, so that knowledge of one is equivalent to knowledge of the other. The PDF, $p(x)$, is obtained from the inverse Fourier transform of the characteristic function $\phi_x(k)$, namely

$$p(x) = \frac{1}{2\pi} \int_{-\infty}^{\infty} \phi_x(k) e^{-ikx} dk.$$

The moments of $p(x)$ can be obtained by differentiating the characteristic function $\phi_x(k)$ m times and evaluating the resulting expression at $k = 0$; this yields the relation

$$\left\{ \frac{d^m}{dk^m} \phi_x(k) \right\}_{k=0} = \left\{ \frac{d^m}{dk^m} \int e^{ikx} p(x) dx \right\}_{k=0} = i^m \int x^m p(x) dx = i^m \nu_m,$$

where $\nu_m = E(x^m)$ is the m th raw moment (about the origin) of x . For easy reference, ► [Table 2](#) lists characteristic functions for some commonly used probability functions.

Related to the characteristic function is the *moment generating function* (MGF), usually denoted by $M_x(t)$, and defined as the expectation of e^{tx} , namely:

$$M_x(t) = E(e^{tx}) = \int_{-\infty}^{\infty} e^{tx} p(x) dx,$$

where x is a random variable and t is a real number, $t \in \mathbb{R}$. Occasionally, t may be restricted to an interval subspace of the real line, say, $t \in (a, b) \subset \mathbb{R}$, but the interval (a, b) must necessarily contain the value $t = 0$. For convenience, one occasionally refers to t as a transform variable. The k th-derivative of $M_x(t)$ with respect to t , denoting as $M_x^{(k)}(t)$ has the property that $M_x^{(k)}(0) = E(x^k) = \nu_k$. Thus, if the expression of the MGF, $M_x(t)$, is known for a probability distribution of x , then all the raw moments of the respective distribution can be calculated

Table 2
Characteristic functions

Distribution	PDF	$\phi(k)$
Binomial	$p(x) = \frac{n!}{x!(n-x)!} s^x (1-s)^{n-x}$	$[s(e^{ik} - 1) + 1]^n$
Poisson	$p(x) = \frac{v^x}{x!} e^{-v}$	$\exp[v(e^{ik} - 1)]$
Uniform	$p(x) = \begin{cases} \frac{1}{\beta - \alpha}, & \alpha \leq x \leq \beta, \\ 0, & \text{otherwise} \end{cases}$	$\frac{e^{i\beta k} - e^{i\alpha k}}{(\beta - \alpha) ik}$
Exponential	$p(x) = \frac{1}{\xi} e^{-x/\xi}$	$\frac{1}{1 - ik\xi}$
Gaussian	$p(x) = \frac{1}{\sqrt{2\pi\sigma^2}} \exp\left(-\frac{(x-v)^2}{2\sigma^2}\right)$	$\exp\left(ivk - \frac{1}{2}\sigma^2 k^2\right)$
Chi-square	$p(x) = \frac{1}{2^{n/2}\Gamma(n/2)} x^{n/2-1} e^{-z/2}$	$(1 - 2ik)^{-n/2}$
Cauchy	$f(x) = \frac{1}{\pi} \frac{1}{1+x^2}$	$e^{- k }$

by taking derivatives of the MGF with respect to t and evaluating them at $t = 0$. Note also the following four theorems, which deal with random-variable translation and scaling:

1. If the MGF, $M_x(t)$, of the PDF of a random variable x exists, and if c is a constant, then $M_{x+c}(t) = e^{ct} M_x(t)$.
2. If the conditions of the preceding theorem apply, and if $m_o = v_1$ is the mean value, then the MGF, $M_{x-m_o}(t)$, is the generator of the central moments of the underlying probability function.
3. If the MGF, $M_x(t)$, of the PDF of a random variable x exists, and if c is a constant, then $M_{cx}(t) = M_x(ct)$.
4. The MGF for the PDF of a random variable x is related to the MGF of the PDF for the standard random variable $u = (x - m_o)/\sigma$ by the formula $M_u(t) = \exp(-m_o t/\sigma) M_x(t/\sigma)$.

The development of MGFs for probability functions of several random variables (random vectors) is analogous to the development for the univariate case. Thus, consider that $\mathbf{x} = (x_1, x_2, \dots, x_n)$ denotes a random vector with n components, where each $x_i \in \mathbb{R}$, ($i = 1, \dots, n$). Furthermore, consider that S_x represents the corresponding space of all such random vectors \mathbf{x} , and that $p(\mathbf{x})$ denotes the associated probability density. Then the multivariate MGF is defined as

$$M_x(\mathbf{t}) = E\left(\exp\left(\sum_{i=1}^n x_i t_i\right)\right) = \int_{S_x} \exp\left(\sum_{i=1}^n x_i t_i\right) p(\mathbf{x}) d\mathbf{x},$$

where the vector (t_1, t_2, \dots, t_n) has components t_i defined symmetrically around the origin $(0, 0, \dots, 0)$, namely $-t_{oi} < t_i < t_{oi}$, with $t_{oi} > 0$, ($i = 1, \dots, n$). Note that, MGFs for discrete

multivariate distributions are defined similarly as above, except that the multiple integrals are replaced by corresponding multiple sums.

The raw moments of multivariate probability functions can be generated from the partial derivatives of $M_x(t)$ with respect to the parameters t_i , ($i = 1, \dots, n$), evaluated at $t = 0$. For example,

$$m_{oi} = v_i = E(x_i) = [\partial M_x(t)/\partial t_i]_{t=0} \quad (i = 1, \dots, n),$$

$$E(x_i x_j) = [\partial^2 M_x(t)/\partial t_i \partial t_j]_{t=0} \quad (i, j = 1, \dots, n),$$

and so on. In particular, the elements of the covariance matrix V_x , ($i, j = 1, \dots, n$), can be readily generated by using the above relations, in conjunction with the relation

$$\text{cov}(x_i, x_j) = E[(x_i - m_{oi})(x_j - m_{oj})] = \mu_{ij} = E(x_i x_j) - m_{oi} m_{oj},$$

and using the convention $\text{var}(x_i) = \text{cov}(x_i, x_i)$, ($i = 1, \dots, n$).

7.5 Commonly Encountered Probability Distributions

This section presents the most important features of the probability distributions and density functions most commonly used for evaluation of data and models.

Degenerate distribution: Consider that x is a random variable which can assume only a single value, namely, $x = c$, where c is a real number. The distribution for x is called the degenerate distribution, and the corresponding probability density is given by $p(x) = \delta(x-c)$, where $-\infty \leq x \leq \infty$, and δ denotes the Dirac delta functional. The MGF for this distribution is $M_x(t) = e^{tc}$, ($t \in \mathbb{R}$), while the mean value is $m_o = c$, and the variance is $\mu_2 = 0$.

Discrete uniform distribution: Consider that x is a random variable, which can assume only the integer values $x = 1, \dots, n$. Each of these values carries equal probability. The distribution for x is called the discrete uniform distribution, and the corresponding probability is given by

$$p(x) = (1/n) \sum_{i=1, n} \delta(x - i) \quad \text{or} \quad p(x) = \begin{cases} 1/n, & (x = 1, 2, \dots, n), \\ 0, & \text{otherwise.} \end{cases}$$

The MGF for this distribution is

$$M_x(t) = [e^t(1 - e^{nt})]/[n(1 - e^t)], \quad (t \in \mathbb{R}).$$

Using either the above MGF or by direct calculations, the mean value of x is obtained as $m_o = (n + 1)/2$, while the variance of x is obtained as $\mu_2 = (n^2 - 1)/12$.

Continuous uniform distribution: Consider that x is a random variable, which can assume any real value in the nondegenerate (i.e., $a < b$) interval $I(a, b)$. The distribution for x is called the continuous uniform distribution, and the corresponding PDF is given by

$$p(x) = \begin{cases} 1/(b - a), & a \leq x < b; a, b \in \mathbb{R}, \\ 0, & \text{otherwise.} \end{cases}$$

The *MGF* for this distribution is

$$M_x(t) = \begin{cases} [(e^{tb} - e^{ta})/[(b-a)t]], & t \in \mathbb{R}, t \neq 0, \\ 1, & t = 0. \end{cases}$$

From the above *MGF*, the mean value is obtained as $m_o = (a + b)/2$, while the variance is obtained as $\mu_2 = (b - a)^2/12$. This distribution is employed wherever the range of a finite random variable is bounded and there is no a priori reason for favoring one value over another within that range. In practical applications, the continuous uniform distribution is often used in Monte Carlo analysis or computational methods, and as a prior for applying Bayes' theorem in the extreme situation when no information is available prior to performing an experiment.

Bernoulli distribution: Bernoulli trials are defined as random trials in which the outcomes can be represented by a random variable having only two values, say $x = 0$ and $x = 1$. Such a model can be applied to a random trial whose outcomes (events) are described by "yes or no," "on or off," "black or white," "success or failure," etc. Suppose that only one Bernoulli trial is performed, for which the probability of "success" ($x = 1$) is denoted by s , for $0 < s < 1$, while the probability of "failure" ($x = 0$) is $(1 - s)$. The probability distribution that describes this trial is called the Bernoulli distribution, and has the form

$$P(x) = \begin{cases} s^x(1-s)^{1-x}, & x = 0, 1, \\ 0, & \text{otherwise.} \end{cases}$$

The *MGF* for this distribution is given by

$$M_x(t) = se^t + 1 - s, \quad (t \in \mathbb{R}).$$

From the above *MGF*, the mean value is obtained as $m_o = s$, while the variance is obtained as $\mu_2 = s(1 - s)$. The Bernoulli distribution provides a basis for the binomial and related distributions.

Binomial and multinomial distributions: Consider a series of n independent trials or observations, each having two possible outcomes, usually referred to as "success" and "failure," respectively. Consider further that the probability for success takes on a constant value, s , and consider that the quantity of interest is the accumulated result of n such trials (as opposed to the outcome of just one trial). The set of n trials can thus be regarded as a single measurement characterized by a discrete random variable x , defined to be the total number of successes. Thus, the sample space is defined to be the set of possible values of x successes given n observations. If the measurement were repeated many times with n trials each time, the resulting values of x would occur with relative frequencies given by the binomial distribution, which is defined as

$$P(x) = \frac{n!}{x!(n-x)!} s^x(1-s)^{n-x}, \quad (x = 0, 1, \dots, n),$$

where x is the random variable, while n and s are parameters characterizing the binomial distribution. Note that the binomial distribution is symmetric for $s = 1/2$. The *MGF* is $M_x(t) = (se^t + 1 - s)^n$, ($t \in \mathbb{R}$). The mean value of x is given by $m_o = ns$, while the variance is given by $\mu_2 = ns(1 - s)$.

If the space \mathcal{E} of all possible simple events is partitioned in $m + 1$ (instead of just two, as was the case for the binomial distribution) compound events A_i , ($i = 1, \dots, m + 1$), the binomial

distribution can be generalized to the multinomial distribution by considering a set of nonnegative integer variables $(x_1, x_2, \dots, x_{m+1})$, satisfying the conditions $\sum_{i=1}^{m+1} x_i = n$, $\sum_{i=1}^{m+1} A_i = \mathcal{E}$, and $\sum_{i=1}^{m+1} s_i = 1$ (since one of the outcomes must ultimately be realized). Then, the multinomial distribution for the joint probability for x_1 outcomes of type 1, x_2 of type 2, etc. is given by

$$P(x_1, \dots, x_{m+1}) = \frac{n!}{x_1! \dots x_{m+1}!} s_1^{x_1} \dots s_{m+1}^{x_{m+1}}.$$

The MGF for this distribution is

$$M_{x_1 \dots x_{m+1}}(t_1, \dots, t_m) = \left(\sum_{i=1}^m s_i e^{t_i} + s_{m+1} \right)^n, \quad (t_i \in \mathbb{R}, i = 1, \dots, m).$$

The variances and covariances for this distribution are, respectively: $\mu_{ii} = \sigma_i^2 = ns_i(1 - s_i)$ for $i = j$, and $\mu_{ij} = -n s_i s_j$ for $i \neq j (i, j = 1, \dots, m + 1)$. Since μ_{ij} is negative (anti-correlated variables), it follows that, if in n trials, bin i contains a larger than average number of entries ($x_i > n s_i$), then the probability is increased that bin j will contain a smaller than average number of entries.

Geometric distribution: The geometric distribution is also based on the concept of a Bernoulli trial. Consider that s , $0 < s < 1$, is the probability that a particular Bernoulli trial is a success, while $1 - s$ is the corresponding probability of failure. Also, consider that x is a random variable that can assume the infinite set of integer values $(1, 2, \dots)$. The geometric distribution gives the probability that the first $x - 1$ trials will be failures, while the x^{th} trial will be a success. Therefore, the geometric distribution can be interpreted as the distribution of the “waiting time” for a success. The probability function characterizing the geometric distribution is

$$P(x) = s(1 - s)^{x-1}, \quad (x = 1, 2, \dots).$$

The MGF for this distribution is

$$M_x(t) = se^t / [1 - (1 - s)e^t], \quad (t < -\ln(1 - s)).$$

From the above MGF, the mean value is obtained as $m_o = (1/s)$, while the variance is obtained as $\mu_2 = (1 - s)/s^2$.

Negative binomial (Pascal) distribution: The negative binomial (Pascal) distribution also employs the concept of a Bernoulli trial. Thus, consider that s , $0 < s < 1$, is the probability of success in any single trial and $1 - s$ is the corresponding probability of failure. This time, though, the result of interest is the number of trials that are required in order for r successes to occur, ($r = 1, 2, \dots$). Note that at least r trials are needed in order to have r successes. Consider, therefore, that x is a random variable that represents the number of additional trials required (beyond r) before obtaining r successes, so that ($x = 0, 1, 2, \dots$). Then, the form of the Pascal probability distribution is

$$P(x) = C_{mx} s^r (1 - s)^n, \quad (x = 0, 1, 2, \dots),$$

where $m = x + r - 1$ and C_{mx} is the binomial coefficient. The MGF for the binomial distribution is $M_n(t) = [s/(1 - (1 - s)e^t)]^r$, ($t < -\ln(1 - s)$). The mean value for the Pascal distribution is $m_o = [r(1 - s)/s]$, while the variance is $\mu_2 = r(1 - s)/s^2$.

Poisson distribution: In the limit of many trials, as n becomes very large and the probability of success s becomes very small, but such that the product ns (i.e., the expectation value of the number of successes) remains equal to some finite value ν , the binomial distribution takes on the form

$$P(x) = \frac{\nu^x}{x!} e^{-\nu}, \quad (x = 0, 1, \dots),$$

which is called the Poisson distribution for the integer random variable x . The corresponding MGF is given by the expression $M_x(t) = \exp[\nu(e^t - 1)]$, ($t \in \mathbb{R}$). The expectation value of the Poisson random variable x is obtained as $m_o = \nu$, and the variance is $\mu_2 = \nu$. Although the Poisson variable x is discrete, it can be treated as a continuous variable if it is integrated over a range $\Delta x \gg 1$. An example of a Poisson random variable is the number of decays of a certain amount of radioactive material in a fixed time period, in the limit that the total number of possible decays (i.e., the total number of radioactive atoms) is very large and the probability for an individual decay within the time period is very small.

Exponential distribution: The exponential PDF, $p(x)$, of the continuous variable x ($0 \leq x < \infty$) is defined by

$$p(x) = \frac{1}{\xi} e^{-x/\xi},$$

where ξ is a real-valued parameter. The expectation value of x is $m_o = \xi$ and the variance of x is $\mu_2 = V(x) = \xi^2$. The MGF is

$$M_x(t) = \lambda/(\lambda - t), \quad \lambda \equiv 1/\xi, \quad (t \in \mathbb{R}, t < \lambda).$$

The exponential distribution is widely used in radioactivity applications and in equipment failure rate analysis. The failure rate is defined as the reciprocal of the mean time to failure, i.e., $\xi = 1/\lambda$. The quantity $R(t_o) = e^{-\lambda t_o}$ is usually denoted as the reliability (of the equipment) at time $t_o > 0$. It should not be surprising that the reliability of a piece of equipment should decline with age, and statistical experience has shown that this decline is well represented by the exponential distribution.

Gaussian distribution: Perhaps the single most important distribution in theoretical as well as in applied statistics is the Gaussian (or normal) PDF of the continuous random variable x (with $-\infty < x < \infty$), defined as

$$p(x) = \frac{1}{\sqrt{2\pi\sigma^2}} \exp\left(-\frac{(x - \nu)^2}{2\sigma^2}\right).$$

Note that, the Gaussian distribution has two parameters, ν and σ^2 , which are, by design, the mean, i.e., $E(x) = \nu$ and variance $V(x) = \sigma^2$. The MGF for the Gaussian distribution is $M_x(t) = \exp[\nu t + (\sigma^2 t^2/2)]$, ($t \in \mathbb{R}$).

The function

$$P(x) = \int_{-x}^x p(z) dz, \quad (x > 0),$$

with $p(z)$ given by the above Gaussian, represents the integrated probability of an event with $-x \leq z < x$, for the standard normal distribution. The first four derivatives of the MGF, $M_x(t)$, of the standard normal distribution are:

$$\begin{aligned} M_x^{(1)}(t) &= t \exp(t^2/2), & M_x^{(2)}(t) &= (1 + t^2) \exp(t^2/2), \\ M_x^{(3)}(t) &= (3t + t^3) \exp(t^2/2), & M_x^{(4)}(t) &= (3 + 6t^2 + t^4) \exp(t^2/2). \end{aligned}$$

Evaluating the above expressions at $t = 0$ yields:

$$\begin{aligned} M_x^{(1)}(0) &= v_1 = m_o = 0, & M_x^{(2)}(0) &= v_2 = \mu_2 = \sigma^2 = 1, \\ M_x^{(3)}(0) &= v_3 = \mu_3 = \alpha_3 = 0, & M_x^{(4)}(0) &= v_4 = \mu_4 = \alpha_4 = 3. \end{aligned}$$

Thus, a normal distribution is symmetric (since it has skewness $\alpha_3 = 0$) and is mesokurtic (since it has kurtosis $\alpha_4 = 3$). Furthermore, since $m_o = 0$ for all standard distributions, the respective raw and central moments are equal to each other. In particular, it can be shown that $\mu_{2k-1} = 0$, ($k = 1, 2, \dots$), which indicates that all the odd central moments of the normal distribution vanish. Furthermore, it can be shown that the even central moments are given by $\mu_{2k} = (1)(3) \dots (2k - 1) \sigma^{2k}$, ($k = 1, 2, \dots$). These results highlight the very important feature of the normal distribution that all its nonzero higher-order central moments can be expressed in terms of a single parameter, namely the standard deviation. This is one of several reasons why the Gaussian distribution is arguably the single most important PDF in statistics.

Another prominent practical role played by the Gaussian distribution is as a replacement for either the binomial distribution or the Poisson distribution. The circumstances under which such a replacement is possible are given by *DeMoivre–Laplace theorem* (given below without proof), which can be stated as follows: Consider the binomial distribution, denoted as $p_b(k)$, ($k = 1, \dots, n$) (n and s denote the usual parameters of the binomial distribution, while the subscript “b” denotes “binomial”), and consider that a and c are two nonnegative integers satisfying $a < c < n$. Furthermore, consider the standard normal distribution, denoted as $p_{sn}(x)$ (the subscript “sn” denotes “standard normal”). Finally, define the quantities α and β as

$$\alpha \equiv (a - ns - 0.5)/[ns(1 - s)]^{1/2} \quad \text{and} \quad \beta \equiv (c - ns + 0.5)/[ns(1 - s)]^{1/2}.$$

Then, for large n , the following relation holds

$$\sum_{k=a}^c p_b(k) \approx \int_{\alpha}^{\beta} p_{sn}(x) dx.$$

Thus, the DeMoivre–Laplace theorem indicates that the sum of the areas of contiguous histogram segments, representing discrete binomial probabilities, approximately equals the area under the corresponding continuous Gaussian curve spanning the same region. The binomial becomes increasingly symmetrical as $s \rightarrow 0.5$, so the approximation provided by the DeMoivre–Laplace theorem is accurate even for relatively small n , since the Gaussian is intrinsically symmetric. When $s \ll 1$, and n is so large that $\sigma^2 = ns(1 - s) = v(1 - v/n) \approx v$, even though $v \gg 1$, then the normal distribution can be shown to be a reasonably good approximation to both the corresponding Poisson distribution and to the binomial distribution (particularly when $x \approx v$).

Another very important role played by the Gaussian distribution is highlighted by the *Central Limit Theorem*, which essentially states that the sum of n independent continuous random variables x_i with means μ_i and variances σ_i^2 becomes a Gaussian random variable with mean $\mu = \sum_{i=1}^n \mu_i$ and variance $\sigma^2 = \sum_{i=1}^n \sigma_i^2$ in the limit that n approaches infinity. This statement holds under fairly general conditions, regardless of the form of the individual *PDFs* of the respective random variables x_i . The central limit theorem provides the formal justification for treating measurement errors as Gaussian random variables, as long as the total error is the sum of a large number of small contributions.

The behavior of certain distributions for limiting cases of their parameters can be investigated more readily by using characteristic or MGFs, rather than their *PDFs*. For example, taking the limit $s \rightarrow 0, n \rightarrow \infty$, with $v = sn$ (constant), in the characteristic function for the binomial distribution yields the characteristic function of the Poisson distribution:

$$\phi(k) = [s(e^{ik} - 1) + 1]^n = \left(\frac{v}{n}(e^{ik} - 1) + 1\right)^n \rightarrow \exp[v(e^{ik} - 1)].$$

Note also that a Poisson variable x with mean v becomes a Gaussian variable in the limit as $v \rightarrow \infty$. This fact can be shown as follows: although the Poisson variable x is discrete, when it becomes large, it can be treated as a continuous variable as long as it is integrated over an interval that is large compared to unity. Next, the Poisson variable x is transformed to the variable $z = (x - v)/\sqrt{v}$. The characteristic function of z is

$$\phi_z(k) = E(e^{ikz}) = E(e^{ikx/\sqrt{v}} e^{-ik\sqrt{v}}) = \phi_x\left(\frac{k}{\sqrt{v}}\right) e^{-ik\sqrt{v}},$$

where ϕ_x is the characteristic function of the Poisson distribution. Expanding the exponential term and taking the limit as $v \rightarrow \infty$ yields

$$\phi_z(k) = \exp[v(e^{ik/\sqrt{v}} - 1) - ik\sqrt{v}] \rightarrow \exp\left(-\frac{1}{2}k^2\right).$$

The last term on the right side of the above expression is the characteristic function for a Gaussian with zero mean and unit variance. Transforming back to the original Poisson variable x , one finds, therefore, that for large v , x follows a Gaussian distribution with mean and variance both equal to v .

Multivariate normal distribution: Consider that \mathbf{x} is a (column) vector of dimension n , with components $x_i \in \mathbb{R}$, ($i = 1, \dots, n$). Consider further that \mathbf{m}_0 is a (column) vector of constants with components denoted as $m_{0i} \in \mathbb{R}$, ($i = 1, \dots, n$). Finally, consider that \mathbf{V} is a real, symmetric, and positive definite $n \times n$ matrix with elements denoted by μ_{ij} , ($i, j = 1, \dots, n$). Then, the multivariate normal distribution for n variables is defined by the PDF

$$p(\mathbf{x}) = (2\pi)^{-n/2} [\det(\mathbf{V})]^{-1/2} \exp[-(1/2)(\mathbf{x} - \mathbf{m}_0)^+ \mathbf{V}^{-1}(\mathbf{x} - \mathbf{m}_0)],$$

where the superscript “+” denotes matrix transposition, and where \mathbf{V}^{-1} is the inverse of \mathbf{V} . The quantity $Q \equiv (\mathbf{x} - \mathbf{m}_0)^+ \mathbf{V}^{-1}(\mathbf{x} - \mathbf{m}_0)$ is called a multivariate quadratic form. The *MGF* is given by

$$M_x(t) = \exp[t^+ \mathbf{m}_0 + (1/2)t^+ \mathbf{V}^{-1}t], \quad (t_i \in \mathbb{R}; i = 1, \dots, n).$$

Note that \mathbf{m}_o is the mean vector, while \mathbf{V} is actually the covariance matrix for this distribution; note also that

$$E(x_i) = [\partial M_x(t)/\partial t_i]_{t=0} = m_{oi}, \quad E(x_i x_j) = [\partial^2 M_x(t)/\partial t_i \partial t_j]_{t=0} = m_{oi} m_{oj} + \mu_{ij}.$$

In particular, the Gaussian PDF for two random variables x_1 and x_2 becomes

$$p(x_1, x_2; m_{o1}, m_{o2}, \sigma_1, \sigma_2, \rho) = \frac{1}{2\pi\sigma_1\sigma_2\sqrt{1-\rho^2}} \times \exp \left\{ -\frac{1}{2(1-\rho^2)} \left[\left(\frac{x_1 - m_{o1}}{\sigma_1} \right)^2 + \left(\frac{x_2 - m_{o2}}{\sigma_2} \right)^2 - 2\rho \left(\frac{x_1 - m_{o1}}{\sigma_1} \right) \left(\frac{x_2 - m_{o2}}{\sigma_2} \right) \right] \right\},$$

where $\rho = \text{cov}(x_1, x_2)/(\sigma_1\sigma_2)$ is the correlation coefficient.

The following properties of the multivariate normal distribution are often used in applications to data evaluation and analysis:

1. If \mathbf{x} is a normally distributed random vector of dimension n with corresponding mean vector \mathbf{m}_o and positive definite covariance matrix \mathbf{V} , and if \mathbf{A} is an $m \times n$ matrix of rank m , with $m \leq n$, then the m -dimensional random vector $\mathbf{y} = \mathbf{A}\mathbf{x}$ is also normally distributed, with a mean (vector) equal to $\mathbf{A}\mathbf{m}_o$ and a positive definite covariance matrix equal to $\mathbf{A}\mathbf{V}\mathbf{A}^+$.
2. If \mathbf{x} is a normally distributed random vector of dimension n , with corresponding mean vector \mathbf{m}_o and positive definite covariance matrix \mathbf{V} , and if \mathbf{A} is a nonsingular $n \times n$ matrix such that $\mathbf{A}^+\mathbf{V}^{-1}\mathbf{A} = \mathbf{I}$ (the diagonal unit matrix), then $\mathbf{y} = \mathbf{A}^{-1}(\mathbf{x} - \mathbf{m}_o)$ is a random vector with a zero mean vector, $\mathbf{0}$, and unit covariance matrix, \mathbf{I} . This linear transformation is the multivariate equivalent of the standard-variable transformation for the univariate Gaussian distribution.
3. If \mathbf{x} is a normally distributed random vector of dimension n with corresponding mean vector \mathbf{m}_o and positive definite covariance matrix \mathbf{V} , then the quadratic form $Q = (\mathbf{x} - \mathbf{m}_o)^+\mathbf{V}^{-1}(\mathbf{x} - \mathbf{m}_o)$ is a statistic distributed according to the chi-square distribution with n degrees of freedom.
4. If \mathbf{x} is a normally distributed vector with mean vector \mathbf{m}_o and covariance matrix \mathbf{V} , then the individual variables x_1, x_2, \dots, x_n are mutually independent iff all the elements μ_{ij} in \mathbf{V} are equal to zero for $i \neq j$.

Log-normal distribution: The random variable $x = e^y$, where y is a Gaussian random variable with mean μ and variance σ^2 , is distributed according to the log-normal distribution

$$p(x) = \frac{1}{\sqrt{2\pi\sigma^2}} \frac{1}{x} \exp \left(-\frac{(\log x - \mu)^2}{2\sigma^2} \right).$$

Since the log-normal and Gaussian distributions are closely connected to one another, they share many common properties. For example, the moments of the log-normal distribution can be obtained directly from those of the normal distribution, by noting that $E(x^k) = E(e^{ky}) = M_y(t)|_{t=k}$. Thus, the expectation value and variance, respectively, for the log-normal distribution are $E(x) = \exp(\mu + \frac{1}{2}\sigma^2)$, $V(x) = \exp(2\mu + \sigma^2)[\exp(\sigma^2) - 1]$.

Applying the central limit theorem to the variable $x = e^y$ shows that a variable x that stems from the product of n factors (i.e., $x = x_1 x_2 \dots x_n$) will follow a log-normal distribution in the

limit as $n \rightarrow \infty$. Therefore, the log-normal distribution is often used to model random errors which change a result by a multiplicative factor. Since the log-normal function is distributed over the range of positive real numbers, and has only two parameters, it is particularly useful for modeling nonnegative phenomena, such as analysis of incomes, classroom sizes, masses or sizes of biological organisms, evaluation of neutron cross sections, scattering of subatomic particles, etc.

Cauchy distribution: The Cauchy distribution is defined by the PDF

$$p(x) = (\lambda/\pi)[\lambda^2 + (x - \nu)^2]^{-1},$$

for $x \in \mathbb{R}$, $\nu \in \mathbb{R}$, and $\lambda \in \mathbb{R}(\lambda > 0)$. Although this distribution is normalized (i.e., the zeroth raw moment exists), the expectations that define the higher-order raw moments are divergent. Mathematical difficulties can be alleviated, however, by confining the analysis to the vicinity of $x = \nu$; if needed, this distribution can be arbitrarily truncated.

Gamma distribution: Consider that x is a nonnegative real variable ($x \in \mathbb{R}$, $x > 0$), and α and β are positive real constants ($\alpha \in \mathbb{R}$, $\alpha > 0$; $\beta \in \mathbb{R}$, $\beta > 0$). Then the PDF for the gamma distribution is defined as

$$p(x) = x^{\alpha-1} e^{-(x/\beta)} / [\beta^\alpha \Gamma(\alpha)].$$

The *MGF* for the gamma distribution is

$$M_x(t) = 1/(1 - \beta t)^\alpha, \quad (t \in \mathbb{R}, t < 1/\beta),$$

while the mean value and variance are $m_o = \alpha\beta$ and $\mu_2 = \alpha\beta^2$, respectively. Note that when $\alpha = 1$ and $\beta = 1/\lambda$, the gamma distribution reduces to the exponential distribution.

Beta distribution: Consider that x is a real variable in the range $0 \leq x \leq 1$, and α and β are positive real parameters ($\alpha \in \mathbb{R}$, $\alpha > 0$; $\beta \in \mathbb{R}$, $\beta > 0$). The PDF for the beta distribution is defined as

$$p(x) = \{\Gamma(\alpha + \beta)/[\Gamma(\alpha)\Gamma(\beta)]\}x^{\alpha-1}(1-x)^{\beta-1}.$$

Since the *MGF* for the beta distribution is inconvenient to use, it is easier to derive the mean value and the variance; this yields $m_o = \alpha/(\alpha + \beta)$ and $\mu_2 = \alpha\beta/[(\alpha + \beta)^2(\alpha + \beta + 1)]$. The beta distribution is often used for weighting probabilities along the unit interval.

Student's t-distribution: The t-distribution was discovered by W. Gosset (who published it under the pseudonym "Student"). It arises when considering the quotient of two random variables. For x a real variable ($x \in \mathbb{R}$), the probability density for the t-distribution is defined as

$$p(x) = \Gamma[(n+1)/2][1 + (x^2/n)]^{-(n+1)/2} / [(n\pi)^{1/2}\Gamma(n/2)], \quad (n = 1, 2, 3, \dots).$$

The t-distribution function does not have an *MGF*. However, certain moments do exist: the mean value is $m_o = 0$, for $n > 1$, and the variance is $\mu_2 = n/(n-2)$, for $n > 2$. Note that, the conditions $n > 1$ and $n > 2$ for the existence of the mean value and variance, respectively, arise from the fact that the t-distribution for $n = 1$ is equivalent to the Cauchy distribution for $\nu = 0$ and $\lambda = 1$.

F-distribution: Just as the t-distribution, the F-distribution also arises when considering the quotient of two random variables; its probability density is given by

$$p(x) = (n/m)^{n/2} \Gamma[(n+m)/2] x^{(n/2)-1} / \{ \Gamma(n/2) \Gamma(m/2) [1 + (nx/m)]^{(n+m)/2} \},$$

where $x \in \mathbb{R}, x > 0$, and the parameters m and n are positive integers called degrees of freedom. The MGF for the F-distribution does not exist, but the mean value is $m_o = m/(m-2)$, for $m > 2$, and the variance is

$$\mu_2 = m^2(2m+2n-4)/[n(m-2)^2(m-4)], \quad \text{for } m > 4.$$

Few-parameter distribution and Pearson's equation: Pearson made the remarkable discovery that the differential equation $(dp/dx) = p(x)(d-x)/(a+bx+cx^2)$ yields several of the univariate PDFs considered in the foregoing, e.g.:

- The normal distribution if $a > 0, b = c = 0$, while d is arbitrary
- The exponential distribution if $a = c = d = 0, b > 0$
- The gamma distribution if $a = c = 0, b > 0$, and $d > -b$
- The beta distribution if $a = 0, b = -c$, and $d > 1 - b$

Chi-square χ^2 -distribution: The χ^2 (chi-square) distribution of the continuous variable x ($0 \leq x < \infty$) is defined as

$$p(x) = \frac{1}{2^{n/2} \Gamma(n/2)} x^{n/2-1} e^{-x/2}, \quad (n = 1, 2, \dots),$$

where the parameter n is the number of degrees of freedom. The mean value and variance of x are given by $m_o = n$ and $\mu_2 = 2n$, respectively.

The χ^2 -distribution is related to the sum of squares of normally distributed variables: given N independent Gaussian random variables x_i with known mean μ_i and variance σ_i^2 , the random variable $x = \sum_{i=1}^N (x_i - \mu_i)^2 / \sigma_i^2$ is distributed according to the χ^2 -distribution with N degrees of freedom. More generally, if the random variables x_i are not independent but are described by an N -dimensional Gaussian PDF, then the random variable $Q = (\mathbf{x} - \boldsymbol{\mu})^+ \mathbf{V}^{-1} (\mathbf{x} - \boldsymbol{\mu})$ also obeys a χ^2 -distribution with N degrees of freedom. Random variables following the χ^2 -distribution play an important role in tests of goodness-of-fit, as highlighted, for example, by the method of least squares.

7.6 Central Limit Theorem

Consider that (x_1, x_2, \dots, x_n) is a random sample of the parent random variable x , whose MGF $M_x(t)$ exists in a range $-t_o < t < t_o$, $t_o > 0$, around $t = 0$. This requirement implies that the mean value m_o and $\text{var}(x) = \sigma^2$ both exist, while the sample average is $\xi_n = (\sum_{i=1}^n x_i) / n$. Note that, the MGF of ξ_n is $M_{\xi_n}(t) = [M_x(t/n)]^n$. Furthermore, define $z_n \equiv (\xi_n - m_o) / (\sigma / n^{1/2})$ to be the reduced random-variable equivalent of ξ_n . Then, the central limit theorem states that z_n , ξ_n , and $n\xi_n$ are all asymptotically normal in the limit as $n \rightarrow \infty$.

The conditions stated in the preceding theorem are more restrictive than they need to be; in particular, the condition that (x_1, x_2, \dots, x_n) be equally distributed can be eliminated. The

least restrictive necessary and sufficient condition for the validity of the central limit theorem is the *Lindeberg condition*, which states that if the sequence of random variables (x_1, x_2, \dots, x_n) is uniformly bounded (i.e., if there exists a positive real constant C such that $|x_i| < C$ for each x_i and all possible n) and the sequence is not degenerate, then the central limit theorem holds. In practice, the Lindeberg condition requires that the mean values and variances exist for each of these variables, and that the overall variance in the sum ξ_n of these random variables be not dominated by just a few of the components. Application of the central limit theorem to correlated random variables is still an open field of research in mathematical statistics.

Rather than specifying the conditions under which the central limit theorem holds exactly in the limit $n \rightarrow \infty$, in practice it is more important to know the extent to which the Gaussian approximation is valid for finite n . This is difficult to quantify exactly, but the rule of thumb is that the central limit theorem holds as long as the sum is built up of a large number of small contributions. Discrepancies arise if, for example, the distributions of the individual terms have long tails, so that occasional large values make up a large part of the sum. Such contributions lead to “non-Gaussian” tails in the sum, which can significantly alter the probability to find values with large departures from the mean. In such cases, the main assumption underlying the central limit theorem, namely the assumption that the measured value of a quantity is a normally distributed variable centered about the mean value, breaks down. Since this assumption is often used when constructing a confidence interval, such intervals can be significantly underestimated if non-Gaussian tails are present. In particular, the relationship between the confidence level and the size of the interval will differ from the Gaussian prescription (i.e., 68.3% for a “ 1σ ” interval, 95.4% for “ 2σ ,” etc.). A better understanding of the non-Gaussian tails can often be obtained from a detailed Monte Carlo simulation of the individual variables making up the sum.

7.7 Statistical Estimation

In practice, the exact form of mathematical models and/or exact values of data are rarely, if ever, available. Rather, the available information comes in the form of observations, usually associated with a frequency distribution, which must be used, in turn, to estimate the mathematical form and/or the parameters describing the underlying probability distribution function. The use of observations to estimate the underlying features of probability functions forms the objective of a branch of mathematical sciences called statistics. Conceptually, therefore, the objective of statistical estimation is to estimate the parameters $(\theta_1, \dots, \theta_k)$ that describe a particular statistical model, by using observations, x_n , of a frequency function $f(x; \theta_1, \dots, \theta_k)$. Furthermore, this statistical estimation process must provide reasonable assurance that the model based on these estimates will fit the observed data within acceptable limits. Furthermore, the statistical estimates obtained from observational data must be consistent, unbiased, and efficient. Therefore, the science of statistics embodies both inductive and deductive reasoning, encompassing procedures for estimating parameters from incomplete knowledge and for refining prior knowledge by consistently incorporating additional information. Hence, the solution to practical problems requires a synergetic use of the various interpretations of probability, including the axiomatic, frequency, and Bayesian interpretations and methodologies.

Consider that x represents a random variable that describes events in a certain event space. For simplicity, the symbol x will be used in this section to represent both the random variable and a typical value; a distinction between these two uses will be made only when necessary to avoid confusion. Thus, x is considered to be described by a probability density $p(x)$, with a

mean value $E(x) = m_o$ and $\text{var}(x) = \sigma^2$. Without loss of generality, x can be considered to be continuous, taking values in an uncountably infinite space \mathcal{S}_x ; the statistical formalisms to be developed in the following can be similarly developed for finite or countably infinite random variables.

In both classical and Bayesian statistics, the estimation procedures are applied to samples of data. A sample, \mathbf{x}_s , of size n is defined as a collection of n equally distributed random variables (x_1, x_2, \dots, x_n) ; each x_i is associated with the same event space and has the same probability density, $p_i(x_i) = p(x_i)$. The random variable x , which each x_i resembles, is usually called the parent random variable. Each sampling step corresponds to the selection of a sample; thus, the first step selects sample 1, which corresponds to x_1 , while the last step (the n th-step) selects sample n , which corresponds to x_n . The selection of values x_i is called a *sampling process*, and the result of this process is the n -tuple of values $\mathbf{x}_s \equiv (x_1, x_2, \dots, x_n)$. If the sampling is random (i.e., the selection of each x_i is unaffected by the selection of all other x_j , $j \neq i$), then the collection of random variables can be treated as a random vector $\mathbf{x}_s \equiv (x_1, x_2, \dots, x_n)$ distributed according to the multivariate probability density $p(x_1, x_2, \dots, x_n) = p(x_1)p(x_2) \dots p(x_n)$. For random sampling, the components x_i are uncorrelated (i.e., the covariance matrix is diagonal), and have mean values $E(x_i) = m_o$ and variances $\text{var}(x_i) = E[(x_i - m_o)^2] = \sigma^2$, identical to the mean value and standard deviation of the parent distribution x .

A function $\Theta(x_1, \dots, x_n)$ that acts only on the sample random variables (and, possibly, on well-defined constants) is called a *statistic*. An *estimator*, $T = \Theta(x_1, \dots, x_n)$, is a statistic specifically employed to provide estimated values for a particular, true yet unknown, constant value T_o of the underlying probability distribution for the parent variable x ; the function Θ is called the *estimation rule*. Since this rule is designed to provide specific values of T that are meant to approximate the constant T_o , the estimator T is called a *point estimator*. The process of selecting estimators is not unique, so the criteria used for particular selections are very important, since they determine the properties of the resulting estimated values for the parameters of the chosen model.

An *estimator* T of a physical quantity T_o is called *consistent* if it approaches the true value T_o of that quantity (i.e., it converges in probability to T_o) as the number of observations x_n of T_o increases: $T(x_1, \dots, x_n) \xrightarrow{n \rightarrow \infty} T_o$. An *estimator* T of T_o is called *unbiased* if its expectation is equal to the true value of the estimated quantity: $E(T) = T_o$. The bias $B(T, T_o)$ of an estimator is defined as $B(T, T_o) \equiv E(T) - T_o$. If $B(T, T_o) > 0$, then T tends to overestimate T_o ; if $B(T, T_o) < 0$, then T tends to underestimate T_o . The quantity $E[(T - T_o)^2]$ is called the *mean-squared error*.

If the estimator $T = \Theta(x_1, \dots, x_n)$ utilizes all the information in the sample that pertains to T_o , then the respective estimator is called a *sufficient estimator*. In practice, the choice of estimators is further limited by considering unbiased estimators, which, among all similar estimators, have the smallest variance. A consistent, unbiased, and minimum variance estimator is called an *efficient estimator*.

Intuitively, it would be expected that the smaller the variance of an unbiased estimator, the closer the estimator is to the respective parameter value. This intuitive expectation is indeed correct. For example, $T(x_1, x_2, \dots, x_n) = \sum_{i=1}^n a_i x_i$, where the quantities a_i are constants, would be a *best linear unbiased estimator (BLUE)* of a parameter θ , if $T(x_1, \dots, x_n)$ is a linear unbiased estimator such that $\text{var}\{T(x_1, \dots, x_n)\} \leq \text{var}\{T'(x_1, \dots, x_n)\}$, where $T'(x_1, \dots, x_n)$ is any other linear unbiased estimator of θ .

The *sample moment of order k* , x_k^S , is the statistic defined as $x_k^S \equiv (1/n) \sum_{i=1}^n x_i^k$, ($k = 1, 2, \dots$). In this definition, the superscript “S” denotes “sample.” The *sample mean* value,

$x^S \equiv (1/n) \sum_{i=1}^n x_i$, is defined in the special case when $k=1$. Note that $E(x^S) = (1/n) \sum_{i=1}^n E(x_i) = (1/n)nE(x) = m_o$, which indicates that the expectation value, $E(x^S)$, of the sample mean is an unbiased estimator for the distribution mean value $E(x) = m_o$. It can also be shown that the variance of the sample mean, $\text{var}(x^S)$, is related to $\sigma^2 = \text{var}(x)$ by means of the relation $\text{var}(x^S) = \sigma^2/n = \text{var}(x)/n$.

The *sample central moment statistic of order k* is defined as $\mu_k^S \equiv (1/n) \sum_{i=1}^n (x_i - x^S)^k$, ($k = 2, 3, \dots$). In particular, the sample variance is defined by setting $k = 2$, to obtain: $\mu_2^S \equiv (1/n) \sum_{i=1}^n (x_i - x^S)^2$, while the sample standard deviation is calculated using the formula $SD(x^S) = \sqrt{(1/(n-1)) \sum_{i=1}^n (x_i - x^S)^2}$.

The properties of sampling distributions from a normally distributed parent random variable x are of particular practical importance due to the prominent practical and theoretical role played by the central limit theorem. Thus, consider a normally distributed parent random variable x , with mean m_o and variance σ^2 . Furthermore, consider a sample (x_1, x_2, \dots, x_n) with sample mean value x^S and sample variance μ_2^S , respectively. Then, the following theorems hold and are often used in practice:

1. The quantities x^S and μ_2^S are independent random variables; note that the converse also holds, namely, if x^S and μ_2^S are independent, then the distribution for x must be normal.
2. The random variable $(n\mu_2^S/\sigma^2)$ is distributed according to a chi-square distribution with $(n - 1)$ degrees of freedom.

If y is a random variable distributed according to a χ^2 -square distribution with n degrees of freedom, and z is distributed as a standard normal random variable, and y and z are independent, then the ratio random variable $r \equiv z/\sqrt{y/n}$ is distributed according to Student's t-distribution with n degrees of freedom. In particular, this theorem holds when r, y, z are random variables defined as $(n\mu_2^S/\sigma^2) \equiv y$, $(x^S - m_o)/\sigma \equiv z$, and $r \equiv z/\sqrt{y/n}$; the ratio r is frequently used in practice to measure the scatter of the actual data relative to the scatter that would be expected from the parent distribution with standard deviation σ .

If y is distributed according to a χ^2 -square distribution with n degrees of freedom, and w is distributed according to a χ^2 -square distribution with m degrees of freedom, and y and w are independent, then the ratio variable $R \equiv (w/m)/(y/n)$ is distributed according to an F-distribution with degrees of freedom m and n . It is important to note that the sample mean $x^S \equiv (1/n) \sum_{i=1}^n x_i$ is the BLUE for the mean $E(x) = m_o$ of the parent distribution.

A concept similar to the BLUE is the *maximum likelihood estimator (MLE)*, which can be introduced, for simplicity, by considering that a single parameter, say θ_o , is to be estimated from a random sample (x_1, x_2, \dots, x_n) of size n . Since each sample is selected independently, the conditional multivariate probability density for the observed sample data set (x_1, x_2, \dots, x_n) is

$$\prod_{i=1}^n p(x_i|\theta) \equiv L(x_1, \dots, x_n|\theta),$$

where $p(x_i|\theta)$ is the conditional probability density that the value x_i will be observed in a single trial. The function $L(x_1, \dots, x_n|\theta)$ is called the *likelihood function*. The *maximum-likelihood method* for estimating θ_o consists of finding the particular value, say $\hat{\theta} \equiv \hat{\theta}(x_1, \dots, x_n)$, which maximizes $L(x_1, \dots, x_n|\theta)$ for the observed data set (x_1, x_2, \dots, x_n) . Thus, the MLE, $\hat{\theta}$, of θ_o is found as the solution to the equation

$$\left. \frac{d \ln L(x_1, \dots, x_n|\theta)}{d\theta} \right|_{\theta=\hat{\theta}} = 0.$$

If the above equation admits multiple solutions, then the solution that yields the largest likelihood function $L(x_1, \dots, x_n | \theta)$ is defined to be the *MLE*. The maximum likelihood method sketched above can, of course, be extended to more than a single parameter θ_o . For a normally distributed sample (x_1, \dots, x_n) , the sample mean x^S is the *MLE* for the parent's distribution mean value, m_o , while the sample variance, μ_2^S , is the *MLE* for the variance σ^2 of the parent's distribution. Since, $E(\mu_2^S) \rightarrow \sigma^2$ as $n \rightarrow \infty$, the *MLE* estimate μ_2^S is consistent; however, the *MLE* estimate μ_2^S is biased. Multiplying μ_2^S with the correction factor $n/(n-1)$ yields the estimate $[n/(n-1)]\mu_2^S = [1/(n-1)] \sum_{i=1}^n (x_i - x^S)^2$, which deviates from the *MLE* value but, on the other hand, is both consistent and unbiased. In practice, a small deviation from the maximum of the likelihood function is less important than a potential bias in the estimate. The sample standard deviation is computed using the formula $SD(x^S) = \sqrt{\sum_{i=1}^n (x_i - x^S)^2 / n - 1}$. The quantity $\hat{V}_{xy} \equiv 1/(n-1) \sum_{i=1}^n (x_i - x^S)(y_i - y^S)$ is an unbiased estimator of the covariance V_{xy} of two random variables x and y of unknown mean.

In many practical instances when estimating a set of parameters $(\theta_1, \dots, \theta_k)$, a certain amount of relevant knowledge is already available prior to performing the experiment. Such a priori knowledge is usually available in the form of a regression (or fitting) model $y = f(x; \theta_1, \dots, \theta_k)$, a priori parameter values $\theta_a = (\theta_1^a, \dots, \theta_k^a)$, and corresponding a priori covariance matrix V_a (the letter "a" indicates a priori). In such instances, it is important to combine the a priori information consistently with the new information derived from the experimental data set (η_1, \dots, η_n) , of observations of y , with a covariance V . The most popular method to accomplish such a consistent combination of a priori with newly obtained information is the *generalized least-squares method*. For example, when the a priori information is uncorrelated with the current information, the least squares method yields the array of values $(\theta_1, \dots, \theta_k)$ obtained by satisfying the condition

$$\chi^2 = (\boldsymbol{\theta} - \boldsymbol{\theta}_a)^+ \mathbf{V}_a^{-1} (\boldsymbol{\theta} - \boldsymbol{\theta}_a) + (\boldsymbol{\eta} - \mathbf{y})^+ \mathbf{V}^{-1} (\boldsymbol{\eta} - \mathbf{y}) = \min.$$

The above expression can be generalized to include also the case when the prior information is correlated with the newly obtained information. The statistic χ^2 to be minimized follows a χ^2 -square distribution, and provides a very valuable index for testing the consistency of data and numerical solutions (if applicable) of the regression model $y = f(x; \theta_1, \dots, \theta_k)$.

The estimators of the form $T = \Theta(x_1, \dots, x_n)$ that have been discussed in the foregoing are specifically employed to provide estimated values for a particular, true yet unknown, value $T_o = \Theta(x_1^o, \dots, x_n^o)$ of the underlying probability distribution. Since the estimation rule Θ is designed to provide specific values of T for approximating T_o , the estimator T is called a *point estimator*. Once the estimator T has been obtained, it becomes of interest to determine by how much the estimator can change when measurements are repeatedly performed under the same conditions. This question is addressed by constructing the so-called *confidence interval* for the true value $T_o = \Theta(x_1^o, \dots, x_n^o)$ of the measured quantity. The confidence interval is an interval that contains, with a prescribed probability called the confidence probability, the true value of the measured quantity. This concept can be illustrated by considering that (x_1, \dots, x_n) is a set of random variables defining the sample of data under study, and θ_p is a fundamental parameter of the underlying distribution that produced the data. If it were now possible to introduce two statistics, say $\theta_1 = \Theta_1(x_1, \dots, x_n)$ and $\theta_2 = \Theta_2(x_1, \dots, x_n)$ which would guarantee that $P\{\theta_1 < \theta_p < \theta_2\} = \alpha$, then the interval $I(\theta_1, \theta_2)$ would be called the $100\alpha\%$ confidence interval. The procedure employed to determine an estimate of the confidence interval is called *interval estimation*. Note that a single experiment involving n samples would produce a single sample

of data, say (x_1, \dots, x_n) ; in turn, this sample would yield a single interval. Additional similar experiments would generate different data and, consequently, different intervals. However, if $I(\theta_1, \theta_2)$ is the $100\alpha\%$ confidence interval, then $100\alpha\%$ of all intervals that might be generated this way would contain the true value, θ_p , of the parameter in question.

There are several methods for constructing confidence intervals. Perhaps the simplest and the most general method for constructing confidence intervals is based on Chebyshev's theorem, although the intervals obtained by using Chebyshev's theorem are too large for practical purposes. When the distribution of the sample observations can be assumed to follow a normal distribution with sample mean x^S and known standard deviation σ , then the confidence interval which would contain the true value, θ_p , of the parameter in question is constructed based on the expression

$$P\left\{|x^S - \theta_p| \leq z_\alpha \frac{\sigma}{\sqrt{n}}\right\} = \alpha,$$

where z_α is the quantile of the normalized Gaussian distribution corresponding to the selected confidence probability α . In practice, however, the sample standard deviation is rarely known; only its estimate, $SD(x^S)$, can be calculated. In such case, the confidence intervals are constructed based on Student's t-distribution, which is the distribution of the random quantity $t \equiv x^S - \theta_p / SD(x^S)$, where $SD(x^S)$ is the sample standard deviation. The confidence interval $[x^S - t_q SD(x^S), x^S + t_q SD(x^S)]$ corresponds to the probability $P\{|x^S - \theta_p| \leq t_q SD(x^S)\} = \alpha$, where t_q is the q -percent point of Student's t-distribution with $(n - 1)$ degrees of freedom and significance level $q \equiv (1 - \alpha)$. The significance level, q , should be consistent with the significance level adopted for verifying the normality of the sample. Although it is possible to verify the admissibility of the hypothesis that the observations are described by a normal distribution (and therefore verify the hypothesis that Student's t-distribution is admissible), in practice, however, confidence intervals are directly constructed based on Student's t-distribution without verifying its admissibility. The observation that this procedure works in practice indirectly confirms the tacit assumption that the truncated distributions usually obeyed by experimental data are often even narrower than normal distributions. In practice, the confidence probability is usually set equal to 0.95.

Confidence intervals for the standard deviation can also be constructed by using the χ^2 -distribution. The confidence interval thus constructed has the limits $(\sqrt{n-1}/\chi_L)SD(x^S)$ and $(\sqrt{n-1}/\chi_U)SD(x^S)$ for the probability

$$P\left\{\left(\frac{\sqrt{n-1}}{\chi_L}\right)SD(x^S) < \sigma < \left(\frac{\sqrt{n-1}}{\chi_U}\right)SD(x^S)\right\} = \alpha,$$

where χ_U^2 and χ_L^2 are found from tables, with χ_U^2 corresponding to $(1+\alpha)/2$, and χ_L^2 corresponding to $(1-\alpha)/2$. Note that the purpose of a confidence interval is to obtain a set of values which, despite sampling variations, yields a reasonable range of values for the estimated parameter, based on the data available. Thus, a confidence interval is an interval estimator of the parameter under investigation.

Another context in which inferences are made about parameters is the test of hypotheses. A *statistical hypothesis* is an assumption about the distribution (frequency function) of a

random variable. If the frequency function involves parameters, then the hypothesis can be an assumption concerning the respective parameters. A test of hypothesis is a rule by which the sample space is divided into two regions: the region in which the hypothesis is accepted and the region in which the hypothesis is rejected. A statistical hypothesis that is being tested is termed the null hypothesis, and is usually denoted by H_0 . In general, the alternative hypothesis is the complement of the null hypothesis. Rejection of the null hypothesis H_0 when it is true is called *type I error*. The size of type I error is the probability of rejecting H_0 when it is true. Acceptance of H_0 when it is false is called *type II error*. The size of type II error is the probability of accepting H_0 when it is false. The sizes of type I and type II errors are usually termed α and β , respectively. By definition, the *power of a test* is $1 - \beta$. The concept of power of a test is used to choose between (among) two or more procedures in testing a given null hypothesis, in that the test with the greater power, i.e., the smaller value of β (if one exists), is chosen. Occasionally, the power of a test depends on the value of the specific alternative when H_0 is not true; in such cases, a “most powerful” test does not exist. Tests that are “most powerful” against all alternatives are called *uniformly most powerful tests*.

7.8 Stationary Random Sequence and White Noise

Let $\mathbf{x} = \{x_0, x_1, x_2, x_3, \dots\}$ be a sequence of (scalar) random variables (also called a *time series*). Let $p(x_t)$ be the PDF of x_t for $t = 0, 1, 2, \dots$. In general, $p(x_t)$ may vary with time t . Then $E(x_t) = \mu_t = \int_{\mathbb{R}} x_t p(x_t) dx_t$ is the mean of x_t , while

$$E[(x_t - \mu_t)(x_{t-j} - \mu_{t-j})] = \gamma_{t,j} = \int_{\mathbb{R}} \int_{\mathbb{R}} (x_t - \mu_t)(x_{t-j} - \mu_{t-j}) p(x_t, x_{t-j}) dx_t dx_{t-j},$$

where $p(x_t, x_{t-j})$ is the joint density of x_t and x_{t-j} , is the covariance between x_t and x_{t-j} . The sequence x is said to be *weakly (or second-order) stationary* if $E(x_t) \equiv \mu$ and the mean and the covariance are *independent* of t , i.e., $E[(x_t - \mu_t)(x_{t-j} - \mu_{t-j})] = \gamma_j$. If $\gamma_j \equiv 0$ for $j \neq 0$, then the sequence x is *uncorrelated*. A weakly stationary random sequence that is uncorrelated is called a *stationary white noise*. In addition, if each of the elements x_t of the sequence has a common normal distribution, e.g., $N(0, \sigma^2)$ then the respective sequence is called *Gaussian white noise*. All of these notions carry over to sequences of random vectors.

8 Fourier Transforms

8.1 Fourier Transforms of Continuous Functions

Consider a function $g : \mathbb{R} \rightarrow \mathbb{R}$ which is piecewise smooth and absolutely integrable, i.e., $\int_{-\infty}^{\infty} |g(t)| dt < \infty$. The (direct or forward) *continuous time Fourier transform* $G(f)$ of a function $g(t)$ is a function $G : \mathbb{R} \rightarrow \mathbb{R}$ defined by $G(f) = F[g(t)] = \int_{-\infty}^{\infty} g(t) e^{-i2\pi ft} dt$, f is called the *rotational frequency* and $\omega = 2\pi f$ is called the *angular frequency*. The *inverse transform* of $G(f)$ is defined by $g(t) = F^{-1}[G(f)] = 1/2\pi \int_{-\infty}^{\infty} G(f) e^{i2\pi ft} df$. $G(f)$ is customarily called the *spectral representation* of $g(t)$. Note that $g(t)$ and $G(f)$ are two equivalent but different representations of the same function because

$$g(t) = F^{-1}[G(f)] = F^{-1}[F(g(t))] \quad \text{and} \quad G(f) = F[g(t)] = F[F^{-1}(G(f))].$$

8.2 Properties of Fourier Transform

1. *Linearity:* $F[ag(t) + bh(t)] = aF[g(t)] + bF[h(t)]$, for any two piecewise smooth and absolutely integrable functions $g(t)$ and $h(t)$ are, and any two real constants a and b .
2. *Shifting property:* $F[g(t - \tau)] = e^{-i2\pi f\tau} F[g(t)]$, for any real τ .
3. *Stretching property:* $F[g(at)] = \frac{1}{|a|} G\left(\frac{f}{a}\right)$, any nonzero real constant a .
4. *Derivative of a function:* $F\left[\frac{dg(t)}{dt}\right] = i2\pi fG(f)$.
5. *Integral of a function:* $F\left[\int_{-\infty}^t g(\tau)d\tau\right] = \frac{G(f)}{i2\pi f}$.
6. *Parseval's theorem:* $\int_{-\infty}^{\infty} |g(t)|^2 dt = \int_{-\infty}^{\infty} \|G(f)\|^2 df$, which signifies that the *total energy* is the same in both the representations.
7. *Time reversal property:* $F[g(-t)] = \int_{-\infty}^{\infty} g(-t)e^{-i2\pi ft} dt = G(-f)$.
8. *Convolution theorem:* the integral $(g * h)(t) = \int_{-\infty}^{\infty} g(r)h(t-r)dr$ is defined as the convolution of $g(t)$ and $h(t)$, and is denoted by $(g * h)(t)$. The convolution is commutative [$g * h = h * g$], associative [$g * (h * f) = (g * h) * f$], and distributive [$g * (f + h) = (g * f) + (g * h)$]; note that $F[g * h] = F(g)F(h)$.

8.3 Fourier Transform of Discrete Functions

The real-valued function $g = \{g_n\} = \{\dots, g_{-2}, g_{-1}, g_0, g_1, g_2, \dots\}$ is absolutely summable if $\sum_{n=-\infty}^{\infty} |g_n| < \infty$. The *discrete time Fourier transform* $G(f)$ of g is defined by $G(f) = \sum_{n=-\infty}^{\infty} g_n e^{-i2\pi fn}$. Note that, $G(f)$ is periodic with period = 1, i.e., $G(f + 1) = G(f)$.

Discrete convolution theorem: The (discrete) convolution of two sequences $g = \{g_n\}$ and $h = \{h_n\}$ is a sequence $s = \{s_n\}$, denoted by $s = g * h$, where $s_n = \sum_{k=-\infty}^{\infty} g_k h_{n-k}$. Note that

$$\begin{aligned} S(f) &= \sum_{n=-\infty}^{\infty} s_n e^{-i2\pi fn} = \sum_{n=-\infty}^{\infty} \left(\sum_{k=-\infty}^{\infty} g_k h_{n-k} \right) e^{-i2\pi fn} \\ &= \sum_{r=-\infty}^{\infty} \sum_{k=-\infty}^{\infty} g_k h_r e^{-i2\pi f(k+r)} \\ &= \sum_{r=-\infty}^{\infty} h_r e^{-i2\pi fr} \sum_{k=-\infty}^{\infty} g_k e^{-i2\pi fk} \\ &= H(f)G(f) = G(f)H(f). \end{aligned}$$

8.4 Fourier Series

Functions in one dimension: A sequence of functions $\{g_k(x)\}_{k=0}^{\infty}$ is a (pair-wise) *orthogonal system* if $\langle g_m, g_n \rangle = 0$, for $m \neq n$, and $\|g_n\|^2 = \lambda_n^2 > 0$, for all m . If $\lambda_n = 1$, then $\{g_k(x)\}_{k=0}^{\infty}$ is called an *orthonormal system*. The inner product is defined as $\langle f, g \rangle = \int_a^b f(x)g(x)dx$ and the *norm* is defined as $\|f\| = \langle f, f \rangle = \int_a^b f^2(x)dx > 0$.

Fourier series expansion: Given an orthogonal system $\{g_k(x)\}_{k=0}^{\infty}$ over the interval $[a, b]$, any piecewise continuous function $f(x)$ over $[a, b]$ can be represented by the (formal) series,

called the *Fourier series* of $f(x)$, $f(x) = \sum_{k=0}^{\infty} c_k g_k(x)$, where the *Fourier coefficients* c_k are obtained from the integral $c_k = \frac{1}{\|g_k\|} \int_a^b f(x) g_k(x) dx$.

Least squares property: Consider that $\{g_k\}_{k=0}^{\infty}$ is an orthogonal system over $[a, b]$, and consider that the finite linear combination $\sum_{k=0}^N a_k g_k(x)$ with arbitrary coefficients a_0, a_1, \dots, a_N denotes an approximation of $f(x)$ over $[a, b]$. Then the norm of the error $[f(x) - \sum_{k=0}^N a_k g_k(x)]$ is a minimum exactly when $a_k = c_k = \frac{1}{\|g_k\|} \int_a^b f(x) g_k(x) dx$, i.e., $\|f(x) - \sum_{k=0}^N c_k g_k(x)\| \leq \|f(x) - \sum_{k=0}^N a_k g_k(x)\|$, for any arbitrary set of coefficients a_0, a_1, \dots, a_N .

Functions in two dimensions: The system $\{g_k(x, y)\}_{k=0}^{\infty}$ is *orthogonal* over a rectangle $[a, b] \times [c, d]$ in \mathbb{R}^2 , $a < b$ and $c < d$, if

1. $\langle g_m, g_n \rangle = \int_c^d \int_a^b g_m(x, y) g_n(x, y) dx dy = 0$ for $m \neq n$.
2. $\|g_m\|^2 = \langle g_m, g_m \rangle = \int_c^d \int_a^b g_m^2(x, y) dx dy > 0$ for all m .

When $\|g_k\| = 1$ for all k , then $\{g_k(x, y)\}$ is called an *orthonormal system*.

Fourier series expansion: A piecewise continuous function $f(x, y)$ over $[a, b] \times [c, d]$ can be expanded in the Fourier series $f(x, y) = \sum_{k=0}^{\infty} c_k g_k(x, y)$, where $c_k = \frac{1}{\|g_k\|^2} \int_c^d \int_a^b f(x, y) g_k(x, y) dx dy$ are the respective Fourier coefficients.

If $\{g_k(x)\}_{k=0}^{\infty}$ and $\{h_j(y)\}_{j=0}^{\infty}$ are two orthogonal systems over the one-dimensional intervals $[a, b]$ and $[c, d]$, respectively, then the product system $\{g_i(x)h_j(y)\}_{0 \leq i < \infty \text{ and } 0 \leq j < \infty}$ is an orthogonal system over $[a, b] \times [c, d]$. In particular, the system

$$\{\cos mx \cos ny, \cos mx \sin ny, \sin mx \cos ny, \sin mx \sin ny, |0 \leq m < \infty, 0 \leq n < \infty\}$$

is orthogonal over $[-\pi, \pi] \times [-\pi, \pi]$. Hence, any piecewise continuous function $f(x)$ over $[a, b] \times [c, d]$ can be expressed in a *double Fourier Series* as

$$f(x, y) = \sum_{m,n} \lambda_{mn} [A_{mn} \cos mx \cos ny + B_{mn} \sin mx \cos ny + C_{mn} \cos mx \sin ny + D_{mn} \sin mx \sin ny],$$

where

$$\lambda_{mn} = \begin{cases} \frac{1}{4}, & \text{if } m = 0, n = 0, \\ \frac{1}{2}, & \text{if } m = 0, n \neq 0, \text{ or } m \neq 0, n = 0, \\ 1 & \text{if } m \neq 0, n \neq 0, \end{cases}$$

$$A_{mn} = \frac{1}{\pi^2} \int_{-\pi}^{\pi} \int_{-\pi}^{\pi} f(x, y) \cos mx \cos ny dx dy,$$

$$B_{mn} = \frac{1}{\pi^2} \int_{-\pi}^{\pi} \int_{-\pi}^{\pi} f(x, y) \sin mx \cos ny dx dy,$$

$$C_{mn} = \frac{1}{\pi^2} \int_{-\pi}^{\pi} \int_{-\pi}^{\pi} f(x, y) \cos mx \sin ny dx dy,$$

$$D_{mn} = \frac{1}{\pi^2} \int_{-\pi}^{\pi} \int_{-\pi}^{\pi} f(x, y) \sin mx \sin ny dx dy.$$

Bibliography

- Bauer H (1981) Probability theory and elements of measure theory, 2nd edn. Academic, New York
- Bogaevski VN, Povzner A (1991) Algebraic methods in nonlinear perturbation theory. Springer, New York
- Box GEP, Hunter WG, Hunter JS (1978) Statistics for experimenters. Wiley, New York
- Debnath L, Bhatta D (2007) Integral transforms and their applications, 2nd edn. Chapman & Hall/CRC Press, Boca Raton
- Deif AS (1982) Advanced matrix theory for scientists and engineers. Abacus Press-Halsted Press, New York
- Dieudonne J (1969) Foundations of modern analysis, vols I–VI. Academic, New York
- Drazin PG (1994) Nonlinear systems. Cambridge University Press, Cambridge
- Erdelyi A, Magnus W, Oberhettinger F, Tricomi FG (1953) Higher transcendental functions. McGraw-Hill, New York
- Erdelyi A, Magnus W, Oberhettinger F, Tricomi FG (1954) Tables of integral transforms. McGraw-Hill, New York
- Golub G, van Loan C (1989) Matrix computations. John Hopkins University Press, Baltimore
- Gradshteyn IS, Ryzhik IM (1965) Table of integrals, series, and products, 4th edn. Academic, New York
- Hestenes M (1980) Conjugate direction methods in optimization. Springer, New York
- Horn RA, Johnson CR (1996) Matrix analysis. Cambridge University Press, Cambridge
- Kanwal RP (1971) Linear integral equations, theory and technique. Academic, New York
- Kato T (1963) Perturbation theory for linear operators. Springer, Berlin
- Kendal M, Stuart A (1976) The advanced theory of statistics, 3rd edn., vols 1–3. Hafner Press, New York
- Liusternik LA, Sobolev VJ (1961) Elements of functional analysis. Frederick Ungar, New York
- Marichev O I (1982) Handbook of integral transforms of higher transcendental functions: theory and algorithmic tables. Ellis Horwood Ltd, Chichester
- Nowinski JL (1981) Applications of functional analysis in engineering. Plenum Press, New York
- Ortega JM, Rheinboldt WC (1970) Iterative solution of nonlinear equations in several variables. Academic, New York
- Pontryagin LS et al (1962) The mathematical theory of optimal processes. Wiley, New York
- Rall LB (ed) (1971) Nonlinear functional analysis and applications. Academic, New York
- Reed M, Simon B (1980) Methods of modern mathematical physics, vols I–IV. Academic, New York
- Rockafeller R T (1970) Convex analysis. Princeton University Press, Princeton
- Sagan H (1969) Introduction to the calculus of variations. McGraw-Hill, New York
- Schechter M (1977) Modern methods in partial differential equations, an introduction. McGraw-Hill, New York
- Varga RS (1971) Matrix iterative analysis. Prentice-Hall, Englewood Cliffs
- Walker J S (1988) Fourier analysis. Oxford University Press, Oxford
- Yosida K (1962) Functional analysis. Springer, Berlin
- Zemanian H (1965) Distribution theory and transform analysis. McGraw-Hill, New York
- Zwillinger D (1992) Handbook of differential equations, 2nd edn. Academic, New York

8 Multigroup Neutron Transport and Diffusion Computations

Alain Hébert

Institut de Génie Nucléaire, École Polytechnique de Montréal,
Montréal, Québec, Canada
alain.hebert@polymtl.ca

1	<i>The Steady-State Boltzmann Equation</i>	753
1.1	The Integro-Differential Form of the Transport Equation	760
1.2	The Characteristic Form of the Transport Equation	760
1.3	The Integral Form of the Transport Equation	761
1.4	Boundary and Continuity Conditions	762
1.5	The Steady-State Source Density	763
1.6	The Transport Correction	766
1.7	Multigroup Discretization	768
2	<i>The First-Order Streaming Operator</i>	772
2.1	Cartesian Coordinate System	772
2.2	Cylindrical Coordinate System	774
2.3	Spherical Coordinate System	777
3	<i>The Spherical Harmonics Method</i>	778
3.1	The P_n Method in 1D Slab Geometry	779
3.1.1	Discretization in Angle	779
3.1.2	Boundary Conditions	779
3.1.3	Difference Relations	781
3.2	The P_n Method in 1D Cylindrical Geometry	783
3.2.1	Discretization in Angle	783
3.2.2	Boundary Conditions	785
3.2.3	Difference Relations	787
3.3	The P_n Method in 1D Spherical Geometry	789
3.3.1	Discretization in Angle	789
3.3.2	Boundary Conditions	790
3.3.3	Difference Relations	790
3.4	The Simplified P_n Method in 2D Cartesian Geometry	792
3.4.1	Discretization in Angle	792
3.4.2	Difference Relations	793
4	<i>The Collision Probability Method</i>	794
4.1	The Interface Current Method	796

4.2	Scattering-Reduced Matrices and Power Iteration.....	799
4.3	Slab Geometry	800
4.4	Cylindrical 1D Geometry.....	805
4.5	Spherical 1D Geometry	812
4.6	Unstructured 2D Finite Geometry.....	814
5	<i>The Discrete Ordinates Method</i>	821
5.1	Quadrature Sets in the Method of Discrete Ordinates	821
5.2	The Difference Relations in 1D Slab Geometry.....	827
5.3	The Difference Relations in 1D Cylindrical Geometry	829
5.4	The Difference Relations in 1D Spherical Geometry	833
5.5	The Difference Relations in 2D Cartesian Geometry.....	836
5.6	Synthetic Acceleration	838
6	<i>The Method of Characteristics</i>	840
6.1	The MOC Integration Strategy	841
6.2	Unstructured 2D Finite Geometry.....	847
6.3	The Algebraic Collapsing Acceleration.....	853
7	<i>The Steady-State Diffusion Equation</i>	859
7.1	The Fick Law	862
7.2	Continuity and Boundary Conditions.....	864
7.3	The Finite Homogenous Reactor.....	866
7.3.1	Cartesian Coordinate System	867
7.3.2	Spherical Coordinate System	867
7.3.3	Cylindrical Coordinate System.....	868
7.4	The Heterogenous 1D Slab Reactor	869
7.4.1	Two-Region Example	872
8	<i>Discretization of the Neutron Diffusion Equation</i>	874
8.1	Mesh-Corner Finite Differences.....	875
8.2	Mesh-Centered Finite Differences	878
8.3	A Primal Variational Formulation	880
8.4	The Lagrangian Finite-Element Method	883
8.5	The Analytic Nodal Method in 2D Cartesian Geometry	887
	<i>Appendix: Tracking of 1D and 2D Geometries</i>	895
1	<i>Tracking of 1D Cylindrical and Spherical Geometries</i>	895
2	<i>The Theory Behind sybt1d</i>	898
3	<i>Tracking of 2D Square Pincell Geometries</i>	900
4	<i>The Theory Behind sybt2d</i>	906
	<i>References</i>	909

Abstract: The *transport equation* is introduced to describe a population of neutral particles such as neutrons or photons, in a close domain, under steady-state (i.e., stationary) conditions. Its derivation is based on the principle of *particle conservation*. The transport equation describes the statistical behavior of a large population of particles. The exact number of particles per unit volume is continuously varying with time, even at steady-state conditions. Under steady-state conditions, the number density of particles oscillates about an average value related to the solution of the steady-state transport equation. A solution of the transport equation is required in many fields of nuclear engineering, notably in *reactor physics*, in *safety and criticality*, and in *radiation shielding and protection*. We review legacy approaches for solving the steady-state transport equation, namely, the method of spherical harmonics, the collision probability method, the discrete ordinates method, and the method of characteristics. The full-core calculation consists of solving a simplified transport equation, either the diffusion equation or the simplified P_n equation.

1 The Steady-State Boltzmann Equation

We first introduce the fundamental quantities used in the context of the transport equation. We use an approach of *statistical mechanics* in which each particle is moving in a six-dimensional *phase space* made of three positions and three velocity coordinate axes. The position of a single particle is identified by a set of seven quantities as follows:

- Three position coordinates $\mathbf{r} = x \mathbf{i} + y \mathbf{j} + z \mathbf{k}$
- Three velocity coordinates. We use the velocity module $V_n \equiv |\mathbf{V}_n|$ with $\mathbf{V}_n = d\mathbf{r}/dt$ and the two components of the direction $\mathbf{\Omega} \equiv \mathbf{V}_n/V_n$
- The time t , used in transient situations, when the steady-state hypothesis is not valid

A population of particles is represented by a distribution, the *population density* $n(\mathbf{r}, V_n, \mathbf{\Omega}, t)$ such that $n(\mathbf{r}, V_n, \mathbf{\Omega}, t) d^3r dV_n d^2\Omega$ is the number of particles, at time t , in the volume element d^3r surrounding point \mathbf{r} , in the velocity element dV_n surrounding V_n , and in the solid angle element $d^2\Omega$ surrounding $\mathbf{\Omega}$. We note that $n(\mathbf{r}, V_n, \mathbf{\Omega}, t)$ is a distribution with respect to variables \mathbf{r} , V_n , and $\mathbf{\Omega}$. It is a function of t .

The dependent variable used in reactor physics is the *particle flux*. The *angular flux* is a distribution related to the population density and is defined as

$$\phi(\mathbf{r}, V_n, \mathbf{\Omega}, t) \equiv V_n n(\mathbf{r}, V_n, \mathbf{\Omega}, t). \quad (1)$$

It is more convenient to use angular flux as the dependent variable of the transport equation. The angular flux has no precise physical significance; it is a mathematical definition. However, the probability for a particle to collide depends on each of the factors n and V_n . Increasing the number of particles in one cubic centimeter volume makes it more likely that one of them will collide. Increasing the particle speed increases the number of visits in the one cubic centimeter volume each second.

The angular flux defined in (1) gives the maximum information about the population of particles. In many applications a more global representation is preferred. The *integrated flux* is obtained by performing a distribution reduction on variable $\mathbf{\Omega}$, so that

$$\phi(\mathbf{r}, V_n, t) = \int_{4\pi} d^2\Omega \phi(\mathbf{r}, V_n, \mathbf{\Omega}, t), \quad (2)$$

where we have used the same symbol to represent the two distributions.

In physical terms, the integrated flux is the total distance traveled in one second by all the particles in the one cubic centimeter volume, as it is obtained by multiplying the number of particles in that cubic centimeter by the speed of each one. This is equivalent to the total length of all the particle tracks laid down in one cubic centimeter in one second.

The integrated flux may be written with the particle energy E or lethargy u as independent variable, replacing V_n . The change of variables can be performed, so that


$$E = \frac{1}{2} m V_n^2 \quad \text{and} \quad u = \ln \frac{E_0}{E}, \quad (3)$$


where m is the mass of a particle and E_0 is the maximum energy of a particle, so that

$$\phi(\mathbf{r}, E, t) = \frac{1}{m V_n} \phi(\mathbf{r}, V_n, t), \quad 0 < E \leq E_0 \quad (4)$$

and

$$\phi(\mathbf{r}, u, t) = E \phi(\mathbf{r}, E, t), \quad 0 \leq u < \infty. \quad (5)$$

We now define the *angular current*, another fundamental distribution. In  Fig. 1, we present an element of surface d^2S with a unit normal vector \mathbf{N} located on point \mathbf{r} .

The number of particles crossing d^2S in  Fig. 1 is

$$d^3n = n(\mathbf{r}, V_n, \Omega, t) [d^2S (V_n dt) \Omega \cdot \mathbf{N}]. \quad (6)$$

The angular current $\mathbf{J}(\mathbf{r}, V_n, \Omega, t)$ is a vector defined in such a way that

$$\frac{d^3n}{d^2S dt} = \mathbf{J}(\mathbf{r}, V_n, \Omega, t) \cdot \mathbf{N} \quad (7)$$

so that

$$\mathbf{J}(\mathbf{r}, V_n, \Omega, t) = \Omega \phi(\mathbf{r}, V_n, \Omega, t). \quad (8)$$

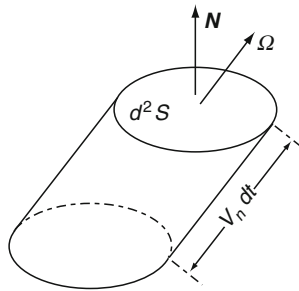


 Figure 1

Definition of the particle current. The number d^3n of particles, of velocity V_n and direction Ω , crossing d^2S during an element of time dt is equal to the number of particles located in the represented slanted cylinder

In similarity with the integrated flux, we can define the *integrated current* as

$$J(\mathbf{r}, V_n, t) = \int_{4\pi} d^2\Omega J(\mathbf{r}, V_n, \Omega, t) = \int_{4\pi} d^2\Omega \Omega \phi(\mathbf{r}, V_n, \Omega, t). \tag{9}$$

The angular current is positive if the particle crosses d^2S in the direction of \mathbf{N} , and negative otherwise. We can also define the *outgoing current* J^+ and *incoming current* J^- by integrating the angular current over outgoing and incoming directions, respectively. We write


$$J^+(\mathbf{r}, V_n, t) = \int_{\Omega \cdot \mathbf{N} > 0} d^2\Omega (\Omega \cdot \mathbf{N}) \phi(\mathbf{r}, V_n, \Omega, t) \tag{10}$$

and

$$J^-(\mathbf{r}, V_n, t) = - \int_{\Omega \cdot \mathbf{N} < 0} d^2\Omega (\Omega \cdot \mathbf{N}) \phi(\mathbf{r}, V_n, \Omega, t) \tag{11}$$

so that

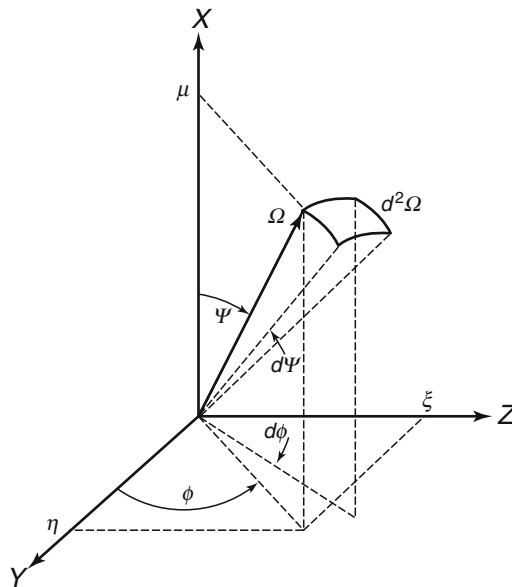
$$J(\mathbf{r}, V_n, t) \cdot \mathbf{N} = J^+(\mathbf{r}, V_n, t) - J^-(\mathbf{r}, V_n, t). \tag{12}$$


The velocity vector V_n of the particle is pointing in the direction of the solid angle Ω , as depicted in  Fig. 2, so that

$$V_n = V_n \Omega, \tag{13}$$

where

$$V_n = |V_n| \quad \text{and} \quad |\Omega| = 1. \tag{14}$$



 **Figure 2**
 Definition of the solid angle. The direction of a moving particle in a three-dimensional (3D) domain is represented by its *solid angle*, a unit vector pointing in the direction of the particle

The solid angle Ω is defined in terms of its three *direction cosines*, μ , η , and ξ , using

$$\Omega = \mu \mathbf{i} + \eta \mathbf{j} + \xi \mathbf{k} \quad (15)$$

with the constraint

$$\mu^2 + \eta^2 + \xi^2 = 1, \quad (16)$$

where the symbols \mathbf{i} , \mathbf{j} , and \mathbf{k} are used to denote the unit vectors in the x -, y -, and z -direction, respectively.

Here, we have used the x -axis as the *principal axis* to define the *colatitude* or *polar angle* $\psi = \cos^{-1} \mu$ and the *azimuth* ϕ . The definition domain is $0 \leq \psi \leq \pi$ for the colatitude and $0 \leq \phi \leq 2\pi$ for the azimuth. On a case-by-case basis, any other axis can be used. The last two direction cosines are written in terms of the azimuthal angle ϕ using

$$\eta = \sqrt{1 - \mu^2} \cos \phi \quad \text{and} \quad \xi = \sqrt{1 - \mu^2} \sin \phi. \quad (17)$$

An increase in ψ by $d\psi$ and in ϕ by $d\phi$ sweeps out the area $d^2\Omega$ on a unit sphere. The solid angle encompassed by a range of directions is defined as the area swept out on the surface of a sphere divided by the square of the radius of the sphere. Thus, the differential solid angle associated with solid angle Ω is

$$d^2\Omega = \sin \psi \, d\psi \, d\phi. \quad (18)$$

The solid angle is a dimensionless quantity. Nevertheless, to avoid confusion when referring to a directional distribution function, units of steradians, abbreviated sr, are attributed to the solid angle.

In reactor physics, many quantities are continuous and bounded distributions of the particle direction cosine μ or solid angle Ω . In the first case, such a quantity is written as $f(\mu)$ and can be approximated in terms of an L -order *Legendre polynomial* expansion using

$$f(\mu) = \sum_{\ell=0}^L \frac{2\ell+1}{2} f_{\ell} P_{\ell}(\mu), \quad (19)$$

where the ℓ th order coefficient is obtained using

$$f_{\ell} = \int_{-1}^1 d\mu P_{\ell}(\mu) f(\mu). \quad (20)$$

The Legendre polynomials are defined by the relations

$$P_0(\mu) = 1, \quad P_1(\mu) = \mu \quad (21)$$

and

$$P_{\ell+1}(\mu) = \frac{1}{\ell+1} [(2\ell+1)\mu P_{\ell}(\mu) - \ell P_{\ell-1}(\mu)] \quad \text{if } \ell \geq 1. \quad (22)$$

In the more general case, a bounded distribution of the particle solid angle is written as $f(\Omega)$ and can be approximated in terms of an L -order *real spherical harmonics* expansion using

$$f(\Omega) = \sum_{\ell=0}^L \frac{2\ell+1}{4\pi} \sum_{m=-\ell}^{\ell} f_{\ell}^m R_{\ell}^m(\Omega), \quad (23)$$

where $R_{\ell}^m(\Omega)$ is a real spherical harmonics component, a distribution of the solid angle Ω .

The first component μ of the solid angle is the cosine of the polar angle and ϕ represents the azimuthal angle. These components are expressed in terms of the associated Legendre functions $P_\ell^{m_l}(\mu)$ using

$$R_\ell^m(\Omega) = \sqrt{(2 - \delta_{m,0}) \frac{(\ell - |m|)!}{(\ell + |m|)!}} P_\ell^{|m|}(\mu) \mathcal{T}_m(\phi), \quad (24)$$

where $P_\ell^m(\mu)$ is defined in terms of the ℓ th-order Legendre polynomial $P_\ell(\mu)$ as

$$P_\ell^m(\mu) = (1 - \mu^2)^{m/2} \frac{d^m}{d\mu^m} P_\ell(\mu), \quad m \geq 0 \quad (25)$$

and where

$$\mathcal{T}_m(\phi) = \begin{cases} \cos m\phi & \text{if } m \geq 0, \\ \sin |m|\phi & \text{otherwise.} \end{cases} \quad (26)$$

Note that we have used the Ferrer definition of the associated Legendre functions $P_\ell^m(\mu)$, in which the factor $(-1)^m$ is absent. They can be obtained using the following Matlab script:

```
function f=plgndr(l,m,x)
% return the Ferrer definition of the associated Legendre function.
% function f=plgndr(l,m,x)
% (c) 2008 Alain Hebert, Ecole Polytechnique de Montreal
if m < 0
    error('bad arguments in plgndr 1')
elseif m > l
    error('bad arguments in plgndr 2')
elseif abs(x) > 1.
    error('bad arguments in plgndr 3')
end
pmm=1.;
if m > 0, pmm=prod(1:2:2*m)*sqrt((1.-x).*(1.+x)).^m; end
if l == m
    f=pmm;
else
    pmmp1=(2*m+1)*x.*pmm;
    if l == m+1
        f=pmmp1;
    else
        for ll=m+2:l
            pll=((2*ll-1)*x.*pmmp1-(ll+m-1)*pmm)/(ll-m);
            pmm=pmmp1; pmmp1=pll;
        end
        f=pll;
    end
end
```

The Ferrer definition helps to simplify low-order angular expansions since

$$\mathbf{\Omega} = \begin{pmatrix} \frac{\mu}{\sqrt{1-\mu^2}} \cos \phi \\ \sqrt{1-\mu^2} \cos \phi \\ \sqrt{1-\mu^2} \sin \phi \end{pmatrix} = \begin{pmatrix} R_1^0(\mathbf{\Omega}) \\ R_1^1(\mathbf{\Omega}) \\ R_1^{-1}(\mathbf{\Omega}) \end{pmatrix}. \quad (27)$$

Real spherical harmonics are to be preferred to classical ones because they permit us to eliminate imaginary components in 3D problems. The trigonometric functions, associated Legendre functions, and real spherical harmonics obey the following orthonormal conditions:

$$\int_{-\pi}^{\pi} d\phi \mathcal{T}_m(\phi) \mathcal{T}_{m'}(\phi) = \pi (1 + \delta_{m,0}) \delta_{m,m'}, \quad (28)$$

$$\int_{-1}^1 d\mu P_\ell^m(\mu) P_{\ell'}^m(\mu) = \frac{2(\ell+m)!}{(2\ell+1)(\ell-m)!} \delta_{\ell,\ell'} \quad (29)$$

and

$$\int_{4\pi} d^2\Omega R_\ell^m(\mathbf{\Omega}) R_{\ell'}^{m'}(\mathbf{\Omega}) = \frac{4\pi}{2\ell+1} \delta_{\ell,\ell'} \delta_{m,m'} \quad (30)$$

with $d^2\Omega = d\mu d\phi$, so that the components of the source distribution are written as

$$f_\ell^m = \int_{4\pi} d^2\Omega R_\ell^m(\mathbf{\Omega}) f(\mathbf{\Omega}). \quad (31)$$

In the previous relations, we have introduced the integral over 4π to represent an integration over all possible directions. This integral is defined as

$$\int_{4\pi} d^2\Omega f(\mathbf{\Omega}) \equiv \int_{-1}^1 d\mu \int_0^{2\pi} d\phi f(\mu, \phi). \quad (32)$$

The real spherical harmonics satisfy the *addition theorem* which can be written in terms of two different solid angles, $\mathbf{\Omega}$ and $\mathbf{\Omega}'$, as

$$P_\ell(\mathbf{\Omega} \cdot \mathbf{\Omega}') = \sum_{m=-\ell}^{\ell} R_\ell^m(\mathbf{\Omega}) R_\ell^m(\mathbf{\Omega}'), \quad \ell \geq 0. \quad (33)$$

The real spherical harmonics can be written as polynomials in direction cosines as follows:

$$R_0^0 = 1, \quad (34)$$

$$R_1^{-1} = \xi, \quad R_1^0 = \mu, \quad R_1^1 = \eta, \quad (35)$$

$$R_2^{-2} = \sqrt{3} \eta \xi, \quad R_2^{-1} = \sqrt{3} \mu \xi, \quad R_2^0 = \frac{1}{2}(3\mu^2 - 1),$$

$$R_2^1 = \sqrt{3} \mu \eta, \quad R_2^2 = \frac{\sqrt{3}}{2}(\eta^2 - \xi^2), \quad (36)$$

$$\begin{aligned}
R_3^{-3} &= \sqrt{\frac{5}{8}} \xi(3\eta^2 - \xi^2), & R_3^{-2} &= \sqrt{15} \mu \xi \eta, & R_3^{-1} &= \sqrt{\frac{3}{8}} \xi(5\mu^2 - 1), \\
R_3^0 &= \frac{1}{2} \mu(5\mu^2 - 3), & R_3^1 &= \sqrt{\frac{3}{8}} \eta(5\mu^2 - 1), & R_3^2 &= \sqrt{\frac{15}{4}} \mu(\eta^2 - \xi^2), \\
R_3^3 &= \sqrt{\frac{5}{8}} \eta(\eta^2 - 3\xi^2).
\end{aligned} \tag{37}$$

Another common approximation consists in developing the angular flux in spherical harmonics. We are using the standard closure condition, assuming that the $(L + 1)$ th Legendre coefficients of the angular flux are zero at all spatial points. The angular flux is expanded as

$$\phi(\mathbf{r}, V_n, \mathbf{\Omega}, t) = \sum_{\ell=0}^L \frac{2\ell+1}{4\pi} \sum_{m=-\ell}^{\ell} \phi_{\ell}^m(\mathbf{r}, V_n, t) R_{\ell}^m(\mathbf{\Omega}), \tag{38}$$

where the real spherical harmonics $R_{\ell}^m(\mathbf{\Omega})$ are defined in (24). The summation over index ℓ in (38) corresponds to the more general case of a three-dimensional (3D) geometry. In one-dimensional (1D) slab and spherical geometries, only the $m = 0$ value is required, due to symmetry reasons. In 1D cylindrical geometry, only $0 \leq m \leq \ell$ values with $m + \ell$ even are required. In 2D geometries defined in the x - y plane, only even $m + \ell$ values are required.

There are important relations between the spherical harmonic moments of the angular flux and the integrated flux and current values. We can show that

$$\phi(\mathbf{r}, V_n, t) = \phi_0^0(\mathbf{r}, V_n, t) \tag{39}$$

and that

$$\mathbf{J}(\mathbf{r}, V_n, t) = \phi_1^0(\mathbf{r}, V_n, t) \mathbf{i} + \phi_1^1(\mathbf{r}, V_n, t) \mathbf{j} + \phi_1^{-1}(\mathbf{r}, V_n, t) \mathbf{k}. \tag{40}$$

However, (40) is only consistent with the Ferrer definition of the associated Legendre polynomials.

Equation (38) can be truncated after the $\ell = 1$ component, leading to the *linearly anisotropic flux approximation*. We write

$$\begin{aligned}
\phi(\mathbf{r}, V_n, \mathbf{\Omega}, t) &= \frac{1}{4\pi} \left[\phi_0^0(\mathbf{r}, V_n, t) + 3 \sum_{m=-1}^1 \phi_1^m(\mathbf{r}, V_n, t) R_1^m(\mathbf{\Omega}) \right] \\
&= \frac{1}{4\pi} [\phi(\mathbf{r}, V_n, t) + 3 \mathbf{\Omega} \cdot \mathbf{J}(\mathbf{r}, V_n, t)].
\end{aligned} \tag{41}$$

Analytical expressions for $J^+(\mathbf{r}, V_n, t)$ and $J^-(\mathbf{r}, V_n, t)$ can be found in the special case of the linearly anisotropic flux approximation. We substitute (41) into (10) and set $\mathbf{N} = \mathbf{i}$ with $\mathbf{\Omega} = \mu \mathbf{i} + \sqrt{1 - \mu^2} \cos \omega \mathbf{j} + \sqrt{1 - \mu^2} \sin \omega \mathbf{k}$, so that

$$\begin{aligned}
J^+(\mathbf{r}, V_n, t) &= \frac{1}{4\pi} \int_{\mathbf{\Omega} \cdot \mathbf{N} > 0} d^2 \Omega (\mathbf{\Omega} \cdot \mathbf{N}) [\phi(\mathbf{r}, V_n, t) + 3 \mathbf{\Omega} \cdot \mathbf{J}(\mathbf{r}, V_n, t)] \\
&= \frac{1}{4\pi} \int_0^1 d\mu \mu \int_0^{2\pi} d\omega [\phi(\mathbf{r}, V_n, t) + 3\mu J_x(\mathbf{r}, V_n, t) \\
&\quad + 3\sqrt{1 - \mu^2} \cos \omega J_y(\mathbf{r}, V_n, t) + 3\sqrt{1 - \mu^2} \sin \omega J_z(\mathbf{r}, V_n, t)] \\
&= \frac{1}{4} \phi(\mathbf{r}, V_n, t) + \frac{1}{2} \mathbf{J}(\mathbf{r}, V_n, t) \cdot \mathbf{N}.
\end{aligned}$$

Similarly, we can show that

$$J^-(\mathbf{r}, V_n, t) = \frac{1}{4} \phi(\mathbf{r}, V_n, t) - \frac{1}{2} \mathbf{J}(\mathbf{r}, V_n, t) \cdot \mathbf{N} \quad (42)$$

and

$$\phi(\mathbf{r}, V_n, t) = 2 [J^-(\mathbf{r}, V_n, t) + J^+(\mathbf{r}, V_n, t)]. \quad (43)$$

1.1 The Integro-Differential Form of the Transport Equation

The Boltzmann equation is obtained as the phase-space balance relation for the neutral particles located in a control volume. The absence of particle-particle interactions produces a linear form of the *Boltzmann equation*. In steady-state conditions, it is written (Hébert 2009) as

$$\Omega \cdot \nabla \phi(\mathbf{r}, V_n, \Omega) + \Sigma(\mathbf{r}, V_n) \phi(\mathbf{r}, V_n, \Omega) = Q(\mathbf{r}, V_n, \Omega). \quad (44)$$

The source density can be written in a spherical harmonic expansion similar to (38) as

$$Q(\mathbf{r}, V_n, \Omega) = \sum_{\ell=0}^L \frac{2\ell+1}{4\pi} \sum_{m=-\ell}^{\ell} Q_{\ell}^m(\mathbf{r}, V_n) R_{\ell}^m(\Omega), \quad (45)$$

where the value of L is smaller or equal to the value used in (38).

1.2 The Characteristic Form of the Transport Equation

The characteristic form of the transport equation corresponds to an integration of the *streaming operator* $\Omega \cdot \nabla \phi$ over the *characteristic*, a straight line direction Ω is corresponding to the particle trajectory. At each time of its motion, the particle is assumed to be at distance s from a reference position \mathbf{r} on its characteristic, so that its actual position is $\mathbf{r} + s \Omega$. The streaming operator can be transformed using a derivation in series. We first write

$$\frac{d}{ds} = \frac{dx}{ds} \frac{\partial}{\partial x} + \frac{dy}{ds} \frac{\partial}{\partial y} + \frac{dz}{ds} \frac{\partial}{\partial z} \quad (46)$$

with

$$ds \Omega = d\mathbf{r} = dx \mathbf{i} + dy \mathbf{j} + dz \mathbf{k}. \quad (47)$$

Taking the dot product of (47) with \mathbf{i} , we obtain $ds \Omega \cdot \mathbf{i} = dx$. Similarly, $ds \Omega \cdot \mathbf{j} = dy$ and $ds \Omega \cdot \mathbf{k} = dz$. After substitution into (46), we obtain

$$\frac{d}{ds} = (\Omega \cdot \mathbf{i}) \frac{\partial}{\partial x} + (\Omega \cdot \mathbf{j}) \frac{\partial}{\partial y} + (\Omega \cdot \mathbf{k}) \frac{\partial}{\partial z} = \Omega \cdot \nabla. \quad (48)$$

Substituting (48) into (44), we obtain the backward *characteristic form of the transport equation* as

$$\frac{d}{ds} \phi(\mathbf{r} + s \Omega, V_n, \Omega) + \Sigma(\mathbf{r} + s \Omega, V_n) \phi(\mathbf{r} + s \Omega, V_n, \Omega) = Q(\mathbf{r} + s \Omega, V_n, \Omega). \quad (49)$$

Equation (49) can also be written in the forward form as

$$-\frac{d}{ds}\phi(\mathbf{r}-s\boldsymbol{\Omega}, V_n, \boldsymbol{\Omega}) + \Sigma(\mathbf{r}-s\boldsymbol{\Omega}, V_n)\phi(\mathbf{r}-s\boldsymbol{\Omega}, V_n, \boldsymbol{\Omega}) = Q(\mathbf{r}-s\boldsymbol{\Omega}, V_n, \boldsymbol{\Omega}). \quad (50)$$

1.3 The Integral Form of the Transport Equation

The integral transport equation is obtained by integrating the angular flux along its characteristic, for a given value of the source density $Q(\mathbf{r}, V_n, \boldsymbol{\Omega})$. We first introduce an integrating factor $e^{-\tau(s, V_n)}$ where the *optical path* is defined as a function of the macroscopic total cross-section $\Sigma(\mathbf{r}, V_n)$ using

$$\tau(s, V_n) = \int_0^s ds' \Sigma(\mathbf{r}-s'\boldsymbol{\Omega}, V_n). \quad (51)$$

We next compute the following relation:

$$\begin{aligned} \frac{d}{ds} \left[e^{-\tau(s, V_n)} \phi(\mathbf{r}-s\boldsymbol{\Omega}, V_n, \boldsymbol{\Omega}) \right] &= e^{-\tau(s, V_n)} \left[-\Sigma(\mathbf{r}-s\boldsymbol{\Omega}, V_n) \phi(\mathbf{r}-s\boldsymbol{\Omega}, V_n, \boldsymbol{\Omega}) \right. \\ &\quad \left. + \frac{d}{ds} \phi(\mathbf{r}-s\boldsymbol{\Omega}, V_n, \boldsymbol{\Omega}) \right], \end{aligned} \quad (52)$$

where we used the identity

$$\frac{d}{ds} \int_0^s ds' g(s') = g(s).$$

Substitution of (50) into (52) leads to

$$-\frac{d}{ds} \left[e^{-\tau(s, V_n)} \phi(\mathbf{r}-s\boldsymbol{\Omega}, V_n, \boldsymbol{\Omega}) \right] = e^{-\tau(s, V_n)} Q(\mathbf{r}-s\boldsymbol{\Omega}, V_n, \boldsymbol{\Omega}). \quad (53)$$

Equation (53) can be integrated between 0 and ∞ , so that

$$-\int_0^\infty ds \frac{d}{ds} \left[e^{-\tau(s, V_n)} \phi(\mathbf{r}-s\boldsymbol{\Omega}, V_n, \boldsymbol{\Omega}) \right] = \int_0^\infty ds e^{-\tau(s, V_n)} Q(\mathbf{r}-s\boldsymbol{\Omega}, V_n, \boldsymbol{\Omega}) \quad (54)$$

or

$$\phi(\mathbf{r}, V_n, \boldsymbol{\Omega}) = \int_0^\infty ds e^{-\tau(s, V_n)} Q(\mathbf{r}-s\boldsymbol{\Omega}, V_n, \boldsymbol{\Omega}). \quad (55)$$

Equation (55) is the integral form of the transport equation for the infinite-domain case.

The path of the particle between points \mathbf{r}' and \mathbf{r} is depicted in  Fig. 3.

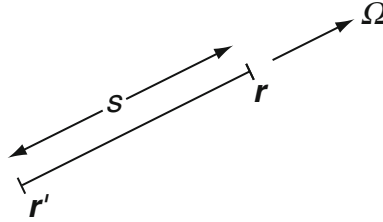
If the domain is finite, it is possible to integrate only over the s values corresponding to a value of \mathbf{r}' inside the domain. In this case, the integral form of the transport equation is written as

$$\phi(\mathbf{r}, V_n, \boldsymbol{\Omega}) = e^{-\tau(b, V_n)} \phi(\mathbf{r}-b\boldsymbol{\Omega}, V_n, \boldsymbol{\Omega}) + \int_0^b ds e^{-\tau(s, V_n)} Q(\mathbf{r}-s\boldsymbol{\Omega}, V_n, \boldsymbol{\Omega}), \quad (56)$$

where $\phi(\mathbf{r}-b\boldsymbol{\Omega}, V_n, \boldsymbol{\Omega})$ can be assimilated to a boundary flux.

The integral form of the transport equation is generally limited to isotropic sources in the laboratory (LAB) frame of reference, so that

$$Q(\mathbf{r}, V_n, \boldsymbol{\Omega}) = \frac{1}{4\pi} Q(\mathbf{r}, V_n). \quad (57)$$



■ Figure 3

Characteristic of the particle between two positions. A particle from source $Q(r', V_n, \Omega)$ will travel with an exponential attenuation factor in direction Ω and contribute to the flux at point r

1.4 Boundary and Continuity Conditions

The domain V where the particles move may be surrounded by a boundary ∂V where *boundary conditions* are imposed. We also introduce $N(\mathbf{r}_s)$, the outward normal at $\mathbf{r}_s \in \partial V$. Solution of the transport equation in V requires the knowledge of the angular flux $\phi(\mathbf{r}_s, V_n, \Omega)$ for $\Omega \cdot N(\mathbf{r}_s) < 0$.

The *albedo boundary condition* is used to relate the incoming flux with the known outgoing flux. This condition is written as

$$\phi(\mathbf{r}_s, V_n, \Omega) = \beta \phi(\mathbf{r}_s, V_n, \Omega') \quad (58)$$

with $\Omega \cdot N(\mathbf{r}_s) < 0$, the solid angle Ω' representing the direction of the outgoing particle. The albedo β is equal to zero and one for a vacuum and reflective boundary condition, respectively. Intermediate values can also be used. *Specular reflection* corresponds to the case where

$$\Omega \cdot N(\mathbf{r}_s) = -\Omega' \cdot N(\mathbf{r}_s) \quad \text{and} \quad (\Omega \times \Omega') \cdot N(\mathbf{r}_s) = 0. \quad (59)$$

The *white boundary condition* is a reflective condition where all particles striking the boundary turn back to V with an isotropic angular distribution. In this case,

$$\phi(\mathbf{r}_s, V_n, \Omega) = \beta \frac{\int_{\Omega' \cdot N(\mathbf{r}_s) > 0} d^2 \Omega' [\Omega' \cdot N(\mathbf{r}_s)] \phi(\mathbf{r}_s, V_n, \Omega')}{\int_{\Omega' \cdot N(\mathbf{r}_s) > 0} d^2 \Omega' [\Omega' \cdot N(\mathbf{r}_s)]} \quad (60)$$

with $\Omega \cdot N(\mathbf{r}_s) < 0$ and where β is the albedo, defined as before. Equation (60) simplifies to

$$\phi(\mathbf{r}_s, V_n, \Omega) = \frac{\beta}{\pi} \int_{\Omega' \cdot N(\mathbf{r}_s) > 0} d^2 \Omega' [\Omega' \cdot N(\mathbf{r}_s)] \phi(\mathbf{r}_s, V_n, \Omega') \quad (61)$$

with $\Omega \cdot N(\mathbf{r}_s) < 0$.

The *periodic boundary condition* corresponds to the case where the flux on one boundary is equal to the flux on another parallel boundary in a periodic lattice grid. In this case,

$$\phi(\mathbf{r}_s, V_n, \Omega) = \phi(\mathbf{r}_s + \Delta \mathbf{r}, V_n, \Omega), \quad (62)$$

where $\Delta \mathbf{r}$ is the lattice pitch.

The *zero-flux boundary condition* corresponds to the absence of particles on ∂V . This condition is nonphysical as particles are continuously leaving the domain V , producing a nonzero number density on ∂V . The vacuum boundary condition must always be preferred to represent an external boundary. In cases where a zero-flux boundary condition must be applied, it is obtained by setting to zero all *even moments* of the spherical harmonic expansion of ϕ as

$$\phi_\ell^m(\mathbf{r}_s, V_n) = 0 \quad \text{with } \ell \text{ even.} \quad (63)$$

Inside the domain V , the angular flux $\phi(\mathbf{r}, V_n, \mathbf{\Omega})$ must be continuous across all internal interfaces in the direction $\mathbf{\Omega}$ of the moving particle. Discontinuities along $\mathbf{\Omega}$ can occur only if the source density contains Dirac delta contributions. The continuity condition is not required along directions which are not parallel to the path of travel.

1.5 The Steady-State Source Density

In reactor physics, the neutral particles are neutrons and the source density is a multiplicative source of secondary fission, scattering, and (n, xn) secondary neutrons. Expressions for the source density are given in steady-state and transient conditions. The steady-state source density is used in both lattice and static full-core calculations. The transient source density is only meaningful for full-core calculations. In the following developments, the energy variable $E = mV_n^2/2$ is used as a replacement for the neutron velocity V_n as independent variable.

In the case of a multiplying medium with neutrons, the differential form of the steady-state transport equation is given by (44) as

$$\mathbf{\Omega} \cdot \nabla \phi(\mathbf{r}, E, \mathbf{\Omega}) + \Sigma(\mathbf{r}, E) \phi(\mathbf{r}, E, \mathbf{\Omega}) = Q(\mathbf{r}, E, \mathbf{\Omega}). \quad (64)$$

Assuming that the fission reactions are isotropic in the LAB, the steady-state source density is written as

$$Q(\mathbf{r}, E, \mathbf{\Omega}) = \int_{4\pi} d^2\Omega' \int_0^\infty dE' \Sigma_s(\mathbf{r}, E \leftarrow E', \mathbf{\Omega} \leftarrow \mathbf{\Omega}') \phi(\mathbf{r}, E', \mathbf{\Omega}') + \frac{1}{4\pi K_{\text{eff}}} Q^{\text{fiss}}(\mathbf{r}, E), \quad (65)$$

where

$\Sigma_s(\mathbf{r}, E \leftarrow E', \mathbf{\Omega} \leftarrow \mathbf{\Omega}')$ = macroscopic differential-scattering cross-section taking into account diffusion *and* (n, xn) reactions.

K_{eff} = *effective multiplication factor*. If the sum of absorption and leakage rates does not equal the production rate of new-fission neutrons, the steady-state condition is lost. K_{eff} is the factor used to divide the fission sources in order to maintain the steady-state condition.

$Q^{\text{fiss}}(\mathbf{r}, E)$ = isotropic fission sources.

In isotropic media, the scattering cross-section is only a function of the scattering angle, so that (65) can be rewritten as

$$Q(\mathbf{r}, E, \mathbf{\Omega}) = \frac{1}{2\pi} \int_{4\pi} d^2\Omega' \int_0^\infty dE' \Sigma_s(\mathbf{r}, E \leftarrow E', \mathbf{\Omega} \cdot \mathbf{\Omega}') \phi(\mathbf{r}, E', \mathbf{\Omega}') + \frac{1}{4\pi K_{\text{eff}}} Q^{\text{fiss}}(\mathbf{r}, E). \quad (66)$$

In this case, it is convenient to expand the scattering cross-section in terms of Legendre polynomials as

$$\Sigma_s(\mathbf{r}, E \leftarrow E', \boldsymbol{\Omega} \cdot \boldsymbol{\Omega}') = \sum_{\ell=0}^L \frac{2\ell+1}{2} \Sigma_{s,\ell}(\mathbf{r}, E \leftarrow E') P_\ell(\boldsymbol{\Omega} \cdot \boldsymbol{\Omega}'), \quad (67)$$

where L is the scattering order of the medium where the neutron is moving. $L = 0$ and $L = 1$ correspond to *isotropic scattering* and to *linearly anisotropic scattering* in the LAB, respectively. The Legendre coefficients $\Sigma_{s,\ell}(E \leftarrow E')$ are defined as

$$\Sigma_{s,\ell}(E \leftarrow E') = \int_{-1}^1 d\mu \Sigma_s(E \leftarrow E', \mu) P_\ell(\mu). \quad (68)$$

Using the addition theorem of spherical harmonics (see (33)), it is possible to rewrite the scattering source of (66) in terms of the spherical harmonics components of the flux as

$$Q(\mathbf{r}, E, \boldsymbol{\Omega}) = \int_0^\infty dE' \sum_{\ell=0}^L \frac{2\ell+1}{4\pi} \Sigma_{s,\ell}(\mathbf{r}, E \leftarrow E') \sum_{m=-\ell}^{\ell} R_\ell^m(\boldsymbol{\Omega}) \phi_\ell^m(\mathbf{r}, E') + \frac{1}{4\pi K_{\text{eff}}} Q^{\text{fiss}}(\mathbf{r}, E), \quad (69)$$

where

$$\phi_\ell^m(\mathbf{r}, E) = \int_{4\pi} d^2\Omega R_\ell^m(\boldsymbol{\Omega}) \phi(\mathbf{r}, E, \boldsymbol{\Omega}). \quad (70)$$

We assume that the isotropic fission source is independent of the energy of the incident neutron. For each fissionable nuclide i , the energy of emitted neutrons is distributed according to a probability density known as *fission spectrum* $\chi_i(E)$. The quantity $\chi_i(E) dE$ is the probability for an emitted neutron to have an energy equal to E (within a dE interval) in the LAB. As expected, the normalization is

$$\int_0^\infty dE \chi_i(E) = 1. \quad (71)$$

The isotropic fission source is written as

$$Q^{\text{fiss}}(\mathbf{r}, E) = \sum_{j=1}^{j^{\text{fiss}}} \chi_j(E) \int_0^\infty dE' \nu_{\Sigma_{f,j}}(\mathbf{r}, E') \phi(\mathbf{r}, E'), \quad (72)$$

where j^{fiss} is the total number of fissionable isotopes and $\nu_{\Sigma_{f,j}}(\mathbf{r}, E)$ is the number of emitted neutrons per fission times the macroscopic fission cross-section of the j th-fissionable isotope.

Substitution of (72) into (69) gives the complete expression of a multiplicative source in reactor physics:

$$\begin{aligned} Q(\mathbf{r}, E, \boldsymbol{\Omega}) &= \int_0^\infty dE' \sum_{\ell=0}^L \frac{2\ell+1}{4\pi} \Sigma_{s,\ell}(\mathbf{r}, E \leftarrow E') \sum_{m=-\ell}^{\ell} R_\ell^m(\boldsymbol{\Omega}) \phi_\ell^m(\mathbf{r}, E') \\ &+ \frac{1}{4\pi K_{\text{eff}}} \sum_{j=1}^{j^{\text{fiss}}} \chi_j(E) \int_0^\infty dE' \nu_{\Sigma_{f,j}}(\mathbf{r}, E') \phi(\mathbf{r}, E'), \end{aligned} \quad (73)$$

where $\phi(\mathbf{r}, E) \equiv \phi_0^0(\mathbf{r}, E)$.

Substitution of (73) into (64) leads to the singular form of the transport equation. This is an *eigenproblem* featuring a number of properties as follows:

- The neutron flux ϕ appears in each term, so that $\phi = 0$ is a trivial solution. A set of nontrivial solutions (also called *eigensolutions*) exists for some discrete values of K_{eff} . We clearly obtain an *eigenvalue* problem, with K_{eff} as the eigenvalue and ϕ as the eigenvector. The *fundamental solution* corresponds to the maximum possible value of K_{eff} and is the only eigensolution with a physical meaning.
- Only the flux distribution of the fundamental solution is almost positive everywhere in the domain. The other eigensolutions are the harmonics of the flux and are partly positive and partly negative.
- The flux distributions of each eigensolution can be arbitrarily normalized. If $\phi(\mathbf{r}, E)$ is a nontrivial solution, then $C\phi(\mathbf{r}, E)$ is also a nontrivial solution for any nonzero value of the constant C . The value of the normalization constant C is generally computed from the thermal power P of the reactor using

$$\int_0^\infty dE \int_V d^3r H(\mathbf{r}, E) \phi(\mathbf{r}, E) = P, \quad (74)$$

where V is the volume of the reactor and $H(\mathbf{r}, E)$ is the *power factor* giving the recoverable energy in terms of the flux.

- It is possible to define a mathematical *adjoint problem* with the same eigenvalues as the original problem.

A multiplicative domain with $K_{\text{eff}} > 1$ is said to be overcritical because its flux level will increase with time if we remove the eigenvalue. Similarly, a multiplicative domain with $K_{\text{eff}} < 1$ is said to be undercritical.

Each term of the steady-state transport equation is an operator for which an adjoint operator can be found. The general rules for creating the adjoint of an operator are

1. Transpose the matrix operators.
2. Change the sign of odd-parity differential operators.
3. Interchange the arguments of the kernels of integral operators.

Using these rules, the adjoint of (64) is written as

$$-\mathbf{\Omega} \cdot \nabla \phi^*(\mathbf{r}, E, \mathbf{\Omega}) + \Sigma(\mathbf{r}, E) \phi^*(\mathbf{r}, E, \mathbf{\Omega}) = Q^*(\mathbf{r}, E, \mathbf{\Omega}), \quad (75)$$

where the adjoint source density is

$$Q^*(\mathbf{r}, E, \mathbf{\Omega}) = \int_0^\infty dE' \sum_{\ell=0}^L \frac{2\ell+1}{4\pi} \Sigma_{s,\ell}(\mathbf{r}, E' \leftarrow E) \sum_{m=-\ell}^{\ell} R_{\ell}^m(\mathbf{\Omega}) \phi_{\ell}^{*m}(\mathbf{r}, E') + \frac{1}{4\pi K_{\text{eff}}} \sum_{j=1}^{j_{\text{fiss}}} \nu \Sigma_{f,j}(\mathbf{r}, E) \int_0^\infty dE' \chi_j(E') \phi^*(\mathbf{r}, E'). \quad (76)$$

A close inspection of (76) reveals that the adjoint flux is a *function* of E . The adjoint flux cannot be a distribution of E because the term $\chi_j(E') \phi^*(\mathbf{r}, E')$ in (76) cannot involve the product of two distributions of E' . In some textbooks, the adjoint flux is referred to as the *importance function*.

The adjoint flux solution is generally normalized to an arbitrary value as

$$\int_0^\infty dE \int_V d^3r \phi^*(\mathbf{r}, E) = 1. \quad (77)$$

The adjoint transport equation is also an eigenvalue problem. Its eigenvalues are the same as those of the original transport equation. Each eigenvalue, such as the K_{eff} in (73) or (76), can be expressed in terms of the corresponding eigenvectors $\phi(\mathbf{r}, E)$ and $\phi^*(\mathbf{r}, E)$ using the *Rayleigh ratio*:

$$K_{\text{eff}} = \frac{\sum_{j=1}^{\text{fiss}} \int_0^\infty dE' \chi_j(E') \phi^*(\mathbf{r}, E') \int_0^\infty dE \nu \Sigma_{f,j}(\mathbf{r}, E) \phi(\mathbf{r}, E)}{\int_0^\infty dE' \phi^*(\mathbf{r}, E') \left[\Sigma(\mathbf{r}, E') \phi(\mathbf{r}, E') - \int_0^\infty dE \Sigma_{s,0}(\mathbf{r}, E' \leftarrow E) \phi(\mathbf{r}, E) \right]}. \quad (78)$$

The interest of the Rayleigh ratio is that it is stationary with respect to a small variation $\delta\Sigma$ of the cross-section terms. The first-order variation δK_{eff} corresponding to such a variation in cross-sections can be written in terms of ϕ , ϕ^* , Σ , and $\delta\Sigma$, *without* using $\delta\phi$ or $\delta\phi^*$. This observation is at the origin of the *perturbation theory*.

1.6 The Transport Correction

The transport equation is frequently solved by assuming the isotropy of the scattering sources in the LAB. This approximation is generally not valid but can be mitigated by performing a *transport correction* on the cross-sections appearing in the transport equation.

The basic principle is to add a forward-peaked component in the Legendre expansion of the differential-scattering cross-section. This additional component takes the form of a Dirac delta term in (67) as

$$\Sigma_s(\mathbf{r}, E \leftarrow E', \mu) = \sum_{\ell=0}^L \frac{2\ell+1}{2} \bar{\Sigma}_{s,\ell}(\mathbf{r}, E \leftarrow E') P_\ell(\mu) + \Delta\Sigma_{\text{tr}}(\mathbf{r}, E \leftarrow E') \delta(\mu-1), \quad (79)$$

where $\bar{\Sigma}_{s,\ell}(\mathbf{r}, E' \leftarrow E)$ is a modified Legendre coefficient and $\Delta\Sigma_{\text{tr}}(\mathbf{r}, E' \leftarrow E)$ is the additional coefficient multiplying the Dirac delta term. These coefficients are computed so as to preserve the Legendre moments of (68). We write

$$\int_{-1}^1 d\mu \Sigma_s(\mathbf{r}, E \leftarrow E', \mu) P_\ell(\mu) = \Sigma_{s,\ell}(\mathbf{r}, E \leftarrow E') \quad (80)$$

for $0 \leq \ell \leq L+1$. Substituting (79) into (80) and using the relation $P_\ell(1) = 1$, we obtain

$$\bar{\Sigma}_{s,\ell}(\mathbf{r}, E \leftarrow E') + \Delta\Sigma_{\text{tr}}(\mathbf{r}, E' \leftarrow E) = \Sigma_{s,\ell}(\mathbf{r}, E \leftarrow E') \quad \text{if } 0 \leq \ell \leq L \quad (81)$$

and

$$\Delta\Sigma_{\text{tr}}(\mathbf{r}, E' \leftarrow E) = \Sigma_{s,L+1}(\mathbf{r}, E \leftarrow E'). \quad (82)$$

Writing $L = 0$, (79) and (82) reduce to

$$\begin{aligned} \Sigma_s(\mathbf{r}, E \leftarrow E', \mu) = & \frac{1}{2} \left[\Sigma_{s,0}(\mathbf{r}, E \leftarrow E') - \Sigma_{s,1}(\mathbf{r}, E \leftarrow E') \right] \\ & + \Sigma_{s,1}(\mathbf{r}, E \leftarrow E') \delta(\mu-1) \end{aligned} \quad (83)$$

so that the substitution of (83) into the steady-state transport equation (64) leads to

$$\mathbf{\Omega} \cdot \nabla \phi(\mathbf{r}, E, \mathbf{\Omega}) + \Sigma(\mathbf{r}, E) \phi(\mathbf{r}, E, \mathbf{\Omega}) - \int_0^\infty dE' \Sigma_{s,1}(\mathbf{r}, E \leftarrow E') \phi(\mathbf{r}, E', \mathbf{\Omega}) = \bar{Q}(\mathbf{r}, E, \mathbf{\Omega}), \quad (84)$$

where the transport-corrected steady-state source density is now given by

$$\begin{aligned} \bar{Q}(\mathbf{r}, E, \mathbf{\Omega}) = & \frac{1}{4\pi} \int_0^\infty dE' [\Sigma_{s,0}(\mathbf{r}, E \leftarrow E') - \Sigma_{s,1}(\mathbf{r}, E \leftarrow E')] \phi(\mathbf{r}, E') \\ & + \frac{1}{4\pi K_{\text{eff}}} \sum_{j=1}^{j_{\text{fiss}}} \chi_j(E) \int_0^\infty dE' \nu \Sigma_{f,j}(\mathbf{r}, E') \phi(\mathbf{r}, E'). \end{aligned} \quad (85)$$

Another approximation is required to simplify the LHS of (84). Two alternative approaches can be used as follows:

- The *micro-reversibility* approximation (MRA) is valid in the thermal energy domain where the neutrons are in quasi-equilibrium with the nucleus. This approximation can be written as

$$\Sigma_{s,1}(\mathbf{r}, E \leftarrow E') \phi(\mathbf{r}, E', \mathbf{\Omega}) = \Sigma_{s,1}(\mathbf{r}, E' \leftarrow E) \phi(\mathbf{r}, E, \mathbf{\Omega}). \quad (86)$$

- The *one-over-E* weighting approximation (OEWA) consists of introducing a weighting function $W(E', E)$, so that

$$\Sigma_{s,1}(\mathbf{r}, E \leftarrow E') \phi(\mathbf{r}, E', \mathbf{\Omega}) = \Sigma_{s,1}(\mathbf{r}, E \leftarrow E') \phi(\mathbf{r}, E, \mathbf{\Omega}) W(E', E), \quad (87)$$

where $W(E', E)$ is given in terms of the neutron energy as

$$W(E', E) = \frac{E}{E'}. \quad (88)$$

In principle, the OEWA is more accurate than the MRA at neutron energies > 4 eV. However, it is common in reactor physics to perform an MRA-based transport correction over the complete energy spectrum.

Substitution of (86) or (87) in (84) leads to

$$\mathbf{\Omega} \cdot \nabla \phi(\mathbf{r}, E, \mathbf{\Omega}) + \bar{\Sigma}(\mathbf{r}, E) \phi(\mathbf{r}, E, \mathbf{\Omega}) = \bar{Q}(\mathbf{r}, E, \mathbf{\Omega}), \quad (89)$$

where the transport-corrected macroscopic cross-section is written as

$$\bar{\Sigma}(\mathbf{r}, E) = \Sigma(\mathbf{r}, E) - \Delta\Sigma_{\text{tr}}(\mathbf{r}, E) \quad (90)$$

with

$$\Delta\Sigma_{\text{tr}}(\mathbf{r}, E) = \begin{cases} \int_0^\infty dE' \Sigma_{s,1}(\mathbf{r}, E' \leftarrow E) & \text{if MRA,} \\ \int_0^\infty dE' W(E', E) \Sigma_{s,1}(\mathbf{r}, E \leftarrow E') & \text{if OEWA.} \end{cases} \quad (91)$$

The transport-corrected steady-state source density can also be simplified, so that

$$\begin{aligned} \bar{Q}(\mathbf{r}, E, \Omega) = & \frac{1}{4\pi} \int_0^\infty dE' \bar{\Sigma}_{s,0}(\mathbf{r}, E \leftarrow E') \phi(\mathbf{r}, E') \\ & + \frac{1}{4\pi K_{\text{eff}}} \sum_{j=1}^{j_{\text{fiss}}} \chi_j(E) \int_0^\infty dE' \nu \Sigma_{f,j}(\mathbf{r}, E') \phi(\mathbf{r}, E'), \end{aligned} \quad (92)$$

where the P_0 transport-corrected component of the differential scattering cross-section is now written as

$$\bar{\Sigma}_{s,0}(\mathbf{r}, E \leftarrow E') = \Sigma_{s,0}(\mathbf{r}, E \leftarrow E') - \delta(E' - E) \Delta \Sigma_{\text{tr}}(\mathbf{r}, E). \quad (93)$$

The transport [equation \(89\)](#) with the transport-corrected source density [\(92\)](#) is as easy to solve as the transport equation for an isotropic collision in the LAB, but includes a correction for anisotropic scattering effects. This technique of transport correction is very useful with the integral form of the transport equation, as presented in [\(55\)](#) and [\(56\)](#), as these equations are otherwise limited to isotropic scattering in the LAB. In this case, the optical path defined in [\(51\)](#) is computed using the transport corrected total cross-section defined in [\(90\)](#). Lattice calculations are generally performed this way.

1.7 Multigroup Discretization

The numerical solution of the transport equation is greatly facilitated by using a *multigroup discretization* in energy. This approach consists in dividing the energy domain in a set of G *energy groups* inside which the neutrons are assumed to behave as one-speed particles and to take averages of all energy-dependent quantities over these groups. This procedure is also named *energy condensation*.

It is advantageous to define the groups in terms of the lethargy variable. As neutron energy approaches the thermal-energy range, the number of collisions required to slow down increases and the average energy loss per collision decreases. Conversely, the average gain in lethargy per collision is almost constant over the complete energy range. We are going to assume constant cross-sections in each group. The definition of the lethargy limits is made after close inspection of the cross-section behavior of all major isotopes present in the reactor, including the position of the resolved resonances. The cross-sections of low-energy resonances (such as the 0.3 eV resonance of ^{239}Pu) must be precisely discretized with a sufficient number of groups; and other resolved resonances must be enclosed in an energy group, in order to avoid numerical problems.

Multigroup discretization may be performed in many instances of the global computational scheme. The first energy condensation occurs in the GROUPR module, during the NJOY-processing step. Energy condensation of continuous-energy cross-sections produces multigroup cross-sections defined over the energy structure of the cross-section library, typically with $50 \leq G \leq 400$. The next energy condensation occurs in the lattice code, in order to produce cross-sections defined over the energy structure of the reactor calculation with $2 \leq G \leq 8$. In some cases, the lattice code uses a *multilevel energy representation* and performs two energy condensations: the first toward an intermediate energy structure with $20 \leq G \leq 35$ and the second toward the energy structure of the reactor calculation. The values of G actually used after each condensation step are carefully chosen by the computational scheme specialists.

The reference energy E_0 used to define the lethargy $u = \ln(E_0/E)$ is generally taken above 10 MeV in order to correspond to the maximum energy of neutrons in a nuclear reactor. The lethargy is zero for the neutrons of energy E_0 and increases as neutrons slow down. We divide the energy domain $0 \leq E \leq E_0$ into G groups W_g , so that

$$W_g = \{u; u_{g-1} \leq u < u_g\} = \{E; E_g < E \leq E_{g-1}\}, \quad g = 1, G,$$

where $u_g = \ln(E_0/E_g)$ and $u_0 = 0$.

Before proceeding with energy condensation, we shall define the average $\langle X \rangle_g$ of a function or of a distribution $X(E)$ over group g . The following definition is used:

$$\langle X \rangle_g = \int_{u_{g-1}}^{u_g} du X(u) = \int_{E_g}^{E_{g-1}} dE X(E) \quad (94)$$

if $X(E)$ is a distribution, and

$$\langle X \rangle_g = \frac{1}{u_g - u_{g-1}} \int_{u_{g-1}}^{u_g} du X(u) = \frac{1}{\ln(E_{g-1}/E_g)} \int_{E_g}^{E_{g-1}} \frac{dE}{E} X(E) \quad (95)$$

if $X(E)$ is a function.

The group-averaged values of the flux, cross-section, differential cross-section, and source density are, therefore, defined as

$$\phi_g(\mathbf{r}, \boldsymbol{\Omega}) \equiv \langle \phi(\mathbf{r}, \boldsymbol{\Omega}) \rangle_g = \int_{u_{g-1}}^{u_g} du \phi(\mathbf{r}, u, \boldsymbol{\Omega}), \quad (96)$$

$$\phi_g(\mathbf{r}) \equiv \langle \phi(\mathbf{r}) \rangle_g = \int_{u_{g-1}}^{u_g} du \phi(\mathbf{r}, u), \quad (97)$$

$$\langle \Sigma(\mathbf{r}) \phi(\mathbf{r}) \rangle_g = \int_{u_{g-1}}^{u_g} du \Sigma(\mathbf{r}, u) \phi(\mathbf{r}, u), \quad (98)$$

$$\langle \Sigma_{s,\ell}(\mathbf{r}) \phi(\mathbf{r}) \rangle_{g \leftarrow h} = \int_{u_{g-1}}^{u_g} du \int_{u_{h-1}}^{u_h} du' \Sigma_{s,\ell}(\mathbf{r}, u \leftarrow u') \phi(\mathbf{r}, u') \quad (99)$$

and

$$\langle Q(\mathbf{r}, \boldsymbol{\Omega}) \rangle_g = \int_{u_{g-1}}^{u_g} du Q(\mathbf{r}, u, \boldsymbol{\Omega}). \quad (100)$$

The angular and integrated *multigroup flux* components are defined as $\phi_g(\mathbf{r}, \boldsymbol{\Omega}) \equiv \langle \phi(\mathbf{r}, \boldsymbol{\Omega}) \rangle_g$ and $\phi_g(\mathbf{r}) \equiv \langle \phi(\mathbf{r}) \rangle_g$. The *multigroup cross-section* components are defined in such a way as to preserve the values of the reaction rates. We write

$$\Sigma_g(\mathbf{r}) = \frac{1}{\phi_g(\mathbf{r})} \langle \Sigma(\mathbf{r}) \phi(\mathbf{r}) \rangle_g, \quad (101)$$

$$\Sigma_{s,\ell,g \leftarrow h}(\mathbf{r}) = \frac{1}{\phi_h(\mathbf{r})} \langle \Sigma_{s,\ell}(\mathbf{r}) \phi(\mathbf{r}) \rangle_{g \leftarrow h}, \quad (102)$$

and

$$v\Sigma_{f,j,g}(\mathbf{r}) = \frac{1}{\phi_g(\mathbf{r})} \langle v\Sigma_{f,j}(\mathbf{r}) \phi(\mathbf{r}) \rangle_g. \quad (103)$$

The multigroup transport correction obtained by energy condensation of (91) leads to

$$\Delta\Sigma_{\text{tr},g}(\mathbf{r}) = \begin{cases} \sum_{h=1}^G \Sigma_{s,1,h\leftarrow g}(\mathbf{r}) & \text{if MRA,} \\ \sum_{h=1}^G W_{gh} \Sigma_{s,1,g\leftarrow h}(\mathbf{r}) & \text{if OEWA.} \end{cases} \quad (104)$$

The multigroup transport-corrected cross-sections are obtained by energy condensation of (90) and (93). The multigroup transport-corrected macroscopic cross-section is written as

$$\bar{\Sigma}_g(\mathbf{r}) = \Sigma_g(\mathbf{r}) - \Delta\Sigma_{\text{tr},g}(\mathbf{r}) \quad (105)$$

and the multigroup P_0 transport-corrected component of the differential-scattering cross-section is written as

$$\bar{\Sigma}_{s,0,g\leftarrow h}(\mathbf{r}) = \Sigma_{s,0,g\leftarrow h}(\mathbf{r}) - \delta_{gh} \Delta\Sigma_{\text{tr},g}(\mathbf{r}), \quad (106)$$

where δ_{gh} is the Kronecker delta function and where

$$W_{gh} = \frac{\int_{E_g}^{E_{g-1}} \frac{dE}{E}}{\int_{E_h}^{E_{h-1}} \frac{dE}{E}} = \frac{u_g - u_{g-1}}{u_h - u_{h-1}}. \quad (107)$$

The transport equation for neutrons can be written in multigroup form, leading to a set of G -coupled integro-differential equations. We will now present the steady-state transport equations.

The multigroup and differential form of the steady-state transport equation in group g is written as

$$\boldsymbol{\Omega} \cdot \nabla \phi_g(\mathbf{r}, \boldsymbol{\Omega}) + \Sigma_g(\mathbf{r}) \phi_g(\mathbf{r}, \boldsymbol{\Omega}) = Q_g(\mathbf{r}, \boldsymbol{\Omega}), \quad (108)$$

where $1 \leq g \leq G$. The multigroup source density is

$$Q_g(\mathbf{r}, \boldsymbol{\Omega}) = \sum_{h=1}^G \sum_{\ell=0}^L \frac{2\ell+1}{4\pi} \Sigma_{s,\ell,g\leftarrow h}(\mathbf{r}) \sum_{m=-\ell}^{\ell} R_{\ell}^m(\boldsymbol{\Omega}) \phi_{\ell,h}^m(\mathbf{r}) + \frac{1}{4\pi K_{\text{eff}}} \sum_{j=1}^{J^{\text{fiss}}} \chi_{j,g} \sum_{h=1}^G \nu \Sigma_{f,j,h}(\mathbf{r}) \phi_h(\mathbf{r}) \quad (109)$$

and the average fission spectrum in group g is

$$\chi_{j,g} \equiv \langle \chi_j \rangle_g = \int_{u_{g-1}}^{u_g} du \chi_j(u). \quad (110)$$

It is always possible to perform a transport correction on the transport equation, whatever its form. This operation will only be illustrated in the case of (108). The substitution of (105) and (106) into (108) leads to a differential-transport equation with a first-order transport correction as

$$\boldsymbol{\Omega} \cdot \nabla \phi_g(\mathbf{r}, \boldsymbol{\Omega}) + \bar{\Sigma}_g(\mathbf{r}) \phi_g(\mathbf{r}, \boldsymbol{\Omega}) = Q_g(\mathbf{r}, \boldsymbol{\Omega}) - \frac{1}{4\pi} \Delta\Sigma_{\text{tr},g}(\mathbf{r}) \phi_g(\mathbf{r}). \quad (111)$$

The characteristic form of (108), without transport correction, is

$$\frac{d}{ds} \phi_g(\mathbf{r} + s \boldsymbol{\Omega}, \boldsymbol{\Omega}) + \Sigma_g(\mathbf{r} + s \boldsymbol{\Omega}) \phi_g(\mathbf{r} + s \boldsymbol{\Omega}, \boldsymbol{\Omega}) = Q_g(\mathbf{r} + s \boldsymbol{\Omega}, \boldsymbol{\Omega}) \quad (112)$$

and the integral infinite-domain form is

$$\phi_g(\mathbf{r}, \boldsymbol{\Omega}) = \int_0^\infty ds e^{-\tau_g(s)} Q_g(\mathbf{r} - s \boldsymbol{\Omega}, \boldsymbol{\Omega}) \quad (113)$$

or, in the case of a finite domain,

$$\phi_g(\mathbf{r}, \boldsymbol{\Omega}) = e^{-\tau_g(b)} \phi_g(\mathbf{r} - b \boldsymbol{\Omega}, \boldsymbol{\Omega}) + \int_0^b ds e^{-\tau_g(s)} Q_g(\mathbf{r} - s \boldsymbol{\Omega}, \boldsymbol{\Omega}), \quad (114)$$

where the optical path in group g is

$$\tau_g(s) = \int_0^s ds' \Sigma_g(\mathbf{r} - s' \boldsymbol{\Omega}). \quad (115)$$

We have obtained an eigenproblem taking the form of a set of coupled differential equations. This problem is not self-adjoint, due to slowing-down effects. The corresponding adjoint equation is written in terms of the multigroup *adjoint flux* $\phi_g^*(\mathbf{r}, \boldsymbol{\Omega}) \equiv \langle \phi^*(\mathbf{r}, \boldsymbol{\Omega}) \rangle_g$ and $\phi_g^*(\mathbf{r}) \equiv \langle \phi^*(\mathbf{r}) \rangle_g$. At this point, an important distinction must be made. The adjoint flux is a *function* of energy, *not* a distribution. It is therefore defined as

$$\phi_g^*(\mathbf{r}, \boldsymbol{\Omega}) \equiv \langle \phi^*(\mathbf{r}, \boldsymbol{\Omega}) \rangle_g = \frac{1}{u_g - u_{g-1}} \int_{u_{g-1}}^{u_g} du \phi^*(\mathbf{r}, u, \boldsymbol{\Omega}), \quad (116)$$

and

$$\phi_g^*(\mathbf{r}) \equiv \langle \phi^*(\mathbf{r}) \rangle_g = \frac{1}{u_g - u_{g-1}} \int_{u_{g-1}}^{u_g} du \phi^*(\mathbf{r}, u). \quad (117)$$

The adjoint, multigroup, and differential form of the steady-state transport equation in group g is written as

$$-\boldsymbol{\Omega} \cdot \nabla \phi_g^*(\mathbf{r}, \boldsymbol{\Omega}) + \Sigma_g(\mathbf{r}) \phi_g^*(\mathbf{r}, \boldsymbol{\Omega}) = Q_g^*(\mathbf{r}, \boldsymbol{\Omega}), \quad (118)$$

where $1 \leq g \leq G$. The adjoint multigroup source density is

$$\begin{aligned} Q_g^*(\mathbf{r}, \boldsymbol{\Omega}) &= \sum_{h=1}^G \sum_{\ell=0}^L \frac{2\ell+1}{4\pi} \Sigma_{s,\ell,h \leftarrow g}(\mathbf{r}) \sum_{m=-\ell}^{\ell} R_{\ell}^m(\boldsymbol{\Omega}) \phi_{\ell,h}^{*m}(\mathbf{r}) \\ &+ \frac{1}{4\pi K_{\text{eff}}} \sum_{j=1}^{j_{\text{fiss}}} \nu \Sigma_{f,j,g}(\mathbf{r}) \sum_{h=1}^G \chi_{j,h} \phi_h^*(\mathbf{r}). \end{aligned} \quad (119)$$

Different approaches can be used to solve the transport equation for neutral particles. The most accurate, and most expensive, technique is the *Monte-Carlo method*. Many millions of particle histories are simulated based on a sequence of random numbers. The simulation of each particle takes into account its interactions with an accurate representation of the geometric domain, using a continuous-energy or multigroup representation of the cross-sections.

The second class of approaches comprises *deterministic-solution* techniques. These approaches do not use any random-number generator. They are based on the application of numerical analysis techniques to the transport equation, either in differential (see (44)), characteristic (see (49)), or integral (see (56)) form. The particle flux is used as a dependent variable and the transport equation is solved with its boundary conditions. A multigroup representation of the cross-sections is generally imposed. The deterministic approaches are based on many approximations related to their energetic and spatial discretization and to the limitation of the angular representation. They are used in legacy lattice and full-core codes such as Dragon and Trivac (Marleau et al. 1992; Hébert 1987).


The Monte-Carlo method is used to study difficult or nonstandard situations and to validate the deterministic results, principally in the lattice-calculation step. The design- and operation-related calculations are generally deterministic. The remaining sections of this chapter are devoted to a description of standard deterministic solution approaches.

2 The First-Order Streaming Operator

We now study the behavior of the first-order streaming operator $\Omega \cdot \nabla \phi(\mathbf{r}, \Omega)$ in different geometries. The energy is not represented as an independent variable, in order to simplify the notation. The streaming operator actually represents the rate of change of the angular flux along the streaming path of the particle, in the direction of its motion Ω . Two coordinate systems can be used to express this term. The position \mathbf{r} of the particle is defined in a Cartesian, cylindrical or spherical coordinate system consistent with the type of geometry being analyzed. The direction of the particle is a solid-angle Ω defined in an *angular-direction coordinate system* that is moving with the particle. Ω is, therefore, defined in terms of its direction cosines in this moving coordinate system using

$$\Omega = \mu \mathbf{e}_\mu + \eta \mathbf{e}_\eta + \xi \mathbf{e}_\xi \quad \text{with} \quad \mu^2 + \eta^2 + \xi^2 = 1. \quad (120)$$

2.1 Cartesian Coordinate System

The 3D Cartesian coordinate system is shown in  Fig. 4. The particle is located at position (x, y, z) , corresponding to the origin of the angular-direction coordinate system. The three axes of the angular-direction coordinate system, denoted as $\mathbf{e}_x = \mathbf{i}$, $\mathbf{e}_y = \mathbf{j}$, and $\mathbf{e}_z = \mathbf{k}$, are parallel to the X , Y , and Z axes of the Cartesian system.

The direction Ω of the particle is uniquely defined by the direction cosine μ of the polar angle Ψ and by the azimuthal angle ϕ . The first-order streaming operator is, therefore, a distribution of x , y , z , μ , and ϕ . Consequently, it can be written as

$$\Omega \cdot \nabla = \frac{d}{ds} = \frac{dx}{ds} \frac{\partial}{\partial x} + \frac{dy}{ds} \frac{\partial}{\partial y} + \frac{dz}{ds} \frac{\partial}{\partial z} + \frac{d\mu}{ds} \frac{\partial}{\partial \mu} + \frac{d\phi}{ds} \frac{\partial}{\partial \phi}, \quad (121)$$

where ds is a differential element of the particle path in direction Ω . Here, we have

$$\frac{dx}{ds} = \mu, \quad \frac{dy}{ds} = \eta, \quad \frac{dz}{ds} = \xi, \quad \text{and} \quad \frac{d\mu}{ds} = \frac{d\phi}{ds} = 0 \quad (122)$$

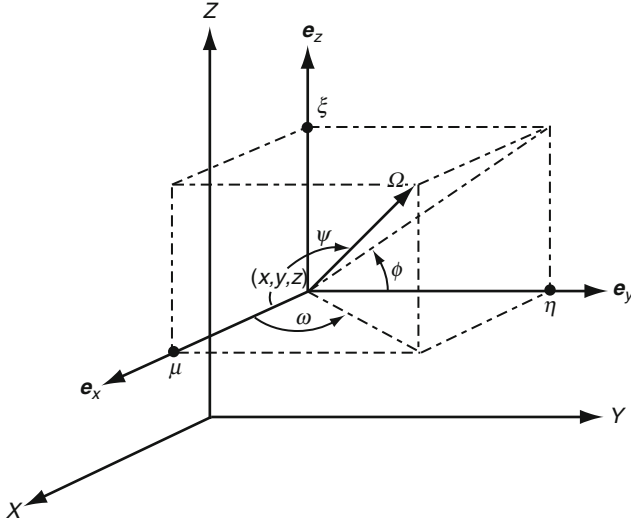


Figure 4
Cartesian coordinate system

so that

$$\mathbf{\Omega} \cdot \nabla = \mu \frac{\partial}{\partial x} + \eta \frac{\partial}{\partial y} + \xi \frac{\partial}{\partial z}. \quad (123)$$

In the particular case of 1D x -oriented slab geometry, the flux and source density are independent of y , z , and of the azimuthal angle ϕ . The source density components with $m \neq 0$ vanish, so that (45) is written as

$$Q(\mathbf{r}, \mathbf{\Omega}) = \sum_{\ell=0}^L \frac{2\ell+1}{4\pi} Q_{\ell}(\mathbf{r}) R_{\ell,0}(\mathbf{\Omega}) = \sum_{\ell=0}^L \frac{2\ell+1}{4\pi} Q_{\ell}(\mathbf{r}) P_{\ell}(\mu), \quad (124)$$


where $P_{\ell}(\mu)$ is the ℓ -order Legendre polynomial. The source density is reduced by integration over the azimuthal angle, using $Q(\mathbf{r}, \mathbf{\Omega}) d^3r d^2\Omega = Q(x, \mu) dx d\mu$, $d^3r = dx dy dz$, and $d^2\Omega = d\mu d\phi$. We obtain

$$Q(x, \mu) = \sum_{\ell=0}^L \frac{2\ell+1}{2} Q_{\ell}(x) P_{\ell}(\mu) \quad (125)$$

so that using the streaming operator (123), the first-order form of the linear Boltzmann equation (44) in slab geometry is written as

$$\left[\mu \frac{\partial}{\partial x} + \Sigma(x) \right] \phi(x, \mu) = \sum_{\ell=0}^L \frac{2\ell+1}{2} Q_{\ell}(x) P_{\ell}(\mu). \quad (126)$$

Another useful geometry is the 2D Cartesian geometry defined on the (x, y) plane. It is convenient to represent the angular variation of the flux using the direction cosine ξ and the

azimuthal angle ω , as represented in  Fig. 4. In this case, the flux and the source density are independent of z and are symmetric with respect to the direction cosine ξ , so that

$$\phi(x, y, \xi, \omega) = \phi(x, y, -\xi, \omega) \quad \text{and} \quad Q(x, y, \xi, \omega) = Q(x, y, -\xi, \omega). \quad (127)$$

In this case, the source density components with odd values of $\ell + m$ vanish, so that (45) is written as

$$Q(x, y, \Omega) = \sum_{\ell=0}^L \frac{2\ell+1}{4\pi} \sum_{\substack{m=-\ell \\ \ell+m \text{ even}}}^{\ell} Q_{\ell}^m(x, y) R_{\ell}^m(\Omega) \quad (128)$$


and the first-order form of the linear Boltzmann equation (44) in Cartesian 2D geometry is written as

$$\begin{aligned} & \left[\sqrt{1-\xi^2} \cos \omega \frac{\partial}{\partial x} + \sqrt{1-\xi^2} \sin \omega \frac{\partial}{\partial y} + \Sigma(x, y) \right] \phi(x, y, \xi, \omega) \\ & = \sum_{\ell=0}^L \frac{2\ell+1}{4\pi} \sum_{\substack{m=-\ell \\ \ell+m \text{ even}}}^{\ell} Q_{\ell}^m(x, y) R_{\ell}^m(\xi, \omega), \end{aligned} \quad (129)$$

where

$$R_{\ell}^m(\xi, \omega) = \sqrt{(2-\delta_{m,0}) \frac{(\ell-|m|)!}{(\ell+|m|)!}} P_{\ell}^{|m|}(\xi) \mathcal{T}_m(\omega). \quad (130)$$

2.2 Cylindrical Coordinate System


The 3D cylindrical coordinate system is shown in  Fig. 5. The particle is located at position (ρ, θ, z) , corresponding to the origin of the angular-direction coordinate system. The three axes of the angular-direction coordinate system, denoted as \mathbf{e}_{ρ} , \mathbf{e}_{θ} , and \mathbf{e}_z , are defined in such a way that \mathbf{e}_{ρ} is colinear with the projection of \mathbf{r} on the XY plane and that \mathbf{e}_z is parallel to the Z axis.

The direction Ω of the particle is uniquely defined by the direction cosine ξ of the polar angle and by the azimuthal angle ω . The first-order streaming operator is, therefore, a distribution of ρ , θ , z , ξ , and ω . Consequently, it can be written as

$$\Omega \cdot \nabla = \frac{d}{ds} = \frac{d\rho}{ds} \frac{\partial}{\partial \rho} + \frac{d\theta}{ds} \frac{\partial}{\partial \theta} + \frac{dz}{ds} \frac{\partial}{\partial z} + \frac{d\xi}{ds} \frac{\partial}{\partial \xi} + \frac{d\omega}{ds} \frac{\partial}{\partial \omega}, \quad (131)$$

where

$$\frac{d\rho}{ds} = \mu, \quad \frac{d\theta}{ds} = \frac{\eta}{\rho}, \quad \frac{dz}{ds} = \xi \quad \text{and} \quad \frac{d\mu}{ds} = 0. \quad (132)$$

The term $d\omega/ds$ is not zero because the particle direction changes as the particle moves. This phenomenon, called *angular redistribution*, is specific to curvilinear geometries. The angular redistribution term is computed with the help of  Fig. 6, representing the projection of the particle path on the $\mathbf{e}_{\rho}-\mathbf{e}_{\theta}$ plane.

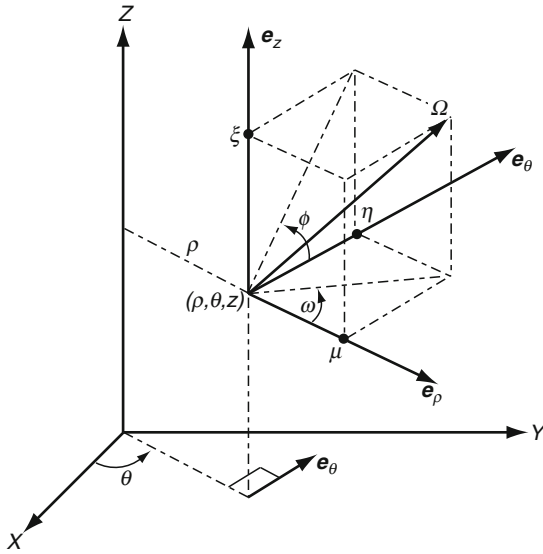


Figure 5
Cylindrical coordinate system

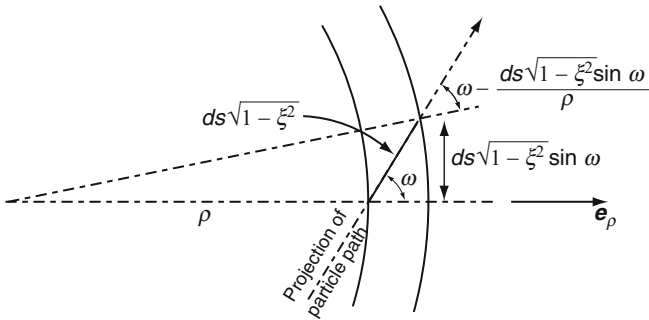


Figure 6
Angular redistribution of particles in cylindrical geometry

We see that

$$\frac{d\omega}{ds} = -\frac{1}{\rho} \sqrt{1-\xi^2} \sin \omega = -\frac{\eta}{\rho}, \tag{133}$$

where the negative sign indicates that the azimuthal angle ω decreases as the particle goes forward. The first-order streaming operator in cylindrical geometry is obtained after substituting (132) and (133) into (131) as

$$\mathbf{\Omega} \cdot \nabla = \mu \frac{\partial}{\partial \rho} + \frac{\eta}{\rho} \frac{\partial}{\partial \theta} + \xi \frac{\partial}{\partial z} - \frac{\eta}{\rho} \frac{\partial}{\partial \omega}. \tag{134}$$

When this operator is applied on the angular flux, the terms can be rearranged in a form that facilitates the representation of particle conservation as

$$\Omega \cdot \nabla \phi = \frac{\mu}{\rho} \frac{\partial}{\partial \rho} (\rho \phi) + \frac{\eta}{\rho} \frac{\partial \phi}{\partial \theta} + \xi \frac{\partial \phi}{\partial z} - \frac{1}{\rho} \frac{\partial}{\partial \omega} (\eta \phi). \quad (135)$$

The angular flux and source are distributions of the solid angle only through direction cosine ξ and azimuthal angle ω . The angular flux and source vary parametrically with μ and η through relations

$$\mu = \sqrt{1 - \xi^2} \cos \omega \quad \text{and} \quad \eta = \sqrt{1 - \xi^2} \sin \omega. \quad (136)$$

Equations (136) can also be used to show that $\partial \eta / \partial \omega = \mu$ and to transform (134) into (135).

In the particular case of a 1D cylindrical geometry, the flux and source density are independent of θ , z and are symmetric with respect to both the direction cosine ξ and azimuthal angle ω , so that

$$\begin{aligned} \phi(\rho, \xi, \omega) &= \phi(\rho, \xi, -\omega), & Q(\rho, \xi, \omega) &= Q(\rho, \xi, -\omega), \\ \phi(\rho, \xi, \omega) &= \phi(\rho, -\xi, \omega), & \text{and} & \quad Q(\rho, \xi, \omega) = Q(\rho, -\xi, \omega). \end{aligned} \quad (137)$$

Under these conditions, the source density components with $m < 0$ and with odd values of $m + \ell$ vanish, so that (45) is written as

$$Q(\rho, \Omega) = \sum_{\ell=0}^L \frac{2\ell+1}{4\pi} \sum_{\substack{m=0 \\ \ell+m \text{ even}}}^{\ell} Q_{\ell}^m(\rho) R_{\ell}^m(\Omega) \quad (138)$$

and the first-order form of the linear Boltzmann equation (44) in cylindrical 1D geometry is written as

$$\begin{aligned} &\mu \frac{\partial}{\partial \rho} \phi(\rho, \xi, \omega) - \frac{\eta}{\rho} \frac{\partial}{\partial \omega} \phi(\rho, \xi, \omega) + \Sigma(\rho) \phi(\rho, \xi, \omega) \\ &= \sum_{\ell=0}^L \frac{2\ell+1}{4\pi} \sum_{\substack{m=0 \\ \ell+m \text{ even}}}^{\ell} Q_{\ell}^m(\rho) R_{\ell}^m(\xi, \omega), \end{aligned} \quad (139)$$

where

$$R_{\ell}^m(\xi, \omega) = \sqrt{(2 - \delta_{m,0})} \frac{(\ell - m)!}{(\ell + m)!} P_{\ell}^m(\xi) \cos m\omega. \quad (140)$$

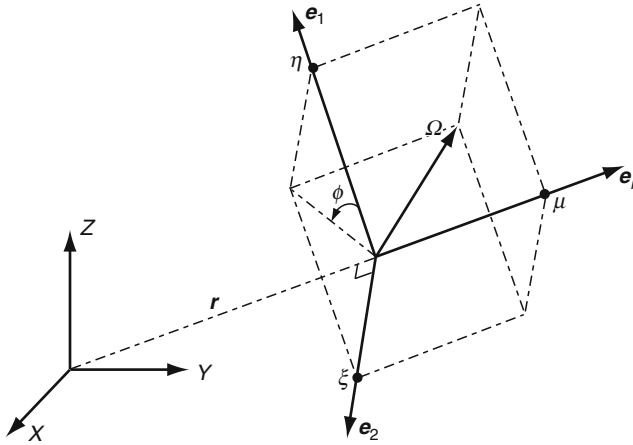
The conservative form of (139) is written as

$$\begin{aligned} &\frac{\mu}{\rho} \frac{\partial}{\partial \rho} [\rho \phi(\rho, \xi, \omega)] - \frac{1}{\rho} \frac{\partial}{\partial \omega} [\eta \phi(\rho, \xi, \omega)] + \Sigma(\rho) \phi(\rho, \xi, \omega) \\ &= \sum_{\ell=0}^L \frac{2\ell+1}{4\pi} \sum_{\substack{m=0 \\ \ell+m \text{ even}}}^{\ell} Q_{\ell}^m(\rho) R_{\ell}^m(\xi, \omega), \end{aligned} \quad (141)$$

where it can be shown that

$$\int_{4\pi} d^2 \Omega \frac{\partial}{\partial \omega} [\eta \phi(\rho, \xi, \omega)] = 0. \quad (142)$$

2.3 Spherical Coordinate System

The 3D spherical coordinate system is shown in  Fig. 7. The particle is located at the origin of the angular-direction coordinate system. The three axes of the angular-direction coordinate system, denoted as \mathbf{e}_r , \mathbf{e}_1 , and \mathbf{e}_2 , are defined in such a way that \mathbf{e}_r is colinear with the position vector of the particle.

The direction Ω of the particle is uniquely defined by the direction cosine μ of the polar angle and by the azimuthal angle ϕ . For 1D spheres, the first-order streaming operator is only a distribution of r and μ so that it can be written as

$$\Omega \cdot \nabla = \frac{d}{ds} = \frac{dr}{ds} \frac{\partial}{\partial r} + \frac{d\mu}{ds} \frac{\partial}{\partial \mu}, \quad (143)$$

where $dr/ds = \mu$ and where the angular redistribution term $d\mu/ds$ is evaluated using an expression similar to (133). Writing $\mu = \cos \theta$, we can show that $r d\theta = -ds \sin \theta$ and

$$\frac{d\mu}{ds} = \frac{\sin^2 \theta}{r} = \frac{1 - \mu^2}{r} \quad (144)$$

so that

$$\Omega \cdot \nabla = \mu \frac{\partial}{\partial r} + \frac{1 - \mu^2}{r} \frac{\partial}{\partial \mu}. \quad (145)$$

When this operator is applied on the angular flux, the terms can be rearranged in a form that facilitates the representation of particle conservation as

$$\Omega \cdot \nabla \phi = \frac{\mu}{r^2} \frac{\partial}{\partial r} (r^2 \phi) + \frac{1}{r} \frac{\partial}{\partial \mu} [(1 - \mu^2) \phi]. \quad (146)$$

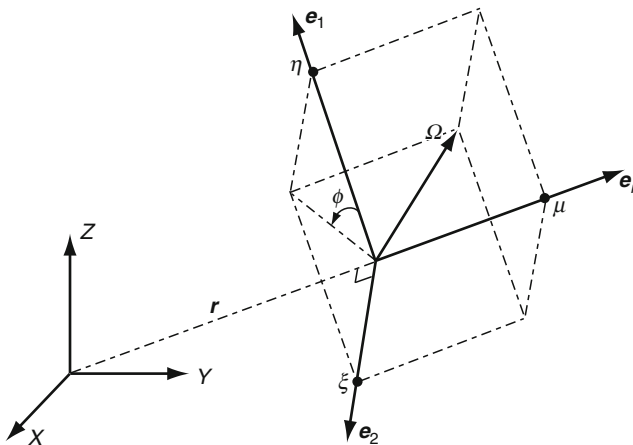


 Figure 7
Spherical coordinate system

In the particular case of a 1D spherical geometry, the flux and source density are only dependent upon r and μ , so that the source density components with $m \neq 0$ vanish. In this case, (45) is written as

$$Q(r, \mu) = \sum_{\ell=0}^L \frac{2\ell+1}{2} Q_{\ell}(r) P_{\ell}(\mu) \quad (147)$$

so that using the streaming operator (145), the first-order form of the linear Boltzmann equation (44) in 1D spherical geometry is written as

$$\mu \frac{\partial}{\partial r} \phi(r, \mu) + \frac{1-\mu^2}{r} \frac{\partial}{\partial \mu} \phi(r, \mu) + \Sigma(r) \phi(r, \mu) = \sum_{\ell=0}^L \frac{2\ell+1}{2} Q_{\ell}(r) P_{\ell}(\mu). \quad (148)$$

The conservative form of this equation is

$$\frac{\mu}{r^2} \frac{\partial}{\partial r} [r^2 \phi(r, \mu)] + \frac{1}{r} \frac{\partial}{\partial \mu} [(1-\mu^2) \phi(r, \mu)] + \Sigma(r) \phi(r, \mu) = \sum_{\ell=0}^L \frac{2\ell+1}{2} Q_{\ell}(r) P_{\ell}(\mu). \quad (149)$$

3 The Spherical Harmonics Method

The spherical harmonics, or P_n method, is a discretization of the differential form of the transport equation. The angular flux is represented as a limited development in real spherical harmonics, as defined in (24). This approach is by far the oldest way to solve transport equations and was used by astrophysicists at the beginning of the twentieth century (Eddington 1926). More recently, this approach was used in neutron-transport theory and has been called the P_n method (Gelbard 1968; Lewis and Miller 1984). A closely-related approximation is based on the solution of the *simplified P_n equation*, leading to an efficient solution technique that can be used for full-core calculations (Gelbard 1960).

We have chosen a *weighted residual* derivation of the relations between values of the particle flux defined at specific points of the spatial domain. A presentation of modern spherical harmonics approximations, based on variational principles and consistent with this text, can be found in Hébert (2006).

It is useful to recall the one-speed steady-state transport (108) as

$$\boldsymbol{\Omega} \cdot \nabla \phi(\mathbf{r}, \boldsymbol{\Omega}) + \Sigma(\mathbf{r}) \phi(\mathbf{r}, \boldsymbol{\Omega}) = Q(\mathbf{r}, \boldsymbol{\Omega}), \quad (150)$$

where the group index g is omitted to simplify the notation.

The spherical harmonics method is based on the expansion of $\phi(\mathbf{r}, \boldsymbol{\Omega})$ and $Q(\mathbf{r}, \boldsymbol{\Omega})$ in spherical harmonics. The expansions are truncated after a few terms, leading to the so-called P_n method. We write

$$\phi(\mathbf{r}, \boldsymbol{\Omega}) = \sum_{\ell=0}^n \frac{2\ell+1}{4\pi} \sum_{m=-\ell}^{\ell} \phi_{\ell}^m(\mathbf{r}) R_{\ell}^m(\boldsymbol{\Omega}) \quad (151)$$

and

$$Q(\mathbf{r}, \boldsymbol{\Omega}) = \sum_{\ell=0}^L \frac{2\ell+1}{4\pi} \sum_{m=-\ell}^{\ell} Q_{\ell}^m(\mathbf{r}) R_{\ell}^m(\boldsymbol{\Omega}), \quad (152)$$

where n is odd and $L \leq n$. The within-group scattering component can be made explicit in (152), leading to

$$Q(\mathbf{r}, \boldsymbol{\Omega}) = \sum_{\ell=0}^L \frac{2\ell+1}{4\pi} \sum_{m=-\ell}^{\ell} [\Sigma_{w,\ell}(\mathbf{r}) \phi_{\ell}^m(\mathbf{r}) + Q_{\ell}^{\circ m}(\mathbf{r})] R_{\ell}^m(\boldsymbol{\Omega}), \quad (153)$$

where $\Sigma_{w,\ell}(\mathbf{r})$ is the macroscopic within-group scattering cross section and $Q_{\ell}^{\circ m}(\mathbf{r})$ is the out-of-group source density.

It is possible to use symmetry properties of specific geometries to reduce the number of components in (151)–(153). This will be the subject of the following sub-sections.

3.1 The P_n Method in 1D Slab Geometry

3.1.1 Discretization in Angle

The P_n method will first be studied for the simple case of a 1D x -oriented slab geometry. In this case, the flux and source density are independent of y , z , and of the azimuthal angle. The flux and source density components with $m \neq 0$ vanishes, so that the angular variation of the flux is only a function of the direction cosine μ . The flux components can be developed using the first $n+1$ Legendre polynomials, n being an odd number. Equation (150) simplifies to (126), so that

$$\left[\mu \frac{\partial}{\partial x} + \Sigma(x) \right] \phi(x, \mu) = Q(x, \mu), \quad (154)$$

where (151) and (152) are now written

$$\phi(x, \mu) = \sum_{\ell=0}^n \frac{2\ell+1}{2} \phi_{\ell}(x) P_{\ell}(\mu) \quad \text{and} \quad Q(x, \mu) = \sum_{\ell=0}^L \frac{2\ell+1}{2} Q_{\ell}(x) P_{\ell}(\mu), \quad (155)$$

where $L \leq n$, so that the components of the flux are written as

$$\phi_{\ell}(x) = \int_{-1}^1 d\mu P_{\ell}(\mu) \phi(x, \mu) \quad (156)$$

with the scalar flux and current given by $\phi_0(x)$ and $\phi_1(x)$, respectively.

We next substitute (155) into (154), multiply by $P_{\ell}(\mu)$, integrate from -1 to $+1$, and use the orthogonality and recurrence relations for the Legendre polynomials. Recurrence relations were previously introduced as (21) and (22). The result is

$$\frac{\ell}{2\ell+1} \frac{d}{dx} \phi_{\ell-1}(x) + \frac{\ell+1}{2\ell+1} \frac{d}{dx} \phi_{\ell+1}(x) + \Sigma(x) \phi_{\ell}(x) = Q_{\ell}(x). \quad (157)$$

3.1.2 Boundary Conditions

A boundary condition with a specular reflection on surface x_- is imposed as a symmetry in direction cosine μ as

$$\phi(x_-, \mu) = \phi(x_-, -\mu) \quad (158)$$

so that the odd moments of the flux are set to zero at point x_- .

There is no straightforward way to represent a vacuum boundary condition. If the domain is bounded on the left by vacuum, then

$$\phi(x_-, \mu) = 0 \quad \text{if } \mu > 0. \quad (159)$$

No sum of Legendre polynomials can fulfill (159) exactly. We are limited to use an approximation in which this condition is projected on the polynomial basis, as proposed by Marshak. Another well-known approximation was proposed by Mark, but will not be considered until we introduce the *discrete ordinate*, or S_n , method in [Sect. 5](#). A Marshak boundary condition on the left boundary x_- is written as

$$\int_0^1 d\mu \phi(x_-, \mu) P_\ell(\mu) = \sum_{m=0}^n \frac{2m+1}{2} \phi_m(x_-) \int_0^1 d\mu P_\ell(\mu) P_m(\mu) = 0, \quad (160)$$

where ℓ is odd and $1 \leq \ell \leq n$.

[Equation \(160\)](#) can be generalized by introducing an albedo β^- representing the fraction of outgoing particles undergoing specular reflection. The revised condition is

$$\begin{aligned} & \sum_{m=0}^n (2m+1) \phi_m(x_-) \int_0^1 d\mu P_\ell(\mu) P_m(\mu) \\ &= -\beta^- \sum_{m=0}^n (2m+1) \phi_m(x_-) \int_{-1}^0 d\mu P_\ell(\mu) P_m(\mu), \end{aligned} \quad (161)$$

where ℓ is odd and $1 \leq \ell \leq n$. This equation can be rewritten as

$$(1 + \beta^-) \phi_\ell(x_-) + (1 - \beta^-) \sum_{\substack{m=0 \\ m \text{ even}}}^{n-1} \mathcal{M}_{\ell,m} \phi_m(x_-) = 0, \quad (162)$$

where ℓ is odd, $1 \leq \ell \leq n$, and where the Marshak coefficients $\mathcal{M}_{\ell,m}$ are given in [Table 1](#). They are defined as

$$\mathcal{M}_{\ell,m} = (2m+1) \int_0^1 d\mu P_\ell(\mu) P_m(\mu). \quad (163)$$

■ **Table 1**

Marshak coefficients in slab geometry

ℓ	$m = 0$	$m = 2$	$m = 4$	$m = 6$	$m = 8$
1	0.5	0.625	-0.1875	0.101562	-0.066406
3	-0.125	0.625	0.632812	-0.203125	0.116211
5	0.0625	-0.195312	0.632812	0.634766	-0.207520
7	-0.039063	0.109375	-0.205078	0.634765	0.635528
9	0.027344	-0.073242	0.118652	-0.208283	0.635528

The Marshak coefficients in slab geometry can be obtained with the following Matlab script:

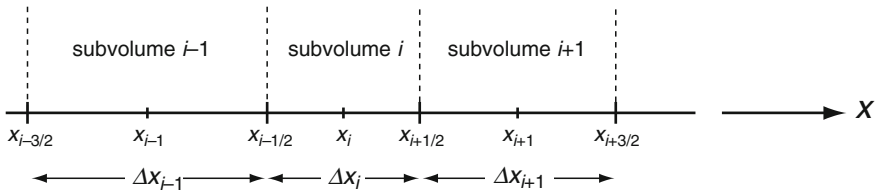
```
function f=pnmars (l, m)
% return the Marshak boundary coefficients in slab geometry. These
% coefficients are specific to the left boundary.
% function f=pnmars (l, m)
% (c) 2008 Alain Hebert, Ecole Polytechnique de Montreal
if mod (l, 2) == 0
    error('odd first index expected')
end
zgksi=[ 0.00529953837 0.0277124941 0.0671843886 0.122297794 ...
0.191061884 0.270991623 0.359198213 0.452493757 0.547506273 ...
0.640801787 0.729008377 0.808938146 0.877702236 0.932815611 ...
0.972287536 0.994700432 ];
wgksi=[ 0.01357623 0.0311267618 0.047579255 0.0623144843 ...
0.0747979954 0.0845782608 0.0913017094 0.0947253034 0.0947253034 ...
0.0913017094 0.0845782608 0.0747979954 0.0623144843 0.047579255 ...
0.0311267618 0.01357623 ];
f=(2*m+1)*sum(wgksi(:).*plgndr(l,0,zgksi(:)).*plgndr(m,0,zgksi(:)));
```

Similarly, a Marshak condition on the right boundary at x_+ would be written as

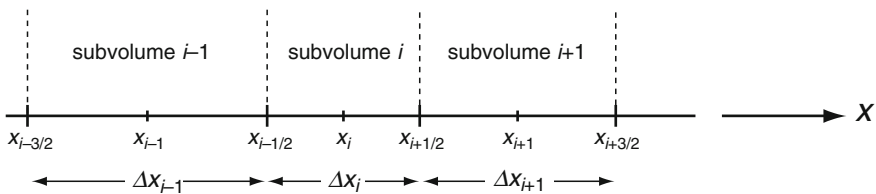
$$(1 + \beta^+) \phi_\ell(x_+) - (1 - \beta^+) \sum_{\substack{m=0 \\ m \text{ even}}}^{n-1} \mathcal{M}_{\ell,m} \phi_m(x_+) = 0, \quad (164)$$

where ℓ is odd and $1 \leq \ell \leq n$.

3.1.3 Difference Relations

A *first-order numerical solution* of the spherical harmonics equations requires the application of finite-difference discretization to every order ℓ of (157), resulting in a symmetric linear system of $n + 1$ coupled relations. The domain is divided into subvolumes, or *elements*, with constant cross-sections, as depicted in  Fig. 8.

The odd-parity variables are discretized over mesh-centered coordinates (x_{i-1}, x_i, x_{i+1}) and the even-parity variables are discretized over interface coordinates $(x_{i-1/2}, x_{i+1/2}, x_{i+3/2})$.



 **Figure 8**
Spatial discretization for slab geometry

We define the corresponding volumes as

$$\Delta x_i = x_{i+1/2} - x_{i-1/2}. \quad (165)$$

Let us now consider the spherical harmonics-discretized relations for even indices ℓ . First consider the case where surface $i + 1/2$ is not a boundary. The finite-difference relations can be applied in many different ways, leading to linear-order accuracy. The specific relations selected here have been selected to enforce consistency with the *diamond differencing scheme* of the discrete ordinates method presented in [5.2](#).

We first consider even-parity indices ℓ . The approximation consists in writing (157) at x_i and x_{i+1} , using the average of even-parity variables on these points. We write

$$\begin{aligned} \ell \frac{d}{dx} \phi_{\ell-1,i}^- + (\ell + 1) \frac{d}{dx} \phi_{\ell+1,i}^- + \frac{2\ell + 1}{2} \Sigma_i (\phi_{\ell,i-1/2}^+ + \phi_{\ell,i+1/2}^+) \\ = \frac{2\ell + 1}{2} (Q_{\ell,i-1/2}^+ + Q_{\ell,i+1/2}^+) \end{aligned} \quad (166)$$

and

$$\begin{aligned} \ell \frac{d}{dx} \phi_{\ell-1,i+1}^- + (\ell + 1) \frac{d}{dx} \phi_{\ell+1,i+1}^- + \frac{2\ell + 1}{2} \Sigma_{i+1} (\phi_{\ell,i+1/2}^+ + \phi_{\ell,i+3/2}^+) \\ = \frac{2\ell + 1}{2} (Q_{\ell,i+1/2}^+ + Q_{\ell,i+3/2}^+) \end{aligned} \quad (167)$$

together with the finite difference relations

$$\frac{d}{dx} \phi_{\ell\mp 1,i}^- = \frac{\phi_{\ell\mp 1,i+1/2}^- - \phi_{\ell\mp 1,i}^-}{\Delta x_i/2}$$

and

$$\frac{d}{dx} \phi_{\ell\mp 1,i+1}^- = \frac{\phi_{\ell\mp 1,i+1}^- - \phi_{\ell\mp 1,i+1/2}^-}{\Delta x_{i+1/2}}, \quad (168)$$

so that

$$\begin{aligned} \ell (\phi_{\ell-1,i+1}^- - \phi_{\ell-1,i}^-) + (\ell + 1) (\phi_{\ell+1,i+1}^- - \phi_{\ell+1,i}^-) \\ + (2\ell + 1) \frac{\Delta x_i}{4} (\Sigma_i \phi_{\ell,i-1/2}^+ - Q_{\ell,i-1/2}^+) + (2\ell + 1) \frac{\Delta x_i}{4} (\Sigma_i \phi_{\ell,i+1/2}^+ - Q_{\ell,i+1/2}^+) \\ + (2\ell + 1) \frac{\Delta x_{i+1}}{4} (\Sigma_{i+1} \phi_{\ell,i+1/2}^+ - Q_{\ell,i+1/2}^+) \\ + (2\ell + 1) \frac{\Delta x_{i+1}}{4} (\Sigma_{i+1} \phi_{\ell,i+3/2}^+ - Q_{\ell,i+3/2}^+) = 0, \end{aligned} \quad (169)$$

where $1 \leq i \leq I$.

Similarly, the left- and right-boundary relations are obtained using difference relations. The derivative of odd-parity variables at $x_{1/2}$ are written with the help of (162) as

$$\frac{d}{dx} \phi_{\ell\mp 1,1}^- = \frac{\phi_{\ell\mp 1,1}^- - \phi_{\ell\mp 1,1/2}^-}{\Delta x_{1/2}} = \frac{2}{\Delta x_1} \left(\phi_{\ell\mp 1,1}^- + \frac{1 - \beta^-}{1 + \beta^-} \sum_{\substack{m=0 \\ m \text{ even}}}^{n-1} \mathcal{M}_{\ell\mp 1,m} \phi_{m,1/2}^+ \right). \quad (170)$$

The left- and right-boundary relations are finally written as

$$\begin{aligned} \ell \phi_{\ell-1,1}^- + (\ell+1) \phi_{\ell+1,1}^- + (2\ell+1) \frac{\Delta x_1}{4} (\Sigma_1 \phi_{\ell,1/2}^+ - Q_{\ell,1/2}^+) + (2\ell+1) \frac{\Delta x_1}{4} (\Sigma_1 \phi_{\ell,3/2}^+ - Q_{\ell,3/2}^+) \\ + (2\ell+1) \frac{1-\beta^-}{1+\beta^-} \sum_{\substack{m=0 \\ m \text{ even}}}^{n-1} \hat{\mathcal{M}}_{\ell,m} \phi_{m,1/2}^+ = 0 \end{aligned} \quad (171)$$

and

$$\begin{aligned} -\ell \phi_{\ell-1,I}^- - (\ell+1) \phi_{\ell+1,I}^- + (2\ell+1) \frac{\Delta x_I}{4} (\Sigma_I \phi_{\ell,I-1/2}^+ - Q_{\ell,I-1/2}^+) \\ + (2\ell+1) \frac{\Delta x_I}{4} (\Sigma_I \phi_{\ell,I+1/2}^+ - Q_{\ell,I+1/2}^+) \\ + (2\ell+1) \frac{1-\beta^+}{1+\beta^+} \sum_{\substack{m=0 \\ m \text{ even}}}^{n-1} \hat{\mathcal{M}}_{\ell,m} \phi_{m,I+1/2}^+ = 0, \end{aligned} \quad (172)$$

where

$$\hat{\mathcal{M}}_{\ell,m} = (2m+1) \int_0^1 d\mu \mu P_\ell(\mu) P_m(\mu) = \frac{1}{2\ell+1} [\ell \mathcal{M}_{\ell-1,m} + (\ell+1) \mathcal{M}_{\ell+1,m}]. \quad (173)$$

Finally, the spherical harmonics-discretized relations for odd-parity indices ℓ are obtained by integrating (157) between $x_{i-1/2}$ and $x_{i+1/2}$ and by assuming that $\phi_{\ell,i}^-$ is equal to the averaged value over subvolume i . We obtain

$$\begin{aligned} -\ell (\phi_{\ell-1,i+1/2}^+ - \phi_{\ell-1,i-1/2}^+) - (\ell+1) (\phi_{\ell+1,i+1/2}^+ - \phi_{\ell+1,i-1/2}^+) - (2\ell+1) \Delta x_i \Sigma_i \phi_{\ell,i}^- \\ = -(2\ell+1) \Delta x_i Q_{\ell,i}^-, \end{aligned} \quad (174)$$

where $1 \leq i \leq I$.

Equations (169)–(174) are the difference equations corresponding to the discretized transport equation in 1D slab geometry. They are solved iteratively, taking two successive Legendre orders at each iteration. The scattering reduction is done in a straightforward way, by extracting the within-group scattering rates from $Q_{\ell,i\pm 1/2}^+$ and $Q_{\ell,i}^-$.

3.2 The P_n Method in 1D Cylindrical Geometry

3.2.1 Discretization in Angle

Due to specific symmetries, the flux is a function of the radius ρ , of the direction cosine ξ , of the azimuthal angle ω , and can be developed in terms of the even $\ell + m$ positive components of an expansion in spherical harmonics, where $1 \leq \ell \leq n$, n being an odd number. Equation (150) simplifies to (139) which can be rewritten, with the help of (136), as

$$\sqrt{1-\xi^2} \cos \omega \frac{\partial}{\partial \rho} \phi(\rho, \xi, \omega) - \frac{\sqrt{1-\xi^2} \sin \omega}{\rho} \frac{\partial}{\partial \omega} \phi(\rho, \xi, \omega) + \Sigma(\rho) \phi(\rho, \xi, \omega) = Q(\rho, \xi, \omega), \quad (175)$$

where the angular source is expanded at order $L \leq n$. The spherical harmonic expansions are written as

$$\phi(\rho, \xi, \omega) = \sum_{\ell=0}^n \frac{2\ell+1}{4\pi} \sum_{\substack{m=0 \\ \ell+m \text{ even}}}^{\ell} \phi_{\ell}^m(\rho) R_{\ell}^m(\xi, \omega) \quad (176)$$

and

$$Q(\rho, \xi, \omega) = \sum_{\ell=0}^L \frac{2\ell+1}{4\pi} \sum_{\substack{m=0 \\ \ell+m \text{ even}}}^{\ell} Q_{\ell}^m(\rho) R_{\ell}^m(\xi, \omega) \quad (177)$$

so that the components of the flux are written as

$$\phi_{\ell}^m(\rho) = \int_{-1}^1 d\xi \int_{-\pi}^{\pi} d\omega R_{\ell}^m(\xi, \omega) \phi(\rho, \xi, \omega) \quad (178)$$

with the scalar flux and current given by $\phi_0^0(\rho)$ and $\phi_1^1(\rho)$, respectively.

We next substitute (176) into (175), multiply by $\rho R_{\ell'}^m(\xi, \omega)$, integrate over 4π , and use the orthogonality relation (30). The result is

$$\begin{aligned} & \mathcal{A}_{\ell}^m \left[\rho \frac{d}{d\rho} - (m-1) \right] \phi_{\ell-1}^{m-1}(\rho) + \mathcal{B}_{\ell}^m \left[\rho \frac{d}{d\rho} - (m-1) \right] \phi_{\ell+1}^{m-1}(\rho) \\ & + \mathcal{C}_{\ell}^m \left[\rho \frac{d}{d\rho} + (m+1) \right] \phi_{\ell-1}^{m+1}(\rho) + \mathcal{D}_{\ell}^m \left[\rho \frac{d}{d\rho} + (m+1) \right] \phi_{\ell+1}^{m+1}(\rho) \\ & + \rho \Sigma(\rho) \phi_{\ell}^m(\rho) = \rho Q_{\ell}^m(\rho), \end{aligned} \quad (179)$$

where we used the following relations:

$$\begin{aligned} & \frac{2\ell'+1}{4\pi} \int_{-1}^1 d\xi \sqrt{1-\xi^2} \int_{-\pi}^{\pi} d\omega \cos \omega R_{\ell}^m(\xi, \omega) R_{\ell'}^m(\xi, \omega) \\ & = \mathcal{A}_{\ell}^m \delta_{\ell', \ell-1} \delta_{m', m-1} + \mathcal{B}_{\ell}^m \delta_{\ell', \ell+1} \delta_{m', m-1} + \mathcal{C}_{\ell}^m \delta_{\ell', \ell-1} \delta_{m', m+1} \\ & + \mathcal{D}_{\ell}^m \delta_{\ell', \ell+1} \delta_{m', m+1}, \end{aligned} \quad (180)$$

$$\begin{aligned} & \frac{2\ell'+1}{4\pi} \int_{-1}^1 d\xi \sqrt{1-\xi^2} \int_{-\pi}^{\pi} d\omega \sin \omega R_{\ell}^m(\xi, \omega) \frac{\partial}{\partial \omega} R_{\ell'}^m(\xi, \omega) \\ & = (m-1) \mathcal{A}_{\ell}^m \delta_{\ell', \ell-1} \delta_{m', m-1} + (m-1) \mathcal{B}_{\ell}^m \delta_{\ell', \ell+1} \delta_{m', m-1} \\ & - (m+1) \mathcal{C}_{\ell}^m \delta_{\ell', \ell-1} \delta_{m', m+1} - (m+1) \mathcal{D}_{\ell}^m \delta_{\ell', \ell+1} \delta_{m', m+1} \end{aligned} \quad (181)$$

and

$$\begin{aligned} & \frac{2\ell'+1}{4\pi} \int_{-1}^1 d\xi \sqrt{1-\xi^2} \int_{-\pi}^{\pi} d\omega \sin \omega \left(\frac{\partial}{\partial \omega} R_{\ell}^m(\xi, \omega) \right) R_{\ell'}^m(\xi, \omega) \\ & = -m \mathcal{A}_{\ell}^m \delta_{\ell', \ell-1} \delta_{m', m-1} - m \mathcal{B}_{\ell}^m \delta_{\ell', \ell+1} \delta_{m', m-1} \\ & + m \mathcal{C}_{\ell}^m \delta_{\ell', \ell-1} \delta_{m', m+1} + m \mathcal{D}_{\ell}^m \delta_{\ell', \ell+1} \delta_{m', m+1} \end{aligned} \quad (182)$$

with the definitions:

$$\begin{aligned}
 \mathcal{A}_\ell^m &= \frac{1}{2(2\ell+1)} \sqrt{(1-\delta_{m,0})(1+\delta_{m,1})(\ell+m)(\ell+m-1)}, \\
 \mathcal{B}_\ell^m &= -\frac{1}{2(2\ell+1)} \sqrt{(1-\delta_{m,0})(1+\delta_{m,1})(\ell-m+1)(\ell-m+2)}, \\
 \mathcal{C}_\ell^m &= -\frac{1}{2(2\ell+1)} \sqrt{(1+\delta_{m,0})(\ell-m)(\ell-m-1)}, \\
 \mathcal{D}_\ell^m &= \frac{1}{2(2\ell+1)} \sqrt{(1+\delta_{m,0})(\ell+m+1)(\ell+m+2)}.
 \end{aligned} \tag{183}$$

These coefficients were obtained using the following identities:

$$\begin{aligned}
 &\int_{-1}^1 d\xi \sqrt{1-\xi^2} P_\ell^m(\xi) P_{\ell'}^{m+1}(\xi) \\
 &= \frac{2}{2\ell+1} \left[\frac{(\ell+m+2)!}{(2\ell+3)(\ell-m)!} \delta_{\ell,\ell'-1} - \frac{(\ell+m)!}{(2\ell-1)(\ell-m-2)!} \delta_{\ell,\ell'+1} \right],
 \end{aligned} \tag{184}$$

$$\begin{aligned}
 &\int_{-1}^1 d\xi \sqrt{1-\xi^2} P_\ell^m(\xi) P_{\ell'}^{m-1}(\xi) \\
 &= \frac{2(\ell+m)!}{(2\ell+1)(\ell-m)!} \left[\frac{1}{2\ell-1} \delta_{\ell,\ell'+1} - \frac{1}{2\ell+3} \delta_{\ell,\ell'-1} \right],
 \end{aligned} \tag{185}$$

$$\int_{-\pi}^{\pi} d\phi \cos \phi \cos m\phi \cos m'\phi = \frac{\pi}{2} [(1+\delta_{m,0})\delta_{m,m'-1} + (1+\delta_{m',0})\delta_{m,m'+1}] \tag{186}$$

and

$$\int_{-\pi}^{\pi} d\phi \sin \phi \cos m\phi \sin m'\phi = \frac{\pi}{2} [(1+\delta_{m,0})\delta_{m,m'-1} - \delta_{m,m'+1}] \quad \text{where } m' > 0. \tag{187}$$

3.2.2 Boundary Conditions

The $\rho = \rho_- \equiv 0$ condition is set by forcing the flux to be an even function of ζ at the origin. Consequently, all components of the flux with an odd value of ℓ are forced to zero.

The external boundary condition of a 1D cylindrical geometry is introduced by choosing an albedo β^+ set to zero for representing a voided boundary, or set to one for representing reflection of particles. The voided boundary condition is similar to the Marshak condition used for 1D slab geometry. The inward flux, written as

$$\phi(\rho_+, \xi, \omega) = 0 \quad \text{if } \pi/2 < \omega < 3\pi/2 \tag{188}$$

is projected onto a space of trial functions. Such a boundary condition is useful in criticality problems for computing the critical radius of tubes. The more general albedo boundary condition is written as


$$(1+\beta^+) \phi_\ell^m(\rho_+) - (1-\beta^+) \sum_{\substack{\ell'=0 \\ \ell' \text{ even}}}^{n-1} \sum_{\substack{m'=0 \\ m' \text{ even}}}^{\ell'} \mathcal{M}_{\ell,\ell'}^{m,m'} \phi_{\ell'}^{m'}(\rho_+) = 0, \tag{189}$$

where ℓ and m are odd integers, $1 \leq \ell \leq n$ and $1 \leq m \leq \ell$. The cylindrical-geometry Marshak coefficients are defined as

$$\mathcal{M}_{\ell, \ell'}^{m, m'} = \frac{2\ell' + 1}{2\pi} \int_{-1}^1 d\xi \int_{-\pi/2}^{\pi/2} d\omega R_{\ell}^m(\xi, \omega) R_{\ell'}^{m'}(\xi, \omega). \quad (190)$$

They can be obtained using the following Matlab script:

```
function f=pncmar (l1,l2,m1,m2)
% return the Marshak boundary coefficients in 1D tube geometry.
% function f=pncmar (l1,l2,m1,m2)
% (c) 2008 Alain Hebert, Ecole Polytechnique de Montreal
if mod(l1,2) == 0
    error('odd legendre order expected.')
elseif mod(m1,2) == 0
    error('odd azimuthal order expected.')
end
zgksi=[ -0.989400923 -0.944575012 -0.865631223 -0.755404413 ...
-0.617876232 -0.458016783 -0.281603545 -0.0950125083 0.0950125083 ...
0.281603545 0.458016783 0.617876232 0.755404413 0.865631223 ...
0.944575012 0.989400923 ];
wgksi=[ 0.0271524601 0.0622535236 0.0951585099 0.124628969 ...
0.149595991 0.169156522 0.182603419 0.189450607 0.189450607 ...
0.182603419 0.169156522 0.149595991 0.124628969 0.0951585099 ...
0.0622535236 0.0271524601 ];
coef=1.0;
if m1 > 0, coef=coef*sqrt(2.0*factorial(l1-m1)/factorial(l1+m1)); end
if m2 > 0, coef=coef*sqrt(2.0*factorial(l2-m2)/factorial(l2+m2)); end
sum1=sum(wgksi(:).*plgndr(l1,m1,zgksi(:)).*plgndr(l2,m2,zgksi(:)));
if m1 == m2
    sumphi=0.25;
elseif mod(m1+m2,2) == 0
    sumphi=0.0;
else
    sumphi=(-1.)^fix((m1-m2)/2)*sign(m1-m2)*(1./(m1-m2)+1./(m1+m2))/(2.*pi);
end
f=sum1*coef*sumphi*(2.*l2+1.);
```

Implementing the reflecting-boundary condition is less straightforward. Such a condition is useful in the context of the *Wigner–Seitz approximation* for lattice calculations in reactor physics. An elementary cell of a nuclear reactor can be represented with a reflecting rectangular or hexagonal boundary. The Wigner–Seitz approximation consists of replacing the exact boundary with an *equivalent cylindrical boundary*, as shown in  Fig. 9, taking care to conserve the amount of moderator present in the cell.

However, a specular boundary condition cannot be used with Wigner–Seitz approximation, because a neutron incident on the boundary would be reflected in such a way that its path could not intersect the fuel element without being scattered. The correct condition in this case is the

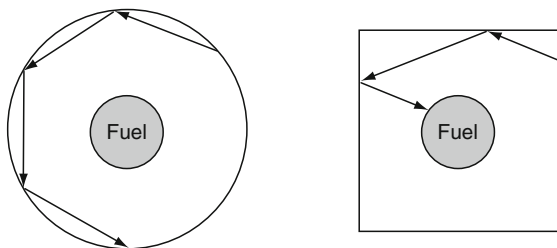


Figure 9
Wigner-Seitz boundary approximation

white boundary condition in which the particles are reflected back, on the cylindrical boundary, with an isotropic angular distribution in the radial plane. Such a condition can be represented by forcing to zero the components of the incoming odd-parity fluxes with $m = 1$ and by treating the remaining components with a vacuum boundary condition.

3.2.3 Difference Relations

Equation (179) with the Marshak-boundary condition (189) can be discretized in ρ by replacing the differential terms with difference relations, taking care to preserve the symmetry of the resulting matrices. The odd-parity variables are discretized over mesh-centered coordinates $(\rho_{i-1}, \rho_i, \rho_{i+1})$ and the even-parity variables are discretized over interface coordinates $(\rho_{i-1/2}, \rho_{i+1/2}, \rho_{i+3/2})$. We also define

$$\Delta\rho_i = \rho_{i+1/2} - \rho_{i-1/2}, \quad \rho_i = \frac{1}{2}(\rho_{i-1/2} + \rho_{i+1/2}), \quad \text{and} \quad V_i = 2\pi \rho_i \Delta\rho_i. \quad (191)$$

We first consider even-parity indices ℓ and m in the case where surface $i + 1/2$ is not a boundary. The approximation consists in writing (179) at ρ_i and ρ_{i+1} , using the average of even-parity variables on these points. We write

$$\begin{aligned} & \mathcal{A}_\ell^m \left[\frac{d}{d\rho} (\rho \phi_{\ell-1,i}^{-,m-1}) - m \phi_{\ell-1,i}^{-,m-1} \right] + \mathcal{B}_\ell^m \left[\frac{d}{d\rho} (\rho \phi_{\ell+1,i}^{-,m-1}) - m \phi_{\ell+1,i}^{-,m-1} \right] \\ & + \mathcal{C}_\ell^m \left[\frac{d}{d\rho} (\rho \phi_{\ell-1,i}^{-,m+1}) + m \phi_{\ell-1,i}^{-,m+1} \right] + \mathcal{D}_\ell^m \left[\frac{d}{d\rho} (\rho \phi_{\ell+1,i}^{-,m+1}) + m \phi_{\ell+1,i}^{-,m+1} \right] \\ & + \frac{\Sigma_i \rho_i}{2} (\phi_{\ell,i-1/2}^{+,m} + \phi_{\ell,i+1/2}^{+,m}) = \frac{\rho_i}{2} (Q_{\ell,i-1/2}^{+,m} + Q_{\ell,i+1/2}^{+,m}) \end{aligned} \quad (192)$$

and

$$\begin{aligned} & \mathcal{A}_\ell^m \left[\frac{d}{d\rho} (\rho \phi_{\ell-1,i+1}^{-,m-1}) - m \phi_{\ell-1,i+1}^{-,m-1} \right] + \mathcal{B}_\ell^m \left[\frac{d}{d\rho} (\rho \phi_{\ell+1,i+1}^{-,m-1}) - m \phi_{\ell+1,i+1}^{-,m-1} \right] \\ & + \mathcal{C}_\ell^m \left[\frac{d}{d\rho} (\rho \phi_{\ell-1,i+1}^{-,m+1}) + m \phi_{\ell-1,i+1}^{-,m+1} \right] + \mathcal{D}_\ell^m \left[\frac{d}{d\rho} (\rho \phi_{\ell+1,i+1}^{-,m+1}) + m \phi_{\ell+1,i+1}^{-,m+1} \right] \\ & + \frac{\Sigma_{i+1} \rho_{i+1}}{2} (\phi_{\ell,i+1/2}^{+,m} + \phi_{\ell,i+3/2}^{+,m}) = \frac{\rho_{i+1}}{2} (Q_{\ell,i+1/2}^{+,m} + Q_{\ell,i+3/2}^{+,m}) \end{aligned} \quad (193)$$

together with the finite difference relations

$$\frac{d}{d\rho}(\rho \phi_{\ell\mp 1, i}^{-, m\mp 1}) = \frac{\rho_{i+1/2} \phi_{\ell\mp 1, i+1/2}^{-, m\mp 1} - \rho_i \phi_{\ell\mp 1, i}^{-, m\mp 1}}{\Delta\rho_i/2} \quad (194)$$

and

$$\frac{d}{d\rho}(\rho \phi_{\ell\mp 1, i+1}^{-, m\mp 1}) = \frac{\rho_{i+1} \phi_{\ell\mp 1, i+1}^{-, m\mp 1} - \rho_{i+1/2} \phi_{\ell\mp 1, i+1/2}^{-, m\mp 1}}{\Delta\rho_{i+1/2}}, \quad (195)$$

so that

$$\begin{aligned} & 2\pi\mathcal{A}_\ell^m \left[(\rho_{i+1} \phi_{\ell-1, i+1}^{-, m-1} - \rho_i \phi_{\ell-1, i}^{-, m-1}) - \frac{m}{2} (\Delta\rho_i \phi_{\ell-1, i}^{-, m-1} + \Delta\rho_{i+1} \phi_{\ell-1, i+1}^{-, m-1}) \right] \\ & + 2\pi\mathcal{B}_\ell^m \left[(\rho_{i+1} \phi_{\ell+1, i+1}^{-, m-1} - \rho_i \phi_{\ell+1, i}^{-, m-1}) - \frac{m}{2} (\Delta\rho_i \phi_{\ell+1, i}^{-, m-1} + \Delta\rho_{i+1} \phi_{\ell+1, i+1}^{-, m-1}) \right] \\ & + 2\pi\mathcal{C}_\ell^m \left[(\rho_{i+1} \phi_{\ell-1, i+1}^{-, m+1} - \rho_i \phi_{\ell-1, i}^{-, m+1}) + \frac{m}{2} (\Delta\rho_i \phi_{\ell-1, i}^{-, m+1} + \Delta\rho_{i+1} \phi_{\ell-1, i+1}^{-, m+1}) \right] \\ & + 2\pi\mathcal{D}_\ell^m \left[(\rho_{i+1} \phi_{\ell+1, i+1}^{-, m+1} - \rho_i \phi_{\ell+1, i}^{-, m+1}) + \frac{m}{2} (\Delta\rho_i \phi_{\ell+1, i}^{-, m+1} + \Delta\rho_{i+1} \phi_{\ell+1, i+1}^{-, m+1}) \right] \\ & + \frac{V_i}{4} (\Sigma_i \phi_{\ell, i-1/2}^{+, m} - Q_{\ell, i-1/2}^{+, m}) + \frac{V_i}{4} (\Sigma_i \phi_{\ell, i+1/2}^{+, m} - Q_{\ell, i+1/2}^{+, m}) \\ & + \frac{V_{i+1}}{4} (\Sigma_{i+1} \phi_{\ell, i+1/2}^{+, m} - Q_{\ell, i+1/2}^{+, m}) + \frac{V_{i+1}}{4} (\Sigma_{i+1} \phi_{\ell, i+3/2}^{+, m} - Q_{\ell, i+3/2}^{+, m}) = 0, \quad (196) \end{aligned}$$

where ℓ and m are even integers and $1 \leq i < I$.

Let us now consider the case where $\rho_{I+1/2}$ is the outer boundary. The derivative of odd-parity variables at $\rho_{I+1/2}$ is written with the help of (189) as

$$\begin{aligned} \frac{d}{d\rho}(\rho \phi_{\ell\mp 1, I}^{-, m\mp 1}) &= \frac{\rho_{I+1/2} \phi_{\ell\mp 1, I+1/2}^{-, m\mp 1} - \rho_I \phi_{\ell\mp 1, I}^{-, m\mp 1}}{\Delta\rho_I/2} \\ &= \frac{2}{\Delta\rho_I} \left(\rho_+ \frac{1 - \beta^+}{1 + \beta^+} \sum_{\substack{\ell'=0 \\ \ell' \text{ even}}}^{n-1} \sum_{\substack{m'=0 \\ m' \text{ even}}}^{\ell'} \mathcal{M}_{\ell\mp 1, \ell'}^{m\mp 1, m'} \phi_{\ell', I+1/2}^{+, m'} - \rho_I \phi_{\ell\mp 1, I}^{-, m\mp 1} \right) \quad (197) \end{aligned}$$

so that

$$\begin{aligned} & 2\pi\mathcal{A}_\ell^m \left[-\rho_I \phi_{\ell-1, I}^{-, m-1} - \frac{m}{2} \Delta\rho_I \phi_{\ell-1, I}^{-, m-1} \right] + 2\pi\mathcal{B}_\ell^m \left[-\rho_I \phi_{\ell+1, I}^{-, m-1} - \frac{m}{2} \Delta\rho_I \phi_{\ell+1, I}^{-, m-1} \right] \\ & + 2\pi\mathcal{C}_\ell^m \left[-\rho_I \phi_{\ell-1, I}^{-, m+1} + \frac{m}{2} \Delta\rho_I \phi_{\ell-1, I}^{-, m+1} \right] + 2\pi\mathcal{D}_\ell^m \left[-\rho_I \phi_{\ell+1, I}^{-, m+1} + \frac{m}{2} \Delta\rho_I \phi_{\ell+1, I}^{-, m+1} \right] \\ & + \frac{V_I}{4} (\Sigma_I \phi_{\ell, I-1/2}^{+, m} - Q_{\ell, I-1/2}^{+, m}) + \frac{V_I}{4} (\Sigma_I \phi_{\ell, I+1/2}^{+, m} - Q_{\ell, I+1/2}^{+, m}) \\ & + 2\pi\rho_+ \frac{1 - \beta^+}{1 + \beta^+} \sum_{\substack{\ell'=0 \\ \ell' \text{ even}}}^{n-1} \sum_{\substack{m'=0 \\ m' \text{ even}}}^{\ell'} \mathcal{M}_{\ell, \ell'}^{m, m'} \phi_{\ell', I+1/2}^{+, m'} = 0 \quad (198) \end{aligned}$$

if ℓ and m are even, where $\rho_+ \equiv \rho_{I+1/2}$ and

$$\begin{aligned} \mathcal{M}_{\ell,\ell'}^{m,m'} &= \frac{2\ell'+1}{2\pi} \int_{-1}^1 d\xi \sqrt{1-\xi^2} \int_{-\pi/2}^{\pi/2} d\omega \cos \omega R_\ell^m(\xi, \omega) R_{\ell'}^{m'}(\xi, \omega) \\ &= \mathcal{A}_\ell^m \mathcal{M}_{\ell-1,\ell'}^{m-1,m'} + \mathcal{B}_\ell^m \mathcal{M}_{\ell+1,\ell'}^{m-1,m'} + \mathcal{C}_\ell^m \mathcal{M}_{\ell-1,\ell'}^{m+1,m'} + \mathcal{D}_\ell^m \mathcal{M}_{\ell+1,\ell'}^{m+1,m'}. \end{aligned} \quad (199)$$

Finally, the spherical harmonics-discretized relations for odd-parity indices ℓ and m are obtained by integrating (179) between $\rho_{i-1/2}$ and $\rho_{i+1/2}$ and by assuming that $\phi_{\ell,i}^{-,m}$ is equal to the averaged value over subvolume i . We obtain

$$\begin{aligned} &-2\pi \mathcal{A}_\ell^m \left[\rho_i (\phi_{\ell-1,i+1/2}^{+,m-1} - \phi_{\ell-1,i-1/2}^{+,m-1}) - \frac{m-1}{2} \Delta \rho_i (\phi_{\ell-1,i-1/2}^{+,m-1} + \phi_{\ell-1,i+1/2}^{+,m-1}) \right] \\ &-2\pi \mathcal{B}_\ell^m \left[\rho_i (\phi_{\ell+1,i+1/2}^{+,m-1} - \phi_{\ell+1,i-1/2}^{+,m-1}) - \frac{m-1}{2} \Delta \rho_i (\phi_{\ell+1,i-1/2}^{+,m-1} + \phi_{\ell+1,i+1/2}^{+,m-1}) \right] \\ &-2\pi \mathcal{C}_\ell^m \left[\rho_i (\phi_{\ell-1,i+1/2}^{+,m+1} - \phi_{\ell-1,i-1/2}^{+,m+1}) + \frac{m+1}{2} \Delta \rho_i (\phi_{\ell-1,i-1/2}^{+,m+1} + \phi_{\ell-1,i+1/2}^{+,m+1}) \right] \\ &-2\pi \mathcal{D}_\ell^m \left[\rho_i (\phi_{\ell+1,i+1/2}^{+,m+1} - \phi_{\ell+1,i-1/2}^{+,m+1}) + \frac{m+1}{2} \Delta \rho_i (\phi_{\ell+1,i-1/2}^{+,m+1} + \phi_{\ell+1,i+1/2}^{+,m+1}) \right], \\ &-V_i \Sigma_i \phi_{\ell,i}^{-,m} = -V_i Q_{\ell,i}^{-,m}, \end{aligned} \quad (200)$$

where ℓ and m are odd integers and $1 \leq i \leq I$.

3.3 The P_n Method in 1D Spherical Geometry

3.3.1 Discretization in Angle

The P_n method will be studied for the simple case of a 1D spherical geometry. In this case, the angular variation of the flux is only a function of the direction cosine μ and can be developed using the first $n + 1$ Legendre polynomials, n being an odd number. Equation (150) simplifies to (148), so that

$$\mu \frac{\partial}{\partial r} \phi(r, \mu) + \frac{1-\mu^2}{r} \frac{\partial}{\partial \mu} \phi(r, \mu) + \Sigma(r) \phi(r, \mu) = Q(r, \mu), \quad (201)$$

where the angular source is expanded at order $L \leq n$. The spherical harmonic expansions are written as

$$\phi(r, \mu) = \sum_{\ell=0}^n \frac{2\ell+1}{2} \phi_\ell(r) P_\ell(\mu) \quad \text{and} \quad Q(r, \mu) = \sum_{\ell=0}^L \frac{2\ell+1}{2} Q_\ell(r) P_\ell(\mu) \quad (202)$$

so that the components of the flux are written as

$$\phi_\ell(r) = \int_{-1}^1 d\mu P_\ell(\mu) \phi(r, \mu) \quad (203)$$

with the scalar flux and current given by $\phi_0(r)$ and $\phi_1(r)$, respectively.

We next substitute (202) into (201), multiply by $P_{\ell'}(\mu)$, integrate from -1 to $+1$, and use the orthogonality and recurrence relation for Legendre polynomials. The result is

$$\begin{aligned} \frac{\ell}{2\ell+1} \left[r \frac{\partial}{\partial r} - (\ell-1) \right] \phi_{\ell-1}(r) + \frac{\ell+1}{2\ell+1} \left[r \frac{\partial}{\partial r} + (\ell+2) \right] \phi_{\ell+1}(r) \\ + r \Sigma(r) \phi_{\ell}(r) = r Q_{\ell}(r). \end{aligned} \quad (204)$$

3.3.2 Boundary Conditions

The boundary conditions are similar to those in cylindrical 1D geometry. The $r = r_- \equiv 0$ condition is set by forcing the flux to be an even function of μ at the origin. Consequently, all components of the flux with an odd value of ℓ are forced to zero.

Vacuum and general albedo (β^+) boundary conditions at $r = r_+$, on the external surface, are set using the Marshak coefficients already introduced for slab geometry in [3.1](#).

A *white-boundary condition* can be applied at $r = r_+$, in which case the particles are reflected back with an isotropic angular distribution. Such a condition can be represented by forcing to zero the component of the incoming odd-parity fluxes with $\ell = 1$ and by treating the remaining components with a vacuum-boundary condition.

3.3.3 Difference Relations

Equations (204) with the Marshak-boundary condition (164) can be discretized in r by replacing the differential terms with difference relations, taking care to preserve the symmetry of the resulting matrices. The odd-parity variables are discretized over mesh-centered coordinates (r_{i-1} , r_i , r_{i+1}) and the even-parity variables are discretized over interface coordinates ($r_{i-1/2}$, $r_{i+1/2}$, $r_{i+3/2}$).

We first consider even-parity indices ℓ in the case where surface $i + 1/2$ is not a boundary. The finite difference approximation is set as before, leading to

$$\begin{aligned} 4\pi\ell \left(\bar{r}_{i+1}^2 \phi_{\ell-1,i+1}^- - \bar{r}_i^2 \phi_{\ell-1,i}^- \right) + 4\pi(\ell+1) \left(\bar{r}_{i+1}^2 \phi_{\ell+1,i+1}^- - \bar{r}_i^2 \phi_{\ell+1,i}^- \right) \\ - 4\pi\ell(\ell+1) \left(\mathcal{B}_i \phi_{\ell-1,i}^- + \mathcal{A}_{i+1} \phi_{\ell-1,i+1}^- - \mathcal{B}_i \phi_{\ell+1,i}^- - \mathcal{A}_{i+1} \phi_{\ell+1,i+1}^- \right) \\ + 4\pi r_i^2 \Delta r_i \sum_{p=0}^1 \left[\mathcal{R}_{p,1} + \frac{2\Delta r_i}{r_i} \mathcal{R}_{p,1}^s + \left(\frac{\Delta r_i}{r_i} \right)^2 \mathcal{R}_{p,1}^{ss} \right] \left(\Sigma_i \phi_{\ell,i-1/2+p}^+ - Q_{\ell,i-1/2+p}^+ \right) \\ + 4\pi r_{i+1}^2 \Delta r_{i+1} \sum_{p=0}^1 \left[\mathcal{R}_{p,0} + \frac{2\Delta r_{i+1}}{r_{i+1}} \mathcal{R}_{p,0}^s + \left(\frac{\Delta r_{i+1}}{r_{i+1}} \right)^2 \mathcal{R}_{p,0}^{ss} \right] \\ \times \left(\Sigma_{i+1} \phi_{\ell,i+1/2+p}^+ - Q_{\ell,i+1/2+p}^+ \right) = 0, \end{aligned} \quad (205)$$

where ℓ is even and $1 \leq i \leq I$. The geometric coefficients are defined as

$$\begin{aligned} \Delta r_i &= r_{i+1/2} - r_{i-1/2}, \\ r_i &= \frac{1}{2} (r_{i-1/2} + r_{i+1/2}), \end{aligned}$$

$$\tilde{r}_i^2 = \frac{1}{3} (r_{i-1/2} r_{i-1/2} + r_{i-1/2} r_{i+1/2} + r_{i+1/2} r_{i+1/2}),$$

$$V_i = 4\pi \tilde{r}_i^2 \Delta r_i,$$

$$\mathcal{A}_i = \Delta r_i \left(\frac{r_{i-1/2}}{3} + \frac{r_{i+1/2}}{6} \right),$$

and

$$\mathcal{B}_i = \Delta r_i \left(\frac{r_{i-1/2}}{6} + \frac{r_{i+1/2}}{3} \right). \quad (206)$$

The mass-matrix components $\mathcal{R}_{p,q}$, $\mathcal{R}_{p,q}^s$, and $\mathcal{R}_{p,q}^{ss}$ are defined as (Hébert 2005)

$$\mathbf{R} = \begin{bmatrix} 1/4 & 1/4 \\ 1/4 & 1/4 \end{bmatrix}, \quad \mathbf{R}^s = \begin{bmatrix} -5/144 & -1/144 \\ -1/144 & 7/144 \end{bmatrix}$$

and

$$\mathbf{R}^{ss} = \begin{bmatrix} 1/108 & 1/54 \\ 1/54 & 1/27 \end{bmatrix}. \quad (207)$$

Let us now consider the case where $r_{I+1/2}$ is the outer boundary. In this case, the even-parity difference relation is written as

$$\begin{aligned} & -4\pi\ell \tilde{r}_I^2 \phi_{\ell-1,I}^- - 4\pi(\ell+1) \tilde{r}_I^2 \phi_{\ell+1,I}^- + 4\pi\mathcal{B}_I \ell(\ell+1) (\phi_{\ell-1,I}^- - \phi_{\ell+1,I}^-) \\ & + 4\pi r_I^2 \Delta r_I \sum_{p=0}^1 \left[\mathcal{R}_{p,1} + \frac{2\Delta r_I}{r_I} \mathcal{R}_{p,1}^s + \left(\frac{\Delta r_I}{r_I} \right)^2 \mathcal{R}_{p,1}^{ss} \right] (\Sigma_I \phi_{\ell,I-1/2+p}^+ - Q_{\ell,I-1/2+p}^+) \\ & + (2\ell+1) 4\pi r_+^2 \frac{1-\beta^+}{1+\beta^+} \sum_{\substack{m=0 \\ m \text{ even}}}^{n-1} \hat{\mathcal{M}}_{m,\ell} \phi_{m,I+1/2}^+ = 0 \quad \text{where } \ell \text{ is even.} \end{aligned} \quad (208)$$

Finally, the spherical harmonics-discretized relations for odd-parity indices ℓ are obtained by integrating (204) between $r_{i-1/2}$, and $r_{i+1/2}$, and by assuming that $\phi_{\ell,i}^-$ is equal to the averaged value over subvolume i . We obtain

$$\begin{aligned} & -4\pi \tilde{r}_i^2 \ell (\phi_{\ell-1,i+1/2}^+ - \phi_{\ell-1,i-1/2}^+) - 4\pi \tilde{r}_i^2 (\ell+1) (\phi_{\ell+1,i+1/2}^+ - \phi_{\ell+1,i-1/2}^+) \\ & + 4\pi [\ell(\ell-1) (\mathcal{A}_i \phi_{\ell-1,i-1/2}^+ + \mathcal{B}_i \phi_{\ell-1,i+1/2}^+) \\ & - (\ell+1)(\ell+2) (\mathcal{A}_i \phi_{\ell+1,i-1/2}^+ + \mathcal{B}_i \phi_{\ell+1,i+1/2}^+)] - (2\ell+1) V_i \Sigma_i \phi_{\ell,i}^- \\ & = - (2\ell+1) V_i Q_{\ell,i}^-, \end{aligned} \quad (209)$$

where ℓ is odd and $1 \leq i \leq I$.

3.4 The Simplified P_n Method in 2D Cartesian Geometry

Application of the spherical harmonics method in 2D and 3D cases produces a linear system with complicated couplings between the discretized unknowns in space and angle. For this reason, the discrete-ordinates method of [Sect. 5](#) is generally a more practical choice. The SP_n method, on the other hand, is based on an expansion of the angular flux in an incomplete basis of orthogonal functions, and its discretization produces a linear system with a simplified structure that can be solved effectively in 2D and 3D cases. A few important facts must be understood concerning the use of SP_n methods:

- The SP_1 method is equivalent to the P_1 method in 1D, 2D, and 3D cases. Assuming $L = 0$ in these cases produces an approximation that is equivalent to the diffusion approximation of [Sect. 7](#).
- The SP_n method is equivalent to the P_n method in 1D, for all values of n .
- Using an incomplete basis does not guarantee the convergence of the numerical results as n increases in 2D and 3D cases. However, SP_3 or SP_5 results have proven to be more accurate than SP_1 results in many situations, leading to production codes with improved accuracy when compared with the diffusion approximation.

3.4.1 Discretization in Angle

The SP_n is *not* based on a spherical harmonics expansion. This approach is an heuristics presented in the original work of Gelbard (1960). We start with the 1D slab-geometry P_n equations, obtained in [3.1.1](#). These equations are written as

$$\frac{\ell}{2\ell+1} \frac{d}{dx} \phi_{\ell-1}(x) + \frac{\ell+1}{2\ell+1} \frac{d}{dx} \phi_{\ell+1}(x) + \Sigma(x) \phi_{\ell}(x) = Q_{\ell}(x), \quad (210)$$

where $\phi_{\ell}(x)$ is the ℓ th Legendre moment of the angular flux, $\Sigma(x)$ is the macroscopic total cross-section, and $Q_{\ell}(x)$ is the ℓ th Legendre moment of the angular source. These equations are written for $0 \leq \ell \leq n$. The closure relation consists to assume that $\phi_{n+1}(x)$ is identically zero.

The Gelbard approach to obtain the SP_n equations is based on the following procedure:

1. Replace the operator d/dx in (210) for even ℓ with the divergence operator.
2. Replace the operator d/dx in (210) for odd ℓ with the gradient operator.

Carrying out this procedure, we obtain

$$\frac{\ell}{2\ell+1} \nabla \cdot \Phi_{\ell-1}(\mathbf{r}) + \frac{\ell+1}{2\ell+1} \nabla \cdot \Phi_{\ell+1}(\mathbf{r}) + \Sigma(\mathbf{r}) \phi_{\ell}(\mathbf{r}) = Q_{\ell}(\mathbf{r}) \quad (211)$$

if $0 \leq \ell \leq n-1$ and ℓ is even, and

$$\frac{\ell}{2\ell+1} \nabla \phi_{\ell-1}(\mathbf{r}) + \frac{\ell+1}{2\ell+1} \nabla \phi_{\ell+1}(\mathbf{r}) + \Sigma(\mathbf{r}) \Phi_{\ell}(\mathbf{r}) = Q_{\ell}(\mathbf{r}) \quad (212)$$

if $1 \leq \ell \leq n$ and ℓ is odd.

Similarly, the albedo boundary condition of (162) can be generalized to the SP_n method by writing

$$(1 + \beta(\mathbf{r})) \Phi_\ell(\mathbf{r}) \cdot \mathbf{N}(\mathbf{r}) - (1 - \beta(\mathbf{r})) \sum_{\substack{m=0 \\ m \text{ even}}}^{n-1} \mathcal{M}_{\ell,m} \phi_m(\mathbf{r}) = 0 \quad \text{if } \mathbf{r} \in \partial V_\beta, \quad (213)$$

where ℓ is an odd integer, ∂V_β is the boundary with an albedo condition, $\beta(\mathbf{r})$ is the albedo, and $\mathbf{N}(\mathbf{r})$ is an outgoing normal unit vector.

Equations (211) and (212) are the differential formulation of the SP_n method. The scalar even-parity flux $\phi_\ell(\mathbf{r})$ and vector odd-parity flux $\Phi_\ell(\mathbf{r})$ are the dependent variables of this equation system.

3.4.2 Difference Relations

The Cartesian domain is discretized in an $I \times J$ grid of rectangular subvolumes. The odd-parity variables are discretized over mesh-centered coordinates, so that $\phi_{i,j}^- \equiv \phi^-(x_i, y_j)$. The even-parity variables are defined over the surfaces surrounding subvolumes, so that $\phi_{i\mp 1/2, j}^+ \equiv \phi^+(x_{i\mp 1/2}, y_j)$ and $\phi_{i, j\mp 1/2}^+ \equiv \phi^+(x_i, y_{j\mp 1/2})$. We define the corresponding mesh widths and volumes as

$$\Delta x_i = x_{i+1/2} - x_{i-1/2}, \quad \Delta y_j = y_{j+1/2} - y_{j-1/2}, \quad \text{and} \quad V_{i,j} = \Delta x_i \Delta y_j. \quad (214)$$

The difference relations are obtained by similarity with the slab-geometry derivation of [3.1](#), so that 2D Cartesian results are identical to 1D slab results in cases where $I = 1$ or $J = 1$. Let us first consider the difference relation, for even-parity values of ℓ , in the case where surface $i + 1/2$ is not a boundary. We obtain

$$\begin{aligned} \Delta y_j \frac{\ell}{2\ell+1} (\phi_{\ell-1, i+1, j}^- - \phi_{\ell-1, i, j}^-) + \Delta y_j \frac{\ell+1}{2\ell+1} (\phi_{\ell+1, i+1, j}^- - \phi_{\ell+1, i, j}^-) \\ + \frac{V_{i,j}}{4} (\Sigma_{i,j} \phi_{\ell, i-1/2, j}^+ - Q_{\ell, i-1/2, j}^+) + \frac{V_{i,j}}{4} (\Sigma_{i,j} \phi_{\ell, i+1/2, j}^+ - Q_{\ell, i+1/2, j}^+) \\ + \frac{V_{i+1, j}}{4} (\Sigma_{i+1, j} \phi_{\ell, i+1/2, j}^+ - Q_{\ell, i+1/2, j}^+) + \frac{V_{i+1, j}}{4} (\Sigma_{i+1, j} \phi_{\ell, i+3/2, j}^+ - Q_{\ell, i+3/2, j}^+) = 0, \end{aligned} \quad (215)$$

where ℓ is even, $1 \leq i < I$ and $1 \leq j < J$.

We next consider the case where surface $j + 1/2$ is not a boundary. We obtain

$$\begin{aligned} \Delta x_i \frac{\ell}{2\ell+1} (\phi_{\ell-1, i, j+1}^- - \phi_{\ell-1, i, j}^-) + \Delta x_i \frac{\ell+1}{2\ell+1} (\phi_{\ell+1, i, j+1}^- - \phi_{\ell+1, i, j}^-) \\ + \frac{V_{i,j}}{4} (\Sigma_{i,j} \phi_{\ell, i, j-1/2}^+ - Q_{\ell, i, j-1/2}^+) + \frac{V_{i,j}}{4} (\Sigma_{i,j} \phi_{\ell, i, j+1/2}^+ - Q_{\ell, i, j+1/2}^+) \\ + \frac{V_{i, j+1}}{4} (\Sigma_{i, j+1} \phi_{\ell, i, j+1/2}^+ - Q_{\ell, i, j+1/2}^+) + \frac{V_{i, j+1}}{4} (\Sigma_{i, j+1} \phi_{\ell, i, j+3/2}^+ - Q_{\ell, i, j+3/2}^+) = 0, \end{aligned} \quad (216)$$

where ℓ is even, $1 \leq i < I$ and $1 \leq j < J$.

Let us now consider the case where the external right boundary, located at $x_{I+1/2}$, has an albedo condition. The difference equation is written as

$$\begin{aligned}
 & -\frac{\ell}{2\ell+1} \Delta y_j \phi_{\ell-1,I,j}^- - \frac{\ell+1}{2\ell+1} \Delta y_j \phi_{\ell+1,I,j}^- + \frac{V_{i,j}}{4} (\Sigma_{I,j} \phi_{\ell,I-1/2,j}^+ - Q_{\ell,I-1/2,j}^+) \\
 & + \frac{V_{i,j}}{4} (\Sigma_{I,j} \phi_{\ell,I+1/2,j}^+ - Q_{\ell,I+1/2,j}^+) + \Delta y_j \frac{1-\beta^+}{1+\beta^+} \sum_{\substack{\ell'=0 \\ \ell' \text{ even}}}^{n-1} \mathcal{M}_{\ell,\ell'} \phi_{\ell',I+1/2,j}^+ = 0, \quad (217)
 \end{aligned}$$

where ℓ is even and $1 \leq j < J$.

Finally, the spherical harmonics-discretized relations for odd-parity indices ℓ are obtained by integrating (212) over subvolume $\{i, j\}$ and by assuming that $\phi_{\ell-1,j}^-$ is equal to the averaged value over this subvolume. We obtain

$$\begin{aligned}
 & -\frac{\ell}{2\ell+1} \Delta y_j (\phi_{\ell-1,i+1/2,j}^+ - \phi_{\ell-1,i-1/2,j}^+) - \frac{\ell+1}{2\ell+1} \Delta y_j (\phi_{\ell+1,i+1/2,j}^+ - \phi_{\ell+1,i-1/2,j}^+) \\
 & -\frac{\ell}{2\ell+1} \Delta x_i (\phi_{\ell-1,i,j+1/2}^+ - \phi_{\ell-1,i,j-1/2}^+) - \frac{\ell+1}{2\ell+1} \Delta x_i (\phi_{\ell+1,i,j+1/2}^+ - \phi_{\ell+1,i,j-1/2}^+) \\
 & -V_{i,j} \Sigma_{i,j} \phi_{\ell,i,j}^- = -V_{i,j} Q_{\ell,i,j}^-, \quad (218)
 \end{aligned}$$

where ℓ is odd, $1 \leq i \leq I$ and $1 \leq j \leq J$.

4 The Collision Probability Method

The *collision probability* (CP) method results from the spatial discretization of the integral transport equation in multigroup form, assuming isotropic particle sources (Carlvik 1965). For a problem containing I regions, this approach produces an $I \times I$ matrix in each energy group. This method is preferred for treating general unstructured meshes and few-region problems. Collision probabilities can be defined over an infinite domain (such as a lattice of identical cells or assemblies) or over a finite (or *open*) domain D surrounded by a surface ∂D . The formalism of the first case is simpler but brings some difficulties related to the practical evaluation of the CPs. It will be examined first. The second case requires that *boundary conditions* be added to close the domain.

Let us first integrate (113) over the solid angles to directly obtain the integrated flux $\phi_g(\mathbf{r})$ as

$$\phi_g(\mathbf{r}) = \int_{4\pi} d^2\Omega \phi_g(\mathbf{r}, \Omega) = \frac{1}{4\pi} \int_{4\pi} d^2\Omega \int_0^\infty ds e^{-\tau_g(s)} Q_g(\mathbf{r} - s\Omega), \quad (219)$$

where the optical path $\tau_g(s)$ is given by (115).

We now introduce the change of variable $\mathbf{r}' = \mathbf{r} - s\Omega$ with $d^3r' = s^2 d^2\Omega ds$. We obtain

$$\phi_g(\mathbf{r}) = \frac{1}{4\pi} \int_\infty^\infty d^3r' \frac{e^{-\tau_g(s)}}{s^2} Q_g(\mathbf{r}') \quad (220)$$

with $s = |\mathbf{r} - \mathbf{r}'|$.

This form of transport equation is generally used to represent an infinite lattice of identical (or *unit*) cells or assemblies, repeating themselves by symmetric- or periodic-boundary conditions. We next perform a partition of the *unit cell* or assembly into regions V_i . We also use the

symbol V_i^∞ to represent the infinite set of regions V_i belonging to all the cells or assemblies in the lattice. We also suppose that the sources of secondary neutrons are uniform and equal to $Q_{i,g}$ on each region V_i . After multiplication by $\Sigma_g(\mathbf{r})$ and integration over each region V_i , (220) can be written as

$$\int_{V_j} d^3r \Sigma_g(\mathbf{r}) \phi_g(\mathbf{r}) = \frac{1}{4\pi} \int_{V_j} d^3r \Sigma_g(\mathbf{r}) \sum_i Q_{i,g} \int_{V_i^\infty} d^3r' \frac{e^{-\tau_g(s)}}{s^2}, \quad (221)$$

where

$$Q_{i,g} = \sum_h \Sigma_{s0,i,g \leftarrow h} \phi_{i,h} + \frac{1}{K_{\text{eff}}} Q_{i,g}^{\text{fiss}}. \quad (222)$$

The fission source in (222) is defined as

$$Q_{i,g}^{\text{fiss}} = \sum_{j=1}^{\text{fiss}} \chi_{j,g} \sum_h \nu \Sigma_{f,j,h} \phi_{i,h}, \quad (223)$$

where j is a fissionable isotope index, $\chi_{j,g}$ is the fission spectrum of isotope j , and $\Sigma_{f,j,h}$ is the macroscopic fission cross-section of isotope j for neutrons in group h .

Equation (221) simplifies to

$$V_j \Sigma_{j,g} \phi_{j,g} = \sum_i Q_{i,g} V_i P_{ij,g}, \quad (224)$$

where

$$\phi_{j,g} = \frac{1}{V_j} \int_{V_j} d^3r \phi_g(\mathbf{r}), \quad (225)$$

$$\Sigma_{j,g} = \frac{1}{V_j \phi_{j,g}} \int_{V_j} d^3r \Sigma_g(\mathbf{r}) \phi_g(\mathbf{r}) \quad (226)$$

and

$$P_{ij,g} = \frac{1}{4\pi V_i} \int_{V_i^\infty} d^3r' \int_{V_j} d^3r \Sigma_g(\mathbf{r}) \frac{e^{-\tau_g(s)}}{s^2}. \quad (227)$$

The *collision probability* $P_{ij,g}$ is the probability for a neutron born uniformly and isotropically in *any* of the regions V_i of the lattice to undergo its first collision in region V_j of a unit cell or assembly.

If the total cross-section $\Sigma_g(\mathbf{r})$ is constant and equal to $\Sigma_{j,g}$ in region V_j , *reduced* CPs can be defined from (227) as

$$P_{ij,g} = \frac{P_{ij,g}}{\Sigma_{j,g}} = \frac{1}{4\pi V_i} \int_{V_i^\infty} d^3r' \int_{V_j} d^3r \frac{e^{-\tau_g(s)}}{s^2}. \quad (228)$$

Reduced CPs generally remain finite in the limit where $\Sigma_{j,g}$ tends to zero. This ensures the correct behavior of the collision probability theory in cases where some regions of the lattice are voided.

Other interesting properties of CPs are the *reciprocity* and *conservation* properties, which can be written as

$$p_{ij,g} V_i = p_{ji,g} V_j \quad (229)$$

and

$$\sum_j P_{ij,g} \Sigma_{j,g} = 1, \quad \forall i. \quad (230)$$

Using the reciprocity property, (224) can be further simplified to

$$\phi_{i,g} = \sum_j Q_{j,g} P_{ij,g}. \quad (231)$$

The CP method generally proceeds in three steps as follows:

1. A *tracking* process is applied over the lattice geometry to span a sufficiently large number of neutron trajectories. In a 2D domain, the tracking parameters are the number of azimuthal angles and the number of parallel tracks per centimeter. The tracking process is dependent on the energy index g only if the domain is infinite (i.e., if boundary conditions are not used) and if the tracks are not cyclic in the lattice.
2. A numerical integration process is required to compute the CPs, using tracking information and knowledge of the macroscopic total cross-sections in each region. This integration should be done for each energy group, but the process is completely parallelizable as there is no interaction between the groups. Parallelization is greatly facilitated in cases where the same tracking file is used for all the energy groups.
3. Once the CPs are known, the integrated flux can be computed from (222) to (231).

Collision probability techniques can also be applied to the case of a domain D surrounded by a surface ∂D . In this case, the free path lengths are restricted to finite lengths defined inside ∂D and (114) is used as the basic integral transport equation. Infinite lattices can still be described by incorporating *reflective* or *periodic* boundary conditions over ∂D .

4.1 The Interface Current Method

Another important category of collision probability techniques is the *interface current* (IC) methods (Sanchez and McCormick 1982). In this case, a unit assembly is subdivided into cells and CP matrices are computed for each uncoupled cell. The detailed flux can then be reconstructed from the knowledge of interface currents surrounding each cell.

In each point \mathbf{r}_s of the surface ∂V surrounding a cell, the outgoing angular flux can be expressed as a double P_n expansion as

$$\phi^+(\mathbf{r}_s, \boldsymbol{\Omega}) = \frac{1}{4\pi} \sum_{\rho} \phi_{\rho}^+(\mathbf{r}_s) \psi_{\rho}(\boldsymbol{\Omega}, \mathbf{N}^+), \quad \text{where } \boldsymbol{\Omega} \cdot \mathbf{N}^+ > 0, \quad (232)$$

where \mathbf{N}^+ is a unit-outgoing vector, normal to ∂V , and located at point \mathbf{r}_s . In this section, we do not show the group g dependence of the various physical quantities. This will help to lighten the mathematical notation.

The base functions are chosen so as to satisfy the following orthogonality condition:

$$\int_{\boldsymbol{\Omega} \cdot \mathbf{N} > 0} d^2\boldsymbol{\Omega} (\boldsymbol{\Omega} \cdot \mathbf{N}) \psi_{\nu}(\boldsymbol{\Omega}, \mathbf{N}) \psi_{\rho}(\boldsymbol{\Omega}, \mathbf{N}) = \pi \delta_{\nu\rho}, \quad (233)$$

where $\delta_{\nu\rho}$ is the delta Kronecker function.

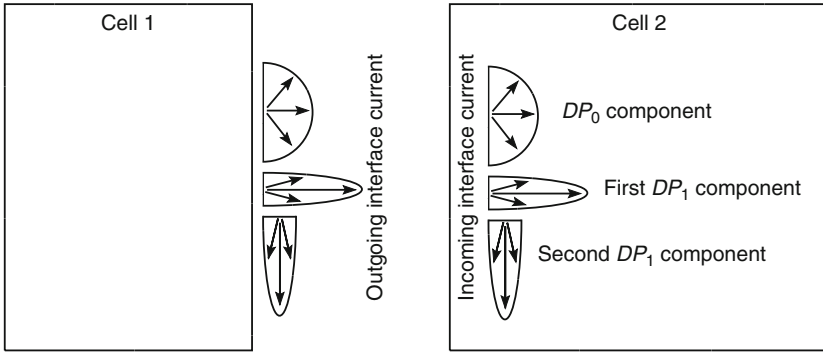


Figure 10
The interface current method

In 2D cases, the base functions corresponding to a double P_1 expansion are illustrated in **Fig. 10** and are obtained as

$$\begin{aligned}
 \psi_0(\mathbf{\Omega}, \mathbf{N}) &= 1 \quad (DP_0 \text{ component}), \\
 \psi_1(\mathbf{\Omega}, \mathbf{N}) &= 3\sqrt{2} (\mathbf{\Omega} \cdot \mathbf{N}) - 2\sqrt{2} \quad (\text{first } DP_1 \text{ component}), \\
 \psi_2(\mathbf{\Omega}, \mathbf{N}) &= 2 (\mathbf{\Omega} \cdot \mathbf{N}_\perp) \quad (\text{second } DP_1 \text{ component}),
 \end{aligned}
 \tag{234}$$

where \mathbf{N}_\perp is a unit vector perpendicular to \mathbf{N} and located in the 2D plane.

The neutron balance equation is ensured by using the same expansion for the outgoing angular flux in a cell and for the incoming angular flux in the neighboring cell. Using \mathbf{N}^- as the incoming unit normal vector in the neighboring cell, we write

$$\varphi^-(\mathbf{r}_s, \mathbf{\Omega}) = \frac{1}{4\pi} \sum_{\rho} \varphi_{\rho}^-(\mathbf{r}_s) \psi_{\rho}(\mathbf{\Omega}, \mathbf{N}^-), \quad \text{where } \mathbf{\Omega} \cdot \mathbf{N}^- > 0.
 \tag{235}$$

Another usual approximation consists in assuming that the expansion coefficients $\varphi_{\rho}^+(\mathbf{r}_s)$ and $\varphi_{\rho}^-(\mathbf{r}_s)$ are uniform along each side of the cell. They are taken equal to $\varphi_{\rho, \alpha}^+$ and $\varphi_{\rho, \alpha}^-$ on surface S_{α} . Uniform- DP_0 and Uniform- DP_1 are the two usual IC approximations.

A cell may contain one or several regions defining the fuel, clad, and coolant. A CP method is used to compute the response matrices of each cell. The following matrices are computed:

- p_{ij} = reduced CP for a neutron born uniformly and isotropically in region i to have its first collision in region j without leaving the cell.
- $P_{S_{\alpha}j}^{(\rho)}$ = reduced CP for a neutron entering from surface S_{α} uniformly and with an angular distribution $\psi_{\rho}(\mathbf{\Omega}, \mathbf{N}^-)$ to have its first collision in region j without leaving the cell.
- $P_{iS_{\beta}}^{(v)}$ = escape probability for a neutron born uniformly and isotropically in region i to leave the cell by surface S_{β} with an angular distribution $\psi_{\nu}(\mathbf{\Omega}, \mathbf{N}^+)$.
- $P_{S_{\alpha}S_{\beta}}^{(\rho\nu)}$ = transmission probability for a neutron entering from surface S_{α} uniformly and with an angular distribution $\psi_{\rho}(\mathbf{\Omega}, \mathbf{N}^-)$ to leave the cell by surface S_{β} , with an angular distribution $\psi_{\nu}(\mathbf{\Omega}, \mathbf{N}^+)$.

The reduced collision probability component p_{ij} is given by an equation similar to (228), taking care to replace the integration over V_i^∞ by an integration over the unique volume V_i in the cell being processed. We write

$$p_{ij} = \frac{P_{ij}}{\Sigma_j} = \frac{1}{4\pi V_i} \int_{V_i} d^3 r' \int_{V_j} d^3 r \frac{e^{-\tau(s)}}{s^2}. \quad (236)$$

The $p_{S_\alpha j}^{(\rho)}$ components are defined as

$$p_{S_\alpha j}^{(\rho)} = \frac{P_{S_\alpha j}^{(\rho)}}{\Sigma_j} = \frac{1}{\pi S_\alpha} \int_{S_\alpha} d^2 r'_s \int_{V_j} d^3 r (\mathbf{\Omega} \cdot \mathbf{N}^-) \psi_\rho(\mathbf{\Omega}, \mathbf{N}^-) \frac{e^{-\tau(s)}}{s^2} \quad (237)$$

and the other CP components are defined as

$$P_{iS_\beta}^{(\nu)} = \frac{1}{4\pi V_i} \int_{V_i} d^3 r' \int_{S_\beta} d^2 r_s (\mathbf{\Omega} \cdot \mathbf{N}^+) \psi_\nu(\mathbf{\Omega}, \mathbf{N}^+) \frac{e^{-\tau(s)}}{s^2} \quad (238)$$

and

$$P_{S_\alpha S_\beta}^{(\rho\nu)} = \frac{1}{\pi S_\alpha} \int_{S_\alpha} d^2 r'_s \int_{S_\beta} d^2 r_s (\mathbf{\Omega} \cdot \mathbf{N}^-) (\mathbf{\Omega} \cdot \mathbf{N}^+) \psi_\rho(\mathbf{\Omega}, \mathbf{N}^-) \psi_\nu(\mathbf{\Omega}, \mathbf{N}^+) \frac{e^{-\tau(s)}}{s^2}. \quad (239)$$

Again, these probabilities satisfy reciprocity relations written as

$$p_{ij} V_i = p_{ji} V_j, \quad p_{S_\alpha i}^{(\rho)} = \frac{4V_i}{S_\alpha} P_{iS_\alpha}^{(\rho)} \quad (240)$$

and

$$P_{S_\alpha S_\beta}^{(\rho\nu)} S_\alpha = P_{S_\beta S_\alpha}^{(\nu\rho)} S_\beta \quad (241)$$

and conservation relations written as

$$\sum_\beta P_{iS_\beta}^{(0)} + \sum_j p_{ij} \Sigma_j = 1, \quad \forall i \quad (242)$$

and

$$\sum_\beta P_{S_\alpha S_\beta}^{(00)} + \sum_j P_{S_\alpha j}^{(0)} \Sigma_j = 1, \quad \forall \alpha. \quad (243)$$

The flux equation for neutrons in each group can be cast into a response-matrix form where the unknowns are the averaged integrated flux ϕ_i in region i and the uniform components of the angular fluxes along surface S_α (related to the *interface currents*). We obtain

$$\begin{aligned} \phi_i &= \sum_\beta \sum_\nu \varphi_{\nu, \beta}^- P_{iS_\beta}^{(\nu)} + \sum_j Q_j p_{ij}, \\ \varphi_{\rho, \alpha}^+ &= \sum_\beta \sum_\nu \varphi_{\nu, \beta}^- P_{S_\alpha S_\beta}^{(\rho\nu)} + \sum_j Q_j p_{S_\alpha j}^{(\rho)}, \end{aligned} \quad (244)$$

where Q_j is the scattering and fission sources in region j .

Finally, a purely geometric equation is required to connect the outgoing and incoming angular fluxes, $\varphi_{\rho,\alpha}^+$ and $\varphi_{\nu,\beta}^-$. This relation is written as

$$\varphi_{\rho,\beta}^- = \sum_{\alpha} A_{\alpha,\beta}^{(\rho)} \varphi_{\rho,\alpha}^+. \quad (245)$$

The complete set of (244) and (245) form a closed system that can be solved iteratively. Another technique consists in simplifying the outgoing and incoming angular fluxes and transforming this coupled system into a simple matrix equation similar to (231).

4.2 Scattering-Reduced Matrices and Power Iteration

The within-group scattering term is first included on the left-hand side of (231) to obtain

$$\phi_{i,g} - \sum_j p_{ij,g} \Sigma_{s0,j,g \leftarrow g} \phi_{j,g} = \sum_j Q_{j,g}^{\diamond} p_{ij,g}, \quad (246)$$

where $Q_{i,g}^{\diamond}$ includes the fission sources and the diffusion sources from all groups except group g . It is obtained from (222) as

$$Q_{i,g}^{\diamond} = \sum_{h \neq g} \Sigma_{s0,i,g \leftarrow h} \phi_{i,h} + \frac{1}{K_{\text{eff}}} Q_{i,g}^{\text{fiss}}. \quad (247)$$

Equation (246) can be written in matrix form as

$$\Phi_g = \mathbb{W}_g \mathbf{Q}_g^{\diamond}, \quad (248)$$

where $\Phi_g = \{\phi_{i,g}; \forall i\}$ and $\mathbf{Q}_g^{\diamond} = \{Q_{i,g}^{\diamond}; \forall i\}$.

The \mathbb{W}_g matrix is the scattering-reduced collision probability matrix and is used in the power iteration of the lattice code. It is defined as

$$\mathbb{W}_g = [\mathbb{I} - \mathbb{P}_g \mathbb{S}_{s0,g \leftarrow g}]^{-1} \mathbb{P}_g, \quad (249)$$

where \mathbb{I} is the identity matrix, $\mathbb{P}_g = \{p_{ij,g}; \forall i \text{ and } j\}$ and $\mathbb{S}_{s0,g \leftarrow g} = \text{diag}\{\Sigma_{s0,i,g \leftarrow g}; \forall i\}$.

Two iterative processes are generally superimposed on these monoenergetic flux solution methods. First, the inner process iterates over the diffusion up-scattering sources until an adequate multigroup thermal flux distribution is obtained. This iteration process is accelerated using two different techniques. The rebalancing technique produces a group-dependent factor which restores the exact multigroup flux distribution homogenized over all regions. Then the variational acceleration technique is used to compute an over-relaxation factor to be used at the next iteration. The outer (or *power*) iteration process is over the eigenvalue and is not required for fixed source problems. It is generally not accelerated in a lattice code and consists in computing neutron flux at outer iteration $k + 1$ from source at iteration k , using

$$\Phi_g^{(k+1)} = \mathbb{W}_g \mathbf{Q}_g^{\diamond(k)}. \quad (250)$$

The critical parameter (K_{eff}) is then adjusted at the end of each power iteration.

4.3 Slab Geometry

The CP formulation in one-dimensional (1D) slab geometry makes possible the analytical integration of (55) or (56) with respect to some dependent variables. We will first consider the case of a geometry made of an infinite lattice of identical unit cells. Each unit cell is made of a succession of I regions, each of volume V_i with $1 \leq i \leq I$. The reference unit cell is defined in $x_{1/2} \leq x \leq x_{I+1/2}$ and the reference region i is defined in $x_{i-1/2} \leq x \leq x_{i+1/2}$. We will represent as \mathcal{C}_i the infinite set of all instances of region i , repeating itself by translation of the unit cell.

Equation (228) is the expression of a CP component in the infinite domain case. It can be rewritten in a more convenient form. We use the relations $\mathbf{r} = \mathbf{r}' + s \boldsymbol{\Omega}$ and $d^3 r = s^2 d^2 \Omega ds$, so that

$$p_{ij} = \frac{1}{4\pi V_i} \int_{V_i^\infty} d^3 r' \int_{4\pi} d^2 \Omega \int_{\mathcal{I}_j} ds e^{-\tau(s)}, \quad (251)$$

where we have omitted the energy group index in order to simplify the equations. The quantity \mathcal{I}_j is the set of points belonging simultaneously to

- The half straight line of origin \mathbf{r} and direction $-\boldsymbol{\Omega}$
- A single instance of volume V_j

We also define the direction $\boldsymbol{\Omega}$ of the particle in terms of the colatitude θ and azimuth ε using $\boldsymbol{\Omega} = \cos \theta \mathbf{i} + \sin \theta \cos \varepsilon \mathbf{j} + \sin \theta \sin \varepsilon \mathbf{k}$. With this definition and with the help of Fig. 11, we can write

$$\begin{aligned} d^2 \Omega &= d\theta d\varepsilon \sin \theta, \\ \ell(\rho) &= \tau(s) |\cos \theta|, \\ dx &= ds |\cos \theta|, \end{aligned} \quad (252)$$

where ρ is a positive number representing the projection of s on the x -axis. The material properties are independent of ε so that the integration in this variable can be performed analytically. Equation (251) can be simplified as

$$p_{ij} = \frac{1}{2 \Delta x_i} \sum_{i' \in \mathcal{C}_i} \int_{x_{i'-1/2}}^{x_{i'+1/2}} dx' \int_0^{\pi/2} d\theta \tan \theta \int_{x_{j-1/2}}^{x_{j+1/2}} dx e^{-\frac{|\ell(x',x)|}{\cos \theta}}, \quad (253)$$

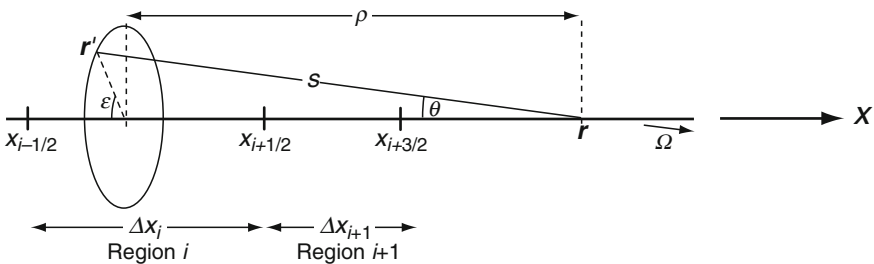


Figure 11
Spatial discretization for slab geometry

where

$$\Delta x_i = V_i = x_{i+1/2} - x_{i-1/2} \tag{254}$$

and $\ell(x', x) = -\ell(x, x')$ is the projected optical path $\ell(\rho)$ defined between points x' and x as

$$\ell(x', x) = \int_{x'}^x dx'' \Sigma(x'') \tag{255}$$

so that $\ell(x', x_{j+1/2}) = \ell(x', x_{j-1/2}) + \Delta x_j \Sigma_j$.

Summation over V_i^∞ includes instances of V_i belonging to all unit cells of the lattice. The presence of neighboring cells will be taken into account in a specular way, using the *periodic boundary condition* introduced in **1.4. Equation (253)** can be rewritten so as to explicitly represent all contributions from other cells. A unit-cell optical path ℓ_{cell} is defined as

$$\ell_{\text{cell}} = \int_{x_{1/2}}^{x_{I+1/2}} dx' \Sigma(x') \tag{256}$$

so that

$$p_{ij} = \frac{1}{2 \Delta x_i} \sum_{m=0}^{\infty} \int_{x_{i-1/2}}^{x_{i+1/2}} dx' \int_0^{\pi/2} d\theta \tan \theta \int_{x_{j-1/2}}^{x_{j+1/2}} dx \left[e^{-\frac{m \ell_{\text{cell}} + \ell(x', x)}{\cos \theta}} + e^{-\frac{(m+1) \ell_{\text{cell}} - \ell(x', x)}{\cos \theta}} \right], \tag{257}$$

where $1 \leq i < j \leq I$ and

$$p_{ii} = \frac{1}{2 \Delta x_i} \sum_{m=0}^{\infty} \int_{x_{i-1/2}}^{x_{i+1/2}} dx' \int_0^{\pi/2} d\theta \tan \theta \left\{ \int_{x_{i-1/2}}^{x'} dx \left[e^{-\frac{m \ell_{\text{cell}} + \ell(x, x')}{\cos \theta}} + e^{-\frac{(m+1) \ell_{\text{cell}} - \ell(x, x')}{\cos \theta}} \right] + \int_{x'}^{x_{i+1/2}} dx \left[e^{-\frac{m \ell_{\text{cell}} + \ell(x', x)}{\cos \theta}} + e^{-\frac{(m+1) \ell_{\text{cell}} - \ell(x', x)}{\cos \theta}} \right] \right\}, \tag{258}$$

where $1 \leq i \leq I$.

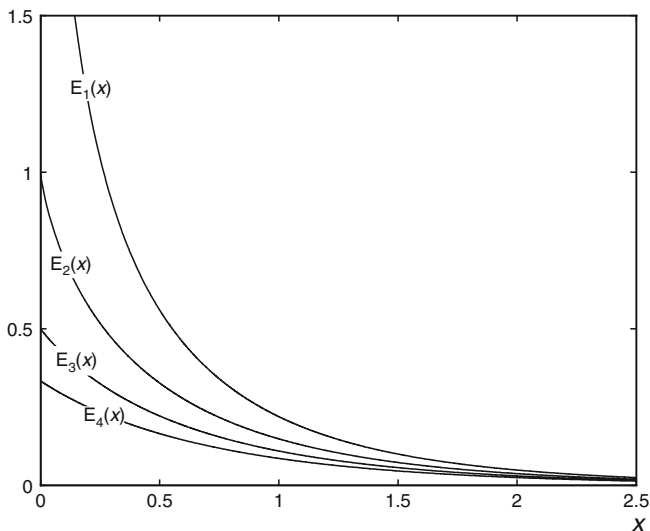
In the case where the domain is not a lattice made of repeating unit cells, (257) must be modified accordingly. If the domain is a set of I regions surrounded by vacuum left- and right-boundary conditions, the CP components are simply

$$p_{ij} = \frac{1}{2 \Delta x_i} \int_{x_{i-1/2}}^{x_{i+1/2}} dx' \int_0^{\pi/2} d\theta \tan \theta \int_{x_{j-1/2}}^{x_{j+1/2}} dx e^{-\frac{|\ell(x', x)|}{\cos \theta}}, \quad \text{where } 1 \leq i \leq j \leq I, \tag{259}$$

and the conservation (230) is no longer valid. Whether (257) or (259) is used, the values of p_{ij} with $i > j$ are computed using the reciprocity (229).

The Kavenoky method is presented as a numerical technique for obtaining the values of the CP components in slab geometry (Kavenoky 1969). We will limit ourselves to (257), (258), and (259), although other boundary conditions were treated in Kavenoky (1969). The principle of this method is to keep the sum over n in (257) and (258) and to introduce *exponential functions* $E_n(x)$, with $n \geq 1$, defined as

$$E_n(x) = \int_0^1 du u^{n-2} e^{-x/u} = \int_1^\infty du u^{-n} e^{-xu}. \tag{260}$$



■ **Figure 12**
Exponential functions

Exponential functions are depicted in [Fig. 12](#). They can be evaluated efficiently using the Matlab script `taben` of Hébert (2009).

The exponential functions satisfy the following two relations:

$$\int_x^{x'} du E_n(u) = E_{n+1}(x) - E_{n+1}(x') \quad (261)$$

and

$$E_n(x) = -\frac{d}{dx} E_{n+1}(x) \quad (262)$$

so that the Taylor expansion of $E_3(x)$ is

$$E_3(x) = E_3(x_0) - E_2(x_0)(x - x_0) + \frac{1}{2}E_1(x_0)(x - x_0)^2 + \mathcal{O}(x - x_0)^3. \quad (263)$$

Integration of (257) in θ leads to

$$p_{ij} = \frac{1}{2\Delta x_i} \sum_{m=0}^{\infty} \int_{x_{i-1/2}}^{x_{i+1/2}} dx' \int_{x_{j-1/2}}^{x_{j+1/2}} dx \{E_1[m \ell_{\text{cell}} + \ell(x', x)] + E_1[(m+1)\ell_{\text{cell}} - \ell(x', x)]\} \quad (264)$$

if $i \leq j$ and

$$\begin{aligned}
 p_{ii} = & \frac{1}{2 \Delta x_i} \sum_{m=0}^{\infty} \int_{x_{i-1/2}}^{x_{i+1/2}} dx' \left\{ \int_{x_{i-1/2}}^{x'} dx \{E_1[m \ell_{\text{cell}} + \ell(x, x')]\right. \\
 & + E_1[(m+1) \ell_{\text{cell}} - \ell(x, x')]\} \\
 & + \left. \int_{x'}^{x_{i+1/2}} dx \{E_1[m \ell_{\text{cell}} + \ell(x', x)] + E_1[(m+1) \ell_{\text{cell}} - \ell(x', x)]\} \right\}. \quad (265)
 \end{aligned}$$

Equations (264) and (265) involve two types of spatial integration which can be written in functional form as

$$\mathcal{R}_{ij,m} \{\pm \ell\} = \frac{1}{2} \int_{x_{i-1/2}}^{x_{i+1/2}} dx' \int_{x_{j-1/2}}^{x_{j+1/2}} dx E_1[m \ell_{\text{cell}} \pm \ell(x', x)], \quad \text{where } i < j \quad (266)$$

and

$$\begin{aligned}
 \mathcal{R}_{ii,m} \{\pm \ell\} = & \frac{1}{2} \int_{x_{i-1/2}}^{x_{i+1/2}} dx' \left\{ \int_{x_{i-1/2}}^{x'} dx E_1[m \ell_{\text{cell}} \pm \ell(x, x')]\right. \\
 & + \left. \int_{x'}^{x_{i+1/2}} dx E_1[m \ell_{\text{cell}} \pm \ell(x', x)] \right\} \quad (267)
 \end{aligned}$$

so that

$$p_{ij} = \frac{1}{\Delta x_i} \sum_{m=0}^{\infty} \mathcal{R}_{ij,m} \{\ell\} + \mathcal{R}_{ij,m+1} \{-\ell\}, \quad \text{where } i \leq j. \quad (268)$$

Similarly, (259) reduces to

$$p_{ij} = \frac{1}{\Delta x_i} \mathcal{R}_{ij,0} \{\ell\}, \quad \text{where } i \leq j. \quad (269)$$

The collision probabilities defined in (268) represent an infinite lattice and are normalized as

$$\sum_{j=1}^I p_{ij} \Sigma_j = 1, \quad \forall i. \quad (270)$$

In contrast, the collision probabilities defined in (269) have boundary leakage and are, therefore, *not* normalized to unity.

We will now find analytical reductions for functionals $\mathcal{R}_{ij,m} \{\pm \ell\}$ and use them to evaluate the CP components in slab geometry. Using (261), it is possible to perform a first integration and obtain

$$\begin{aligned}
 & \int_{x_{i-1/2}}^{x_{i+1/2}} dx E_n[f(x, x')] \\
 = & \begin{cases} \pm \frac{1}{\Sigma_i} \{E_{n+1}[f(x_{i+1/2}, x')] - E_{n+1}[f(x_{i-1/2}, x')]\} & \text{if } \Sigma_i \neq 0, \\ \Delta x_i E_n[f(x_{i-1/2}, x')] & \text{otherwise} \end{cases} \quad (271)
 \end{aligned}$$

and

$$\int_{x_{j-1/2}}^{x_{j+1/2}} dx E_n [f(x', x)] = \begin{cases} \mp \frac{1}{\Sigma_j} \{E_{n+1}[f(x', x_{j+1/2})] - E_{n+1}[f(x', x_{j-1/2})]\} & \text{if } \Sigma_j \neq 0, \\ \Delta x_j E_n [f(x', x_{j-1/2})] & \text{otherwise,} \end{cases} \quad (272)$$

where the upper sign is used if $f \equiv m\ell_{\text{cell}} + \ell$ and the lower sign is used if $f \equiv m\ell_{\text{cell}} - \ell$.

Integration in x' is next performed, leading to the following relations:

(a) $i < j$, $\Sigma_i \neq 0$ and $\Sigma_j \neq 0$:

$$\mathcal{R}_{ij,m} \{\pm \ell\} = \frac{1}{2\Sigma_i \Sigma_j} \{E_3[m\ell_{\text{cell}} \pm \ell(x_{i+1/2}, x_{j-1/2})] - E_3[m\ell_{\text{cell}} \pm \ell(x_{i+1/2}, x_{j+1/2})] + E_3[m\ell_{\text{cell}} \pm \ell(x_{i-1/2}, x_{j+1/2})] - E_3[m\ell_{\text{cell}} \pm \ell(x_{i-1/2}, x_{j-1/2})]\}. \quad (273)$$

(b) $i < j$, $\Sigma_i = 0$ and $\Sigma_j \neq 0$:

$$\mathcal{R}_{ij,m} \{\pm \ell\} = \pm \frac{\Delta x_i}{2\Sigma_j} \{E_2[m\ell_{\text{cell}} \pm \ell(x_{i-1/2}, x_{j-1/2})] - E_2[m\ell_{\text{cell}} \pm \ell(x_{i-1/2}, x_{j+1/2})]\}. \quad (274)$$

(c) $i < j$, $\Sigma_i \neq 0$ and $\Sigma_j = 0$:

$$\mathcal{R}_{ij,m} \{\pm \ell\} = \pm \frac{\Delta x_j}{2\Sigma_i} \{E_2[m\ell_{\text{cell}} \pm \ell(x_{i+1/2}, x_{j-1/2})] - E_2[m\ell_{\text{cell}} \pm \ell(x_{i-1/2}, x_{j-1/2})]\}. \quad (275)$$

(d) $i < j$ and $\Sigma_i = \Sigma_j = 0$:

$$\mathcal{R}_{ij,m} \{\pm \ell\} = \frac{\Delta x_i \Delta x_j}{2} E_1[m\ell_{\text{cell}} \pm \ell(x_{i-1/2}, x_{j-1/2})]. \quad (276)$$

(e) $i = j$ and $\Sigma_i \neq 0$:

$$\mathcal{R}_{ii,m} \{\pm \ell\} = \pm \frac{\Delta x_i E_2[m\ell_{\text{cell}}]}{\Sigma_i} - \frac{1}{\Sigma_i^2} \{E_3[m\ell_{\text{cell}}] - E_3[m\ell_{\text{cell}} \pm \ell(x_{i-1/2}, x_{i+1/2})]\}. \quad (277)$$

(f) $i = j$ and $\Sigma_i = 0$:

$$\mathcal{R}_{ii,m} \{\pm \ell\} = \frac{E_1[m\ell_{\text{cell}}] \Delta x_i^2}{2}. \quad (278)$$

The above relations are implemented in Matlab using the following two scripts:

```
function f=rif_f(sg,tau0,sigi,sigj,segmenti,segmentj)
% function f=rif_f(sg,tau0,sigi,sigj,segmenti,segmentj)
% (c) 2006 Alain Hebert, Ecole Polytechnique de Montreal
```



```

if sigi == 0 && sigj == 0
    f=0.5*(taben(3,tau0)-taben(3,tau0+sg*sigi*segmenti)- ...
        taben(3,tau0+sg*sigj*segmentj)+ ...
        taben(3,tau0+sg*sigi*segmenti+sg*sigj*segmentj))/(sigi*sigj) ;
elseif sigi == 0 && sigj == 0
    f=sg*0.5*segmenti*(taben(2,tau0)-taben(2,tau0+sg*sigj*segmentj))/sigj ;
elseif sigi == 0 && sigj == 0
    f=sg*0.5*segmentj*(taben(2,tau0)-taben(2,tau0+sg*sigi*segmenti))/sigi ;
else
    f=0.5*segmenti*segmentj*taben(1,tau0) ;
end

```

and


```

function f=rri_f(sg,tau0,sigi,segmenti)
% function f=rri_f(sg,tau0,sigi,segmenti)
% (c) 2006 Alain Hebert, Ecole Polytechnique de Montreal
if sigi == 0
    f=sg*segmenti*taben(2,tau0)/sigi- ...
        (taben(3,tau0)-taben(3,tau0+sg*sigi*segmenti))/sigi^2 ;
else
    f=0.5*segmenti^2*taben(1,tau0) ;
end

```

In the case where $m = 0$, (278) reduces to $\mathcal{R}_{ii,0}\{\ell\} = \infty$. This singularity has no effect on the solution of the transport equation because region i is voided and $\mathcal{R}_{ii,0}\{\ell\}$ is multiplied by a zero cross-section value. The value of the neutron flux in region i remains finite in this case. In all other cases, the reduced collision probability components remain finite as a cross-section is set to zero. All the collision probability components with $i > j$ are computed using the reciprocity (229).

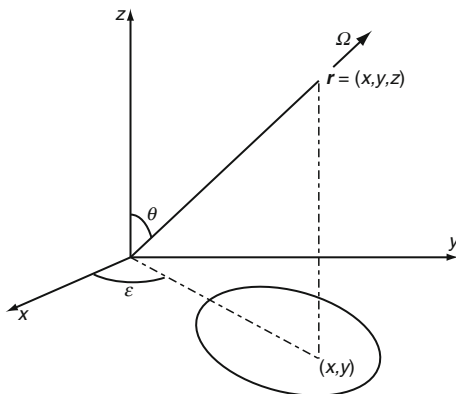
4.4 Cylindrical 1D Geometry

We will now study the case of a 2D geometry defined in the x - y plane and homogenous along the z -axis. A cylinder or tube of infinite length is an example of such a geometry. In this case, it is possible to analytically integrate (228) or (236)–(239) along the axial angle θ , as depicted in  Fig. 13.

The direction of the particle is $\Omega = \sin \theta \cos \varepsilon i + \sin \theta \sin \varepsilon j + \cos \theta k$. Integration over θ is possible by taking the projection of each particle free path on the x - y plane. We write

$$\begin{aligned}
 d^2\Omega &= d\theta d\varepsilon \sin \theta, \\
 \tau(\rho) &= \tau(s) \sin \theta, \\
 d\rho &= ds \sin \theta,
 \end{aligned} \tag{279}$$

where ρ is the projection of s on the x - y plane.



■ Figure 13

Projection of a particle trajectory on the x - y plane. Angle θ is used to define the direction cosine of the particle relative to the z -axis

For reasons that will be explained later, we will limit ourselves to the integration of (236), defined on the domain of a unique unit cell. As before, we use the relations $\mathbf{r} = \mathbf{r}' + s \boldsymbol{\Omega}$ and $d^3 r = s^2 d^2 \Omega ds$ and obtain an equation similar to (251) as follows:

$$p_{ij} = \frac{1}{4\pi V_i} \int_{V_i} d^3 r' \int_{4\pi} d^2 \Omega \int_{\mathcal{I}_j} ds e^{-\tau(s)}, \quad (280)$$

where the quantity \mathcal{I}_j is the set of points belonging simultaneously

- To the half straight line of origin \mathbf{r} and direction $-\boldsymbol{\Omega}$
- To volume V_j of the unit cell

With the help of ► Fig. 13, (280) can be rewritten as

$$p_{ij} = \frac{1}{4\pi V_i} \int_0^{2\pi} d\epsilon \int_{V_i} d^2 r' \int_0^\pi d\theta \int_{\mathcal{I}_j} d\rho e^{-\frac{\tau(\rho)}{\sin \theta}}, \quad (281)$$

where V_i now represents a surface in the x - y plane and \mathcal{I}_j is the set of points belonging simultaneously

- To the half straight line of origin \mathbf{r}' and direction ϵ
- To surface V_j of the unit cell

Equation (281) can be simplified by introducing the *Bickley functions* $Ki_n(x)$, with $n \geq 1$, defined as

$$Ki_n(x) = \int_0^{\pi/2} d\theta \sin^{n-1} \theta e^{-\frac{x}{\sin \theta}} = \int_0^{\pi/2} d\theta \cos^{n-1} \theta e^{-\frac{x}{\cos \theta}} \quad (282)$$

and depicted in ► Fig. 14. They can be evaluated using the Matlab script `aki_n` of Hébert (2009).

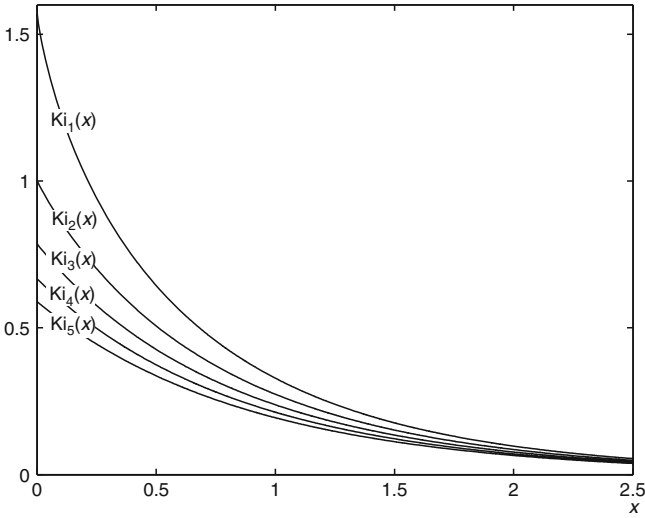


Figure 14
Bickley functions

The following equations present the relationships between Bickley functions of different orders:

$$\int_x^{x'} du \text{Ki}_n(u) = \text{Ki}_{n+1}(x) - \text{Ki}_{n+1}(x'), \tag{283}$$

$$\frac{d}{dx} \text{Ki}_n(x) = -\text{Ki}_{n-1}(x) \tag{284}$$

so that the Taylor expansion of $\text{Ki}_3(x)$ is

$$\text{Ki}_3(x) = \text{Ki}_3(x_0) - \text{Ki}_2(x_0)(x - x_0) + \frac{1}{2} \text{Ki}_1(x_0)(x - x_0)^2 + \mathcal{O}(x - x_0)^3 \tag{285}$$

and

$$n \text{Ki}_{n+1}(x) = (n - 1) \text{Ki}_{n-1}(x) + x [\text{Ki}_{n-2}(x) - \text{Ki}_n(x)]. \tag{286}$$

We obtain

$$p_{ij} = \frac{1}{2\pi V_i} \int_0^{2\pi} d\varepsilon \int_{V_i} d^2r' \int_{\mathcal{I}_j} d\rho \text{Ki}_1[\tau(\rho)]. \tag{287}$$

Sets of integration lines, referred to as *tracks*, are drawn over the complete domain. Each set is characterized by a given angle ε and contains parallel tracks covering the domain. Tracks in a set can be separated by a constant distance Δh or can be placed at optimal locations, as depicted in **Fig. 15a** and **b**, respectively. Each track is used forward and backward, corresponding to angles ε and $-\varepsilon$. The track generation procedure is described in Appendices **Section 1** and **Section 2**.

In the case of convex volumes i and j , as depicted in **Fig. 16**, (287) can be rewritten as

$$p_{ij} = \frac{1}{2\pi V_i} \int_0^{2\pi} d\varepsilon \int_{h_{\min}}^{h_{\max}} dh \int_0^{\ell_i} d\ell' \int_0^{\ell_j} d\ell \text{Ki}_1(\tau_{ij} + \Sigma_i \ell' + \Sigma_j \ell) \quad \text{if } i \neq j, \tag{288}$$

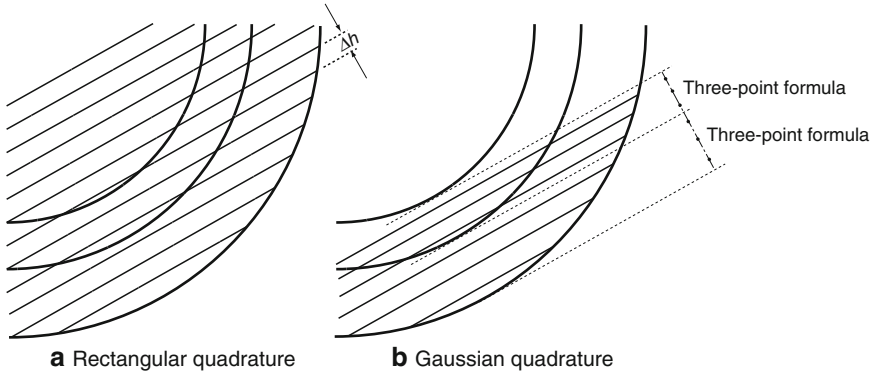


Figure 15 Tracking a 1D cylindrical geometry (a) Rectangular quadrature and (b) Gaussian quadrature

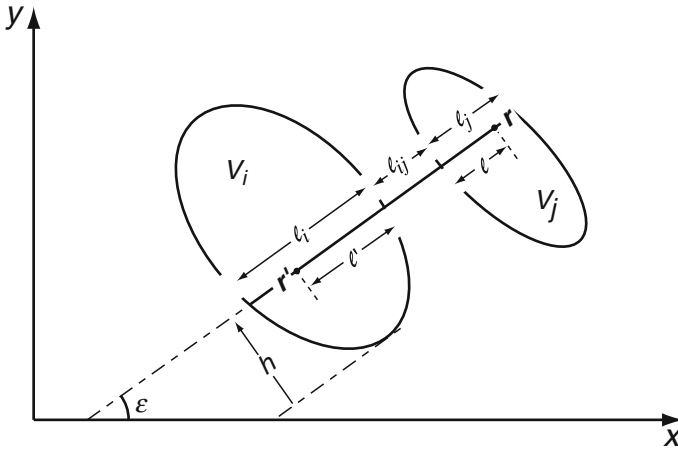


Figure 16 Integration of collision probabilities in 2D x-y geometry

where τ_{ij} is the optical path of the materials between regions i and j and

$$p_{ii} = \frac{1}{2\pi V_i} \int_0^{2\pi} d\epsilon \int_{h_{\min}}^{h_{\max}} dh \int_0^{\ell_i} d\ell' \int_{\ell'}^{\ell_i} d\ell \text{Ki}_1[\Sigma_i(\ell - \ell')]. \quad (289)$$

In the case of 1D cylindrical geometry, the tracks are identical for any value of the angle ϵ . However, the tubular volumes are concave, causing extra terms to appear. The corresponding geometry is depicted in Fig. 17. Two tracks are represented, both contributing to collision probability components p_{ij} with $i < j$ and p_{ii} . Track ① corresponds to the integration domain where region i is concave and track ② corresponds to the integration domain where it is convex. In this figure, τ_{ij} and τ_{ii} are the optical paths of the materials located between the regions i and j or between two instances of region i .

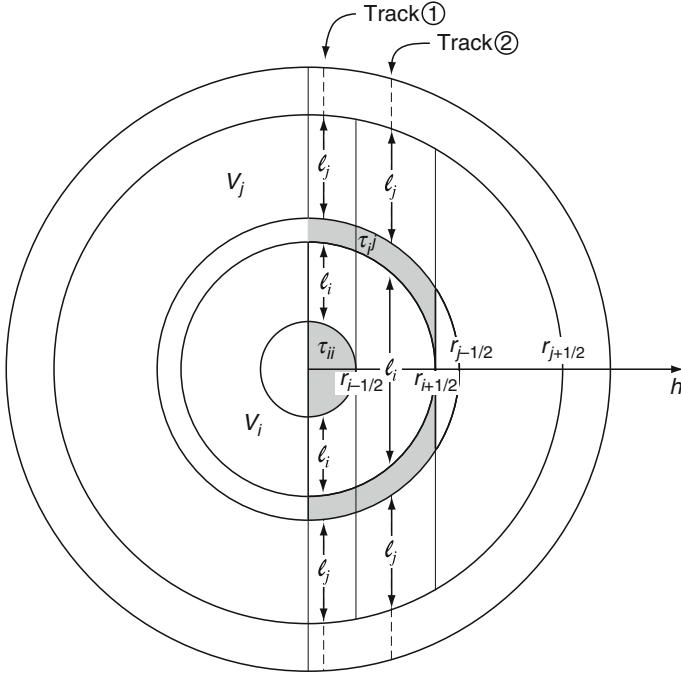


Figure 17
 Integration of collision probabilities in 1D cylindrical geometry

In this case, (287) can be rewritten as

$$\begin{aligned}
 p_{ij} = \frac{2}{V_i} \left\{ \int_0^{r_{i-1/2}} dh \int_0^{\ell_i} d\ell' \int_0^{\ell_j} d\ell \left[\text{Ki}_1[(\tau_{ij} + \tau_{ii} + \Sigma_i \ell_i) + \Sigma_i \ell' + \Sigma_j \ell] \right. \right. \\
 \left. \left. + \text{Ki}_1(\tau_{ij} + \Sigma_i \ell' + \Sigma_j \ell) \right] \right. \\
 \left. + \int_{r_{i-1/2}}^{r_{i+1/2}} dh \int_0^{\ell_i} d\ell' \int_0^{\ell_j} d\ell \text{Ki}_1(\tau_{ij} + \Sigma_i \ell' + \Sigma_j \ell) \right\} \quad \text{if } i < j, \quad (290)
 \end{aligned}$$

where $r_{i\pm 1/2}$ are the radii bounding region i and

$$\begin{aligned}
 p_{ii} = \frac{2}{V_i} \left\{ \int_0^{r_{i-1/2}} dh \int_0^{\ell_i} d\ell' \left[2 \int_{\ell'}^{\ell_i} d\ell \text{Ki}_1[\Sigma_i (\ell - \ell')] + \int_0^{\ell_i} d\ell \text{Ki}_1[\tau_{ii} + \Sigma_i (\ell' + \ell)] \right] \right. \\
 \left. + \int_{r_{i-1/2}}^{r_{i+1/2}} dh \int_0^{\ell_i} d\ell' \int_{\ell'}^{\ell_i} d\ell \text{Ki}_1[\Sigma_i (\ell - \ell')] \right\}, \quad (291)
 \end{aligned}$$

where the first and second terms of (290) and (291) are the contributions from tracks ① and ②, respectively. All the collision probability components with $i > j$ are computed using the reciprocity (229).

These equations can be simplified by introducing the following definitions:

$$C_{ij}(\tau_0) = \int_0^{\ell_i} d\ell' \int_0^{\ell_j} d\ell \text{Ki}_1(\tau_0 + \Sigma_i \ell' + \Sigma_j \ell) \quad (292)$$

and

$$\mathcal{D}_i = \int_0^{\ell_i} d\ell' \int_{\ell'}^{\ell_i} d\ell \text{Ki}_1[\Sigma_i(\ell - \ell')] \quad (293)$$

so that

$$p_{ij} = \frac{2}{V_i} \left\{ \int_0^{r_{i-1/2}} dh [C_{ij}(\tau_{ij} + \tau_{ii} + \Sigma_i \ell_i) + C_{ij}(\tau_{ij})] + \int_{r_{i-1/2}}^{r_{i+1/2}} dh C_{ij}(\tau_{ij}) \right\} \quad \text{if } i < j \quad (294)$$

and

$$p_{ii} = \frac{2}{V_i} \left\{ \int_0^{r_{i-1/2}} dh [2\mathcal{D}_i + C_{ii}(\tau_{ii})] + \int_{r_{i-1/2}}^{r_{i+1/2}} dh \mathcal{D}_i \right\}. \quad (295)$$

Integration in ℓ and ℓ' is performed next, leading to the following relations:

(a) $\Sigma_i \neq 0$ and $\Sigma_j \neq 0$:

$$C_{ij}(\tau_0) = \frac{1}{\Sigma_i \Sigma_j} [\text{Ki}_3(\tau_0) - \text{Ki}_3(\tau_0 + \Sigma_i \ell_i) - \text{Ki}_3(\tau_0 + \Sigma_j \ell_j) + \text{Ki}_3(\tau_0 + \Sigma_i \ell_i + \Sigma_j \ell_j)]. \quad (296)$$

(b) $\Sigma_i = 0$ and $\Sigma_j \neq 0$:

$$C_{ij}(\tau_0) = \frac{\ell_i}{\Sigma_j} [\text{Ki}_2(\tau_0) - \text{Ki}_2(\tau_0 + \Sigma_j \ell_j)]. \quad (297)$$

(c) $\Sigma_i \neq 0$ and $\Sigma_j = 0$:

$$C_{ij}(\tau_0) = \frac{\ell_j}{\Sigma_i} [\text{Ki}_2(\tau_0) - \text{Ki}_2(\tau_0 + \Sigma_i \ell_i)]. \quad (298)$$

(d) $\Sigma_i = \Sigma_j = 0$:

$$C_{ij}(\tau_0) = \ell_i \ell_j \text{Ki}_1(\tau_0). \quad (299)$$

(e) $\Sigma_i \neq 0$:

$$\mathcal{D}_i = \frac{\ell_i}{\Sigma_i} - \frac{1}{\Sigma_i^2} [\text{Ki}_3(0) - \text{Ki}_3(\Sigma_i \ell_i)]. \quad (300)$$

(f) $\Sigma_i = 0$:

$$\mathcal{D}_i = \frac{\pi \ell_i^2}{4}. \quad (301)$$

The above relations are implemented in Matlab using the following two scripts:

```
function f=cij_f(tau0,sigi,sigj,segmenti,segmentj)
% function f=cij_f(tau0,sigi,sigj,segmenti,segmentj)
% (c) 2006 Alain Hebert, Ecole Polytechnique de Montreal
if sigi ~= 0 && sigj ~= 0
    f=(akin(3,tau0)-akin(3,tau0+sigi*segmenti)-akin(3,tau0+sigj*segmentj)+ ...
        akin(3,tau0+sigi*segmenti+sigj*segmentj))/(sigi*sigj);
```

```

elseif sigi == 0 && sigj ~ = 0
    f=(akin(2,tau0)-akin(2,tau0+sigj*segmentj))*segmenti/sigj ;
elseif sigi ~ = 0 && sigj == 0
    f=(akin(2,tau0)-akin(2,tau0+sigi*segmenti))*segmentj/sigi ;
else
    f=akin(1,tau0)*segmenti*segmentj ;
end

```

and

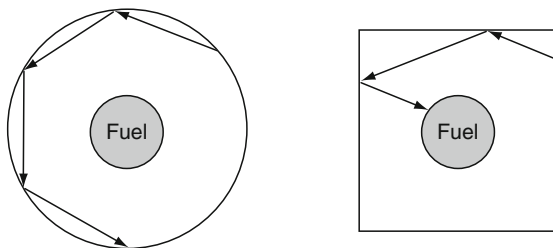
```

function f=di_f(sig,segment)
% function f=di_f(sig,segment)
% (c) 2006 Alain Hebert, Ecole Polytechnique de Montreal
if sig ~ = 0
    f=segment/sig-(akin(3,0)-akin(3,sig*segment))/sig^2 ;
else
    f=pi*segment^2/4 ;
end

```

The external-boundary condition of a 1D cylindrical geometry is introduced by choosing an albedo β^+ set to zero for representing a voided boundary, or set to one for representing reflection of particles. The voided-boundary condition is similar to the vacuum condition used for 1D slab geometry. Such a boundary condition is useful in criticality problems for computing the critical radius of tubes. On the other hand, the reflecting boundary condition is implemented in the context of the *Wigner–Seitz approximation* for lattice calculations in reactor physics. As introduced in [▶ 3.2](#), the Wigner–Seitz approximation consists of replacing the exact boundary with an *equivalent cylindrical boundary*, as shown in [▶ Fig. 18](#), taking care to conserve the amount of moderator present in the cell. The correct condition in this case is the *white-boundary condition* in which the particles are reflected back, on the cylindrical boundary, with an isotropic angular distribution in the radial plane.

We present two cylinderization techniques on the unit cell of [▶ Fig. 18](#). The square boundary of side a must be replaced by a cylindrical boundary of radius R^* . Moreover, all



■ **Figure 18**
Wigner–Seitz boundary approximation

cross-sections Σ_x in the outer-most region must be replaced by cross-sections Σ_x^* . The *Wigner cylinderization* consists in preserving the volume of the outermost region. We write

$$R^* = \sqrt{\frac{a^2}{\pi}} \quad \text{and} \quad \Sigma_x^* = \Sigma_x. \quad (302)$$

The *Askew cylinderization* consists in preserving the outer surface of the unit cell and modifying the number density of the nuclei present in the outermost region. We write

$$R^* = \frac{2a}{\pi} \quad \text{and} \quad \Sigma_x^* = \frac{a^2 - \pi R^2}{\pi[(R^*)^2 - R^2]} \Sigma_x. \quad (303)$$

The application of a white-boundary condition is based on the transformation of the reduced collision probability matrix $\mathbb{P} = \{p_{ij}, i = 1, I \text{ and } j = 1, I\}$ corresponding to a vacuum-boundary condition. We first compute the *escape probability* vector $\mathbf{P}_{iS} = \{P_{iS}, i = 1, I\}$, a column vector whose components are obtained from

$$P_{iS} = 1 - \sum_{j=1}^I p_{ij} \Sigma_j \quad (304)$$

representing the probability for a neutron born in region i to escape from the unit cell without collision.

We define P_{Si} as the probability for a neutron, entering the unit cell through its boundary with an isotropic angular distribution, to first collide in region i . It is possible to show that

$$p_{Si} = \frac{P_{Si}}{\Sigma_i} = \frac{4V_i}{S} P_{iS}, \quad (305)$$

where S is the surface of the boundary.

The *transmission probability* P_{SS} is, therefore, given as

$$P_{SS} = 1 - \sum_{i=1}^I p_{Si} \Sigma_i. \quad (306)$$

The reduced-collision probability matrix $\tilde{\mathbb{P}} = \{\tilde{p}_{ij}, i = 1, I \text{ and } j = 1, I\}$ corresponding to a white-boundary condition can now be obtained using

$$\tilde{\mathbb{P}} = \mathbb{P} + \frac{\beta^+}{1 - \beta^+ P_{SS}} \mathbf{P}_{iS} \mathbf{P}_{Sj}^\top. \quad (307)$$

The collision-probability matrix $\tilde{\mathbb{P}}$ can be scattering-reduced using (249) and used in the matrix-flux equation of (248).

4.5 Spherical 1D Geometry

Computing the tracking and collision probabilities in 1D spherical geometry is similar to the cylindrical geometry case. The tracking is obtained by the `sybt1d` procedure

of Appendices [Section 1](#) and [Section 2](#). Equation (287) is replaced by

$$p_{ij} = \frac{1}{V_i} \int_{V_i} d^3 r' \int_{\mathcal{I}_j} ds e^{-\tau(s)} \quad (308)$$

which can be rewritten as

$$p_{ij} = \frac{2\pi}{V_i} \left\{ \int_0^{r_{i-1/2}} dh h \int_0^{\ell_i} d\ell' \int_0^{\ell_j} d\ell \left[e^{-[(\tau_{ij} + \tau_{ii} + \Sigma_i \ell_i) + \Sigma_i \ell' + \Sigma_j \ell]} + e^{-(\tau_{ij} + \Sigma_i \ell' + \Sigma_j \ell)} \right] \right. \\ \left. + \int_{r_{i-1/2}}^{r_{i+1/2}} dh h \int_0^{\ell_i} d\ell' \int_0^{\ell_j} d\ell e^{-(\tau_{ij} + \Sigma_i \ell' + \Sigma_j \ell)} \right\} \quad \text{if } i < j, \quad (309)$$

where $r_{i\pm 1/2}$ are the radii-bounding region i and

$$p_{ii} = \frac{2\pi}{V_i} \left\{ \int_0^{r_{i-1/2}} dh h \int_0^{\ell_i} d\ell' \left[2 \int_{\ell'}^{\ell_i} d\ell e^{-[\Sigma_i (\ell - \ell')]} + \int_0^{\ell_i} d\ell e^{-[\tau_{ii} + \Sigma_i (\ell' + \ell)]} \right] \right. \\ \left. + \int_{r_{i-1/2}}^{r_{i+1/2}} dh h \int_0^{\ell_i} d\ell' \int_{\ell'}^{\ell_i} d\ell e^{-[\Sigma_i (\ell - \ell')]} \right\}, \quad (310)$$

where the first- and second terms of (309) and (310) are the contributions from tracks ① and ②, respectively. All the collision probability components with $i > j$ are computed using the reciprocity (229).

These equations can be simplified by introducing the following definitions:

$$C_{ij}(\tau_0) = \int_0^{\ell_i} d\ell' \int_0^{\ell_j} d\ell e^{-(\tau_0 + \Sigma_i \ell' + \Sigma_j \ell)} \quad (311)$$

and

$$\mathcal{D}_i = \int_0^{\ell_i} d\ell' \int_{\ell'}^{\ell_i} d\ell e^{-\Sigma_i (\ell - \ell')} \quad (312)$$

so that

$$p_{ij} = \frac{2\pi}{V_i} \left\{ \int_0^{r_{i-1/2}} dh h [C_{ij}(\tau_{ij} + \tau_{ii} + \Sigma_i \ell_i) + C_{ij}(\tau_{ij})] + \int_{r_{i-1/2}}^{r_{i+1/2}} dh h C_{ij}(\tau_{ij}) \right\} \quad (313)$$

if $i < j$, and

$$p_{ii} = \frac{2\pi}{V_i} \left\{ \int_0^{r_{i-1/2}} dh h [2\mathcal{D}_i + C_{ii}(\tau_{ii})] + \int_{r_{i-1/2}}^{r_{i+1/2}} dh h \mathcal{D}_i \right\}. \quad (314)$$

Integration in ℓ and ℓ' is performed next, leading to the following relations:

(a) $\Sigma_i \neq 0$ and $\Sigma_j \neq 0$:

$$C_{ij}(\tau_0) = \frac{1}{\Sigma_i \Sigma_j} \left[e^{-\tau_0} - e^{-(\tau_0 + \Sigma_i \ell_i)} - e^{-(\tau_0 + \Sigma_j \ell_j)} + e^{-(\tau_0 + \Sigma_i \ell_i + \Sigma_j \ell_j)} \right]. \quad (315)$$

(b) $\Sigma_i = 0$ and $\Sigma_j \neq 0$:

$$C_{ij}(\tau_0) = \frac{\ell_i}{\Sigma_j} \left[e^{-\tau_0} - e^{-(\tau_0 + \Sigma_j \ell_j)} \right]. \quad (316)$$

(c) $\Sigma_i \neq 0$ and $\Sigma_j = 0$:

$$C_{ij}(\tau_0) = \frac{\ell_j}{\Sigma_i} \left[e^{-\tau_0} - e^{-(\tau_0 + \Sigma_i \ell_i)} \right]. \quad (317)$$

(d) $\Sigma_i = \Sigma_j = 0$:

$$C_{ij}(\tau_0) = \ell_i \ell_j e^{-\tau_0}. \quad (318)$$

(e) $\Sigma_i \neq 0$:

$$D_i = \frac{\ell_i}{\Sigma_i} - \frac{1}{\Sigma_i^2} \left[1 - e^{-\Sigma_i \ell_i} \right]. \quad (319)$$

(f) $\Sigma_i = 0$:

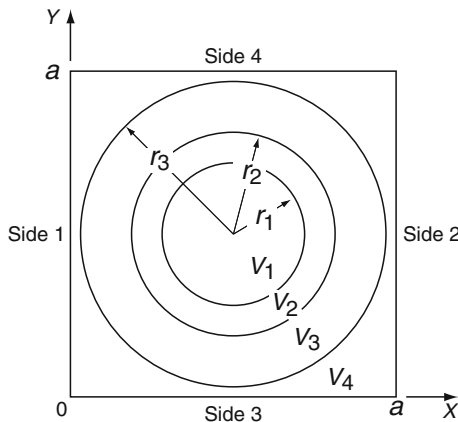
$$D_i = \frac{\ell_i^2}{2}. \quad (320)$$

4.6 Unstructured 2D Finite Geometry

The calculation of collision, escape, and transmission probabilities in unstructured 2D geometry is based on the generalization of (288) and (289) to concave volumes (Hébert 1981). In the general unstructured 2D case, the tracks are no longer identical for different values of the azimuthal angle ε . The integration domain for computing the collision probabilities can be either an infinite lattice or a finite geometry V surrounded by an external boundary ∂V . The former case is similar to the approach introduced in [4.3](#) and is beyond the level of this handbook. However, the calculation of collision probabilities in finite-geometry cases will be studied in detail.

We have chosen to present the *square pincell* geometry as an illustration of the more general unstructured 2D geometry. This simplified geometry is illustrated in [Fig. 19](#).

The approach used for this simple pincell geometry can be generalized to more complex 2D unstructured geometries, such as the BASALA assembly, depicted in [Fig. 20](#). This assembly



■ Figure 19

2D square pincell geometry. This geometry is among the simplest type of unstructured 2D finite geometry that can be processed using a tracking approach

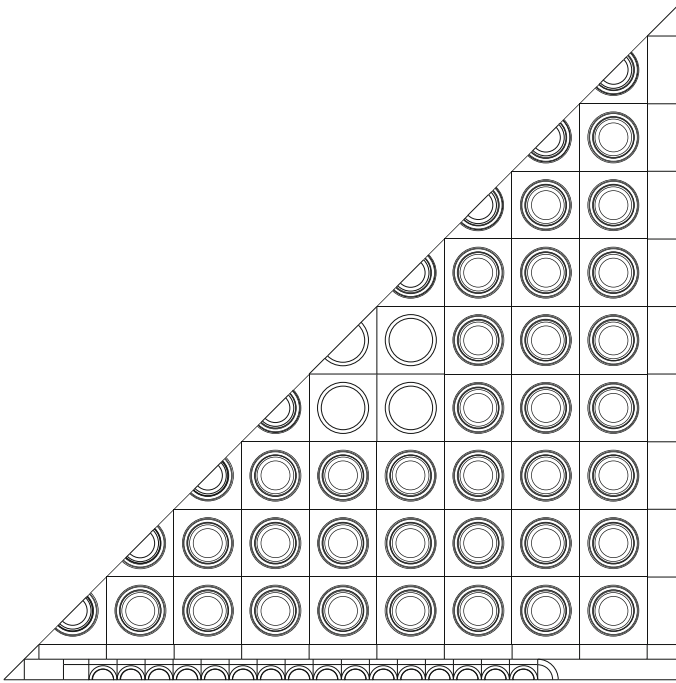


Figure 20
2D BASALA geometry

represents an experimental setup for studying mixed-oxide recycling in boiling water reactors (BWR) (Le Tellier et al. 2008). The tracking procedure presented in Appendices Section 3 and Section 4 can be generalized to these types of geometries, but the complexity of the corresponding tracking algorithms is far beyond the level of this handbook.

Sets of tracks are drawn over the complete 2D domain. Each set is characterized by a given angle ε and contains parallel tracks covering the domain. Tracks in a set can be separated by a constant distance Δh or can be placed at optimal locations, as depicted in Fig. 21a and b, respectively. Each track is used forward and backward, corresponding to angles ε and $-\varepsilon$. The track-generation procedure is described in Appendices Section 3 and Section 4 for the particular case of a 2D square pincell.

In the case of convex volumes i and j , a collision-probability component is given by (288) and (289) as

$$p_{ij} = \frac{1}{2\pi V_i} \int_0^{2\pi} d\varepsilon \int_{h_{\min}}^{h_{\max}} dh \int_0^{\ell_i} d\ell' \int_0^{\ell_j} d\ell \text{Ki}_1(\tau_{ij} + \Sigma_i \ell' + \Sigma_j \ell) \quad \text{if } i \neq j, \quad (321)$$

where τ_{ij} is the optical path of the materials between regions i and j and

$$p_{ii} = \frac{1}{2\pi V_i} \int_0^{2\pi} d\varepsilon \int_{h_{\min}}^{h_{\max}} dh \int_0^{\ell_i} d\ell' \int_{\ell'}^{\ell_i} d\ell \text{Ki}_1[\Sigma_i (\ell - \ell')]. \quad (322)$$

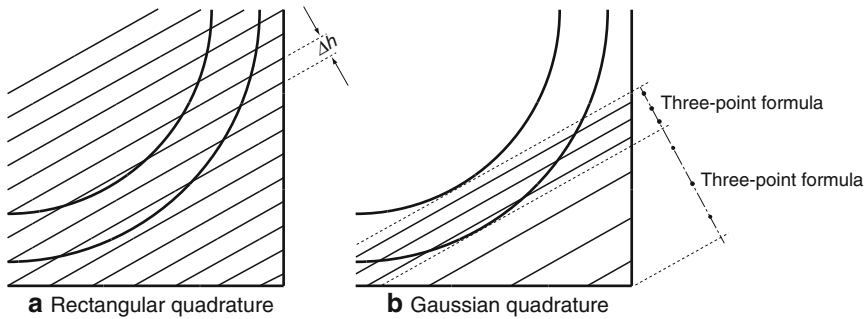


Figure 21
Tracking a 2D pincell geometry (a) Rectangular quadrature and (b) Gaussian quadrature

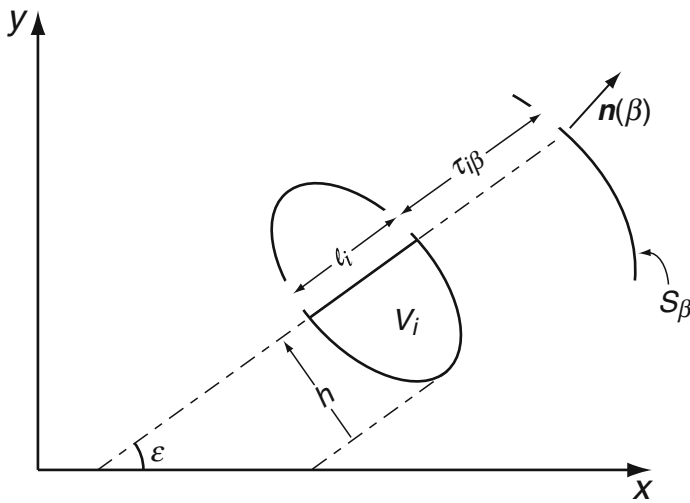


Figure 22
Integration of escape probabilities in 2D x - y geometry

Similarly, escape and transmission probability components are obtained after integration of (238) and (239) as

$$P_{iS_\beta} = \frac{1}{2\pi V_i} \int_0^{2\pi} d\varepsilon \int_{h_{\min}}^{h_{\max}} dh \int_0^{\ell_i} d\ell \text{Ki}_2(\tau_{i\beta} + \Sigma_i \ell), \quad (323)$$

where $\tau_{i\beta}$ is the optical path between region i and surface S_β , as depicted in Fig. 22, and

$$P_{S_\alpha S_\beta} = \frac{2}{\pi S_\alpha} \int_0^{2\pi} d\varepsilon \int_{h_{\min}}^{h_{\max}} dh \text{Ki}_3(\tau_{\alpha\beta}). \quad (324)$$

These equations can be simplified by introducing (294) and (295), together with the following definition:

$$\mathcal{E}_i(\tau_0) = \int_0^{\ell_i} d\ell \text{Ki}_2(\tau_0 + \Sigma_j \ell), \quad (325)$$

where $\tau_{\alpha\beta}$ is the optical path between surface S_α and surface S_β , so that

$$p_{ij} = \frac{1}{2\pi V_i} \int_0^{2\pi} d\varepsilon \int_{h_{\min}}^{h_{\max}} dh \mathcal{C}_{ij}(\tau_{ij}) \quad \text{if } i \neq j, \quad (326)$$

$$p_{ii} = \frac{1}{2\pi V_i} \int_0^{2\pi} d\varepsilon \int_{h_{\min}}^{h_{\max}} dh \mathcal{D}_i \quad (327)$$

and

$$P_{iS_\beta} = \frac{1}{2\pi V_i} \int_0^{2\pi} d\varepsilon \int_{h_{\min}}^{h_{\max}} dh \mathcal{E}_i(\tau_{i\beta}). \quad (328)$$

The analytical reduction of (294) and (295) is given in (296)–(301). Analytical reduction of $\mathcal{E}_i(\tau_0)$ leads to the following relations:

(a) $\Sigma_i \neq 0$:

$$\mathcal{E}_i(\tau_0) = \frac{1}{\Sigma_i} [\text{Ki}_3(\tau_0) - \text{Ki}_3(\tau_0 + \Sigma_i \ell_i)]. \quad (329)$$

(b) $\Sigma_i = 0$:


$$\mathcal{E}_i(\tau_0) = \ell_i \text{Ki}_2(\tau_0). \quad (330)$$

The above relations are implemented in Matlab using the following script:

```
function f=ei_f(tau0,sig,segment)
% function f=ei_f(tau0,sig,segment)
% (c) 2008 Alain Hebert, Ecole Polytechnique de Montreal
if sig ~= 0
    f=(akin(3,tau0)-akin(3,tau0+sig*segment))/sig;
else
    f=segment*akin(2,tau0);
end
```

The algorithm for computing p_{ij} , P_{iS_β} , and $P_{S_\alpha S_\beta}$ is greatly simplified by the definition of a symmetric matrix \mathbb{T} of order $\Lambda + I$, where Λ is the total number of surfaces and I is the total number of volumes. The components of \mathbb{T} are defined as

$$t_{\alpha,\beta} = \frac{S_\alpha}{4} P_{S_\alpha S_\beta}, \quad t_{\Lambda+i,\beta} = V_i P_{iS_\beta} \quad \text{and} \quad t_{\Lambda+i,\Lambda+j} = V_i p_{ij}. \quad (331)$$

Unstructured geometries may contain concave volumes, causing additional terms to appear in (321)–(324). These terms exist even for the simple pincell geometry of  Fig. 19. A straightforward way to present the integration algorithm of (321)–(324) in the presence of concave volumes is to provide a Matlab script implementing their practical evaluation. The simplicity of this script is remarkable. Matrix \mathbb{T} is obtained using the tracking information of the 2D geometry and the array of macroscopic total cross-sections in each region as input. This script follows:

```

function tij=tij_2d(track,sigt)
% integration of the collision, escape and transmission probabilities
% in unstructured finite 2D geometry.
% function tij=tij_2d(track,sigt)
% (c) 2009 Alain Hebert, Ecole Polytechnique de Montreal
indpos=@(i,j) max(i,j).*(max(i,j)-1)./2+min(i,j);
nsurf=track(1); nreg=track(2) ; k=5+track(1)+track(2)+2*track(3) ;
tij=zeros(1,(nreg+nsurf)*(nreg+nsurf+1)/2) ;
for itrk=1:track(4)
    isurf=track(k+2) ; jsurf=track(k+3) ; wei=track(k+4) ; km=track(k+5) ;
    kgar=k+5 ; k=k+5+km ; irs=isurf ; seg1=0. ; sig1=0. ;
    for ixi=1:km
        irt=irs ; irs=track(kgar+ixi) ; seg2=track(k+ixi) ; sig2=sigt(irs) ;
        irs=irs+nsurf ; iij=indpos(irs,irs) ;
        tij(iij)=tij(iij)+2.0*wei*di_f(sig2,seg2) ; tau0=0. ;
        for ixj=ixi:km
            jrs=track(kgar+ixj) ; seg3=track(k+ixj) ; sig3=sigt(jrs) ;
            jrs=jrs+nsurf ; iij=indpos(irt,jrs) ;
            if irt <= nsurf
                tij(iij)=tij(iij)+wei*ei_f(tau0,sig3,seg3) ;
            else
                wi3=cij_f(tau0,sig1,sig3,seg1,seg3) ;
                if jrs == irt, wi3=2.0*wi3 ; end
                tij(iij)=tij(iij)+wei*wi3 ;
            end
            tau0=tau0+seg3*sig3 ;
        end
        iij=indpos(irt,jsurf) ;
        if irt <= nsurf
            wi3=akin(3,tau0) ;
            if isurf == jsurf, wi3=2.0*wi3 ; end
            tij(iij)=tij(iij)+wei*wi3 ;
        else
            tij(iij)=tij(iij)+wei*ei_f(tau0,sig1,seg1) ;
        end
        seg1=seg2 ; sig1=sig2 ;
    end
    iij=indpos(irs,jsurf) ; tij(iij)=tij(iij)+wei*ei_f(0.0,sig1,seg1) ;
    k=k+km ;
end
tij(:)=tij(:).*track(5)^2 ;

```

Script `tij_2d` implements the core algorithm for computing the \mathbb{T} matrix corresponding to finite 2D unstructured geometries. The symmetric matrix \mathbb{T} is returned in triangular storage mode. The tracking script `sybt2d` of Appendices [Section 3](#) and [Section 4](#) is limited to pincell geometries, but the \mathbb{T} integration script `tij_2d` is general, as long as the geometry domain is

finite. The script calls functions `cij_f`, `di_f` and `ei_f`, the former two defined in [4.4](#). We also note that these three functions do not deal with situations where the cross-section values are small and approach zero. A production implementation should take this possibility into consideration using power series. Finally, it is worth noting that the evaluation of functions `akin` is time consuming. Typical production implementations generally rely on piecewise linear or quadratic fits to evaluate these functions.

There is no guarantee that the collision, escape, and transmission probability matrices obtained that way are conservative. Conservation relations can be forced using a consistent normalization of the collision probability matrices. Many normalization techniques are available, but the approach promoted by Villarino (1992) is highly recommended.

The Villarino–Stamm’ler normalization is based on the symmetric matrix \mathbb{T} defined by (331) and on the definition of two vectors defined as

$$\mathbf{s} = \text{col}\{(1; \alpha = 1, \Lambda), (\Sigma_i; i = 1, I)\}$$

and

$$\mathbf{g} = \text{col}\{(S_\alpha/4; \alpha = 1, \Lambda), (V_i; i = 1, I)\}. \quad (332)$$

Using this definition, reciprocity (240) and (241) are satisfied if matrix \mathbb{T} remains symmetric. Conservation (242) and (243) are written as

$$\mathbb{T} \mathbf{s} = \mathbf{g}. \quad (333)$$

Conservation relations are imposed *a posteriori* by computing a normalized matrix $\hat{\mathbb{T}}$ preserving its symmetry and satisfying (333). The additive normalization proposed by Villarino and Stamm’ler consists in finding a set of $\Lambda + I$ factors z_ℓ defined in such a way that

$$\tilde{t}_{\ell m} = (z_\ell + z_m) t_{\ell m}, \quad \ell, m = 1, \Lambda + I. \quad (334)$$

Substitution of (334) into (333) leads to

$$z_\ell \sum_m t_{\ell m} s_m + \sum_m z_m t_{\ell m} s_m = \sum_m \left[\delta_{\ell m} \sum_k t_{\ell k} s_k + t_{\ell m} s_m \right] z_m = g_\ell, \quad \ell = 1, \Lambda + I. \quad (335)$$

A fixed-point iteration for solving this linear equation can be written as

$$z_\ell^{(n+1)} = \frac{g_\ell - \left[\sum_{m < \ell} t_{\ell m} s_m z_m^{(n+1)} + \sum_{m > \ell} t_{\ell m} s_m z_m^{(n)} \right]}{t_{\ell \ell} s_\ell + \sum_m t_{\ell m} s_m}, \quad (336)$$

where $\ell = 1, \Lambda + I$, and where n is the iteration index.

Fixed-point iterations are initialized using $z_\ell^{(0)} = 1/2; \forall \ell$. Convergence can be accelerated by using a residue-minimizing approach.

The final assembly step consists in introducing albedo-boundary conditions to our unstructured finite geometry. A *white-boundary condition*, similar to the condition presented at the end of [4.4](#), can be implemented in a straightforward way. The normalized $\hat{\mathbb{T}}$ matrix can be transformed into collision, escape, and transmission probabilities using (331). The resulting matrices

are defined as

$$\mathbb{P}_{\text{vv}} = \{p_{ij}; i = 1, I \text{ and } j = 1, I\}, \quad \mathbb{P}_{\text{vS}} = \{P_{iS_\alpha}; i = 1, I \text{ and } \beta = 1, \Lambda\},$$

$$\mathbb{P}_{\text{Sv}} = \{P_{S_\alpha j}; \alpha = 1, \Lambda \text{ and } j = 1, I\}$$

and

$$\mathbb{P}_{\text{SS}} = \{P_{S_\alpha S_\beta}; \alpha = 1, \Lambda \text{ and } \beta = 1, \Lambda\}. \quad (337)$$

The flux and outgoing boundary current values are related to incoming boundary current and source values using (244). They are written in matrix form as

$$\begin{aligned} \Phi &= \mathbb{P}_{\text{vS}} J^- + \mathbb{P}_{\text{vv}} Q, \\ J^+ &= \mathbb{P}_{\text{SS}} J^- + \mathbb{P}_{\text{Sv}} Q, \end{aligned} \quad (338)$$

where $J^+ = \{\varphi_{0,\alpha}^+; \alpha = 1, \Lambda\}$, $J^- = \{\varphi_{0,\beta}^-; \beta = 1, \Lambda\}$, $Q = \{Q_i; i = 1, I\}$, and $\Phi = \{\phi_j; j = 1, I\}$.

A white-boundary condition is set by assigning unit albedos ($\beta_\alpha = 1$) on each boundary surface. A geometric equation can be written in terms of albedo values β_α as

$$\mathbb{A} = \text{diag}\{\beta_\alpha; \alpha = 1, \Lambda\} \quad (339)$$

and used to relate outgoing and incoming boundary currents using

$$J^- = \mathbb{A} J^+. \quad (340)$$

Combining (338) and (340) leads to a standard collision probability matrix equation, written as

$$\Phi = \hat{\mathbb{P}}_{\text{vv}} Q, \quad (341)$$

where the *closed* collision probability matrix is given as

$$\hat{\mathbb{P}}_{\text{vv}} = \mathbb{P}_{\text{vv}} \hat{\mathbb{P}}_{\text{SS}} \mathbb{P}_{\text{Sv}}, \quad (342)$$

where

$$\hat{\mathbb{P}}_{\text{SS}} = \mathbb{A} (\mathbb{I} - \mathbb{P}_{\text{SS}} \mathbb{A})^{-1}. \quad (343)$$

The complete assembly sequence implementing the collision-probability method in unstructured 2D finite geometry can be summarized as follows:

1. A tracking file is produced after analysis of the geometry. This approach is presented in **► Sects. 3** and **► 4** for the particular case of a 2D square pincell. The same tracking can usually be used in all energy groups.
2. The diagonal matrix \mathbb{T} is obtained by integration of the tracking using the algorithm of script `t i j _ 2 d`. This operation must be repeated in every energy group.
3. The \mathbb{T} matrix is normalized using the Villarino–Stamm’ler method.
4. A *closed*-reduced collision probability matrix is computed using (342) and (343).
5. The scattering-reduced collision probability matrix \mathbb{W} is computed using (249).

5 The Discrete Ordinates Method

The discrete ordinates method, also called the S_N method, is a discretization of the differential form of the transport equation. The angular flux is discretized according to discrete values and the particle flux is solved along each angular base point. This method is the evolution of an approach used in radiation transfer theory for stellar atmospheres (Chandrasekhar 1960). It was later adapted in reactor physics by Carlson and Bell (1958).

The basic difference relations of the S_N method are obtained from the straightforward discretization of the one-speed Boltzmann equation, evaluated at specific angles. The number of angles is a function of N , an even integer. Different relations are obtained, depending on the geometry. In each case, a fixed-point iterative strategy will emerge from the difference relations. However, powerful preconditioners and acceleration strategies will be required to ensure convergence in many practical cases.

5.1 Quadrature Sets in the Method of Discrete Ordinates

The discrete ordinate, or S_N method, is based on the discretization of the angular variable Ω as a set of discrete directions Ω_n defined in terms of specific-direction cosines. The direction cosines are chosen so as to integrate polynomials in direction cosines with maximum accuracy. Moreover, the S_N method must be consistent with diffusion theory, even at low N values. Different quadrature sets are used, depending on the type of geometry.

In 1D slab and spherical geometries, the transport equation is a function of only one direction cosine μ . In this case, a N -point Gauss-Legendre quadrature is generally used. This quadrature is written as

$$\int_{-1}^1 d\mu f(\mu) \simeq \sum_{n=1}^N \mathcal{W}_n f(\mu_n), \quad (344)$$

where the weights \mathcal{W}_n and base points μ_n are those of the classical Gauss-Legendre quadrature. This quadrature is known to be exact for polynomial functions $f(\mu)$ of degree equal or less than $2N - 1$, so that

$$\int_{-1}^1 d\mu \mu^k = \sum_{n=1}^N \mathcal{W}_n \mu_n^k = \begin{cases} \frac{2}{k+1} & \text{if } k \text{ is even,} \\ 0 & \text{if } k \text{ is odd,} \end{cases} \quad \forall 0 \leq k \leq 2N - 1. \quad (345)$$

In the more general case where the transport equation is a function of all the direction cosines, a two-dimensional quadrature is required to approximate integrals in angular variables. The S_N quadrature over the positive octant is written as


$$\frac{2}{\pi} \int_0^1 d\mu \int_0^{\pi/2} d\phi f(\mu, \eta, \xi) \simeq \sum_{n=1}^M \mathcal{W}_n f(\mu_n, \eta_n, \xi_n), \quad (346)$$

where $\eta = \sqrt{1 - \mu^2} \cos \phi$, $\xi = \sqrt{1 - \mu^2} \sin \phi$, and $M = N(N + 2)/8$. A solid angle is associated to each direction Ω_n , so that

$$\mathcal{W}_n = \frac{1}{4\pi} \int_{\Omega_n} d^2\Omega \quad (347)$$

with

$$\sum_{n=1}^M \mathcal{W}_n = 1. \quad (348)$$

In this case, it is generally recommended to use a two-dimensional quadrature where the base points are selected on the unit sphere in such a way as to preserve the symmetry of the eight octants with respect to $\pi/2$ rotations. This approach leads to the *level-symmetric* quadratures as represented in  Fig. 23. The projection of the base points on each Cartesian axis leads to the same set of N -direction cosine values. This choice reduces the number of degrees of freedom for the positioning of base points. It can be shown that the set of direction cosine values on each axis is represented by

$$\mu_p^2 = \mu_1^2 + (p-1) \frac{2(1-3\mu_1^2)}{N-2}, \quad 1 \leq p \leq \frac{N}{2}, \quad (349)$$

where μ_1 is the projection of the first base point in the interval $0 < \mu_1^2 \leq 1/3$. The choice of μ_1 is arbitrary, except in S_2 case where the only available value is $\mu_1^2 = 1/3$. For μ_1 small, the base points are located near the limits of the $[0, 1]$ interval and are concentrated around the Cartesian axis. If the value of μ_1 is close to $1/\sqrt{3}$, the base points are located around the middle direction of each octant.

Weights associated with each base point a subject to symmetry constraints. For $N = 2$, there is only one direction per octant and one corresponding weight. For $N = 4$, the three directions

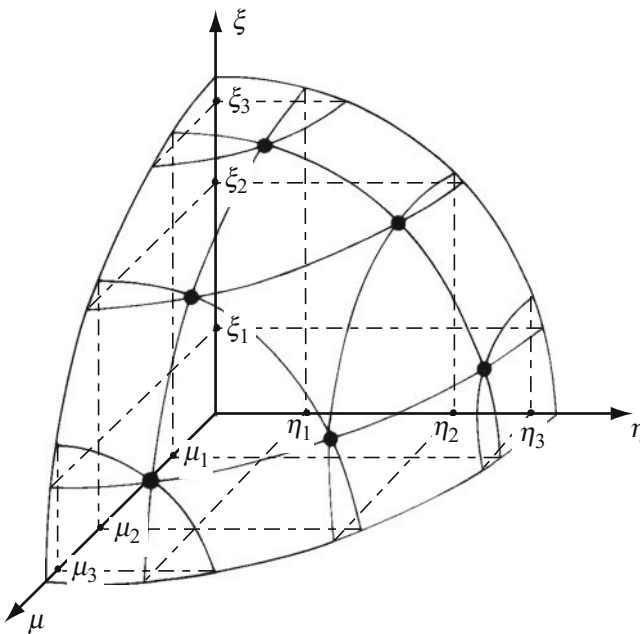


 Figure 23

S_6 level-symmetric quadrature

per octant must share the same weight, for symmetry reasons. In general, for all orders $N \geq 6$, the symmetry imposes equal weights for all directions belonging to a set of positions invariant with respect to $\pi/2$ rotations. For low values of N , the number of distinct weights per octant is equal to

$$N_w = 1 + \frac{N(N + 8) - 1}{48}. \tag{350}$$

► *Figure 24* represents the level-symmetric weight configuration for one octant showing base points of equal weight. Considering the free choice for μ_1 , the total number of degrees of freedom for a level-symmetric quadrature is $N_w + 1$. These degrees of freedom can be used in many ways to try to satisfy as many even-moments of direction cosines as possible. There is no need to include odd-moment conditions since these are automatically satisfied by level-symmetric quadrature sets when the integral is performed over 4π solid angles. Depending on the choice of even-moment conditions, different level-symmetric quadrature sets are obtained.

A first set of level-symmetric quadratures has been proposed in Carlson (1971) so as to integrate a polynomial function in direction cosines with maximum accuracy. These quadratures are represented in ► *Table 2*. They are exact for integrating the following polynomials for low values of k and ℓ :

$$\frac{2}{\pi} \int_0^1 d\mu \int_0^{\pi/2} d\phi \mu^k \eta^\ell = \sum_{m=1}^M \mathcal{W}_m \mu_m^k \eta_m^\ell = \begin{cases} \frac{1}{k+1} & \text{if } \ell = 0, \\ \frac{1}{k+\ell+1} \prod_{i=1, \text{ odd}}^{\ell-1} \frac{i}{k+i} & \text{if } \ell \geq 2, \end{cases} \tag{351}$$

where k and ℓ are even integers. Quadratures in ► *Table 2* are exact for $k + \ell \leq N$ if $N \leq 6$, for $k \leq 12$ ($\ell = 0$) and $k + \ell \leq 8$ if $N = 8$, for $k \leq 20$ ($\ell = 0$) and $k + \ell \leq 10$ if $N = 12$, and for $k \leq 30$ ($\ell = 0$) and $k + \ell \leq 14$ if $N = 16$.

Jenal et al. (1977) proposes a root-mean square approach for obtaining the quadrature sets in such a way that polynomials (351) are integrated exactly for all values of k and ℓ with

1	1
11	22
S_4 weight configuration	343
	3553
	24542
	123321
	S_{12} weight configuration
1	1
22	22
121	353
S_6 weight configuration	4664
	47874
	368863
	2567652
	12344321
1	S_{16} weight configuration
22	
232	
1221	
S_8 weight configuration	

► **Figure 24**

Level-symmetric weight configurations for one octant showing base points of equal weight

Table 2
Level-symmetric S_N quadratures of type 1^a

Level	μ_1	Distinct weights				
S_2	0.5773503	1.0				
S_4	0.3500212	0.3333333				
S_6	0.2666355	0.1761263	0.1572071			
S_8	0.2182179	0.1209877	0.0907407	0.0925926		
S_{12}	0.1672126	0.0707626	0.0558811	0.0373377	0.0502819	0.0258513
S_{16}	0.1389568	0.0489872	0.0413296	0.0212326	0.0256207	0.0360486
		0.0144589	0.0344958	0.0085179		

^a The weights are normalized to 1 in one octant

$0 \leq k + \ell < N$. In this work, the first base point is always taken equal to

$$\mu_1 = \frac{1}{\sqrt{3(N-1)}}. \quad (352)$$

It is possible to gain one order of accuracy by choosing the optimal value of μ_1 . The quadrature sets given in [Table 3](#) can integrate polynomials (351) exactly for all values of k and ℓ such that $0 \leq k + \ell \leq N$. An S_N quadrature is therefore able to integrate the spherical harmonics orthogonality in (30) exactly up to order of $\ell = N/2$.

Finally, [Table 4](#) reproduces quadrature sets used in the discrete ordinates code SNOW (Gunther and Kinnebrock 1973). They are given only for historical reasons.

In the particular case of cylindrical 1D geometry, two variables (ξ and ω) are required to determine the direction of the particle. The previous level-symmetric quadratures are consistent with this geometry. However, it is recommended to use the combination of a Gauss–Legendre and Gauss–Chebychev quadrature with the main axis (ξ) parallel to the cylinder axis and the μ axis joining the position of the particle with the cylinder axis, as shown in [Fig. 25](#).

The corresponding S_N quadrature is defined in terms of integer indices p and q as

$$\mu_{p,q} = \sqrt{1 - \xi_p^2} \cos \omega_{p,q} \quad \text{with} \quad 1 \leq p \leq \frac{N}{2} \quad \text{and} \quad 1 \leq q \leq N - 2p + 2, \quad (353)$$

where the values ξ_p are the positive base points of a Gauss–Legendre quadrature and where

$$\omega_{p,q} = \frac{\pi}{2} \left(1 - \frac{N - 2q - 2p + 3}{N - 2p + 2} \right). \quad (354)$$

The corresponding weights of the S_N quadrature are given in terms of the Gauss–Legendre weights \mathcal{W}_p using

$$\mathcal{W}_{p,q} = \frac{\pi \mathcal{W}_p}{N - 2p + 2}. \quad (355)$$

Table 3
Level-symmetric S_N quadratures of type 2^a

Level	μ_1	Distinct weights				
S_2	0.5773503	1.0				
S_4	0.3500212	0.3333333				
S_6	0.2666354	0.1761262	0.1572071			
S_8	0.2182178	0.1209876	0.0907408	0.0925925		
S_{10}	0.1893227	0.0893043	0.0725281	0.0450455	0.0539274	
S_{12}	0.1672308	0.0707734	0.0558760	0.0373436	0.0502654	0.0258553
S_{14}	0.1519951	0.0580031	0.0488943	0.0228095	0.0393955	0.0380920
		0.0258382	0.0082759			
S_{16}	0.1389747	0.0489967	0.0413235	0.0203158	0.0265468	0.0378883
		0.0135404	0.0326129	0.0103825		
S_{18}	0.1300795	0.0426910	0.0370806	0.0139198	0.0297556	0.0100159
		0.0306093	0.0160431	0.0197011	0.0011939	0.0158226
S_{20}	0.1206339	0.0370368	0.0332667	0.0112149	0.0244882	0.0136043
		0.0317999	0.0068205	0.0307489	0.0000038	0.0056654
		0.0045702	0.0281998			

^a The weights are normalized to 1 in one octant

Table 4
Level-symmetric S_N quadratures used in code SNOW

Level	μ_1	Distinct weights		
S_2	0.5773503	1.0		
S_4	0.3333333	0.3333333		
S_6	0.2581989	0.1608612	0.1724721	
S_8	0.2182179	0.1066008	0.1011727	0.0731616

The weights \mathcal{W}_p are normalized to one so that $\mathcal{W}_{p,q}$ is normalized to the solid angle of an octant as

$$\sum_{p=1}^{N/2} \mathcal{W}_p = 1, \quad \sum_{p=1}^{N/2} \sum_{q=1}^{N-2p+2} \mathcal{W}_{p,q} = \pi. \tag{356}$$

A set of $N/2$ zero-weight points is also defined in a direction where the angular redistribution term of the Boltzmann equation vanishes. These points are set at $\omega = \pi$, so that

$$\tilde{\mu}_p \equiv \mu_{p,N-2p+(5/2)} = -\sqrt{1 - \xi_p^2}. \tag{357}$$

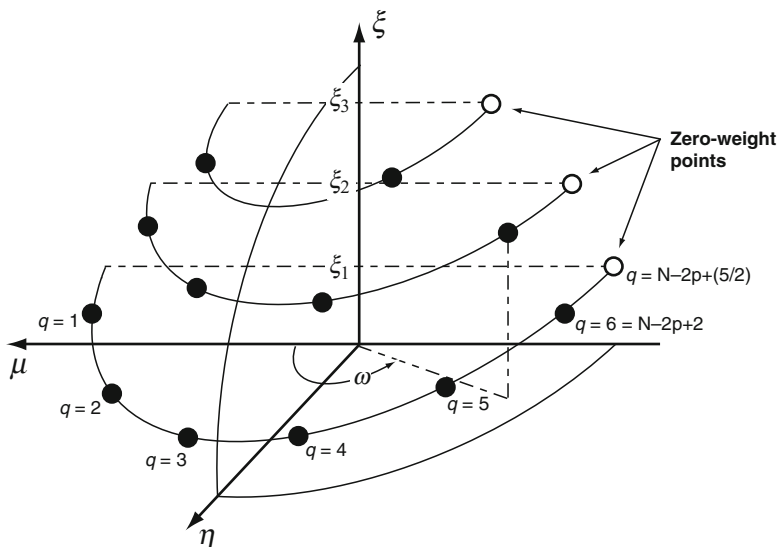


Figure 25
 S_6 Gauss–Chebyshev quadrature

Product quadratures can also be used in 1D cylindrical geometry. They are defined in such a way that $\mu_{p,q}$ and $\omega_{p,q}$ can be set as the product of an index p value with an index q value. The product of a Gauss–Legendre and a Gauss–Chebyshev quadrature is defined as

$$\mu_{p,q} = \sqrt{1 - \xi_p^2} \cos \omega_q \quad \text{with } 1 \leq p \leq \frac{N}{2} \quad \text{and } 1 \leq q \leq N, \tag{358}$$

where the values ξ_p are the positive base points of a Gauss–Legendre quadrature and where

$$\omega_q = \frac{\pi}{2} \left(1 - \frac{N - 2q + 1}{N} \right). \tag{359}$$

The corresponding weights of the S_N quadrature are given in terms of the Gauss–Legendre weights \mathcal{W}_p using

$$\mathcal{W}_{p,q} = \frac{\pi \mathcal{W}_p}{N}. \tag{360}$$

The weights \mathcal{W}_p are normalized to one so that $\mathcal{W}_{p,q}$ is normalized to the solid angle of an octant as

$$\sum_{p=1}^{N/2} \mathcal{W}_p = 1, \quad \sum_{p=1}^{N/2} \sum_{q=1}^N \mathcal{W}_{p,q} = \pi. \tag{361}$$

As before, a set of $N/2$ zero-weight points are set at $\omega = \pi$. These points are written as

$$\tilde{\mu}_p \equiv \mu_{p,N+(1/2)} = -\sqrt{1 - \xi_p^2}. \tag{362}$$

5.2 The Difference Relations in 1D Slab Geometry

The first-order form of the linear Boltzmann equation in 1D slab geometry is given in (126). The base points μ_n and weights \mathcal{W}_n are those of an N -point Gauss–Legendre quadrature. After discretization of the direction cosine, we obtain

$$\left[\mu_n \frac{\partial}{\partial x} + \Sigma(x) \right] \phi_n(x) = \sum_{\ell=0}^L \frac{2\ell+1}{2} Q_\ell(x) P_\ell(\mu_n), \quad n = 1, N, \tag{363}$$

where $\phi_n(x) \equiv \phi(x, \mu_n)$. The Legendre moments of the flux are given in terms of the S_N components using

$$\phi_\ell(x) = \sum_{n=1}^N \mathcal{W}_n \phi_n(x) P_\ell(\mu_n), \quad 0 \leq \ell \leq L. \tag{364}$$

The domain is divided in submeshes with constant cross-sections, as depicted in Fig. 26. The mesh-edge and mesh-centered values of the flux are given as $\phi_{n,i\pm 1/2}$ and $\phi_{n,i}$, respectively. The size of submesh i is given by

$$\Delta x_i = x_{i+1/2} - x_{i-1/2}. \tag{365}$$

The next step of the discretization procedure is to integrate (363) over each sub-mesh to obtain the following balance relation:

$$\mu_n \left(\phi_{n,i+1/2} - \phi_{n,i-1/2} \right) + \Delta x_i \Sigma_i \phi_{n,i} = \Delta x_i Q_{n,i}, \quad n = 1, N. \tag{366}$$

Using (125), the source components are defined as

$$Q_{n,i} = \sum_{\ell=0}^L \frac{2\ell+1}{2} Q_{\ell,i} P_\ell(\mu_n) \tag{367}$$

and where the mesh-centered values are given by

$$\phi_{n,i} = \frac{1}{\Delta x_i} \int_{x_{i-1/2}}^{x_{i+1/2}} dx \phi_n(x) \quad \text{and} \quad Q_{\ell,i} = \frac{1}{\Delta x_i} \int_{x_{i-1/2}}^{x_{i+1/2}} dx Q_\ell(x). \tag{368}$$

Equation (366) is an exact relation resulting from integration of (363) over each submesh. We will assume that the incoming left-hand side mesh-edge flux $\phi_{n,i-1/2}$ is known for $\mu_n > 0$

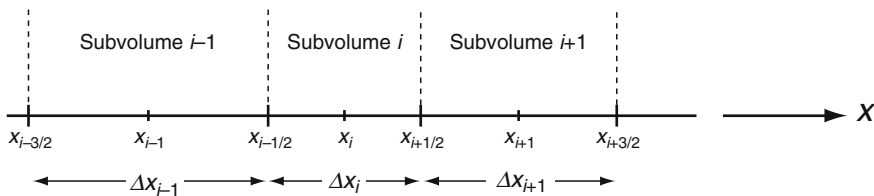


Figure 26
Spatial discretization for slab geometry

and that the incoming right-hand side mesh-edge flux $\phi_{n,i+1/2}$ is known for $\mu_n < 0$. Using these known values, it is possible to compute the outgoing fluxes in each direction, providing that an auxiliary relation is introduced to close the system. One of the most common auxiliary equations is the *diamond-differencing scheme* written as

$$\phi_{n,i} = \frac{1}{2} (\phi_{n,i-1/2} + \phi_{n,i+1/2}). \quad (369)$$

An inner iteration is initiated by assuming incoming fluxes at one boundary and proceeds by computing the other mesh-edge and mesh-centered fluxes recursively using

$$\begin{aligned} \phi_{n,i-1/2} = 2\phi_{n,i} - \phi_{n,i+1/2} & \quad \text{with } \phi_{n,i} = \frac{\Delta x_i Q_{n,i} - 2\mu_n \phi_{n,i+1/2}}{\Delta x_i \Sigma_i - 2\mu_n} & \text{if } \mu_n < 0, \\ \phi_{n,i+1/2} = 2\phi_{n,i} - \phi_{n,i-1/2} & \quad \text{with } \phi_{n,i} = \frac{\Delta x_i Q_{n,i} + 2\mu_n \phi_{n,i-1/2}}{\Delta x_i \Sigma_i + 2\mu_n} & \text{if } \mu_n > 0. \end{aligned} \quad (370)$$

The procedure generally starts from a vacuum boundary if one exists. A linear shooting approach can be used in other cases, in order to match the boundary incoming and outgoing fluxes at the starting boundary. At the end of each inner iteration, we have obtained matching boundary fluxes for a given set of sources $Q_{\ell,i}$. Inner iterations are required because the scattering rate components in $Q_{\ell,i}$ are generally a function of the flux moments $\phi_{\ell,i}$. Note that outer iterations are also required for convergence to the eigenvalue in criticality cases.

At the end of each inner iteration, the Legendre moments of the flux are computed using (364). These values are used to compute the Legendre moments $Q_{\ell,i}$ of the source for the next iteration.

Combining (370), we eliminate edge-mesh fluxes and obtain

$$\phi_{n,i \mp 1/2} = \frac{2\Delta x_i Q_{n,i} + (2|\mu_n| - \Delta x_i \Sigma_i) \phi_{n,i \pm 1/2}}{\Delta x_i \Sigma_i + 2|\mu_n|}. \quad (371)$$

The resulting mesh-averaged flux becomes negative if the numerator becomes negative. The condition for positive flux $\phi_{n,i}$ is

$$(2|\mu_n| - \Delta x_i \Sigma_i) \phi_{n,i \pm 1/2} < 2\Delta x_i Q_{n,i}. \quad (372)$$

This relation must be valid even for zero sources. The positive flux condition becomes

$$\Delta x_i \Sigma_i < 2|\mu_n|. \quad (373)$$

Negative fluxes can be generated if $\Delta x_i \Sigma_i$ is large or if some values of the base points μ_n are small. They are likely to occur when the mesh sizes are large, in high cross-section zones or with high-order angular quadratures.

There is an equivalence between a spherical harmonics solution of order $N-1$, as presented in [3.1](#), and the S_N solution of a 1D slab geometry. We observe that any discrepancy between the two numerical solutions is only due to the Marshak versus Mark treatment of vacuum-boundary conditions. Infinite lattice solutions are identical.

5.3 The Difference Relations in 1D Cylindrical Geometry

The first-order form of the linear Boltzmann equation in 1D cylindrical geometry is given in (141). After integration over the angular subdomain surrounding direction Ω_n , we obtain

$$\begin{aligned} & \frac{1}{\rho} \int_{\Omega_n} d^2\Omega \mu \frac{\partial}{\partial \rho} [\rho \phi(\rho, \xi, \omega)] - \frac{1}{\rho} \int_{\Omega_n} d^2\Omega \frac{\partial}{\partial \omega} [\eta \phi(\rho, \xi, \omega)] \\ & + \Sigma(\rho) \int_{\Omega_n} d^2\Omega \phi(\rho, \xi, \omega) = \sum_{\ell=0}^L \frac{2\ell+1}{4\pi} \sum_{\substack{m=0 \\ \ell+m \text{ even}}}^{\ell} Q_{\ell}^m(\rho) \int_{\Omega_n} d^2\Omega R_{\ell}^m(\xi, \omega). \end{aligned} \quad (374)$$

In cylindrical geometry, the direction Ω_n is defined in terms of base points ξ_p and $\omega_{p,q}$. The integration must be done over two octants with $N/2$ axial levels in interval $0 \leq \xi \leq 1$. Each axial level contains $2\mathcal{F}(p)$ base points in interval $0 \leq \omega_{p,q} \leq \pi$, with

$$\mathcal{F}(p) = \begin{cases} N/2 & \text{for a product quadrature,} \\ (N/2) - p + 1 & \text{otherwise,} \end{cases} \quad \text{with } 1 \leq p \leq \frac{N}{2} \quad (375)$$

so that the total number of positive-weight discrete directions is equal to $N^2/4$ for a product quadrature and equal to $N(N+2)/4$ otherwise.

The integrals in (374) can be evaluated as


$$\int_{\Omega_n} d^2\Omega \mu \frac{\partial}{\partial \rho} [\rho \phi(\rho, \xi, \omega)] = \mathcal{W}_{p,q} \mu_{p,q} \frac{\partial}{\partial \rho} [\rho \phi(\rho, \xi_p, \omega_{p,q})], \quad (376)$$

$$\begin{aligned} \int_{\Omega_n} d^2\Omega \frac{\partial}{\partial \omega} [\eta \phi(\rho, \xi, \omega)] &= \mathcal{W}_p [\eta_{p,q+1/2} \phi(\rho, \xi_p, \omega_{p,q+1/2}) \\ &\quad - \eta_{p,q-1/2} \phi(\rho, \xi_p, \omega_{p,q-1/2})], \end{aligned} \quad (377)$$

$$\int_{\Omega_n} d^2\Omega \phi(\rho, \xi, \omega) = \mathcal{W}_{p,q} \phi(\rho, \xi_p, \omega_{p,q}) \quad (378)$$

and

$$\int_{\Omega_n} d^2\Omega R_{\ell}^m(\xi, \omega) = \mathcal{W}_{p,q} R_{\ell}^m(\xi_p, \omega_{p,q}). \quad (379)$$

We now present the approach proposed by Alcouffe and O'Dell to compute the $\eta_{p,q\pm 1/2}$ values (Alcouffe and O'Dell 1986). For each level ξ_p , the first value η lies on the ξ - μ plane and is therefore zero. These values correspond to the zero-weight points in  Fig. 25. We can write

$$\eta_{p,2\mathcal{F}(p)+(1/2)} = 0 \quad \text{with } 1 \leq p \leq \frac{N}{2}. \quad (380)$$

The other values of $\eta_{p,q\pm 1/2}$ are obtained in such a way as to preserve the constant flux in a case where an infinite, homogenous, and nonabsorbing medium contains a population

of particles, in the absence of sources. In this case, $\phi(\rho, \xi, \omega) = C$, a constant, and (374) reduces to

$$\mathcal{W}_{p,q} \mu_{p,q} C - \mathcal{W}_p (\eta_{p,q+1/2} C - \eta_{p,q-1/2} C) = 0 \quad (381)$$

so that the $\eta_{p,q\pm 1/2}$ values can be computed recursively using

$$\eta_{p,q+1/2} = \eta_{p,q-1/2} + \frac{\mathcal{W}_{p,q}}{\mathcal{W}_p} \mu_{p,q}. \quad (382)$$

Defining $\alpha_{p,q\pm 1/2} = \mathcal{W}_p \eta_{p,q\pm 1/2}$, the recurrence relation simplifies to

$$\alpha_{p,q+1/2} = \alpha_{p,q-1/2} + \mathcal{W}_{p,q} \mu_{p,q}. \quad (383)$$

Equation (374) can therefore be rewritten as

$$\begin{aligned} \mu_{p,q} \frac{\partial}{\partial \rho} [\rho \phi_{p,q}(\rho)] - \frac{1}{\mathcal{W}_{p,q}} [\alpha_{p,q+1/2} \phi_{p,q+1/2}(\rho) - \alpha_{p,q-1/2} \phi_{p,q-1/2}(\rho)] \\ + \rho \Sigma(\rho) \phi_{p,q}(\rho) = \rho \sum_{\ell=0}^L \frac{2\ell+1}{4\pi} \sum_{\substack{m=0 \\ \ell+m \text{ even}}}^{\ell} Q_{\ell}^m(\rho) R_{\ell}^m(\xi_p, \omega_{p,q}), \end{aligned} \quad (384)$$

where $\phi_{p,q}(\rho) \equiv \phi(\rho, \xi_p, \omega_{p,q})$. The spherical harmonics moments of the flux are given in terms of its S_N components using

$$\phi_{\ell}^m(\rho) = 4 \sum_{p=1}^{N/2} \sum_{q=1}^{2\mathcal{F}(p)} \mathcal{W}_{p,q} \phi_{p,q}(\rho) R_{\ell}^m(\xi_p, \omega_{p,q}), \quad (385)$$

with $0 \leq \ell \leq L$ and $0 \leq m \leq \ell$ with $\ell + m$ even.

The domain is divided in submeshes with constant cross-sections, with $\rho_{1/2} = 0$. The mesh-edge and mesh-centered values of the flux are given as $\phi_{p,q,i\pm 1/2}$ and $\phi_{p,q,i}$, respectively. The volume and surfaces of submesh i are given by

$$V_i = \pi (\rho_{i+1/2}^2 - \rho_{i-1/2}^2) \quad \text{and} \quad S_{i\pm 1/2} = 2\pi \rho_{i\pm 1/2} \quad (386)$$

with $\Delta S_i = S_{i+1/2} - S_{i-1/2}$.

The next step of the discretization procedure is to integrate (384) over each submesh to obtain the following balance relation:

$$\begin{aligned} \mu_{p,q} (S_{i+1/2} \phi_{p,q,i+1/2} - S_{i-1/2} \phi_{p,q,i-1/2}) - \frac{\Delta S_i}{\mathcal{W}_{p,q}} (\alpha_{p,q+1/2} \phi_{p,q+1/2,i} \\ - \alpha_{p,q-1/2} \phi_{p,q-1/2,i}) + V_i \Sigma_i \phi_{p,q,i} = V_i Q_{p,q,i}, \end{aligned} \quad (387)$$

where $1 \leq p \leq N/2$ and $1 \leq q \leq 2\mathcal{F}(p)$. Using (138), the source components are defined as

$$Q_{p,q,i} = \sum_{\ell=0}^L \frac{2\ell+1}{4\pi} \sum_{\substack{m=0 \\ \ell+m \text{ even}}}^{\ell} Q_{\ell,i}^m R_{\ell}^m(\xi_p, \omega_{p,q}) \quad (388)$$

and the mesh-centered values are given by

$$\phi_{p,q,i} = \frac{2\pi}{V_i} \int_{\rho_{i-1/2}}^{\rho_{i+1/2}} d\rho \rho \phi_{p,q}(\rho) \quad \text{and} \quad Q_{\ell,i}^m = \frac{2\pi}{V_i} \int_{\rho_{i-1/2}}^{\rho_{i+1/2}} d\rho \rho Q_{\ell}^m(\rho). \quad (389)$$

In this case, the *diamond-differencing scheme* is written as

$$\phi_{p,q,i} = \frac{1}{2} (\phi_{p,q,i-1/2} + \phi_{p,q,i+1/2}) = \frac{1}{2} (\phi_{p,q-1/2,i} + \phi_{p,q+1/2,i}). \quad (390)$$

We first need knowledge of mesh-centered values of the flux $\phi_{p,1/2,i}$ over the zero-weight points, in order to initialize the recursive solution procedure. We observe that these directions correspond to particles entering the external surface and moving toward the central axis, for discrete values of ξ . The angular redistribution term vanishes on these points so that (139) simplifies to

$$\mu \frac{\partial}{\partial \rho} \phi(\rho, \xi, \pi) + \Sigma(\rho) \phi(\rho, \xi, \pi) = \sum_{\ell=0}^L \frac{2\ell+1}{4\pi} \sum_{\substack{m=0 \\ \ell+m \text{ even}}}^{\ell} Q_{\ell}^m(\rho) R_{\ell}^m(\xi, \pi), \quad (391)$$

where $\omega = \pi$ since the particle is moving toward the central axis. Discretization of (391) leads to

$$2\pi\tilde{\mu}_p (\tilde{\phi}_{p,i+1/2} - \tilde{\phi}_{p,i-1/2}) + \Delta S_i \Sigma_i \tilde{\phi}_{p,i} = \Delta S_i \tilde{Q}_{p,i}, \quad (392)$$

where $\tilde{\phi}_{p,i} \equiv \phi_{p,2\mathcal{F}(p)+(1/2),i}$ and $\tilde{Q}_{p,i} \equiv Q_{p,2\mathcal{F}(p)+(1/2),i}$.

The average flux $\tilde{\phi}_{p,i}$ is given in terms of the right-hand side components as

$$\tilde{\phi}_{p,i} = \frac{\Delta S_i \tilde{Q}_{p,i} - 4\pi\tilde{\mu}_p \tilde{\phi}_{p,i+1/2}}{\Delta S_i \Sigma_i - 4\pi\tilde{\mu}_p}, \quad \tilde{\mu}_p < 0, \quad (393)$$

and the corresponding angular edge values are

$$\tilde{\phi}_{p,i-1/2} = 2\tilde{\phi}_{p,i} - \tilde{\phi}_{p,i+1/2}. \quad (394)$$

At completion of this initialization sweep, the angular edge values are discarded and the mesh-centered values $\tilde{\phi}_{p,i}$ are kept.

The finite-weight points are next processed, taking into account the angular redistribution term. In this case, the average flux $\phi_{p,q,i}$ is given in terms of the right-hand side components as

$$\begin{aligned} \phi_{p,q,i} = & \frac{V_i Q_{p,q,i} - \mu_{p,q} (S_{i-1/2} + S_{i+1/2}) \phi_{p,q,i+1/2}}{V_i \Sigma_i - 2\mu_{p,q} S_{i-1/2} + 2\Delta S_i \alpha_{p,q-1/2} / \mathcal{W}_{p,q}} \\ & + \frac{\Delta S_i (\alpha_{p,q-1/2} + \alpha_{p,q+1/2}) \phi_{p,q+1/2,i} / \mathcal{W}_{p,q}}{V_i \Sigma_i - 2\mu_{p,q} S_{i-1/2} + 2\Delta S_i \alpha_{p,q-1/2} / \mathcal{W}_{p,q}} \end{aligned} \quad (395)$$

if $\mu_{p,q} < 0$. The corresponding edge values are

$$\phi_{p,q,i-1/2} = 2\phi_{p,q,i} - \phi_{p,q,i+1/2} \quad \text{and} \quad \phi_{p,q+1/2,i} = 2\phi_{p,q,i} - \phi_{p,q-1/2,i}. \quad (396)$$




Moreover, the average flux $\phi_{p,q,i}$ is given in terms of the left-hand side components as

$$\begin{aligned} \phi_{p,q,i} = & \frac{V_i Q_{p,q,i} + \mu_{p,q} (S_{i-1/2} + S_{i+1/2}) \phi_{p,q,i-1/2}}{V_i \Sigma_i + 2\mu_{p,q} S_{i+1/2} + 2\Delta S_i \alpha_{p,q-1/2} / \mathcal{W}_{p,q}} \\ & + \frac{\Delta S_i (\alpha_{p,q-1/2} + \alpha_{p,q+1/2}) \phi_{p,q+1/2,i} / \mathcal{W}_{p,q}}{V_i \Sigma_i + 2\mu_{p,q} S_{i+1/2} + 2\Delta S_i \alpha_{p,q-1/2} / \mathcal{W}_{p,q}} \end{aligned} \quad (397)$$

if $\mu_{p,q} > 0$. The corresponding edge values are

$$\phi_{p,q,i+1/2} = 2\phi_{p,q,i} - \phi_{p,q,i-1/2} \quad \text{and} \quad \phi_{p,q+1/2,i} = 2\phi_{p,q,i} - \phi_{p,q-1/2,i}. \quad (398)$$

Equations (396) and (398) are used to iterate the flux for particles moving toward the central axis and the external surface, respectively.

The sweep strategy is represented in  Fig. 27 for a fixed ξ level. The iteration is started by assuming a fixed incoming current (either zero or positive) on the external boundary at ρ_I , for all negative (entering) μ values. These points correspond to symbol \otimes in  Fig. 27. The initialization sweep corresponds to the line with $\omega = \pi$ and is indicated by symbol \circ . Using the same incoming current at all angles leads to the *white-boundary condition*, currently used with cylindrical geometry. Next, for each remaining negative μ direction, we perform a backward sweep (from ρ_I to ρ_1) immediately followed by a forward sweep (from ρ_1 to ρ_I) in the corresponding positive μ direction. The complete inner iteration terminates when the flux is available over each point in  Fig. 27, for all ξ levels.

At the end of each inner iteration, the spherical harmonics moments of the flux are computed using mesh-centered values of the flux in (385). These values are used to compute the spherical harmonics moments $Q_{m,i}^{\ell}$ of the source for the next iteration. The outgoing current

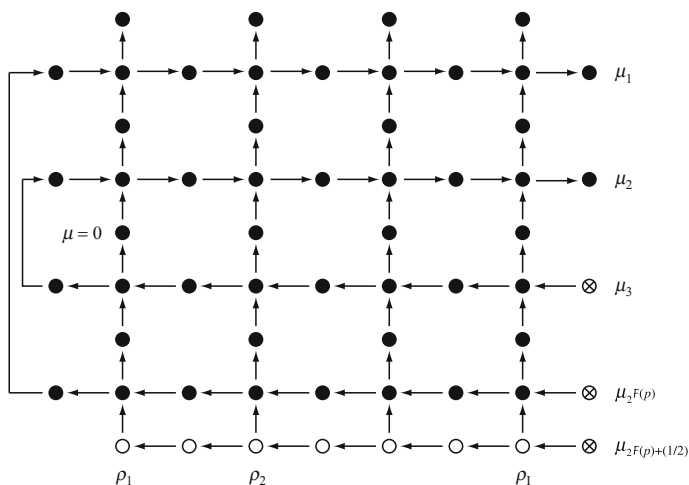


 Figure 27

Sweep strategy for one-dimensional cylindrical geometry

on the external boundary is also computed using mesh-edge values of the boundary flux with

$$J^+ = 4 \sum_{p=1}^{N/2} \sum_{q=1}^{(N/2)-p+1} \mathcal{W}_{p,q} \mu_{p,q} \phi_{p,q,I+1/2}. \quad (399)$$

The boundary flux used to start an elementary sweep is a function of the incoming current $J^- = \beta J^+$ using

$$\phi_{p,q,I+1/2} = \frac{J^-}{4 \sum_{p'=1}^{N/2} \sum_{q'=1}^{(N/2)-p'+1} \mathcal{W}_{p',q'} \mu_{p',q'}} \quad \forall p \text{ and } q, \quad (400)$$

where the denominator is a normalization constant used to ensure particle conservation in cases where the albedo β is set to one. Equation (399) corresponds to a white-boundary condition.

A vacuum-boundary condition is represented by setting $J^- = 0$. In this case, a single pair of backward and forward sweeps is sufficient to compute J^+ and complete a single inner iteration. A reflective ($\beta = 1$) or general albedo-boundary condition involves finding the incoming current matching the outgoing current. This operation can be done with a *shooting method* involving two pairs of backward–forward sweeps. The first pair is performed with $J_{\bar{a}}^- = 0$ and leads to a corresponding value of $J_{\bar{a}}^+$. The second pair is performed with $J_{\bar{b}}^- = 1$ and leads to a corresponding value of $J_{\bar{b}}^+$. Using the linear characteristic of the transport operator, one can obtain the correct value of J^- as

$$J^- = \frac{\beta J_{\bar{a}}^+}{1 + \beta (J_{\bar{a}}^+ - J_{\bar{b}}^+)}. \quad (401)$$

5.4 The Difference Relations in 1D Spherical Geometry

The first-order form of the linear Boltzmann equation in 1D spherical geometry is given in (149). After integration over the angular subdomain, we obtain

$$\begin{aligned} & \frac{1}{r^2} \int_{\mu_{n-1/2}}^{\mu_{n+1/2}} d\mu \mu \frac{\partial}{\partial r} [r^2 \phi(r, \mu)] + \frac{1}{r} \int_{\mu_{n-1/2}}^{\mu_{n+1/2}} d\mu \frac{\partial}{\partial \mu} [(1 - \mu^2) \phi(r, \mu)] \\ & + \Sigma(r) \int_{\mu_{n-1/2}}^{\mu_{n+1/2}} d\mu \phi(r, \mu) = \sum_{\ell=0}^L \frac{2\ell + 1}{2} Q_{\ell}(r) \int_{\mu_{n-1/2}}^{\mu_{n+1/2}} d\mu P_{\ell}(\mu). \end{aligned} \quad (402)$$

In spherical geometry, the base points μ_n and weights \mathcal{W}_n are those of an N -point Gauss–Legendre quadrature.

The integrals in (402) can be evaluated as

$$\int_{\mu_{n-1/2}}^{\mu_{n+1/2}} d\mu \mu \frac{\partial}{\partial r} [r^2 \phi(r, \mu)] = \mathcal{W}_n \mu_n \frac{\partial}{\partial r} [r^2 \phi(r, \mu_n)], \quad (403)$$

$$\int_{\mu_{m-1/2}}^{\mu_{m+1/2}} d\mu \frac{\partial}{\partial \mu} [(1 - \mu^2) \phi(r, \mu)] = [\alpha_{m+1/2} \phi(r, \mu_{m+1/2}) - \alpha_{m-1/2} \phi(r, \mu_{m-1/2})], \quad (404)$$

$$\int_{\mu_{m-1/2}}^{\mu_{m+1/2}} d\mu \phi(r, \mu) = \mathcal{W}_n \phi(r, \mu_n) \quad (405)$$

and

$$\int_{\mu_{m-1/2}}^{\mu_{m+1/2}} d\mu P_\ell(\mu) = \mathcal{W}_n P_\ell(\mu_n). \quad (406)$$

We now present the approach to compute the $\alpha_{n\pm 1/2}$ values. The first value α is equal to $1 - (-1)^2 = 0$. The other values of $\alpha_{n\pm 1/2}$ are obtained in such a way as to preserve the constant flux in a case where an infinite, homogeneous and nonabsorbing medium contains a population of particles, in the absence of sources. In this case, $\phi(r, \mu) = C$, a constant, and (402) reduces to

$$2\mathcal{W}_n \mu_n C + (\alpha_{n+1/2} C - \alpha_{n-1/2} C) = 0 \quad (407)$$

so that the $\alpha_{n\pm 1/2}$ values can be computed recursively using

$$\alpha_{n+1/2} = \alpha_{n-1/2} - 2\mathcal{W}_n \mu_n. \quad (408)$$

Equation (402) can therefore be rewritten as

$$\begin{aligned} \mu_n \frac{\partial}{\partial r} [r^2 \phi_n(r)] + \frac{r}{\mathcal{W}_n} [\alpha_{n+1/2} \phi_{n+1/2}(r) - \alpha_{n-1/2} \phi_{n-1/2}(r)] + r^2 \Sigma(r) \phi_n(r) \\ = r^2 \sum_{\ell=0}^L \frac{2\ell+1}{2} Q_\ell(r) P_\ell(\mu_n), \quad n = 1, N, \end{aligned} \quad (409)$$

where $\phi_n(r) \equiv \phi(r, \mu_n)$. The Legendre moments of the flux are given in terms of its S_N components using

$$\phi_\ell(r) = \sum_{n=1}^N \mathcal{W}_n \phi_n(r) P_\ell(\mu_n) \quad \text{with } 0 \leq \ell \leq L. \quad (410)$$

The domain is divided in submeshes with constant cross-sections, with $r_{1/2} = 0$. The mesh-edge and mesh-centered values of the flux are given as $\phi_{n,i\pm 1/2}$ and $\phi_{n,i}$, respectively. The volume and surfaces of submesh i are given by

$$V_i = \frac{4\pi}{3} (r_{i+1/2}^3 - r_{i-1/2}^3) \quad \text{and} \quad S_{i\pm 1/2} = 4\pi r_{i\pm 1/2}^2 \quad (411)$$

with $\Delta S_i = S_{i+1/2} - S_{i-1/2}$.

The next step of the discretization procedure is to integrate (409) over each submesh to obtain the following balance relation:

$$\begin{aligned} \mu_n (S_{i+1/2} \phi_{n,i+1/2} - S_{i-1/2} \phi_{n,i-1/2}) + \frac{\Delta S_i}{2\mathcal{W}_n} [\alpha_{n+1/2} \phi_{n+1/2,i} - \alpha_{n-1/2} \phi_{n-1/2,i}] \\ + V_i \Sigma_i \phi_{n,i} = V_i Q_{n,i}, \end{aligned} \quad (412)$$

where $1 \leq n \leq N$. Using (147), the source components are defined as

$$Q_{n,i} = \sum_{\ell=0}^L \frac{2\ell+1}{2} Q_{\ell,i} P_{\ell}(\mu_n) \quad (413)$$

and the mesh-centered values are given by

$$\phi_{n,i} = \frac{4\pi}{V_i} \int_{\rho_{i-1/2}}^{r_{i+1/2}} dr r^2 \phi_n(r) \quad \text{and} \quad Q_{\ell,i} = \frac{4\pi}{V_i} \int_{r_{i-1/2}}^{r_{i+1/2}} dr r^2 Q_{\ell}(r). \quad (414)$$

In this case, the *diamond differencing scheme* is written as

$$\phi_{n,i} = \frac{1}{2} (\phi_{n,i-1/2} + \phi_{n,i+1/2}) = \frac{1}{2} (\phi_{n-1/2,i} + \phi_{n+1/2,i}). \quad (415)$$

We first need knowledge of mesh-centered values of the flux $\phi_{1/2,i}$ over the zero-weight points, in order to initialize the recursive-solution procedure. We observe that these directions correspond to particles entering the external surface and moving toward the central axis with $\mu = -1$. The angular redistribution term vanishes on these points so that (148) simplifies to

$$-\frac{\partial}{\partial r} \phi_{-1/2}(r) + \Sigma(r) \phi_{-1/2}(r) = \sum_{\ell=0}^L \frac{2\ell+1}{2} Q_{\ell}(r) P_{\ell}(-1). \quad (416)$$

Discretization of (416) leads to

$$-(\tilde{\phi}_{i+1/2} - \tilde{\phi}_{i-1/2}) + \Delta r_i \Sigma_i \tilde{\phi}_i = \Delta r_i \tilde{Q}_i, \quad (417)$$

where $\tilde{\phi}_i \equiv \phi_{1/2,i}$, $\tilde{Q}_i \equiv Q_{1/2,i}$, and $\Delta r_i = r_{i+1/2} - r_{i-1/2}$.

The average flux $\tilde{\phi}_i$ is given in terms of the right-hand side components as

$$\tilde{\phi}_i = \frac{\Delta r_i \tilde{Q}_i + 2\tilde{\phi}_{i+1/2}}{\Delta r_i \Sigma_i + 2}, \quad (418)$$

and the corresponding angular edge values are

$$\tilde{\phi}_{i-1/2} = 2\tilde{\phi}_i - \tilde{\phi}_{i+1/2}. \quad (419)$$

At completion of this initialization sweep, the angular edge values are thrown away and the mesh-centered values $\phi_{1/2,i}$ are kept.

The finite-weight points are processed next, taking into account the angular redistribution term. In this case, the average flux $\phi_{n,i}$ is given in terms of the right-hand side components as

$$\phi_{n,i} = \frac{V_i Q_{n,i} - \mu_n (S_{i-1/2} + S_{i+1/2}) \phi_{n,i+1/2} + \Delta S_i (\alpha_{n-1/2} + \alpha_{n+1/2}) \phi_{n-1/2,i} / 2\mathcal{W}_n}{V_i \Sigma_i - 2\mu_n S_{i-1/2} + \Delta S_i \alpha_{n+1/2} / \mathcal{W}_n} \quad (420)$$

if $\mu_n < 0$. The corresponding edge values are

$$\phi_{n,i-1/2} = 2\phi_{n,i} - \phi_{n,i+1/2} \quad \text{and} \quad \phi_{n+1/2,i} = 2\phi_{n,i} - \phi_{n-1/2,i}. \quad (421)$$

Moreover, the average flux $\phi_{n,i}$ is given in terms of the left-hand side components as

$$\phi_{n,i} = \frac{V_i Q_{n,i} + \mu_n (S_{i-1/2} + S_{i+1/2}) \phi_{n,i-1/2} + \Delta S_i (\alpha_{n-1/2} + \alpha_{n+1/2}) \phi_{n-1/2,i} / 2 \mathcal{W}_n}{V_i \Sigma_i + 2\mu_n S_{i+1/2} + \Delta S_i \alpha_{n+1/2} / \mathcal{W}_n} \quad (422)$$

if $\mu_n > 0$. The corresponding edge values are

$$\phi_{n,i+1/2} = 2\phi_{n,i} - \phi_{n,i-1/2} \quad \text{and} \quad \phi_{n+1/2,i} = 2\phi_{n,i} - \phi_{n-1/2,i}. \quad (423)$$

Equations (421) and (423) are used to iterate the flux for particles moving toward the central axis and the external surface, respectively. The sweep strategy is identical to the one used in the cylindrical 1D case. At the end of each inner iteration, the Legendre moments of the flux are computed using (410). These values are used to compute the Legendre moments $Q_{\ell,i}$ of the source for the next iteration.

5.5 The Difference Relations in 2D Cartesian Geometry

The first-order form of the linear Boltzmann equation in 2D Cartesian geometry is given in (129). The direction Ω_n is defined in terms of base points μ_n and η_n . The integration must be done over four octants, using $N(N+2)/2$ discrete directions, corresponding to a level-symmetric quadrature. After discretization of the direction cosines, we obtain

$$\left[\mu_n \frac{\partial}{\partial x} + \eta_n \frac{\partial}{\partial y} + \Sigma(x, y) \right] \phi_n(x, y) = \sum_{\ell=0}^L \frac{2\ell+1}{4\pi} \sum_{\substack{m=-\ell \\ \ell+m \text{ even}}}^{\ell} Q_{\ell}^m(x, y) R_{\ell}^m(\Omega_n), \quad (424)$$

$n = 1, N(N+2)/2$, where $\phi_n(x, y) \equiv \phi(x, y, \mu_n, \eta_n)$. The spherical harmonics moments of the flux are given in terms of the S_N components using

$$\phi_{\ell}^m(x, y) = 2 \sum_{n=1}^{N(N+2)/2} \mathcal{W}_n \phi_n(x, y) R_{\ell}^m(\mu_n, \eta_n, \xi_n). \quad (425)$$

The domain is divided in rectangular submeshes $\{i, j\}$ with constant cross-sections. The x -directed mesh-edge and mesh-centered values of the flux are given as $\phi_{n,i\pm 1/2,j}$ and $\phi_{n,i,j}$, respectively. Similar definitions are used along the y -axis. The dimensions of each sub-mesh are

$$\Delta x_i = x_{i+1/2} - x_{i-1/2} \quad \text{and} \quad \Delta y_j = y_{j+1/2} - y_{j-1/2} \quad (426)$$

corresponding to a volume $V_{i,j} = \Delta x_i \Delta y_j$.

The next step of the discretization procedure is to integrate (424) over each submesh to obtain the following balance relation:

$$\frac{\mu_n}{\Delta x_i} (\phi_{n,i+1/2,j} - \phi_{n,i-1/2,j}) + \frac{\eta_n}{\Delta y_j} (\phi_{n,i,j+1/2} - \phi_{n,i,j-1/2}) + \Sigma_{i,j} \phi_{n,i,j} = Q_{n,i,j}, \quad (427)$$

where $n = 1, N(N+2)/2$. Using (128), the source components are defined as

$$Q_{n,i,j} = \sum_{\ell=0}^L \frac{2\ell+1}{4\pi} \sum_{\substack{m=-\ell \\ \ell+m \text{ even}}}^{\ell} Q_{\ell,i,j}^m R_{\ell}^m(\mu_n, \eta_n, \xi_n) \quad (428)$$

and where the mesh-centered values are given by

$$\phi_{n,i,j} = \frac{1}{V_{i,j}} \int_{x_{i-1/2}}^{x_{i+1/2}} dx \int_{y_{j-1/2}}^{y_{j+1/2}} dy \phi_n(x, y) \quad (429)$$

and

$$Q_{\ell,i,j}^m = \frac{1}{V_{i,j}} \int_{x_{i-1/2}}^{x_{i+1/2}} dx \int_{y_{j-1/2}}^{y_{j+1/2}} dy Q_{\ell}^m(x, y). \quad (430)$$

Equation (427) is an exact relation between one mesh-centered and four mesh-edge flux values. Assuming two mesh-edge values, two supplementary equations are required to obtain the other three values. Again, *diamond-differencing scheme* relations are written as

$$\phi_{n,i,j} = \frac{1}{2} (\phi_{n,i-1/2,j} + \phi_{n,i+1/2,j}) = \frac{1}{2} (\phi_{n,i,j-1/2} + \phi_{n,i,j+1/2}). \quad (431)$$

The flux values are computed by following the particle path. The sweep strategy can be described using generic relations. We first define

$$\begin{aligned} \phi_{n,i-,j} &= \begin{cases} \phi_{n,i-1/2,j} & \text{if } \mu > 0, \\ \phi_{n,i+1/2,j} & \text{if } \mu < 0, \end{cases} & \phi_{n,i+,j} &= \begin{cases} \phi_{n,i+1/2,j} & \text{if } \mu > 0, \\ \phi_{n,i-1/2,j} & \text{if } \mu < 0, \end{cases} \\ \phi_{n,i,j-} &= \begin{cases} \phi_{n,i,j-1/2} & \text{if } \eta > 0, \\ \phi_{n,i,j+1/2} & \text{if } \eta < 0, \end{cases} & \phi_{n,i,j+} &= \begin{cases} \phi_{n,i,j+1/2} & \text{if } \eta > 0, \\ \phi_{n,i,j-1/2} & \text{if } \eta < 0, \end{cases} \end{aligned} \quad (432)$$


so that the sweep relations are

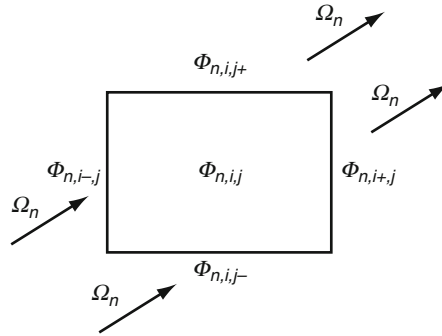
$$\phi_{n,i,j} = \frac{Q_{n,i,j} + (2|\mu_n|/\Delta x_i) \phi_{n,i-,j} + (2|\eta_n|/\Delta y_j) \phi_{n,i,j-}}{\Sigma_{i,j} + (2|\mu_n|/\Delta x_i) + (2|\eta_n|/\Delta y_j)} \quad (433)$$

with

$$\phi_{n,i+,j} = 2\phi_{n,i,j} - \phi_{n,i-,j} \quad \text{and} \quad \phi_{n,i,j+} = 2\phi_{n,i,j} - \phi_{n,i,j-}. \quad (434)$$

The sweep relations can be solved without iterations, provided that the angular flux is known on the domain boundary. The numerical approximation of the flux $\phi_{n,i,j}$ in each mesh, for a given angle Ω_n , is computed from the known components of the source $Q_{n,i,j}$ and from the incoming fluxes $\phi_{n,i-,j}$ and $\phi_{n,i,j-}$ using (433). The outgoing flux components $\phi_{n,i+,j}$ and $\phi_{n,i,j+}$ are computed from (434). The outgoing flux from a cell is the incoming flux of the following mesh in the direction of the traveling particle.

The spatial swapping starts from the boundary meshes where the angular flux is known and proceeds forward in the direction of the particle, as depicted in  Fig. 28. We selected sides $X+$ and $Y+$ as starting boundaries, so that we expect that any vacuum-boundary condition shall be assigned to these two sides in priority. The particles are next assumed to reflect on $X-$ and $Y-$ boundaries (possibly with an albedo condition) and pursue their path toward the $X+$ and $Y+$ boundaries. If a nonvacuum boundary condition is assigned on $X+$ or $Y+$ boundaries, initial flux components are assumed to initiate the spatial swapping on these surfaces. These initial values are taken as equal to one or are recovered from the last inner iteration. No shooting approach is used in 2D Cartesian geometry, so that we need to keep the S_N boundary fluxes $\phi_{n,i+,j}$ and $\phi_{n,i,j+}$ on $X+$ and $Y+$ in the unknown vector, in addition to the spherical harmonic moments $\phi_{\ell,i,j}^m$ inside the domain.



■ Figure 28

Cartesian 2D spatial swapping. The spatial swapping start from the boundary meshes where the angular flux is known and proceed forward in the direction of the particle

At the end of each inner iteration, the spherical harmonics moments of the flux are computed using mesh-centered values of the flux in (425). These values are used to compute the spherical harmonic moments $Q_{m,i,j}^\ell$ of the source for the next iteration.

The above procedure can be generalized to higher spatial discretization orders. The *diamond-differencing scheme* can be written at quadratic and cubic orders for Cartesian approximations (Hébert 2006).

As pointed out in an important paper by Lathrop, the discrete ordinates method in 2D and 3D suffers from a limitation called *ray effect* (Lathrop 1968). The ray effect is an oscillation of the flux distribution about its exact value that can be observed in cases with very little scattering and localized sources. This is caused by the discretization of the angular variable over precise directions Ω_n , producing a numerical solution which is represented as a sum of delta distributions in angle although the exact solution is a continuous distribution in angle. Ray effects do not occur in 1D geometries, since even a plane source produces uncollided neutrons traveling in all $\mu > 0$ and $\mu < 0$ directions (Lewis and Miller 1984). The most straightforward approach to reduce ray effects is to simply increase the order of the discrete ordinates approximation, at the cost of increased CPU resources.

5.6 Synthetic Acceleration

The particle source distribution $Q(\mathbf{r}, \Omega)$ appearing in the right-hand side of the transport equation is written in terms of the within-group scattering-reaction rate using

$$Q(\mathbf{r}, \Omega_n) = \sum_{\ell=0}^L \frac{2\ell+1}{4\pi} \sum_{m=-\ell}^{\ell} [\Sigma_{w,\ell}(\mathbf{r}) \phi_l^m(\mathbf{r}) + Q_\ell^{\diamond m}(\mathbf{r})] R_\ell^m(\Omega_n), \quad (435)$$

where $\Sigma_{w,\ell}(\mathbf{r})$ is the ℓ th Legendre moment of the macroscopic within-group scattering cross-section, $\phi_l^m(\mathbf{r})$ is a spherical harmonic component of the flux, and $Q_\ell^{\diamond m}(\mathbf{r})$ is a spherical harmonic component of the source representing other contributions such as fission and out-of-group scattering rates. Scattering source iterations are always required with the discrete

ordinates method because the flux component $\phi_l^m(\mathbf{r})$ is obtained in terms of the dependent variable using (425). Introducing an iteration index (κ), the basic *scattering source iterative scheme* is written as

$$\begin{aligned} & \Omega \cdot \nabla \phi^{(\kappa+1)}(\mathbf{r}, \Omega) + \Sigma(\mathbf{r}) \phi^{(\kappa+1)}(\mathbf{r}, \Omega) \\ &= \sum_{\ell=0}^L \frac{2\ell+1}{4\pi} \sum_{m=-\ell}^{\ell} \left[\Sigma_{w,\ell}(\mathbf{r}) \phi_l^{m,(\kappa)}(\mathbf{r}) + Q_{\ell}^{\diamond m}(\mathbf{r}) \right] R_{\ell}^m(\Omega), \end{aligned} \quad (436)$$

where $\phi_l^{m,(\kappa)}(\mathbf{r})$ are the spherical harmonic flux component computed from the S_N components of the flux obtained at the (κ)th iteration.

As pointed out in Alcouffe (1977), the fixed-point convergence of (436) becomes difficult when the scattering ratio approaches one, a situation that occurs in the presence of purely scattering media. In this case, Alcouffe proposed a preconditioning known as *synthetic acceleration*, based on the following scheme:

$$\begin{aligned} & \Omega \cdot \nabla \phi^{(\kappa+1/2)}(\mathbf{r}, \Omega) + \Sigma(\mathbf{r}) \phi^{(\kappa+1/2)}(\mathbf{r}, \Omega) \\ &= \sum_{\ell=0}^L \frac{2\ell+1}{4\pi} \sum_{m=-\ell}^{\ell} \left[\Sigma_{w,\ell}(\mathbf{r}) \phi_l^{m,(\kappa)}(\mathbf{r}) + Q_{\ell}^{\diamond m}(\mathbf{r}) \right] R_{\ell}^m(\Omega), \end{aligned} \quad (437)$$

$$\begin{aligned} & \Omega \cdot \nabla \delta \phi^{(\kappa+1/2)}(\mathbf{r}, \Omega) + \Sigma(\mathbf{r}) \delta \phi^{(\kappa+1/2)}(\mathbf{r}, \Omega) \\ & - \sum_{\ell=0}^L \frac{2\ell+1}{4\pi} \sum_{m=-\ell}^{\ell} \Sigma_{w,\ell}(\mathbf{r}) \delta \phi_l^{m,(\kappa+1/2)}(\mathbf{r}) R_{\ell}^m(\Omega) \\ &= \sum_{\ell=0}^L \frac{2\ell+1}{4\pi} \sum_{m=-\ell}^{\ell} \Sigma_{w,\ell}(\mathbf{r}) \left[\phi_l^{m,(\kappa+1/2)}(\mathbf{r}) - \phi_l^{m,(\kappa)}(\mathbf{r}) \right] R_{\ell}^m(\Omega) \end{aligned} \quad (438)$$

and

$$\phi^{(\kappa+1)}(\mathbf{r}, \Omega) = \phi^{(\kappa+1/2)}(\mathbf{r}, \Omega) + \delta \phi^{(\kappa+1/2)}(\mathbf{r}, \Omega). \quad (439)$$

The above scheme leads to the converged solution of the within-group transport equation in only one iteration, provided that (438) can be solved. This fact can be easily demonstrated by adding (437) and (438) and by canceling the term in $\phi_l^{m,(\kappa)}(\mathbf{r})$. However, (438) is just as difficult to solve as the original transport equation itself. The approach proposed by Alcouffe is to replace (438) by a form of the transport equation that is simpler to solve. He proposed to use a compatible *diffusion equation*, leading to the *diffusion-synthetic acceleration* (DSA) scheme. In his work, (438) is replaced by

$$\begin{aligned} & -\nabla \cdot \frac{1}{3\Sigma(\mathbf{r})} \nabla \delta \phi^{(\kappa+1/2)}(\mathbf{r}) + [\Sigma(\mathbf{r}) - \Sigma_{w,0}(\mathbf{r})] \delta \phi^{(\kappa+1/2)}(\mathbf{r}) \\ &= \Sigma_{w,0}(\mathbf{r}) \left[\phi_0^{0,(\kappa+1/2)}(\mathbf{r}) - \phi_0^{0,(\kappa)}(\mathbf{r}) \right]. \end{aligned} \quad (440)$$

The spherical harmonic flux component with $m = \ell = 0$ at iteration ($\kappa + 1$) are set as

$$\phi_0^{0,(\kappa+1)}(\mathbf{r}) = \phi_0^{0,(\kappa+1/2)}(\mathbf{r}) + \delta \phi^{(\kappa+1/2)}(\mathbf{r}). \quad (441)$$

Alcouffe also pointed out that not any discretization scheme can be used to solve (440). Only specific differentiation approaches are compatible with the diamond-differencing scheme used to solve (437). A compatible diffusion approximation consists in setting $L = 0$ in (438) and using a Raviart-Thomas discretization of the P_1 spherical harmonic equations with Gauss-Legendre integration of the mass matrices, as explained in Hébert (2006). This type of discretization has the greatest compatibility with the diamond-differencing scheme.

Specific attention should be made to the S_N boundary fluxes used to represent nonvacuum boundary conditions in Cartesian 2D geometry. These components of the unknown vector must be accelerated using a relation similar to (441). The solution of the DSA equation is evaluated on each boundary point \mathbf{r}_s and is applied isotropically on each angular component n using

$$\phi_n^{(\kappa+1)}(\mathbf{r}_s) = \phi_n^{(\kappa+1/2)}(\mathbf{r}_s) + \frac{1}{4\pi} \delta\phi^{(\kappa+1/2)}(\mathbf{r}_s). \quad (442)$$

It is important to note that the above synthetic acceleration scheme is equivalent to a preconditioning of the nonaccelerated scheme in (436). We first recognize that (438) or (440) can be written in matrix-operator form as

$$\mathbb{D} \delta\Phi^{(\kappa+1/2)} = \mathbb{E}(\Phi^{(\kappa+1/2)} - \Phi^{(\kappa)}), \quad (443)$$

where Φ (or $\delta\Phi$) is a column vector containing all the spherical harmonic components of the flux (or of the flux increments) in the domain. Equations (437) and (443) can be rewritten in matrix-operator form as

$$\begin{aligned} \Phi^{(\kappa+1/2)} &= \mathbb{W} \Phi^{(\kappa)} + \mathbf{S}, \\ \Phi^{(\kappa+1)} &= \Phi^{(\kappa)} + \mathbb{M}(\Phi^{(\kappa+1/2)} - \Phi^{(\kappa)}) \end{aligned} \quad (444)$$

so that

$$\Phi^{(\kappa+1)} = \Phi^{(\kappa)} + \mathbb{M}(\mathbf{S} - \mathbb{A}\Phi^{(\kappa)}), \quad (445)$$

where

$$\mathbb{M} = \mathbb{I} + \mathbb{D}^{-1} \mathbb{E} \quad \text{and} \quad \mathbb{A} = \mathbb{I} - \mathbb{W}. \quad (446)$$

Equation (445) is a standard preconditioned fixed-point recursion. Setting $\mathbb{M} = \mathbb{I}$ reduces the preconditioned form to the nonaccelerated scheme in (436). This form is compatible with an acceleration procedure based on the minimization of its residual. The *Livolant acceleration* and GMRES(m) methods are efficient acceleration procedures based on this principle. The Livolant method is the simplest approach, requiring minimal storage resources. The GMRES(m) is more efficient at reducing the total number of iterations but relies on sophisticated orthogonalization processes (Saad and Schultz Kelley 1986; 1995).

6 The Method of Characteristics

The method of characteristics (MOC) solves the characteristic form of the transport equation by following the straight neutron paths of the neutral particle as it moves across the complete domain (Askew 1972). This approach is based on an iterative calculation of the particle flux by

solving the transport equation over tracks crossing the complete domain. The MOC is generally applied to the multigroup form of the transport equation and to spatial domains made of regions with piecewise-uniform nuclear properties. The scalar flux per region and energy group is constructed by collecting all mean angular fluxes in terms of the entering angular flux and the source inside the region. Interestingly, the MOC has the capability to use the same tracking information as the collision probability method.

The MOC offers an alternative to the collision probability (CP) method in order to overcome its two main limitations: (1) the CP method produces full square matrices of order equal to the number of regions in the domain, and (2) the CP method is limited to isotropic sources in the LAB. In particular, the MOC is to be preferred in cases where the number of regions exceeds a few hundred.

The application of the MOC to reactor physics was first reported by Askew (1972), followed by a first-production implementation, known as the CACTUS module of WIMS-E (Halsall 1980). CACTUS is based on the concept of *cyclic tracking* where the characteristics are infinite in length and periodic with respect to the lattice. The same idea of periodic characteristics has also been implemented in the MOCC module of DRAGON V3 (Roy 1998) and MCCG module of DRAGON V4 (Le Tellier and Hébert 2006).

Another class of characteristic solvers is based on the explicit representation of boundary conditions and on the use of finite-length characteristics. This class of solvers is noticeably faster than those based on the cyclic-tracking approach and is used in production lattice calculations. The most widely known implementations are those of codes CASMO-4 Knott and Edenius (1993) and MCCG3D (Suslov 1993). Similar techniques were subsequently implemented in codes APOLLO2 (Sanchez and Chetaine 2000) and DRAGON (Wu and Roy 2003). We have chosen to present this approach in the upcoming subsections.

Our presentation of the MOC follows the terminology and the guidelines proposed by Roy (1998). Many technical details have been recovered from Le Tellier (2006).

6.1 The MOC Integration Strategy

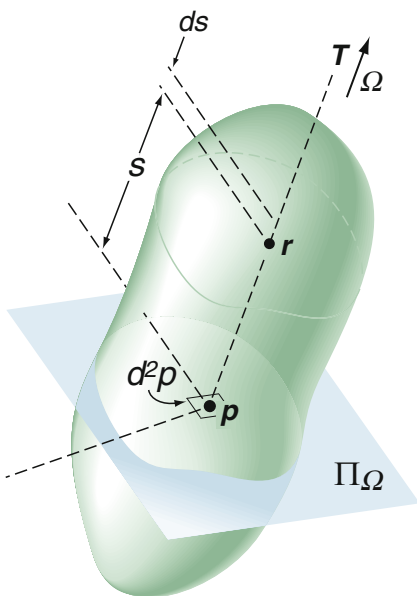
The backward *characteristic form of the transport equation* was obtained as (49) in 1.2. The one-speed and steady-state form of this equation is written as

$$\frac{d}{ds} \phi(\mathbf{r} + s \boldsymbol{\Omega}, \boldsymbol{\Omega}) + \Sigma(\mathbf{r} + s \boldsymbol{\Omega}) \phi(\mathbf{r} + s \boldsymbol{\Omega}, \boldsymbol{\Omega}) = Q(\mathbf{r} + s \boldsymbol{\Omega}, \boldsymbol{\Omega}) \quad (447)$$

where \mathbf{r} is the starting point of the particle, s is the distance traveled by the particle on its characteristic, $\boldsymbol{\Omega}$ is the direction of the characteristic, $\Sigma(\mathbf{r})$ is the value of the macroscopic total cross-section at \mathbf{r} , $\phi(\mathbf{r}, \boldsymbol{\Omega})$ is the particle angular flux at \mathbf{r} , and $Q(\mathbf{r}, \boldsymbol{\Omega})$ is the fixed source at \mathbf{r} .

The spatial integration domain is partitioned into regions of volume $\{V_i; i = 1, I\}$, each of them characterized by uniform nuclear properties and surrounded by boundary surfaces $\{S_\alpha; \alpha = 1, \Lambda\}$. The MOC is based on the discretization of (447) along each path of the particle and on the integration of the flux contributions using spatial integrals of the form

$$\begin{aligned} V_i \phi_i &= \int_{V_i} d^3 r \int_{4\pi} d^2 \Omega \phi(\mathbf{r}, \boldsymbol{\Omega}) \\ &= \int_Y d^4 T \int_{-\infty}^{\infty} ds \chi_{V_i}(T, s) \phi(\mathbf{p} + s \boldsymbol{\Omega}, \boldsymbol{\Omega}) \end{aligned} \quad (448)$$

where ϕ_i is the average flux in region i and $Y = \{T\}$ is the tracking domain. A single characteristic T is determined by its orientation Ω and its starting point p defined on a reference plane Π_Ω perpendicular to T , as depicted in  Fig. 29. The characteristics are selected in domain $Y = 4\pi \times \Pi_\Omega$ which is characterized by an order-four differential $d^4 T = d^2 \Omega d^2 p$. The local coordinate s defines the distance of point r with respect to plane Π_Ω . Finally, the characteristic function $\chi_{V_i}(T, s)$ is equal to 1 if point $p + s\Omega$ of characteristic T is located inside V_i , and zero otherwise.

The MOC requires knowledge of region indices N_k and segment lengths ℓ_k describing the overlapping of characteristic T with the domain. This information is written as $\{N_k, \ell_k; k = 1, K\}$, where K is the total number of regions crossed by T . It is important to note that segment lengths ℓ_k are *always* defined in 3D, even for prismatic 2D geometries. The intersection points of a characteristic with the region boundaries, and the corresponding angular flux on these boundaries, are written as

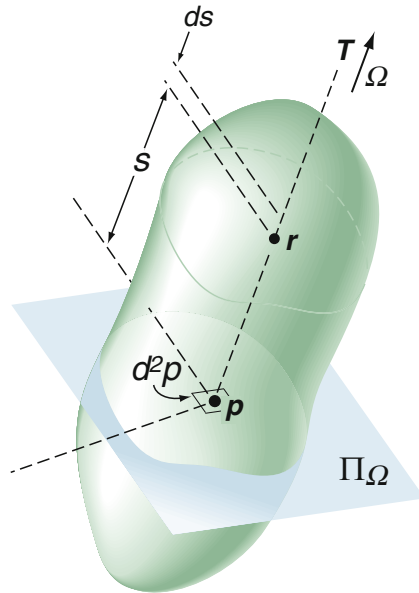
$$\mathbf{r}_{k+1} = \mathbf{r}_k + \ell_k \Omega, \quad k = 1, K \quad (449)$$


and

$$\phi_k(T) = \phi(\mathbf{r}_k, \Omega), \quad k = 1, K + 1. \quad (450)$$

The average flux over each segment is defined as

$$\bar{\phi}_k(T) = \frac{1}{\ell_k(T)} \int_0^{\ell_k(T)} ds \phi(\mathbf{r}_k + s \Omega, \Omega), \quad k = 1, K. \quad (451)$$



 **Figure 29**
Spatial integration domain

Using this relation, it is possible to rewrite (448) as

$$V_i \phi_i = \int_Y d^4 T \sum_k \delta_{iN_k} \ell_k(\mathbf{T}) \bar{\phi}_k(\mathbf{T}), \quad (452)$$

where δ_{ij} is the Kronecker delta function and where the summation over k is performed over all the existing indices. All the characteristics \mathbf{T} are spanned in (452), but only those that effectively cross region i contribute to the integral.

Using the same approach that leads to (452), the volume of region i is written as

$$4\pi V_i = \int_Y d^4 T \sum_k \delta_{iN_k} \ell_k(\mathbf{T}). \quad (453)$$

The MOC equations also use the average fixed source over each segment, defined as

$$\bar{Q}_k(\mathbf{T}) = \frac{1}{\ell_k(\mathbf{T})} \int_0^{\ell_k(\mathbf{T})} ds Q(\mathbf{r}_k + s \boldsymbol{\Omega}, \boldsymbol{\Omega}), \quad k = 1, K. \quad (454)$$

Based on (449), \mathbf{r}_1 and \mathbf{r}_{K+1} are the incoming and outgoing boundary points for \mathbf{T} . The incoming (-) and outgoing (+) boundary currents are given as

$$\begin{aligned} \frac{S_\alpha}{4} \varphi_\alpha^- &= - \int_{\partial D_\alpha} d^2 r_\alpha \int_{\boldsymbol{\Omega} \cdot \mathbf{N}_\alpha < 0} d^2 \boldsymbol{\Omega} (\boldsymbol{\Omega} \cdot \mathbf{N}_\alpha) \phi(\mathbf{r}_\alpha, \boldsymbol{\Omega}), \\ \frac{S_\beta}{4} \varphi_\beta^+ &= \int_{\partial D_\beta} d^2 r_\beta \int_{\boldsymbol{\Omega} \cdot \mathbf{N}_\beta > 0} d^2 \boldsymbol{\Omega} (\boldsymbol{\Omega} \cdot \mathbf{N}_\beta) \phi(\mathbf{r}_\beta, \boldsymbol{\Omega}), \end{aligned} \quad (455)$$

where \mathbf{r}_α is a point of the domain boundary ∂D_α and \mathbf{N}_α is an outgoing unit normal vector at that point. The corresponding MOC integrals are written

$$\begin{aligned} \frac{S_\alpha}{4} \varphi_\alpha^- &= - \int_Y d^4 T \chi_\alpha(\mathbf{T}, \mathbf{r}_1) \phi_1(\mathbf{T}), \\ \frac{S_\beta}{4} \varphi_\beta^+ &= \int_Y d^4 T \chi_\beta(\mathbf{T}, \mathbf{r}_{K+1}) \phi_{K+1}(\mathbf{T}), \end{aligned} \quad (456)$$

where the characteristic function $\chi_\alpha(\mathbf{T}, \mathbf{r})$ is equal to 1 if point \mathbf{r} of characteristic \mathbf{T} is located on surface ∂D_α , and zero otherwise.

Using the same approach that leads to (456), the values of surfaces α and β are written as

$$\pi S_\alpha = \int_Y d^4 T \chi_\alpha(\mathbf{T}, \mathbf{r}_1) \quad \text{and} \quad \pi S_\beta = \int_Y d^4 T \chi_\beta(\mathbf{T}, \mathbf{r}_{K+1}). \quad (457)$$

The MOC is similar to a discrete ordinates approach in the way the integrals in $d^4 T$ are handled. These integrals are systematically replaced by weighted summations of the form

$$\int_Y d^4 T f(\mathbf{T}) \simeq 4\pi \sum_{m=1}^M \omega_m f(\mathbf{T}_m), \quad (458)$$

where M is the number of discrete characteristic. The discrete characteristic \mathbf{T}_m and weights ω_m are recovered from a collision probability-type tracking, but defined in 3D.

Each characteristic T_m is associated with another one of opposite direction. In the practical implementation of the MOC, only characteristics with $\Omega > 0$ are computed and stored, so that every available characteristic travels two ways, back and forth.

These numerical quadratures can also be applied to the evaluation of volumes and surfaces, using (453) and (457), respectively. These approximate values are used as a denominator to normalize the MOC quadratures, leading to the following values of ϕ_i , φ_α^- and φ_β^+ :

$$\frac{\phi_i}{4\pi} = \frac{\sum_{m=1}^M \omega_m \sum_k \delta_{iN_k} \ell_k(T_m) \bar{\phi}_k(T_m)}{\sum_{m=1}^M \omega_m \sum_k \delta_{iN_k} \ell_k(T_m)} \quad (459)$$

and

$$\begin{aligned} \frac{\varphi_\alpha^-}{4\pi} &= -\frac{\sum_{m=1}^M \omega_m \chi_\alpha(T_m, \mathbf{r}_1) \phi_1(T_m)}{\sum_{m=1}^M \omega_m \chi_\alpha(T_m, \mathbf{r}_1)}, \\ \frac{\varphi_\beta^+}{4\pi} &= \frac{\sum_{m=1}^M \omega_m \chi_\beta(T_m, \mathbf{r}_{K+1}) \phi_{K+1}(T_m)}{\sum_{m=1}^M \omega_m \chi_\beta(T_m, \mathbf{r}_{K+1})}. \end{aligned} \quad (460)$$

Integration of the characteristics (447) requires a hypothesis concerning the spatial variation of the fixed source along each characteristic T . The *step-characteristic* (SC) *scheme* is a widely used approximation written as

$$Q(\mathbf{r}_k + s \mathbf{\Omega}, \mathbf{\Omega}) = Q_{N_k}(\mathbf{\Omega}); \quad \forall s \in [0, \ell_k]. \quad (461)$$

The SC scheme is prevalent for the following reasons: (1) The SC scheme is *positive*, leading to positive values for $Q_i(\mathbf{\Omega})$, $\phi_k(T)$, and $\bar{\phi}_k(T)$. (2) The SC scheme leads to a number of unknowns equal to the number of regions plus the number of boundary surfaces; more advanced schemes may require storing an amount of information proportional to the tracking. (3) The SC scheme has the same level of approximation as the collision probability method. (4) The SC scheme is conservative.

Introduction of the SC scheme in the characteristics in (447) and integration of the resulting equation over a single segment ℓ_k leads to the following analytical solution for the segment-boundary and segment-averaged fluxes:

$$\begin{aligned} \phi_{k+1}(T) &= \mathcal{A}_k(T) \phi_k(T) + \mathcal{B}_k(T) Q_{N_k}(\mathbf{\Omega}), \\ \bar{\phi}_k(T) &= \frac{1}{\ell_k} [\mathcal{B}_k(T) \phi_k(T) + \mathcal{C}_k(T) Q_{N_k}(\mathbf{\Omega})], \end{aligned} \quad (462)$$

where the SC coefficients are written as,

(a) $\Sigma_{N_k} \neq 0$:

$$\begin{aligned}\mathcal{A}_k(\mathbf{T}) &= e^{-\tau_k(\mathbf{T})}, \\ \mathcal{B}_k(\mathbf{T}) &= \frac{1}{\Sigma_{N_k}} \left(1 - e^{-\tau_k(\mathbf{T})}\right), \\ \mathcal{C}_k(\mathbf{T}) &= \frac{\ell_k(\mathbf{T})}{\Sigma_{N_k}} \left(1 - \frac{1 - e^{-\tau_k(\mathbf{T})}}{\tau_k(\mathbf{T})}\right),\end{aligned}\quad (463)$$

(b) $\Sigma_{N_k} = 0$:

$$\mathcal{A}_k(\mathbf{T}) = 1, \quad \mathcal{B}_k(\mathbf{T}) = \ell_k(\mathbf{T}), \quad \text{and} \quad \mathcal{C}_k(\mathbf{T}) = \frac{\ell_k(\mathbf{T})^2}{2}.\quad (464)$$

Equation (463) use the optical paths $\tau_k(\mathbf{T})$ defined as

$$\tau_k(\mathbf{T}) = \Sigma_{N_k} \ell_k(\mathbf{T}).\quad (465)$$

In the case of an isotropic source in the LAB, (462) is rewritten as

$$\begin{aligned}\phi_{k+1}(\mathbf{T}) &= \mathcal{A}_k(\mathbf{T}) \phi_k(\mathbf{T}) + \frac{1}{4\pi} \mathcal{B}_k(\mathbf{T}) Q_{N_k}, \\ \bar{\phi}_k(\mathbf{T}) &= \frac{1}{\ell_k} \left[\mathcal{B}_k(\mathbf{T}) \phi_k(\mathbf{T}) + \frac{1}{4\pi} \mathcal{C}_k(\mathbf{T}) Q_{N_k} \right],\end{aligned}\quad (466)$$

where Q_i is written in terms of fission, out-of-group scattering and/or fixed sources Q_i^\diamond , and macroscopic within-group scattering cross-sections $\Sigma_{w,i}$ using

$$Q_i = Q_i^\diamond + \Sigma_{w,i} \phi_i.\quad (467)$$

Substitution of (466b) into (459) leads to

$$\phi_i = \mathcal{P}_{ii} Q_i + 4\pi \frac{\sum_{m=1}^M \omega_m \sum_k \delta_{iN_k} \mathcal{B}_k(\mathbf{T}_m) \phi_k(\mathbf{T}_m)}{\sum_{m=1}^M \omega_m \sum_k \delta_{iN_k} \ell_k(\mathbf{T}_m)},\quad (468)$$

where we defined the *self-collision factor* \mathcal{P}_{ii} as

$$\mathcal{P}_{ii} = \frac{\sum_{m=1}^M \omega_m \sum_k \delta_{iN_k} \mathcal{C}_k(\mathbf{T}_m)}{\sum_{m=1}^M \omega_m \sum_k \delta_{iN_k} \ell_k(\mathbf{T}_m)}.\quad (469)$$

The self-collision factor should not be confused with the collision probability component p_{ii} introduced in [Sect. 4](#). The self-collision factor is computed using only the particle paths that are not intercepting regions with indices other than i . All the self-collision factors can be computed in the assembly phase of the transport calculation, outside the scattering iterations.

The MOC integration strategy can be further simplified by performing a partial scattering reduction based on (467). It is written as

$$\begin{aligned} \phi_i &= \frac{1}{1 - \sum_{w,i} \mathcal{P}_{ii}} \left[\mathcal{P}_{ii} Q_i^\diamond + 4\pi \frac{\sum_{m=1}^M \omega_m \sum_k \delta_{iN_k} \mathcal{B}_k(\mathbf{T}_m) \phi_k(\mathbf{T}_m)}{\sum_{m=1}^M \omega_m \sum_k \delta_{iN_k} \ell_k(\mathbf{T}_m)} \right], \\ \phi_\alpha^- &= -4\pi \frac{\sum_{m=1}^M \omega_m \chi_\alpha(\mathbf{T}_m, \mathbf{r}_1) \phi_1(\mathbf{T}_m)}{\sum_{m=1}^M \omega_m \chi_\alpha(\mathbf{T}_m, \mathbf{r}_1)}, \\ \phi_\beta^+ &= 4\pi \frac{\sum_{m=1}^M \omega_m \chi_\beta(\mathbf{T}_m, \mathbf{r}_{K+1}) \phi_{K+1}(\mathbf{T}_m)}{\sum_{m=1}^M \omega_m \chi_\beta(\mathbf{T}_m, \mathbf{r}_{K+1})}, \end{aligned} \quad (470)$$

where the swapping relations are simplified to

$$\phi_{k+1}(\mathbf{T}) = \mathcal{A}_k(\mathbf{T}) \phi_k(\mathbf{T}) + \frac{1}{4\pi} \mathcal{B}_k(\mathbf{T}) Q_{N_k}. \quad (471)$$

This approach based on self-collision factors is referred to as the *source isolation method* in (Le Tellier 2006). It can be generalized to anisotropic cases by introducing angular-dependent self-collision factors.

There is one more issue of the MOC that is worth mentioning. It is possible to replace the SC scheme with a *diamond-differencing scheme* similar to (369). Using this relation, the average flux on a track segment is assumed to be

$$\bar{\phi}_k(\mathbf{T}) = \frac{1}{2} [\phi_k(\mathbf{T}) + \phi_{k+1}(\mathbf{T})]. \quad (472)$$

The diamond-differencing (DD) scheme leads to the same (462) with the corresponding coefficients now written as

$$\begin{aligned} \mathcal{A}_k(\mathbf{T}) &= \frac{2 - \tau_k(\mathbf{T})}{2 + \tau_k(\mathbf{T})}, \\ \mathcal{B}_k(\mathbf{T}) &= \frac{2\ell_k(\mathbf{T})}{2 + \tau_k(\mathbf{T})}, \\ \mathcal{C}_k(\mathbf{T}) &= \frac{\ell_k(\mathbf{T})^2}{2 + \tau_k(\mathbf{T})}. \end{aligned} \quad (473)$$

As pointed out by Suslov, the DD scheme can be obtained from the SC scheme by performing a Padé approximation of the exponential function (Suslov 1997). Suslov has shown that the DD scheme is related to the linear characteristic (LC) scheme, based on the assumption that the angular flux varies linearly in each region. Assuming that the slope of the fixed sources is proportional to the slope of the flux, the LC scheme reduces to the DD scheme. Consequently, the DD scheme has numerical properties that make it more accurate than the SC scheme in many practical situations. Another successful linear scheme is the linear surface characteristic (LSC) scheme proposed by Santandrea and Mosca (2006).

6.2 Unstructured 2D Finite Geometry

Let us consider an unstructured finite geometry in the x - y plane, infinite and uniform along the z -axis. This type of geometry is commonly used in lattice codes. The projection on the x - y plane is performed as depicted in **Fig. 30**. The direction of the particle is $\Omega = \sin \theta \cos \varepsilon \mathbf{i} + \sin \theta \sin \varepsilon \mathbf{j} + \cos \theta \mathbf{k}$. Integration over θ is possible by taking the projection of each particle free path on the x - y plane. The differential element $d^4 T$ is written as

$$d^4 T = d^2 p d^2 \Omega = dr (\sin \theta dr) (\sin \theta d\varepsilon) d\theta. \quad (474)$$

Defining $\mu = \cos \theta$ and $d^2 T_{xy} = dr d\varepsilon$, (474) can be rewritten as

$$d^4 T = d^2 T_{xy} \sin^2 \theta d\theta dz. \quad (475)$$

The tracking domain $Y_{xy} = \{T_{xy}\}$ is now defined in the x - y plane. The discrete tracking information $\{T_{xy,m}; m = 1, M\}$ is computed using the *same* tracking operator available with the collision probability method in unstructured 2D finite geometry. A useful example of 2D tracking is presented in Appendices **Sects. 3** and **4** for the particular case of a square pincell geometry.

The 3D track lengths corresponding to the tabulated segments are given as

$$\ell_k(T) = \frac{\ell_k(T_{xy})}{\sin \theta} \quad (476)$$

so that (452) and (456) are now written as

$$V_i \phi_i = 2 \int_{Y_{xy}} d^2 T \sum_k \delta_{iN_k} \ell_k(T_{xy}) \int_0^{\pi/2} d\theta \sin \theta \check{\phi}_k(T) \quad (477)$$

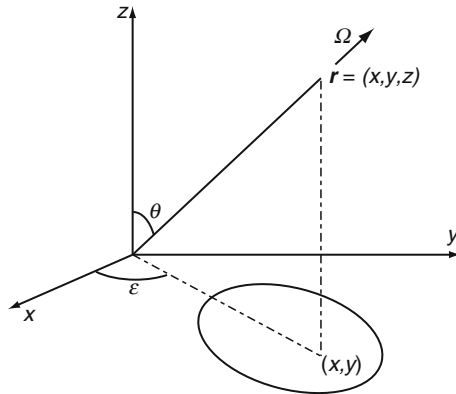


Figure 30


Projection of a particle trajectory on the x - y plane. The polar angle θ is used to define the direction cosine of the particle relative to the z -axis

and

$$\begin{aligned}\frac{S_\alpha}{4} \varphi_\alpha^- &= -2 \int_{Y_{xy}} d^2 T \chi_\alpha(\mathbf{T}_{xy}, \mathbf{r}_1) \int_0^{\pi/2} d\theta \sin^2 \theta \phi_1(\mathbf{T}), \\ \frac{S_\beta}{4} \varphi_\beta^+ &= 2 \int_{Y_{xy}} d^2 T \chi_\beta(\mathbf{T}_{xy}, \mathbf{r}_{K+1}) \int_0^{\pi/2} d\theta \sin^2 \theta \phi_{K+1}(\mathbf{T}).\end{aligned}\quad (478)$$

Leonard and McDaniel (1995) introduced *optimized polar quadratures* for the MOC, in such a way as to generate numerical results close to those obtained via the collision probability method with isotropic scattering. They proposed approaches to obtain quadratures that optimize the integration of *Bickley functions*, as defined in (282). Later, the two-base point Leonard–McDaniel optimized polar quadratures were generalized to three and four base points in Le Tellier and Hébert (2008). These quadratures are written as

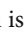
$$\int_0^{\pi/2} d\theta \sin \theta f\left(\frac{1}{\sin \theta}\right) \simeq \sum_{\lambda=1}^L \mathcal{W}_\lambda f(z_\lambda), \quad (479)$$

where θ is the polar angle depicted in  Fig. 30. Using this quadrature, the $Ki_3(x)$ function is approximated as

$$Ki_3(x) = \int_0^{\pi/2} d\theta \sin^2 \theta e^{-\frac{x}{\sin \theta}} \simeq \sum_{\lambda=1}^L \mathcal{W}_\lambda e^{z_\lambda x}. \quad (480)$$

The Leonard–McDaniel-optimized polar quadratures can be recovered from the following Matlab script:

```
function [zmu,wzmu]=lmcd(nmu)
% set the Leonard-McDaniel quadrature base points and weights
% function [zmu,wzmu]=lmcd(nmu)
% (c) 2008 Alain Hebert, Ecole Polytechnique de Montreal
if nmu == 2
    zmu=[1.15511584 3.65419436 ]; wzmu=[ 0.744970262 0.03816792 ];
elseif nmu == 3
    zmu=[ 1.12178171 2.52822733 10.0188332 ];
    wzmu=[ 0.707642138 0.0745818987 0.00175868778 ];
elseif nmu == 4
    zmu=[ 1.10098934 2.15439725 6.02394629 23.7072144 ];
    wzmu=[ 0.677962959 0.10134203 0.00533553911 0.000130677523 ];
else
    error('invalid number of base points.')
end
```

where variables K , z_λ , and \mathcal{W}_λ are represented by Matlab variables `nmu`, `zmu`, and `wzmu`, respectively. Errors observed in the (480) evaluation are plotted in  Fig. 31. Other optimized polar quadratures are presented in Le Tellier and Hébert (2008) for situations with source anisotropy.

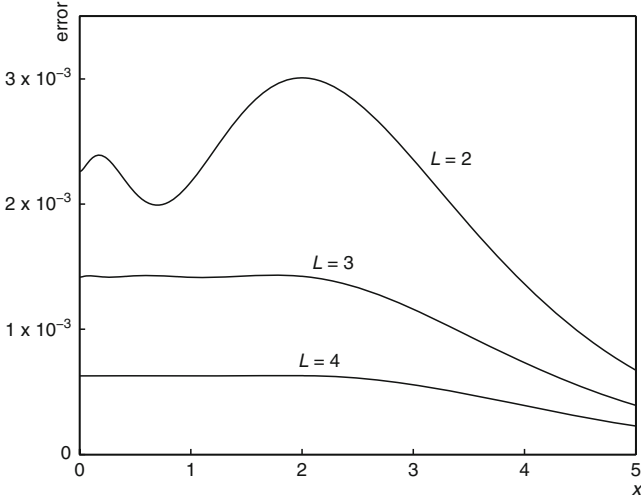


Figure 31 Error of the Leonard–McDaniel quadratures for evaluating $Ki_3(x)$ functions

Using the polar quadrature of (479), (470) are now rewritten as

$$\begin{aligned} \phi_i &= \frac{1}{1 - \sum_{w,i} \mathcal{P}_{ii}} \left[\mathcal{P}_{ii} Q_i^\diamond + 4\pi \frac{\sum_{m=1}^M \omega_m \sum_k \delta_{iN_k} \sum_{\lambda=1}^L \mathcal{W}_\lambda \mathcal{B}_k(\mathbf{T}_m) \phi_k(\mathbf{T}_m)}{\sum_{m=1}^M \omega_m \sum_k \delta_{iN_k} \sum_{\lambda=1}^L \mathcal{W}_\lambda \ell_k(\mathbf{T}_m)} \right], \\ \phi_\alpha^- &= -4\pi \frac{\sum_{m=1}^M \omega_m \chi_\alpha(\mathbf{T}_m, \mathbf{r}_1) \sum_{\lambda=1}^L \mathcal{W}_\lambda \phi_1(\mathbf{T}_m)}{\sum_{m=1}^M \omega_m \chi_\alpha(\mathbf{T}_m, \mathbf{r}_1) \sum_{\lambda=1}^L \mathcal{W}_\lambda}, \\ \phi_\beta^+ &= 4\pi \frac{\sum_{m=1}^M \omega_m \chi_\beta(\mathbf{T}_m, \mathbf{r}_{K+1}) \sum_{\lambda=1}^L \mathcal{W}_\lambda \phi_{K+1}(\mathbf{T}_m)}{\sum_{m=1}^M \omega_m \chi_\beta(\mathbf{T}_m, \mathbf{r}_{K+1}) \sum_{\lambda=1}^L \mathcal{W}_\lambda}, \end{aligned} \tag{481}$$

where the self-collision factors are now written as

$$\mathcal{P}_{ii} = \frac{\sum_{m=1}^M \omega_m \sum_k \delta_{iN_k} \sum_{\lambda=1}^L \mathcal{W}_\lambda \mathcal{C}_k(\mathbf{T}_m)}{\sum_{m=1}^M \omega_m \sum_k \delta_{iN_k} \sum_{\lambda=1}^L \mathcal{W}_\lambda \ell_k(\mathbf{T}_m)}, \tag{482}$$

and where

$$\ell_k(\mathbf{T}_m) = z_\lambda \ell_k(\mathbf{T}_{xy,m}). \tag{483}$$

The self-collision factors \mathcal{P}_{ii} are not a function of the fluxes or sources. They are computed during the assembly phase of the calculation using the algorithm reproduced in Matlab script `mcppii`. The tracking in `track` is produced using the script `sybt2d` of Appendix Section 3 for a square pincell. The script parameters are defined as

`track`=tracking information,
`sig`=array of size `nreg` containing the macroscopic total cross-sections,
`nmu`=order of the optimized polar quadrature, and
`pii`=array of size `nreg` containing the self-collision factors.

The script `mcgp ii` is written as

```
function pii=mcgp ii(track,sigt,nmu)
% compute the pii components for source isolation with the MOC.
% function pii=mcgp ii(track,sigt,nmu)
% (c) 2008 Alain Hebert, Ecole Polytechnique de Montreal
nreg=track(2); nbtr=track(4);
[zmu,wzmu]=lmcd(nmu);
k=5+track(1)+track(2)+2*track(3);
volnum=zeros(nreg,1); pii=zeros(nreg,1);
for iline=1:nbtr
    weitf=track(k+4); km=track(k+5); kgar=k+5; k=k+5+km;
    nom=track(kgar+1:kgar+km); htf=track(k+1:k+km); h=zeros(1,km);
    for imu=1:nmu
        ww=weitf*wzmu(imu); h(:)=htf(:).*zmu(imu);
        b=mcgscs(nom,h,sigt);
        for i=1:km
            nomi=nom(i);
            volnum(nomi)=volnum(nomi)+h(i)*ww;
            pii(nomi)=pii(nomi)+b(2,i)*ww;
        end
    end
    k=k+km;
end
pii=pii./volnum;
```

where the script `mcgscs` is implemented as

```
function b=mcgscs(nom,h,xst)
% calculate coefficients of a track for the characteristics integration.
% step-characteristic scheme with exact exponential calls.
% function b=mcgscs(nom,h,xst)
% (c) 2008 Alain Hebert, Ecole Polytechnique de Montreal
km=length(h); b=zeros(2,km);
for i=1:km
    nomi=nom(i);
    if xst(nomi) == 0.
        b(1,i)=h(i);
        b(2,i)=0.5*h(i)^2;
```

```

else
    b(1,i)=(1.-exp(-h(i)*xst(nomi)))/xst(nomi);
    b(2,i)=(h(i)-b(1,i))/xst(nomi);
end
end
end

```

The basic algorithm for computing the fluxes and interface current in the innermost scattering iteration is reproduced in Matlab script `mcgsis`. The script parameters are defined as

`phi` = dependent variables. The first `nsurf` components of column array `phi` contain the interface currents and the following `nreg` components contain the fluxes ϕ_i in each region.

`q` = source array. The array `q` of length `nreg` contains Q_i^\diamond , the fission, out-of-group scattering, and/or fixed sources.

`track` = tracking information.

`sigt` = array of size `nreg` containing the macroscopic total cross-sections.

`sigw` = array of size `nreg` containing the macroscopic within-group scattering cross-sections.

`pii` = self-collision factors as computed by script `mcgpii`.

`nmu` = order of the optimized polar quadrature.

The script `mcgsis` is written as

```

function phi=mcgsis(phi,q,track,sigt,sigw,pii,nmu)
% single MOC scattering iteration with source isolation
% function phi=mcgsis(phi,q,track,sigt,sigw,pii,nmu)
% (c) 2008 Alain Hebert, Ecole Polytechnique de Montreal
    nsurf=track(1); nreg=track(2); nbtr=track(4);
    s=q+phi.*[ones(1,nsurf) sigw]';
    [zmu,wzmu]=lmcd(nmu);
%--
%      flux calculation
%--
    k=5+track(1)+track(2)+2*track(3);
    volsur=zeros(nsurf+nreg,1); phi=zeros(nsurf+nreg,1);
    for iline=1:nbtr
        isurf=track(k+2); jsurf=track(k+3); weitf=track(k+4); km=track(k+5);
        kgar=k+5; k=k+5+km;
        nom=track(kgar+1:kgar+km); htf=track(k+1:k+km); h=zeros(1,km);
        for imu=1:nmu
            ww=weitf*wzmu(imu); h(:)=htf(:).*zmu(imu);
            b=mcgscs(nom,h,sigt);
            rp=s(isurf); rm=s(jsurf);
            for i=1:km
                nomi=nom(i);
                volsur(nsurf+nomi)=volsur(nsurf+nomi)+2.*h(i)*ww;
            end
        end
    end
end

```

```

    phi(nsurf+nomi)=phi(nsurf+nomi)+b(1,i)*rp*ww ;
    rp=rp+b(1,i)*(s(nsurf+nomi)-sigt(nomi)*rp);
end
for i=km:-1:1
    nomi=nom(i) ;
    phi(nsurf+nomi)=phi(nsurf+nomi)+b(1,i)*rm*ww ;
    rm=rm+b(1,i)*(s(nsurf+nomi)-sigt(nomi)*rm) ;
end
phi(jsurf)=phi(jsurf)+rp*ww ; phi(isurf)=phi(isurf)+rm*ww ;
volsur(jsurf)=volsur(jsurf)+ww ; volsur(isurf)=volsur(isurf)+ww ;
end
k=k+km ;
end
phi=phi./volsur ;
unk=phi(nsurf+1:nsurf+nreg)+pii.*q(nsurf+1:nsurf+nreg) ;
phi(nsurf+1:nsurf+nreg)=unk./(ones(nreg,1)-pii.*sigw') ;

```

The largest fraction of CPU resources required to execute the MOC algorithm is spent in script `mcgscs` and in the two inner loops of script `mcgsls`. These few lines of code must be highly optimized to ensure a good performance for production calculations. The `mcgscs` script requires the evaluation of $\exp(x)$ and $\mathcal{B}_k(T)$ functions. It is recommended to compute these functions from piecewise linear or parabolic fits instead of using the hardwired $\exp(x)$ operator of the CPU.

It is possible to analytically integrate the MOC equations in polar angle θ , leading to a version of the MOC written in terms of $Ki_3(x)$ functions instead of exponentials. Such a method leads to numerical results equivalent to those obtained with a polar quadrature, as L goes to infinity. However, Bickley functions do not satisfy the same properties as exponentials, so that $Ki_3(x+y) \neq Ki_3(x)Ki_3(y)$. Consequently, the practical implementation of a script similar to `mcgsls` would require the addition of an inner loop of the form “for $j=i-1:-1:1$ ” and “for $j=i+1:km$ ” inside the “for $i=1:km$ ” and “for $i=km:-1:1$ ” loops, respectively. The extra loops make this MOC inefficient if too many tracks have a number of segments greater than K .

Once the MOC single-iteration capability is implemented, the complete scattering iteration can be set using a fixed-point iterative approach. A free-iteration fixed-point approach would be implemented as

```
[phi err iter]=free(phi,q,'mcgsls',errtol,maxit,track,sigt,sigw,pii,nmu)
```

where the Matlab script `free` is programmed as

```

function [x, error, iter] = free(x, b, atv, errtol, maxit, varargin)
% free-iteration linear equation solver
% function [x, error, total_iters] = free(x0, b, atv, errtol, maxit, varargin)
% input parameters:
% x    initial iterate

```



```

% b   right-hand side
% atv character name of a matrix-vector product routine returning x+(b-Ax)
%     when x is input. The format for atv is "function x = atv(x,b,p1,p2,...)"
%     where p1 and p2 are optional parameters
% errtol relative residual reduction factor
% maxit maximum number of iterations
% varargin optional parameters (p1,p2,...) for atv
% output parameters:
% x     solution of the linear system
% error vector of residual norms for the history of the iteration
% iter  number of iterations
% (c) 2007 Alain Hebert, Ecole Polytechnique de Montreal
errtol=errtol*norm(b);
error=[];
rho=Inf;
iter=0;
while((rho > errtol) && (iter < maxit))
    iter=iter+1;
    r=feval(atv,x,b,varargin)-x;
    rho=norm(r); error=[error;rho];
    x=x+r;
end

```

6.3 The Algebraic Collapsing Acceleration

The algebraic collapsing acceleration (ACA) method was introduced by Suslov as a general technique for the acceleration of the MOC in 2D and 3D (see Suslov 1993; Le Tellier and Hébert 2007). The core of the ACA is the solution of a simplified transport equation, referred to as the ACA operator, leading to even-parity fluxes similar to those obtained with the diffusion theory. The discretization process is based on a weighted summation of all trajectories over the global angular domain. The resulting sparse matrix system, of order $\Lambda + I$, can be scattering reduced and solved for the even-parity flux and boundary currents. The solution of the sparse matrix system requires only small computer resources and is therefore a good candidate for synthetic acceleration. The scattering iteration of the MOC is preconditioned with the ACA operator using the synthetic acceleration approach already presented in [5.5](#).

Other types of simplified transport equations have been used within a synthetic acceleration approach, leading to competing acceleration strategies. The asymptotic synthetic acceleration (ASA) and DP_1 acceleration methods, based on the interface current formalism of [4.1](#), are alternative approaches proposed in Sanchez and Chetaine (2000), Santandrea and Sanchez (2002) and Santandrea and Sanchez (2005). A presentation of ASA and DP_1 strategies is outside the scope of this handbook.

The ACA operator is based on a set of relations between the isotropic flux and boundary currents on a single track. Each of these relations is expected to couple an unknown with its

two neighbors, leading to a tridiagonal matrix system for the single-track unknown numbering. The contribution of all tracks T_m and the introduction of the global unknown numbering lead to a sparse matrix system that can be solved using sparse matrix algebra techniques.

We first obtain the tridiagonal matrix system for a single-track T . Any function of the position s can be written in terms of even- and odd-parity functions, defined as

$$f^s(T, s) = \frac{1}{2} [f(T, s) + f(-T, s)] \quad \text{and} \quad f^a(T, s) = \frac{1}{2} [f(T, s) - f(-T, s)]. \quad (484)$$

The k th segment on track T is located between positions s_k and s_{k+1} . Using (462), the segment-boundary and segment-averaged flux are related as

$$\bar{\phi}_k(T) = \frac{1 + \alpha(T)}{2} \phi_{k+1}(T) + \frac{1 - \alpha(T)}{2} \phi_k(T), \quad (485)$$

$$\bar{\phi}_k(-T) = \frac{1 - \alpha(T)}{2} \phi_{k+1}(-T) + \frac{1 + \alpha(T)}{2} \phi_k(-T), \quad (486)$$

where $k = 1, K$. The coefficient $\alpha_k(T)$ is written in terms of the SC or DD coefficients as

$$\alpha(T) = \frac{2}{1 - \mathcal{A}(T)} - \frac{2}{\tau_k(T)} - 1 \quad (487)$$

with the asymptotic limit

$$\lim_{\tau_k \rightarrow 0} \alpha(T) = 0. \quad (488)$$

Equation (486) is substituted into (484), leading to a first set of flux relations:

$$\bar{\phi}_k^s(T) = \frac{1}{2} [\phi_{k+1}^s(T) + \phi_k^s(T) + \alpha(T) (\phi_{k+1}^a(T) - \phi_k^a(T))], \quad (489)$$

$$\bar{\phi}_k^a(T) = \frac{1}{2} [\phi_{k+1}^a(T) + \phi_k^a(T) + \alpha(T) (\phi_{k+1}^s(T) - \phi_k^s(T))]. \quad (490)$$

A second set of flux equations can now be obtained. The integration of the characteristics in (447) over the k th segment leads to

$$\phi_{k+1}(T) - \phi_k(T) + \tau_k(T) \bar{\phi}_k(T) = \frac{\ell_k(T)}{4\pi} Q_{N_k}, \quad (491)$$

where we assumed an isotropic source. Equation (490) can be rewritten in terms of $-T$, leading to its even- and odd-parity formulation. We have obtained

$$\phi_{k+1}^a(T) - \phi_k^a(T) + \tau_k(T) \bar{\phi}_k^s(T) = \frac{\ell_k(T)}{4\pi} Q_{N_k}, \quad (492)$$

$$\phi_{k+1}^s(T) - \phi_k^s(T) + \tau_k(T) \bar{\phi}_k^a(T) = 0. \quad (493)$$

Substitution of (490) into (493) leads to

$$\phi_{k+1}^s(T) = \phi_k^s(T) - \frac{\tau_k(T)}{2 + \tau_k(T) \alpha_k(T)} (\phi_k^a(T) + \phi_{k+1}^a(T)). \quad (494)$$

Substitution of (494) and (489) into (492) leads to

$$\phi_k^s(\mathbf{T}) = \zeta_k(\mathbf{T}) \phi_k^a(\mathbf{T}) + (1 - \tilde{b}_k(\mathbf{T})) \bar{\phi}_k^s(\mathbf{T}) + b_k(\mathbf{T}) \frac{Q_{N_k}}{4\pi}, \quad (495)$$

where

$$\zeta_k(\mathbf{T}) = \frac{\tau_k(\mathbf{T})}{2 + \tau_k(\mathbf{T}) \alpha_k(\mathbf{T})}, \quad b_k(\mathbf{T}) = \frac{\ell_k(\mathbf{T})}{2} (\zeta_k(\mathbf{T}) - \alpha_k(\mathbf{T})) \quad (496)$$

and

$$\tilde{b}_k(\mathbf{T}) = b_k(\mathbf{T}) \Sigma_{N_k}. \quad (497)$$

Similarly, we can show that

$$\phi_{k+1}^s(\mathbf{T}) = -\zeta_k(\mathbf{T}) \phi_{k+1}^a(\mathbf{T}) + (1 - \tilde{b}_k(\mathbf{T})) \bar{\phi}_k^s(\mathbf{T}) + b_k(\mathbf{T}) \frac{Q_{N_k}}{4\pi}. \quad (498)$$

We combine (495) for segment k with (498) for segment $k - 1$, so that

$$\begin{aligned} \phi_k^a(\mathbf{T}) = & \frac{1}{\zeta_{k-1}(\mathbf{T}) + \zeta_k(\mathbf{T})} \left[(1 - \tilde{b}_{k-1}(\mathbf{T})) \bar{\phi}_{k-1}^s(\mathbf{T}) - (1 - \tilde{b}_k(\mathbf{T})) \bar{\phi}_k^s(\mathbf{T}) \right. \\ & \left. + \left(b_{k-1}(\mathbf{T}) \frac{Q_{N_{k-1}}}{4\pi} - b_k(\mathbf{T}) \frac{Q_{N_k}}{4\pi} \right) \right]. \end{aligned} \quad (499)$$

Next, we combine (495) for segment $k + 1$ with (498) for segment k , so that

$$\begin{aligned} \phi_{k+1}^a(\mathbf{T}) = & \frac{1}{\zeta_k(\mathbf{T}) + \zeta_{k+1}(\mathbf{T})} \left[(1 - \tilde{b}_k(\mathbf{T})) \bar{\phi}_k^s(\mathbf{T}) - (1 - \tilde{b}_{k+1}(\mathbf{T})) \bar{\phi}_{k+1}^s(\mathbf{T}) \right. \\ & \left. + \left(b_k(\mathbf{T}) \frac{Q_{N_k}}{4\pi} - b_{k+1}(\mathbf{T}) \frac{Q_{N_{k+1}}}{4\pi} \right) \right]. \end{aligned} \quad (500)$$

Finally, the boundary conditions can be written in terms of fixed incoming currents \mathcal{J}_1^- and \mathcal{J}_{K+1}^- , and of albedo values β_1 and β_{K+1} at each end of track \mathbf{T} . They are written as

$$\phi_1(\mathbf{T}) = \mathcal{J}_1^-(\mathbf{T}) + \beta_1 \phi_1(-\mathbf{T}') \quad \text{and} \quad \phi_{K+1}(-\mathbf{T}) = \mathcal{J}_{K+1}^-(-\mathbf{T}) + \beta_{K+1} \phi_{K+1}(\mathbf{T}'), \quad (501)$$

where \mathbf{T}' is the *mirror image* track corresponding to a specular reflection of track \mathbf{T} on the boundary. Here, we will assume $\mathbf{T}' \equiv \mathbf{T}$ which is consistent with the hypothesis of a *white-boundary condition*. The weighted summation approach of the ACA naturally leads to white-boundary conditions. The even- and odd-parity boundary fluxes are therefore written as

$$\phi_1^a(\mathbf{T}) = \frac{1}{2} [\mathcal{J}_1^-(\mathbf{T}) - (1 - \beta_1) \phi_1(-\mathbf{T})], \quad (502)$$

$$\phi_{K+1}^a(\mathbf{T}) = \frac{1}{2} [-\mathcal{J}_{K+1}^-(-\mathbf{T}) + (1 - \beta_{K+1}) \phi_{K+1}(\mathbf{T})] \quad (503)$$

and

$$\phi_1^s(\mathbf{T}) = \frac{1}{2} [\mathcal{J}_1^-(\mathbf{T}) + (1 + \beta_1) \phi_1(-\mathbf{T})], \quad (504)$$

$$\phi_{K+1}^s(\mathbf{T}) = \frac{1}{2} [\mathcal{J}_{K+1}^-(\mathbf{T}) + (1 + \beta_{K+1}) \phi_{K+1}(\mathbf{T})]. \quad (505)$$

Substitution of (499), (500), (502), and (503) into (492) leads to K ACA relations, one for each segment of \mathbf{T} . Two relations are still missing to close our linear system. The first is obtained by combining (495) for segment 1 with (502) and (504). The second is obtained by combining (498) for segment K with (503) and (505).

The ACA linear system is written in terms of global unknown numbering for the flux, outgoing boundary current, and source components. We are representing the starting and ending surfaces of \mathbf{T} as α_{st} and α_{end} , respectively. The relation between the local and global numbering is set as

$$\phi_1(-\mathbf{T}) = \frac{1}{4\pi} \varphi_{\alpha_{st}}^+, \quad \phi_{K+1}(\mathbf{T}) = \frac{1}{4\pi} \varphi_{\alpha_{end}}^+, \quad \text{and} \quad \mathcal{J}_1^-(\mathbf{T}) = \frac{1}{4\pi} J_{\alpha_{st}}^-, \quad (506)$$

$$\mathcal{J}_{K+1}^-(\mathbf{T}) = \frac{1}{4\pi} J_{\alpha_{end}}^- \quad \text{and} \quad \bar{\phi}_k^s(\mathbf{T}) = \frac{1}{4\pi} \phi_{N_k}. \quad (507)$$

The complete linear system for a single track \mathbf{T}_m is made of $2 + K$ relations. The dependence of parameters on \mathbf{T}_m has been removed to simplify the notation. The ACA linear system is written as

$$\frac{1}{2} [1 + \beta_{\alpha_{st}} + \zeta_1(1 - \beta_{\alpha_{st}})] \varphi_{\alpha_{st}}^+ - (1 - \bar{b}_1) \phi_{N_1} = -\frac{1}{2} (1 - \zeta_1) J_{\alpha_{st}}^- + b_1 Q_{N_1} \quad (508)$$

$$\frac{1}{2} [1 + \beta_{\alpha_{end}} + \zeta_K(1 - \beta_{\alpha_{end}})] \varphi_{\alpha_{end}}^+ - (1 - \bar{b}_K) \phi_{N_K} = -\frac{1}{2} (1 - \zeta_K) J_{\alpha_{end}}^- + b_K Q_{N_K}. \quad (509)$$

If $K = 1$:

$$\frac{1}{2} (1 - \beta_{\alpha_{st}}) \varphi_{\alpha_{st}}^+ + \tau_1 \phi_{N_1} + \frac{1}{2} (1 - \beta_{\alpha_{end}}) \varphi_{\alpha_{end}}^+ = \frac{1}{2} J_{\alpha_{st}}^- + \ell_1 Q_{N_1} + \frac{1}{2} J_{\alpha_{end}}^- \quad (510)$$

If $K > 1$:

$$\begin{aligned} & \frac{1}{2} (1 - \beta_{\alpha_{st}}) \varphi_{\alpha_{st}}^+ + \left(\frac{1 - \bar{b}_1}{\zeta_1 + \zeta_2} + \tau_1 \right) \phi_{N_1} - \frac{1 - \bar{b}_2}{\zeta_1 + \zeta_2} \phi_{N_2} \\ & = \frac{1}{2} J_{\alpha_{st}}^- - \left(\frac{b_1}{\zeta_1 + \zeta_2} - \ell_1 \right) Q_{N_1} + \frac{b_2}{\zeta_1 + \zeta_2} Q_{N_2}, \end{aligned} \quad (511)$$

$$\begin{aligned} & - \frac{1 - \bar{b}_{k-1}}{\zeta_{k-1} + \zeta_k} \phi_{N_{k-1}} + \left[\left(\frac{1}{\zeta_{k-1} + \zeta_k} + \frac{1}{\zeta_k + \zeta_{k+1}} \right) (1 - \bar{b}_k) + \tau_k \right] \phi_{N_k} \\ & - \frac{1 - \bar{b}_{k+1}}{\zeta_k + \zeta_{k+1}} \phi_{N_{k+1}} = \frac{b_{k-1}}{\zeta_{k-1} + \zeta_k} Q_{N_{k-1}} - \left[\left(\frac{1}{\zeta_{k-1} + \zeta_k} + \frac{1}{\zeta_k + \zeta_{k+1}} \right) b_k - \ell_k \right] Q_{N_k} \\ & + \frac{b_{k+1}}{\zeta_k + \zeta_{k+1}} Q_{N_{k+1}}, \quad k = 1, K - 1 \end{aligned} \quad (512)$$

and

$$\begin{aligned}
 & -\frac{1-\tilde{b}_{K-1}}{\zeta_{K-1}+\zeta_K}\phi_{N_{K-1}}+\left(\frac{1-\tilde{b}_K}{\zeta_{K-1}+\zeta_K}+\tau_K\right)\phi_{N_K}+\frac{1}{2}(1-\beta_{\alpha_{\text{end}}})\varphi_{\alpha_{\text{end}}}^+ \\
 & =\frac{b_{K-1}}{\zeta_{K-1}+\zeta_K}Q_{N_{K-1}}-\left(\frac{b_K}{\zeta_{K-1}+\zeta_K}-\ell_K\right)Q_{N_K}+\frac{1}{2}J_{\alpha_{\text{end}}}^-.
 \end{aligned} \tag{513}$$

Equations (508) to (513) can be obtained for a single-track T_m and written as

$$\mathbb{A}_m \Phi_m = \mathbb{B}_m \mathbf{Q}_m, \tag{514}$$

where the first Λ components of Φ_m and \mathbf{Q}_m are related to boundary surfaces and the following I components are related to regions. The coefficients of the above linear system are computed for *each* track T_m . The source components are written in terms of \mathbf{Q}_m^\diamond (fission, out-of-group scattering, and/or fixed sources) and in terms of within-group scattering sources, so that

$$\mathbf{Q}_m = \mathbf{Q}_m^\diamond + \mathbb{S} \Phi_m, \tag{515}$$

where $\mathbb{S} = \text{diag}\{0; \alpha = 1, \Lambda \text{ and } \Sigma_{w,i}; i = 1, I\}$ is a diagonal matrix containing the macroscopic within-group scattering cross-sections in each region. The first Λ diagonal terms of \mathbb{S} are set to zero.

The linear system (514) is equivalent to the MOC solution on a single track. The ACA approximation comes from the weighted summation of all individual \mathbb{A}_m and \mathbb{B}_m matrices, assuming the isotropy of flux and boundary currents. Individual matrices are weighted with the ω_m -values of (458) and summed as

$$\mathbb{A} = \sum_m \omega_m \mathbb{A}_m \quad \text{and} \quad \mathbb{B} = \sum_m \omega_m \mathbb{B}_m, \tag{516}$$

so that the ACA approximation leads to a unique sparse matrix system written as

$$\mathbb{A} \Phi = \mathbb{B} \mathbf{Q} = \mathbb{B} (\mathbf{Q}^\diamond + \mathbb{S} \Phi). \tag{517}$$

A scattering reduction can be performed on (517), so that

$$\Phi = \tilde{\mathbb{A}}^{-1} \mathbb{B} \mathbf{Q}^\diamond, \tag{518}$$

where the scattering-reduced matrix $\tilde{\mathbb{A}}$ is defined as

$$\tilde{\mathbb{A}} = \mathbb{A} - \mathbb{B} \mathbb{S}. \tag{519}$$

Equation (518) is the ACA discretization of the one-speed transport equation for neutral particles. It can be used to obtain an approximate solution of the flux and outgoing boundary currents as required in our synthetic acceleration method.

The synthetic ACA is implemented in three phases:

1. The sparsity graph of matrices $\tilde{\mathbb{A}}$ and \mathbb{B} is only a function of the tracking. It is independent of the particle energy and can therefore be obtained at the end of the tracking operation.

Obtaining the sparsity graph at this point greatly reduces the CPU resources required to construct matrices $\tilde{\mathbb{A}}$ and \mathbb{B} in production calculations. This phase is omitted in our simple Matlab implementation.

2. The construction of matrices $\tilde{\mathbb{A}}$ and \mathbb{B} in sparse storage mode and their incomplete factorization is performed in the assembly phase of the calculation, just after the calculation of the self-collision factors \mathcal{P}_{ii} .

This construction of matrices \mathbb{A} and \mathbb{B} can be implemented in Matlab using the script `mcgaca` taking as input the tracking (`track`), the macroscopic total cross sections (`sigt`), the polar quadrature order (`nmu`), and the albedo (`beta`). The programming of this script is left as an exercise for the reader. Scattering reduction of matrix \mathbb{A} is performed next, using the macroscopic within-group scattering cross-sections (`sigw`). Then, an incomplete LU factorization of matrix $\tilde{\mathbb{A}}$ is performed in such a way as to avoid any fill-in. These operations are set in Matlab as

```
pii=mcgpri(track,sigt,nmu);
beta=1.0; [A B]=mcgaca(track,sigt,nmu,beta);
A=sparse(A-B*diag([zeros(nsurf,1); sigw']));
[L1 U1]=luinc(A,'0');
```

3. An ACA-preconditioned scattering iteration can be set, using information already available from the assembly phase. The preconditioning operations are based on Eqs. (437) to (439). This step makes use of incomplete LU factors obtained previously and the solution of (518) is based on the *Bi-CGSTAB* algorithm (see Kelley 1995). It is possible to combine the ACA preconditioning with Livolant or GMRES(m) acceleration in order to further reduce the number of scattering iterations. We are using a special version of script `gmres_m`, as implemented in (Hébert 2009). Here, our Matlab prototype is based on ACA preconditioning together with GMRES(m) convergence of the scattering iterations:

```
phi=[zeros(track(1),1); ones(track(2),1)];
errtol=1.e-10; maxit=300;
[phi err iter]=gmres_m(phi,q,'mcgsis_aca',errtol,nstart,maxit, ...
    track,sigt,sigw,pii,nmu,A,B,L1,U1);
```


where a single-scattering iteration of the preconditioned MOC is implemented as

```
function phi=mcgsis_aca(phi,q,track,sigt,sigw,pii,nmu,A,B,L1,U1)
% single MOC scattering iteration with source isolation and ACA
% function phi=mcgsis_aca(phi,q,track,sigt,sigw,pii,nmu,A,B,L1,U1)
% (c) 2008 Alain Hebert, Ecole Polytechnique de Montreal
nsurf=track(1);
phi_half=mcgsis(phi,q,track,sigt,sigw,pii,nmu);
qaca=(phi_half - phi).*[ones(1,nsurf),sigw]';
[delta_phi flag]=bicgstab(A,B*qaca,1e-6,20,L1,U1);
phi=phi_half+delta_phi;
```

7 The Steady-State Diffusion Equation

In the previous sections, we have studied the notions of neutron cross-section, reaction rates, and neutron flux. The calculation of the energy-dependent neutron flux in each reactor region is required to obtain reaction rates in general and thermal reactor power in particular. Thermal reactor power is a measure of the *recoverable energy* production rate due to decay and neutron-induced reactions, the fission reaction being the most important source of energy release. As explained in the previous sections, neutron-induced reaction rates can be computed from knowledge of the *neutron flux* distribution, the solution of the *transport equation* for neutrons.

The geometric complexity of most nuclear reactors prevents the detailed solution of the neutron transport equation on the full-core geometry. Moreover, the resonant behavior in the energy of many cross-sections introduces another level of complexity along the energy independent variable. The computation of full-core reaction rates is generally the result of a *two-level computational scheme* based on the observation that the reactor is an assembly of unit cells or assemblies organized in a Cartesian or hexagonal lattice layout. The unit cell of a CANDU reactor is composed of the fuel bundle, pressure tube, calandria tube, and moderator zone. The unit assembly of a pressurized water reactor (PWR) is composed of the fuel assembly (generally a 15×15 or 17×17 assembly), including the control poisons and the interstitial light water. The unit cells or assemblies present in the reactor are supposed to be similar, only differing by a set of *global* or *local parameters*. These parameters generally include a measure of the fuel burnup (expressed in MW-day/tons of initial heavy isotopes), the fuel temperature, the coolant density and/or temperature, and any other parameter having an effect on the nuclear properties.

The first level of our computational scheme is the *lattice calculation*. Such a calculation is performed for *every* combination of global and local parameters that are likely to occur. The lattice calculation involves the solution of the steady-state transport equation over the unit cell or assembly, using a few hundred energy groups, as depicted in  Fig. 32. The dependent variable of this calculation is the neutron flux in each energy group, written as $\phi_g(\mathbf{r})$, with $1 \leq g \leq G$. The steady-state condition requires an exact balance between neutron loss and production. If this condition is not fulfilled, the production rate is divided by an adjustment factor, the *effective multiplication factor* K_{eff} , defined as

$$K_{\text{eff}} = \frac{\text{production rate by fission}}{\text{absorption rate} + \text{leakage rate}}. \quad (520)$$

In general, the steady-state condition $K_{\text{eff}} = 1$ is obtained by adjusting the *buckling* B^2 of the lattice calculation. The selected parameter used to force steady-state conditions is the *eigenvalue* of the calculation. At the end of a lattice calculation, the homogenized and condensed information is stored in the *reactor database*.

The second level of our computational scheme is the *full-core calculation*, aimed at producing the neutron flux and reaction rates over the complete reactor. This calculation is an assembly of homogenized cells or assemblies whose condensed nuclear properties are recovered from the reactor database. The homogenized cells or assemblies are generally arranged over a regular Cartesian or hexagonal mesh, so that the transport equation can be solved using standard numerical analysis techniques such as the *finite-difference* or *finite-element method* (FEM).

The full-core calculation consists of solving a simplified transport equation, either the *diffusion equation* or the *simplified P_n equation*, already presented in [3.4](#). This solution can be performed either in transient or steady-state conditions, in which case it can also be depicted by [Fig. 32](#), using a small number of energy groups (generally, $G = 2$ is sufficient). A steady-state full-core calculation generally uses the effective multiplication factor K_{eff} as eigenvalue. Another possible choice of eigenvalue is to select a poison concentration or the position of a reactivity device.

Full-core calculations offer the possibility of accurately representing the reactor boundary. A correct representation of neutron leakage will be possible, as neutrons effectively escape the reactor domain through its boundary. Consequently, 3D full-core calculations do not need a leakage model.

We will first investigate the steady-state solution of the transport equation over the complete reactor domain. The neutron balance over any control domain in energy group g will be written as

$$\text{Leakage rate} + \text{Collision rate} = \text{Sources}$$

or, in symbolic form, as

$$\nabla \cdot \mathbf{J}_g(\mathbf{r}) + \Sigma_g(\mathbf{r})\phi_g(\mathbf{r}) = Q_g(\mathbf{r}), \quad (521)$$

where $\mathbf{J}_g(\mathbf{r})$ is the *neutronic current*, as defined by (9). The definition of the neutronic current involves the introduction of an arbitrary surface whose unit normal vector is set to \mathbf{N} . The scalar product of the neutronic current with \mathbf{N} is equal to the net number of neutrons crossing the arbitrary surface per unit surface and time.

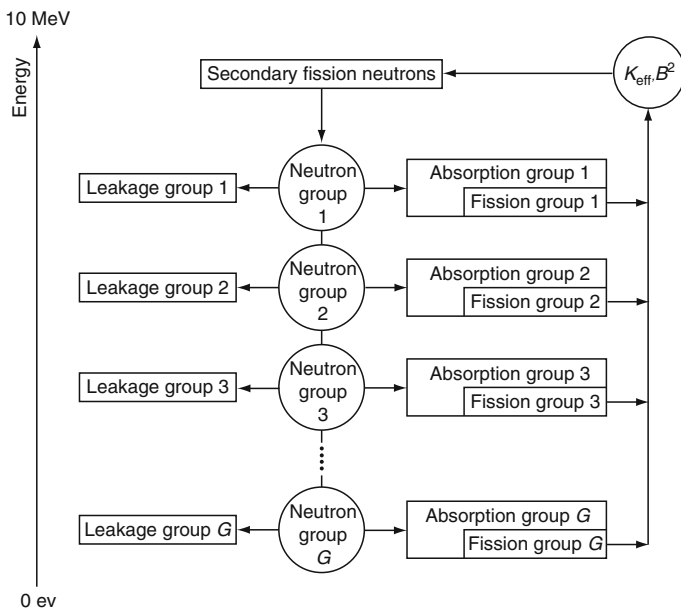


Figure 32
G-energy group transport calculation

The neutronic sources $Q_g(\mathbf{r})$ represent the production of secondary neutrons from scattering (including neutrons from (n,xn) reactions) and fission reactions. This term is written as

$$Q_g(\mathbf{r}) = \sum_{h=1}^G \Sigma_{g \leftarrow h}(\mathbf{r}) \phi_h(\mathbf{r}) + \frac{\chi_g(\mathbf{r})}{K_{\text{eff}}} \sum_{h=1}^G \nu \Sigma_{fh}(\mathbf{r}) \phi_h(\mathbf{r}), \tag{522}$$

where

- G = total number of energy groups
- $\Sigma_{g \leftarrow h}(\mathbf{r})$ = macroscopic-scattering cross-section from group h toward group g
- $\chi_g(\mathbf{r})$ = fission spectrum in group g
- $\nu \Sigma_{fh}(\mathbf{r})$ = product of the macroscopic fission cross-section by the average number of neutrons emitted per fission in group h

In the particular case where $G = 2$, as depicted in Fig. 33, two approximations will be made:

- A neutron cannot be accelerated from group 2 (thermal) toward group 1 (fast)
- All the secondary neutrons from fission are produced in group 1

The approximations are written as

$$\Sigma_{1 \leftarrow 2}(\mathbf{r}) = 0, \quad \chi_1(\mathbf{r}) = 1, \quad \text{and} \quad \chi_2(\mathbf{r}) = 0. \tag{523}$$

Using these approximations, the sources $Q_g(\mathbf{r})$ simplify to

$$\begin{aligned} Q_1(\mathbf{r}) &= \Sigma_{1 \leftarrow 1}(\mathbf{r}) \phi_1(\mathbf{r}) + \frac{1}{K_{\text{eff}}} [\nu \Sigma_{f1}(\mathbf{r}) \phi_1(\mathbf{r}) + \nu \Sigma_{f2}(\mathbf{r}) \phi_2(\mathbf{r})], \\ Q_2(\mathbf{r}) &= \Sigma_{2 \leftarrow 1}(\mathbf{r}) \phi_1(\mathbf{r}) + \Sigma_{2 \leftarrow 2}(\mathbf{r}) \phi_2(\mathbf{r}). \end{aligned} \tag{524}$$

We have obtained a balance equation for a steady-state reactor, corresponding to the situation where the leakage and absorption rates are exactly equal to the production rate of new neutrons, at all times, in each energy group. In this case, the effective multiplication factor K_{eff} is an artifact (or an *eigenvalue*) that satisfies this equality. This factor is expected to be

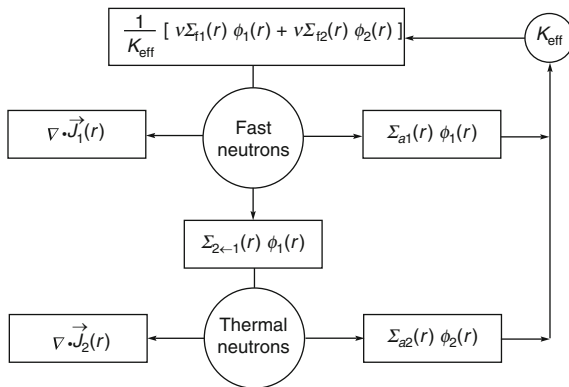


Figure 33 Two-group full-core calculation. This multigroup approximation is frequently used in full-core production calculations

close to one for a reactor in a nominal situation. An additional term can be added to the transport equation to represent transient behavior of the reactor in cases where the equality is not met.

Equation (521) must be solved on the scale of the complete reactor, correctly taking into account the position of its boundaries. Its solution requires additional information to relate the neutron flux and current. Two approaches are possible to obtain this information:

- Use a spherical harmonics (P_n) or discrete ordinate (S_N) approach, as proposed in Sects. 3 or 5. A legacy alternative is to use a variant of the P_n method based on the *simplified P_n equation*, as presented in 3.4. Gelbard (1960)
- Relate the neutron current to the gradient of the neutron flux using the *Fick law*.

This second choice will lead to the *diffusion equation*, used in this section.

7.1 The Fick Law

The *neutron diffusion equation* can be readily obtained by introducing the Fick law into (521). The Fick law is a heuristic relation between the neutron current and the gradient of the neutron flux, translating the fact that neutrons have a tendency to migrate from regions where they are more numerous to regions where they are less. This relation is known to be acceptable on the scale of the complete reactor, but not at the level of lattice calculations where it breaks down. It is written as

$$\mathbf{J}_g(\mathbf{r}) = -\mathbb{D}_g(\mathbf{r})\nabla\phi_g(\mathbf{r}), \quad (525)$$

where $\mathbb{D}_g(\mathbf{r})$ is a 3×3 diagonal tensor containing *directional diffusion coefficients*. Nondirectional diffusion coefficients are generally sufficient to represent streaming effects in the lattice. In this case, the three diagonal components are simply set to the same value. Directional diffusion coefficients are more closely related to the B_1 *heterogeneous streaming* effect occurring when long streaming channels or planes are open in the reactor. The unit of the diffusion coefficient is the centimeter (cm).

Substituting (525) into (521), we get

$$-\nabla \cdot \mathbb{D}_g(\mathbf{r})\nabla\phi_g(\mathbf{r}) + \Sigma_g(\mathbf{r})\phi_g(\mathbf{r}) = Q_g(\mathbf{r}). \quad (526)$$

The next step consists in subtracting the within-group scattering rate from both sides of (526). We obtain the one-speed neutron diffusion equation as

$$-\nabla \cdot \mathbb{D}_g(\mathbf{r})\nabla\phi_g(\mathbf{r}) + \Sigma_{rg}(\mathbf{r})\phi_g(\mathbf{r}) = Q_g^\diamond(\mathbf{r}), \quad (527)$$

where $\Sigma_{rg}(\mathbf{r}) = \Sigma_g(\mathbf{r}) - \Sigma_{g\leftarrow g}(\mathbf{r})$ is the *removal cross section* and where $Q_g^\diamond(\mathbf{r})$ is written as

$$Q_g^\diamond(\mathbf{r}) = \sum_{\substack{h=1 \\ h \neq g}}^G \Sigma_{g\leftarrow h}(\mathbf{r}) \phi_h(\mathbf{r}) + \frac{\chi_g(\mathbf{r})}{K_{\text{eff}}} \sum_{h=1}^G \nu \Sigma_{fh}(\mathbf{r}) \phi_h(\mathbf{r}). \quad (528)$$

In the two-energy group case ($G = 2$), (528) simplifies to

$$\begin{aligned} Q_1^\circ(\mathbf{r}) &= \frac{1}{K_{\text{eff}}} [v\Sigma_{f1}(\mathbf{r})\phi_1(\mathbf{r}) + v\Sigma_{f2}(\mathbf{r})\phi_2(\mathbf{r})], \\ Q_2^\circ(\mathbf{r}) &= \Sigma_{2\leftarrow 1}(\mathbf{r})\phi_1(\mathbf{r}). \end{aligned} \quad (529)$$

The neutron diffusion equation can be solved analytically in academic cases or using standard numerical analysis techniques such as the *finite difference* or *finite-element method*.

Substituting the source term from (528) into (527), we get the multigroup form of the steady-state neutron diffusion equation:

$$-\nabla \cdot \mathbb{D}_g(\mathbf{r})\nabla\phi_g(\mathbf{r}) + \Sigma_{rg}(\mathbf{r})\phi_g(\mathbf{r}) = \sum_{\substack{h=1 \\ h \neq g}}^G \Sigma_{g\leftarrow h}(\mathbf{r})\phi_h(\mathbf{r}) + \frac{\chi_g(\mathbf{r})}{\lambda} \sum_{h=1}^G v\Sigma_{fh}(\mathbf{r})\phi_h(\mathbf{r}). \quad (530)$$

Equation (530) is an *eigenproblem*, whose solution behaves in a typical way:

- A trivial solution of (530) is $\phi_g(\mathbf{r}) = 0, \forall \mathbf{r}$. Many nontrivial solutions of (530) exist for different eigenvalues λ . The largest eigenvalue in absolute value corresponds to the *fundamental solution* of the eigenproblem and is equal to the *effective multiplication factor* K_{eff} of the reactor. Only the fundamental solution has a physical meaning. The *eigenspectrum* of (530) is the set of all its eigenvalues (including K_{eff}).
- Only the fundamental solution can lead to a positive neutron flux $\phi_g(\mathbf{r})$ over the reactor domain. The other solutions are called *neutron flux harmonics* and lead to oscillating values of the flux, sometime positive, sometime negative. The knowledge of these harmonics is useful in some stability analysis as they correspond to natural excitation modes of the reactor.
- Every solution of (530) can be renormalized with an arbitrary normalization constant. If $\phi_g(\mathbf{r})$ is a solution, then $C\phi_g(\mathbf{r})$ is also a solution for any value of constant C . The normalization constant is generally computed from the knowledge of the reactor power using

$$\sum_{g=1}^G \int_V d^3r H_g(\mathbf{r})\phi_g(\mathbf{r}) = P, \quad (531)$$

where V is the volume of the reactor, $H_g(\mathbf{r})$ is the *H-factor*, and P is the power of the reactor. The H-factor permits the computation of the recoverable energy produced by the reactor.

- It is possible to find a *mathematical adjoint* to (530). This adjoint equation has the same *eigenspectrum* as (530).

The mathematical adjoint of (530) is obtained by permuting primary and secondary group indices. It is written as

$$-\nabla \cdot \mathbb{D}_g(\mathbf{r})\nabla\phi_g^*(\mathbf{r}) + \Sigma_{rg}(\mathbf{r})\phi_g^*(\mathbf{r}) = \sum_{\substack{h=1 \\ h \neq g}}^G \Sigma_{h\leftarrow g}(\mathbf{r})\phi_h^*(\mathbf{r}) + \frac{v\Sigma_{fg}(\mathbf{r})}{\lambda} \sum_{h=1}^G \chi_h(\mathbf{r})\phi_h^*(\mathbf{r}), \quad (532)$$

where $\phi_g^*(\mathbf{r})$ is the adjoint flux or adjoint-flux harmonics. The particular case with $G = 1$ is said to be *self-adjoint* as it corresponds to the case where $\phi_g^*(\mathbf{r}) = \phi_g(\mathbf{r})$. The adjoint flux can also be renormalized with an arbitrary normalization constant. It is generally normalized using the following arbitrary relation:

$$\sum_{g=1}^G \int_V d^3r \chi_g(\mathbf{r})\phi_g^*(\mathbf{r}) = 1. \quad (533)$$

7.2 Continuity and Boundary Conditions

The neutron flux is a continuous distribution of \mathbf{r} and the neutron current must be continuous across any imaginary surface (of unit normal \mathbf{N}) placed at any point of the reactor. Let's first imagine an infinite plane placed at abscissa x_0 . The flux continuity condition at this point is written as

$$\phi_g(x_0^-, y, z) = \phi_g(x_0^+, y, z) \quad \forall y \text{ and } z. \quad (534)$$

The neutron current continuity condition is written after introducing the unit normal $\mathbf{N} = (1, 0, 0)$, perpendicular to the infinite plane. We write

$$\mathbf{J}_g(x_0^-, y, z) \cdot \mathbf{N} = \mathbf{J}_g(x_0^+, y, z) \cdot \mathbf{N} \quad \forall y \text{ and } z. \quad (535)$$


Using the Fick law from (525), we obtain

$$-\mathbb{D}_g(x_0^-, y, z) \nabla \phi_g(x_0^-, y, z) \cdot \mathbf{N} = -\mathbb{D}_g(x_0^+, y, z) \nabla \phi_g(x_0^+, y, z) \cdot \mathbf{N} \quad \forall y \text{ and } z \quad (536)$$

or with the help of the first diagonal component $D_{x,g}(x, y, z)$ in $\mathbb{D}_g(x, y, z)$,

$$D_{x,g}(x_0^-, y, z) \left. \frac{d}{dx} \phi_g(x, y, z) \right|_{x=x_0^-} = D_{x,g}(x_0^+, y, z) \left. \frac{d}{dx} \phi_g(x, y, z) \right|_{x=x_0^+} \quad \forall y \text{ and } z. \quad (537)$$

Equation (537) clearly indicates that the neutron flux gradient is discontinuous at each point of the domain where the diffusion coefficient is discontinuous.

Boundary conditions must be applied at each point of the spatial domain boundary ∂V . We will identify the real boundaries and the symmetry boundaries, as depicted in  Fig. 34.

The most straightforward way to represent a real boundary is to set a *zero-flux boundary condition* on it. In this case, we simply write

$$\phi_g(\mathbf{r}) = 0 \quad \text{if } \mathbf{r} \in \partial W_i, \quad (538)$$

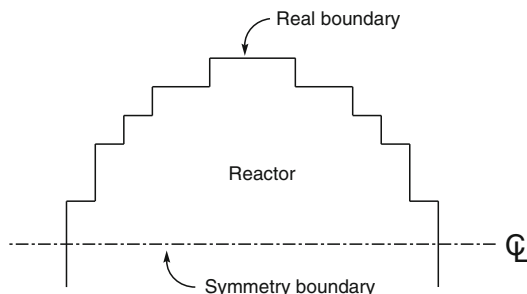


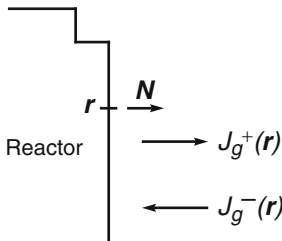
 Figure 34

Spatial domain with symmetries. The spatial boundary generally includes the complete reactor with its reflector, but it may happen that symmetries exist so that the domain may correspond to a fraction of the complete reactor

where ∂W_i is the fraction of ∂V where the zero-flux condition is applied. However, this condition is not fully satisfactory, as it assumes the *absence* of neutrons on ∂W_i . It would be more exact to assume a *zero-incoming current condition* translating the fact that neutrons can escape from the real boundary but cannot be reflected back. Such a condition can be seen as a particular case of the more general *albedo-boundary condition*.

To implement this condition, we first identify the incoming and outgoing net currents using


$$\mathbf{J}_g(\mathbf{r}) \cdot \mathbf{N}(\mathbf{r}) = J_g^+(\mathbf{r}) - J_g^-(\mathbf{r}) \quad \text{if } \mathbf{r} \in \partial W_i, \quad (539)$$

where $\mathbf{N}(\mathbf{r})$ is a unit vector, located at \mathbf{r} , normal to ∂W_i , and pointing in the outgoing direction, as depicted in  Fig. 35.

The *albedo* at \mathbf{r} is defined by the relation

$$\beta_g(\mathbf{r}) = \frac{J_g^-(\mathbf{r})}{J_g^+(\mathbf{r})} \quad \text{if } \mathbf{r} \in \partial W_i. \quad (540)$$

In general, we use the same albedo in all energy groups. The most usual values are $\beta(\mathbf{r}) = 0$ to represent a *zero-incoming current condition* and $\beta(\mathbf{r}) = 1$ to represent a symmetry condition. However, any positive value of $\beta(\mathbf{r})$ can be set at a boundary.

We have shown in  Sect. 1 that the incoming and outgoing net currents can be obtained from the neutron current and flux distributions provided the angular flux is represented by a limited P_1 expansion. In this case, we recall (42) and (43) as

$$J_g^-(\mathbf{r}) = \frac{1}{4} \phi_g(\mathbf{r}) - \frac{1}{2} \mathbf{J}_g(\mathbf{r}) \cdot \mathbf{N}(\mathbf{r})$$

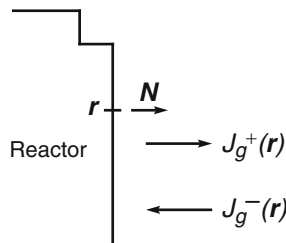
and


$$J_g^+(\mathbf{r}) = \frac{1}{4} \phi_g(\mathbf{r}) + \frac{1}{2} \mathbf{J}_g(\mathbf{r}) \cdot \mathbf{N}(\mathbf{r}). \quad (541)$$

Substituting (541) into (540) and using the Fick law (525), we obtain the *albedo boundary condition* as

$$\mathbb{D}_g(\mathbf{r}) \nabla \phi_g(\mathbf{r}) \cdot \mathbf{N}(\mathbf{r}) + \frac{1 - \beta(\mathbf{r})}{2(1 + \beta(\mathbf{r}))} \phi_g(\mathbf{r}) = 0 \quad \text{if } \mathbf{r} \in \partial W_i, \quad (542)$$

where ∂W_i is the fraction of ∂V where the albedo-boundary condition is applied.



 **Figure 35**
Definition of incoming and outgoing net currents

The zero-incoming current condition ($J_g^-(\mathbf{r}) = 0$) is obtained by setting $\beta(\mathbf{r}) = 0$. However, it can be shown that the Fick law and the P_1 approximation used in [Sect. 1](#) introduce an error that can be reduced by using a value of $\beta(\mathbf{r})$ slightly above zero. It is sometimes recommended to represent the zero-incoming current condition using the value $\beta(\mathbf{r}) = 0.031758$.

Another particular case is the symmetry condition obtained by setting the albedo to value $\beta(\mathbf{r}) = 1$. In this case, (542) reduces to

$$\nabla \phi_g(\mathbf{r}) \cdot \mathbf{N}(\mathbf{r}) = 0 \quad \text{if } \mathbf{r} \in \partial W_i. \quad (543)$$

7.3 The Finite Homogenous Reactor

We will now study the particular case of a homogenous and finite reactor surrounded by zero-flux or symmetry-boundary conditions, represented by (538) and (543), respectively. We will also use nondirectional diffusion coefficients. With all these simplifications, it is now possible to obtain an analytical solution for the diffusion equation, whatever the form of the reactor or the number of energy groups. This analytic solution is similar to the relations obtained with a homogenous fundamental mode approximation. In this case, the nuclear properties of the reactor are independent of space and (530) simplifies to

$$-D_g \nabla^2 \phi_g(\mathbf{r}) + \Sigma_{rg} \phi_g(\mathbf{r}) = \sum_{\substack{h=1 \\ h \neq g}}^G \Sigma_{g \leftarrow h} \phi_h(\mathbf{r}) + \frac{\chi_g}{K_{\text{eff}}} \sum_{h=1}^G \nu \Sigma_{fh} \phi_h(\mathbf{r}). \quad (544)$$

It is possible to factorize the flux according to

$$\phi_g(\mathbf{r}) = \psi(\mathbf{r}) \varphi_g. \quad (545)$$

Substituting (545) into (544), we obtain

$$-\frac{\nabla^2 \psi(\mathbf{r})}{\psi(\mathbf{r})} = -\frac{\Sigma_{rg}}{D_g} + \frac{1}{D_g \varphi_g} \left\{ \sum_{\substack{h=1 \\ h \neq g}}^G \Sigma_{g \leftarrow h} \varphi_h + \frac{\chi_g}{K_{\text{eff}}} \sum_{h=1}^G \nu \Sigma_{fh} \varphi_h \right\}. \quad (546)$$

We note that the left side of (546) is independent of the neutron energy, whereas its right side is independent of the position in the reactor. This fact is only possible if each side of (546) is itself equal to the same constant. The choice of this constant is arbitrary, and any real number can be selected. Here, by analogy to the fundamental mode approximation, this constant was set equal to B^2 , the *buckling* of the reactor. We therefore obtain two independent equations as

$$\nabla^2 \psi(\mathbf{r}) + B^2 \psi(\mathbf{r}) = 0 \quad (547)$$

and

$$[D_g B^2 + \Sigma_{rg}] \varphi_g = \sum_{\substack{h=1 \\ h \neq g}}^G \Sigma_{g \leftarrow h} \varphi_h + \frac{\chi_g}{K_{\text{eff}}} \sum_{h=1}^G \nu \Sigma_{fh} \varphi_h. \quad (548)$$

Equation (547) is a Laplace equation, an eigenproblem whose eigenvalue is the buckling B^2 . Its solution is a function of the shape and size of the reactor and of the boundary conditions. Substituting the factorization (545) in the boundary conditions (538) and (543), we get

- Zero-flux-boundary condition:

$$\psi(\mathbf{r}) = 0 \quad \text{if } \mathbf{r} \in \partial W_i \quad (549)$$

- Symmetry-boundary condition:

$$\nabla\psi(\mathbf{r}) \cdot \mathbf{N}(\mathbf{r}) = 0 \quad \text{if } \mathbf{r} \in \partial W_i. \quad (550)$$

Here, the more general albedo-boundary condition (542) cannot be factorized and cannot be used in this analytical solution technique of a finite homogenous reactor.

Equation (547) has many nontrivial solutions, each of them corresponding to an element of its eigenspectrum. Only the fundamental solution corresponds to a positive neutron flux everywhere in the domain.

The Laplace operator ∇^2 can be written in different ways, depending on the coordinate system selected to solve the problem. We will present the three most usual coordinate systems.

7.3.1 Cartesian Coordinate System

The Cartesian coordinate system is the most usual choice for real application problems. In this case, the Laplace operator is written as

$$\nabla^2\psi = \frac{\partial^2\psi}{\partial x^2} + \frac{\partial^2\psi}{\partial y^2} + \frac{\partial^2\psi}{\partial z^2}. \quad (551)$$

Let us consider a prismatic homogenous reactor of dimension $L_x \times L_y \times L_z$. In this case, the fundamental solution of (547) is

$$\psi(x, y, z) = C \sin \frac{\pi x}{L_x} \sin \frac{\pi y}{L_y} \sin \frac{\pi z}{L_z}. \quad (552)$$

The Cartesian domain is defined over $0 \leq x \leq L_x$, $0 \leq y \leq L_y$, and $0 < z < L_z$. A *zero-flux-boundary condition* is imposed on the surface of the domain. The normalization constant C is arbitrary as both (547) and (548) are eigenproblems.

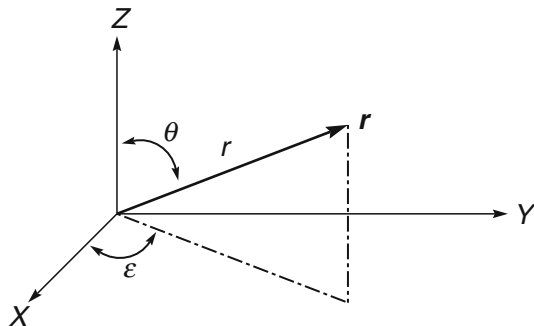
The corresponding critical buckling is

$$B^2 = \left(\frac{\pi}{L_x}\right)^2 + \left(\frac{\pi}{L_y}\right)^2 + \left(\frac{\pi}{L_z}\right)^2. \quad (553)$$

7.3.2 Spherical Coordinate System

The spherical coordinate system is depicted in  Fig. 36. In this case, the Laplace operator is written as

$$\nabla^2\psi = \frac{1}{r^2 \sin \theta} \left[\sin \theta \frac{\partial}{\partial r} \left(r^2 \frac{\partial \psi}{\partial r} \right) + \frac{\partial}{\partial \theta} \left(\sin \theta \frac{\partial \psi}{\partial \theta} \right) + \frac{1}{\sin \theta} \frac{\partial^2 \psi}{\partial \varepsilon^2} \right]. \quad (554)$$



■ **Figure 36**
Definition of the spherical coordinate system

The fundamental solution of (547) represents the neutron flux in a spherical reactor of radius R . A *zero-flux-boundary condition* is imposed at $r = R$ (i.e., $\psi(R) = 0$). The fundamental solution is written as

$$\psi(r) = \frac{C}{r} \sin \frac{\pi r}{R} \quad (555)$$

with the critical buckling equal to

$$B^2 = \left(\frac{\pi}{R}\right)^2. \quad (556)$$

7.3.3 Cylindrical Coordinate System

The cylindrical coordinate system is depicted in ► Fig. 37. In this case, the Laplace operator is written as

$$\nabla^2 \psi = \frac{1}{\rho} \left[\frac{\partial}{\partial \rho} \left(\rho \frac{\partial \psi}{\partial \rho} \right) + \frac{1}{\rho} \frac{\partial^2 \psi}{\partial \varepsilon^2} + \rho \frac{\partial^2 \psi}{\partial z^2} \right]. \quad (557)$$

The fundamental solution of (547) represents the neutron flux in a cylindrical reactor of radius R and height L_z . The spatial domain is defined as $0 \leq \rho \leq R$ and $0 \leq z \leq L_z$. A *zero-flux-boundary condition* is imposed on the surface of the domain. The fundamental solution is

$$\psi(\rho, z) = C J_0 \left(\frac{2.405 \rho}{R} \right) \sin \frac{\pi z}{L_z} \quad (558)$$

with the critical buckling equal to

$$B^2 = \left(\frac{2.405}{R}\right)^2 + \left(\frac{\pi}{L_z}\right)^2, \quad (559)$$

where $J_0(x)$ is a zeroth-order ordinary Bessel function, such as $J_0(2.405) = 0$.

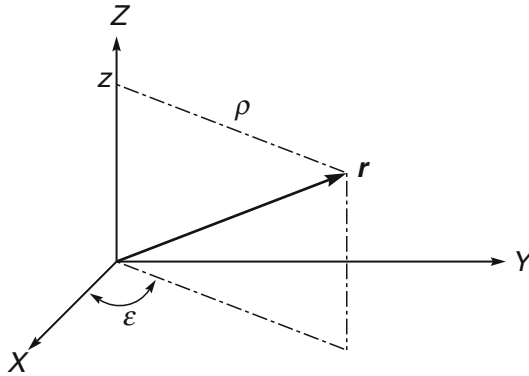


Figure 37 Definition of the cylindrical coordinate system

7.4 The Heterogenous 1D Slab Reactor

The one-dimensional (1D) heterogenous reactor configurations correspond to the case where the neutron flux is a function of a unique spatial variable. These cases can be solved analytically, whatever the type of conditions imposed at boundaries. These academic cases are useful to validate solutions based on numerical analysis techniques. Here, we are limiting our investigations to a 1D Cartesian domain made from the assembly of many infinite slabs.

In this case, the nuclear properties of the reactor are only a function of the independent variable x . Equation (530) simplifies to

$$-\frac{d}{dx} D_g(x) \frac{d\phi_g}{dx} + \Sigma_{rg}(x) \phi_g(x) = Q_g^\diamond(x), \tag{560}$$

where

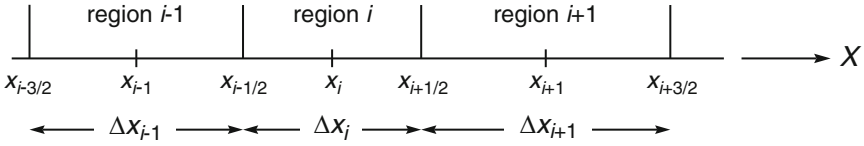
$$Q_g^\diamond(x) = \sum_{\substack{h=1 \\ h \neq g}}^G \Sigma_{g \leftarrow h}(x) \phi_h(x) + \frac{\chi_g(x)}{K_{\text{eff}}} \sum_{h=1}^G \nu \Sigma_{fh}(x) \phi_h(x). \tag{561}$$

The boundary conditions are either a zero-flux condition ($\phi_g(x) = 0$) or an albedo condition written as

$$\mp D_g(x) \frac{d\phi_g}{dx} + \frac{1 - \beta(x)}{2(1 + \beta(x))} \phi_g(x) = 0, \tag{562}$$

where the sign “-” or “+” is used for a left ($x = x_{l/2}$) or a right boundary ($x = x_{l+1/2}$), respectively.

Each slab is assumed to be homogenous, so that the corresponding nuclear properties $D_g(x)$, $\Sigma_{rg}(x)$, $\Sigma_{g \leftarrow h}(x)$, $\chi_g(x)$, and $\nu \Sigma_{fh}(x)$ are piecewise continuous. As shown in Fig. 38, the reactor domain is divided into I regions of indices $1 \leq i \leq I$, in such a way that the nuclear properties in region i are constant and equal to $D_{g,i}$, $\Sigma_{rg,i}$, $\Sigma_{g \leftarrow h,i}$, $\chi_{g,i}$, and $\nu \Sigma_{fh,i}$.



■ Figure 38

Definition of the regions in 1D slab geometry

Equation (560) can be written in such a way as to be valid in region i as

$$-D_{g,i} \frac{d^2 \phi_g}{dx^2} + \Sigma_{rg,i} \phi_g(x) = Q_g^\diamond(x), \quad (563)$$

where

$$Q_g^\diamond(x) = \sum_{\substack{h=1 \\ h \neq g}}^G \Sigma_{g \leftarrow h,i} \phi_h(x) + \frac{\chi_{g,i}}{K_{\text{eff}}} \sum_{h=1}^G v \Sigma_{fh,i} \phi_h(x) \quad (564)$$

if $x_{i-1/2} < x < x_{i+1/2}$.

At this point, we introduce the analytical solution approach for (563). It is based on a *linear transformation technique*, valid only for multigroup 1D problems. Equation (563) is first rewritten in matrix form as

$$\frac{d^2}{dx^2} \Phi(x) + \mathbb{F}_i \Phi(x) = \mathbf{0} \quad \text{if } x_{i-1/2} < x < x_{i+1/2} \quad (565)$$

with

$$\Phi(x) = \begin{pmatrix} \phi_1(x) \\ \vdots \\ \phi_G(x) \end{pmatrix} \quad (566)$$

and

$$\mathbb{F}_i = \begin{pmatrix} f_{11,i} & f_{12,i} & \cdots & f_{1G,i} \\ f_{21,i} & f_{22,i} & \cdots & f_{2G,i} \\ \vdots & \vdots & \ddots & \vdots \\ f_{G1,i} & f_{G2,i} & \cdots & f_{GG,i} \end{pmatrix}, \quad (567)$$

where the components $f_{gh,i}$ of this matrix are written as

$$f_{gh,i} = \frac{1}{D_{g,i}} \left[-\Sigma_{rg,i} \delta_{gh} + \Sigma_{g \leftarrow h,i} (1 - \delta_{gh}) + \frac{\chi_{g,i}}{K_{\text{eff}}} v \Sigma_{fh,i} \right]. \quad (568)$$

The next step consists in finding all eigenvectors $\mathbf{t}_{\ell,i}$ of matrix \mathbb{F}_i with the associated eigenvalues $\lambda_{\ell,i}$. We build a matrix \mathbb{T}_i whose columns are the eigenvectors of \mathbb{F}_i . This matrix is written as

$$\mathbb{T}_i = (\mathbf{t}_{1,i} \quad \mathbf{t}_{2,i} \quad \cdots \quad \mathbf{t}_{G,i}) \quad (569)$$

so that

$$\mathbb{F}_i \mathbb{T}_i = \mathbb{T}_i \text{diag}(\lambda_{\ell,i}). \quad (570)$$

The linear transformation technique used to solve (560) is based on the introduction of an unknown vector $\Psi(x)$ defined as

$$\Phi(x) = \mathbb{T}_i \Psi(x) = \begin{pmatrix} t_{11,i} & t_{12,i} & \dots & t_{1G,i} \\ t_{21,i} & t_{22,i} & \dots & t_{2G,i} \\ \vdots & \vdots & \ddots & \vdots \\ t_{G1,i} & t_{G2,i} & \dots & t_{GG,i} \end{pmatrix} \begin{pmatrix} \psi_1(x) \\ \psi_2(x) \\ \vdots \\ \psi_G(x) \end{pmatrix} \quad (571)$$

and to its substitution in (565). We obtain

$$\frac{d^2}{dx^2} \mathbb{T}_i \Psi(x) + \mathbb{F}_i \mathbb{T}_i \Psi(x) = \mathbf{0} \quad \text{if } x_{i-1/2} < x < x_{i+1/2}. \quad (572)$$

We next left-multiply each side of (572) by $[\mathbb{T}_i]^{-1}$ and use (570) to obtain

$$\frac{d^2}{dx^2} \Psi(x) + \text{diag}(\lambda_{\ell,i}) \Psi(x) = \mathbf{0} \quad \text{if } x_{i-1/2} < x < x_{i+1/2}. \quad (573)$$

Equation (573) is similar to (565) with the difference that all the energy groups are uncoupled. Its resolution is reduced to the solution of G one-speed problems. In each energy group g , we assume an analytical solution of the form

$$\psi_g(x) = \begin{cases} A_{g,i} \cos(\sqrt{\lambda_{g,i}} x) + B_{g,i} \sin(\sqrt{\lambda_{g,i}} x) & \text{if } \lambda_{g,i} \geq 0, \\ C_{g,i} \cosh(\sqrt{-\lambda_{g,i}} x) + E_{g,i} \sinh(\sqrt{-\lambda_{g,i}} x) & \text{otherwise,} \end{cases} \quad (574)$$

if $x_{i-1/2} < x < x_{i+1/2}$.

The analytical expression of the flux $\phi_g(x)$ is obtained after substitution of (574) into (571) as

$$\phi_g(x) = \sum_{h=1}^G t_{gh,i} \psi_h(x) \quad \text{if } x_{i-1/2} < x < x_{i+1/2}. \quad (575)$$

The final step consists of coupling together the analytical solutions of each region i and applying the boundary conditions. If region $i-1$ exists (i.e., if the left side of region i is not a boundary), the solution obeys the continuity relations (534) and (537), so that

$$\phi_g(x_{i-1/2}^-) = \phi_g(x_{i-1/2}^+) \quad (576)$$

and

$$D_{g,i-1} \phi_g'(x_{i-1/2}^-) = D_{g,i} \phi_g'(x_{i-1/2}^+), \quad (577)$$

where we defined $\phi'_g(x_{i-1/2}^-) = (d\phi_g/dx)|_{x=x_{i-1/2}^-}$. Similarly, if region $i + 1$ exists, we write

$$\phi_g(x_{i+1/2}^-) = \phi_g(x_{i+1/2}^+) \quad (578)$$

and

$$D_{g,i} \phi'_g(x_{i+1/2}^-) = D_{g,i+1} \phi'_g(x_{i+1/2}^+). \quad (579)$$

The boundary conditions are imposed in the same way, by forcing the value of $\phi_g(x)$ or $\phi'_g(x)$ on a boundary abscissa.

An analytical solution of (563) with its continuity and boundary conditions can always be found, with a computational effort increasing with the number of energy groups and regions. We will now apply this analytical technique to a simple two-region problem.

7.4.1 Two-Region Example

We now apply the linear transformation technique to the one-speed, two-region problem depicted in  Fig. 39. In this case, (563) simplifies to

$$-D_i \frac{d^2\phi}{dx^2} + \Sigma_{r,i} \phi(x) = \frac{1}{K_{\text{eff}}} \nu \Sigma_{f,i} \phi(x) \quad \text{if } x_{i-1/2} < x < x_{i+1/2}. \quad (580)$$

We assume an analytical solution of the form

$$\phi(x) = \begin{cases} A_{11} \cos(\kappa_1 x) + A_{21} \sin(\kappa_1 x), & \text{if } 0 \leq x \leq \frac{1}{2}; \\ A_{12} \cos(\kappa_2 x) + A_{22} \sin(\kappa_2 x), & \text{if } \frac{1}{2} \leq x \leq 1, \end{cases} \quad (581)$$

so that

$$\phi'(x) = \begin{cases} -A_{11} \kappa_1 \sin(\kappa_1 x) + A_{21} \kappa_1 \cos(\kappa_1 x), & \text{if } 0 \leq x \leq \frac{1}{2}, \\ -A_{12} \kappa_2 \sin(\kappa_2 x) + A_{22} \kappa_2 \cos(\kappa_2 x), & \text{if } \frac{1}{2} \leq x \leq 1 \end{cases} \quad (582)$$

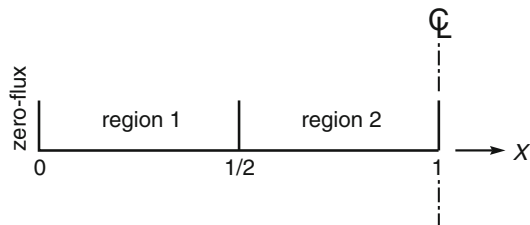


 Figure 39

Two-region 1D slab reactor

and

$$\frac{d^2\phi}{dx^2} = \begin{cases} -A_{11} \kappa_1^2 \cos(\kappa_1 x) - A_{21} \kappa_1^2 \sin(\kappa_1 x), & \text{if } 0 \leq x \leq \frac{1}{2}, \\ -A_{12} \kappa_2^2 \cos(\kappa_2 x) - A_{22} \kappa_2^2 \sin(\kappa_2 x), & \text{if } \frac{1}{2} \leq x \leq 1. \end{cases} \quad (583)$$

The left zero-flux boundary condition is written as

$$\phi(0) = A_{11} = 0. \quad (584)$$

The continuity conditions at $x = \frac{1}{2}$ are written as

$$A_{11} \cos\left(\frac{\kappa_1}{2}\right) + A_{21} \sin\left(\frac{\kappa_1}{2}\right) = A_{12} \cos\left(\frac{\kappa_2}{2}\right) + A_{22} \sin\left(\frac{\kappa_2}{2}\right) \quad (585)$$

and

$$\begin{aligned} & -A_{11} \kappa_1 D_1 \sin\left(\frac{\kappa_1}{2}\right) + A_{21} \kappa_1 D_1 \cos\left(\frac{\kappa_1}{2}\right) \\ & = -A_{12} \kappa_2 D_2 \sin\left(\frac{\kappa_2}{2}\right) + A_{22} \kappa_2 D_2 \cos\left(\frac{\kappa_2}{2}\right). \end{aligned} \quad (586)$$

Finally, the right-symmetry-boundary condition is written as

$$-A_{12} \kappa_2 \sin(\kappa_2) + A_{22} \kappa_2 \cos(\kappa_2) = 0$$

so that

$$A_{22} = A_{12} \tan(\kappa_2). \quad (587)$$

Substituting (584) and (587) into (585) and (586), we find the following matrix equation:

$$\begin{pmatrix} \sin\left(\frac{\kappa_1}{2}\right) & -\frac{1}{\cos(\kappa_2)} \cos\left(\frac{\kappa_2}{2}\right) \\ \kappa_1 D_1 \cos\left(\frac{\kappa_1}{2}\right) & -\frac{\kappa_2 D_2}{\cos(\kappa_2)} \sin\left(\frac{\kappa_2}{2}\right) \end{pmatrix} \begin{pmatrix} A_{21} \\ A_{12} \end{pmatrix} = \begin{pmatrix} 0 \\ 0 \end{pmatrix}. \quad (588)$$

Equation (588) has a nontrivial solution only if its determinant is zero. We write

$$\det \begin{pmatrix} \sin\left(\frac{\kappa_1}{2}\right) & -\frac{1}{\cos(\kappa_2)} \cos\left(\frac{\kappa_2}{2}\right) \\ \kappa_1 D_1 \cos\left(\frac{\kappa_1}{2}\right) & -\frac{\kappa_2 D_2}{\cos(\kappa_2)} \sin\left(\frac{\kappa_2}{2}\right) \end{pmatrix} = 0 \quad (589)$$

so that the resulting characteristic equation is a nonlinear relation in κ_1 and κ_2 , written as

$$\tan\left(\frac{\kappa_1}{2}\right) \tan\left(\frac{\kappa_2}{2}\right) = \frac{\kappa_1 D_1}{\kappa_2 D_2}. \quad (590)$$

Substituting (581) and (583) into (580), we find the expressions of κ_1 and κ_2 as

$$\kappa_1 = \sqrt{\frac{v\Sigma_{f,1} - K_{\text{eff}}\Sigma_{r,1}}{K_{\text{eff}}D_1}} \quad \text{and} \quad \kappa_2 = \sqrt{\frac{v\Sigma_{f,2} - K_{\text{eff}}\Sigma_{r,2}}{K_{\text{eff}}D_2}}. \quad (591)$$

Combining (590) and (591), we obtain the nonlinear expression of the effective multiplication factor K_{eff} as

$$\tan\left(\frac{1}{2}\sqrt{\frac{\nu\Sigma_{f,1} - K_{\text{eff}}\Sigma_{r,1}}{K_{\text{eff}}D_1}}\right)\tan\left(\frac{1}{2}\sqrt{\frac{\nu\Sigma_{f,2} - K_{\text{eff}}\Sigma_{r,2}}{K_{\text{eff}}D_2}}\right) = \sqrt{\frac{D_1(\nu\Sigma_{f,1} - K_{\text{eff}}\Sigma_{r,1})}{D_2(\nu\Sigma_{f,2} - K_{\text{eff}}\Sigma_{r,2})}}. \quad (592)$$

The effective multiplication factor is obtained by solving (592) using a numerical technique for the solution of a nonlinear equation with one unknown. Knowledge of K_{eff} permits the computation of κ_1 and κ_2 , and the determination of the analytical expression of the neutron flux $\phi(x)$, the eigenvector corresponding to K_{eff} . Its value is

$$\phi(x) = \begin{cases} A_{21} \sin(\kappa_1 x), & \text{if } 0 \leq x \leq \frac{1}{2}, \\ A_{21} \frac{\sin\left(\frac{\kappa_1}{2}\right)}{\cos\left(\frac{\kappa_2}{2}\right)} \cos[\kappa_2(1-x)], & \text{if } \frac{1}{2} \leq x \leq 1. \end{cases} \quad (593)$$

The neutron flux can be renormalized to the power of the reactor by adjusting the remaining constant A_{21} .

8 Discretization of the Neutron Diffusion Equation

We refer to as *discretization* the technique we use to transform an algebraic operator, similar to those present in a differential equation, into a matrix operator. A discretization of the neutron diffusion equation allows its transformation into a matrix system that can be solved by standard numerical analysis techniques. A variety of different discretization techniques exists and many techniques, at first view different, produce *identical* matrix systems. A discretization technique is characterized by the following criteria:

- A discretization technique is said to be *consistent* if the discretization of a *Laplace operator* $\nabla^2\phi(\mathbf{r})$ produces a symmetric, positive-definite- and diagonally dominant matrix. Consistent discretization techniques are generally based on polynomial approximation of the dependent variable (here, the neutron flux) in each region. Each homogeneous region of the reactor can be subdivided into subregions in order to increase the number of piecewise polynomials. This operation is called *sub-meshing*. Moreover, a numerical solution of a consistent discretization technique must tend to the exact solution of the differential problem
 - As the number of subregions increases to infinity, for a given order of the polynomial basis,
 - As the polynomial order of the polynomial basis increases to infinity, for a given number of subregions.

The criterion relative to the symmetry of the matrix operator is important to ensure that the discretization of an adjoint differential equation, similar to (532), leads to the transposed matrix operator obtained from the discretization of the direct differential equation ((530)

in this case). Moreover, the positive-definite and diagonally dominant criteria ensure the success of the standard numerical analysis techniques used to solve the matrix system.

- Discretization techniques can be derived from the *differential formulation* of the neutron diffusion equation by replacing the dependent variable with *Taylor's expansions* or by using a *weighted residual approach*. They can also be obtained from a *variational formulation* by finding a *stationary point* of an ad-hoc functional. In this case, the choice of the functional is arbitrary, the only condition being that the *Euler equations* of the functional must be identical to the neutron diffusion equation with its continuity and boundary conditions. The variational approach and the FEM are presented in [▶ 8.3](#) and [▶ 8.4](#).
- A discretization technique can be *primal* if it belongs to the family of *mesh-corner-finite differences*, or *dual* if it belongs to the family of *mesh-centered finite differences*. A discretization technique can be simultaneously primal and dual; this property is called *primal-dual agreement* and is a characteristic of *superconvergent* approximations (Hébert 2005).

Both mesh-corner and mesh-centered techniques are consistent discretization approaches that can be obtained from the differential formulation of the neutron diffusion equation. These two basic formulations are presented in [▶ 8.1](#) and [▶ 8.2](#).

8.1 Mesh-Corner Finite Differences

The 1D Cartesian mesh-corner finite-difference formulation can be derived from the differential formulation of the neutron diffusion equation. This approach consists of replacing the flux derivative terms in (560) and (562) by finite-difference relations written in terms of the neutron flux values at specific abscissa points. These finite-difference relations can be obtained from the Taylor expansion of the neutron flux between successive points.

The choice of the abscissa points where the neutron flux is explicitly calculated determines the type of finite-difference approximation. In its mesh-corner formulation, these points are chosen on the boundary between subregions and are numbered as depicted in [▶ Fig. 38](#). We will use Taylor expansions to represent the flux at points $x_{i-3/2}$ and $x_{i+1/2}$ in terms of the flux at point $x_{i-1/2}$, so that

$$\phi(x_{i-3/2}) = \phi(x_{i-1/2}) - \Delta x_{i-1} \phi'(x_{i-1/2}^-) + \frac{1}{2} \Delta x_{i-1}^2 \phi''(x_{i-1/2}^-) \quad (594)$$

and

$$\phi(x_{i+1/2}) = \phi(x_{i-1/2}) + \Delta x_i \phi'(x_{i-1/2}^+) + \frac{1}{2} \Delta x_i^2 \phi''(x_{i-1/2}^+), \quad (595)$$

where the energy group index was omitted, in order to simplify the notation.

Care must be taken to correctly represent the discontinuous behavior of the first derivative of the neutron flux at material discontinuities. The neutron current continuity condition at $x_{i-1/2}$ causes a discontinuity in the first derivative of the neutron flux at this point. This relation is written as

$$D_{i-1} \phi'(x_{i-1/2}^-) = D_i \phi'(x_{i-1/2}^+). \quad (596)$$

We multiply (594) and (595) by $D_{i-1}/\Delta x_{i-1}$ and $D_i/\Delta x_i$, respectively, add the resulting relations, and introduce (596). We obtain

$$\begin{aligned} & \frac{1}{2} \left[\Delta x_{i-1} D_{i-1} \phi''(x_{i-1/2}^-) + \Delta x_i D_i \phi''(x_{i-1/2}^+) \right] \\ &= \frac{D_i}{\Delta x_i} \left[\phi(x_{i+1/2}) - \phi(x_{i-1/2}) \right] - \frac{D_{i-1}}{\Delta x_{i-1}} \left[\phi(x_{i-1/2}) - \phi(x_{i-3/2}) \right]. \end{aligned} \quad (597)$$

Equation (597) is used as a finite-difference relation valid for the internal points. We also need relations valid on the left- and right-boundary points where an *albedo boundary condition* is imposed. In this case, a Taylor expansion is written as

$$\phi(x_{3/2}) = \phi(x_{1/2}) + \Delta x_1 \phi'(x_{1/2}) + \frac{1}{2} \Delta x_1^2 \phi''(x_{1/2}) \quad (598)$$

for the left boundary and

$$\phi(x_{I-1/2}) = \phi(x_{I+1/2}) - \Delta x_I \phi'(x_{I+1/2}) + \frac{1}{2} \Delta x_I^2 \phi''(x_{I+1/2}) \quad (599)$$

for the right boundary. We multiply these two relations by $D_1/\Delta x_1$ and $D_I/\Delta x_I$, respectively, and introduce (562). We obtain

$$\frac{1}{2} \Delta x_1 D_1 \phi''(x_{1/2}) = \frac{D_1}{\Delta x_1} \left[\phi(x_{3/2}) - \phi(x_{1/2}) \right] - \frac{1}{2} \frac{1 - \beta_-}{1 + \beta_-} \phi(x_{1/2}) \quad (600)$$

and

$$\frac{1}{2} \Delta x_I D_I \phi''(x_{I+1/2}) = \frac{D_I}{\Delta x_I} \left[\phi(x_{I-1/2}) - \phi(x_{I+1/2}) \right] - \frac{1}{2} \frac{1 - \beta_+}{1 + \beta_+} \phi(x_{I+1/2}), \quad (601)$$

where β_- and β_+ are the left- and right-domain albedos, respectively.

Our Taylor expansions are truncated after the term in Δx_i^2 . Consequently, the difference relations (597), (600), and (601) are accurate only to the second order in Δx_i^2 . *This order is the smallest one that leads to a consistent discretization of the diffusion equation.* This choice will limit the accuracy of the discretization process in terms of the selected mesh Δx_i^2 .

The final step of our discretization process consists in substituting the finite difference relations into the differential equation, that is, into the neutron diffusion equation. On both sides of point $x_{i-1/2}$, the nuclear properties are uniform, so that the neutron diffusion equation reduces to

$$-D_{i-1} \phi''(x_{i-1/2}^-) + \Sigma_{r,i-1} \phi(x_{i-1/2}) = Q_{i-1}^\diamond$$

and

$$-D_i \phi''(x_{i-1/2}^+) + \Sigma_{r,i} \phi(x_{i-1/2}) = Q_i^\diamond, \quad (602)$$

where the flat-source approximation leading to constant terms Q_{i-1}^\diamond and Q_i^\diamond is compatible with the truncation order of the Taylor series. A higher truncation order would have required spatially dependent neutron sources in the right term.

We multiply each of (602) with Δx_{i-1} and Δx_i , respectively, and we add the resulting relations. Introducing the finite-difference relations (597), (600), and (601), we obtain

- In mesh points internal to the domain:

$$\begin{aligned} & \frac{D_i}{\Delta x_i} [\phi_{i+1/2} - \phi_{i-1/2}] - \frac{D_{i-1}}{\Delta x_{i-1}} [\phi_{i-1/2} - \phi_{i-3/2}] \\ &= \frac{1}{2} \phi_{i-1/2} [\Delta x_i \Sigma_{r,i} + \Delta x_{i-1} \Sigma_{r,i-1}] - \frac{1}{2} [\Delta x_i Q_i^\diamond + \Delta x_{i-1} Q_{i-1}^\diamond], \end{aligned} \quad (603)$$

where we used the notation $\phi_{i-1/2} = \phi(x_{i-1/2})$.

- On zero-flux-boundary points:

$$\phi_{1/2} = 0 \quad \text{or} \quad \phi_{I+1/2} = 0. \quad (604)$$

- On the left-boundary point, assuming an *albedo-boundary condition*:

$$\frac{D_I}{\Delta x_1} [\phi_{3/2} - \phi_{1/2}] - \frac{1}{2} \frac{1 - \beta_-}{1 + \beta_-} \phi_{1/2} = \frac{1}{2} \Delta x_1 \Sigma_{r,1} \phi_{1/2} - \frac{1}{2} \Delta x_1 Q_1^\diamond. \quad (605)$$

- On the right-boundary point, assuming an *albedo-boundary condition*:

$$\frac{D_I}{\Delta x_I} [\phi_{I-1/2} - \phi_{I+1/2}] - \frac{1}{2} \frac{1 - \beta_+}{1 + \beta_+} \phi_{I+1/2} = \frac{1}{2} \Delta x_I \Sigma_{r,I} \phi_{I+1/2} - \frac{1}{2} \Delta x_I Q_I^\diamond. \quad (606)$$

The discretization process involves the transformation of (560) with its continuity and boundary conditions into a matrix system whose unknown vector, denoted Φ , is a set of neutron flux values selected at specific abscissa:

$$\Phi = \begin{pmatrix} \phi_{1/2} \\ \phi_{3/2} \\ \vdots \\ \phi_{I+1/2} \end{pmatrix}. \quad (607)$$

The matrix system is written as


$$\mathbb{A} \Phi = \mathbf{Q}, \quad (608)$$

where coefficient matrix \mathbb{A} and source vector \mathbf{Q} components correspond to the various terms of (603) to (606). Matrix \mathbb{A} is symmetric, positive definite, and diagonally dominant.

The numerical solution of (608) is greatly simplified by the particular structure of matrix \mathbb{A} . All its components are located in a *tridiagonal structure*, each component $\phi_{i-1/2}$ being related only to its two closest neighbors, $\phi_{i-3/2}$ and $\phi_{i+1/2}$. The wide acceptance of the mesh-corner finite-difference method is due to the observation that similar tridiagonal layouts are observed with two- and three-dimensional domains.

8.2 Mesh-Centered Finite Differences

The mesh-centered finite-difference method is an alternative to the mesh-corner finite-difference method frequently implemented in production codes for solving the neutron diffusion equation. It basically offers the same accuracy and the same advantages as the mesh-corner finite-difference method. However, the discretization errors originating from these two types of finite-difference methods are often of opposite sign: an overestimation of a power peak with one method is often associated with an underestimation with the other method. A careful mathematical study of this phenomenon reveals that the mesh-corner and mesh-centered finite-difference methods are the *Euler equations* of *primal* and *dual* variational formulations, respectively (Hébert 1993).

The mesh-centered finite-difference relations can be obtained in many different ways. We are presenting the simplest approach, which consists in assuming that the average neutron flux in a subregion is equal to the neutron flux at the center of this subregion. We consider the subregion surrounding the abscissa point x_i and write the neutron flux at this point, using  Fig. 38 to define the other abscissa values. We obtain

$$\phi_i = \phi(x_i) = \frac{1}{\Delta x_i} \int_{x_{i-1/2}}^{x_{i+1/2}} dx \phi(x). \quad (609)$$

The next step consists in integrating (563) over each subregion, so that

$$-D_i \int_{x_{i-1/2}}^{x_{i+1/2}} dx \frac{d^2 \phi}{dx^2} + \Sigma_{r,i} \int_{x_{i-1/2}}^{x_{i+1/2}} dx \phi(x) = \Delta x_i Q_i^\diamond, \quad (610)$$

where we assumed that neutron sources $Q^\diamond(x)$ are uniform and equal to Q_i^\diamond over subregion i .

The first term on the left can be integrated analytically. Introducing (609), we get

$$-D_i [\phi'(x_{i+1/2}^-) - \phi'(x_{i-1/2}^+)] + \Delta x_i \Sigma_{r,i} \phi(x_i) = \Delta x_i Q_i^\diamond. \quad (611)$$

The differential terms of (611) are replaced with finite-difference relations. These relations can be obtained from the following two Taylor expansions:

$$\phi(x_{i-1}) = \phi(x_{i-1/2}) - \frac{\Delta x_{i-1}}{2} \phi'(x_{i-1/2}^-) \quad (612)$$

and

$$\phi(x_i) = \phi(x_{i-1/2}) + \frac{\Delta x_i}{2} \phi'(x_{i-1/2}^+). \quad (613)$$

We also remember the neutron-current continuity condition at point $x_{i-1/2}$. This condition is written as

$$D_{i-1} \phi'(x_{i-1/2}^-) = D_i \phi'(x_{i-1/2}^+). \quad (614)$$

We multiply (612) and (613) by $D_{i-1}/\Delta x_{i-1}$ and $D_i/\Delta x_i$, respectively, and add these relations in such a way as to eliminate the derivatives of the flux with the help of (614). We obtain

$$\phi(x_{i-1/2}) = \frac{\Delta x_i D_{i-1} \phi(x_{i-1}) + \Delta x_{i-1} D_i \phi(x_i)}{\Delta x_i D_{i-1} + \Delta x_{i-1} D_i}. \quad (615)$$

After substitution of (615) into (613), we obtain our first mesh-centered finite-difference relation as

$$\phi' (x_{i-1/2}^+) = 2D_{i-1} \frac{\phi(x_i) - \phi(x_{i-1})}{\Delta x_i D_{i-1} + \Delta x_{i-1} D_i}. \quad (616)$$

Using a similar approach, we obtain a second mesh-centered finite-difference relation as

$$\phi' (x_{i+1/2}^-) = 2D_{i+1} \frac{\phi(x_{i+1}) - \phi(x_i)}{\Delta x_{i+1} D_i + \Delta x_i D_{i+1}}. \quad (617)$$

Let us now consider the case where the left-most surface is characterized by a *zero-flux boundary condition*. Setting $\phi(x_{1/2}) = 0$ in (613) leads to the corresponding finite-difference relation. It is written as

$$\phi' (x_{1/2}^+) = \frac{2}{\Delta x_1} \phi(x_1). \quad (618)$$

Similarly, if the left-most surface is characterized by an *albedo-boundary condition*, we combine (562) and (613) to obtain

$$\phi' (x_{1/2}^+) = \frac{2(1 - \beta_-)}{4D_1(1 + \beta_-) + \Delta x_1(1 - \beta_-)} \phi(x_1). \quad (619)$$

The substitution of finite-difference (616) to (619) into (611) leads to the complete set of mesh-centered finite-difference relations. A specific relation is written for each of the following situations:

- The subregion i is internal to the domain:

$$\begin{aligned} & 2 \left[D_i D_{i+1} \frac{\phi_{i+1} - \phi_i}{\Delta x_{i+1} D_i + \Delta x_i D_{i+1}} - D_i D_{i-1} \frac{\phi_i - \phi_{i-1}}{\Delta x_i D_{i-1} + \Delta x_{i-1} D_i} \right] \\ & = \Delta x_i \Sigma_{r,i} \phi_i - \Delta x_i Q_i^\diamond. \end{aligned} \quad (620)$$

- The left surface of subregion $i = 1$ is characterized by a zero-flux-boundary condition:

$$2 \left[D_1 D_2 \frac{\phi_2 - \phi_1}{\Delta x_2 D_1 + \Delta x_1 D_2} - \frac{D_1}{\Delta x_1} \phi_1 \right] = \Delta x_1 \Sigma_{r,1} \phi_1 - \Delta x_1 Q_1^\diamond. \quad (621)$$

- The left surface of subregion $i = 1$ is characterized by an albedo-boundary condition:

$$\begin{aligned} & 2 \left[D_1 D_2 \frac{\phi_2 - \phi_1}{\Delta x_2 D_1 + \Delta x_1 D_2} - \frac{D_1(1 - \beta_-)}{4D_1(1 + \beta_-) + \Delta x_1(1 - \beta_-)} \phi_1 \right] \\ & = \Delta x_1 \Sigma_{r,1} \phi_1 - \Delta x_1 Q_1^\diamond \end{aligned} \quad (622)$$

- The right surface of subregion $i = I$ is characterized by a zero-flux-boundary condition:

$$2 \left[-\frac{D_I}{\Delta x_I} \phi_I - D_I D_{I-1} \frac{\phi_I - \phi_{I-1}}{\Delta x_I D_{I-1} + \Delta x_{I-1} D_I} \right] = \Delta x_I \Sigma_{r,I} \phi_I - \Delta x_I Q_I^\diamond. \quad (623)$$

- The right surface of subregion $i = I$ is characterized by an albedo-boundary condition:

$$2 \left[-\frac{D_I(1 - \beta_+)}{4D_I(1 + \beta_+) + \Delta x_I(1 - \beta_+)} \phi_I - D_I D_{I-1} \frac{\phi_I - \phi_{I-1}}{\Delta x_I D_{I-1} + \Delta x_{I-1} D_I} \right] = \Delta x_I \Sigma_{r,I} \phi_I - \Delta x_I Q_I^\diamond \quad (624)$$

The matrix system produced by the mesh-centered finite-difference method is similar and has the same numerical properties as the matrix system produced by the mesh-corner finite-difference method. The principal distinction comes from the fact that the unknown vector is the set of all mesh-centered neutron flux values. It is written as

$$\Phi = \begin{pmatrix} \phi_1 \\ \phi_2 \\ \vdots \\ \phi_I \end{pmatrix}. \quad (625)$$

As before, the matrix system is written as

$$\mathbb{A} \Phi = \mathbf{Q}, \quad (626)$$

where coefficient matrix \mathbb{A} and source vector \mathbf{Q} components correspond to the various terms of Eqs. (620) to (624). Matrix \mathbb{A} is symmetric, positive definite, and diagonally dominant.

The spatial discretization order of the mesh-centered finite-difference method can be increased beyond the linear order presented in this text, leading to the *nodal collocation method* Hébert (1987).

8.3 A Primal Variational Formulation

It is possible to rewrite the diffusion equation (527), together with its continuity and boundary conditions, into a *variational formulation* that is mathematically equivalent. This approach is also known as the *Rayleigh–Ritz method* and provides a means to obtain approximate solutions to a differential equation by finding a stationary point of a related functional. Many variational formulations exist, but we will restrict ourselves to the kind based on the *one-speed primal functional*. This formulation enables us to obtain a solution for (527) inside a space of basic functions. The *Sobolev space* is the most general space that can be used. It is a vector space of functions $f(\mathbf{r})$ defined over domain V and bounded in the Sobolev sense. Elements of the Sobolev space $W_1(V)$ are L^2 -integrable over domain V and possess first derivatives that are also L^2 -integrable over domain V . Functions that are elements of $W_1(V)$ are therefore continuous over V . We write

$$W_1(V) = \left\{ f(\mathbf{r}); f(\mathbf{r}) \in L^2(V) \text{ and } \nabla f(\mathbf{r}) \in [L^2(V)]^3 \right\}, \quad (627)$$

where $L^2(V)$ is the set of functions defined over domain V , whose quadratic norm is bounded, so that

$$L^2(V) = \left\{ f(\mathbf{r}); \sqrt{\int_V d^3r [f(\mathbf{r})]^2} < \infty \right\}. \quad (628)$$

The elements of $W_1(V)$ are functions with less-restrictive continuity requirements than those imposed on the solution of (527). For example, it is possible to choose basis functions that do not satisfy (536). In this sense, a variational formulation is a *weak formulation*.

It is also possible to choose basis functions within a subset of $W_1(V)$. For example, a primal formulation restricts the choice to the set $\mathcal{D}(V)$ of functions that vanish over ∂V_0 , the domain boundary where a zero-flux condition is imposed. It is also possible to restrict ourselves to piecewise polynomial functions, leading to the *Lagrangian FEM*. Use of a primal variational formulation together with the Lagrangian FEM was first reported by Semenza (1972).

A variational formulation makes it possible to solve (527) by seeking a stationary point of a corresponding functional. The one-speed primal functional is written as

$$\begin{aligned} \mathcal{F} \{ \phi(\mathbf{r}) \} = & \frac{1}{2} \int_V d^3r \{ D(\mathbf{r}) \nabla \phi(\mathbf{r}) \cdot \nabla \phi(\mathbf{r}) + \Sigma_r(\mathbf{r}) [\phi(\mathbf{r})]^2 \\ & - 2\phi(\mathbf{r}) Q^\circ(\mathbf{r}) \} + \frac{1}{2} \int_{\partial V_\beta} d^2r \frac{1-\beta(\mathbf{r})}{2+\beta(\mathbf{r})} [\phi(\mathbf{r})]^2, \end{aligned} \quad (629)$$

where $\phi(\mathbf{r}) \in W_1(V) \cap \mathcal{D}(V)$, $\beta(\mathbf{r})$ is the albedo, and ∂V_β is the fraction of ∂V where the *albedo-boundary condition* is applied, so that $\partial V = \partial V_0 \cup \partial V_\beta$. We have suppressed the group index g in order to simplify the notation.

A stationary point of this functional is defined by the relation

$$\delta_{\delta\phi} \mathcal{F} \{ \phi(\mathbf{r}) \} = \lim_{\varepsilon \rightarrow 0} \left\{ \frac{d}{d\varepsilon} \mathcal{F} \{ \phi(\mathbf{r}) + \varepsilon \delta\phi(\mathbf{r}) \} \right\} = 0, \quad (630)$$

where $\delta\phi(\mathbf{r})$ is an arbitrary element of vector space $W_1(V) \cap \mathcal{D}(V)$. We thus obtain

$$\begin{aligned} \int_V d^3r \{ D(\mathbf{r}) \nabla \delta\phi(\mathbf{r}) \cdot \nabla \phi(\mathbf{r}) + \Sigma_r(\mathbf{r}) \delta\phi(\mathbf{r}) \phi(\mathbf{r}) \\ - \delta\phi(\mathbf{r}) Q^\circ(\mathbf{r}) \} + \int_{\partial V_\beta} d^2r \frac{1-\beta(\mathbf{r})}{2+\beta(\mathbf{r})} \delta\phi(\mathbf{r}) \phi(\mathbf{r}) = 0 \end{aligned} \quad (631)$$

$\forall \delta\phi(\mathbf{r}) \in W_1(V) \cap \mathcal{D}(V)$.

We divide the total reactor volume V into a set of subvolumes $\{V_i; i = 1, N\}$ over which constant diffusion coefficient $\{D_i; i = 1, N\}$ and constant removal cross-sections $\{\Sigma_{r,i}; i = 1, N\}$ are defined. Moreover, $\nabla\phi(\mathbf{r})$ and $\nabla\delta\phi(\mathbf{r})$ are assumed continuous inside each subvolume V_i . With the help of \blacktriangleright Fig. 40, we also define $\{\partial V_i; i = 1, N\}$ as surfaces surrounding each subvolume and $\mathbf{N}_i(\mathbf{r})$ as the normal unit vector pointing out of ∂V_i at \mathbf{r} . We note from \blacktriangleright Fig. 40 that $\mathbf{N}_i(\mathbf{r}) = -\mathbf{N}_j(\mathbf{r})$.

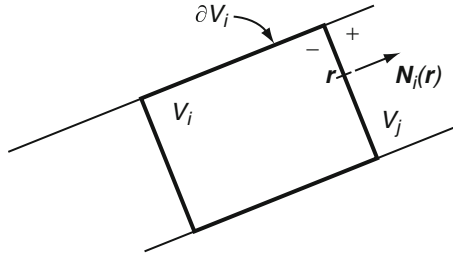


Figure 40

Variational formulation in diffusion theory

Let us now apply the Gauss divergence theorem over subvolume V_i , so that

$$\begin{aligned} \int_{V_i} d^3r D(\mathbf{r}) \nabla \delta \phi(\mathbf{r}) \cdot \nabla \phi(\mathbf{r}) &= - \int_{V_i} d^3r \delta \phi(\mathbf{r}) \nabla \cdot D(\mathbf{r}) \nabla \phi(\mathbf{r}) \\ &+ \int_{\partial V_i} d^2r \delta \phi(\mathbf{r}) D(\mathbf{r}_-) \nabla \phi(\mathbf{r}_-) \cdot \mathbf{N}_i(\mathbf{r}); \quad i = 1, N. \end{aligned} \quad (632)$$

We separate each surface ∂V_i into three parts, as

$$\partial V_i = \partial W_i + \partial V_{\beta,i} + \partial V_{0,i}, \quad (633)$$

where ∂W_i is the part of ∂V_i internal to domain V . Surfaces $\partial V_{\beta,i}$ and $\partial V_{0,i}$ are the part of ∂V_i belonging to ∂V_β and ∂V_0 , respectively.

Substituting (632) into (631), we obtain

$$\begin{aligned} \sum_{i=1}^N \int_{V_i} d^3r \delta \phi(\mathbf{r}) \left[- \nabla \cdot D(\mathbf{r}) \nabla \phi(\mathbf{r}) + \Sigma_r(\mathbf{r}) \phi(\mathbf{r}) - Q^\circ(\mathbf{r}) \right] \\ + \int_{\partial W_i} d^2r \delta \phi(\mathbf{r}) D(\mathbf{r}_-) \nabla \phi(\mathbf{r}_-) \cdot \mathbf{N}_i(\mathbf{r}) \\ + \int_{\partial V_{\beta,i}} d^2r \left[D(\mathbf{r}) \nabla \phi(\mathbf{r}) \cdot \mathbf{N}_i(\mathbf{r}) + \frac{1-\beta(\mathbf{r})}{2(1+\beta(\mathbf{r}))} \phi(\mathbf{r}) \right] = 0 \end{aligned} \quad (634)$$

$\forall \delta \phi(\mathbf{r}) \in W_1(V) \cap \mathcal{D}(V)$.

Hence $\phi(\mathbf{r})$ is a stationary point of functional (629) for all arbitrary variations $\delta \phi(\mathbf{r}) \in W_1(V) \cap \mathcal{D}(V)$ if, and only if,

$$- \nabla \cdot D(\mathbf{r}) \nabla \phi(\mathbf{r}) + \Sigma_r(\mathbf{r}) \phi(\mathbf{r}) = Q^\circ(\mathbf{r}), \quad \mathbf{r} \in V, \quad (635)$$

$$\sum_{i=1}^N \delta_i(\mathbf{r}) D_i \nabla \phi(\mathbf{r}_-) \cdot \mathbf{N}_i(\mathbf{r}) = 0 \quad (636)$$

with

$$\delta_i(\mathbf{r}) = \begin{cases} 1, & \text{if } \mathbf{r} \in \delta W_i, \\ 0, & \text{otherwise,} \end{cases} \quad (637)$$

and

$$D(\mathbf{r}) \nabla \phi(\mathbf{r}) \cdot \mathbf{N}(\mathbf{r}) + \frac{1}{2} \frac{1 - \beta(\mathbf{r})}{1 + \beta(\mathbf{r})} \phi(\mathbf{r}) = 0, \quad \mathbf{r} \in \partial V_\beta. \tag{638}$$

We have obtained the *Euler equations* of functional (629). Equation (635) is none other than the diffusion (527). Equation (636) is the current continuity condition for the particles inside the domain. Lastly, (638) is the *albedo-boundary condition* (542). In conclusion, a function $\phi(\mathbf{r})$ corresponding to a stationary point of functional (629) will respect current continuity and albedo-boundary conditions in addition to satisfying the diffusion equation. Conditions satisfied as a stationary point of a functional are said to be *natural conditions*. Conditions imposed on the trial functions, such as flux continuity or zero-flux boundary conditions, are said to be *essential conditions*.

8.4 The Lagrangian Finite-Element Method

The FEM is used for finding approximate solutions of partial differential equations. It is based on an expansion of the dependent variable(s), the particle flux in our case, into a linear combination of polynomial *trial functions* defined over subvolumes. The trial function space must be chosen so as to ensure that improvement in the numerical approximation occurs with an increase in the number I of subvolumes *and/or* with the degree K of the polynomial trial functions. The trial functions are known a priori and the corresponding coefficients can be found using a *weighted residual approach* or a *variational formulation* as introduced in [8.3](#). We have chosen to present the latter approach, as it brings two important benefits: (1) the intrinsic symmetry of the one-speed diffusion equation is always preserved by the discretization process and (2) the boundary conditions are introduced in a consistent way.

The polynomial basis $\{u_m(\mathbf{r}); m = 1, M\}$ with $u_m(\mathbf{r}) \in W_1(V) \cap \mathcal{D}(V)$ is used to span the neutron flux $\phi(\mathbf{r})$ and flux variation $\delta\phi(\mathbf{r})$ over V , according to

$$\phi(\mathbf{r}) = \sum_{m=1}^M \phi_m u_m(\mathbf{r}) \quad \text{and} \quad \delta\phi(\mathbf{r}) = \sum_{m=1}^M \delta\phi_m u_m(\mathbf{r}), \tag{639}$$

where the set of *variational coefficients* $\{\phi_m; m = 1, M\}$ represents the unknown vector or the numerical solution to be obtained by the FEM.

The FEM can be applied to various types and forms of subvolumes or *elements*. Cartesian and hexagonal elements are the most widely used in reactor physics for full-core calculations. A Cartesian domain is first partitioned into rectangular parallelepipeds over which the nuclear properties are assumed to be uniform. A polynomial basis is defined over each element by using full tensorial products of 1D polynomials up to a given order. In the case of a primal variational formulation, as introduced in [8.3](#), Lagrange polynomials are chosen as polynomial basis in order to satisfy the requirement that $u_m(\mathbf{r}) \in W_1(V) \cap \mathcal{D}(V)$.

We will consider a 1D Cartesian domain with I subvolumes, as depicted in [Fig. 38](#). Trial functions in space are transformed from the global coordinate x defined over element i with $x_{i-1/2} \leq x \leq x_{i+1/2}$ to local coordinate u defined over the unit domain, with $-1/2 \leq u \leq 1/2$. The following change of variable will be used:

$$u = \frac{1}{\Delta x_i} \left[x - \frac{1}{2} (x_{i-1/2} + x_{i+1/2}) \right], \tag{640}$$

where

$$\Delta x_i = x_{i+1/2} - x_{i-1/2}. \quad (641)$$

The polynomial trial functions are written as

$$u_m(x) = \sum_{i=1}^I \sum_{k=0}^K \delta_{i,k}^m L_k(u), \quad m = 1, M, \quad (642)$$

where I is the total number of elements and $\delta_{i,k}^m$ is the finite-element delta function, equal to 1 if the local unknown k in element i corresponds to the global unknown m , and 0 otherwise. Each element i serves as support for a local basis of order- K Lagrange polynomials. These polynomials are defined so as to preserve the continuity of the global trial functions, as required by our primal variational formulation.

- Linear Lagrange polynomials ($K = 1$): This local basis contains two linear Lagrange polynomials in 1D, defined for local base points $u_0 = -1/2$ and $u_1 = 1/2$. They are written as

$$L_0(u) = \frac{1}{2} - u \quad \text{and} \quad L_1(u) = \frac{1}{2} + u \quad (643)$$

so that $L_0(-1/2) = L_1(1/2) = 1$ and $L_0(1/2) = L_1(-1/2) = 0$.

In this case, the variational coefficients ϕ_m are the flux values at abscissas $x_{i-1/2}$ and $x_{i+1/2}$. Continuity of the trial functions is preserved if each coefficient ϕ_m , corresponding to an internal mesh, is shared by two elements. This condition is reached by using the correct values of the finite-element delta function. For example, if a domain has left- and right-albedo boundary conditions, then $\delta_{i,k}^m$ is defined as

$$\delta_{i,k}^m = \begin{cases} 1, & \text{if } m = i + k, \\ 0, & \text{otherwise.} \end{cases} \quad (644)$$

Similarly, if a domain has left- and right *zero-flux-boundary conditions*, then $\delta_{i,k}^m$ is defined as

$$\delta_{i,k}^m = \begin{cases} 0, & \text{if } i = 1 \text{ and } k = 0, \\ 0, & \text{if } i = I \text{ and } k = 1, \\ 1, & \text{if } m = i + k - 1, \\ 0, & \text{otherwise.} \end{cases} \quad (645)$$

- Parabolic Lagrange polynomials ($K = 2$): This local basis contains three parabolic Lagrange polynomials in 1D. They are written as

$$L_0(u) = -\frac{1}{8} - u + \frac{5u^2}{2}, \quad L_1(u) = \frac{5}{4} - 5u^2, \quad \text{and} \quad L_2(u) = -\frac{1}{8} + u + \frac{5u^2}{2}. \quad (646)$$

Again, the continuity of trial functions will be satisfied if some coefficients ϕ_m are shared by two elements. For example, if a domain has left- and right-albedo boundary conditions, then $\delta_{i,k}^m$ is defined as

$$\delta_{i,k}^m = \begin{cases} 1, & \text{if } m = 2i + k - 1, \\ 0, & \text{otherwise.} \end{cases} \quad (647)$$

Similarly, if a domain has left- and right zero-flux-boundary conditions, then $\delta_{i,k}^m$ is defined as

$$\delta_{i,k}^m = \begin{cases} 0, & \text{if } i = 1 \text{ and } k = 0, \\ 0, & \text{if } i = I \text{ and } k = 2, \\ 1, & \text{if } m = 2i + k - 2, \\ 0, & \text{otherwise.} \end{cases} \tag{648}$$

- Cubic Lagrange polynomials ($K=3$): This local basis contains four parabolic Lagrange polynomials in 1D. They are written as

$$\begin{aligned} L_0(u) &= -\frac{1}{8} + \frac{3u}{4} + \frac{5u^2}{2} - 7u^3, & L_1(u) &= \frac{5}{8} - \frac{5\sqrt{7}u}{4} - \frac{5u^2}{2} + 5\sqrt{7}u^3, \\ L_2(u) &= \frac{5}{8} + \frac{5\sqrt{7}u}{4} - \frac{5u^2}{2} - 5\sqrt{7}u^3, & \text{and } L_3(u) &= -\frac{1}{8} - \frac{3u}{4} + \frac{5u^2}{2} + 7u^3. \end{aligned} \tag{649}$$

Again, the continuity of trial functions will be satisfied if some coefficients ϕ_m are shared by two elements. For example, if a domain has left- and right-albedo-boundary conditions, then $\delta_{i,k}^m$ is defined as

$$\delta_{i,k}^m = \begin{cases} 1, & \text{if } m = 3i + k - 2, \\ 0, & \text{otherwise.} \end{cases} \tag{650}$$

Similarly, if a domain has left- and right-zero-flux-boundary conditions, then $\delta_{i,k}^m$ is defined as

$$\delta_{i,k}^m = \begin{cases} 0, & \text{if } i = 1 \text{ and } k = 0, \\ 0, & \text{if } i = I \text{ and } k = 3, \\ 1, & \text{if } m = 3i + k - 3, \\ 0, & \text{otherwise.} \end{cases} \tag{651}$$

Having defined our space of polynomial trial functions, we need to find the variational coefficients corresponding to the solution of the diffusion equation. Using the variational approach introduced in [8.3](#), we first rewrite (631) for the particular case of a Cartesian 1D domain. We have

$$\begin{aligned} \sum_{i=1}^I \int_{x_{i-1/2}}^{x_{i+1/2}} dx [D_i \nabla \delta \phi(x) \cdot \nabla \phi(x) + \Sigma_{r,i} \delta \phi(x) \phi(x) - \delta \phi(x) Q^\circ(x)] \\ + \mathcal{B}_- \delta \phi(x_{1/2}) \phi(x_{1/2}) + \mathcal{B}_+ \delta \phi(x_{I+1/2}) \phi(x_{I+1/2}) = 0 \end{aligned} \tag{652}$$

$\forall \delta \phi(x) \in W_1(V) \cap \mathcal{D}(V)$. The two boundary terms \mathcal{B}_- and \mathcal{B}_+ are defined as

$$\mathcal{B}_- = \begin{cases} \frac{1}{2} \frac{1 - \beta_-}{1 + \beta_-}, & \text{if the domain has a left-albedo condition,} \\ 0, & \text{otherwise.} \end{cases} \tag{653}$$

and

$$\mathcal{B}_+ = \begin{cases} \frac{1}{2} \frac{1 - \beta_+}{1 + \beta_+}, & \text{if the domain has a right-albedo condition,} \\ 0, & \text{otherwise.} \end{cases} \tag{654}$$

We next define a linear product and two different types of bilinear products:

$$\langle Q^\diamond u_m \rangle = \sum_{i=1}^I \int_{x_{i-1/2}}^{x_{i+1/2}} dx Q^\diamond(x) u_m(x), \quad (655)$$

$$\langle \nabla u_m, D \nabla u_n \rangle = \sum_{i=1}^I \int_{x_{i-1/2}}^{x_{i+1/2}} dx D_i \nabla u_m(x) \cdot \nabla u_n(x) \quad (656)$$

and

$$\langle u_m, \Sigma u_n \rangle = \sum_{i=1}^I \int_{x_{i-1/2}}^{x_{i+1/2}} dx \Sigma_i u_m(x) u_n(x). \quad (657)$$

These bilinear products can be expressed for a Lagrangian FEM as

$$\langle \nabla u_m, D \nabla u_n \rangle = \sum_{i=1}^I \frac{D_i}{\Delta x_i} \sum_{k=0}^K \sum_{\ell=0}^K \delta_{i,k}^m \delta_{i,\ell}^n Q_{k,\ell} \quad (658)$$

and

$$\langle u_m, \Sigma u_n \rangle = \sum_{i=1}^I \Delta x_i \Sigma_i \sum_{k=0}^K \sum_{\ell=0}^K \delta_{i,k}^m \delta_{i,\ell}^n M_{k,\ell}. \quad (659)$$

Substitution of (655) to (657) into (652) leads to the discretized linear system, corresponding to the one-speed neutron diffusion equation. We write

$$\left\{ \sum_{m=1}^M \phi_m [\langle \nabla u_m, D \nabla u_n \rangle + \langle u_m, \Sigma_r u_n \rangle] \right\} + \phi_1 \mathcal{B}_- \delta_{n,1} + \phi_M \mathcal{B}_+ \delta_{n,M} = \langle Q^\diamond u_n \rangle, \quad (660)$$

where $n = 1, M$.

System (660) is a linear matrix system of the form $\mathbb{A} \Phi = \mathbf{Q}$ where the coefficient matrix \mathbb{A} is symmetric, positive definite, and diagonally dominant. Its resolution can be performed using standard numerical techniques.

Equations (658) and (659) are written in terms of the FEM *mass matrix* $\{M_{k,\ell}, k = 0, K \text{ and } \ell = 0, K\}$ and *stiffness matrix* $\{Q_{k,\ell}, k = 0, K \text{ and } \ell = 0, K\}$, defined as

$$M_{k,\ell} = \int_{-1/2}^{1/2} du L_k(u) L_\ell(u) \quad (661)$$

and

$$Q_{k,\ell} = \int_{-1/2}^{1/2} du \frac{d}{du} L_k(u) \frac{d}{du} L_\ell(u). \quad (662)$$

These unit matrices can be integrated analytically, leading to

- Linear Lagrange polynomials ($K = 1$):

$$\mathbb{M}_1 = \begin{bmatrix} \frac{1}{3} & \frac{1}{6} \\ \frac{1}{6} & \frac{1}{3} \end{bmatrix} \quad \text{and} \quad \mathbb{Q}_1 = \begin{bmatrix} 1 & -1 \\ -1 & 1 \end{bmatrix}. \quad (663)$$

- Parabolic Lagrange polynomials ($K = 2$):

$$\mathbb{M}_2 = \begin{bmatrix} \frac{1}{8} & 0 & -\frac{1}{24} \\ 0 & \frac{5}{6} & 0 \\ -\frac{1}{24} & 0 & \frac{1}{8} \end{bmatrix} \quad \text{and} \quad \mathbb{Q}_2 = \begin{bmatrix} \frac{37}{12} & -\frac{25}{6} & \frac{13}{12} \\ -\frac{25}{6} & \frac{25}{3} & -\frac{25}{6} \\ \frac{13}{12} & -\frac{25}{6} & \frac{37}{12} \end{bmatrix}. \quad (664)$$

- Cubic Lagrange polynomials ($K = 3$):

$$\mathbb{M}_3 = \begin{bmatrix} \frac{1}{15} & 0 & 0 & \frac{1}{60} \\ 0 & \frac{5}{12} & 0 & 0 \\ 0 & 0 & \frac{5}{12} & 0 \\ \frac{1}{60} & 0 & 0 & \frac{1}{15} \end{bmatrix} \quad (665)$$

and

$$\mathbb{Q}_3 = \begin{bmatrix} \frac{83}{15} & -\frac{21\sqrt{7}+25}{12} & \frac{21\sqrt{7}-25}{12} & -\frac{41}{30} \\ -\frac{21\sqrt{7}+25}{12} & \frac{65}{6} & -\frac{20}{3} & \frac{21\sqrt{7}-25}{12} \\ \frac{21\sqrt{7}-25}{12} & -\frac{20}{3} & \frac{65}{6} & -\frac{21\sqrt{7}+25}{12} \\ -\frac{41}{30} & \frac{21\sqrt{7}-25}{12} & -\frac{21\sqrt{7}+25}{12} & \frac{83}{15} \end{bmatrix}. \quad (666)$$

We have presented the FEM in its simplest implementation. The Lagrangian formulation can be modified by using numerical integration to obtain the mass and stiffness matrices of (661) and (662). Using a *Gauss–Lobatto quadrature* with linear Lagrange polynomials produces a numerical solution that is equivalent to the mesh-corner finite-difference method of [8.1](#). Using a *Gauss–Legendre quadrature* leads to *superconvergent* approximations. Discretization of 2D and 3D domains with a Lagrangian FEM produces a matrix system that is not compatible with the alternating direction implicit (ADI) method. This incompatibility is due to the off-diagonal term present in the mass matrices of (663) to (665). This off-diagonal term can be suppressed by using a Gauss–Lobatto quadrature, leading to the primal finite-element approximations of the TRIVAC code (Hébert 1987).

The *Raviart–Thomas (1977) finite element* method introduces an important class of approximations, based on a *mixed-dual variational formulation*. These methods have been applied to the solution of the neutron diffusion equation in 3D Cartesian and hexagonal domains in Hébert (1993) and Hébert (2008), respectively. A linear Raviart–Thomas FEM, with Gauss–Lobatto integration of the unit matrices, is equivalent to the mesh-centered finite-difference method of [8.2](#). All Raviart–Thomas FEMs produce approximations that are compatible with the ADI method and with the TRIVAC code.

8.5 The Analytic Nodal Method in 2D Cartesian Geometry

The 2D Cartesian heterogeneous-reactor configurations correspond to the case where the neutron flux is a function of two spatial variables. These cases cannot be solved analytically and the analytic nodal method (ANM) is an attempt to find the solution with the *smallest possible approximation*. Here, we are limiting our investigations to a 2D Cartesian domain made from the assembly of many x – y rectangular nodes which are infinite in the z direction.

In this case, the nuclear properties of the reactor are only a function of the independent variables x and y . Equation (530) simplifies to

$$\begin{aligned} & -\frac{\partial}{\partial x} D_g(x, y) \frac{\partial \phi_g}{\partial x} - \frac{\partial}{\partial y} D_g(x, y) \frac{\partial \phi_g}{\partial y} + \Sigma_{rg}(x, y) \phi_g(x, y) = Q_g^\circ(x, y) \\ & = \sum_{\substack{h=1 \\ h \neq g}}^G \Sigma_{g \leftarrow h}(x, y) \phi_h(x, y) + \frac{\chi_g(x, y)}{K_{\text{eff}}} \sum_{h=1}^G v \Sigma_{fh}(x, y) \phi_h(x, y). \end{aligned} \quad (667)$$

Each node is assumed to be homogenous, so that the corresponding nuclear properties $D_g(x, y)$, $\Sigma_{rg}(x, y)$, $\Sigma_{g \leftarrow h}(x, y)$, $\chi_g(x, y)$, and $v \Sigma_{fh}(x, y)$ are piecewise continuous. As shown in Fig. 41, the reactor domain is divided into $I \times J$ regions of indices $1 \leq i \leq I$ and $1 \leq j \leq J$, in such a way that the nuclear properties in region i, j are constant and equal to $D_{g,i,j}$, $\Sigma_{rg,i,j}$, $\Sigma_{g \leftarrow h,i,j}$, $\chi_{g,i,j}$, and $v \Sigma_{fh,i,j}$.

The linear transformation technique of 7.4 is applied on each node, leading to the linear transformation $G \times G$ matrix $\mathbb{T}_{i,j}$ and to a set of G eigenvalues $\lambda_{\ell,i,j}$. The transformation process is repeated for each node, leading to $I \times J$ matrix equations written as

$$\frac{\partial^2}{\partial x^2} \Psi(x, y) + \frac{\partial^2}{\partial y^2} \Psi(x, y) + \text{diag}(\lambda_{\ell,i,j}) \Psi(x, y) = \mathbf{0} \quad (668)$$

if $x_{i-1/2} < x < x_{i+1/2}$ and $y_{j-1/2} < y < y_{j+1/2}$. Each equation is uncoupled in energy, and can be written as G differential equations of the form

$$\frac{\partial^2}{\partial x^2} \psi_g(x, y) + \frac{\partial^2}{\partial y^2} \psi_g(x, y) + \lambda_{g,i,j} \psi_g(x, y) = 0, \quad g = 1, G. \quad (669)$$

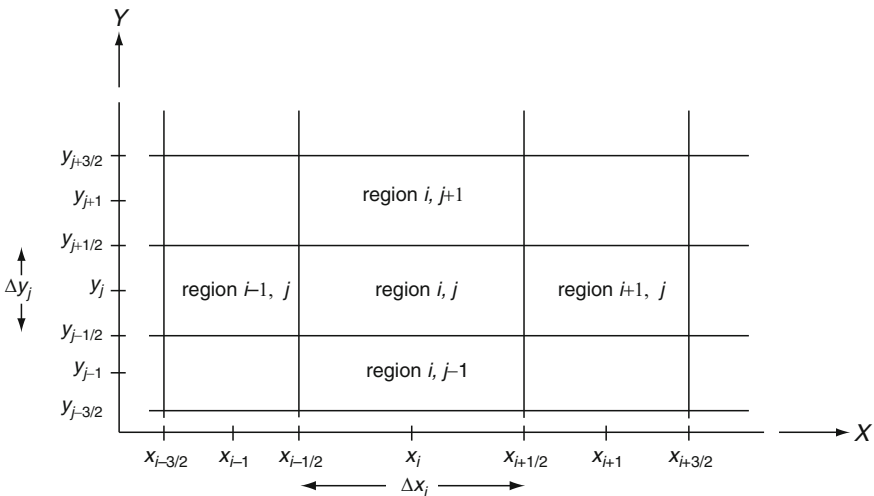


Figure 41

Definition of the regions in 2D Cartesian geometry

Unfortunately, it is impossible to find the analytical solution of (669) because its dependent variable $\psi_g(x, y)$ is generally not separable. The ANM is based on *transverse integration* of (669). Transverse integration along the Y -axis leads to

$$\int_{y_{j-1/2}}^{y_{j+1/2}} dy \frac{\partial^2}{\partial x^2} \psi_g(x, y) + \int_{y_{j-1/2}}^{y_{j+1/2}} dy \frac{\partial^2}{\partial y^2} \psi_g(x, y) + \lambda_{g,i,j} \int_{y_{j-1/2}}^{y_{j+1/2}} dy \psi_g(x, y) = 0, \quad (670)$$

which can be rewritten as

$$\frac{\partial^2}{\partial x^2} \psi_{g,j}^y(x) + \lambda_{g,i,j} \psi_{g,j}^y(x) = \frac{1}{\Delta y_j} \mathcal{F}_{g,j}^y(x), \quad (671)$$

where $\Delta y_j = y_{j+1/2} - y_{j-1/2}$,

$$\psi_{g,j}^y(x) = \frac{1}{\Delta y_j} \int_{y_{j-1/2}}^{y_{j+1/2}} dy \psi_g(x, y) \quad (672)$$

and where we introduced the X -directed *transverse-leakage* term as

$$\mathcal{F}_{g,j}^y(x) = - \int_{y_{j-1/2}}^{y_{j+1/2}} dy \frac{\partial^2}{\partial y^2} \psi_g(x, y) = - \left. \frac{\partial}{\partial y} \psi_g(x, y) \right|_{y_{j-1/2}}^{y_{j+1/2}}. \quad (673)$$

Similarly, the transverse integration along the X -axis leads to

$$\frac{\partial^2}{\partial y^2} \psi_{g,i}^x(y) + \lambda_{g,i,j} \psi_{g,i}^x(y) = \frac{1}{\Delta x_i} \mathcal{F}_{g,i}^x(y), \quad (674)$$

where $\Delta x_i = x_{i+1/2} - x_{i-1/2}$,

$$\psi_{g,i}^x(y) = \frac{1}{\Delta x_i} \int_{x_{i-1/2}}^{x_{i+1/2}} dx \psi_g(x, y) \quad (675)$$

and where we introduced the Y -directed *transverse-leakage* term as

$$\mathcal{F}_{g,i}^x(y) = - \int_{x_{i-1/2}}^{x_{i+1/2}} dx \frac{\partial^2}{\partial x^2} \psi_g(x, y) = - \left. \frac{\partial}{\partial x} \psi_g(x, y) \right|_{x_{i-1/2}}^{x_{i+1/2}}. \quad (676)$$

Equations (671) and (674) can be solved analytically, provided that the x and y variation of the transverse-leakage terms $\mathcal{F}_{g,j}^y(x)$ and $\mathcal{F}_{g,i}^x(y)$ are known. This is where we introduce the *unique* approximation of the ANM. Many possibilities exist to predict this variation, and have been investigated in the 1970s. Shober (1976) initially assumed that the transverse leakages and the 1D fluxes had the same shape. He wrote

$$\begin{aligned} \mathcal{F}_{g,j}^y(x) &= B_{g,i,j}^y \psi_{g,j}^y(x), \\ \mathcal{F}_{g,i}^x(y) &= B_{g,i,j}^x \psi_{g,i}^x(y). \end{aligned} \quad (677)$$

This *buckling*-type approximation would be exact if the dependent-variable $\psi_g(x, y)$ were spatially separable within node (i, j) . However, Shober found that the use of the buckling

approximation led to large errors in highly nonseparable cases. As an alternative to the buckling approximation, Shober proposed to use a *flat leakage approximation* in which the transverse-leakage shape is spatially flat over each node, leading to

$$\begin{aligned}\mathcal{F}_{g,j}^y(x) &= \bar{\mathcal{F}}_{g,i,j}^y = \mathcal{J}_{g,i}^x(y_{j+1/2}) - \mathcal{J}_{g,i}^x(y_{j-1/2}), \\ \mathcal{F}_{g,i}^x(y) &= \bar{\mathcal{F}}_{g,i,j}^x = \mathcal{J}_{g,j}^y(x_{i+1/2}) - \mathcal{J}_{g,j}^y(x_{i-1/2}),\end{aligned}\quad (678)$$

where the *transformed currents* are defined as

$$\mathcal{J}_{g,j}^y(x) \equiv -\frac{\partial}{\partial x} \psi_{g,j}^y(x) \quad \text{and} \quad \mathcal{J}_{g,i}^x(y) \equiv -\frac{\partial}{\partial y} \psi_{g,i}^x(y). \quad (679)$$

Later, Smith introduced a *quadratic-leakage approximation* in the ANM, leading to the version that is now currently used in legacy codes (Smith 1979). The expansion coefficients of the leakage fit are calculated by assuming that the quadratic polynomial extends over the two neighboring nodes and satisfies the average leakages in the central and two neighboring nodes. The quadratic leakage fit does not rely on the diffusion equation itself and can only be justified if the transverse leakages vary smoothly across the three nodes. Such an approximation can be constructed for node (i, j) , in the X -direction, using $\bar{F}_{g,i-1,j}^y$, $\bar{F}_{g,i,j}^y$ and $\bar{F}_{g,i+1,j}^y$, the transverse-leakage terms *without* linear transformation. In his thesis, Smith developed the ANM with a quadratic leakage approximation in two-group, 3D-Cartesian geometry. In this handbook, we will restrict ourselves to the flat-leakage approximation in G -group, 2D-Cartesian geometry.

Under these conditions, (671) is rewritten as

$$\frac{\partial^2}{\partial x^2} \psi_{g,j}^y(x) + \lambda_{g,i,j} \psi_{g,j}^y(x) = \frac{1}{\Delta y_j} [\mathcal{J}_{g,i}^x(y_{j+1/2}) - \mathcal{J}_{g,i}^x(y_{j-1/2})]. \quad (680)$$

Integration of (680) over node (i, j) leads to the transformed *nodal balance equation*, written as

$$\begin{aligned}\bar{\psi}_{g,i,j} &= \frac{1}{\Delta x_i \lambda_{g,i,j}} [\mathcal{J}_{g,j}^y(x_{i+1/2}) - \mathcal{J}_{g,j}^y(x_{i-1/2})] \\ &+ \frac{1}{\Delta y_j \lambda_{g,i,j}} [\mathcal{J}_{g,i}^x(y_{j+1/2}) - \mathcal{J}_{g,i}^x(y_{j-1/2})].\end{aligned}\quad (681)$$

Let us first consider the case where $\lambda_{g,i,j} \geq 0$. In energy group g and in node (i, j) , (680) has an analytical solution of the form

$$\begin{aligned}\psi_{g,j}^y(x) &= \frac{1}{\Delta y_j \lambda_{g,i,j}} [\mathcal{J}_{g,i}^x(y_{j+1/2}) - \mathcal{J}_{g,i}^x(y_{j-1/2})] \\ &+ A_{g,i,j} \cos(\sqrt{\lambda_{g,i,j}} x) + B_{g,i,j} \sin(\sqrt{\lambda_{g,i,j}} x)\end{aligned}\quad (682)$$

if $x_{i-1/2} < x < x_{i+1/2}$.

Integrating (682) over the node leads to

$$\begin{aligned}\bar{\psi}_{g,i,j} &= \frac{1}{\Delta y_j \lambda_{g,i,j}} [\mathcal{J}_{g,i}^x(y_{j+1/2}) - \mathcal{J}_{g,i}^x(y_{j-1/2})] + \frac{A_{g,i,j}}{\Delta x_i \sqrt{\lambda_{g,i,j}}} \sin(\sqrt{\lambda_{g,i,j}} x) \Big|_{x_{i-1/2}}^{x_{i+1/2}} \\ &- \frac{B_{g,i,j}}{\Delta x_i \sqrt{\lambda_{g,i,j}}} \cos(\sqrt{\lambda_{g,i,j}} x) \Big|_{x_{i-1/2}}^{x_{i+1/2}}.\end{aligned}\quad (683)$$

Differentiating (682) over the node leads to

$$\mathcal{J}_{g,j}^y(x) = A_{g,i,j} \sqrt{\lambda_{g,i,j}} \sin(\sqrt{\lambda_{g,i,j}} x) - B_{g,i,j} \sqrt{\lambda_{g,i,j}} \cos(\sqrt{\lambda_{g,i,j}} x). \quad (684)$$

Equations (682) to (684) can be rewritten, if $\lambda_{g,i,j} \leq 0$, as

$$\begin{aligned} \psi_{g,j}^y(x) &= \frac{1}{\Delta y_j \lambda_{g,i,j}} [\mathcal{J}_{g,i}^x(y_{j+1/2}) - \mathcal{J}_{g,i}^x(y_{j-1/2})] \\ &\quad + C_{g,i,j} \cosh(\sqrt{-\lambda_{g,i,j}} x) + E_{g,i,j} \sinh(\sqrt{-\lambda_{g,i,j}} x), \end{aligned} \quad (685)$$

$$\begin{aligned} \bar{\psi}_{g,i,j} &= \frac{1}{\Delta y_j \lambda_{g,i,j}} [\mathcal{J}_{g,i}^x(y_{j+1/2}) - \mathcal{J}_{g,i}^x(y_{j-1/2})] \\ &\quad + \frac{C_{g,i,j}}{\Delta x_i \sqrt{-\lambda_{g,i,j}}} \sinh(\sqrt{-\lambda_{g,i,j}} x) \Big|_{x_{i-1/2}}^{x_{i+1/2}} \\ &\quad + \frac{E_{g,i,j}}{\Delta x_i \sqrt{-\lambda_{g,i,j}}} \cosh(\sqrt{-\lambda_{g,i,j}} x) \Big|_{x_{i-1/2}}^{x_{i+1/2}} \end{aligned} \quad (686)$$

and

$$\mathcal{J}_{g,j}^y(x) = -C_{g,i,j} \sqrt{-\lambda_{g,i,j}} \sin h(\sqrt{-\lambda_{g,i,j}} x) - E_{g,i,j} \sqrt{-\lambda_{g,i,j}} \cos h(\sqrt{-\lambda_{g,i,j}} x). \quad (687)$$

To proceed further, we need to rewrite Eqs. (682) to (687) in matrix algebra. We define

$$\begin{aligned} \Psi_j^y(x) &= \{\psi_{g,j}^y(x), g = 1, G\}, \\ \bar{\Psi}_{i,j} &= \{\bar{\psi}_{g,i,j}, g = 1, G\}, \\ \mathcal{J}_j^y(x) &= \{\mathcal{J}_{g,j}^y(x), g = 1, G\}, \\ \mathcal{J}_i^x(y) &= \{\mathcal{J}_{g,i}^x(y), g = 1, G\}, \\ \mathbf{A}_{i,j} &= \{A_{g,i,j}, g = 1, G\}, \\ \mathbf{B}_{i,j} &= \{B_{g,i,j}, g = 1, G\} \end{aligned}$$

so that the above equations can be cast into

$$\begin{bmatrix} \bar{\Psi}_{i,j} \\ \mathcal{J}_j^y(x_{i-1/2}) \end{bmatrix} = \mathbb{M}_{i,j}^- \begin{bmatrix} \mathbf{A}_{i,j} \\ \mathbf{B}_{i,j} \end{bmatrix} + \begin{bmatrix} -\mathbb{Y}_{i,j} & \mathbb{Y}_{i,j} \\ \mathbb{O} & \mathbb{O} \end{bmatrix} \begin{bmatrix} \mathcal{J}_i^x(y_{j-1/2}) \\ \mathcal{J}_i^x(y_{j+1/2}) \end{bmatrix}, \quad (688)$$

$$\begin{bmatrix} \bar{\Psi}_{i,j} \\ \mathcal{J}_j^y(x_{i+1/2}) \end{bmatrix} = \mathbb{M}_{i,j}^+ \begin{bmatrix} \mathbf{A}_{i,j} \\ \mathbf{B}_{i,j} \end{bmatrix} + \begin{bmatrix} -\mathbb{Y}_{i,j} & \mathbb{Y}_{i,j} \\ \mathbb{O} & \mathbb{O} \end{bmatrix} \begin{bmatrix} \mathcal{J}_i^x(y_{j-1/2}) \\ \mathcal{J}_i^x(y_{j+1/2}) \end{bmatrix}, \quad (689)$$

$$\Psi_j^y(x_{i-1/2}) = \mathbb{N}_{i,j}^- \begin{bmatrix} \mathbf{A}_{i,j} \\ \mathbf{B}_{i,j} \end{bmatrix} + \begin{bmatrix} -\mathbb{Y}_{i,j} & \mathbb{Y}_{i,j} \\ \mathbb{O} & \mathbb{O} \end{bmatrix} \begin{bmatrix} \mathcal{J}_i^x(y_{j-1/2}) \\ \mathcal{J}_i^x(y_{j+1/2}) \end{bmatrix} \quad (690)$$

and

$$\Psi_j^y(x_{i+1/2}) = \mathbb{N}_{i,j}^+ \begin{bmatrix} \mathbf{A}_{i,j} \\ \mathbf{B}_{i,j} \end{bmatrix} + \begin{bmatrix} -\mathbb{Y}_{i,j} & \mathbb{Y}_{i,j} \\ \mathbb{O} & \mathbb{O} \end{bmatrix} \begin{bmatrix} \mathcal{J}_i^x(y_{j-1/2}) \\ \mathcal{J}_i^x(y_{j+1/2}) \end{bmatrix}, \quad (691)$$

where $\mathbb{M}_{i,j}^\mp$ are two $2G \times 2G$ matrices, $\mathbb{N}_{i,j}^\mp$ are two $G \times 2G$ matrices, and $\mathbb{Y}_{i,j}$ is a $G \times G$ matrix whose coefficients are recovered from (682) to (687). Coefficients $\mathbf{A}_{i,j}$ and $\mathbf{B}_{i,j}$ from (690) can be eliminated using (688) and coefficients $\mathbf{A}_{i,j}$ and $\mathbf{B}_{i,j}$ from (691) can be eliminated using (689). The resulting equations can be cast into

$$\Psi_j^y(x_{i-1/2}) = \mathbb{P}_{i,j} \begin{bmatrix} \tilde{\Psi}_{i,j} \\ \mathcal{J}_j^y(x_{i-1/2}) \\ \mathcal{J}_i^x(y_{j-1/2}) \\ \mathcal{J}_i^x(y_{j+1/2}) \end{bmatrix} \quad \text{and} \quad \Psi_j^y(x_{i+1/2}) = \mathbb{Q}_{i,j} \begin{bmatrix} \tilde{\Psi}_{i,j} \\ \mathcal{J}_j^y(x_{i+1/2}) \\ \mathcal{J}_i^x(y_{j-1/2}) \\ \mathcal{J}_i^x(y_{j+1/2}) \end{bmatrix}, \quad (692)$$

where $\mathbb{P}_{i,j}$ and $\mathbb{Q}_{i,j}$ are two $G \times 4G$ matrices.

The transformed nodal balance equation (681) can be written in matrix form as

$$\tilde{\Psi}_{i,j} = [-\mathbb{X}_{i,j} \quad \mathbb{X}_{i,j}] \begin{bmatrix} \mathcal{J}_j^y(x_{i-1/2}) \\ \mathcal{J}_j^y(x_{i+1/2}) \end{bmatrix} + [-\mathbb{Y}_{i,j} \quad \mathbb{Y}_{i,j}] \begin{bmatrix} \mathcal{J}_i^x(y_{j-1/2}) \\ \mathcal{J}_i^x(y_{j+1/2}) \end{bmatrix}. \quad (693)$$

Finally, the linear transformation can be inverted, with the help of the following definitions:

$$\begin{aligned} \Phi_j^y(x) &= \{ \phi_{g,j}^y(x); \quad g = 1, G \} = \mathbb{T}_{i,j} \Psi_j^y(x), \\ \tilde{\Phi}_{i,j} &= \{ \tilde{\phi}_{g,i,j}^y; \quad g = 1, G \} = \mathbb{T}_{i,j} \tilde{\Psi}_{i,j}, \\ J_j^y(x) &= \left\{ -D_{g,i,j} \frac{d}{dx} \phi_{g,j}^y(x); \quad g = 1, G \right\} = \text{diag}(D_{g,i,j}) \mathbb{T}_{i,j} \mathcal{J}_j^y(x), \\ S_{i,j} &= \mathbb{T}_{i,j}^{-1} \text{diag}(D_{g,i,j})^{-1}. \end{aligned}$$

We can show that

$$\Phi_j^y(x_{i-1/2}) = \mathbb{L}_{i,j} \begin{bmatrix} \tilde{\Phi}_{i,j} \\ J_j^y(x_{i-1/2}) \\ J_i^x(y_{j-1/2}) \\ J_i^x(y_{j+1/2}) \end{bmatrix} \quad \text{and} \quad \Phi_j^y(x_{i+1/2}) = \mathbb{R}_{i,j} \begin{bmatrix} \tilde{\Phi}_{i,j} \\ J_j^y(x_{i+1/2}) \\ J_i^x(y_{j-1/2}) \\ J_i^x(y_{j+1/2}) \end{bmatrix}, \quad (694)$$

where

$$\mathbb{L}_{i,j} = \mathbb{T}_{i,j} \mathbb{P}_{i,j} \begin{bmatrix} \mathbb{T}_{i,j}^{-1} & \mathbb{O} & \mathbb{O} & \mathbb{O} \\ \mathbb{O} & \mathbb{S}_{i,j} & \mathbb{O} & \mathbb{O} \\ \mathbb{O} & \mathbb{O} & \mathbb{S}_{i,j} & \mathbb{O} \\ \mathbb{O} & \mathbb{O} & \mathbb{O} & \mathbb{S}_{i,j} \end{bmatrix} \quad (695)$$

and

$$\mathbb{R}_{i,j} = \mathbb{T}_{i,j} \mathbb{Q}_{i,j} \begin{bmatrix} \mathbb{T}_{i,j}^{-1} & \mathbb{O} & \mathbb{O} & \mathbb{O} \\ \mathbb{O} & \mathbb{S}_{i,j} & \mathbb{O} & \mathbb{O} \\ \mathbb{O} & \mathbb{O} & \mathbb{S}_{i,j} & \mathbb{O} \\ \mathbb{O} & \mathbb{O} & \mathbb{O} & \mathbb{S}_{i,j} \end{bmatrix}. \quad (696)$$

The X-directed ANM-coupling relations are therefore written by imposing the flux continuity on $x_{i-1/2}$ as

$$\mathbb{R}_{i-1,j} \begin{bmatrix} \tilde{\Phi}_{i-1,j} \\ J_j^y(x_{i-1/2}) \\ J_{i-1}^x(y_{j-1/2}) \\ J_{i-1}^x(y_{j+1/2}) \end{bmatrix} = \mathbb{L}_{i,j} \begin{bmatrix} \tilde{\Phi}_{i,j} \\ J_j^y(x_{i-1/2}) \\ J_i^x(y_{j-1/2}) \\ J_i^x(y_{j+1/2}) \end{bmatrix}. \quad (697)$$

The nodal balance equation can be written in terms of nontransformed variables as

$$\bar{\Phi}_{i,j} = \mathbb{B}_{i,j} \begin{bmatrix} J_j^y(x_{i-1/2}) \\ J_j^y(x_{i+1/2}) \end{bmatrix} + \mathbb{C}_{i,j} \begin{bmatrix} J_i^x(y_{j-1/2}) \\ J_i^x(y_{j+1/2}) \end{bmatrix}, \quad (698)$$

where

$$\mathbb{B}_{i,j} = \mathbb{T}_{i,j} \begin{bmatrix} -\mathbb{X}_{i,j} & \mathbb{X}_{i,j} \\ \mathbb{O} & \mathbb{S}_{i,j} \end{bmatrix} \quad (699)$$

and

$$\mathbb{C}_{i,j} = \mathbb{T}_{i,j} \begin{bmatrix} -\mathbb{Y}_{i,j} & \mathbb{Y}_{i,j} \\ \mathbb{O} & \mathbb{S}_{i,j} \end{bmatrix}. \quad (700)$$

Relations (697) are used together with the Y -directed ANM-coupling relations and with the nodal balance equation (698) to build the global matrix system.

Calculation of matrices $\mathbb{L}_{i,j}$, $\mathbb{R}_{i,j}$, $\mathbb{B}_{i,j}$, and $\mathbb{C}_{i,j}$ for each node represents the core of the ANM. These matrices are a function of the G -group cross-sections and diffusion coefficients, of the node size *and* of the effective multiplication factor K_{eff} . They must be updated during the power iteration, as K_{eff} changes. A straightforward way to present the core of the ANM is to provide a Matlab script implementing the linear transformation and the calculation of the nodal-coupling matrices for a single node. The script parameters are defined as

keff = effective multiplication factor,
 xm = value of $x_{i-1/2}$ (cm),
 xp = value of $x_{i+1/2}$ (cm),
 dely = node size Δy_j along the Y -axis (cm),
 diff = diffusion-coefficient array of size G (cm),
 sigr = macroscopic removal cross-section array of size G (cm^{-1}),
 chi = fission-spectrum array of size G ,
 nusigf = ν times the macroscopic-fission cross-section array of size G (cm^{-1}),
 [L, R, B] = nodal-coupling matrices,

The script `anm_coupling_2D` follows:

```
function [L, R, B] = anm_coupling_2D(keff, xm, xp, dely, diff, sigr, chi, ...
    nusigf)
% Compute the 2D ANM coupling matrices for a single node. Flat transverse
% leakage approximation.
% function [L, R, B] = anm_coupling_2D(keff, xm, xp, dely, diff, sigr, ...
%     chi, nusigf)
% (c) 2008 Alain Hebert, Ecole Polytechnique de Montreal
G=size(diff,2);
F=inv(diag(diff))*(chi*nusigf/keff-sigr); [T,Lambda]=eig(F);
delx=xp-xm;
Mm=zeros(2*G,2*G); Mp=zeros(2*G,2*G); Nm=zeros(G,2*G); Np=zeros(G,2*G);
B=zeros(G,2*G); Y=zeros(G,G);
```

```

for g=1:G
  sqla=sqrt(abs(Lambda(g,g)));
  if Lambda(g,g) >= 0
    Mm(g,g) = (sin(sqla*xp)-sin(sqla*xm))/(delx*sqla);
    Mm(g,G+g) = -(cos(sqla*xp)-cos(sqla*xm))/(delx*sqla);
    Mm(G+g,g) = sqla*sin(sqla*xm); Mm(G+g,G+g)=-sqla*cos(sqla*xm);
    Mp(G+g,g) = sqla*sin(sqla*xp); Mp(G+g,G+g)=-sqla*cos(sqla*xp);
    Nm(g,g) = cos(sqla*xm); Nm(g,G+g)=sin(sqla*xm);
    Np(g,g) = cos(sqla*xp); Np(g,G+g)=sin(sqla*xp);
  else
    Mm(g,g) = (sinh(sqla*xp)-sinh(sqla*xm))/(delx*sqla);
    Mm(g,G+g) = (cosh(sqla*xp)-cosh(sqla*xm))/(delx*sqla);
    Mm(G+g,g) = -sqla*sinh(sqla*xm); Mm(G+g,G+g)=-sqla*cosh(sqla*xm);
    Mp(G+g,g) = -sqla*sinh(sqla*xp); Mp(G+g,G+g)=-sqla*cosh(sqla*xp);
    Nm(g,g) = cosh(sqla*xm); Nm(g,G+g)=sinh(sqla*xm);
    Np(g,g) = cosh(sqla*xp); Np(g,G+g)=sinh(sqla*xp);
  end
  Mp(g,g) = Mm(g,g); Mp(g,G+g)=Mm(g,G+g);
  B(g,g) = -1.0/(delx*Lambda(g,g)); B(g,G+g)=1.0/(delx*Lambda(g,g));
  Y(g,g) = 1.0/(dely*Lambda(g,g));
end
warning off
GAR1 = Nm*inv(Mm); GAR2=Np*inv(Mp);
warning on
MAT1 = [GAR1,-Y+GAR1(:,1:G)*Y,Y-GAR1(:,1:G)*Y];
MAT2 = [GAR2,-Y+GAR2(:,1:G)*Y,Y-GAR2(:,1:G)*Y];
S = inv(T)*inv(diag(diff));
L = T*MAT1*blkdiag(inv(T),S,S,S); R=T*MAT2*blkdiag(inv(T),S,S,S);
B = T*B*blkdiag(S,S);

```

Equations (694) are written in a convenient form to introduce a *zero-flux-* or *albedo-boundary condition* on the left or right boundary. The relation between the surfacic flux and current, required to implement an albedo-boundary condition, is obtained directly from (542). We also note that the above Matlab script does not deal with situations where $\lambda_{g,i,j}$ approaches zero. A production implementation should take this possibility into consideration.

The ANM unknowns are the average fluxes on the node volumes and the average net currents on the node surfaces. This choice of unknowns is a characteristic of *dual discretization* approaches such as the *mesh-centered finite-difference* method of ▶ 8.2 or the *Raviart-Thomas finite-element* technique of Hébert (1993). The ANM belongs to the family of dual-discretization approaches.

The ANM in 2D leads to a matrix system of order approximately equal to $3GN$ where G is the number of energy groups and N is the number of nodes. About one-third of the system equations are nodal-balance relations and the remaining equations corresponds to X - or Y -directed nodal-coupling relations.

Appendix: Tracking of 1D and 2D Geometries

1 Tracking of 1D Cylindrical and Spherical Geometries

The tracking of 1D cylindrical and spherical geometries is similar and can be generated with the same algorithm. A Matlab script `f=sybt1d(rad,lg sph,ngauss)` is presented to produce a tracking object in these cases. **Figure 42** presents an example with $I = 2$ regions and $K = 2$ tracks per regions. Tracks ① and ② have two segments, identified as ℓ_1 and ℓ_2 . Tracks ③ and ④ have only one segment, identified as ℓ_2 . Each track is making an angle ϕ with respect to the outgoing normal vector.

The purpose of the tracking object is to permit the numerical evaluation of the integrals in a collision probability approach or with the MOC. A K -point Gauss-Jacobi quadrature is used as follows:

$$\int_{r_1}^{r_2} dh f[\ell(h)] = \frac{1}{2} \sum_{k=1}^K w_k f[\ell(h_k)], \tag{701}$$

where r_1 and r_2 are the integration limits, corresponding to consecutive radii of the geometry. The Matlab-tracking object is a 2D-cell array containing $I \times K$ elements, one per track. The i index refers to the tracks located in $r_{i-1/2} < h < r_{i+1/2}$. The (i, j) -th cell is also a cell array containing three elements:

- The weight w_k of the track
- The product $w_k \cos \phi$
- A 1D array of dimension $I - i + 1$ containing the track segments

The Matlab script uses three arguments: a 1D array of dimension I containing the radii (the 0.0 radius is not given), a logical variable set to `false` in cylindrical geometry or `true`

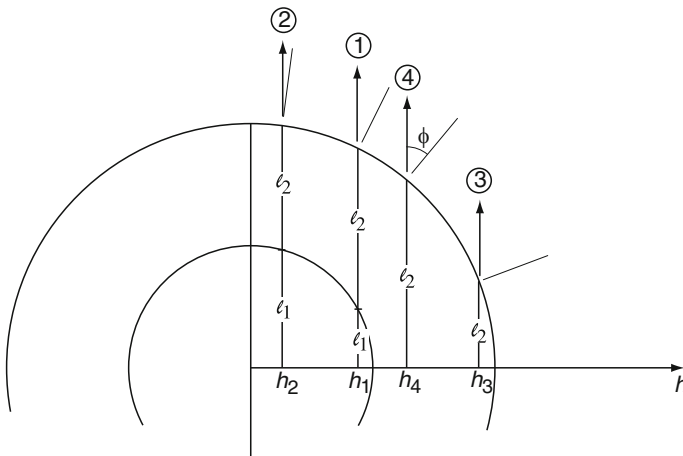


Figure 42
Tracking in 1D cylindrical and spherical geometries

in spherical geometry, and the number of Gauss–Jacobi points. The script is implemented as follows:

```
function f=sybt1d(rad, lgsph, ngauss)
% produce a Gauss-Jacobi tracking in 1D curvilinear geometry
% function f=sybt1d(rad, lgsph, ngauss)
% (c) 2005 Alain Hebert, Ecole Polytechnique de Montreal
    npij=size(rad,2);
    if ngauss == 1
        alp=.6666666667; pwr=.5;
    elseif ngauss == 2
        alp=[.3550510257, .8449489743]; pwr=[.1819586183, .3180413817];
    elseif ngauss == 3
        alp=[.2123405382, .5905331356, .9114120405];
        pwr=[.0698269799, .2292411064, .2009319137];
    elseif ngauss == 4
        alp=[.1397598643, .4164095676, .7231569864, .9428958039];
        pwr=[.0311809710, .1298475476, .2034645680, .1355069134];
    elseif ngauss == 5
        alp=[.0985350858, .3045357266, .5620251898, .8019865821, .9601901429];
        pwr=[.0157479145, .0739088701, .1463869871, .1671746381, .0967815902];
    elseif ngauss == 6
        alp=[.0730543287, .2307661380, .4413284812, .6630153097, .8519214003, ...
            .9706835728];
        pwr=[.0087383018, .0439551656, .0986611509, .1407925538, .1355424972, ...
            .0723103307];
    else
        error('invalid number of Gauss-Jacobi points.')
    end
    rik1=0;
    for ik=1:npij
        rik2=rad(ik);
        rd=rik2-rik1;
        for il=1:ngauss
            r=rik2-rd*alp(il)^2;
            aux=4*rd*pwr(il);
            if lgsph
                aux=aux*r*pi;
            end
            ct1=0.;
            z=zeros(1,npij-ik+1);
            for i=ik:npij;
                ct2=sqrt(rad(i)^2-r^2);
                z(i-ik+1)=ct2-ct1;
                ct1=ct2;
            end
            cell {1} = aux;
        end
    end
end
```

```

cell {2} = aux*ct2/rad(npj);
cell {3} = z;
f {ik,il} = cell;
end
rik1=rik2;
end

```

Using this script, the four tracks of [Fig. 42](#) are obtained using

```

rad=[0.075 0.15];
track=sybt1d(rad,false,2);

```

The ℓ_1 -segment length of track ② is

```
l2=track{1,2} {3} (1)
```

leading to $l_2 = 0.07186585$. Any length $\text{track}\{ik, il\} \{3\} (1)$ corresponding to a segment that crosses the h -axis must be multiplied by 2, as depicted in [Fig. 17](#).

This tracking can be used to compute the p_{11} component of an infinite cylinder of radius R and cross-section Σ surrounded by a vacuum-boundary condition. According to (295), this component is

$$p_{11} = \frac{2}{\pi R^2} \int_0^R dh \left\{ \frac{\ell(h)}{\Sigma} - \frac{1}{\Sigma^2} [\text{Ki}_3(0) - \text{Ki}_3(\Sigma \ell(h))] \right\} \quad \text{if } \Sigma \neq 0 \quad (702)$$

and

$$p_{11} = \frac{1}{2R^2} \int_0^R dh \ell(h)^2 = \frac{4R}{3} \quad \text{if } \Sigma = 0. \quad (703)$$

The following script will perform a numerical integration of p_{11} in a 1D cylindrical tube of radius rad and macroscopic total cross-section sigt :

```

function f=p11_cyl(rad,sigt)
% compute the p11 component in 1D cylindrical geometry
track=sybt1d(rad,false,5);
val=0;
for i=1:5
    segment=2*track{1,i} {3} (1);
    if sigt == 0
        d=segment/sigt-(akin(3,0)-akin(3,sigt*segment))/sigt^2;
    else
        d=pi*segment^2/4;
    end
    val=val+track{1,i} {1} *d;
end
f=val/(pi*rad^2);

```

where $\text{akin}(n, x)$ is a script used to compute $Ki_n(x)$.

Similarly, the following script will perform a numerical integration of p_{11} in a 1D spherical sphere of radius rad and macroscopic total cross-section sigt :

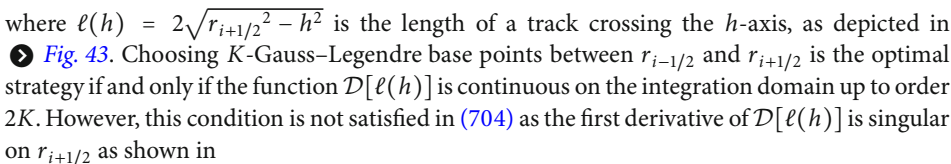
```
function f=p11_sphere(rad,sigt)
% compute the p11 component in 1D spherical geometry
track=sybt1d(rad,true,5);
val=0;
for i=1:5
    segment=2*track{1,i}{3}(1);
    if sigt == 0
        d=segment/sigt*(1-exp(-sigt*segment))/sigt^2;
    else
        d=segment^2/2;
    end
    val=val+track{1,i}{1}*d;
end
f=val/(4*pi*rad^3/3);
```

2 The Theory Behind sybt1d

The tracking strategy consists in drawing K tracks (Matlab variable `ngauss`) in each subdomain $r_{i-1/2} < h < r_{i+1/2}$. It is important to find the optimal location for these tracks, in order to keep the total number of tracks in the complete domain as low as possible. Such an optimization strategy helps to reduce round-off errors in the collision probability or characteristics calculation.

We will concentrate our investigation on the second term of components p_{ii} in (295), which can be written as

$$I = \int_{r_{i-1/2}}^{r_{i+1/2}} dh \mathcal{D}[\ell(h)], \quad (704)$$

where $\ell(h) = 2\sqrt{r_{i+1/2}^2 - h^2}$ is the length of a track crossing the h -axis, as depicted in  **Fig. 43**. Choosing K -Gauss-Legendre base points between $r_{i-1/2}$ and $r_{i+1/2}$ is the optimal strategy if and only if the function $\mathcal{D}[\ell(h)]$ is continuous on the integration domain up to order $2K$. However, this condition is not satisfied in (704) as the first derivative of $\mathcal{D}[\ell(h)]$ is singular on $r_{i+1/2}$ as shown in

$$\frac{d\mathcal{D}}{dh} = \frac{d\mathcal{D}}{d\ell} \frac{d\ell}{dh} = \frac{d\mathcal{D}}{d\ell} \frac{-2h}{\sqrt{r_{i+1/2}^2 - h^2}}. \quad (705)$$

This singularity is purely geometric and is not related to the presence of Bickley or exponential functions that may appear in $\mathcal{D}[\ell(h)]$. The behavior of the singularity was studied in the sixties by Carlvik (1965) and Kavenoky (1969) in the context of the collision probability method in 1D cylindrical and spherical geometry. The proposed solution is to remove the singularity by performing a change of variable in (704).

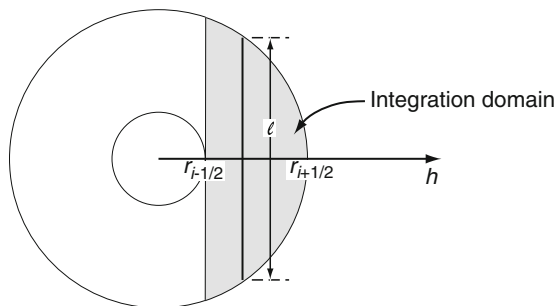


Figure 43 The Flurig scheme allows to take into account the singularity of tracks tangent to a circular arc

The *Flurig scheme* is a change of variable of the form $y = \sqrt{r_{i+1/2} - h}$, so that (704) is rewritten as

$$I = 2 \int_0^{\sqrt{r_{i+1/2} - r_{i-1/2}}} dy y \mathcal{D}[\ell(r_{i+1/2} - y^2)]. \tag{706}$$

With this transformation, the first derivative of the integrand is

$$\frac{d\mathcal{D}}{dy} = \frac{d\mathcal{D}}{d\ell} \frac{d\ell}{dh} \frac{dh}{dy} = \frac{d\mathcal{D}}{d\ell} \frac{-2h}{\sqrt{r_{i+1/2}^2 - h^2}} (-2\sqrt{r_{i+1/2} - h}) \tag{707}$$

so that

$$\lim_{h \rightarrow r_{i+1/2}} \frac{d\mathcal{D}}{dy} = 2\sqrt{2r_{i+1/2}} \left. \frac{d\mathcal{D}}{d\ell} \right|_{h=r_{i+1/2}}. \tag{708}$$

There is no singularity in the integral of (706) and an efficient Gauss–Legendre quadrature can be used to determine its value. However, it is possible to gain one more order of accuracy by using a Gauss–Jacobi quadrature where the factor y is taken into account implicitly, as proposed in Article 25.4.33 of Abramowitz and Stegun (1970).

A second change of variable is made in order to transform the support $0 \leq y \leq \sqrt{r_{i+1/2} - r_{i-1/2}}$ into a normalized support $0 \leq u \leq 1$. We define


$$u = \frac{y}{\sqrt{r_{i+1/2} - r_{i-1/2}}} \tag{709}$$

so that

$$\begin{aligned} I &= 2(r_{i+1/2} - r_{i-1/2}) \int_0^1 du u \mathcal{D}[\ell(r_{i+1/2} - (r_{i+1/2} - r_{i-1/2}) u^2)] \\ &= 2(r_{i+1/2} - r_{i-1/2}) \sum_{k=1}^K \omega_k \mathcal{D}[\ell(r_{i+1/2} - (r_{i+1/2} - r_{i-1/2}) u_k^2)], \end{aligned} \tag{710}$$

where $\{\omega_k, u_k; k = 1, K\}$ are the weights and base points of a Gauss–Jacobi quadrature.

3 Tracking of 2D Square Pincell Geometries

The tracking of unstructured 2D geometries is performed using a *tracking operator*, leading to a *tracking file* containing straight-line particle trajectories spread over the complete domain. The complexity of this operator increases with the complexity of the geometry, so that general algorithms involve large production softwares. Here, we have chosen to define a specification for a general-purpose tracking file and to present a Matlab script for generating this file in the particular case of a 2D-square *pincell* geometry. This geometry features one-eighth symmetry with concentric annuli not crossing the external perimeter, as depicted in  Fig. 19. This simple geometry is sufficient to introduce solution algorithms of the particle-transport equation based on the method of collision probabilities or on the MOC.

A general-purpose tracking file can be implemented as a binary sequential file. It is described using the following Fortran instructions:

```
WRITE (IUNIT)  NSURF, NREG, NANGLE, NBTRK, FNORM
WRITE (IUNIT)  (SURF ( I ), I=1, NSURF) , (VOL ( I ), I=1, NREG)
WRITE (IUNIT)  (SINANG ( I ), I=1, NANGLE) , (COSANG ( I ), I=1, NANGLE)
DO  ITRK=1, NBTRK
  WRITE (IUNIT)  IANGL, ISURF, JSURF, WEIGHT, NSEG
  WRITE (IUNIT)  (NRSEG ( I ), I=1, NSEG)
  WRITE (IUNIT)  (SEGLN ( I ), I=1, NSEG)
ENDDO
```

where

IUNIT = Fortran unit associated with this sequential binary file

NSURF = number of surfaces surrounding the geometry

NREG = number of regions in the geometry

NANGLE = number of trajectory angles

NBTRK = number of trajectories (tracks) in tracking file

FNORM = angular normalization factor

SURF = perimeter length of each surface

VOL = volume of each region

SINANG = sine of trajectory angles

COSANG = cosine of trajectory angles

IANGL = angle index for this track ($1 \leq \text{IANGL} \leq \text{NANGLE}$)

ISURF = entering surface index for this track ($1 \leq \text{ISURF} \leq \text{NSURF}$)

JSURF = exit surface index for this track ($1 \leq \text{JSURF} \leq \text{NSURF}$)

WEIGHT = weight for this track

NSEG = number of regions crossed by this track. If a single region is crossed many times, NSEG must be increased accordingly.

NRSEG = indices of the regions crossed by this track ($1 \leq \text{NRSEG} (I) \leq \text{NREG}$)

SEGLN = segment lengths corresponding to each region crossed by this track.

We have implemented a simple Matlab script to generate the tracking information for a 2D square pincell. The Matlab script `track=sybt2d(a, rad, nangle, ngauss)` stores this information in a Matlab array `track` instead of using a sequential binary file. Variables `nangle` and `ngauss` (≤ 6) are the number of trajectory angles in $(0, \pi/4)$ and the number of Gauss-Jacobi points in each subdomain, respectively. A partial tracking is first

computed on the subdomain depicted in  Fig. 44 and is unfolded to cover the full pincell geometry. The script is implemented as follows:

```
function track=sybt2d(a,rad,nangle,ngauss)
% produce a Gauss-Jacobi tracking in 2D square pincell geometry
% function track=sybt2d(a,rad,nangle,ngauss)
% (c) 2009 Alain Hebert, Ecole Polytechnique de Montreal
nreg=1+size(rad,2); radd = [0. rad]; na2=2*nangle;
if ngauss == 1
    alp= .6666666667; pwr= .5; zx= 0.; wx= 2.;
elseif ngauss == 2
    alp= [.3550510257, .8449489743]; pwr=[.1819586183, .3180413817];
    zx= [-.577350259, .577350259]; wx=[1.,1.];
elseif ngauss == 3
    alp= [.2123405382, .5905331356, .9114120405];
    pwr= [.0698269799, .2292411064, .2009319137];
    zx= [-.774596691,0., .774596691];
    wx= [.555555556, .888888889, .555555556];
elseif ngauss == 4
    alp= [.1397598643, .4164095676, .7231569864, .9428958039];
    pwr= [.0311809710, .1298475476, .2034645680, .1355069134];
    zx= [-.861136317,-.339981049, .339981049, .861136317];
    wx= [.347854853, .652145147, .652145147, .347854853];
elseif ngauss == 5
    alp= [.0985350858, .3045357266, .5620251898, .8019865821, .9601901429];
    pwr= [.0157479145, .0739088701, .1463869871, .1671746381, .0967815902];
    zx= [-.906179845,-.538469315,0., .538469315, .906179845];
    wx= [.236926883, .478628665, .568888843, .478628665, .236926883];
elseif ngauss == 6
    alp= [.0730543287, .2307661380, .4413284812, .6630153097, .8519214003,
        .9706835728];
    pwr= [.0087383018, .0439551656, .0986611509, .1407925538, .1355424972,
        .0723103307];
    zx= [-.932469487,-.661209404,-.238619193, .238619193, .661209404,
        .932469487];
    wx= [.171324492, .360761583, .467913926, .467913926, .360761583, .171324492];
else
    error('invalid number of Gauss-Jacobi points.')
end
if 2.0*radd(nreg) > a
    error('a radius is greater than half a side.')
end
track_w=zeros(1,9+nreg+4*na2*(2+ngauss*nreg*(5+2*(2*nreg-1)))));
kstart=9+nreg+8*na2; track_w(1:3)=[4, nreg, 4*na2]; zn1=0.;
ao2=a/2.; wa=2./real(na2); track_w(6:9)=a; vol=a*a;
for jjj=nreg:-1:1
    r2=pi*radd(jjj)^2; track_w(9+jjj)=vol-r2; vol=r2;
end
```

```

%----
% track generation
%----
k=kstart ;
for ia=1 : na2
    za=(2.0*real(ia)-1.)/real(na2)-1. ; phi=0.25*pi*(za+1.) ;
    zn1=zn1+sin(phi)*wa ; si=sin(phi) ; co=cos(phi) ; ta=si/co ;
    track_w(9+nreg+ia)=si ; track_w(9+nreg+4*na2+ia)=co ;
    track_w(9+nreg+na2+ia)=-si ; track_w(9+nreg+5*na2+ia)=co ;
    if phi <= 0.25*pi
        track_w(9+nreg+2*na2+ia)=co ; track_w(9+nreg+6*na2+ia)=-si ;
        track_w(9+nreg+3*na2+ia)=si ; track_w(9+nreg+7*na2+ia)=co ;
        jsu=4 ; x1=0. ; xlim=a ; dlim=ao2*co+(ao2-xlim)*si ;
    else
        track_w(9+nreg+2*na2+ia)=co ; track_w(9+nreg+6*na2+ia)=si ;
        track_w(9+nreg+3*na2+ia)=si ; track_w(9+nreg+7*na2+ia)=-co ;
        jsu=2 ; x1=a/ta ; xlim=0.5*(a+a/ta) ; dlim=0. ;
    end
end
for k0=nreg:-1:1
    km=nreg-k0+1 ; x2=min(xlim,xlim-(radd(k0)-dlim)/si) ;
    if ((x1 < xlim) && (phi <= 0.25*pi)) || ((x1 < x2) && (phi > 0.25*pi))
        l3=k ; vap=zeros(1,nreg) ;
        for ix=1:ngauss
            if k0 == nreg
                s=0.5*(x2-x1)*si*wx(ix) ;
                x=x1+0.5*(x2-x1)*(1.0+zx(ix)) ;
            else
                % Flurig change of variable.
                s=2.*(x2-x1)*si*pwr(ix) ;
                x=x1+(x2-x1)*alp(ix)^2 ;
            end
            track_w(k+1:k+5)=[ia, 1, jsu, s*wa/4., 2*km-1] ;
            track_w(k+6:k+2*km+4)=abs(km-1:-1:1-km)+1+nreg-km ;
            k=k+5+(2*km-1) ;
            c=ao2*si-(ao2-x)*co ; d=(ao2*co+(ao2-x)*si)^2 ; sumtrk=0. ;
            for kk=nreg:-1:k0+1
                corde=sqrt(rad(kk-1)^2-d) ; del=c-corde ; sumtrk=sumtrk+del ;
                track_w(k+nreg-kk+1)=del ; vap(kk)=vap(kk)+del*s ;
                c=corde ;
            end
            if km ~= 1
                del=2.0*corde ; track_w(k+km)=del ; vap(k0)=vap(k0)+del*s ;
                sumtrk=sumtrk+del+sum(track_w(k+km-1:-1:k+2)) ;
                track_w(k+km+1:k+2*km-2)=track_w(k+km-1:-1:k+2) ;
                vap(k0+1:k0+km-2)=vap(k0+1:k0+km-2)+track_w(k+km-1:-1:k+2).*s ;
            end
        end
    end
end

```

```

k=k+2*km-1;
if phi <= 0.25*pi
    del=x/co-sumtrk;
else
    del=a/si-sumtrk;
end
track_w(k)=del; vap(nreg)=vap(nreg)+del*s;
end
%-----
% volume normalization
%-----
if k0 < nreg
    dlim1=ao2*co+(ao2-x2)*si; dlim2=ao2*co+(ao2-x1)*si;
    vw1=0.; sumvap=0.;
    for i=k0:nreg-1
        sumvap=sumvap+vap(i); rw=rad(i);
        vex1=rw*rw*acos(dlim1/rw)-dlim1*sqrt(rw*rw-dlim1*dlim1);
        if rw > dlim2
            vex1=vex1-(rw*rw*acos(dlim2/rw)-dlim2*sqrt(rw*rw-dlim2*dlim2));
        end
        vap(i)=(vex1-vw1)/vap(i); vw1=vex1;
    end
    vex1=0.5*(a*si-(a-x1-x2)*co)*(x2-x1)*si;
    if phi <= 0.25*pi
        vex2=0.5*ta*(x2*x2-x1*x1)-vex1;
    else
        vex2=(x2-x1)*a-vex1;
    end
    vex1=(vex1-0.5*vw1)/(vex1-0.5*sumvap);
    vex2=(vex2-0.5*vw1)/(vex2-0.5*sumvap);
    for ix=1:ngauss
        l3=l3+5; km=(track_w(l3)+1)/2; l3=l3+2*km-1;
        track_w(l3+km)=track_w(l3+km)*vap(k0);
        fact=vap(k0+1:k0+km-2);
        track_w(l3+km-1:l3+2)=track_w(l3+km-1:l3+2).*fact;
        track_w(l3+km+1:l3+2*km-2)=track_w(l3+km+1:l3+2*km-2).*fact;
        track_w(l3+1)=track_w(l3+1)*vex1;
        track_w(l3+2*km-1)=track_w(l3+2*km-1)*vex2;
        l3=l3+2*km-1;
    end
end
track_w(4)=track_w(4)+ngauss; x1=x2;
end
end
track_w(5)=1./sqrt(0.25*pi*zn1); kend=k;

```

```

%----
% apply symmetries
%----
track_w(kend+1:2*kend-kstart)=track_w(kstart+1:kend) ;
for itrk=1:track_w(4)
    track_w(k+1)=na2+track_w(k+1) ; nseg=track_w(k+5) ;
    if track_w(k+3) == 2 ;
        track_w(k+2)=4 ; track_w(k+3)=3 ;
    elseif track_w(k+3) == 4 ;
        track_w(k+3)=3 ;
    end
    track_w(k+6+nseg:k+5+2*nseg)=track_w(k+5+2*nseg-1:k+6+nseg) ;
    k=k+5+2*track_w(k+5) ;
end
track_w(4)=2*track_w(4) ; kend=k ;
track_w(kend+1:2*kend-kstart)=track_w(kstart+1:kend) ;
for itrk=1:track_w(4)
    track_w(k+1)=2*na2+track_w(k+1) ;
    if track_w(k+3) == 4
        track_w(k+2)=4 ; track_w(k+3)=2 ;
    elseif track_w(k+3) == 2
        track_w(k+2)=3 ; track_w(k+3)=4 ;
    elseif track_w(k+2) == 1 ; && track_w(k+3) == 3
        track_w(k+2)=3 ; track_w(k+3)=2 ;
    elseif track_w(k+2) == 4 && track_w(k+3) == 3
        track_w(k+2)=1 ; track_w(k+3)=2 ;
    end
    k=k+5+2*track_w(k+5) ;
end
track_w(4)=2*track_w(4) ;
%
track=track_w(1:k) ;

```

The tracking algorithm of script `sybt2d` originates from Appendix A in Hébert (1981). The I regions (Matlab variable `npj`) of the 2D square pincell are numbered from center toward perimeter. Their volumes are computed as

$$\begin{aligned}
 V_i &= \pi R_{i+1}^2 - \pi R_i^2, \quad i = 1, I - 1 \\
 V_I &= a^2 - \pi R_I^2,
 \end{aligned} \tag{711}$$

where a is the side length and where R_i and R_{i+1} are the internal and external radii of region i , respectively. The first radius is set as $R_1 = 0$. The geometry is homogenous if $I = 1$.

The tracking information is used for the numerical integration of functions $F_{S_\alpha, S_\beta} \{f_i(x, \varepsilon)\}$ defined as

$$F_{3,2} \{f_i(x, \varepsilon)\} = \frac{1}{\pi} \int_0^a dx \int_0^{\pi/4} d\varepsilon \sin \varepsilon f_i(x, \varepsilon) \tag{712}$$

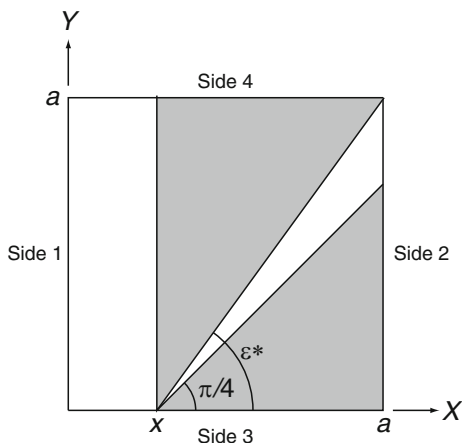


Figure 44
Integration domain for a 2D square pincell

and

$$F_{3,4}\{f_i(x, \varepsilon)\} = F_{1,2}\{f_i(x, \varepsilon)\} = \frac{1}{\pi} \int_0^a dx \int_{\varepsilon^*}^{\pi/2} d\varepsilon \sin \varepsilon f_i(x, \varepsilon), \quad (713)$$

where

$$\varepsilon^* = \tan^{-1} \frac{a}{a-x}. \quad (714)$$

The transmission probability matrix P_{S_α, S_β} of a square pincell is a 4×4 matrix that can be computed using (712) and (713). The angular integration domain is illustrated in Fig. 44, taking care of the pincell symmetries. A simple Matlab script can be used to obtain this matrix as a function of the tracking and of the macroscopic total cross-sections sigt in each region:

```
function pss=sybpss(track,sigt)
% integration of transmission probabilities. The tracks are computed by
% sybt2d.
% function pss=sybpss(track,sigt)
% (c) 2008 Alain Hebert, Ecole Polytechnique de Montreal
%–
% define anonymous function indpos
%–
indpos=(i,j) max(i,j).*(max(i,j)-1)./2+min(i,j);
%–
% pss integration
%–
nsurf=track(1) ; surfa=track(6:5+nsurf) ;
k=5+track(1)+track(2)+2*track(3) ; tij=zeros(1,nsurf*(nsurf+1)/2) ;
for itrk=1:track(4)
    isurf=track(k+2) ; jsurf=track(k+3) ; ind=indpos(isurf,jsurf) ;
    z1=track(k+4) ; km=track(k+5) ; kgar=k+5 ; k=k+5+km ;
    pop=sum(sigt(track(kgar+1:kgar+km)).*track(k+km:-1:k+1));
```

```

    tij(ind)=tij(ind)+akin(3,pop)*z1 ; k=k+km ;
end
pss=zeros(nsurf,nsurf) ;
for i=1:nsurf
    pss(i,1:nsurf)=tij(indpos(i,1:nsurf)).*(4.*track(5)^2/surfa(i)) ;
end

```

4 The Theory Behind sybt2d

The practical evaluation of (712) and (713) first involves the permutation of variables x and ε . The angular domain between 0 and $\pi/2$ is divided into J equidistant values (Matlab variable `nanngle`), with J even. We write

$$\varepsilon_j = \frac{\pi}{2J} (j - 1/2), \quad j = 1, J, \quad (715)$$

$$\Delta\varepsilon_j = \frac{\pi}{2J}, \quad j = 1, J. \quad (716)$$

For each angle ε_j , we trace a set of parallel trajectories, each of them made of m individual segments, with $1 \leq m \leq 2I-1$. The global integration domain is next subdivided into subdomains where all the trajectories have the same number of segments. In each subdomain, K trajectories (Matlab variable `ngauss`) are set according to the Flurig scheme presented in [Sect. 2](#). The set $\{\Delta s_k; k = 1, K\}$ contains the perpendicular distances associated with the K trajectories for angle ε_j in a given subdomain. The corresponding distances on the X -axis are therefore written as

$$\Delta x_k = \frac{\Delta s_k}{\sin \varepsilon_k}, \quad k = 1, K \quad (717)$$

so that the trajectory weights, corresponding to Fortran variable `WEIGHT`, are computed as a function of spacings Δs_k using

$$\omega_k = \frac{\Delta s_k}{2J}. \quad (718)$$

We can now rewrite (712) and (713) in their discretized form as

$$F_{3,2}\{f_i(x, \varepsilon)\} = \sum_{j=1}^{J/2} \sum_{k \in D_{3,2}} \omega_k f_i(x_k, \varepsilon_j) \quad (719)$$

and

$$F_{3,4}\{f_i(x, \varepsilon)\} = F_{1,2}\{f_i(x, \varepsilon)\} = \sum_{j \in C_{3,4}} \sum_{k \in D_{3,4}} \omega_k f_i(x_k, \varepsilon_j), \quad (720)$$

where

$$D_{3,2} = \{k \mid x_k > a - a \tan \varepsilon_j\}, \tag{721}$$

$$D_{3,4} = \{k \mid x_k < a - a \tan \varepsilon_j\} \tag{722}$$

and

$$C_{3,4} = \{j \mid \varepsilon_j > \pi/4\}. \tag{723}$$

The segment lengths $X_i(x, \varepsilon)$ depicted in **Fig. 45** are obtained using the following two trigonometric formulas:

$$\begin{aligned} d &= \frac{a}{2} \cos \varepsilon_j + \left(x_k - \frac{a}{2}\right) \sin \varepsilon_j, \\ c &= \left[\frac{a}{2} \sin \varepsilon_j - \left(x_k - \frac{a}{2}\right) \cos \varepsilon_j\right] - \sqrt{R^2 - d^2}. \end{aligned} \tag{724}$$

A spatial subdomain E_i is depicted in gray in **Fig. 46**, corresponding to an angle ε_j . It is possible to use the tracking to obtain a numerical approximation W_i of this volume, as

$$W_i = \sum_{k \in E} \Delta s_k X_i(x_k, \varepsilon_j), \quad i = 1, I. \tag{725}$$

Subdomain E_i is bounded by two straight lines set at distances d_1 and d_2 from the pincell center, as depicted in **Fig. 46**. We also define an area $G_i(d)$, with $1 \leq i \leq I$, as

$$G_i(d) = \begin{cases} R_i^2 + \cos^{-1} \frac{d}{R_i} - d\sqrt{R_i^2 - d^2} & \text{if } 0 \leq d \leq R_i, \\ 0 & \text{otherwise.} \end{cases} \tag{726}$$

The exact value of subvolume W_i is given in terms of these areas as

$$\begin{aligned} W_1^+ &= G_2(d_1) - G_2(d_2), \\ W_i^+ &= G_{i+1}(d_1) - G_{i+1}(d_2) - \sum_{\ell=1}^{i-1} W_\ell^+; \quad i = 2, I-1 \end{aligned} \tag{727}$$

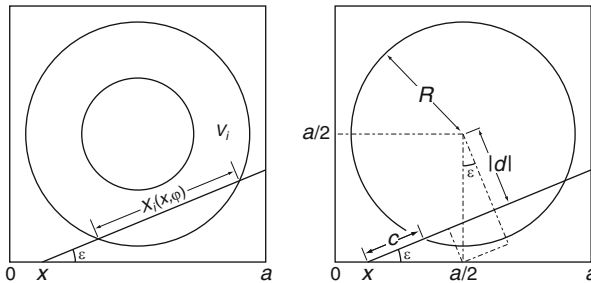
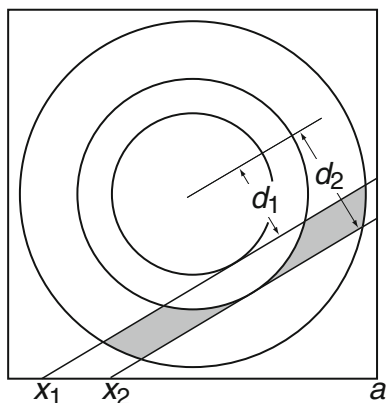


Figure 45
Interception of a trajectory with pincell geometry



■ Figure 46

Calculation of subvolume W_i^+ (in gray in the figure)

and

$$W_i^+ = \begin{cases} \frac{1}{2} \tan \varepsilon_j [(a - x_1)^2 - (a - x_2)^2] - \sum_{\ell=1}^{I-1} W_\ell^+, & \text{if } x_1 > a - a \tan \varepsilon_j, \\ b(x_2 - x_1) - \sum_{\ell=1}^{I-1} W_\ell^+, & \text{if } x_2 < a - a \tan \varepsilon_j. \end{cases} \quad (728)$$

The numerical value W_i of the subvolume evaluated from the tracking is different from its analytical value W_i^+ , due to discretization error during the integration process. This error is expected to become smaller as the number of trajectories increases, i.e., as Matlab variables `nangle` and `ngauss` increase. However, increasing the size of the tracking has undesirable effects:

- The CPU time required to compute the collision probabilities or to solve the characteristics equations increases strongly with the size of the tracking. Moreover, large domains can lead to tracking sizes exceeding the limits of the computer.
- As the number of tracks increases, the collision probability components (or the solution of the characteristics equations) are obtained as the summation of increments that become smaller and smaller. Consequently, numerical instabilities are likely to produce oscillations in the transport calculation.

Two remedies exist to increase the accuracy of the integration process using small tracking files. The first remedy is the *Flurig scheme* and is already incorporated into Matlab script `sybt2d`. This approach is very efficient but breaks down in complex 2D geometries due to its inherent difficulty in isolating each subdomain E_i .

A second remedy consists in normalizing the segment lengths $X_i(x_k, \varepsilon_j)$ in such a way that (725) leads to exact volumes, whatever the size of the tracking. It is important to perform segment normalization one angle ε_j at a time. Our Matlab script `sybt2d` performs an improved normalization that preserves the exact volumes W_i^+ for each angle ε_j and for each

subdomain E_i . This normalization is written as

$$\tilde{X}_i(x_k, \varepsilon_j) = \frac{W_i^+}{W_i} X_i(x_k, \varepsilon_j), \quad k \in E_i. \quad (729)$$

It is also possible to normalize the angular integral values. The idea here is to multiply the angular summations by the factor e_1^2 chosen in such a way that

$$e_1^2 \left[\frac{\pi}{2J} \sum_{j=1}^J \sin \varepsilon_j \right] = \int_0^{\pi/2} d\varepsilon \sin \varepsilon = 1. \quad (730)$$

An angular normalization factor e_1 is written in position `track(5)` of the Matlab tracking (Fortran variable `FNORM`), defined as

$$e_1 = \frac{1}{\sqrt{\frac{\pi}{2J} \sum_{j=1}^J \sin \varepsilon_j}}. \quad (731)$$

References

- Abramowitz M and Stegun IA (1970) Handbook of mathematical functions. Dover Publications, Inc., New York
- Alcouffe RE (1977) Diffusion synthetic acceleration methods for the diamond differenced discrete ordinates equations. Nucl Sci Eng 64:344
- Alcouffe RE, O'Dell D (1986) Florida, transport calculations for nuclear reactors. In: Ronen Y (ed) CRC Handbook of nuclear reactors calculations, vol I. CRC Press, Boca Raton
- Askew JR (1972) A characteristics formulation of the neutron transport equation in complicated geometries. Report AEEW-M 1108, United Kingdom atomic energy establishment, Winfrith
- Carlson BG, Bell GI (1958) Solution of the transport equation by the S_N Method. Proceedings of the United Nations international conference on peaceful uses of atomic energy, 2nd Geneva P/2386
- Carlson BG (1971) On a more precise definition of discrete ordinates methods. Proceedings of the 2nd conference on transport theory, April 1971, Los Alamos, N. M., pp. 348–390, CONF-710107, U. S. Atomic Energy Commission
- Carlvik I (1965) A Method for Calculating Collision Probabilities in General Cylindrical Geometry and Applications to Flux Distributions and Dancoff Factors, Proceedings of the United Nations international conference on peaceful uses of atomic energy, vol. 2. Geneva, p 225
- Chandrasekhar S (1960) Radiative transfer. Dover, New York
- Eddington A (1926) The internal constitution of the stars. Dover, New York
- Gelbard EM (1960) Application of spherical harmonics method to reactor problems. WAPD-BT-20, Bettis Atomic Power Laboratory
- Gelbard EM (1968) Computing methods in reactor physics (chap. 4). In: Greenspan H, Kelber CK, Okrent D (eds). Gordon and Breach, New York
- Gunther G, Kinnebrock W (1973) SNOW: a two-dimensional SN program for solving the neutron-transport equation in rectangular and cylindrical geometry, Report EURFNR-1130 (KFK 1826)
- Hébert A (1981) Développement de la méthode SPH: Homogénéisation de cellules dans un réseau non uniforme et calcul des paramètres de réflecteur, Note CEA-N-2209, Commissariat à l'Énergie Atomique, France
- Hébert A (1987) Development of the nodal collocation method for solving the neutron diffusion equation Ann Nucl Energy 14(10): 527
- Hébert A (1987) TRIVAC, a modular diffusion code for fuel management and design applications. Nucl J Canada 1(4):325. Available at <http://www.polymtl.ca/merlin/>

- Hébert A (1993) Application of a dual variational formulation to finite element reactor calculations. *Ann Nucl Energy* 20:823
- Hébert A (2006) The search for superconvergence in spherical harmonics approximations *Nucl Sci Eng* 154:134
- Hébert A (2006) High order diamond differencing schemes. *Ann Nucl Energy* 33:1479
- Hébert A (2008) A Raviart–Thomas–Schneider solution of the diffusion equation in hexagonal geometry *Ann Nucl Energy*, 35, 363–376
- Hébert A (2009) Applied reactor physics. Presses internationales polytechnique, Montréal (See the home page at <http://www.polymtl.ca/pub/>)
- Halsall MJ (1980) CACTUS, a characteristics solution to the neutron transport equation in complicated geometries. Report AEEW-R 1291, United Kingdom Atomic Energy Establishment, Winfrith
- Jenal JP, Erickson PJ, Rhoades WA, Simpson DB, Williams ML (1977) The generation of a computer library for discrete ordinates quadrature sets. Report ORNL/TM-6023, Oak Ridge National Laboratory, Tennessee
- Kavenoky A (1969) Calcul et utilisation des probabilités de première collision pour les milieux hétérogènes à une dimension: Les programmes ALCOLL et CORTINA, Note CEA-N-1077, Commissariat à l'Énergie Atomique, France
- Kelley CT (1995) Iterative methods for linear and nonlinear equations. SIAM, Philadelphia
- Knott D, Edenius M (1993) Validation of the CASMO-4 transport solution. In: Kusters H, Stein E, Werner W (eds) Proceedings of the international conference on mathematical methods and supercomputing in nuclear applications, vol 2, Kernforschungszentrum Karlsruhe GmbH, Karlsruhe, Germany, p 547, April 19–23.
- Lathrop KD (1968) Ray effects in discrete ordinates equations. *Nucl Sci Eng* 32:357
- Leonard A, McDaniel CT (1995) Optimal polar angles and weights for the characteristics method. *Trans Am Nucl Soc* 73:172
- Lewis EE, Miller WF, Jr (1984) Computational methods of neutron transport. John Wiley, New York. (Republished by American Nuclear Society, Inc., 1993)
- Marleau G, Hébert A, Roy R (1992) New computational methods used in the lattice code dragon. Proceedings of the international top1 meeting on advances in reactor physics, Charleston, USA, March 8–11. American Nuclear Society. Available at <http://www.polymtl.ca/merlin/>
- Raviart P, Thomas J (1977) A mixed finite element method for second order elliptic equations. In *Mathematical aspects of the finite element method*. Lecture notes in mathematics, vol 606. Springer, Berlin, pp 292–315
- Roy R (1998) The cyclic characteristics method International conference on physics of nuclear science and technology, Long Island, New York, October 5–8
- Saad Y, Schultz MH (1986) GMRES: a Generalized Minimal RESidual algorithm for solving non-symmetric linear systems. *SIAM J Sci Stat Comput* 7:856–869
- Sanchez R, McCormick NJ (1982) A review of neutron transport approximations. *Nucl Sci Eng* 80:481
- Sanchez R, Chetaine A (2000) A synthetic acceleration for a two-dimensional characteristic method on unstructured meshes *Nucl Sci Eng* 136:122
- Santandrea S, Sanchez R (2002) Acceleration techniques for the characteristic method in unstructured meshes. *Ann Nucl Energy* 29:323
- Santandrea S, Sanchez R (2005) Analysis and improvements of the DP_N acceleration technique for the method of characteristics in unstructured meshes. *Ann Nucl Energy* 32:163
- Santandrea S, Mosca P (2006) Linear surface characteristic scheme for the neutron transport equation in unstructured geometries. Proceedings of the international meeting on advances in nuclear analysis and simulation, September 10 – 14, Vancouver, Canada
- Semenza LA, Lewis EE, Rossow EC (1972) The application of the finite element method to the multigroup neutron diffusion equation. *Nucl Sci Eng* 47:302
- Shober RA, Henry AF (1976) Nonlinear methods for solving the diffusion equation. M.I.T. Report MITNE-196
- Smith KS (1979) An analytic nodal method for solving the two-group, multidimensional, static and transient neutron diffusion equation. Nuclear Engineer's Thesis, Massachusetts Institute of Technology, Department of Nuclear Engineering
- Suslov IR (1993) Solution of transport equation in 2- and 3-dimensional irregular geometry by the method of characteristics. In: Kusters H, Stein E, Werner W (eds) Proceedings of the international conference on mathematical methods and supercomputing in nuclear applications, vol 1, Kernforschungszentrum
- Suslov IR (1997) An improved transport theory scheme based on the quasi-stationary derivatives principle International conference on

- mathematical methods and supercomputing in nuclear applications, Saratoga Springs, New York, October 5-9
- Le Tellier R (2006) Développement de la méthode des caractéristiques pour le calcul de réseau, Ph.D. thesis presented at the École Polytechnique de Montréal, Canada
- Le Tellier R, Hébert A (2006) On the integration scheme along a trajectory for the characteristics method. *Ann Nucl Energy* 33:1260
- Le Tellier R, Hébert A (2007) An improved algebraic collapsing acceleration with general boundary conditions for the characteristics method. *Nucl Sci Eng* 156:121
- Le Tellier R, Hébert A (2008) Anisotropy and particle conservation for trajectory-based deterministic methods. *Nucl Sci Eng* 158:28
- Le Tellier R, Hébert A, Santamarina A, Litaize O (2008) A modeling of BWR-MOX assemblies based on the characteristics method combined with advanced self-shielding models *Nucl Sci Eng* 158:231
- Villarino EA, Stamm'ler RJJ, Ferri AA, Casal JJ (1992) HELIOS: angularly dependent collision probabilities. *Nucl Sci Eng* 112:16
- Wu GJ, Roy R (2003) A new characteristics algorithm for 3D transport calculations. *Ann Nucl Energy* 30:1



9 Lattice Physics Computations

Dave Knott¹ · Akio Yamamoto²

¹Studsvik Scandpower, Inc., Wilmington, NC, USA

Dave.Knott@studsvik.com

²Graduate School of Engineering, Nagoya University, Nagoya, Japan

a-yamamoto@nucl.nagoya-u.ac.jp

I	Overview	918
1.1	Introduction	918
1.2	Brief History	920
1.3	Cross Section Library	922
1.4	Entering the Resonance Tables	925
1.4.1	Determining Microscopic Background Cross Sections	925
1.4.2	Resonance Interference Effects	926
1.5	Condensation Scheme	928
1.5.1	Pin-Cell Calculations	929
1.5.2	Coupling Calculation	930
1.6	Assembly Fine-Mesh Transport Calculation	932
1.6.1	The CCCP Method	932
1.6.2	The Method of Characteristics	934
1.7	Fundamental Mode Calculation	935
1.8	Gamma Transport Calculation	937
1.9	Power Distribution Calculation	939
1.10	Burnup Calculation	939
1.11	Edits	940
1.12	Summary	941
2	Cross Section Library	941
2.1	Objective	941
2.2	Choice of Energy Group Structure	943
2.2.1	WIMS 69 Groups	944
2.2.2	XMAS 172 Groups	945
2.2.3	SHEM 281 Groups	946
2.2.4	Other Energy Group Structures	949
2.3	Cross Sections Used in Lattice Physics Computations	952
2.4	Cross Section Processing	954
2.4.1	Generation of Multigroup Cross Section Data	955
2.4.2	Execution Control of NJOY	958
2.4.3	Post-Processing for Cross Section Library	959
2.5	Tabulation and Contents of Cross Section Library	961
2.5.1	General File Format	962

2.5.2	Nuclide Identifiers	962
2.5.3	Dependency of Cross Sections	964
2.5.4	General Data	966
2.5.5	One-Dimensional Data	966
2.5.6	Two-Dimensional Data	968
2.5.7	Burnup-Related Data	968
2.5.8	Gamma Cross Section Library	969
2.6	Summary	969
3	<i>Resonance Treatment</i>	969
3.1	Objective	969
3.2	Effective Cross Sections	970
3.3	Physics of Self-Shielding and Major Resonance Calculations	972
3.3.1	Physics of Self-Shielding	972
3.3.2	Ultrafine Energy Group Calculation	973
3.3.3	Equivalence Theory	973
3.3.4	Subgroup Method	974
3.4	Resonance Self-Shielding in a Homogeneous System	975
3.4.1	Slowing Down of Neutrons in a Homogeneous System	975
3.4.2	Narrow Resonance Approximation	977
3.4.3	Wide Resonance Approximation	980
3.4.4	Intermediate Resonance Approximation	983
3.5	Resonance Self-Shielding in a Heterogeneous Systems	991
3.5.1	Neutron Slowing Down in a Heterogeneous Isolated System	991
3.5.2	Equivalence Theory	997
3.5.3	Various Approximations for Escape Probability	998
3.5.4	Neutron Slowing Down in a Heterogeneous Lattice System	1005
3.5.5	Calculation of the Dancoff Factor and Background Cross Sections	1012
3.5.6	Stamm'ler's Method for a Heterogeneous Lattice System	1020
3.5.7	Potential Limitations of the Equivalence Theory	1023
3.6	Tabulation of Self-Shielding Factors	1026
3.6.1	Cross Section Processing and Effective Cross Sections	1026
3.6.2	Interpolation of Self-Shielding Factor Table	1027
3.7	Ultrafine Group Method	1029
3.7.1	Homogeneous System	1029
3.7.2	Heterogeneous System	1032
3.7.3	Limitations of the Ultrafine Energy Groups Method	1033
3.8	Subgroup Method	1035
3.8.1	General Concept	1035
3.8.2	Direct Approach	1036
3.8.3	Probability Table Approach	1038
3.8.4	Fitting Method	1041
3.8.5	Moment Method	1043
3.8.6	Improvements in the Probability Table Approach	1047
3.9	Other Methods	1047
3.9.1	Tone's Method	1047

3.9.2	The Stoker–Weiss Method and the Space-Dependent Dancoff Method (SDDM)	1051
3.10	Resonance Overlap Effect	1061
3.10.1	Overview	1061
3.10.2	Resonance Interference Factor (RIF) Table	1062
3.10.3	Utilization of an Ultrafine Energy Group Cross Section	1063
3.11	Other Topics in Resonance Calculations	1065
3.11.1	Effective Temperature Used in Resonance Calculation	1065
3.11.2	Temperature Distribution in a Resonance Region	1066
3.11.3	Treatment of Number Density Distribution in a Pellet	1067
3.11.4	Resonance Calculation for Non-Heavy Nuclides	1068
3.11.5	Verification and Validation of Resonance Calculation Model	1068
3.12	Summary	1069
4	<i>Energy Condensation Scheme</i>	1069
4.1	Introduction	1069
4.2	Pin-Cell Spectral Calculations	1070
4.2.1	General Theory	1071
4.2.2	The Method of Collision Probabilities in Slab Geometry	1075
4.2.3	The Method of Collision Probabilities in Cylindrical Geometry	1080
4.2.4	White Boundary Conditions	1085
4.2.5	Buffer Zone	1087
4.2.6	Numerics of the Pin-Cell Spectral Calculation	1088
4.3	Coupling Calculation	1091
4.3.1	The Method of Transmission Probabilities	1092
4.3.2	Numerics of the Coupling Calculation	1094
4.3.3	Solution to the Response Matrix Equations	1097
4.3.4	Geometry of the Coupling Calculation	1099
4.4	Cross Section Condensation	1101
4.5	Sundries	1103
5	<i>Fine-Mesh Assembly Calculation</i>	1104
5.1	Introduction	1104
5.2	General Theory of the Method of Characteristics	1104
5.2.1	Introduction	1104
5.2.2	Solution to the Characteristics Form of the Transport Equation	1105
5.3	Quadrature Sets	1108
5.3.1	Introduction	1108
5.3.2	Azimuthal Angles	1109
5.3.3	Polar Angles	1111
5.4	Geometry Routine	1113
5.4.1	Introduction	1113
5.4.2	Neutron Streaming and Symmetry in Slab Geometry	1114
5.4.3	Ray Tracing in Slab Geometry	1115
5.5	Solution to the Characteristics Equation	1116
5.5.1	Introduction	1116
5.5.2	Initialization of the Flux	1117

5.5.3	Calculating the Source Term	1117
5.5.4	Boundary Conditions	1120
5.5.5	Convergence	1121
5.5.6	Accelerating the Flux Convergence	1123
5.6	Cylindrical Geometry	1125
5.6.1	Introduction	1125
5.6.2	Choosing the Azimuthal Angles of Motion	1127
5.6.3	An Alternative Tracking Approach	1130
5.6.4	Modification to the Characteristics Equation	1133
5.7	Two-Dimensional Geometry	1134
5.8	Mesh Subdivisions for Two-Dimensional Problems	1138
5.8.1	Assigning Material Regions	1138
5.8.2	Meshing	1140
5.8.3	Defining Various Cell Types	1141
5.8.4	Meshing of Control Blade Cells	1144
5.8.5	Final Mesh Layout	1144
5.9	Two-Dimensional Ray Tracing	1145
5.9.1	The Cyclic Tracking Approach	1145
5.9.2	The Macro-Band Approach	1151
5.10	Quadrature Sets for Two-Dimensional LWR Lattice Calculations	1152
5.10.1	Quadratures for Modeling Polar Motion	1152
5.10.2	Quadratures for Modeling Azimuthal Motion	1153
5.11	Acceleration Schemes for Two-Dimensional Calculations	1155
5.11.1	Coarse Mesh Rebalance	1155
5.11.2	Coarse Mesh Finite Difference	1156
5.12	Treating Very Thin Cylindrical Regions	1158
5.13	Final Comments	1160
6	<i>Burnup Calculation</i>	1161
6.1	Objective	1161
6.2	The Physics of Burnup and its Modeling	1162
6.2.1	Phenomena during Burnup	1162
6.2.2	Burnup Chain	1163
6.2.3	Burnup Equation	1170
6.2.4	Burnup, Burnup Time, and Normalization of Neutron Flux	1174
6.3	Numerical Scheme	1176
6.3.1	Potential Causes of Error in a Numerical Solution	1176
6.3.2	General Remarks on Numerical Solutions for the Burnup Equation	1177
6.3.3	The Euler Method	1178
6.3.4	The Runge–Kutta Method	1179
6.3.5	The Matrix Exponential Method	1181
6.3.6	The Matrix Decomposition Method	1183
6.3.7	Bateman Method	1186
6.3.8	The Padé Approximation	1187
6.3.9	The Krylov Subspace Method	1188
6.3.10	Numerical Example	1189
6.3.11	Predictor–Corrector Method	1195

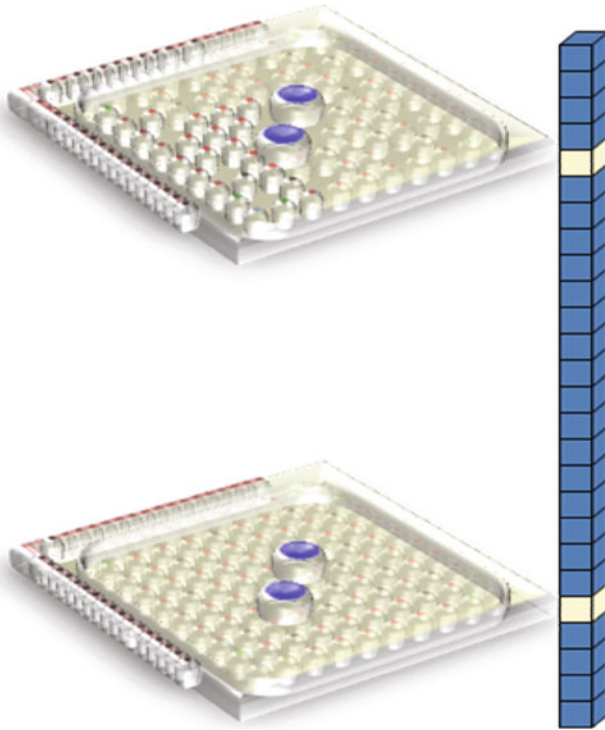
6.3.12	Sub-Step Method	1198
6.3.13	Cooling Calculation	1200
6.4	Burnup in Gadolinia-Bearing Fuel	1201
6.4.1	Onion-Skin Effect	1202
6.4.2	Asymmetry Effect in Gadolinium Depletion	1204
6.4.3	Various Numerical Techniques for Gadolinium Depletion	1205
6.5	Summary	1207
7	<i>Case Matrix</i>	1207
7.1	Introduction	1207
7.2	Cross Section Dependencies in BWRs	1208
7.3	Cross Section Dependencies in PWRs	1218
7.4	Summary	1221
8	<i>Edits</i>	1222
8.1	Nomenclature	1223
8.2	Various Edits	1223
8.3	Neutron Balance	1230
9	<i>Concluding Remarks</i>	1231
	<i>References</i>	1232

Abstract: This chapter presents a detailed description of the elements that comprise a lattice physics code. Lattice physics codes are used to generate cross section data for nodal codes, where the nodal codes are used to model the coupled neutronics and thermal-hydraulics behavior of the entire reactor core during steady state and transient operation. Lattice physics codes analyze axial segments of fuel assemblies, referred to as *lattices*, to determine the detailed spatial and spectral distribution of neutrons and photons across the segment. Once the flux distribution is known, the cross sections can be condensed and homogenized into the structure needed by the nodal code. The nodal code then pieces the various lattices together to construct the various fuel assemblies in the reactor core. This chapter is split into individual sections representing the major pieces of a lattice physics code. ➤ [Section 1](#) presents a general overview of the computational scheme used for a typical lattice physics code (*Knott*). The remaining sections of this chapter are used to describe the major pieces in detail. ➤ [Section 2](#) describes the contents of the cross section library that accompanies a lattice physics code (*Yamamoto*). ➤ [Section 3](#) discusses the various resonance treatments used in lattice physics calculations (*Yamamoto*). ➤ [Section 4](#) describes a method for removing cross section energy detail without sacrificing too much accuracy (*Knott*). ➤ [Section 5](#) describes the fine-mesh transport calculation on the heterogeneous lattice geometry (*Knott*). ➤ [Section 6](#) discusses the burnup calculation (*Yamamoto*). ➤ [Section 7](#) describes some of the details of a typical case matrix (*Knott*), and ➤ [Sect. 8](#) discusses some of the edits that are provided by the lattice physics code (*Knott*). This chapter provides the interested reader with a broad understanding of a typical lattice physics code.

1 Overview

1.1 Introduction

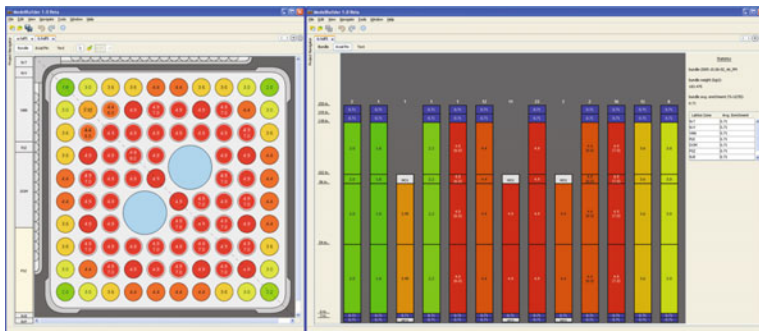
Our primary interest in reactor analysis is to be able to model day-to-day steady state operation of the reactor core, or to model brief periods of time during which the reactor is experiencing some sort of operational transient due to an unexpected insertion or removal of reactivity. Such analyses are performed using a three-dimensional nodal code with thermal-hydraulic feedback. The nodal code models the entire reactor core as a collection of homogeneous prisms, referred to as *nodes*. The nodes are homogeneous in the sense that the material cross sections, used to represent the neutronic properties of the fuel, are constant and there is no geometry detail within a node, such as the explicit representation of fuel pins, guide tubes, or control rods. In other words, everything gets smeared together. A model of a full-sized reactor core will use anywhere from 15,000 to 20,000 nodes. Material cross sections for a node have traditionally been represented by just two energy groups – a fast group typically above 0.625 eV and a thermal group typically below 0.625 eV – although current nodal codes have begun to expand on this number. The material cross sections for a node are obtained from tables generated by a *lattice physics code*. The lattice physics code is used to perform a very detailed neutronic analysis on each unique axial portion of a fuel design, where the characteristics of the fuel might change due to changes in geometry or materials from the surrounding elevations. We refer to these unique axial zones as *lattices*, two of which are illustrated in ➤ [Fig. 1](#). A typical fuel bundle may contain seven or eight different axial zones. This is illustrated in ➤ [Fig. 2](#) for a boiling water reactor (BWR) bundle design, where the panel on the left shows the radial distribution of pin enrichments in the bundle design and the panel on the right shows the axial zoning of each



■ Figure 1
Lattices within homogeneous nodes

of the unique pin types that have been included in the design. In this example, of the 92 fuel pins contained in the bundle design, 13 happen to be unique, differing from each other either in enrichment, burnable absorber content (i.e., Gadolinium mixed into the Uranium fuel pellet), or height. Several pins in the bundle are referred to as part-length rods and span only a portion of the total height of the assembly. The lattice physics code analyses each zone at various snap shots in time (i.e., burnup) and at different core conditions to create tables of homogenized two-group cross sections, which are needed by the nodal code. The collection of cases analyzed to create the tables is referred to as the *case matrix*. The nodal code then interpolates the tables between snap shots to determine the characteristics of the fuel at each specific core elevation, for a given reactor condition. The challenge is to come up with a scheme for the lattice physics code that can accurately reduce the continuous energy raw cross section data for the strongly heterogeneous fuel assembly into a single, homogenized material in two representative energy groups that can be used by the nodal code to produce accurate results.

To create the homogenized, two-group cross sections for each lattice, the lattice physics code needs to calculate an accurate flux distribution in energy and space for the heterogeneous problem. It will then use this flux distribution to spatially and spectrally homogenize the lattice. The main difference between various lattice physics codes in use today is the way in which they go about determining the flux.



■ Figure 2

Panels showing the radial and axial enrichment distribution of pins in a BWR bundle

Ideally, the flux distribution in the lattice would be determined by solving the transport equation in the exact geometry of the lattice using continuous energy cross sections, the way a Monte Carlo code might. But because of time constraints, such a calculation is outside the realm of today's design requirements, where thousands of lattice physics calculations are needed to fully functionalize a single fuel design's characteristics. To this end, the calculational scheme within a lattice physics code is intended to reduce the overall computation time without sacrificing too much accuracy.

In this chapter, we will describe the concept of the lattice physics code. The details of the scheme that will be discussed follow the path outlined in ► Fig. 3. The lattice physics code draws upon many of the topics discussed in other chapters of this handbook, so it provides a nice way of tying many of the topics together. Application to BWR fuel designs are used as examples. Concepts developed to analyze a BWR fuel design can be extended directly to pressurized water reactor (PWR) fuel designs.

1.2 Brief History

In the early days (i.e., late 1950s and early 1960s), the method for analyzing a reactor core consisted of a series of simplistic calculations performed using separate pieces of software that formed a calculational chain. Each piece of software in the chain served a specific purpose and results from one piece of software were used to feed the next piece of software in the chain. The procedure began by calculating a spatially independent fast flux spectrum above 0.625 eV, such as the one generated on a grid of 54 energy groups using the MUFT code (Bohl et al. 1957). The companion thermal flux spectrum below 0.625 eV was generated on a grid of 172 energy groups using the SOFOCATE code (Amster and Suarez 1957). The 0.625 eV energy was used as the thermal cut-off, above which up-scattering effects were neglected. Both MUFT and SOFOCATE were dimensionless codes that simply supplied a general flux spectrum for a given material.

The flux spectrum from the MUFT–SOFOCATE analysis was used to collapse cross sections to a very small number of groups – typically 4. Using the four-group energy structure, a one-dimensional cylindrical pin-cell calculation was performed using the THERMOS code

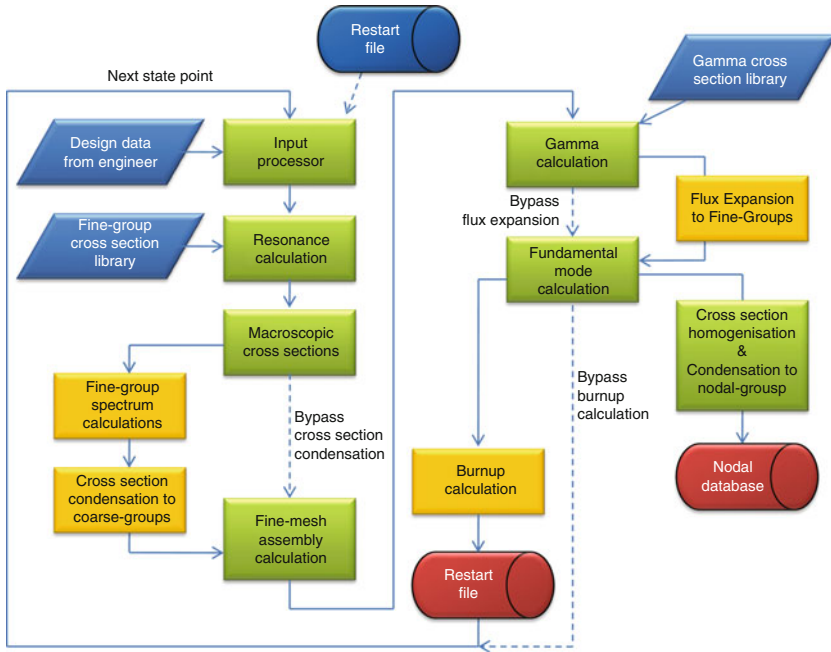


Figure 3
Typical lattice physics calculation scheme

(Honeck 1961). The pin-cell calculation provided representative flux spectrums for the fuel, clad, and coolant regions of the reactor. The flux in the fuel region from the THERMOS pin-cell calculation was passed to a burnup code, such as LEOPARD (Barry 1963), which performed the depletion analysis on selected isotopes. The whole process was very crude by today's standards and offered little in the way of accuracy.

The development of lattice physics codes for reactor analysis began in the mid-1960s with the introduction of WIMS (Winfrith Improved Multigroup Scheme) at Winfrith in the UK (Askew et al. 1966a). The concept gathered all the processes for generating few-group cross section data into a modular collection of software that automated many of the tasks in a systematic fashion, thereby relieving the engineer of a great deal of tedious data transfer and manipulation. But the major evolutionary step was to add a two-dimensional calculation, which analyzed a fuel assembly at a specific elevation. (It should be noted here that the lattice physics code models each lattice as being infinitely tall; i.e., there are no boundaries along the z -axis. This is what we refer to as a two-dimensional problem, i.e., boundaries along two axes.) This two-dimensional calculation provided a way of explicitly capturing the response of each pin due to the influence of its neighbors (other fuel pins, absorber rods, water rods, channel box walls, water gaps, etc.). The original WIMS code provided a framework for research in reactor analysis and could be applied to a very wide range of problems, such as gas-cooled reactors of the Magnox and AGR types that are prevalent in the UK. In the early 1970s, a special version of WIMS was released, LWRWIMS (Fayers et al. 1972), which was streamlined for analyzing light water reactor (LWR) fuel designs. These first versions of WIMS made use of gross approximations at all stages of the

calculational scheme in order to reduce execution time and memory requirements to a manageable level. For LWR analysis, the standard way of determining the flux at the lattice level was based on a few-group diffusion calculation applied to a coarse Cartesian grid.

In the 1970s and early 1980s, a series of lattice physics codes were developed in the Scandinavian countries. These included CASMO (Ahlin and Edenius 1977), CPM (Ahlin and Edenius 1978), and PHOENIX (Stamm'ler 1992). These codes, together with LWRWIMS, the General Electric/Toshiba code TGBLA (Yamamoto et al. 1984), the Combustion Engineering code DIT (Jonsson and Loretz 1991), and the Cadarache code APOLLO (Hoffman et al. 1973), provided a stable platform for LWR lattice physics analysis throughout the 1980s. Most codes were very similar in concept, but differed in detail. All employed significant approximations in order to reduce execution time to a manageable level. However, the newer codes had begun to introduce transport effects into the lattice calculation. Throughout the 1990s, CPM and DIT faded from routine use. During the same period of time, drastic improvements in computer architecture allowed for significant improvements in accuracy in CASMO (CASMO-4 (Knott et al. 1995)), APOLLO (APOLLO-2 (Sanchez et al. 1988)), and the development of HELIOS (Casal et al. 1991). Most lattice physics codes in production use today share many of the ideas from these codes.

The content of this chapter relies heavily on experiences from the development of CASMO-4, LANCER02 (Knott and Wehlage 2007), and AEGIS (Sugimura et al. 2007). When appropriate, deviations from the approaches in these codes are discussed.

1.3 Cross Section Library

The first step in building a lattice physics code is to create an energy group-dependent cross section library. This is our first approximation – that we assume we can accurately represent cross sections over a range of energies using constant values as opposed to point-wise data. The number of energy groups needed and the location of the group boundaries are determined by the lattice physics code's range of application. For example, analysis on mixed-oxide fuel requires different energy detail than does analysis on Uranium-oxide fuel; analysis on fast reactors requires different energy detail than does analysis on thermal reactors; analysis on light water reactors requires different energy detail than does analysis on heavy water reactors, and so on. From the early WIMS days through the 1980s, the cross section libraries associated with production-level lattice physics codes were limited to 100 energy groups or fewer. The original WIMS library contained 69 energy groups (Taubman 1975) and many early lattice physics codes replicated that structure. In the early 1990s, HELIOS was released with a master library containing 190 energy groups, although this group structure was rarely used for analysis. Instead, a smaller library with 35 groups was routinely utilized. Today, it is common for libraries to contain hundreds of energy groups (Rhodes 2009). The more energy groups contained in the library, the more time consuming the analysis becomes. In [▶ 1.5](#) – and in much more detail in [▶ Sect. 4](#) – we will discuss the ways of reducing this computational burden.

In addition to determining the energy group structure of the cross section library, it is also necessary to determine the isotopes that will be carried in the library. Not all isotopes need to be included in the library. For instance, deuterium data might only be required if the lattice physics code is going to be applied to heavy water reactor analysis; graphite data might only be required if the lattice physics code is going to be applied to gas-cooled reactors and so on. The number of isotopes included in the library is primarily dictated by the depletion chains that will be solved during the burnup calculation and by the fission products that will be treated explicitly.

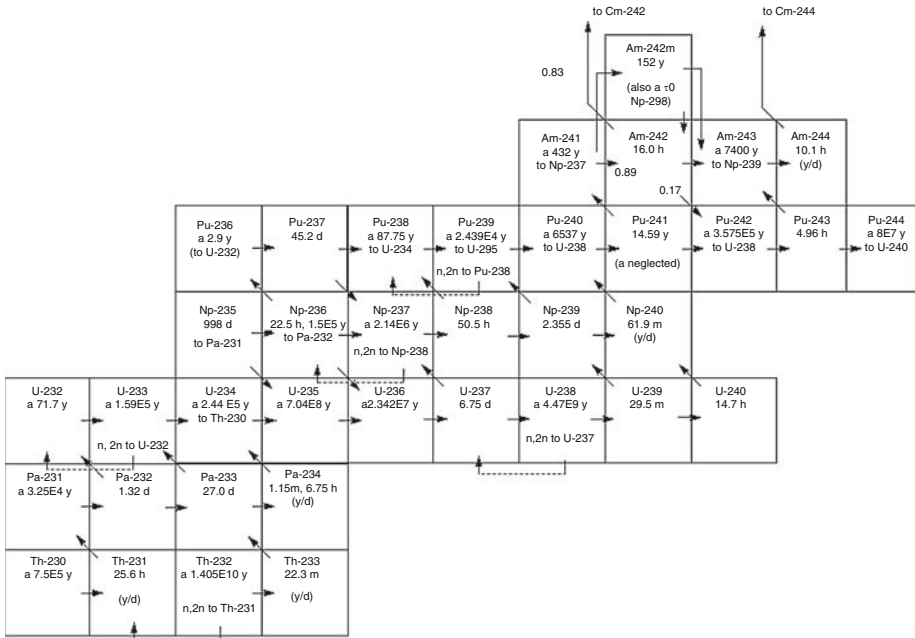


Figure 4
Typical actinide chain

Figure 4 contains an example of the lower portion of the actinide chain modeled in a typical lattice physics code (Rhodes 2009). In order to model this burnup chain, data for every isotope in the chain would need to be contained in the cross section library, although an exception can be made for the extremely short-lived isotopes (i.e., those isotopes that decay within a matter of minutes). Early libraries typically linearized the depletion chains in order to reduce the computational burden and memory requirements (Stamm’ler and Abbate 1983). In addition, only the most important fission products were modeled explicitly in the library. The fission products that were not modeled explicitly were rolled up into a couple of pseudo isotopes, typically one pseudo isotope for all the slowly saturating fission products and one pseudo isotope for all the non-saturating fission products. The total number of isotopes contained in the early libraries was often limited to 100. Today, it is common practice to include several hundred isotopes in a library and to solve the depletion chains explicitly in their matrix representation (Knott and Wehlage 2007); (Rhodes 2009). Section 2 is devoted to a discussion on the cross section library associated with a lattice physics code.

Creation of a multigroup cross section library for a lattice physics code begins with the code that processes the continuous energy cross section data. In the case of the ENDF/B data, the major processing code is NJOY (MacFarlane and Muir 1994a). To create a group-wise library from the continuous energy point-wise data, NJOY must have a flux spectrum with which to combine point-wise data over an energy range,

$$\sigma_x^g = \frac{\int_E^{E+\Delta E} \sigma_x(E)\phi(E)dE}{\int_E^{E+\Delta E} \phi(E)dE} \tag{1}$$

where x is a reaction type (e.g., fission, capture); g is an energy group over the energy interval ΔE ; $\sigma_x(E)$ is the microscopic cross section at energy point E ; and $\phi(E)$ is the flux spectrum used to weigh the continuous energy cross section over the energy interval from E to $E + \Delta E$.

The flux contained in (1) is meant to represent the spectrum found in a typical LWR. Unfortunately, NJOY does not contain the capability of solving the transport equation for a specific flux spectrum. Instead, NJOY contains a couple of options that can be selected to generate an estimate to the true flux found in an LWR. The options available in NJOY assume that the flux behaves as defined by the following expression,

$$\phi(E) \propto \frac{1/E}{\sigma_{t,iso}(E) + \sigma_0} \quad (2)$$

where $\sigma_{t,iso}(E)$ is the microscopic total cross section for the isotope under consideration, iso ; and σ_0 is the microscopic background cross section, which represents the scattering strength of all isotopes in the system other than isotope of interest, iso . In this context, the term *system* refers to the material mixture plus anything else in the immediate vicinity that can contribute to scattering, such as moderator surrounding a fuel pellet. Equation (2) is often referred to as the Bondarenko model based on the narrow resonance (NR) approximation (Lamarsh 1972). If possible, group boundaries in the cross section library should be chosen such that results are insensitive to the flux from (2) used to generate the library.

For each isotope containing resonances, NJOY creates a base cross section set at a base temperature (e.g., 300 K), for infinitely dilute conditions by setting σ_0 equal to a very large value (e.g., 10^{10}) in (2). In this context, the term *infinitely dilute* refers to a system in which the background cross section (i.e., the scattering strength of all the other isotopes in the material and surrounding environment) is so large as to render the presence of the resonance absorber unrecognizable. That is, scattering is the dominant process even at resonance energies.

Once the base set of cross sections are generated, NJOY can create correction factors to the infinitely dilute values to account for changes in the cross sections caused by different temperatures and different background cross sections. We will refer to these tables as the f -tables, $f(T, \sigma_0)$. When the lattice physics code obtains microscopic cross sections from the cross section library, the code reads the infinitely dilute values and enters the f -tables to obtain the appropriate correction factor as a function of temperature and microscopic background cross section,

$$\sigma_{x,iso}^g = \sigma_{x,iso}^g(300 \text{ K}, \infty) \cdot f_{x,iso}^g(T, \sigma_0) \quad (3)$$

Interpolation in the f -tables is performed as a quadratic function of the square root of the fuel temperature, $\sqrt{T_f}$, and the logarithm of the microscopic background cross section, $\log(\sigma_0)$. Self-shielded data for each resonance absorber are generated at many different temperatures between 300 and 2,500 K, and at many different background cross section conditions between 10 barns and 10^{10} barns.

In a lattice physics code, the fuel temperature is typically set to a specific value by the user, removing all ambiguity for that particular parameter. The various microscopic background cross sections for the resonance absorbers in the bundle, however, are not obvious and must be determined by the code. If the calculated microscopic background cross section for a particular isotope is incorrect, the lattice physics code will enter the f -tables in the wrong location and pick up the wrong cross sections for the resonance region. This introduces a certain amount of error into the analysis, so it becomes very important that the lattice physics code have a way of accurately calculating the background cross section for each material in the fuel assembly.

1.4 Entering the Resonance Tables

1.4.1 Determining Microscopic Background Cross Sections

To calculate a proper *microscopic* background cross section for each isotope in a material mixture, we begin by determining the *macroscopic* background cross section for the system as a whole and then back-out the microscopic contribution for each isotope.

The calculation of a macroscopic background cross section for a system, Σ_0 , can be separated into two contributions: (1) a volume component, Σ_p ; and (2) a surface component, Σ_e (Wigner et al. 1955). That is, $\Sigma_0 = \Sigma_p + \Sigma_e$.

Volume Component

The volume component, Σ_p , accounts for neutrons that are scattered into a resonance energy by the material mixture (i.e., not the moderator). It is calculated in a very straightforward way as the sum of the potential scattering cross sections for all isotopes in the mixture (hence the use of the subscript p for potential),

$$\Sigma_p = \sum_{iso} N_{iso} \sigma_{p,iso} \quad (4)$$

where N_{iso} is the number density for isotope iso ; and $\sigma_{p,iso}$ is the microscopic potential scattering cross section for isotope iso . The potential scattering cross section is energy-independent and represents the forces that act upon a neutron as it moves in or near the nucleus of an atom. It is a function only of the effective scattering radius of the nucleus, which depends on the way in which the different wavelengths of the incident neutron (e.g., s -wave, p -wave) interact with the target nucleus. The effective scattering radius of each isotope is obtained from the ENDF/B files and the potential scattering cross section is then calculated as $\sigma_{p,iso} = 4\pi R_{0,iso}^2$, where $R_{0,iso}$ is the effective scattering radius of the nuclide.

Surface Component

The surface component, Σ_e , accounts for neutrons that escape the fuel material and are scattered into a resonance energy by the surrounding moderator (hence the use of the subscript e for escape). They are then free to reenter the material, where they may be absorbed. It is the solution to this component that has been studied extensively since the 1960s.

There are many different ways to estimate the contribution from the surface component and different lattice physics codes address it using different approximations. For an isolated fuel pellet, the surface component may be grossly approximated using the Wigner rational expression (Wigner et al. 1955), where a macroscopic escape cross section is expressed as the inverse of the mean chord length for a simple convex body,

$$\Sigma_e = \left(\frac{4V}{S} \right)^{-1} = \frac{1}{2r} \quad (5)$$

In (5), V refers to the volume of the fuel pellet; S refers to the surface area of the pellet; and r is the pellet radius.

The Wigner rational expression is a surprisingly good approximation under certain circumstances. For modern LWR fuel designs, though, the escape cross section calculated using the

Wigner approximation can be in error by far more than is tolerable for the accuracy we desire. Hence, few lattice physics codes rely on the Wigner approximation. Those that do must augment the approximation with a correction factor to produce acceptable results. When this method is chosen, the correction factor is usually determined from a Monte Carlo analysis. ▶ [Section 3](#) is devoted to a thorough description of resonance approximations in lattice physics codes.

For an array of tightly packed fuel pins, such as those in a fuel assembly, some neutrons may escape from one pellet and suffer their first collision in a neighboring pellet rather than in the surrounding moderator. This shadowing effect changes the escape cross section of the isolated pellet and can be taken into account through the use of a Dancoff factor, Γ , and applied to the escape cross section (Carlvik [1966b](#))

$$\Sigma_0 = \Sigma_p + \Gamma \Sigma_e \quad (6)$$

A detailed description of Dancoff factors is included in ▶ [Sect. 3](#).

For each isotope in the fuel mixture, the associated microscopic background cross section is calculated as

$$\sigma_{0,iso} = \frac{\Sigma_0}{N_{iso}} - \sigma_{p,iso} \quad (7)$$

The microscopic background cross section from (7) is used to enter the resonance tables and obtain the appropriate cross sections for each isotope in each fuel mixture in the lattice.

1.4.2 Resonance Interference Effects

Resonance interference refers to the way in which cross section resonances from one nuclide affect resonance absorption or scattering in another nuclide when multiple resonance absorbers exist in the same fuel mixture. During creation of the cross section library, resonance interference effects were neglected. That is, microscopic cross sections for each isotope in the library were created as if none of the resonances from any of the other isotopes existed. In practice, such a condition will never exist since all LWR fuel consists of several Uranium isotopes and/or Plutonium isotopes – all of which contain many resonances over a wide range of energies. In addition, many major fission products contain large resonances. The presence of the additional resonances will exaggerate the spectral flux dips and change the results when using (1). In lattice physics codes, resonance interference effects between different resonance absorbers in the same material mixture can be taken into account through a separate calculation that determines a resonance interference correction factor to the NJOY-generated cross sections (Williams [1983](#); Wehlage [2005](#)).

For this model, a separate ultrafine-group cross section library is utilized that contains tens of thousands of group-wise data points with equal lethargy widths in the resolved resonance energy range from about 40 eV to 10 keV, or possibly even extended up to 100 keV. The narrow resonance (NR) approximation is used to generate a flux spectrum for each resonance absorber in isolation, ϕ_{iso}^u , and a separate flux spectrum for the material mixture as a whole, ϕ_{Mix}^u . Here, u represents the ultrafine-group energy structure. The narrow resonance approximation assumes that the energy lost by a neutron suffering a scattering collision is large compared to the width of a resonance. Under such circumstances, it is unlikely that a neutron will experience more than a single collision within any resonance peak and the neutron is, therefore, somewhat unlikely to be absorbed by a resonance absorber. This approximation tends to be very good for all neutron

energies above 40 eV. Below 40 eV, it is important that the energy group structure of the lattice physics cross section library contains enough detail such that the group-wise cross sections are not strongly shielded.

The ultrafine-group flux for each isotope, ϕ_{iso}^u , and for the material mixture as a whole, ϕ_{Mix}^u , can be described by the following expressions:

$$\phi_{iso}^u = \frac{1/E^u}{\Sigma_{t,iso}^u + \Sigma_0} \quad (8)$$

$$\phi_{Mix}^u = \frac{1/E^u}{\Sigma_{t,Mix}^u + \Sigma_0} \quad (9)$$

where the only difference between (8) and (9) is in the value for the total cross section in the denominator. $\Sigma_{t,iso}^u$ is the ultrafine-group total cross section for isotope *iso*; and $\Sigma_{t,Mix}^u$ is the ultrafine-group total cross section for the material mixture as a whole.

Equations (8) and (9) may be solved directly using the macroscopic background cross section for the material mixture, Σ_0 , from (6). The fluxes from (8) are used to create parallel sets of cross sections, in the energy group structure of the lattice physics cross section library, for each individual resonance absorber,

$$\sigma_{x,iso}^g = \frac{\sum_{u \in g} \sigma_x^u \phi_{iso}^u}{\sum_{u \in g} \phi_{iso}^u} \quad (10)$$

And the flux from (9) is used to create cross sections for the material mixture as a whole,

$$\sigma_{x,Mix}^g = \frac{\sum_{u \in g} \sigma_x^u \phi_{Mix}^u}{\sum_{u \in g} \phi_{Mix}^u} \quad (11)$$

where *x* is the reaction type; *iso* is a resonance absorber; *g* is the energy group structure of the lattice physics cross section library; and *u* is the energy group structure of the ultrafine-group cross section library. Resonance interference correction factors are then calculated as the ratio of (11) to (10),

$$\text{RIF}_{x,iso}^g = \frac{\sigma_{x,Mix}^g}{\sigma_{x,iso}^g} \quad (12)$$

and are applied to the cross sections from the lattice physics library,

$$\sigma_{x,iso}^g = \sigma_{x,iso}^g(300 \text{ K}, \infty) \cdot f_{x,iso}^g(T, \sigma_0) \cdot \text{RIF}_{x,iso}^g \quad (13)$$

RIFs for capture, fission, and elastic scattering cross sections for each major resonance absorber in any material mixture should be calculated. In most cases, the effect of the resonance interference calculation on the results from the lattice physics code is small and serves to basically fine-tune any reactivity coefficients that rely on spectrum hardening effects. A more thorough description of resonance interference effects is contained in [Sect. 3](#).


1.5 Condensation Scheme

Once microscopic cross sections have been obtained from the cross section library and the macroscopic cross sections for each material region in the problem have been created, the lattice physics code is ready to determine the flux distribution throughout the lattice. Solution to the steady state Boltzmann transport equation in the energy group structure of the cross section library is usually supported by modern lattice physics codes, but the calculation is often too time consuming for production-level analysis, where several thousand state points are analyzed to generate nodal cross section data for a single bundle design.

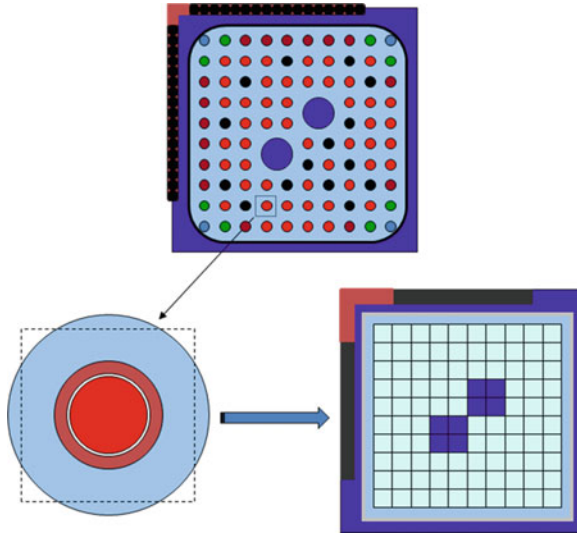
One common approach for reducing execution time to a reasonable level is to condense the cross sections from the energy group structure of the library to a smaller, more manageable energy group structure. When doing this, it is imperative that accuracy is maintained by the smaller cross section set, so an adequate condensation scheme is very important.

HELIOS addressed this issue by performing a single calculation on a generic LWR lattice in the energy group structure of the master cross section library (Casal et al. 1991). The lattice-averaged flux from the reference calculation was then used to condense the entire master cross section library from the fine-group structure (190 groups) into a smaller energy group structure (~35 groups). The smaller library was then used in all production-level analyses without any further condensation. Since the condensation scheme was applied to the microscopic cross sections, the resonance tables (i.e., f -tables) had to be condensed, as well.

CASMO-4 used a different approach (Knott et al. 1995). The cross section library for CASMO-4 contained 70 energy groups and at the beginning of each individual case the code performed a series of calculations in the energy group structure of the library in order to generate a unique condensation spectrum for each different material region of the problem. Macroscopic cross sections for each material region in the problem were condensed from 70-groups to a much smaller group structure, which depended on the type of problem being analyzed, but in general was kept below a dozen energy groups. The approach in LANCER02 is very similar (Knott and Wehlage 2007). The LANCER02 cross section library contains 118 energy groups (or a 190 group library for mixed oxide analysis) and the flux from the condensation scheme is used to collapse macroscopic cross sections to approximately 25 energy groups. The approaches in both CASMO-4 and LANCER02 are based on the scheme described in Knott (1991). This scheme will be described in this chapter.

The condensation scheme in CASMO-4 and LANCER02 consists of a two-step process involving, first, a series of one-dimensional pin-cell calculations and, second, a fast two-dimensional coupling calculation, as illustrated in  Fig. 5. Both calculations could be performed in the energy group structure of the cross section library. An alternative approach would be to perform the coupling calculation in an intermediate energy group structure, somewhere between the fine-group structure of the library and the broad-group structure of the assembly fine-mesh transport solution, in order to reduce execution time even further. Either approach is acceptable, keeping in mind that the level of accuracy used at this stage of the computational scheme will affect the number of energy groups that must be maintained for the assembly fine-mesh transport solution.

In contrast to the two-step approach, CASMO-5 has removed the coupling calculation from the condensation scheme and relies solely on the pin-cell calculations to generate a condensation flux. The lattice physics code AEGIS contains no condensation scheme and performs the assembly fine-mesh transport calculation in the energy group structure of the cross section



■ **Figure 5**
Progression of condensation scheme

library. This is the approach taken for ultimate accuracy, although at the price of a much longer run time.

1.5.1 Pin-Cell Calculations

For the series of one-dimensional pin-cell calculations in the CASMO-4 and LANCER02 condensation scheme, the flux in the system is determined by solving the integral form of the transport equation using the method of collision probabilities (CP). The CP method is ideal for physically small systems containing a small number of mesh. Each pin cell in the lattice – including water rods and vanish locations (i.e., locations above the top of part-length fuel rods) – should take part in its own unique pin-cell calculation. The square coolant region of each cell can be cylindricalized by preserving volume. This converts the two-dimensional nature of the square cell into a one-dimensional problem, where the flux can be determined very rapidly without significantly affecting accuracy. A buffer zone, made up of average fuel and moderator material, can be added to the outside of each cell to help drive the flux across inert pins (e.g., water rods, control rods) and pins containing strong absorbers (e.g., gadolinium, erbium). The system can be represented as a fixed source problem, where the fission spectrum can be used as the neutron source and can be placed in the buffer zone. This helps to facilitate a speedy convergence to the transport solution.

The scalar flux is determined by solving the following integral equation (the derivation of which is presented in detail in [Sect. 4](#)),

$$\phi(\vec{r}_i, E) = \int_{-\infty}^0 Q(\vec{r}_j, E) \cdot T(\vec{r}_j \rightarrow \vec{r}_i, E) \cdot dV_j \quad (14)$$

where $Q(\vec{r}_j, E)$ is the total neutron source in mesh j ; $\phi(\vec{r}_i, E)$ is the scalar flux in mesh i ; and $T(\vec{r}_j \rightarrow \vec{r}_i, E)$ is the first-flight transmission probability of neutrons from mesh j to mesh i , given by the expression

$$T(\vec{r}_j \rightarrow \vec{r}_i, E) = \frac{e^{-\tau(\vec{r}_i - \vec{r}_j, E)}}{4\pi |\vec{r}_i - \vec{r}_j|^2} \quad (15)$$

In order to arrive at the expression for the scalar flux in (14), the source term was assumed to be isotropic. Such an assumption necessitates the use of transport-corrected cross sections in order to account for anisotropic scattering effects. The transport-correction is derived by expanding the scattering kernel using spherical harmonics and keeping only the first two terms. This leads us to the diffusion equations for the scalar flux, ϕ_0^g , and current, ϕ_1^g , and the corresponding definition for the diffusion coefficient

$$D^g = \frac{1/3}{\Sigma_{t1}^g - \sum \Sigma_{s1}^{g' \rightarrow g} \left(\phi_1^{g'} / \phi_1^g \right)} \quad (16)$$

The denominator in (16) represents the definition for the transport cross section, which is a function of the ratio of currents in various energy groups. Unfortunately, we do not know the currents in our problem a priori and we are forced to make the assumption that the current-induced scattering of neutrons into an energy group is equal to the current-induced scattering of neutrons out of the energy group,

$$\sum_{g'} \Sigma_{s1}^{g' \rightarrow g} \phi_1^{g'} \approx \sum_{g'} \Sigma_{s1}^{g \rightarrow g'} \phi_1^g \quad (17)$$

This is a fair assumption when scattering is the dominant reaction and relatively little neutron absorption is taking place. It is a poor assumption when absorption is the dominant reaction.

From (17) it follows that,

$$\Sigma_{tr}^g = \Sigma_t^g - \sum_{g'} \Sigma_{s1}^{g \rightarrow g'} = \Sigma_t^g - \Sigma_{s1}^g \quad (18)$$

which is our definition for the transport cross section. In (18), Σ_t^g is the total cross section in group g ; and Σ_{s1}^g is the first moment to the total scattering cross section in group g . The transport cross section can be created internally from the total cross section and the first moment to the scattering cross section, both of which should be contained in the cross section library.

Specular reflection boundary conditions are used on the outside of the one-dimensional pin-cell geometry to simulate perfect reflection in the square coolant system (i.e., Weiner-Seitz cell).

1.5.2 Coupling Calculation

The solution to the CP equation yields a flux distribution in each region of each pin cell in the energy group structure of the cross section library. This flux distribution is generated without considering the true surroundings of each pin cell (water gaps, water rods, strong absorber pins, control blades, etc.). Before condensing cross sections to a smaller energy group structure, the

fluxes from the one-dimensional pin-cell calculations should be updated to account for the effects on the energy distribution from the surrounding components of the lattice. This can be accomplished by performing a two-dimensional coupling calculation on the entire lattice using a simplified geometry and a simplified solution to the transport equation.

Since this coupling calculation will use a simplified geometry of the lattice, all solutions techniques to the Boltzmann transport equation are viable. At this stage of the calculational scheme, speed is of essence. A very good choice for the two-dimensional coupling calculation is one that solves the integral transport equation using a response matrix (RM) method based on simplified transmission probabilities. In this method, each pin cell is homogenized into an equivalent material set of cross sections using the fluxes from the corresponding one-dimensional pin-cell calculation. Cells are coupled to each other via surface currents, which are assumed to be isotropically distributed in angle and spatially constant along a given cell surface. The equations representing the scalar flux and outward-directed current are, respectively,

$$\phi_I^g = T_{I \leftarrow I}^g Q_I^g V_I + 4 \sum_s T_{I \leftarrow s}^g J_{s, in}^g A_s \quad (19)$$

$$J_{I, out}^g = T_{s \leftarrow I}^g Q_I^g V_I + \sum_{s'} T_{I \leftarrow s'}^g J_{s', in}^g A_{s'} \quad (20)$$

where I represents a spatial mesh, such as an homogenized pin cell; s represents a surface to mesh I ; the T 's are transmission probabilities between volumes and/or surfaces; V represents the volume of mesh I ; and A represents the surface area of surface s . Outward-directed currents from one mesh become the inward-directed currents to the neighboring mesh. The calculation of transmission probabilities will be discussed in [Sect. 4](#).

Following the two-dimensional RM calculation, the energy distribution of neutrons from each one-dimensional pin-cell calculation is updated,

$$\tilde{\phi}_i^g = \phi_i^g \cdot \frac{\phi_I^g V_I}{\sum_{i \in I} \phi_i^g V_i} \quad (21)$$

Fluxes for the surrounding regions of the lattice – channel box wall, water gaps, etc. – are obtained directly from the RM solution. Fluxes for the various regions of a control blade can be obtained from a special series of pin-cell calculations performed on each absorber tube in a control blade and updated with the flux from the RM solution. [Equation \(21\)](#) represents the flux for each material region of the problem that will be used to condense the macroscopic cross sections. The final energy group structure for the two-dimensional assembly transport calculation depends on the accuracy of the condensation scheme, the energy group boundaries in the cross section library, and the types of problems to be analyzed by the lattice physics code.

Today, many lattice physics codes are attempting to move away from cross section condensation and rely solely on solving the fine-mesh transport problem in the energy group structure of the cross section library. Although this approach produces the most accurate solution possible, it is still far too time consuming for a lattice physics code used at a fuel vendor, where millions of lattice calculations must be performed each year in order to support reload core design work. Because of this, the need for a suitable condensation scheme will not go away anytime soon.


[Section 4](#) is devoted to a thorough description of the condensation scheme used in CASMO-4 and LANCER02.

1.6 Assembly Fine-Mesh Transport Calculation

Due to severe heterogeneities present in most modern bundle designs, the final two-dimensional lattice calculation (in the condensed energy group structure if a condensation scheme is employed) should be performed by modeling the lattice in its true geometry. This need renders many solution techniques obsolete due to the complex geometries of LWR fuel designs (cylinders arranged in square arrays, surrounded by channels with partial arcs, etc.). The most feasible techniques are those that solve the integral form of the transport equation. These techniques include the method of collision probabilities (CP) and its current coupling derivatives; the method of characteristics (MoC), and Monte Carlo methods. Monte Carlo methods are far too time consuming when detailed flux tallies in small regions are required, such as those needed for providing the means to solve the depletion chains in fuel pellets. For this reason, we will abandon the idea of using Monte Carlo techniques directly and focus on the other two possibilities.

1.6.1 The CCCP Method

The CP method is an outstanding choice for small problems, such as one-dimensional pin cells. However, because execution times and memory requirements increase with the square of the number of mesh, the straightforward CP method is a very poor choice for large problems, such as full-size lattices. One way around this is to decouple cells and connect them via surface currents, as we did for the coupling calculation in the condensation scheme. This is the approach used for the assembly fine-mesh transport calculation in HELIOS and derivatives thereof. In order to do this, however, an assumption must be made about the distribution of the current in both angle and space as it leaves or enters a cell. Such an assumption will introduce a certain error into the solution, which will manifest itself around cells containing strong absorbers (control rods, control blades, absorber pins, fuel pins containing Gadolinium, etc.). This is highly undesirable for lattice physics code modeling LWR assemblies, since all of the above-mentioned absorbers are present, to some degree, in every assembly design. In addition, anisotropic scattering effects are nearly impossible to model explicitly in the CP method and we are forced to rely solely on transport-corrected cross sections, which tend to be more than adequate for single assembly calculations using perfectly reflective boundary conditions.

The transmission probabilities method used in the first release of HELIOS is referred to as the CCCP method (Current Coupling of the space elements, which are internally treated by collision probabilities (Casal et al. 1991)). It is a method that has since been employed in other lattice physics codes, such as LANCER01 (Azekura et al. 2003) and PARAGON (Ouisloumen et al. 2001). The premise is to perform a very detailed transport solution within a cell, which for fuel pins is made up of the fuel pellet, cladding, and coolant, and possibly including the initial expansion gap between the pellet and the cladding. The surface of each cell is split into multiple regions and a separate current is calculated for each unique region of the surface, as illustrated in  Fig. 6 where each surface has been split in half. This provides a means for modeling spatial changes in the surface current. In the original HELIOS work, the angular distribution of the current is represented using the quadrature used to model neutron transport within the cell: that is, which ever quadrature is used to integrate the collision probabilities within the cell, the same is also used to subdivide the current as it leaves one cell and enters the neighboring cell.

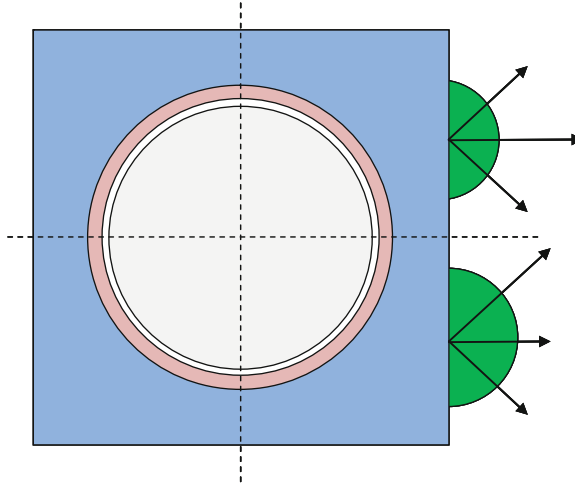


Figure 6
Outward directed currents split along a cell surface

The surface coupling is performed at different polar levels as well as different azimuthal angles, producing a current that can be anisotropic in all directions.

The coupled multigroup equations to be solved are

$$\sum_i^g \varphi_i^g V_i = \sum_{n,m,l} \Gamma_{nml \rightarrow i}^g J_{nml}^{-g} A_{nm} + \sum_j P_{j \rightarrow i}^g \sum_{g'} \left(\Sigma_j^{g' \rightarrow g} + \frac{\chi_j^g}{\lambda} \nu \Sigma_{f,j}^{g'} \right) \varphi_j^{g'} V_j \quad (22)$$

$$J_{nml}^{+,g} = \sum_j P_{j \rightarrow nml}^g \sum_{g'} \left(\Sigma_j^{g' \rightarrow g} + \frac{\chi_j^g}{\lambda} \nu \Sigma_{f,j}^{g'} \right) \varphi_j^{g'} V_j + \sum_{n',m',l'} \Gamma_{n',m',l' \rightarrow nml}^g J_{n',m',l'}^{-g} A_{n'm'} \quad (23)$$

where $J_{nml}^{\pm,g}$ is the out-going/in-coming current from/to the cell in group g , through surface segment m , of cell boundary n , in direction l ; φ_i^g is the neutron flux in group g , mesh i of the cell; $P_{j \rightarrow i}^g$ is the probability for a neutron emitted in group g , mesh j , to suffer its first collision in mesh i ; $P_{j \rightarrow nml}^g$ is the probability for a neutron emitted in group g , mesh j , to leave the cell through segment m of node boundary n in directional l ; $\Gamma_{n',m',l' \rightarrow i}^g$ is the probability for a neutron in group g , in-coming through segment m' , of cell surface n' , in directional l' , to suffer its first collision in mesh i ; $\Gamma_{n',m',l' \rightarrow nml}^g$ is the probability for a neutron in group g , in-coming through segment m' ; cell surface n' ; in directional l' , to leave the cell through segment m of cell surface n in directional l ; A_{nm} is the area of segment m of surface n ; V_i is the volume of mesh i ; $\Sigma_i^g, \nu \Sigma_{f,i}^g, \Sigma_i^{g' \rightarrow g}$ are the macroscopic neutron cross sections in group g , mesh i ; χ_j^g is the fission neutron spectrum in mesh j ; and λ is the neutron multiplication factor.

Ray tracing is used to calculate collision probabilities between mesh within a given cell. The various regions of a cell (e.g., fuel, clad, and coolant) are subdivided further into flat source/flat flux mesh and the collision probabilities are used to redistribute the neutrons between the various mesh of a cell, based on the neutron source distribution in the mesh layout and the neutron current distribution across cell surfaces.

This whole effort is implemented in order to reduce the number of coupled mesh in the CP matrix. In a typical LWR lattice, there may be 5,000 mesh needed to accurately capture the physics of the problem using flat source regions. For a straightforward CP solution, this would require inverting a $5,000 \times 5,000$ matrix for every energy group – a rather daunting task even by today’s standards. By decoupling cells from the CP solution, the problem is reduced to a collection of much smaller “mini” CP matrices – one for each cell in the problem (on the order of a couple of hundreds). The size of each mini CP matrix is on the order of 40×40 , except in cells containing fuel pellets with multiple depletion rings, where the mini CP matrix can be as large as 100×100 – still a much more manageable size compared to $5,000 \times 5,000$. The method still suffers from the approximation imposed by coupling cells via currents.

1.6.2 The Method of Characteristics

In contrast to the drawbacks associated with the method of collision probabilities and Monte Carlo methods, the method of characteristics has few drawbacks. Execution times and memory requirements increase linearly with the angular and spatial detail of the problem; the accuracy of the method can be virtually precise – assuming enough angular detail is used and the spatial mesh are small enough and the method can accommodate explicit modeling of anisotropic scattering, if needed. Additionally, the method is relatively simple to implement, compared with other methods.

The method of characteristics was originally introduced into WIMS in the early 1980s as the CACTUS module (Halsall 1980). That first incarnation of the method saw limited success, though, due to memory requirements and limitations in computers of the day. The first serious application in a commercial lattice physics code was introduced into CASMO-4 in the early 1990s, at a time when workstations had progressed to the point where memory was no longer a major issue (although it remained a minor issue for many more years to come). Since then, the method has found widespread use in other lattice physics codes, including a reawakening in WIMS and additional applications in DRAGON (Marleau et al. 1994), AEGIS (Sugimura et al. 2007), LANCER02 (Knott and Wehlage 2007), APOLLO-2 (Masiello et al. 2009), and most ironically HELIOS-2 (Wemple et al. 2008).

The MoC implemented in CASMO-4 and LANCER02 is the most basic of all the characteristic methods and is a direct derivative of the CACTUS module, first proposed by Askew in the 1970s (Askew 1972). The multigroup equation to be solved is the characteristic form of the Boltzmann equation,

$$\frac{d\Phi_{m,i}^G}{ds_m} + \Sigma_{tr,i}^G \Phi_{m,i}^G = Q_{m,i}^G \quad (24)$$

where s_m is a streaming track across a mesh at angle Ω_m ; $\Phi_{m,i}^G$ is the angular flux in direction Ω_m , across mesh i , in energy group G ; and $Q_{m,i}^G$ is the corresponding angular source, which can be calculated using transport-corrected cross sections or can be modeled using anisotropic scattering effects explicitly.

To solve the characteristic equation, streaming tracks are traced over the problem geometry at a number of different angles. Each angle has associated with it a weight, and each track has associated with it a width. Solution to the characteristics equation, in terms of the angular flux, is obtained along streaming rays and is of the form

$$\Phi_{m,i}^G(s_m) = \Phi_{m,i}^G(0)e^{-\Sigma_{tr,i}^G s_m} + \frac{Q_{m,i}^G}{\Sigma_{tr,i}^G}(1 - e^{-\Sigma_{tr,i}^G s_m}) \quad (25)$$

where the source across a mesh is considered constant (i.e., flat source approximation).

The scalar flux for a given mesh is calculated by integrating the angular flux along all streaming tracks that cross the mesh, and integrating over all directions of motion,

$$\phi_i^G = \int_{4\pi} \bar{\Phi}_i^G(\Omega) d\Omega = 4\pi \sum_m \bar{\Phi}_{m,i}^G \omega_m \quad (26)$$


where ω_m is the weight associated with each direction of motion and the average angular flux in a specific direction across a given mesh, $\bar{\Phi}_{m,i}^G$, is obtained from

$$\bar{\Phi}_{m,i}^G = \frac{\sum_k \bar{\Phi}_{m,k,i}^G \cdot s_{m,k,i} \cdot \delta A_m}{\sum_k s_{m,k,i} \cdot \delta A_m} \quad (27)$$

In (27), δA_m is the separation between parallel streaming tracks; $s_{m,k,i}$ is the length of the streaming track crossing mesh i ; and k represents the different streaming tracks that cross mesh i in direction Ω_m . To obtain an expression for the average value of the angular flux along a streaming track, $\bar{\Phi}_{m,k,i}^G$, (25) is integrated along track k , in direction Ω_m , crossing mesh i , and divided by the length of the track,

$$\bar{\Phi}_{m,k,i}^G = \frac{\int_0^{s_{m,k,i}} \Phi_{m,k,i}^G(s') ds'}{\int_0^{s_{m,k,i}} ds'} \quad (28)$$

Solution to the characteristic equation reduces to finding the intersections between rays and mesh boundaries and calculating the angular flux between intersections. The final solution to the equation produces a very detailed, very accurate flux distribution throughout the lattice (in the condensed energy group structure, if a condensation scheme is employed).

Due to its prominence in lattice physics,  Sect. 5 is devoted to a thorough description of the method of characteristics as applied to the two-dimensional fine-mesh lattice calculation.

1.7 Fundamental Mode Calculation

The fine-mesh assembly calculation assumes perfect reflection on all surfaces of the bundle. In this way, there are no neutrons leaking into or out of the system. However, the data generated by the lattice physics code will be used in a nodal code to model an entire reactor core and, within the reactor core, there are almost always neutrons leaking into or out of each node in the system. To be consistent with the way in which the nodal cross sections are to be used, the lattice physics code should somehow account for neutron leakage at the assembly level.

Leakage effects can be included in an ad hoc way by performing a buckling calculation on the system. The leakage calculation typically involves solving the fundamental mode equation in the diffusion approximation for the material buckling of the system,

$$\bar{\Sigma}_r^g \Psi^g + B_m^2 \bar{D}^g \Psi^g = \sum_{g' \neq g} \bar{\Sigma}_s^{g' \rightarrow g} \Psi^{g'} + \chi^g \quad (29)$$

where the lattice-averaged diffusion coefficient, \bar{D}^g , is calculated as

$$\bar{D}^g = \frac{1}{3 \bar{\Sigma}_{tr}^g} \quad (30)$$

The lattice-averaged removal cross section, $\bar{\Sigma}_r^g$ is calculated as

$$\bar{\Sigma}_r^g = \bar{\Sigma}_{tr}^g - \bar{\Sigma}_s^{g \rightarrow g} \quad (31)$$

and the lattice-averaged cross sections are calculated by volume and flux weighting the cross sections from the various regions of the problem,

$$\bar{\Sigma}_x^g = \frac{\sum_i \Sigma_{x,i}^g \phi_i'^g V_i}{\sum_i \phi_i'^g V_i} \quad (32)$$

In (32), x is a reaction type and $\phi_i'^g$ is the MoC flux distribution expanded back to the energy group structure of the cross section library,

$$\phi_i'^g = \bar{\phi}_i^g \cdot \frac{\phi_i^G}{\sum_{g \in G} \bar{\phi}_i^g} \quad (33)$$

To create a lattice-averaged fission spectrum using the averaging technique represented in (32), $\bar{\chi}^g$, the summation should include only the fuel regions in the lattice.

The flux distribution in (33) has been expanded back to the energy group structure of the cross section library in order to more accurately account for leakage effects in the fast energy group range, where the majority of neutron leakage occurs. In (33), $\bar{\phi}_i^g$ is the condensation flux from (21), and ϕ_i^G is the flux from the broad-group MoC calculation, given by (26).

Equation (27) assumes that the flux has been normalized such that a single absorption occurs in the system, $\sum_g (\bar{\Sigma}_a^g + \bar{D}^g B_m^2) \Psi^g = 1$. The multiplication factor of the system is then calculated from

$$k_{eff} = \sum_g \nu \bar{\Sigma}_f^g \Psi^g \quad (34)$$

The material buckling is adjusted until $k_{eff} = 1.0$. That is, an initial calculation is performed by setting $B_m^2 = 0$. This reproduces the infinite lattice multiplication factor. Next, a second calculation is performed by setting the buckling to a very small positive value, for example, $B_m^2 = 10^{-6}$. The multiplication factors from the first two calculations are used to extrapolate the buckling value to a new value and the corresponding multiplication factor is calculated using

(34). This process continues until a multiplication factor sufficiently close to unity is obtained (i.e., $|k_{eff} - 1| < 0.00001$). This produces the flux spectrum for a critical system and the expanded flux distribution from the MoC solution is adjusted to account for leakage effects,

$$\phi_i''^g = \phi_i'^g \cdot \frac{\Psi^g \cdot \sum_i V_i}{\sum_i \phi_i'^g V_i} \quad (35)$$

Equation (35) represents the final flux distribution for the lattice. The leakage flux can be used to create the nodal data and to deplete the burnable isotopes in the fuel. We also need the adjoint flux in order to accurately generate nodal kinetics data for the effective delayed neutron fraction, β_{eff}^m , and the prompt neutron lifetime, l_p ,

$$\beta_{eff}^d = \frac{\sum_{iso} \left[\sum_g \beta_{iso}^d \chi_d^g \Psi^{\dagger g} \cdot \sum_g \nu \sigma_{f,iso}^g N_{iso} \Psi^g \right]}{\sum_g \chi^g \Psi^{\dagger g} \cdot \sum_g \nu \Sigma_f^g \Psi^g} \quad (36)$$

$$l_p = \frac{\sum_g \frac{1}{v^g} \Psi^{\dagger g} \Psi^g}{\sum_g \chi^g \Psi^{\dagger g} \cdot \sum_g \nu \Sigma_f^g \Psi^g} \quad (37)$$

where the outer summation in (36) is over all isotopes in the fuel and d represents a delayed neutron group.

The adjoint flux is obtained by solving the adjoint to the fundamental mode equation,

$$\Sigma_r^g \Psi^{\dagger g} = \sum_{g' \neq g} \Sigma_s^{g \rightarrow g'} \Psi^{\dagger g'} + \nu \Sigma_f^g \quad (38)$$

where the removal cross section now contains the leakage term

$$\bar{\Sigma}_r^g = \bar{\Sigma}_{tr}^g - \bar{\Sigma}_s^{g \rightarrow g} - B_m^2 \bar{D}^g \quad (39)$$

In this derivation, the spatial component of the adjoint flux is assumed to be equivalent to the spatial component of the forward flux and only the energy distribution of the adjoint flux is assumed to differ from that of the forward flux. This is a very good assumption when there is no spatial leakage explicitly modeled in the system, as is the case for our lattice physics calculations.

1.8 Gamma Transport Calculation

The gamma transport calculation is used to generate a detailed rod-by-rod gamma energy deposition that can be used to determine the gamma heating contribution to the total power distribution. The calculation can also provide a gamma detector response for reactors that contain a gamma TIP (Traversing Incore Probe) system or that use gamma thermometers as a stationary detector system. In BWRs, the detector tube is located in the corner of the lattice that is diagonally opposite to the corner in which the control blade resides.

The gamma transport calculation can be performed using the same computational module as that used to solve the neutron transport problem. Steady state gamma sources are calculated for each region of the lattice in the energy group structure of the accompanying gamma library. The gamma calculation is a fixed source calculation, where the sum of prompt and delayed gamma sources, due to neutron capture and fission, are given by the following expressions:

$$q_{\text{capture}}^y = \sum_g N_{\text{iso}} \sigma_{\text{capture},\text{iso}}^g V_i \phi_i''^g q_{\text{capture},\text{iso}}^g \chi_{\text{capture},\text{iso}}^{g \rightarrow y} \quad (40)$$

$$q_{\text{fission}}^y = q_{\text{fission},\text{iso}}^y \chi_{\text{fission},\text{iso}}^y \sum_g N_{\text{iso}} \sigma_{\text{fission},\text{iso}}^g V_i \phi_i''^g \quad (41)$$

Here, $q_{\text{capture},\text{iso}}^g$ is the gamma energy (in MeV/fission) released by neutron capture in isotope iso , neutron energy group g ; $q_{\text{fission},\text{iso}}^y$ is the total gamma energy (in MeV/fission) released through fission in isotope iso ; $\chi_{\text{capture},\text{iso}}^{g \rightarrow y}$ is the gamma spectrum that distributes the energy released from neutron capture in neutron energy group g , isotope iso , to gamma energy group y ; $\chi_{\text{fission},\text{iso}}^y$ is the gamma spectrum that distributes the energy released from fission in isotope iso ; $\sigma_{\text{capture},\text{iso}}^g$ and $\sigma_{\text{fission},\text{iso}}^g$ are the gamma microscopic cross sections; V_i is the volume of material region i ; and $\phi_i''^g$ is the neutron flux in material region i , neutron energy group g obtained from (35). The total fixed source in each region of the problem is the sum of (40) and (41).

The gamma transport calculation can use the same geometry and angular detail to solve the transport equation as is used to determine the neutron flux distribution. There is no condensation applied to the gamma cross sections and the flux is determined in the energy group structure of the gamma library. Typical gamma libraries contain no more than a couple of dozen energy groups.

For lattice physics codes based on the MoC, the equation to be solved is (25), where the total fixed source per mesh, i , is given by

$$q_i^y = q_{\text{capture},i}^y + q_{\text{fission},i}^y + \sum_{y'} \Sigma_{s,i}^{y' \rightarrow y} \phi_i^{y'} \quad (42)$$

In (42), $\Sigma_{s,i}^{y' \rightarrow y}$ is the macroscopic gamma scattering cross section. From (42), the isotropic angular source needed in (25) is calculated as $Q_{m,i}^y = q_i^y / 4\pi$, m being the angular direction.

Gamma energy deposition in each unique material region of the lattice is calculated by using the converged gamma fluxes and macroscopic energy deposition cross sections,

$$E_i = \sum_y \Sigma_{e,i}^y V_i \phi_i^y \quad (43)$$

where the energy deposition cross section, $\Sigma_{e,i}^y$, accounts for contributions from the photoelectric effect, pair production, and Compton scattering.

The detector response is defined as the energy deposited to the detector and normalized to the lattice power level. A good approximation for the energy deposition cross section for the detector is to use the value for Fe. The equation for calculating the gamma detector response is given by

$$R = \frac{\sum_y \sigma_{e,\text{Fe}}^y \Phi_{\text{DET}}^y}{P} \quad (44)$$

where ϕ_{DET}^γ is the gamma flux at the location of the detector tube and $\sigma_{e,\text{Fe}}^\gamma$ is the microscopic gamma energy deposition cross section for some representative material, for example, Fe. P is the lattice power level, in MeV.

1.9 Power Distribution Calculation

The power generated in a fuel rod is the sum of energy from gamma and beta decay, as well as kinetic energy from fission. The various contributions to the power can be calculated from the following relationships;

Kinetic energy:

$$E_{\text{kinetic}} = \sum_{\text{iso}} q_{\text{fission,iso}} \sum_i \sum_g N_{\text{iso},i} \sigma_{f,\text{iso},i}^g V_i \phi_i^g \quad (45)$$

Total gamma energy:

$$E_\gamma = \sum_i \sum_\gamma \Sigma_{e,i}^\gamma V_i \phi_i^\gamma \quad (46)$$

Beta energy due to capture (a very minor contributor):

$$E_{\beta,i} = \sum_{\text{iso}} q_{\beta,\text{iso}} \sum_i \sum_g N_{\text{iso},i} \sigma_{a,\text{iso},i}^g V_i \phi_i^g \quad (47)$$

Neutron slowing down:

$$E_{\text{SD},i} = \sum_{\text{iso}} \sum_i \sum_g \sum_{g' > g} N_{\text{iso},i} \sigma_{s,\text{iso},i}^{g' \rightarrow g} V_i \phi_i^g \cdot (\bar{E}^g - \bar{E}^{g'}) \quad (48)$$

where i is a material region; g is a neutron energy group; and γ is a gamma energy group. The microscopic neutron cross sections per isotope are for fission, σ_f^g , absorption, σ_a^g , and scattering, $\sigma_s^{g \rightarrow g'}$. \bar{E}^g is the average energy per neutron group. The summations for i are over all mesh in a specific fuel region.

1.10 Burnup Calculation

The last step of the lattice physics calculation is to determine the change in fuel isotopics over a specified period of time, referred to as a *burnup step*. The equation to be solved is the first-order differential equation of the type (Knott and Wehlage 2007)

$$\begin{aligned} \frac{dN_{\text{iso}}}{dt} = & \sum_{\text{iso}'} u_{\text{iso},\text{iso}'} \lambda_{\text{iso}'} N_{\text{iso}'} + \sum_{\text{iso}'} v_{\text{iso},\text{iso}'} \left(\sum_g \sigma_{c,\text{iso}'}^g \phi''^g N_{\text{iso}'} \right) \\ & + \sum_{\text{iso}'} w_{\text{iso},\text{iso}'} \left(\sum_g \sigma_{(n,2n),\text{iso}'}^g \phi''^g N_{\text{iso}'} \right) + \sum_{\text{iso}'} \gamma_{\text{iso},\text{iso}'} \left(\sum_g \sigma_{f,\text{iso}'}^g \phi''^g N_{\text{iso}'} \right) \\ & - \left\{ \lambda_{\text{iso}} + \left(\sum_g \sigma_{a,\text{iso}}^g \phi''^g \right) + \left(\sum_g \sigma_{(n,2n),\text{iso}}^g \phi''^g \right) \right\} \cdot N_{\text{iso}} \quad (49) \end{aligned}$$

where $\mathbf{u}_{iso,iso'}$, $\mathbf{v}_{iso,iso'}$, $\mathbf{w}_{iso,iso'}$ are branching ratios for decay, neutron capture, and (n, 2n) reactions, respectively; λ_{iso} is the decay constant; $\gamma_{iso,iso'}$ is the fission yield; and ϕ''^g is the flux distribution from (35). The symbols iso and iso' in (49) represent different isotopes. Equation (49) has a solution of the form

$$N_{iso}(\Delta t) - N_{iso}(0) = (Q - \tilde{\lambda}_{iso}N_{iso}(0)) \frac{(1 - e^{-\tilde{\lambda}_{iso}\Delta t})}{\tilde{\lambda}_{iso}} \quad (50)$$

where the effective decay constant, $\tilde{\lambda}_{iso}$, is equal to

$$\tilde{\lambda}_{iso} = \lambda_{iso} + \left(\sum_g \sigma_{a,iso}^g \phi''^g \right) + \left(\sum_g \sigma_{n2n,iso}^g \phi''^g \right) \quad (51)$$

and the production term, Q , is assumed constant over a small time interval, Δt .

The analytical solution to (49) can be obtained using a fourth order Runge–Kutta–Gill numerical algorithm for the predictor step, or by several other methods. **► Section 6** is devoted to a detailed description of the burnup solution in lattice physics codes.

1.11 Edits

Results from the lattice physics code to the corresponding three-dimensional nodal code are produced in two distinct categories: (1) cross sections that have been condensed and homogenized to represent the characteristics of the entire lattice, and (2) form factors that represent pin-by-pin distributions across the lattice.

The condensed and homogenized cross sections can be created by flux and volume weighting cross sections from every region of the lattice

$$\Sigma_x^h = \frac{\sum_i \sum_{g \in h} \Sigma_{x,i}^g V_i \phi_i''^g}{\sum_i \sum_{g \in h} V_i \phi_i''^g} \quad (52)$$

where x is a reaction type, such as absorption, fission, etc.; the flux, $\phi_i''^g$, includes leakage and is obtained from (35), and h represents the energy group structure of the nodal code, which has commonly been defined as two energy groups with the boundary between the fast and thermal groups at 0.625 eV, although there is some variation to this within the industry.

Form factors typically take the form of a two-dimensional normalized distribution. These factors can represent many physical properties from the lattice calculation, such as a pin-by-pin power distribution, multiple pin-by-pin isotopic distributions, and a pin-by-pin exposure distribution etc. The form factors are usually normalized to an average value of unity with a corresponding scaling factor that is passed to the nodal code. The nodal code can then superimpose the pin-by-pin shape from the lattice physics calculation onto the intra-nodal flux shape. For a more accurate super-positioning, form factors can be broken into individual pieces for each nodal energy group. For instance, the pin-by-pin power distribution can be broken into a fast group distribution and a thermal group distribution before being edited by the lattice physics code. Fast group distributions tend to be fairly flat across the assembly, while thermal group distributions tend to vary significantly from one pin location to another, especially in BWR assemblies.

Along with the form factors, the lattice physics code must also edit surface fluxes, surface currents, and assembly discontinuity factors. These data are used to transfer information about the heterogeneous assembly that would otherwise be lost from the homogeneous cross sections. The surface currents and surface fluxes are used in conjunction with the 2-D form factors in reconstructing the various pin distributions across the node.

Discontinuity factors are used by nodal codes to preserve surface currents from the lattice physics calculation. For a lattice calculation using reflective boundary conditions, the discontinuity factors are defined as

$$DF_S^h = \frac{\sum_{s \in S} \sum_{g \in h} A_s \psi_s^g}{\bar{\phi}^h} \quad (53)$$

where S is a specific surface of the assembly (north, south, etc.) and s are all the mesh that lie along that surface; A_s are the various surface areas that lie along the assembly surface, S ; ψ_s^g are the scalar fluxes lying along the assembly surface (i.e., the heterogeneous flux); $\bar{\phi}^h$ is the assembly homogeneous flux, and h is the nodal energy group structure. The homogeneous flux is the average flux across the assembly that would be produced by the homogenized cross sections,

$$\bar{\phi}^h = \frac{\sum_i \sum_{g \in h} V_i \phi_i^g}{\sum_i V_i} \quad (54)$$

where the heterogeneous fluxes are those obtained prior to the fundamental mode calculation.

Several parameters commonly edited by a lattice physics code are discussed in [Sect. 8](#).

1.12 Summary

This section has provided an overview of the calculational scheme used for a typical lattice physics code. The remainder of this chapter is devoted to describing, in depth, many of the features mentioned in this overview section. We will concentrate our discussions on methods that are considered to be somewhat current in lattice physics computations. The reader is directed to (Stamm'ler and Abbate 1983) for an in-depth discussion of legacy methods in lattice physics computations.

2 Cross Section Library

2.1 Objective

Various data for nuclear reactions are necessary for lattice physics computations, for example, fission, capture, absorption, scattering, $(n, 2n)$, and fission spectrum. The typical energy range considered in lattice physics computations ranges from 20 MeV down to 10^{-5} eV – from fast to thermal neutrons. The sources of these nuclear data are evaluated in nuclear data files such as ENDF, JEFF, and JENDL. These nuclear data files are collected for general-purpose utilization and thus contain highly detailed information on cross section data, for example, continuous energy (or “point-wise”) cross section data can be reconstructed from them. They contain cross

sections not only for neutrons but also for other particles, for example, electrons and photons. Covariance data that represent the uncertainty of cross section data are also included for some nuclides. A detailed description of a nuclear data file is, however, far beyond the scope of this section, but can be found in [▶ Chap. 4](#).

In principle, since a nuclear data file contains “everything,” it can be directly used in lattice physics computations. Such direct utilization of a nuclear data file, however, is not very efficient, for the following reasons:

First, since a nuclear data file is designed for general-purpose utilization, from the viewpoint of lattice physics computations, it contains much excess data. For example, the neutron fission cross section is sometimes classified according to the probability of fission. The inelastic scattering cross sections for different levels are tabulated independently. However, because such detailed classification is not necessary in common lattice physics computations appropriate data preprocessing becomes necessary.

Second, a nuclear data file adopts various formulae to describe the complicated behavior of cross sections, for example, the single and multilevel Bright Wigner and the Rich–Moore formulae used in the resonance peak. With some processing, these data can be used to reconstruct point-wise (or “continuous”) cross sections. The reconstructed point-wise cross sections are discrete (cross sections are given at discrete energy points), but have sufficient resolution to accurately reproduce the original continuous cross sections for nuclides. Since medium-to-heavy nuclides have many resolved resonances, a detailed description of these resonances is necessary. Consequently, for many nuclides, the typical number of energy points for point-wise cross sections ranges from several dozen to several hundred thousand. The reconstruction of a cross section requires considerable computation time, as discussed in [▶ Chap. 4](#). Furthermore, a great deal of memory is necessary when point-wise cross sections are directly used in lattice physics computations. As the above points make clear, preprocessing of cross sections is both necessary and useful.

What is much needed, then, is a dedicated database for the processed cross sections of various nuclides. In fact, a lattice physics code has its own dedicated cross section database, which is usually called a cross section library. We must note here that the source of cross sections (e.g., ENDF) is called a nuclear data file. The distinctions between a cross section library and cross section file can be confusing, and will be clarified in this section.

Since lattice physics computations are usually carried out in multiple groups (typically, several dozen to a few hundred groups), the number of energy groups in a cross section library is chosen to suit the calculation. A detailed discussion on the number of energy groups and the energy group structure is given in [▶ Sect. 2.2](#).

The major objective of a lattice physics computation is to provide a set of cross sections for successive core analysis. Therefore, a portion of the cross section data in a nuclear data file is not necessary in lattice computations. In [▶ Sect. 2.3](#), some typical cross sections used in lattice physics computation will be discussed.

Various processing steps are necessary for the preparation of a cross section library, and nuclear data processing codes are used for this purpose. A general-purpose cross section processing code (e.g., NJOY) and a dedicated post-processing code for library tabulation are commonly used to prepare a cross section library. Though a detailed discussion of nuclear data processing codes is presented in [▶ Chap. 4](#), a brief discussion that is relevant to cross section library preparation is offered in [▶ Sect. 2.4](#).

Since numerous data are necessary for cross section data, the methods of tabulation for cross section data are essential for their efficient storage and usage. [▶ Section 2.5](#) addresses some

key considerations on the tabulation of cross section data, and the structure and contents of a cross section library.

2.2 Choice of Energy Group Structure

The number of energy groups in a cross section library has a significant impact on lattice physics computations from two important points of view, namely, accuracy and computation time. And expectedly, there exists a trade-off between these two parameters. When the number of energy groups is small, the computation time will be short but the accuracy of the calculations might be insufficient. On the other hand, a large number of energy groups can be favorable in terms of accuracy, yet can be impractical due to the long computation time required. If we are to mitigate these contradictions, then the choice of energy group structure becomes crucial. There are two areas in which we can influence this: the number of energy groups, and their structure. We should note that some resonance calculation methods (the subgroup method, and ultrafine energy group calculation) may require a dedicated energy group structure. This topic will be discussed in [Sect. 3](#).

For typical light water reactors, anywhere from several dozen to a few hundred energy groups are adopted in a cross section library used in lattice physics computations. As a general trend, the number of energy groups used in the most recent lattice physics codes is increasing. This is due to improvements in storage capacity, and the higher processing speed of the affordable computers used for production calculations.

As discussed above, a larger number of energy groups allows for a more detailed representation of the energetic behavior of the neutron spectrum, which in turn can be applied with improved accuracy to a wider range of fuel assembly designs. Though the number of energy groups is quite important, the structure of the energy groups is crucial as well. These two factors are strongly interdependent, that is, the number of energy groups depends on the energy group structure, and vice versa.


The choice of an energy group structure is quite difficult. In general, this choice requires that four important physical phenomena in the reactor must be taken into account. The first of these is the generation of fission neutrons in the fast energy range. The second is the slowing down and diffusion of neutrons in the fast to resonance energy range. The third is the resonance absorption, and the final factor is the thermalization of neutrons in the thermal energy range. In order to appropriately incorporate these four phenomena, the energy range of a cross section library is typically divided into three parts: fast, resonance, and thermal regions. The fast range (typically 20 MeV to 10 keV) is usually divided into groups of equal lethargy width to capture the fission, slowing down, and diffusion phenomena. We must note that a sufficiently high upper energy boundary (20 MeV) is important in order to accurately capture an $(n, 2n)$ reaction.

In the resonance energy range (typically 10 keV to 1 eV), the widths of the energy groups should be small when a cross section shows rapid variations in energy, that is, in the resonance region. However, when all the resonances of all nuclides are explicitly taken into account, the energy group structure will be very fine, that is, comparable to point-wise energy groups (a few hundred thousand). From this point of view, the choice of energy group structure also depends on resonance calculation methods, which will be discussed in [Sect. 3](#).

For accurate resonance calculations, the significant resonance peaks should generally be located in the center of the energy group. Since the “significant” resonance depends on the


dominant nuclides appearing in lattice physics computations, it inherently depends on the given type of target reactor. In the case of light water reactor analyses, the first priority is given to major resonances of ^{238}U , and then those of ^{235}U and plutonium isotopes. However, care should also be taken for intermediate weight nuclides such as Fe and Ni, which are important as structural materials. These nuclides also have many resonances in the medium-to-high energy range, and accurate consideration of these resonances is very important, especially for PWR, in which baffle plates or heavy reflectors are made of stainless steel.

The thermal energy range (typically 1 to 10^{-5} eV) is divided into groups of equal lethargy or equal energy width to capture the Maxwell energy distribution of thermal neutrons. Special care must be taken at the boundary of resonance and thermal energy regions, which is usually called the thermal cut-off energy. In the typical thermal energy range, neutron up-scatter, which is caused by the thermal vibration of the nucleolus, is considered through up-scattering cross sections. Therefore, the thermal cut-off energy is set in order to cover the up-scattering effect. In light water reactor analysis, a few electronvolts (eV) is usually sufficient. In the case of graphite-moderated reactors, however, a higher thermal cut-off energy (~ 4 eV) is necessary, due to the greater up-scattering by graphite.

Up-scattering may also pose a challenge in the treatment of resonances at low energy around the thermal cut-off energy. Two issues may need to be addressed for resonance treatment at low energy. The first is the preparation of effective cross sections. In the usual resonance calculations, the neutron slowing down equation is solved from a higher to a lower energy without consideration of up-scattering. By using the neutron spectrum obtained by the neutron slowing down equation, effective cross sections can be evaluated; the effect of up-scattering on the neutron spectrum (and thus on effective cross sections) is therefore not taken into account. Next, many cross section libraries do not have a self-shielding table to evaluate effective cross sections in the thermal energy range, since resonances appear in the epithermal – resonance (i.e., higher than thermal) energy range. Therefore, when large resonances in the thermal energy range have a considerable impact on calculation results, their treatment should be carefully considered. A typical example of such resonances is the giant resonance of ^{240}Pu around 1 eV shown in  [Fig. 7](#).

In many cross section libraries for light water reactor analyses, the above resonance is treated by a fine energy group structure around 1 eV, as will be described later. In the following section, the principal energy group structures used in light water reactor analyses are briefly introduced.

2.2.1 WIMS 69 Groups

The 69 group energy structure of WIMS, which is designed for light water reactor analysis, is shown in  [Table 1](#) (Askew et al. 1966; WIMS-D/4 2000). The WIMS energy group structure and those derived from it (e.g., 70 energy groups used in CASMO) have been widely used not only in academic investigations, but also for production calculations for light water reactors.

The WIMS library is divided into three parts: fast, resonance, and thermal energy ranges. The fast energy range (10 MeV to 9.118 keV) has 14 groups with an equal lethargy width of 0.5. This structure is selected to capture neutron slowing down and diffusion in the fast energy range, and the fast fission of ^{238}U . The resonance energy range (9.118 keV to 4 eV) is divided into 13 groups. The lethargy width in the resonance energy range is basically 0.5, but several energy boundaries are adjusted in order to put important resonances close to the center of groups. For

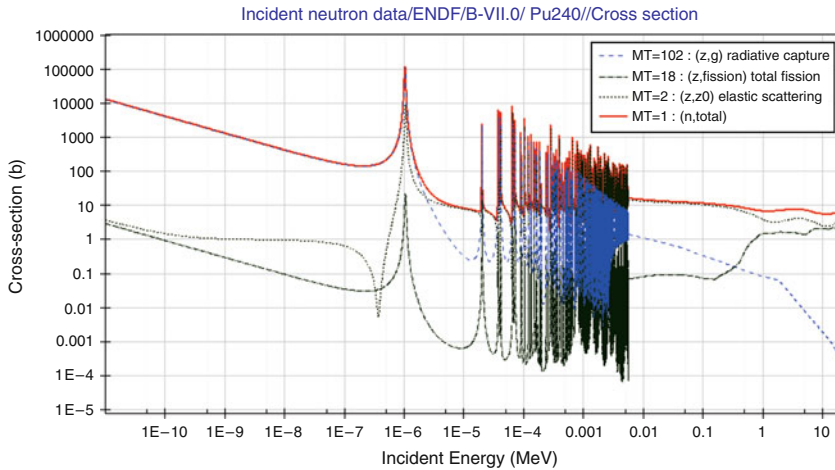


Figure 7
Large resonance of ^{240}Pu around the thermal cut-off energy

example, large resonances of ^{238}U located at 6.7, 20, and 33 eV are included in the 27th group (9.877 – 4.0 eV), 25th group (27.7 – 15.698 eV), and 24th group (48.052 – 27.7 eV), respectively.

A considerable number of energy groups are devoted to the description of the large resonance of ^{240}Pu at 1.0 eV. Since this large resonance is located near the thermal cut-off energy and is affected by thermal up-scattering, it is handled by fine energy discretization, rather than the utilization of a self-shielding table. The approximately 0.02 eV energy mesh is assigned near 1.0 eV. In the preparation of a self-shielding table, slowing down calculations are carried out in a very fine energy group structure, as described in [Sect. 3](#). This slowing down calculation is carried out without consideration of thermal up-scattering, so the utilization of a self-shielding table for resonances below the thermal cut-off energy should be carefully performed.

The thermal energy range is divided into 42 groups, which allows for a detailed description of the Maxwell spectrum of thermal neutrons. We must note that a fine energy mesh is also assigned around 0.3 eV, in which there is a broad resonance of ^{239}Pu .

2.2.2 XMAS 172 Groups

The XMAS 172 group structure is also designed for light water reactor analysis (Sartori 1990; Santamarina et al. 2004). Therefore, the XMAS 172 group structure has features similar to those in WIMS 69 groups, for example, fine energy discretization around 1 eV, an energy boundary suitable for large resonances of ^{238}U at low energy. In fact, the XMAS group structure is derived from the WIMS 69 and APOLLO1 99 group structures.

This energy group structure was developed in France and is widely used in light water reactor analyses, particularly in European countries. Since the XMAS group structure has more detailed energy discretization than the WIMS structure, the XMAS group structure can be applied to more generic applications. For example, the XMAS group structure is more suitable for MOX or high burnup fuel analyses, since spectrum variations and resonance absorption by higher plutonium (^{242}Pu) and minor actinides can be taken into account more precisely. In order to accurately consider an (n, 2n) reaction that plays an important part in the burnup

■ Table 1
WIMS 69 group structure

Group	E_{\max} [eV]	Δu	Group	E_{\max} [eV]	Δu	Group	E_{\max} [eV]	Δu
1	1.000E+07	0.500	24	4.805E+01	0.551	47	5.000E-01	0.223
2	6.066E+06	0.500	25	2.770E+01	0.551	48	4.000E-01	0.134
3	3.679E+06	0.500	26	1.597E+01	0.480	49	3.500E-01	0.090
4	2.231E+06	0.500	27	9.877E+00	0.904	50	3.200E-01	0.065
5	1.353E+06	0.500	28	4.000E+00	0.192	51	3.000E-01	0.069
6	8.210E+05	0.496	29	3.300E+00	0.238	52	2.800E-01	0.113
7	5.000E+05	0.503	30	2.600E+00	0.214	53	2.500E-01	0.128
8	3.025E+05	0.503	31	2.100E+00	0.336	54	2.200E-01	0.201
9	1.830E+05	0.500	32	1.500E+00	0.143	55	1.800E-01	0.251
10	1.110E+05	0.500	33	1.300E+00	0.123	56	1.400E-01	0.336
11	6.734E+04	0.500	34	1.150E+00	0.024	57	1.000E-01	0.223
12	4.085E+04	0.500	35	1.123E+00	0.023	58	8.000E-02	0.177
13	2.478E+04	0.500	36	1.097E+00	0.024	59	6.700E-02	0.144
14	1.503E+04	0.500	37	1.071E+00	0.025	60	5.800E-02	0.148
15	9.118E+03	0.500	38	1.045E+00	0.024	61	5.000E-02	0.174
16	5.530E+03	0.452	39	1.020E+00	0.024	62	4.200E-02	0.182
17	3.519E+03	0.452	40	9.960E-01	0.024	63	3.500E-02	0.154
18	2.239E+03	0.452	41	9.720E-01	0.023	64	3.000E-02	0.182
19	1.425E+03	0.452	42	9.500E-01	0.043	65	2.500E-02	0.223
20	9.069E+02	0.904	43	9.100E-01	0.068	66	2.000E-02	0.288
21	3.673E+02	0.904	44	8.500E-01	0.086	67	1.500E-02	0.405
22	1.487E+02	0.678	45	7.800E-01	0.222	68	1.000E-02	0.693
23	7.550E+01	0.452	46	6.250E-01	0.223	69	5.000E-03	6.215

Δu : lethargy width.

calculation of heavy nuclides, the upper boundary of the energy groups is increased to 20 MeV. The energy group structure of XMAS is shown in [▶ Table 2](#).

2.2.3 SHEM 281 Groups

The SHEM 281 group structure was designed to overcome certain potential deficiencies in the XMAS group structure (Hfaïdedh and Santamarina 2005; Hebert and Santamarina 2008). The SHEM group structure is especially designed to avoid the resonance overlap effect among different nuclides. The resonances of major nuclides (heavy nuclides, fission products, structural

■ Table 2

XMAS 172 group structure

Group	E_{\max} [eV]	Δu	Group	E_{\max} [eV]	Δu	Group	E_{\max} [eV]	Δu
1	1.964E+07	0.125	59	7.485E+02	0.100	117	1.150E+00	0.022
2	1.733E+07	0.150	60	6.773E+02	0.400	118	1.125E+00	0.014
3	1.492E+07	0.075	61	4.540E+02	0.200	119	1.110E+00	0.012
4	1.384E+07	0.175	62	3.717E+02	0.200	120	1.097E+00	0.024
5	1.162E+07	0.150	63	3.043E+02	0.400	121	1.071E+00	0.025
6	1.000E+07	0.200	64	2.040E+02	0.317	122	1.045E+00	0.010
7	8.187E+06	0.200	65	1.486E+02	0.083	123	1.035E+00	0.015
8	6.703E+06	0.100	66	1.367E+02	0.400	124	1.020E+00	0.024
9	6.065E+06	0.100	67	9.166E+01	0.192	125	9.960E-01	0.010
10	5.488E+06	0.200	68	7.567E+01	0.108	126	9.860E-01	0.014
11	4.493E+06	0.200	69	6.790E+01	0.200	127	9.720E-01	0.023
12	3.679E+06	0.200	70	5.560E+01	0.075	128	9.500E-01	0.021
13	3.012E+06	0.200	71	5.158E+01	0.067	129	9.300E-01	0.022
14	2.466E+06	0.100	72	4.825E+01	0.058	130	9.100E-01	0.057
15	2.231E+06	0.100	73	4.552E+01	0.125	131	8.600E-01	0.012
16	2.019E+06	0.200	74	4.017E+01	0.075	132	8.500E-01	0.073
17	1.653E+06	0.200	75	3.727E+01	0.100	133	7.900E-01	0.013
18	1.353E+06	0.100	76	3.372E+01	0.100	134	7.800E-01	0.101
19	1.225E+06	0.100	77	3.051E+01	0.100	135	7.050E-01	0.120
20	1.108E+06	0.100	78	2.761E+01	0.100	136	6.250E-01	0.146
21	1.003E+06	0.100	79	2.498E+01	0.100	137	5.400E-01	0.077
22	9.072E+05	0.100	80	2.260E+01	0.150	138	5.000E-01	0.030
23	8.209E+05	0.300	81	1.945E+01	0.200	139	4.850E-01	0.113
24	6.081E+05	0.100	82	1.593E+01	0.150	140	4.330E-01	0.079
25	5.502E+05	0.100	83	1.371E+01	0.200	141	4.000E-01	0.023
26	4.979E+05	0.100	84	1.122E+01	0.125	142	3.910E-01	0.111
27	4.505E+05	0.100	85	9.906E+00	0.075	143	3.500E-01	0.090
28	4.076E+05	0.300	86	9.190E+00	0.100	144	3.200E-01	0.017
29	3.020E+05	0.100	87	8.315E+00	0.100	145	3.145E-01	0.047
30	2.732E+05	0.100	88	7.524E+00	0.200	146	3.000E-01	0.069
31	2.472E+05	0.300	89	6.160E+00	0.142	147	2.800E-01	0.121
32	1.832E+05	0.400	90	5.346E+00	0.058	148	2.480E-01	0.120
33	1.228E+05	0.100	91	5.043E+00	0.200	149	2.200E-01	0.152

■ Table 2 (continued)

Group	E_{\max} [eV]	Δu	Group	E_{\max} [eV]	Δu	Group	E_{\max} [eV]	Δu
34	1.11E+05	0.300	92	4.129E+00	0.032	150	1.890E-01	0.049
35	8.230E+04	0.200	93	4.000E+00	0.168	151	1.800E-01	0.118
36	6.738E+04	0.200	94	3.381E+00	0.024	152	1.600E-01	0.134
37	5.517E+04	0.300	95	3.300E+00	0.176	153	1.400E-01	0.044
38	4.087E+04	0.100	96	2.768E+00	0.017	154	1.340E-01	0.153
39	3.698E+04	0.233	97	2.720E+00	0.045	155	1.150E-01	0.140
40	2.928E+04	0.067	98	2.600E+00	0.019	156	1.000E-01	0.051
41	2.739E+04	0.100	99	2.550E+00	0.077	157	9.500E-02	0.172
42	2.479E+04	0.400	100	2.360E+00	0.103	158	8.000E-02	0.038
43	1.662E+04	0.100	101	2.130E+00	0.014	159	7.700E-02	0.139
44	1.503E+04	0.300	102	2.100E+00	0.039	160	6.700E-02	0.144
45	1.114E+04	0.200	103	2.020E+00	0.046	161	5.800E-02	0.148
46	9.119E+03	0.200	104	1.930E+00	0.048	162	5.000E-02	0.174
47	7.466E+03	0.300	105	1.840E+00	0.047	163	4.200E-02	0.182
48	5.531E+03	0.100	106	1.755E+00	0.050	164	3.500E-02	0.154
49	5.005E+03	0.350	107	1.670E+00	0.049	165	3.000E-02	0.182
50	3.527E+03	0.050	108	1.590E+00	0.058	166	2.500E-02	0.223
51	3.355E+03	0.400	109	1.500E+00	0.017	167	2.000E-02	0.288
52	2.249E+03	0.100	110	1.475E+00	0.021	168	1.500E-02	0.405
53	2.035E+03	0.300	111	1.445E+00	0.053	169	1.000E-02	0.371
54	1.507E+03	0.050	112	1.370E+00	0.024	170	6.900E-03	0.322
55	1.434E+03	0.150	113	1.338E+00	0.028	171	5.000E-03	0.511
56	1.234E+03	0.200	114	1.300E+00	0.051	172	3.000E-03	5.704
57	1.010E+03	0.100	115	1.235E+00	0.054			
58	9.142E+02	0.200	116	1.170E+00	0.017			

Δu : lethargy width.

material nuclides, and burnable nuclides) are treated in different energy groups as much as possible up to 23 eV. The descriptions of slowing down and resonance scattering in coolant and structural material (^{16}O , ^{23}Na , ^{27}Al , ^{56}Fe , ^{58}Ni , and ^{55}Mn) are improved. Threshold reactions such as the inelastic scattering of ^{238}U and fission (1 – 0.1 MeV) are considered in the design of a library structure. Though the number of the energy group is increased (from 172 to 281), it offers higher calculation accuracy than conventional energy group structures. Since the maximum lethargy width in the SHEM structure is less than 0.2 in the slowing down energy region, it is applicable not only to LWR, but also to fast reactors.

The energy group structure of SHEM is shown in [▶ Table 3](#).

2.2.4 Other Energy Group Structures

Looking at recent improvements in cross section libraries, we find an increased number of energy groups in the resonance region. For example, in the latest version of CASMO, resonances in the low-energy ranges (<10 eV) are divided into fine energy groups in which a self-shielding table is not necessary. As a result, the number of energy groups in the cross section library

■ Table 3

SHEM 281 group structure

Group	Emax [eV]	Δu	Group	Emax [eV]	Δu	Group	Emax [eV]	Δu
1	1.964E+07	0.275	95	2.238E+01	0.010	189	5.320E+00	0.021
2	1.492E+07	0.075	96	2.216E+01	0.007	190	5.210E+00	0.019
3	1.384E+07	0.175	97	2.200E+01	0.014	191	5.110E+00	0.035
4	1.162E+07	0.150	98	2.170E+01	0.010	192	4.933E+00	0.034
5	1.000E+07	0.100	99	2.149E+01	0.007	193	4.768E+00	0.076
6	9.048E+06	0.100	100	2.134E+01	0.005	194	4.420E+00	0.025
7	8.187E+06	0.100	101	2.123E+01	0.004	195	4.310E+00	0.021
8	7.408E+06	0.100	102	2.114E+01	0.004	196	4.220E+00	0.054
9	6.703E+06	0.100	103	2.106E+01	0.004	197	4.000E+00	0.030
10	6.065E+06	0.200	104	2.098E+01	0.010	198	3.882E+00	0.045
11	4.966E+06	0.200	105	2.077E+01	0.004	199	3.712E+00	0.047
12	4.066E+06	0.200	106	2.068E+01	0.004	200	3.543E+00	0.120
13	3.329E+06	0.200	107	2.060E+01	0.004	201	3.142E+00	0.013
14	2.725E+06	0.200	108	2.052E+01	0.005	202	2.884E+00	0.039
15	2.231E+06	0.160	109	2.042E+01	0.007	203	2.775E+00	0.012
16	1.901E+06	0.150	110	2.028E+01	0.010	204	2.741E+00	0.008
17	1.637E+06	0.152	111	2.007E+01	0.024	205	2.720E+00	0.007
18	1.406E+06	0.050	112	1.960E+01	0.011	206	2.700E+00	0.022
19	1.337E+06	0.038	113	1.939E+01	0.010	207	2.640E+00	0.008
20	1.287E+06	0.102	114	1.920E+01	0.006	208	2.620E+00	0.012
21	1.162E+06	0.100	115	1.908E+01	0.060	209	2.590E+00	0.016
22	1.051E+06	0.100	116	1.796E+01	0.011	210	2.550E+00	0.032
23	9.511E+05	0.101	117	1.776E+01	0.011	211	2.470E+00	0.058
24	8.600E+05	0.197	118	1.756E+01	0.006	212	2.330E+00	0.025
25	7.065E+05	0.200	119	1.745E+01	0.036	213	2.273E+00	0.025
26	5.784E+05	0.158	120	1.683E+01	0.017	214	2.217E+00	0.027

Table 3 (continued)

Group	E_{\max} [eV]	Δu	Group	E_{\max} [eV]	Δu	Group	E_{\max} [eV]	Δu
27	4.940E+05	0.080	121	1.655E+01	0.031	215	2.157E+00	0.041
28	4.560E+05	0.100	122	1.605E+01	0.017	216	2.070E+00	0.039
29	4.125E+05	0.072	123	1.578E+01	0.059	217	1.990E+00	0.046
30	3.839E+05	0.180	124	1.487E+01	0.009	218	1.900E+00	0.065
31	3.206E+05	0.180	125	1.473E+01	0.009	219	1.780E+00	0.064
32	2.678E+05	0.152	126	1.460E+01	0.009	220	1.669E+00	0.050
33	2.300E+05	0.165	127	1.447E+01	0.015	221	1.588E+00	0.044
34	1.950E+05	0.167	128	1.425E+01	0.014	222	1.520E+00	0.051
35	1.650E+05	0.164	129	1.405E+01	0.036	223	1.444E+00	0.024
36	1.400E+05	0.131	130	1.355E+01	0.016	224	1.410E+00	0.021
37	1.228E+05	0.060	131	1.333E+01	0.056	225	1.381E+00	0.037
38	1.156E+05	0.200	132	1.260E+01	0.010	226	1.331E+00	0.029
39	9.466E+04	0.140	133	1.247E+01	0.013	227	1.293E+00	0.033
40	8.230E+04	0.200	134	1.231E+01	0.015	228	1.251E+00	0.030
41	6.738E+04	0.200	135	1.213E+01	0.012	229	1.214E+00	0.037
42	5.517E+04	0.100	136	1.198E+01	0.013	230	1.170E+00	0.019
43	4.992E+04	0.200	137	1.182E+01	0.009	231	1.148E+00	0.016
44	4.087E+04	0.100	138	1.171E+01	0.010	232	1.130E+00	0.012
45	3.698E+04	0.100	139	1.159E+01	0.028	233	1.116E+00	0.011
46	3.346E+04	0.133	140	1.127E+01	0.020	234	1.104E+00	0.011
47	2.928E+04	0.067	141	1.105E+01	0.023	235	1.092E+00	0.013
48	2.739E+04	0.048	142	1.080E+01	0.021	236	1.078E+00	0.041
49	2.610E+04	0.043	143	1.058E+01	0.108	237	1.035E+00	0.014
50	2.500E+04	0.097	144	9.500E+00	0.039	238	1.021E+00	0.012
51	2.270E+04	0.200	145	9.140E+00	0.018	239	1.009E+00	0.012
52	1.858E+04	0.137	146	8.980E+00	0.020	240	9.965E-01	0.015
53	1.620E+04	0.084	147	8.800E+00	0.014	241	9.820E-01	0.019
54	1.490E+04	0.091	148	8.674E+00	0.017	242	9.640E-01	0.021
55	1.360E+04	0.200	149	8.524E+00	0.027	243	9.440E-01	0.026
56	1.114E+04	0.200	150	8.300E+00	0.021	244	9.200E-01	0.044
57	9.119E+03	0.200	151	8.130E+00	0.020	245	8.800E-01	0.071
58	7.466E+03	0.200	152	7.970E+00	0.016	246	8.200E-01	0.130
59	6.113E+03	0.200	153	7.840E+00	0.013	247	7.200E-01	0.141
60	5.005E+03	0.200	154	7.740E+00	0.018	248	6.250E-01	0.049

■ Table 3 (continued)

Group	E_{\max} [eV]	Δu	Group	E_{\max} [eV]	Δu	Group	E_{\max} [eV]	Δu
61	4.097E+03	0.163	155	7.600E+00	0.029	249	5.950E-01	0.070
62	3.481E+03	0.150	156	7.380E+00	0.033	250	5.550E-01	0.065
63	2.996E+03	0.150	157	7.140E+00	0.021	251	5.200E-01	0.091
64	2.579E+03	0.150	158	6.994E+00	0.011	252	4.750E-01	0.096
65	2.220E+03	0.150	159	6.918E+00	0.007	253	4.316E-01	0.101
66	1.910E+03	0.168	160	6.870E+00	0.005	254	3.900E-01	0.100
67	1.614E+03	0.182	161	6.835E+00	0.004	255	3.530E-01	0.083
68	1.345E+03	0.170	162	6.811E+00	0.003	256	3.250E-01	0.064
69	1.135E+03	0.064	163	6.792E+00	0.002	257	3.050E-01	0.086
70	1.065E+03	0.160	164	6.776E+00	0.002	258	2.800E-01	0.094
71	9.075E+02	0.193	165	6.760E+00	0.003	259	2.550E-01	0.098
72	7.485E+02	0.200	166	6.742E+00	0.004	260	2.312E-01	0.098
73	6.128E+02	0.200	167	6.717E+00	0.013	261	2.096E-01	0.098
74	5.017E+02	0.200	168	6.631E+00	0.004	262	1.900E-01	0.160
75	4.108E+02	0.150	169	6.606E+00	0.003	263	1.619E-01	0.160
76	3.536E+02	0.100	170	6.588E+00	0.002	264	1.380E-01	0.140
77	3.199E+02	0.120	171	6.572E+00	0.002	265	1.200E-01	0.140
78	2.838E+02	0.160	172	6.556E+00	0.003	266	1.043E-01	0.150
79	2.418E+02	0.200	173	6.539E+00	0.004	267	8.980E-02	0.160
80	1.980E+02	0.200	174	6.515E+00	0.005	268	7.650E-02	0.160
81	1.621E+02	0.200	175	6.482E+00	0.008	269	6.520E-02	0.161
82	1.327E+02	0.200	176	6.432E+00	0.011	270	5.550E-02	0.160
83	1.086E+02	0.200	177	6.360E+00	0.013	271	4.730E-02	0.160
84	8.895E+01	0.170	178	6.280E+00	0.019	272	4.030E-02	0.158
85	7.505E+01	0.200	179	6.160E+00	0.016	273	3.440E-02	0.160
86	6.144E+01	0.154	180	6.060E+00	0.017	274	2.930E-02	0.161
87	5.267E+01	0.140	181	5.960E+00	0.027	275	2.494E-02	0.220
88	4.579E+01	0.040	182	5.800E+00	0.014	276	2.001E-02	0.300
89	4.400E+01	0.091	183	5.720E+00	0.018	277	1.483E-02	0.350
90	4.017E+01	0.175	184	5.620E+00	0.016	278	1.045E-02	0.380
91	3.372E+01	0.200	185	5.530E+00	0.008	279	7.145E-03	0.450
92	2.761E+01	0.116	186	5.488E+00	0.014	280	4.556E-03	0.600
93	2.459E+01	0.088	187	5.410E+00	0.006	281	2.500E-03	3.124
94	2.252E+01	0.006	188	5.380E+00	0.011			

Δu : lethargy width.

reaches approximately 600 (Rhodes et al. 2006). Such fine groups are being used in production calculation due to the ongoing improvements in the capacity of affordable computers.

Another energy group structure sometimes used in lattice physics computation is that of so-called ultrafine energy groups (MC** 2-2 1999; Ishiguro 1974; Tsuchihashi et al. 1982; Williams et al. 2005; Huria and Ouislomen 2008; Sugimura and Yamamoto 2007). A very fine energy group structure is used in an ultrafine group's spectrum calculation in which resolved resonances are explicitly treated without self-shielding factors. Unfortunately, since the number of energy groups reaches from several thousand to several dozens of thousands, the preparation of an explicit scattering matrix becomes difficult on account of the storage it requires. To overcome this obstacle, a one-dimensional cross section (e.g., absorption, fission, capture, and elastic scattering) is stored in a cross section library. Neutron slowing down is evaluated from slowing down calculations that assume elastic scattering. A more detailed discussion of this will be provided in [▶ Sect. 3](#).

2.3 Cross Sections Used in Lattice Physics Computations

Various cross sections are used in lattice physics computations. The following cross sections are usually necessary.

Total cross section: A total cross section is necessary for transport calculations in order to obtain neutron spatial distribution. In the principal lattice physics codes, transport-corrected (P0) cross sections are used instead of explicit treatment of anisotropic scattering.

Capture cross section: A capture cross section is necessary for burnup calculations.

Fission cross section: A fission cross section is necessary for burnup calculations as well as pin-power distribution calculations.

Production cross section: A production cross section, which is the product of a fission cross section and the average number of neutrons released per fission, is used in transport calculations to evaluate the reactivity of the fuel assembly.

Absorption cross section: For many nuclides, an absorption cross section can be obtained by the summation of the capture and fission cross sections. However, especially for light nuclides, other reactions may play significant role in neutron absorption. For example, most of the absorption reaction for ^{10}B is (n, α) . Therefore, the absorption cross section should be treated independently from the capture and fission reactions. In lattice physics computations, the absorption cross section is used to evaluate the reactivity of the fuel assembly. Neutron emission reactions other than fission may be considered as absorption cross sections, as described below.

$(n, 2n)$ cross section: This reaction is important both in burnup calculation and in its contribution to reactivity. Since an $(n, 2n)$ reaction increases the number of neutrons, its contribution to reactivity is positive. Note that an $(n, 3n)$ reaction has a similar effect, but has a smaller impact than an $(n, 2n)$ reaction since the cross section of $(n, 3n)$ has a higher threshold energy and is smaller than that of $(n, 2n)$. It is for this reason that in many lattice physics codes, only an $(n, 2n)$ reaction is considered. In order to rigorously incorporate an $(n, 2n)$ reaction, a dedicated treatment that is similar to fission is necessary. Many transport codes, however, do not incorporate the capability of such treatment. Therefore, an $(n, 2n)$ cross section is usually subtracted from the absorption cross section since the “net neutron emission” in an $(n, 2n)$ reaction is one (one absorption, two emissions). This apparently has a positive effect on reactivity. In this simplified treatment, the neutron emission spectrum is disregarded, and emitted neutrons are assumed to have the same energy as the absorbed neutron. When an $(n, 3n)$ reaction is taken into account,

twice the $(n, 3n)$ cross section is subtracted from the absorption cross section. As described in [2.2](#), since $(n, 2n)$ is a threshold reaction, the upper limit of an energy group in a cross section library is important –20 MeV is necessary in order to accurately incorporate an $(n, 2n)$ reaction. *Scattering cross section:* A scattering cross section is treated in matrix form. Though other reactions (e.g., fission) do not have anisotropy on the angular distribution of emitted neutrons, the elastic scattering reaction has considerable anisotropy. This anisotropy on the scattering reaction is expanded by the Legendre functions of the scattering angle. Not just the isotropic (P0) component of a scattering matrix, but also higher-order anisotropic components (P1, P2, and so on) can be considered. Light nuclides (e.g., hydrogen) have greater anisotropy since the neutrons are scattered in a more forward direction by these nuclides. Since the anisotropic scattering of hydrogen, which is a major nuclide in LWRs, has a large impact on neutron leakage from the core, this effect must be taken into account.

Anisotropic scattering may be explicitly taken into account when the transport calculation module in a lattice physics code has such capability. In fact, the method of characteristics, which is commonly used in the most recent lattice physics codes, can account for anisotropic scattering, though larger memory and longer computation time are required. However, the anisotropic component of a scattering matrix is also approximately taken into account by the transport-corrected total cross section (transport cross section), with a P0 scattering cross section. When we use the transport-corrected cross section, the self-scattering cross section is also modified to maintain balance in the cross section. Described in more detail, the difference between the total and transport-corrected cross sections is subtracted from the self-scattering cross section.

The effect of anisotropic scattering becomes more important when the angular distribution of the neutron flux is far from isotropic. Since neutron absorption in MOX fuel is much greater than that in UO₂ fuel, the angular distribution of the neutron flux is more anisotropic. The effect of anisotropic scattering therefore becomes more important in MOX fuel analysis.

Another consideration in this regard is the order of anisotropic scattering that should be taken into account. Higher-order anisotropic scattering gives more accurate results, but requires more memory because of the higher-order scattering matrix. In a typical light water reactor analysis, the incorporation of P1 scattering gives fair results. When up to P3 components are taken into account, it gives an almost converged result on the treatment of anisotropic scattering. Note that when transport-corrected scattering is used, up to P1 component is commonly taken into account.

Fission spectrum: Fission spectra are slightly different in each fissionable nuclide, as each fissionable nuclide has an independent fission spectrum. Furthermore, strictly speaking, a given fission spectrum also depends upon the incident neutron energy. In common lattice physics computations, however, such rigorous treatment is not necessary, and an approximate treatment can be applied, as will be described later.

Gamma cross sections: In fission and the successive decays of fission products, many photons (gamma rays) are emitted. The gamma ray plays an important role in the distribution of power in a reactor core since considerable energy (heat) is deposited due to the scattering and absorption of gamma rays. Since the mean free path of a gamma ray is larger than that of typical neutrons, gamma ray “removes” heat from pellet as the form of its energy and releases it at other places. In this sense, a gamma ray “smears” heat generation in a core, which is why this effect is known as gamma smearing. The gamma-smearing effect is important for the accurate evaluation of heat distribution in a fuel assembly.

Table 4
Example of energy release per fission of ^{235}U

Form of released energy	MeV	Note
Kinetic energy of fission fragment	168	Heat deposit mainly in pellet
Prompt gamma ray	7	Gammer smearing
Kinetic energy of prompt neutrons	5	Possible heat deposit in moderator
Beta ray originated by decay of fission fragment	8	
Gamma ray originated by decay of fission fragment	7	Gammer smearing
Anti-neutrino	(12)	Cannot be recovered (escapes from reactor)
Gamma ray emitted by capture of fission neutron	3 ~ 12	Gammer smearing
Total	~ 202	

Source: Stacy (2001).

In many cases, the gamma-smearing effect flattens the power distribution in a core, but it may also increase pin-power for pellets with low power density. For example, the power density of a gadolinia-bearing fuel pellet is very low at the beginning of life (BOL) due to the extremely large absorption cross section of gadolinium isotopes. The gamma-smearing effect pushes up the pin-power of a gadolinia-bearing fuel rod at BOL.

Note that gamma smearing is also significant in a reflector that uses medium-heavy nuclides, such as stainless-steel reflectors in advanced type PWRs, and shielding fuel elements in fast breeder reactors. Gamma transport calculation is sometimes carried out to accurately estimate heat deposition by gamma rays. In this case, cross sections for the gamma rays are also necessary. The gamma production cross section is also necessary in order to estimate the gamma source.

Energy release per fission: The value of energy release per fission is not a “cross section,” but is a very important parameter in lattice physics computation, since it defines the normalization condition of the absolute value of neutron flux. Elementary textbooks on reactor physics tell us that the energy release per fission is approximately 200 MeV for ^{235}U . This is not incorrect, but we must be careful how we regard the breakdown of its contents. ▶ *Table 4* shows the breakdown of energy release by fission of ^{235}U . Since the energy balance due to fission and successive phenomena is complicated, one needs to be careful when setting values for energy release per fission.

2.4 Cross Section Processing

The source of nuclear data is an evaluated nuclear data file. In order to generate a cross section library for use in lattice physics computations, the processing of nuclear data files is necessary (Marcille and Mills 2003; Yamamoto et al. 2006; Yamamoto and Sugimura 2006). In general, nuclear data processing is divided into two parts. The first part is the generation of

general-purpose multigroup cross section data by a nuclear data processing code. The second part is the editing of cross section data into a suitable format of a lattice physics code. Some detailed description of these processes is presented below.

2.4.1 Generation of Multigroup Cross Section Data

As described before, nuclear data files such as ENDF/B, JEFF, and JENDL are not suitable for direct utilization in lattice physics codes (McLane 2001). Therefore, cross section processing codes are used to generate multigroup cross section data. Many lattice physics codes utilize the NJOY code, which is widely used not only in academia, but also in industry (MacFarlane and Muir 1994b). Though a detailed description of the NJOY code and the theoretical background of cross section processing are given in [Chaps. 1 and 4](#), a brief description of cross section processing is given in this section, with a focus on the preparation of a lattice physics code for a cross section library.

The common nuclear data processing scheme by NJOY is described as follows. The modules of NJOY used in processing are given along with brief descriptions of the outline of processing.

MODER

Since a nuclear data file is given in text format, it is converted to binary format in order to perform rapid input/output during cross section processing.

RECONR

Though the original cross section data is “continuous,” it is energetically discretized for processing. The point-wise cross section data, which accurately reproduces the original continuous cross section data with cross sections at discrete energy grid points, are reconstructed from an original nuclear data file. The accuracy of a reconstructed cross section is determined by the number of energy grid points, and the structure of their point-wise cross sections. In order to reduce the number of energy grid points while retaining accuracy, a dedicated algorithm is used to thin out the energy grid points. In general, grid points are chosen so that the accuracy of the interpolated cross section data satisfies the required tolerance given by the user. The number of grid points of a point-wise cross section may reach a few hundred thousand for heavy nuclides with many resonances. The reconstructed data is written to an intermediate (working) file in the PENDF (point-wise ENDF) format.

BROARDR

The point-wise cross section data are generated at a base temperature (typically room temperature) in RECONR. Cross sections, however, are temperature dependent. Thus, cross section data in the resonance region are broadened by considering the Doppler effect in BROARDR. Specific temperatures are given by users for consideration of the Doppler effect.

THERMR

A cross section in the thermal energy range (~ 4 eV) is created by considering the thermal vibration of the nucleolus. When the chemical binding of a molecule is taken into account (e.g., H in H₂O, D in D₂O, and graphite), $S(\alpha, \beta)$ data, which describe the secondary energy distribution

of a scattered neutron, are also necessary as an input file. The $S(\alpha, \beta)$ data are given as a part of the evaluated nuclear data file.

UNRESR

Multigroup cross section data in the unresolved resonance energy region is given as a function of the background cross sections given in the input data. A narrow resonance approximation is used to evaluate an effective multigroup cross section. The NJOY code provides another approach for the resonance treatment of an unresolved resonance region by PURR. The PURR module can provide a probability table in addition to a self-shielding table for multigroup cross sections. The probability table can be used through the subgroup method, which will be described in [Sect. 3](#).

GROUPR

Since the reconstructed data is “point-wise,” an adequate neutron spectrum is necessary in order to evaluate effective (average) multigroup cross sections. The GROUPR module provides the capability of evaluating the neutron spectrum with the reconstructed point-wise cross sections. Therefore, the present module is highly important in the generation of a multigroup cross section library for lattice physics codes. The GROUPR module provides two different ways to estimate the point-wise neutron spectrum. The first is a very quick, simple approach based on the narrow resonance approximation. In this approach, the neutron flux is simply expressed as

$$\phi(E) = \frac{C(E)}{\sigma_t(E) + \sigma_0} \quad (55)$$

where

- $\phi(E)$: neutron flux,
- $C(E)$: base spectrum function,
- $\sigma_t(E)$: microscopic total cross section of a nuclide,
- σ_0 : background cross section.

Note that the theoretical background for resonance calculation will be described in [Sect. 3](#). Since no slowing down calculation is carried out, the generation of a multigroup cross section takes place quite quickly. However, since (55) is based on a narrow resonance approximation, its accuracy is not sufficient for broad resonances that appear in the epithermal energy region, for example, resonance of ^{238}U at 6.7 eV. That said, the above approach is usually satisfactory for the high-energy region in which each resonance is narrow enough, compared to the energy width of neutron slowing down. Note that various options are provided as $C(E)$ in the GROUPR module, that is, $1/E$, fission spectrum $+1/E$, fission spectrum $+1/E + \text{Maxwell}$. A suitable base spectrum function would be preferable for the generation of a cross section library. The base spectrum function can also be given as input data. Therefore, a typical spectrum (e.g., cell average spectrum in the operating condition of light water reactors) can be used. Some sensitivity analyses of the base spectrum function are desirable before the preparation of a cross section library.

The second option is a direct numerical solution of the neutron slowing down equation. In the GROUPR module, the second option can be used for the resolved resonance energy range, and the following equation is usually solved:


$$(\sigma_t(E) + \sigma_0) \phi(E) = \int_E^{E/\alpha} \frac{\sigma_s(E') \phi(E')}{(1 - \alpha)E'} dE' + \int_E^{E/\alpha_0} \frac{\sigma_0 \phi(E')}{(1 - \alpha_0)E'} dE' \quad (56)$$

where

$$\alpha := \left(\frac{A-1}{A+1} \right)^2, \quad A \text{ is the relative mass of a nuclide to a neutron,}$$

$$\alpha_0 := \left(\frac{A_0-1}{A_0+1} \right)^2, \quad A_0 \text{ is the relative mass of a background nuclide to a neutron,}$$

$$\sigma_s(E): \text{ elastic scattering cross section.}$$

As commonly calculated, hydrogen is assumed as a background nuclide; thus α_0 is set at a very small value (e.g., 10^{-7}). When the mass effect of a moderator is taken into account as the lambda parameter, different A_0 values are used to solve (56). A detailed discussion of this issue will be presented in  Sect. 3.

Though the direct numerical solution of (56) is quite accurate, it may also be time consuming. The computation time depends on the number of points of reconstructed cross sections. In the case of heavy nuclides (e.g., ^{238}U and ^{239}Pu), the number of the reconstructed cross section point may reach a few hundred thousand. Since slowing down calculations are repeatedly carried out for different background cross sections (typically 10–20 different background cross sections for major resonance isotopes), and for different temperatures (typically several temperature points), the computation time needed to process a heavy nuclide may be more than several hours on a modern PC or Workstation.

The obtained effective multigroup cross sections are written into a file in a GENDF (group-wise ENDF) format. The GROUPT module has various options for the energy group structure. The major energy group structures are hardwired in the GROUPT module, for example, WIMS 69 groups and XMAS 172 groups. Of course, an arbitrary energy group structure can be also given for the GROUPT module.

MATXS

The multigroup cross section (GENDF) generated by GROUPT is converted to the MATXS format that can be used in some application codes. Since the MATXS format is versatile, it is useful for many lattice physics codes.

Other Modules

When gamma transport calculations are carried out in a lattice physics code, multigroup cross sections for gamma rays are necessary (Wemple et al. 2008; Mertyurek 2007). In this case, a KERMA (kinetic energy released in material) factor evaluation by the HEATR module, and gamma cross section evaluations by the GAMINR module, are necessary.

The NJOY code can provide a cross section library for the MCNP code, which is a continuous energy Monte Carlo code frequently used for the validation and verification of lattice physics codes. The ACER module is used for the preparation of an MCNP library. When a cross section library for MCNP is generated by the NJOY code and is used for verification, “consistent comparison” between a Monte Carlo code and a lattice physics code can be carried out. Such comparisons (verification and validation) yield rich information regarding the soundness of lattice physics codes.

A cross section library for the widely used lattice physics code WIMS, can be generated through the WIMSR module. Even if direct utilization of the WIMS code is not considered, the output of the WIMSR module provides an invaluable benchmark for a cross section library of


lattice physics codes. As discussed later, the post-processing of NJOY outputs is usually carried out to generate a cross section library of a lattice physics code. Certain aspects of this post-processing are highly complicated, for example, the processing of a fission matrix. Therefore, in order to check the correctness of edited multigroup cross section data, a comparison with the WIMSR output sometimes proves quite useful.

Some Notes on NJOY

The NJOY code is well maintained and is continuously updated with improvements and bug-fixes. These improvements and fixes can be downloaded from the Web site as a collection of patches, and can be applied to the NJOY code by a dedicated update system. The latest version has fewer flaws, and is thus recommended for use. Furthermore, there are various options as input data that are sometimes difficult to use. It is therefore highly recommended that calculation results be verified. A comparison with independent calculations (e.g., continuous energy Monte Carlo calculations) can provide a good means for such verification.

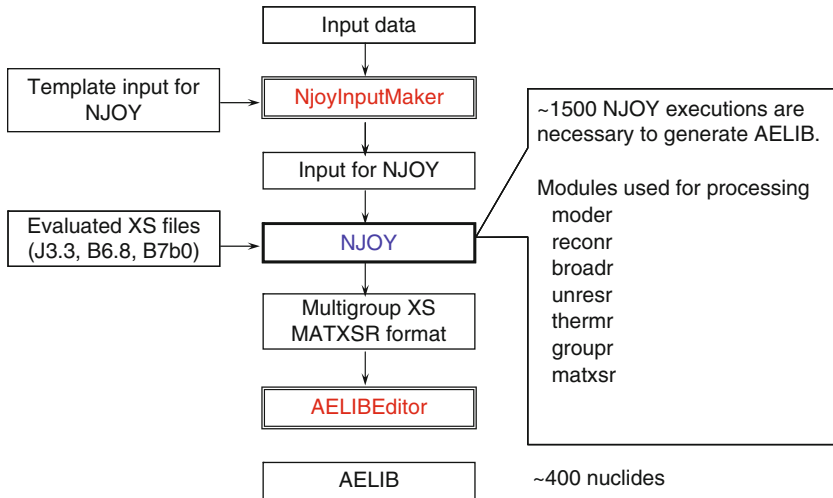
2.4.2 Execution Control of NJOY

In common lattice physics codes, more than a few hundred nuclides may be processed in order to generate a cross section library. When this processing is carried out manually, quality control for the generation of a cross section library becomes difficult. Therefore, a dedicated cross section generation system that automatically generates NJOY inputs and can manage subsequent post-processing steps with minimal user input is often developed and used.

In this section, the cross section library generation system of AELIB, which is a cross section library for the lattice physics code AEGIS, is described as an example (Yamamoto et al. 2006; Yamamoto and Sugimura 2006). A calculation flowchart of the system is shown in  Fig. 8. The NjoyInputMaker code generates input data for NJOY by using short user input that contains the following information:

- Nuclide identification name in AELIB
- Upper energy boundary of resolved energy range
- Potential scattering cross section
- Order of anisotropic scattering
- Temperature points
- Background cross section points

NjoyInputMaker automatically generates not only the input data but also the execution shell. The NJOY code is executed using the automatically generated shell. The calculation result of NJOY is dumped onto a file in the MATXS format. The AELIBEditor code performs post-processing of the NJOY results shown in the next section, and generates AELIB, which is a binary file of a particular format. The details of post-processing will be described in the next section. Note that the AELIBEditor code can generate AELIB not only from the NJOY result, but also from user input data. For example, some fission product nuclides that have a short half-life are defined as “dummy” nuclides with a zero cross section, that is, only decay is considered for these nuclides. In such a case, a zero cross section is given from an input file. Since an ideal nuclide that has a particular multigroup cross section can be defined, a multigroup benchmark calculation, in which a given cross section is used, can easily be performed. Note that using a



■ **Figure 8**
Example of automatic calculation flowchart of NJOY

common PC, it takes approximately two CPU days to generate an entire set of AELIB in which more than 400 nuclides are stored.

2.4.3 Post-Processing for Cross Section Library

The NJOY code can output a multigroup cross section in various formats (e.g., MATXS, WIMS, CCCC, and DTF). These output formats, however, may not be suitable for direct utilization as a cross section library of lattice physics codes. For example, while the MATXS format can be used for very general purposes, it may contain cross sections that are too detailed for lattice physics codes, such as a fission matrix. The WIMS format may require additional data for higher-order anisotropic scattering ($>P1$).

For the reasons given above, many lattice physics codes use their own (dedicated) formats in their cross section library – formats that are suitable for lattice physics computations. In order to generate such a cross section library, post-processing of the NJOY output becomes necessary. A description of post-processing of the MATXS format into a lattice physics code is given below as an example.

Absorption Cross Section

In the MATXS format, various reactions may be tabulated as neutron absorption reactions. However, in lattice physics computations, an absorption cross section is necessary for the neutron transport calculation. Therefore, various neutron absorption reactions are summed in order to obtain an absorption cross section:

$$\begin{aligned} \sigma_a = & \sigma(n, \gamma) + \sigma(n, f) + \sigma(n, p) + \sigma(n, d) + \sigma(n, t) + \sigma(n, \alpha) + \sigma(n, 2\alpha) + \dots \\ & - \sigma(n, 2n) - 2\sigma(n, 3n) - 3\sigma(n, 4n) \end{aligned} \quad (57)$$

The $(n, 2n)$ cross section is subtracted since its “net emission” of neutrons is 1, that is, “net absorption” is -1 . Similarly, the “net absorptions” for $(n, 3n)$ and $(n, 4n)$ reactions are -2 and -3 , respectively. By using (57), various neutron absorption reactions can be taken into account.

Nu-Value and Fission Spectrum

Energy distribution and the number of released neutrons in fission depend on the incident neutron energy. Therefore, in a nuclear data file, the fission cross sections of major fissionable nuclides are given not only as ordinary (total) fission cross sections, but also in the form of a fission matrix. In the MATXS format, a similar expression is used for the fission cross section. Unfortunately, the transport modules of many lattice physics codes cannot directly handle the fission matrix.

For a fission matrix, the fission neutron is evaluated by

$$f_g = \sum_{g'} \sigma_{f,g' \rightarrow g} \phi_{g'} + \chi_{d,g} \sum_{g'} \nu_{d,g'} \sigma_{f,g'} \phi_{g'} \quad (58)$$

where

f_g : fission neutrons appeared in group g ,

$\sigma_{f,g' \rightarrow g}$: fission matrix for prompt neutrons, whose incident and emission energy groups are g' and g , respectively,

$\phi_{g'}$: neutron flux of group g' ,

$\chi_{d,g}$: fission spectrum for delayed neutrons,

$\nu_{d,g}$: number of delayed neutrons per fission,

$\sigma_{f,g}$: (total) fission cross section (MT = 18 in the ENDF format).

However, many lattice physics codes evaluate fission neutrons as follows, since the dependence of fission spectra upon incident neutron energy is fairly minor:

$$f_g = \chi_g \sum_{g'} \nu_{g'} \sigma_{f,g'} \phi_{g'} \quad (59)$$

In order to fit the fission-related data in the MATXS format into ordinary representation, the following post-processing is carried out for a cross section library of lattice physics codes.

$$\chi_g = \frac{\sum_{g'} \sigma_{f,g' \rightarrow g} \phi_{g'} + \chi_{d,g} \sum_{g'} \nu_{d,g'} \sigma_{f,g'} \phi_{g'}}{\sum_g \sum_{g'} \sigma_{f,g' \rightarrow g} \phi_{g'} + \sum_{g'} \nu_{d,g'} \sigma_{f,g'} \phi_{g'}} \quad (60)$$

$$\nu_g = \frac{\sum_{g'} \sigma_{f,g' \rightarrow g}}{\sigma_{f,g}} + \nu_{d,g} \quad (61)$$

where

χ_g : fission spectrum for neutrons (including both prompt and delayed),

ν_g : number of neutrons per fission (including both prompt and delayed).

Equation (60) indicates that a neutron spectrum is necessary to evaluate the fission spectrum, that is, the fission spectrum depends on the neutron spectrum. However, the neutron spectrum is, of course, unknown during the preparation of the cross section library. Fortunately,

the fission spectrum is not strongly dependent on the neutron spectrum, so we can use a typical neutron spectrum for (60), for example, a cell average neutron spectrum in the operating condition of a typical LWR.

Scattering Matrix

In the MATXS format, various scattering cross sections are independently given as the matrix form. Therefore, these scattering matrixes should be summed up for utilization in lattice physics codes:

$$\begin{aligned} \sigma_{s,g' \rightarrow g} = & \sigma_{el,g' \rightarrow g} + \sigma_{n,2n,g' \rightarrow g} + \sigma_{n,3n,g' \rightarrow g} + \sigma_{n,4n,g' \rightarrow g} + \sigma_{n,n\alpha,g' \rightarrow g} + \sigma_{n,np,g' \rightarrow g} \\ & + \sigma_{n,nd,g' \rightarrow g} + \sigma_{n,nt,g' \rightarrow g} + \sum_i \sigma_{inel,i,g' \rightarrow g} + \sigma_{inel,c,g' \rightarrow g}, \end{aligned} \quad (62)$$

where

- $\sigma_{s,g' \rightarrow g}$: scattering cross section used for lattice physics computation,
- $\sigma_{el,g' \rightarrow g}$: elastic scattering cross section,
- $\sigma_{n,2n,g' \rightarrow g}$, $\sigma_{n,3n,g' \rightarrow g}$, $\sigma_{n,4n,g' \rightarrow g}$: (n, 2n) cross section, and so on,
- $\sigma_{n,n\alpha,g' \rightarrow g}$, $\sigma_{n,np,g' \rightarrow g}$, $\sigma_{n,nd,g' \rightarrow g}$, $\sigma_{n,nt,g' \rightarrow g}$: (n, n + α) cross section, and so on,
- $\sigma_{inel,i,g' \rightarrow g}$: inelastic cross section of *i*th level,
- $\sigma_{inel,c,g' \rightarrow g}$: inelastic cross section of continuous level.

Note that the above treatment is an approximation for (n, 2n) cross sections, and so on, since the “scattering” reaction changes only the energy of an incident neutron and does not affect the number of neutrons. Variations in the number of neutrons through (n, 2n), along with other reactions, are taken into account approximately through modification of the absorption cross section, in which the energy of the incident neutron does not change, as described in “Absorption cross section”. However, the impact of the present approximation is considered negligible, since the total reactivity effect of (n, 2n) and similar reactions are not of a significant degree.

Editing for Cross Section Library

Multiple NJOY calculation results are usually necessary to generate a complete cross section library for an isotope, since variations in temperatures and background cross sections must be taken into account. Furthermore, additional data (e.g., cross section identifiers, names of isotopes, and burnup-related data) may be supplemented by the input data. In order to gather and handle multiple NJOY outputs and fit the cross section data of NJOY outputs into a cross section library format of a lattice physics code, some post-editing is carried out at the end of the post-processing of cross sections.

2.5 Tabulation and Contents of Cross Section Library

The tabulation and contents of a cross section library are very important for utilization by lattice physics codes (Stammler and Abbate 1983; Okumura et al. 2007; Marleau et al. 2000; Hébert et al. 2000). This section provides some practical information on tabulation methods and the contents of a cross section library.

2.5.1 General File Format

Cross section data are stored in a cross section library. There are two approaches to the configuration of a file(s) for a cross section library.

The first approach is an “integrated” cross section library, that is, all cross sections and related data are stored in a file. For example, the WIMS code utilizes one file for a cross section library.

The second approach is an “indexed” cross section library. In this approach, there are two file types in regard to a cross section, that is, an index file and cross sections files. An index file indicates the correspondence between a cross section file and each nuclide and miscellaneous data. A cross section file contains cross sections for a nuclide, that is, each nuclide is stored in an independent file. The MCNP code adopts such a cross section configuration.

There are advantages and disadvantages to both approaches. From the point of view of the integrity of the cross section data, the “integrated” approach is better than the “indexed” approach, since part of the cross section library cannot be replaced. On the other hand, the “indexed” approach is better in terms of flexibility, since the replacement, removal, and addition of cross sections for a particular nuclide(s) are easily accomplished. During routine production calculations, such manipulations are not necessary. However, when research and development works, for example, the incorporation of new burnable absorbers and the adjustment of cross sections to obtain better prediction accuracy, are considered, such flexibility becomes invaluable. The “indexed” approach is also advantageous in the input of cross sections in lattice physics codes, since the nuclides used in the calculation can be read on a “demand-basis.”

The structure of cross section files for the “index” type cross section library is shown in

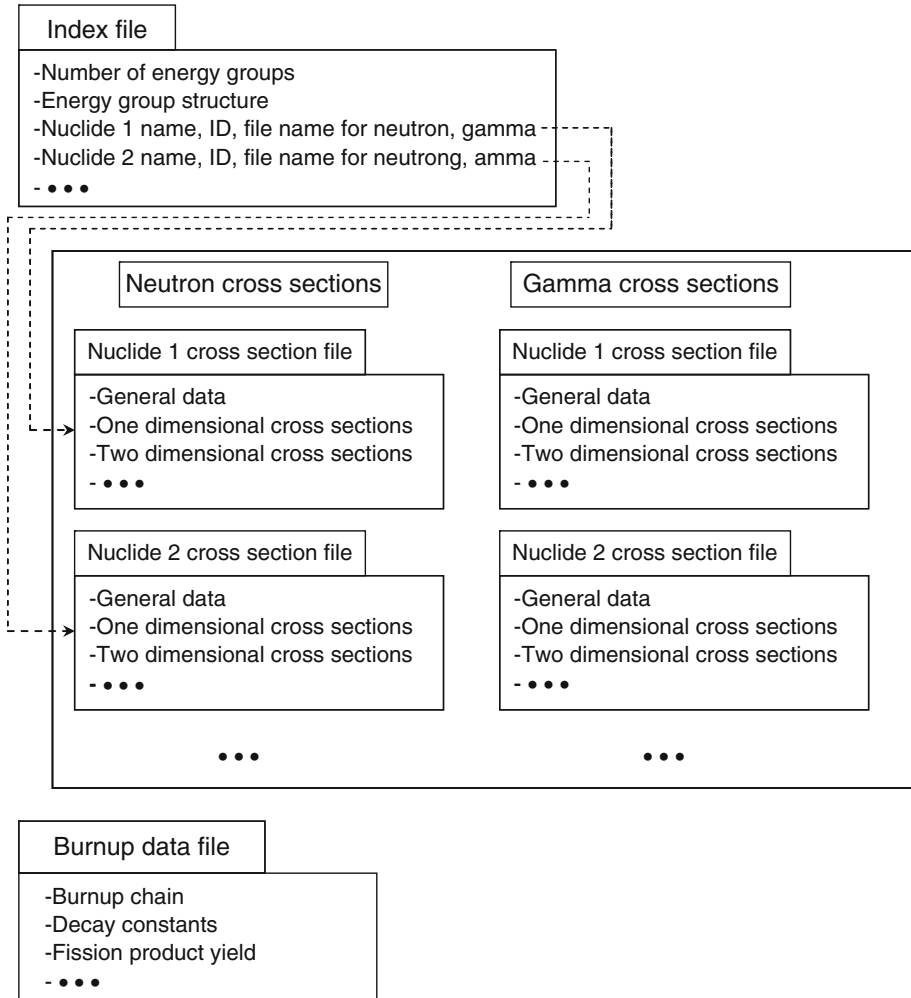
► [Fig. 9.](#)

Though the manipulation of many files requires a considerable effort for conventional main-frame computers, it is very easy for the modern Unix, Linux, or Windows operating systems. Many files can quite practically be treated and managed by a directory. If we consider the ongoing progress being made in the computer industry, the second approach, that is, the index-type cross section library, will be more suitable for future lattice physics codes. In this approach, a cross section library is no longer “a file,” but rather, is “a directory.” Note that burnup-related data may also be prepared by an independent file, since the selection of a burnup chain to be used in calculations is easily accomplished.

2.5.2 Nuclide Identifiers

Nuclide identifiers are very important for a lattice physics code since they are the bridge between users and the lattice physics codes. Nuclide identifiers should include the following information:

- Nuclide information (name of element, atomic number, and mass number)
- State of nuclide (ground/meta-stable)
- Fission product or not
- Chemical binding form (e.g., H in H₂O)
- Source of cross section data (e.g., ENDF/B-VII.0)
- Additional information (e.g., adjustment of cross section data)



■ **Figure 9**
Structure of cross section library ("index" type)

The identifiers can be a string of characters or digits. In conventional lattice physics codes, digits are usually used, for example, "92238" represents ^{238}U . However, when the above information is taken into account, the design of identifiers should be done quite carefully, especially from the viewpoint of extensibility.

Though identifiers based on digits are "computer friendly," they are not "user friendly." On the other hand, identifiers based on a string of characters are "user friendly" but are not "computer friendly." In order to resolve this contradiction, each nuclide can have two identifiers, that is, one consisting of a string of characters, and one of a string of digits. The character identifiers are used in input data, while the digit identifiers are used in the internal calculations of a lattice physics code.

Some nuclides play two roles in lattice physics computations. For example, ^{155}Gd is used as a burnable absorber, but it also appears as a fission product. The number density of ^{155}Gd in a burnable absorber is high, but that of the fission product is low. Therefore, though the self-shielding (resonance) effect of ^{155}Gd in a burnable absorber must be accurately accounted for, the resonance of ^{155}Gd as a fission product may be simply accounted for by assuming an appropriate (fixed) background cross section. Since the scattering matrix of ^{155}Gd as a fission product has a negligible impact from the point of view of neutronics, it may be truncated in a cross section library.

Furthermore, burnable absorber nuclides sometimes have a burnup chain that is independent of that of fission products. In such a case, though the same nuclides (^{155}Gd) appear as both a burnable absorber and fission product, they are considered as different nuclides from the viewpoint of the implementation of lattice physics codes. In order to distinguish “different” ^{155}Gd , different identifiers are necessary for the burnable absorber and fission product. We encounter a similar situation for other nuclides, for example, ^{109}Ag (control rod absorber and fission product), ^{103}Rh (Rh detector and fission product), and Zr (cladding and fission products).

2.5.3 Dependency of Cross Sections

Microscopic cross sections stored in a cross section library are usually dependent on the background cross section and temperature. In a given case, the mass effect of moderator nuclides may be taken into account (a detailed description of the mass effect will be given in [▶ Sect. 3](#)).

In order to account for these dependencies, multiple NJOY calculations are carried out for different calculation conditions (different temperatures and background cross sections). Some typical examples of temperatures and background cross sections used in the NJOY code are shown in [▶ Tables 5](#) and [▶ 6](#), respectively.

The temperatures for the major nuclides cover a range from room temperature (293 K) almost to the melting point of UO_2 (2,800 K). The maximum average pellet temperature of light water reactor fuel in a typical nominal operating condition is approximately 1,100 K. Higher temperatures (>1,100 K) are necessary for transient and accident analyses. Hydrogen has more detailed temperature grid points between 300 and 600 K, due to the considerable variation in scattering cross sections in the thermal energy region. For less important nuclides (e.g., fission product with small absorption) less detailed temperature grid points (or even one fixed temperature) can be applied in order to reduce the size of a cross section library with no loss of accuracy.

The grid points for a background cross section cover a range from infinite dilution (10^8 barn) to a fully shielded condition (10 or 1 barn). Dedicated grid points are assigned to ^{238}U since it is a dominant resonance absorber in many currently used reactor fuels. The grid points for ^{238}U have a fine resolution between 10–100 barn, since the typical background cross section for ^{238}U in light water reactor fuel pins is ~50 barn. Since the number densities of other nuclides (e.g., ^{235}U and ^{239}Pu) vary considerably during burnup, their background cross sections should also cover a wide range. For example, a background cross section for ^{235}U in typical UO_2 fuel is ~1,000 barn at beginning of life (BOL), but it increases up to ~5,000 barn at end of life (EOL), since the number density of ^{235}U reduces with burnup. In the case of ^{239}Pu , its background cross

■ **Table 5**
Example of temperatures used in the NJOY code

Major nuclides (K)	Hydrogen (K)
293	296
373	350
559	400
748	450
793	500
833	600
963	800
1,273	1,000
1,773	
2,573	

Source: Marcille and Mills (2003).

■ **Table 6**
Example of background cross sections used in the NJOY code

^{238}U (barns)	Heavy nuclides (barns)	FP (barns)	Others (barns)
1.00E+08	1.00E+08	1.00E+08	1.00E+08
1.00E+06	1.00E+06	1.00E+06	1.00E+06
1.00E+05	1.00E+05	1.00E+05	1.00E+05
1.00E+04	3.00E+04	1.00E+04	1.00E+04
1.00E+03	1.00E+04	1.00E+03	1.00E+03
3.00E+02	3.00E+03	1.00E+02	1.00E+02
1.00E+02	1.00E+03	1.00E+01	1.00E+01
5.00E+01	3.00E+02		1.00E+00
2.00E+01	1.00E+02		
1.00E+01	1.00E+01		

Source: Marcille and Mills (2003).

section is very large (almost infinite dilution) at BOL, since the number density of ^{239}Pu is very small. At EOL, the background cross section is reduced to approximately several thousands barn due to buildup during burnup.

Due to a current limitation of the NJOY code, the number of background cross sections is limited to less than or equal to 10. When more detailed grid points for a background cross section are necessary, two NJOY executions and the coupling of their results in post-processing becomes necessary.

2.5.4 General Data

When the index file approach is adopted, we have two different files, that is, the index file, and the cross section file for each nuclide. The general data contained in the index file and cross section file are described as follows:

a. Index file

- Numbers of total, fast, and thermal energy groups (note that thermal groups have up-scattering)
- Energy boundaries
- Directory in which cross section files are stored
- Correspondence among name of nuclide (character string identifier), nuclide id (digit identifier), and file name that stores cross section data

b. Cross section file

- Name of nuclide (character string identifier)
- Nuclide id (digit identifier)
- Atomic number, mass number
- Atomic weight (in units of amu is useful for slowing down calculation)
- Number of energy groups
- Fissionable (yes/no)
- Scattering matrix (present/no)
- Upper boundary of resolved resonance range
- Potential scattering cross section
- IR (intermediate resonance) parameter, if necessary
- Energy released per fission
- Kinetic parameters (delayed neutron fraction and decay constant for delayed neutron precursor)
- Number of grid points for temperature
- Number of grid points for background cross section
- Number of grid points for moderator mass effect
- Grid points for temperature
- Grid points for background cross section
- Grid points for moderator mass
- Generation time and date
- Comments
- Others

2.5.5 One-Dimensional Data

In the cross section file for each nuclide, the following one-dimensional cross section data are tabulated:

- Total cross section
- Absorption cross section
- Fission cross section

- Production cross section (number of neutrons released by a fission multiplied by fission cross section)
- (n, 2n) cross section
- Capture cross section
- Fission spectrum
- Neutron source intensity (e.g., by spontaneous fission)
- Other parameters (e.g., (n, 3n), (n, γ), and so on, if necessary)

Additional parameters may be necessary if a lattice physics code adopts a particular resonance calculation method. When the subgroup method is used, the band cross sections and band probabilities are necessary. Almost continuous energy (point-wise) cross sections are necessary for the ultrafine group calculation method.

The above data are tabulated for each energy group, temperature, background cross section, and moderator mass. Since the volume of data is quite considerable and several elements of the above data are zero, compression of the above data is of practical importance. The following two approaches can be used to reduce data size.

Elimination of Zero Elements

For example, an (n, 2n) cross section has a nontrivial value for energy groups above 1 MeV. In other words, (n, 2n) cross sections are zero for most energy groups. Many nuclides are not fissionable; thus, fission, production cross sections, and the fission spectrum are zero for these nuclides. In order to eliminate the zero elements, the upper and bottom energy groups with significant values are stored with nonzero values between the (stored) upper and bottom energy groups. This approach is adopted in the MATXS format.

Storage of Variations in Cross Sections

Certain one-dimensional cross sections, for example, cross sections in the fast energy range, are insensitive to variations in temperature and background cross section. This means that almost identical cross sections are repeatedly tabulated for different temperatures and background cross sections. In such a case, the difference between cross sections from a base condition (e.g., room temperature and infinite dilution condition) will be zero when variations due to temperature and/or background cross section are considered, as follows:

$$\begin{aligned}\sigma(T, \sigma_0) &= \sigma(T_0, \sigma_{0,\infty}) + (\sigma(T, \sigma_0) - \sigma(T_0, \sigma_{0,\infty})) \\ &= \sigma(T_0, \sigma_{0,\infty}) + \Delta\sigma(T, \sigma_0)\end{aligned}\quad (63)$$

where

$\sigma(T, \sigma_0)$: effective microscopic cross section for temperature T and background cross section σ_0 ,

$\sigma(T_0, \sigma_{0,\infty})$: effective microscopic cross section for temperature T_0 and background cross section $\sigma_{0,\infty}$,

$\Delta\sigma(T, \sigma_0)$: difference of effective microscopic cross section,

T_0 : base temperature, for example, 293 K,

$\sigma_{0,\infty}$: background cross section for infinite dilute condition, for example, 10^8 barn.

Since the zero element of a cross section can be compressed by elimination, as discussed above, consideration through variation of a cross section is effective at reducing the volume of cross section data. The present method is also adopted in the MATXS format.

Reduction of Grid Points for Temperature/Background Cross Sections

For less important nuclides such as minor fission products, full tabulation of the cross sections for all temperatures/background cross sections is not necessary, since they have little impact on the calculation results. For these nuclides, a typical temperature (e.g., that of the operating condition) and background cross section (e.g., average value during burnup) can be used, instead of full tabulation of temperatures/background cross sections.

2.5.6 Two-Dimensional Data

Scattering matrixes for both isotropic component (P0) and anisotropic components are tabulated here. In light water reactor analysis, the transport-corrected total cross section, which considers anisotropic components up to P1, is usually used with acceptable results. However, for fuels with a steep angular flux distribution, an explicit anisotropic scattering calculation is desirable. Higher-order anisotropic scattering matrixes are necessary for such calculations. Several studies have demonstrated that anisotropic scattering up to a P3 component is sufficient for ordinary light water reactor core calculations. Therefore, anisotropic scattering up to P3 components for nuclides with large anisotropic scattering (light nuclides) and reflector materials (e.g., Fe, Ni, and Cr) would be included in the cross section data. For other materials, anisotropic scattering up to a P1 component is sufficient for lattice physics computation. Note that if sensitivity calculations on anisotropic scattering will be carried out, the order of anisotropic scattering in a cross section library should be higher.

Since the size of a scattering matrix is large, the compression of data is crucial. The techniques for one-dimensional cross sections described previously can also be applied to two-dimensional data, that is, scattering matrixes. Furthermore, scattering matrixes for nuclides with a small number density and small cross section (e.g., minor fission products) can be omitted, since the scattering matrix of such nuclides has a negligible impact on reactor physics parameters. This is another reason to provide independent nuclide identifiers for fission products. For example, the number density of ^{155}Gd used as a burnable absorber is high, so its scattering matrix should be explicitly taken into account. However, since the number density of ^{155}Gd as a fission product is small, its scattering matrix can be omitted. Therefore, we can have two different cross section files for ^{155}Gd : one that (for a burnable absorber) contains a scattering matrix, and one that does not.

2.5.7 Burnup-Related Data

For burnup-related data, the following information is necessary:

- Burnup chain (including branching ratio)
- Decay constant for each nuclide
- Yields for fission products

A burnup chain used in a lattice physics code would depend on the purpose of the analysis. Therefore, various burnup chains may be used with the same cross section library. Therefore, burnup-related data might be stored in a file that is independent of the cross section data. More detailed discussion on burnup chains will be presented in [▶ Sect. 6](#).

2.5.8 Gamma Cross Section Library

In order to evaluate detailed pin-wise energy deposition by gamma rays, a transport calculation of gamma rays is necessary. For such gamma transport calculation, the following data are necessary (Mertyurek 2007):

- Gamma energy released by a photonuclear reaction, mainly (n, γ)
- Gamma spectra of a photonuclear reaction (from neutron group n to gamma group g)
- Gamma energy released by a fission reaction
- Gamma spectra of a fission reaction (to gamma group g)
- Gamma total cross section
- Gamma absorption cross section
- Gamma scattering cross section (isotropic and anisotropic components)
- Energy deposition cross section from gamma

Since gamma cross sections have contents similar to those of neutron cross sections, a similar format for neutron cross sections can be used.

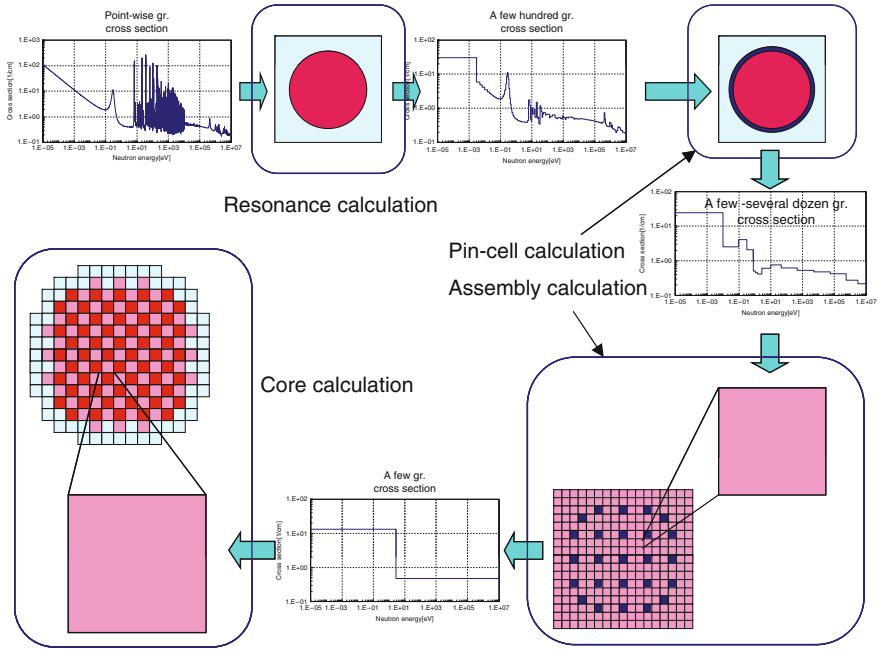
2.6 Summary

In [▶ Sect. 2](#), a detailed discussion of a cross section library for lattice physics code is provided. Though a cross section library is a crucial part of a lattice physics code, a description of its contents and preparation is rarely found in references. This section will be useful not only for the design and generation of a new cross section library, but also for an understanding of the contents and generation process of a current cross section library.

3 Resonance Treatment

3.1 Objective

All reactor physics calculations are carried out with cross sections. The actual cross-sectional data for each nuclide describe the very detailed (fine) energy structure, typically comprising several hundreds of thousands of energy points for major resonance nuclides. In fact, direct utilization of such ultrafine energy groups in lattice physics computations and subsequent core calculations is so time consuming as to be impractical, even on today's computers. For this reason, the fine energy structures of cross sections, especially in the resonance energy range, are condensed during lattice physics computations, as shown in [▶ Fig. 10](#). The first step in such energy condensation for cross sections is the resonance calculation. In this context, the resonance calculation is the “sole interface with the real world,” since the “actual” cross section



■ Figure 10

General calculation flow for core analysis

appears only in the resonance calculation, while only the condensed (i.e., artificial) cross sections are used in subsequent calculations. The consequence is that if the resonance calculation were inaccurate, subsequent calculations would be meaningless.

Since the resonance calculation is one of the most difficult and challenging part of reactor physics calculations, significant effort and study have been directed to the development of various innovative calculation methods. A complete review of these resonance calculation methods would, however, require an entire book, and hence, the discussion in ► 3.2 is limited to the major calculation methods being used in current lattice physics codes.

In the following subsection, the concept of an effective cross section is introduced, along with a discussion of the major resonance calculation methods used in current lattice physics codes (Weinberg and Wigner 1958; Dresner 1960; Goldstein and Cohen 1962; Rothenstein 1980; Stamm'ler and Abbate 1983; Rothenstein and Segev 1986; Cullen 1986; Kobayashi 1995; Hall-sall 1995; Loubiere et al. 1999; Hwang 2003; Reuss and Coste-Delclaux 2003; Hébert 2005b; Karthikeyan and Hébert 2008).

3.2 Effective Cross Sections

The Boltzmann transport equation in continuous energy is given as follows:

$$\vec{\Omega} \cdot \nabla \psi(\vec{r}, E, \vec{\Omega}) + \Sigma_t(\vec{r}, E) \psi(\vec{r}, E, \vec{\Omega}) = Q(\vec{r}, E, \vec{\Omega}) \quad (64)$$

In principle, (64) can be accurately solved with a very fine energy structure, but for the reasons discussed in the previous section, such treatment remains impractical. Thus, the Boltzmann transport equation in a multigroup form is usually used in lattice physics computations:

$$\vec{\Omega} \cdot \nabla \psi_g(\vec{r}, \vec{\Omega}) + \Sigma_{t,g}(\vec{r}, \vec{\Omega}) \psi_g(\vec{r}, \vec{\Omega}) = Q_g(\vec{r}, \vec{\Omega}) \quad (65)$$

With the following definition of a multigroup microscopic cross section, (64) and (65) are consistent.

$$\sigma_g(\vec{r}, \vec{\Omega}) = \frac{\int_{E_g}^{E_{g-1}} dE \sigma(E) \psi(\vec{r}, E, \vec{\Omega})}{\int_{E_g}^{E_{g-1}} dE \psi(\vec{r}, E, \vec{\Omega})} \quad (66)$$

It should be noted that the multigroup cross sections given in (66) is not a common expression since it depends not only on the location, but also on angle. Since neutron transport calculations in a lattice physics code assumes a constant cross section in a small spatial region (e.g., a fuel pellet), the spatially averaged cross section is necessary:

$$\sigma_{i,g}(\vec{\Omega}) \psi_{i,g}(\vec{\Omega}) V_i = \int_{V_i} d\vec{r} \sigma_g(\vec{r}, \vec{\Omega}) \psi_g(\vec{r}, \vec{\Omega}). \quad (67)$$

The cross section expressed in (67) still has angular dependence, which is not usually taken into account in the transport calculations in lattice physics codes. Therefore, the following definition is of practical value for microscopic cross sections in the multigroup neutron transport calculation:

$$\sigma_g(\vec{r}) = \frac{\int_{E_g}^{E_{g-1}} dE \sigma(E) \phi(\vec{r}, E)}{\int_{E_g}^{E_{g-1}} dE \phi(\vec{r}, E)} \quad (68)$$

where $\phi(\vec{r}, E)$ is the total (or scalar) flux, which is defined as

$$\phi(\vec{r}, E) = \int^{4\pi} \psi(\vec{r}, E, \vec{\Omega}) d\vec{\Omega}$$

The cross section given in (68) is called the effective cross section because it can effectively preserve the total reaction rate for the group. The group-wise definition of reaction leads also to scattering matrices for various angular moments. The scattering matrices are not covered in detail here though. It should be noted that detailed information regarding angular flux is implicitly taken into account.

The above discussion clarifies the fact that the essence of the resonance calculation is the energy collapsing and the spatial averaging (homogenization) that uses the detailed angular flux distribution to be obtained by solving (64). The above discussion also suggests a significant contradiction: the detailed angular fluxes used in (66) and (67) are, of course, unknown, since they are exactly what we would like to know. If the exact angular flux were known, the reactor physics calculation would have already been completed with ideal accuracy.

Herein lies the difficulty of the resonance calculation. We need to estimate the neutron flux distribution in a resonance region without a complete knowledge of the entire calculation system, such as a fuel assembly or a reactor core. In this sense, the resonance calculation methods must to a significant degree rely on approximations, which are considered valid from an engineering perspective.

3.3 Physics of Self-Shielding and Major Resonance Calculations

3.3.1 Physics of Self-Shielding

In the resonance energy range, the cross sections of many nuclides (especially heavy nuclides) exhibit a severely varying behavior. Since the peak of a resonance is often quite high, neutrons at the resonance peak energy are often easily absorbed by resonance nuclides. In such a case, the neutron flux also exhibits very complicated energetic behavior due to resonance absorption, as shown in [Fig. 11](#). Since the neutron absorption rate is obtained as a product of the microscopic cross section and the neutron flux, the dip in the neutron flux at a resonance peak reduces absorption at that peak. The resonance peak thus appears to be “energetically” shielded from neutrons around the resonance peak energy. For this reason, the reduction of neutron absorption around the resonance peak by the above mechanism is referred to as the energetic self-shielding effect. It is apparent that the energetic self-shielding effect appears not only in a heterogeneous geometry, but also in a homogeneous geometry, since the slowing down of the neutrons (energetic transport of neutrons) and absorption are the principal physical phenomena behind the energetic self-shielding effect.

There is another important shielding effect related to resonance absorption. In heterogeneous geometry, neutrons that flow from a moderator into a fuel (i.e., into the resonance region) are captured in the peripheral area, as shown in [Fig. 12](#). The neutron flux distribution thus shows a profound depression from the surface to the center part of the fuel near the resonance peak energy. The spatial variation in neutron absorption becomes very large in the resonance energy range due to the large resonance absorption cross section of fuel. This phenomenon is known as the spatial self-shielding effect, since the resonance material “shields” the inflow of neutrons, thus reducing the neutron absorption in the resonance material.

The essence of the resonance calculation is, in other words, the accurate evaluation of the energetic and spatial self-shielding effects in resonance material.

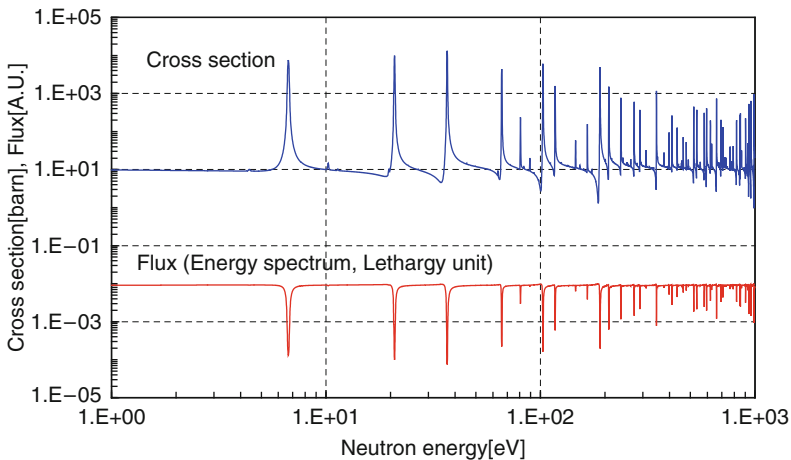


Figure 11

Neutron spectrum obtained by ultra-fine energy groups calculation

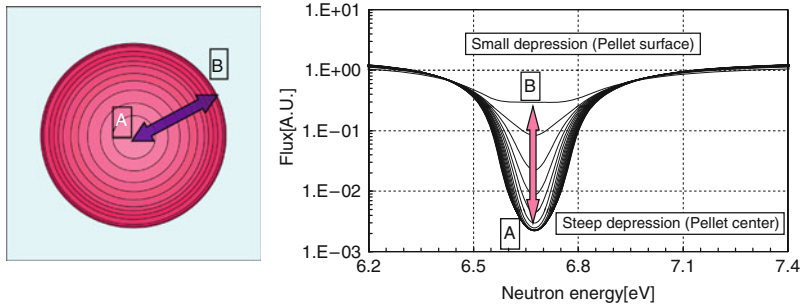


Figure 12
Space dependency of neutron spectrum in a fuel pellet

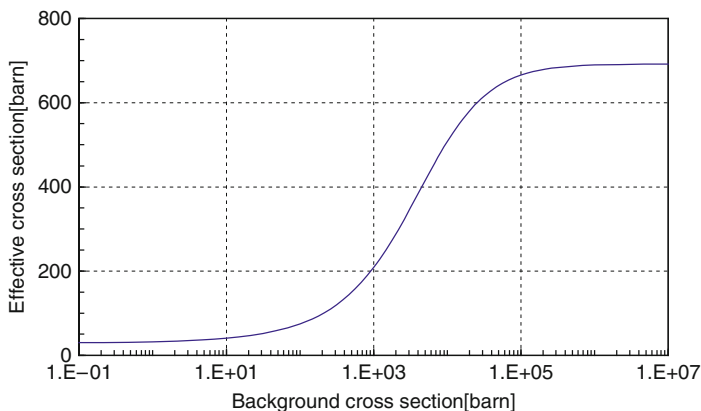
Even though there are various approaches to resonance calculations, they are generally classified into three categories: ultrafine energy group calculation, the equivalence theory, and the subgroup (or multiband) method.

3.3.2 Ultrafine Energy Group Calculation

The ultrafine energy group calculation is a quite simple and direct approach, in which neutron flux distribution (both energetic and spatial) is calculated with very fine energy groups (Ishiguro 1974; Tsuchihashi et al. 1982; Rothenstein et al. 1988; MC²-2 1999; Chiba 2003; Sugimura and Yamamoto 2007). In this approach, the effective multigroup cross section is evaluated with a very detailed neutron spectrum distribution, as shown in [Fig. 11](#), and since it is based on first principles, it clearly gives quite accurate, effective cross sections. We must recall, however, the necessity of the resonance calculation. If a neutron transport calculation in very fine energy groups can be carried out, a conventional resonance calculation is not necessary. Currently, the direct practical application of ultrafine energy group calculation is, however, limited to a pin cell or to small multicells, because of the enormous amount of computational resource required for the ultrafine group transport calculation.

3.3.3 Equivalence Theory

The second approach, that is, the equivalence theory, is a historical method that is widely used in current lattice physics codes (Weinberg and Wigner 1958; Dresner 1960; Goldstein and Cohen 1962; Bitelli et al. 1970; Chao and Martinez 1978; Chao et al. 1981; Stamm'ler and Abbate 1983; Rothenstein and Segev 1986; Cullen 1986). In this approach, the neutron escape probability from the fuel (resonance) material is approximated by a rational function of the total cross section of a resonance nuclide. With some additional assumptions, the neutron flux spectrum in a heterogeneous resonance region can be expressed as an analytic formula that is applicable to a homogeneous medium as well. During this derivation, the effect of heterogeneity is taken into account by the macroscopic escape cross section. The escape cross section plays the same role as the background cross section does in the self-shielding effect in a homogeneous system. The notion of escape and background cross sections will be addressed in more detail in [3.4](#) and [3.5](#). Therefore, an effective cross section can be tabulated with a background cross section



■ Figure 13

Effective cross section versus background cross section (^{238}U , 293 K, 6.16–7.52 eV)

(which may include the escape cross section) as an index, as shown in [▶ Fig. 13](#). Consequently, the effective cross sections in homogeneous and heterogeneous configurations will be the same if they have the same background cross sections. In this sense, the treatment of homogeneous and heterogeneous geometries is unified through the background cross section. In other words, the spatial self-shielding effect (captured by the escape cross section) and the energetic self-shielding effect (captured by the background cross section) are unified.

Though the equivalence theory offers a very simple and effective approach to resonance calculation, one must remember that it incorporates many approximations that are implicitly used. Therefore, the application of the equivalence theory is inherently limited to simple configurations, such as an isolated pin cell or regular lattices. Very heterogeneous geometries with complicated resonance material distribution require a more sophisticated approach.

3.3.4 Subgroup Method

The previous approach, the subgroup method, provides a calculation route that offers a compromise, by using a correlation between the neutron flux and the resonance cross section shown in [▶ Fig. 11](#) (Nikoleav et al. 1971; Levitt 1972; Cullen 1986). Generally speaking, neutron flux is inversely proportional to the macroscopic total cross section of a resonance material. This dynamic suggests that neutron energy groups would be subdivided not by the order of energy (the conventional approach), but by the magnitude of the cross section, as show in [▶ Fig. 14](#). When neutron energy groups are defined according to the magnitude of the cross section, the variations in neutron flux in a subdivided energy group will be smaller than those in a conventional subdivision, since the variation of the cross section (and thus that of the neutron flux) in a sub-energy group is smaller. The dependence of the effective cross section in each subgroup on a shielding condition (in the equivalence theory, on a background cross section) is clearly weaker, and it is this condition, which guarantees the robustness of the subgroup method. Although a very fine energy group structure is necessary in the ultrafine energy group calculation, a few subgroups within a conventional group offer high accuracy, which makes the subgroup method computationally efficient.

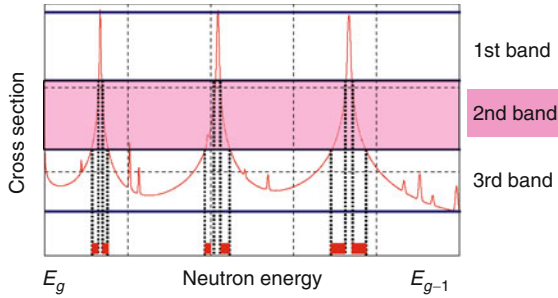


Figure 14
Concept of the subgroup method

The above discussion describes the concept of the subgroup method, in which the energy group structure in each subgroup is explicitly defined. In other words, all energy points are explicitly classified into corresponding subgroups. However, the subgroup method currently used in lattice physics codes does not have such an explicit energy group structure. Each subgroup is probabilistically defined in terms of its band probability and the corresponding band cross sections. The band probability and band cross sections are chosen to be independent of the self-shielding condition (i.e., the background cross section in the equivalence theory). Since each band does not have an explicit energy range, direct application of the current subgroup method is difficult when the shape of the cross section of a nuclide is different in each resonance region. The radial temperature distribution in a pellet poses just such a situation, since the shape of a cross section in a resonance energy range depends on the temperature, due to the Doppler effect. Furthermore, since the common subgroup method relies on the narrow resonance approximation that will be presented in the [3.4](#), its accuracy might be limited.

The advantages and disadvantages of the three major resonance calculation methods are summarized in [Table 7](#). This table suggests that there is no method of “last resort,” so the choice of a resonance calculation method greatly depends on the design concept of a given lattice physics code.

In the following subsection, the theoretical basis of the resonance calculation methods will be described. Beginning with the resonance theory in a homogeneous medium, the discussion is then extended to heterogeneous geometries.

3.4 Resonance Self-Shielding in a Homogeneous System (Dresner 1960; Rothenstein and Segev 1986; Cullen 1986)

3.4.1 Slowing Down of Neutrons in a Homogeneous System

In a homogeneous system, where the neutron flux is isotropic, the Boltzmann transport equation can be written as follows:

$$\Sigma_t(E)\phi(E) = \int_0^\infty \Sigma_s(E' \rightarrow E)\phi(E')dE' + \frac{\chi(E)}{k_{eff}} \int_0^\infty v\Sigma_f(E')\phi(E')dE' \quad (69)$$

■ Table 7

Advantages and disadvantages of the major resonance calculation methods

Methods	Advantages	Disadvantages
Equivalence theory	Simple	Inability to treat space-dependent resonance shielding
	Fast	Inability to treat complicated geometry Limited accuracy due to assumptions for simplification Inability to treat the resonance interference effect
Subgroup method	Reasonably accurate	Longer computation time than the equivalence theory
	Applicable to general geometry	Inability to treat temperature distribution Inability to treat resonance interference effect
Ultrafine group method	Accurate	Longer computation time and larger memory storage
	Applicable to general geometry Ability to treat resonance interference effect	Impractical for large system (e.g., a fuel assembly)

where

$\Sigma_t(E)$: macroscopic total cross section,
 $\Sigma_s(E' \rightarrow E)$: macroscopic scattering cross section,
 $\nu\Sigma_f(E)$: macroscopic production cross section,
 $\chi(E)$: fission spectrum,
 $\phi(E)$: scalar flux, and
 k_{eff} : k -effective.

In the resonance region (e.g., 1 eV–10 keV and 10–300 keV for the resolved and unresolved resonance energy ranges, respectively, for ^{238}U), fission neutrons can be neglected, and elastic scattering is the dominant mechanism for the slowing down of neutrons. Under these assumptions, (69) can be simplified into

$$\left(\sum_k N_k \sigma_{t,k}(E) \right) \phi(E) = \sum_k \frac{1}{1 - \alpha_k} \int_E^{E/\alpha_k} N_k \sigma_{s,k}(E') \phi(E') \frac{dE'}{E'} \quad (70)$$

where

$\sigma_{t,k}(E')$: microscopic total cross section of nuclide k ,
 $\sigma_{s,k}(E')$: microscopic elastic scattering of nuclide k ,
 $\phi(E)$: total (scalar) neutron flux, and
 $\alpha_k = \left(\frac{A-1}{A+1} \right)^2$ when A is the atomic mass in atomic mass units (amu).

If a material is a pure scatterer that consists of a single nuclide, (70) becomes

$$N_k \sigma_{t,k}(E) \phi(E) = \frac{1}{1 - \alpha_k} \int_E^{E/\alpha_k} N_k \sigma_{t,k}(E') \phi(E') \frac{dE'}{E'} \quad (71)$$

It is easily confirmed that the solution to (71) is given by

$$\phi(E) = \frac{C}{N_k \sigma_{t,k}(E) E} \quad (72)$$

where

C: a constant that is defined by the source intensity.

Equation (72) suggests that the asymptotic neutron spectrum in a pure scatterer is inversely proportional to the macroscopic total cross section and the neutron energy. In fact, in an LWR lattice, the overall behavior of the neutron spectrum in the resonance region is approximately given by $1/E$ even with absorption, since the moderator (H_2O) is almost a pure scatterer in the resonance energy region.

Unfortunately, the analytic solution to the equation for the slowing down of neutrons can be derived only under a very limited condition. Additional approximations will thus be necessary as a basis for further derivation. In the following sections, we discuss the major approximations that are behind the resonance calculations of many lattice physics codes.

3.4.2 Narrow Resonance Approximation

First, let us assume that the homogeneous material is composed of a resonance nuclide and other (nonresonant) nuclides. Even though the material may contain multiple resonance nuclides, the narrow resonance (NR) approximation to be discussed below will be valid when there is no coincident resonance overlap among nuclides (which will be discussed in more detail in a later section). Now, assume that the energy dependence of cross sections for nonresonant nuclides is assumed to be constant, with no absorption, that is, their total cross sections are equal to the potential scattering cross sections ($\sigma_{t,k} = \sigma_{s,k} = \sigma_{p,k}$). This assumption can be justified by the fact that this potential scattering, which is independent of the incident neutron energy, is dominant for nonresonant nuclides in the resonance energy range. With this assumption, (70) becomes as follows:

$$\left(N_r \sigma_{t,r}(E) + \sum_{k \neq r} N_k \sigma_{p,k} \right) \phi(E) = \frac{1}{1 - \alpha_r} \int_E^{E/\alpha_r} N_r \sigma_{s,r}(E') \phi(E') \frac{dE'}{E'} + \sum_{k \neq r} \frac{1}{1 - \alpha_k} \int_E^{E/\alpha_k} N_k \sigma_{p,k} \phi(E') \frac{dE'}{E'} \quad (73)$$

where the subscript r denotes a resonance nuclide.

It should be noted again that (73) assumes that only a resonance nuclide has energy dependence on cross sections, that is, other nuclides have a constant total and scattering cross sections. As discussed later, this simplification (which neglects the resonance overlap effect) is one of the weaknesses of this resonance calculation method. In actual fuel, a fuel material could have a

very diverse composition due to burnup (through the generation of minor actinides and fission products, which have many distinct resonances) and/or its initial mixed loading (e.g., MOX fuel, which includes both uranium and plutonium isotopes).

Unfortunately, the right-hand side of (73) contains an unknown function of energy E' , that is, neutron flux. Therefore, some assumptions are necessary in order to analytically solve (73).

For the purpose of further simplification, the resonance width of nuclide r is assumed to be narrow compared to the slowing down width. This means that most neutrons that appear near the resonance peak energy come from outside of the resonance peak (i.e., the nonresonant energy range) due to much higher energies. Furthermore, from (72), we see that the neutron spectrum in the nonresonant part is assumed to be proportional to $1/E$, since the energy dependence of the total cross section in the nonresonant part is fairly flat. Though the neutron spectrum around the resonance peak does not have a $1/E$ shape, its contribution to the integration of the energy is small because of the narrow resonance width. With these assumptions, the second term in the right-hand side of (73) can be reduced into the following:

$$\begin{aligned} \sum_{k \neq r} \frac{1}{1 - \alpha_k} \int_E^{E/\alpha_k} N_k \sigma_{p,k} \phi(E') \frac{dE'}{E'} &= \sum_{k \neq r} \frac{N_k \sigma_{p,k}}{1 - \alpha_k} \int_E^{E/\alpha_k} \phi(E') \frac{dE'}{E'} \\ &\approx \sum_{k \neq r} \frac{N_k \sigma_{p,k}}{1 - \alpha_k} \int_E^{E/\alpha_k} \frac{1}{E'} \frac{dE'}{E'} \\ &= \sum_{k \neq r} N_k \sigma_{p,k} \frac{1}{E} \end{aligned} \quad (74)$$

Note that the proportional constant C in (72) has been taken arbitrarily as 1 for normalization of the flux such that $E\phi(E) = 1$ above the resonance.

Next, we will estimate the first term in the right-hand side of (73). For this estimation, two additional approximations are introduced. The scattering cross section of a resonant nuclide in the nonresonant part is considered as a constant, since it is dominated by the potential scattering in this energy range. Furthermore, the shape of the neutron spectrum is approximated by $1/E$, as are the treatments for other nuclides. Using these assumptions, we have

$$\begin{aligned} \frac{1}{1 - \alpha_r} \int_E^{E/\alpha_r} N_r \sigma_{s,r}(E') \phi(E') \frac{dE'}{E'} &\approx \frac{N_r \sigma_{p,r}}{1 - \alpha_r} \int_E^{E/\alpha_r} \phi(E') \frac{dE'}{E'} \\ &\approx \frac{N_r \sigma_{p,r}}{1 - \alpha_r} \int_E^{E/\alpha_r} \frac{1}{E'} \frac{dE'}{E'} = N_r \sigma_{p,r} \frac{1}{E} \end{aligned} \quad (75)$$

By substituting (74) and (75) into (73), we obtain the following equation:

$$\left(N_r \sigma_{t,r}(E) + \sum_{k \neq r} N_k \sigma_{p,k} \right) \phi(E) = \frac{N_r \sigma_{p,r} + \sum_{k \neq r} N_k \sigma_{p,k}}{E} \quad (76)$$

Finally, the energy dependence of the neutron flux is given by

$$\begin{aligned} \phi(E) &= \frac{N_r \sigma_{p,r} + \sum_{k \neq r} N_k \sigma_{p,k}}{N_r \sigma_{t,r}(E) + \sum_{k \neq r} N_k \sigma_{p,k}} \frac{1}{E} \\ &= \frac{\sigma_{p,r} + \sigma_0}{\sigma_{t,r}(E) + \sigma_0} \frac{1}{E} \end{aligned} \quad (77)$$

In (77), the background cross section (σ_0), is defined as

$$\sigma_0 = \left(\sum_{k \neq r} N_k \sigma_{p,k} \right) / N_r \quad (78)$$

Equation (77) is the analytic form for the energy dependence of the neutron flux obtained by the narrow resonance (NR) approximation. Note that the absolute value of the neutron flux is not necessary in the resonance calculation, since the neutron flux is used as the weighting function. Though (72) is limited to a pure scatter, (77) is an extension that accounts for absorption, and can thus be used in the case of general homogeneity.

The background cross section defined by (78) is a fictitious microscopic cross section that determines the depression of the neutron flux at resonance peak energy. When the background cross section is very small, the energetic neutron flux behavior given by (77) approaches that in (72), in which the contribution of scattering from other nuclides is not considered. In this case, the neutron flux is inversely proportional to the microscopic total cross section of the resonance nuclide. Note that the variation due to the $1/E$ part is much smoother than that in the microscopic cross section. On the contrary, when the background cross section is very large, the neutron flux given by (77) approaches $1/E$, which is an asymptotic neutron spectrum in which no absorption is considered, that is, the scattering of other nonresonant nuclides dictates the spectrum. The actual neutron flux variation will be between the two extreme cases above, and would be interpolated by the background cross section.

The background cross section plays a very important role in resonance calculation theory, as will be described later.

During the derivation of (77), many assumptions were used. It is worthwhile to summarize the assumptions used in the NR approximation:

- No resonance overlap is considered.
- Nonresonant nuclides have constant scattering cross sections, which are dominated by the potential scattering.
- The resonant nuclide has a constant scattering cross section above the resonance, which is dominated by the potential scattering.
- The slowing down of neutrons is dominated by elastic scattering.
- The energy dependence of the neutron flux in the nonresonant part is asymptotic ($1/E$ shape).
- The neutron source within the resonance energy range is dominated by scattered neutrons coming from outside of the resonance peak. In other words, the resonance peak is so narrow compared to the average energy loss of neutrons due to elastic scattering.
- The source of neutron scattering is calculated by the asymptotic $1/E$ spectrum.

Though the above assumptions help to greatly simplify the expression of the energy dependence of the neutron flux, some of them may be a source of significant error. Since a resonance peak is assumed to be narrow, the NR approximation is more appropriate for a higher energy region in which the resonance is narrower than the slowing down width, in a relative sense. On the other hand, the accuracy of the NR approximation diminishes for broad resonances in the epithermal energy region (e.g., the resonance of ^{238}U at 6.7 eV). The accuracy of the NR approximation will be discussed later in more detail.

3.4.3 Wide Resonance Approximation

The first term in the right-hand side of (73) can be simplified by another assumption, namely the assumption that a resonant nuclide has infinite mass. This means that the width of the resonance peak is “wide” compared to the average energy loss due to scattering. In this regard, this approximation is called the wide resonance (WR) approximation, or the wide resonance infinite (mass) absorber (WRIA) approximation. When the mass of a nuclide is infinite, no energy loss is expected in the elastic scattering reaction. This physical observation suggests that the first term in (73), which is the energy integral of an in-scatter neutron by the resonant nuclide, is equal to the out-scatter reaction at energy E , that is,

$$\begin{aligned}
 \lim_{\alpha_r \rightarrow 1} \frac{1}{1 - \alpha_r} \int_E^{E/\alpha_r} N_r \sigma_{s,r}(E') \phi(E') \frac{dE'}{E'} &\approx \lim_{\alpha_r \rightarrow 1} \frac{1}{1 - \alpha_r} N_r \sigma_{s,r}(E) \phi(E) \int_E^{E/\alpha_r} \frac{dE'}{E'} \\
 &= N_r \sigma_{s,r}(E) \phi(E) \lim_{\alpha_r \rightarrow 1} \frac{1}{1 - \alpha_r} \ln \left(\frac{1}{\alpha_r} \right) \\
 &= N_r \sigma_{s,r}(E) \phi(E) \lim_{\alpha_r \rightarrow 1} \frac{-\ln \alpha_r}{1 - \alpha_r} \\
 &= N_r \sigma_{s,r}(E) \phi(E)
 \end{aligned} \tag{79}$$

Here, the energy dependence of the scattering cross section and the neutron flux is assumed to be constant within the narrow integration range, $E/\alpha_r \sim E$. By substituting (79) into (73) and applying the NR approximation for nonresonant nuclides, we obtain

$$\left(N_r \sigma_{t,r}(E) + \sum_{k \neq r} N_k \sigma_{p,k} \right) \phi(E) = N_r \sigma_{s,r}(E) \phi(E) + \frac{\sum_{k \neq r} N_k \sigma_{p,k}}{E} \tag{80}$$

Since $\sigma_{a,r}(E) = \sigma_{t,r}(E) - \sigma_{s,r}(E)$, (80) is rewritten as

$$\left(N_r \sigma_{a,r}(E) + \sum_{k \neq r} N_k \sigma_{p,k} \right) \phi(E) = \frac{\sum_{k \neq r} N_k \sigma_{p,k}}{E} \tag{81}$$

The final form of flux, is then

$$\begin{aligned}
 \phi(E) &= \frac{\sum_{k \neq r} N_k \sigma_{p,k}}{N_r \sigma_{a,r}(E) + \sum_{k \neq r} N_k \sigma_{p,k}} \frac{1}{E} \\
 &= \frac{\sigma_0}{\sigma_{a,r}(E) + \sigma_0} \frac{1}{E}
 \end{aligned} \tag{82}$$

where $\sigma_0 = \left(\sum_{k \neq r} N_k \sigma_{p,k} \right) / N_r$.

Note that the narrow resonance approximation is still applied to the nonresonant nuclides to derive (82). Therefore, the above derivation is sometimes called the WR–NR approximation, which means that the WR approximation is applied to the resonant nuclide, while the NR approximation is applied to the nonresonant nuclides. In this context, the above approximation

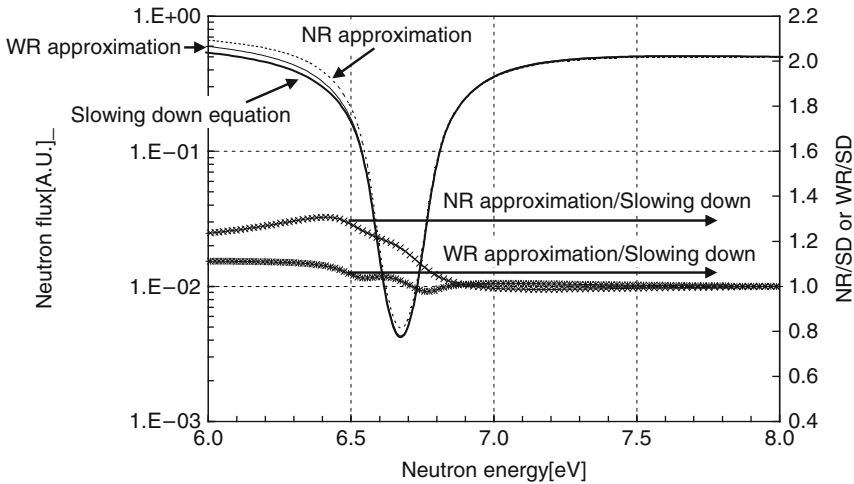


Figure 15

Neutron fluxes $\phi(E)$ obtained by the NR, WR approximations, and the numerical solution of the slowing down equation (SD) (homogeneous mixture of ^{238}U and hydrogen, 293 K, $\sigma_0 = 50$ barn)

is also referred to as the narrow resonance infinite mass (NRIM) approximation. The above assumption is justified by the fact that the energy loss from the slowing down by nonresonant nuclides (e.g., hydrogen) is generally much larger than the width of a resonance peak.

A comparison of (77) and (82) provides useful insight into the energy dependence of the neutron flux at the resonance peak. In fact, when the scattering reaction of the resonant nuclide is neglected (i.e., $\sigma_{p,r}$ and $\sigma_{s,r}(E)$ are zero), (77) and (82) become identical. This observation is adequate, since the scattering reaction of a resonant nuclide is essentially “neglected” in the WR approximation. Due to the assumptions in the WR approximation, it is more appropriate to treat broad resonances appearing in the epithermal-low energy range.

Figure 15 shows neutron spectra in a homogeneous mixture of ^{238}U and hydrogen around 7 eV, as obtained by different methods. The background cross section (σ_0) is 50 barn and the temperature is 293 K. The neutron flux is normalized at 8 eV. The ratios of the two approximated results to the reference are also shown. The reference result is obtained by the numerical solution of the slowing down equation, and the two approximate solutions (the NR and WR approximations) are also depicted in Fig. 15. Since the resonance of ^{238}U at 6.7 eV is located in a lower energy region and is relatively wide, the WR approximation is in better agreement with the reference solution.

Differences in the neutron spectrum affect the effective cross section during energy condensation. Tables 8 and 9 show a comparison of the effective microscopic capture cross sections of ^{238}U and ^{235}U obtained by the NR and WR approximations, and offer an accurate slowing down equation. Table 8 indicates that the NR approximation gives higher accuracy than the WR approximation in the higher energy range, while the WR approximation works better in the lower energy range. In comparison with ^{238}U shown in Table 8, the capture cross section of ^{235}U shown in Table 9 is accurately calculated by both the NR and WR

■ Table 8

Comparison of the effective microscopic capture cross section of ^{238}U obtained through the numerical solution of the slowing down equation (SD), and the narrow resonance (NR) and the wide resonance (WR) approximations (background cross section = 50 barn, 293 K, homogeneous mixture of ^{238}U and hydrogen; values are in barn)

Group number (XMAS 172 group)	Upper energy [eV]	Calculation method			Difference [%]	
		S.D.	N.R.	W.R.	(N.R.-S.D.)/S.D.	(W.R.-S.D.)/S.D.
45	1.11E+04	0.649	0.648	0.661	-0.19	1.80
46	9.12E+03	0.592	0.592	0.640	-0.03	7.97
47	7.47E+03	0.730	0.730	0.817	0.00	11.93
48	5.53E+03	0.776	0.773	0.838	-0.33	7.97
49	5.00E+03	0.736	0.734	0.875	-0.24	18.93
50	3.53E+03	0.749	0.747	1.020	-0.24	36.13
51	3.35E+03	0.940	0.937	1.229	-0.28	30.75
52	2.25E+03	0.745	0.746	1.027	0.17	37.82
53	2.03E+03	0.878	0.873	1.385	-0.54	57.77
54	1.51E+03	0.663	0.665	0.946	0.32	42.73
55	1.43E+03	0.999	0.983	1.406	-1.63	40.76
56	1.23E+03	1.334	1.322	1.833	-0.91	37.44
57	1.01E+03	1.084	1.064	2.159	-1.89	99.18
58	9.14E+02	1.289	1.261	1.750	-2.23	35.73
59	7.49E+02	1.390	1.374	1.685	-1.11	21.22
60	6.77E+02	1.323	1.291	1.855	-2.44	40.20
61	4.54E+02	1.397	1.374	1.502	-1.65	7.50
62	3.72E+02	0.751	0.680	1.143	-9.45	52.19
63	3.04E+02	1.814	1.654	2.297	-8.78	26.65
64	2.04E+02	1.567	1.262	2.184	-19.49	39.33
65	1.49E+02	1.287	1.289	1.217	0.15	-5.44
66	1.37E+02	2.757	2.085	3.304	-24.38	19.84
67	9.17E+01	2.129	2.103	1.993	-1.23	-6.38
68	7.57E+01	0.370	0.363	0.373	-1.87	0.84
69	6.79E+01	4.700	3.599	4.845	-23.43	3.09
70	5.56E+01	0.101	0.101	0.101	0.00	0.00
71	5.16E+01	0.144	0.144	0.144	-0.04	-0.01
72	4.83E+01	0.173	0.173	0.173	-0.06	0.01
73	4.55E+01	0.516	0.512	0.517	-0.82	0.20
74	4.02E+01	5.747	5.296	6.111	-7.85	6.32

Table 8 (continued)

Group number (XMAS 172 group)	Upper energy [eV]	Calculation method			Difference [%]	
		S.D.	N.R.	W.R.	(N.R.-S.D.)/S.D.	(W.R.-S.D.)/S.D.
75	3.73E+01	25.430	16.285	25.851	-35.96	1.66
76	3.37E+01	0.874	0.881	0.874	0.78	0.03
77	3.05E+01	0.398	0.399	0.398	0.08	0.00
78	2.76E+01	0.459	0.459	0.459	-0.03	0.00
79	2.50E+01	1.151	1.143	1.153	-0.64	0.17
80	2.26E+01	27.522	24.430	26.354	-11.23	-4.24
81	1.95E+01	1.175	1.193	1.175	1.56	0.04
82	1.59E+01	0.349	0.349	0.349	0.05	-0.01
83	1.37E+01	0.342	0.342	0.342	-0.07	0.00
84	1.12E+01	0.849	0.850	0.847	0.11	-0.24
85	9.91E+00	0.507	0.507	0.507	-0.01	0.00
86	9.19E+00	0.866	0.866	0.867	-0.04	0.02
87	8.32E+00	2.403	2.400	2.404	-0.12	0.08
88	7.52E+00	45.674	48.196	45.455	5.52	-0.48
89	6.16E+00	5.218	5.259	5.212	0.80	-0.12
90	5.35E+00	1.903	1.903	1.903	0.02	-0.01
91	5.04E+00	1.215	1.216	1.215	0.03	-0.02
92	4.13E+00	0.783	0.783	0.783	0.00	0.00

Background cross section = 50 barn, 293 K, homogeneous mixture of ^{238}U and hydrogen; values are in barn.

approximations, since the background cross section (1,000 barn, which is typical for ^{235}U in an LWR lattice) is much larger than that of ^{238}U in this calculation, and the peak of the resonance cross section is smaller and narrower than ^{238}U . Note that the typical peak values of the resonance cross sections are 10,000 barns and 1,000 barns for the microscopic total cross sections of ^{238}U and ^{235}U , respectively. In the case of a more shielded condition, the difference between the NR and WR approximations will be larger for ^{235}U .

3.4.4 Intermediate Resonance Approximation

Concept

The NR and WR approximations give the two limiting conditions in neutron slowing down for a resonant nuclide. Actual resonance peaks, however, appear to have an “intermediate” resonance width, which would be a blend of the “narrow” and “wide” ones. The intermediate resonance (IR) approximation offers a compromise approach for resonances of intermediate width (Sehgal and Goldstein 1966; Goldstein 1967; Ishiguro 1968; Ishiguro and Takano 1969).

■ Table 9

Comparison of the effective capture cross section of ^{235}U obtained through the numerical solution of the slowing down equation (SD), the narrow resonance approximation (NR), and the wide resonance approximation (WR)

Group number (XMAS 172 group)	Upper energy [eV]	Calculation method			Difference [%]	
		S.D.	N.R.	W.R.	(N.R. – S.D.)/ S.D.	(W.R. – S.D.)/S.D.
45	1.11E+04	1.063	1.063	1.063	0.00	0.00
46	9.12E+03	1.216	1.216	1.216	0.00	0.00
47	7.47E+03	1.261	1.261	1.261	0.00	0.00
48	5.53E+03	1.246	1.246	1.246	0.00	0.00
49	5.00E+03	1.458	1.458	1.458	0.01	0.00
50	3.53E+03	1.667	1.667	1.667	0.00	0.00
51	3.35E+03	1.825	1.825	1.825	0.00	0.00
52	2.25E+03	3.948	3.948	3.950	0.00	0.04
53	2.03E+03	3.292	3.292	3.293	-0.01	0.03
54	1.51E+03	2.801	2.801	2.802	0.00	0.04
55	1.43E+03	3.460	3.460	3.462	-0.02	0.04
56	1.23E+03	4.392	4.392	4.395	0.00	0.06
57	1.01E+03	5.085	5.084	5.088	-0.01	0.06
58	9.14E+02	4.505	4.505	4.507	-0.01	0.03
59	7.49E+02	4.798	4.796	4.806	-0.04	0.17
60	6.77E+02	5.226	5.225	5.232	-0.02	0.12
61	4.54E+02	5.069	5.069	5.073	-0.01	0.06
62	3.72E+02	7.121	7.120	7.128	-0.02	0.09
63	3.04E+02	8.422	8.423	8.449	0.01	0.32
64	2.04E+02	10.840	10.837	10.861	-0.03	0.20
65	1.49E+02	10.432	10.427	10.440	-0.05	0.07
66	1.37E+02	12.841	12.834	12.855	-0.06	0.11
67	9.17E+01	12.150	12.128	12.162	-0.17	0.10
68	7.57E+01	11.336	11.322	11.323	-0.12	-0.11
69	6.79E+01	13.380	13.381	13.394	0.01	0.11
70	5.56E+01	18.998	18.985	19.001	-0.07	0.02
71	5.16E+01	31.862	31.845	31.854	-0.05	-0.02
72	4.83E+01	15.778	15.768	15.763	-0.07	-0.09
73	4.55E+01	20.648	20.639	20.653	-0.04	0.02
74	4.02E+01	18.433	18.380	18.408	-0.29	-0.13

■ Table 9 (continued)

Group number (XMAS 172 group)	Upper energy [eV]	Calculation method			Difference [%]	
		S.D.	N.R.	W.R.	(N.R. – S.D.)/ S.D.	(W.R. – S.D.)/S.D.
75	3.73E+01	38.266	38.331	38.328	0.17	0.16
76	3.37E+01	37.883	37.813	37.856	–0.18	–0.07
77	3.05E+01	9.621	9.622	9.621	0.01	0.00
78	2.76E+01	6.655	6.653	6.652	–0.03	–0.04
79	2.50E+01	41.271	41.293	41.279	0.05	0.02
80	2.26E+01	28.951	28.899	28.927	–0.18	–0.08
81	1.95E+01	33.076	32.867	32.933	–0.63	–0.43
82	1.59E+01	14.145	14.135	14.134	–0.07	–0.08
83	1.37E+01	66.431	66.467	66.524	0.05	0.14
84	1.12E+01	6.232	6.233	6.234	0.02	0.03
85	9.91E+00	17.173	17.189	17.186	0.09	0.08
86	9.19E+00	63.474	63.361	63.344	–0.18	–0.21
87	8.32E+00	4.426	4.427	4.426	0.01	0.00
88	7.52E+00	56.860	57.016	56.963	0.27	0.18
89	6.16E+00	5.579	5.578	5.577	–0.02	–0.05
90	5.35E+00	3.515	3.515	3.515	0.00	0.00
91	5.04E+00	21.761	21.734	21.716	–0.13	–0.21
92	4.13E+00	2.133	2.133	2.133	0.00	0.00

Background cross section = 1,000 barn, 293 K, homogeneous mixture of ^{235}U and hydrogen; values are in barn.

The discussion in [3.4.3](#) clarifies that the difference between the NR and WR approximations can be found in their differing treatment of the scattering cross section of a resonant nuclide. In other words, the scattering cross section of a resonant nuclide is fully incorporated in the NR approximation, but is completely neglected in the WR approximation. This observation naturally provides for an intermediate approach, that is, only a part of the scattering cross section of a resonant nuclide is taken into account:

$$\begin{aligned}
 \phi(E) &= \frac{\lambda N_r \sigma_{p,r} + \sum_{k \neq r} N_k \sigma_{p,k}}{N_r \sigma_{a,r}(E) + \lambda N_r \sigma_{p,r} + \sum_{k \neq r} N_k \sigma_{p,k}} \frac{1}{E} \\
 &= \frac{\lambda \sigma_{p,r} + \sigma_0}{\sigma_{a,r}(E) + \lambda \sigma_{p,r} + \sigma_0} \frac{1}{E} \tag{83}
 \end{aligned}$$

where λ is the IR parameter. The NR and WR approximations correspond to $\lambda = 1$ and $\lambda = 0$, respectively. By choosing an appropriate IR parameter, (83) gives better accuracy for resonances of intermediate width.

Historically, the IR parameter was introduced to provide an analytical expression for the energy dependence of the neutron flux at resonances of intermediate width. However, in the practical world of lattice physics computing, slowing down calculations are carried out by the numerical solution of (70) during the stage of cross section libraries; we can thus accurately evaluate the energy dependence of the neutron flux even for resonances of intermediate width. In this sense, an analytical expression for the energetic behavior of neutron flux is no longer necessary in order to evaluate the effective cross section.

In spite of the above description, the IR parameter still plays a very important role in today's lattice physics computation. In the slowing down calculations, the "effective" width of a resonance depends not only on the actual width of the resonance peak, but also on the average increment of lethargy (average energy loss) in the collision between a neutron and a target nuclide.

Let us assume a resonance peak. This resonance peak is "narrow" when hydrogen is used as a moderator nuclide. The same resonance peak, however, would be "wide" when a neutron loses its energy due to collisions with a heavier nuclide (e.g., oxygen, uranium). This discussion suggests that the width of resonance effectively depends also on the mass of the moderator nuclide. The IR parameter can be used to correct the mass effect of a moderator nuclide. \blacktriangleright Table 10 shows the effective capture cross sections of ^{238}U in the 172 XMAS groups when various nuclides are assumed as moderator. This result was obtained through a numerical solution of the slowing down equation. The background cross section in \blacktriangleright Table 10, which influences the magnitude of the self-shielding effect, is assumed to be 50 barns.

\blacktriangleright Table 10 clearly indicates that the mass of the moderator nuclide has a significant impact on the effective cross sections even if the background cross section is the same. The actual dependence of the effective cross section on the mass of the moderator nuclide is somewhat complicated, as can be seen in this table. However, heavy nuclides generally contribute less to the background cross section than do light nuclides such as hydrogen, since the energy loss of a neutron through a collision is much smaller and also the IR factor is small for resonant nuclides. Since the variation in the effective cross section in \blacktriangleright Table 10 comes from the superficial "relative width" of a resonance peak, it would be adequately captured by the IR parameter. In order to apply the IR parameter to all nuclides, (83) is extended as follows:

$$\phi(E) = \frac{\lambda_r \sigma_{p,r} + \sigma_0}{\sigma_{a,r}(E) + \lambda_r \sigma_{p,r} + \sigma_0} \frac{1}{E} \quad (84)$$

$$\sigma_0 = \left(\sum_{k \neq r} \lambda_k N_k \sigma_{s,k} \right) / N_r \quad (85)$$

where λ_r and λ_k are the IR parameters for resonance nuclide r and the non-resonance nuclide k , respectively. Equation (84) indicates that the scattering of all nuclides is taken into account with use of the IR parameter, that is, the "effective" scattering cross section is used through $\lambda_k \sigma_{s,k}$. When nuclide k is hydrogen, $\lambda_k = 1$, while $\lambda_k < 1$ for other nuclides. In general, the value of the IR parameter becomes smaller when the mass of a nuclide becomes heavier.

■ Table 10

Moderator mass effect on effective microscopic capture cross section of ^{238}U . Hydrogen, oxygen, and uranium are considered as the moderator nuclides

Group number (XMAS 172 group)	Upper energy [eV]	Moderator nuclide			Difference [%]	
		H	^{16}O	^{238}U	$(^{16}\text{O}-\text{H})/\text{H}$	$(^{238}\text{U}-\text{H})/\text{H}$
45	1.11E+04	0.649	0.649	0.652	0.03	0.40
46	9.12E+03	0.594	0.594	0.596	0.03	0.38
47	7.47E+03	0.732	0.731	0.726	-0.06	-0.79
48	5.53E+03	0.779	0.779	0.778	0.01	-0.06
49	5.00E+03	0.738	0.738	0.740	0.03	0.34
50	3.53E+03	0.754	0.754	0.749	-0.07	-0.73
51	3.35E+03	0.943	0.942	0.934	-0.11	-1.00
52	2.25E+03	0.748	0.747	0.750	-0.12	0.20
53	2.03E+03	0.881	0.881	0.877	-0.07	-0.54
54	1.51E+03	0.666	0.665	0.664	-0.10	-0.23
55	1.43E+03	1.003	1.003	0.999	-0.08	-0.44
56	1.23E+03	1.341	1.340	1.329	-0.07	-0.91
57	1.01E+03	1.091	1.087	1.053	-0.30	-3.50
58	9.14E+02	1.296	1.297	1.300	0.04	0.29
59	7.49E+02	1.406	1.402	1.375	-0.32	-2.21
60	6.77E+02	1.331	1.329	1.295	-0.12	-2.72
61	4.54E+02	1.406	1.405	1.402	-0.08	-0.33
62	3.72E+02	0.755	0.752	0.696	-0.38	-7.77
63	3.04E+02	1.826	1.814	1.703	-0.65	-6.76
64	2.04E+02	1.577	1.571	1.375	-0.37	-12.80
65	1.49E+02	1.294	1.317	1.422	1.83	9.91
66	1.37E+02	2.791	2.752	1.882	-1.41	-32.57
67	9.17E+01	2.137	2.113	2.116	-1.14	-0.99
68	7.57E+01	0.371	0.369	0.359	-0.56	-3.30
69	6.79E+01	4.747	4.930	7.026	3.84	47.99
70	5.56E+01	0.101	0.101	0.101	0.01	0.01
71	5.16E+01	0.144	0.144	0.144	0.00	-0.09
72	4.83E+01	0.173	0.173	0.173	-0.03	-0.13
73	4.55E+01	0.517	0.516	0.507	-0.08	-1.91
74	4.02E+01	5.799	5.731	4.711	-1.16	-18.76
75	3.73E+01	25.817	27.635	51.450	7.04	99.29

■ Table 10 (continued)

Group number (XMAS 172 group)	Upper energy [eV]	Moderator nuclide			Difference [%]	
		H	¹⁶ O	²³⁸ U	(¹⁶ O-H)/H	(²³⁸ U-H)/H
76	3.37E+01	0.873	0.885	0.898	1.40	2.89
77	3.05E+01	0.398	0.398	0.399	-0.13	0.31
78	2.76E+01	0.459	0.459	0.458	-0.03	-0.13
79	2.50E+01	1.154	1.152	1.119	-0.11	-3.04
80	2.26E+01	27.675	27.550	13.338	-0.45	-51.81
81	1.95E+01	1.172	1.237	1.309	5.53	11.64
82	1.59E+01	0.349	0.350	0.351	0.17	0.43
83	1.37E+01	0.343	0.342	0.339	-0.09	-1.09
84	1.12E+01	0.849	0.848	0.829	-0.11	-2.40
85	9.91E+00	0.508	0.507	0.506	-0.02	-0.22
86	9.19E+00	0.868	0.867	0.859	-0.08	-1.07
87	8.32E+00	2.411	2.405	2.299	-0.23	-4.64
88	7.52E+00	45.716	42.732	12.215	-6.53	-73.28
89	6.16E+00	5.207	5.686	6.598	9.19	26.71
90	5.35E+00	1.905	1.896	1.919	-0.49	0.71
91	5.04E+00	1.216	1.220	1.238	0.31	1.75
92	4.13E+00	0.783	0.783	0.784	0.00	0.05

Background cross section = 50 barn, ²⁹³K, edited in 172 XMAS groups.

Numerical Procedure

A detailed procedure to evaluate the IR parameter is presented below (MacFarlane and Muir 1994a):

1. Case 1: Perform the slowing down calculation with a homogeneous mixture of hydrogen and a resonance nuclide (e.g., ²³⁸U). The composition of the homogeneous mixture is adjusted to give a typical background cross section for a resonance nuclide. For example, in the case of ²³⁸U in a light water reactor lattice, 50 barn may be used. The evaluated effective cross section is σ_{Case1} .
2. Case 2: Perform another slowing down calculation with a homogeneous mixture of hydrogen and the resonance nuclide used in Case 1. The composition of the homogeneous mixture is slightly changed from that in Case 1 so that the background cross section for the resonance nuclide is increased slightly. If the background cross section cannot be directly specified in the slowing down calculation, the number density of the moderator nuclide is adjusted. In Case 2, for example, 55 barn is used, a number density that is 10% more than that in Case 1. The evaluated effective cross section is σ_{Case2} .
3. Case 3: Perform the third slowing down calculation with a homogeneous mixture of another moderator nuclide (e.g., oxygen) and the resonance nuclide used in Case 1. The composition of the homogeneous mixture is adjusted to give the same background cross section as in Case 2. Since the (potential) scattering cross section is different among nuclides, the

■ Table 11

IR parameter for the microscopic absorption cross section of ^{238}U in 172-groups XMAS energy structure

Group number (XMAS172)	Upper energy [eV]	a= 16 Background XS (barn)			a= 40 Background XS (barn)			a= 238 Background XS (barn)		
		50	1,000	10,000	50	1,000	10,000	50	1,000	10,000
57	1.01E+03	0.995	0.997	0.998	0.990	0.993	0.994	0.897	0.949	0.956
60	6.77E+02	0.998	0.999	0.999	0.997	0.999	0.999	0.899	0.942	0.946
63	3.04E+02	0.991	0.994	0.994	0.980	0.987	0.987	0.764	0.872	0.890
64	2.04E+02	0.965	0.983	0.990	0.916	0.951	0.968	0.494	0.704	0.808
66	1.37E+02	0.970	0.988	0.990	0.919	0.968	0.975	0.357	0.715	0.793
69	6.79E+01	1.000	1.000	1.000	0.992	0.982	0.985	0.328	0.682	0.776
75	3.73E+01	1.000	1.000	1.000	1.000	1.000	1.000	0.191	0.466	0.648
80	2.26E+01	0.986	0.993	0.994	0.949	0.983	0.984	0.148	0.415	0.591
88	7.52E+00	0.872	0.977	0.988	0.654	0.938	0.969	0.043	0.198	0.348

293 K; a represents the mass number; Lower energy for group 88 is 6.16 eV.

composition of the homogeneous mixture is changed accordingly from that in Case 2. In the case of oxygen, the potential scattering cross section is approximately 3.9 barn, while that of hydrogen is 20.5 barn. Thus, the number density of oxygen in Case 3 will be $20.5/3.9 \approx 5.25$ times larger than that of hydrogen in Case 2. The evaluated effective cross section is σ_{Case3} . When the NJOY code is used, one can arbitrarily set the mass of the admixed moderator. Therefore, we can easily perform Case 3 in the NJOY code, as will be described later (MacFarlane and Muir 1994a).

4. Compute the IR parameter by

$$\lambda = \frac{\sigma_{\text{Case3}} - \sigma_{\text{Case1}}}{\sigma_{\text{Case2}} - \sigma_{\text{Case1}}} \quad (86)$$

In (86), the variation in the effective cross section and that of the background cross section is assumed to have a linear relationship. This treatment is justified since the background cross section and the effective cross section has smooth correlation as shown in Fig. 22 and variation of the background cross section is very small in the above calculation.

Examples of evaluation results of the IR parameter for the ^{238}U and ^{235}U absorption cross section are shown in Tables 11 and 12, respectively. In both tables, the 172-group XMAS-type energy group structure is assumed. In the 88th group (7.52 eV–6.16 eV), which includes the large resonance of ^{238}U , the IR parameters for oxygen ($a = 16$), light nuclides ($a = 40$), and uranium ($a = 238$) are approximately 0.87, 0.65, and 0.04, respectively, when the background cross section is 50 barn. This result clearly shows the significance of the IR parameter in the resonance calculation.

Table 12 provides other interesting observations. The IR parameters for ^{235}U are clearly different from those for ^{238}U . For example, the IR parameters of the ^{235}U absorption cross section for oxygen, light nuclide, and uranium are 1.0, 0.77, and 0.15, respectively, in the 88th group. Since the width of the resonance peak for ^{235}U is generally narrower than that for ^{238}U , the IR

■ Table 12

IR parameter for the microscopic absorption cross section of ^{235}U in 172-groups XMAS energy structure

Group number (XMAS172)	Upper energy [eV]	a= 16 Background XS (barn)			a= 40 Background XS (barn)			a= 238 Background XS (barn)		
		50	1,000	10,000	50	1,000	10,000	50	1,000	10,000
62	3.72E+02	0.999	0.996	1.000	0.980	0.979	1.000	0.926	0.925	0.923
63	3.04E+02	0.952	0.972	0.975	0.932	0.961	0.963	0.824	0.869	0.877
64	2.04E+02	0.992	0.997	0.988	0.995	0.999	1.000	0.814	0.867	0.866
66	1.37E+02	1.000	1.000	1.000	1.000	1.000	1.000	0.911	0.917	0.918
67	9.17E+01	1.000	1.000	1.000	1.000	1.000	1.000	0.669	0.718	0.739
68	7.57E+01	1.000	1.000	1.000	1.000	1.000	1.000	0.922	0.924	0.927
69	6.79E+01	0.955	0.960	0.964	0.811	0.873	0.885	0.430	0.526	0.554
70	5.56E+01	0.958	0.988	0.990	1.000	1.000	1.000	0.629	0.692	0.711
71	5.16E+01	1.000	1.000	1.000	0.958	0.933	0.929	0.767	0.784	0.797
75	3.73E+01	0.956	0.970	0.972	0.981	0.973	0.976	0.183	0.461	0.540
79	2.50E+01	0.989	0.987	0.988	0.915	0.941	0.947	0.747	0.711	0.712
81	1.95E+01	0.990	1.000	1.000	0.954	0.955	0.968	0.350	0.443	0.522
83	1.37E+01	0.974	0.985	0.986	0.990	0.961	0.967	0.370	0.485	0.537
86	9.19E+00	1.000	1.000	1.000	1.000	1.000	1.000	0.331	0.327	0.374
88	7.52E+00	1.000	1.000	1.000	0.775	0.874	0.889	0.154	0.287	0.333

293 K; a represents mass number; Lower energy for group 88 is 6.16 eV.

parameter becomes larger than that of ^{238}U . The systematic estimation of the IR parameter clarifies that the IR parameter depends not only on the resonance nuclide, but also on the magnitude of the background cross section, the temperature, and the energy range (energy group).

The above observation highlights a conflict with (84), which is commonly used in many lattice physics codes. In that equation, the IR parameter is assumed to be a constant that is inherent to each moderator nuclide, that is, the dependency of the IR parameter on various other parameters (temperature, background cross section, and energy range) cannot be directly incorporated. This is a limitation of the conventional IR method, in which only one IR parameter is considered for each nuclide.

We should therefore choose an appropriate IR parameter for each nuclide. First, since ^{238}U is a dominant resonance absorber in light water reactor calculations, ^{238}U can be assumed as a typical resonance absorber. For the background cross section, a typical value for ^{238}U (e.g., 50 barn) can be assumed. For the energy range, the major resonance of ^{238}U in 6.7 eV is considered a typical resonance. Fortunately, temperature has less impact on the IR parameter, since hot operating conditions will be used in the evaluation of the IR parameter.

Some additional discussion related to the IR parameter will be useful. In today's lattice physics codes, the tabulation of an effective cross section (more generally, a cross section library) is performed through a nuclear data processing code such as NJOY (MacFarlane and Muir 1994a). In NJOY, the mass of a moderator nuclide and its background cross section are given

independently through user input. The former is given as the $\alpha = \left(\frac{A-1}{A+1}\right)^2$ parameter for the admixed moderator, and the latter is given by a combination of the fraction of the admixed moderator cross section γ and the background cross section σ_0 . Note that the cross section of the admixed moderator is given by $\gamma\sigma_0$. The remaining part, that is, $(1 - \gamma)\sigma_0$, is generally assumed to be hydrogen.

In conventional lattice physics codes, the mass effect of the moderator is treated through the above approach, that is, correction by the IR parameter. However, when we can freely draw a blueprint of a cross section library for a lattice physics code, the mass effect of the moderator can be incorporated by a correction table that is similar to a self-shielding factor table. In this case, the library has a correction table for each nuclide, which gives the correction factor of the effective cross section for various masses of the moderator. Although the size of such a library will be larger than that of the current one, one can expect it to yield a more accurate treatment. Such a consideration becomes especially useful when lattice physics codes are applied to non-LWRs, for example, heavy water reactors, graphite reactors, and fast reactors.

3.5 Resonance Self-Shielding in a Heterogeneous Systems

3.5.1 Neutron Slowing Down in a Heterogeneous Isolated System

Formulation of Neutron Slowing Down Equation

In this subsection, we will discuss resonance self-shielding in a heterogeneous system (Dirac 1943; Weinberg and Wigner 1958; Dresner 1960; Rosenstein 1960; Goldstein and Cohen 1962; Stamm'ler and Abbate 1983; Rothenstein and Segev 1986). Since various difficulties arise in the treatment of a heterogeneous system, we will start with an isolated system, in which there is an isolated lump of resonance material in a large moderator. A fuel rod in a large moderator region, for example, is an isolated system.

Since it is necessary to know the energy dependence of the neutron spectrum in detail in order to evaluate the effect of resonance shielding, we will consider the neutron slowing down equation in an isolated heterogeneous system:

$$\begin{aligned} \Sigma_{t,f}(E)\phi_f(E)V_f = P_{f \rightarrow f}(E)V_f \int_0^\infty dE' \Sigma_{s,f}(E' \rightarrow E)\phi_f(E') \\ + P_{m \rightarrow f}(E)V_m \int_0^\infty dE' \Sigma_{s,m}(E' \rightarrow E)\phi_m(E') \end{aligned} \quad (87)$$

where

$\Sigma_{t,f}(E)$: macroscopic total cross section in fuel,

$\Sigma_{s,f}(E' \rightarrow E)$: macroscopic scattering cross section in fuel,

$\Sigma_{s,m}(E' \rightarrow E)$: macroscopic scattering cross section in moderator,

$\phi_f(E), \phi_m(E')$: neutron fluxes in fuel and moderator, respectively,

V_f, V_m : volumes of fuel and moderator, respectively, and

$P_{f \rightarrow f}(E), P_{m \rightarrow f}(E)$: fuel-to-fuel, and moderator-to-fuel collision probabilities, respectively.

Space dependent neutron transport can be described in various ways, for example, the discrete-ordinates method, or the method of characteristics. However, the collision probability method is well suited to describe the neutron balance in fuel and moderator regions, since in a simple system, analytical approaches with some approximations can be applied to collision probabilities.

The approximations involved for the collision probability calculation have a crucial meaning in the equivalence theory, as will be discussed later.

If we assume that the neutron slowing down is dominated by elastic scattering, the right-hand side of (87) can be written as

$$\begin{aligned} \Sigma_{t,f}(E)\phi_f(E)V_f &= P_{f\rightarrow f}(E)V_f \sum_{k\in f} \int_E^{E/\alpha_k} \frac{dE' N_k \sigma_{es,k}(E') \phi_f(E')}{(1-\alpha_k)E'} \\ &+ P_{m\rightarrow f}(E)V_m \sum_{k\in m} \int_E^{E/\alpha_k} \frac{dE' N_k \sigma_{es,k}(E') \phi_m(E')}{(1-\alpha_k)E'} \end{aligned} \quad (88)$$

where k is a nuclide index.

When the NR approximation discussed in 3.4.2 is applied to the right-hand side of (88), it becomes

$$\Sigma_{t,f}(E)\phi_f(E)V_f = \frac{1}{E} (P_{f\rightarrow f}(E)V_f \Sigma_{p,f} + P_{m\rightarrow f}(E)V_m \Sigma_{p,m}) \quad (89)$$

where

$\Sigma_{p,f}$: macroscopic potential scattering cross section of fuel, and
 $\Sigma_{p,m}$: macroscopic potential scattering cross section of moderator.

In an isolated system, the fuel-to-fuel collision probability can be written as the fuel-to-moderator collision probability

$$P_{f\rightarrow f}(E) = 1 - P_{f\rightarrow m}(E) \quad (90)$$

where

$P_{f\rightarrow m}(E)$: fuel-to-moderator collision probability.

Equation (90) can be derived from the normalization condition of collision probability, that is, the sum of the collision probabilities for fuel-to-fuel, and fuel-to-moderator, is unity. By substituting (90) into (89), we obtain

$$\Sigma_{t,f}(E)\phi_f(E)V_f = \frac{1}{E} ((1 - P_{f\rightarrow m}(E)) V_f \Sigma_{p,f} + P_{m\rightarrow f}(E) V_m \Sigma_{p,m}) \quad (91)$$

Reciprocity Theorem

Two different collision probabilities now appear in (91). A further simplification can be made to derive the analytic form for the energy dependence of the neutron spectrum in the fuel region. Next, we will consider the reciprocity theorem

$$P_{m\rightarrow f}(E) V_m \Sigma_{p,m} = P_{f\rightarrow m}(E) V_f \Sigma_{t,f}(E) \quad (92)$$

In (92), the total cross section of the moderator is assumed to be equal to the potential scattering cross section, which is energy independent.

An intuitive understanding of (92) is as follows. Equation (92) is rewritten as

$$\frac{P_{m\rightarrow f}(E)}{V_f \Sigma_{t,f}(E)} = \frac{P_{f\rightarrow m}(E)}{V_m \Sigma_{p,m}} \quad (93)$$

Since $P_{m \rightarrow f}(E)$ is the collision probability from moderator to fuel, it is proportional to the attenuation between moderator and fuel, the fuel volume, and the total cross section of the fuel. Therefore, $P_{m \rightarrow f}(E)/(V_f \Sigma_{t,f}(E))$ represents the attenuation between moderator and fuel. A similar consideration of $P_{f \rightarrow m}(E)$ yields $P_{f \rightarrow m}(E)(V_m \Sigma_{p,m})$ that is the attenuation between fuel and moderator. Since the neutron attenuation between two points does not have directional dependence (i.e., attenuation from A to B is equivalent to attenuation from B to A), we achieve the equality of (93). Note that $\Sigma_{p,m}$ and $\Sigma_{t,m}$ are assumed to be equal in the above discussion.

By substituting (92) into (91), we obtain

$$\phi_f(E) = \frac{1}{E} \left((1 - P_{f \rightarrow m}(E)) \frac{\Sigma_{p,f}}{\Sigma_{t,f}(E)} + P_{f \rightarrow m}(E) \right) \quad (94)$$

If an accurate value for the fuel-to-moderator collision probability $P_{f \rightarrow m}(E)$ is known, the accurate energy dependence of the neutron flux can be evaluated using (94). A detailed numerical calculation for $P_{f \rightarrow m}(E)$ would give, of course, an accurate result, but such numerical calculation would require considerable computation time. An approximate analytic expression for $P_{f \rightarrow m}(E)$ is therefore needed for an efficient evaluation of the energy dependence of the neutron flux. This approach yields an important by-product: the concept of equivalence between heterogeneous and homogeneous systems, which will be discussed later.

Estimation of Escape Probability and Average Chord Length

In an isolated system, the collision probability from the fuel-to-moderator region is equivalent to the neutron escape probability from the fuel, $P_e(E)$, which is defined by the probability that a neutron born in the fuel region will escape from the fuel without a collision in the fuel, and will suffer its first collision in the moderator.


The escape probability of a neutron, which is flying in direction $\vec{\Omega}$, and whose distance to the fuel lump surface is s , is given by $\exp(-\Sigma_{t,f}(E)s)$. Since the small volume around the neutron is expressed as $(\vec{n} \cdot \vec{\Omega}) dS ds$, the volume average of the escape probability for direction $\vec{\Omega}$ is given by

$$\begin{aligned} P_e(E, \vec{\Omega}) &= \frac{1}{V_f} \int_S (\vec{n} \cdot \vec{\Omega}) dS \int_0^l \exp(-\Sigma_{t,f}(E)s) ds \\ &= \frac{1}{\Sigma_{t,f}(E)V_f} \int_S (\vec{n} \cdot \vec{\Omega}) dS \{1 - \exp(-\Sigma_{t,f}(E)l)\} \end{aligned} \quad (95)$$

where

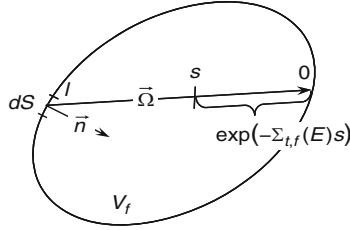
- $\vec{\Omega}$: neutron flight direction,
- \vec{n} : normal vector to surface,
- S : surface area of a fuel lump,
- l : track length of neutron in a fuel lump (chord length), and
- s : coordinate along neutron flight direction.

Note that the integration of (95) is carried out for $\vec{n} \cdot \vec{\Omega} > 0$.

The physical meaning of (95) can be explained by  Fig. 16.

Since $P_e(E, \vec{\Omega})$ depends on $\vec{\Omega}$, the average on $\vec{\Omega}$ is considered in order to obtain the final form of $P_e(E)$, that is,

$$P_e(E) = \frac{1}{4\pi} \int_{\vec{n} \cdot \vec{\Omega} > 0} P_e(E, \vec{\Omega}) d\vec{\Omega} \quad (96)$$



■ **Figure 16**
Calculation of escape probability

Using (95) and (96), the escape probability from an isolated fuel lump is given as follows:

$$\begin{aligned} P_e(E) &= \frac{1}{4\pi V_f} \int_{\vec{n} \cdot \vec{\Omega} > 0} d\vec{\Omega} \int_S (\vec{n} \cdot \vec{\Omega}) dS \int_0^l \exp(-\Sigma_{t,f}(E)s) ds \\ &= \frac{1}{4\pi \Sigma_{t,f}(E) V_f} \int_{\vec{n} \cdot \vec{\Omega} > 0} d\vec{\Omega} \int_S dS (\vec{n} \cdot \vec{\Omega}) \{1 - \exp(-\Sigma_{t,f}(E)l)\} \end{aligned} \quad (97)$$

In order to obtain a detailed form of (97), the distribution function of chord length l , which also depends on $\vec{\Omega}$, is necessary. The distribution function of the chord length is given as follows (Dirac 1943):

$$f(l)dl = \frac{\int_l^{l+dl} d\vec{\Omega} \int_S dS (\vec{n} \cdot \vec{\Omega})}{\int_{\vec{n} \cdot \vec{\Omega} > 0} d\vec{\Omega} \int_S dS (\vec{n} \cdot \vec{\Omega})} \quad (98)$$

The value of $f(l)dl$ represents the probability of the chord length's appearance between l and $l + dl$. ► **Figure 16** presents $(\vec{n} \cdot \vec{\Omega})dS$ as the weight of a chord, whose direction is $\vec{\Omega}$, and which cuts the surface area of dS . As a result, the numerator of (98) shows the summation of the weights of chords whose lengths are between l and $l + dl$, and the denominator shows the summation of the weight of all chords.

The denominator of (98) can be rewritten as follows:

$$\begin{aligned} \int_{\vec{n} \cdot \vec{\Omega} > 0} d\vec{\Omega} \int_S dS (\vec{n} \cdot \vec{\Omega}) &= \int_{\cos \theta > 0} d\vec{\Omega} \int_S dS \cos \theta = \int_0^1 \mu d\vec{\Omega} \int_S dS \\ &= \int_0^1 2\pi \mu d\mu \int_S dS = \pi S \end{aligned} \quad (99)$$

where

$$\begin{aligned} \mu &= \cos \theta, \\ d\vec{\Omega} &= \cos \theta d\theta \int_0^{2\pi} d\varphi = 2\pi d\mu. \end{aligned}$$

The average chord length \bar{l} is given by

$$\bar{l} = \int_0^\infty l f(l) dl \quad (100)$$

■ Table 13

Parameters for resonance calculation in simple heterogeneous geometry

Geometry	Surface area	Volume	Average chord length
Slab (H : width of slab)	$2S$	SH	$2H$
Cylinder (R : radius)	$2\pi R$	πR^2	$2R$
Hollow cylinder*	$2\pi(R+r)$	$\pi(R^2-r^2)$	$2(R-r)$
Sphere (R : radius)	$4\pi R^2$	$4\pi R^3/3$	$4R/3$

*Void is assumed for hollow part. Inner radius is r .

By substituting (98) and (99) into (100), we obtain

$$\bar{l} = \frac{1}{\pi S} \int_{4\pi} d\vec{\Omega} \int_S dS l(\vec{n} \cdot \vec{\Omega}) = \frac{1}{\pi S} \int_{4\pi} d\vec{\Omega} V = \frac{V \cdot 4\pi}{\pi S} = \frac{4V}{S} \quad (101)$$

Note that the following relationship is used in the above derivation:

$$\int_S dS l(\vec{n} \cdot \vec{\Omega}) = V \quad (102)$$

A chord in a lump and its nearby volume constitutes a small “cylinder,” whose bottom area and height are dS and $l(\vec{n} \cdot \vec{\Omega})$, respectively. Thus, $dS l(\vec{n} \cdot \vec{\Omega})$ indicates the volume of the small cylinder in which a chord is contained. Therefore, the integration of the volume of each small cylinder gives the total volume of a lump.

Equation (101) suggests that the average chord length is given by the volume and the surface area of a lump. Typical average chord lengths using simple geometry, which frequently appear in lattice physics computations, are summarized in ► Table 13.

Using (98), (99), and (101), (98) can be rewritten as

$$\int_l^{l+dl} d\vec{\Omega} \int_S dS(\vec{n} \cdot \vec{\Omega}) = \pi S \cdot f(l) dl = \frac{4\pi V}{\bar{l}} f(l) dl \quad (103)$$

By substituting (103) into (97), we obtain

$$\begin{aligned} P_e(E) &= \frac{1}{4\pi \Sigma_{t,f}(E) V_f} \int_{\vec{n} \cdot \vec{\Omega} > 0} d\vec{\Omega} \int_S dS(\vec{n} \cdot \vec{\Omega}) \{1 - \exp(-\Sigma_{t,f}(E)l)\} \\ &= \frac{1}{4\pi \Sigma_{t,f}(E) V_f} \int_0^\infty \int_l^{l+dl} d\vec{\Omega} \int_S dS(\vec{n} \cdot \vec{\Omega}) \{1 - \exp(-\Sigma_{t,f}(E)l)\} \\ &= \frac{1}{4\pi \Sigma_{t,f}(E) V_f} \int_0^\infty \frac{4\pi V_f}{\bar{l}} f(l) dl \{1 - \exp(-\Sigma_{t,f}(E)l)\} \\ &= \frac{1}{\Sigma_{t,f}(E) \bar{l}} \int_0^\infty dl f(l) \{1 - \exp(-\Sigma_{t,f}(E)l)\} \end{aligned} \quad (104)$$

When the actual form of the chord distribution function is known, an analytic form of the escape probability can be derived. Though the actual chord distribution function depends on the shape of the fuel lump, we assume it is given by the following:

$$f(l) dl = \frac{1}{\bar{l}} \exp(-l/\bar{l}) dl \quad (105)$$

Equation (105) indicates the probability of a longer chord existing exponentially decreases as the length of the chord increases (Sauer 1963). Such a distribution is, clearly, a poor approximation for many shapes. The form of (105) remains important, however, if we are to derive the equivalence between heterogeneous and homogeneous systems.

By substituting (105) into (104), we obtain

$$\begin{aligned}
 P_e(E) &= \frac{1}{\Sigma_{t,f}(E)\bar{l}} \int_0^\infty dl f(l) \{1 - \exp(-\Sigma_{t,f}(E)l)\} \\
 &= \frac{1}{\Sigma_{t,f}(E)\bar{l}} \int_0^\infty dl \frac{1}{l} \exp(-l/\bar{l}) \{1 - \exp(-\Sigma_{t,f}(E)l)\} \\
 &= \frac{1}{\Sigma_{t,f}(E)\bar{l} + 1}
 \end{aligned} \tag{106}$$

Equation (106) is Wigner's rational approximation for the escape probability (Weinberg and Wigner 1958). Equation (106) suggests that the escape probability from a lump, which has a great optical thickness $\Sigma_{t,f}(E)\bar{l}$, becomes smaller. This is the case for a large total cross section and/or large average chord length. On the contrary, when the optical thickness of a lump is small, the escape probability approaches unity. Such a situation can be observed in a small lump with a small total cross section. We see then, that Wigner's rational approximation satisfies our intuitive sense of the physical properties of the escape probability. In fact, Wigner's rational approximation gives an accurate value for the black limit (infinite $\Sigma_{t,f}(E)\bar{l}$, $P_e(E) = 0$) and the white limit (zero $\Sigma_{t,f}(E)\bar{l}$, $P_e(E) = 1$).

Approximations of Neutron Spectrum in a Heterogeneous System

By approximating the escape probability using the rational approximation in (106), we can derive the "equivalence" between heterogeneous and homogeneous systems, as follows.

Equation (94) is rewritten as follows:

$$\begin{aligned}
 \phi_f(E) &= \frac{1}{E} \left((1 - P_{f \rightarrow m}(E)) \frac{\Sigma_{p,f}}{\Sigma_{t,f}(E)} + P_{f \rightarrow m}(E) \right) \\
 &= \frac{1}{E} \left((1 - P_e(E)) \frac{\Sigma_{p,f}}{\Sigma_{t,f}(E)} + P_e(E) \right)
 \end{aligned} \tag{107}$$

By substituting (106) into (107), we can derive the following equation:

$$\begin{aligned}
 \phi_f(E) &= \frac{1}{E} \left(\left(1 - \frac{1}{\Sigma_{t,f}(E)\bar{l} + 1} \right) \frac{\Sigma_{p,f}}{\Sigma_{t,f}(E)} + \frac{1}{\Sigma_{t,f}(E)\bar{l} + 1} \right) \\
 &= \frac{1}{E} \frac{\Sigma_{p,f}\bar{l} + 1}{\Sigma_{t,f}(E)\bar{l} + 1} \\
 &= \frac{1}{E} \frac{\Sigma_{p,f} + 1/\bar{l}}{\Sigma_{t,f}(E) + 1/\bar{l}}
 \end{aligned}$$

$$\begin{aligned}
&= \frac{1}{E} \frac{\Sigma_{p,f} + \Sigma_e}{\Sigma_{t,f}(E) + \Sigma_e} \\
&= \frac{1}{E} \frac{N_r(\sigma_{p,r} + \sigma_{0,f}) + \Sigma_e}{N_r(\sigma_{t,r}(E) + \sigma_{0,f}) + \Sigma_e} \\
&= \frac{1}{E} \frac{\sigma_{p,r} + (\sigma_{0,f} + \Sigma_e/N_r)}{\sigma_{t,r}(E) + (\sigma_{0,f} + \Sigma_e/N_r)} \tag{108}
\end{aligned}$$

where

Σ_e : macroscopic escape cross section,

N_r : number density of the resonance nuclide,

$\sigma_{p,r}$: potential scattering cross section of the resonance nuclide, and

$\sigma_{0,f} = \sum_{k \neq r} N_k \sigma_{s,k} / N_r$: background cross section for the resonance nuclide.

The escape cross section is defined by the inverse of the average chord length ($\Sigma_e = 1/\bar{l}$). When the average chord length is small, the escape cross section becomes large, and vice versa. This suggests that the escape cross section is related to the escape probability from a fuel lump.

Various assumptions are used to derive the above equivalence between heterogeneous and homogeneous systems. They are summarized as follows:

- No resonance overlap is considered.
- Nonresonant nuclide has a constant scattering cross section.
- Resonant nuclide has a constant scattering cross section.
- Neutron slowing down is dominated by elastic scattering.
- Energy dependence of neutron flux at nonresonant part is asymptotic ($1/E$).
- Use of narrow resonance (NR) approximation for neutron slowing down source.
- The escape probability from a lump is approximated by Wigner's rational approximation, that is, (106).

The accuracy of (108) thus depends on the validity of the above assumptions. The approximation for the escape probability, particularly, has a significant impact on the equivalence theory.

3.5.2 Equivalence Theory

When we compare (77) and (108), an apparent similarity can be found. Indeed, by adding the escape cross section to both the numerator and the denominator of (77), we can derive (108). The physical interpretation of this relationship is given as follows.

When a fuel lump has a large escape probability (i.e., an optically thin lump), neutrons entering from the moderator can easily reach everywhere in the fuel lump. This means that the energy dependence (depression) of the neutron flux at the resonance peak is mitigated by the incoming neutrons from the moderator. In other words, neutrons in a fuel lump with a large escape probability will likely experience a collision in the moderator, so that the depression of the neutron flux in the fuel becomes smaller. This effect is captured through the escape cross section. This is analogous to our discussion of the background cross section given by (78). In the previous discussion of a homogeneous system, we noted that the depression of the neutron flux at the resonance peak is mitigated by the background cross section.

The above discussion is the essence of the equivalence theory between heterogeneous and homogeneous systems, that is, the energy dependence of neutron flux can be approximated in the same analytic form by a different argument, σ_0 or $\sigma_{0,f} + \Sigma_e/N_r$.

To sum up, the background cross section with the NR approximation is given by
In a homogeneous system:

$$\sigma_{0,r} = \sum_{k \neq r} N_k \sigma_{p,k} / N_r = \sum_{k \neq r} N_k \sigma_{s,k} / N_r \quad (109)$$

In heterogeneous system:

$$\sigma_{0,r} = \sigma_{0,f} + \Sigma_e / N_r = \sum_{k \neq r} N_k \sigma_{s,k} / N_r + \Sigma_e / N_r \quad (110)$$

In other words, the effect of heterogeneity on the energy dependence of the neutron flux is represented by the fictitious escape cross section, which is equivalent to, and has the same effect as, the background cross section. Therefore, when the effective cross sections are tabulated for various background cross sections, the result can be used not only for a homogeneous system, but also for a heterogeneous system. From the viewpoint of cross section preparation, this equivalence significantly reduces the size of the tabulation table for effective cross sections. If the equivalence is not used, the effective cross sections for various heterogeneous systems will be tabulated independently. The tabulation of effective cross sections will be discussed in more detail in [3.6](#).

The distribution function of the chord length given by (105) is chosen in order to derive an analytic form of neutron flux that is consistent with that of a homogeneous system. This is a key point of the equivalence theory. In this context, other expressions for the escape probability can be used in the framework of the equivalence theory, as is discussed in [3.5.3](#).

3.5.3 Various Approximations for Escape Probability

Incorporation of the Bell Factor

In [3.5.1](#), the escape probability from a fuel lump was approximated by Wigner's rational approximation of (106) in order to achieve equivalence between heterogeneous and homogeneous systems. Though Wigner's rational approximation reflects our intuition regarding the behavior of the escape probability, better approximations can be used (Levine 1963; Carlvik 1967; Chiarella and Keane 1969; Mizuta 1970; Stamm'ler and Abbate 1983; Hébert and Marleau 1991). One of the improved rational approximations involves a correction by the Bell factor, as follows:

$$P_e(E) = \frac{a_B}{\Sigma_{t,f}(E)\bar{l} + a_B} = \frac{a_B \Sigma_e}{\Sigma_{t,f}(E) + a_B \Sigma_e} \quad (111)$$

where

a_B : the Bell factor.

The escape probability, $P_e(E)$, is a function of the total cross section and the shape of the fuel lump (i.e., the average chord length). Therefore, when the escape probability is evaluated by

an accurate method (e.g., numerical calculation by the collision probability method), the Bell factor can be evaluated by

$$a_B = \frac{P_e}{1 - P_e} \Sigma_{t,f} \bar{l} \quad (112)$$

In a typical situation that appears in LWR lattice physics computations, $a_B = 1.1$ – 1.4 gives adequate results (Levine 1963). By substituting (111) into (107), we obtain

$$\phi_f(E) = \frac{1}{E} \frac{\sigma_{p,r} + (\sigma_{0,f} + a_B \Sigma_e / N_r)}{\sigma_{t,r}(E) + (\sigma_{0,f} + a_B \Sigma_e / N_r)} \quad (113)$$

A comparison of (113) and (108) clarifies the merit of (111). In fact, the escape cross section is modified from Σ_e to $a_B \Sigma_e$ in (113). In other words, the escape probability (which is equivalent to the neutron inflow effect) is underestimated in Wigner's rational approximation as it is conventionally used, as given by (106).

Though the Bell factor is considered as an adjustment parameter, its range of validity can be mathematically derived as follows. When the value of $\Sigma_{t,f}(E) \bar{l}$ is small, (104) is approximated by the Taylor series expansion

$$\begin{aligned} P_e(E) &= \frac{1}{\Sigma_{t,f}(E) \bar{l}} \int_0^\infty dl f(l) \{1 - \exp(-\Sigma_{t,f}(E)l)\} \\ &\cong \frac{1}{\Sigma_{t,f}(E) \bar{l}} \int_0^\infty dl f(l) \left[1 - \left\{1 - \Sigma_{t,f}(E)l + (\Sigma_{t,f}(E)l)^2/2\right\}\right] \\ &= \frac{1}{\bar{l}} \int_0^\infty dl f(l)l - \frac{1}{2} \frac{\Sigma_{t,f}(E)}{\bar{l}} \int_0^\infty dl f(l)l^2 \\ &= 1 - \frac{1}{2} \Sigma_{t,f}(E) \frac{\bar{l}^2}{\bar{l}} \\ &\cong \frac{1}{1 + \frac{1}{2} \Sigma_{t,f}(E) \frac{\bar{l}^2}{\bar{l}}} \\ &= \frac{a_B}{\Sigma_{t,f}(E) \bar{l} + a_B} \end{aligned} \quad (114)$$

where

$$a_B = 2 \frac{(\bar{l})^2}{\bar{l}^2}.$$

The Schwarz inequality is established for arbitrary function $f(l)$.

$$\int l^2 f(l) dl > \left\{ \int l f(l) dl \right\}^2 \quad (115)$$

From (115), we have the following relationship:

$$\bar{l}^2 > (\bar{l})^2 \quad (116)$$

Therefore,

$$a_B = 2 \frac{(\bar{l})^2}{\bar{l}^2} < 2 \quad (117)$$

Utilization of the Bell factor increases the accuracy of the escape probability, which can be rigorously reproduced for a particular energy point (i.e., particular fuel cross section) by choosing an appropriate value for the Bell factor. However, such rigorous reproduction of the escape probability for all energy ranges (i.e., for various fuel cross sections) is impossible, so it still includes an error factor that has the potential to impact resonance calculations.

N-Terms Rational Approximations

Further improvement of the escape probability can be achieved by using the summation form of the rational approximations. In order to derive this approximation, the distribution function of the chord length is approximated by a summation of the exponential functions

$$f(l)dl = \sum_{n=1}^N c_n \exp(-d_n l) dl \quad (118)$$

By substituting (118) into (104), we obtain

$$\begin{aligned} P_e(E) &= \frac{1}{\Sigma_{t,f}(E)\bar{l}} \int_0^\infty dl \sum_{n=1}^N c_n \exp(-d_n l) \{1 - \exp(-\Sigma_{t,f}(E)l)\} \\ &= \frac{1}{\Sigma_{t,f}(E)\bar{l}} \sum_{n=1}^N c_n \int_0^\infty dl \exp(-d_n l) \{1 - \exp(-\Sigma_{t,f}(E)l)\} \\ &= \sum_{n=1}^N \frac{c_n/d_n}{\Sigma_{t,f}(E)\bar{l} + d_n\bar{l}} \\ &= \sum_{n=1}^N \frac{b_n a_n}{\Sigma_{t,f}(E)\bar{l} + a_n} \end{aligned} \quad (119)$$

where

$$\begin{aligned} a_n &= d_n \bar{l}, \\ b_n a_n &= c_n / d_n. \end{aligned}$$

For a very small optical length, (119) can be reduced into

$$P_e(E) = \lim_{\Sigma_{t,f}(E)\bar{l} \rightarrow 0} \sum_{n=1}^N \frac{b_n a_n}{\Sigma_{t,f}(E)\bar{l} + a_n} = \sum_{n=1}^N b_n \quad (120)$$

Since $P_e(E)$ should be approaching unity for a very small optical length, we obtain the normalization condition as follows:

$$\sum_{n=1}^N b_n = 1 \quad (121)$$

Wigner's rational approximation of (106) gives an accurate result for an escape probability with a large $\Sigma_{t,f}(E)\bar{l}$. In order to be consistent with the derivatives of (106) when there is large $\Sigma_{t,f}(E)\bar{l}$, the following constraint on the coefficients of (119) should be satisfied:

$$\sum_{n=1}^N b_n a_n = 1 \quad (122)$$

Note that (122) is an additional constraint, and may not necessarily be satisfied. For example, (111) and (124) do not satisfy (122).

Equation (119) is considered as a superposition of the rational approximations with the Bell factor, that is, a_n and b_n are the Bell factor for each rational approximation and the corresponding weight of each term.

Carlvik's Two-Term Rational Approximation

A well-known approximation for the escape probability for the cylindrical geometry in (119) is given by Carlvik et al. (Carlvik 1967; Stamm'ler and Abbate 1983):

$$P_e(E) = 2 \frac{2}{\Sigma_{t,f}(E)\bar{l} + 2} - \frac{3}{\Sigma_{t,f}(E)\bar{l} + 3} \quad (123)$$

For slab geometry, Roman gives the following (Stamm'ler and Abbate 1983):

$$P_e(E) = 1.1 \frac{1.4}{\Sigma_{t,f}(E)\bar{l} + 1.4} - 0.1 \frac{5.4}{\Sigma_{t,f}(E)\bar{l} + 5.4} \quad (124)$$

The three term rational approximation is also considered to increase the accuracy of the escape probability from a fuel lump (Hébert and Marleau 1991).

By substituting (119) into (107), we obtain

$$\begin{aligned} \phi_f(E) &= \frac{1}{E} \left((1 - P_e(E)) \frac{\Sigma_{p,f}}{\Sigma_{t,f}(E)} + P_e(E) \right) \\ &= \frac{1}{E} \left(\left(1 - \sum_{n=1}^N \frac{b_n a_n}{\Sigma_{t,f}(E)\bar{l} + a_n} \right) \frac{\Sigma_{p,f}}{\Sigma_{t,f}(E)} + \sum_{n=1}^N \frac{b_n a_n}{\Sigma_{t,f}(E)\bar{l} + a_n} \right) \\ &= \frac{1}{E} \left(\left(\sum_{n=1}^N b_n - \sum_{n=1}^N \frac{b_n a_n}{\Sigma_{t,f}(E)\bar{l} + a_n} \right) \frac{\Sigma_{p,f}}{\Sigma_{t,f}(E)} + \sum_{n=1}^N \frac{b_n a_n}{\Sigma_{t,f}(E)\bar{l} + a_n} \right) \\ &= \frac{1}{E} \left(\sum_{n=1}^N b_n \frac{\Sigma_{t,f}(E)\bar{l}}{\Sigma_{t,f}(E)\bar{l} + a_n} \frac{\Sigma_{p,f}}{\Sigma_{t,f}(E)} + \sum_{n=1}^N \frac{b_n a_n}{\Sigma_{t,f}(E)\bar{l} + a_n} \right) \\ &= \frac{1}{E} \sum_{n=1}^N b_n \frac{\Sigma_{p,f}\bar{l} + a_n}{\Sigma_{t,f}(E)\bar{l} + a_n} \\ &= \frac{1}{E} \sum_{n=1}^N b_n \frac{\sigma_{p,r} + \sigma_{0,f} + a_n/\bar{l}/N_r}{\sigma_{t,r}(E) + \sigma_{0,f} + a_n/\bar{l}/N_r} \\ &= \frac{1}{E} \sum_{n=1}^N b_n \frac{\sigma_{p,r} + \sigma_{0,f} + a_n \Sigma_e / N_r}{\sigma_{t,r}(E) + \sigma_{0,f} + a_n \Sigma_e / N_r} \\ &= \frac{1}{E} \sum_{n=1}^N b_n \frac{\sigma_{p,r} + \sigma_{0,n}}{\sigma_{t,r}(E) + \sigma_{0,n}} \end{aligned} \quad (125)$$

where

$$\sigma_{0,n} = \sigma_{0,f} + a_n \Sigma_e / N_r.$$

Evaluation of the Effective Cross Section from N-Term Rational Approximation

Equation (125) is given by the superposition of (113). Though the background cross section for each term in (125) is given by $\sigma_{0,n} = \sigma_{0,f} + a_n \Sigma_e / N_r$, it cannot be directly applied to the interpolation of effective cross sections, due to the superposition of several terms. In this case, the equivalent background cross section for (125) is given as follows:

$$\begin{aligned}
 \sigma_{g,x} &= \frac{\int_{E_g}^{E_{g-1}} dE \sigma_x(E) \phi_f(E)}{\int_{E_g}^{E_{g-1}} dE \phi_f(E)} \\
 &= \frac{\int_{E_g}^{E_{g-1}} dE \sigma_x(E) \frac{1}{E} \sum_{n=1}^N b_n \frac{\sigma_{p,r} + \sigma_{0,n}}{\sigma_{t,r}(E) + \sigma_{0,n}}}{\int_{E_g}^{E_{g-1}} dE \frac{1}{E} \sum_{m=1}^N b_m \frac{\sigma_{p,r} + \sigma_{0,m}}{\sigma_{t,r}(E) + \sigma_{0,m}}} \\
 &= \sum_{n=1}^N b_n \frac{\int_{E_g}^{E_{g-1}} dE \sigma_x(E) \frac{1}{E} \frac{\sigma_{p,r} + \sigma_{0,n}}{\sigma_{t,r}(E) + \sigma_{0,n}}}{\int_{E_g}^{E_{g-1}} dE \frac{1}{E} \frac{\sigma_{p,r} + \sigma_{0,n}}{\sigma_{t,r}(E) + \sigma_{0,n}}} \frac{\int_{E_g}^{E_{g-1}} dE \frac{1}{E} \frac{\sigma_{p,r} + \sigma_{0,n}}{\sigma_{t,r}(E) + \sigma_{0,n}}}{\int_{E_g}^{E_{g-1}} dE \frac{1}{E} \sum_{m=1}^N b_m \frac{\sigma_{p,r} + \sigma_{0,m}}{\sigma_{t,r}(E) + \sigma_{0,m}}} \quad (126)
 \end{aligned}$$

In order to simplify (126), we can use the following relationship:

$$\sigma_{g,x,n} = \frac{\int_{E_g}^{E_{g-1}} dE \sigma_x(E) \phi_n(E)}{\int_{E_g}^{E_{g-1}} dE \phi_n(E)} = \frac{\int_{E_g}^{E_{g-1}} dE \sigma_x(E) \frac{1}{E} \frac{\sigma_{p,r} + \sigma_{0,n}}{\sigma_{t,r}(E) + \sigma_{0,n}}}{\int_{E_g}^{E_{g-1}} dE \frac{1}{E} \frac{\sigma_{p,r} + \sigma_{0,n}}{\sigma_{t,r}(E) + \sigma_{0,n}}} \quad (127)$$

In (127), $\sigma_{g,x,n}$ is a effective cross section whose background cross section is given by $\sigma_{0,n}$.

Next, we use the following relationship:

$$\begin{aligned}
 \sigma_{g,a,n} &= \frac{\int_{E_g}^{E_{g-1}} dE \sigma_{a,r}(E) \phi_n(E)}{\int_{E_g}^{E_{g-1}} dE \phi_n(E)} = \frac{\int_{E_g}^{E_{g-1}} dE \frac{1}{E} \sigma_{a,r}(E) \frac{\sigma_{p,r} + \sigma_{0,n}}{\sigma_{t,r}(E) + \sigma_{0,n}}}{\int_{E_g}^{E_{g-1}} dE \frac{1}{E} \frac{\sigma_{p,r} + \sigma_{0,n}}{\sigma_{t,r}(E) + \sigma_{0,n}}} \\
 &= \frac{\int_{E_g}^{E_{g-1}} dE \frac{1}{E} \sigma_{a,r}(E) \frac{\sigma_{p,r} + \sigma_{0,n}}{\sigma_{t,r}(E) + \sigma_{0,n}}}{\int_{E_g}^{E_{g-1}} dE \frac{1}{E} \frac{\sigma_{p,r} + \sigma_{a,r}(E) - \sigma_{a,r}(E) + \sigma_{0,n}}{\sigma_{t,r}(E) + \sigma_{0,n}}} \\
 &= \frac{\int_{E_g}^{E_{g-1}} dE \frac{1}{E} \sigma_{a,r}(E) \frac{\sigma_{p,r} + \sigma_{0,n}}{\sigma_{t,r}(E) + \sigma_{0,n}}}{\int_{E_g}^{E_{g-1}} dE \frac{1}{E} - \int_{E_g}^{E_{g-1}} dE \frac{1}{E} \sigma_{a,r}(E) \frac{\sigma_{p,r} + \sigma_{0,n}}{\sigma_{t,r}(E) + \sigma_{0,n}} \frac{1}{\sigma_{p,r} + \sigma_{0,n}}} \\
 &= \frac{\int_{E_g}^{E_{g-1}} dE \frac{1}{E} \sigma_{a,r}(E) \frac{\sigma_{p,r} + \sigma_{0,n}}{\sigma_{t,r}(E) + \sigma_{0,n}}}{\int_{E_g}^{E_{g-1}} dE \frac{1}{E} - \frac{1}{\sigma_{p,r} + \sigma_{0,n}} \int_{E_g}^{E_{g-1}} dE \frac{1}{E} \sigma_{a,r}(E) \frac{\sigma_{p,r} + \sigma_{0,n}}{\sigma_{t,r}(E) + \sigma_{0,n}}} \quad (128)
 \end{aligned}$$

From (128), we have

$$\int_{E_g}^{E_{g-1}} dE \frac{1}{E} \sigma_{a,r}(E) \frac{\sigma_{p,r} + \sigma_{0,n}}{\sigma_{t,r}(E) + \sigma_{0,n}} \bigg/ \int_{E_g}^{E_{g-1}} dE \frac{1}{E} = \frac{\sigma_{g,a,n}}{1 + \frac{\sigma_{g,a,n}}{\sigma_{p,r} + \sigma_{0,n}}} \quad (129)$$

By using (129), we can derive the following equation:

$$\begin{aligned} & \frac{\int_{E_g}^{E_{g-1}} dE \frac{1}{E} \frac{\sigma_{p,r} + \sigma_{0,n}}{\sigma_{t,r}(E) + \sigma_{0,n}}}{\int_{E_g}^{E_{g-1}} dE \frac{1}{E} \sum_{m=1}^N b_m \frac{\sigma_{p,r} + \sigma_{0,m}}{\sigma_{t,r}(E) + \sigma_{0,m}}} \\ &= \frac{\int_{E_g}^{E_{g-1}} dE \frac{1}{E} \frac{\sigma_{p,r} + \sigma_{0,n}}{\sigma_{t,r}(E) + \sigma_{0,n}}}{\sum_{m=1}^N b_m \int_{E_g}^{E_{g-1}} dE \frac{1}{E} \frac{\sigma_{p,r} + \sigma_{0,m}}{\sigma_{t,r}(E) + \sigma_{0,m}}} \\ &= \frac{\int_{E_g}^{E_{g-1}} dE \frac{1}{E} \frac{\sigma_{p,r} + \sigma_{a,r}(E) - \sigma_{a,r}(E) + \sigma_{0,n}}{\sigma_{t,r}(E) + \sigma_{0,n}}}{\sum_{m=1}^N b_m \int_{E_g}^{E_{g-1}} dE \frac{1}{E} \frac{\sigma_{p,r} + \sigma_{a,r}(E) - \sigma_{a,r}(E) + \sigma_{0,m}}{\sigma_{t,r}(E) + \sigma_{0,m}}} \\ &= \frac{\int_{E_g}^{E_{g-1}} dE \frac{1}{E} - \int_{E_g}^{E_{g-1}} dE \frac{1}{E} \sigma_{a,r}(E) \frac{\sigma_{p,r} + \sigma_{0,n}}{\sigma_{t,r}(E) + \sigma_{0,n}} \frac{1}{\sigma_{p,r} + \sigma_{0,n}}}{\sum_{m=1}^N b_m \left(\int_{E_g}^{E_{g-1}} dE \frac{1}{E} - \int_{E_g}^{E_{g-1}} dE \frac{1}{E} \sigma_{a,r}(E) \frac{\sigma_{p,r} + \sigma_{0,m}}{\sigma_{t,r}(E) + \sigma_{0,m}} \frac{1}{\sigma_{p,r} + \sigma_{0,m}} \right)} \\ &= \frac{1 - \frac{1}{\sigma_{p,r} + \sigma_{0,n}} \int_{E_g}^{E_{g-1}} dE \frac{1}{E} \sigma_{a,r}(E) \frac{\sigma_{p,r} + \sigma_{0,n}}{\sigma_{t,r}(E) + \sigma_{0,n}} \bigg/ \int_{E_g}^{E_{g-1}} dE \frac{1}{E}}{\sum_{m=1}^N b_m \left(1 - \frac{1}{\sigma_{p,r} + \sigma_{0,m}} \int_{E_g}^{E_{g-1}} dE \frac{1}{E} \sigma_{a,r}(E) \frac{\sigma_{p,r} + \sigma_{0,m}}{\sigma_{t,r}(E) + \sigma_{0,m}} \bigg/ \int_{E_g}^{E_{g-1}} dE \frac{1}{E} \right)} \\ &= \frac{1 - \frac{1}{\sigma_{p,r} + \sigma_{0,n}} \frac{\sigma_{g,a,n}}{1 + \sigma_{g,a,n}/(\sigma_{p,r} + \sigma_{0,n})}}{\sum_{m=1}^N b_m \left(1 - \frac{1}{\sigma_{p,r} + \sigma_{0,m}} \frac{\sigma_{g,a,m}}{1 + \sigma_{g,a,m}/(\sigma_{p,r} + \sigma_{0,m})} \right)} \\ &= \frac{f_n}{\sum_{m=1}^N b_m f_m} \quad (130) \end{aligned}$$

where

$$f_n = \frac{\sigma_{p,r} + \sigma_{0,n}}{\sigma_{p,r} + \sigma_{0,n} + \sigma_{g,a,n}}.$$

Finally, by using (127) and (130), (126) is rewritten as follows:

$$\sigma_{g,x} = \frac{\sum_{n=1}^N w_n \sigma_{g,x,n}}{\sum_{n=1}^N w_n} \quad (131)$$

where

$$w_n = b_n f_n.$$

Resonance Integral and Effective Cross Section

When the resonance integral is tabulated in a cross section library, the following relationship can be used (Stamm'ler et al. 1973):

$$\begin{aligned}
 \sigma_{g,x} &= \frac{\int_{E_g}^{E_{g-1}} dE \sigma_x(E) \phi_f(E)}{\int_{E_g}^{E_{g-1}} dE \phi_f(E)} \\
 &= \frac{\int_{E_g}^{E_{g-1}} dE \sigma_x(E) \frac{1}{E} \sum_{n=1}^N b_n \frac{\sigma_{p,r} + \sigma_{0,n}}{\sigma_{t,r}(E) + \sigma_{0,n}}}{\int_{E_g}^{E_{g-1}} dE \frac{1}{E} \sum_{n=1}^N b_n \frac{\sigma_{p,r} + \sigma_{0,n}}{\sigma_{t,r}(E) + \sigma_{0,n}}} \\
 &= \frac{\sum_{n=1}^N b_n \int_{E_g}^{E_{g-1}} dE \sigma_x(E) \frac{1}{E} \frac{\sigma_{p,r} + \sigma_{0,n}}{\sigma_{t,r}(E) + \sigma_{0,n}}}{\sum_{n=1}^N b_n \int_{E_g}^{E_{g-1}} dE \frac{1}{E} \frac{\sigma_{p,r} + \sigma_{0,n}}{\sigma_{t,r}(E) + \sigma_{0,n}}} \\
 &= \frac{\sum_{n=1}^N b_n \left(\int_{E_g}^{E_{g-1}} (dE/E) \right) \cdot I_{g,x}(\sigma_{0,n})}{\sum_{n=1}^N b_n \int_{E_g}^{E_{g-1}} dE \frac{1}{E} \left(1 - \frac{\sigma_{a,r}(E)}{\sigma_{t,r}(E) + \sigma_{0,n}} \right)} \\
 &= \frac{\sum_{n=1}^N b_n \left(\int_{E_g}^{E_{g-1}} (dE/E) \right) \cdot I_{g,x}(\sigma_{0,n})}{\sum_{n=1}^N b_n \left(\int_{E_g}^{E_{g-1}} (dE/E) \right) - \sum_{n=1}^N b_n \int_{E_g}^{E_{g-1}} dE \sigma_{a,r}(E) \frac{1}{E} \frac{\sigma_{p,r} + \sigma_{0,n}}{\sigma_{t,r}(E) + \sigma_{0,n}} \frac{1}{\sigma_{p,r} + \sigma_{0,n}}} \\
 &= \frac{\sum_{n=1}^N b_n \left(\int_{E_g}^{E_{g-1}} (dE/E) \right) \cdot I_{g,x}(\sigma_{0,n})}{\left(\int_{E_g}^{E_{g-1}} (dE/E) \right) - \sum_{n=1}^N b_n \left(\int_{E_g}^{E_{g-1}} (dE/E) \right) \cdot I_{g,a}(\sigma_{0,n}) / (\sigma_{p,r} + \sigma_{0,n})} \\
 &= \frac{\sum_{n=1}^N b_n I_{g,x}(\sigma_{0,n})}{1 - \sum_{n=1}^N b_n I_{g,a}(\sigma_{0,n}) / (\sigma_{p,r} + \sigma_{0,n})} \tag{132}
 \end{aligned}$$

where $I_{g,x}$ is the resonance integral per unit lethargy width as defined by

$$I_{g,x}(\sigma_{0,n}) = \frac{\int_{E_g}^{E_{g-1}} dE \sigma_x(E) \phi_n(E)}{\int_{E_g}^{E_{g-1}} dE \frac{1}{E}} \approx \frac{\int_{E_g}^{E_{g-1}} dE \sigma_x(E) \left(\frac{1}{E} \frac{\sigma_{p,r} + \sigma_{0,n}}{\sigma_{t,r}(E) + \sigma_{0,n}} \right)}{\int_{E_g}^{E_{g-1}} dE \frac{1}{E}}$$

The resonance integral, which is the energy integration of the reaction rate that is defined by $\int_{E_g}^{E_{g-1}} dE \sigma_x(E) \phi(E)$, is used instead of the effective cross section in the resonance calculation of

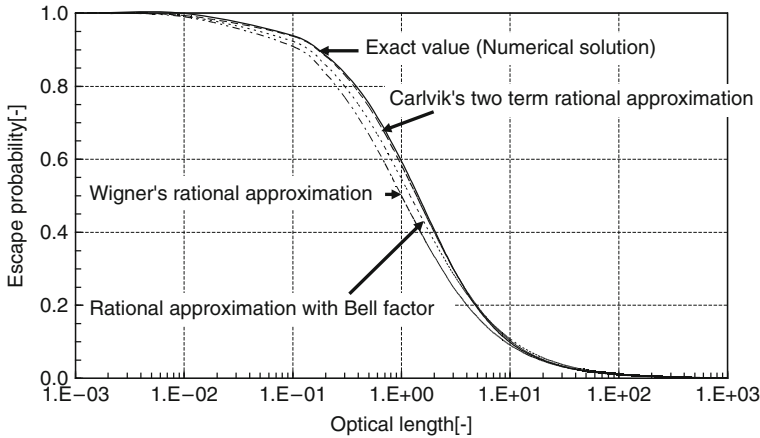


Figure 17

Comparison of various approximations for the escape probability from an infinite cylinder. The horizontal axis shows the average optical length of an infinite cylinder, that is, diameter multiplied by the macroscopic total cross section

some lattice physics codes, for example, the WIMS code. The resonance integral and the effective cross section can be converted into each other using (181), and can thus be considered as almost “equivalent” quantities. As a shortcut for (132), the following can be used as an “equivalent” background cross section:

$$\bar{\sigma}_0 = \left(\sum_{n=1}^N b_n \sqrt{\sigma_{0,n}} \right)^2 \quad (133)$$

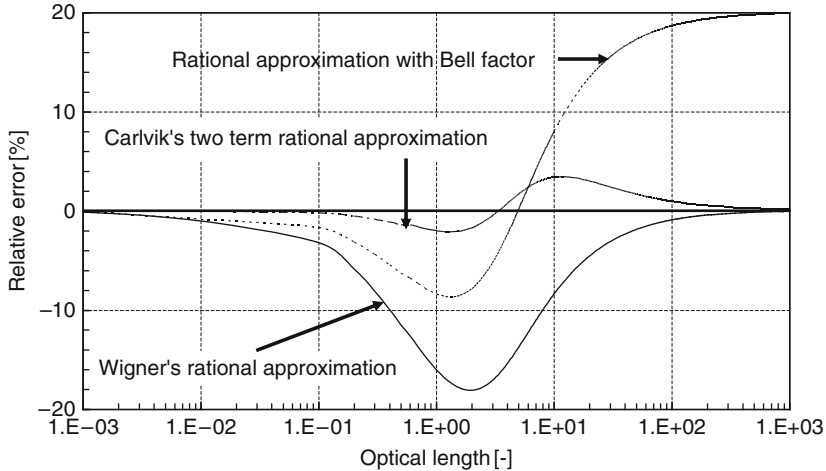
The above relationship is justified, since the resonance integral has a strong correlation with the square root of the background cross section for the practical value of background cross sections, as will be discussed in Sect. 3.6.3 with reference to Fig. 22.

We have thus far described three different approximations for the escape probability. Figures 17 and 18 show the accuracy of these approximations for an infinite cylindrical fuel lump. Carlvik’s two-term rational approximation of (123) clearly gives better results than the others, and Wigner’s approximation with the Bell factor is the next best. Wigner’s rational approximation as conventionally used gives accurate results for the white and the black limits, but shows a considerable discrepancy at a medium optical thickness, which is mainly the case in common LWR lattice calculations.

3.5.4 Neutron Slowing Down in a Heterogeneous Lattice System

Formulation of Slowing Down Equation in Lattice System

In Sect. 3.5.1, we discussed the energy dependence of the neutron flux in an isolated fuel lump, in which a neutron escaping from one fuel lump never enters other fuel lumps. In an actual fuel assembly, however, many fuel rods are packed in one assembly, so that neutrons that escape from one fuel rod do in fact enter other fuel rods. In this case, the “effective” escape



■ Figure 18

Accuracy of various approximations for the escape probability from an infinite cylinder. The horizontal axis shows the average optical length of the infinite cylinder, that is, the diameter multiplied by the macroscopic total cross section

from a fuel is reduced, so the energy dependence of the neutron flux is affected (Dresner 1960; Rosenstein 1960).

Let us consider an ideal fuel assembly in which the fuel rods are very tightly packed. If there is no gap between fuel pellets (i.e., no moderator and cladding in a fuel assembly), the energy dependence of the neutron flux will be identical to that in a homogeneous system composed of only fuel material. This suggests that the energy dependence of the neutron flux can be roughly expressed as an intermediate dynamic between that found in isolated heterogeneous and homogeneous systems.

The equivalence theory gives a unified description of the energy dependence of the neutron flux in isolated and homogeneous systems. From (108), the neutron flux in an isolated fuel lump is expressed as

$$\phi_f(E) = \frac{1}{E} \frac{\sigma_{p,r} + (\sigma_{0,f} + \Sigma_e/N_r)}{\sigma_{t,r}(E) + (\sigma_{0,f} + \Sigma_e/N_r)} \quad (134)$$

When the escape cross section Σ_e becomes zero, (134) is reduced into that in the homogeneous system given by (77). That is, (134), which is based on the equivalence theory, can express the neutron flux in both heterogeneous and homogeneous systems. We can therefore expect that the neutron flux in a heterogeneous lattice system can also be described in the framework of the equivalence theory, if we adjust the escape cross section. The final goal of this subsection, then, is to derive a definition of the escape cross section in lattice systems.

In the following part, we first discuss a regular lattice system, which consists of an infinite regular array of fuel rods. A regular lattice system, however, does not apply to actual fuel assemblies because they contain many irregularities, for example, guide and instrumentation thimbles in PWR, water channels, gap water, and part length rods in BWR. Such irregularities

have, of course, an impact on neutron flux. Treatment to account for these irregularities will be also discussed later in this subsection.

We begin with the neutron balance equation for a heterogeneous system:

$$\Sigma_{t,f}(E)\phi_f(E)V_f = \sum_j P_{j \rightarrow f}(E)V_j \int_0^\infty dE' \Sigma_{s,j}(E' \rightarrow E)\phi_j(E') \quad (135)$$

where

j : region number in a heterogeneous system, which includes the fuel in question, the moderator, and other fuels.

Recalling the derivation of (89), (135) can be transformed with the NR approximation into the following:

$$\phi_f(E) = \frac{1}{E} \sum_j \frac{P_{j \rightarrow f}(E)V_j \Sigma_{p,j}}{\Sigma_{t,f}(E)V_f} \quad (136)$$

We then consider (137) and (138), which are the normalization conditions of the collision probabilities, and the reciprocity theorem discussed in (92), respectively

$$\sum_{j \neq m} P_{f \rightarrow j}(E) = 1 - P_{f \rightarrow m}(E) \quad (137)$$

$$P_{j \rightarrow f}(E)V_j \Sigma_{t,j}(E) = P_{f \rightarrow j}(E)V_f \Sigma_{t,f}(E) \quad (138)$$

In an actual system composed of multiple regions, m in (137) includes not only the moderator, but also other regions, with the exception of fuel (e.g., cladding). By substituting (137) and (138) into (136), (136) can be rewritten as follows:

$$\begin{aligned} \phi_f(E) &= \frac{1}{E} \sum_j \frac{P_{j \rightarrow f}(E)V_j \Sigma_{p,j}}{\Sigma_{t,f}(E)V_f} \\ &= \frac{1}{E} \sum_j \frac{P_{f \rightarrow j}(E)V_f \Sigma_{t,f}(E)}{\Sigma_{t,j}(E)} \frac{\Sigma_{p,j}}{\Sigma_{t,f}(E)V_f} \\ &= \frac{1}{E} \sum_j \frac{P_{f \rightarrow j}(E)\Sigma_{p,j}}{\Sigma_{t,j}(E)} \\ &= \frac{1}{E} \left(\sum_{j \neq m} \frac{P_{f \rightarrow j}(E)\Sigma_{p,j}}{\Sigma_{t,j}(E)} + \frac{P_{f \rightarrow m}(E)\Sigma_{p,m}}{\Sigma_{t,m}(E)} \right) \\ &\cong \frac{1}{E} \left(\frac{\Sigma_{p,f}}{\Sigma_{t,f}(E)} \sum_{j \neq m} P_{f \rightarrow j}(E) + P_{f \rightarrow m}(E) \right) \\ &= \frac{1}{E} \left((1 - P_{f \rightarrow m}(E)) \frac{\Sigma_{p,f}}{\Sigma_{t,f}(E)} + P_{f \rightarrow m}(E) \right) \end{aligned} \quad (139)$$

In the above derivation, we applied an important assumption, namely, that the macroscopic total cross sections in the fuel regions are spatially constant. This assumption is justified because identical or similar compositions are used in an LWR fuel assembly. However, the above assumption could introduce a crucial error for fuel assemblies of various compositions. Furthermore, no absorption is assumed for the moderator region; that is, the total cross section and the (potential) scattering cross section are identical in the moderator region. Also, the scattering reaction is dominated by the potential scattering, which has an energetically constant cross section.

Dancoff Correction or Dancoff Factor

When (139) and (94) are compared, we can find that they have an identical form, that is, the neutron fluxes in both isolated and lattice systems can be described by a unified analytical form. Note that the above discussion assumes the same composition of fuel, but the regularity of the lattice is not assumed. In this context, (139) can be applied to irregular and general arrangements of heterogeneous fuel.

In the case of an isolated system, the collision probability from the fuel to the moderator is evaluated as the escape probability from the fuel, and is approximated by the rational approximation in order to derive the equivalence between heterogeneous and homogeneous systems. Thus, a similar approach will be useful for (139).

In a lattice system, the number of neutrons entering a fuel region decreases, since part of the neutrons in the moderator region is absorbed into “other” fuels. In other words, other fuels make “shadows” for the fuel we consider. In order to consider the shadowing effect in a lattice system, the Dancoff correction C is used (Stamm’ler and Abbate 1983; Sugimura and Yamamoto 2006):

$$C = \frac{I_0 - I}{I_0} \quad (140)$$

where

I_0 : number of neutrons entering the fuel region in an isolated system,

I : number of neutrons entering the fuel region in question in a lattice system.

When the number of entering neutrons is the same in both isolated and lattice systems, the Dancoff correction is zero ($I = I_0$). On the contrary, when the number of neutrons from the moderator region is fully shadowed, that is, $I = 0$, the Dancoff correction is 1. Thus, the Dancoff correction represents the degree of the shadowing effect by other fuel rods.

The Dancoff correction can also be defined in terms of the reduction of the escape probability. That is, some of the neutrons escaping from a fuel may have their next collision in other fuels. On the contrary, in the case of an isolated fuel (with a convex shape), all neutrons escaping from a fuel have their next collision in the moderator. Thus, the “effective” neutron escape probability from a fuel is reduced in lattice geometry.

Dancoff Correction and Collision Probability in the Moderator

When the thickness of the moderator is l , the un-collided probability between fuels is given by $\exp(-\Sigma_{t,m}l)$. Here l is defined by the distance between one fuel from which a neutron escapes, and another fuel in which the neutron has a collision. Thus, the Dancoff correction is given by the following equation:

$$C = \frac{\int_{\vec{n} \cdot \vec{\Omega} > 0} d\vec{\Omega} \int_S dS (\vec{n} \cdot \vec{\Omega}) \exp(-\Sigma_{t,m}l)}{\int_{\vec{n} \cdot \vec{\Omega} > 0} d\vec{\Omega} \int_S dS (\vec{n} \cdot \vec{\Omega})} \quad (141)$$

In the case of isolated geometry, the Dancoff correction is zero, since $\exp(-\Sigma_{t,m}l)$ is zero for infinite l . When the isotropic neutron source is uniformly distributed, (140) and (141) give identical results, which can be proved through selected formulations (Kobayashi 1995). Since approximations for (141) can be derived more easily than those for (140), in the following discussion we will consider (141). Note that (140) is used for the neutron current method and the

enhanced neutron current method, which are suitable for the evaluation of the Dancoff correction in complicated and large geometries (Sugimura and Yamamoto 2006; Yamamoto 2009). Explanations of these methods will be given later.

In order to discuss the characteristics of the Dancoff correction, an approximate expression for the Dancoff correction will be derived, though it is not used in actual lattice physics calculations. We now consider the chord length distribution in the moderator region, $f(l)dl$, which is a concept similar to the escape probability from a fuel discussed in [3.5.1](#). With the chord distribution function, the Dancoff correction is given by

$$C = \int_0^{\infty} dl f(l) \exp(-\Sigma_{t,m} l) \quad (142)$$

[Equation \(142\)](#) indicates that the Dancoff correction is given by the average of probability that there will not be a collision with the moderator. In some lattice physics computations, the Dancoff factor D is also used:

$$\begin{aligned} D &= 1 - C = 1 - \int_0^{\infty} dl f(l) \exp(-\Sigma_{t,m} l) \\ &= \int_0^{\infty} dl f(l) - \int_0^{\infty} dl f(l) \exp(-\Sigma_{t,m} l) \\ &= \int_0^{\infty} dl f(l) \{1 - \exp(-\Sigma_{t,m} l)\} \end{aligned} \quad (143)$$

In order to incorporate the Dancoff correction into the equivalence theory, approximations similar to those used for the escape probability from fuel are applied to the Dancoff correction. First, the chord length distribution is approximated by the exponential function, which is used for the escape probability from fuel, that is, [\(105\)](#):

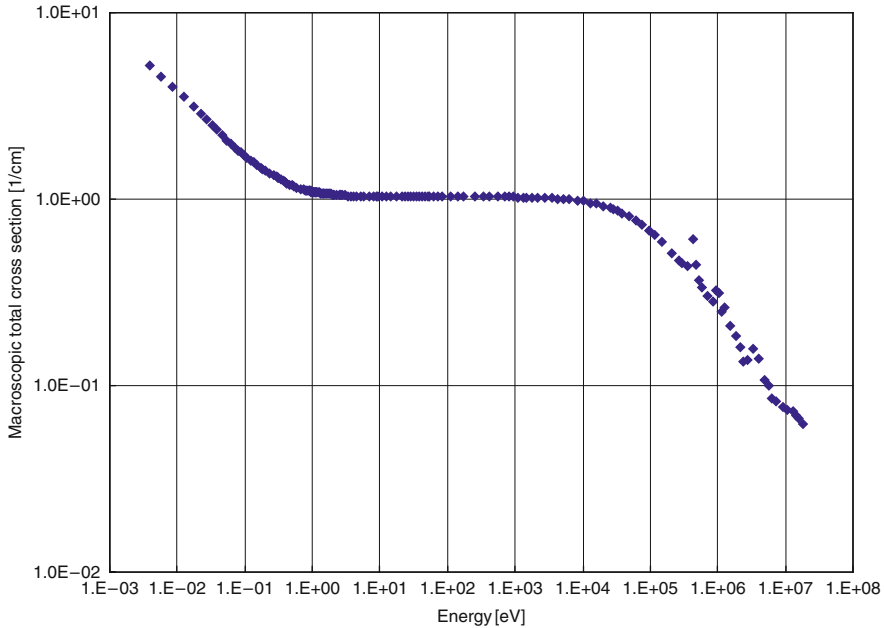
$$f(l)dl = \begin{cases} 0 & (l < l_m) \\ \frac{1}{\bar{l} - l_m} \exp\{-(l - l_m)/(\bar{l} - l_m)\} d(l - l_m) & (l \geq l_m) \end{cases} \quad (144)$$

where l_m is the minimum thickness of the moderator between two fuels. From the definition, the chord length function is zero for $l < l_m$. Therefore, the chord length distribution for the moderator is defined by the parallel translation of the chord length distribution for a fuel region, which is given by [\(105\)](#). By substituting [\(144\)](#) into [\(142\)](#), we obtain

$$\begin{aligned} C &= \int_0^{\infty} dl f(l) \exp(-\Sigma_{t,m} l) \\ &= \int_{l_m}^{\infty} \frac{1}{\bar{l} - l_m} \exp\{-(l - l_m)/(\bar{l} - l_m)\} \exp(-\Sigma_{t,m} l) d(l - l_m) \\ &= \frac{\exp(-\Sigma_{t,m} l_m)}{\Sigma_{t,m} \cdot (\bar{l} - l_m) + 1} \end{aligned} \quad (145)$$

[\(145\)](#), particularly, becomes Wigner's rational approximation for the escape probability from the moderator when $l_m = 0$:

$$C = \frac{1}{\Sigma_{t,m} \bar{l} + 1}. \quad (146)$$



■ Figure 19

Example of the macroscopic cross section of light water (under typical LWR operating conditions)

Note that the moderator region among the fuel is “isolated” when $l_m = 0$. In this case, (146) gives the escape probability for an isolated “moderator” lump. A corresponding equation for a fuel is given by (106). From the perspective of its physical meaning, the Dancoff correction is similar to that of the escape probability from fuel, that is, the escape probability from the moderator. However, since the total cross section of the moderator is fairly constant in the resonance energy range, as shown in ► Fig. 19, the Dancoff correction is incorporated in the equivalence theory as an independent energy constant. It depends only on the chord length distribution of the moderator region and the total cross section of the moderator, and does not depend on the fuel cross section.

Dancoff Correction and Escape Probability for an Isolated Fuel Lump

When the angular distribution of neutrons entering from the moderator region into the fuel is isotropic, the collision probability from the fuel to the moderator in a lattice system is expressed as follows (Kobayashi 1995):

$$P_{f \rightarrow m}(E) = \frac{(1 - C)P_e(E)}{1 - (1 - \Sigma_{t,f}(E)\bar{l}P_e(E))C} \quad (147)$$

where

$P_{f \rightarrow m}(E)$: collision probability from the fuel to the moderator in a lattice system, and
 $P_e(E)$: escape probability from the fuel (i.e., collision probability from the fuel to the moderator in an isolated system).

When Wigner's rational approximation with the Bell factor is applied to (147), we obtain

$$\begin{aligned}
 P_{f \rightarrow m}(E) &= \frac{(1-C)P_e(E)}{1 - (1 - \Sigma_{t,f}(E)\bar{l})P_e(E)} C \\
 &= \frac{(1-C) \cdot \frac{a_B}{\Sigma_{t,f}(E)\bar{l} + a_B}}{1 - \left(1 - \Sigma_{t,f}(E)\bar{l} \cdot \frac{a_B}{\Sigma_{t,f}(E)\bar{l} + a_B}\right) C} \\
 &= \frac{g(C, a_B)}{\Sigma_{t,f}(E)\bar{l} + g(C, a_B)} \tag{148}
 \end{aligned}$$

where

$$g(C, a_B) = \frac{(1-C)a_B}{1 + C(a_B - 1)} \tag{149}$$

By comparing (111) and (148), we have the following relationship:

$$\frac{\bar{l}^{iso}}{\bar{l}^{lat}} = \frac{4V}{S^{iso}} \frac{S^{lat}}{4V} = \frac{S^{lat}}{S^{iso}} = \frac{\Sigma_e^{lat}}{\Sigma_e^{iso}} = \frac{g(C, a_B)/\bar{l}}{a_B/\bar{l}} = \frac{(1-C)}{1 + C(a_B - 1)} \tag{150}$$

Therefore, the "effective" surface area of the fuel from which the inflow of neutrons is reduced in the lattice system due to the shadowing effect of other fuels. In the case of Wigner's rational approximation ($a_B = 1$):

$$\frac{S^{lat}}{S^{iso}} = (1-C) \tag{151}$$

Thus, the Dancoff correction directly shows the reduction in the effective surface area of the fuel in the lattice system.

Equivalence Theory in Lattice System

By substituting (148) into (139), we obtain

$$\begin{aligned}
 \phi_f(E) &= \frac{1}{E} \left((1 - P_{f \rightarrow m}(E)) \frac{\Sigma_{p,f}}{\Sigma_{t,f}(E)} + P_{f \rightarrow m}(E) \right) \\
 &= \frac{1}{E} \left(\left(1 - \frac{g(C, a_B)}{\Sigma_{t,f}(E)\bar{l} + g(C, a_B)} \right) \frac{\Sigma_{p,f}}{\Sigma_{t,f}(E)} + \frac{g(C, a_B)}{\Sigma_{t,f}(E)\bar{l} + g(C, a_B)} \right) \\
 &= \frac{1}{E} \frac{\Sigma_{p,f}\bar{l} + g(C, a_B)}{\Sigma_{t,f}(E)\bar{l} + g(C, a_B)} \\
 &= \frac{1}{E} \frac{\Sigma_{p,f} + g(C, a_B)/\bar{l}}{\Sigma_{t,f}(E) + g(C, a_B)/\bar{l}} \\
 &= \frac{1}{E} \frac{\Sigma_{p,f} + g(C, a_B)\Sigma_e}{\Sigma_{t,f}(E) + g(C, a_B)\Sigma_e}
 \end{aligned}$$

$$\begin{aligned}
&= \frac{1}{E} \frac{N_r(\sigma_{p,r} + \sigma_{0,f}) + g(C, a_B)\Sigma_e}{N_r(\sigma_{t,r}(E) + \sigma_{0,f}) + g(C, a_B)\Sigma_e} \\
&= \frac{1}{E} \frac{\sigma_{p,r} + (\sigma_{0,f} + g(C, a_B)\Sigma_e/N_r)}{\sigma_{t,r}(E) + (\sigma_{0,f} + g(C, a_B)\Sigma_e/N_r)} \quad (152)
\end{aligned}$$

If we invoke the relevant discussion of the equivalence theory, the background cross section for nuclide r is given by

$$\sigma_{0,r} = \sigma_{0,f} + g(C, a_B)\Sigma_e/N_r \quad (153)$$

When (113) and (153) are compared, the background cross section in a lattice system becomes smaller than that in an isolated system, since $g(C, a_B) \leq a_B$. In a lattice system, the self-shielding effect is larger than it is in an isolated system, as was discussed previously. Equation (153) represents this physical phenomenon. When $a_B = 1$, the background cross section is given by

$$\sigma_{0,r} = \sigma_{0,f} + D\Sigma_e/N_r \quad (154)$$

In the case of an isolated system ($D = 1$), the background cross section for nuclide r given by (154) is equivalent to (110), which was originally derived for an isolated system.

3.5.5 Calculation of the Dancoff Factor and Background Cross Sections

Calculation of Dancoff Factor Using the Collision Probability Method

Once the Dancoff correction has been calculated, we can estimate the background cross section in a lattice geometry, as shown in (154). Though various analytical methods have been developed for the estimation of the Dancoff correction in simple geometries (i.e., slab, cylinder), the following numerical procedure with the collision probability method is actually used in today's lattice physics codes. We will now consider the value of $\Sigma_{t,f}(E)\bar{I}P_{f \rightarrow m}(E)$, whose detailed analytic form is derived from (147)

$$\Sigma_{t,f}(E)\bar{I}P_{f \rightarrow m}(E) = \Sigma_{t,f}(E) \frac{(1-C)\bar{I}P_e(E)}{1 - (1 - \Sigma_{t,f}(E)\bar{I}P_e(E))C} \quad (155)$$

In conventional equivalence theory, we treat a fuel as black, that is, the total cross section of a fuel is very large. By applying this assumption, we obtain


$$\begin{aligned}
\lim_{\Sigma_{t,f}(E) \rightarrow \infty} \Sigma_{t,f}(E)\bar{I}P_{f \rightarrow m}(E) &= \lim_{\Sigma_{t,f}(E) \rightarrow \infty} \frac{\Sigma_{t,f}(E)\bar{I}(1-C)P_e(E)}{1 - C + \Sigma_{t,f}(E)\bar{I}P_e(E)C} \\
&= \lim_{\Sigma_{t,f}(E) \rightarrow \infty} \frac{(1-C)P_e(E)}{(1-C)/(\Sigma_{t,f}(E)\bar{I}) + P_e(E)C} \\
&= \lim_{\Sigma_{t,f}(E) \rightarrow \infty} \frac{(1-C)P_e(E)}{P_e(E)C} = \frac{(1-C)}{C} \quad (156)
\end{aligned}$$

where

$$\bar{I} = 4V/S.$$

In actual numerical computations, the total cross section of a fuel region is set at a sufficiently large value (e.g., 10^5 cm^{-1}), and then the collision probability from a fuel to the moderator is calculated (Tsuchihashi et al. 1982; Stamm'ler and Abbate 1983; Ishiguro 1985). Once the collision probability from a fuel to the moderator is obtained, the Dancoff correction is evaluated by (156). Note that the chord length is calculated by the volume and surface area of the fuel region, that is, $\bar{l} = 4V/S$, as given in (101). Once the Dancoff correction is obtained, we can easily evaluate the background cross section, which is used for the calculation of effective cross sections.

The above derivation also represents a potential source of error in the Dancoff correction method. For example, let us consider a fuel pellet that is annularly subdivided into multiple regions. Such a subdivision is usually used for a Gadolinia-bearing fuel pellet. The Dancoff correction for the inner region of a subdivided fuel pellet is clearly unity, since the collision probability from the inner region of the fuel to the moderator approaches zero, due to the large total cross section in a pellet. In other words, neutrons cannot “escape” from the inner region of the fuel to the moderator at resonance peak energy, because they always experience collisions in the outer regions of the fuel pellet, which have a very large total cross section. When the Dancoff correction is unity ($C = 1$ or $D = 0$), the background cross section becomes identical to that of a homogeneous system. The above discussion suggests that spatial dependent self-shielding cannot be directly handled by the Dancoff correction given by (156), which represents a major drawback of the conventional equivalence theory.

That said, the above discussion of the Dancoff correction also shows the advantage it offers. The Dancoff correction does not depend on the composition (cross section) of a fuel; it is calculated by the geometry and the cross section of the moderator. Variations in the cross section in the moderator region are very smooth, especially in the resonance energy range, as shown in  Fig. 19. The calculation of the Dancoff correction is thus greatly simplified, and once the Dancoff correction is obtained (with a representative moderator cross section), it can be used for all resonance energy groups.

In the equivalence theory, the heterogeneity effect for a fuel region is incorporated through the escape cross section, and the property of a moderator is taken into account through the Dancoff correction. The escape cross section and the Dancoff correction are both constants. In reality, interaction takes place between the fuel and moderator regions through the “communication” of neutrons, that is, the neutron spectrum in each region is affected by the spectrum in the other region. In the equivalence theory, this situation is simplified, and the effects of the moderator, and of other fuels on the neutron spectrum, are treated independently through the escape cross section, and the Dancoff correction, respectively. Such simplicity contributes greatly to the success of the equivalence theory in conventional resonance calculations. Again, however, it should be noted that such simplification could restrict the application of the Dancoff correction.

Neutron Current Method for Dancoff Correction Calculation

In the following part of this subsection, two numerical methods to evaluate the Dancoff correction and the background cross section are introduced, that is, the neutron current method and the enhanced neutron current method (Sugimura and Yamamoto 2006; Yamamoto 2008, 2009). In conventional equivalence theory, the heterogeneous effect (the Dancoff correction) is evaluated by the collision probability method, as was previously discussed. Though the collision probability method is very efficient for a simple geometry, its applicability to large and

complicated geometries is quite limited due to its computational inefficiency. For example, a collision probability calculation of an LWR fuel assembly still requires considerable computation time, even with the latest computers. For this reason, direct calculation of the Dancoff correction for a large geometry using the collision probability method would be limited by the computation time it requires.

Recently, the method of characteristics has been widely used for neutron transport calculations in lattice physics computations. The neutron current and the enhanced neutron current methods utilize the method of characteristics, rather than the collision probability method, to evaluate the Dancoff correction and the background cross section in a heterogeneous geometry (Sugimura and Yamamoto 2006; Yamamoto 2008, 2009). Using these methods, the Dancoff correction and the background cross section in a large and complicated geometry, such as that of an LWR fuel assembly, can be easily calculated.

The neutron current method and the enhanced neutron current method are based on the approximations used in the equivalence theory, that is, the NR approximation, the rational approximation for the escape probability, and the black-limit approximation of a fuel lump. Thus, they are mathematically equivalent to the equivalence theory used in current lattice physics codes. In other words, the accuracy of these methods is the same as that of the conventional equivalence theory. Though many lattice physics codes utilize collision probability methods for the evaluation of the Dancoff correction in a simple geometry, in a large geometry (even in an entire LWR core) the Dancoff correction is easily calculated by the neutron current and the enhanced neutron current methods.

The original definition of the Dancoff correction is given by the reduction of the incoming neutron current into fuel regions, as shown in (140). In the neutron current method, the Dancoff correction is calculated by the neutron flux in the fuel region as follows:

$$C = \frac{\phi_0 - \phi}{\phi_0} \quad (157)$$

where

ϕ_0 : neutron flux of fuel region at isolated system, and

ϕ : neutron flux of fuel region at lattice system.

When we assume that there is no neutron (slowing down) source in a fuel region, and that the fuel is purely an absorber material with a very large absorption cross section, the average neutron flux in a fuel region will be proportional to the incoming neutron current into the fuel. In such a case, (157) can be rewritten as follows:

$$C = \frac{I_0 - I}{I_0} = \frac{\phi_0 - \phi}{\phi_0} \quad (158)$$

Since the transport codes used in lattice physics computations have the capability to estimate the neutron flux in each region, the definition of the Dancoff correction given by (157) is useful, and is easily adopted in current lattice physics codes. That is, when a lattice physics code utilizes the method of characteristics for transport calculations, the transport module can be directly used for estimation of the Dancoff correction.

A detailed discussion of the validity of (158) is given as follows. For the sake of simplicity, we will consider a fuel-moderator two-region system.

Recalling (94), the energy dependence of the neutron flux in an isolated fuel lump is given by

$$\phi_f(E) = \frac{1}{E} \left((1 - P_{f \rightarrow m}(E)) \frac{\Sigma_{p,f}}{\Sigma_{t,f}(E)} + P_{f \rightarrow m}(E) \right) \quad (159)$$

With (139), that in a lattice system is

$$\phi_f(E) = \frac{1}{E} \left((1 - P_{F \rightarrow M}(E)) \frac{\Sigma_{p,f}}{\Sigma_{t,f}(E)} + P_{F \rightarrow M}(E) \right) \quad (160)$$

Note that the fuel and moderator regions in a lattice system are indicated by F and M , respectively, to distinguish them from those in an isolated system (f and m). When the black-limit approximation is applied to the fuel region, (159) can be simplified as follows:

$$\begin{aligned} \phi_0 &= \lim_{\Sigma_{t,f}(E) \rightarrow \infty} \phi_f(E) \\ &= \lim_{\Sigma_{t,f}(E) \rightarrow \infty} \frac{1}{E} \left((1 - P_{f \rightarrow m}(E)) \frac{\Sigma_{p,f}}{\Sigma_{t,f}(E)} + P_{f \rightarrow m}(E) \right) \\ &= \frac{1}{E} \lim_{\Sigma_{t,f}(E) \rightarrow \infty} P_{f \rightarrow m}(E) \\ &= \frac{1}{E} \left(1 - \lim_{\Sigma_{t,f}(E) \rightarrow \infty} P_{f \rightarrow f}(E) \right) \end{aligned} \quad (161)$$

Note that the normalization condition for collision probability, that is, $P_{f \rightarrow m}(E) = 1 - P_{f \rightarrow f}(E)$, is used. Similarly, for the lattice system

$$\begin{aligned} \phi &= \lim_{\Sigma_{t,f}(E) \rightarrow \infty} \phi_F(E) \\ &= \lim_{\Sigma_{t,f}(E) \rightarrow \infty} \frac{1}{E} \left((1 - P_{F \rightarrow M}(E)) \frac{\Sigma_{p,f}}{\Sigma_{t,f}(E)} + P_{F \rightarrow M}(E) \right) \\ &= \frac{1}{E} \lim_{\Sigma_{t,f}(E) \rightarrow \infty} P_{F \rightarrow M}(E) \\ &= \frac{1}{E} \left(1 - \lim_{\Sigma_{t,f}(E) \rightarrow \infty} P_{F \rightarrow F}(E) - \lim_{\Sigma_{t,f}(E) \rightarrow \infty} P_{F \rightarrow F'}(E) \right) \end{aligned} \quad (162)$$

where

$P_{F \rightarrow M}(E) = \sum_{j \neq F, F'} P_{F \rightarrow j}(E)$: collision probability from fuel F to other regions, except for fuel (F and F'), and

$P_{F \rightarrow F'}(E) = \sum_{j=F'} P_{F \rightarrow j}(E)$: collision probability from fuel F to other fuels F' (fuel F is not included in fuel F').

Here, the relationship $P_{F \rightarrow M}(E) = 1 - P_{F \rightarrow F}(E) - P_{F \rightarrow F'}(E)$ is used.

By substituting (161) and (162) into (157), we obtain

$$\begin{aligned}
 C &= \frac{\phi_0 - \phi}{\phi_0} \\
 &= \frac{\frac{1}{E} \left(1 - \lim_{\Sigma_{i,f}(E) \rightarrow \infty} P_{f \rightarrow f}(E) \right) - \frac{1}{E} \left(1 - \lim_{\Sigma_{i,f}(E) \rightarrow \infty} P_{F \rightarrow F}(E) - \lim_{\Sigma_{i,f}(E) \rightarrow \infty} P_{F \rightarrow F'}(E) \right)}{\frac{1}{E} \left(1 - \lim_{\Sigma_{i,f}(E) \rightarrow \infty} P_{f \rightarrow f}(E) \right)} \\
 &= \frac{\lim_{\Sigma_{i,f}(E) \rightarrow \infty} P_{F \rightarrow F}(E) - \lim_{\Sigma_{i,f}(E) \rightarrow \infty} P_{f \rightarrow f}(E) + \lim_{\Sigma_{i,f}(E) \rightarrow \infty} P_{F \rightarrow F'}(E)}{1 - \lim_{\Sigma_{i,f}(E) \rightarrow \infty} P_{f \rightarrow f}(E)} \\
 &= \frac{\lim_{\Sigma_{i,f}(E) \rightarrow \infty} P_{F \rightarrow F'}(E)}{1 - \lim_{\Sigma_{i,f}(E) \rightarrow \infty} P_{F \rightarrow F}(E)} \tag{163}
 \end{aligned}$$

Note that the fuel-to-fuel self-collision probabilities are identical in both isolated and lattice systems (i.e., $P_{f \rightarrow f}(E) = P_{F \rightarrow F}(E)$), since the fuel-to-fuel self-collision probabilities depend only upon the property of the fuel lump we are considering.


The original definition of the Dancoff correction states that a fraction of the neutrons escaping from a fuel lump suffer their first collision in other fuel lumps. The numerator and denominator of (163) represent the collision probability in other fuel lumps, and the escape probability from the fuel we are considering. Thus (163), which is derived from an analytic expression of the neutron flux, is mathematically identical to that of the original definition of the Dancoff correction. The above discussion can easily be extended to more complicated systems with more than two materials.

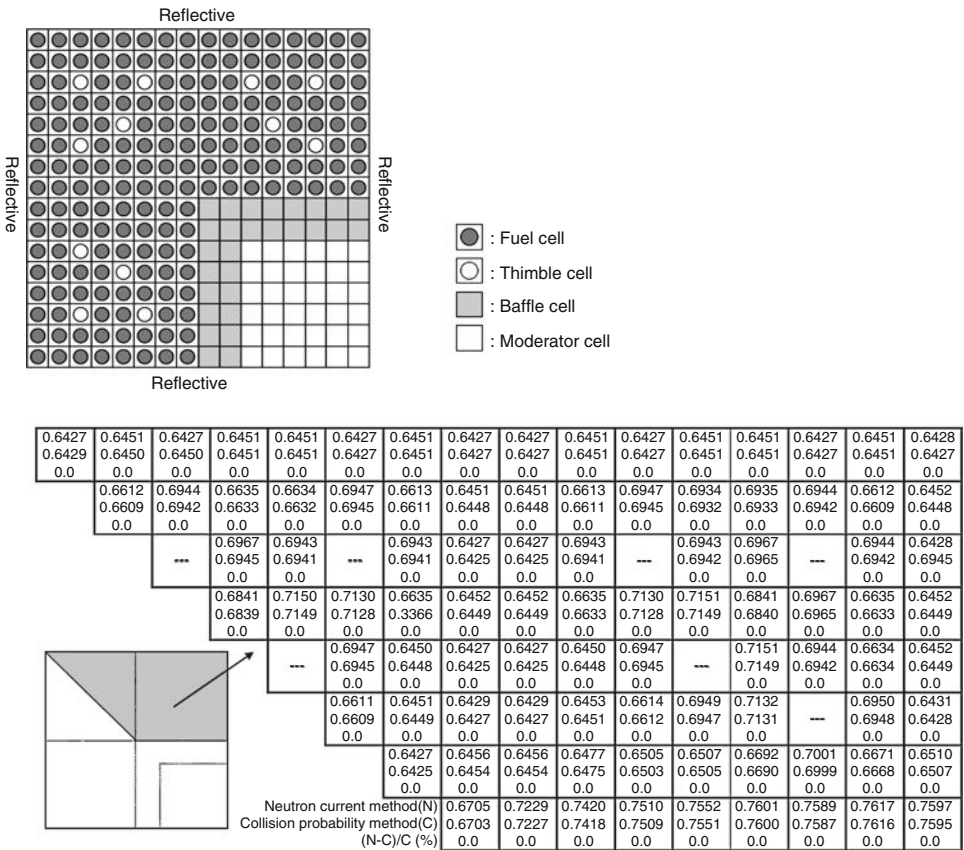
In the actual numerical computation of the Dancoff factor, the following procedure is followed:


- a. The total cross section of each material in the system, except for the fuel, is set to be equivalent to the value of the potential scattering cross section of each material. No scattering is assumed (scattering cross section is set at zero), so the total and absorption cross sections are identical for each material.
- b. The neutron source intensity of each material in the system, except for the fuel, is set to be equivalent to the value of the potential scattering cross section (the NR approximation).
- c. The total cross section of the fuel is set to be sufficiently large, for example, 10^5 cm^{-1} . No scattering is assumed (scattering cross section is set at zero), so the total and the absorption cross sections are identical, in terms of fuel.
- d. The neutron source intensity in the fuel is set at zero.
- e. Perform a one-group fixed-source neutron transport calculation in an isolated system, in which the fuel lump in question is put in a sufficiently large moderator.
- f. Evaluate the neutron flux in the fuel region obtained in step (e).
- g. Perform a one-group fixed-source neutron transport calculation in a lattice system.
- h. Evaluate the neutron flux in the fuel region obtained in step (g).
- i. Evaluate the Dancoff correction by (157).

Using the neutron current method, the Dancoff correction can be evaluated not only for a fuel, but for other resonance materials as well. For example, zirconium isotopes, which are used

in cladding, channel boxes and water rods, have resonances, so that appropriate self-shielding should be taken into account. Since cladding, channel boxes and water rods form a complicated geometry in a BWR fuel assembly, it becomes quite difficult to calculate the Dancoff correction accurately. However, the neutron current method offers an easy way to evaluate the Dancoff correction for zirconium isotopes in a complicated geometry.

An example of the calculation results of the Dancoff factors D ($D = 1 - C$) for fuel pins is shown in  Fig. 20, which represents a typical setting of a fuel assembly adjacent to a baffle plate in a PWR (Sugimura and Yamamoto 2006). The Dancoff factor depends on the position of the fuel rod, and it becomes large for fuel rods that are adjacent to a baffle plate. Since the same resonance material (uranium) does not exist in the baffle and reflector regions, neutrons from the baffle–reflector region are not “shadowed.” Thus, the Dancoff factor becomes large; that is, the Dancoff correction becomes small in the region near the baffle–reflector. Furthermore, the Dancoff factors obtained by the neutron current method are consistent with those obtained by the conventional collision probability method.



 **Figure 20**
Example of Dancoff factors in a large and complicated geometry

Enhanced Neutron Current Method for Background Cross Section Evaluation

In the neutron current method, two transport calculations are needed to evaluate the Dancoff correction in isolated and lattice systems. The enhanced neutron current method offers a simpler way to calculate the background cross section; one fixed-source transport calculation in one group is sufficient to evaluate the background cross section, including the heterogeneous effect (Yamamoto 2008, 2009). In the enhanced neutron current method, the total reaction rate of fuel region $\Sigma_{t,f}(E)\phi_f(E)$ is considered. By using (152), we obtain

$$\Sigma_{t,f}(E)\phi_f(E) = \Sigma_{t,f}(E) \frac{\Sigma_{p,f} + g(C, a_B)\Sigma_e}{\Sigma_{t,f}(E) + g(C, a_B)\Sigma_e} \quad (164)$$

Note that the term $1/E$ is omitted since its variation is much smoother than that due to the resonance peak, and the source intensity can be adjusted. That is, the source intensity due to slowing down by the potential scattering is considered to be $\Sigma_{p,f}$, instead of $\Sigma_{p,f}/E$.

When the black-limit approximation is applied to the fuel, (164) can be reduced as follows:

$$\begin{aligned} \lim_{\Sigma_{t,f}(E) \rightarrow \infty} \Sigma_{t,f}(E)\phi_f(E) &= \lim_{\Sigma_{t,f}(E) \rightarrow \infty} \Sigma_{t,f}(E) \frac{\Sigma_{p,f} + g(C, a_B)\Sigma_e}{\Sigma_{t,f}(E) + g(C, a_B)\Sigma_e} \\ &= \Sigma_{p,f} + g(C, a_B)\Sigma_e \\ &= N_r(\sigma_{p,r} + \sigma_{0,f}) + g(C, a_B)\Sigma_e \\ &= N_r\sigma_{p,r} + N_r(\sigma_{0,f} + g(C, a_B)\Sigma_e/N_r) \end{aligned} \quad (165)$$

By using (165), we can derive the background cross section, including the heterogeneous effect, as follows:

$$\begin{aligned} \sigma_0 &= \sigma_{0,f} + g(C, a_B)\Sigma_e/N_r \\ &= \frac{\lim_{\Sigma_{t,f}(E) \rightarrow \infty} \Sigma_{t,f}(E)\phi_f(E) - N_r\sigma_{p,r}}{N_r} \\ &= \frac{\lim_{\Sigma_{t,f}(E) \rightarrow \infty} \Sigma_{t,f}(E)\phi_f(E)}{N_r} - \sigma_{p,r} \end{aligned} \quad (166)$$

In lattice geometry, the Dancoff correction can also be derived using (166), that is,

$$g(C, a_B) = \frac{\lim_{\Sigma_{t,f}(E) \rightarrow \infty} \Sigma_{t,f}(E)\phi_f(E) - N_r\sigma_{p,r} - N_r\sigma_{0,f}}{\Sigma_e} \quad (167)$$

The value of $\lim_{\Sigma_{t,f}(E) \rightarrow \infty} \Sigma_{t,f}(E)\phi_f(E)$, which is the total reaction rate, can be evaluated by means of a transport calculation by using the method of characteristics. The escape cross section is given by $S/(4V)$. The number density and the potential scattering cross sections are known values. Therefore, the right-hand side of (167) can be evaluated. When the Bell factor is unity, $g(C, a_B)$ becomes the Dancoff factor D ($D = 1 - C$), from the definition of $g(C, a_B)$ given by (149).

The actual calculation procedure of the enhanced neutron current method is as follows:

- a. The total cross sections of a material in the system, except for the fuel, are set to be equivalent to the potential scattering cross section. No scattering is assumed, so the total and absorption cross sections are identical in these materials.
- b. The neutron source intensities of the materials in the system (including the fuel region) are set to be equivalent to the potential scattering cross section (the NR approximation).
- c. The total cross section of the fuel is set to be sufficiently large, for example, 10^5 cm^{-1} . No scattering is assumed, so the total and the absorption cross sections in the fuel are identical.
- d. Perform a one-group fixed-source neutron transport calculation in the lattice system.
- e. Evaluate the total reaction rate $\Sigma_{t,f}(E)\phi_f(E)$ in each fuel region.
- f. Evaluate the background cross section by (166). The Dancoff factor can be evaluated by (167) with the Bell factor $a_B = 1$, if necessary.

The enhanced neutron current method gives a different background cross section for each fuel rod, which reflects the spatial source distribution in the moderator region, and the spatial variation of the neutron inflow to the fuels. In this method, the shadowing effect from the other fuel rods is naturally taken into account.

Since the fuel region is considered as a completely black material, that is, all fuels are treated as being made of the same material with a very large absorption cross section, the difference in fuel cross sections among fuel rods cannot be taken into account in this method. In this context, the enhanced neutron current method is consistent with the conventional equivalence theory, with Wigner's rational approximation and the Dancoff correction. Therefore, the enhanced neutron current method cannot be applied to self-shielding calculations in which the grayness of a fuel must be taken into account, for example, calculation of the space-dependent effective cross section in a pellet.

One may consider the possibility of applying the N -term rational approximation in the derivation of the enhanced neutron current method. However, since the accuracy of Wigner's rational approximation is the same as that of the N -term rational approximation, the accuracy of the enhanced neutron current method cannot be improved by incorporation of the N -term rational approximation. The following formulation will clarify this discussion.

First, by recalling the discussion for (119) and (148), we assume that the fuel-to-moderator collision probability can be expressed by the following rational approximation:

$$P_{f \rightarrow m}(E) = \sum_{n=1}^N \frac{g(C, a_B) b_n a_n}{\Sigma_{t,f}(E) \bar{l} + g(C, a_B) a_n} \quad (168)$$

By substituting (168) into (139) and using (121), we obtain

$$\phi_f(E) = \frac{1}{E} \sum_{n=1}^N b_n \frac{\Sigma_{p,f} + g(C, a_B) a_n \Sigma_e}{\Sigma_{t,f}(E) + g(C, a_B) a_n \Sigma_e} \quad (169)$$

Therefore, the total reaction rate is given by

$$\begin{aligned}
 \lim_{\Sigma_{t,f}(E) \rightarrow \infty} \Sigma_{t,f}(E) \phi_f(E) &= \lim_{\Sigma_{t,f}(E) \rightarrow \infty} \Sigma_{t,f}(E) \sum_{n=1}^N b_n \frac{\Sigma_{p,f} + g(C, a_B) a_n \Sigma_e}{\Sigma_{t,f}(E) + g(C, a_B) a_n \Sigma_e} \\
 &= \sum_{n=1}^N b_n \lim_{\Sigma_{t,f}(E) \rightarrow \infty} \Sigma_{t,f}(E) \frac{\Sigma_{p,f} + g(C, a_B) a_n \Sigma_e}{\Sigma_{t,f}(E) + g(C, a_B) a_n \Sigma_e} \\
 &= \sum_{n=1}^N b_n \{ \Sigma_{p,f} + g(C, a_B) a_n \Sigma_e \} \\
 &= \sum_{n=1}^N b_n \Sigma_{p,f} + \sum_{n=1}^N b_n g(C, a_B) a_n \Sigma_e \\
 &= \Sigma_{p,f} \sum_{n=1}^N b_n + g(C, a_B) \Sigma_e \sum_{n=1}^N b_n a_n \\
 &= \Sigma_{p,f} + g(C, a_B) \Sigma_e \tag{170}
 \end{aligned}$$

Equation (170) indicates that the total reaction rate is the same as that in (165), which is derived with the one-term rational approximation. In other words, the obtained background cross section is independent of the number of terms in the rational approximation. This is to be expected, since the behavior of the N -term rational approximation converges with that of the one-term rational approximation at the black limit.

In the enhanced neutron current method, the black limit is assumed for evaluation of the background cross section. However, it can be extended to include the “grayness” of the fuel by including the total reaction rate obtained by the moderate magnitude of the total cross sections, that is, a_n and b_n is determined by the least square fitting of $\Sigma_{t,f}(E) \phi_f(E) = \Sigma_{t,f}(E) \sum_{n=1}^N b_n \frac{\Sigma_{p,f} + g(C, a_B) a_n \Sigma_e}{\Sigma_{t,f}(E) + g(C, a_B) a_n \Sigma_e}$. This approach is a generalization of Hébert and Marleau (1991), in which the collision probability method is used (Koike et al. 2010).

3.5.6 Stamm’ler’s Method for a Heterogeneous Lattice System

In [3.5.5](#), the lattice effect was considered in terms of the Dancoff correction, and the escape probability from a fuel lump in a lattice system was corrected (reduced) by applying the Dancoff correction.

There is another approach to treating the lattice effect in the equivalence theory, which is discussed in detail by Stamm’ler et al. and is currently being adopted in major lattice physics codes, such as CASMO, WIMS, and PHOENIX (Stamm’ler and Abbate 1983). In this subsection, Stamm’ler’s treatment of the lattice effect will be briefly reviewed.

In an infinite lattice system, the collision probability from region I to J is assumed to be expressed by

$$p_{IJ} = p_{ij} + p_{ib} R p_{bj} + p_{ib} R p_{bb} R p_{bj} + p_{ib} R p_{bb} R p_{bb} R p_{bj} + \dots \tag{171}$$

where

- p_{IJ} : collision probability from region I to J in a lattice system,
- p_{ij} : collision probability from i to j in an isolated system,
- p_{bb} : transmission probability of a neutron from cell boundary b to another cell boundary b ,
- p_{ib} : transmission probability of a neutron born in region i to reach cell boundary b ,
- p_{bj} : collision probability that a neutron entering cell boundary b will suffer its first collision in region j , and
- R : reflection probability at cell boundary b .

In (171), several paths from region I to J in the lattice system are taken into account, so that the collision probability becomes larger than it is in an isolated system. The first term of the right-hand side of (171) is the direct collision from region i to j inside a cell. The second term represents a collision from region i to the cell boundary, then from the cell boundary to region j in another cell. The third term represents a collision from region i to the cell boundary, then from the cell boundary to another cell boundary (transmission of the cell), and finally from the cell boundary to region j . When a neutron is passing through a cell boundary, the reflection probability is taken into account by considering the neutron reflection at the fuel assembly boundary. When a fuel assembly becomes large, the reflection probability approaches unity, since most of the fuel cells are not adjacent to the assembly boundary.

Equation (171) can be transformed as follows:

$$p_{IJ} = p_{ij} + \frac{Rp_{ib}p_{bj}}{1 - Rp_{bb}} \quad (172)$$

By incorporating several physical considerations, whose details are given by Stamm'ler and Abbate (1983), we obtain the following formula:

$$p_{FF} = p_{ff} + \frac{x(1 - p_{ff})^2}{x(1 - p_{ff}) + A + B} \quad (173)$$

where

$$x = \frac{4V_f}{S_f} \Sigma_{t,f}$$

$$A = \frac{S_b}{S_f t_{fb}^2} \gamma_b^0$$

$$B = \frac{S_b}{S_f t_{fb}^2} \frac{f(1 - g)}{1 - f(1 - g)}$$

S_b : surface area of cell boundary,

S_f : surface area of fuel lump (pellet),

V_f : volume of fuel lump,

t_{fb} : transmission probability that neutrons leaving a fuel surface with cosine angular distribution will reach the cell boundary,

γ_b^0 : blackness of a cell when the total cross section of the fuel is zero,

f : ratio of assembly surface area to that of the sum of all cell surface areas,

g : first-flight reflection probability across the gap between fuel assemblies.

Note that $B = 0$ in the case of an infinite regular lattice, that is, pin cell geometry.

In contrast to the Dancoff correction, this method naturally incorporates the energy dependence of the shadowing effect among fuel rods. The relationship between the Dancoff factor and Stamm'ler's method is shown as follows:

$$D = \lim_{\Sigma_{t,f} \rightarrow \infty} \frac{1 - p_{FF}}{1 - p_{ff}} = 1 - \frac{1}{1 + A + B} \quad (174)$$

Therefore, the Dancoff correction method is considered to be an asymptotic case with a black-limit approximation.

Next, we will try to express (173) with a rational approximation in order to derive an equivalence relationship. For an isolated fuel lump with a cylindrical shape, we can apply Carlvik's two-term rational approximation, as defined by (123):

$$P_e(E) = 1 - P_{ff}(E) = 2 \frac{2}{\Sigma_{t,f}(E)\bar{l} + 2} - \frac{3}{\Sigma_{t,f}(E)\bar{l} + 3} \quad (175)$$

Substituting (175) into (173), and after some algebra, we obtain

$$p_e^{lat} = 1 - p_{FF} = \beta_1 \frac{\alpha_1}{x + \alpha_1} + \beta_2 \frac{\alpha_2}{x + \alpha_2} \quad (176)$$

where

$$\begin{aligned} \alpha_{1,2} &= \frac{(5C + 6) \mp \sqrt{C^2 + 36C + 36}}{2(C + 1)} \\ C &= A + B \\ \beta_1 &= \frac{C' - \alpha_1}{\alpha_2 - \alpha_1} \\ \beta_2 &= 1 - \beta_1 \\ C' &= \frac{4C + 6}{C + 1} \end{aligned}$$

By substituting (176) into (139) we obtain

$$\phi_f(E) = \frac{1}{E} \sum_{n=1}^2 \beta_n \frac{\sigma_{p,r} + \sigma_{0,n}}{\sigma_{t,r}(E) + \sigma_{0,n}} \quad (177)$$

where

$$\sigma_{0,n} = \sigma_{0,f} + \alpha_n \Sigma_e / N_r$$

Now we have a form identical to that in (125). Therefore, with (131), (132), or (133), we can derive the effective cross section using Stamm'ler's method.

The advantages and disadvantages of Stamm'ler's method are summarized as follows:

- Energy dependence of the shadowing effect for a regular lattice is taken into account approximately.
- Boundary effect of a fuel assembly is taken into account approximately using an average.
- Approximate treatment of the assembly boundary effect.

- Rational approximation for the escape probability.
- This method only yields the effective cross section for an “average pin cell” in a fuel assembly. Effective cross sections that are position-dependent due to lattice irregularity (e.g., gap water, water holes, or water rods) cannot be evaluated. The Dancoff correction is still needed to evaluate such effects.

3.5.7 Potential Limitations of the Equivalence Theory

In [3.5](#), the equivalence theory for resonance calculations, which is widely used for current lattice physics computations, is discussed. In the explanation of each method, several crucial approximations used in the equivalence theory were pointed out (Mizuta 1970). Since these approximations largely determine the accuracy and applicability of the equivalence theory, a review of the approximations used in the equivalence theory is most useful. They are summarized as follows:

1. No resonance overlap is considered.

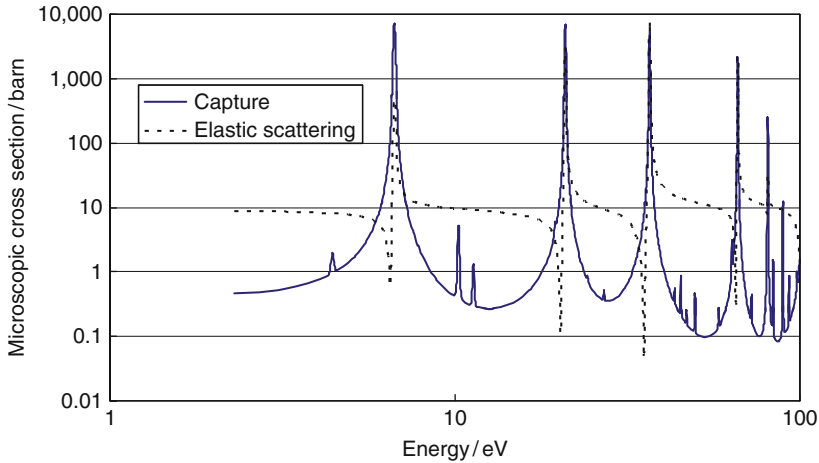
In the neutron slowing down calculation, the cross section variation is considered only for a resonance isotope, and the scattering cross section is assumed to be constant and dominated by the potential scattering, which is independent of energy. Since various nuclides exist in fuel, especially in a burnt fuel, coincident overlaps among resonance peaks of different nuclides are inevitable. The effect of such resonance overlap has an impact on the energy dependence of the neutron flux. In the preparation of a cross section library, the slowing down calculation for an ultrafine energy group structure is usually carried out with point-wise cross sections. The slowing down calculation is numerically carried out with a resonance nuclide and an energetically constant background cross section. In a common multigroup cross section library, therefore, the resonance overlap effect is not taken into account. The resonance overlap effect will be discussed in more detail in [3.10](#), since it has a considerable impact on effective cross section evaluation.

2. Nonresonant nuclide has a constant scattering cross section.

In an LWR lattice, the major contributors to the slowing down of neutrons are hydrogen and oxygen. In the resonance energy range, these nuclides have fairly constant cross sections, so this assumption is appropriate. Note that in the preparation of a cross section, a constant background cross section is assumed in the slowing down calculation.

3. Resonant nuclide has a constant scattering cross section.

In reality, the scattering cross section of a resonance nuclide in the resonance energy range is not constant, and sometimes has peaks of the scattering cross section (resonance scattering), as shown in [Fig. 21](#). Though the constant scattering cross section is assumed in the NR, WR, and IR approximations, the explicit energy dependence of the scattering cross section of a resonance nuclide is taken into account in the slowing down calculation in cross section library preparation. This inconsistency would be a source of error in the equivalence theory.



■ Figure 21

Microscopic capture and elastic scattering cross sections of ^{238}U (ENDF/B-VII, 300 K)

4. Neutron slowing down is dominated by elastic scattering.

In the resonance energy range, this assumption is appropriate. However, we should take care that neutron slowing down due to elastic scattering does not incorporate the thermal vibration of the target nuclides. If the thermal vibration is taken into account, the energy dependence of the neutron flux will be changed. This simplification (no thermal vibration in the slowing down calculation in the resonance energy range) could be a source of error not only for the equivalence theory, but also for other resonance calculation methods, including the continuous-energy Monte Carlo method (Lee et al. 2009).

5. Energy dependence of the neutron flux in the nonresonant part is asymptotic.

In the equivalence theory, the energy dependence of the neutron flux in the nonresonant part is assumed to be asymptotic ($1/E$). However, in cross section library preparation, the neutron slowing down calculation is usually explicitly carried out for a resonance nuclide with a constant background cross section. In reality, therefore, the energy dependence of the neutron flux in the nonresonant part is not assumed to be asymptotic. This inconsistency would be a cause of error in the equivalence theory.

6. The NR, WR, and IR approximations.

In cross section library preparation, hydrogen is usually used as a background nuclide. Therefore, when the moderator in a system consists of only hydrogen, the homogeneous term in the background cross section (except for the escape cross section) will not be a source of error. However, since various nuclides exist in a system, the slowing down of neutrons by these nuclides should be accurately taken into account in an actual situation. In this context, both the NR and WR approximations will be a source of error, since these methods incorporate approximations to evaluate the source of the slowing down. The IR approximation offers an adjustment

factor for various nuclides with a heavier mass. As discussed in [▶ 3.4.4](#), the conventional IR approximation, which utilizes one IR parameter for a nuclide, is still a source of error since one IR parameter cannot be applied to all self-shielding situations.

7. Escape probability from a fuel lump.

In the equivalence theory, the escape probability from a fuel lump is approximated by the rational approximation to derive the equivalence between homogeneous and heterogeneous systems. However, since the rational approximation cannot rigorously reproduce the escape probability from a fuel lump for all fuel cross section values, it is a source of error in the equivalence theory.

8. Dependence of the Dancoff correction on the moderator cross section.

The Dancoff correction depends on the cross section of the moderator, which is theoretically energy dependent. However, in actual lattice physics computations, the Dancoff correction is usually assumed to be constant throughout the resonance energy range. Though the cross section of the moderator is fairly flat in this energy range, this assumption could be a source of error.

9. The same fuel material (cross section) for all fuel.

The lattice effect, that is, the shadowing effect by other fuels, is incorporated through the Dancoff correction or Stamm'ler's method. These methods are based on the assumption that all fuels in the system consist of the same material (cross section). However, various fuel materials are used in a single fuel assembly, and different types of fuel assemblies may be loaded into adjacent positions in a core. The shadowing effect that is evaluated using the above assumption may not be accurate.

10. Spatially constant cross section in fuel and moderator.

In the evaluation of the escape probability from a fuel lump, the cross section in a fuel lump is assumed to be spatially constant. This situation captures a fuel pellet well, before burnup. However, once a fuel pellet experiences burnup, the fuel composition has a spatial variation due to the gradient of flux in the fuel pellet and the space-dependent resonance shielding effect. For example, ^{239}Pu is generally produced on the pellet surface due to the spatially self-shielding effect of ^{238}U . Therefore, this assumption might be a source of error in the equivalence theory. Fortunately, as several studies have confirmed, the spatial average treatment does not have a significant impact on the accuracy of resonance calculations (Rothenstein et al. 1988; Stoker and Weiss 1996).

11. Black approximation in the Dancoff correction evaluation.

In the evaluation of the Dancoff correction, a fuel lump is assumed to be black, that is, is assumed to behave as a completely absorbent material. This is a source of error in the capture of the lattice effect. For example, let us consider the resonance shielding of ^{239}Pu in a UO_2 pellet. In the beginning of life, the number density of ^{239}Pu is small. In this situation, the self-shielding of ^{239}Pu is not black, that is, it is in an intermediate, diluted (or "gray") condition. However, in the estimation of the Dancoff correction, the entire nuclide is assumed to be black, and could thus be a source of error. The Dancoff correction for a resonance nuclide with a low concentration would therefore be overestimated, since the resonance nuclide is assumed to be completely black, that is, is assumed to have a very large macroscopic cross section.

3.6 Tabulation of Self-Shielding Factors

3.6.1 Cross Section Processing and Effective Cross Sections

In the framework of the equivalence theory, multigroup cross sections are prepared by solving the slowing down equation in a homogeneous medium, as was discussed in [Sect. 2](#). A number of cross section processing codes, such as NJOY, are used for cross section preparation. Cross section processing codes perform slowing down calculations for various background cross sections and temperature conditions, since the self-shielding effect significantly depends on these parameters. Finally, cross section processing codes output the relationship among the background cross section, the temperature, and the effective cross section. These parameters are tabulated in the cross section library of lattice physics codes.

In a typical cross section library, the effective cross sections are not directly tabulated as a function of the background cross section and temperature. Instead, the base cross section for the reference temperature (e.g., 293 K) and infinite background cross section (e.g., 10^{10} barn), and their ratios to the base cross sections for other temperatures and background cross sections, are tabulated in a cross section library (Abagyan et al. 1980). The ratio is the self-shielding factor, which is defined as

$$f(\sigma_0, T) = \frac{\sigma(\sigma_0, T)}{\sigma(\sigma_0^{\text{inf}}, T_{\text{ref}})} \quad (178)$$

where

$f(\sigma_0, T)$: self-shielding factor for the background cross section (σ_0) and temperature (T);
 $\sigma(\sigma_0^{\text{inf}}, T_{\text{ref}})$: base cross section and σ_0^{inf} is a sufficiently large background cross section, for example, 10^{10} barn, and T_{ref} is a reference temperature, for example, room temperature; and
 $\sigma(\sigma_0, T)$: effective cross section at the background cross section (σ_0) and temperature (T).

The shielded cross section is reconstructed as

$$\sigma(\sigma_0, T) = \sigma(\sigma_0^{\text{inf}}, T_{\text{ref}})f(\sigma_0, T) \quad (179)$$

A cross section library that tabulates the reference cross sections and the shielding factors is referred to as a Bondarenko-type cross section library.

Another choice is the tabulation of the base cross section at a reference condition and the deviation of a cross section from the base cross section. The design of the MATXS format, for example, was based on this concept (Macfarlane and Muir 1994a). In this case, the shielded cross section is reconstructed by

$$\sigma(\sigma_0, T) = \sigma(\sigma_0^{\text{inf}}, T_{\text{ref}}) + \Delta\sigma(\sigma_0, T) \quad (180)$$

where $\Delta\sigma(\sigma_0, T)$: difference of effective cross section at the background cross section (σ_0) and temperature (T).

When a cross section does not have resonance, the difference of the cross section in (180) will be zero at the same temperature. Therefore, we can naturally compress the size of a cross section library by truncating (or compressing) the zero values in the self-shielding factor table. This explains the superiority of the MATXS format.

The resonance integral given in (132) can be also used instead of the effective cross section. The resonance integral is converted into the effective cross section as follows:

$$\sigma_{g,x} = \frac{I_{g,x}(\sigma_0, T)}{1 - I_{g,a}(\sigma_0, T)/(\sigma_{p,r} + \sigma_0)} \quad (181)$$

where

$\sigma_{g,x}$: effective cross section of reaction type x ,

$I_{g,x}(\sigma_0, T)$: resonance integral of reaction type x for background cross section (σ_0) and temperature T ,

$I_{g,a}(\sigma_0, T)$: resonance integral of absorption reaction for background cross section (σ_0), and temperature T ,


σ_0 : background cross section, and

$\sigma_{p,r}$: potential scattering cross section of the resonance nuclide.

In the case of the N -term rational approximation, (132) is used to obtain the effective cross section.

3.6.2 Interpolation of Self-Shielding Factor Table

Since the self-shielding factor table is tabulated for discrete values of background cross sections and temperatures, interpolation is necessary in order to obtain an effective cross section for a desired background cross section and temperature.

Since the range of the background cross section is very wide (typically 10–10¹⁰ barn), linear interpolation is not a suitable approach. The grid point for the background cross section is often chosen as the equal interval on a logarithmic axis. In fact, the dependence of an effective cross section on the background cross section is expressed as a reasonably smooth function when the background cross section is expressed on a logarithmic axis, as shown in  Fig. 22.

Therefore, interpolation by the background cross section should be performed on a logarithmic basis. A higher-order polynomial function could be used to increase the accuracy of the interpolation. However, an unphysical polynomial dip would degrade the accuracy of the interpolation when the grid points of the background cross section are not appropriate and/or the variation in the effective cross sections is steep.

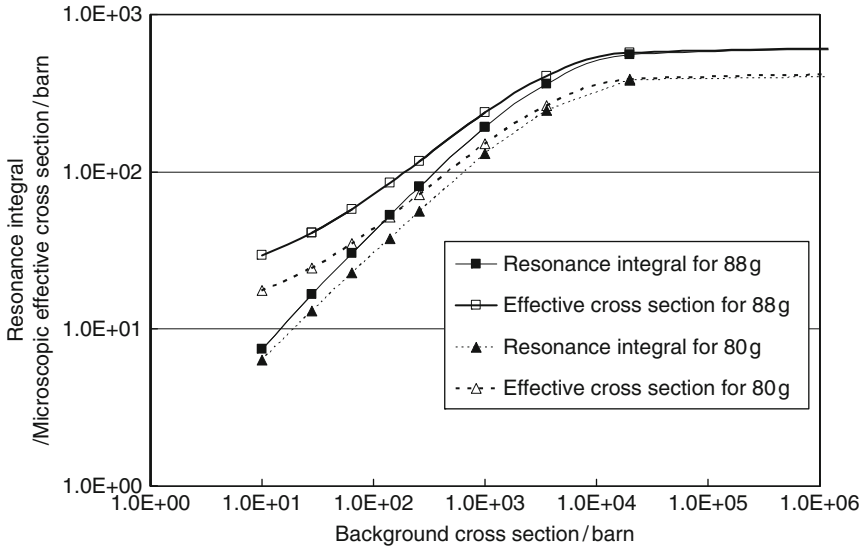
Though the accuracy of linear interpolation on a log–log scale is generally lower than that of a higher-order polynomial, the method of linear interpolation is more robust. Therefore, one should carefully check the validity of the cross section interpolation method when it is implemented in a lattice physics code. In general, the reproducibility of the effective cross section should be checked against various background cross sections and temperatures, including the intervals between tabulation points.

When the property of the neutron spectrum is taken into account, the following formula will be also suitable for interpolation:

$$\sigma_{g,x}(\sigma_0) = \sigma_{g,x}(\sigma_0 = \infty) \cdot \frac{\sigma_0^{-1} + a - \sigma_0 b}{\sigma_0^{-1} + c - \sigma_0 d} \quad (182)$$

where

a, b, c, d : parameters for interpolation.



■ Figure 22

Variations in the resonance integral and effective cross section (absorption) of ^{238}U at 900 K, for 80 g (22.6–19.45 eV) and 88 g (7.52–6.16 eV) of 172 XMAS group structure

Equation (182) was originally derived for subgroup cross sections (to be described later) based on the NR approximation for neutron flux in a resonance peak (Yamamoto 2003, 2004).

In the original derivation, the four coefficients in (182) were analytically derived. In the actual interpolation procedure, however, the coefficients in (182) (a , b , c , and d) can be evaluated by the tabulated data set for the background cross section and the effective cross section. Since (182) well reproduces the behavior of the effective cross section for a wide range of background cross sections, (182) offers an accurate approach to interpolation.

Examples of a number of interpolation schemes are shown below:

$$RI(\sigma_0) = a + b\sqrt{\sigma_0} \quad (183)$$

$$\sigma_{eff}(\sigma_0)/\sigma_{eff}(\sigma_0 = \infty) = \sqrt{\sigma_0} \exp[-f\sigma_0] \quad (184)$$

$$\sigma_{eff}(\sigma_0)/\sigma_{eff}(\sigma_0 = \infty) = 1 + a(\tan h(b \ln[\sigma_0] + c) - 1) \quad (185)$$

$$\sigma_{eff}(\sigma_0)/\sigma_{eff}(\sigma_0 = \infty) = \sqrt{(a + \sigma_0)/(a + b + \sigma_0)} \quad (186)$$

$$RI(\sigma_0)/RI(\sigma_0 = \infty) = (\sigma_0/(a + \sigma_0))^b. \quad (187)$$

Equations (183)–(185) are used in the WIMS (Askew et al. 1966), EPRICELL, and IDX (Kidmon 1975) codes, respectively, and (186) and (187) have been proposed by Segev (1975, 1981).

When the resonance integral is used, the root of the background cross section can be used as an interpolation variable, since the resonance integral has a strong linear relationship with the root of the background cross section, as discussed in (133).

The effective cross section is generally a very smooth function of temperature. It can be therefore be interpolated by a quadratic polynomial, or by a combination of constant, root, and linear terms of temperature in Kelvin. Since the resonance integral has a strong correlation with the root of temperature in Kelvin, it could be interpolated with the root of temperature in Kelvin. However, for more accurate interpolation, the root and linear terms of temperature in Kelvin are both necessary.

Interpolation of the self-shielding factor table may dominate the accuracy of the effective cross section. One should therefore be careful in the choice and application of an interpolation scheme, and the accuracy of the interpolation should be confirmed though comparison with other interpolation schemes and/or integration tests of a lattice physics code. For example, variations in the assembly k -infinity should show a smooth dependence on the variations in fuel temperature. Similarly, the assembly k -infinity should be a smooth function of the number density of a resonance absorber. Some anomalies in the calculated k -infinity could signify inappropriate interpolation of the effective cross section.

Finally, it should be noted that, taking into account the advances in affordable PCs, the fine grid points of the background cross section and temperature in a cross section library are recommended, rather than utilization of a sophisticated interpolation scheme.

3.7 Ultrafine Group Method

3.7.1 Homogeneous System

In a homogeneous system, the Boltzmann transport equation shown in (64) can be simplified as follows:

$$\Sigma_t(E)\phi(E) = \int_0^\infty dE' \Sigma_s(E' \rightarrow E)\phi(E') + \chi(E) \int_0^\infty dE' \nu \Sigma_f(E')\phi(E') \quad (188)$$

The scattering term, that is, the first term of the right-hand side of (188), can be reduced as follows when the elastic scattering is dominant:

$$\begin{aligned} \int_0^\infty dE' \Sigma_s(E' \rightarrow E)\phi(E') &= \int_0^\infty dE' \Sigma_{es}(E')P(E' \rightarrow E)\phi(E') \\ &= \sum_k \int_E^{E/\alpha_k} \frac{dE' N_k \sigma_{es,k}(E')\phi(E')}{(1 - \alpha_k)E'} \end{aligned} \quad (189)$$

In the ultrafine group method, the fission source in (188) can be approximated as a fixed source, which is assumed to be independent of neutron flux. In this case, since the absolute value of the fixed source can be arbitrarily set, the sum of the fission source is set at unity, that is, $\int_0^\infty dE' \nu \Sigma_f(E')\phi(E') = 1$. Finally, (188) is rewritten as follows:

$$\Sigma_t(E)\phi(E) = \sum_k \int_E^{E/\alpha_k} \frac{dE' N_k \sigma_{es,k}(E')\phi(E')}{(1 - \alpha_k)E'} + \chi(E) \quad (190)$$

Unfortunately, (190) cannot be analytically solved, except for the particular case ($\alpha_k = 0$, $\sigma_{es,k} = \text{const.}$). A numerical solution, however, can be easily obtained by means of sufficient energy discretization (Ishiguro 1974; Tsuchihashi et al. 1982; Rothenstein et al. 1988; Macfarlane and Muir 1994a; Kobayashi 1995; MC** 2-2 1999; Hazama et al. 2006; Sugimura and Yamamoto 2007).

When the variations in the cross sections and neutron flux in an energy range (energy group) is assumed to be constant, (190) can be converted into a multigroup form as follows:

$$\Sigma_{t,fg}\phi_{fg} = \sum_k \sum_{fg'} \frac{\Sigma_{es,k,fg'}\phi_{fg'}\Delta E_{fg'}}{(1-\alpha_k)\overline{E}_{fg'}} + \chi_{fg} \quad (191)$$

where

$$\begin{aligned} fg &= \{E|E_{fg} \leq E \leq E_{fg-1}\} \\ \Delta E_{fg} &= E_{fg-1} - E_{fg} \\ \overline{E}_{fg} &= \sqrt{E_{fg}E_{fg-1}} \\ fg' &= \{\overline{E}_{fg'} | \overline{E}_{fg} \leq \overline{E}_{fg'} \leq \overline{E}_{fg}/\alpha_k\} \end{aligned}$$

In (191), neutron flux is defined as the average value in a group, and is different from that in a common multigroup equation (integrated value in a group). It should be again noted that the width of an energy group should be narrow enough to neglect variations in the cross section and the neutron flux inside a group. The typical width of this ultrafine energy group is $\Delta U_{fg} = \ln(E_{fg}/E_{fg-1}) = 0.0002 \sim 0.001$, which is sufficiently narrower than that of the energy loss of elastic scattering by a heavy nuclide (e.g., 0.0168 for ^{238}U) and the widths of the major resonance peaks (Ishiguro 1974).

Equation (191) can be solved by the following procedure. The neutron flux for the first group is given by

$$\phi_1 = \frac{\chi_1}{\Sigma_{t,1}} \quad (192)$$

For the second group

$$\phi_2 = \frac{1}{\Sigma_{t,2}} \left(\sum_k \frac{\Sigma_{es,k,1}\phi_1\Delta E_1}{(1-\alpha_k)\overline{E}_1} + \chi_2 \right) \quad (193)$$

For the third group

$$\phi_3 = \frac{1}{\Sigma_{t,3}} \left(\sum_k \left(\frac{\Sigma_{es,k,1}\phi_1\Delta E_1}{(1-\alpha_k)\overline{E}_1} + \frac{\Sigma_{es,k,2}\phi_2\Delta E_2}{(1-\alpha_k)\overline{E}_2} \right) + \chi_3 \right) \quad (194)$$

By repeating the above procedure, the neutron fluxes for successive energy groups can be recursively solved unless up-scattering is taken into account.

Note that the removal cross section, which is defined by

$$\Sigma_{r,fg} = \Sigma_{t,fg} - \frac{\Sigma_{es,k,fg}\Delta E_{fg}}{(1-\alpha_k)\overline{E}_{fg}} \quad (195)$$

could be used in (192)–(194) in order to be consistent with (191). However, the second term in the right-hand side of (195), which represents self-scattering, is sufficiently small in the ultrafine energy group structure. Thus, direct utilization of the total cross section is justified.

Direct implementation of the above procedure entails considerable computation cost, since the summation of the slowing down source that appears in the right-hand side of (192)–(194) will be large, especially when a material contains hydrogen, whose α_k is nearly zero. For this reason, several numerical techniques can be applied.

The slowing down source terms for group fg and $fg - 1$ are given as follows:

$$S_{fg} = \sum_k \sum_{fg'=fg'_{k,fg}}^{fg-1} \frac{\Sigma_{es,k,fg'} \phi_{fg'} \Delta E_{fg'}}{(1 - \alpha_k) \bar{E}_{fg'}} \quad (196)$$

$$S_{fg-1} = \sum_k \sum_{fg'=fg'_{k,fg-1}}^{fg-2} \frac{\Sigma_{es,k,fg'} \phi_{fg'} \Delta E_{fg'}}{(1 - \alpha_k) \bar{E}_{fg'}} \quad (197)$$

where

$fg'_{k,fg}$: upper energy group from which neutrons are down-scattered into fg , for nuclide k ,
 $fg'_{k,fg-1}$: upper energy group from which neutrons are down-scattered into $fg - 1$, for nuclide k .

By subtracting (196) and (197), we obtain

$$\begin{aligned} S_{fg} - S_{fg-1} &= \sum_k \sum_{fg'=fg'_{k,fg}}^{fg-1} \frac{\Sigma_{es,k,fg'} \phi_{fg'} \Delta E_{fg'}}{(1 - \alpha_k) \bar{E}_{fg'}} - \sum_k \sum_{fg'=fg'_{k,fg-1}}^{fg-2} \frac{\Sigma_{es,k,fg'} \phi_{fg'} \Delta E_{fg'}}{(1 - \alpha_k) \bar{E}_{fg'}} \\ &= \sum_k \sum_{fg'=fg'_{k,fg}}^{fg-2} \frac{\Sigma_{es,k,fg'} \phi_{fg'} \Delta E_{fg'}}{(1 - \alpha_k) \bar{E}_{fg'}} + \sum_k \frac{\Sigma_{es,k,fg-1} \phi_{fg-1} \Delta E_{fg-1}}{(1 - \alpha_k) \bar{E}_{fg-1}} \\ &\quad - \sum_k \sum_{fg'=fg'_{k,fg}}^{fg-2} \frac{\Sigma_{es,k,fg'} \phi_{fg'} \Delta E_{fg'}}{(1 - \alpha_k) \bar{E}_{fg'}} - \sum_k \sum_{fg'=fg'_{k,fg-1}}^{fg'_{k,fg}-1} \frac{\Sigma_{es,k,fg'} \phi_{fg'} \Delta E_{fg'}}{(1 - \alpha_k) \bar{E}_{fg'}} \\ &= \sum_k \frac{\Sigma_{es,k,fg-1} \phi_{fg-1} \Delta E_{fg-1}}{(1 - \alpha_k) \bar{E}_{fg-1}} - \sum_k \sum_{fg'=fg'_{k,fg-1}}^{fg'_{k,fg}-1} \frac{\Sigma_{es,k,fg'} \phi_{fg'} \Delta E_{fg'}}{(1 - \alpha_k) \bar{E}_{fg'}} \end{aligned} \quad (198)$$

Equation (198) indicates that the slowing down source of group fg can be calculated by adding the contribution from group $fg-1$ (the first term in the right-hand side of (198)), and subtracting the contributions of $fg'_{k,fg-1} \leq fg' \leq fg'_{k,fg} - 1$ (the second term in the right-hand side of (198)) from the slowing down source of group $fg - 1$. Since the number of energy groups that satisfies $fg'_{k,fg-1} \leq fg' \leq fg'_{k,fg} - 1$ is small, the computational load for estimating the slowing down source is significantly reduced.

Finally, (191) can be rewritten as follows:

$$\Sigma_{t,fg} \phi_{fg} = S_{fg-1} + \sum_k \frac{\Sigma_{es,k,fg-1} \phi_{fg-1} \Delta E_{fg-1}}{(1 - \alpha_k) \bar{E}_{fg-1}} - \sum_k \sum_{fg'=fg'_{k,fg-1}}^{fg'_{k,fg}-1} \frac{\Sigma_{es,k,fg'} \phi_{fg'} \Delta E_{fg'}}{(1 - \alpha_k) \bar{E}_{fg'}} + \chi_{fg} \quad (199)$$

The number of nuclides can reach several hundred for a burnt pellet, in which there are many heavy and fission product nuclides. In such a case, the computational load for the right-hand side of (199) would be heavy. In order to reduce this load, the nuclides can be categorized by their atomic mass, since slowing down due to elastic scattering depends on atomic mass. For example, in a typical LWR analysis, zirconium and uranium can be considered as representative nuclides for cladding, fission products, and heavy nuclides, in addition to hydrogen and oxygen (Sugimura and Yamamoto 2007).

The above numerical solution is used to solve the neutron slowing down equation in a homogeneous system, and is used in major codes such as NJOY. Furthermore, (199) is also used to evaluate the neutron slowing down source in the heterogeneous calculation that will be discussed in the next subsection.

Once the neutron flux in each energy group is obtained, the effective cross section is given by (200), which is the common definition

$$\sigma_g = \frac{\sum_{fg \in g} \Delta E_{fg} \sigma_{fg} \phi_{fg}}{\sum_{fg \in g} \Delta E_{fg} \phi_{fg}} \quad (200)$$

3.7.2 Heterogeneous System

In a heterogeneous system, the neutron slowing down equation is given by (201), when the collision probability is used for the transport kernel.

$$\Sigma_{t,i}(E) \phi_i(E) V_i = \sum_j P_{j \rightarrow i}(E) V_j \left(\int_0^\infty dE' \Sigma_{s,j}(E' \rightarrow E) \phi_j(E') + \chi_j(E) \int_0^\infty dE' \nu \Sigma_{f,j}(E') \phi_j(E') \right) \quad (201)$$

By applying the same approximations (multigroup and fixed source) used in [Sect. 3.7.1](#), we obtain

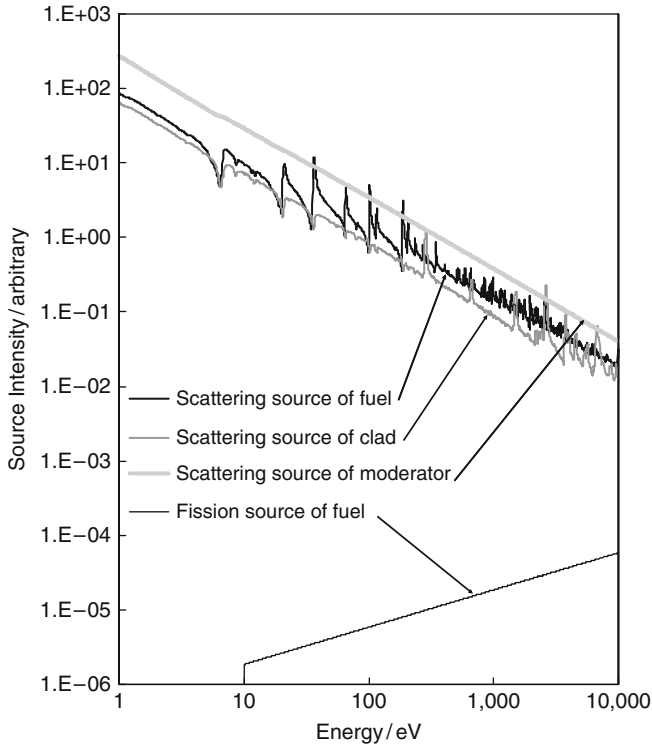
$$\Sigma_{t,f,fg} \phi_{f,fg} V_f = \sum_j P_{j \rightarrow f,fg} V_j (S_{j,fg} + \chi_{j,fg}) \quad (202)$$

When the collision probability in each group is evaluated, (202) can be easily solved. Since (202) contains neutron transport in space, its application is practically limited to a small system, such as a pin cell. Since (202) is a common multigroup form of the transport equation, other transport theories, for example, the discrete-ordinate method or the method of characteristics, can be used. However, the collision probability method is a practical choice due to its superiority for a small system, as discussed in [Sect. 4](#).

Even if a small system is considered, estimation of the collision probability for each group may require considerable computational effort, since in ultrafine energy group calculations, the typical number of energy groups ranges from some tens of thousand to a hundred thousand. Since the collision probability calculation in a one-dimensional system (e.g., cylinder) is quite rapid, a cylindrical approximation with a white boundary condition is a practical choice for an ultrafine energy group calculation in a heterogeneous system.

However, since typical LWR lattices adopt a square shape, a cylindrical approximation would introduce considerable error to the evaluation of neutron flux. Since estimation of the collision probability in a general two-dimensional geometry requires the numerical integration of angle and space with a ray-tracing method, its direct implementation becomes impractical due to the longer computation time required. Collision probabilities are therefore pre-tabulated for various cross sections in each region, and the collision probabilities in each group are obtained by an interpolation of the table (Ishiguro 1974). Though such table interpolation offers a simple, practical approach to the estimation of collision probability, its application is practically limited to a small system, in which there are just a few regions.

The number of regions in a heterogeneous system is, of course, larger than that in a homogeneous system. Thus, evaluations of the slowing down sources for all regions require a longer



■ Figure 23

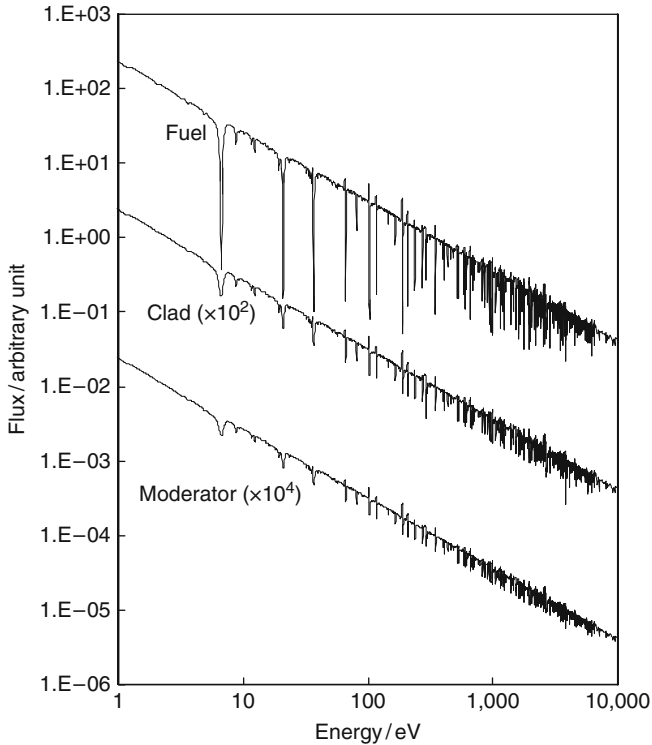
Typical neutron slowing down source in an LWR cell. Note that the fission source is assigned above 10 eV

computation time. Some typical slowing down sources and neutron fluxes in an LWR cell are shown in [Figs. 23](#) and [24](#). These figures suggest that the neutron source in the moderator region is fairly close to $1/E$, in which the NR approximation is well established for the neutron slowing down source. Therefore, the neutron source in the moderator region can be given $1/E$ as a fixed source, and no slowing down calculation would be carried out for the moderator region. Such an approximation not only gives good results, but also considerably reduces the computation time required (Sugimura and Yamamoto 2007).

3.7.3 Limitations of the Ultrafine Energy Groups Method

The approximations used in the ultrafine energy groups method are summarized as follows:

- Neutron slowing down is dominated by elastic scattering.
- Fission source is treated as a fixed source.
- Cross section and neutron flux are assumed to be constant in a group.
- Thermal up-scattering is not taken into account.



■ Figure 24
Typical neutron fluxes in an LWR cell

For a heterogeneous system, the following additional approximations would be taken into account, which are common in typical transport calculations:

- Angular/spatial discretization, and
- Treatment of anisotropic scattering.


The above assumptions usually have small impact on common lattice physics computations for an LWR, if sufficient considerations are taken into account. The ultrafine group method thus offers much greater accuracy than the equivalence theory, and can also overcome a number of deficiencies of that theory (NR/WR/IR approximations, escape probability approximations, resonance overlap, and so on). In fact, the result of the ultrafine group method is usually comparable to that of the continuous-energy Monte Carlo method. The largest and most crucial drawback of this method is its applicability to a large geometry, for example, its direct application to an entire fuel assembly will require hours of calculation with a modern PC, which would be prohibitive in production lattice physics computations. Therefore, the ultrafine group method would be coupled with other resonance calculation methods in order to reinforce its weak points. For example, the ultrafine group calculation can be carried out in a homogeneous system to correct the resonance overlap effect, or it can be carried out in pin cell geometry, with

the position dependency corrected by the conventional equivalence theory with the Dancoff factor (Sugimura and Yamamoto 2007).

3.8 Subgroup Method

3.8.1 General Concept

In the subgroup method, an energy group is subdivided into several subgroups in order to accurately consider variations in the cross section within a group. Since the subgroup method can accurately calculate the effective cross section even if the number of the subgroups in an energy group is a few to several, some lattice physics codes (e.g., APOLLO, WIMS, and HELIOS) incorporate the subgroup method for evaluation of the effective cross section (Nikoleav et al. 1971, 1973; Levitt 1972; Sinitsa and Nikoleav 1973; Cullen 1974, 1986; Ribon 1986; Halsall 1995; Hébert 1998; Loubiere et al. 1999; Yamamoto and Takeda 2000; Sublet and Ribon 2002; Hébert and Coste 2002; Yamamoto 2003, 2004; Hébert 2004, 2005a; Chiba and Unesaki 2006; Yamamoto and Takeda 2006).

The basic concept of the subgroup method is as follows. Variations in neutron flux mainly depend on the magnitude of the cross section, as described in the resonance theory for a homogeneous system, for example, (77). Therefore, when a group is divided into several subgroups according to the magnitude of the cross section, the variations in the neutron flux in a subgroup would be smaller than that in the original group structure. The concept of the subgroup method based on the above explanation is shown in  Fig. 14.

A subgroup structure defined by the above approach has one distinguishing feature: the energy range for a subgroup is no longer contiguous as in the conventional multigroup method. Direct utilization of this physical concept in a resonance calculation is referred to as the direct approach. Though the direct approach yields a clear and intuitive insight into the subgroup method, it also has drawbacks. The most significant drawback is that the subgroup averaged cross section still has dependency on the background cross section, though its dependency on the background cross section is much smaller than that of the effective cross section as defined in a conventional multigroup structure.

On account of this deficiency, the direct approach is not widely used in present day lattice physics codes. Instead of the direct approach, the concept of the probability table method is widely used in practical applications. In this approach, the cross sections of subgroups and their weights (corresponding to the energy group width of each subgroup in the direct method) are chosen so that they are independent of the background cross section. In the probability table approach, the parameters for subgroups (their cross sections and weights) become nonphysical, and no longer have corresponding distinguishing energy ranges as in the direct method.

Though the concept of the probability table is widely used in lattice physics computations, we will discuss the direct approach first, since an intuitive physical understanding of the direct approach is much easier than the probability table approach. An explanation of the probability table approach will be provided after we discuss the direct approach. Two separate methods to generate the probability table are also discussed in this subsection.

3.8.2 Direct Approach

The neutron transport equation for the “direct” subgroup approach is obtained by the energy integration of the following transport equation for a subgroup sg :

$$\vec{\Omega} \cdot \nabla \psi(\vec{r}, E, \vec{\Omega}) + \Sigma_t(\vec{r}, E, \vec{\Omega}) \psi(\vec{r}, E, \vec{\Omega}) = Q(\vec{r}, E, \vec{\Omega}) \quad (203)$$

We obtain

$$\vec{\Omega} \cdot \nabla \psi_{sg}(\vec{r}, \vec{\Omega}) + \Sigma_{t,sg}(\vec{r}) \psi_{sg}(\vec{r}, \vec{\Omega}) = Q_{sg}(\vec{r}) \quad (204)$$

Cross section for subgroup sg is given as follows:


$$\sigma_{sg}(\vec{r}) = \frac{\int_{sg} dE \sigma(E) \phi(\vec{r}, E)}{\int_{sg} dE \phi(\vec{r}, E)} \quad (205)$$

Note that the angular dependence of the neutron source and of the effective cross section in sg is neglected for the sake of simplicity. Such simplification is also used for conventional effective cross sections in a multigroup energy structure. The effective cross section for a conventional multigroup structure is obtained with the neutron scalar flux of subgroup sg , which is obtained as a solution of (204)

$$\sigma_g(\vec{r}) = \frac{\sum_{sg \in g} \sigma_{sg}(\vec{r}) \phi_{sg}(\vec{r})}{\sum_{sg \in g} \phi_{sg}(\vec{r})} \quad (206)$$

In the equivalence theory, the spatial distribution of the neutron flux is evaluated approximately by the escape probability from a fuel lump. In contrast to the equivalence theory, the spatial distribution of the neutron flux is evaluated by the explicit transport calculation in each subgroup. Therefore, the subgroup method can give more accurate results than the equivalence theory. Furthermore, application of the conventional equivalence theory is limited to the average value of a fuel lump, and the spatial distribution of the self-shielding effect cannot be evaluated, since it relies on the escape probability from a fuel lump. The subgroup method can, however, be applied to more general conditions, which include the spatial distribution of the self-shielding effect.

When a subgroup structure is sufficiently fine, variations in the cross section and neutron spectrum in a subgroup can be neglected. Under such conditions, the subgroup method will be consistent with the ultrafine group method. That said, the essential usefulness of the subgroup method is due to the high accuracy that can be obtained even with a small number of subgroups. In this context, the subgroup method is considered as a resonance calculation method that is different from the ultrafine group method.

The effectiveness of the subgroup method depends on the accuracy or appropriateness of the subgroup parameters when a small (i.e., practical) number of subgroups is used in calculations. Since a cross section in a subgroup depends on the neutron spectrum in a subgroup, its evaluation is important. In the direct approach, we have the freedom to choose the energy group structure for subgroups, so we should find a better energy group structure for a subgroup. The neutron flux is approximately inversely proportional to the magnitude of the cross section. Therefore, a subgroup structure, which is defined by the magnitude of the cross section and has discrete ranges, as shown in  Fig. 14, is clearly better than the conventional approach

(sequential division of energy range), since variations in the cross section in a group (and thus variations in the neutron flux in a group) are smaller than those in a conventional group structure with a contiguous energy range.

The subgroup cross section becomes independent of the background cross section (or the shielding condition) when the resonance cross section has a “step shape,” that is, the cross section in each subgroup is constant. In reality, however, we cannot neglect variations in the cross section in a subgroup, so the subgroup cross section inevitably has dependency on the neutron spectrum. Therefore, in the direct approach of the subgroup method, the subgroup cross section is evaluated by

$$\sigma_{sg}(\sigma_0) = \frac{\int_{sg} dE \sigma(E) \phi(E, \sigma_0)}{\int_{sg} dE \phi(E, \sigma_0)}$$

$$sg = \{ E | \sigma_{sg,\min} \leq \sigma(E) \leq \sigma_{sg,\max} \} \quad (207)$$

where

σ_{sg} : subgroup cross section in subgroup sg .

$\phi(E, \sigma_0)$ is obtained by solving a slowing down equation in a homogeneous system composed of hydrogen and the resonance nuclide in question. By performing slowing down calculations for different background cross sections, we can tabulate the dependency of subgroup cross sections on the background cross sections. Once the background cross section in a heterogeneous geometry is evaluated, the subgroup cross section can be obtained through interpolation of the pre-tabulated data. This approach is the same as in the conventional equivalence method, but provides better accuracy, since the sensitivity (variation) of the subgroup cross section on the background cross section is smaller. However, since the above approach still relies on the equivalence between homogeneous and heterogeneous systems, it presents a potential source of error.

When the direct approach of the subgroup method is applied to a general geometry, the evaluation of the background cross section becomes difficult, especially in the evaluation of the space-dependent effective cross section. Since the equivalence theory relies on the rational approximation for the neutron escape probability from a fuel lump, it cannot directly treat the inner regions of a resonance lump. In fact, the heterogeneous term in the background cross section for the inner region of a fuel lump will be zero, since the Dancoff correction becomes unity in such a case. The inner region of a fuel lump is surrounded by fuels, which in a Dancoff factor evaluation are black; thus, the Dancoff correction is unity for such inner regions. In other words, the appropriate derivation of the background cross section for general geometry is difficult, which is why application of the direct approach of the subgroup method has been limited (Yamamoto 2003).

A recent study, however, presents the possible resolution of this issue by using the effective cross section as an index of the self-shielding condition. In this approach, the following procedures are used to evaluate the effective cross section in a general heterogeneous system (Yamamoto et al. 2009a, b):

1. Tabulate the subgroup and the effective cross sections, which are defined by (205) and (206), respectively, versus the background cross section. The subgroup and effective cross sections are evaluated through slowing down calculations in a homogeneous system with various background cross sections.

2. Perform a transport calculation using the tabulated subgroup cross sections. For the first iteration, the subgroup cross sections with an infinite-dilution condition can be used as a starting point.
3. Evaluate the effective cross section by (206) with the subgroup neutron flux obtained in (2).
4. A corresponding background cross section that reproduces the effective cross section obtained in (3) is then estimated from the tabulated data.
5. Update the subgroup cross sections with the background cross section obtained in (4).
6. Repeat (2)–(5) until convergence; a few iterations are sufficient to obtain converged results.

By using the above approach, the evaluation of the background cross section, which is a difficult step in the application of the direct approach of the subgroup method, can be avoided. The above procedure can thus be a practical way to apply the direct approach of the subgroup method in general geometry.

3.8.3 Probability Table Approach

In the direct approach of the subgroup method, the energy group structure for each subgroup is explicitly specified. Contrary to this, in the probability table approach, the energy group structure is not explicitly defined (Levitt 1972; Cullen 1974, 1986; Ribon 1986; Halsall 1995; Hébert 1998; Sublet and Ribon 2002; Hébert and Coste 2002; Hébert 2005a; Chiba and Unesaki 2006). In the mathematical context, it is considered as a utilization of the Lebesgue integration, that is, the integration of neutron spectrum $f(E)$ into energy is converted to that on a cross section

$$\int_{E_g}^{E_{g-1}} dE f(E) = \int_{\sigma_{\min,g}}^{\sigma_{\max,g}} d\sigma f(\sigma) p(\sigma) \quad (208)$$

where

σ : cross section,

$f(E)$: neutron spectrum (dependence of neutron flux on energy),

$f(\sigma)$: neutron spectrum (dependence of neutron flux on cross section),

$p(\sigma)$: probability that cross section in group g is σ ,


$\sigma_{\min,g}$: minimum value of cross section in group g ,

$\sigma_{\max,g}$: maximum value of cross section in group g .

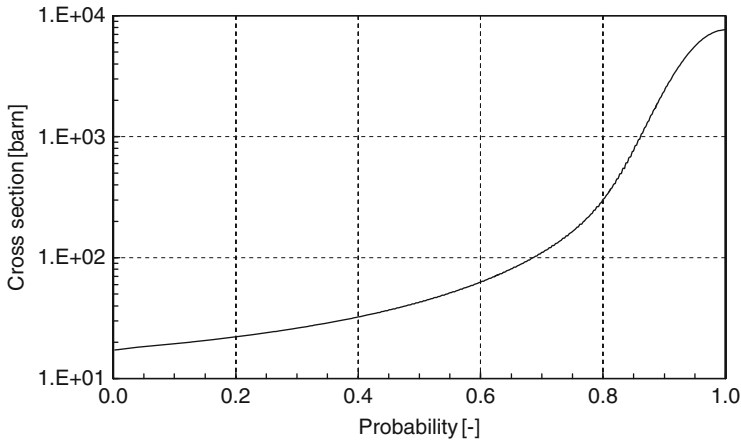
Note that $f(\sigma)$ and $f(E)$ represent the same physical quantity but have different formulas. Variations in $f(\sigma)$ are much smoother than those of $f(E)$ since the neutron spectrum is a smooth function of the magnitude of the cross section. Recalling the NR approximation, the neutron flux is expressed as

$$f(\sigma) = \frac{\sigma_0}{\sigma(E) + \sigma_0} \quad (209)$$

which is a smooth function of the cross section (σ) of a resonant nuclide.

In (209), the $1/E$ dependence is omitted since variations in neutron flux due to $1/E$ are not very large. The probability density function for the cross section, $p(\sigma)$, is also a smooth function of the cross section. An example of $p(\sigma)$ is shown in  Fig. 25.

The above discussion suggests that the integration in the right-hand side of (208) is easier than that in the left-hand side, since the behavior of the integrand is much smoother. Coarse discretization can therefore be used in the integration of the right-hand side of (208).



■ Figure 25

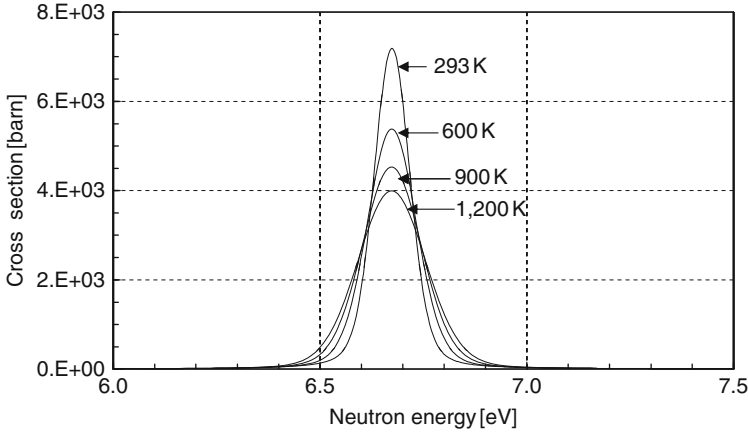
Cumulative probability density function of cross section for ^{238}U (88 group in the 172-group XMAS structure (7.52–6.16 eV), in which there is a large resonance of ^{238}U)

By adopting the concept of the probability density of the cross section, we can define a set of subgroup cross sections and their associated weights that are independent of the background cross section, that is, generalized subgroup cross sections and weights can be derived. Since these parameters are independent of the magnitude of self-shielding, they can be used in any configuration, including the space-dependent self-shielding in a fuel lump, which is difficult to handle using the conventional direct approach of the subgroup method.

The above approach, however, also has a significant drawback. By adopting the integration procedure on the cross section, energy-dependent information is lost. That is, each subgroup defined by the probability table method has no physical energy group structure. This creates difficulty in the treatment of the temperature distribution in a configuration. The shape of a resonance cross section depends on temperature, due to the Doppler broadening effect, as shown in [Fig. 26](#).

When there is temperature distribution in a system, we have different sets of subgroup cross sections and their associated probabilities (weights), even for a nuclide. However, since the implicit energy group structure for each subgroup is different, direct utilization of subgroup parameters with different temperatures cannot be justified in transport calculations. Let us assume two different multigroup cross section sets with totally different energy group structures, but with the same number of energy groups. We can perform a transport calculation that simultaneously uses these two multigroup cross section sets, since the number of energy groups is the same. However, such calculation is, clearly, meaningless. Because direct application of the probability table method for a temperature-dependent problem causes the above inconsistency, care must be taken.

We now consider a set of subgroup cross sections and their associated probabilities, σ_{sg} and p_{sg} . Note that σ_{sg} is constant in a subgroup. Intuitive interpretation of the probability is the fraction of the energy range of the corresponding subgroup within an energy group. When the probability is larger, the corresponding subgroup occupies a larger fraction in an energy group. The subgroup cross section physically represents the average cross section in a subgroup.



■ **Figure 26**
Variations in a ^{238}U capture cross section due to Doppler broadening

However, it must again be remembered that each subgroup has no explicit energy range, and thus these remain abstract and rather mathematical properties.

With the subgroup parameters (subgroup cross sections and probabilities), we have the following equations:

$$\int_{E_g}^{E_{g-1}} dE f(E) = \int_{\sigma_{\min,g}}^{\sigma_{\max,g}} d\sigma f(\sigma) p(\sigma) = \sum_{sg \in g} f_{sg} p_{sg} \quad (210)$$

$$\sum_{sg \in g} p_{sg} = 1 \quad (211)$$

where

$$f_{sg} = f(\sigma_{sg})$$

Equation (210) means that the neutron flux can be integrated through a quadrature set, whose quadrature points and associated weights are σ_{sg} and p_{sg} , respectively. Under this assumption, the effective cross section can be obtained by

$$\sigma_g = \frac{\int_{E_g}^{E_{g-1}} dE \sigma(E) \phi(E)}{\int_{E_g}^{E_{g-1}} dE \phi(E)} = \frac{\int_{\sigma_{\min,g}}^{\sigma_{\max,g}} d\sigma \sigma \phi(\sigma) p(\sigma)}{\int_{\sigma_{\min,g}}^{\sigma_{\max,g}} d\sigma \phi(\sigma) p(\sigma)} = \frac{\sum_{sg \in g} \sigma_{sg} \phi_{sg} p_{sg}}{\sum_{sg \in g} \phi_{sg} p_{sg}} \quad (212)$$

Once the subgroup parameters, that is, σ_{sg} and p_{sg} are known, we can evaluate the effective cross section through the neutron flux for subgroup ϕ_{sg} , which is obtained by a transport calculation for each subgroup. A set of subgroup parameters is called a probability table, which is obtained by a number of numerical calculations that will be discussed later.

Since subgroup parameters are chosen to be independent of the background cross section, they can in principle be used in any configuration. Such flexibility is the advantage of the probability method. However, as discussed previously, an explicit energy group structure cannot be

defined (or is lost) in the derivation of the subgroup cross section. Therefore, application of this method to a problem with temperature distribution is limited.

The fitting and the moment methods are major approaches to the derivation of subgroup parameters. From a historical point of view, they represent the origin of the subgroup method. A more intuitive approach, that is, the direct approach discussed [▶ 3.8.2](#), was devised as a physical interpretation of the subgroup method based on the probability table approach.

3.8.4 Fitting Method

The fitting method is a numerical calculation procedure to derive a set of probability tables used in the subgroup method (Nikoleav et al. 1971; Levitt 1972). In the following, we will discuss the derivation based on the NR approximation.

When the NR approximation for the neutron flux is applied to the formulation of the subgroup cross section, we obtain the following equation:

$$\sigma_{t,sg}(\sigma_0) = \frac{\int_{sg} dE \sigma_t(E) \phi(E, \sigma_0)}{\int_{sg} dE \phi(E, \sigma_0)} = \frac{\int_{sg} dE \sigma_t(E) \frac{1}{\sigma_t(E) + \sigma_0}}{\int_{sg} dE \frac{1}{\sigma_t(E) + \sigma_0}} \quad (213)$$

The band probability is defined by the width of the energy range for each subgroup, as follows:

$$p_{sg} = \frac{\int_{sg} dE}{\int_g dE} \quad (214)$$

The numerator in (213) can be written as follows:

$$\begin{aligned} \int_{sg} dE \sigma_t(E) \frac{1}{\sigma_t(E) + \sigma_0} &= \int_{sg} dE \frac{\sigma_t(E) + \sigma_0 - \sigma_0}{\sigma_t(E) + \sigma_0} \\ &= \int_{sg} dE - \sigma_0 \int_{sg} dE \frac{1}{\sigma_t(E) + \sigma_0} \end{aligned} \quad (215)$$

By substituting (214) and (215) into (213), we obtain the following:

$$\begin{aligned} \sigma_{t,sg}(\sigma_0) &= \frac{\int_{sg} dE - \sigma_0 \int_{sg} dE \frac{1}{\sigma_t(E) + \sigma_0}}{\int_{sg} dE \frac{1}{\sigma_t(E) + \sigma_0}} \\ &= \frac{p_{sg} \int_g dE}{\int_{sg} dE \frac{1}{\sigma_t(E) + \sigma_0}} - \sigma_0 \end{aligned} \quad (216)$$

From (216), we have the following relationship:

$$\int_{sg} dE \frac{1}{\sigma_t(E) + \sigma_0} = \frac{p_{sg} \int_g dE}{\sigma_{t,sg}(\sigma_0) + \sigma_0} \quad (217)$$

By substituting (214) and (217) into (215), we obtain

$$\begin{aligned} \int_{s_g} dE \sigma_t(E) \frac{1}{\sigma_t(E) + \sigma_0} &= p_{sg} \int_g dE - \sigma_0 \frac{p_{sg} \int_g dE}{\sigma_{t,sg}(\sigma_0) + \sigma_0} \\ &= \frac{\sigma_{t,sg}(\sigma_0) p_{sg} \int_g dE}{\sigma_{t,sg}(\sigma_0) + \sigma_0} \end{aligned} \quad (218)$$

With (213), (217) and (218), the total cross section is given as follows:

$$\begin{aligned} \sigma_{t,g}(\sigma_0) &= \frac{\int_{E_g}^{E_{g-1}} dE \sigma_t(E) \frac{1}{\sigma_t(E) + \sigma_0}}{\int_{E_g}^{E_{g-1}} dE \frac{1}{\sigma_t(E) + \sigma_0}} \\ &= \frac{\sum_{sg \in g} \int_{s_g} dE \sigma_t(E) \frac{1}{\sigma_t(E) + \sigma_0}}{\sum_{sg \in g} \int_{s_g} dE \frac{1}{\sigma_t(E) + \sigma_0}} \\ &= \frac{\sum_{sg \in g} \frac{\sigma_{t,sg}(\sigma_0) p_{sg} \int_g dE}{\sigma_{t,sg}(\sigma_0) + \sigma_0}}{\sum_{sg \in g} \frac{p_{sg} \int_g dE}{\sigma_{t,sg}(\sigma_0) + \sigma_0}} \\ &= \frac{\sum_{sg \in g} \frac{\sigma_{t,sg}(\sigma_0) p_{sg}}{\sigma_{t,sg}(\sigma_0) + \sigma_0}}{\sum_{sg \in g} \frac{p_{sg}}{\sigma_{t,sg}(\sigma_0) + \sigma_0}} \end{aligned} \quad (219)$$

In (219), the subgroup cross section has dependency on the background cross section. However, we assume that the subgroup cross sections are independent of the background cross section, so the effective cross section is defined as

$$\sigma_{t,g}(\sigma_0) = \frac{\sum_{sg \in g} \frac{\sigma_{t,sg} p_{sg}}{\sigma_{t,sg} + \sigma_0}}{\sum_{sg \in g} \frac{p_{sg}}{\sigma_{t,sg} + \sigma_0}} \quad (220)$$

In the fitting method, the subgroup parameters (a set of subgroup cross sections and associated probabilities) are chosen to satisfy (220) through a fitting procedure. When the number of subgroup is N , we have $2N$ unknowns for the subgroup cross sections and the probabilities. The normalization condition for the probabilities can be used as a constraint.

$$\sum_{sg \in g} p_{sg} = 1 \quad (221)$$

In addition, we should consider at least $2N - 1$ relations between the background cross section and the effective cross section in order to complete a set of equations with which to estimate

unknowns:

$$\sigma_{t,g}(\sigma_{0,l}) = \frac{\sum_{sg \in g} \frac{\sigma_{t,sg} p_{sg}}{\sigma_{t,sg} + \sigma_{0,l}}}{\sum_{sg \in g} \frac{p_{sg}}{\sigma_{t,sg} + \sigma_{0,l}}} \quad (l = 1, 2, \dots, 2N - 1) \quad (222)$$

We can use more than $2N - 1$ relations for the background cross section and the effective cross section. In this case, the subgroup parameters are evaluated through the least square fitting. Therefore, this approach is usually called the fitting method.

In principle, there is not a general set of subgroup parameters that is independent of the background cross section. Therefore, even if we use the fitted subgroup parameters, the effective cross section cannot be exactly reproduced for every background cross section. This is a shortcoming of the fitting method. Furthermore, when the number of subgroups increases, the fitting procedure used for (222) sometimes runs into numerical difficulties and may provide a nonphysical solution for the subgroup parameters, for example, negative and/or imaginary probabilities and subgroup cross sections.

Despite this deficiency, the fitting method remains a major approach to the derivation of subgroup cross sections since it gives the “general” subgroup parameters that can be used for any geometry, and estimation of the effective cross section in general geometry becomes easy once the subgroup is obtained. Furthermore, in the fitting method, the band probabilities and subgroup cross sections are chosen to reproduce the effective multigroup cross section, which in a homogeneous system, is usually generated through an accurate numerical solution of the slowing down equation (ultrafine group calculation). In this context, the fitting method can implicitly incorporate the “slowing down” effect, which is obtained by the ultrafine group calculation.

3.8.5 Moment Method

The moment method is another approach to estimating subgroup parameters (Ribon 1986; Hébert and Coste 2002; Hébert 2005a). In this method, we use the following “moment” of a cross section:

$$M_{t,n} = \frac{\int_{E_g}^{E_{g-1}} dE \sigma_t(E)^n}{\int_{E_g}^{E_{g-1}} dE} \quad (223)$$

where n is the order of a moment. Using the probability density function of the cross section and applying the integration with a cross section, (223) can be rewritten as follows:

$$\begin{aligned} M_{t,n} &= \frac{\int_{E_g}^{E_{g-1}} dE \sigma_t(E)^n}{\int_{E_g}^{E_{g-1}} dE} = \frac{\int_{\sigma_{t,\min,g}}^{\sigma_{t,\max,g}} d\sigma_t \sigma_t^n p(\sigma_t)}{\int_{\sigma_{t,\min,g}}^{\sigma_{t,\max,g}} d\sigma_t p(\sigma_t)} \\ &\approx \frac{\sum_{sg \in g} \int_{\sigma_{t,\min,g}}^{\sigma_{t,\max,g}} d\sigma_t \sigma_t^n \delta(\sigma_t - \sigma_{t,sg}) p_{sg}}{\sum_{sg \in g} \int_{\sigma_{t,\min,g}}^{\sigma_{t,\max,g}} d\sigma_t \delta(\sigma_t - \sigma_{t,sg}) p_{sg}} \\ &= \frac{\sum_{sg \in g} \sigma_{t,sg}^n p_{sg}}{\sum_{sg \in g} p_{sg}} = \sum_{sg \in g} \sigma_{t,sg}^n p_{sg} \end{aligned} \quad (224)$$

The moment of a cross section using the subgroup parameters is given by

$$m_{t,n} = \sum_{sg \in g} \sigma_{t,sg}^n p_{sg} \quad (225)$$

In the moment method, we also have $2N$ unknowns for the subgroup cross sections and probabilities, just as in the fitting method. Since the normalization condition for probability is also used in the moment method, we should consider the $2N - 1$ constraints for different moments:

$$\sum_{sg \in g} p_{sg} = 1 \quad (226)$$

$$\frac{\int_{E_g}^{E_{g-1}} dE \sigma_t(E)^n}{\int_{E_g}^{E_{g-1}} dE} = \sum_{sg \in g} \sigma_{t,sg}^n p_{sg} \quad (n = I + 1, I + 2, \dots, I + 2N - 1, I : \text{integer}) \quad (227)$$

When $n = 0$, (227) is reduced to (226). By solving (226) and (227), (i.e., $\sum_{sg \in g} p_{sg} = 1$ and $M_{t,n} = m_{t,n}$), we can obtain the subgroup parameters. However, (226) and (227) require the solution of the n th degree equation, which would be difficult to obtain. In the following part, a numerical procedure for the evaluation of subgroup parameters using the Pade approximation, as proposed by Ribon et al. is described (Ribon 1986).

First, in the case of $I = 0$, we define a polynomial of order $2N - 1$, which contains the moments of a cross section in its coefficients:

$$F(z) = \sum_{n=0}^{\infty} m_{t,n} z^n = \sum_{n=0}^{2N-1} m_{t,n} z^n + r(z^{2N}) \quad (228)$$

where $r(z^{2N})$ indicates a residual term.

When the value of z is chosen to satisfy $\sigma_{t,sg} z < 1$, (228) can be rewritten as follows:

$$\begin{aligned} F(z) &= \sum_{n=0}^{2N-1} m_{t,n} z^n + r(z^{2N}) \\ &= \sum_{n=0}^{2N-1} \sum_{sg \in g} \sigma_{t,sg}^n p_{sg} z^n + r(z^{2N}) \\ &= \sum_{sg \in g} p_{sg} \sum_{n=0}^{2N-1} (\sigma_{t,sg} z)^n + r(z^{2N}) \\ &= \sum_{sg \in g} p_{sg} \frac{1}{1 - \sigma_{t,sg} z} + r'(z^{2N}) \end{aligned} \quad (229)$$

$F(z)$ can be also expressed by $M_{t,n}$ since $m_{t,n}$ should reproduce $M_{t,n}$, that is, $M_{t,n} = m_{t,n}$. Using the Pade approximation, $F(z)$ can be written as follows:

$$F(z) = \sum_{n=0}^{2N-1} M_{t,n} z^n + R(z^{2N}) = \frac{\sum_{n=0}^{N-1} a_n z^n}{\sum_{n=0}^N b_n z^n} + R'(z^{2N}) \quad (230)$$

where $R(z^{2N})$ is a residual term, which is slightly different from $r(z^{2N})$.

Note that the summation of the polynomial order in the numerator and denominator of the Pade approximation should be $2N - 1$, in order to approximate a polynomial of order $2N - 1$. Thus, the order of polynomials for the numerator and denominator in (230) is chosen to be $N - 1$ and N , respectively ($N - 1 + N = 2N - 1$). In the Pade approximation, the coefficients in (230) can be determined by the following set of $2N$ linear equations:

$$\begin{aligned} a_n &= \sum_{m=0}^n M_{t,n-m} b_m & (n = 0, 1, \dots, N-1) \\ 0 &= \sum_{m=0}^N M_{t,N+n-m} b_m & (n = 0, 1, \dots, N-1) \end{aligned} \quad (231)$$

where

$$b_0 = 1$$

Once we know the coefficients of a_n and b_n , (230) can be transformed into the following:

$$\begin{aligned} F(z) &= \frac{\sum_{n=0}^{N-1} a_n z^n}{\sum_{n=0}^N b_n z^n} + R'(z^{2N}) = \frac{\sum_{n=0}^{N-1} a_n z^n}{1 + \sum_{n=1}^N b_n z^n} + R'(z^{2N}) \\ &= \frac{\sum_{n=0}^{N-1} a_n z^n}{\prod_{n=1}^N \left(1 - \frac{z}{z_n}\right)} + R'(z^{2N}) = \sum_{n=1}^N \frac{\omega_n}{1 - \frac{z}{z_n}} + R'(z^{2N}) \end{aligned} \quad (232)$$

where

ω_n : a coefficient defined by a_n and b_n .

In (232), the denominator is factorized with the roots of $1 + \sum_{n=0}^N b_n z^n = 0$, expressed by z_n . By comparing (229) and (232), we find that the subgroup cross section is given by

$$\sigma_{t,sg=n} = \frac{1}{z_n} \quad (234)$$

Therefore, the subgroup cross section can be evaluated using the roots of $1 + \sum_{n=0}^N b_n z^n = 0$. Once we have the subgroup cross sections, the associated probabilities are calculated by

$$M_{t,n} = m_{t,n} = \sum_{sg \in g} \sigma_{t,sg}^n p_{sg} \quad (n = 1, 2, \dots, N) \quad (235)$$

The moments for other cross sections (except for the total cross section) are defined by

$$M_{x,n} = \frac{\int_{E_g}^{E_{g-1}} dE \sigma_x(E) \sigma_t(E)^n}{\int_{E_g}^{E_{g-1}} dE} \quad (236)$$

$$m_{x,n} = \sum_{sg \in g} \sigma_{x,sg} \sigma_{t,sg}^n p_{sg} \quad (237)$$

When the values of $\sigma_{t,sg}$ and p_{sg} are known, the moments for other cross sections can be derived by equating (236) and (237), that is,

$$M_{x,n} = m_{x,n} \quad (238)$$

In the above derivation, the moments of the cross sections with an integer order are preserved. The above procedure is generally used in the moment method. However, it could also be extended to non-integer moments (Chiba and Unesaki 2006). Let us consider an effective cross section based on the NR approximation:

$$\sigma_{x,g}(\sigma_0) = \frac{\int_{E_g}^{E_{g-1}} dE \sigma_x(E) \frac{1}{\sigma_t(E) + \sigma_0}}{\int_{E_g}^{E_{g-1}} dE \frac{1}{\sigma_t(E) + \sigma_0}} \quad (239)$$

By considering very small and large values for the background cross section, we have the following expressions for the infinite-dilute and fully shielded conditions:

$$\begin{aligned} \sigma_{x,g}(\sigma_0 = \infty) &= \frac{\int_{E_g}^{E_{g-1}} dE \sigma_x(E)}{\int_{E_g}^{E_{g-1}} dE} = \frac{\int_{E_g}^{E_{g-1}} dE \sigma_x(E) \sigma_t(E)^0}{\int_{E_g}^{E_{g-1}} dE \sigma_t(E)^0} \\ &= \frac{M_{x,0}}{M_{t,0}} \end{aligned} \quad (240)$$

$$\begin{aligned} \sigma_{x,g}(\sigma_0 = 0) &= \frac{\int_{E_g}^{E_{g-1}} dE \sigma_x(E) \frac{1}{\sigma_t(E)}}{\int_{E_g}^{E_{g-1}} dE \frac{1}{\sigma_t(E)}} = \frac{\int_{E_g}^{E_{g-1}} dE \sigma_x(E) \sigma_t(E)^{-1}}{\int_{E_g}^{E_{g-1}} dE \sigma_t(E)^{-1}} \\ &= \frac{M_{x,-1}}{M_{t,-1}} \end{aligned} \quad (241)$$

In the above equations, the asymptotic neutron flux ($1/E$) is assumed to be unity. Equations (240) and (241) suggest that an effective cross section for a particular background cross section may be given by an interpolation of n :

$$\sigma_{x,g}(\sigma_0) = \frac{M_{x,n}}{M_{t,n}} \quad (242)$$

in which $-1 \leq n \leq 0$, since all shielded conditions appear between two extreme conditions, that is, the infinite-dilute ($n = 0$) and the fully shielded ($n = -1$) conditions.

The above discussion justifies the preservation of the cross section moments of a non-integer order. A previous study also indicates that the accuracy of the effective cross sections in a homogeneous geometry is improved by preservation of the non-integer moments of the cross sections (Chiba and Unesaki 2006).

In the conventional moment method, which preserves the integer moments of cross sections, no distinct physical properties are directly taken into account during the derivation process. On the contrary, in the non-integer approach, neutron flux behavior is partly (at least in the infinite-dilute and the fully shielded conditions) taken into account in the generation process of the subgroup cross sections. Thus, the accuracy of the subgroup parameters derived by the preservation of non-integer moments becomes higher.

3.8.6 Improvements in the Probability Table Approach

Various efforts are still being made to improve the probability table approach. Some of the issues addressed by these improvements are introduced below.

In general, subgroup parameters are generated with the slowing down calculation in a homogeneous system. However, the subgroup parameters generated in a homogeneous system may not exactly reproduce the effective cross section in a heterogeneous system. Therefore, the generation of subgroup parameters using the slowing down calculation in a heterogeneous geometry is proposed, in order to increase the accuracy of the actual calculation results in a heterogeneous fuel assembly (Joo et al. 2009).

Direct application of the probability table approach for nonuniform temperature problems poses difficulties, as was discussed earlier. However, because nonuniform temperature distribution appears in actual reactor core analyses, a countermeasure to this is important. Several methods have thus far been proposed to address this issue (Joo et al. 2005; Wemple et al. 2007).

Resonance overlap (or interference), which will be discussed in ▶ 3.10, may also have an impact on the calculation accuracy of the subgroup method. This topic has also been investigated by several researchers (Hébert 2004).

3.9 Other Methods

3.9.1 Tone's Method

In fast reactor calculations, a resonance calculation based on Tone's method is sometimes used (Tone 1975). In this method, a resonance absorber is not approximated as black, the escape probability from a fuel lump is directly evaluated by the collision probability method, and the rational approximation in the equivalence theory is not explicitly used. Therefore, the background cross section for a general heterogeneous geometry can be evaluated with approximated treatment of the space-dependent self-shielding effect.

Recalling (136), the neutron flux in region i can be calculated by considering the contribution of neutron sources in other regions:

$$\phi_i(E) = \frac{1}{E} \sum_j \frac{P_{j \rightarrow i}(E) V_j \Sigma_{p,j}}{\Sigma_{t,i}(E) V_i} \quad (243)$$

Note that the NR approximation is used for the neutron slowing down source in each region. In Tone's method, we introduce the following key approximation:

$$\frac{P_{j \rightarrow i}(E)}{\Sigma_{t,i}(E)} = \alpha_i(E) \frac{P_{j \rightarrow i,g}}{\Sigma_{t,i,g}} \quad (244)$$

where g denotes a group averaged property. For example, the collision probability $P_{j \rightarrow i,g}$ is the group average collision probability, which is obtained by a set of multigroup cross sections. Equation (244) indicates that the fine energy dependency of the collision probability inside an energy group relies only on target region i . In reality, the energy dependence of the collision probability relies not only on region i , but on other regions as well, including the source region. In other words, with the exception of region i , cross sections are assumed to be energetically

constant in an energy group. In a more physical interpretation, a resonance nuclide in question is not included (or can be neglected) in other regions, in the evaluation of the background cross section. This is a major assumption in Tone's method that represents a potential cause of error.

By substituting (244) into (243), we obtain

$$\phi_i(E) = \frac{1}{E} \alpha_i(E) \sum_j \frac{P_{j \rightarrow i, g} V_j \Sigma_{p, j}}{\Sigma_{t, i, g} V_i} \quad (245)$$

In addition to the above equation, the reciprocity theorem and the normalization condition for collision probabilities are also taken into account:

$$P_{j \rightarrow i}(E) V_j \Sigma_{t, j}(E) = P_{i \rightarrow j}(E) V_i \Sigma_{t, i}(E) \quad (246)$$

$$\sum_j P_{i \rightarrow j}(E) = 1 \quad (247)$$

Equation (247) can be transformed as follows, by substituting (244) and (246) into (247):

$$\begin{aligned} 1 &= \sum_j P_{i \rightarrow j}(E) \\ &= \sum_j \frac{P_{j \rightarrow i}(E) V_j \Sigma_{t, j}(E)}{V_i \Sigma_{t, i}(E)} \\ &= \sum_j \alpha_i(E) \frac{P_{j \rightarrow i, g} V_j \Sigma_{t, j}(E)}{\Sigma_{t, i, g} V_i} \\ &= \alpha_i(E) \frac{1}{\Sigma_{t, i, g} V_i} \sum_j P_{j \rightarrow i, g} V_j \Sigma_{t, j}(E) \end{aligned} \quad (248)$$

Finally, using (248), α is expressed as follows:

$$\alpha_i(E) = \frac{\Sigma_{t, i, g} V_i}{\sum_j P_{j \rightarrow i, g} V_j \Sigma_{t, j}(E)} \quad (249)$$

By substituting (249) into (245), we obtain:

$$\begin{aligned} \phi_i(E) &= \frac{1}{E} \alpha_i(E) \sum_j \frac{P_{j \rightarrow i, g} V_j \Sigma_{p, j}}{\Sigma_{t, i, g} V_i} \\ &= \frac{1}{E} \frac{\Sigma_{t, i, g} V_i}{\sum_j P_{j \rightarrow i, g} V_j \Sigma_{t, j}(E)} \sum_j \frac{P_{j \rightarrow i, g} V_j \Sigma_{p, j}}{\Sigma_{t, i, g} V_i} \\ &= \frac{1}{E} \frac{\sum_j P_{j \rightarrow i, g} V_j \Sigma_{p, j}}{\sum_j P_{j \rightarrow i, g} V_j \Sigma_{t, j}(E)} \end{aligned}$$

$$\begin{aligned}
& \cong \frac{1}{E} \frac{\sum_j P_{j \rightarrow i, g} V_j \cdot \left(N_{r, j} \sigma_{p, r} + \sum_{k \neq r} N_{k, j} \sigma_{p, k} \right)}{\sum_j P_{j \rightarrow i, g} V_j \cdot \left(N_{r, j} \sigma_{t, r}(E) + \sum_{k \neq r} N_{k, j} \sigma_{p, k} \right)} \\
& = \frac{1}{E} \frac{\sigma_{p, r} \sum_j P_{j \rightarrow i, g} V_j N_{r, j} + \sum_j P_{j \rightarrow i, g} V_j \sum_{k \neq r} N_{k, j} \sigma_{p, k}}{\sigma_{t, r}(E) \sum_j P_{j \rightarrow i, g} V_j N_{r, j} + \sum_j P_{j \rightarrow i, g} V_j \sum_{k \neq r} N_{k, j} \sigma_{p, k}} \\
& = \frac{1}{E} \frac{\sigma_{p, r} + \left(\sum_j P_{j \rightarrow i, g} V_j \sum_{k \neq r} N_{k, j} \sigma_{p, k} \right) / \left(\sum_j P_{j \rightarrow i, g} V_j N_{r, j} \right)}{\sigma_{t, r}(E) + \left(\sum_j P_{j \rightarrow i, g} V_j \sum_{k \neq r} N_{k, j} \sigma_{p, k} \right) / \left(\sum_j P_{j \rightarrow i, g} V_j N_{r, j} \right)} \\
& = \frac{1}{E} \frac{\sigma_{p, r} + \sigma_0}{\sigma_{t, r}(E) + \sigma_0} \tag{250}
\end{aligned}$$

where



$$\sigma_0 = \frac{\sum_j \sum_{k \neq r} P_{j \rightarrow i, g} V_j N_{k, j} \sigma_{p, k}}{\sum_j P_{j \rightarrow i, g} V_j N_{r, j}} \tag{251}$$

We assume that with the exception of a resonance nuclide, cross sections are approximated by a constant potential scattering cross section.

Equation (251) indicates that the background cross section is obtained by the collision probabilities among regions, volume, number densities, and potential cross sections. Since collision probabilities depend on the effective cross sections, which in turn depend on the background cross sections, an iteration calculation procedure is necessary, which is as follows:

1. Assume initial background cross sections for resonance nuclides. They can be evaluated using the conventional equivalence method with the Dancoff correction.
2. Evaluate the effective cross sections of resonance nuclides using the conventional equivalence theory.
3. Evaluate group-wise collision probability using the effective cross section evaluated in (2).
4. Update the background cross section using (251).
5. Repeat (2)–(4) until convergence. A few iterations are usually sufficient to obtain the converged result.

Tone's method seeks to incorporate actual collision probabilities among regions through the approximation of (244). Therefore, it is more applicable to general geometry than the conventional equivalence method. Furthermore, since only the definition of the background cross section is changed, it has a closer affinity to the conventional equivalence method than to the subgroup method.

An example of a performance comparison between the subgroup and Tone's methods in a fast reactor fuel assembly is shown in  Fig. 27 (Chiba 2003). The fuel assembly used for the comparison is shown on the left side of  Fig. 27, in which there are 169 fuel pins. The effective microscopic capture cross section of ^{238}U in each fuel rod is evaluated at 300 K. JENDL3.2 is used throughout the comparison. The number of energy groups (70 groups) and the energy group structure used in this comparison, is the same as in JSF-3-3.2R. The moment method is

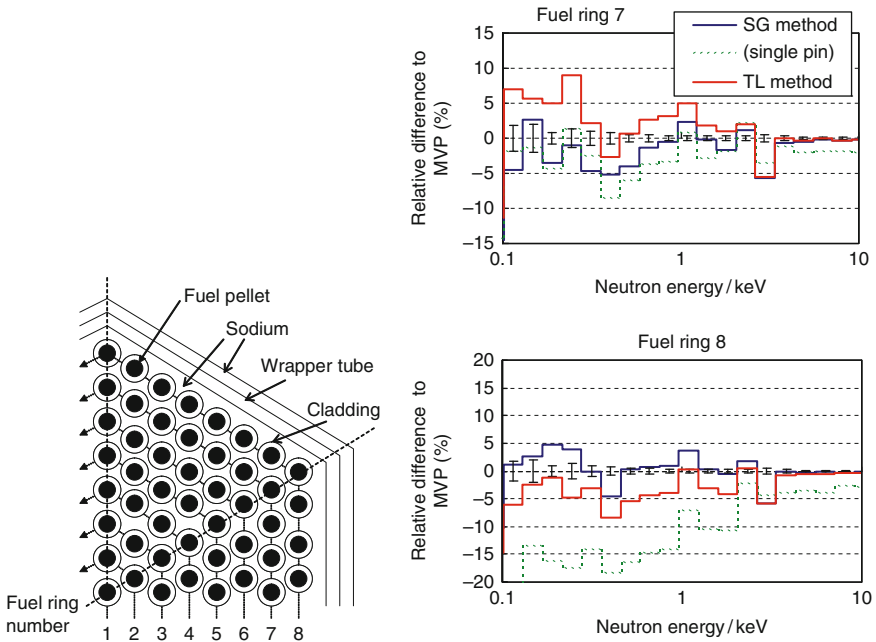


Figure 27

Schematic view of fast reactor fuel assembly, and the difference between effective cross sections obtained by the subgroup method and Tone's method (SG; subgroup, TL; table lookup by Tone's method) (Chiba 2003)

used to generate the subgroup parameters in the subgroup method. The number of subgroups is set at less than or equal to five.

The wrapper tube and sodium in the peripheral region of the assembly create position dependency on the effective cross sections in a fuel assembly. That is, the effective cross sections in the outer ring of the fuel assembly become larger, since ^{238}U is not included in the wrapper tube and sodium, and they act as a neutron source of heavy nuclides in the resonance energy region. In fast reactor calculations, this effect is called the double heterogeneity effect: pellet, cladding, and coolant for the primary and fuel rods, and wrapper and sodium for the secondary heterogeneity.

In order to verify the significance of the position dependency, the subgroup method is also applied to a single pin-cell geometry, which does not consider the wrapper tube and sodium in the peripheral region.

A comparison of the effective cross section for ^{238}U is shown on the right side of Fig. 27. The reference result is obtained by the continuous-energy Monte Carlo code, MVP. In this comparison, the subgroup method gives better accuracy than Tone's method. In the outermost fuel ring (ring 8), the double heterogeneity effect exerts a considerable effect on the effective cross sections, so such an effect must be accurately taken into account. Since BWR fuel assembly also has a similar structure (channel box with gap water around the fuel assembly), the position dependency of the effective cross section is also important.

The above results suggest that the subgroup method gives better accuracy than Tone's method. In this context, Tone's method can be considered as a simple and reasonably accurate resonance calculation method that can be applied to general geometry. Due to this feature, some lattice physics codes adopt this method as the resonance calculation method.

The advantages and disadvantages of Tone's method are summarized as follows:

- Contributions to a background cross section from other regions are taken into account approximately through region-wise and group-wise collision probabilities.
- Its affinity to the conventional equivalence theory is high. Cross section libraries and self-shielding factors prepared for the conventional method with equivalence theory can be directly used in Tone's method.
- The "gray regions" from the viewpoint of the resonance calculation can be approximately treated. Thus the space-dependent self-shielding effect in a fuel lump could be evaluated approximately.
- The NR approximation is used. Note that this method is primarily intended for fast reactor calculations, in which the NR approximation displays a high degree of accuracy. In this context, this method can be accurately applied to resonances in a higher energy range in LWR calculations, in which the NR approximation is valid.
- The energy dependence of collision probabilities among regions are approximated using (244).
- Iteration calculations are required for effective cross sections, in which calculation of the collision probabilities is included, though only a few iterations are needed to obtain converged results. If one's initial rough predictions for effective cross sections is reasonably good, no iteration may be necessary.

3.9.2 The Stoker–Weiss Method and the Space-Dependent Dancoff Method (SDDM)

The Stoker–Weiss Method

The Stoker–Weiss method is another approach to estimating the space-dependent self-shielding effect for the annular regions of a cylindrical fuel rod (Stoker and Weiss 1996; Matsumoto et al. 2005; Matsumoto et al. 2006). This method derives an approximate expression of the escape probability from the annular regions in a fuel pellet not only for an outer ring, but for the inner rings as well.

From a practical point of view, the space-dependent self-shielding effect is important because

- Larger resonance capture of ^{238}U on the pellet surface area causes a higher plutonium buildup in the outer region of a fuel pellet.
- The power distribution inside a pellet is significantly affected by the plutonium buildup and power distribution as the outer region becomes higher at middle to end of life. Consequently, burnup on the pellet surface becomes higher than that of the pellet average, which has an impact on the fission gas release from a pellet, which could be a one of the mechanical limitations of a fuel rod.
- The temperature distribution in a pellet is influenced by the power distribution inside it, for example, the pellet centerline and the average temperature.

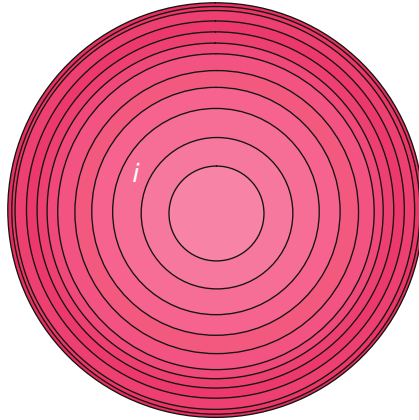


Figure 28

Annular subdivisions of a fuel pellet

Therefore, a simple method to estimate the self-shielding effect inside a pellet is important, mainly for the mechanical evaluation of a fuel rod and a fuel assembly.

From the viewpoint of the resonance calculation, many studies have clarified that the subdivision of a fuel pellet into multiple annular regions does not have a major impact on the accuracy of the resonance calculation, even if the spatial distribution of the number density due to burnup is taken into account. This means that the average treatment of resonance nuclides can be justified for a fuel pellet, at least from the viewpoint of the resonance calculation. A more detailed discussion of this will be offered in [3.11.3](#).

Though the major objective of a lattice physics computation is to provide cross section sets for a core calculation code, the calculation results are also used in mechanical design and safety analyses (e.g., decay heat is dominated by the number densities of heavy and fission product nuclides, which are calculated by a lattice physics code).

Let us now assume that an isolated fuel pellet is annularly subdivided into multiple annular rings, as shown in [Fig. 28](#). The final objective of the Stoker–Weiss method is to derive an expression of the energy dependence of a neutron spectrum for an annular region i with the N -term rational approximation.

When the macroscopic cross section is assumed to be spatially constant inside a pellet region, and the NR approximation is applied to calculate the slowing down source, the neutron flux in region i is expressed as

$$\phi_i(E) = \frac{1}{E} \left((1 - P_{i \rightarrow m}(E)) \frac{\Sigma_{p,f}}{\Sigma_{t,f}(E)} + P_{i \rightarrow m}(E) \right) \quad (252)$$

where i is a region in a pellet ($i \in f$); a detailed derivation of the above equation is given in [\(139\)](#).

In the Stoker–Weiss method, the escape probability from region i to the moderator region m , $P_{i \rightarrow m}(E)$ is assumed to be expressed as

$$P_{i \rightarrow m}(E) = DP_{e,i}(E) \quad (253)$$

where $P_{e,i}(E)$ is the escape probability of a neutron from a fuel, which includes region i , and D is the Dancoff factor (which is unity for isolated fuel). When the number of annular regions in a pellet is one, (253) is reduced into the conventional equivalence theory with the Dancoff factor.

Theoretically, the Dancoff factor should be an energy-dependent parameter in (253). However, the energy dependence of the Dancoff factor is neglected in the derivation of this method.

In order to evaluate $P_{e,i}(E)$, we start from the escape probability for an isolated lump, that is, (106):

$$P_e(E) = \frac{1}{\Sigma_{t,f}(E)\bar{l}} \int_0^\infty dl f(l) \{1 - \exp(-\Sigma_{t,f}(E)l)\} \tag{254}$$

In (254), $\exp(-\Sigma_{t,f}(E)l)$ denotes the transmission probability of a fuel lump, and thus $1 - \exp(-\Sigma_{t,f}(E)l)$ is the probability that a neutron entering from the surface of a fuel lump will suffer a collision in the fuel lump. Consequently, $\int_0^\infty dl f(l) \{1 - \exp(-\Sigma_{t,f}(E)l)\}$ gives the expected value of the collision probability in a fuel lump.

When a neutron entering a fuel pellet has its first collision in region i (in the fuel pellet) with the probability of $\gamma_i(E)$, the escape probability from region i can be expressed as

$$P_{e,i}(E) = \frac{1}{\Sigma_{t,f}(E)\bar{l}_i} \int_0^\infty dl f(l) \{1 - \exp(-\Sigma_{t,f}(E)l)\} = \frac{\gamma_i(E)}{\Sigma_{t,f}(E)\bar{l}_i} \tag{255}$$

where

$\bar{l}_i = 4V_i/S_f$, which is the ‘‘average chord length’’ of region i , expressed by the volume of region i (V_i) and the surface of a fuel pellet (S_f). Note that the definition of the average chord length in this derivation (\bar{l}_i) is different from the conventional one, which is defined by $\bar{l}_i = 4V_i/S_i$. In (255), a neutron that enters from the pellet surface (S_f) collides at region i (V_i). However, in the conventional definition, a neutron that enters from region i (S_i) collides at region i (V_i).

In (255), $\gamma_i(E)$ is also considered as the blackness of region i . The blackness of a solid cylinder that includes region i (ABC in \blacktriangleright Fig. 29) is approximated by

$$\gamma_{i,ABC}(E) = (\gamma_{i,OBC}(E) - \gamma_{i,OAB}(E)) \tag{256}$$

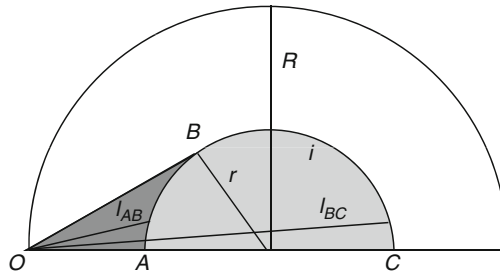


Figure 29
Calculation geometry of blackness for a cylinder

A similar expression for the solid cylinder that includes region $i - 1$ is given by

$$\gamma_{i-1,ABC}(E) = (\gamma_{i-1,OBC}(E) - \gamma_{i-1,OAB}(E)) \quad (257)$$

Equations (256) and (257) assume that the blackness of each region can be synthesized by the subtraction that is shown in  Fig. 29.

Finally, in the Stoker–Weiss method, the blackness of region i is evaluated by (258), since the blackness of ring i can be approximated by subtraction of the blackness for the solid cylinders, including regions i and $i - 1$:

$$\gamma_i(E) = (\gamma_{i,OBC}(E) - \gamma_{i,OAB}(E)) - (\gamma_{i-1,OBC}(E) - \gamma_{i-1,OAB}(E)) \quad (258)$$

Next, we will try to estimate each component on the right-hand side of (258). Recalling (254), the collision probability in a region can be expressed by the product of the optical length of a region $(\Sigma_{t,f}(E)\bar{l})$ and the escape probability $P_e(E)$:

$$\int_0^\infty dl f(l) \{1 - \exp(-\Sigma_{t,f}(E)l)\} = \Sigma_{t,f}(E)\bar{l} \times P_e(E) \quad (259)$$

Using the above observation, the blackness for solid region OBC can be evaluated by the following:

$$\begin{aligned} \gamma_{i,OBC}(E) &= (\text{Entering probability to the region } OBC \text{ for a neutron entering the fuel}) \\ &\quad \times (\text{Collision probability in the solid region } OBC) \\ &= (\text{Entering probability to the region } OBC \text{ for a neutron entering the fuel}) \\ &\quad \times (\text{Optical length of the solid region } OBC) \\ &\quad \times (\text{Escape probability from the solid region } OBC) \\ &= \rho_i \times \Sigma_{t,f}(E)\bar{l}_{i,BC} \times \sum_{n=1}^N \frac{b_n a_n}{\Sigma_{t,f}(E)\bar{l}_{i,BC} + a_n} \end{aligned} \quad (260)$$

The entering probability into region OBC is given by

$$\rho_i = r_i/R \quad (261)$$

where r_i and R are the radii of region i , and the fuel pellet, respectively, and the escape probability from the solid region OBC is approximated by the N -term rational approximation.

The average chord length from O (origin of a neutron entering a fuel pellet) to arc BC , is analytically derived through some algebra, and given by

$$\bar{l}_{i,BC} = \frac{2R}{\pi} \left(\sqrt{1 - \rho_i^2} + \frac{1}{\rho_i} \sin^{-1} \rho_i + \frac{\pi}{2} \rho_i \right) \quad (262)$$

Similarly, the average chord length from O to arc AB is

$$\bar{l}_{i,AB} = \frac{2R}{\pi} \left(\sqrt{1 - \rho_i^2} + \frac{1}{\rho_i} \sin^{-1} \rho_i - \frac{\pi}{2} \rho_i \right) \quad (263)$$

By applying the above derivation to the other terms in (258), we have the following relationship for the blackness of ring i :

$$\begin{aligned}
 \gamma_i(E) &= (\gamma_{i,OBC}(E) - \gamma_{i,OAB}(E)) - (\gamma_{i-1,OBC}(E) - \gamma_{i-1,OAB}(E)) \\
 &= \rho_i \Sigma_{t,f}(E) \overline{l_{i,BC}} \sum_{n=1}^N \frac{b_n a_n}{\Sigma_{t,f}(E) \overline{l_{i,BC}} + a_n} - \rho_i \Sigma_{t,f}(E) \overline{l_{i,AB}} \sum_{n=1}^N \frac{b_n a_n}{\Sigma_{t,f}(E) \overline{l_{i,AB}} + a_n} \\
 &\quad - \rho_{i-1} \Sigma_{t,f}(E) \overline{l_{i-1,BC}} \sum_{n=1}^N \frac{b_n a_n}{\Sigma_{t,f}(E) \overline{l_{i-1,BC}} + a_n} \\
 &\quad + \rho_{i-1} \Sigma_{t,f}(E) \overline{l_{i-1,AB}} \sum_{n=1}^N \frac{b_n a_n}{\Sigma_{t,f}(E) \overline{l_{i-1,AB}} + a_n}
 \end{aligned} \tag{264}$$

By substituting (264) into (255), we obtain

$$\begin{aligned}
 P_{e,i}(E) &= \frac{\gamma_i(E)}{\Sigma_{t,f}(E) \overline{l_i}} \\
 &= \frac{1}{\Sigma_{t,f}(E) \overline{l_i}} \left[\begin{aligned} &\rho_i \Sigma_{t,f}(E) \overline{l_{i,BC}} \sum_{n=1}^N \frac{b_n a_n}{\Sigma_{t,f}(E) \overline{l_{i,BC}} + a_n} \\ &- \rho_i \Sigma_{t,f}(E) \overline{l_{i,AB}} \sum_{n=1}^N \frac{b_n a_n}{\Sigma_{t,f}(E) \overline{l_{i,AB}} + a_n} \\ &- \rho_{i-1} \Sigma_{t,f}(E) \overline{l_{i-1,BC}} \sum_{n=1}^N \frac{b_n a_n}{\Sigma_{t,f}(E) \overline{l_{i-1,BC}} + a_n} \\ &+ \rho_{i-1} \Sigma_{t,f}(E) \overline{l_{i-1,AB}} \sum_{n=1}^N \frac{b_n a_n}{\Sigma_{t,f}(E) \overline{l_{i-1,AB}} + a_n} \end{aligned} \right] \\
 &= \frac{\rho_i \overline{l_{i,BC}}}{\overline{l_i}} \sum_{n=1}^N \frac{b_n a_n}{\Sigma_{t,f}(E) \overline{l_{i,BC}} + a_n} - \frac{\rho_i \overline{l_{i,AB}}}{\overline{l_i}} \sum_{n=1}^N \frac{b_n a_n}{\Sigma_{t,f}(E) \overline{l_{i,AB}} + a_n} \\
 &\quad - \frac{\rho_{i-1} \overline{l_{i-1,BC}}}{\overline{l_i}} \sum_{n=1}^N \frac{b_n a_n}{\Sigma_{t,f}(E) \overline{l_{i-1,BC}} + a_n} + \frac{\rho_{i-1} \overline{l_{i-1,AB}}}{\overline{l_i}} \sum_{n=1}^N \frac{b_n a_n}{\Sigma_{t,f}(E) \overline{l_{i-1,AB}} + a_n} \\
 &= \sum_{m=1}^4 c_m \sum_{n=1}^N \frac{b_n a_n}{\Sigma_{t,f}(E) \overline{l_m} + a_n}
 \end{aligned} \tag{265}$$

The coefficients c_m and average chord length $\overline{l_m}$ that appear in (265) are summarized in **Table 14**.

The coefficient c_m satisfies the following relationship:

$$\sum_{m=1}^4 c_m = 1 \tag{266}$$

■ **Table 14**
Coefficients and average chord length used in (265) of the Stoker–Weiss method

M	c_m	\bar{l}_m
1	$\rho_i \bar{l}_m / l_i$	$\bar{l}_{i,BC}$
2	$-\rho_i \bar{l}_m / l_i$	$\bar{l}_{i,AB}$
3	$\rho_{i-1} \bar{l}_m / l_i$	$\bar{l}_{i-1,BC}$
4	$-\rho_{i-1} \bar{l}_m / l_i$	$\bar{l}_{i-1,AB}$

With (253) and (265), $1 - P_{i \rightarrow m}(E)$ can be expressed as

$$\begin{aligned}
 1 - P_{i \rightarrow m}(E) &= \sum_{m=1}^4 c_m \sum_{n=1}^N b_n - D \sum_{m=1}^4 c_m \sum_{n=1}^N \frac{b_n a_n}{\Sigma_{t,f}(E) \bar{l}_m + a_n} \\
 &= \sum_{m=1}^4 c_m \sum_{n=1}^N b_n \left(1 - D \frac{a_n}{\Sigma_{t,f}(E) \bar{l}_m + a_n} \right) \\
 &= \sum_{m=1}^4 c_m \sum_{n=1}^N b_n \frac{\Sigma_{t,f}(E) \bar{l}_m + (1-D)a_n}{\Sigma_{t,f}(E) \bar{l}_m + a_n} \tag{267}
 \end{aligned}$$

where $\sum_{n=1}^N b_n = 1$ is used by recalling (121).

Finally, by substituting (267) into (252), the energy dependence of the neutron flux in region i is given by

$$\begin{aligned}
 \phi_i(E) &= \frac{1}{E} \left((1 - P_{i \rightarrow m}(E)) \frac{\Sigma_{p,f}}{\Sigma_{t,f}(E)} + P_{i \rightarrow m}(E) \right) \\
 &= \frac{1}{E} \frac{\Sigma_{p,f}}{\Sigma_{t,f}(E)} \sum_{m=1}^4 c_m \sum_{n=1}^N b_n \frac{\Sigma_{t,f}(E) \bar{l}_m + (1-D)a_n}{\Sigma_{t,f}(E) \bar{l}_m + a_n} \\
 &\quad + D \frac{1}{E} \sum_{m=1}^4 c_m \sum_{n=1}^N \frac{b_n a_n}{\Sigma_{t,f}(E) \bar{l}_m + a_n} \tag{268}
 \end{aligned}$$

When the macroscopic total cross section is very large, the energy dependence of the neutron flux can be approximated as follows:

$$\begin{aligned}
 \phi_i(E) &= \frac{1}{E} \frac{\Sigma_{p,f}}{\Sigma_{t,f}(E)} \sum_{m=1}^4 c_m \sum_{n=1}^N b_n \frac{\Sigma_{t,f}(E) \bar{l}_m + (1-D)a_n}{\Sigma_{t,f}(E) \bar{l}_m + a_n} + \frac{1}{E} D \sum_{m=1}^4 c_m \sum_{n=1}^N \frac{b_n a_n}{\Sigma_{t,f}(E) \bar{l}_m + a_n} \\
 &\approx (1-D) \frac{1}{E} \sum_{m=1}^4 c_m \sum_{n=1}^N b_n \frac{\Sigma_{p,f} \bar{l}_m}{\Sigma_{t,f}(E) \bar{l}_m} + D \frac{1}{E} \sum_{m=1}^4 c_m \sum_{n=1}^N b_n \frac{\Sigma_{p,f} \bar{l}_m + a_n}{\Sigma_{t,f}(E) \bar{l}_m + a_n} \\
 &= (1-D) \frac{1}{E} \sum_{m=1}^4 c_m \sum_{n=1}^N b_n \frac{\sigma_0}{\sigma_{a,r}(E) + \sigma_0} + D \frac{1}{E} \sum_{m=1}^4 c_m \sum_{n=1}^N b_n \frac{\sigma_{0,mn}}{\sigma_{a,r}(E) + \sigma_{0,mn}} \tag{269}
 \end{aligned}$$

where

$$\begin{aligned}\sigma_0 &= \Sigma_{p,f} / N_r \\ \sigma_{0,mn} &= (\Sigma_{p,f} + a_n / \bar{l}_m) / N_r\end{aligned}$$

In the above derivation, the following approximations are used:

$$\begin{aligned}\frac{1}{E} \frac{\Sigma_{p,f}}{\Sigma_{t,f}(E)} \sum_{m=1}^4 c_m \sum_{n=1}^N b_n \frac{(1-D)a_n}{\Sigma_{t,f}(E)\bar{l}_m + a_n} &\approx 0 \\ \frac{1}{E} \sum_{m=1}^4 c_m \sum_{n=1}^N b_n \frac{\Sigma_{p,f}\bar{l}_m}{\Sigma_{t,f}(E)\bar{l}_m + a_n} &\approx \frac{1}{E} \sum_{m=1}^4 c_m \sum_{n=1}^N b_n \frac{\Sigma_{p,f}\bar{l}_m}{\Sigma_{t,f}(E)\bar{l}_m}\end{aligned}$$

In (125) and (132) we derived a formula for the effective cross section when the energy dependence of the neutron flux is given by the N -term rational approximation. Considering the similarity between (125) and (269), and by applying (132), we can derive the following formula for the effective cross section:

$$\begin{aligned}\sigma_{g,x,i} &= \frac{\int_{E_g}^{E_{g-1}} dE \sigma_x(E) \lim_{\Sigma_{t,f}(E) \rightarrow \infty} \phi_i(E)}{\int_{E_g}^{E_{g-1}} dE \lim_{\Sigma_{t,f}(E) \rightarrow \infty} \phi_i(E)} \\ &= \frac{(1-D)I_{g,x}(\sigma_0) + D \sum_{m=1}^4 c_m \sum_{n=1}^N b_n I_{g,x}(\sigma_{0,mn})}{1 - (1-D)I_{g,a}/\sigma_0 - D \sum_{m=1}^4 c_m \sum_{n=1}^N b_n I_{g,a}(\sigma_{0,mn})/\sigma_{0,mn}}\end{aligned}\quad (270)$$

Once the Dancoff factor D is evaluated, the effective cross section in each annular ring can be evaluated by (270). Since the background cross section for each annular ring is evaluated by the potential scattering cross section and the geometry information of an annularly divided fuel pellet, the application and implementation of the Stoker–Weiss method for common lattice physics codes are easy.

Space-Dependent Dancoff Method (SDDM)

The above method can be modified by incorporating Stamm'ler's method for the evaluation of blackness, as described in [3.5.6](#) (Matsumoto et al. 2005; Matsumoto et al. 2006). The improved approach is called the spatially dependent Dancoff method, or SDDM. Recalling (173), we have the following relationship between the fuel-to-fuel collision probability in isolated and lattice systems in Stamm'ler's method:

$$p_{FF} = p_{ff} + \frac{x(1-p_{ff})^2}{x(1-p_{ff}) + A + B}\quad (271)$$

Recalling (255), the blackness for the fuel regions in the isolated and the lattice systems are given by

$$\gamma_F = \frac{4V_f}{S_f} \Sigma_{t,f}(1-p_{FF}) = x(1-p_{FF})\quad (272)$$

and

$$\gamma_f = \frac{4V_f}{S_f} \Sigma_{t,f}(1 - p_{ff}) = x(1 - p_{ff}) \quad (273)$$

respectively. By substituting (272) and (273) into (271), we obtain

$$\gamma_F = \frac{\gamma_f C}{\gamma_f + C} \quad (274)$$

where

$$C = A + B \text{ (} A \text{ and } B \text{ is given in (173)).}$$

Care should be taken that C in (274) is different from the Dancoff correction. The term expressed by C represents the effect of a finite fuel assembly. In SDDM, this term is assumed to be proportional to the fractional radius of region i , that is, $\rho_i = r_i/R$.

By utilizing (274) and considering the above discussion, (258) can be written as

$$\gamma_i^{lat} = \left(\frac{\rho_i C \gamma_{i,OBC}}{\gamma_{i,OBC} + \rho_i C} - \frac{\rho_i C \gamma_{i,OAB}}{\gamma_{i,OAB} + \rho_i C} \right) - \left(\frac{\rho_{i-1} C \gamma_{i-1,OBC}}{\gamma_{i-1,OBC} + \rho_{i-1} C} - \frac{\rho_{i-1} C \gamma_{i-1,OAB}}{\gamma_{i-1,OAB} + \rho_{i-1} C} \right) \quad (275)$$

By applying Carlvik's two-term rational approximation for $\gamma_{i,OBC}$, $\gamma_{i,OAB}$, $\gamma_{i-1,OBC}$, $\gamma_{i-1,OAB}$, we have the following formula for escape probability based on SDDM:

$$P_{e,i}(E) = \sum_{m=1}^4 c_m \sum_{n=1}^2 \frac{\beta_n \alpha_n}{\Sigma_{t,f}(E) \overline{l}_m + \alpha_n} \quad (276)$$

where

$$\begin{aligned} \alpha_{1,2} &= \frac{(5C + 6) \mp \sqrt{C^2 + 36C + 36}}{2(C + 1)} \\ \beta_1 &= \frac{C' - \alpha_1}{\alpha_2 - \alpha_1} \\ \beta_2 &= 1 - \beta_1 \\ C' &= \frac{4C + 6}{C + 1} \\ C &= A + B \text{ (} A \text{ and } B \text{ is given in (173)).} \end{aligned}$$

Therefore, the energy dependence of the neutron flux is

$$\phi_i(E) = \frac{1}{E} \sum_{m=1}^4 c_m \sum_{n=1}^2 \beta_n \frac{\sigma_{0,mn}}{\sigma_{t,r}(E) + \sigma_{0,mn}} \quad (277)$$

where

$$\sigma_{0,mn} = \sigma_{0,f} + \alpha_n \Sigma_e / N_r = \sigma_{0,f} + \alpha_n / N_r / \bar{l}_m \text{ and}$$

$$\sigma_{0,f} = \sum_{k \neq r} N_k \sigma_{s,k} / N_r$$

Finally, the effective cross section can be obtained by

$$\sigma_{g,x,i} = \frac{\sum_{m=1}^4 c_m \sum_{n=1}^2 \beta_n I_{g,x}(\sigma_{0,mn})}{1 - \sum_{m=1}^4 c_m \sum_{n=1}^2 \beta_n I_{g,a}(\sigma_{0,mn}) / \sigma_{0,mn}} \quad (278)$$

When (270) and (278) are compared, (278), that is, SDDM, gives a more consistent formula than the original Stoker–Weiss method.

The advantages and disadvantages of the Stoker–Weiss method (or SDDM method) are summarized as follows:

- It is an extension of the equivalence method and can be easily implemented in conventional lattice physics codes.
- The calculation procedure for the background cross section in each region is simple.
- Since the derivation of the background cross section is based on the analytic approach for a cylinder with annular divisions, its extension to a general geometry is impossible.
- The NR approximation is used.
- The Dancoff factor is used to incorporate the shadowing effect of other fuel rods. In the case of SDDM, Stamm'ler's method is used.
- The macroscopic total cross section is assumed to be spatially constant in a fuel pellet, which means no variations in the temperature and/or number density distribution in a pellet.

Previous studies have revealed that the spatial variation of the number density of a resonance nuclide does not have a significant impact on the calculation accuracy of the effective cross section. Thus, the Stoker–Weiss method can be applied to a resonance calculation in which the distribution of the number density in a pellet exists. On the contrary, when the temperature profile in a pellet is taken into account, the Stoker–Weiss method will not be very accurate. In such a case, particular considerations need to be incorporated (Matsumoto et al. 2006).

◆ *Figure 30* shows the space-dependent effective cross section in a UO_2 fuel pellet that was obtained by the Stoker–Weiss method. In the outer region, the effective cross section is larger than that in the inner regions, due to neutron inflow from the moderator region. Thus, this method reproduces the trend intuited for the space-dependent effective cross sections.

◆ *Figure 31* shows a comparison of the number density distributions obtained by SDDM and by the continuous-energy Monte Carlo method. SDDM well produces the plutonium buildup on the pellet surface, which is referred to as the rim effect. This comparison clarifies that SDDM can be applied to evaluate not only the space-dependent effective cross sections, but also the number density distribution in a pellet. Therefore, the power depression inside a pellet, which is an important factor in the mechanical design of a fuel rod, can also be evaluated by this method. Burnup calculation by the continuous-energy Monte Carlo method can also provide such results, but the Stoker–Weiss and SDDM methods are more suitable for production calculations, due to the short computation time they require.

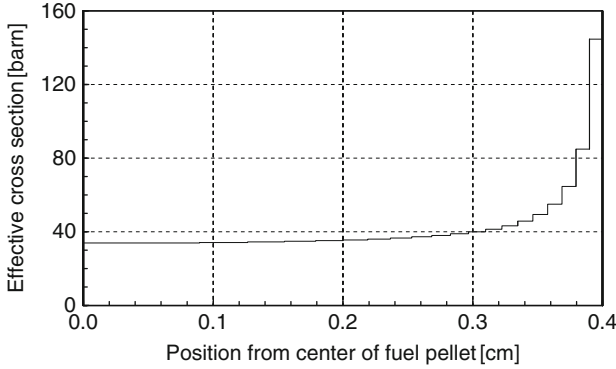


Figure 30

Example of space dependency of the effective cross section of ^{238}U in a fuel pellet calculated by the Stoker–Weiss method (293 K, typical PWR cell, pellet radius is 0.4 cm) (Matsumoto et al. 2005)

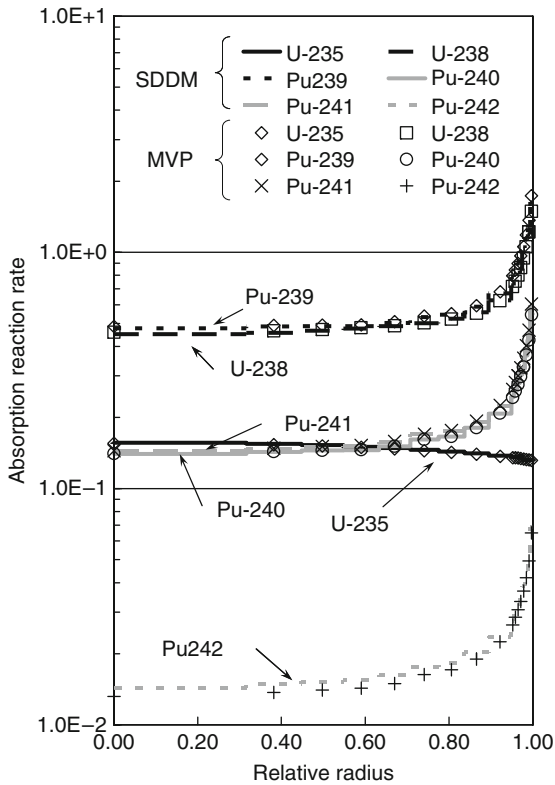


Figure 31


Comparison of absorption reaction rates obtained by SDDM and continuous-energy Monte Carlo code MVP, at the end of life of UO_2 fuel (Matsumoto et al. 2005)

3.10 Resonance Overlap Effect

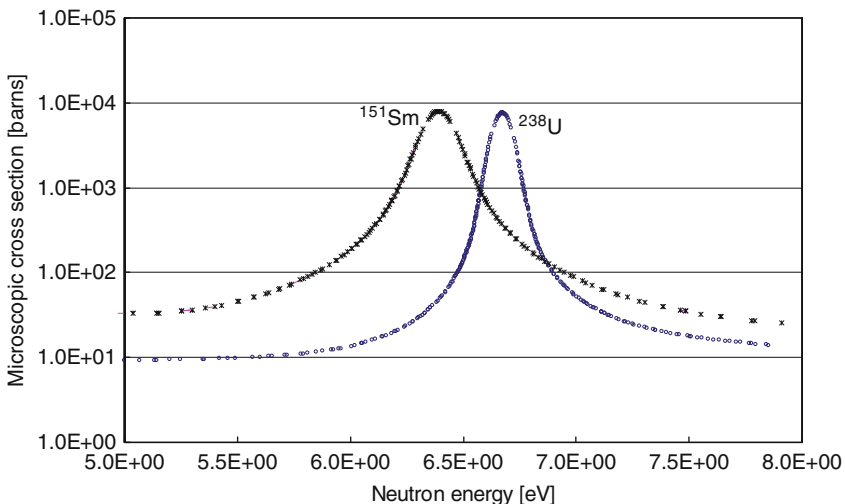
3.10.1 Overview

Various resonance calculation methods have been discussed in this section thus far. These resonance calculation methods (except for the ultrafine group method) assume just one resonance nuclide in a system – no interference of the resonance peaks of different nuclides is considered. In reality, however, a fuel pellet contains many resonance nuclides, especially in burnt fuels. Consequently, a discrepancy arises between the calculation model (i.e., resonance theory) and the actual situation regarding prediction error of the effective cross section. This discrepancy is referred to as the resonance overlap (or interference) effect (Hébert 2004).

From the viewpoint of the “gross” neutronics characteristics of a fuel assembly, the impact of the resonance overlap effect is, fortunately, not very large. However, if more detailed information is necessary, such as the nuclide number densities of burnt fuel or the reaction rate of a particular nuclide, then the resonance overlap effect might play a very important role. Consideration of the resonance overlap effect, therefore, should not be neglected in the resonance calculation of a lattice physics code.

For example, let us consider the effective cross section of ^{151}Sm at 6.16–7.524 eV (88th group of the 172 XMAS groups). In this energy range, ^{238}U has a large resonance peak at 6.7 eV, as shown in  Fig. 32. Therefore, the typical neutron spectrum in the fuel shows a significant depression in this energy range due to the resonance absorption of ^{238}U . The neutron slowing down source in this energy range is also far from the asymptotic one (which is typically constant in the NR approximation).

^{151}Sm also has large resonance in this energy range. When the resonance overlap between ^{151}Sm and ^{238}U is not taken into account, the effective cross section for ^{151}Sm at 6.16–7.524 eV



 **Figure 32**
Resonance overlap between ^{238}U and ^{151}Sm (microscopic absorption cross section at 300 K)

with a low number density (nearly the infinite-dilution condition) is 1,185 barn, while it becomes 898 barn when distortion of the neutron spectrum due to the presence of ^{238}U is taken into account. The resulting difference in the effective cross sections is approximately 25%, which has a significant impact on the absorption reaction rate of ^{151}Sm . Though the impact on the k -infinity of a fuel assembly is limited due to the low contribution of ^{151}Sm , the number density of ^{151}Sm during burnup is significantly mispredicted if the resonance interference effect is not taken into account.

We can see similar observations for more important nuclides, for example, ^{235}U . Since there are coincident resonance overlaps between ^{238}U and ^{235}U , the accuracy of the effective cross section of ^{235}U in some energy groups becomes lower if the overlap effect is neglected. A previous study suggests that the resonance overlap effect between ^{235}U and ^{238}U is approximately 0.2% dk/k on k -infinity for a typical UO_2 LWR fuel assembly. In MOX fuel, similar resonance interference is observed between ^{239}Pu and ^{238}U . The effect is reported to be approximately 0.2% dk/k , which is close to that between ^{235}U and ^{238}U .

In the following subsection, a countermeasure for the resonance overlap effect will be discussed.

3.10.2 Resonance Interference Factor (RIF) Table

In principle, the resonance overlap effect can occur between any two resonance nuclides. However, in the typical situation of LWR lattices, the resonance overlap effect between ^{238}U and other resonance nuclides is dominant, and the interferences among other resonance nuclides can be considered as a second-order effect. This can be justified by the fact that the number density of ^{238}U is usually much larger than that of other resonance nuclides, so that the neutron spectrum in a fuel pellet is dominated by the resonance absorption of ^{238}U . Thus, from an engineering perspective, the treatment of the resonance overlap effect can be simplified to those between ^{238}U and other resonance nuclides.

Since the effective cross section is affected by the resonance overlap effect, it can be corrected by the resonance interference (overlap) factor, which is prepared in advance of lattice physics computations. In more detail, the resonance interference factors defined by the following equation are evaluated and tabulated in a cross section library:

$$\text{RIF}_{k,g,N_{^{238}\text{U}}} = \frac{\sigma_{\text{eff},k,g}(N_{^{238}\text{U}})}{\sigma_{\text{eff},k,g}(0)} \quad (279)$$

where

$\text{RIF}_{k,g,N_{^{238}\text{U}}}$: resonance interference factor for nuclide k and energy group g , when the number density of ^{238}U is $N_{^{238}\text{U}}$;

$\sigma_{\text{eff},k,g}(N_{^{238}\text{U}})$: effective cross section for nuclide k and energy group g , when the number density of ^{238}U is $N_{^{238}\text{U}}$; and

$\sigma_{\text{eff},k,g}(0)$: effective cross section for nuclide k and energy group g , when the number density of ^{238}U is zero, that is, no resonance overlap effect is considered.

In the resonance calculation, the effective cross section without consideration of the resonance overlap is evaluated first, then the RIF is multiplied by the obtained effective cross section in order to capture the resonance overlap effect.

The RIF table can be prepared by the NJOY code or by utilization of the ultrafine group spectrum calculations. In the usual spectrum calculation based on the NR approximation, a typical asymptotic neutron spectrum with $1/E$ (or similar shape) is used as a starting point, then the actual neutron spectrum with the depression due to a resonance peak is evaluated by

$$\phi(E) = \phi_{\text{asymptotic}}(E) \frac{\sigma_0}{\sigma_t(E) + \sigma_0} \quad (280)$$

The neutron spectrum obtained by (280) is then used to collapse the cross section to obtain a group averaged effective cross section. The NJOY code also has the following option:

$$\phi(E) = \phi_{\text{input}}(E) \frac{\sigma_0}{\sigma_t(E) + \sigma_0} \quad (281)$$

where

$\phi_{\text{input}}(E)$: user-specified neutron spectrum.

In order to consider the resonance overlap effect, the following procedure can be followed:

1. Perform the spectrum calculation for ^{238}U using (280).
2. Use the spectrum obtained in (1) as the user-specified spectrum in (281).
3. Collapse the cross section to obtain the effective cross section using the neutron spectrum obtained in (2).

The effective cross section obtained in (3) includes the resonance overlap effect with ^{238}U . It can therefore be used as the numerator in (279). Since the neutron spectrum obtained in (1) depends on the background cross section (number density) of ^{238}U , several calculations with different shielding conditions (different background cross sections and/or number densities of ^{238}U) should be carried out. The evaluated RIFs are edited as a table for the utilization of resonance calculations in lattice physics codes.

3.10.3 Utilization of an Ultrafine Energy Group Cross Section

We can also use an ultrafine energy group cross section to correct the resonance overlap effect. The ultrafine energy group spectrum calculation discussed in 3.7 can precisely capture any resonance overlap effect, so it can be used to incorporate the effect. However, as previously discussed in 3.7, direct application of the ultrafine energy group calculation for a whole fuel assembly still requires an impractical amount of computation time, so the appropriate combination with other methods would be required. For example, an ultrafine energy group calculation is carried out in simple pin cell geometry, and the position-dependence of the effective cross section due to the shadowing effect of other fuel rods is evaluated through the Dancoff correction (Sugimura and Yamamoto 2007).

Since a neutron spectrum calculation for an ultrafine energy group requires some computation time, a more simplified approach can be used to capture the resonance interference effect. Since an approximate neutron spectrum can be obtained by the NR (or IR)

approximation, the following procedures can be used to evaluate the resonance overlap factor “on the fly”:

1. By recalling (108), evaluate the neutron spectrum using the NR approximation with one resonance nuclide,

$$\begin{aligned}\phi_{f,\text{no-RI}}(E) &= \frac{1}{E} \frac{\Sigma_{p,f} + \Sigma_e}{\Sigma_{t,f}(E) + \Sigma_e} \\ &= \frac{1}{E} \frac{N_r(\sigma_{p,r} + \sigma_{0,f}) + \Sigma_e}{N_r(\sigma_{t,r}(E) + \sigma_{0,f}) + \Sigma_e}\end{aligned}\quad (282)$$

where

Σ_e : macroscopic escape cross section,

$$\sigma_{0,f} = \sum_{k \neq r} N_k \sigma_{p,k} / N_r.$$

2. Evaluate the neutron spectrum using the NR approximation with multiple resonance nuclides,

$$\begin{aligned}\phi_{f,\text{with-RI}}(E) &= \frac{1}{E} \frac{\Sigma_{p,f} + \Sigma_e}{\Sigma_{t,f}(E) + \Sigma_e} \\ &= \frac{1}{E} \frac{\sum_k N_k \sigma_{p,k} + \Sigma_e}{\sum_k N_k \sigma_{t,k}(E) + \Sigma_e}\end{aligned}\quad (283)$$

3. The resonance interference factor is evaluated by

$$\begin{aligned}\text{RIF}_g &= \frac{\sigma_{k,g,\text{with-RI}}(\vec{r})}{\sigma_{k,g,\text{no-RI}}(\vec{r})} = \frac{\int_{E_g}^{E_{g-1}} dE \sigma_k(E) \phi_{f,\text{with-RI}}(\vec{r}, E)}{\int_{E_g}^{E_{g-1}} dE \phi_{\text{with-RI}}(\vec{r}, E)} \\ &\quad \times \frac{\int_{E_g}^{E_{g-1}} dE \phi_{f,\text{no-RI}}(\vec{r}, E)}{\int_{E_g}^{E_{g-1}} dE \sigma_k(E) \phi_{\text{no-RI}}(\vec{r}, E)}\end{aligned}\quad (284)$$

Note that the IR approximation can be also used in the above procedure.

The advantages and disadvantages of this method are summarized as follows:

- The resonance interference factor can be evaluated with the actual composition of the resonance material. Therefore, the resonance interference not only for ^{238}U , but also for other nuclides can be taken into account.
- Since the resonance interference factor is evaluated “on the fly,” additional computation time is necessary. The ultrafine energy group calculation, particularly, requires some computation time, though it is accurate. The second approach with the NR (or IR) approximation could yield a solution that offers a compromise between calculation accuracy and computation time.
- The ultrafine energy group calculation is applied to the resolved resonance energy range, which is ~ 10 keV for heavy resonance isotopes. In order to accurately cover this energy range,

a few to several tens of thousand energy group is necessary. If the number of nuclides considered in the evaluation of the resonance interference factor increases, these cross sections with fine energy resolution require considerable memory storage.

Some of the most recent lattice physics codes adopt this approach to capture the resonance interference effect (Wehlage et al. 2005; Sugimura and Yamamoto 2007).

3.11 Other Topics in Resonance Calculations

3.11.1 Effective Temperature Used in Resonance Calculation

The effective cross section depends not only on the background cross section, but also on the temperature, due to the Doppler broadening of the cross section. The temperature of a fuel pellet varies across its volume during power generation. The shape of the temperature distribution is approximately parabolic in a pellet during steady-state operation. In lattice physics computations, a fuel pellet is commonly treated as a single region, since equivalence theory is widely used. In this case, the choice of “average temperature” is very important in resonance calculations.

Resonance absorption generally takes place on the surface of a resonance lump, due to neutron injection from the moderator. Thus, the surface region should assume more importance than the center region.

Several estimation methods have been developed to date:

- Simple volume average model

$$T_{f,eff} = \frac{1}{V_f} \int_{V_f} T_f(\vec{r}) d\vec{r} \quad (285)$$

- Rowland’s model (for parabolic temperature distribution) (Rowlands 1962)

$$T_{f,eff} = T_s + \frac{4}{9}(T_c - T_s) \quad (286)$$

where

T_s : surface temperature, and

T_c : centerline temperature

- Arnold and Dannels’s model (for parabolic temperature distribution) (Arnold and Dannels 1960)

$$T_{f,eff} = T_s + 0.35(T_c - T_s) \quad (287)$$

- Chord average model (Kruijff 1994; Kruijff and Jansen 1996)

$$T_{f,eff} = \int_S \int_{\vec{n} \cdot \vec{\Omega} > 0} d\vec{\Omega} g(\vec{r}_s, \vec{\Omega}) \frac{\int_0^{L(\vec{r}_s, \vec{\Omega})} T(l) dl}{L(\vec{r}_s, \vec{\Omega})} \quad (288)$$

■ **Table 15**
Weight factors of temperature for the chord average model (10 equi-volumes in an annularly divided cylindrical pellet). Regions 1 and 10 indicate the center and surface, respectively

Region	Weight
1	0.079560
2	0.081776
3	0.084304
4	0.087240
5	0.090726
6	0.094994
7	0.100461
8	0.107987
9	0.119917
10	0.153034

Source: Matsumoto et al. (2006).

where

$L(\vec{r}_s, \vec{\Omega})$: chord length at position \vec{r}_s on surface S and in direction $\vec{\Omega}$,

$g(\vec{r}_s, \vec{\Omega})$: probability distribution of a chord, which is given by $g(\vec{r}_s, \vec{\Omega}) = n \cdot \vec{\Omega} / (\pi S)$ in the case of isotropic and uniform incident incoming neutrons.

From the viewpoint of integrated parameters such as k-infinity, the above definitions do not yield a considerable discrepancy. However, with respect to the temperature coefficients of a fuel pellet (i.e., the Doppler coefficient), the chord average model more accurately reproduces reference results obtained using a continuous-energy Monte Carlo method. Under transient conditions, the temperature distribution inside a pellet may not have a parabolic shape. For example, during very fast transitions such as a reactivity initiated accident (RIA), which occurs as a rapid increase in reactivity on control rod ejection for LWRs, the temperature distribution may be proportional to the power distribution inside a pellet because of the adiabatic variation of the temperature. The power density is greater on the pellet surface than in the center, so the maximum temperature may appear near the surface in a rapid transition. Both the Rowland and the Arnold and Dannels models assume a parabolic temperature distribution, which is appropriate for the steady state, but which might not be applicable in transient cases. Therefore, the chord average model becomes useful in such a case.

When a fuel pellet is divided into ten annularly equi-volume regions, the weight factors used in the chord average model are those given in ➤ [Table 15](#).

3.11.2 Temperature Distribution in a Resonance Region

Several resonance calculation methods that can handle the spatial resonance self-shielding effect were discussed in ➤ [3.7–3.9](#). When a fuel pellet is subdivided into annular regions, it


is straightforward to consider the temperature distribution in each annular region. However, direct utilization of space-dependent resonance shielding methods with a temperature profile may go beyond the assumptions used in the resonance calculation model.

Since the ultrafine energy group calculation is based on the “first principle,” it can handle the temperature distribution in a fuel lump, and gives a reliable result even with the temperature profile.


The subgroup parameters are generated by the fitting or the moment methods, which assume a certain temperature. Since the probability (weight) of each subgroup and of the subgroup cross section are temperature-dependent, they cannot be directly applied to a space-dependent self-shielding calculation with a temperature profile. Let us consider a subgroup. This subgroup has a certain probability, which “physically” corresponds to the ratio of the energy range in an energy group. This probability depends on the temperature, and takes on another value for a different temperature. This means that the ratio of the energy range for a particular subgroup in an energy group changes due to temperature. Subgroup parameters with different temperatures have different and inconsistent “energy group structures,” so they cannot be used in the same calculation. On the contrary, when a subgroup parameter is generated through the direct method with a fixed energy group structure, it can be applied to a temperature distribution problem because there is no inconsistency in the subgroup parameters for different temperatures. Several studies have been carried out to address this inconsistency in the probability table approach to a temperature-dependent problem (Joo et al. 2005).

The Tone method and the Stoker–Weiss method (or SDDM) also assume a constant macroscopic cross section throughout a fuel lump. Thus, the direct application of these methods to a temperature distribution problem would result in misprediction, and particular considerations would be necessary (Matsumoto et al. 2006).

3.11.3 Treatment of Number Density Distribution in a Pellet

Resonance capture by ^{238}U mainly occurs on the pellet surface due to the spatial self-shielding effect. As a result, plutonium buildup in the surface region becomes dominant, as shown in  [Fig. 31](#).

Resonance calculation methods based on the equivalence theory (including Tone, Stoker–Weiss, SDDM) assumes a constant macroscopic cross section in a fuel lump. Strictly speaking, then, the spatial distributions of resonance nuclides cannot be taken into account and are neglected. Fortunately, previous studies have clarified that the distribution of number density in a pellet has a small impact on the calculation results, so it can be treated as a constant throughout the fuel region in common lattice physics computations (Stoker and Weiss 1996). Therefore, the simple average of number density can be applied to a fuel region in the resonance calculation. Such treatment greatly simplifies the resonance treatment in actual calculations. Note that the subgroup method and the ultrafine energy group calculation method accurately handle these effects, since no assumption regarding the constant cross section is taken into account.

As will be discussed in  [Sect. 6](#), a gadolinia-bearing fuel pellet is subdivided into several annular regions in order to capture the depletion characteristics of gadolinia (the onion skin effect). In this case, we can apply the space-dependent self-shielding method to evaluate the space-dependent effective cross section in each ring. However, in common lattice physics computation such detailed treatment is not necessary, that is, a pellet’s average number density can be used in the resonance calculation, and the same effective cross section can be used in all regions inside a pellet. Note that the number densities in each region are independently

tracked through the burnup calculation, since the reaction rates in each region are different due to spatial variations in the neutron spectrum (even if an identical effective cross section is used in all regions).

3.11.4 Resonance Calculation for Non-Heavy Nuclides

➤ Section 3 mainly considers the resonance calculation for heavy nuclides, for example, ^{238}U . However, a resonance treatment for other nuclides also has important role.

In LWR fuel, gadolinia is commonly used as a burnable absorber. Since the major isotopes of Gd have large resonances and are used with high-content, the self-shielding effect should be taken into account. As described in ➤ Sect. 3.11.3, the spatial dependence of the number densities of Gd isotopes can be handled through the simple average over a pellet in the resonance treatment.

The absorbers used in LWRs also have large resonances, that is, Ag, In, and Cd for PWR, and Hf for BWR. Since the number densities of these resonance nuclides in the absorber are high, the resonance treatment is important in order to accurately predict the reactivity value of the control rod. When an infinite-dilute cross section is used for absorber nuclides, the reactivity value of a control rod will be significantly over-predicted.

Zircaloy is used not only as a cladding material, but also as a structural material such as a water rod, channel box, and grid spacer. Because zirconium isotopes have resonances in the medium energy range, the self-shielding effect of these isotopes would be taken into account, even though absorption by zirconium isotopes is low. In a typical LWR cell, the self-shielding effect of the zirconium isotopes reaches $0.1\% \Delta k/k$, which is considerable. The number densities of the zirconium isotopes in Zircaloy are almost constant, and the shapes of Zircaloy are limited (e.g., cladding and channel box). Pre-tabulation of these isotopes for a particular background cross section might therefore be efficient in practical applications.

Structural material such as Fe, Ni, and Cr have many sharp resonances in the medium energy range. These materials are used for the reflector material in APWR/EPR, and the resonance shielding effect should be taken into account in the reflector calculations. Since the angular dependency of the neutron flux is very large in the reflector, particular care becomes necessary in the resonance calculation for the reflector material. A similar situation can be found in the blanket calculation for a fast breeder reactor. In this case, application of the subgroup method is effective (Yamamoto and Takeda 2000).

3.11.5 Verification and Validation of Resonance Calculation Model

Since many assumptions and approximations are used in resonance calculation models, the verification and validation of these models is very important. Since the verification and validation of a resonance calculation model can be carried out in a small geometry, utilization of a continuous-energy Monte Carlo code is very useful.

In comparison with the results achieved using Monte Carlo code, the effective cross section is usually considered as a benchmark quantity. We must remember, however, that the effective cross sections in lattice physics computations are just intermediate products. Our final objective is the evaluation of neutronics characteristics such as k -infinity and fission rate distribution. In

this sense, the microscopic reaction rates are rather more important than the effective cross sections. Indeed, even if the effective cross sections show excellent agreement in their Monte Carlo and the resonance calculation results, this does not necessarily mean that the resonance calculation model has given accurate reaction rates (Sugimura and Yamamoto 2007). When the effective cross section obtained by a resonance calculation model exactly reproduces the Monte Carlo result, they would still produce inconsistent reaction rates, due to the energy collapsing process that is inevitably included in a resonance calculation model (Rothenstein et al. 1988; Sugimura and Yamamoto 2007). This consideration should not be neglected in the validation and verification process.

3.12 Summary

In [▶ Sect. 3](#), resonance calculation methods to estimate the effective cross section for successive pin cell and/or assembly calculations are described. Since a direct numerical solution to the neutron slowing down equation in a general heterogeneous geometry is still time consuming for practical applications, various calculation models, for example, the equivalence theory, the subgroup method, ultrafine group calculation in small geometry, the Tone method, the Stoker-Weiss (or SDDM) method, have been developed, and are applied in current lattice physics codes.

These models adopt various approximations that could be valid under certain conditions. One should therefore carefully consider the limitations of resonance calculation models and the potential prediction errors associated with the approximations. In this context, the current major resonance methods are still an approximate science, as opposed to the science of approximation, in which prediction errors associated with approximations are well controlled. Therefore, validation and verification of a resonance calculation model in a lattice physics code is quite important.

4 Energy Condensation Scheme

4.1 Introduction

Energy condensation refers to the generation of a unique flux spectrum in each material region of the problem that can be used to condense cross sections from the energy group structure of the cross section library (e.g., hundreds of energy groups) to a smaller energy group structure in preparation for the fine-mesh assembly transport solution (e.g., at most, a couple dozen energy groups). The scheme that will be discussed in this section was used in CASMO-4 and LANCER02 and consists of a series of one-dimensional pin-cell calculations followed by a two-dimensional coupling calculation. This section develops the theory behind the scheme and describes the numerics used to solve the system of equations.

Note that not all lattice physics codes use a condensation scheme. Those that do not use a condensation scheme perform the fine-mesh assembly transport calculation in the energy group structure of the cross section library. For the major fuel vendors who design dozens of reload cores each year requiring the need to design and analyze hundreds of different bundles on their way to finding the best fit for their cores, the need to perform millions of lattice calculations annually almost necessitates the need for a condensation scheme. For small fuel vendors or

utilities that may analyze a very limited number of reload core designs annually, the need for a condensation scheme in the lattice physics code is not so great.

It is important to keep in mind that, at this point in our lattice physics computational scheme, we are only concerned with generating a good condensation flux with which to collapse cross sections. We are allowed to sacrifice accuracy – especially spatial accuracy – for execution speed. However, the number of energy groups required for the fine-mesh assembly transport solution is directly proportional to the accuracy of the condensation spectra, so it is in our best interest to produce a reasonably accurate condensation flux.

4.2 Pin-Cell Spectral Calculations

Our condensation scheme begins with a series of one-dimensional pin-cell spectral calculations. The pin-cell spectral calculations are used to generate a flux spectrum in each region of each pin cell in the lattice, where the term *pin cell* implies a system consisting of a fuel rod plus the coolant in the immediate vicinity. It is also meant to include each of the inert rods present in the assembly, such as water rods and any absorber pins. The flux spectra in each region of the cell are generated in the energy group structure of the cross section library. During the pin-cell spectral calculations, each pin cell in the lattice is isolated from the influence of all other cells. Once all the pin-cell spectral calculations have been completed, we will perform a two-dimensional coupling calculation to modify the flux spectrum in each region of each cell to account for the influence of the surroundings.

For each pin cell, the square coolant region is approximated by a cylinder, preserving the volume of the outer coolant region and allowing for a purely one-dimensional analysis to be performed. White boundary conditions are applied to the outer edge of the cell to simulate perfect reflection in the true square geometry.

To help drive the flux across each pin cell, a buffer zone of average fuel material may be placed on the outside of the coolant zone. The pin-cell analysis is a fixed source calculation, where the neutron fission spectrum is used as the neutron source and may be placed in the buffer zone, exclusively, or in both the buffer zone and the fuel pellet. Either approach works equally well. The use of a fixed source helps to speed up convergence of the solution to the transport equation without adversely affecting the accuracy of the solution.

Because the pin-cell calculation is a purely one-dimensional problem, any solution technique to the transport equation is a viable choice. We can choose to solve the integrodifferential form of the transport equation using discrete ordinates, or we can choose to solve the integral form of the transport equation using the method of collision probabilities. Our choice is to use the method of collision probabilities because of its superior performance on physically small problems containing only a few mesh. ➤ Sections 4.2.1 and ➤ 4.2.2 will be devoted to the method of collision probabilities as applied to the pin-cell spectral calculations in a lattice physics code. The contents of this section have been taken from lectures given to postgraduate students in a course on computational reactor analysis at The Pennsylvania State University in 1990 (Knott 1990). Citations are absent from the bulk of the text because the material has been derived from first principles. The interested reader is directed to Lewis and Miller (1984) and Stamm'ler and Abbate (1983), from which much of the material have been culled. For an excellent discussion on the method of collision probabilities, the interested reader is directed to the seven publications that comprise Ingvar Carlvik's Ph.D. thesis (Carlvik 1967a, b, c, d, 1965,

1966a, b; Carlvik and Pershagen 1959) along with one additional publication that did not appear in his thesis (Carlvik 1966c).

4.2.1 General Theory

The spectral calculation determines the neutron flux distribution across the pin cell by solving the integral form of the transport equation using the method of collision probabilities. The integral equation is derived from the integrodifferential form of the Boltzmann transport equation

$$\frac{1}{|v|} \frac{\partial \Phi(\vec{r}, E, \hat{\Omega}, t)}{\partial t} = Q(\vec{r}, E, \hat{\Omega}, t) - \Omega \cdot \nabla \Phi(\vec{r}, E, \hat{\Omega}, t) - \Sigma_t(\vec{r}, E) \Phi(\vec{r}, E, \hat{\Omega}, t) \quad (289)$$

where the source term, $Q(\vec{r}, E, \hat{\Omega}, t)$, is the total source of neutrons at location \vec{r} , with energy E , traveling in direction $\hat{\Omega}$, at time t , and is given by

$$Q(\vec{r}, E, \hat{\Omega}, t) = \iint \Sigma_s(\vec{r}, E' \rightarrow E, \hat{\Omega}' \rightarrow \hat{\Omega}) \Phi(\vec{r}, E', \hat{\Omega}', t) dE' d\hat{\Omega}' + S(\vec{r}, E, \hat{\Omega}, t) \quad (290)$$

In the above expressions, $\Phi(\vec{r}, E, \hat{\Omega}, t)$ is the angular flux, $\Sigma_t(\vec{r}, E)$ is the total macroscopic cross section, and $\Sigma_s(\vec{r}, E' \rightarrow E, \hat{\Omega}' \rightarrow \hat{\Omega})$ is the macroscopic scattering cross section. $S(\vec{r}, E, \hat{\Omega}, t)$ is the source of neutrons at location \vec{r} , either internal (i.e., due to fission) or external.

In lattice physics calculations, only time-independent problems are considered and the steady state Boltzmann equation to be solved is expressed as

$$\Omega \cdot \nabla \Phi(\vec{r}, E, \hat{\Omega}) + \Sigma_t(\vec{r}, E) \Phi(\vec{r}, E, \hat{\Omega}) = Q(\vec{r}, E, \hat{\Omega}) \quad (291)$$


Equation (291) describes neutron motion as viewed from a fixed reference point, giving rise to the partial derivative in the streaming term. If neutron motion were viewed from the neutron's frame of reference, the partial derivative in the streaming term reduces to a total derivative along the path of motion of the neutron

$$\frac{d\Phi(\vec{r}, E, \hat{\Omega})}{ds} + \Sigma_t(\vec{r}, E) \Phi(\vec{r}, E, \hat{\Omega}) = Q(\vec{r}, E, \hat{\Omega}) \quad (292)$$

where s is the track along which the neutron is traveling across the region at location \vec{r} .

Equation (292) may be solved to obtain an expression for the angular flux. We first solve the homogeneous portion of the equation, where the source term, $Q(\vec{r}, E, \hat{\Omega})$, is set to zero. The homogeneous solution is

$$\Phi^h(\vec{r}, E, \hat{\Omega}) = C e^{-\int_0^s \Sigma_t(s', E) ds'} \quad (293)$$

where s is measured along the streaming path from the differential volume element dV' to the differential volume element of interest, dV , as illustrated in  Fig. 33.

Next Lagrange's method of varying the constant is used, where the integration constant in (293), C , is assumed to be a function of the streaming length, $C(s)$. This solution is back-substituted into (292) and the entire differential equation is integrated along s from $-\infty$

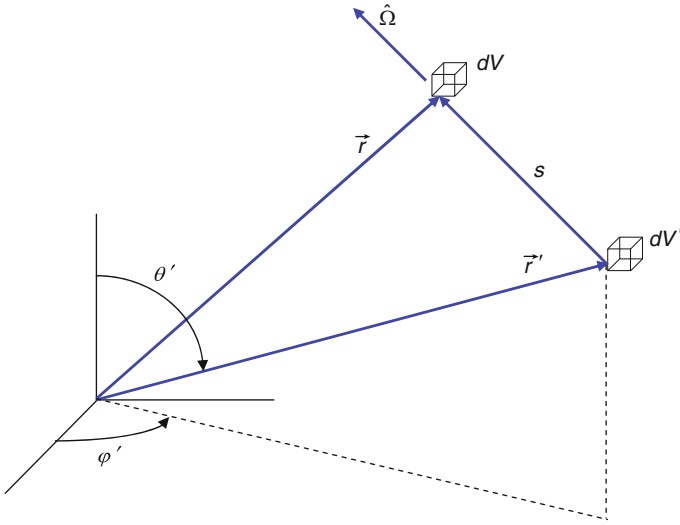


Figure 33
Coordinate system for the integral transport equation

to the differential volume of interest, dV . The final expression for the integrating constant is given by

$$\int_{-\infty}^s dC(s') ds' = \int_{-\infty}^s Q(s', E, \hat{\Omega}) \cdot e^{\int_0^{s'} \Sigma_t(s'', E) ds''} ds' \quad (294)$$

$$C(s) = C(-\infty) + \int_{-\infty}^s Q(s', E, \hat{\Omega}) \cdot e^{\int_0^{s'} \Sigma_t(s'', E) ds''} ds' \quad (295)$$

Back-substituting (295) into (293) gives the general form of the integral equation for the angular flux at location \vec{r} ,

$$\Phi(\vec{r}, E, \hat{\Omega}) = \int_{-\infty}^s Q(s', E, \hat{\Omega}) \cdot e^{-\int_{s'}^s \Sigma_t(s'', E) ds''} ds' \quad (296)$$

where the $C(-\infty)$ term in (295) has been taken to be zero since it would take a neutron, infinitely far away, an infinite length of time to travel along the streaming path in order to reach the volume element located at \vec{r} and, infinitely long ago, there were no neutrons.

To visualize the integral equation, imagine standing at a point in space. If you wished to calculate the neutron flux at that point, you would look around yourself in all directions and count up all the neutrons that are streaming toward you along lines that originate from the location of each neutron's most recent collision (i.e., birth). The angular fluxes would be the number of neutrons streaming toward you along each specific line. Each time you moved your head to look in a different direction, you would be viewing a different angular flux. To calculate a scalar flux, you would simply count up all neutrons moving toward you from all directions.

The energy dependence in (296) is represented by neutrons that are moving at different speeds along each of those lines. As we move to [Sect. 5](#), we will refer to these lines as *characteristics* and we will view our system from the neutron's point of view as it moves along the line, instead of viewing our system while standing still and watching the neutron move toward us.

If we assume that all self-scattering and total cross sections in the library have been transport corrected, then scattering can be modeled, mathematically, in the same way as an isotropic source is modeled. In addition, the only source of neutrons are those due to fission, which is inherently isotropic, and the angular source term, $Q(\vec{r}, E, \hat{\Omega})$, may be expressed in terms of the total source term, $q(\vec{r}, E)$, as

$$Q(\vec{r}, E, \hat{\Omega}) = \frac{q(\vec{r}, E)}{4\pi} = \int \frac{\Sigma_s(\vec{r}, E' \rightarrow E)}{4\pi} \int_{4\pi} \Phi(\vec{r}, E', \hat{\Omega}') d\hat{\Omega}' dE' + \frac{s(\vec{r}, E)}{4\pi} \quad (297)$$

where the fixed scalar source term, $s(\vec{r}, E)$, can be due to fission or may be a constant external source. The angular source due to fission has the following appearance:

$$S(\vec{r}, E, \hat{\Omega}) = \frac{s(\vec{r}, E)}{4\pi} = \frac{\chi(E)}{k^\infty} \int \frac{\nu \Sigma_f(\vec{r}, E')}{4\pi} \int_{4\pi} \Phi(\vec{r}, E', \hat{\Omega}') d\hat{\Omega}' dE' \quad (298)$$

Here, k^∞ is the infinite multiplication factor, which assumes no leakage of neutrons from the system, and is calculated as

$$k^\infty = \frac{\iint \nu \Sigma_f(\vec{r}, E) \phi(\vec{r}, E) \cdot d^3\vec{r} \cdot dE}{\iint \Sigma_a(\vec{r}, E) \phi(\vec{r}, E) \cdot d^3\vec{r} \cdot dE} \quad (299)$$

and the scalar flux at location \vec{r} in (299) is the integration of the angular flux over all directions,

$$\phi(\vec{r}, E) = \int_{4\pi} \Phi(\vec{r}, E, \hat{\Omega}) d\hat{\Omega} \quad (300)$$

Using (300), the source term in (297) may be expressed in terms of the scalar flux alone, as

$$Q(\vec{r}, E, \hat{\Omega}) = \frac{q(\vec{r}, E)}{4\pi} = \frac{1}{4\pi} \left[\int \Sigma_s(\vec{r}, E' \rightarrow E) \phi(\vec{r}, E') dE' + \frac{\chi(E)}{k^\infty} \int \nu \Sigma_f(\vec{r}, E') \phi(\vec{r}, E') dE' \right] \quad (301)$$

Substituting (301) into (296) yields

$$\Phi(\vec{r}, E, \hat{\Omega}) = \int_{-\infty}^s \frac{q(s', E)}{4\pi} \cdot e^{-\int_{s'}^s \Sigma_t(s'', E) ds''} ds' \quad (302)$$

Equation (302) is the integral equation for the angular flux, where all sources are considered to be isotropic (using transport-corrected cross sections to account for anisotropic effects). The

integral equation may be formulated directly for the scalar flux by using (300) and integrating (302) over all angles. Hence,

$$\phi(\vec{r}, E) = \int_{4\pi} \Phi(\vec{r}, E, \hat{\Omega}) \cdot d\hat{\Omega} = \int_{4\pi} \int_{-\infty}^{\infty} \frac{q(s', E)}{4\pi} \cdot e^{-\int_{s'}^{\infty} \Sigma_t(s'', E) ds''} ds' \cdot d\hat{\Omega} \quad (303)$$

Since the path of integration over s' stretches to infinity in all directions, all space is included in the integral $ds' d\hat{\Omega}$. As such, the line integral in (303) may be converted to a volume integral by the following change of variables:

$$\vec{r}' = \vec{r} - s' \cdot \hat{\Omega} \quad (304)$$

Rearranging (304)


$$s' = |\vec{r} - \vec{r}'| \quad (305)$$

Multiplying and dividing the integrand in (303) by s'^2 we get

$$\phi(\vec{r}, E) = \int_{4\pi} d\hat{\Omega} \int_0^{\infty} s'^2 \frac{q(\vec{r}', E) e^{-\tau(\vec{r}' \rightarrow \vec{r}, E)}}{|\vec{r} - \vec{r}'|^2} ds' \quad (306)$$

where $\tau(\vec{r}' \rightarrow \vec{r}, E)$ is the distance between points \vec{r}' and \vec{r} in mean free paths (i.e., the optical distance), represented by

$$\tau(\vec{r}' \rightarrow \vec{r}, E) = \int_{r'}^r \Sigma_{tr}(s', E) ds' \quad (307)$$

If we now take a spherical coordinate system with \vec{r} at the origin, as illustrated in  Fig. 34, the incremental volume centered about \vec{r}' is

$$dV' = 4\pi \cdot d\hat{\Omega} \cdot ds' \cdot s'^2 \quad (308)$$

where we have made use of the definition for the incremental solid angle $d\hat{\Omega} = d\varphi \cdot \sin \theta \cdot d\theta / 4\pi$. Combining (308) with (306), we obtain our new expression of the integral equation for the scalar flux with isotropic sources,

$$\phi(\vec{r}, E) = \int q(\vec{r}', E) \cdot \frac{e^{-\tau(\vec{r}' \rightarrow \vec{r}, E)}}{4\pi |\vec{r} - \vec{r}'|^2} \cdot dV' \quad (309)$$

The exponential term in (309) represents the non-collision probability along a streaming path, which may intersect regions of different material properties (i.e., cross sections). We may write (309) in a more compact form as

$$\phi(\vec{r}, E) = \int_{-\infty}^0 dV' \cdot T(\vec{r}' \rightarrow \vec{r}, E) \cdot q(\vec{r}', E) \quad (310)$$

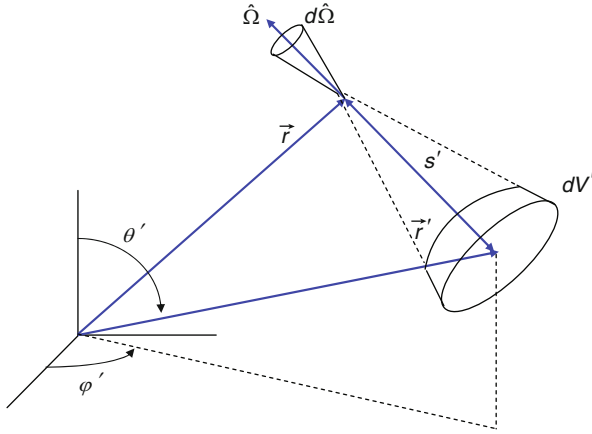


Figure 34
Spherical coordinate system centered at r

where $T(\vec{r}' \rightarrow \vec{r}, E)$ is referred to as the transport matrix between \vec{r}' and \vec{r} for neutrons at energy E ,

$$T(\vec{r}' \rightarrow \vec{r}, E) = \frac{1}{4\pi |\vec{r} - \vec{r}'|^2} \cdot \exp \left\{ - \int_{\vec{r}'}^{\vec{r}} \Sigma_{tr}(s, E) ds \right\} \quad (311)$$

To convert (310) into a form that is amenable for computations, we split the problem geometry into regions where the flux is considered to be flat and, therefore, the source distribution will be constant across the region. The discretized form of the integral equation becomes

$$\phi_i^g = \sum_{i'} T_{i' \rightarrow i}^g \cdot q_{i'}^g \cdot V_{i'} \quad (312)$$

where i is the mesh in which the flux is being calculated and the summation is over all mesh in the problem, including the mesh i itself; g is the energy group. The solution to the integral equation reduces to determining the transport matrix for the geometry of the system.

4.2.2 The Method of Collision Probabilities in Slab Geometry

In all solutions to the transport equation, we must solve for the motion of neutrons in all three dimensions. This is true regardless of the dimensionality of the problem. The dimensionality of the problem merely reflects the number of axes along which material boundaries exist. For example, a one-dimensional problem contains material boundaries along one axis and is infinite along the other two axes. Similarly, a two-dimensional problem contains material boundaries along two axes and is infinite along the third axis. Regardless of the dimensionality of the problem, we must always model neutron motion in all three dimensions. In most transport solution techniques, such as the method of characteristics or discrete ordinates, we must model neutron motion explicitly in all directions through the use of a quadrature set. In the method of collision

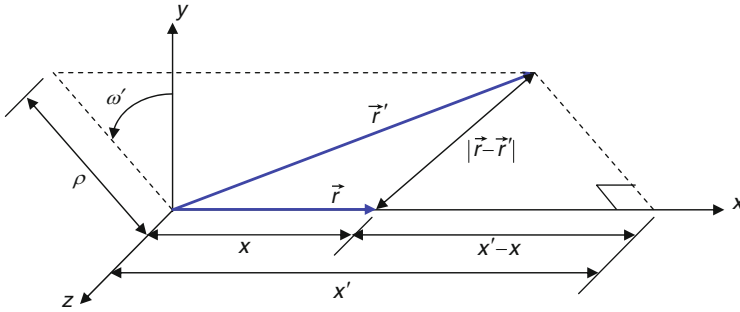


Figure 35
Cylindrical coordinate system for slab geometry

probabilities with isotropic sources, though, it is possible to integrate over all polar directions of motion analytically. This removes a great deal of the computational burden. Once we do this, we need only compute neutron motion numerically in the plane of the problem.

We begin our derivation for the method of collision probabilities in slab geometry. We will then move into cylindrical geometry, which is our desired geometry for the pin-cell calculation. In slab geometry, to perform the polar integration, we begin by expressing the volume element in cylindrical coordinates,

$$dV' = \rho \cdot d\rho \cdot d\omega' \cdot dx' \quad (313)$$

The coordinates to (313) are illustrated in Fig. 35. Using the cylindrical coordinate system, the integral equation can be expressed as

$$\phi(x, E) = \int_{-\infty}^{\infty} dx' \cdot q(x', E) \int_0^{\infty} \rho \cdot d\rho \int_0^{2\pi} \frac{e^{-\tau(\vec{r}' \rightarrow \vec{r}, E)}}{4\pi |\vec{r}' - \vec{r}|^2} \cdot d\omega' \quad (314)$$

where $\tau(\vec{r}' \rightarrow \vec{r}, E)$ now represents the distance, in mean free paths, between \vec{r}' and \vec{r} at some energy, E .

Integrating over $d\omega'$, we get 2π , and (314) becomes

$$\phi(x, E) = 2\pi \int_{-\infty}^{\infty} dx' \cdot q(x', E) \int_0^{\infty} \rho \cdot d\rho \cdot \frac{e^{-\tau(\vec{r}' \rightarrow \vec{r}, E)}}{4\pi |\vec{r}' - \vec{r}|^2} \quad (315)$$

Since the cross sections change only in the x -direction of motion, the optical path between \vec{r}' and \vec{r} , $\tau(\vec{r}' \rightarrow \vec{r}, E)$, may be expressed in terms of the projected length onto the x -axis. Here, we let γ be the projected ratio,

$$\gamma = \frac{|\vec{r}' - \vec{r}|}{|x' - x|} = \frac{\text{true}}{\text{projected}} \quad (316)$$

Then, $\tau(\vec{r}' \rightarrow \vec{r}) = \gamma \cdot \tau(x' - x)$. Using the right triangle illustrated in Fig. 35

$$|\vec{r}' - \vec{r}|^2 = \rho^2 + |x' - x|^2 \quad (317)$$

and, therefore, we can rearrange (317) to get an expression for $\rho \cdot d\rho$,

$$\begin{aligned}
 \rho^2 &= |\vec{r}' - \vec{r}|^2 - |x' - x|^2 \\
 &= y^2 \cdot |x' - x|^2 - |x' - x|^2 \\
 &= (y^2 - 1) \cdot |x' - x|^2 \\
 \rho &= \sqrt{(y^2 - 1)} \cdot |x' - x| \\
 d\rho &= \frac{1}{2\sqrt{(y^2 - 1)}} \cdot 2y \cdot dy \cdot |x' - x| \\
 &= \frac{1}{\sqrt{(y^2 - 1)}} \cdot y \cdot dy \cdot |x' - x|
 \end{aligned} \tag{318}$$

Now, we may express the integral in ρ in terms of the projected ratio, γ ,

$$\rho \cdot d\rho = y \cdot dy \cdot |x' - x|^2 \tag{319}$$

Substituting (319) into (315) we get the equation for the flux expressed in terms of the projected ratio

$$\begin{aligned}
 \phi(x, E) &= 2\pi \int_{-\infty}^{\infty} dx' \cdot q(x', E) \int_0^{\infty} \rho \cdot d\rho \cdot \frac{e^{-\tau(\vec{r}' \rightarrow \vec{r}, E)}}{4\pi |\vec{r}' - \vec{r}|^2} \\
 &= \int_{-\infty}^{\infty} dx' \cdot q(x', E) \int_1^{\infty} \gamma \cdot dy \cdot |x' - x|^2 \cdot \frac{e^{-\gamma\tau(x' \rightarrow x, E)}}{2y^2 \cdot |x' - x|^2} \\
 &= \int_{-\infty}^{\infty} dx' \cdot q(x', E) \int_1^{\infty} \frac{dy}{2y} \cdot e^{-\gamma\tau(x' \rightarrow x, E)}
 \end{aligned} \tag{320}$$

Although the above transformation may seem pointless, it actually simplifies things because the integral over γ may be expressed in terms of the exponential integral, $E_n(\tau)$,

$$E_n(\tau) = \int_1^{\infty} \frac{dy}{y^n} e^{-\gamma\tau} \tag{321}$$

Our integral equation for the scalar flux with isotropic sources now becomes much more compact,

$$\phi(x, E) = \int_{-\infty}^{\infty} dx' \cdot q(x', E) \cdot \frac{1}{2} E_1 \tau [(x' \rightarrow x, E)] \tag{322}$$

Numerical recipes for exponential integrals are widely available in the literature. The interested reader is directed to the Appendix contained in citation (Stamm'ler and Abbate 1983).

For our slab, we divide the interval between the left boundary and the right boundary of the slab into I number of mesh, where the scalar flux is constant (flat) across each mesh. The width of mesh i is $\Delta_i = x_i - x_{i-1}$.

The scalar flux in mesh i is calculated as

$$\phi_i^g = \frac{1}{\Delta_i} \int_{x_{i-1}}^{x_i} dx \cdot \phi(x, E) = \frac{1}{\Delta_i} \int_{x_{i-1}}^{x_i} dx \int_1^\infty dx' \cdot \frac{1}{2} E_1 [\tau(x' \rightarrow x, E)] \cdot q(x', E) \quad (323)$$

where the flat flux approximation leads to the following expression for the source:

$$q(x, E) = q_i^g = \sum_{g'} \Sigma_{s,i}^{g' \rightarrow g} \phi_i^{g'} + \frac{\chi^g}{k^\infty} \sum_{g'} \nu \Sigma_{f,i}^{g'} \phi_i^{g'} \quad (324)$$

Multiplying (323) through by $\Sigma_{tr,i}^g \cdot \Delta_i$, we get

$$\Sigma_{tr,i}^g \cdot \Delta_i \cdot \phi_i^g = \sum_{i'=1}^I P_{i' \rightarrow i}^g \cdot \Delta_{i'} \cdot q_{i'}^g \quad (325)$$

The left-hand side of (325) represents the total number of interactions in mesh i . On the right-hand side of the equation, $\Delta_{i'} \cdot q_{i'}^g$ represents the total number of neutrons born in mesh i' , and $P_{i' \rightarrow i}^g$ represents the probability that a neutron travels undisturbed from mesh i' to mesh i , where it suffers its first collision. In this context, $P_{i' \rightarrow i}^g$ is a true probability in the sense that $\sum_i P_{i' \rightarrow i}^g = 1$. That is, the neutron must eventually interact with something, somewhere.

Comparing (323) against (325), the collision probability can be expressed as

$$P_{i' \rightarrow i}^g = \frac{\Sigma_{tr,i'}^g}{\Delta_{i'}} \int_{x_{i-1}}^{x_i} dx \int_{x_{i'-1}}^{x_{i'}} dx' \cdot \frac{1}{2} E_1 [\tau(x' \rightarrow x, E)] \quad (326)$$

Integrating, we get the following expression for the collision probability between mesh i' and i :

$$P_{i' \rightarrow i}^g = \frac{1}{2 \Sigma_{tr,i'}^g \cdot \Delta_{i'}} \left[\begin{array}{l} E_3(\tau_{i' \rightarrow i}^g) \\ -E_3(\tau_{i' \rightarrow i}^g + \Sigma_{tr,i}^g \cdot \Delta_i) \\ -E_3(\tau_{i' \rightarrow i}^g + \Sigma_{tr,i'}^g \cdot \Delta_{i'}) \\ +E_3(\tau_{i' \rightarrow i}^g + \Sigma_{tr,i}^g \cdot \Delta_i + \Sigma_{tr,i'}^g \cdot \Delta_{i'}) \end{array} \right] \quad (327)$$

and the collision probability within mesh i ,

$$P_{i \rightarrow i}^g = 1 - \frac{1}{2 \Sigma_{tr,i}^g \cdot \Delta_i} [1 - 2E_3(\Sigma_{tr,i}^g \cdot \Delta_i)] \quad (328)$$

where $\tau_{i' \rightarrow i}^g$ is the optical path between mesh i' and i along the x -axis, in energy group g . Note that the optical path does not rely on the direction of motion of the neutron. In other words, $\tau_{i' \rightarrow i}^g = \tau_{i \rightarrow i'}^g$, which is the *optical reciprocity relationship*. In arriving at our final expression in (327) and (328), we have made use of the relationship $E_n(\tau) = \int_\tau^\infty E_{n-1}(x) dx$.

For a slab with vacuum boundary conditions, a neutron can only make it from mesh i' to mesh i if it starts off streaming in the direction of mesh i . If it streams in the opposite direction, it will have a collision or leak through the vacuum boundary without ever reaching mesh i . The

collision probabilities represented by (327) are referred to as *black body* CP's since, should a neutron reach the system boundary, it is lost forever. In this way, the boundary acts as a perfect absorber (i.e., black).

For reflective boundary conditions, all neutrons have some chance of reaching mesh i from mesh i' . To account for this, we can take one of two approaches to correct our black body CP's. We may extend the calculation of $P_{i' \rightarrow i}^g$ to include the reflection off each surface to the slab. Usually, the calculation of collision probabilities will proceed until $\tau_{i' \rightarrow i}^g$ is beyond a preset value, typically between 6 and 10 mean free paths. A neutron that is born 6 mean free paths from mesh i has an e^{-6} chance of reaching the mesh without suffering a collision. This probability is only 1 in 400, which can usually be ignored without impacting the results. The trouble with this approach is the sheer amount of bookkeeping required, especially in the fast energy groups where the mean free paths can be very large. Neutrons may bounce from boundary to boundary many times before reaching the preset limit on mean free path.

An alternative approach would be to calculate the total current on both boundaries caused by the flux in each mesh. Once the surface currents are known, the contribution to the flux in each mesh caused by the current on each surface can be calculated. To do this, we need to calculate the collision probability from mesh i to surface j , which ends up appearing as

$$P_{i \rightarrow j}^g = \int_{S_j} dS \int_{A_i} dA \cdot \hat{n} \cdot |\vec{r} - \vec{r}'| \frac{E_2[\tau(\vec{r} \rightarrow \vec{r}')] }{|\vec{r} - \vec{r}'|^2} \\ = [E_3(\tau_{i \rightarrow j}^g) - E_3(\tau_{i \rightarrow j}^g) + \Sigma_{tr,i}^g \Delta i] \quad (329)$$

Then the current on surface j is the sum of all neutrons arriving on the surface from all mesh in the problem and also from the other surface to the slab. The contribution from each mesh can be expressed as

$$J_j^g = \sum_{i=1}^I P_{i \rightarrow j}^g \cdot q_i^g \cdot \Delta i \quad (330)$$

The contribution from the other surface of the slab will be addressed shortly.

The τ values in (327) and (329) are measured as the shortest distance between two mesh, or between a mesh and a surface. For mesh that share a common surface (i.e., mesh that neighbor each other), $\tau_{i' \rightarrow i}^g = 0$ and $E_3(0) = 1/2$. Similarly, for mesh that neighbor a slab boundary, $\tau_{i \rightarrow j}^g = 0$.

To represent the boundary condition ideally, we would need to know the angular distribution of the flux as it reaches the surface. Since we are solving directly for the scalar flux, we do not know the angular flux distribution. Therefore, we must make some sort of assumption. For illustrative purposes, we will say that the angular flux is distributed isotropically as it reaches the surface. Then, for example, the current along the west surface of the slab is given by

$$J_{\text{west}}^g = \int_{\hat{\Omega} \cdot \hat{n} < 0} d\hat{\Omega} |\hat{\Omega} \cdot \hat{n}| \Phi_{\text{west}}^g(\hat{\Omega}) = \int_{\hat{\Omega} \cdot \hat{n} < 0} d\hat{\Omega} |\hat{\Omega} \cdot \hat{n}| \frac{\phi_i^g}{4\pi} = \frac{1}{4} \phi_{\text{west}}^g \quad (331)$$

where we are only concerned with neutrons traveling to the west. Rearranging (331) we get an expression for the flux along the west surface of the slab,

$$\phi_{\text{west}}^g = 4J_{\text{west}}^g \quad (332)$$

The expression for the scalar flux can now include the contribution from the surface currents (assuming an isotropic angular flux distribution)

$$\phi_i^g = \sum_{i'=1}^I T_{i' \rightarrow i}^g \cdot \Delta_{i'} \cdot q_{i'}^g + 4 \sum_{j=1}^J T_{j \rightarrow i}^g \cdot J_j^g \quad (333)$$

where the transport matrices are given by

$$T_{i' \rightarrow i}^g = \frac{1}{\Sigma_{tr,i}^g \cdot \Delta_i} P_{i' \rightarrow i}^g$$

$$T_{j \rightarrow i}^g = \frac{1}{2\Sigma_{tr,i}^g \cdot \Delta_i} P_{j \rightarrow i}^g$$

and the currents are calculated from


$$J_j^g = \sum_{i=1}^I T_{i \rightarrow j}^g \cdot q_i^g \cdot \Delta_i \quad (334)$$

Note that the transport matrices are insensitive to the direction of motion of the neutron,

$$T_{i' \rightarrow i}^g = T_{i \rightarrow i'}^g \quad (335)$$

(335) is the optical reciprocity relationship, where the transport matrices are diagonally symmetric and only the diagonal elements and upper triangle elements need to be calculated; the lower triangle elements of the matrix can be filled in with the values from the upper triangle.

4.2.3 The Method of Collision Probabilities in Cylindrical Geometry

In slab geometry, we are able to represent neutron streaming in all directions through the slab by using the exponential integral in the streaming term during the calculation of collision probabilities. This is extremely efficient because we now need only know the width of each mesh in order to determine all the first flight collision probabilities. We are able to express the collision probability this way because the neutron's angle of motion with respect to the slab normal is constant. As a result, the track length of the neutron through the slab is the same regardless of the point at which the neutron enters the slab. This is illustrated schematically in  Fig. 36, where the angle of motion with respect to the x -axis is referred to as ω .

We cannot do the same thing in cylindrical geometry because the face of the cylinder is not flat, as the face of the slab is. In cylindrical geometry, we can only perform the integration analytically over all polar directions. To perform the integration over azimuthal directions of motion, we must use streaming tracks.

For cylindrical geometry, infinite in the z -direction, the integration over the polar angle, θ , is equivalent to determining the flux at a point caused by a line source. If the line source is isotropic, and the point at which the flux is to be determined is a distance t from the line source, then the flux may be calculated by integrating along the line source

$$\phi(P) = \int_{-\infty}^{\infty} \frac{e^{-\Sigma R}}{4\pi R^2} dz = \int_{-\infty}^{\infty} \frac{e^{-\rho}}{4\pi R^2} dz \quad (336)$$

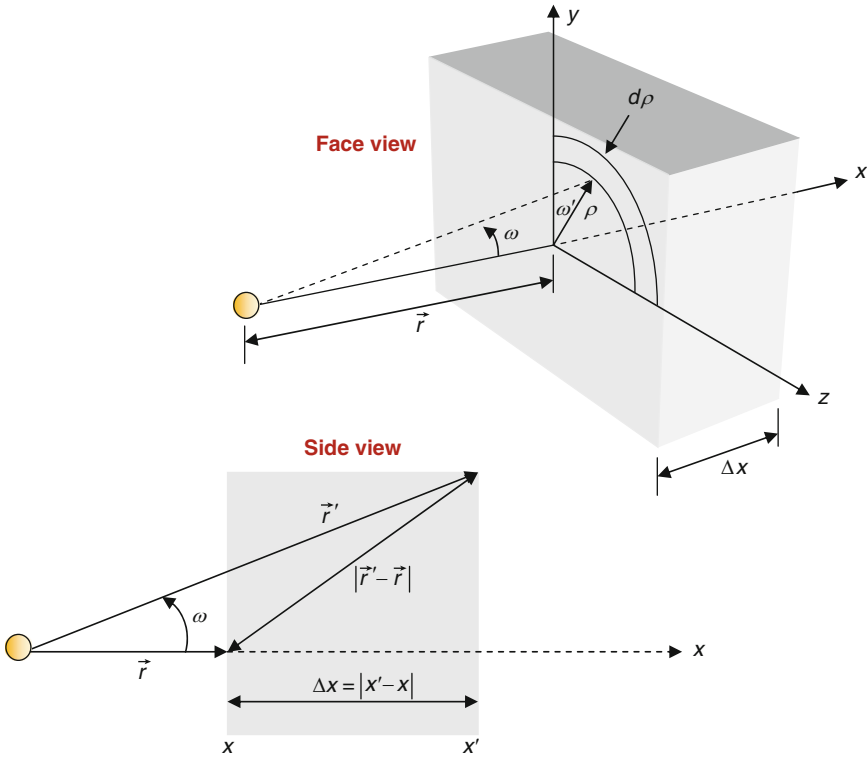


Figure 36
A neutron streaming through a slab

where we have defined $\rho = \Sigma_{tr}R$ to be the optical distance from a point on the line source to the point at which the flux is to be calculated. And the length of R can be expressed as $R = t / \cos \theta$, where t is the closest distance of point P to the line source. The coordinates for this system are illustrated in Figs. 37 and 38.

If we define $\tau = \Sigma_{tr}t$, then $\rho = \tau / \cos \theta$, where τ is in mean free paths. Then (336) becomes

$$\phi(P) = \int_{-\infty}^{\infty} \frac{e^{-(\tau/\cos \theta)}}{4\pi(t^2/\cos^2 \theta)} dz = \int_0^{\infty} \frac{e^{-(\tau/\cos \theta)}}{2\pi(t^2/\cos^2 \theta)} dz \tag{337}$$

where we have made use of the symmetry of the system about the plane of the problem.

Using Fig. 38, we make the following change of variables:

$$\begin{aligned} dz &= \frac{R \cdot d\theta}{\cos \theta} \\ &= \frac{t \cdot d\theta}{\cos^2 \theta} \end{aligned} \tag{338}$$

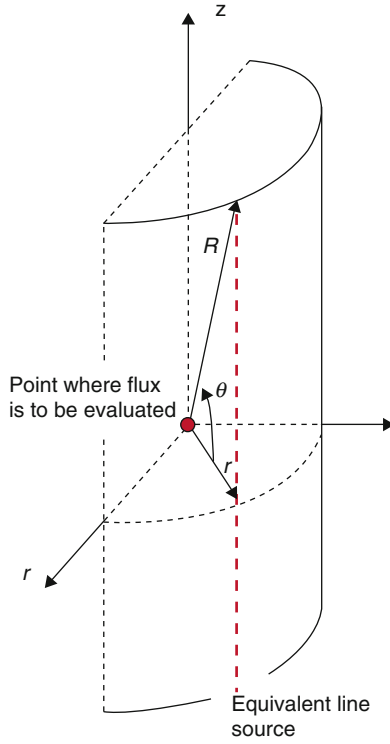


Figure 37
Coordinate system for calculating the flux at a point

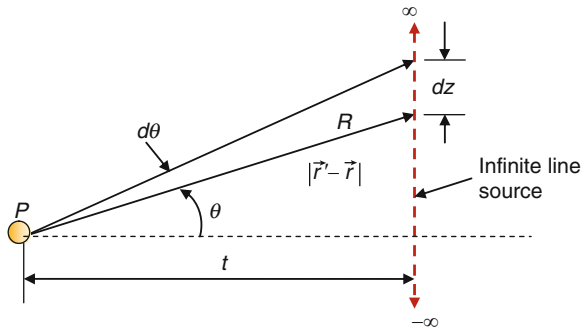


Figure 38
Variables in cylindrical geometry

Substituting (338) into (337) we get

$$\begin{aligned}\phi(P) &= \int_0^{\pi/2} \frac{e^{-(\tau/\cos\theta)}}{2\pi t} d\theta \\ &= \frac{Ki_1(\tau)}{2\pi t}\end{aligned}\quad (339)$$



where $Ki_1(\tau)$ is the first order Bickley–Naylor function, defined as

$$Ki_n(\tau) = \int_0^{\pi/2} \exp\left\{-\frac{\tau}{\cos\theta}\right\} \cos^{n-1}\theta \cdot d\theta \quad (340)$$

The probability of a neutron actually traveling the projected distance, $\tau = \Sigma_{tr}t$, is given by

$$p(\tau) = \int_{\tau}^{\infty} Ki_1(\tau') \cdot d\tau' = Ki_2(\tau) \quad (341)$$

In cylindrical geometry, the Bickley–Naylor functions serve the same purpose as the exponential integral serves in slab geometry. The main difference is that the exponential integral accounts for motion in all directions, whereas the Bickley–Naylor function accounts for motion only out of the plane of the problem. However, by using the Bickley–Naylor functions, we need now only account for neutron streaming in the plane of the problem. This is much more efficient than having to numerically account for streaming in three dimensions and helps to simplify our analysis. This is the great benefit of using the method of collision probabilities over other transport solution techniques. As with the exponential functions, numerical recipes for Bickley–Naylor functions are contained in the Appendix in citation (Stamm'ler and Abbate 1983).

The coordinate system for the azimuthal and spatial integration is shown in  Fig. 39, where φ represents the azimuthal angle, and h represents the spatial dimension. For this particular geometry, the azimuthal integration can be rolled into the spatial integration. Also, due to symmetry in the azimuthal plane, we need only model 1/4 of the cylinder – applying perfect reflection along the x - and y -axes and a vacuum boundary condition along the outer edge of the cylinder. The resulting coordinate system is shown in  Fig. 40, where each track drawn at a different h value represents a different φ angle. Collision probabilities will be integrated along these tracks in order to calculate the corresponding transport matrix.

Going through the same exercise for the scalar flux as was followed for slab geometry, we come out with the following expressions for the collision probabilities in cylindrical geometry:

$$\begin{aligned}P_{i' \rightarrow i}^g &= Ki_3(\tau_{i' \rightarrow i}^g) - Ki_3(\tau_{i' \rightarrow i}^g + \tau_{i' \rightarrow i'}^g) - Ki_3(\tau_{i' \rightarrow i}^g + \tau_{i \rightarrow i}^g) \\ &\quad + Ki_3(\tau_{i' \rightarrow i}^g + \tau_{i \rightarrow i}^g + \tau_{i' \rightarrow i'}^g) \\ P_{i \rightarrow i}^g &= \Sigma_{tr,i}^g V_i - \left[\frac{\pi}{4} - Ki_3(\tau_{i \rightarrow i}^g) \right] \\ P_{s \rightarrow i}^g &= Ki_3(\tau_{s \rightarrow i}^g) - Ki_3(\tau_{s \rightarrow i}^g + \tau_{i \rightarrow i}^g) \\ P_{s' \rightarrow s}^g &= Ki_3(\tau_{s' \rightarrow s}^g)\end{aligned}\quad (342)$$

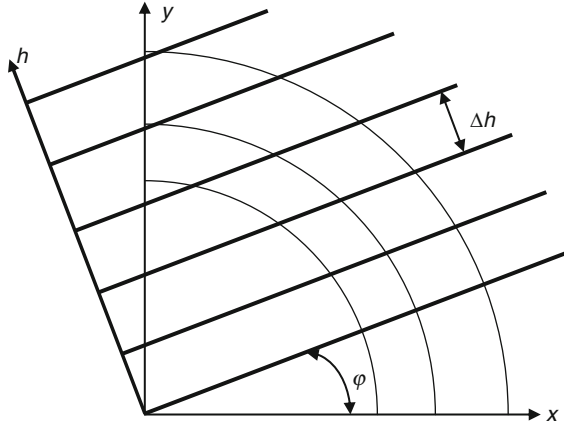


Figure 39

Spatial and angular variables for cylindrical geometry

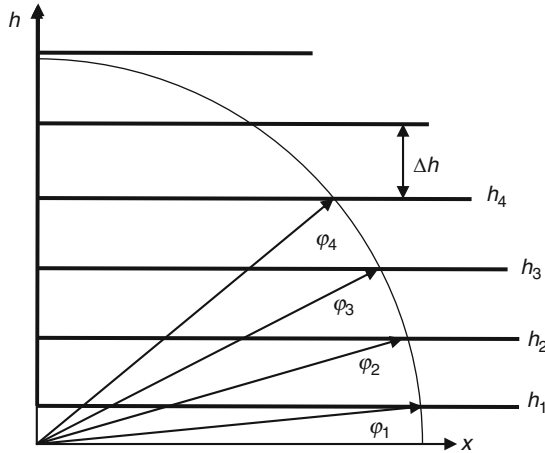


Figure 40

Angular variable combined with spatial variable

where i and i' represent mesh in the problem; and s and s' represent surfaces in the problem. The elements of the transport matrix are given by

$$\begin{aligned}
 T_{i' \rightarrow i}^g &= \frac{1}{\sum_{tr,i}^g V_i \sum_{tr,i'}^g V_{i'}} \int P_{i' \rightarrow i}^g(h) \cdot dh = \frac{1}{\sum_{tr,i}^g V_i \sum_{tr,i'}^g V_{i'}} \sum_m P_{i' \rightarrow i}^g(h_m) \cdot \Delta h \\
 T_{i \rightarrow i}^g &= \frac{1}{(\sum_{tr,i}^g V_i)^2} \int P_{i \rightarrow i}^g(h) \cdot dh = \frac{1}{(\sum_{tr,i}^g V_i)^2} \sum_m P_{i \rightarrow i}^g(h_m) \cdot \Delta h \\
 T_{s' \rightarrow i}^g &= \frac{1}{\sum_{tr,i}^g V_i A_{s'}} \int P_{s' \rightarrow i}^g(h) \cdot dh = \frac{1}{\sum_{tr,i}^g V_i A_{s'}} \sum_m P_{s' \rightarrow i}^g(h_m) \cdot \Delta h \\
 T_{s' \rightarrow s}^g &= \frac{1}{A_s A_{s'}} \int P_{s' \rightarrow s}^g(h) \cdot dh = \frac{1}{A_s A_{s'}} \sum_m P_{s' \rightarrow s}^g(h_m) \cdot \Delta h
 \end{aligned} \tag{343}$$

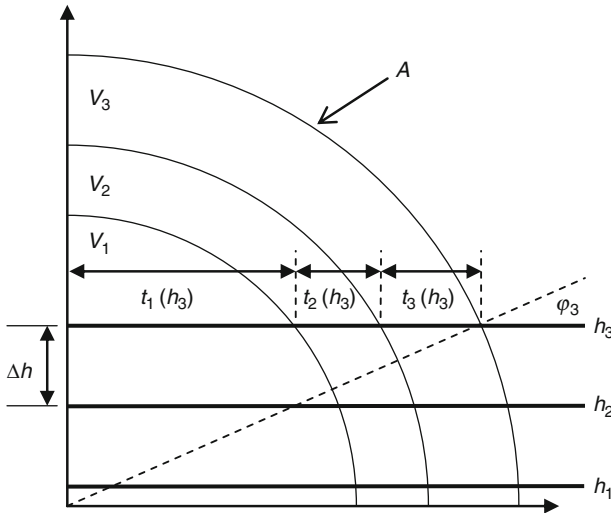


Figure 41 Integration variables associated with annular geometry

where V_i represents the volume of a mesh, which in our one-dimensional cylinder is actually the area of the mesh; and A_s represents the surface area of each outer surface of the cylinder, which in our one-dimensional cylinder is actually the outer perimeter of the cylinder. This is shown in Fig. 41. The figure also contains an example of the track distances across the different mesh of the cylinder. These are the track lengths used to calculate the τ values in (342).

To apply the method of collision probabilities, the cylindrical problem is subdivided into a number of small annular mesh. The scalar flux and, hence, the source across each mesh is assumed to be constant. To obtain an accurate solution to the integral equation, the size of each mesh must be small enough such that the flat source approximation is valid. If the source exhibits large variations across a given mesh, the mesh in question would need to be subdivided into smaller mesh where the source variations were not so extreme.

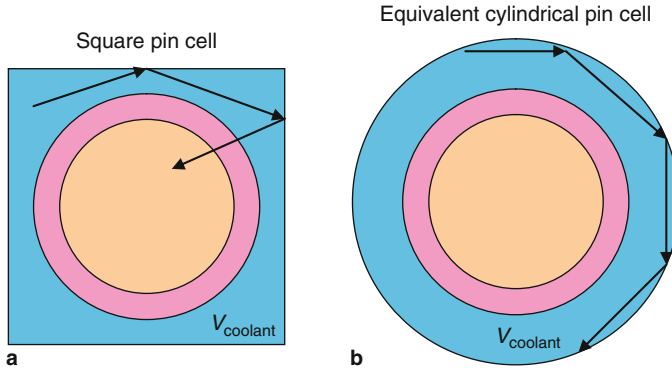
For cylindrical geometry, the equation for the scalar flux is given by

$$\phi_i^g = T_{i \rightarrow i}^g \cdot q_i^g \cdot V_i + \sum_{i' \neq i} q_{i'}^g \cdot V_{i'} \cdot T_{i' \rightarrow i}^g \tag{344}$$

In this formulation, the surface of the cylinder is considered to be non reentrant. That is, if a neutron reaches the surface of the cylinder, it leaks out of the system and does not return. In this respect, the collision probabilities represented in (342) are for a black boundary. We will correct these accordingly in Sect. 4.2.4 to account for reflection along the edge of the cylinder.

4.2.4 White Boundary Conditions

As mentioned earlier, the spectral calculation takes the true geometry of each pin cell – cylindrical fuel and clad regions imbedded in a square coolant zone – and cylindricalizes the coolant



■ **Figure 42**
Neutron streaming effects in a cylindrical cell

region of the cell, preserving the coolant volume, in order to allow for a one-dimensional calculation to be performed on the cell. To isolate the cell from its assembly surroundings, the surfaces along the square coolant region are assumed to be perfectly reflecting. In this way, the spectral calculation generates an infinite spectrum for each pin cell.

Once the pin cell has been cylindricalized, the boundary conditions applied to the equivalent cylindrical coolant region must be consistent with those that would be applied to the square coolant region. Applying perfect reflection along the outer surface of the cylindrical cell will not, however, produce results equivalent to the results generated from a two-dimensional pin-cell calculation. The reason for this is best illustrated in [▶ Fig. 42](#). Here, [▶ Fig. 42a](#) illustrates a neutron streaming across a square coolant region of the true pin-cell geometry at a rather shallow angle relative to the top surface of the cell. Following a few reflections off the boundary of the cell, the neutron streams into the fuel region and is potentially absorbed. [▶ Figure 42b](#) illustrates the same neutron streaming across the coolant region of the cylindrical cell geometry at the same shallow angle relative to the boundary of the cell. Regardless of the number of times the neutron reaches the boundary of the cell, it will never be reflected through the fuel region unless it suffers a scattering collision. As a result, the flux in the coolant region of the cylindrical cell will be overestimated and the cylindrical cell geometry will produce results that are not entirely representative of the results generated in the true geometry of the cell. In even simpler terms, perfect reflection imposes the constraint that a neutron will forever stream back and forth along the same ray trace shown in [▶ Fig. 41](#) unless it suffers a scattering collision. It is easy to see from [▶ Fig. 42a](#) that this is not the case for a square boundary.

To provide a more accurate estimate of the flux in the coolant region of the equivalent cylindrical cell, a “white” boundary condition is applied at the outer surface of the one-dimensional pin-cell geometry, rather than perfect reflection. Here, a neutron reaching the boundary of the system is reflected back into the system with a cosine distribution. In this way, neutrons moving at steep angles relative to the surface of the cylinder are weighed more heavily than neutrons that move at shallow angles relative to the surface of the cylinder, thereby minimizing the streaming effect illustrated in [▶ Fig. 42](#). By using the white boundary condition, most results from the equivalent cell geometry agree nicely with results from the true cell geometry that uses perfect reflection.

Carlvik's method is used to update all collision probabilities from a black boundary to a white boundary (Carlvik 1967a). Here, the vector R_i^g is determined following the calculation of the black boundary $P_{i' \rightarrow i}^g$,

$$R_i^g = \sum_{tr,i}^g V_i - \sum_{i'} \sum_{tr,i'}^g V_{i'} P_{i' \rightarrow i}^g \quad (345)$$

The black boundary collision probabilities are all updated using the relationship

$$\sum_{tr,i}^g V_i \hat{P}_{i' \rightarrow i}^g = \sum_{tr,i}^g V_i P_{i' \rightarrow i}^g - \frac{R_{i'} R_i}{\sum_j R_j} \quad (346)$$

where $P_{i' \rightarrow i}^g$ is a black boundary collision probability, and $\hat{P}_{i' \rightarrow i}^g$ is a white boundary collision probability. Once the collision probabilities have been updated, (344) may be solved directly for the scalar flux. (344) should be rewritten to reflect the fact that we have modified the collision probabilities in (342). Our new expression for the scalar flux is

$$\phi_i^g = \hat{T}_{i \rightarrow i}^g \cdot q_i^g \cdot V_i + \sum_{i' \neq i} q_{i'}^g \cdot V_{i'} \cdot \hat{T}_{i' \rightarrow i}^g \quad (347)$$

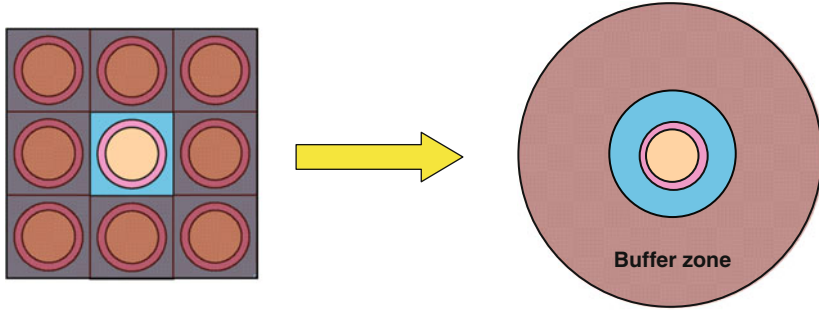
where the modified transport matrix elements are given by

$$\begin{aligned} \hat{T}_{i' \rightarrow i}^g &= \frac{1}{\sum_{tr,i}^g V_i \sum_{tr,i'}^g V_{i'}} \sum_m \hat{P}_{i' \rightarrow i}^g(h_m) \cdot \Delta h \\ \hat{T}_{i \rightarrow i}^g &= \frac{1}{\left(\sum_{tr,i}^g V_i\right)^2} \sum_m \hat{P}_{i \rightarrow i}^g(h_m) \cdot \Delta h \\ \hat{T}_{s' \rightarrow i}^g &= \frac{1}{\sum_{tr,i}^g V_i A_{s'}} \sum_m \hat{P}_{s' \rightarrow i}^g(h_m) \cdot \Delta h \\ \hat{T}_{s' \rightarrow s}^g &= \frac{1}{A_s A_{s'}} \sum_m \hat{P}_{s' \rightarrow s}^g(h_m) \cdot \Delta h \end{aligned} \quad (348)$$

4.2.5 Buffer Zone

For normal fuel pin cells, the fuel pellet itself produces neutrons via the fission process and the cell can sustain its own chain reaction for the pin-cell spectral calculation. For inert cells, such as water rods, control rods, or vanish portions of part length rods, there is no neutron source within the pin cell and, hence, there is no way of generating a solution to the integral transport equation. Similarly for fuel pins containing Gadolinium, the Gd cross sections are so large at energies below 1 eV that it becomes difficult to produce a realistic thermal flux spectrum within the pin cell without an external source of neutrons.

In an effort to impose consistency between different pin-cell spectral calculations, all pin cells can be modeled with an outer buffer zone comprised of a representative amount of fuel, cladding, and water. For normal fuel pins, the buffer zone is slightly detrimental because it places fuel material too close to the coolant region. But for inert rods and rods containing Gadolinium, the buffer zone helps to drive the neutron flux across the problem. The size of the buffer zone is somewhat irrelevant to the solution of the problem. For application in most lattice physics codes, the buffer zone can be chosen to be equivalent in size to eight pin cells.



■ **Figure 43**
Geometry of a pin cell with a buffer zone attached

The buffer zone is placed on the outside of each pin cell, as illustrated in ► [Fig. 43](#), and the white boundary condition described in ► [4.2.4](#) is applied at the outer surface of the buffer zone.

The cross sections for the buffer zone can be created in many different ways. The results to the analysis are highly insensitive to the method used. The easiest way to create cross sections for the buffer zone is to simply volume-average all materials in the problem into a single, homogenized material. When applying this simple averaging technique, one should ensure that none of the strong absorbers in the assembly are included in the buffer material. That is, materials for the control blade, control rods, absorber pins, and any fuel pins containing Erbium or Gadolinium should be left out of the average. Inclusion of the strong absorbers into the material will produce a spectrum that is too hard. Another alternative for creating the cross sections for the buffer zone material is to perform a single pin-cell calculation on a representative pin cell (that does not contain a buffer zone) and use the flux from that calculation to flux- and volume-weight the cross sections into a homogenized material. Either approach is perfectly acceptable.

4.2.6 Numerics of the Pin-Cell Spectral Calculation

The pin-cell spectral calculations can be treated as fixed source problems. The fission cross sections of all fuel regions are set to zero and a fixed source of neutrons is defined to exist in the buffer zone only, using the fission spectrum as the neutron source. This is done to help speed up convergence of the solution without adversely affecting the final neutron distribution.

The routine begins by calculating the collision probabilities between all mesh in the problem, using [\(342\)](#). The surface terms are dropped from consideration because they are now rolled into the white boundary correction,

$$\begin{aligned}
 P_{i' \rightarrow i}^g(h) &= Ki_3(\tau_{i' \rightarrow i}^g) - Ki_3(\tau_{i' \rightarrow i}^g + \tau_{i' \rightarrow i'}^g) - Ki_3(\tau_{i' \rightarrow i}^g + \tau_{i \rightarrow i}^g) \\
 &\quad + Ki_3(\tau_{i' \rightarrow i}^g + \tau_{i \rightarrow i}^g + \tau_{i' \rightarrow i'}^g) \\
 P_{i \rightarrow i}^g(h) &= \sum_{i'r,i}^g V_i - \left[\frac{\pi}{4} - Ki_3(\tau_{i \rightarrow i}^g) \right]
 \end{aligned}
 \tag{349}$$

The black boundary collision probabilities are then modified for a white boundary condition using (346). Next, the transport kernel is calculated using (343), where a Gaussian quadrature is used to perform the integration over angle. Once again, the surface terms are dropped from the explicit calculation because they are implicit in the modified collision probability terms,

$$\begin{aligned}\hat{T}_{i' \rightarrow i}^g &= \frac{1}{\Sigma_{tr,i}^g V_i \Sigma_{tr,i'}^g V_{i'}} \sum_m \hat{P}_{i' \rightarrow i}^g(h_m) \cdot \Delta h \\ \hat{T}_{i \rightarrow i}^g &= \frac{1}{(\Sigma_{tr,i}^g V_i)^2} \sum_m \hat{P}_{i \rightarrow i}^g(h_m) \cdot \Delta h\end{aligned}\quad (350)$$

Once the transport kernel has been calculated for the system, the iteration scheme begins. The one-group expression for the flux can be written from (312) as

$$\phi_i = \sum_{i'} q'_{i'} V_{i'} \hat{T}_{i' \rightarrow i} + \sum_{i' \neq i} \Sigma_{s,i'} \phi_{i'} V_{i'} \hat{T}_{i' \rightarrow i} + \Sigma_{s,i} \phi_i V_i \hat{T}_{i \rightarrow i} \quad (351)$$

where the superscript representing the energy group has been dropped and the self-scattering portion of the source has been isolated from the in-scattering and the fixed source, $q'_{i'}$. Rearranging (351) to isolate the in-scattering source term, we get

$$\phi_i - \Sigma_{s,i} \phi_i V_i \hat{T}_{i \rightarrow i} - \sum_{i' \neq i} \Sigma_{s,i'} \phi_{i'} V_{i'} \hat{T}_{i' \rightarrow i} = \sum_{i'} q'_{i'} V_{i'} \hat{T}_{i' \rightarrow i} \quad (352)$$

$$\sum_{i'} \phi_{i'} (\delta_{i,i'} - \Sigma_{s,i'} V_{i'} \hat{T}_{i' \rightarrow i}) = \sum_{i'} q'_{i'} V_{i'} \hat{T}_{i' \rightarrow i} \quad (353)$$

where the in-scattering and fixed source term is given by

$$q'_{i'}{}^g = \sum_{g' \neq g} \Sigma_{s,i'}^{g' \rightarrow g} \phi_{i'}^{g'} + \chi_{i'}^g \quad (354)$$

recalling that the fixed source is zero everywhere other than in the buffer zone.

(352) may be expressed in one-group matrix notation as

$$\underline{\underline{A}}_{ii'} \phi_i = \underline{\underline{B}}_i \quad (355)$$

where

$$\begin{aligned}\underline{\underline{A}}_{ii'} &= \delta_{i,i'} - \Sigma_{s,i'} V_{i'} \hat{T}_{i' \rightarrow i} \\ \underline{\underline{B}}_i &= \sum_{i'} q'_{i'} V_{i'} \hat{T}_{i' \rightarrow i}\end{aligned}\quad (356)$$

The solution to (355) is of the form

$$\phi_i = \underline{\underline{A}}_{ii'}^{-1} \underline{\underline{B}}_i \quad (357)$$

where the $\underline{\underline{A}}$ matrix is inverted only once, prior to beginning the iteration process, using Gaussian elimination.

The iteration scheme consists of a series of inner iterations that are used to converge the scalar flux in each energy group. The inner iterations are contained within outer iterations that

are used to converge the source distribution. Since the pin-cell spectral calculations are treated as a fixed source problem, the flux in the fast energy groups can be solved directly without the need for an outer iteration. The outer iterations are used only to treat up-scattering in the thermal energy groups below ~ 2 eV.

The calculation begins by initializing all scalar flux values in all groups, all mesh, to unity. This represents the flux distribution from the 0 outer iteration. Using this flux initialization, the total (scalar) source in each region of the problem is calculated as

$$q_{i,iter}^g = \sum_{g' < g} \Sigma_{s,i}^{g' \rightarrow g} \phi_{i,iter}^{g'} + \sum_{g' > g} \Sigma_{s,i}^{g' \rightarrow g} \phi_{i,iter-1}^{g'} + \chi_{i,iter-1}^g \quad (358)$$

where *iter* refers to the current outer iteration. The first summation in (358) is over all energy groups above the current group, *g*. The second summation in (358) is over all energy groups below the current group, *g*. The value χ_i^g is the fixed source and is present only in the buffer zone. For energy groups above the thermal up-scattering threshold, the second summation in (358) is always zero and (357) can be solved directly to obtain the fast flux distribution across the pin cell. For thermal energy groups, the flux distribution in lower energies influences the flux distribution in higher energies via thermal up-scattering and the outer iterations are used to drive the flux distribution to a converged solution.

Following the completion of an outer iteration, a fundamental mode rebalancing of the group flux distribution is performed in order to properly normalize the flux and ensure neutron conservation in the thermal groups. The fundamental mode calculation is performed on an equivalent homogeneous system using flux and volume weighted cross sections from the pin-cell calculation

$$\bar{\Sigma}_x^g = \frac{\sum_i \Sigma_{x,i}^g \phi_i^g V_i}{\sum_i \phi_i^g V_i} \quad (359)$$

The fundamental mode equation to be solved is a simple balance equation

$$\begin{aligned} \bar{\Sigma}_{tr}^g \psi^g &= \sum_{g' \neq g} \bar{\Sigma}_s^{g' \rightarrow g} \psi^{g'} + \bar{\Sigma}_s^{g \rightarrow g} \psi^g + \bar{\chi}^g \\ (\bar{\Sigma}_{tr}^g - \bar{\Sigma}_s^{g \rightarrow g}) \psi^g &= \sum_{g' \neq g} \bar{\Sigma}_s^{g' \rightarrow g} \psi^{g'} + \bar{\chi}^g \\ \psi^g &= \frac{\bar{q}^g}{\bar{\Sigma}_r^g} \end{aligned} \quad (360)$$

where the source term does not contain self-scattering and $\bar{\Sigma}_r^g$ is the removal cross section, given by $\bar{\Sigma}_r^g = \bar{\Sigma}_{tr}^g - \bar{\Sigma}_s^{g \rightarrow g}$.

Following the solution to (360), the scalar flux distribution is scaled using

$$\hat{\phi}_i^g = \phi_i^g \cdot \frac{\psi^g}{\sum_i \phi_i^g V_i} \quad (361)$$

Once the flux has converged, the infinite multiplication factor for the pin cell can be calculated from

$$k^\infty = \frac{\sum_g v \bar{\Sigma}_f^g \psi^g}{\sum_g \bar{\Sigma}_a^g \psi^g} \quad (362)$$

4.3 Coupling Calculation

The flux from the pin-cell calculations can be used, directly, as a condensation spectrum to generate broad-group cross sections for the fine-mesh transport solution. Since each pin-cell calculation was performed by isolating the pin from the rest of the assembly, the spectra are only a fair approximation of the actual distribution of neutrons in energy in the various regions of the pin cell (fuel pellet, cladding, and coolant region). If we choose to use these spectra to condense cross sections, we will end up having to carry a lot of broad energy groups in order to preserve accuracy at the fine-mesh assembly level. We will also run into a dilemma with respect to condensing cross sections in the outer regions of the assembly. For example, we have no specific flux spectrum from the series of pin-cell calculations with which to condense the outer water gaps of a BWR fuel assembly, the channel shroud, or regions of the control blade. We will need to use either the spectrum from one of the pin-cell regions, or possibly from the buffer zone – neither of which is an adequate choice. By performing a two-dimensional coupling calculation, we can avoid this dilemma.

The coupling calculation is used to adjust the energy distribution of neutrons from the pin-cell spectral calculations to account for the effects of the true surroundings. Once the energy distribution from the series of pin-cell calculations is adjusted, the resulting flux spectra are used to condense macroscopic cross sections in each material region of the problem from the energy group structure of the cross section library to a smaller, broad-group energy structure in preparation for the fine-mesh transport calculation. The coupling calculation is performed on the entire lattice using homogenized pin-cell cross sections. As such, the solution may be obtained in a straightforward Cartesian geometry and any solution technique to the transport equation is a viable candidate for the coupling calculation.

The solution techniques considered for the coupling calculation include the explicit transport techniques of discrete ordinates, collision probabilities, and the method of characteristics. Approximate techniques considered for the coupling calculation include transmission probabilities (TP) and diffusion theory. Obviously, the explicit transport techniques offer the greatest accuracy. Their main deficiency is execution speed, especially for the large number of energy groups we are considering. In addition, one might wonder why we would bother performing a coupling calculation at all if we are going to use an explicit transport technique to do it. That is, we should simply perform the fine-mesh assembly transport calculation in the energy group structure of the cross section library and be done with it. So, our only real choices for the coupling calculation are the two approximate techniques – TP and diffusion theory. The major assumption used in the derivation of the diffusion approximation is that scattering is the dominant process taking place in the problem. For normal fuel regions and water regions, this assumption is true. For strongly absorbing regions, however, such as control blades, control rods, absorber pins, and fuel pins containing Erbium or Gadolinium, this assumption is very

poor and the use of diffusion theory becomes questionable. Around highly absorbing regions, diffusion theory underestimates the gradient of the flux dip across the absorber and calculates a much flatter flux profile than other solution techniques. The result is too many neutrons being placed directly in, and around, the absorber region and a resulting flux spectrum that is too hard. This is highly undesirable from the point of view of producing a condensation spectrum. As a result, in this section we will focus on a coupling scheme based on a response matrix formulation that uses a simplified transmission probabilities method. The method is accurate in terms of distributing neutrons in energy, and is extremely fast.

4.3.1 The Method of Transmission Probabilities

As in the pin-cell spectral calculations, the transmission probabilities method solves the integral form of the transport equation. In collision probabilities, (347) represent contributions to the scalar flux in mesh i from all other mesh in the system, as well as from the system boundary. The number of solutions to (347) required to calculate a new flux distribution for each energy group is equal to the square of the number of mesh in the problem. If the system being analyzed has many mesh and many energy groups, the number of times (347) must be solved may become very large indeed. In addition, the amount of memory needed to store the transport matrix, (348), for large problems with hundreds of energy groups is excessive, and it may become necessary to store only portions of the matrix in memory at any given time.

This burden on the computer system renders the collision probabilities technique, in its present form, a rather poor choice for large problems such as a whole fuel assembly. The burden on the computer system can be relaxed significantly by coupling mesh together via their surface currents, rather than via their scalar fluxes.

In the transmission probabilities technique, an outgoing current is calculated along each surface of each mesh. The outgoing current will become the incoming current to the neighboring mesh. This eliminates the first summation in (347) for the scalar flux and leaves only the contribution to the scalar flux from neutrons born within a particular mesh, and from the incoming currents along all surfaces to the mesh. The equations to be solved are then reduced to

$$\phi_i^g = T_{i \rightarrow i}^g \cdot q_i^g \cdot V_i + 4 \sum_{s'_i} T_{s'_i \rightarrow i}^g \cdot J_{s'_i, in}^g \cdot A_{s'_i} \quad (363)$$

$$J_{s_i, out}^g = q_{i'}^g \cdot V_{i'} \cdot T_{i' \rightarrow s_i}^g + 4 \sum_{s'_i \neq s_i} T_{s'_i \rightarrow s_i}^g \cdot J_{s'_i, in}^g \cdot A_{s'_i} \quad (364)$$

where $J_{s_i, out}^g$ becomes $J_{s'_i, in}^g$ to the subsequent mesh. All summations in (363) and (364) are over surfaces to mesh i only. It should be remembered that, in the derivation of these equations, the source – and hence the scalar flux – was assumed to be constant across a mesh.

The average neutron current crossing a mesh surface is calculated from the outward directed angular flux distribution along the surface as

$$J_{s_i}^g = \int |\hat{n} \cdot \hat{\Omega}_m| \cdot \Phi_{m, i}^g \cdot d\hat{\Omega}_m = \sum_m \sin \varphi_m \cdot \cos \theta_m \cdot \Phi_{m, i}^g \cdot \omega_m \quad (365)$$

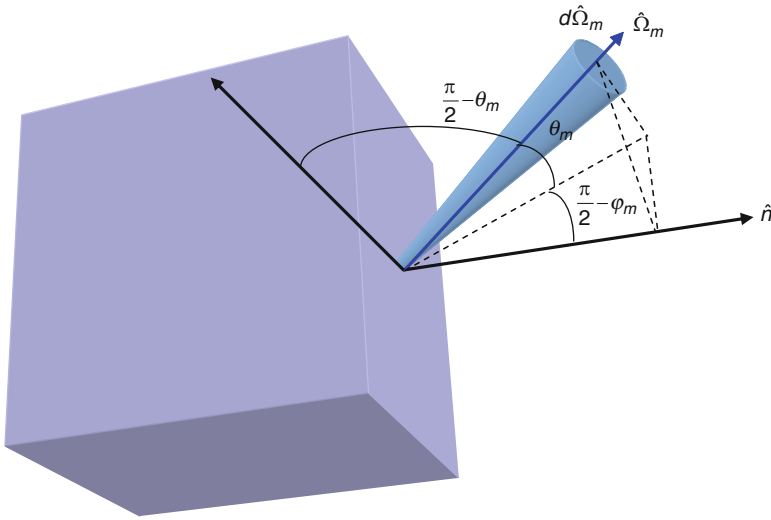


Figure 44
Variables for calculating the surface current leaving a mesh

where the current is normal to the mesh surface. The meanings of the variables used in (365) are illustrated in Fig. 44.

In methods that solve the integrodifferential form of the Boltzmann transport equation, such as the discrete ordinates method, the equations are formulated in terms of the angular flux and the current can be easily calculated, if desired. In integral transport theory, though, the angular dependency of the flux is integrated out of the equation prior to formulating the numerical solution. By doing so, the integral equation is solved directly in terms of the scalar flux, which is usually the desired quantity. The one drawback to this process, in relation to transmission probabilities, is that the angular flux is needed in order to determine the current.

To calculate a current passing through each surface of each mesh, the angular flux must now be approximated in some manner. In the response matrix technique that uses a simplified transmission probabilities method, the angular flux crossing each surface of each mesh is assumed to be distributed isotropically in angle and uniformly in space along the surface

$$\Phi_{m,i}^g = \frac{\phi_i^g}{4\pi} \tag{366}$$

where m represents a specific direction of motion, of which there are a total of 4π radian. (366) leads to the following expression for the current crossing a surface:

$$J_{s_i}^g = \int_{\hat{\Omega} \cdot \hat{n} > 0} d\hat{\Omega} |\hat{\Omega} \cdot \hat{n}| \Phi(\vec{r}, \hat{\Omega}) = \frac{\phi_i^g}{4} \tag{367}$$

From (367), the relationship between the scalar flux and the current is given by

$$4J_{s_i}^g = \phi_i^g \tag{368}$$

where s is a surface to mesh i .

In the coupling calculation routine, the current crossing any boundary is assumed to be isotropically distributed in angle. For a very detailed calculation in space, this would be a very poor approximation. For homogenized pin cells, however, this is actually a better approximation than one might think and allows the simplified transmission probabilities method to be used successfully to generate a reasonably accurate condensation flux. Remember that, at this stage of the calculational scheme, we are focusing on obtaining an accurate energy distribution of neutrons and not so much an accurate spatial distribution.

4.3.2 Numerics of the Coupling Calculation

As in the method of collision probabilities, the transmission probabilities technique reduces to calculating reasonably accurate transport probabilities between all surfaces of a mesh. The equations to be solved here are similar to those introduced for the collision probabilities method

$$\begin{aligned} T_{i \rightarrow i}^g &= \frac{1}{(\sum_{tr,i}^g V_i)^2} \int \frac{d\varphi}{2\pi} \int P_{i \rightarrow i}^g(\varphi, h) dh \\ T_{s \rightarrow i}^g &= \frac{1}{\sum_{tr,i}^g V_i A_s} \int \frac{d\varphi}{2\pi} \int P_{s \rightarrow i}^g(\varphi, h) dh \\ T_{s' \rightarrow s}^g &= \frac{1}{A_s A_{s'}} \int \frac{d\varphi}{2\pi} \int P_{s' \rightarrow s}^g(\varphi, h) dh \end{aligned} \quad (369)$$

where the $P_{i \rightarrow i}^g(\varphi, h)$'s represent the collision probabilities, given by

$$\begin{aligned} P_{i \rightarrow i}^g(\varphi, h) &= \sum_{tr,i}^g V_i - \left[\frac{\pi}{4} - Ki_3(\tau_{i \rightarrow i}^g) \right] \\ P_{s \rightarrow i}^g(\varphi, h) &= \frac{1}{2} \left[\frac{\pi}{4} - Ki_3(\tau_{s \rightarrow i}^g) \right] \\ P_{s' \rightarrow s}^g(\varphi, h) &= Ki_3(\tau_{s' \rightarrow s}^g) \end{aligned} \quad (370)$$

In the above equation, the A_s 's represent the surface areas of a mesh, and the $\tau_{i \rightarrow i}^g$'s represent the optical distances between surfaces of a mesh, in mean free paths, in the xy -plane of the problem. The $Ki_3(\tau_{i \rightarrow i}^g)$ values are the Bickley–Naylor functions arising from the integration over polar angle performed analytically, as discussed previously. Note that collision probabilities for the coupling calculation are calculated on a mesh by mesh basis and are, therefore, much simpler than the collision probabilities calculated for the pin-cell spectral calculations.

The integrations in (369) are performed numerically using sets of parallel, equidistant tracks (separated by a distance dh), which are traced over each mesh individually at several evenly spaced angles (distributed every $\Delta\varphi$ radians). The collision probabilities between the various surfaces are then calculated along these tracks.

The numerics of the coupling calculation are very similar to those of the pin-cell spectral calculations. Here, though, streaming tracks are traced over each mesh in the system individually in order to obtain the optical distances, τ , needed to solve (370) and to perform the integrations over angle and space contained in (369).

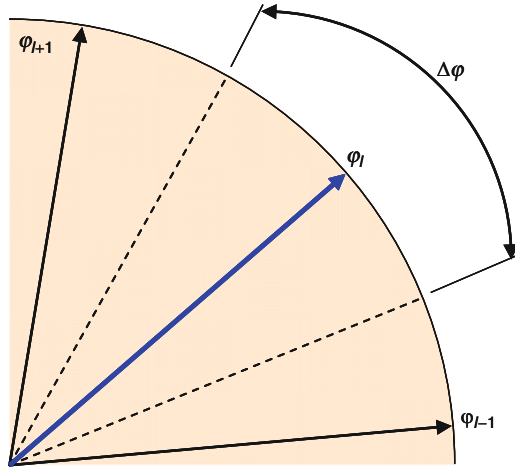


Figure 45
Area between different angles of motion

For a specified number of azimuthal angles, L , the azimuthal boundaries are evenly spaced and the direction of the streaming tracks are distributed according to

$$\varphi_l = \left(l - \frac{1}{2} \right) \cdot \Delta\varphi \quad (371)$$

The weight associated with each direction, $d\varphi = \Delta\varphi$, is then given by

$$\Delta\varphi = \frac{2\pi}{L} \quad (372)$$

The weight represents the area between different directions, as illustrated in Fig. 45. Since the integration over polar angles was performed analytically, giving rise to the Bickley–Naylor functions, polar angles of motion out of the plane of the problem need not be specified.

Tracks are traced across each mesh individually and the distance of each track is calculated by determining the intersection of each track with each surface of the mesh, as illustrated in Fig. 46. The optical distance along each track is then calculated as

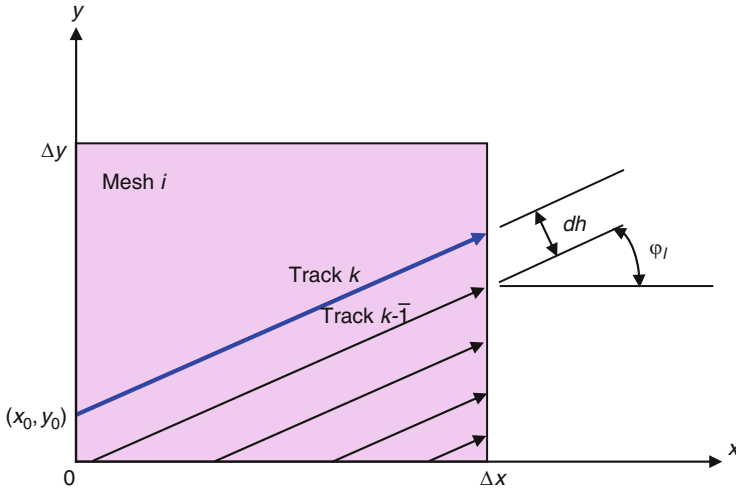
$$\tau_{k,l,i}^g = \sum_{tr,i}^g s_{k,l,i} \quad (373)$$

where k is a specific track number; l is a specific angle of motion; and i is a specific mesh in the system.

The total length of the line segment across the mesh is calculated as

$$s_{k,l,i} = \frac{\Delta x - x_0}{\cos \varphi_l}, \quad \text{for } \varphi_l < \frac{\pi}{2}$$

$$s_{k,l,i} = \frac{x_0}{\cos \varphi_l}, \quad \text{for } \varphi_l > \frac{\pi}{2} \quad (374)$$



■ **Figure 46**
Streaming rays traced across a mesh at a specific angle

The exiting point of the line segment along the y -axis is calculated as

$$y_{\text{out}} = y_0 + s_{k,l,i} \cdot \sin \varphi_l \quad (375)$$

If $y_{\text{out}} > \Delta y$, then the track exits along the top of the mesh and the track length is re-calculated as

$$s_{k,l,i} = \frac{\Delta y - y_0}{\sin \varphi_l} \quad (376)$$

During the ray tracing, the code keeps track of the surface along which the segment enters and leaves the mesh. These surfaces will be used in the calculation of volume-to-surface and surface-to-surface transmission probabilities.

Rays are traced over each individual mesh at azimuthal angles from 0 to π and neutrons are assumed to flow in both directions along a single segment, thus integration for all azimuthal angles (2π) is not necessary.

The transport matrices, (369), are then calculated as

$$\begin{aligned} T_{i \rightarrow i}^g &= \frac{1}{(\sum_{tr,i}^g V_i)^2} \sum_l \frac{\Delta \varphi}{2\pi} \sum_k dh \cdot \left\{ \sum_{tr,i}^g V_i - \left[\frac{\pi}{4} - Ki_3(\tau_{k,l,i}^g) \right] \right\} \\ T_{i,s \rightarrow i}^g &= \frac{1}{2\sum_{tr,i}^g V_i A_{i,s}} \sum_l \frac{\Delta \varphi_l}{2\pi} \sum_k dh \cdot \left[\frac{\pi}{4} - Ki_3(\tau_{k,l,i}^g) \right] \\ T_{i,s' \rightarrow i,s}^g &= \frac{1}{A_{i,s} A_{i,s'}} \sum_l \frac{\Delta \varphi_l}{2\pi} \sum_k Ki_3(\tau_{k,l,i}^g) \end{aligned} \quad (377)$$

where the surface areas and volumes in (377) are those that are approximated by the ray tracing,

$$\begin{aligned} V_i &= \sum_l \sum_k dh \cdot \frac{\Delta\varphi_l}{2\pi} \cdot s_{k,l,i} \\ A_{i,s} &= \sum_l \sum_k dh \cdot \frac{\Delta\varphi_l}{2\pi} \end{aligned} \quad (378)$$

Note that the surface summations in (377) and (378) include only those tracks, k , that actually intersect the specific surface, whereas the volume summations include all tracks, k , traced at each azimuthal angle, l .

4.3.3 Solution to the Response Matrix Equations

For the coupling calculation, the scalar flux in all groups, all mesh, is initialized to unity prior to the start of the first iteration. All inward directed currents along the boundaries of the problem, in all energy groups, are initialized to $1/4$, from (367). This initialization supplies an initial guess to the solution technique and the iterative algorithm may begin.

Inner Iterations

The inner iterations are used to converge the scalar flux distribution throughout the entire problem domain in a single energy group. The inner iterations will also drive the current along the system boundaries to converge. These are the solutions to (363) and (364).

The scalar flux distribution is considered converged when the following criterion is met within each mesh of the problem:

$$\frac{|\phi_{i,iter}^g - \phi_{i,iter-1}^g|}{\phi_{i,iter}^g} < \varepsilon \quad (379)$$

where ε is the convergence criterion on the scalar flux, which can be loosely set to 10^{-4} .

The outward directed current coming in contact with the boundary of the system is considered converged when the following criterion is met within each mesh along the problem boundary:

$$\frac{|J_{s,i,out,iter}^g - J_{s,i,out,iter-1}^g|}{J_{s,i,out,iter}^g} < \varepsilon \quad (380)$$

where ε is the convergence criterion on the current, which can be loosely set to 10^{-4} . The subscripts in (380) represent only the mesh, and surfaces of those mesh, which lie along the system boundary.

During an inner iteration, the source term of neutrons born into the energy group of interest, g , is constantly being updated using the scalar flux from inner iterations in higher energy groups. In this way the source takes on the appearance

$$q_i^g = \sum_{g' < g} \Sigma_{s,i}^{g' \rightarrow g} \phi_{i,iter}^{g'} + \sum_{g' \geq g} \Sigma_{s,i}^{g' \rightarrow g} \phi_{i,iter-1}^{g'} + \frac{\chi_i^g}{k_\infty} \left[\sum_{g'} \nu \Sigma_{f,i}^{g'} \phi_{i,iter-1}^{g'} \right] \quad (381)$$

where group 1 is the highest energy group of the cross section library. This defines a Gauss–Seidel scheme for the inner iterations.

In lattice physics computations, the fission source can be represented as a production kernel, similar to the way in which the scattering source is represented as a kernel, and the fission source term may be rolled up into the scattering source term as

$$q_i^g = \sum_{g' < g} \Sigma_{s,i}^{g' \rightarrow g} \phi_{i,iter}^{g'} + \sum_{g' \geq g} \Sigma_{s,i}^{g' \rightarrow g} \phi_{i,iter-1}^{g'} + \frac{1}{k^\infty} \sum_{g'} \Sigma_{p,i}^{g' \rightarrow g} \phi_{i,iter-1}^{g'} \quad (382)$$

where the production kernel is defined as

$$\Sigma_{p,i}^{g' \rightarrow g} = \chi_i^g \nu \Sigma_{f,i}^{g'} \quad (383)$$

Outer Iterations

Just as mesh are coupled together via their surface currents, energy groups are coupled together via the scattering and fission sources. The outer iterations are used to converge the source distribution and, hence, the eigenvalue to the problem. The outer iterations redistribute the source neutrons resulting from the updated scalar flux distribution generated during the sweep through the inner iterations. A complete sweep of inner iterations through all energy groups of the problem defines one outer iteration.

The source is considered to be converged when the following criterion is met during two successive iterations,

$$\frac{|k_{iter}^\infty - k_{iter-1}^\infty|}{k_{iter}^\infty} < \varepsilon \quad (384)$$

where ε is the convergence criterion on the eigenvalue, which can be loosely set to 10^{-4} .

During an outer iteration, the fission source distribution is held constant and the scattering distribution is updated continuously using results from the most recent inner iteration.

Fundamental Mode Rebalance

Following completion of an outer iteration, a fundamental mode rebalancing of the group flux distribution is performed in order to properly normalize the flux and ensure neutron conservation. The fundamental mode calculation is performed on an equivalent homogeneous system using flux and volume weighted cross sections from the heterogeneous calculation. The resulting group flux values from the homogeneous calculation are then used to rebalance the magnitude of the heterogeneous group flux values.

The equation to be solved here is equivalent to (360)

$$\phi_{FM}^g = \frac{\bar{q}^g}{\bar{\Sigma}_r^g} \quad (385)$$

where the source term does not include self scattering and the fission source is normalized to unity by the multiplication factor. Hence,

$$\bar{q}^g = \sum_{g' \neq g} \bar{\Sigma}_s^{g' \rightarrow g} \phi_{FM}^{g'} + \frac{\bar{\chi}^g}{k^\infty} \sum_{g'} \nu \bar{\Sigma}_f^{g'} \phi_{FM}^{g'} \quad (386)$$

where the flux and volume weighted cross sections for the fundamental mode calculation are calculated from

$$\bar{\Sigma}_x^g = \frac{\sum_i \Sigma_{x,i}^g \phi_i^g V_i}{\sum_i \phi_i^g V_i} \quad (387)$$

In (387), x represents the desired reaction (e.g., fission, absorption, etc.).

Since there are no neutron leakage effects across the boundaries of the problem (i.e., perfect reflection is assumed along all boundaries), the multiplication factor in (387) can be calculated directly as the ratio of neutron production in the system to neutron destruction

$$k^\infty = \frac{\sum_{g'} \nu \bar{\Sigma}_f^{g'} \phi_{\text{FM}}^{g'}}{\sum_{g'} \bar{\Sigma}_a^{g'} \phi_{\text{FM}}^{g'}} \quad (388)$$

If we normalize the flux in such a way that there is only one neutron being absorbed in the entire problem, then the denominator to (388) becomes unity and the multiplication factor is simply the sum of all neutrons born through fission

$$k^\infty = \sum_{g'} \nu \bar{\Sigma}_f^{g'} \phi_{\text{FM}}^{g'} \quad (389)$$

Plugging (389) into (386) yields the final expression for the fundamental mode homogeneous source

$$\bar{q}^g = \sum_{g'} \bar{\Sigma}_s^{g' \rightarrow g} \phi_{\text{FM}}^{g'} + \bar{\chi}^g \quad (390)$$

Due to up-scattering in the thermal energy groups, the solution to (385) defines an iterative process and the fundamental mode equation is solved directly with no acceleration. Following the solution to (385), the scalar flux distribution from the solution to (363) is scaled using the solution from the fundamental mode calculation

$$\hat{\phi}_{i,iter}^g = \phi_{i,iter}^g \cdot \frac{\phi_{\text{FM}}^g}{\sum_i \phi_{i,iter}^g V_i} \quad (391)$$

4.3.4 Geometry of the Coupling Calculation

The coupling calculation takes the true geometry of the lattice and homogenizes all non-rectangular regions into an equivalent rectangular geometry and an equivalent set of material cross sections. Homogenization of the material sets is done using a straightforward flux and volume weighting of the heterogeneous material sets. The flux used in the homogenization process is obtained from the pin-cell spectral calculations. If there exists no flux from the pin-cell spectral calculations for regions that are to be homogenized, then the homogenization is done in a straightforward volume weighting process.


For a typical LWR lattice, all pin cells are homogenized into a single equivalent material set

$$\bar{\Sigma}_{x,I}^g = \frac{\sum_{i \in I} \Sigma_{x,i}^g \phi_i^g V_i}{\sum_{i \in I} \phi_i^g V_i} \quad (392)$$

where i represents a region of the pin cell (fuel, clad, and coolant), and I represents the homogenized square.

For the inner regions of the fuel bundle, most cells take part in the pin-cell spectral calculations and, therefore, there exist flux spectrums for each of the various regions of the cell. In rare circumstances, there may not exist a flux spectrum for the various regions of a cell. In such cases, the materials are volume weighted into a single homogeneous set

$$\bar{\Sigma}_{x,I}^g = \frac{\sum_{i \in I} \Sigma_{x,i}^g V_i}{\sum_{i \in I} V_i} \quad (393)$$

For BWR lattices, (393) is also used to homogenize the inner water gap, along the inside wall of the channel, with the channel wall itself. For absorber pins of a cruciform control blade, fluxes can be obtained from a special series of pin-cell spectral calculations performed on each absorber tube and (392) can be used to homogenize all absorber tubes into a single homogeneous material set. The final geometry of the coupling calculation appears as in  Fig. 47, where the red mesh lines represent the geometry of the coupling calculation.

For regions containing strong absorbers, such as control blades, control rods, burnable absorber pins, or fuel pins containing Gadolinium or Erbium, the homogenized cross sections will grossly overestimate the actual absorption rate in the heterogeneous cell. One way of accounting for this is to calculate correction factors for the homogenized material. The correction factors are determined by performing one additional pin-cell calculation on the absorber cell that uses the homogenized cross sections in all regions of the cell – fuel, clad, and coolant.

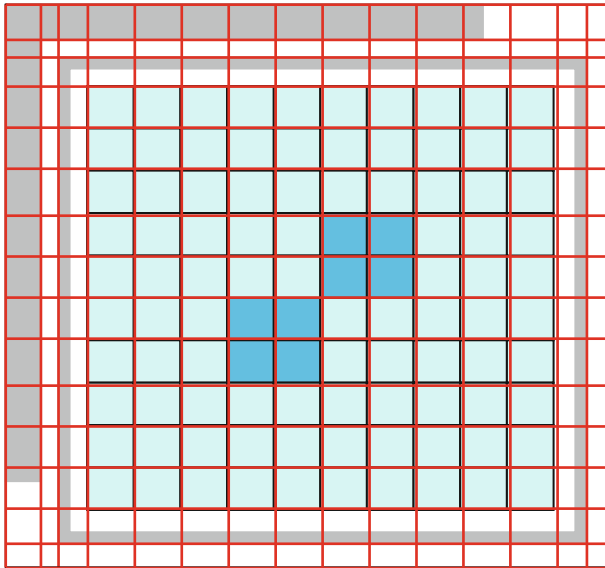


 Figure 47

Typical geometry of coupling calculation

The cross sections for the buffer zone are the same as those used in the heterogeneous pin-cell calculation.


The reaction rate in the homogenized cell is then compared against the averaged reaction rate in the combined regions of the heterogeneous cell. Correction factors are determined that, when applied to the homogenized cross sections, produce equivalent reaction rates in the homogenized cell. This involves an iterative process, where the correction factors are estimated using the results from the first homogenized pin-cell analysis,

$$R^g = \frac{\sum_i \Sigma_{tr,i}^g \phi_i^g V_i}{\overline{\Sigma_{tr}^g} \bar{V}} \quad (394)$$

The new homogenized cross sections are estimated to be $\overline{\Sigma_{x,\text{new}}^g} = R^g \cdot \overline{\Sigma_{x,\text{old}}^g}$. Using these new homogenized cross sections, the homogenized pin-cell calculation is re-performed. This process continues until the reaction rates using the homogenized cross sections match those from the heterogeneous pin cell. Note that there is a unique correction factor for each energy group.

For normal fuel pins, the correction factors will be unity or close enough to unity that no correction needs to be applied to the homogenized cross section set. For strong absorber pins, such as fuel pins containing Gadolinium, the correction factors will be far from unity in the thermal energy groups. They will be close to unity above the thermal energy cut-off of 0.625 eV.

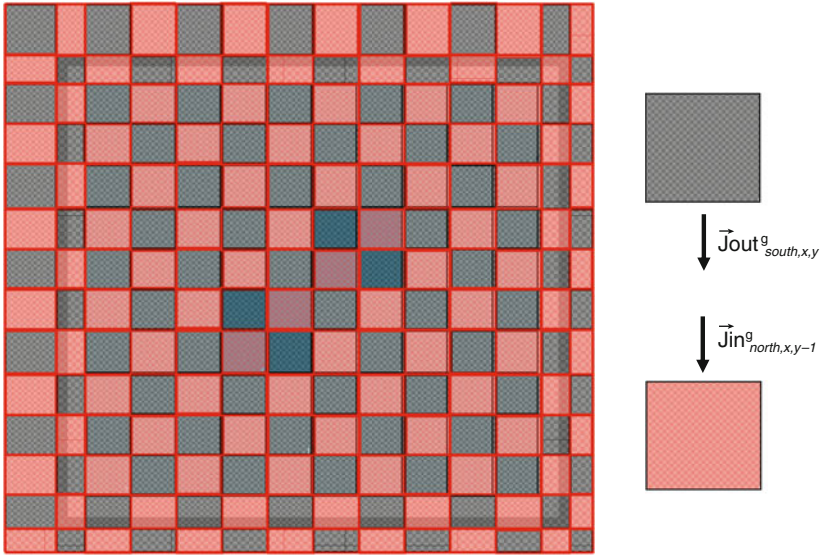
Use of the correction factors will produce a slightly better condensation spectrum, depending on the number of strong absorber pins present in the fuel assembly. For problems containing a cruciform control blade, the use of correction factors is almost a necessity in order to obtain meaningful results.

Once the homogenized materials have been constructed, the material layout has been assigned, and the transmission matrices have been calculated, the code can proceed to solve for the flux and current in each mesh by the use of a red–black iteration scheme. The layout for this scheme is illustrated in  Fig. 48, where each mesh is assigned either a “red” or “black” declaration. Here, the flux and outward directed currents for all red mesh are solved first. The inward currents to all black mesh are set equal to the newly calculated outward currents from the corresponding red mesh. The flux and outward directed currents for all black mesh are then solved. The inward currents to all red mesh are then set equal to the outward currents from the corresponding black mesh. And so on and so forth. An inner iteration is complete when the outward currents and mesh fluxes have converged for a given source distribution in a given energy group.

4.4 Cross Section Condensation

The energy distribution of neutrons from the series of one-dimensional pin-cell calculations are updated with the flux spectra from the two-dimensional response matrix calculation

$$\tilde{\phi}_i^g = \phi_i^g \cdot \frac{\phi_I^g V_I}{\sum_{i \in I} \phi_i^g V_i} \quad (395)$$



■ **Figure 48**
Red–black iteration scheme

where i represents a region of the pin cell (fuel, clad, and coolant), and I represents the homogenized rectangle from the coupling calculation.

Fluxes for the surrounding regions of the lattice – channel box wall, water gaps, etc. – are obtained directly from the response matrix solution. Fluxes for the absorber tubes of a control blade are obtained from the special series of pin-cell calculations performed on each absorber tube and updated with the flux from the response matrix solution. Equation (395) represents the flux for each material region of the problem that will be used to condense the macroscopic cross sections. The final energy group structure for the fine-mesh transport calculation depends on the accuracy of the condensation scheme, the energy group boundaries in the original cross section library, and the types of problems to be analyzed by the lattice physics code. The broad-group cross sections are created using the following expression:

$$\Sigma_{x,i}^G = \frac{\sum_{g \in G} \Sigma_{x,i}^g \tilde{\phi}_i^g}{\sum_{g \in G} \tilde{\phi}_i^g} \quad (396)$$

where g represents the fine-group energy structure of the cross section library, and G represents the broad-group energy structure of the condensed cross sections. The summations in (396) are performed for all fine-groups within a broad-group.

The primary assumptions used in the derivation of the response matrix method are as follows: the scalar flux is flat across each mesh; the angular flux is distributed isotropically across the surface of each mesh; and the angular flux is spatially constant along the surface of each mesh. For normal fuel cells and water regions, these assumptions are not entirely bad. In fact,

when grouped together for such situations, the errors associated with each assumption tend to balance and one is left with a surprisingly better-than-expected solution to the transport equation. For strongly absorbing, relatively thin regions, though, the angular flux emerging from a mesh is highly anisotropic. This is most noticeable in mesh used to model the presence of the cruciform control blade. Under such conditions, neutrons that strike the blade surface head-on, have a much greater chance of streaming across the blade without interacting than do neutrons that strike the blade surface at a steep angle. The assumption of an isotropic current, however, tends to suppress the transmission probability of the neutrons that strike the blade head-on. This results in an excess of absorptions taking place in the black regions of the model, including Gadolinium pins. The increased strength of the control blade will tend to cause the flux to be pushed away from the control blade corner of the problem, across the lattice to the corner where the detector resides. The increased strength of Gadolinium pins will tend to push neutrons away from Gd pins, to pins along the edge of the bundle.

4.5 Sundries

Due to the limitations mentioned above, there is a lower limit to the number of energy groups that must be maintained for the broad-group, fine-mesh transport calculation in order to preserve the accuracy of the fine-group library structure. It is up to the developer to determine the appropriate energy boundaries for the broad-group cross section set.

The most direct way of determining the broad-group energy structure is via trial and error. To do this, the lattice physics code must be developed in such a way as to ensure that the fine-mesh transport calculation is capable of providing a solution in the energy group structure of the cross section library. This provides the code with the ability to generate a reference solution for any condensed group structure. Once a fine-group reference solution exists, groups can be combined to determine which boundaries are necessary for the broad-group solution and which groups can be combined. In general, the more energy groups that exist in the fine-group cross section library, the more groups are needed in the broad-group structure to maintain a desired accuracy.

The energy boundaries required for a desired accuracy will depend on the problem being analyzed and the materials present in the bundle design. Fuel designs containing Gadolinium as an absorber require more thermal energy groups for a desired accuracy than do fuel designs containing, say, Erbium or Boron as an absorber. Fuel designs containing a cruciform control blade require more fast energy groups for a desired accuracy than do fuel designs, which contain pin-sized control fingers inserted directly into the assembly. Fuel designs containing mixed-oxide fuel require more thermal and epithermal energy groups for a desired accuracy than do fuel designs containing, say, uranium-oxide fuel.

In general, it is perfectly acceptable to determine unique broad-group energy structures for different types of problems, so long as the lattice physics code is capable of accurately determining the type of problem being analyzed. Alternatively, the lattice physics code may contain a single broad-group energy structure that is applicable to all problems. This single group structure will likely contain more detail than needed for most problems being analyzed, but will remove the chance that the code will accidentally use the wrong group structure on a certain type of problem.

5 Fine-Mesh Assembly Calculation

5.1 Introduction

Once the cross sections have been condensed to the broad-group structure (if, indeed, there exists a cross section condensation scheme to the specific lattice physics code), we are ready to perform the fine-mesh, two-dimensional heterogeneous transport calculation on the entire lattice. Since we are interested in modeling the lattice in its exact geometry, we are limited to techniques that solve the integral form of the transport equation. Due to the overwhelming benefits associated with the method of characteristics (MoC), as discussed in [Sect. 1](#), we will dedicate this section to developing that method and not discuss other alternatives any further.

Unless otherwise indicated, the content of this section is based on unpublished lectures given to postgraduate students in a course on computational reactor analysis at The Pennsylvania State University in 1990 (Knott 1990). The interested reader is directed to the original paper by Askew (Askew 1972), or the follow-up paper by Halsall (Halsall 1980), for a brief introduction to the MoC. Similar information can be found in Knott (1991), Knott and Edenius (1993), Goldgerg et al. (1995), Cho and Hong (1996), Roy (1998), Postma and Vujic (1999), Kosaka and Saji (2000), Kim et al. (2002), Jevremovic et al. (2002). This section presents a much broader description of the method of characteristics than is found in any of the references.

5.2 General Theory of the Method of Characteristics

5.2.1 Introduction

The characteristics form of the steady state Boltzmann transport equation is derived from the integrodifferential form of the equation

$$\frac{1}{|v|} \frac{\partial \Phi(\vec{r}, E, \hat{\Omega}, t)}{\partial t} = Q(\vec{r}, E, \hat{\Omega}, t) - \Omega \cdot \nabla \Phi(\vec{r}, E, \hat{\Omega}, t) - \Sigma_t(\vec{r}, E) \Phi(\vec{r}, E, \hat{\Omega}, t) \quad (397)$$

Which, after rearranging for steady state applications, becomes

$$\Omega \cdot \nabla \Phi(\vec{r}, E, \hat{\Omega}) - \Sigma_t(\vec{r}, E) \Phi(\vec{r}, E, \hat{\Omega}) = Q(\vec{r}, E, \hat{\Omega}) \quad (398)$$

where the source term, $Q(\vec{r}, E, \hat{\Omega})$, is the total angular source of neutrons at location \vec{r} , with energy E , traveling in direction $\hat{\Omega}$, and is expressed as

$$Q(\vec{r}, E, \hat{\Omega}) = \iiint \Sigma_s(\vec{r}, E' \rightarrow E, \hat{\Omega}' \rightarrow \hat{\Omega}) \Phi(\vec{r}, E', \hat{\Omega}') dE' d\hat{\Omega}' + S(\vec{r}, E, \hat{\Omega}) \quad (399)$$

In the above expressions, $\Phi(\vec{r}, E, \hat{\Omega})$ is the angular flux, $\Sigma_t(\vec{r}, E)$ is the total macroscopic cross section, and $\Sigma_s(\vec{r}, E' \rightarrow E, \hat{\Omega}' \rightarrow \hat{\Omega})$ is the macroscopic scattering cross section. $S(\vec{r}, E, \hat{\Omega})$ is the angular source of neutrons at location \vec{r} , either internal (i.e., due to fission) or external.

[Equation \(398\)](#) describes neutron motion as viewed from a fixed reference point, giving rise to the partial derivative in the streaming term. If neutron motion is viewed from the neutron's

frame of reference, the partial derivative in the streaming term reduces to a total derivative along the path of motion of the neutron and (398) becomes

$$\frac{d\Phi(\vec{r}, E, \hat{\Omega})}{ds} + \Sigma_t(\vec{r}, E)\Phi(\vec{r}, E, \hat{\Omega}) = Q(\vec{r}, E, \hat{\Omega}) \quad (400)$$

where s is the track along which the neutron is traveling across the region at location \vec{r} (i.e., the location relative to the fixed reference point).

Equation (400) is the characteristics form of the transport equation and describes neutron motion as viewed through the eyes of the neutron – if, indeed, neutrons do have eyes.

5.2.2 Solution to the Characteristics Form of the Transport Equation

At this point in our derivation of the MoC, we will focus exclusively on one-dimensional slab problems. A little later in this section, we will move into one-dimensional cylindrical geometry, which is a prelude to moving into two-dimensional geometries for orthogonal systems. We choose to start with one-dimensional slab geometry because many of the most important features of the method of characteristics can be described easily for such a system. We will use slab geometry to introduce all features of the MoC, including simple quadrature sets, flat source regions, a simple iteration scheme, and a simple acceleration technique. Once we get into two-dimensional geometry, we will describe the more complicated features used in modern lattice physics codes.

To make things as simple as possible, we will assume that all scattering and all sources (fission and fixed) are isotropic. That is, there are no preferred angles of emission. Anisotropic effects can easily be represented using transport-corrected cross sections, which were briefly alluded to in [Sect. 1](#).

For an isotropic scalar source of total strength q , the isotropic angular source in each direction of travel will be $Q = q/4\pi$ and the transport equation becomes

$$\frac{d\Phi}{ds} + \Sigma_{tr}\Phi = \frac{q}{4\pi} \quad (401)$$

where Σ_{tr} is the transport cross section and the arguments associated with each variable have been dropped to simplify the equation. Equation (401) has the solution

$$\Phi(s) = \Phi(0)e^{-\Sigma_{tr}s} + \frac{q}{4\pi\Sigma_{tr}}(1 - e^{-\Sigma_{tr}s}) \quad (402)$$

where s is the characteristic along which the neutron is traveling and $s=0$ is the location of the neutron at time $t=0$, as illustrated in [Fig. 49](#).

Equation (402) is only applicable if we can assume that the source of neutrons inside the region of interest is constant. In such cases, the scalar flux will also be constant and we can solve directly for the value of the angular flux exiting the mesh, based on the value of the angular flux entering the mesh,

$$\Phi_{\text{out}} = \Phi_{\text{in}}e^{-\Sigma_{tr}t/\cos\varphi} + \frac{q}{4\pi\Sigma_{tr}}(1 - e^{-\Sigma_{tr}t/\cos\varphi}) \quad (403)$$

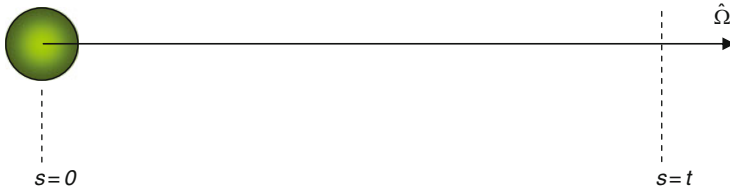


Figure 49

Coordinate system for the characteristics equation

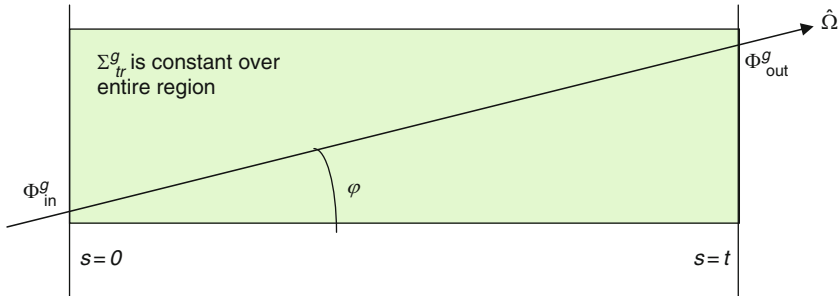


Figure 50

Angular flux across a region of constant material properties

The variables in (403) are illustrated in [Fig. 50](#).

The average value of the angular flux, $\bar{\Phi}$, along any track segment is calculated by integrating the value of the angular flux along the entire length of the track segment and dividing by the length of the segment,

$$\bar{\Phi} = \frac{\int_0^{t/\cos\varphi} \Phi(s) ds}{\int_0^{t/\cos\varphi} ds} = \frac{\int_0^{t/\cos\varphi} \left\{ \Phi(0)e^{-\Sigma s} + \frac{q}{4\pi\Sigma}(1 - e^{-\Sigma s}) \right\} ds}{t/\cos\varphi} \quad (404)$$

After carrying out the integration in the numerator of (404), we are left with the following expression for the average value of the angular flux along a track segment

$$\bar{\Phi} = \frac{\frac{1}{\Sigma} \left\{ \Phi(0) - \Phi(0)e^{-\Sigma t/\cos\varphi} + \frac{qt}{4\pi\cos\varphi} - \frac{q}{4\pi\Sigma}(1 - e^{-\Sigma t/\cos\varphi}) \right\}}{t/\cos\varphi} \quad (405)$$

Combining the second and fourth terms in the numerator, we can express the average value of the angular flux along a track segment in a more compact form

$$\bar{\Phi} = \frac{q}{4\pi\Sigma} + \frac{\Phi(0) - \Phi(t)}{\Sigma t/\cos\varphi} = \frac{q}{4\pi\Sigma} + \frac{\Delta}{\Sigma t'} \quad (406)$$

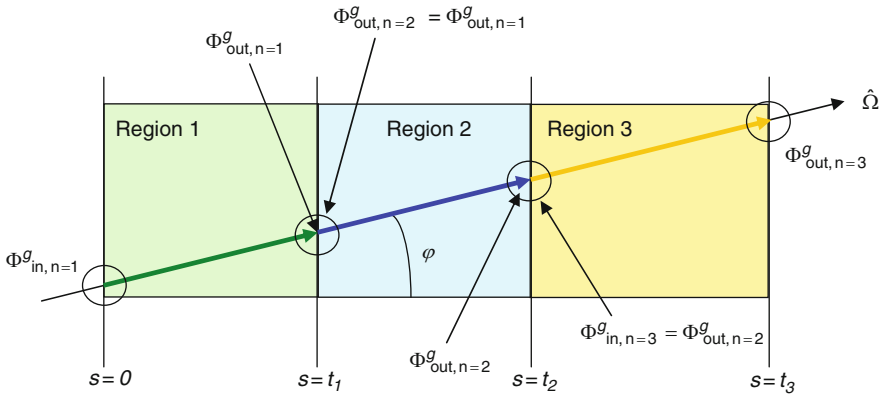


Figure 51
Angular flux across multiple regions

where $\Delta = \Phi(0) - \Phi(t)$ is the change in the angular flux along the track segment; and $t' = t / \cos \varphi$ is the true length of the segment in the xy -plane of the problem across the mesh. Note that the average angular flux in (406) is the value along a specific track segment, across a specific mesh, at a specific angle, in a specific energy group. There will be many such values crossing each slab at different angles, in different energy groups.

If we have multiple slabs, the angular flux exiting each successive slab can be calculated as

$$\begin{aligned} \Phi(t_1) &= \Phi(0)e^{-\Sigma_1 t'_1} + \frac{q_1}{4\pi\Sigma_1}(1 - e^{-\Sigma_1 t'_1}) \\ \Phi(t_2) &= \Phi(t_1)e^{-\Sigma_2 t'_2} + \frac{q_2}{4\pi\Sigma_2}(1 - e^{-\Sigma_2 t'_2}) \\ \Phi(t_3) &= \Phi(t_2)e^{-\Sigma_3 t'_3} + \frac{q_3}{4\pi\Sigma_3}(1 - e^{-\Sigma_3 t'_3}) \\ \Phi(t_n) &= \Phi(t_{n-1})e^{-\Sigma_n t'_n} + \frac{q_n}{4\pi\Sigma_n}(1 - e^{-\Sigma_n t'_n}) \end{aligned} \quad (407)$$

where the calculation of the angular flux exiting one slab is a cascading effect into the next slab, as illustrated in Fig. 51. Note that the energy dependence has been omitted from (407) and that the parameter Σ is understood to represent the transport-corrected total cross section of each material region.

If we apply this principle to a number of different directions, L , then the scalar flux in each slab can be calculated from the average angular flux across each slab at each of the different angles,

$$\phi_n^g = \int_{\hat{\Omega}} \overline{\Phi}_n^g(\hat{\Omega}) d\hat{\Omega} = \sum_i \overline{\Phi}_n^g(\varphi_i) \cdot \Delta\varphi_i \quad (408)$$

where $\Delta\varphi_i$ is the solid angle subtended by the direction φ_i (i.e., the weight associated with direction φ_i), and is illustrated in Fig. 52.

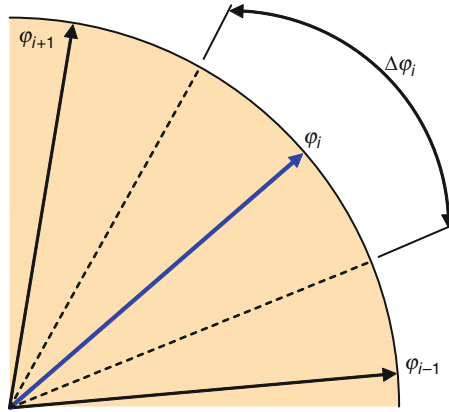


Figure 52

Weight associated with angular direction

Equation (408) can be rewritten as

$$\phi_n^g = \sum_m \bar{\Phi}_{m,n}^g \omega_m = \sum_m \left(\frac{q_n^g}{4\pi \Sigma_{tr,n}^g} + \frac{\Delta_{m,n}^g}{\Sigma_{tr,n}^g t'_{m,n}} \right) \omega_m \quad (409)$$

where $\sum_m \omega_m = 4\pi$, noting that the directions cover polar angles out of the xy -plane of the problem as well as azimuthal angles in the xy -plane of the problem.

For our isotropic source and transport-corrected cross sections

$$\sum_m \frac{q_n^g}{4\pi \Sigma_{tr,n}^g} \omega_m = \frac{q_n^g}{\Sigma_{tr,n}^g} \quad (410)$$

and we arrive at our final expression for the scalar flux in each slab

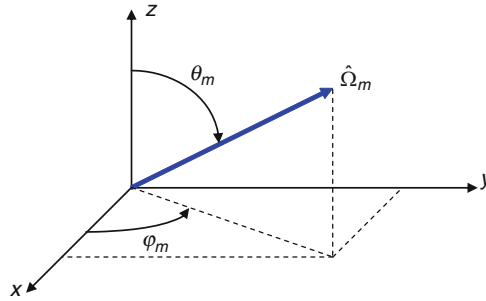
$$\phi_n^g = \frac{q_n^g}{\Sigma_{tr,n}^g} + \frac{1}{\Sigma_{tr,n}^g} \sum_m \frac{\Delta_{m,n}^g}{t'_{m,n}} \cdot \omega_m \quad (411)$$

The flux in (411) is assumed to be a constant value within a given mesh (i.e., the flat flux approximation).

5.3 Quadrature Sets

5.3.1 Introduction

The $d\hat{\Omega}$ in (408) represents the weight associated with each particular direction, $\hat{\Omega}$, which together make up the quadrature set. Here it should be pointed out that neutrons always travel in three dimensions. The problem being studied may be a one- or two-dimensional problem, but



■ **Figure 53**
Coordinates describing the direction of motion of a neutron

neutrons are always moving in all directions. The only detail that separates a one-dimensional problem from a two-dimensional or three-dimensional problem is the fact that there are material boundaries along only one axis of the coordinate system – the material regions all stretching to infinity along the remaining axes. Neutrons, however, are traveling at every imaginable angle to the one finite dimension. Therefore, we must model neutron motion in all three dimensions regardless of the dimensionality of the problem.

The direction of a neutron may be described using an azimuthal angle, φ , and a polar angle, θ . For all of our discussions, the azimuthal angle is measured from the positive x direction in the xy -plane of the problem. The polar angle is measured down from the positive z -direction, as illustrated in [► Fig. 53](#).

To model neutron transport, we need to trace streaming paths (i.e., characteristics) across the system in a number of directions. We then solve for $\bar{\Phi}_n^g(\hat{\Omega}_m)$ along each characteristic, across each slab, n , in each direction, $\hat{\Omega}_m$, using (406), and calculate ϕ_n^g using (411). This is done best by choosing a set of azimuthal angles and a set of polar angles, which together will determine each unique direction of motion, as illustrated by the quadrature ball contained in [► Fig. 54](#).

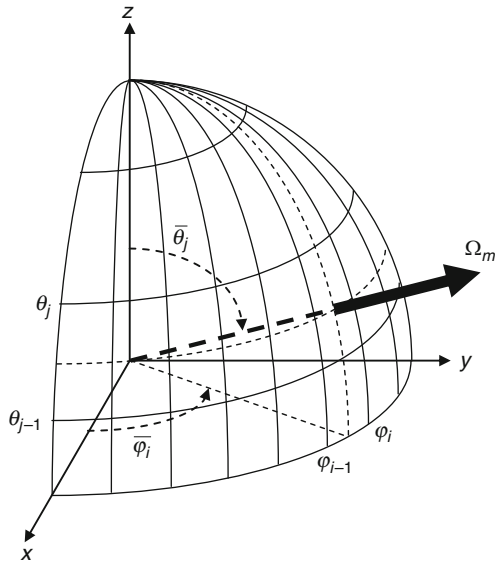
5.3.2 Azimuthal Angles

For lattice physics calculations, the azimuthal angles in the characteristics method are evenly spaced in the xy -plane of the problem. If we wish to model four azimuthal directions of motion, say, we would split the directions up evenly in the xy -plane such that the *boundaries* of motion occur at intervals calculated from the following expression:

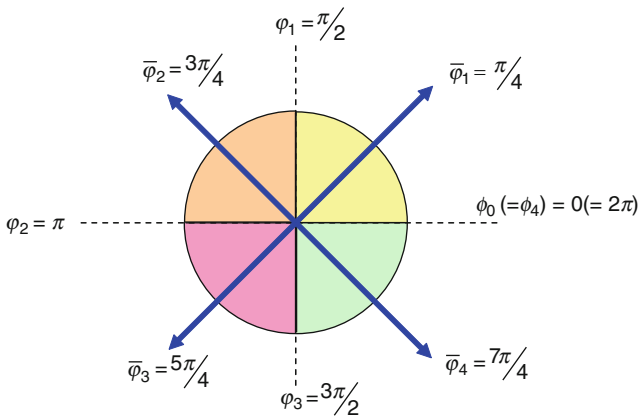
$$\Delta\varphi = \frac{2\pi}{I} = \frac{2\pi}{4} = \frac{\pi}{2} \quad (412)$$

In this way, the azimuthal *boundaries* are located at angles: $\varphi_0 = 0$, $\varphi_1 = \pi/2$, $\varphi_2 = \pi$, $\varphi_3 = 3\pi/2$, and $\varphi_4 = 2\pi (= 0)$. The azimuthal *direction of motion* takes place through the center of two neighboring *boundaries*,

$$\bar{\varphi}_i = \frac{1}{2}(\varphi_{i-1} + \varphi_i) \quad (413)$$



■ Figure 54
Typical quadrature ball



■ Figure 55
Azimuthal boundaries and angles of motion for $l = 4$

Each azimuthal direction of motion represents neutrons that travel at all angles in between the two surrounding azimuthal boundaries, as illustrated in [Fig. 55](#). The neutrons that are modeled as traveling along the $\bar{\varphi}_1 = \pi/4$ characteristic, for instance, actually represent all neutrons traveling at angles between $\varphi_0 = 0$ and $\varphi_1 = \pi/2$. The neutrons that are modeled as traveling along the $\bar{\varphi}_2 = 3\pi/4$ characteristic represent all neutrons traveling at angles between $\varphi_1 = \pi/2$ and $\varphi_2 = \pi$. And so on, and so forth.

The weight associated with each azimuthal direction of motion is then given by

$$\omega_i = \frac{2\pi}{I} \quad (414)$$

where I is the total number of azimuthal directions of motion in the quadrature set.

5.3.3 Polar Angles

Choosing polar directions of motion is somewhat more complicated than choosing azimuthal directions of motion and is open to one of several different methods. We will discuss a couple of very simple methods and then make mention of the more complicated, more accurate methods, that are used in most lattice physics codes. The two methods to be discussed in this section are those associated with *equal weights* and *equal angles*.

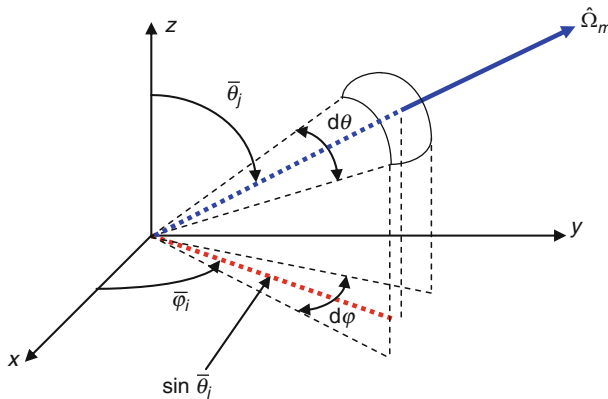
Equal Weights Quadrature Set

To generate an *equal weights* quadrature set, we choose polar directions of motion that will result in all directions having equal polar weights (and, hence, equal weights in all directions of motion). The weights associated with each direction are calculated from the differential area on a unit sphere subtended by all boundaries for a given direction of motion, such as that illustrated in [► Fig. 54](#). To calculate *equal weights* for all directions of motion, we proceed in the following manner: The differential area on a unit sphere associated with each direction, $\hat{\Omega}_m$, is given by

$$dA = \hat{\Omega}_m^2 \sin \bar{\theta}_m d\theta d\varphi \quad (415)$$

where the variables are defined in [► Fig. 56](#). For a unit sphere, $|\hat{\Omega}| = 1$, and (415) can be expressed as

$$dA = \sin \bar{\theta}_m \cdot d\theta \cdot d\varphi \quad (416)$$



■ Figure 56
Differential surface area on a unit sphere

The total area associated with each direction, $\hat{\Omega}_m$, subtended on the unit sphere is then calculated as

$$A = \int_{\theta_{j-1}}^{\theta_j} \int_{\phi_{i-1}}^{\phi_i} dA = \int_{\theta_{j-1}}^{\theta_j} \int_{\phi_{i-1}}^{\phi_i} \sin \bar{\theta} \cdot d\theta \cdot d\phi = (\phi_i - \phi_{i-1})(\cos \theta_{j-1} - \cos \theta_j) \quad (417)$$

Since the spacing between azimuthal angles is $\Delta\varphi = \varphi_i - \varphi_{i-1}$, equal areas on the unit sphere require

$$A = \frac{4\pi}{I \cdot J} \quad (418)$$

where I is the total number of azimuthal angles, and J is the total number of polar angles. Rearranging (417) and setting it equal to (418) yields

$$(\cos \theta_{j-1} - \cos \theta_j) = \frac{4\pi}{I \cdot J \cdot \Delta\varphi} \quad (419)$$

From (412), $\Delta\varphi = 2\pi/I$ so the boundaries to the polar directions can be expressed as

$$\theta_j = \cos^{-1} \left\{ \cos \theta_{j-1} - \frac{2}{J} \right\} \quad (420)$$

where $\theta_0 = 0$.

We would like the polar direction of motion to pass through the centroid of the surface area subtended by the polar boundaries. Therefore, the polar directions of motion are calculated as

$$\bar{\theta}_j = \cos^{-1} \left\{ \frac{1}{2} (\cos \theta_j + \cos \theta_{j-1}) \right\} \quad (421)$$

The corresponding polar weights associated with the polar directions are the differential areas on the surface of the unit sphere created by the polar boundaries

$$\omega_j = \cos \theta_j - \cos \theta_{j-1} \quad (422)$$

Equal Angles Quadrature Set

For the *equal angles* quadrature set, we run through exactly the same scenario as we went through to generate the *equal weights* quadrature set. For the *equal angles* quadrature set, we are interested in distributing the angles uniformly in the polar direction, just as we have done with the azimuthal angles in the xy -plane of the problem. Without actually showing the mathematics associated with the derivation, the *equal angles* requirement leads us to make the following choices for the polar boundaries, polar directions of motion, and associated weights, respectively,

$$\Delta\theta = \frac{\pi}{J} \quad (423)$$

$$\bar{\theta}_j = \cos^{-1} \left\{ \frac{1}{2} (\cos \theta_j + \cos \theta_{j-1}) \right\} \quad (424)$$

$$\omega_j = \cos \theta_j - \cos \theta_{j-1} \quad (425)$$

where the polar boundaries are distributed from $\theta_0 = 0$ to $\theta_j = \pi$. Note that, in the *equal weights* quadrature set, only the distribution of polar *boundaries* is different from that in the *equal areas* distribution. The equations used to calculate the angles of motion and associated weights are the same for the *equal angles* quadrature as they are for the *equal weights* quadrature.

This section has described the generation of two slightly different quadrature sets – *equal weights* and *equal angles*. Both of these quadrature sets are perfectly acceptable for use with the method of characteristics. Different quadrature sets will require a different number of polar angles to obtain the same accuracy. That is, the *equal weights* quadrature set places more emphasis on neutrons that stream at angles close to the plane of the problem. In contrast, the *equal angles* quadrature set places the same emphasis on neutrons streaming in any direction out of the plane of the problem. The *equal angles* quadrature set is preferable for three-dimensional transport problems because it distributes the angles symmetrically in all directions, similar to the way in which our azimuthal directions are distributed symmetrically in the *xy*-plane of the problem. The *equal weights* quadrature set is preferable for one- and two-dimensional problems because angles are weighted toward the plane of motion.

For one- and two-dimensional problems, better distributions of angles are generated using Legendre and Gaussian quadratures. These quadrature sets will be discussed later in this section, once we reach the subject of two-dimensional applications. For now, we can say that the MoC problem reduces to tracing characteristics across the system at several angles, along each of which we will solve the transport equation. For the cases being described presently, we will focus solely on systems where all sources are isotropic and all cross sections have been transport-corrected such that scattering can be treated mathematically as being isotropic.

5.4 Geometry Routine

5.4.1 Introduction

The first step we take in writing a computer code to solve the characteristics form of the transport equation is to lay down the streaming paths along which our neutrons will travel. In order to do this, we must first assign material IDs to each region of the problem and then subdivide each material region into a suitable number of mesh that represent the flat source regions. This is illustrated in [▶ Fig. 57](#).

In an arrangement such as this, we might hold data in arrays structured by both mesh and region. That is, the array that holds the scalar flux in each mesh of the problem, say, might be structured as flux (mesh, region). Alternatively, mesh could be numbered sequentially beginning from the left side of the problem and moving to the right. This approach is depicted in

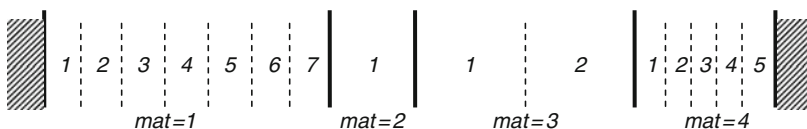
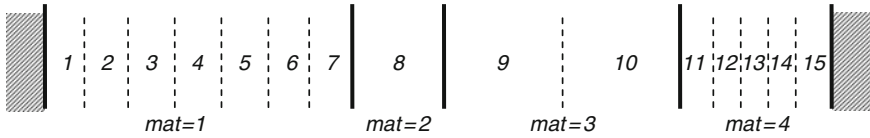


Figure 57
Example of flat source mesh and material numbers



■ Figure 58

Alternative example of flat source mesh and material numbers

► Fig. 58. The scalar flux in each mesh would be held in an array such as `flux (mesh)`. Then we would need another array, `material (mesh)`, which defined the material for each mesh. Either approach is acceptable. At one time, when memory was scarce, we would choose the most economical approach, that is, the one that used the least amount of memory. Nowadays, though, memory is plentiful and it is more important to choose the most intuitive approach, that is, the one that provides the most clarity to the programmer and especially to subsequent programmers who need to decipher the original programmer's work.

To begin our application of the MoC, we first lay down the paths in the azimuthal direction only (i.e., in the xy -plane of the problem). Once we calculate all the t 's in (411) – through all mesh of the system, at all azimuthal angles of motion – we can ratio each of the path lengths with the sine of the various polar angles to obtain the true track length at each of the directions of motion, $\hat{\Omega}_m$.

So, we have some system of slabs (i.e., mesh) with boundaries at $\{x_0, x_1, x_2, \dots, x_N\}$, where N is the total number of slabs in the problem. In each of these regions we have a set of constant cross sections and, possibly, an external source that is also spatially constant across the slab region.

Now we choose the number of azimuthal angles and polar angles at which we would like to solve the transport equation. Let I be the total number of azimuthal angles we choose and let J be the total number of polar angles we choose. We calculate the azimuthal boundaries, $\bar{\varphi}_i$'s, to the quadrature set using (412), and we calculate the azimuthal directions of motion, $\bar{\varphi}_i$'s, using (413). The weights associated with each azimuthal direction of motion, ω_i 's, are calculated using (414).

5.4.2 Neutron Streaming and Symmetry in Slab Geometry

There are a couple of points that can be made here regarding neutron motion in the xy -plane of the problem and out of the xy -plane of the problem.

To begin with, when we lay down tracks for the neutrons to stream along, we lay them down such that each track has a counter-track in the opposite direction. This is a requirement in order to model perfectly reflecting (i.e., mirror symmetric) boundary conditions. For instance, if we choose to lay four tracks down in the azimuthal direction, we have tracks at $\bar{\varphi}_1 = \pi/4$, $\bar{\varphi}_2 = 3\pi/4$, $\bar{\varphi}_3 = 5\pi/4$, and $\bar{\varphi}_4 = 7\pi/4$. The $\bar{\varphi}_3 = 5\pi/4$ track is in the opposite direction to the $\bar{\varphi}_1 = \pi/4$ track, and the $\bar{\varphi}_4 = 7\pi/4$ track is in the opposite direction to the $\bar{\varphi}_2 = 3\pi/4$ track. Since neutrons are indifferent to the direction at which they stream along a given track, we may – if we so desire – lay down tracks only between $0 \leq \bar{\varphi} \leq \pi$ in the problem and allow neutrons to travel in both directions along each track. This will help simplify our ray-tracing routine.

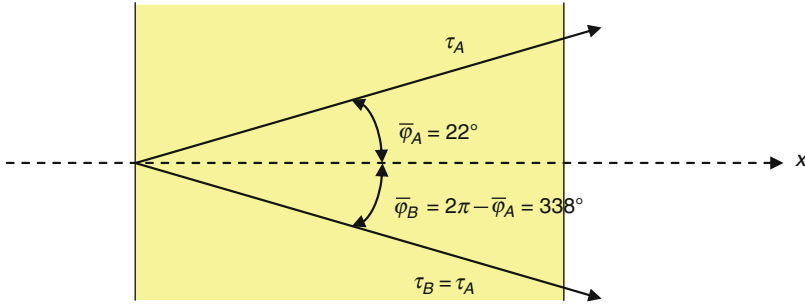


Figure 59
Neutrons moving at equivalent azimuthal angles

Secondly, in a one-dimensional problem such as a slab problem, neutrons travel at azimuthal angles between $0 \leq \bar{\varphi} \leq \pi$ in an identical fashion to the way in which they travel at azimuthal angles between $\pi \leq \bar{\varphi} \leq 2\pi$, as illustrated in [Fig. 59](#).

We may take advantage of these observations within our geometry routine, if we care to, by only having to trace tracks over our slab system at azimuthal angles between $0 \leq \bar{\varphi} \leq \pi$. If we choose to do this, we must compensate for the neglected directions by modifying our azimuthal weights, to wit,

$$\omega_i = 2 \times \frac{2\pi}{I} = \frac{4\pi}{I} \tag{426}$$

where I still represents the number of azimuthal directions of motion distributed between $0 \leq \bar{\varphi} \leq 2\pi$.

Lastly, in one- and two-dimensional geometries, neutrons travel at polar angles between $0 \leq \bar{\theta} \leq \pi/2$ in an identical fashion to the way in which they travel at polar angles between $\pi/2 \leq \bar{\theta} \leq \pi$. We may take advantage of this point in a manner similar to the azimuthal symmetry condition described for slab geometry. That is, we can trace tracks in the upper hemisphere of the problem, only, and modify the polar weights to account for symmetry in the lower hemisphere of the problem

$$\omega_j = 2(\cos \theta_j + \cos \theta_{j-1}) \tag{427}$$

where J now represents the total number of polar directions between $0 \leq \bar{\theta} \leq \pi/2$.

5.4.3 Ray Tracing in Slab Geometry

We now have a set of azimuthal angles, $\{\bar{\varphi}_1, \bar{\varphi}_2, \bar{\varphi}_3, \dots, \bar{\varphi}_I\}$, which are distributed between $0 \leq \bar{\varphi} \leq 2\pi$ (although we will only trace rays between $0 \leq \bar{\varphi} \leq \pi$), and associated weights, $\{\omega_1, \omega_2, \omega_3, \dots, \omega_I\}$, which are all equal and sum to 2π . We know, from the problem definition, the widths of all N slabs in the system, $\{\Delta x_1, \Delta x_2, \Delta x_3, \dots, \Delta x_N\}$. We may determine the track lengths through each slab, at each azimuthal angle, in the xy -plane of the problem,

$$t_{i,n} = \frac{\Delta x_n}{\cos \bar{\varphi}_i} \tag{428}$$

where each direction carries with it a weight of ω_i .

Once we have all the track lengths traced through all the slabs at all the desired azimuthal angles, and we have a weight associated with each of the azimuthal directions of motion, we can generate the polar angles of neutron motion, which will complete our quadrature set. Once again, as with the generation of the azimuthal angles, we take advantage of the symmetry of the problem and generate angles only between $0 \leq \bar{\theta} \leq \pi/2$. Each direction represents neutrons moving in both the upper and lower hemispheres of the problem. We generate our set of polar angles, $\{\bar{\theta}_1, \bar{\theta}_2, \bar{\theta}_3, \dots, \bar{\theta}_J\}$, and associated weights, $\{\omega_1, \omega_2, \omega_3, \dots, \omega_J\}$, based on either the *equal weights or equal angles* equations – or perhaps from a Legendre or Gaussian quadrature. The polar weights sum to 2.

With our polar angles of motion, we can ratio the track lengths from the plane of the problem into the upper hemisphere

$$t_{i,j,n} = \frac{t_{i,n}}{\sin \bar{\theta}_j} \quad (429)$$

We now have our quadrature set and our track lengths, which have been measured in the xy -plane of the problem and ratioed to their proper lengths in the polar direction. Now we can begin to solve the transport equation for the flux distribution.

5.5 Solution to the Characteristics Equation

5.5.1 Introduction

We have, really, only one equation to solve, namely,

$$\Phi_{\text{out}} = \Phi_{\text{in}} e^{-\Sigma_{tr} t} + \frac{q}{4\pi\Sigma_{tr}} (1 - e^{-\Sigma_{tr} t}) \quad (430)$$

which is to be solved using the assumptions mentioned before and restated below:

1. All scattering is transport corrected and can be modeled as isotropic
2. All sources are inherently isotropic
3. The source and, hence, scalar flux is constant within a mesh (i.e., flat flux approximation).

Equation (430) represents two physical processes: $\Phi_{\text{in}} e^{-\Sigma_{tr} t}$ are the number of neutrons that stream across the mesh without suffering a collision; and $q \cdot (1 - e^{-\Sigma_{tr} t}) / 4\pi\Sigma_{tr}$ are the number of neutrons that are picked up along the track from scatterings and sources as the track crosses the mesh. Together, these two processes determine the number of neutrons that reach the end of the track on the other side of the mesh.

Equation (430) is very simple to solve. For any problem we analyze, we will always know the cross sections beforehand. These will be the cross sections that are created from the energy condensation scheme (i.e., if one exists for the lattice physics code). In our geometry routine, we have already calculated the ratioed track lengths crossing every mesh, $t_{i,j,n}$. All we need to know in order to solve (430) is the angular flux entering the mesh at the beginning of the track, and the total source term within the mesh – Φ_{in} and q , respectively.

5.5.2 Initialization of the Flux

The need to know Φ_{in} and q brings us to the flux initialization. For lack of a better choice, we may simply guess at what Φ_{in} and q are everywhere. This constitutes our initial flux guess that will be used to start solving (430). We set $\phi = 1.0$ in every energy group, every mesh of the problem. For the Φ_{in} 's, we only need to guess these values along one boundary of the slab problem since Φ_{out} will become Φ_{in} as we move along each track. So, a good guess for Φ_{in} is to set it equal to $\Phi_{in} = 1/4\pi$ in all groups, in all directions, along one edge of the slab problem.

Now we may calculate the $\Phi_{in} e^{-\Sigma_{tr} t}$ part of the Φ_{out} equation, leaving us to determine the q part.

5.5.3 Calculating the Source Term

The total angular source term is a combination of three separate sources:

1. Scattering: $Q_s(\vec{r}, E, \hat{\Omega}) = \int \int \Sigma_s(\vec{r}, E' \rightarrow E, \hat{\Omega}' \rightarrow \hat{\Omega}) \Phi(\vec{r}, E', \hat{\Omega}') dE' d\hat{\Omega}'$
2. Fission: $Q_f(\vec{r}, E, \hat{\Omega}) = \chi(\vec{r}, E) \int \nu \Sigma_f(\vec{r}, E', \hat{\Omega}) \phi(\vec{r}, E') dE'$
3. Fixed external: $Q_{ext}(\vec{r}, E, \hat{\Omega}) = S(\vec{r}, E, \hat{\Omega})$

Scattering Source

As mentioned earlier, all scattering is assumed isotropic for our purposes. Anisotropic scattering effects are accounted for by transport-correcting the self scattering and total cross sections. By doing so, we can express the scattering cross section as

$$\Sigma_s(\vec{r}, E' \rightarrow E, \hat{\Omega}' \rightarrow \hat{\Omega}) = \frac{1}{4\pi} \Sigma_s(\vec{r}, E' \rightarrow E) \quad (431)$$

Then the integral over angle in the scattering source term becomes

$$\begin{aligned} Q_s(\vec{r}, E, \hat{\Omega}) &= \int \int \Sigma_s(\vec{r}, E' \rightarrow E, \hat{\Omega}' \rightarrow \hat{\Omega}) \Phi(\vec{r}, E', \hat{\Omega}') dE' d\hat{\Omega}' \\ &= \frac{1}{4\pi} \int \Sigma_s(\vec{r}, E' \rightarrow E) \phi(\vec{r}, E') dE' \end{aligned} \quad (432)$$

In multigroup theory, where the entire range of energies is discretized into a number of energy groups, the scattering kernel is defined as elements which make up a matrix

$$Q_{s,n}^g = \frac{1}{4\pi} \int \Sigma_s(\vec{r}, E' \rightarrow E) \phi(\vec{r}, E') dE' = \frac{1}{4\pi} \sum_{g'} \Sigma_{s,n}^{g' \rightarrow g} \phi_n^{g'} \quad (433)$$

Here, the quantity $\Sigma_{s,n}^{g' \rightarrow g} \phi_n^{g'}$ defines the total number of neutrons within the mesh n , within energy group g' , which have scattering collisions and are scattered into an energy within group g – our energy of interest. Out of all the neutrons that are scattered into energy group g , only $1/4\pi$ of them are traveling in direction Ω – our direction of interest.

Fission Source

For criticality problems, the only source of fresh neutrons are those born into the fast energy groups of the problem via fission. Neutrons born via fission are assumed to be distributed

isotropically (a good assumption) and integration of the angular fission source over all angles reduces to

$$\begin{aligned} Q_f(\vec{r}, E, \hat{\Omega}) &= \chi(\vec{r}, E) \int v\Sigma_f(\vec{r}, E', \hat{\Omega})\phi(\vec{r}, E') dE' \\ &= \chi(\vec{r}, E) \int \frac{v\Sigma_f(\vec{r}, E')}{4\pi} \phi(\vec{r}, E') dE' \end{aligned} \quad (434)$$

In multigroup form,

$$Q_{f,n}^g = \chi(\vec{r}, E) \int \frac{v\Sigma_f(\vec{r}, E')}{4\pi} \phi(\vec{r}, E') dE' = \chi_n^g \sum_{g'} \frac{v\Sigma_{f,n}^{g'}}{4\pi} \phi_n^{g'} \quad (435)$$

Here, we sum up all the fissions that occur in mesh n per unit volume,

$$\sum_{g'} v\Sigma_{f,n}^{g'} \phi_n^{g'} \quad (436)$$

and distribute those neutrons within the various fast energy groups using the fission spectrum, χ_n^g , which can be unique for each fuel material in the problem. The fission spectrum is normalized to unity,

$$\sum_{g'} \chi_n^g = 1.0 \quad (437)$$

The fission neutrons are then distributed isotropically by dividing the total scalar fission source by 4π . Equation (435) can be expressed as a production kernel, $\Sigma_{p,n}^{g' \rightarrow g}$, in a manner similar to the scattering kernel,

$$Q_{f,n}^g = \chi_n^g \sum_{g'} \frac{v\Sigma_{f,n}^{g'}}{4\pi} \phi_n^{g'} = \sum_{g'} \frac{\Sigma_{p,n}^{g' \rightarrow g}}{4\pi} \phi_n^{g'} \quad (438)$$

where

$$\Sigma_{p,n}^{g' \rightarrow g} = \chi_n^g \sum_{g'} v\Sigma_{f,n}^{g'} \quad (439)$$

External Source

For an external source of neutrons with energy E , located at position \vec{r} , with total (scalar) strength $s(\vec{r}, E)$, we distribute the neutrons isotropically such that

$$Q_{ext}(\vec{r}, E, \hat{\Omega}) = \frac{s(\vec{r}, E)}{4\pi} \quad (440)$$

or in multigroup form

$$Q_{ext,n}^g = \frac{s_n^g}{4\pi} \quad (441)$$

Total Source for a Non-Multiplying System

For a non-multiplying system, there is no source due to fission. For such a system, we are interested only in the flux distribution and not the multiplication factor. This is the type of problem solved when determining a gamma distribution. The external source in such instances is the gamma source resulting from the neutron flux distribution and contains contributions from neutron slowing down (scattering), from the fission process, and from the decay of fission products from an excited state to a more stable state. The final total (scalar) source distribution for a non-multiplying system would be expressed as

$$q_n^g = q_{s,n}^g + q_{ext,n}^g = \sum_{g'} \Sigma_{s,n}^{g' \rightarrow g} \phi_n^{g'} + s_n^g \quad (442)$$

Total Source for a Multiplying System

For a multiplying system, we may or may not have an external source. If we have an external source, then we are concerned with a subcritical system where the total source term is expressed as

$$q_n^g = q_{s,n}^g + q_{f,n}^g + q_{ext,n}^g = \sum_{g'} \left(\Sigma_{s,n}^{g' \rightarrow g} + \Sigma_{p,n}^{g' \rightarrow g} \right) \phi_n^{g'} + s_n^g \quad (443)$$

Lattice physics applications consist of multiplying systems with no external sources. For these types of problems the total scalar source is expressed as

$$q_n^g = q_{s,n}^g + q_{f,n}^g = \sum_{g'} \left(\Sigma_{s,n}^{g' \rightarrow g} + \frac{\Sigma_{p,n}^{g' \rightarrow g}}{k^\infty} \right) \phi_n^{g'} \quad (444)$$

which is similar to the expression of the source in (443) with the external source having been removed from the equation. The parameter k^∞ in (444) is the infinite multiplication factor and, for a system with no neutron leakage, is equal to the volume integrated number of neutrons born through fission divided by the volume integrated number of neutrons absorbed in the system,

$$k^\infty = \frac{\sum_n \sum_g \nu \Sigma_{f,n}^g \phi_n^g V_n}{\sum_n \sum_g \Sigma_{a,n}^g \phi_n^g V_n} \quad (445)$$

where V_n is the volume of each mesh in the system.

Physically, (445) describes a mesh, n , where there are $\sum_g \nu \Sigma_{f,n}^g \phi_n^g$ fission neutrons being born *per unit volume*. To calculate the total number of fission neutrons born in mesh n , we simply multiply by the volume of the mesh. This is only possible because we have assumed that the scalar flux is constant across mesh n , as are the cross sections. In a similar manner, there are $\sum_g \Sigma_{a,n}^g \phi_n^g$ neutrons absorbed in mesh n *per unit volume*. To calculate the total number of neutrons absorbed in mesh n , we once again multiply by the volume of the mesh. As before, this is possible because we have assumed that the scalar flux and the cross sections are constant across the volume. Mathematically, k^∞ is used to stabilize the source of neutrons from one flux iteration to the next.


So, now we can calculate q for each slab in the problem and we have all the information we need to solve the transport equation

$$\Phi_{\text{out}} = \Phi_{\text{in}} e^{-\Sigma_{tr}t} + \frac{q}{4\pi\Sigma_{tr}} (1 - e^{-\Sigma_{tr}t}) \quad (446)$$

5.5.4 Boundary Conditions


Boundary conditions in the characteristics method are applied to the angular flux only. There are two types of boundary conditions we will examine for slab geometry – periodic and reflective. Each of these will be discussed below. We will not examine vacuum boundary conditions because they are not applied in single assembly lattice physics analysis, although they can be applied when generating nodal discontinuity factors for water reflector regions. Such applications, however, are beyond the scope of this chapter.

Periodic Boundary Conditions

Periodic boundary conditions require the value of the angular flux in group g , in direction $(\bar{\varphi}_i, \bar{\theta}_j)$, entering the western-most surface of the system of slabs ($n = 1$) to be equal to the value of the angular flux in group g , moving in direction $(\bar{\varphi}_i, \bar{\theta}_j)$, leaving the eastern-most surface of the system of slabs ($n = N$). This is illustrated in  Fig. 60 and expressed mathematically as

$$\begin{aligned} \Phi_{\text{in},n=1}^g(\bar{\varphi}_i, \bar{\theta}_j) &= \Phi_{\text{out},n=N}^g(\bar{\varphi}_i, \bar{\theta}_j) \quad \text{for } 0 \leq \bar{\varphi}_i \leq \pi/2 \\ \Phi_{\text{in},n=N}^g(\bar{\varphi}_i, \bar{\theta}_j) &= \Phi_{\text{out},n=1}^g(\bar{\varphi}_i, \bar{\theta}_j) \quad \text{for } \pi/2 \leq \bar{\varphi}_i \leq \pi \end{aligned} \quad (447)$$

Reflective Boundary Conditions

Reflective boundary conditions require a fraction, α , of the value of the angular flux hitting the boundary of the system along the characteristic traveling in direction $\bar{\varphi}_i$ to be reflected back along the companion characteristic traveling in direction $\pi - \bar{\varphi}_i$. This is illustrated in  Fig. 61 and expressed mathematically as

$$\Phi_{\text{in},n=N}^g(\bar{\varphi}'_i, \bar{\theta}'_j) = \alpha \cdot \Phi_{\text{out},n=N}^g(\bar{\varphi}_i, \bar{\theta}_j) \quad (448)$$

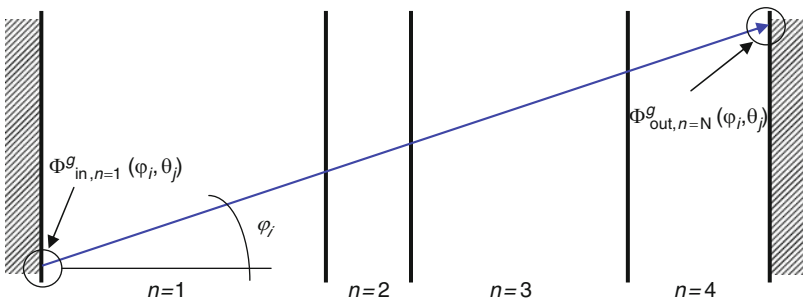


 Figure 60

Periodic boundary condition in slab geometry

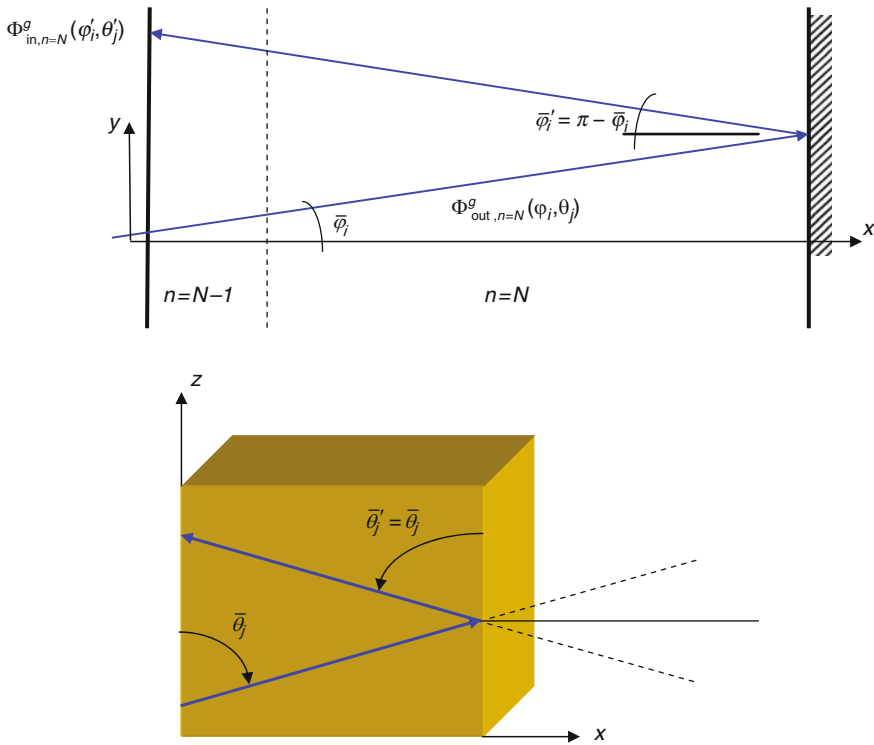


Figure 61
Reflective boundary condition in slab geometry

where the primes on the azimuthal and polar angles represent the reflective counterparts to the incident angles. For $\alpha = 1.0$, we have perfect reflexion. For $\alpha = 0.0$, we have a perfect vacuum condition.

For the reflective boundary condition, we must make sure we have distributed the azimuthal angles in such a way that there exists a reflective counterpart for each incident direction. For the equally distributed set of azimuthal angles we use in our implementation of the method of characteristics, this criterion is satisfied automatically. For I azimuthal directions distributed evenly between $0 \leq \bar{\varphi}_i \leq \pi$, the reflected counterpart to angle i is angle $i' = I - i + 1$.

5.5.5 Convergence

Convergence of the Angular Flux

For each energy group, g , we have an initial value for the inward flux along the surface of the problem, in azimuthal direction i , polar direction j , which is represented by $\Phi_{in,n=1}^g(\bar{\varphi}_i, \bar{\theta}_j)$. We march along the track until we reach the opposite boundary of the slab system, at which point we have an outwardly directed angular flux, $\Phi_{out,n=N}^g(\bar{\varphi}_i, \bar{\theta}_j)$. This then becomes the inward value for the angular flux in the reflected (or periodic) direction, using (448). This replaces the

previous value for the inward directed angular flux in direction $(\bar{\varphi}'_i, \bar{\theta}'_j)$. The difference in the two values – the value of the angular flux at the end of the previous iteration, and the value of the angular flux at the end of the present iteration – is a measure of how close we are to the true solution to the problem. When the difference between the two angular flux values is within a certain criterion, ε , for all inward directions, along both surfaces of the slab system, the angular flux for that particular energy group is assumed to be converged,

$$\left| \frac{\Phi_{\text{new,in},n}^g(\bar{\varphi}_i, \bar{\theta}_j) - \Phi_{\text{old,in},n}^g(\bar{\varphi}_i, \bar{\theta}_j)}{\Phi_{\text{new,in},n}^g(\bar{\varphi}_i, \bar{\theta}_j)} \right| < \varepsilon \quad (449)$$

where $n = 1$ represents the western-most surface to the slab system and $n = N$ represents the eastern-most surface to the slab system. (449) must hold true for all i 's and j 's in order to satisfy a fully converged solution to the problem in a given energy group.

Convergence of the Scalar Flux

At the end of each inner iteration, in addition to testing for convergence of the angular flux, the scalar flux is also tested for convergence. The same principle applies here as for the angular flux.

We begin the iteration with some value for the scalar flux in group g , $\phi_n^g(\text{old})$. This value for the scalar flux is used to calculate the source term prior to solving for the new flux distribution. With the source distribution frozen, we solve for a new scalar flux distribution, $\phi_n^g(\text{new})$. The new scalar flux is calculated by solving the equation

$$\phi_n^g(\text{new}) = \frac{q_n^g}{\Sigma_{tr,n}^g} + F_n^g \quad (450)$$

where

$$q_n^g = \sum_{g' < g} \left(\Sigma_{s,n}^{g' \rightarrow g} + \frac{\Sigma_{p,n}^{g' \rightarrow g}}{k^\infty} \right) \phi_n^{g'}(\text{new}) + \sum_{g' \geq g} \left(\Sigma_{s,n}^{g' \rightarrow g} + \frac{\Sigma_{p,n}^{g' \rightarrow g}}{k^\infty} \right) \phi_n^{g'}(\text{old}) \quad (451)$$

$$F_n^g = \sum_j \sum_i \frac{\Delta_{i,j,n}^g \cdot \omega_i \cdot \omega_j}{\Sigma_{tr,n}^g t_{i,j,n}} \quad (452)$$

In (452), $\Delta_{i,j,n}^g = \Phi_{\text{in},n}^g(\bar{\varphi}_i, \bar{\theta}_j) - \Phi_{\text{out},n}^g(\bar{\varphi}_i, \bar{\theta}_j)$ is the change in the angular flux value along the characteristic as it passes through a mesh.

The difference between the old and new value of the scalar flux will approach zero as the solution converges. Typically, as in the case of the angular flux, convergence is declared when the following statement is satisfied in every mesh:

$$\left| \frac{\phi_n^g(\text{new}) - \phi_n^g(\text{old})}{\phi_n^g(\text{new})} \right| < \varepsilon \quad (453)$$

Convergence of the Multiplication Factor

Prior to starting an outer iteration, the multiplication factor for the old flux distribution is calculated, k^∞ . As the fission source distribution converges, so too will the multiplication factor.

From one iteration to the next, we check for convergence of the multiplication factor

$$\left| \frac{k^\infty(\text{new}) - k^\infty(\text{old})}{k^\infty(\text{new})} \right| < \varepsilon \quad (454)$$

Equation (454) will always be satisfied if both (449) and (453) are satisfied. That is, the multiplication factor will always be converged if the flux distribution is converged. For this reason, satisfying (454) is relatively irrelevant.

5.5.6 Accelerating the Flux Convergence

For large problems, the number of iterations needed for convergence may become extreme if the initial flux guess is far from the converged solution. In order to reduce the number of iterations needed to satisfy convergence requirements, we would like to accelerate the convergence rate. We wish to accelerate the energy convergence as well as the spatial convergence. This section presents two methods that can be applied to accelerate the convergence of the scalar flux.

Energy Acceleration

Following completion of an outer iteration, a fundamental mode rebalancing of the group flux distribution is performed in order to properly normalize the flux and ensure neutron conservation. The fundamental mode calculation is performed on an equivalent homogeneous system using flux and volume weighted cross sections from the heterogeneous calculation. The resulting group flux values from the homogeneous calculation are then used to rebalance the magnitude of the heterogeneous group flux values. The description of the fundamental mode rebalancing calculation for the MoC is identical to that found in [Sect. 4](#) for the rebalance applied to the coupling calculation.

The equation to be solved here is equivalent to (310),

$$\phi_{\text{FM}}^g = \frac{\bar{q}^g}{\bar{\Sigma}_r^g} \quad (455)$$

where the source term does not include self scattering and the fission source is normalized to unity by the eigenvalue. Hence,

$$\bar{q}^g = \sum_{g' \neq g} \bar{\Sigma}_s^{g' \rightarrow g} \phi_{\text{FM}}^{g'} + \frac{\bar{\chi}^g}{k^\infty} \sum_{g'} \nu \bar{\Sigma}_f^{g'} \phi_{\text{FM}}^{g'} \quad (456)$$

The flux and volume weighted cross sections for the fundamental mode calculation are calculated from

$$\bar{\Sigma}_x^g = \frac{\sum_i \Sigma_{x,i}^g \phi_i^g V_i}{\sum_i \phi_i^g V_i} \quad (457)$$

where x represents the desired reaction.

For problems exhibiting no neutron leakage across the boundaries (i.e., perfect reflection along all boundaries), the multiplication factor in (457) can be calculated directly as the ratio of neutron production in the system to neutron destruction, as in (445),

$$k^\infty = \frac{\sum_{g'} \nu \bar{\Sigma}_f^{g'} \phi_{\text{FM}}^{g'}}{\sum_{g'} \bar{\Sigma}_a^{g'} \phi_{\text{FM}}^{g'}} \quad (458)$$

If we normalize the flux in such a way that there is only one neutron being absorbed in the entire problem, then the denominator to (458) becomes unity and the multiplication factor is simply the sum of all neutrons born through fission,

$$k^\infty = \sum_{g'} \nu \bar{\Sigma}_f^{g'} \phi_{\text{FM}}^{g'} \quad (459)$$

Plugging (459) into (456) yields the final expression for the fundamental mode homogeneous source

$$\bar{q}^g = \sum_{g'} \bar{\Sigma}_s^{g' \rightarrow g} \phi_{\text{FM}}^{g'} + \bar{\chi}^g \quad (460)$$

Due to up-scattering in the thermal energy groups, the solution to (455) defines an iterative process and the fundamental mode equation is solved directly, with no acceleration. Following the solution to (455), the scalar flux distribution from the solution to (411) is scaled using the rebalance factors,

$$\hat{\phi}_n^g = \phi_n^g \cdot \frac{\phi_{\text{FM}}^g}{\sum_n \phi_n^g V_n} \quad (461)$$


where the summation in (461) is over all mesh in the problem.

Spatial Acceleration

The scalar flux can be accelerated spatially using a simple coarse mesh rebalance (CMR) throughout the system. This is especially important since the characteristics equations are not based on a neutron balance and solution to the equations does not necessarily conserve neutrons from one iteration to the next. Coarse mesh are determined by material region. Each material region may be subdivided into smaller mesh to improve the accuracy of the flat flux approximation. The CMR is performed to ensure neutron conservation within each material region – or coarse mesh – of the problem.

The balance equation to be solved in each coarse mesh is defined as

$$\left[\sum_{m \in n} \Sigma_{r,m}^g \phi_m^g V_m + \sum_{s \in n} J_{\text{out},s,n}^g \right] \cdot f_n^g = \sum_{m \in n} q_m^g V_m + \sum_{s' \in n'} J_{\text{in},s',n'}^g \cdot f_{n'}^g \quad (462)$$

where m represents the mesh subdivisions within a coarse mesh material region, n ; s represents the surfaces to the coarse mesh, n ; s' represents the surfaces to the neighboring coarse mesh, n' . The variables in (462) are illustrated in  Fig. 62.

The currents must be accumulated as the inner iterations are performed. The contribution to the outgoing current along a coarse mesh surface is calculated as

$$J_{\text{out},s,n}^g = \sum_j \sum_i \sum_{k_m} \Phi_{k_m,i,j}^g \cdot \omega_i \cdot \omega_j \cdot |\cos \varphi_i \cdot \sin \theta_j| \quad (463)$$

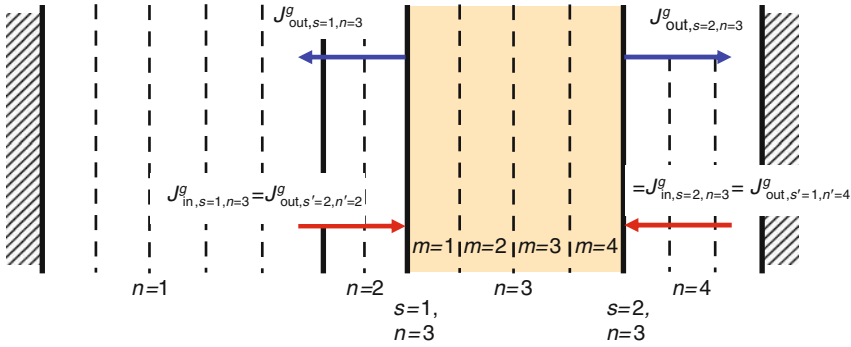


Figure 62
Variables for the coarse mesh rebalance calculation

where k_m represents a track segment crossing mesh m , and the accumulation is only performed if mesh m is along the edge of coarse mesh n .

Equation (462) is solved iteratively for the balance factors, f_n^g . Once the balance factors are determined, the scalar flux is updated,

$$\phi_m^g = \phi_m^g \cdot f_n^g \tag{464}$$

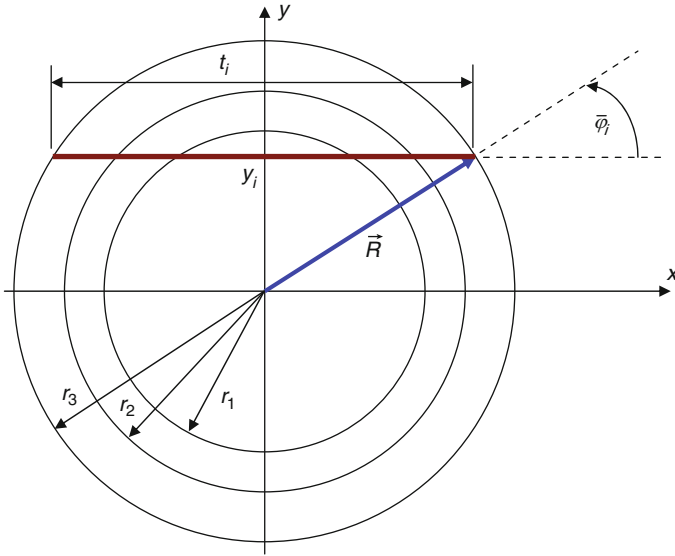
for all mesh subdivisions, m , within coarse mesh region n . The CMR calculation is performed at the end of each inner iteration. Note that the CMR method is not inherently stable and the acceleration scheme can diverge or oscillate when mesh become optically very thin or very thick. The interested reader is directed to refer to, for instance, Reed (1971), Yamamoto et al. (2004), Cefus and Larsen (1990), Adams and Larsen (2002), Cho and Park (2003), and Lee and Downar (2003) for more information on convergence issues associated with acceleration techniques.

5.6 Cylindrical Geometry

5.6.1 Introduction

So far, only slab geometry has been discussed. The remaining one-dimensional geometries are cylindrical and spherical. For the characteristics method, spherical geometry is a special case of cylindrical geometry. Cylindrical geometry also forms the basis for moving on to complex geometries in two dimensions. Therefore, cylindrical geometry will be discussed in this section as a prelude to the discussion of two-dimensional analysis.

For our one-dimensional geometry, we consider a cylinder that is infinite in the z -direction and may contain many annular regions. If we use the coordinate system shown in **Fig. 63**, then the azimuthal angles of motion are constructed from the radius vector, \vec{R} , and a track parallel with the x -axis and perpendicular to the y -axis. The two lines are located such that the radius vector intersects the track at the outer radius of the cylinder.



■ **Figure 63**
Coordinates used for MoC cylindrical geometry

The intersection of the track occurs at some height along the y -axis. This height, or y -intersection, may be calculated by equating the equations of the two lines

$$\vec{R}^2 = x_i^2 + y_i^2 \text{ radius of outer annulus} \quad (465)$$

$$t_i = 2\vec{R} \cos \bar{\varphi}_i \quad (466)$$

where t_i is the track length spanned across the cylinder by the characteristic associated with azimuthal angle $\bar{\varphi}_i$.

We know \vec{R} from the problem definition, and we have chosen $\bar{\varphi}_i$ from our quadrature set. The value of x_i is the point along the x -axis at which the track intersects the outer radius of the cylinder and is easily calculated as

$$x_i = \vec{R} \cos \bar{\varphi}_i = \frac{1}{2} t_i \quad (467)$$

and the y -intercept is calculated as

$$y_i = \vec{R} \sin \bar{\varphi}_i \quad (468)$$

From (468), if $r_n > y_i$, then track t_i passes through annulus n , where r_n is the radius of annulus n .

$$r_n^2 = x_n^2 + y_i^2 \quad \text{or} \quad x_n = \sqrt{r_n^2 - y_i^2} \quad (469)$$

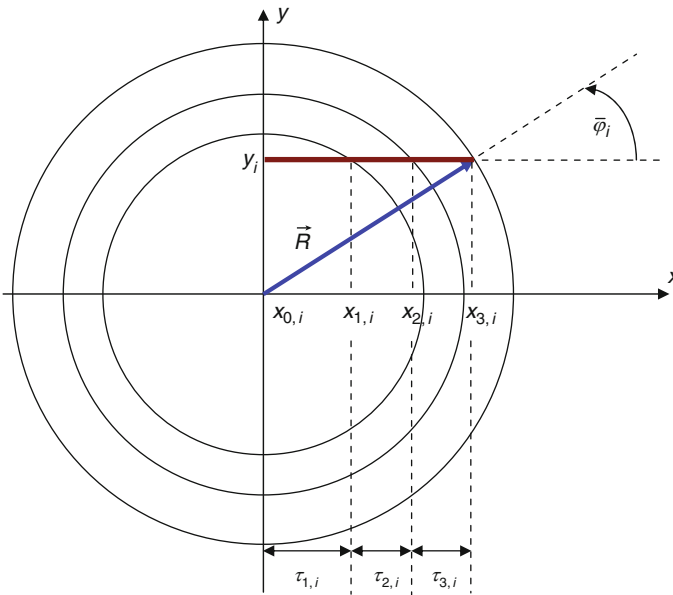


Figure 64
Track segments along a single characteristic

and track segment $\tau_{n,i}$ at azimuthal angle i , passing through region n , may be calculated as

$$\tau_{n,i} = x_n - x_{n-1} \tag{470}$$

This is illustrated in Fig. 64.

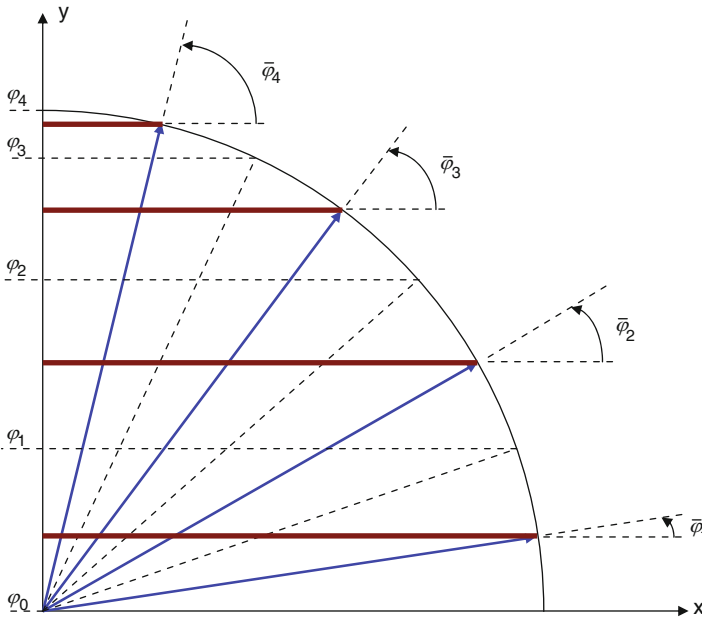
5.6.2 Choosing the Azimuthal Angles of Motion

Even Angle Distribution

As in the case of slab geometry, we wish to model neutron motion in the azimuthal plane of the problem in several unique directions. We could stick with our original choice of an evenly spaced set of azimuthal directions and boundaries, φ_i and $\bar{\varphi}_i$, respectively. To this end, we would have tracks crossing the system as shown in Fig. 65.

The above choice of four unique directions evenly distributed between $0 \leq \bar{\varphi}_i \leq \pi/2$ generates the boundaries, directions, and associated weights on a unit cylinder listed in Table 16. Note that the weight associated with each direction of motion is equivalent to the distance between parallel lines.

It can be seen from the table that, for our equal angle quadrature set, we will have more characteristics concentrated toward the top of the cylinder than we have near the center of the cylinder. This distribution is highly undesirable.



■ Figure 65
Evenly distributed angles in the azimuthal plane of a cylinder

■ Table 16
Evenly distributed angles in azimuthal plane of unit cylinder

i	φ_i	$\bar{\varphi}_i$	y_i	\bar{y}_i	ω_i
0	0°	–	0.00000	–	–
1	22.5°	11.25°	0.38268	0.19509	0.38268
2	45°	33.75°	0.70711	0.55557	0.32443
3	67.5°	56.25°	0.92388	0.83147	0.21677
4	90°	78.75°	1.00000	0.98079	0.07612

To correct for this skewed distribution, we wish to distribute the characteristics evenly, or more precisely we wish to produce azimuthal angles with the same weights, which requires the characteristic boundaries to be distributed evenly.

Even Boundary Distribution

From our previous example, if we wish to distribute the four characteristic boundaries evenly, we choose to enforce the following constraint:

$$\Delta y = \frac{R}{I} \quad (471)$$

where R is the outer radius of the cylinder and I is the total number of azimuthal angles. Then the y -intercepts of the boundaries are calculated as

$$y_i = R \sin \varphi_i \quad (472)$$

and the angles of motion are defined by rearranging (472)

$$\varphi_i = \sin^{-1} \left(\frac{y_i}{R} \right) \quad (473)$$

The location of the characteristic passing between the boundaries should be chosen to preserve the mean chord length of the prism being intersected. In the xy -plane, the mean chord length of a circle is simply the ratio of the area to the diameter,

$$\frac{A}{D} = \frac{\pi R^2}{2R} = \frac{\pi R}{2} \quad (474)$$

To convert this to the mean chord of a cylinder, we multiply by the mean secant of the azimuthal angle, where the mean secant is calculated as

$$\sec \varphi = \frac{\int_0^{\pi/2} \sec \varphi \cdot \cos^2 \varphi \cdot d\varphi}{\int_0^{\pi/2} \cos^2 \varphi \cdot d\varphi} = \frac{4}{\pi} \quad (475)$$

and the mean chord length for a complete cylinder then becomes $2R$.

The mean chord length for a horizontal slice through a cylinder can be calculated in a similar manner. This calculation results in an expression for the angle of travel for the characteristic passing through the slice

$$\begin{aligned} \sec \bar{\varphi}_i &= \frac{\omega_i}{\frac{1}{2}(\varphi_i - \varphi_{i-1}) + \frac{1}{4}(\sin 2\varphi_i - \sin 2\varphi_{i-1})} \\ &= \frac{\sin \varphi_i - \sin \varphi_{i-1}}{\frac{1}{2}(\varphi_i - \varphi_{i-1}) + \frac{1}{4}(\sin 2\varphi_i - \sin 2\varphi_{i-1})} \end{aligned} \quad (476)$$

Inverting (476) gives

$$\cos \bar{\varphi}_i = \frac{\frac{1}{2}(\varphi_i - \varphi_{i-1}) + \frac{1}{4}(\sin 2\varphi_i - \sin 2\varphi_{i-1})}{\sin \varphi_i - \sin \varphi_{i-1}} \quad (477)$$

From (477), the expression for the angle of travel for the characteristic passing through the centroid of the horizontal slice in the xy -plane of the problem is

$$\begin{aligned} \bar{\varphi}_i &= \cos^{-1} \left\{ \frac{\frac{1}{2}(\varphi_i - \varphi_{i-1}) + \frac{1}{4}(\sin 2\varphi_i - \sin 2\varphi_{i-1})}{\sin \varphi_i - \sin \varphi_{i-1}} \right\} \\ &= \cos^{-1} \left\{ \frac{\frac{1}{2}(\varphi_i - \varphi_{i-1}) + \frac{1}{4}(\sin 2\varphi_i - \sin 2\varphi_{i-1})}{\omega_i} \right\} \end{aligned} \quad (478)$$

For our previous example of four azimuthal directions of motion between $0 \leq \bar{\varphi}_i \leq \pi/2$, the new angles and weights using the *equal weights* quadrature will be those listed in [Table 17](#).

Table 17

Evenly distributed boundaries in azimuthal plane of unit cylinder

i	φ_i	$\bar{\varphi}_i$	y_i	\bar{y}_i	ω_i
0	0°	–	0.00	–	–
1	14.4775°	8.3168°	0.25	0.19509	0.25
2	30°	22.5209°	0.50	0.55557	0.25
3	48.5904°	39.1897°	0.75	0.83147	0.25
4	90°	63.0437°	1.00	0.98079	0.25

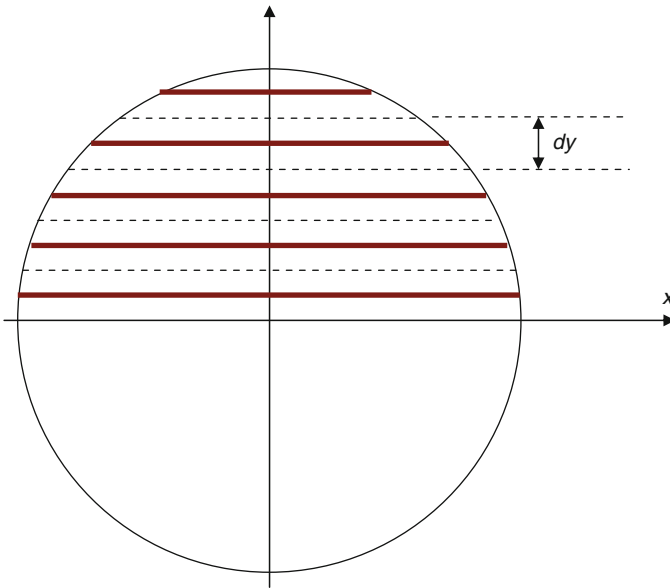


Figure 66

Evenly distributed characteristics in the azimuthal plane of a cylinder

5.6.3 An Alternative Tracking Approach

General Theory

Rather than concerning ourselves with the azimuthal boundaries and positioning of the azimuthal angle of motion, there is a somewhat simpler, more direct way to track across our cylindrical system. We may lay tracks across the system, evenly spaced at increments of dy , as shown in [Fig. 66](#). Each characteristic has associated with it a “width,” which extends from the characteristic, half the way to the next characteristic on either side, as illustrated in [Fig. 67](#). The weight that is associated with each characteristic is then equal to the width of the characteristic, dy . The width of each characteristic is easily calculated by dividing the radius of the cylinder by the number of azimuthal directions of motion (i.e., the number of characteristics),

$$dy = \frac{R}{I} \quad (479)$$

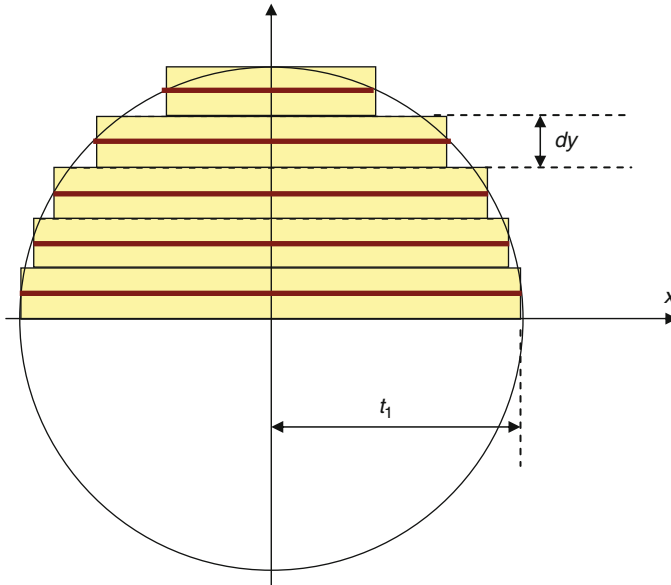


Figure 67
Characteristic “widths”

Here, I is the number of characteristics in the NE quadrant of the cylinder and dy is the spacing between tracks and also between boundaries.

For one-dimensional cylinders, which exhibit azimuthal symmetry, we need only trace in the NE quadrant of the problem, since all other quadrants would be reflections of the NE quadrant. Since each characteristic has associated with it a width, we have two cylinder areas – (1) the *true* area of the NE quadrant $A_{\text{true}} = \pi R^2/4$, and (2) the area *approximated* by the characteristic widths,

$$A_{\text{approx}} = \sum_i t_i \cdot dy \tag{480}$$

where t_i is the length of the i th characteristic across the NE quadrant of the cylinder in the xy -plane of the problem.

Example

If we have many annular rings, but only a few characteristics, then we may end up with A_{approx} being much different from the A_{true} value. To illustrate this, let us suppose we have the system contained in **Fig. 68**.

If we look at the innermost ring – region 1 – then the true area of that region is

$$A_{\text{true}} = \frac{\pi r_1^2}{4} = \frac{\pi(0.74'')^2}{4} = 0.43 \text{ in}^2$$

and the x -intercept of the first characteristic with the radius of region 1 occurs at

$$\tau_{1,1} = \sqrt{r_1^2 - y_1^2} = \sqrt{(0.74'')^2 - (0.45'')^2} = 0.58745''$$

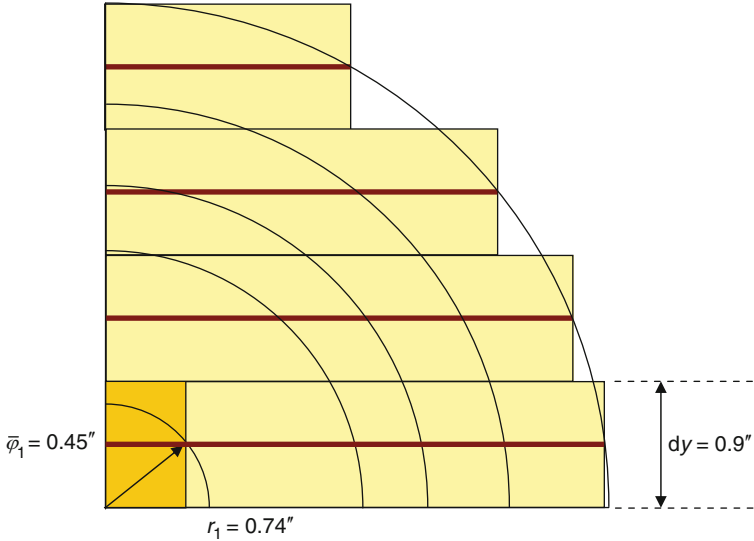


Figure 68
System with many annular rings and few characteristics

The approximated area of region 1 is calculated using (480)

$$A_{\text{approx}} = \tau_{1,1} \cdot dy = 0.58745'' \times 0.9'' = 0.52871 \text{ in}^2$$

In this example, the approximated area through region 1 is overestimated by

$$\% \text{diff} = \frac{|A_{\text{approx}} - A_{\text{true}}|}{A_{\text{true}}} \times 100\% = \frac{|0.52871 \text{ in}^2 - 0.43 \text{ in}^2|}{0.43 \text{ in}^2} \times 100\% = 23\%$$

Therefore, $\tau_{1,1}$ is really 23% longer than it should be and we will get too few neutrons being passed from region 1 to region 2 along this track segment if we leave it to remain as it is.

Track Adjustments

To correct for the poor estimation of the region area, we can adjust the track length until $A_{\text{approx}} = A_{\text{true}}$. We do this using the ratio below,

$$\tau'_{1,1} = \tau_{1,1} \cdot \frac{A_{\text{true}}}{A_{\text{approx}}} \quad (481)$$

For our example above, we would perform the following ratio:

$$\tau'_{1,1} = 0.58745'' \times \frac{0.43 \text{ in}^2}{0.52871 \text{ in}^2} = 0.47777''$$

In this way, we have reduced the true track length by 23% to ensure that the approximated area is correct. This will help to ensure that a proper number of neutrons are passed through region 1 to region 2, and vice versa.

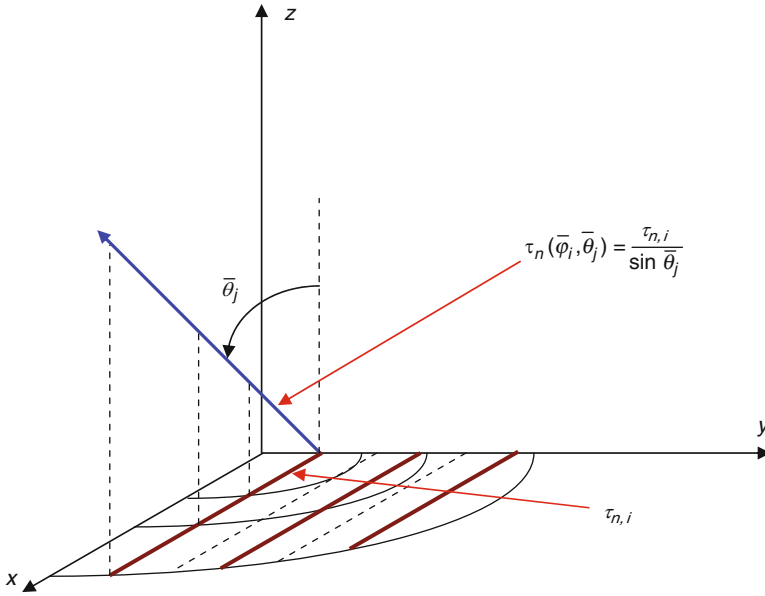


Figure 69 Definition of track segments in MoC cylindrical coordinates

In general, then, we keep a running tally of the approximated area in each region using (480) and ratio all track segments following the completion of the tracking routine

$$\tau'_{n,i} = \tau_{n,i} \cdot \frac{A_{\text{true}}}{A_{\text{approx}}} = \tau_{n,i} \cdot \frac{\pi(r_n^2 - r_{n-1}^2)}{4 \sum \tau_{n,i} dy} \tag{482}$$

where the parameters in (482) are illustrated in Fig. 69. The transport equation may then be solved using the ratioed track lengths

$$\Phi_{\text{out},n}^g(\bar{\varphi}_i, \bar{\theta}_j) = \Phi_{\text{in},n}^g(\bar{\varphi}_i, \bar{\theta}_j) e^{-\sum_n^g \tau'_n(\bar{\varphi}_i, \bar{\theta}_j)} + \frac{q_n^g}{4\pi \sum_n^g} \left(1 - e^{-\sum_n^g \tau'_n(\bar{\varphi}_i, \bar{\theta}_j)} \right) \tag{483}$$

5.6.4 Modification to the Characteristics Equation

The solution to the transport equation must now be modified in order to apply our new tracking approach. In slab geometry, our ray tracing was precise and we kept track of the following summation in (411):

$$\sum_j \sum_i \frac{\Delta_n^g(\bar{\varphi}_i, \bar{\theta}_j) \cdot \omega_i \cdot \omega_j}{\tau_n(\bar{\varphi}_i, \bar{\theta}_j)} \tag{484}$$

where $\Delta_n^g(\bar{\varphi}_i, \bar{\theta}_j)$ is the change in the value of the angular flux across a mesh, moving in azimuthal direction $\bar{\varphi}_i$ and polar direction $\bar{\theta}_j$; and $\tau_n(\bar{\varphi}_i, \bar{\theta}_j)$ is the length of the track segment crossing the mesh. These lengths are always precise in slab geometry and all characteristics cross all slab regions in the problem.

In cylindrical geometry, the situation is different because not all characteristics cross each of the annular cylindrical regions and the characteristics do not preserve the true volume of each annular region. We can modify the summation in (484) to compensate for this. First, we rewrite (484) in a form that includes the length of the track segment projected onto the xy -plane of the problem

$$\sum_j \sum_i \frac{\Delta_n^g(\bar{\varphi}_i, \bar{\theta}_j) \cdot \omega_i \cdot \omega_j}{\tau'_{n,i} / \sin \bar{\theta}_j} = \sum_j \sum_i \frac{\Delta_n^g(\bar{\varphi}_i, \bar{\theta}_j) \cdot \omega_i \cdot \omega_j \cdot \sin \bar{\theta}_j}{\tau'_{n,i}} \quad (485)$$

Now we can substitute our expression for the approximated volume into (485) to replace the length of the projected track segment

$$\sum_j \sum_i \frac{\Delta_n^g(\bar{\varphi}_i, \bar{\theta}_j) \cdot \omega_i \cdot \omega_j \cdot \sin \bar{\theta}_j}{\tau_{n,i} \cdot \frac{A_{\text{true}}}{A_{\text{approx}}}} = \frac{1}{A_{\text{true}}} \sum_j \sum_i \Delta_n^g(\bar{\varphi}_i, \bar{\theta}_j) \cdot \omega_i \cdot \omega_j \cdot \sin \bar{\theta}_j \cdot dy \quad (486)$$

Substituting (486) into (411) gives us our modified expression for the scalar flux in cylindrical geometry,

$$\phi_n^g = \frac{q_n^g}{4\pi \Sigma_{tr,n}^g} + \frac{dy}{\Sigma_{tr,n}^g A_{\text{true}}} \sum_j \left(\omega_j \cdot \sin \bar{\theta}_j \sum_i \Delta_n^g(\bar{\varphi}_i, \bar{\theta}_j) \cdot \omega_i \right) \quad (487)$$

5.7 Two-Dimensional Geometry

For two-dimensional characteristics calculations, we take an approach similar to the approach we took for the one-dimensional cylindrical geometry. We assign a width to each characteristic and trace characteristics across the entire system at several azimuthal angles between $0 \leq \bar{\varphi} \leq 2\pi$. In one dimension, neutrons traveled at angles between $0 \leq \bar{\varphi} \leq \pi$ in an identical fashion to the way in which they traveled at angles between $\pi \leq \bar{\varphi} \leq 2\pi$. Therefore, we needed only to model neutron motion between $0 \leq \bar{\varphi} \leq \pi$ and account for the remaining azimuthal angles by doubling the associated weight, ω_i . Similarly, neutrons traveled at polar angles between $0 \leq \bar{\theta} \leq \pi/2$ in an identical fashion to the way in which they traveled at angles between $\pi/2 \leq \bar{\theta} \leq \pi$ and we accounted for this symmetry by modeling neutron motion only between $0 \leq \bar{\theta} \leq \pi/2$ and doubling the associated polar weight, ω_j .

In two dimensions, neutron motion in the polar direction is still symmetric about the xy -plane of the problem. That is, neutron motion above the plane is symmetric to neutron motion below the plane. Neutron motion within the xy -plane, though, is not symmetric about either the x -axis or y -axis and we must model neutron motion explicitly at all azimuthal angles between $0 \leq \bar{\varphi} \leq 2\pi$. The tracking routine may be eased somewhat by tracing across the system at angles between $0 \leq \bar{\varphi} \leq \pi$ only, and allowing neutrons to travel in both directions along each track during the characteristics solution.

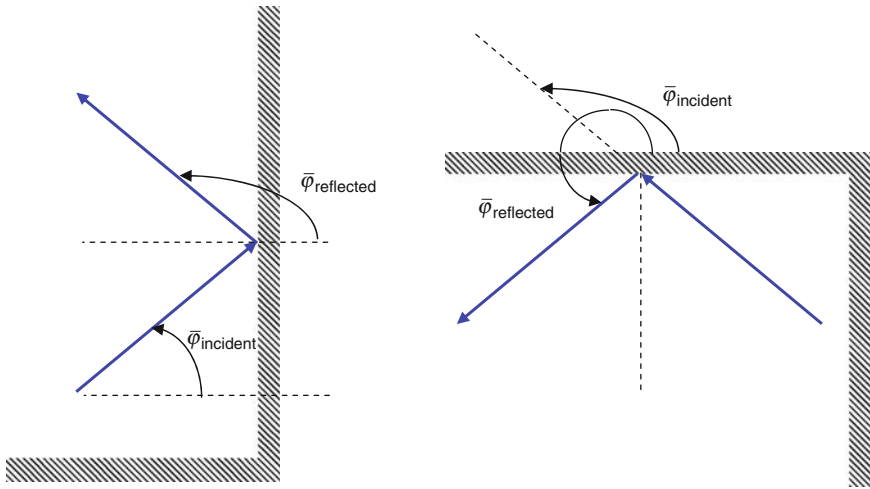


Figure 70
Reflected tracks off different boundaries to the two-dimensional problem

As in the one-dimensional case for reflective boundary conditions, we have a set of unique characteristics, which are distributed between $0 \leq \bar{\varphi} \leq \pi/2$. In one-dimension, we had the associated reflected tracks distributed between $\pi/2 \leq \bar{\varphi} \leq \pi$. In two-dimensional problems, we have tracks reflecting off the top and bottom boundaries of the problem, as well as off the side boundaries to the problem, as illustrated in **Fig. 70**. This leads to three reflected angles between $\pi/2 \leq \bar{\varphi} \leq 2\pi$ – one reflected angle in each directional quadrant of the problem. To this end, then, we must make sure that the end of each incident characteristic aligns precisely with the beginning of its reflected counterpart.

To ensure perfect reflection in two dimensions, track separations and streaming angles in the xy -plane of the problem must be altered based on the overall dimensions of the problem. We specify the number of azimuthal angles of motion that are to be used to model neutron streaming, I , and the separation of the set of parallel, equidistantly spaced tracks, d , at each azimuthal angle. The unadjusted set of azimuthal angles will be evenly spaced at angles defined by the following expressions:

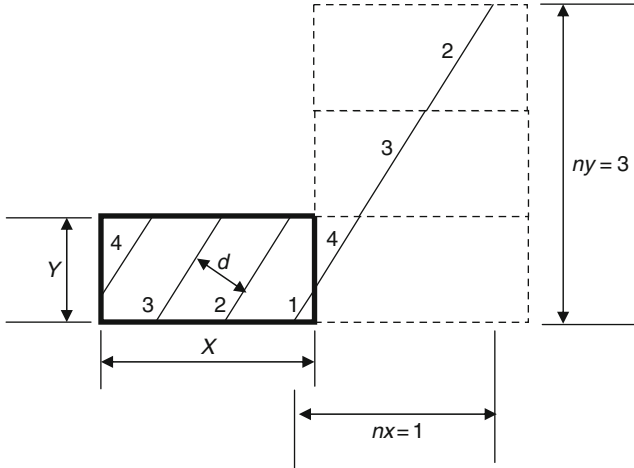
$$\bar{\varphi}_i = \frac{1}{2}(\varphi_i + \varphi_{i-1}), \quad \text{where } \varphi_0 = 0^\circ \tag{488}$$

$$\varphi_i - \varphi_{i-1} = \frac{2\pi}{I} \tag{489}$$

where I is the number of azimuthal angles distributed between $0 \leq \varphi_i \leq 2\pi$.

If the system is of total width X and total height Y , then the total number of system widths spanned by a characteristic moving in the azimuthal direction of motion i , with a characteristic separation of distance d , is

$$nx = \frac{X \sin \bar{\varphi}_i}{d} \tag{490}$$



■ **Figure 71**
System heights and widths spanned by characteristic

and the total number of system heights spanned is

$$ny = \frac{X \cos \bar{\varphi}_i}{d} \quad (491)$$

This is illustrated in ► [Fig. 71](#).

In order to ensure that all tracks in direction $\bar{\varphi}_i$ align themselves with their reflective counterparts at the boundaries of the system, nx and ny are rounded up to the nearest integer values and the updated angle of streaming is then calculated as

$$\bar{\varphi}'_i = \tan^{-1} \left(\frac{ny_i}{nx_i} \right) \quad (492)$$

along with the updated separation distance

$$d'_i = \frac{X}{\sqrt{ny_i^2 + nx_i^2}} \quad (493)$$

Using these angles and separations, the azimuthal set of parallel, equidistantly spaced tracks are traced across the system at angles between $0 \leq \bar{\varphi}'_i \leq \pi$. For the angles between $\pi \leq \bar{\varphi}'_i \leq 2\pi$, the previous tracks are used, allowing neutrons to travel in the opposite direction.

For reflection cases, we have a separate reflected angle for each boundary of the system – north, south, east, and west.

For two-dimensional cases, the solution to the characteristics form of the transport equation is slightly different from the slab geometry case, since now each characteristic has associated

with it a width, d'_i . The average angular flux through mesh n at angle $(\bar{\varphi}'_i, \bar{\theta}_j)$ is equivalent to the cylindrical geometry case and is calculated by averaging the contribution from all tracks that pass through mesh n at angle i ,

$$\bar{\Phi}_n^g(\bar{\varphi}'_i, \bar{\theta}_j) = \frac{\sum_k \bar{\Phi}_{k,n}^g(\bar{\varphi}'_i, \bar{\theta}_j) \cdot t_{k,n}(\bar{\varphi}'_i, \bar{\theta}_j) \cdot d'_i}{\sum_k t_{k,n}(\bar{\varphi}'_i, \bar{\theta}_j) \cdot d'_i} \quad (494)$$

where the sum over k are the tracks at azimuthal angle $\bar{\varphi}'_i$, polar angle $\bar{\theta}_j$, which pass through mesh n .

As before, the scalar flux is considered flat across mesh n and is given by

$$\begin{aligned} \phi_n^g &= \sum_j \sum_i \bar{\Phi}_n^g(\bar{\varphi}'_i, \bar{\theta}_j) \cdot \omega_i \cdot \omega_j \\ \phi_n^g &= \frac{q_n^g}{4\pi \sum_{tr,n}^g} + \sum_j \sum_i \frac{\sum_k \frac{\Delta_{k,n}^g(\bar{\varphi}'_i, \bar{\theta}_j)}{\sum_{tr,n}^g \cdot t_{k,n}(\bar{\varphi}'_i, \bar{\theta}_j)} \cdot t_{k,n}(\bar{\varphi}'_i, \bar{\theta}_j) \cdot d'_i}{\sum_k t_{k,n}(\bar{\varphi}'_i, \bar{\theta}_j) \cdot d'_i} \cdot \omega_i \cdot \omega_j \\ \phi_n^g &= \frac{q_n^g}{4\pi \sum_{tr,n}^g} + \frac{1}{\sum_{tr,n}^g} \sum_j \sum_i \sum_k \frac{\Delta_{k,n}^g(\bar{\varphi}'_i, \bar{\theta}_j)}{t_{k,n}(\bar{\varphi}'_i, \bar{\theta}_j)} \cdot \omega_i \cdot \omega_j \end{aligned} \quad (495)$$

where the expression for the average angular flux along track segment k , crossing mesh n , in azimuthal direction $\bar{\varphi}'_i$, polar direction $\bar{\theta}_j$, represented by the variable $\bar{\Phi}_{k,n}^g(\bar{\varphi}'_i, \bar{\theta}_j)$, has been expanded using (406).

As with the cylindrical geometry calculation, each track length should be ratioed with the quotient of the approximated-to-true area of the mesh being subtended by the characteristic. This leads to an expression equivalent to (482),

$$t'_{k,n}(\bar{\varphi}'_i, \bar{\theta}_j) = t_{k,n}(\bar{\varphi}'_i, \bar{\theta}_j) \cdot \frac{A_{\text{approx}}}{A_{\text{true}}} \quad (496)$$

This, in turn, leads to an expression for the scalar flux equivalent to (487),

$$\phi_n^g = \frac{q_n^g}{4\pi \sum_{tr,n}^g} + \frac{1}{\sum_{tr,n}^g \cdot A_{\text{true},n}} \sum_j \sum_i \omega_i \cdot \omega_j \cdot d_i \cdot \sin \bar{\theta}_j \cdot \sum_k \Delta_{k,n}^g(\bar{\varphi}'_i, \bar{\theta}_j) \quad (497)$$

where

$$\Delta_{k,n}^g = \Phi_{k,n}^g(s=0) - \Phi_{k,n}^g(s=t'_{k,n}), \text{ in direction } \bar{\varphi}'_i, \bar{\theta}_j \quad (498)$$

The angular fluxes are calculated along each characteristic in the same manner as before,

$$\begin{aligned} \Phi_{\text{out},k,n}^g(\bar{\varphi}'_i, \bar{\theta}_j) &= \Phi_{\text{in},k,n}^g(\bar{\varphi}'_i, \bar{\theta}_j) \cdot \exp\{-\sum_{tr,n}^g \cdot t'_{k,n}(\bar{\varphi}'_i, \bar{\theta}_j)\} \\ &+ \frac{q_n^g}{4\pi \sum_{tr,n}^g} \left[1 - \exp\{-\sum_{tr,n}^g \cdot t'_{k,n}(\bar{\varphi}'_i, \bar{\theta}_j)\} \right] \end{aligned} \quad (499)$$

The main difference between the slab geometry calculation and the two-dimensional calculation is that, in slab geometry, there was one characteristic per azimuthal angle and each characteristic passed through all regions of the problem. In two-dimensions, there are many characteristics per azimuthal angle (the k subscript in the summations) and no single characteristic passes through all regions of the problem. We must, therefore, keep track of the region through which each characteristic, k , in azimuthal direction i , passes.


5.8 Mesh Subdivisions for Two-Dimensional Problems

The ray-tracing routine is the most complex module associated with the MoC. Ray tracing, itself, is not all that complicated. However, the calculation of true areas for all the complicated mesh shapes requires a great effort and is fairly cumbersome to implement. The true area of each mesh is required to accurately solve (496) and (497). Alternatively, one could make the assumption that enough ray-tracing detail will be used that the approximated area will be close enough to the true area to remove the need to ratio the track lengths. Such an assumption would simplify the ray-tracing module significantly, hopefully without overly penalizing the accuracy of the solution.

There are different approaches to ray tracing. The details that will be described in this section are based on the approach used in CASMO-4 and LANCER02. This approach has been shown to be extremely advantageous, in terms of execution speed. It uses predefined cell types that are commonly found in all LWR lattice designs and is preferred because it simplifies the calculation of true mesh areas. Alternative approaches include generalized geometry routines, such as those routinely used in Monte Carlo codes, and factorial geometry, such as that used in AEGIS. For such routines, the calculation of true mesh areas can become complicated and the correction in (496) might need to be abandoned. The other benefit of using predefined cell types is that meshing can be predetermined by the programmer and, therefore, is guaranteed to be adequate. For generalized ray-tracing routines, the meshing is typically left to the user, who may or may not have an adequate feel for the meshing needs of the problem being solved. The accuracy of the MoC depends on the size of the flat source mesh – especially those used in the thermal energy range – so inadequate meshing can produce misleading results. The interested reader is directed to refer Jevremovic et al. (2001), Yamamoto et al. (2005), Sugimura et al. (2007), West and Emmet (1980), and Weiss and Ball (1991).

5.8.1 Assigning Material Regions

Before we begin to ray trace, we first define the various material regions of the problem and then split each material region into an adequate number of flat source/flat flux mesh. The materials are the broad-group macroscopic cross section sets from the condensation scheme (if one exists).

To do this, we must first assign *cell* numbers to the problem. We define a *cell* to be a large region of the lattice that may contain multiple material regions, such as a whole pin cell or a portion of a control blade that contains one or more absorber pins and sheathing. All *cells* are rectangular, as illustrated in  Fig. 72, and are part of a Cartesian grid. The *cells* are numbered sequentially starting, for example, in the upper left-hand corner of the problem and working across the row and then down the columns. Note that the oversized water rod in the center

1	2	3	4	5	6	7	8	9	10
11	(12)	(13)	(14)	(15)	(16)	(17)	(18)	(19)	20
21	(22)	(23)	(24)	(25)	(26)	(27)	(28)	(29)	30
31	(32)	(33)	(34)	(35)	(36)	(37)	(38)	(39)	40
41	(42)	(43)	(44)	(45)	(46)	(47)	(48)	(49)	50
51	(52)	(53)	(54)	(55)	(56)	(57)	(58)	(59)	60
61	(62)	(63)	(64)	(65)	(66)	(67)	(68)	(69)	70
71	(72)	(73)	(74)	(75)	(76)	(77)	(78)	(79)	80
81	(82)	(83)	(84)	(85)	(86)	(87)	(88)	(89)	90
91	92	93	94	95	96	97	98	99	100

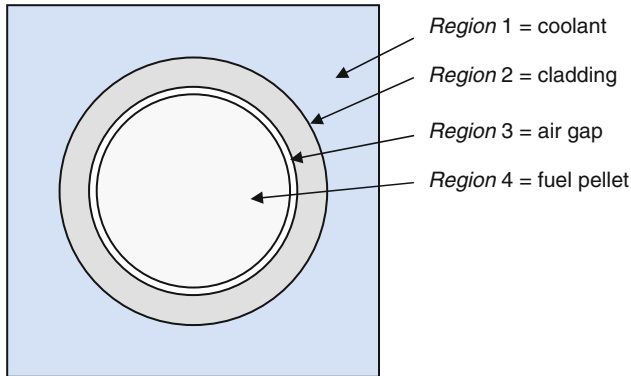
Figure 72
Definition of cells

of the lattice in Fig. 72 has been divided into four *cells* by our Cartesian grid. This will be addressed by four separate ray-tracing routines.

The cell numbers are held by a two-dimensional array, such as “CellNumber(maxx,maxy),” where “maxx” is the number of *cells* along the *x*-axis of our lattice, and “maxy” is the number of *cells* along the *y*-axis of our lattice, which in Fig. 72 would be 10 × 10.

Within each *cell*, there may be multiple material *regions*, each one representing a different material type. For instance, within a pin *cell*, there is a coolant *region*, a cladding *region*, possibly an air gap *region* between the fuel pellet and the cladding, and a fuel pellet *region*. If the fuel pellet contains Gadolinium, there may be multiple pellet *regions* defined in order to accurately model the spatial self-shielding nature of the Gadolinium. Each of the pellet *regions* is its own unique material type. The *regions* within a *cell* can be thought of as levels in our lattice physics code, where the base level is the outermost material in the *cell* and you add levels as you move further into the *cell*. This is illustrated for a simple pin *cell* in Fig. 73, where the coolant material forms the base *region* and the *region* numbers (i.e., levels) increase as the cylinders become smaller.

From a programming point of view, we would represent this using a two-dimensional array. For instance, we may define material sets for each *region* of each *cell* using an array



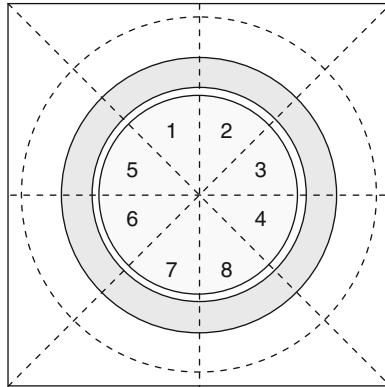
■ **Figure 73**
Definition of regions within a cell

such as “MaterialPerRegion(regions,cells).” Then we would need a one-dimensional array that described the number of *regions* per *cell*, such as “RegionsPerCell(cells).” The value of “cells” in the two arrays would come from our “CellNumber(maxx,maxy)” variable.

5.8.2 Meshing

Each *cell* in the problem needs to be broken into a number of *mesh* that are small enough to accurately represent the source and the flux as being perfectly flat within the *mesh*. In an LWR lattice, the *regions* within each *cell* are usually small enough to accurately be used as flat source *mesh* without further subdivision for neutron energies in the epithermal and fast range. That is, for neutron energies above roughly 2 eV, the cross sections are small enough and consistent enough from one material region to the next to use a *mesh* such as that illustrated in ► Fig. 72 to represent the flux and the source as being perfectly flat. In the thermal energy range below 2 eV, though, some cross sections can be very large indeed and the size of the cross sections may vary wildly from one material region to the next. This is especially true for regions containing strong thermal absorbers, such as the B4C or hafnium absorber pins in a control blade, or fuel pellets containing Gadolinium. In such cases, the flux will change rapidly across a material *region* and the material *region* will need to be subdivided into much smaller *mesh* in order to produce an accurate solution to the characteristics equation.

During the initial development of CASMO-4 (early 1990s), computer memory was at a premium and it was necessary to devise clever schemes to save memory wherever possible. One way of minimizing the memory required by the MoC solution was by using two separate mesh – a coarse mesh for all energy groups above 2 eV, and a fine mesh for all energy groups below 2 eV. This was acceptable for all lattice calculations except BWRs containing a cruciform control blade in one corner of the problem. For those cases, it was necessary to apply the fine mesh to all energy groups in order to properly model the steep flux gradient across the bundle that was created by the presence of the control blade. The use of the dual mesh system allowed the MoC to be applied on machines with small memory, but at a price. Accuracy – primarily at cold



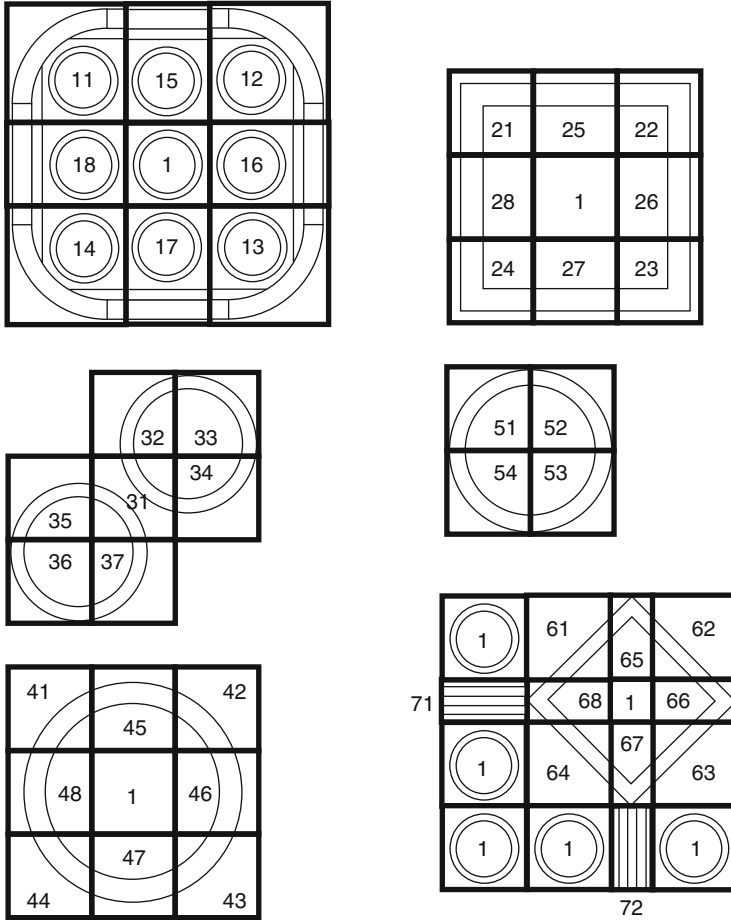
■ **Figure 74**
Example of *mesh* ordering

conditions – was somewhat compromised. Also, since the mesh changed for different energy groups, there had to be a way of superimposing the fine mesh onto the coarse mesh and vice versa. This complicated bookkeeping within the code. Today, memory is plentiful and there is no need to micro-manage memory on a scale like that, so the fine mesh is always used for all energy groups. This makes bookkeeping within the code much simpler.

➤ *Figure 74* contains an example of a pin cell that has been subdivided into octants of equal areas. The cell has been subdivided in this way because it lends itself to an easy calculation of true areas for each *mesh*. The figure contains an example of a numbering scheme used for the *mesh* layout. Any numbering scheme is valid – the important point being that a consistent scheme exists that allows the ray-tracing routine to determine the *mesh* through which the characteristic passes. In this scheme, we might have a three-dimensional array to hold the flux or area of each mesh, such as “MeshArea(mesh,regions,cells).”

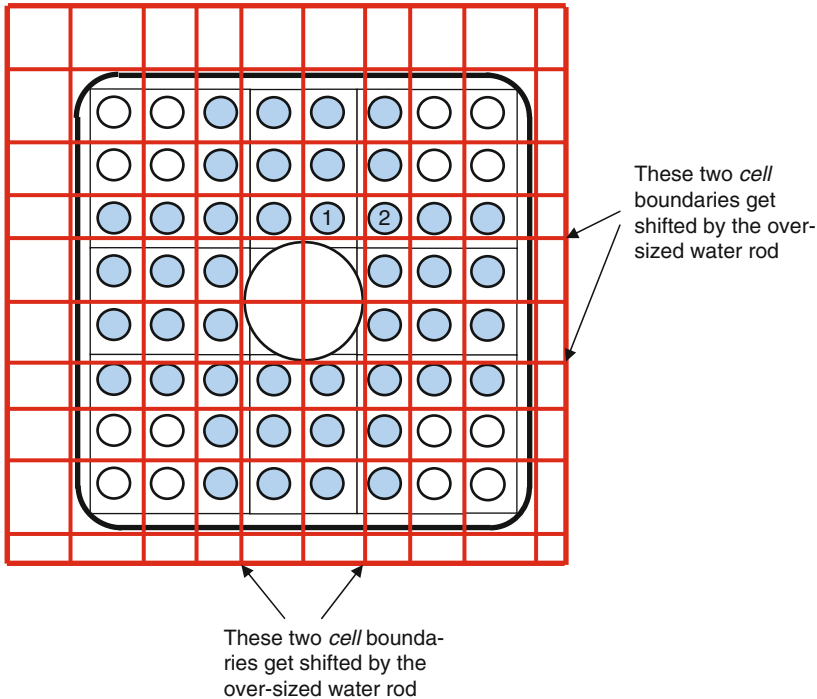
5.8.3 Defining Various Cell Types

The different types of *cells* are distinguished by their contents. ➤ *Figure 75* contains examples of some of the *cells* that might be defined internally by the MoC ray-tracing module. The most common *cell* found in a typical problem is a square or rectangular cell that may or may not contain imbedded cylinders. The origin of the imbedded annular cylinders is typically centered in the cell, although this is not necessarily a requirement and is sometimes modified by the code internally, as will be explained later in this section. Other *cells* may contain imbedded slabs at different angles. A collection of *cells* can be created to handle pins along the edge of the bundle that abut the channel shroud of a BWR. Unique *cells* exist along each different face of the channel and in each corner of the channel. The corner *cells* are created to handle the specific intricacies of the rounded channel corners and the thick–thin nature of channel walls on modern BWR assembly designs. Additional *cells* can be created to handle the oversized water rods and water boxes found in designs from the various fuel vendors.



■ Figure 75
Examples of different type of cells

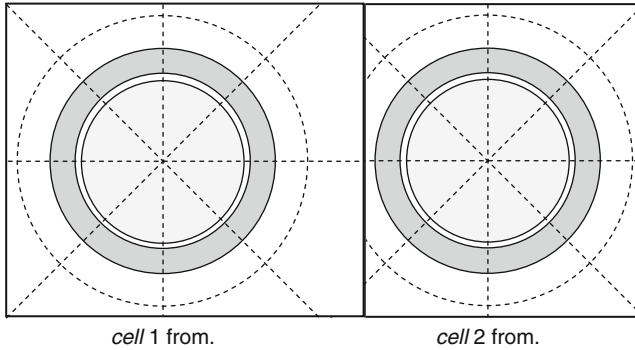
For such a scheme, we should define a two-dimensional array to carry the type of each *cell* in the lattice, such as “CellType(maxx,maxy).” For each *cell* type, we create a unique ray-tracing routine that is specific for the contents of that *cell*, that is, imbedded cylinders, or orthogonal slabs, or whatever. Then, for any characteristic we trace across the geometry of the problem, we will know what type of *cell* we are traversing at any point in the lattice and we will enter the appropriate ray-tracing routine, which has been written specifically for the type of geometry contained within the *cell*. If the lattice physics code is being developed for a specific application, such as analyzing BWR or PWR fuel designs, this is the preferred approach, in terms of execution speed and ease of use. The major drawback is that the code requires modifications if a new geometry is introduced into a fuel design. But that rarely happens. The different geometries that exist in fuel designs today have remained unchanged for decades.



■ **Figure 76**
Modifying cell boundaries to accommodate oversized rods

For most LWR applications, the MoC ray-tracing routine can be limited to dealing with imbedded cylinders that have a common origin within the cell of interest. A special exception to this rule-of-thumb is made for some legacy BWR fuel designs that contained water rods whose center of origin was located in a neighboring cell. This situation is illustrated in [▶ Fig. 75](#) as cell types 31 through 37, where the two water rods were centered in cells 33 and 36, respectively, and cell 31 contained contributions from each. But for most cells, the physical dimensions of the rod can safely be prohibited from crossing the cell boundaries. For bundles containing water rods that occupy multiple cell locations, for example, cells 51 through 54 in [▶ Fig. 75](#), the MoC ray-tracing routine can be written to modify the Cartesian grid boundaries in such a way that the water rods fit entirely within four cells. When this happens, the pins in rows of cells neighboring the water rod will be shifted from their cell centers and the cells themselves will be modified from a square to a rectangular shape, as illustrated in [▶ Fig. 76](#). In the figure, all pins shaded in blue are those whose origins have been shifted from the center of the cell by the new grid boundaries.

[▶ Figure 77](#) contains details of two cells taken from [▶ Fig. 76](#). These are the two cells labeled “1” and “2” in [▶ Fig. 76](#). Both cells have had a grid boundary adjusted by the presence of the oversized water rod in the center of the lattice. Cell “1” has had its east boundary moved further to the east, increasing the area of the cell. Cell “2” has had its west boundary moved to the east, reducing the area of the cell. Mesh subdivisions are always centered in the



■ **Figure 77**
Mesh subdivisions centered in annular regions

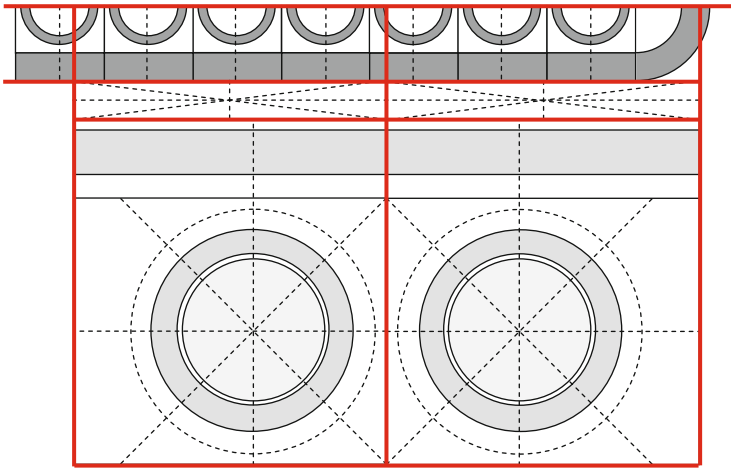
middle of the annular cylinders. This is done to simplify the ray-tracing logic. Unfortunately, this action results in somewhat uncommon mesh shapes and complicates the calculation of the true area of some mesh subdivisions. In contrast, if no imbedded annular cylinders exist in the mesh, the azimuthal subdivisions can be drawn between diagonal corners of the mesh. Note that annular *mesh* subdivisions are allowed to intersect with the *cell* boundaries, whereas annular *material boundaries* are not allowed to intersect with the *cell* boundaries. The coding must be capable of distinguishing between *mesh boundaries* and *material boundaries* when imposing this limitation.

5.8.4 Meshing of Control Blade Cells

The presence of the control blade presents its own challenge, in terms of the *cells* that are created by the Cartesian grid, not only for the ray tracing, but especially for the calculation of the true area for each mesh subdivision in the control blade. In essence, the same Cartesian grid as that illustrated in ► [Fig. 76](#) is placed over the geometry of the bundle with or without the control blade being present. In instances when the control blade is present, the interior of some of the *cells* take on more complicated geometries, as illustrated in ► [Fig. 78](#). Each *cell* of the control blade will contain multiple absorber tubes and it is possible that each absorber tube can be made up of a unique material (B₄C, Hafnium, etc.). The Cartesian grid boundaries can intersect the control blade at any point, which complicates the calculation of the true areas of the mesh subdivisions in each *cell*.

5.8.5 Final Mesh Layout

The final geometry layout consists of a mesh that resembles that illustrated in ► [Figs. 77](#) and [78](#). That is, the fine mesh are very small and are used to model the steep flux gradients present primarily in the thermal energy groups. The mesh layout for a typical BWR assembly is illustrated in ► [Fig. 79](#). The lavender colored pins in the figure represent pellets containing Gd₂O₃.



■ **Figure 78**
An example of control blade cells

For such locations, the pellets will be subdivided annularly into multiple concentric rings. Each ring in the pellet is represented by a set of unique material cross sections. This allows for an accurate modeling of the Gadolinium radial depletion rate.

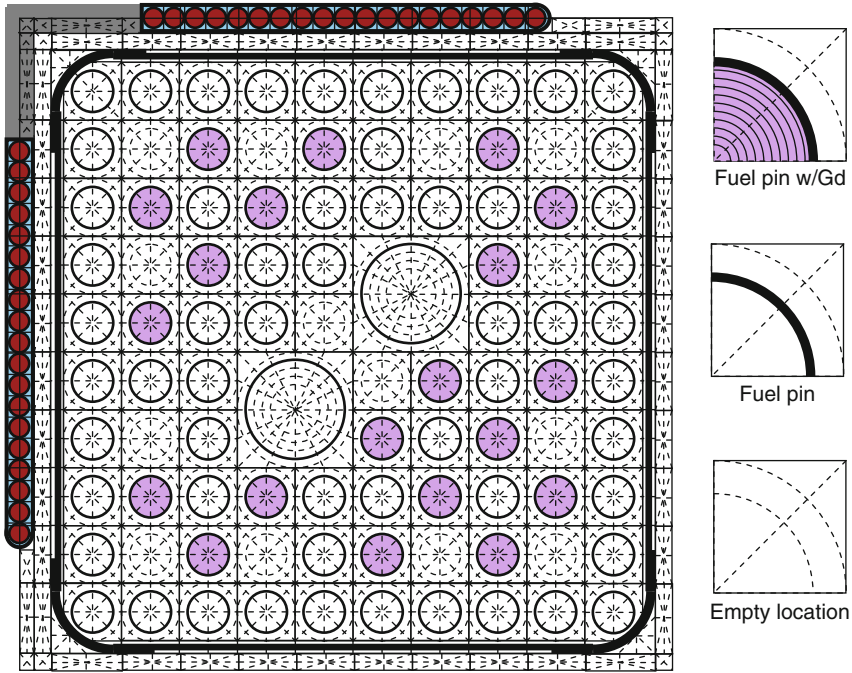
For a typical modern fuel design, the fine-mesh layout will contain approximately 5,000 flat source/flat flux mesh. The water gaps should be subdivided vertically and horizontally such that no gap mesh is wider than 0.5 cm. After the outer gaps have been subdivided, additional azimuthal mesh should be applied to further subdivide each gap mesh into octants, as illustrated in ► [Fig. 79](#). Large water rods should be subdivided annularly into smaller fine-mesh sizes to better model thermal flux gradients across the rod.

5.9 Two-Dimensional Ray Tracing

5.9.1 The Cyclic Tracking Approach

Once the problem has been segmented into various *cell* types, the MoC routine is ready to begin ray tracing across the problem. Ray tracing takes place only for the azimuthal directions of motion. The resulting track lengths are raised out of the plane of the problem to each of the various polar angles and the track lengths are adjusted accordingly. For any given azimuthal angle of motion, $\overline{\varphi}'_i$, the ray-tracing routine will first determine the number of characteristics that begin along the x -axis and the y -axis and will then determine the coordinates of the origin of each characteristics. The separation of the characteristics along the x and y axes is calculated as

$$\delta x_i = \frac{d_i}{|\sin \overline{\varphi}'_i|} \quad (500)$$



■ **Figure 79**
 Typical *mesh* layout for a BWR assembly calculation

and

$$\delta y_i = \frac{d_i}{|\cos \bar{\varphi}_i|} \quad (501)$$

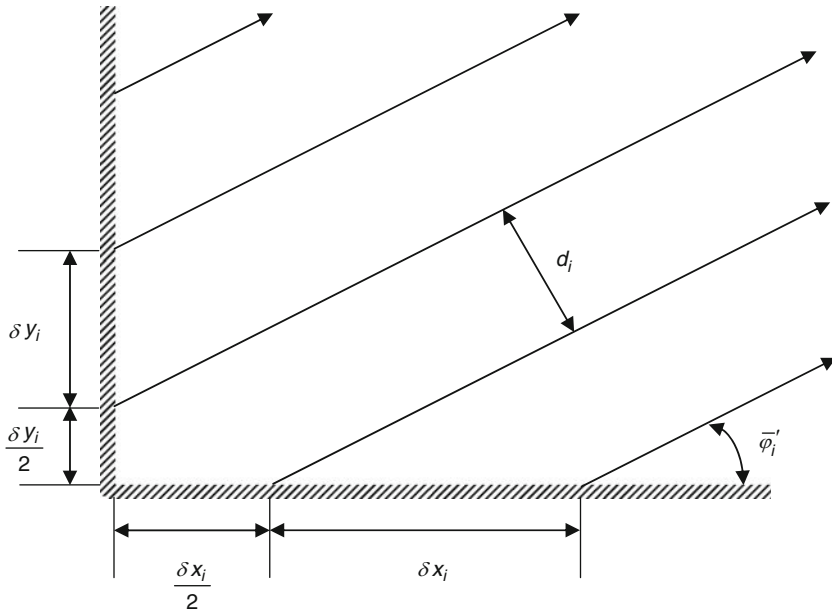
as illustrated in ► [Fig. 80](#).

As described in ► [5.7](#), the azimuthal angle has been slightly modified to ensure that each characteristic aligns with its reflective counterpart along each boundary of the problem, and the separation between parallel characteristics has been slightly adjusted to ensure that there are a perfect integral number of characteristics covering the problem geometry. To avoid a characteristic originating in a corner of the problem, the entire set of characteristics is centered along the axes. This results in the first characteristic along each axis being shifted by an amount equal to half the separation distance along that particular axis,

$$\delta x_{i,0} = \frac{\delta x_i}{2} \quad (502)$$

and

$$\delta y_{i,0} = \frac{\delta y_i}{2} \quad (503)$$



■ Figure 80
Origin of each characteristic at a given angle

Once the origin of each track is determined, the code may begin to trace the characteristics across the geometry of the problem. The module first determines the *cell* being crossed by the characteristic. Based on the specific *cell* type, the module will enter the appropriate ray-tracing routine and proceed to determine all intersections of *mesh* lines with the crossing characteristic. The basic principles of each ray-tracing routine are illustrated in ► Fig. 81.

Within any *cell* containing imbedded cylinders, the origin of the *cell* is placed at the center of the annular rings. The fine-*mesh* subdivisions are also centered in the middle of the annular cylinders. This simplifies the ray-tracing routine for *cells* that contain imbedded cylinders whose origin is not located in the center of the *cell*. The entrance point to the *cell*, (x_{in}, y_{in}) , is known either from the exit point from the neighboring *cell*, or from the origin of the characteristic along one of the outer problem boundaries. The width of the *cell* in the x and y directions is also known, x_{dim} and y_{dim} , respectively. The total length of the characteristic across the *cell* can then be calculated as

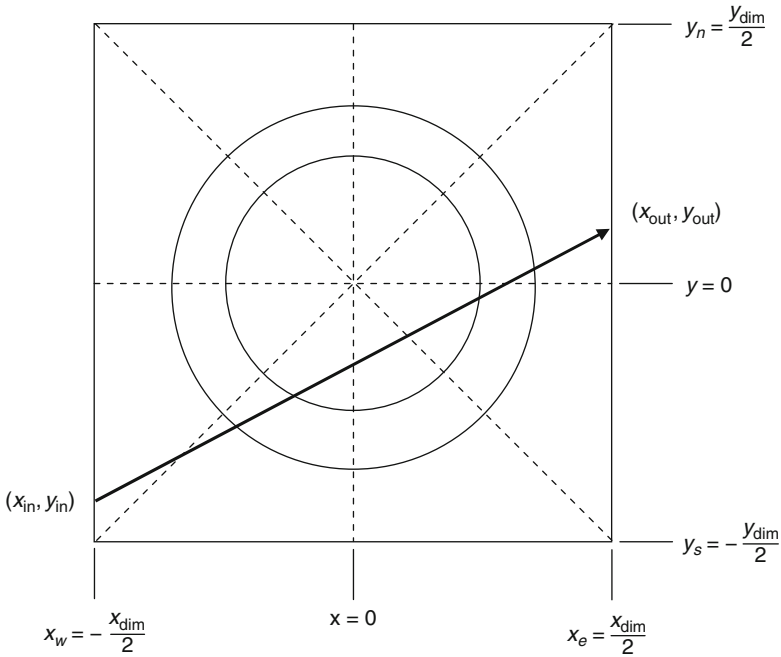
$$l = \frac{x_e - x_{in}}{\cos \bar{\varphi}'_i}, \quad \text{if } \bar{\varphi}'_i < \pi/2 \quad (504)$$

or

$$l = \frac{x_w - x_{in}}{\cos \bar{\varphi}'_i}, \quad \text{if } \bar{\varphi}'_i > \pi/2 \quad (505)$$

The exiting point of the characteristic along the y -axis is calculated as

$$y_{out} = y_{in} + l \cdot \sin \bar{\varphi}'_i \quad (506)$$



■ **Figure 81**
Intersections of *mesh* with a passing characteristic

If y_{out} is determined to lie outside the boundaries of the *cell*, then the track length is recalculated as

$$l = \frac{y_n - y_{\text{in}}}{\sin \bar{\varphi}'_i} \quad (507)$$

y_{out} is then equal to y_n and x_{out} is calculated as

$$x_{\text{out}} = x_{\text{in}} + l \cdot \cos \bar{\varphi}'_i \quad (508)$$

The ray-tracing routine keeps track of the surface of the *cell* that is crossed when the characteristic enters and exits the *cell*. This information is later used during the coarse mesh rebalance acceleration scheme, described later in this section.

Once the entrance and exit points are known, all intersections within the *cell* may be determined. This is done by equating the equation of the line for the characteristic with the equation of the line/arc for each *mesh* or material *region* in the *cell*. The equation of the line for the characteristic is expressed as

$$y = m_c x + b_c \quad (509)$$

where m_c is the slope of the line of the characteristic, calculated as $\tan \bar{\varphi}'_i$; and b_c is the point at which the characteristic intersects the y -axis, as illustrated in ► [Fig. 82](#).

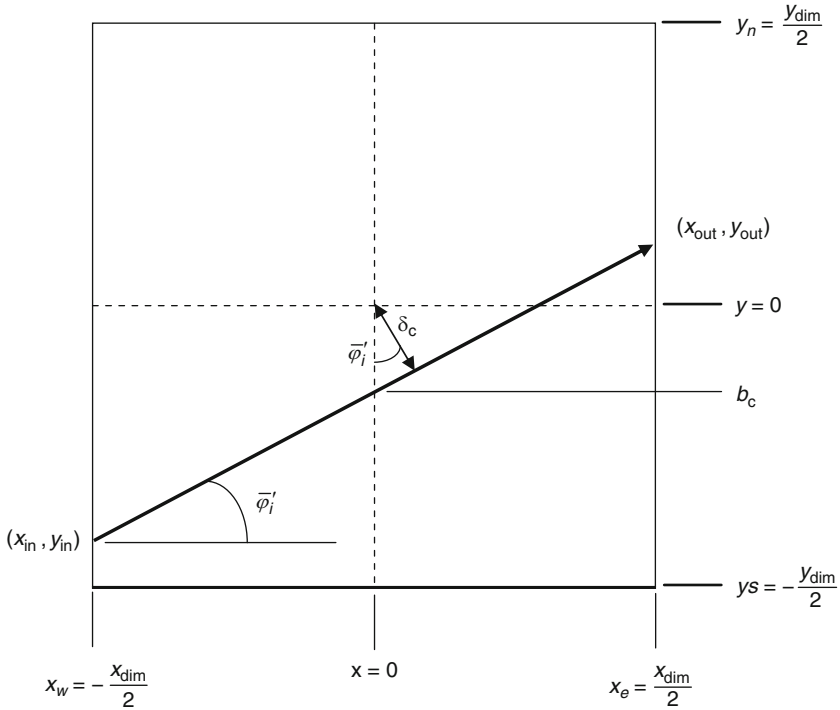


Figure 82
Variables associated with the equation of the characteristic

The y -axis intercept is calculated as

$$b_c = y_{in} - (x_{in} \cdot \tan \bar{\varphi}'_i) \quad (510)$$

And the closest the characteristic approaches to the origin of the *cell* is

$$\delta_c = |b_c \cdot \cos \bar{\varphi}'_i| \quad (511)$$

The equation for any annular cylinder in the *cell* is given by

$$r_{cyl}^2 = x^2 + y^2 \quad (512)$$

or

$$y = \sqrt{r_{cyl}^2 - x^2} \quad (513)$$

Equating (513) with (509) produces the two values for the x -intercept of the characteristic with the cylinder,

$$x = \frac{-m_c b_c \pm \sqrt{m_c^2 r_{cyl}^2 + r_{cyl}^2 - b_c^2}}{m_c^2 + 1} \quad (514)$$

The corresponding y -intercept values can be obtained by plugging the x -intercept values into (513) or (509). These intercepts are only calculated if $\delta_c < r_{\text{cyl}}$, otherwise, the characteristic cannot cross the boundary of the cylinder. After determining the coordinate intercepts of the characteristic with the cylinder, the routine checks to make sure that the intercepts lie within the *cell* boundaries. This is necessary because the cylindrical *fine-mesh* subdivision in the coolant is allowed to cross the *cell* boundaries.

Similar logic is used to determine the intercept of the characteristic with a slab imbedded in a *cell*. Slabs are typically vertical or horizontal and the equation of the line representing the slab is then of the form

$$x = \text{const} \quad (515)$$

or

$$y = \text{const} \quad (516)$$

The constants that represent the equation of the line for the various vertical slabs may be plugged directly into (509) to determine the corresponding y -intercepts. For horizontal slabs, (509) is rearranged prior to plugging in the constants and is subsequently solved for the corresponding x -intercept. After determining the intercepts, the routine checks to make sure the intercepts lie within the *cell* boundaries. If not, the characteristic cannot cross the slab within the *cell* and the intercepts are discarded. Intersections of the characteristic with the *fine-mesh* subdivisions are determined in a similar manner.

The number of intersections resulting from ray tracing over a typical LWR lattice is usually on the order of one million. That is, we will end up having to solve the transport equation approximately one million times for each inner iteration we perform. Even on today's computers, this is a rather daunting task. The solution to our problem will go much faster if we hold the ray-tracing results in tightly packed one-dimensional arrays. In the early days, this was also necessary in order to manage memory properly. However, that is no longer a consideration for single assembly calculations.

In any event, we wish to hold the ray-tracing data in tightly packed, one-dimensional arrays. One way to do this is to simply allocate enough space that we could not possibly surpass it. That is, we could allocate an array, such as "TrackLengths(2000000)." A more economical approach is the one taken in CASMO-4 and LANCER02. In this approach, the ray-tracing routine is entered twice in a row. The first time the routine is entered, none of the information is retained except for the total number of track lengths traced. Using this one value, all ray-tracing arrays are dimensioned to the minimum size needed and the ray-tracing routine is entered for the second time. The second time through, all information is retained.

From the ray-tracing routine, we need only save: the track lengths; the *mesh*, *region*, and *cell* through which each track passes; and the *cell* surface across which each track crosses (if, indeed, it does cross a *cell* surface). The last bit of information is used for the acceleration scheme.

Once we have the tracking information, our best approach is to calculate all mean free paths in all energy groups and hold them in memory in preparation for the iteration scheme. That is, we calculate the following portion of (499):

$$\exp \left\{ -\Sigma_{tr,n}^g \cdot t'_{k,n} (\bar{\varphi}'_i) / \sin \bar{\theta}_j \right\} \quad (517)$$

If there are one million track segments, three polar angles of motion in the quadrature set, and 20 energy groups, the entire size of the array needed to hold (517) will be 60 million words, or

240 Mb. A sizeable amount of memory, but worth every bit of it (pun intended) based on the amount of execution time it saves during the iteration process. The alternative is to evaluate the exponential for every track segment in the problem, for every iteration we perform. This is a very expensive proposition, in terms of computation time.

To employ (517), (499) should be rearranged in a simplified form

$$\Phi_{k,n,\text{out}}^g(\bar{\varphi}'_i, \bar{\theta}_j) = \hat{Q}_n^g + \exp[-\Sigma_{tr,n}^g \tau_{k,n}(\bar{\varphi}'_i, \bar{\theta}_j)] \cdot (\Phi_{k,n,\text{in}}^g(\bar{\varphi}'_i, \bar{\theta}_j) - \hat{Q}_n^g) \quad (518)$$


where $\tau_{k,n}(\bar{\varphi}'_i, \bar{\theta}_j) = t'_{k,n}(\bar{\varphi}'_i) / \sin \bar{\theta}_j$ is the modified track length after being lifted out of the xy -plane of the problem to the appropriate polar angle; and $\hat{Q}_n^g = q_n^g / 4\pi \Sigma_{tr,n}^g$ is the term containing the angular source. The scalar source term concealed in (518) is expressed as

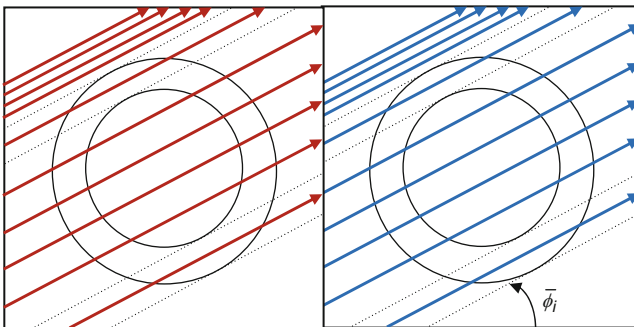
$$q_n^g = \sum_{g'} \left(\Sigma_{s,n}^{g' \rightarrow g} + \frac{\Sigma_{p,n}^{g' \rightarrow g}}{k^\infty} \right) \phi_n^{g'} \quad (519)$$

where the production cross section is defined as $\Sigma_{p,n}^{g' \rightarrow g} = \chi_n^g \sum_{g'} \nu \Sigma_{f,n}^{g'}$.

The scalar flux in (519) – for any given *mesh*, n – is obtained using (497).

5.9.2 The Macro-Band Approach

In the cyclic tracking approach, all characteristics were traced across the entire width of the problem and the end of each characteristic aligned precisely with the beginning of its reflective counterpart along the problem boundaries. An alternative approach to the cyclic tracking method is to employ a macro-band method. In this method, ray tracing takes place on an individual *cell* basis only and characteristics are not forced to align along the boundaries of each *cell*. Instead, angular fluxes at the beginning of a track segment are inferred from the interpolation of the two closest track segments exiting the neighboring *cell*. This is illustrated in  Fig. 83 where the ends of the red characteristics do not align precisely with the beginning of the blue



 **Figure 83**
Macro-bands and characteristics

characteristics. To get the value of the angular flux entering a *cell*, the angular flux exiting the neighboring *cell* is linearly interpolated.

The macro-bands are the dotted lines in the pin cells in [▶ Fig. 83](#). They bound the singularities that arise from the intercept of the mesh in the *cell* with the characteristic at angle $\bar{\varphi}_i$. The macro-bands ensure that no characteristic ever passes through a singularity. In our cyclic tracking routine, this was ensured by continuously nudging the track away from a local singularity. We want to avoid singularities because, in such cases, it is unclear which mesh is being intersected. By nudging the characteristic in one direction or another, we force the track to pass through one of the multiple mesh that are part of the singularity.

In the macro-band method, which was first implemented commercially in the HELIOS CCCP method, characteristics are distributed evenly between macro-bands. If desired, characteristics can take on different spacing between different macro-bands, as illustrated in the figure. In subsequent implementations of the concept, such as in the AEGIS lattice physics code, the bands are distributed according to a Gauss–Legendre quadrature set, which improves the accuracy of integration (Yamamoto et al. 2005).

The macro-band method is superior to the cyclic tracking method at treating singularities, but at the price of having to estimate the angular flux at the cell boundaries. Either ray-tracing approach is perfectly adequate for an LWR lattice physics code. The choice is up to the programmer’s own preference.

5.10 Quadrature Sets for Two-Dimensional LWR Lattice Calculations

5.10.1 Quadratures for Modeling Polar Motion

The quadrature sets described previously in this section were based on simple formulas that either forced all weights to be equal, or forced all angle increments to be equal. These types of quadratures serve as very good examples for developing the theory of the MoC, but are rather inefficient when used to represent neutron streaming out of the plane of the problem, resulting in the need to model many angles of motion in order to arrive at an accurate solution to the transport equation. The integration can be performed much more efficiently with the use of other quadrature sets that will be discussed in this section.

The use of a Legendre quadrature set is far more efficient for two-dimensional transport problems than either the equal weights or equal angles quadrature sets described in [▶ 5.3.3](#). An adequate set of Legendre quadratures are given in [▶ Table 18](#) (Lewis and Miller 1984). There are six separate Legendre quadratures contained in the table from which to choose. For the majority of production analyses, the $N = 6$ quadrature set should be sufficient. This set of angles and weights models neutron motion out of the plane of the problem in three unique polar directions. Solutions using the $N = 6$ quadrature set are virtually saturated and there is little measurable improvement in results by going to a quadrature set that contains more polar directions of motion. The μ values in [▶ Table 18](#) represent the cosine of the polar angle of motion, that is, $\mu_j = \cos \theta_j$. For problems containing mixed-oxide pellets, more polar angles are usually needed in order to account for changes in the flux out of the plane of the problem due to the much larger thermal absorption cross sections.

An even more efficient set of angles and weights can be obtained by minimizing the error involved in numerically integrating the Bickley functions of the collision probability method.

Table 18

Legendre quadratures for modeling polar motion

$P_N(\mu_j)$	j	$\pm\mu_j$	ω_j
$N = 2$	1	0.57735 02691	1.00000 00000
$N = 4$	1	0.33998 10435	0.65214 51549
	2	0.86113 63115	0.34785 48451
$N = 6$	1	0.23861 91860	0.46791 39346
	2	0.66120 93864	0.36076 15730
	3	0.93246 95142	0.17132 44924
$N = 8$	1	0.18343 46424	0.36268 37834
	2	0.52553 24099	0.31370 66459
	3	0.79666 64774	0.22238 10344
	4	0.96028 98564	0.10122 85363
$N = 10$	1	0.14887 43387	0.29552 42247
	2	0.43339 53941	0.26926 67193
	3	0.67940 95682	0.21908 63625
	4	0.86506 33666	0.14945 13492
	5	0.97390 65285	0.06667 13443
$N = 12$	1	0.12523 34085	0.24914 70458
	2	0.36783 14989	0.23349 25365
	3	0.58731 79542	0.20316 74267
	4	0.76990 26741	0.16007 83286
	5	0.90411 72563	0.10693 93260
	6	0.98156 06342	0.04717 53364

This approach leads to the set of angles and weights contained in [Table 19](#) (Yamamoto et al. 2007). Using this quadrature set, an accurate solution to the transport equation can usually be obtained from $N = 2$ for typical uranium-oxide problems. As with all other quadrature sets, more detail may be necessary for problems containing mixed-oxide pellets. Note that the values in the table are the $\mu_j = \sin \theta_j$, not the $\mu_j = \cos \theta_j$.

Alternative polar angle quadrature sets are available in Leonard and McDaniel (1995) and Sanchez et al. (2002).

5.10.2 Quadratures for Modeling Azimuthal Motion

Azimuthal angles of motion are distributed evenly throughout the plane of the problem. There is really no other reasonable choice for distributing the angles in the azimuthal direction for LWR lattice physics calculations. The same set of angles can be used for all energy groups or different quadratures can be used for different energy ranges. In general, the energy ranges that are of interest in lattice physics problems can be split into three separate distributions. This is

■ **Table 19**
Tabuchi–Yamamoto quadratures for modeling
polar motion

$P_N(\mu_j)$	j	$\pm\mu_j$	ω_j
$N = 2$	1	0.798184	1.000000
$N = 4$	1	0.363900	0.212854
	2	0.899900	0.787146
$N = 6$	1	0.166648	0.046233
	2	0.537707	0.283619
	3	0.932954	0.670148

done in an effort to accurately capture the distinct features of neutron motion as the neutrons lose energy via scattering collisions.

A very large number of angles are required to accurately model neutron motion above 500 keV in order to capture the streaming effect exhibited between isolated fuel pellets. The streaming effect occurs as a result of the neutrons being born in the isolated fuel pellets at very high energies. As the neutrons stream away from the pellets, they suffer very few collisions, and those collisions that do take place tend to result in the neutron losing a substantial amount of energy and slowing down below the 500 keV threshold. Because of this, the angular flux is highly anisotropic and many azimuthal angles are needed in order to properly model the phenomenon. Below the 500 keV threshold, many collisions are taking place in the coolant and, to a lesser extent, in the oxide pellet itself and the angular flux becomes more isotropic such that fewer azimuthal angles are needed to capture the physics of the problem. To produce accurate results, as many as 128 evenly spaced azimuthal angles of motion should be used in all energy groups above 500 keV and 64 evenly spaced azimuthal angles of motion should be used in all energy groups below 500 keV.

In addition to using a different number of directions to model neutron streaming over different energy ranges, a different track spacing between parallel characteristics can be used over different energy ranges. The track spacing is dictated by the variation in cross sections from one material region of the problem to another. Above the up-scatter cut-off point of ~ 2 eV most material cross sections are of a similar size and flux gradients are considered to be relatively mild across the problem. This is true even across the resonance energy range. For energy ranges exhibiting a relatively flat flux profile, the characteristics can be widely spread apart without affecting the accuracy of the solution. As the flux begins to exhibit larger gradients, though, the characteristics must be much closer together in order to accurately capture the physics of the problem. Typical values for track separation are 1 to 2 mm in all groups above the up-scatter cut-off energy of 2 eV and 0.5 to 1 mm in all groups below the up-scatter cut-off energy.

The combination of variations in the number of azimuthal angles and the spacing of parallel characteristics typically produces three separate quadratures for the MoC solution. The three quadrature sets are listed in ▶ [Table 20](#). Note that a single quadrature set can be used, but should include the maximum detail from each of the three sets listed in ▶ [Table 20](#). That is, 128 azimuthal angles, two polar angles, and a characteristic separation of between 0.05 and 0.1 cm.

■ **Table 20**

Typical quadrature sets for different energy ranges

Range	Upper energy	Lower energy	I^\dagger	$J^{\dagger\dagger}$	d_j [cm]
Fast	20 MeV	500 keV	128	2	0.1–0.2
Epithermal	500 keV	2 eV	64	2	0.1–0.2
Thermal	2 eV	10^{-5} eV	64	2	0.05–0.1

[†] Number of azimuthal angles distributed over 2π rad.

^{††} Number of polar angles distributed over $\pi/2$ rad.

This will increase execution time with no improvement in accuracy, but will ease some of the bookkeeping within the code.

5.11 Acceleration Schemes for Two-Dimensional Calculations


The method of characteristics is notoriously slow to converge. Thankfully, this is not much of a problem for lattice physics calculations, for a couple of reasons. First, there exist a couple of sufficient acceleration schemes to speed up convergence. Second, there almost always exists a very good flux guess from which to begin the iteration process for a new calculation. Because of this second reason, the flux is rarely far from a converged solution and the acceleration scheme becomes less important. This is a consequence of the sheer number of state points that must be analyzed by the lattice physics code in order to provide the needed data to the three-dimensional nodal code. Each state point differs little from the previous point analyzed and the flux from one point is an excellent starting guess for the following point.

In this section, we will discuss two very reasonable and easily implemented acceleration schemes for the MoC. Both schemes are equally acceptable for single assembly lattice physics calculation. The CMFD scheme is superior for very large problems that contain multiple assemblies. Such calculations, though, are outside the scope of providing cross section data to three-dimensional nodal codes.

5.11.1 Coarse Mesh Rebalance

Coarse mesh rebalance, discussed in “Spatial acceleration” for one-dimensional slabs, is an adequate scheme for accelerating the spatial convergence rate of the two-dimensional characteristics solution. Once again, we want to solve the balance equation given in (462) and reproduced below,

$$\left[\sum_{m \in n} \Sigma_{r,m}^g \phi_m^g V_m + \sum_{s \in n} J_{\text{out},s,n}^g \right] \cdot f_n^g = \sum_{m \in n} q_m^g V_m + \sum_{s' \in n'} J_{\text{in},s',n'}^g \cdot f_{n'}^g \quad (520)$$

where m represents the *fine mesh* within a *cell*, n ; s represents the surfaces to the *cell*; and s' represents the surfaces to neighboring *cell*, n' . The coarse mesh are the *cells* of the problem, such as those illustrated in  Fig. 72. The solutions to the coupled balance equations are the

f_n^g values – one for each coarse mesh in the problem. Once the f_n^g values are known, the scalar flux can be modified as

$$\phi_m^g = \phi_m^g \cdot f_n^g \quad (521)$$

for all *fine mesh*, m , within *cell* n . The angular flux along the cell boundaries can also be modified,

$$\Phi_{k,i,j,m}^g = \Phi_{k,i,j,m}^g \cdot f_n^g \quad (522)$$

Equation (520) is solved using a red–black iteration scheme, just as was done for the two-dimensional coupling calculation in [Sect. 4](#). All values of f_n^g are initialized to unity to begin the iterations. With these initial values, a sweep is performed across the entire problem, solving the balance equation for the f_n^g values in all red *cells*. Following this, a second sweep is performed across the entire problem, solving the balance equation for the f_n^g values in all black *cells* – using the newly calculated f_n^g values in all red *cells* from the previous sweep. This process continues, un-accelerated, until the f_n^g value in all *cells* converge. The currents in (520) are calculated as

$$J_{\text{out},s,n}^g = \sum_j \sum_i \sum_k \Phi_{k,i,j,m}^g \cdot \omega_i \cdot \omega_j \cdot |\cos \varphi_i \cdot \sin \theta_j| \quad (523)$$

where i is an azimuthal angle; j is a polar angle; and k is a specific characteristic crossing the *cell*. The inward-directed current across a surface is calculated in the same way, but for the opposite azimuthal angles. For instance, along the east face of a *cell*, the outward-directed angles of motion extend from $-\pi/2$ to $\pi/2$, whereas the inward-directed angles of motion extend from $\pi/2$ to $3\pi/2$. Along the west surface to the cell, the situation is exactly the opposite.

The acceleration is performed following each inner iteration. For this acceleration scheme, there should only be one inner iteration performed per energy group. This scheme is not guaranteed to converge, so it is prudent to include a check for oscillations or divergence between applications. It is very rare that the scheme not converge for typical LWR lattice physics calculations. However, for somewhat extreme cases, such as 100% voided coolant cases at hot conditions, it is possible for the scheme to fail. If it appears that the scheme is diverging or oscillating, the scheme can simply be disengaged for the problem and the MoC iterations can continue un-accelerated. A more rigorous formulation can be found in Yamamoto (2005) as applied to generalized geometries, not just LWRs. In Yamamoto (2005), the CMR is applied to accelerate the solution both spectrally and spatially.

5.11.2 Coarse Mesh Finite Difference

A slightly different approach that can be used to accelerate both the spatial and spectral convergence rate simultaneously is the coarse mesh finite difference scheme (CMFD) that has been applied very successfully to nodal iterations (Smith 1983). Here, we are solving the diffusion equation using a diffusion coefficient that preserves the details from the MoC solution. The information needed to apply the CMFD scheme is similar to that needed to apply the CMR.

For lattice physics calculations, the CMFD acceleration technique is applied on a cell basis, just like the CMR technique (Smith and Rhodes 2000; Cho 2002; Joo et al. 2002; Smith and

Rhodes 2002; Clarno 2007). For a given energy group, the contents of a cell are homogenized using the typical formula (we have dropped the broad energy group symbol from the following variables for conciseness)

$$\bar{\Sigma}_{x,I} = \frac{\sum_{i \in I} \Sigma_{x,i} \phi_i V_i}{\bar{\phi}_I V_I} \quad (524)$$

where the average scalar flux in the cell is given by

$$\bar{\phi}_I = \frac{\sum_{i \in I} \phi_i V_i}{V_I} \quad (525)$$

and V_I is just the total volume of the cell.

To solve the diffusion equation, we make reference to the variables depicted in [Fig. 84](#). We want to solve for the flux in a given coarse mesh (i.e., cell), namely $\bar{\psi}_I$. Within each coarse mesh, the diffusion equation is given by

$$\frac{\partial J_I}{\partial u} + \bar{\Sigma}_{r,I} \bar{\psi}_I = S_I \quad (526)$$

where, along the surface of each coarse mesh, the current is defined as

$$J_I = -D_I \frac{\partial \psi(u)}{\partial u} \quad (527)$$

Here, u is the direction either along the x -axis or the y -axis; and $\bar{\Sigma}_{r,I}$ is the removal cross section, $\bar{\Sigma}_{r,I} = \bar{\Sigma}_{tr,I} - \bar{\Sigma}_{s,I}^{g \rightarrow g}$. The total source, S_I , is defined in the usual way (i.e., scatterings plus fissions).

Using the current from our MoC solution, that is, (523), we can define a diffusion coefficient along each surface of each cell that preserves the details from the fine-mesh calculation. For the u_i^+ surface we would have

$$\hat{D}(u_i^+) = -\frac{\hat{J}(u_i^+) + \bar{D}(u_i^+) \{\bar{\phi}_{I+1} - \bar{\phi}_I\}}{\bar{\phi}_{I+1} + \bar{\phi}_I} \quad (528)$$

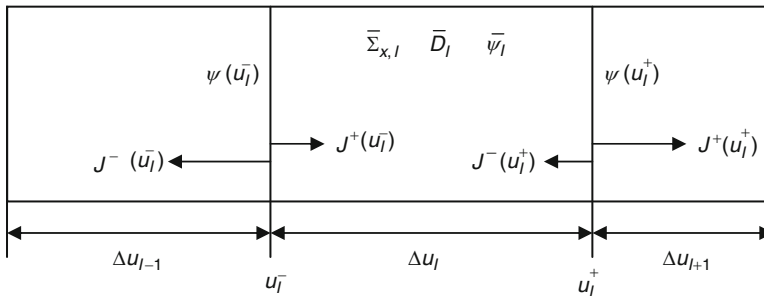


Figure 84
Parameters for the CMFD scheme

where

$$\tilde{D}(u_I^+) = \frac{2\bar{D}_{I+1}\bar{D}_I}{\bar{D}_{I+1}\Delta u_I + \bar{D}_I\Delta u_{I+1}} \quad (529)$$

The current in (528) is the net current from the MoC solution. It is defined as $\hat{J}(u_I^+) = J_{\text{out}}(u_I^+) - J_{\text{in}}(u_I^+)$ along the east surface to the cell, and as $\hat{J}(u_I^-) = J_{\text{in}}(u_I^-) - J_{\text{out}}(u_I^-)$ along the west surface to the cell. That is, it is the net current moving in the positive u direction. The cell-averaged diffusion coefficient is calculated in the usual way, $\bar{D}_I = (3\bar{\Sigma}_{tr,I})^{-1}$. The surface current can be expressed by rearranging (529), to wit,

$$\hat{J}(u_I^+) = -\tilde{D}(u_I^+) \{\bar{\phi}_{I+1} - \bar{\phi}_I\} - \hat{D}(u_I^+) \{\bar{\phi}_{I+1} + \bar{\phi}_I\}.$$

Using these parameters, we solve the diffusion equation for the average flux in each cell,


$$\left\{ \hat{J}(x_I^-) - \hat{J}(x_I^+) \right\} - \left\{ \hat{J}(y_I^-) - \hat{J}(y_I^+) \right\} + \bar{\Sigma}_{r,I} \bar{\psi}_I V_I = S_I V_I \quad (530)$$

$$S_I = S_I^g = \sum_{g' \neq g} \bar{\Sigma}_{s,I}^{g' \rightarrow g} \psi_I^{g'} + \frac{\chi_I^g}{k^\infty} \sum_{g'} \nu \Sigma_{f,I}^{g'} \psi_I^{g'} \quad (531)$$

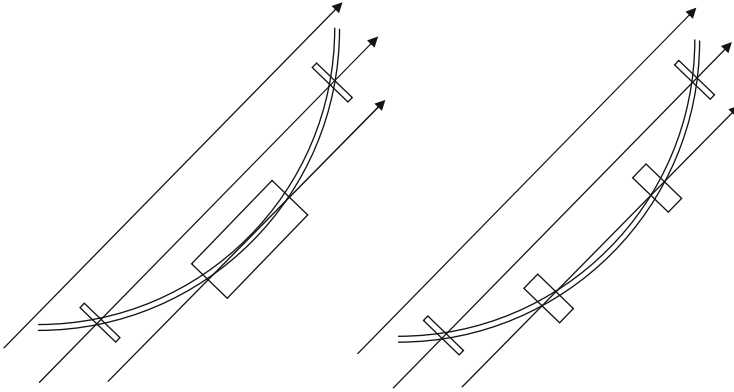
More information on acceleration techniques for the MoC can be found in Yamamoto (2005), Smith and Rhodes (2000), Cho (2002), Joo et al. (2002), Smith and Rhodes (2002), and Clarno (2007).

5.12 Treating Very Thin Cylindrical Regions

One of the few drawbacks with the method of characteristics is in its treatment of very thin, highly absorbing cylindrical regions. Unfortunately, these regions are very common in certain PWR fuel designs, where they arise in the form of a very thin layer of ZrB₂ sprayed onto the outside of fuel pellets as a burnable absorber, referred to as IFBA pellets. The layer is, on average, no thicker than 0.002 cm.

The issue is depicted in  Fig. 85, where three rays are illustrated to bisect the fuel pellet and the absorber coating. The rectangles depicted in the figure represent the area associated with the track lengths that bisect the absorber coating. In the case on the left, the characteristics are arranged in such a way that one of the tracks just happens to skim along the edge of the thin absorber region. In the case on the right, the characteristics are shifted ever so slightly and no track skims the edge of the thin absorber region. Because the region is so strongly absorbent, the solution is very sensitive to the length of track that bisects it and we will get two very different solutions to the situation depicted in the figure. This is highly undesirable. With our cyclic tracking method, the only way to truly avoid this sensitivity is to distribute characteristics with a spacing equal to the width of the region – 0.002 cm – which is out of the question.

An alternative solution to our dilemma is to homogenize the thin coating with the fuel pellet. If we have performed a pin-cell spectral calculation on this pin to generate a spectrum with which to condense cross sections, then we have a good flux distribution to use for the homogenization. Assuming that our flux from the pin-cell spectral calculation is represented



■ **Figure 85**
Characteristics skimming a thin, strongly absorbent region

as ϕ_{fuel}^g in the fuel pellet and ϕ_{absorber}^g in the absorber coating, where g is our fine-group energy structure, we first collapse the individual cross sections using the typical formula

$$\begin{aligned}\Sigma_{x,\text{fuel}}^G &= \frac{\sum_{g \in G} \Sigma_{x,\text{fuel}}^g \phi_{\text{fuel}}^g}{\sum_{g \in G} \phi_{\text{fuel}}^g} \\ \Sigma_{x,\text{absorber}}^G &= \frac{\sum_{g \in G} \Sigma_{x,\text{absorber}}^g \phi_{\text{absorber}}^g}{\sum_{g \in G} \phi_{\text{absorber}}^g}\end{aligned}\quad (532)$$

where G represents the broad-group energy structure. While we are collapsing cross sections, we must also collapse the flux in the two regions since we will need the flux to homogenize the broad-group cross sections of the two regions, to wit,

$$\begin{aligned}\psi_{x,\text{fuel}}^G &= \sum_{g \in G} \phi_{\text{fuel}}^g \\ \psi_{x,\text{absorber}}^G &= \sum_{g \in G} \phi_{\text{absorber}}^g\end{aligned}\quad (533)$$

Now we homogenize the two regions using flux and volume weighting to preserve the reaction rates

$$\bar{\Sigma}_x^G = \frac{\Sigma_{x,\text{fuel}}^G \psi_{\text{fuel}}^G V_{\text{fuel}} + \Sigma_{x,\text{absorber}}^G \psi_{\text{absorber}}^G V_{\text{absorber}}}{\psi_{\text{fuel}}^G V_{\text{fuel}} + \psi_{\text{absorber}}^G V_{\text{absorber}}}\quad (534)$$

After homogenizing the regions, we still want to maintain the true geometry of the pellet and the coating during the MoC solution in order to simplify the bookkeeping in the code. To account for this, the cross sections represented by (534) are applied to both the fuel pellet and the absorber coating.

Following the MoC solution, we must back out the true flux in the absorber coating and the fuel pellet. To do this, we first average the MoC flux in the fuel pellet and the absorber coating using a straightforward volume weighting

$$\bar{\phi}_{\text{fuel}}^G = \frac{\phi_{\text{fuel}}^G V_{\text{fuel}} + \phi_{\text{absorber}}^G V_{\text{absorber}}}{V_{\text{fuel}} + V_{\text{absorber}}} \quad (535)$$

With this average flux, we can superimpose the condensed flux from the pin-cell spectral calculation and obtain the true flux for each region,

$$\begin{aligned} \phi_{\text{fuel}}^G &= \frac{\psi_{\text{fuel}}^G}{\bar{\phi}_{\text{fuel}}^G} \cdot \left\{ \frac{\psi_{\text{fuel}}^G V_{\text{fuel}} + \psi_{\text{absorber}}^G V_{\text{absorber}}}{V_{\text{fuel}} + V_{\text{absorber}}} \right\} \\ \phi_{\text{absorber}}^G &= \frac{\psi_{\text{absorber}}^G}{\bar{\phi}_{\text{fuel}}^G} \cdot \left\{ \frac{\psi_{\text{fuel}}^G V_{\text{fuel}} + \psi_{\text{absorber}}^G V_{\text{absorber}}}{V_{\text{fuel}} + V_{\text{absorber}}} \right\} \end{aligned} \quad (536)$$

This approach works remarkably well to provide consistently accurate results when extremely thin cylindrical regions are present in the fuel design. Alternatively, this entire issue can be avoided by moving to a ray-tracing method based on macro-bands.

5.13 Final Comments

This section has presented a very detailed derivation of the method of characteristics, in its most fundamental, simplistic form. Within this derivation, it was assumed that scattering effects could be treated as being isotropic, with transport-corrected cross sections accounting for the majority of effects caused by anisotropic scattering. When analyzing a single lattice employing perfectly reflective or periodic boundaries, such an assumption is quite adequate – especially for neutron calculations, but even for gamma calculations. If particles are allowed to leak out of the system through the boundaries, though, this assumption may be invalidated.

It was also assumed that the use of a flat flux/flat source approximation was valid and would produce accurate results, so long as the fine-mesh were small enough to capture all flux gradient effects in the thermal groups. Once again, when analyzing a single lattice employing perfectly reflective or periodic boundaries, such an assumption is quite adequate. If multiple bundles are to be analyzed, or if large areas of water are to be included in the problem, such an assumption may be invalidated.

In any case, the fundamental concepts described in this section are contained in many of today's lattice physics codes and an understanding of this section should provide the reader with a reasonably good grasp of current lattice physics transport methods.

It is interesting to note that, in the not too distant past, the fine-mesh transport solution in a lattice physics code accounted for the overwhelming majority of computer resources (memory use and execution time). Back in the day, when it was common – almost necessary – for cross section libraries to be limited to 100 energy groups and 100 different isotopes, and when burnup chains were linearized, the fine-mesh transport solution could easily account for two-thirds of the total execution time, or more. In some current lattice physics codes employing a cross section condensation scheme, the fine-mesh transport solution accounts for less than one-third of the total execution time and is, by no means, limiting on memory requirements. The biggest

burden on computer resources in these lattice physics codes is in constructing the macroscopic scattering matrices from the microscopic data contained in the cross section library. Here, we are referring to the construction of a matrix containing possibly 600×600 elements from as many as 200 isotopes (if the contribution from fission products is included). This has to be done in every fuel region in the lattice. An equal amount of execution time can be spent solving the burnup chains in their matrix form. Like the calculation of the macroscopic scattering matrix, this has to be done in every fuel region of the lattice, which can easily exceed 200 unique regions in a BWR lattice containing 20 or so Gadolinium pins, each split into 10 or 12 multiple depletion rings. These two pieces of the lattice physics code – constructing macroscopic scattering matrices and solving the burnup matrix – can easily account for two-thirds of the total execution time of a modern lattice physics code.

6 Burnup Calculation

6.1 Objective

Nuclear fission is one of the principal mechanisms in the generation of energy from nuclear fuels. The composition of fuels varies during irradiation in a nuclear reactor core. In the vocabulary of reactor physics, the change in fuel composition due to nuclear fission, neutron capture, radioactive decay, and other factors, is referred to as “burnup.” The burnup of a nuclear fuel is different from the conventional concept of burnup, which is based on chemical reactions. Therefore, when uranium “burns” in a nuclear reactor core, there is no emission of CO_2 since the burnup of a nuclear fuel is based on nuclear reactions. While energy is released by changes in the chemical bonding states of materials in conventional burnup, in nuclear burnup, energy is generated by the changes in nuclear binding. If burnup is viewed as a “process of energy generation through changes in a material,” then nuclear fission can quite naturally be considered a burnup phenomenon. In this sense, the technical term burnup seems quite aptly and carefully chosen.

The properties of nuclear fuels depend on the composition of the fuel. The characteristics of the reactor core therefore undergo changes during burnup. In practice, precise prediction of core lifetime and reactor behavior during burnup is an essential part of reactor core analysis. In fact, the prediction accuracy of burnup calculations is a critical factor in the reactor analysis sequence.

In this section, the physics of the burnup of nuclear fuel is discussed. The fundamental theoretical basis for burnup phenomena will first be discussed, and then the major numerical solution schemes for solving the burnup equation will be presented. The burnup behavior of gadolinium, a burnable poison in nuclear fuel, is quite important in actual core analysis, but its behavior is somewhat complicated, requiring special treatment in numerical modeling and calculations. ➤ 6.4 will therefore be devoted to the treatment of gadolinium-bearing fuels. Finally, some discussion will be presented on power normalization, which plays an inevitable role in burnup calculations.

In reactor core analysis, there are two levels of burnup calculation, that is, burnup in lattice physics analysis, and burnup in core analysis. This section focuses on the former, that is, burnup calculation in lattice physics computations.

6.2 The Physics of Burnup and its Modeling

6.2.1 Phenomena during Burnup

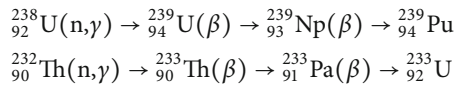
During burnup in a nuclear reactor, the following phenomena occur in nuclear fuels:

Depletion of Fissile Nuclides (a)

The fissile nuclides (e.g., $^{235}_{92}\text{U}$, $^{239}_{94}\text{Pu}$) deplete during burnup due to fission reactions. This effect has a negative impact on fuel reactivity since the number of fissile nuclides decreases during burnup.

Conversion from Fertile Nuclide to Fissile Nuclide (b)

Fertile nuclides become fissile nuclides through neutron capture and beta decay, for example,



The conversion effect increases the number of fissile nuclides, and thus has a positive impact on fuel reactivity during burnup.

Production of Fission Products (c)

The fissions of fissionable nuclides yield various fission products. Since these fission products are neutron absorbers, they have a negative impact on fuel reactivity.

The above three phenomena, that is, (a)–(c), take place simultaneously in nuclear fuel during burnup. In thermal reactors (e.g., light water reactors), the conversion effect is rather small, and the absorption by fission products is large, due to the thermal neutron spectrum. Note that this conversion takes place by means of the resonance capture of fertile material in the epithermal energy region; thus, the conversion is generally small in thermal reactors.

Absorption cross sections of some fission products are large in the thermal energy region. Therefore, since the negative effects on reactivity ((a) and (c)) are large, and the positive effect (b) is small in thermal reactors, the multiplication factor of nuclear fuel decreases as burnup proceeds.

The above dynamic is different in typical fast reactors. Since fast neutrons dominate nuclear reactions in a fast reactor core, the conversion effect is much larger than it is in thermal reactors. Furthermore, the absorption by fission products is small due to the absence of thermal neutrons. Consequently, due to greater conversion (the positive reactivity effect) and smaller absorption by fission products (negative reactivity effect), the reduction of the multiplication factor of nuclear fuel during burnup becomes smaller than that in thermal reactors.

In addition to the above effects, which have a major impact on fuel reactivity, the following phenomena must also be considered as contributors to fuel reactivity:

Decay

Various nuclides are produced during burnup but many of them are unstable, so they are transformed into other nuclides through α -, β -decay, spontaneous fission, and other processes. This decay has a considerable impact on fuel reactivity, as will be described later.

Transmutation of Nuclides due to Neutron Absorption

Conversion is included in this category. During burnup, various reactions due to neutron absorption take place as follows:

- (n, 2n): neutron absorption followed by emission of two neutrons
- (n, 3n): neutron absorption followed by emission of three neutrons
- (n, 4n): neutron absorption followed by emission of four neutrons
- (n, γ): neutron absorption followed by emission of gamma radiation
- (n, p): neutron absorption followed by emission of a proton
- (n, d): neutron absorption followed by emission of a deuteron
- (n, t): neutron absorption followed by emission of a triton
- (n, α): neutron absorption followed by emission of an alpha particle
- Other

The transmutation of nuclides due to neutron absorption is very important, especially for burnup calculations of burnable poison in a light water reactor analysis. Burnable poison is used to flatten out the variations in reactivity during burnup and to improve the characteristics of the core neutronics. The burnable absorber nuclides loaded in a reactor core at the beginning of cycle (BOC) are depleted and converted to other nuclides during burnup through neutron capture. Thus, the negative reactivity of the burnable poison diminishes or disappears at the end of cycle (EOC); that is, the burnable poison is “burnt-out” at EOC.

The flattening of variations in reactivity provides several merits in actual core design. In the case of PWR, a higher reactivity of fresh fuel assemblies at BOC requires a higher boron concentration to suppress excess reactivity in the core. However, a high boron concentration may create problems related to water chemistry, for example, excess deposition of crud on the cladding. A high boron concentration may also have a negative impact on core safety, since the moderator temperature coefficient tends to be positive, and reactivity insertion during a boron dilution accident tend to be large. In the case of BWR, higher core reactivity may reduce the shutdown margin, making core design difficult. The above discussion clearly indicates the important role of burnable poison in light water reactor core design. In fact, a burnable poison is almost always used in light water reactor core designs, with a few exceptions (e.g., no burnable poison is used in the short operating cycle).

Boron, gadolinium, and erbium are the major burnable absorber materials in light water reactor designs. The actual implementation and design of these burnable poisons in a fuel assembly is a key topic in fuel design for which lattice physics computation is used.

6.2.2 Burnup Chain

Design and Setup of Burnup Chain

As described in the previous section, various transmutations of nuclides occur during burnup in a reactor core. In a burnup analysis, a series of nuclide changes is treated by the concept of a “chain,” since the transmutations of nuclides occur successively. In reactor physics calculations, this chain is known as the burnup chain. For example, the conversion from a fertile to a fissile nuclide, $^{238}\text{U} \rightarrow ^{239}\text{U} \rightarrow ^{239}\text{Np} \rightarrow ^{239}\text{Pu}$, is a typical burnup chain that appears in reactor analysis.

In general, burnup chains are classified in terms of the following nuclides:

- a. Heavy nuclides (Th, U, Pu, Am, Cm, etc.)
- b. Fission products (Xe, Sm, Pm, etc.)
- c. Burnable absorber or burnable poison nuclides (B, Gd, Er, etc.)

The actual nuclide transmutations in nuclear fuels are highly complicated, with several thousands of nuclides being produced and disappearing through various nuclear reactions. Since the direct modeling of such complex nuclide behavior is not feasible, lattice physics computation treats the specific nuclides that have significant or considerable impact on the characteristics of neutronics.

From the viewpoint of calculation accuracy, of course, detailed modeling is desirable; that is, the treatment of as many nuclides as possible. However, many cross section libraries for these nuclides must be prepared, and their effective cross sections must be evaluated in resonance calculations in order to treat the many nuclides. Since such detailed treatment is quite burdensome in terms of memory storage and computation time, the number of nuclides used in a burnup calculation must be selectively limited. In the case of a burnup calculation in a small configuration, for example, single pin-cell geometry or a fuel assembly, a very detailed burnup chain can be used. In actual reactor core calculations, however, the scale of the calculation configuration must be carefully assessed, as discussed below.

Let us assume that a set of burnup chains, which includes 300 nuclides, is used for a reactor core analysis. Note that a set of burnup chains with 300 nuclides is a detailed one in current burnup analysis. When the variations in nuclide number densities are tracked in each fuel pin, the required memory storage for a three-dimensional PWR whole-core analysis is evaluated as follows:

$$1[\text{byte/nuclide}] \times 300[\text{nuclides/burnup region}] \times 300[\text{burnup regions/fuel assembly(radial)}] \\ \times 193[\text{fuel assemblies/core}] \times 60[\text{meshes/fuel assembly(axial)}] = 10^9[\text{byte}].$$

The above rough estimate suggests that 1 GB of memory storage is necessary to hold the nuclide number densities when 300 nuclides are tracked in pin-by-pin whole-core analysis.

In order to reduce the computational burden, the number of nuclides explicitly (independently) treated in burnup calculations may be limited to the major nuclides that have a considerable impact on the neutronics characteristics. Those that have a lesser impact would be gathered and treated in an approximate manner as one or several groups. Fission products, in particular, are often modeled as several groups of pseudo fission product nuclides that comprise multiple fission products. The modeling of pseudo fission products depends on the burnup chain, and there are variations on this, ranging from a very simple one-group model (combine all fission products that are not explicitly treated), to a complicated model (which considers dependency on fissile nuclide, saturation, and the non-saturation behaviors of number density during burnup). For example, the MVP-BURN code, which is a continuous energy Monte Carlo code with burnup capability, has several burnup chains, as shown in [Table 21](#).

The burnup chain used in the MVP-BURN code is depicted in [Figs. 86–88](#).

In the case of a Monte Carlo burnup calculation, since continuous energy (point-wise) cross section data for each nuclide are stored in memory, utilization of a detailed burnup chain requires a larger amount of memory. Furthermore, the reaction rate estimate (tally) of each nuclide, which is inevitable in a burnup calculation, requires a longer computation time when

Table 21
Burnup chains implemented in the MVP-BURN code

Name	Number of heavy nuclides	Number of FPs	Number of pseudo FPs	Note
Standard	21 (^{234}U to ^{246}Cm)	49	1	Conventional UO_2/MOX analysis
General	21 (^{234}U to ^{246}Cm)	103	1	PIE analysis, etc.
Developer	28 (^{232}Th to ^{246}Cm)	193	0	Verification of a burnup chain
Simplified	19 (^{235}U to ^{245}Cm)	30	4	Conventional UO_2/MOX analysis

Source: Okumura et al. (2000, 2007).

the number of nuclides in a calculation configuration is large. In general, therefore, the utilization of a simple burnup chain model that satisfies the purpose and accuracy requirements of the analysis is desirable. Note that “pseudo” treatment, which is sometimes used for fission products, is not usually applied to heavy nuclides; the less important heavy nuclides are simply omitted from the burnup chain.

Our discussion thus far has focused particularly on the neutronics characteristics, which is major objective of lattice physics computing. In high burnup and MOX fuels, however, evaluation of the source term, that is, the neutron/gamma source intensities and heat generation rate, becomes important for fuel storage and reprocessing. These source terms depend on the isotopic composition of the fuel. For example, the neutron source intensity and heat generation rate are generally dominated by ^{242}Cm , ^{244}Cm , and ^{238}Pu , respectively.

A dedicated code that has an extensive burnup chain, for example, ORIGEN2, is commonly used to estimate the source term, since the important nuclides may not be included in the burnup chain of a common lattice physics code, in which nuclides are selected from the point of view of neutronics. A detailed burnup analysis code such as ORIGEN2, however, applies an approximate treatment to the cross section of each nuclide. For example, ORIGEN2 has one-group cross section libraries that are generated and collapsed under the neutron spectra of several typical reactor types. Users can select a cross section library that is suitable for their analysis. Though various cross section libraries are provided, the neutron spectrum assumed for library generation may not well reproduce that of the analysis configuration. As a consequence, dedicated burnup analysis codes are not superior to lattice physics codes in terms prediction accuracy for nuclide number density.

The above discussion suggests that any new burnup chain developed for lattice physics computations might have capability of source term estimation. In fact, instead of pseudo fission products, most recent lattice physics codes adopt detailed burnup chains in which 20–30 heavy and 200–300 fission-product nuclides that are explicitly considered.

Evaluation of Fission-Product Yield

One of the most troublesome tasks in the design of a burnup chain is the evaluation of fission-product yields. The fission-product yield is given in a nuclear data file (e.g., the ENDF

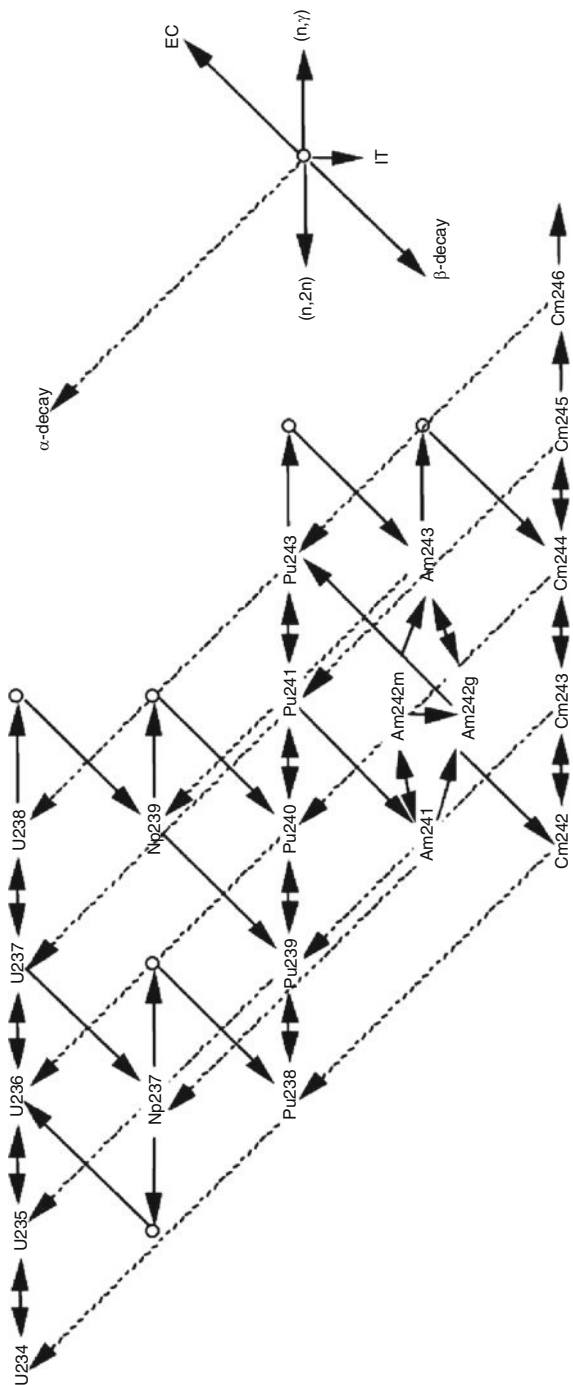


Figure 86
Burnup chain of MVP-BURN code for heavy nuclides (Standard burnup chain) (Okumura et al. 2000, 2007)

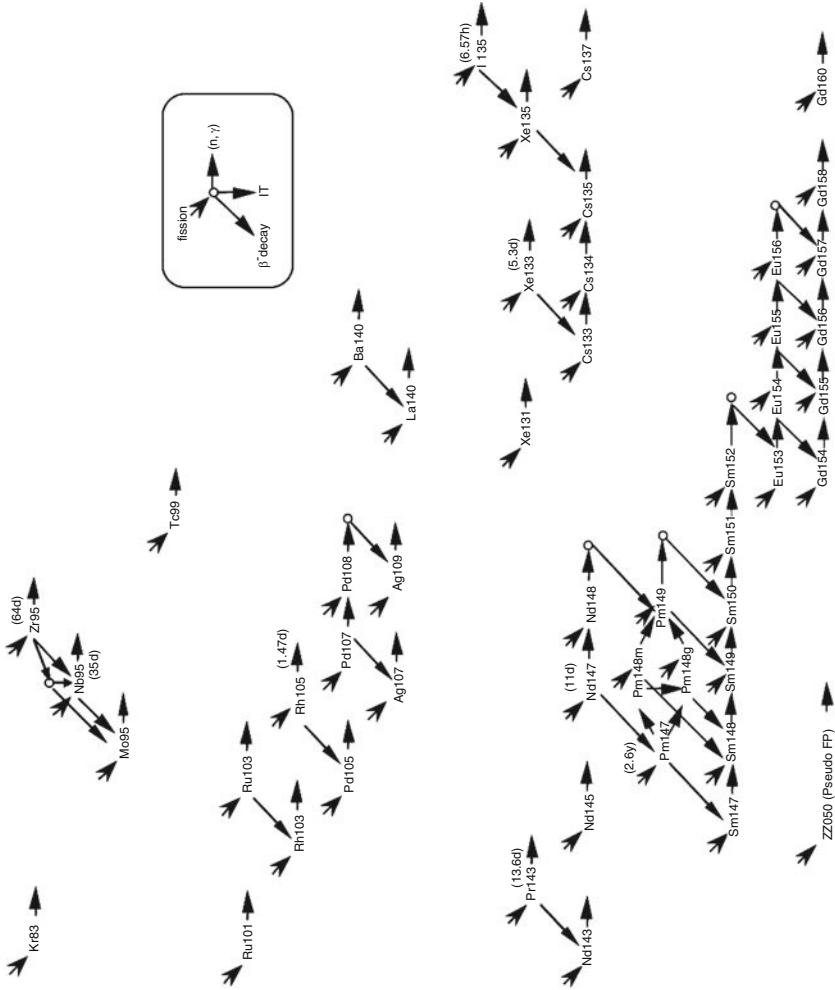
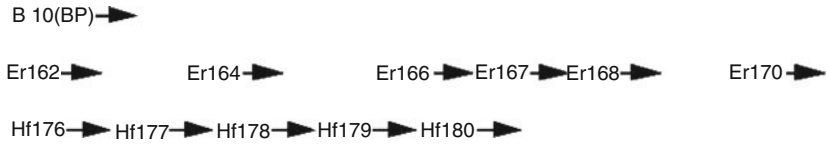
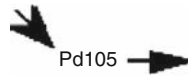


Figure 87 Burnup chain of MVP-BURN code for fission product nuclides (Standard burnup chain) (Okumura et al. 2000, 2007)



■ Figure 88

Burnup chain of MVP-BURN code for burnable poison nuclides (Standard burnup chain) (Okumura et al. 2000, 2007)



■ Figure 89

Simplified chain for ^{105}Pd in the MVP-BURN code

fission-product data or the JNDC nuclear data library of fission products), in which the yield values for more than 1,000 fission products are given (McLane 2001; Ihara 1989). In contrast, just a few dozen to a few hundred fission products are independently treated in lattice physics codes. This difference (more than a thousand versus a few hundred) should be carefully taken into account when the fission-product yield is being set. A simple treatment that neglects the yields of nuclides not included in the burnup chain is not appropriate.

For example, let us consider the part of the burnup chain in [Fig. 87](#), namely $^{105}\text{Rh} \rightarrow ^{105}\text{Pd}$. This part of the burnup chain is expressed somewhat differently in the Simplified and the Developer chains of the MVP-BURN code, as shown in [Figs. 89](#) and [90](#).

In the Simplified chain, ^{105}Pd is produced directly from a fission reaction. But in the Standard chain shown in [Fig. 87](#), ^{105}Pd is partly produced from the beta decay of ^{105}Rh , and the rest is produced from a fission reaction. Finally, in the Developer chain, the production of ^{105}Pd has three paths: a neutron capture of ^{104}Pd , a beta decay of ^{105}Rh , and a fission reaction. The fission-product yields for these chains are compared in [Table 22](#).

[Table 22](#) clearly indicates that the yields of ^{105}Rh and ^{105}Pd are very different in the different burnup chains. In the Developer chain, the yields for ^{105}Rh and ^{105}Pd are very small (effectively zero). These are the independent yields, that is, the number of fission products directly produced from a fission reaction. In the Standard chain, though the yield for ^{105}Pd is the same as that from the Developer chain, ^{105}Rh has a larger yield of 9.63844×10^{-3} . This is the cumulative yield, which is obtained by summing the yields of the “upstream” fission products of ^{105}Rh , for example, ^{104}Ru and ^{105}Ru . In other words, the “upstream” fission products of ^{105}Rh are assumed to be immediately transformed into ^{105}Rh along the burnup chain. The cumulative yield is estimated based upon this consideration. A similar assumption is used for the Simplified chain, in which the upstream fission products of ^{105}Pd are immediately transformed into ^{105}Pd after a fission reaction.

The above discussion suggests that the estimation of fission yields (whether independent or cumulative) depends on the design of a burnup chain, and is a very complicated task. A common practice today is to adopt an ad hoc approach, that is, the utilization of small ad hoc codes that calculate the independent and cumulative yield.

Table 22
Yields of ^{105}Rh and ^{105}Pd in the burnup chains of the MVP-BURN code

Name	^{105}Rh	^{105}Pd
Developer	1.70062E-08	9.99776E-13
Standard	9.63844E-03	9.99776E-13
Simplified	–	9.63844E-03

Estimation of Cross Sections and Yields for Pseudo Fission Products

When the number of fission products in a burnup chain is small, the pseudo fission products should be used in order to maintain the prediction accuracy of the burnup dependency of fuel reactivity (Garrison and Roos 1962; Iijima and Yoshida 1982; Ikehara et al. 1998). The cross sections and yields of the pseudo fission products are evaluated and adjusted with the calculation results of a detailed burnup chain, for example, the Developer chain in the MVP-BURN code. Therefore, in a strict sense, the cross section and yield of pseudo fission products depend on the reactor types being analyzed. Different pseudo fission-product nuclides may therefore need to be prepared for different reactor types.

The utilization of a detailed burnup chain with many independent fission products reduces the importance of the pseudo fission products. For example, when 112 fission products are independently considered in a BWR burnup analysis, we can capture more than 98% of the neutron absorption by the fission products. In this case, the reactivity discrepancy caused by the utilization of pseudo fission products is less than $0.1\% \Delta k/k$ up to 100 GW d/t (Ikehara et al. 1998). Utilization of a more detailed burnup chain, such as the Developer chain of the MVP-BURN code, allows for the elimination of the pseudo fission product. If we take into account the ongoing improvements in computer platforms, the incorporation of a detailed burnup chain is recommended.

Branching Ratio

Some nuclides can produce different daughter nuclides after the decay of the neutron capture reaction. For example, ^{241}Am can be transformed into $^{242\text{m}}\text{Am}$ or ^{242}Am after the capture of a neutron. The ratio of branch (branching ratio) is inherent to the reaction and the nuclide. Though the branching ratio depends on the neutron energy, there are not many experimental results on this relationship. The branching ratio can therefore be a source of error in burnup calculations. Though the major sources of error in burnup calculations are sometimes considered to be the accuracy of the effective cross section and neutron spectrum, etc., the branching ratio can also be an important factor.

6.2.3 Burnup Equation

Burnup of a Fissile Nuclide

As a first step, a very simple burnup model is discussed here. The variation of the number density of ^{235}U number is treated as an example.

The variation of ^{235}U during burnup can be described by (537).

$$\frac{dN^{235}\text{U}(t)}{dt} = -N^{235}\text{U}(t) \times \sigma_a(t) \times \phi(t) \quad (537)$$

where

$N^{235}\text{U}(t)$: number density of ^{235}U [cm^{-3}],
 $\sigma_a(t)$: microscopic absorption cross section of ^{235}U (= capture + fission) [cm^2],
 $\phi(t)$: neutron flux [$\text{cm}^{-2} \text{s}^{-1}$].

Equation (537) indicates that the reduction rate of the fissile (i.e. ^{235}U) number density is given by the absorption reaction rate. Note that the absorption includes not only the fission reaction but also the capture reaction. In an actual situation, the production of ^{235}U (e.g., by the neutron capture of ^{234}U) and its decay may be considered, but they are omitted here for the sake of simplicity. Note that the reaction rate is given by (538).

$$R = N \times \sigma \times \phi \quad (538)$$

where

R : reaction rate (e.g., [$\text{cm}^{-3} \text{s}^{-1}$]),
 N : number density (e.g., [cm^{-3}]),
 σ : microscopic cross section (e.g., [cm^2]),
 ϕ : neutron flux (e.g., [$\text{cm}^{-2} \text{s}^{-1}$]).

When the neutron flux and microscopic absorption cross section are assumed to be constant, (537) can be written as follows:

$$\frac{dN^{235}\text{U}(t)}{dt} = -N^{235}\text{U}(t) \times \sigma_a \times \phi \quad (539)$$

Equation (539) is a basic differential equation and its solution is analytically expressed by

$$N^{235}\text{U}(t) = N^{235}\text{U}(0) \exp(-\sigma_a \phi t) \quad (540)$$

In common burnup analyses, the initial number density, the microscopic cross section, and neutron flux are given as input data. Therefore, the number density of ^{235}U is expressed as a function of burnup time. For example, when the microscopic absorption cross section of ^{235}U and the neutron flux are approximately given by 1,000 [barn] (=1,000 $\times 10^{-24}$ [cm^2]) and 10^{13} [$\text{cm}^{-2} \text{s}^{-1}$], respectively, the variation of the number density of ^{235}U is expressed by

$$N^{235}\text{U}(t) = N^{235}\text{U}(0) \exp(-10^{-8}t) \quad (541)$$

where unit of t is [s].

In the above derivation, the microscopic cross section and neutron flux are assumed to be constant. However, these parameters generally depend on the burnup time, so (540) cannot be directly applied to a reactor core analysis. In actual burnup analyses, the microscopic cross section and neutron flux are assumed to be constant during a short period Δt , and number density is evaluated by

$$N^{235}\text{U}(t + \Delta t) = N^{235}\text{U}(t) \exp(-\sigma_a \phi \Delta t) \quad (542)$$

This is the fundamental temporal discretization in burnup calculation. Further discussion will be provided in [6.3](#).

Burnup Equation with Multiple Nuclides

In the previous section, we focused on a simple burnup equation with a nuclide. In our next step, more complicated burnup equations with multiple nuclides ($^{238}\text{U} \sim ^{241}\text{Pu}$) will be discussed. These burnup equations are important in common reactor analyses as conversion reactions. The burnup equations for these nuclides are as follows:

$$^{238}\text{U} : \frac{dN^{238}\text{U}(t)}{dt} = -N^{238}\text{U}(t) \times \sigma_a^{238}\text{U} \times \phi \quad (543)$$

$$^{239}\text{Pu} : \frac{dN^{239}\text{Pu}(t)}{dt} = -N^{239}\text{Pu}(t) \times \sigma_a^{239}\text{Pu} \times \phi + N^{238}\text{U}(t) \times \sigma_c^{238}\text{U} \times \phi \quad (544)$$

$$^{240}\text{Pu} : \frac{dN^{240}\text{Pu}(t)}{dt} = -N^{240}\text{Pu}(t) \times \sigma_a^{240}\text{Pu} \times \phi + N^{239}\text{Pu}(t) \times \sigma_c^{239}\text{Pu} \times \phi \quad (545)$$

$$^{241}\text{Pu} : \frac{dN^{241}\text{Pu}(t)}{dt} = -N^{241}\text{Pu}(t) \times \sigma_a^{241}\text{Pu} \times \phi + N^{240}\text{Pu}(t) \times \sigma_c^{240}\text{Pu} \times \phi \quad (546)$$

Note that decays are omitted for the sake of simplicity. Though ^{239}Pu is generated from ^{238}U through ^{239}U and ^{239}Np , it is assumed to be produced directly from ^{238}U .

Care should be taken that both the absorption and capture cross sections are used in (543)–(546). The vanishing rate of a nuclide is given by its absorption rate, but the conversion rate of a nuclide, for example, transmutation from ^{238}U to ^{239}Pu , is given by the capture rate. Therefore, the absorption cross section is used for the vanishing term and the capture cross section is used for the production term, which corresponds to a conversion from an ancestor nuclide.

As described previously, since microscopic cross sections, neutron flux, and initial number densities are given as input parameters, variations in the number densities of $^{238}\text{U} - ^{241}\text{Pu}$ can be evaluated by the analytical solutions in (543)–(546). Though this example treats only four nuclides, the analytical solutions are highly complicated. In an actual burnup analysis, the number of nuclides is much larger than in the above example.

Burnup Equation in General Form

Based on the discussion in this section so far, we will now derive a general burnup equation in which the production and disintegration of nuclides are considered. In general, the production or disintegration of a nuclide is described by (547)

$$\frac{dN_i}{dt} = \text{production rate} - \text{absorption rate} - \text{decay rate} \quad (547)$$

Equation (547) is written in the form of a burnup equation as follows:

$$\frac{dN_i}{dt} = \sum_j \gamma_{ji} \sigma_{f,j} N_j \phi + \sigma_{c,i-1} N_{i-1} \phi + \sum_k \lambda_{ki} N_k - \sigma_{a,i} N_i \phi - \lambda_i N_i \quad (548)$$

where

N_i : number density of nuclide i [cm^{-3}],

γ_{ji} : yield of nuclide i from a fission of nuclide j [-],

- $\sigma_{f,j}$: microscopic fission cross section of nuclide j [cm^2],
 ϕ : neutron flux [$\text{cm}^{-2} \text{s}^{-1}$],
 $\sigma_{c,i-1}$: capture cross section of nuclide $i - 1$ [cm^2],
 λ_{ki} : decay constant of nuclide k to nuclide i [s^{-1}],
 λ_i : decay constant of nuclide i [s^{-1}],
 $\sigma_{a,i}$: absorption cross section of nuclide i [cm^2].


The first term on the right side of (548) shows the direct production from a fission. When the nuclide i is not a fission product, this term is zero. The second term is the production due to neutron capture, that is, (n, γ) reaction. The third term is the production due to decay of other nuclides, which considers α - and β -decays. The fourth and last terms are the disintegration by the neutron absorption, and the decay, respectively. Note that (548) is not truly rigorous since some nuclear reactions have been omitted. For example, $(n, 2n)$, $(n, 3n)$, and (n, p) reactions are not taken into account. If these reactions are important, they would be also considered as additional terms in (548).

Equation (548) is an extension of the burnup equation, as discussed in this section so far, and is a differential equation of the first order (Bateman 1910). When the number densities of nuclides are considered as a vector, (548) can be written in a more general form:

$$\frac{d\vec{N}}{dt} = \mathbf{A}\vec{N} \quad (549)$$

where

- \vec{N} : vector of nuclide number density,
 \mathbf{A} : the burnup matrix.

When the nuclides in a vector \vec{N} are arranged in order of atomic mass (light fission products appear first, then heavy fission products, and finally heavy nuclides), the typical structure of the burnup matrix \mathbf{A} is that shown in  Fig. 91.

The analytical solution of (549) is formally given by the following formula, when the element of the burnup matrix is constant.

$$\vec{N}(t) = \exp(\mathbf{A}t)\vec{N}(0) \quad (550)$$

Equation (550) is a natural extension of (540), which is derived for a single nuclide. The term $\exp(\mathbf{A}t)$ is called the matrix exponential, but its analytical expression for a general case cannot, unfortunately, be obtained. For example, when the rank of matrix \mathbf{A} is two, $\exp(\mathbf{A})$ is given as follows:

$$\text{MatrixExp} \left[\begin{pmatrix} a & b \\ c & d \end{pmatrix} \right] = \begin{pmatrix} \frac{e^{\frac{a+d}{2}} \left(\alpha \cosh\left(\frac{\alpha}{2}\right) + (a-d) \sinh\left(\frac{\alpha}{2}\right) \right)}{\alpha} & \frac{2be^{\frac{a+d}{2}} \sinh\left(\frac{\alpha}{2}\right)}{\alpha} \\ \frac{2ce^{\frac{a+d}{2}} \sinh\left(\frac{\alpha}{2}\right)}{\alpha} & \frac{e^{\frac{a+d}{2}} \left(\alpha \cosh\left(\frac{\alpha}{2}\right) + (d-a) \sinh\left(\frac{\alpha}{2}\right) \right)}{\alpha} \end{pmatrix}$$

where $\alpha = \sqrt{(a-d)^2 + 4bc}$.

The above result suggests that when the number of nuclides is from several dozen to a few hundred, it is impractical to seek a direct solution through the analytical approach; some approximations should be used in order to practically obtain the analytical solution, as will be discussed later. Therefore, in an actual burnup calculation, the numerical solution of (550) is necessary.

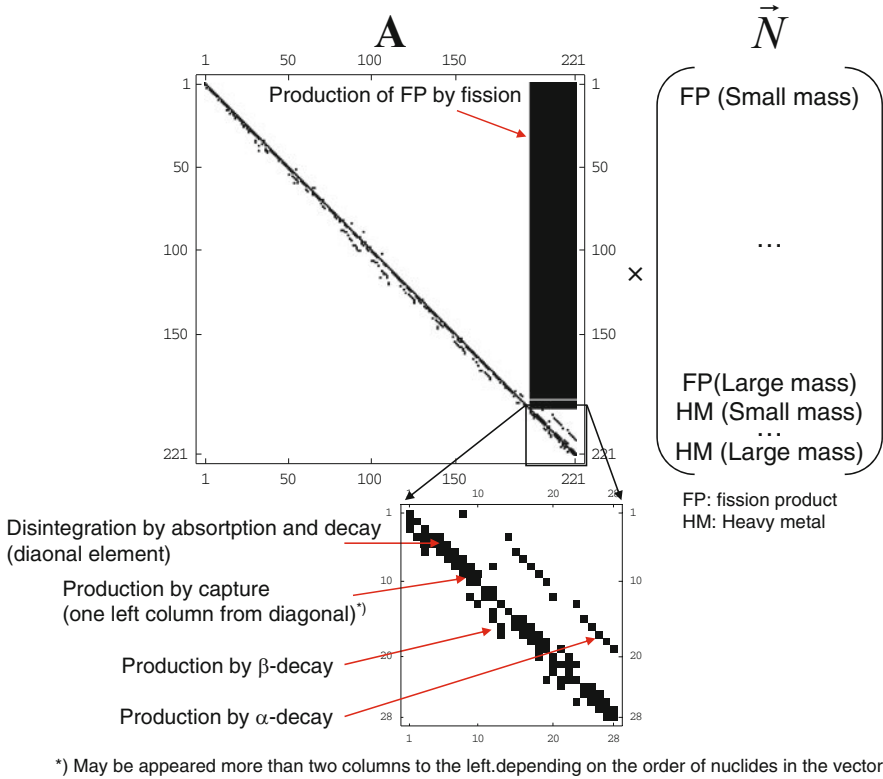


Figure 91
Typical structure of a burnup matrix

6.2.4 Burnup, Burnup Time, and Normalization of Neutron Flux

Burnup and Burnup Time

Burnup is expressed as the cumulative energy output per unit weight of the initial heavy metal loading. Since the cumulative energy release from a nuclear fuel is very large, MWd/t or GWd/t is commonly used as the unit of burnup. ISO states that “M” (mega, 10^6), “G” (giga, 10^9), and “W” (Watt) must be written in upper case letters, while “d” (day) and “t” (ton) must be written in the lower case. The value of 1 MWd/t indicates that 1 t of heavy metal sustains 1 MW energy production for 1 d, and that a value of 1 GWd/t shows that 1 t of heavy metal sustains 1 GW energy production for 1 d.

One must be careful when defining the weight of the heavy metal used in burnup. Since the weight of heavy metal diminishes during burnup due to fission reactions, the weight of the heavy metal at initial loading (i.e., beginning of life) is used for the definition of a burnup unit.

In burnup calculations, not only burnup (e.g., MWd/t) but also burnup time (e.g., in second) is important. In actual in-core fuel management calculations, the planned cycle length is given

as burnup time (days or months). The conversion of these two parameters (burnup and burnup time) is therefore quite important. The conversion of units can be carried out as follows:

- a. Conversion from Burnup Time (e.g., Day) to Burnup (e.g., MWd/t)

$$\text{Burnup (MWd/t)} = \text{Thermal output (MW)} \times \text{duration (day)} \div \text{heavy metal weight (t)}$$

Note that the initial (beginning of life) value of the heavy metal weight should be used in the above relationship. The thermal output and the initial heavy metal weight of a fuel assembly for unit axial length are usually used in lattice physics computations, while those for the entire core are used in core calculations.

- b. Conversion from Burnup to Burnup Time

$$\text{Duration (day)} = \text{Burnup (MWd/t)} \div \text{Thermal output (MW)} \times \text{Heavy metal weight (t)}$$

Normalization of Neutron Flux

The neutron transport calculation in a lattice physics computation is carried out as an eigenvalue calculation; thus, the neutron flux is obtained as a relative value. However, the absolute value of the neutron flux is necessary in order to perform the burnup calculation. Normalization of the neutron flux to an absolute value is performed as follows:

1. Integrate the thermal output by fission reaction over the entire configuration.
2. Evaluate the normalization factor by (input thermal output)/(integrated thermal output).
3. Normalize the neutron flux by the normalization factor obtained in (2).

Normalization of the neutron flux and the conversion between burnup time and burnup can be sources of error. Furthermore, since errors related to these calculations are often not apparent, care must be taken in actual lattice physics/in-core fuel management calculations. The following points in the analyses should be checked:

- a. Unit of thermal output (W/kW/MW)

The input unit of thermal output depends on the codes used in the calculation. Some lattice physics/core calculation codes may use non-SI units.

- b. Specification of power normalization (whole core, an assembly, an assembly per unit axial height, power density, etc.)

Care must be taken with the power normalization input of a lattice physics code. The power normalization input greatly depends on the lattice physics codes, and various specifications are possible, that is, thermal output for a whole assembly, power linear density for fuel assembly or fuel pin, power density per unit heavy metal weight (W/gHM), and power density per unit volume (W/cm³). One should be careful regarding the specification used in the lattice physics code for the analysis.

- c. Specification of Heavy Metal Weight

In the USA, a non-SI unit, for example, short ton (st) may be used instead of ton (t). Since the difference between the two is not very large (1 st = 0.907 t), it is quite difficult to find out their discrepancy in a burnup calculation. However, when the conversion from MWd/t to d, or d to MWd/t is carried out with an incorrect weight unit, a difference of approximately 10% takes place, which is completely unacceptable in actual in-core fuel management calculations.

Furthermore, in lattice physics and core calculations, the precise value of the total heavy metal weight is necessary in order to estimate burnup. We would again emphasize

here that the initial heavy metal weight is used for burnup calculations. In the evaluation of heavy metal weight, detailed specifications of the fuel assembly should be taken into account. For example, a gadolinia-bearing fuel rod contains less heavy metal than an ordinary fuel rod without burnable poison. Fuel assemblies from different fuel vendors may have different heavy metal weights. Since heavy metal weight has a direct impact on the value of a burnup, it should be accurately calculated with this in mind.

d. Lattice/Core Volume

Since the total thermal output is calculated through the integration of power density over configuration, the volume of the calculation configuration is important. If an inaccurate volume is given, the normalized power will reflect that discrepancy.

As discussed above, there can be various reasons for wrong power normalization, that is, an inaccurate estimate of the absolute value of the neutron flux. Since common lattice physics codes internally use both burnup and burnup time, they are both printed in the output list. Therefore, when the specification for burnup is given in MWd/t or GWd/t, the burnup time (day) should be confirmed. The inverse, of course, is also true: when the burnup time is used in the input data, the burnup in units of MWd/t or GWd/t should be checked. This double checking is very useful for preventing errors related to burnup specifications.

6.3 Numerical Scheme

6.3.1 Potential Causes of Error in a Numerical Solution

As discussed in the previous subsections, a general solution for the burnup equation is given by (550). However, it is difficult to obtain a general analytic solution of (550) that can be used for numerical calculations. A numerical solution is therefore inevitable in practical burnup calculations. Before we present a detailed discussion of a numerical solution, potential causes of error in a numerical solution for the burnup equation are discussed below.

Error in Reaction Rate (Production, Absorption, and Decay Rates)

The microscopic reaction rate (e.g., $\sigma_a(t)\phi(t)$) is given as the product of a microscopic cross section and the neutron flux. In order to accurately evaluate microscopic reaction rates, effective microscopic cross sections and the neutron fluxes in burnup regions must be precisely evaluated. However, since precise evaluation of these parameters is still a major research topic in reactor physics, some errors are still inevitable when present calculation methods are used. This is especially true for nuclides with resonances, in which the resonance interference effect and other factors can become a source of error. Furthermore, the number densities of resonant nuclides (especially fission products and higher heavy nuclides) vary during burnup, so the magnitude of the self-shielding effect also changes. In the beginning of life, their self-shielding effect is very small, and infinite-dilute treatment is appropriate. But the self-shielding effect gradually becomes larger as the burnup proceeds, so it must be accurately taken into account.

Temporal Discretization Error of the Differential Equation of Burnup Equation

In order to numerically solve the differential equation, temporal discretization may be necessary, which introduces some error. This issue will be discussed later in more detail.

Temporal Discretization Error in Reaction Rates of Burnup Equation

The reaction rates that appear in the burnup equation depend on the burnup time, since both the microscopic cross section and neutron flux vary during burnup. They are usually assumed to be constant, however, within a particular time-step in the numerical solution of the burnup equation. This assumption introduces some error in the reaction rates used in the burnup equation. The discrepancy could be large when the temporal variation of the reaction rate is large. A detailed discussion of this point will be offered in the latter part of this section.

Normalization Error of Thermal Output

As described previously, the neutron flux used in a burnup calculation should be an absolute value rather than the relative one obtained in the eigenvalue calculation. The absolute value of the neutron flux is normalized with the thermal output of a reactor. The thermal output of an actual reactor is estimated by the heat balance of the primary cooling system. Since it requires measurement values for the inlet/outlet temperatures, the flow rate of the primary coolant and so on, these measured values contain errors. Therefore, the thermal output of a reactor core based on the measured value may also include some uncertainty. Consequently, the absolute neutron flux evaluated from the measured core thermal output may also be in error. Generally speaking, though the error in the core thermal output is not very large, it is nonetheless a potential cause of error in the burnup analysis.

Error in Initial Composition of Fuel

The initial composition of the fuel can be a source of error in burnup calculation and is often overlooked. Actual fuels inevitably have fluctuations in their properties, for example, ^{235}U enrichment and heavy metal loading. The tolerances of these fluctuations in the manufacturing process are set based on their impact upon the neutronics properties. Therefore, they have a limited impact on core behavior, for example, core k -effective. That said, fluctuations in the initial fuel composition may not be negligible in regard to the calculation of nuclide number densities, which are often required in the post-irradiation examination (PIE) of fuel assemblies. An error in initial number density has an especially large impact on nuclides whose number density is small. In any case, the nominal value of the fuel's isotopic composition should not be used without cross-checking the mill-sheet.

6.3.2 General Remarks on Numerical Solutions for the Burnup Equation

The general form of the burnup equation is (549) and its solution is formally given by (550). Solution methods for the burnup equation have long been the subject of investigation (England 1962; Ball and Adams 1967; Lapidus and Luus 1967; Vondy 1962; Bell 1973; Tasaka 1977), and the major results of this inquiry are implemented in the ORIGEN2 code, which is a dedicated burnup analysis code for general purposes (Croff 1980). The reference manual of the ORIGEN2 code well summarizes the numerical solution methods for the burnup equation, and also provides useful information. Since the numerical methods used in the ORIGEN2 code are sophisticated, many burnup calculation codes adopt the one used in the ORIGEN2 code.

In fact, this type of burnup equation, that is, the first-order differential equation, has frequently appeared not only in the field of reactor physics, but also in the fields of physics, chemistry, economics, and systems analysis. Studies of this type of equation have also been independently carried out in the field of applied mathematics. Moler and Loan (2003) summarizes the results of the investigations in this field, and reviews various methods used to solve the matrix exponential, that is, (550). Though more than 20 methods are described by Moler and Loan (2003), only 3~4 of them have been applied in the field of reactor physics.

In the following sections, a fundamental method to solve the differential equation (the Euler method), and typical numerical solutions used in burnup analysis (the Runge-Kutta method, the matrix exponential method, the matrix decomposition method, the Bateman method) are described. Furthermore, the Padé approximation, which is a general numerical method used to solve the matrix exponential, and the Krylov subspace method, which is suitable for estimating the matrix exponential of a sparse matrix, are also explained.

Note that the microscopic reaction rate ($\sigma\phi$) is assumed to be constant throughout a particular burnup step. In other words, the elements of burnup matrix \mathbf{A} remain constant during a burnup step. A consideration of variations in the microscopic reaction rate will be presented in [6.3.11](#).

6.3.3 The Euler Method

The Euler method is a quite simple numerical method based on the finite-difference scheme. When (549) is differentiated with respect to the temporal variable, we obtain (551):

$$\frac{d\vec{N}}{dt} \approx \frac{\vec{N}^{l+1} - \vec{N}^l}{\Delta t} = \mathbf{A}\vec{N}^l \quad (551)$$

where l shows the number of burnup steps. Equation (551) can be transformed into the following:

$$\vec{N}^{l+1} = (\mathbf{I} + \mathbf{A}\Delta t)\vec{N}^l \quad (552)$$

where \mathbf{I} shows the unit matrix. Since the value of \vec{N}^l is known (input values), the nuclide number densities at $l + 1$ step can be obtained by (552).

Equation (549) can be also differentiated as (553):

$$\frac{d\vec{N}}{dt} \approx \frac{\vec{N}^{l+1} - \vec{N}^l}{\Delta t} = \mathbf{A}\vec{N}^{l+1} \quad (553)$$

Equation (553) can be transformed into (554)

$$\vec{N}^{l+1} = (\mathbf{I} - \mathbf{A}\Delta t)^{-1}\vec{N}^l \quad (554)$$

The nuclide number densities at step $l + 1$ can be obtained by (554).

The numerical method shown in (551) and (552) is an explicit method, and that of (553) and (554) is an implicit method. Though the computation time for a burnup step is short in the explicit method, the time-step size must be fine in order for a reliable result to be obtained. When a coarser burnup step is used in the explicit method, we often encounter numerical instability. In the case of the implicit method, the inverse of the matrix, that is, $(\mathbf{I} - \mathbf{A}\Delta t)^{-1}$, is

necessary, so that a longer computation time is required for a complicated burnup chain. However, the numerical stability of the implicit method for a coarse burnup step is much higher than that of the explicit method.

Temporal discretization errors from both methods diminish as finer burnup step sizes are used in calculations. However, since the number of burnup steps to achieve a particular burnup is increased with a finer burnup step, there can be a considerable accumulation of round-off errors in the numerical solution. Furthermore, the computation time naturally increases with an increasing number of burnup steps. The appropriate burnup step should be chosen with consideration for these observations. Note that though the Euler method is a simple numerical method, it does not offer a high degree of accuracy under practical calculation conditions. For this reason it is not usually used for actual lattice physics computations.

6.3.4 The Runge–Kutta Method

The Runge–Kutta method is one of the most widely used numerical methods applied to differential equations, and is frequently offered as illustrative material for lectures on numerical methods. Though there are several formulations for the Runge–Kutta method, the second- or fourth-order Runge–Kutta methods are commonly used for numerical calculations.


In the second-order Runge–Kutta method, (555)–(557) are used:

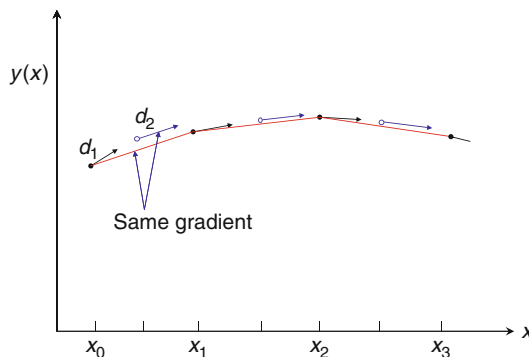
$$\vec{d}_1 = \frac{d\vec{N}}{dt}(t^l, \vec{N}^l) \Delta t = \mathbf{A} \vec{N}^l \Delta t \quad (555)$$

$$\vec{d}_2 = \frac{d\vec{N}}{dt} \left(t^l + \frac{\Delta t}{2}, \vec{N}^l + \frac{\vec{d}_1}{2} \right) \Delta t = \mathbf{A} \left(\vec{N}^l + \frac{\vec{d}_1}{2} \right) \Delta t \quad (556)$$

$$\vec{N}^{l+1} = \vec{N}^l + \vec{d}_2 \quad (557)$$

where $\frac{d\vec{N}}{dt}(t^l, \vec{N}^l)$ shows $\frac{d\vec{N}}{dt}$ at time t^l and number density \vec{N}^l .

The governing concept of the Runge–Kutta method is shown in  Fig. 92: the gradient at the midpoint of burnup steps is estimated by (556), and is used to obtain the number density



 **Figure 92**
Concept of the second-order Runge–Kutta method

at the next step. Since the gradient at the midpoint of a burnup step gives better accuracy than that at the beginning, the calculation accuracy exceeds that of the Euler method, which uses the gradient at the beginning of the burnup step.

The fourth-order Runge–Kutta method utilizes the following equations:


$$\vec{d}_1 = \frac{d\vec{N}}{dt}(t^l, \vec{N}^l)\Delta t = \mathbf{A}\vec{N}^l\Delta t \quad (558)$$

$$\vec{d}_2 = \frac{d\vec{N}}{dt}\left(t^l + \frac{\Delta t}{2}, \vec{N}^l + \frac{\vec{d}_1}{2}\right)\Delta t = \mathbf{A}\left(\vec{N}^l + \frac{\vec{d}_1}{2}\right)\Delta t \quad (559)$$

$$\vec{d}_3 = \frac{d\vec{N}}{dt}\left(t^l + \frac{\Delta t}{2}, \vec{N}^l + \frac{\vec{d}_2}{2}\right)\Delta t = \mathbf{A}\left(\vec{N}^l + \frac{\vec{d}_2}{2}\right)\Delta t \quad (560)$$

$$\vec{d}_4 = \frac{d\vec{N}}{dt}(t^l + \Delta t, \vec{N}^l + \vec{d}_3)\Delta t = \mathbf{A}(\vec{N}^l + \vec{d}_3)\Delta t \quad (561)$$

$$\vec{N}^{l+1} = \vec{N}^l + \frac{\vec{d}_1 + 2\vec{d}_2 + 2\vec{d}_3 + \vec{d}_4}{6} \quad (562)$$

Though the governing concept of the fourth-order Runge–Kutta method is similar to that of the second-order method, the “average gradient” between burnup steps is estimated in a more sophisticated manner, as shown in  Fig. 93.

The accuracy of the fourth-order Runge–Kutta method is high and its computation time is short. Furthermore, since it can handle any form of burnup matrix, it can be applied to very complicated burnup chains. The above features make the fourth-order Runge–Kutta method a practical numerical method for the burnup equation, which is adopted by some lattice physics codes (Morimoto et al. 1989).

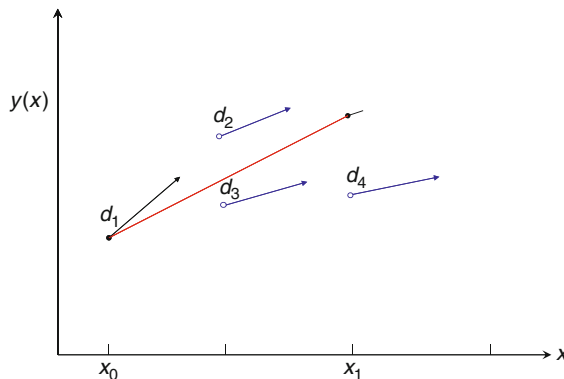


 Figure 93

Concept of the fourth-order Runge–Kutta method

6.3.5 The Matrix Exponential Method

The matrix exponential method directly performs the numerical calculation of (550), which is a general solution of the burnup equation. The matrix exponential can be evaluated by the Taylor series expansion as follows:

$$\exp(\mathbf{A}\Delta t) = \mathbf{I} + (\mathbf{A}\Delta t) + \frac{(\mathbf{A}\Delta t)^2}{2!} + \frac{(\mathbf{A}\Delta t)^3}{3!} + \dots \quad (563)$$

Since the evaluation of (563) directly gives a general numerical solution to the burnup equation, the matrix exponential method seems to be an ideal numerical method. In actual computation, however, the convergence of the expansion series given in (563) can pose a numerical problem. For example, let us numerically estimate the value of $\exp(-100)$ by applying the Taylor series expansion:

$$\exp(-100) = 1 + (-100) + \frac{(-100)^2}{2!} + \frac{(-100)^3}{3!} + \dots \quad (564)$$

Note that the value of $\exp(-100)$ is approximately 4×10^{-44} . The salient point is whether or not the present value can be obtained through the numerical computation of (564). The actual numerical computation shows that the maximum value of a term on the right side of (564) appears to be approximately $n = 100$, that is, $(-100)^{100}/100! \sim 1 \times 10^{42}$. Therefore, in order to estimate $\exp(-100)$ with five significant digits, at least $42 + 44 + 5 = 92$ significant digits will be necessary during computation, due to the severe round-off error. The number of digits in double-precision calculations in common computer languages (e.g., Fortran, C, C++) is 16, and so 92 significant digits is for all purposes impractical.

A similar consideration becomes relevant in the evaluation of (563). Roughly speaking, the diagonal elements, that is, absolute value of the disintegration term due to absorption and decay, are largest in matrix \mathbf{A} . When a burnup matrix is a diagonal matrix, its matrix exponential can be obtained through exponentials of the diagonal elements. Therefore, the convergence of (563) is dominated by the largest diagonal elements. In other words, when short-lived nuclides exist in the burnup chain, the absolute values of these disintegration terms ($-\lambda - \sigma_a \phi$) in the diagonal position of the burnup matrix become large, so that the convergence of the Taylor series expansion becomes slower. Note that a higher absorption reaction could have a similar impact on a numerical calculation, but a large decay constant is far more important in actual burnup calculations.

To address this more precisely, the maximum norm of burnup matrix \mathbf{A} must be considered. When the norm of a matrix is defined by (565), the maximum (absolute) term that appears in the Taylor series expansion of (563) does not exceed $(|\mathbf{A}|\Delta t)^n/n!$, where n is the largest integer that does not exceed $|\mathbf{A}|\Delta t$ (Lapidus and Luus 1967).

$$|\mathbf{A}| = \min \left\{ \max_i \sum_j |a_{ij}|, \max_j \sum_i |a_{ij}| \right\} \quad (565)$$

In the ORIGEN2 code, (566) is used to limit the value of $|\mathbf{A}|\Delta t$ (Croff 1980):

$$|\mathbf{A}|\Delta t \leq -2 \ln(0.001) \leq 13.855 \quad (566)$$

In this case, the maximum value of $(|\mathbf{A}|\Delta t)^n/n!$ is obtained at $n = 13$, which is approximately 1.1×10^5 . When double-precision calculations (16 significant digits) are used for the numerical

computation of (563), the elements of the matrix exponential for the burnup matrix have significant digits up to 10^{-11} . Therefore, when five significant digits are required in calculation results, a value as small as 10^{-6} can be treated by applying the above limitation.

The limitation of (566) can be satisfied by forcing $\exp(-d\Delta t) < 0.001$, where d is the maximum (absolute) value of the diagonal elements. Since d is the disintegration rate (= absorption rate + decay rate), the value of $|\mathbf{A}|$ does not exceed $2d$. For example, in the case of ^{135}Xe , it transforms into ^{136}Xe due to neutron capture or into ^{135}Cs due to decay. Let us assume that the diagonal element of a burnup matrix for ^{135}Xe is -1.0 , and the transformation ratio to ^{136}Xe , and the decay ratio to ^{135}Cs , are 0.4 and 0.6 , respectively. In this case, the summation of absolute values of the row elements for ^{135}Xe is $|-1.0| + |0.4| + |0.6| = 2.0$, which corresponds to twice the absolute value of the diagonal element (-1.0). Consequently, we have the following relationship:

$$|\mathbf{A}|\Delta t \leq 2d\Delta t \leq -2\ln(\exp(-d\Delta t)) \leq -2\ln(0.001) \quad (567)$$

In the case of actual burnup calculations, the above relationship can be satisfied by limiting d or Δt . The most direct approach is to limit Δt as follows:

$$\Delta t \leq \frac{-2\ln(0.001)}{2d} \quad (568)$$

The apparent drawback of this method is that an impractically small Δt may be obtained for a large d . For example, in the case of the ‘‘Developer’’ burnup chain of the MVP-BURN code, the maximum value of d is given by ^{106}Rh , whose half-life is 29.8 s:

$$d = \ln(2)/29.8 \approx 0.0233[\text{s}^{-1}] \quad (569)$$

By substituting (569) into (568), we obtain Δt in order to satisfy (567) as follows:

$$\Delta t \leq \frac{-2\ln(0.001)}{2 \times 0.0233} \approx 297[\text{s}] \quad (570)$$

A typical burnup step in lattice physics computations is 100–1,000 MWd/t. When a typical power density for a PWR is used, these burnup steps correspond to 3–30 d. Since this burnup step (3–30 d) is much larger than that in (570), some compensatory measures become necessary.

There are two possible ways to resolve this issue. The first is to utilize the scaling and squaring method, which utilizes the following nature of a matrix:

$$\exp(\mathbf{A}\Delta t) = \exp\left(m \frac{\mathbf{A}\Delta t}{m}\right) = \left[\exp\left(\frac{\mathbf{A}\Delta t}{m}\right)\right]^m = \left[\exp\left(\mathbf{A} \frac{\Delta t}{m}\right)\right]^m \quad (571)$$

By using (571), an integer m is defined to satisfy $\Delta t/m \leq \frac{-2\ln(0.001)}{2d}$. The scaling and squaring method is a very effective way to compute a matrix exponential. This is especially true when $m = 2^n$. In the above case, however, m would be approximately 1,000, so the round-off error and computational cost would be considerable.

The second approach is the modification of the burnup chain, which eliminates nuclides with a high disintegration rate (d) and treats them independently. Nuclides with a high disintegration rate attain a radiation equilibrium state with precursors in a short time. Therefore, an

equilibrium solution that is obtained by ignoring the temporal differentiation on the left side of (548) can be used:

$$0 = \sum_j \gamma_{ji} \sigma_{f,j} N_j \phi + \sigma_{c,i-1} N_{i-1} \phi + \sum_k \lambda_{ki} N_k - \sigma_{a,i} N_i \phi - \lambda_i N_i \quad (572)$$

Equation (572) yields the following solution:

$$N_i = \frac{\sum_j \gamma_{ji} \sigma_{f,j} N_j \phi + \sigma_{c,i-1} N_{i-1} \phi + \sum_k \lambda_{ki} N_k}{\sigma_{a,i} \phi + \lambda_i} \quad (573)$$

A nuclide with a very high disintegration rate may be treated by the Bateman method, as described in Sect. 8.3.7, since neither the matrix exponential method nor application of the equilibrium solution yields appropriate results. The equilibrium solution, the Bateman method, and the matrix exponential method are used in the ORIGEN2 code in order to compensate for the weakness of each method.

Finally, we will discuss an important relationship among the matrix exponential method, the Euler method and the Runge–Kutta method. In many textbooks on numerical computation, these methods are explained independently. The Euler method, however, is an approximation that considers up to the second terms (i.e., up to the first order) in the Taylor series expansion shown in (563). This becomes obvious when (552) and (563) are compared.

When the elements of the burnup matrix are constant in a burnup step, the Runge–Kutta method of the second order considers up to the third terms (i.e., up to the second order) in the Taylor series expansion. This can be confirmed by substituting (555) and (556) into (557), then comparing the result with (563). Similarly, the Runge–Kutta method of the fourth order considers up to the fifth terms (i.e., up to the fourth order) in the Taylor series expansion, which can be confirmed by substituting (558)–(561) into (562), then comparing the result with (563).

To sum up, in the Taylor series expansion of the burnup matrix:

Consideration up to the second terms (the first order): the Euler method.

Consideration up to the third terms (the second order): the Runge–Kutta method of the second order.

Consideration up to the fifth terms (the fourth order): the Runge–Kutta method of the fourth order.

From the above viewpoint, both the Euler and Runge–Kutta methods can be considered as variations of the matrix exponential method. Furthermore, the above discussion also suggests the limitation of the Euler and Runge–Kutta methods for nuclides with a high disintegration rate. Since both methods truncate the Taylor series expansion, the limitations of the burnup step in these methods are expected to be smaller than that shown in (568).

6.3.6 The Matrix Decomposition Method

Let us assume that a burnup matrix \mathbf{A} can be decomposed by two matrixes \mathbf{L} and \mathbf{D} :

$$\mathbf{A} = \mathbf{L}\mathbf{D}\mathbf{L}^{-1} \quad (574)$$

The substitution of (574) into (563) yields

$$\begin{aligned}
 \exp(\mathbf{A}\Delta t) &= \mathbf{I} + (\mathbf{LDL}^{-1}\Delta t) + \frac{(\mathbf{LDL}^{-1}\Delta t)^2}{2!} + \dots \\
 &= \mathbf{LL}^{-1} + \mathbf{L}(\mathbf{D}\Delta t)\mathbf{L}^{-1} + \frac{(\mathbf{LDL}^{-1}\mathbf{LDL}^{-1}\Delta t^2)}{2!} + \dots \\
 &= \mathbf{LL}^{-1} + \mathbf{L}(\mathbf{D}\Delta t)\mathbf{L}^{-1} + \frac{(\mathbf{LD}^2\mathbf{L}^{-1}\Delta t^2)}{2!} + \dots \\
 &= \mathbf{LL}^{-1} + \mathbf{L}(\mathbf{D}\Delta t)\mathbf{L}^{-1} + \mathbf{L}\frac{(\mathbf{D}\Delta t)^2}{2!}\mathbf{L}^{-1} + \dots \\
 &= \mathbf{L}\left(\mathbf{I} + (\mathbf{D}\Delta t) + \frac{(\mathbf{D}\Delta t)^2}{2!}\dots\right)\mathbf{L}^{-1} \\
 &= \mathbf{L}\exp(\mathbf{D}\Delta t)\mathbf{L}^{-1}
 \end{aligned} \tag{575}$$

Equation (575) indicates that the matrix exponential of \mathbf{A} can be replaced by that of \mathbf{D} . When \mathbf{D} is a matrix with a general form, the transformation shown in (575) is not of value, though it requires a computational cost similar to that of $\exp(\mathbf{D}\Delta t)$. However, if \mathbf{D} is a diagonal matrix, which has nonzero elements only at diagonal positions, then the above formulation has practical merit

$$\mathbf{D} = \begin{bmatrix} \alpha_1 & & & 0 \\ & \alpha_2 & & \\ & & \dots & \\ 0 & & & \alpha_n \end{bmatrix}. \tag{576}$$

In this case, the matrix exponential of \mathbf{D} is expressed by

$$\exp(\mathbf{D}\Delta t) = \begin{bmatrix} \exp(\alpha_1\Delta t) & & & 0 \\ & \exp(\alpha_2\Delta t) & & \\ & & \dots & \\ 0 & & & \exp(\alpha_n\Delta t) \end{bmatrix}, \tag{577}$$

thus $\exp(\mathbf{A}\Delta t)$ can be easily obtained by (575). In this method, once a matrix is decomposed, then the matrix exponential is evaluated by the decomposed matrixes; this is called the matrix decomposition method.

Next, we should consider a numerical procedure that evaluates the matrixes of \mathbf{D} and \mathbf{L} . Such a procedure is common in the field of linear algebra, that is, the diagonalization of a matrix, which is equivalent to evaluate all eigenvalues and eigenvectors of matrix \mathbf{A} . Note that the diagonal elements of matrix \mathbf{D} correspond to the eigenvalues, and the matrix \mathbf{L} is composed of eigenvectors. In general, the calculation of eigenvalues and eigenvectors requires computation time, so that matrix decomposition is inevitably time consuming. However, the diagonal matrix \mathbf{D} can be obtained easily when the burnup equation is approximated as follows:

$$\begin{aligned}
 \frac{dN_i}{dt} &= \sum_j \gamma_{ji}\sigma_{f,j}N_j\phi + \sigma_{c,i-1}N_{i-1}\phi + \lambda_{i-1}N_{i-1} - \sigma_{a,i}N_i\phi - \lambda_iN_i \\
 &= F_i + (\sigma_{c,i-1}\phi + \lambda_{i-1})N_{i-1} - (\sigma_{a,i}\phi + \lambda_i)N_i
 \end{aligned} \tag{578}$$

Equation (578) is different from (548) in the following points:

- a. The production rate from a fission is assumed to be constant.
- b. The production from a “previous” nuclide, only, is taken into account.

By incorporating the above assumptions, the burnup equation and the burnup matrix become as follows:

$$\frac{d\vec{N}}{dt} = \mathbf{A}\vec{N} + \vec{F} \tag{579}$$

$$\mathbf{A} = \begin{bmatrix} -\sigma_{a,1} - \lambda_1 & 0 & 0 & \dots & 0 \\ \sigma_{c,1} + \lambda_1 & -\sigma_{a,2} - \lambda_2 & \dots & \dots & \dots \\ 0 & \dots & \dots & \dots & \dots \\ \dots & 0 & \dots & -\sigma_{a,n-1} - \lambda_{n-1} & 0 \\ 0 & \dots & 0 & \sigma_{c,n-1} + \lambda_{n-1} & -\sigma_{a,n} - \lambda_n \end{bmatrix} \tag{580}$$

The diagonalization of matrix **A** given by (580) is easy. The matrixes of **L** and **D** are assumed as follows:

$$\mathbf{L} = \begin{bmatrix} l_{1,1} & l_{2,1} & \dots & \dots & l_{n,1} \\ l_{1,2} & l_{2,2} & \dots & \dots & \dots \\ \dots & \dots & \dots & \dots & \dots \\ \dots & \dots & \dots & l_{n-1,n-1} & \dots \\ l_{1,n} & \dots & \dots & \dots & l_{n,n} \end{bmatrix}, \quad \mathbf{D} = \begin{bmatrix} \alpha_1 & 0 & \dots & \dots & 0 \\ 0 & \alpha_2 & \dots & \dots & \dots \\ \dots & \dots & \dots & \dots & \dots \\ \dots & \dots & \dots & \alpha_{n-1} & 0 \\ 0 & \dots & \dots & 0 & \alpha_n \end{bmatrix} \tag{581}$$

Equation (574) can be transformed into

$$\mathbf{AL} = \mathbf{LD} \tag{582}$$

Therefore, by comparing each element of the matrixes in (582), the following relationship can be obtained:

$$(-\sigma_{a,1} - \lambda_1)l_{1,1} = l_{1,1}\alpha_1 \tag{583}$$

$$(\sigma_{c,1} + \lambda_1)l_{1,1} + (-\sigma_{a,2} - \lambda_2)l_{1,2} = l_{1,2}\alpha_1 \tag{584}$$

Since (583) and (584) are the recurrence relationships, the elements in matrixes **L** and **D** can be easily obtained. Here, column vector of matrix **L** is eigenvector thus they can be normalized arbitrary. The analytical solution of (579) is

$$\begin{aligned} \vec{N}^{l+1} &= \exp(-\mathbf{A}\Delta t) \left[\vec{N}^l - \mathbf{A}^{-1}\vec{F} \right] + \mathbf{A}^{-1}\vec{F} \\ &= \mathbf{L} \exp(\mathbf{D}\Delta t) \mathbf{L}^{-1} \left[\vec{N}^l - \mathbf{A}^{-1}\vec{F}^l \right] + \mathbf{A}^{-1}\vec{F}^l \end{aligned} \tag{585}$$

The inverse of matrix **A** is given as follows:

$$\mathbf{A}^{-1} = \mathbf{LD}^{-1}\mathbf{L}^{-1} \tag{586}$$

since


$$\mathbf{AA}^{-1} = \mathbf{I} \tag{587}$$

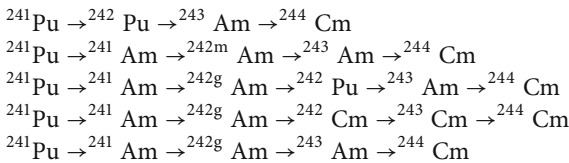
The matrix decomposition method can estimate an accurate solution but has the following drawbacks:

- a. A complicated burnup chain that includes the neutron capture, α -, β -decay, and (n, 2n) reactions cannot be directly treated

As shown in (578), the production of a nuclide is limited by a fission and the “previous” nuclide, that is, there are only two paths. Therefore, even if there are multiple production paths, for example, ^{239}Pu is produced from α -, β -decay and (n, 2n) reactions, direct treatment of these production paths is not possible; the “linearization” of the burnup chain is necessary.

- b. All burnup chains must be linearized

For example, let us consider the production of ^{244}Cm from ^{241}Pu in the burnup chains shown in  Fig. 86. In order to linearize a burnup chain, all production paths should be treated independently. Therefore, the following five linearized burnup chains need to be solved.



Once the solutions for these five burnup equations are obtained, the final solution can be reconstructed through the summation of these solutions. This is a somewhat complicated treatment in the actual implementation of a numerical solution.

The above discussion suggests that number of burnup equations significantly increases when linearization is carried out for a complicated burnup chain.

- c. A numerical difficulty (divide by zero) appears when two nuclides have identical disintegration rates (= absorption + decay rate)
- d. A burnup chain with a “circuit shape” cannot be treated

For example, the burnup chain of $^{241}\text{Pu} \rightarrow ^{242}\text{Pu} \rightarrow ^{243}\text{Am} \rightarrow ^{244}\text{Cm} \rightarrow ^{240}\text{Pu} \rightarrow ^{241}\text{Pu}$ is an example of a circuit-shaped chain.

The matrix decomposition method is a numerically efficient method (Knott and Edenius 1993). However, it is not very suitable for treating very complicated burnup chains.

6.3.7 Bateman Method

The Bateman method utilizes an analytic solution for first-order linear differential equations (Okumura et al. 2007; Bateman 1910; Tasaka 1977; Villarino et al. 1992). The general solution for the linearized burnup equation shown in (578) is given as follows:

$$\begin{aligned}
 N_i(t + \Delta t) &= N_i(t) \exp(-d_i \Delta t) \\
 &+ \sum_{k=1}^{i-1} N_k(t) \left[\sum_{j=k}^{i-1} \frac{\exp(-d_j \Delta t) - \exp(-d_i \Delta t)}{d_i - d_j} a_{j+1,j} \prod_{\substack{n=k \\ n \neq j}}^{i-1} \frac{a_{n+1,n}}{d_n - d_j} \right] \quad (588)
 \end{aligned}$$

where $a_{i,j}$ is the element of matrix \mathbf{A} and $d_i = -a_{i,i}$. Note that F_i is assumed to be zero in the above derivation. Equation (588) has a very complicated form that includes several summation and multiplication operations.

The matrix decomposition method and the Bateman method solve the identical equation since both methods treat the same linearized burnup chain. The difference between these methods is the actual solution method: numerical calculation for a matrix is used in the matrix decomposition method, and the analytic solution is used in the Bateman method.

Though the accuracy of the Bateman method is superior due to its utilization of the analytic solution, it presents several problems that are identical to those of the matrix decomposition method:

- Since linearization of the burnup chain is necessary, some approximations may be necessary for a complicated burnup chain.
- Numerical difficulty arises when two nuclides have identical disintegration rates. In this case, the denominator in (588) becomes zero.
- A circulating burnup chain cannot be directly treated.

The issue of (b) can be avoided by deriving the analytical solution with the assumption of an identical disintegration rate (i.e., $d_i = d_j$ or $d_n = d_j$). Issue (c) can be approximately treated by terminating and cutting the circuit burnup chain at a certain point. Note that the degree of error due to the approximation of terminating the burnup chain is negligible when the number of burnup steps is sufficiently large.

The Bateman method is used in the ORIGEN2 code for short-lived nuclides, as described ▶ 6.3.5. The MVP-BURN code (Okumura et al. 2000) also utilizes the Bateman method, whose burnup module is based on the DCHAIN code developed by JAERI (former JAEA) (Tasaka 1977).

6.3.8 The Padé Approximation

The Padé approximation of (p, q) -order for the exponential function is given as follows:

$$\exp(x) \cong \frac{N_{pq}(x)}{D_{pq}(x)} \quad (589)$$

where

$$N_{pq}(x) = \sum_{k=0}^p \frac{(p+q-k)!p!}{(p+q)!k!(p-k)!} x^k$$

$$D_{pq}(x) = \sum_{k=0}^q \frac{(p+q-k)!q!}{(p+q)!k!(q-k)!} (-x)^k$$

Equation (589) can be reduced into the Taylor series expansion when $q = 0$:

$$\frac{N_{p0}(x)}{D_{p0}(x)} = 1 + x + \frac{x^2}{2!} + \cdots + \frac{x^p}{p!} \quad (590)$$


The Padé approximation for the matrix exponential utilizes (589) rather than the conventional Taylor series expansion, that is,

$$\exp(A\Delta t) \cong \frac{N_{pq}(A\Delta t)}{D_{pq}(A\Delta t)} \quad (591)$$

In general, convergence of the Padé approximation is faster than that of the Taylor series expansion. The Padé approximation with $p = q$ (the diagonal Padé approximation) is frequently used due to the special advantages it offers in computation time and numerical stability.

The Padé approximation is, of course, a series of expansion, so the problems of slower convergence and round-off error manifest when the norm of $\mathbf{A}\Delta t$ is large. For this reason, the scaling and squaring method is also used to efficiently estimate for a matrix exponential with a large norm.

The Padé approximation is widely used as the numerical solution of the matrix exponential method (Moler and Loan 2003). For example, Mathematica and Matlab adopt the Padé approximation and the scaling and squaring method to evaluate a matrix exponential.

The Padé approximation has also been successfully applied to the burnup calculation for a complicated burnup chain (Yamamoto et al. 2007). However, since the Padé approximation is best suited to calculation for a dense-matrix, the Krylov subspace method is more suitable for a burnup calculation when the burnup matrix is very sparse, as shown in  Fig. 91.

6.3.9 The Krylov Subspace Method

The matrix exponential method and the Padé approximation offer a general numerical scheme to evaluate the matrix exponential. Burnup calculations in lattice physics computing, however, have the following features:

- a. Only the number densities are necessary as calculation results, that is, the matrix exponential itself is not necessary.
- b. The burnup matrix is a sparse matrix with many zero elements.

The Krylov subspace method is a new numerical method that utilizes the above features and is being applied in the fields of molecular dynamics and computational finance (Moler and Loan 2003). By using the Krylov subspace method, stiff burnup calculations with short-lived nuclides, which are difficult to treat by conventional methods, for example, the matrix exponential and the Runge–Kutta methods, have been successfully carried out in short computation time (Yamamoto et al. 2007). A detailed theoretical description of this method is shown by Yamamoto et al. (2007). A theoretical outline of the Krylov subspace method is offered as follows.

When (563) is truncated by m -1th order, we have the following polynomial:

$$\vec{N}(t + \Delta t) \cong c_0 \vec{N}(t) + c_1 (\mathbf{A}\Delta t)^1 \vec{N}(t) + c_2 (\mathbf{A}\Delta t)^2 \times \vec{N}(t) + \cdots + c_{m-1} (\mathbf{A}\Delta t)^{m-1} \times \vec{N}(t) \quad (592)$$

where

$$c_k = \frac{1}{k!}$$

The group of the vectors appearing in (592) is known as the Krylov subspace, which is defined as follows:

$$\mathbf{K}_m(\mathbf{A}\Delta t, \vec{N}(t)) = \text{Span} \{ \vec{N}(t), (\mathbf{A}\Delta t)\vec{N}(t), (\mathbf{A}\Delta t)^2\vec{N}(t), \dots, (\mathbf{A}\Delta t)^{m-1}\vec{N}(t) \}$$

Equation (592) is an example of a polynomial that approximately estimates $\vec{N}(t + \Delta t)$ with the m th order Krylov subspace. Therefore, when the appropriate coefficients, that is, c_k , can be chosen, a better estimate of $\vec{N}(t + \Delta t)$ may become possible. In the Krylov subspace method, c_k are chosen to minimize the square residual of the prediction error for $\vec{N}(t + \Delta t)$. Roughly speaking, appropriate c_k , which depend on matrix \mathbf{A} , are chosen by the least square fitting in the Krylov subspace method, while the conventional method (e.g., the matrix exponential method) utilizes $c_k = \frac{1}{k!}$ regardless of the burnup matrix.

The above explanation suggests that the Krylov subspace method offers an advantage in the choice of expansion coefficients, and is thus different from conventional methods. Since the matrix exponential method and the Runge–Kutta method also utilize a part of the Krylov subspace, they might be classified as a variation of the Krylov subspace method with fixed expansion coefficients.

6.3.10 Numerical Example

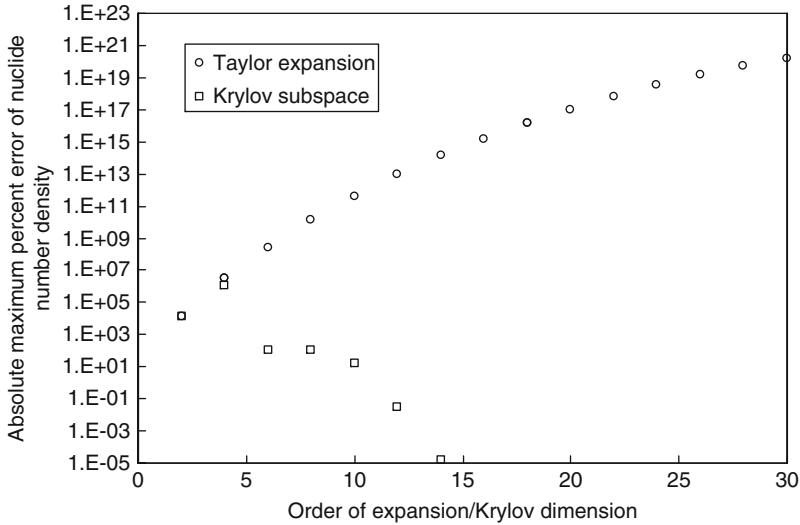
Test calculations to confirm the validity of the Krylov subspace method are offered and explained below. The calculation configuration is the pin-cell geometry of UO₂ fuel in PWR whose enrichment is 4.1 wt%. The initial number densities and geometry of this configuration are shown in [Table 23](#).

The linear power density is set at 179 W/cm. The burnup calculation up to 1 MWd/t (~2,300 s) is carried out by the matrix exponential method (the Taylor series expansion) and the

Table 23
Specifications of a pin cell for test calculation

	Pellet	Clad	Moderator
Radius [cm]	0.4095	0.4750	0.6300 [*])
Temperature [K]	900	600	559
Number density [1/cm ³]			
²³⁴ U	7.6551E+18		
²³⁵ U	9.5264E+20		
²³⁸ U	2.1994E+22		
¹⁶ O	4.5888E+22		
Nat-Zr		3.7375E+22	
¹ H			4.9848E+22
¹⁶ O			2.4926E+22

Square cell with 1.26 cm pitch is used in this analysis.



■ Figure 94

Maximum absolute error of number densities versus order of Taylor series expansions or dimensions of Krylov subspace

Krylov subspace method. The burnup chain used in this calculation is the “Developer” burnup chain of the MVP-BURN code, which consists of 28 heavy nuclides and 193 fission products (a total of 221 nuclides). The nuclide with the shortest half-life in this burnup chain is ^{106}Rh (29.8 s), and the norm of the burnup matrix ($\mathbf{A}\Delta t$) is $\ln(2)/29.8 \times 2,300 = 0.0233 \times 2,300 = 53.6$, which is quite large. The reference solution is obtained by Mathematica, in which evaluation of the matrix exponential is performed by the Padé approximation.

The maximum (absolute) error of number densities at 1 MW d/t is shown in [Fig. 94](#). In the case of Taylor series expansion, the maximum absolute error increases as the order of Taylor series expansion increases, which suggests that a very large expansion order will be necessary to obtain the converged result. Even if such Taylor series expansion is numerically evaluated, the reliability of the result is doubtful because of the severe numerical round-off error, as discussed in [6.3.5](#). In the Krylov subspace method, on the other hand, the maximum absolute error of nuclide number densities rapidly decreases with an increasing order of expansion (i.e., the order of Krylov subspace dimensions), and sufficient accuracy is obtained when the order of dimension is 14. The number densities of the nuclides and their associated errors are presented in [Figs. 95–99](#).

Next, burnup calculations up to 100, 1,000, 10,000 and 100,000 MW d/t are carried out by the fourth-order Runge–Kutta, Padé (order $p = 2, 4, 6, 8$) and Krylov subspace (order of dimension = 5, 10, 20, 30, 40, 50, 60) methods, and the accuracy of their calculations are compared. Note that three different time-steps, that is, 0.0001, 0.001, and 0.002 d are used in the fourth-order Runge–Kutta method. In the Padé and Krylov subspace methods, burnup steps are automatically adjusted in order to keep the error of nuclide number densities sufficiently small. Once again, the burnup chain used in the calculation is the “Developer” chain of the MVP-BURN code. The reference solution is obtained by the Mathematica.

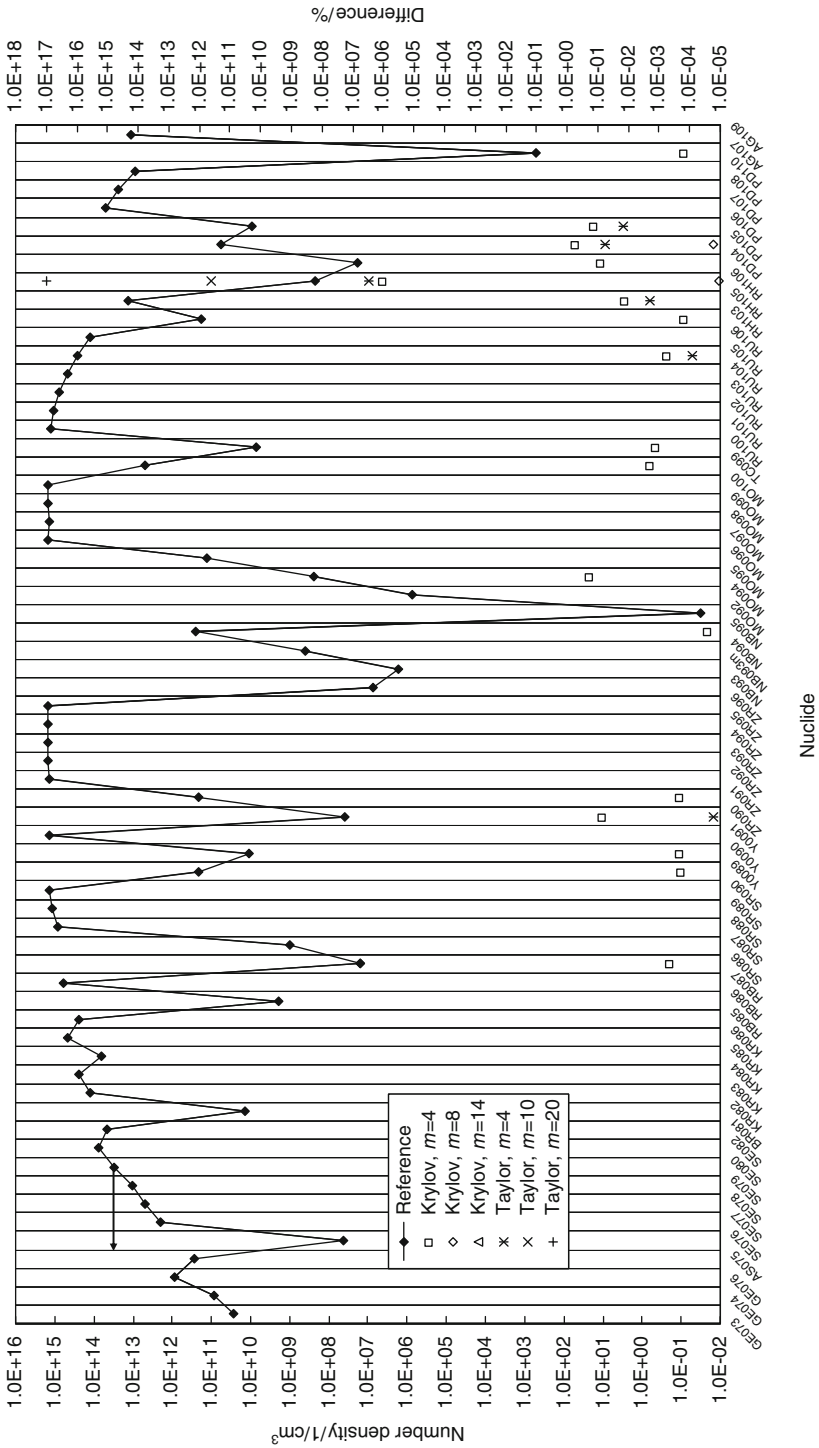


Figure 95 Number densities and their errors at 1 MW d/t. (⁷³Ge-¹⁰⁹Ag) Note that errors less than 10⁻⁵% are not shown

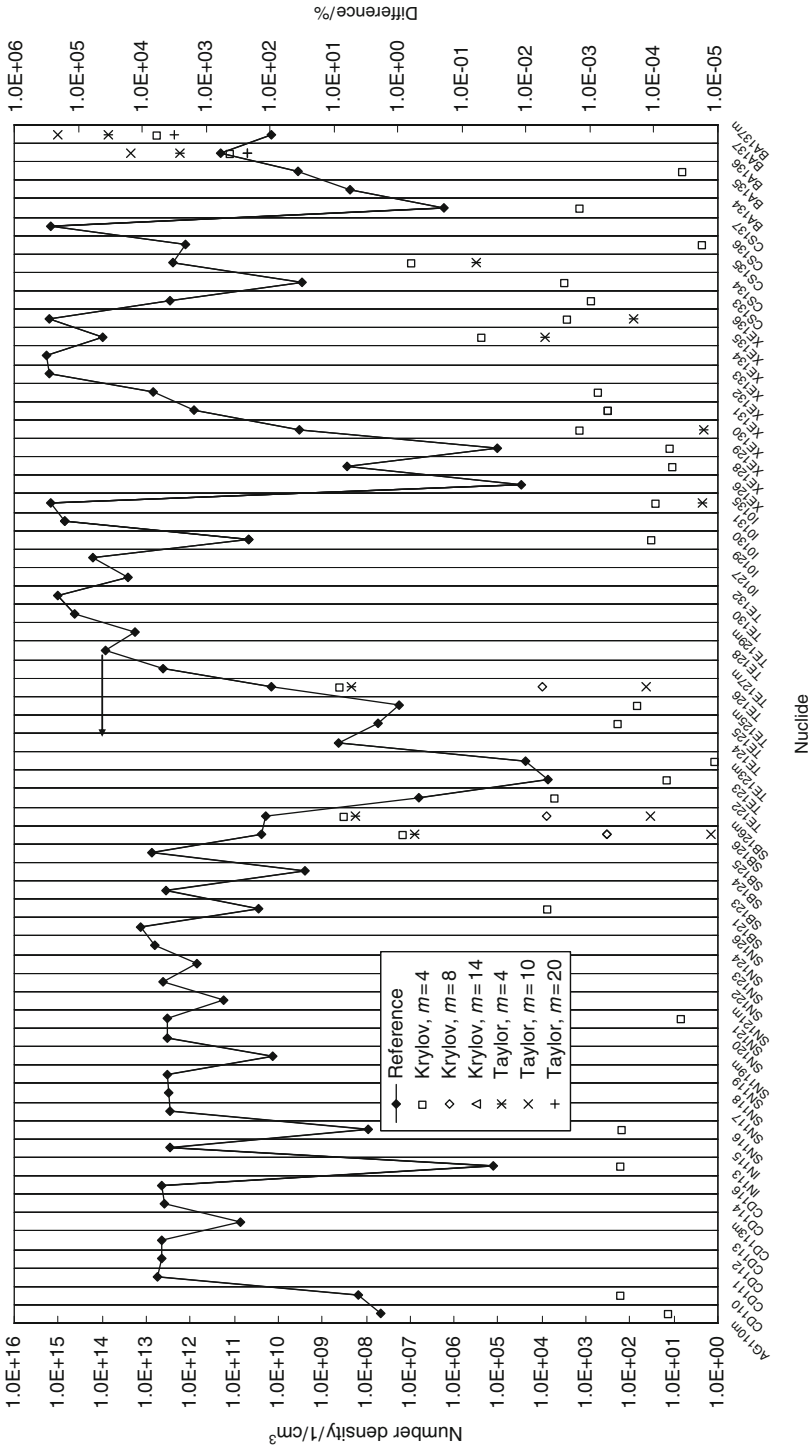
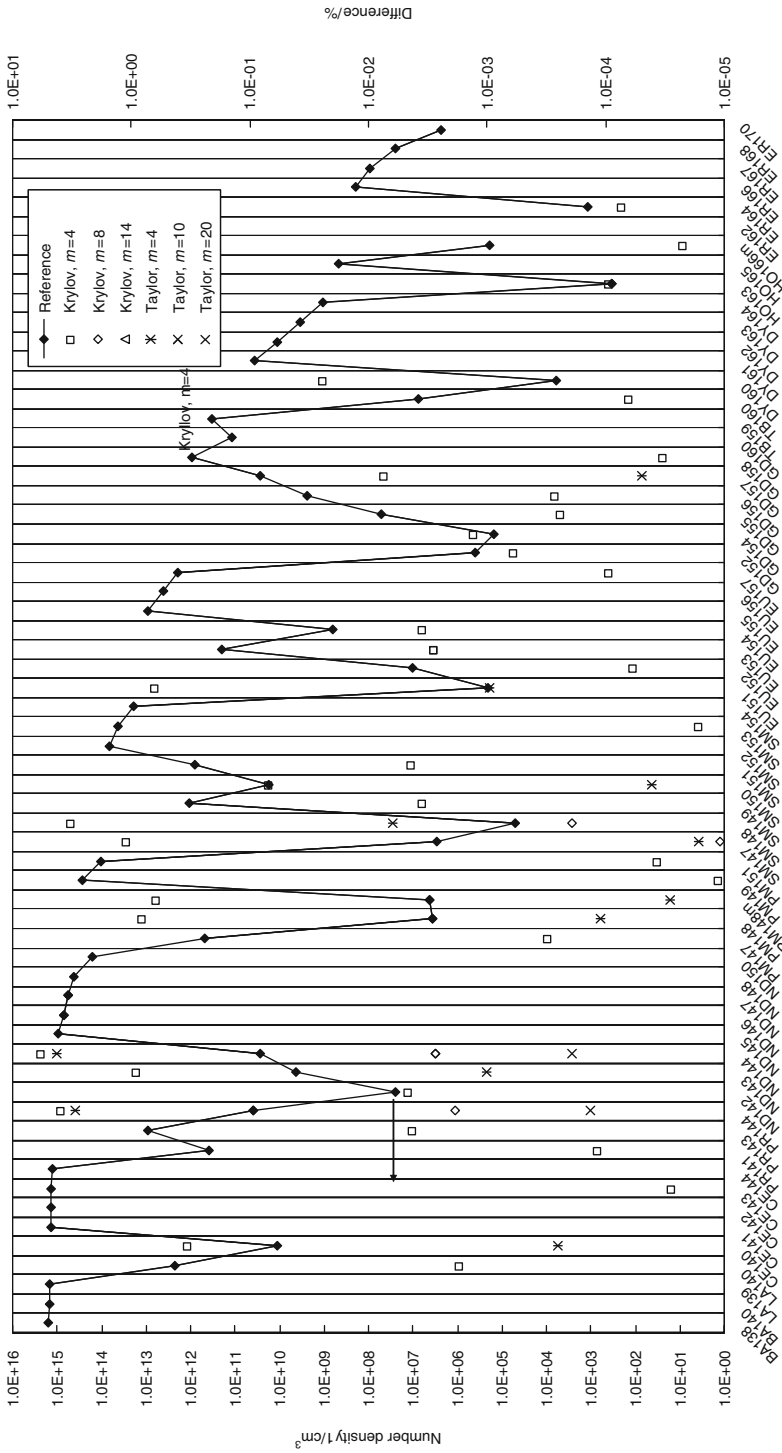


Figure 96 Number densities and their errors at 1 MW d/t. ($^{110\text{m}}\text{Ag}$, $^{137\text{m}}\text{Ba}$) Note that errors less than $10^{-5}\%$ are not shown



Nuclide

Figure 97
 Number densities and their errors at 1 MW d/t. (¹³⁸Ba-¹⁷⁰Er) Note that errors less than 10⁻⁵% are not shown

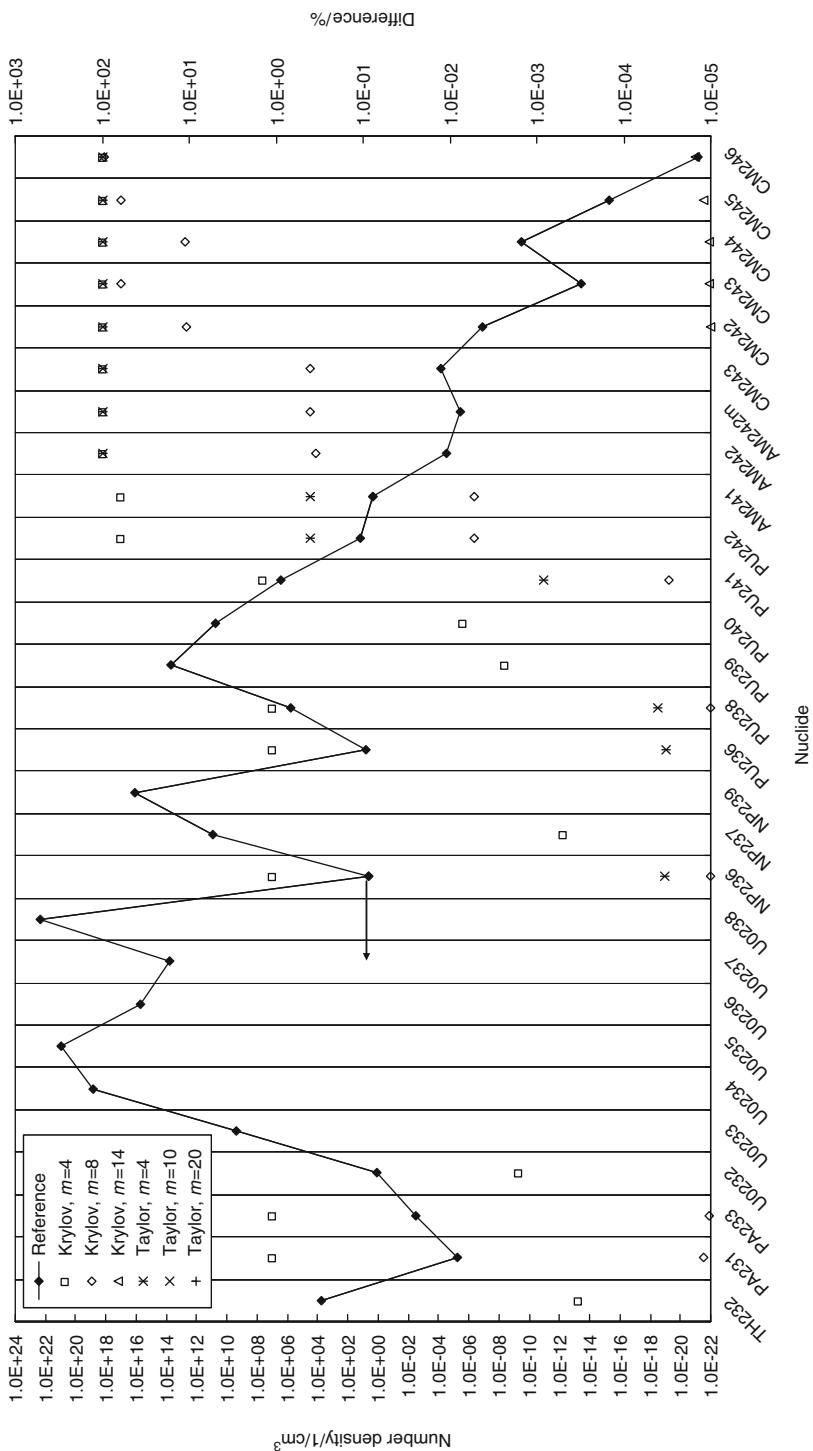
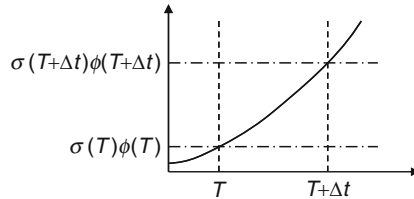


Figure 98 Number densities and their errors at 1 MW d/t. (^{232}Th - ^{246}Cm) Note that errors less than $10^{-5}\%$ are not shown



■ **Figure 99**

Example of microscopic absorption rate during burnup

The maximum errors of nuclide number densities after burnup, and calculation times, are summarized in [▶ Tables 24](#) and [▶ 25](#). From these tables we can make the following observations:

- In the Runge–Kutta method, a very fine burnup step is necessary in order to obtain the appropriate result. The burnup step should be set at less than 0.001 d (~ 90 s) in the present burnup calculation, due to the presence of a short-lived nuclide (^{106}Rh). Consequently, the computation time becomes impractically long.
- Both the Padé and Krylov subspace methods give accurate results from a practical point of view.
- The Krylov subspace method is between several and several hundred times faster than the Padé method.
- When the dimension of subspace is increased, the accuracy of the expansion by the subspace increases; thus, the width of the burnup step can be reduced in order to achieve sufficient accuracy. The computation time for matrix manipulations, however, then becomes longer. On the contrary, when the dimension of subspace is decreased, the accuracy of the expansion decreases; thus, the burnup step must be increased. The computation time for matrix manipulations, however, then becomes shorter. Consequently, in terms of computation time, there is an adequate dimension of the Krylov subspace.

The above observations suggest that the Krylov subspace method can provide an accurate solution in a short computation time for a complicated burnup chain with short-lived nuclides.

In the actual implementation of the Krylov subspace method, a well-established package such as EXPOKIT can be used (Sidje 1998). The utilization of such sophisticated software reduces the work of implementation.

6.3.11 Predictor–Corrector Method

There are two sources of error in the numerical simulation of a burnup calculation, that is, temporal discretization errors in the sections so far, and the reaction rate. The former topic has been addressed in the previous subsections. The latter topic, the temporal discretization error in the reaction rate, is treated in this section.

First, we consider a very simple burnup equation for an absorber nuclide:

$$\frac{dN}{dt} = -\sigma_a(t)\phi(t)N \quad (593)$$

■ **Table 24**
Maximum error of nuclide number densities (unit: %)

Method	Burnup time			
	10 ² MWd/t (2.67 days)	10 ³ MWd/t (26.7 days)	10 ⁴ MWd/t (267 days)	10 ⁵ MWd/t (2,670 days)
Reference (Mathematica)	0.0E+00	0.0E+00	0.0E+00	0.0E+00
Runge-Kutta				
Substep = 0.0001 day	8.3E-01	-**	-	-
Substep = 0.001 day	8.3E-01	-	-	-
Substep = 0.002 day	NA*	-	-	-
Pade				
Order = 2	3.8E-05	3.7E-05	4.9E-05	4.9E-05
Order = 4	3.8E-05	3.7E-05	4.9E-05	4.9E-05
Order = 6	3.8E-05	3.7E-05	4.9E-05	4.9E-05
Order = 8	3.8E-05	3.7E-05	4.9E-05	4.9E-05
Krylov				
Dimension = 5	1.0E+02	1.0E+02	1.0E+02	1.8E+03
Dimension = 10	7.5E-06	4.6E-06	1.0E+02	1.7E+03
Dimension = 20	7.5E-06	4.6E-06	1.2E-05	4.9E-06
Dimension = 30	1.0E-05	4.6E-06	1.2E-05	4.9E-06
Dimension = 40	7.5E-06	4.6E-06	1.2E-05	4.9E-06
Dimension = 50	7.5E-06	3.3E-04	1.2E-05	4.9E-06
Dimension = 60	7.5E-06	3.3E-04	1.2E-05	4.9E-06

* Diverged.

** Not evaluated.

The analytic solution of (593) is given as follows:

$$N(T + \Delta t) = N(T) \exp\left(-\int_T^{T+\Delta t} \sigma_a(t)\phi(t)dt\right) \quad (594)$$

In a common burnup calculation, the absorption cross section and the neutron flux are given as constants at the discrete burnup step (T). Thus (594) can be written as

$$N(T + \Delta t) = N(T) \exp\left(-\int_T^{T+\Delta t} \sigma_a(t)\phi(t)dt\right) \cong N(T) \exp(-\sigma_a(T)\phi(T)\Delta t) \quad (595)$$


When the absorption cross section and neutron flux is fairly constant throughout a burnup step, the accuracy of (595) is high. However, when the behavior of the absorption rate is not constant, as shown in  Fig. 99, the integrated absorption rate during $T \sim T + \Delta t$ is underestimated. The number density of a nuclide is therefore overestimated; that is, a nuclide appears to have burned more slowly than it actually did.


Table 25
Computation time (unit: s)

Method	Burnup time			
	10 ² MWd/t (2.67 days)	10 ³ MWd/t (26.7 days)	10 ⁴ MWd/t (267 days)	10 ⁵ MWd/t (2,670 days)
Reference (Mathematica)	1.24	1.47	14.38	30.41
Runge-Kutta				
Substep = 0.001 day	>1,000*	–***	–	–
Substep = 0.001 day	>100	–	–	–
Substep = 0.002 day	NA**	–	–	–
Pade				
Order = 2	1.29	1.49	1.63	1.64
Order = 4	1.31	1.50	1.63	1.65
Order = 6	1.29	1.50	1.64	1.65
Order = 8	1.30	1.50	1.65	1.65
Krylov				
Dimension = 5	1.03	1.05	0.97	0.82
Dimension = 10	0.61	1.50	1.71	1.64
Dimension = 20	0.01	0.07	0.31	1.51
Dimension = 30	0.01	0.03	0.11	0.58
Dimension = 40	0.02	0.04	0.09	0.36
Dimension = 50	0.04	0.05	0.09	0.33
Dimension = 60	0.11	0.12	0.18	0.48

*Precise measurement was not carried out since the code was not optimized for computation speed.

** Diverged.

*** Not evaluated.

Variations in the reaction rate, such as those shown in  Fig. 99, frequently occur in actual burnup calculations. Such a trend is especially apparent when a burnable absorber, for example, gadolinium, is used in a fuel. The number density of a burnable absorber decreases as burnup proceeds. Consequently, the neutron flux in the burnable absorber becomes higher since the macroscopic absorption cross section of the absorber becomes smaller. Furthermore, the neutron spectrum shifts to a lower energy region (becomes “softer”) since the macroscopic thermal absorption cross section of the burnable absorber becomes smaller. A multigroup (energy-averaged) microscopic cross section becomes larger during burnup due to its softer neutron spectrum. Consequently, the microscopic reaction rate ($\sigma\phi$) becomes larger during burnup.

The temporal discretization error due to (595) can be suppressed by reducing the time-step in a burnup calculation. In other words, utilization of a finer burnup step can limit the temporal

discretization error. However, evaluation of the reaction rate, that is, evaluations of an effective microscopic cross section and neutron flux, is the most time-consuming part of actual burnup calculations. Therefore, the number of reaction rate calculations (i.e., those of an effective microscopic cross section and neutron flux) should be minimized in terms of computation time.

One way to resolve the above conflict is the predictor–corrector (PC) method. Roughly speaking, the PC method performs burnup calculation using a time-averaged absorption reaction rate during a time-step, through pre-evaluation of the absorption rate at $T + \Delta t$.

The actual calculation procedure of the PC method is as follows (Method 1):

- a. Evaluate the microscopic reaction rate with the number density of burnup step n .
- b. Perform the burnup calculation to burnup step $n + 1$ using the reaction rate obtained in (a). This calculation step is called the predictor step.
- c. The number density of burnup step $n + 1$ is estimated using the calculation result of (b). The microscopic reaction rates at this point (burnup step $n + 1$) are then evaluated.
- d. Again perform the burnup calculation using the average microscopic reaction rates of (a) and (c). This step is called the corrector step.

The following alternative method (Method 2) can also be used:

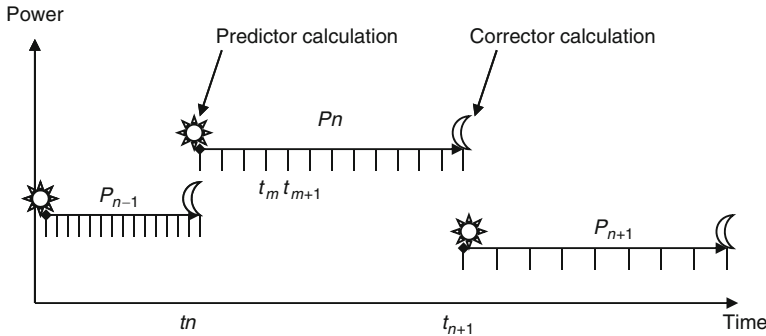
- a. Evaluate the microscopic reaction rate with the number density of burnup step n .
- b. Perform burnup calculation to burnup step $n + 1$ using the reaction rate obtained in (a). This calculation step is called the predictor step.
- c. The number density of burnup step $n + 1$ is estimated using the calculation result of (b). The microscopic reaction rates at this point (burnup step $n + 1$) are then evaluated.
- d. Again perform burnup calculation using the microscopic reaction rates of (c). This step is called the corrector step.
- e. Average the number densities obtained in (b) and (d) to obtain the final results.

Because two reaction rate calculations (predictor and corrector) are necessary for a burnup step in the PC method, it would seem to require longer computation time. However, since the PC method enables the width of the burnup step to be increased by a factor of 10, the computational efficiency of the PC method is actually much greater than that of the conventional method. Therefore, the PC method is the inevitable choice for production lattice physics and core simulation codes.

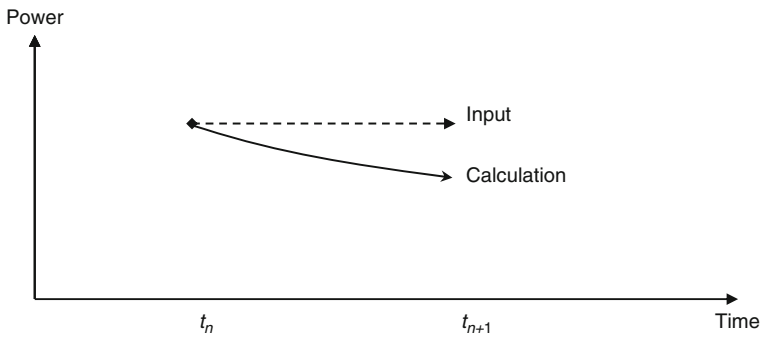
6.3.12 Sub-Step Method

As described in [▶ 6.3.11](#), reaction rate calculations dominate the computation time of a lattice physics computation. Therefore, the time-step size for reaction rate calculations can be longer than that for temporal discretization of the burnup equation, as shown in [▶ Fig. 100](#). Such “double” time-step setting is called the sub-stepping method.

In common lattice physics codes, the burnup steps for reaction rate evaluations are given as input data. Since the sub-step is automatically (and internally) set by the lattice physics codes, users are usually not aware of this. For example, the MVP-BURN code subdivides an input burnup step into 20 sub-steps to which the numerical solution of the burnup calculation is applied, using the Bateman method.



■ Figure 100
Concept of sub-stepping method for burnup calculation




■ Figure 101
Variation of power density during a time-step

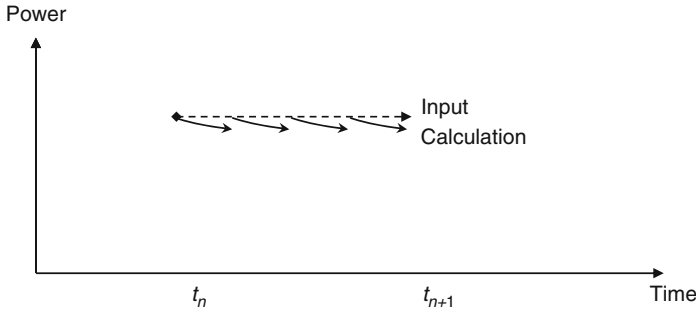
There are two objectives to incorporating the sub-stepping method:

Reduction of Temporal Discretization Error

Temporal discretization error inevitably occurs in a numerical solution by the Euler, Runge–Kutta, matrix exponential, Padé, and Krylov subspace methods, all of which contain a degree of error due to truncation of the expansion series of a matrix exponential. The temporal discretization error can be reduced by the sub-stepping method (though the discretization error from the reaction rate cannot be reduced). Since the matrix decomposition and Bateman methods utilize the “analytic solution” for the burnup equation, temporal discretization error might not be produced by these methods. However, they still suffer from temporal discretization error since in actual calculations, the burnup chain is approximated (e.g., cut the “circuit chain”). Therefore, the sub-stepping method is also useful for these methods.

Power Normalization during Burnup Step

In light water reactor calculations, fissile nuclides are depleted during burnup. Since the neutron flux is normalized at the beginning of the time-step, power density gradually decreases during burnup, as shown in  Fig. 101.



■ Figure 102

Variation of power with power normalization at sub-step during burnup step

Since burnup is evaluated by the time integration of power, the calculated burnup will be underestimated in [Fig. 101](#). Therefore, the following power normalization is carried out at sub-step m , that is, the normalized factor Norm_m is multiplied by the reaction rate.

$$P = \text{Norm}_m \sum_i \left(\sum_k \kappa_k \sigma_{f,k,i} N_{k,i} \right) \phi_i V_i \quad (596)$$

where

P : power (input data) [J s^{-1}],

κ_k : released energy per fission of nuclide k [J],

$\sigma_{f,k,i}$: microscopic fission cross section of nuclide k in region i [cm^2],

$N_{k,i}$: number density of nuclide k in region i [cm^{-3}],

ϕ_i : neutron flux [$\text{cm}^{-2} \text{s}^{-1}$],

V_i : region volume [cm^3].

By using the above power normalization, the underestimation of burnup can be avoided, as shown in [Fig. 102](#).

6.3.13 Cooling Calculation

The composition of fuels varies during shutdown due to the decay of nuclides. This variation of fuel composition during shutdown has a considerable impact on core characteristics, so this effect must be taken into account in actual in-core fuel management calculations.

In light water reactor analyses, the following decays are important:



This decay has an impact on criticality during the immediate return to power after a scram. It is also a cause of Xe oscillation. Since the half-life of ^{135}Xe is also short (9 h), in a startup analysis after refueling, all Xe is assumed to have decayed (no Xe).

$^{149}\text{Pm} \rightarrow (\text{Half-Life } 54 \text{ h}) \rightarrow ^{149}\text{Sm}$

This has an impact on the core characteristics during the startup operation. Since ^{149}Sm is a stable isotope, all ^{149}Pm is assumed to have decayed into ^{149}Sm (peak condition of Sm) in the startup analysis.

 $^{239}\text{Np} \rightarrow (\text{Half-Life } 2.4 \text{ days}) \rightarrow ^{239}\text{Pu}$

This has an impact on the criticality during return to power after a scram. The positive reactivity effect of this decay is partly canceled out by the negative reactivity effect of $^{149}\text{Pm} \rightarrow ^{149}\text{Sm}$, whose half-life is similar to that of ^{239}Np . Therefore, in an analysis of return to power during a few days after a shutdown, the decay of both $^{149}\text{Pm} \rightarrow ^{149}\text{Sm}$ and $^{239}\text{Np} \rightarrow ^{239}\text{Pu}$ should either be taken into account, or not considered at all.

 $^{148\text{m}}\text{Pm} \rightarrow (\text{Half-Life } 41 \text{ days}) \rightarrow ^{148}\text{Sm}$

This has an impact on the core characteristics of a startup physics test after a normal periodic inspection and refueling that requires a few months.

 $^{148}\text{Pm} \rightarrow (\text{Half-Life } 2.6 \text{ years}) \rightarrow ^{148}\text{Sm}$

Since the half-life of this decay is quite long, it has an impact on the reactivity of reinserted fuels, which were irradiated during a cycle then temporarily stored in the spent fuel pool for future use. When reinserted fuels with long-term cooling are used, the present decay will affect the core characteristics.

 $^{155}\text{Eu} \rightarrow (\text{Half-Life } 4.7 \text{ years}) \rightarrow ^{155}\text{Gd}$


This also has an impact on the reactivity of reinserted fuels. It is a major cause of reactivity variations in reinserted fuels that have been stored for a long time.

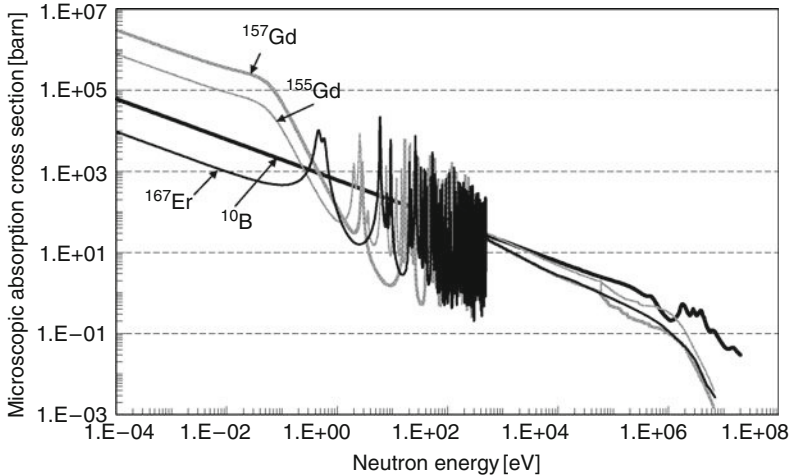
 $^{241}\text{Pu} \rightarrow (\text{Half-Life } 14.4 \text{ years}) \rightarrow ^{241}\text{Am}$

This has a major impact on the reactivity of reinserted fuels. This decay reaction is especially important for MOX fuels, since a considerable amount of ^{241}Pu is initially loaded in them. In a core design loaded with MOX fuels, this cooling effect should be taken into account not only for spent MOX fuels, but also for fresh MOX fuels. In order to estimate the decay amount, an accurate cooling time (the span of time from fuel composition characterization to fuel loading) is necessary.

A cooling calculation can be carried out as a burnup calculation with a very low power density. Note that zero power density might cause numerical problems, so the utilization of a very low power density might be appropriate in actual cooling calculations.

6.4 Burnup in Gadolinia-Bearing Fuel

Gadolinia (Gd_2O_3) is a common burnable absorber used in light water reactors. A comparison of the microscopic absorption cross sections of major nuclides used as burnable absorber is shown in  Fig. 103. This figure indicates that the absorption cross section of gadolinium (^{155}Gd , ^{157}Gd) is considerably larger than those of other nuclides. This blackness, that is, the



■ Figure 103

Comparison of microscopic absorption cross sections of major burnable absorber nuclides

strong neutron absorption property of gadolinia, requires some particular consideration in a burnup analysis.

First, since the absorption cross section of gadolinium is very large, gadolinia-bearing fuel rods are generally sparsely located (scattered) in fuel assemblies. Therefore, a gadolinia-bearing fuel assembly has a higher neutronics heterogeneity due to the presence of the “black” regions. Such “black” regions should be handled through sophisticated calculation methods, for example, a neutron transport calculation with explicit geometry treatment. Otherwise, the prediction error will be greater than that of conventional fuel assemblies without gadolinia-bearing fuel rods.

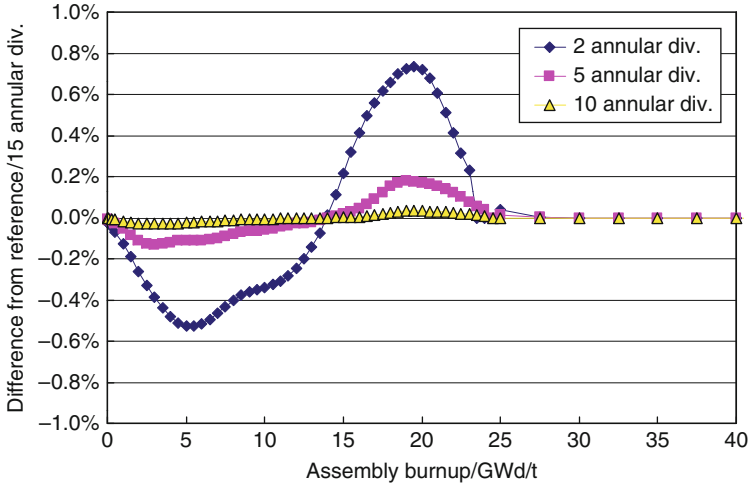
The second point is the unique burnup properties of a gadolinia-bearing fuel rod. This point will be discussed in detail in the next section.

In the following sections, modeling considerations in the accurate handling of a gadolinia-bearing fuel assembly are discussed.

6.4.1 Onion-Skin Effect

The mean free path of thermal neutrons in a gadolinia-bearing fuel pellet is very short, due to the large absorption cross section of gadolinia isotopes. At the beginning of life, thermal neutrons entering from a moderator into a pellet are immediately absorbed by gadolinium nuclides at the surface. Therefore, gadolinium nuclides are depleted from the pellet surface like the layered skins of an onion. This particular burnup behavior of gadolinium isotopes is called the “onion-skin” effect.

In the numerical modeling of a gadolinia-bearing fuel pellet, the onion-skin effect should be carefully treated since it has a significant impact on the neutronics characteristics of a gadolinia-bearing fuel assembly. To accurately capture the onion-skin effect, a gadolinia-bearing fuel pellet



■ Figure 104

Effect of annular division of gadolinia-bearing fuel pellet (17×17 PWR fuel assembly with 24 Gd-bearing fuel rods of 10 wt% Gd_2O_3)

is annularly divided into regions ranging in number from several to more than a dozen, and the depletion of gadolinium isotopes is explicitly tracked in each annular region. Note that ordinary UO_2 fuel usually has one spatial region in a pellet.

The effect of the annular divisions of a gadolinia-bearing fuel pellet on fuel assembly k -infinity is shown in [Fig. 104](#). This figure shows that the annular division of a gadolinia-bearing fuel pellet has a significant impact on the k -infinity of a fuel assembly, and more than several annular regions are necessary to obtain an accurate result.

The onion-skin effect requires detailed spatial modeling of the gadolinia-bearing fuel pellet. Such modeling, however, requires a very burdensome calculation, which is why various numerical techniques have been used in practical lattice physics computations. Previously, the “off-line” depletion calculation for a gadolinia-bearing fuel pellet was used in conventional lattice physics codes. In this approach, a gadolinia-bearing fuel pellet is depleted in one-dimensional cylindrical geometry, which consists of an annularly divided pellet, clad, moderator, and buffer regions. The buffer region simulates the spectrum environment of adjacent fuel cells in order to reproduce the neutron spectrum in a gadolinia-bearing fuel pellet. The depletion calculation in one-dimensional geometry is carried out prior to the assembly calculation, and spatially homogenized and energetically collapsed cross sections for a gadolinia-bearing fuel pellet or fuel cell are provided in the subsequent assembly calculation. Since the “off-line” depletion calculation is carried out in one-dimensional geometry, detailed spatial discretization (annular divisions) of a gadolinia-bearing fuel pellet can be used within a short computation time.

Though the off-line approach has merit in terms of computation time, its accuracy depends on the calculation conditions used in the one-dimensional transport calculation. Since the actual assembly configuration in two-dimensional geometry is approximated by one-dimensional geometry, there is some ambiguity in the setting of the buffer region. In fact, the difference between the neutron spectrum obtained by one-dimensional geometry and that

obtained by explicit two-dimensional geometry sometimes becomes considerable, and can be a major cause of error in the burnup calculation of a gadolinia-bearing fuel assembly.

Ongoing progress in the computational environment and the requirement of increased accuracy strongly promote the utilization of more advanced and sophisticated treatment of a gadolinia-bearing fuel assembly. As described in [▶ Sect. 5](#), the latest lattice physics codes explicitly treat the heterogeneous geometry of the entire fuel assembly in the spectrum calculation, in which annular divisions of the gadolinia-bearing fuel pellet are also explicitly and directly taken into account. Such detailed modeling of fuel assembly improves the prediction accuracy of burnup behavior of a gadolinia-bearing fuel assembly, since the neutron spectrum in a gadolinia-bearing fuel pellet (and thus the absorption reaction rate of gadolinium isotopes) is more accurately evaluated than it is by the conventional model that utilizes the buffer region.

6.4.2 Asymmetry Effect in Gadolinium Depletion

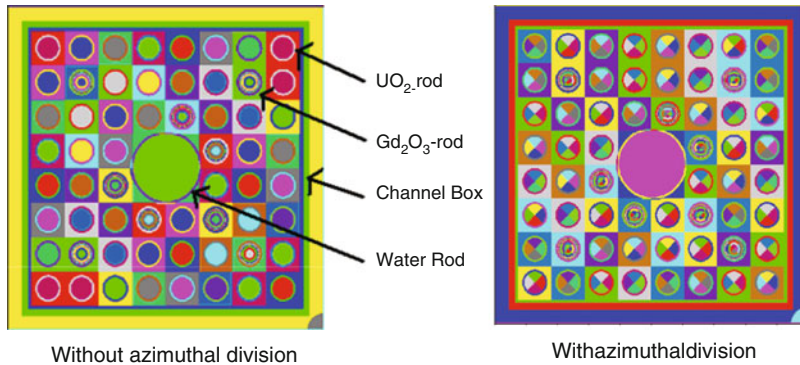
The previous section describes the necessity of the annular division of a gadolinia-bearing fuel pellet due to the onion-skin effect. Such modeling is appropriate when the adjacent fuel cells are similar from the viewpoint of the neutron spectrum. In other words, when the neutron spectra entering into a gadolinia-bearing fuel pellet are fairly uniform in azimuthal direction, the annular division (without azimuthal division) of a pellet is adequate, since the depletion rate of gadolinium isotopes is azimuthally uniform.

However, in actual situations, especially in a BWR fuel assembly, the neutron spectrum is highly space-dependent due to the presence of gap water and large water holes. Therefore, the azimuthal dependence of the gadolinium depletion rate (asymmetry effect in gadolinium depletion) should be taken into account for an accurate prediction of the burnup behavior of a gadolinia-bearing fuel assembly.

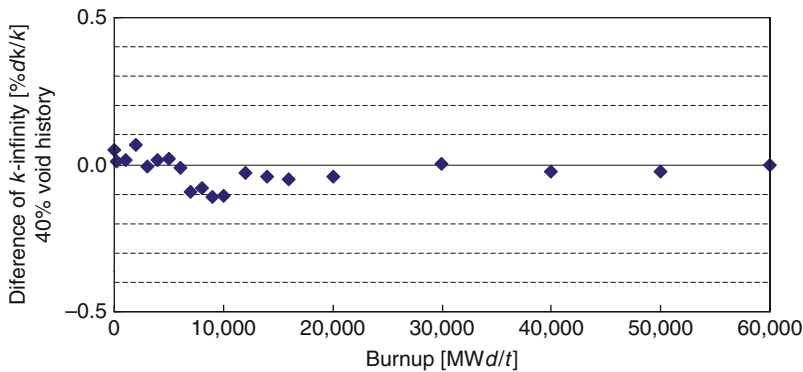
In order to capture the asymmetry effect, a gadolinia-bearing fuel pellet should be azimuthally divided, in addition to the annular division. The magnitude of the asymmetry effect is evaluated in an 8×8 BWR fuel assembly with gadolinia-bearing fuel rods (Tohjo et al. 2006). A continuous energy Monte Carlo calculation code is used to evaluate the asymmetry effect in this calculation, since detailed spatial discretization in the azimuthal direction cannot be directly modeled by many lattice physics codes.

Calculation geometries are shown in [▶ Fig. 105](#). The left model is an ordinary spatial (material) discretization used in lattice physics computations. Unlike this, the right model has an azimuthal division in addition to the discretization used in the left one. These two calculation models are used for burnup calculation by the continuous energy Monte Carlo burnup code. The difference of the k -infinity at 40% voided condition is shown in [▶ Fig. 106](#). This figure indicates that the asymmetry effect reaches $0.15\% \Delta k/k$ at 10,000 MW d/t, where gadolinium is almost burned out. When the gadolinia-bearing fuel pellet is azimuthally divided, the depletion of gadolinium isotopes is independently tracked in each azimuthal region. Consequently, the k -infinity of the Gd-bearing fuel assembly changes, due to variations in the burnup behavior of gadolinium isotopes.

Though the asymmetry depletion effect is not very large in this case, it could be larger when the azimuthal variation of the neutron spectrum becomes more significant. For example, in a conventionally designed fuel assembly, the gadolinia-bearing fuel rods are sparsely located,



■ **Figure 105**
Calculation geometries used for asymmetry effect of gadolinium depletion



■ **Figure 106**
Difference of assembly k -infinity with and without azimuthal division in 8×8 BWR assembly. Difference is defined by (without – with)/with

but they may be placed side-by-side in order to improve their performance. In such a case, the asymmetry depletion effect should be carefully investigated and its impact should be estimated.

6.4.3 Various Numerical Techniques for Gadolinium Depletion

The predictor–corrector method to reduce the effect of the constant reaction rate approximation in a burnup step is discussed in 6.3.11. However, even if the PC method is used, the typical time-step size used for a Gd-bearing fuel assembly is 0.2 GW d/t (Knott and Wehlage 2007), since the absorption reaction rate of gadolinium isotopes changes rapidly during burnup. Since gadolinium typically burns out at 10–20 GW d/t, from several dozen to a hundred burnup steps are still necessary to accurately deplete a Gd-bearing fuel assembly with the PC method.


In order to reduce this computational burden, some numerical techniques have been developed. One of these is the dual-time depletion method (Rhodes et al. 2006; Knott and Wehlage 2007). In this approach, only the pin-cell calculation for the Gd-bearing fuel rods is performed at a fine time-step size, and the time-consuming assembly calculation is executed at a coarser time-step. By synthesizing these two different calculations (i.e., pin cell and assembly), we can obtain the assembly calculation results that are equivalent to a fine time-step analysis. The reference suggests that the time-step size for assembly calculations can be increased to five times larger than that of the conventional burnup method, without dual-time stepping.

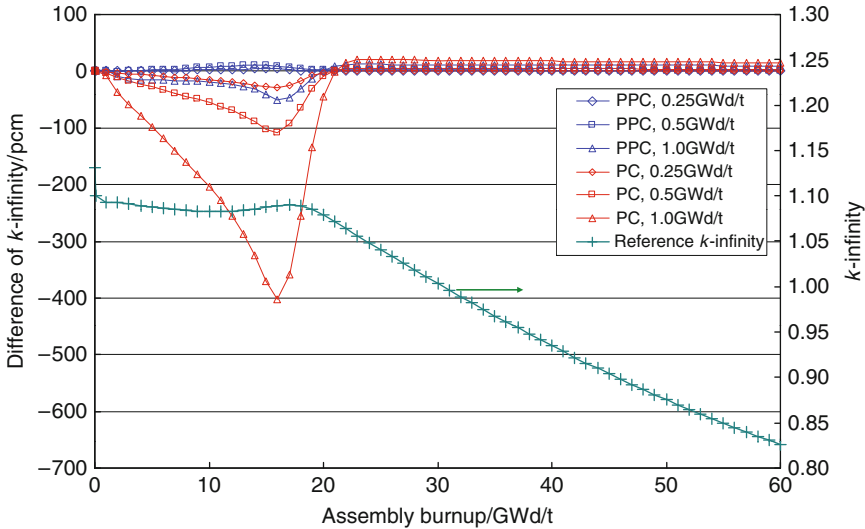
Another approach is the consideration of reaction rate variation during a time-step. In the conventional approach, the coefficients of the burnup equation (i.e., the reaction rates) are assumed to be constant during a time-step. This assumption is used for both the predictor and corrector burnup calculations. The final results are obtained by averaging the predictor and corrector burnup calculation results in order to cancel out the discretization error caused by the assumption of a constant reaction rate. In order to more accurately capture the depletion of each nuclide, the variation of reaction rates within a burnup step can be taken into account. These variations are incorporated by using the linear (Knott and Wehlage 2007) or the quadratic (Rhodes et al. 2006) function of the burnup time.

One of the problems with the conventional PC method is the error in the estimate of reaction rates in a corrector step. The reaction rates of a corrector step are estimated based on the number density obtained by a predictor step. Therefore, when the calculation accuracy of the predictor step is not sufficient, the number densities used in the corrector step may contain some error. Thus, the estimated corrector reaction rates might not be predicted accurately. This is especially true for a Gd-bearing fuel assembly, since the neutron flux in a Gd-bearing fuel rod rapidly increases before the burnout of gadolinia. In this case, the reaction rates in Gd-bearing fuel rods at a predictor step are smaller than the “true” (or the average during the time-step) values, so that the depletion of gadolinium isotopes will be smaller. Since the gadolinia content will be higher than the appropriate (or “true”) value in the corrector calculation, the reaction rates in the Gd-bearing fuel rod are also underestimated. Consequently, the reaction rates in the Gd-bearing fuel rod will be underestimated, since both the predictor and the corrector reaction rates are underestimated. This, in fact, is one of the dominant errors in the conventional PC method.

The traditional countermeasure for this problem is the iteration of the corrector calculations. That is, corrector calculations are carried out until the corrector reaction rates are converged with the best-estimated number densities (obtained by the average of the predictor and updated corrector results). The apparent drawback of this approach is the computation time it requires. Since the corrector calculations need to be repeated, the computation time per time-step will increase.

Another approach is to utilize the relationship between gadolinium number density and the microscopic reaction rate of gadolinium isotopes. In fact, the microscopic reaction rates (i.e., reaction rate per atom) of gadolinium isotopes are approximately proportional to their number densities, at least within a moderate burnup step-size. By using this relationship, improved corrector reaction rates are estimated by the projection (or extrapolation) of the conventional PC results. This approach does not require additional corrector calculation; it is computationally efficient (Yamamoto et al. 2009).

A comparison of the accuracy achieved with the conventional PC and the “projected” PC (PPC) methods is presented in  Fig. 107. Apparently, the PPC method gives better accuracy than the conventional PC method. By using the PPC method, the width of the burnup step-size



■ Figure 107

Comparison of k -infinity for Gd-bearing fuel assembly (17×17 PWR fuel, 4.1 wt% enrichment, 10 wt% Gd_2O_3)

can be increased (less than doubled), that is, the number of the burnup step can be reduced (by less than half). Note that we can apply higher-order polynomials to represent the relationship between the number densities of gadolinium and their microscopic reaction rates. The drawback of the higher-order method is the amount of memory it requires. For example, in order to use the second-order polynomial, additional memory storage to maintain the microscopic reaction rates at three burnup points is necessary.

6.5 Summary

In this section, various aspects of the burnup calculations used in lattice physics computation, that is, physics, modeling, numerical methods, and other topics are summarized. Since the burnup calculation is one of the dominant factors contributing to the overall accuracy of calculations, its treatment is important. Though the burnup calculation is a major part of a lattice physics code, a detailed description of this issue can be hardly be found in common textbooks. This subsection would be helpful for both the users and developers of lattice physics codes.

7 Case Matrix

7.1 Introduction

All the individual state points that need to be analyzed by the lattice physics code to fully characterize the fuel design for use in a specific three-dimensional nodal code are referred to as

the *case matrix*. The case matrix will vary between different nodal codes and between different reactor types (i.e., between BWRs and PWRs). The necessity for a case matrix arises from our need to condense and homogenize cross sections over the entire lattice in order to generate two-group nodal data. To perform the condensation and homogenization, we need a very detailed flux distribution. The flux distribution changes as the conditions in the core change, and as the isotopics of the fuel change. This requires us to analyze the lattice every time the isotopics change substantially (i.e., burnup calculation) or every time a core parameter changes substantially (i.e., branch calculation), giving rise to a large collection of different cases. In this section, we will describe the approach used to build cross sections for use in a nodal code such as SIMULATE-3 (Dean et al. 2005). This is by no means an exhaustive discussion on case matrices and the reader should be aware that there are other ways of designing a case matrix to support a nodal code.

7.2 Cross Section Dependencies in BWRs

In general, macroscopic nodal cross sections for a specific reactor condition (e.g., exposure, fuel temperature, and moderator density) can be pieced together as the sum of a base cross section and a collection of partial cross sections, where each partial cross section is used to account for changes in the base cross section due to perturbations in various reactor conditions. To a good approximation, this can be expressed for BWRs as

$$\begin{aligned} \Sigma_x^g = & \Sigma_{x,V}^g(E, U) + \delta\Sigma_{x,TF}^g(E, V) + \delta\Sigma_{x,TM}^g(E, V) + \delta\Sigma_{x,CR}^g(E, V) \\ & + \delta\Sigma_{x,HCR}^g(E) + \delta\Sigma_{x,HTF}^g(E) + \delta\Sigma_{x,SDC}^g(E) \end{aligned} \quad (597)$$

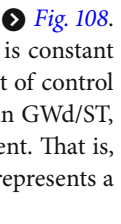
where x is a reaction type (e.g., absorption and fission); g is one of the two energy groups (either fast or thermal). The various cross sections have the following definitions:

- $\Sigma_{x,V}^g(E, U)$ is the base cross section as a function of instantaneous void content in the coolant, V ; exposure, E ; and historical void content, U (to be explained soon).
- $\delta\Sigma_{x,TF}^g(E, V)$ is the change in the base cross section at different exposures and different void conditions due to a change in fuel temperature, TF .
- $\delta\Sigma_{x,TM}^g(E, V)$ is the change in the base cross section at different exposures and different void conditions due to a change in the moderator temperature, TM .
- $\delta\Sigma_{x,CR}^g(E, V)$ is the change in the base cross section at different exposures and different void conditions due to the insertion of a control blade, CR .
- $\delta\Sigma_{x,HCR}^g(E)$ is the change in the base cross section at different exposures due to the removal of a control blade following a period of time during which the blade was inserted, HCR . This is referred to as the *control blade history* effect.
- $\delta\Sigma_{x,HTF}^g(E)$ is the change in the base cross section at different exposures due to extended operation at a fuel temperature other than the average fuel temperature, HTF . This is referred to as the *fuel temperature history* effect.
- $\delta\Sigma_{x,SDC}^g(E)$ is the change in the base cross section at different exposures following an extended period of inactivity, SDC . This is referred to as the *shutdown cooling* effect.

Historical Void

In (597), the *historical* void content in the coolant, U , is the void level at which the fuel has been depleted. In contrast, the *instantaneous* void content, V , is the amount of void currently in the coolant. To illustrate, a node may deplete for the first 6 months of operation with a void content of 50% (i.e., half vapor, half liquid). This 50% represents the *historical* void content, which is a function of time. It is also the instantaneous void content because it is the void level at which the node is currently operating. If, after 6 months of operation, the conditions in the core change and the void redistributes itself such that the node is filled with 35% void (i.e., 35% vapor, 65% liquid), we would say that our *instantaneous* void content is now 35%, but our *historical* void content remains 50% until we begin to deplete the node at this new void level. Then, assuming the void content remains at 35% for the foreseeable future, the new historical void content will slowly change from 50 to 35% over time.

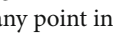
The *historical* void content determines the isotopics of the fuel with time: higher void content produces a harder spectrum, which produces more Plutonium through U^{238} capture and depletes less U^{235} due to less thermal fission. When the node changes void instantaneously, the effect of the change is determined by the isotopes present in the fuel, which are determined by the historical void content. So, a node at an exposure of 20 GWd/ST that instantaneously changes from $U = 50\%$, $V = 50\%$ to $U = 50\%$, $V = 35\%$ will differ in reactivity from a node at an exposure of 20 GWd/ST that instantaneously changes from $U = 60\%$, $V = 60\%$ to $U = 60\%$, $V = 35\%$, simply because the isotopes will have built up differently over time in the two nodes. Although the two nodes currently contain the same void at the same exposure, their reactivities are different because their operating histories have been different.

The relationship between *instantaneous* void and *historical* void is illustrated in  [Fig. 108](#). In the figure, the saw tooth green line represents the void level over time, which is constant for long periods, but changes abruptly as core conditions change (e.g., adjustment of control blades, changes in core flow rate). In the graph, the abscissa is burnup, expressed in GWd/ST, and the ordinate is water density, expressed in g/cc, which is inverse to void content. That is, as void content increases, the water density decreases. The blue line in the graph represents a straightforward averaging of the void over time using the relationship

$$U = \frac{\sum V_i \cdot \Delta E_i}{\sum \Delta E_i} \quad (598)$$

This would be considered a crude estimate of void history. The orange line in the graph represents the true historical void content, defined by the reactivity worth of the node at any point in time. It can be closely approximated by the expression

$$U = \frac{\sum \exp\{0.08 \cdot \Delta E_i\} \cdot V_i \cdot \Delta E_i}{\sum \exp\{0.08 \cdot \Delta E_i\} \cdot \Delta E_i} \quad (599)$$

In (599), the exponential term is a weighting function that describes the decay of spectral effects from past void levels. In (598), the weighting function was set to unity for the straightforward averaging with time. The graph in  [Fig. 108](#) should be interpreted as follows: At any point in time, the reactivity of a node that has operated with the void levels represented by the V curve, is equivalent to having depleted the node at a constant void level defined by the U (*exact*) curve and then branching to the instantaneous void level represented by V . So, for example, the reactivity of the node at an exposure of 30 GWd/ST and an instantaneous water density of 0.742 g/cc in the figure (i.e., 0% void at hot operating conditions), can be determined by depleting the node

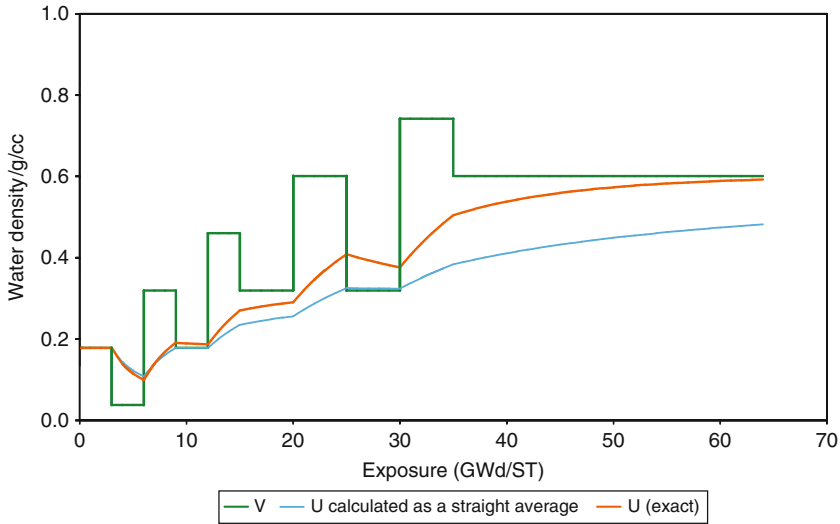


Figure 108

Relationship between instantaneous and historical void

at a constant water density of 0.377 g/cc (i.e., approximately 50% void at hot operating conditions) for 30 GWd/ST and then instantaneously branching to a water density of 0.742 g/cc. In this way, the lattice physics code does not have to follow the exact operating history of a node in order to supply cross sections to the nodal code. We simply need to deplete each lattice at several different historical void levels and perform back branch calculations periodically to different instantaneous void levels in order to generate sufficient cross section information for the nodal code. The nodal code can then interpolate between the explicit points analyzed by the lattice physics code in order to obtain cross sections for a specific core condition.

We now need to determine the number of different historical void levels that need to be analyzed by the lattice physics code in order to supply the nodal code with sufficient information to achieve the accuracy we desire. This number can be ascertained by inspecting [Fig. 109](#), which contains a graph of the fast group macroscopic cross section as a function of void fraction in the coolant (void fraction is defined as void percentage divided by 100, so a void fraction of 0.1 is 10% void, and so on). In the figure, there are two separate curves represented. The first curve is the magenta line, which is the fast group absorption cross section for the node. It has been generated by performing a detailed analysis of the lattice at void fraction increments of 0.1 (i.e., 10% void increments). This is the reference solution. The second curve is the black line that has been generated by fitting a quadratic through the explicit points at void fractions of 0, 0.4, and 0.8 (highlighted by the blue squares on the graph). Here, it can be seen that the cross section can be accurately represented as a quadratic between void fractions of 0 and 0.8. However, beyond a void fraction of 0.8, the cross section no longer behaves as a quadratic and the extrapolated points beyond a void fraction of 0.8 deviate significantly from the reference solution.

The implications of [Fig. 109](#) are rather significant. Years ago, when power densities at most BWRs were consistently at or below 50 kW/L, exit void fractions from fuel bundles were within the 0.8 range. From the quadratic fit in [Fig. 109](#), it can be seen that very little error

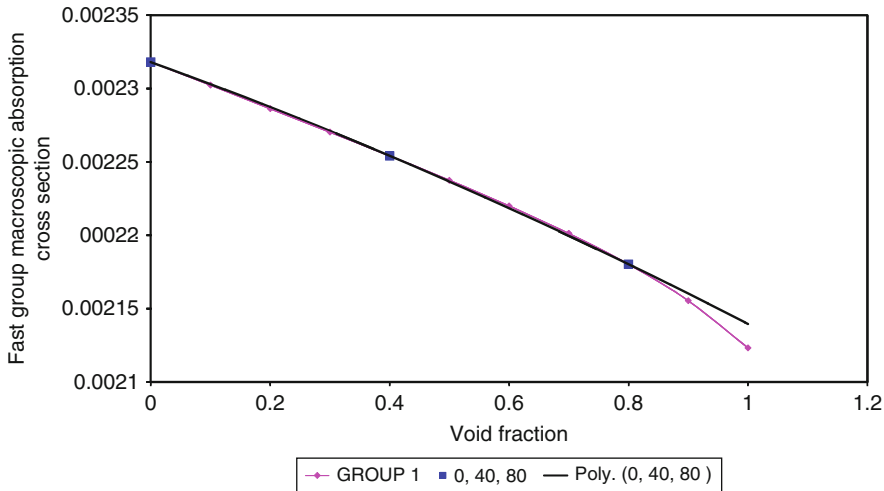
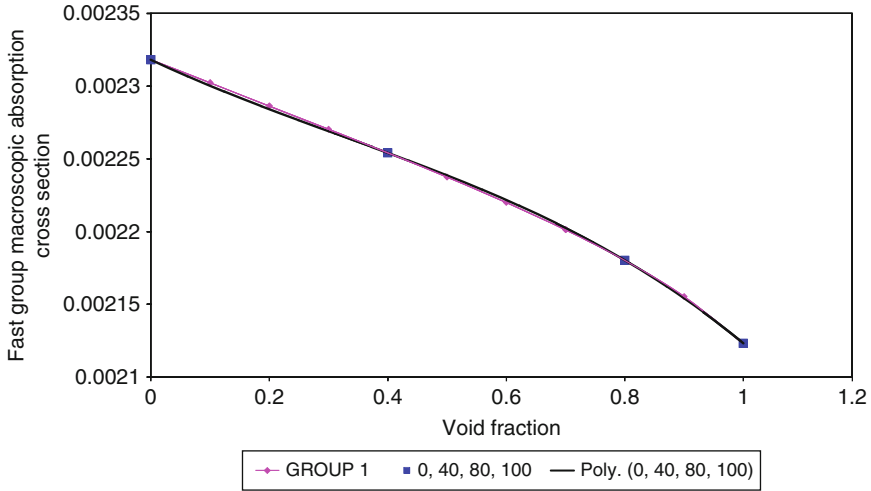


Figure 109
Behaviour of cross section as a function of void fraction

would be incurred by producing explicit data at void fractions of 0, 0.4, and 0.8 and then fitting a quadratic through the three points. Today, after years of power up-rates at many BWRs, the exit void fraction is close to 1.0. If the nodal code uses data from the lattice code that has been generated at explicit void fractions of 0, 0.4, and 0.8, the reactivity at the top of the core will be underestimated and the nodal code will model the axial power shape as being too bottom-peaked early in the cycle. This will result in the nodal code depleting the fuel in the bottom of the core too rapidly, causing the power shape to become too top-peaked during the second half of the cycle.

In order for the nodal code to provide us with the accuracy we desire, the lattice physics code will have to provide cross section data at four different void levels and then the nodal code can use a polynomial to interpolate between explicit data points. This is illustrated in [Fig. 110](#), where a polynomial has been fit through explicit data points at void fractions of 0, 0.4, 0.8, and 1. Note that there will be an inherent error in our cross sections from our polynomial interpolation scheme. That is, the black polynomial trend does not lie precisely on the magenta line. This is the error we will have to live with if we choose to implement this particular case matrix scheme.

The lattice physics code must supply the nodal code with tables of all the cross sections needed to solve the nodal diffusion equation. This includes fast and thermal group data for absorption and production cross sections, as well as the diffusion coefficient. In addition, the nodal code requires data for the fast group removal cross section, energy release values (κ), and a few parameters needed for modeling Xenon transients. If there are 15,000 nodes in the reactor model, then the nodal code has to perform approximately $12 \times 15,000$ interpolations for every analysis, or nearly 200,000 interpolations. This number does not include all the other tables of data that need to be interpolated, such as pin power form functions. If we want the nodal code to use a third-order polynomial fit to interpolate between points in our tables of cross sections, this could become very time consuming.



■ Figure 110

Polynomial fit to cross section data

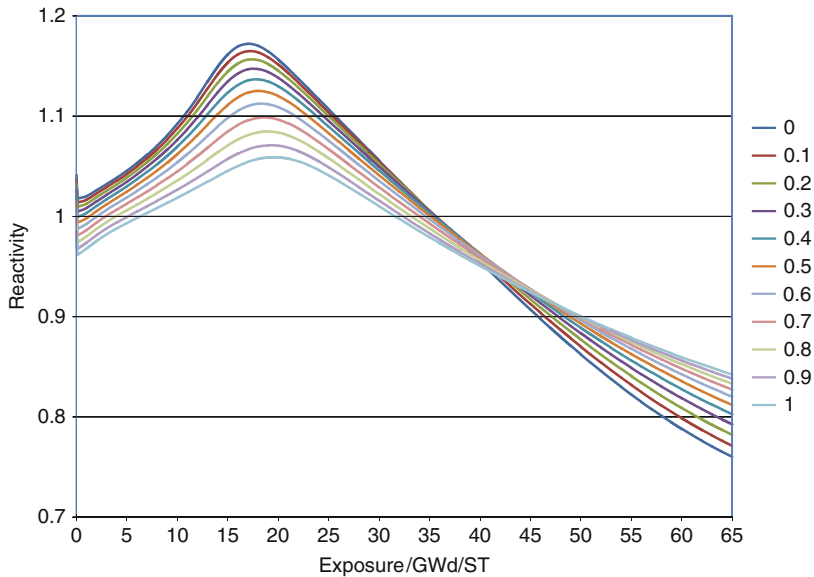
A more economical approach is to allow the nodal code to interpolate linearly between explicit points in the cross section tables. But interpolating linearly between the four explicit data points is not going to provide us with the accuracy we desire. So we break the process into two steps. Our first step is to gather the explicit data points from the lattice physics code with a processing code that fits the data with a polynomial and creates intermediate points in our tables. That is, we gather the data points at void fractions of 0, 0.4, 0.8, and 1 from the lattice physics code and then allow the processing code to create additional points at void fractions of, say, 0.2 and 0.6 using a polynomial interpolation. The processing code creates tables for the nodal code that include data at void fractions of 0, 0.2, 0.4, 0.6, 0.8, and 1. Then the nodal code can interpolate linearly between all points in the table. This saves us a great deal of time during the nodal analysis without appreciably affecting our accuracy. It also saves us from having to analyze six explicit void fractions with the lattice physics code, which also saves us a great deal of time.

We will return to the topic of void in a later section.

Exposure

► *Figure 111* contains several graphs of reactivity from the depletion of a BWR lattice at various void fractions. The graph can be broken into three distinct regions. The first region consists of exposures between 0 and 0.25 GWd/ST. To help put these numbers in perspective, a single day of full power operation at a typical BWR accounts for approximately 0.025 GWd/ST of exposure, so the first region on the graph accounts for roughly 10 days of full power operation. During this period, the fuel is building in fission products, which account for a drop in reactivity of roughly 2% (i.e., $-0.02 \Delta\rho$ of reactivity).

The second region on the graph encompasses the rise in reactivity from an exposure of 0.25 GWd/ST to approximately 20 GWd/ST. During this period of time, the Gadolinium in the fuel design, which is used to hold down reactivity during the bundle's first cycle of operation, is



■ **Figure 111**
Reactivity as a function of exposure and void fraction

being depleted. The rise in reactivity, and the length of time that the rise lasts, is proportional to the Gadolinium loading. Different designs will have different rises and also different slopes to that rise. However, the point that is being made here is that there will be such a rise whenever Gadolinium is present. The reactivity peak is reached when the Gadolinium has been completely depleted from the bundle.

The third region of the curve consists of all data beyond the reactivity peak – in this case from an exposure of approximately 20 to 65 GWd/ST. This represents the typical reactivity let-down as the U^{235} depletes. It is not linear because there is Pu^{239} being bred due to U^{238} capture, and the Pu^{239} is producing energy during the depletion. Note that the reactivity letdown curve has a steeper slope for the smaller void fractions. As the void fraction increases, the flux spectrum hardens and more U^{238} capture takes place. As a result, there is more Pu available at the higher void fractions and the bundle's energy is consumed more slowly.

It is very important for the lattice physics code – and the nodal code – to accurately capture the detail of the bundle depletion around the reactivity peak. Since we never know exactly where this peak will occur until after the fuel design has been analyzed, the lattice physics code must be able to track the Gadolinium isotopes in the fuel and automatically take time-steps small enough to capture the details of this depletion. As a rule of thumb, time-step sizes for BWR fuel designs should probably not exceed 0.5 GWd/ST until the bundle has surpassed the reactivity peak. This ensures that the onion-skin style of depletion of the Gadolinium pins will be modeled with sufficient accuracy. Once the Gadolinium has been exhausted, it is customary to take time-steps that can range in size from 2.5 to 5 GWd/ST. When the lattice physics results are tabularized for use in the nodal code, it is crucial to ensure that enough exposure detail is maintained such that the reactivity peak is explicitly captured.

Void Coefficient

$\Sigma_{x,V}^g(E, U)$ in (597) represents the base cross section, which accounts for changes in reactivity due to changes in void content. These are the tables of cross sections alluded to in “Historical void” of this section, when we discussed depleting the lattice at several different void levels (i.e., void histories) and then performing a series of back branches at various exposures to various instantaneous void levels. In practice, we would choose our four base void fractions – 0, 0.4, 0.8, and 1 – and, for each void fraction, perform lattice depletions to a final exposure that is guaranteed to encompass the entire operating lifetime of the bundle (e.g., 65 GWd/ST). During the depletion analysis, we save the pin-by-pin isotopic concentrations at each depletion step in a binary file that we will refer to as a *restart file*. The restart file allows us to go back to any point during the depletion of the lattice and perturb one of the system parameters, such as void, and re-perform the step to determine the change in cross sections due to the perturbed parameter.

For the base cross sections, we would like to generate a full three-dimensional table as a function of exposure, historical void, and instantaneous void. To do this, we deplete the lattice at our first void fraction – 0 – and then go back and perform branch calculations to the other three void fractions – 0.4, 0.8, and 1 – at various exposures. Next, we deplete the lattice at our second void fraction – 0.4 – and then go back and perform back branches to the other three void fractions – 0, 0.8, and 1 – at various exposures. And so on with the remaining two void fractions. This will create our three-dimensional table of base cross sections.

For BWRs, the instantaneous void coefficient is more than an order of magnitude larger (i.e., more negative) than any of the other reactivity coefficients.

Fuel Temperature Coefficient

$\delta\Sigma_{x,TF}^g(E, V)$ in (597) represents changes in the cross sections due to changes in fuel temperature. This is referred to as the Doppler coefficient, which varies linearly with the square root of the fuel temperature, $\sqrt{T_f}$, and changes as the composition of the fuel changes. That is, the Doppler coefficient is dependent upon the amount of Uranium, Plutonium, and Gadolinium in the fuel. The cases performed with the lattice physics code to generate the Doppler coefficient consist of back branches at various exposures to a different fuel temperature from each of the uncontrolled depletions. Since the Doppler coefficient is linear, it makes no difference what fuel temperature is chosen for the back branches, so long as the change in reactivity is large enough to be captured by the lattice physics code. Often times, users prefer to branch from the full power fuel temperature used for the base depletions at the four different void fractions, to the hot zero power fuel temperature of 561 K (550 °F).

Moderator Temperature Coefficient

$\delta\Sigma_{x,TM}^g(E, V)$ in (597) represents changes in the cross sections due to changes in the moderator temperature. In BWRs at hot operating conditions, the coolant enters the reactor at a slightly subcooled temperature, but reaches saturation conditions within the first foot or so of the bottom of the core. Once the temperature reaches saturation conditions, it does not change and all heat from the fuel goes into boiling the water. As a result, there really is no cross section dependence on moderator temperature at operating conditions. The moderator temperature dependence comes into play at shutdown conditions. Unlike PWRs, which warm the reactor vessel up to hot zero power conditions before going critical, BWRs can go critical at any zero power temperature. Consequently, the lattice physics code needs to generate enough cross section data so as to enable the nodal code to accurately model criticality conditions at any

temperature below hot zero power conditions. This can usually be accomplished by performing back branches at various exposures from each of the uncontrolled depletions to three separate temperatures between cold conditions (293 K, 68 °F) and hot zero power (approximately 561 K, 550 °F). The back branches have to be performed at both uncontrolled and controlled conditions. The nodal code can then use a straightforward quadratic fit through the cross sections to obtain data at any cold temperature.

Control Blade Coefficient

$\delta\Sigma_{x,CR}^g(E, V)$ in (597) represents changes in the cross sections due to the presence of the control blade. This is perhaps the most direct dependency in (597). The data for this coefficient is generated by performing back branches at various exposures from each of the uncontrolled depletions to an identical condition with the control blade inserted.

Control Blade History Coefficient

$\delta\Sigma_{x,HCR}^g(E)$ in (597) is usually referred to as the *control blade history* effect. When a control blade is present next to a fuel bundle, the blade hardens the spectrum by removing thermal neutrons from the surroundings. The hardened spectrum enhances neutron capture in U^{238} and promotes the build-up of Plutonium in the controlled bundle – primarily in the fuel pins along the edge of the bundle closest to the control blade. If the control blade is present for several weeks of full power operation, the Pu build-up can be substantial. When the blade is removed, the bundle will have a different isotopic composition from its composition prior to being controlled and its reactivity may have actually increased over the controlled period of time. If the bundle is now operated uncontrolled for a long period of time, the Pu will eventually be exhausted. This effect is usually modeled at the lattice physics level by depleting the fuel segment with the control blade present and then performing uncontrolled back branches at various exposures. The uncontrolled back branches are compared against uncontrolled depletions of the fuel segment and the appropriate adjustments are made to the cross sections to capture the effect. The control blade history effect is typically modeled at the nominal void level (e.g., 40% void).

Fuel Temperature History Coefficient

$\delta\Sigma_{x,HTF}^g(E)$ in (597) represents changes in the cross sections due to extended periods of operation at a fuel temperature other than the nominal fuel temperature. The fuel temperature is directly proportional to the power level. Higher fuel temperatures represent higher power levels and harden the flux spectrum. Lower fuel temperatures represent lower power levels and soften the flux spectrum. Operating a fuel segment at a higher or lower fuel temperature, relative to the nominal temperature, for an extended period of time will change the isotopic concentration of the fuel and, hence, its reactivity. The data for this effect is generated by depleting the fuel at either an elevated or diminished fuel temperature and then performing back branches to the nominal fuel temperature at various exposures. The depletion at the elevated fuel temperature can be performed at a single void fraction – say the nominal value of 0.4 – and applied to all void levels. The partial cross sections are determined by comparing the back branches against results from the base depletion for the nominal void fraction. In a BWR, fuel temperature history is a very minor effect compared to the other reactivity coefficients and can be ignored without significantly affecting the accuracy of the cross sections.

Shutdown Cooling Coefficient

$\delta\Sigma_{x,SDC}^g(E)$ in (597) represents the decay of certain important isotopes as the bundle cools during a period of inactivity – often referred to as *shutdown cooling*. For short periods of inactivity (i.e., days), the isotopes that are of most interest are the fission products Promethium and Iodine, which decay to Samarium and Xenon, respectively. These decays are important because the Sm^{149} and Xe^{135} absorption cross sections are very large in the thermal energy range and have a profound effect on the reactivity of the fuel. The Xe^{135} is also an unstable isotope and will eventually decay to Cs^{135} , which is neutronically inert. For long periods of inactivity (i.e., years), we are most interested in the decay of Pu^{241} to Am^{241} and, to a lesser extent, the decay of Eu^{155} to Gd^{155} .

To model shutdown cooling effects, the lattice physics code can perform back branches at various exposures from one of the voided depletions – say the nominal value of 40%. Several shutdown cooling times are analyzed at each exposure point. These cooling times are usually spaced to cover a wide range of periods of inactivity. For example, 1 day, 10 days, 30 days, 1 year, and 4 years. This is usually adequate to cover all bundles that would be discharged from the core at the end of a given cycle and possibly be reinserted into the core at the beginning of a future cycle. The partial cross sections are created by comparing the values from the branch cases against values for the base set at the nominal void.

Our final set of BWR cross section tables will consist of a three-dimensional table of base cross sections augmented by a combination of two-dimensional and three-dimensional tables of various partial cross sections. For the case matrix described in this section, we will have a total of five depletions: four uncontrolled depletions at void fractions of 0, 0.4, 0.8, and 1; and one controlled depletion at a void fraction of 0.4. We will then have a very large series of back branches needed to generate the partial cross sections to (597). A generic CASMO-4 case matrix for generating a BWR cross section model at hot operating conditions is shown in [Table 26](#). The case matrix for generating a corresponding BWR cross section model at cold shutdown conditions is shown in [Table 27](#). In the tables: U represents the historical void level; V represent the instantaneous void level; CR represents the presence of the control blade; TFU represents the fuel temperature; TMO represents the moderator temperature; SDC represents shutdown cooling time; and BOR represents the boron concentration in the coolant, which is included only to analyze the effectiveness of the standby liquid control system (SLCS). All cases in the hot case matrix are performed at hot saturation conditions (i.e., an average coolant temperature of approximately 550 °F at a vessel dome pressure of 1,040 psi). The hot, full power fuel temperature of 900 K contained in the two tables is meant for illustration purposes only. The true value for the fuel temperature is typically obtained from a fuel-mechanical analysis of the fuel rod.

The exposure vector for depletion cases consists of time-step sizes of 0.5 GWd/MTU up to an exposure of 20 GWd/MTU, which can be considered at or beyond the Gadolinium burnout point. Beyond the Gadolinium burnout point, time-step sizes of 2.5 GWd/MTU are taken. In general, branch cases are performed at exposure increments of 2.5 GWd/MTU up to an exposure of 20 GWd/MTU. Beyond that, branch cases are performed at exposure increments of 10 GWd/MTU. Note that it is important for the lattice physics code to be able to determine the Gadolinium burnout point because the point will change as a function of void content in the coolant. At very high void fractions, such as 0.8 and 1, the Gadolinium depletes extremely slowly due to the diminished number of thermal neutrons present and the burnout point can be several GWd/MTU beyond the equivalent point at lower void fractions. For the depletion case with the control blade present, the Gadolinium will take a very long time to deplete.

■ Table 26

An example of a BWR hot case matrix

Case#	DEPL#	Branch from DEPL#	U [%]	V [%]	CR	TFU [K]	SDC [days]
1	1		0	0	No	900	0
2	2		40	40	No	900	0
3	3		80	80	No	900	0
4	4		100	100	No	900	0
5	5		40	40	Yes	900	0
6		1	0	40	No	900	0
7		1	0	80	No	900	0
8		1	0	100	No	900	0
9		2	40	0	No	900	0
10		2	40	80	No	900	0
11		2	40	100	No	900	0
12		3	80	0	No	900	0
13		3	80	40	No	900	0
14		3	80	100	No	900	0
15		4	100	0	No	900	0
16		4	100	40	No	900	0
17		4	100	80	No	900	0
18		1	0	0	No	561	0
19		2	40	40	No	561	0
20		3	80	80	No	561	0
21		4	100	100	No	561	0
22		2	40	40	No	900	1
23		2	40	40	No	900	10
24		2	40	40	No	900	30
25		2	40	40	No	900	365
26		2	40	40	No	900	1,460
27		1	0	0	Yes	900	0
28		2	40	40	Yes	900	0
29		3	80	80	Yes	900	0
30		4	100	100	Yes	900	0
31		5	40	40	No	900	0

■ Table 27

An example of a BWR cold case matrix

Case#	Branch from DEPL#	U [%]	V [%]	CR	TMO [K]	SDC [days]	BOR [ppm]
32	1	0	0	No	293	0	0
33	2	40	0	No	293	0	0
34	3	80	0	No	293	0	0
35	4	100	0	No	293	0	0
36	1	0	0	Yes	293	0	0
37	2	40	0	Yes	293	0	0
38	3	80	0	Yes	293	0	0
39	4	100	0	Yes	293	0	0
40	3	80	0	No	353	0	0
41	3	80	0	No	475	0	0
42	3	80	0	Yes	353	0	0
43	3	80	0	Yes	475	0	0
44	3	80	0	No	293	0	1,000
45	3	80	0	No	475	0	1,000
46	3	80	0	No	293	1	0
47	3	80	0	No	293	10	0
48	3	80	0	No	293	30	0
49	3	80	0	No	293	365	0
50	3	80	0	No	293	1,460	0

7.3 Cross Section Dependencies in PWRs

To a good approximation, the macroscopic cross section for a PWR can be expressed as

$$\begin{aligned} \Sigma_x^g = & \Sigma_{x,HTM}^g(E) + \delta\Sigma_{x,HBOR}^g(E) + \delta\Sigma_{x,TF}^g(E) + \delta\Sigma_{x,TM}^g(E) \\ & + \delta\Sigma_{x,BOR}^g(E) + \delta\Sigma_{x,CRD}^g(E) + \delta\Sigma_{x,HTF}^g(E) + \delta\Sigma_{x,SDC}^g(E) \end{aligned} \quad (600)$$

where x and g are as previously defined in (597). The various cross sections have the following definitions:

- $\Sigma_{x,HTM}^g(E)$ is the base cross section as a function of exposure and historical moderator temperature, *HTM*.
- $\delta\Sigma_{x,HBOR}^g(E)$ is the change in the base cross section at different exposures due to changes in the historical boron concentration, *HBOR*.
- $\delta\Sigma_{x,TF}^g(E)$ is the change in the base cross section at different exposures due to a change in fuel temperature, *TF*.

- $\delta\Sigma_{x, TM}^g(E)$ is the change in the base cross section at different exposures due to a change in the instantaneous moderator temperature, TM .
- $\delta\Sigma_{x, BOR}^g(E)$ is the change in the base cross section at different exposures due to a change in the instantaneous boron concentration, BOR .
- $\delta\Sigma_{x, CR}^g(E)$ is the change in the base cross section at different exposures due to the insertion of a control rod cluster, CR .
- $\delta\Sigma_{x, HTF}^g(E)$ and $\delta\Sigma_{x, SDG}^g(E)$ are as previously defined in (597).

Historical Moderator Temperature

In (600), the *instantaneous* and *historical* moderator temperatures fill a role similar to the role filled by the instantaneous and historical void concentrations in the BWR cross section model. In a PWR, the vessel is pressurized to approximately 2,250 psi and the coolant is not meant to boil. As the liquid coolant flows up the assembly, it picks up heat from the fuel rods and the temperature of the coolant steadily rises with elevation. As a result, the coolant is relatively cool at the bottom of the fuel and is relatively hot at the top of the fuel, with a difference in temperature of approximately 75 °F (i.e., approximately 40 K) between the inlet to and exit from the core. The fuel at the bottom of the core consistently experiences a softer spectrum (i.e., higher water density) compared to the fuel at the top of the core, which consistently experiences a harder spectrum (i.e., lower water density). As time goes by, this difference in the flux spectrum produces a difference in isotopic concentrations between the bottom of a fuel rod and the top of the rod.

In order to model the effect this axial variation in the flux spectrum has on the fuel, the nodal code applies an *historical moderator temperature* model that is similar to the historical void model applied for BWRs. However, since it is rare for the axial moderator temperature profile to change appreciably during PWR operation, there is no real need to perform back branches off the historical moderator temperature depletions the way we performed back branches off the historical void depletions for BWRs. Therefore, it is acceptable to use a two-dimensional table for the base set of cross sections as opposed to the three-dimensional table we used for our BWR model. To generate the cross sections, the lattice is depleted at multiple moderator temperatures, using a nominal fuel temperature and a nominal boron concentration in the coolant. The instantaneous moderator temperature is assumed to be equal to the historical moderator temperature.

Historical Boron Concentration

By now, the reader should be developing a fairly good understanding behind historical parameters. These parameters change the isotopic concentrations of the fuel during extended operation, caused by changes in the flux spectrum – either a hardening or softening effect. The instantaneous parameters are those that have an instantaneous effect on reactivity, but no effect on isotopic concentrations. In (600), the *historical* boron concentration is used to account for changes in the fuel isotopics caused by extended periods of operation at boron concentrations in the coolant, which are different from the nominal value used to generate the base set of cross sections.

The presence of soluble boron in the coolant has a hardening effect on the flux spectrum by removing thermal neutrons. To properly model the dependency of the cross sections on boron, we can simply re-deplete the lattice with multiple boron concentrations, at the nominal moderator temperature and the nominal fuel temperature. The partial cross sections, $\delta\Sigma_{x, HBOR}^g(E)$,

are then calculated simply as the difference between the depletion using the perturbed boron concentrations and the depletion using the nominal boron concentration. The instantaneous boron concentration is assumed to be equal to the historical boron concentration (i.e., no back branches).

Moderator Temperature Coefficient

$\delta\Sigma_{x, TM}^g(E)$ in (600) represents changes in the cross sections due to instantaneous changes in the moderator temperature. The data for this effect is generated by performing back branches at various exposures to a different moderator temperature from the nominal historical moderator temperature. This accounts for spectrum softening effects caused by a drop in moderator temperature (i.e., an increase in moderator density) or spectrum hardening effects caused by a rise in moderator temperature (i.e., a decrease in moderator density). The cross sections behave as a quadratic versus moderator temperature, so data should be generated at three separate moderator temperatures (e.g., 560, 580, and 600 K). The nominal level is typically the middle level (i.e., core mid-plane temperature at full power conditions).

Boron Coefficient

$\delta\Sigma_{x, BOR}^g(E)$ in (600) represents changes in the cross sections due to instantaneous changes in the soluble boron concentration in the coolant. The data for this effect are generated by performing back branches at various exposures to different boron concentrations from the nominal historical boron concentration. This accounts for spectrum softening effects caused by a reduction in boron concentration or spectrum hardening effects caused by an increase in boron concentration. The absorption cross sections behave as a quadratic versus boron concentration, so data should be generated at three separate boron levels (e.g., 0, 800, and 1,600 ppm). The nominal level is typically the middle level (i.e., middle of cycle level).

The remainder of the partial cross sections contained in (600) has been discussed in [7.2](#), so we will not revisit them here. All PWR reactivity coefficients are of a similar magnitude, so they are all equally important to the overall accuracy of the nodal cross section sets. This includes the historical fuel temperature coefficient, which was considered somewhat insignificant in the BWR cross section model because it was so much smaller than all the other effects.

For the case matrix described in this section, we will have a total of four depletions: the base depletion; a depletion at a perturbed moderator temperature; a depletion at a perturbed boron condition; and a depletion at a perturbed fuel temperature condition. A generic CASMO-4 case matrix for generating a PWR cross section model at hot operating conditions is contained in [Table 28](#). The case matrix for generating a corresponding PWR cross section model at cold shutdown conditions is contained in [Table 29](#). In the tables: *HTMO* represents the historical moderator temperature; *TMO* represent the instantaneous moderator temperature; *CR* represents the presence of the control blade; *HTFU* represents the historical fuel temperature; *TFU* represents the instantaneous fuel temperature; *HBOR* represents the historical boron concentration; *BOR* represents the instantaneous boron concentration; and *SDC* represents shutdown cooling times.

The exposure vector for PWR depletion cases consists of time-step sizes of 1 GWd/MTU up to an exposure of 15 GWd/MTU (assuming Gadolinium is not being used as a burnable absorber in the fuel design). Beyond that, time-step sizes of 2.5 GWd/MTU are taken. In general, branch cases are performed at exposure increments of 2 GWd/MTU up to an

■ Table 28

An example of a PWR hot case matrix

Case#	DEPL#	Branch from DEPL#	HTMO [K]	TMO [K]	CR	HTFU [K]	TFU [K]	HBOR [ppm]	BOR [ppm]	SDC [days]
1	1		580	580	No	900	900	800	800	0
2	2		560	560	No	900	900	800	800	0
3	3		580	580	No	900	900	1,600	1,600	0
4	4		580	580	No	560	560	800	800	0
5		1	580	580	No	900	900	800	0	0
6		1	580	580	No	900	900	800	1,600	0
7		1	580	580	No	900	900	800	2,400	0
8		1	580	560	No	900	900	800	800	0
9		1	580	600	No	900	900	800	800	0
10		1	580	580	No	900	560	800	800	0
11		1	580	580	Yes	900	900	800	800	0
12		1	580	580	No	900	900	800	800	1
13		1	580	580	No	900	900	800	800	10
14		1	580	580	No	900	900	800	800	30
15		1	580	580	No	900	900	800	800	365
16		1	580	580	No	900	900	800	800	1,460

exposure of 20 GWd/MTU. Beyond that, branch cases are performed at exposure increments of 10 GWd/MTU.

7.4 Summary

This section has provided a description of one possible way of constructing a case matrix for a nodal code. The models described in this section are by no means exhaustive and are meant only to provide the reader with a glimpse at the types of analyses performed using a lattice physics code to support a nodal code. There are other ways of designing a case matrix for a nodal code. The main premise, though, is to provide the reader with an appreciation for the number of cases needed to be performed by the lattice physics code in order to accurately capture the behavior of the fuel over its anticipated lifetime in the core. For BWRs, the case matrix we have described will require approximately 1,200 state points per lattice. If the fuel design contains 8 lattices, it will take approximately 10,000 lattice physics state point calculations to fully functionalize the behavior of the fuel. The PWR case matrix we described contains substantially less – approximately 800 state points, 300 of which are needed to model hot

■ Table 29

An example of a PWR cold case matrix

Case#	DEPL#	Branch from DEPL#	HTMO [K]	TMO [K]	CR	HTFU [K]	TFU [K]	HBOR [ppm]	BOR [ppm]	SDC [days]
17		1	580	293	No	900	293	800	0	0
18		1	560	293	No	900	293	800	800	0
19		1	580	293	No	900	293	800	1,600	0
20		1	580	425	No	900	425	800	0	0
21		1	580	425	No	900	425	800	800	0
22		1	580	425	No	900	425	800	1,600	0
23		1	580	560	No	900	560	800	0	0
24		1	580	560	No	900	560	800	800	0
25		1	580	560	No	900	560	800	1,600	0
26		1	580	560	No	900	560	800	2,400	0
27		1	580	293	Yes	900	293	800	1,600	0
28		1	580	475	Yes	900	475	800	1,600	0
29		1	580	560	Yes	900	560	800	1,600	0
30		1	580	293	No	900	293	800	1,600	1
31		1	580	293	No	900	293	800	1,600	10
32		1	580	293	No	900	293	800	1,600	30
33		1	580	293	No	900	293	800	1,600	365
34		1	580	293	No	900	293	800	1,600	1,460
35		2	560	293	No	900	293	800	1,600	0
36		3	580	293	No	900	293	1,600	1,600	0

operating conditions. With this knowledge, the reader can begin to appreciate the effort required to accurately model the fuel in the core of a nuclear power plant.

8 Edits

This section presents some of the more common data passed from a lattice physics code to a nodal code. It is by no means an exhaustive list and there are often times more than one way of calculating a parameter. A perfect example of this would be the diffusion coefficient, which has no precise definition at the lattice physics level. Nevertheless, this section should provide the reader with an understanding of some of the back-end calculations performed by the lattice physics code.

The contents of this section have been taken from various information edited from LANCER02 (Knott and Wehlage 2007) for use in the nodal codes PANACEA (Moore et al. 1999) and AETNA (Iwamoto et al. 2003), and from various information edited from CASMO-4 (Knott et al. 1995) for use in the nodal code SIMULATE-3 (Dean 2005).

8.1 Nomenclature

g = energy group structure of the nodal code (typically two groups)

r = material region (e.g., fuel, clad, and coolant)

s = surface length of a particular mesh (cm)

S = surface length of an entire side of the lattice (cm)

h = six-group delayed neutron structure

i = energy group structure of the lattice physics code's neutron cross section library

j = energy group structure of the lattice physics code's gamma library

dr = volume of material region r per unit height (cm^3/cm)

$V(r) = dr$

V_{ass} = volume of entire lattice per unit height (cm^3/cm)

V_{fuel} = total volume of all fuel pellets per unit height (cm^3/cm)

$N_m(r)$ = atomic number density for nuclide m ; at position r

A_m = atomic mass of nuclide m

ρ_m = density for nuclide m , in (g/cm^3)

$\sigma_{xm}(g, r)$ = microscopic cross section for reaction type x ; of nuclide m ; in energy group g ; at position r .

$\phi(g, r)$ = neutron flux in energy group g ; at position r

$\psi(g, s)$ = neutron surface flux in energy group g ; at surface position s

$\chi_m(i, h)$ = delayed neutron fission spectrum of nuclide m ; for neutrons born in energy group i ; to be deposited in delayed group h

$\Psi(i)$ = neutron flux in group i from fundamental mode calculation

$\Psi^\dagger(i)$ = adjoint flux in group i from fundamental mode calculation

8.2 Various Edits

Parameters that need to be edited by the lattice physics code for use in the accompanying nodal code may include some of the following:

Lattice-averaged atomic number densities of nuclide m

$$\bar{N}_m = \frac{\int V_{ass} N_m(r) dr}{\int V_{ass} dr} \quad (601)$$

Fuel-averaged atomic number density of heavy isotope m

$$\bar{N}_m = \frac{\int V_{fuel} N_m(r) dr}{\int V_{fuel} dr} \quad (602)$$

Decay constant of delayed neutrons in delayed group h

$$\bar{\lambda}(h) = \frac{\sum_m \lambda_m(h) \cdot \beta_m(h) \cdot \sum_g N_m \nu \sigma_{f,m}(g) \phi(g)}{\bar{\beta}(h) \cdot \sum_g \nu \bar{\Sigma}_f(g) \phi(g)} \quad (603)$$

where $\beta_m(h)$ is the delayed neutron fraction for nuclide m , in delayed group h ; and $\lambda_m(h)$ is its decay constant. The summation over m is performed over all fissile isotopes. The averaged delayed neutron fraction, $\bar{\beta}(h)$, is calculated as

$$\bar{\beta}(h) = \frac{\sum_m \beta_m(h) \cdot \sum_g N_m \nu \sigma_{f,m}(g) \phi(g)}{\sum_g \nu \bar{\Sigma}_f(g) \phi(g)} \quad (604)$$

Lattice-averaged flux per nodal group

$$\bar{\phi}(g) = \frac{\int_{V_{ass}} \phi(g, r) dr}{\int_{V_{ass}} dr} \quad (605)$$

where the fine-mesh flux in the nodal-group energy structure, $\phi(g, r)$, is calculated by a straightforward condensation

$$\phi(g, r) = \sum_{i \in g} \phi(i, r) \quad (606)$$

Boundary diffusion coefficient per nodal group for each assembly surface

$$\bar{D}_s(g) = \frac{\int_{S_{ass}} D(g, r) \psi(g, r) dS}{\int_{S_{ass}} dS} \quad (607)$$

where the integral is performed over one assembly surface only. There are four $\bar{D}_s(g)$ values edited: (1) north; (2) east; (3) south; and (4) west.

Effective delayed neutron fraction for delayed group h

The effective delayed neutron fraction accounts for the fact that delayed neutrons are born at energies lower than those of prompt neutrons and, hence, do not contribute to fast fission and have smaller leakage rates into (or out of) the system than prompt neutrons. The effective delayed neutron fraction is calculated as

$$\beta(h) = \frac{\sum_m \left[\sum_i \beta_m(h) \bar{\chi}_{d,m}(i, h) \Psi^\dagger(i) \cdot \sum_i \nu \bar{\sigma}_{f,m}(i) \bar{N}_m \Psi(i) \right]}{\sum_m \left\{ \left(1 - \sum_h \beta_m(h) \right) \left(\sum_i \bar{\chi}_{p,m}(i) \Psi^\dagger(i) \right) + \sum_h \beta_m(h) \left(\sum_i \bar{\chi}_{d,m}(i, h) \Psi^\dagger(i) \right) \right\} \cdot \sum_i \nu \bar{\Sigma}_f(i) \Psi(i)}$$

$$\begin{aligned} & \frac{\sum_m \left[\sum_i \beta_m(h) \bar{\chi}_{d,m}(i, h) \Psi^\dagger(i) \cdot \sum_i v \bar{\sigma}_{f,m}(i) \bar{N}_m \Psi(i) \right]}{\sum_i \bar{\chi}(i) \Psi^\dagger(i) \cdot \sum_i v \bar{\Sigma}_f(i) \Psi(i)} \\ & \frac{\sum_m \left[\sum_i \beta_m(h) \bar{\chi}_{d,m}(i, h) \Psi^\dagger(i) \cdot \sum_i v \bar{\sigma}_{f,m}(i) \bar{N}_m \Psi(i) \right]}{k^\dagger \sum_i v \bar{\Sigma}_f(i) \Psi(i)} \end{aligned} \quad (608)$$

where the summation over m includes the isotopes: Th²³², U²³³, U²³⁴, U²³⁵, U²³⁶, U²³⁸, Pu²³⁹, Pu²⁴⁰, Pu²⁴¹, and Pu²⁴²; $\bar{\chi}_{d,m}(i, h)$ is the delayed neutron fission spectrum from energy group i to delayed group h , for isotope m ; $\bar{\chi}_{p,m}(i)$ is the prompt neutron fission spectrum for isotope m ; and $\bar{\chi}(i)$ is the total fission spectrum for the homogeneous system. The adjoint flux, $\Psi^\dagger(i)$, can be obtained by solving the non-leakage adjoint form of the fundamental mode equation

$$\bar{\Sigma}_{tr}(i) \cdot \Psi^\dagger(i) = \sum_{i'} \left[\bar{\Sigma}_s(i \rightarrow i') + \frac{v \bar{\Sigma}_f(i)}{k^\dagger} \cdot \bar{\chi}(i') \right] \Psi^\dagger(i') \quad (609)$$

where the adjoint multiplication factor is given by

$$k^\dagger = \sum_{i'} \bar{\chi}(i') \Psi^\dagger(i') \quad (610)$$

All cross sections are flux-volume weighted over the entire assembly using the forward flux from the MoC solution after expanding it to the energy group structure of the cross section library (i.e., the fine-group structure). In this formulation, it is assumed that the flux-volume weighted assembly-averaged cross sections using the forward flux are not significantly different from the equivalent cross sections that would be created using a spatial adjoint flux distribution. This assumption is perfectly adequate when non-leakage boundary conditions are used (either perfect reflexion or periodic).

The effective delayed neutron fraction can be calculated a slightly different way by considering neutron leakage effects. The adjoint flux, $\Psi^\dagger(i)$, is obtained by solving the adjoint form of the fundamental mode equation that includes neutron leakage effects

$$\left[\bar{\Sigma}_{tr}(i) + \bar{D}(i) B^2 \right] \cdot \Psi^\dagger(i) = \sum_{i'} \left[\bar{\Sigma}_s(i \rightarrow i') + \frac{v \bar{\Sigma}_f(i)}{k^\dagger} \cdot \bar{\chi}(i') \right] \Psi^\dagger(i') \quad (611)$$

where B^2 is the value of the material buckling from the solution to the forward form of the fundamental mode calculation, (29). The value of $\beta(h)$ should be more accurate when including leakage effects into the adjoint flux spectrum, since neutron leakage out of the system occurs predominately in the fast energy groups.

Total effective delayed neutron fraction

$$\beta_{\text{total}} = \sum_{h=1}^6 \beta(h) \quad (612)$$

Lattice-averaged diffusion coefficient per nodal group

$$D(g) = \sum_{i \in g} \left\{ \frac{1/3}{\int_{V_{ass}} \Sigma_{tr}(i, r) \phi(i, r) dr} \right\} \quad (613)$$

where the lattice-averaged diffusion coefficient is calculated in the fine-group energy structure and collapsed directly to the nodal-group energy structure. Note that it is important that the spatial homogenization be performed on the transport cross section, not the diffusion coefficient. If the spatial homogenization is performed on the diffusion coefficient, any vacuum regions in the lattice (e.g., air gaps between fuel pellet and cladding) will skew the value of the coefficient.

In the context of (613), the lattice-averaged diffusion coefficient in each energy group is being condensed. That is, we calculate a diffusion coefficient in the fine-group energy structure of the cross section library and condense it to the nodal-group structure. An alternative approach would be to condense the transport cross section to the nodal-group structure and calculate a diffusion coefficient from that. The equation would then take the form

$$D(g) = \frac{1/3}{\sum_{i \in g} \left\{ \int_{V_{ass}} \Sigma_{tr}(i, r) \phi(i, r) dr \right\}} \quad (614)$$

Equations (613) and (614) will give different values for the diffusion coefficients, especially in the fast energy group. Neither approach is incorrect – nor correct. Most nodal methods modify the diffusion coefficient during the iteration process, so the choice is somewhat irrelevant. Nodal results should be somewhat insensitive to the method chosen in the lattice physics code.

Absorption reaction rates per isotope m

$$\Sigma_{a,m} = \sum_g \int_{V_{ass}} N_m(r) \sigma_{a,m}(g) \phi_g(r) dr \quad (615)$$

Effective energy release per fission, per fuel rod

$$\kappa(r) = \frac{E_{kinetic}(r) + E_\gamma(r) + E_\beta(r) + E_s(r)}{\sum_g \Sigma_f(g, r) \phi(g, r) V(r)} \quad (616)$$

where the energy terms are defined in (45)–(48).

Flux discontinuity factor per nodal group

$$DF_S(g) = \frac{\int_S \psi(g, s) ds}{\int_{V_{ass}} \phi(g, r) dr} \quad (617)$$

Lattice-averaged fast flux (above 1 MeV)

$$\bar{\Psi}_{fast} = \sum_{E_i \geq 1 \text{ MeV}} \Psi(i) \quad (618)$$

where the summation over energy group runs from 20 MeV (group 1) to the energy boundary closest to 1 MeV.

Relative fission rate per fuel rod

$$\text{FRR}(r) = \frac{\sum_g \int_{V_{x,y}} \Sigma_f(g, r) \phi(g, r) dr}{\left\{ \frac{\sum_g \int_{V_{\text{fuel}}} \Sigma_f(g, r) \phi(g, r) dr}{\int_{V_{\text{fuel}}} dr} \right\}} \quad (619)$$

Relative gamma energy deposition per fuel rod

$$\text{GRR}(r) = \frac{\sum_j \int_{V_{x,y}} \Sigma_e(j, r) \phi(j, r) dr}{\left\{ \frac{\sum_j \int_{V_{\text{fuel}}} \Sigma_e(j, r) \phi(j, r) dr}{\int_{V_{\text{fuel}}} dr} \right\}} \quad (620)$$

where $\Sigma_e(j, r)$ is the macroscopic energy deposition cross section for material region r in the energy group structure of the gamma library, j .

Gamma detector response

$$D^y = \left(\frac{1}{P} \right) \sum_j \sigma_{e,m}(j) \phi(j, r) \quad (621)$$

where $\phi(j, r)$ is the gamma flux in the narrow–narrow corner of the problem for BWRs, or in the location of the instrument thimble for PWRs; and $\sigma_{e,m}(j)$ is the microscopic energy deposition cross section for some nuclide of choice (e.g., Fe). P is the lattice power level, in MeV.

Fission detector response

$$D^n = \left(\frac{1}{P} \right) \sum_i \sigma_{f,U^{235}}(i) \phi(i, r) \quad (622)$$

where $\phi(i, r)$ is the fine-group flux in the narrow–narrow corner of the problem for BWRs, or in the location of the instrument thimble for PWRs; and $\sigma_{f,U^{235}}(i)$ is the fine-group microscopic fission cross section for U^{235} . P is the lattice power level, in MeV.

Nodal infinite multiplication factor

This is the multiplication factor obtained from the two-group cross sections. The two-group cross sections are created using the fine-group critical flux spectrum following the fundamental mode calculation. Since the cross sections are collapsed using the critical spectrum, the two-group multiplication factor will not be precisely equal to the multiplication factor from the fine-mesh assembly transport calculation unless the multiplication factor for the system just happens to be 1.0.

$$k = \frac{v\bar{\Sigma}_f(1) + v\bar{\Sigma}_f(2) \cdot \frac{\bar{\Sigma}_{\text{rem}}}{\bar{\Sigma}_a(2)}}{\bar{\Sigma}_a(1) + \bar{\Sigma}_{\text{rem}}} \quad (623)$$

Lattice-averaged microscopic cross section per isotope

$$\bar{\sigma}_x(g) = \frac{\int_{V_{ass}} N_m(r) \sigma_{x,m}(g, r) \phi(g, r) dr}{\int_{V_{ass}} N_m(r) \phi(g, r) dr} \quad (624)$$

where x is a reaction type, such as absorption, capture, fission, or production.

Average nodal-group neutron velocity

$$\bar{v}(g) = \frac{\sum_{i \in g} \Psi^\dagger(i)}{\sum_{i \in g} \frac{\Psi^\dagger(i)}{v(i)}} \quad (625)$$

where $v(i)$ is the neutron velocity in the fine-group energy structure (i.e., velocity at the mid-point of the energy group); and $\Psi^\dagger(i)$ is the adjoint flux from the fundamental mode solution, including leakage. The value can also be calculated using the forward flux if the adjoint flux is not available.

$$\bar{v}(g) = \frac{\sum_{i \in g} \Psi(i)}{\sum_{i \in g} \frac{\Psi(i)}{v(i)}} \quad (626)$$

where $\Psi(i)$ is the critical forward flux from the fundamental mode solution.

Lattice-averaged macroscopic cross section per nodal group

$$\bar{\Sigma}_a(g) = \frac{\sum_{i \in g} \int_{V_{ass}} \Sigma_a(i, r) \phi(i, r) dr}{\sum_{i \in g} \int_{V_{ass}} \phi(i, r) dr} \quad (627)$$

where x is a reaction type, such as absorption, fission, or production.

Lattice-averaged macroscopic scattering kernel per nodal group

$$\bar{\Sigma}_s(g' \rightarrow g) = \frac{\sum_{i \in g} \sum_{i' \in g'} \int_{V_{ass}} \Sigma_s(i' \rightarrow i, r) \phi(i', r) dr}{\sum_{i \in g} \sum_{i' \in g'} \int_{V_{ass}} \phi(i', r) dr} \quad (628)$$

Lattice-averaged macroscopic removal cross section per nodal group

$$\bar{\Sigma}_{rem}(1) = \bar{\Sigma}(1 \rightarrow 2) - \frac{\bar{\phi}(2)}{\bar{\phi}(1)} \bar{\Sigma}(2 \rightarrow 1) \quad (629)$$

Equation (629) represents the value for a two-group energy structure, where there is a nonzero removal cross section only for the fast group (i.e., group 1). For a three-group energy structure, the expressions for the various group-dependent removal cross sections become

$$\begin{aligned}\bar{\Sigma}_{\text{rem}}(1) &= \frac{v\bar{\Sigma}_f(1) + v\bar{\Sigma}_f(2) \cdot \frac{\bar{\phi}(2)}{\bar{\phi}(1)} + v\bar{\Sigma}_f(3) \cdot \frac{\bar{\phi}(3)}{\bar{\phi}(1)}}{k^\infty} - \bar{\Sigma}_a(1) \\ \bar{\Sigma}_{\text{rem}}(2) &= \bar{\Sigma}_{\text{rem}}(1) \cdot \frac{\bar{\phi}(1)}{\bar{\phi}(2)} - \bar{\Sigma}_a(2) \\ \bar{\Sigma}_{\text{rem}}(3) &= 0\end{aligned}\quad (630)$$

In the expression for the fast group removal cross section, $\bar{\Sigma}_{\text{rem}}(1)$, the infinite multiplication factor is calculated as

$$k^\infty = \frac{v\bar{\Sigma}_f(1) \cdot \bar{\phi}(1) + v\bar{\Sigma}_f(2) \cdot \bar{\phi}(2) + v\bar{\Sigma}_f(3) \cdot \bar{\phi}(3)}{\bar{\Sigma}_a(1) \cdot \bar{\phi}(1) + \bar{\Sigma}_a(2) \cdot \bar{\phi}(2) + \bar{\Sigma}_a(3) \cdot \bar{\phi}(3)}\quad (631)$$

The above formulations closely preserve the reactivity from the fine-mesh assembly calculation. The reactivity will not be preserved precisely because the flux used to condense cross sections from the fine-group structure to the nodal-group structure is the critical spectrum, not the infinite spectrum.

Microscopic fission cross section at TIP location

$$\sigma_f(g, r') = \frac{\sum_{i \in g} \sigma_{f, \text{U}^{235}}(i) \phi(i, r')}{\sum_{i \in g} \phi(i, r')}\quad (632)$$

where r' is the location of the TIP tube in the narrow–narrow water gap corner of a BWR problem. The microscopic fission cross section is the unshielded (i.e., infinitely dilute) value.

Lattice-averaged fission yield of various isotopes

$$Y_m = \frac{\sum_{m' \in V_{\text{fuel}}} Y_{m', m} N_{m'}(r) \sigma_{f, m'}(g, r) \phi(g, r) dr}{\int_{V_{\text{fuel}}} N_{m'}(r) \sigma_{f, m'}(g, r) \phi(g, r) dr}\quad (633)$$

where $Y_{m', m}$ is the yield from actinide m' to isotope m ; and the summation is performed over all actinides Th²²⁸ through Cm²⁴⁶. The isotopes, m , of interest are typically La¹⁴⁰, Ba¹⁴⁰, Ce¹⁴⁴, I¹³⁵, Xe¹³⁵, Pm¹⁴⁹, and Sm¹⁴⁹.

Thermal–hydraulic data

In addition to cross section data, the lattice physics code usually edits thermal–hydraulic related data to the nodal code, which may include some or all of the following:

- In-channel flow area (not including water rods) (cm²).
- Out-channel flow area (not including control blade) (cm²).
- Water rod flow area (cm²).
- Control blade flow area (cm²).
- Total flow area (cm²).

- Density of in-channel water (g/cm^3).
- Density of out-channel water (g/cm^3).
- Density of water in water rods (g/cm^3).
- Density of water in control blade (g/cm^3).
- Lattice-averaged water density (g/cm^3).
- Heated perimeter of all fuel rods (cm).
- Wetted perimeter of in-channel coolant (cm).
- Wetted perimeter of out-channel coolant (cm).
- Hydraulic diameter of in-channel coolant (cm).
- Number of heated pins.

8.3 Neutron Balance

Neutron balances typically include the following definitions:

Region integrated flux

$$\text{RIF}(g, r) = \sum_{r' \in r} \bar{\phi}(g, r') \cdot V(r') \quad (634)$$

In this nomenclature, the neutron balance is being performed over all the mesh included in the region of choice, r . They could be all the mesh in the lattice, or a subset defined by the user.

Region averaged flux

$$\text{RAF}(g, r) = \frac{\text{RIF}(g, r)}{\sum_{r' \in r} V(r')} \quad (635)$$

Integrated absorptions

$$\text{ABS}(g, r) = \text{RIF}(g, r) \cdot \bar{\Sigma}_a(g, r) \quad (636)$$

Integrated fissions

$$\text{FISS}(g, r) = \text{RIF}(g, r) \cdot \bar{\Sigma}_f(g, r) \quad (637)$$

Integrated neutron production

$$\text{NUFISS}(g, r) = \text{RIF}(g, r) \cdot \bar{\nu} \bar{\Sigma}_f(g, r) \quad (638)$$

Integrated neutron leakage

$$\text{LEAK}(g, r) = \text{RIF}(g, r) \cdot \bar{D}(g) \cdot B^2 \quad (639)$$

Integrated out-scattering

$$\text{OUTSC}(g, r) = \text{RIF}(g, r) \cdot \sum_{g' \neq g} \bar{\Sigma}_s(g \rightarrow g', r') \quad (640)$$

Integrated in-scattering

$$\text{INSC}(g, r) = \sum_{g' \neq g} \text{RIF}(g', r) \cdot \bar{\Sigma}_s(g' \rightarrow g, r') \quad (641)$$

Integrated neutron source

$$\text{SOURCE}(g, r) = \bar{\chi}(g) \sum_{g'} \frac{\text{RIF}(g', r) \cdot \overline{\nu \Sigma_f}(g, r)}{k_{eff}} \quad (642)$$

Net neutron in-current

$$\begin{aligned} \text{INCURR}(g, r) = & \text{ABS}(g, r) + \text{EAK}(g, r) + \text{OUTSC}(g, r) \\ & - \text{INSC}(g, r) - \text{SOURCE}(g, r) \end{aligned} \quad (643)$$

All cross sections in (636)–(642) are region-averaged, using the following expression:

$$\bar{\Sigma}_x(g, r) = \frac{\sum_{r' \in r} \Sigma_x(g, r') \cdot \phi(g, r') \cdot V(r')}{\sum_{r' \in r} \phi(g, r') \cdot V(r')} \quad (644)$$

The fluxes and cross sections have been condensed directly from the fine-group energy structure to the nodal-group energy structure

$$\Sigma_x(g, r') = \frac{\sum_{i \in g} \Sigma_x(i, r') \cdot \phi(i, r')}{\sum_{i \in g} \phi(i, r')} \quad (645)$$

$$\phi(g, r') = \sum_{i \in g} \phi(i, r') \quad (646)$$

9 Concluding Remarks

In this chapter, we have presented a rather verbose treatise on current lattice physics methodology. The salient features of a lattice physics code include the following:

- The generation of energy group-dependent neutron and gamma cross section libraries;
- A resonance calculation used to obtain cross sections from the neutron cross section library for resonance absorbers;
- A means of combining energy groups in order to accelerate the solution to the Boltzmann transport equation;
- A detailed solution to the Boltzmann transport equation to determine the spectral and spatial distribution of neutrons throughout the exact planar geometry of the fuel design;
- A fundamental mode calculation to account for neutron leakage effects in an ad hoc manner;
- The calculation of gamma sources and a detailed solution to the fixed-source Boltzmann transport equation to determine the spectral and spatial distribution of gamma particles throughout the exact planar geometry of the fuel design;
- Editing of nodal constants and various form functions;
- The saving of isotopic data to some sort of a restart file;
- And the solution to the burnup chains, assuming the analysis involves a time-step.

For some of these topics, there may exist multiple approaches that are equally well suited to solving the problem at hand. In such cases, we have tried to provide a broad description of the

various techniques. This is most notable in [▶ Sects. 3](#) and [▶ 6](#), which cover the resonance calculation and the solution to the burnup chains, respectively. In both sections, many different techniques have been presented. For other topics – most notably those concerned with solving the Boltzmann transport equation – there is one approach that is so vastly superior to all other approaches that we have simply concentrated on describing that one method in great detail such that the reader can fully appreciate its intricacies. This includes [▶ Sects. 4](#) and [▶ 5](#), which cover the group condensation scheme and the fine-mesh lattice transport calculation, respectively.

The accuracy of current state-of-the-art lattice physics codes for light water reactor analysis has now approached the level of accuracy of the Monte Carlo codes that are being used to generate reference solutions for benchmarking. As such, potential improvements stand to gain little in the way of accuracy and are little more than minor tweaks to the current methods. As computers become more powerful, the most significant improvements may be realized by adding more energy groups to the lower resonance region of the cross section library (i.e., below 100 eV), creating unshielded cross section groups and minimizing the importance of the resonance calculation described in [▶ Sect. 3](#). Beyond that, improvements in accuracy will most likely come from improvements to the raw cross section data and the processing of the data (e.g., the NJOY methodology), both of which are beyond the scope of the lattice physics code.

Recent developments in lattice physics are almost universally related to expanding the analysis to a collection of bundles, as opposed to analyzing a single bundle. Such two-dimensional multi-bundle analyses are not needed in order to generate cross sections for use in nodal codes, but rather are used as reference solutions for comparison to equivalent nodal calculations. These comparisons can sometimes serve to help uncover modeling deficiencies at the nodal level. This type of development really falls outside the traditional definition of a lattice physics code and could be thought of more appropriately as a convenient way of replacing the Monte Carlo analysis as a reference solution, since such analyses can be cumbersome to implement and time consuming to execute. In any event, this seems to be an area that is experiencing a great deal of attention at the moment with the promise that, at some point in the future, it will translate into a full three-dimensional modeling capability with thermal–hydraulic feedback and include an explicit thermal–mechanical treatment of the stresses experienced by the fuel cladding. Once again, such calculations would serve to provide reference solutions against which the nodal production code could be benchmarked.

References

-
- Abagyan LN, Bazazyants NO, Nikoleav MN, Tsiulya AM (1980) A new system of group constants for the calculation of fast reactors. *Sov At Energy* 48:117
- Adams ML, Larsen EW (2002) Fast iterative methods for discrete-ordinates particle transport calculations. *Prog Nucl Energy* 40:3
- Ahlin A, Edenius M (1977) CASMO – a fast transport theory assembly depletion code for LWR analysis. *Trans Am Nucl Soc* 26:604
- Ahlin A, Edenius M (1978) The collision probability module EPRI-CPM, Pt II, Chap 6. EPRI CCM-1, Electric Power Research Institute
- Amster HJ, Suarez R (1957) The calculation of thermal constants averaged over a Wigner-Wilkins flux spectrum: description of the SOFOGATE code. U.S. AEC Report WAPD-TM-39
- Arnold WH, Dannels RA (1960) The Doppler coefficient of $U^{238}O_2$. *Trans Am Nucl Soc* 3:229
- Askew JR (1972) A characteristics formulation of the neutron transport equation in complicated geometries. AEEW-M 1108
- Askew JR, Fayers FJ, Kemshell PB (1966) A general description of the lattice code WIMS. *J Brit Nucl Ener Soc* 5:564

- Azekura K, Maruyama H, Ikehara T, Yamamoto M, Mills V, Marcille T (2003) Development of a BWR lattice analysis code LANCER based on an improved CCCP method. In: Advances in nuclear fuel management III, Hilton Head Island
- Ball SJ, Adams RK (1967) MATEXP: a general purpose digital computer program for solving ordinary differential equations by the matrix exponential method, ORNL/TM-1933, Union Carbide Corporation, Nuclear Division, Oak Ridge National Laboratory
- Barry FR (1963) LEOPARD – a spectrum dependent non-spatial depletion code for the IBM-7094. U.S. AEC Report WCAP-3741
- Bateman H (1910) The solution of differential equations occurring in the theory of radioactive transformations. Proc Cambridge Phil Soc 15:423
- Bell MJ (1973) ORIGEN – the ORNL isotope depletion and generation code, ORNL-4628
- Bitelli G, Salvatores M, Cecchini G (1970) Heterogeneity effects on neutron self-shielding factors for fast reactors. Nucl Sci Eng 40:138
- Bohl H Jr, Gelbard EM, Ryan GH (1957) MUFT-4, fast neutron spectrum code for the IBM-704. U.S. AEC Report WAPD-TM-72
- Carlvik I (1965) A method for calculating collision probabilities in general cylindrical geometry and applications to flux distributions and Dancoff factors. In: U.N. international conference on the peaceful uses of atomic energy, vol 2. Geneva, p 225
- Carlvik I (1966a) Integral transport theory in one-dimensional geometries. AB Atomenergi, Stockholm, Sweden, AE-227
- Carlvik I (1966b) The Dancoff correction in square and hexagonal lattices. Part of Carlvik's PhD thesis, Chalmers University, Göteborg, Sweden, AE-257
- Carlvik I (1966c) On the use of integral transport theory for the calculation of the neutron flux distribution in a Wigner-Seitz cell, vol 8. Nukleonik, p 226
- Carlvik I (1967a) Studies of integral neutron transport methods for nuclear reactor calculations, Ph.D. thesis, Chalmers University, Göteborg, Sweden
- Carlvik I (1967b) Calculations of neutron flux distributions by means of integral transport methods. AB Atomenergi, Stockholm, Sweden, AE-279
- Carlvik I (1967c) Collision probabilities for finite cylinders and cuboids. AB Atomenergi, Stockholm, Sweden, AE-281
- Carlvik I (1967d) Monoenergetic critical parameters and decay constants for small spheres and thin slabs. AB Atomenergi, Stockholm, Sweden, AE-273
- Carlvik I, Pershagen B (1959) The Dancoff correction in various geometries. AB Atomenergi, Stockholm, Sweden, AE-16
- Casal JJ, Stamm'ler RJJ, Villarino E, Ferri A (1991) HELIOS: geometric capabilities of a new fuel assembly program. In: Proceedings of the international topical meeting on advances in mathematics, computations, and reactor physics, Pittsburgh
- Cefus CR, Larsen EW (1990) Stability analysis of coarse-mesh rebalance. Nucl Sci Eng 105:31
- Cho NZ, Hong SG (1996) CRX: a transport theory code for cell and assembly calculations based on the characteristics method. In: Proceedings of the international conference on physics of reactors, PHYSOR96, vol 1, September 16–20, 1996, Mito, Japan, p A-80
- Chao YA, Martinez AS (1978) On approximations to the neutron escape probability from an absorbing body. Nucl Sci Eng 66:254
- Chao YA, Yarbrough MB, Martinez AS (1981) Approximations to neutron escape probability and Dancoff corrections. Nucl Sci Eng 78:89
- Chiarella C, Keane A (1969) Equivalence relation based on an improved rational approximation. J Nucl Sci Technol 6:273
- Chiba G (2003) A combined method to evaluate the resonance self shielding effect in power fast reactor fuel assembly calculation. J Nucl Sci Technol 40:537
- Chiba G, Unesaki H (2006) Improvement of moment-based probability table for resonance self-shielding calculation. Ann Nucl Energy 33:1141
- Cho NZ, Park CJ (2003) A comparison of coarse mesh rebalance and coarse mesh finite difference accelerations for the neutron transport calculations. In: Proceedings of the nuclear mathematical and computational sciences: a century in review, April 6–11, 2003, American Nuclear Society, Gatlinburg [CD-ROM]
- Cho JY et al (2002) Cell based CMFD formulation for acceleration of whole-core method of characteristics calculations. J Korean Nucl Soc 34(3):250
- Croff AG (1980) ORIGEN2 – a revised and updated version of the Oak Ridge isotope generation and depletion code, ORNL-5621, 22
- Clarno K (2007) Implementation of generalized coarse-mesh rebalance in NEWTRNX for acceleration of parallel block-Jacobi transport. Trans Am Nucl Soc 97:498
- Cullen DE (1974) Application of the probability table method to multi-group calculations of neutron transport. Nucl Sci Eng 55:387
- Cullen DE (1986) Nuclear cross section preparation. In: CRC handbook of nuclear reactor calculations I. CRC Press, Boca Raton

- Dean D, Rempe K, Umbarger J (2005) SIMULATE-3 – an advanced three-dimensional two-group reactor analysis code, User's Manual. STUDSVIK/ SOA-95/15, rev. 3, Studsvik of America
- Dirac PAM (1943) Approximate rate of neutron multiplication for a solid of arbitrary shape and uniform density. British Report MS-D-5, Part I
- Dresner L (1960) Resonance absorption in nuclear reactors. Pergamon Press, Elmsford
- England TR (1962) CINDER – a one-point depletion and fission product program, WAPD-TM-334, Bettis Atomic Power Laboratory
- Fayers FJ, Davidson W, George CH, Halsall MJ (1972) LWRWIMS, a modular computer code for the evaluation of light water reactor lattices – part I: description of methods. UKAEA Report AEEW-R 785, Winfrith
- Garrison JD, Roos BW (1962) Fission-product capture cross sections, a compilation of yields for U233T, U235T, and PU239T. Nucl Sci Eng 12:115
- Goldberg L, Vujic J, Leonard A (1995) The method of characteristics in general geometry. Trans Am Nucl Soc 73:173
- Goldstein R (1967) Intermediate resonance absorption including interference scattering and Doppler broadening. Trans Am Nucl Soc 6:161
- Goldstein R, Cohen ER (1962) Theory of resonance absorption of neutrons. Nucl Sci Eng 13:132
- Halsall MJ (1980) CACTUS, a characteristics solution to the neutron transport equation in complicated geometries. AEEW-R 1291, Atomic Energy Establishment, Winfrith, Dorchester, Dorset, UK
- Halsall MJ (1995) The WIMS subgroup method for resonance absorption. Trans Am Nucl Soc 72:354
- Hazama T, Chiba G, Sugino K (2006) Development of a fine and ultra-fine group cell calculation Code SLAROM-UF for fast reactor analyses. J Nucl Sci Technol 43:908
- Hébert A (1998) A comparison of three methods for computing probability tables. In: Proceedings of the international conference on physics of nuclear science and technology, October 5–8, 1998, Hauppauge
- Hébert A (2004) A mutual resonance self-shielding model consistent with subgroup equations. In: Proceedings of the international meeting on physics of fuel cycles and advanced nuclear systems: global developments, PHYSOR2004, April 25–29, 2004, Chicago
- Hébert A (2005a) The ribbon extended self-shielding model. Nucl Sci Eng 151:1
- Hébert A (2005b) A review of legacy and advanced self-shielding models for lattice calculations. In: Proceedings of the mathematics and computation, supercomputing, reactor physics and nuclear and biological applications (M&C2005), September 12–15, 2005, Avignon, France
- Hébert A, Coste M (2002) Computing moment-based probability tables for self-shielding calculations in lattice codes. Nucl Sci Eng 142:245
- Hébert A, Marleau G (1991) Generalization of the Stamm'ler method for the self-shielding of resonant isotopes in arbitrary geometries. Nucl Sci Eng 108:230
- Hébert A, Marleau G, Roy R (2000) A description of the DRAGON data structures. Version DRAGON_000331 Release 3.04, Report IGE-232 Rev. 3, Institut de génie nucléaire, École Polytechnique de Montréal, Montréal, Québec
- Hébert A, Santamarina A (2008) Refinement of the Santamarina-Hfaiedh energy mesh between 22.5 eV and 11.4 keV. In: Proceedings international conference on reactor physics, nuclear power: a sustainable resource (Physor2008), September 2008, Interlaken, Switzerland [CD-ROM]
- Hfaiedh N, Santamarina A (2005) Determination of the optimized SHEM mesh for neutron transport calculations. In: Proceedings of the mathematics and computation, supercomputing, reactor physics and nuclear and biological applications (MC&SNA2007), September 2005, Avignon, France [CD-ROM]
- Hoffman A et al (1973) APOLLO: code Multigroupe de résolution de l'équation du transport pour les neutrons thermiques et rapides. Note CEA-N-1610, Commissariat à l'énergie Atomique, France
- Honeck HC (1961) THERMOS, a thermalization transport code for reactor lattice calculations. U.S. AEC Report BNL-5826
- Huria H, Ouislomen M (2008) An optimized ultra-fine energy group structure for neutron transport calculations. In: Proceedings of the international conference on the physics of reactors (PHYSOR2008), September 2008, Interlaken, Switzerland [CD-ROM]
- Hwang RN (2003) Resonance theory in reactor applications. In: Review lecture in topical meeting nuclear mathematical and computational sciences: a century in review – a century anew (M&C 2003), Gatlinburg, April 6–10, 2003, American Nuclear Society, LaGrange Park, pp 1–15
- Ihara H (ed) (1989) Tables and figures from JNDC nuclear data library of fission products, version 2, JAERI-M 89–204
- Iijima S, Yoshida T (1982) Fission product model for BWR lattice calculation code. J Nucl Sci Technol 19:96

- Ikehara T, Ando Y, Yamamoto M (1998) Fission product model for BWR analysis with improved accuracy in high burnup. *J Nucl Sci Technol* 35:527
- Ishiguro Y (1968) Exact treatment of the resonance absorption of neutrons of intermediate energy. *Nucl Sci Eng* 32:422
- Ishiguro Y (1974) PEACO-II: a code for calculation of effective cross sections in heterogeneous systems, JAERI-M 5527
- Ishiguro Y (1985) Generalized Dancoff factor in complex lattice arrangement. *J Nucl Sci Technol* 22:853
- Ishiguro Y, Takano K (1969) Intermediate neutron resonance absorption with interference scattering in heterogeneous systems. *J Nucl Sci Technol* 6:380
- Iwamoto T, Tamitani M, Moore B (2003) Methods, benchmarking, and applications of the BWR core simulator code AETNA. In: Proceedings of the International Conference on Advances in Nuclear Fuel Management III (ANFM 2003), CD-ROM, American Nuclear Society, Hilton Head Island
- Jevremovic T, Ito T, Inaba Y (2002) ANEMONA: multiassembly neutron transport modelling. *Ann Nucl Energy* 29:2105
- Jevremovic T, Vujic J, Tsuda K (2001) ANEMONA—a neutron transport code for general geometry reactor assemblies based on the method of characteristics and R-function solid modeller. *Ann Nucl Energy* 28:125
- Jonsson A, Loretz RA (1991) Historical and recent developments, applications, and performance of the DIT assembly lattice code. In: Proceedings of the international topical meeting on advances in mathematics, computations, and reactor physics, Pittsburgh
- Joo HG, Cho JY, Kim HY et al (2002) Dynamic implementation of the equivalence theory in the heterogeneous whole core transport calculation. In: Proceedings of the international conference on the new frontiers of nuclear technology: reactor physics, safety and high-performance computing (PHYSOR2002), October 7–10, 2002, Seoul, Korea, p 13A-02 [CD-ROM]
- Joo HG, Han BS, Kim CH (2005) Implementation of subgroup method in direct whole core transport calculation involving non-uniform temperature distribution. In: Proceedings of the mathematics and computation, supercomputing, reactor physics and nuclear and biological applications (M&C2005), September 12–15, 2005, Avignon, France [CD-ROM]
- Joo HG, Kim GY, Pogobekyan L (2009) Subgroup weight generation based on shielded pin-cell cross section conservation. *Ann Nucl Energy* 36:859
- Karthikeyan R, Hébert A (2008) Performance of advanced self-shielding models in DRAGON version 4 on analysis of a high conversion light water reactor lattice. *Ann Nucl Energy* 35:396
- Kidmon RB (1975) The shielding factor method for generating multigroup cross sections for fast reactor analysis. *Nucl Sci Eng* 44:189
- Kim KS, Kim HY, Zee SQ (2002) Benchmark calculations of DENT-2D code for PWR fuel assemblies. In: Proceedings of the international conference on the new frontiers of nuclear technology: reactor physics, safety and high-performance computing, vol 14, October 7–10, 2002, Seoul, Korea, p A-05
- Knott D (1990) NUC ENG 521, computational methods in steady state neutron transport theory. Department of Nuclear Engineering, The Pennsylvania State University
- Knott D (1991) KRAM, a lattice physics code for modelling the detailed depletion of Gadolinia isotopes from BWR fuel designs. PhD thesis, The Pennsylvania State University, University Park
- Knott D, Edenius M (1993) Validation of CASMO-4 transport solution. In: Proceedings of the international meeting mathematical methods and supercomputing in nuclear applications, vol 2, April 19–23, 1993, Karlsruhe, Germany, p 547
- Knott D, Forssen B-H, Edenius M (1995) CASMO-4 – a fuel assembly burnup program, methodology. STUDEVK/SOA-95/2, Studsvik of America
- Knott D, Wehlage E (2007) Description of the LANCER02 lattice physics code for single-assembly and multibundle analysis. *Nucl Sci Eng* 155:331
- Kobayashi K (1995) Genshiro Butsuri (Reactor Physics). Corona, Tokyo [in Japanese]
- Koike H, Yamaji K, Sato D et al (2010) A resonance calculation method based on the multi-terms rational approximation for general geometry with gray resonance absorbers, Proc. PHYSOR2010, Pittsburgh
- Kosaka S, Saji E (2000) Transport theory calculation for heterogeneous multi-assembly problem by the characteristics method with direct path linking technique. *J Nucl Sci Technol*, 37:1015
- Kruijff WJ (1994) Reactor physics analysis of the pin-cell Doppler effect in a thermal nuclear reactor, Ph.D. thesis, Delft University
- Kruijff W, Jansen A (1996) The effective fuel temperature to be used for calculating resonance

- absorption in a $^{238}\text{UO}_2$ lump with a nonuniform temperature profile. *Nucl Sci Eng* 123:121
- Lamarsh JR (1972) Introduction to nuclear reactor theory. Addison-Wesley, Reading, ISBN 0-201-04120-X
- Lapidus L, Luus R (1967) Optimal control of engineering processes. Blaisdell, Waltham
- Lee D, Downar TJ (2003) Convergence analysis of the nonlinear coarse mesh finite difference method. In: Proceedings of the nuclear mathematical and computational sciences: a century in review, April 6–11, 2003, American Nuclear Society, Gatlinburg [CD-ROM]
- Lee D, Smith K, Rhodes J (2009) The impact of ^{238}U resonance elastic scattering approximations on thermal reactor Doppler reactivity. *Ann Nucl Energy* 36:274
- Leonard A, McDaniel CT (1995) Optimal polar angles and weights. *Trans Am Nucl Soc* 73:171
- Levine M (1963) Resonance integral calculations for ^{238}U lattices. *Nucl Sci Eng* 18:271
- Levitt LB (1972) The probability table method for treating unresolved neutron resonances in Monte Carlo calculations. *Nucl Sci Eng* 49:450
- Lewis EE, Miller WF (1984) Computational methods of neutron transport. Wiley, New York, ISBN 0-471-09245-2
- Loubiere S, Sanchez R, Coste M et al (1999) APOLLO2 twelve years later. In: Proceedings Of the international conference on mathematics and computation, reactor physics and environmental analysis in nuclear applications, September 27–30, 1999, Madrid
- MacFarlane RE, Muir DW (1994a) The NJOY nuclear data processing system, Version 91. LA-12740-M, Los Alamos National Laboratory, Los Alamos
- MacFarlane RE, Muir DW (1994b) The NJOY nuclear data processing system, Version 91, LA-17740-M, Los Alamos National Laboratory, Los Alamos
- Marcille TF, Mills VW (2003) An automated multi-group cross section processing technique using NJOY. In: Proceedings of the advances in nuclear fuel management III, October 5–8, 2003, Hilton Head Island [CD-ROM]
- Marleau G, Hébert A, Roy R (2000) A user guide for DRAGON. Version DRAGON_000331 Release 3.04, Report IGE-174 Rev. 5, Institut de génie nucléaire, École Polytechnique de Montréal, Montréal, Québec
- Marleau G, Roy R, Hébert A (1994) DRAGON: a collision probability transport code for cell and supercell calculations. Report IGE-157, Institut de génie nucléaire, École Polytechnique de Montréal, Montréal, Québec
- Masiello E, Sanchez R, Zmijarevic I (2009) New numerical solution with the method of short characteristics for 2-D heterogeneous Cartesian cells in the APOLLO2 code: numerical analysis and tests. *Nucl Sci Eng* 161:257
- Matsumoto H, Ouisloumen M, Takeda T (2005) Development of spatially dependent resonance shielding method. *J Nucl Sci Technol* 42:688
- Matsumoto H, Ouisloumen M, Takeda T (2006) Spatially dependent self-shielding method with temperature distribution for the two-dimensional transport code PARAGON. *J Nucl Sci Technol* 43:1311
- MC**2-2 (1999) Multigroup neutron spectra, slowing-down calculation using ENDF/B, P1 and B1 approximation, NESC0355, NEA/OECD (last updated November 1999)
- McLane V (ed) (2001) ENDF-102 data formats and procedures for the evaluated nuclear data file ENDF-6, BNL-NCS-44945-01/04-Rev
- Mertyurek U (2007) Gamma flux calculations in lattice physics code LANCER02. *Trans Am Nucl Soc* 97:580
- Mizuta H (1970) Accuracy of approximations used in resonance integral calculation. *J Nucl Sci Technol* 7:264
- Moler C, Loan CV (2003) Nineteen dubious ways to compute the exponential of a matrix, twenty-five years later. *SIAM Rev* 45:3
- Moore B, Zhang H, Congdon S (1999) Comparison of methods for BWR prediction accuracy as applied to a small BWR/4. In: Proceedings of the mathematical and computational reactor physics, and environmental analysis in nuclear Applications, Madrid, Spain, p 679
- Morimoto Y, Maruyama H, Ishii K et al (1989) Neutronic analysis code for fuel assembly using a vectorized Monte Carlo method. *Nucl Sci Eng* 103:351
- Nikolaev MN (1976) Comments on the probability table method. *Nucl Sci Eng* 61:286
- Nikoleav MN, Ignatcv AA, Isaev NV, Khokhlov VF (1971) The method of subgroups for considering the resonance structure of cross sections in neutron calculations. *Sov At Energy* 5:426
- Nikoleav MN, Germogenova TA, Isaev NV, Khokhlov VF (1973) Computations of neutron propagation, allowing for the resonance structure of the cross sections. *Sov At Energy* 35:29
- Okumura K, Kugo T, Kaneko K, Tsuchihashi K (2007) SRAC2006: a comprehensive neutronics calculation code system, JAEA-Data/Code 2007-004
- Okumura K, Mori T, Nakagawa M, Kanako K (2000) Validation of a continuous-energy Monte Carlo burn-up code MVP-BURN and its application to

- analysis of post irradiation experiment. *J Nucl Sci Technol* 37:128
- Ouisloumen M et al (2001) PARAGON: the New Westinghouse assembly lattice code. In: ANS international topical meeting on mathematical methods for Nuclear Applications, Salt Lake City
- Postma T, Vujic J (1999) The method of characteristics in general geometry with anisotropic scattering. In: Proceedings of the international conference on mathematics and computation, reactor physics and environmental analysis in nuclear applications, vol 2, September 27–30, 1999, Madrid, Spain, p 1215
- Reed WH (1971) The effectiveness of acceleration techniques for iterative methods in transport theory. *Nucl Sci Eng* 45:245
- Reuss P, Coste-Delclaux M (2003) Development of computational models used in France for neutron resonance absorption in light water lattices. *Prog Nucl Energy* 42:237
- Rhodes JD III (2009) ENDF/B-VII.0 586 group neutron data library for CASMO-5 and CASMO-5M. SSP-07/402, rev. 5, Studsvik Scandpower, Inc
- Rhodes J, Smith K, Lee D (2006) CASMO-5 development and applications. In: Proceedings of the PHYSOR-2006, ANS topical meeting on reactor physics, September 2006, Vancouver, Canada
- Ribon P (1986) Probability tables and Gauss quadrature application to neutron cross-sections in the unresolved energy range. In: Proceedings of the topical meeting on advances in reactor physics and safety, September 17–19, 1986, vol 1. Saratoga Springs, p 280
- Rosenstein W (1960) Collision probabilities and resonance integrals for lattice. *Nucl Sci Eng* 7:162
- Rothenstein W (1980) Resonance absorption calculations in thermal reactors. *Prog Nucl Energy* 5:95
- Rothenstein W, de Oliveira CRE, Brandman N (1988) Accurate resonance absorption calculations including 2-D effects and their representation in multigroup lattice physics codes. *Ann Nucl Energy* 15:293
- Rothenstein W, Segev M (1986) Unit cell calculations. In: CRC handbook of nuclear reactor calculations I. CRC Press, Boca Raton
- Rowlands G (1962) Resonance absorption and non-uniform temperature distributions. *J Nucl Energy Parts A/B* 16:235
- Roy R (1998) The cyclic characteristics method. In: Proceedings of the international topical meeting on the physics of nuclear science and technology, vol 1, October 5–8, 1998, Long Island, p 407
- Sanchez R, Mao L, Santandrea S (2002) Treatment of boundary conditions in trajectory-based deterministic transport methods. *Nucl Sci Eng* 140:23
- Sanchez R, Mondot J, Stancovski Z, Cosic A, Zmi-jarevic I (1988) APOLLO II: a user-oriented, portable, modular code for multi-group transport assembly calculations. *Nucl Sci Eng* 100:352
- Santamarina A, Collignon C, Garat A (2004) French calculation schemes for light water reactor analysis. In: Proceedings of the International Conference on PHYSOR2004-The physics of fuel cycles and advanced nuclear systems, April, 2004, Chicago [CD-ROM]
- Sartori E (1990) OECD/NEA Data Bank, Standard energy group structures of cross section libraries for reactor shielding, reactor cell and fusion neutronics applications: VITAMIN-J, ECCO-33, ECCO-2000 and XMAS, JEF/DOC-315 Revision 3 – DRAFT (December 11, 1990)
- Sauer A (1963) Approximate escape probabilities. *Nucl Sci Eng* 16:329
- Segev M (1975) A theory of resonance group self-shielding. *Nucl Sci Eng* 56:72
- Segev M (1981) Interpolation of resonance integrals. *Nucl Sci Eng* 79:113
- Sehgal BR, Goldstein R (1966) Intermediate resonance absorption in heterogeneous media. *Nucl Sci Eng* 25:174
- Sidje RB (1998) EXPOKIT: software package for computing matrix exponentials. *ACM Trans Math Software* 24:130
- Sinitsa VV, Nikoleav MN (1973) Analytic determination of subgroup parameters. *Sov At Energy* 35:429
- Smith KS (1983) Nodal method storage reduction by nonlinear iteration. *Trans Am Nucl Soc* 44:265
- Smith KS, Rhodes JD (2000) CASMO-4 characteristics method for two-dimensional PWR and BWR core calculations. *Trans Am Nucl Soc* 83:292
- Smith KS, Rhodes JD III (2002) Full-core, 2-D, LWR core calculation with CASMO-4E. In: Proceedings of the international conference on the new frontiers of nuclear technology: reactor physics, safety and high-performance computing (PHYSOR2002), October 7–10, 2002, Seoul, Korea, p 13A-04 [CD-ROM]
- Stacy WM (2001) Nuclear reactor physics. Wiley, New York
- Stamm'ler RJJ (1992) PHOENIX – User's guide. ABB-Atom AB Report UR 92–054, Rev. 5
- Stamm'ler RJJ, Abbate MJ (1983) Methods of steady state reactor physics in nuclear design. Academic, London, New York, ISBN 0-12-663320-7
- Stamm'ler RJJ, Blomstrand J, Weiss ZJ (1973) Equivalence relations for resonance integral calculations. *J Nucl Energy* 27:885

- Stoker CC, Weiss ZJ (1996) Spatially dependent resonance cross sections in a fuel rod. *Ann Nucl Energy* 23:765
- Sublet J, Ribon P (2002) A probability table based cross section processing system: CALENDF-2001. *J Nucl Sci Technol* 2(Suppl):856
- Sugimura N, Yamamoto A (2006) Evaluation of Dancoff factors in complicated geometry using the method of characteristics. *J Nucl Sci Technol* 43:1182
- Sugimura N, Yamamoto A (2007) Resonance treatment based on ultra-fine-group spectrum calculation in the AEGIS code. *J Nucl Sci Technol* 44:958
- Sugimura N, Yamamoto A, Ushio T, Mori M, Tabuchi M, Endo T (2007) Neutron transport models of AEGIS: an advanced next-generation neutronics design system. *Nucl Sci Eng* 155:276
- Tasaka K (1977) DCHAIN: code for analysis of build-up and decay of nuclides, JAERI 1250, Japan Atomic Energy Research Institute [in Japanese]
- Taubman CJ (1975) The WIMS 69-group library tape 166259. Report AEEW-M1324, U.K. Atomic Energy Authority, Winfrith
- Tohjih M, Watanabe M, Yamamoto A (2006) Study on spatial discretization and temperature distribution approximation effects on BWR assembly calculations, *Ann Nucl Energy* 33:242
- Tone T (1975) A numerical study of heterogeneity effects in fast reactor critical assemblies. *J Nucl Sci Technol* 12:467
- Tsuchihashi K, Takano H, Horikami K et al (1982) SRAC: JAERI thermal reactor standard code system for reactor design and analysis, JAERI-1302, Japan Atomic Energy Research Institute
- Villarino EA, Stamm'ler RJJ, Ferri AA, Casal JJ (1992) HELIOS: angularly dependent collision probabilities. *Nucl Sci Eng* 112:16
- Vondy DR (1962) Development of a general method of explicit solution to the nuclide chain equations for digital machine calculations, ORNL/TM-361, Union Carbide Corporation, Nuclear Division, Oak Ridge National Laboratory
- Wehlage EM (2005) Modeling resonance interference effects in the LANCER02 lattice physics code. MSc thesis, The Ohio State University, Columbus
- Wehlage E, Knott D, Mills VW (2005) Modeling resonance interference effects in the lattice physics code LANCER02. In: Proceedings of the mathematics and computation, supercomputing, reactor physics and nuclear and biological applications (M&C2005), September 12–15, 2005, Avignon, France [CD-ROM]
- Weinberg AM, Wigner EP (1958) The physical theory of neutron chain reactors. University of Chicago Press, Chicago
- Weiss Z, Ball G (1991) Ray-tracing in complicated geometries. *Ann Nucl Energy* 18:483
- Wemple CA, Gheorghiu H-NM, Stamm'ler RJJ, Villarino EA (2008) Recent advances in the HELIOS-2 lattice physics code. In: Proceedings of the international conference on the physics of reactors (PHYSOR2008), September 2008, Interlaken, Switzerland [CD-ROM]
- Wemple CA, Stamm'ler RJJ, Ferri AA (2007) Improved temperature-dependent resonance treatment in HELIOS-1.9. *Trans Am Nucl Soc* 96:657
- West JT, Emmet MB (1980) MARS: a multiple array system using combinatorial geometry. Oak Ridge National Laboratory, Radiation Shielding Information Center
- Wigner EP, Creutz E, Jupnik H, Snyder T (1955) Resonance absorption of neutrons by spheres. *J Appl Phys* 26:260
- Williams ML (1983) Correction of multigroup cross sections for resolved resonance interference in mixed absorbers. *Nucl Sci Eng* 83:37
- Williams ML, Asgari M, Hollenbach DF (2005) CENTRM: a one-dimensional neutron transport code for computing pointwise energy spectra. Sect. F18 of SCALE: a modular code system for performing standardized computer analyses for licensing evaluations, ORNL/TM-2005/39, Version 5, vols I–III, April 2005. Available from Radiation Safety Information Computational Center at Oak Ridge National Laboratory as CCC-725
- WIMS-D/4 (2000) Multi-group reactor lattice calculation for thermal reactor and fast reactor, NEA-0329, NEA/OECD (last updated March, 2000)
- Yamamoto A (2005) Generalized coarse-mesh rebalance method for acceleration of neutron transport calculations. *Nucl Sci Eng* 151:274
- Yamamoto A (2008) Evaluation of background cross-section for heterogeneous and complicated geometry by the enhanced neutron current method. *J Nucl Sci Technol* 45:1287
- Yamamoto A (2009) Applicability of the enhanced neutron current method for non-convex fuel shapes. *Ann Nucl Energy* 36:193
- Yamamoto T (2003) Background-cross-section-dependent subgroup parameters. *J Nucl Sci Technol* 40:370
- Yamamoto T (2004) Generalized approach to optimize subgroup parameters. *J Nucl Sci Technol* 41:425

- Yamamoto M et al (1984) Development and validation of TGBLA lattice physics methods. In: Proceedings of the topical meeting on reactor physics and shielding, Chicago
- Yamamoto A, Kitamura Y, Ushio T, Sugimura N (2004) Convergence improvement of coarse mesh rebalance method for neutron transport calculations. *J Nucl Sci Technol* 41:781
- Yamamoto A, Koike H, Yamane Y (2009a) A new framework of resonance calculation method based on the sub-group method (1); theory. *Trans Am Nucl Soc* 100:647
- Yamamoto A, Koike H, Yamane Y (2009b) A new framework of resonance calculation method based on the sub-group method (2); calculation. *Trans Am Nucl Soc* 100:650
- Yamamoto A, Sugimura N (2006) Improvement on multi-group scattering matrix in thermal energy range generated by NJOY. *Ann Nucl Energy* 33:555
- Yamamoto A, Tabushi M, Sugimura N, Ushio T, Mori M (2007) Derivation of optimum polar angle quadrature set for the method of characteristics based on approximation error for the Bickley function. *J Nucl Sci Technol* 44:129
- Yamamoto A, Tabuchi M, Sugimura N et al (2005) Non-equidistant ray tracing for the method of characteristics. In: Proceedings of the international topical meeting on mathematics and computation, super-computing, reactor physics and nuclear and biological applications (M&C2005), Sept. 12–15, 2005, Avignon, France [CD-ROM]
- Yamamoto A, Tada K, Sugimura N, Ushio T, Mori M (2006) Generation of cross section library for lattice physics code, AEGIS. In: Proceedings of the Physor-2006, September 10–14, 2006, Vancouver, Canada [CD-ROM]
- Yamamoto T, Takeda T (2000) Reaction rate calculation in fast reactor blanket using multiband Sn theory. *J Nucl Sci Technol* 37:428
- Yamamoto T, Takeda T (2006) A complement proposal for optimization of subgroup parameters. *J Nucl Sci Technol* 43:765
- Yamamoto A, Tatsumi M, Sugimura N (2007) Numerical solution of stiff burnup equation with short half lived nuclides by the Krylov subspace method. *J Nucl Sci Technol* 44:147
- Yamamoto A, Tatsumi M, Sugimura N (2009) Projected predictor-corrector method for lattice physics burnup calculations. *Nucl Sci Eng* 163:144



10 Core Isotopic Depletion and Fuel Management

Paul J. Turinsky

Department of Nuclear Engineering, North Carolina State
University, Raleigh, NC, USA
turinsky@ncsu.edu

1	<i>Burnup and Conversion</i>	1243
1.1	Introduction	1243
1.2	The Bateman Equation	1244
1.3	Solution of the Bateman Equation	1245
1.4	Results of Burnup Calculations	1247
1.5	The Breeding (Conversion) Ratio	1247
1.6	Transmutation	1249
1.7	Burnable Poisons	1249
2	<i>Transient Fission Products</i>	1252
2.1	Transient Fission Product Equations	1252
2.2	Xenon Transient Phenomena and Control	1252
2.2.1	Global Phenomena	1252
2.2.2	Spatial Phenomena	1253
3	<i>Nuclear Fuel Management</i>	1254
3.1	Introduction	1254
3.2	Out-of-Core Nuclear Fuel Management	1255
3.3	LWR In-Core Nuclear Fuel Management	1266
3.3.1	LWR Loading Pattern Selection	1266
3.3.2	LWR Control Rod Programming Selection	1271
3.3.3	LWR Lattice and Assembly Selection	1275
3.4	Non-LWR In-Core Nuclear Fuel Management	1283
3.4.1	Introduction	1283
3.4.2	Heavy Water Reactors	1284
3.4.3	Very High Temperature Gas-Cooled Reactors	1284
3.4.4	Advanced Recycle Reactor	1285
3.5	Applications of Mathematical Optimization in Nuclear Fuel Management	1286
3.5.1	Introduction	1286
3.5.2	Mathematical Optimization Approaches Utilized for Nuclear Fuel Management	1286
3.5.3	Application of Mathematical Optimization to Out-of-Core Nuclear Fuel Management	1291

3.5.4	Application of Mathematical Optimization to In-Core Nuclear Fuel Management	1293
3.6	Computational Design Sequences	1303
3.6.1	Design Calculations Needed	1303
3.6.2	Cross-Section Generation	1304
3.6.3	Core Simulation	1307
4	Conclusions	1309
	References	1310

Abstract: This chapter discusses how core isotopic depletion and fuel management are completed for reactor cores of nuclear power plants. First, core isotopic depletion is discussed, in particular, how the Bateman equation is numerically solved, and the behaviors of the fissile, fertile, burnable poison and transient fission products isotopes. The concepts of breeding, conversion, and transmutation are introduced. Nuclear fuel management is discussed next, with a strong emphasis on the fuel management for light water reactors (LWRs), given their predominance. The discussion utilizes the components of design optimization, those being objectives, decision variables, and constraints. The fuel management discussion first addresses out-of-core fuel management, which involves such decisions as cycle length; stretch out operations; and feed fuel number, fissile enrichment, and burnable poison loading and partially burnt fuel to reinsert, for each cycle in the planning horizon. In-core fuel management is introduced by focusing on LWRs, with the basis of making decisions associated with determining the loading pattern, control rod program, lattice design, and assembly design presented. This presentation is followed by a brief review of in-core fuel management decisions for heavy water reactors, very high temperature gas-cooled reactors, and advanced recycle reactors. Mathematical optimization techniques appropriate for making nuclear fuel management decisions are next discussed, followed by their applications in out-of-core and in-core nuclear fuel management problems. Next presented is a review of the computations that are required to support nuclear fuel management decision making and the tools that are available to accomplish this. The chapter concludes with a summary of the current state of depletion and nuclear fuel management capabilities, and where further enhancements are required to increase capabilities in these areas.

1 Burnup and Conversion

1.1 Introduction

To understand the behavior of a reactor's core over its operating lifetime, it is necessary to be able to predict the changes in the isotopic composition of the core as a function of both time and space. Given the isotopic composition of the core, macroscopic cross-section values as a function of time and space can be determined as follows.

$$\Sigma_x(\vec{r}, E, t) = \sum_j \sigma_{x_j}(\vec{r}, E, t) N_j(\vec{r}, t) \quad (1)$$

where

$\Sigma_x(\vec{r}, E, t)$ = macroscopic cross-section for reaction type x

$\sigma_{x_j}(\vec{r}, E, t)$ = microscopic cross-section for reaction type x of isotope j

$N_j(\vec{r}, t)$ = number density of isotope j

\vec{r}, E, t = spatial position, neutron energy, and time-independent variables

Equation (1) indicates that the microscopic cross-section is not only a function of neutron energy, but also of spatial position and time. These latter dependencies arise because of the temperature dependence originating from Doppler broadening and the thermal scattering kernel. Solving the neutron transport equation or an approximation to it, e.g., neutron diffusion equation, yields the flux distribution throughout the core, which in turn can be used to determine the power distribution and many other core attributes of interest.

The isotopic composition of the core is also of interest to access the performance of other stages of the nuclear fuel cycle than core performance. Concerns about criticality, radiation intensity, and heat load are relevant to back-end stages, e.g., storage, partitioning, and waste disposal, and even front-end stages when considering a closed fuel cycle, e.g., MOX fuel fabrication. Further, knowledge of isotopic compositions are used when a fuel pin failure has occurred in narrowing down the possible core location of the failed pin, and when completing gamma scans on a discharged fuel assembly to infer power production and discharge burnup. The composition of the fuel, now elemental rather than isotopic, is also utilized in materials' simulations to predict fuel performance attributes, e.g., swelling, fission product gas release, thermal conductivity, and melting temperature. It follows that what isotopes need to be tracked is dependent upon the intended usage.

1.2 The Bateman Equation

The Bateman balance equation mathematically describes the time dependency of the isotopic number densities. Assuming that the isotopes' spatial movement from their place of origination does not occur, the spatial dependence of the isotopic number densities can be suppressed if it is recognized that the Bateman equation is written for a specific spatial position \vec{r} as now indicated

$$\begin{aligned} \frac{dN_i(t)}{dt} = & \sum_j \left[\int_0^\infty \gamma_{ji}(E, t) \sigma_{f_j}(E, t) \phi(E, t) dE \right] N_j(t) \\ & + \sigma_{c_{i-1}}(E, t) \phi(E, t) N_{i-1}(t) + \lambda_{i'} N_{i'}(t) \\ & - \left\{ \left[\int_0^\infty (\sigma_{f_i}(E, t) + \sigma_{c_i}(E, t)) \phi(E, t) dE \right] + \lambda_i \right\} N_i(t) \end{aligned} \quad (2)$$

where

$\left[\int_0^\infty \gamma_{ji}(E, t) \sigma_{f_j}(E, t) \phi(E, t) dE \right] N_j(t)$ = creation rate of isotope i due to fission of isotope j

$\sigma_{c_{i-1}}(E, t) \phi(E, t) N_{i-1}(t)$ = creation rate of isotope i due to radiative neutron capture in isotope $i - 1$

$\lambda_{i'} N_{i'}(t)$ = creation rate of isotope i due to radioactive decay of isotope i'

$\left[\int_0^\infty (\sigma_{f_i}(E, t) + \sigma_{c_i}(E, t)) \phi(E, t) dE \right] N_i(t)$ = destruction rate of isotope i due to fission and radiative neutron capture

$\lambda_i N_i(t)$ = destruction rate of isotope i due to radioactive decay

Needless to say, for a specific isotope i not all destruction terms in (2) may appear. The implication is that not all isotopes are coupled to each other, which from a mathematical viewpoint means that the balance equation for a specific isotope i does not couple to all other isotopic balance equations.

It is noted that the neutron flux appears in the Bateman equation. But the neutron flux depends on the isotopic number density distributions in the core, which implies that a nonlinear problem must be solved. Assuming for now that the neutron flux is known, (2) can be written in compact matrix notation

$$\frac{d\bar{N}(t)}{dt} = \bar{A}(t)\bar{N}(t) \quad (3)$$

where the single bar denotes a column vector, the double bar denotes a matrix, and the elements of the coefficient matrix given by $(\overline{\overline{A}}(t))_{ij} = a_{ij}(t)$ denote the coefficient of one of the creation or destruction terms in (2).

1.3 Solution of the Bateman Equation

Assuming for now that the neutron flux is known so that the nonlinear coupling between the Bateman equation and neutron transport equation can be ignored, there are a number of approaches to solve (3) utilizing numerical methods. A challenge to numerically solve this equation is addressing the potential for a wide range of timescales associated with the different isotopes, implying that methods appropriate for solving a stiff system of equations may be necessary. Alternatively, those isotopes which are relatively short lived could be separated from (3), allowing the altered equation to be solved for isotopes with longer lives using nonstiff solvers and the isotopes with shorter lives treated separately using a different method. Mathematically, this implies that the coefficient matrix is partitioned into block submatrices and written as

$$\overline{\overline{A}} = \begin{bmatrix} \overline{\overline{A}}_{ll} & \overline{\overline{A}}_{ls} \\ \overline{\overline{A}}_{sl} & \overline{\overline{A}}_{ss} \end{bmatrix} \quad (4)$$

where l and s denote, respectively, the isotopes associated with the longer and shorter lives, and subscripts mn (where m and n equate to s or l) indicate the matrix elements associated with creation of isotopes m from isotopes n . If it is assumed now that the short-lived isotopes do not produce the long-lived isotopes, then $\overline{\overline{A}}_{ls} = 0$ and (4) reduces to a two-step solution given by

$$\frac{d\overline{N}_l(t)}{dt} = \overline{\overline{A}}_{ll}(t)\overline{N}_l(t) \quad (5)$$

and

$$\frac{d\overline{N}_s(t)}{dt} = \overline{\overline{A}}_{ss}(t)\overline{N}_s(t) + \overline{\overline{A}}_{sl}(t)\overline{N}_l(t) \quad (6)$$

enabling these two equations to be numerically solved utilizing different methods.

Methods that can be considered in solving the Bateman equations include all those methods associated with solving coupled first-order ordinary differential equations, e.g., finite difference, Runge-Kutta, matrix exponential, and under certain conditions analytic approaches, e.g., integrating factor technique or Laplace transforms. Nearly all these methods have been employed sometime in the past, but today two solution methods dominate.

The matrix exponential method (Moler and Van Loan 2003) is widely employed to solve problems where all sorts of coupling between isotopes can be accounted for. This is the method utilized in the ORNL-produced ORIGEN code (Bell 1973) and the CEA DARWIN code (Roque et al. 2002). Using the concepts of the integrating method to solve an ordinary differential equation and Taylor's series expansion, one can show that the solution to (3) can be written

$$\overline{N}(t_n) = \overline{N}(t_{n-1})e^{\int_{t_{n-1}}^{t_n} \overline{\overline{A}}(t)dt} \quad (7)$$

where

$$e^{\int_{t_{n-1}}^{t_n} \bar{\bar{A}}(t) dt} = \bar{I} + \sum_{m=1}^{\infty} \frac{\left(\int_{t_{n-1}}^{t_n} \bar{\bar{A}}(t) dt \right)^m}{m!} \quad (8)$$

where t_n and t_{n-1} denote the current and former discrete times associated with discretizing the time variable. If it is assumed that $\bar{\bar{A}}(t) = \bar{\bar{A}}(t_{n-1})$ for $t \in [t_{n-1}, t_n]$, then $\int_{t_{n-1}}^{t_n} \bar{\bar{A}}(t) dt = \bar{\bar{A}}(t_{n-1}) \Delta t_n$ defining $\Delta t_n = t_n - t_{n-1}$. To assure more rapid convergence of the infinite series, which in practice is approximated using a finite number of terms, note that

$$e^{\bar{\bar{A}}(t_{n-1}) \Delta t_n} = \left(e^{\bar{\bar{A}}(t_{n-1}) (\Delta t_n / q)} \right)^q \quad (9)$$

allowing scaling to be introduced. If the scale factor q is selected to be a power of 2, then (9) can be evaluated by successive squaring starting with the term $\left(e^{\bar{\bar{A}}(t_{n-1}) (\Delta t_n / q)} \right)$ evaluated using (8). It can be shown that the first few terms in the summation may have norms larger than one, but eventually they will become smaller than one and decrease in norm size as m increases. This is referred to as the “hump” effect. It is possible to determine the value of q such that at a specified value of m , the expansion will be over the “hump.” Also, one can obtain a series truncation error bound that indicates how many terms in the summation must be carried to assure a specified accuracy and a round-off error bound.

For the short-lived isotope chains, an analytic solution can be employed, again assuming that the coefficient matrix is constant over a time step. This avoids the necessity to introduce small time steps associated with numerical approximations. Vondy (1962) has analytically solved the Bateman equation for an arbitrary forward-branching chain





$$N_i(t_n) = N_i(t_{n-1}) e^{-|a_{ii}| \Delta t_n} + \sum_{k=1}^{i-1} N_k(t_{n-1}) \left[\sum_{j=k}^{i-1} \frac{e^{-|a_{jj}| \Delta t_n} - e^{-|a_{ii}| \Delta t_n}}{|a_{ii}| - |a_{jj}|} a_{j+1,j} \prod_{\substack{n=k \\ n \neq j}}^{i-1} \frac{a_{n+1,n}}{|a_{nn}| - |a_{jj}|} \right] \quad (10)$$

where N_i for $i = 1, 2, \dots$ denote the concentrations of the short-lived isotopes. This equation can be rearranged so that it can be programmed in a recursive manner, thereby minimizing the computational burden. As written, (10) assumes that only one long-lived isotope N_0 serves as the precursor for the short-lived isotopes, which can be corrected. Equation (10) can be extended to predict the concentration of the long-lived isotope that has associated with it short-lived precursors, i.e., those associated with the $\bar{\bar{A}}_s$ submatrix. Details on how this is accomplished in the case of the ORIGEN code can be found in Bell (1973).

When completing reactor physics calculations, one needs only to specifically treat isotopes where at least one of its macroscopic cross-section is large enough to affect the calculational solution. In this case the majority of the isotopes that exist in partially burnt fuel can be ignored. It is not uncommon to just specifically treat the fissile–fertile, transient fission products (if a thermal spectrum reactor), and reactivity control materials isotopes. Given the resulting limited number of linear chains, (10) can be used directly to predict the concentrations of the isotopes

in each linear chain. Use of (10) in this context denotes the second dominant solution method noted above. To account for fission products beyond the transient fission products, i.e., Pm^{149} , Sm^{149} , I^{135} , and Xe^{135} , one or more lumped fission products are introduced. Each lumped fission product is characterized by an effective fission product yield and capture cross-section so selected to approximately produce the correct capture rates as a function of exposure for a subset of fission products.

1.4 Results of Burnup Calculations

It is informative to look at the time behavior of several of the more important isotopes for reactor physics as the core is burned. What isotopes are present and their behaviors will be dependent upon the specific reactor type, e.g., boiling water reactor, heavy water reactor, and fast sodium reactor, and its associated fuel cycle, e.g., open fuel cycle and closed fuel cycle recycling only U and Pu.  [Figures 1](#) and  [2](#) present isotopic number densities for a representative Pressurized Water Reactor (PWR) lattice, which utilizes a lattice average fuel enrichment of 4.07 w/o and Erbium in the form of Erbium (Er_2O_3) as the burnable poison material.  [Figure 1](#) shows the fissile–fertile chain associated with uranium. As expected, this figure indicates that U235 is depleting in an approximately exponential fashion with time with a reduction to about 1 w/o at the time of discharge. For U238 the amount of depletion is very small.  [Figure 2](#) presents the plutonium isotopes, where, as expected, the lower mass isotopes build up and reach an equilibrium concentration sooner. The equilibrium concentration occurs when the creation rate equals the destruction rate.

1.5 The Breeding (Conversion) Ratio

The breeding (conversion) ratio is defined as the number of fissionable atoms produced to the number of fissionable atoms consumed in a reactor. If this ratio is greater or equal to 1, it is referred to as the breeding ratio. If less than 1, it is referred to as the conversion ratio. In terms of the coefficient matrix introduced in (3) it is mathematically defined by

Breeding (Conversion) Ratio at time t

$$= \frac{\sum_{i \in s_{\text{Capture}}} \left[\int_0^\infty \sigma_{c_i}(E, t) \phi(E, t) dE \right] N_i(t) + \sum_{i' \in s_{\text{Decay}}} \lambda_{i'} N_{i'}(t)}{\sum_{j \in s_{\text{Fissile}}} \left[\int_0^\infty (\sigma_{f_j}(E, t) + \sigma_{c_j}(E, t)) \phi(E, t) dE + \lambda_j \right] N_j(t)} \quad (11)$$

where s_{Fissile} refers to the set of fissile isotopes, e.g., U235, Pu239, and Pu241, s_{Capture} and s_{Decay} refer to the set of isotopes that either through neutron capture, e.g., Pu240, or decay, e.g., Np239, respectively, produces fissile isotopes. [Equation \(11\)](#) in reality is of little value since it refers to a specific time and spatial position (recall the spatial dependence has been suppressed). To obtain the value for a core over a reactor cycle, one reintroduces the spatial variable and integrates the numerator and denominator over the core volume and time from the beginning to the end of cycle rendering.

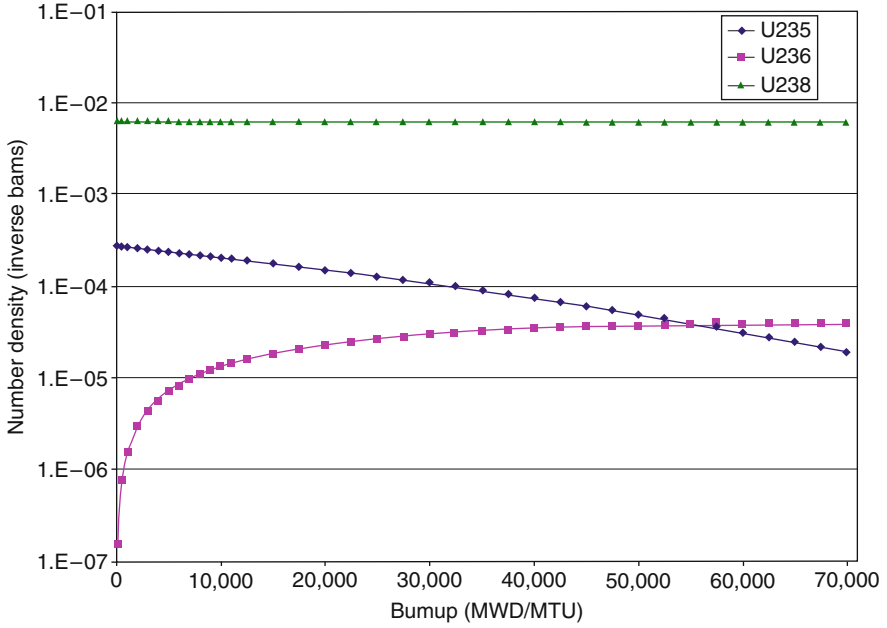


Figure 1
Uranium isotope concentrations versus burnup for a lattice

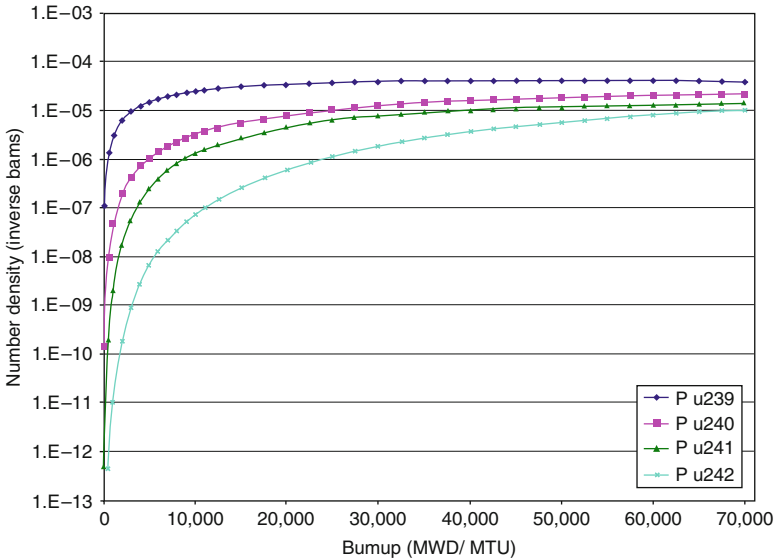


Figure 2
Plutonium isotopes concentrations versus burnup for a lattice

Breeding (Conversion) Ratio

$$= \frac{\int_{V_{Core}} d\vec{r} \int_{t_{BOC}}^{t_{EOC}} dt \left(\sum_{j \in S_{Capture}} \left[\int_0^\infty \sigma_{c_j}(\vec{r}, E, t) \phi(\vec{r}, E, t) dE \right] N_j(\vec{r}, t) + \sum_{i' \in S_{Decay}} \lambda_{i'} N_{i'}(\vec{r}, t) \right)}{\int_{V_{Core}} d\vec{r} \int_{t_{BOC}}^{t_{EOC}} dt \sum_{j \in S_{Fissile}} \left[\int_0^\infty (\sigma_{f_j}(\vec{r}, E, t) + \sigma_{c_j}(\vec{r}, E, t)) \phi(\vec{r}, E, t) dE + \lambda_j \right] N_j(\vec{r}, t)} \quad (12)$$

A high ratio can be obtained by selecting isotopes, which have a high number of fission neutrons produced per neutron capture.

1.6 Transmutation

Transmutation involves, via a nuclear reaction, the transmuting of a long half-life isotope into a stable or short half-life isotope. This is one possible manner of minimizing the heat and radio toxicity loads of high-level nuclear waste by transmitting Pu, minor actinides, and certain fission products. Minor actinides consist of the isotopes associated with elements of the actinide series of the periodic table minus U and Pu, which for spent fuel mainly implies Np237, Am241, Am243, Cu242-Cu248, and Ca249-Ca252. For isotopes that can fission, one desires to operate in a neutron energy range where the fission to capture cross-section is large, thereby avoiding the production of additional heavy isotopes via neutron capture. For Pu and minor actinides, a hard neutron spectrum accomplishes this. For fission products of interest, in particular Tc99, Cs135, and I129, which do not fission, they are best transmuted in a thermal spectrum via neutron capture.

Both critical and noncritical facilities are being considered as the source of neutrons. For critical facilities, a low conversion ratio design is desired, achieved by designing a fast reactor with a high fuel to coolant volume ratio. For a subcritical facility, an external neutron source is required, obtained using an accelerator-driven system (ADS), which creates neutrons by having high-energy protons collide with a high atomic number target, e.g., tungsten, mercury, and lead. By using a subcritical system, it is thought that some of the safety design requirements of a critical system that are more difficult to satisfy, such as having a proper reactivity power coefficient, can be avoided.

1.7 Burnable Poisons

As the fuel depletes, for a typical thermal reactor or any reactor where the conversion ratio is less than 1, the core reactivity decreases. The implication is to keep the reactor critical for the desired energy production; the core must start up with considerable excess reactivity. This excess reactivity must be offset with negative reactivity sources to make the core critical at the desired power level. If done by just utilizing control rods the cost would be high and the fuel duty increased due to the large number of control rods required, assuming this was even possible from a reactivity hold-down viewpoint. For a boiling water reactor (BWR) where the coolant flow rate through the core can be adjusted by the recirculation system, by operating at lower flow

rate core reactivity can be decreased. This occurs via the increased resonance capture from the reduced moderation due to the higher coolant void fraction. Since the majority of resonance capture is associated with U238, which produces Pu239 after neutron capture and beta decays, using coolant flow rate to control excess core reactivity is a desirable approach since excess neutrons are utilized to generate fissile material that is consumed later in the cycle. Flow stability and critical heat flux limit the flow reduction, hence reactivity reduction that can be achieved, implying the need for another source of excess reactivity control. For a PWR one can utilize soluble boron for excess reactivity control, which has neither an adverse cost nor fuel duty consequence. But as the soluble boron concentration is increased, the moderator density coefficient turns from positive to negative, which is adverse for overpower accidents that result in the decrease of moderator density. So even for PWRs as cycle length increases, requiring higher soluble boron concentrations to maintain criticality, at some point another reactivity control mechanism is required.

Burnable poisons consist of the introduction of a highly neutron-capturing material in the core, which depletes due to neutron capture. Since isotopes with large neutron capture cross-sections occur mainly in the thermal energy range, burnable poisons are only utilized in thermal reactors. Ideally, the rate of burnable poison material depletion is such that the associated reduction in negative reactivity introduced is equal to the reduction in positive reactivity associated with fuel depletion. Such a perfect balance is not possible in practice. Burnable poisons come in two varieties: discrete and integral burnable poisons. Discrete burnable poisons are only used in PWRs, where they are encased in a cladding material and displace fuel pin locations in the fuel assembly. A boron compound is normally selected as the burnable poison material. Integral burnable poisons do not displace fuel pins but are blended into the fuel matrix or coated on the fuel pellet surface. If blended with the UO_2 powder, gadolinia (Gd_2O_3) or erbia (Er_2O_3) powder is used, the powder subsequently pressed and baked to form the solid ceramic pellet. If coated on the pellet surface, this is done by a spraying application of a boron compound dissolved in a solvent, which subsequently evaporates. Both forms of burnable poisons suffer from not all the burnable poison material depleting, in particular, the isotopes with large thermal capture cross-sections. This introduces negative reactivity in the core requiring higher fuel enrichments to be used to satisfy the cycle energy requirement beyond what would have been required. Higher fuel enrichments are also required because burnable poison material is displacing fuel material. Discrete burnable poisons suffer from the additional penalties of neutron captures in the cladding material and for LWRs displacement of moderator, both of which introduce negative reactivity which is not desired near the end of cycle.

Natural erbium consists mainly of Er166, Er167, Er168, and Er170, with Er167 having a large thermal capture cross-section. The concentrations of the first three isotopes versus time are presented in [▶ Fig. 3](#) for the lattice design introduced in [▶ 1.4](#). Two behaviors are to be noted in this figure. Firstly, at representative discharge burnups the Erbium isotope with the large thermal capture cross-section (Er167) still exists with some abundance, implying a reactivity penalty that will increase the required fuel enrichment to achieve a desired discharge burnup. Secondly, the significant reason why Er167 exists with some abundance at higher burnups is due to the capture of neutrons in Er166, which produces Er167. [▶ Figure 4](#) shows the reactivity hold down associated with using an Erbia burnable poison using natural erbium and 100% enriched in Er167 material. The reactivity penalty of Er166 capturing a neutron and producing Er167 is evident in this figure.

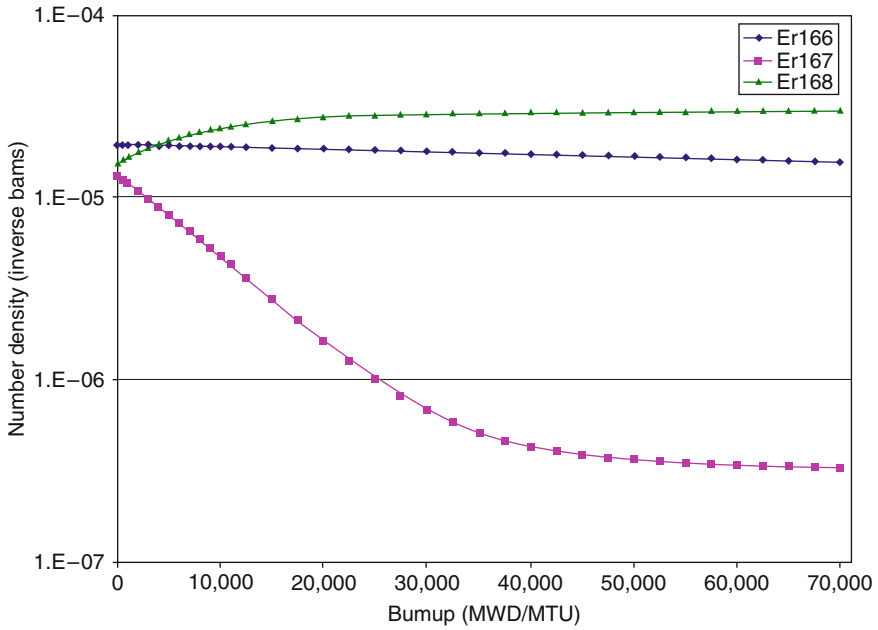


Figure 3
Erbium isotopes concentrations versus burnup for a lattice

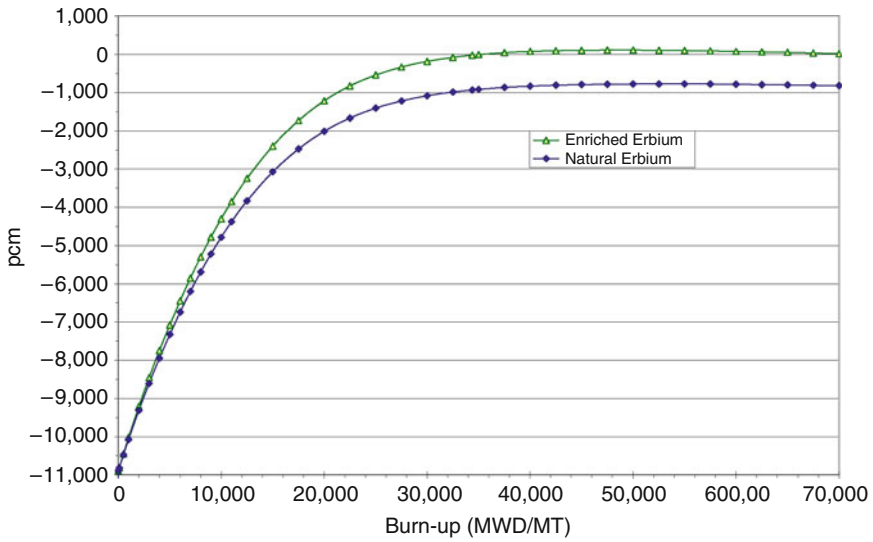
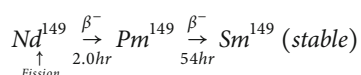


Figure 4
Erbium burnable poison reactivity penalty versus burnup for natural erbium and 100% enriched Er¹⁶⁷

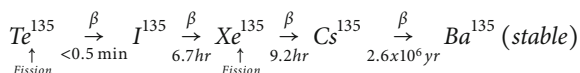
2 Transient Fission Products

2.1 Transient Fission Product Equations

Transient fission products are defined as fission products, which can change concentrations over hours to weeks, and whose capture reaction rates are significant enough to affect the core's attributes. They are mainly of interest for thermal reactors, since the thermal capture cross-sections for certain fission products can be very large. The transient fission products of interest for thermal reactors are Pm^{149} , Sm^{149} , I^{135} , and Xe^{135} . These particular isotopes are of interest because Sm^{149} and Xe^{135} possess large thermal capture cross-sections so are poisons in thermal reactors. They are created by the following simplified paths:



and



2.2 Xenon Transient Phenomena and Control

The xenon concentration in a nuclear reactor core can vary over a time period of hours. This can occur during core escalation to power and shutdown, during load follow maneuvers, and during changes in the power distribution from control rod motion. The resulting xenon concentration transient will impact the core reactivity, a global phenomenon, and the core power distribution, a spatial phenomenon.

2.2.1 Global Phenomena

➤ *Figure 5* displays the behaviors of the transient fission products Sm^{149} and Xe^{135} for the lattice introduced in ➤ 1.4. For fresh fuel, there are no fission products present. Within several days of operation, Xe^{135} approaches its equilibrium concentration and hence appears in the figure at equilibrium all the time due to the scale used. After plant shutdown, a substantial increase in the concentration of Xe^{135} will occur over the first 10 hours or so, since the I^{135} decay rate is larger than the Xe^{135} decay rate, and destruction of Xe^{135} by neutron capture no longer exists. Subsequently, the Xe^{135} will decay away since the I^{135} decay source is substantially diminished. When load following using a nuclear reactor, a less severe Xe^{135} concentration transient is experienced. When reducing power, the Xe^{135} concentration will build up as in complete plant shutdown, but at a slower rate. If the reduced power is maintained the Xe^{135} concentration will eventually decrease to reach the equilibrium concentration associated with the reduced power. When performing an up power maneuver, the reverse behavior occurs. Initially, the Xe^{135} concentration will decrease rapidly due to destruction by neutron capture, but latter the Xe^{135} concentration will increase to reach the equilibrium concentration associated with the higher power. The effect of the changes in concentration on core reactivity along with that associated with the power

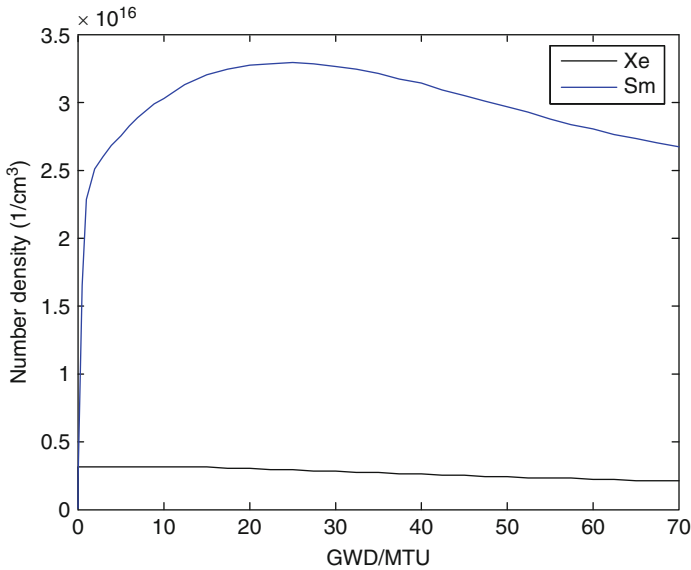


Figure 5
Xe135 and Sm149 isotopic concentrations versus burnup for a lattice

reactivity coefficient must be compensated for via the reactivity control system to maintain the reactor critical at the desired power level. If attempted by solely using control rods (blades), the resulting axially partial control rod insertions may result in unacceptable power distributions, so additional reactivity control devices will need to be employed, e.g., PWR soluble poison and BWR recirculation flow rate.

The buildup of Sm^{149} to its equilibrium concentration can be seen in Figure 4, which takes several weeks. The subsequent variation with burnup is due to the flux magnitude, flux energy-spatial spectra and fission product effective yield changing. Upon plant shutdown, the concentration of Sm^{149} reaches a maximum since the Pm^{149} decays to Sm^{149} , which is stable. The only source of Sm^{149} destruction is via neutron capture, which is now zero. The implication is that partially burnt fuel that is used in a reload cycle will start with zero concentrations of Pm^{149} , I^{135} , and Xe^{135} and maximum concentration of Sm^{149} . With regard to daily load follow, the more sluggish time behavior of Sm^{149} makes its effect on core reactivity much less important than that of Xe^{135} .

2.2.2 Spatial Phenomena

The behavior of Xe^{135} on a local basis can complicate power maneuvering for a thermal reactor, in particular in light water reactors (LWRs). Performing a down power maneuver, the moderator's density decreases as it flows up through the core, due to either the temperature rise in a PWR or void fraction increase in a BWR. Without compensatory action, the negative reactivity gradient due to the moderator density decrease with elevation is reduced with a power

reduction shifting the axial power distribution toward the upper core region. This results in an initial increase in the Xe^{135} concentration due to power reduction being less pronounced in the upper core region, which further shifts the axial power distribution toward the upper core region. Several hours later the top peaked axial power distribution will result in increased Xe^{135} production once the I^{135} has had time to decay. This introduces preferentially negative reactivity in the upper core region, which causes the axial power distribution to shift toward the lower core region. Now the same phenomena that occurred in the upper core region takes place in the lower core region. The resulting oscillation can either decay or grow with time, the determination dependent on the moderator reactivity density coefficient and its rate of change with moderator density. For a PWR the core becomes axially unstable later in life due to the more positive moderator reactivity density coefficient that occurs as the soluble boron concentration is decreased in order to keep the reactor critical as the fuel depletes. Regarding radial core oscillations due to Xe^{135} , they are not expected to occur over the entire cycle for both PWR and BWR.

3 Nuclear Fuel Management

3.1 Introduction

The focus of this section will be mainly on LWRs, both PWRs and BWRs, but much of the content is applicable to reactors of a different type. Nuclear fuel management is concerned with making the following decisions:

1. Cycle length between refueling outages, i.e., cycle energy requirement
2. Utilization of stretch out, i.e., operating reactor beyond when criticality can be maintained at full-rated power with nominal plant conditions
3. Fresh fuel assemblies number and compositions
4. Burnt fuel assemblies to reinsert
5. Burnable poison type and total loadings
6. Core loading pattern, i.e., fresh fuel, burnt fuel, and burnable poisons core locations
7. Control rod (blades) locations and core flow rate (only for BWRs) as function of burnup

These decisions are for each cycle in the planning horizon, which typically number between five and ten cycles for Decisions 1–5, and three to five cycles for Decisions 6 and 7.

Commercial nuclear power plants are reloaded on some frequency. This is necessary even if core criticality at full-rated power can be maintained, i.e., breeder reactor, because of material limitations of the nuclear fuel, which limit the time it can spend for producing power. Further, from an economic viewpoint periodic partial refueling of the reactor is desirable. Indeed, the maximum energy that can be extracted from nuclear fuel is obtained when continuous refueling is possible, e.g., approached by online refueling used in CANDU reactors.

Nuclear fuel management is typically subdivided into out-of-core nuclear fuel management and in-core nuclear fuel management. Out-of-core decisions address Decisions 1–5; whereas, in-core decisions address Decisions 6 and 7. This subdivision is convenient but should be recognized as artificial in that out-of-core and in-core nuclear fuel management decisions are truly coupled. The following presentation utilizes this subdivision.

3.2 Out-of-Core Nuclear Fuel Management

Out-of-core nuclear fuel management is concerned with making Decisions 1–5 noted in [3.1](#). Since any of those decisions will impact future reload cycles, out-of-core decision making involves a multicycle analysis. The overall fuel cycle is not mentioned as an out-of-core decision, but could be considered as one of the decisions. The overall fuel cycle refers to decisions associated with material flows throughout the various stages of the fuel cycle, i.e., mining and milling, conversion, enrichment, fuel fabrication, power generation, storage, separations, and waste disposal. Not all fuel cycle stages may be associated with a specific fuel cycle, e.g., the separation stage would be absent in an open fuel cycle and the enrichment stage could be absent for a heavy water thermal reactor. Possible fuel cycles include the U thermal reactor open fuel cycle, U-Pu thermal or fast reactor closed fuel cycle, U-Th thermal reactor closed fuel cycle, and various closed fuel cycles that recycle specific minor actinides and fission products either in homogenous or heterogeneous core designs. Several of these fuel cycles could work in tandem, which has been extensively studied considering merits such as resource utilization, proliferation resistance, high-level waste disposal, and economics (Dixon et al. 2008). To limit the following discussion, it has been assumed that the decision concerning the overall fuel cycle has been made.

Decision 1, the operating cycle length, is selected considering the seasonal energy demands of the electric utilities customers and electrical energy costs. The seasonal energy demand is highly dependent upon the geographic area that the electric utility services. Weather conditions will dictate the heating and air conditioning loads as a function of time of year. The mix of consumer and industry loads, and the types of industry, will also impact the electrical energy demands as a function of time of year. Peak loads may occur in the winter if heating using electrical energy, e.g., heat pumps or resistance heating, is dominant or in the summer if air conditioning load dominates. For a service territory where the industrial load dominates the consumer load, the load variation throughout the year may be slight. For many service territories, fall or spring will be the lowest demand sessions. Since nuclear electric plants have the lowest fuel costs, it is not desirable to take these plants off line for refueling outages during peak load sessions since loss of their generating capabilities would need to be offset by generation of electrical energy using higher fuel cost generating capability or intra-grid purchases.

The fuel cycle cost of a nuclear power plant also influences the selected cycle length. As the cycle energy requirement is increased, the fuel cycle cost of a nuclear power plant increases, as can be seen in [Fig. 6](#). The reason for this behavior will be explained later. So when selecting the cycle length, say 6, 12, 18, or 24 months minus the time for the refueling outage, one needs to consider the nuclear fuel cycle cost, replacement power fuel cycle cost, and outage operation and maintenance (O&M) cost. Mathematically this can be expressed as

$$\text{Grid Energy Cost} = \frac{\sum_p c_p E_p}{\sum_p E_p} \quad (13)$$

where c_p is the cost per unit energy and E_p is the energy produced over some time period for power plant p . Now customer demand requires that $\sum_p E_p = E_{\text{Grid}}$ where E_{Grid} denotes this demand. The cost per unit energy consists of capital, O&M, and fuel cost components. The capital cost component of the product $c_p E_p$ can be assumed nearly independent of whether power plant p is running or not, since it is related to retiring the debt and earning a return on

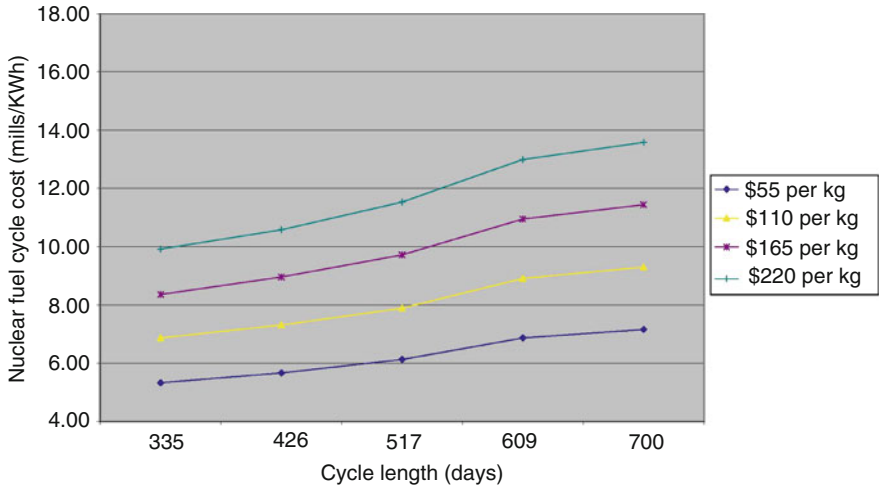


Figure 6

Fuel cycle cost versus cycle length for different assumed costs of uranium ore (\$/kg of yellowcake)

the capital investments, so it does not enter the decision about desired cycle length. Fixing this term in (13), and focusing on a specific nuclear power plant and its replacement power

$$\text{Effective Nuclear Energy Cost} = \text{Capital Energy Cost} + \frac{(c_{nuc}^{fuel} + c_{nuc}^{O\&M})E_{nuc} + \Delta C_{nuc}^{O\&M} + c_{rep}\Delta E_{rep}}{E_{nuc} + \Delta E_{rep}} \quad (14)$$

where the delta terms refer to the refueling outage either in terms of nuclear power plant O&M costs or replacement energy required. As the nuclear cycle length is increased, both the fuel cycle cost and the nuclear energy output increase. If it is assumed that the refueling outage length, replacement power cost, and replacement energy needed per outage are independent of cycle length, (14) implies that there is an optimum cycle length resulting from the trade-off of higher nuclear fuel cycle power cost versus lower nuclear outage O&M and replacement energy costs as cycle length is increased. This is shown in Fig. 7. If the ratio of replacement power cost to nuclear fuel cycle power cost increases, the optimum cycle length increases. Seasonal demand discussed above comes into play in (14) when it is recognized that the unit replacement power cost and/or amount of replacement power needed would increase if refueling outages occurred during periods of high electrical energy demand.

Once the operating cycle length is selected, the cycle energy requirement (E_{Cycle}), effective full power days ($EFPD$), and cycle burnup (BU_{Cycle}) can be determined. This is done as follows:

$$E_{Cycle} = Q \cdot CF \cdot T_{Cycle} \quad (15)$$

$$EFPD = CF \cdot T_{Cycle} \quad (16)$$

$$BU_{Cycle} = \frac{E_{Cycle}}{M_{HM}} \quad (17)$$

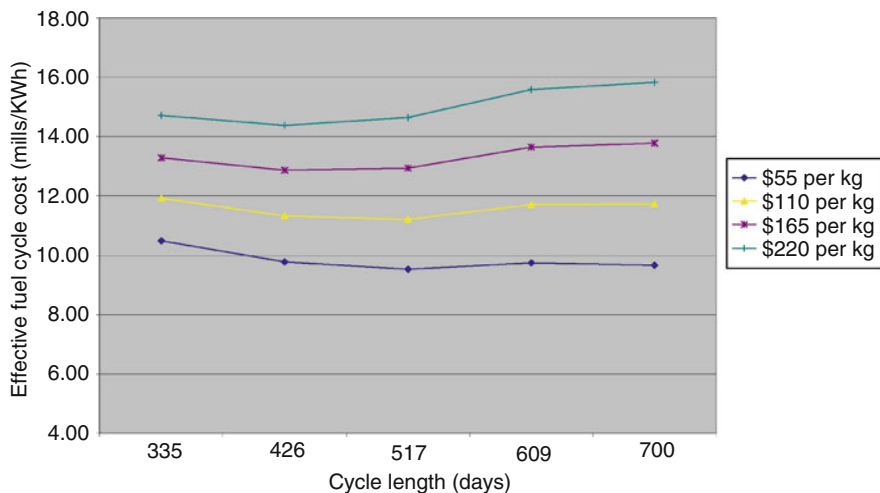


Figure 7

Effective fuel cycle cost versus cycle length for replacement power cost = 35 mills/kWh

where Q denotes the rated core thermal power (MWth), CF the capacity factor over the cycle, T_{Cycle} the cycle length (days), and M_{HM} the heavy metal (fissile + fertile) loading (MT or ST) for the total core when fresh fuel. The following example illustrates the utilization of these equations.

Example:

Rated Power = 3411MWth, Cycle Length = 548 days (18 months),

CF = 90%, Heavy Metal Loading 89.9 MTU

Cycle Energy Requirement = $3411 * 548 * 0.9 = 1,682,305 \text{ MWDth}$

Effective Full Power Days = $548 * 0.9 = 493.2$ days

Cycle Burnup = $1,682,305 / 89.9 = 18,713 \text{ MWD / MTU}$

Decision 2, utilization of stretch out, concerns operating the reactor beyond when criticality can be maintained at full-rated power with nominal plant conditions. Without consideration of stretch out, for a reactor with a conversion ratio less than 1, end-of-cycle (EOC) is assumed to occur when all excess reactivity control systems are such that minimum negative reactivity is inserted in the core, the core is at full-rated power at nominal conditions, and the core is just critical. The implication is that one additional fission event will cause the core to be marginally subcritical. Stretch out changes the definition of EOC by not demanding that the core be at full-rated power at nominal conditions when determining EOC. Since power reactors must possess a negative power reactivity coefficient for safety reasons, core reactivity increases as power decreases. This occurs due to less resonance capture from the lower fuel temperatures and more effective moderation in a light water reactor due to higher coolant density. Further, core reactivity will increase due to the reduced equilibrium xenon concentration that exists at a lower power. If no action is taken, when the core reaches nominal EOC, the power will thereafter

reduce with time since any additional fission will cause the core to go subcritical and therefore on a power reduction transient until criticality is restored. For this reason, such operation is referred to as coast down. For a limited time period during coast down in a PWR, full-rated power electrical energy production may be possible by further opening the turbine inlet valves, thereby maintaining high pressure turbine impulse pressure and decreasing the entropy loss across these valves. Eventually, the electric output will decrease, which may necessitate the generation or purchase of more expensive replacement power to meet customer needs.

Before commencing stretch out by coast down, alternatives do exist that minimize the loss of reduction in electric power output. For LWRs, which are substantially under-moderated near EOC, if the coolant density could be increased core reactivity would increase allowing full core power operation to be maintained beyond nominal EOC. For a BWR, this is accomplished by increasing the core flow rate above nominal 100% via the recirculation system, limited by the recirculation systems capability and moisture separators/dryers capabilities to produce dry steam. For a PWR that operates on a programmed reactor vessel average coolant temperature, by decreasing the programmed value the average coolant density in the reactor will increase, which in turn inserts positive reactivity. The average coolant temperature reduction is achieved by decreasing the reactor vessel inlet coolant temperature by reducing the preheating of the secondary side feed water. Again moisture separators/dryers ability to produce dry steam limits the extent that feed water temperature reduction can be utilized. Also note that decreasing feed water temperature will decrease steam generator pressure and eventually high pressure turbine impulse pressure once the turbine inlet valves go fully open, resulting in reduced electric power due to reduced thermodynamic efficiency.

The economically optimum extent of stretch out to utilize is determined by considering the reduced nuclear fuel cycle cost due to more energy being extracted from the core and the offsetting cost of replacement power. Early in stretch out, the logical thing to do is to utilize a coolant density increase because this minimizes the need for replacement power since rated or nearly rated electric power can be maintained. Thereafter, coast down can be commenced, necessitating the purchase of replacement power. At some point, the reduction in nuclear fuel cycle cost will be offset by the cost of replacement power, this point defining the economic optimum extent of stretch out to utilize. In practice, BWRs tend to routinely utilize stretch out, whereas PWRs seldom utilize stretch out.

Decisions 3, 4, and 5, which are fresh fuel assemblies number and compositions, burnt fuel assemblies to reinsert, and burnable poison type and total loadings, are highly coupled decisions. The objectives of making these decisions are

- Satisfying the cycle energy requirements
- Minimizing the fuel cycle cost

To discuss how these decisions are made, some definitions are useful.


Fuel Region: A group of fuel assemblies loaded into the reactor for the first time (fresh fuel) together. Note that these assemblies need not be identical, i.e., have the same average enrichment.

Fuel Batch: A subgroup of fuel assemblies from a fuel region, which has the same assembly average enrichment and also experiences the same irradiation (burnup) history.

The number of fuel assemblies in each fuel region and batch is one of the decisions that must be made. The result of making these decisions can be expressed in a cycling scheme table as illustrated in [▶ Table 1](#).

■ **Table 1**
Example of cycling scheme table

Cycle	1	2	3	4	5	...
Cycle length	500 days	325 days	325 days	325 days	325 days	...
Stretch out	No	No	No	No	No	...
BP loading	8% $\Delta\rho$	0% $\Delta\rho$	0% $\Delta\rho$	0% $\Delta\rho$	0% $\Delta\rho$...
Region/batch						
1/a	50 F/A	0	0	0	0	...
1/b	1	1	0	0	0	...
1/c	1	0	1	0	0	...
1/d	1	0	0	1	0	...
2	52	52	0	0	0	...
3	52	52	52	0	0	...
4/a	0	51	51	51	0	...
4/b	0	1	1	1	1	...
5/a	0	0	51	51	51	...
5/b	0	0	1	1	1	...
...

This table is for a PWR core with a total of 157 fuel assemblies in the core, as indicated by adding the number of assemblies in a column. Region 1 subdivides into Batches a, b, c, and d because of different irradiation histories. Actually, the Batches b, c, and d serve as the center fuel assembly in the core for Cycles 2, 3, and 4, respectively. Deviating from the normal definition of a fuel region for Cycle 1, Regions 1, 2, and 3 are designated even though these fuel assemblies are all loaded as fresh fuel at the same time, distinguished by differing enrichments and irradiation histories. Examining  [Table 1](#) along rows indicates the number of cycles a Region–Batch pairing is irradiated.

Assuming that the cycling scheme table is determined, which specifies the number of fuel assemblies in each region–batch pairing, the only free variable in a reload cycle to satisfy the cycle energy requirement is the fuel assembly enrichments for the region–batch pairings of the fresh fuel.

The following constraints are very important in making nuclear fuel management decisions.

- Maximum fuel enrichment must be less than or equal to the maximum enrichment allowed, e.g., enrichment specified in the Critical Materials License used to assure subcriticality throughout various stages of the nuclear fuel cycle, e.g., LWR: 5.0 w/o.
- Fuel discharge burnup must be less than or equal to the maximum burnup dictated by materials limitations.

The following types of burnup limits may be imposed:

- Region average burnup – Average of burnup of all assemblies in a region
- Batch average burnup – Average burnup of all assemblies in a batch
- Assembly burnup – Average burnup of an assembly, i.e., axially and radially averaged burnup of all rods in an assembly
- Rod burnup – Average burnup of a rod, i.e., axially averaged burnup of a rod
- Pellet burnup – Individual pellet burnup

Typical values for the region average discharge burnup limit, denoted $\langle BU \rangle_{\max}$, are (45–50) GWD/MTU for PWRs and (40–45) GWD/MTU for BWRs, where GWD denotes giga-watt days.

To understand how burnup limits impact out-of-core nuclear fuel management decisions, consider the impact of the region average discharge burnup limit, $\langle BU \rangle_{\max}$. To simplify the discussion, consider an equilibrium reload cycle, which is a cycle that has an infinite repetition of the same cycle energy requirement utilizing the same cycling scheme in each cycle. For an equilibrium cycle, the number of cycles a region is burned is equal to the number of fuel regions in the core. To see this, consider a PWR core with a total number of assemblies equal to 156 (removed center fuel assembly to simplify the example). Now assume that three regions are utilized in each equilibrium cycle, which produces the cycling scheme table shown in [Table 2](#).

It is clear that a three-region core produces three cycles of irradiation of each region. This implies that the region average discharge burnup is calculated by

$$\text{Region Average Discharge Burnup} = (\text{Number of Regions}) * (\text{Cycle BU})$$

Imposing the region average discharge burnup limit

$$\langle BU \rangle_{\text{Disc}} = (\text{Number of Regions}) * BU_{\text{Cycle}} \leq \langle BU \rangle_{\max}$$

and solving for the constraint on the number of regions

$$\text{Number of Regions} \leq \langle BU \rangle_{\max} / BU_{\text{Cycle}}$$

Table 2

Example of three-region core for equilibrium cycles

Cycle	n	$n+1$	$n+2$	$n+3$	$n+4$
Region ^a					
...
m	52	0	0	0	0
m + 1	52	52	0	0	0
m + 2	52	52	52	0	0
m + 3	0	52	52	52	0
m + 4	0	0	52	52	52
...	

^aBatch ID not shown since only one batch per region

The implication is that the maximum number of fuel regions that can be utilized is fixed. If the limit on number of regions allowed is exceeded, the region average discharge burnup limit will be violated. As region average discharge burnup limit is increased or cycle burnup is decreased, the number of fuel regions allowed increases. Consider the following PWR example.

$$\text{Given } \langle BU \rangle_{\max} = 48 \text{ GWD/MTU}, BU_{\text{Cycle}} = 16 \text{ GWD/MTU}$$

(determined from cycle length and capacity factor)

$$\text{Maximum Number of Regions} = 48/16 = 3$$

Now the number of feed (fresh) fuel assemblies for an equilibrium cycle is given by

$$\text{Number of Feed Fuel Assemblies} = \frac{\text{Total Number of Fuel Assemblies in Core}}{\text{Number of Regions}}$$

which for the PWR example noted above with a total number of fuel assemblies equal to 156 and using the maximum number of regions of 3 produces

$$\text{Number of Feed Fuel Assemblies} = 156/3 = 52$$

This example produces the cycling scheme table shown in [▶ Table 2](#).

What if the number of regions is not equal to an integer number as in our example? This of course is the more likely situation. Consider the following example.

$$\text{Cycle Length} = 589 \text{ days}, \text{CF} = 91\% \Rightarrow \text{Cycle BU} = 20.34 \text{ GWD/MTU}$$

$$\text{Maximum Number of Regions} = 48/20.34 = 2.36$$

This result implies that if the maximum number of regions is employed, that all fuel assemblies will be burnt two cycles and subset of assemblies (36%) will be burnt three cycles. The number of feed fuel assemblies is given for this example by

$$\text{Number of Feed Fuel Assemblies} = 156/2.36 = 66.1 \Rightarrow 67$$

which has been rounded up to obtain a whole assembly and avoid exceeding the region average discharge burnup limit. Since some assemblies are only burnt two cycles and others three cycles, the region splits into two batches due to different irradiation histories. To determine the number of fuel assemblies in each batch, one first calculates the number of assemblies in the batch burnt three cycles based upon filling the core, followed by a calculation of the number of assemblies in the batch burnt two cycles.

$$\text{Number of assemblies burnt 3 cycles} = 156 - 2 * 67 = 22$$

$$\text{Number of assemblies burnt just 2 cycles} = 67 - 22 = 45$$

■ **Table 3**

Example of 2.33 region core for equilibrium cycles

Cycle	n	$n+1$	$n+2$	$n+3$
Region/batch				
...
m/b	22	0	0	0
m + 1/a	45	0	0	0
m + 1/b	22	22	0	0
m + 2/a	45	45	0	0
m + 2/b	22	22	22	0
m + 3/a	0	45	45	0
m + 3/b	0	22	22	22
m + 4/a	0	0	45	45
m + 4/b	0	0	22	22
...

The associated cycling scheme table for this example is presented in [Table 3](#), where the figure caption has denoted that this cycling scheme corresponds to a 2.33 region core due to rounding up to a whole fuel assembly.

In practice, when loading the core with fuel assemblies, one wishes to retain quarter core symmetry. This implies that region and batch sizes must be a multiple of 4, which for our example has the following effect.

$$\text{Region Size} = 67 \Rightarrow 68$$

$$\text{Batch "b" Size} = 156 - 2^* 68 = 21 \Rightarrow 20$$

$$\text{Batch "a" Size} = 68 - 20 = 48$$

Note that the number of fuel assemblies in Batch b, which is the batch burnt three cycles, is rounded down to assure that the region average discharge burnup limit is not violated.

So far examples have been worked using the maximum number of regions allowed. Any number of regions less than the maximum allowed would be acceptable with regard to satisfying the region average discharge burnup limit. What determines the desired number of fuel regions is economics, in particular, minimization of the fuel cycle cost. In fact, the fuel cycle cost is minimized by using the maximum number of regions allowed. The inclination is to think that because using the maximum number of regions equates with using the least number of feed fuel assemblies, the economics is most favorable. But the favorable economics results for another reason. Two examples will show this.

Consider the case of an equilibrium cycle, uniform core power distribution, fixed $\langle BU \rangle_{Disc}$, variable feed enrichment selected to take the fuel to $\langle BU \rangle_{Disc}$, and variable cycle length. Now

for a one- and two-region core, the EOC core average burnup, i.e., average burnup of all fuel assemblies in the core at EOC, is

$$\begin{aligned} \text{Number of Regions} &= 1 \\ \langle BU \rangle_{\text{Core}} &= \langle BU \rangle_{\text{Disc}} \\ \text{Number of Regions} &= 2 \\ \langle BU \rangle_{\text{Core}} &= (BU_{\text{Disc}}/2)(1/2) + (BU_{\text{Disc}})(1/2) = 3/4 BU_{\text{Disc}} \end{aligned}$$

So a two-region core has 25% less core average burnup than a one-region core at EOC, implying that a lower feed fuel enrichment than anticipated could be utilized, resulting in fuel cycle cost reduction. For an N region core, one obtains

$$\begin{aligned} \text{Number of Regions} &= N \\ \langle BU \rangle_{\text{Core}} &= [(N + 1) / 2N] BU_{\text{Disc}} \end{aligned}$$

So the benefits of a reduced core average burnup at EOC become greater as more fuel regions are utilized, but the incremental benefits in increasing the number of regions by one decrease as the number of regions increases. In the limit of a very large number of regions, which would be associated with frequent online refueling, the core average burnup at EOC is reduced by 50% from that of a one-region core.

An alternative justification for why utilizing the maximum number of regions allowed is economically preferred can be obtained utilizing the linear reactivity model (LRM) (Driscoll et al. 1990). LRM assumes that the fuel's reactivity decreases linearly with burnup. Now assuming an equilibrium cycle, uniform core power distribution, variable $\langle BU \rangle_{\text{Disc}}$, fixed feed enrichment, and variable cycle length, one can determine the cycle energy production and $\langle BU \rangle_{\text{Disc}}$ as a function of the number of regions utilized.

$$\begin{aligned} \text{Number of Regions} &= 1 \\ \text{Core Reactivity} &= \rho = \rho_0 \left(1 - \frac{BU}{BU_1} \right) \end{aligned} \quad (18)$$

where ρ_0 denotes the beginning-of-life (BOL) core reactivity (set by feed enrichment) and BU the cycle burnup at any time during the cycle. At EOC core reactivity is zero and cycle burnup $BU = BU_{\text{Cycle}}$ so

$$0 = \rho_0 \left(1 - \frac{BU_{\text{Cycle}}}{BU_1} \right) \quad (19)$$

implying for a one-region core $BU_{\text{Cycle}} = BU_1$ and $\langle BU \rangle_{\text{Disc}} = 1^* BU_{\text{Cycle}} = BU_1$.

$$\begin{aligned} \text{Number of Regions} &= 2 \\ \text{Core Reactivity} &= \rho \approx \rho_0 \left(1 - \frac{BU}{BU_1} \right) \cdot \frac{1}{2} + \rho_0 \left(1 - \frac{BU_{\text{Cycle}}}{BU_1} - \frac{BU}{BU_1} \right) \cdot \frac{1}{2} \end{aligned} \quad (20)$$

where BU_{Cycle} denotes the EOC cycle burnup for this two-region core. Again at EOC core reactivity is zero and $BU = BU_{\text{Cycle}}$ so

$$0 = \rho_0 \left(1 - \frac{BU_{\text{Cycle}}}{BU_1} \right) \cdot \frac{1}{2} + \rho_0 \left(1 - \frac{BU_{\text{Cycle}}}{BU_1} - \frac{BU_{\text{Cycle}}}{BU_1} \right) \cdot \frac{1}{2} \quad (21)$$

■ **Table 4**
Increased energy output relative to a one-region core

Number of regions	Fuel energy output increase versus one-region core (%)
1	0
2	33
3	50
4	60
5	67
∞	100

which when solved indicates $BU_{Cycle} = (2/3)BU_1$ and $\langle BU \rangle_{Disc} = 2BU_{Cycle} = (4/3)BU_1$. The implication is that a two-region core produces 33% more energy than a one-region core when using the same fuel, i.e., for fuel of the same cost per unit mass. The results can be generalized to an N region core.

$$\begin{aligned}
 \text{Number of Regions} &= N \\
 \text{Core Reactivity} = \rho &\approx \sum_{i=1}^N \rho_0 \left(1 - (i-1) \frac{BU_{Cycle}}{BU_1} - \frac{BU}{BU_1} \right) \cdot \frac{1}{N} \quad (22)
 \end{aligned}$$

Completing similar operations as above finds $BU_{Cycle} = (2/[N+1])BU_1$ and $\langle BU \rangle_{Disc} = N \cdot BU_{Cycle} = (2N/[N+1])BU_1$. ➤ **Table 4** indicates the increased energy output per unit mass of fuel with reference to a one-region core.

It is clear that one wishes to utilize the maximum number of regions allowed, or equivalently the minimum number of feed fuel assemblies allowed. This will take the fuel close to but not exceed the region average discharge burnup limit. The logic for reaching this conclusion has been based on an equilibrium cycle and several other assumptions, but the same conclusion is drawn when considering nonequilibrium cycles and relaxing assumptions. The key is to load the core in successive cycles with a sufficient number of feed fuel assemblies such that they will be close to but not exceed the region average discharge burnup limit.

Having determined the cycling scheme table, i.e., the number of feed fuel assemblies in each cycle of the planning horizon, the only free design variables to assure that the cycle energy requirement is satisfied in each cycle in the planning horizon are the feed fuel enrichments. This follows since the reactivity of the partially burnt fuel that back fills the core has a fixed reactivity. If a required feed enrichment exceeds the maximum enrichment limit, which is not uncommon for high-energy BWR cores, this will necessitate loading more feed fuel assemblies than dictated by the region average discharge burnup limit.

When a region contains more than one batch due to irradiation history, e.g., 2.33 region core example, one has freedom what the batches' enrichments should be with the constraint that they be chosen to satisfy the cycle energy requirement. When one batch is going on for an extra cycle of irradiation, it is desirable to use a higher enrichment in this batch to carry reactivity forward into the extra cycle of irradiation. The enrichment difference between the two batches is limited by core power distribution and/or maximum enrichment limit considerations.

With regard to the partially burnt fuel to utilize to back fill the core, assemblies are selected such that discharge burnup limits are not violated with one more cycles of irradiation, the assemblies are mechanically sound ascertained by visual inspection during the refueling outage, and they carry maximum reactivity of the available assemblies.

Burnable poisons were previously introduced in [1.7](#). They are required to be utilized all the time in BWRs and sometimes in PWRs when larger cycle energy production, i.e., longer cycle lengths, occurs. Since they are affixed in the core either permanently, e.g., integral burnable poison, or for a cycle, e.g., discrete burnable poison, ideally they should burn out via neutron capture such that the resulting decrease in their negative reactivity just offsets the loss of reactivity due to the fuel burning. This cannot be accomplished, with the implication that the net core reactivity without other means of reactivity control could be increasing or decreasing as the core burns during the earlier portion of the cycle and eventually decreasing later in the cycle.

For PWRs the amount of burnable poison required is determined such that the soluble boron concentration required to produce criticality, with control rods mostly withdrawn and the core at full-rated power conditions, is reduced to a level that assures the moderator density coefficient is positive, i.e., moderator temperature coefficient is negative. The implication is that for shorter cycle lengths, such as 12 months, no burnable poison is required, but for cycle lengths of 18 months or longer, burnable poisons are normally required. Needless to say, the longer the cycle energy requirement, the higher the core reactivity at BOC, so the greater need for negative reactivity introduction via burnable poisons.

The need for burnable poisons in BWRs is based on the cold shutdown margin (CSM) requirement. A BWR must be capable of going from full-rated power (HFP) conditions to cold zero power (CZP) conditions based on the insertion of cruciform control blades. A PWR has the benefit of being able to increase the soluble boron concentration during the cool down either in a normal fashion or by utilizing the emergency boron injection system. Given the extensive bulk boiling in a BWR, utilization of a soluble poison is undesirable due to deposition on the fuel cladding surface. The reactivity swing due to moderator density, fuel temperature, and xenon concentration changes in going from HFP critical to CZP subcritical conditions clearly must be addressed via the cruciform control blades. However, to adjust the absolute core reactivity that exists at CZP, which must satisfy the CSM subcriticality limit assuming the most reactive control blade is stuck out, requires another source of negative reactivity. That source is burnable poisons, with the amount loaded such that the CSM limit is satisfied.

Discrete burnable poisons depending upon the PWR fuel assembly design either can be located in the guide tubes of a fuel assembly or displace fuel pins. The difference is that if placed in guide tubes, they can be removed after a cycle of irradiation; whereas, if displacing a fuel pin this is not possible. Discrete burnable poison designs have varied with time, with the burnable material being boron either contained in borosilicate glass tubing or B4C dispersed in an Al pellet matrix. Cladding material is typically the same as used for the fuel pin, so a zirconium alloy. By varying the number of burnable poison rods in a fuel assembly and the number of fuel assemblies containing burnable poison rods of a certain count, the amount of negative reactivity inserted can be matched against the need. Given the residual negative reactivity effect at EOC due to neutron capture in the burnable poison's cladding, and displacement of the moderator, and need to handle during refueling operations discrete burnable poison designs that are removable, there is a preference to utilize integral burnable poisons.

As noted in [1.7](#), integral burnable poisons introduce the burnable poison material by either coating the fuel pellet surface with the poison or mixing it with the fuel. A boron compound, which can be enriched in B10, is utilized for the integral fuel burnable absorber

(IFBA) design that coats the pellet surface. In addition to inserting negative reactivity via captures in the burnable poison, the coating is effective in maximizing the thermal self-shielding effect. For high cycle energy requirements, IFBA may burn out too quickly resulting in the critical boron concentration increasing to a level that the moderator temperature coefficient becomes positive at HFP. In this case, a combination of discrete burnable poisons and IFBA is necessary. For burnable poison material mixed with the fuel, Gadolinia (Gd_2O_3) and Erbium (Er_2O_3) are both utilized. Since the fuel is an oxide (UO_2), mixing the burnable poison oxide with the fuel power produces a ceramic pellet after baking. Typically Gadolinia concentrations are limited to about 8 w/o and Erbium concentrations to 2 w/o, which assures that the pellet's thermal and mechanical properties are still acceptable. Needless to say, the displacement of fuel material with burnable poison material will result in a higher fuel enrichment being required. An advantage of integral burnable poisons, in addition to overcoming some of the disadvantages of discrete burnable poisons, is that by a combination of concentration and number of fuel pins in the core containing burnable poison the rate of decrease of negative reactivity with burnup can be controlled. By using a higher concentration in fewer fuel pins, the rate of decrease of negative reactivity can be reduced while still maintaining the same initial total negative reactivity hold down. This occurs due to the increased thermal self-shielding associated with the higher concentration.

Independent of the type of burnable poison utilized, there is cost associated with utilizing them. The obvious cost is that of the burnable poison, but a more significant cost may be that associated with the increased fuel enrichment required to meet the cycle energy requirement so as to offset the residual burnable poison reactivity penalty at EOC.

Where to locate the burnable poison material in the core within the feed fuel assemblies is a decision that falls within the domain of in-core nuclear fuel management. Their location can have a significant impact on the power distribution, but also on the burnable poison worth as a function of the cycle depleting.

3.3 LWR In-Core Nuclear Fuel Management

In-core nuclear fuel management addresses Decision 6, core loading pattern, i.e., fresh fuel, burnt fuel, and burnable poisons core locations, and Decision 7, control rod (blades) locations and core flow rate (only for BWRs) as functions of burnup.

3.3.1 LWR Loading Pattern Selection

The major design objectives associated with selecting the core loading pattern are

- Minimization of the power peaking by making the core's power distribution as flat as possible (to increase margins to thermal limits, e.g., critical heat flux and fuel temperatures)
- Maximization of the cycle energy production for fuel to be loaded into the core

Maximization of the cycle energy production is achievable by minimization of neutron leakage, which implies a low flux on the core periphery. But if the flux is low on the core periphery so is the power, which implies that the power must be higher in the core interior to maintain the rated core power. This produces a conflict with the objective of minimizing power peaking, implying that a trade-off must be struck between these two objectives.

Focusing first on addressing the objective of minimizing power peaking, which one could view as a constraint versus an objective, this arises because of thermal limits on the fuel. The thermal limits that are most likely to be active include the

- Loss of coolant accident (LOCA) peak clad temperature (PCT) limit of 1, 205°C, which limits the maximum pellet linear power density to approximately 48 kW/m at HFP
- Critical heat flux (CHF), which denotes departure from nuclear boiling (DNB) for a PWR and Dryout for a BWR, not being exceeded during anticipated transients, which limits the maximum average fuel pin linear power density to approximately 29 kW/m at HFP
- Fuel cladding strain limit not be exceeded during anticipated transients

For PWRs the LOCA linear power density limit on the pellet is expressed in terms of the total peaking factor defined as

$$F_Q \equiv \frac{\text{Power}_{\text{Peak}}^{\text{Pellet}}}{\langle \text{Power}^{\text{Pellet}} \rangle} = \frac{\text{Max}_{x,y,z} P(x, y, z)}{\frac{1}{V_{\text{Core}}} \iiint_{V_{\text{Core}}} P(x, y, z) dx dy dz}$$

which in practice is likely to also have an axial dependence due to LOCA blow down and reflood characteristics, obtained by completing the numerator's maximization only over x, y . The DNB linear power density limit on the fuel pin is expressed in terms of the enthalpy rise (radial) peaking factor defined as

$$F_{\Delta H} \equiv \frac{\text{Power}_{\text{Peak}}^{\text{Rod}}}{\langle \text{Power}^{\text{Rod}} \rangle} = \frac{\text{Max}_{x,y} \frac{1}{L} \int_0^L P(x, y, z) dz}{\frac{1}{V_{\text{Core}}} \iiint_{V_{\text{Core}}} P(x, y, z) dx dy dz}$$

where the x, y dependence should be recognized as being on a unit rod discretization.

For BWRs the LOCA linear power density limit is expressed in terms of the Maximum fraction of Average Power RATio to the limiting value (MAPRAT) defined as

$$\text{MAPRAT} = \max_{x,y,z} \frac{\langle P(x, y, z) \rangle_{\text{Actual}}}{\langle P(x, y, z) \rangle_{\text{Limit}}}$$

where the powers have been radially averaged across a fuel assembly and the limit is fuel assembly type and burnup dependent. The Dryout limit is expressed as the Maximum Fraction of Limiting Critical Power Ratio (MFLCPR) defined as

$$\text{MFLCPR} = \max_{x,y,z} \frac{\text{CPR}(x, y, z)_{\text{Limit}}}{\text{CPR}(x, y, z)_{\text{Actual}}}$$

where CPR denotes the critical power. Finally, the cladding strain limit is expressed as the Maximum Fraction of Limiting Power Density (MFLPD) defined as

$$\text{MFLPD} = \max_{x,y,z} \frac{P(x, y, z)_{\text{Actual}}}{P(x, y, z)_{\text{Limit}}}$$

where powers are evaluated on a pellet-wise basis. Working with the PWR limits, since they are easier to interpret, the core average linear power density plays a key role and is defined by

$$\langle q' \rangle = \frac{Q \text{ (unit of kW)}}{(\text{Total Number of Fuel Assemblies in Core}) \left(\frac{\text{Fuel Rods}}{\text{Fuel Assembly}} \right) L \text{ (unit of m)}}$$

where Q denotes the full-rated core power and L the active fuel height, i.e., fuel pellet stack height. For a reload core with a fixed mechanical fuel design, the average linear power density is fixed. This implies in terms of peaking factors that the maximum pellet and rod linear powers are given by

$$\begin{aligned} \text{Maximum Pellet Power} &= F_Q * \langle q' \rangle * P_{Rel} \\ \text{Maximum Rod Power} &= F_{\Delta H} * \langle q' \rangle * P_{Rel} \end{aligned}$$

where P_{Rel} denotes the core relative power, so $P_{Rel} \in [0, 1]$. By imposing the thermal limits obtained is

$$F_Q \leq \frac{q'_{LOCA}}{\langle q' \rangle * P_{rel}} \quad (23)$$

and

$$F_{\Delta H} \leq \frac{q'_{CHF}}{\langle q' \rangle * P_{rel}} \quad (24)$$

Using (23) and (24) with the previously stated LOCA and DNB limits along with a typical average linear power density of 18.5 kW/m, one finds at full power that $F_Q \leq 2.5$ and $F_{\Delta H} \leq 1.5$.

Using these power peaking factors as representative limits, alternate core loading patterns will be assessed for their effectiveness. First consider a right cylindrical core employing one region, i.e., homogenous core, and no reflector. The one group diffusion equation solution for this core design is a Bessel function of the first type for the radial direction and a cosine function in the axial direction. This implies $F_Q = 3.63$ and $F_{\Delta H} = 2.31$, which to satisfy the thermal limits would necessitate approximately limiting core power to about 65% of rated power, i.e., $P_{Rel} = 0.65$. The unacceptable high power peaks originate because of high neutron leakage from the core periphery.

Addition of radial and axial core reflectors would reduce the power peaking but not to any acceptable level. In fact, all LWRs utilize reflectors in the form of the coolant surrounding the core, and make possible the addition of metallic radial core reflectors. Recognizing that cores utilize multiple fuel regions for improved economics, advantage can be taken of this by locating the most reactive region nearest to the core periphery, and regions of lesser and lesser reactivity further and further away from the core periphery. Such a loading will counteract the neutron leakage from the core radial periphery and is referred to as Out-In loading because of the fuel movement each successive cycle. Considering a three-region core, what one finds is indeed the flux and hence power is held up on the core periphery where the most reactive feed fuel is located, but the power is very low about the core center where the least reactive twice burnt fuel is located. This results in high power peaking in the mid-core where the mid-reactive once burnt fuel is located. The cause of this is the relative reactivity differences between the feed, once and twice burnt fuel, which cannot be adjusted since the initial enrichment of each fuel region is determined to satisfy the cycle energy requirement.

The correction to this problem is to mix in a checker-board pattern the mid and least reactive fuel in the core interior and retain the most reactive fuel on the core periphery, which is displayed in **Fig. 8** for a PWR. In this manner the least reactive fuel's flux and power are held up by neutron leakage from the mid-reactive fuel, which in turn holds down the power peaking in the mid-reactive fuel. **Figure 9** displays the assembly relative power distribution at BOC of an Out-In Check-board loading pattern for a three-region PWR core. The power peaking factors throughout the cycle are such that $F_Q \leq 1.8$ and $F_{\Delta H} \leq 1.35$ under HFP conditions with equilibrium xenon and samarium. The Xe^{135} spatial transients induced by load following will increase the F_Q value but it will still remain considerable below the LOCA imposed limit. The

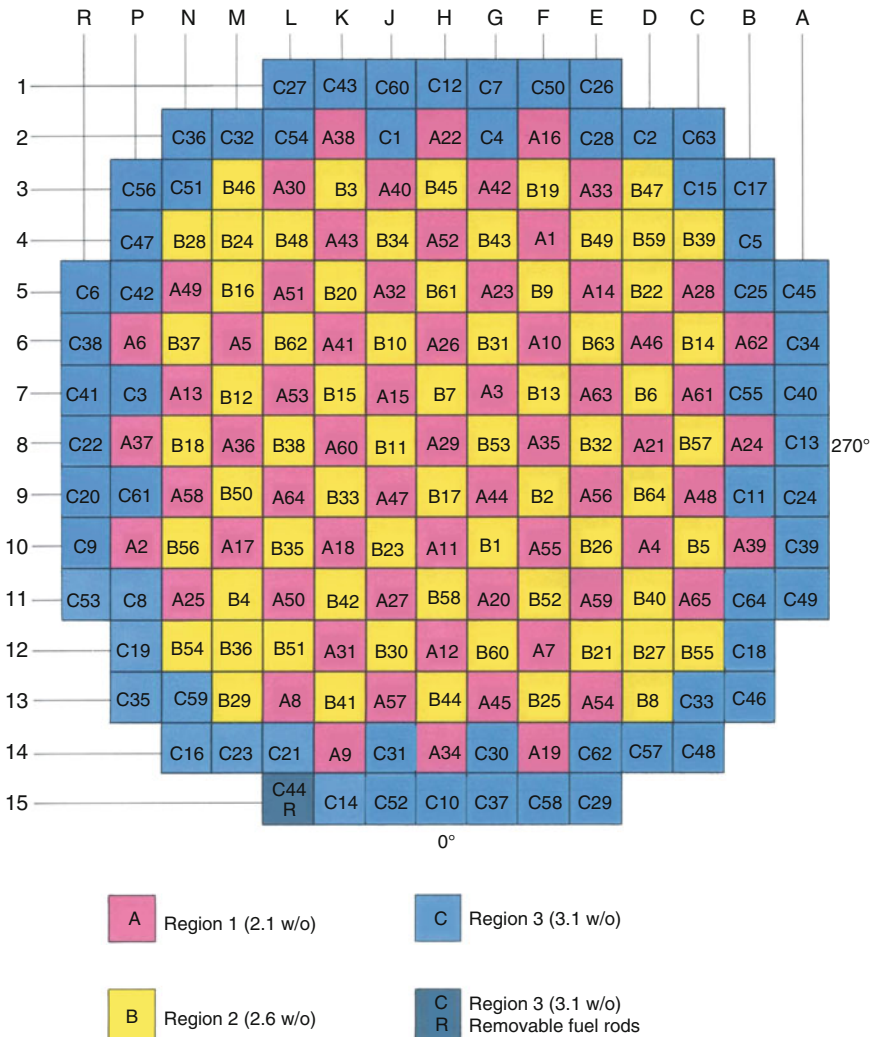


Figure 8
Out-in checker-board loading pattern for a PWR

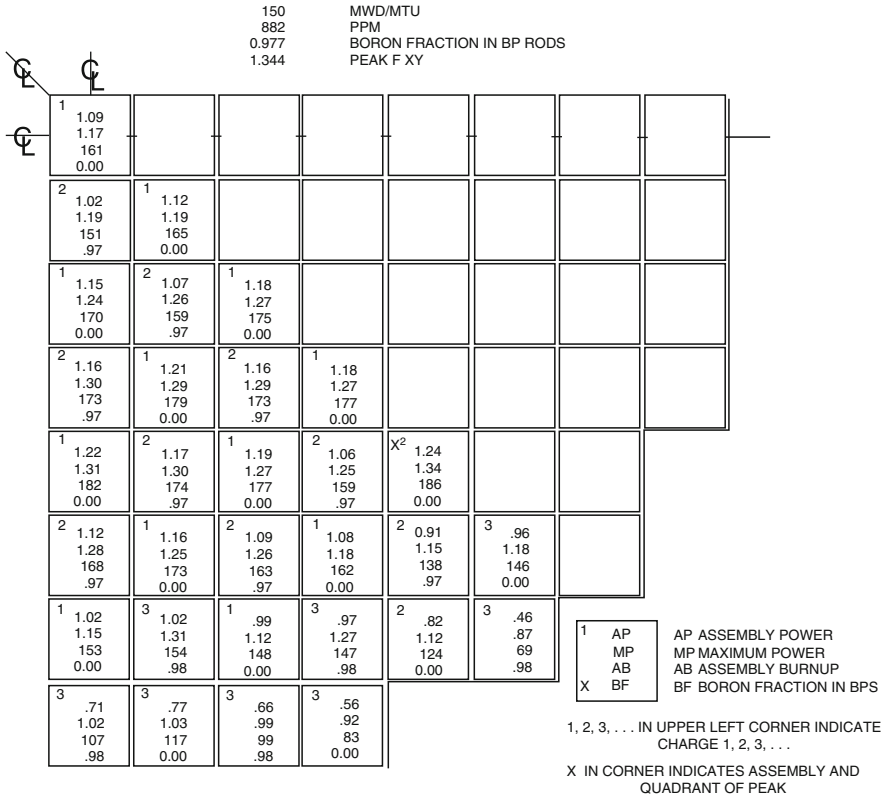
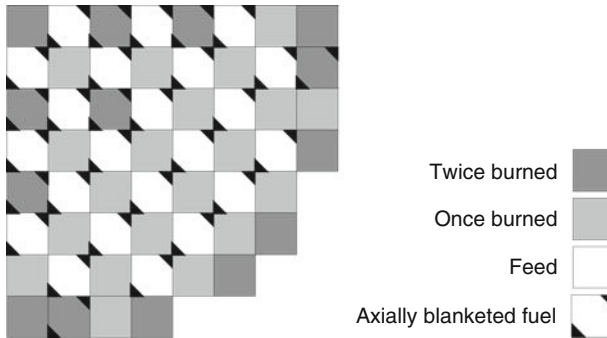


Figure 9
Relative radial power distribution at the beginning of cycle associated with Fig. 8 loading pattern

Out-in checker-board loading pattern served for many years as the preferred loading pattern given its effectiveness in satisfying the objective of minimizing power peaks. However, as noted earlier in satisfying this objective the radial neutron leakage is increased resulting in less energy being extracted from the core, so conflicts with this economically motivated objective.

Consider now how the objective of maximizing the cycle energy production for the fuel to be loaded into the core is to be achieved. This could be accomplished by minimizing neutron leakage and by maximizing the flux in the most reactive fuel in accordance with reactivity importance weighting. Clearly an In-Out loading strategy would accomplish this, where the most reactive fuel is placed in the core center spatial zone and lesser and lesser reactive fuel is placed further and further out from the core center. However, highly unacceptable power peaking would occur. If burnable poisons were required for reactivity hold down they could be preferentially placed in the high power, feed fuel assemblies to suppress power peaking. What is found is that more burnable poison is required to suppress the power peaking than required for reactivity hold down, and that the resulting additional burnable poison reactivity penalty more than offsets any savings due to the lower neutron leakage. An In-Out-In strategy which associates directly with a three-fuel region core would seem to be a compromise between an Out-In and In-Out loading strategy; however, it is again found that the residual burnable poison penalty associated with the excess burnable poisons required to suppress unacceptable power peaking



■ Figure 10

Ring of Fire low leakage loading pattern for a PWR for two different objective functions



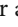

now just about offsets the reduced neutron leakage reactivity effect, resulting in no net gain in cycle energy produced.

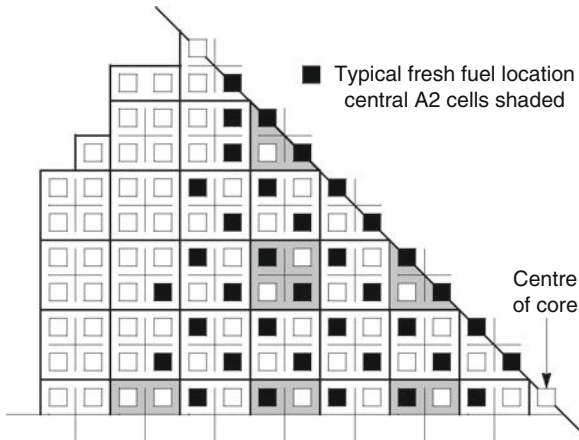
What has evolved is a more complicated loading pattern strategy referred to as a Low Leakage Loading Pattern (L^3P) with a Ring of Fire. In this approach some of the least reactive fuel assemblies are placed in the highest leakage locations, i.e., those with two sides of the assembly on the core periphery, and adjacent high leakage locations. Much of the feed fuel, which is the most reactive fuel, is placed one or two assembly pitches from the core periphery forming an approximate ring about the core center. These assemblies tend to operate at the highest powers, hence the reference to the Ring of Fire. The remaining least reactive and most reactive fuels are then check-boarded with the mid-reactive fuel, with a preference for locating the least reactive fuel assembly side-by-side with the most reactive fuel to both drive the least reactive fuel and decrease power peaking in the most reactive fuel. For a PWR, [▶ Fig. 10](#) displays an L^3P with a Ring of Fire. Very acceptable power peaking is obtained without the need to introduce additional burnable poison material beyond that required for reactivity hold down, hence no additional burnable poison reactivity penalty is experienced. This general approach to loading patterns is utilized for PWR cores. A difference for BWR cores is that the Ring of Fire is now composed of mid-reactive fuel assemblies versus the most reactive fuel. This is done to increase the CSM at BOC. Further there may be some clumping of fresh fuel in the interior about a control blade to increase the CSM at EOC.

3.3.2 LWR Control Rod Programming Selection

In addition to determining the core loading pattern, BWRs have the additional requirement of determining the control blade insertion patterns as a function of cycle exposure, referred to as Control Rod Programming (CRP). There is no such need for PWRs since at HFP most control rods are totally withdrawn from the core, with only a few control rods shallowly inserted. This is possible since the excess core reactivity is controlled by the soluble boron concentration. To position a group of control rods to the proper insertion depth, the soluble boron concentration is adjusted and the core is maintained critical by offsetting the reactivity change associated with the concentration change with the insertion depth of the control rods. The only reason why any control rods are shallowly inserted at HFP is because the automatic control system utilizes

control rod motion to maintain the programmed power level at the programmed vessel average coolant temperature. Since BWRs cannot utilize a soluble poison, the only mechanisms for controlling the core reactivity, e.g., maintaining the core critical, are via the control blades and core flow rate. At EOC clearly the control blades will be all withdrawn and the core flow rate will be maximized to keep the core critical at HFP as long as possible. But prior to EOC there are many control blade insertion patterns and core flow rate combinations that maintain the core critical. This freedom can be utilized to assure that the thermal limits are all satisfied. However, if not done properly a burnup distribution will develop that prevents the thermal limits from all being satisfied later in the cycle when control blades need to be more shallowly inserted, so less capable of power distribution control. In particular, if the control blades inserted stay longer covering a certain zone of the core, this zone will experience less burnup because the flux and hence power is suppressed in the vicinity of the control blade, referred to as burnup shadowing. At some point the control blade will need to be withdrawn to maintain the core critical, exposing a fuel zone with lower burnup and reduced equilibrium xenon concentration. This will result in a large local power increase that could cause a violation of a thermal margin and unacceptable fuel mechanical duty, e.g., Pellet–Clad Interaction. Two approaches to CRP have evolved, referred to as Conventional Core and Control Cell Core, to minimize burnup shadowing and fuel duty.

The Conventional Core approach focuses on not allowing a control blade to shadow a zone of the core too long. By switching on some frequency, which control blades are utilized to control core reactivity and perform power distribution control, the buildup of burnup shadowing is minimized to an acceptable level. When switching of control blades occur, referred to as a rod swap, the zones of the core that were previously shadowed will experience a local power increase which is within the acceptable range. This increase in local power increases the rate of local burnup, tending to heal the shadowed zone. To assure that the local power increase does not cause unacceptable fuel duty, the rod swap is completed at reduced power, normally about 85% of full-rated power. Since the resulting loss of energy production is economically undesirable, the time between rod swaps is desired to be maximized, which tends to occur at a time interval of several months.  [Figure 11](#) displays the layout of a conventional core for a BWR.  [Figure 12](#) shows the CRP for a BWR operating by using the Conventional Core approach. The numbers indicate the position of a control blade, which defines a control cell composed of the control blade and four face adjacent fuel assemblies. The unit utilized is a notch, which corresponds to a 0.0762 m (3 in.) movement. For a 3.66 m (144 in.) active fuel height, 48 notches implies complete withdrawal of the control blade and is not shown in the figure. The subset of control blades utilized over a specific time is specified. For the example presented in  [Fig. 12](#), there are four subsets utilized, referred to as A1, A2, B1, and B2 as illustrated in  [Fig. 13](#). A1 is utilized up to Burnup Step 5, at which time a rod swap occurs to A2. At Burnup Step 6 a rod swap occurs to B1, which is utilized up to Burnup Step 7 when a swap to B2 occurs. B2 is then maintained until Burnup Step 10 when a rod swap to A1 occurs and the sequence is repeated. At Burnup Step 18, which corresponds to EOC, as expected all control blades are withdrawn. The withdrawal positions as a function of burnup are so selected to keep the core critical and shape the power distribution such that the thermal limits are satisfied not only at the current time, but also at future times by avoiding unacceptable burnup shadowing. As noted earlier, the core's reactivity can be changed by changing the core flow rate, which is controlled by the recirculation flow rate. The implication is that the CRP is impacted by the selected core flow as a function of cycle exposure. To minimize fuel cycle cost i.e., minimize the feed enrichment required, core flow is selected to be as low as permitted early in the cycle, increasing coolant



■ Figure 11
Conventional core layout for a BWR

voiding, which hardens the neutron energy spectrum resulting in more Pu239 production via resonance capture in U238. Later in the cycle the core flow will need to be increased to maintain the core critical.

The Control Cell Core approach was developed to minimize or eliminate the need to do down powers during rod swaps by removing the need to do rod swaps. The basic idea is to select a single subgroup of control elements that will be utilized throughout the cycle to control core reactivity and the power distribution. By selecting the fuel assemblies in the control cells of this subgroup of control blades to be less reactive, burnup shadowing effects can be minimized since the rate of putting burnup on these fuel assemblies is reduced. Further, when control blade withdrawal does occur, neither thermal nor fuel duty limits will be violated since the local power increase starts from a lower power density and after the increase still is at an acceptable power density. To assure that the control cells involved utilize fuel assemblies that display an acceptable low reactivity, restrictions must be placed on the fuel assemblies that are located there. Further, to avoid multicycle buildup of burnup shadowing, including the concern of a significant burnup gradient across the fuel assembly, a fuel assembly is restricted over its lifetime to occupy a control cell only one cycle. So employing a Control Cell Core places further restrictions on the loading pattern. ➤ [Table 5](#) contrasts the key LP and CRP attributes of a Conventional Core and Control Cell Core. ➤ [Figure 14](#) indicates the positions of the control cells utilized and ➤ [Fig. 15](#) displays the CRP for a Control Cell Core. For high-energy cores, associated with extended cycle lengths and power uprates, it has proven difficult to utilize a Control Cell Core approach because the feed region size needs to be large to satisfy discharge burnup and enrichment limits, implying that it is not possible to load control cells to have lower reactivity.

What should be obvious at this point is that for BWRs, the determination of the loading pattern and the CRP is linked together, implying that their determinations must be completed together. As shall be seen shortly, things are even more complicated in that the determinations of the lattice and assembly designs are also linked to the determinations of the loading pattern and CRP.

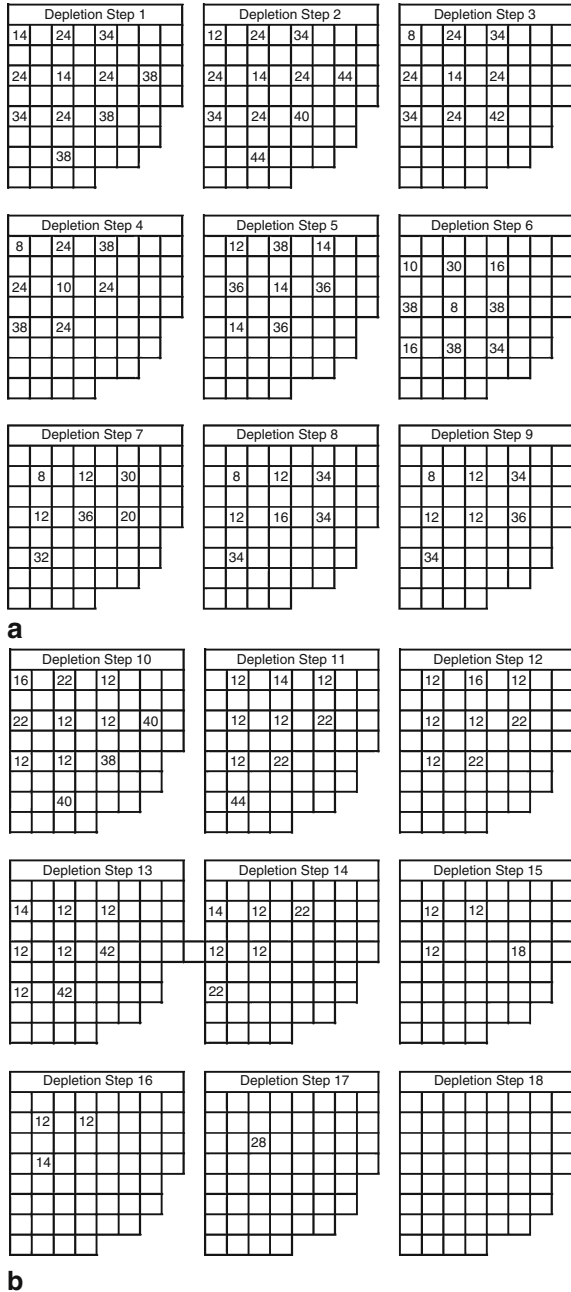


Figure 12

Control rod program associated with a conventional core for a BWR

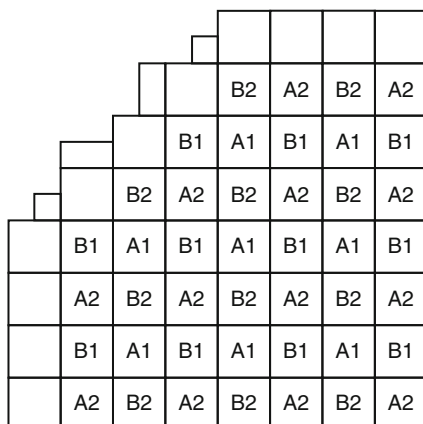


Figure 13

Control blade groups sequence layout associated with a conventional core for a BWR

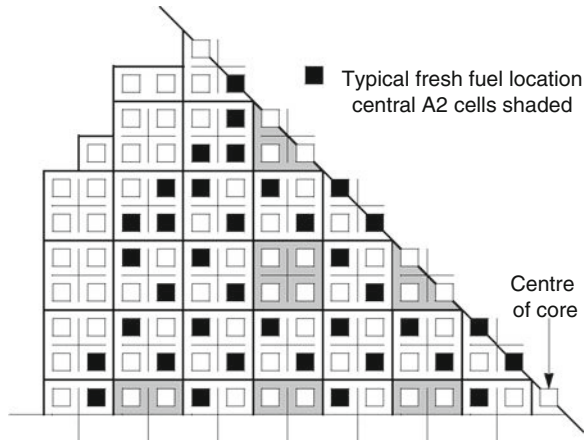
Table 5

Key attributes of a conventional core and control cell core

Attribute	Conventional core	Control cell core
LP	Scatter load fuel assembly of different reactivities throughout core (L ³ P)	Load less reactive fuel assemblies about control rods to be inserted at power. Only allow fuel assembly to be in CC for one cycle. Note still L ³ P.
CRP	Group control rods into patterns A-1, A-2, B-1, and B-2. Sequence through (swap) A and B patterns, e.g., A-1, A-2, B-1, B-2, with cycle burnup with regard to deep insertions. Slight down power must be done during swap to avoid pellet-clad interaction failures.	Use fixed group of control rods in control cells throughout the cycle with no or minimum need for rod swaps.

3.3.3 LWR Lattice and Assembly Selection

The loading pattern mainly effects the radial power distribution of the core. Is there any need to also do fuel management to effect the axial power distribution? Since axially the LWR fuel assembly is a single structural unit, the only manner of affecting the axial power distribution via the fuel assembly is by its design. Axial blankets are utilized in both PWRs and BWRs. They are introduced by replacing approximately 0.15 m (6 in.) at the top and bottom of the enriched typically 3.66 m (144 in.) fuel pellet stack with either natural solid or slightly enriched annular pellets. In doing this the cost of the uranium ore and enrichment service per unit energy produced is reduced, so the motivation is economic. As expected, axial neutron leakage is reduced



■ Figure 14
Control cell core layout for a BWR

due to the lower flux on the axial periphery, but in doing so axial power peaking is increased. So axial blankets work against a reduction in axial power peaking.

Returning to the need to address axial power peaking, PWRs via burnup naturally tend to suppress axial power peaking. For a Cycle 1 loaded with all fresh fuel, approximately a chopped cosine shape exists, which causes the higher power zone about the core mid-plane to receive burnup at a higher rate. If burnable poisons are not present or present such that reactivity decreases with fuel irradiation, this implies that about the core mid-plane the reactivity decreases faster than in the lower and upper axial zones of the core. This causes the characteristic double-hump axial power distribution associated with PWRs as displayed in [Fig. 16](#) to develop with burnup in Cycle 1. Since reload cores will have typically anywhere from one-half to two-thirds of the fuel being burnt from earlier cycles of irradiation, the double-hump shape appears throughout reload cycle cores. Given that PWRs only experience higher axial power peaking early in Cycle 1, and even then the power peaks are of acceptable magnitude, there is reduced need to address via assembly design axial power peaking control. What needs to be addressed is power peaking due to axial xenon transients as discussed in [2.2.2](#) and improper partial insertion of control rods, which is accomplished via control strategies, e.g., axial offset control, and power level-dependent control rod insertion limits.

The situation for BWRs in regard to the need to address axial power peaking is very different than for PWRs. Due to the increased voiding as the coolant flows up through the core, the moderating power decreases, hence reactivity decreases with elevation. If no counteractions were taken, the axial power distribution would be skewed toward the core bottom and high axial power peaking would occur. Burnup would partially mitigate this effect but not to an acceptable level. Given that BWRs utilize bottom entry control blades, since it is difficult to have top entry given the steam separators and dryers above the core, they can be partially inserted introducing negative reactivity in the core bottom somewhat offsetting the negative reactivity in the core top from coolant voiding. Near EOC the control blades will need to be nearly totally withdrawn making them not useful for axial power distribution control, and perhaps more important fuel duty would be increased by first inserting and later withdrawing the control

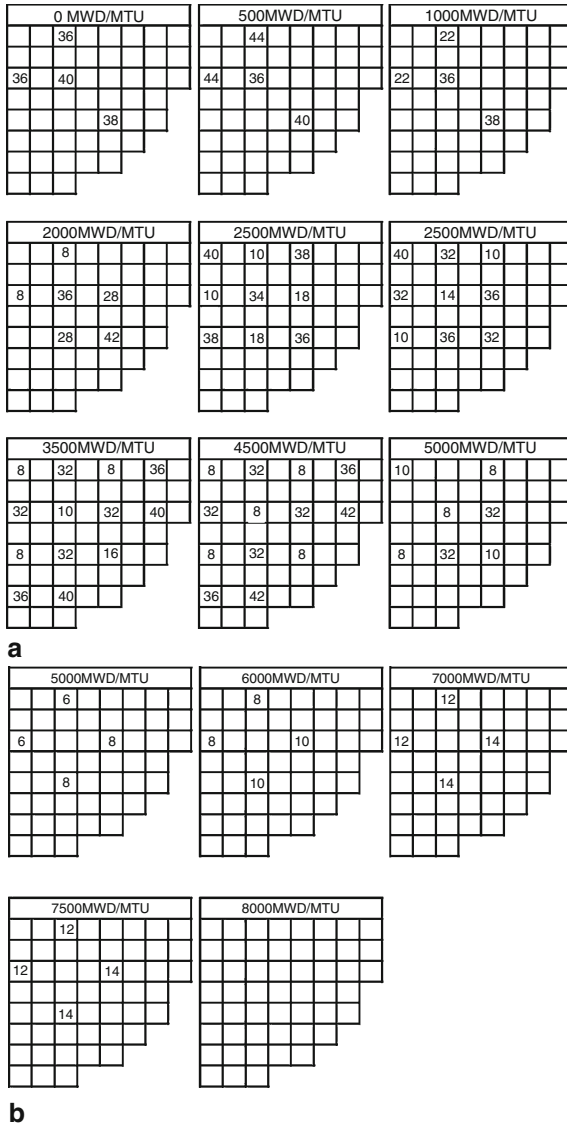
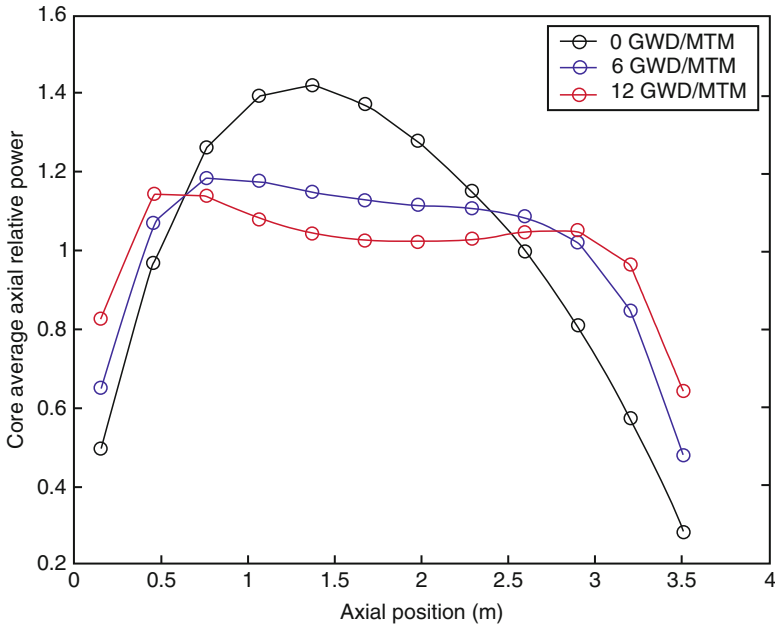


Figure 15
Control rod program associated with a control cell core for a BWR

blades. To minimize but not eliminate the need for partial control blades insertions, additional burnable poison material, which is Gadolinia in BWRs, is introduced in the lower portion of fuel assemblies. Note that about 15% of the fuel pins in an assembly may be part length, i.e., 2.74 m (108 in.) versus 3.66 m (144 in.) in stack height. This is mainly done to increase flow stability by minimizing the two-phase pressure drop and to increase the CSM by reducing the reactivity increase due to flux axial redistribution, but also impacts the axial power distribution during



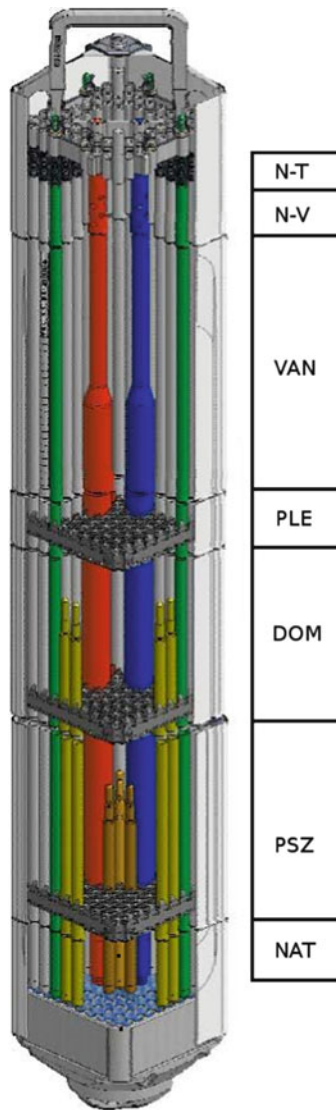
■ Figure 16

Core average relative axial power distribution as a function of cycle burnup during Cycle 1 for a PWR

power operation. ➤ *Figure 17* displays how different lattice designs are used at different axial elevations. ➤ *Figure 18* shows the possible variability of axial power distributions for a fresh assembly as it burns in a BWR core due to a combination of partial control blade insertions and Gadolinia depletion. Such variability of the axial power distribution occurs from assembly to assembly at a fixed cycle burnup. The upper portion of this figure showing uncertainty will be discussed later.

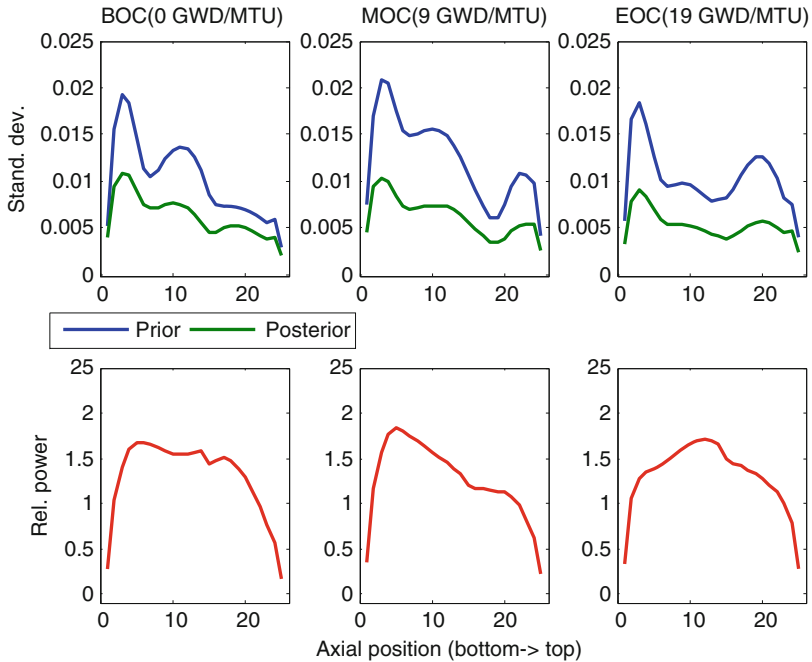
How axial heterogeneities are introduced into a fuel assembly is done by utilizing different lattice designs at different elevations as noted in ➤ *Fig. 17*. Recall that a lattice describes the geometry and composition of a fuel assembly in the x, y radial plane. With axial elevation, from a neutronics viewpoint one is concerned with axial power distribution shaping at operating conditions and minimizing the reactivity swing due to axial flux redistribution when going from operating to shutdown conditions, implying that the fuel assemblies' radially averaged axial reactivity profile is of interest. Radially, one is mainly concerned with the local power peaking that can occur within an assembly at elevations where the power may be higher. So fuel assembly design, which encompasses lattice design and at what elevations different lattice designs should be utilized, must address both axial and radial behavior requirements. The desirable features of the fuel assembly have been discussed above, but not in detail as to how this is accomplished and which is the subject of lattice design.

Local radial power peaking occurs in lattices mainly because of local concentrations of coolant. This follows since LWR cores are under-moderated for safety reasons, so any local zone of concentration of coolant will increase the reactivity in the fuel pins adjacent to this zone, resulting in local power peaking. This effect can be minimized by utilizing a geometry that



■ **Figure 17**
Fuel assembly and location of different lattice designs for a BWR

minimizes local zones of coolant concentration. Such an approach is utilized for some PWR fuel assembly designs. By displacing only a single fuel pin for either a guide tube or instrumentation sheath, which will be occupied by coolant if a control rod, discrete burnable poison rod or instrumentation thimble is not inserted within an assembly, the extent of power peaking in the adjacent fuel pins can be minimized. Likewise, by minimizing the inter-assembly gap, power peaking on fuel pins on the periphery of the fuel assembly can be minimized. As can be seen in ► [Fig. 19](#) for a fresh 17×17 PWR fuel assembly, this approach of minimizing local zones of coolant concentration is sufficiently effective that acceptable levels of local power peaking



■ Figure 18

Fresh assembly axial power distribution as a function of cycle burnup for a BWR

are achieved without the need for using different enrichments in the fuel pins. Other PWR fuel designs elect to displace a 2×2 array of unit cells for guide tubes and instrumentation sheath. Using this approach, lower enrichment fuel pins need to be utilized around their locations to obtain acceptable local power peaking. ➤ [Figure 20](#) presents an example of doing this by the so-called island design. With the introduction of burnable poison material, whether discrete or integral, local power peaking is increased while there is significant burnable poison material present. However, within the core if significant burnable poison material is present, the power density in this zone will be suppressed so that higher local power peaking can be accommodated. This is not to say that when using an integral burnable poison, which allows the freedom to decide where burnable poison material is placed, consideration of local power peaking is ignored.

Local power peaking is of much greater concern when designing BWR lattices. This occurs due to the large inter-assembly gap that is necessary to accommodate control blades and instrumentation, which in the case of a BWR are located outside the assembly channel box. Not only is the inter-assembly gap large, but it also contains higher density, subcooled coolant. Given that inside the channel box at all but the lower elevations will exist lower density, voided coolant, the fuel pins on the assembly periphery will experience much more effective neutron moderation, leading to a significant increase in flux and power density. This will be particularly true for the fuel pins on the corners since they are adjacent to where the inter-assembly gap forms a cross. Without the introduction of design features to counter the inter-assembly gap local

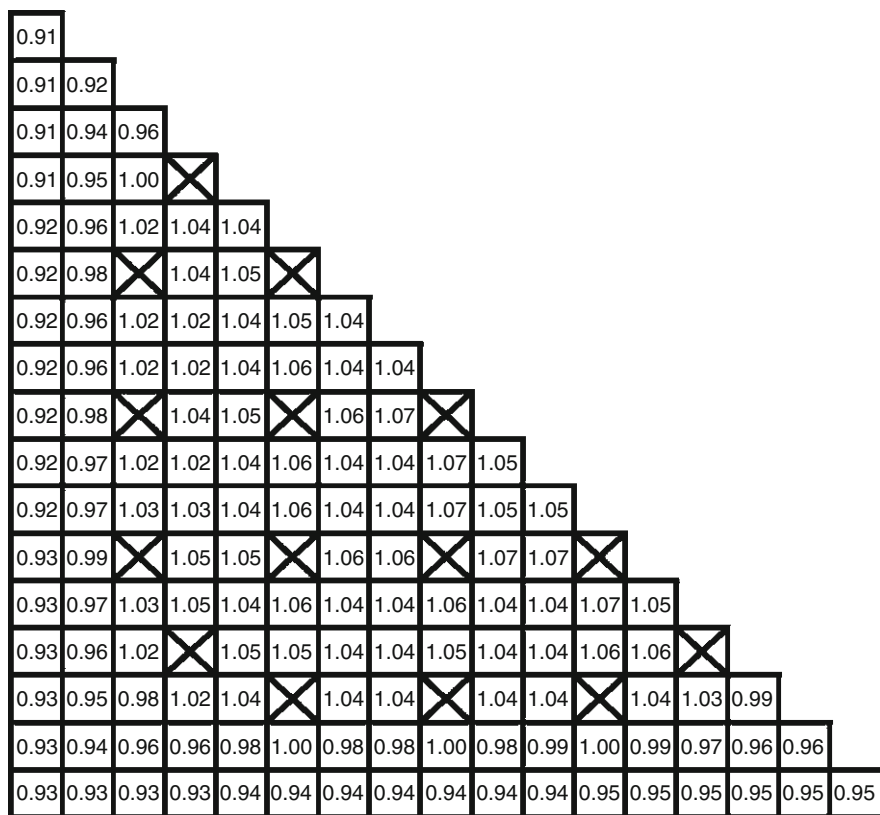
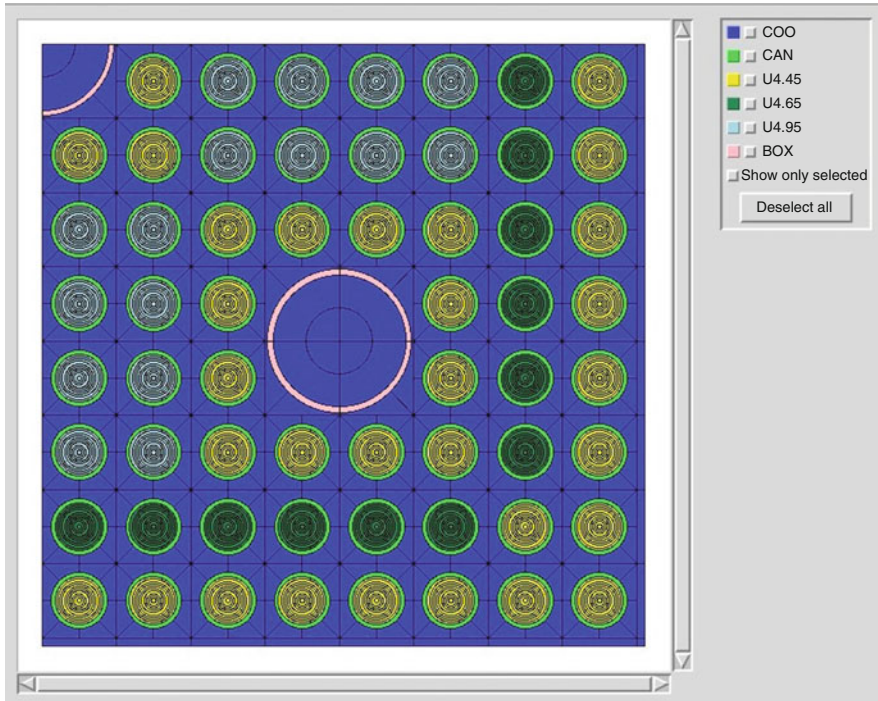


Figure 19

Pin-wise relative radial power distribution in a fuel assembly that utilizes small water holes for a PWR

moderation, unacceptable local power peaking would occur. For this reason fuel pins with different enrichments are utilized within the lattice. As expected and illustrated in [Figure 21](#) for the dominant lattice, the lowest enrichment pins will occupy some of the corner pin locations, and the enrichment of pins will increase for the fuel pins that are further away from the corners and periphery. The reason why the pin enrichments are generally lower in symmetric locations above versus below the diagonal axis running from the southwest corner to northeast corner can be due to a difference in the inter-assembly gap size, which is larger on the north and west surfaces to accommodate control blade insertion.

Without an additional design feature, a significant number of fuel pins of different enrichment would be required. Further, at the coolant void fractions BWRs operate at the core would be very under-moderated without an additional design feature. Now unit cell pitch could be increased, but that presents a structural challenge to designing spacers that would support fuel pins. So to both balance the local moderation effect caused by the inter-assembly gap and under moderation, fuel pins are displaced and replaced by water rods or slots. [Figure 21](#) indicates a lattice design that elects to displace 2×2 unit fuel cells. An alternative design forms an internal



■ Figure 20

Pin-wise fuel and Erbium enrichments in a fuel assembly that utilized large water holes for a PWR

cross within the fuel assembly formed by a 2×2 array of 5×5 unit fuel cells for a 10×10 fuel assembly design.

As mentioned earlier, BWR fuel assemblies have utilized part-length fuel pins in the upper core elevations as a mechanism to introduce more coolant and improve moderation. This actually introduces not one but two lattice designs, one associated with the axial span where the part-length fuel pin plenum volume exists and the other where the part-length rod is vanished. A typical number of fuel pins that are part length in a 10×10 array is 14 fuel pins or approximately 15% of all the fuel pins. Also mentioned previously was an assembly design that loaded more Gadolinia at lower elevations to improve the axial power distribution. ➤ *Figure 21* shows the addition of two additional 2 w/o Gadolinia-loaded fuel pins to the twelve 6 w/o Gadolinia-loaded fuel pins. As with the pin-wise enrichment distribution, the additional Gadolinia-loaded fuel pins are loaded closer to the wider inter-assembly gap.

➤ *Figure 17* indicates the lattice designs that can be found in a typical BWR fuel assembly. For this example, seven different lattice designs are utilized. Recognizing that each lattice design involved decisions concerning geometry and pin-wise isotopic compositions, and that lattice, assembly, loading pattern, and CRP design decisions are coupled, one begins to realize the complexity of BWR in-core nuclear fuel management. But on the positive side, where there is complexity due to the large number of design decisions that need to be made, there is opportunity for design creativity.

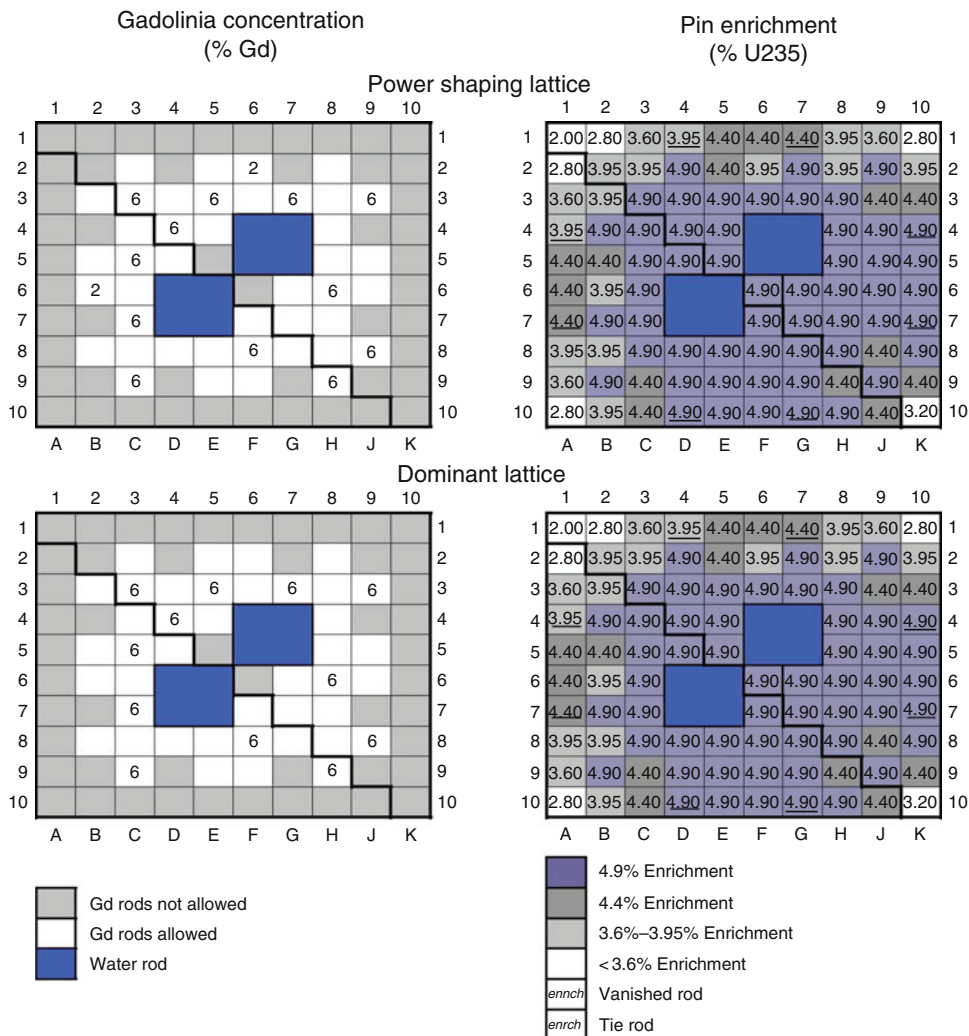


Figure 21
Pin-wise fuel and Gadolinia enrichments in the dominant and power shaping fuel lattices for a BWR

3.4 Non-LWR In-Core Nuclear Fuel Management

3.4.1 Introduction

In the following sections very brief descriptions of fuel management for reactor types other than LWRs, in particular heavy water reactors (HWR), very high temperature gas-cooled reactors (VHTR), and advanced recycle reactors (ARR) will be presented. Since VHTRs and ARRs have not been widely deployed on a commercial scale, the state of sophistication of nuclear fuel

management decision making in regard to meeting the various objectives within constraints in an optimum manner is less than that for LWRs.

3.4.2 Heavy Water Reactors

HWRs have many of the same limitations that are imposed on LWRs. A major difference with LWRs is online refueling, which is necessary since the reactors are designed to operate using natural uranium, hence the fuel's lifetime is short, e.g., 8 GWD/MTU versus that of LWR fuel, e.g., 45–50 GWD/MTU. The implication is that the fuel management decisions about cycle length between refueling outages, utilization of stretch out, fresh fuel assembly compositions, burnt fuel assemblies to reinsert, and burnable poison type and total loadings do not apply to an HWR. The core loading pattern decision now addresses, which fuel channel should be reloaded, how many bundles should be pushed (loaded), and at what frequency should this occur. The decisions regarding number of bundles to push and frequency of doing this is simple, determined by the requirement to keep the core critical for a certain period of time between pushes. Which fuel channels to push feed bundles into is done in such a way that the burnup of the fuel being discharged is approximately uniform factoring in power distribution constraint limits. Given a total of 380 fuel channels and 12 fuel bundles per channel, each with a length of about 0.5 m, over a typical week of operation at full power ten channels will be reloaded each with four or eight feed fuel bundles. Regarding control rod locations, the HWR has a diversity of reactivity control devices. They are utilized to both do power distribution shaping and control excess core reactivity. Zone controllers, which introduce light water (a poison in an HWR) in selected axial and radial core positions, provide excess core reactivity and power distribution controls. Adjusters, a weak absorber control device, are also used for controlling core reactivity and power distribution as required, and mechanical control absorbers, a strong absorber control device, are used mainly for controlling core reactivity. For a Cycle 1 core, a soluble poison may be added to the heavy water moderator, which for an HWR is distinct from the coolant. In no time the core takes on an equilibrium characteristic. Mathematical optimization software has been developed to assist in making the push decisions. In contrast to LWRs, HWRs do permit a positive coolant void coefficient. Fuel bundles, using a combination of slightly enriched uranium, central fuel rod blended burnable poison, and altered water to uranium ratio, have been designed to minimize the magnitude of the positive coolant void coefficient.

3.4.3 Very High Temperature Gas-Cooled Reactors

VHTR core designs being considered fall into two categories: prismatic and pebble bed. In the prismatic design, hexagonal blocks containing fuel, burnable poison, coolant channels, and control rod penetrations if appropriate, are placed side-by-side and stacked axially to create the core. For both designs TRISO particle fuel is employed, embedded within the graphite moderator. This adds an additional fuel management decision, which is the packing fraction of TRISO particle fuel within the graphite moderator. Like LWRs, VHTRs are batch refueled. So the nuclear fuel management decisions concerning cycle length between refueling outages, fresh fuel assemblies number and compositions, burnt fuel assemblies to reinsert, burnable poison type and total loadings, core loading pattern, and CRP all come into play. A multi-batch core design, like for LWRs, is planned to be employed, composed of fuel of different number of

cycles of irradiation. A major difference for a VHTR core is the ability to do three-dimensional loading patterns, since the fuel block can be located not only radially, but also axially within the core. Radial column shuffling, where all the blocks in a radial location move from one radial location to another with their axial positions retained (Kim and Venneri 2007), is one form of shuffling that has been examined. Given that the blocks in a radial column located in a control rod position may have additional holes in the block for control rod insertion, this will limit radial columns without these additional holes to noncontrol rod positions. Axial column shuffling has also been considered, where now radial position is retained but the axial position of blocks are shuffled (Kim et al. 2007). Commonly used is a ring loading pattern, where all the fuel blocks within a given radial ring will have the same number of cycles of irradiation. Given that a gas coolant is utilized, thermal limits for a VHTR are associated with fuel temperature limits.

Pebble bed reactor utilize online refueling, so a number of the nuclear fuel management decisions appropriate for LWRs are not applicable. Replacement of a burnt pebble by a feed pebble is done when the burnt pebble reaches a desired level of burnup. It follows that fuel enrichment is determined so as to take the pebble to the desired level of discharge burnup while retaining the reactor with sufficient excess core reactivity. Pebbles may differ in TRISO particle fuel packing fraction, burnable poison loading, and fuel enrichment. The rate of circulation of pebbles, which equates to the residence time of a pebble in the core for one of its multiple core passes, is determined factoring fuel composition, discharge burnup limit, desired number of passes, and power distribution. The lower the rate of circulation, the lower the number of passes of the pebble before discharge due to the longer residence time in the core. Like the prismatic design, the power distribution is limited by fuel temperature limits. The radial placement of pebbles on the top of the stack when feed, versus a random placement, accounting for their reactivity does influence the core's characteristics and can be considered an additional decision variable.

3.4.4 Advanced Recycle Reactor

Several different reactor types are being considered to fill the role of an ARR. The sodium fast reactor (SFR) is the prime candidate of these different types, so shall be discussed. SFRs can be designed to have a range of conversion ratios. If breeding is desired, use of axial and radial blankets composed of depleted uranium is the preferred configuration. In addition to the utilization of plutonium, one of the goals of ARRs is the destruction of minor actinides, which are the actinide elements above plutonium in the Periodic Table. Concepts being considered vary on whether minor actinides are mixed with the uranium and plutonium or contained in separate targets. Exactly what minor actinides will be recycled from spent fuel, which is dependent upon ease of separation, heat loading, fuel performance, and benefit of recycle, have yet to be decided. Regarding fuel management decisions, fissile material composition now becomes more complicated given that multiple elements each with multiple isotopes are involved. Given a closed fuel cycle, the isotopic composition of the recycled material available is variable. If a low conversion ratio is desired to maximize destruction of minor actinides, this implies a low fuel to sodium ratio, achieved by utilizing a smaller fuel pin radius. Some fuel management constraints include peak linear power density, maximum excess core reactivity, maximum cladding

fluence, maximum discharge burnup, and limits on various reactivity coefficients and reactivity device worths. A typical in-core fuel management scheme consists of two or three different fuel reactivities achieved by elemental mixtures, each loaded into a radial ring zone of the core, all done to flatten the power distribution. A no-fuel shuffling scheme may be employed, where in each refueling outage a fraction of the fuel in each radial ring zone may be replaced with fresh fuel assemblies without movement of any partially burnt assemblies. Given the long mean free path of neutrons in a fast reactor makes more possible the utilization of a no-fuel shuffling scheme.

3.5 Applications of Mathematical Optimization in Nuclear Fuel Management

3.5.1 Introduction

Earlier sections of this chapter have revealed the complexity of making nuclear fuel management decisions. This has motivated the development of capabilities to apply mathematical optimization to nuclear fuel management problem. Such capabilities should be viewed as an aid to the core design engineer since factors need to be considered, such as risk associated with a decision, which cannot be easily quantified and hence captured within a mathematical optimization capability. Since the majority of effort in applying mathematical optimization has been for LWR cores, the following discussion will reflect this. However, some of the capabilities developed for LWR cores could be adapted for utilization to non-LWR cores.

3.5.2 Mathematical Optimization Approaches Utilized for Nuclear Fuel Management

There are a wide range of mathematical optimization approaches available to consider for application to nuclear fuel management problems. Consistent with the language of mathematical optimization and what has been used throughout this chapter, the purpose of mathematical optimization is to minimize an objective function by the determination of the values of decision variables as limited by the imposed constraints. If the objective is to maximize an objective, this can be accomplished by minimization of the original negated objective function, so in the following minimization will always be assumed as the objective. Broadly speaking mathematical optimization approaches can be classified as deterministic or stochastic approaches. Linear programming and dynamic programming are two examples of widely used deterministic approach. Simulated annealing (SA) and genetic algorithms (GAs) are examples of widely used stochastic approach. When possible, a deterministic approach is to be preferred over a stochastic approach because of reduced computational effort and many times the capability to assure that the global optimum decisions have been determined. Unfortunately for many nuclear fuel management problems due to their characteristics deterministic approaches appear not to be applicable, implying that a stochastic approach needs to be utilized. Typical attributes of a nuclear fuel management problem are

- Nonlinear dependence of objective function and constraints on decision variables
- Multi-objective decision-making problem
- Lack of derivative information of objective function with respect to decision variables
- Mixed integer-continuous or integer-decision variables
- Highly constrained problem with feasible decision subdomains disjointed
- Multiple local minima of objective function for feasible solutions whose quality is nearly as good as the global minima solution
- A very large decision space

Clearly, for certain optimization problems that are nonlinear, one could attempt linearizing the problem about some assumed values of the decision variables, optimizing the linear problem using a deterministic approach, and relinearizing the problem about the updated decision variables, continuing this process until convergence of the decision variables. This approach has in the past been attempted to be utilized without success for the in-core optimization problem using the branch-and-bound linear programming approach to address the integer-decision variables. So the focus will be on stochastic optimization approaches, in particular SA and GAs. These two approaches have been selected for discussion because of their wide utilization in solving the nuclear fuel management optimization problem, but one should recognize that other stochastic optimization approaches have been utilized with success.

SA is based upon the physical analogy of cooling of a metal. It builds upon the statistical mechanics algorithm due to Metropolis (Metropolis et al., 1953) that was first introduced as a means of finding the equilibrium configuration of a collection of particles at a given temperature. The connection between the Metropolis algorithm and minimization was first noted by Pincus (1970), but it was Kirkpatrick (Kirkpatrick et al. 1983) who proposed that it forms the basis of an optimization technique for combinatorial problems, in which a set of candidate solutions to minimize an objective function is generated by random trial moves. The physical analogy is that if a metal is cooled too quickly, it will assume a structure that does not correspond to the lowest energy state. If a metal is cooled very slowly, it will assume a structure that does correspond to the lowest energy state but at the cost of increased cooling time. What one desires is the maximum cooling rate, which will assure that the metal will assume a structure that does correspond to the lowest energy state. Using this analogy, the SA stochastic optimization approach has been developed. Let f_C denote the current value of the objective function, which is associated with a set of values for the decision variables. Now randomly sample one or more of the decision variable values to form a perturbed state and determine f_P , the perturbed value of the objective function. Now determine whether the perturbed state replaces the current state by

$$f_C = \begin{cases} f_P & \text{if } f_P < f_C \text{ or } r \leq e^{(f_C - f_P)/T} \text{ if } f_P \geq f_C \\ f_C & \text{otherwise} \end{cases} \quad (25)$$

where r is a random number between 0 and 1 and T denotes the annealing temperature. What this acceptance criterion does is not only accept superior solutions, but also inferior solutions with some probability dependent upon the annealing temperature. This allows the optimization search to escape from local minima in its search for the global minima.

Key to SA is the rate of decreasing of the annealing temperature as the search progresses. The initial annealing temperature is selected to be high allowing the decision variables' search space to be spanned. Its specific value is set by randomly, successively sampling the set of decision

variables, evaluating the objective function values and standard deviation of the objective function values, σ_f , and specifying the initial annealing temperature by $T_o = A\sigma_f$. When substituting this expression into (25) it is recognized that by the selection of the value of A the initial annealing temperature is being selected so that a desired probability of accepting inferior solutions is attained. As the search progresses, the annealing temperature is decreased, with one possible way of doing this based upon

$$T_{k+1} = \alpha_k T_k \quad (26)$$

where k denotes the cooling step. A cooling step is completed after a certain number of histories, i.e., perturbation cases, are evaluated at annealing temperature T_k , which forms a Markov Chain. The length of Markov Chain has to be sufficient to establish an equilibrium Boltzmann distribution, which by an analogy to statistical mechanics indicates that the annealing temperature decrement should be determined by

$$\alpha_k = \max \left(\alpha_{\min}, e^{-[vT_k/(\sigma_f)_k]} \right) \quad (27)$$


where α_{\min} and v are selected, and $(\sigma_f)_k$ denotes the standard deviation of the objective function for the k th cooling step. Various attributes are evaluated to determine the length of the Markov Chain to assure that an equilibrium Boltzmann distribution has been approximately established.

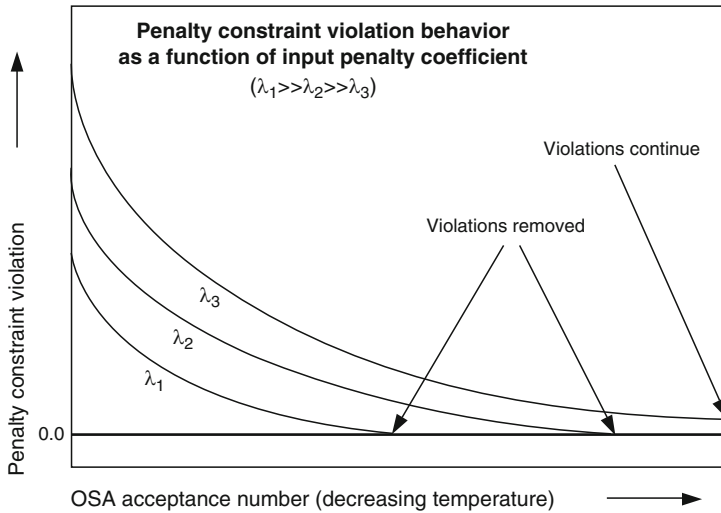
Constraints need to be imposed during the optimization search. If a constraint is directly on the value a decision variable can take, this is simply enforced in the sampling of decision variable values. If the constraint relates to some limitation of the system being analyzed, e.g., maximum allowed fuel pin burnup, it can be imposed as a hard or soft constraint. If imposed as a hard constraint, if a history violates the constraint it is rejected from further consideration by SA. If imposed as a soft constraint, a penalty function is introduced where

$$P_k^m(\eta_{limit}^m, \eta_P^m) = \begin{cases} 0 & \text{if constraint not violated} \\ > 0 & \text{if constraint violated and increases with violation magnitude} \end{cases} \quad (28)$$

where m indicates the specific constraint, k denotes the fact that the penalty function magnitude increases with cooling steps for the same violation magnitude, and η_{limit}^m and η_P^m denote the attributes associated with constraint m and its limit and perturbed state value, respectively. Using the soft constraints the augmented objective function is formed

$$f_P^{Aug} = f_P + \sum_m P_k^m(\eta_{limit}^m, \eta_P^m) \quad (29)$$

and used in place of the true objective function in the SA selection of acceptance or rejection of a history. The rate of increase of the penalty function has to be such that the constraint violations are removed as the optimization search progresses, but not so fast that the search gets locked into a local minimum. This behavior is illustrated in  Fig. 22. Just as there are adaptive techniques for controlling the cooling rate of the annealing temperature, there are also adaptive techniques for controlling the rate of increase of each of the penalty functions. By using adaptive methods, the optimization search can proceed with greater assurance that the solutions within the vicinity of the global optimum solution can be located while minimizing the



■ **Figure 22**
Impact of penalty function multiplier on removing constraint violations

computational effort, which still can be substantial. To further reduce the computational burden, an early rejection approach can be utilized. In early rejection, one first determines the random number, r that appears in (25) and back calculates the value of f_p^{Aug} that would cause rejection of the perturbed history being evaluated. Many times constraints can be evaluated prior to the complete analysis of the perturbed history. Using a conservative low estimate of the true objective function value, f_p , and adding to (29) constraint violation penalty functions as the value of constraint violations become available, early rejection causing termination of further perturbed history evaluation will occur if the resulting value of (29) exceeds the predetermined rejection value. An example of where early rejection is most useful is in determining the loading pattern, where cycle depletion is required to assure that no constraints are violated throughout the cycle. If violations occur at some cycle depletion step, early rejection could then trigger termination of further cycle depletion steps.

Since a number of histories are generated, the best of the feasible solutions can be archived for later consideration by the designer when considering attributes that cannot be quantified. This is a nice feature associated with stochastic optimization and particularly attractive for nuclear fuel management optimization, where a number of local minima may exist nearly as good as the global minima but associated with quite different decision parameter values.

GAs are another class of popular stochastic optimization approaches (Goldberg 1989) used to complete the mathematical optimization of nuclear fuel management decisions. GAs' potential advantage over SA is the ability to efficiently locate the vicinity of the global optimum decisions by allowing large perturbations, but in doing so they have the potential disadvantage of not being able to efficiently determine the family of near optimum decisions because of the large perturbations. They are based on an analogy of the evolution of a biological system.

GAs employ a random search procedure in which the members of a population of solutions are either crossed over with one another, or mutated to form a new population of solutions which, on average, should be more fit than the previous generation of solutions. Unlike SA, which seeks to minimize a cost function, GAs seek to maximize the fitness of the population. To accomplish this, the GAs take the negation of the SA objective function as the fitness. A GA parameter known as the selection pressure takes the place of the SA temperature. The selection pressure is a measure of how greatly the more fit solutions are favored for reproduction into the next generation. A selection pressure of 1.0 implies no selection pressure, i.e., all solutions are equally likely to be allowed to reproduce. Increasing positive selection pressures makes it more likely that the more fit solutions will be the solutions allowed to reproduce offspring, which form the new solutions for the next generation. This results in an algorithm, which has all the advantages of SA, along with the drawback of SA of requiring the evaluation of a large number of histories. Because GAs operate on a population of solutions, rather than a single solution at a time, this permits GAs to explore numerous solution possibilities simultaneously. GA's ability to explore numerous solution possibilities simultaneously also provides a highly effective capability for multi-objective optimization. Like SA, hard and soft constraints can be utilized and archiving of the family of near optimum solutions is possible. Unlike adaptive SA, there are many more tuning features that need to be specified when using GAs, the specific features employed dependent upon the attributes of the optimization problem. Tuning features include population size, selection, archiving and elitism, mutation fraction, number of mutation changes per history (also a feature of SA), nature of crossover operator, and crowding and niching. These tuning features provide the opportunity to develop a robust and efficient mathematical optimization capability for a specific optimization problem, but also require more expertise and development time than SA to do this correctly.

Key measures of success in implementing any stochastic optimization approach are robustness and computational efficiency. Robustness denotes the ability to determine the family of near optimum decision variable values for a range of applications, e.g., determination of loading pattern for different LWR plants and reload cycles, independent of the initial guess of the decision variables values. This is demonstrated by analyzing a range of applications, and for each application completing the optimization several times for different initial guesses of the decision variables values. From these different applications and initial guesses the robustness of satisfying all the constraints can be judged, and from the different initial guesses for a specific application the standard deviation in the objective function value associated with the optimum decision variable values can be determined. What one seeks is a small standard deviation since one desires the minimum objective function value determined to be independent of the initial guess of decision variable values. To assure that the minimum objective function value found is close to the value associated with the true global optimum is a more difficult task to complete, since the true global optimum is not known for realistic problems. In this case, a brute force approach of sampling a very large number of histories using whatever optimization capability has been developed, e.g., a very slow annealing temperature cooling schedule may serve to provide some knowledge of the value of the objective function in the vicinity of the true optimum. Regarding computational efficiency, clearly the objective is to minimize the number of histories that must be analyzed to determine the family of near optimum solutions. Unfortunately, the minimum number of histories to accomplish this is not known, so comparison of one optimization approach versus another seems the only manner of getting some measure of computational efficiency.

3.5.3 Application of Mathematical Optimization to Out-of-Core Nuclear Fuel Management

In [3.1](#) the out-of-core nuclear fuel management decisions were presented as

- 1 Cycle length between refueling outages, i.e., cycle energy requirement
- 2 Utilization of stretch out, i.e., operating reactor beyond when criticality can be maintained at full-rated power with nominal plant conditions
- 3 Fresh fuel assemblies number and compositions
- 4 Burnt fuel assemblies to reinsert
- 5 Burnable poison type and total loadings

There are not many, perhaps no, examples of the capability to make all these out-of-core nuclear fuel management decisions simultaneously employing mathematical optimization. However, there are a few examples of making Decisions 3, 4, and 5 simultaneously employing mathematical optimization. The OCEON-P computer code (Comes and Turinsky 1988) is an example of having this capability, so will be discussed at length to provide some insight into what features need to be incorporated into such a code. OCEON-P, which completes Out-of-Core Nuclear Fuel Management Optimization for PWRs, has as its objectives minimization of the leveled fuel cycle cost over the planning horizon and minimization of engineering effort to accomplish this.

The decision variables determined for each cycle in the planning horizon include

- 1 Feed enrichment and number of assemblies for region/batch pairings
- 2 Partially burnt fuel assemblies to reinsert
- 3 Total burnable poison types and loadings
- 4 Batch power shares

Decision 4 is introduced to provide some degree of coupling between the out-of-core and in-core nuclear fuel management problems. By optimizing power shares, i.e., fraction of core energy produced by a region/batch pairing over the cycle, in the out-of-core optimization, the power shares can then be employed as input constraints for in-core fuel management optimization when determining loading patterns. The optimum power shares are determined by inputting multiple target EOC reactivities as a function of core location and feed region size, which are used to determine associated loading patterns during the out-of-core optimization search from which power shares are calculated.

The constants imposed on the optimization are the following:

- 1 Cycle energy requirements
- 2 Discharge burnup limits (region and batch averages)
- 3 Assembly lifetime
- 4 Moderator temperature coefficient
- 5 Minimum and maximum feed enrichments
- 6 Minimum and maximum feed batch sizes
- 7 Feed enrichment palette
- 8 Feed enrichment split options
- 9 Enrichment smoothing

Constraint 7 restricts feed enrichments to predefined values, so to satisfy cycle energy requirements split enrichments must generally be used. This constraint arises to minimize fuel manufacturing costs, in particular, the conversion of UF₆ to UO₂ powder. Constraint 9 is introduced to force the cycling scheme to approach equilibrium in the later cycles of the planning horizon. This is necessary since cycles beyond the last cycle in the planning horizon must be modeled to assure that no constraint violations occur due to decisions made within the planning horizon, and to evaluate the leveled fuel cycle cost since fresh fuel loaded in the planning horizon must be followed to final discharge, i.e., no further energy production.

The OCEON-P code major modules consist of an economic model, neutronics models, and optimization engine. The economic model uses a carrying charge model. The neutronics models consist of three models of different fidelity and computational burden, allowing the user to select which model or combination of models are to be utilized. The neutronics models available are the following:

- Linear Reactivity Model (LRM) (Driscoll et al. 1990) accounting for radial leakage effects
- FLAC model (Beard 1978) using coarse mesh, nodal FLARE technique
- Nuclear design core simulator via MPI linkage

Several optimization engines have been developed for OCEON-P that a user can select from:

- Single objective, biased Integer Monte Carlo Programming with hard constraints
- Single objective, biased, adaptive SA with soft constraints and early rejection (Anderson et al. 2007)
- Single objective GA (Du and Turinsky 2008) with soft constraints.

Of these optimization approaches, biased SA appears most robust and efficient for this particular application. By biased is inferred that the feed region sizes of each cycle and enrichment difference if using split enrichments are determined not by purely random sampling, but using probability distributions determined and updated during the optimization search based upon the economically attractive feasible solutions so far identified.

➤ *Figures 23* and ➤ *24* present the results of an OCEON-P optimization. ➤ *Figure 23* presents the feed/batch sizes and enrichments for the top 50 cases as ranked by leveled fuel cycle cost. All these cases are feasible. ➤ *Figure 24* shows the associated burnable poison loadings, where the burnable poison number refers to a specific burnable poison design, e.g., 12 Gadolinia rods of 6 w/o in an assembly, and the percentage of assemblies so loaded. ➤ *Figure 25* presents the cycling scheme table associated with one of the top 50 cases, identified by history number. This particular optimization did not optimize power shares, so their values are not presented.

A shortcoming of OCEON-P is its lack of tight coupling between out-of-core and in-core decision making. As mentioned, power shares derived from selecting among loading patterns characterized in terms of EOC assembly reactivity loading pattern candidates is employed to provide some degree of coupling. Given increased computational power, in particular, multiprocessors and multicores, capability has been developed to more tightly couple the out-of-core and in-core decisions. Capability to make out-of-core Decisions 3, 4, and 5 simultaneously with in-core Decision 6, which concerns determining the core loading pattern for a PWR over a limited number of reload cycles has been demonstrated utilizing SA as the optimization approach (Kropaczek 2009).

		CYCLE / REGION NUMBER											
		4/4	5/5	6/6	7/7	8/8	9/9	10/10	11/11	12/12	13/13		
RANK	HISTORY	FCC [M/KWHR]	NUMBER OF FEED ASSEMBLIES / FEED ENRICHMENT										
1	2954	9.4563	16 / 4.22 68 / 4.62	88 / 4.51	20 / 4.45 64 / 4.85	92 / 4.27	24 / 4.55 60 / 4.95	20 / 4.18 68 / 4.58	20 / 4.22 68 / 4.62	20 / 4.44 64 / 4.84	24 / 4.16 64 / 4.56	24 / 4.26 64 / 4.66	
2	3984	9.4571	16 / 4.22 68 / 4.62	24 / 4.26 64 / 4.66	20 / 4.41 64 / 4.81	92 / 4.25	24 / 4.57 60 / 4.97	24 / 4.20 64 / 4.60	20 / 4.21 68 / 4.61	20 / 4.24 68 / 4.64	20 / 4.41 64 / 4.81	24 / 4.18 64 / 4.58	
3	4922	9.4572	16 / 4.22 68 / 4.62	88 / 4.51	20 / 4.45 64 / 4.85	92 / 4.27	24 / 4.55 60 / 4.95	20 / 4.38 64 / 4.78	24 / 4.19 64 / 4.59	24 / 4.25 64 / 4.65	24 / 4.25 64 / 4.65	24 / 4.24 64 / 4.64	
4	4654	9.4621	16 / 4.22 68 / 4.62	24 / 4.26 64 / 4.66	20 / 4.41 64 / 4.81	24 / 3.99 68 / 4.39	24 / 4.53 60 / 4.93	28 / 4.21 60 / 4.61	24 / 4.03 68 / 4.43	20 / 4.32 68 / 4.72	20 / 4.40 64 / 4.80	24 / 4.17 64 / 4.57	
5	4207	9.4623	16 / 4.22 68 / 4.62	24 / 4.26 64 / 4.66	20 / 4.41 64 / 4.81	92 / 4.25	24 / 4.57 60 / 4.97	24 / 4.40 60 / 4.80	28 / 4.00 64 / 4.40	24 / 4.34 64 / 4.74	24 / 4.23 64 / 4.63	24 / 4.23 64 / 4.63	
6	2469	9.4625	16 / 4.22 68 / 4.62	88 / 4.51	20 / 4.45 64 / 4.85	92 / 4.27	24 / 4.55 60 / 4.95	20 / 4.18 68 / 4.58	24 / 4.24 64 / 4.64	24 / 4.46 60 / 4.86	28 / 4.00 64 / 4.40	24 / 4.33 64 / 4.73	
7	4001	9.4633	16 / 4.22 68 / 4.62	24 / 4.26 64 / 4.66	20 / 4.41 64 / 4.81	28 / 4.02 64 / 4.42	24 / 4.52 60 / 4.92	28 / 4.01 64 / 4.41	20 / 4.27 68 / 4.67	20 / 4.24 68 / 4.64	20 / 4.39 64 / 4.79	24 / 4.20 64 / 4.60	
8	4898	9.4634	16 / 4.22 68 / 4.62	88 / 4.51	20 / 4.45 64 / 4.85	28 / 4.23 60 / 4.63	28 / 4.25 60 / 4.65	24 / 4.07 68 / 4.47	20 / 4.28 68 / 4.68	20 / 4.42 64 / 4.82	24 / 4.16 64 / 4.56	24 / 4.26 64 / 4.66	
9	1644	9.4636	16 / 4.22 68 / 4.62	24 / 4.26 64 / 4.66	20 / 4.41 64 / 4.81	92 / 4.25	24 / 4.57 60 / 4.97	24 / 4.20 64 / 4.60	24 / 4.24 64 / 4.64	24 / 4.26 64 / 4.66	24 / 4.23 64 / 4.63	24 / 4.25 64 / 4.65	
10	2015	9.4640	16 / 4.22 68 / 4.62	88 / 4.51	20 / 4.45 64 / 4.85	92 / 4.27	24 / 4.55 60 / 4.95	20 / 4.18 68 / 4.58	24 / 4.47 60 / 4.87	28 / 4.20 60 / 4.60	28 / 4.08 64 / 4.48	24 / 4.33 64 / 4.73	
11	2378	9.4644	16 / 4.22 68 / 4.62	24 / 4.26 64 / 4.66	24 / 4.44 60 / 4.84	28 / 4.01 64 / 4.41	20 / 4.30 68 / 4.70	20 / 4.30 68 / 4.63	20 / 4.40 64 / 4.80	24 / 4.20 64 / 4.60	24 / 4.24 64 / 4.64	24 / 4.26 64 / 4.66	
12	2979	9.4646	16 / 4.22 68 / 4.62	24 / 4.26 64 / 4.66	24 / 4.44 60 / 4.84	28 / 4.01 64 / 4.41	24 / 4.32 64 / 4.72	20 / 4.22 68 / 4.62	20 / 4.20 68 / 4.60	20 / 4.44 64 / 4.84	24 / 4.17 64 / 4.57	24 / 4.25 64 / 4.65	
13	3988	9.4651	16 / 4.22 68 / 4.62	24 / 4.26 64 / 4.66	24 / 4.44 60 / 4.84	28 / 4.01 64 / 4.41	24 / 4.32 64 / 4.72	24 / 4.25 64 / 4.65	20 / 4.19 68 / 4.59	20 / 4.24 68 / 4.64	24 / 4.42 64 / 4.82	24 / 4.18 64 / 4.58	
14	2910	9.4651	16 / 4.22 68 / 4.62	88 / 4.51	20 / 4.45 64 / 4.85	92 / 4.27	32 / 4.60 52 / 5.00	24 / 4.00 68 / 4.40	20 / 4.32 68 / 4.72	20 / 4.41 64 / 4.81	24 / 4.16 64 / 4.56	24 / 4.27 64 / 4.67	
15	4581	9.4672	16 / 4.22 68 / 4.62	20 / 4.23 68 / 4.63	20 / 4.42 64 / 4.82	24 / 4.18 64 / 4.58	20 / 4.22 68 / 4.62	20 / 4.24 68 / 4.64	28 / 4.47 56 / 4.87	32 / 4.22 56 / 4.62	32 / 3.93 64 / 4.33	24 / 4.39 64 / 4.79	

Figure 23

Feed fuel assembly numbers and enrichments for PWR determined by mathematical optimization

3.5.4 Application of Mathematical Optimization to In-Core Nuclear Fuel Management

A great deal of work has been successfully completed on using mathematical optimization to optimize in-core nuclear fuel management decisions. Recall that these decisions are:

- Core loading pattern, i.e., fresh fuel, burnt fuel, and burnable poisons core locations
- Control rod (blades) locations and core flow rate (only for BWRs) as function of burnup

These in turn involve additional design decisions about the lattice and assembly designs. Much of the mathematical optimization capability developed has been limited to only addressing one or two of the decisions that need to be made. In lattice design, there have been a number of successful efforts to incorporate mathematical optimization in the decision-making process (Francois et al. 2005; Hernandez-Noyola and Maldonado 2009). Examples of using various optimization approaches, such as linear programming and SA, exist. Many times the method of solution to the lattice physics problem, required to evaluate the objective function and constraints, is simplified to minimize the computational effort, e.g., using successive linear or quadratic functionalization of the objective function or constraint value dependences upon the decision variables. The problem with decoupling lattice optimization with the other in-core optimization aspects is how to define a meaningful objective function and constraints. Many

		CYCLE/REGION NUMBER											
		4/4	5/5	6/6	7/7	8/8	9/9	10/10	11/11	12/12	13/13		
RANK	HISTORY	FCC [M/KWHR]	BE TYPE OF FEED ASSEMBLIES/BP FRACTION										
1	2954	9.4563	1/1.000	13/0.982	1/1.000	13/0.991	1/1.000	1/1.000	1/1.000	1/1.000	1/1.000	1/1.000	1/1.000
			20/0.802		20/0.802		20/0.890	20/0.768	20/0.788	20/0.790	20/0.840	20/0.853	
2	3984	9.4571	1/1.000	1/1.000	1/1.000	13/0.993	1/1.000	1/1.000	1/1.000	1/1.000	1/1.000	1/1.000	1/1.000
			20/0.802	20/0.845	20/0.786		20/0.891	20/0.833	20/0.785	20/0.786	20/0.787	20/0.842	
3	4922	9.4572	1/1.000	13/0.982	1/1.000	13/0.991	1/1.000	1/1.000	1/1.000	1/1.000	1/1.000	1/1.000	1/1.000
			20/0.802		20/0.802		20/0.890	20/0.772	20/0.846	20/0.851	20/0.849	20/0.848	
4	4654	9.4621	1/1.000	1/1.000	1/1.000	1/1.000	1/1.000	1/1.000	1/1.000	1/1.000	1/1.000	1/1.000	1/1.000
			20/0.802	20/0.845	20/0.786	20/0.834	20/0.873	20/0.912	20/0.840	20/0.794	20/0.784	20/0.842	
5	4207	9.4623	1/1.000	1/1.000	1/1.000	13/0.993	1/1.000	1/1.000	1/1.000	1/1.000	1/1.000	1/1.000	1/1.000
			20/0.802	20/0.845	20/0.786		20/0.891	20/0.840	20/0.905	20/0.861	20/0.845	20/0.849	
6	2469	9.4625	1/1.000	13/0.982	1/1.000	13/0.991	1/1.000	1/1.000	1/1.000	1/1.000	1/1.000	1/1.000	1/1.000
			20/0.802		20/0.802		20/0.890	20/0.768	20/0.855	20/0.857	20/0.902	20/0.861	
7	4001	9.4633	1/1.000	1/1.000	1/1.000	13/0.991	1/1.000	1/1.000	1/1.000	1/1.000	1/1.000	1/1.000	1/1.000
			20/0.802	20/0.845	20/0.786	20/0.907	20/0.868	20/0.900	20/0.792	20/0.784	20/0.787	20/0.843	
8	4898	9.4634	1/1.000	13/0.982	1/1.000	1/1.000	1/1.000	1/1.000	1/1.000	1/1.000	1/1.000	1/1.000	1/1.000
			20/0.802		20/0.802	20/0.918	20/0.925	20/0.838	20/0.792	20/0.787	20/0.841	20/0.853	
9	1644	9.4636	1/1.000	1/1.000	1/1.000	13/0.993	1/1.000	1/1.000	1/1.000	1/1.000	1/1.000	1/1.000	1/1.000
			20/0.802	20/0.845	20/0.786		20/0.891	20/0.833	20/0.852	20/0.848	20/0.848	20/0.849	
10	2015	9.4640	1/1.000	13/1.000	1/1.000	13/0.991	1/1.000	1/1.000	1/1.000	1/1.000	1/1.000	1/1.000	1/1.000
			20/0.802		20/0.802		20/0.890	20/0.768	20/0.865	20/0.914	20/0.913	20/0.857	
11	2378	9.4644	1/1.000	1/1.000	1/1.000	1/1.000	1/1.000	1/1.000	1/1.000	1/1.000	1/1.000	1/1.000	1/1.000
			20/0.802	20/0.845	20/0.857	20/0.903	20/0.792	20/0.783	20/0.788	20/0.843	20/0.851	20/0.849	
12	2979	9.4646	1/1.000	1/1.000	1/1.000	1/0.991	1/1.000	1/1.000	1/1.000	1/1.000	1/1.000	1/1.000	1/1.000
			20/0.802	20/0.845	20/0.857	20/0.903	20/0.860	20/0.779	20/0.785	20/0.791	20/0.840	20/0.852	
13	3988	9.4651	1/1.000	1/1.000	1/1.000	1/1.000	1/1.000	1/1.000	1/1.000	1/1.000	1/1.000	1/1.000	1/1.000
			20/0.802	20/0.845	20/0.857	20/0.903	20/0.860	20/0.846	20/0.782	20/0.786	20/0.787	20/0.842	
14	2910	9.4651	1/1.000	13/0.982	1/1.000	13/0.991	2/0.767	1/1.000	1/1.000	1/1.000	1/1.000	1/1.000	1/1.000
			20/0.802		20/0.802		20/1.000	20/0.824	20/0.796	20/0.784	20/0.842	20/0.853	
15	4581	9.4672	1/1.000	1/1.000	1/1.000	1/1.000	1/1.000	1/1.000	1/1.000	2/0.056	1/1.000	1/1.000	1/1.000
			20/0.802	20/0.779	20/0.789	20/0.842	20/0.785	20/0.785	20/0.946	20/1.000	20/0.976	20/0.865	

■ Figure 24

Feed fuel burnable poison types and fraction loadings in zones for PWR determined by mathematical optimization

times target lattice reactivity versus burnup is given as a constraint with the objective of minimizing the cost of enriched material in the lattice. Sometimes the local peaking factor is either imposed as an objective to be minimized or as a constraint. Clearly, the target lattice reactivity must be dependent upon where this lattice is located throughout the core. Likewise, the local peaking factor cannot be considered in isolation of what the lattice average powers are for all the locations of this lattice throughout the core. But the lattice locations throughout the core are determined by the loading pattern, and the associated lattice average powers are also dependent upon the CRP for a BWR. To address this coupling, one could consider iterating between the lattice optimization and loading pattern optimization, but when done in this loose fashion robustness of the optimization becomes questionable.

Some progress has been made on coupling the lattice and assembly optimization with the core's response to lattice designs (Jessee and Kropaczek 2005). In this work done for a BWR, it is assumed that the core loading pattern and CRP are fixed, and that there is a limited number of fuel pins characterized by fuel enrichment and Gadolinia w/o as a function of axial position. The decision variable is the radial positions of the candidate fuel pins within the feed fuel assemblies for a specified number of fuel assembly designs, which equates to the number of batches in a region assuming that irradiation history is not also used as a discriminator to define a batch. In BWR lingo, each feed fuel assembly design refers to a stream, so if N feed fuel assembly designs

BATCH / CYCLE SCHEMATIC FOR HISTORY # 2954

BATCH #	CYCLE NUMBER															
	1	2	3	4	5	6	7	8	9	10	11	12	13	14	15	16
1A	23	23	23	-	-	-	-	-	-	-	-	-	-	-	-	-
1B	64	64	64	-	-	-	-	-	-	-	-	-	-	-	-	-
1C	1	1	1	-	-	-	-	-	-	-	-	-	-	-	-	-
2A	-	19	19	-	-	-	-	-	-	-	-	-	-	-	-	-
2B	-	5	5	5	-	-	-	-	-	-	-	-	-	-	-	-
2C	-	64	64	64	-	-	-	-	-	-	-	-	-	-	-	-
3A	-	-	19	19	-	-	-	-	-	-	-	-	-	-	-	-
3B	-	-	5	5	5	-	-	-	-	-	-	-	-	-	-	-
3C	-	-	64	64	64	-	-	-	-	-	-	-	-	-	-	-
4A	-	-	-	15	15	-	-	-	-	-	-	-	-	-	-	-
4B	-	-	-	68	68	68	-	-	-	-	-	-	-	-	-	-
4C	-	-	-	1	1	1	-	-	-	-	-	-	-	-	-	-
5A	-	-	-	-	23	23	-	-	-	-	-	-	-	-	-	-
5B	-	-	-	-	64	64	64	-	-	-	-	-	-	-	-	-
5C	-	-	-	-	1	1	1	1	-	-	-	-	-	-	-	-
6A	-	-	-	-	-	20	20	-	-	-	-	-	-	-	-	-
6B	-	-	-	-	-	64	64	64	-	-	-	-	-	-	-	-
7A	-	-	-	-	-	-	23	23	-	-	-	-	-	-	-	-
7B	-	-	-	-	-	-	64	64	64	-	-	-	-	-	-	-
7C	-	-	-	-	-	-	5	5	5	5	-	-	-	-	-	-
8A	-	-	-	-	-	-	-	24	24	-	-	-	-	-	-	-
8B	-	-	-	-	-	-	-	60	60	60	-	-	-	-	-	-
9A	-	-	-	-	-	-	-	-	19	19	-	-	-	-	-	-
9B	-	-	-	-	-	-	-	-	68	68	68	-	-	-	-	-
9C	-	-	-	-	-	-	-	-	1	1	1	-	-	-	-	-
10A	-	-	-	-	-	-	-	-	-	19	19	-	-	-	-	-
10B	-	-	-	-	-	-	-	-	-	68	68	68	-	-	-	-
10C	-	-	-	-	-	-	-	-	-	1	1	1	-	-	-	-
11A	-	-	-	-	-	-	-	-	-	-	19	19	-	-	-	-
11B	-	-	-	-	-	-	-	-	-	-	64	64	64	-	-	-
11C	-	-	-	-	-	-	-	-	-	-	1	1	1	-	-	-
12A	-	-	-	-	-	-	-	-	-	-	-	23	23	-	-	-
12B	-	-	-	-	-	-	-	-	-	-	-	64	64	64	-	-
12C	-	-	-	-	-	-	-	-	-	-	-	1	1	1	-	-
13A	-	-	-	-	-	-	-	-	-	-	-	-	23	23	-	-
13B	-	-	-	-	-	-	-	-	-	-	-	-	64	64	64	-
13C	-	-	-	-	-	-	-	-	-	-	-	-	1	1	1	-

Figure 25

Cycling scheme for lowest fuel cycle cost scheme for PWR determined by mathematical optimization

were specified to be utilized, an N-streaming core design would occur. In addition to imposing the number of streams as a constraint, the maximum number of different pin-type designs that can be utilized in a single stream and also for all streams from the candidate pin-type designs can be imposed as constraints. Since fuel manufacturing cost is increased by using more pin types, this constraint attempts to control fuel manufacturing cost. Using SA perturbations are made of the current fuel pin layout using the fuel-type pin designs provided for each stream of feed assemblies. The resulting lattices are analyzed using a linear superposition approach to reduce computational effort, with linearization recompleted at some frequency about the current optimized lattice designs. The results of the lattice analysis, i.e., homogenized few-group cross-sections, local pin power distribution, and F-factors used in CHF analysis, are then provided to the 3D core simulator to evaluate the objective function, i.e., minimization of feed fuel cost, and constraints on the core, e.g., cycle energy requirement, CSM, and thermal limits.

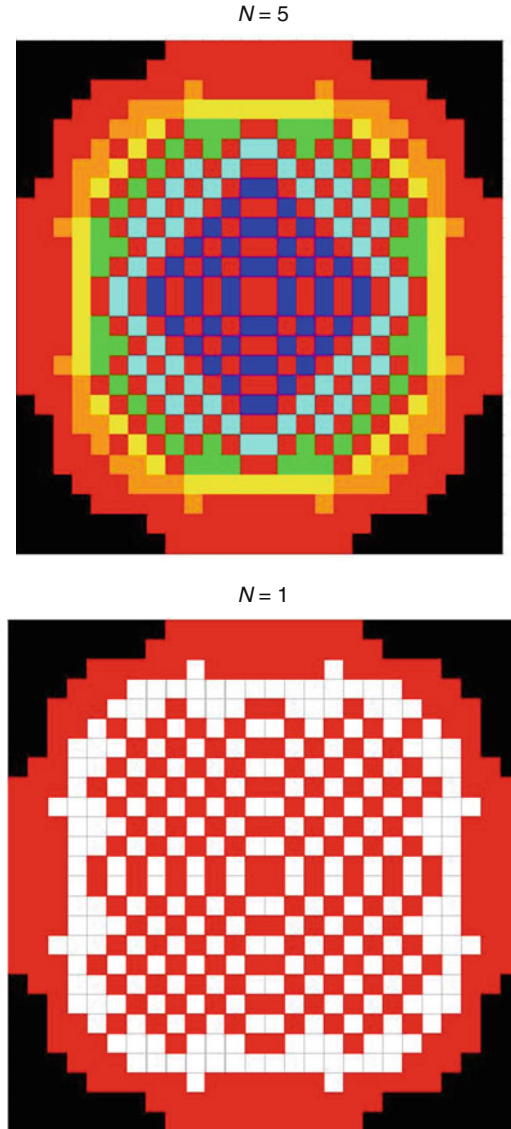


Figure 26

Core loading pattern for $N = 1$ and $N = 5$ streaming using mathematical optimization for a BWR

In addition, constraints on pin-type placement based on experience can be imposed, which are treated as hard constraints and limit the pin configurations that need to be considered.

► Figure 26 shows the loading patterns that are found when using $N = 1$ and $N = 5$ fresh fuel assembly types, where both loading patterns satisfying all constraints imposed but fuel cycle cost savings of about \$1 million for a cycle result for $N = 5$ over $N = 1$ due to a reduction of four fresh fuel assemblies.

Work has also been completed on BWR assembly optimization using mathematical optimization (Martin-del-Campo et al. 2002). Here again the lack of significantly tight coupling with the other design decisions that must be made likely compromises the quality of the overall optimum decision making.

The most work on using mathematical optimization in support of making fuel management decisions has been in making loading pattern decisions. SA, GAs, evolutionary algorithms, linear programming, steepest descent, and other methods have been historically utilized to complete the mathematical optimization. Here the SA and GAs approaches will be discussed. In particular, results for the FORMOSA-P (Kropaczek and Turinsky 1991; Maldonado and Turinsky 1995), a PWR loading pattern optimization code, and FORMOSA-B (Moore et al. 1998; Karve and Turinsky 1999; Karve and Turinsky 2001), a BWR loading pattern and CRP optimization code, will be presented.

FORMOSA-P can complete single- or multi-objective optimization selecting from the following objectives:

- 1 Minimize feed fuel enrichment (including split feed enrichments)
- 2 Maximize EOC core reactivity
- 3 Minimize radial peaking factor
- 4 Maximize region average discharge burnup
- 5 Minimize reactor vessel fluence

The decision variables optimized include:

- 1 Location of fuel assemblies
- 2 Rotation of fuel assemblies
- 3 Burnable poison loading in each fresh fuel assembly (type and quantity)
- 4 Partially burned fuel assemblies to reinsert
- 5 Feed fuel enrichment (if not fixed)

The decision variable for the core loading pattern is described mathematically by the binary values of $X_{l,m,n,o}$, where,

$$X_{l,m,n,o} = \begin{cases} 1 & \text{if fuel assembly of shade } m \text{ burnable poison type } n, \text{ and orientation } o \\ & \text{is located in core location } l \\ 0 & \text{otherwise} \end{cases}$$

where shade refers to a fuel assembly of the same feed enrichment and BOC burnup distribution. For example, if all the feed fuel assemblies were identical they would form a single shade, and if quarter core symmetry was applicable groups of four shuffled fuel assemblies would form shades.

The optimization is completed with the ability to impose the following constraints:

- 1 Discharge burnup limits: node, pin, assembly, and region averages
- 2 Radial power peaking factor (multi-rodged and unrodged configurations)
- 3 Target EOC critical soluble boron concentration for specified cycle energy production
- 4 Maximum soluble boron
- 5 Maximum moderator temperature coefficient at 0%, 50%, and 100% of rated power
- 6 Axial offset anomaly criteria

- 7 Maximum feed enrichment
- 8 Maximum number of burnable poison types to utilize
- 9 Maximum number of discrete burnable poison rods (if applicable)
- 10 Maximum reactor vessel fluence
- 11 Minimum excore detector response
- 12 Octant power tilt
- 13 Octant orientation mix
- 14 Region/batch maximum and minimum power sharing
- 15 Fuel assembly core placement and rotation restrictions
- 16 Fuel assembly position freeze constraint
- 17 Fresh fuel assembly burnable loading restrictions

The FORMOSA-P code major modules consist of an economic model, neutronics models, and optimization engine. The economic model evaluates the overnight feed fuel cost. The neutronics models consist of several different models of different fidelity and computational burden, allowing the user to select which model or combination of models are to be utilized. The neutronics models available are the following:

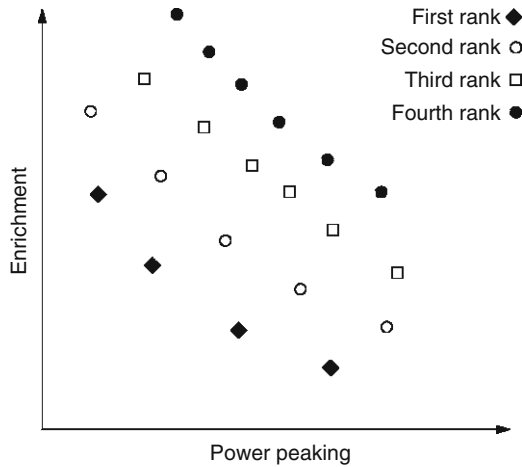
- Built-in modern nodal core simulator with the following capabilities: Cartesian or hexagonal geometries, microscopic or macroscopic cross-section models, thermal-hydraulic and transient fission product treatments, 3D to 2D consistent geometry collapse models (Keller and Turinsky 2001), generalized perturbation theory capability to reduce CPU time, and pin reconstruction with surface spectral history model.
- Nuclear design core simulator via MPI linkage, with capability to execute on multi-processor or networked computers.

Several optimization engines have been developed for FORMOSA-P that a user can select from:

- Single- or multi-objective, adaptive SA with soft constraints and early rejection (Engrand 1997)
- Single- or multi-objective GA with soft constraints (Keller 2001)

Note that multi-objective optimization capability has been included. The implementation utilizes true multi-objective optimization rather than an approach that forms a single objective from a sum of weighted objectives. This later approach causes the optimum family of solutions found to be dependent upon the weights selected, but how to select the values of the weights lacks a mathematical basis. By true multi-objective optimization is implied that the values of the decision variables that define the Pareto surface, which can be thought of as a trade-off surface of several objectives, are determined. It is easiest to describe this considering just two objectives. Given a value of Objectives A, one seeks to determine the minimum value of Objective B. By continuously changing the specific value of Objective A and determining the minimum value of Objective B, the Pareto surface is determined. This could be done by multiple single objective optimizations treating Objective A value as a constraint. Alternatively and with enhanced computational efficiency this can be done using the following multi-objective mathematical optimization approach, which requires the creation of a nondominated archive of solutions. Given N objectives, a solution X is said to be dominated by solution Y if

$$f^{(i)}(Y) < f^{(i)}(X) \quad \forall i = 1, N \quad (30)$$



■ **Figure 27**
Display of nondominated solutions when there are two objective functions

i.e., if solution Y is superior for all objectives. This is pictorially shown in [Fig. 27](#) for two objective functions. If a candidate solution dominates any solutions in the archives, then those solutions are removed from the archive, and the new solution is added. If the new solution is dominated by any solution in the archive, then the candidate solution is not archived. If the candidate solution neither dominates nor is dominated by any member of the archive, it is added to the archive.

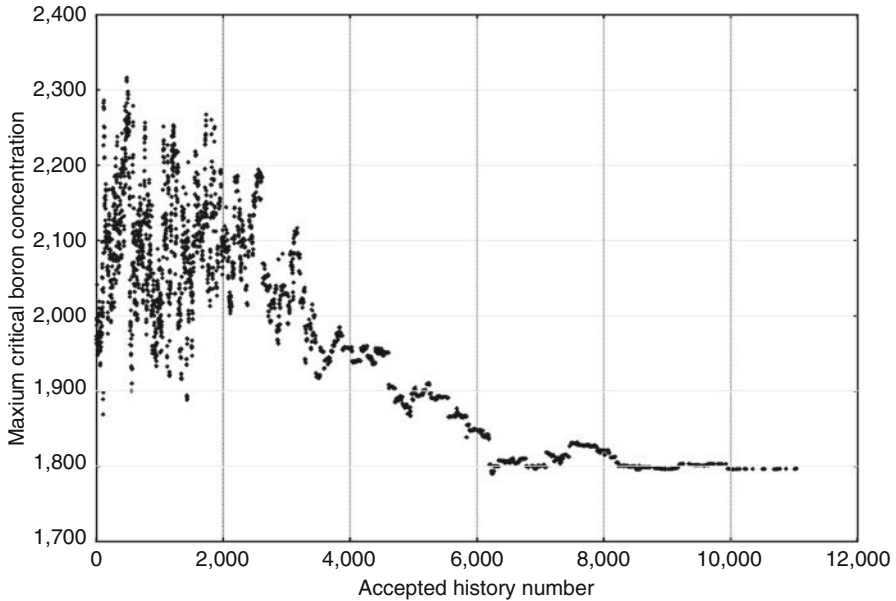
In the Multi-Objective SA (MOSA) approach (Engrand 1997), a perturbed loading pattern is tested for possible inclusion into the nondominated archive before the simulated annealing acceptance test is performed. If a perturbed loading pattern solution is archived, then it is automatically accepted by SA as the new current loading pattern solution. For loading pattern solutions, which are not added to the nondominated archive, and thus accepted at the nondominated archiving stage, then, the loading pattern is accepted with a probability p given by

$$p = \prod_{i=1}^N e^{-(f_p^{(i)} - f_c^{(i)})/T_n} = e^{-\sum_{i=1}^N (f_p^{(i)} - f_c^{(i)})/T_n} \quad (31)$$

The implementation of Multi-Objective GA (MOGA) is much simpler because the concept of an archive already exists, that being the population of a generation (Parks 1996).

FORMOSA-P also has the capability to complete multicycle optimization, but this is done by optimizing each cycle's loading pattern without consideration of the other cycles, hence does not possess the capability to perform true multicycle optimization. It also lacks the capability to determine the optimum equilibrium cycle, which exists in other codes (Quist et al. 1999).

► [Figure 28](#) shows the behavior of the true objective function values and constraints as a single objective SA optimization progresses. This optimization was completed with the objective of maximizing the critical boron at the end of cycle. Note how the augmented objective function value can climb out of local minima due to the higher annealing temperatures early in the search. Constraint limits are removed at some point and the optimization search than



■ Figure 28

Objective function value versus history number for a single objective PWR loading pattern optimization

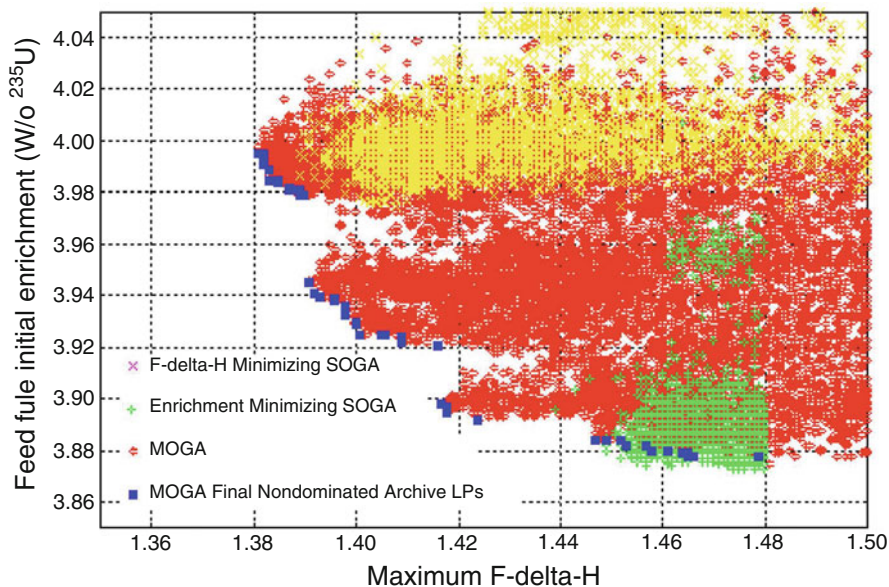
focuses on decreasing the true objective function value. This is because of how the constraint penalty functions increase in magnitude as the search progresses.

➤ [Figure 29](#) shows the results of a multi-objective optimization utilizing MOGA. Two objectives are being traded-off against each other, those being enrichment and radial peaking factor. As expected, as the radial peaking factor assumes large values, more freedom in selecting the loading pattern is taken advantage of in decreasing the feed enrichment.

Presented in ➤ [Table 6](#) are the standard deviations and other metrics of robustness of three optimization methods: MOSA, Single Objective SA (SOSA), and Single Objective GA (SOGA). The objectives are minimization of radial power peaking and minimization of feed enrichment. These metrics were obtained by rerunning FORMOSA-P a number of times, changing the random number seed, which results in a different optimization path to the vicinity of the global minima.

FORMOSA-B shares many of the features of FORMOSA-P, differing in the unique features of BWR versus PWR loading pattern determination and the need to determine the CRP coincident with the loading pattern. FORMOSA-B can complete single objective optimization by selecting from the following objectives:

1. Minimize total reload cost (i.e., overnight fresh fuel loading cost)
2. Maximize plant cycle length for fixed fresh fuel inventory (either maximization of EOC core reactivity or minimization of EOC critical flow)
3. Minimize the Maximum Linear Heat Generation Rate (MLHGR)
4. Maximize region average discharge burnup



■ Figure 29

Objective function values as search progresses for a dual-objective PWR loading pattern optimization

The decision variables optimized include:

1. Location of fuel assemblies
2. Fresh assembly types to load from palette of fresh assembly design types, including burnable poison configurations
3. Partially burned fuel assemblies to reinsert
4. Control rod program

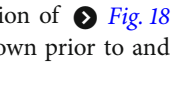
The optimization is completed with the ability to impose the following constraints:

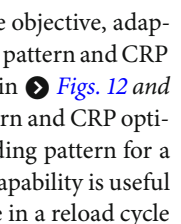
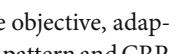
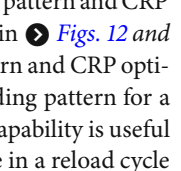
1. Fuel assembly placement restrictions associated with conventional or control cell cores
2. Maximum hot excess reactivity
3. Minimum and maximum core flows versus cycle burnup
4. Discharge burnup limits: node, pin, assembly, and region averages
5. Peak Linear Heat Generation Rate (MLHGR)
6. Maximum Average Planar Linear Heat Generation Rate (MAPLHGR)
7. Core Thermal Margin to Boiling Transition (MCPR)
8. Cold Shutdown Margin
9. Target core reactivity versus cycle burnup
10. Maximum number of fresh fuel assembly types to utilize
11. Octant power tilt
12. Fuel assembly core placement restrictions
13. Fuel assembly position freeze constraint

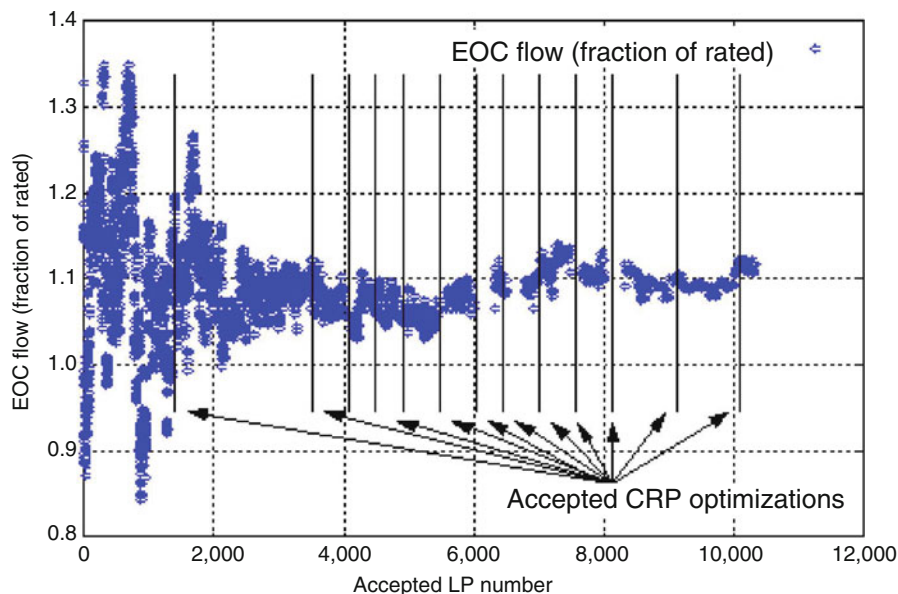
■ **Table 6**
Comparison of optimization performance of different methods

Attribute	MOGA	SOGA	SOSA
Mean Lowest Radial Peaking Factor	1.381	1.396	1.391
Standard Deviation of Mean Lowest Radial Peaking Factor	0.007	0.018	0.008
Lowest Radial Peaking Factor for all optimizations	1.371	1.377	1.383
Mean Enrichment at Minimum Radial Peaking Factor	3.97	4.06	4.06
Standard Deviation of Mean Enrichment at Minimum Radial Peaking Factor	0.03	0.13	0.13
Mean Number of Loading Patterns Evaluated	45,300	24,717	25,592

14. Numerous heuristic rules associated with Control Rod Programming, e.g., exchange sequence, exchange frequency, deep and shallow allowed notch position ranges, and fixed full insertions (to shadow leakers), and associated restrictions on fuel assembly placement, e.g., Conventional and Control Cell Cores.

The FORMOSA-B code major modules consist of an economic model, neutronics models, and optimization engine. The economic model evaluates the overnight feed fuel cost. The neutronics model has the following features: 3D Cartesian geometry, microscopic or macroscopic cross-section models, two-phase thermal-hydraulic using drift flux model with by-pass flow and flow redistribution (with capability to insert proprietary constituents relationships, e.g., GEXL correlation), transient fission product treatment, 3D sub-core collapse model for CSDM evaluations, pin-wise reconstruction, and adaptive core simulator (Jessee et al. 2009) to enhance agreement with design basis core simulators as may be necessary. Note that the adaptive core simulator feature is important if using a core simulator during the optimization search that is not the design simulator. This follows since if these two simulators differ in their prediction of core attributes used to evaluate the objective function or constraints, it is likely that when the family of near optimum loading patterns and CRP pairings are reevaluated using the design simulator, some constraint violations could be predicted rendering the optimization not useful. Clearly, the best approach is to utilize the design simulator during the optimization if the computational burden can be tolerated. The other usage of adaptive simulation is to adapt the core simulator to reduce the uncertainties in the cross-section, which is displayed in the upper portion of  where the relative power uncertainty due to cross-section uncertainty is shown prior to and after adaptation.

The optimization engine developed for FORMOSA-B is based upon single objective, adaptive SA with soft constraints and early rejection. Results for a combined loading pattern and CRP optimization are presented in . Note that the CRPs presented earlier in  and  were generated using FORMOSA-B also in a combined loading pattern and CRP optimization. Needless to say, FORMOSA-B has the capability to optimize a loading pattern for a specified CRP or to optimize a CRP for a specified loading pattern. This later capability is useful for an operating BWR core, where the actual CRP used up to the current time in a reload cycle



■ Figure 30

Objective function value versus history number for a single objection BWR loading pattern and control rod pattern optimization

differs from the optimized CRP. In this case, one would want to reoptimize the CRP over the rest of the cycle.


3.6 Computational Design Sequences

This section discusses the design calculations needed to complete nuclear fuel management, and the methods employed to accomplish this. The discussion of the methods employed will be limited since other chapters in this handbook present in detail the methodologies.

3.6.1 Design Calculations Needed

From the presentation so far it is apparent that one must establish a core simulator model, deplete this model over the cycle, and perform branch calculations at various burnup steps to access whether the constraints placed on the core are being satisfied. ➤ Section 3.5 presents the out-of-core constraints for a PWR that are imposed in the OCEON-P code, the in-core constraints for a PWR that are imposed in the FORMOSA-P code, and the in-core constraints for a BWR that are imposed in the FORMOSA-B code. With the exception of the CSM constraint for a BWR, all these constraints are imposed within the normal power operating range. In addition to these constraints, there are numerous other constraints that originate due to safety limits. Many times these constraints can be expressed in terms of limits on point kinetic parameters,

power peaking factors, and control rod worths under normal or abnormal conditions. An example of such constraints is the Doppler temperature coefficient under normal, ejected control rod, and $N-1$ control rod, i.e., all control rods inserted except highest worth rod stuck out, conditions, for fuel temperatures and coolant densities that span the normal operating range and beyond. Other examples are the power peaking factor for an ejected control rod condition, and the control rod ejected rod worth. Such constraints originate because the associated constraint values are utilized in safety analysis where system transient codes are employed to assess nuclear safety. In the past it was common to utilize a point kinetics model to represent the neutronics behavior, i.e., core nuclear power, as a function of time. This capability has evolved to utilize 1D axial models of the core's neutronics behavior, and further to utilize 3D models of the core's neutronics behavior. In doing so, the simple approach of imposing constraints on core characteristics that could be represented by point kinetic parameters, power peaking factors, and control rod worths has become more challenging to utilize because how does one do bounding calculations where these characteristics are set to their limits within the context of using a 1D or 3D core simulator. Many times, technical specifications and startup acceptance test criteria relate to these core characteristics, so it is difficult to move beyond using them as constraints. Further, from a computational burden viewpoint, one does not wish to repeat all the safety analyses for every reload core, which would become more necessary if a core model is utilized that could not be characterized by bounding values.

The sequence of calculations required to complete a reload core analysis is presented in  **Fig. 31**. It starts with utilizing an evaluated nuclear data library such as ENDF/B, JEDL, or JEF. That library is processed to produce a many energy-group cross-section set and some characterization of resonances by codes such as NJOY (McFarlane et al. 1982), AMPX (Greene et al. 1976), or proprietary buffer codes associated with a specific lattice physics code. The many energy-group cross-sections are based upon an assumed flux energy spectrum, e.g., LWR spectrum, with the dependence of the many-group cross-sections on the spectrum assumed decreasing as more energy groups are utilized. In the case of the scattering kernel in the thermal energy range when considering a thermal reactor, it will be generated at several moderator temperatures. Representation of resonance effects has been done in terms of infinitely dilute resonance integrals or resonance probability tables using the many-group structure given as a function of temperature. The specific representation is dependent upon how resonances will be treated in the lattice physics code that the many-group library is being prepared for. Numerous lattice physics calculations are then completed to determine few-group, spatially homogenized cross-sections. Clearly, spatial homogenization does remove details that will need to be recaptured, e.g., pin powers, but it does have the benefit of making the diffusion theory assumption used at the core simulator level more appropriate since strong heterogeneities, e.g., burnable poison rods, have been minimized. Finally, core simulator calculations are completed to evaluate the core's characteristics, normally based upon a few-group neutron diffusion theory model. The following sections provide more details for the lattice physics and core simulator calculations required.

3.6.2 Cross-Section Generation

The goal of lattice physics calculations is to generate the few-group, spatially homogenized cross-sections that are utilized as input to the core simulator. Elsewhere in this handbook is

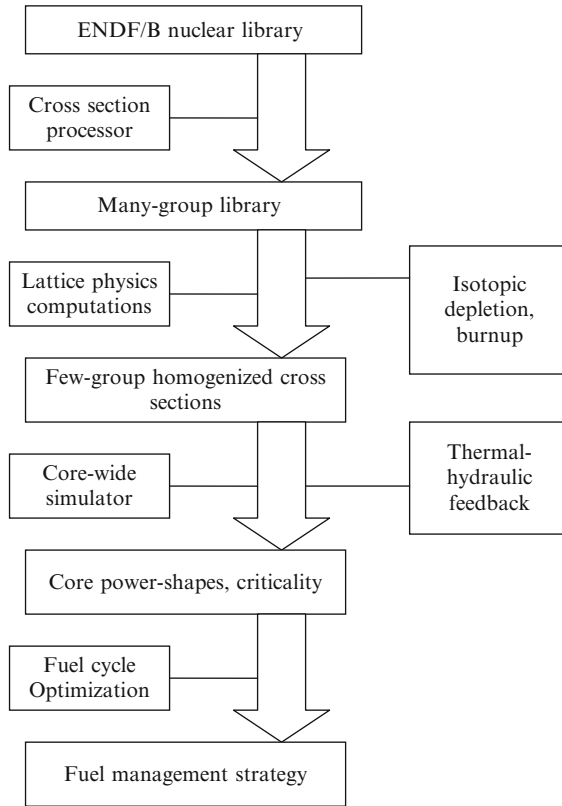


Figure 31
Sequence of calculations required to complete a reload core analysis

presented in detail the methodologies utilized by lattice physics codes. There are a number of assumptions that are generally made in addition to those associated with the numerical solution approach. Some of the key assumptions are:

- Zero current boundary condition used on lattice boundaries
- Two-dimensional radial geometry
- Isotropic or linear anisotropic scattering
- Resonance treatment assumptions, e.g., multiple isotopes additive contributions to resonance self-shielding
- Uniform thermal conditions, i.e., uniform fuel temperature, cladding temperature, and coolant temperature and density.

The validity of these and other assumptions are dependent on the application at hand. For example, the zero current boundary condition assumption appears to work well for LWRs loaded with LEU assemblies for the normal operating range, but mixed LEU-MOX assembly cores require further treatment to minimize the errors introduced by this assumption.

The number of energy groups used and range of spatial homogenization are dependent upon the core type being analyzed. LWRs and HWRs typically utilize two energy groups, thermal gas-cooled reactors may add one or two epithermal groups due to weaker moderation, and finally fast reactors may be using a dozen or more groups. Clearly, fidelity required will influence the number of groups selected to be used. Spatial homogenization for PWRs and BWRs are typically 2×2 and 1×1 , respectively, meshing per lattice when using a nodal method for the core simulator. If a finite difference method is used by the core simulator, which is not common for LWRs, a unit cell mesh would likely be used. Because the unit cell meshing retains strong heterogeneities, which compromises diffusion theory, transport corrected cross-sections would need to be determined and utilized by a diffusion theory-based core simulator. Spatial homogenization across the lattice is typical for fast spectrum cores.

What specific lattice cases need to be executed depends on the core simulator's need and range of applications that the core simulator will have to address, e.g., CZP conditions. Some core simulators utilize a macroscopic cross-section model, i.e., only complete depletion calculations for a limited number of isotopes such as those associated with the transient fission products and burnable poisons, where others utilize a microscopic cross-section model, i.e., complete depletion calculations for the fissile, fertile, selected fission products, and lumped fission products isotopes in addition to those treated by the macroscopic model. The usage of a macroscopic cross-section model could influence the number of history depletion cases that need to be executed. History depletion cases attempt to capture the effects of fuel temperature, coolant temperature and density, control rod insertion, and for PWRs soluble boron concentration, variations throughout the cycle on the isotopic number densities, which originate due to their impact on the neutron energy spectrum. For each history depletion case, there is a need to execute instantaneous branch cases at various burnup points. The instantaneous branch cases utilize fixed isotopic number densities except for the ones that are instantaneously changed. Needless to say, the history and instantaneous branch cases need to be executed for every lattice type, so require a large number of lattice physics calculations. The following are examples of typical cases that may need to be executed for an LWR.

History cases

- Nominal conditions, unrodded depletion
- Nominal conditions, rodded depletion
- Off nominal spectral cases, e.g., coolant density or soluble boron concentration, unrodded depletion
- Off nominal fuel temperature, unrodded depletion

Instantaneous branches cases

- Fuel temperature
- Coolant density (void for BWR and temperature for PWR)
- Rodded to unrodded or unrodded to rodded
- Discrete burnable poison rod pull
- Cold conditions
- Soluble boron for a PWR

The resulting few-group, spatially homogenized cross-sections, whether macroscopic or microscopic, are then characterized in some fashion in terms of history depletion and instantaneous

conditions, e.g., dependence on fuel temperature characterized as square root of absolute fuel temperature. This characterization is either done inside or outside the core simulator. If done inside the core simulator, so-called table sets are prepared from the lattice physics code output and provided as core simulator input. If done outside the core simulator, various fitting coefficients are prepared from the lattice physics code output and provided as core simulator input. In doing this a reference condition for the cross-sections is defined from which corrections to their values for changes in the reference condition are subsequently applied by the cross-section characterization. A typical reference condition would be HFP thermal conditions (fuel temperature, coolant density and temperature), no transient fission products, unrodded state, and for a PWR soluble boron-free.

Clearly given the volume of history depletion and instantaneous branch cases required, this sequence of lattice physics code executions tends to be automated. At the risk of leaving out the reader's favorite lattice physics code, LWR lattice physics codes used commonly today include the following: PARAGON (Ouisloumen et al. 2001), LANCER (Knott et al. 2002), CASMO (Edenius et al. 1995), HELIOS (Casal et al. 1991), APOLLO (Hoffman 1971), WIMS (Halsall 1996), and TRITON (Dehart et al. 2007). For fast spectrum reactors, MC² (Toppel et al. 1967) and APOLLO are examples of applicable lattice physics codes. Needless to say, a Monte Carlo code can serve as a lattice physics code, but given the computational burden per case and the number of cases that need to be run, this approach is rarely utilized in a production environment.

In addition to determining the few-group, spatially homogenized cross-sections, for core simulators based upon a nodal method, discontinuity factors are also determined by the lattice physics code and characterized in some fashion utilizing the history depletion and instantaneous branch cases results. Recall that the discontinuity factors are introduced to correct the spatial homogenization error introduced into the neutron leakage term. When considering the fuel-reflector interface, the discontinuity factors are also correcting the diffusion theory introduced error into the neutron leakage term. Any degree of spatial homogenization beyond the unit cell span implies that pin-wise attributes, such as power and burnup, are no longer available. Since such information is required to evaluate fuel pin and pellet power, burnup, and clad fluence limits, pin reconstruction methods have been developed to be utilized with the information that is available from a coarser mesh core simulator model, typical when using a nodal method. These pin reconstruction methods either utilize the pin-by-pin flux or power predicted by the lattice physics code, combined mathematically with the intra-nodal flux or power available from the coarser mesh core simulator model. Again this pin-by-pin information, referred to as form factors, is characterized in some manner based upon the history depletion and instantaneous branch cases and used by the core simulator. Corner point discontinuity factors may be required in the pin reconstruction to obtain the intra-nodal flux or power. Depending upon the core simulator, other information determined by the lattice physics code will need to be characterized using the history depletion and instantaneous branch cases.

3.6.3 Core Simulation

Core simulation is required to determine whether the values selected for fuel management decision variables, e.g., feed enrichment and loading pattern, minimize/maximize the objectives while satisfying normal operating and safety constraints. In addition, core simulation is required to validate the core simulator utilizing normal operating data and special tests, e.g.,

zero power startup physics tests, and as an aide to the reactor operating staff. Few-group diffusion theory is widely employed to analyze thermal, epithermal, and fast reactor cores. This is due to the computational efficiency of this method and what is considered acceptable fidelity. To minimize modeling-introduced errors, discrete solution of the transport equation or some higher-order approximation to it, e.g., SPN or quasi-diffusion theory, and Monte Carlo may be utilized. The overall benefits so derived in increased fidelity need to be judged in its totality since it may be that cross-section uncertainties dominate the overall uncertainty in a core simulation. Note when utilizing a continuous energy Monte Carlo model or very large number of groups in a many-group transport equation model (or lower order approximation of), with a fine spatial mesh there is no longer a need for lattice physics calculations.

In addition to cross-section and geometry input, core simulators require isotopic and thermal-hydraulic data to be input. For feed fuel, the isotopic data can be passed from the lattice physics code since it is needed to be input to this code. It may be based upon design values, or if the fuel has been fabricated as built values. For the shuffled fuel, the isotopic data is obtained from the previous cycles' core simulations sometimes adjusted to better agree with in-core detector readings. For production quality core simulators, they will have the ability to simulate the fuel shuffle in order to facilitate establishment of the core simulator model for the upcoming reload core. Within the core simulator or coupled to it will be a depletion model that will calculate the isotopics as a function of core lifetime. The capabilities required of the depletion model will be dependent upon whether a macroscopic or microscopic cross-section approach is being utilized. In either instance some form of history depletion model will be needed to utilize the characterized lattice physics produced cross-sections.

For the thermal-hydraulic input data, what are required is dependent upon the thermal-hydraulic model used within or coupled to the core simulator. In many cases a simplified thermal-hydraulic model is utilized since one is mainly interested in using the results of the thermal-hydraulic model to correct cross-sections for thermal-hydraulic feedback, which would have lower fidelity requirements than evaluating whether a thermal limit has been violated. Further, the range of thermal-hydraulic conditions that the core simulator will be utilized to evaluate may be more limiting than those conditions spanned by a complete safety analysis, e.g., core is subcritical during an LOCA. Common to all core types, fuel temperature input to the core simulator for steady-state calculations may consist of tables or functional fits of fuel temperature as a function of power density and burnup for a fixed coolant temperature. The information to provide this input will come from a separate fuel thermal-mechanical code. For transient analysis, more data must be provided as input, such as cladding and fuel thermal conductivity as a function of temperature and burnup, and a gap closure model. Again an external fuel thermal-mechanical model will be used to provide such data. For the hydraulic model, for PWRs it is common to utilize a closed channel, Homogenous Equilibrium Mixture (HEM) model for normal operating conditions. For a BWR, again a closed channel, now accurate if radial meshing is 1×1 for the lattice due to presence of the BWR channel, in conjunction with a drift flux model to capture slip, would be commonly used in core simulators. In addition, by-pass flow and inlet flow redistribution models would be utilized, and a Dryout correlation incorporated to predict the critical power ratio (CPR). Under accident conditions when needed, coupling of the core simulator to a subchannel hydraulic code, such as COBRA (Stewart et al. 1977) or VIPRE (Stewart et al. 1989), has been utilized to more accurately represent the thermal-hydraulic feedback on the cross-sections.

The core simulator cases that must be executed are numerous, as indicated by the following list of intended applications that core simulations must support.

1. Determination of loading pattern, feed enrichments, and for BWRs CRP
2. Determination of core attributes over normal operating range, e.g., power distribution, burnup distribution, reactivity coefficients, transient fission product worths, control rod worths, for PWRs soluble boron worths, and point kinetic parameters
3. Determination of core attributes for safety analysis done by point kinetics via providing point kinetic parameter values outside normal operating range and for unique rodged conditions, e.g., ejected rod, dropped rod, and stuck rod, along with determination of associated power peaking factors and rod worths
4. Three-dimensional core simulation within or coupled to a system transient code for analysis of selected accidents
5. Data to interpret zero power reactor physics and other testing
6. Data to interpret in-core and excore detector readings

Applications 2, 3, and 4 are required to be completed to various degrees to complete Application 1 since they are involved in evaluating whether constraints have been satisfied. What is obvious from the above list of applications is that to complete a first or reload core design, a substantial number of core simulations must be completed. For LWRs where there are numerous reload cores that must be analyzed, in practice automation has been implemented to minimize both the calendar time and core nuclear designer time to complete these simulations. The compression of calendar time is not only beneficial from a cost viewpoint, but also minimizes the uncertainty that the currently operating reload cycle will not operate as assumed in the upcoming reload core design and analysis. Do note that it is a common practice in LWR reload core design to design for a “burnup window” of several weeks shorter or longer than the planned EOC to accommodate this uncertainty.

4 Conclusions

This section presents conclusions regarding the current state of depletion and nuclear fuel management capabilities, and where further enhancements are required to increase capabilities in these areas.

Isotopic depletion modeling capability is well developed. Its major limitation originates not so much from the mathematical limitations of solving the Bateman equation, but from the quality of the input data provided. Nuclear data for certain isotopes and reaction types are not sufficiently accurate to support the needs of nuclear fuel management, particularly for some advanced nuclear systems under consideration, e.g., ARR. As more advanced physics-based models of core materials performance are developed and utilized, very fine spatial and time detail of the isotopic concentrations will be needed. This will produce a heavy computational burden on modeling isotopic depletion. Fortunately, since the spatial component of solving the Bateman equation lends itself to parallel processing, utilization of multi-processor multi-core architectures should be able to address the enhanced computational burden.

Nuclear fuel management practices are very well established for nuclear power plant types that have enjoyed wide deployment, such as PWRs, BWRs, and HWRs. For nuclear power plant types not yet widely deployed, there is considerable opportunity to consider more creative nuclear fuel management practices. VHTRs, whether PBR or PRISMATIC, involve three-dimensional fuel movement, so offer another degree of freedom in in-core nuclear fuel

management. ARRs involve the complexity of feed material of variable elemental and isotopic composition, which can be viewed as a design complexity but offers opportunity due to the increased number of decision variables. For current LWRs and HWRs that elect to employ slightly enriched uranium, nuclear fuel management optimization using mathematical optimization has advanced greatly but still has not addressed the entirely coupled, i.e., out-of-core and in-core, nuclear fuel management problem. The grand challenge for nuclear fuel management optimization remains to address the lattice–assembly–core coupled problem over the multiple cycles in the planning horizon. For closed fuel cycles, one can add additional decisions associated with what elements to recycle, in what quantity, and how to physically introduce them into the core, e.g., heterogeneous or homogenous.

Concerning methods, by the introduction of sufficient margin nuclear fuel management decisions for nearly any nuclear power plant type can be implemented. However, the introduction of margin implies a higher cost, so the focus on methods development in support of nuclear fuel management has been to reduce the uncertainty in predicted core attribute values of importance. This involves not only the methods introduced uncertainties, but also all the other sources of uncertainties, e.g., manufacturing and nuclear data. Here the further development of adaptive simulation capability may play an important role complementary to refinement of models and numerical methods. Also since nuclear fuel management involves multiphysics modeling, e.g., radiation transport, thermal-hydraulics, depletion, and material behavior, a need to understand how all these physics pieces contribute to quantifying uncertainty and approaches to minimizing uncertainty need to be developed.

References

- Anderson KA, Turinsky PJ, Keller PM (2007) Improvement of OCEON-P Optimization Capabilities. *Trans Am Nucl Soc* (96):201–202
- Bell MJ (1973) ORIGEN: the ORNL Isotope Generation and Depletion Code. Oak Ridge National Lab, Oak Ridge, doi:10.2172/4480214
- Beard CL (1978) FLAC, Unpublished Master of Science Thesis, Massachusetts Institute of Technology, Cambridge
- Casal JJ, Stamm'ler RJJ, Villarino E, Ferri A, (1991). "HELIOS: Geometric Capabilities of a New Fuel Assembly Program," *Proc. Int. Topl. Mtg Advances in Mathematics, Computations, and Reactor Physics*, Pittsburgh
- Comes SA, Turinsky, PJ (1987). Out-of-core nuclear fuel cycle economic optimization for nonequilibrium cycles. *Nucl Tech* 83:31
- DeHart MD, Gauld IC, Williams ML (2007) High fidelity lattice physics capabilities of the SCALE code system using TRITON. *Joint International Topical Meeting on Mathematics Computation and Supercomputing in Nuclear Applications*, Monterey, pp 15–19
- Dixon B, Kim S, Shropshire D, Piet S, Matthern G, Halsey B (2008) Dynamic systems analysis report for nuclear fuel recycle. Idaho National Laboratory, doi: 10.2172/963737
- Driscoll MJ, Downar TJ and Pilat EE (1990) The linear reactivity model for nuclear fuel management. American Nuclear Society, La Grange Park
- Du S, Turinsky PJ (2008) Implementation of genetic algorithms to the out of core economic optimization PWR (OCEON-P) code. *Trans Am Nucl Soc* (99):195–196
- Edenius M, Ekberg K, Forssen BH, Knott D (1995) CASMO-4: a fuel assembly burnup program, *User's Manual, SOA-95/1*, Studsvik of America
- Engrand P (1997) A multi-objective approach based on simulated annealing and its application to nuclear fuel management. *Proceedings of 5th International Conference on Nuclear Engineering*, Nice France
- Francois JL, Martin-del-Campo C, Morales LB, Palomera MA (2005) BWR fuel lattice optimization using scatter search. *Trans Am Nucl Soc* (92):615–617
- Goldberg DE (1989) Genetic algorithms in search, optimization, and machine learning. Addison-Wesley, New York

- Greene NM, Lucius JL, Petrie LM, Ford WE III, White JE, Wright RQ (1976) AMPX: a modular code system for generating coupled multi-group neutron-gamma libraries from ENDF/B. Oak Ridge National Lab, Oak Ridge
- Halsall MJ (1996) WIMS7, an overview, Proc. Int. Conf Reactor Physics PHYSOR96 – breakthrough of nuclear energy by reactor physics, Mito, JAEIU, B-1
- Hernandez-Noyola H, Maldonado GI (2009) Added features and MPI-based parallelization of the FORMOSA-L lattice loading optimization code. Advances in Nuclear Fuel Management Fuel Management IV, Hilton Head
- Hoffman A (1971) The Code APOLLO a general description. CEA Departement des Etudes de Piles, Service de Physique Mathematique, France
- Jessee MA, Kropaczek DJ (2005) Coupled bundle-core design using fuel rod optimization for boiling water reactors. Nucl Sci Eng (155): 378–385
- Jessee M, Turinsky PJ, Abdel-Khalik H (2009) Cross-section uncertainty propagation and adjustment algorithms for BWR core simulation. Advances in Nuclear Fuel Management Fuel Management IV, Hilton Head
- Karve AA, Turinsky PJ (1999) FORMOSA-B: a boiling water reactor in-core fuel management optimization package II. Nucl Technol 131(1):48–68
- Karve AA, Turinsky PJ (2001) FORMOSA-B: a boiling water reactor in-core fuel management optimization package III. Nucl Technol 135(3): 241–251
- Keller PM (2001) FORMOSA-P Constrained multiobjective simulated annealing methodology. Proc. Int. Mtg. Mathematical Methods for Nuclear Applications, Salt Lake City, Utah
- Keller PM, Turinsky PJ (2001) FORMOSA-P three-dimensional/two-dimensional geometry collapse methodology. Nucl Sci Eng 139(3): 235–247
- Kim Y, Jo CK, Noh J (2007) Optimization of axial fuel shuffling strategy in a block-type VHTR. Trans Am Nucl Soc (97):406–407
- Kim Y, Venneri F (2007) Optimization of TRU burnup in modular helium reactor. ICAPP '07, Niece, France
- Kirkpatrick S, Gelatt Jr. CD, Vecchi MP (1983) Optimization by simulated annealing. Science 220(4598):671–680
- Knott D, Mills VW, Wehlage E (2002) Validation of the GE lattice physics code LANCER 02. Trans Am Nucl Soc (92):505–507
- Kropaczek DJ (2009) COPERNICUS: a multi-cycle nuclear fuel optimization code based on coupled in-core constraints. Advances in Nuclear Fuel Management Fuel Management IV, Hilton Head
- Kropaczek DJ, Turinsky PJ (1991) In-core nuclear fuel management optimization for pressurized water reactors utilizing simulated annealing. Nucl Technol 95(1):9–32
- MacFarlane RE, Muir DW, Boicourt RM (1982) The NJOY nuclear data processing system: Volume 1: user's manual. Los Alamos National Laboratory, Los Alamos
- Maldonado GI, Turinsky PJ (1995) Application of nonlinear nodal diffusion generalized perturbation theory to nuclear fuel reload optimization. Nucl Technol 110(2):198–219
- Martin-del-Campo C, Francois JL, Morales LB (2002) BWR fuel assembly axial design optimization using tabu search. Nucl Sci Eng 142: 107–115
- Metropolis N, Rosenbluth AW, Rosenbluth MN, Teller AH, Teller E (1953) Equation of state calculations by fast computing machines. J Chem Phys 21(6):1087–1092
- Moler C, Van Loan CF (2003) Nineteen dubious ways to compute the exponential of a matrix, twenty-five years later. SIAM Rev 45(1):3–49
- Moore BR, Turinsky PJ, Karve AA (1998) FORMOSA-B: a boiling water reactor in-core fuel management optimization package. Nucl Technol 126(1):153–169
- Ouisloumen M et al (2001) PARAGON: the new Westinghouse lattice code. Proc ANS Int Meeting on Mathematical Methods for Nuclear Applications
- Parks GT (1996) Multiobjective pressurized water reactor reload core design by nondominated genetic algorithm search. Nucl Sci Eng 124: 178–187
- Pincus M (1970) A Monte Carlo method for the approximate solution of certain types of constrained optimization problems. Operat Res 18(6):1225–1228
- Quist AJ, Van Geemert R, Hoogenboom JE, Illes T, De Klerk E, Roos C, Terlaky T (1999) Finding optimal nuclear reactor core reload patterns using nonlinear optimization and search heuristics. Eng Optimization 32(2):143–176, doi:10.1080/03052159908941295
- Roque B et al (2002) "Experimental Validation of the Code System "DARWIN" for spent fuel isotopic predictions in fuel cycle applications," PHYSOR 2002, Seoul Korea
- Stewart CW, Cuta JM, Montgomery SD, Kelly JM, Basehore KL, George TL, Rowe DS (1989) VIPRE-01: a thermal-hydraulic code for reactor cores. Electric Power Research Institute (EPRI), Palo Alto

- Stewart CW, Wheeler CL, Cena RJ, McMonagle CA, Cuta JM, Trent DS (1977) COBRA-IV: the model and the method. Pacific Northwest Lab, Richland, doi: 10.2172/5358588
- Toppel BJ, Rago AL, O'Shea DM (1967). MC2, a code to calculate multigroup cross-sections. USAEC Report ANL-7318
- Vondy DR (1962) Development of a general method of explicit solution to the nuclide chain equations for digital machine calculations, ORNL/TM-361, Union Carbide Corporation, Nuclear Division, Oak Ridge National Laboratory, Oak Ridge

11 Radiation Shielding and Radiological Protection

J. Kenneth Shultis · Richard E. Faw

Department of Mechanical and Nuclear Engineering, Kansas
State University, Manhattan, KS, USA

jks@ksu.edu

fawre@triad.rr.com

1	<i>Radiation Fields and Sources</i>	1316
1.1	Radiation Field Variables	1317
1.1.1	Direction and Solid Angle Conventions	1317
1.1.2	Radiation Fluence	1318
1.1.3	Radiation Current or Net Flow	1319
1.1.4	Directional Properties of the Radiation Field	1320
1.1.5	Angular Properties of the Flow and Flow Rate	1320
1.2	Characterization of Radiation Sources	1321
1.2.1	General Considerations	1321
1.2.2	Neutron Sources	1322
1.2.3	Gamma-Ray Sources	1328
1.2.4	X-Ray Sources	1336
2	<i>Conversion of Fluence to Dose</i>	1339
2.1	Local Dosimetric Quantities	1340
2.1.1	Energy Imparted and Absorbed Dose	1340
2.1.2	Kerma	1341
2.1.3	Exposure	1341
2.1.4	Local Dose Equivalent Quantities	1342
2.2	Evaluation of Local Dose Conversion Coefficients	1345
2.2.1	Photon Kerma, Absorbed Dose, and Exposure	1345
2.2.2	Neutron Kerma and Absorbed Dose	1345
2.3	Phantom-Related Dosimetric Quantities	1346
2.3.1	Characterization of Ambient Radiation	1346
2.3.2	Dose Conversion Factors for Geometric Phantoms	1347
2.3.3	Dose Coefficients for Anthropomorphic Phantoms	1349
2.3.4	Comparison of Dose Conversion Coefficients	1352
3	<i>Basic Methods in Radiation Attenuation Calculations</i>	1353
3.1	The Point-Kernel Concept	1353
3.1.1	Exponential Attenuation	1354
3.1.2	Uncollided Dose from a Monoenergetic Point Source	1354
3.2	Uncollided Doses for Distributed Sources	1356
3.2.1	The Superposition Procedure	1356

3.2.2	Example Calculations for Distributed Sources	1356
4	<i>Photon Attenuation Calculations</i>	1359
4.1	The Photon Buildup-Factor Concept	1359
4.2	Isotropic, Monoenergetic Sources in Infinite Media	1360
4.3	Buildup Factors for Point and Plane Sources	1362
4.3.1	Empirical Approximations for Buildup Factors	1365
4.3.2	Point-Kernel Applications of Buildup Factors	1365
4.4	Buildup Factors for Heterogenous Media	1369
4.4.1	Boundary Effects in Finite Media	1369
4.4.2	Treatment of Stratified Media	1370
4.5	Broad-Beam Attenuation of Photons	1372
4.5.1	Attenuation Factors for Photon Beams	1372
4.5.2	Attenuation of Oblique Beams of Photons	1372
4.5.3	Attenuation Factors for X-Ray Beams	1373
4.5.4	The Half-Value Thickness	1376
4.6	Shield Heterogeneities	1376
4.6.1	Limiting Case for Small Discontinuities	1377
4.6.2	Small Randomly Distributed Discontinuities	1378
5	<i>Neutron Shielding</i>	1378
5.1	Neutron Versus Photon Calculations	1379
5.2	Fission Neutron Attenuation by Hydrogen	1379
5.3	Removal Cross Sections	1382
5.4	Extensions of the Removal Cross Section Model	1384
5.4.1	Effect of Hydrogen Following a Nonhydrogen Shield	1384
5.4.2	Homogenous Shields	1385
5.4.3	Energy-Dependent Removal Cross Sections	1386
5.5	Fast-Neutron Attenuation Without Hydrogen	1387
5.6	Intermediate and Thermal Fluences	1389
5.6.1	Diffusion Theory for Thermal Neutron Calculations	1389
5.6.2	Fermi Age Treatment for Thermal and Intermediate-Energy Neutrons	1391
5.6.3	Removal-Diffusion Techniques	1392
5.7	Capture-Gamma-Photon Attenuation	1394
5.8	Neutron Shielding with Concrete	1396
5.8.1	Concrete Slab Shields	1396
6	<i>The Albedo Method</i>	1400
6.1	Differential Number Albedo	1401
6.2	Integrals of Albedo Functions	1402
6.3	Application of the Albedo Method	1402
6.4	Albedo Approximations	1403
6.4.1	Photon Albedos	1403
6.4.2	Neutron Albedos	1405
7	<i>Skyshine</i>	1407
7.1	Approximations for the LBRF	1408
7.1.1	Photon LBRF Approximation	1409
7.1.2	Neutron LBRF Approximation	1409

7.2	Open Silo Example	1409
7.3	Shielded Skyshine Sources	1411
7.4	Computational Resources for Skyshine Analyses	1412
8	<i>Radiation Streaming Through Ducts</i>	1412
8.1	Characterization of Incident Radiation	1413
8.2	Line-of-Sight Component for Straight Ducts	1414
8.2.1	Line-of-Sight Component for the Cylindrical Duct	1414
8.2.2	Line-of-Sight Component for the Rectangular Duct	1415
8.3	Wall-Penetration Component for Straight Ducts	1415
8.4	Single-Scatter Wall-Reflection Component	1416
8.5	Photons in Two-Legged Rectangular Ducts	1418
8.6	Neutron Streaming in Straight Ducts	1420
8.7	Neutron Streaming in Ducts with Bends	1421
8.7.1	Two-Legged Ducts	1421
8.7.2	Neutron Streaming in Ducts with Multiple Bends	1423
8.8	Empirical and Experimental Results	1423
9	<i>Shield Design</i>	1424
9.1	Shielding Design and Optimization	1424
9.2	Shielding Materials	1425
9.2.1	Natural Materials	1425
9.2.2	Concrete	1427
9.2.3	Metallic Shielding Materials	1428
9.2.4	Special Materials for Neutron Shielding	1428
9.2.5	Materials for Diagnostic X-Ray Facilities	1429
9.3	A Review of Software Resources	1429
9.4	Shielding Standards	1430
10	<i>Health Physics</i>	1430
10.1	Deterministic Effects from Large Acute Doses	1431
10.1.1	Effects on Individual Cells	1431
10.1.2	Deterministic Effects in Organs and Tissues	1431
10.1.3	Potentially Lethal Exposure to Low-LET Radiation	1432
10.2	Hereditary Illness	1433
10.2.1	Classification of Genetic Effects	1434
10.2.2	Estimates of Hereditary Illness Risks	1435
10.3	Cancer Risks from Radiation Exposures	1435
10.3.1	Estimating Radiogenic Cancer Risks	1436
10.4	The Dose and Dose-Rate Effectiveness Factor	1437
10.4.1	Dose-Response Models for Cancer	1437
10.4.2	Average Cancer Risks for Exposed Populations	1438
10.5	Radiation Protection Standards	1439
10.5.1	Risk-Related Dose Limits	1440
10.5.2	The 1987 NCRP Exposure Limits	1441
	<i>References</i>	1442

Abstract: This chapter deals with shielding against nonionizing radiation, specifically gamma rays and neutrons with energies less than about 10 MeV, and addresses the assessment of health effects from exposure to such radiation. The chapter begins with a discussion of how to characterize mathematically the energy and directional dependence of the radiation intensity and, similarly, the nature and description of radiation sources. What follows is a discussion of how neutrons and gamma rays interact with matter and how radiation doses of various types are deduced from radiation intensity and target characteristics. This discussion leads to a detailed description of radiation attenuation calculations and dose evaluations, first making use of the point-kernel methodology and then treating the special cases of “skyshine” and “albedo” dose calculations. The chapter concludes with a discussion of shielding materials, radiological assessments, and risk calculations.

1 Radiation Fields and Sources

The transmission of directly and indirectly ionizing radiation through matter and its interaction with matter is fundamental to radiation shielding design and analysis. Design and analysis are but two sides of the same coin. In *design*, the source intensity and permissible radiation dose or dose rate at some location are specified, and the task is to determine the type and configuration of shielding that is needed. In *analysis*, the shielding material is specified, and the task is to determine the dose, given the source intensity, or the latter, given the former.

The radiation is conceptualized as particles – photons, electrons, neutrons, and so on. The term *radiation field* refers collectively to the particles and their trajectories in some region of space or through some boundary, either per unit time or accumulated over some period of time.

Characterization of the radiation field, for any one type of radiation particle, requires a determination of the spatial variation of the joint distribution of the particle’s energy and direction. In certain cases, such as those encountered in neutron scattering experiments, properties such as spin may be required for full characterization. Such infrequent and specialized cases are not considered in this chapter.

The sections to follow describe how to characterize the radiation field in a region of space in terms of the particle fluence and how to characterize the radiation field at a boundary in terms of the particle flow. The fluence and flow are called *radiometric* quantities, as distinguished from *dosimetric* quantities. The fluence and flow concepts apply both to measurement and calculation. Measured quantities are inherently stochastic, in that they involve enumeration of individual particle trajectories. Measurement, too, requires finite volumes or boundary areas. The same is true for fluence or flow calculated by Monte Carlo methods, because such calculations are, in large part, computer simulations of experimental determinations. In the methods of analysis discussed in this chapter, the fluence or flow is treated as a deterministic point function and should be interpreted as the expected value, in a statistical sense, of a stochastic variable. It is perfectly proper to refer to the fluence, flow, or related dosimetric quantity at a point in space. But it must be recognized that any measurement is only a single estimate of the expected value.

1.1 Radiation Field Variables

1.1.1 Direction and Solid Angle Conventions

The directional properties of radiation fields are commonly described using spherical polar coordinates as illustrated in [Fig. 1](#). The direction vector is a unit vector, given in terms of the orthogonal Cartesian unit vectors \mathbf{i} , \mathbf{j} , and \mathbf{k} by

$$\boldsymbol{\Omega} = \mathbf{i}u + \mathbf{j}v + \mathbf{k}w = \mathbf{i} \sin \theta \cos \psi + \mathbf{j} \sin \theta \sin \psi + \mathbf{k} \cos \theta. \quad (1)$$

An increase in θ by $d\theta$ and ψ by $d\psi$ sweeps out the area $dA = \sin \theta d\theta d\psi$ on a sphere of unit radius. The solid angle encompassed by a range of directions is defined as the area swept out on the surface of a sphere divided by the square of the radius of the sphere. Thus, the differential solid angle associated with the differential area dA is $d\Omega = \sin \theta d\theta d\psi$. The solid angle is a dimensionless quantity. Nevertheless, to avoid confusion when referring to a directional distribution function, units of *steradians*, abbreviated sr, are attributed to the solid angle.

A substantial simplification in notation can be achieved by making use of $w \equiv \cos \theta$ as an independent variable instead of the angle θ , so that $\sin \theta d\theta = -dw$. The benefit is evident when one computes the solid angle subtended by “all possible directions,” namely,

$$\Omega = \int_0^\pi d\theta \sin \theta \int_0^{2\pi} d\psi = \int_{-1}^1 dw \int_0^{2\pi} d\psi = 4\pi. \quad (2)$$

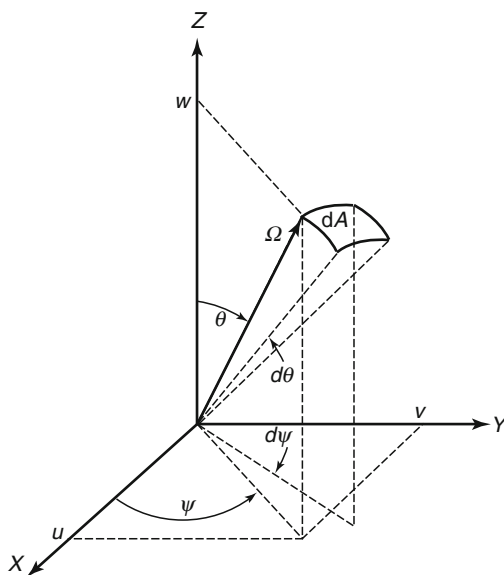




Figure 1

Spherical polar coordinate system for specification of the unit direction vector $\boldsymbol{\Omega}$, polar angle θ , azimuthal angle ψ , and associated direction cosines (u, v, w)

1.1.2 Radiation Fluence

A fundamental way of characterizing the intensity of a radiation field is in terms of the number of particles that enter a specified volume. To make this characterization, the radiometric concept of *fluence* is introduced. The particle fluence, or simply fluence, at any point in a radiation field may be thought of in terms of the number of particles ΔN_p that, during some period of time, penetrate a hypothetical sphere of cross section ΔA centered on the point, as illustrated in  Fig. 2a. The fluence is defined as

$$\Phi \equiv \lim_{\Delta A \rightarrow 0} \left[\frac{\Delta N_p}{\Delta A} \right]. \quad (3)$$

An alternative, and often more useful definition of the fluence, is in terms of the sum $\sum_i s_i$ of path-length segments within the sphere, as illustrated in  Fig. 2b. The fluence can also be defined as

$$\Phi \equiv \lim_{\Delta V \rightarrow 0} \left[\frac{\sum_i s_i}{\Delta V} \right]. \quad (4)$$

Although the difference quotients of (3) and (4) are useful conceptually, beginning in 1971, the ICRU prescribed that the fluence should be given in terms of differential quotients, in recognition that ΔN_p is the expectation value of the number of particles entering the sphere. Thus, $\Phi \equiv dN_p/dA$, where dN_p is the number of particles which penetrate into a sphere of cross-sectional area dA .

The fluence rate, or *flux*, is expressed in terms of the number of particles entering a sphere, or the sum of path segments traversed within a sphere, per unit time, namely,

$$\phi \equiv \frac{d\Phi}{dt} = \frac{d^2 N_p}{dA dt}. \quad (5)$$

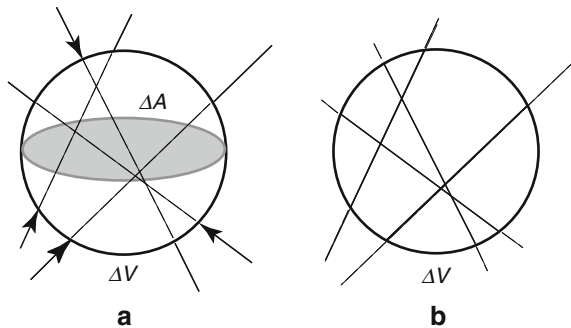


 Figure 2

Element of volume ΔV in the form of a sphere with cross-sectional area ΔA . In (a) the attention is on the number of particles passing through the surface *into* the sphere. In (b) the attention is on the paths traveled within the sphere by particles passing through the sphere

1.1.3 Radiation Current or Net Flow

Another radiometric measure of a radiation field is the net number of particles crossing a surface with a well-defined orientation, as illustrated in **Fig. 3**. The *net particle flow* (or simply *net flow*) at a point on a surface is the net number of particles in some specified time interval that flow across a unit differential area on the surface, in the direction specified as positive. As shown in the figure, one side of the surface is characterized as the positive side and is identified by a unit vector \mathbf{n} normal to the area ΔA . If the number of particles crossing ΔA from the negative to the positive side is ΔM_p^+ and the number from the positive to the negative side is ΔM_p^- , then the *net* number crossing toward the positive side is $\Delta M_p \equiv \Delta M_p^+ - \Delta M_p^-$. The net flow at the given point is designated as J_n , with the subscript denoting the unit normal \mathbf{n} from the surface, and is defined as

$$J_n \equiv \lim_{\Delta A \rightarrow 0} \frac{\Delta M_p}{\Delta A} = \frac{dM_p}{dA}. \quad (6)$$

The total flow of particles in the positive and negative directions, J_n^+ and J_n^- , are defined in terms of ΔM_p^+ and ΔM_p^- in a similar manner. The relation between the net flow and the positive and negative flows is $J_n \equiv J_n^+ - J_n^-$.

The net flow *rate* is expressed in terms of the net number of particles crossing an area perpendicular to unit vector \mathbf{n} , per unit area and per unit time, namely, $j_n \equiv j_n^+ - j_n^-$.

The concepts of fluence and particle flow appear to be very similar, both being defined in terms of a number of particles per unit area. However, for the concept of the fluence, the area presented to incoming particles is independent of the direction of the particles, whereas for the particle flow concept, the orientation of the area is well defined.

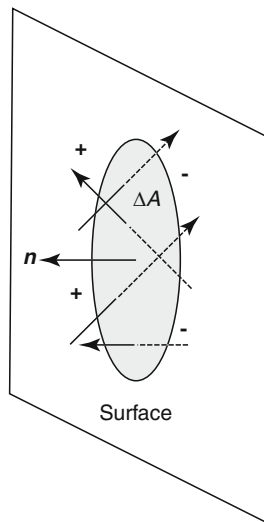


Figure 3
Element of area ΔA in a surface. Particles cross the area from either side

1.1.4 Directional Properties of the Radiation Field


The computed fluence is a point function of position \mathbf{r} . Measurement of the fluence requires a radiation detector of finite volume; therefore, there is not only uncertainty due to experimental error but also ambiguity in identification of the “point” at which to attribute the measurement. The nature of the particles is implicit, and the argument \mathbf{r} in $\Phi(\mathbf{r})$ is sometimes implicit. With no other arguments, Φ or $\Phi(\mathbf{r})$ represents the total fluence irrespective of particle energy or particle direction, that is, integrated over all particle energies and directions.


In many circumstances, it is necessary to broaden the concept of the fluence to include information about the energies and directions of particles. To do so requires the use of *distribution functions*. Particle energies and directions require, in general, fluences expressed as distribution functions. For example, $\Phi(\mathbf{r}, E) dE$ is, at point \mathbf{r} , the *fluence energy spectrum* – the fluence of particles with energies between E and $E + dE$.

The angular dependence of the fluence is a bit more complicated to write. The angular variable itself is the vector direction Ω . The direction is a function of the polar and azimuthal angles, θ and ψ . Similarly, the differential element of solid angle is a function of the same two variables, namely $d\Omega = \sin \theta d\theta d\psi = d\omega d\psi$. Thus, $\Phi(\mathbf{r}, \Omega) d\Omega$ or $\Phi(\mathbf{r}, \omega, \psi) d\omega d\psi$ is, at point \mathbf{r} , the angular fluence – the fluence of particles with directions in $d\Omega$ about Ω . The joint energy and angular distribution of the fluence is defined in such a way that $\Phi(\mathbf{r}, E, \Omega) dE d\Omega$ is the fluence of particles with energies in dE about E and with directions in $d\Omega$ about Ω .

In the system of notation adopted here, it is necessary that the energy and angular variables appear specifically as arguments of Φ to identify the fluence as a distribution function in these variables. The ICRU notation refers to the energy distribution as the *spectral distribution* and to the angular distribution as the *radiance*.

1.1.5 Angular Properties of the Flow and Flow Rate

Just as it is very often necessary to account for the variation of the fluence with particle energy and direction, the same is true for the flow and flow rate. Treatment of the energy dependence is no different from the treatment used for the fluence, so here only the angular dependence of the flow is examined. With an element of area and its orientation as illustrated in  Fig. 3, it is perfectly proper to define the angular flow in such a way that $J_n(\mathbf{r}, \Omega) d\Omega$ is the flow of particles through a unit area with directions in $d\Omega$ about Ω . The corresponding angular flow rate is written as $j_n(\mathbf{r}, \Omega)$.

 Figure 4 illustrates particles within a differential element of direction $d\Omega$ about direction Ω crossing a surface perpendicular to unit vector \mathbf{n} . Also shown in the figure is a sphere whose surface just intercepts all the particles. It is apparent that if ΔA is the cross-sectional area of the sphere, then the corresponding area in the surface is $\Delta A \sec \theta$, where $\cos \theta = \mathbf{n} \cdot \Omega$. Thus, because the same number of particles pass through the sphere and through the area in $J_n(\mathbf{r}, \Omega) \Delta A = \cos \theta \Delta A \Phi(\mathbf{r}, \Omega)$, or

$$J_n(\mathbf{r}, \Omega) = \mathbf{n} \cdot \Omega \Phi(\mathbf{r}, \Omega). \quad (7)$$

The net flow is given by

$$\begin{aligned} J_n(\mathbf{r}) &\equiv \int_{4\pi} d\Omega J_n(\mathbf{r}, \Omega) \\ &= \int_{4\pi} d\Omega \mathbf{n} \cdot \Omega \Phi(\mathbf{r}, \Omega). \end{aligned} \quad (8)$$

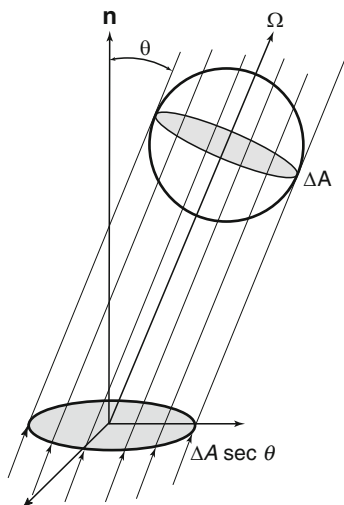


Figure 4
 $J_n(\mathbf{r}, \Omega)$ versus $\Phi(\mathbf{r}, \Omega)$

The fluence is a positive quantity; however, $J_n(\mathbf{r}, \Omega)$ is positive or negative as $\mathbf{n} \cdot \Omega$ is positive or negative. That part of the integral for which $\mathbf{n} \cdot \Omega$ is positive is the flow $J_n^+(\mathbf{r})$, and that part for which $\mathbf{n} \cdot \Omega$ is negative is $-J_n^-(\mathbf{r})$. The algebraic sum of the two parts gives the net flow $J_n(\mathbf{r})$.

1.2 Characterization of Radiation Sources

1.2.1 General Considerations

The most fundamental type of source is a point source. A real source can be approximated as a point source provided that (1) the volume is sufficiently small, that is, with dimensions much smaller than the dimensions of the attenuating medium between the source and detector, and (2) there is negligible interaction of radiation with the matter in the source volume. The second requirement may be relaxed if source characteristics are modified to account for source self-absorption and other source-particle interactions.

In general, a point source may be characterized as depending on energy, direction, and time. In almost all shielding practices, time is not treated as an independent variable because the time delay between a change in the source and the resulting change in the radiation field is usually negligible. Therefore, the most general characterization of a point source used here is in terms of energy and direction, so that $S_p(E, \Omega) dE d\Omega$ is the number of particles emitted with energies in dE about E and in $d\Omega$ about Ω . Common practical units for $S_p(E, \Omega)$ are $\text{MeV}^{-1} \text{sr}^{-1}$ or $\text{MeV}^{-1} \text{s}^{-1}$.

Most radiation sources treated in the shielding practice are isotropic, so that source characterization requires only knowledge of $S_p(E) dE$, which is the number of particles emitted with energies in dE about E (per unit time), and has common practical units of MeV^{-1} (or $\text{MeV}^{-1} \text{s}^{-1}$). Radioisotope sources are certainly isotropic, as are fission sources and capture gamma-ray sources.

A careful distinction must be made between the activity of a radioisotope and its source strength. *Activity* is precisely defined as the expected number of atoms undergoing radioactive transformation per unit time. It is *not* defined as the number of particles emitted per unit time. Decay of two very common laboratory radioisotopes illustrate this point. Each transformation of ^{60}Co , for example, results in the emission of two gamma rays, one at 1.173 MeV and the other at 1.333 MeV. Each transformation of ^{137}Cs , accompanied by a transformation of its decay product ^{137m}Ba , results in emission of a 0.662-MeV gamma ray with probability 0.85.

The SI unit of activity is the becquerel (Bq), equivalent to 1 transformation per second. In medical and health physics, radiation source strengths are commonly calculated on the basis of *accumulated activity*, Bq s. Such time-integrated activities account for the cumulative number of transformations in some biological entity during the transient presence of radionuclides in the entity. Of interest in such circumstances is not the time-dependent dose rate to that entity or some other nearby region, but rather the total dose accumulated during the transient. Similar practices are followed in dose evaluation for reactor transients, solar flares, nuclear weapons, and so on.

Radiation sources may be distributed along a line, over an area, or within a volume. Source characterization requires, in general, spatial and energy dependence, with $S_l(\mathbf{r}, E) dE$, $S_a(\mathbf{r}, E) dE$, and $S_v(\mathbf{r}, E) dE$ representing, respectively, the number of particles emitted in dE about E per unit length, per unit area, and per unit volume. Occasionally, it is necessary to include angular dependence. This is especially true for effective area sources associated with computed angular flows across certain planes. Clearly, for a fixed surface, $S_a(\mathbf{r}, E, \Omega)$ and $J_n(\mathbf{r}, E, \Omega)$ are equivalent specifications.

Energy dependence may be discrete, such as for radionuclide sources, or continuous, as for bremsstrahlung or fission neutrons and photons. When discrete energies are numerous, an energy multigroup approach is often used. The same multigroup approach may be used to approximately characterize a source whose emissions are continuous in energy.

1.2.2 Neutron Sources

Fission Sources

Many heavy nuclides fission after the absorption of a neutron, or even spontaneously, producing several energetic fission neutrons. Fission neutrons may produce secondary radiation sources, such as inelastic-scattering photons and capture gamma photons, and may transmute stable isotopes into radioactive ones.

Almost all of the fast neutrons produced from a fission event are emitted within 10^{-7} s of the fission event. Less than 1% of the total fission neutrons are emitted as *delayed neutrons*, which are produced by the neutron decay of fission products at times up to many minutes after the fission event. Except for very specialized situations, these delayed neutrons, which are emitted with significantly less energy than the prompt neutrons, are of little importance in shield design because of their relatively small yield and low energies.

As the energy of the neutron which induces the fission in a heavy nucleus increases, the average number of fission neutrons also increases. Yields in thermal-neutron induced fission of ^{235}U , ^{239}Pu , and ^{233}U are respectively 2.43, 2.87, and 2.48. See Keepin (1965) for information on epithermal- and fast-neutron induced fission.

Many transuranic isotopes have appreciable, spontaneous fission probabilities; and consequently, they can be used as very compact sources of fission neutrons. For example, 1 g of ^{252}Cf releases 2.3×10^{12} neutrons per second, and very intense neutron sources can be made from this isotope, limited in size only by the need to remove the fission heat through the necessary encapsulation. Properties of the spontaneously fissioning isotopes of greatest importance in spent nuclear fuel are listed in [Table 1](#). Almost all of these isotopes decay much more rapidly by α emission than by spontaneous fission.

The energy dependence of the fission neutron spectrum has been investigated extensively, especially that for ^{235}U . All fissionable nuclides produce a distribution of prompt fission-neutron energies which goes to zero at low and high energies and reaches a maximum at about 0.7 MeV. The fraction of prompt fission neutrons emitted per unit energy about E , $\chi(E)$, can be described quite accurately by a modified two-parameter Maxwellian distribution (a Maxwellian corrected for the average energy of the fission fragments in the laboratory coordinate system), namely,

$$\chi(E) = \frac{e^{-(E+E_\omega)/T_\omega}}{\sqrt{\pi E_\omega T_\omega}} \sinh \sqrt{\frac{4E_\omega E}{T_\omega^2}}. \quad (9)$$

In many shielding applications, the spectrum for thermal-neutron-induced fission of ^{235}U has often been used, at least as a first approximation for other fissioning isotopes, although ^{233}U , ^{239}Pu , and ^{252}Cf have somewhat greater high-energy components; and consequently, their fission neutrons are slightly more penetrating than those of ^{235}U . Please refer to [Table 2](#) for parameter values.

Photoneutrons

A gamma photon with energy sufficiently larger to overcome the neutron-binding energy (about 7 MeV in most nuclides) may cause a (γ, n) reaction. Very intense and energetic photoneutron production can be realized in an electron accelerator where the bombardment of an appropriate target material with the energetic electrons produces intense bremsstrahlung with a distribution of energies up to that of the incident electrons.

Table 1

Selected nuclides which spontaneously fission. All also decay by alpha emission, which is usually the only other decay mode

Nuclide	Half-life	Fission prob. per decay (%)	Neutrons per fission	α per fission	Neutrons per (g s)
^{238}Pu	87.7 y	1.9×10^{-7}	2.28	5.4×10^8	2.7×10^3
^{240}Pu	6569 y	5.7×10^{-6}	2.21	2.0×10^7	920
^{242}Pu	3.76×10^5 y	5.5×10^{-4}	2.24	1.8×10^5	1.8×10^3
^{242}Cm	163 d	6.2×10^{-6}	2.70	1.5×10^7	2.3×10^7
^{244}Cm	18.11 y	1.37×10^{-4}	2.77	7.5×10^5	1.1×10^7
^{246}Cm	4730 y	0.02615	2.86	3.8×10^3	8.5×10^6
^{252}Cf	2.645 y	3.092	3.73	31	2.3×10^{12}

Sources: Data compiled from Dillman (1980), Kocher (1981), and Reilly et al. (1991), and from the NuDat data resource of the National Nuclear Data Center at Brookhaven National Laboratory

■ **Table 2**

Parameters for the Watt approximation for the prompt fission-neutron distribution for various fissionable nuclides. Values for ^{252}Cf are from Fröhner (1990). The other values were obtained by a logarithmic fit of the Watt formula to the calculated spectra by Walsh (1989)

Nuclide	Type of fission	Equation (9)	
		E_w	T_w
^{233}U	Thermal	0.3870	1.108
^{235}U	Thermal	0.4340	1.035
^{239}Pu	Thermal	0.4130	1.159
^{232}Th	Fast (2 MeV)	0.4305	0.971
^{238}U	Fast (2 MeV)	0.4159	1.027
^{252}Cf	Spontaneous	0.359	1.175

■ **Table 3**

Important nuclides for photoneutron production

Nuclide	Threshold E_t (MeV) ($-Q$ value)	Reaction
^2H	2.225	$^2\text{H}(\gamma, n)^1\text{H}$
^6Li	3.698	$^6\text{Li}(\gamma, n + p)^4\text{He}$
^6Li	5.664	$^6\text{Li}(\gamma, n)^5\text{Li}$
^7Li	7.251	$^7\text{Li}(\gamma, n)^6\text{Li}$
^9Be	1.665	$^9\text{Be}(\gamma, n)^8\text{Be}$
^{13}C	4.946	$^{13}\text{C}(\gamma, n)^{12}\text{C}$

In reactor shielding analyses, the gamma photons encountered have energies too low, and most materials have a photoneutron threshold too high for photoneutrons to be of concern. Only for a few light elements, listed in [Table 3](#), are the thresholds for photoneutron production sufficiently low that these secondary neutrons may have to be considered. In heavy water- or beryllium-moderated reactors, the photoneutron source may be very appreciable, and the neutron-field deep within a hydrogenous shield is often determined by photoneutron production in deuterium, which constitutes about 0.015 at% of the hydrogen. Capture gamma photons arising from neutron absorption have particularly high energies and, thus, may cause a significant production of energetic photoneutrons.

The photoneutron mechanism can be used to create laboratory neutron sources by mixing intimately a beryllium or deuterium compound with a radioisotope that decays with the emission of high-energy photons. Alternatively, the encapsulated radioisotope may be surrounded

by a beryllium- or deuterium-bearing shell. One common laboratory photoneutron source is an antimony–beryllium mixture, which has the advantage of being rejuvenated by exposing the source to the neutrons in a reactor to transmute the stable ^{123}Sb into the required ^{124}Sb isotope (half-life of 60.2 days). Other common sources are mixtures of ^{226}Ra and beryllium or heavy water.

One very attractive feature of such (γ, n) sources is the nearly monoenergetic nature of the neutrons if the photons are monoenergetic. However, in large sources, the neutrons may undergo significant scattering in the source material, and thereby degrade the nearly monoenergetic nature of their spectrum. These photoneutron sources generally require careful usage because of their inherently large, photon emission rates. Because only a small fraction of the high-energy photons (typically, 10^{-6}) actually interact with the source material to produce a neutron, these sources generate gamma rays that are of far greater biological concern than the neutrons.

Neutrons from (α, n) Reactions

Many compact neutron sources use energetic alpha particles from various radioisotopes (*emitters*) to induce (α, n) reactions in appropriate materials (*converters*). Although a large number of nuclides emit neutrons if bombarded with alpha particles of sufficient energy, the energies of the alpha particles from radioisotopes are capable of penetrating the Coulombic potential barriers of only the lighter nuclei.

Of particular interest are those light isotopes for which the (α, n) reaction is exothermic ($Q > 0$) or, at least, has a low threshold energy (see [Table 4](#)). For endothermic reactions, the threshold alpha energy is $-Q(1 + 4/A)$. Thus, for an (α, n) reaction to occur, the alpha particle must (1) have enough energy to penetrate the Coulomb barrier, and (2) exceed the threshold energy. Alpha particles emitted by uranium and plutonium range between 4 and 6 MeV and can cause (α, n) neutron production when in the presence of oxygen or fluorine. Neutrons from (α, n) reactions often exceed the spontaneous fission neutrons in UF_6 or in aqueous mixtures of uranium and plutonium such as found in nuclear waste (Reilly et al. 1991).

A neutron source can be fabricated by mixing intimately one of the converter isotopes listed in [Table 4](#) with an alpha-particle emitter. Most of the practical alpha emitters are actinide elements, which form intermetallic compounds with beryllium. Such a compound (e.g., PuBe_{13})

■ **Table 4**

Important (α, n) reactions

Target	Natural abundance (%)	Reaction	energy (MeV) (Q value)	Threshold energy (MeV)	Coulomb barrier (MeV)
^9Be	100	$^9\text{Be}(\alpha, n)^{12}\text{C}$	5.702	Exothermic	2.6
^9Be	100	$^9\text{Be}(\alpha, n)3\alpha$	-1.573	2.272	2.6
^{10}B	19.8	$^{10}\text{B}(\alpha, n)^{13}\text{N}$	1.060	Exothermic	3.2
^{11}B	80.2	$^{11}\text{B}(\alpha, n)^{14}\text{N}$	0.157	Exothermic	3.2
^{18}O	0.2	$^{18}\text{O}(\alpha, n)^{21}\text{Ne}$	-0.697	0.852	4.6
^{19}F	100	$^{19}\text{F}(\alpha, n)^{22}\text{Na}$	-1.950	2.361	5.1

ensures both that the emitted alpha particles immediately encounter converter nuclei, thereby producing a maximum neutron yield, and that the radioactive actinides are bound into the source material, thereby reducing the risk of leakage of the alpha-emitting component. Some characteristics of selected (α, n) sources are listed in ► [Table 5](#).

The neutron yield from an (α, n) source varies strongly with the converter material, the energy of the alpha particle, and the relative concentrations of the emitter and converter elements. The degree of mixing between the converter and emitter, and the size, geometry, and source encapsulation may also affect the neutron yield.

The energy distributions of neutrons emitted from all such sources are continuous below some maximum neutron energy with definite structure at well-defined energies determined by the energy levels of the converter and the excited product nuclei. The use of the same converter material with different alpha emitters produces similar neutron spectra with different portions of the same basic spectrum accentuated or reduced as a result of the different alpha-particle energies.

Generally, neutrons emitted from the ${}^9\text{Be}(\alpha, n)$ reaction have higher energies than those produced by other (α, n) sources because Be has a larger Q value than that of other converters. The structure in the Be-produced neutron spectrum above 1 MeV can be interpreted in terms of structure in the ${}^9\text{Be}(\alpha, n){}^{12}\text{C}$ cross section, which in turn depends on the excitation state in which the ${}^{12}\text{C}$ nucleus is left. A large peak below 1 MeV in the Be neutron spectrum arises not from the direct (α, n) reaction, but from the “breakup” reaction ${}^9\text{Be}(\alpha, \alpha'){}^9\text{Be}^* \rightarrow {}^8\text{B} + n$. As the alpha-particle energy increases, both the fraction of neutrons emitted from the breakup reaction ($E_n < 1$ MeV) and the probability that the product nucleus is left in an excited state ($E_n < 6$ MeV) increase, thereby decreasing slightly the average neutron energy (see ► [Table 5](#)).

In all (α, n) sources, there is a maximum neutron energy corresponding to the reaction in which the product nucleus is left in the ground state and the neutron appears in the same direction as that of the incident alpha particle ($\theta = 0$). Thus, unlike fission neutron sources, there are no very high energy neutrons generated in an (α, n) source.

■ **Table 5**
Characteristics of some (α, n) sources

Source	Half-life	Principal alpha energies (MeV)	Average neutron energy (MeV)	Optimum neutron yield per 10^6 primary alphas ^a
${}^{239}\text{Pu}$ / Be	24100 y	5.155, 5.143, 5.105	4.6	60
${}^{210}\text{Po}$ / Be	138.4 d	5.305	4.5	70
${}^{238}\text{Pu}$ / Be	87.8 y	5.499, 5.457, 5.358	4.5	80
${}^{241}\text{Am}$ / Be	432 y	5.486, 5.443, 5.388	4.4	75
${}^{226}\text{Ra}$ / Be + daughters	1600 y	7.687, 6.003, 5.490 5.304, 4.785, 4.602	3.9	500 ^b

Sources: Jaeger (1968), GPO (1970), and Knoll (1989)

^aYield for alpha particles incident on a target thicker than the alpha-particle ranges

^bYield is dependent on the proportion of daughters present. Value for ${}^{226}\text{Ra}$ corresponds to a 22-year-old source (50% contribution for ${}^{210}\text{Po}$)


With appropriate (α, n) cross-section data for a converter, ideal neutron energy spectra can be calculated for the monoenergetic alpha particles emitter by different alpha emitters (Geiger and Van der Zwan 1975). However, these ideal spectra are modified somewhat in actual (α, n) sources. The monoenergetic alpha particles lose variable amounts of energy through ionization interactions in the source material before inducing an (α, n) reaction. This effectively continuous nature of the alpha-particle energy spectrum tends to smooth out many of the fine features of the ideal neutron spectrum. Further, if the source is physically large as a result of requiring a large activity (e.g., a $^{239}\text{Pu}/\text{Be}$ source emitting 10^7 neutrons per second requires about 73 g of plutonium), neutron interactions within the source itself may alter the emitted neutron spectrum. Neutron scattering, $(n, 2n)$ reactions with beryllium, and even neutron-induced fission of the actinide converter change the neutron energy spectrum slightly. Finally, impurity nuclides, which also emit alpha particles, as well as the buildup of alpha-emitting daughters, affect the neutron energy spectrum. In general, the neutron energy spectrum as well as the yield depend in a very complicated manner on the composition, size, geometry, and encapsulation of the source. Fortunately, in most shielding applications only approximate energy information is needed and idealized spectra are often adequate.

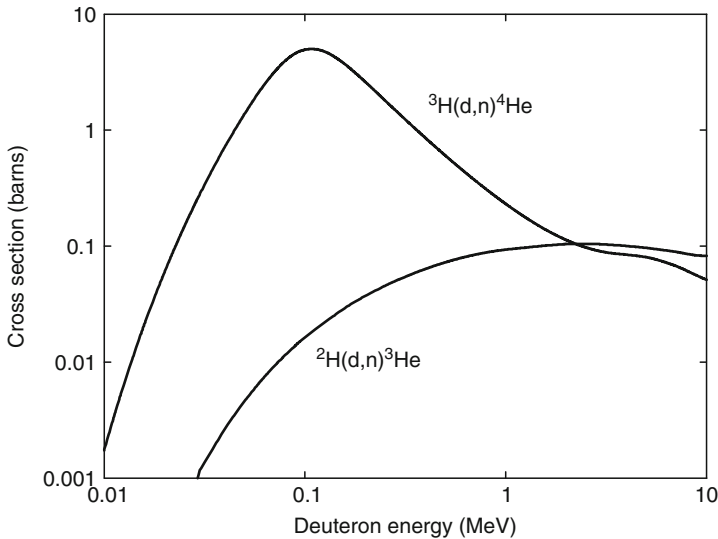
Activation Neutrons

A few highly unstable nuclides decay by the emission of a neutron. The delayed neutrons associated with fission arise from such decay of the fission products. However, there are nuclides other than those in the fission-product decay chain which also decay by neutron emission. Only one of these nuclides, ^{17}N , is of importance in shielding situations. This isotope is produced in water-moderated reactors by an (n, p) reaction with ^{17}O (threshold energy, 8.0 MeV), with a small cross section of about $5.2 \mu\text{b}$ averaged over the fission spectrum. The decay of ^{17}N by beta emission (half-life 4.4 s) produces ^{17}O in a highly excited state, which in turn decays rapidly by neutron emission. Most of the decay neutrons are emitted within ± 0.2 MeV of the most probable energy of about 1 MeV, although a few neutrons with energies up to 2 MeV may be produced.

Fusion Neutrons

Many nuclear reactions induced by energetic charged particles can produce neutrons. Most of these reactions require incident particles of very high energies for the reaction to take place and, consequently, are of little concern to the shielding analyst. Only near accelerator targets, for example, would such reaction neutrons be of concern.

From a shielding viewpoint, one major exception to the insignificance of charged particle-induced reactions are those fusion reactions in which light elements fuse exothermally to yield a heavier nucleus and which are accompanied quite often by the release of energetic neutrons. The resulting fusion neutrons are usually the major source of radiation to be shielded against. Prompt gamma photons are not emitted in the fusion process, and the bremsstrahlung produced by charged-particle deflections are easily shielded by any shielding adequate for protection from the neutrons. On the other hand, activation and capture gamma photons may arise as a result of neutrons being absorbed in the surrounding material. Cross sections for the two neutron-producing fusion reactions of most interest in the development of thermonuclear fusion power are illustrated in  Fig. 5. In the D-D reaction and D-T reactions, 2.45 and 14.1 MeV neutrons, respectively, are released.



■ Figure 5

Cross sections for the two most easily induced thermonuclear reactions as a function of the incident deuteron energy. Tritium data are from ENDF/B-VI.8 and deuterium data from ENDF/B-VII.0

1.2.3 Gamma-Ray Sources

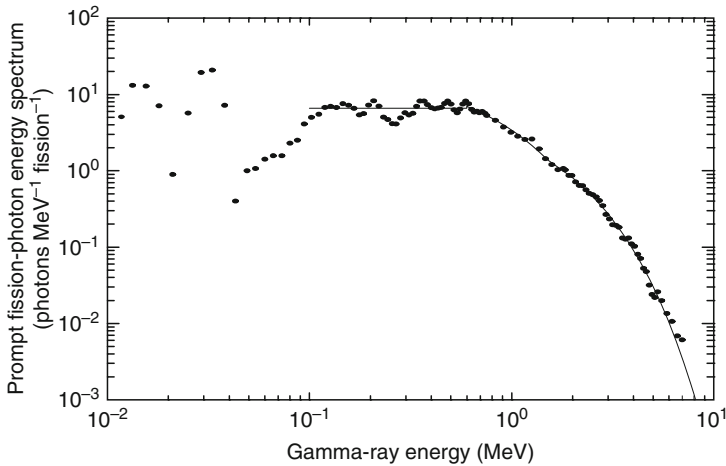
Radioactive Sources

There are many data sources for characterizing such sources. Printed documents include compilations by Kocher (1981), Weber et al. (1989), Eckerman et al. (1994), and Firestone et al. (1996). There are also many online data sources. One is the NuDAT (nuclear structure and decay data) and Chart of the Nuclides, www.nndc.bnl.gov, supported by the National Nuclear Data Center at Brookhaven National Laboratory. Another is the WWW table of radioisotopes (TORI) <http://nucleardata.nuclear.lu.se/nucleardata/toi> supported by the Lund/LBNL Nuclear Data Search. For detailed information on secondary X-rays and Auger electrons, the computer program of Dillman (1980) is invaluable.

Prompt Fission Gamma Photons

The fission process produces copious gamma photons. The *prompt fission-gamma photons* are released in the first 50 ns after the fission event. Those emitted later are the *fission product gamma photons*. Both are of extreme importance in the shielding and gamma-heating calculations for a reactor.

Investigations of prompt fission-gamma photons have centered on the thermal-neutron-induced fission of ^{235}U . For this nuclide, it has been found that the number of prompt fission photons is 8.13 ± 0.35 photons per fission over the energy range of 0.1 to 10.5 MeV, and the energy carried by this number of photons is 7.25 ± 0.26 MeV per fission (Peele and Maienschein 1970). In ► Fig. 6, the measured prompt fission-photon spectrum per thermal fission is shown for thermal fission of ^{235}U . The large peaks observed at 15 and 30 keV are X-rays emitted by the light- and heavy-fission fragments, respectively. Although some structure is evident between



■ Figure 6

Energy spectrum of prompt fission photons emitted within the first 69 ns after the fission of ^{235}U by thermal neutrons. Data are from Peele and Maienschein (1970) and the line is the fission-spectrum approximation of (10)

0.1 and 0.6 MeV, the prompt fission-gamma spectrum is approximately constant at $6.6 \text{ photons MeV}^{-1} \text{ fission}^{-1}$. At higher energies, the spectrum falls off sharply with increasing energy. For shielding purposes, the measured energy distribution shown in [Fig. 6](#) can be represented by the following empirical fit over the range of 0.1 to 10.5 MeV (Peele and Maienschein 1970):

$$N_{py}(E) = \begin{cases} 6.6 & 0.1 < E < 0.6 \text{ MeV} \\ 20.2e^{-1.78E} & 0.6 < E < 1.5 \text{ MeV} \\ 7.2e^{-1.09E} & 1.5 < E < 10.5 \text{ MeV,} \end{cases} \quad (10)$$

where E is in MeV and $N_{py}(E)$ is in units of $\text{photons MeV}^{-1} \text{ fission}^{-1}$. The low-energy prompt fission photons (i.e., those below 0.6 MeV) are not of concern for shielding considerations, although they may be important for gamma-heating problems. For this purpose, 3.74 photons with an average energy of 0.324 MeV may be considered as emitted below 0.6 MeV per fission. Relatively little work has been done to determine the characteristics of prompt fission photons from the fission of nuclides other than ^{235}U , but it is reasonable for shielding purposes to use ^{235}U spectra to approximate those for ^{233}U , ^{239}Pu , and ^{252}Cf .

Gamma Photons from Fission Products

One of the important concerns for the shielding analyst is the consideration of the very long lasting gamma activity produced by the decay of fission products. The total gamma-ray energy released by the fission product chains at times greater than 50 ns after the fission is comparable with that released as prompt fission gamma photons. About three-fourths of the delayed gamma-ray energy is released in the first thousand seconds after fission. In the calculations

involving spent fuel, the gamma activity at several months or even years after the removal of fuel from the reactor is of interest and only the long-lived fission products need be considered.

The gamma energy released from fission products is not very sensitive to the energy of the neutrons causing the fissions. However, the gamma-ray energy released and the photon energy spectrum depend significantly on the fissioning isotope, particularly in the first 10 s after fission. Generally, fissioning isotopes having a greater proportion of neutrons to protons produce fission-product chains of longer average length, with isotopes richer in neutrons and hence, with greater available decay energy. Also, the photon energy spectrum generally becomes "softer" (i.e., less energetic) as the time after the fission increases. Fission products from ^{235}U and ^{239}Pu release, on average, photon energy of 6.84 and 6.15 MeV/fission, respectively (Keepin 1965).

For very approximate calculations, the energy spectrum of delayed gamma photons from the fission of ^{235}U , at times up to about 500 s, may be approximated by the proportionality

$$N_{dy}(E) \sim e^{-1.1E}, \quad (11)$$

where $N_{dy}(E)$ is the delayed gamma yield (photons MeV^{-1} fission $^{-1}$) and E is the photon energy in MeV. The time dependence for the total gamma photon energy emission rate $F_T(t)$ (MeV s^{-1} fission $^{-1}$) is often described by the simple decay formula

$$F_T(t) = 1.4t^{-1.2}, \quad 10 \text{ s} < t < 10^8 \text{ s}, \quad (12)$$

where t is in seconds. More detailed, yet conservative expressions are available in the industrial standards [ANSI/ANS 2005]. ^{235}U and ^{239}Pu have roughly the same total gamma-ray-energy decay characteristics for up to 200 days after fission, at which time ^{235}U products begin to decay more rapidly until at 1 year after fission, the ^{239}Pu gamma activity is about 60% greater than that of ^{235}U .

Gamma-photon source data for the use in reactor design and analysis are readily available from software such as the ORIGEN code, which accounts for mixed oxide fuels and differing operating conditions, namely, BWR, PWR, or CANDU concentrations and temperatures. Activation products are also taken into account, as are spontaneous fission. Both gamma-photon and neutron spectra are available at user-selected times and energy group structures. As of this writing, the ORIGEN code is available as code package C00732 SCALE5.1/ORIGEN from the Radiation Safety Information Computational Center, Oak Ridge National Laboratory, Oak Ridge, Tennessee.

Sample ORIGEN results are given in [Table 6](#) for two extreme cases: time dependent (a) gamma-ray decay power from fission products created by a single fission event, and (b) gamma-ray decay power from fission products created during a 30,000-h period of operation at a constant rate of one fission per second. These particular results are for fission products only and are for fission of ^{235}U . The results do not account for bremsstrahlung or for neutron absorption, during operation, by previously produced fission products.

With these or similar results, the gamma-energy emission rate can be calculated for a wide variety of operation histories and decay times. Let $F_j(t)$ be the rate of energy emission via gamma photons in energy group j from fission products created by a single fission event t seconds earlier. Then, the photon energy emission rates can be calculated readily in terms of $F_j(t)$ for a sample of fissionable material which has experienced a prescribed power or fission history $P(t)$. Data fits are provided by George et al. (1980) and Labauve et al. (1982) for both ^{235}U and

Table 6

Fission-product gamma-photon energy release rates (MeV/s) for thermal fission of ^{235}U , computed using the ORIGEN code (RSIC 1991), Hermann and Westfall (1995)

Mean Energy (MeV)	Cooling time t (s)								
	10	100	1000	10^4	10^5	10^6	10^7	10^8	10^9
Single instantaneous fission event ^a									
0.010	1.69-04 ^a	1.70-05	2.14-06	1.34-07	6.98-09	3.78-10	2.79-11	1.16-12	1.61-13
0.030	1.78-04	2.05-05	2.42-06	1.65-07	1.40-08	1.25-09	3.78-11	1.54-12	2.02-13
0.055	2.33-04	2.28-05	2.41-06	1.65-07	1.01-08	4.65-10	3.19-11	1.45-12	1.84-13
0.085	2.27-04	2.28-05	2.73-06	1.72-07	8.59-09	1.35-09	2.83-11	1.43-12	1.58-13
0.120	2.72-04	2.85-05	2.55-06	1.83-07	1.51-08	9.77-10	4.17-11	2.56-12	1.51-13
0.170	4.42-04	5.96-05	8.72-06	5.70-07	2.13-08	2.07-09	1.21-10	1.78-12	2.09-13
0.300	1.39-03	2.17-04	3.43-05	1.35-06	1.60-07	8.07-09	7.31-11	3.56-12	3.81-13
0.650	3.91-03	5.86-04	1.06-04	1.40-05	8.01-07	4.29-08	4.81-09	3.20-11	1.29-11
1.130	2.10-03	6.95-04	1.19-04	6.09-06	2.27-07	5.45-09	3.08-11	1.41-12	7.47-14
1.580	1.14-03	2.40-04	5.51-05	6.95-06	1.09-07	3.84-08	1.39-10	8.17-13	1.33-14
2.000	4.93-04	1.25-04	3.46-05	3.02-06	2.48-08	5.86-10	2.10-11	1.68-12	1.01-15
2.400	4.26-04	1.23-04	2.74-05	4.01-06	9.80-09	2.74-09	9.87-12	5.54-14	7.08-19
2.800	5.03-04	1.37-04	9.74-06	1.03-06	2.91-10	4.42-11	2.26-13	9.04-15	2.67-23
3.250	2.89-04	1.11-04	6.89-06	4.87-07	7.50-11	2.29-11	9.13-14	1.46-15	5.32-24
3.750	2.53-04	5.77-05	3.84-06	2.65-07	1.51-11	7.15-18	5.19-18	7.43-19	2.71-27
4.250	2.89-04	1.15-04	2.89-06	3.40-09	2.64-12	1.64-30	1.69-30	1.99-30	2.27-30
4.750	2.57-04	2.44-05	4.84-07	9.77-09	2.19-11	9.20-31	9.45-31	1.12-30	1.27-30
5.500	2.87-04	1.72-05	3.43-07	7.27-11	1.62-13	7.91-31	8.11-31	9.61-31	1.09-30
Total	1.28-02	2.62-03	4.23-04	3.84-05	1.41-06	1.05-07	5.38-09	4.93-11	1.44-11
Long-term operation for 30,000 h at 1 fission per second									
0.010	2.00-02	1.32-02	8.78-03	4.68-03	2.26-03	1.22-03	4.81-04	6.34-05	1.55-05
0.030	2.63-02	1.90-02	1.36-02	8.78-03	5.51-03	2.24-03	6.31-04	8.27-05	1.97-05
0.055	2.56-02	1.64-02	1.08-02	6.15-03	3.03-03	1.44-03	5.90-04	7.69-05	1.76-05
0.085	2.75-02	1.85-02	1.27-02	7.31-03	4.55-03	2.04-03	5.70-04	7.21-05	1.50-05
0.120	3.18-02	2.05-02	1.44-02	9.23-03	5.74-03	2.03-03	1.03-03	1.09-04	1.45-05
0.170	7.27-02	5.32-02	3.68-02	1.80-02	1.05-02	5.16-03	1.05-03	9.23-05	1.99-05
0.300	2.62-01	1.92-01	1.31-01	6.50-02	3.59-02	1.02-02	1.45-03	1.80-04	3.62-05
0.650	1.16+00	9.80-01	7.82-01	4.81-01	2.80-01	1.42-01	4.61-02	3.24-03	1.33-03
1.130	6.86-01	5.51-01	3.43-01	1.24-01	2.95-02	6.41-03	6.98-04	9.42-05	8.78-06

Table 6 (continued)

Mean Energy (MeV)	Cooling time t (s)								
	10	100	1000	10^4	10^5	10^6	10^7	10^8	10^9
1.580	4.93-01	4.39-01	3.59-01	1.87-01	1.03-01	5.90-02	5.61-04	4.23-05	1.44-06
2.000	1.89-01	1.64-01	1.14-01	3.65-02	4.17-03	1.32-03	6.89-04	5.61-05	9.61-08
2.400	1.94-01	1.70-01	1.33-01	4.39-02	7.31-03	4.23-03	3.91-05	3.00-06	6.73-11
2.800	9.13-02	6.54-02	3.56-02	7.24-03	1.26-04	7.34-05	4.26-06	5.29-07	1.73-15
3.250	5.99-02	4.36-02	1.62-02	3.62-03	5.99-05	3.68-05	7.85-07	9.45-08	3.46-16
3.750	3.46-02	2.33-02	8.84-03	1.88-03	1.87-07	4.10-10	3.36-10	4.81-11	1.76-19
4.250	4.23-02	2.68-02	8.72-04	2.13-05	3.52-08	1.87-22	1.90-22	2.10-22	2.28-22
4.750	1.38-02	5.16-03	3.30-04	1.30-04	2.91-07	1.05-22	1.07-22	1.18-22	1.28-22
5.500	1.20-02	3.72-03	7.21-05	9.64-07	2.16-09	9.04-23	9.16-23	1.01-22	1.10-22
Total	3.43+00	2.81+00	2.02+00	1.00+00	4.90-01	2.37-01	5.38-02	4.10-03	1.47-03

^aRead as 1.69×10^{-4}

²³⁹Pu and for all fission products or gaseous products only. Shultis and Faw (2000) reproduce the data and address procedures in detail. Calculations mirroring the data of Table 6 are illustrated in Figs. 7 and 8.

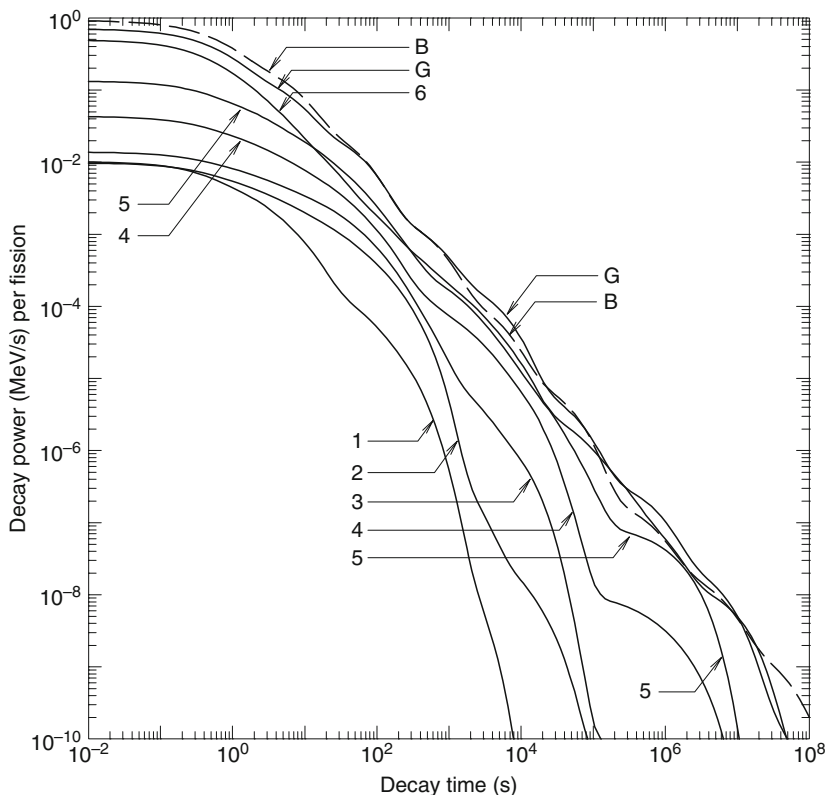
Capture Gamma Photons

The compound nucleus formed by neutron absorption is initially created in a highly excited state with excitation energy equal to the kinetic energy of the incident neutron plus the neutron-binding energy, which averages about 7 MeV. The decay of this nucleus, within 10^{-12} s and usually by way of intermediate states, typically produces several energetic photons. Such capture photons may be created intentionally by placing a material with a high thermal-neutron (n, γ) cross section in a thermal-neutron beam. The energy spectrum of the resulting capture gamma photons can then be used to identify trace elements in the sample. More often, however, capture gamma photons are an undesired secondary source of radiation encountered in neutron shielding. The estimation of the neutron absorption rate and the subsequent production of the capture photons is an important aspect of shielding analyses.

To calculate at some position in a shield the total source strength per unit volume of capture photons of energy E_γ , it is first necessary to know the energy-dependent fluence of neutrons, $\Phi(E)$, and the macroscopic absorption coefficient, $N^i \sigma_\gamma^i(E)$, where N^i and σ_γ^i are the atomic density and microscopic, radiative-capture cross section for the i th type of nuclide in the shield medium. If $F^i(E, E_\gamma) dE_\gamma$ represents the probability of obtaining a capture photon with energy in dE_γ about E_γ when a neutron of energy E is absorbed in the i th-type nuclide, the production, per unit volume, of capture photons with energy in unit energy about E_γ is

$$S_v(E_\gamma) = \sum_{i=1}^n \int_0^{E_{\max}} dE F^i(E, E_\gamma) N^i \sigma_\gamma^i(E) \Phi(E), \quad (13)$$

where E_{\max} is the maximum neutron energy and n is the number of nuclide species in the shield material. The evaluation of (13) can be accomplished only by using sophisticated computer codes for neutron transport calculations.

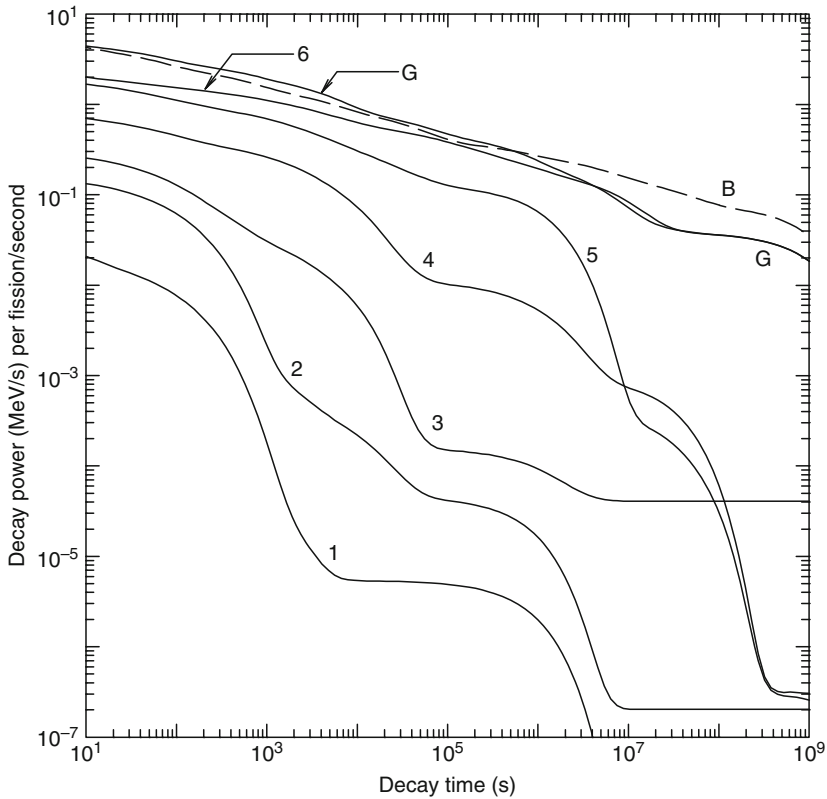


■ Figure 7

Total gamma-ray (G) and beta-particle (B) energy emission rates as a function of time after the thermal fission of ^{235}U . The curves identified by the numbers 1–6 are gamma emission rates for photons in the energy ranges 5–7.5, 4–5, 3–4, 2–3, 1–2, and 0–1 MeV, respectively

Fortunately, in most shielding situations, the evaluation of the capture photon source can be simplified considerably. The absorption cross sections are very small for energetic neutrons, typically no more than a few hundred millibarns for neutrons with energies between 10 keV and 10 MeV, and they are known with far less certainty than the scattering cross sections. The scattering cross-section for fast neutrons is always at least an order of magnitude greater than the absorption cross-section and, thus, in shielding analysis, the absorption of neutrons while they scatter and slow down is often ignored. Except in a few materials with isolated absorption resonances in the range of 1–100 eV, most of the neutron absorption occurs after the neutrons have completely slowed and assumed a speed distribution which is in equilibrium with the thermal motion of the atoms of the shielding medium. The thermal-neutron (n, γ) cross sections may be very large and in practice, the capture-gamma source calculation is usually based only on the absorption of thermal neutrons, with the epithermal and high-energy absorptions being neglected. Thus, (13) reduces to

$$S_v(E_\gamma) \simeq \sum_{i=1}^n F_{th}^i(E_\gamma) \bar{\sigma}_\gamma^i N^i \Phi_{th}, \quad (14)$$



■ Figure 8

Total gamma-ray (G) and beta-particle (B) energy-emission rates from a ^{235}U sample that has experienced a constant thermal-fission rate of one fission per second for effectively an infinite time so that the decay and production of fission products are equal. These data thus represent the worst-case situation for estimating radiation source strengths for fission products. The curves identified by the numbers 1–6 are gamma-emission rates for photons in the energy ranges 5–7.5, 4–5, 3–4, 2–3, 1–2, and 0–1 MeV, respectively

where F_{th}^i is the capture gamma spectrum arising from thermal neutron (n, γ) reactions and Φ_{th} is the neutron fluence integrated over all thermal energies. The thermal-averaged cross section $\bar{\sigma}_\gamma^i$ may be related to the 2200-m/s cross sections σ_γ^i given in ► Table 7 for selected elements, by $\bar{\sigma}_\gamma^i \approx \sqrt{\pi} \sigma_\gamma^i / 2$ (Lamarsh 1966). Capture cross sections and energy spectra of the capture photons, $F_{th}^i(E_\gamma)$ are given in ► Table 7 for selected elements.

Gamma Photons from Inelastic Neutron Scattering

The excited nucleus formed when a neutron is inelastically scattered decays to the ground state within about 10^{-14} s, with the excitation energy being released as one or more photons. Because of the constraints imposed by the conservation of energy and momentum in all scattering interactions, inelastic neutron scattering cannot occur unless the incident neutron energy is greater

Table 7

Radiative capture cross sections σ_y , and the number of capture gamma rays produced in common elements with natural isotopic abundances. The thermal capture cross sections are for 2200 m s^{-1} (0.0253 eV) neutrons in units of the barn (10^{-24} cm^2). Listed are the numbers of gamma rays produced, per neutron capture, in each of 11 energy groups

	σ_y (b)	Energy group (MeV)										
		0-1	1-2	2-3	3-4	4-5	5-6	6-7	7-8	8-9	9-10	10-11
H	3.32E-1	0.0000	0.0000	1.0000	0.0000	0.0000	0.0000	0.0000	0.0000	0.0000	0.0000	0.0000
Li	3.63E-2	0.1242	0.0491	0.8933	0.0000	0.0000	0.0000	0.0107	0.0402	0.0000	0.0000	0.0000
Be	9.20E-3	0.2641	0.0000	0.2356	0.4530	0.0000	0.0175	0.6375	0.0000	0.0000	0.0000	0.0000
B	1.03E-1	0.0000	0.0000	0.0000	0.0000	1.1014	0.0000	0.3950	0.4785	0.0000	0.0000	0.0000
Ti	6.10E+0	0.3213	0.9772	0.0832	0.1221	0.1187	0.0283	0.6089	0.0109	0.0043	0.0022	0.0003
V	5.04E+0	0.3837	0.2486	0.1335	0.0591	0.0877	0.3158	0.3947	0.1972	0.0000	0.0000	0.0000
Cr	3.10E+0	0.4051	0.1608	0.2067	0.0921	0.0421	0.1103	0.1189	0.2461	0.3766	0.1097	0.0000
Mn	1.33E+1	0.7128	0.1242	0.3838	0.2199	0.2049	0.2981	0.0949	0.3257	0.0000	0.0000	0.0000
Fe	2.55E+0	0.2781	0.2383	0.1018	0.1328	0.1137	0.1097	0.1045	0.5865	0.0087	0.0415	0.0011
Co	3.72E+1	0.9375	0.1737	0.0794	0.0920	0.1121	0.2991	0.2893	0.0980	0.0000	0.0000	0.0000
Ni	4.43E+0	0.2616	0.0658	0.0604	0.0364	0.0371	0.0746	0.1703	0.1404	0.5898	0.0000	0.0000
Cu	3.79E+0	0.8176	0.0602	0.0458	0.0588	0.0917	0.1018	0.1621	0.6488	0.0000	0.0000	0.0000
Zr	1.85E-1	0.8081	0.3048	0.2119	0.1361	0.0847	0.0820	0.1745	0.0042	0.0082	0.0000	0.0000
Mo	2.65E+0	0.8097	0.2000	0.0816	0.0416	0.0590	0.0542	0.0611	0.0074	0.0054	0.0000	0.0000
Ag	6.36E+1	0.6831	0.0166	0.0105	0.0102	0.0312	0.0877	0.0266	0.0112	0.0000	0.0000	0.0000
Cd	2.45E+3	1.0399	0.2239	0.1895	0.0736	0.0410	0.0957	0.0129	0.0073	0.0036	0.0025	0.0000
In	1.94E+2	0.3362	0.3534	0.1365	0.0311	0.0381	0.0328	0.0029	0.0000	0.0000	0.0000	0.0000

Source: Lone, Leavitt, and Harrison (1981)

than $(A+1)/A$ times the energy required to excite the scattering nucleus to its first excited state. Except for the heavy nuclides, neutron energies above about 0.5 MeV are typically required for inelastic scattering. The secondary photons produced by inelastic scattering of low-energy neutrons from heavy nuclides are generally not of interest in a shielding situation because of their low energies and the ease with which they are attenuated. Even the photons arising from inelastic scattering of high-energy neutrons (above 1 MeV) are rarely of importance in shielding analyses unless they represent the only source of photons.

The detailed calculation of secondary photon source strengths from inelastic neutron scattering requires knowledge of the fast-neutron fluence, the inelastic scattering cross sections, and spectra of resultant photons, all as functions of the incident neutron energy. Accounting accurately for inelastic scattering can be accomplished only with neutron transport codes using very detailed nuclear data. The cross sections and energy spectra of the secondary photons depend strongly on the incident neutron energy and the particular scattering nuclide. Such inelastic scattering data are known only for the more important nuclides and shielding materials, and even that known data require extensive data libraries such as that provided by

Roussin et al. (1980). Fortunately, in most analyses, these secondary photons are of little importance when compared with the eventual capture photons. Although inelastic neutron scattering is usually neglected with regard to its secondary-photon radiation, such scattering is a very important mechanism in the attenuation of the fast neutrons, better even than elastic scattering in some cases.

Activation Gamma Photons

For many materials, absorption of a neutron produces a radionuclide with a half-life ranging from a fraction of a second to many years. The radiation produced by the subsequent decay of these activation nuclei may be very significant for materials that have been exposed to large neutron fluences, especially structural components in a reactor core. Most radionuclides encountered in research laboratories, medical facilities, and industry are produced as activation nuclides from neutron absorption in some parent material. Such nuclides decay, usually by beta emission, leaving the daughter nucleus in an excited state which usually decays quickly (within 10^{-14} s) to its ground state with the emission of one or more gamma photons. Thus, the apparent half-life of the photon emitter is that of the parent (or activation nuclide), while the number and energy of the photons is characteristic of the nuclear structure of the daughter.

Although most activation products of concern in shielding problems arise from neutron absorption, there is one important exception in water-moderated reactors. The ^{16}O in the water can be transmuted to ^{16}N in the presence of fission neutrons by an (n, p) reaction with a threshold energy of 9.6 MeV. The activation cross section, averaged over the fission spectrum, is 0.019 mb (Jaeger 1968) and although reactions with such small cross sections are rarely important, ^{16}N decays with a 7.4-s half-life emitting gamma photons of 6.13 and 7.10 MeV (yields of 0.69 and 0.05 per decay). This activity may be very important in coolant channels of power reactors.

1.2.4 X-Ray Sources

As photons and charged particles interact with matter, secondary X-rays are inevitably produced. Because X-rays in most shielding applications usually have energies $\lesssim 100$ keV, they are easily attenuated by any shield adequate for the primary radiation. Consequently, the secondary X-rays are often completely neglected in analyses involving higher-energy photons. However, for those situations in which X-ray production is the only source of photons, it is important to estimate the intensity, energies, and the resulting exposure of the X-ray photons. There are two principal methods whereby secondary X-ray photons are generated: the rearrangement of atomic electron configurations leads to characteristic X-rays, and the deflection of charged particles in the nuclear electric field results in bremsstrahlung. Both mechanisms are briefly discussed as follows.

Characteristic X Rays

If the normal electron arrangement around a nucleus is altered through ionization of an inner electron or through excitation of electrons to higher energy levels, the electrons begin a complex series of transitions to vacancies in the lower shells (thereby acquiring higher binding energies) until the unexcited state of the atom is achieved. In each electronic transition, the difference in the binding energy between the final and initial states is either emitted as a photon, called a

characteristic X ray, or given up to an outer electron, which is ejected from the atom and is called an *Auger electron*. The discrete electron energy levels and the transition probabilities between levels vary with the Z number of the atom and, thus, the characteristic X rays provide a unique signature for each element.

The number of X rays with different energies is greatly increased by the multiplicity of electron energy levels available in each shell (1, 3, 5, 7,... distinct energy levels for the K, L, M, N, \dots shells, respectively). Fortunately, in shielding applications such detail is seldom needed, and often only the dominant K series of X rays is considered, with a single representative energy being used for all X rays.

There are several methods commonly encountered in shielding applications, whereby atoms may be excited and characteristic X rays produced. A photoelectric absorption leaves the absorbing atom in an ionized state. If the incident photon energy is sufficiently greater than the binding energy of the K -shell electron, which ranges from 14 eV for hydrogen to 115 keV for uranium, it is most likely (80–100%) that a vacancy is created in the K shell and, thus, that the K series of X rays dominates the subsequent secondary radiation. These X-ray photons produced from photoelectric absorption are often called *fluorescent radiation*.

Characteristic X rays can also arise following the decay of a radionuclide. In the decay process known as *electron capture*, an orbital electron, most likely from the K shell, is absorbed into the nucleus, thereby decreasing the nuclear charge by one unit. The resulting K -shell vacancy then gives rise to the K series of characteristic X rays. A second source of characteristic X rays, which occurs in many radionuclides, is a result of *internal conversion*. Most daughter nuclei formed as a result of any type of nuclear decay are left in excited states. This excitation energy may be either emitted as a gamma photon or transferred to an orbital electron which is ejected from the atom. Again it is most likely that a K -shell electron is involved in this internal conversion process.

Bremsstrahlung

A charged particle gives up its kinetic energy either by collisions with electrons along its path or by photon emission as it is deflected, and hence accelerated, by the electric fields of nuclei. The photons produced by the deflection of the charged particle are called *bremsstrahlung* (literally, “braking radiation”).

The kinetic energy lost by a charged particle of energy E , per unit path length of travel, to electron collisions (which excites and ionizes ambient atoms) and to bremsstrahlung is denoted by L_{coll} and L_{rad} , the collisional and radiative *stopping powers*, respectively. For a relativistic particle of rest mass M (i.e., $E \gg Mc^2$) slowing in a medium with atomic number Z , it can be shown that the ratio of radiative to ionization losses is approximately (Evans 1955)

$$\frac{L_{\text{rad}}}{L_{\text{coll}}} \simeq \frac{EZ}{700} \left(\frac{m_e}{M} \right)^2, \quad (15)$$

where E is in MeV. From this result, it is seen that bremsstrahlung is more important for high-energy particles of small mass incident on high- Z material. In shielding situations, only electrons ($m_e/M = 1$) are ever of importance for their associated bremsstrahlung. All other charged particles are far too massive to produce significant amounts of bremsstrahlung. Bremsstrahlung from electrons, however, is of particular radiological interest for devices that accelerate electrons, such as betatrons and X-ray tubes, or for situations involving radionuclides that emit only beta particles.

For monoenergetic electrons of energy E_o incident on a target thick when compared with the electron range, the number of bremsstrahlung photons of energy E , per unit energy and per incident electron, emitted as the electron is completely slowed down can be approximated by the distribution (Wyrd 1952)

$$N_{br}(E_o, E) = 2kZ \left[\left(\frac{E_o}{E} - 1 \right) - \frac{3}{4} \ln \left(\frac{E_o}{E} \right) \right], \quad E \leq E_o, \quad (16)$$

where k is a normalization constant independent of E . The fraction of the incident electron's kinetic energy that is subsequently emitted as bremsstrahlung can then be calculated from this approximation as

$$Y(E_o) = \frac{1}{E_o} \int_0^{E_o} dE E N_{br}(E_o, E) = \frac{13}{16} kZE_o, \quad (17)$$


which is always a small fraction for realistic shielding situations. For example, only 4% of the energy of a 0.5-MeV electron, when stopped in lead, is converted into bremsstrahlung. Equation (17) can be used to express the normalization constant k in terms of the radiation yield $Y(E_o)$, namely $kZ = 16Y(E_o)/(13E_o)$, where $Y(E_o)$ can be found from tabulated values (ICRU 1984). With this choice for k , the approximation of (16) agrees quite well with the thick-target bremsstrahlung spectrum calculated by much more elaborate methods, such as the continuous slowing-down model.

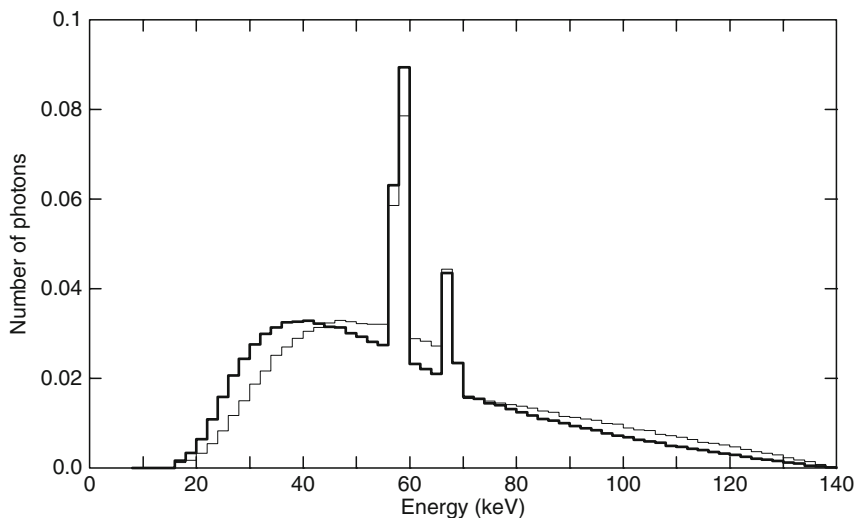
The electrons and positrons emitted by radionuclides undergoing beta decay produce bremsstrahlung as they slow down in the source material. However, these photons generally are of negligible importance in radiation shielding situations because the gamma and X-ray photons usually produced in radioactive decay are more numerous and penetrating than the bremsstrahlung. Only for the case of pure beta-particle emitters is beta-particle bremsstrahlung possibly of interest.

During the beta-decay process, the beta particle is accelerated, and consequently, a small amount of bremsstrahlung is emitted. These X rays, called "inner" bremsstrahlung, can be ignored in shielding analyses because only a small fraction of the beta-decay energy, on the average, is emitted as this type of radiation.

X-Ray Machines

The production of X-ray photons as bremsstrahlung and fluorescence occurs in any device that produces high-energy electrons. Devices that can produce significant amount of X rays are those in which a high voltage is used to accelerate electrons, which then strike an appropriate target material. Such is the basic principle of all X-ray tubes used in medical diagnosis and therapy, industrial applications, and research laboratories.

The energy spectrum of X-ray photons emitted from an X-ray tube has a continuous bremsstrahlung component up to the maximum electron energy (i.e., the maximum voltage applied to the tube). If the applied voltage is sufficiently high as to cause ionization in the target material, there will also be characteristic X-ray lines superimposed on the continuous bremsstrahlung spectrum. In  Fig. 9, two X-ray energy spectra are shown for the same operating voltage but for different amounts of beam filtration (i.e., different amounts of material attenuation in the X-ray beam). As the beam filtration increases the low-energy X rays are preferentially attenuated, and the X-ray spectrum hardens and becomes more penetrating. Also readily apparent in these spectra are the tungsten $K_{\alpha 1}$ and $K_{\beta 1}$ characteristic X rays.



■ Figure 9

Measured photon spectra from a Machlett Aeromax X-ray tube (tungsten anode) operated at a constant 140 kV potential. This tube has an inherent filter thickness of 2.50-mm aluminum equivalent and produces the spectrum shown by the thick line. The addition of an external 6-mm aluminum filter hardens the spectrum shown by the thin line. Both spectra are normalized to unit area. Data are from Fewell, Shuping, and Hawkins [1981]

Traditionally, the output from a particular X-ray machine is expressed by a parameter K_o ($R\text{ mA}^{-1}\text{ min}^{-1}$), which is the exposure in the beam (expressed in roentgens) at a specified distance from the tube focal spot (usually 1 m) that would be produced by a 1-mA tube current of 1-min duration. This performance parameter is usually assumed to be known when making analyses for X-ray shielding around a particular machine because it depends greatly on the operating voltage and the degree of beam filtering.

2 Conversion of Fluence to Dose

The *dose conversion coefficient* (ICRP 1987) provides the link between the physical description of a radiation field, namely the fluence and some measure of radiation dose or radiation sensor response. There are two main classes of dose conversion coefficients. One class, the *local* conversion coefficient, converts the energy spectrum of the fluence at a point, $\Phi(\mathbf{r}, E)$ to the point value of the dose (kerma, exposure, absorbed dose, or effective dose). The other class of dose conversion coefficients, sometimes called *phantom related*, makes use of local fluences and dose coefficients within geometric or anthropomorphic phantoms to evaluate risk-related average or effective doses of various types. Geometric phantoms are used for evaluation of operational dose quantities such as the ambient dose, which is correlated with monitored occupational exposure. Effective doses associated with anthropomorphic phantoms are used prospectively for planning and optimization of protection, and retrospectively for demonstration of compliance with dose limits or for comparing with dose constraints or reference levels. These phantom related

coefficients account for the relative radiation sensitivities of the various organs and tissues and the relative biological effectiveness of different radiations.

In the extreme, a receiver with volume V might have a sensitivity that depends on the radiation's energy and direction and where in V the radiation interacts, so the dose or response is

$$R = \int_0^\infty dE \int_{4\pi} d\Omega \int_V dV \mathcal{R}(\mathbf{r}, E, \Omega) \Phi(\mathbf{r}, E, \Omega), \quad (18)$$

in which R is the response, $\Phi(\mathbf{r}, E, \Omega)$ is the fluence, and $\mathcal{R}(\mathbf{r}, E, \Omega)$ is the dose conversion coefficient or response function. For many cases, the receiver is a point and the response is isotropic, so that

$$R(\mathbf{r}) = \int_0^\infty dE \mathcal{R}(E) \Phi(\mathbf{r}, E). \quad (19)$$

Fluence-to-dose conversion is accomplished internally within calculations using point-kernel codes such as Isoshield, Microshield, and the QAD series of codes. The same is true for multi-group codes such as the DOORS and PARTISN series and, in general, it is necessary for the user to provide data tables for dose conversion coefficients. With Monte Carlo codes, such as MCNP, the absorbed dose or kerma may be computed directly or the energy-dependent fluence may be first computed and then dose conversion coefficients applied to the results.

2.1 Local Dosimetric Quantities

Dosimetric quantities are intended to provide, at a point or in a region of interest, a physical measure correlated with a radiation effect. The radiometric quantity called the fluence is not closely enough related to most radiation effects to be a useful determinant. Energy fluence appears to be more closely correlated with radiation effect than is fluence alone, because the energy carried by a particle must have some correlation with the damage it can do to material such as biological matter. This choice is not entirely adequate – not even for particles of a single type. One must examine more deeply the mechanism of the effect of radiation on matter in order to determine what properties of the radiation are best correlated with its effects, especially its biological hazards. One must account for energy transfer from the primary radiation, neutrons or photons in this context, to the absorbing medium at the microscopic level. One must then account for the creation of secondary charged particles and, as well, tertiary particles such as X-rays created as charged particles are stopped.

2.1.1 Energy Imparted and Absorbed Dose

For a given volume of matter of mass m , the energy ϵ imparted in some time interval is the sum of the energies (excluding rest-mass energies) of all charged and uncharged ionizing particles entering the volume minus the sum of the energies (excluding rest-mass energies) of all charged and uncharged ionizing particles leaving the volume, further corrected by subtracting the energy equivalent of any increase in rest-mass energy of the material in the volume. Thus, the energy imparted is that which is involved in the ionization and excitation of atoms and molecules within the volume and the associated chemical changes. This energy is eventually degraded almost entirely into thermal energy. The *specific energy* $z \equiv \epsilon/m$, the energy imparted per unit mass, leads to the absorbed dose quantity.

The *absorbed dose* is the quotient of the *mean* energy imparted $\bar{\epsilon}$ to matter of mass m , in the limit as the mass approaches zero (ICRU 1971). Or it may be written in differential form, namely,

$$D \equiv \lim_{m \rightarrow 0} \bar{z} = \frac{d\bar{\epsilon}}{dm}. \quad (20)$$

The standard unit of absorbed dose is the gray (Gy), 1 Gy being equal to an imparted energy of 1 joule per kilogram. A traditional unit for absorbed dose is the rad, defined as 100 ergs per gram. Thus, 1 rad = 0.01 Gy.

The concept of absorbed dose is very useful in radiation protection. Energy imparted per unit mass in tissue is closely, but not perfectly, correlated with radiation hazard.

2.1.2 Kerma

The absorbed dose is a measurable quantity, but in many circumstances it is difficult to calculate from the incident radiation fluence and material properties because such a calculation would require a detailed accounting of the energies of all secondary particles leaving the volume of interest. A closely related deterministic quantity, used only in connection with indirectly ionizing (uncharged) radiation, is the *kerma*, an acronym for *kinetic energy of radiation produced per unit mass in matter*. If E_{tr} is the sum of the initial kinetic energies of all the charged ionizing particles released by interaction of indirectly ionizing particles in matter of mass m , then

$$K \equiv \lim_{m \rightarrow 0} \frac{\bar{E}_{tr}}{m} = \frac{d\bar{E}_{tr}}{dm}, \quad (21)$$

where \bar{E}_{tr} is the mean or expected energy transferred to the secondary charged particles in the mass m . That some of the initial kinetic energy may be transferred ultimately to bremsstrahlung and lost from m , for example, is irrelevant. The kerma is relatively easy to calculate (requiring knowledge of only the initial interactions), but is hard to measure (because all the initial kinetic energy of the charged particles may not be deposited in m).

The use of the kerma requires the specification of the material present in the incremental volume, possibly hypothetical, used as an idealized receptor of radiation. Thus, one may speak conceptually of tissue kerma in a concrete shield or in a vacuum, even though the incremental volume of tissue may not be actually present.

Absorbed dose and kerma are frequently almost equal in magnitude. Under a condition known as *charged particle equilibrium*, they are equal. This equilibrium exists in an incremental volume about a point of interest if, for every charged particle leaving the volume, another of the same type and with the same kinetic energy enters the volume traveling in the same direction. In many practical situations, this charged particle equilibrium is closely achieved so that the kerma is a close approximation of the absorbed dose.

2.1.3 Exposure

The quantity called *exposure*, with abbreviation X , is used traditionally to specify the radiation field of gamma or X-ray photons. It is defined as the absolute value of the ion charge of one

sign produced anywhere in air by the complete stoppage of all negative and positive electrons, except those produced by bremsstrahlung, that are liberated in an incremental volume of air, per unit mass of air in that volume. The exposure is closely related to air kerma but differs in one important respect. The phenomenon measured by the interaction of the photons in the incremental volume of air is not the kinetic energy of the secondary electrons but the ionization caused by the further interaction of these secondary electrons with air. The SI unit of exposure is coulombs per kilogram. The traditional unit is the roentgen, abbreviated R, which is defined as precisely 2.58×10^{-4} coulomb of separated charge of one sign per kilogram of air in the incremental volume where the primary photon interactions occur.

Kerma in air and exposure are very closely related. A known proportion of the initial kinetic energy of secondary charged particles results in ionization of the air, namely, 33.85 ± 0.15 electron volts of kinetic energy per ion pair (ICRU 1979). The product of this factor and the air kerma, with appropriate unit conversions, is the exposure X . The product, however, must be reduced slightly to account for the fact that some of the original energy of the secondary electrons may result in bremsstrahlung, not in ionization or excitation.

2.1.4 Local Dose Equivalent Quantities

If the energy imparted by ionizing radiation per unit mass of tissue were by itself an adequate measure of biological hazard, absorbed dose would be the best dosimetric quantity to use for radiation protection purposes. However, there are also other factors to consider that are related to the spatial distribution of radiation-induced ionization and excitation. The charged particles responsible for the ionization may themselves constitute the primary radiation, or may arise secondarily from interactions of uncharged, indirectly ionizing, primary radiation.

Relative Biological Effectiveness

In dealing with the fundamental behavior of biological material or organisms subjected to radiation, one needs to take into account variations in the sensitivity of the biological material to different types or energies of radiation. For this purpose, radiobiologists define a *relative biological effectiveness* (RBE) for each type and energy of radiation, and, indeed, for each biological effect or *endpoint*. The RBE is the ratio of the absorbed dose of a reference type of radiation (typically, 250-kVp X-rays or ^{60}Co gamma rays) producing a certain kind and degree of biological effect to the absorbed dose of the radiation under consideration required to produce the same kind and degree of effect. RBE is normally determined experimentally and takes into account all factors affecting biological response to radiation in addition to absorbed dose.

Linear Energy Transfer

As a charged particle moves through matter it slows, giving up its kinetic energy through (a) Coulombic interactions with ambient atomic electrons causing ionization and excitation of the atoms and (b) radiative energy loss by the emission of bremsstrahlung (important only for electrons). The *stopping power* or unrestricted linear energy transfer, LET, L_∞ , often denoted as $-dE/dx$, is the expected energy loss per unit distance of travel by the charged particle.

The larger the LET of a radiation particle the more the ionization, and hence the biological damage, it causes per unit travel distance. Calculation of the LET is accomplished efficiently using one of the STAR Codes (Berger et al. 2005). Representative results are summarized by Shultis and Faw (2000).

Radiation Weighting Factor and Dose Equivalent

The RBE depends on many variables: the physical nature of the radiation field, the type of biological material, the particular biological response, the degree of response, the radiation dose, and the dose rate or dose fractionation. For this reason, it is too complicated a concept to be applied in the routine practice of radiation protection or in the establishment of broadly applied standards and regulations. Since 1964, a surrogate quantity called the *quality factor* Q (not to be confused with the Q value of a nuclear reaction) has been applied to the local value of the absorbed dose to yield a quantity called the *dose equivalent* H , recognized as an appropriate measure of radiation risk when applied to operational dosimetry. As is discussed below, the quality factor is also applied to evaluation of geometric-phantom related doses such as the ambient dose. Note that “the dose equivalent is based on the absorbed dose at a point in tissue which is weighted by a distribution of quality factors which are related to the LET distribution at that point” (NCRP 1993).

Because the spatial density of ionization and excitation along particle tracks is believed to be an important parameter in explaining the variations in biological effects of radiation of different types and energies, and because the density is clearly proportional to linear energy transfer (LET), the quality factor was defined in terms of LET. In particular, because tissue is largely water and has an average atomic number close to that of water, the quality factor was made a mathematical function of the unrestricted LET in water, L_∞ (ICRP 2007).

$$Q(L_\infty) = \begin{cases} 1 & L_\infty < 10 \text{ keV}/\mu\text{m} \\ 0.32L_\infty - 2.2 & 10 \leq L_\infty \leq 100 \text{ keV}/\mu\text{m} \\ 300/\sqrt{L_\infty} & L_\infty > 100 \text{ keV}/\mu\text{m}. \end{cases} \quad (22)$$

To ascribe a quality factor to some particular primary radiation, whether that primary radiation be directly or indirectly ionizing, more information is needed about the nature of the energy deposition. In principle, one must first determine how the absorbed dose is apportioned among particles losing energy at different LETs. One may then account for the variability of Q with L_∞ and determine an average quality factor \bar{Q} .

Quality factors can be ascribed to uncharged ionizing radiation through a knowledge of the properties of the secondary charged particles they release upon interaction with matter. Because secondary electrons released by gamma rays or X-rays are always assigned a quality factor of unity, the same factor applies universally to all ionizing photons. The situation for neutrons is not so simple, and average values must be determined as indicated in the following discussion.

Closely related to the quality factor is the *radiation weighting factor* w_R , introduced by the ICRP in 1991 and modified in 2007, for use with the dose equivalent in tissues of the anthropomorphic phantom and addressed in [2.3.3](#). The SI unit of the dose equivalent H is the sievert, abbreviated as Sv. [Table 8](#) compares quality factors specified by

■ Table 8

Mean quality factors Q or radiation weighting factors w_R adopted by the ICRP (2007) and by the US Nuclear Regulatory Commission (1991), based on NCRP (1971). They apply to the radiation incident on the body or, for internal sources, emitted from the source

Radiation	USNRC ^a	ICRP (2007) ^b
Gamma- and X-rays of all energies	1	1
Electrons and muons of all energies	1	1
Protons, other than recoil	10	2
Alpha particles, fission fragments, heavy nuclei	20	20
Neutrons		
MeV		
0.0001	2	2.5
0.001	2	2.5
0.01	2.5	3.0
0.1	7.5	10.0
0.5	11	19.3
1	11	20.7
2.5	9	16.0
5	8	12.0
7	7	10.3
10	6.5	8.8
14	7.5	7.7
20	8	6.8
40	7	5.7
60	5.5	5.4
100	4	4.9

^aNeutron data based on a 30-cm diameter cylinder tissue-equivalent phantom

^bThe neutron radiation weighting factor is computed from (23)

the US Nuclear Regulatory Commission (NCRP 1971, USNRC 1991) and radiation weighting factors specified by the ICRP (2007). The 2007 formulation computes neutron weighting factors as

$$\omega_R = \begin{cases} 2.5 + 18.2 \exp[-\ln^2(E)/6], & E < 1 \text{ MeV}, \\ 5.0 + 17 \exp[-\ln^2(2E)/6], & 1 \text{ MeV} \leq E \leq 50 \text{ MeV}, \\ 2.5 + 3.25 \exp[-\ln^2(0.04E)/6], & E > 50 \text{ MeV}. \end{cases} \quad (23)$$

2.2 Evaluation of Local Dose Conversion Coefficients

2.2.1 Photon Kerma, Absorbed Dose, and Exposure

If $\mu(E)$ is the total interaction coefficient (less coherent scattering), $f(E)$ is the fraction of the photon's energy E transferred to secondary charged particles and ρ is the material density, the kerma is given by

$$K = \left(\frac{f(E)\mu(E)}{\rho} \right) E\Phi(E). \quad (24)$$

The quantity $f(E)\mu(E)$ is called the linear *energy transfer* coefficient μ_{tr} . For energy E in units of MeV, Φ in units of cm^{-2} , the mass energy transfer coefficient $\mu_{tr}(E)/\rho$ in units of cm^2/g , and the conversion coefficient \mathcal{R}_K in units of Gy cm^2 ,

$$\mathcal{R}_K(E) = 1.602 \times 10^{-10} E \left(\frac{\mu_{tr}(E)}{\rho} \right), \quad (25)$$

in which $\mu_{tr}(E)$ is averaged on the basis of weight fractions of each element in the transport medium at the point of interest.

If the secondary charged particles produce substantial bremsstrahlung, a significant portion of the charged-particles' kinetic energy is reradiated away as bremsstrahlung from the region of interest. Even under charged-particle equilibrium, the kerma may overpredict the absorbed dose. The production of bremsstrahlung can be taken into account by the substitution in (25) of the mass energy absorption coefficient $\mu_{en}/\rho = [1 - G(E)]\mu_{tr}/\rho$, where $G(E)$ is the fraction of the secondary-charged particle's initial kinetic energy radiated away as bremsstrahlung. Then, under the assumptions of charged-particle equilibrium and no local energy transfer from bremsstrahlung,

$$\mathcal{R}_D(E) = 1.602 \times 10^{-10} E \left(\frac{\mu_{en}(E)}{\rho} \right). \quad (26)$$

Extensive table of μ_{en}/ρ values are available on line (Hubbell and Seltzer 2004).

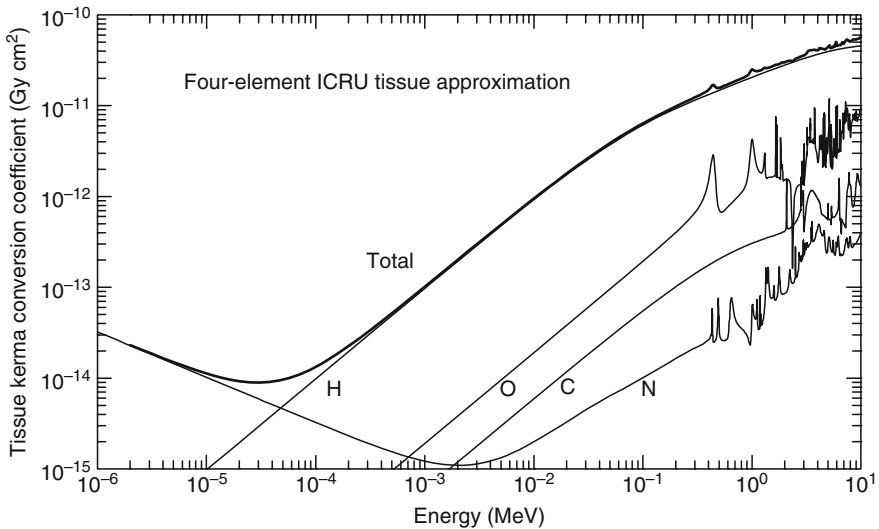
For exposure in units of roentgen, E in MeV, (μ_{en}/ρ) for air in cm^2/g , and Φ in cm^{-2} ,

$$X = 1.835 \times 10^{-8} E \left(\frac{\mu_{en}(E)}{\rho} \right)_{\text{air}} \Phi. \quad (27)$$

2.2.2 Neutron Kerma and Absorbed Dose

Charged particle equilibrium is, in most instances, closely approached in neutron transport, so that the kerma is an excellent approximation of the absorbed dose. The local dose conversion coefficient, in units of Gy cm^2 is given by

$$\mathcal{R}_K(E) = 1.602 \times 10^{-10} \sum_i \frac{N_i}{\rho} \sum_j \sigma_{ji}(E) \epsilon_{ji}(E), \quad (28)$$



■ Figure 10

Kerma dose conversion coefficient for neutron interactions in the ICRU four-element approximation for tissue, with mass fractions: 0.101 H, 0.111 C, 0.026 N, and 0.762 O. Computed using NJOY-processed ENDF/B-V data

in which ρ is the material density (g/cm^3), N_i (cm^{-3}) is the density of atomic species i , $\sigma_{ji}(E)$ is the cross-section (cm^2) for nuclear reaction j with atomic species i , and $\epsilon_{ji}(E)$ (MeV) is the energy transferred to the medium in that same reaction. ➤ Figure 10 illustrates the neutron-kerma dose conversion coefficient for a four-element tissue approximation.

2.3 Phantom-Related Dosimetric Quantities

2.3.1 Characterization of Ambient Radiation

A problem very often encountered in radiation shielding is as follows. At a given reference point representing a location accessible to the human body, the radiation field has been characterized in terms of the fluxes or fluences of radiations of various types computed in the *free field*, that is, in the absence of the body. Suppose for the moment that only a single type of radiation is involved, say either photons or neutrons, and the energy spectrum $\Phi(E)$ of the fluence is known at the reference point. What is needed is the ability to define and to calculate, at *that point* and for *that single type of radiation*, a dose quantity R for a phantom representation of the human subject, which can be calculated using an appropriate conversion coefficient, or response function \mathcal{R} , as

$$R = \int_0^{\infty} dE \mathcal{R}(E) \Phi(E), \quad (29)$$

analogous to (19). Here \mathcal{R} is a phantom-related conversion coefficient and Φ is the fluence energy spectrum, not perturbed by the presence of the phantom. Generation of the conversion coefficient, of course, requires determination of the absorbed dose and accounting for the radiation transport inside a phantom resulting from incident radiation with a carefully defined angular distribution (usually, a parallel beam).

Suppose one knows the angular and energy distributions of the fluence of ionizing radiation at a point in space, that is, the radiation field at the point. Both operational and limiting dose quantities are evaluated as radiation doses in phantoms irradiated by a *uniform* radiation field derived from the actual radiation field at the point. In the *expanded field*, the phantom is irradiated over its entire surface by radiation whose energy and angular distributions are the same as those in the actual field at the point of interest. In the *expanded and aligned field*, the phantom is irradiated by unidirectional radiation whose energy spectrum is the same as that in the actual field at the point.

2.3.2 Dose Conversion Factors for Geometric Phantoms

Of the geometrically simple mathematical phantoms, the more commonly used is the *ICRU sphere* of 30 cm diameter with density 1.0 g/cm^3 and of tissue-equivalent composition, by weight—76.2% oxygen, 11.1% carbon, 10.1% hydrogen, and 2.6% nitrogen. The dose quantity may be the maximum dose within the phantom or the dose at some appropriate depth.

Dose conversion coefficients for the phantoms are computed for a number of irradiation conditions, for example, a broad parallel beam of monoenergetic photons or neutrons. At selected points or regions within the phantom, absorbed-dose values, often approximated by kerma values, are determined. In this determination, contributions by all secondary-charged particles at that position are taken into account; and for each type of charged particle of a given energy, the L_∞ value in water and, therefore, Q are obtained. These are then applied to the absorbed-dose contribution from each charged particle to obtain the dose-equivalent contribution at the given location in the phantom. The resulting distributions of absorbed dose and dose equivalent throughout the phantom are then examined to obtain the maximum value, or the value otherwise considered to be in the most significant location, say at 10 mm depth. The prescribed dose conversion coefficient is then that value of either absorbed dose or dose equivalent divided by the fluence of the incident beam.

These conversion coefficients are intended for operational dose quantities and are designed to provide data for radiation protection purposes at doses well below limits for public exposure. The dose quantities may be treated as point functions, determined exclusively by the radiation field in the vicinity of a point in space. Application of the conversion coefficients for these dose quantities is explained in depth by the ICRU (1988).

Deep Dose Equivalent Index

For this dose quantity, $H_{1,d}$, the radiation field is assumed to have the same fluence and energy distribution as those at a reference point, but expanded to a broad parallel beam striking the phantom. The dose is the maximum dose equivalent within the 14-cm-radius central core of the ICRU sphere. There are difficulties in using this dose quantity when the incident radiation is polyenergetic or consists of both neutrons and gamma rays. The reason is that the depth at

which the dose is maximum varies from one type of radiation to another or from one energy to another. Thus, this quantity is nonadditive.

Shallow Dose Equivalent Index

This dose quantity, $H_{I,s}$, is very similar to the deep dose-equivalent index, except that the dose equivalent is the maximum value between depths 0.007 and 0.010 cm from the surface of the ICRU sphere (corresponding to the depths of radiosensitive cells of the skin).

Ambient Dose Equivalent

For this dose, $H^*(d)$, the radiation field is assumed to have the same fluence and energy distribution as those at a reference point but expanded to a broad parallel beam striking the phantom. The dose equivalent is evaluated at depth d , on a radius opposing the beam direction. This calculated dose quantity is associated with the measured *personal dose equivalent* $H_p(d)$, the dose equivalent in soft tissue below a specified point on the body, at depth d . For weakly penetrating radiation, depths of 0.07 mm for the skin and 3 mm for the lens of the eye are employed. For strongly penetrating radiation, a depth of 10 mm is employed.

Directional Dose Equivalent

For this dose quantity, $H'(d, \Omega)$, the angular and energy distributions of the fluence at a point of reference are assumed to apply over the entire phantom surface. The depths at which the dose equivalent is evaluated are the same as those for the ambient dose equivalent. The specification of the angular distribution, denoted symbolically by argument Ω , requires specification of a reference system of coordinates in which directions are expressed. In the particular case of a unidirectional field, $H'(d, \Omega)$ may be written as $H'(d)$ and is equivalent to $H^*(d)$.

Irradiation Geometries for Spherical Phantoms

Photon and neutron conversion coefficients for deep and shallow indices and for directional dose equivalents at depths of 0.07, 3, and 10 mm have been calculated for radiation protection purposes and have been tabulated by the ICRP (1987) for the following irradiation geometries: (a) PAR, a single-plane parallel beam, (b) OPP, two opposed plane parallel beams, (c) ROT, a rotating-plane parallel beam (i.e., a plane-parallel beam with the sphere rotating about an axis normal to the beam), and (d) ISO, an isotropic radiation field.

For a single plane parallel beam, the more conservative of the irradiation geometries, the conversion coefficients for $H_{I,d}$ and $H^*(d)$ at 10 mm are almost identical for photons. For neutrons, the two differ only at low energies, with the deep dose equivalent index being greater and thus more conservative.

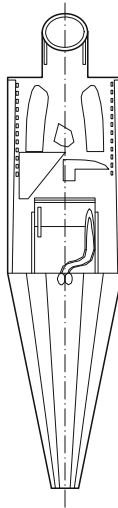
Slab and Cylinder Phantoms

Dose conversion coefficients are also available for plane parallel beams incident on slabs and on cylinders with axes normal to the beam. Slab-phantom deep-dose conversion coefficients are tabulated by the ICRP (1987) for high-energy photons and neutrons. Cylinder-phantom deep-dose coefficients reported by the NCRP (1971) are of special interest in that they are employed in US federal radiation protection regulations (USNRC 1991).

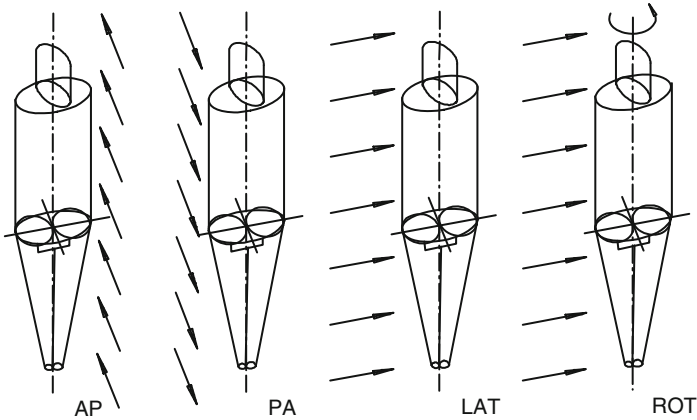
2.3.3 Dose Coefficients for Anthropomorphic Phantoms

The effective dose equivalent H_E and the effective dose \mathcal{E} are limiting doses based on an anthropomorphic phantom for which doses to individual organs and tissues may be determined. Averaging the individual doses with weight factors related to radiosensitivity leads to the effective dose or effective dose equivalent. In many calculations, a single phantom represents the adult male or female. In other calculations, separate male and female phantoms are used. These dose quantities have been developed for radiation-protection purposes in occupational and public health and, to some extent, in internal dosimetry as applied to nuclear-medicine procedures. The dose quantities apply, on average, to large and diverse populations, at doses well below annual limits. Their use in assessment of health effects for an individual subject requires a very careful judgment. One male phantom, Adam, is illustrated in ► Fig. 11. Adam has a companion female phantom, named Eva (Kramer et al. 1982). In yet other calculations (Cristy and Eckerman 1987), a suite of phantoms is available for representation of the human at various ages from the newborn to the adult. The many phantoms used for measurements or calculations are described in ICRU Report 48 (1992).

Anthropomorphic phantoms are mathematical descriptions of the organs and tissues of the human body, formulated in such a way as to permit calculation or numerical simulation of the transport of radiation throughout the body. In calculations leading to conversion coefficients, monoenergetic radiation is incident on the phantom in fixed geometry. One geometry leading to conservative values of conversion coefficients is *anteroposterior* (AP), irradiation from the front to the back with the beam at right angles to the long axis of the body. Other geometries, *posteroanterior* (PA), *lateral* (LAT), *rotational* (ROT), and *isotropic* (ISO) are illustrated in ► Fig. 12. The ROT case is thought to be an appropriate choice for the irradiation pattern experienced by a person moving unsystematically relative to the location of a radiation



■ Figure 11
Sectional view of the male anthropomorphic phantom used in calculation of the effective dose



■ Figure 12

Irradiation geometries for the anthropomorphic phantom. From ICRP (1987)

source. However, the AP case, being most conservative, is the choice in the absence of particular information on the irradiation circumstances.

Effective Dose Equivalent

In 1977, the ICRP introduced the effective dose equivalent H_E , defined as a weighted average of mean dose equivalents in the tissues and organs of the human body, namely,

$$H_E = \sum_T \omega_T D_T Q_T, \quad (30)$$

in which D_T is the mean absorbed dose in organ T and Q_T is the corresponding mean quality factor. If m_T is the mass of organ or tissue T , then

$$Q_T = \frac{1}{m_T} \int dm QD = \frac{1}{m_T} \int dm \int dL_\infty D(L_\infty) Q(L_\infty), \quad (31)$$

in which $D(L_\infty) dL_\infty$ is that portion of the absorbed dose attributable to charged particles with LETs in the range dL_∞ about L_∞ . Tissue weight factors to be used with the effective dose equivalent are listed in [Table 9](#). They are determined by the relative sensitivities for stochastic radiation effects such as cancer and first-generation hereditary illness. The 1977 values are still of importance because of their implicit use in federal radiation protection regulations [USNRC 1991] in the United States.

Effective Dose

In 1991, the ICRP recommended a replacement of the effective dose equivalent by the effective dose. This recommendation was endorsed in 1993 by the NCRP in the United States and modified by the ICRP in 2007. The effective dose \mathcal{E} is defined as follows. Suppose that the body is irradiated externally by a mixture of particles of different type and different energy, the different radiations being identified by the subscript R . The effective dose may then be determined as

$$\mathcal{E} = \sum_T \omega_T H_T = \sum_T \omega_T \sum_R \omega_R D_{T,R}, \quad (32)$$

■ **Table 9**

Tissue weight factors adopted by the ICRP (1991, 2007) and the NCRP (1993) for use in determination of the effective dose

Organ	ICRP (1977) USNRC (1991)	ICRP (1991) NCRP (1993)	ICRP (2007)
Gonads	0.25	0.20	0.08
Bone marrow (red)	0.12	0.12	0.12
Lung	0.12	0.12	0.12
Breast	0.15	0.05	0.12
Thyroid	0.03	0.05	0.04
Bone surfaces	0.03	0.01	0.01
Remainder	0.30 ^a	0.05 ^b	0.12 ^c
Colon ^d	–	0.12	0.12
Stomach	–	0.12	0.12
Bladder	–	0.05	0.04
Liver	–	0.05	0.04
Oesophagus	–	0.05	0.04
Skin	–	0.01	0.01
Salivary glands	–	–	0.01
Brain	–	–	0.01

^aA weight of 0.06 is applied to each of the five organs or tissues of the remainder receiving the highest dose equivalents, the components of the GI system being treated as separate organs

^bThe remainder is composed of the following additional organs and tissues: adrenals, brain, small intestine, large intestine, kidney, muscle, pancreas, spleen, thymus, uterus, and others selectively irradiated. With certain exceptions, the weight factor of 0.05 is applied to the average dose in the remainder tissues and organs

^cThe remainder tissues are adrenals, extrathoracic tissues, gall bladder, heart wall, kidneys, lymphatic nodes, muscle, oral mucosa, pancreas, prostate, small intestine, spleen, thymus, and uterus/cervix. The weight factor for the remainder is applied to the average of the male and female remainder doses, each being the unweighted average dose to the 13 organs or tissues appropriate to the male or female

^dIn both the 1991 and 2007 formulations, the dose to the colon is the mass-weighted mean of upper and lower intestine doses

in which H_T is the *equivalent dose* in organ or tissue T , $D_{T,R}$ is the mean absorbed dose in organ or tissue T from radiation R , ω_R is a radiation weighting factor for radiation R as determined from ► [Table 8](#), and ω_T is a tissue weight factor given in ► [Table 9](#). Note that in this formulation, ω_R is independent of the organ or tissue and ω_T is independent of the radiation.

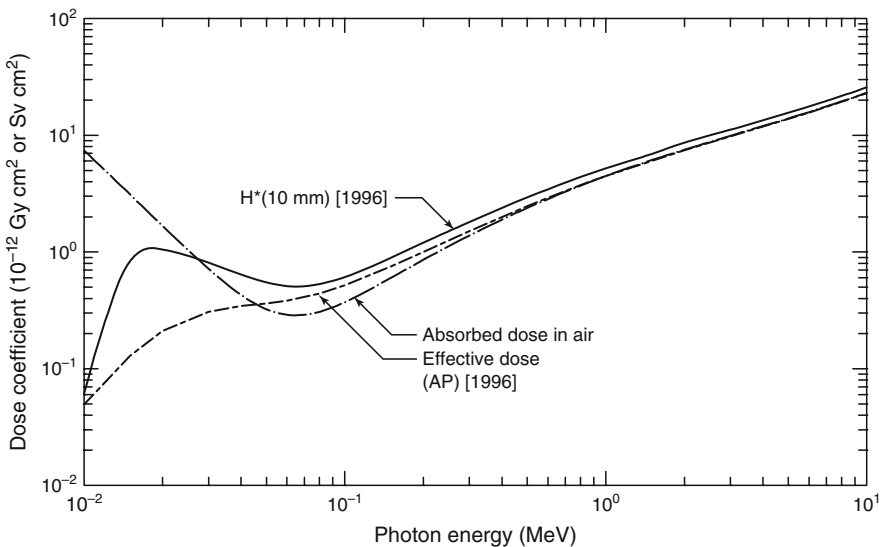
In computing the dose conversion coefficient for the effective dose, one assumes that the phantom is irradiated by unit fluence of monoenergetic particles of energy E . Neither local values nor tissue-average dose equivalents but only tissue-average absorbed doses are calculated. The tissue-average absorbed doses are multiplied by quality factors determined not by the LET distributions in the tissues and organs but by quality factors characteristic of the incident

radiation. This is a fundamental departure from the methodology used in determination of the conversion coefficients for the effective dose equivalent.

2.3.4 Comparison of Dose Conversion Coefficients

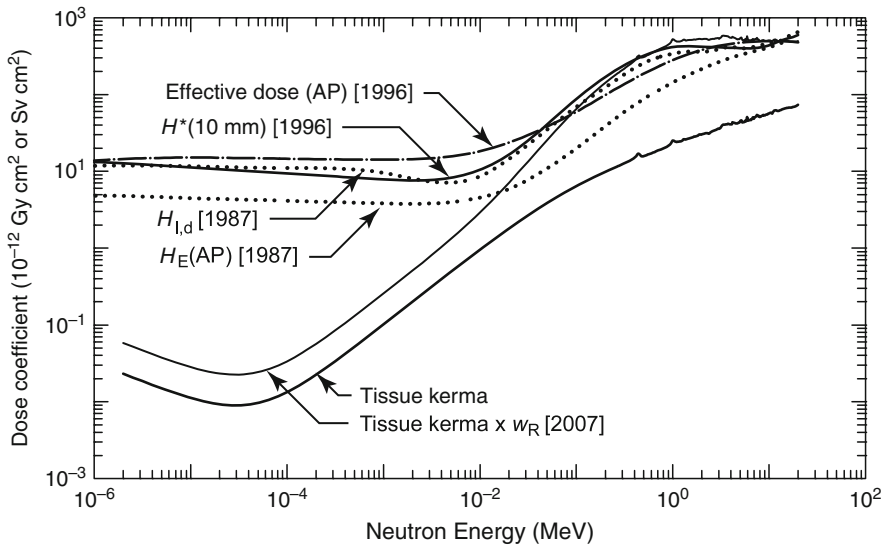
► *Figures 13* and ► *14* compare the dose conversion coefficients for photons and neutrons, respectively. At energies above about 0.1 MeV, the various photon coefficients are very nearly equal. This is a fortunate situation for radiation dosimetry and surveillance purposes. Instruments such as ion chambers respond essentially in proportion to absorbed dose in air. Personnel dosimeters are usually calibrated to give responses proportional to the ambient dose. Both the ambient dose and the absorbed dose in air closely approximate the effective dose equivalent. However, below 100 keV the three conversion coefficients are quite different. At the scale of the graph, the 1996 ambient dose coefficients are indistinguishable from the 1987 deep dose index.

The comparison of conversion coefficients for neutrons is not so straightforward. The tissue kerma always has the smallest value, largely because no quality factor is applied to the kinetic energy of a secondary charged particle. Fortunately, the ambient dose and the deep dose equivalent index have conversion coefficients that are very similar at energies above about 5 keV. Therefore, historic dosimetry records based on personnel dosimeters calibrated in terms of the deep dose equivalent index do not diverge significantly from those that would have been recorded using more modern dose standards. Furthermore, the ambient dose coefficient exceeds that for the effective dose equivalent index above about 0.01 MeV. Thus, calibration of personnel dosimeters in terms of ambient dose is a conservative practice. It should be noted that neutron dose conversion factors in the U.S. N.R.C. regulations (10CFR Part 20) are based on very early calculations (NCRP 1971).



■ **Figure 13**

Comparison of photon dose conversion coefficients. Data are from ICRP (1996)



■ Figure 14

Comparison of neutron dose conversion coefficients. Data are from ICRP (1987, 1996, 2007). The 1987 deep dose index and effective dose equivalent are based on quality factors defined prior to ICRP Report 45 (1985)

3 Basic Methods in Radiation Attenuation Calculations

In this section, simplified methods for estimating the dose under specialized source and geometric conditions are reviewed. The methods apply in circumstances in which there is a direct path from source to receiver and a significant portion of the dose is from uncollided radiation. A spatially distributed source is divided conceptually into a set of contiguous small sources, each of which can be treated as a point source. With an *uncollided point kernel*, the uncollided dose can be calculated for each point source. Summation or integration over the source volume then yields the total uncollided dose. In general, a correction factor may be applied to the uncollided point kernel to yield the point kernel for combined uncollided and collided radiation. For monoenergetic gamma rays, the correction factor is referred to as the *buildup factor*. For polyenergetic X-rays, an *attenuation factor* jointly accounts for both collided and uncollided radiation. Similarly, for polyenergetic neutron sources in hydrogenous media, the dose from collided and uncollided fast neutrons is estimated with a total-dose point kernel.

3.1 The Point-Kernel Concept

The fluence or dose at some point of interest is in many situations determined primarily by the uncollided radiation that has streamed directly from the source without any interaction in the surrounding medium. For example, if only air separates a gamma-ray or neutron source from a detector, interactions in the intervening air or in nearby solid objects, such as the ground or

building walls, are often negligible, and the radiation field at the detector is due almost entirely to uncollided radiation coming directly from the source. Scattered and other secondary radiation in such situations is of minor importance. In this section, some basic properties of the uncollided radiation field are presented, and methods for estimating the dose from this radiation are derived.

3.1.1 Exponential Attenuation

The *linear interaction coefficient* for indirectly ionizing radiations such as gamma rays or neutrons, $\mu(E)$, also called the *macroscopic cross section* $\Sigma(E)$, in the limit of small distances, is the probability per unit distance of travel that a particle of energy E experiences an interaction such as scattering or absorption. From this definition, it is easily shown that the probability of a particle traveling a distance x without interaction is given by


$$P(x) = e^{-\mu x}. \quad (33)$$

From this result, the *half-value thickness* x_2 that is required to reduce the uncollided radiation to one-half of its initial value can readily be found, namely, $x_2 = \ln 2/\mu$. Similarly, the *tenth-value thickness* x_{10} , which is the distance the uncollided radiation must travel to be reduced to 10% of its initial value, is found to be $x_{10} = \ln 10/\mu$. The concepts of half-value and tenth-value thicknesses, although stated here for uncollided radiation, are also often used to describe the attenuation of the total radiation dose. The average distance λ that a particle streams from the point of its birth to the point at which it makes its first interaction is called the *mean-free-path length*. It is easily shown that $\lambda = 1/\mu$.

3.1.2 Uncollided Dose from a Monoenergetic Point Source

In the following subsections, basic expressions are derived for the dose from uncollided radiation produced by isotropic point sources.

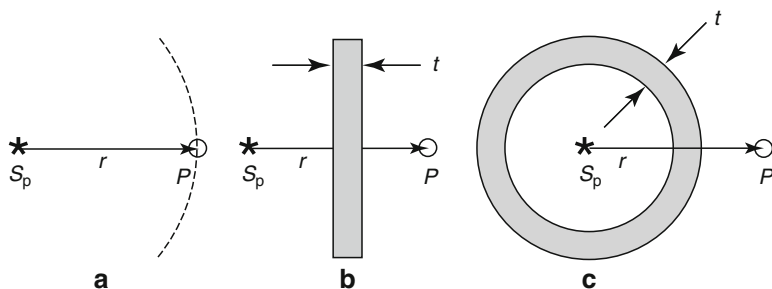
Point Source in a Vacuum

Consider a point-isotropic source that emits S_p particles into an infinite vacuum as in  Fig. 15a. All particles move radially outward without interaction, and because of the source isotropy, each unit area on an imaginary spherical shell of radius r has the same number of particles crossing it, namely, $S_p/(4\pi r^2)$. It then follows from the definition of the fluence that the fluence Φ^o of uncollided particles at a distance r from the source is

$$\Phi^o(r) = \frac{S_p}{4\pi r^2}. \quad (34)$$

If all the source particles have the same energy E , the response of a point detector at a distance r from the source is obtained by multiplying the uncollided fluence by the appropriate dose-conversion coefficient \mathcal{R} , which usually depends on the particle energy E , namely,

$$D^o(r) = \frac{S_p \mathcal{R}(E)}{4\pi r^2}. \quad (35)$$



■ Figure 15

Point isotropic source (a) in a vacuum, (b) with a slab shield, and (c) with a spherical-shell shield. Point P is the location of the receiver or point detector

Notice that the dose and fluence decrease as $1/r^2$ as the distance from the source is increased. This decreasing dose with increasing distance is sometimes referred to as *geometric attenuation*.

Point Source in a Homogenous Attenuating Medium

Now consider the same point monoenergetic isotropic source embedded in an infinite homogenous medium characterized by a total interaction coefficient μ . As the source particles stream radially outward, some interact before they reach the imaginary sphere of radius r and do not contribute to the uncollided fluence. The number of source particles that travel at least a distance r without interaction is $S_p e^{-\mu r}$, so that the uncollided dose is

$$D^o(r) = \frac{S_p \mathcal{R}(E)}{4\pi r^2} e^{-\mu(E)r}. \quad (36)$$

The term $e^{-\mu r}$ is referred to as the *material attenuation* term to distinguish it from the $1/r^2$ geometric attenuation term.

Point Source with a Shield

Now suppose that the only attenuating material separating the source and the detector is a slab of material with attenuation coefficient μ and thickness t as shown in ► Fig. 15b. In this case, the probability that a source particle reaches the detector without interaction is $e^{-\mu t}$, so that the uncollided dose is

$$D^o(r) = \frac{S_p \mathcal{R}(E)}{4\pi r^2} e^{-\mu(E)t}. \quad (37)$$

This same result holds if the attenuating medium has any shape (e.g., a spherical shell of thickness t as shown in ► Fig. 15c) provided that a ray drawn from the source to the detector passes through a thickness t of the attenuating material.

If the interposing shield is composed of a series of different materials such that an uncollided particle must penetrate a series of thicknesses t_i of materials with attenuation coefficients μ_i before reaching the detector, the uncollided dose is

$$D^o(r) = \frac{S_p \mathcal{R}(E)}{4\pi r^2} \exp(-\sum_i \mu_i(E) t_i). \quad (38)$$

Here $\sum_i \mu_i t_i$ is the total number of mean-free-path lengths of attenuating material that an uncollided particle must traverse without interaction, and $\exp(-\sum_i \mu_i t_i)$ is the probability that a source particle traverses this number of mean-free-path lengths without interaction.

3.2 Uncollided Doses for Distributed Sources

3.2.1 The Superposition Procedure


The results for the uncollided dose from a point source can be used to derive expressions for the uncollided dose arising from a wide variety of distributed sources such as line sources, area sources, and volumetric sources. One widely used approach is to divide the distributed source conceptually into a set of equivalent point sources and then to sum (integrate) the dose contribution from each point source.


The examples presented later for a line source are selected because of their simplicity or utility. In all these examples, it is assumed that the source is monoenergetic and isotropic and the detector is a point isotropic one. For polyenergetic sources, the monoenergetic result can be summed (or integrated) over all source energies.

The superposition technique of decomposing a source into a set of simpler sources is very powerful and has been applied to line, surface, and volumetric sources of complex shapes. Many important practical cases have been examined and generalized results have been published. Among the special cases are cylindrical and spherical surface and volume sources, with and without external shields, and with interior as well as exterior receptor locations. The examples below are but a few of the known results. For other source and shield configurations, the reader is referred to the publications of Rockwell (1956), Blizard and Abbott (1962), Hungerford (1966), Blizard et al. (1968), Schaeffer (1973), Courtney (1975), Chilton et al. (1984), and Shultis and Faw (2000).

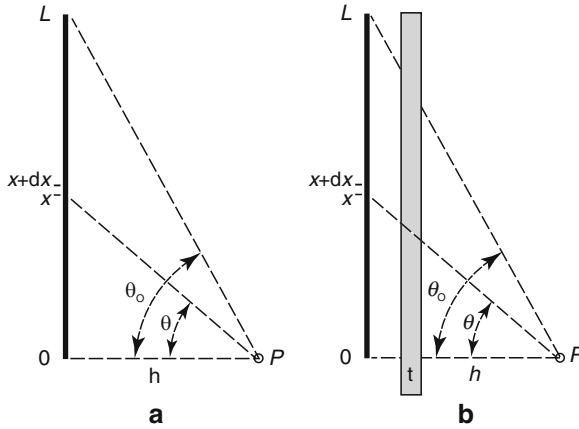
3.2.2 Example Calculations for Distributed Sources

The Line Source

A straight-line source of length L emitting isotropically S_1 particles per unit length at energy E is depicted in  Fig. 16. A detector is positioned at point P , a distance h from the source along a perpendicular to one end of the line. Consider a segment of the line source between distance x and $x + dx$ measured from the bottom of the source. The source within this segment may be treated as an effective point isotropic source emitting $S_1 dx$ particles which produces an uncollided dose at P of dD^0 . To obtain the total dose at P from all segments of the line source, one then must sum, or rather integrate, dD^0 over all line segments. Several cases are discussed as follows.

Line Source in a Nonattenuating Medium. In the absence of material interaction () Fig. 16a), the differential uncollided dose produced by particles emitted in dx about x is, from (36),

$$dD^0(P) = \frac{1}{4\pi} \frac{S_1 \mathcal{R} dx}{x^2 + h^2} \quad (39)$$



■ **Figure 16**
Isotropic line source (a) in a homogenous medium and (b) with a slab shield

and thus,

$$D^o(P) = \frac{S_l \mathcal{R}}{4\pi} \int_0^L \frac{dx}{x^2 + h^2} = \frac{S_l \mathcal{R} \theta_0}{4\pi h}. \quad (40)$$

The angle $\theta_0 = \tan^{-1} L/h$ in this result must be expressed in radians.

Line Source in a Homogenous Attenuating Medium. Now suppose that the source and receptor are present in a homogenous medium with a total interaction coefficient μ . Attenuation along the ray from x to P reduces the uncollided dose at P to

$$dD^o(P) = \frac{1}{4\pi} \frac{S_l \mathcal{R} dx}{x^2 + h^2} \exp[-\mu \sqrt{x^2 + h^2}], \quad (41)$$

where \mathcal{R} and μ generally depend on the particle energy E . The total uncollided dose now is described by the integral

$$D^o(P) = \frac{S_l \mathcal{R}}{4\pi h} \int_0^{\theta_0} d\theta e^{-\mu h \sec \theta}. \quad (42)$$

This integral cannot be evaluated analytically. However, it can be expressed in terms of the *Sievert integral* or the *secant integral*, defined as

$$F(\theta, b) \equiv \int_0^\theta dx e^{-b \sec x}. \quad (43)$$

This integral is widely available in the previously cited text and reference works. With it, the dose from a line source may be expressed as

$$D^o(P) = \frac{S_l \mathcal{R}}{4\pi h} F(\theta_0, \mu h). \quad (44)$$

Line Source Behind a Slab Shield. Now suppose that the only material separating the line source and the receptor is a parallel slab or concentric cylindrical-shell shield of thickness t and total attenuation coefficient μ_s , as shown in **► Fig. 16b**. For this case, the analysis above using only attenuation in the slab yields

$$D^o(P) = \frac{S_L \mathcal{R}}{4\pi h} F(\theta_o, \mu_s t). \tag{45}$$

If the shield is made up of layers of thicknesses t_i and attenuation coefficients μ_{si} , then $\mu_s t$ must be replaced by $\sum_i \mu_{si} t_i$, the total mean-free-path thickness of the shield.

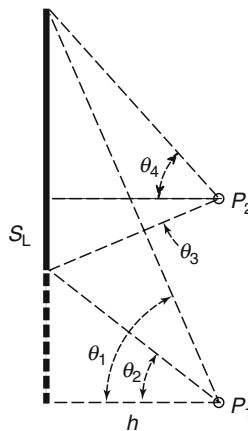
A Superposition Procedure for Line Sources. The restriction in the foregoing examples that the detector be perpendicularly opposite one end of the line source is easily relaxed by use of the principle of *superposition of sources*. **► Figure 17** illustrates two receptor points in relation to a line source in a homogenous attenuating medium. Determination of the uncollided dose at either point may be obtained by conceptually decomposing the line source into two adjacent line sources each of which has an end perpendicular to the detector. Point P_1 , for example, is on a normal from the end of a projection of the line source. Were the line source truly of the extended length, then the dose would be given by (44) with angle argument θ_1 . However, that result would be too high by just the amount contributed by a line source of the same strength subtending angle θ_2 . Thus, at point P_1 ,

$$D^o(P_1) = \frac{S_L \mathcal{R}}{4\pi h} [F(\theta_1, \mu h) - F(\theta_2, \mu h)]. \tag{46}$$

By similar reasoning, at point P_2 ,

$$D^o(P_2) = \frac{S_L \mathcal{R}}{4\pi h} [F(\theta_3, \mu h) + F(\theta_4, \mu h)]. \tag{47}$$

As illustrated by these line source examples, the superposition of multiple distributed sources, for each of which the dose is readily calculated, to create a more complex source configuration is an extremely useful procedure that can be used effectively for all types of sources.



► Figure 17
Application of the superposition principle to an isotropic line source

Indeed, part of the art of shield analysis is to devise how to reduce a complex source problem to a set of simpler problems, and the source superposition principle is a valuable tool in this reduction.

4 Photon Attenuation Calculations

This section describes the engineering methodology that has evolved for the design and analysis of shielding for gamma and X-rays with energies from about 1 keV to about 20 MeV. To support this methodology, very precise radiation transport calculations have been applied to a wide range of carefully prescribed situations. The results are in the form of buildup factors, attenuation factors, albedos or reflection factors, and line-beam response functions.

Buildup factors relate the total dose to the dose from uncollided photons alone and are most applicable to point monoenergetic-radiation sources with shielding well distributed between the source point and points of interest. Attenuation factors apply equally well to monoenergetic sources and to polyenergetic sources such as X-ray machines and are most applicable when a shield wall separates the source and points of interest, the wall being sufficiently far from the source that radiation strikes it as a nearly parallel beam. There are many common features of buildup and attenuation factors and it is possible to represent one factor in terms of the other. Albedos, which describes how radiation is reflected from a surface, and line-beam response functions, which are used in skyshine analyses, are taken up in other sections of this chapter.

Discussed first in this section are buildup factors for point isotropic and monoenergetic sources in infinite media. Incorporation of these buildup factors into the uncollided point kernel is treated next. Then addressed are three topics associated with the use of buildup factors. The first is the use of empirical buildup-factor approximations designed to simplify engineering design and analysis. The second is the use of buildup factors with point kernels to treat spatially distributed radiation sources. The third is the application of approximate methods to permit the use of buildup factors in media with variations in composition.

4.1 The Photon Buildup-Factor Concept

Whatever the photon source and the attenuating medium, the energy spectrum of the total photon fluence $\Phi(\mathbf{r}, E)$ at some point of interest \mathbf{r} may be divided into two components. The *unscattered* component $\Phi^o(\mathbf{r}, E)$ consists of just those photons that have reached \mathbf{r} from the source without having experienced any interactions in the attenuating medium. The *scattered* component $\Phi^s(\mathbf{r}, E)$ consists of source photons scattered one or more times, as well as secondary photons such as X-rays and annihilation gamma rays. Accordingly, the dose or detector response $D(\mathbf{r})$ at point of interest \mathbf{r} may be divided into unscattered (primary) and scattered (secondary) components $D^o(\mathbf{r})$ and $D^s(\mathbf{r})$. The buildup factor $B(\mathbf{r})$ is defined as the ratio of the total dose to the unscattered dose, i.e.,

$$B(\mathbf{r}) \equiv \frac{D(\mathbf{r})}{D^o(\mathbf{r})} = 1 + \frac{D^s(\mathbf{r})}{D^o(\mathbf{r})}. \quad (48)$$

The doses may be evaluated using response functions described in [Sect. 2](#), so that

$$B(\mathbf{r}) = 1 + \frac{\int dE \mathcal{R}(E) \Phi^s(\mathbf{r}, E)}{\int dE \mathcal{R}(E) \Phi^o(\mathbf{r}, E)}, \quad (49)$$

in which the integrations are over all possible E .

It is very important to recognize that in (49), the fluence terms depend only on the source and medium, and not on the type of dose or response. The conversion factors or response function $\mathcal{R}(E)$ depends only on the type of dose, and not on the attenuating medium. For these reasons, it is imperative to associate with buildup factors the nature of the source, the nature of the attenuating medium, and the nature of the response.

When the source is monoenergetic, with energy E_o , then $\Phi^o(\mathbf{r}, E) = \Phi^o(\mathbf{r}) \delta(E - E_o)$, so that

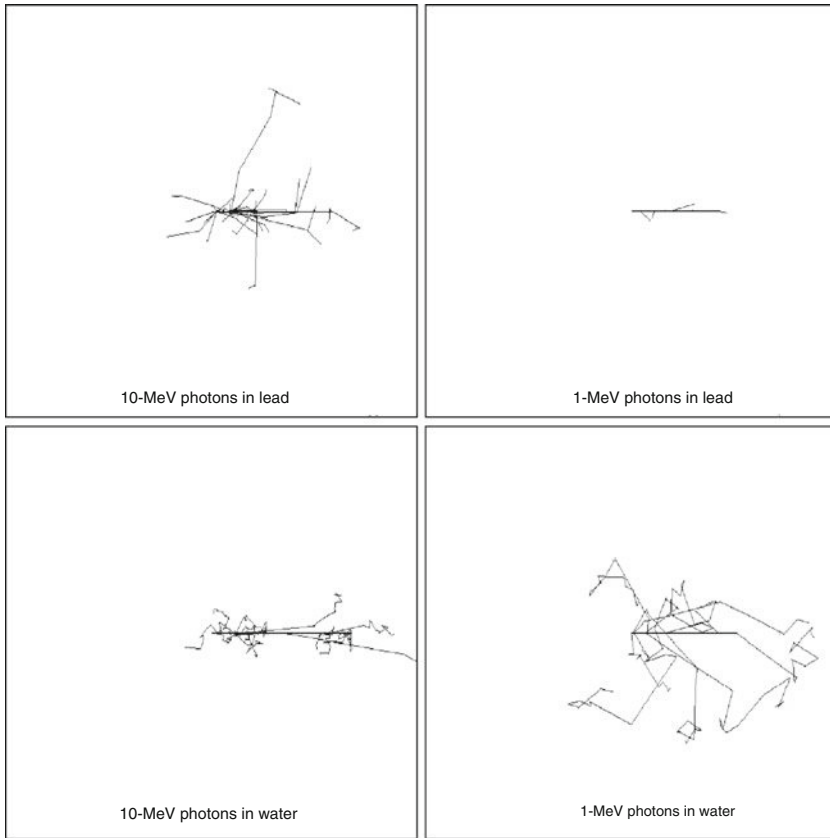
$$B(\mathbf{r}) = 1 + \frac{1}{\Phi^o(\mathbf{r})} \int_0^{E_o} dE \frac{\mathcal{R}(E)}{\mathcal{R}(E_o)} \Phi_s(\mathbf{r}, E). \quad (50)$$

In this case, the response nature is fully accounted for in the ratio $\mathcal{R}(E)/\mathcal{R}(E_o)$.

4.2 Isotropic, Monoenergetic Sources in Infinite Media

By far, the largest body of buildup-factor data is for point, isotropic, and monoenergetic sources of photons in infinite homogenous media. The earliest data (Fano et al. 1959; Goldstein 1959; Goldstein and Wilkins 1954) were based on moments-method calculations (Shultis and Faw 2000) and accounted only for buildup of Compton-scattered photons. Subsequent moments-method calculations (Eisenhauer and Simmons 1975; Chilton et al. 1980) accounted for buildup of annihilation photons as well. Buildup-factor calculations using the discrete-ordinates ASFIT code (Subbaiah et al. 1982) and the integral-transport PALLAS code (Takeuchi, Tanaka, and Kinno 1981) account for not only Compton-scattered and annihilation photons, but also for fluorescence and bremsstrahlung. These calculations, which supplement later moments-method calculations, are the basis for the data prescribed in the American National Standard for buildup factors (ANSI/ANS 1991). Calculation of buildup factors for high-energy photons requires consideration of the paths traveled by positrons from their creation until their annihilation. Such calculations have been performed by Hirayama (1987) and by Faw and Shultis (1993a) for photon energies as great as 100 MeV. Most point-source buildup-factor compilations exclude coherently scattered photons and treat Compton scattering in the free-electron approximation. This is also true for the buildup factors in the standard. Thus, in computing the dose or response from unscattered photons, coherent scattering should be excluded and the total Klein–Nishina cross section should be used. Correction for coherent scattering, significant for only low-energy photons at deep penetration, is discussed in ANSI/ANS (1991).

➤ [Figure 18](#) gives a qualitative impression of the buildup of secondary photons during the attenuation of primary photons. For 10-MeV photons in lead, there is considerable buildup of annihilation photons, which are emitted isotropically, and bremsstrahlung, which deviates little in direction from the path of the decelerating electron or positron. For 1-MeV photons in lead, there is very little buildup of secondary photons, owing to the strong photoelectric absorption of the primary photons. In water, both 1- and 10-MeV photons experience Compton scattering principally. However, for the higher-energy primary photons, the scattering leads to relatively small change in direction. ➤ [Figure 19](#) illustrates the energy spectrum of the energy fluence

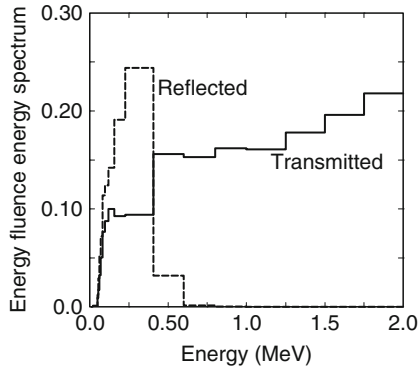


■ Figure 18

Comparison of photon transport in lead and water. Each box has 10 mean-free paths on a side. Each depicts the projection in a plane of primary and secondary photon tracks arising from 10 primary photons originating at the box center, moving to the right in the plane of the paper. Tracks computed using the EGS4 code, courtesy of Robert Stewart, Kansas State University

$E\Phi(E)$ of reflected and transmitted photons produced by 2-MeV primary photons, normally incident on a concrete slab two mean free paths in thickness. These fluences are normalized to unit incident flow and, thus, are dimensionless. Note that transmitted photons have energies up to the energy of the primary photons. However, the reflected photons, mostly single scattered, are much more restricted in energy.

Tables of buildup factors are available in standards (ANSI/ANS 1991), the technical literature (Eisenhauer and Simmons 1975; Takeuchi and Tanaka 1984; Goldstein and Wilkins 1954) and many textbooks. Buildup-factor data are generally more broadly applicable than might be thought at first glance. As indicated in (50), it is the ratio $\mathcal{R}(E)/\mathcal{R}(E_o)$ that defines the dependence of the buildup factor on the type of dose or response. For responses such as kerma or absorbed dose in air or water, exposure, or dose equivalent, the ratio is not very sensitive to the type of response. Thus, buildup factors for air kerma may be used with little error for exposure or dose equivalent.



■ Figure 19

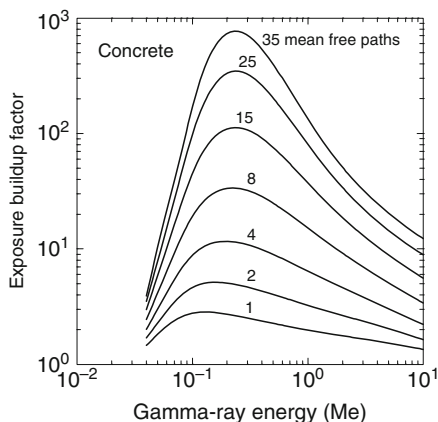
Transmitted and reflected energy fluences for 2-MeV photons normally incident on a concrete slab of two mean free path thickness

It can be shown that, for a point isotropic source of monoenergetic photons in an infinite homogenous medium, the buildup factor depends spatially only on the number of mean free paths μr separating the source and the point of interest. Here, μ is the total interaction coefficient (excluding coherent scattering) in the attenuating medium at the source energy, namely $\mu(E_0)$. Thus, we write the buildup factor as $B(\mu r)$, but it must be recognized that there is an implicit dependence on the source energy, the nature of the attenuating medium, and the nature of the response.

► Figure 20 illustrates the buildup factor for concrete, plotted with the photon energy as the independent variable and the number of mean free paths as a parameter. That there are maxima in the curves is due to the relative importance of the photoelectric effect, as compared to Compton scattering, in the attenuation of lower-energy photons and to the very low fluorescence yields exhibited by the low- Z constituents of concrete. ► Figure 21 illustrates the buildup factor for lead, plotted with the number of mean free paths as the independent variable and the photon energy as a parameter. For high-energy photons, pair production is the dominant attenuation mechanism in lead, the cross section exceeding that for Compton scattering at energies above about 5 MeV. The buildup is relatively large because of the production of 0.511-MeV annihilation gamma rays. As may also be seen from the figure, the attenuation factor increases greatly at photon energies just above the 0.088-MeV K -edge for photoelectric absorption, each absorption resulting in a cascade of X-rays. For these reasons, buildup factors may be extraordinarily large, as evidenced by the line for 0.089-MeV photons in ► Fig. 21. At energies below the K -edge, the buildup factors are very small. The importance of fluorescence in the buildup of low-energy photons is addressed by Tanaka and Takeuchi (1986) and by Subbaiah and Natarajan (1987).

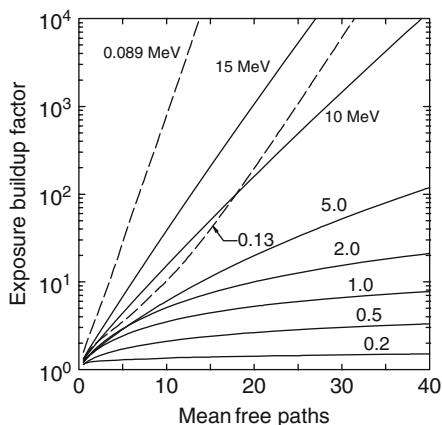
4.3 Buildup Factors for Point and Plane Sources

Many so-called “point-kernel codes” finding wide use in radiation shielding design and analysis make exclusive use of buildup factors for point isotropic sources in infinite media. This is true even when the source and shield configuration is quite different from that of an infinite



■ Figure 20

Air-kerma buildup factors for gamma-ray attenuation in concrete, excluding bremsstrahlung, fluorescence, and coherent scattering. Data from Eisenhauer and Simmons (1975)



■ Figure 21

Exposure buildup factors for gamma-ray attenuation in lead, calculated using the PALLAS code, excluding coherent scattering. Data from ANSI/ANS (1991)

medium. A good example is that of a point source and point receptor, each at some distance in air from an intervening shielding wall. Is the use of infinite-medium buildup factors a conservative approximation? That question is addressed in ► [Table 10](#), prepared for shielding of 1-MeV gamma rays by iron. This table lists exposure buildup factors, in some cases for infinite media and in other cases for vacuum-bounded finite media. The first column in the table is the number of mean free paths from source to receptor location. Six columns of buildup factors follow, three for point isotropic (PTI) sources and three for plane monodirectional (PLM) sources.

The PTI source in an infinite medium is the reference case. Data for the PTI source in a finite medium refer to the exposure rate at the surface of a sphere whose radius corresponds to

■ **Table 10**
Exposure buildup factors for 1-MeV gamma rays in iron

Thickness (mfp)	Source type and attenuating medium					
	PTI			PLM		
	Infinite ^a	Finite ^b	Slab ^c	Infinite ^d	Semi-infinite ^e	Finite ^f
0.5	1.41	1.36	1.35		1.49	
1	1.85	1.77	1.73	1.92	1.88	1.72
2	2.85	2.68	2.63	2.74	2.68	2.45
3	4.00	3.75	3.65		3.54	
4	5.30	4.95	4.43	4.57	4.46	3.97
5	6.74	6.26	6.47		5.44	
6	8.31	7.70	6.67		6.51	5.77
7	10.0	9.41	8.98	8.81	7.63	
8	11.8	11.1			8.82	7.91
10	15.8	14.5		11.6	11.3	9.77
15	27.5	26.1		18.9	18.5	

^aStandard ANSI/ANS-6.4.3-1991;

^bEGS4 calculations, courtesy Sherrill Shue, Kansas State University;

^cDunn et al. (1992);

^dGoldstein (1959);

^eTakeuchi and Tanaka (1984);

^fChen and Faw (1994)

the mean free path thickness. Data for the PTI source and slab shield are for a point source on one side of a slab of given thickness and a receptor point directly on the opposite side of the slab. Data for the PLM source in an infinite medium are for the buildup factor as a function of distance from a hypothetical plane source emitting a parallel beam of photons perpendicular to the plane. Data for the PLM source in a semi-infinite medium are for the buildup factor as a function of depth in a half-space illuminated by a normally incident parallel beam of photons. Data in the last column, for the PLM source in a finite medium, refer to the exposure on one side of a slab shield of given thickness which is illuminated by a parallel beam of photons normally incident on the opposite side of the slab.

It is apparent from [Table 10](#) that for the cases examined, use of buildup factors for point sources in an infinite medium, with few exceptions, is a conservative approximation in shield design, that is, predicted doses are slightly higher than the actual doses. However, the PLM examples are all for beams *normally* incident on slab shields. When beams are obliquely incident on slab shields, point kernel codes routinely determine the number of mean free paths along the oblique path through the slab shield and apply infinite-medium buildup factors for the corresponding thickness. This practice can underestimate shielding requirements because buildup factors for slant penetration of beams can greatly exceed those for point sources computed at the same optical thicknesses (mean free paths) as is addressed later in this section.

Buildup factors are available for plane isotropic (PLI) and plane monodirectional (PLM) gamma-ray sources in infinite media. Indeed, Fano et al. (1959), Goldstein (1959), and Spencer

(1962), in their moments-method calculations, obtained buildup factors for plane sources first and, from these, buildup factors for point sources. Buildup factors at depth in a half-space shield are also available for the PLM source, that is, normally incident photons (Takeuchi et al. 1981; Takeuchi and Tanaka 1984; Hirayama 1987).

Special methods have been developed for treating buildup when source and receptor are separated by many shielding slabs, such as walls and floors of a structure, at various orientations. For example, Dunn et al. (1992) address shipboard radiation shielding problems and provide buildup factors for common shielding materials.

4.3.1 Empirical Approximations for Buildup Factors

A great deal of effort has been directed toward the approximation of point-source buildup factors by mathematical functions which can be used directly in calculations. These efforts have dealt almost exclusively with buildup factors for point-isotropic and monoenergetic sources in infinite media. Two forms of approximation have been in use for many years. One is the *Taylor form* (Chilton 1977; Foderaro and Hall 1981; Shure and Wallace 1988). The other is the *Berger form* (Chilton 1979; Chilton et al. 1980). While both forms still see a wide application in computer codes used in engineering practice, a more modern, more accurate, but much more complicated approximation is the *geometric progression* (GP) form, and without question it is the preferred approximation to use if possible.

The Geometric Progression Approximation

An extraordinarily precise formulation, called the *geometric progression approximation* of the buildup factor, was developed in recent years (Harima 1986; Harima et al. 1986, 1991). The approximation is in the form

$$B(E_o, \mu r) \simeq \begin{cases} 1 + (b - 1)(K^{\mu r} - 1)/(K - 1), & K \neq 1 \\ 1 + (b - 1)\mu r, & K = 1, \end{cases} \quad (51)$$

where

$$K(\mu r) = c(\mu r)^a + d \frac{\tanh(\mu r/\xi - 2) - \tanh(-2)}{1 - \tanh(-2)}, \quad (52)$$

in which a , b , c , d , and ξ are parameters dependent on the gamma-ray energy, the attenuating medium, and the nature of the response. Example values of the parameters for kerma in air as the response, and for attenuation in air, water, concrete, iron, and lead are listed in [► Tables 11 and 12](#). The parameters are based on PALLAS code calculations (Takeuchi et al. 1981).

4.3.2 Point-Kernel Applications of Buildup Factors

For a distributed source of monoenergetic photons $S_v(\mathbf{r}_s)$ of energy E_o , the dose from uncollided photons at some position \mathbf{r} is

$$D^o(\mathbf{r}) = \int_{V_s} dV_s \frac{S_v(\mathbf{r}_s)\mathcal{R}(E_o)}{4\pi|\mathbf{r}_s - \mathbf{r}|^2} e^{-\ell}, \quad (53)$$

■ Table 11

Coefficients for the geometric progression form of the gamma-ray buildup factor

Photon energy (MeV)	Air kerma / air medium					Air kerma / concrete medium				
	<i>b</i>	<i>c</i>	<i>a</i>	ξ	<i>d</i>	<i>b</i>	<i>c</i>	<i>a</i>	ξ	<i>d</i>
0.015	1.170	0.459	0.175	13.73	-0.0862	1.029	0.364	0.240	14.12	-0.1704
0.020	1.407	0.512	0.161	14.40	-0.0819	1.067	0.389	0.214	12.68	-0.1126
0.030	2.292	0.693	0.102	13.34	-0.0484	1.212	0.421	0.201	14.12	-0.1079
0.040	3.390	1.052	-0.004	19.76	-0.0068	1.455	0.493	0.171	14.53	-0.0925
0.050	4.322	1.383	-0.071	13.51	0.0270	1.737	0.628	0.115	15.82	-0.0600
0.060	4.837	1.653	-0.115	13.66	0.0511	2.125	0.664	0.118	11.90	-0.0615
0.080	4.929	1.983	-0.159	13.74	0.0730	2.557	0.895	0.042	14.37	-0.0413
0.100	4.580	2.146	-0.178	12.83	0.0759	2.766	1.069	0.001	12.64	-0.0251
0.150	3.894	2.148	-0.173	14.46	0.0698	2.824	1.315	-0.049	8.66	-0.0048
0.200	3.345	2.147	-0.176	14.08	0.0719	2.716	1.430	-0.070	18.52	0.0108
0.300	2.887	1.990	-0.160	14.13	0.0633	2.522	1.492	-0.082	16.59	0.0161
0.400	2.635	1.860	-0.146	14.24	0.0583	2.372	1.494	-0.085	15.96	0.0194
0.500	2.496	1.736	-0.130	14.32	0.0505	2.271	1.466	-0.082	16.25	0.0195
0.600	2.371	1.656	-0.120	14.27	0.0472	2.192	1.434	-0.078	17.02	0.0199
0.800	2.207	1.532	-0.103	14.12	0.0425	2.066	1.386	-0.073	15.07	0.0202
1.000	2.102	1.428	-0.086	14.35	0.0344	1.982	1.332	-0.065	15.38	0.0193
1.500	1.939	1.265	-0.057	14.24	0.0232	1.848	1.227	-0.047	16.41	0.0160
2.000	1.835	1.173	-0.039	14.07	0.0161	1.775	1.154	-0.033	14.35	0.0100
3.000	1.712	1.051	-0.011	13.67	0.0024	1.671	1.054	-0.010	10.47	-0.0008
4.000	1.627	0.983	0.006	13.51	-0.0051	1.597	0.988	0.008	12.53	-0.0115
5.000	1.558	0.943	0.017	13.82	-0.0117	1.527	0.951	0.020	9.99	-0.0184
6.000	1.505	0.915	0.025	16.37	-0.0231	1.478	0.940	0.021	13.11	-0.0163
8.000	1.418	0.891	0.032	12.06	-0.0167	1.395	0.917	0.028	13.45	-0.0213
10.00	1.358	0.875	0.037	14.01	-0.0226	1.334	0.901	0.035	12.56	-0.0267
15.00	1.267	0.844	0.048	14.55	-0.0344	1.260	0.823	0.065	14.28	-0.0581

Source: Extracted from American National Standard ANSI/ANS-6.4.3-1991, *Gamma-Ray Attenuation Coefficients and Buildup Factors for Engineering Materials*, published by the American Nuclear Society. Data are also available from Data Library DLC-129/ANS643, issued by the Radiation Shielding Information Center, Oak Ridge National Laboratory, Oak Ridge, TN

■ Table 12

Coefficients for the geometric progression form of the gamma-ray buildup factor

Photon energy (MeV)	Air kerma / iron medium					Air kerma / lead medium				
	<i>b</i>	<i>c</i>	<i>a</i>	ξ	<i>d</i>	<i>b</i>	<i>c</i>	<i>a</i>	ξ	<i>d</i>
0.015	1.004	1.561	-0.554	5.60	0.3524					
0.020	1.012	0.130	0.620	11.39	-0.6162					
0.030	1.028	0.374	0.190	29.34	-0.3170	1.007	0.322	0.246	13.67	-0.1030
0.040	1.058	0.336	0.248	11.65	-0.1188	1.014	0.317	0.245	14.95	-0.0867
0.050	1.099	0.366	0.232	14.01	-0.1354	1.023	0.312	0.252	14.17	-0.1005
0.060	1.148	0.405	0.208	14.17	-0.1142	1.033	0.320	0.260	13.89	-0.1223
0.080	1.267	0.470	0.180	14.48	-0.0974	1.058	0.362	0.233	13.91	-0.1127
0.088						1.067	0.382	0.220	14.14	-0.1048
0.089						2.368	1.580	0.075	12.44	-0.0635
0.090						2.187	1.693	0.050	18.21	-0.0415
0.100	1.389	0.557	0.144	14.11	-0.0791	1.930	1.499	0.061	29.65	-0.1162
0.110						1.821	1.196	0.102	16.64	-0.0756
0.120						1.644	0.970	0.136	16.10	-0.1135
0.130						1.540	0.718	0.194	15.69	-0.1685
0.140						1.472	0.479	0.273	16.50	-0.2153
0.150	1.660	0.743	0.079	14.12	-0.0476	1.402	0.352	0.269	17.09	-0.0247
0.160						1.334	0.329	0.145	11.38	-0.0643
0.200	1.839	0.911	0.034	13.23	-0.0334	1.201	0.158	0.426	14.12	-0.1873
0.300	1.973	1.095	-0.009	11.86	-0.0183	1.148	0.422	0.203	13.49	-0.1013
0.400	1.992	1.187	-0.027	10.72	-0.0140	1.187	0.562	0.137	14.19	-0.0706
0.500	1.967	1.240	-0.039	8.34	-0.0074	1.233	0.634	0.109	14.20	-0.0556
0.600	1.947	1.247	-0.040	8.20	-0.0096	1.269	0.685	0.089	13.78	-0.0440
0.800	1.906	1.233	-0.038	7.93	-0.0110	1.329	0.759	0.065	13.69	-0.0317
1.000	1.841	1.250	-0.048	19.49	0.0140	1.367	0.811	0.051	13.67	-0.0283
1.500	1.750	1.197	-0.040	15.90	0.0110	1.369	0.942	0.020	14.65	-0.0207
2.000	1.712	1.123	-0.021	7.97	-0.0057	1.384	0.980	0.014	13.51	-0.0216
3.000	1.627	1.059	-0.005	11.99	-0.0132	1.367	1.006	0.017	13.33	-0.0377
4.000	1.553	1.026	0.005	12.93	-0.0191	1.337	1.009	0.024	14.15	-0.0455
5.000	1.483	1.009	0.012	13.12	-0.0258	1.360	0.957	0.049	14.04	-0.0683

Table 12 (continued)

Photon energy (MeV)	Air kerma / iron medium					Air kerma / lead medium				
	<i>b</i>	<i>c</i>	<i>a</i>	ξ	<i>d</i>	<i>b</i>	<i>c</i>	<i>a</i>	ξ	<i>d</i>
6.000	1.442	0.980	0.023	13.37	-0.0355	1.363	0.965	0.054	14.21	-0.0715
8.000	1.354	0.974	0.029	13.65	-0.0424	1.441	0.994	0.061	14.18	-0.0800
10.000	1.297	0.949	0.042	13.97	-0.0561	1.464	1.148	0.032	14.08	-0.0554
15.000	1.199	0.957	0.049	14.37	-0.0594	1.573	1.337	0.016	13.54	-0.0463

Source: Extracted from American National Standard ANSI/ANS-6.4.3-1991, *Gamma-Ray Attenuation Coefficients and Buildup Factors for Engineering Materials*, published by the American Nuclear Society. Data are also available from Data Library DLC-129/ANS643, issued by the Radiation Shielding Information Center, Oak Ridge National Laboratory, Oak Ridge, TN

where the integration is over all source locations and ℓ is the optical thickness between \mathbf{r}_s and \mathbf{r} , namely,

$$\ell = \int_0^{|\mathbf{r}_s - \mathbf{r}|} ds \mu(s), \quad (54)$$

with s measured along a straight line from \mathbf{r}_s to \mathbf{r} . To correct for the buildup of secondary radiation, an appropriate buildup factor is included in the integrand of (53). If an infinite-medium, point-source buildup factor is used and the medium is of uniform composition but possibly of variable density, the total dose at \mathbf{r} is

$$D(\mathbf{r}) = \int_{V_s} dV_s \frac{S_v(\mathbf{r}_s) \mathcal{R}(E_o)}{4\pi|\mathbf{r}_s - \mathbf{r}|^2} B(E_o, \ell) e^{-\ell} \equiv \int_{V_s} dV_s S_v(\mathbf{r}_s) \mathcal{G}(\mathbf{r}_s, \mathbf{r}). \quad (55)$$

Here,

$$\mathcal{G}(\mathbf{r}_s, \mathbf{r}) \equiv \frac{\mathcal{R}(E_o)}{4\pi|\mathbf{r}_s - \mathbf{r}|^2} B(E_o, \ell) e^{-\ell} \quad (56)$$

is the dose Green's function or point kernel that gives the dose at \mathbf{r} due to a photon emitted isotropically at \mathbf{r}_s .

From this approximate result, it is seen that the total dose at \mathbf{r} from radiation emitted isotropically from \mathbf{r}_s depends only on the material properties along a line between \mathbf{r}_s and \mathbf{r} and on the distance $|\mathbf{r}_s - \mathbf{r}|$ between these two points. This approximation, based on the infinite-medium, point-source buildup factor, is sometimes called *ray theory*, indicative that the total dose is determined simply by the material and distance along the ray joining the source and detector points. In many situations, it is an excellent approximation and is widely used in photon shielding calculations. To illustrate the use of ray theory, two examples are given as follows.

Line Source in an Infinite Attenuating Medium

With reference to Fig. 16 and (41), one sees that the total dose at detector point P due to photons arising from the differential source length dx is

$$dD(P) = \frac{\mathcal{R}(E_o) S_1 dx}{4\pi(x^2 + h^2)} e^{-\mu\sqrt{x^2 + h^2}} B(E_o, \mu\sqrt{x^2 + h^2}). \quad (57)$$

In analogy to (41), the response due to the entire line source is given by the integral

$$D(P) = \mathcal{R}(E_o) \frac{S_l}{4\pi h} \int_0^{\theta_o} d\theta e^{-\mu h \sec \theta} B(E_o, \mu h \sec \theta). \quad (58)$$

In general, the integral must be evaluated numerically. However, if the Taylor form of buildup-factor approximation is employed, the integral yields a sum of Sievert integrals (Shultis and Faw 2000).

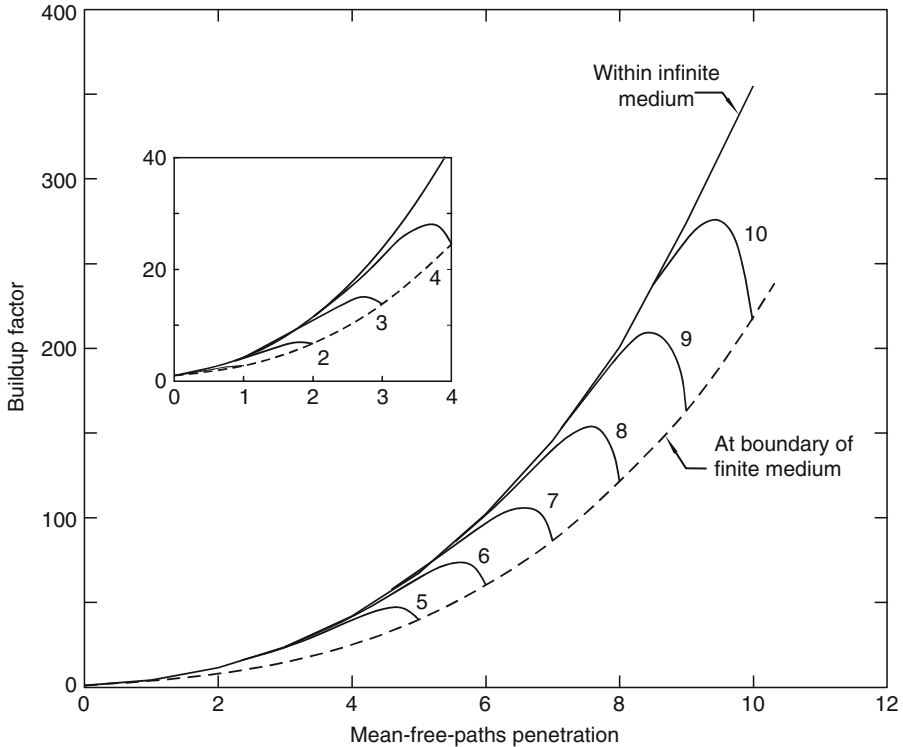
4.4 Buildup Factors for Heterogenous Media

4.4.1 Boundary Effects in Finite Media

Consider a point isotropic source at the center of a finite sphere of shielding material and a dose point at the surface. The sphere is surrounded by air, which may be approximated as a vacuum. The use of an infinite-medium buildup factor in calculating the dose at the boundary leads to an overestimate because, in fact, no photons are reflected back to the sphere from the space beyond the spherical surface. Because the error is on the side of overestimation of the dose, corrections are very often ignored.

► *Figure 22* illustrates the magnitude of the effect of a vacuum interface for a tissue medium. The lower bounding dashed lines are buildup factors for the dose at the surface of a sphere of given radius. The upper bounding solid lines are for the dose at the same radius in an infinite medium. The intervening lines are for points interior to the finite sphere. It is apparent that the effect of the boundary is insignificant for points more than about one mean free path from the surface. Buildup factors at vacuum boundaries of finite media are conveniently presented as the ratio $(B_x - 1)/(B_\infty - 1)$, in which B_x is the finite-medium buildup factor and B_∞ is the infinite-medium buildup factor. This ratio, which is illustrated in ► *Fig. 23*, can be used in many applications, because it has been found to be insensitive to whether the source is a point isotropic, plane isotropic, or plane perpendicular, and to the distance x from the source to the boundary.

Consider the same point isotropic source at the center of a finite sphere of shielding material and a dose point at the surface. The sphere is bounded not by a vacuum but by a tissue medium. This model is appropriate for determination of the phantom dose outside a shielding structure. For use in such calculations, Gopinath et al. (1987) determined adjustment factors to be applied to infinite-medium buildup factors. The adjustment factors, which are listed in ► *Table 13*, were adopted in the ANSI/ANS Standard (1991) for buildup factors. They were computed for parallel beam sources normally incident on shielding slabs, but may be used for point sources as well. The adjustment factor is to be used as follows. For the given shield material, first compute the absorbed dose in tissue at the location of the interface but within an infinite medium of the shielding material. Then multiply the result by the adjustment factor to yield the maximum absorbed dose in the tissue medium surrounding the shielding medium. The adjustment factor is insensitive to the thickness of the shielding medium.



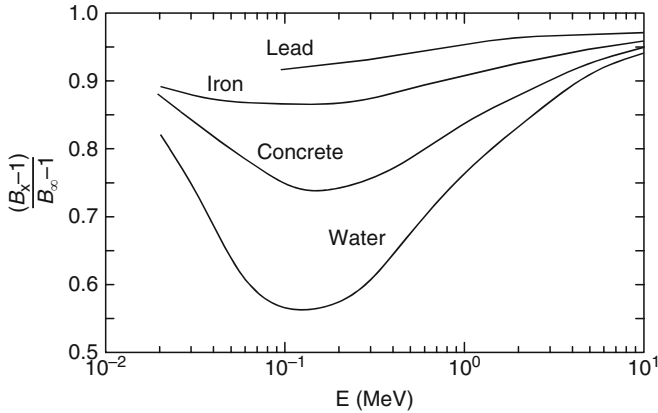
■ Figure 22

Finite-medium versus infinite-medium buildup factors for a 0.1-MeV point isotropic gamma-ray source in tissue. Calculations performed using the EGS4 code, courtesy of Sherrill Shue (1994), Kansas State University

4.4.2 Treatment of Stratified Media

The use of the buildup-factor concept for heterogenous media is of dubious merit, for the most part. Nevertheless, implementation of point-kernel codes for shielding design and analysis demands some way of treating buildup when the path from source point to dose point is through more than one shielding material. Certain regularities do exist, however, which permit at least an approximate use of homogenous-medium buildup factors for stratified shields. In general, though, the user of a point-kernel code must make the choice of a single material to characterize buildup. That choice is usually either the material with the greatest number of mean free paths between the source and the receiver or the material nearest the receiver.

For hand calculations, greater flexibility may often be used. For example, consider two-layer shields of optical thicknesses (mean free paths) l_1 and l_2 and effective atomic numbers Z_1 and Z_2 , numbered in the direction from source to detector. A commonly applied rule is that if $Z_1 < Z_2$, then the overall buildup factor is approximately equal to the buildup factor B_2 for material 2 evaluated at the total optical thickness $l_1 + l_2$. However, if $Z_1 > Z_2$, then the overall



■ Figure 23

Adjustment factor for the buildup factor at the boundary of a finite medium in terms of the infinite-medium buildup factor for the same depth of penetration. Exposure buildup calculations were performed for point isotropic sources in finite spheres and infinite media, using the EGS4 code, courtesy of Sherrill Shue, Nuclear Engineering Department, Kansas State University

■ Table 13

Adjustment factors to be applied to infinite-medium buildup factors when the maximum dose equivalent is to be evaluated in a thick-tissue medium bounding the shielding medium


E (MeV)	Shielding medium			
	Water	Concrete	Iron	Lead
0.05	0.95	1.29	1.60	1.65
0.06	0.95	1.29	1.66	1.72
0.08	0.96	1.24	1.60	1.72
0.10	0.97	1.20	1.48	1.46
0.15	0.98	1.14	1.31	1.37
0.20	0.98	1.11	1.22	1.36
0.30	0.99	1.08	1.15	1.29
0.40	0.99	1.06	1.11	1.22
0.50	0.99	1.05	1.09	1.18
0.60	0.99	1.05	1.08	1.15
0.80	0.99	1.04	1.06	1.12
1.00	0.99	1.03	1.06	1.10
1.50	1.00	1.02	1.03	1.07
2.00	1.00	1.02	1.02	1.04
3.00	1.00	1.01	1.01	1.02

Source: ANSI/ANS (1991)


buildup factor is the product $B_1(\ell_1) \times B_2(\ell_2)$. More precise methods have been suggested by Kalos (Goldstein 1959), Broder et al. (1962), Kitazume (1965), Bünemann and Richter (1968), Harima (1983), Su and Jiang (1989), Harima and Hirayama (1993), and Shin and Hirayama (1994, 1995).

4.5 Broad-Beam Attenuation of Photons

4.5.1 Attenuation Factors for Photon Beams

It is often the case in dealing with the shielding requirements for a radionuclide or X-ray source that the source is located some distance in air from a wall or shielding slab, and the concern is with the radiation dose on the exterior (cold) side of the wall. Often too, the source is sufficiently far from the wall that the radiation reaches the wall in nearly parallel rays, and the attenuation in the air is quite negligible in comparison to that provided by the shielding wall. Shielding design and analysis in the circumstances just described, and illustrated in  Fig. 24, are addressed by the National Council on Radiation Protection and Measurements (NCRP 1976) in their widely used Report 49. Attenuation of photons from both monoenergetic and polyenergetic sources can be established in terms of the formula

$$D(P) = D^{\circ}(P)A_f, \quad (59)$$

in which $D(P)$ is the dose or response at point P (the receiver in  Fig. 24), $D^{\circ}(P)$ is the response in the absence of the shield wall, accounting only for the inverse-square attenuation, and A_f is an *attenuation factor* which depends on the nature and thickness of the shielding material, the source energy characteristics, and the angle of incidence θ . The attenuation factor incorporates the response function and combines buildup and exponential attenuation into a single factor A_f .

4.5.2 Attenuation of Oblique Beams of Photons

When monoenergetic beams of gamma rays are obliquely incident on shielding slabs, attenuation-factor and conventional ray-theory methods are not successful. The reason is that

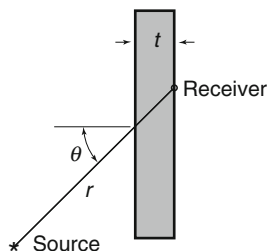


 Figure 24

Attenuation of gamma and X-rays from a point source in air by a shielding wall

the uncollided component of penetrating radiation is likely very small when compared with the collided component, and that the collided component is likely only very weakly dependent on the uncollided component. Obliquely incident beams, however, may be treated using a modified buildup factor that is a function of the angle of incidence. With respect to [Fig. 24](#), the beam attenuation factor in [\(59\)](#) may be written as

$$A_f = B(E_o, \cos \theta, \mu t) e^{-\mu t / \cos \theta}. \quad (60)$$

Values of the special buildup factor $B(E_o, \cos \theta, \mu t)$ are available in Shultis and Faw (2000) for concrete, iron, and lead shields for thicknesses as great as 10 mean free paths for wide ranges of photon energy and angle of incidence. Attenuation factors for concrete are listed in [Table 14](#). Attenuation factors for other materials may be found in the standard ANSI/ANS-6.4 (2006).

4.5.3 Attenuation Factors for X-Ray Beams

The appropriate measure of source strength for X-ray sources is the electron-beam current, and the appropriate characterization of photon energies, in principle, involves the peak accelerating voltage (kVp), the wave form, and the degree of filtration (e.g., mm Al) through which the X rays pass. Although the degree of filtration of the X rays would affect their energy spectra, there is only a limited range of filtrations practical for any one voltage, and within that limited range, the degree of filtration has little effect on the attenuation factor (NCRP 1976). Most diagnostic radiographic procedures for adult patients are conducted with an X-ray-beam quality of 2–3 mm Al half-value-layer (HVL) (Keriakes and Rosenstein 1980), which is consistent with 2.5–3.5 mm Al filtration of the X-ray source. The National Council on Radiation Protection and Measurements (NCRP 1989) requires at least 3.1 mm HVL and 3.1 mm Al filtration for three-phase generators with voltages 90 kVp or greater. Similar requirements are stated for lower voltages and for single-phase generators. Data on energy spectra from a wide variety of X-ray tubes and filtrations are available (Fewell and Shuping 1978; Fewell et al. 1981). For a given voltage, the greatest penetration would occur for a constant potential generator, but it has been found that X rays from modern three-phase generators are very nearly as penetrating (Simpkin 1989; Archer et al. 1994). Less penetrating are X rays from single-phase generators. Conservatism in design, allowing for upgrade in generators, dictates use of attenuation data for multiphase or constant-potential generators. If i is the beam current (mA) and r is the source–detector distance (m), then [\(59\)](#), with dose rate ($cGy \text{ min}^{-1} \simeq R \text{ min}^{-1}$) as the response, takes the form

$$\dot{D}(P) = \frac{i}{r^2} K_o A_f, \quad (61)$$

in which K_o is the *radiation output factor* with units of dose rate in vacuum (or air), per unit beam current at a distance of 1 m from the source in the absence of any shield. The dose unit was recently changed from exposure to air kerma (NCRP 1989). For the same voltage, the radiation output factor for a single-phase generator is less than that for a three-phase generator by a factor of $\sqrt{3}$ (NCRP 1989).

Attenuation factors for X rays normally incident on various shielding materials have been fit by Simpkin (1989, 1995) and by Archer et al. (1994) to the following expression, which was

Table 14

Attenuation factors for monoenergetic beams of gamma rays obliquely incident on slabs of ordinary concrete, expressed as the ratio of transmitted to incident air kerma

Photon energy (MeV)	Slab thickness (mfp)	$\cos \theta$						
		1.0	0.875	0.75	0.625	0.5	0.375	0.25
0.2	1	7.28E-01	6.53E-01	5.67E-01	4.57E-01	3.33E-01	2.15E-01	1.05E-01
	2	4.13E-01	3.28E-01	2.58E-01	1.77E-01	1.11E-01	6.09E-02	2.92E-02
	4	9.89E-02	6.77E-02	4.15E-02	2.61E-02	1.37E-02	7.87E-03	3.71E-03
	8	4.02E-03	2.15E-03	1.15E-03	6.08E-04	3.21E-04	1.65E-04	7.61E-05
0.661	1	6.78E-01	6.08E-01	5.25E-01	4.26E-01	3.11E-01	1.91E-01	8.49E-02
	2	3.69E-01	2.98E-01	2.24E-01	1.54E-01	9.23E-02	4.65E-02	1.96E-02
	4	8.86E-02	5.92E-02	3.62E-02	2.00E-02	9.95E-03	4.68E-03	2.01E-03
	8	3.51E-03	1.73E-03	7.86E-04	3.46E-04	1.50E-04	6.32E-05	2.47E-05
1.25	1	6.37E-01	5.73E-01	4.95E-01	4.01E-01	2.92E-01	1.76E-01	7.37E-02
	2	3.36E-01	2.69E-01	2.01E-01	1.35E-01	7.78E-02	3.60E-02	1.33E-02
	4	7.59E-02	4.92E-02	2.86E-02	1.45E-02	6.39E-03	2.54E-03	9.25E-04
	8	2.72E-03	1.21E-03	4.72E-04	1.67E-04	5.59E-05	1.85E-05	5.73E-06
2.5	1	5.94E-01	5.34E-01	4.62E-01	3.74E-01	2.71E-01	1.60E-01	6.29E-02
	2	2.99E-01	2.39E-01	1.77E-01	1.16E-01	6.41E-02	2.67E-02	8.02E-03
	4	6.30E-02	3.98E-02	2.20E-02	1.02E-02	3.76E-03	1.13E-03	3.08E-04
	8	2.04E-03	8.11E-04	2.88E-04	6.93E-05	1.64E-05	3.61E-06	7.23E-07
6.13	1	5.31E-01	4.76E-01	4.09E-01	3.30E-01	2.37E-01	1.36E-01	4.85E-02
	2	2.49E-01	1.97E-01	1.43E-01	9.21E-02	4.79E-02	1.74E-02	3.68E-03
	4	4.75E-02	2.91E-02	1.53E-02	6.37E-03	1.92E-03	3.78E-04	5.90E-05
	8	1.37E-03	5.03E-04	1.42E-04	2.67E-05	3.58E-06	4.17E-07	3.85E-08
10	1	4.98E-01	4.43E-01	3.82E-01	3.04E-01	2.11E-01	1.23E-01	3.96E-02
	2	2.23E-01	1.76E-01	1.27E-01	8.05E-02	3.99E-02	1.39E-02	2.51E-03
	4	4.08E-02	2.47E-02	1.24E-02	5.12E-03	1.46E-03	2.35E-04	2.41E-05
	8	1.14E-03	4.02E-04	1.08E-04	1.88E-05	2.16E-06	1.83E-07	1.20E-08

Source: MCNP calculations extending the work of Fournie and Chilton (1981) and Chen and Faw (1994)

originally recommended by Archer, Thornby, and Bushong (1983):

$$A_f = \left[\left(1 + \frac{\beta}{\alpha} \right) e^{\alpha y x} - \frac{\beta}{\alpha} \right]^{-1/\gamma}, \quad (62)$$

in which x is the material thickness, in units of millimeters. The coefficients for lead and concrete attenuation factors are listed in [Table 15](#) based on measurements and calculations of Archer et al. (1994), Simpkin (1987a), and Légaré et al. (1977). Conservative values of the output factor K_o given in the table conform to those given by Keriakes and Rosenstein (1980) and in NCRP Report 102 (1989).

In the design and analysis of shield walls for X-ray installations, it is necessary to account for a number of factors: (1) the *maximum permissible dose* for an individual situated beyond the shield wall during some prescribed time interval, such as 1 week, (2) the *workload*, which is the cumulative sum during the prescribed time interval of the product of the beam current and the duration of machine operation, (3) the *use factor*, which is the fraction of machine operation time that the X-ray beam is directed toward the shield wall, and (4) the *occupancy factor*, which is the fraction of the time during which the X-ray machine is in use and the beam is directed toward the shield wall behind which the individual at risk is actually present. All these factors are taken into account in the methodology of NCRP Reports 49 and 147. In addition, that methodology also treats leakage radiation from the X-ray machine and radiation scattered from patients or other objects present in the X-ray beam. The methodology is discussed at length by Simpkin (1987a,b, 1989, 1990) and by Chilton et al. (1984). A computer code for routine X-ray-shielding design and analysis [Simpkin 1987a] is available as code packages CCC-515/KUX and CCC-594/CALKUX from the Radiation Safety Information Computational Center, Oak Ridge National Laboratory, Oak Ridge, Tennessee.

Table 15

Fitting parameters for constant-potential X-ray attenuation factors computed for typical energy spectra from modern three-phase generators. The data for 30 and 35 kV are for low-voltage units with molybdenum anodes and beryllium windows. Otherwise, data are for tungsten anodes

kVcp	K_o^a	α (mm ⁻¹)	β (mm ⁻¹)	γ	α (mm ⁻¹)	β (mm ⁻¹)	γ
		Lead, $\rho = 11.35$ g/cm ³			Concrete, $\rho = 2.35$ g/cm ³		
30	2.61	38.80	178.0	0.3473	0.3173	1.698	0.3593
35	4.04	29.55	164.7	0.3948	0.2528	1.807	0.4648
50	0.87	8.801	27.28	0.2957	0.09032	0.1712	0.2324
70	2.19	5.369	23.49	0.5881	0.05087	0.1696	0.3847
100	4.69	2.500	15.28	0.7557	0.03925	0.08567	0.4273
120	7.62	2.246	8.950	0.5873	0.03566	0.07109	0.6073
140	8.74	2.009	5.916	0.4018	0.03345	0.07476	1.0470

^aRadiation output in units (mGy mA⁻¹ min⁻¹ at 1 m).

Source: Parameters α , β , γ , and K_o are from NCRP (2004); those for K_o are based on data of Archer et al. (1994)

4.5.4 The Half-Value Thickness

The half-value thickness, or half-value layer (HVL), is defined in terms of the attenuation of a parallel beam gamma or X rays, namely,

$$\text{HVL}(x) = \frac{-\ln 2}{d \ln A_f(x)/dx}. \quad (63)$$

For the special case of uncollided monoenergetic photons, $A_f(x) = e^{-\mu x}$, and

$$\text{HVL} = \frac{-\ln 2}{d \ln A_f/dx} = \frac{\ln 2}{\mu}. \quad (64)$$

However, when dealing with X rays or accounting for scattered gamma rays, the half-value thickness is a function of the depth of penetration, namely,

$$\text{HVL}(x) = \frac{-\ln 2}{d \ln A_f(x)/dx}. \quad (65)$$

At shallow penetrations, lower-energy photons are selectively removed and the HVL is relatively small. As the beam spectrum “hardens” with increasing penetration, the HVL increases. As may be shown from (62), the following relationships apply to X-ray data fit by that equation:

$$\lim_{x \rightarrow 0} \text{HVL} = \frac{\ln 2}{\alpha + \beta} \quad (66)$$

and


$$\lim_{x \rightarrow \infty} \text{HVL} = \frac{\ln 2}{\alpha}. \quad (67)$$

One other important application of the HVL. Values of the HVL at shallow penetration, usually for aluminum or copper, are widely used to characterize the penetration ability of X rays and as a parameter in the assessment of radiation doses from medical X rays. HVL data for a wide variety of materials and a wide variety of gamma- and X-ray source energies may be found in NCRP Reports 49 and 147 (1976, 2005).

4.6 Shield Heterogeneities

Occasionally, an analyst encounters a shield that includes regions of composition different from the bulk shield material. These regions may be large with a well-defined geometry, such as embedded pipes or instrumentation channels transverse to the direction of radiation penetration. By contrast, there may be incorporated into the shield material small irregularly shaped and randomly distributed voids or lumps of other material, such as pieces of scrap iron used to increase the effectiveness of a concrete shield against gamma radiation. For a large, well-defined heterogeneity in the shield (most often a single void or region of low-interaction coefficient), ray theory can often be used effectively. For simple geometry (e.g., a spherical or cylindrical void in a slab shield), (53) can be evaluated analytically. Otherwise, numerical integration techniques are used. Examples are given by Rockwell (1956), Burrus (1968b), and Chilton et al. (1984).

Rigorous calculation of the effect of such heterogenous regions in a shield usually requires Monte Carlo techniques. In this section, some simplified techniques, based on ray theory, illustrate the effect of shield heterogeneities.

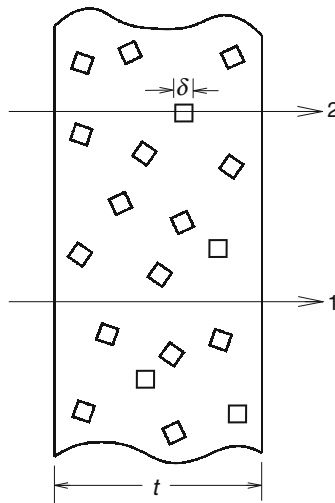
Consider two rays through a shield (see  Fig. 25) containing randomly distributed small voids in a continuous phase which has an effective linear attenuation coefficient μ . Ray 1 travels a distance t with transmission probability $T_1 = e^{-\mu t}$. Ray 2 travels a distance $t - \delta$ with transmission probability $T_2 = e^{-\mu(t-\delta)}$. The average path length for these two rays is $\bar{t} = t - \delta/2$, and the average transmission probability is


$$\bar{T} = \frac{1}{2}(T_1 + T_2) = e^{-\mu \bar{t}} \cosh(\mu \delta/2) > e^{-\mu \bar{t}}. \quad (68)$$

Thus, it is seen that the use of the average path length of a ray through the shield material underpredicts the average transmission probability. If the voids are replaced by a material with an attenuation coefficient different from that of the shield material, a similar analysis shows that use of the average path length (in mean free paths) also underestimates the average transmission probability. This effect is known as *channeling* and its neglect leads to an overestimation of the effectiveness of a shield. Channeling is seen in shields with randomly included heterogeneities as well as in shields with well-defined placement of voids and heterogenous regions.

4.6.1 Limiting Case for Small Discontinuities

Suppose in (68) that $\delta \ll \mu^{-1}$, that is, the lumps or voids are much smaller in size than the radiation mean free path length in the continuous phase. In this case, the channeling effect is negligible, and shield transmission factors may be estimated using an average mass attenuation coefficient $\bar{\mu}/\rho$. Suppose that μ , ρ , and w are the effective linear attenuation coefficient, density,



 **Figure 25**
Shield containing randomly distributed voids

and weight fraction of the continuous phase, and μ' , ρ' , and w' are the same quantities for the discontinuous phase. If v is the volume fraction of the voids or lumps in the shield and $\bar{\rho}$ is the average shield density, the average mass attenuation coefficient is

$$\overline{\mu/\rho} = \omega \left(\frac{\mu}{\rho} \right) + \omega' \left(\frac{\mu'}{\rho'} \right) = \frac{\rho(1-v)}{\bar{\rho}} \left(\frac{\mu}{\rho} \right) + \frac{\rho'v}{\bar{\rho}} \left(\frac{\mu'}{\rho'} \right), \quad (69)$$

and the transmission probability is thus

$$T(t) = e^{-(\overline{\mu/\rho})\bar{\rho}t} = e^{-(1-v)\mu + v\mu'}t} = e^{-\mu t} e^{-(\mu' - \mu)v t}. \quad (70)$$

This transmission probability is the same as if the shield materials (continuous and discontinuous components) were conceptually homogenized and the average attenuation coefficient for the homogenous mixture was used.

4.6.2 Small Randomly Distributed Discontinuities

Channeling effects have been treated by a statistical technique attributed to Coveyou (Burrus 1968a). Consider an infinite slab shield of thickness t , uniformly and normally illuminated on one side by radiation. The shield contains randomly distributed lumps with a different linear attenuation coefficient (μ') from that of the shield material (μ). Suppose that the mean chord length through a lump is δ . Then it can be shown that

$$T(t) = e^{-\mu t} e^{-(\mu' - \mu)v t / c_o}. \quad (71)$$

Here, c_o is the *cross-section effectiveness ratio*, namely,

$$c_o = \frac{-(\mu' - \mu)v\delta}{\ln[(1-v) + v e^{-(\mu' - \mu)\delta}]}. \quad (72)$$

For an arbitrary convex lump, the mean chord length is just four times the volume/surface area ratio. For concave and irregularly shaped lumps, the value of δ must be determined by specific calculation or by measurement of slices of the shield material.

5 Neutron Shielding

Neutron shielding analysis is often quite complex, involving not only attenuation of primary or source neutrons but also production and attenuation of secondary particles. These associated problems include the production of photons from neutron inelastic scattering, slowing down and thermalization of neutrons, capture of thermal neutrons leading to capture gamma photons, and even production of secondary neutrons as a result of fission or ($n, 2n$) reactions. Moreover, none of these associated problems is accurately solved using elementary techniques. To obtain accurate results with errors of only a few percentage, it is necessary to use sophisticated numerical techniques based on the exact descriptions of photon and neutron transport in the shield.

In this section, several of the simplified techniques developed for neutron shielding over the past 50 years are reviewed. Although these techniques are seldom used directly in modern shield analysis, the ideas behind them provide an insight into important mechanisms that determine the effectiveness of a neutron shield. Such insight allows the analyst to interpret and assess more critically results obtained with large computer codes.

5.1 Neutron Versus Photon Calculations

The development of simplified techniques for neutron shielding analysis is considerably more difficult than for photon shielding. The use of buildup factors, while theoretically applicable to any type of indirectly ionizing radiation, is much more difficult to apply to the neutron problem. The buildup of scattered neutrons depends strongly on the isotopic composition of the medium, on the neutron energy spectrum, and above all, on the problem geometry. Near a free surface, neutron densities generally decrease much more dramatically than in the photon case. Consequently, the use of infinite-medium buildup factors, which work so well for photon analyses, may introduce serious errors for neutron analyses.

Another serious difference between photon and neutron calculations arises from the evolution of thinking about fluence-to-dose conversion coefficients. Many different response-function sets have been issued by various national and international institutions over the past 50 years. Because the photon quality factor is independent of the photon energy, the ratio of different conversion coefficients, except at very low energies, is nearly constant, as is seen in [▶ Fig. 13](#). Thus, measured or calculated photon doses based on one conversion coefficient can be converted easily to another type of dose by an appropriate multiplicative constant. By contrast, the many neutron response functions that have been used at one time or another are not simply related to each other by a multiplicative constant (see, for example, [▶ Fig. 14](#)). Thus, much neutron shielding data (e.g., point kernels, albedos, transmission factors, etc.) reported in obsolete units cannot be rigorously used in modern shielding analysis. At best, only approximate conversions can be made; and if accurate results are needed, then there is no recourse but to repeat the original calculations or measurements using modern dose units.

5.2 Fission Neutron Attenuation by Hydrogen

There is one widely encountered situation for which the attenuation of a fast-neutron beam can be expected to be somewhat insensitive to the buildup of scattered neutrons. Elastic scattering from light elements results in a significant portion of the neutron's kinetic energy being lost, on the average, in a single scatter. In particular, for scattering from hydrogen the average energy loss is one-half of the initial neutron energy and, consequently, the scattering of a fast neutron on hydrogen acts essentially as an effective absorption or removal interaction because the neutron is, on the average, removed from the fast-neutron energy region by a single scatter. Thus, for the deep penetration of fast neutrons, the fast-neutron fluence might be expected to be very nearly equal to that of uncollided fast neutrons deep in an hydrogenous medium. In addition, the cross section for hydrogen in the MeV-energy region increases as the neutron energy decreases; hence, a low-energy neutron is much more likely to scatter from hydrogen than is a high-energy neutron. In effect, this characteristic of the hydrogen cross section implies

that, once a fast neutron interacts in an hydrogenous medium, the subsequent scattering or slowing-down interactions occur relatively near the point of the first scattering interaction.

From these arguments, it is then possible to derive a point kernel for the uncollided fast-neutron fluence in an infinite hydrogenous medium (Albert and Welton 1950). Consider a point-fission source which emits S_p fission neutrons with an energy spectrum given by $\chi(E)$ in an infinite hydrogenous medium with a hydrogen atom density of $N_H \text{ cm}^{-3}$. The uncollided fluence $\Phi_H^o(r, E)$ at distance r from the source, if one neglects any nonhydrogen collisions, is

$$\Phi_H^o(r, E) = \frac{S_p \chi(E)}{4\pi r^2} \exp[-N_H \sigma_H(E)r]. \quad (73)$$

Because the total fast-neutron fluence is of interest, (73) must be integrated over all fission energies. To perform such an integration, the functional form of $\chi(E)$ and $\sigma_H(E)$ must be used, and because the fast fluence is dominated by those neutrons with energies greater than 4 MeV, a simpler form from that of (9) may be used, namely,

$$\chi(E) \simeq A e^{-aE}, \quad (74)$$

where the parameters A and a depend on the fissile isotope and the energy range of the fit. For the energy range 2–12 MeV, the hydrogen total cross section (which is essentially the scattering cross section) may be approximated by (Blizard 1962)

$$\sigma_H(E) \simeq B E^{-b}, \quad (75)$$

where $B = 5.13 \times 10^{-24}$, $b = 0.725$, and σ_H is in units of cm^2 when E is in units of MeV.

As is shown by Chilton, Shultis, and Faw (1984), integration of (73) over all energy yields

$$\Phi_H^o(r) = \frac{S_p A \beta}{4\pi r^2} r^{\gamma/2} \exp(-\alpha r^\gamma), \quad (76)$$

where

$$\gamma \equiv 1/(1+b), \quad (77)$$

$$\beta \equiv \left[\frac{2\pi\gamma(N_H B b)^\gamma}{a^{1+\gamma}} \right]^{1/2}, \quad (78)$$

and

$$\alpha \equiv \frac{1}{\gamma} \left(\frac{a}{b} \right)^{b\gamma} (N_H B)^\gamma. \quad (79)$$

The presence of heavier components in the attenuating medium (e.g., the oxygen in a water shield) also degrades the fast neutrons in energy, although not nearly as well as the hydrogen. Many experiments have been performed to measure the attenuation of fast fission neutrons in hydrogenous media. Experimentally, it is found that the fast-neutron fluence falls off slightly faster with increasing distance from the source than (76) would indicate. In particular, experimental data for attenuation in water reveal that the spatial distribution of the total fast-neutron fluence can be related to that in hydrogen by

$$\Phi^o(r) = \Phi_H^o(r) \exp(-\mu_{r,O} r); \quad (80)$$

that is, the nonhydrogen component (oxygen) contributes an exponential attenuation factor. The constant $\mu_{r,O}$, although given the symbol of an attenuation coefficient, is an empirically derived constant to account for the nonhydrogen attenuation. Because of the similarity of this constant to the coefficient in the usual exponential attenuation of uncollided radiation, it is called the *removal coefficient*, although numerically it is usually significantly less than the actual total attenuation coefficient. More is said in the next section about the physical basis of the removal coefficient. Thus, by correcting for the attenuation of the oxygen, the fast-neutron fluence in water for a point fission source may be written as

$$\Phi^o(r) = \frac{A\beta S_p}{4\pi r^2} r^{\gamma/2} \exp(-\alpha r^\gamma - \mu_{r,O}r). \quad (81)$$

It should be emphasized at this point that the fast-neutron fluence kernel obtained from (81), with $S_p = 1$, is not adequate for detector-response evaluation because no account is taken of the buildup of small-angle-scattered neutrons which have lost very little energy. The usefulness of the kernel, however, is to suggest how the uncollided fluence (and hence, dose) can be expected to vary with distance from the source. Consequently, by fitting the functional form of the kernel to experimental data, one could expect to obtain a reasonably accurate semiempirical result. Such a fitting technique could be expected to lead to better agreement with experiment because the buildup of fast neutrons could be incorporated empirically. One widely used result is due to Casper (1960), who obtained the following fast-neutron tissue-absorbed-dose kernel for a point ^{235}U fission source in water:

$$\mathcal{G}(r) = \frac{5.39 \times 10^{-11}}{4\pi r^2} r^{0.349} \exp(-0.422r^{0.698} - 0.0308r), \quad (82)$$

where r has units of centimeters and \mathcal{G} has units of Gy for a source strength of one fission neutron.

Other functional forms have been fit to experimental dose data or to values calculated by the more elaborate neutron transport techniques. One particularly simple form for a ^{235}U fission source, which can be readily incorporated into analytical kernel calculations, expresses the fast-neutron tissue-absorbed dose kernel for water in terms of exponential functions (Grotenhuis 1962; Glasstone and Sesonske 1963), in the same units as used above, as

$$\mathcal{G}(r) = \frac{10^{-12}}{4\pi r^2} (23.9e^{-0.129r} + 2.89e^{-0.091r}). \quad (83)$$

Another empirical result, with the same units, which fits the experimental water kernel for absorbed dose in tissue more accurately than do the previous two results and which is valid over a much wider range of r ($0 \leq r \leq 300$ cm), is given by Brynjolfsson [1975] as

$$\mathcal{G}(r) = \frac{2.6 \times 10^{-11}}{4\pi r^2} e^{-br}, \quad (84)$$

where

$$b = \left[0.126 - 0.0001773 \left(r - \frac{r^2}{600} \right) \right] \left[1 - \left(2 + \frac{r^4}{5000} \right)^{-1} \right]. \quad (85)$$

A comparison of the foregoing three empirical tissue-absorbed dose-point-kernels in water with accurately calculated values is presented in [Table 16](#).

■ Table 16

Absorbed dose kernels in tissue from a point ^{235}U fission source in water (\mathcal{G}_o) obtained by the moments method (Goldstein 1959)

Distance from source (cm)	$4\pi r^2 \mathcal{G}_o(r)$ moments methods (Gy cm ²)	Ratio to \mathcal{G}_o^a		
		$\mathcal{G}_1/\mathcal{G}_o$	$\mathcal{G}_2/\mathcal{G}_o$	$\mathcal{G}_3/\mathcal{G}_o$
0	2.63×10^{-11}	0	1.02	0.98
10	1.05×10^{-11}	1.03	0.74	0.97
20	2.30×10^{-12}	1.19	0.99	1.04
30	7.08×10^{-13}	1.06	0.97	0.99
60	2.43×10^{-14}	0.94	0.94	0.99
90	9.89×10^{-16}	0.95	1.03	1.05
120	5.53×10^{-17}	0.85	1.03	0.98

^a \mathcal{G}_1 calculated from (82); \mathcal{G}_2 calculated from (83); and \mathcal{G}_3 calculated from (84)

5.3 Removal Cross Sections

In many realistic situations, fission neutrons are attenuated not only by an hydrogenous medium but also by an interposed nonhydrogenous shield such as the wall of a steel pressure vessel. Many experimental data have been obtained for such situations; and under special circumstances, the effect of the nonhydrogen component can be very simply accounted for by an exponential attenuation factor, much as was done for the oxygen correction examined in the preceding section.

An idealized fast-neutron attenuation experiment is shown in ► Fig. 26. A point isotropic fission source in an infinite homogenous hydrogenous medium is surrounded by a spherical shell of thickness t composed of a nonhydrogenous material. Experimental results reveal that under certain circumstances, the tissue-absorbed dose D' with the shell in position (i.e., at a distance $r_1 + r_2$ of hydrogenous medium plus a thickness t of the nonhydrogenous component) is related to the dose D at a distance $r = r_1 + r_2$ from the source, without the shell, by

$$D' = D \left(\frac{r}{r+t} \right)^2 e^{-\mu_r t}, \quad (86)$$

where μ_r is called the *removal coefficient* and is a constant characteristic of the nonhydrogenous component for a given fission-neutron energy spectrum.

Two important restrictions on the experimental arrangement are required for the validity of (86). First, it is important that there be at least 6 g cm^{-2} of hydrogen, equivalent to 50 cm of water, between the nonhydrogenous component and the observation position. Second, the thickness t must be such that $\mu_r t$ is less than about 5.

Although the factor $\exp(-\mu_r t)$ in (86) appears to indicate that absorption of neutrons is taking place in the nonhydrogenous component, the principal interactions are scattering interactions in which the fission neutrons are degraded in energy only slightly. However, the

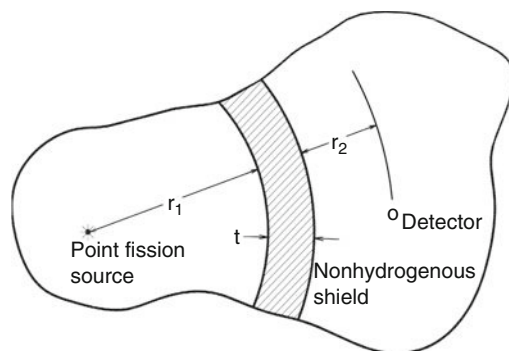


Figure 26

Idealized experimental geometry for the measurement of the removal cross-section in which a nonhydrogenous shield of thickness t is placed between the point-fission source and the detector in an infinite hydrogenous medium

hydrogen in the material following the nonhydrogenous component (one of the two experimental restrictions) moderates or removes the slightly slowed-down neutrons more quickly than those neutrons which traverse the nonhydrogenous component without any energy loss. If, following the nonhydrogenous component, there is sufficient hydrogen to effect the removal of the neutrons which are slightly moderated, the spatial variation of the fast-neutron tissue-absorbed dose D can be obtained from one of the kernels of (82) to (84), for the case that the hydrogenous medium is water.

If a series of different materials is inserted into the hydrogenous medium, the removal term $\exp(-\mu_r t)$ of (86) becomes simply $\exp(-\sum_i \mu_{r,i} t_i)$, where $\mu_{r,i}$ is the removal coefficient for the i th slab of thickness t_i . Similarly, if a slab of a mixture of elements is inserted, the removal coefficient μ_r for the slab is given by $\sum_i N_i \sigma_{r,i}$, where N_i is the atom density of the i th element with microscopic removal cross section $\sigma_{r,i}$. This additive nature of the relaxation lengths for the nonhydrogen components, which is a direct consequence of (86), has generally been supported by experiment, although some deviations have been noted.

The (n, γ) absorption cross-section for most materials in the MeV-energy region is negligible and plays no significant role in the removal of fast neutrons. Conceptually, the removal cross-section is that fraction of the total fast-neutron cross section, averaged over energies of fission neutrons, representing inelastic and elastic scattering through a large scattering angle (i.e., scattering in which there is significant energy loss). Thus, the removal cross section can be expected to be somewhat less than the total cross section. As an approximation, $\mu_r \approx \frac{2}{3} \bar{\mu}_t$, where $\bar{\mu}_t$ is the average total attenuation coefficient in the energy range 6–8 MeV (Goldstein and Aronson 1954).

There is no firm theoretical reason for the removal cross section to be a material constant, and indeed, it might be expected to vary with the fission neutron energy spectrum, the thickness of the nonhydrogenous shield, amount of hydrogenous material on either side of the slab, and the geometry of the experiment. However, experimental results have shown that for most situations (provided that the slab is less than five removal relaxation lengths thick), μ_r can often be taken as a constant for a given incident fission spectrum. In Table 17, the measured values of removal cross sections for several materials are presented. To obtain removal cross sections

■ Table 17

Measured microscopic removal cross sections of various elements and compounds for ^{235}U fission neutrons

Material	σ_r (b/atom)	Material	σ_r (b/atom)
Aluminum	1.31 ± 0.05	Oxygen	0.99 ± 0.10
Beryllium	1.07 ± 0.06	Tungsten	3.36
Bismuth	3.49 ± 0.35	Zirconium	2.36 ± 0.12
Boron	0.97 ± 0.10	Uranium	3.6 ± 0.4
Carbon	0.81 ± 0.05	Boric oxide, B_2O_3	4.30 ± 0.41^a
Chlorine	1.2 ± 0.8	Boron carbide, B_4C	4.7 ± 0.3^a
Copper	2.04 ± 0.11	Fluorothene, $\text{C}_2\text{F}_3\text{Cl}$	6.66 ± 0.8
Fluorine	1.29 ± 0.06	Heavy water, D_2O	2.76 ± 0.11^a
Iron	1.98 ± 0.08	Heavimet ^b	3.22 ± 0.18
Lead	3.53 ± 0.30	Lithium fluoride, LiF	2.43 ± 0.34^a
Lithium	1.01 ± 0.05	Oil, CH_2 group	2.84 ± 0.11^a
Nickel	1.89 ± 0.10	Paraffin, $\text{C}_{30}\text{H}_{62}$	80.5 ± 5.2

^aRemoval cross-section is in barns per molecule or per group.

^b90 wt% W, 6 wt% Ni, 4 wt% Cu; cross-section is weighted average.

Source: Blizard (1962); Chapman and Storrs (1955)

for other elements, the following empirical formulas (in units of cm^2/g) have been obtained to permit interpolation between these measured values (Zoller 1964):

$$\frac{\mu_r}{\rho} = \begin{cases} 0.190Z^{-0.743} & Z \leq 8 \\ 0.125Z^{-0.565} & Z > 8 \end{cases} \quad (87)$$

or

$$\frac{\mu_r}{\rho} = 0.206A^{-1/3}Z^{-0.294}, \quad (88)$$

where A and Z are the atomic mass and atomic number, respectively, for the element of concern.

5.4 Extensions of the Removal Cross Section Model

5.4.1 Effect of Hydrogen Following a Nonhydrogen Shield

In the preceding section, it was emphasized that the applicability of the removal cross section model of (86) was dependent on whether there is sufficient hydrogen following the nonhydrogenous component to complete the removal of neutrons which have been degraded slightly in energy by the nonhydrogen component. If there is insufficient hydrogen following the

nonhydrogenous component, not all the neutrons are removed, and the removal cross-section appears to have a smaller value. In such a situation, the removal cross-section is no longer simply a material property, but it is also a function of the hydrogen thickness following the nonhydrogen component (Shure et al. 1969).

Values of removal cross sections are insensitive to the lower cutoff energy used to define the lower limit of the fast-neutron fluence. However, for hydrogen-deficient shields, the lower cutoff energy yields slightly smaller values for the removal cross section, as would be expected, because the limited hydrogen available is unable to remove all the degraded neutrons and consequently, leaves relatively more fast neutrons to penetrate the shield.

5.4.2 Homogenous Shields

For homogenous systems in which the nonhydrogen material is uniformly dispersed in a hydrogenous medium such as concrete, the removal cross section concept can also be applied if the hydrogen concentration is sufficiently high. For such situations, the fast-neutron tissue-absorbed dose $D(r)$ from a point fission source of strength S_p can be related to the dose $D_H(r)$ in a pure hydrogen medium of equivalent hydrogen density by the equation

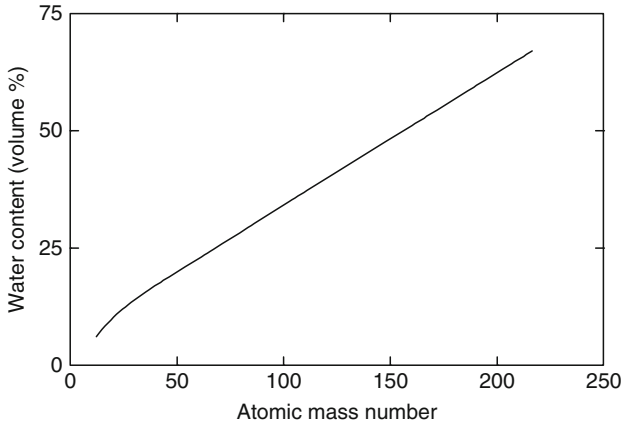
$$D(r) = D_H(r) \exp\left(-\sum_{i=1}^N N_i \sigma_{r,i}^{\text{homo}} r\right), \quad (89)$$

where $\sigma_{r,i}^{\text{homo}}$ is the microscopic removal cross section of the i th nonhydrogen component for a fission neutron source, and N_i is the atom density of the i th nonhydrogen species. The pure hydrogen dose $D_H(r)$ in this result can be calculated in terms of a point-source dose kernel $\mathcal{G}_H(r)$ as $D_H(r) = S_p \mathcal{G}_H(r)$, where $\mathcal{G}_H(r)$ can be inferred from the water kernels of (82) to (85) by eliminating the oxygen contribution and correcting for the different hydrogen atomic density. For example, using Casper's semiempirical kernel of (82), with the oxygen removal term eliminated, $\mathcal{G}_H(r)$ can be expressed as

$$\mathcal{G}_H(r) = \frac{5.39 \times 10^{-11}}{4\pi r^2} \left\{ (Yr)^{0.349} \exp[-0.422(Yr)^{0.698}] \right\}, \quad (90)$$

where Y is the ratio of the hydrogen atom density in the mixture to that in pure water. For most elements, the homogenous removal cross sections in (89) can be taken equal to the heterogenous removal cross section (see [Table 17](#)); although for lighter elements, the homogenous removal cross sections appear to be 5–10% smaller than those for heterogenous media (Tsy-pin and Kukhtevich 1968).

For (89) to be valid, it is imperative that there be sufficient hydrogen present to remove neutrons degraded in energy by collisions with the heavy component. In [Fig. 27](#), the lowest concentration of water required for the validity of (89) is presented as a function of the atomic mass of the nonwater component. Note that the heavier the nonhydrogen component, the more the water is required. It should also be noted that the concrete, which is a very important neutron-shielding material, is just barely able to pass this criterion. One should be cautious therefore in the application of (89) to a very dry concrete.



■ Figure 27

Lowest volume concentration of water in a homogenous mixture containing heavy components with an average atomic mass A for (89) to be valid. From Tsypin and Kukhovich (1968)

5.4.3 Energy-Dependent Removal Cross Sections

In many situations, the neutron spectrum incident on an hydrogenous shield is not that of a fission source, but may have a completely different energy dependence, $\chi(E)$, as a result of penetration through other materials or from a difference in the physical source of the fast neutrons (e.g., a fusion reaction). In such situations, the removal concept can again be used by employing energy-dependent removal cross sections. As with the fission-spectrum case, it is important that sufficient hydrogen be present to remove those neutrons which have been slightly degraded by collisions with the nonhydrogenous components in the shield. For any point isotropic source of strength S_p and energy spectrum $\chi(E)$, the tissue-absorbed dose in a distance r away from the source in an infinite homogenous medium can, by analogy with our previous results, be written as

$$D = \int_0^{\infty} dE S_p \chi(E) \mathcal{G}_H(r, E) \exp\left[-\sum_{i=1}^N N_i \sigma_{r,i}(E) r\right], \quad (91)$$

where $\mathcal{G}_H(r, E)$ is the neutron dose kernel at a distance r from a unit-strength isotropic source emitting neutrons of energy E in a pure hydrogen medium of density equivalent to that in the shield material; $\sigma_{r,i}(E)$ is the microscopic removal cross section of the i th nonhydrogen shield component for neutron energy E ; and N_i is the atom density of the i th shield component.

The use of (91) to calculate the dose depends on two crucial pieces of information: the hydrogen dose kernel $\mathcal{G}_H(r, E)$ and the energy-dependent removal coefficient $\mu_{r,i}$. As a rough approximation for the energy-dependent hydrogen dose kernel, one may use the following result [Tsypin and Kukhovich 1968]:

$$\mathcal{G}_H(r, E) = \frac{1}{4\pi r^2} \exp[-\mu_H(E)r][1 + \mu_H(E)r]\mathcal{R}_D(E), \quad (92)$$

which is simply the uncollided dose kernel times an approximate buildup-factor correction, $[1 + \mu_H(E)r]$, times the tissue-absorbed dose-response function $\mathcal{R}_D(E)$. Here $\mu_H(E)$ is

the total hydrogen attenuation coefficient at energy E . An alternative is to use the following empirical result for the tissue-absorbed dose kernel (Shultis and Faw 2000) as

$$\mathcal{G}_H(r, E) = \frac{A_0(E)}{4\pi r^2} \exp[-A_1(E)Yr - A_2(E)(Yr)^2 + \mu_{r,O}(E)Yr], \quad (93)$$

in which Y is the ratio of the hydrogen atom density to that in water, and $\mu_{r,O}(E)$ is the energy-dependent removal coefficient for oxygen in water. The parameters $A_0(E)$, $A_1(E)$, and $A_3(E)$ are given in ► [Table 18](#).

A more severe limitation of the energy-dependent removal-cross-section theory is the availability of values for removal cross sections. Only sparse experimental data are available, and those have rather large associated uncertainties (Gronroos 1968; Tsypin and Kukhtevich 1968). In many cases, it is necessary to use theoretical values of removal cross sections. Generally, the lack of information about energy-dependent removal cross sections as well as a lack of an accurate hydrogen-attenuation dose kernel limit the use of removal-cross-section theory for dose calculations. Of particular concern in shield calculations are those energy regions for which these removal cross-sections have minima, that is, those energies for which neutrons can stream through the shield material with a little chance of being removed. To obtain accurate results for nonfission spectra, more elaborate transport-theory based methods are called for. However, for an approximate calculation, (91) may be useful.

5.5 Fast-Neutron Attenuation without Hydrogen

In nonhydrogenous material, accurate calculation of the attenuation of fast neutrons requires numerical procedures based on transport theory or removal-diffusion theory. For rough estimates of fast-neutron penetration, however, a few empirical results have been obtained and are summarized in this section.

■ **Table 18**

Constants for the empirical fit of the tissue-absorbed dose kernel for a point-monoenergetic neutron source in water as given by (93).^a

Source energy (MeV)	A_0 (Gy cm ²)	A_1 (cm ⁻¹)	A_2 (cm ⁻²)	Range of fit (cm)
2	7.31×10^{-11}	0.1716	6.274×10^{-4}	10 to 80
4	9.55×10^{-11}	0.1115	3.792×10^{-4}	10 to 110
6	8.63×10^{-11}	0.07953	1.913×10^{-4}	10 to 140
8	7.04×10^{-11}	0.06362	1.634×10^{-4}	10 to 140
10	6.09×10^{-11}	0.05723	1.414×10^{-4}	10 to 140
14	5.42×10^{-11}	0.04925	1.318×10^{-4}	10 to 140

^aThese values were obtained by a least-squares fit to the results of moments calculations (Brynjolfsson 1975; Goldstein 1959). Agreement is within $\pm 10\%$ over the indicated range of each fit

Important nonhydrogenous materials frequently encountered in shield design include iron, lead, and aluminum used as structural material or for photon shielding. Fast neutrons are attenuated very poorly by these materials. For Po–Be neutrons, relaxation lengths are found to be 16 cm for iron, 24 cm for lead, and 30 cm for aluminum (Dunn 1957). Hence, fast-neutron attenuation through only a few centimeters of these materials can be neglected for practical purposes.

However, for thick nonhydrogenous shields, fast neutrons may be appreciably attenuated. Beyond a few mean-free-path lengths from a fast-neutron source in an infinite nonhydrogenous medium, the fast-neutron fluence has been observed to decrease exponentially. However, the relaxation length is a characteristic not only of the material but also of the source energy and the low-energy limit used to define the fast-neutron region (i.e., the “fast group” of neutrons). Specifically, the total fast-neutron fluence $\Phi_\alpha(r)$ above some threshold energy E_α at a distance r greater than three mean-free-path lengths from a point monoenergetic source of strength S_p and energy E_o in an infinite homogenous medium, can be calculated by (Broder and Tsy-pin 1968)

$$\Phi_\alpha(r) \simeq \int_{E_\alpha}^{E_o} \Phi(r, E) dE = \frac{S_p B_o}{4\pi r^2} \exp(-r/\lambda_r). \quad (94)$$

The factor B_o corrects for the initial buildup of scattered fast neutrons and, after a few mean-free-path lengths, becomes a constant. Both the initial buildup factor and the relaxation length λ_r are empirical constants and depend on the attenuating material, the source energy, and the threshold energy E_α . In \blacklozenge Table 19, values of B_o and λ_r are presented for a few materials.

If the fast-neutron source is distributed in energy, the technique above can still be applied by dividing the source energy region into several contiguous narrow energy ranges and then treating the neutrons in each range as monoenergetic neutrons, governed by (94). Thus,

$$\Phi_\alpha = \frac{S_p}{4\pi r^2} \sum_i f_i B_o^i \exp(-r/\lambda_r^i), \quad (95)$$

where f_i is the fraction of neutrons emitted in the i th energy range and B_o^i and λ_r^i are the initial buildup factor and relaxation length, respectively, for neutrons at the mean energy of the i th

\blacksquare **Table 19**
Initial Buildup Factors and Relaxation Lengths in Different Media for Monoenergetic Neutron Sources. The energy range for the fast-neutron flux density is 1.5 MeV to E_o

Medium	Density (g cm ⁻³)	$E_o = 4$ MeV		$E_o = 14.9$ MeV	
		B_o	λ_r (cm)	B_o	λ_r (cm)
B ₄ C	1.67	2	12.0	2	17.2
C	1.67	2	11.4	2	19.2
Al	2.70	2.5	14.1	2.5	15.8
Fe	7.83	2.5	7.6	2.7	8.2
Pb	11.3	4	15	2.9	15.3

Source: Broder and Tsy-pin (1968)

energy range. At large distances into the shield, only a few terms in the summation of (95) are significant, those corresponding to neutrons whose energies are at minima in the total effective nuclear cross section.

The exponential attenuation of the fluence given empirically by the equations above can also be applied to media composed of a mixture of elements by using a weighted average of the relaxation lengths for the individual components, that is,

$$\lambda_r = \left(\sum_i \frac{\rho'_i}{\rho_i} \frac{1}{\lambda_r^i} \right)^{-1}, \quad (96)$$

where λ_r^i is the relaxation distance of the i th material at density ρ_i , and ρ'_i is the actual density of the i th material in the mixture, which may be different from ρ_i .

One of the major difficulties in applying the above technique is the lack of empirical data for initial buildup or, more important, for values of the relaxation lengths. Often, values for λ_r are chosen as the reciprocal of the removal coefficient μ_r for neutrons above 3 MeV. In reality, one can expect the relaxation length to be somewhat larger because hydrogen is not present to remove the slightly degraded neutrons. Typically, the removal coefficient should as a rule of thumb be reduced by a factor of about 2 to compute λ_r . However, the use of such inferred values for the relaxation lengths introduces a great deal of uncertainty in the fast-neutron fluences calculated, and consequently, such estimates must be used cautiously.

The procedures described here for estimating the fast-neutron fluence are, at best, only approximate. For design work, it is necessary to employ more elaborate methods based on the neutron-transport equation.

5.6 Intermediate and Thermal Fluences

The attenuation of fast neutrons in a shield necessarily leads to neutrons with intermediate and, eventually, thermal energies. The resulting intermediate-energy neutrons can contribute appreciably to the transmitted neutron dose in a shield, and the thermal neutrons, which are readily absorbed in the shield material, lead to the production of high-energy capture gamma photons. In many instances, the capture gamma-ray dose at the shield surface is the dominant consideration in the shield design. Thus, an important aspect of neutron shield analyses is the calculation of thermal and intermediate neutron fluences.

The thermal and intermediate neutrons in a shield arise from the thermalization of fast neutrons as well as from thermal and intermediate-energy neutrons incident on the shield's surface. Many elaborate techniques have been developed to compute accurately the thermal and intermediate neutron fluences; however, two simplified methods, based on diffusion and Fermi age theory, are first presented.

5.6.1 Diffusion Theory for Thermal Neutron Calculations

For hydrogenous shields, the fast neutrons are rapidly thermalized once they are removed from the fast group, as a result of the higher hydrogen cross section experienced by the neutrons removed. Consequently, as a rough approximation, the neutrons can be assumed to become

thermalized at the point at which they are removed from the fast group. In effect, the migration of intermediate-energy neutrons is neglected. The diffusion of the thermal neutrons then establishes the thermal-neutron fluence inside the shield. The thermal neutron flux density Φ_{th} can be calculated by use of the steady-state, one-speed, diffusion model for neutron transport (Lamarsh 1966),

$$D\nabla^2\Phi_{th}(\mathbf{r}) - \mu_a\Phi_{th}(\mathbf{r}) + S_{th}(\mathbf{r}) = 0, \quad (97)$$

where D and μ_a are the diffusion coefficient and linear absorption coefficient (macroscopic absorption cross section), respectively, for thermal neutrons.

Neutrons appear in the thermal group as they are lost from the fast group. Thus, the thermal neutron source term in (97) can be determined from the spatial rate of change of the fast neutrons traveling in direction Ω , namely,

$$S_{th}(\mathbf{r}) = -\nabla \cdot \int_{4\pi} d\Omega \Omega \Phi_f(\mathbf{r}, \Omega). \quad (98)$$

To a good approximation, the fast neutrons can be considered to be moving directly away from their source because there is little change in direction from the time the neutron leaves the source until it is removed from the fast region. Also, far from the fast neutron sources, the fast neutrons are all traveling in approximately the same direction \mathbf{n} directly away from their source, so that $\int_{4\pi} d\Omega \Omega \Phi_f(\mathbf{r}, \Omega) \simeq \mathbf{n}\Phi_f(\mathbf{r})$. Thus, the source of the thermal neutrons can be estimated from the fast-neutron fluence as

$$S_{th}(\mathbf{r}) \simeq -\nabla \cdot \mathbf{n}\Phi_f(\mathbf{r}). \quad (99)$$

The vector \mathbf{n} is a unit vector directed away from the fast-neutron source in the direction of fast-neutron travel or, equivalently, the direction in which the fast fluence decreases the most rapidly (i.e., opposite to the direction of the gradient of Φ_f).

For example, consider a plane shield ($0 < x < T$) in which the fast-neutron fluence is represented by an exponential function, or more generally, by a sum of N exponentials; that is,

$$\Phi_f(x) = \sum_{i=1}^N \Phi_f^i(0) \exp[-k_f^i x], \quad (100)$$

where $\Phi_f^i(0)$ and k_f^i are adjusted to give the best fit to the given fast-neutron fluence. For this case, the diffusion equation becomes

$$\frac{d^2\Phi_{th}(x)}{dx^2} - \frac{\mu_a}{D}\Phi_{th}(x) = -\frac{1}{D} \sum_{i=1}^N k_f^i \Phi_f^i(0) \exp[-k_f^i x], \quad (101)$$

whose general solution is

$$\Phi_{th}(x) = Ae^{-x/L} + Ce^{x/L} - \sum_{i=1}^N \frac{k_f^i \Phi_f^i(0)}{(k_f^i)^2 D - \mu_a} \exp[-k_f^i x], \quad (102)$$

where $L \equiv \sqrt{D/\mu_a}$. The constants A and C are then evaluated from the presumably known thermal neutron fluence incident at $x = 0$, and by setting Φ_{th} to zero at the outer surface of the shield, or, for thick shields, setting C equal to zero.

Instead of representing the fast-neutron fluence by a sum of exponentials as in (8.39), the shield could be divided into contiguous regions, with the fluence in each region represented by a single exponential, that is,

$$\Phi_f(x) = \Phi_f(x_j) \exp[-k_f^i(x - x_j)], \quad x_j < x < x_{j+1}. \quad (103)$$

Such a fit is easily performed by a series of straight-line fits to a plot of $\ln \Phi_f(x)$ versus x , and the relaxation constant k_f^j is obtained from

$$k_f^j = \frac{1}{x_j - x_{j+1}} \ln \left[\frac{\Phi_f(x_{j+1})}{\Phi_f(x_j)} \right]. \quad (104)$$

Once the exponential fit of the fast-neutron fluence is obtained for each region, the thermal neutron diffusion equation is solved in each region. The constants of integration are evaluated by requiring the solution and its first derivative to be continuous at the interfaces x_j or equal to specified values of the thermal neutron fluence at the shield surfaces. For preliminary analyses, it is often sufficient to fit the fast-neutron fluence by a single exponential over the whole shield volume. In **Table 20**, values for D and μ_a are presented for a few important shield materials, together with values of k_f for attenuation of fast neutrons.

5.6.2 Fermi Age Treatment for Thermal and Intermediate-Energy Neutrons

A refinement of the diffusion-theory procedure is to use Fermi age theory to correct for the migration of neutrons as they slow down to thermal energies (Blizard 1962). Age theory describes the slowing down of neutrons by a continuous energy-loss process which results in the same average energy loss as in the actual discrete energy losses from each scattering interaction. With this theory, neutrons are found to be distributed spatially in a Gaussian manner about the point at which they begin to slow down.

Table 20

Neutron properties of hydrogenous shield materials

Material	Density (g cm ⁻³)	k_f (cm ⁻¹) ^a	D (cm)	μ_a (cm)
Water	1.0	0.14	0.17	0.022
Ordinary concrete	2.35	0.085	0.65	0.0094
Barytes	3.50	0.125	0.44	0.019
Iron concrete	4.30	0.16	0.29	0.081

^aApproximate value for fast-neutron attenuations for a single exponential fit by (100). Actual fit values should be used whenever available.

Source: Glasstone and Sesonske (1963)

The number of fast neutrons reaching thermal energies per unit time at some point x inside the shield, $S_{th}(x)$, can be shown to be (Shultis and Faw 2000)

$$S_{th}(x) \simeq k_f \Phi_f(0) \exp[-k_f(x - k_f \tau_{th})], \quad (105)$$

where τ_{th} is the age to thermal energy. This result is valid for a shield whose thickness $T \gg \sqrt{\tau_{th}}$.

If the thermal neutrons are absorbed near the point at which they reach thermal energies, then under steady conditions the number absorbed, $\mu_a \Phi_{th}(x)$, must equal the number thermalized, $S_{th}(x)$. Thus, from (105),

$$\Phi_{th}(x) \simeq \frac{k_f}{\mu_a} \Phi_f(0) \exp[-k_f(x - k_f \tau_{th})] = \frac{k_f}{\mu_a} \Phi_f(x - k_f \tau_{th}). \quad (106)$$

This result implies that inside the shield the thermal neutron fluence is proportional to the fast-neutron fluence displaced toward the source by a *displacement distance* $k_f \tau_{th}$. The thermal neutron fluence inside a shield can thus be expected to parallel the fast-neutron fluence – a result usually observed.

5.6.3 Removal-Diffusion Techniques

Although diffusion theory can be used for initial estimates, more accurate techniques are often needed without the effort and expense of a full-scale multigroup transport calculation. Multigroup diffusion theory, which is considerably less expensive and complex to use than the transport theory, is remarkably successful at describing the slowing down and thermalization of neutrons in a reactor core. However, for describing neutrons deep within a shield, it has met with only limited success (Taylor 1951), although better accuracy has been obtained by introducing extraneous renormalization techniques to describe the penetration of the fast neutrons (Anderson and Shure 1960; Haffner 1968). That strict diffusion models should be of limited use to describe fast-neutron penetration, and subsequent thermalization is not surprising since diffusion theory requires both the differential scattering cross sections, and the angular fluence to be well described by first-order Legendre expansions. Such conditions usually hold in a reactor core where the neutron fluence is approximately isotropic; however, the fluence deep within a shield is determined by those very energetic neutrons which are highly penetrating and whose angular distribution is therefore highly anisotropic.

The penetrating fast neutrons are described very successfully by removal theory. The migration of the neutrons, once they are removed from the anisotropic fast group and begin to thermalize, is small compared to the distance traveled by the unremoved neutrons. Further, during thermalization, the fluence becomes more isotropic as more scatters occur. Consequently, one would expect multigroup diffusion theory to be applicable for the description of the slowing-down process and the subsequent diffusion at thermal energies. One approach to compute the buildup of low-energy neutrons inside a shield is to combine removal theory (to describe the penetration of fast neutrons) with multigroup diffusion theory (to describe the subsequent thermalization and thermal diffusion). This combination of removal and diffusion theory, in many formulations, has proved very successful.

Original Spinney Method

The first wedding of removal theory to diffusion theory was introduced by Spinney in 1958 (Avery et al. 1960). In the original formulation, the fast-source region, 0–18 MeV, is divided into 18 equal-width energy bands. The source neutrons in each band penetrate the shield in accordance with the removal theory. The density of removal collisions from all bands is then used as the source of neutrons in the first diffusion group. Explicitly, this diffusion source density at \mathbf{r} is given by

$$S_d(\mathbf{r}) = \sum_{i=1}^{18} \int_V \frac{S_v(\mathbf{r}') \chi_i \mu_{r,i} \exp(-\mu_{r,i} |\mathbf{r} - \mathbf{r}'|)}{4\pi |\mathbf{r}' - \mathbf{r}|^2} dV(\mathbf{r}'), \quad (107)$$

where $S_v(\mathbf{r}')$ is the production of source neutrons per unit volume at \mathbf{r}' in the source region, χ_i is the fraction of source neutrons in the i th removal band, and $\mu_{r,i}(\mathbf{r})$ is the removal coefficient for the i th band at position \mathbf{r} . The term $\mu_{r,i} |\mathbf{r} - \mathbf{r}'|$ is the total number of removal relaxation lengths between \mathbf{r} and \mathbf{r}' for a fast neutron in the i th band.

These removal neutrons are inserted as source neutrons into the top energy group of five energy groups, with the fifth group representing the thermal neutrons. The transfer of neutrons from one diffusion group to another diffusion group is determined by Fermi age theory (Lamarsh 1966), a continuous slowing-down model, and consequently neutrons can be transferred only to the energy group directly below. Thus, the diffusion group equations are written as

$$\nabla^2 \Phi_i(\mathbf{r}) - \frac{\mu_{a,i}}{D_i} \Phi_i(\mathbf{r}) - \frac{1}{\tau_i} \Phi_i(\mathbf{r}) = -\frac{S_i(\mathbf{r})}{D_i}, \quad (108)$$

where Φ_i is the fluence for group i , $\mu_{a,i}$ is the linear absorption coefficient for group i , D_i is the i th group diffusion coefficient, and τ_i is the square of the slowing-down length from group i to the next lower group $i + 1$, or equivalently, the Fermi age of neutrons starting from group i and slowing down to group $i + 1$ (for the thermal group, $\tau_i^{-1} = 0$).

The source term for the i th diffusion group is then given by

$$S_i(x) = \begin{cases} S_d(\mathbf{r}) & \text{from (107), } i = 1, \\ D_{i-1} \tau_{i-1}^{-1} \Phi_{i-1}(\mathbf{r}), & i > 1. \end{cases} \quad (109)$$

Improved Removal-Diffusion Methods

The original Spinney method, just described, was quite successful in predicting the low-energy neutron fluences in the concrete shields around early graphite reactors. However, to obtain better accuracy for a wider range of shield configurations, several obvious improvements could be made. First, more diffusion groups could be used to better describe the continuous slowing-down model implied by Fermi age theory. Second, neutrons should be allowed to transfer past intermediate diffusion groups in a single step to account for the possibility of large energy losses in inelastic scattering or elastic scattering from light nuclei. Third, more detail should be given for the removal of fast neutrons from the removal bands to the diffusion groups. Fast-neutron diffusion cannot be neglected altogether; and hence, the upper diffusion groups should overlap the same energy region spanned by the lower-energy removal bands. Further, when neutrons suffer a removal interaction, they should be allowed to enter any one of several diffusion groups, depending on the severity of the removal interaction. This improved description of the removed neutrons would give more information about the fast-neutron fluence, an important consideration for radiation damage studies.

Shortly after the introduction of the Spinney method, several variations of it were introduced which implement some or all of the improvements described above. Three such codes are RASH-E (Bendall 1962), MAC (Peterson 1962), and NRN (Hjärne 1964).

For thick shields with attenuation factors as low as 10^{-12} , this removal-diffusion method gives very accurate results even for layered shields, provided that penetration takes place mainly at the source energies (Peterson 1962). It is least accurate when significant attenuation occurs after diffusion (e.g., water followed by a thick iron shield). The greatest disadvantage of this method is the need to calculate many energy-group and removal-band constants (although considerably fewer than are needed for multigroup transport calculations). The removal-diffusion technique is a very powerful tool for the reactor designer, offering accuracies for many shield configurations comparable to those of the much more computationally expensive neutron transport methods.

With the advent of computing power undreamed of only decades ago, the use of removal-diffusion theory has waned and transport theory codes are now almost universally used in place of removal-diffusion codes. However, we include this section, not only for historical completeness, but for the insight it affords the analyst on how fast neutrons migrate through a shield.

5.7 Capture-Gamma-Photon Attenuation

Often, a significant contribution to the total dose at the surface of a shield is made by capture gamma photons produced deep within the shield as a result of neutron absorption. Another source of secondary photons arises from the inelastic scattering of fast neutrons. The resulting photons generally have much lower energies than the capture gamma photons (see [Table 7](#)) and are frequently ignored in the analysis of thick shields.

Most neutrons are not absorbed until they are thermalized, and consequently, one needs to consider only the absorption of thermal neutrons in most shield analyses. For this reason, it is important to calculate accurately the thermal neutron fluence $\Phi_{th}(\mathbf{r})$ in the shield. The volumetric source strength of capture photons per unit energy about E is, thus, given by (13), namely

$$S_{\gamma}(\mathbf{r}, E) = \Phi_{th}(\mathbf{r})\mu_{\gamma}(\mathbf{r})f(\mathbf{r}, E), \quad (110)$$

where $\mu_{\gamma}(\mathbf{r})$ is the absorption coefficient at \mathbf{r} for thermal neutrons and $f(\mathbf{r}, E)$ is the number of photons produced in unit energy about E per thermal neutron absorption at \mathbf{r} . Although the capture-photon-energy distribution for any material is composed of a set of monoenergetic photons, a great many different energies can generally be expected as a result of multiple nuclear transitions following neutron capture and the usual presence of many different nuclear species in the shield material. Consequently, the capture-gamma-photon yield is usually “binned” into energy groups. Thus, the source strength for the i th energy group of width ΔE_i is

$$S_{\gamma i}(\mathbf{r}) \equiv \int_{\Delta E_i} S(\mathbf{r}, E) dE = \Phi_{th}(\mathbf{r})\mu_{\gamma}(\mathbf{r})f_i(\mathbf{r}), \quad (111)$$

where f_i is the number of photons produced in group i per thermal neutron absorbed at \mathbf{r} , averaged over all isotopes at \mathbf{r} , namely,

$$f_i(\mathbf{r}) = \frac{1}{\mu_{\gamma}(\mathbf{r})} \sum_m \mu_{\gamma}^m(\mathbf{r})f_i^m, \quad (112)$$

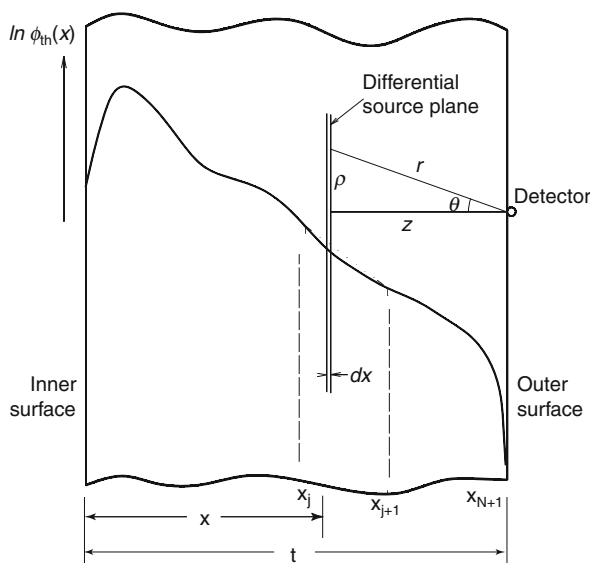
where the superscript m refers to the m th nuclide and summation is over all nuclear species. The quantity f_i^m is the number of capture photons emitted in group i arising from the absorption of a thermal neutron by the m th nuclide (see [Table 7](#)).

The calculation of the dose from capture gamma photons is based on the distributed source of (111). The calculational procedure is illustrated for an infinite slab shield in which the thermal-neutron fluence has been previously obtained (see [Fig. 28](#)). The slab is generally composed of laminates, that is, a series of adjacent homogenous regions. If the thermal-neutron fluence depends only on the distance into the slab (plane geometry), then with the technique involving the point kernel and point-source buildup factors, the dose or detector response $D(t)$ at the shield surface from capture-gamma photons in all G groups is

$$D(t) = \sum_{i=1}^G \mathcal{R}_i \int_0^t dx S_{\gamma i}(x) \int_0^\infty d\rho 2\pi\rho B_i(r) \frac{\exp[-\mu_i r]}{4\pi r^2}, \quad (113)$$

where \mathcal{R}_i is a fluence-to-dose conversion factor for photons in energy group i , B_i is a composite buildup factor for photons in group i traveling from the source to the detector through the various interposed laminates, and $\mu_i r$ is the total number of mean free paths for photons in group i between the source and the detector.

[Equation \(113\)](#) could be evaluated numerically for a given B_i and $S_{\gamma i}$; however, considerable simplification is possible if we assume functional forms for these two quantities that allow analytical evaluation of the integrals. In particular, the shield is subdivided into N contiguous regions such that each region is composed of a single material and over which the thermal-neutron fluence could be fit reasonably well by a single exponential (see [Fig. 28](#)). Thus, for



■ **Figure 28**

Profile of the thermal neutron fluence in a multilaminar shield showing the coordinate system used for calculation of the capture-gamma-photon dose at the shield surface

the j th region bounded by x_j and x_{j+1} , the thermal-neutron fluence is represented by

$$\Phi_{th}^j(x) \simeq \Phi^j \exp[-k^j x], \quad x_j < x < x_{j+1}, \quad (114)$$

where Φ^j and k^j are constants. Thus, the capture-gamma-source strength for the i th energy group is

$$S_{\gamma i}^j(x) = C_i^j \exp[-k^j x], \quad (115)$$

with $C_i^j \equiv \Phi^j \mu_{\gamma i}^j f_i^j$, where the superscript j refers to material properties in the j th region and the subscript i refers to the energy group of the photons. Equation (113) can then be evaluated analytically for the uncollided dose ($B = 1$), and for the collided dose, if the Berger-buildup factor approximation is used (Stevens and Trubey 1968).

5.8 Neutron Shielding with Concrete

Of all shielding materials, concrete is probably the most widely used because of its relatively low cost and the ease with which it can be cast into large and variously shaped shields. Concrete is prepared from a mixture, by weight, of about 13% cement, 7% water (including water in the aggregate), and 80% aggregate. Many different types of concrete can be prepared by varying the nature of the aggregate. For example, to improve photon-attenuation properties, scrap iron or iron ore may be incorporated into the sand-and-gravel aggregate.

The amount of hydrogen in concrete strongly influences its effectiveness for shielding against neutrons. Generally, the more water content, the less concrete is needed to thermalize and absorb incident-fast neutrons. Virtually, all the hydrogen in concrete is in the form of water, which is present not only as *fixed water* (i.e., water of hydration in the cement and aggregate) but also as *free water* in the pores of the concrete. At elevated temperatures, both may be lost, thereby greatly reducing the ability of the concrete to attenuate fast neutrons. Even at ambient temperatures, free water may be lost slowly over time by diffusion and evaporation. Typically, the free water is initially about 3% by weight of the concrete, and this water is lost by evaporation during curing of the concrete. Over a 20- to 30-year period at ambient temperatures, half the fixed water may be lost.

Neutron attenuation calculations for concrete, especially by the simplified methods presented in this chapter, are usually problematic, partly as a result of the variation in elemental compositions of different concretes, and partly because the hydrogen content of many concretes is only marginal for the application of removal theory. Neutron transport methods generally must be used if accurate results are desired.

5.8.1 Concrete Slab Shields

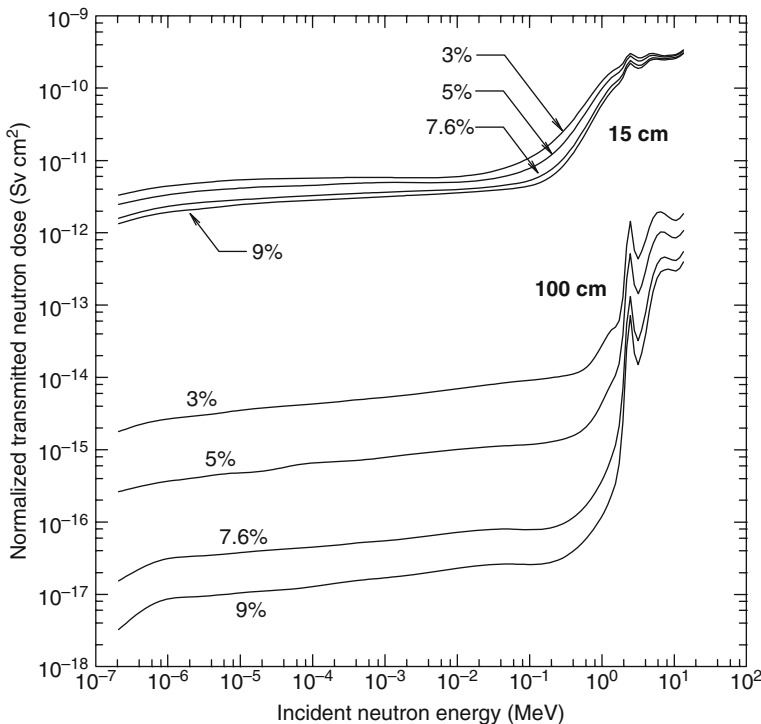
A particularly important shielding geometry is that of a plane slab of ordinary concrete on which a monoenergetic, broad, parallel beam of neutrons is normally incident. This problem has been studied in some detail (Alsmiller et al. 1969; Chilton 1971; Roussin and Schmidt 1971; Roussin et al. 1973; Wyckoff and Chilton 1973; Wang and Faw 1995). Extensive tables of dose transmission factors $\tau_i(t, E, \cos \theta)$ are available for neutrons ($i = n$) and the secondary photon

dose ($i = p$), for plane parallel beams of neutrons of energy E incident at the concrete slab (NBS Type 04), at an angle θ with respect to the slab normal (ANSI/ANS-2006). The transmitted dose rates for a neutron flux of Φ is then simply calculated as

$$D_i(t) = \Phi \cos \theta \tau_i(t, E, \cos \theta), \quad i = n, p. \quad (116)$$

Effect of Water Content

If the proportion of water is changed in concrete, the concrete's attenuation ability also changes, especially for thicker shields. An example of the effect of water content in ordinary concrete (NBS Type 04 of [Table 24](#)) is shown in [Fig. 29](#). Detailed data must be obtained from the literature (Chilton 1971); but as an example, it can be shown that a reduction from 5.5% water to 4.5% water requires that the prescribed dose-equivalent values be multiplied by a factor of about 1.6 for incident neutrons in the energy range 1–15 MeV and for a shield thickness of about 400 g cm^{-2} . A reduction to 3.5% requires a multiplicative factor of about 2.6 under these circumstances; and a reduction to 2.5% implies a factor of about 4.1 (NCRP 1977).



■ Figure 29

Transmitted dose equivalent per unit incident fluence for neutrons, normally incident on slabs of ordinary concrete (NBS Type 04), with two thicknesses and four water contents (by weight). Response functions used are for the deep dose index (PAR) as specified by the ICRP (1987). Data courtesy of X. Wang, Kansas State University

Effect of Slant Incidence

Data are also available for neutron penetration through concrete slabs under slant incidence conditions (Chilton 1971; Wang and Faw 1995; ANS/ANSI 2006). In [▶ Fig. 30](#), the transmitted phantom-related dose equivalent for several slab thicknesses and incident angles is shown for a slab composed of a 5.5%-water calcareous concrete. These dose-equivalent results, which also included the capture-photon contribution, are normalized to a unit incident flow on the slab surface; that is, to an incident beam that irradiates each square centimeter of the surface with one neutron regardless of the beam direction. The transmitted dose equivalent when normalized this way is called the *transmission factor*. In ANSI/ANS-6.4-2006, tables are provided for the neutron and secondary-photon transmission factors for several thicknesses of concrete slabs uniformly illuminated by monoenergetic and monodirectional neutrons. Data for different concretes, incident energies, and incident directions can be found in the literature cited.

The transmission factor for a given slab thickness is seen from [▶ Fig. 30](#), to decrease by a multiplicative factor of between only 2–5 as the incident beam changes from normal incidence to a grazing incidence of 75° (from the normal), for a wide range of incident neutron energies. This variation of the transmission factor for neutrons, while appreciable, is not nearly as severe as it is for photons (see [▶ Table 14](#)).

Effect of the Aggregate

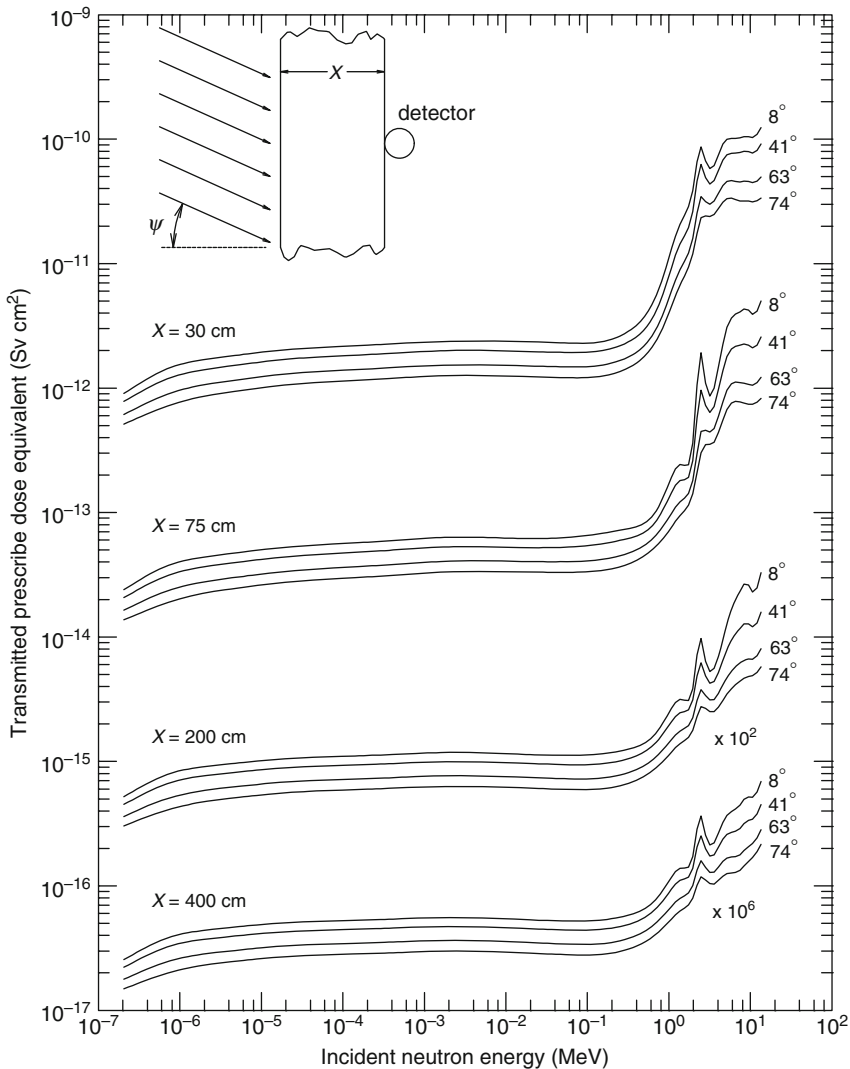
Aside from water variation, the other major change possible in the composition of ordinary concrete is the use of quartz-based sand and aggregate (SiO_2), instead of limestone in ordinary concrete. This siliceous type of concrete allows more dose-equivalent penetration than does the same mass thickness of calcareous concrete with the same water content; in general, it has neutron shielding properties about the same as calcareous concrete with about 2% less water (i.e., as if a 5.5% water content had been reduced to 3.5%) (Chilton 1971; Wyckoff and Chilton 1973).

It should be noted that none of the data presented in this section apply to “heavy concretes,” that is, to concretes with minerals containing high- Z elements included as part of the aggregate, nor to any other concrete of a composition deviating markedly from those proportions considered “ordinary.”

Effect of the Fluence-to-Dose Conversion Factor

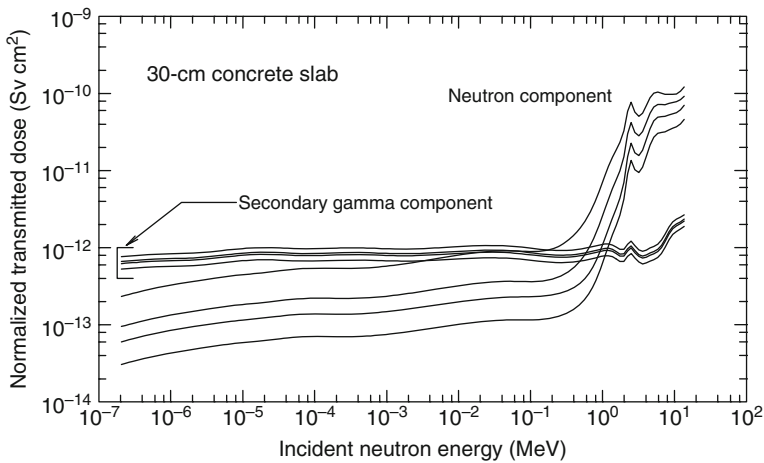
Finally, the dose units used to measure the transmitted dose can have an appreciable effect on the transmission factor, far more so for neutrons than for photons. In [▶ Fig. 31](#), the neutron and secondary-gamma-ray transmission factors are shown for four response functions. It is seen that the transmitted secondary-photon dose is insensitive to the type of response function when compared with the neutron dose. For this reason, it is very important to pay careful attention to the dose-conversion coefficient used when trying to apply results found in the literature to a particular neutron shielding problem.

One final comment on the data presented in this section is appropriate as a cautionary statement. The data presented here are based on results of theoretical calculations. No experimental verification is available. Under such circumstances, the data should be used with some caution, especially for the greater thicknesses, and a factor of safety of at least two in dose is advised.



■ Figure 30

Transmitted deep dose equivalent (including the capture-gamma-photon contribution) through a concrete slab illuminated obliquely at four angles as a function of the incident neutron energy. The transmitted dose is normalized to a unit flow on the slab surface. Note that the curves at $x = 200$ cm and $x = 400$ cm have been multiplied by factors of 10^2 and 10^6 , respectively. Concrete composition (in 10^{21} atoms cm^{-3}): H, 8.50; C, 20.20; O, 35.50; Mg, 1.86; Al, 0.60; Si, 1.70; Ca, 11.30; and Fe, 0.19; density is 2.31 g cm^{-3} and water (percent by weight) is 5.5%. From data of Chilton (1971)



■ Figure 31

Transmitted dose per unit incident fluence for neutrons normally incident on a 30-cm slab of ordinary concrete (NBS Type 03) for four different dose units. The four response functions (from top to bottom) are for the NCRP-38 phantom (ANS/ANSI 1977), and the ICRP-51 anthropomorphic phantom for AP, PA, and LAT irradiation conditions (ICRP 1987). Data courtesy of X. Wang, Kansas State University

6 The Albedo Method

The calculation of how radiation incident on a surface is reemitted through the surface toward some point of interest is a frequently encountered problem in radiation shielding. Transport techniques are generally required for detailed estimation of reflected doses. But under certain circumstances, a simplified approach based on the albedo concept can be used with great effect. These conditions are (1) that the displacement on the surface between the entrance and exit of the radiation is very small when compared with the problem dimensions, (2) that the reflecting medium is about two or more mean free paths thick, and (3) that scattering between the radiation source and surface and between the surface and point of interest is insignificant.

Of course, reflection does not take place exactly at the point of incidence, but results from scattering by nuclei or electrons within the medium, with perhaps very many interactions taking place before an incident particle emerges or is “reflected” from the surface, as indicated in ► Fig. 32. Nevertheless, in radiation shielding calculations in which the character of the incident radiation does not change greatly over the surface in distances of about one mean free path, as measured in the reflecting medium, a reasonably accurate assumption can be made that the particles emerging from an incremental area result directly from those incident on that same area. Similarly, it has been found that for a reflecting medium thicker than about two mean free paths, it is an excellent approximation to treat the medium as a half-space. For discussion of these approximations and for more advanced treatments, the reader is referred to Leimdorfer (1968) and Selph (1973). The use of albedo techniques is central to many radiation-streaming codes and has been widely used as an alternative to much more expensive transport calculations.

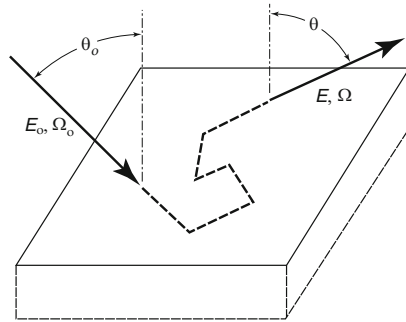


Figure 32
Particle reflection from a scattering medium

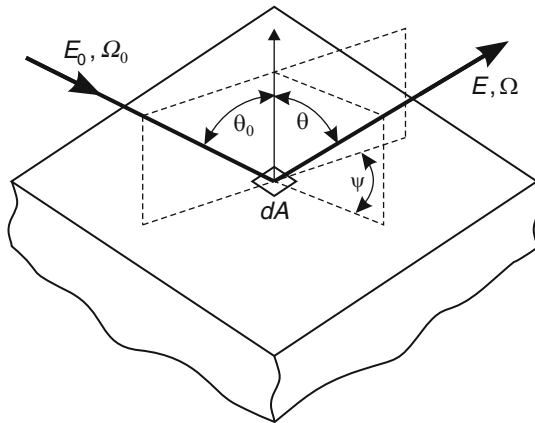


Figure 33
Angular and energy relationships in the albedo formulation

6.1 Differential Number Albedo

Radiation reflection may be described in terms of the geometry shown in Fig. 33. Suppose that a broad beam of incident particles, all of energy E_0 and traveling in the same direction, strike area dA in the reflecting surface at angle θ_0 measured from the normal to the surface. If Φ_0 is the fluence of the incident particles and J_{n0} is the corresponding flow, the number of incident particles striking dA is $dA J_{n0} = dA \Phi_0 \cos \theta_0$. Suppose that the energy spectrum of the angular distribution of the fluence of reflected particles emerging from the surface with energy E and direction characterized by angles θ and ψ is $\Phi_r(E, \theta, \psi)$ and the corresponding differential flow is $J_{nr}(E, \theta, \psi)$. The number of particles emerging from dA with energies in dE about E and with directions in solid angle $d\Omega$ about direction (θ, ψ) is $dA J_{nr}(E, \theta, \psi) dE d\Omega = dA \cos \theta \Phi_r(E, \theta, \psi) dE d\Omega$. The *number albedo* $\alpha(E_0, \theta_0; E, \theta, \psi)$ is defined as

$$\alpha(E_0, \theta_0; E, \theta, \psi) \equiv \frac{J_{nr}(E, \theta, \psi)}{J_{n0}} = \frac{\cos \theta \Phi_r(E, \theta, \psi)}{\cos \theta_0 \Phi_0}. \quad (117)$$

6.2 Integrals of Albedo Functions

Occasionally of interest as reference albedos or in verification of particle conservation in transport calculations are the following integrals over all possible energies and all possible directions:

$$\alpha_N(E_o, \theta_o; \theta, \psi) \equiv \int_0^{E_o} dE \alpha(E_o, \theta_o; E, \theta, \psi) \quad (118)$$

and


$$A_N(E_o, \theta_o) \equiv \int_0^{2\pi} d\psi \int_0^1 d(\cos \theta) \alpha_N(E_o, \theta_o; \theta, \psi). \quad (119)$$

Of much more interest and utility is the *differential dose albedo*, defined as the ratio of the reflected flow, in dose units, to the incident flow, also in dose units. If $\mathcal{R}(E)$ is the dose-conversion coefficient, then

$$\alpha_D(E_o, \theta_o; \theta, \psi) \equiv \frac{\int_0^{E_o} dE \mathcal{R}(E) J_{nr}}{\mathcal{R}(E_o) J_{no}} = \int_0^{E_o} dE \frac{\mathcal{R}(E)}{\mathcal{R}(E_o)} \alpha(E_o, \theta_o; E, \theta, \psi). \quad (120)$$

It is important to recognize that dose-conversion coefficients affect $\alpha_D(E_o, \theta_o; \theta, \psi)$ only in the *ratio* $\mathcal{R}(E)/\mathcal{R}(E_o)$. For this reason, the photon dose albedo is not strongly dependent on the nature of the response. Photon albedos are commonly evaluated for exposure as the dose, but used in estimation of dose-equivalent or even effective dose. However, greater care must be taken with neutron albedos because $\mathcal{R}(E)/\mathcal{R}(E_o)$ can be quite different for different conversion coefficients.

6.3 Application of the Albedo Method

Refer to  [Fig. 33](#) and suppose that a point isotropic and monoenergetic photon source of strength S_p is located at distance r_1 from area dA along incident direction Ω_o and that a dose point is located distance r_2 from area dA along emergent direction Ω . Suppose that an isotropic radiation detector at the dose point is a vanishingly small sphere with cross-sectional area δ . At area dA , the flow of incident photons is $J_{no} = (S_p/4\pi r_1^2) \cos \theta_o$. Since the solid angle subtended by the detector at dA is δ/r_2^2 , the number of photons emerging from dA with energies in dE and with directions intercepting the detector is $J_{nr}(E, \theta, \psi) dA (\delta/r_2^2)$. This quantity, divided by the cross-sectional area of the spherical detector, is just that part of the energy spectrum of the fluence at the detector attributable to reflection of photons from area dA , namely,

$$d\Phi(E) dE = J_{nr}(E, \theta, \psi) \frac{dA}{r_2^2} dE = J_{no} \alpha(E_o, \theta_o; E, \theta, \psi) \frac{dA}{r_2^2} dE \quad (121)$$

or

$$d\Phi(E) dE = \frac{S_p \cos \theta_o}{4\pi r_1^2} \alpha(E_o, \theta_o; E, \theta, \psi) \frac{dA}{r_2^2} dE. \quad (122)$$

That part dD_r of the dose D_r owing to reflection of photons from dA is $\int dE \mathcal{R}(E) d\Phi(E)$, namely,

$$dD_r = \frac{S_p \cos \theta_o}{4\pi r_1^2} \frac{dA}{r_2^2} \int_0^{E_o} dE \mathcal{R}(E) \alpha(E_o, \theta_o; E, \theta, \psi) \quad (123)$$

or

$$dD_r = \left[\frac{S_p \mathcal{R}(E_o)}{4\pi r_1^2} \right] \frac{dA \cos \theta_o}{r_2^2} \alpha_D(E_o, \theta_o; \theta, \psi). \quad (124)$$

If the source were not isotropic but had an angular distribution $S(\Omega)$, then

$$dD_r = \left[\frac{S(\theta_o) \mathcal{R}(E_o)}{r_1^2} \right] \frac{dA \cos \theta_o}{r_2^2} \alpha_D(E_o, \theta_o; \theta, \psi), \quad (125)$$

in which $S(\theta_o)$ denotes symbolically the source intensity per steradian, evaluated at the direction from the source to reflecting area dA . Note that the bracketed term on the right side of either of the two previous equations is just the dose D_o at dA due to incident photons. Thus,

$$dD_r = D_o \alpha_D(E_o, \theta_o; \theta, \psi) \frac{dA \cos \theta_o}{r_2^2}. \quad (126)$$

Determination of the total reflected dose D_r requires an integration over the area of the reflecting surface. In doing such an integration, it must be remembered that as the reflecting location on the surface changes, all the variables θ_o , θ , ψ , r_1 , and r_2 change as well.

6.4 Albedo Approximations

Key to the albedo technique is the availability of either a large set of albedo data or, preferably, an empirical formula that approximates the albedo over the range of source energies and incident and exit radiation directions involved in a particular problem. Many albedo approximations have been proposed over the past four decades. However, many of these must be used with caution because they are based on limited energy-angular ranges, a single reflecting material, old cross section data, and, for neutron albedos, obsolete fluence-to-dose conversion factors.

6.4.1 Photon Albedos

A two-parameter approximation for the photon-dose albedo was devised by Chilton and Huddleston (1963), later extended by Chilton, Davisson, and Beach (1965), in the following form:

$$\alpha_D(E_o, \theta_o; \theta, \psi) \approx \frac{C(E_o) \times 10^{26} [\sigma_{ce}(E_o, \theta_s)/Z] + C'(E_o)}{1 + \cos \theta_o / \cos \theta}, \quad (127)$$

in which $C(E_o)$ and $C'(E_o)$ are empirical parameters that depend implicitly on the composition of the reflecting medium. Here, θ_s is the scattering angle, whose cosine is

$$\cos \theta_s = \sin \theta_o \sin \theta \cos \psi - \cos \theta_o \cos \theta \quad (128)$$

and $\sigma_{ce}(E_o, \theta_s)$ is the Klein–Nishina *energy scattering* cross section

$$\sigma_{ce}(E, \theta_s) = Zr_e^2 q^2 [1 + q^2 - q(1 - \cos^2 \theta_s)]/2, \quad (129)$$

where $q = E/E_o$, r_e is the classical electron radius, and Z is the atomic number of the medium. The approximation of (127) was fit to data obtained by Monte Carlo calculations using modern dose units to produce the albedo parameters shown in ► Table 21.

Chilton (1967) found that albedo data for concrete could be fit even better by the formula

$$\alpha_D(E_o, \theta_o; \theta, \psi) = F(E_o, \theta_o; \theta, \psi) \frac{C(E_o) \times 10^{26} [\sigma_{ce}(E_o, \theta_s)/Z] + C'(E_o)}{1 + (\cos \theta_o / \cos \theta)(1 + 2E_o \text{ vers } \theta_s)^{1/2}}, \quad (130)$$

in which the factor F is a purely empirical multiplier, given by

$$F(E_o, \theta_o; \theta, \psi) = A_1(E_o) + A_2(E_o) \text{ vers}^2 \theta_o + A_3(E_o) \text{ vers}^2 \theta + A_4(E_o) \text{ vers}^2 \theta_o \text{ vers}^2 \theta + A_5(E_o) \text{ vers } \theta_o \text{ vers } \theta \text{ vers } \psi, \quad (131)$$

in which $\text{vers } \theta = 1 - \cos \theta$. The seven parameters in this approximation are tabulated by Shultis and Faw (2000).

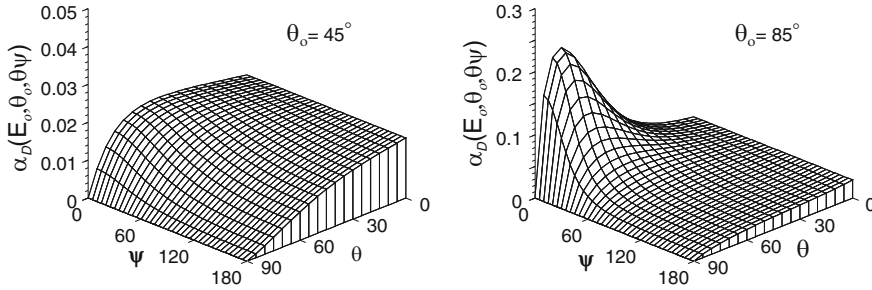
It should be emphasized that, to estimate an albedo for a photon energy between the tabulation energies, the interpolation should *not* be made with interpolated values of the parameters; rather, an interpolation of calculated albedos obtained with coefficients at bracketing tabulated energies should be used. Examples of the dose albedo from (130) are shown in ► Fig. 34.

■ Table 21

Parameters for the two-term Chilton–Huddleston approximation, (127), for the 10-mm H*(10) ambient-dose-equivalent albedo

Energy (MeV)	Water		Concrete		Iron		Lead	
	10 ³ C	10 ³ C'	10 ³ C	10 ³ C'	10 ³ C	10 ³ C'	10 ³ C	10 ³ C'
0.10	3.83956	156.682	15.0806	53.5702	6.01974	6.30725	-0.99254	71.4260
0.20	12.8933	95.1294	19.5317	56.3968	22.8818	4.52419	2.54139	13.6862
0.40	26.9251	49.4120	31.0515	34.8623	34.9866	10.5355	12.3140	-4.16344
0.60	36.2690	35.5403	38.5117	26.5358	44.7663	10.5212	23.0250	-6.35561
0.80	44.6428	27.7803	46.5630	20.9768	52.9704	9.63214	32.4332	-6.21926
1.00	52.7863	22.5602	54.4830	17.3114	55.7093	8.65893	41.5937	-5.71107
1.25	61.9729	18.5551	65.3668	14.2054	70.5985	7.65120	51.2948	-4.89882
2.00	86.5642	12.6338	86.5215	10.6027	91.4505	7.81777	72.0777	0.65892
4.00	137.182	8.63979	134.941	8.84981	131.920	10.5014	93.2920	7.47707
6.00	172.511	7.47389	162.904	8.47375	148.934	11.5784	107.474	8.80086
8.00	195.014	6.97739	178.589	8.36158	170.405	11.9144	125.587	9.07966
10.00	218.439	6.58747	196.888	8.15070	173.252	11.9926	139.207	9.03810

Source: Data courtesy of R.C. Brockhoff, Nuclear Engineering Department, Kansas State University



■ **Figure 34**
Ambient-dose-equivalent albedos for reflection of 1.25-MeV photons from concrete

6.4.2 Neutron Albedos

There is much data in the literature for neutron albedos and for the associated secondary-photon doses. For a review of these earlier studies, see Shultis and Faw (2000) and Brockhoff and Shultis (2007). Unlike compilations or formulas for albedos for monoenergetic incident photons, it is difficult to interpolate similar neutron albedos because of the many resonances in the neutron cross sections. To account for the usual continuous distribution of fast or intermediate-energy neutrons, it is preferable to obtain albedos for incident neutrons in various contiguous energy bins. However, many early albedo studies are for monoenergetic sources, and hence, are of limited practical utility. Moreover, most neutron-albedo approximating formulas are based on the very old neutron-interaction data, on only a few incident directions, and are available only for a single reflecting material. With rare exception, neutron-albedo studies consider only concrete, the material most frequently subject to reflection analyses.

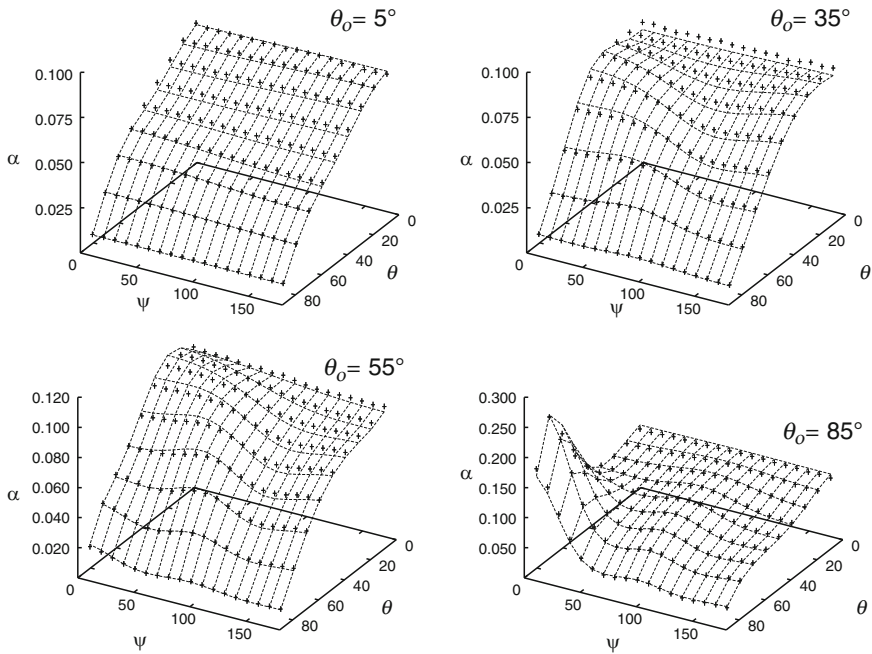
Recently, neutron dose albedos have been calculated for reflection from concrete, water, iron, and lead (Brockhoff and Shultis 2007). From these data, a variety of approximating formulas were adjusted to the calculated data. The formula that best fit the data for all materials and energy groups was

$$\alpha_D(\Delta E_o, \theta_o; \theta, \psi) = \frac{H(\kappa_1, \cos \theta_o)H(\kappa_2, \cos \theta)}{1 + K_1(E_o, \theta_o; \theta) / \cos \theta} \sum_{i=0}^N B_i P_i(\cos \theta_s), \quad (132)$$

where

$$K_1(E_o, \theta_o; \theta) = \sum_{i=0}^2 \cos^i \theta \sum_{j=0}^2 A_{ij} \cos \theta_o^j. \quad (133)$$

The number of fitting parameters is $N+12$ [κ_1 , κ_2 , $9 A_{ij}$, and $(N+1) B_i$]. The number of terms used in the Legendre expansion, $N+1$, determines the accuracy of the approximation. For most reflecting media and neutron energies, the use of a 9-term expansion results in fits with a maximum deviation of less than 10%. However, for extreme cases such as 8–10 MeV neutrons incident on concrete, water, iron, and lead, an $N = 13$ (24 parameters) results in maximum deviations of 6.95, 9.08, 8.97, and 8.13% for the four reflecting media, respectively. Besides approximating the albedo for all the discrete fast-energy groups, the 24-parameter formula also worked well for thermal neutrons, ^{252}Cf fission neutrons, and 14-MeV neutrons. Tabulations of the 24 parameters are provided by Brockhoff and Shultis (2007) and by ANS/ANSI (2006). A sample comparison between the calculated albedo data and approximation is shown in ► [Fig. 35](#).



■ Figure 35

Neutron differential ambient-dose equivalent albedo $\alpha_D(E_o, \theta_o; \theta, \psi)$ for 6–8 MeV neutrons, incident on a slab of concrete for $\theta_o = 5, 35, 55,$ and 85 degrees. Comparison of MCNP results (crosses) and the results obtained using the approximation of (132) (surface)

Secondary-Photon Albedos


The secondary albedo arises from the production of inelastic and capture gamma rays that are radiated from the reflecting surface. In general, the secondary-photon albedo is independent of the azimuthal angle as a consequence of the isotropic emission of secondary gamma rays. Also of note is that the magnitude of the secondary-photon dose albedo is usually considerably less than that of the neutron dose albedo and, consequently, a high accuracy for the secondary-photon albedo is generally not needed.

Maerker and Muckenthaler provided detailed calculations for thermal neutrons incident on concrete, and proposed a relation to approximate the secondary-photon albedo, namely, (Maerker and Muckenthaler 1965)

$$\alpha_{D_2}^{(n,\gamma)}(\theta_o, \theta) = \cos^{A_1}(\theta) [A_2 + A_3 \cos(\theta_o) + A_4 \cos^2(\theta_o)] A_5, \quad (134)$$

where the parameters $A_1, A_2, A_3, A_4,$ and A_5 are functions of the reflecting media and the energy of the incident neutrons. This approximation was used by Shultis and Brockhoff (2007) to approximate their calculated secondary-photon albedos.

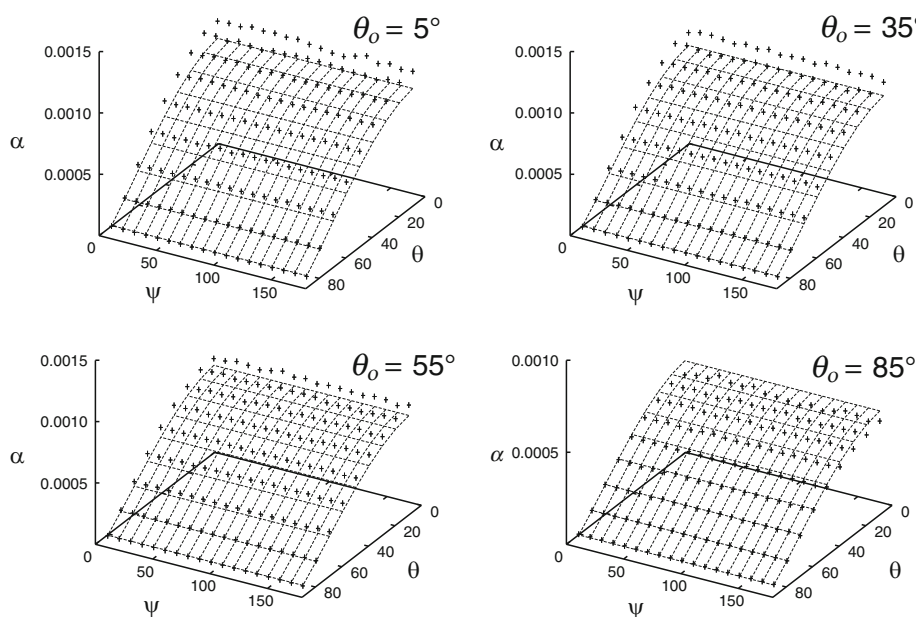
This approximation is not as accurate as the approximations presented for the neutron albedo. Use of this approximation can result in deviations in excess of 20% in some cases. Therefore, for problems in which the secondary-photon albedo needs to be calculated accurately over a small range of reflected directions, (134) should be used carefully. For most problems,

the secondary-photon albedo is usually small in comparison with the neutron albedo; and the use of this approximation should yield acceptable results. A sample comparison between the calculated albedo data and approximation is shown in  Fig. 36.

7 Skyshine

In many facilities with intense localized sources of radiation, the shielding against radiation that is directed skyward is usually far less than that for the radiation emitted laterally. However, the radiation emitted vertically into the air undergoes interactions and some secondary radiation is reflected back to the ground, often at distances far from the source. This atmospherically reflected radiation, referred to as *skyshine*, is of concern both to workers at a facility and to the general population outside the facility site.

A rigorous treatment of the skyshine problem requires the use of computationally expensive methods based on multidimensional transport theory. Alternatively, several approximate procedures have been developed for both gamma-photon and neutron-skyshine sources. See Shultis et al. (1991) for a review. This section summarizes one approximate method, which has been found useful for bare or shielded gamma-ray and neutron skyshine sources. This method, termed the *integral line-beam skyshine method*, is based on the availability of a *line-beam response function* (LBRF) $\mathcal{R}(E, \Phi, x)$ that gives the dose at a distance x from a point source



 **Figure 36**

The differential secondary-photon effective-dose-equivalent (AP) albedo $\alpha_D(E_o, \theta_o; \theta, \psi)$ for 1–2 MeV monidirectional neutrons, incident on a slab of concrete for $\theta_o = 5, 35, 55,$ and 85 degrees. Comparison of MCNP results (crosses) and the results obtained using the approximation of (134) (surface)

emitting a particle (neutron or photon) of energy E , at an angle Φ from the source-to-detector axis into an infinite air medium.

To obtain the skyshine dose $D(d)$ at a distance d from a bare collimated source, the line-beam response function, weighted by the energy and angular distribution of the source, is integrated over all source energies and emission directions. Thus, if the collimated source emits $S(E, \Omega)$ particles, the skyshine dose is

$$D(d) = \int_0^\infty dE \int_{\Omega_s} d\Omega S(E, \Omega) \mathcal{R}(E, \Phi, d), \quad (135)$$

where the angular integration is over all emission directions allowed by the source collimation Ω_s . Here Φ is a function of the emission direction Ω . To obtain this result, it has been assumed that the presence of an air-ground interface can be neglected by replacing the ground by an infinite air medium. The effect of the ground interface on the skyshine radiation, except at positions very near to a broadly collimated source, has been found to be small. At positions near the source (near-field), the ground augments slightly the dose, although at large distances from the source; it depresses slightly the dose when compared with results obtained with the infinite-air approximation. To account for the generally small air-ground interface effect, empirical *ground correction factors* are available to correct the infinite-air result of (135) (Kahn 1994; Gui, Shultis and Faw 1997a and 1997b).

Implicit in the integral line-beam approach is the assumption that the radiation source can be treated as a point source and that the source containment structure has a negligible perturbation on the skyshine radiation field, that is, once source radiation enters the atmosphere, it does not interact again with the source structure. With this assumption, the energy and angular distribution of source radiation penetrating any overhead source shield or escaping from the containment structure is independent of the subsequent transport of the radiation through the air to the detector. In most skyshine calculations at distances far from the source, this is true; however, for detectors near the source, this second assumption is not always valid.

7.1 Approximations for the LBRF

The LBRF for both photons, neutrons, and secondary photons from neutron interactions in the air can all be approximated over a large range of x by the following three-parameter empirical formula, for a fixed value of E and Φ (Lampley et al. 1988):

$$\mathcal{R}(x, E, \Phi) = \kappa E(\rho/\rho_o)^2 [\rho x/\rho_o]^b \exp[a - (c\rho x/\rho_o)], \quad (136)$$

in which ρ is the air density in the same units as the reference density $\rho_o = 0.0012 \text{ g cm}^{-3}$ and κ is a constant that depends on the dose unit used. The parameters a , b , and c depend on the neutron or photon source energy E (in MeV), the emission direction Φ , and dose unit employed. Various compilations of the parameters a , b , and c have been produced by fitting (136) to results of Monte Carlo calculations of the LBRF.

A double linear interpolation scheme can be used to obtain the logarithm of $\mathcal{R}(E, \Phi, x)$ for any E or Φ in terms of values at the discrete tabulated energies and angles. In this way, the approximate line-beam response function can be rendered completely continuous in the x , E , and Φ variables. With these approximate LBRFs, the skyshine dose is readily evaluated from (135) using standard numerical integration.

7.1.1 Photon LBRF Approximation

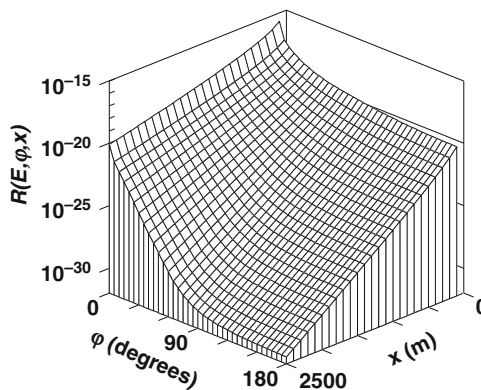
Tables of the parameters for (136), suitable for estimating the LBRF $\mathcal{R}(E, \Phi, x)$, were provided first by Lampley et al. (1988) and later, in more modern dosimetric units, by Shultis and Faw (1994) for a source-to-detector range of about $1 \text{ m} < x < 3000 \text{ m}$ for 12 discrete energies from 0.04 to 10 MeV and for 20 discrete angles Φ are available. Brockhoff et al. (1996) later extended to the energy range from 20 to 100 MeV. These later compilations are available from the Radiation Safety Information Computational Center (RSICC) as part of the Data Library Collection DLC-188/SKYDATA-KSU. \blacktriangleright Figure 37 illustrates $\mathcal{R}(E, \Phi, x)$ for 6.13-MeV photons. Such high-energy photons arise from decay of ^{16}N and are important in the design of water-cooled nuclear power plants.

7.1.2 Neutron LBRF Approximation

The neutron and secondary-photon LBRFs have been evaluated with the MCNP code at 14 discrete energies from 0.01 to 14 MeV, at 18 emission angles from 1 to 170 degrees, and at 24 source-to-detector distances from 10 to 2450 m (Gui et al. 1997a). Equation (136) was fit to these data and a compilation of the fitting parameters for modern neutron dosimetry units produced and is also part of the RSICC Data Library Collection DLC-188/SKYDATA-KSU. Examples of these approximate neutron LBRFs are shown in \blacktriangleright Fig. 38.

7.2 Open Silo Example

The general result of (135) can be reduced to explicit forms suitable for calculation for special geometries and source characteristics (Shultis et al. 1991). As an example, consider the case in which an isotropic, monoenergetic point source [(i.e., $S(E', \Omega) = S_p \delta(E' - E)/4\pi$], is located on the vertical axis of a cylindrical-shell shield (silo) of inner radius r (see \blacktriangleright Fig. 39). The wall of the silo is assumed to be *black* (i.e., no source radiation penetrates it). The source is distance h_s



\blacksquare Figure 37

Line-beam response function for 6.13-MeV photons in the atmosphere

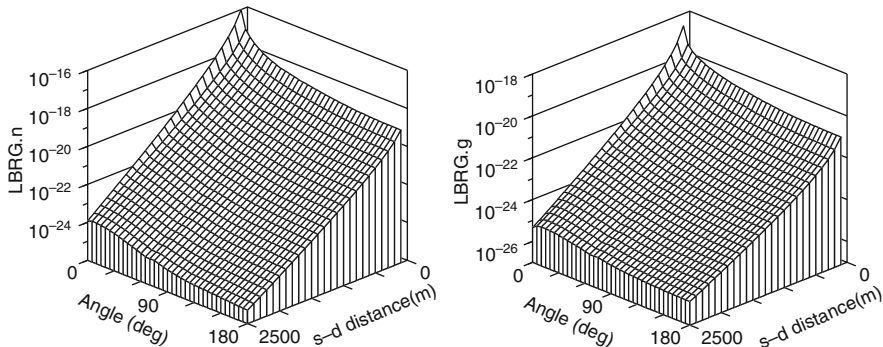


Figure 38

The neutron line-beam response functions (Sv/source-neutron) for a 14-MeV source in an infinite air medium. The left figure shows the neutron dose as a function of the source-to-detector distance and the angle of neutron emission with respect to the source–detector axis. The right figure shows the dose from secondary photons

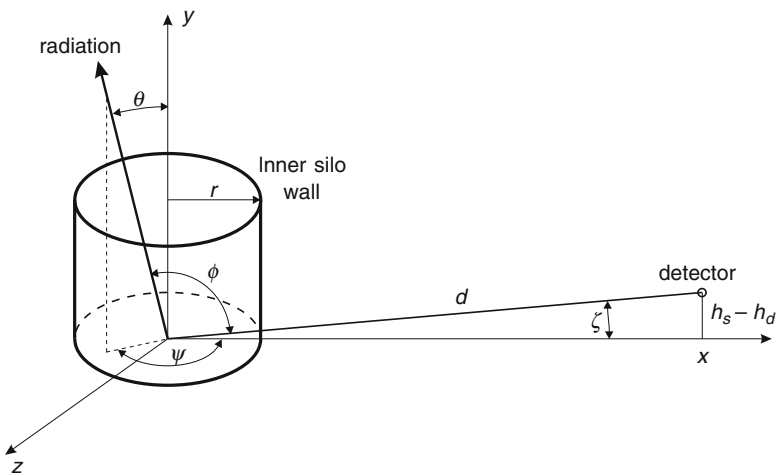


Figure 39

Geometry for skyshine analysis of an isotropic point source in an open silo

below the horizontal top of the silo which collimates the emergent radiation into a cone with a polar angle θ_{max} measured from the vertical axis and defined by

$$\omega_o \equiv \cos \theta_{max} = 1 / \sqrt{1 + r^2 / h_s^2}. \tag{137}$$

A detector (dose point) is located in air at radial distance x from the silo axis and at distance h_d below the silo top. If h_d is above the top of the silo wall, this distance is negative. The distance

from the source to the detector is

$$d = \sqrt{x^2 + (h_s - h_d)^2} \quad (138)$$

and the angle ζ between the horizontal and the source-to-detector axis is

$$\zeta = \tan^{-1}[(h_s - h_d)/x]. \quad (139)$$

Consider a particle emitted at polar angle θ , measured from the silo axis, and at azimuthal angle ψ , measured from the vertical plane through the source and detector. The cosine of the angle of emission Φ between the photon direction and the source–detector axis is the dot product of the unit vector in the emission direction and a unit vector along the source–detector axis, namely,

$$\cos \Phi = \sin \theta \cos \psi \cos \zeta + \cos \theta \sin \zeta. \quad (140)$$

For this unshielded-silo, monoenergetic-source problem, the skyshine dose at the detector is given by (135), which, upon using the azimuthal symmetry of the geometry and the monoenergetic nature of the source, reduces to

$$D(d) = \frac{S_p}{2\pi} \int_0^\pi d\psi \int_{\omega_o}^1 d\omega \mathcal{R}(E, \Phi, d). \quad (141)$$

This double integral is readily evaluated using standard numerical integration techniques.

7.3 Shielded Skyshine Sources

Most skyshine sources have some shielding over them, for example, a building roof, that reduces the amount of radiation escaping into the atmosphere. Such shielding causes some of the source radiation penetrating the shield to be degraded in energy and angularly redirected before entering the atmosphere. The effect of an overhead shield on the skyshine dose far from the source can be accurately treated by a two-step hybrid method (Shultis et al. 1991; Stedry et al. 1996; Shultis 2000). First, a transport calculation is performed to determine the energy and angular distribution of the radiation penetrating the shield, and then, with this distribution as an effective point, bare, skyshine source, the integral line-beam method is used to evaluate the skyshine dose at distances far from the source.

Although the two-step hybrid method can give very accurate results (e.g., Hertel et al. (2005)) the shield transport calculation requires considerable effort when compared with the subsequent integral line-beam calculation. A simpler, albeit less-accurate method to account for an overhead shield for photon skyshine is to assume that source photons are exponentially attenuated and that the buildup of secondary radiation can be estimated by an infinite-medium buildup factor for the source-energy photons (Shultis et al. 1991). In this simplified method, the energy and angular redistribution of the photons scattered in the shield is ignored (i.e., the scattered photons are assumed to emerge from the shield with the same energy and direction as the uncollided photons). The skyshine dose rate for a shielded source is thus

$$D(d) = \int_0^\infty dE \int_{\Omega_s} d\Omega e^{-\lambda} B(E, \lambda) S(E, \Omega) \mathcal{R}(E, \Phi, d), \quad (142)$$

where λ is the mean-free-path length that a photon emitted in direction Ω travels through the shield without collision. Clearly, when there is no source shielding ($\lambda = 0$), this result reduces to the unshielded result of (135).

An alternative approach for skyshine sources of photons shielded by a horizontal slab shield is to use a simple one-dimensional Monte Carlo calculation to determine the scattered and annihilation photons that subsequently escape into the atmosphere. These escaping photons are then transported through the air with the LBFR to the point of interest far from the source (Stedry et al. 1996). In this approach, the exact energy and angular distributions of the photons are used and very accurate results can be obtained with minimal computational effort.

The integral line-beam method for photon and neutron skyshine calculations has been applied to a variety of source configurations and found to give generally an excellent agreement with benchmark calculations and experimental results (Shultis et al. 1991; Shultis and Faw 1994; Hertel et al. 2005).

7.4 Computational Resources for Skyshine Analyses

As an alternative to computationally expensive transport calculations of far-field skyshine doses, several codes, based on the line-beam response function, are available that allow evaluation of skyshine doses with minimal computational effort. SKYSHINE-III, developed by Lampley, Andrews, and Wells (1988), is the original photon LBRF code, and can be obtained from RSICC. MicroSkyshine is a commercially available code (Grove 1987) for photon skyshine using improved LBRFs (Shultis and Faw 1987). More recent photon skyshine codes include SKYDOSE, which treats source energies between 0.4 and 100 MeV and distances out to 2500 m, and McSKY, which treats shielded skyshine sources by the Monte Carlo shield approach discussed above. For neutron skyshine problems there is SKYNEUT, which computes skyshine dose out to 2500 m from an arbitrary spectrum of neutron energies, and SKYCONES, which treats sources with polar angle variations and is used in the hybrid method discussed in the previous section. With the exception of MicroSkyshine, all these codes are available from RSICC.

8 Radiation Streaming Through Ducts

Except for the simplest cases, the analysis of radiation streaming through gaps and ducts in a shield requires advanced computational procedures. Because neutron albedos, especially for thermal neutrons, are generally much higher than those for photons, multiple scattering from duct walls is more severe for neutrons than for photons, for which a single scatter analysis is often sufficient. Moreover, placing bends in a duct, which is very effective for reducing gamma-ray penetration, is far less effective for neutrons. Fast neutrons entering a duct in a neutron shield become thermalized and, thereafter, are capable of scattering many times, allowing neutrons to stream along the duct, even one with several bends. Also, unlike gamma-ray streaming, the duct need not be a void (or gas filled) but can be any part of a heterogenous shield that is “transparent” to neutrons. Neutrons can navigate many bends and twists of the streaming channel, and consequently, the design of neutron shields containing ducts or regions with low hydrogen content must be done with great care.

The albedo concept has been found useful for simple duct analyses, and even for more complex geometries in which Monte Carlo techniques are used. Albedo methods are widely used in

the treatment of streaming, and special data sets, primarily for photons, have been developed for such use. Among these are SAIL (Simmons et al. 1979) and BREESE-II (Cain and Emmett 1979). The STORM method (Gomes and Stevens 1991) was especially devised to account for random variations in the displacement between point of entry and point of emergence in particle reflection, an important consideration in the analysis of radiation streaming. Among the few codes that deal exclusively with radiation streaming through ducts are DCTDOS (Spencer 1987) and ALBEDO/ALBEZ (Baran and Grun 1990).

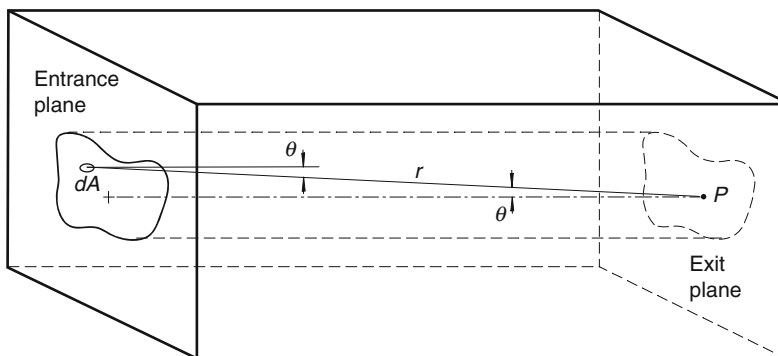
This section provides an introduction to the topic of radiation streaming through ducts, with emphasis on axisymmetric illumination of straight cylindrical ducts and two-legged ducts void of any attenuating medium. First addressed are techniques that can be applied to both neutrons and photons, and then later methods are presented that were developed for a specific type of radiation.

8.1 Characterization of Incident Radiation

Here it is assumed that radiation incident upon a duct is uniform across the entrance plane (☛ Fig. 40). The incident radiation intensity may vary with polar angle θ , but it is assumed that it does not vary azimuthally about the duct axis. The natural polar axis for describing the angular variation is the duct axis. If the angular fluence of the incident radiation at the duct entrance plane is $\Phi_o(\theta)$, then the angular flow in the plane is just $J_{no}(\theta) = \cos \theta \Phi_o(\theta)$. It is often useful to use $\omega \equiv \cos \theta$ rather than θ as the independent angular variable so that $J_{no}(\omega) = \omega \Phi_o(\omega)$. Note that θ varies from 0 to $\pi/2$ and ω from 0 to 1. The flow J_n^+ within this range, which is the total flow into the duct (per unit area of the entrance plane), is given by

$$J_n^+ = 2\pi \int_0^1 d\omega J_{no}(\omega) = 2\pi \int_0^1 d\omega \omega \Phi_o(\omega), \quad (143)$$

in which the positive superscript designates directions within the hemisphere toward the duct entrance.




■ Figure 40
Detector response at point P on duct axis due to passage of particles through area dA in duct-entrance plane

Now suppose that the incident angular flow $J_{no}(\omega)$ is expanded in a power series. Each portion of the incident radiation characterized by a single term in a power series may be treated independently. Thus, suppose that $J_{no}(\omega) = (m+1)\omega^m J_n^+ / 2\pi$. The corresponding angular fluence is $\Phi_o(\omega) = (m+1)\omega^{m-1} J_n^+ / 2\pi$. Also, suppose that the incident radiation has energy E_o . The dose at the entrance plane is denoted by $D^o(0)$, where the superscript denotes incident radiation and the zero argument denotes the entry plane. Here,

$$D^o(0) = 2\pi \mathcal{R}(E_o) \int_0^1 d\omega \Phi_o(\omega) = \frac{m+1}{m} \mathcal{R} J_n^+, \quad (144)$$

where $\mathcal{R}(E_o)$ is the fluence-to-dose conversion factor for particles of energy E_o .

8.2 Line-of-Sight Component for Straight Ducts

Consider a dose point P in the exit plane of a straight duct illustrated in  Fig. 40. The dose at P in the exit plane, caused by radiation incident from an element of area dA in the entrance plane, is $dD^o(P) = \mathcal{R} dA J_{no}(\omega)/r^2$, in which the zero superscript denotes uncollided radiation and r is the distance from dA to point P . The uncollided dose from the entire entrance plane is

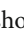
$$D^o(P) = \mathcal{R} \int_A \frac{dA}{r^2} J_{no}(\omega), \quad (145)$$

in which the integration is over the total area A of the source plane covering the duct entrance. Because $dA \omega/r^2$ is the solid angle $d\Omega$ subtended by dA at P , the dose can be expressed as an integration over the solid angle Ω subtended by the entrance area A at point P , namely,

$$D^o(P) = \mathcal{R} \int_A d\Omega \omega^{-1} J_{no}(\omega) = \mathcal{R} \int_{\Omega} d\Omega \Phi_o(\omega). \quad (146)$$

It is an important but subtle point that the line-of-sight dose *in the exit plane* of a duct is given by integrating the angular distribution of the fluence *in the entrance plane*.

8.2.1 Line-of-Sight Component for the Cylindrical Duct

Consider a duct of length Z , radius a , and aspect ratio $\beta \equiv a/Z$ as shown in  Fig. 41, but, for the line-of-sight analysis, with $\rho \leq a$, that is, with the element of area $2\pi\rho d\rho$ inside the duct entrance. The dose contribution $dD^o(P)$ at point P due to the differential annular area is $2\pi\rho d\rho \mathcal{R} J_n(\theta)/r^2$. Because $\rho d\rho = r dr$, $r = Z/\omega$, $\omega = \cos \theta$, and $dr = -Zd\omega/\omega^2$, it follows that

$$dD^o(P) = (m+1)J_n^+ \mathcal{R} d\omega \omega^{m-1}, \quad (147)$$

and upon integrating,

$$D^o(P) = (m+1)J_n^+ \mathcal{R} \int_{\omega_o}^1 d\omega \omega^{m-1}. \quad (148)$$

Because $D^o(0) = J_n^+ \mathcal{R}(m+1)/m$ for $m > 0$, this result may be written as

$$\frac{D^o(P)}{D^o(0)} = m \int_{\omega_o}^1 d\omega \omega^{m-1} = 1 - \omega_o^m = 1 - (1 + \beta^2)^{-m/2}. \quad (149)$$

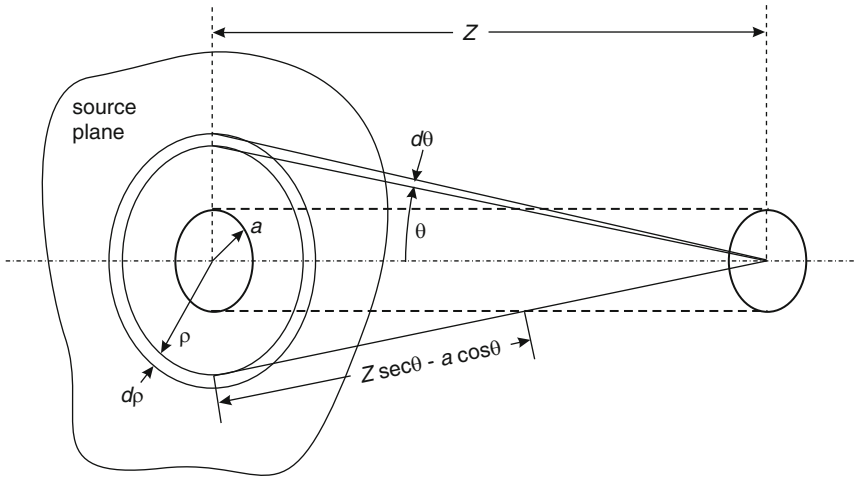


Figure 41
Geometry for evaluation of the line-of-sight and wall-penetration components of dose for a straight cylindrical duct

For the special case of $m = 1$, that is, for isotropic incident fluence, $D^o(P)/D^o(0) = \Omega/(2\pi)$, where Ω is the solid angle subtended by the duct entrance at the center of the duct exit.

The line-of-sight component of the dose at the exit of a cylindrical duct is illustrated in **Fig. 42** and **Fig. 44**. As is quite evident from these figures, for $a \ll Z$, $D^o(P)/D^o(0) \simeq (m/2)\beta^2$, which is just the inverse-square law for attenuation of radiation from a point source.

8.2.2 Line-of-Sight Component for the Rectangular Duct

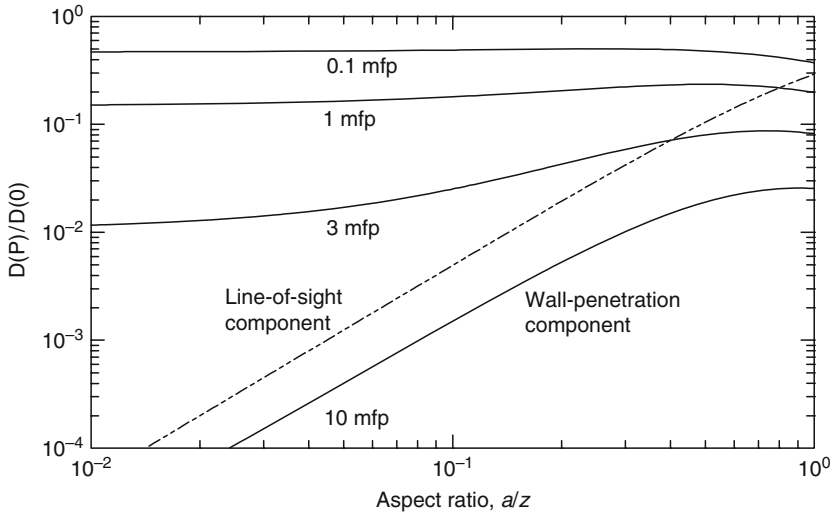
The line-of-sight component for a rectangular ducts with dimensions $W \times L$, for $J_{no}(\omega) = (m + 1)\omega^m J_n^+ / 2\pi$, is given by (Shultis and Faw 2000)

$$D^o(P) = \frac{2}{\pi} \mathcal{R}(m + 1) J_n^+ \int_0^{L/2} dy \int_0^{W/2} dx Z^m (x^2 + y^2 + Z^2)^{-(m+2)/2}. \quad (150)$$

For the special case of $m = 1$, that is, for isotropic incident fluence and just as for the cylindrical duct, $D^o(P)/D^o(0) = \Omega/(2\pi)$, where Ω is the solid angle subtended by the duct entrance at the center of the duct exit.

8.3 Wall-Penetration Component for Straight Ducts

The following discussion applies to photons, or to fast neutrons penetrating a duct wall with sufficient hydrogen content so that removal theory can be used. In the later case, the photon-attenuation coefficient μ is replaced by the appropriate removal coefficient μ_r . However, for



■ Figure 42

Line-of-sight and wall-transmission components for photons incident with isotropic fluence on a straight cylindrical duct. The independent variable is β , the aspect ratio, and the parameter is the wall thickness expressed as μZ , the number of mean free paths

thermal neutrons emitted by the source plane at the duct entrance, no simple formulas for the wall-penetration component exist.

Consider the cylindrical duct illustrated in [Fig. 41](#). Of interest is the radiation penetrating the wall through the lip of the duct entrance. This component $D^w(P)$ may be evaluated in a way very similar to that for the line-of-sight component, (147) through (149), except that $\rho \geq a$ and attenuation in the wall material must be accounted for, as is illustrated in the figure. Suppose that the effective linear-interaction coefficient for the wall material is μ . Then, the attenuation factor for a ray toward P from radius ρ is $\exp[-\mu(Z \sec \theta - a \csc \theta)]$. The analog of (149) is

$$\frac{D^w(P)}{D^o(0)} = m \int_0^{\omega_0} d\omega \omega^{m-1} \exp\left[-\mu Z \left(\frac{1}{\omega} - \frac{\beta}{\sqrt{1-\omega^2}}\right)\right]. \quad (151)$$

This ratio, which depends on *both* β as well as the mean free paths μZ of wall thickness, is illustrated in [Fig. 42](#). Obviously, for thinner walls and narrower ducts, the wall-penetration component can dominate the dose at the duct exit.

8.4 Single-Scatter Wall-Reflection Component

To evaluate this component, it is assumed that the particles entering the duct at its entrance may be treated as though coming from a point source on the duct axis. Only singly reflected particles are taken into account. Although this is a reasonable approximation for gamma rays, which

experience relatively very low albedos peaked in directions along the duct axis, it is not reasonable for thermal neutrons, which experience relatively very high albedos with more nearly isotropic reflection.

The geometry and notation for duct-wall reflection are illustrated in **Fig. 43**. The equivalent point source on the axis is located at point P_0 at the duct entrance, and dose is evaluated at point P on the axis at the other end of the duct. The source emits $S(\theta)$ monoenergetic particles per steradian, with azimuthal symmetry about the duct axis. If $J_n(\theta) = [(m+1)/2\pi]J_n^+ \cos^m \theta$ is the fluence at the duct-entry plane, then $S(\theta) = \pi a^2 J_n(\theta) = [(m+1)/2]a^2 J_n^+ \cos^m \theta = [(m+1)/2]a^2 J_n^+ \omega^m$. In accord with (124), the incident flow J_{n0} at reflecting area $dA = 2\pi a dz$ is given by $\cos \theta_1 S(\theta)/4\pi r_1^2$, and because $\cos \theta_1 = a/r_1$, it follows that the portion of the dose at P due to reflection from area dA is given by

$$dD^1 = \frac{2\pi a^2 dz \mathcal{R} S(\theta)}{r_1^3 r_2^2} \alpha_D(E_o, \theta_1; \theta_2, 0). \quad (152)$$

Note that all reflections leading to the dose point require zero change in azimuthal angle ψ . The total reflected dose is given by

$$D^1(P) = 2\pi a^2 \mathcal{R} \int_0^Z dz \frac{S(\theta)}{r_1^3 r_2^2} \alpha_D(E_o, \theta_1; \theta_2, 0). \quad (153)$$

By using dimensionless variables, namely, $u \equiv z/Z$ and the *aspect ratio* $\beta \equiv a/Z$, this result can be expressed as

$$D^1(P) = \pi(m+1)J_n^+ \mathcal{R} \beta^4 \int_0^1 du u^m \frac{\alpha_D(E_o, \theta_1; \theta_2, 0)}{(\beta^2 + u^2)^{(m+3)/2} [\beta^2 + (1-u)^2]}. \quad (154)$$

For $m > 0$, this can be expressed in terms of the dose at the source plane $D^0(0)$. From (144), $D^0(0) = [(m+1)/m] \mathcal{R} J_n^+$ for the broadly illuminated duct entrance, and because $\omega = \cos \theta = z/\sqrt{z^2 + a^2} = 1/\sqrt{1 + \beta^2/u^2}$, the ratio of the single-reflection dose at the duct exit to the dose at the center of the broadly illuminated duct entrance is, for $m > 0$,

$$\frac{D^1(P)}{D^0(0)} = \pi m \beta^4 \int_0^1 du u^m \frac{\alpha_D(E_o, \theta_1; \theta_2, 0)}{(\beta^2 + u^2)^{(m+3)/2} [\beta^2 + (1-u)^2]}, \quad (155)$$

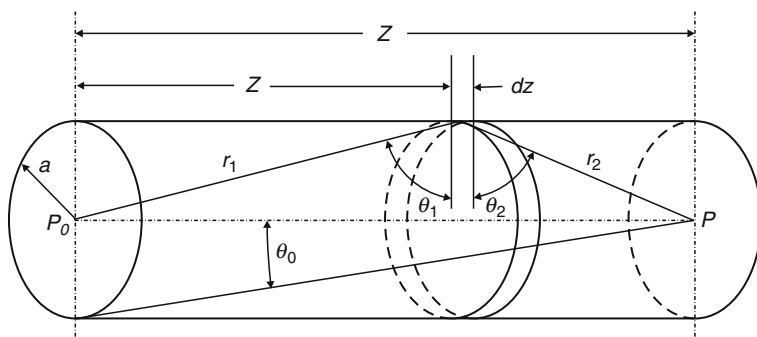
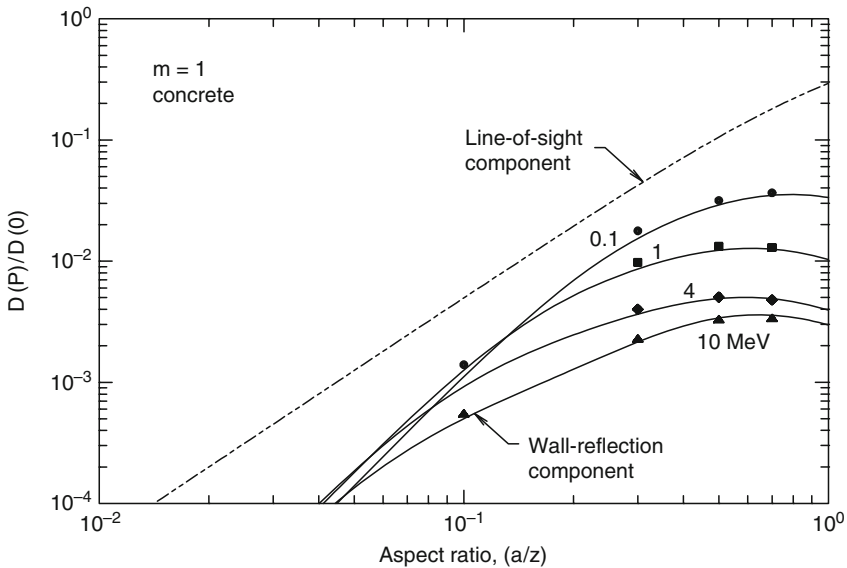


Figure 43

Geometry for evaluation of single-wall reflection in a straight cylindrical duct



■ Figure 44

Line-of-sight and single wall-reflection component for photons incident with isotropic fluence on a straight cylindrical duct in a concrete wall. The independent variable is β , the aspect ratio, and the parameter is the photon energy. The data points represent the multiple-reflection dose for a 0.1-MeV equivalent point source at the entry of a cylindrical duct in a 2-m-thick concrete wall, computed using the MCNP Monte Carlo radiation-transport computer code

in which $\theta_1 = \cot^{-1}[\beta/u]$ and $\theta_2 = \cot^{-1}[\beta/(1-u)]$. The reader will note that, for specified photon energy and wall material, the reflection component of the exit dose is a function of only the aspect ratio. Representative results are illustrated in [► Fig. 44](#). Even for concrete, which has higher albedos than iron or lead, the wall-reflection component of the dose is generally much less than the line-of-sight component.

8.5 Photons in Two-Legged Rectangular Ducts

Photon transmission through multiple-legged ducts of arbitrary cross section is beyond the scope of this chapter. However, an albedo approach that might be employed in general cases is illustrated here for a two-legged rectangular duct. Details of this analysis and refinements to account for lip and corner penetration are described by LeDoux and Chilton (1959).

The geometry is illustrated in [► Fig. 45](#). It is assumed here that the lengths of the duct's legs are appreciably greater than the widths and heights of the legs and that the duct walls are of uniform composition and at least two mean-free-path-lengths thick. The dose $D(P)$ is evaluated at the center of the duct exit. Photons entering the duct are approximated by an anisotropic source $S(\theta)$ at the center of the duct entrance. For example, if the axisymmetric angular flow at the duct entrance plane is $J_n(\theta)$ and the cross-sectional area of the duct entrance is A ,

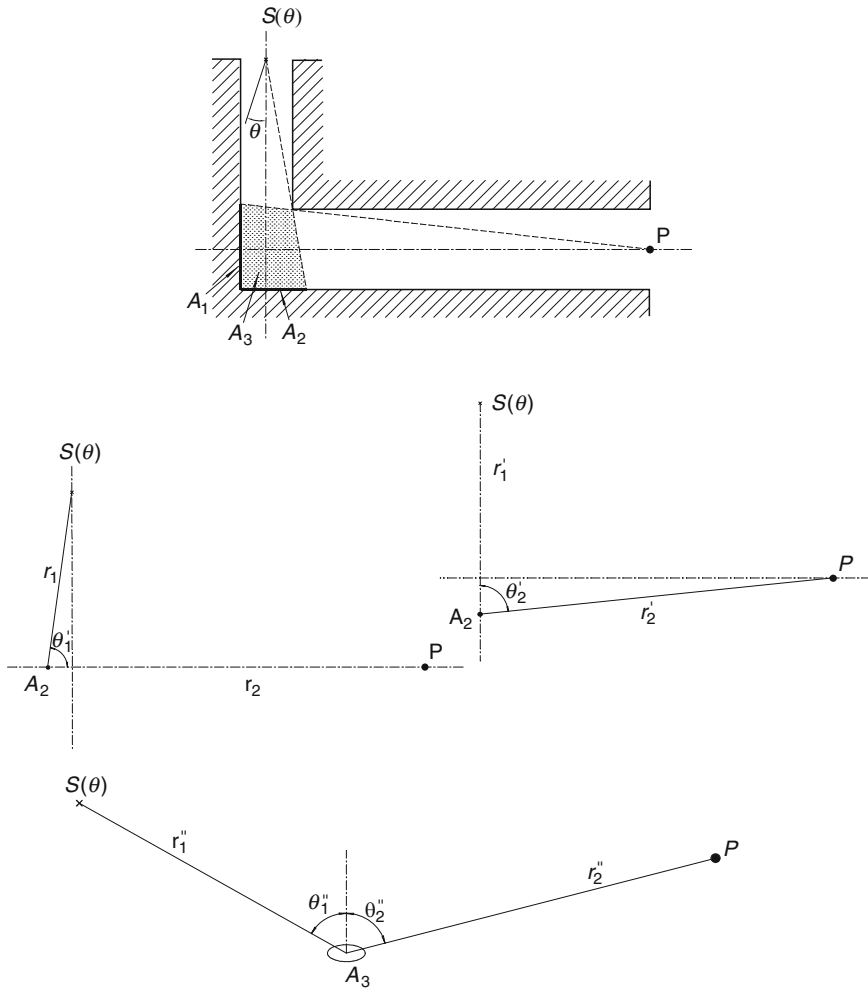


Figure 45 Prime scattering areas in radiation transmission through two-legged rectangular ducts

$S(\theta) = AJ_n(\theta)$. Here a monoenergetic photon source is assumed, although generalization of the method to polyenergetic sources is straightforward.

The analysis by LeDoux and Chilton is based on the approximation that the dose at $P, D(P)$, consists principally of responses to radiation reflected from *prime scattering areas*, that is, areas on the duct walls visible to both source and detector and from which radiation may reach the detector after only a single reflection. There are four prime scattering areas as can be seen in **► Fig. 45**, namely, areas A_1 and A_2 on the walls, and areas A_3 and A_4 on the floor and ceiling (considering the figure to be a plan view). Photon reflection from each area is treated as though it occurred from the centroid of the area. Thus, the transmitted dose may be expressed as

$$D(P) = D_1(P) + D_2(P) + 2D_3(P). \tag{156}$$


According to (124),

$$D_1(P) = \frac{\mathcal{R}A_1S(\pi/2 - \theta'_1) \cos \theta'_1 \alpha_D(E_o, \theta'_1; 0, 0)}{(r_1 r_2)^2}, \quad (157)$$

$$D_2(P) = \frac{\mathcal{R}A_2S(0) \alpha_D(E_o, 0; \theta'_2, 0)}{(r'_1 r'_2)^2}, \quad (158)$$

and


$$D_3(P) = \frac{\mathcal{R}A_3S(\pi/2 - \theta''_1) \cos \theta''_1 \alpha_D(E_o, \theta''_1; \theta''_2, \pi/2)}{(r''_1 r''_2)^2}, \quad (159)$$

in which the various arguments of the albedo function α_D are identified in  Fig. 45. Penetration of radiation through the corner lip can also be estimated in a similar manner (Shults and Faw 2000).

8.6 Neutron Streaming in Straight Ducts

Neutron streaming in straight ducts can be treated in the same context as gamma-ray streaming (see (148) and (150)). Neutron streaming may be treated similarly if the material surrounding the duct is a hydrogenous medium for which removal theory can be applied by replacing the attenuation coefficient μ for photons by the appropriate removal coefficient μ_r . However, for thermal neutrons no simple approximation is available. In this section, the albedo method is used to estimate the wall-scattered component. First, single-wall scattering is considered for neutrons.

Single-Wall Scattering

To describe the neutron albedo from the duct walls, it is assumed that neutrons are reflected partially isotropically and partially with a cosine distribution. In particular, the differential-wall dose albedo is approximated (using the notation of  Fig. 43) as

$$\alpha_D(E_o, \theta_1; \theta_2, 0) \simeq A_D \frac{\gamma + 2(1 - \gamma) \cos \theta_2}{2\pi}, \quad (160)$$

where A_D is the *dose reflection factor*, the fraction of incident dose reemitted in all outward directions from the wall surface, γ is the fraction of neutrons reemitted isotropically, and $(1 - \gamma)$ is the fraction reemitted with a cosine distribution. With this albedo approximation, the single-scatter dose given by (154) can be written as

$$D^1(P) = \frac{1}{2} J_n^+ \mathcal{R} \beta^2 A_D [\gamma I_{0,m} + 2\beta(m+2)(1-\gamma)I_{1,m}], \quad (161)$$

where the $I_{n,m}$ integral is defined for $n = 0, 1$ and $m \geq 0$ as

$$I_{n,m}(\beta) \equiv \beta^2 \frac{m+1}{(m+2)^n} \int_0^1 du \frac{u^m}{(\beta^2 + u^2)^{(m+3)/2} [\beta^2 + (1-u)^2]^{(n+2)/2}}. \quad (162)$$

The integral $I_{n,m}$ approaches unity (Chilton et al. 1984), as the aspect ratio becomes very small (i.e., for $\beta \equiv a/Z \ll 1$). For such ducts, illuminated by an isotropic source plane ($m = 0$), (161) reduces to

$$D^1(P) = \frac{1}{2} J_n^+ \mathcal{R} \beta^2 A_D [\gamma + 4\beta(1 - \gamma)]. \quad (163)$$

This result is known as the Simon and Clifford (1956) single-scatter duct formula.

Multiple-Wall Scattering

Because of the relatively high albedo for neutrons, they can scatter many times from a duct wall before reaching the duct exit. An analytical estimation of the multiple wall-scatter component is a formidable task. Simon and Clifford (1956) showed that, for the albedo of (160) and a long cylindrical duct ($Z \gg a$) illuminated by a source plane with isotropic incident fluence, that the wall-scattered component, including all orders of scatters, is given by (163), with the total albedo A_D replaced by

$$A'_D = 1 + A_D + A_D^2 + A_D^3 + A_D^4 + \dots = \frac{A_D}{1 - A_D}. \quad (164)$$

Thus, the dose from both the line-of-sight and multiple wall-scattered components at the duct exit is

$$D(P) = J_n^+ \mathcal{R} \beta^2 \left\{ 1 + \frac{A_D}{1 - A_D} [\gamma + 4(1 - \gamma)\beta] \right\}. \quad (165)$$

Here the line-of-sight component is obtained by treating the entrance as a disk source of radius a and evaluating the uncollided dose at a distance Z from the disk's center. The result is $D^0(P) \simeq J_n^+ \mathcal{R} \beta^2$ (Shultis and Faw 2000).


The result above holds for cylindrical ducts with a small aspect ratio a/Z . For larger ratios, the importance of the infinite number of internal reflections implied by (164) becomes less. Artigas and Hungerford (1969) have produced a more complicated version of (165), which gives better results for $a/Z > 0.3$ (Selph 1973).

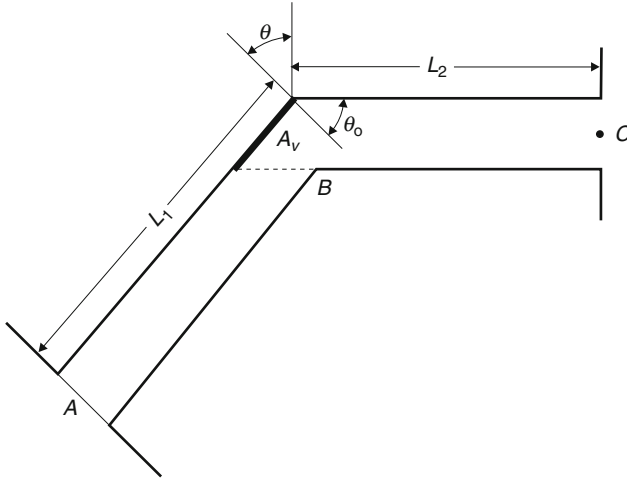
8.7 Neutron Streaming in Ducts with Bends

To reduce radiation reaching the duct exit, shield designers often put one or more bends in the duct. Analyzing the effect of bends is an important but difficult task for the designer. However, a few simplified techniques are available for estimating transmitted neutron doses through ducts with bends. Albedo methods are widely used for treating neutron streaming through bent ducts. These methods range from simple analytical models, such as those presented in this section, to Monte Carlo methods that use albedos to reflect neutrons from duct walls and, thereby, allow them to travel large distances along the duct (Brockhoff and Shultis 2007).

8.7.1 Two-Legged Ducts

Neutron Streaming in a Two-Legged Cylindrical Duct

A two-legged cylindrical duct of radius a , shown in  Fig. 46, is first considered. The two legs are bent at an angle θ such that neutrons emitted from the source plane across the duct



■ **Figure 46**
Geometry for the two-legged duct model

entrance at A cannot stream directly to the duct exit at C . Both legs are assumed to have small aspect ratios, that is, $a/L_1 \ll 1$ and $a/L_2 \ll 1$. The uniform source plane emits neutrons into the duct with a general cosine flow distribution $J_n^+(\psi) = (m+1)J_n^+ \cos^m \psi / (2\pi)$, where ψ is the angle with respect to the normal to the source plane.

The uncollided dose on the duct centerline at the duct bend B arising from the disk source at the duct entrance is, for $a/L_1 \ll 1$, (Shultis and Faw 2000)

$$D^o(B) = (m+1)\mathcal{R}(E_o) \frac{J_n^+}{2} \left(\frac{a}{L_1}\right)^2. \quad (166)$$

Neutrons that reach the bend enter the duct-wall material, interact, and some are scattered back into the duct. Those neutrons reaching the duct exit at C are those that are reradiated from the portion of the duct wall visible from C , namely from the area $A_v = \pi a^2 / \sin \theta$. With the albedo concept [cf. (122)], the reflected or reradiated dose at C can be expressed as (recall that $a/L_2 \ll 1$)

$$D(C) = D^o(B) \cos \xi \widehat{\alpha}_D(\theta_o) \frac{A_v}{L_2^2}, \quad (167)$$

where ξ is some effective incident angle at the bend, and $\theta_o = (\pi/2) - \theta$ is the angle with respect to the normal to A_v at which reradiated neutrons reach the duct exit. Here $\widehat{\alpha}_D$ is a *differential reradiation probability*, analogous to the differential dose albedo. Assume that a fraction γ of the reradiated neutron flow from A_v is isotropic and a fraction $(1-\gamma)$ has a cosine distribution, so that

$$\widehat{\alpha}_D(\theta_o) = \widehat{A}_D \frac{\gamma + 2(1-\gamma) \cos \theta_o}{2\pi}. \quad (168)$$

The quantity \widehat{A}_D is the fraction of all the neutrons incident on the wall surfaces at the bend that are reradiated from A_v .

Finally, substitution of (166) and (168) into (167), along with the relation $\cos \theta_o = \sin \theta$, gives the transmitted dose at C as

$$D(C) = (m+1)J_n^+ K \mathcal{R}(E_o) \left(\frac{a^2}{2L_1^2} \right) \left(\frac{a^2}{2L_2^2} \right) \frac{\gamma + 2(1-\gamma) \sin \theta}{\sin \theta}, \quad (169)$$

where $K \equiv \widehat{A}_D \cos \xi$ is treated as an empirical constant. This result for the case of isotropic source flow ($m = 0$) was first obtained by Simon and Clifford (1956). Although cylindrical ducts have been used in this somewhat heuristic derivation, any simple duct shape could be used and only a slightly different expression would result.

Neutron Streaming in a Two-Legged Rectangular Duct

The LeDoux–Chilton albedo analysis of a two-legged L-shaped duct discussed in Section 8.5 cannot be applied directly to the neutron duct problem because of the importance of multiple scattering from the duct walls for the neutron case. However, Chapman (1962) extended the LeDoux–Chilton model to include second-order scattering effects, and Song (1965) used this refined model successfully to treat neutron transmission.

8.7.2 Neutron Streaming in Ducts with Multiple Bends

The Simon–Clifford model for a two-legged cylindrical duct can be extended to a duct with N legs. With this extension, the dose at the exit of the N th leg is

$$D(L_N) = (m+1)J_n^+ \mathcal{R}(E_o) \left(\frac{a^2}{2L_1^2} \right) \times \prod_{i=2}^N \left[K \left(\frac{a^2}{2L_i^2} \right) \left(\frac{\gamma + 2(1-\gamma) \sin \theta_i}{\sin \theta_i} \right) \right]. \quad (170)$$

This result can be applied to a duct that makes a curved path through the shield by dividing the duct into a series of straight-line segments of length equal to the maximum chord length that can be drawn internal to the duct (Selph 1973). In particular, if the duct is conceptually represented by a series of N equal-length (L) and equally bent (θ) legs, the dose at the duct exit is

$$D(L_N) = (m+1)J_n^+ \mathcal{R}(E_o) \left(\frac{a^{2N} K^{N-1}}{2^N L^{2N}} \right) \left(\frac{\gamma + 2(1-\gamma) \sin \theta}{\sin \theta} \right)^{N-1}. \quad (171)$$

8.8 Empirical and Experimental Results

There is much literature on experimental and calculational studies of gamma-ray and neutron streaming through ducts. In many of these studies, empirical formulas, obtained by fits to the data, have been proposed. These formulas are often useful for estimating duct-transmitted doses under similar circumstances. As a starting point for finding such information, the interested reader is referred to Rockwell (1956), Selph (1973), NCRP (1977, 1984), and Weise (1994).

9 Shield Design

9.1 Shielding Design and Optimization

Shielding design embodies essentially the same considerations as shielding analysis. Both require thorough characterization of radiation sources and receptors as well as comprehensive information on shield properties. Such properties encompass not only the nuclear characteristics but also the thermal properties and certainly, structural properties. Shield optimization may have the goal of minimizing weight, volume, or cost. Minimum weight is a common goal, but it is easy to envision cases where shield volume or shield cost might control.

Source characterization is a major task. Usually, the source emits gamma rays or a mixture of neutrons and gamma rays. In either case, the energy spectra and spatial distributions must be known. On occasion, a surface such as the outside of a nuclear reactor pressure vessel is identified as a “(secondary) source surface.” Then, it is necessary to specify angular distribution as well as energy spectrum. When thermal effects are important, it may be necessary to account for charged particles or low-energy X-rays or Auger electrons released from the primary source. Similarly, such low energy particles may be released in the course of reactions taking place as primary radiations are attenuated.

Receptor characterization is another important task. What are dose and dose rate limitations and are they specified at a point or averaged over a region? Does the dose apply to a physical or anthropomorphic phantom? Is the shielding designed to protect workers, individual members of the public, or population groups? Otherwise, is the shielding designed to protect materials or equipment?

Materials characterization poses broad demands for information ranging from nuclear properties to structural properties. Some materials are effective in attenuating gamma rays but ineffective in attenuating neutrons. Therefore, in many instances, composite materials, perhaps homogenous and perhaps layered, are demanded. Thereby, shield geometry – numbers and thicknesses of layers – enters into the shield-optimization problem. Elemental compositions and densities of material components must be known. Cross sections must be known by element. In some cases, for example, dealing with boron- or lithium-shield components, isotopic compositions and cross sections must also be known. Structural properties, including thermal expansion characteristics, must also be known. Other considerations include sensitivity to heat, relative humidity, and radiation damage. Long-term composition changes such as water loss from concrete may also play a role in material selection and shield optimization.

Shield optimization may well be a “brute force” trial-and-error procedure, tempered by experience. As computational resources continue to improve, the trial-and-error approach gains favor. However, there are elegant, well-known optimization procedures calling on the application of variational principles to find an optimal design for the given design criteria and constraints. Blizard (1962) describes shield optimization by weight using methods of variational calculus. Mooney and Schaeffer (1973) also address variational methods and cite a number of applications. Claiborne and Schaeffer (1973) integrate the many design considerations into a comprehensive review of the three distinct phases in reactor shielding design: (1) preliminary conceptual design, (2) correlation of phase (1) with mechanical design to obtain a final conceptual design, and (3) translation of the final conceptual design into a detailed engineering design. In doing so, they draw on the experience of Hungerford (1966) in the design of the shielding for the Enrico Fermi sodium-cooled nuclear power plant. Hungerford (1968) put forth six

principles of shield design to be followed in developing the shield system for a nuclear power reactor:

1. *Reactor Shield Unity*: A shield is an integral part of a reactor system and must be designed at the same time as, and as an entity with, the overall reactor system.
2. *Shield Integrity*: Adjacent parts of a shield, having the same design criteria, must be designed with equal performance characteristics.
3. *Shield Safety*: Because the reactor shield is a safety device and must be considered as a part of the safety system of the reactor, there can be no compromise with expediency in its design.
4. *Shield Accommodation*: A shield should be adapted to provide for the mechanical requirements of the reactor, its supporting structure, and its component systems, without sacrificing the principles of reactor shield unity, shield integrity, or shield safety.
5. *Shield Economy*: The best possible shield should be designed at the lowest possible cost, consistent with the overall reactor design, without sacrificing safety, integrity, or accommodation.
6. *Shield Simplicity*: A shield should be designed to be as simple in configuration as possible, with the minimum number of voids, ducts, and cutouts for the reactor components and auxiliary systems, consistent with the principle of shield accommodation.

Two comprehensive resources for shielding design are Vols. II and III of the Engineering Compendium on Radiation Shielding (Jaeger et al. 1975, 1970). Volume III (1970) addresses the following individual topics in shielding design: the design of shielding for research and testing reactors, stationary power reactors, and ship-propulsion reactors. Also addressed are the design of shipping and storage containers, hot cells, medical irradiation facilities, accelerators, and nuclear fuel processing plants. In the preface to the volume, Jaeger points out that radiation attenuation analysis is a design tool in two states: first, in an approximate comparative assessment of design alternatives, then, in complex engineering considerations reaching a balance between the aspects of safety and economy and the functional requirements of nuclear facilities. Volume II (1975) provides a wealth of information on mechanical, thermal, and technological properties of gamma-ray and neutron shields, as well as optimal choices of shielding materials. Two American National Standards, ANSI/ANS-6.4-2006 and ANSI/ANS-6.4.2-2006, not only address shielding standards but also provide comprehensive guidance on shielding materials and fabrication, especially for concrete.

9.2 Shielding Materials

In this section, essential properties and compositions of shielding materials are summarized. These materials include natural materials such as air, water, and soil as well as materials of construction. Specialized materials for X-ray facilities are addressed, as are special materials for neutron shielding.

9.2.1 Natural Materials

Air and water, the most natural of materials, require an understanding of their shielding properties. Air properties are critical in dealing with design or analysis involving atmospheric skyshine and when irradiated by neutrons. Dry air, at 1 atmosphere and 20°C has a density of 0.00120 g/cm³. Ordinarily ideal gas laws may be applied to account for different temperatures

■ **Table 22**
Compositions of Five Representative Soil Types

	Weight Fractions for Soil Types				
	Nominal	Dry porous	Dry dense	Wet porous	Wet dense
Hydrogen	0.023	0.015	0.015	0.030	0.030
Oxygen	0.559	0.529	0.529	0.585	0.585
Silicon	0.223	0.243	0.243	0.206	0.206
Aluminum	0.065	0.071	0.071	0.060	0.060
Iron	0.040	0.044	0.044	0.037	0.037
Calcium	0.029	0.032	0.032	0.027	0.027
Potassium	0.021	0.023	0.023	0.019	0.019
Sodium	0.023	0.025	0.025	0.021	0.021
Magnesium	0.017	0.018	0.018	0.015	0.015

Source: Shue et al. (1998)

■ **Table 23**
Characteristics of Five Representative Soil Types

	Soil Type				
	Nominal	Dry porous	Dry dense	Wet porous	Wet dense
Porosity ^a	0.5	0.6	0.4	0.6	0.4
Free water content ^b	0.2	0.1	0.1	0.3	0.3
Bound water content ^c	0.05	0.05	0.05	0.05	0.05
Mineral density (g/cm ³) ^d	2.684	2.684	2.684	2.684	2.684
In situ density (g/cm ³)	1.610	1.181	1.771	1.396	2.094

^aFraction of total volume occupied by water and air.

^bRatio of free water mass to mineral mass.

^cRatio of bound water mass to mineral mass.

^dMineral density includes bound water.

Source: Shue et al. (1998)

or pressures as well as to account for humidity. In dry air, weight fractions by element are N: 0.7553, O: 0.2318, C: 0.0001, and Ar: 0.0128. ⁴⁰Ar, present at 0.996 atomic fraction, captures thermal neutrons with the cross section of 0.66 b. The product ⁴¹Ar decays with a half-life of 110 m, releasing a beta particle and, with 99.6% frequency, a 1.293-MeV gamma ray.

Hydrogen present in water with 0.112 weight fraction, captures thermal neutrons with a cross section of 0.33 b and, in the process, releases a 2.23-MeV-capture gamma ray. In a complementary reaction with 2.23-MeV threshold, photoneutrons are produced in the interaction of gamma rays with deuterium.

Soils often find use as radiation shields; however, water content is highly variable, depending on environmental conditions. ➤ [Tables 22](#) and [23](#) list characteristics of a range of soil types. Similarly, untreated wood, though useful for neutron attenuation, loses water over time and is, therefore, generally found unacceptable as a shield material.

9.2.2 Concrete

Cost, density, compressive strength, ease of placement, and effectiveness in attenuation of both neutrons and gamma rays make concrete a highly desirable shielding material. Neutron shielding by concrete and the importance of water (hydrogen) content are addressed earlier in this chapter and is not repeated here. Types of concrete are characterized by the type of aggregate, *siliceous* referring to quartz based aggregate and *calcareous* referring to limestone based aggregate. Table 24 lists components of three types of “ordinary” concrete: NBS Type 03, Type 04, and the current NIST ordinary concrete (Hubbell & Seltzer 2004). Type 04 is commonly cited and appears to be accepted as “representative.” High-density concrete is often used to provide greater attenuation for a given thickness. Additives for this type of concrete include scrap metal such as steel punchings and metallic ores. Magnetite concrete ($\rho = 3.53 \text{ g/cm}^3$) contains in the mix iron oxide to the extent 4900 lb/yd³. Barite concrete ($\rho = 3.35 \text{ g/cm}^3$) contains barium sulfate ore to the extent 5000 lb/yd³. ANSI/ANS-6.4-2006 lists other high-density concretes plus a low-density ($\rho = 2.1 \text{ g/cm}^3$) serpentine concrete for high temperature applications.

Reinforcing steel, or *rebar*, provides tensile strength and adds density to concrete. For gamma-ray shielding, it is generally satisfactory to conceptually homogenize the reinforced concrete. For neutron shielding, however, channeling effects very often call for treatment of the reinforced concrete as a combination of a continuous concrete phase with steel heterogeneities.

Table 24
Compositions of Types 03 and 04 and NIST Ordinary Concretes

Elemental Composition (partial g/cm ³)			
Element	Type 03	Type 04	NIST
Hydrogen	0.020	0.013	0.051
Carbon	0.118		0.006
Oxygen	1.139	1.171	1.322
Sodium		0.040	0.035
Magnesium	0.057	0.006	0.003
Calcium	0.582	0.194	0.099
Aluminum	0.085	0.107	0.046
Sulfur	0.007	0.003	
Silicon	0.342	0.742	0.701
Potassium	0.004	0.045	0.023
Iron	0.003	0.029	0.015
Nickel	0.026		
Phosphorus	0.007		
Total	2.39	2.35	2.300

Source: ANL-5800 (2nd ed.), ANSI/ANS-6.4-2006, Hubbell and Seltzer (2004)

9.2.3 Metallic Shielding Materials

Very often it is necessary to address shielding properties of alloy (carbon) steels and stainless steels. Alloy steel has a nominal density of 7.86 g/cm^3 , contains 0.2 to 0.4% carbon by weight plus varying concentrations of Si, Mn, Cr, Ni, Mo, P, and S. Stainless steel, with density typically $7.9\text{--}8.0 \text{ g/cm}^3$, contains up to about 0.08% carbon by weight and large concentrations of Mn, Cr, Ni, and Mo. In the presence of neutrons, cobalt must be held to the lowest concentration possible to prevent activation yielding the gamma-ray emitter ^{60}Co .

Other important metallic shielding materials are lead, tungsten, and uranium. Next to concrete, lead is no doubt the most common shield material. It has low strength, a low melting point (327°C), and a high density (11.34 g/cm^3). Tungsten has high strength and a high melting point (3410°C). Uranium, especially uranium depleted in ^{235}U , has high strength, intermediate melting point (857°C), and a high density ($18.5\text{--}19.0 \text{ g/cm}^3$).

9.2.4 Special Materials for Neutron Shielding

Shielding of epithermal or fast neutrons requires a two stage process. Fast neutrons can rarely be captured or absorbed; thus, it is first necessary to slow neutrons to thermal energies, as the first step, and then to absorb them. The slowing-down process itself may be in two stages. Neutrons with many MeV of energy may be slowed by inelastic scattering with atoms of, for example, iron. This is the removal process discussed in [5.3](#). At neutron energies below about 6 MeV, the elastic scattering cross section of hydrogen exceeds the inelastic scattering cross section of iron. Thus, in addition to a component such as iron, a hydrogenous component is needed for efficient neutron thermalization. Thermal neutrons are readily captured, unfortunately, in most instances releasing high-energy capture-gamma rays. Thus, for an effective neutron shield, a strong absorber such as boron or lithium, perhaps indium or cadmium, is needed to avoid significant capture-gamma rays.

Boron for Neutron Attenuation

Natural boron contains 19.9 atomic percent ^{10}B and 80.1 percent ^{11}B , the former with a 3840-b (2200-m/s) absorption cross section, the latter with only 5 mb. The absorption of a neutron by ^{10}B releases a 0.48-MeV gamma ray – significant, but of lower energy than most capture gamma rays. Boron shielding materials are available in the form of boron carbide, B_4C , with density 2.51 g/cm^3 , borated graphite, boron carbide mixed in graphite, and boral (a mixture of boron carbide in aluminum cladding). Plates or sheets of boral commonly contain 35% boron by weight and are available up to 1 by 3 m^2 in area and thicknesses of 0.125 and 0.25 in. Boron shielding is also available as borated polyethylene in a wide range of shapes and compositions, in a wide range of boron concentrations, and even in castable form. For mixed neutron and gamma-ray shielding, lead-loaded borated polyethylene is also available.

Lithium for Neutron Attenuation

Natural lithium contains 7.5 atomic percent ^6Li and 92.5 percent ^7Li . The former has an exceptionally high cross section (941 b) for thermal-neutron absorption and

produces no secondary gamma rays. It is light in weight and available enriched in ^6Li . It is offered commercially as lithium polyethylene, with 7.5% lithium by weight and in a variety of shapes.

9.2.5 Materials for Diagnostic X-Ray Facilities

There are six materials of prime concern in the design of diagnostic facilities. Of these, concrete, steel, and lead have already been addressed. Others are wood, plate glass, and gypsum wallboard. Shielding design considerations are documented by Jaeger et al. (1975), Archer et al. (1994), and NCRP (2005).

Depending on hydrogen content, wood density varies from 0.5 to 0.8, nominally 0.55 g/cm^3 , and is essentially cellulose, water, and lignin. Crown glass, a silica soda lime glass, is durable and has a low index of refraction. Density is $2.5\text{--}2.7\text{ g/cm}^3$. Lead oxide may be added at up to about 0.75 weight fraction Pb to yield lead glass with density up to about 6.2 g/cm^3 . Sheets are available with lateral dimensions up to about 140 cm and thicknesses up to about 40 cm. Plaster board, or gypsum wallboard, has a density typically 2.32 g/cm^3 . By weight fraction, gypsum composition is H 0.0234, O 0.5576, S 0.1862, and Ca 0.2328. Typical thickness is 14 mm of gypsum plus 1 mm of paper. Sheets may be lined with lead in thicknesses 1/32 in to 1/8 in.

9.3 A Review of Software Resources

Listed below are selected software packages of interest in shielding design and analysis. All are available from the Radiation Safety Information Computational Center, accessible on line at <http://www-rsicc.ornl.gov/>.

- **QAD-CGGP**: point kernel code featuring combinatorial 3D geometry and source options with geometric progression buildup factors for gamma rays
- **QADMOD-GP**: point kernel code featuring faster 3D geometry and source options with geometric-progression buildup factors for gamma rays
- **G-33**: point kernel code featuring multi-group gamma-ray scattering with QAD geometry and GP-buildup factors
- **ISOSHLD**: point kernel code featuring multiple isotope sources, limited geometry, and source description
- **DOORS**: discrete ordinates code package incorporating ANISN, DORT, and TORT codes for 1, 2, and 3D discrete ordinates calculations
- **PARTISN**: discrete ordinates code featuring multidimensional, time-dependent, multigroup discrete ordinates transport code system
- **COHORT**: Monte Carlo code featuring radiation transport; flexible geometry
- **MORSE**: Monte Carlo code featuring multigroup neutron and gamma-ray transport; combinatorial geometry
- **MCNP**: Monte Carlo code featuring continuous energy, neutral particle transport; flexible geometry
- **ORIGEN**: neutron activation code featuring neutron activation, radioactive decay, and source-term analysis

9.4 Shielding Standards

Listed below are ANSI/ANS standards pertinent to shielding design. Standards 6.4 and 6.4.2 cite standards of other sponsors such as ASME and IEEE as well as selected international standards.

- ANSI/ANS-5.1-2005: Decay Heat Power in Light Water Reactors
- ANSI/ANS-6.1.2-1999: Neutron and Gamma-Ray Cross Sections for Nuclear Radiation Protection Calculations for Nuclear Power Plants
- ANSI/ANS-6.3.1-1987;R1998;R2007 (R=Reaffirmed): Program for Testing Radiation Shields in Light Water Reactors (LWR)
- ANSI/ANS-6.4-2006: Nuclear Analysis and Design of Concrete Radiation Shielding for Nuclear Power Plants
- ANSI/ANS-6.4.2-2006: Specification for Radiation Shielding Materials
- ANSI/ANS-6.6.1-1987;R1998;R2007 (R=Reaffirmed): Calculation and Measurement of Direct and Scattered Gamma Radiation from LWR Nuclear Power Plants
- ANSI/ANS-18.1-1999: Radioactive Source Term for Normal Operation for Light Water Reactors
- ANSI/ANS-19.1-2002: Nuclear Data Sets for Reactor Design Calculations
- ANSI/ANS-19.3.4-2002: The Determination of Thermal Energy Deposition Rates in Nuclear Reactors

10 Health Physics

As it passes through biological tissue, radiation interacts with ambient atoms and produces chemical free radicals that, in turn, cause oxidation–reduction reactions with cell biomolecules. However, how such reactions affect the cell and produce subsequent detrimental effects to an organism is not easily determined. Because of the obvious concern about the biological effects of radiation, much research has been directed toward understanding the hazards associated with ionizing radiation.

There are two broad categories of radiation hazards to humans. *Hereditary effects* result in damage to the genetic material in germ cells that, although not detrimental to the individual exposed, may result in hereditary illness to succeeding generations. *Somatic effects* affect the individual exposed and are further classified by the nature of the exposure, for example, *acute* or *chronic*, and by the time scale of the hazard, for example, short term or long term. The short-term acute effects on the gastrointestinal, respiratory, and hematological systems are referred to as the *acute radiation syndrome*.

The effects of human exposure to ionizing radiation depend on both the exposure as well as its duration. Acute, life-threatening exposures lead to *deterministic* consequences requiring medical treatment. For such exposures, illness is certain, with the type and severity depending on the exposure and the physical condition of the individual exposed.

By contrast, minor acute or chronic low-level exposures produce stochastic damage to cells and subsequent ill effects are quantifiable only in a probabilistic sense; hereditary illness or cancer may or may not occur. Only the probability of illness, not its severity, is dependent on the radiation exposure. Such consequences are, thus, *stochastic* as distinct from *deterministic*. Although the effects of low-level radiation exposures to a large number of individuals can be estimated, the effect to a single individual can be described only probabilistically.

10.1 Deterministic Effects from Large Acute Doses

There are two circumstances under which a person can receive high doses of ionizing radiation. The first is accidental, and most likely involves a single exposure of short duration. The second is from medical treatments, and often involves doses delivered daily for several weeks and which may be delivered under conditions designed to intensify the response of certain organs and tissues to the exposures. Here, only single acute exposures to all or part of the body are considered. Issues such as fractionation and effect modification, which pertain largely to medical exposures, are not addressed.

10.1.1 Effects on Individual Cells

The probability that a particular radiation exposure kills a cell or prevents it from dividing depends on many factors. The two most important factors are the dose rate and the LET of the radiation. Doses delivered at low dose rates allow the cell's natural repair mechanism to repair some of the damage, so that the consequences are generally not as severe as if the doses were delivered at high dose rates. High LET radiation, like alpha particles, creates more ion–electron pairs closer together than does low LET radiation. Consequently, high LET radiation produces more damage to a cell it passes through than would, say, a photon.

The position in a cell's life cycle at the time of exposure also greatly affects the damage to the cell. Cell death is more likely if the cell is in the process of division than if it is in a quiescent state. Thus, radiation exposure results in more cell death in organs and tissues with rapidly dividing cells, such as the fetus (especially in the early stages of gestation), the bone marrow, and the intestinal lining. Whole-body absorbed doses of several Gy are life-threatening largely because of stem cell killing in the bone marrow and lining of the intestines. However, in these tissues and in most other tissues and organs of the body, there are ample reserves of cells, and absorbed doses of much less than one Gy are tolerable without significant short-term effect. Similarly, radiation doses which would be fatal if delivered in minutes or hours may be tolerable if delivered over significantly longer periods of time. Age, general health, and nutritional status are also factors in the course of events following radiation exposure.

For those tissues of the body for which cell division is slow, absorbed doses which might be fatal if delivered to the whole body may be sustained with little or no effect. On the other hand, much higher absorbed doses may lead ultimately to such a high proportion of cell death that, because replacement is so slow, structural or functional impairment appears perhaps long after exposure and persists perhaps indefinitely.

10.1.2 Deterministic Effects in Organs and Tissues

In this section, only deterministic somatic effects – effects in the person exposed – are considered. These effects have well-defined patterns of expression and thresholds of dose, below which the effects do not occur. The severity of the effect is a function of dose. The stochastic carcinogenic and genetic effects of radiation are addressed later.

The risk, or probability of suffering a particular effect or degree of harm, as a function of radiation dose above a threshold dose D_{th} , can be expressed in terms of a 50th-percentile dose D_{50} , or median effective dose, which would lead to a specified effect or degree of harm in half the persons receiving that dose. The D_{50} dose depends, in general, on the rate at which the dose is received. For doses below a threshold dose D_{th} , the effect does not occur.

A summary of important deterministic effects is given in [Table 25](#). Information about these and other effects on particular organs and tissues can be found in the following sources: Information is taken from the following sources: (Langham 1967; Upton and Kimball 1967; Wald 1967; NCRP 1971a; Vogel and Motulsky 1979; Pochin 1983; ICRP 1984, 1991; UN 1988; Shultis and Faw 2008).

10.1.3 Potentially Lethal Exposure to Low-LET Radiation

The question of what constitutes a *lethal dose* of radiation has, of course, received a great deal of study. There is no simple answer. Certainly, the age and general health of the exposed person are key factors in the determination. So, too, are the availability and administration of specialized medical treatment. Inadequacies of dosimetry make interpretation of sparse human data difficult. Data from animal studies, when applied to human exposure, are subject to uncertainties in extrapolation. Delay times in the response to radiation, and the statistical variability in response have led to expression of the lethal dose in the form, for example, $LD_{50/60}$, meaning the dose is fatal to 50% of those exposed within 60 days. The *dose* itself requires a careful interpretation. One way of defining the *dose* is the free-field exposure, in roentgen units, for gamma or

Table 25

Median effective absorbed doses D_{50} and threshold doses D_{th} for exposure of different organs and tissues in the human adult to gamma photons at dose rates $\leq 0.06 \text{ Gy h}^{-1}$

Organ/Tissue	Endpoint	D_{50} (Gy)	D_{th} (Gy)
Skin	Erythema	6 ± 1	3 ± 1
	Moist desquamation	30 ± 6	10 ± 2
Ovary	Permanent ovulation suppression	3 ± 1	0.6 ± 0.4
Testes	Sperm count suppressed for 2 y	0.6 ± 0.1	0.3 ± 0.1
Eye lens	Cataract	3.1 ± 0.9	0.5 ± 0.5
Lung	Death ^a	70 ± 30	40 ± 20
	Vomiting	2 ± 0.5	0.5
	Diarrhea	3 ± 0.8	1
GI system	Death	15 ± 5	8
	Death	3.8 ± 0.6	1.8 ± 0.3

^aDose rate 0.5 Gy/h

Source: Scott and Hahn (1989)

X-rays. A second is the average absorbed dose to the whole body. A third is the *mid-line* absorbed dose, that is, the average absorbed dose near the abdomen of the body. For gamma rays and X-rays, the mid-line dose, in units of rads, is about two-thirds the free-field exposure, in units of roentgens. The evaluation by Anno et al. (1989) for the lethal doses of ionizing radiation are given in ► [Table 26](#). The effects of large doses below the threshold for lethality are summarized in NCRP Report 38 (1971) and by Anno et al. (1989). For extremely high doses (>500 Gy), death is nearly instantaneous, resulting from enzyme inactivation or possibly from immediate effects on the electrical response of the heart (Kathren 1985). Lesser, but still fatal doses, lead promptly to symptoms known collectively as the *prodromal syndrome*. The symptoms, which are expressed within a 48-h period are primarily gastrointestinal (e.g., nausea, diarrhea, cramps, and dehydration) and neuromuscular (e.g., fatigue, sweating, fever, headache, and hypotension). For high doses with potential survival, the prodromal stage is followed by a latent stage, a stage of manifest illness, and a recovery stage beyond 6–8 weeks post-exposure.

10.2 Hereditary Illness

In 1927, Hermann Muller discovered that fruit flies receiving high doses of radiation could produce offspring with genetic abnormalities. Subsequent animal and plant studies have demonstrated a nearly linear relationship between dose and mutation frequency, for doses as low as 3 mSv. However, there is almost no evidence of radiation-induced mutations in humans. Indeed, the only unequivocal evidence relates to chromosomal rearrangement in spermatocytes. Nevertheless, animal studies clearly indicate that radiation can produce heritable mutational effects in the humans. Because radiation-induced mutation rates in humans are unknown, even for atom bomb survivors, estimation of risks to human populations are based largely on extrapolation of studies of radiation effects in other mammals, notably the mouse. The estimation of human hereditary risks from animal studies involve many assumptions, and the estimates turn out to be a very small fraction of the natural incidence of such illness, thereby, explaining why radiation-induced hereditary illness has not been observed in humans.

■ **Table 26**
Lethal doses of radiation

Lethality	Mid-line absorbed dose (Gy)
$LD_{5/60}$	2.0–2.5
$LD_{10/60}$	2.5–3.0
$LD_{50/60}$	3.0–3.5
$LD_{90/60}$	3.5–4.5
$LD_{99/60}$	4.5–5.5

10.2.1 Classification of Genetic Effects

► *Table 27* reports estimates of the natural incidence of human hereditary or partially hereditary traits causing serious handicap at some time during life. Inheritance of a deleterious trait results from mutation(s) in one or both maternal and paternal lines of germ cells. Here a mutation is either a microscopically visible chromosome abnormality or a submicroscopic disruption in the DNA making up the individual genes within the chromosomes. Mutations take place in both germ cells and somatic cells, but only mutations in germ cells are of concern here.

Regularly inherited traits are those whose inheritance follows Mendelian laws. These are autosomal dominant, X-linked, and recessive traits. Examples of autosomal dominant disorders, that is, those which are expressed even when the person is heterozygous for that trait, are certain types of muscular dystrophy, retinoblastoma, Huntington's chorea, and various skeletal malformations. Examples of recessive disorders, that is, those which are expressed only when the individual is homozygous for the trait, include Tay-Sachs disease, phenylketonuria, sickle-cell anemia, and cystic fibrosis. X-linked disorders, that is, those traits identified with genes in the X chromosome of the X-Y pair and which are expressed mostly in males, include hemophilia, color blindness, and one type of muscular dystrophy. In the X-Y chromosome pair, otherwise recessive genetic traits carried by the "stronger" maternal X chromosome are expressed as though the traits were dominant. *Chromosome abnormalities* are of two types:

■ **Table 27**

Genetic risks from continuing exposure to low-LET, low-dose, or chronic radiation as estimated by the BEIR and UNSCEAR committees on the basis of a doubling-dose of 1 Gy

Type of Disorder	Per million progeny		
	Natural frequency	Cases/Gy in first generation	Cases/Gy in second generation ^a
Mendelian autosomal			
Dominant and X-linked	16,500	750–1500	1300–2500
Recessive	7,500	0	0
Chromosomal	4,000	^b	^b
Irregularly inherited traits			
Chronic multifactorial	650,000	250–1200	250–1200
Congenital abnormalities	60,000	2000	2400–3000
Total	738,000	3000–4700	3950–6700
Total risk (% of baseline)		0.41–0.64	0.53–0.91

^aRisk to the second generation includes that to the first except for congenital abnormalities for which it is assumed that between 20% and 50% of the abnormal progeny in the first generation may transmit the damage to the second post-radiation generation, the remainder causing lethality.

^bAssumed to be included with Mendelian diseases and congenital abnormalities.

Source: UN (2001); adopted by NAS (2006) and ICRP (2007)

those involving changes in the numbers of chromosomes and those involving the structure of the chromosomes themselves. Down syndrome is an example of the former. With natural occurrence, numerical abnormalities are more common. By contrast, radiation-induced abnormalities are more frequently structural abnormalities.

There is a very broad category comprising what are variously called *irregularly inherited traits*, multifactorial diseases, or traits of complex etiology. This category includes abnormalities and diseases to which genetic mutations doubtlessly contribute, but which have inheritances much more complex than result from chromosome abnormalities or mutations of single genes. They are exemplified by inherited predispositions for a wide variety of ailments and conditions. One or more other multifactorial disorders, including cancer, are thought to afflict nearly all persons sometime during life; however, the mutational components of these disorders are unknown even as to orders of magnitude (NAS 1990). Also included in [▶ Table 27](#) is a subgroup of irregularly inherited traits identified as *congenital abnormalities*. These are well-identified conditions such as spina bifida and cleft palate, with reasonably well-known degrees of heritability.

10.2.2 Estimates of Hereditary Illness Risks

[▶ Table 27](#) also summarizes the 2001 UNSCEAR genetic risk estimates. The results are for low LET radiation (quality factor $Q = 1$); thus, the absorbed dose and dose equivalent are the same. These estimates are based on a population-averaged *gonad*-absorbed dose of 1 Gy (100 rad) to the reproductive population which produce one-million live-born. Because of the linearity of the dose-effect models used, these estimated hereditary risks are the same whether the gonad dose is received in a single occurrence or over the 30-year reproduction interval. The population for these results is assumed static in number, so that one million born into one generation replace one million in the parental generation.

Data in [▶ Table 27](#) give the expected number of genetic illness cases appearing in the first and second generations, each receiving radiation exposure. Except as indicated, cases in the second generation include the new cases from exposure of the first generation plus cases resulting from exposure of the previous generation, for example, 550–1000 cases of autosomal dominant and X-linked class and no cases of the autosomal recessive class. The ICRP (2007) suggests overall risk coefficients for heritable disease up to the second generation as 0.002 Sv^{-1} for the whole population and 0.001 Sv^{-1} for adult workers.

10.3 Cancer Risks from Radiation Exposures

A large body of evidence leaves no doubt that ionizing radiation, when delivered in high doses, is one of the many causes of cancer in the human. Excess cancer risk cannot be observed at doses less than about 0.2 Gy and, therefore, risks for lower doses cannot be determined directly (UN 1988). At high doses, in almost all body tissues and organs, radiation can produce cancers that are indistinguishable from those occurring naturally. Consequently, radiation-induced cancer can be inferred only from a statistical excess above natural occurrence. [▶ Table 28](#) summarizes natural incidence and mortality for the male and female. ICRP Report 103 (2007) provides comprehensive age and gender dependent incidence and mortality data for Euro-American and Asian populations.

■ **Table 28**

Annual cancer incidence and death rates per 100,000 population in the 2002 United States population

Primary site	Incidence per 10 ⁵ per year		Deaths per 10 ⁵ per year	
	Males	Females	Males	Females
Leukemia	14.6	8.8	10.1	5.7
Lymphoma	25.1	17.9	10.2	6.5
Respiratory	94.7	55.8	76.2	42.2
Digestive	106.9	71.4	59.1	35.9
Breast		124.9		25.5
Genital	167.3	48.9	28.6	16.7
Urinary	56.3	19.1	13.9	5.3
Other	80.6	58.2	41.8	24.9
Total	545.5	405.0	239.9	162.7

Source: HHS (2005)

There is a large variation in the sensitivity of tissues and organs to cancer induction by radiation. For whole-body exposure to radiation, solid tumors are of greater numerical significance than leukemia. The excess risk of leukemia appears within a few years after radiation exposure and largely disappears within 30 years after exposure. By contrast, solid cancers, which occur primarily in the female breast, the thyroid, the lung, and some digestive organs, characteristically have long latent periods, seldom appearing before 10 years after radiation exposure and continuing to appear for 30 years or more. It is also apparent that age at exposure is a major factor in the risk of radiation-induced cancer. Various host or environmental factors influence the incidence of radiation-induced cancer. These may include hormonal influences, immunological status, and exposure to various oncogenic agents.

10.3.1 Estimating Radiogenic Cancer Risks

Our knowledge about radiation-induced cancer is based on epidemiological studies of people who have received large radiation doses. These populations include atomic bomb survivors, radiation therapy patients, and people who have received large occupational doses. Some 91,000 survivors of the atomic weapon attacks on Hiroshima and Nagasaki and their offspring remain under continuing study, and much of our knowledge about radiation-induced cancer derives from this group. Occupational groups include medical and industrial radiologists and technicians, women who ingested large amounts of radium while painting instrument dials during World War I, and miners exposed to high concentrations of radon and its daughter radionuclides. Finally, radiation therapy patients have provided much information on radiation carcinogenesis. These include many treated with X-rays between 1930 and 1950 for severe spinal arthritis, Europeans given ²²⁶Ra injections, and many women given radiation therapy for cervical cancer.

10.4 The Dose and Dose-Rate Effectiveness Factor

Assessment of cancer risks from radiation exposure is concerned primarily with exposures of population groups to low doses at low dose rates. As just indicated, however, there is little choice but to base risk estimates on consequences of exposures at high doses and dose rates. Furthermore, organizations such as the ICRP and the NCRP have endorsed, and government organizations have agreed, to base risk estimates on a linear no-threshold relationship between cancer risk and radiation dose. An exception applies to radiation-induced leukemia, for which a quadratic, no-threshold relationship has been adopted. How does one reconcile low-dose risk estimates based on high-dose data? The answer is addressed in [Fig. 47](#). Symbols display a limited base of data for high doses and dose rates. A central curved line displays what may be the true dose response (say a linear quadratic relationship). The upper straight line, with slope α_H is the linear, no-threshold approximation for the high-dose data. The lower straight line, with slope α_L is tangent to the true response curve in the limit of low dose and low-dose rate, conditions allowing for partial repair of radiation damage. Risks at low doses and dose rates, if computed on the basis of α_H , need to be corrected by division by the ratio α_H/α_L defined as the *DDREF*, the *dose and dose rate correction factor*.

10.4.1 Dose-Response Models for Cancer

Evidence is clear that absorbed doses of ionizing radiation at levels of 1 Gy or greater may lead stochastically to abnormally high cancer incidence in exposed populations. However, there is no direct evidence that chronic exposure to low levels of ionizing radiation may likewise lead to abnormally high cancer incidence. Risk estimates for chronic, low-level exposure requires extrapolation of high-dose and high-dose-rate response data to low doses. Methods used for extrapolation are often controversial, any one method being criticized by some as overpredictive and by others as underpredictive.

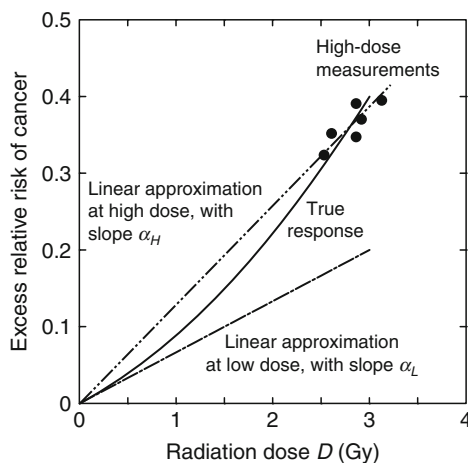


Figure 47
Basis for the dose and dose-rate effectiveness factor

Current risk estimates for cancer have as the basic elements dose responses that are functions of the cancer site or type, the age a_o (y) at exposure, the age a (y) at which the cancer is expressed or the age at death, and the sex s of the subject. The radiogenic cancer risk is expressed as

$$\text{risk} = R_o(s, a) \times EER(D, s, a_o, a). \quad (172)$$

Here, R_o is the natural cancer risk as a function of sex, site, and age at cancer expression, for both incidence and mortality; and EER is the *excess relative risk* function that is determined by fitting a model to observed radiogenic cancer incidence or mortality for cancer at a particular site. For example, the excess relative risk for all solid cancer, except thyroid and nonmelanoma skin cancer, is expressed as (NAS 2006)

$$ERR(D, s, a_o, a) = \beta_s D \exp[e^* \gamma] (a/60)^\eta, \quad (173)$$

in which D is the dose in Sv. In this particular model, the empirical parameter $e^* = (a_o - 30)/10$ for $a_o < 30$ and zero for $a_o \geq 30$. Parameters β_s , γ , and η depend on whether the estimate is for incidence or mortality. For example, for cancer incidence, $\gamma = -0.30$, $\eta = -1.4$, and $\beta_s = 0.33$ for males and 0.57 for females.

To use (172), the natural risk $R_o(s, a)$ for the type of cancer of concern must be known. Data for natural risk are available, but are too extensive to be presented here. They may be found in publications of the Centers for Disease Control (HHS 2005) and on-line at <http://www.cdc.gov/cancer/ncpr/uscs> or <http://seer.cancer.gov/statistics>. For example, US death rates per 100,000 US males, for all races and all cancer sites combined increase from 2.1 for infants to 11.3 at age 30–34, and 520 at age 60–64. For females, the corresponding rates are 1.6, 13.8, and 382, respectively.

It should be emphasized that, in examining these risks of cancer from radiation exposure, one should keep in mind the overall or natural risk of cancer. As indicated in **► Table 28**, two persons per thousand in the United States die each year from cancer. As will be seen in the next section, the overall lifetime risk of cancer mortality is about one in five for males and about one in six for females.

10.4.2 Average Cancer Risks for Exposed Populations

The BEIR-VII Committee of the National Academy of Sciences (NAS 2006) made various estimates of the risk of excess cancer incidence and mortality resulting from low-LET (gamma-ray) exposures. These risks are summarized in **► Table 29** by sex and by age at exposure. Although the data are for conditions of low dose and dose rate, they were generated in large part from cancer incidence and mortality experienced by survivors of atomic weapons at Hiroshima and Nagasaki. At lower doses and dose rates, risks are somewhat less because biological repair mechanisms can repair a greater fraction of the genetic damage produced by the radiation. This effect is accounted for in risk estimates for leukemia, which are based on a linear-quadratic dose–response model. For solid cancers, risks have been modified by application of a dose and dose-rate effectiveness factor, namely, by dividing high-dose and dose-rate data by the DDREF value of 1.5. The ICRP (1991, 2007) continues to recommend a DDREF value of 2.0.

The BEIR-VII Committee also calculated risks to the US population under three low-LET exposure scenarios: (1) single exposure to 0.1 Gy, (2) continuous lifetime exposure to 1 mGy

Table 29

Excess lifetime cancer incidence and mortality for the US population by age at exposure for a whole-body dose of 0.1 Gy (10 rad) from low LET radiation to populations of 10^5 males or females

	Age at exposure (years)								
	0	10	20	30	40	50	60	70	80
Females									
Incidence									
Leukemia	185	86	71	63	62	62	57	51	37
All solid	4592	2525	1575	1002	824	678	529	358	177
Mortality									
Leukemia	53	53	51	51	52	54	55	52	38
All solid	1717	1051	711	491	455	415	354	265	152
Males									
Incidence									
Leukemia	237	120	96	84	84	84	82	73	48
All solid	2326	1325	881	602	564	507	407	270	126
Mortality									
Leukemia	71	71	67	64	67	71	73	69	51
All solid	1028	641	444	317	310	289	246	181	102

Source: based on (NAS 2006)

per year, and (3) exposure to 10 mGy per year from age 18 to age 65. Results are summarized in Table 30. The first scenario is representative of accidental exposure of a large population (the 1999 US population), the second of chronic exposure, and the third of occupational exposure. For example, for leukemia mortality, with 95% confidence limits (not given in Table 30), for a single exposure of the US population to 0.1 Gy, the risk per 100,000 is 70 (20–220) for the male and 50 (10–190) for the female. For nonleukemia mortality per 100,000 fatalities are 410 (200–830) for the male and 610 (300–1200) for the female. For this case, the total low-dose cancer mortality risk for the US population is $0.5 \times (480 + 660) / (0.1 \text{ Gy} \times 10^5) = 0.057$ per Gy, which can be rounded to 0.05 per Gy, or 5×10^{-4} per rem. This risk should be used as an overall cancer risk factor for environmental exposures, that is, small exposures obtained at low dose rates. The ICRP (2007) nominal risk recommendations are 0.055 Sv^{-1} for the whole population and 0.041 Sv^{-1} for adult workers.

10.5 Radiation Protection Standards

It was recognized near the beginning of the twentieth century that standards were needed to protect workers and patients from the harmful consequences of radiation. Many sets of standards, based on different philosophies, have been proposed by several national and international

■ Table 30

Excess cancer incidence and mortality per 100,000 males and 100,000 females in the stationary US population for three low-dose exposure scenarios

Cancer Type	Cases per 10 ⁵		Deaths per 10 ⁵	
	Males	Females	Males	Females
Single Exposure to 0.1 Gy (10 rad):				
Radiation Induced:				
leukemia	100	70	70	50
nonleukemia	800	1300	410	610
total	900	1370	480	660
Natural Expectation:				
leukemia	830	590	710	530
nonleukemia	45500	36900	22100	17500
total	46330	37490	22810	18030
Continuous Lifetime Exposure to 1 mGy (100 mrad) per year:				
Radiation Induced:				
leukemia	67	51	47	38
nonleukemia	554	968	285	459
total	621	1019	332	497
Continuous Exposure to 10 mGy (1 rad) per year from age 18 to 65:				
Radiation Induced:				
leukemia	360	270	290	220
nonleukemia	2699	4025	1410	2169
total	3059	4295	1700	2389

Source: based on (NAS 2006)

standards groups. The earliest standards were based on the concept of *tolerable doses* below which no ill effects would occur. This was replaced in 1948 by the National Council on Radiation Protection and Measurements (NCRP) in the United States which introduced standards based on the idea of *permissible doses*, that is, a dose of ionizing radiation which was not expected to cause appreciable body injury to any person during his or her lifetime.

10.5.1 Risk-Related Dose Limits

Today it is understood that low-level radiation exposure leads to stochastic hazards and that modern radiation standards should be based on probabilistic assessments of radiation hazards.

This new line of thinking is exemplified by a 1972 report to the ICRP by the Task Group on Dose Limits. Key portions of the report are summarized as follows. It must be noted that the report is unpublished and not necessarily reflective of the official ICRP position. The tentative dose limits examined in the report were not based on explicit balancing of risks and benefits, then thought to be an unattainable ideal. Rather, they were based on the practical alternative of identifying acceptable limits of occupational radiation risk in comparison with risks in other occupations generally identified as having a high standard of safety and also having risks of environmental hazards generally accepted by the public in everyday life.

Linear, no-threshold dose-response relationships were assumed for carcinogenic and genetic effects, namely, a 1×10^{-4} probability per rem whole-body dose equivalent for malignant illness or a 4×10^{-5} probability per rem for hereditary illness within the first two generations of descendants (ICRP 1977). For other radiation effects, absolute thresholds were assumed.

To illustrate the reasoning for risk-based limits, consider the occupational whole-body dose-equivalent limit of 5 rem/y. For occupational risks, it was observed that “occupations with a high standard of safety” are those in which the average annual death rate due to occupational hazards is no more than 100 per million workers. An *acceptable risk* was taken as 50 per million workers per year, or a 40-year occupational lifetime risk of 2 fatalities per 1000 workers, that is, 0.002. It was also observed that in most facilities in which radiation may expose workers, the average annual doses are about 10 percent of the doses of the most highly exposed individuals, with the distribution highly skewed toward the lower doses. To ensure an *average* lifetime risk limit of 0.002, an upper limit of 10 times this value was placed on the lifetime risk for any one individual. The annual whole-body dose-equivalent limit for stochastic effects was thus taken as $(10 \times 0.002)/(40 \text{ y} \times 0.01 \text{ malignancies/Sv}) = 0.05 \text{ Sv}$ (5 rem) per year. Similar reasoning is used to set public dose limits and limits for nonstochastic effects (Shultis and Faw 2008).

10.5.2 The 1987 NCRP Exposure Limits

The concept of “risk-based” or “comparable-risk” dose limits provides the rationale for the 1977 ICRP and the 1987 NCRP recommendations for radiation protection, and which serve as the present basis for the US radiation protection standards. A summary of these dose limits is given in [▶ Table 31](#).

Acknowledgments

The authors of this chapter gratefully acknowledge the guidance and support of their colleagues and mentors in the field of radiation shielding and radiation protection. The late Arthur Chilton, our colleague and friend, will be known to readers of this chapter for his breadth of interest and experience in radiation shielding. He was the coauthor of and the inspiration for our first book on radiation shielding. Of the many who taught us, we particularly acknowledge Lewis Spencer, Martin Berger, Herbert Goldstein, and Norman Schaeffer. We acknowledge the American Nuclear Society too for their continuing publication of our textbooks on radiation shielding and radiological assessment, from which much of the material in this chapter has been taken.

■ **Table 31**
The 1987 NCRP recommendations for exposure limits

Type of Dose	mSv	rem
<i>Occupational exposures (annual):</i>		
1. Limit for stochastic effects	50	5
2. Limit for nonstochastic effects:		
a. Lens of the eye	150	15
b. All other organs	500	50
3. Guidance: cumulative exposure age (y) ×	10	1
<i>Public exposures (annual):</i>		
1. Continuous or frequency exposure	1	0.1
2. Infrequent exposure	5	0.5
3. Remedial action levels	5	0.5
4. Lens of the eyes, skin and extremities	50	5
<i>Embryo–fetus exposure:</i>		
1. Effective-dose equivalent	5	0.5
2. Dose-equivalent limit in a month	0.5	0.05
<i>Negligible individual risk level (annual):</i>		
1. Effective-dose equivalent per source or practice	0.01	0.001

Source: NCRP (1987)

References

- Albert RD, Welton TA (1950) A simplified theory of neutron attenuation and its application to reactor shield design. USAEC Report WAPD-15 (Del.), Westinghouse Electric Corporation, Atomic Power Division, Pittsburgh, PA
- Alsmiller RG Jr, Mynatt RR, Barish J, Engle WW Jr (1969) Shielding against neutrons in the energy range 50 to 400 MeV. Nucl Instrum Methods 72:213
- Anno GH, Baum SJ, Withers HR, Young RW (1989) Symptomatology of acute radiation effects in humans after exposure to doses of 0.5–30 Gy. Health Phys 56:821–838
- ANSI/ANS-6.1.1-1977, American National Standard (1977) Neutron and gamma-ray flux-to-dose-rate factors. American Nuclear Society, La Grange Park, IL
- ANSI/ANS-6.6.1-1987, American National Standard (1987) Calculation and measurement of direct and scattered gamma radiation from LWR nuclear power plants. American Nuclear Society, La Grange Park, IL
- ANSI/ANS-6.4.3-1991, American National Standard (1991) Gamma ray attenuation coefficients and buildup factors for engineering materials. American Nuclear Society, La Grange Park, IL (Available as Data Library Collection DLC-129/ANS-643 from the Radiation Shielding Information Center, Oak Ridge National Laboratory, Oak Ridge, TN)
- ANSI/ANS-5.1-2005, American National Standard (2005) Decay heat power in light water reactors. American Nuclear Society, La Grange Park, IL
- ANSI/ANS-6.4-2006, American National Standard (2006) Nuclear analysis and design of concrete

- radiation shielding for nuclear power plants. American Nuclear Society, La Grange Park, IL
- ANSI/ANS-6.4.2-2006 (2006) Specification for radiation shielding materials. American Nuclear Society, La Grange Park, IL
- Archer BR, Fewell TR, Conway BJ, Quinn PW (1994) Attenuation properties of diagnostic X-ray shielding materials. *Med Phys* 21:1499–1507
- Archer BR, Thornby JL, Bushong SC (1983) Diagnostic X-ray shielding design based on an empirical model of photon attenuation. *Health Phys* 44:507–517
- Artigas R, Hungerford HE (1969) A numerical treatment of the attenuation of neutrons by air ducts in shields. *Nucl Sci Eng* 36:295
- Avery AF, Bendall DE, Butler J, Spinney KT (1960) Methods of calculation for use in the design of shields for power reactors. Report AERE-R 3216, Atomic Energy Research Establishment, Oxfordshire, England
- Baran A, Grun M (1990) ALBEDO/ALBEZ: PC-programs for the calculation of the attenuation of radiation in single and double bends. NUKEM GmbH informal document (RSIC Code Collection CCC-555), Alzenau, Germany
- Bendall DE (1962) RASH D-A mercury programme for neutron shielding calculations. Report AEEW-M 261, Atomic Energy Weapons Establishment, Winfrith, Dorset, England
- Blizard EP (1962) Shield optimization with respect to weight. In: Blizard EP (ed) *Reactor handbook*, Part B: shielding, 2nd edn, vol III. Interscience, New York
- Blizard EP, Abbott LS (eds) (1962) *Reactor handbook*, Part B: shielding, 2nd edn, vol III. Interscience, New York
- Blizard EP, Foderaro A, Goussev NG, Kovaiev EE (1968) Extended radiation sources (point kernel integrations). In: Jaeger RG (ed) *Engineering compendium on radiation shielding*, chap 6, vol I. Springer, New York
- Brockhoff RC, Shultis JK (2007) A new approximation for the neutron Albedo. *Nucl Sci Eng* 155:1–17
- Brockhoff RC, Shultis JK, Faw RE (1996) Skyshine line-beam response functions for 20- to 100-MeV photons. *Nucl Sci Eng* 123:282–288
- Broder DL, Kayurin Yu P, Kutrezov AA (1962) An iterative method for calculating gamma-ray buildup factors in multi-layer shields. *Sov J At Energy* 12:26–31
- Broder DL, Tsypin SG (1968) Attenuation in non-hydrogenous media. In: Jaeger RG (ed) *Engineering compendium on radiation shielding*, vol I. Springer, New York, p 322
- Brynjolfsson A (1975) Water. In: Jaeger RG (ed) *Engineering compendium on radiation shielding*, vol II. Springer, New York, p 288
- Bünemann D, Richter G (1968) Multilayered shields. In: Jaeger RG (ed) *Engineering compendium on radiation shielding*, vol I. Springer, New York, p 230
- Burrus WR (1968a) Random voids and lumps. In: Jaeger RG (ed) *Engineering compendium on radiation shielding*, vol I. Springer, New York, p 490
- Burrus WR (1968b) Regular geometric void shapes. In: Jaeger RG (ed) *Engineering compendium on radiation shielding*, vol I. Springer, New York, p 495
- Casper AW (1960) Modified fast neutron attenuation functions. USAEC Report XDC-60-276, General Electric Corporation, Atomic Products Division, Cincinnati, OH
- Chapman GT, Storrs CL (1955) Effective neutron removal cross sections for shielding. USAEC Report ORNL-1843 (AEC-D-3978), Oak Ridge National Laboratory, Oak Ridge, TN
- Chapman JM (1962) Computer calculation of dose rates in two-legged ducts using the Albedo concept. USAEC file number NP-13652 (TR-264), Naval Civil Engineering Laboratory, Port Hueneme, CA
- Chen MF, Faw RE (1994) Build-up factors for gamma rays obliquely incident on slab shields of concrete, iron and lead. *Radiat Protect Dosimetry* 51:27–33
- Chilton AB (1967) A modified formula for differential exposure Albedo for gamma rays reflected from concrete. *Nucl Sci Eng* 27:481–482
- Chilton AB (1971) Effect of material composition on neutron penetration of concrete slabs. Report 10425, National Bureau of Standards, Washington, DC
- Chilton AB (1977) Optimized Taylor parameters for concrete buildup factor data. *Nucl Sci Eng* 64:799–800
- Chilton AB (1979) Tschebycheff-fitted Berger coefficients for Eisenhauer-Simmons gamma-ray buildup factors in ordinary concrete. *Nucl Sci Eng* 69:436–438
- Chilton AB, Davisson CM, Beach LA (1965) Parameters for C-H Albedo formula for Gamma rays reflected from water, concrete, iron, and lead. *Trans Amer Nucl Soc* 8:656
- Chilton AB, Eisenhauer CM, Simmons GL (1980) Photon point source buildup factors for air, water, and iron. *Nucl Sci Eng* 73:97–107
- Chilton AB, Huddleston CM (1963) A semi-empirical formula for differential dose Albedo for gamma rays on concrete. *Nucl Sci Eng* 17:419

- Chilton AB, Shultis JK, Faw RE (1984) Principles of radiation shielding. Prentice Hall, Englewood Cliffs, NJ
- Claiborne HC, Schaeffer NM (1973) Shield design. In: Schaeffer NM (ed) Reactor shielding for nuclear engineers, USAEC, TID-25951. (Available from NTIS, U.S. Department of Commerce, Springfield, VA)
- Courtney JC (ed) (1975) A handbook of radiation shielding data. A Publication of the Shielding and Dosimetry Division of the American Nuclear Society, La Grange Park, IL
- Cristy M, Eckerman KF (1987) Specific absorbed fractions of energy at various ages from internal photon sources. Report ORNL/TM-8381 (6 vols), Oak Ridge National Laboratory, Oak Ridge, TN
- Dillman LT (1980) EDISTR – A computer program to obtain a nuclear data base for nuclear dosimetry. Report ORNL/TM-6689, Oak Ridge National Laboratory, Oak Ridge, TN
- Dunn WL, Yacout AM, O’Foghluda F, Riel G (1992) Gamma-Ray and neutron dose-equivalent buildup factors for infinite slabs. Nucl Sci Eng 110:134–156
- Dunn WW (1957) Transmission of fast neutrons through aluminum, iron and lead. Dissertation, Air Force Institute of Technology (Armed Services Technical Information Agency 124760)
- Eckerman KF, Westfall RJ, Ryman JC, Cristy M (1994) Availability of nuclear decay data in electronic form, including beta spectra not previously published. Health Phys 67:338–345. (Available as DLC-172, NUCDECAY Data Library, Radiation Shielding Information Center, Oak Ridge National Laboratory, Oak Ridge, TN)
- Eisenhauer CM, Simmons GL (1975) Point isotropic buildup factors in concrete. Nucl Sci Eng 46:263–270
- EPA (1986) A citizen’s guide to radon. Report OPA-86-004 of the U.S. Environmental Protection Agency and the Centers for Disease Control of the U.S. Department of Health and Human Services, U.S. Government Printing Office
- Evans RD (1955) The atomic nucleus. McGraw-Hill, New York
- Fano U, Spencer LV, Berger MJ (1959) Penetration and diffusion of X rays. In: Flügge S (ed) Handbuch der physik, vol 38/2. Springer, Berlin
- Faw RE, Shultis JK (1993a) Absorbed dose buildup factors in air for 10- to 100-MeV photons. Nucl Sci Eng 114:76–80
- Faw RE, Shultis JK (1993b) Radiological assessment. Prentice Hall, Englewood Cliffs, NJ
- Fewell TR, Shuping RE (1978) Handbook of mammographic X-ray spectra. HEW Publication (FDA) 79-8071, U.S. Department of Health, Education, and Welfare, Rockville, MD
- Fewell TR, Shuping RE, Hawkins KR Jr (1981) Handbook of computed tomography X-ray spectra. HHS Publication (FDA) 81-8162, U.S. Department of Health and Human Services, Rockville, MD
- Firestone RB et al (1996) Table of isotopes, 8th edn, the book and CD-ROM. Wiley, New York
- Foderaro A, Hall RJ (1981) Application of three-exponential representation of photon buildup factors to water. Nucl Sci Eng 78. (Data are also tabulated in Chilton, Shultis, and Faw (1984))
- Fournie EM, Chilton AB (1981) Gamma-ray buildup factors for concrete slab shields under slant incidence conditions. Nucl Sci Eng 77: 66–69
- Fröhner FH (1990) Evaluation of ^{252}Cf prompt fission neutron data from 0 to 20 MeV by Watt spectrum fit. Nucl Sci Eng 106:345–352
- Geiger KW, Van der Zwan L (1975) Radioactive neutron source spectra from $^{11}\text{B}(\alpha, n)$ cross section data. Nucl Instrum Methods 131:315
- George DC et al (1980) Delayed photon sources for shielding applications. Trans Am Nucl Soc 35:463
- Glasstone S, Sesonske A (1963) Nuclear reactor engineering. Van Nostrand, Princeton, NJ
- Goldstein H (1959) Fundamental aspects of reactor shielding. Addison-Wesley, Reading, MA (Reprinted by Johnson Reprint Corporation, New York, 1971)
- Goldstein H, Aronson R (1954) Effective removal cross sections – theory. React Sci Technol 4:149 (USAEC Report TID-2015)
- Goldstein H, Wilkins JE Jr (1954) Calculations of the penetrations of gamma rays, NDA/AEC Report NYO-3075, U.S. Government Printing Office, Washington, DC
- Gopinath DV, Subbaiah KV, Trubey DK (1987) Gamma-ray transport in a shield-tissue composite system and the buildup factor implications. Nucl Sci Eng 97:362–373
- GPO (1970) Radiological health handbook. U.S. Government Printing Office, Washington, DC
- Gronroos H (1968) Energy dependent removal cross-sections in fast neutron shielding theory. In: Jaeger RG (ed) Engineering compendium on radiation shielding, vol I. Springer, New York, p 305
- Grotenhuis M (1962) Lecture notes on reactor shielding. Report ANL-6000, Argonne National Laboratory, Argonne, IL
- Grove (1987) Engineering, MicroSkyshine user’s manual. Grove Engineering, Rockville, MD

- Gui AA, Shultis JK, Faw RE (1997a) Response functions for neutron skyshine analyses. *Nucl Sci Eng* 125:111–127
- Gui AA, Shultis JK, Faw RE (1997b) Neutron skyshine calculations with the integral line-beam method. *Nucl Sci Eng* 127:230–237
- Harima Y (1983) An approximation of gamma-ray buildup factors for two-layer shields. *Nucl Sci Eng* 85:45–79
- Harima Y (1986) An approximation of gamma-ray buildup factors by modified geometric progression. *Nucl Sci Eng* 83:299–309
- Harima Y, Hirayama H (1993) Detailed behavior of exposure buildup factor in stratified shields for plane-normal and point isotropic sources, including the effects of Bremsstrahlung and fluorescent radiation. *Nucl Sci Eng* 113: 367–378
- Harima Y, Sakamoto Y, Tanaka S, Kawai M (1986) Validity of the geometric progression gamma-ray buildup factors. *Nucl Sci Eng* 94:24–35
- Harima Y, Tanaka S, Sakamoto Y, Hirayama H (1991) Development of new gamma-ray buildup factors and applications to shielding calculations. *J Nucl Sci Technol* 28:74–78
- Hermann OW, Westfall RM (1995) ORIGEN-S: SCALE system module to calculate fuel depletion, actinide transmutation, fission product buildup and decay, and associated radiation source terms, Sec F7 of SCALE: a modular code system for performing standardized computer analyses for licensing evaluation, Report NUREG/CR-0200, Revision 5(draft), vol 2, Oak Ridge National Laboratory, Oak Ridge, TN. Reference data libraries are from J.C. Ryman, ORIGEN-S Data Libraries, Sec M6 of SCALE: a modular code system for performing standardized computer analyses for licensing evaluation, Report NUREG/CR-0200, Oak Ridge National Laboratory, Oak Ridge, TN, vol 3, Revision 5 (draft) 1995
- Hertel NE, Sweezy JE, Shultis JK, Warkentin JK, Rose ZJ (2005) A comparison of skyshine computational methods. *Radiat Protect Dosimetry* 116:525–533
- HHS (2005) U.S. Cancer Statistics, 2002 incidence and mortality, U.S. Cancer Statistics Working Group, U.S. Department of Health and Human Services, Center for Disease Control and Prevention and National Cancer Institute
- Hirayama H (1987) Exposure buildup factors of high-energy gamma rays for water, concrete, iron, and lead. *Nucl Technol* 77:60–67
- Hjärne L (1964) A user's manual for the N.R.N. shield design method, Report AE-145, AB Atomenergi, Stockholm
- Hubbell JH, Seltzer SM (2004) Tables of X-ray mass attenuation coefficients and mass energy-absorption coefficients, (version 1.4). Available online: <http://physics.nist.gov/xaamdi>, National Institute of Standards and Technology, Gaithersburg, MD. Accessed 2 Nov 2009
- Hungerford HE (1966) Shielding. In: Yevick JG, Amorosi A (eds) *Fast reactor technology: plant design*. MIT Press, Cambridge, MA
- Hungerford HE (1968) Problems in design of fast reactor shields. *Trans Amer Nucl Soc* 11:702
- ICRP (1977) Recommendations of the international commission on radiological protection. *Annals of the ICRP, Publication 26*, International commission on radiological protection, vol 1, no 3. Pergamon Press, Oxford
- ICRP (1984) Nonstochastic effects of ionizing radiation, Publication 41, International commission on radiological protection. Pergamon Press, Oxford
- ICRP (1987) Data for use in protection against external radiation. *Annals of the ICRP, Publication 51*, International commission on radiological protection, vol 17, no 2/3. Pergamon Press, Oxford
- ICRP (1991) 1990 recommendations of the international commission on radiological protection, *Annals of the ICRP, Publication 60*, International commission on radiological protection, vol 21, no 1–3. Pergamon Press, Oxford
- ICRP (1996) Coefficients for use in radiological protection. *Annals of the ICRP, Publication 74*, International commission on radiological protection, vol 26, no 3–4
- ICRP (2007) Recommendations of the ICRP, *Annals of the ICRP, Publication 103*, International commission on radiological protection, vol 37, no 2–4
- ICRU (1971) Radiation quantities and units. Report 19, International commission on radiation units and measurements, Washington, DC
- ICRU (1979) Average energy required to produce an ion pair. Report 31, International commission on radiation units and measurements, Washington DC
- ICRU (1988) Determination of dose equivalents from external radiation sources – Part 2. Report 43, International commission on radiation units and measurements, Bethesda, MD
- ICRU (1992) Phantoms and computational models in therapy, diagnosis and protection. Report 48, International commission on radiation units and measurements, Bethesda, MD
- Jaeger RG (ed) (1968) *Engineering compendium on radiation shielding. Shielding fundamentals and methods*, vol I. Springer, New York

- Jaeger RG et al (eds) (1970) Engineering compendium on radiation shielding. Shield design and engineering, vol III. Springer, New York
- Jaeger RG et al (eds) (1975) Engineering compendium on radiation shielding. Shielding materials, vol II. Springer, New York
- Keepin GR (1965) Physics of nuclear kinetics. Addison-Wesley, Reading, MA
- Keriakes JG, Rosenstein M (1980) Handbook of radiation doses in nuclear medicine and diagnostic X ray. CRC Press, Boca Raton, FL
- Kitazume M (1965) Some considerations of buildup factors in γ ray penetration for multiple layers. Nippon Genshiryoku Gakkaishi 7:496
- Knoll GF (1989) Radiation detection and measurement, 2nd edn. Wiley, New York
- Kocher DC (1981) Radioactive decay data tables. DOE/TIC-11026, Technical Information Center, U.S. Department of Energy, Washington, DC
- Kramer R, Zankl M, Williams G, Drexler G (1982) The calculation of dose from external photon exposures using reference human phantoms and Monte Carlo methods, Part I: the male (Adam) and female (Eva) adult mathematical phantoms. Report GSF-Bericht S-885, Gesellschaft für Umweltforschung, Munich (Reprinted 1986)
- LaBaume RJ, England TR, George DC, Maynard CW (1982) Fission product analytic impulse source functions. Nucl Technol 56:322-339
- Lamarsh JR (1966) Introduction to nuclear reactor theory. Addison-Wesley, Reading, MA
- Lampley CM, Andrews MC, Wells MB (1988) The SKYSHINE-III procedure: calculation of the effects of structure design on neutron, primary gamma-ray and secondary gamma-ray dose rates in air. RRA T8209A (RSIC Code Collection CCC-289), Radiation Research Associates, Fort Worth, TX
- Langham WH (ed) (1967) Radiobiological factors in manned space flight. Report of the Space Radiation Study Panel, National Academy of Sciences, National Research Council, Washington, DC
- LeDoux JC, Chilton AB (1959) Gamma-ray streaming through two-legged rectangular ducts. Nucl Sci Eng 11:362-368
- Légaré JM, Carrieres PE, Manseau A, Bibeau C, Robert J, Robidoux N (1977) Blindage contre les grands champs de rayons X primaires et diffusés des appareils triphasés au moyen de panneaux de verre, de gypse et de plomb acoustique. Radio-protection 13:79-95
- Leimdorfer M (1968) The backscattering of photons. In: Jaeger RG (ed) Engineering compendium on radiation shielding, vol I. Springer, New York
- Maerker RE, Muckenthaler FJ (1965) Calculation and measurement of the fast-neutron differential dose Albedo for concrete. Nucl Sci Eng 22:455
- Mooney LG, Schaeffer NM (1973) Shield heating, air transport shield materials, and shield optimization. In: Schaeffer NM (ed) Reactor shielding for nuclear engineers, USAEC, TID-25951. Available from NTIS, U.S. Department of Commerce, Springfield, VA
- NAS, National Research Council, Advisory Committee on the Biological Effects of Ionizing Radiations (1990) Health effects of exposure to low levels of ionizing radiation. National Academy of Sciences, Washington, DC. (The BEIR-V Report)
- NCRP (1971a) Basic radiation protection criteria. NCRP Report 39, National Council on Radiation Protection and Measurements, Washington, DC
- NCRP (1971b) Protection against neutron radiation, Recommendations of the National Council on Radiation Protection and Measurements. Report 38, National Council on Radiation Protection and Measurements, Washington, DC
- NCRP (1976) Structural shielding design and evaluation for medical use of X rays and gamma rays of energies up to 10 MeV. Report 49, National Council on Radiation Protection and Measurements, Washington, DC
- NCRP (1977) Radiation protection design guidelines for 0.1-100 MeV Particle accelerator facilities. NCRP Report 51, National Council on Radiation Protection and Measurements, Washington, DC
- NCRP (1984) Neutron contamination from medical accelerators. Report 79, National Council on Radiation Protection and Measurements, Bethesda, MD
- NCRP (1987) Radiation exposure of the U.S. population from consumer products and miscellaneous sources. Report 95, National Council on Radiation Protection and Measurements, Washington, DC
- NCRP (1989) Medical X-ray, electron beam, and gamma-ray Protection for energies up to 50 MeV. Report 102, National Council on Radiation Protection and Measurements, Bethesda, MD
- NCRP (1993) Recommendations on limits for exposure to ionizing radiation. Report 116, National Council on Radiation Protection and Measurements, Bethesda, MD
- NCRP (2004) Structural shielding design for medical X-ray imaging facilities. Report 147, National Council on Radiation Protection and Measurements, Bethesda, MD (Rev 2005)

- Peele RW, Maienschein FC (1970) The absolute spectrum of photons emitted in coincidence with thermal-neutron fission of Uranium-235. ORNL-4457, Oak Ridge National Laboratory, Oak Ridge, TN
- Peterson EG (1962) MAC – a bulk shielding code. USAEC Report HW-73381, Hanford Atomic Products Operation, Hanford, WA
- Pochin E (1983) Nuclear radiation risks and benefits. Clarendon Press, Oxford
- Reilly D, Ensslin N, Smith H Jr, Kreiner S (1991) Passive nondestructive assay of nuclear materials. NUREG/CR-5550, U.S. Nuclear Regulatory Commission, Washington, DC
- Rockwell T, III (ed) (1956) Reactor shielding design manual. D Van Nostrand, Princeton, NJ
- Roussin RW, Alsmiller RG Jr, Barish J (1973) Calculations of the transport of neutrons and secondary gamma-rays through concrete for incident neutrons in the energy range 15 to 75 MeV. Nucl Eng Des 24:2
- Roussin RW, Schmidt FAR (1971) Adjoint Sn calculations of coupled neutron and gamma-ray transport calculations through concrete slabs. Nucl Eng Des 15:319
- Roussin RW, Weisbin CR, White JE, Green NM, Wright RQ, Wright JB (1980) VITAMIN-C: the CRT processed multigroup cross section library for neutronics studies. Report ORNL/RSIC-37 (ENDF-296), Radiation Shielding Information Center, Oak Ridge National Laboratory, Oak Ridge, TN
- RSIC (1991) ORIGEN 2.1: isotope generation and depletion code matrix exponential method. Code Package CCC-371, Radiation Shielding Information Center, Oak Ridge National Laboratory, Oak Ridge, TN
- Schaeffer NM (ed) (1973) Reactor shielding for nuclear engineers. USAEC, TID-25951. Available from NTIS, U.S. Department of Commerce, Springfield, VA
- Scott BR, Hahn FF (1989) Early occurring and continuing effects. In: Health effects models for nuclear power plant accident consequence analysis – low LET radiation, Part II: scientific bases for health effects models. Report NUREG/CR-4214, Rev. 1, Part II, U.S. Nuclear Regulatory Commission
- Selph WE (1973) Albedos, ducts and voids. In: Schaeffer NM (ed) Reactor shielding for nuclear engineers, TID 25951, Chap 7. National Technical Information Service, U.S. Department of Commerce, Springfield, VA
- Shin K, Hirayama H (1994) A new approximating model for gamma-ray buildup factors of stratified shields. Nucl Sci Eng 118:91–102
- Shin K, Hirayama H (1995) Approximating model for multilayer gamma-ray buildup factors by transmission matrix method: application to point isotropic source geometry. Nucl Sci Eng 120:211–222
- Shue S (1994) Calculating specific absorbed fractions using finite-medium buildup factors. M.S. Thesis, Nuclear Engineering Department, Kansas State University, Manhattan, KS
- Shue SL, Faw RE, Shultis JK (1998) Thermal-neutron intensities in soils irradiated by fast neutrons from point sources. Chem Geol 144:47–61
- Shultis JK (2000) Hybrid Skyshine calculations for complex neutron and gamma-ray sources. Nucl Sci Eng 136:294–304
- Shultis JK, Faw RE (1987) Improved line-beam response functions for the MicroSkyshine method. Report 189, Engineering Experiment Station, Kansas State University, Manhattan, KS
- Shultis JK, Faw RE (1994) Extensions to the integral line-beam method for gamma-ray Skyshine analyses, SAND94-2019, Sandia National Laboratory, Albuquerque, NM
- Shultis JK, Faw RE (2000) Radiation shielding. American Nuclear Society, La Grange Park, IL
- Shultis JK, Faw RE (2008) Fundamentals of nuclear science and engineering, 2nd edn. CRC Press, Boca Raton, FL
- Shultis JK, Faw RE, Bassett MS (1991) The integral line-beam method for gamma Skyshine analyses. Nucl Sci Eng 107:228–245
- Shure KJ, O'Brien KA, Rothberg DM (1969) Neutron dose rate attenuation by iron and lead. Nucl Sci Eng 35:371
- Shure K, Wallace OJ (1988) Taylor parameters for gamma-ray buildup factors in the proposed American National Standard. Report WAPD-TM-1628, Bettis Atomic Power Laboratory, West Mifflin, PA. (See data tabulation in ANSI/ANS (1991))
- Simmons GL, Albert TE, Gritzner ML (1979) The SAI/EPRI Albedo information library. Report SAI-013-79-525-LJ (RSIC Code Collection DLC-57), Science Applications, La Jolla, CA
- Simon A, Clifford CE (1956) The attenuation of neutrons by air ducts in shields. Nucl Sci Eng 1:156–166
- Simpkin DJ (1987a) A general solution to the shielding of medical X and γ rays by the NCRP Report 49 methods. Health Phys 52:431–436
- Simpkin DJ (1987b) Shielding requirements for mammography. Health Phys 53:267–279
- Simpkin DJ (1989) Shielding requirements for constant potential diagnostic X-ray beams determined by a Monte Carlo calculation. Health Phys 56:151–154

- Simpkin DJ (1990) Transmission of scatter radiation from computed tomography (ct) scanners determined by a Monte carlo calculation. *Health Phys* 58:363–367
- Simpkin DJ (1995) Transmission data for shielding diagnostic X-ray facilities. *Health Phys* 68:704–709
- Song YT (1965) Fast neutron streaming through two-legged concrete ducts. Report AD-457746 (TR-354), Naval Civil Engineering Laboratory, Port Hueneme, CA
- Spencer LV (1962) Structure shielding against fallout radiation from nuclear weapons. NBS Monograph 42, National Bureau of Standards, Washington, DC
- Stedry MH, Shultis JK, Faw RE (1996) Effect of an overhead shield on gamma-ray Skyshine. *Nucl Sci Eng* 123:289–294
- Stevens PA, Trubey DK (1968) Methods for calculating neutron and gamma ray attenuation. In: Weapons radiation shielding handbook, chap 3. USAEC Report DASA-1892-3, Oak Ridge National Laboratory, Oak Ridge, TN
- Su M, Jiang S (1989) Gamma-ray buildup factors for a point isotropic source in stratified spherical shields. *Nucl Sci Eng* 102:64–73
- Subbaiah KV, Natarajan A (1987) Effect of fluorescence in deep penetration of gamma rays. *Nucl Sci Eng* 96:330–342
- Subbaiah KV, Natarajan A, Gopinath DV, Trubey DK (1982) Effect of fluorescence, Bremsstrahlung, and annihilation radiation on the spectra and energy deposition of gamma rays in bulk media. *Nucl Sci Eng* 81:172–195
- Swanson WP (1979) Radiological safety aspects of the operation of electron linear accelerators. Report 188, International Atomic Energy Agency, Vienna
- Takeuchi K, Tanaka S (1984) Buildup factors of gamma rays including Bremsstrahlung and annihilation radiation for water, concrete, iron, and lead. *Nucl Sci Eng* 87:478–489
- Takeuchi K, Tanaka S, Kinno M (1981) Transport calculations of gamma rays, including Bremsstrahlung by the discrete ordinates code PALLAS. *Nucl Sci Eng* 78:272–283
- Tanaka M, Takeuchi K (1986) Detailed investigation of the buildup factors and spectra for point isotropic gamma-ray sources in the vicinity of the k-edge in lead. *Nucl Sci Eng* 93:376–385
- Taylor JJ (1951) Report WAPD-23, Westinghouse Corporation, Pittsburgh, PA. (See Rockwell (1956) for a summary of this technique)
- Tsypin SG, Kukhtevich VI (1968) Removal theory. In: Jaeger RG (ed) Engineering compendium on radiation shielding, vol I. Springer, New York
- UN (1988) Sources, effects and risks of ionizing radiation. United Nations Scientific Committee on the Effects of Atomic Radiation, New York
- UN (2001) Hereditary effects of radiation. United Nations Scientific Committee on the Effects of Atomic Radiation, New York
- Upton AC, Kimball RF (1967) Radiation biology. In: Morgan KZ, Turner JE (eds) Principles of radiation protection. Wiley, New York
- USNRC (1991) Standards for protection against radiation, Title 10, Code of Federal Regulations, Part 20, 56FR23360. U.S. Nuclear Regulatory Commission, Washington, DC
- Vogel F, Motulsky AG (1979) Human genetics. Springer, Berlin
- Wald N (1967) Evaluation of human exposure data. In: Morgan KZ, Turner JE (eds) Principles of radiation protection, Wiley, New York
- Walsh RL (1989) Spin-dependent calculation of fission neutron spectra and fission spectrum integrals for six fissioning systems. *Nucl Sci Eng* 102:119–133
- Wang X, Faw RE (1995) Transmission of neutrons and secondary gamma rays through concrete slabs. *Radiat Protect Dosimetry* 60:213–222
- Weber DA, Eckerman KF, Dillman LT, Ryman JC (1989) MIRD: radionuclide data and decay schemes. Society of Nuclear Medicine, New York
- Weise H-P (1994) Neutron leakage from the entrance maze of medical electron accelerators. In: Proceedings of the 8th international conference on radiation shielding, American Nuclear Society, La Grange Park, IL, p 934
- Wyard SJ (1952) Intensity distribution of Bremsstrahlung from beta rays. *Proc Phys Soc London* A65:377
- Wyckoff JM, Chilton AB (1973) Dose due to practical neutron energy distributions incident on concrete shielding slabs. In: Proceedings of the 3rd international congress IRPA, Washington, DC, p 694
- Zoller LK (1964) Fast-neutron removal cross sections. *Nucleonics* 22:128

12 High Performance Computing in Nuclear Engineering

Christophe Calvin¹ · David Nowak²

¹CEA/DEN/DANS/DM2S CEA Saclay, Gif-sur-Yvette, France
christophe.calvin@cea.fr

²Mathematics and Computer Science Division Argonne
National Laboratory, Argonne, IL, USA
nowak@mcs.anl.gov

1	<i>Introduction</i>	1452
2	<i>Main Computer and Processor Architectures</i>	1452
2.1	Main Architecture Classes for High Performance Computing	1452
2.2	SIMD Architectures	1454
2.3	MIMD Architectures	1455
2.4	Dataflow and Systolic Architectures: Specialized Architectures Versus Generic Ones	1456
2.5	Vector Architectures	1456
3	<i>Parallelism Models</i>	1458
3.1	Overview	1458
3.2	Shared Memory Model	1459
3.3	Threads Model	1459
3.4	Message Passing Model	1461
3.5	Data Parallel Model	1462
3.6	Other Models	1463
3.6.1	Hybrid	1463
3.6.2	Single Program Multiple Data (SPMD)	1463
3.6.3	Multiple Program Multiple Data (MPMD)	1463
3.7	The Different Levels of Parallelism	1464
3.7.1	First Level: Distributed Computing	1464
3.7.2	Second Level: Coarse Grain Parallel Computing	1464
3.7.3	Third Level: Fine Grain Parallel Computing	1465
4	<i>Designing Parallel Programs</i>	1466
4.1	Automatic Versus Manual Parallelization	1466
4.2	Understand the Problem and the Program	1467
4.3	Partitioning	1468

4.3.1	Domain Decomposition	1468
4.3.2	Functional Decomposition	1468
4.4	Communications	1470
4.4.1	Who Needs Communications?	1470
4.4.2	Factors to Consider	1471
4.5	Synchronization	1473
4.5.1	Types of Synchronization	1473
4.6	Data Dependencies	1474
4.6.1	Definition	1474
4.6.2	Examples	1474
4.6.3	How to Handle Data Dependencies	1475
4.7	Load Balancing	1475
4.7.1	How to Achieve Load Balance	1475
4.8	Granularity	1476
4.8.1	Computation/Communication Ratio	1476
4.8.2	Fine Grain Parallelism	1476
4.9	Limits and Costs of Parallel Programming	1476
4.9.1	Amdahl's Law	1476
4.9.2	Complexity	1477
4.9.3	Portability	1477
4.9.4	Resource Requirements	1478
4.9.5	Scalability	1478
5	<i>Use of HPC for Nuclear Energy Application: Overview</i>	1478
5.1	The Virtual Power Plant Challenge	1479
5.1.1	Description	1479
5.1.2	Motivation	1479
5.1.3	Main Challenges	1479
5.2	Other Examples and Use	1482
6	<i>Illustration of HPC Use on Different Applications</i>	1483
6.1	HPC for Reactor Core Simulation	1483
6.1.1	Introduction	1483
6.1.2	Major Challenges	1483
6.1.3	HPC in Monte Carlo Simulations	1484
6.1.4	HPC in Deterministic Simulations	1488
6.2	HPC for CFD and DNS	1491
6.2.1	Main Industrial Issues	1491
6.2.2	The Multi-Scale Approach	1493
6.2.3	HPC for DNS	1494
6.2.4	HPC for LES	1496
6.2.5	Other Fields	1497
6.3	High Performance Computing for Materials Science	1499
6.3.1	Introduction	1499
6.3.2	Theoretical and Computational Methods	1500
6.3.3	Models and Simulations of Nuclear Fuels and Structural Materials	1504
6.3.4	Fuel Performance Codes	1508

6.3.5	Conclusions	1512
7	<i>Conclusion and Open Issues</i>	<i>1513</i>
	<i>References</i>	<i>1514</i>

Abstract: The aim of this chapter is to give some key points on the use of high performance computing (HPC) in the field of nuclear engineering.

This chapter is divided into two main parts. This first one is an introduction to parallel computing. In this first part, we will describe not only the main computer and processor architectures which are used today but also some which are not so usual but which will allow the readers to better understand the key point of parallelism from the hardware point of view. Still in this first part, we will continue by describing the main parallelism models, in the same point of view as the description of the parallel architecture. In [Sect. 4](#), we will give some basic ideas on how to design parallel programs. This section is the last of the first part.

The second part is dedicated to the use of high performance computing in nuclear engineering. We will give first the main challenges which can be addressed using HPC. Some of them are illustrated in [Sect. 6](#) on some of the main scientific domains in nuclear engineering (reactor physics, material sciences and thermal-hydraulic). For each of them we have tried to describe the main problems which can be addressed using HPC but some of them remain as scientific and industrial challenges.

1 Introduction

The aim of this chapter is to give some key points on the use of high performance computing (HPC) in the field of nuclear engineering.

In this chapter we will give an introduction to high performance computing, by describing the main computer and processor architectures, parallel programming models, and some elements concerning the design of parallel software.

After this short introduction to parallel computing, we will discuss the main challenges concerning HPC in nuclear engineering and give illustrations of them in three main fields, namely, reactor physics, computational fluid dynamics, and material sciences.

2 Main Computer and Processor Architectures

2.1 Main Architecture Classes for High Performance Computing

One of the main ways to classify the different kinds of architectures is the well-known Flynn's classification (Butenhof 1997; Duncan 1990). Flynn's taxonomy (Flynn 1972) is a classification of computer architectures, proposed by Michael J. Flynn in 1966. The four classifications defined by Flynn are based upon the number of concurrent instruction (or control) and data streams available in the architecture ([Table 1](#)). This classification can be summarized as follows:

- Single Instruction, Single Data stream (SISD): A sequential computer which exploits no parallelism in either the instruction or data streams. Examples of SISD architecture are the traditional uni-processor machines like a PC or old mainframes.
- Single Instruction, Multiple Data streams (SIMD): A computer which exploits multiple data streams against a single instruction stream to perform operations which may be naturally parallelized, for example, an array processor or graphical processor unit (GPU).

Table 1
Flynn's classification

		Data flow	
		Simple	Multiple
Instruction flow	Simple	SISD	SIMD
	Multiple	MISD	MIMD

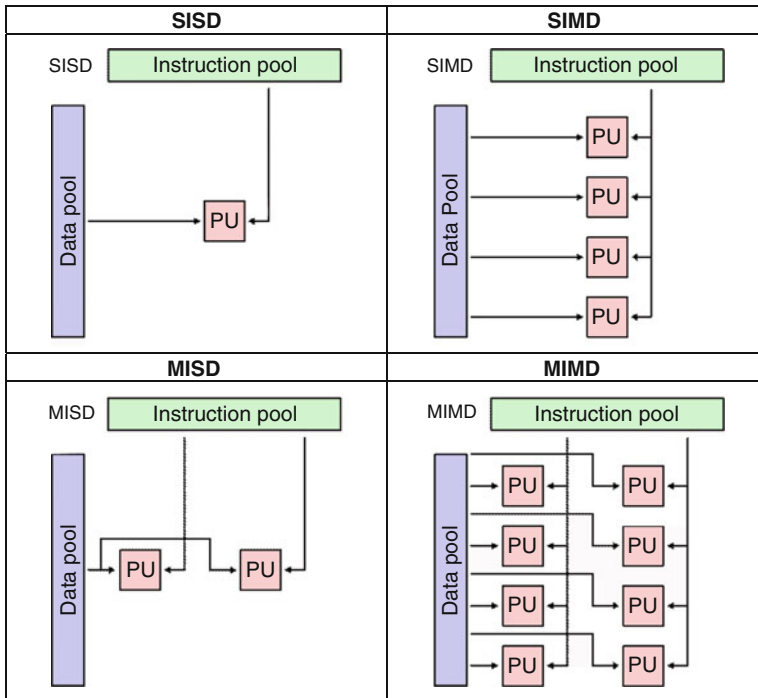


Figure 1
Flynn's classification

- Multiple Instruction, Single Data stream (MISD): This architecture is rarely seen due to the fact that multiple instruction streams generally require multiple data streams to be effective. However, this architecture is used for systems requiring redundant parallelism, as for example on airplanes that need to have several backup systems in case one fails. Some theoretical computer architectures have also been proposed which make use of MISD, but none have entered mass production.
- Multiple Instruction, Multiple Data streams (MIMD): Multiple autonomous processors simultaneously executing different instructions on different data (➤ Fig. 1). Distributed systems are generally recognized to be MIMD architectures, either exploiting a single shared memory space or a distributed memory space.

Today, even PC could not be considered as SISD architecture, since standard processors execute at least two instructions per cycle.

Most of the existing architectures are now MIMD architectures. Some processors, like GPU (Hong and Kim 2009), accelerators, Cell (Gschwind et al. 2006), etc. are considered as SIMD processor architectures.

Concerning today's architecture, other possible classifications exist. One of them is the following:

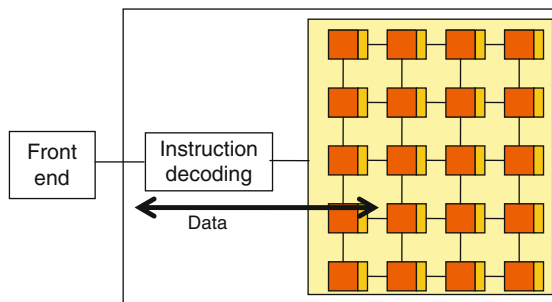
- Standard components architecture: based on standard processors and interconnection networks
- Semi-custom architectures: based on standard processors and specific interconnection networks
- Full-custom architectures: based on specific processors and interconnection networks

In principle, full-custom architectures should be the most performing but also the most expensive, since the development time is greater, and the market for this kind of architecture is thinner.

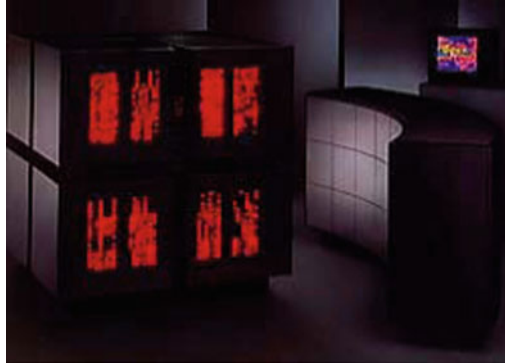
The readers can find in (Leighton 1992; King et al. 1988; Hwang 1993) many details and explanations on parallel computer architecture.

2.2 SIMD Architectures

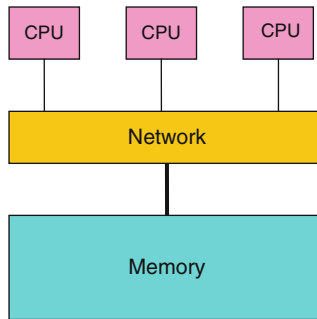
As presented below, SIMD architectures are based on a unique synchronism mechanism (🔍 Figs. 2 and 🔍 Figure 3). At each clock cycle the same instruction is executed by all the processing units on the data located in the processing unit. One of the best examples of this kind of architecture in the past is the CM2 (Hillis 1982; Tucker and Robertson 1988; Trew and Wilson 1991). This kind of architecture is similar to systolic arrays. SIMD architectures had all but disappeared with the emergence of standard component architectures, but they should be reexamined with the emergence of custom processing units, like GPGPU (Hong and Kim 2009).



🔍 Figure 2
SIMD architecture



■ Figure 3
CM2 machine



■ Figure 4
Shared memory MIMD architecture model

2.3 MIMD Architectures

In MIMD architecture, the different computing units are dealing with different instructions and different data at the same time. Moreover, no more global synchronization is needed, since each computing unit is independent.

There exist different architectures based on this model:

- Shared memory multiprocessors (SMP): each computing unit shares the same memory (see [▶ Fig. 4](#))
- Distributed memory multiprocessors: each computing unit has its own memory (see [▶ Fig. 5](#))
- Hybrid MIMD architecture: a combination of the two previous architecture models. Computing units are gathered into shared memory nodes. These nodes are then linked using distributed memory architecture model (see [▶ Fig. 6](#)).

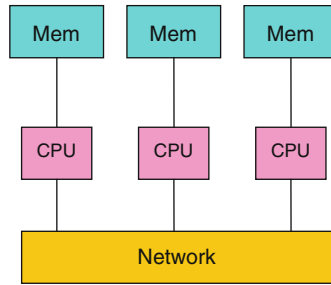


Figure 5
Distributed memory MIMD architecture model

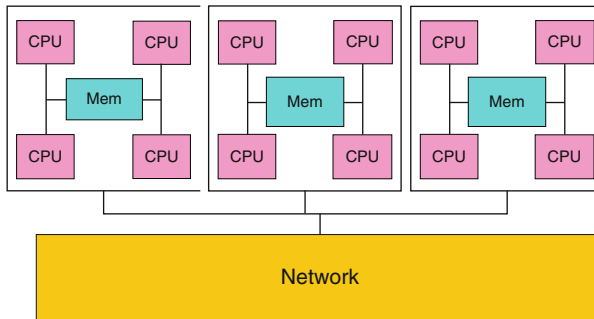


Figure 6
Hybrid MIMD architecture model

2.4 Dataflow and Systolic Architectures: Specialized Architectures Versus Generic Ones

These architectures are potentially more powerful on data flow, SIMD, systolic algorithms, but need customized processors. The relatively long time required to design these custom powerful architectures results in performance increases over time, which lags behind the rate of performance increase seen in commodity components.

However, there are situations where this strategy yields high returns. One of them is to consider architectures where the custom processor is not the main computing element but a coprocessor dedicated to increase the power of the main component. One typical example is the graphical processor unit (GPU). This point will be developed later.

2.5 Vector Architectures

A vector processor, or array processor, is a CPU design where the instruction set includes operations that can perform mathematical operations on multiple data elements simultaneously.

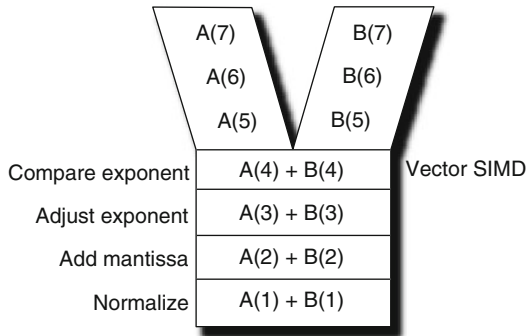


Figure 7
Principle of vector processing

This is in contrast to a scalar processor which handles one element at a time using multiple instructions.

Single instruction results in multiple operands being updated. Scalar processing operates on single data elements. Vector processing operates on whole vectors (groups) of data at a time (see ► [Fig. 7](#)).

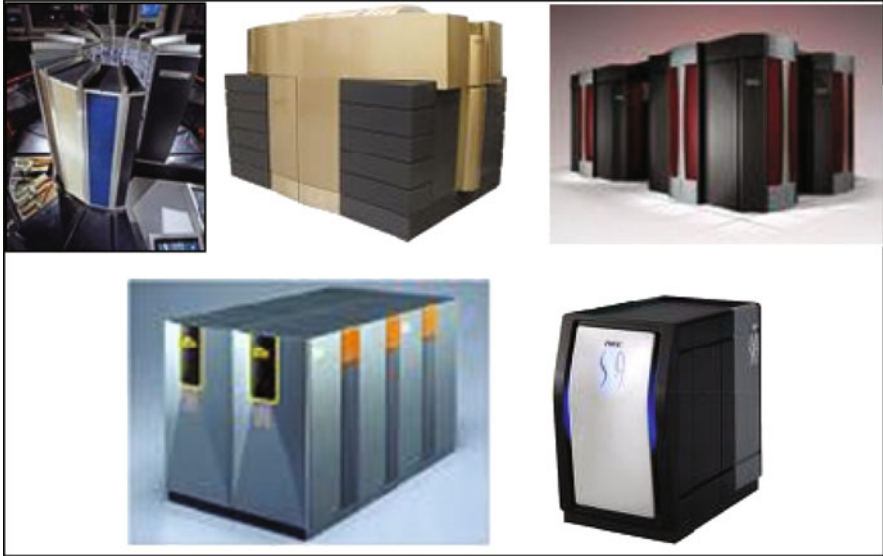
In general terms, CPUs are able to manipulate one or two pieces of data at a time. For instance, many CPUs have an instruction that essentially says “add A to B and put the result in C,” while others require two or three instructions to perform these types of operations.

The data for A, B, and C could be – in theory at least – encoded directly into the instruction. However, things are rarely that simple. In general, the data is rarely sent in raw form and is instead “pointed to” by passing in an address to a memory location that holds the data. Decoding this address and getting the data out of the memory takes some time. As CPU speeds have increased, this memory latency has historically become a large impediment to performance.

In order to reduce the amount of time this takes, most modern CPUs use a technique known as instruction pipelining in which the instructions pass through several subunits in turn. The first subunit reads the address and decodes it, the next “fetches” the values at those addresses, and the next does the math itself. With pipelining the “trick” is to start decoding the next instruction even before the first has left the CPU, in the fashion of an assembly line, so that the address decoder is constantly in use. Any particular instruction takes the same amount of time to complete, a time known as the latency, but the CPU can process an entire batch of operations much faster than if it did so one at a time.

Vector processors take this concept one step further. Instead of pipelining just the instructions, they also pipeline the data itself. They are fed instructions that say not just to add A to B, but to add all of the numbers “from here to here” to all of the numbers “from there to there.” Instead of constantly having to decode instructions and then fetch the data needed to complete them, it reads a single instruction from memory, and “knows” that the next address will be one larger than the last. This allows for significant savings in decoding time.

In fact, vector processors work best only when there are large amounts of data to be worked on. For this reason, these sorts of CPUs were found primarily in supercomputers, as the supercomputers themselves were generally found in places such as weather prediction centers and physics labs, where huge amounts of data are “crunched.”



■ Figure 8

Examples of vector architecture – from *top to bottom and left to right*: CRAY 1, CRAY T90, CRAY X1, Fujitsu VPP5000 and NEC SX9

Main examples of these architectures are the Cray supercomputers (Cray 1, YMP, C90, T90, X1), Fujitsu VP family, NEC SX family (see ➤ [Fig. 8](#)).

3 Parallelism Models

3.1 Overview

There are several parallel programming models in common use (Butenhof [1997](#)):

- Shared memory
- Threads
- Message passing
- Data parallel
- Hybrid

Parallel programming models exist as an abstraction above hardware and memory architectures. Although it might not seem apparent, these models are not specific to a particular type of machine or memory architecture. In fact, any of these models can (theoretically) be implemented on any underlying hardware.

Two examples:

- Shared memory model on a distributed memory machine: Kendall Square Research (KSR) (Singh et al. [1993](#); Burkhardt et al. [1992](#)) approach.

Machine memory was physically distributed, but appeared to the user as a single shared memory (global address space). Generically, this approach is referred to as “virtual shared memory.” Note: although KSR is no longer in business, there is no reason to suggest that a similar implementation will not be made available by another vendor in the future.

- Message passing model on a shared memory machine: MPI on SGI Origin

The SGI Origin employed the CC-NUMA (Chapman et al. 2001) type of shared memory architecture where every task has direct access to global memory. However, the ability to send and receive messages with MPI, as is commonly done over a network of distributed memory machines, is not only easily implementable but is widely used.

Which model to use is often a combination of what is available and personal choice? There is no “best” model, although there certainly are better implementations of some models over others.

The following sections describe each of the models mentioned above, and also discuss some of their actual implementations.

3.2 Shared Memory Model

In the shared memory programming model, tasks share a common address space, which they read and write asynchronously. Various mechanisms such as locks/semaphores may be used to control access to the shared memory.

An advantage of this model from the programmer’s point of view is that the notion of data “ownership” is lacking, and so there is no need to specify explicitly the communication of data between tasks. Program development can often be simplified.

An important disadvantage in terms of performance is that it becomes more difficult to understand and manage data locality.

Implementations:

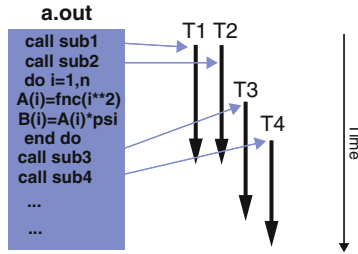
On shared memory platforms, the native compilers translate user program variables into actual memory addresses, which are global.

No common distributed memory platform implementations currently exist.

3.3 Threads Model

In the threads model of parallel programming (Tanenbaum 1992), a single process can have multiple, concurrent execution paths. Perhaps the simplest analogy that can be used to describe threads is the concept of a single program that includes a number of subroutines:

- The main program `a.out` is scheduled to run by the native operating system. `a.out` loads and acquires all of the necessary system and user resources to run.
- `a.out` performs some serial work, and then creates a number of tasks (threads) that can be scheduled and run by the operating system concurrently.
- Each thread has local data, but also, shares the entire resources of `a.out`. This saves the overhead associated with replicating a program’s resources for each thread. Each thread also benefits from a global memory view because it shares the memory space of `a.out`.
- A thread’s work may best be described as a subroutine within the main program. Any thread can execute any subroutine at the same time as other threads.



■ **Figure 9**

Thread programming model

- Threads communicate with each other through global memory (updating address locations). This requires synchronization constructs to insure that no more than one thread is updating the same global address at any time.
- Threads can come and go, but `a.out` remains present to provide the necessary shared resources until the application has completed.

Threads are commonly associated with shared memory architectures and operating systems (👉 [Fig. 9](#)).

Implementations:

From a programming perspective, threads implementation commonly comprises:

- A library of subroutines that are called from within parallel source code
- A set of compiler directives imbedded in either serial or parallel source code

In both cases, the programmer is responsible for determining all parallelism. Threaded implementations are not new in computing. Historically, hardware vendors have implemented their own proprietary versions of threads. These implementations differed substantially from each other making it difficult for programmers to develop portable threaded applications. Unrelated standardization efforts have resulted in two very different implementations of threads: POSIX threads and OpenMP.

- POSIX threads (Butenhof [1997](#))
 - Library based; requires parallel coding.
 - Specified by the IEEE POSIX 1003.1c standard (1995).
 - C Language only.
 - Commonly referred to as Pthreads.
 - Most hardware vendors now offer Pthreads in addition to their proprietary threads implementations.
 - Very explicit parallelism; requires significant programmer attention to detail.
- OpenMP (Chandra [2001](#); Chapman et al. [2007](#))
 - Compiler directive based; can use serial code.
 - Jointly defined and endorsed by a group of major computer hardware and software vendors. The OpenMP Fortran API was released October 28, 1997. The C/C++ API was released in late 1998.
 - Portable/multi-platform, including Unix and Windows NT platforms.

- Available in C/C++ and Fortran implementations.
- Can be very easy and simple to use – provides for “incremental parallelism.”

Microsoft has its own implementation for threads, which is not related to the UNIX POSIX standard or OpenMP.

3.4 Message Passing Model (Roosta 2000)

The message passing model demonstrates the following characteristics:

- Sets of tasks that use their own local memory during computation. Multiple tasks can reside on the same physical machine as well across an arbitrary number of machines.
- Tasks exchange data through communications by sending and receiving messages.
- Data transfer usually requires cooperative operations to be performed by each process (➤ Fig. 10). For example, a send operation must have a matching receive operation.

Implementations:

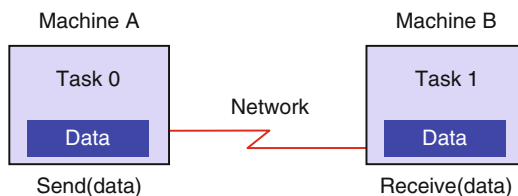
From a programming perspective, message passing implementations commonly comprise a library of subroutines that are imbedded in source code. The programmer is responsible for determining all parallelism.

Historically, a variety of message passing libraries have been available since the 1980s. These implementations differed substantially from each other making it difficult for programmers to develop portable applications. In 1992, the MPI Forum was formed with the primary goal of establishing a standard interface for message passing implementations (The MPI Forum 1993).

Part 1 of the message passing interface (MPI) was released in 1994. Part 2 (MPI-2) was released in 1996. Both MPI specifications are available on the web at www.mcs.anl.gov/Projects/-mpi/standard.html.

MPI is now the “de facto” industry standard for message passing, replacing virtually all other message passing implementations used for production work. Most, if not all of the popular parallel computing platforms offer at least one implementation of MPI. A few offer a full implementation of MPI-2.

For shared memory architectures, MPI implementations usually do not use a network for task communications. Instead, they use shared memory (memory copies) for performance reasons.



■ Figure 10
Principle of the message passing model

3.5 Data Parallel Model (Roosta 2000)

The data parallel model demonstrates the following characteristics:

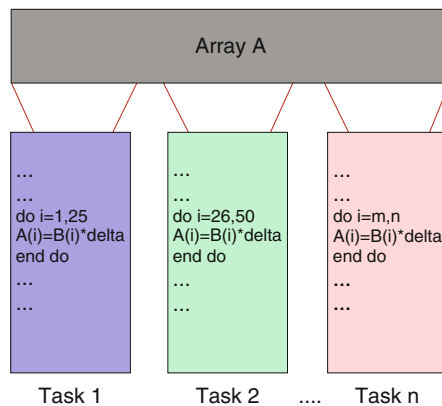
- Most of the parallel work focuses on performing operations on a data set. The data set is typically organized into a common structure, such as an array or cube.
- A set of tasks work collectively on the same data structure; however, each task works on a different partition of the same data structure.
- Tasks perform the same operation on their partition of work, for example, “add 4 to every array element.”

On shared memory architectures, all tasks may have access to the data structure through global memory. On distributed memory architectures the data structure is split up and resides as “chunks” in the local memory of each task (🔗 Fig. 11).

Implementations:

Programming with the data parallel model is usually accomplished by writing a program with data parallel constructs. The constructs can be calls to a data parallel subroutine library or, compiler directives recognized by a data parallel compiler. For example, one can cite:

- Fortran 90 and 95 (F90, F95) (Metcalf and Reid 1999): this is an ISO/ANSI standard extensions to Fortran 77 like pointers and dynamic memory allocation added array processing (arrays treated as objects), recursive and new intrinsic functions, and many other new features. Implementations are available for most common parallel platforms.
- High Performance Fortran (HPF) (H.P.F. Forum 1993): it consists of extensions to Fortran 90 to support data parallel programming. Directives to tell compiler how to distribute data have been added, assertions that can improve optimization of generated code have been added, and data parallel constructs have also been added (now part of Fortran 95). Implementations are available for most common parallel platforms.
- Compiler Directives: Allow the programmer to specify the distribution and alignment of data. Fortran implementations are available for most common parallel platforms.



🔗 Figure 11

Principle of data parallel programming model

Distributed memory implementations of this model usually have the compiler convert the program into standard code with calls to a message passing library (MPI usually) to distribute the data to all the processes. All message passing is done invisibly to the programmer.

3.6 Other Models

Other parallel programming models besides those previously mentioned certainly exist, and will continue to evolve along with the ever changing world of computer hardware and software. Only three of the more common ones are mentioned here.

3.6.1 Hybrid

In this model, any two or more parallel programming models are combined.

Currently, a common example of a hybrid model is the combination of the message passing model (MPI) with either the threads model (POSIX threads) or the shared memory model (OpenMP) (Rabenseifner et al. 2006). This hybrid model lends itself well to the increasingly common hardware environment of networked SMP machines.

Another common example of a hybrid model is combining data parallel with message passing. As mentioned in the data parallel model section previously, data parallel implementations (F90, HPF) on distributed memory architectures actually use message passing to transmit data between tasks, transparently to the programmer.

3.6.2 Single Program Multiple Data (SPMD) (Roosta 2000)

SPMD is actually a “high level” programming model that can be built upon any combination of the previously mentioned parallel programming models (► Fig. 12).

A single program is executed by all tasks simultaneously. At any moment in time, tasks can be executing the same or different instructions within the same program.

SPMD programs usually have the necessary logic programmed into them to allow different tasks to branch or conditionally execute only those parts of the program they are designed to execute. That is, tasks do not necessarily have to execute the entire program – perhaps only a portion of it. All tasks may use different data.

3.6.3 Multiple Program Multiple Data (MPMD) (Roosta 2000)

Like SPMD, MPMD is actually a “high level” programming model that can be built upon any combination of the previously mentioned parallel programming models.

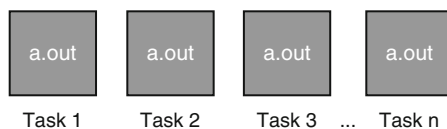


Figure 12
SPMD model

MPMD applications typically have multiple executable object files (programs). While the application is being run in parallel, each task can be executing the same or different program as other tasks. All tasks may use different data (► Fig. 13).

3.7 The Different Levels of Parallelism

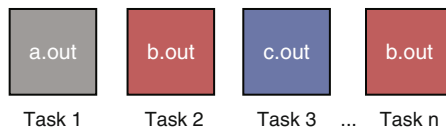
3.7.1 First Level: Distributed Computing

This means that “quasi” independent simulation can be achieved in parallel. Only a light central control could be performed in order to control the whole simulation. This is used for all parameterized calculations (uncertainties reduction, design optimization, safety and operating optimization). In this case the major problems to deal with are the dataflow and workflow management (► Fig. 14).

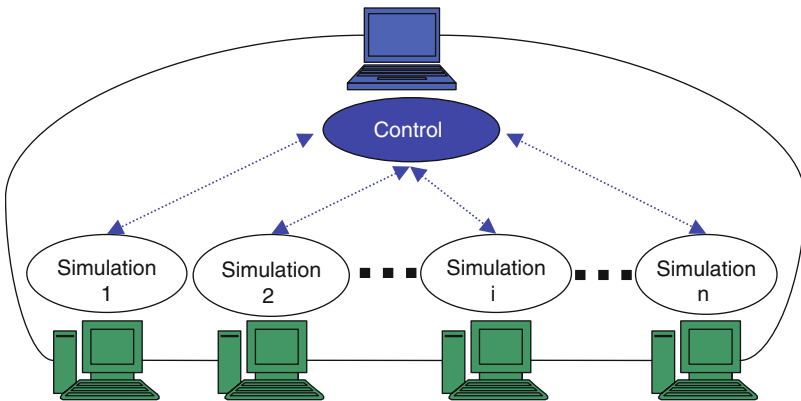
For the distributed level, the architecture of the simulation does not suppose specific constraint on the hardware. The only need is to have a connection between the unit in charge of the control of the simulation and the units in charge of the simulation itself.

3.7.2 Second Level: Coarse Grain Parallel Computing

For this case, we cannot suppose independent simulation. We consider either a unique problem which can be solved by concurrent calculation but needs synchronization and communication



■ Figure 13
MPMD programming model



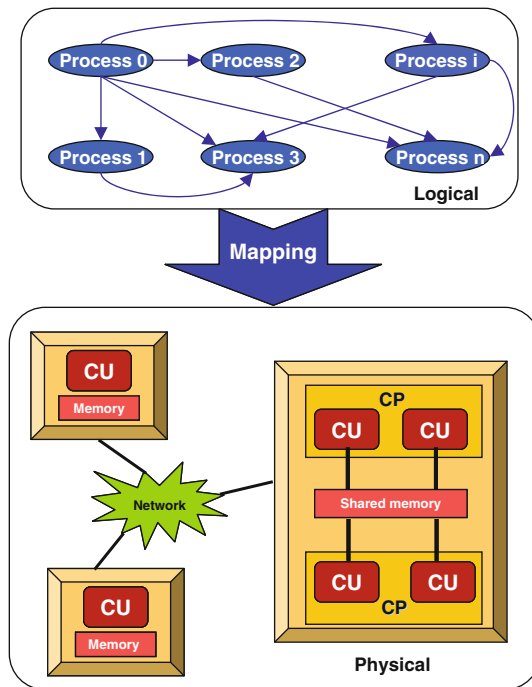
■ Figure 14
Sketch of a distributed computing simulation

between processes. In that case, one can have either a centralized control for the simulation of a distributed one. Of course, since the simulation needs communication, the hardware has a strong influence on the performance of simulation. For this kind of simulation, we consider an ideal parallel machine, that is to say specific communication hardware which minimizes the latency and offers the greater bandwidth as possible.

We have to define the graph of processes (dependency graph) and the communication graph. These two graphs have then to be mapped on the target architecture. We can suppose each process will be mapped on one different computational unit (CU), or many processes could be mapped on the same physical process unit. Moreover, even, we assume that each process is mapped on a different computational unit; the communication media can be different depending on the target architecture. The communication can be achieved either using a communication network between different memory units or through the memory in case of a shared memory machine (► [Fig. 15](#)).

3.7.3 Third Level: Fine Grain Parallel Computing

In this level, we consider the very fine level of parallelism that can be achieved in a single program. Usually this level is implemented using a multithreaded programming model on shared



■ Figure 15

Sketch of a parallel computing simulation – mapping of a logical graph onto a real architecture

memory architecture. This level is not very different from the previous one, but in order to achieve good performance, one has to be cautious in the use of the different memory hierarchies.

The most popular way to implement this model is to use the OpenMP (Chandra 2001) standard, where the parallelism is expressed using directives. So it is quite easy to obtain quite good performances with a moderate effort and reduced modification of the source code.

This model can be used in a standalone way in order to increase performance of a program on a reduced architecture or used in a combined way with coarse grain approach.

This model becomes more and more popular with multicore architectures. Most of the desktops have now between four and eight cores, and server can have up to 32 cores sharing a common memory.

4 Designing Parallel Programs

4.1 Automatic Versus Manual Parallelization

Designing and developing parallel programs has characteristically been a very manual process. The programmer is typically responsible for both identifying and actually implementing parallelism. Very often, manually developing parallel codes is a time consuming, complex, error-prone, and iterative process.

For a number of years now, various tools have been available to assist the programmer with converting serial programs into parallel programs. The most common type of tool used to automatically parallelize a serial program is a parallelizing compiler or preprocessor (Feautrier 2006).

A parallelizing compiler generally works in two different ways:

- Fully automatic
 - The compiler analyzes the source code and identifies opportunities for parallelism.
 - The analysis includes identifying inhibitors to parallelism and possibly a cost weighting on whether or not the parallelism would actually improve performance.
 - Loops (do, for) are the most frequent target for automatic parallelization.
- Programmer directed
 - Using “compiler directives” or possibly compiler flags, the programmer explicitly tells the compiler how to parallelize the code.
 - May be able to be used in conjunction with some degree of automatic parallelization also.

If you are beginning with an existing serial code and have time or budget constraints, then automatic parallelization may be the answer. However, there are several important caveats that apply to automatic parallelization:

- Wrong results may be produced.
- Performance may actually degrade.
- Much less flexible than manual parallelization.
- Limited to a subset (mostly loops) of code.
- May actually not parallelize the code if the analysis suggests there are inhibitors or the code is too complex.

- Most automatic parallelization tools are for Fortran.

The remainder of this section applies to the manual method of developing parallel codes.

4.2 Understand the Problem and the Program

Undoubtedly, the first step in developing parallel software is to first understand the problem that you wish to solve in parallel. If you are starting with a serial program, this necessitates understanding the existing code also.

Before spending time in an attempt to develop a parallel solution for a problem, determine whether or not the problem is one that can actually be parallelized.

Example of parallelizable problem:

Calculate the potential energy for each of several thousand independent conformations of a molecule. When done, find the minimum energy conformation.

This problem is able to be solved in parallel. Each of the molecular conformations is independently determinable. The calculation of the minimum energy conformation is also a parallelizable problem.

Example of a nonparallelizable problem:

Calculation of the Fibonacci series (1, 1, 2, 3, 5, 8, 13, 21, ...) by use of the formula: $F(k + 2) = F(k + 1) + F(k)$

This is a nonparallelizable problem because the calculation of the Fibonacci sequence as shown would entail dependent calculations rather than independent ones. The calculation of the $k + 2$ values uses those of both $k + 1$ and k . These three terms cannot be calculated independently and therefore, not in parallel.

Identify the program's *hotspots*:

- Know where most of the real work is being done. The majority of scientific and technical programs usually accomplish most of their work in a few places.
- Profilers and performance analysis tools can help here.
- Focus on parallelizing the hotspots and ignore those sections of the program that account for little CPU usage.

Identify *bottlenecks* in the program

- Are there areas that are disproportionately slow, or cause parallelizable work to halt or be deferred? For example, I/O is usually something that slows a program down.
- May be possible to restructure the program or use a different algorithm to reduce or eliminate unnecessary slow areas.

Identify inhibitors to parallelism

- One common class of inhibitor is *data dependence*, as demonstrated by the Fibonacci sequence above.

Investigate other algorithms if possible

- This may be the single most important consideration when designing a parallel application.

4.3 Partitioning

One of the first steps in designing a parallel program is to break the problem into discrete “chunks” of work that can be distributed to multiple tasks. This is known as decomposition or partitioning.

There are two basic ways to partition computational work among parallel tasks: *domain decomposition* and *functional decomposition*.

4.3.1 Domain Decomposition (Smith et al. 1996)

In this type of partitioning, the data associated with a problem is decomposed. Each parallel task then works on a portion of the data (see ▶ Fig. 16).

There are different ways to partition data as illustrated on ▶ Fig. 17.

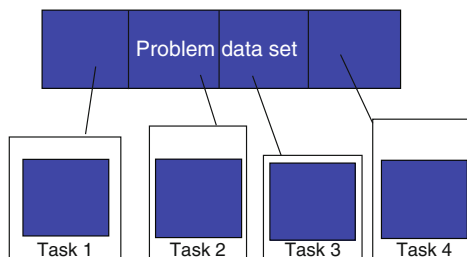
4.3.2 Functional Decomposition (Andrade et al. 2003)

In this approach, the focus is on the computation that is to be performed rather than on the data manipulated by the computation. The problem is decomposed according to the work that must be done. Each task then performs a portion of the overall work (see ▶ Fig. 18).

Functional decomposition lends itself well to problems that can be split into different tasks. For example:

Ecosystem Modeling

Each program calculates the population of a given group, where each group’s growth depends on that of its neighbors. As time progresses, each process calculates its current state, then exchanges



■ Figure 16

Sketch of a domain decomposition technique

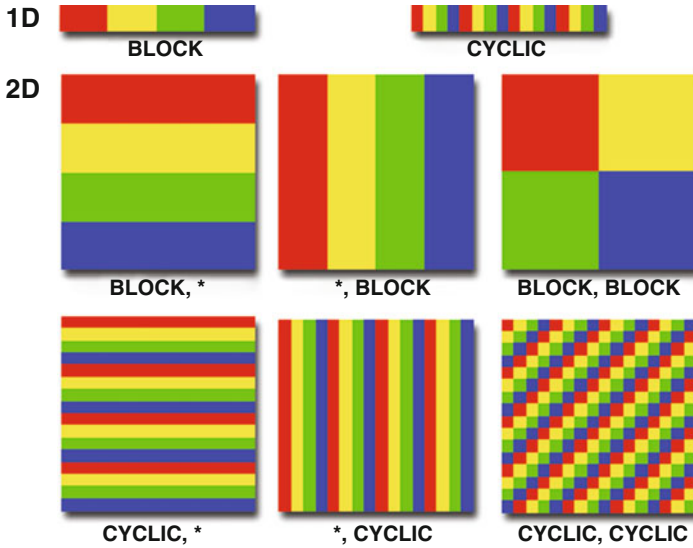


Figure 17
Different kinds of data partitioning

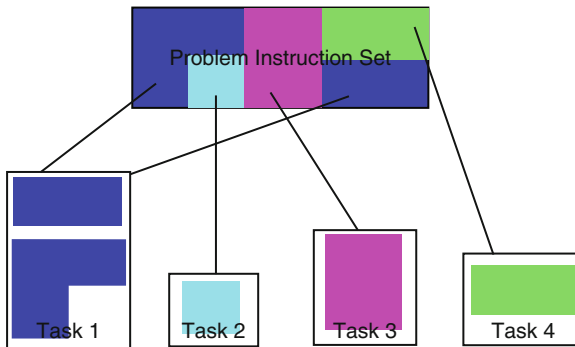


Figure 18
Sketch of a functional decomposition technique

information with the neighbor populations. All tasks then progress to calculate the state at the next time step (see Fig. 19).

Signal Processing

An audio signal data set is passed through four distinct computational filters. Each filter is a separate process. The first segment of data must pass through the first filter before progressing to the second. When it does, the second segment of data passes through the first filter. By the time the fourth segment of data is in the first filter, all four tasks are busy (Fig. 20).

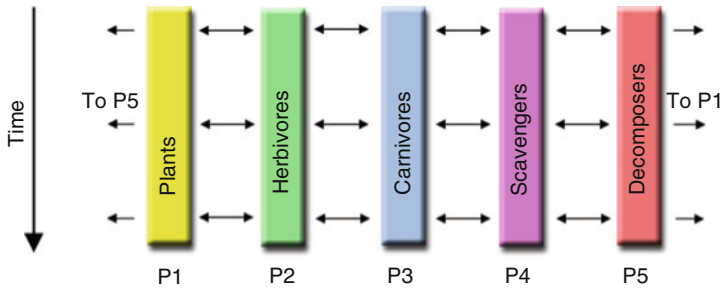


Figure 19
Ecosystem modeling

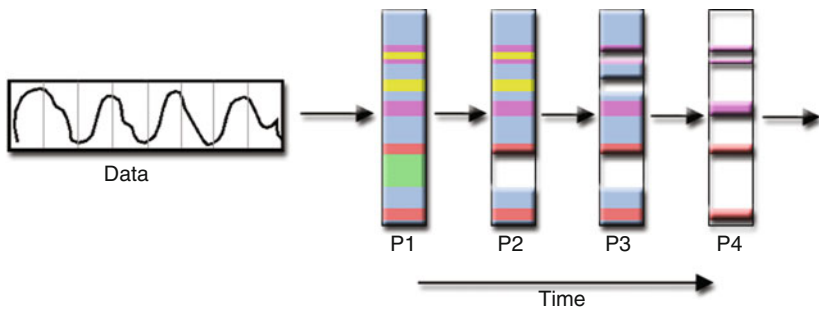


Figure 20
Signal processing parallelization

Climate Modeling

Each model component can be thought of as a separate task. Arrows represent exchanges of data between components during computation: the atmosphere model generates wind velocity data that are used by the ocean model, the ocean model generates sea surface temperature data that are used by the atmosphere model, and so on (► [Fig. 21](#)).

Combining these two types of problem decomposition is common and natural.

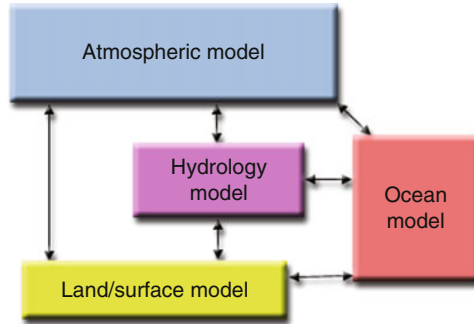
4.4 Communications (Saad and Schultz 1989; Gannon and Rosendale 1984)

4.4.1 Who Needs Communications?

The need for communications between tasks depends upon your problem:

You Do Not Need Communications

Some types of problems can be decomposed and executed in parallel with virtually no need for tasks to share data. For example, imagine an image processing operation where every pixel



■ **Figure 21**
Climate modeling – coupled model components

in a black and white image needs to have its color reversed. The image data can easily be distributed to multiple tasks that then act independently of each other to do their portion of the work.

These types of problems are often called *embarrassingly parallel* because they are so straightforward. Very little inter-task communication is required.

You Do Need Communications

Most parallel applications are not quite so simple, and do require tasks to share data with each other. For example, a 3D heat diffusion problem requires a task to know the temperatures calculated by the tasks that have neighboring data. Changes to neighboring data has a direct effect on that task's data.

4.4.2 Factors to Consider

There are a number of important factors to consider when designing your program's inter-task communications:

Cost of Communications

Inter-task communication virtually always implies overhead. Machine cycles and resources that could be used for computation are instead used to package and transmit data. Communications frequently require some type of synchronization between tasks, which can result in tasks spending time "waiting" instead of doing work. Competing communication traffic can saturate the available network bandwidth, further aggravating performance problems.

Latency Versus Bandwidth

Latency is the time it takes to send a minimal (0 byte) message from point A to point B, commonly expressed as microseconds.

Bandwidth is the amount of data that can be communicated per unit of time, commonly expressed as megabytes/seconds.

Sending many small messages can cause latency to dominate communication overheads. Often it is more efficient to package small messages into a larger message, thus increasing the effective communications bandwidth.

Visibility of Communications

With the Message Passing Model, communications are explicit and generally quite visible and under the control of the programmer.

With the Data Parallel Model, communications often occur transparently to the programmer, particularly on distributed memory architectures. The programmer may not even be able to know exactly how inter-task communications are being accomplished.

Synchronous Versus Asynchronous Communications

Synchronous communications require some type of “handshaking” between tasks that are sharing data. This can be explicitly structured in code by the programmer, or it may happen at a lower level unknown to the programmer.

Synchronous communications are often referred to as *blocking* communications since other work must wait until the communications have completed.

Asynchronous communications allow tasks to transfer data independently from one another. For example, task 1 can prepare and send a message to task 2, and then immediately begin doing other work. When task 2 actually receives the data does not matter.


Asynchronous communications are often referred to as *nonblocking* communications since other work can be done while the communications are taking place.

Interleaving computation with communication is the single greatest benefit for using asynchronous communications.

Scope of Communications

Knowing which tasks must communicate with each other is critical during the design stage of a parallel code. Both of the two scopings described below can be implemented synchronously or asynchronously.

Point-to-point – involves two tasks with one task acting as the sender/producer of data, and the other acting as the receiver/consumer.

Collective – involves data sharing between more than two tasks, which are often specified as being members in a common group, or collective. Some common variations (there are more) are illustrated on  [Fig. 22](#).

Efficiency of Communications

Very often, the programmer will have a choice with regard to factors that can affect communications performance. Only a few are mentioned here.

Which implementation for a given model should be used? Using the Message Passing Model as an example, one MPI implementation may be faster on a given hardware platform than another.

What type of communication operations should be used? As mentioned previously, asynchronous communication operations can improve overall program performance.

Network media – some platforms may offer more than one network for communications. Which one is best?

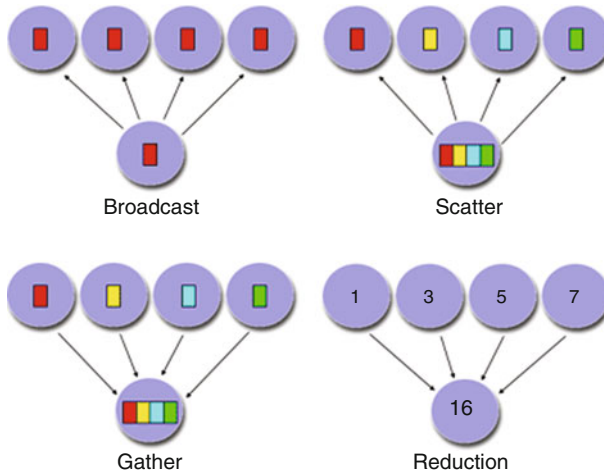


Figure 22
Main global communication schemes

Finally, realize that this is only a partial list of things to consider!!!

4.5 Synchronization

4.5.1 Types of Synchronization

Barrier

Usually implies that all tasks are involved

Each task performs its work until it reaches the barrier. It then stops, or “blocks.”

When the last task reaches the barrier, all tasks are synchronized.

What happens from here varies. Often, a serial section of work must be done. In other cases, the tasks are automatically released to continue their work.

Lock/Semaphore

- Can involve any number of tasks.
- Typically used to serialize (protect) access to global data or a section of code. Only one task at a time may use (own) the lock/semaphore/flag.
- The first task to acquire the lock “sets” it. This task can then safely (serially) access the protected data or code.
- Other tasks can attempt to acquire the lock but must wait until the task that owns the lock releases it.
- Can be blocking or nonblocking.

Synchronous Communication Operations

Involves only those tasks executing a communication operation. When a task performs a communication operation, some form of coordination is required with the other task(s)

participating in the communication. For example, before a task can perform a send operation, it must first receive an acknowledgment from the receiving task that it is OK to send.

Discussed previously in the [Sect. 4.4](#).

4.6 Data Dependencies

4.6.1 Definition

A *dependence* exists between program statements when the order of statement execution affects the results of the program.

A *data dependence* results from multiple use of the same location(s) in storage by different tasks.

Dependencies are important to parallel programming because they are one of the primary inhibitors to parallelism.

4.6.2 Examples

Loop Carried Data Dependence

```
DO 500 J = MYSTART, MYEND
  A(J) = A(J-1) * 2.0
500 CONTINUE
```

The value of $A(J - 1)$ must be computed before the value of $A(J)$; therefore, $A(J)$ exhibits a data dependency on $A(J - 1)$. Parallelism is inhibited.

If task 2 has $A(J)$ and task 1 has $A(J - 1)$, computing the correct value of $A(J)$ necessitates the following:

- Distributed memory architecture – task 2 must obtain the value of $A(J - 1)$ from task 1 after task 1 finishes its computation.
- Shared memory architecture – task 2 must read $A(J - 1)$ after task 1 updates it.

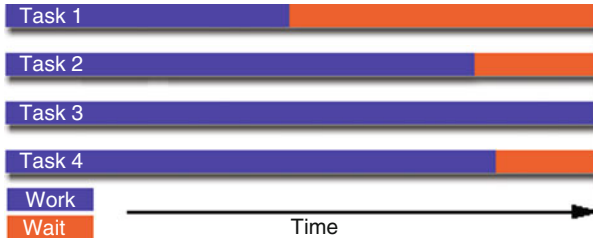
Loop Independent Data Dependence

task 1	task 2
-----	-----
X = 2	X = 4
.	.
.	.
Y = X**2	Y = X**3

As with the previous example, parallelism is inhibited. The value of Y is dependent on:

- Distributed memory architecture – if or when the value of X is communicated between the tasks
- Shared memory architecture – which task last stores the value of X

Although all data dependencies are important to identify when designing parallel programs, loop carried dependencies are particularly important since loops are possibly the most common target of parallelization efforts.



■ Figure 23

Example of time-dependent diagram of a parallel computation using four tasks. Illustration of load imbalance between tasks

4.6.3 How to Handle Data Dependencies

In distributed memory architectures, communicate required data at synchronization points.
In shared memory architectures, synchronize read/write operations between tasks.

4.7 Load Balancing

Load balancing refers to the practice of distributing work among tasks so that *all* tasks are kept busy *all* of the time. It can be considered a minimization of task idle time.

Load balancing is important to parallel programs for performance reasons. For example, if all tasks are subject to a barrier synchronization point, the slowest task will determine the overall performance (🕒 Fig. 23).

4.7.1 How to Achieve Load Balance

Equally Partition the Work Each Task Receives

For array/matrix operations where each task performs similar work, evenly distribute the data set among the tasks.

For loop iterations where the work done in each iteration is similar, evenly distribute the iterations across the tasks.

If a heterogeneous mix of machines with varying performance characteristics are being used, be sure to use some type of performance analysis tool to detect any load imbalances. Adjust work accordingly.

Use Dynamic Work Assignment

Certain classes of problems result in load imbalances even if data is evenly distributed among tasks:

- Sparse arrays – some tasks will have actual data to work on while others have mostly “zeros.”
- Adaptive grid methods – some tasks may need to refine their mesh while others do not.

- N-body simulations – where some particles may migrate to/from their original task domain to another task's; where the particles owned by some tasks require more work than those owned by other tasks.

When the amount of work each task will perform is intentionally variable, or is unable to be predicted, it may be helpful to use a *scheduler – task pool* approach. As each task finishes its work, it queues to get a new piece of work.

It may become necessary to design an algorithm which detects and handles load imbalances as they occur dynamically within the code.

4.8 Granularity

4.8.1 Computation/Communication Ratio

In parallel computing, granularity is a qualitative measure of the ratio of computation to communication.

Periods of computation are typically separated from periods of communication by synchronization events.

4.8.2 Fine Grain Parallelism

This parallelism is characterized by relatively small amounts of computational work done between communication events and a low computation to communication ratio.

4.9 Limits and Costs of Parallel Programming

4.9.1 Amdahl's Law

Amdahl's Law states that potential program speedup is defined by the fraction of code (P) that can be parallelized:

$$\text{Speedup} = \frac{1}{1 - P}$$

If none of the code can be parallelized, $P = 0$ and the speedup = 1 (no speedup). If all of the code is parallelized, $P = 1$ and the speedup is infinite (in theory).

If 50% of the code can be parallelized, maximum speedup = 2, meaning the code will run twice as fast.

Introducing the number of processors performing the parallel fraction of work, the relationship can be modeled by:

$$\text{Speedup} = \frac{1}{S + (P/N)}$$

where P = parallel fraction, N = number of processors, and S = serial fraction.

It soon becomes obvious that there are limits to the scalability of parallelism. For example, at $P = .50, .90,$ and $.99$ (50%, 90%, and 99% of the code is parallelizable):

N	Speedup		
	$P = .50$	$P = .90$	$P = .99$
10	1.82	5.26	9.17
100	1.98	9.17	50.25
1,000	1.99	9.91	90.99
10,000	1.99	9.91	99.02

However, certain problems demonstrate increased performance by increasing the problem size. For example:

2D Grid calculations	85 s	85%
Serial fraction	15 s	15%

We can increase the problem size by doubling the grid dimensions and halving the time step. This results in four times the number of grid points and twice the number of time steps. The timings then look like:

2D Grid calculations	680 s	75.84%
Serial fraction	15 s	2.16%

Problems that increase the percentage of parallel time with their size are more *scalable* than problems with a fixed percentage of parallel time.

4.9.2 Complexity

In general, parallel applications are much more complex than corresponding serial applications, perhaps in the order of magnitude. Not only do you have multiple instruction streams executing at the same time, but you also have data flowing between them.

The costs of complexity are measured in programmer time in virtually every aspect of the software development cycle:

- Design
- Coding
- Debugging
- Tuning
- Maintenance

Adhering to “good” software development practices is essential when working with parallel applications – especially if somebody besides you will have to work with the software.

4.9.3 Portability

Thanks to standardization in several APIs, such as MPI, POSIX threads, HPF, and OpenMP, portability issues with parallel programs are not as serious as in the past years. However, all

of the usual portability issues associated with serial programs apply to parallel programs. For example, if you use vendor “enhancements” to Fortran, C, or C++, portability will be a problem.

Even though standards exist for several APIs, implementations will differ in a number of details, sometimes to the point of requiring code modifications in order to effect portability.

Operating systems can play a key role in code portability issues.

Hardware architectures are characteristically highly variable and can affect portability.

4.9.4 Resource Requirements

The primary intent of parallel programming is to decrease execution wall clock time; however, in order to accomplish this, more CPU time is required. For example, a parallel code that runs in 1 h on eight processors actually uses 8 h of CPU time.

The amount of memory required can be greater for parallel codes than serial codes, due to the need to replicate data and for overheads associated with parallel support libraries and subsystems.

For short running parallel programs, there can actually be a decrease in performance compared to a similar serial implementation. The overhead costs associated with setting up the parallel environment, task creation, communications, and task termination can comprise a significant portion of the total execution time for short runs.

4.9.5 Scalability

The ability of a parallel program’s performance to scale is a result of a number of interrelated factors. Simply adding more machines is rarely the answer.

The algorithm may have inherent limits to scalability. At some point, adding more resources causes performance to decrease. Most parallel solutions demonstrate this characteristic at some point.

Hardware factors play a significant role in scalability. Examples:

- Memory–CPU bus bandwidth on an SMP machine
- Communications network bandwidth
- Amount of memory available on any given machine or set of machines
- Processor clock speed

Parallel support libraries and subsystems software can limit scalability independent of your application.

5 Use of HPC for Nuclear Energy Application: Overview

As for many scientific and technological fields, high performance computing brings many benefits for nuclear energy domain. As for other fields, basic disciplines, like material sciences, thermo- hydraulics, and structural mechanics, can benefit from HPC. Moreover, typical discipline likes neutronics is very time and memory consuming, and HPC is very important for this kind of simulation.

Of course, one cannot imagine high accuracy simulation without S modeling. So the coupling complexity becomes an added challenge each of the disciplines.

One of main illustration of the need and use of HPC is the Virtual Power Plant Challenge. Even if this goal is not fully reachable, it is interesting to describe it as an illustration of the potential needs in terms of simulation and high performance computing for nuclear energy.

5.1 The Virtual Power Plant Challenge

5.1.1 Description

The virtual power plant is intended to provide 3D, multi-physics, multi-scale simulation tools dedicated to the operation and safety of today's power plants, the design optimization of advanced reactors, the design of next generation systems, and the management of nuclear waste storage. These tools will involve various disciplines such as materials, reactor physics, thermal-hydraulics, thermal-mechanics, fuel management, and geological disposal.

5.1.2 Motivation

For today's power plants (GEN III: PWR, BWR) the challenges are the lifespan extension of nuclear installations, the optimization of the fuel use, and the preparation for their dismantlement. Advanced reactors (GEN III+: EPR) have to be tuned in order to increase their economic competitiveness, safety, and reliability. For next generation systems (GEN IV: SFR, HTR, FGCR) a technological jump has to be achieved in order to enable: the transition away from fossil fuel, the control of waste management, optimization of the use of resources, and the nonproliferation of nuclear material.

The main needs can be grouped along the following lines: coupling models of vibration and structure ageing, simulating the degradation mechanisms of materials under irradiation, guaranteeing optimum use of the fuel, simulating earthquake resistance of cooling towers, using real geometries to study accidental scenario, predicting the life span of vessels, and simulating the geological long-term storage of waste material.

The main disciplines involved are thermal-hydraulics (DNS, LES), thermal-mechanics, material (Ab initio – molecular dynamics – kinetic Monte Carlo/by chemical kinetics – discrete dislocation dynamics – crystal plasticity), neutron physics (deterministic and Monte Carlo simulations), and coupling between these disciplines.

5.1.3 Main Challenges

For the main challenges, we discuss the state-of-the-art, and a possible roadmap for the future.

- Coupled thermo-hydro-mechanical problems: Predicting long-term safety of civil engineering installations, like nuclear power plants containment walls or underground nuclear waste

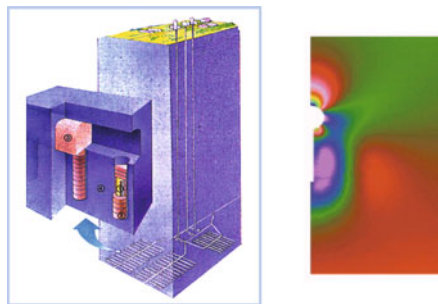
disposal facilities, requires numerical simulations with the following features:

- 3D geometries due to geometrical configuration of the installations and anisotropic properties of materials.
- Nonlinear coupled problems: multiphase transport phenomenon and mechanical behavior are two examples.
- Wide uncertainties on material data imply parametric studies or inverse problem resolution.

Today, we are able to solve coupled problems in near field which means less than 100 m. Long-term behavior taking care of transport phenomenon and creep effects will need to solve these problems for domains 10 times bigger. Solving such a problem with 30,000 unknowns and 5,000 time steps takes 4 days of calculation on one node today. The target 3D problem will have 600,000 unknowns: with the same machine execution time it would be $500 \times 4 = 2,000$ days = 10 years. Clearly, we expect a gain of a factor between 100 and 500 on the calculation time (👉 Fig. 24).

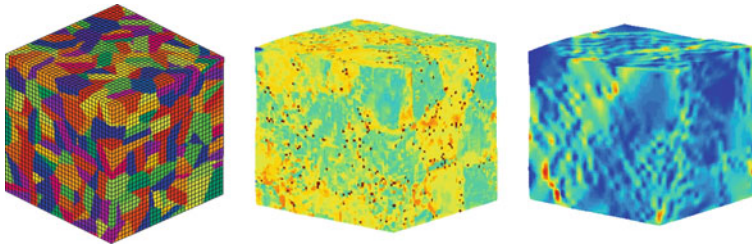
- Multi-scale modeling of behavior and degradation mechanisms of materials: Detailed prediction of high nonlinear mechanical behavior of metallic materials but also concrete require the introduction of micro structural features into the modeling. This is even more crucial for prediction of degradation due to natural ageing, environment, or irradiation. Following features are required:
 - Very complex 3D geometries to represent real microstructures
 - Calibration of complex mechanical formulation by inverse problem resolution
 - Weak multi-scale coupling between discrete dislocations dynamics (DDD) and finite element (FE) codes

Today, material behavior on the scale of $200 \mu\text{m}^3$ can be computed with a coarse representation of microstructure (500,000 degrees of freedom), which represents 0.1 TeraFlops. Solving real problems without technical rupture (what is this?) will lead to problems with a few millions



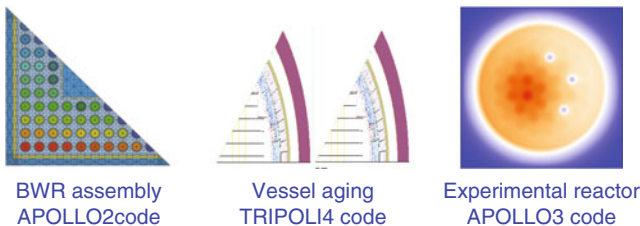
■ Figure 24

Example of complex system to model (subsurface waste repository) and an illustration of a coupled thermo-hydro-mechanical simulation using FEM approach (EDF courtesy)



■ Figure 25

Material simulation using domain decomposition (figure on the left) and results of the simulation. (EDF courtesy)



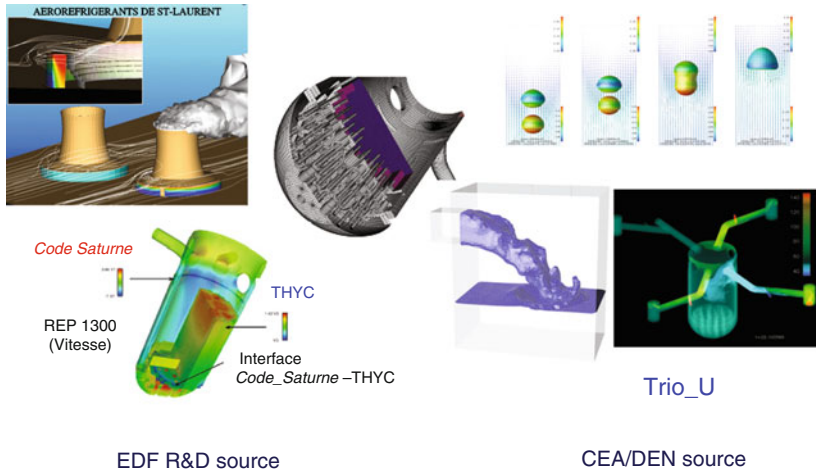
■ Figure 26

Illustration of different neutronic reference calculation using different approaches (Monte Carlo and deterministic) (CEA DEN courtesy)

degrees of freedom and a few TeraFlops. Development and implementation of new computational methods will lead to a few 10 million degrees of freedom and a few 10 TeraFlops (► Fig. 25).

- Neutronics reference calculations: In the field of neutron physics, in order to validate the different models, one needs reference calculations which can be achieved using Monte Carlo simulations and deterministic simulations. An example of what could be achieved is the simulation of one reactor cycle using a probabilistic approach in order to establish reference values concerning the fine 3D power distribution inside a reactor. Such a calculation using a Monte Carlo approach requires about 50 ExaFlops (50.10e18 floating point operations) or 26 PetaFlops (25.10e15 floating point operations) using an unstructured transport solver (► Fig. 26).
- Multi-scale and multi-model simulations: In the field of thermal-hydraulics, the problem can be illustrated by the simulation of two-phase turbulent flows. It implies the coupling of different scales (multi-scale/multi-resolution approaches) and models (two-phase flows and turbulent flows). In order to have a detailed description of the phenomena, it is compulsory to deal with very fine mesh. In the context of power plants, the complexity of geometries combined with fine mesh resolution lead to over $1e9$ meshing elements. It can be considered that one simulation step represents around 10 TeraFlops ($10 \cdot 10^{E12}$ floating point operations).

In the field of thermal-mechanics, the problem is the computation of the whole structure (pipe) and the modeling of much localized damage (thermal fatigue on surface). At the



■ Figure 27

Illustration of different scales for thermal-hydraulic simulations (EDF R&D and CEA DEN courtesy)

finest level, very precise results from thermal-hydraulics are expected and specific complex mechanical formulations are required (🔗 Fig. 27).

- Multi-physics problems: In order to ensure the safety of the installations, the simulation tools have to offer the capability to simulate coupled phenomena (like thermal-hydraulics and neutron physics or thermal-hydraulics and thermal-mechanics) in the transient state. The appropriate level of precision is compulsory for realistic simulations for each physical field. For instance a reference calculation using a Monte Carlo approach has to be coupled with the right level of precision coming from the thermal-hydraulics side. These lead to coupled simulations requiring more than 100 ExaFlops. The different estimates of floating point operations presented above may be reduced by both improved more efficient physical models and better numerical optimizations, but the needs lie between two to three orders of magnitude of what can be handled today. Same coupling schemes and corresponding challenges are required to compute full 3D response of reactor pressure vessel during pressurized thermal shocks or real deformation (due to geometrical evolution under neutron flux, vibration/erosion) of a complete set of fuel assemblies.

5.2 Other Examples and Use

Of course, many other uses of HPC exist. They require the different levels of parallelism described in 🔗 Sect. 3.7.

For example, the first level, distributed computing one, is used for parametric studies or for sensibility calculations. It is also used for embarrassing applications like Monte Carlo simulations in neutronic calculations.

The second level, the coarse grain parallel computing one, is used by all the parallel applications in the different scientific domains involved in nuclear energy simulations: material

sciences, thermo-mechanic, thermo-hydraulic, neutronic, etc. In this case, usually the parallelism is a data parallel one (see ▶ Sects. 3.5 and ▶ 4.3.1). It is also used for coupled simulations like described in ▶ Sect. 4.3.2.

Finally, the third level, the fine grain one, is usually used in combination with the second one for massively parallel applications, or in a stand alone way for applications which do not need massively parallel computations. One can cite some structural mechanic applications, or some solvers in which implementation is much more efficient using a thread model parallelism (see ▶ Sect. 3.3) using a reduced number of threads.

The aim of the next section is to illustrate the use of HPC in some of the basic scientific fields used in nuclear energy simulation.

6 Illustration of HPC Use on Different Applications

The goal of this section is to illustrate the different applications of the use of HPC, and not to deal with the physical part. The goal is not to go deeper into the technical stuff in order to explain how different applications are parallelized but more to explain what are the benefits of using HPC, the main techniques used, the state-of-the-art use of HPC in the different fields, and of course the challenges and needs.

6.1 HPC for Reactor Core Simulation

6.1.1 Introduction

In this section, we will focus on the three main scientific fields involved in the numerical simulation of nuclear reactors, namely: neutronics, thermal-hydraulic, and fuel modeling. Of course, the true modeling of a reactor core is much more complex and should involve many more physical fields (structural mechanics, chemistry, materials); but for a first level of modeling, either the three fields listed above are sufficient or simplified model and embedded modeling are used (for instance, structural mechanics and chemistry in fuel simulation).

Some of these scientific fields are treated in the following sections (material sciences, structural mechanics).

We propose to consider each field independently and then address specific problem of coupling.

6.1.2 Major Challenges

As explained before, we can consider different targets of use for high performance computing in reactor physics. Depending on the target, different level and techniques can be used. Nevertheless, the different techniques will allow us to fall back on to higher level of simulation, like:

- Parameterized calculations: this is the basic technique for optimization. HPC is a great opportunity to take into account more parameters and to reduce “time to market.” This

allows too the use of optimization techniques, like neural networks, in order to find and optimize a set of parameters automatically.

- A high resolution physics: greater memory capacity and greater CPU power are required for more refined models in each discipline, for instance CFD in thermal-hydraulic, instead of porous media modeling, deterministic or Monte Carlo transport instead of few groups diffusion approach.
- A more realistic physics by using systematically real physical model instead of simplified model or pretabulated values. This implies, not only greater CPU power, but robust and easy of use coupled system.
- Real time simulation: this already exists, but we can imagine improving modeling in order to obtain more realistic simulators and decreases the number of assumptions.

All these improvements are needed in order to:

- Increase margin by reducing uncertainties.
- Optimize designs.
- Improve safety.
- Optimize operations.
- Increase physics knowledge.

We are not too far from being able to design a virtual reactor system which allows the virtual design and optimization of existing or new design of reactors or part of reactors.

6.1.3 HPC in Monte Carlo Simulations

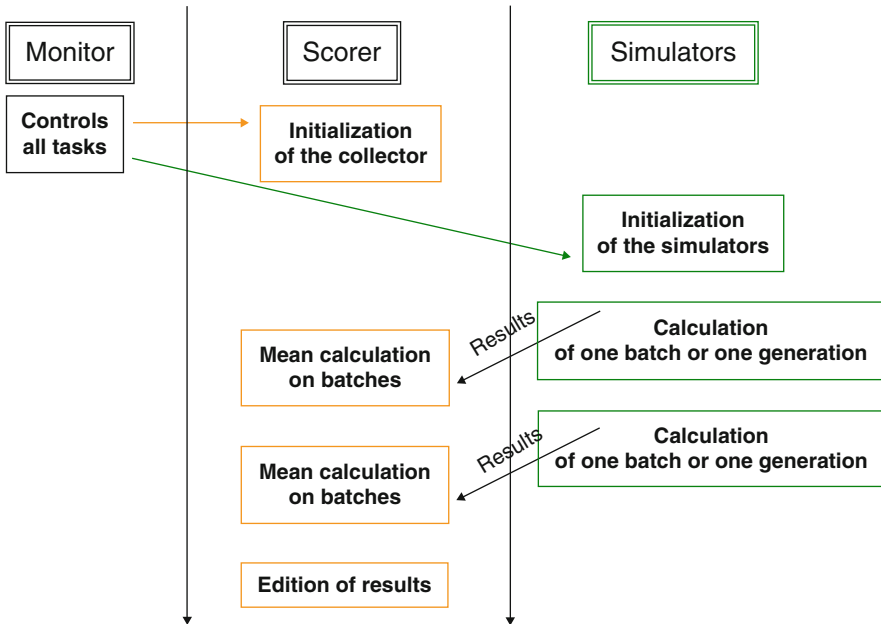
Monte Carlo method to solve the transport equation is the best candidate for parallelism. Since the simulation process is based on a statical approach of independent particle trajectories, each particle can be computed by a different processor. Monte Carlo simulation is embarrassingly parallel (see “Principles for a parallel implementation”).

Principles for a Parallel Implementation

This is for the main principle. For a true implementation, there are some more details. In order to control the simulation process, one needs a monitor which is in charge to control the whole simulation and another process which is in charge to collect the simulations results. These two processes could be executed on a same processor or on different ones. For this implementation part, the model used is an MPMD one (see [Sect. 3.6.3](#)), based on master/slave model with the identification of a master in charge of the simulation control and the separation of simulation process and collector process (Trama and Hugot 2007; Deng and Xie 1999; Goorley et al. 2003).

This implementation principle is used in the TRIPOLI-4^Z (Trama 2008; Hugot et al. 2008; Trama and Hugot 2007) code and is illustrated in [Fig. 28](#).

The main advantages of this model are that it is very easy to implement and port (very basic exchange of information between processes); it is well adapted to independent particles simulation. The last advantage is that this implementation allows fault tolerant simulation. Indeed, if one simulator falls down, either due to a material fault or a numerical one, the monitor can launch the corresponding batches to another simulator. Using these features, even if we lost more than half of the simulators, the whole simulation can still go on.



■ **Figure 28**
Parallel implementation principle in Monte Carlo code

Other features have been also implemented in the TRIPOLI-4^Z, like checkpoint/restart functionalities: the current state of the TRIPOLI-4^Z simulation is stored in different files which allow the restart of the simulation at anytime.

In the area of mathematical and algorithmic development, the main problem concerns the parallel version of the random number generator (Hellekalek 1998). This one has to fulfill the following properties:

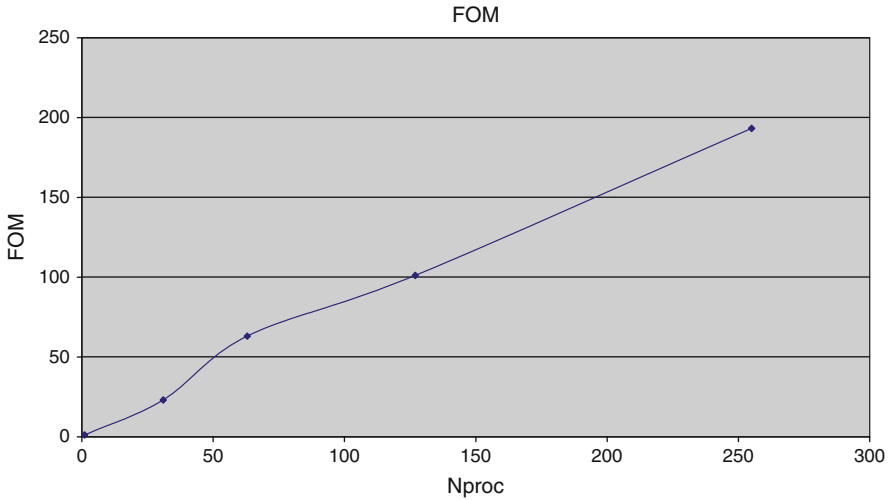
- Independent from the number of processors.
- No correlation between suites for different processors.
- On each processor, the generator can be initialized independently (no communication between processes).

One example of this parallel random generator is based on the generalized feedback shift register (GFSR) algorithm (Lewis and Payne 1973). The main advantages of this random number generator are that it is very fast and has very long period (2,607). However, one can have two identical integers before the end of the generator period (which limits to 2^{32} , which is the maximum number of integer) and it is quite tricky to parameter and tune.

Performances

The way for evaluating the parallel performances of Monte Carlo simulations is quite different from the classical speedup of efficiency (see ► Sect. 4.1.1) and is based on the “figure of merit” (FOM) formula. The FOM quantity is defined as follow:

$$Q = \frac{1}{\sigma^2 \times \tau},$$



■ **Figure 29**
FOM of parallel execution of TRIPOLI-4 code

where σ is the standard deviation, τ is the elapsed time

It is expected that the speedup or the FOM is linear with the number of processor (🔍 Fig. 29). It is almost true.

The same behavior has been measured until 1,000 processors using TRIPOLI-4 code with efficiency over 90%.

One of the advantages of the parallel implementation of TRIPOLI-4 code is that the monitor can control dynamically the load balance of each simulator, and the number and size of the batch can be adjusted in order that the simulators are not waiting and thus maximize the global efficiency of the simulation.

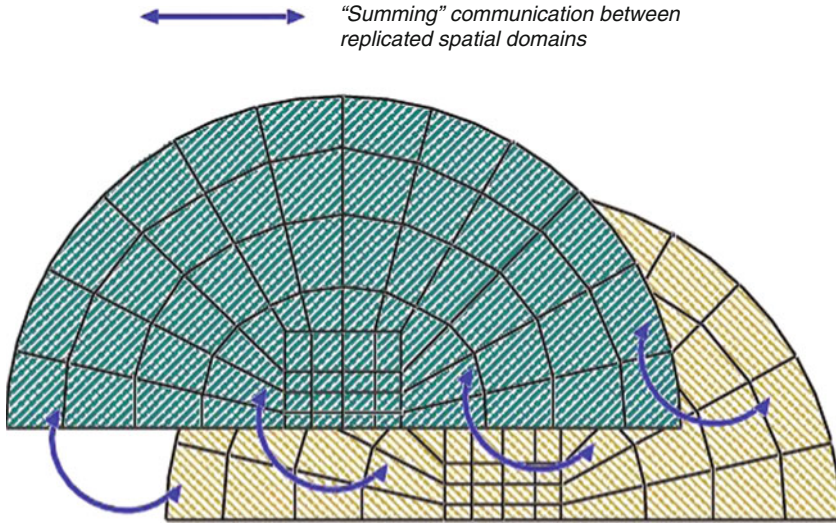
However, there are some bottlenecks to obtain ideal efficiency. Even if the performance can be adjusted, the scorer could be a bottleneck to an ideal efficiency for very large number of simulators ($\gg 1,000$). Some solutions could be investigated, like implementing a tree of collector, in order to share the load of collecting results. Another solution could be to avoid the online collecting and accumulate the results after the simulation. One has to be cautious with the amount of data to store.

Future Challenges

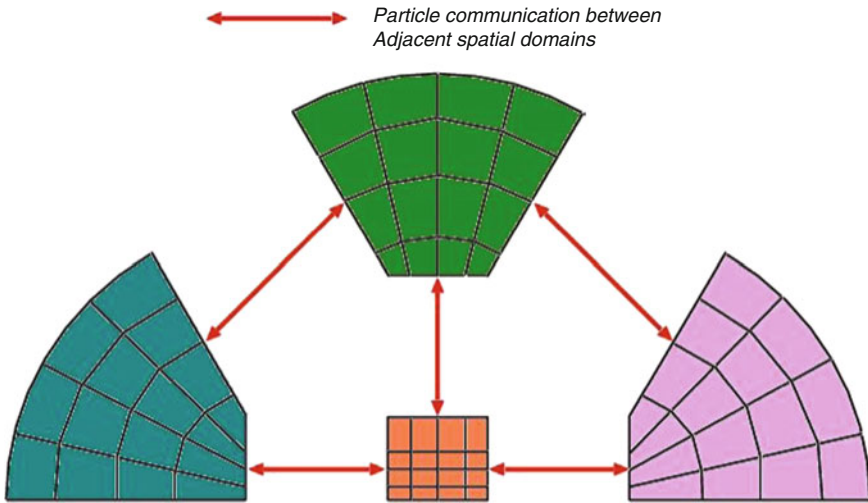
Even if, as we have seen, Monte Carlo simulations are embarrassingly parallel, access to petascale class simulation will however be a challenge, as for many other applications.

As we mentioned earlier, we will have to deal with the huge amount of data, either on the network or the file system, in order to store the simulations results.

But if we still increase the complexity of the geometry, the refinement of the details and the amount of computing variables (for instance, detailed reaction rates on a whole core), the storage of all these information in memory will be a problem. Indeed, in the parallelism model described below, all the input (geometry, nuclear data) and output data are duplicated on each processor (see 🔍 Fig. 30).

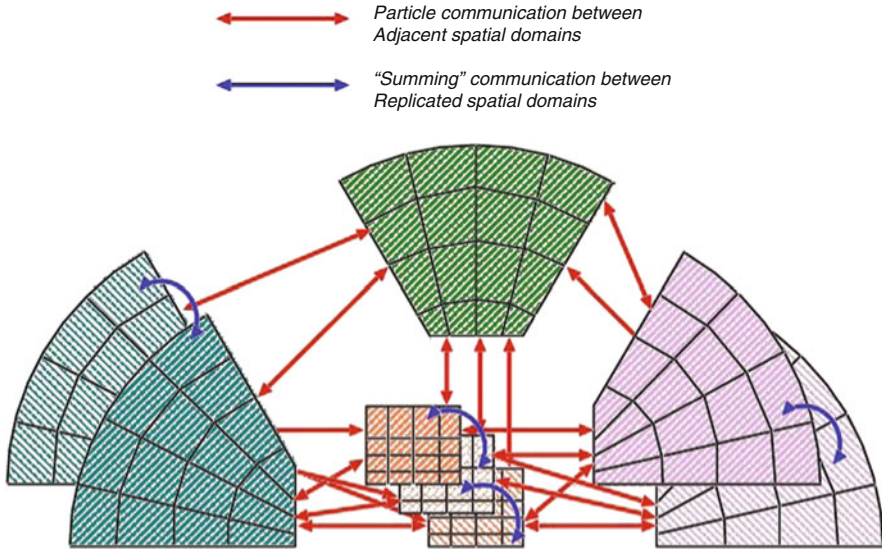


■ **Figure 30**
Domain replication (particle parallelism)



■ **Figure 31**
Domain decomposition (spatial parallelism)

Thus, the future limit will be not only the CPU time as now, but the memory limit. One solution would be to mix the task parallelism with a data parallelism, and to split the computational domain and distribute it among the different processors (see ➤ [Fig. 31](#)).



■ **Figure 32**

Domain decomposition and domain replication (spatial and particle parallelism)

But, it is against the natural way of parallelizing Monte Carlo simulations and will lead to tricky problems like load imbalance and efficiency decrease due to communications traffic between processors.

In the MERCURY code, both models are implemented (Procassini et al. 2005) in order to take advantage of both spatial and particles parallelism (see ► [Fig. 32](#)).

6.1.4 HPC in Deterministic Simulations

The Different Level of Parallelism

In deterministic simulation, we can consider three main levels of parallelism:

- The first level concerns multiparameterized calculations. This level is typically implanted using a distributed computing approach (see ► [Sect. 3.7.1](#)), since each calculation is an independent one from the other. Classical example is a multiparameter assembly's calculation, where one has to compute different kinds of reactor assemblies for core code calculation.
- The second is what we can call multi-domain calculations. It is implemented using a coarse grain parallelism approach (see ► [Sect. 3.7.2](#)). For example, it concerns all the treatment dealing with cross sections, depletion process, thermal-hydraulic feedback, etc. In this level, usually we can consider that the spatial dependency of the data is very tight and a massively parallel approach is well suited. Concerning the case where the spatial dependency of the data is strong, domain decomposition techniques are used. It concerns, for example, the transport equation resolution.

- The third level is based on a fine grain parallelism model (see [Sect. 3.7.3](#)) and mainly concerns the fine grain parallelization of solvers by exploiting intrinsic parallelism of the involved numerical methods.

In the following we will illustrate these different levels by describing some typical examples.

First Level: Multiparameterized Calculations

The main interest of this level is to use the brute force of HPC to solve problems with huge amount of independent calculation in a “human” time. (Some examples have been presented by Prof. Turinsky in this talk during the M&C-SNA conference in 2007 in Monterey.) Different uses of HPC for reducing uncertainties in simulator predictions of limiting nuclear plant attributes or how to gain margins using optimization techniques are discussed below.

One way to reduce uncertainties is of course to use deterministic (forward and adjoint) approaches. Another way is to use a less-intrusive method and is based on a stochastic (sampling) approach. Of course this approach is challenged in regard to computational resources required. This sampling approach is also very interesting in case of problem where deterministic approach is too complex. One can cite coupled problems (thermo-hydraulic–neutronic) or depletion ones.

Concerning optimization problems, one very good example is fuel optimization. Grand challenge problem attributes include:

- Multiobjective
- Multicycle

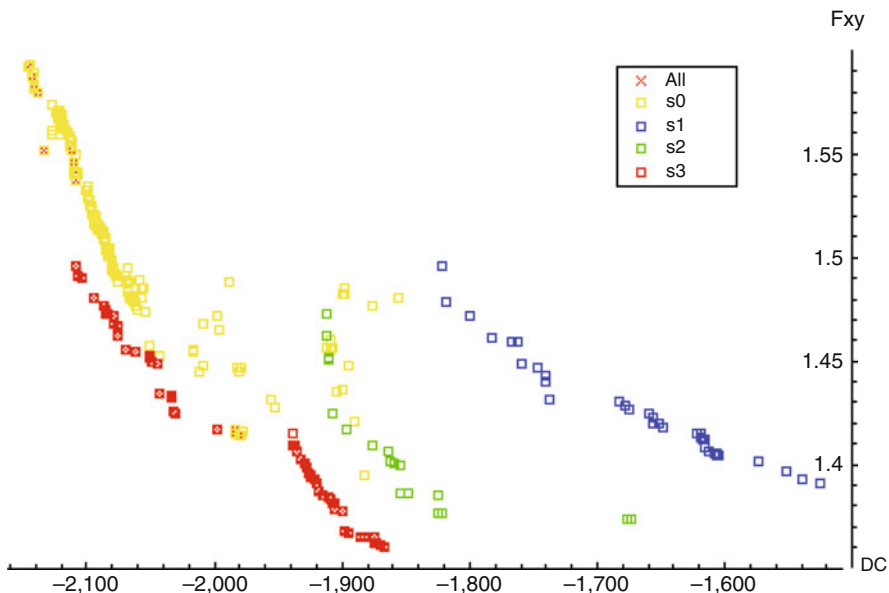
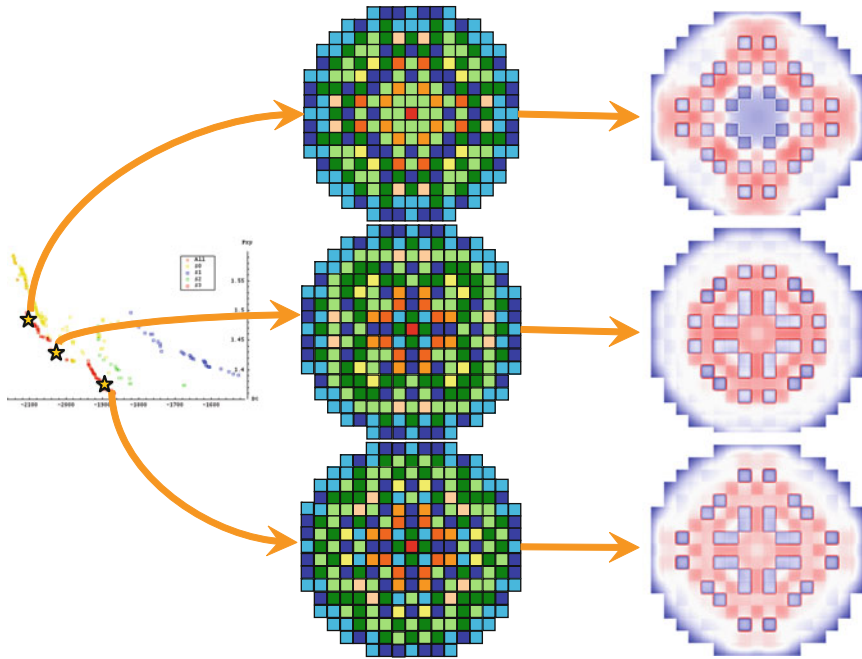


Figure 33

Example of set of solutions found by the genetic algorithm depending on different strategies (Pareto front)



■ Figure 34

Illustration of different solutions: Pareto front on the *left* – loading pattern on the *middle* – corresponding power map on the *right*

- Lattice optimization
- Bundle optimization
- Loading pattern optimization
- Excess reactivity control optimization (e.g., BWR: CRP and core flow)

As an example of this topic, one can cite an exercise achieved for fuel loading pattern optimization with genetic algorithm (Do et al. 2009). A tool based on URANIE/VIZIR and APOLLO3² (Golfier et al. 2009) code has been designed and has been successfully applied to the optimization of fuel loading pattern in the case of high heterogeneous LWR cores. This tool allows the evaluation of more than ten million different configuration in less than 10 h using more than 4,000 processors. An illustration of different kinds of solutions is provided in [Fig. 33](#).

The main advantage of this kind of approach is to allow engineers to test many different kinds of configurations and relax some constraints which are not possible without genetic algorithms and HPC. An example of different solutions found is given in [Fig. 34](#).

Second Level: Multi-Domain Calculations

This level is the most classical one. In most of parallel scientific applications this one is used through domain decomposition techniques. To be more precise, one could say that this domain is mainly based on spatial decomposition. Applied to neutronics applications, all the calculations which are spatially independent are included. For instance, in a typical two-stage calculation, at the core level, all the steps concerning cross-sections loading and management,

thermal feedback, isotopic depletion, etc. are local to the cell of the geometrical domain, and thus could be done in parallel. To summarize in a standard deterministic 3D core calculation, all the steps are spatially independent and thus could be done naturally in parallel, except one, the flux calculation. Even if all the precedent steps could be done in parallel, the main problem is still the data flow management and the data distribution between the processes. One has to think about it in the architecture code design in order to have optimum data structures to mitigate this problem.

Concerning the flux calculation itself, classical domain decomposition techniques can be used (see ▶ Sect. 4.3.1, Smith et al. 1996). Concerning the Boltzmann transport equation solver (Roy and Stankovski 1997), other parallelism degree can be found, since the other dimensions of the equations can be used, for instance the angular or energetic ones. Many solvers have been implemented in parallel, exploiting either angular and energetic parallelism (Zeyao and Lianxiang 2004; Stankovski et al. 1997), spatial one (Guérin et al. 2007; Ragusa 2003a, b) or both (Sjoden 1997).

Another degree of parallelism can be used when exploiting multilevel techniques. For instance, fine transport solution on one assembly coupled with full 3D coarse solution. Typical examples of such techniques can be found in the COBAYA code (see ▶ Fig. 35) (Herrero et al. 2007) or applied to the MINOS diffusion solver within an original approach based on a component mode synthesis (Guérin et al. 2005; Guérin et al. 2006).

Multilevel parallelism approach is also well suited for 3D calculations, especially when the method is intrinsically parallel or very difficult to parallelize. One typical example is the method of characteristics solver used to find the solution of the neutron transport equation. Indeed it is possible to parallelize this method, but one needs to employ very advanced parallelism techniques in order to obtain interesting efficiency (Dahmani and Roy 2006; Wu and Roy 2001; Dahmani and Roy 2005). Another way is to couple a 2D approach with a coupling one in the third direction and to compute 2D plans in parallel (see ▶ Fig. 36). This approach is used for instance in the Dekart code (Han Gyu et al. 2004) in UNIC code (Palmiotti et al. 2007).

Third Level: Fine Grain Parallelism Model

This level is usually used on shared memory architecture and exploits intrinsic parallelism of the algorithms. These techniques had a great infatuation in early 2000's with HPF language and after that OpenMP (Ragusa 2003a,b; Coulomb 1997). It becomes more and more interesting in today's computing environment with the many-core architectures which have to be combined with the second level of parallelism in order to improve the overall performances of the algorithm.

6.2 HPC for CFD and DNS

Benoit Mathieu, CEA/DEN/DER/SSTH – CEA Grenoble

6.2.1 Main Industrial Issues

As mentioned in Simulation and Modeling for Advanced Nuclear Energy Systems Workshop, modeling fluid flow and heat transfer is necessary, not only for core modeling, but also for

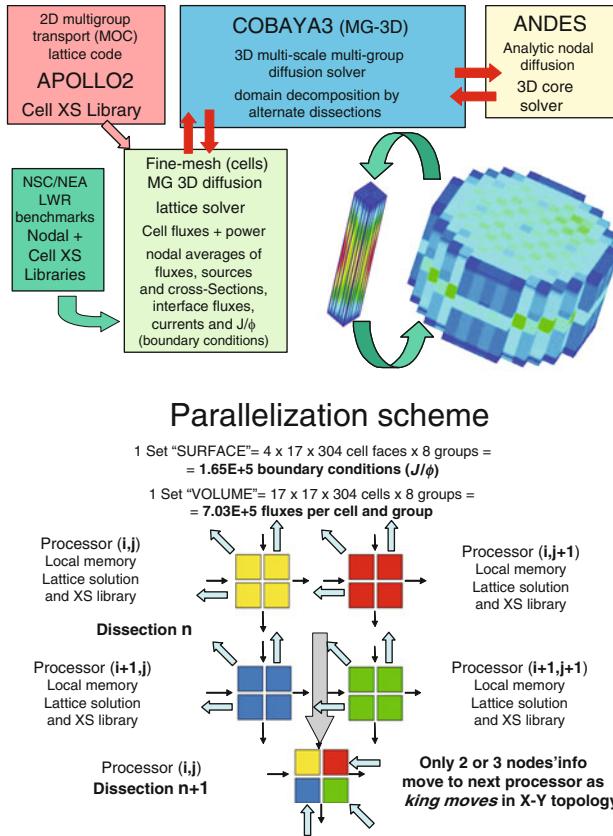


Figure 35

Parallelism principle used in COBAYA code (Courtesy NURESIM project)

the whole plant, including steam generators, pipes, pumps, and condensers. Because of the complexity of the phenomena and geometries involved, current codes often rely on empirical correlations. It is often not clear whether these correlations can be readily extrapolated to new situations. The scientific challenges are in physical modeling, numerical methods, and computer science. Physical modeling must rely on more first principles methods for single-phase and multiphase-multi-fluid flows, for steady and unsteady flows, and with or without heat transfer. Numerical methods must be more robust and provide the optimal mix between accuracy and stability. Codes must deal with billions of mesh elements and enable easy multi-scale and multi-physics coupling.

The main problems to solve in the short term (2–5 years) for light water reactors (LWRs) are pressurized thermal shock, gravity-driven flows, and fluid–structure interactions. For sodium-cooled fast reactors (SFRs) detailed core flow modeling is needed. In the intermediate term (5–10 years) reflooding and thermal fatigue of LWRs and transients and severe accidents for SFRs must be addressed. In the long-term (>10 years) critical heat flux for LWRs and the fluids and heat transfer portion of the numerical reactor simulation for both LWRs and SFRs must be developed. Development is needed in four areas:

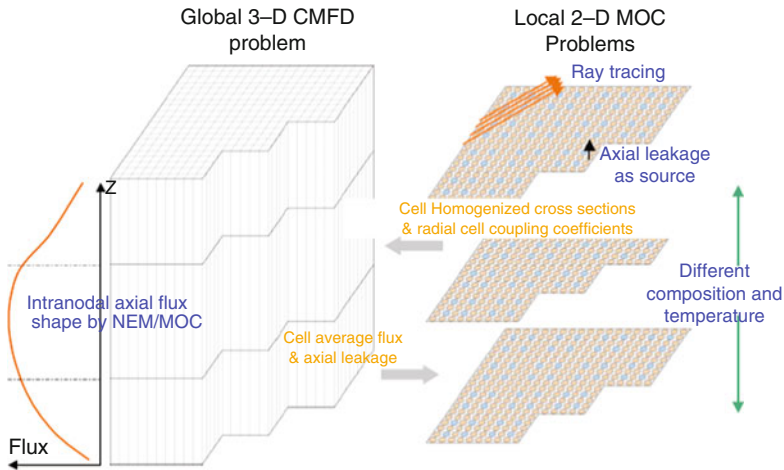


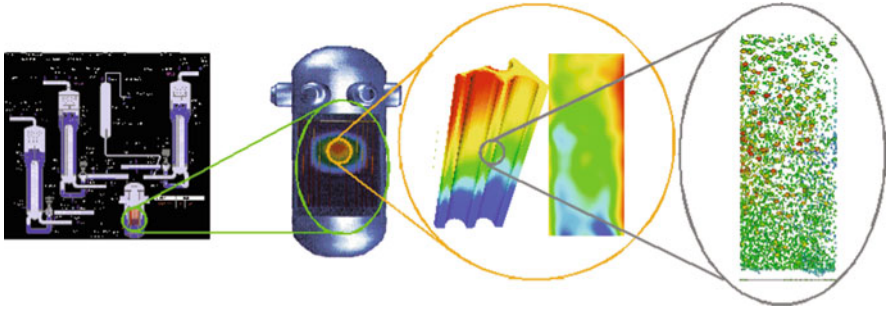
Figure 36
Planar MOC Solution-based 3D CMFD (Downar 2007)

- Direct numerical simulation (DNS), the closest scale to first principles approach: front-tracking, diffuse interface models, particle methods, and lattice Boltzmann techniques
- Computational fluid dynamics (CFD) in open media (detailed calculation within one subchannel or within plena), with a focus on large eddy simulation and high Reynolds numbers
- CFD in porous media (for multichannel analysis)
- System scale (overall plant calculation)

6.2.2 The Multi-Scale Approach

Studies in fluid mechanics for civil nuclear engineering cover a broad range of applications that involve different length scales and time scales. To address these needs, engineers usually use different physical and numerical methods, implemented in various dedicated and sometimes application-specific software packages. In order to provide a unified and comprehensive view of these tools, a framework called “multi-scale approach” has been defined. This framework not only provides a classification of the different modeling scales, but it also suggests a methodology to simultaneously use several of them to solve a given problem. For example, many complex situations cannot be reliably modeled with one single simulation tool without a preliminary qualification process. The multi-scale approach facilitates the selection of an appropriate model as well as the definition of a procedure to qualify for the given application. Moreover, this framework underlines the possibility to couple codes at different scales which extend by several orders of magnitude the range of scales that can be represented within a single simulation. High performance computing can be used at all scales to improve the quality of the results in general or to simulate particularly complex problems (🔗 Fig. 37).

Simulation tools dedicated to the largest scales (system scale or component scale) very often require complex physical models to account for subgrid-scale phenomena. Hence, system-scale



■ Figure 37

The four identified scales of the multi-scale approach for thermal-hydraulics (system scale, component scale, local averaged scale, DNS scale)

codes might use a 1D or 0D descriptions of some system components, together with complex correlations to take into account the different flow patterns that might be found in these components (see, e.g., the CATHARE code (<http://www-cathare.cea.fr/>; Barre and Bernard 1990)). Some of these models do not rely on any mesh convergence property and the mesh can therefore be very coarse. Due to the small number of degrees of freedom (a few thousands in system models), these models can run on single processor computers. HPC is used for these codes though, in order to perform sensitivity analysis by running thousands of simulations.

When the study requires a more accurate representation of the flow pattern at smaller scales, 3D simulations are used and the assessment of the model can partially rely on mesh convergence properties. Therefore, a higher number of degrees of freedom is expected to produce a better result and HPC is massively exploited to run the most refined simulations.

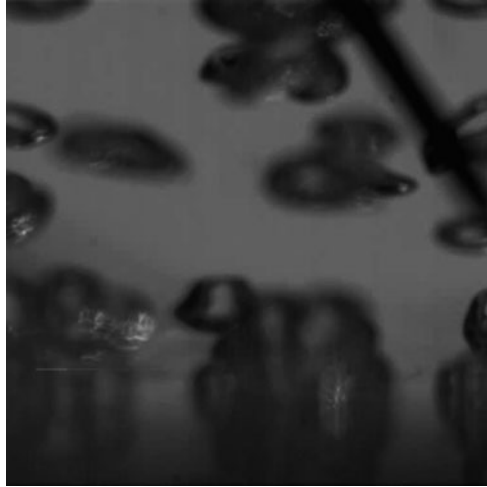
6.2.3 HPC for DNS

DNS stands for direct numerical simulation and traditionally consists in solving the Navier–Stokes equations down to the Kolmogorov scales to achieve mesh convergence of the numerical scheme without any subgrid turbulence model. It is the preferred way to study general properties of turbulent incompressible single-phase flows in academic geometries (infinite 3D periodic domain or channels with flat parallel walls) because it does not rely on any questionable subgrid-scale model but, for a majority of real flows, the physical size of simulated channels cannot exceed a few millimeters.

Despite the academic nature of DNS-based studies, this kind of methodology already provided useful results for the study of turbulent flows, particularly in the field of averaged equations models (closure laws for LES and K-epsilon models, wall laws, etc.).

In the framework of the multi-scale approach, two new fields of research recently arose, for which using DNS is quite natural:

- Porous medium modeling
- Study of two-phase flows and boiling



■ Figure 38

The QLOVICE experiment: pool heating in a transparent test section (CEA/DEN)

Both subjects are treated for the purpose of the multi-scale approach. Porous medium studies with DNS will help tuning the component-scale models that rely on a porous medium description of the component (for instance, the reactor core). Studies of two-phase flows with DNS have at least two purposes:

- Improving models at larger scales (for instance, closure laws for six equations models)
- Studying some complex physical mechanisms like the DNB (departure from nucleate boiling)

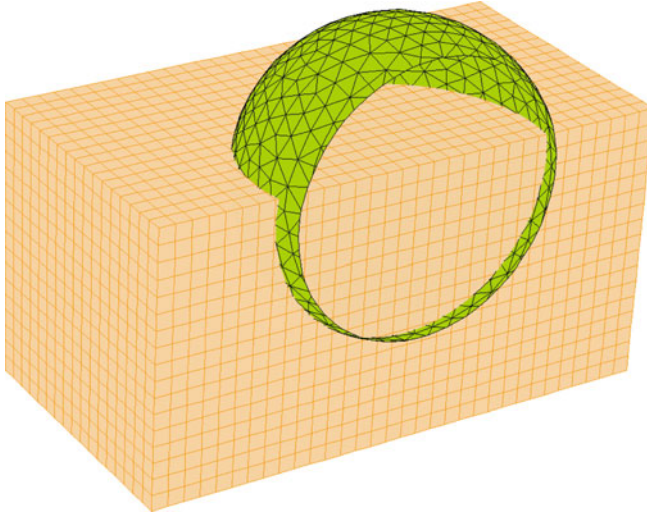
If we illustrate the DNB problem, today, we use hundreds of correlations for DNB. Using a multi-scale approach the idea is to better understand the basic phenomena through close interaction between numerical experiments and experimental observations, like coalescence of bubbles, spreading of one bubble (➤ Fig. 38).

Whereas single-phase DNS codes in structured grids are quite simple, DNS of two-phase flows or porous medium face serious algorithmic difficulties which have found satisfactory solutions only recently.

DNS codes for the incompressible Navier–Stokes equations are usually based on efficient FFT-based Poisson solvers to solve for a divergence free velocity field at each time step. For different reasons, both of these two new applications of DNS do not fit very well in this framework and require more complex codes:

- Porous media have a nonregular geometry.
- Two-phase flows need a Poisson solver for nonuniform density, plus a proper treatment of surface tension and jumps of some physical quantities at the interface (density, viscosity, velocity, etc.).

For example, the Trio_U code (CEA) (<http://www-trio-u.cea.fr>; Calvin et al. 2002) implements a sophisticated mixed Lagrangian–Eulerian method to track the interface (➤ Fig. 39).



■ Figure 39

Mixed front-tracking-based DNS method for two-phase flows (Trio_U code). A dynamic surface mesh tracks the phase interfaces

In order to run this method on massively parallel computers, proper algorithms for dynamic load balancing of the Lagrangian mesh must be implemented (Laucoin and Calvin 2004).

In this field of research, meshes typically have 10–100 million elements (Eulerian mesh) and computations typically cost several hundreds of thousand hours of CPU time.

One typical example of actual capabilities is a two-phase flow intermittent, relatively difficult to reproducibly achieve experimentally, and especially difficult to orchestrate. Only some magnitude of most important physical parameters can be measured by direct experiences; these include the interfacial area (total surface interfaces between the liquid and gas), the void fraction (fraction of gas per unit volume), and drag (friction force between the liquid and gas). The numerical model provides much more information such as speed, size, and possible collisions of thousands of gas bubbles from the flow (see ► Fig. 40).

The calculation was performed on 1,000 cores representing 300,000 h of computing total and was executed in 10 days.

6.2.4 HPC for LES

LES stands for Large Eddy Simulation and sits on the next level just above DNS in the multi-scale approach. The goal of LES is to model the effect of small-scale turbulence eddies on the large scales in order to use a coarser mesh, while capturing the nonstationary nature of the flow due to large eddies. It essentially consists of modeling the turbulent viscosity that accounts for the subgrid-scale kinetic energy dissipation. LES will be used at larger scales where an accurate description of the wall geometry must be used. Hence, meshes are usually not regular.

Typical application examples related to the field of nuclear safety include:

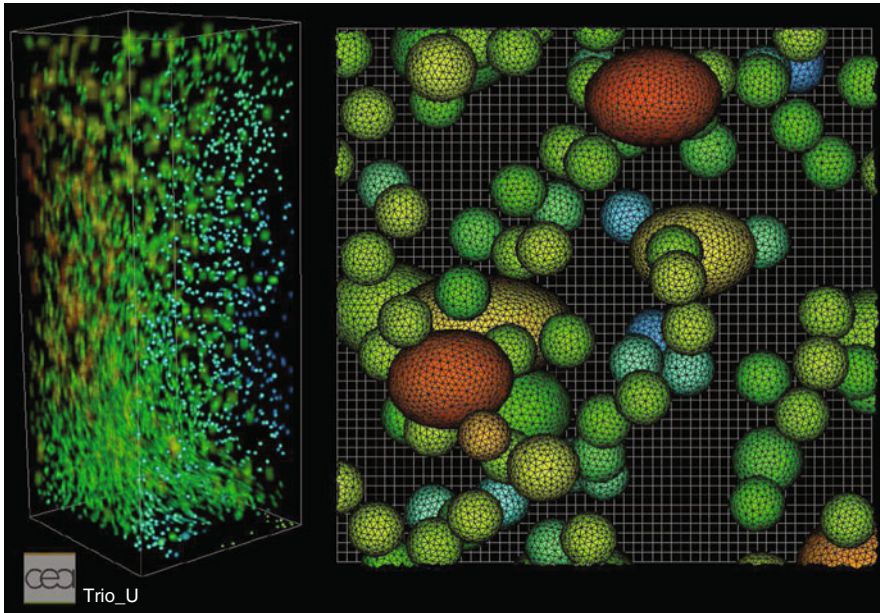


Figure 40
Example of DNS simulation, flow bubble column using Trio_U code

- Modeling of thermal oscillations at a T-junction (thermal fatigue) (see Fig. 41)
- Finding absolute extremas of boron concentration (location and value) during a clean water injection (see Fig. 42) (Bieder and Calvin 2003; Calvin 2003)
- Finding peak temperatures in a fuel assembly (see Fig. 43)

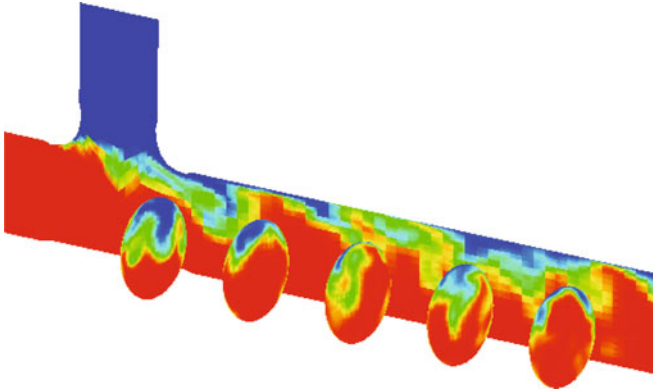
Some codes will use hexahedral elements (which sometimes requires a difficult meshing process), while some other rely on tetrahedral elements. Tetrahedral meshes will need more elements to accurately represent channel flows but can be quickly generated even for complex geometries. Moreover, they do not tend to artificially drive the flow in particular directions (e.g., main directions given by mesh lines in hexahedral meshes).

The main issues in LES are:

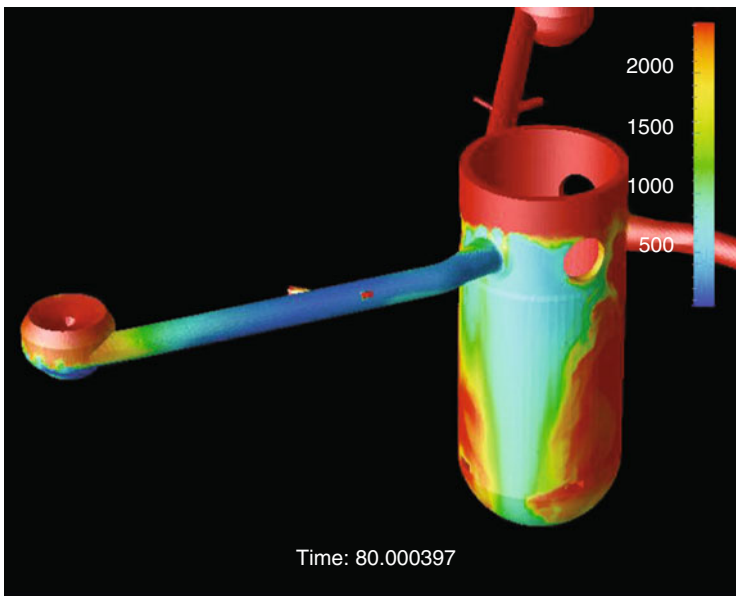
- Designing wall laws to account for the non-isotropic turbulence at walls
- Obtaining appropriate numerical schemes for unstructured grids (many cell or vertex-based methods require a questionable smoothing step to kill spurious velocity fields that are not seen by the pressure correction step).
- Being able to run unsteady simulations with appropriate meshes (10–100 million mesh elements).

6.2.5 Other Fields

We have illustrated in the previous sections the main fields where HPC is involved in CFD, but lots of other fields can address the use of HPC, like RANS models.



■ Figure 41
Modeling of thermal oscillations at a T-junction



■ Figure 42
Boron dilution in a PWR using LES approach with Trio_U code

Major problems, which one has to deal with are standard ones but have to be addressed in order to progress in the physical modeling of phenomena while conserving very good performances.

Among these problems one can cite implicit methods and code coupling.

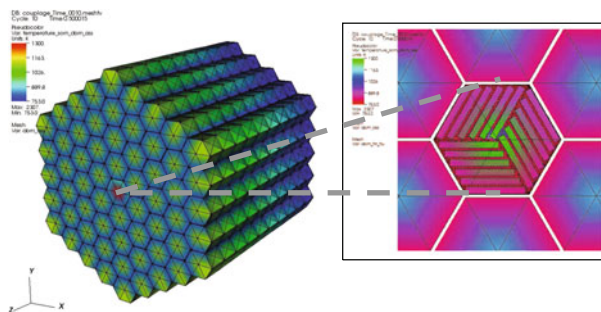


Figure 43
SFR modeling

6.3 High Performance Computing for Materials Science

Marius Stan and Stephen R. Lee – Los Alamos National Laboratory, Los Alamos, NM 87545, USA.

6.3.1 Introduction

In nuclear reactors, severe radiation environments continuously alter thermo-mechanical properties of nuclear fuels (actinide-based alloys and ceramics) (Olander 1976) and structural materials (alloys) (Hecker and Stan 2008). The physics and chemistry of such materials increase in complexity due to irradiation effects. To address these issues, several projects have been developed all over the world to assess the properties of multicomponent materials.

One of the most challenging aspects of developing a comprehensive understanding of nuclear reactor fuels and structural materials is their complex, evolving composition. The study of multicomponent systems containing U, Np, Pu, Am, Cm or Fe, C, Cr, and their oxides, nitrides, and alloys, is considerably complicated by the presence of fission products such as Xe, Cs, Sr, He, I, and Tc. Most commercial reactor and fuel performance codes assume the reactor materials to be homogenous and average the properties over the computational domain. By including the heterogeneous character of the fuels, the precision and accuracy of predictions can be significantly improved.

There is an increasing need for a multi-physics approach to develop a fundamental understanding of properties of complex nuclear fuel materials in the reactor environment, leading to improved tools for predicting phenomena such as heat transfer, phase stability, species diffusion, and fission products retention.

Recently, combined theoretical, computational, and experimental efforts have provided valuable information about material properties and important phenomena associated with nuclear fuels (Stan et al. 2007). However, as of today, models and simulations are still not regarded as critical tools for fuel design and optimization. One of the reasons is the lack of predictability, often associated with the empirical correlations used in computational tools. The applicability of such correlations is limited to a regime where experimental data is available.

Another reason is the lack of available computational power during previous design eras, which limited the fidelity and reach of simulations.

The idea of replacing empirical correlations with theory-based models for the purpose of improving high performance simulation tools is not new. For example, in USA the last nuclear test was fired in 1992, and shortly thereafter, the Comprehensive Test Ban Treaty was adopted. This led to the creation of the Stockpile Stewardship Program (SSP) and the Advanced Simulation and Computing Initiative (ASCI), started in 1996. The SSP was an integrated program of experimentation and simulation directed to certify the US nuclear weapons stockpile without full nuclear tests. ASCI was the simulation component of the overall SSP. For various reasons, ASCI did not have a counterpart in the nuclear fuels area. However, the ASCI program redefined high performance computing and applications for coupled computational multi-physics problems, all of which are available for advanced nuclear fuel performance codes today, enabling them to incorporate theory-based models and simulations rather than empirical correlations. The ASCI program also affected the type, pace, and ultimately the widespread availability of high performance computing for scientific endeavors.

The definitions below are intended to ensure a coherent framework for the presentation of results and discussions in this section:

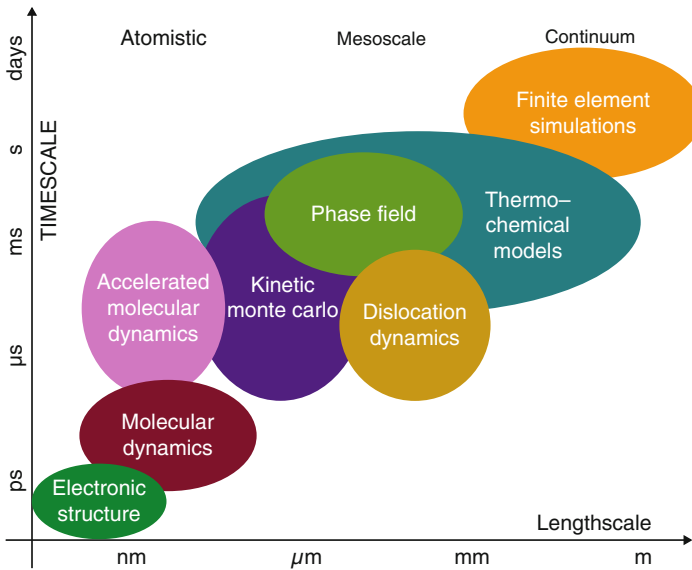
A *model* is a logical description of how a system (nuclear fuel material, in our case) performs. Models are based either on a theory or empirical knowledge and are validated by experiment (rarely by computation). Most models are presented as mathematical expressions. For example, “enthalpy depends linearly on temperature” and “enthalpy is quadratic in temperature” are different models.

Empirical models are collections of experimental observations fitted to mathematical expressions, such as (but not only) polynomial functions. When accurate, they allow for concise descriptions of material properties and are extremely valuable for technological applications. However, empirical models are only valid within the range of parameters and irradiation conditions covered in the data set on which they have been developed. Interpolation and extrapolation of empirical models is a dangerous practice that can lead to errors. Since the uncertainty associated with empirical models is often large, confidence intervals are difficult to calculate. *Theory-based models* are developed to include and explain the physics, chemistry, and materials science of fuel materials. These models are often referred to as “mechanistic” descriptions of properties. They are expected to provide a deeper understanding of the nature of the properties and to have improved predictive character.

A *simulation* is the process of running computer programs to reproduce, in a simplified way, the behavior of a system. Simulations describe the evolution of the system along a certain coordinate, most often the time. For example, a simulation of heat transport in a fuel element can describe the enthalpy content of a specific volume at different moments in time. The simulation is likely to involve a model of enthalpy, similar or more sophisticated than the ones mentioned above.

6.3.2 Theoretical and Computational Methods

To account for all the important material properties and reactor phenomena, models and simulations must address a wide range of space and time scales, starting with the nucleus, the electronic structure, atomistic, nanoscale, mesoscale, all the way to the fuel element size



■ Figure 44

Length and time scales involved in simulating phenomena relevant for nuclear materials as covered by computational methods (Stan et al. 2007)

(centimeters), and from picoseconds to seconds, all the way to the operating and storage characteristic times (months, years). The characteristic time step and space length associated with various phenomena cannot be estimated. For example, diffusion involves the electronic structure properties of the atoms at nanoscale lengths and nanosecond times. Still, the kinetics of bulk diffusion processes can be characterized from a continuum, macroscopic point of view (microns) using characteristic times of minutes, hours, and even days for the fuel-clad interaction.

To address all relevant properties and phenomena that occur in materials in general and nuclear fuels in particular, numerous theoretical and computational methods have been developed. The methods cover various time and space scales, as shown in [Fig. 44](#). The information is transferred between scales via characteristic parameters such as density, energy, temperature, or average grain size.

Nuclear methods are often reviewed as part of reactor physics books (Stacey 2001) and revolve around nuclear reactions and neutron transport theory. Sophisticated mathematical methods and computational techniques are used to calculate nuclear cross sections. Although very important for criticality calculations and reactor energy balance, the nuclear methods have, as of now, little impact on materials models. Since the thermo-mechanical and chemical properties of the nuclear fuels appear to be more influenced by the electron bands rather than the nuclear structure of the atoms, the nuclear data and associated models will not be reviewed in this section.

Atomistic methods account for the evolution of each atom in the computation domain and typically focus on point properties that are then used as a basis for statistical mechanics evaluations of bulk properties.

Electronic structure (ES) calculations are quantum mechanical (QM) calculations aimed at describing properties such as energy levels or bands, cohesive energy, lattice parameters, and phonon spectra solely based on the electronic structure of the materials. They provide invaluable information about materials, especially when no experimental data is available (Martin 2004; Singleton 2001; Sutton 1993). The QM information feeds into higher-scale models and is often used to determine interatomic potentials and forces. One of the most popular approximations is the Density Functional Theory (DFT) (Kohn and Sham 1965; March 1992), sometimes coupled with the direct force method (Frank et al. 1995; Kunc and Martin 1982). Most reliable results from electronic structure calculations are obtained at 0 K temperatures, for single-element substances. Unfortunately, it is quite common to compare these results with room or high temperature experimental, in an attempt to achieve a weak form of validation. Another challenge is calculating properties of mixtures and solutions, for specific compositions. That is related to the relative small number of atoms involved in the calculation cell (often less than 100). In spite of the limitations, ES methods are the most theoretically sound and most promising tools for predicting materials properties. To improve the quality of the results, ES methods must be run on high performance computational platforms that allow calculations involving thousands of atoms.

Molecular dynamics (MD) methods typically operate at time scales no larger than hundreds of picoseconds and involve up to one million atoms (Frenkel and Smit 2002). Although MD methods are capable of capturing lower-scale properties, they do not directly incorporate quantum mechanical properties and only operate within the framework of classical mechanics. MD methods are however very powerful and can evaluate both equilibrium properties and parameters of chemical kinetics models (Billing and Mikkelsen 1996).

The most challenging component of MD is defining the interatomic potentials and the associated interatomic forces. The atoms are given initial velocities and then the structure is relaxed until minimum free energy is reached. Many-body potentials, such as the embedded atom method (EAM) (Daw and Baskes 1984) and the modified embedded atom method (MEAM) (Baskes 1992) have been successfully used for calculations of metals and alloys properties, but rarely for actinide-based ceramics. The main reason is the very difficult process of adding charge transfer. As of today, the most reliable models for actinide-based ceramics involve pair-potentials, such as the Buckingham (Busker et al. 1999) or the shell model 0.

MD methods are successful in calculating equilibrium energy and thermal properties of nuclear materials and are very efficient in studies of point defect formation and interactions. As of today, the simulations cannot address real times t long enough to describe phenomena such as diffusion (milliseconds) or even cascade effects during irradiation (microseconds). Recent implementations of ASC high performance codes (e.g., SPaSM) at Los Alamos on the BlueGene/L Livermore architecture and the sustained petaFLOPS Los Alamos Roadrunner supercomputer (an advanced, hybrid architecture) give hope that MD simulations of species diffusion in bulk materials (seconds or minutes) will be available soon.

A temporary solution for achieving longer simulation times is the temperature-accelerated dynamics (TAD) method that increases the rate of events by increasing the temperature of the simulation (Voter et al. 2002). The behavior at temperature of interest is then determined by a mapping technique. To allow for the investigation of more atoms, MD and TMD are often coupled with Monte Carlo (MC) (Metropolis and Ulam 1949) and kinetic Monte Carlo (KMC) (Voter 2005) methods. During MC calculations, the solution space is sampled and only points that satisfy certain criteria are accepted. The quantum Monte Carlo method (QMC) is deemed

to be the most advanced tool for evaluating properties of materials at scales that allow for direct experimental validation (Foulkes et al. 2005).

Mesoscale methods operate in time and space intervals that are characteristic to material's nano- or microstructure. The methods are sometimes “atomistically informed,” in the sense that some of the parameters in the mesoscale method are optimized against the output of atomistic calculations.

The phase field (PF) method is derived from the Ginzburg–Landau theory of phase transitions (Ginzburg and Landau 1950). It assigns a set of phase variables to a target function, such as the free energy of the system, and then solves a set of evolution equations. For the case of microstructure evolution, the equations typically involve solving the Cahn–Hilliard equations (Cahn 1961; Karma 2001).

Dislocations are essentially two-dimensional (2D) defects in a continuum three-dimensional (3D) material and are typically investigated by electron microscopy. The early dislocation dynamics (DD) models were 2D (Van der Giessen and Needleman 1995; Lepinoux and Kubin 1987; Wang and LeSar 1995) but recent 3D discrete dislocation dynamics (DDD) computational approaches (Bulatov et al. 2001; Hirth et al. 1996) allow for dislocation motion and interactions with other defects, particles, and surfaces.

Most continuum computational methods involve solving relevant partial differential equations (PDE) in which a dependent variable, such as density, is a function of independent variables, usually time and spatial position (Bird 2002; Incopera and DeWitt 1996). The PDEs are solved together with equations reflecting conservation of mass, energy, and momentum. The computational space is discretized using a 3D mesh that is either fixed (Eulerian framework) or moves with the computational volume (Lagrangian framework). In the finite difference method (FDM) the solution is obtained using a discrete representation to the PDE. When more flexibility is necessary in complicated geometries, the finite element method (FEM) can provide higher-order approximations and more accurate solutions (Reddy and Gartling 2001). Rather than using point approximations on a grid, the finite volume method (FVM) approximates the average integral value of the desired property on a reference volume. Although continuum level methods capture properties of the bulk materials, they are often “informed” by atomistic and mesoscale results.

Several theoretical and computational methods can be grouped under thermo-chemical methods (TCM) (Aybar and Ortego 2005; Glicksman 2000; Sandler 1999). They are based on statistical mechanics, solid state physics, and thermodynamics and describe chemical properties of the fuel from point defect clusters to species diffusivity, all the way to the free energy and the kinetics of chemical reactions. Experimental and atomistic results are often the input data for the TCM and the predictive character is tested at continuum level, through experimental characterization of the fuel and the fuel–clad interaction.

For studies of phase stability, the calculation of phase diagrams (CALPHAD) method provides an efficient way to assess the Gibbs free energy models that are consistent with a given set of phase diagram data (Hillert 1998; Kaufman and Bernstein 1970; Sounders and Miodownik 1998). For example, the CALPHAD method and the temperature integration of the free energy from MD calculations have been coupled to produce phase boundaries in binary systems (Baskes and Stan 2003). In recently published methodologies, part of the free energy models are retrieved from QM calculations (Baskes et al. 2003).

To model known material properties and validate the calculations it is often necessary to use corrective parameters. In these cases, referring to electronic structure calculations as “first principles” is sometimes an abuse of scientific language. The use of “first principles”

should be reserved for calculations that do not involve fitting to experiment to derive model parameters.

6.3.3 Models and Simulations of Nuclear Fuels and Structural Materials

A key component is the understanding of the relationships between thermo-mechanical properties such as enthalpy, heat capacity, thermal conductivity, and thermal expansion, and parameters such as temperature, composition, porosity, pressure, and irradiation level. For example, although a review UO₂ thermal conductivity (Fink 2000) shows a wealth of models that account for temperature dependence, rarely the models include composition as a parameter (Ramirez et al. 2006). Several materials properties are implicitly dependent on the burnup level (Olander 1976; Stacey 2001). However, directly correlating thermo-mechanical properties to burnup is a challenging task. A certain burnup level can be associated with a variety of thermo-mechanical properties of the fuel, depending on the history of the fuel element and damage mechanisms involved. In other words: predicting fuel properties as function of burnup is highly desirable; using experimental information that involves burnup as the characteristic parameter may lead to mathematically ill-posed problems.

Understanding the materials microstructure (grain size, porosity, and chemistry) and the behavior under irradiation and temperature are also important areas of research. For example, the influence of self and external radiation on void and fission gas bubble formation, swelling, and creep can be incorporated in the thermo-mechanical models (Olander 1976). Unfortunately, due to the complexity of the phenomenon and the lack of a good theory, modeling creep turns out to be very difficult and semi-empirical approaches are the only solution, for now.

Reactor materials are not perfect crystals. In the absence of properties-defective structures, many fuel performance codes are modeled using values from databases that have been measured or calculated for perfect crystals. It is important that the new models incorporate point, line, 2D, and 3D defects (Phillips 2001). Models of dislocations and fracture can play a central role in improving the finite element simulations of heat and species transport in nuclear fuel elements.

The phase stability of nuclear fuels, especially during transient regimes, is a subject of concern for nuclear energy industry and regulators. Uncertainty evaluations of rather simple phase diagrams, such as UO₂ – PuO₂, revealed that the solidus and liquidus lines are known with an error as large as 100 K (Stan and Reardon 2003). Ceramic fuels tend to be less likely to melt but may experience local phase transformations. Metallic fuels are more at risk due the presence of low temperature eutectics in their phase diagram (Hecker and Stan 2008) and the potential for redistribution of the constituents in the fuel rod. Some structural materials, such as cladding alloys, are also at risk during transient regimes. Since temperature and pressure are the control parameters in most processes, the Gibbs free energy of all phases is the critical thermodynamic property for phase stability calculations (Lindemer and Besmann 1985). When taking into account the fission products and the chemical dynamics of the fuel material, it becomes necessary to study systems with five to ten components to achieve a good description of the thermo-chemical properties of the fuel. Although free energy functions are available for many phases of interest (mostly oxides and alloys) more work is necessary to cover the nitrides and the advanced (minor actinide containing) fuels. In France, the Atomic Energy

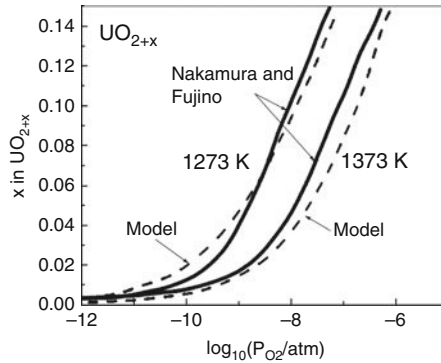


Figure 45

Cross section of UO_2 fuel rod operated at a linear power high enough to cause extensive melting [LYO65]

Commission (CEA) has developed one of the most advanced databases for thermodynamic properties of fuels, named FUELBASE. Similar studies are under development in USA, at the National Institute for Standards and Technology (NIST).

Reactor materials are subject to severe radiation environments and their thermal, chemical, and mechanical properties change significantly with time and irradiation level. The major factors that influence the properties are temperature, stoichiometry, and microstructure (especially porosity and point defects). It was discovered early on (Lyons et al. 1965) that the accumulation of fission products in gas bubbles can decrease the heat transfer, leading to overheating of the fuel element and local melting (► Fig. 45).

Recent work at LANL was focused on irradiation effects on properties such as thermal conductivity, oxygen diffusivity, and thermal expansion. The methods cover a large spectrum of time and space scales, from electronic structure to atomistic, to mesoscale, to continuum (Stan et al. 2007). As an example of the coupling between atomistic models of point defect and thermo-chemical method, ► Fig. 46 shows a calculation of UO_{2+x} nonstoichiometry as a function of partial pressure of oxygen. The model is further used to predict point defect concentrations and oxygen diffusivity at various temperatures and oxygen pressures.

In these results, the migration rates of the oxygen interstitials and vacancies are calculated using activation energies obtained from experiments (Kim and Olander 1981).

Another example, this time at the mesoscale, is given in ► Fig. 47 and shows a comparison of simulated and experimental gas bubbles formation and evolution (Hu et al. 2007, 2009). This type of simulations requires intensive computation and is most suitable for high performance computing. However, at the time of this writing, no parallel phase field codes for this purpose was available. Current work in this area in USA, France, and Japan is focused on developing models of advanced, multicomponent fuels that contain transuranic elements (minor actinides) as well as advanced structural materials, such as oxygen deficient steels (ODS) (Samaras et al. 2009). The next step is to include fission products as system components.

Uranium-oxide-based nuclear fuels are commonly used in thermal, light water reactors and have been recently considered as the potential fuel for fast, breeder reactors. As shown in ► Fig. 48, the oxide nuclear fuel rods consist of oxide fuel pellets stacked in a cylindrical

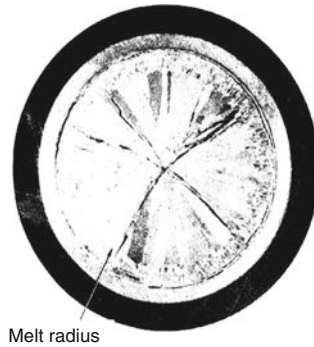


Figure 46

UO_{2+x} non-stoichiometry as a function of partial pressure of oxygen. Solid lines: Nakamura model. Dashed lines: calculated with the present model (Stan and Cristea 2005; Stan et al. 2007)

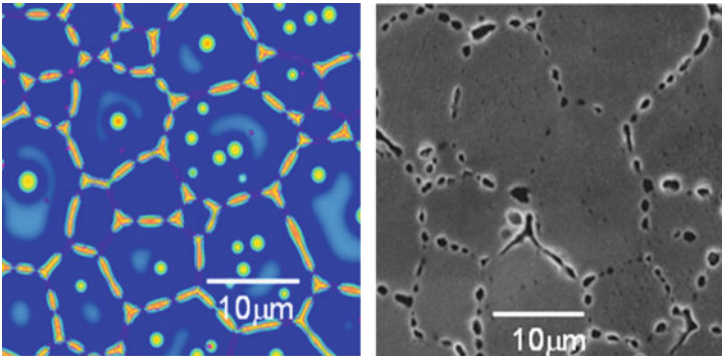


Figure 47

Left panel: phase field simulations of gas bubbles evolution in UO_2 (Hu et al. 2009). The color scheme represents the He concentration (high = yellow and low = blue). *Right panel:* Experimental microstructure of irradiated UO_2 fuel (Zacharie et al. 1998)

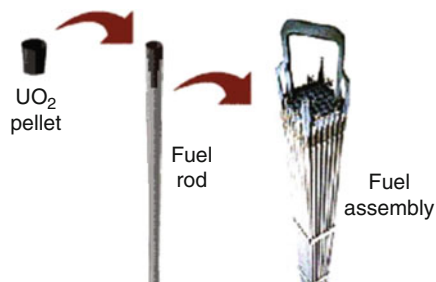


Figure 48

Schematic of the nuclear fuel rod and assembly (United States Nuclear Regulatory Commission, Emergency Preparedness)

metal cladding and then bundled in a fuel assembly, operating at temperatures up to 2,000 K (United States Nuclear Regulatory Commission, Emergency Preparedness).

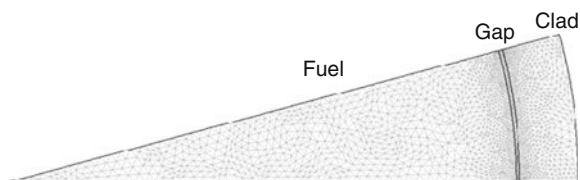
There are many additional fuel types, and evaluating them all is beyond the scope of this work. The most popular, with the richest history, are based on uranium oxide (Belle 1961). Plutonium oxide was introduced as a component of the mixed oxide fuels (MOX) for reasons that include reprocessing of the weapons grade plutonium metal for energy purposes. Metallic fuels have been investigated with success but are less popular (Hecker and Stan 2008).

Given the tremendous resources (cost, time, people) required to conduct experiments in the nuclear reactors, the studies of nuclear fuels are sometimes replaced by studies of surrogate ceramic materials, such as ceria (CeO_2) or zirconia (ZrO_2). The problem with such studies is the transferability of the results. For example, although ceria is considered a good surrogate for plutonia (Stan et al. 2002) it is not clear if the study of the fission product diffusion mechanism in the $\text{UO}_{2+x} - \text{CeO}_{2-x}$ system can provide a definitive answer to the questions related to fission products accumulation in a mixed oxide fuel $\text{UO}_{2+x} - \text{PuO}_{2-x}$. Another reason to use lower atomic number elements such as Ce as surrogate for high atomic number actinides (U, Pu, Th, etc.) is the complexity of the ES calculation. High performance computing may help completing the necessary calculations to fully describe properties of complex, actinide materials and reduce the need for surrogates.

Researchers at Los Alamos National Laboratory (LANL) have examined the influence of temperature and stoichiometry changes on the UO_{2+x} fuel properties and on the coupling of heat and species transport in a fuel element with stainless steel cladding (Ramirez et al. 2006). The objective was to improve the understanding of fuel damage and performance. Several parametric models have been created for these properties using the temperature, pressure, burnup, and other reactor parameters (Cristea et al. 2007; Stan and Cristea 2005; Stan et al. 2007). The main advantage of the LANL models is the fact that they include the dependence of the properties on the stoichiometry x in UO_{2+x} .

The finite element simulations of coupled heat and oxygen transport (Ramirez et al. 2006) were performed using COMSOL Multiphysics^{texttrademark} which provides an ideal tool for studying coupled phenomena and allows for mesh and time step refinement in 3D configurations (► Fig. 49). Quadratic Lagrange elements and a nonlinear iterative technique with a nested unsymmetric multi-frontal (UMFPACK) linear solver have been used to solve the coupled heat and species equations.

The steady-state parametric studies were focused on determining the centerline temperature in the fuel rod as a function of non-stoichiometry and the rate of heat generation during



■ **Figure 49**
Representative “slice” of the computational domain, showing a 22.5 deg. angular sector of the fuel element. The mesh was refined at the gap, where temperature and stoichiometry gradients are steeper.

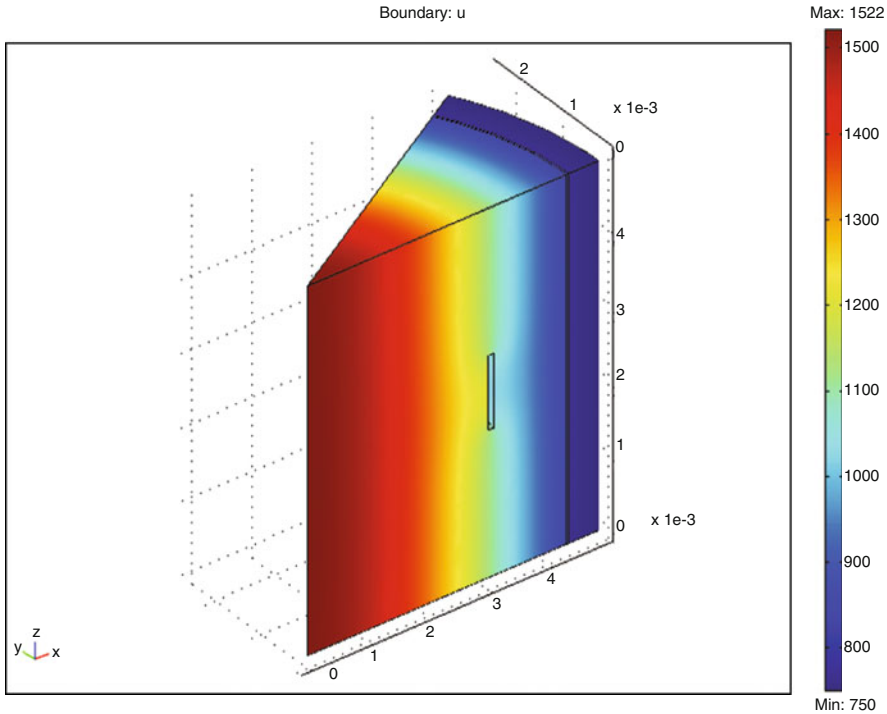


Figure 50

FEM simulations of heat transport in a fuel element. A disc-shaped macroscopic defect was placed in the fuel pellet to simulate the effect of a macroscopic defect. The simulation predicts that the temperature (color scale in K) will locally increase by 190 K (Lyons et al. 1965; Stan et al. 2009)

fission. Given the strong temperature gradients in the reactor, the effect of thermally driven diffusion of species, also known as the Soret effect, had to be included. The results show that the counterbalancing of the Soret (Janek and Timm 1998; Korte et al. 1997) and Fickian fluxes is responsible for the variation of oxygen concentration in the fuel pellet (Ramirez et al. 2006). The simulations demonstrate that including macroscopic defects in the fuel pellet can lead to significant changes in the local temperature. Additional simulations involved transient regimes and examination of the time lag in the response of the temperature and non-stoichiometry distributions with respect to sudden changes in heat generation rate intensity and oxygen removal rate. Current work includes studies of the effects of macroscopic defects such as porosity (Fig. 50) and simulations of fuel-cladding interactions involving simulations on high performance computational platforms.

6.3.4 Fuel Performance Codes

Evaluating the properties of the fuel and predicting the changes caused by the reactor environment is a challenging task. Most nuclear technological processes are complex combinations of

the above reviewed properties and phenomena. As an example, sintering of ceramic fuel materials involves heat and mass transport, phase transformations, irradiation effects, and changes in mechanical properties. A complex simulation of the sintering process must be developed as soon as possible, to assist with fuel design and fabrication.

Fuel performance is one of the areas that already benefited from models and simulations. A fuel performance capability (FPC) consists of a computer code or a set of codes that contain models of fuel properties and are able to simulate phenomena in the nuclear fuel during operation. In a more general version of this concept, the fuel performance is evaluated in the fuel element (fuel plus clad) and the applicability is extended to cover manufacturing and storage. The FPCs are sometimes classified according to their history and complexity into “generations” starting with Generation 1 (1D, serial codes based on empirical models) and ending with Generation 4 (future, parallel, 3D codes that contain theory-based models).

Besides extensive experimental post irradiation examination (PIE), the fuel performance capabilities are increasingly complex tools in support of fuel characterization and optimization (Aybar and Ortego 2005).

For this section, we have extended the review of FPCs and found that most countries tend to develop their own simulation capabilities. Here is a list (by no means exhaustive) of some of the most popular fuel performance codes: COMETHE (Belgonucleaire, Belgium), COPERNIC (FRAMATOME, Germany), ENIGMA (British Energy, BNFL, UK), FALCON (EPRI, USA), FRAPCON (PNNL, USA), FRAPTRAN (PNNL, USA), LIFE (ANL, USA), MACROS (SCK-CEN, Belgium), ORIGEN (ORNL, USA), PARFUME (INEEL, USA), SPHERE (PSI, Switzerland), and TRANSURANUS (ITU, Germany).

The major drawback of most FPCs is the fact that they are too dedicated to a specific fuel form and composition. The use of empirical correlations in describing material properties and the much simplified description of heat and mass transport phenomena make extrapolations and information transfer impossible. In order to achieve a consistent predictive character, many codes are moving away from empirical models and include theory-based models.

Neutron transport *fission processes*, although not the main subject of this section, are a critical component of fuel behavior. Phenomena such as fission products release, diffusion, and accumulation have a strong impact on material properties and influence the heat and mass transport. Up to now, due to computational power limitations, nuclear reactions have been decoupled from the study of material properties. For example, in many FPCs, the heat generated during fission is only added as a source term to the finite element calculations. Modern high performance computing opens the door for fully coupled simulations of neutrons, heat, and species transport in the reactor.

Since in the nuclear fuels community heat and species transport phenomena have been studied in much more detail, most commercial fuel performance codes, such as FRAPCON (FRAPCON simulation code) have capabilities for a global evaluation of heat transfer and species diffusion simulations. Some codes can address transient regimes and solve for the time-dependent transport equations. More challenging are the simulations of heat transfer in heterogeneous materials, with porosity and defects distributed in the fuel rod according to experimental data.

Although extremely important, the diffusion of fission products is not well understood due to the lack of “in situ” characterization methods. Also, the role of diffusion at the grain boundaries is still unclear. This phenomenon is strongly related to microstructure evolution and must be further studied using experimental and theoretical tools. Unfortunately, accurate models of

microstructure evolution (point defects and dislocations along with grain boundary movement) during service are most often lacking in FPCs.

Our review shows that many codes do not address the thermo-chemistry of chemical reactions, such as oxidation/reduction or the effect of the coolant on the radiation-enhanced corrosion of reactor materials. One exception is TRANSURANUS, which accounts for radial redistribution of oxygen in fast breeder reactor fuels.

All FPCs focus on thermo-mechanical properties and phenomena. Still, mechanical phenomena that involve 3D simulations, such as pellet fragmentation and clad–pellet interactions are difficult to address at this stage. Most codes do not allow for simulations of large changes in the gap and clad geometry. That leads to simulation tools for rather idealized geometries, difficult to validate against experimental results on real fuel elements.

From a computational point of view, a major problem is the fact that most FPCs cannot run in parallel on high performance supercomputers and use simplified, and often empirical, models reflective of the limited computational horsepower available to these codes at the time they were created. This both increases the computation time and reduces the computation fidelity. It is unfortunate that current FPCs do not take advantage of this technology and are still running on personal computers. There is, therefore, a tremendous opportunity for moving to high performance computing for nuclear fuels applications and increasing their fidelity and speed. Each of the top 500 fastest supercomputers in the world today can now reach over a teraflop per second. At the time of writing this article, the number one position in the world was claimed by the Roadrunner computer at LANL (Roadrunner supercomputer. <http://www.lanl.gov/roadrunner>), a joint development of Los Alamos, IBM, Toshiba, and DOE's National Nuclear Security Administration (NNSA). The second place position was held by the Jaguar computer at Oak Ridge National Laboratory. The European Union and Japan are also working on systems that will compete for first place in the future. Already, neutron diffusion calculations, as well as some safety and security simulations, are performed on such resources. FPCs can and must become more complex to run on supercomputing networks. This involves innovative code design and advance algorithms which are capable of taking advantage of the hardware developments. The codesign of such an application with emerging computational architectures, along with improvements in physics models and numerical methods made available by such systems, provide a path for enhanced fidelity and performance, pointing toward predictive capability and quantified uncertainties.

Another major difficulty is the lack of compatibility between the FPCs. The codes have very useful and complementary features but cannot be coupled and executed together, nor even easily feed information to each other. Software engineering issues prevent a full coupling of the codes and modifying them to run in parallel very difficult, as required for large-scale simulations on advanced computational platforms. To solve this problem, France has developed an integrating platform SALOME (<http://www.salome-platform.org/home/presentation/overview/>) intended to facilitate the creation of industrial simulation applications. It is currently used by CEA for nuclear energy simulations that incorporate independent fuel performance and reactor codes. Using this platform and the associated codes, CEA researchers have been able to produce integrated, multi-scale simulations in irradiated fuel elements.

The question remains: is it better to attempt to modify existing codes to make them structured, run in parallel on high performance computational platforms, and possibly become object oriented, or create new codes from scratch? The answer to this question is complex, and ultimately depends on available human resources and expertise and how the code will be used.

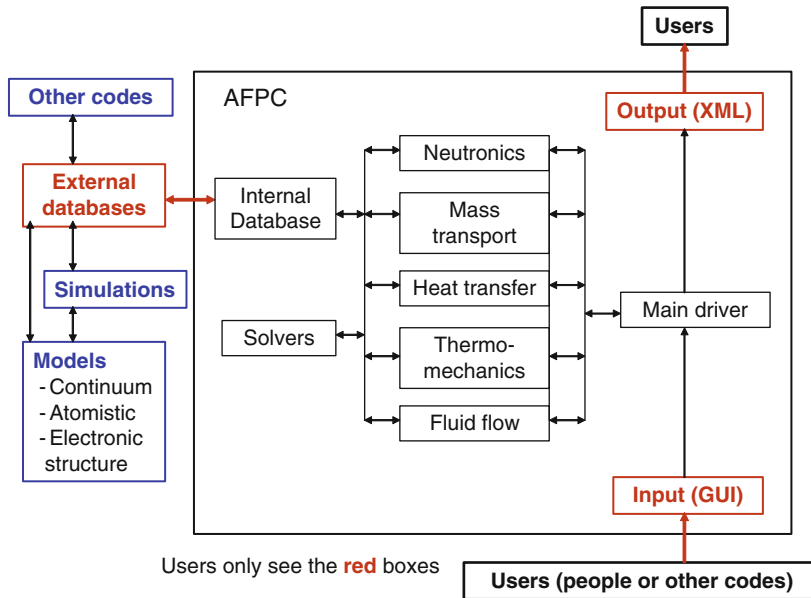


Figure 51

Preliminary design of the advanced fuel performance capability (AFPC) (Stan 2005; Stan et al. 2009)

Modifying a large existing legacy code can be very difficult and time consuming, and in some cases, impossible, due to the limitations of the data structures embedded in the code. Repeatability of computational results achieved from a re-factored legacy code can also be an issue, particularly if previously unknown errors are found. However, legacy codes represent a wealth of integrated experience and knowledge that require preservation. Creating a new code from scratch is also a difficult endeavor for different reasons – validation of an entirely new code with no historical pedigree being one of the most difficult. There are several options for developing new fuel performance capabilities, going from integration of existing codes to the design of new ones.

The real answer to this question lies in a combination of approaches. It is particularly important to carefully plan verification and validation activities as empirical methods are replaced with more advanced and accurate methods on faster computers. It is given that, as legacy codes are re-factored and reborn, previously achieved results will change due to an unknown canceling of errors that occurred in legacy codes.

This challenging endeavor involves both model development and software engineering.

► Figure 51 shows a preliminary design of a new generation, advanced fuel performance capability (AFPC) (Stan 2005). To address the nuclear fuels material properties and phenomena, the code must include at the minimum the following components:

- Neutronics (fission and neutrons diffusion)
- Heat transfer (conduction, convection, and radiation)
- Mass transport (species diffusion and gas accumulation)
- Thermo-mechanics (deformation, such as swelling)

- Fluid flow (to model the coolant, if necessary)

There are also requirements related to numerical algorithm design, uncertainty quantification, and software engineering. For example, using nested (linear + nonlinear) solvers, multilevel preconditioning, running parallel on large-scale supercomputers, and easy adaptation to hybrid platforms are all requirements. Additionally, the code must interact with an external database that is continuously updated with the most advanced models of fuel and material properties and the necessary nuclear data.

Another vital component of this strategy is creating the framework for active national and international collaborations. For example, the Materials Models and Simulations for Nuclear Fuels (MMSNF) workshop series (<http://itu.jrc.ec.europa.eu/index.php?id=36&type=&iEntryUID=164&iEntryPID=68>) and the OECD/NEA Working Party on Multi-Scale Modelling of Fuels and Structural Materials for Nuclear Systems (WPMM) (<http://www.nea.fr/html/science/wpmm/index.html>.) have the goals of establishing multi-scale models and simulations as validated predictive tools for the design of nuclear systems, fuel fabrication, and performance.

Given the improvements in precision and accuracy, and the full validation of the methods, the computer simulation capabilities (sets of codes) are likely to soon become part of the fuel qualification process. The most challenging aspect of this process is building the trust of the national regulatory agencies. To achieve the necessary level of confidence, the codes must be thoroughly validated against experimental data.

6.3.5 Conclusions

The radiation environment specific to nuclear reactors continuously alters the properties of nuclear fuels and structural materials. There is a need for an integrated theoretical, experimental, and computational approach to develop a fundamental understanding of properties of complex materials in the reactor environment. A key component of such approach is relating the models of thermo-mechanical properties such as enthalpy, heat capacity, thermal conductivity, and thermal expansion, to parameters such as temperature, composition, porosity, pressure, and irradiation level. Such a methodology can lead to improved tools for simulation and predicting reactor phenomena, including heat transfer, phase stability, species diffusion, and fission products retention.

In this work we distinguish between models (mathematical representations of how materials perform) and simulations (the process of running computer programs to reproduce, in a simplified way, the behavior of materials). Models and simulations address a wide range of space and time scales, starting with the nucleus to the electronic structure, atomistic, nanoscale, mesoscale, all the way to the fuel element size (centimeters), and from picoseconds to seconds, all the way to the operating and storage characteristic times (months, years).

A review of recent model and simulation results in USA, Europe, and Japan shows the importance of accounting for radiation effects on properties such as thermal conductivity, oxygen diffusivity, and thermal expansion. By coupling atomistic models of point defect and thermo-chemical methods into a model of oxygen diffusivity in UO_{2+x} , predictions of point defect concentrations and fuel stoichiometry at various temperatures and oxygen pressures are now available. Based on the same models, the simulations of coupled heat transfer and species diffusion demonstrated that including the dependence of thermal conductivity and

density on composition can lead to changes in the calculated centerline temperature and thermal expansion displacements that exceed 5%.

The major drawback of most commercial fuel performance capabilities (FPCs) is the fact that they are dedicated to a specific fuel form and composition. The use of empirical correlations in describing material properties and the much simplified calculations of heat and mass transport make accurate extrapolations very difficult. Many codes are moving away from empirical models toward including theory-based models, to achieve a consistent predictive character. From a computational point of view, a major problem is that the majority of commercial codes are not designed to take advantage of the high performance (tera- and petascale) computational platforms. In this work we propose a preliminary design of an advanced fuel performance capability (AFPC) that is able to interact with the material properties database and provide an efficient way of performing multi-physics simulations of coupled phenomena, such as neutron, heat, and chemical species diffusion.

The most important resource for achieving the goal of conducting high performance simulations of material's properties in nuclear reactors is the people: computer and computational scientists, physicists, chemists, and materials scientists. Their contribution is essential in ensuring the relevance of the modeling and simulation work for the nuclear engineering community. A large pool of experts is necessary to cover all theoretical, experimental, and computational tasks. That can be achieved by including "Models and Simulation" in the materials science and nuclear engineering programs at universities all over the world and by increasing national and international collaborations.

We hope that, given the improvements in precision and accuracy and the full validation of the models, the high performance computer simulations will soon become part of the fuel qualification process.

7 Conclusion and Open Issues

We have presented in this chapter a short introduction to high performance computing and some illustrations of this use in nuclear engineering.

This chapter could neither cover all the fields of parallel computing nor all the uses of HPC in nuclear engineering. We have tried to figure out how HPC tools can be useful and even sometimes be the unique way to progress and go beyond some limits.

Of course the domain of computer science and HPC permanently moves, and it is a tricky exercise to describe the state of the art of this domain. We do not have the pretention to be exhaustive but we have tried to show the major challenges involved in the field of nuclear energy and HPC. But there are still many of them which are open issues for HPC in nuclear engineering.

First of all, concerning architecture and processors, one of the biggest challenges is to reach the desired performances (many petaflops, exaflops, etc.) within a controlled thermal envelope. Moreover, tomorrow's architecture will be based on hundreds of thousands of cores, and the failure probability will grow dramatically. Thus, in order to use these supercomputers, fault tolerance will have to be taken into account at different levels: hardware level, middleware level, and application ones. Another great challenge is the programmability of these architectures, since the number of parallelism levels is increasing more and more (multi-instructions in one core, multi-threading between cores in a same node, concurrency between cores and accelerators, task parallelism between nodes, etc.) and it becomes more and more difficult to express parallelism in an efficient way.

All these hardware and software challenges have of course direct consequences on applications, especially on the design and the methods to “embed parallelism” into scientific applications. Thus, applications have to be more and more modular and versatile in order to be as polymorphic as possible and at the same time the most efficient as possible for a given parallel architecture at a given time and able to move to other parallelism models for the future, since the code life cycles are much more longer than supercomputer architectures.

References

- Andrade H, Kurc T, Sussman A, Saltz J (2003) Exploiting functional decomposition for efficient parallel processing of multiple data analysis queries. In: Proceedings parallel and distributed processing symposium, Nice, France
- Aybar HS, Ortego P (2005) A review of nuclear fuel performance codes. *Prog Nucl Energy* 46: 127–141
- Barre F, Bernard M (1990) The CATHARE code strategy and assessment. *Nucl Eng Des J* 124(3): 257–284
- Baskes MI (1992) Modified embedded-atom potentials for cubic materials and impurities. *Phys Rev B* 46:2727
- Baskes MI, Stan M (2003) An atomistic study of solid/liquid interfaces and phase equilibrium in binary systems. *Metall Mater Trans* 34A: 435–439
- Baskes MI, Muralidharan K, Stan M, Valone SM, Cherne FJ (2003) Using the modified embedded-atom method to calculate the properties of pu-ga alloys. *JOM* 55:41–50
- Belle J (ed) (1961) Uranium oxide: properties and nuclear applications. Naval Reactors, Division of Reactor Development USAEC
- Bieder U, Calvin C et al (2003) Detailed thermal hydraulic analysis of induced break severe accidents using the massively parallel CFD code Trio_U/PRICELES. In: 5th international conference on supercomputing for nuclear applications (SNA – 2003), 22–24 September 2003, Paris, France
- Billing GD, Mikkelsen KV (1996) Introduction to molecular dynamics and chemical kinetics. Wiley, New York
- Bird RB (2002) Transport phenomena. Wiley, New York
- Brown F, Goorley J, Sweezy J (2003) MCNP5 parallel processing workshop, workshop M&C. http://mcnp-green.lanl.gov/publication/mcnp_publications.html
- Bulatov V, Tang M, Zbib HM (2001) Crystal plasticity from dislocation dynamics. *Mater Res Soc Bull* 26:191–195
- Burkhardt H et al (February 1992) Overview of the KSR1 computer system. Technical Report KSR-TR-9202001. Kendall Square Research, Boston
- Busker G et al (1999) Solution mechanisms for dopant oxides in yttria. *J Am Ceram Soc* 82: 1553–1559
- Butenhof DR 1997 Programming with POSIX(R) threads. Addison-Wesley Professional Computing Series
- Cahn JW (1961) On spinodal decomposition. *Acta Metall* 9:795–801
- Calvin C (2003) A development framework for parallel CFD applications: Trio-U project. 5th international conference on supercomputing for nuclear applications (SNA – 2003), 22–24 September 2003, Paris, France
- Calvin C, Cueto O, Emonot P (2002) An object-oriented approach to the design of fluid mechanics software. *M2AN* 36(5):907–921
- Chandra R (2001) Parallel programming in OpenMP. Academic, San Diego
- Chapman B et al (2001) Program development environment for OpenMP programs on ccNUMA architectures. In: Large-scale scientific computing. 3rd international symposium, Sozopol, Bulgaria, vol 2179, pp 210–217
- Chapman B, Jost G, van der Pas R (2007) Using OpenMP – portable shared memory parallel programming. MIT Press, Cambridge
- Coulomb F (1997) Parallelization of the DSN multi-group neutron transport equation on the CRAY-T3D using CRAFT. In Proceedings of the 8th SIAM conference on parallel processing for scientific computing, PPSC, Minneapolis, Minnesota
- Cristea P, Stan M, Ramirez JC (2007) Point defects and oxygen diffusion in fluorite type oxides. *J Optoelectr Adv Mater* 9:1750–1756

- Dahmani M, Roy R (2005) Parallel solver based on the three-dimensional characteristics method: design and performance analysis. *Nucl Sci Eng* 150(2):155–169.
- Dahmani M, Roy R (2006) Scalability modeling for deterministic particle transport solvers. *Int J High Perform Comput Appl* 20(4): 541–556
- Do JM et al (2009) Fuel loading pattern for heterogeneous EPR core configuration using a distributed evolutionary algorithm. In: *Proceedings of M&C, Saratoga Springs, New York*
- Daw MS, Baskes MI (1984) Embedded-atom method: Derivation and application to impurities and other defects in metals. *Phys Rev B* 29:6443
- Deng L, Xie Z-S (1999) Parallelization of MCNP Monte Carlo neutron and photon transport code in parallel virtual machine and message passing interface. *J Nucl Sci Technol* 36(7): 626–629
- Duncan R (1990) A survey of parallel computer architectures. *IEEE Comput* February:5–16
- Feautrier P (2006) Automatic parallelization in the polytope model. In: *The data parallel programming model*. LCNS. Springer
- Fink JK (2000) Thermophysical properties of uranium dioxide. *J Nucl Mater* 279:1–18
- Flynn M (1972) Some computer organizations and their effectiveness. *IEEE Trans Comput* C-21:948
- Foulkes WMC, Mitas L, Needs RJ, Rajagopal G (2005) Quantum monte carlo simulations of solids. *Rev Mod Phys* 73:33–83
- Frank W, Elsasser C, Fahnle M (1995) AB initio force-constant method for phonon dispersions in alkali metals. *Phys Rev Lett* 74:1791–1794
- FRAPCON simulation code. <http://www.pnl.gov/frapcon3/>
- Frenkel D, Smit B (2002) *Understanding molecular dynamics*. Academic Press, San Diego
- Gannon DB, Rosendale JV (1984) On the impact of communication complexity on the design of parallel numerical algorithms. *IEEE Trans Comput* 33:1180–1194
- Ginzburg VL, Landau LD (1950) On the theory of superconductivity. *Zh Eksp Teor Fiz* 20:1064
- Glicksman ME (2000) *Diffusion in solids*. Wiley, New York
- Golfier H et al (2009) APOLLO3: a common project of CEA, AREVA and EDF for the development of a new deterministic multi-purpose code for core physics analysis. In: *Proceedings of M&C, Saratoga Springs, New York*
- Goorley T, Brown F, Cox LJ (2003) MCNP 5TM improvements for windows PCs. In: *Nuclear mathematical and computational sciences, Gatlinburg, Tennessee, 6–11 April 2003 (CD-ROM)*. American Nuclear Society, LaGrange Park
- Gschwind M et al (2006) Synergistic processing in cell's multicore architecture. *IEEE Micro* 26(2):10–24
- Guérin P, Baudron A-M, Lautard J-J (2005) A component mode synthesis method for 3D cell by cell SPn core calculation using the mixed dual finite element solver MINOS. M&C, Avignon, France
- Guérin P, Baudron A-M, Lautard J-J (2006) Component mode synthesis methods applied to 3D heterogeneous core calculations, using the mixed dual finite element solver MINOS. PHYSOR, Vancouver, Canada
- Guérin P, Baudron A-M, Lautard J-J (2007) Domain decomposition methods for core calculations using the MINOS solver. M&C, Arignon, France
- Han Gyu J et al (2004) Methods and performance of a three-dimensional whole-core transport code DeCART. PHYSOR, Chicago, USA
- Hecker SS, Stan M (2008) Plutonium metallic fuels for fast reactors. *J Nucl Mater* 383:112–118
- Hellekalek P (July 1998) Don't trust parallel Monte Carlo! *ACM SIGSIM Simul Digest Arch* 28(1)
- Herrero JJ, Ahnert C, Aragonés JM (2007) Spatial domain decomposition for LWR cores at the pin scale. *ANS Winter meeting*
- Hillert M (1998) *Phase equilibria, phase diagrams and phase transformations*. Cambridge University Press, New York
- Hillis D (1982) New computer architectures and their relationship to physics or why CS is no good. *Int J Theor Phys* 21(3/4):255–262
- Hirth JP, Rhee M, Zbib HM (1996) Modelling of deformation by a 3D simulation of multipole, curved dislocations. *J Comput-Aided Mater Des* 3:164–166
- Hong S, Kim H (June 2009) An analytical model for a GPU architecture with memory-level and thread-level parallelism awareness. *ACM SIGARCH Comput Archit News Arch* 37(3): 152
- H.P.F. Forum (1993) *High Performance Fortran language specification (version 1.0)*. <http://www.netlib.org/hpf/>
- Hu SY, Baskes MI, Stan M, Tome C (2007) Phase-field modeling of microvoid evolution under elastic-plastic deformation. *Appl Phys Lett* 90:81921–81923
- Hu S, Henager Jr CH, Heinisch HL, Stan M, Baskes MI, Valone SM (2009) Phase-field modeling of gas bubbles and thermal conductivity evolution in nuclear fuels. *J Nucl Mater* 392: 292–300

- Hugot FX, Lee YK, Malvagi F (2008) Recent R&D around the Monte Carlo code Tripoli4 for criticality calculations. In: Proceedings of PHYSOR conference, Interlaken, Switzerland
- Hwang K (1993) Advanced computer architecture – parallelism, scalability, programmability. McGraw-Hill/MIT Press, New York/Cambridge
- Incopera FP, DeWitt DP (1996) Fundamentals of heat and mass transfer. Wiley, New York
- Janek J, Timm H (1998) Thermal diffusion and Soret effect in $(U,Me)O_{2+\delta}$: the heat of transport of oxygen. *J Nucl Mater* 255:116–127
- Karma A (2001) Phase-field formulation for quantitative modeling of alloy solidification. *Phys Rev Lett* 87:115701
- Kaufman L, Bernstein H (1970) Computer calculations of phase diagrams. Academic, New York
- Kim KC, Olander DR (1981) *J Nucl Mater* 102:192
- King CT, Chu WH, Ni LM (1988) Pipelined data parallel algorithms – concept and modeling. In: Proceedings of the international conference on supercomputing, Saint-Malo, France, pp 385–395
- Kohn W, Sham LJ (1965) *Phys Rev* 140:A1133
- Korte C, Janek J, Timm H (1997) Transport processes in temperature gradients: thermal diffusion and Soret effect in crystalline solids. *Solid State Ionics* 101/103:465–470
- Kunc K, Martin RM (1982) Ab initio force constants of GaAs: a new approach to calculation of phonons and dielectric properties. *Phys Rev Lett* 48:406–409
- Laucoin É, Calvin C (2004) A parallel front-tracking method for two-phase flows simulations. Parallel Cfd, Gran Canaria Las Palmas City, Spain
- Leighton FT (1992) Introduction to parallel algorithms and architectures: arrays – trees – hypercubes. Morgan Kaufman Publishers, San Mateo
- Lepinoux J, Kubin LP (1987) The dynamic organization of dislocation structures: A simulation. *Scr Metall* 21:833–838
- Lewis TG, Payne WH (July 1973) Generalized feedback shift register pseudorandom number algorithm. *ACM* 20(3):456–468
- Lindemer TB, Besmann TM (1985) Chemical thermodynamic representation of $\langle PuO_2-x \rangle$ and $\langle U_1-zPuzO_w \rangle$. *J Nucl Mater* 130:473
- Lyons MF et al (1965) *Trans Am Nucl Soc* 8:42
- March NH (1992) Electron density theory of atoms and molecules. Academic, New York
- Martin RM (2004) Electronic structure. Cambridge University Press, New York
- Metcalf M, Reid J (1999) FORTRAN 90/95 explained, 2nd edn. Oxford University Press, Oxford
- Metropolis N, Ulam S (1949) The Monte Carlo method. *J Am Statist Assoc* 44:335–341
- Olander DR (1976) Fundamental aspects of nuclear reactor fuel elements. TID-26711-P1. Technical Information Service, U.S. Department of Commerce, Springfield, Virginia
- Palmiotti G et al (2007) UNIC: Ultimate Neutronic Investigation Code. M&C, Monterey, USA
- Phillips RB (2001) Crystals, defects, and microstructures. Cambridge University Press, Cambridge
- Procassini R, O'Brien M, Taylor J (2005) Load balancing of parallel Monte Carlo transport calculations. M&C, Avignon, France
- Rabenseifner R et al (2006) Hybrid MPI and OpenMP parallel programming. In: Recent advances in parallel virtual machine and message passing interface. LNCS. Springer, Berlin
- Ragusa J (April 2003a) Implementation of multithreaded computing in the neutronics FEM solver Minos. In: Proceedings of the ANS mathematics and computations international conference, Gatlinburg, Tennessee
- Ragusa J (September 2003b) Application of multithread computing and domain decomposition to the 3-D neutronics FEM code CRONOS. In: International conference on supercomputing in nuclear applications, Paris, France
- Ramirez JC, Stan M, Cristea P (2006) Simulations of heat and oxygen diffusion in UO_2 nuclear fuel rods. *J Nucl Mater* 359:174–184
- Reddy JN, Gartling DK (2001) The finite element method in heat transfer and fluid dynamics. CRC Press, LLC, Boca Raton
- Roadrunner supercomputer. <http://www.lanl.gov/roadrunner/>
- Roosta SH (2000) Parallel processing and parallel algorithms: theory and computation. Springer, LCNS
- Roy R, Stankovski Z (1997) Parallelization of neutron transport solvers. In: Recent advances in parallel virtual machine and message passing interface. LCNS, vol 1332, pp 494–501
- Saad Y, Schultz MH (1989) Data communication in parallel architectures. *Parallel Comput* 11: 13–150
- SALOME platform. <http://www.salome-platform.org/home/presentation/overview/>
- Samaras M, Victoria M, Hoeffelner W (2009) Nuclear energy materials prediction: application of the multiscale modelling paradigm. *Nucl Eng Technol* 41:1–10
- Sandler SI (1999) Chemical engineering and thermodynamics. Wiley, New York
- Simulation and modeling for advanced nuclear energy systems workshop. <https://www.cels.anl.gov/events/workshops/anes/>

- Singh JP et al (1993) An empirical comparison of the Kendall Square Research KSR-1 and Stanford DASH multiprocessors. In: Proceedings of the 1993 ACM/IEEE conference on supercomputing, Portland, Oregon
- Singleton J (2001) Band theory and electronic properties of solids. Oxford University Press, Oxford
- Sjoden GE (November 1997) PENTRAN: a parallel 3-D S(N) transport code with complete phase space decomposition, adaptive differencing, and iterative solution methods. PhD thesis. The Pennsylvania State University, Source DAI-B 58/05, p. 2652. 301 pp
- Smith BF, Bjorstad P, Gropp W (1996) Domain decomposition – parallel multilevel methods for elliptic partial differential equations. Cambridge University Press, New York
- Sounders N, Miodownik AP (1998) CALPHAD. Elsevier Science Limited, New York
- Stacey WM (2001) Nuclear reactor physics. Wiley, New York
- Stan M (2005) Materials models and simulations in support of nuclear fuels development. Los Alamos National Laboratory Report. LA-UR-05-5652
- Stan M (2009) Multi-Scale models and simulations of nuclear fuels. J Nucl Eng Technol 41:39–52
- Stan M, Cristea P (2005) Thermochemistry of defects and oxygen diffusion in PuO₂-x. J Nucl Mater 344:213–218
- Stan M, Reardon B (2003) CALPHAD J 27:319
- Stan M, Armstrong TJ, Butt DP, Wallace Sr TC, Park YS, Haertling CL, Hartmann T, Hanrahan Jr RJ (2002) Stability of the perovskite compounds in the Ce-Ga-O and Pu-Ga-O systems. J Am Ceram Soc 85:2811–2816
- Stan M, Ramirez JC, Cristea P et al (2007) Models and simulations of nuclear fuel materials properties. J Alloys Comp 444–445:415–423
- Stan M et al (2009) Discovery and design of nuclear fuels. J Nucl Mater, in press
- Stankovski Z, Puill A, Dullier L (1997) Advanced plutonium assembly parallel calculations using the APOLLO2 code. M&C, Saratoga, USA
- Sutton AP (1993) Electronic structure of materials. Oxford University Press, Oxford
- Tanenbaum A (1992) Modern operating systems. Prentice-Hall, Englewood Cliffs
- The MPI Forum (1993) MPI: a message passing interface. Technical Report. University of Tennessee, Knoxville
- Trama JC (2008) Overview of TRIPOLI-4.5. In: Proceedings of ICRS conference, Pine Mountain
- Trama JC, Hugot FX (2007) TRIPOLI-4: parallelism capability. ANS Winter meeting
- Trew A, Wilson G (1991) Past, present, parallel: a survey of available parallel computing systems. Springer-Verlag, New York
- Tucker LW, Robertson GG (August 1988) Architecture and applications of the connection machine. Computer 21(8):26–38
- United States Nuclear Regulatory Commission, Emergency Preparedness. <http://www.nrc.gov/about-nrc/emerg-preparedness/images/fuel-pellet-assembly.jpg>
- Van der Giessen E, Needleman A (1995) Discrete dislocation plasticity: a simple planar model. Model. Simul. Mater Sci Eng 3:689–735
- Voter AF (2005) Introduction to the kinetic Monte Carlo method. In: Sickafus KE, Kotomin EA (eds) Radiation effects in solids. Springer, NATO Publishing Unit, Dordrecht, The Netherlands
- Voter AF, Montalenti F, Germann TC (2002) Extending the time scale in atomistic simulation of materials. Ann Rev Mater Res 32:321
- Wang HY, LeSar R (1995) O(N) algorithm for dislocation dynamics. Philos Magazine A 71: 149–164
- Wu G, Roy R (2001) Parallelization of characteristics solvers for 3D neutron transport. In: Recent advances in parallel virtual machine and message passing interface. 1, Springer, LCNS, pp 344–351
- Zacharie I et al (1998) Springer, J Nucl Mater 255:92–104
- Zeyao M, Lianxiang F (2004) Parallel flux sweep algorithm for neutron transport on unstructured grid. J Supercomput 30(1):5–17

13 Analysis of Reactor Fuel Rod Behavior

Paul Van Uffelen¹ · Rudy J.M. Konings² · Carlo Vitanza³ · James Tulenko⁴

¹European Commission, Joint Research Centre, Institute for Transuranium Elements, Karlsruhe, Germany
paul.van-uffelen@ec.europa.eu

²European Commission, Joint Research Centre, Institute for Transuranium Elements, Karlsruhe, Germany
rudy.konings@ec.europa.eu

³OECD Halden Reactor Project, Halden, Norway
Carlo.Vitanza@hrp.no

⁴202 Nuclear Science Center, University of Florida, Gainesville, FL, USA
tulenko@ufl.edu

1	<i>Introduction</i>	1522
2	<i>The LWR Fuel Element: A General Outline</i>	1523
2.1	The Fuel Pellet	1523
2.2	The Fuel Rod	1526
2.3	The Fuel Element	1526
3	<i>Properties of Oxide Nuclear Fuel</i>	1527
3.1	Structure and Thermal Expansion	1527
3.2	Thermal Conductivity	1529
3.2.1	UO ₂	1529
3.2.2	Mixed Oxides	1530
3.2.3	Effects of Irradiation	1533
3.3	Heat Capacity	1534
3.4	Melting Temperature	1536
4	<i>Properties of Cladding Materials for LWRs Fuel</i>	1537
4.1	Composition	1537
4.2	Microstructure	1538
4.3	Thermal Properties	1541
4.3.1	Linear Thermal Expansion	1541
4.3.2	Thermal Conductivity	1541
4.3.3	Specific Heat Capacity	1542
4.3.4	Emissivity	1542
4.4	Mechanical Properties	1543

4.4.1	Elastic Constants	1543
4.4.2	Plastic Deformation	1543
4.5	Irradiation Effects	1543
4.5.1	Irradiation-Induced Growth	1543
4.5.2	Irradiation-Induced Hardening	1544
4.5.3	Irradiation-Induced Creep	1544
4.5.4	Corrosion and Hydrogen Pickup	1545
4.6	High-Temperature Effects	1549
4.6.1	High-Temperature Corrosion	1549
4.6.2	High-Temperature Deformation	1551
5	<i>Basic Phenomena for In-Reactor Performance</i>	1551
5.1	Neutronic Aspects of Nuclear Fuel Rods	1552
5.1.1	Nuclide Evolution in Nuclear Fuel	1552
5.1.2	The Basic Equations	1552
5.1.3	Burnable Absorbers	1556
5.2	Heat Transfer and Thermal Characteristics	1557
5.2.1	Axial Heat Transport in the Coolant	1558
5.2.2	Heat Transport through the Cladding	1559
5.2.3	Heat Transport from the Cladding to the Fuel Pellet	1560
5.2.4	Effects of Irradiation on Gap Conductance	1561
5.2.5	Heat Transport in the Fuel Pellet	1561
5.3	Mechanical Behavior	1563
5.3.1	Main Assumptions and Equations	1563
5.3.2	Calculation of Strains	1564
5.3.3	Boundary Conditions	1571
5.4	Fission Gas Behavior	1572
5.4.1	Basic Mechanisms	1573
5.4.2	Modeling the Fission Gas Behavior	1577
6	<i>Typical Phenomena and Issues in the Design and Licensing of LWR Fuels</i>	1582
6.1	High Burnup Structure	1582
6.1.1	Characteristics of the High Burnup Structure	1582
6.1.2	Importance of the High Burnup Structure	1584
6.1.3	Modeling of the High Burnup Structure	1586
6.2	Pellet-Cladding Interaction	1589
6.2.1	Pellet-Cladding Mechanical Interaction	1589
6.2.2	Irradiation-Induced Stress Corrosion Cracking	1591
6.2.3	Outside-In Cracking Caused by Power Ramps	1596
6.3	Pellet-Coolant Interaction	1596
6.4	Loss-of-Coolant Accidents	1599
6.4.1	Sequence of Events during a LOCA	1599
6.4.2	Main Characteristics of a LOCA Failure	1600
6.4.3	Current LOCA Safety Criteria	1600
6.4.4	Extension to High Burnup Fuel	1604
6.5	Reactivity-Initiated Accidents	1608
6.5.1	Sequence of Events during a RIA	1608

6.5.2	Main Characteristics of RIA Failures	1609
6.5.3	RIA Safety Criteria	1610
7	<i>Uncertainty Analysis</i>	1618
8	<i>Outlook</i>	1619
	<i>References</i>	1620

Abstract: The analysis of the behavior of light water reactor (LWR) fuel rods is described. The properties of relevant fuel and cladding materials are discussed and numerical data are given. The basic phenomena taking place in pellet-in-cladding nuclear reactor fuel are described systematically, including neutronic aspect of the fuel, the thermal and mechanical behavior, the fission gas behavior, and radiation effects. Finally typical phenomena and issues in the design and licensing of LWR fuels and their effects on fuel behavior are discussed: the high burnup structure, pellet-cladding interaction, pellet-coolant interaction, loss-of-coolant accidents (LOCA), and reactivity-initiated accidents (RIA).

1 Introduction

The nuclear fuel is the basic element of a nuclear reactor core, providing the material for generating the energy that is used for the production of electricity or process heat. The process taking place in the nuclear fuel is fission, by which a fissile nuclide disintegrates in two fragments after it has captured a neutron. There are two basic nuclear fuels that fission with thermal neutrons ($E < 1$ eV): uranium (^{235}U) and plutonium (^{239}Pu and ^{241}Pu). Of these, ^{235}U is the only one found in nature, its natural abundance being 0.72%. ^{239}Pu is generated in reactor from ^{238}U , when a ^{238}U atom captures a neutron. These two elements produce basically all the nuclear energy generated in the current generation thermal neutron reactors (light water reactors, heavy water reactors). Fast neutrons ($E > 10$ keV) can also be used to fission uranium and plutonium, and eventually other actinides in fast neutron reactors (FNRs). These reactors can also be used to breed fissile plutonium from uranium. An additional fuel cycle utilizes ^{233}U , which is created when ^{232}Th captures a neutron.

The fission process taking place in the reactor core produces about 200 MeV of energy per fissioned atom. This energy is transferred for the majority as kinetic energy to the two fission fragments that are produced. During the trajectory from the site of their creation to the site where they come to a halt, the fission fragments transfer their energy to the crystal lattice of the host material, principally by exciting thermal vibrations in the lattice. At the same time the fission fragments knock atoms from their crystal lattice sites causing lattice damage that leads to material degradation.

The science and technology of nuclear fuel deals principally with describing the fundamental processes that are governing and affecting the heat transport in the fuel, and that are limiting the in-reactor lifetime of a fuel rod or fuel element. This is a complex set of processes depending on the initial state of the material, the linear power, the burnup, and the operating temperature. Since the operation of the first reactors in the 1950s, the need for an understanding these processes has been manifest and an enormous knowledge base has been created. This knowledge base is built on observations of irradiated nuclear fuel from commercial reactors or irradiation tests in research reactors by destructive and nondestructive examination, on separate effect studies performed in-reactor or out-of-reactor, and on theoretical calculations and simulations.

Uranium oxide fuel in the form of pellets-in-clad type fuel rods is used in all light water reactors (LWRs) and heavy water reactors (HWRs) around the world, which constitute more than 90% of the installed nuclear power. Due to the industrial relevance, extensive studies on conventional uranium oxide fuels have been performed and an adequate knowledge of the behavior now exists to ensure safe and economic operation of present-day reactors, as will be detailed in this chapter. In some countries, especially in Europe, also mixed oxide fuel, (U,Pu) O_2 , is used

to fuel LWRs with the intention to consume separated plutonium, originally intended for fast reactor operation. Also for MOX fuel an acceptable understanding of the fuel behavior exist.

The goal of this chapter is to describe the fundamental issues in the science and technology of nuclear fuel required to analyze and simulate the in-pile behavior of nuclear fuel. The emphasis will be on pellet-in-clad type oxide fuel for LWRs, which represent the majority of power reactors operated presently.

2 The LWR Fuel Element: A General Outline

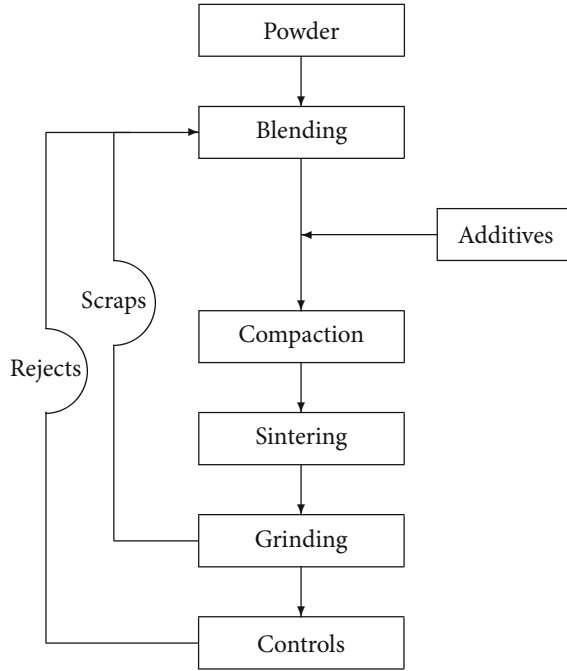
2.1 The Fuel Pellet

The basic building block of the traditional pellet-in-pin fuel element is the fuel pellet. The fuel pellet is a cylindrical compact produced from a powder, that is, UO_2 or $(\text{U,Pu})\text{O}_2$. It can be a full pellet, as is normally the case in Western boiling water reactors (BWR) and pressurised water reactors (PWR), or an annular pellet as is the case for the Russian pressurized water reactors (known under the acronym VVER).

In case of UO_2 fuel, the starting powder is the product of the mining-conversion-enrichment chain, during which the uranium is purified and eventually enriched in ^{235}U to meet the specification. The uranium dioxide is produced from UF_6 in either a dry or wet process. In the dry process, the solid UF_6 is sublimed to its gaseous form and is reacted with superheated steam and then passed through a rotating drying kiln to produce UO_2 powder. In the wet process, the solid UF_6 is sublimed to its gaseous form and is bubbled through water to form UO_2F_2 , which is then mixed with aqueous ammonia causing the uranium to precipitate as ammonium diuranate (ADU, $(\text{NH}_4)_2\text{U}_2\text{O}_7$). The precipitate is dried and calcined to form U_3O_8 , which is then further reduced in a cracked ammonia atmosphere to form UO_2 . The UO_2 powder is blended in a batch mode, where binder materials, lubricant and eventually pore formers are mixed with the fuel (► Fig. 1). The powder is cold pressed at 150–300 MPa to form “green” pellets of 50–60% theoretical density (TD). The green pellets are then placed in a furnace and sintered in a hydrogen–argon atmosphere at 1,600–1,700 °C for 5–10 h to produce pellets of 95–96% TD. Eventually, further annealing in hydrogen gas ensures a final product of the correct stoichiometric composition. Finally, a centerless grinding is applied to adjust the diameter to the specified dimensions. Although designs vary from core to core, typical final dimensions of LWR fuel pellets are on the order of 1 cm in diameter and 1–2 cm in height.

In general, reactor grade UO_2 fuel pellets must meet a number of very specific criteria related to their physical state (Assmann 1982):

1. *Density and porosity:* During the high-temperature sintering the density of the compacted pellet changes to above 90% TD. A fully dense material is not wanted as it cannot accommodate the radiation-induced matrix swelling nor the fission gases that are produced during irradiation; a too low density cannot be tolerated as it will impact the thermal conductivity (see below). In practice a density of about 95% TD is the best compromise. This means that the pellet contains about 5% porosity. The pore structure and distribution in the pellet should be homogeneous, with the ideal mono-modal pore size between 1 and 10 μm . Since some starting powders have a high sinterability and contain only little intragranular porosity, pore formers can be added to control the porosity. In that case a bi-modal pore structure is obtained made of small intergranular pores and larger pores resulting from the pore former.



■ Figure 1

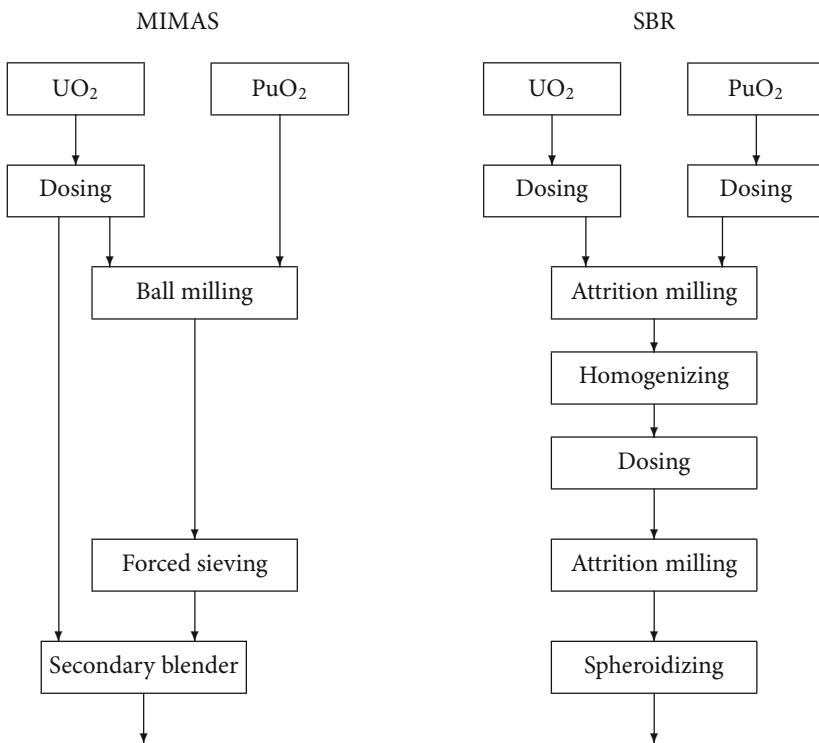
Schematic representation of the nuclear fuel pellet fabrication processes

2. *Grain size*: The grain size of the UO_2 strongly depends on the powder properties and the sintering conditions. Normally a mono-modal grain size distribution is obtained, with average grain size in the order of 8–12 μm . Additives (e.g., chromium oxide, aluminosilicate, or niobium oxide) can be used to increase the grain size, which can have a positive impact on the in-reactor behavior, as a larger grain size can improve fission gas retention.
3. *Stoichiometry (O/M)*: The stoichiometry (or oxygen-to-metal ratio, O/M) is an important parameter for the UO_2 fuel as it strongly affects the physicochemical properties, as discussed ▶ Sect. 3. The sintering process is a reductive process, normally performed in an argon/hydrogen gas mixture, that yields $\text{O/M} = 2.00$ as required for LWR fuel.
4. *Dimensions and surface roughness*: It is evident that pellets with defects cannot be accepted for fuel rod fabrication. Furthermore the outer dimensions of the pellets and the outer surface roughness must be assured within a small tolerance to the specification in view of the fuel rod characteristics. Since after pressing and sintering the pellets generally do not fulfill this requirement, a (centerless) grinding step is generally used to achieve conformity with the specification.

In the case of mixed oxide fuel (MOX), powders of uranium oxide and reprocessed plutonium oxide are mixed mechanically. Since a homogeneous distribution is the aim and this is not reached by simply co-milling of the powders, various processes have been developed, two of which are currently used on an industrial scale. Since fissile plutonium (^{239}Pu and ^{241}Pu) is

approximately equivalent to ^{235}U on a gram for gram basis, equal weight percentages of ^{235}U in UO_2 and fissile plutonium in MOX are needed to reach the same discharge exposures. The total plutonium enrichment will however be higher because of the presence of non-fissile ^{240}Pu and ^{242}Pu isotopes.

The most widely used process to fabricate MOX fuel is the MIMAS (Micronized MASTer blend) process. The process consists of two steps, first a mixture of plutonium dioxide, uranium dioxide, and recycled scrap is finely grounded (● Fig. 2). The obtained powder is sifted and diluted in uranium dioxide until the desired plutonium content is obtained. This secondary mixture is pressed into green pellets and the green pellets are sintered to the desired density. In the SBR (short binderless route) process, the UO_2 and PuO_2 powders are mixed and milled in several stages in an attrition mill to obtain a homogeneous powder. In both processes, however, the distribution of plutonium in the final product is not homogeneous. Plutonium-rich spots can be observed in a matrix of $(\text{U,Pu})\text{O}_2$, though much more pronounced in the MIMAS fuel compared to the SBR fuel. A variation of the MIMAS process is selected for the Japanese MOX fabrication plant in Rokkasho-Mura, the master blend being produced from mixing of UO_2 and a $\text{UO}_2\text{-PuO}_2$ mixture (50:50) obtained from reprocessing, avoiding the handling of pure PuO_2 .



■ Figure 2

Schematic representation of the MIMAS and SBR processes used for the production of powders for mixed oxide fuel

Also fuels with dopants such as Gd are generally produced by powder technology. The technology is similar to that used for MOX fuel. First a master blend is made that is then blended down with UO_2 to the required Gd concentration.

In many LWR fuels, the pellets have dished faces (concave central recess) to anticipate for the radial anisotropic expansion behavior of the fuel pellets during irradiation. Also chamfering of the pellet faces is often used, as this eases loading into the fuel rod and also reduces the pellet-cladding mechanical interaction (PCMI) (6.2.1).

2.2 The Fuel Rod

The fuel rod (or pin) is the principal confinement of the nuclear fuel in the reactor core. The fuel rod is a cylindrical metallic sheath in which the stack of pellets is loaded. The size of thermal reactor fuel rods differs significantly between the various reactor designs (about 400 cm in length and 9–11 mm in diameter in PWRs, 400 cm in length, and 12–14 mm in diameter in BWRs) but in all cases zirconium alloys are used for the cladding. The fuel does not cover the complete length of the pins, but a free volume (plenum) is generally kept at the top of the pin to accommodate some release of fission gases. The pellets are kept in place by a plenum spring. To avoid contact between the top pellet and the spring, an insulator pellet (Al_2O_3) is placed in between. Similarly an insulator pellet is placed between the bottom fuel pellet and the lower end plug. The fuel rods are pressurized with helium (about 20–25 bar in PWRs and 3 bar in BWRs), to assure a good thermal conduction of the gap between the pellet and the cladding, and then end-capped with the upper end plug. A schematic drawing of a fuel rod is given in Fig. 3.

2.3 The Fuel Element

For the loading into the reactor the fuel rods are assembled into fuel elements (also called bundles or subassemblies), whose design vary strongly per reactor type, depending on the thermal–hydraulic and neutronic characteristics. In general three different geometries are used: square, hexagonal, and circular.

In western PWRs the fuel rods are assembled in a square geometry generally ranging between 14×14 to 17×17 (Fig. 4). The fuel elements for the Russian VVERs in contrast have a hexagonal geometry, containing around 300 fuel rods. The fuel rods are kept together by a support structure that consists of the following elements:

- A top and a bottom nozzle, that support the element stability and directs the coolant flow. The nozzles are generally made of stainless steel (e.g., AISI 304L). The top grid is also designed to allow handling during loading and unloading.

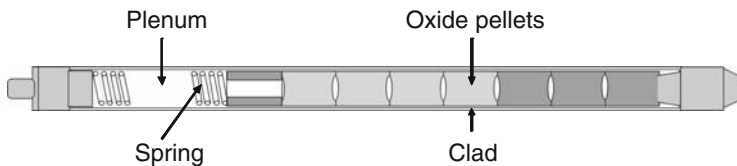
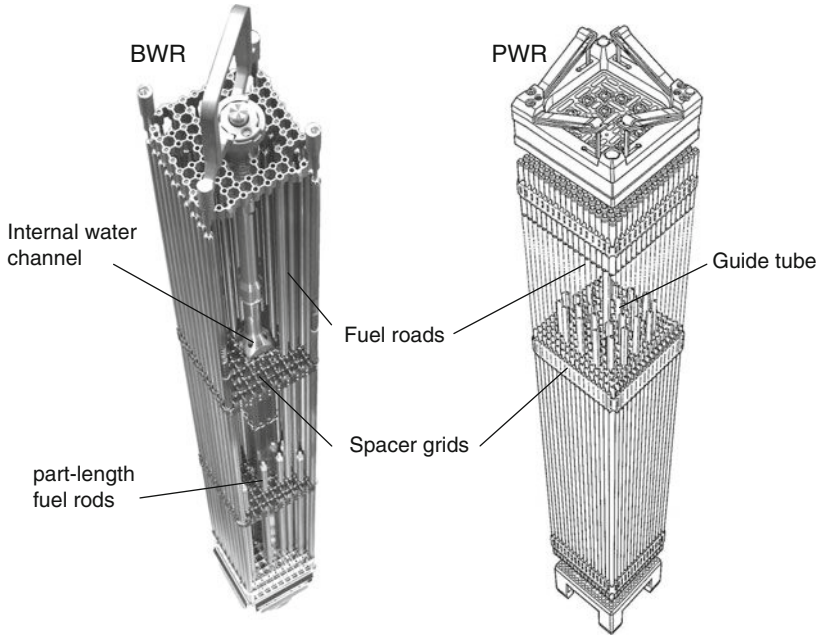


Figure 3
Schematic representation of a LWR fuel rod



■ **Figure 4**
Fuel elements for BWR and PWR. ©AREVA, reproduced with permission

- Guide tubes, that are needed for the movement of the control rods, are made of zirconium alloy, as the fuel cladding.
- A central instrumentation tube for the introduction of core instrumentation. It is also made of zirconium alloy.
- Several axially spaced grids along the height of the assembly, to ensure the spacing between the fuel rods during irradiation. The spacer grids are made of zirconium alloy and are normally welded to the guide tubes and instrumentation tubes.

For boiling water reactors (BWRs) the fuel rods are generally assembled in a 8×8 to 10×10 square geometry and also kept together by spacer grids and supported by top and bottom nozzles (► *Fig. 4*). In modern BWR fuel bundles, there are either 91, 92, or 96 fuel rods per assembly depending on the manufacturer. Each element also contains several flow channels.

3 Properties of Oxide Nuclear Fuel

3.1 Structure and Thermal Expansion

Uranium dioxide (UO_2) has a cubic crystal structure, with uranium in a face centered array and the oxide ions occupying the tetrahedral holes. This cubic structure gives the uranium oxide

pellet uniform expansion properties. The lattice parameter of the UO_2 unit cell is 546.92 pm at $T = 293$ K, which yields a theoretical density is $10.963 \text{ g}\cdot\text{cm}^{-3}$.

Upon heating, the UO_2 crystalline lattice expands. Martin (1988) evaluated the lattice expansion and recommended the following polynomial equations for solid UO_2 , as also selected by an IAEA expert group (IAEA 2006):

$$\begin{aligned} L/L_{273} = & 0.9973 + 9.082 \times 10^{-6}(T/K) - 2.705 \times 10^{-10}(T/K)^2 \\ & + 4.391 \times 10^{-13}(T/K)^3 \quad (273 < (T/K) < 923) \end{aligned} \quad (1)$$

$$\begin{aligned} L/L_{273} = & 0.99672 + 1.179 \times 10^{-5}(T/K) - 2.429 \times 10^{-9}(T/K)^2 \\ & + 1.219 \times 10^{-12}(T/K)^3 \quad (973 < (T/K) < 3110) \end{aligned} \quad (2)$$

The density of solid UO_2 can be derived from this equation using the formula

$$\rho(T) = \rho(273) \frac{L(T)}{L(273)} \quad (3)$$

using $\rho(273) = 10.963 \text{ g}\cdot\text{cm}^{-3}$ based on the recommended lattice parameter. For practical reason the density can be represented by the following polynomial equation

$$\begin{aligned} \rho(T) = & 11.049 - 3.34 \times 10^{-4}(T/K) + 3.9913 \times 10^{-8}(T/K)^2 \\ & - 2.7649 \times 10^{-11}(T/K)^3 \end{aligned} \quad (4)$$

Plutonium oxide (PuO_2) also crystallizes in the face centered fluorite structure and forms a solid solution with UO_2 in the complete composition range. The lattice parameter of PuO_2 is 539.60 pm at $T = 273$ K, which yields a theoretical density of $11.46 \text{ g}\cdot\text{cm}^{-3}$. The thermal expansion of PuO_2 is almost similar to that of UO_2 and since UO_2 and PuO_2 form an ideal solid solution, Eqs. 1 and 3 can thus also be used for the $(\text{U}_{1-y}\text{Pu}_y)\text{O}_2$ solid solution. Carbajo et al. Carbajo et al. (2001) suggested that the density of $(\text{U}_{1-y}\text{Pu}_y)\text{O}_2$ at 273 K can be interpolated linearly between the two end-members, which becomes

$$\rho(273.15 \text{ K}) = 10.963 + 0.497y \quad (5)$$

with the density value for UO_2 used here.

The International Atomic Energy Agency (IAEA) expert group (IAEA 2006) gave recommendations for the thermal expansion of $(\text{U}_{1-y}\text{Gd}_y)\text{O}_2$ based on critical review of the existing experimental data. The recommended equation is

$$\begin{aligned} L(T)/L_{273} = & 0.99866 + 7.2512 \times 10^{-6}(T/K) \\ & + (2.0463 \times 10^{-13}y^2 + 3.4846 \times 10^{-11}y + 2.0653 \times 10^{-9})(T/K)^2 \end{aligned} \quad (6)$$

3.2 Thermal Conductivity

3.2.1 UO₂

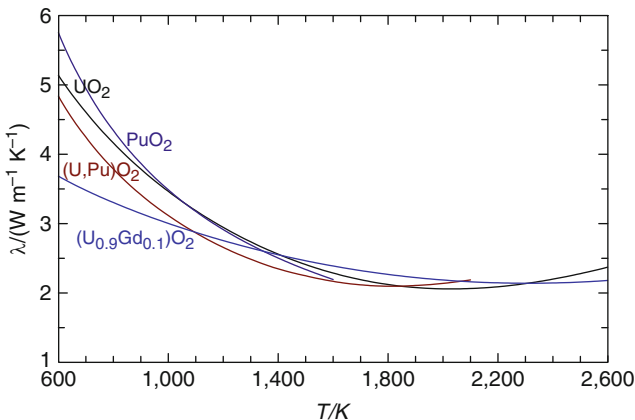
The thermal conductivity is an important property of a nuclear fuel, as we will explain in [Sect. 5.2.3](#). UO₂ has a relatively poor thermal conductivity, which has a minimum at approximately 2,000°C ([Fig. 5](#)). Many measurements have been reported for UO₂ and were carefully evaluated by an expert group of the IAEA ([2006](#)).

Conduction of heat in the pellets occurs by phonons or by the kinetic energy of electrons: $\lambda = \lambda_{ph} + \lambda_{el}$. At temperatures below 1,500 K the phonon contribution predominates. When applying the kinetic gas theory to the propagation of atomic vibrations (phonons) or quasi-particles, it appears that the phonon conductivity in the temperature range of interest can be expressed as

$$\lambda_{ph} = \frac{1}{A + BT} \quad (7)$$

where A corresponds to the scattering of phonons by imperfections such as point defects, line and planar defects, fission gas bubbles. The parameter B corresponds to the scattering by phonon–phonon (Umklapp) interactions. When the burnup (bu) in the pellets increases, the accumulation of point defects and fission products will increase the phonon scattering (A -term). The same happens if the fuel (e.g., UO₂) is doped with a neutron absorber such as Gd₂O₃, or if a deviation from stoichiometry occurs ($x \neq 0$, where $x = |2 - O/M|$ and O/M is the oxygen-to-metal ratio in UO₂), that is, in general $A = A(bu, Gd, Pu, x)$.

[Equation \(7\)](#) also suggests that the thermal conductivity decreases with increasing temperature, which is the case for UO₂ up to about 2,000 K. Above this temperature the electronic contribution becomes important as a result of which the thermal conductivity slightly increases



■ Figure 5

The thermal conductivity of UO₂, PuO₂, (U,Pu)O₂, and (U_{0.9}Gd_{0.1})O₂ as a function of temperature

again (● Fig. 5). The temperature dependent creation of electronic carriers leading to λ_{el} is typically expressed as (Harding and Martin 1989)

$$\lambda_{el} = \frac{C}{T^n} \exp\left(-\frac{W}{kT}\right) \quad (8)$$

where λ is expressed in $\text{W m}^{-1} \cdot \text{K}$, T is the absolute temperature, $k_B = 8.6144 \times 10^{-5}$ is Boltzmann's constant (eV/K), n is a constant, usually 2, $\frac{5}{2}$ or 3, $C = 4.715 \times 10^9$ and $W = 1.41$ is related to the energy gap between conduction and valence bands. More complex dependencies of the temperature have been proposed more recently (IAEA 1997).

Besides temperature and composition, the porosity is an important factor affecting the overall thermal conductivity of a ceramic such as UO_2 . Pores, which are generally filled with gas, poorly conduct the heat and thus act as thermal barriers. Many formulas have been suggested to correct for this effect, mainly assuming that in highly dense materials the pores have a spherical shape, which is indeed the case for sintered UO_2 . One of the most common expressions is the Maxwell–Eucken correction:

$$\lambda = \lambda_0 \frac{1 - P}{1 + \beta P} \quad (9)$$

Here λ_0 is the thermal conductivity of the fully (100%) dense material, P is the porosity, and β is a constant, which is unity for perfect spherical pores. For complex pore shapes, other corrections are needed.

Another popular correction factor is derived from the Loeb correction:

$$\lambda = \lambda_0(1 - \alpha P) \quad (10)$$

where $\alpha = 1.7$ –3.

The thermal conductivity of stoichiometric UO_2 has been measured by many authors and these measurements were evaluated by an IAEA expert group (IAEA 2006). The recommended equation for 95% dense material is

$$\lambda = \frac{100}{7.5408 + 17.692t + 3.6142t^2} + \frac{6400}{t^{5/2}} \exp\left(\frac{-16.35}{t}\right) \quad (11)$$

where λ is the thermal conductivity in $\text{W} \cdot \text{m}^{-1} \cdot \text{K}^{-1}$, and $t = T/1,000$ in Kelvin.

3.2.2 Mixed Oxides

The substitution of Pu^{4+} or Gd^{3+} ions in the UO_2 lattice will substantially affect the thermal conductivity. These ions act as phonon-scattering centers in the crystal lattice, as a result of which the thermal conductivity of $(\text{U,Pu})\text{O}_2$ or $(\text{U,Gd})\text{O}_2$ will be lower than that of pure UO_2 . For these solid solutions Eq. 7 can be changed to

$$\lambda = \frac{1}{A_0 + A_1(x) + BT} \quad (12)$$

where the parameter A_0 describes the temperature independent phonon scattering in the pure compound. The parameter $A_1(x)$ represents the influence of substitution or non-stoichiometry

on the temperature independent phonon scattering and x represents the amount of non-stoichiometry or substitution. The parameter B is less sensitive to substitutions or other scattering centers.

The thermal conductivity of solid solutions can be described adequately by the theory developed by Ambegaokar (1959) and Abeles (1963), as discussed by Gibby (1971) and Fukushima et al. (1986). The parameter $A_1(x)$ in (12) can be represented by

$$A_1(x) = \frac{\pi^2 V \Theta}{3v^2 h} \Gamma \quad (13)$$

where V is the average atomic volume, Θ is the Debye temperature, v is the average phonon velocity, h is Planck's constant. Γ is the scattering cross section parameter of the phonon by the impurity type. Γ is given by

$$\Gamma = x(1-x) \left(\frac{M_1 - M_2}{(1-x)M_1 + xM_2} \right)^2 + \varepsilon x(1-x) \left(\frac{r_1 - r_2}{(1-x)Mr_1 + xr_2} \right)^2 \quad (14)$$

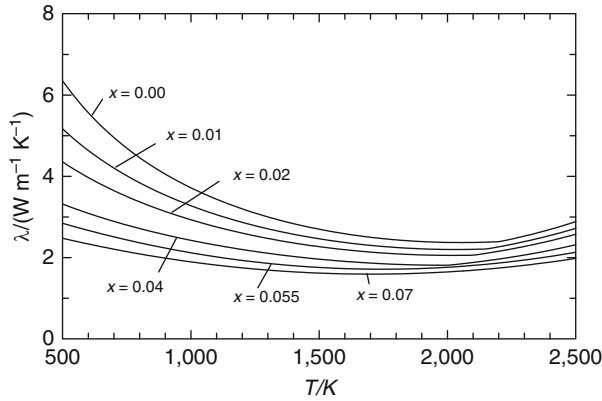
where x is the mole fraction of impurity atoms, M_1 is the mass of the host ion, M_2 is the mass of the substituted ion, r_1 is the ionic radius of the host atom, and r_2 is the ionic radius of the impurity atom. ε is a parameter that represents the strain generated in the lattice and is assumed to be about 100, which is obtained from an analysis of various solid solutions by Fukushima et al. (1986).

Gibby (1971) systematically measured the effect of the Pu content on the thermal conductivity of (U,Pu)O₂ solid solutions up to 30 mol% PuO₂, observing a small but systematic decrease with increasing PuO₂ content. This could be explained by the fact that the Pu⁴⁺ ions substitute on the uranium positions of the UO₂ lattice where they act as phonon-scattering centers, in line with theory. However, Schmidt (1970) found a different dependence on the PuO₂ content with a peak at about 15 mol% in the thermal conductivity, particularly evident at low temperatures. Beauvy (1992) reported similar results, and attributed this to differences in the defect cluster concentrations below and above 12.5 mol% PuO₂. Clearly, further studies are needed as also the strong variation of the thermal conductivity close to O/M = 2.00 (see below) might have affected the results, as well as auto-irradiation effects.

Duriez et al. (2000) made systematic measurements of the thermal conductivity of (U,Pu)O₂ mixed oxide fuel, for average Pu concentrations from 3 to 15 wt% and in the temperature range 700–2,300 K. They used both homogeneous samples and industrial MIMAS samples. The thermal conductivity was found to be significantly lower than that of the UO₂, although no dependence on the Pu concentration was found, neither was a difference between the homogeneous and MIMAS samples observed. Similar to the results of Schmidt, a clear decrease of the thermal conductivity as a function of the O/M ratio was observed. Their results expressed for 95% TD in this concentration range were represented by the equation

$$\lambda = \frac{1}{A(x) + B(x)(T/K)} + \frac{C}{(T/K)^2} \exp \frac{-D}{(T/K)} \quad (15)$$

with $A(x) = 2.85x + 0.035$ m K W⁻¹, $B(x) = (2.86 - 7.15x)10^{-4}$ m W⁻¹, $C = 1.689 \cdot 10^9$ W K m⁻¹, and $D = 13,520$ K. However, Carbajo et al. (2001) argued that this equation does not reproduce



■ Figure 6

The thermal conductivity of $(U_{0.8}Pu_{0.2})O_{2\pm x}$ for various values of x ; after Schmidt (1971)

the high-temperature data ($>2,000$ K) correctly and suggested a combination of the results of Duriez et al. (2000) and Ronchi et al. (1999):

$$\lambda = \frac{1}{A(x) + B(x)(T/K)} + \frac{6,400}{t^{5/2}} \exp\left(\frac{-16.35}{t}\right) \quad (16)$$

Schmidt (1971) studied the effect of O/M ratio on the thermal conductivity of $(U_{0.8}Pu_{0.2})O_{2-x}$ in the temperature range 373–2,073 K, observing a strong decrease as a function of x , particularly at the lowest temperatures (● Fig. 6), which is due to the fact that Pu^{3+} and oxygen vacancies act as scattering centers. Schmidt also studied the $(U_{0.8}Pu_{0.2})O_{2+x}$ (see Mattys (1968)), revealing a similar trend as for $UO_{2\pm x}$, that is, the thermal conductivity decreases for positive as well as negative values of x , though slightly asymmetric around O/M = 2.00.

The presence of Gd^{3+} ions in the UO_2 lattice causes local distortion, lattice strain, and an increase of oxygen defects (vacancies). This has an impact on the phonon–lattice and phonon–phonon interactions, leading to a decrease of the thermal conductivity of $(U,Gd)O_{2-x}$. Following the recommendation by an IAEA expert group (IAEA 2006), the recommended thermal conductivity equation for $(U,Gd)O_{2-x}$ (95% TD) is that by Ishimoto et al. (1994), valid for the temperature range 300–3,000 K:

$$\lambda = \frac{\lambda_0}{x} \arctan(x) + 3.94 \times 10^{-11} (T/K)^3 \quad (17)$$

$$x = 3.31 \exp(-7.61 \times 10^{-4} (T/K)) \sqrt{y\lambda_0} \quad (18)$$

where y is the Gd_2O_3 content, and λ_0 is the thermal conductivity of point defect free UO_2 :

$$\lambda_0 = \frac{1}{0.0245 + 2.46 \times 10^{-4} (T/K)} \quad (19)$$

3.2.3 Effects of Irradiation

The thermal conductivity of nuclear fuel decreases with burnup. The decrease is mainly caused by the buildup of fission product atoms and point defects resulting from radiation damage in the UO_2 lattice, both of which act as scattering centers for phonons. Thermal annealing of the spent fuel results in the recovery of the thermal conductivity (Walker et al. 2006). This occurs in two distinct steps. The first step occurs in the temperature range 800–1,000 K (527–727°C) and is associated with the removal of point defects produced by out-of-pile radiation damage. The second step occurs in the temperature range 1,150–1,400 K (877–1,127°C) and is attributed to further annealing of self-irradiation, the onset of annihilation of in-pile radiation damage and the removal of fission product atoms in solid solution in the fuel matrix to form voids and precipitates. Thermal annealing at temperatures below 800 K (527°C) results in slight recovery of the thermal conductivity amounting to less than 10% of the value for the irradiated fuel. This recovery is due to the partial healing of point defects created by self-irradiation in the time interval between discharge of the spent fuel from the reactor and the measurement of the thermal diffusivity. The bulk of the damage created during this time is removed in the first recovery step.

As discussed above, the thermal conductivity of nuclear fuel degrades continuously during irradiation as a result of fission product accumulation and radiation damage. In-pile experiments with instrumented fuel rods (centerline thermocouples) have revealed this effect for LWR fuel, taking into account supplementary information about the linear power and the fuel-cladding gap conductance. Based on the experiments performed in the Halden boiling water reactor (Wiesenack 1997) the following equation is recommended for the thermal conductivity of irradiated UO_2 :

$$\lambda = \frac{1}{0.1148 + 0.0035bu + 2.47510^{-4} \times (1 - 0.0033bu)(T/K) + 0.0132 \exp(0.00188(T/K))} \quad (20)$$

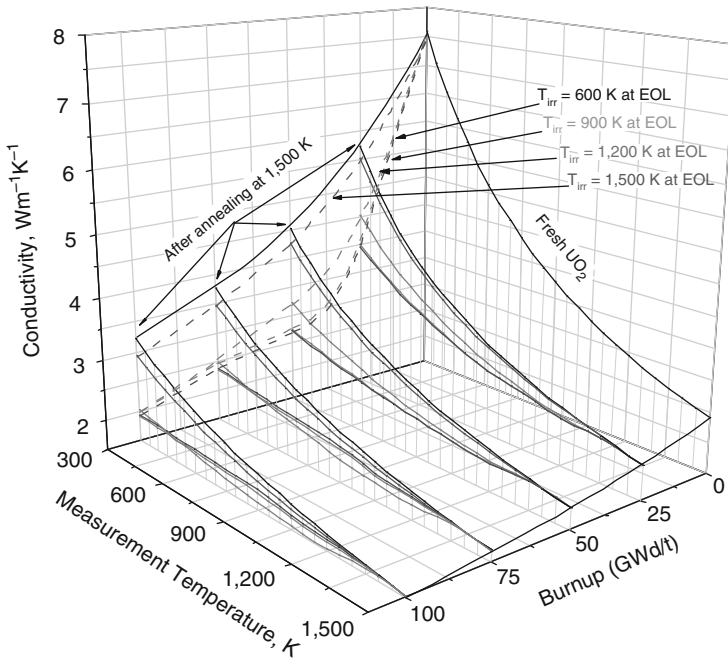
where bu is burnup in MWd/kgU. This correlation is based on a burnup correction to the MATPRO thermal conductivity data for unirradiated UO_2 (Hagrman and Reymann 1979).

The thermal conductivity degradation has also been studied directly by out-of-pile experiments. Ronchi et al. (2004) studied the thermal conductivity of irradiated UO_2 up to 92 MWd/kgHM and different in-pile temperatures. By systematic studies of the thermal conductivity of samples irradiated at different burnup and temperature using thermal annealing cycles, these authors established the complex thermal conductivity dependence (Fig. 7). Ronchi et al. (2004) proposed a thermal conductivity expression based on the classical phonon heat transport equation (Eq. 7) with coefficients A and B depending on the irradiation temperature T_{irr} (700–1,450 K), the maximum temperature reached during annealing T_{ann} (700–1,450 K) following irradiation at T_{irr} , and the local burnup bu (0–100 MWd/kgHM):

$$\lambda = \frac{1}{A(T_{irr}, T_{ann}, bu) + B(T_{irr}, T_{ann}, bu)T} \quad (21)$$

Here T is the instant application temperature (300–1,500 K), which for in-pile applications $T = T_{irr} = T_{ann}$. The set of relevant equations to use this expression is summarized in Table 1.

There is limited information on the thermal conductivity of irradiated MOX in the open literature. Cozzo et al. (2010) reported the results for homogeneous SBR MOX of 35 MWd/kgHM



■ Figure 7

The thermal conductivity of irradiated UO₂ fuel (Ronchi et al. 2004) © Elsevier, 2004, reprinted with permission

obtained from out of pile studies. The results agree well with those for irradiated UO₂ by Ronchi et al. (2004) for the same burnup. This can be explained by the fact that the composition of UO₂ and low Pu content MOX fuel converge during irradiation, the UO₂ producing Pu and the MOX consuming Pu, both accumulating fission products and radiation damage in an homogeneous way.

3.3 Heat Capacity

The heat capacity of UO₂ has been evaluated by many authors and various expressions have been suggested. The difficulty is that the heat capacity of UO₂ shows an anomalous behavior above 2,000 K as a result of Frenkel pair formation on the oxygen lattice and excitation of the electronic levels of U⁴⁺. The recommendation by Fink (2000) for the temperature range 298.15 K < T < 3,120 K is generally accepted, and can be represented by

$$C_p(T)/(J \cdot K^{-1} \cdot mol^{-1}) = 52.1743 + 87.951t - 84.2411t^2 + 31.542t^3 - 2.6334t^4 - 0.71391t^{-2} \quad (22)$$

Table 1
Dependencies of the parameters of Eq. 21

$A(T_{irr}, T_{ann}, bu)/m \cdot W^{-1} \cdot K^{-1}$	$= 0.046 + \Gamma(bu, GIS) + \delta A^{a,b}$
$\Gamma(bu, GIS)$	$= 9.02 \times 10^{-4} bu GIS + 1.74 \times 10^{-3} bu + 7.51 \times 10^{-3} a$
δA	$= \delta A_{self}(T_m, bu) + \delta A_{EOL}(T_m, bu)^c$
$\delta A_{EOL}/m \cdot K \cdot W^{-1}$	$= \frac{bu}{850} \left[\left(1 + \exp\left(\frac{T_m - 950}{25}\right) \right)^{-1} + \left(1 + \exp\left(\frac{T_m - 1,300}{35}\right) \right)^{-1} - 0.0525 \right]$
$\delta A_{self}(T_{ann}, bu)/m \cdot K \cdot W^{-1}$	$= 0.02F(bu)$ for $T_{ann} < 900$ K
	$= 0.02F(bu) \frac{1,450 - T_{ann}}{1,450 - 900}$ for $900 < T_{ann} < 1,450$ K
	$= 0$ for $T_{ann} > 1,450$ K
$B(T_{irr}, T_{ann}, bu)/m \cdot W^{-1}$	$= B_0 + (B_1 - B_0) + \frac{6.5 \times 10^{-5} - \delta B}{6.5 \times 10^{-5}}$
$B_0/m \cdot W^{-1}$	$= 1.65 \times 10^{-6} bu + 2.55 \times 10^{-4} + 3.6 \times 10^{-5} IRIM^d$
B_1	$= 4.2 \times 10^{-7} bu + 2.75 \times 10^{-4}$
δB	$= F(bu) \delta B_{EOL}(T_m, bu)$
$\delta B_{EOL}/m \cdot W^{-1}$	$= \frac{bu}{34} \left[\left(4.0 \times 10^{-5} \left(1 + \exp\left(\frac{T_m - 950}{25}\right) \right)^{-1} \right. \right.$
	$\left. + 2.5 \times 10^{-5} \left(1 + \exp\left(\frac{T_m - 1,300}{35}\right) \right)^{-1} \right]$
$GIS(bu, T_{ann}, T_{irr})$	$= \frac{1 - 0.9 \left[1 + \exp\left(\frac{T_{irr} - 950}{30}\right) \right]^{-1} \left[1 + \exp\left(\frac{73 - bu}{2}\right) \right]^{-1}}{\left[1 + \exp\left(\frac{T_{irr} - 1,350}{200}\right) \right] \left[1 + \exp\left(\frac{T_{ann} - 1,350}{200}\right) \right]}$
$IRIM$	$= \left[1 + \exp\left(\frac{T_{irr} - 950}{30}\right) \right]^{-1} \times \left[1 + \exp\left(\frac{73 - bu}{2}\right) \right]^{-1} d$
$F(bu)$	$= \left(1 - \exp\left(\frac{20 - bu}{6}\right) \right)^{-1} - 0.015267$

^a GIS is the fraction of gas in solid defined as the ratio of the gas amount present in dynamical solution to the total produced inventory.

^b Γ is the total scattering coefficient.

^c $T_m = \max(T_{irr}, T_{ann})$.

^d $IRIM$ is the correction associated with the hbs formation.

where $t = T/1,000$ with temperature T in Kelvin. This equation does not reproduce the λ type transition at $(2,670 \pm 30)$ K in heat capacity measurements in the pre-melting range that was observed by Ronchi and coworkers (Hiernaut et al. 1993; Ronchi et al. 1999).

Carbajo et al. (2001) critically evaluated the heat capacity and enthalpy data for $(U,Pu)O_2$ and concluded that the results for the solid phase can be described well by the Neumann–Kopp rule:

$$C_p(T, U_{1-y}Pu_yO_2) = (1 - y)C_p(T, UO_2) + yC_p(T, PuO_2) \quad (23)$$

which is in line with the fact that this solid solution is ideal. Measurements by Duriez et al. (2000) confirmed this conclusion.

The recommended equation for the heat capacity of $(U_{1-y}Gd_y)O_2$ by the IAEA expert group (IAEA 2006) is (298.15–2,000 K):

$$C_p = C_{p0} + \Delta C_p \quad (24)$$

$$C_{p0} = 79.8 + (0.1263y^2 - 0.0073y + 0.0061)(T/K) - (1.68 - 1.48y) \times 10^6 (T/K)^{-2} \quad (25)$$


where ΔC_p is expressed as

$$\Delta C_p = \frac{\Delta H^*}{\sqrt{2}RT^2} \exp\left(\frac{\Delta S^*}{2R}\right) \exp\left(\frac{\Delta H^*}{\sqrt{2}RT}\right) \quad (26)$$

where $\Delta H^* = (-73,880y^3 + 10,190y^2 - 612.13y + 310) \times 10^3 \text{ J}\cdot\text{mol}^{-1}$ is the enthalpy of formation of Frenkel pair formation and $\Delta S^* = 61.969 - 45.564y \text{ J}\cdot\text{K}^{-1}\cdot\text{mol}^{-1}$ is the entropy of formation of Frenkel pair formation. These Frenkel pairs of oxygen are formed because the substitution of Gd^{3+} on the uranium lattice creates oxygen vacancies on the oxygen sub-lattice. To maintain a nearly stoichiometric composition for $(U,Gd)O_2$, an oxygen interstitial must be formed (together with U^{5+} formation). As discussed in IAEA (2006) the entropy and enthalpy of formation per Frenkel pair thus obtained are higher than the values known from UO_2 , but when extrapolated to zero Gd content, they are in fair agreement with the estimated values for UO_2 .

3.4 Melting Temperature

The melting point of UO_2 has been the subject of many studies. In the most recent reviews (Carbajo et al. 2001; Fink 2000; IAEA 2006) the recommended melting point is $T_{fus} = (3,120 \pm 20) \text{ K}$, the value suggested by Adamson et al. (1985). Recent measurements confirm this value.

The melting temperature of $(U,Pu)O_2$ is strongly dependent on the composition. The UO_2 – PuO_2 phase diagram, as shown in  Fig. 8, indicates that the liquidus and solidus lines steadily decrease with increasing PuO_2 concentration, which can be represented by the following equations (Adamson et al. 1985):

$$T_{\text{solidus}}/K = 3120 - 655.3x + 336.4x^2 - 99.9x^3 \quad (27)$$

$$T_{\text{liquidus}}/K = 3120 - 388.1x - 30.4x^2 \quad (28)$$

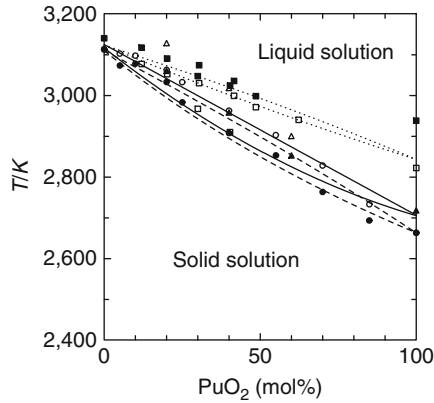
These recommendations are based on the results of Aitken and Evans (1968) and Lyon and Bailey (1967) from the 1960s, among others. However, the recent measurements by Kato et al. (2008) are in disagreement with these results, and suggest a melting point for pure PuO_2 about 200 K higher than the recommended value. Further experiments are required to solve this discrepancy.

The phase diagram of the UO_2 – Gd_2O_3 system has been studied by Beals et al. (1969) and more recently by Kang et al. (2007). Their results for the liquidus are close but those for the solidus differ significantly. The results by Kang et al. (2007) can be represented by

$$T_{\text{solidus}}/K = 3120 - 48.01x + 1.31x^2 \quad (29)$$

$$T_{\text{liquidus}}/K = 3120 - 8.0x \quad (30)$$

where x is the weight fraction of Gd_2O_3 .



■ Figure 8

The pseudobinary phase diagram $\text{UO}_2\text{-PuO}_2$. The circles give the experimental data by (Lyon 1967), the triangles by (Aitken and Evans 1968), and the squares by (Kato et al. 2008). The solid lines represent the recommended liquidus and solidus by (Adamson et al. 1985), the broken line represents the ideal liquidus and solidus based on the results of Lyon and Baily, and the dotted line represents the liquidus and solidus suggested by Kato et al.

The effect of irradiation on the melting temperature of UO_2 has been studied by several authors. Christensen (1962) reported an increase of more than 100 K for the melting point of UO_2 irradiated to 1.12×10^{19} fissions/ cm^3 . At higher exposures, he observed a decrease of 40 K at approximately 2×10^{19} fission/ cm^3 and of 130 K at approximately 2.7×10^{19} fissions/ cm^3 . Subsequent work by Christensen et al. (1964) showed a nearly linear decrease of approximately 10 K per 10^{19} fissions/ cm^3 in melting temperature with exposure between 6.3×10^{19} and 1.6×10^{21} fissions/ cm^3 . Bates (1970), repeating the work of Christensen, found no difference between the melting temperatures of nonirradiated and UO_2 irradiated up to 1.9×10^{20} fissions/ cm^3 . This was further confirmed by measurements by Yamanouchi et al. (1988) for irradiated UO_2 and $\text{UO}_2\text{-}2\text{wt}\%\text{Gd}_2\text{O}_3$ fuel with burnup up to 30 MWd/kgHM.

4 Properties of Cladding Materials for LWRs Fuel

4.1 Composition

The selection of zirconium as main component for cladding material in light water reactors was made on the basis of its mechanical strength, its low thermal neutron capture cross section, and its high corrosion resistance in high-temperature water. Several alloying elements have been added for different reasons:

- *Oxygen*: The addition of the soluble alloying element oxygen raises the yield strength of zirconium, thanks to solution strengthening or its interaction with mobile dislocations. The addition of approximately 1,000 ppm doubles the yield strength at room temperature from 150 to 300 MPa.

■ **Table 2**

Nominal composition of commercial Zr-based alloys for claddings

Alloy	Sn (wt.%)	Nb (wt.%)	O (wt.%)	Fe (wt.%)	Cr (wt.%)	Ni (wt.%)	Zr
Zry 2	1.45	–	0.125	0.14	0.10	0.06	Balance
Zry 4	1.45	–	0.125	0.21	0.10	–	Balance
Zirlo	1.1	1.1	0.120	0.1	–	–	Balance
M5	–	1.0	0.135	0.038	–	–	Balance
E110	–	1.0	0.06	0.009	–	–	Balance

- *Tin*: The solution of Sn aims at promoting the corrosion resistance of the cladding material and is typically on the order of 1.2–1.7% .
- *Iron, Chromium, and Nickel*: These elements are mainly soluble in the high temperature body-centered cubic BCC β phase. In the low-temperature hexagonal closed packed HCP α phase, they form intermetallic precipitates such as $Zr(Cr,Fe)_2$ and $Zr_2(Ni,Fe)$ because of their maximum solubility limit being 20 and 200 ppm for Fe and Cr in the α phase respectively. The size and stability of the precipitates strongly affects the corrosion rate (cf. ➤ Sect. 4.5).
- *Niobium*: Niobium stabilizes the β phase and improves several properties related to irradiation damage such as corrosion and growth (cf. ➤ Sect. 4.5). Given the reduced corrosion of zirconium–niobium alloys in comparison with the zirconium–tin alloys during normal operation, niobium has been added in recent years to alloys used in Western type PWRs. In advanced cladding materials, with a typical concentration of 1%, niobium forms intermetallic particles of cubic $[(Zr,Nb)_4Fe_2]$ and hexagonal $[Zr(Nb,Fe)_2]$ structure. This is in contrast to tin that is completely soluble in zirconium.

The chemical composition of the main cladding materials applied in the nuclear industry is listed in ➤ Table 2. Zircaloy-2 (Zry-2) cladding is used in boiling water reactors. In Western type pressurized water reactors Zircaloy-4 (Zry-4), ZIRLO, and M5 are used, whereas in Russian-type WWERS the alloy E110 is applied.

The density of the zirconium alloy is about $6,550 \text{ kg/m}^3$ at room temperature, and has a melting temperature of about 2,100 K (➤ Figs. 9 and ➤ 10).

4.2 Microstructure

The lattice structure of pure zirconium at room temperature is the HCP α phase, with a lattice parameter of 0.323 nm in the basal plane and 0.515 nm along the c -axis. Above 865°C , pure zirconium transforms to the BCC β phase (➤ Fig. 9). The phase transformation from α to β and vice versa affects the strength of the cladding during accidental conditions such as loss-of-coolant accidents. The transformation is influenced by the composition (e.g., oxygen and niobium content) as well as the microstructure resulting from the fabrication process, and the temperature rate because of the diffusion processes involved. Specific correlations are therefore proposed for different cladding materials. As an example, Forgeron et al. (2000) provide a dynamic model

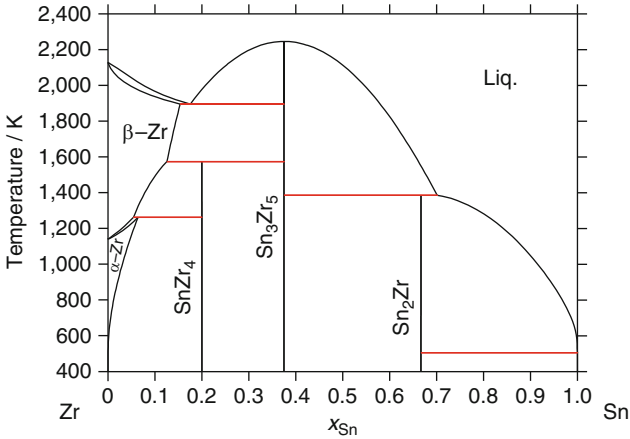


Figure 9
The Zr–Sn phase diagram after Dupin et al. (1999)

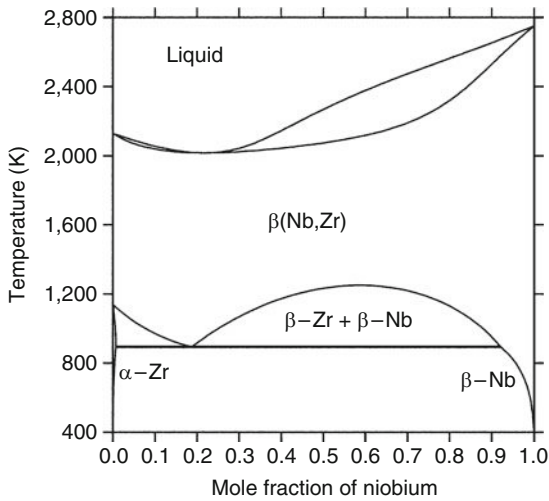


Figure 10
The Zr–Nb phase diagram; after Jerlerud Pérez and Massih (2007) ©Elsevier, 2007, reprinted with permission

for the fraction of the β phase as a function of the heating or cooling rate for Zircaloy-4:

$$\frac{d\beta}{dt} = K(T) \cdot \beta \cdot (1 - \beta) \tag{31}$$

where $K(T)$ is an empirical formula of the temperature:

$$K = \pm |T - T_{eq}| \cdot \exp(c_1 + c_2 \cdot |T - T_{eq}|) \tag{32}$$

Table 3
Examples of Kearns factors for various textures of Zircaloy

	f_r	f_θ	f_z
Isotropic	$\frac{1}{3}$	$\frac{1}{3}$	$\frac{1}{3}$
Purely radial	1	0	0
Stress relieved annealed	0.59	0.32	0.09
Recrystallized	0.54	0.32	0.14

where $c_1 = -5.725$ and $c_2 = 0.05$, and T_{eq} represents the thermodynamic equilibrium temperature between the α and β phase, and is the inverse function of the equilibrium curve:

$$\beta_{\text{eq}} = 1 - \exp\left(-[k(T - T_0)^z]\right) \quad (33)$$

where β_{eq} represents the equilibrium fraction of the β phase, T_0 is the incubation temperature (1,085.15 K), and $k = 1/(T_{\beta_{\text{eq}}=0.632} - T_0)$, where $T_{\beta_{\text{eq}}=0.632} = 1,170.15$ K and $z = 2.1$.

The fabrication process of Zircaloy results in an anisotropic polycrystalline material. The basic deformation mechanisms of HCP Zry consist of slip and twinning, depending on the relative orientation of the grain with respect to the stress field. The mechanical processing during fabrication results in interactions between both the slip and the twin systems. Consequently, the slip systems tend to align the basal planes parallel to the direction of the main deformation. The cold-rolled cladding material has a texture or preferred crystallographic orientation that is characterized by a majority of grains having their c -axis tilted 30–40° away from the normal of the clad surface toward the tangential direction.

The cold work (rolling) during the fabrication process therefore induces a texture-induced anisotropy. The anisotropy is determined by the degree of cold work (area reduction), but also by temperature and hold-time of the heat treatment. The cladding texture is generally characterized by means of Kearns texture factors f_r, f_θ, f_z , corresponding to resolved fractions of basal poles of the c -direction in the various cladding directions, as illustrated by a few examples in [Table 3](#). These factors are used in the expressions for the irradiation-induced growth (cf. [Sect. 4.5](#)).

Unless specifically mentioned otherwise the following sections will provide information and properties about standard cladding materials Zircaloy-2 and Zircaloy-4. Most of those properties can be applied to other zirconium-based alloys such as ZIRLO and M5 as a first approximation, except for

- Thermal properties: specific heat, thermal expansion
- Mechanical properties: density, elastic constants, yield stress, creep
- Irradiation properties: corrosion, irradiation growth

As a matter of fact, for the advanced cladding materials some of the properties are not available in the open literature.

4.3 Thermal Properties

4.3.1 Linear Thermal Expansion

The linear thermal expansion coefficient of the Zircaloy cladding material is smaller than that of the oxide fuel, contributing to the closure of the fuel-to-clad gap during operation. Thermal expansion of Zircaloy cladding is more pronounced in the c -direction, although the anisotropy reduces with temperature. For single crystals with a temperature between 300 and 1,083 K (MATPRO 1993)

$$\varepsilon_{11} = 4.95 \times 10^{-6} T - 1.485 \times 10^{-3} \quad (34)$$

$$\varepsilon_{33} = 1.26 \times 10^{-5} T - 3.78 \times 10^{-3} \quad (35)$$

where ε_{11} is the circumferential thermal expansion, ε_{33} is the axial thermal expansion and T is the temperature (K). For temperatures between 1,083 and 1,244 K

$$\varepsilon_{11} = \left[8.76758 + 1.09822 \cos \left(\frac{T - 1,083}{161} \pi \right) \right] \times 10^{-3} \quad (36)$$

$$\varepsilon_{33} = \left[2.77763 + 1.09822 \cos \left(\frac{T - 1,083}{161} \pi \right) \right] \times 10^{-3} \quad (37)$$

where the arguments of the cosines are in radian. For $1,244 \leq T \leq 2,098$ K

$$\varepsilon_{11} = 9.7 \times 10^{-6} T - 1.04 \times 10^{-2} \quad (38)$$

$$\varepsilon_{33} = 9.7 \times 10^{-5} T - 4.4 \times 10^{-3} \quad (39)$$

For $T > 2,098$ K (liquid)

$$\varepsilon_p = \frac{2}{3} \varepsilon_{11} + \frac{1}{3} \varepsilon_{33} + 0.0067 \quad (40)$$

where ε_{11} is the circumferential thermal expansion strain of a single Zircaloy crystal at 2,098 K, ε_{33} is the axial thermal expansion strain of a single Zircaloy crystal at 2,098 K, and ε_p is the thermal expansion of molten Zircaloy. In order to infer the cladding strains on the basis of the strain in a single crystal, it is necessary to perform a volume-weighted averaging over the entire cladding section.

4.3.2 Thermal Conductivity

The thermal conductivity of Zircaloy mainly depends on temperature, rather than crystal orientation, and minor composition differences such as those between Zry-2 and Zry-4. Texture may have an effect in the α phase temperature region, in which Zircaloy is crystallized in a hexagonal, close-packed configuration. Indeed, there may be some difference in the thermal conductivity along the prismatic and basal directions. At higher temperatures, the material is body-centered

cubic and will not exhibit texture effects. In any case, contributions to the thermal conductivity due to texture are well within the scatter of the experimental data.

According to the MATPRO library (1981, 1990), the following correlations are recommended for the thermal conductivity (W/m·K) of both Zircaloy-2 and Zircaloy-4 when $300 \text{ K} < T < 2,098 \text{ K}$

$$\lambda = 7.51 + 2.09 \times 10^{-2} T - 1.45 \times 10^{-5} T^2 + 7.67 \times 10^{-9} T^3 \quad (41)$$

and when $T \geq 2,098 \text{ K}$

$$\lambda = 36 \quad (42)$$

where T is the temperature (K).

4.3.3 Specific Heat Capacity

The specific heat capacity for Zircaloy 2 and Zircaloy 4 at constant pressure (J/(g · K)) is given by (Zimmerer 1978)

$$c_p = 286 + 9.286 \times 10^{-2} T \quad (43)$$

for $T \leq 800^\circ\text{C}$. When the temperature lies between 800 and 907°C

$$c_p = -3340.512 + 4.626 T \quad (44)$$

and if $907 \leq T \leq 985^\circ\text{C}$

$$c_p = 6611.092 - 6.346 T \quad (45)$$

For temperatures beyond 985°C a constant value of $c_p = 350.282$ is recommended.

For E110 cladding with 1% Nb, applied for instance in Russian-type WWER reactors, Volkov et al. (1989) have published values for $T < 866.5 \text{ K}$

$$c_p = -1.660714 \times 10^{-4} T^2 + 2.866393 \times 10^{-1} T + 2.612246 \times 10^{-2} \quad (46)$$

where c_p is expressed in J/(g · K). When $T < 131.3 \text{ K}$

$$c_p = -2.740292 T - 1.989514 \times 10^3 \quad (47)$$

and when $T < 116 \text{ K}$ then

$$c_p = -3.236827 T + 4.174431 \times 10^3 \quad (48)$$

Finally, for β -Zry above 1,168 K, a constant value of $c_p = 393.817 \text{ J/(g · K)}$ is suggested.

4.3.4 Emissivity

In principle, the total emissivity depends on the surface roughness and oxide thickness. However, a constant value of 0.8 is recommended in the MATPRO library (1981, 1990) and in the review of thermophysical properties for oxidized Zircaloy from the IAEA. In contrast, a constant value of approximately 0.2 is recommended for unoxidized Zircaloy.

4.4 Mechanical Properties

In view of the texture of the Zircaloy, the mechanical properties are generally anisotropic in the α phase, whereas the anisotropy disappears in the β phase.

4.4.1 Elastic Constants

Elastic moduli are required to relate stresses to strains. The elastic moduli are defined by the generalized form of Hooke's law as elements of the fourth rank tensor that relates the second rank stress and strain tensors prior to yielding. In practice, however, cladding is frequently assumed to be an isotropic material. In such a case, only two independent elastic moduli are needed to describe the relation between elastic stress and strain: Young's modulus and the shear modulus.

Cladding elastic moduli are affected primarily by temperature and oxygen content. Fast neutron fluence, cold work, and texture effects should also be included in the models, such as in the MATPRO library, but they are not as important as temperature and oxygen content for typical LWR fuel rod cladding. Therefore, codes often adopt a temperature dependent correlation for the elastic modulus (MPa)

$$E = 1.088 \times 10^3 - 5.475 \times T \quad (49)$$

where the temperature is expressed in degree Celsius and the oxygen concentration resulting from fabrication is in the range of 1,200 to 1,400 ppm. Similarly, the shear modulus is often approximated by a constant value of 0.3 or by a temperature dependent expression

$$G = 4.04 \times 10^3 - 2.168 \times T \quad (50)$$

4.4.2 Plastic Deformation

The plastic deformation in metals takes place by movements of linear lattice defects or dislocations and is controlled by shear stresses. It is therefore made possible and hindered by lattice defects, follows crystallographic planes and preserves the volume. More precisely, plastic deformation through dislocation slip is hindered by clusters of point defects such as alloying elements, oxygen and irradiation damage (or cold work). Furthermore, the second-phase particles formed by alloying elements and hydrides (cf. [Sect. 4.5](#)) also hinder dislocation slip, as well as dislocation pileup, referred to as deformation hardening. These factors thus increase the yield strength and make it dependent on both the composition and fabrication route, that is, it is specific for each cladding type and generally on the order of 550 MPa.

4.5 Irradiation Effects

4.5.1 Irradiation-Induced Growth

Clustering of irradiation-induced point defects caused primarily by fast neutrons can occur in an anisotropic manner. For instance, when all the vacancies form loops that are perpendicular to a plane, while the interstitials form loops parallel to the same plane, the crystal will shrink

and expand (at constant total volume) in the direction parallel to and perpendicular to that plane, respectively. In the Zircaloy cladding, irradiation growth is also due to partitioning of interstitials and vacancies to various sinks that are not isotropically distributed in the material. For Zr single crystals, irradiation growth consists of an expansion along the $\langle a \rangle$ direction and a corresponding contraction along the $\langle c \rangle$ axis. In polycrystalline zircaloy the situation is of course more complex, although on average expansion and contraction also occur along the same directions as in single crystals. Due to the texture caused by the fabrication, however, prism planes are preferentially aligned perpendicular to the axial direction. Irradiation growth therefore causes axial elongation. Since the irradiation growth is influenced by microstructural variables such as the amount of cold work, residual stresses, tubing texture, and composition (alloying additions) there are various correlations available. One that is generally applicable for both standard Zircaloy-2 and Zircaloy-4 can be found in MATPRO (1981, 1990):

$$\frac{\Delta L}{L} = a[\exp(240.8/T)](\Phi t)^{1/2}(1 - 3f_z)(1 + 2CW) \quad (51)$$

where $\frac{\Delta L}{L}$ represents the fractional change in length due to irradiation growth, $a = 1.407 \times 10^{-16} (\text{n/m}^2)^{1/2}$, T is the cladding temperature (K), Φt corresponds to the fast neutron fluence (n/m^2) ($E > 1 \text{ MeV}$), f_z is the texture factor for the tubing axis, that is, the effective fraction of grains aligned with their $\langle 0001 \rangle$ axis parallel to the tubing axis, and CW designates the fraction of cross-sectional area reduction due to cold work.

In normal operating conditions, the change in length of fuel rods due to irradiation growth is small. However, it can be a significant fraction of the clearance between the rod and the top and bottom assembly nozzles. Contact with those nozzles can cause rods bowing and possibly failure at points where rods contact each other.

In addition to normal growth as expressed above, a breakaway phenomena has been observed after a fluence of about $3 \times 10^{25} \text{ n/m}^2$, which has been linked to the development of $\langle c \rangle$ component dislocations. Nevertheless, in recrystallized ternary alloy of Zr, Nb, and O referred to as M5TM, very few $\langle c \rangle$ component basal loops have been observed so that no sign of accelerated growth regime is expected for fuel burnup values of PWR fuel rods up to 70 GWd/t.

4.5.2 Irradiation-Induced Hardening

Due to the high concentration of point defects and dislocations produced by the neutron irradiation, dislocation slip is inhibited, hence the yield strength increases. The increase in yield strength is associated with a reduction in ductility and affects the total elongation from 20% to a few percent. Nevertheless, both the yield strength and the ultimate tensile stress saturate beyond a fluence of about $5 \times 10^{24} \text{ n/m}^2$ in both stress relieved and recrystallized Zircaloys. Saturation is caused by the overlapping absorption volumes for interstitials and vacancies by an increasing loop concentration.

4.5.3 Irradiation-Induced Creep

Generally, the creep of materials comprises three successive domains:

- The primary creep where the specimen begins to deform relatively quickly whereupon the creep rate decreases with time,

- The secondary creep that is characterized by a constant strain rate,
- The tertiary creep that corresponds to an increase of the strain rate and finally leads to the failure of the material.

At high temperature, there are two kinds of creep mechanisms, namely creep controlled by dislocation movements, and creep controlled by diffusion. For the first kind, when the plastic flow is mainly ensured by the thermally activated movement of dislocations, creep follows a power law of the Norton type:

$$\dot{\epsilon} = A \cdot \sigma^n \cdot \exp\left(-\frac{\Delta E}{RT}\right) \quad (52)$$

where $\dot{\epsilon}$ represents the effective strain rate, σ is the effective stress, A and n are constants, ΔE is the molar activation enthalpy, R the gas constant, and T is the absolute temperature.

When creep is controlled by core diffusion (Nabarro–Herring creep), the power-law does not apply anymore and the strain rate is a function of the applied stress, the vacancies diffusion coefficient D , and the grain size d :

$$\dot{\epsilon} = K \cdot \frac{\sigma D}{d^2} \cdot \exp\left(-\frac{\Delta E}{RT}\right) \quad (53)$$

where K is a constant.

During normal operating conditions in a reactor, slow deformation under an external stress experienced by the cladding material under irradiation can occur due to creep that is promoted by the neutron flux. The total creep strain is therefore dependent on the temperature, stress level, and neutron flux. For practical purposes the cladding creep strain in fuel performance codes generally consists of two components. The first corresponds to high-temperature creep and depends only on temperature and stress, while the second component is irradiation induced and only depends on the stress and the neutron flux:

$$\dot{\epsilon} = A \cdot \sigma^n \cdot \exp\left(-\frac{Q}{k \cdot T}\right) + B \cdot \sigma^m \cdot \phi^n \quad (54)$$

The usual values of those exponents are $m = 0.6$ to 1 , and n close to 1 , while the activation energy Q is in the range of 0.05 to 0.16 eV per atom. It is assumed that irradiation creep deformation occurs by dislocation climb and glide, where climb is controlled by the absorption of point defects at dislocations.

4.5.4 Corrosion and Hydrogen Pickup

Zirconium alloys are very corrosion resistant in general. Under stringent conditions (300°C , 7 – 15 MPa) in light water reactors, however, corrosion determines the design life of fuel rods and other components. A number of different corrosion morphologies have been observed under irradiation in power reactors. First of all, in PWRs, usually a *uniform oxide growth* is observed, provided that enough dissolved hydrogen is present to suppress water radiolysis. When these films exceed approximately $100 \mu\text{m}$, oxide delamination and spalling can occur. A second distinct corrosion morphology is *nodular corrosion* and has been observed in BWRs, where water radiolysis and boiling allow oxygen to accumulate in water. Rigorous control of the second-phase particle sizes in Zry-2 has largely eliminated the nodular corrosion problem, although

at the expense of an enhanced uniform oxide growth, and sometimes with late development of nodules. A third and last corrosion morphology was observed in BWRs as well and was referred to as *shadow corrosion* because it appeared when *shadows* of the stainless steel control-blade handles were observed on the outsides of fuel boxes, or when small patches of thicker oxide appeared at contact points between fuel cladding and spacer grids from stainless steel or nickel alloys due to a galvanic effect.

In general, cladding oxidation during normal LWR operation occurs in two stages. At the beginning, a protective black oxide film develops. The corrosion layer is dense and contains mostly tetragonal zirconium, an allotropic form that is stable at high pressure and temperature.

The oxidation of zirconium alloys by water in the temperature range from 573 to 673 K proceeds by the migration of oxygen vacancies from the oxide metal interface through the oxide layer along grain boundaries to the oxide coolant surface (and the accompanying migration of oxygen as O^{2-} in the opposite direction). The vacancies at the metal oxide surface are generated by the large chemical affinity of zirconium for oxygen. Although the rate of oxidation is controlled in part by vacancy migration, the process of oxygen transfer from coolant to metal is not complete until the vacancy is annihilated by an oxygen ion at the oxide coolant surface. It is thus reasonable to expect the complex combination of both bulk oxide properties effects and surface or coolant chemistry to affect the initial corrosion rate. Since there is presently no consensus about the detailed mechanisms modelers have recourse to an empirical relation to describe the time dependency of zircaloy oxidation (MATPRO 1981, 1990, 1993):

$$\dot{\epsilon}_{ox} = k \cdot t^n \exp\left(-\frac{Q}{T}\right) \quad (55)$$

where ϵ_{ox} represents the oxidation thickness expressed either as a size (μm) or a weight gain (mg/dm^2), k is the pre-exponential factor, T is the absolute temperature, and Q the oxidation activation energy.

If the low-temperature oxidation would have been controlled by diffusion alone in the protective layer, the oxygen concentration would obey Fick's law:

$$J = -D \frac{\partial O}{\partial x} \quad (56)$$

where J represents the flux of oxygen atoms expressed in atoms per unit of surface and time, D is the diffusion coefficient expressed in surface per second, O corresponds to the oxygen concentration expressed in atoms per unit volume, and x is the distance in the direction perpendicular to the oxide surface. Assuming that O is fixed on both sides of the protective layer, corresponding to the saturation concentration in the metal phase (O_m) on one side and to the oxygen concentration in the coolant (O_{cool}) on the other side, the oxide growth rate can be expressed as

$$\frac{dw_{ox}}{dt} = -D \frac{O_m - O_{cool}}{O_{av} w_{ox}} \quad (57)$$

whereby the oxide growth rate is obtained by dividing the flux of oxygen atoms arriving at the metal oxide interface by the average oxygen concentration in the oxide layer (O_{av}). As a consequence, Eq. (57) indicates that the oxide layer growth rate becomes inversely proportional with the oxide thickness when diffusion controls the oxygen migration in the protective layer, leading to a parabolic time dependence: $n = -\frac{1}{2}$. However, it is generally observed

that the initial oxidation rate is inversely proportional to the square of the oxide thickness, corresponding to $n = -\frac{2}{3}$. This has been interpreted (MATPRO 1993) as being due to the short lifetime of the oxygen vacancies during their migration toward the coolant with respect to the time to diffuse across the protective layer. Indeed, for an infinite lifetime, the oxygen vacancy flux would obey Eq. (56), whereas for a short lifetime the flux of oxygen vacancies arriving at the coolant would be inversely proportional to the time required to arrive at the oxide coolant interface. This duration is proportional to the square of the average diffusion distance, hence the oxygen flux or the oxide growth rate in Eq. (57) would become inversely proportional with the square of the oxide thickness, resulting in $n = -\frac{2}{3}$. Nevertheless, the actual mechanism reducing the lifetime of the oxygen vacancies remains unexplained.

After a certain oxidation time, commonly referred to as the transition time, the second stage of the corrosion starts. This occurs when the compressive stresses in the oxide layer cannot be compensated by the tensile stresses in the metallic substrate and plastic yield in the metal limits the compression in the oxide. The tetragonal phase becomes unstable and the oxide transforms to a monoclinic form. An interconnected porosity develops, creating shortcuts for oxidizing water. Once this transformation occurred, only a portion of the oxide layer remains protective and the corrosion is controlled by diffusion through the dense protective layer only. Since the thickness of this layer remains almost constant (in the order of 1 μm) the corrosion rate is constant for this transition, hence $n = 1$.

Careful out of pile experiments have been used to infer the constants in the oxidation rate equation in the two phases van der Linde (1965):

$$\dot{w} = 27.1 \times 10^3 \cdot t^{\frac{1}{3}} \exp\left(-\frac{5,220}{T}\right) \quad (58)$$

for pre-transition oxidation, where the temperature T is expressed in Kelvin and the oxidation rate in weight gain (mg/dm^2). After the transition the oxidation rate can be expressed as

$$\dot{w} = 23.0 \times 10^8 \cdot t \exp\left(-\frac{14,400}{T}\right) \quad (59)$$

In general, the transition is a function of temperature and oxide layer thickness. Considering that the oxidation is expressed in weight gain (mg/dm^2), the weight gain at transition is given by (MATPRO 1981, 1990)

$$w_{tr} = 123 \cdot \exp\left(-\frac{790}{T}\right). \quad (60)$$

The above-mentioned equations for Zircaloy cannot be applied directly to predict in-pile oxidation. There is a need to apply an enhancement factor A : $\hat{w}_{tr} = A \cdot w_{tr}$ where \hat{w}_{tr} is the corrected value. The correction factor has been ascribed to either an increased supply of oxygen ions, or to irradiation damage in the oxide layer. Since no definite answer could be provided, the enhancement factor is fitted to experimental data. For BWR reactors, the enhancement factor proposed between 500 and 673 K is (MATPRO 1993)

$$A = 4.84 \times 10^5 \exp\left(-1.945 \times 10^{-2} T_c\right) \quad (61)$$

where T_c is the oxide outer surface temperature (K). For PWRs, the equation for A in the same temperature range reads

$$A = 1.203 \times 10^2 \exp(-7.118 \times 10^{-3} T_c) \quad (62)$$

It should be underlined that the rate enhancement factor A does not result in a linear change in the oxide thickness, even though the post-transition oxidation thickness varies linearly with time. This is due to the effect of the enhancement factor on the pretransition oxidation rate, which is nonlinear. It should also be underlined that the scatter in experimental data for oxidation of individual rods is considerable, with the maximum measured value deviating by as much as a factor two from the average value. These differences are caused by temperature variations and/or local variations in coolant quality or chemistry due to nucleate boiling and contaminants for instance.

Since the ZrO_2 layer is much more brittle than the underlying Zircaloy metal, and contains micro-cracks and pores, cracks will initiate in a cladding subjected to a tensile stress during a pellet-clad mechanical interaction. Since stress concentration increases with crack length, the localization effect increases with oxide thickness.

Another important consequence of cladding oxidation is hydrogen production:



Hydrogen is also produced by radiolysis of water.



A fraction of the hydrogen ions penetrates the oxide and diffuses to the metallic part. When the hydrogen content in the metal exceeds the solubility limit, it precipitates and forms brittle hydrides.



The latter form as single platelets or as elongated groups of platelets. The degree of cladding embrittlement in hydrided zirconium alloys depends on both the hydride morphology and its relative orientation to the stress field. A crack usually propagates through hydrides perpendicular to the hydride layer. It is relevant for high burnup fuel, and in particular for its resistance during ramps and accidents such as reactivity-initiated accidents (RIA).

In the case of niobium-containing cladding materials (e.g., M5 and ZIRLO), a uniform distribution of α and β grains is obtained after fabrication. The β grains are metastable and decompose on aging into a mixture of α -Zr and β -Nb. The α -Zr phase itself is supersaturated in Nb and an irradiation-induced precipitation occurs, which is believed to improve corrosion resistance, and therefore also inhibit the hydrogen uptake. In comparison with Zircaloy-4, the corrosion resistance of the M5 alloy (Bossis et al. 2006) is improved by a factor 3 to 4, and a hydrogen content reduction by a factor 5 to 6 at burnups up to 60 GWd/t. The low tin Zircaloy-4 reaches a corrosion layer thickness of about 90 μm , whereas for M5 this layer remains below 20 μm after irradiation in a PWR to 70 GWd/t. No hydride precipitation is therefore expected in M5 during service.

4.6 High-Temperature Effects

During a loss-of-coolant accident (cf. ► Sect. 6.4) the cladding temperature generally exceeds 600°C. Under these circumstances specific material properties are required for the interaction of the cladding with steam and for the mechanical strength.

4.6.1 High-Temperature Corrosion

The cladding-steam reaction model is often based on parabolic kinetic correlations for both the oxygen mass gain and or the ZrO₂ layer thickness growth. The actual reaction rate constant is defined as a function of the temperature through an Arrhenius relation

$$K_m = A_m \exp\left(-\frac{Q_m}{T}\right) \quad (67)$$

where K_m is the oxygen mass gain rate in mg/cm²/s^{1/2}, A_m is the pre-exponential factor, Q_m is the activation energy divided by the perfect gas constant, and T is the cladding temperature in Kelvin.

The kinetics of high-temperature oxidation of Zircaloy were described by Baker and Just (1962) by the following equation: (B-J)

$$w = 2029t^{0.5} \exp\left(\frac{-11,450}{T}\right) \quad (68)$$

where w is the weight of metal zirconium reacted per unit surface in mg/cm², T is the temperature in Kelvin, and t is the time (at the constant temperature T) in seconds. Although a more precise correlation was derived subsequently, the Baker-Just correlation is quoted here because it is the reference correlation for expressing the cladding zero ductility criterion for LOCA accidents, as will be discussed in ► 6.4. An improved correlation (C-P) was developed by Cathcart et al. (1977):

$$w = 601.8t^{0.5} \exp\left(\frac{-10050}{T}\right) \quad (69)$$

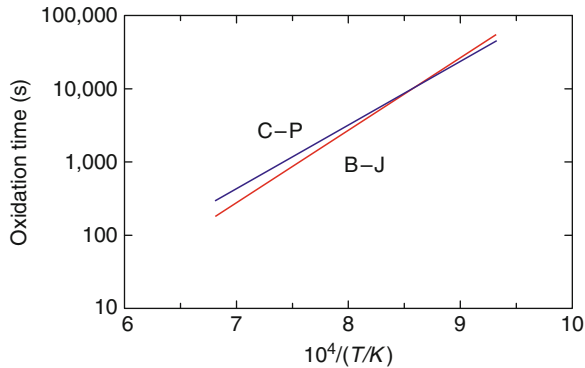
The two above correlations are compared in ► Fig. 11, in terms of temperature and time needed to achieve the same level of oxidation (17% of metal) for a two-side oxidation of a PWR 17 × 17 cladding. As one can notice, the B-J correlation is somewhat more conservative in that in the high-temperature range the given oxidation level (17%) is predicted for somewhat lower temperature and/or lower time as compared with the C-P correlation. The difference is of approximately 50°C in the temperature interval 1100–1200°C, whereas it is practically negligible in the 800–1000°C range.

Typical correlations for the Zr1%Nb-specific alloy were published by Solyany et al. (1983).

$$K_m = 920 \exp\left(-\frac{10,410}{T}\right) \quad (70)$$

and Gyori et al. (2003, 2008)

$$K_m = 658 \exp\left(-\frac{10,200}{T}\right) \quad (71)$$



■ Figure 11

Comparison of the Baker–Just (B–J) (Baker and Just 1962) and the Cathcart–Powel (C–P) (Cathcart et al. 1977) correlations in terms of time–temperature dependence to achieve 17% oxidation (PWR 17×17 cladding)

At higher temperatures, only data published by Urbanic et al. (1978) are available for Zircaloy. At 1,853 K, which is close to the monoclinic to cubic transformation of the oxide, a discontinuity has been observed in the oxidation rate.

The equations above indicate that the oxidation rate (at constant temperature) is not constant with time but decreases as it progresses, since the metal reacted progresses with the square root of time. In other words, as the oxidation progresses, there appears to be a protective effect induced by the oxide layer created in the oxidation process itself. Hence the question arises as to whether this protective effect is also effective for cladding that has been subjected to corrosion during base irradiation, as it would be the case for high burnup cladding. The experimental evidence on this particular point is scarce and to some extent contradictory. Tests done in Japan (JAEA) indicated that corroded cladding does not offer any protection against the effects of high-temperature oxidation (Nagase and Fuketa 2004). Experiments done at Argonne National Laboratory (ANL) on the other hand, indicated a “partial” protective effect of the preexisting corrosion oxide layer (Billone et al. 2008).

The reason for this difference might be due to the different experimental technique used at JAEA and ANL, or to the different morphology of the preexisting oxide layer, but is at present unclear. From the application viewpoint it thus appears that since the experimental evidence is inconclusive, LOCA analyses should not take credit of any beneficial effect of the preexisting corrosion layer on the high temperature oxidation process, unless clear and consistent evidence of a protective effect is produced. In other words, high burnup fuel with a certain corrosion layer should be treated as fresh (non-corroded cladding) for the purpose of computing the oxidation kinetics in a LOCA, unless further experimental evidence is brought forward on this particular point.

An additional observation regards the way the high-temperature oxidation correlations Eq. (68) and Eq. (69) are to be used in practice. In fact, these correlations were derived from constant temperature tests, whereas in practical LOCA applications the temperature varies with time. The procedure suggested here is to calculate the oxidation at the end of a time-step t by

means of the following algorithm (e.g., for the C-P correlation):

$$w = 0.6018(t_e + \delta t_n)^{0.5} \exp(-10050/T_n) \quad (72)$$

where T_n is the average temperature in the time interval δt_n and t_e is an equivalent time, defined as the time that would be needed to achieve the oxidation present at start of the time-step δt_n , if the temperature up to that moment had always been constant and equal to T_n .

4.6.2 High-Temperature Deformation

In fuel performance codes, usually a one-dimensional mechanical model is applied for the radial cladding deformation. For dealing with large high-temperature deformation (i.e., ballooning), typically during a LOCA-type accident, generally a strain rate correlation in the form of a Norton power equation is applied:

$$\frac{d\varepsilon_{eff}}{dt} = A \cdot \sigma_{eff}^n \cdot \exp\left(-\frac{Q}{R \cdot T}\right) \quad (73)$$

where ε_{eff} is the effective strain, σ_{eff} represents the effective stress, R is the universal gas constant, T is the temperature, A is the strength coefficient, Q is the activation energy for the plastic deformation, and n is the stress exponent.

The parameters of the Norton equation (A , Q , and n) are generally defined separately for the α and the β phases of the different cladding alloys. Indeed, at high temperatures, such as during a LOCA, the cladding may undergo a phase transition from the HCP α phase to the FCC β phase. In order to define the effective strain rate of the cladding in the metallurgical phase transition range there are two different approaches proposed in the literature. According to the first approach, the Norton parameters A , n , and Q are interpolated in the transition range using the fractions of the α and β phases as weighting factors. The second approach is based on micro-mechanical considerations for composite materials assuming a statistically homogeneous distribution of α -phase inclusions embedded in the β -phase matrix, that is, each representative volume element has the same α to β volume fraction corresponding to the macroscopic average value. According to the basic relation of self-consistency the overall average strain, and consequently the macroscopic strain rate of the two-phase cladding is expressed as the weighted average of the strain rates of each phases:

$$\dot{\varepsilon} = (1 - \phi) \cdot \dot{\varepsilon}_\alpha + \phi \cdot \dot{\varepsilon}_\beta \quad (74)$$

where ϕ is the fraction of β phase.

5 Basic Phenomena for In-Reactor Performance

The main objective of this section is the review of the main equations and boundary conditions required to describe the thermal-mechanical behavior of the nuclear fuel rods. The accurate description of the fuel rod's behavior, however, involves various disciplines ranging from chemistry, nuclear and solid state physics, metallurgy, ceramics and applied mechanics. The strong interrelationship between these disciplines calls for the development of computer codes describing the general fuel behavior. Fuel designers and safety authorities rely heavily on this type of

codes since they require minimal costs in comparison with the costs of an experiment or an unexpected fuel rod failure.

5.1 Neutronic Aspects of Nuclear Fuel Rods

5.1.1 Nuclide Evolution in Nuclear Fuel

A part of each fuel performance code deals with the calculation of the local concentrations of various actinide isotopes such as U, Pu, and some fission products (e.g., Xe, Kr, Cs, I, He) as a function of the radial position across a fuel pellet. These local quantities are required for the determination of the local power density, the local burnup, and the source term of fission products.

The radial variation of the power is due to the self-shielding effect, which is both energetic and spatial in nature. The energy self-shielding results from the resonances in the various cross sections of the nuclides present in the fuel. The spatial self-shielding effect results from the heterogeneity of a reactor. Indeed, neutron absorption at the outside of a fuel pellet will effectively shield the inside of the pellet, resulting in a neutron flux depression in the center of a fuel rod. This is strongly influenced by the neutron spectrum of the reactor.

With the present fuel discharge burnup levels in excess of 50 GWd/t, the large radial gradient of the concentrations of fissile isotopes in the fuel leads to a strong radial dependence of the power generation and the related discharge burnup. The power density provides the source term for the temperature calculation, affecting most mechanisms in the fuel. In view of the primary importance of the relative radial power profile for the thermal and mechanical analysis of nuclear fuel rods, priority is given to relative rather than absolute concentrations in fuel performance codes. Such a code receives the absolute linear heat rate (kW/m) on input at each time-step. In order to compute that radial power profile as a function of time various models are available. The main equations will be presented in the next section.

5.1.2 The Basic Equations

Rather than solving the Boltzmann transport equation for neutrons as in the WIMS (Newton and Hutton 2002) or HELIOS (Stammler 1996) lattice reactor physics codes, which are in use by the nuclear industry in fuel management calculations for nuclear power reactors, fuel performance codes must make use of simpler models for the sake of calculation time. Most of them were derived from the RADAR model (Palmer 1983), which is based on thermal neutron diffusion theory and was validated with WIMS calculations. The original TUBRNP (Lassmann et al. 1994) model for power and burnup calculations included in the TRANSURANUS fuel performance code (Lassmann 1992), and later also in other codes such as FRAPCON3 (Berna 1997), extended the RADAR model by including higher Pu isotopes, and modifying the radial shape function that accounts for resonance absorption by ^{238}U . TUBRNP was originally validated for UO_2 fuel in LWRs with experimental data from fuel with burnup values between 35 and 64 MWd/kgHM. Later the RAPID model (Lee et al. 2000) was developed for the COSMOS code (Lee et al. 2007), and PLUTON (Lemehov et al. 2001) was developed for the FEMAXI code (Suzuki 2000), while a specific burnup model for the RTOP code (Kurchatov et al. 2002) was developed for fuel rods in

Russian-type WWER reactors. RAPID was validated purely on the basis of profiles calculated by HELIOS up to 150 MWd/kgHM, while the others were validated against experimental data up to 83 MWd/kgHM.

The main equations of the simple diffusion-based models consist of a differential equation for the ^{235}U concentration, a differential equation for the ^{239}Pu concentration, and the solution of diffusion theory for the thermal flux, by assuming proportionality of the local power density $q'''(r)$ to the neutron flux $\phi(r)$, the concentrations of the relevant isotopes $N_k(r)$, and to the corresponding one-group fission cross sections $\sigma_{f,k}$ that are averaged over the neutron spectrum:

$$q'''(r) \propto \sigma_{f,k} N_k(r) \phi(r) \quad (75)$$

In order to determine ϕ thermal flux diffusion theory can be applied:

$$\nabla \phi - \kappa^2 \phi(r) = 0 \quad (76)$$

where the inverse diffusion length

$$\kappa = \sqrt{\frac{\sum_{a,tot}}{D}} \quad (77)$$

is derived from the macroscopic absorption and scattering cross sections:

$$\sum_{a,tot} \approx \sum_k \sigma_{a,k} N_k \quad (78)$$

$$D = \frac{1}{3 \sum_s} = \frac{1}{3 \sigma_s N_{tot}} \quad (79)$$

The resulting solutions of the differential equation are based on the modified Bessel functions (of the first and second type):

$$\phi(r) \propto I_0(\kappa r) \quad (80)$$

for the solid cylinder and

$$\phi(r) \propto I_0(\kappa r) + \frac{I_1(\kappa R)}{K_1(\kappa R)} K_0(\kappa r) \quad (81)$$

for the hollow cylinder, where R denotes the fuel at the outer radius.

The main disadvantage of models derived from RADAR is that they take only the formation of ^{239}Pu into account, that is, the formation of ^{240}Pu and higher Pu isotopes is neglected. In order to eliminate some of the high burnup limitations of the RADAR model, more elaborated models have been developed. The modeling of the radial power profiles is hence split into the approximation of the neutron flux through thermal diffusion theory and the computation of the local concentrations of the relevant actinide isotopes that are either fissile or fertile. As an example the equations implemented in the most recent TUBRNP model (Schubert et al. 2008) are given in [Table 5](#). In this table $N_k(r)$ denotes the local concentration of the isotope N_k , σ_a and σ_b are the one-group effective cross sections for total neutron absorption and neutron capture, respectively, and "A" is a conversion constant

$$A = 0.8815 \frac{\rho_{fuel}}{\alpha \sum_k \sigma_{f,k} N_k} \quad (82)$$

where ρ_{fuel} represents the fuel density, and the time-step or the increment of the neutron fluence Φdt has been replaced by a burnup increment

$$dbu = \frac{q'''dt}{\rho_{fuel}} = \frac{\alpha}{\rho_{fuel}} \sum_k \sigma_{f,k} N_k \phi dt \quad (83)$$

This evaluation assumes a quasi-immediate β -decay of ^{237}U and ^{238}Np analogous to modeling the generation of ^{239}Pu by neutron capture of ^{238}U and quasi-immediate β -decay of ^{239}U and ^{239}Np . The concept of one group, spectrum-averaged cross sections is also used in codes such as ORIGEN (Croff et al. 1978) and KORIGEN (Fischer and Wiese 1983).

Resonance absorptions of epithermal neutrons in ^{238}U and ^{240}Pu give rise to enhanced plutonium production near the surface of the pellet. This plutonium is distributed radially according to an empirical function for the sake of simplicity:

$$f(r) = 1 + 3 \exp\left(-9.7\sqrt{R-r}\right) \quad (84)$$

in the original RADAR model (Palmer et al. 1983), and

$$f(r) = 1 + p_1 \exp\left(-p_2(R-r)^{p_3}\right) \quad (85)$$

in the TUBRNP model (Lassmann et al. 1994), where R is the fuel outer radius. While the value of p_1 differs between LWRs ($p_1 = 3.45$) and the Halden HWR ($p_1 = 2.21$), the values of $p_2 = 3.0$ and $p_3 = 0.45$ hold for both reactor types. Owing to the asymptotic behavior of expression for $f(r)$ at the minimum and maximum pellet radii, the main parameter p_1 can be interpreted as an estimate of the ratio of integrals for resonance and thermal neutrons:

$$p_1 = \frac{\int_{res} \sigma_c(E) \phi(E) dE}{\int_{th} \sigma_c(E) \phi(E) dE} \quad (86)$$

where $\sigma_c(E)$ is the differential neutron capture cross section and $\phi(E)$ denotes the neutron flux per energy. As a result, the parameter $p_1(^{240}\text{Pu})$ can be estimated on the basis of $p_1(^{238}\text{U})$ as follows:

$$\frac{p_1(^{240}\text{Pu})}{p_1(^{238}\text{U})} = \frac{RI(^{240}\text{Pu})}{\sigma_{c,th}(^{240}\text{Pu})} \frac{\sigma_{c,th}(^{238}\text{U})}{RI(^{238}\text{U})} \quad (87)$$

where RI are the resonance integrals and $\sigma_{c,th}$ are the thermal neutron capture cross-sections of the given isotopes. The applied values (► Table 4) originate from (Chadwick et al. 2006; Nichols et al. 2005) and a recent reanalysis of the thermal neutron capture cross section in ^{238}U (Trkov et al. 2005).

The system of ordinary differential equations is solved incrementally. For each average burnup increment a new radial power density profile is calculated from which the radial burnup profile is updated. Finally, the local concentrations of Kr, Xe, Cs, and Nd, are obtained by multiplying the local burnup increment by the appropriate fission yields.

Under irradiation conditions of UO_2 and $(\text{U,Pu})\text{O}_2$ fuels, three main sources for production of He have to be considered: (n,α) reactions on oxygen, ternary fission of actinides, and α -decay of actinides. The last nuclide in the above-mentioned set of ordinary differential equations is ^4He and accounts for α -decay from ^{242}Cm , ^{238}Pu , and ^{244}Cm .

■ **Table 4**
Resonance integrals (RI) and thermal neutron capture cross sections ($\sigma_{c,th}$) of the isotopes ^{238}U and ^{240}Pu

	^{238}U	^{240}Pu
RI	277 b	2.68 b
$\sigma_{c,th}$	8450 b	290 b

■ **Table 5**
Basic equations for modeling the radial burnup profile in nuclear fuels

$\frac{d^{235}\text{U}(r)}{dbu}$	$= -\sigma_{\alpha,235\text{U}}^{235}\text{U}(r)A$
$\frac{d^{236}\text{U}(r)}{dbu}$	$= -\sigma_{\alpha,236\text{U}}^{236}\text{U}(r)A + \sigma_{c,235\text{U}}^{235}\text{U}(r)A$
$\frac{d^{237}\text{Np}(r)}{dbu}$	$= -\sigma_{\alpha,237\text{Np}}^{237}\text{Np}(r)A + \sigma_{c,236\text{U}}^{236}\text{U}(r)A + \sigma_{(n,2n),238\text{U}}^{238}\text{U}(r)A$
$\frac{d^{238}\text{U}(r)}{dbu}$	$= -\sigma_{\alpha,238\text{U}}^{238}\text{U}(r)f_{238\text{U}}(r)A - \sigma_{(n,2n),238\text{U}}^{238}\text{U}(r)A$
$\frac{d^{238}\text{Pu}(r)}{dbu}$	$= -\sigma_{\alpha,238\text{Pu}}^{238}\text{Pu}(r)A + \sigma_{c,237\text{Np}}^{237}\text{Np}(r)A + \frac{\lambda_{242\text{Cm}}^{242}\text{Cm}(r)A}{\Phi} - \frac{\lambda_{238\text{Pu}}^{238}\text{Pu}(r)A}{\Phi}$
$\frac{d^{239}\text{Pu}(r)}{dbu}$	$= -\sigma_{\alpha,239\text{Pu}}^{239}\text{Pu}(r)A + \sigma_{c,238\text{Pu}}^{238}\text{Pu}(r)A + \sigma_{c,238\text{U}}^{238}\text{U}(r)f_{238\text{U}}(r)A$
$\frac{d^{240}\text{Pu}(r)}{dbu}$	$= -\sigma_{\alpha,240\text{Pu}}^{240}\text{Pu}(r)f_{240\text{Pu}}(r)A + \sigma_{c,239\text{Pu}}^{239}\text{Pu}(r)A + \frac{\lambda_{244\text{Cm}}^{244}\text{Cm}(r)A}{\Phi}$
$\frac{d^{241}\text{Pu}(r)}{dbu}$	$= -\sigma_{\alpha,241\text{Pu}}^{241}\text{Pu}(r)A + \sigma_{c,240\text{Pu}}^{240}\text{Pu}(r)A - \frac{\lambda_{241\text{Pu}}^{241}\text{Pu}(r)A}{\Phi}$
$\frac{d^{242}\text{Pu}(r)}{dbu}$	$= -\sigma_{\alpha,242\text{Pu}}^{242}\text{Pu}(r)A + \sigma_{c,241\text{Pu}}^{241}\text{Pu}(r)A$
$\frac{d^{243}\text{Pu}(r)}{dbu}$	$= -\sigma_{\alpha,243\text{Pu}}^{243}\text{Pu}(r)A + \sigma_{c,242\text{Pu}}^{242}\text{Pu}(r)A - \frac{\lambda_{243\text{Pu}}^{243}\text{Pu}(r)A}{\Phi}$
$\frac{d^{241}\text{Am}(r)}{dbu}$	$= -\sigma_{\alpha,241\text{Am}}^{241}\text{Am}(r)A + \sigma_{c,241\text{Pu}}^{241}\text{Pu}(r)A$
$\frac{d^{242}\text{Am}(r)}{dbu}$	$= -\sigma_{\alpha,242\text{Am}}^{242}\text{Am}(r)A + \sigma_{c,241\text{Am}}^{241}\text{Am}(r)A - \frac{\lambda_{242\text{Am}}^{242}\text{Am}(r)A}{\Phi}$
$\frac{d^{243}\text{Am}(r)}{dbu}$	$= -\sigma_{\alpha,243\text{Am}}^{243}\text{Am}(r)A + \sigma_{c,242\text{Am}}^{242}\text{Am}(r)A + \sigma_{c,242\text{Pu}}^{242}\text{Pu}(r)A$
$\frac{d^{244}\text{Am}(r)}{dbu}$	$= -\sigma_{\alpha,244\text{Am}}^{244}\text{Am}(r)A + \sigma_{c,243\text{Am}}^{243}\text{Am}(r)A - \frac{\lambda_{244\text{Am}}^{244}\text{Am}(r)A}{\Phi}$
$\frac{d^{242}\text{Cm}(r)}{dbu}$	$= -\sigma_{\alpha,242\text{Cm}}^{242}\text{Cm}(r)A + \sigma_{c,241\text{Am}}^{241}\text{Am}(r)A - \frac{\lambda_{242\text{Cm}}^{242}\text{Cm}(r)A}{\Phi}$
$\frac{d^{243}\text{Cm}(r)}{dbu}$	$= -\sigma_{\alpha,243\text{Cm}}^{243}\text{Cm}(r)A + \sigma_{c,242\text{Cm}}^{242}\text{Cm}(r)A$
$\frac{d^{244}\text{Cm}(r)}{dbu}$	$= -\sigma_{\alpha,244\text{Cm}}^{244}\text{Cm}(r)A + \sigma_{c,243\text{Cm}}^{243}\text{Cm}(r)A + \sigma_{c,243\text{Am}}^{243}\text{Am}(r)A - \frac{\lambda_{244\text{Cm}}^{244}\text{Cm}(r)A}{\Phi}$
$\frac{d^{245}\text{Cm}(r)}{dbu}$	$= -\sigma_{\alpha,245\text{Cm}}^{245}\text{Cm}(r)A + \sigma_{c,244\text{Cm}}^{244}\text{Cm}(r)A$
$\frac{d^{246}\text{Cm}(r)}{dbu}$	$= +\sigma_{c,245\text{Cm}}^{245}\text{Cm}(r)A$
$\frac{d^4\text{He}(r)}{dbu}$	$= \frac{\lambda_{242\text{Cm}}^{242}\text{Cm}(r)A}{\Phi} + \frac{\lambda_{244\text{Cm}}^{244}\text{Cm}(r)A}{\Phi} + \frac{\lambda_{238\text{Pu}}^{238}\text{Pu}(r)A}{\Phi}$

For a typical UO_2 fuel, the contributions of the decay of ^{244}Cm , ^{242}Cm , and ^{238}Pu amount to at least 90% of the total ^4He generation at end of irradiation. The discrepancy becomes more significant with higher power density and during a storage period. The total amount of generated ^4He in UO_2 fuel is, however, rather low – the maximum corresponding to approximately 20% of the ^4He present in MOX fuel. On the other hand, in MOX fuel the contribution of the nuclides ^{244}Cm , ^{242}Cm , and ^{238}Pu is almost equal to the total generation of ^4He by α -decay.

5.1.3 Burnable Absorbers

The need to improve reactor performance through longer cycle lengths or improved fuel utilization has been apparent since the beginning of commercial nuclear power generation. The fuel initial enrichment has been increased to almost 5%, with the consequence that the additional amount of fissile material in the core at beginning of life has had to be compensated for by the introduction of additional absorber material in the core (IAEA 1995). This additional absorber can be introduced in the form of control rods, soluble absorber (boric acid) in the coolant, integral burnable absorbers (IBA), or burnable poison rod assemblies (BPRA). IBAs are nonremovable, neutron-absorbing materials used as components of a fuel assembly. BPRAs are assemblies that contain only rods with neutron-absorbing materials that can be inserted in PWR assembly guide tubes. There are two disadvantages to the use of BPRA's. First their use results in a separate radioactive waste item, which is normally placed in a discharged fuel assembly and must be separately disposed of. Secondly, the BPRA creates a water displacement reactivity penalty at the end of cycle by virtue of it taking up the space in the guide tubes where the water moderator would otherwise be, thus hardening the spectrum. Both type of burnable absorbers can be used to control core reactivity and local power peaking and optimize fuel utilization. In general, both are designed to function during the first cycle of irradiation of a fresh, unirradiated fuel assembly.

For all BWRs integral burnable absorbers in the fuel are chosen. For PWRs the use of soluble absorber in the coolant was for many years the only burnable poison control required. However, the increase of initial fuel enrichment and the development of the ultra low leakage in-in-out fuel management scheme could not be indefinitely compensated for by increasing the boric acid concentration and therefore integral burnable absorbers and discrete burnable poison rod absorbers are also utilized in PWR designs nowadays. Burnable poisons allow fresh fuel to be placed in the center of a reactor core in an “ultra low leakage” design. The burnable poisons quench the high reactivity of the new fuel and help maintain a constant power and flux within the reactor core that is below the maximum safety standard allowed for the reactor. This low-leakage core also converts more fertile material to fissile material than a core with the fresh fuel loaded on the outside of the reactor allowing a greater proportion of the fuel to be burned by the end of life (EOL). The low-leakage design also helps eliminate damage to the pressure vessel due to neutrons escaping from the core. In addition, the highly efficient shuffle schemes made possible by the BPRA and integral burnable poisons have reduced ore requirements by >3% and separative work requirements by >4%.

Two concepts of integral burnable absorbers are treated in general, namely Gadolinia (Gd_2O_3) and Zirconium diboride (ZrB_2). Gadolinium addition to the fuel is considered to have several significant effects on fuel performance, such as degrading the thermal conductivity

of the fuel (see [Sect. 3.2.2](#)), reducing the melting point and producing a distorted, rapidly changing radial power profile. Only the last aspect will be treated here.

Natural gadolinium consists of seven isotopes with mass numbers 152, 154, 155, 156, 157, 158, and 160. The natural percent abundances are 0.002, 0.021, 0.148, 0.206, 0.157, 0.248, and 0.218 respectively. This burnable absorber works by neutron capture of two isotopes, ^{155}Gd and ^{157}Gd , with extremely high absorption cross sections. The isotopes produced by this reaction, ^{156}Gd and ^{158}Gd have a small absorption cross section and need not to be further considered.

The methodology to describe the neutron absorption of ^{155}Gd and ^{157}Gd is the same as in previous burnup equations, that is,

$$\frac{d\text{Gd}_{155}}{dbu} = -\sigma_{a,155}\text{Gd}_{155}A \quad (88)$$

$$\frac{d\text{Gd}_{157}}{dbu} = -\sigma_{a,157}\text{Gd}_{157}A \quad (89)$$

The difficulty of this simplified treatment is the definition of the effective absorption cross section σ_a . The absorption cross section is extremely high for neutron energies below 1 eV. The consequence is (1) a local shift of the neutron spectrum of the thermal flux (hardening) and (2) a significant spatial self-shielding of the fuel. One can try to fit the effective absorption cross section so that the local change of the neutron spectrum is approximately taken into account. Nevertheless, the self-shielding is solved with the diffusion approximation, which is not valid in strong absorbing media. It leads to an underestimation of the power and the central temperature by the fuel performance code at beginning-of-life (BOL). In order to cope with Gd more accurately, it is therefore recommended to apply tables with relative power profiles obtained by means of transport codes such as WIMS or HELIOS.

The second burnable absorber was developed by Westinghouse under the name IFBA (Integral Fuel Burnable Absorber). This fuel consists of a thin layer ZrB_2 ($\sim 200 \mu\text{m}$) deposited by sputtering on the surface of the UO_2 pellets. The resulting loading is $1.7 \text{ mg }^{10}\text{B}$ per cm and the layer adheres perfectly to the UO_2 substrate (IAEA 1995). This burnable absorber in the form of a thin layer works through the (n,α) reaction, for example, He is produced. As a result there is a need to reduce the pre-pressurization level of the fuel rod. Apart from this, the methodology to describe the neutron absorption of boron is the same as in the case of Gadolinia.

5.2 Heat Transfer and Thermal Characteristics

The objective of this section is to describe how the temperature distribution in a nuclear fuel rod is calculated in a fuel rod performance code. The scope is limited to a description of the important physical phenomena, along with the basic equations and the main assumptions. Detailed numerical aspects as well as mathematical derivations are provided in (Bailly et al. 1999; Lassmann and Van Uffelen 2004; Olander 1976).

The temperature distribution in a fuel rod is of primary importance for several reasons. First of all, the commercial oxide fuels have poor thermal conductivity, resulting in high temperatures even at modest power ratings. Secondly, fuel performance codes are used for safety cases where one has to show that no fuel melting will occur, or that the rod internal pressure will remain below a certain limit. Finally, many other properties and mechanisms are exponentially dependent on temperature.

The most important quantity is of course the local power density q''' , that is, the produced energy per unit volume and time. It is usually assumed that q''' depends only on the radius and the time. The linear rating q' is then simply given by

$$q' = \int_{r_{f,i}}^{r_{cl,o}} q''' 2\pi r dr = \int_{r_{f,i}}^{r_{f,o}} \bar{q}_f''' f(r) 2\pi r dr + \int_{r_{cl,i}}^{r_{cl,o}} \bar{q}_{cl}''' 2\pi r dr \quad (90)$$

where $r_{f,i}/r_{cl,i}$ is the inner fuel/cladding radius, $r_{f,o}/r_{cl,o}$ is the outer fuel/cladding radius, \bar{q}_f''' and \bar{q}_{cl}''' are the average power density in the fuel and cladding, respectively, and $f(r)$ is a radial distribution (form) function obtained from the neutronic calculations (cf. ► 5.1). Generally, the linear rating is a prescribed quantity and is a function of the axial coordinate z and the time t . For some phenomena (e.g., cladding creep), the neutron flux is also needed. It can be prescribed as well but may also be calculated from the local power density.

5.2.1 Axial Heat Transport in the Coolant

In general, three regimes must be covered in a LWR:

1. The subcooled regime, where only surface boiling occurs. This regime is typical for PWR's under normal operating conditions.
2. The saturated, two-phase regime. This regime is typical for BWRs under normal operating conditions.
3. The saturated or overheated regime. This regime may be reached in all off-normal situations. A typical example is a LOCA.

The fuel rod performance codes use one-dimensional (axial) fluid dynamic equations that can only cope with the first two regimes. For simulating the third type of regime, the whole reactor coolant system needs to be analyzed by means of thermo-hydraulic system codes such as RELAP or ATHLET.

The temperature calculation in the coolant serves two purposes. First of all, the axial coolant temperature in the basic (fictional) channel provides the (Dirichlet) boundary condition for the radial temperature distribution in the fuel rod. It results from the combined solution of the mass, momentum, and energy balance equations. The simplified equation used in fuel performance codes reads

$$c\rho \frac{\partial T}{\partial t} + c\rho w \frac{\partial T}{\partial Z} = q_{cl,c}'' \frac{2\pi r_{cl,o}}{A} + q_c''' \quad (91)$$

where c represents the heat capacity, ρ the density, w the velocity, T the temperature, $q_{cl,c}''$ the heat flux from the cladding to the coolant, A the channel cross-sectional area, $r_{cl,o}$ the cladding outer radius, and q_c''' the power density in the coolant. In general, the heat flux from cladding to coolant should be computed by means of a thermo-hydraulic code. Mathematically, the boundary condition is of the convective type

$$q_{cl,c}'' = -\lambda \frac{\partial T(r,t)}{\partial r} \Big|_{r_{cl,o}} = \alpha \{T(r=r_{cl,o}) - T_c\} \quad (92)$$

where α is the heat transfer coefficient between cladding and coolant and $T_c = T_c(z, t)$ is the (bulk) coolant temperature. Only for a steady-state condition

$$c\rho w \frac{dT}{dZ} = \frac{q'}{A} + q''' \quad (93)$$

the heat flux from the cladding to the coolant is known and is given by

$$q''_{cl,c} = \frac{q'}{2\pi r_{cl,o}} \quad (94)$$

Under normal operational conditions, the mass flow rate, the coolant inlet temperature, and pressure are prescribed. In an off-normal or accidental situation the normal operational condition is the initial condition, but the boundary conditions must be provided by the thermo-hydraulic system codes.

The second objective of the heat flow calculation in the coolant is the derivation of the radial temperature drop between the coolant and the cladding $T_{cl} - T_c$, resulting from convection:

$$q'' = \alpha_{\text{film}}(T_{cl} - T_c) = \frac{q'_c}{2\pi r_{cl,o}} \quad (95)$$

The heat transfer coefficient in the film depends on the type of convection (forced or natural) and the type of coolant (gas, liquid, liquid metal). In the subcooled regime of a PWR, the Dittus-Boelter correlation is largely applied, whereas in the saturated regime of a BWR the Jens-Lottes correlation is applied.

5.2.2 Heat Transport through the Cladding

The heat transport through the cladding occurs through conduction:

$$\frac{1}{r} \frac{\partial}{\partial r} \left(r \lambda_c \frac{\partial T}{\partial r} \right) + q'''_{cl} = 0 \quad (96)$$

where λ_c is the cladding conductivity (~ 20 W/mK for Zircaloy), and q'''_{cl} the heat generation in the cladding (gamma-heating, as well as the exothermic clad oxidation process). In order to account for the presence of an outside oxide layer with a thermal conductivity on the order of 2 W/mK for ZrO_2 (thickness < 100 μm), the total equivalent cladding conductivity can be obtained by applying the formula for serial thermal resistances. In a similar manner, the appearance of crud on the outer cladding surface is sometimes accounted for through an additional heat transfer coefficient. The word crud stems from Chalk River unidentified deposits, that is, the filtered reactor coolant that contained metal fragments. Crud builds up in the reactor coolant over time and becomes extremely radioactive. It gathers in elbows of the piping system and when coolant pumps are started or shifted, the rapid change in turbulent water flow in the pipes causes a crud burst. Some of the crud is deposited on the cladding, but because of its varying composition and attachment, it is difficult to predict accurately its contribution to the heat transfer in the fuel rod.

5.2.3 Heat Transport from the Cladding to the Fuel Pellet

The temperature difference in the pellet-cladding gap, ΔT_{gap} , is calculated as follows (Lassmann and Hohlefeld 1987):

$$\Delta T_{gap} = \frac{q''}{h_{gap}} \quad (97)$$

where q'' is the heat flux in W per unit area and h_{gap} is the heat transfer coefficient between fuel and cladding (gap conductance). Heat transfer by convection can be neglected. In general, the heat transfer coefficient h_{gap} depends on

- Gap width or contact pressure between fuel and cladding;
- Gas pressure and composition;
- Surface characteristics of cladding and fuel.

In fact, there are three parallel conduction routes:

$$h_{gap} = h_{rad} + h_{con} + h_{gas} \quad (98)$$

The contribution of the radiative component is given by

$$h_{rad} = \left(\frac{C_s}{\frac{1}{\varepsilon_f} + \frac{1}{\varepsilon_{cl}} - 1} \right) \frac{T_f^4 - T_{cl}^4}{T_f - T_{cl}} \quad (99)$$

where C_s is the Stefan–Boltzmann constant, ε the emissivity, and T the temperature. The radiative component is less than 1% during normal operating conditions, because of the limited surface temperatures.

The component h_{con} reproduces the improvement in heat transfer due to contact pressure

$$h_{con} = \alpha \bar{\lambda} \delta \left(\frac{P}{\delta^2 H} \right)^\beta \quad (100)$$

where $\bar{\lambda}$ and δ are the mean values of the thermal conductivity and the arithmetic mean roughness, respectively, P is the contact pressure, H is the Meyer hardness of the softer material, α and β are model parameters.

The heat transfer by conduction in the gas is often based on the model of Ross and Stoute (1962):


$$h_{gas} = \frac{\lambda_{gas}}{\delta + s + g_f + g_{cl}} \quad (101)$$

where the thermal conductivity of a multicomponent gas is only composition dependent and calculated by means of

$$\lambda_{gas} = \sum_{j=1}^n \left[\frac{\lambda_j}{\left(1 + \sum_{k=1, j \neq k}^n w_{jk} \frac{c_k}{c_j} \right)} \right] \quad (102)$$


with c and w being molar concentrations and weighting factors respectively. The gas extrapolation lengths g_f and g_{cl} (or temperature jump distance) account for the imperfect heat transport across the solid–gas interface, which is material and gas-pressure dependent. Detailed formulations are discussed in Lassmann and Hohlefeld (1987).

5.2.4 Effects of Irradiation on Gap Conductance

As a result of the release of fission gases from the fuel pellets, the thermal conductivity of the plenum gas will change. As shown in  Fig. 12 the released fission gases (Kr, Xe) have a much lower thermal conductivity than the helium-filling gas. According to Eq. 102 the thermal conductivity of the He–Kr–Xe mixtures can be written as

$$\lambda_{gas} = \frac{\lambda_1}{1 + A_{12}(x_2/x_1) + A_{13}(x_3/x_1)} + \frac{\lambda_2}{1 + A_{21}(x_1/x_2) + A_{23}(x_3/x_2)} + \frac{\lambda_3}{1 + A_{32}(x_1/x_3) + A_{32}(x_2/x_3)} \quad (103)$$

where subscripts $j, k = 1, 2,$ and 3 denote He, Kr, and Xe, respectively, and A_{jk} are empirical coefficients. Since the fission gas release in LWR fuel during normal operation is around 1% of the inventory, the fraction of (Xe + Kr) steadily increases as a function of burnup, which according to Eq. 103 leads to a lower thermal conductance of the gap. For example, the thermal conductivity decreases by about a factor of 2 when the concentration of Xe and Kr released to the gap and plenum increases to about 27%. At the same time the pressure in the free volume of the pin increases. This latter effect on the thermal conductivity is, however, small and can be neglected on the basis of the known data for helium (Tsederberg et al. 1971).

 Figure 13 shows the thermal conductivity of a (He + Kr + Xe) gas mixture typical for a PWR fuel rod as a function of burnup calculated using Eq. 103. The A_{jk} coefficients are taken from (Yamnikov and Malanchenko 1977):

$$\begin{aligned} A_{12} &= 2.7 & A_{13} &= 3.6 \\ A_{21} &= 1.7 & A_{23} &= 0.6 \\ A_{31} &= 0.5 & A_{32} &= 3.5 \end{aligned}$$

It is important to note that, despite very detailed formulations for the gap conductance, there is an unavoidable uncertainty in the gap sizes due to input uncertainties, but also because of uncertainties in the mechanical computation (e.g., cracking and fuel swelling, as discussed below).

5.2.5 Heat Transport in the Fuel Pellet

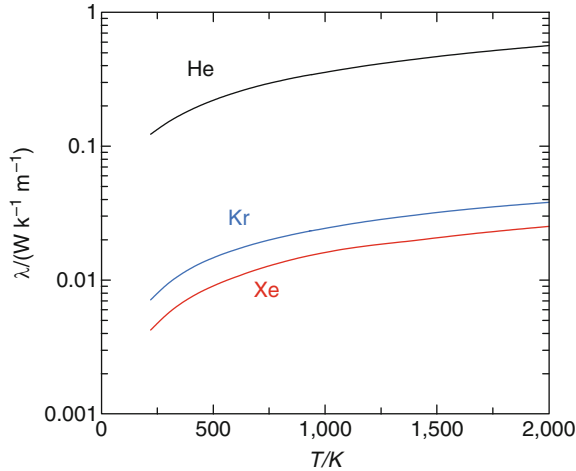
The heat produced by the slowing down of the fission fragments in the fuel pellets is removed through conduction in the pellets:

$$\rho c \frac{\partial T}{\partial t} = \frac{1}{r} \frac{\partial}{\partial r} \left(\lambda r \frac{\partial T}{\partial r} \right) + q''' \quad (104)$$

where c is the specific heat at constant pressure for fuel. The boundary conditions are

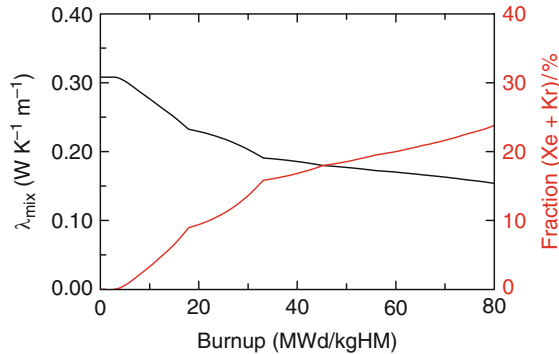
$$\text{Inner boundary : } \frac{\partial T(r = r_i, t)}{\partial r} = 0 \text{ (radial symmetry)}$$

$$\text{Outer boundary : } \Delta T_{gap} = \frac{q''}{h_{gap}} \text{ (pellet surface temperature is known)}$$



■ Figure 12

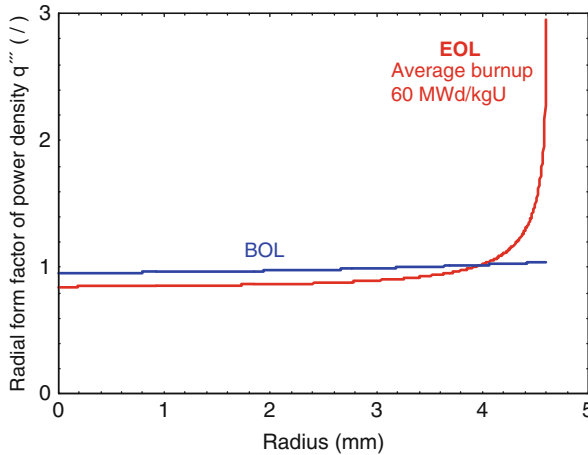
The thermal conductivity of helium and the fission gases krypton and xenon at atmospheric pressure as a function of temperature (Hanley 1973; Häussinger et al. 1991)



■ Figure 13

The thermal conductivity of the (He + Kr + Xe) gas mixture in the free volume of a PWR fuel rod at $T = 800$ K (black curve) as a function of burnup as calculated from Eq. (103) and the corresponding fraction of krypton and xenon (red curve). The discontinuities in the curves correspond to changes in the power between reactor cycles

The temperature distribution in the pellets is therefore affected by two terms: the heat source and the fuel thermal conductivity. At beginning-of-life (BOL), the heat production in LWRs is subject to a slight (typically in the range of 10%) depression, that is, $q''_{BOL} \approx l_0(r)$, where $l_0(r)$ is the modified Bessel function. During the irradiation of the fuel, epithermal neutrons are captured preferentially near to the surface of the fuel by ^{238}U . This leads to an enrichment of ^{239}Pu at the outer periphery of the fuel. At end of life (EOL), $q''_{f,0} \propto (2 - 2)q''_{f,i}$, that is, the power density distribution is a steep function of the radius (see Fig. 14). This effect needs



■ Figure 14

Radial form factor of the power density q''' at beginning and end of life for “typical” LWR conditions according to the TUBRNP model (Lassmann et al. 1998). The radial distribution of the power density depends on enrichment, rod diameter, neutron spectrum, and other parameters

therefore to be considered and a specific model for the radial power density such as TUBRNP is a prerequisite for any temperature analysis at high burnup.

The thermal conductivity of the fuel is specified in ➤ Sect. 3.2.

5.3 Mechanical Behavior

The first barrier against release of radioactive fission products to the environment is the cladding of the nuclear fuel rod. The stress and associated deformation assessment of the cladding are therefore essential in fuel performance calculations. Furthermore, the deformation of both the pellets and the cladding affects the gap width, which in turn affects the conductance of the gap, hence the temperature distribution in the pellets. The thermal and mechanical analyses are therefore equally important and closely coupled. In principle, both problems should therefore be solved simultaneously. In practice, however, all fuel performance codes solve them separately but provide coupling through an iterative scheme. This important numerical aspect will not be dealt with here. The interested reader is referred to a general discussion on this issue in Lassmann (1980, 1992) and Lassmann and Hohlefeld (1987).

The following sections summarize how stress and strains are calculated in both the ceramic pellets and the metallic cladding, while underlining the main assumptions and limitations.

5.3.1 Main Assumptions and Equations

The main assumptions generally made in fuel performance codes are as follows:

- The system is axisymmetric, that is, variables do not vary tangentially.

- Although the fuel and cladding move axially (not necessarily at the same rate), planes perpendicular to the z -axis remain plane during deformation (plain strain condition), that is, the rod remains cylindrical.
- Dynamic forces are in general not treated, and the time dependence inherent in the analysis (creep) is handled incrementally.
- Elastic constants are isotropic and constant within a cylindrical ring.
- The total strain can be written as the sum of elastic and nonelastic components.

The first two assumptions reduce the problem to one dimension. The third assumption indicates that the stresses are related through a local equilibrium condition for the radial force in the following form:

$$\frac{d\sigma_r}{dR} = \frac{\sigma_t - \sigma_r}{R} \quad (105)$$

where σ_r and σ_t represent the normal radial and tangential stress, respectively, and R corresponds to the radius of the deformed geometry.

Since the fuel stack and cladding are treated as a continuous, uncracked medium, no discontinuities are allowed in their displacements. This is translated by the compatibility relations for the strains

$$\varepsilon_r = \frac{dU}{dR} \quad (106)$$

$$\varepsilon_t = \frac{u}{R} \quad (107)$$

$$\varepsilon_a = \text{constant} = C_3 \quad (108)$$

where u represents the radial deformation and ε_i are the normal strains.

Finally, the last equation relates the stresses to the strains. Based on the fifth assumption, the constitutive relations read

$$\underline{\varepsilon}^{\text{total}} = \underline{\varepsilon}^{\text{elastic}} + \sum \underline{\varepsilon}^{\text{nonelastic}} \quad (109)$$

where

$$\underline{\varepsilon} = \begin{Bmatrix} \varepsilon_r \\ \varepsilon_t \\ \varepsilon_a \end{Bmatrix} \quad (110)$$

5.3.2 Calculation of Strains

Elastic Strain

The elastic strains for an isotropic material are reversible and given by

$$\varepsilon_r^{\text{elastic}} = \frac{1}{E} [\sigma_r - \nu(\sigma_t + \sigma_a)] \quad (111)$$

$$\varepsilon_t^{\text{elastic}} = \frac{1}{E} [\sigma_t - \nu(\sigma_r + \sigma_a)] \quad (112)$$

$$\varepsilon_a^{\text{elastic}} = \frac{1}{E} [\sigma_a - \nu(\sigma_r + \sigma_t)] \quad (113)$$

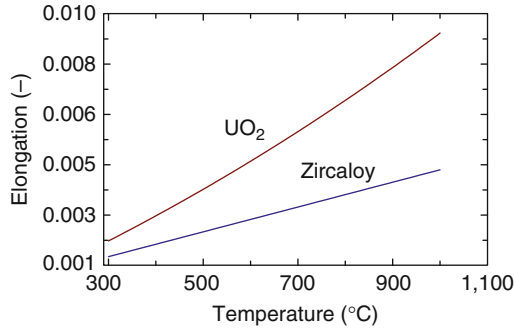


Figure 15

Elongation of UO_2 fuel and Zircaloy cladding due to thermal expansion (-), as a function of the temperature

Nonelastic Strain

The nonelastic strains consist of various contributions. First of all, there is the thermal strain resulting from temperature differences, which is assumed to be isotropic and reversible

$$\varepsilon_i^t = \alpha(T - T_0) \quad i \in r, t, a \quad (114)$$

The thermal expansion coefficients depend on the material and the temperature itself, as shown in Fig. 15. The larger thermal expansion of UO_2 with respect to that of zircaloy explains why thermal expansion is one of the largest contributions to the gap closure in a nuclear fuel rod at beginning-of-life.

The second contribution to the nonelastic strain in the fuel pellets comes from swelling, and is also assumed to be isotropic. The fuel swelling in turn has four contributions:

$$\varepsilon_{fuel}^s = \frac{1}{3} \left[\left(\frac{\Delta V}{V} \right)_{solid FP} + \left(\frac{\Delta V}{V} \right)_{gaseous FP} - \left(\frac{\Delta V}{V} \right)_{densification} - \left(\frac{\Delta V}{V} \right)_{hotpressing} \right] \quad (115)$$

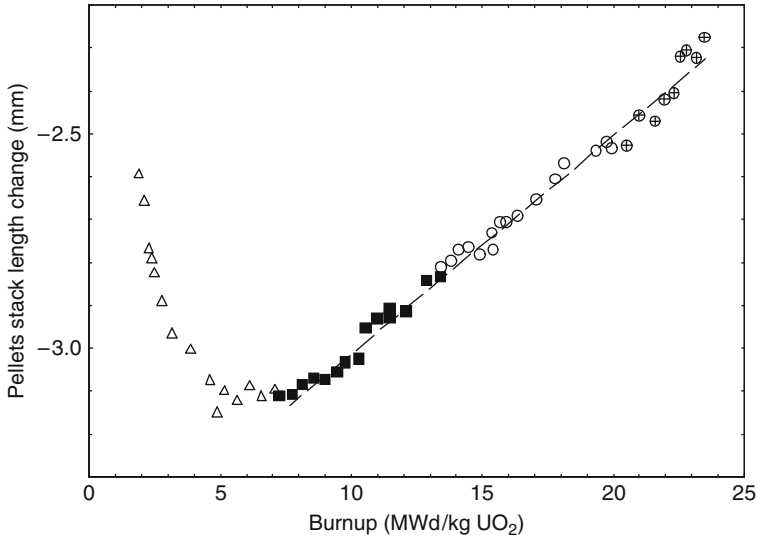
where the first term is attributed to the inexorable swelling of solid fission products:

$$\left(\frac{\Delta V}{V} \right)_{solid FP} = bu \left(\sum_{solid FP} Y_i \frac{v_i}{v_u} - 1 \right) \quad (116)$$

which is linearly dependent on burnup, the fission product yield (Y_i), and on the partial volume of the species (v_i). In general, the solid fission product swelling is on the order of 1% per 10 GWd/t. The second term comes from gaseous fission product swelling:

$$\left(\frac{\Delta V}{V} \right)_{gaseous FP} = \frac{4\pi}{3} \int_0^{R_{max}} R^3 N(R) dR \quad (117)$$

and requires a model to predict the gaseous fission product behavior, more precisely the gas bubble formation due to the low solubility of rare gases in UO_2 (cf. below). During the initial



■ Figure 16

Change of the fuel pellet stack length (mm) at beginning-of-life as a function of the burnup (MWd/kgUO₂), showing the combined effect of densification and solid fission product swelling

stages of the irradiation ($bu < 10$ MWd/kgHM), the density increases as some fabrication porosity disappears as a result of the impact of fission fragments on the (small) pores. In general, the shrinkage process depends on the temperature, burnup, fission rate as well as a combination of the initial density, the pore size distribution, and the grain size. The ideal situation is thus to have a fundamental model for densification, such as those proposed by Assmann and Stehle (1978) and Suk et al. (1992). However, values for the parameters involved are not always well known. Therefore, many code developers have implemented empirical correlations for the fraction of the original porosity, which has annealed out as a function of the local burnup, the temperature and the grain size, for example (Jackson et al. 1990):

$$\frac{\Delta P}{P_0} = \alpha [1 - \beta \exp(-a_1 bu) - (1 - \beta) \exp(-a_2 bu)] \quad (118)$$

where $\alpha = (T/^\circ\text{C} - 83)/(288D_{gr})$, $\beta = 5.12 \exp(-5,100/(T/K))$, $a_2 = 0.0016 \text{ tUO}_2/\text{MWd}$, $a_1 = 100a_2$. The densification, together with the solid fission product swelling is illustrated in

► Fig. 16.

Under the influence of high temperatures, stress levels, and defect production rates during irradiation, a fraction of the fabrication porosity will disappear. This fourth contribution to fuel swelling is referred to as hot pressing and is similar to creep (see below). Therefore, either vacancy diffusion:

$$\frac{dP}{dt} = -K\alpha \left(\frac{\Omega D_{vol}}{kT} \right) \frac{P}{R_{gr}^2} \sigma \quad (119)$$

or plastic flow (i.e., dislocation climb or other model of creep)

$$\frac{dP}{dt} = -\frac{9}{4}\alpha\sigma P \quad (120)$$

are considered.

The isotropic swelling strain in the cladding is due solely to void formation, hence it requires a model for the evolution of voids in the metal.

The third contribution to the nonelastic strain in the fuel is visco-plastic in nature. It consists of instantaneous plastic deformation when the yield stress is exceeded and of time-dependent creep. For the fuel and cladding a simple isotropic plastic flow model can be applied. Nevertheless, as creep is the main contributor to stress relaxation after cracking (see below) in the oxide pellets, it is often only considered in the cladding.

In a multiaxial state of stress a method of relating the onset of plastic deformation to the results of a uniaxial test is required. Furthermore, when plastic deformation takes place one needs to determine (1) how much plastic deformation has occurred and (2) how that deformation is distributed among the individual components of strain. For the first requirement a so-called yield-function is needed. This may be one-dimensional such as the Mises criterion (Cunningham et al. 2001; Suzuki 2000):

$$\sigma_{eff} = \frac{1}{\sqrt{2}} [(\sigma_r - \sigma_t)^2 + (\sigma_r - \sigma_a)^2 + (\sigma_t - \sigma_a)^2]^{1/2} \quad (121)$$

so that yielding only occurs when the effective or equivalent stress (σ_{eff}) exceeds the yield stress determined from a uniaxial tensile test. Others have introduced the anisotropic factors according to Hill's methodology (Lassmann and Van Uffelen 2004). Finally, a multidimensional yield surface (Garcia et al. 2002; Oguma 1983) has also been proposed. In order to account for work hardening, one generally assumes that the yield stress changes with the total permanent deformation. The plastic strain is therefore computed incrementally.

In order to answer the second question, each increment of effective plastic strain is related to the individual plastic strain components by a flow rule

$$\Delta \varepsilon_i = \Delta \varepsilon_{eff} \frac{\partial \sigma_{eff}}{\partial \sigma_i} \quad i \in r, t, a \quad (122)$$

When using the above-mentioned definition of the equivalent stress, one obtains the Prandtl-Reuss flow rule

$$\Delta \varepsilon_i^p = \frac{3\Delta \varepsilon_{eff}^p}{2\sigma_i} S_i \quad (123)$$

indicating that the plastic strain increment is proportional to the deviatoric stress $S_i = \sigma_i - \sigma_h$ where $\sigma_h = (\sigma_r + \sigma_t + \sigma_a)/3$.

For the time-dependent creep one needs strain rate equations, although the total creep strain is also computed incrementally by multiplying the strain rate with the time-step length. For primary creep, typically an empirical expression is applied:

$$\dot{\varepsilon}_{eff} = K \sigma_{eff}^n t^m \quad (124)$$

where K , n , m are constants.

For the secondary or steady-state creep, there are three parallel processes. The vacancy diffusion or Nabarro–Herring creep and the dislocation climb are dominating at high temperature and high stresses, respectively:

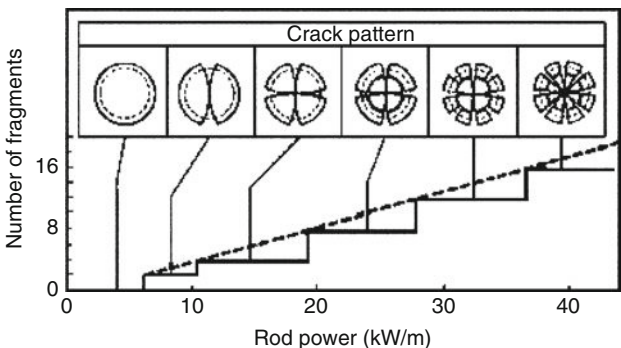
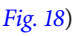
$$\dot{\epsilon}_{eff}^c = \frac{Bq''' \sigma_{eff}}{R_{gr}^2} \exp\left(-\frac{E}{kT}\right) \quad \text{vacancy diffusion} \quad (125)$$

$$\dot{\epsilon}_{eff}^c = B' q''' \sigma_{eff}^{4.5} \exp\left(-\frac{E}{kT}\right) \quad \text{dislocation climb} \quad (126)$$

The third process is irradiation-induced creep, dominating at low temperatures and assumed to be proportional to the effective stress and the local fission rate density or q''' .

The fourth and last nonelastic strain component stems from the pellet cracking. Pellet cracking already occurs at startup due to the differential thermal expansion since the hot pellet center expands more than the cold periphery. In order to assess the linear heat generating rate at which cracking in cylindrical pellet occurs, the maximum thermal stress ($= \sigma_{t,max} = \sigma_{a,max}$ at pellet periphery) in an uncracked pellet submitted to a parabolic temperature gradient

$$\sigma_{t,max} = -\frac{\alpha E q'}{8\pi(1-\nu)\lambda} \quad (127)$$

must be compared with the (uniaxial) fracture stress, which is approximately 130 MPa. When using $E = 200$ GPa, $\nu = 0.31$, the thermal diffusivity $\alpha = 10^{-5} \text{ K}^{-1}$, and an average thermal conductivity of $\lambda = 3 \text{ W/mK}$ radial cracks are predicted to be initiated in the pellet periphery at a linear heat rate q' of the order of 5 kW/m. The number of cracks (N_{cr}) is dependent on the linear heat rate. Oguma (1983) proposed a linear model for the number of radial cracks that is illustrated in  Fig. 17. In addition to radial, also axial and (especially under ramping conditions) circumferential cracks are formed ( Fig. 18).

The consequences of cracking are very important in fuel performance modeling. Owing to the larger thermal expansion of the fuel fragments in comparison with that of a monolithic

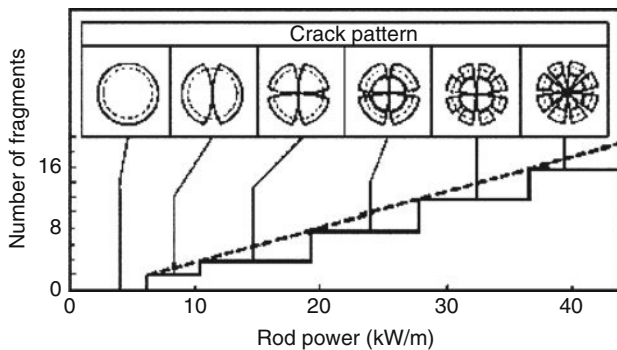


 Figure 17

Calculated crack pattern from thermoelastic stress (Oguma 1983) ©Elsevier, 1983, reprinted with permission

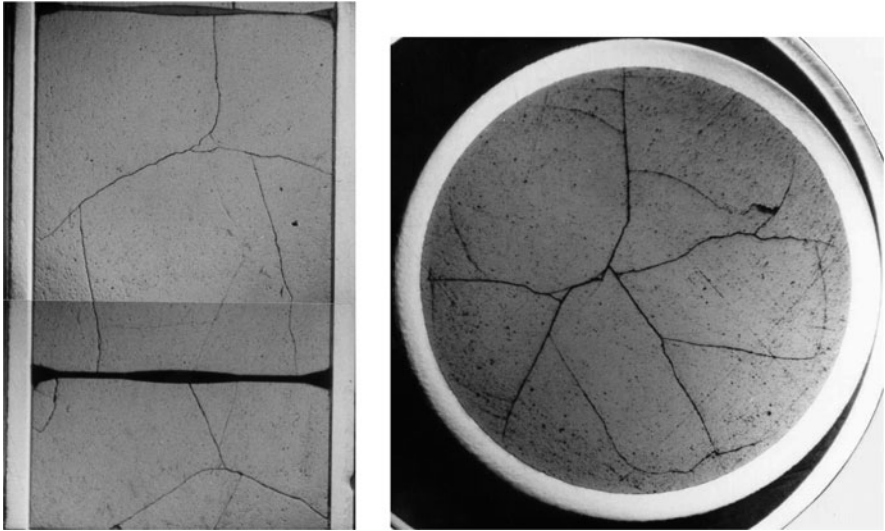


Figure 18
 Illustration of cracks in axial (left) and horizontal (right) cross sections of irradiated fuel pellets.
 ©European Communities, reproduced with permission

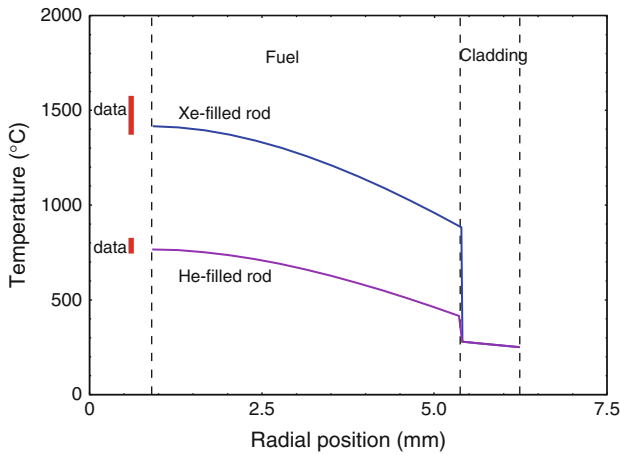
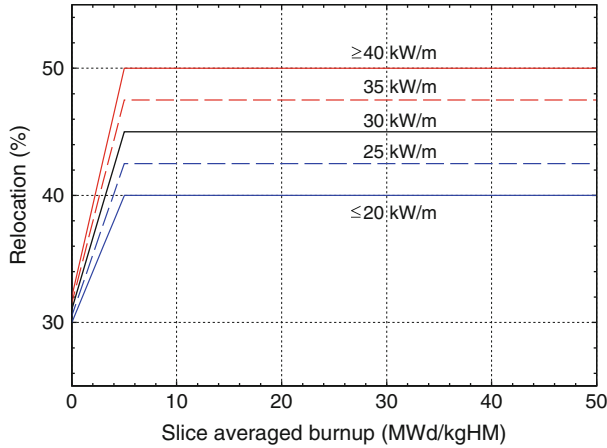


Figure 19
 Radial temperature distribution in a BWR-rod (IFA-505) at beginning-of-life (BOL) calculated by the TRANSURANUS code. Comparison between the analysis of a Xe-filled rod with (full line) and without (dashed line) taking relocation into account



■ Figure 20

Fraction of gap closure due to pellet fragment relocation (δ_g), derived from the relocation model in the `frapcon3` code

cylinder, and due to vibration-induced motion they move outward. This is called pellet “relocation” and has a strong impact on the thermal behavior as shown in [Fig. 19](#). It reduces the pellet-cladding gap size, thereby reducing the temperature levels in the fuel at beginning-of-life. This constitutes the largest contribution to the gap closure (approximately 30–50%, depending on q') but is also the one that is subject to the largest uncertainty, because of the stochastic nature of the cracking process. This also raises questions about the usefulness of applying three-dimensional stress calculations.

The contribution from relocation is generally accounted for in the tangential strain component as a (linear) function of the linear heat rate: $\varepsilon_t = u/r$, where $u = s\delta_g$, s being the initial radial gap size and δ_g the fraction of the gap size closing as a result of relocation. An example based on the relocation model in the `FRAPCON3` code (Berna et al. 1997) is illustrated in [Fig. 20](#) (Lassmann et al. 2005).

When the pellets relocate to such an extent that they come into contact with the cladding, which creeps down under influence of the pressure difference between the coolant pressure and the fill gas pressure, then relocation may be (partly) reversed.

The effect of relocation on the mechanical behavior is also of primary importance since it reduces the overall stress in the pellets and may even change the sign of the stress in central part of the pellet from compression (in a cylinder) to traction (in fragments) (Van Uffelen et al. 2004). To account for the cracks exactly would require the exact location and size of every crack and to solve a three-dimensional stress-strain problem in each block. Instead, one simply modifies either the material constants (Lassmann et al. 2005; Suzuki 2000) or modifies the constitutive equations. An example of the former approach is that of Jankus and Weeks (1972), where a reduction of the elastic constants is proposed:

$$E' = \left(\frac{2}{3}\right)^{N_{cr}} E \quad (128)$$

$$v' = \left(\frac{1}{2}\right)^{N_{cr}} v \quad (129)$$

which means that an equivalent continuous and homogeneous solid body with directionally dependent (anisotropic) properties is considered. As the pellet-clad gap closes during irradiation the contact pressure can press the fragments inward, thereby reducing the relocated radius to a minimum value. Some codes also account for the restoration of the elastic constants as the relocation is reversed (partially) (Suzuki 2000).

In order to modify the constitutive equations, a plane stress condition has been proposed (Garcia et al. 2002), that is the tangential stress is set equal to the fill gas pressure once the radial crack appears. Both types of approaches, however, do not account for crack healing.

5.3.3 Boundary Conditions

In order to solve the main equations summarized in the previous sections, boundary conditions are required.


Radial Boundary Conditions

In general, continuity of the radial stress and displacement at each radial zone is imposed and the radial stress at the outer cladding surface is determined by the coolant pressure: $\sigma_r(r_{cl,o}) = -p_{cool}$.

The boundary condition in the rod depends on the configuration. When pellet-cladding mechanical interaction is not established, the radial stress at the pellet periphery is determined by the fill gas pressure in the fuel rod (p_{gas}): $\sigma_r(r_{f,o}) = -p_{gas}$. For the boundary condition in the pellet center, two possibilities exist. In hollow pellets, the radial stress at the pellet center is equal to fill gas pressure as well: $\sigma_r(r_{f,i}) = -p_{gas}$, whereas in the event of full cylindrical pellets the radial and tangential stresses are equal in the pellet center.

When the fuel and cladding are in contact, a fuel pellet interfacial pressure exists (p_{fc}) and determines the boundary condition at the pellet surface: $\sigma_r(r_{f,o}) = \sigma_r(r_{cl,i}) = -p_{fc}$. The other radial boundary conditions remain unchanged.

Axial Boundary Conditions

The plane strain assumption entails that the axial strain is constant in the plane perpendicular to the axial axis. The axial strain is therefore determined by an axial force balance equation including the fill gas pressure, the plenum spring pressure, the fuel column weight, and the friction forces. The latter depend on the fuel-cladding interaction and can only be taken into account iteratively. Indeed, when a section i is analyzed it is not known whether friction forces between fuel and cladding originating from a section above/below i need to be considered in the axial balance of forces. This is schematically shown in  Fig. 21. In the case of a radial contact between fuel and cladding both bodies may stick to each other, but some sliding may be possible in specific conditions (sticking or static vs. sliding friction). Part of the fuel rod may be “trapped,” which means that rather high axial forces may act on cladding and fuel.

One advantage of two-dimensional and three-dimensional finite element models is that such effects are automatically included in the analysis through the use of specific gap elements.

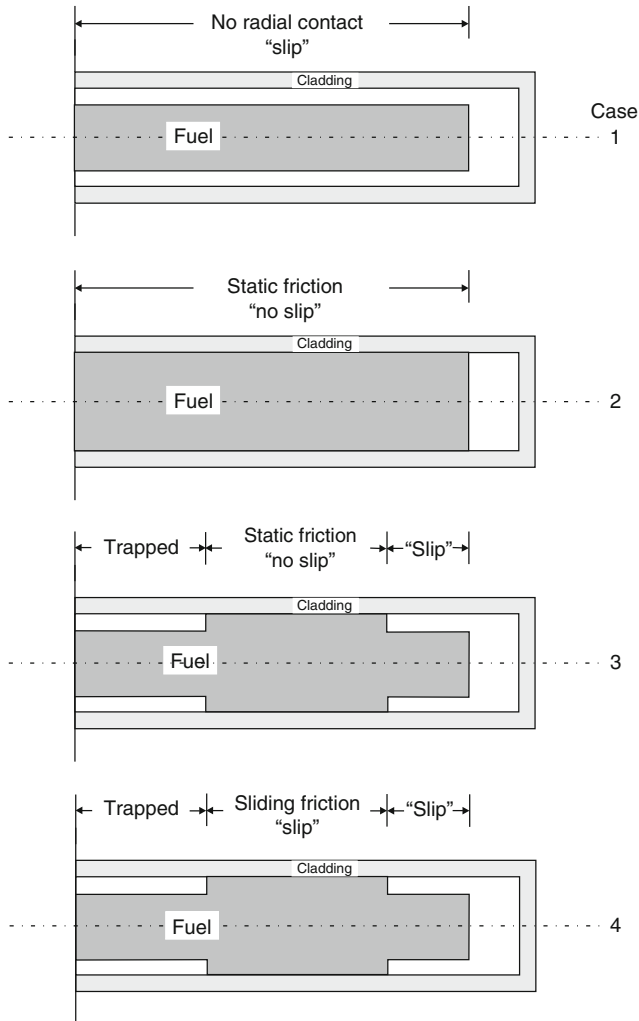


Figure 21

Four possible modes of an interaction between fuel and cladding

5.4 Fission Gas Behavior

On average, each fission event produces 0.3 Xe and Kr atoms. These inert fission gas atoms are basically insoluble, causing two important life-limiting phenomena in the fuel rod: either they remain in the pellets and contribute to the swelling, or they are released from the pellets and increase the rod internal gas pressure while reducing the thermal heat transfer in the gap (see [Sect. 5.2.4](#)). The fuel swelling may lead to pellet-cladding mechanical interaction and even cladding failure under certain conditions. Likewise, the fission gas release may lead to higher fuel rod temperatures, which in turn could lead to higher fission gas release until the rod fails due to clad ballooning and clad burst.

Because of its implications for fuel performance, the basic mechanisms involved in the fission gas release and swelling in LWR fuel will be summarized first, before outlining how these phenomena are implemented in a code. The interested reader will find more details in Van Uffelen (2002).

5.4.1 Basic Mechanisms

Recoil, Knockout and Sputtering

In general, a fission event entails – among others – two fission fragments that transfer their kinetic energy to the fuel lattice. A fission fragment, close enough to a free surface ($<6\text{--}7\ \mu\text{m}$), can escape from the fuel due to its high kinetic energy (60–100 MeV). This is called recoil release. When fission fragments make elastic collisions with the nuclei of lattice atoms, a collision cascade appears. The interaction of a fission fragment, a collision cascade, or a fission spike with a stationary gas atom near the surface can also cause the latter to be ejected if it happens within a distance close enough to the surface. This process is called release by knockout. Finally, the energy loss of a fission fragment traveling through the oxide crystal lattice causes a high local heat pulse. When this happens close to the fuel surface, a heated zone will evaporate or sputter, thereby releasing any fission product contained in the evaporated zone.

Recoil, knockout, and sputtering can only be observed at temperatures below 1000°C , when thermally activated processes (cf. below) do not dominate. They are almost temperature independent and therefore called athermal mechanisms. It is generally of little importance in reactor at intermediate burnup levels. The fraction of athermal release is roughly under 1% for rod burnup below 45 MWd/kgU, and accelerates to roughly 3% when the burnup reaches about 60 MWd/kgU.

Lattice Diffusion of Single Gas Atoms

The first and basic step in fission gas release is single gas atom diffusion in the lattice. Possible mechanisms by which the inert gas atoms migrate through the fuel have been studied by Grimes and Catlow (1991) by considering low-energy migration pathways between solution sites as well as the stability of gas atoms at a variety of solution sites within a defective $\text{UO}_{2\pm x}$ lattice ($x = |O/M - 2|$, the deviation of the stoichiometry). They postulate a cation vacancy-controlled migration pathway for Xe atoms. Indeed, according to his calculations, Xe is trapped at a uranium vacancy in UO_{2+x} , at a tri-vacancy cluster in UO_{2-x} and at a di- or tri-vacancy in UO_2 . Since the local environment of the migrating Xe atoms is supposed to become the charged tetra-vacancy for all stoichiometries, the mechanism for diffusion only considers the association of a cation vacancy to the trap sites. (Uranium vacancies as the slower moving species are rate-controlling for most diffusion-related processes in UO_2).

The lattice diffusion coefficient is influenced by the temperature, deviations from stoichiometry and additives (e.g., Cr, Nb), phase changes and therefore also indirectly by the burnup. Also the fission fragments are assumed to contribute to the diffusion process, which is referred to as irradiation-enhanced diffusion. This is due to the interaction of the fission fragments and the associated irradiation damage cascades with the fission gas atoms in the

lattice, resulting in a displacement of the gas atoms. Indeed, there is a constant process of slowing down fission products in the fuel causing fission spikes or tracks to be formed. The spikes have a length in the order of 7 microns, wherein about 15,000 U-Frenkel pairs are produced instantaneously (Matzke 1980). Only 5,000 pairs remain after direct annihilation. The width of the permanently disturbed zone is approximately 7 nm. Significant temperature increases along the axis occur causing larger hydrostatic pressure gradients leading, for example, to a separation of vacancies from interstitials and hence a largely temperature-independent, athermal radiation-enhanced diffusion, as well as resolution of inert gas atoms from bubbles or even complete destruction of bubbles nuclei or small bubbles. Each atom is affected by a fission spike at a rate of once in a few hours to once in a day, depending on the reactor type.

A consistent set of radiation-enhanced diffusion coefficients (D^*) is available for metal self-diffusion (Matzke 1980). In as far as these data may be due to a mixing of atoms in the course of fission spikes, the D^* values will apply for gases as well. However, no firm conclusions emerge as to the mechanism. Atomic scale simulations could shed light on the details of this mechanism. Despite the lack of details, D^* has been shown to be directly proportional to the fission rate density (F'): $D^* = AF'$, where $A = 1.2 \cdot 10^{-29} \text{ cm}^5$ for oxide fuels.

Since $D^{Xe} > D^U$, the thermally activated temperature regime for fission gas diffusion extends to lower temperatures than D_U . A radiation-enhanced diffusion coefficient will therefore only be operative in the cold outer rim of the fuel. However, at temperatures between 1,000 and 1,400°C, there appears to be some influence of the irradiation as well, leading to a lower activation enthalpy for the single gas atom diffusion coefficient.

Irradiation-induced migration dominates the diffusion process at temperatures below 1,000°C and is temperature independent. For temperatures between 1,000 and 1,400°C, vacancies necessary for the gas atom diffusion are assumed to be created both thermally and by the damage cascades related to fission fragments. Above 1,400°C, a purely thermally activated diffusion coefficient is applied, that is, thermally created vacancies for diffusion are predominant. These three temperature regimes are reflected in the three components of the single gas atom diffusion coefficient (m^2/s) often applied in the fuel performance codes (Turnbull et al. 1982):

$$D = D_1 + D_2 + D_3 \quad (130)$$

where

$$D_1 = 7.6 \times 10^{-6} \exp\left(-\frac{35,000}{T}\right) \quad (131)$$

$$D_2 = 5.6 \times 10^{-25} \sqrt{\dot{F}} \exp\left(-\frac{13,800}{T}\right) \quad (132)$$

$$D_3 = 8 \times 10^{-40} \dot{F} \quad (133)$$

where \dot{F} is the fission rate density and T is the absolute temperature.

Unperturbed (intrinsic) diffusion of single inert gas atoms (Xe, Kr) can be observed at low damage and gas concentration (10^{-5} at-%). At higher gas and damage concentrations other effects should be taken into account.

Trapping

In nuclear fuels, either natural (e.g., impurities, dislocation lines, and closed pores) or radiation produced imperfections in the solid (e.g., vacancy clusters in fission tracks, fission gas bubbles, and solid fission product precipitates) depress the amount of fission products available for diffusion by temporarily or permanently trapping the migrating atoms. Experiments show that for burnups characteristic of power reactors, gas atom trapping due to (intragranular) fission gas bubbles in the grains is predominant. The trapping rate depends on the size of the intragranular bubbles, hence on temperature, fission rate, and burnup. A second important effect of trapping occurs at grain boundaries. It deals with the delay for the onset of thermal fission gas release, via the bubble interconnection mechanism (cf. below).

Irradiation-Induced Resolution

A fraction of the gas atoms trapped in bubbles can be re-dissolved in the surrounding matrix through the interaction of a fission fragment with the bubble. Although gamma-rays, neutrons, and fission fragments are all capable of causing resolution of fission gases from bubbles, only fission fragments can account for the high efficiency of the process as observed experimentally. Fission fragments not only have a higher initial kinetic energy (50–100 MeV) than fast neutrons (2 MeV), but also they are charged and consequently have a higher cross section for transferring energy either to lattice or gas atoms.

Two different types of mechanisms are proposed to explain the experimental observations (Olander 1976; Turnbull 1980). On one hand, microscopic models consider the resolution of one gas atom at a time when interacting with a fission fragment or an energetic atom from the collision cascade. These models do not predict complete bubble destruction – as suggested from experimental observations (Blank and Matzke 1973; Turnbull 1980) – since only about 10% of the initial fission fragment energy is lost in direct collisions with lattice ions while the rest is first dissipated in the electronic structure of the material through which it passes by means of Rutherford collisions. Macroscopic models on the other hand consider the complete bubble destruction, but there is still discussion about the detailed mechanisms. Despite this, the balance of opinion favors a mechanism based on fission fragment energy loss via electron excitation leading to a cylindrical heat distribution around the fission track along with a compressive thermoelastic pulse (Blank and Matzke 1973; Olander 1976; Ronchi and Elton 1986; Turnbull 1980). Regardless of the type of model adopted, one can express the rate at which gas atoms are redissolved from a bubble by means of the macroscopic model of Turnbull (1980), which lead to Eq. (140). Nevertheless, for (larger) grain boundary bubbles resolution is supposed to be less effective.

Grain Boundary Diffusion

Grain boundary diffusion is the most commonly observed route for solute migration in polycrystalline materials. It is generally accepted that diffusion in crystalline solids proceeds more rapidly along grain boundaries than through the lattice. This is due to the atomic jump frequency in these planar defects, which is about a million times greater than the jump frequency of regular lattice atoms in stoichiometric materials at 0.6 times the absolute melting temperature. Nevertheless, there is a switch from release assisted by grain boundary diffusion in trace-irradiated UO_2 to trapping and eventual interlinkage of the intergranular bubbles (cf. below). This switch occurs early in life, so that grain boundary diffusion is only considered to

contribute to the precipitation of fission gas atoms in grain boundary bubbles, rather than to the long-range transport along grain boundaries to the free surface of the pellets (Olander and Uffelen 2001).

Grain Boundary Sweeping or Grain Growth


In LWR fuel under normal operating conditions, only normal grain growth is observed, that is, large grains grow at the expense of smaller ones. It affects fission gas release in two ways. First of all, grain boundary sweeping provides another mechanism for the collection of gas at these internal surfaces from which release can occur. The collection results from the low solubility of the fission gas, hence the sweeping grain boundary does not redeposit any gas in the newly formed crystal behind it. The moving grain boundary acts as a fission gas filter. Secondly, the average diffusion distance for the fission products created in the grain increases. Unlike the first consequence this tends to reduce the release rate. Grain boundary sweeping occurs at temperatures above roughly 1,600°C.

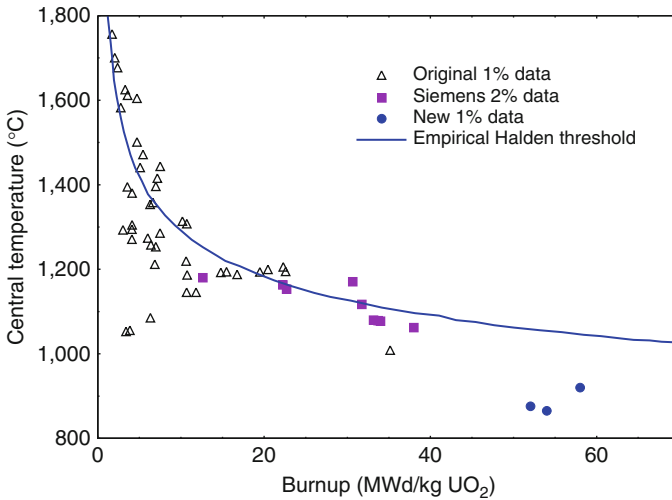
Bubble Migration

The migration of fission gas bubbles provides an alternative to the sequence “bubble formation-resolution-gas atom diffusion” in order to describe fission product release from nuclear fuels. Migration of bubbles in the oxide fuels has two other important consequences, namely the columnar grain growth with the concomitant central void formation (observed in fast breeder reactor fuel), and the coalescence of the bubbles, which gives rise to fuel swelling. Under normal operating conditions, however, fission gas bubbles remain small (typically below 20 nm) due to resolution, and show a small mobility at least up to 1,800°C (Matzke 1980). This is partly explained by the pinning by dislocations and other crystal defects.

Bubble Interconnection

Fission gas bubbles appear along grain boundaries after a certain burnup, depending on the temperature history. When bubbles interconnect, they form a so-called tunnel network through which the gas can be released. The bubble interconnection is a reversible process, for the tunnel network can close again under the influence of the surface tension when the outgoing flux of gas atoms outweighs their supply.

The bubble interconnection has two important consequences. First of all, it determines the onset of release as the release remains small (due to athermal release) before grain boundary bubbles interconnect with open grain edge tunnels. This incubation period is reflected in the Halden threshold for fission gas release, which is shown in  Fig. 22. The ensuing release corresponds to a seepage process. Secondly, when grain face bubbles interconnect and form snake-like tunnels, there will be a sudden release of the gas accumulated in these bubbles, referred to as burst release. This can also be interpreted as a sudden interconnection or opening of grain face bubbles due to micro-cracking along grain boundaries during abrupt power variations. Cracking entails a sudden opening of a fraction of the grain boundaries with the instantaneous venting of the corresponding fraction of the accumulated gas atoms. Interconnection of gas-filled bubbles takes place in general where diffusion-controlled precipitation occurs at the grain boundaries, that is, when both T and the burnup are high enough. The



■ Figure 22

Original Halden criterion for the onset of fission gas release and supporting data (Vitanza et al. 1978)

conditions correspond roughly to the Halden threshold (Vitanza et al. 1978; Wiesenack 1997)

$$T_c(^{\circ}\text{C}) = \frac{9,800}{\ln\left(\frac{bu}{0.005}\right)} \quad (134)$$

where T_c represents the central temperature in degree Celsius, and bu the burnup in MWd/kgUO₂.

5.4.2 Modeling the Fission Gas Behavior

There are various approaches in fission gas release and swelling modeling. They can be classified into two categories. On one hand there are purely empirical models, including those based on soft computing techniques such as neural networks. These models are inexpensive to use and provide an efficient tool for the design of fuel rods within a limited range of application. However, they are not suitable for gaining knowledge about the underlying mechanisms, nor do they enable us to extend their range of application to higher discharge burnup values as required by the industry. On the other hand, there are mechanistic models that aim at the physical description of the underlying phenomena. Despite their need for a large database, such models provide an excellent basis, both for the analysis of the mechanisms, as well as for the extension of the models beyond their range of calibration.

Fuel performance codes nowadays tend to implement more and more mechanistic models, based on very detailed but stand-alone models. They all consider fission gas release to be a two-step process. The first step deals with the gas behavior in the grains (intragranular part),

whereas the second step deals with the gas behavior along the grain boundaries (intergranular part).

Intragranular Behavior

For the behavior in the fuel grains, the following scenario is generally adopted. The gas atoms are created by fission in the fuel matrix. They then diffuse in the grains toward grain boundaries by thermal- and irradiation-enhanced diffusion. Small intragranular bubbles with a diameter of 1 to 2 nm are observed in irradiated fuel. They are created in the wake of fission spikes and then grow by diffusion (trapping). They are continuously destroyed by fission spikes (resolution). There is no bubble migration except at temperatures above roughly 1,800°C. The bubbles act as sinks for gas atoms, thereby reducing the amount of gas available for release.

This scenario leads to solving a diffusion equation in a sphere with a source term proportional to the local fission rate density ($S = Y_f p \dot{F}$), which is based on the pioneering model of Booth (1957a). He proposed the equivalent sphere model. This theory considers a polycrystalline sintered body as a collection of uniform spheres with an equivalent radius in order to simplify the mathematical problem. The hypothetical sphere radius (R_B) is defined so that the effective surface-to-volume ratio of the fuel (S/V) is preserved:

$$\frac{1}{R_B} = \frac{1}{3} \left(\frac{S}{V} \right)_t \quad (135)$$

where $(S/V)_t$ accounts for the sum of the geometric surface of the pellets as well as the surface due to open porosity. As irradiation proceeds, fission gases are generated within the Booth sphere and migrate to the surface, where the concentration is taken to be zero. He proposed that the fractions of stable gas release can be approximated by

$$f_{ann}(t) \simeq 6 \sqrt{\frac{Dt}{\pi R_{gr}^2}} - 3 \frac{Dt}{R_{gr}^2} \quad (136)$$

for so-called annealing conditions (i.e., without source term, but with an initial nonzero concentration), and

$$f_{irr}(t) \simeq 4 \sqrt{\frac{Dt}{\pi R_{gr}^2}} - \frac{3}{2} \frac{Dt}{R_{gr}^2} \quad (137)$$

for irradiation conditions (nonzero source term, but no initial concentration). In a second model Booth (1957b) proposed the approximation for the release-to-birth ratio for unstable gas release under steady-state conditions to be

$$\frac{R}{B} = \frac{3}{R_{grain}} \sqrt{\frac{D}{\lambda}} \left[\coth \left(R_{grain} \sqrt{\frac{\lambda}{D}} - \frac{1}{R_{grain}} \sqrt{\frac{D}{\lambda}} \right) \right] \quad (138)$$

where λ represents the decay constant of the species under consideration. It should be underlined that the diffusion coefficient to be used is subject to an order of magnitude uncertainty. Eq. (130) in the previous section is often being used, with a multiplication or reduction factor of about 5.

Regardless of the uncertainty on the diffusion coefficient, the Booth models themselves suffer from several limitations:

1. They consider a constant temperature and fission rate density
2. They do not account for resolution and trapping at intragranular bubbles
3. They do not account for grain boundary sweeping
4. They cannot reproduce an incubation period (cf. Halden curve)
5. They do not account for resolution at grain boundary bubbles

All of these limitations have been alleviated over time. First, several numerical techniques have been proposed to cope with time-varying conditions, which have been compared in Lassmann and Benk (2000). In order to deal with trapping and resolution, Speight (1969) found that instead of solving one diffusion equation coupled with an equation for the gas balance in the traps, one could solve a single diffusion equation for the sum of the concentration in the matrix and in the traps with an effective diffusion coefficient (D_{eff}):

$$D_{eff} = D \frac{b}{b + g} \quad (139)$$

where $g = 4\pi R_{bubble} d$ corresponds to the trapping rate coefficient and b corresponds to the resolution rate coefficient. Whatever model is being considered for resolution, fission gas behavior models generally introduce a simple resolution rate coefficient that is proportional to the local fission rate density and depends on the bubble size:

$$b = 2\pi(R_{bl} + \delta)^2 \mu_{ff} \dot{F} \quad (140)$$

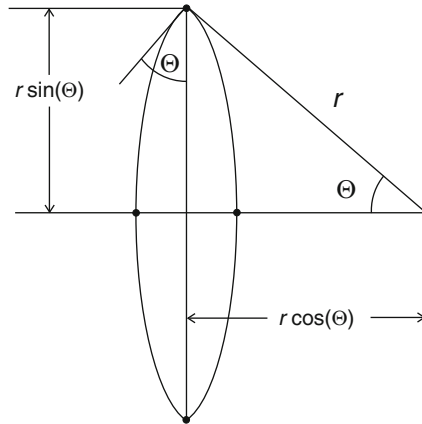
where it is assumed that a bubble can be destroyed if its center lies within a distance δ from the fission fragment track of length $\mu_{ff} = 7-10 \mu m$. The condition for applying D_{eff} , is that the traps are saturated. Experiments show that small intragranular bubbles stabilize rapidly both in size and in diameter. Intragranular bubbles can therefore be considered saturated for irradiation times of practical interest (beyond 0.5 MWd/kgU). Nevertheless, the difference between D and D_{eff} is only important for temperatures above approximately 1,100°C. It should be underlined, however, that during a power ramp the application of D_{eff} provides an overestimation of the trapping effect (Lösönen 2000).

During the course of time several models have been proposed wherein the Booth sphere radius was taken to be equal to the average grain radius of the fuel, in order to be able to account for grain growth. However, it must first be pointed out that although there is no consensus about which grain growth model should be applied, the (Ainscough et al. 1974) model is often used:

$$\frac{dR_{grain}}{dt} = k \left(\frac{1}{R_{grain}} - \frac{1}{R_{max}} \right) \quad (141)$$

where k is a temperature dependent rate constant, and $R_{max} = R_{max}(bu)$ the grain size at which growth stops. This burnup dependent quantity is introduced in order to account for the retarding effect of fission products on grain growth as burnup proceeds.

Most fission gas release models only account for the increase of the average diffusion distance when normal grain growth occurs. Some other models only take into consideration the sweeping effect, assuming either that the fractional release is proportional to the grain boundary velocity, or that the gas in the total fraction of grain volume swept by the grain boundaries



■ Figure 23

Schematic representation of a lenticular grain face bubble with radius of curvature r

is released. So they all fail to properly incorporate boundary motion into the intragranular diffusion equation and artificially separate the two aspects of grain growth on fission gas release. Only some stand-alone models have been proposed so far that account for both simultaneously by solving the diffusion equation in a sphere with a moving boundary (e.g., Forsberg and Massih (2001)).

For alleviating the fourth and fifth limitations of the Booth models, an intergranular module has to be introduced.

Intergranular Behavior

Three main different concepts are being applied. First of all, an intergranular model that does not treat the kinetics at the grain boundaries directly. In a way the Booth model is a special case of this type, in that it considers gas atoms to be released as soon as they arrive at the grain boundary. The other models in this category consider gas arriving at the grain boundaries to precipitate straight away in grain boundary bubbles. An open tunnel network is assumed to be established along the grain boundaries once a so-called saturation value for the intergranular gas atom concentration (N_{\max}) has been collected. In order to derive this saturation value, one assumes that

1. Intergranular bubbles are lenticular, with Θ being the dihedral angle between the grain boundary and the bubble surface (cf. ► Fig. 23)
2. A mechanical equilibrium exists between the bubble gas pressure (p_{gas}), the surface tension (γ), and the hydrostatic pressure (σ_H) in the surrounding matrix: $p_{gas} = \frac{2\gamma}{\rho_{bl}} + \sigma_H$, where ρ_{bl} is the radius of curvature of the grain boundary bubble,
3. A perfect gas law can be applied as equation-of-state.

Under those assumptions, the following expression is obtained for N_{\max} :

$$N_{\max} = \frac{4\rho_{bl}f(\Theta)}{3kT \sin(\Theta)^2} \phi^* \left(\frac{2\gamma}{\rho_{bl}} + \sigma_H \right) \quad (142)$$

where $f(\Theta) = 1 - \frac{3}{2} \cos \Theta + \frac{1}{2} (\cos \Theta)^3$ and ϕ^* stands for the fraction of the grain face surface occupied by the bubbles at interconnection. As soon as N_{\max} is achieved, any excess gas atoms arriving at the grain boundaries are deemed released. It must be pointed out that no consensus has been reached as to what value should be applied for the hydrostatic stress. Often it is neglected, or a value is being used, which is constant and uniform. Obviously this is a rough approximation.

In a second category of models, the intergranular kinetics is being considered directly. As such, an account is made of the reversible character of the tunnel establishment. The first model was proposed by White and Tucker (1983). They considered two parallel processes for release from the Booth sphere: intragranular diffusion and gaseous diffusion through tunnels along grain boundaries. To this end they solve two different diffusion equations in the equivalent Booth sphere. More recently, Koo et al. (1994) proposed two different contributions for the S/V used to compute the equivalent Booth sphere radius. One contribution was attributed to macroscopic radial cracks in the pellet periphery, while the second contribution was ascribed to a fraction of the tunnel network along grain boundaries that was in contact with the open grain corner porosity (based on percolation theory in two dimensions). Recently, several other models have been proposed wherein the gaseous diffusion through the open tunnel network is being modeled according to Darcy's or Poiseuille's law in a tube (e.g., Kogai (1997) and Van Uffelen (2002)). These models enable the effect of the hydrostatic pressure on the release kinetics to be accounted for. More recently, White (2004) went even further with the details and modeled the evolution of the bubble morphological relaxation through differential absorption/emission of vacancies, which is surface-curvature driven. Nevertheless, these models are not yet implemented as standard models in fuel performance codes.

In a third category of models, a comprehensive list of mechanisms (cf. previous section) has been implemented in the form of a set of ordinary differential equations, that is, the intra- and intergranular parts of the model are solved simultaneously (e.g., MARGARET (Noirot 2005)). These models were essentially produced to deal with fission product behavior under severe-accident conditions. Up to now, only the FASTGRASS model of Rest et al. (1992) is being applied in the VICTORIA code (Olander and Mubayi 1999).

Coupling Intra and Intergranular Behavior

In general, the intragranular and intergranular modules of a fission gas behavior model are coupled in two directions. On one hand, the intragranular module provides the source term for the intergranular module. On the other hand, the intergranular module provides the boundary condition for the diffusion equation in the spherical grains and/or the supplementary source term near the grain boundary. In fact most models make use of the Booth approximations, that is, they assume zero boundary conditions, meaning that the grain boundary is considered to be a perfect sink. Some models consider a finite segregation factor. In order to account for the resolution effect on grain boundary bubbles, three different approaches are being utilized. The first group considers a correction factor for the Booth flux, accounting for the fact that the resolution opposes the gaseous diffusion out of the grains. The second group of models applies a time-varying boundary condition that makes use of a time dependent flux balance. In the third and last group, a supplementary source term is defined in a fine layer adjacent to the grain face, either as a uniform source in a fine layer, or as a Dirac distribution at a given distance from the grain boundary. Mainly the first two approaches have been implemented in fuel performance codes.

Swelling

Theoretically speaking, the fission gas release and the fission gas swelling models should be closely related. In most codes, however, semiempirical relations are being used for the gaseous swelling as a function of the temperature and burnup (e.g., MATPRO (1981; 1990)), or as an empirical function of the released fraction, for instance (Billaux 2005):

$$\left(\frac{\Delta V}{V}\right)_{\text{gaseous FP}} = A(1 - \alpha_{FG}FGR - \alpha_{CS}CSR)bu \quad (143)$$

where A is a constant for solid swelling, FGR the local fraction fission gas release from the grain, CSR the fractional release of the volatile fission products (Cs, I) from the grain, bu the local fuel burnup, $\alpha_{FG} = 0.37$ and $\alpha_{CS} = 0.45$. The empirical nature reflects the uncertainty pertaining to both the release and swelling models (in particular during power ramps at high burnup) as can also be inferred from the large variety of models presented above.

6 Typical Phenomena and Issues in the Design and Licensing of LWR Fuels

6.1 High Burnup Structure

6.1.1 Characteristics of the High Burnup Structure

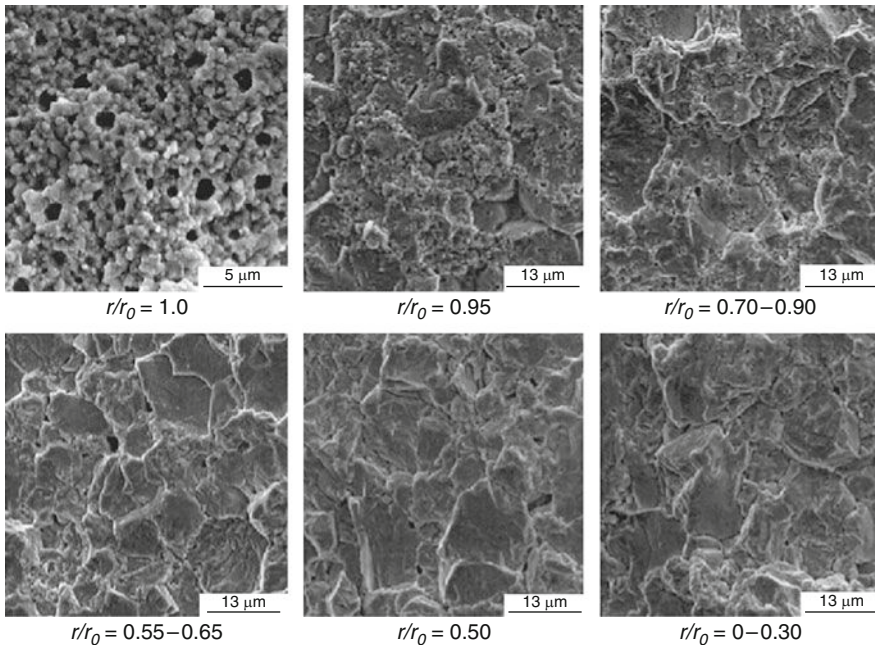
During irradiation, the strong resonance absorption of epithermal neutrons in ^{238}U leads to the production of the isotope ^{239}U , which successively decays by β -emissions to ^{239}Np and ^{239}Pu . For fuel in the form of cylindrical pellets, maximum neutron absorption takes place at the pellet surface, hence the local plutonium concentration in UO_2 exhibits a maximum at this outer surface and decreases exponentially toward the pellet center. Subsequent fissioning of this plutonium results in a near surface enhancement of burnup compared to that throughout the rest of the pellet. At a pellet average burnup ≈ 60 MWd/kg, the local burnup within ~ 100 μm of the pellet surface is increased by a factor 2 or 3 depending on the flux spectrum of the reactor.

In the late 1950s, it was first observed that in very high burnup UO_2 fuel a restructuring process takes place (Barney and Wemble 1958; Belle 1961). It was found that UO_2 irradiated to high burnup, 10%FIMA at relatively low temperatures, did experience a change of crystalline state (Barney and Wemble 1958). From this it was inferred that the material became amorphous. In the mid-1980s the phenomenon was observed again in power reactor fuel (Barner et al. 1990; Baron 1986).

From the various observations it was found that this zone is characterized by

1. Xe depletion (0.25 w%) from the matrix of newly formed small grains, as measured by electron-probe microanalysis EPMA,
2. Coarsened fission gas pores of micrometric size, leading to a swelling contribution up to 15%,
3. Subdivision of the initial grains from typically 10 μm to 0.15–0.30 μm .

At first it was thought that the restructuring and enhanced porosity were a direct result of the production of plutonium in the rim region of the pellet. However, EPMA studies on high burnup LWR fuel by Walker et al. (1992) showed that the restructuring extended much further from the

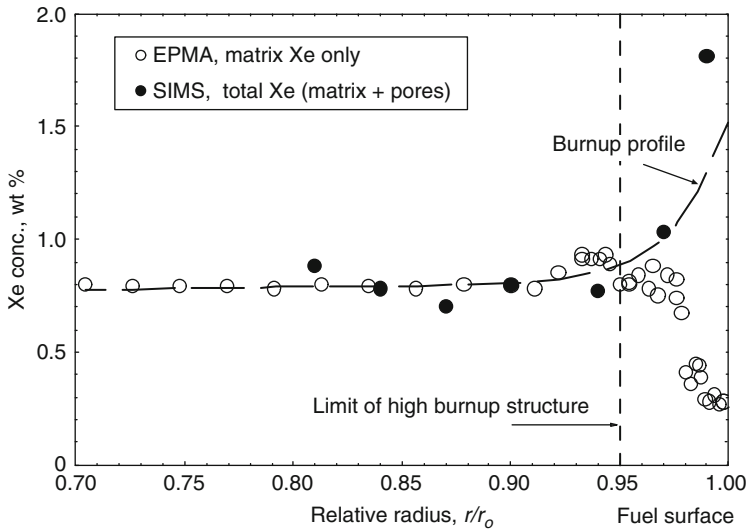


■ Figure 24

Scanning electron micrographs of a nuclear reactor fuel of rod average burnup of 97.8 MWd/kgHM at several radial positions (Manzel and Walker 2002). ©Elsevier, 2002, reprinted with permission

pellet surface than the extent of the plutonium concentration. From these studies it was clear that the restructuring was a result of the local high burnup and not the generation of plutonium. This conclusion was supported further by Kameyama et al. (1994) who investigated the threshold for rim structure formation as a function of burnup in fuels of different initial enrichment in the high burnup effects program (HBEP) (Cunningham et al. 1992; Mogensen et al. 1999). They found that the threshold, which occurred at a local burnup of 70–80 MWd/kgU, was independent of the enrichment, which varied in their study from 1.38 to 8.25 wt% ^{235}U . The contribution of plutonium to the local burnup becomes greater in the lower enriched pellets at high burnup. They concluded that the plutonium/uranium burnup ratios did not change the threshold burnup for rim structure formation. In addition, the different enrichments ensured that the fuels operated at different power densities during irradiation. Thus the invariance of the threshold with enrichment also implied that it was insensitive to power or fission rate.

Further support for the onset of the rim structure depending only on local burnup and not on the U/Pu fission ratio, hence on plutonium concentration and heat rate, comes from the high burnup rim project (HBRP) (Kinoshita et al. 2000; Sonoda et al. 1999, 2002). In this project UO_2 disks fabricated with a ^{235}U enrichment of 26 wt% were irradiated in the Halden reactor, and discharged with a range of burnup levels up to 100 MWd/kg. Despite the extreme uranium enrichment and short time irradiation of 2–2.5 years, the onset of the rim structure occurred at burnup levels very similar to those found in lower enriched LWR fuel as discussed above by Walker et al. and Kameyama et al. Also, in the highest burnup disks, this restructuring



■ Figure 25

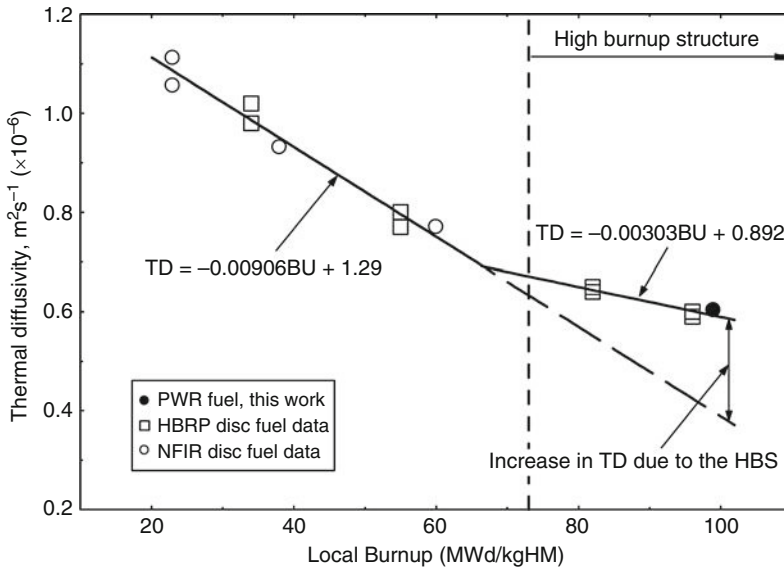
Comparison between measured local xenon concentrations measured by EPMA and SIMS as a function of the pellet radius (Walker et al. 2009). ©Elsevier, 2009, reprinted with permission

occurred throughout the whole volume of the disk. As a consequence, the “rim” structure has been renamed as the “high burnup structure,” HBS, because such microstructure modification can occur anywhere within the pellet at temperatures below 1000°C and depends solely on the local burnup. This is also supported by observations of HBS surrounding Pu-rich regions in some types of MOX fuels whose burnup is in excess of the surrounding matrix.

6.1.2 Importance of the High Burnup Structure

The concomitant measurement of an increase of the fractional fission gas release in LWR fuel once the rod average burnup exceeded 45 MWd/kgHM, and the Xe depletion observed by means of EPMA was first considered as an indication that there was a new release mechanism from the HBS. This was thought to be associated with the percolation through the large porosity that was collecting all the depleted Xe from the surrounding grains. In addition to such direct contribution from the HBS to the fractional release, the porosity formed in the pellet periphery was also assumed to constitute a thermal barrier. The resulting temperature increase would enhance the thermal release from the pellet interior, thereby providing an indirect contribution from the HBS to the observed increase in fission gas release. The thermal effect of the HBS was further supported by the observed thermal conductivity degradation with burnup.

The formation of the high burnup structure, however, seems to have a very positive effect on the thermal conductivity in the outer region of the fuel. The thermal conductivity in this region of the fuel is much higher than would be the case if the high burnup structure was not present. The increase in thermal conductivity caused by the formation of the high burnup structure is a consequence of the removal of fission product atoms and radiation defects from the fuel



■ Figure 26

Thermal diffusivity of the high burnup fuel at 217°C as a function of the local burnup. At $r/r_0 = 0.81$, where the local burnup was 90 MWd/kgHM, the local thermal conductivity of the fuel rod would have been 20% higher in the absence of gas pores. Five percentage porosity is a hypothetical value equating to the porosity of the fresh fuel (Walker et al. 2006); ©Elsevier, 2004, reprinted with permission

lattice during recrystallization of the fuel grains (an integral part of the formation process of the high burnup structure). The role of the pores of the high burnup structure as sinks for fission gas expelled from the fuel lattice during recrystallization is more important than their effect as barriers to heat transfer. In the outer region of the fuel, between $r/r_0 = 0.81$ and 0.66, the porosity of the high burnup structure reduced the increase in thermal conductivity caused by recrystallization between 35 and 50% at 217°C.

Recent observations (Spino et al. 2006) also indicated that the HBS porosity is not interconnected, and that release from the HBS is too small to explain the increase of overall fission gas release measured during post-irradiation examination on commercial fuel rods. Furthermore, new experimental evidence on thermal conductivity indicated that the Xe depletion in the matrix accompanying the grain restructuring results in a restoration of the thermal conductivity, the effect of which is larger than the degradation due to the porosity buildup (● Fig. 26). Combining this with a measured decrease of the hardness (Spino et al. 2006) along with an increase of the fracture toughness (Baron et al. 2005), the overall effect of the HBS on the fuel performance under normal operating conditions even seems beneficial rather than detrimental as originally feared.

The importance of the HBS during off-normal conditions, on the other hand can be of concern. However, it was observed that the gas stored in the HBS porosity may not contribute significantly to the fuel dispersal during a sudden increase of the local temperature, (e.g., during the first instants of a reactivity-initiated accident or RIA in ● Sect. 6.5), while it is still unknown

whether it can contribute to the fuel dispersal during the cooling down when fuel micro-cracks form due to thermal stress relaxation.

6.1.3 Modeling of the High Burnup Structure

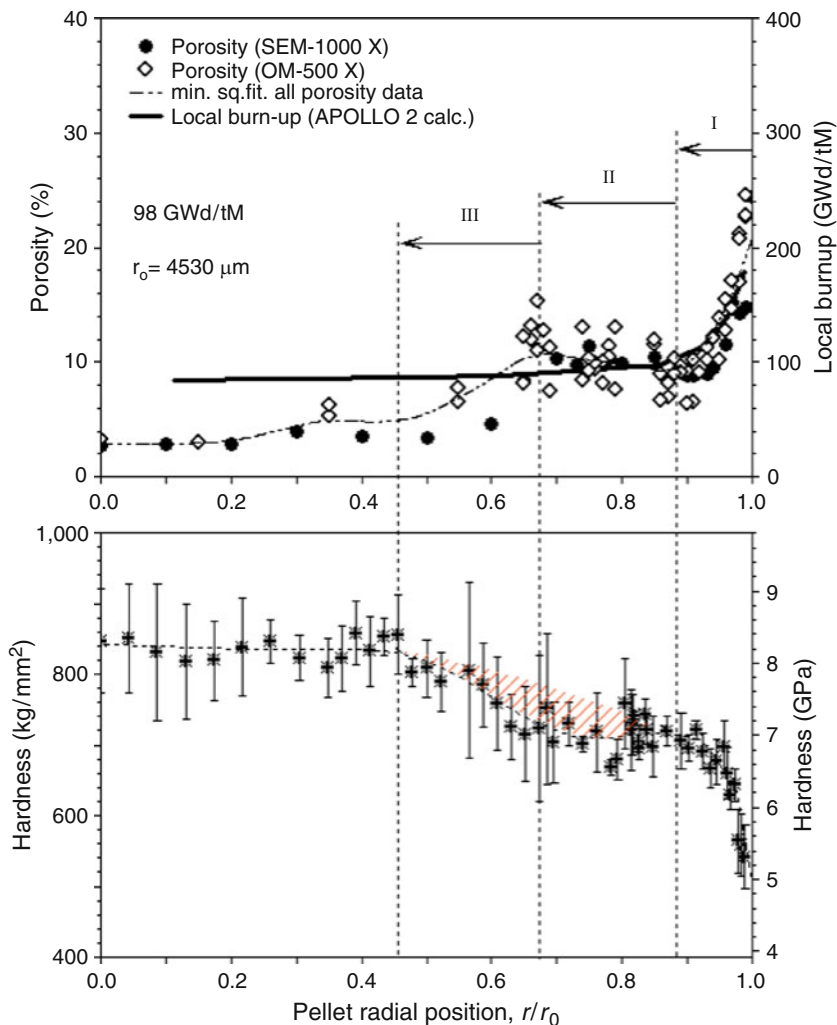
In view of its implications on the fuel rod performance, the HBS has been the subject of many studies. Despite these efforts, no consensus could yet be obtained for several issues (Van Uffelen et al. 2004). The most important differences exist about the scenario describing the nucleation and growth of the HBS. This in turn is related to discussions about the driving force for the HBS formation (radiation damage and/or fission product accumulation), about the nucleation centers for the HBS nucleation (over-pressurized bubbles, grain boundaries, fabrication pores, and dislocations or so-called recrystallization nuclei), and about the parameters affecting the HBS formation and propagation (pellet-cladding contact pressure, initial grain size).

In fuel performance codes, the effect of the HBS on the heat transfer is generally included in a correlation describing the thermal conductivity degradation (cf. ▶ Sect. 3.2.3) and the porosity build up in the HBS as well as in an improved gap conductance in order to account for the bonding layer between the ceramic pellets and the metallic cladding. To this end, for example, the cladding and pellet roughness is empirically reduced above a certain burnup, to account for the filling up by mainly zirconium oxide, which has a higher thermal conductivity than that of the mixture of He and Xe in the residual gap.

Thermal conductivity degradation of the fuel is sometimes considered to saturate (Sontheimer et al. 1998). Occasionally partial thermal conductivity restoration is even considered when the HBS is created. In this way account is made for the *cleaning* of the matrix from point defects and fission products, which relies on an empirical formulation of the lattice parameter variation (Baron 1998). The latter approach seems to be in line with the most recent experimental data shown in ▶ Fig. 26.

The effect of the long irradiation time in the mechanical analysis is mostly accounted for in the cladding properties. The process of outer cladding corrosion liberates hydrogen from the water and can lead to brittle hydride formation. When these hydrides are oriented normal to the cladding surface, the cladding strength is further reduced. Reduction of the microhardness (▶ Fig. 27) and Young's modulus (▶ Fig. 28) observed in high burnup fuel pellets is not yet included in the codes. This also holds for the bond between pellet and cladding, which improves the pellet-cladding interaction resistance since it is much softer than UO_2 .

The impact of the HBS on fission gas release is incorporated in various ways. The simplest way is based on an empirical threshold depending on the local burnup, and/or temperature and/or initial grain size. Others include the burnup as a parameter in the diffusion coefficient or the S/V value (cf. Booth sphere radius in ▶ Sect. 5.4.2), or in the grain boundary saturation value. Quantitative details of most models are not available in the open literature. In the START3 code the grain size reduction observed is modeled in an empirical manner as a function of temperature and burnup (Bibilashvily et al. 2000). As the average distance for intragranular diffusion thereby reduces, an increased release fraction is predicted. Nevertheless, there is evidence that direct release from the HBS is small under normal operating conditions (Spino et al. 2006). Apart from this general statement that the release is small, there is no consensus about

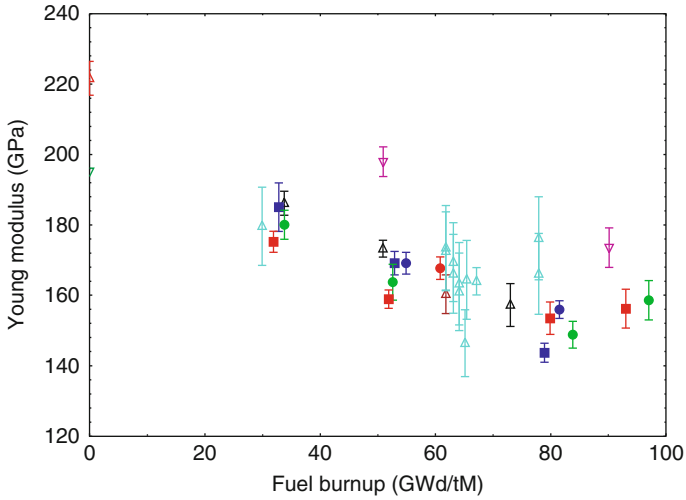


■ Figure 27

Experimental values for microhardness of irradiated UO_2 fuel with a burnup of 98 GWd/tHM (Spino et al. 2006); ©Elsevier, 2004, reprinted with permission

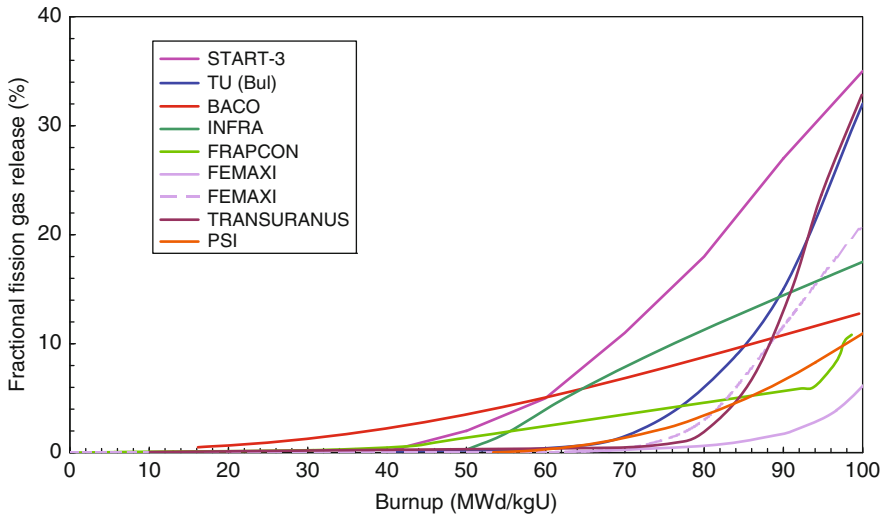
the quantitative contribution from the HBS to the overall release under normal operating conditions. This is very well reflected in the large spread of fission gas release predictions at very high burnup for the codes involved in the FUMEX-II benchmark exercise organized recently by the IAEA (► Fig. 29) (Killeen et al. 2007).

Under design basis accident conditions, the release models disregard the kinetics. Release is assumed to be instantaneous (provided that the gap is open) and comes from grain boundary cracking. The precise modeling of this relies on the modeling of the local conditions of temperature and stress, which is very difficult but is hardly discussed in publications.



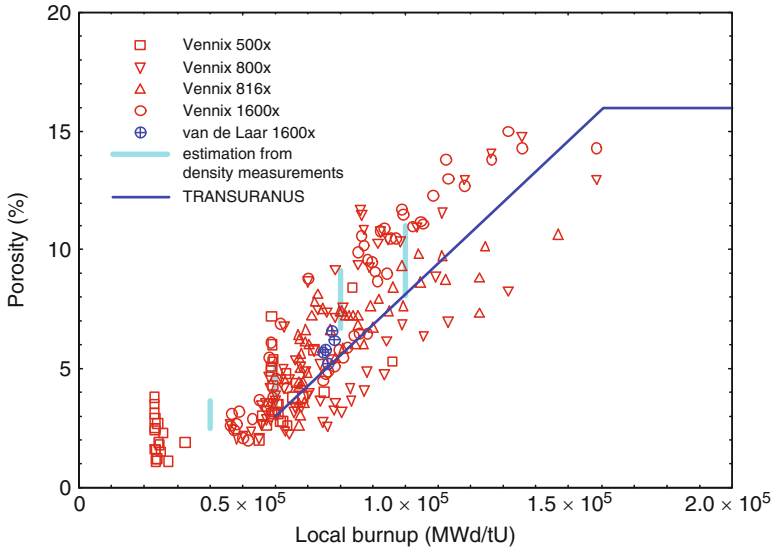
■ Figure 28

Experimental Young's modulus of irradiated LWR fuels as a function of burnup (Baron et al. 2005)



■ Figure 29

Cumulative fractional fission gas release predicted for a constant linear heat rate of 15 kW/m by various fuel performance codes involved in the FUMEX-II round robin exercise of the IAEA (Killeen et al. 2007)



■ Figure 30

Porosity as a function of the local burnup for highly irradiated fuel, and the corresponding correlation adopted in the transuranus code (Lassmann 2000)

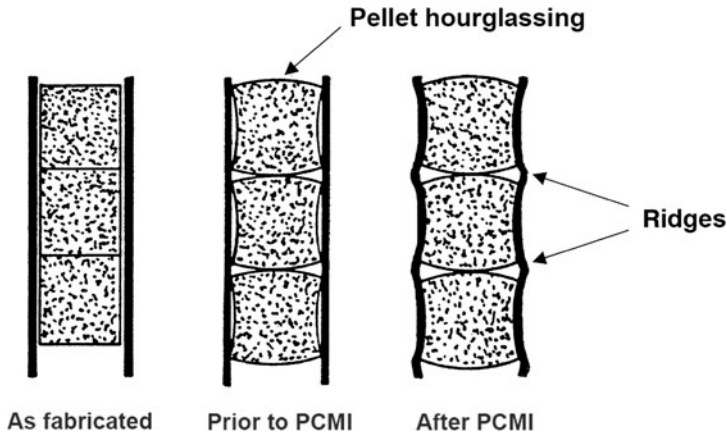
Finally, the swelling in the HBS is mostly modeled separately with a very simple linear or quadratic function of burnup (► Fig. 30). Also the width of the HBS structure is sometimes modeled empirically as a function of the burnup.

6.2 Pellet-Cladding Interaction

6.2.1 Pellet-Cladding Mechanical Interaction

The high radial temperature gradient and the concomitant differential thermal swelling in the ceramic fuel pellet leads to a so-called hourglass type deformation (► Fig. 31). Indeed, even at a low linear heat generation rate of around 5 kW/m, the internal thermal stresses in the cylindrical fresh pellet exceed the fracture stress of UO_2 (around 100 MPa), causing pellet fracture. Once the pellet has fractured, it is able to deform much more readily under the effects of the temperature field, causing the pellet ends to bow outward. The pellets also swell during irradiation (► Sect. 5.3).

In line with the pellet deformation, the cladding creeps toward the pellets during the first part of the irradiation under the action of the differential pressure, that is, the difference between the pressure of the primary water circuit (about 15 MPa in PWR) and the initial internal fill gas pressure in the rod (about 6 MPa in hot conditions). Although the cladding also undergoes thermal expansion, the expansion rate of zircaloy is less than that of UO_2 , leading to a net reduction of the original clearance between both. Due to pellet hourglassing, the onset of pellet-cladding mechanical contact occurs at the inter-pellet planes. This creates primary ridges



■ **Figure 31**
Schematic representation of pellet swelling

at the cladding exterior surface observed after ramps, sometimes referred to as the bamboo structure.

The onset of pellet-cladding mechanical interaction (PCMI) is affected by a number of design and fabrication parameters. First of all, the pellet geometry is adapted to extend the onset and to mitigate PCMI. In particular, the pellet height has been reduced with respect to its diameter while chamfers were applied for delaying PCMI and reducing the probability of fuel chipping. Secondly, the rod geometry is important. More precisely, the width of the original clearance between the pellets and the cladding should be large enough. Nevertheless, the gap size is subject to many uncertainties, the largest being the pellet fragment relocation. In addition, it is generally assumed that the pellets are located concentrically within the cladding, although this is seldom the case. Any eccentricity in the stacking arrangement, resulting from fabrication or fuel rod handling, is likely to lead to premature onset of PCMI even though its effect will diminish as gap closure occurs.

Once PCMI has started, both the pellet geometry and the material properties of the interacting components influence the maximum stresses and strains as well as their evolution. Flat-ended pellet stacks will generate larger axial expansion in comparison with dished stacks, especially in fresh fuel. This is due to the fact that in flat-ended pellets the hot central part determines the maximum length change, whereas for dished pellets there is no contact between pellets along the central axis (when the power is not too high), hence the axial expansion will be controlled by outer (cooler) regions of the pellet. In practice, the ratio of axial to tangential strain can vary between 0.2 for large dishes and 2 for undished pellets (Hoppe 1980). Nevertheless, the axial expansion from flat-ended pellets can diminish with burnup because of in-pile dishing, for instance caused by densification in the hot central parts of the pellets during PCMI.

In addition to the difficulties to reproduce two-dimensional (local) pellet deformations during PCMI by means of one-dimensional fuel performance codes as explained in ► Sect. 5.3, there are other challenges to be dealt with. Apart from pellet and cladding eccentricity, which mostly affects the onset of PCMI, there are uncertainties related to the assessment of the stress

in cracked pellets, to pinching by assembly grids, as well as to the (static and dynamic) friction coefficient between pellets and cladding. In particular, the slipping is severely restricted by the interaction layer that establishes between both components after gap closure at higher burnups.

6.2.2 Irradiation-Induced Stress Corrosion Cracking

Failures during power variations are not only attributed to stress. Stresses increase at the intersection of radial crack planes, the inter-pellet planes, and the inner surface of the cladding. The brittle nature of the failure site, however, has led to the general consensus that although stress is the primary initiator, propagation of the crack is chemically assisted, thus the process is termed stress corrosion cracking (SCC). The chemical assistance for brittle cracking in all probability arises from the environment established by fission products release into the fuel-to-clad interspace with isotopes of iodine as main candidates as the principal corroding species. There is some discussion as to whether or not the corrodent must be freshly released from the fuel or whether it is sufficient for it to have accumulated in the fuel-to-clad gap throughout the irradiation period prior to the over power transient.

The morphology of SCC surfaces in Zircaloy-4 has characteristic aspects of cracking and deformation mechanisms of hexagonal close-packed metals. The vicinities of crack initiation zones are exclusively intergranular. The intergranular cracks observed in experimental reactors can range from a few to about 20 μm . The rest of the cracking surfaces are purely transgranular, a mixture of quasi-cleavage on the basal planes of zirconium and connection of these planes by plastic deformation (flutting). The quasi-cleavage is enhanced by irradiation hardening, which increases the stresses and adsorption of corrosive fission products that in turn lower the surface energy of the basal planes. This explains the limited amount of intergranular crack propagation in irradiated material.

Intergranular cracks initiate above a certain stress level, in the order of 300 MPa. Laboratory experiments on precracked tubes give transgranular crack propagation rates ranging between 0.3 and 3 $\mu\text{m/s}$ in irradiated Zircaloy-4 at 350°C (Rousselier et al. 2003). The intergranular rate is much more difficult to measure, but is in the order of 0.1 $\mu\text{m/s}$. The transition from intergranular to transgranular SCC is supposed to occur at a critical stress intensity factor in the order of 3 $\text{MPa}\sqrt{m}$ for the unirradiated material. It decreases with radiation damage.

Since its discovery in CANDU reactors and BWRs in the 1970s, four factors affect the incidence of PCI-SCC failures and were reviewed by Cox (Cox 1990), as discussed below.

Sufficient Stress

Pellet Cladding Interaction (PCI) failures are induced following substantial local power variations leading to an increase of the loading on cladding: from control-blade movements in BWRs or from load follow, frequency control, and extended reduced power operation for PWRs. However, the calculation of the stress (or stress intensity) sustained by the cladding and its time dependence is very complex and is affected by the fuel geometry and the friction coefficients, as explained above. Moreover, the stress is affected by the maximum power and the change in power. Indeed, stresses imposed on the cladding arise from a combination of the maximum power subjected to the fuel, which determines the overall expansion, and the change in power

during the ramp, which establishes the increment in strain that the cladding sees over the short period during which the power is raised. The relative importance and the actual critical levels of both factors have led to *fuelograms*, providing limits for the two factors at different burnup levels. These fuelograms depend on the fuel design.

Sufficient Time

The overall time to failure can be subdivided into two periods; an incubation time, at the end of which incipient cracks are detectable, and the propagation time during which these cracks grow through the wall. The incubation is considered as a chemical phenomenon, and the propagation time is very difficult to measure in a reactor. It was concluded that as in laboratory tests, the majority of the time to failure was incubation time, during which no apparent damage to the cladding occurred. In order to establish incubation times and crack growth rates, several international research projects have been conducted (Sartori et al. 2007). It was observed that partial through wall cracks could be observed after ramps of about 20 s, and through wall cracks for ramps of less than one minute. However, these rapid failures could only be obtained when the test fuel was submitted to a relatively high power for at least 6 h prior to the ramp, suggesting chemical conditioning of the environment within the fuel rod. Under some conditions, the intergranular crack growth can continue at the start of SCC until the stress intensity factor for transgranular propagation (K_{ISCC}) is reached. Under such conditions an *accumulated damage parameter* could be valuable. However, since the occurrence of intergranular initiation can only be demonstrated a posteriori, and since the short times to failure attained with fast ramps are almost entirely transgranular in nature, the practical value of such an accumulated damage parameter seems limited and has been omitted in modeling (Cox 1990).

Susceptible Material

Cox (1990) reviewed many laboratory experiments that were conducted to identify the metallurgical variables (yield strength, texture, residual stresses, precipitate distribution, etc.) and compositional changes that could influence the susceptibility of the cladding for SCC. The results were quite variable as no standardized test has been adopted. Furthermore, after a critical irradiation dose, it was noticed that the differences disappeared and all materials become susceptible to cracking. The influence of irradiation on SCC susceptibility caused the redirecting of research from varying the base alloy to developing protective coatings in mitigating PCI.

Proper Chemical Environment

Based on examinations of PCI failures obtained in CANDU fuel that always show some intergranular features it was concluded that iodine-induced cracking was the cause (Cox 1990). In LWRs on the other hand, the elongated grains in the stress relieved conditions, or the very small and distorted grains size in β -quenched cladding make it difficult to distinguish transgranular from intergranular features when subsequent corrosion of the fracture surface took place. In the absence of clear evidence for intergranular features on the fracture surface, it has been impossible to reach a firm conclusion about the causative agent for PCI failures. What became

clear, however, was that the right chemical atmosphere must be present inside the cladding before the ramp.

Mitigating PCI

Understanding the important variables for PCI–SCC enables fuel designers to propose solutions. More precisely, fuel designers have adapted the fuel geometry (reducing the height to diameter ratio, introducing dishes and chamfers), imposed restrictions on the power variation, modified the fuel assembly design, and applied coatings on the inner cladding surface.

In CANDU fuel, both carbon and siloxane coatings have been tested successfully, although the former has become the standard because of the lower fabrication costs. Both carbon and siloxane are applied as coating after tubing fabrication and provide a lubricating effect. The friction coefficient of CANLUB cladding is in the range of 0.15 to 0.3 instead of 0.7 to 0.9 for standard Zircaloy (Cox 1990). The benefits of graphite coating are not only limited to the lubricating effect. Tests also revealed that it forms a barrier for establishing the proper chemical environment for SCC.

In BWRs, Cu and Zr barriers were applied in the form of thin metallic layers as an integral part of the tube fabrication process. The pure zirconium (of either crystal bar or sponge origin) (Harbottle et al. 1994; Schire et al. 1994) has been adopted as the standard barrier, because irradiation experience showed that copper offered less protection after high irradiation doses. However, pure zirconium oxidizes more rapidly in comparison with zircaloy while the terminal solubility of hydrogen is lower in the liner (Van Swam 1997). Accordingly, when a primary defect occurs in the cladding for instance due to debris fretting, water ingress will oxidize both the fuel and the liner. This occurs typically in the lower (cooler) part of the fuel rod. The hydride formation near the cladding inner diameter can lead to a *sunburst* hydride and would, due to the volume increase, set up tangential stress in the zircaloy part of the cladding, which can promote crack formation. The local hydrogen absorption can cause more severe hydriding and therefore secondary defects in the form of long axial splits and circumferential cracks. Secondary cladding defects in LWR fuel can cause large releases of uranium and fission products to the primary coolant (Karlsson et al. 2004), and seems to be correlated with PCI caused for instance by control-blade movements in BWRs. Mitigating these secondary failures has been made by means of increasing the number of rods per assembly (Garner et al. 2007) (e.g., from 6×6 to 10×10 in BWR assemblies) in order to reduce the linear heat generation rate per rod, and by alloying the liner with either Fe (Hoffmann and Dewes 2004) or Sn (Sihver et al. 1997).

A more recent component of PCI resistant fuel designs is the use of softer fuel pellets obtained by means of large grained doped UO₂ for both BWR and PWR applications. Since the early 1990s, AREVA has developed an optimized chromia-doped UO₂ fuel that exhibits significantly higher performance compared to standard UO₂ (Delafoy et al. 2007). The grains are on the order 60 μm compared to 10 μm in standard UO₂, and the creep is only controlled by dislocations movements such as sliding and climbing leading to a larger creep rate (Nonon et al. 2004). As a result of the grain size increase the fuel releases less fission gas and is less prone to PCI failures during ramp tests. Post-irradiation examinations after ramp tests revealed a larger number of radial cracks on the pellet periphery. Recent two-dimensional finite element simulations of PCI have shown that this can be attributed to the larger friction due to fuel-clad bonding in high burnup fuel and the reduced fracture stress of the doped fuel (Marchal et al. 2009). The simulations also indicate that, unlike the hoop stress, the

shear stress distribution in the cladding is smoother, thanks to the reduced fracture stress.

Modeling PCI

Modeling PCI has evolved since the first attempts aiming at the fitting of the time to failure (or failure probability), maximum power, and power increase to experimental data, although the uncertainty could reach a factor 5 (Misfeldt 1977).

The initial step is either assumed to occur at preexisting flaws (Zhou et al. 2005) according to a frequency distribution, or to occur spontaneously when a threshold such as the iodine concentration is exceeded (Miller et al. 1981). More recently, Park et al. (2008) postulated that pits would generate preferentially around grain boundaries and coalesce to form a micro-crack, referred to as grain boundary pitting coalescence. The micro-crack is assumed to develop into an incipient crack, initiating and propagating along the grain boundary.

For the simulation of crack propagation, most authors apply linear elastic fracture mechanics (LEFM), in line with Kreyns et al. (1976). By fitting the experimental data of Wood (1972), they advocated that the crack velocities could be related to the fourth power on the stress intensity factor K_I ,

$$\frac{da}{dt} = C \cdot K_I^4 \quad (144)$$

where a is the crack length and C is a constant. The crack intensity factor was shown to be controlled by the elastic stress field at a flaw tip as described by K_I , rather than the nominal applied stress:

$$K_I = \sigma \sqrt{a} Y \quad (145)$$

where σ represents the nominal hoop stress and the factor Y incorporates a correction factor to account for the finite width of a defect-bearing component. Nevertheless, Kreyns et al. (1976) pointed out that small scale plasticity will occur near the crack tip, in a cone with radius r_p :

$$r_p = \frac{1}{\sqrt{6\pi}} \left(\frac{K_I}{\sigma_y} \right)^2 \quad (146)$$

where σ_y corresponds to the yield stress, and $K_I = \sigma \sqrt{a_{eff}} Y$, which results in an effective crack length:

$$a_{eff} = a + r_p \quad (147)$$

and the effective correction factor $Y_{eff} = Y \sqrt{\frac{a_{eff}}{a}}$ becomes

$$Y_{eff} = \frac{Y}{\sqrt{1 - \left(\frac{\sigma}{\sigma_y} \right)^2 \left(\frac{Y^2}{6\pi} \right)}} \quad (148)$$

Anderson (1995) provided a general correction factor so that K_I can be expressed more generally

$$K_I = \frac{pR}{t} \sqrt{\frac{\pi a}{Q}} F \left(\frac{a}{2c}, \frac{a}{t}, \frac{R}{t} \right) \quad (149)$$

where p is the internal pressure on the tube (MPa), R the mean tube radius, t the tube wall thickness, Q the shape factor for an elliptic crack

$$Q = 1 + 1.464 \left(\frac{a}{c} \right)^{1.65} \quad (150)$$

c is the half length of the crack, and F is a boundary correction factor that depends on the shape of the initial crack formed at the inner cladding surface. Park et al. (2008) applied an expression for F within the range of $5 \leq R/t \leq 20$, $2c/a \leq 12$ and $a/t \leq 0.8$:

$$F = 1.12 + 0.053\xi + 0.0055\xi^2 + (1 + 0.02\xi + 0.019\xi^2) \frac{20 - \frac{R}{t}}{1,400} \quad (151)$$

where $x_i = \frac{a}{t} \frac{a}{2c}$. The K_{ISCC} value provided by Park et al. was 3.3 MPa m^{0.5} and 4.8 MPa m^{0.5} for stress relieved and recrystallized Zircaloy-4, respectively.

Zhou et al. (2005) replaced the constant C in Eq. (144) by a function of the iodine concentration and an Arrhenius-type temperature dependency. More importantly, however, they also involved the pellet-cladding contact pressure in the estimation of the stress intensity factor. The local effect of the frictional shear forces is accounted for by adopting the Coulomb friction model, according to which the friction force is proportional with the contact pressure. The extension of Zhou et al. is in line with recent findings of Michel et al. (2008). Based on two-dimensional and three-dimensional finite element computations, they showed that the tangential stress concentration in the cladding is proportional to the shear loading transmitted at the pellet-clad interface. As a result, the peak hoop stress at the inner surface of the cladding depends on the interfacial shear stress and the uniform loading in the hoop direction. Nevertheless, the simulations did not account for cladding anisotropy, neither for stress relaxation.

Stress relaxation was accounted for in an empirical manner by Mattas et al. (1979). They assumed the chemical (intergranular) crack growth rate to have an initial value and to decrease exponentially as the crack depth increases. Chemical crack growth was postulated to continue until a critical stress intensity for cleavage and fluting was achieved, at which point intragranular cleavage initiated until failure.

As pointed out by Rousselier et al. (2003), stress relaxation and the ensuing crack arrest is necessary to explain a so-called discontinuity observed during ramp experiments: depending on the maximum power of the fuel rod, either a through crack is obtained within maximum ten minutes or the SCC damage is limited to a few microns, even after hours at the maximum power. This discontinuous behavior was observed above the SCC initiation threshold of about 300 MPa in Zircaloy-4 (Schuster and Lemaignan 1992). Rousselier et al. attributed this to the stress relaxation and to the fact that the intergranular crack could leave the stress concentration zone at the crack tip. Crack arrest was postulated to occur when at the same time the stress intensity factor would be below a certain threshold ($K_I \leq K_{Ia}$) and the stress intensity factor would decrease. However, quantitative information cannot be directly inferred from their analysis, since the critical stress corresponding to K_{Ia} should depend on the material (stress relieved versus recrystallized), the irradiation as well as the loading history. Furthermore, the LEFM should not be applied without corrections for the visco-plastic behavior and finally, because of the local inhomogeneities of the material at the scale of the crack one should apply local rather than global criteria such as $K_I \leq K_{Ia}$.

With the advent of improved computers and software on one hand, and more detailed experimental data on the other hand, more detailed models are being developed at various scales. At the electronic and atomic scale, first principle computations should enable analyzing the individual effect of impurities such as iodine on the binding energies, in much the same way as Xin et al. (2009) have studied the point defects properties and their interactions with Nb in Zr or Kaji et al. (2002) analyzed the clustering of Ni in Fe. By means of finite element computations on the level of crystallographic grains, Rousselier et al. suggest avoiding the limitations associated with LEFM for crack initiation and propagation. Because of the excessive computation time and the lack of precise data of some model parameters, their model is not applicable in fuel performance codes but should enable analyzing the effect of corrosive fission products on the intergranular damage by coupling the mechanical problem with a diffusion problem. A similar tool has already been developed by Musienko et al. (2009), albeit that the corrosive environment parameters are accounted for by a phenomenological approach, that is, via an effective diffusion coefficient. At the meso-scopic scale, Kaji et al. developed a two-dimensional model for SCC growth, in order to analyze qualitatively the effect of load (normal versus shear stress) and grain boundary corrosion on the branching aspect of crack growth. The macroscopic models are mostly based on finite element simulations (Marchal et al. 2009; Michel et al. 2008). These tools provide deeper insight and qualitative information about the various parameters affecting PCI as explained above. Nevertheless, these models are not yet capable of replacing the simplified one-dimensional models implemented in fuel performance codes, despite the improvements of computers and software. Marchal et al. (2009) are trying to develop analytical “enrichments” for one-dimensional models in fuel performance codes based on the two-dimensional models. The stochastic nature of cracking along with the complex evolution of material properties and boundary conditions during irradiation are the most important difficulties to be tackled.

6.2.3 Outside-In Cracking Caused by Power Ramps

High burnup fuel rods in LWRs are characterized by the absence of a clearance between the pellets and their metallic containment. During power ramp tests with high burnup BWR rods, a failure mechanism therefore occurred from the cladding outside toward the inner surface of the zircaloy (Shimada et al. 2004) as opposed to standard PCI–SCC as discussed above. Post-irradiation examination revealed that the process started an axial split with cracking of radial hydrides that had formed during the power ramp test, followed by a step-by-step cracking of hydrides at the crack tip. The process bears similarities with secondary hydride failures discussed above. The temperature gradient along the cladding and the stress due to the ramp test precipitate radial hydrides in the outer surface of the tube. These hydrides can crack under the influence of stress caused by PCMI and progressing toward the inner tube surface. The main difference with secondary hydride failures that start on the inner surface is that hydrogen is already absorbed at the outer surface due to clad oxidation during normal operation.

6.3 Pellet-Coolant Interaction

Failure of a fuel rod has a probability of between 10^{-4} and 10^{-6} per year. It can be caused by a design fault in the cladding, by fretting of debris or rod to grid fretting, by pellet-cladding mechanical interaction, or stress corrosion cracking. Operational experience during the last

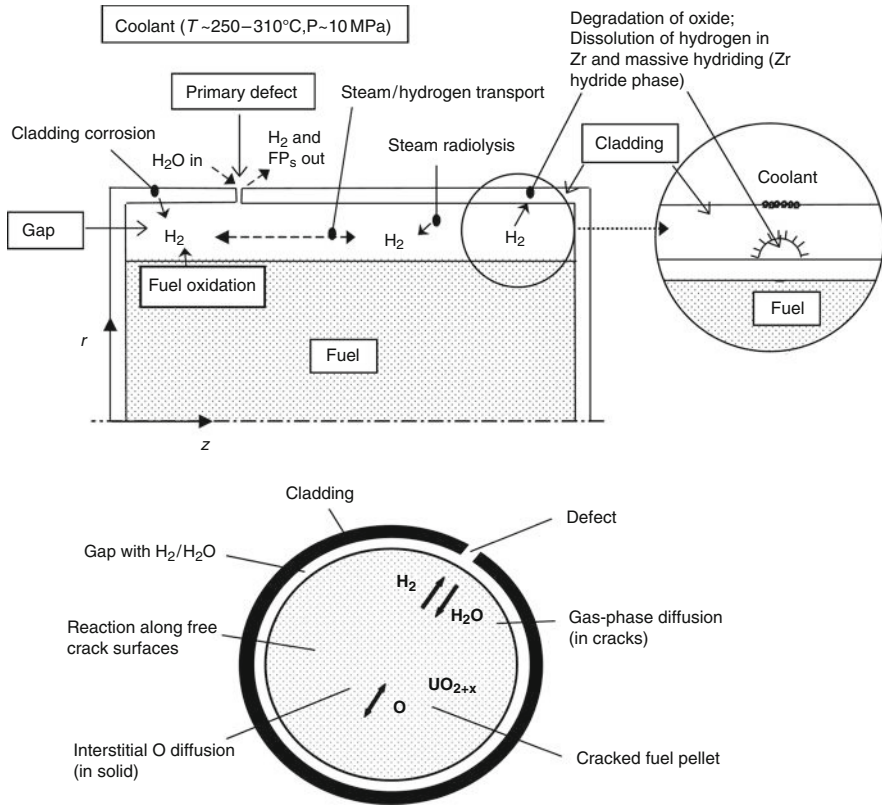
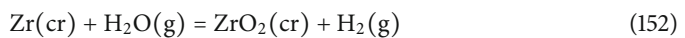


Figure 32

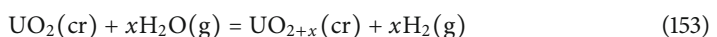
Schematic of physical/chemical processes in defective fuel. Sources of hydrogen and gas-phase transport in the element (upper figure), and cross section of a defective element showing interstitial oxygen diffusion in the solid fuel matrix and gas-phase transport of hydrogen/steam in the fuel cracks (lower figure) (Higgs et al. 2007) © Elsevier, 2007, reprinted with permission

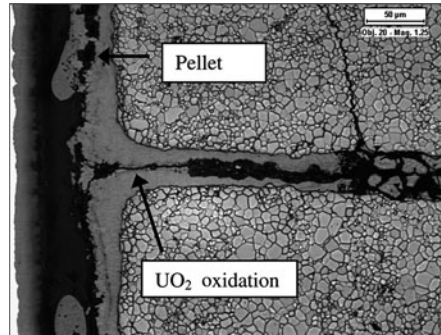
10 years has reduced the failure probability significantly, and rod to grid fretting is now the main cause for failure.

In case of failure of the fuel rod cladding, interaction of steam with the pellet will take place. As discussed by Higgs et al. (2007), this is a complex process, as depicted schematically in Fig. 32. After a breach in the cladding occurs, hot steam will enter the fuel rod, where it will react with the Zircaloy (152) producing hydrogen:



The ratio of the partial pressures of H₂ and H₂O (Eq. 152) will control the oxygen potential of the gap atmosphere. At the same time the fuel pellet surface will be oxidized





■ **Figure 33**

UO₂ oxidation near a primary cladding defect, showing the effects at the pellet surface and in the pellet cracks. (Higgs et al. 2007) © Elsevier, 2007, reprinted with permission

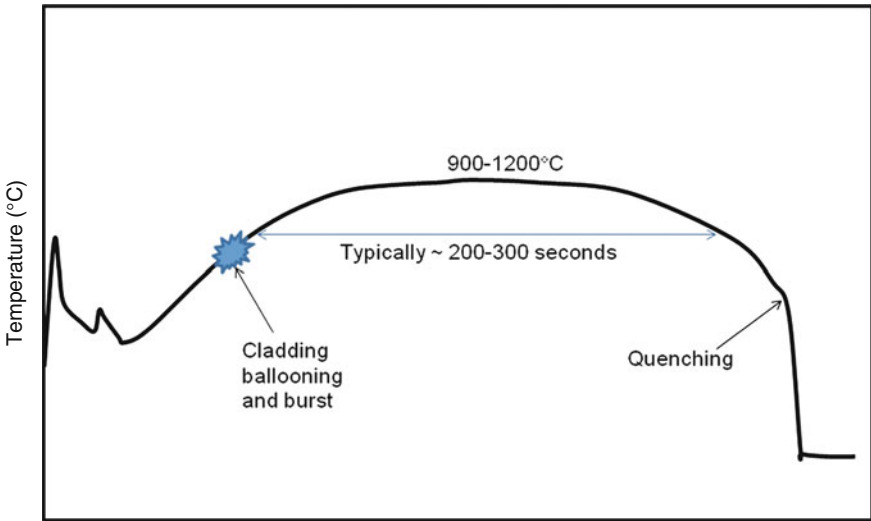
where the value of x is principally controlled by the oxygen potential of the gap gas, as the hydrogen production by thermal oxidation of the fuel in steam is small compared with that due to cladding corrosion (Olander et al. 1999). Similarly the gap gas will diffuse into the hotter regions of open cracks of the fuel, also establishing equilibrium with the solid phase around the crack region (► Fig. 33). The increase of the O/M ratio in the rim and crack regions of the pellet will lead to diffusion of oxygen into the fuel. Considering the temperature regime for LWR fuel and the high fuel density, thermodiffusion of interstitials is considered to be dominant for the redistribution of oxygen in a temperature gradient (Soret effect).

Une et al. (1995) reported post-irradiation examinations of UO₂ pellets from defected fuel Zircaloy-clad BWR fuel rods that had small leaks along both pellet diametral and fuel rod axial directions. They reported that the fuel oxidized to hyperstoichiometric UO_{2+x}, the fuel oxidation significantly depending on the defect size and distance from the defect. The pellet volume-averaged O/M ratio at various axial locations were in the range of 2.02–2.06, whereas higher O/M ratios were detected at the fuel periphery, which decreased toward the pellet center, except for the specimen near the secondary defect at the rod bottom having the opposite O/M distribution. However, Olander et al. (1999) claim that there is no conclusive evidence that oxidation to such O/M ratios can occur with steam during the incubation stage following initial cladding perforation. They argue that experimental and theoretical evidence indicate that UO₂ is resistant to oxidation by irradiated steam as long as even a minor percentage of hydrogen is present. They suggest that direct contact with liquid coolant containing dissolved O₂ can produce highly hyperstoichiometric uranium oxides, or even oxidation with storage pool water.

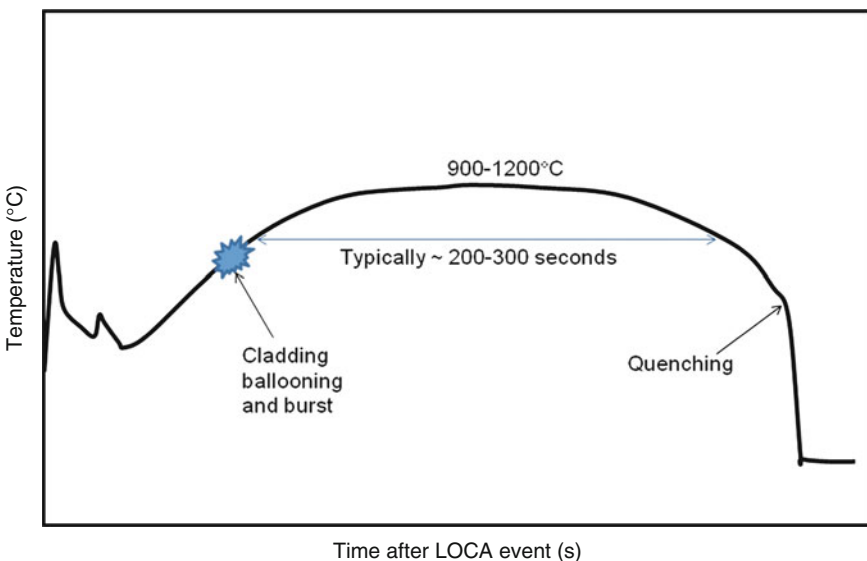
As the oxidized fuel has a much lower thermal conductivity than stoichiometric fuel (see ► Fig. 6) and a lower melting temperature, the coolant-cladding interaction can have a significant impact on the fuel thermal performance. The higher fuel temperature could lead to increased fission gas release. Une et al. (1995) indeed found a remarkable difference in Xe release between the defective and sound fuels. Another consequence can be local fuel melting, as has been observed for CANDU fuel by Lewis et al. (2004).

6.4 Loss-of-Coolant Accidents

6.4.1 Sequence of Events during a LOCA

A loss-of-coolant accident (LOCA) in a water cooled reactor consists of a large break of the coolant primary system and consequent loss of core cooling capacity. A LOCA is a design basis accident, that is, an accident that the plant design must account and accommodate for in terms of ensuring that a core coolable configuration is maintained. Post-LOCA coolability is achieved by an immediate reactor scram, that is, a rapid insertion of control rods in the core, which ends the fission power production in the nuclear fuel, and by the activation of an emergency core cooling system (ECCS) that enters into function upon depressurization, within relatively short time after start of the transient. As schematically shown in  Fig. 34, a typical LOCA sequence in a light water reactor (LWR) consists of the following phases:

1. Depressurization (blow down) of the primary system, accompanied by an automatic reactor scram. During this phase the fuel temperature may oscillate depending on position, timing of the power reduction, and timing of the depressurization. The cladding temperature may even decrease since the water still has enough cooling capacity and because the water temperature is decreasing as pressure decreases.
2. Heat up of the core caused by the remaining heat generation in the fuel (stored and decay heat) and by the loss of water inventory. The decay heat will continue to be active despite shutdown of the fission power. Some amount of water remains in the lower portion of the core, whereas steam prevails at middle and high core elevation, leading to a more pronounced heat-up rate in the upper regions of the core. The heat-up rate varies with plant design, fuel design, and operating power at the time of the LOCA. Normally, the fuel-cladding



 **Figure 34**
A schematic representation of a LOCA sequence

temperature increases at moderate rate, approximately some few degrees per second in the earlier phase of the temperature escalation. When the temperature exceeds 600°C , the cladding becomes more and more prone to plastic deformation and under the effect of the rod inner pressure – which is appreciably larger than in the depressurized reactor vessel – it starts deforming and balloon in the space between the fuel assembly grid spacers. If the ballooning exceeds a certain size, the fuel rod cladding will burst open, breaking the first barrier to radiation containment. In addition, the zircaloy cladding undergoes phase transitions from a so-called α phase to a β phase at temperature exceeding 900°C (cf. [Sect. 4.2](#)), although one should consider that the transition temperature is to some extent affected by the amount of hydrogen contained in the metal cladding as well as the heating rate.

3. The cladding temperature continues to increase but at gradually lower rate due to the increasing radiant and convective heat transfer, exhibiting a relatively flat temperature trend for some period of time normally lasting for a few minutes. Under the ECCS effect, the cladding temperature trend is then reversed and after a period of gradual temperature decrease, the cladding is finally quenched by the ECCS water rising in the core.

6.4.2 Main Characteristics of a LOCA Failure

Important phenomena occur in the fuel as the heat-up progresses. One is the already mentioned ballooning and burst, which normally occurs in the cladding temperature range $600\text{--}800^{\circ}\text{C}$, depending on the rod inner pressure. In fuel performance codes, usually a one-dimensional mechanical model is applied for the radial cladding deformation. For dealing with large high-temperature deformation (i.e., ballooning), typically during a LOCA-type accident, (73) is applied. As described in [Sect. 4.6.2](#), the strain is calculated for the α and β phases separately and weighted [Eq. \(74\)](#).

A number of experimental studies have been conducted in the past to verify that a ballooned fuel assembly remains coolable in spite of the reduced rod-to-rod spacing. The conclusions of these studies, which were conducted decades ago and which evidenced that ballooned assemblies remain coolable, have not been challenged in subsequent times. Hence, the ballooning as such does not constitute a limitation in the current LOCA safety assessment.

Another important phenomenon is the release of fission products from the fuel into the primary system and hence inside the reactor containment. The radiological consequences are assessed through conservative estimates, which may entail assumptions such as complete release of the plenum fission gas and of the inter-granular fission products inventory at the time of the accident, as well as complete fission product release from the fuel region exceeding a certain temperature threshold.

The major concern from the fuel safety criteria viewpoint is the rapid cladding oxidation taking place when the cladding is exposed to high temperature and steam environment, as it occurs in a LOCA.

6.4.3 Current LOCA Safety Criteria

LOCA Criterion Based on Zero-Ductility

In the high-temperature range ($>800^{\circ}\text{C}$), the cladding oxidation kinetics increases dramatically with temperature, typically doubling for a temperature increase of 20°C . This has the

significant consequence that hydrogen is generated in the core due to the zirconium–water reaction (152). One should also consider that the zirconium–water reaction is exothermic and has a heat release of 580 kJ/mol (Powers 2000), which adds to the cladding heat-up caused by the fuel decay heat.

It is known that the zircaloy cladding becomes brittle when subjected to high temperature oxidation in steam environment, mainly due to the hydrogen that remains entrained in the metal itself during the high-temperature oxidation process. This increased cladding brittleness has a major impact on the failure criteria. As stated in the US code of Federal Regulations issued in 1971 “General Design Criteria for Nuclear Power Plants,” US code of Federal Regulations, Title 10, Part 50, Appendix A, 1971, “the cladding temperature transient is terminated at a time when the core geometry is still amenable to cooling, and before the cladding is so embrittled as to fail during or after quenching.” Atomic Energy Commission Rule-making Hearing, Opinion of the Commission, Docket RM50-1, 1973. Since it was deemed difficult or impossible to quantify the type and magnitude of the stress imposed to the cladding during or after quenching (especially in coincidence of, e.g., a seismic event), the US Atomic Energy Commission stated their “belief that retention of ductility in the zircaloy is the best guarantee of its remaining intact during the hypothetical LOCA.” Consistent with the above, the current LOCA safety limits are in most countries based on ductility tests. These are performed by first subjecting tube test specimens to two-side steam oxidation at various temperature levels and for varying duration. Two-side oxidation is used because the cladding is assumed to have ballooned and burst open, giving steam access also to the tube interior. Two-side oxidation provides maximum cladding exposure to steam and is a conservative test configuration, since it represents the most severe oxidation condition.

Upon completion of the high-temperature oxidation phase, the specimen residual ductility is determined by a ring compression test. The results of such ring compression tests for the various specimens are separated in two categories, that is, those showing some residual ductility and those exhibiting brittleness or “zero ductility.” As shown by Hobson and Rittenhouse already in 1972 (Vitanza 2006), the brittle category would expectedly consist of those specimens that experienced longer exposures and/or higher temperature during steam oxidation. When plotted on a oxidation time vs. oxidation temperature diagram (i.e., on a $\text{Log}(\text{time})$ vs. $1/T$ diagram), the Hobson and Rittenhouse ductile and brittle data were separated by a line, which approximately corresponded to a 17% cladding wall oxidation (or 17% ECR, equivalent cladding reacted), when oxidation was calculated with the Baker–Just correlation (see [Sect. 4.6.1](#)) as two-side oxidation (Vitanza 2006). Hence, the Baker–Just 17% ECR was adopted as general LOCA embrittlement criterion, together with the additional requirement that the cladding temperature should not exceed 1204°C, as there was evidence of substantial rapid embrittlement beyond that temperature level. The embrittlement is explained by solid–solution hardening of transformed-beta phase at high oxygen concentrations that are characteristic of oxidation at the high temperature (Chung 2005). Furthermore, prevention of runaway oxidation was another factor in limiting the peak cladding temperature to 1204°C, above which heat generation from metal–water reaction becomes excessive and an autocatalytic type of situation can occur (Chung 2005).

In fact the safety criteria are stated as five requirements dealing with the calculated performance of the cooling system under the most severe loss-of-coolant accident conditions. The first two are the maximum of 17% ECR and 1204°C peak cladding temperature mentioned above. The third requirement addresses the maximum hydrogen generation, the total amount of which shall not exceed 1% of the hypothetical amount generated by the reaction of all the metal in

the surrounding fuel. Finally, the last two requirements are related to the core cooling. More precisely, the calculated changes in core geometry shall leave the core amenable to cooling and after any operation of the ECCS, the core temperature shall be maintained at an acceptable low value and decay heat removed for the extended period of time required by long-lived radioactivity.

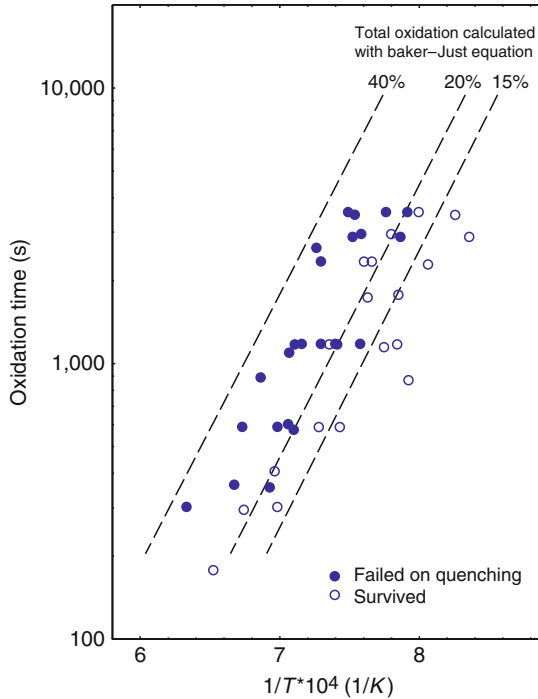
The so-called 17% ECR criterion, established in the early 1970s, is still applied today, although with small variations in some cases. Regarding actual applications in LOCA assessments, the following points should be considered:

1. The 17% ECR limit is a time-temperature limit, not an oxidation limit as such. The criterion precisely states that the 17% ECR must be calculated with the Baker–Just (B–J) correlation. When this is done, the 17% limit is nothing more than a straight line in a time-temperature domain.
2. Unfortunately, the criterion is often misinterpreted, and other correlations are used instead of the B–J correlation. In some cases, for instance, the Cathcart–Powel (C–P) correlation (see ► Sect. 4.6.1) is used in licensing evaluations, with the motivation that it is a better correlation to predict oxidation. While this might well be the case, the 17% limit is not an oxidation limit, but a ductile-to-brittle limit, which happens to coincide with the B–J calculated 17% ECR. Fortunately, the difference between the C–P and the B–J correlation is not very large, as ► Fig. 11 shows. However, this apparently minor change does imply a loss of a $\sim 50^{\circ}\text{C}$ margin in the LOCA assessment.
3. Occasionally, other researchers express experimental ductility data as function of “measured ECR” instead of the calculated one, claiming that the measured value would provide a more realistic reference than the B–J calculated ECR. In reality, a ductility limit expressed vs. measured ECR is meaningless for a LOCA assessment if it is not supported by a sufficiently precise knowledge of the oxidation dependence of time and temperature.
4. Since the LOCA ductility database is founded on two-side oxidation tests, ECR LOCA calculations shall be made with a two-side oxidation assumption. This may be a conservative assumption because access of steam to the interior of a fuel rod may be limited, especially in regions away from the ballooning regions and especially at high burnup, when the pellet-to-cladding gap is very small. However, a sufficiently comprehensive characterization of ID vs. OD corrosion at various axial positions and at realistic conditions does not exist at present. Further, most LOCA ductility assessments assume that the cladding zero-ductility limit should not be encroached anywhere along the cladding. Hence there is no basis for taking credit for cladding being subjected to one-side oxidation only “somewhere” along the fuel rod length.

The zero-ductility criterion is derived from steam oxidation experiments normally carried out at constant temperature. The applicability to a generic temperature transient has been discussed above. However, zero-ductility is not a straightforward cladding characteristic as its definition may depend on several details of the experimental set up used for measuring the residual ductility and on the method for exactly determining it. Important question marks can also be raised on the way it should be applied, as it will be discussed below.

LOCA Criterion Based on Integral Quench Tests

The experimental basis for the LOCA criteria in Japan consists of quench tests conducted on fuel rod simulators made of cladding tube segments filled with alumina pellets. These tests were performed at JAERI (now JAEA) in the 1980s (Uetsuka et al. 1983). The cladding tubes were



■ Figure 35

JAERI quench test database on as-received Zircaloy-4 tubes subjected to high-temperature oxidation and quench, under full constraint condition (Uetsuka et al. 1983)

ballooned, ruptured, subjected to high-temperature two-side oxidation, and then quenched. During quenching there was full constraint, that is, the tubes were held at both ends in order to prevent axial contraction during cooling. The full constraint was used as the bounding case for the actual fuel assembly condition, since a reliable assessment of fuel-grid interaction and consequent loading was difficult to make at that time.

Approximately 50 experiments were carried out on nonirradiated Zry-4 cladding tubes, which served as basis for the Japanese LOCA criteria. The results were divided in two categories, depending on whether the tube had survived or failed during the quenching. ➤ Figure 35 provides a plot of the experimental results, showing the data points for the failed and non-failed tubes on a time vs. temperature diagram. As one can observe, the Baker-Just 15% ECR line represents a conservative rendition of the results. As most phenomena under LOCA conditions, including rupture, secondary hydriding from inner surface and axial loading during the quench, are taken into account in the quench tests, the 15% ECR criteria was adopted as the LOCA failure criterion – and hence coolability criterion – in Japan (Uetsuka et al. 1983).

As already mentioned, the JAEA integral tests constitute an as-close-as possible representation of an actual fuel rod and of all the phenomena that actually incur during a LOCA. In fact, the fuel rod simulator is subjected to heat-up, ballooning and burst, high-temperature oxidation,

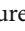

and quenching as it would be in an actual LOCA. In this sense, it appears to be much closer to a realistic simulation of all LOCA phenomena than the ductility tests. This is particularly true for what concerns ballooning, a phenomenon that is incorporated in the integral quench testing while it still represents a question mark for the applicability of the zero-ductility criterion. Setting the coolability limit in correspondence of the fuel failure during quenching ensures conservatism in this approach, hence providing a certain (although unquantified) degree of safety margin. However, an aspect that requires attention is the type and level of stress that can arise in the cladding during quenching. While full axial constraint certainly represents a conservative assumption on axial stress, questions can be raised as to the lack of transversal forces acting on the cladding in the JAEA testing.

6.4.4 Extension to High Burnup Fuel

Zero-Ductility Limit at High Burnup


In an overview of the experimental database performed in 2005 (Vitanza 2006) it was shown that the zero-ductility LOCA limit for high burnup fuel is affected by the amount of corrosion experienced by the fuel cladding during service. In particular, it was found that the zero-ductility limit was decreasing proportionally to the amount of hydrogen picked up by the cladding as a consequence of corrosion. Consistently with the available database, the ECR limit (at 135°C) could be expressed as follows:

$$\text{ECR}(B - J) = 17\% \left[1 - \alpha \frac{H}{1,000} \right] \quad (154)$$

(up to $H = 600$ ppm, stable for $H > 600$ ppm) where H is the hydrogen content in the cladding prior to the high-temperature transient, in ppm. As shown in  Fig. 36, the parameter α was found to vary between 0.5 and 1 depending on the type of test performed. In acknowledgment of the results obtained at JAEA, which showed that the ECR decreased up to 600 ppm and stabilized beyond that (see  Fig. 37), the ECR was assumed to stabilize beyond $H=600$ ppm at a level

$$\text{ECR}(B - J) = 17\% [1 - \alpha \cdot 0.6] \quad (155)$$

This implies that the LOCA zero-ductility limit at high burnup would decrease from 17% to about 7% for the case $\alpha = 1$.

In a subsequent USNRC report issued in 2008 (Billone et al. 2008), a similar linear decrease of the zero-ductility ECR was proposed, but with a more pronounced slope as compared with (154). The results are shown in  Fig. 38. As one can notice, there is no cut for hydrogen content beyond 600 ppm in this case. An in-depth analysis of the database considered in that report is beyond the scope of this chapter. However, it is worth noting that there are only two data points for hydrogen beyond 100 ppm, and that this is indeed a too scarce database.

In particular, much data at high hydrogen content would be needed to justify the continuous decrease of the zero-ductility limit all the way down to $\text{ECR} = 0$, a limit that would imply that fuel with hydrogen content beyond 700 ppm would simply not be allowed to operate in a power reactor. The situation would be even worse if the limit is applied considering local hydrogen content instead of average, a point that is not clarified in Billone et al. (2008).

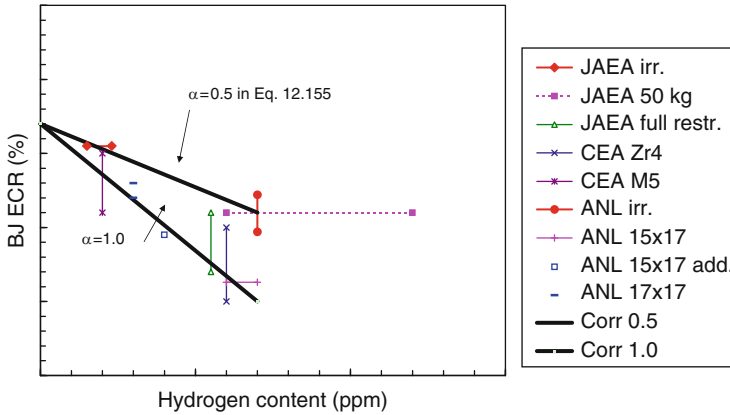


Figure 36

Decrease of the LOCA ECR limit as a function of hydrogen content in the cladding prior to LOCA, as obtained from different types of experiments. All data have been normalized to 17% for zero hydrogen content. The two solid lines are predictions obtained by setting $\alpha = 0$ and $\alpha = 1$ in Eq. (154)

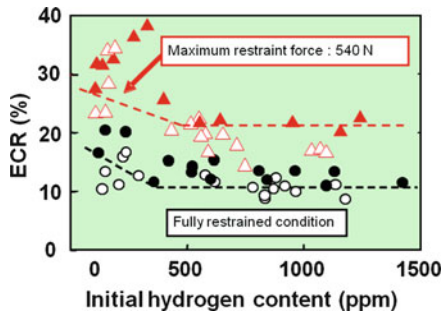


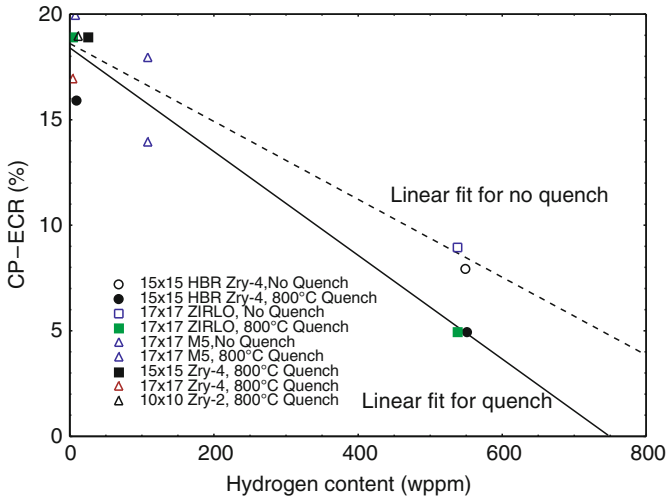
Figure 37

Decrease of LOCA ECR limit as a function of hydrogen content in the cladding prior to LOCA, as obtained from different types of experiments at JAEA

LOCA High Burnup Limit from Integral Quench Tests

Integral tests in the high burnup range have been performed at JAEA. Fuel rods retrieved from power plants were transferred to hot cells and cut in order to extract a test segment at a predetermined position. This was defueled and then refilled with alumina pellets, pressurized to a predetermined pressure and sealed by end plugs. The test segment was then transferred to the experimental equipment in order to be subjected to the integral LOCA sequence, that is, heat-up, ballooning and rupture, high temperature oxidation, and quenching.

Quenching was intended to be performed in the presence of an axial loading of approximately 500 N, which in JAEA’s estimate represents an upper limit for the force expected to be exerted on an actual fuel rod during quenching. In some cases, however, it was difficult to maintain the load, such that some of the tests were in fact carried out with reduced or no loading.



■ Figure 38

Decrease of LOCA ECR limit as a function of hydrogen content in the cladding prior to LOCA, as obtained from different types of experiments published by NUREG (Billone et al. 2008)

Different types of PWR cladding and one BWR cladding were tested and are listed in ▶ Table 6. The fuel burnup in the region corresponding to the cladding test segment ranged between 66 and 76 MWd/kg. The corrosion layer at power reactor discharge was low for the M5 cladding (6–7 μm), while it varied from 32 to 79 μm for the other PWR cladding segments and from 24 to 30 μm for the two BWR segments. Correspondingly, the hydrogen content in the cladding prior to the LOCA test was ~ 70 ppm for the M5 cladding and in the range ~ 200 –850 ppm in the other cases.

The oxidation temperature reached almost 1200°C in all cases, while time ranged from 130 to 280 s except in one case in which it was 719 s. In the latter case, the B–J calculated high-temperature oxidation was large and corresponding to an ECR = 35.6%. The axial loading during quench was 518–530 N in five tests, ~ 200 –400 N in three tests. No loading was applied in two cases.

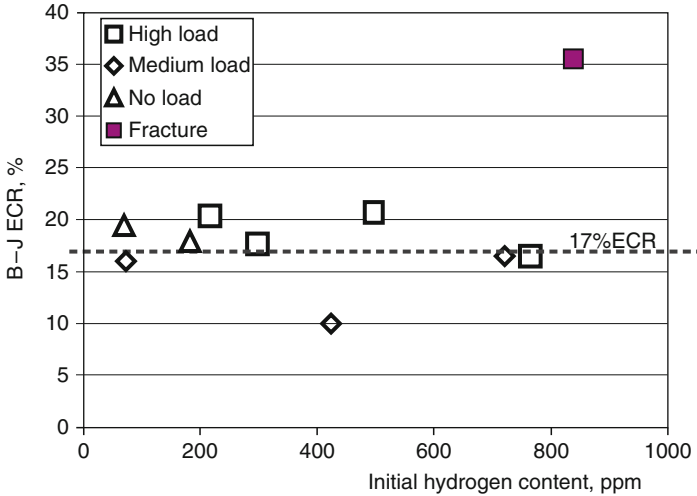
The test segment with highest oxidation (ECR = 35.6%) is the only one that fractured upon quenching. None of the other tests resulted in segment fracture, even if the B–J ECR was close to or higher than 17% B–J ECR.

The outcome of the JAEA results obtained so far are summarized in ▶ Fig. 39. As one can observe, the conclusion of this type of testing is that cladding fracturing does not occur regardless of the initial hydrogen content, unless a very high ECR is achieved. In other words, there would be no need to modify the current 17% (or 15%) ECR limit, as this would remain valid also for high burnup fuel, if the JAEA methodology is adopted. This is quite a different conclusion than the one reached with the zero-ductility approach, which would imply a strong decrease of the ECR limit with initial hydrogen content. This different position is in fact a most important consideration regarding the methodology to be adopted in LOCA tests, an issue that the nuclear community needs to address and resolve in principle.

Table 6
LOCA test results

Test rod ID	LMDA1R	LMDA2R	LMF11	LMF12	LNDA1	LZIR1R	LZIR2R	LZIR3R	LZRT1	LZRT2
Local burnup, GWd/t	76	76	66	66	69	71	71	73	66	73
Cladding material	MDA	MDA	M5	M5	NDA	ZIRLO	ZIRLO	ZIRLO	Zry-2	Zry-2
Corrosion layer (mm)	48	60	6	7	32	36	50	79	30	24
H content (ppm)	720	838	73	69	214	424	496	764	297	182
Burst temperature (°C)	715	---	780	762	715	Weld leak	672	676	763	778
Circumf. strain (%)	9.9	6	20.1	19.2	8.9	8.4	28	20.6	17.7	20.6
Oxidation temp. (°C)	1207	1190	1197	1196	1194	1197	1200	1186	1195	1194
Oxidation time (s)	131	719	151	229	280	122	228	153	222	232
Oxidation amount ^a	18.3	38	19.5	23.6	22.5	10.9	27.3	20.2	21.2	22
(% ECR B-J)	-16.4	-35.6	-15.9	-19.5	-20.4	-10	-20.8	-16.4	-17.7	-17.9
Axial load (N)	<350	530	<400	0	518	<190	518	519	519	0
Fracture/no-fracture	NF	F	NF	NF	NF	NF	NF	NF	NF	NF

^a The value in bracket is B-J calculated ECR for non-deformed cladding, whereas the other value in the table is calculated considering the wall thinning in the ballooning region (circumferential strain is also given in the table).



■ Figure 39

Outcome of the JAEA integral quench test. The results so far show that the 17% ECR criterion holds also at high burnup. This is opposite to the results obtained from ductility tests (see [Fig. 37](#))

6.5 Reactivity-Initiated Accidents

6.5.1 Sequence of Events during a RIA

The reactivity-initiated accident (RIA) is another design basis accident for LWRs, postulated to occur with a very low probability albeit with serious consequences when not appropriately accounted for in the reactor design. The RIA involves the unexpected removal of a control element from the reactor core, resulting in a prompt criticality of the reactor characterized by a rapid power excursion on a time scale of tens of milliseconds in neighboring fuel elements. The power increase in the rods adjacent to the ejected control rods is significant but remains limited, thanks to the natural occurrence of the Doppler effect caused by the temperature increase in the fuel. Afterward, the power is reduced to zero by insertion of fault-free control rods triggered by the reactor criticality.

Among the various scenarios considered for a RIA, the most penalizing in a PWR consists of a control rod ejection at hot standby conditions, and a control rod drop accident at cold zero power (CZP) conditions in a BWR. The form and duration of the power peak depend on the scenario, the fuel and reactor design as well as the condition of the fuel. State-of-the-art three-dimensional neutron kinetics codes indicate that the width of the power pulse is in the range of 25–75 ms in fuel with a burnup exceeding 40 MWd/kgHM (Meyer 1996).

During the pulse, one can distinguish three phases in the fuel rod behavior. The first phase of the RIA is characterized by the quasi-adiabatic temperature increase in the fuel, accompanied by its thermal expansion and the fission gas swelling. This results in a cladding temperature increase at a rate on the order of 1000°C/s and a multiaxial loading on the cladding, driven by the fuel displacement. The hoop strain rate is on the order of $1/\text{s}$ (Federici et al. 2001), being four to five orders of magnitude larger than rate during a normal power ramp of about 10 kW/m per

minute. The clad load is multiaxial: the axial to tangential strain ranges between 0 and 1. The purely tangential strain is only achieved when the friction between fuel and cladding is infinite, whereas the equivalent deformation in axial and tangential direction is obtained when there is no slip between both components. During the first phase of the RIA, the cladding temperature remains moderate, typically below 600°C. Therefore the cladding can fail due to PCMI, depending on the cladding condition properties (irradiation damage, oxide thickness, hydride concentration and orientation, etc.). In some cases the cladding oxide underwent spalling off, causing a local cladding cooling along with a clad ovalization on nonuniform deformation.

During the second phase of the RIA, the cladding temperature continues rising because of the energy generated by the fuel, and can lead to departure of nucleate boiling (DNB). Under these conditions, the cladding temperature could remain above 1,000–1,200 K for up to 10–15 s. During the temperature increase the clad stiffness is strongly impaired, while the inner gas pressure of the rod increases due to gas release and the temperature increase. A local deformation and clad rupture may result.

During the third stage of the RIA, the cladding is submitted to a rewetting or quenching, which may cause a fragile rupture, especially when clad oxidation is important. During this cooling, hydrides that were dissolved at high temperature may precipitate again under influence of the stress in the radial direction. Brittle radial hydrides that are perpendicular to the main (hoop) stress contribute to cladding fragilization, although clad rupture caused by radial hydrides during the quenching phase of a RIA has never been reported.

During the fourth and last stage of a RIA, fuel dispersal can occur. Indeed, when the energy deposition is high enough, fuel melting accompanied by excessive fuel swelling could cause clad failure by overheating or overstraining. When dispersed into the coolant upon clad failure, the hot fuel may cause a pressure pulse in the water due to vaporization, potentially damaging neighboring assemblies or other core components.

6.5.2 Main Characteristics of RIA Failures

Among the four failures modes described in the sequence of events, there are two dominant types of fuel rod failures during a RIA. The first deals with a typical PCMI failure and is predominant for fuel rods irradiated to an average burnup beyond 30–40 MWd/kgHM because of gap closure and clad fragilization. The second type of failure is more typical for fuel rods with a lower burnup level and is caused by gaseous pressure at high temperature during the post-DNB phase. However, the post-DNB phase and the phenomena occurring after rupture have not yet been reproduced properly.

Most research is directed toward the first failure type because of the tendency to increase the average discharge burnup levels for economic reasons, and because this is considered to be the most severe criterion for high burnup rods. The main factors affecting the PCMI failure type are the following:


- The gap size
- The burnup (because of the clad fragilization caused by irradiation damage, oxidation, and hydrogen pickup)
- The friction coefficient (friction will distribute the deformation, hence reduce the failure propensity)

- The width and height of the power pulse (large pulse widths enable the clad temperature to raise along with the stress, reducing the risk of fragile rupture in the first phase of the RIA).

The fragile failure of the cladding during the first phase of the RIA takes place at a hoop strain on the order of 1%, and takes place in two steps. The first step consists of radial crack nucleation in the hydrogen-rich outer (fragile) cladding layer, followed by its propagation in a ductile manner toward the cladding inner surface until the local deformation exceeds the rupture limit, causing cleavage in a shear band oriented 45° away from the radial and tangential directions. There seems to be a transition zone between the fragile and ductile part due to pseudo-cleavage, which is more affected by the hydrogen concentration gradient than by the temperature gradient (Hermann et al. 2007). During the second phase of the failure, a few of the radial cracks will propagate axially, causing long splits along the hydrogen-rich zones (Fuketa et al. 1997).

6.5.3 RIA Safety Criteria

Acceptance criteria for fuel behavior during a RIA were established by the US NRC based on early tests in pulse reactors (US-NRC 1981) and used worldwide, albeit sometimes in a slightly modified form. The first criterion defines a limit on the radial average fuel enthalpy at 1,172 J/g (280 cal/g) to ensure core coolability and reactor pressure vessel integrity by preventing fuel melting, the ensuing fuel expulsion, and violent fuel-coolant interaction and generation of pressure pulses. Nevertheless, a revised criterion of 963 J/g (230 cal/g) has been recommended in 1980 (Hollasky et al. 2000; MacDonald et al. 1980) since some tests also indicated that a fuel rod subject to a radial average peak fuel enthalpy of this amount would be severely damaged, lose its original geometry, and impair post-accident cooling. In Japan, the same threshold energy is imposed by the regulatory body to prevent melting, fragmentation, and fuel dispersal (Fuketa et al. 1997), while in France it is 942 J/g (225 cal/g) and 837 J/g (200 cal/g) for fresh and irradiated fuel respectively (Chung and Kassner 1998). A second criterion aims at limiting the radiological consequences of escaped fission products in the event of fuel rod failure and fixed the upper limit for the average fuel enthalpy at 712 J/g (170 cal/g).

More recent tests on pre-irradiated fuel revealed clad failure at enthalpies below 712 J/g in high burnup rods. The prevalent safety criteria have therefore been questioned, and it was realized that they do not account for cladding embrittlement along with gap closure. This has prompted a new series of experiments. To date, a total of 78 RIA tests on high burnup LWR fuel rods, pre-irradiated in commercial reactors, have been carried out in various test reactors, as summarized in  Table 7. The integral tests in pulse reactors provide valuable information about the fuel behavior under RIA conditions. However, they are costly and do not enable the assessment of the effects of particular parameters. To this end, complementary separate-effect tests are made out-of-pile (Cazalis et al. 2005; Kuroda et al. 2001; Le Saux 2008; Le Saux et al. 2008; Link et al. 1998), enabling the development of models. Nevertheless, correct extrapolation of the results and models of out-of-pile tests to in-pile RIA tests is delicate because the test conditions (e.g., sample geometry, deformation rate, and temperature) are not always fully representative.

The prediction of fuel rod failure during a RIA requires the use of a computer code that accounts for the various aspects of the fuel behavior. In order to guarantee acceptable calculation times, however, only simplified models for the clad rupture can be afforded, rather than complex

■ Table 7

Overview of RIA simulation tests in the CANRI, NSRR, IGR, and BIGR reactors

	CABRI	NSRR	IGR	BIGR
Coolant medium	Flowing sodium	Stagnant water	Stagnant water	Stagnant water
Coolant temperature (K)	553	293–358	293	293
Coolant pressure (MPa)	0.2–0.5	0.1	0.1	0.1
Power pulse width (ms)	9–75	4–7	630–850	2–3
Coolant temperature (K)	553	293–358	293	293
Number of tests	13	45	8	12
Burnup (MWd/kgU)	28–77	26–78	47–51	48–61
Clad oxide thickness (μm)	4–100	4–81	≈ 5	≈ 5
Rod active length (mm)	440–570	122–135	150	150
Peak fuel enthalpy (J/g)	340–950	155–660	255–1050	480–790
Lowest failure enthalpy (J/g)	125	251	737	68
Cladding types	Zry-4, ZIRLO, M5	Zry-4, Zry-2, MDA, NDA, ZIRLO, M5	Zr1%Nb	Zr1%Nb

Source: Jankus and Weeks (1972)

mechanistic models. On the basis of the experimental results and main characteristics, several RIA rupture criteria have been proposed and are adopted in fuel performance codes. The models are either based on the rupture strain, or in terms of a rupture strain energy density (SED). The models based on rupture strain postulate clad failure when

$$\varepsilon_{\theta}^p \geq \varepsilon_{\theta}^*(z, t) \dot{\varepsilon}_{\theta}^p(z, t) > 0 \quad (156)$$

where ε_{θ}^p and $\dot{\varepsilon}_{\theta}^p$ represent the radially averaged clad hoop strain and strain rate, respectively. The uniform hoop elongation is often selected for two reasons. Firstly, the largest strains due to PCMI are in the tangential direction. Secondly, the true failure strain is somewhere between uniform elongation and total elongation (includes both uniform and localized strain) at failure. Geelhood et al. (2004) have implemented such a uniform strain-based failure model in the FRAPTRAN code. The empirical correlation was derived from biaxial burst tests in addition to uniaxial tension tests on irradiated Zircaloy, and is a function of the temperature and excess hydrogen in the cladding (i.e., the quantity of hydrogen above the solubility limit). Therefore, they have had to apply a correction factor because of the nonrepresentative stress conditions. They also implemented a new yield stress correlation, whereby the plastic strain hardening component is dependent on both the temperature and the fast neutron fluence (representing irradiation damage) and has been fitted on the basis of the same set of experiments. As a result their failure predictions account for the temperature, the irradiation damage, the strain rate, and the hydrogen content. In a similar manner, Jernkvist (2006) proposed more recently an empirical correlation for ε_{θ}^p for recrystallized Zry-2 and stress-relieved Zry-4 on the basis of

more than 200 out-of-pile mechanical property tests:

$$\varepsilon_{\theta}^* = \frac{3 \cdot \varepsilon_{\theta}^0 \cdot S \cdot f_1 \cdot f_2 \cdot f_3}{f_1 \cdot f_2 + f_1 \cdot f_3 + f_2 \cdot f_3} \quad (157)$$

where ε_{θ}^0 is the plastic strain to failure of as-fabricated cladding at low strain rate, S is a ductility reduction factor for clad tubes with spalled oxide layer, responsible for detrimental effects of a nonuniform hydride distribution, and f_1 , f_2 , and f_3 are ductility reduction factors accounting for elevated strain rate, hydrogen-induced embrittlement, and irradiation damage, respectively. The functions have been fitted to the experimental data and are as follows:

$$\varepsilon_{\theta}^0(T) = 2.82 \times 10^{-2} + 1.22 \times 10^{-4} T \quad (158)$$

$$f_1(\dot{\varepsilon}_{\theta}) = \begin{cases} 1.0 & \dot{\varepsilon}_{\theta} < 8.37 \times 10^{-4} \text{ s}^{-1} \\ 0.046 - 0.031 \log_{10} \dot{\varepsilon}_{\theta} & 8.37 \times 10^{-4} \leq \dot{\varepsilon}_{\theta} \leq 1 \text{ s}^{-1} \\ 0.046 & \dot{\varepsilon}_{\theta} > 1 \text{ s}^{-1} \end{cases} \quad (159)$$

$$f_2(c_{\text{Hex}}, T, \dot{\varepsilon}_{\theta}) = 0.01 + 0.99 e^{-\gamma(T, \dot{\varepsilon}_{\theta}) c_{\text{Hex}}} \quad (160)$$

$$\gamma(T, \dot{\varepsilon}_{\theta}) = 6.52 \times 10^{-4} + 2.21 \times 10^{-3} (6 + \log_{10} \dot{\varepsilon}_{\theta}) \left(1 - \tanh \left(\frac{T - 298}{8.5} \right) \right) \quad (161)$$

$$f_3(\phi) = 0.05 + 0.95 e^{-2.89 \times 10^{-24} \phi} \quad (162)$$

The empirical correlation for the rupture hoop strain is valid for temperatures between 20 and 400°C, deformation rates between 5×10^{-5} and 1 s^{-1} , hydrogen concentrations in the range of 0 and 1941 ppm, and fluences between 0 and $12 \times 10^{25} \text{ n} \cdot \text{m}^{-2}$. Jernkvist (2006) implemented this rupture threshold in the SCANAIR-3.2 code that was originally developed at the IRSN in France. It was verified on the basis of integral tests in the CABRI and NSRR pulse reactors. The comparison with the experimental data indicates that the strain-based criterion is conservative, and that the standard deviation of the relative differences between calculated and measured failure strain obtained with the modified SCANAIR-3.2 code is 0.57. A part of the scatter has been attributed to the deviation of the loading conditions of the out-of-pile tests from those of the in-pile tests (tangential and axial loading nearly equal), which required the application of a correction factor to the measured hoop strains.

Desquines et al. (2005) adopted a more physical-based modeling for defining the rupture strain. More precisely, they applied the concept of elastoplastic failure mechanics, in line with Kuroda et al. (2001), and combined this with a probabilistic model for the defect size and the oxide layer thickness (or average hydrogen content) in order to determine the failure probability as a function of the hoop strain at failure, the oxide layer thickness, the temperature, and the height of the fuel rod (Le Saux 2008). Although they had a lack of experimental data at temperatures above 400°C, they applied the rupture criterion in the SCANAIR code at IRSN.

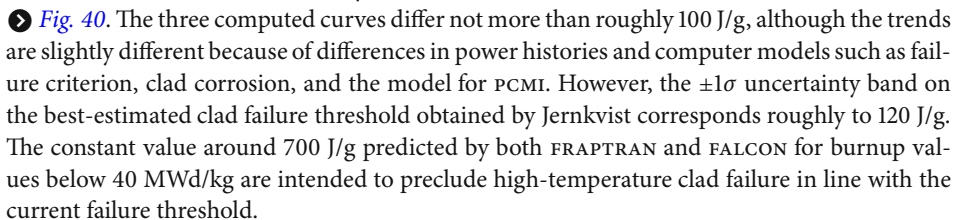
The strain-based failure criterion is conceptually simple, and the correlation can be determined in a rather straightforward manner from total elongation as well as burst strain data. However, these data are not true material properties, and attention must be paid to the impact of the specimen geometry and load biaxiality. Furthermore, the strain-based failure criterion depends on the mechanical loading and temperature history prior to failure. As an alternative, a critical strain energy density (CSED) has been proposed by Rashid et al. (2001) and implemented

in the FALCON code. The measure for the clad to resist failure is formulated as the total mechanical energy (elastic + plastic) per unit volume that can be absorbed by the material before it can fail. The threshold value for SED is derived from the experimental stress-strain curves and is expressed as a function of the fast neutron fluence, temperature, hydrogen concentration, and material type, or alternatively the oxide thickness. A correction factor was applied to account for deviations from the biaxiality of stress during the tests, and it should be underlined that the tests were limited in terms of strain rate ($7 \times 10^{-5} \text{ s}^{-1}$ instead of $1\text{--}5 \text{ s}^{-1}$ for RIA). A similar approach was adopted by Bernaudat and Pupier (2005) and Leclercq et al. (2008) for application in the SCANAIR code applied by EdF, although the CSED limit is expressed as a function of the oxide thickness or the average burnup:

$$\begin{aligned} \text{CSED} &= 95.17 - 4.7653 \cdot \text{OX} + 8.759 \cdot \text{OX}^2 - 5.56 \times 10^{-4} \text{OX}^3 & (163) \\ \text{if } \text{OX} &< 54 \text{ } \mu\text{m} \\ \text{CSED} &= 5.3 \text{ otherwise} \end{aligned}$$

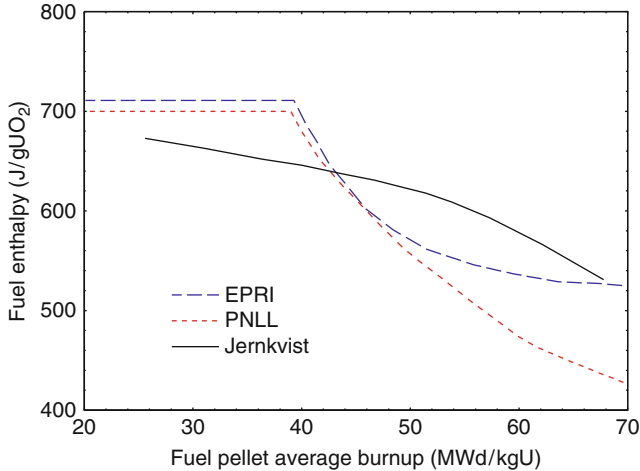
where OX is the oxide thickness in micrometer and CSED is expressed in MPa. The conversion of the oxide thickness in average fuel burnup depends on the material under consideration. Nevertheless, Bernaudat et al. concluded that the correlation derived for Zircaloy-4 could be (conservatively) applied to ZIRLOtm and M5tm.

Nevertheless, the strain energy density is not as easily measured in mechanical property tests as the plastic strain to failure, and direct measurements of this quantity are seldom made. In addition, the derivation of the SED from the (nonrepresentative) experiments relies on a constitutive relation for the material, and is also sensitive to the load and temperature history. There is thus no obvious benefit in using the critical SED instead of a critical strain in clad failure criteria for RIA (Jernkvist 2006).

In order to compare the rupture hoop strain or critical SED with the criteria currently adopted on the basis of the in-pile tests, they must be expressed in terms of maximum enthalpy (or enthalpy increase) in the fuel versus rod average burnup. The conversion requires the implementation in a fuel performance code such as the SCANAIR (Bernaudat and Pupier 2005; Jernkvist 2006) of FALCON code (Rashid et al. 2001), as well as fixing a fuel design and an irradiation history. At various burnup values, a RIA is then simulated by means of the fuel performance code in order to determine the peak enthalpy leading to the failure. Jernkvist (2006) compared the calculated clad failure thresholds for a hot zero power (HZP) rod ejection accident in a PWR obtained by means of the three above-mentioned codes, as shown in  Fig. 40. The three computed curves differ not more than roughly 100 J/g, although the trends are slightly different because of differences in power histories and computer models such as failure criterion, clad corrosion, and the model for PCMI. However, the $\pm 1\sigma$ uncertainty band on the best-estimated clad failure threshold obtained by Jernkvist corresponds roughly to 120 J/g. The constant value around 700 J/g predicted by both FRAPTRAN and FALCON for burnup values below 40 MWd/kg are intended to preclude high-temperature clad failure in line with the current failure threshold.

Because of the above-mentioned limitations and scatter, Vitanza (2006) proposed an empirical model on the basis of the most representative integral tests. The limit is expressed directly in terms of the enthalpy as inferred from the experiments:

$$H_F = \left[200 \frac{25 + 10D}{bu} + 0.3\delta\tau \right] \left(1 - \frac{0.85\text{OX}}{W} \right)^2 - H_0 \quad (164)$$



■ Figure 40

Comparison of calculated clad failure thresholds for PWR hot zero power (HZP) rod ejection accident (Jernkvist 2006)

where H_F is the failure enthalpy in cal/g (if $H_F > 200$, set $H_F = 200$), bu is the burnup in MWd/kg (if $bu > 60$ set $bu = 60$), W is the cladding thickness, as-fabricated, in μm , $\delta\tau$ is the RIA pulse width (if $\delta\tau > 75$ ms, set $\delta\tau = 75$), ms. $H_0 = 0$ for the hot zero power (HZP) and $H_0 = 18(1-D)$ cal/g for the cold zero power (CZP) case. $D = 0$ (brittle) for spalled oxide and when $OX \geq 25\mu\text{m}$ for Zr-2 and Zr-4 and cold conditions and $OX \geq 45\mu\text{m}$ for advanced PWR cladding and cold conditions. $D = 1$ (ductile) for remaining conditions (Vitanza 2007). The term in the right-hand side that depends on the oxide thickness is similar to the function proposed by Chung et al. (1998). When comparing the values with those shown in ► Fig. 40 for low burnup fuel, it is evident that the fuel performance codes provide conservative estimations. Jernkvist attributed this to the penalizing choice of the accident scenarios: a Gaussian pulse shape and a low pulse width as well as an axial peak power chosen at the highest clad oxidation level.

As burnup progresses beyond 55–60 MWd/kg, the experimental data show no evidence of additional cladding strain enhancement (Bernaudat and Pupier 2005; Vitanza 2006; Vitanza and Conde Lopez 2005). This is why the burnup effect in Eq. (164) is limited up to 60 MWd/kg as shown in ► Fig. 41, which is in line with the burnup limit applied by Bernaudat and Pupier (2005). ► Figure 41 shows the predicted failure enthalpy versus burnup obtained for two PWR cases with respectively high and low corrosion. As one can observe, corrosion has a much more pronounced effect for a CZP than for a HZP RIA. This is because corroded cladding is brittle at low temperature (as low as room temperature), whereas it can retain ductility under hot conditions (unless oxide spalling prevails).

The effect of the cladding oxidation is also revealed in ► Fig. 42, which successfully compares the measured and the calculated failure enthalpy for the NSRR PWR tests that resulted in fuel failure. It should be pointed out, that while Eq. (164), predicts a significant impact of corrosion for CZP conditions, the corrosion effect under hot conditions is predicted to be much less pronounced (for non-spalled cladding). Furthermore, Eq. (164) also reflects the observation that corrosion and burnup act in synergy with each other, in that the burnup

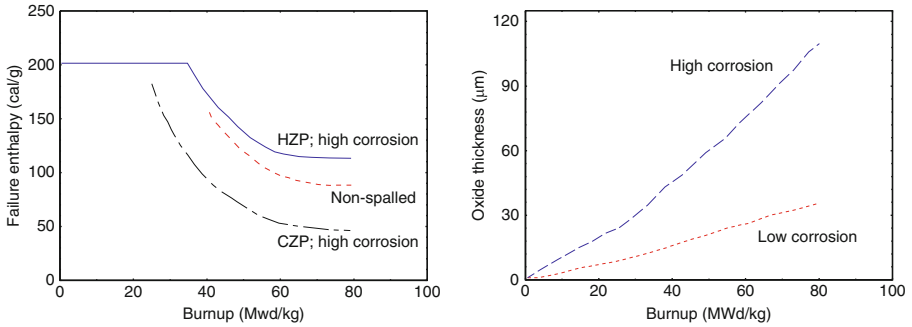


Figure 41
 Calculated failure enthalpy vs. burnup for two PWR instances, respectively with high and low corrosion, the latter for advanced cladding (left) and the corresponding corrosion buildup for the two instances (right). The predicted corrosion effect is very large for CZP conditions and moderate for hzp (with non-spalled fuel cladding)

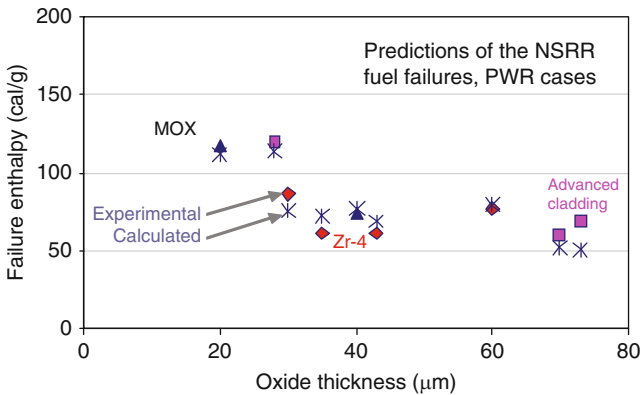
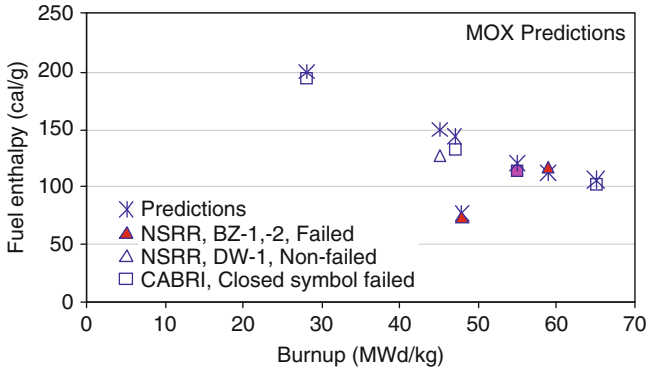


Figure 42
 Calculated and measured failure enthalpy vs. oxide thickness for NSRR PWR tests with PWR fuel

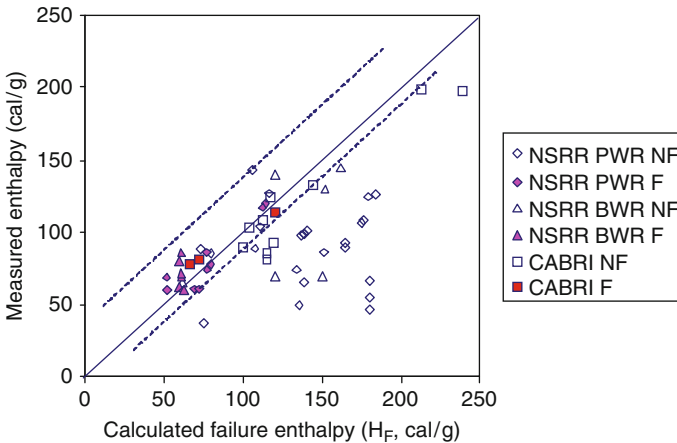
effects become stronger when corrosion is high and corrosion effects become more important when the burnup is high. Thus, expressing the RIA failure limit only in terms of burnup or only in terms of corrosion oxide thickness represents, according to this model, an oversimplification.

The experimental threshold versus burnup for all NSRR and CABRI MOX fuel are plotted in **Fig. 43** and compared with the prediction on the basis of (164). The predictions follow the data very closely. The figure also shows that the failures of MOX fuel can be well predicted by the same failure threshold correlation used for UO₂ fuel, leading to the conclusion that a different treatment of MOX as compared with UO₂ fuel is not needed, at least for what failure threshold is concerned. This, however, does not exclude that other aspects could differ, for instance in relation to the post-failure behavior of the two types of fuel (Koo et al. 1997; Sasajima et al.



■ Figure 43

Calculated failure enthalpy and measured enthalpy for the MOX fuel tests performed in nsrr and CABRI



■ Figure 44

Calculated failure enthalpy on the basis of (164) versus measured fuel enthalpy

2000). More data are therefore required for the MOX behavior under RIA conditions before drawing definite conclusions. The same holds for Gd-doped UO_2 , for which data are scarce. Jernkvist (2006) mentioned tests in the NSRR on fresh fuel rods with Gd_2O_3 additions, where the observed failure threshold and failure behavior were not notably different from those of fresh UO_2 .

When comparing the failure enthalpy predictions of Vitanza with the experimental data in Fig. 44 it can be concluded that the predictions are satisfactory in that 85% of the non-failure data are below the median line and 85% of failures cases are along or above the median line. In addition to the median best-estimate prediction, Vitanza therefore proposed an empirical failure probability defined as a function of the distance from the best-estimate threshold, that

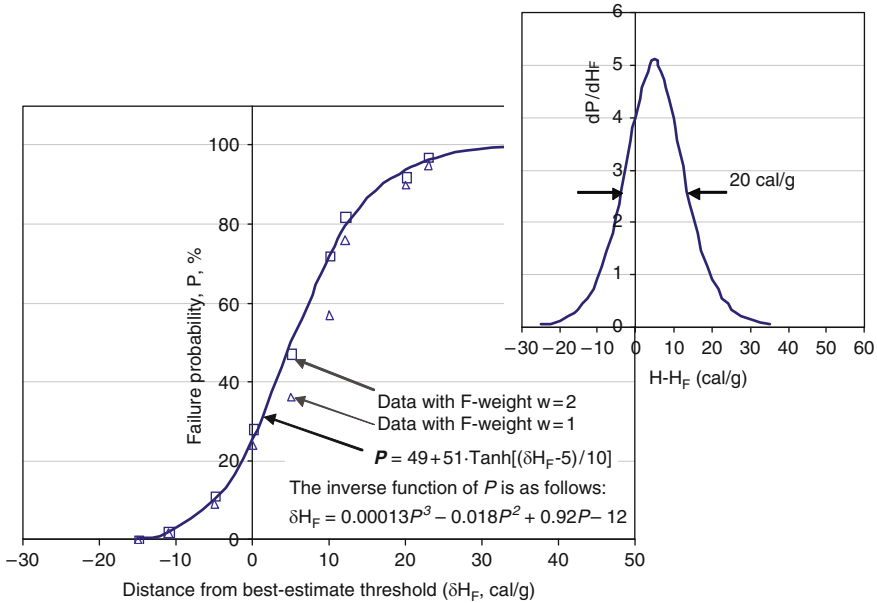


Figure 45

Probability distribution as function of distance from the best-estimate failure threshold, inferred from the prediction distribution shown in the previous figure and calculated with (165). The calculated points are obtained with two different weight factors for failure data. The solid line represents a rendition of the calculated probabilities. The diagram on the upper right side is the probability density obtained by deriving the probability function shown in the main figure

is, for and line parallel to the median line and distant from it by a certain amount δH_F :

$$P = 100N_{F \leq} / [N_{F \leq} + N_{>}] \quad (165)$$

where $N_{F \leq}$ is the number of failure data points that are below or along a given parallel line drawn at a certain distance from the median line of Fig. 44, and $N_{>}$ is the total number of data points (failed and non-failed) that are above such a line. By definition, the zero probability corresponds to the lowest failed data point, while 100% probability corresponds to the uppermost data point, as indicated by the dotted lines in Fig. 44. By applying (165) to the data in Fig. 44, the failure probability has been calculated as a function of distance from the best-estimate failure threshold. The result is shown in Fig. 45.

The same approach could be extended with weighting factors for the non-failure and failure data, or applied with a different best-estimate model when more data become available. The increasing amount of data is likely to reduce the uncertainty, but it should be underlined that the calculated thresholds for clad failure as well as for incipient melting are well above the enthalpy levels anticipated in high burnup fuel. Three-dimensional core kinetics analyses generally show that the peak radial average enthalpy is below 418 J/g (100 cal/g) in high burnup fuel.

7 Uncertainty Analysis

In general, uncertainties to be considered in fuel performance analysis may be grouped into three categories. The first category deals with prescribed quantities. The fuel rod performance code requires as input the fuel fabrication parameters (e.g., rod geometry, composition) and irradiation parameters (e.g., reactor type, coolant conditions, and irradiation history). The second category of uncertainties is the material properties, such as the fuel thermal conductivity or the fission gas diffusion coefficients. The third and last category of uncertainties is the so-called model uncertainties. A good example of such an uncertainty is the plain strain assumption in the axial direction (intuitively, it is clear that for a detailed analysis of pellet-cladding interaction, two- or three-dimensional models are indispensable). In order to assess the technological effect of all sources of uncertainties there are various techniques that may be considered.

First of all, there are various so-called sensitivity methodologies, ranging from multiple runs with input data or model parameters being varied, up to a rigorous mathematical treatment based on perturbation theory. Apart from the numerical noise technique, which is included in the TRANSURANUS code for example, perturbation theory has never been applied to fuel rod modeling, probably because the mathematical effort would be too great to formulate all the nonlinear phenomena in the form of basic differential equations. The numerical noise analysis allows the estimation of the standard deviation for instance of the center line temperature within just one run. For this purpose, the most important parameters of the fuel rod (e.g., q' and λ) are varied slightly on a random basis in an interval, which is similar to introducing numerical noise. These changes of model parameters result in modifications of the resulting quantities, which enables the analysis of the sensitivity of the code with respect to its parameters. The computational effort is therefore identical with that of a deterministic run, but there is no information available about the effect between various uncertain parameters. Furthermore, changes of parameters may only produce modifications in the results that are smaller than the numerical accuracy. This can be overcome with an increased accuracy through a compiler option, along with an appropriate adaptation of the convergence limits.

A second category of probabilistic approaches is the response surface technique. This is based on a careful combination of parameters called the experimental design, such as the Latin hypercube sampling or the Taguchi design. Peck (1980) tried this with the FRAP code. The main problem is that one has to decide in advance which parameter should be selected and how fine the variation of each parameter should be.

Finally, the Monte Carlo method is based on random sampling of all variables that are considered. It seems most attractive in view of its simplicity, but it entails high computational costs (increase by a factor 100–500), the knowledge about the distributions of the variables is rather limited, and it is unclear how much each parameter uncertainty contributes to the variation of the outcome. In order to reduce the computational costs, quasi-Monte Carlo methods may be applied. Instead of random sampling, quasi-random sampling sequences are recommended, which fill the space more uniformly than uncorrelated random numbers. They may be considered as a combination of the variations of parameters in response surface techniques with its experimental design and the standard Monte Carlo technique.

Despite the restrictions, applying a limited variation of some fabrication variable parameters in fuel rod performance calculations is being considered in several countries for two reasons. First of all, it is argued (Heins et al. 1991) that probabilistic calculations can replace a deterministic calculation with superimposed unfavorable tolerance limits on some fabrication

parameters (worst-case data set) in fuel design calculations. The results obtained with the deterministic worst-case calculation are said to be very conservative, with a degree of conservatism that would be difficult to quantify. Probabilistic calculations based on distributions on the other hand would allow the replacement of the worst-case data set by a data set leading to results with a known, defined conservatism. The industry, of course, would like to reduce the margins in this way. Secondly, it has been observed that in some cases the deterministic conservative approach did in fact not predict the worst fuel performance as in a probabilistic approach. This of course, depends on the proper definition of the worst case on one hand, and on the limits of variation of the variable parameters in the Monte Carlo approach on the other hand.

8 Outlook

In this chapter the main models have been outlined that are used for the simulation of the in-pile behavior of traditional pellet-in-clad nuclear oxide fuel and implemented in fuel performance codes. Most of these models contain semiempirical correlations that are valid within the confines of the parameters and irradiation conditions covered in the database used for their development and validation. Extrapolating the models beyond their range of validation is not appropriate, and would require extending the database with the corresponding experimental data, generally obtained from in-pile irradiations of real-scale fuel rods or elements. Because this approach of incremental design through experiments, their (semi)empirical interpretation or description, and validation is time consuming, expensive, and allows only limited progress, a more science-based approach is nowadays advocated. Although this so-called *multi-scale* approach is mainly addressing new fuel types (Stan 2009), the much larger amount of experimental data for conventional fuel enables the establishment and verification of this new approach and it can also help to strengthen the scientific basis for traditional oxide fuel.

Multi-scale here refers to the complex interrelationships of the processes taking place in irradiated material at the various scales of length and time, and the challenge is unraveling them to obtain a fundamental understanding of the basic underlying mechanisms. The multi-scale approach is hierarchical, based on passing information or parameters from the atomic scale up to structural length and time scales. A close coupling of experiments and computations is needed to achieve this goal. In particular the advances in computational sciences are a strong driving force since both software and hardware development allow nowadays reliable computations by means of quantum mechanical and molecular dynamic techniques at the atomistic scale and by phase field simulation, dislocation dynamics, or thermodynamics techniques at the mesoscale and continuum level. But also the advances in experimental sciences using spectroscopic techniques such as those offered by current generation synchrotron sources among others, also allow probing materials at atomistic scale, and eventually in situ.

The need for traditional fuel performance codes will, however, remain, particularly for calculating integral effects at the scale of the fuel rod, fuel element, or reactor core. Of course advances can be expected by integrating improved correlations and models resulting from the multi-scale approach into the codes. Relevant advances can also be expected from the transition from one-dimensional/two-dimensional to three-dimensional modeling using finite element solvers, as has been demonstrated for modeling of pellet-cladding interaction (Michel et al. 2010). Significant improvement in the analysis of reactor fuel rod behavior can therefore be expected in the coming decade.

Acknowledgment

The authors wish to thank D. Staicu (Institute for Transuranium Elements) for fruitful discussions, W. Goll (AREVA NP) and Nathalie Dupin (Calcul Thermo) for providing some of the figures and J. van der Laar for help for the preparation of some of the figures.

References

- Abeles B (1963) Lattice thermal conductivity of disordered semiconductor alloys at high temperatures. *Phys Rev* 131:1906–1911
- Adamson MG, Aitken EA, Caputi RW (1985) Experimental and thermodynamic evaluation of the melting behavior of irradiated oxide fuels. *J Nucl Mater* 130:349–365
- Ainscough JB, Oldfield BW, Ware JO (1973/1974) Isothermal grain growth kinetics in sintered UO_2 pellets. *J Nucl Mater* 49:117–128
- Aitken EA, Evans SK (1968) A thermodynamic data program involving plutonium and uranium. Tech. Rep. USAEC GEAP-5672, General Electric
- Ambegaokar V (1959) Thermal resistance due to isotopes at high temperatures. *Phys Rev* 114:488–489
- Anderson TL (1995) Fracture mechanics – fundamentals and applications, 2nd edn. CRC Press
- Assmann H (1982) Überblick über Zusammenhänge zwischen LWR-brennstoffeigenschaften und verfahrensabläufen bei der Brennstoffproduktion. *J Nucl Mater* 106:15–34
- Assmann H, Stehle H (1978) Thermal and in-reactor densification of UO_2 : mechanisms and experimental results *Nucl Eng Des* 48:49–67
- Bailly H, Ménessier D, Prunier C (1999) The nuclear fuel of pressurized water reactors and fast neutron reactors. Lavoisier
- Baker L, Just LC (1962) Studies of metal-water reactions at high temperatures; III. Experimental and theoretical studies of the zirconium-water reaction. Tech. Rep. ANL-6548, Argonne National Laboratory
- Barner J, Gunningham MD, Freshley DD, Lanning D (1990) Relationship between microstructure and fission gas release in high burnup UO_2 fuel with emphasis on the rim region, International Topical Meeting on LWR Fuel Performance, ANS/ENS, 21-24 April 1991, Avignon, France, Proceedings, pp 538–548
- Barney W, Wemble B (1958) Metallography of UO_2 -containing fuel elements. Tech. Rep. KAPL-1836
- Baron D (1986) Porosity Buildup in the Fuel Periphery at High Burnup. HBEP steering committee meeting
- Baron D (1998) A fuel thermal conductivity correlation based on the latest experimental results. In: Proceedings of the seminar on thermal performance of high burn-up LWR fuel. Cadarache, France, pp 129–143
- Baron D, Masson R, Gatt J, Spino J, Laux D (2005) Evolution of the nuclear fuel mechanical properties with burn-up. An extensive European experimental program. In: Proceedings of the international topical meeting on LWR fuel performance, Track 2, Paper 1040. Kyoto, Japan
- Bates JL (1970) Melting point of irradiated uranium dioxide. *J Nucl Mater* 36:234–236
- Beals RJ, Handwerk JH, Wrona BJ (1969) Behavior of uranium-rare-earth oxides at high temperatures. *J Am Ceram Soc* 52:578–581
- Beauvy M (1992) Nonideality of the solid solution in (U, Pu) O_2 nuclear fuels. *J Nucl Mater* 188:232–238
- Belle J (1961) Uranium dioxide: properties and nuclear applications. Naval reactor handbooks. US Atomic Energy Commission
- Berna GA, Beyer CE, Davis KL, Lanning DD (1997) *Frapcon-3: a computer code for the calculation of steady-state, thermal-mechanical behavior of oxide fuel rods for high burnup*, report NUREG/CR-6534-v2, (PNNL-11513-v2), December 1997
- Bernaudoat C, Pupier P (2005) A new analytical approach to study the rod ejection accident in PWRs. In: Proceedings of the international topical meeting on light water reactor fuel performance. Kyoto, Japan, pp 602–614
- Bibilashvily Y, Medvedev A, Khostov G, Bogatyr S, Korystine L (2000) Development of the fission gas behavior model in the START-3 code and its experimental support. In: Proceedings of the international seminar on fission gas behaviour in water reactor fuels. Cadarache, France

- Billaux M (2005) High burnup fuel for LWRs: fuel performance, limits, operational and safety Issues. The 2005 Frédéric Joliot and Otto Hahn Summerschool. Karlsruhe, Germany
- Billone M et al (2008) Cladding embrittlement during postulated loss-of-coolant accidents. Tech. Rep. NUREG /CR-6967
- Blank H, Matzke H (1973) The effect of fission spikes on fission gas re-solution. *Radiat Eff* 17:57–64
- Booth AH (1957) A method of calculating fission gas diffusion from UO_2 fuel and its application to the x-2-f loop test. Tech. Rep. CRDC-721, AECL, Chalk River, Ontario, Canada
- Booth AH (1957) A suggested method for calculating the diffusion of radioactive rare gas fission products from UO_2 elements and a discussion of proposed in-reactor experiments that may be used to test its validity. Tech. Rep. DCI-27, AECL, Chalk River, Ontario, Canada
- Bossis P, Pêcheur D, Hanifi K, Thomazet J, Blat M (2006) Comparison of the high burn-up corrosion on M5 and low tin Zircaloy-4. *ASTM Int* 3, DOI:10.1520/JAI12,404
- Carbajo JJ, Yoder GL, Popov SG, Ivanov VK (2001) A review of the thermophysical properties of MOX and UO_2 fuels. *J Nucl Mater* 299:181–198
- Cathcart JV, Powel RE et al (1977) Zirconium metal-water oxidation kinetics, w. reaction rate studies. Tech. Rep. ORNLINUREG-17, Oak Ridge National Laboratory
- Cazalis B, Bernaudat C, Yvon P, Desquines J, Poussard C, Averty X (2005) The PROMETRA program: a reliable material database for highly irradiated Zircaloy-4, ZIRLOTM and M5TM fuel cladding. In: Proceedings of the 18th international conference on structural mechanics in reactor technology (SMiRT 18), no. C02-1 in SMiRT
- Chadwick MB, Oblozinsky P, Herman M et al (2006) ENDF/B-VII.0: Next generation evaluated nuclear data library for nuclear science and technology. *Nucl Data Sheets* 107: 2931–3060
- Christensen JA (1962) Irradiation effects on uranium dioxide melting Tech. Rep. Report HW-69234, Hanford, California
- Christensen JA, Allio RJ, Biancheria A (1964) Uranium dioxide thermal conductivity. *Trans Am Nucl Soc* 7:390–391
- Chung H (2005) Fuel behavior under loss-of-coolant accident situations. *Nucl Eng Technol* 37: 327–362
- Chung H, Kassner T (1998) Cladding metallurgy and fracture behavior during reactivity-initiated accidents at high burnup. *Nucl Eng Des* 186: 411–427
- Cox B (1990) Pellet-clad interaction (PCI) failures of zirconium alloy fuel cladding a review. *J Nucl Mater* 172:249–292
- Cozzo C, Staicu D, Pagliosa G, Papaioannou D, Rondinella V, Konings RJM, Walker C, Barker M, Herve PJ (2010) Thermal diffusivity of homogeneous SBR MOX fuel with a burn-up of 35 MWd/kgHM. *J Nucl Mater*, doi:10.1016/j.jnucmat.2010.03.006
- Croff AG, Bjerke MA, Morrison GW, Petrie LM (1978) Revised uranium-plutonium cycle pwr and bwr models for the ORIGEN computer code. Tech. Rep. ORNL/TM-6051, Oak Ridge National Laboratory
- Cunningham M, Feshley M, Lanning D (1992) Development and characteristics of the rim region in high burnup UO_2 fuel pellets. *J Nucl Mater* 188:19–27
- Cunningham ME, Beyer CE, Medvedev PG, Berna GA, Scott H (2001) Fraptan: a computer code for the transient analysis of oxide fuel rods, NUREG/CR-6739, vol 1, PNNL-13576
- Delafoy C, Dewes P, Miles T (2007) AREVA NP Cr_2O_3 -doped fuel development for BWRs. In: Proceedings of the 2007 international LWR fuel performance meeting, Paper 1071. San Francisco, California
- Desquines J, Cazalis B, Bernaudat C, Poussard C, Averty X, Yvon P (2005) Mechanical properties of Zircaloy-4 PWR fuel cladding with burnup 54–64 MWd/kgU and implications for RIA behavior. In: Proceedings of the 14th international symposium on zirconium in the nuclear industry, ASTM STP 1467, pp 851–872
- Dupin N, Ansara I, Servant C, Toffolond C, Lemaignanc C, Brachet JC (1999) A thermodynamic database for zirconium alloys. *J Nucl Mater* 275: 287–295
- Duriez C, Alessandri JP, Gervais T, Philipponneau Y (2000) Thermal conductivity of hypostoichiometric low Pu content $(\text{U,Pu})\text{O}_{2-x}$ mixed oxide. *J Nucl Mater* 277:143–158
- Federici E, Lamare F, Bessiron V, Papin J (2001) The SCANAIR code version 3.2: main features and status of qualification. In: Proceedings of the technical committee meeting on fuel behaviour under transient and LOCA conditions, TECDOC-1320. IAEA, pp 88–101
- Fink JK (2000) Thermophysical properties of uranium dioxide. *J Nucl Mater* 279:1–18
- Fischer U, Wiese HW (1983) Verbesserte konsistente berechnung des nuklearen inventars abge brannter dwr-brennstoffe auf der basis des zell-abbrand-verfahrens mit korigen. Tech. Rep. KfK-3014, Kernforschungszentrum Karlsruhe

- Forgeron T, Brachet JC, Barcelo F, Castaing A, Hivroz J, Mardon J, Bernaudat C (2000) Experiment and modeling of advanced fuel rod cladding behavior under LOCA conditions: alpha-beta phase transformation kinetics and EDGAR methodology ASTM STP 1354, pp 256–279
- Forsberg K, Massih AR (2001) Theory of fission gas release in a growing grain 16th International Conference on Structural Mechanics in Reactor Technology (SMIRT-16), Washington DC, USA, 12–17 August 2001
- Fuketa T, Sasajima H, Mori Y, Ishijima K (1997) Fuel failure and fission gas release in high burnup PWR fuels under RIA conditions. *J Nucl Mater* 248:249–256
- Fukushima S, Ohmichi T, Handa M (1986) The effect of rare earths on thermal conductivity of uranium, plutonium and their mixed oxide fuels. *J Less-Common Met* 121:631–639
- Garcia P, Struzik C, Agard M, Louche V (2002) Monodimensional mechanical modelling of fuel rods under normal and off-normal operating conditions. *Nucl Eng Des* 216:183–201
- Garner N, Rentmeister T, Lippert HJ, Mollard P (2007) Upgraded fuel assemblies for BWRs. In: Proceedings of the 2007 international LWR fuel performance meeting, Paper 1091. San Francisco, California
- Geelhood KJ, Beyer CE, Cunningham ME (2004) Modifications to Fraptran to predict fuel rod failures due to PCMI during RIA-type accidents. In: Proceedings of the 2004 international meeting on LWR fuel performance, Paper 1097. Orlando, Florida, pp 585–595
- Gibby RL (1971) The effect of plutonium content on the thermal conductivity of (U, Pu)O₂ solid solutions *J Nucl Mater* 38:163–177
- Grimes RW, Catlow CRA (1991) The stability of fission products in uranium dioxide. *Phil Trans R Soc London A* 335:609–634
- Gyori C, Hózer Z, Lassmann K, Schubert A, van de Laar J, Cvan M, Hatala B (2003) In: EU Research in Reactor Safety, Conclusion Symposium on Shared-Cost and Concerted Actions (FISA-2003), Proceedings EUR 21026, Luxembourg, November 10–13, 2003, pp 584–589
- Hagman DL, Reyman GA (1979) MATPRO version 11-A, Handbook of materials properties for use in the analysis of light water reactor fuel rod behavior, 3rd edn. TRENUREC-1280, Advanced Inorganic Chemistry
- Hanley HJM (1973) The viscosity and thermal conductivity coefficients of dilute argon, krypton, and xenon. *J Phys Chem Ref Data* 2: 619–642
- Harbottle JE, Kennard MW, Sunderland DJ, Strasser AA (1994) The behaviour of defective BWR barrier and non-barrier fuel. In: Proceedings of the international topical meeting on LWR fuel performance. West Palm Beach, Florida, April 17–21
- Harding J, Martin D (1989) A recommendation for the thermal conductivity of UO₂. *J Nucl Mater* 166:223–226
- Haüssinger P, Glatthaar R, Rhode W, Kick H, Benkmann C, Weber J, Wunschel HJ, Stenke V, Leicht E, Stenger H, Groll G (1991) Noble gases. In: Ullmann's encyclopedia of industrial chemistry. VCH Verlagsgesellschaft AG, Weinheim, pp 485–540
- Heins L, Groß H, Nissen K, Wunderlich F (1991) Statistical analysis of QC data and estimation of fuel rod behavior. *J Nucl Mater* 178:287–295
- Hermann A, Yagnik S, Gavillet D (2007) Effect of local hydride accumulations on Zircaloy cladding mechanical properties. In: 15th international symposium on zirconium in the nuclear industry. Sunriver, Oregon
- Hiernaut JP, Hyland GJ, Ronchi C (1993) Premelting transition in uranium dioxide. *Int J Thermophys* 14:259–283
- Higgs JD, Lewis BJ, Thompson WT, He Z (2007) A conceptual model for the fuel oxidation of defective fuel. *J Nucl Mater* 366:99–128
- Hoffmann PB, Dewes P (2004) Post-irradiation examination and ramp testing of fuel rods with Fe-enhanced Zr liner cladding at high burnup. In: Proceedings of the 2004 international meeting on LWR fuel performance, Paper 1059. Orlando, Florida
- Hollasky N, Valtonen K, Hache G, Gross H, Bakker K, Recio M, Bart G, Zimmermann M, van Duisboerg W, Killeen J, Meyer R (2000) Fuel safety criteria technical review. Tech. Rep. NEA/CSNI/R(99)25, Nuclear Energy Agency, Committee on the safety of nuclear installations
- Hoppe N (1980) Improvements to Cometh III-j fuel rod modelling code. *Nucl Eng Des* 56:123–133
- IAEA (1995) Characteristics and use of uranium-gadolinia fuels. Tech. Rep. IAEA-TECDOC-844, International Atomic Energy Agency
- IAEA (1997) Thermophysical properties of materials for light water reactors. Tech. Rep. IAEA-TECDOC-949
- IAEA (2006) Thermophysical properties database of materials for light water reactors and heavy water reactors. Tech. Rep. IAEA-TECDOC-1496
- Ishimoto S, Hirai M, Ito K, Korei Y (1994) Effects of soluble fission products on thermal conductivities of nuclear fuel pellets. *J Nucl Sci Technol* 31:796–802

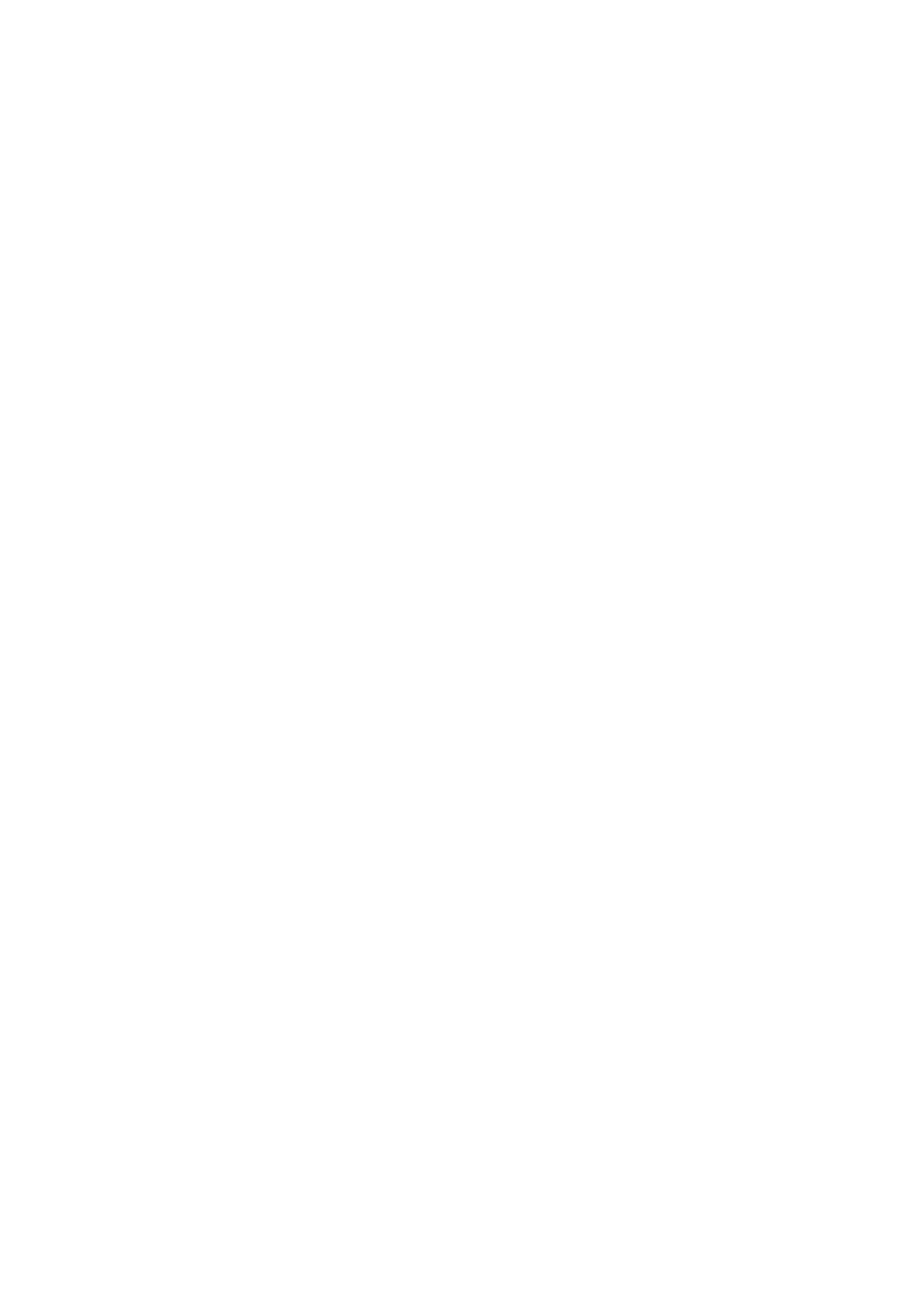
- Jackson PA, Turnbull JA, White RJ (1990) Enigma fuel performance code. *Nucl Energy* 29:107-114
- Jankus VZ, Weeks RW (1972) LIFE-II — A computer analysis of fast-reactor fuel-element behavior as a function of reactor operating history. *Nucl Eng Des* 18:83-96
- Jerlerud Pérez R, Massih AR (2007) Thermodynamic evaluation of the Nb-O-Zr system. *J Nucl Mater* 360:242-254
- Jernkvist L (2006) Computational assessment of burnup-dependent fuel failure thresholds for reactivity initiated accidents. *J Nucl Sci Technol* 43:546-561
- Kaji Y, Tsuru T (2008) Investigation of model for stress corrosion cracking of cladding materials. In: *Proceedings of the 7th international workshop materials modelling and simulations or nuclear fuel MMSNF 7*, EUR 23556 EN. Karlsruhe, Germany
- Kamemaya T, Matsumura T, Kinoshita M (1994) Numerical analysis for microstructure change of a light water reactor fuel pellet at high burnup. *Nucl Technol* 106:334-341
- Kang KW, Yang JH, Kim JH, Rhee YW, Kim DJ, Kim KS, Song KW (2007) The solidus and liquidus temperatures of $\text{UO}_2\text{-Gd}_2\text{O}_3$ and $\text{UO}_2\text{-Er}_2\text{O}_3$ fuels. *Thermochim Acta* 455:134-137
- Karlsson J, Lysell G, Pettersson H, Rönnerberg G (2004) In-pile testing of liner-cladding and pellet performance in failed fuel rods. In: *Proceedings of the international topical meeting on LWR fuel performance*, Paper 1046. Orlando, Florida
- Kato M, Morimoto K, Sugata H, Konashi K, Kashimura M, Abe T (2008) Solidus and liquidus temperatures in the $\text{UO}_2\text{-PuO}_2$ system. *J Nucl Mater* 373:237-245
- Killeen J, Turnbull J, Sartori E (2007) Fuel modelling at extended burnup: IAEA coordinated research project FUMEX-II. In: *Proceedings of the 2007 international LWR fuel performance meeting*, paper 1102. San Francisco, California, pp 261-273
- Kinoshita M, Sonoda T, Kitajima S, Kolstad E, Matzke H, Rondinella V, Stalios A, Walker C, Ray I, Sheindlin M, Halton D, Ronchi C (2000) High burn-up rim project, (ii) irradiation and examination to investigate rim-structured fuel. In: *Proceedings of the international topical meeting on LWR fuel performance*. Park City, Utah
- Kogai T (1997) Modelling of fission gas release and gaseous swelling of light water reactor fuels. *J Nucl Mater* 244:131-140
- Koo YH, Sohn DS, Volkov B (1997) A comparative analysis of UO_2 and MOX fuel behaviour under reactivity initiated accident conditions. *Ann Nucl Energy* 24:859-870
- Koo YH, Sohn DS, Yoon YK (1994) An analysis method for the fuel rod gap inventory of unstable fission products during steady-state operation. *J Nucl Mater* 209:62-78
- Kreyens P, Spahr G, McCauley J (1976) An analysis of iodine stress corrosion cracking of Zircaloy-4 tubing. *J Nucl Mater* 61:203-212
- Kurchatov SY, Likhanskii VV, Sorokin AA, Khoruzhii OV (2002) RTOP-code simulation of the radial distribution of heat release and plutonium isotope accumulation in high burnup oxide fuel. *Atom Energy* 92:349-356
- Kuroda M, Yamanaka S, Nagase F, Uetsuka H (2001) Analysis of the fracture behavior of hydrided fuel cladding by fracture mechanics. *Nucl Eng Des* 203:185-194
- Lassmann K (1980) The structure of fuel element codes. *Nucl Eng Des* 57:17-39
- Lassmann K (1992) TRANSURANUS: a fuel rod analysis code ready for use. *J Nucl Mater* 188:295-302
- Lassmann K, Benk H (2000) Numerical algorithms for intragranular fission gas release. *J Nucl Mater* 280: 127-135
- Lassmann K, Hohlefeld F (1987) The revised URGAP model to describe the gap conductance between fuel and cladding. *Nucl Eng Des* 103:215-221
- Lassmann K, O'Carroll C, van de Laar J, Walker CT (1994) The radial distribution of plutonium in high burnup UO_2 fuels. *J Nucl Mater* 208: 223-231
- Lassmann K, Schubert A, van de Laar J, Venix C (2000) Recent developments of the TRANSURANUS code with emphasis on high burnup phenomena. In: *Proceedings of the IAEA technical committee meeting on nuclear fuel behaviour modelling at high burnup*, IAEA-TECDOC-1233. Windermere, UK, pp 387-406
- Lassmann K, Schubert A, Van Uffelen P, van de Laar J (2005) TRANSURANUS Handbook v1mlj09 (2009), European Commission, Joint Research Centre, Institute for Transuranium Elements, Karlsruhe, Germany
- Lassmann K, Van Uffelen P (2004) The structure of fuel rod codes. *Tech. Rep. EUR 21400 EN*, JRC Publications, European Commission
- Lassmann K, Walker CT, van de Laar J (1998) Extension of the TRANSURANUS burnup model to heavy water reactor conditions. *J Nucl Mater* 255: 222-233
- Le Saux M (2008) Comportement et rupture de gaines en Zircaloy-4 détendu vierges, hydrurées ou irradiées en situation accidentelle de type RIA. Ph.D. thesis, Ecole National Supérieure des Mines, MINES Paris Tech
- Le Saux M, Besson J, Carassour S, Poussard C, Averty X (2008) A model to describe the

- anisotropic viscoplastic mechanical behaviour of fresh and irradiated Zircaloy-4 fuel claddings under RIA loading conditions. *J Nucl Mater* 378:60–69
- Leclercq S, Parrot A, Leroy M (2008) Failure characteristics of cladding tubes under RIA conditions. *Nucl Eng Des* 238: 2206–2218
- Lee BH, Koo YH, Oh JY, Cheon JS, Sohn DS (2007) Improvement of fuel performance code COSMOS with recent in-pile data for MOX and UO₂. *Fuels Nucl Technol* 157:53–64
- Lee CB, Kim BG, Song JS, Bang JG, Jung YH (2000) RAPID model to predict radial burnup distribution in LWR UO₂ fuel. *J Nucl Mater* 282: 196–204
- Lemehov S, Nakamura J, Suzuki M (2001) PLUTON: A three-group model for the radial distribution of plutonium, burnup, and power profiles in highly irradiated LWR fuel rods. *Nucl Technol* 133:153–168
- Lewis BJ, Thompson WT, Akbari F, Thompson DM, Thurgood C, Higgs J (2004) Thermodynamic and kinetic modelling of fuel oxidation behaviour in operating defective fuel. *J Nucl Mater* 328:180–196
- Link T, Koss D, Motta A (1998) Failure of Zircaloy cladding under transverse plane-strain deformation. *Nucl Eng Des* 186:379–394
- Lösönen P (2000) On the behaviour of intragranular fission gas in UO₂ fuel. *J Nucl Mater* 280:56–72
- Lyon WL, Bailey WE (1967) The solid-liquid phase diagram for the UO₂-PuO₂ system. *J Nucl Mater* 22:332–339
- MacDonald P, Seiffert S, Martinson Z, McCardell R, Owen D, Fukuda S (1980) Assessment of light-water-reactor fuel damage during a reactivity-initiated-accident. *Nucl Safety* 21:582–602
- Manzel R, Walker CT (2002) EPMA and SEM of fuel samples from PWR rods with an average burn-up of around 100 MWd/kgHM. *J Nucl Mater* 301:170–182
- Marchal N, Campos C, Garnier C (2009) Finite element simulation of pellet-cladding interaction PCI. *Comput Mat Sci* 821–826
- Martin DG (1988) The thermal expansion of solid UO₂ and (U, Pu) mixed oxides - a review and recommendations. *J Nucl Mater* 152:94–101
- MATPRO (1981) Version 11 (Revision 2), A handbook of material properties for use in the analysis of light water reactor fuel rod behaviour
- MATPRO (1990) Report NUREG/CR-5273, EGG-2555
- MATPRO (1993) NUREG/CR-6150, EGG-2720, SCDAP/RELAP5/MOD3.1 Code Manual volume IV. In: Hagrman DT (ed) MATPRO – A library of materials properties for Light-Water Reactor accident analysis. November 1993, Idaho National Engineering Laboratory
- Mattys R, Yaggee F, Neimark L (1979) Iodine stress-corrosion cracking in irradiated Zircaloy cladding. In: Proceedings topical meeting LWR fuel. Portland, Oregon
- Mattys HM (1968) Plutonium oxide as nuclear fuel. *Actinides Rev* 1:165–182
- Matzke H (1980) Gas release mechanisms in UO₂—a critical review *Radiat Eff* 53:219–242
- Meyer R, McCardell R, Chung H, Diamond H, Scott H (1996) A regulatory assessment of test data for reactivity initiated accidents. *Nucl Safety* 37:271–288
- Michel B, Sercombe J, Nonon C, Fandeur O (2010) Modelling of pellet cladding interaction. In: Konings RJM, Allen TR, Stoller RE, Yamanaka S (eds) *Comprehensive Nuclear Materials*. Elsevier, Oxford
- Michel B, Sercombe J, Thouvenin G (2008) A new phenomenological criterion for pellet cladding interaction. *Nucl Eng Des* 238:1612–1628
- Miller A, Ocken H, Tasooji A (1981) Iodine stress corrosion cracking of Zircaloy: laboratory data, a phenomenological model, and predictions of in-reactor behavior. *J Nucl Mater* 254–268
- Misfeldt I (1977) A stress corrosion failure model. In: Proceedings of IAEA specialists' meeting on fuel element performance computer modelling blackpool. Report SRE-14-77. Risoe National Laboratory
- Mogensen M, Pearce J, Walker C (1999) Behaviour of fission gas in the rim region of high burn-up UO₂ fuel pellets with particular reference to results from XRF investigation. *J Nucl Mater* 264:99–112
- Musienko A, Cailletaud G (2009) Simulation of inter- and intragranular crack propagation in polycrystalline aggregates due to stress corrosion cracking. *Acta Mater* 57:3840–3855
- Nagase F, Fuketa T (2004) Effects of pre-hydrating on thermal resistance of Zircaloy-4 cladding under simulated loss-of-coolant accident conditions. *J Nucl Sci Tech* 41(7):723–730
- Newton TD, Hutton JL (2002) The next generation WIMS lattice code: WIMS9 In: PHYSOR 2002 – international conference on the new frontiers of nuclear technology: reactor physics, safety and high-performance computing, 14A-04, American Nuclear Society, Seoul, Korea, October 7–10, 2002, ISBN 0-89448-672-1
- Nichols AL, Aldama DL, Verpelli M (2008) Handbook of nuclear data for safeguards. Tech. Rep. INDC(NDS)-0502, IAEA – International Nuclear Data Committee, Vienna

- Noiroi L (2005) MARGARET: an advanced mechanistic model of fission gas behavior in nuclear fuel. In: International topical meeting on light water reactor fuel performance. ANS, Kyoto, Japan, October 2–5, 2005. OECD paper No. 1067
- Nonon C, Menard J, Lansiard S, Noiroi J, Martin S, Decroix G, Rabouille O, Delafoy C, Petitprez B (2004) PCI behaviour of chromium oxide doped fuel. In: Proceedings of the international seminar on pellet-clad interaction in water reactor fuels. OECD-NEA, Aix-en Provence, France
- Oguma M (1983) Cracking and relocation behavior of nuclear fuel pellets during rise to power. *Nucl Eng Des* 76:35–45
- Olander D (1976) Fundamental aspects of nuclear reactor fuel elements. Tech. Rep. TID-26711-P1, Technical Information Center, Office of Public Affairs Energy Research and Development Administration
- Olander DR, Kim YS, Wang WE, Yagnik SK (1999) Steam oxidation of fuel in defective LWR rods. *J Nucl Mater* 270:11–20
- Olander DR, Mubayi V (1999) Review of the materials-chemistry models in the VICTORIA code. *J Nucl Mater* 270:1–10
- Olander DR, Uffelen PV (2001) On the role of grain boundary diffusion in fission gas release. *J Nucl Mater* 288:137–147
- Palmer ID, Hesketh KW, Jackson PA (1983) Water reactor fuel element performance computer modelling. Applied Science Barking, UK, p 321
- Park S, Kim J, Lee MH, Jeon YH (2008) Stress-corrosion crack initiation and propagation behavior of Zircaloy-4 cladding under iodine environment. *J Nucl Mater* 372:293–303
- Peck SO (1980) Automated uncertainty analysis methods in the FRAP computer codes, IAEA Specialist's Meeting on Fuel Element Performance Computer Modeling, Blackpool, UK, March 17–21, 1980, pp 260–266, IAEA Summary report IWGFPT/7
- Powers DA (2000) Technical issues associated with air ingress during core degradation. Tech. Rep. SAND2000, 1935C, SANDIA National Laboratory
- Rashid J, Montgomery R, Lyon W, Yang R (2001) A cladding failure model for fuel rods subjected to operational transients and accident transients. In: Nuclear fuel behaviour modeling at high burn-up and its experimental support. Proceedings of a Technical Committee meeting, June 19–23, 2000. Windermere, UK, IAEA-TECDOC-1233. IAEA, pp 187–199
- Rest J, Zawadski SA (1992) Fastgrass: a mechanistic model for the prediction of Xe, I, Cs, Te, Ba and Sr release from nuclear fuel under normal and severe-accident conditions. Tech. Rep. NUREG/CR-5840, ANL-92/3, Argonne National Laboratory
- Ronchi C, Elton PT (1986) Radiation re-solution of fission gas in uranium dioxide and carbide. *J Nucl Mater* 140:228–244
- Ronchi C, Sheindlin M, Staicu D, Kinoshita M (2004) Effect of burn-up on the thermal conductivity of uranium dioxide up to 100,000 MWd t⁻¹. *J Nucl Mater* 327:58–76
- Ronchi C, Shindlin M, Musella M, Hyland GJ (1999) Thermal conductivity of uranium dioxide up to 2900 K from simultaneous measurement of the heat capacity and thermal diffusivity. *J Appl Phys* 85:776–789
- Ross AM, Stoute RL (1962) Heat transfer coefficient between UO₂ and Zircaloy-2. Tech. Rep. AECL-1552, AECL
- Rousselier G, Leclercq S, Diard O (2003) Scenario for the damage of PWR fuel cladding in situations of pellet-cladding interaction. In: Transactions of the 17th international conference on structural mechanics in reactor technology (SMiRT 17). Prague, Czech Republic, pp C03–3
- Sartori E, Killeen J, Turnbull J (2007) International fuel performance experiments (IFPE) database (January 2010). URL <http://www.nea.fr/html/science/fuel/ifpelst.html> 2009.
- Sasajima H, Fuketa T, Nakamura T, Nakamura J, Kikuchi K (2000) Behavior of irradiated atr/mox fuel under reactivity initiated accident conditions. *J Nucl Sci Technol* 37:455
- Schire D, Grapengiesser B, Hallstadius L, Lundholm L, Lysell G, Frenning G, Ronnberg G, Jonsson A (1994) Secondary defect behaviour in sc abb bwr fuel. In: Proceedings international topical meeting on LWR fuel performance. West Palm Beach, Florida, pp 398–409
- Schmidt HE (1970) Commission of the European Communities. European Institute for Transuranium Elements, Karlsruhe, Tech. Rep. Progress Report No. 9, July-December 1969, No. 2576, p. 29
- Schmidt HE (1971) Die Wärmeleitfähigkeit von Uran- und Uran-Plutonium dioxyd. *High Temp-High Press* 3:345–353
- Schubert A, Van Uffelen P, van de Laar J, Walker CT, Haec W (2008) Extension of the TRANSURANUS burn-up model. *J Nucl Mater* 376:1–10
- Schuster I, Lemaignan C (1992) Influence of texture on iodine-induced stress corrosion cracking

- of Zircaloy-4 cladding tubes. *J Nucl Mater* 189: 157-166
- Shimada S, Etoh E, Hayashi H, Tukuta Y (2004) A metallographic and fractographic study of outside-in cracking caused by power ramp tests. *J Nucl Mater* 327:97-113
- Shhver L, Hallstadius L, Wikmark G (1997) Recent ABB BWR failure experience. In: *Proceedings international topical meeting on LWR fuel performance*. Portland, Oregon, pp. 356-364
- Solyany VI, Bibilashvily YK, Tonkov VY (1983) In: *Proceeding OECD-NEA-CSNI/IAEA Specialists meeting on water reactor fuel safety and fission product release in off-normal and accident conditions*, May 16-20, 1983. Risoe, Denmark, p 163
- Sonoda T, Kinoshita M, Ray I, Wiss T, Thiele H, Pellottiero D, Matzke H (2002) Transmission electron microscopy observation on irradiation-induced microstructural evolution in high burnup UO_2 disk fuel. *Nucl Instr Methods Phys Res B* 191:622-628
- Sonoda T, Matzke H, Kinoshita M (1999) High burnup rim project: (iv) threshold burnup of rim structure formation. In: *Project OHR (ed) Proceedings of the enlarged Halden program group meeting*. Loen, Norway
- Sontheimer F, Landskron H, Billaux M (1998) A fuel thermal conductivity correlation based on the latest experimental results. In: *Proceedings of the seminar on thermal performance of high burn-up LWR fuel*. Cadarache, France, p 119
- Speight MV (1969) A calculation on the migration of fission gas in material exhibiting precipitation and re-solution of gas atoms under irradiation. *Nucl Sci Eng* 37:180-185
- Spino J, Stalios A, Santa Cruz H, Baron D (2006) Stereological evolution of the rim structure in PWR-fuels at prolonged irradiation. *J Nucl Mater* 354:66-84
- Stan, M. (2009) *Discovery and Design of Nuclear Fuels*. *Materials Today* 12, 36-44.
- Stammler JJ, Boerresen S, Casal JJ, Forslund P (1996) Helios - Verification against Kritz and other critical experiments. In: *PHYSOR 1996 - international conference on physics of reactors*, September 16-20, 1996, American Nuclear Society, Mito, Ibaraki, Japan
- Suk HC, Wang W, Kim BG, Kim KS, Heo YH (1992) In: *Technical committee meeting on fission gas release and fuel chemistry related to extended burnup*, April 1992, Pembroke, Ontario, Canada, pp 193-201
- Suzuki M (2000) Analysis of high burnup fuel behavior in Halden reactor by FEMAXI-V code. *Nucl Eng Des* 201:99-106
- Suzuki M (2000) Light water reactor fuel analysis code Femaxi-v (ver.1)
- Trkov A, Molnár GL, Révay Z, Mughabghab SF, Firestone RB, Pronyaev V, Nichols AL, Moxon MC (2005) Revisiting the ^{238}U thermal capture cross section and gamma-ray emission probabilities from ^{239}Np Decay. *Nucl Sci Eng* 150: 336-348
- Tsederberg NV, Popov VN, Morozova NA (1971) *Thermodynamic and thermophysical properties of Helium*. Israel Program for Scientific Translations, Jerusalem
- Turnbull JA (1980) A review of irradiation induced re-solution in oxide fuels. *Rad Effects* 53:243-250
- Turnbull JA, Friskney C, Findlay J, Johnson E, Walter AJ (1982) The diffusion coefficients of gaseous and volatile species during the irradiation of uranium dioxide. *J Nucl Mater* 107:168-184
- Uetsuka H, Furuta T, Kawasaki S (1983) failure-bearing capability of oxidized zircaloy-4 cladding under simulated loss-of-coolant Condition *J Nucl Sci Techn* 20:941-950
- Une K, Amaya M, Imamura M, Korei Y (1995) Fission gas release from defective BWR fuels. *J Nucl Mater* 226:323-326
- Une K, Imamura M, Amaya M, Korei Y (1995) Fuel oxidation and irradiation behaviors of defective BWR fuel rods. *J Nucl Mater* 223:40-50
- Urbanic VF, Heidrick TR (1978) High-temperature oxidation of Zircaloy-2 and Zircaloy-4 in steam. *J Nucl Mater* 75:251-261
- US-NRC (1981) Standard review plan for the review of safety analysis reports for nuclear power plants, LWR edition.
- van der Linde A (1965) Calculation of the safe life time expectancy of zirconium alloy canning in the fuel Tech. Rep. RCN-41, Reactor Centrum Nederland
- Van Swam L, Strasser A, Cook J, Burger J (1997) Behaviour of Zircaloy-4 and zirconium liner Zircaloy-4 cladding at high burnup. In: *Proceedings international topical meeting on LWR fuel performance*. Portland, Oregon, pp 421-431
- Van Uffelen P (2002) Contribution to the modelling of fission gas release in light water reactor fuel. Ph.D. thesis, University of Liege, Nuclear Engineering
- Van Uffelen P, Gyori C, Schubert A, van de Laar J, Hózer Z, Spykman G (2008) Extending the application range of a fuel performance code from

- normal operating to design basis accident conditions. *J Nucl Mater* 383:137–143
- Van Uffelen P, Jonnet J, Ronchi C (2004) Open questions related to the high burnup structure in nuclear fuels. In: Proceedings of the workshop on materials modelling and simulations for nuclear fuels. Washington, DC
- Van Uffelen P, Sheindlin M, Rondinella V, Ronchi C (2004) On the relations between the fission gas behaviour and the pellet-cladding mechanical interaction in LSR fuel rods In: Seminar on Pellet-clad interaction in water reactor fuels (PCI-2004), CEA Cadarache/DEN/DEC, Aix en Provence, France, March 9–11 2004, OECD, Paper 14
- Vitanza C (2006) RIA failure threshold and LOCA limit at high burn-up. *J Nucl Sci Technol* 43:1074–1079
- Vitanza C (2007) A review and interpretation of RIA experiments. *Nucl Eng Technol* 39:591–602
- Vitanza C, Conde Lopez JM (2005) PCMI implications for high burn-up light water reactor fuel in reactivity-initiated accidents. In: Seminar on pellet-clad interaction in water reactor fuels (PCI-2004) Aix-en-Provence, March 9–11, 2004, OECD, Paper 5
- Vitanza C, Graziani U, Fordestrommen NT, Vilpponen KO (1978) Fission gas release from in-pile measurements. Tech. Rep. HPR-221.10, OECD Halden Reactor Project
- Volkov BY, Viktorov VF, Platonov PA, Rjazantzeva A (1989) Library of subprograms on physical and mechanical properties of the ni-alloy fuel rod cladding material. Tech. Rep. KIAE-4941/11, Institute of Atomic Energy I.V. Kurchatov
- Walker C, Kamemaya T, Kitajama S, Kinoshita M (1992) Concerning the microstructure changes that occur at the surface of UO_2 pellets on irradiation to high burnup. *J Nucl Mater* 188: 73–79
- Walker CT, Bremier S, Portier S, Hasnaoui R, Goll W (2009) SIMS analysis of an UO_2 fuel irradiated at low temperature to 65 MWd/kgHM. *J Nucl Mater* 393:212–223
- Walker CT, Staicu D, Sheindlin M, Papaioannou D, Goll W, Sontheimer F (2006) On the thermal conductivity of UO_2 nuclear fuel at burnup of around 100 MWd/kgHM. *J Nucl Mater* 350:19–39
- White RJ (2004) The development of grain-face porosity in irradiated oxide fuel. *J Nucl Mater* 325:61–77
- White RJ, Tucker MO (1983) A new fission-gas release model. *J Nucl Mater* 118: 1–38
- Wiesenack W (1997) In: Proceedings of the international topical meeting on light water reactor fuel performance, March 2–6, 1997, Portland, Oregon. Assessment of UO_2 conductivity degradation based on in-pile temperature data
- Wood J (1972) Factors affecting stress corrosion cracking of Zircaloy in iodine vapour. *J Nucl Mater* 45:105–122
- Xin X, Lai W, Liu B (2009) Point defect properties in hcp and bcc Zr with trace solute Nb revealed by ab initio calculations. *J Nucl Mater* 393: 197–202
- Yamanouchi S, Tachibana T, Tsukui K, Oguma M (1988) Melting Temperature of Irradiated UO_2 and UO_2 -2wt% Gd_2O_3 Fuel Pellets up to Burnup of about 30 GWd/tU. *J Nucl Sci Technol* 25:528–533
- Yamnikov VM, Malanchenko LL (1977) Variation of thermal conductivity of a gas mixture under the fuel-element jacket during burn-up. *Atomic Energy* 42:358–360
- Zhou G, Lindbäck JE, Schutte HC, Jernkvist LO, Massih AR (2005) Modelling pellet clad interaction during power ramps. In: Proceedings international seminar on pellet-clad interaction in water reactor fuels. OECD-NEA, Aix-en Provence, France
- Zimmerer W (1978) Darstellung der neu integrierten stoffdaten-funktionen im system maplib in tabellarischer und graphischer form. Tech. Rep. KfK-Ext.8/78-3, Kernforschungszentrum Karlsruhe



14 Noise Techniques in Nuclear Systems

Imre Pázsit^{1,2} · Christophe Demazière¹

¹Department of Nuclear Engineering, Chalmers University of Technology, Göteborg, Sweden

²Department of Nuclear Engineering and Radiological Sciences, University of Michigan, Ann Arbor, Michigan, USA

1	Introduction	1631
2	Zero Power Reactor Noise	1632
2.1	Methodology of Zero Power Neutron Noise	1632
2.1.1	Forward Approach	1634
2.1.2	Backward Approach	1637
2.2	Reactivity Measurements in Traditional Systems with Stationary Poisson Sources	1641
2.2.1	The Feynman-Alpha (Variance to Mean) Method	1644
2.2.2	The Rossi-Alpha (Correlation) Method	1647
2.2.3	The Bennett Variance Method	1649
2.2.4	Mogilner's Zero Crossing Method	1650
2.2.5	The Cf-252 Method	1651
2.3	Reactivity Measurements in ADS	1653
2.3.1	Spallation Source	1654
2.3.2	Pulsed Source in Feynman- and Rossi-Alpha Applications	1656
2.3.3	Feynman-Alpha with Deterministic Pulsing	1657
2.3.4	Feynman-Alpha with Stochastic Pulsing	1658
2.3.5	Rossi-Alpha with Stochastic Pulsing	1658
2.4	Pulse Counting Techniques in Nuclear Material Management (Safeguards)	1659
2.4.1	Neutron Factorial Moments	1661
2.4.2	Gamma Photon Factorial Moments	1661
2.4.3	Mixed Moments	1662
2.4.4	Multiplicity Detection Rates	1663
3	Power Reactor Noise Theory	1664
3.1	Basic Principles	1666
3.2	Space-Time Dependent Reactor Kinetics in Diffusion Theory	1670
3.2.1	Static Equations	1671
3.2.2	Time-Dependent One-Group Diffusion Equations	1674
3.2.3	The Flux Factorization and the Kinetic Approximations	1675

3.3	Small Space-Time Dependent Fluctuations: Power Reactor Noise	1677
3.3.1	Neutron Noise in One-Group Diffusion Theory	1678
3.3.2	The Factorization of the Neutron Noise	1679
3.3.3	Neutron Noise in Two-Group Diffusion Theory: The Local Component ...	1685
4	<i>Applications of Power Reactor Noise Diagnostics</i>	1691
4.1	Unfolding Noise Source Parameters with Noise Diagnostics	1691
4.1.1	Localization of Absorbers of Variable Strength	1692
4.1.2	Localization of Vibrating Control Rods	1696
4.1.3	Flow Velocity Estimations	1699
4.1.4	Miscellaneous Other Applications	1704
5	<i>Special Noise Techniques: Determination of Core Global Dynamical Parameters</i>	1711
5.1	Determination of the Decay Ratio in BWRs	1711
5.1.1	Stability Indicator	1713
5.1.2	Stability Mechanism of a BWR	1714
5.1.3	Types of BWR Instabilities	1715
5.1.4	Combined Types of Oscillations	1718
5.2	Determination of the Moderator Temperature Coefficient of Reactivity in PWRs	1723
5.2.1	Definition of the MTC	1723
5.2.2	Derivation of the MTC Noise Estimate	1724
5.2.3	Measurement by Noise Analysis Technique	1725
5.2.4	Elaboration of a Correct MTC Noise Estimator	1728
6	<i>Conclusions and Open Issues</i>	1731
	<i>References</i>	1734

Abstract: This chapter deals with neutron fluctuations in nuclear systems. Such neutron fluctuations, or neutron noise, fall into two categories: neutron noise in zero power systems and neutron noise in power reactors. The concepts, the theory, and the methodology of these fluctuations as well as their various applications for extracting information in a nonintrusive way about the system in question are described. A number of specific applications are described, where detection and analysis of zero power and power reactor noise make it possible to extract diagnostic information about the system by determining some parameters of the system during normal operation, or by detecting, identifying, and quantifying developing anomalies at an early stage and determining their severity. This chapter ends with an outline of future developments and actual issues in the field.

1 Introduction

This chapter deals with the methods and techniques used in reactor surveillance and diagnostics, which are based on the analysis of fluctuations in the neutron population in a reactor core. These fluctuations appear as random variations of the detector counts at low power, or as fluctuations of the detector current at high power, representing two classes of neutron fluctuations, respectively. These two classes of neutron fluctuations, termed as zero power noise and power reactor noise, respectively, differ in their physical origin, hence their field of utilization, as well as have different mathematical description, and as the name indicates, they dominate at two different extremes of the magnitude of the neutron population in the core.

In low-power systems, the core material is constant in time. In such systems, the nontrivial (over-Poisson) distribution of the neutron population is brought about by the fact of branching, that is, the generation of several neutrons concurrently in the fission process. The fission process generates fission chains, and the neutrons in the same chain are time-correlated. Their joint detection has a non-Poisson distribution, and the deviation from the Poisson distribution can be used for different purposes. The theory of zero power noise is based on probability balance equations (master equations). The major applications are the measurement of the subcritical reactivity of a core, and the detection and quantification of fissile nuclear material in nuclear safeguards.

In power reactors, the effect of branching on the statistics of the neutron population is suppressed by another dominating effect. In such systems, several technological processes (boiling of the coolant/moderator in a BWR, vibrations of mechanical constructions in a PWR, etc., commonly called “noise sources”), cause the medium in which the neutron transport and multiplication takes place to fluctuate in time and space. These fluctuations again have a non-Poisson character, although not because of branching, rather because several neutrons in the system are affected simultaneously in the core in a *random* manner, and hence their parameters become correlated. A deterministic variation of the reactor material does not induce such correlations. The primary use of the information content of the neutron fluctuations so induced is to detect, identify, and quantify the noise sources. Both operational parameters in the normal state as well as changes of the reactor state to the abnormal state can be quantified as well as the occurrence of new anomalies can be detected and quantified. The methodology used to describe these stochastic processes is based on the linearized form of the Langevin technique.

In the following subsections, these phenomena and corresponding methods and applications will be described. This chapter starts with the theory and methodology of neutron noise in low-power systems. Applications for determining subcritical reactivity by various

fluctuation-based methods are described. Two newer areas of application, calculation, and use of zero power noise methods in accelerator-driven systems (ADSs) and in nuclear safeguards are then described. Thereafter, the concept of power reactor noise and the basics of the calculation of the dynamical response of a reactor to external perturbations are developed. The kinetic approximations in the theory of neutron noise and the different spatial components are defined and discussed. Expressions are given in one- and two-group diffusion theory for the Green's function, and the dynamic adjoint and the noise induced by some basic types of perturbations are calculated. The final two sections concern the application of neutron noise diagnostics for detecting and quantifying various anomalies as well as for determining some global core parameters of safety interest in BWRs and PWRs. This chapter concludes by giving an outlook on future trends of noise techniques.

2 Zero Power Reactor Noise

Historically, neutron fluctuations in a chain reaction were first studied in connection with “start-up with a weak source” (Harris 1964). In a multiplying system, including supercritical ones, when starting up the chain reaction with an external source, at the onset, the total number of neutrons is small; hence the relative fluctuations in the process are large. Thus, the time it takes before the avalanche of the supercritical behavior is established, and thus before the behavior of the system has a deterministic character, can vary from case to case significantly. This posed the question: what is the probability that, due to fluctuations in the neutron chain, criticality or prompt criticality could be attained in a system during start-up without an experimental indication. Another aspect of the start-up procedure, known from the much earlier studies of Watson and Galton (1873), is that the probability of the extinction of a supercritical branching process is larger than zero. This aspect has a bearing on the mechanism and success of detonating a nuclear device. Early work on this subject, constituting the real beginnings of these studies, is classified still as of this writing.

As is self-evident, all the above refers to the random aspects of transient behavior. However, the main use of zero power noise methods is found in utilizing the fluctuations in stationary low-power systems, such as a subcritical core with an extraneous source to measure the subcritical reactivity. A power reactor core during start-up and stepwise approaching criticality is an example. A low-power ADS that runs in subcritical state driven by an accelerator-based source is another example. In the following subsections, the principles and the main types of noise-based reactivity measurement methods are described. We also refer to the existing monographs and review articles, such as Thie (1963), Harris (1964), Uhrig (1966, 1970), Stacey (1969), Pacilio (1970), Williams (1974), Saito (1979), and the recent monograph by Pázsit and Pál (2008).

2.1 Methodology of Zero Power Neutron Noise

Zero power noise is concerned with the determination of the statistics of the neutron population in a multiplying system, and the statistics of detector counts during a time period or within two time gates a certain time apart. The emphasis is on the temporal evolution of the distributions, of which usually only that of the few lowest-order moments are determined explicitly. In the conventional description, space and energy effects are neglected, and only an integral parameter, the effective multiplication constant or the reactivity of the system, is sought. The description

assumes an infinite homogeneous system, into which an infinite homogeneous source and a detector are embedded. The approximation is often referred to as the “point reactor model.”

The theory of neutron fluctuations can of course be formulated in a general setting with space-energy-angular dependence included in a finite material, as it was already done in the first rigorous descriptions of the theory (Pál 1958, Bell 1965). However, the general treatment has the pragmatic drawback that the moment equations cannot be solved in a closed form, and the conceptual drawback that in a concrete case of applying the theory to reactivity measurement, the material and geometrical composition of the system is not known exactly (e.g., due to deviations from the assumed core composition by erroneous loading). If the composition of the system was known in all detail, the reactivity of the system could be determined purely by calculation. Space-energy corrections of the point model results can still be feasible and serve a better result than pure calculations when the composition of the system is only known approximately, such that this approximate knowledge can be used to improve the result of the measurement evaluated by the results of the space-independent theory. A crucial step in the correction methods is that the errors incurred by the imprecise knowledge of the system composition should only have a second-order small effect on the accuracy of the correction. The efficiency and accuracy of such correction methods is a subtle question whose discussion is beyond the scope of this chapter.

The methodology is based on probability balance equations, also called Kolmogorov or Chapman–Kolmogorov equations, and more recently just master equations. To calculate the transition probabilities of the system, one needs to define lumped parameters for the intensities of the various neutron processes and reactions. Hence, λ_c , λ_d and λ_f will denote the intensities of capture, fission, and detection of/by one neutron, respectively (these are often referred to in the literature as “transition probabilities per unit time”). These are, in turn, given as $\lambda_c = \nu \Sigma_c$, etc., where Σ_c is the macroscopic cross section of capture and ν the neutron speed. Further, λ is the intensity (decay constant) of the decay of the delayed neutron precursors. The generation of neutrons and delayed neutron precursors is characterized by the probability $p_f(n, m)$ of emitting n neutrons and m delayed neutron precursors in a fission event. The distribution $p_f(n, m)$ has the property

$$\sum_{n,m} p_f(n, m) = 1$$

The above description corresponds to the simplified assumption of having one single averaged delayed neutron group. Using six delayed neutron groups instead of one is completely straightforward, and final results will be given also for six delayed neutron groups; however, such a more general treatment would spoil the transparency of the illustration here. Readers interested in the details of calculations with six delayed neutron groups are referred to the literature, for example, Pál (1958), Williams (1974), Kuang and Pázsit (1999), and Pázsit and Pál (2008).

Similarly to traditional (deterministic) transport theory, the problem can be formulated by two equivalent ways, namely through either forward (direct) or backward (adjoint) type master equations, respectively. The difference in the structure of the forward and backward equations is larger in the stochastic treatment than in the deterministic one, or one can say that the differences between the forward and backward equations increase with the moment order. Generally, for calculating higher moments, the backward approach is considered more effective and rigorous than the forward one. For illustration purposes, which is our goal here, the forward approach is more suitable; hence it will be used here to demonstrate the principles of the master equations for neutron fluctuations. In general, however, the backward approach is more

effective, and the majority of the publications is based on the backward equation, including the seminal work by Pál (1958) and in general when space and energy dependence is involved (Bell 1965; Munoz-Cobo et al. 1987). The very essence of the backward equations will also be shown, just to illustrate the differences between the two methods.

A typical quantity sought in neutron fluctuation problems is the probability

$$P(N, C, Z, t) \quad (1)$$

of having N neutrons and C delayed neutron precursors in the system at time t , and having detected Z neutrons in the time interval $[0, t]$, given that the process was started with zero neutrons and precursors in the system at $t = -\infty$, when an extraneous neutron source of intensity S was switched on. The reason for starting the process at $t = -\infty$ is that by $t = 0$, all transients will have decayed, and the neutron and precursor numbers can be assumed to be stationary processes. A more rigorous treatment would be to set the start of the neutron injection at a finite time t_0 and seek the probability of having N neutrons and C delayed neutron precursors at time t , and having detected Z neutrons in the time interval $[t - T, t]$, and then take the limit $t \rightarrow \infty$.

2.1.1 Forward Approach

The master equation is derived by constructing the probability $P(N, C, Z, t + dt)$ from that of $P(N, C, Z, t)$ by accounting for all possible transitions during dt . Assuming the mutually exclusive character of the events source emission, capture, detection, fission, and decay of a precursor within an infinitesimal time interval dt , and accounting for all possible transitions from the accessible states at time t to the state $\{N, C, Z\}$ at time $t + dt$, and by using the theorem of total probability and rearranging, the following master equation can be derived for $P(N, C, Z, t)$:

$$\begin{aligned} \frac{dP(N, C, Z, t)}{dt} = & \lambda_c P(N + 1, C, Z, t)(N + 1) + \lambda_d P(N + 1, C, Z - 1, t)(N + 1) \\ & + \lambda_f \sum_n \sum_m P(N + 1 - n, C - m, Z, t)(N + 1 - n)p_f(n, m) \\ & + SP(N - 1, C, Z, t) + \lambda P(N - 1, C + 1, Z, t)(C + 1) \\ & - P(N, C, Z, t)[N(\lambda_f + \lambda_c + \lambda_d) + \lambda C + S]. \end{aligned} \quad (2)$$

The terms on the right-hand side can all be easily interpreted by accounting for the fact that the intensities of reactions refer to a single neutron, hence the multipliers N , $(N + 1)$, etc. in the corresponding expressions. Note that here it is assumed that the detector is embedded in the multiplying medium, and capture in the detector competes with the other processes. Usually, the detector efficiency ε is introduced, defined as $\varepsilon = \lambda_d/\lambda_f$, which gives the ratio of the intensities of capture in the detector to the intensity of fissions in the system. A large detector efficiency in such a case means the introduction of a strong “parasitic” absorber, which hence modifies the reactivity of the original system. If the detector is placed outside the system, which is the case with the safeguards measurements treated later, a different formulation is necessary, where the escape of the neutrons from the system must be incorporated into the formalism. In such a case, just as in reality, the detector efficiency does not influence the progress of the chain reaction in the medium.

Since in a stationary system, the effect of the initial state has already decayed by $t = 0$, no initial condition needs to be specified for N and C . However, since the measurement starts at $t = 0$, one has the initial condition of $Z = 0$ at $t = 0$.

The solution of (2) cannot be given in a compact analytical form. However, one only needs the few lowest-order moments, which can be calculated in a straightforward manner, even if at the expense of some extensive algebra. In order to derive equations for the moments, it is practical and customary to introduce the generating functions of the probability distributions occurring in the equation. The generating functions are defined as

$$G(x, y, v, t) = \sum_N \sum_C \sum_Z x^N y^C v^Z P(N, C, Z, t) \quad (3)$$

and

$$g_f(x, y) = \sum_n \sum_m x^n y^m p_f(n, m) \quad (4)$$

The factorial moments of the random variables N , C , and Z are obtained as derivatives of G taken at its variables equal to unity, that is,

$$\langle \mathbf{N}(t) \rangle \equiv N(t) = \left. \frac{\partial G(x, y, v, t)}{\partial x} \right|_{x=y=v=1} \quad (5)$$

and

$$\langle \mathbf{N}(t)(\mathbf{N}(t) - 1) \rangle = \left. \frac{\partial^2 G(x, y, v, t)}{\partial x^2} \right|_{x=y=v=1} \quad (6)$$

etc. The moments of the generating function

$$p(n, m) \quad (7)$$

are neutron physics constants, and the following notations will be used:

$$\left. \frac{\partial g_f(x, y)}{\partial x} \right|_{x=y=1} = \sum_n \sum_m n p_f(n, m) \equiv \langle v_p \rangle \equiv \langle v \rangle (1 - \beta) \quad (8)$$

and

$$\left. \frac{\partial g_f(x, y)}{\partial y} \right|_{x=y=1} = \sum_n \sum_m m p_f(n, m) \equiv \langle v_d \rangle \equiv \langle v \rangle \beta \quad (9)$$

where $\langle v \rangle = \langle v_p \rangle + \langle v_d \rangle$ is the expectation of the total (prompt plus delayed) neutron number per fission, and the delayed neutron fraction β was also introduced.

Using the above definitions, (2) is converted into

$$\begin{aligned} \frac{\partial G(x, y, v, t)}{\partial t} = & \{ \lambda_f [g_f(x, y) - x] - \lambda_c(x - 1) - \lambda_d(x - v) \} \frac{\partial G(x, y, v, t)}{\partial x} \\ & + \lambda(x - y) \frac{\partial G(x, y, v, t)}{\partial y} + (x - 1)SG(x, y, v, t) \end{aligned} \quad (10)$$

This is the typical form of the forward master equation for branching processes. It is a linear partial differential equation. The various equations for the moments are then obtained by taking the derivatives of G with respect to the auxiliary variables x , y , and u , leading to a system of coupled ordinary differential equations.

Before giving an illustration of the technique, at this point, it is worth to make a small diversion. Assume that the neutrons are injected into a medium not containing fissile material, that is, $\lambda_f = 0$; hence delayed neutrons do not occur either, and we are not concerned with the number of detections (one takes $\nu = 1$), rather we only study the statistics of the neutron number. Then, (10) is converted to

$$\frac{\partial G(x, t)}{\partial t} = \lambda_a(1-x) \frac{\partial G(x, t)}{\partial x} + (x-1)S(t)G(x, t) \quad (11)$$

where $\lambda_a = \lambda_c + \lambda_d$. In the above, a time-dependent source is allowed for, to indicate the generality of the statement for non-multiplying systems. From (11), it follows for the expectations that

$$\frac{d \langle N(t) \rangle}{dt} = -\lambda_a \langle N(t) \rangle + S(t) \quad (12)$$

Here, and only here, to avoid confusion, we kept the notation on the expectation value for the first moment. With this, it is seen that the full solution of (11) is obtained as

$$G(x, t) = e^{(x-1)\langle N(t) \rangle} \quad (13)$$

since substituting (13) into (11) will lead to (12). Equation (13) is, on the other hand, the generating function of the Poisson distribution

$$P(N, t) = \frac{e^{-\langle N(t) \rangle} \langle N(t) \rangle^N}{N!} \quad (14)$$

It is thus seen that the number of particles in a non-multiplying medium (i.e., one in which branching does not occur) follows Poisson statistics even with a (deterministically) time-varying source intensity. (If the source intensity is a random process, as in some of the cases of pulsed ADS experiments described in the forthcoming sections, the statement is not true). It will be seen soon that branching, that is, the presence of fission, will bring about deviation from the Poisson statistics.

Turning back to (10), we illustrate its use for deriving the first moments; obtaining the higher moments goes in a similar way. Taking the derivatives with respect to x , y , and ν at $x = y = \nu = 1$ yields the coupled equation system

$$\frac{dN(t)}{dt} = \frac{\rho - \beta}{\Lambda} N(t) + \lambda C(t) + S \quad (15)$$

$$\frac{dC(t)}{dt} = \frac{\beta}{\Lambda} N(t) - \lambda C(t) \quad (16)$$

and

$$\frac{dZ(t)}{dt} = \lambda_d N(t) = \epsilon \lambda_f N(t), \quad t \geq 0. \quad (17)$$

Here the conventional notations

$$\rho = \frac{\langle v \rangle \lambda_f - (\lambda_f + \lambda_c + \lambda_d)}{\langle v \rangle \lambda_f} \quad (18)$$

and

$$\Lambda = \frac{1}{\langle v \rangle \lambda_f} \quad (19)$$

were introduced, where ρ is the reactivity and Λ is the prompt neutron generation time. Also, in these equations, a stationary source was assumed with a constant intensity. Equations (15) and (16) are recognized as the standard point-kinetic equations, as expected.

As is seen from the above, the forward master equation leads to a coupled system of ordinary differential equations for the moments, whereas as we shall see, in the backward approach, each moment can be calculated independently of the others.

Due to the stationary state of the system, the neutron and precursor numbers are constants; hence the time derivatives on the left-hand sides of (15) and (16) are zero. This yields a solution for the stationary neutron and precursor numbers as

$$N = \frac{\Lambda S}{-\rho} \quad (20)$$

and

$$C = \frac{\beta N}{\lambda \Lambda} = \frac{\beta S}{\lambda(-\rho)} \quad (21)$$

The solution of (17) with the initial condition $Z(0) = 0$ is obtained as

$$Z(t) = \varepsilon \lambda_f N t = \varepsilon \lambda_f \frac{\Lambda S}{-\rho} t \quad (22)$$

The derivation of higher moments goes in an analogous manner and is quite straightforward. It can be found in the literature, so the details will not be given here.

2.1.2 Backward Approach

Here only the principles will be given in a very cursory way. When using the backward equations with a source, it is necessary to progress in two steps. Since the backward equation operates on initial variables, the master equation that describes the evolution of the population concerns a cascade that was started by one initial neutron. In order to calculate the distributions of a cascade induced by a source of particles with an intensity S , one needs to use a second master equation, connecting the single-particle induced and source-induced distributions, or their generating functions. The probability distributions and corresponding generating functions and moments will be distinguished by using lower-case-letters for the single-particle induced processes, and upper-case-letters for the quantities corresponding to the extraneous source.

In the backward approach, the probability of finding the system in the state $\{N, C, Z\}$ at time t is calculated by following up the first reaction of the particle in $[t_0, t]$ (integral form of the backward equation) or within $[t_0, t_0 + dt_0]$ (differential form). However, due to time homogeneity in a stationary system, the distributions depend only on $t - t_0$, hence operation on t_0 can be transferred to operating on t . Thus, to simplify the notations, we will set $t_0 = 0$, and will derive a master equation by considering the possible events within $[0, dt]$. By this approach, we will arrive to the so-called “mixed” form of the master equations, in that the time variable (and only this variable) will refer to the terminal value and not the initial one. In all other respects, the equations will have the property of the backward approach. In fact, the mixed-type equations are often referred to as backward equations in the literature.

Hence we will seek the probability distribution

$$p(n, c, z, T, t) \quad (23)$$

that there will be n neutrons and c precursors in the system at time t , induced by one initial neutron at $t = 0$, and that there have been z detector counts registered between $t - T$ and t . The stationary state of the system is attained by considering the solution for $t \rightarrow \infty$. The source emission is taken into account by deriving another backward master equation to connect the single-particle induced distribution function $p(n, c, z, T, t)$ with the probability distribution $P(N, C, Z, T, t)$ of the source emission case, when the source was switched on at $t = 0$.

The construction of the differential backward equation connecting the two distributions is based on summing up the probabilities of the mutually exclusive events of not having or having a source emission event in dt , respectively:

$$P(N, C, Z, T, t) = (1 - Sdt)P(N, C, Z, T, t - dt) + Sdt \sum_{\substack{N_1 + n_2 = N \\ C_1 + c_2 = C \\ Z_1 + z_2 = Z}} P(N_1, C_1, Z_1, T, t) p(n_2, c_2, z_2, T, t) \quad (24)$$

Here the last product term on the right-hand side expresses the fact that the initial particle injected at $t = 0$ and the source particle injected within dt at t lead to independent chains of neutrons and precursors as well as detector counts, and one has add up to all possible combinations of the mutually exclusive events of the source neutron leading to N_1 neutrons while the initial particle leads to $N - N_1 = n_1$ neutrons at time t etc.

The summation in the last term of (24) is of the form of a discrete convolution, which, in analogy with the continuous Laplace transform, will be converted to a simple product of the generating functions of the corresponding probabilities. Introducing the generating functions $G(x, y, v, T, t)$ and $g(x, y, v, T, t)$ of $P(N, C, Z, T, t)$ and $p(n, c, z, T, t)$, respectively, one arrives from (24) at

$$\frac{dG(x, y, v, T, t)}{dt} = SG(x, y, v, T, t) \{g(x, y, v, T, t) - 1\} \quad (25)$$

In this equation, the variables x , y , and v are only parameters, on which no operations are made. Hence, once an equation for $g(x, y, v, T, t)$ or its moments are obtained, the corresponding moments of $G(x, y, v, T, t)$ can be determined independently from the other moments. This

is a definite difference between the two approaches: the forward approach leads to a coupled system of differential equations of increasing order for the higher moments; in the backward approach, the higher moments of a random variable can be determined by performing nested integrals of increasing order of nesting for the moments of increasing order. Besides, it turns out that the single-particle induced first moment of the neutron number is the kernel (or Green's function) of all higher-order moments. Thus, once this simple expectation $n(t)$ is determined, there are no more equations to solve, only integrals to be performed. This feature of the backward equation makes it more straightforward than the forward approach, although technically, calculating the integrals is not necessarily simpler than solving the coupled system of ordinary differential equations.

By accounting for the initial conditions

$$g(x, y, \nu, T, 0) = x \quad \text{and} \quad G(x, y, \nu, T, 0) = 1, \tag{26}$$

equations (25) can be easily integrated to obtain the solution

$$G(x, y, \nu, T, t) = \exp \left\{ S \int_0^t [g(x, y, \nu, T, t') - 1] dt' \right\}. \tag{27}$$

The stationary value of this distribution, from which the moments can be calculated, is given by

$$G(x, y, \nu, T) = \lim_{t \rightarrow \infty} G(x, y, \nu, T, t) = \exp \left\{ S \int_0^\infty [g(x, y, \nu, T, t') - 1] dt' \right\} \tag{28}$$

The moments of $G(x, y, \nu, T)$ can be obtained by taking the derivatives, which will lead to expressions supplying the moments in terms of integrals of corresponding moments of $g(x, y, \nu, T)$.

The calculation of the single-particle induced moments goes as follows. In addition to the already defined probability $p(n, c, z, T, t)$, one needs also to define

$$w(n, c, z, T, t)$$

as the probability that there are n neutrons and c precursors at time t in the system, induced by one initial precursor at $t = 0$, and that there have been z detector counts between $t - T$ and t . The corresponding probability generating function, defined in the usual way, will be denoted as $h(x, y, \nu, T, t)$.

The master equations for g and h can be obtained as follows. With the usual arguments one writes

$$\begin{aligned} p(n, c, z, T, t) = & (1 - \lambda_a dt)p(n, c, z, T, t - dt) + \lambda_c \delta_{n,0} \delta_{c,0} \delta_{z,0} dt \\ & + \lambda_f dt \sum_{k,\ell} p_f(k, \ell) \sum_{\substack{n_1+n_2=n \\ c_1+c_2=c \\ z_1+z_2=z}} A_k(n_1, c_1, z_1, T, t) B_\ell(n_2, c_2, z_2, T, t) \tag{29} \\ & + \lambda_d dt \delta_{n,0} \delta_{c,0} [\bar{\Delta}(t, T) \delta_{z,1} + \bar{\Delta}(t, T) \delta_{z,0}], \end{aligned}$$

where

$$A_k(n_1, c_1, z_1, T, t) = \sum_{\substack{n_{11} + \dots + n_{1k} = n_1 \\ c_{11} + \dots + c_{1k} = c_1 \\ z_{11} + \dots + z_{1k} = z_1}} \prod_{j=1}^k p(n_{1j}, c_{1j}, z_{1j}, T, t), \quad (30)$$

and

$$B_\ell(n_2, c_2, z_2, T, t) = \sum_{\substack{n_{21} + \dots + n_{2k} = n_2 \\ c_{21} + \dots + c_{2k} = c_2 \\ z_{21} + \dots + z_{2k} = z_2}} \prod_{j=1}^{\ell} w(n_{2j}, c_{2j}, z_{2j}, T, t). \quad (31)$$

The function $\Delta(t, T)$ is defined as

$$\Delta(t, T) = \begin{cases} 1 & \text{for } 0 \leq t \leq T, \\ 0 & \text{otherwise} \end{cases} \quad (32)$$

and $\bar{\Delta}(t, T) = 1 - \Delta(t, T)$.

With similar arguments, for the precursor-induced cascade one obtains

$$w(n, c, z, T, t) = (1 - \lambda dt)w(n, c, z, T, t - dt) + \lambda dt p(n, c, z, T, t). \quad (33)$$

Turning to the generating functions, eliminating the generating function $h(x, y, \nu, T, t)$ of the precursor-initiated distributions by solving the equation obtained from (33), one arrives to an equation containing only the generating function $g(x, y, \nu, T)$ that is to be used in (28) to calculate the moments of the source-induced distributions. The equation reads as

$$\frac{\partial g(x, y, \nu, T, t)}{\partial t} = \lambda_f \sum_k \sum_\ell p_f(k, \ell) [g(x, y, \nu, T, t)]^k \left[\lambda \int_0^t e^{-\lambda(t-t')} g(x, y, \nu, T, t') dt' \right. \\ \left. + ye^{-\lambda t} \right]^\ell + \lambda_c - \lambda_a g(x, y, \nu, T, t) + \lambda_d \{(\nu - 1)\Delta(t, T) + 1\}. \quad (34)$$

Here one can note a significant difference compared to the forward equation. As (34) shows, in the backward formalism, one gets one single equation for the generating function g . Since the equation does not contain any derivatives with respect to the variables x , y , or ν , one single equation can be derived for any individual moment of any order, which can be solved separately from the other moment equations. This property holds also for (28) which is used for the calculation of the moments of the source-induced distributions from those of the single-particle induced ones. The only technical difficulty of the solution is the calculation of nested integrals of increasing order with increasing moment order. In the forward formalism, there is also one single master equation as a starting point. However, the equation contains derivatives with respect to x and y (see (10)). Because of this, for any moment except the first moment of the detector count, a coupled system of differential equations arises. The order of the system is increasing with the order of the moments. This, in general, constitutes more difficulties in the solution than the performing of the multiple integrals in the backward case.

2.2 Reactivity Measurements in Traditional Systems with Stationary Poisson Sources

The typical situation of measuring reactivity in a subcritical system is shown in **Fig. 1**. One approaches criticality gradually either by adding more fuel to the core, or lifting out a control rod. At each step, the level of criticality is determined, in order to know the margins to criticality. It is obvious that one single static measurement of the detector counts and using (22) is not practical, since in order to determine ρ , one has to know both the detector efficiency and the source strength in absolute terms. Besides, equation (22) was derived in the infinite homogeneous reactor approximation in which the detector efficiency is defined as the ratio of the fission cross sections, but in reality, it will include also geometrical factors due to the finite size of the detector. Hence, this efficiency can also change when new fuel is added to the core. In a more formal way of expressing it, the source S , the detector efficiency ε , and the prompt neutron generation time Λ in (22) can be expressed as adjoint-weighted integrals of the underlying space- and energy-dependent quantities (source spectrum, detector, and fission cross sections) (Ott and Neuhold 1985), and the weighting adjoint changes with the system configuration. In either case, this means that both ε and S are unknowns, and they need to be considered as dependent on the core configuration. Since the detector count depends linearly on the measurement time gate, comparing measurements of different lengths does not help either.

Therefore, in all cases the reactivity is determined from ratios of measurements of some kind, such as in two different configurations in the system or using time-dependent measurements and using detector counts at different times. The use of ratios of detector counts plays two different roles. Partly, in principle it can eliminate the unknown parameters from the corresponding expressions, which is the main goal. Partly, in a fortunate case, the inaccuracy of the method, caused by the deviations between the point model in which the formulas were derived and the real practical case, might be decreased by taking ratios if both quantities are biased toward the same direction.

However, taking the ratios may also introduce new problems. Consider for instance the most straightforward case of performing two static measurements, one in a state with a known

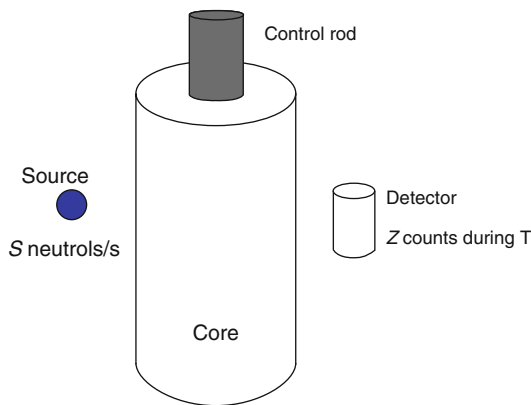


Figure 1
Illustration of the reactivity measurement method

reactivity ρ_1 , and one with an unknown reactivity ρ_2 . Using (22) one has

$$Z_1(t) = \varepsilon \lambda_f \frac{\Lambda S}{|\rho_1|} t; \quad Z_2(t) = \varepsilon \lambda_f \frac{\Lambda S}{|\rho_2|} t; \quad \rho_2 = \rho_1 \frac{Z_1(t)}{Z_2(t)} \quad (35)$$

The problem with this method is that, as indicated above, the parameters ε , Λ , and S are in general different in the two states, hence the last expression of (35) still contains ratios of unknown quantities.

One way of avoiding this difficulty is to perform time-dependent measurements, and extract the sought parameters from the time-dependence of the detector response in one single measurement. This is the essence of the pulsed neutron measurements. An analysis of (15) and (16) shows that the detector count rate, taken to be proportional to the temporary neutron level, decays in time with two different decay constants, given by the characteristic equation of (15) and (16), which is also the so-called inhour equation. With one delayed neutron group in a subcritical system, there are only two negative roots ω_0 and ω_1 , respectively. In practical work, one uses their positive values instead, and these are called the prompt and delayed neutron decay constant. In systems not too far from critical, they are given with a good approximation as


$$\alpha_p \equiv \alpha = -\omega_1 = \frac{\beta - \rho}{\Lambda} \quad (36)$$

and

$$\alpha_d = -\omega_0 = \frac{\lambda \rho}{\rho - \beta} \quad (37)$$

The experiment is performed by injecting a pulse in the system and analyzing the temporal decay of the detector count rate. After a transient period of pulse injection and a subsequent period during which the shape of the neutron distribution has to readjust to the fundamental mode, the temporal variation of the neutron population can be described asymptotically as

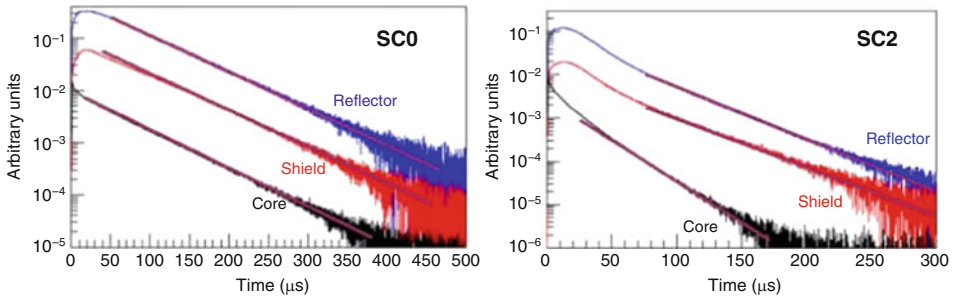
$$N(t) = N(0) e^{-\alpha t} = N(0) \exp \left\{ -\frac{\beta - \rho}{\Lambda} \right\} \quad (38)$$

From such a measurement, the prompt neutron decay constant α can be determined. An illustration of such a measurement is seen in  Fig. 2, taken from two different configurations of the MUSE experiments, performed by the MUSE collaboration (Mellier 2005).

The parameter α contains, in addition to the reactivity, also the effective delayed neutron fraction β and the prompt neutron generation time Λ , which are also unknown. It is often desirable to obtain either the reactivity ρ directly, or the reactivity in dollars ρ/β , and determine Λ in a separate measurement. One possibility would seem to be to perform a measurement at prompt critical to determine $\alpha_c = \beta/\Lambda$, and hence to determine the reactivity as

$$\frac{\rho}{\beta} = \frac{\alpha_c - \alpha}{\alpha_c} \quad (39)$$

However, this method suffers from the problem mentioned before, namely that the values of Λ and β differ in the critical and subcritical case.



■ **Figure 2**

Pulsed neutron experiments made on the fast research reactor core MASURCA in the MUSE project (The MUSE collaboration, Mellier 2005)

To avoid this problem, an ingenious method was devised by Sjöstrand (1956) usually referred to as the area ratio method. A simple analysis of (15) and (16) shows that taking the ratio of the area A_p of the prompt peak and the delayed area A_d , one has

$$\frac{A_p}{A_d} = \frac{-\rho}{\beta} \quad (40)$$

This is the celebrated Sjöstrand-formula or area ratio formula (Sjöstrand 1956). With this method the reactivity in dollars can be determined without the need of knowing either of Λ , ε , or S quantitatively. The key to this success was to use both a dynamic method *and* the ratio of two measured quantities, taken from the same system.

By using only one single pulse, practical application of the method would be hard, due to low neutron levels and interference from the background, making the determination of the delayed area impossible. Hence the method is used with periodic pulsing with a repetition period T such that $1/\alpha \ll T \ll 1/\alpha_d$. This way the prompt peak has sufficient time to die away between the pulses, whereas the delayed part does not decay significantly. After several hundred pulses, an approximately constant delayed background will be built up, whereas the prompt peak will be practically unchanged. It can be easily shown that calculating A_d as the delayed area within the period will leave (40) unchanged. This way the delayed area A_d can be determined with much bigger accuracy.

The area ratio method has been used with much success in reactivity measurements throughout the years. It has been proven to be very robust and working well in various systems, bare and reflected as well as in thermal and fast systems. Naturally, strong deviations from point kinetics make it work less accurately; thus several modifications of the original method were suggested, such as the extrapolated area ratio method, which under special circumstances can perform better. On the whole, however, the area ratio method is the most reliable pulsed neutron measurement method.

One reason for its success, seldom discussed and even more seldom investigated numerically, is the fact that it uses the ratio of two independent quantities from one and the same measurement. It is surmised that inaccuracies arising from the deviation from point kinetics cancel to a certain degree due to taking the ratio of the two independently measured parameters with the same detector. The Sjöstrand method shares this potential strength with the

fluctuation-based methods described below, which are also based on the ratio of two parameters measured in the same system, often with the same detector.

2.2.1 The Feynman-Alpha (Variance to Mean) Method

From the pragmatic point of view the pulsed neutron experiments described above have the drawback that they require access to a pulsed neutron generator. Radioactive neutron sources lend a much larger flexibility to perform measurements and they are much more readily available. They are not suitable to extract dynamic parameters the same way as the pulsed neutron experiments do, that is, utilizing only the time-dependence of the expectations, but this is where the noise measurements make their presence.

The essence of the noise measurements is that the correlations in the prompt chain between the neutron numbers or detector counts at different times in a subcritical reactor die out with the same prompt neutron decay constant as the one in the pulsed experiments. Although it sounds intuitively very plausible, this statement is far from trivial, and it had to be derived by rigorous methods for verification (Pál 1958). The methods described in the forthcoming sections determine the prompt neutron decay constant by only using a stationary neutron source. In addition, by using the first two moments of the neutron counts and using the dynamics in the evolution of the correlations, they also eliminate the unknown parameters S and ε . Eliminating Λ with using the properties of both the prompt and delayed decay modes is not as simple though as in the case of the pulsed experiments.

The principle of the Feynman-alpha method is to measure the detector counts during a measurement time duration (gate) t repeatedly and to calculate the variance to mean, that is, the relative variance, of the detector counts. Then, the measurement is repeated at different measurement times to obtain the time-dependence of the variance to mean. The time-dependence of the variance to mean will be determined by the prompt and delayed neutron decay constants.

The derivation of the variance to mean formula can be made via the forward approach by continuing the procedure of calculating the moments as outlined in [Sect. 2.1.1](#) Taking all possible second-order derivatives of (10), one obtains a coupled linear ordinary differential equation system with constant coefficients of order six for the six moments $\langle N(N-1) \rangle$, $\langle NC \rangle$, $\langle C(C-1) \rangle$, etc. Solution of this equation system is quite straightforward, and the relative variance of the detector counts as a function of the measurement time can be obtained. The result can be compactly written as

$$\frac{\sigma_Z^2(t)}{Z(t)} = 1 + \varepsilon \frac{\lambda_j^2}{(\alpha + \lambda)} \sum_{i=1}^2 \frac{W(\alpha_i)}{(\alpha_i - \alpha_j)} f_i(t); \quad i, j = p, d; \quad i \neq j \quad (41)$$

or, introducing the Feynman $Y(t)$ function as

$$Y(t) \equiv \frac{\sigma_Z^2(t)}{Z(t)} - 1, \quad (42)$$

alternatively one has

$$Y(t) = \varepsilon \sum_{i=1}^2 A_i f_i(t) = \varepsilon \left[A_1 \left(1 - \frac{1 - e^{-\alpha t}}{\alpha t} \right) + A_2 \left(1 - \frac{1 - e^{-\alpha_d t}}{\alpha_d t} \right) \right] \quad (43)$$

In (41) the following definitions were used:

$$W(s) \equiv \left(1 - \frac{\lambda^2}{s^2}\right) \langle v_p(v_p - 1) \rangle - \frac{\lambda^2}{s^2} 2\langle v_p \rangle \langle v_d \rangle \tag{44}$$

and

$$f_i(t) \equiv 1 - \frac{1 - e^{-\alpha_i t}}{\alpha_i t}; \quad i = p, d. \tag{45}$$

For six delayed neutrons, a completely analogous expression is valid, with the sum in (41) and (43) running from $i = 0$ to 6 (for the details see Pázsit and Pál 2008).

From (41) it is seen that the variance is over-Poisson in the case when branching is present. The sought parameter α is contained in the part of the relative variance exceeding unity. Similarly to the cases discussed earlier when ratios of various measured quantities are calculated, the source intensity S is not present in the formula. The detector efficiency ϵ does not disappear, but due to the nonlinear dependence of the relative variance on time, the parameters $\alpha = \alpha_p$ and α_d can be extracted by a fitting of the theoretical curve to the measurement without knowledge of the detector efficiency. An illustration of Feynman-Y functions with various reactivity values in units of 10^{-4} is shown in [Fig. 3](#).

The approximate expressions for the factors A_1 and A_2 read, for not too deep subcriticalities as

$$A_1 = \frac{D_{v_p}}{(\beta - \rho)^2} \tag{46}$$

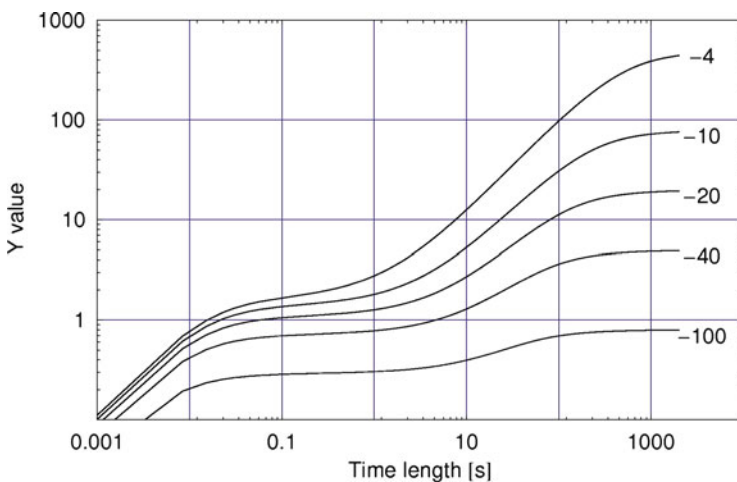


Figure 3 Feynman-Y values as functions of time, for various values of subcritical reactivity in units of 10^{-4}

and

$$A_2 = \frac{D_{v_p}}{(\rho - \beta)^2} \left[\left(\frac{\rho - \beta}{\rho} \right)^2 - 1 \right] = A_1 \left[\left(\frac{\rho - \beta}{\rho} \right)^2 - 1 \right] \quad (47)$$

where the prompt neutron Diven factor D_{v_p} was introduced, whose definition is

$$D_{v_p} = \frac{\langle v_p(v_p - 1) \rangle}{\langle v_p \rangle^2} \quad (48)$$

Since for $1/\alpha \ll t_1 \ll 1/\alpha_d$ one has

$$Y(t_1) = \varepsilon A_1 \quad (49)$$

and for $1/\alpha_d \ll t_2$

$$Y(t_2) = \varepsilon(A_1 + A_2), \quad (50)$$

in principle one has a similar possibility as with the Sjöstrand method, namely to determine ρ/β from $Y(t_1)/Y(t_2)$ without knowledge of Λ . However, unlike in the case of the former method where the pulse repetition could shorten the measurement time, with the Feynman-alpha method one needs long measurement times comparable with the delayed neutron time constants, which are not performed for practical cases. On the other hand, the advantages of determining the reactivity (or prompt neutron decay constant) from the ratio of two independent quantities from the same measurement (the first two moments of the neutron count) are still the same, namely that the method is relatively insensitive to deviations from the point-kinetic behavior.

The Feynman-alpha formula can be derived by accounting for six delayed neutron groups with fractions β_i ; decay constants λ_i , $i = 1 \dots 6$, with the same methods, at the expense of more complicated algebra. For the sake of completeness, the formula is given below. With one prompt and six delayed neutron groups, the time-dependence of the system will be characterized by the seven roots s_i of the characteristic equation, also called the “inhour equation”:

$$s \left(\Lambda + \sum_{i=1}^6 \frac{\beta_i}{s + \lambda_i} \right) - \rho = G^{-1}(s) = 0, \quad (51)$$

where $G(s)$ is the so-called zero power transfer function. With these preliminaries, the Feynman-alpha formula for six delayed neutron groups can now be given as

$$Y(t) = \frac{\mu_{ZZ}(t)}{Z(t)} = \sum_{i=0}^6 Y_i \left(1 - \frac{1 - e^{-\alpha_i t}}{\alpha_i t} \right), \quad (52)$$

where $\alpha_i = -s_i$, $i = 0, 1, \dots, 6$, and where t stands for the measurement time length. An explicit expression for the coefficients Y_i can be given by assuming that the probability of the simultaneous generation of two delayed neutron precursor nuclei, either in the same or in different groups, is zero or negligible, in the form

$$Y_i = 2\varepsilon D_v A_i \frac{G(\alpha_i)}{\alpha_i}, \quad (53)$$

where the A_i are the residues of G at s_i . Explicit expressions for the residues A_i can be found in Pázsit and Pál (2008) and a derivation for the most general case of all second-order precursor generating possibilities retained is given by Kuang and Pázsit (1999, 2002).

With the concrete values of the prompt neutron generation time Λ and the delayed neutron decay constants λ_i , even in a slow (thermal) reactor, the character of the solution given by (52) will be qualitatively very similar to the solution (43), calculated by assuming one average delayed neutron group. There will be a prompt part of the $Y(t)$ curve for short measurement times, and a delayed part for long times. In practical work, the prompt part is usually utilized.

Performing a Feynman-alpha measurement in practice means that one has to count the detector pulses during time intervals of length t repeatedly, in order to estimate the mean and the variance. The repetition is achieved by performing detection during a longer period and then dividing the total time length into sections of equal length and estimating the mean and the variance as arithmetic averages of the counts in these adjacent as well as nonadjacent intervals. Such an estimate will be biased as compared to the theoretical formula for two reasons. One reason is the finite number of samples used in the arithmetic averaging, and the other, more important circumstance is that the detector counts in time slots lying close to each other will not be independent random variables (the covariance is not zero). Theoretical expressions for the bias of the measurement, in terms of the sample population and the separation of the measurement intervals are given by Pázsit and Pál (2008).

Actually, the fact that the number of counts in adjacent or not too far separated intervals is not independent, can be used to construct measurement methods that utilize the information in the covariance of the count numbers in closely lying intervals. Such a method, the Bennett method, will be described below.

2.2.2 The Rossi-Alpha (Correlation) Method

The Rossi-alpha method is similar to the Feynman-alpha method. Instead of measuring the dependence of the relative variance of the detector counts in a time interval t , a covariance-type quantity is considered. Namely, the conditional probability of detecting a neutron in $(t + \tau, dt)$, given that a detection was made at t is considered. Since for an infinitesimal time dt the probability of a detection is equal to the expectation of the detections, this conditional probability can be written in terms of a covariance function. Based on the previous definitions, the Rossi-alpha formula is defined as

$$R(\tau)d\tau = \frac{\langle Z(t, dt)Z(t + \tau, d\tau) \rangle}{\langle Z(t, dt) \rangle} = \frac{C_{ZZ}(\tau)}{Z dt} + Z d\tau \quad (54)$$

where Z is the constant detection rate in the stationary system, and $C_{ZZ}(\tau)$ is the covariance function, defined as

$$C_{ZZ}(\tau) = \langle Z(t, dt)Z(t + \tau, d\tau) \rangle - \langle Z(t, dt) \rangle \langle Z(t + \tau, d\tau) \rangle \quad (55)$$

In a stationary system, the right-hand side obviously does not depend on t , only on the delay time τ . In the literature, the first term in the last equality of (54) is often referred to as the “correlated counts,” and the last term as the “uncorrelated background.” The information on the sought parameter α is contained in the covariance to the mean, that is, the first of these

two terms, through its dependence on τ . Thus, due to its simpler form and the fact that the information is contained in that term, we shall refer to the Rossi-alpha formula as the covariance to the mean, $P_r(\tau)d\tau$, that is,

$$P_r(\tau)d\tau = \frac{C_{ZZ}(\tau)}{Z dt}, \quad (56)$$

but in the literature the $R(\tau)$ of (54) is also referred to as the Rossi-alpha formula. The $P_r(\tau)$ above can be calculated from a two-point (in time) master equation in a way similar to the calculation of the Feynman-alpha formula. With the details we refer to Pázsit and Pál (2008). The final result can be written in a form similar to that of the Feynman-alpha:

$$P_r(\tau)d\tau = \varepsilon \frac{\lambda_j^2 d\tau}{2(\alpha + \lambda)} \sum_{i=1}^2 \frac{W(\alpha_i)}{(\alpha_i - \alpha_j)} f_i(t); \quad i, j = p, d; \quad i \neq j \quad (57)$$

where the functions $W(s)$ are identical with those in (44), but now the functions $f_i(t)$ are different from those of the Feynman-formula:

$$f_i(\tau) \equiv \alpha_i e^{-\alpha_i \tau}, \quad i = p, d. \quad (58)$$

Hence the Rossi-alpha formula can be written in the form

$$P_r(\tau)d\tau = \varepsilon(\alpha A_1 e^{-\alpha \tau} + \alpha_d A_2 e^{-\alpha_d \tau})d\tau \quad (59)$$

It is thus seen that the correlated part of the Rossi-alpha formula decays with the same decay constants as the detector count rate in the pulsed experiments. As is usual with the Feynman-alpha method, only the prompt part of the measurement is utilized, for the determination of the prompt neutron decay constant α . Similar to the Feynman-alpha method, space effects are suppressed by the ratio of the second- and first-order moments, although the domains of validity are not exactly the same for the two methods.

In a way analogous to the Feynman-alpha method, the Rossi-alpha formula can be calculated for six delayed neutron precursor groups with the result

$$P_r(\tau) = \frac{1}{2} \sum_{i=0}^6 Y_i \alpha_i e^{-\alpha_i \tau}, \quad (60)$$

where the coefficients Y_i are the same as in (53).

It may be interesting to note that an analogue of the fact that the second factorial moment of a discrete random variable in a volume of the phase space can be obtained from an integral of its two-point distribution (correlation function), exists to connect the Rossi- and Feynman-alpha expressions. Namely, once the Rossi-alpha formula for a process is known (or the two-point distribution of particle detection at two infinitesimal times), the Feynman-alpha formula, based on the variance of the detection number over a finite time period, can be calculated from the former by a temporal integration. Such derivations of the Feynman-alpha formula, using also a heuristic derivation of the Rossi-alpha formula, can be found in the literature (Yamane and Pázsit 1998; Baeten 2004).

2.2.3 The Bennett Variance Method

The Bennett variance method (Bennett 1981) utilizes the fact, mentioned above, that the detector counts in repeated time intervals are not independent random variables; for example, the covariance of the counts in neighbor or second neighbor intervals is larger than zero. This fact can be used to construct a measurement method and corresponding formula that can be used as a complement to the Feynman- and Rossi-alpha methods. Namely, the Bennett formula, similarly to the above two, expresses a higher moment of the detection statistics in terms of the reactivity and the delayed neutron precursor fraction, but in a functionally different form. The information content is equivalent with the Feynman- and Rossi-alpha methods, but the application has some practical advantages.

The principle of the method is to define adjacent nonoverlapping time intervals of length τ , separated by the time instants lying at $m\tau$. In the measurement, counts from two different detectors are used, indexed by $i = 1, 2$. Denoting the detector counts in detector i in the interval $(m-1)\tau \leq t \leq m\tau$ as $C_m^{(i)}(\tau)$, first the estimate of the expectation is defined as

$$\langle C^{(i)}(\tau) \rangle = \frac{1}{M} \sum_{m=1}^M C_m^{(i)}(\tau) \quad (61)$$

Next, a quantity called the “local fluctuation” is defined as

$$\delta u_m^{(i)}(\tau) = \frac{C_m^{(i)}(\tau) - \frac{1}{2} \{C_{m-1}^{(i)}(\tau) + C_{m+1}^{(i)}(\tau)\}}{\langle C^{(i)}(\tau) \rangle} \quad (62)$$

The covariance $\sigma_{1,2}^2(\tau)$ is then defined as

$$\sigma_{1,2}^2(\tau) = \frac{1}{M-2} \sum_{m=2}^{M-1} \{ \delta u_m^{(1)}(\tau) \cdot \delta u_m^{(2)}(\tau) \} \quad (63)$$

The evaluation of the right-hand side of (63) requires calculation of the joint expectations $\langle C_k^{(i)}(\tau) C_l^{(i)}(\tau) \rangle$ with $l = k-1, k, k+1$. These are available from Yamane et al. (1999) and were also calculated in Pázsit and Pál (2008). After straightforward but lengthy calculations one obtains the expression

$$\sigma_{1,2}^2(\tau) = \frac{D_{v_p}}{F \left(\frac{\beta}{1-\beta} \right)^2 (1+\$)^2 \tau} \left\{ \frac{3}{2} - \frac{10 - 15e^{-\alpha\tau} + 6e^{-2\alpha\tau} - e^{-3\alpha\tau}}{4\alpha\tau} \right\} \quad (64)$$

where D_{v_p} is the Diven factor of the prompt neutrons, defined in (48), and F is the mean fission rate. By determining the dependence of the Bennett covariance $\sigma_{1,2}^2(\tau)$ on the gate length τ in a measurement and fitting the measurement to (64), the coefficient

$$A_0 = \frac{D_{v_p}}{F \left(\frac{\beta}{1-\beta} \right)^2 (1+\$)^2} \quad (65)$$

can be determined. From A_0 , in possession of the fission rate F and the subcritical reactivity in dollars, $\$,$ which can be determined from the same measurement with the Feynman- or Rossi-alpha methods, as well as knowing the Diven factor, the effective delayed neutron fraction β can be determined. Having determined $\$$ and β , the reactivity ρ can also be obtained in absolute units.

A modified version of the Bennett method was proposed and tested by Yamane et al. (1999) and was shown to have advantages over the original Bennett method. The modified version is an extension of the original one by using more time intervals in the definition of the local fluctuation as

$$\delta u_m^{(i)}(\tau) = \frac{C_m^{(i)}(\tau) - \frac{1}{2K} \left\{ \sum_{k=1}^K [C_{m-k}^{(i)}(\tau) + C_{m+k}^{(i)}(\tau)] \right\}}{\langle C^{(i)}(\tau) \rangle} \quad (66)$$

With this, the covariance is now defined as

$$\sigma_{1,2}^2(\tau) = \frac{1}{N-2K} \sum_{m=K+1}^{N-K} \left\{ \delta u_m^{(1)}(\tau) \cdot \delta u_m^{(2)}(\tau) \right\} \quad (67)$$

The τ dependence of the covariance $\sigma_{1,2}^2(\tau)$ of (67) is similar to, but more involved than that of (64). Nevertheless, the value of the coefficient A_0 remains the same as in (65), and can be determined similarly, that is, by fitting the measured data to the theoretical expression.

The original Bennett method has the advantage of being insensitive to a slow drift in the expectations (reactor power) due to the definition of the local fluctuations. The modified Bennett method, while keeping this advantage, is also more robust for low-frequency oscillations.

2.2.4 Mogilner's Zero Crossing Method

This is yet another technique for the determination of the prompt neutron decay constant α from the statistics of neutron detection. Mogilner suggested an expression for the generating function of the probability distribution $P_M(Z, t)$ of detecting Z neutrons during time t such that $P_M(Z, t)$ is a special negative binomial distribution (Mogilner and Zolotukhin 1961). Hence his heuristic generating function

$$G_M(z, t) = \sum_{Z=0}^{\infty} P_M(Z, t) z^Z \quad (68)$$

was of the form

$$G_M(z, t) = [1 + (1-z)\psi(t)]^{-Z(t)/\psi(t)} \quad (69)$$

where $Z(t)$ is the expectation of the neutron counts, given by (22), and $\psi(t) = Y f(t)$ is equal to the prompt term of the Feynman-alpha expression given by the combination of (43) and (46). This can be written as

$$\psi(t) = \varepsilon \left(\frac{\lambda_f}{\alpha} \right)^2 \langle v_p \rangle^2 D_{v_p} \left(1 - \frac{1 - e^{-\alpha t}}{\alpha t} \right) \quad (70)$$

The first two factorial moments of this expression are equal to those of the exact solution.

The essence of the Mogilner method is to utilize an expression for the dependence of the probability of obtaining no counts in a time interval t on the length of this interval. From (69), one obtains

$$P_M(0, t) = G_M(0, t) = [1 + \psi(t)]^{-Z(t)/\psi(t)} \quad (71)$$

and from here it follows that

$$\ln \frac{1}{P_M(0, t)} = Z(t) \frac{\ln [1 + \psi(t)]}{\psi(t)} \quad (72)$$

The use of this formula in measurements is analogous to that of the Feynman-alpha method. The zero detection probability $P_M(0, t)$ is estimated by repeated measurements with a given measurement time and the time-dependence is determined by repeating the procedure with varying the measurement time. After that $\psi(t)$, or rather the prompt neutron decay constant α is determined by a curve-fitting procedure using (72) and (70).

It has to be kept in mind that (71) is only approximately valid. Comparing with the exact expression for the zero detection probability shows that (71) is accurate only if $Y \ll 1$. On the other hand, determination of Y is difficult for such cases. Hence, one has to exercise care with the use of this method.

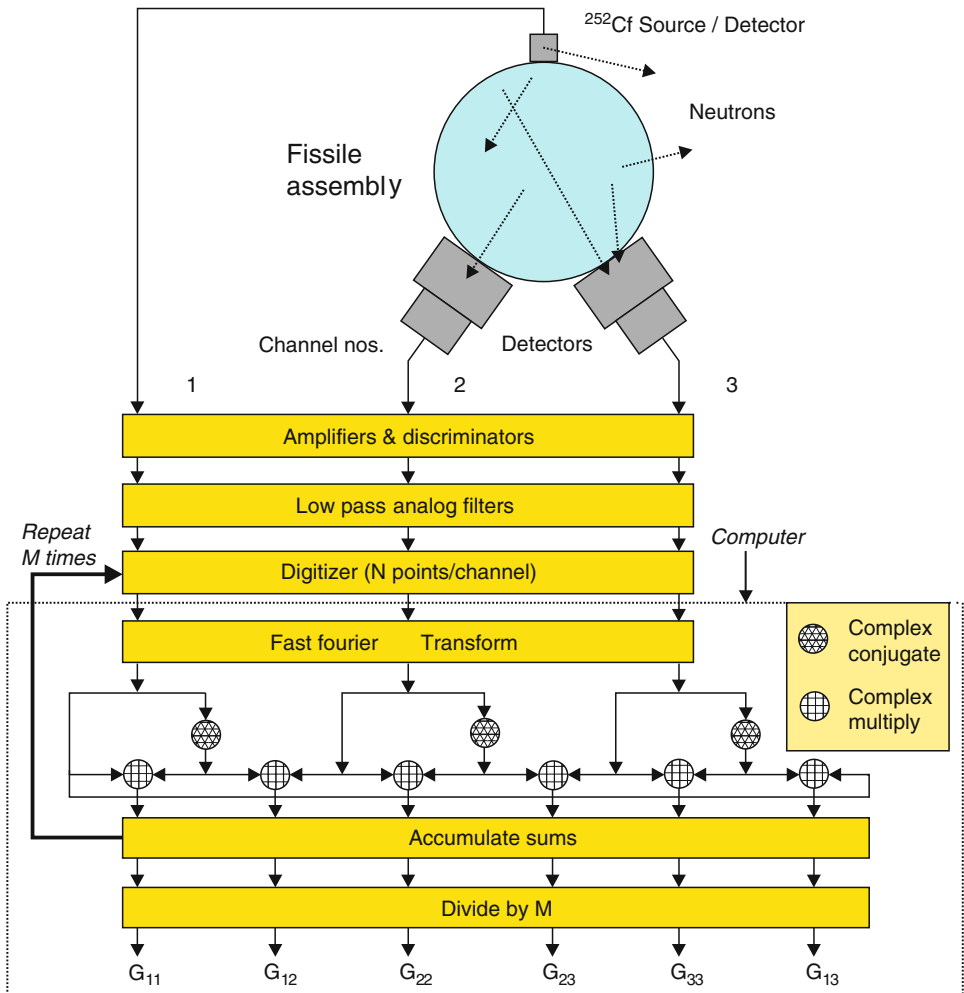
2.2.5 The Cf-252 Method

This method is different from the above methods, which are all based on pulse counting techniques in the time domain, in that it is based on spectral features of the detector signals in the frequency domain (Mihalczko et al. 1990). A detailed description of all aspects of the method is found in a recently published tutorial (Blakeman 2009), which contains a very extensive list of original publications. Here only a very brief summary is given.

The essence of the method is to use a ^{252}Cf neutron source, which is built together with an ionization chamber. The ^{252}Cf is brought up electrochemically on one of the plates of a parallel-plate ionization chamber. Such an arrangement is called a “ ^{252}Cf detector.” The detector identifies each spontaneous fission event leading to neutron emission by measuring the ionized fission products, but without absorbing any neutron. This way, the time origin of the fission is known, and correlated neutrons can be easily discriminated, and hence an increased signal-to-noise ratio can be obtained.

In the method three detectors are used: one Cf-252 detector (detector #1), and two “ordinary” neutron detectors (#2 and #3) that measure the time-dependent flux fluctuations in current mode. The Cf-252 detector only detects the fission events, which lead to the emission of neutrons (► Fig. 4).

The Cf-252 method also starts with pulse counting and rejecting the pulses of the Cf-252 detector arising from reactions other than spontaneous fission, most notably alpha decay. However, after that the pulses are smoothed by low-pass filtering to a continuous signal, similar to a detector signal in current mode. This signal is then digitized and processed with frequency analysis methods, similar to the methods of power reactor noise, as described in ► Sects. 3–5. The principle of the method is to calculate the pairwise cross-spectra between all three detectors and the auto-spectrum of the Californium detector in the frequency domain.



■ Figure 4

Schematics of the Cf-252 reactivity measurement method (From Blakeman 2009)

In the original applications of the method (Mihalcz 1990), the multiplication factor is obtained from the following expression:

$$\frac{G_{12}^* G_{13}}{G_{11} G_{23}} = \frac{\nu_c I_c}{\nu I} \frac{1}{R D_\nu} \frac{1 - k_{eff}}{k_{eff}} \quad (73)$$

Here, G_{12} is the cross-spectrum between detector #1 (containing the Cf source) and detector #2, etc.; ν_c and ν are the mean value of source (Cf) and core (U-235) fission neutrons per fission; I_c and I , the average importance of source and fission chain neutrons; D_ν is the Diven factor of the fission chain prompt neutrons (the same as (48)); finally, R is a factor that corrects for deviations from point kinetics.

The quantities on the left-hand side are measured. The quantities on the right-hand side are either nuclear constants or flux-type quantities that need to be calculated in advance, except k_{eff} . The source strength and detector efficiencies do not appear in the expression. The method yields the absolute value of k_{eff} , that is, not in dollars. However, the knowledge of certain parameters, notably I , I_C and R , is assumed. These need to be determined from transport calculations which, as discussed in the foregoing, in a general case cannot be exact, since the core configuration is only known in an approximate way. However, use of the corrections usually improves the accuracy of the method, even when the correction factors are calculated with a certain inaccuracy.

As described by Blakeman (2009), the method has lately been used in a modified form. The left-hand side of equation (73) is defined as the spectral ratio $R(\omega)$ (independent of the frequency in the frequency range of interest), and the relationship between the spectral ratio and the reactivity is written as

$$R(\omega) = R = \frac{\rho}{C_2\rho - C_1}$$

where C_1 and C_2 are constants, consisting of the Diven factors of the Cf-252 fission and that of the fissile material as well as detector efficiencies and fission rates. For reactivities close to critical, $C_2\rho - C_1 \approx -C_1$, moreover $C_1 \approx 1$, hence for such cases, the spectral ratio is approximately equal to the subcritical reactivity.

The method has some advantages over other methods. It does not require the knowledge of β and Λ . This is sometimes expressed such as no calibration close to delayed critical is necessary. The method is fast, such that a short measurement period (a few seconds) is sufficient for a reliable measurement. Thus, the method can be applied on-line (following dynamic changes in the reactivity) and it works also with deep subcriticalities. For the same reasons, the method can be used in large cores. Currently, this is the only method that is effective for reactivity control in power reactor cores during loading. A recent application is reported by Baeten et al. (2010), which also discusses the principles of the technique.

2.3 Reactivity Measurements in ADS

The neutron fluctuation-based methods of measuring subcritical reactivity described earlier have been elaborated and tested a long time back. However, recently these methods have received a renewed attention due to the appearance of the concept of accelerator-driven subcritical systems (ADSs). In these systems, various methods of reactivity measurement were investigated both conceptually as well as in some experimental programs. Regarding the Rossi and Feynman-alpha methods, these needed some theoretical development. In contrast to the traditional methods that use a neutron source with pure Poisson statistics, the neutron source in an ADS, based on the spallation process, has a so-called compound Poisson statistics with a time-dependent source intensity. The first characteristic, that is, the compound Poisson statistics, is due to the fact that several source neutrons are generated simultaneously in each spallation event, whose descendants have the same temporal correlation properties as neutrons belonging to the same fission chain. The second characteristic, the temporal intensity, arises since the accelerator, serving as the neutron source, is usually run in a pulsed mode, that is, with a periodically varying intensity. Hence the process is not stationary, only periodically stationary in such systems.

Because of these differences in the source properties, the corresponding Rossi- and Feynman-formulas will be modified as compared to their traditional counterparts in the literature. In this section, an account will be given of the formulas used in ADS experiments.

2.3.1 Spallation Source

In the target of a spallation source, a large and random number of neutrons (typically several tens of neutrons) are generated by each impinging high-energy proton. In a thick target, a whole shower of spallation reactions will take place. It is usually assumed that the target is small enough such that all neutrons in one reaction can be assumed as being born simultaneously. Such sources will be called multiple emission sources. Actually, a Cf-252 source is also a multiple emission source, but the effects of its relatively low multiplicity are negligible.

The number of spallation events in a time interval for a steady source with a constant intensity S will be assumed to follow Poisson statistics. The validity of this assumption is questionable; there is reason to believe that the ions (protons) of an accelerator are time-correlated. This question is discussed in detail by Degweker and Rana (2007) who derive formulas for certain forms of time-correlations between the accelerator ion impinging events. We shall disregard such effects here.

The distribution of the number of particles emitted per spallation event will be denoted by $p_q(n)$, and its generating function will be denoted as

$$r(z) = \sum_{n=0}^{\infty} p_q(n) z^n. \quad (74)$$

Only the first two moments of the above distribution will enter the relevant final formulas, and these will be denoted as

$$r_1 = \langle \mathbf{q} \rangle = \sum_n n p_q(n) \quad \text{and} \quad r_2 = \langle \mathbf{q}(\mathbf{q} - 1) \rangle = \sum_n n(n-1) p_q(n). \quad (75)$$

It is practical to introduce the Diven factor of the source:

$$D_q = \frac{\langle \mathbf{q}(\mathbf{q} - 1) \rangle}{\langle \mathbf{q} \rangle^2} = \frac{r_2}{r_1^2}. \quad (76)$$

Since the difference compared to the traditional case lies entirely in the different statistics of the source, the distributions induced by a single particle will not be affected. Hence it is only the formula connecting the single-particle induced and source-induced distributions, which has to be recalculated; the rest of the calculations will go along a line very similar to that given previously for the backward approach. With the same arguments as with (24), one can write, in first order of dt :

$$P(N, C, Z, T, t) = (1 - S dt) P(N, C, Z, T, t - dt) + S dt \sum_{n,c,z} P(N-n, C-c, Z-z, T, t) \sum_k p_q(k) A_k(n, c, z, T, t), \quad (77)$$

where, analogous to (30), the function $A_k(n, c, z, T, t)$ is defined as

$$A_k(n, c, z, T, t) = \sum_{\substack{n_1 + \dots + n_k = n \\ c_1 + \dots + c_k = c \\ z_1 + \dots + z_k = z}} \prod_{j=1}^k p(n_j, c_j, z_j, T, t). \tag{78}$$

With the usual steps, the solution of the equation connecting the corresponding generating functions of the single-particle induced distribution and that of the source-induced distribution reads as

$$G(x, y, v, T, t) = \exp \left\{ S \int_0^t \{ r [g(x, y, v, T, t')] - 1 \} dt' \right\}. \tag{79}$$

This expression is very similar to the case of a simple Poisson source, (27), except that the single-particle generating function appears as an argument of a power series represented by the generating function $r(z)$ of the source particle number distribution. The form of the relationship is not affected by the presence of delayed neutrons or detectors in the system; those only affect $p(n, c, z, T, t)$, but not the source properties.

Due to the similarity with the formulas for the standard case, and the unchanged form of the single-particle induced distribution, it can be expected that the Feynman- and Rossi-alpha for the case of the spallation source will only be moderately changed compared to the traditional formulas. This is indeed the case. Without the details of the calculations, we quote here the results.

It turns out that the Feynman-alpha formula can be written exactly in the same form as (41), that is,

$$Y(t) = \varepsilon \frac{\lambda_f^2}{(\alpha + \lambda)} \sum_{i=1}^2 \frac{W(\alpha_i)}{(\alpha_i - \alpha_j)} f_i(t); \quad i, j = p, d; \quad i \neq j \tag{80}$$

where, as in the traditional case, the limit $t \rightarrow \infty$ was performed and the measurement time duration T was re-denoted as t . The parameters α_p, α_d and the functions $f_p(t)$ and $f_d(t)$ are the same as before, for example, in (45). The only difference is that the function $W(s)$ is now modified to

$$W(s) = \left(1 - \frac{\lambda^2}{s^2} \right) \left[\langle v_p (v_p - 1) \rangle + r_2 \frac{\langle v \rangle}{r_1} (-\rho) \right] - \frac{\lambda^2}{s^2} 2 \langle v_p \rangle \langle v_d \rangle. \tag{81}$$

Writing the result again in the standard Feynman $Y(t)$ form

$$Y(t) = \varepsilon \sum_{i=1}^2 A_i f_i(t) \tag{82}$$

and considering the prompt term $\varepsilon A_1 f_1(t)$ only with the same simplifications as in the traditional case, that is, with (46), one obtains

$$\begin{aligned} \varepsilon A_1 f_1(t) &= \frac{\varepsilon D_{v_p}}{(\rho - \beta)^2} \left[1 + \frac{r_1 D_q}{\langle v \rangle D_{v_p}} (-\rho) \right] \left(1 - \frac{1 - e^{-\alpha t}}{\alpha t} \right) \\ &= \frac{\varepsilon D_{v_p}}{(\rho - \beta)^2} (1 + \delta) \left(1 - \frac{1 - e^{-\alpha t}}{\alpha t} \right). \end{aligned} \tag{83}$$

Here the parameter

$$\delta = \frac{r_1 D_q}{\langle v \rangle D_{v_p}} (-\rho) \quad (84)$$

was introduced.

It is thus seen that for multiple emission sources, the variance to mean formula changes only very slightly. The time-dependence of the formula, which is the basis of the reactivity determination, is the same as with a simple Poisson source.

It is seen that the presence of the multiple emission is beneficial for the application of the Feynman method for the measurement of the reactivity, since it increases the amplitude of the useful part of the variance, that is, the factor Y , which stands for the deviation from the Poisson statistics in the count rate. The reason for this is the simultaneous emission of several source neutrons in the system by the source, hereby increasing the number of neutrons being time-correlated.

The effect of the presence of the “enhancement factor” $\delta > 0$ on the formula can be estimated quantitatively. According to experimental evidence, the Diven factors show a very little variation whether it regards fission or spallation, that is, the factor D_q/D_{v_p} will be in the order of unity. For a ^{252}Cf source in a core loaded with enriched uranium, the factor $r_1/\langle v \rangle = \langle \mathbf{q} \rangle / \langle v \rangle$ is also in the order of unity, hence for a value of the multiplication factor $k_{eff} = 0.95$, the correction represented by δ is below 10%. For spallation sources, on the other hand, the situation is different. For spallation with protons in the GeV range and a thick Pb target, the yield is $r_1 \approx 40$ neutrons per spallation event, and accordingly, with $k_{eff} = 0.95$, one has $\delta \approx 3$. For deeper subcriticalities the value increases further. Hence, for deeply subcritical systems the large source multiplicity becomes a significant factor in measuring the reactivity of the system.

For the Rossi-alpha formula with a steady spallation source, the differences to the traditional case are the same as for the Feynman-alpha formula. The Rossi-alpha for the multiple emission source case is given as

$$P_r(\tau) d\tau = \frac{C_{ZZ}(\tau)}{Z dt} = \frac{\epsilon \lambda_f^2 d\tau}{2(\alpha + \lambda)} \sum_{i=1}^2 \frac{W(\alpha_i)}{(\alpha_i - \alpha_j)} f_i(t); \quad i, j = p, d; \quad i \neq j \quad (85)$$

where the function $W(s)$ is equal to those in the Feynman-alpha formula for spallation sources, (81), whereas the functions $f_i(\tau)$ are the same as in the traditional case, (58):

$$f_i(\tau) \equiv \alpha_i e^{-\alpha_i \tau}, \quad i = p, d.$$

Hence the same enhancement factor δ appears in the Rossi-alpha formula for spallation sources as in the Feynman-alpha formula.

2.3.2 Pulsed Source in Feynman- and Rossi-Alpha Applications

For technical reasons, accelerator-driven subcritical systems will be most likely run in a pulsed mode. At least this has been the case in some model ADS experiments performed so far.

When considering the description of the source in a pulsed ADS, there are a large number of varieties. The pulsing itself can be treated as strictly periodic. The pulses can be either wide or narrow, on a time scale of the lifetime of the subcritical chains in the core. For wide

pulses, the source events within the pulse can be treated either as a Poisson point process, or to be time-correlated with an exponentially decaying correlation. Various pulse forms can be assumed, the square and the Gaussian distribution of the temporal intensity of the source being two possibilities that have been considered.

For very narrow pulses, it is a good approximation that all neutrons in the pulse are emitted simultaneously. The case of narrow pulses can be described much simpler by assuming strongly periodic processes for the injection, that is, a train of temporal Dirac-delta functions. This is equivalent with the assumption that all neutrons in the short pulse were born concurrently. There is a principal difference between source neutrons born simultaneously in an instantaneous emission, or being born in a finite width pulse with either correlated or uncorrelated statistics of the neutrons being born in the pulse.

A final distinction between further alternatives is whether the pulsing is synchronized with the start of the data collection in the experiment or not. In the latter case, the start of the neutron counting is a random parameter in relation to the pulse starting times. These two alternatives will be referred to as “deterministic pulsing” (detection start synchronized with the pulses) and “stochastic pulsing,” respectively.

Due to the above variety, there is a corresponding collection of Feynman- and Rossi-alpha formulas (Degweker 2000, 2003; Yamane et al. 2002; Kitamura et al. 2005; Ballester and Munoz-Cobo 2005; Munoz-Cobo et al. 2008). A generic and most complete treatment of all cases is given by Degweker and Rana (2007) and we refer the reader to that publication for details. Here we shall only give results for the case of narrow pulses. For the sake of better readability, the delayed neutrons will be neglected and we shall only consider the prompt part of the corresponding Feynman- and Rossi-alpha formulas. The extension to include delayed neutrons is readily possible and is available in the literature.

2.3.3 Feynman-Alpha with Deterministic Pulsing

Here it is assumed that pulses are emitted into the system at times $t = nT_0$, with n running through the integers from $-\infty$ to ∞ . The measurement starts at $t = +0$, and lasts over a gate length T , hence its start coincides with the arrival of a pulse (this case is also called the “pulse-triggered” Feynman-alpha measurement). It is supposed that in one pulse a random number of neutrons are injected with a probability distribution $p_q(n)$, with a corresponding generating function $r(z)$, that is, the same notations are used as before.

The final result for the deterministically pulsed Feynman-alpha formula reads as

$$Y(T) = \frac{\lambda_d \lambda_f \langle v(v-1) \rangle}{\alpha^2 M_1^*(T)} \left\{ \frac{-2\alpha u e^{-\alpha u} + 2(1 - e^{-\alpha T})}{1 - e^{-\alpha T_0}} - \frac{2\alpha T_0 e^{-\alpha T_0} (e^{-\alpha u} - e^{-\alpha T})}{(1 - e^{-\alpha T_0})^2} + (1 + \delta^*) [T/T_0] - (1 - \delta^*) \frac{e^{-2\alpha u} - e^{-2\alpha T} + (1 - e^{-\alpha T})^2}{1 - e^{-2\alpha T_0}} - \delta^* \frac{2(e^{-\alpha u} - e^{-\alpha T})}{(1 - e^{-\alpha T_0})} \right\}. \quad (86)$$

with

$$M_1^*(T) = \frac{1 + [T/T_0] (1 - e^{-\alpha T_0}) - e^{-\alpha u}}{1 - e^{-\alpha T_0}} \quad (87)$$

Here, $[T/T_0]$ stands for the largest integer smaller than or equal to T/T_0 , $u = T - [T/T_0]T_0$, $\alpha = \alpha_p$ is the prompt neutron decay constant, and $M_1^*(T)$ is proportional to the first moment of the detector counts. Further, δ^* is a “source enhancement factor”:

$$\delta^* \equiv \frac{r_1}{\langle v \rangle} \frac{(D_q - 1)}{D_v} |\rho| = \delta - \frac{r_1 |\rho|}{\langle v \rangle D_v} \quad (88)$$

Its form is similar to the factor δ , defined in (84). The difference is that instead of the factor D_q , the expression $D_q - 1$ appears in the numerator.

2.3.4 Feynman-Alpha with Stochastic Pulsing

Here it is assumed that the arrival of the pulses and the start of the measurement are not synchronized. As a result, the corresponding formulas, and in particular that of the expectation of the detector counts, will be smoother functions of time. The result is given as

$$Y(T) = \frac{\lambda_d \lambda_f \langle v(v-1) \rangle}{\alpha^2} [1 + \delta^*] \left(1 - \frac{1 - e^{-\alpha T}}{\alpha T} \right) + \frac{r_1 \lambda_d}{\alpha} \left\{ \frac{u(T_0 - u)}{T_0 T} + \frac{e^{\alpha(u-T_0)} + e^{-\alpha u} - e^{-\alpha T_0} - 1}{\alpha T (1 - e^{-\alpha T_0})} \right\}. \quad (89)$$

The factor δ^* is the same as in (88). This expression consists of two terms; a smooth term, corresponding to the traditional Feynman-alpha solution with stationary sources, although with an amplitude enhanced with the factor δ^* , and a nonnegative oscillating term with an oscillation period equal to T_0 . The smooth, traditional term constitutes a lower envelope of the oscillatory part. This formula is suitable for evaluating measurements, and was experimentally verified.

2.3.5 Rossi-Alpha with Stochastic Pulsing

Again, without details of the derivation, the final result is given as

$$R(\tau) = \frac{P_2(0, \tau)}{Z} = \frac{\lambda_d \lambda_f \langle v(v-1) \rangle}{2\alpha} [1 + \delta^*] e^{-\alpha \tau} + \frac{r_1 \lambda_d}{\alpha T_0} + \frac{r_1 \lambda_d}{2(1 - e^{-\alpha T_0})} \left[e^{-\alpha u} + e^{-\alpha T_0} e^{\alpha u} - \frac{2(1 - e^{-\alpha T_0})}{\alpha T_0} \right] \quad (90)$$

The result contains a traditional smooth Rossi-alpha formula, that is, a decaying exponential and a constant part corresponding to the so-called correlated and uncorrelated counts, plus an oscillating part. The oscillating part has a discontinuous derivative, unlike in the case of the stochastically pulsed Feynman-alpha curve. As the formula shows, in contrast to the pulsed Feynman-alpha method, the oscillations do not decay with time; rather they are periodic. This lends the possibility of eliminating the oscillating part from an experiment, from the tail of the curve at large τ values (Kitamura et al. 2006).

2.4 Pulse Counting Techniques in Nuclear Material Management (Safeguards)

Branching in the fission process, as the physical origin of time correlations and hence nontrivial statistical properties of the neutron distribution, can be used also in areas other than measuring the reactivity (or multiplication factor) in nearly critical systems. One such area, a branch of nuclear safeguards, deals with nuclear material control and accounting. The purpose is to detect, identify, and quantify fissile material with nonintrusive methods (Böhnel 1985; Hage and Cifarelli 1985; Ensslin 1998). This is achieved by detecting radiation, either neutrons or gamma photons, that are emitted either spontaneously (passive methods), or through inducing by neutron or photon irradiation (active methods).

As a rule, such investigations concern samples of fissile material far from being critical. The material, consisting of transuranic elements, is a neutron emitter through spontaneous fission or emission through (α, n) reaction, and the passive way of identification is based on detecting the emitted neutrons, and lately also the associated gamma photons (Pázsit and Pozzi 2005). However, even in small samples, a primary neutron has a nonzero probability to start a short chain before escaping through fission induced in the sample, much like in the case of fast fission in the fuel elements of thermal reactors. The difference in the number and energy distributions in spontaneous and induced fission between the different isotopes gives, theoretically, a possibility of identifying the fissile isotope, and also its mass. In practice, with present technology, only some lumped parameters can be determined. The most relevant material to be quantified is plutonium, and the measurements supply the so-called ^{240}Pu effective mass. The total Pu mass is then extracted from the ^{240}Pu mass by determining the isotopic composition of the sample by other means such as gamma-ray spectroscopy.

Here we only consider the number distributions and will disregard the energy aspects. The number distribution of the fission neutrons is usually quantified by the low-order factorial moments. These are then converted into multiplicity detection rates, which are the quantities observed in measurements. In the safeguards literature, the number of neutrons or gamma photons in a spontaneous fission, as well as the number of particles generated or leaving the sample is often referred to as multiplicities, and the various descriptors as multiplicity distribution, multiplicity moments, etc. For example, experimental determination of the factorial moments is usually referred to as “multiplicity counting.” Whenever it cannot lead to confusion, any of these quantities may be referred to as just multiplicities.

In what follows, the notations used will be briefly summarized, and the master equations for the generating function of the number of neutrons and gamma photons per one initial neutron and one initial source event (spontaneous fission) will be given. After that, without derivation, a mere list of the factorial moments is given, together with the corresponding multiplicity detection rates.

The notations are summarized as follows. Random variables and their moments referring to neutrons are denoted by ν , their probability distributions by $p(n)$, and their generating functions by $q(z)$. The same quantities for gamma photons are denoted by μ , $f(n)$, and $r(z)$. The variables/moments and the number distributions belonging to (known) elementary nuclear reactions, will have indices, indicating which type of reaction they refer to. Those referring to spontaneous fission will have a subscript sf , and those referring to induced fission will have a subscript i . For the factorial moments, there will always be a second index, giving the order of the moment, such as $\nu_{sf,2}$.

In addition, one has to distinguish between two sets of variables for both neutrons and photons, depending on whether they belong to a source event (all processes, i.e., spontaneous fission and (α, n) processes included), or to the *total number* of generated neutrons, which accounts also for the internal multiplication (“superfission.” After Böhnel 1985). The parameters belonging to the first set will be written with a subscript indication (*sf*, *i* or *s*, the latter denoting “source”), whereas those of the second set will be denoted with just a numerical subscript indicating their order. The corresponding probability distributions will be denoted by $p(n)$ and $P(n)$ for neutrons, for the total number of neutrons per one starting neutron or one source event, respectively, and by $f(n)$ and $F(n)$ for gamma photons, respectively. The corresponding generating functions are denoted by $h(z)$, $H(z)$, $g(z)$, and $G(z)$, respectively. Finally, the probability that a neutron will have a collision before escaping will be denoted by the symbol p . This latter parameter is not known in a measurement, hence it is one of the parameters to be determined.

The relationship between the number distribution of the source neutrons, $p_s(n)$, which accounts for both spontaneous fission and (α, n) neutrons, and that of the number distribution of spontaneous fission, $p_{sf}(n)$, is given by

$$p_s(n) = \frac{\alpha v_{sf} \delta_{1,n} + p_{sf}(n)}{1 + \alpha v_{sf}} \quad (91)$$

where the parameter α is defined as the ratio of the average neutron production between (α, n) and spontaneous fission processes:

$$\alpha = \frac{Q_\alpha}{Q_f v_{sf}} \quad (92)$$

Here, Q_α and Q_f are the intensities of the corresponding processes. The introduction of the joint source distribution (91) simplifies the notations while doing the calculations, but in the end one has to go back to the distribution $p_s(n)$ and its moments, since the distribution $p_s(n)$ contains the factor α , which is not known and hence need to be determined together with the other parameters sought, from the detected multiplicity rates.

From the nature of the problem, it follows that the master equations to be derived for the probability distribution of the neutrons or photons leaving the sample has to be a backward type equation. Hence, as described earlier in this chapter, it has to be split into the task of calculating the number distribution of particles leaving the sample as generated by one starting neutron, and by one source event, respectively. Let $w(n_1, n_2)$ denote the probability of *one* starting neutron leading to n_1 neutrons and n_2 gamma photons, and $u(z_1, z_2)$ its generating function. Likewise, let $W(n_1, n_2)$ and $U(z_1, z_2)$ denote the same quantities for one *source* event. Then, by simple considerations it is easy to derive the following master equations for the generating functions (for the details, see Pázsit and Pál 2008):

$$u(z_1, z_2) = (1 - p)z_1 + pr_i(z_2)q_i [u(z_1, z_2)] \quad (93)$$

where $q_i(z)$ and $r_i(z)$ are the generating functions of the number distributions of neutrons and photons generated in an induced reaction, respectively, and

$$U(z_1, z_2) = r_s(z_2)q_s [u(z_1, z_2)]. \quad (94)$$

Equations (93) and (94), together with (91) are fully sufficient to derive individual and mixed factorial moments for the neutrons and gamma photons. The separate equations for neutrons and gamma photons only, which are better known from the literature, can be obtained by substituting $z_1 = 1$ and $z_2 = 1$, respectively. These read for the corresponding generation functions, with the notations defined earlier, as

$$h(z) = (1 - p)z + pq_r [h(z)], \quad (95)$$

$$H(z) = q_s [h(z)] \quad (96)$$

for the neutrons, and

$$g(z) = (1 - p) + pr_r(z)q_r [g(z)], \quad (97)$$

$$G(z) = r_s(z)q_s [g(z)] \quad (98)$$

for the gamma photons.

In what follows, without derivation, we list here the first three individual factorial moments for neutrons and gamma photons, and the first three mixed moments (for the derivation of the full probability distributions see Enqvist et al. 2006).

2.4.1 Neutron Factorial Moments

One defines the so-called *leakage multiplication* as

$$\mathbf{M} \equiv \frac{1 - p}{1 - pv_{i,1}}; \quad pv_{i,1} < 1 \quad (99)$$

With this notation, the moments for the singles, doubles, and triples read as

$$v_1 = \mathbf{M}v_{s,1} \quad (100)$$

$$v_2 = \mathbf{M}^2 \left\{ v_{s,2} + \frac{\mathbf{M} - 1}{v_{i,1} - 1} v_{s,1}v_{i,2} \right\} \quad (101)$$

$$v_3 = \mathbf{M}^3 \left\{ v_{s,3} + \frac{\mathbf{M} - 1}{v_{i,1} - 1} (3v_{s,2}v_{i,2} + v_{s,1}v_{i,3}) + 3 \left(\frac{\mathbf{M} - 1}{v_{i,1} - 1} \right)^2 v_{s,1}v_{i,2}^2 \right\} \quad (102)$$

2.4.2 Gamma Photon Factorial Moments

One defines the gamma leakage multiplicity per one initial neutron

$$\mathbf{M}_\gamma \equiv \frac{p\mu_{i,1}}{1 - pv_{i,1}} \quad (103)$$

and the factorial moments g_n of the number of gamma photons generated by one initial neutron,

$$g_n = \left. \frac{d^n g(z)}{dz^n} \right|_{z=1} \quad (104)$$

Then the moments read as follows:

$$\mu_1 = \frac{\mu_{sf,1} + \alpha v_{sf,1}}{(1 + \alpha v_{sf,1})} + \frac{v_{sf,1}(1 + \alpha)}{(1 + \alpha v_{sf,1})} \mathbf{M}_\gamma, \quad (105)$$

$$\mu_2 = \frac{\mu_{sf,2}}{1 + \alpha v_{sf,1}} + 2 \frac{(\mu_{sf,1} + \alpha v_{sf,1})}{(1 + \alpha v_{sf,1})} \frac{v_{sf,1}(1 + \alpha)}{(1 + \alpha v_{sf,1})} \mathbf{M}_\gamma + \frac{v_{sf,2}}{(1 + \alpha v_{sf,1})} \mathbf{M}_\gamma^2 + \frac{v_{sf,1}(1 + \alpha)}{(1 + \alpha v_{sf,1})} g_2 \quad (106)$$

and

$$\begin{aligned} \mu_3 = & \frac{1}{(1 + \alpha v_{sf,1})} \left[\mu_{sf,3} + 3 \mu_{sf,2} \frac{v_{sf,1}(1 + \alpha)}{(1 + \alpha v_{sf,1})} \mathbf{M}_\gamma \right. \\ & \left. + 3(\mu_{sf,1} + \alpha v_{sf,1}) \left\{ \frac{v_{sf,2}}{(1 + \alpha v_{sf,1})} \mathbf{M}_\gamma^2 + \frac{v_{sf,1}(1 + \alpha)}{(1 + \alpha v_{sf,1})} g_2 \right\} \right. \\ & \left. + v_{sf,3} \mathbf{M}_\gamma^3 + 3 v_{sf,2} g_2 + v_{sf,1}(1 + \alpha) g_3 \right] \quad (107) \end{aligned}$$

with

$$g_2 = \frac{\mathbf{M} - 1}{v_{i,1} - 1} \left\{ \mu_{i,2} + 2 \mu_{i,1} v_{i,1} \mathbf{M}_\gamma + v_{i,2} \mathbf{M}_\gamma^2 \right\} \quad (108)$$

and

$$g_3 = \frac{\mathbf{M} - 1}{v_{i,1} - 1} \left\{ \mu_{i,3} + 3 \mu_{i,2} v_{i,1} \mathbf{M}_\gamma + 3 \mu_{i,1} [v_{i,2} \mathbf{M}_\gamma^2 + v_{i,1} g_2] + v_{i,3} \mathbf{M}_\gamma^3 + 3 v_{i,2} \right\} \quad (109)$$

In (105) the possibility of generating single photons in an (α, n) reaction was taken into account.

2.4.3 Mixed Moments

$$\langle v \mu \rangle = \frac{1}{(1 + \alpha v_{sf,1})} \left[\frac{(\mu_{sf,1} + \alpha v_{sf,1}) v_{sf,1}(1 + \alpha)}{(1 + \alpha v_{sf,1})} \mathbf{M} + v_{sf,2} \mathbf{M} \mathbf{M}_\gamma + v_{sf,1}(1 + \alpha) c_{1,1} \right] \quad (110)$$

$$\begin{aligned} \langle v(v-1)\mu \rangle = & \frac{1}{(1 + \alpha v_{sf,1})} \left\{ (\mu_{sf,1} + \alpha v_{sf,1}) \left[\frac{v_{sf,2}}{(1 + \alpha v_{sf,1})} \mathbf{M}^2 + \frac{v_{sf,1}(1 + \alpha)}{(1 + \alpha v_{sf,1})} h_2 \right] \right. \\ & \left. + v_{sf,3} \mathbf{M}_\gamma \mathbf{M}^2 + v_{sf,2} [2 \mathbf{M} c_{1,1} + \mathbf{M}_\gamma h_2] + v_{sf,1}(1 + \alpha) c_{2,1} \right\} \quad (111) \end{aligned}$$

and

$$\begin{aligned} \langle v \mu(\mu-1) \rangle = & \frac{1}{(1 + \alpha v_{sf,1})} \left\{ \mu_{sf,2} \frac{v_{sf,2}}{(1 + \alpha v_{sf,1})} \mathbf{M} \right. \\ & \left. + 2(\mu_{s,1} + \alpha v_{sf,1}) \left[\frac{v_{sf,2}}{(1 + \alpha v_{sf,1})} \mathbf{M} \mathbf{M}_\gamma + \frac{v_{sf,1}(1 + \alpha)}{(1 + \alpha v_{sf,1})} c_{1,1} \right] \right. \\ & \left. + v_{sf,3} \mathbf{M} \mathbf{M}_\gamma^2 + v_{sf,2} [g_2 \mathbf{M} + 2 \mathbf{M}_\gamma c_{1,1}] + v_{sf,1}(1 + \alpha) c_{1,2} \right\} \quad (112) \end{aligned}$$

Here the following abbreviations were introduced:

$$c_{1,1} = \left\{ p \frac{\mu_{i,1} v_{i,1} \mathbf{M} + v_{i,2} \mathbf{M} \mathbf{M}_\gamma}{1 - p v_{i,1}} \right\}, \quad (113)$$

$$c_{2,1} = \frac{p}{1 - p v_{i,1}} \{ \mu_{r,1} [v_{i,2} \mathbf{M}^2 + v_{i,1} h_2] + v_{i,3} \mathbf{M}^2 \mathbf{M}_\gamma + v_{i,2} [h_2 \mathbf{M}_\gamma + 2 \mathbf{M} c_{1,1}] \}, \quad (114)$$

$$c_{1,2} = \frac{p}{1 - p v_{i,1}} \{ \mu_{i,2} v_{i,1} \mathbf{M} + 2 \mu_{i,1} [v_{i,2} \mathbf{M} \mathbf{M}_\gamma + v_{i,1} c_{1,1}] + v_{i,3} \mathbf{M} \mathbf{M}_\gamma^2 + v_{i,2} [2 \mathbf{M}_\gamma c_{1,1} + \mathbf{M} g_2] \} \quad (115)$$

and

$$h_2 = \frac{\mathbf{M} - 1}{v_{i,1} - 1} v_{i,2} \mathbf{M}^2. \quad (116)$$

2.4.4 Multiplicity Detection Rates

The multiplicity detection rates can be calculated by defining the intensity of the source events by introducing the sample fission rate F , and the detection efficiencies ε_n and ε_γ for the neutrons and photons, respectively. The total source event intensity Q_s can be expressed by the fission rate F and the factor α as

$$Q_s = F + Q_\alpha = F(1 + \alpha v_{sf,1}) \quad (117)$$

It is easy to see that the intensity C_k of detecting the k th order multiplets, by accounting for all possible combinations of selecting a k -tuplelet from a higher-order multiplet and for the detection efficiency, is given by

$$C_k = Q_s \frac{\varepsilon_n^k v_k}{k!} \quad (118)$$

for the neutrons and a similar formula is valid for the gamma photons. Using (117) and (118) together with the expressions for factorial moments and (91), the multiplicity detection rates for the singles, doubles, and triples will read as

$$S = F \varepsilon_n \mathbf{M} v_{sf,1} (1 + \alpha), \quad (119)$$

$$D = \frac{F \varepsilon_n^2 \mathbf{M}^2}{2} \left[v_{sf,2} + \left(\frac{\mathbf{M} - 1}{v_{i,1} - 1} \right) v_{sf,1} (1 + \alpha) v_{i,2} \right] \quad (120)$$

and

$$T = \frac{F \varepsilon_n^3 \mathbf{M}^3}{6} \left\{ v_{sf,3} + \left(\frac{\mathbf{M} - 1}{v_{i,1} - 1} \right) [3 v_{sf,2} v_{i,2} + v_{sf,1} (1 + \alpha) v_{i,3}] + 3 \left(\frac{\mathbf{M} - 1}{v_{i,1} - 1} \right)^2 v_{sf,1} (1 + \alpha) v_{i,2}^2 \right\}. \quad (121)$$

Similar expressions can be derived for the gamma multiplicity detection rates and the mixed detection rates (Enqvist et al. 2010). Such expressions have been derived recently, but since these are not yet in routine use, they will not be given here.

The three multiplicity detection rates above are used to unfold three parameters of an unknown sample, out of which the sample fission rate, most directly related to the sample mass, is the most important. The other two unknowns are the factor α and the leakage multiplication \mathbf{M} , which latter depends on the first collision probability p and hence also on the sample mass, although in a rather implicit manner. This approach assumes that the detection efficiency is the same for all detectors included, and that it is known.

The above equations represent a coupled nonlinear system, which is of fifth order in the leakage multiplication, but can be solved such that at most a third-order algebraic equation needs to be solved. Formally, one has to determine the physical root of the equation

$$a + b\mathbf{M} + c\mathbf{M}^2 + \mathbf{M}^3 = 0 \quad (122)$$

where the coefficients read as

$$a = \frac{-6Tv_{s2}(v_{i1} - 1)}{\varepsilon^2 S [v_{i3}v_{s2} - v_{s3}v_{i2}]} \quad (123)$$

$$b = \frac{2Dv [v_{s3}(v_{i1} - 1) - 3v_{i2}v_{s2}]}{\varepsilon S [v_{i3}v_{s2} - v_{s3}v_{i2}]} \quad (124)$$

and

$$c = \frac{6v_{i2}v_{s2}D}{\varepsilon S [v_{i3}v_{s2} - v_{s3}v_{i2}]} - 1 \quad (125)$$

Having determined \mathbf{M} , the other two parameters (F and α) can be easily obtained by substituting it back to (119) (Cifarelli and Hage 1986). In practice, the doubles and triples gate fraction factors f_d and f_t also appear in the formulas, however these are neglected here for simplicity.

Using the gamma and the mixed multiplicity rates for the unfolding of the sample parameters is more complicated, due to the more complicated nonlinear structure of the equations, and to the larger number of unknowns, it is not possible to use analytical tools for the inversion; rather, nonparametric nonlinear unfolding methods are suggested.

3 Power Reactor Noise Theory

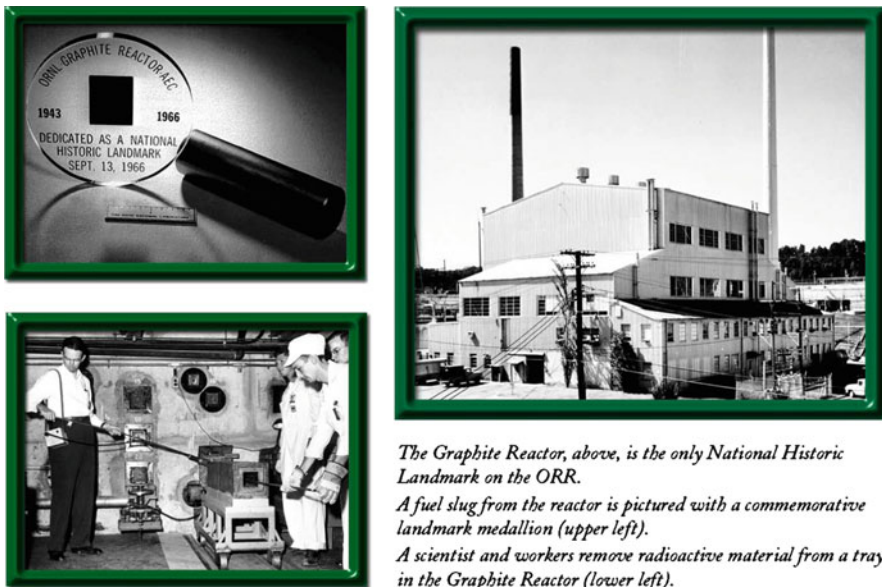
Power reactor noise deals with neutron fluctuations that are induced by fluctuations or oscillations of the reactor properties, that is, displacement of core components, temperature, or density variations. It is clear that any temporal change in the reactor composition manifests itself as changes of the corresponding cross sections. These changes are called “perturbations.” The cross sections are, in turn, coefficients of the pertinent transport or diffusion equations. Time-dependence of the cross sections will naturally lead to the time-dependence of the neutron flux, which is in addition space-dependent. Most often the changes in the cross sections are due to processes that are themselves random in character: turbulent one- or two-phase flow, boiling, flow-induced random vibrations, etc. Hence the induced neutron flux variations

will also become random processes in time, with a deterministic, or sometimes random space-dependence (when then perturbation is random in space). One talks about space- and time- (frequency-) dependent neutron noise in power reactors, or about power reactor noise in short. The use of the neutron noise, by unfolding the noise source properties from the measured neutron noise and by knowledge of the effect of the perturbations on the neutron noise (i.e., through knowledge of the reactor transfer function), is called neutron noise diagnostics.

The origin of neutron noise theory can be traced back to the reactor oscillator experiments performed at the “Clinton Pile” in Oak Ridge. The Clinton Pile was the nickname of the first “real” reactor, the Graphite Reactor or X-10 reactor. It was built already in 1943 (after Fermi’s first reactor in Chicago , 1942) in what is today called the Oak Ridge National Laboratory (ORNL). The reactor today is a historic landmark building and is shown in ► Fig. 5.

Such neutron oscillations were first induced artificially in so-called oscillator experiments. These were, at the beginning, not at all about reactor diagnostics, rather just investigations of nuclear physics data (measurement of cross sections). Various samples were moved back and forth inside the core periodically, and the goal of the measurements was to determine thermal absorption cross sections of the various elements. This was achieved by measuring the amplitude of neutron oscillations and comparing it with measurements with samples of known cross sections.

Already then it was observed that the neutron flux fluctuations, that is, the response of the reactor was considerably more complex than solely reactivity-induced power oscillations,



The Graphite Reactor, above, is the only National Historic Landmark on the ORR.

A fuel slug from the reactor is pictured with a commemorative landmark medallion (upper left).

A scientist and workers remove radioactive material from a tray in the Graphite Reactor (lower left).

■ Figure 5

The building of the graphite reactor (right); a fuel piece (top left); and the removal of an irradiated sample from a horizontal channel (bottom left)

that is, a “point-kinetic response,” in which the neutron distribution maintains its spatial form (equal to the critical neutron flux) and only its amplitude changes. Rather, the response was space-dependent, and consisted of a local term with short spatial relaxation that prevailed in the vicinity of the disturbance (10–20 cm), corresponding to the local flux dip movement with the absorber, and a global component, with a much longer spatial relaxation length. In small, tightly coupled reactors, this global component is equal to the reactivity or point reactor component, but in large reactors a further, slowly varying space-dependent component appears. The theoretical analysis of the Clinton Pile measurements was given in a classic paper by Weinberg and Schweinler (1948).

Later, it was observed in the Oak Ridge Research Reactor (ORR) and the high flux isotope reactor (HFIR) that anomalous vibrations of control rods can be identified from the frequency spectrum of in-core neutron detectors (Fry 1971). In measurements performed in the HFIR, suddenly a peak appeared at 5–6 Hz. The reason for this peculiar frequency-dependence was that a ball bearing to one of the control rods had been broken and the control rod started excessive flow-induced vibrations with this frequency.

This event made it clear that it was possible to obtain information about unwanted or unexpected changes or anomalies by measuring neutron fluctuations in the core. This is how the concept of neutron noise diagnostics was born. Later, similar observations were made in power plants. It was observed in the Palisades plant (USA) that vibrations of the whole core barrel and its support can be detected by ex-core neutron detectors (Fry et al. 1974). German measurements in boiling water reactors (BWRs) showed a linear phase of the coherence between two detectors in the same detector tube, showing the velocity of the two-phase flow (Wach and Kosály 1974). Vibrations of such detectors in BWRs were also detected and quantified by neutron noise methods. Control rod vibrations were observed and the vibrating rod localized from neutron noise measurements in pressurized water reactors (PWRs). The neutron noise can also be used to measure the moderator temperature coefficient of reactivity (MTC), the stability of boiling water reactors (BWRs), and in general for detecting any anomaly at an early stage through the change of the neutron noise spectra.

The process of neutron noise diagnostics consists of first constructing a simple model of the noise source under investigation, which contains only a few parameters to be determined, calculating the induced noise through calculating the dynamic transfer function of the system, and constructing an inversion procedure by which, from the measurements of the neutron noise, one can unfold the searched parameters of the noise source (perturbation). The underlying theory and methods will be expounded in the forthcoming sections. For more details, we can refer the reader to a few monographs, conference proceedings, and review articles, such as Williams (1974), Saito (1979), Kosály (1980), and Thie (1981). Another useful source of information is the proceedings of the eight SMORN symposia held so far in the field, several of which were published in Progress in Nuclear Energy. These can be found at the OECD NEA Web site (OECD 2002)

3.1 Basic Principles

Starting with a critical reactor with time-independent cross sections, any change of the cross sections will lead to changes of the neutron flux in space and time. These changes will occur irrespective of the change of the cross sections is a random process or a deterministic one, but their character (deterministic or not) will match the change of the cross sections (perturbations). A

large class of the changes consists of small variations of the cross sections around an expected value, corresponding to the critical case, in which the perturbation can be called a noise source, and the induced flux fluctuations the neutron noise.

The neutron noise $\delta\phi(\mathbf{r}, t)$ is hence defined through

$$\delta\phi(\mathbf{r}, t) \equiv \phi(\mathbf{r}, t) - \langle \phi(\mathbf{r}, t) \rangle = \phi(\mathbf{r}, t) - \phi_0(\mathbf{r}), \quad (126)$$

with $\phi_0(\mathbf{r})$ being the static flux, and the noise source $\delta\Sigma(\mathbf{r}, t)$ through the fluctuation of the macroscopic cross sections (perturbations) as

$$\delta\Sigma(\mathbf{r}, t) \equiv \Sigma(\mathbf{r}, t) - \langle \Sigma(\mathbf{r}, t) \rangle \quad (127)$$

One would think that these flux fluctuations could also be described by the master equation technique, that is, through the setting up of a probability balance equation for the distribution of the neutrons in space and time. Such a description is possible in principle, but it is associated with severe problems, both conceptual and practical (Pázsit et al. 2002; Pál and Pázsit 2006, 2007). The conceptual ones concern the fact that the master equation approach is based on the transition intensities between the different states of the system, which in the case of neutron chains are related to the nuclear cross sections. In the case of zero power systems, these are constant. In the case of power reactor noise, the cross sections, that is, the transition probabilities, become random processes themselves. Hence, the neutron transport and multiplication in a temporally varying system becomes a “doubly stochastic process.” Such a process can only be formulated for a temporally varying homogeneous medium with two discrete states, which is a poor approximation of the real case.

Such an approach was discussed recently, as is described in Pázsit and Pál (2008). It was shown that even in the case of a homogeneous system with a homogeneous perturbation in the form of a dichotomic Markov process, the solution is rather involved. Solutions for more realistic cases, involving space-dependence and continuous variations of the system properties, are in practice impossible. On the other hand, the case of spatially constant perturbations is completely uninteresting from the point of view of power reactor noise diagnostic problems.

There is one further subtle point to this. Because the changes of the system affect all neutrons in the system over the volume of the perturbation, the neutron chains started in a branching process (fission) will not be independent. Hence the factorization property, based on the independence of the chains, which is a prerequisite for the application of the backward master equation as in (24) and (29)–(31), cannot be applied. Thus, in the case of a temporally varying system, only the forward approach is applicable, which is less powerful than the backward approach.

Hence, in practice, in the theory of power reactor noise another approach is selected. One starts with the space- and time-dependent transport or diffusion equations for the mean (expected) neutron flux. In this equation, the critical (steady-state) cross sections occur as multiplying coefficients. Then, one assumes that there occur fluctuations in some cross sections, corresponding to some ordinary (e.g., boiling) or anomalous (excessive vibrations) process. The fluctuating cross sections are treated as stochastic processes, which are usually described by their autocorrelations and auto-spectra (c.f. (131)–(136)). Because some coefficients of the diffusion equation are now stochastic processes, the equation becomes a stochastic differential equation. Instead of obtaining an explicit solution for $\delta\phi(\mathbf{r}, t)$, its statistical properties (correlations, spectra) can be determined to the same extent as those are known for $\delta\Sigma(\mathbf{r}, t)$. This way, the probability distribution of the noise is not searched, only certain moments. The main

purpose of power reactor noise theory is to find relationships between the statistical properties of the noise source and the induced noise by the solution of the diffusion equation.

It is clear from the above that in the above description of power reactor noise, also called the Langevin technique, the zero power noise (fluctuations inherent in the branching process) is neglected. This is justified because in high-power systems the zero power noise is negligible (its variance is a linear function of the power, whereas the variance of power reactor noise is proportional to the square of the reactor power). Moreover, power reactor noise is indeed generated only in reactors at high power, since the perturbations inducing the noise (boiling, flow-induced vibrations) do not exist in low-power systems and critical assemblies. Hence, for all practical cases, the treatment of power reactor noise through the Langevin technique is fully adequate.

An important fact is that the perturbations (cross section fluctuations) are usually small enough such that the equations can be linearized. This means that the induced noise can be represented as a convolution over the noise source and a system transfer function where the latter is determined by the unperturbed system, that is, it is independent from the properties of the noise source.

The first step of noise diagnostics is to set up a framework for the calculation of the neutron noise for a specified perturbation type. According to the fact mentioned above, an equation for the neutron noise can conceptually be written as

$$\tilde{\mathbf{L}}(\mathbf{r}, t) \delta\phi(\mathbf{r}, t) = S(\mathbf{r}, t) \quad (128)$$

Here, the operator $\tilde{\mathbf{L}}(\mathbf{r}, t)$ is usually the diffusion theory representation of the transport operator, whereas, as it will be shown soon, the perturbation $S(\mathbf{r}, t)$ is simply related to the fluctuations of the cross sections as

$$S(\mathbf{r}, t) = \delta\Sigma(\mathbf{r}, t)\phi_0(\mathbf{r}). \quad (129)$$

This equation is sometimes called a Langevin equation, at least when the right-hand side is a white noise (a Wiener process). A white noise is a process whose correlation function is a Dirac-delta function and thus its power spectrum is a constant.

In (129), the perturbation $S(\mathbf{r}, t)$, also called the driving force, or rather the cross section fluctuation $\delta\Sigma(\mathbf{r}, t)$ cannot be specified explicitly, only its correlation function or spectrum is known (or the correlations or spectra of its individual parameters). All processes will be assumed stationary and ergodic. Thus, the mean value of the perturbation is time-independent and identically zero:

$$\langle \delta\Sigma(\mathbf{r}, t) \rangle = 0. \quad (130)$$

Its correlation function is given as

$$CCF_{\Sigma}(\mathbf{r}, \mathbf{r}', \tau) = \langle \delta\Sigma(\mathbf{r}, t) \delta\Sigma(\mathbf{r}', t + \tau) \rangle = \lim_{T \rightarrow \infty} \frac{1}{2T} \int_{-T}^T \delta\Sigma(\mathbf{r}, t) \delta\Sigma(\mathbf{r}', t + \tau) dt \quad (131)$$

The above quantity is called a cross-correlation because it describes correlations between different spatial points. The cross-spectrum is the Fourier transform of the correlation function

$$CPSD_{\Sigma}(\mathbf{r}, \mathbf{r}', \omega) = \int_{-\infty}^{\infty} CCF_{\Sigma}(\mathbf{r}, \mathbf{r}', \tau) e^{-i\omega\tau} d\tau \quad (132)$$

Usually this is all one can specify about the perturbation. The goal is to calculate the auto- and cross-spectra of the induced noise from this information and (128). That is, one wants to know

$$CCF_{\phi}(\mathbf{r}, \mathbf{r}', \tau) = \langle \delta\phi(\mathbf{r}, t)\delta\phi(\mathbf{r}', t + \tau) \rangle = \lim_{T \rightarrow \infty} \frac{1}{2T} \int_{-T}^T \delta\phi(\mathbf{r}, t)\delta\phi(\mathbf{r}', t + \tau) dt \quad (133)$$

and

$$CPSD_{\phi}(\mathbf{r}, \mathbf{r}', \omega) = \int_{-\infty}^{\infty} CCF_{\phi}(\mathbf{r}, \mathbf{r}', \tau) e^{-i\omega\tau} d\tau \quad (134)$$

In practical work, the power spectra are often calculated by the Wiener–Khinchin theorem, which states that for ergodic processes

$$CPSD_{\Sigma}(\mathbf{r}, \mathbf{r}', \omega) \propto \delta\Sigma(\mathbf{r}, \omega)\delta\Sigma^*(\mathbf{r}', \omega) \quad (135)$$

and hence

$$CPSD_S(\mathbf{r}, \mathbf{r}', \omega) \propto S(\mathbf{r}, \omega)S^*(\mathbf{r}', \omega) \quad (136)$$

The above relationship is useful when the auto- and cross-spectra of the noise are searched as functions of the auto- and cross-spectra of the perturbation. To find such a relationship it is sufficient to find the solution of the Fourier transformed diffusion equations. This means that if one finds the noise in the form

$$\delta\phi(\mathbf{r}, \omega) = \int G(\mathbf{r}, \mathbf{r}', \omega)S(\mathbf{r}', \omega)d\mathbf{r}', \quad (137)$$

where the noise source $S(\mathbf{r}, \omega)$ is given, as will be seen later, as

$$S(\mathbf{r}, \omega) = \phi_0(\mathbf{r})\delta\Sigma(\mathbf{r}, \omega) \quad (138)$$

with $\phi_0(\mathbf{r})$ being the static neutron flux, then, through (135), one has

$$CPSD_{\phi}(\mathbf{r}, \mathbf{r}', \omega) = \int G(\mathbf{r}, \mathbf{r}_1, \omega)G^*(\mathbf{r}', \mathbf{r}'_1, \omega)CPSD_S(\mathbf{r}_1, \mathbf{r}'_1, \omega) d\mathbf{r}_1 d\mathbf{r}'_1 \quad (139)$$

The transfer function or Green's function $G(\mathbf{r}, \mathbf{r}', \omega)$ can be determined from (128) as it will be shown concretely below.

The purpose of power reactor noise studies is to find relationships between noise source and induced noise in the form of (138). In conceptual studies, rather (137) is used, because it is more

transparent. The various forms of noise diagnostics can then be illustrated as follows. In (137), there are three quantities:

1. The induced neutron noise, $\delta\phi(\mathbf{r}, \omega)$, which is always measured;
2. The dynamic transfer function $G(\mathbf{r}, \mathbf{r}', \omega)$, which can be calculated from the time- (frequency-) dependent diffusion equations with the parameters of the unperturbed system;
3. The noise source $S(\mathbf{r}, \omega)$.

If two of these three are known, the third can be determined, in principle. The generic task is that the transfer function is known from calculations, and the noise source is unknown. The objective is to invert (137) to express the noise source with the transfer function and the measured noise.

Mathematically, (137) is a Fredholm-type integral equation which, under some mild circumstances, can be uniquely inverted. However, this requires that the functions $\phi_0(\mathbf{r})$ and $G(\mathbf{r}, \mathbf{r}', \omega)$ are known everywhere in the reactor as continuous functions of their parameters. While this is true for the transfer function, which is determined by calculations, the same is not true for the detected noise. The noise is only measured in the discrete positions of the neutron detectors, which are actually placed quite sparse in the reactor. This means that for arbitrary perturbations $S(\mathbf{r}, \omega)$, the inversion is not possible.

This is where noise diagnostics expertise is invoked to solve this problem. Namely, in most cases of perturbations to be diagnosed, such as a vibrating control rod, two-phase flow in a channel, etc., one can make a simple model of the perturbation in form of a mathematical function, which only contains a few unknown parameters (position of a control rod, void fraction fluctuation, etc). Examples will be given soon. Those few parameters can be determined from the signals of a few neutron detectors.

Another way of performing diagnostics is to determine some parameter of the transfer function. As earlier mentioned, the functional form of the transfer function can always be calculated from the neutron kinetic (diffusion) equations, if all the parameters (cross sections, delayed neutron data, reactivity in case of subcritical systems, etc.) are known. Sometimes certain parameters are not known, and the diagnostics is aimed at determining those parameters. In that case, one needs to measure both the perturbation (e.g., inlet temperature fluctuations) and the induced neutron noise, to determine for example, reactivity coefficients, such as the moderator temperature coefficient. If some assumptions can be made on the driving force, such as in the case of BWR instability, the stability of the system can be determined solely from the measured neutron noise.

3.2 Space-Time Dependent Reactor Kinetics in Diffusion Theory

A suitable starting point is to study the space-time dynamic response of a reactor to perturbations in the deterministic case, and to define some concepts, notably the reactor kinetic approximations, out of which the two lowest order (point kinetic and adiabatic) will come to use in the interpretation of the behavior of the system. The stochastic nature of the perturbations will be considered in the next subsection, treating small perturbations where linear theory is applicable and the effect of the noise source and the system transfer properties factorize.

All derivations will be made in one- or two-group diffusion theory. This level of the description was chosen because it has proven completely satisfactory so far in all known cases of practical interest. In a few cases such as the treatment of voids the use of P_1 theory might be

called for (Kleiss and van Dam 1978), but the general conclusion is that in most cases diffusion theory is fully sufficient (Pázsit 2002; Larsson and Demazière 2009). The number of the energy groups used is dictated by the nature of the perturbation and the diagnostic task considered. In one-group diffusion theory, the characteristic equation, both in the static case and the dynamic case, has only one root, and hence one large spatial relaxation length, on the scale of the migration distance. This solution will be able to describe only the global behavior of the system. This global behavior is point kinetic in small systems and/or low frequencies, but deviates from it, still on a relatively large spatial scale, in larger systems and/or higher frequencies. In this case, we speak about space-dependent noise, and the deviation from the point-kinetic behavior is called “the space-dependent term” of the response. In most cases, this space-dependence of the behavior, as calculated in one-group theory, is sufficient to solve the diagnostic problem, because the spacing of the detectors and the distance of the detectors to the noise source is on the same scale as the relaxation length. However, as mentioned earlier, in the neighborhood of a localized perturbation there exists also a third component with a short spatial relaxation length, comparable with the thermal diffusion length in the system. This is called the local component of the noise. In order to obtain the local component, one needs to use two energy groups, since the characteristic equation in two-group theory has two roots, giving two spatial relaxation lengths. The longer one is approximately the same as the one obtained from one-group theory. The shorter one describes, in the static case, the reflector peak and the local flux dip around control rods. In cases when the detectors are close to the perturbation, such as in the case of BWR in-core detectors sensing the effect of bubbles passing by, one has to account for the local component, and hence has to use two-group theory.

For the transparency of the description, the emphasis of the description will be on one-group theory in the forthcoming sections. Basic features of the two-group description will be mentioned when necessary, but with the details of derivations we will refer to the literature.

3.2.1 Static Equations

One-Group Theory

With obvious notations, the static equation reads as

$$\nabla D(\mathbf{r})\nabla\phi_0(\mathbf{r}) + [\nu\Sigma_f(\mathbf{r}) - \Sigma_a(\mathbf{r})]\phi_0(\mathbf{r}) = 0 \quad (140)$$

with the boundary conditions of vanishing flux at the system boundaries, that is,

$$\phi_0(\mathbf{r}_B) = 0 \quad (141)$$

where \mathbf{r}_B is an arbitrary point on the extrapolated boundary. Usually, we will assume a homogeneous, or piecewise homogeneous system, in which case (140) is simplified to

$$D\nabla^2\phi_0(\mathbf{r}) + [\nu\Sigma_f - \Sigma_a]\phi_0(\mathbf{r}) = 0 \quad (142)$$

Introducing the material buckling

$$B_m^2 = \frac{\nu\Sigma_f - \Sigma_a}{D} \quad (143)$$

the equation is further simplified to

$$\nabla^2 \phi_0(\mathbf{r}) + B_m^2 \phi_0(\mathbf{r}) = 0 \quad (144)$$

The criticality equation is obtained by noticing that only specific values of the material buckling are allowed, which fulfill the boundary condition (141). These values depend on the system geometry, and are denoted by B_g^2 . The criticality equation can be symbolically written as $B_g^2 = B_m^2 \equiv B_0^2$. A system that we will frequently use for illustration is a homogeneous one-dimensional non-reflected reactor with extrapolated boundaries at $x_B = \pm a$. In that case, the critical flux is given as

$$\phi_0(x) = A \cos(B_0 x) \quad (145)$$

with $B_0 = \pi/2a$, and the criticality equation reads as

$$\frac{\nu \Sigma_f - \Sigma_a}{D} = \left(\frac{\pi}{2a} \right)^2 \quad (146)$$

Because of its practical and methodological importance, we shall also treat a nonhomogeneous case by assuming that the system contains a thin absorber rod. As a mathematical simplification, this rod will be described by an absorption cross section, which is a spatial Dirac-delta function. That is, we assume

$$\Sigma_a^{rod}(x) = \gamma \delta(x - x_p) \quad (147)$$

where x_p is the position of the rod, and γ is the so-called Galanin factor, describing the strength of the rod. The static equation for this case reads as

$$D \nabla^2 \phi_0(x) + (\nu \Sigma_f - \Sigma_a) \phi_0(x) - \gamma \delta(x - x_p) \phi_0(x) = 0 \quad (148)$$

Noting that for $x \neq x_p$ the above equation is the same as (144), the solution can be obtained easily in the two half-spaces separated by the rod. Continuity of the flux at $x = x_p$ and the discontinuity of the current, obtained by integrating (148) between $x_p - \varepsilon$ and $x_p + \varepsilon$, leading to


$$\left. \frac{d\phi_0(x)}{dx} \right|_{x_p+\varepsilon} - \left. \frac{d\phi_0(x)}{dx} \right|_{x_p-\varepsilon} = \frac{\gamma}{D} \phi_0(x_p)$$

that leads to the solution

$$\phi_0(x) = A \begin{cases} \sin B_0(a+x) \sin B_0(a-x_p) & x \leq x_p \\ \sin B_0(a-x) \sin B_0(a+x_p) & x \geq x_p \end{cases} \quad (149)$$

where A is an arbitrary constant, and to the criticality equation

$$\cot B_0(x_p - a) - \cot B_0(x_p + a) = \frac{\gamma}{B_0 D} \quad (150)$$

The solution (149), with material and geometrical data corresponding to a light water power reactor, is shown in  Fig. 6.

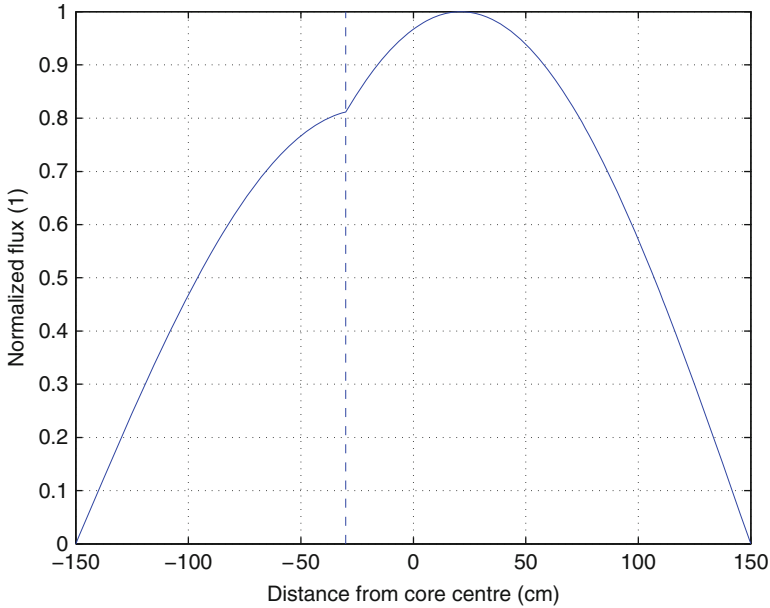


Figure 6
 Static neutron flux in one-group diffusion theory for a bare homogeneous reactor with a thin absorber rod located at $x_p = -30$ cm and a Galanin constant $\gamma = 0.01$

As seen from the figure, the presence of the control rod causes a global change of the flux shape compared to the pure cosine shape without the rod. The local flux dip is not reconstructed by the one-group treatment.

Two-Group Theory

The two-group static equations can be most conveniently written in a matrix notation. For simplicity, a homogeneous system will be assumed only. The equations for the fast and thermal fluxes $\phi_1(\mathbf{r})$ and $\phi_2(\mathbf{r})$, respectively, read as

$$\begin{bmatrix} D_1 \nabla^2 + \nu \Sigma_{f_1} - \Sigma_{a_1} - \Sigma_R & \nu \Sigma_{f_2} \\ \Sigma_R & D_2 \nabla^2 - \Sigma_{a_2} \end{bmatrix} \begin{bmatrix} \phi_1(\mathbf{r}) \\ \phi_2(\mathbf{r}) \end{bmatrix} = 0 \tag{151}$$

Here, subscripts 1 and 2 refer to the fast and the thermal flux, respectively, and Σ_R is the removal cross section.

It is easy to show that both the fast flux and the thermal flux have to obey the same Helmholtz equation

$$\nabla^2 \phi_g(\mathbf{r}) + B^2 \phi_g(\mathbf{r}) = 0; \quad g = 1, 2 \tag{152}$$

where B^2 denotes any of the two roots μ^2 and ν^2 of the characteristic equation, second order in B^2 :

$$\begin{vmatrix} -D_1 B^2 + \nu \Sigma_{f_1} - \Sigma_{a_1} - \Sigma_R & \nu \Sigma_{f_2} \\ \Sigma_R & -D_2 B^2 - \Sigma_{a_2} \end{vmatrix} = 0 \tag{153}$$

The solution of this equation in one dimension can be written as

$$\begin{pmatrix} \phi_1(x) \\ \phi_2(x) \end{pmatrix} = A \begin{pmatrix} 1 \\ c_\mu \end{pmatrix} \cos \mu x + C \begin{pmatrix} 1 \\ c_\nu \end{pmatrix} \cosh \nu x \quad (154)$$

with

$$c_\mu = \frac{\Sigma_R}{D_2\mu^2 + \Sigma_{a_2}} \quad \text{and} \quad c_\nu = \frac{\Sigma_R}{\Sigma_{a_2} - D_2\nu^2} \quad (155)$$

With the data of light water reactors, $\nu \gg \mu$, and correspondingly the first term in (154) describes a smoothly varying term (global term) whereas the second represents a fast decaying local term. The second term is associated with the reflector peak in the thermal flux in a reflected reactor, and it describes the local flux dip around a thin control rod. In a bare homogeneous system, only the first, slowly varying term exists.

3.2.2 Time-Dependent One-Group Diffusion Equations

When describing the temporal variations, we need to account for the presence of the delayed neutrons. Similar to the case of zero power noise, most characteristics of the dynamical response of the core can be satisfactorily described by one, average group of delayed neutrons with decay constant λ and density of delayed neutron precursors $C(\mathbf{r}, t)$. The coupled equations for the neutron flux and the precursor density read as

$$\frac{1}{v} \frac{\partial \phi(\mathbf{r}, t)}{\partial t} = D\nabla^2 \phi(\mathbf{r}, t) + [\nu \Sigma_f(\mathbf{r}, t)(1 - \beta) - \Sigma_a(\mathbf{r}, t)] \phi(\mathbf{r}, t) + \lambda C(\mathbf{r}, t) \quad (156)$$

$$\frac{\partial C(\mathbf{r}, t)}{\partial t} = \beta \nu \Sigma_f(\mathbf{r}, t) \phi(\mathbf{r}, t) - \lambda C(\mathbf{r}, t) \quad (157)$$

Here, for simplicity and according to general praxis, the fluctuations of the diffusion coefficient were disregarded. The second equation can easily be integrated and substituted back to the first, leading to the integrodifferential form

$$\begin{aligned} \frac{1}{v} \frac{\partial \phi(\mathbf{r}, t)}{\partial t} = & D\nabla^2 \phi(\mathbf{r}, t) + [\nu \Sigma_f(\mathbf{r}, t)(1 - \beta) - \Sigma_a(\mathbf{r}, t)] \phi(\mathbf{r}, t) \\ & + \lambda \beta \int_{-\infty}^t \nu \Sigma_f(\mathbf{r}, t') \phi(\mathbf{r}, t') e^{-\lambda(t-t')} dt' \end{aligned} \quad (158)$$

Equations (156) and (157), or (158) are difficult to solve for arbitrary variations of the cross sections analytically, and in the early days it was difficult even numerically. Historically, the so-called reactor kinetics approximations were introduced via the flux factorization technique of Henry (1958, 1975) in order to obtain numerical solutions. The role of the kinetic approximations as a tool for numerical analysis has long been diminished, but their value remains for the interpretation and for solving diagnostic tasks. Therefore, a brief survey will be given here.

3.2.3 The Flux Factorization and the Kinetic Approximations

The basis of the kinetic approximations after Henry (1958, 1975) is a factorization of the space-time dependent flux into an amplitude factor $P(t)$ and a normalized shape function $\psi(\mathbf{r}, t)$ as

$$\phi(\mathbf{r}, t) = P(t)\psi(\mathbf{r}, t) \quad (159)$$

To make the factorization unique, an extra condition is needed. Such a condition will be formulated with the intention to collect all changes of the total reactor power, or the total neutron number in the system, into the amplitude function, and to have the shape function to describe the shape changes of the flux in a normalized manner. In the general space-energy-angularly dependent case, this is specified as

$$\frac{\partial}{\partial t} \int \phi_0^\dagger(\mathbf{r}, E, \Omega)\psi(\mathbf{r}, E, \Omega t) d\mathbf{r} dE d\Omega = 0 \quad (160)$$

where $\phi_0^\dagger(\mathbf{r}, E, \Omega)$ is the static adjoint of the reference critical system (Bell and Glasstone, 1970). In two-group diffusion theory, the angular variable and the corresponding integral are omitted, and the integral with respect to the energy variable is replaced by a summation over the energy groups. In one-group diffusion theory, which is the case that we will be concerned with in the continuation, the situation is even simpler since also the energy variable is missing, and the static flux can be used instead of the static adjoint, since one-group diffusion theory is self-adjoint. Hence, the normalization condition becomes

$$\frac{\partial}{\partial t} \int \phi_0(\mathbf{r})\psi(\mathbf{r}, t) d\mathbf{r} = 0 \quad (161)$$

with

$$\phi_0(\mathbf{r}) = P_0\psi(\mathbf{r}, t = 0) \quad (162)$$

That is, it is assumed that at time $t = 0$ the system was in an unperturbed critical state with a static flux $\phi_0(\mathbf{r})$, obeying (140). Actually in (162) there is still a freedom to choose either P_0 , or the amplitude of the shape function at $t = 0$ (or at $t = -\infty$, which is the usual procedure in noise analysis where the processes are stationary and the transient effects of the “switching on” the perturbation are of no interest) arbitrarily. In the analysis of large reactivity excursions and other transients, P_0 is chosen to be equal to the thermal power generated in the core. In noise analysis work, found frequently in the literature, it is customary to use $P_0 = 1$, which yields $\psi(\mathbf{r}, t = 0) = \phi_0(\mathbf{r})$.

With the above assumptions one can derive coupled equations for the amplitude function and the shape function. Multiplying (140) by $P(t)\psi(\mathbf{r}, t)$ and (156) and (157) by $\phi_0(\mathbf{r})$, integrating and subtracting the static equation from the dynamic ones leads to two coupled equations for the amplitude function, known as the point-kinetic equations:

$$\frac{dP(t)}{dt} = \frac{\rho(t) - \beta}{\Lambda(t)} P(t) + \lambda C(t) \quad (163)$$

and

$$\frac{dC(t)}{dt} = \frac{\beta}{\Lambda(t)} P(t) - \lambda C(t) \quad (164)$$

Here,

$$\rho(t) = \frac{1}{F(t)} \int \{ \delta v \Sigma_f(\mathbf{r}, t) - \delta \Sigma_a(\mathbf{r}, t) \} \phi_0(\mathbf{r}) \psi(\mathbf{r}, t) d\mathbf{r}, \quad (165)$$

$$\Lambda(t) = \frac{1}{F(t)} \int \frac{1}{v} \phi_0(\mathbf{r}) \psi(\mathbf{r}, t) d\mathbf{r} \quad (166)$$

and

$$C(t) = \frac{1}{\Lambda(t)F(t)} \int C(\mathbf{r}, t) \phi_0(\mathbf{r}) d\mathbf{r} \quad (167)$$

with

$$F(t) = \int v \Sigma_f(\mathbf{r}, t) \phi_0(\mathbf{r}) \psi(\mathbf{r}, t) d\mathbf{r} \quad (168)$$

The fluctuations of the cross sections are defined as

$$\delta v \Sigma_f(\mathbf{r}, t) = v \Sigma_f(\mathbf{r}, t) - v \Sigma_f(\mathbf{r}) \quad \text{and} \quad \delta \Sigma_a(\mathbf{r}, t) = \Sigma_a(\mathbf{r}, t) - \Sigma_a(\mathbf{r}) \quad (169)$$

The point-kinetic equations (163) and (164) can be readily solved if the parameters $\rho(t)$ and $\Lambda(t)$ are known. The calculation of these latter requires knowledge of the shape function $\psi(\mathbf{r}, t)$, which obeys a complicated equation. The various reactor kinetic approximations consist of an approximate calculation of the shape function. In linear noise theory, valid for small perturbations, these parameters will be constants, and independent of the shape function.

An equation for the shape function can be obtained by putting $P(t)\psi(\mathbf{r}, t)$ into (158), which will read as

$$\begin{aligned} \frac{1}{v} \left[\frac{\partial \psi(\mathbf{r}, t)}{\partial t} + \frac{1}{P(t)} \frac{dP(t)}{dt} \psi(\mathbf{r}, t) \right] &= D \nabla^2 \psi(\mathbf{r}, t) + [v \Sigma_f(\mathbf{r}, t)(1 - \beta) - \Sigma_a(\mathbf{r}, t)] \psi(\mathbf{r}, t) \\ &+ \frac{Q_d(\mathbf{r}, t)}{P(t)} \end{aligned} \quad (170)$$

where $Q_d(\mathbf{r}, t)$ is the “delayed neutron source,” given as

$$Q_d(\mathbf{r}, t) = \lambda \beta \int_{-\infty}^t v \Sigma_f(\mathbf{r}, t') P(t') \psi(\mathbf{r}, t') e^{-\lambda(t-t')} dt' \quad (171)$$

This equation is considerably more difficult to solve than the original diffusion equation (158) for the full solution, partly because it contains the other unknown, the amplitude function. Thus, in order to make the flux factorization useful, one needs to use simplifications in its calculation. We shall only discuss the two lowest-order approximations, the point reactor approximation, and the adiabatic approximation.

The Point Reactor Approximation

Here it is assumed that the shape function at any time is equal to the time-independent static flux, that is,

$$\psi(\mathbf{r}, t) = \phi_0(\mathbf{r}), \quad \forall t \quad (172)$$

Then the parameters ρ and Λ are constants, and the point-kinetic equations can be readily solved for $P(t)$. The space-time dependent flux is thus given as

$$\phi(\mathbf{r}, t) = P(t)\phi_0(\mathbf{r}) \quad (173)$$

This description is suitable for large power excursions or any other changes where the shape function does not change appreciably during the process. If the reactor behavior can be described by this approximation, then only the information of the time-dependence of the flux can be used to extract information on the perturbation causing the flux change, because the spatial dependence of the flux is independent from that of the perturbation.

The Adiabatic Approximation

A somewhat more effective approximation, in which the shape function has a time-varying space-dependence, but where the equations for the amplitude function and shape function still fully decouple is the adiabatic approximation. In this approximation the shape function at each time instant is assumed to be equal to the normalized (in the sense of (161) and (162)) k -eigenvalue equation of the system, belonging to the momentary values of $v\Sigma_f(\mathbf{r}, t)$ and $\Sigma_a(\mathbf{r}, t)$:

$$D\nabla^2\psi(\mathbf{r}, t) + \left[\frac{v\Sigma_f(\mathbf{r}, t)}{k(t)} - \Sigma_a(\mathbf{r}, t) \right] \psi(\mathbf{r}, t) = 0 \quad (174)$$

Here, the time t is only a parameter, and not a variable, and the equation is a static one. Formally, this equation can be obtained from (170) by neglecting all time derivatives and assuming that the delayed neutron source (171) is a constant. Obviously no dynamics is involved, and it is assumed that both the flux *and* the delayed precursor distribution correspond to an equilibrium distribution. This approximation can be used only for slow changes and preferably for small perturbations, but it is a very effective tool for interpreting the results of noise calculations and in order to devise noise unfolding techniques.

A better approximation, which takes into account that the prompt neutron distribution can readjust to the changed cross sections, while the delayed neutron precursors cannot, is the quasistatic approximation. In this approximation, only the time derivative of the shape function, the first term on the left-hand side of (170), is neglected. Further, in this approximation, the equations for the amplitude function and for the shape function remain coupled, and the solution of the latter is rather complicated. The efficiency of the method as compared to solve the original equations (156) and (157) is that in the numerical solution of the shape function a much larger time step can be used than in the solution of the much simpler ordinary differential equations (163) and (164). On the other hand, the solution of the quasistatic approximation cannot be interpreted in such easy intuitive terms as that of the adiabatic approximation.

3.3 Small Space-Time Dependent Fluctuations: Power Reactor Noise

In power reactor noise theory one concerns with perturbations represented by small, stationary fluctuations of the cross sections about their expectation (mean value). The static values (the expectations) are supposed to constitute a critical reactor. The perturbation is supposed to start at $t = -\infty$, so that all transients have already decayed by finite times, and temporal Fourier transform can be used to solve time-dependent equations. The task of noise theory is to calculate

the space-time (or rather, space-frequency) dependence of the fluctuations of the neutron flux around its static value, and this will be described in this subsection. The task of noise diagnostics is to invert the obtained solutions, which will be described in the following subsections.

3.3.1 Neutron Noise in One-Group Diffusion Theory

The equations giving the time- and space-dependent neutron flux in diffusion theory in [Subsect. 3.2.2, \(156\) and \(157\)](#), were derived in the general case. Now some assumptions will be made in order to estimate the neutron noise in first-order linear theory.

Splitting all the time-dependent terms, generically expressed as $X(\mathbf{r}, t)$, into their mean values $X_0(\mathbf{r})$ (corresponding to the steady state and thus critical configuration of the system) and their fluctuations $\delta X(\mathbf{r}, t)$ around their mean values as

$$X(\mathbf{r}, t) = X_0(\mathbf{r}) + \delta X(\mathbf{r}, t) \quad (175)$$

where X stands for the macroscopic cross sections Σ_α of type α , the concentration C of the delayed neutron precursors, and the neutron flux ϕ , the following assumptions can be made:

- The fluctuations are assumed to be small compared to the mean values, that is,

$$|\delta X(\mathbf{r}, t)| \ll X_0(\mathbf{r}), \quad \forall(\mathbf{r}, t) \quad (176)$$

such that the product of any two fluctuating quantities can be neglected, and

- The processes are assumed to be stationary, that is,

$$\langle \delta X(\mathbf{r}, t) \rangle = 0, \quad \forall(\mathbf{r}, t) \quad (177)$$

which results in

$$\langle X(\mathbf{r}, t) \rangle = X_0(\mathbf{r}), \quad \forall(\mathbf{r}, t) \quad (178)$$

With these assumptions, the fluctuations $\langle \delta X(\mathbf{r}, t) \rangle$ are defined as the first-order noise. The extension of these assumptions for two-group theory is straightforward.

Substituting the generic expression given by [\(175\)](#) for all time-dependent parameters in [\(156\)–\(157\)](#), the second-order terms (i.e., terms of the form $\delta X(\mathbf{r}, t) \cdot \delta Y(\mathbf{r}, t)$) can be neglected because of the assumed smallness of the fluctuations. Subtracting the time-independent equation [\(140\)](#) and performing a Fourier transform leads to

$$\begin{aligned} \nabla \cdot D(\mathbf{r}) \nabla \delta \phi(\mathbf{r}, \omega) + \left\{ \left[1 - \frac{i\omega\beta}{i\omega + \lambda} \right] v\Sigma_f(\mathbf{r}) - \Sigma_a(\mathbf{r}) - \frac{i\omega}{\nu} \right\} \delta \phi(\mathbf{r}, \omega) \\ = \left\{ \delta \Sigma_\alpha(\mathbf{r}, \omega) - \left[1 - \frac{i\omega\beta}{i\omega + \lambda} \right] \delta v\Sigma_f(\mathbf{r}, \omega) \right\} \phi_0(\mathbf{r}) \end{aligned} \quad (179)$$

where the temporal Fourier transform of any quantity $\delta X(\mathbf{r}, t)$ is estimated as

$$\delta X(\mathbf{r}, \omega) = \int_{-\infty}^{\infty} \exp(-i\omega t) \delta X(\mathbf{r}, t) dt \quad (180)$$

Compared to the static equation (140), it can be noticed that the equation for the neutron noise is an inhomogeneous equation, whereas the equation for the static flux is a homogeneous one. From this viewpoint, the equation for the neutron noise is easier to solve, although the quantities in (179) are complex quantities.

With introducing some notations usual in reactor dynamics and neutron noise theory, (179) can be written in the simpler form

$$\Delta \delta \phi(\mathbf{r}, \omega) + B^2(\omega) \cdot \delta \phi(\mathbf{r}, \omega) = \frac{S(\mathbf{r}, \omega)}{D} \quad (181)$$

with

$$B^2(\omega) = B_0^2 \left(1 - \frac{1}{\rho_\infty \cdot G_0(\omega)} \right) \quad (182)$$

where $G_0(\omega)$ is the “zero-power reactor transfer function” defined as

$$G_0(\omega) = \frac{1}{i\omega \left(\Lambda + \frac{\beta}{i\omega + \lambda} \right)} \quad (183)$$

and further,

$$\rho_\infty = 1 - \frac{1}{k_\infty} = 1 - \frac{\Sigma_a}{\nu \Sigma_f} \quad (184)$$

and

$$S(\mathbf{r}, \omega) = \left\{ \delta \Sigma_a(\mathbf{r}, \omega) - \left[1 - \frac{i\omega \beta}{i\omega + \lambda} \right] \delta \nu \Sigma_f(\mathbf{r}, \omega) \right\} \phi_0(\mathbf{r}) \quad (185)$$

The Green’s function of (181) will be calculated later on.

3.3.2 The Factorization of the Neutron Noise

We shall derive the neutron noise in the so-called point-kinetic approximation, which has been often used when evaluating measurements, especially at the early days of power reactor noise. As a starting point, the equations giving the fluctuations of the amplitude factor and of the shape functions are derived in linear theory.

As described earlier, the reactor physics approximations are based on the factorization of the time- and space-dependent neutron flux into an amplitude factor and a shape function as

$$\phi(\mathbf{r}, t) = P(t) \cdot \psi(\mathbf{r}, t) \quad (186)$$

Splitting the time-dependent parameters to mean values and fluctuations according to (175) results in

$$P(t) = P_0 + \delta P(t) \quad (187)$$

$$\psi(\mathbf{r}, t) = \psi(\mathbf{r}, t = 0) + \delta \psi(\mathbf{r}, t) \quad (188)$$

$$\phi(\mathbf{r}, t) = \phi_0(\mathbf{r}) + \delta \phi(\mathbf{r}, t) \quad (189)$$

Due to (162), (188) leads to

$$\psi(\mathbf{r}, t) = \frac{\phi_0(\mathbf{r})}{P_0} + \delta\psi(\mathbf{r}, t) \quad (190)$$

Using (187) and (190) in (189) and neglecting second-order terms gives

$$\delta\phi(\mathbf{r}, t) = \underbrace{\phi_0(\mathbf{r}) \cdot \frac{\delta P(t)}{P_0}}_{\text{point-reactor term}} + \underbrace{P_0 \cdot \delta\psi(\mathbf{r}, t)}_{\text{space-dependent term}} \quad (191)$$

The above composition of the neutron noise from a point reactor term, driven by the reactivity effect of the perturbation, and a space-dependent term, which is driven by the nonuniform (in space) character of the perturbation, is basic in reactor noise theory.

We also see from (161)–(162) that the fluctuation of the shape function, that is, the space-dependent term and the static flux are orthogonal. This reads as

$$\int \phi_0(\mathbf{r}) \delta\psi(\mathbf{r}, t) d\mathbf{r} = 0 \quad (192)$$

Determination of the Fluctuations of the Amplitude Factor

It was shown in ► 5.2.2 that the amplitude factor $P(t)$ fulfills the following time-dependent equations:

$$\frac{dP(t)}{dt} = \frac{\rho(t) - \beta}{\Lambda(t)} P(t) + \lambda C(t) \quad (193)$$

$$\frac{dC(t)}{dt} = \beta \frac{P(t)}{\Lambda(t)} - \lambda C(t) \quad (194)$$

In the static case, these equations result in $\rho_0 = 0$ (critical system).

Noticing that in first-order theory one has $\Lambda(t) = \Lambda, \forall t$ where

$$\Lambda = \frac{1}{\nu \nu \Sigma_f}, \quad (195)$$

splitting all time-dependent parameters into mean values and fluctuating parts according to (175), neglecting second-order terms and performing a temporal Fourier transform lead to

$$\delta P(\omega) = P_0 \cdot G_0(\omega) \cdot \delta\rho(\omega) \quad (196)$$

where $G_0(\omega)$ is the zero-power reactor transfer function defined in (183). The frequency-dependence of the amplitude and phase of this function is shown in ► Fig. 7. As is also seen from this figure, for the “plateau region”

$$\lambda \ll \omega \ll \frac{\beta}{\Lambda_0}, \quad (197)$$

the amplitude is nearly constant and is equal to

$$|G_0(\omega)| \approx \frac{1}{\beta} \quad (198)$$

whereas the phase delay is close to zero within this region.

The fluctuations of the reactivity in (196) are given in first-order approximation as

$$\delta\rho(\omega) = \frac{\int \{ \delta\nu\Sigma_f(\mathbf{r}, \omega) - \delta\Sigma_a(\mathbf{r}, \omega) \} \phi_0^2(\mathbf{r}) d\mathbf{r}}{\delta\Sigma_{f,0}(\mathbf{r})\phi_0^2(\mathbf{r}) d\mathbf{r}} \quad (199)$$

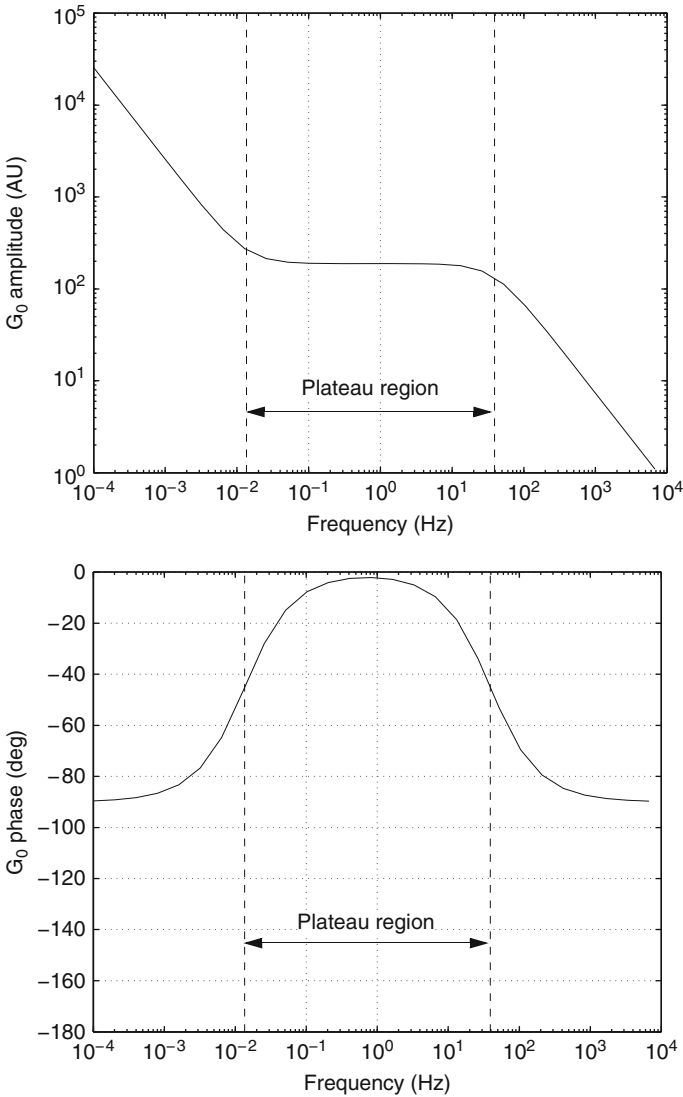


Figure 7
Gain and phase of the transfer function $G_0(\omega)$

Since the kinetic approximations will not be derived and discussed in two-group theory here, we just give the corresponding expression for the reactivity in two-group diffusion theory, to give some flavor of the formalism:

$$r(\omega) = \frac{1}{F} \int \left\{ \left[\delta v \Sigma_{f,1}(r, \omega) - \delta \Sigma_{a,1}(r, \omega) - \delta \Sigma_r(r, \omega) \right] \varphi_{1,0}^\dagger(r) \varphi_{1,0}(r) + \delta v \Sigma_{f,2}(r, \omega) \varphi_{1,0}^\dagger(r) \varphi_{2,0}(r) - \delta \Sigma_{a,1}(r, \omega) - \delta \Sigma_{a,2}(r, \omega) \varphi_{2,0}^\dagger(r) \varphi_{2,0}(r) \right\} dr \quad (200)$$

with

$$F = \int \left[v \Sigma_{f,1,0}(r) \varphi_{1,0}^\dagger(r) \varphi_{1,0}(r) + v \Sigma_{f,2,0}(r) \varphi_{1,0}^\dagger(r) \varphi_{2,0}(r) \right] dr$$

The reason for the appearance of the fast and thermal static adjoints is due to the fact that, as mentioned earlier, in an energy-dependent theory, the normalization condition attached to the factorization assumption is defined through the static adjoint (see (160)).

The above shows that, since in linear theory one only needs to keep first-order terms in the expression for the reactivity, the static flux (in two-group theory the static fluxes and adjoints) can be used for its calculation, hence the reactivity can be calculated without knowledge of the shape function. This means that the point-kinetic equations for the fluctuation of the amplitude factor decouple from those of the shape function.

Determination of the Fluctuations of the Shape Function

The equation for the shape function is derived from (181). Rewriting (191) in the frequency domain as

$$\delta \phi(\mathbf{r}, \omega) = \phi_0(\mathbf{r}) \cdot \frac{\delta P(\omega)}{P_0} + P_0 \cdot \delta \psi(\mathbf{r}, \omega) \quad (201)$$

and using this expression in (181), after rearrangements one obtains

$$P_0 \Delta \delta \psi(\mathbf{r}, \omega) + P_0 \cdot B^2(\omega) \delta \psi(\mathbf{r}, \omega) = \frac{S(\mathbf{r}, \omega)}{D_0} + \frac{v \Sigma_{f,0}}{D_0} \phi_0(\mathbf{r}) \delta \rho(\omega) \quad (202)$$

As the above shows, also the equation for the shape function decouples from the point-kinetic equations. Hence, in linear theory the shape function can be calculated in a simpler way than in the general case. However, the solution of (202) is not simpler than that of the full equation (181), so in general, the solution of (202) is not sought. The representation of the noise as a sum of the point-kinetic term and the space-dependent term is useful in the first place for the interpretation of the results, and in cases when the shape function is calculated in the adiabatic approximation.

From (201) and (196), one finds that the flux noise is given by

$$\delta \phi(\mathbf{r}, \omega) = \phi_0(\mathbf{r}) G_0(\omega) \delta \rho(\omega) + P_0 \delta \psi(\mathbf{r}, \omega) \quad (203)$$

Full Solution in One-Group Diffusion Theory

The exact or full solution of neutron noise in linear one-group diffusion theory can be conveniently calculated using the so-called Green's function technique. The Green's function in the general case is given by the solution to the following equation:

$$\nabla_r \cdot D(\mathbf{r}) \nabla_r G(\mathbf{r}, \mathbf{r}', \omega) + \left\{ \left[1 - \frac{i\omega\beta}{i\omega + \lambda} \right] \times v\Sigma_f(\mathbf{r}) - \Sigma_a(\mathbf{r}) - \frac{i\omega}{\nu} \right\} G(\mathbf{r}, \mathbf{r}', \omega) = \delta(\mathbf{r} - \mathbf{r}') \quad (204)$$

where the ∇_r operator is taken with respect to the \mathbf{r} variable. With the Green's function, the neutron noise is expressed as

$$\delta\phi(\mathbf{r}, \omega) = \int G(\mathbf{r}, \mathbf{r}', \omega) S(\mathbf{r}', \omega) d\mathbf{r}' \quad (205)$$

In the following, a homogeneous system, in which an analytical solution can be obtained, will be considered. A finite one-dimensional reactor of dimension $2a$ will be used. For this case, one has

$$\Delta_x G(x, x', \omega) + B^2(\omega) G(x, x', \omega) = \frac{\delta(x - x')}{D_0} \quad (206)$$

and

$$\delta\phi(x, \omega) = \int G(x, x', \omega) \cdot S(x', \omega) dx' \quad (207)$$


with

$$S(x', \omega) = \left\{ \delta\Sigma_a(\omega) - \left[1 - \frac{i\omega\beta}{i\omega + \lambda} \right] \times \delta v\Sigma_f(\omega) \right\} \phi_0(x') \quad (208)$$

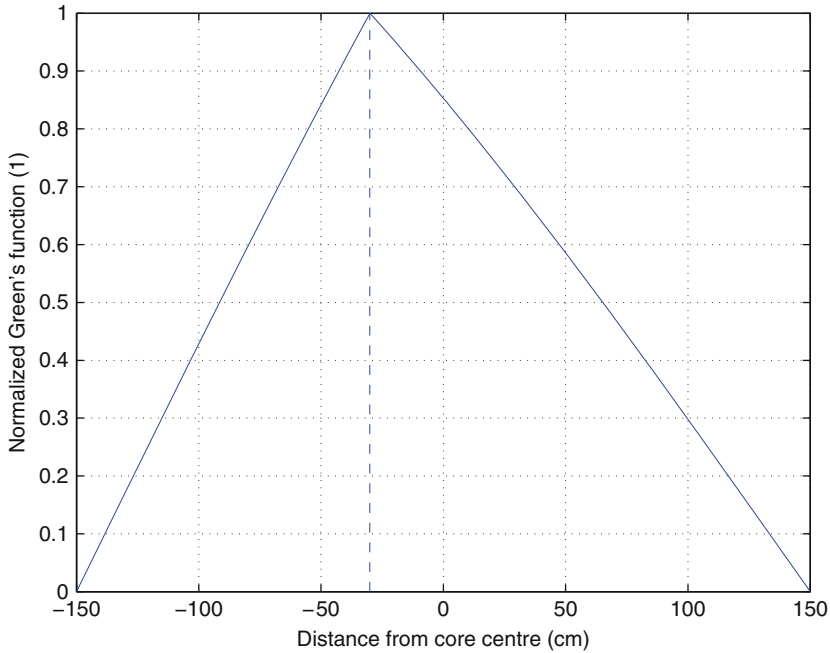
and where $B^2(\omega)$ was defined in (182).

Equation (206) is an inhomogeneous equation and is of the same type as (148), except that the right-hand side does not contain the searched function and therefore it is an inhomogeneous equation with a unique solution. Using the same technique in the solution, accounting for the continuity of Green's function and the discontinuity of its derivative at $x = x'$, one obtains

$$G(x, x', \omega) = \begin{cases} -\frac{\sin[B(\omega)(a+x)] \cdot \sin[B(\omega)(a-x')]}{D_0 B(\omega) \sin[2B(\omega)a]} & x \leq x' \\ -\frac{\sin[B(\omega)(a-x)] \cdot \sin[B(\omega)(a+x')]}{D_0 B(\omega) \sin[2B(\omega)a]} & x > x' \end{cases} \quad (209)$$

An illustration of the space-dependence of the amplitude (absolute value) of the above Green's function $G(x, x', \omega)$ for a non-central perturbation is shown in  Fig. 8 with the data of a power reactor.

The neutron noise that can be determined by (206)–(208) corresponds to the neutron noise induced by a localized perturbation at $x = x'$, which changes its strength with a frequency ω . Such a perturbation is sometimes referred to as the neutron noise induced by an “absorber of variable strength” or “reactor oscillator.”



■ Figure 8

Space-dependence of the amplitude of the one-dimensional Green's function $G(x, x', \omega)$ in one-group diffusion theory for $x' = -30$ cm at 1 Hz

Figure 8 shows that in a power reactor and at a frequency of $f = 1$ Hz, the response of the reactor is not point kinetic, since the shape of the induced noise deviates from the shape of the static flux, that is, from a pure cosine function. For decreasing frequencies or system sizes, the response to a localized perturbation becomes more and more point kinetic with a growing amplitude, whereas the other limit of increasing frequency or system size results in more and more localized response with a decreasing amplitude. In general, in power reactors at plateau frequencies, which is the most important parameter range of noise applications, space-dependent effects are important. Actually a one-dimensional model underestimates the importance of space-dependent effects, which are more pronounced in two- and three-dimensional cases.

In the following, the neutron noise induced by a vibrating perturbation, that is, a perturbation that originates from the variation of the position of an absorber, will be derived. Such a case is sometimes referred to as a “vibrating absorber.” A typical example is a vibrating control rod in a reactor. The control rod, whose diameter is much smaller than the core size, will be described with the same model as used in the static case, (147). Assuming that the vibrations occur with the same amplitude at each axial point, the axial dependence of the noise can be factorized and hence disregarded. Then, the problem can be treated as a two-dimensional one. The steady (i.e., not vibrating) control rod at r_p is described by

$$\Sigma_a^{\text{rod}}(\mathbf{r}) = \gamma \cdot \delta(\mathbf{r} - \mathbf{r}_p), \quad (210)$$

where \mathbf{r}_p is the rod equilibrium position and γ is its Galanin's constant. When vibrating, the rod will move on a two-dimensional stochastic trajectory around the equilibrium position such that its momentary position will be given by $\mathbf{r}_p + \underline{\varepsilon}(t)$, where $|\underline{\varepsilon}(t)| \ll R$ and R is the core radius. The perturbation represented by the vibrations is given as

$$\delta\Sigma_a(\mathbf{r}, t) = \gamma [\delta(\mathbf{r} - \mathbf{r}_p - \underline{\varepsilon}(t)) - \delta(\mathbf{r} - \mathbf{r}_p)]. \quad (211)$$

Equation (211) shows that the vibrating rod is characterized by the parameters \mathbf{r}_p and $\{\varepsilon_x(t), \varepsilon_y(t)\}$. The latter parameters describe the amplitude and the frequency content of the vibrations.



From (185), (205), and (211), everything is available for a formal solution except that $\delta\Sigma_a(\mathbf{r}, \omega)$ is not explicitly available since (211) cannot be Fourier transformed directly. However, performing the spatial integral in (205) first, then utilizing the smallness of the vibration amplitude through a one-term Taylor expansion in $\underline{\varepsilon}(t)$, this latter appears explicitly and can be Fourier transformed. One then obtains for the neutron noise in the frequency domain

$$\begin{aligned} \delta\phi(\mathbf{r}, \omega) &= \gamma \cdot \underline{\varepsilon}(\omega) \cdot \nabla_{\mathbf{r}_p} \{G(\mathbf{r}, \mathbf{r}_p, \omega) \cdot \phi_0(\mathbf{r}_p)\} \\ &= \gamma \cdot \{\varepsilon_x(\omega)G_x(\mathbf{r}, \mathbf{r}_p, \omega) + \varepsilon_y(\omega)G_y(\mathbf{r}, \mathbf{r}_p, \omega)\} \end{aligned} \quad (212)$$

where

$$G_x(\mathbf{r}, \mathbf{r}_p, \omega) = \frac{\partial}{\partial x_p} \{G_x(\mathbf{r}, \mathbf{r}_p, \omega)\phi_0(\mathbf{r}_p)\}, \quad (213)$$

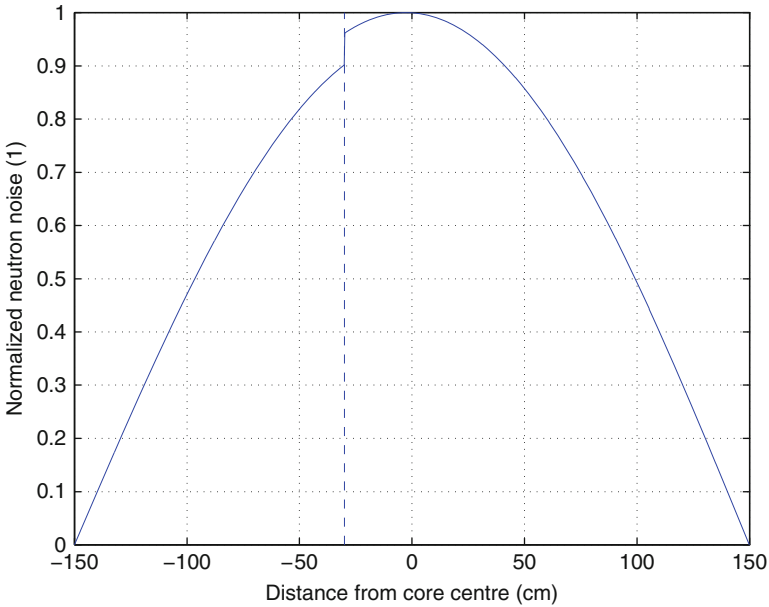
and similarly for $G_y(\mathbf{r}, \mathbf{r}_p, \omega)$.

In a one-dimensional model, the vibrations can only take place in one direction, and the above formulas get simplified. The amplitude of the induced noise with a non-central equilibrium position of the rod is shown in  Fig. 9. The discontinuity at the rod position is due to the interplay between the point-kinetic term and the space-dependent term. The point-kinetic term, which is proportional to the static flux, for weak rods can be taken as a cosine function (the small static dip around the rod can be neglected). The space-dependent component can be visualized with the help of the adiabatic approximation as the difference between two static fluxes, one with the equilibrium position of the rod and the other when the rod is off from the equilibrium position. The space-dependence of the shape function was solved using (148) in the case of a thin absorber. This is illustrated in  Fig. 10.

3.3.3 Neutron Noise in Two-Group Diffusion Theory: The Local Component

Direct Approach: the Green's Function Matrix

Here, only a cursory description is given, just to illustrate the principles. Only the full solution and its Green's function will be considered, the various kinetic approximations will not be discussed. Similar to the static case, (151), a matrix and vector formalism will be used. After the usual procedure of splitting the time-dependent quantities into mean values and fluctuations,



■ Figure 9

Space-dependence of the amplitude of the noise induced by a non-central vibrating rod at $x_p = -30$ at a frequency of 1 mHz and for a Galanin constant of $\gamma = 0.01$; the discontinuity is due to the interference between the space-dependent and the point-kinetic terms

neglecting second-order terms, subtracting the static equations, and eliminating the delayed neutron precursors after a temporal Fourier transform, one obtains

$$\begin{bmatrix} D_1 \nabla^2 - \Sigma_1(\omega) & v \Sigma_{f_2}(\omega) \\ \Sigma_R & D_2 \nabla^2 - \Sigma_{a_2}(\omega) \end{bmatrix} \begin{bmatrix} \phi_1(\mathbf{r}, \omega) \\ \phi_2(\mathbf{r}, \omega) \end{bmatrix} = \begin{bmatrix} S_1(\mathbf{r}, \omega) \\ S_2(\mathbf{r}, \omega) \end{bmatrix} \quad (214)$$

The definitions of the quantities appearing in (214) are as follows:

$$\Sigma_1(\omega) = \Sigma_{a_1} + \frac{i\omega}{v_1} + \Sigma_R - v \Sigma_{f_1} \left(1 - \frac{i\omega\beta}{i\omega + \lambda} \right) \quad (215)$$

$$v \Sigma_{f_2}(\omega) = v \Sigma_{f_2} \left(1 - \frac{i\omega\beta}{i\omega + \lambda} \right) \quad (216)$$

$$\Sigma_{a_2}(\omega) = \Sigma_{a_2} + \frac{i\omega}{v_2} \quad (217)$$

$$\begin{aligned} S_1(\mathbf{r}, \omega) = & \left(\delta \Sigma_R(\mathbf{r}, \omega) + \delta \Sigma_{a_1}(\mathbf{r}, \omega) - \delta \Sigma_{f_1}(\mathbf{r}, \omega) \left(1 - \frac{i\omega\beta}{i\omega + \lambda} \right) \right) \phi_1(\mathbf{r}) \\ & - \delta \Sigma_{f_1}(\mathbf{r}, \omega) \left(1 - \frac{i\omega\beta}{i\omega + \lambda} \right) \phi_2(\mathbf{r}) \end{aligned} \quad (218)$$

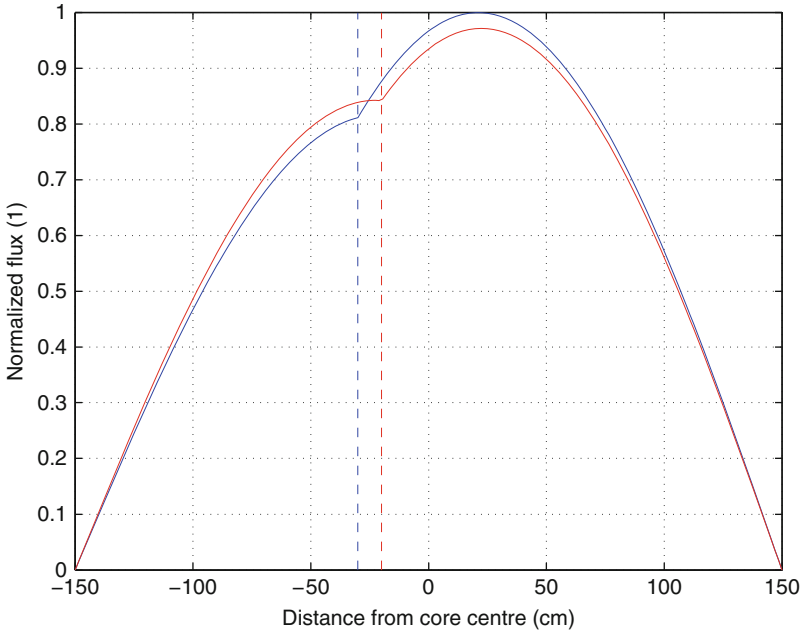


Figure 10

The space-dependent component of the vibration noise for a Galanin constant of $\gamma = 0.01$, calculated as the difference between two static flux calculations with the rod positioned at $x_p = -30$ cm (results plotted in blue) and $x_p = -20$ cm (results plotted in red), respectively (adiabatic approximation)

and

$$S_2(\mathbf{r}, \omega) = (-\delta\Sigma_R(\mathbf{r}, \omega) + \delta\Sigma_{a_1}(\mathbf{r}, \omega)) \phi_2(\mathbf{r}) \tag{219}$$

In view of the matrix character of the equation for the noise components in the two groups, for the application of Green’s function technique, one has to define a Green’s matrix

$$\hat{\mathbf{G}}(\mathbf{r}, \mathbf{r}', \omega) = \begin{bmatrix} G_{1 \rightarrow 1} & G_{2 \rightarrow 1} \\ G_{1 \rightarrow 2} & G_{2 \rightarrow 2} \end{bmatrix} \tag{220}$$

where $G_{i \rightarrow j}$ is the transfer function between the noise source in group i to the neutron noise in group j . Then, the Green’s matrix obeys the equation, written in symbolic form as

$$\hat{\mathbf{L}}(\mathbf{r}, \omega) \hat{\mathbf{G}}(\mathbf{r}, \mathbf{r}', \omega) = \delta(\mathbf{r} - \mathbf{r}') \hat{\mathbf{E}} \tag{221}$$

where $\hat{\mathbf{L}}(\mathbf{r}, \omega)$ is a shorthand notation for the matrix operator on the left-hand side of (214), and $\hat{\mathbf{E}}$ is the unity matrix. The noise in the two groups is then given by

$$\begin{bmatrix} \delta\phi_1(\mathbf{r}, \omega) \\ \delta\phi_2(\mathbf{r}, \omega) \end{bmatrix} = \int_{V_R} \hat{\mathbf{G}}(\mathbf{r}, \mathbf{r}', \omega) \begin{bmatrix} S_1(\mathbf{r}', \omega) \\ S_2(\mathbf{r}', \omega) \end{bmatrix} d\mathbf{r}' \tag{222}$$

In the general case, when there is a noise source present in both groups, and one is interested in the noise in both groups, all four elements of Green's matrix (220) need to be determined. The situation can be simplified if the noise source exists only in the thermal group. In that case, it is sufficient to calculate only the second column of $\hat{\mathbf{G}}$, which obeys the equation

$$\hat{\mathbf{L}}(\mathbf{r}, \omega) \begin{bmatrix} G_{2 \rightarrow 1}(\mathbf{r}, \mathbf{r}', \omega) \\ G_{2 \rightarrow 2}(\mathbf{r}, \mathbf{r}', \omega) \end{bmatrix} = \begin{bmatrix} 0 \\ \delta(\mathbf{r} - \mathbf{r}') \end{bmatrix} \quad (223)$$

This equation can be solved with a combination of the techniques used in the solution of the static matrix equation (151) and the inhomogeneous one-group equation (206) by converting the Dirac-delta function into an interface condition. The solution will be determined by the two roots $\mu^2(\omega)$ and $\nu^2(\omega)$ of the characteristic equation belonging to $\hat{\mathbf{L}}$, which is simply a frequency-dependent generalization of (153). They can be given approximately as

$$\mu(\omega) \cong B_0^2 \left(1 - \frac{k_\infty}{M^2 B_0^2 G_0(\omega)} \right); \quad M^2 = L_1^2 + L_2^2 \quad (224)$$

and

$$\nu(\omega) \approx \frac{1}{L_2} \quad (225)$$

with $L_g = D_g / \Sigma_{a_g}$; $g = 1, 2$ being the diffusion lengths. This shows that for light water power reactors at plateau frequencies, $|\nu^2| \gg |\mu^2(\omega)|$. Taking again the same non-reflected homogeneous one-dimensional system with boundaries at $x = \pm a$, the solution is given as

$$\begin{bmatrix} G_{2 \rightarrow 1}(\mathbf{r}, \mathbf{r}', \omega) \\ G_{2 \rightarrow 2}(\mathbf{r}, \mathbf{r}', \omega) \end{bmatrix} = \begin{pmatrix} 1 \\ c_\mu(\omega) \end{pmatrix} G_\mu(x, x', \omega) + \begin{pmatrix} 1 \\ c_\nu(\omega) \end{pmatrix} G_\nu(x, x', \omega) \quad (226)$$

with

$$G_\mu(x, x', \omega) = -\frac{\Sigma_R}{D_1 D_2 \nu^2(\omega) \mu(\omega) \sin(2\mu(\omega)a)} \begin{cases} \sin[\mu(\omega)(a+x)] \sin[\mu(\omega)(a-x_0)]; & x < x_0 \\ \sin[\mu(\omega)(a-x)] \sin[\mu(\omega)(a+x_0)]; & x > x_0 \end{cases} \quad (227)$$

and

$$G_\nu(x, x', \omega) = \frac{\Sigma_R}{D_1 D_2 \nu^3(\omega) \sin(2\nu(\omega)a)} \begin{cases} \sinh[\nu(\omega)(a+x)] \sinh[\nu(\omega)(a-x_0)]; & x < x_0 \\ \sinh[\nu(\omega)(a-x)] \sinh[\nu(\omega)(a+x_0)]; & x > x_0 \end{cases} \quad (228)$$

Further, $c_\mu(\omega)$ and $c_\nu(\omega)$ are the frequency-dependent extensions of the static quantities in (155):

$$c_\mu = \frac{\Sigma_R}{D_2 \mu^2(\omega) + \Sigma_{a_2} + \frac{i\omega}{\nu_2}} \quad \text{and} \quad c_\nu = \frac{\Sigma_R}{\Sigma_{a_2} + \frac{i\omega}{\nu_2} - D_2 \nu^2(\omega)} \quad (229)$$

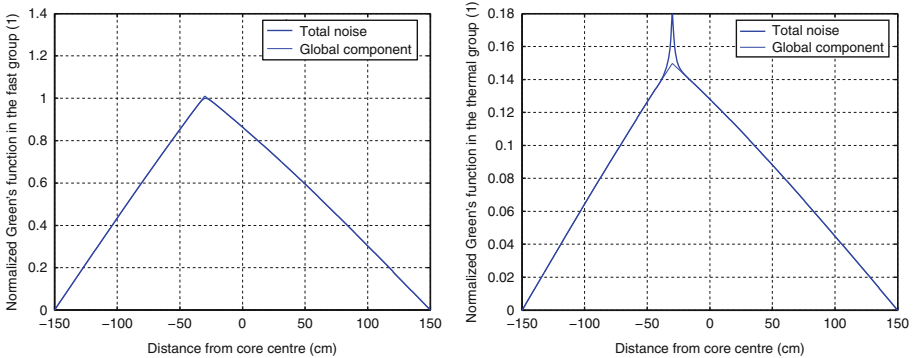


Figure 11
Space-dependence of the amplitude of the one-dimensional Green’s function in two-group diffusion theory for $x' = -30$ cm at 5 Hz in the fast group (left) and in the thermal group (right)

In (226), G_μ is the global component, representing a slow spatial relaxation, and G_ν is the local component, representing the response of the system, which exists only in the vicinity of the perturbation. As mentioned earlier, in quantitative terms, the global component is rather similar to the full solution in one-group theory, whereas the local component adds a small peak to the global component around the position of the perturbation. An illustration of the fast and the thermal components of Green’s function, $G_{2 \rightarrow 1}(x, x', \omega)$ and $G_{2 \rightarrow 2}(x, x', \omega)$, respectively, is given in [Fig. 11](#).

However, in the problem of largest practical importance for the local component, that is, in the interpretation of in-core neutron noise in a BWR induced by a propagating two-phase flow, the most important factor in the driving force is the fluctuations of the removal cross sections. As (218) and (219) show, the fluctuation of the removal cross section generates a noise source both in the fast group and the thermal group. To describe such a case, in the above “direct” or “forward” treatment, both columns of Green’s matrix (220) need to be determined.

At the same time, in noise measurements, only the thermal noise, that is, the fluctuation of the thermal flux, is measured; hence the full information content of Green’s matrix is somewhat redundant. As is also seen from (220), for such a case, it would be sufficient to determine only the second row of Green’s matrix. In the direct (forward) equations used so far, this is not possible by solving one equation. These problems can be remedied by the use of adjoint (“backward”) methods, as described below.

Adjoint Approach: The Dynamic Adjoint Function

To alleviate the problems described above and for several further advantages, the concept of the dynamic adjoint function, basically the adjoint of the noise equations or that of the Green’s function, was introduced by H. van Dam (1975, 1976). The adjoint operator \hat{L}^\dagger corresponding to direct operator \hat{L} given by the left-hand side of (214) is defined as one that obeys the relationship

$$(\bar{\Phi}^\dagger, \hat{L}\bar{\Phi}) = (\hat{L}^\dagger\bar{\Phi}^\dagger, \bar{\Phi}) \tag{230}$$

Here, $\bar{\Phi}$ and $\bar{\Phi}^\dagger$ are flux-type vectors, having a fast component and a thermal component, and both obeying the same boundary conditions of vanishing at the extrapolated boundary, and the

bracket denotes integration over the volume of the reactor. It is easy to show that in two-group diffusion theory the adjoint is simply the transposed of the direct operator, that is,

$$\hat{\mathbf{L}}^\dagger = \hat{\mathbf{L}}^T \quad (231)$$

Then, the corresponding adjoint Green's matrix $\hat{\mathbf{G}}^\dagger$ obeys the equation


$$\hat{\mathbf{L}}^\dagger(\mathbf{r}, \omega) \hat{\mathbf{G}}^\dagger(\mathbf{r}, \mathbf{r}', \omega) = \delta(\mathbf{r} - \mathbf{r}') \hat{\mathbf{E}} \quad (232)$$

Note that in (232) \mathbf{r}' stand for the detection point, and the first and second members of the diagonal on the right-hand side stand for detection in the fast and the thermal group, respectively. Now if we only have a thermal detector, it is sufficient to determine the second column of the Green's matrix $\hat{\mathbf{G}}^\dagger$. Denoting this column vector as $\bar{\Psi}^\dagger$, called the dynamic adjoint for short, it obeys the equation

$$\hat{\mathbf{L}}^\dagger(\mathbf{r}, \omega) \bar{\Psi}^\dagger(\mathbf{r}, \mathbf{r}', \omega) = \begin{bmatrix} 0 \\ \delta(\mathbf{r} - \mathbf{r}') \end{bmatrix} \quad (233)$$

Then, using the properties of the adjoint, one readily obtains that with the dynamic adjoint, the noise $\delta\phi_2(\mathbf{r}, \omega)$ in the thermal group, induced by a perturbation $\bar{S}(\mathbf{r}, \omega)$ having nonzero components in both the fast and thermal groups, can be expressed as

$$\delta\phi_2(\mathbf{r}, \omega) = \int \bar{\Psi}^\dagger(\mathbf{r}', \mathbf{r}, \omega) \bar{S}(\mathbf{r}', \omega) d\mathbf{r}' \quad (234)$$

If the perturbation consists only of the fluctuations of the removal cross section, which is a good approximation for a BWR, then, as (218) and (219) show, the response of the system is determined by the scalar adjoint transfer function $\Psi_1 - \Psi_2$ (sometimes called the "removal adjoint"). The weight of the local component is enhanced in the removal adjoint as compared to the thermal direct Green's function (Behringer et al. 1979).  Figure 11 gives a hint of this fact, although it refers to the direct Green's function.

The use of the dynamic adjoint has a number of further other advantages, which will not be described here. The interested reader is referred to Pázsit (1992, 2003).

As it will be seen in the next two subsections, in many cases of noise diagnostic applications, especially in conceptual ones aimed at method development, the use of a homogeneous non-reflected system in one-group theory, in one or two dimensions, is fully satisfactory. However, for concrete applications in inhomogeneous cores, the Green's function (or the dynamic adjoint), and also the induced neutron noise, need to be calculated by taking into account the inhomogeneous loading of a core. This calculation should have the same precision and spatial resolution as the known in-core fuel management (ICFM) codes. In fact, there is a way to convert existing multigroup static codes to calculate the dynamic adjoint in n -group theory. This method was used by van der Hagen et al. (1992) and tested in applications. An alternative possibility is to develop a code from scratch, dedicated to noise calculations. This alternative also was used to develop a code for the numerical calculation of the dynamic Green's function of the neutron noise and the dynamic adjoint in realistic systems in two-group diffusion theory. The code, also called as the "Neutron noise simulator" (Demazière 2004; Demazière and Pázsit 2008), takes the same input of core parameters as the ICFM code SIMULATE. Some of its applications are described in the next two subsections.

4 Applications of Power Reactor Noise Diagnostics

4.1 Unfolding Noise Source Parameters with Noise Diagnostics

In this subsection some typical applications of noise diagnostics are presented. The objective of noise diagnostics is to monitor the proper operation of nuclear reactors, the early detection of anomalies, and to identify and quantify the type of anomaly and its severity. This is achieved by unfolding the significant parameters of the perturbation $S(\mathbf{r}, \omega)$ from the measured neutron noise. One example of such parameters is the position of a localized source. The two main types of such perturbations are the absorbers of variable strength (channel-type instabilities in BWRs) and the case of vibrating absorbers. Another example is the determination of in-core flow velocity in both BWRs and PWRs. The last two examples in this subsection are the diagnostics of core-barrel vibrations and the detection of vibrating detector strings in BWRs. These last two applications, although they are based on the detection of the neutron noise as measured by ex-core and in-core neutron detectors, respectively, are not based on the dynamic response of the core to perturbations in the core. They are mentioned here only to make the list of noise methods monitoring the integrity of the core with neutron noise methods more complete.

The treatment will be based on the formalism developed in [Subsect. 3.3](#). For simplicity, the basics of unfolding noise source parameters will be outlined in one-group theory with one average delayed neutron group, and the perturbation consisting of the fluctuations of the absorption cross section. Extension to two energy groups or several groups of delayed neutrons as well as fluctuations of other cross sections is straightforward. The quantitative examples in most cases were calculated by the neutron noise simulator, unless specified otherwise.

As described earlier, the equation for the neutron noise, induced by the fluctuation of the absorption cross sections, reads as

$$\nabla^2 \delta\phi(\mathbf{r}, \omega) + B^2(\omega) \delta\phi(\mathbf{r}, \omega) = \frac{S(\mathbf{r}, \omega)}{D}, \quad (235)$$

where

$$S(\mathbf{r}, \omega) = \delta\Sigma_a(\mathbf{r}, \omega)\phi_0(\mathbf{r}). \quad (236)$$

The solution is given with the Green's function or system transfer function $G(\mathbf{r}, \mathbf{r}', \omega)$, which is obtained from the equation

$$\nabla^2 \delta\phi(\mathbf{r}, \omega) + B^2(\omega) \delta\phi(\mathbf{r}, \omega) = \frac{\delta(\mathbf{r} - \mathbf{r}')}{D} \quad (237)$$

as

$$\delta\phi(\mathbf{r}, \omega) = \int G(\mathbf{r}, \mathbf{r}', \omega) S(\mathbf{r}', \omega) d\mathbf{r}'. \quad (238)$$

[Equation \(238\)](#) is the basis of core diagnostics with neutron noise methods. It shows that the effect of a perturbation can be factorized into a noise source term $S(\mathbf{r}, \omega)$, and a system transfer $G(\mathbf{r}, \mathbf{r}', \omega)$. As [\(237\)](#) shows, the system transfer function is only dependent on the parameters of the unperturbed system, which is a consequence of using linear theory. The transfer function

$G(\mathbf{r}, \mathbf{r}', \omega)$ can thus be calculated for a reactor independently of the type of perturbation. Hence, $G(\mathbf{r}, \mathbf{r}', \omega)$ can be assumed to be known in a diagnostic task.

The task of diagnostics is to quantify the noise source $S(\mathbf{r}, \omega)$ from the measured neutron noise $\delta\phi(\mathbf{r}, \omega)$, using the knowledge of the transfer function. Determining $S(\mathbf{r}, \omega)$ from $\delta\phi(\mathbf{r}, \omega)$ through (238) is an inverse task. Formally, if $\delta\phi(\mathbf{r}, \omega)$ and $G(\mathbf{r}, \mathbf{r}', \omega)$ are known as continuous functions of the space coordinates, (238) is a Fredholm-type integral equation for the unknown $S(\mathbf{r}, \omega)$, which may be inverted.

However, a difficulty arises here since $\delta\phi(\mathbf{r}, \omega)$ is only known in a few discrete points, that is, in the detector positions. If nothing is known about $S(\mathbf{r}, \omega)$, inversion of (238) has only a chance if a relatively large number of detectors are available at a time, which is normally not the case in practice. Thus, usually another approach is selected. First, by inspecting the signals of the neutron detectors available, a guess is made on the type of perturbation giving rise to the detected noise (such as, two-phase flow transport, vibrations). Such assumptions are usually made by studying the frequency content of the measured noise and the phase relationships between the detectors, or the type of noise source may be apparent from other, independent measurements. A given noise source is then represented by a simple functional form, in which only a few parameters remain as unknowns. Then, it may be possible to determine those few parameters by using a few neutron detectors.

For an illustration, the case of the neutron noise induced by a central “absorber of variable strength,” as well as that of a vibrating absorber will be considered in a two-dimensional cylindrical geometry (► Fig. 12 and ► 13, respectively). In both figures, the surface plots show the full space-dependence of the amplitude (left figures) and phase (right figures) of the noise as calculated by the noise simulator. The black dots represent the possible locations of five in-core neutron detectors together with the value of the amplitude and phase of their measured signals. It can clearly be seen from these figures, that the neutron noise recorded from these five detectors does not allow a direct determination of the location of the noise source, which is responsible for the measured neutron noise. However, the type of the noise source (either an “absorber of variable strength” or a “vibrating absorber”) can be determined from the phase of the neutron noise. In case of an “absorber of variable strength,” the phase does not vary much throughout the core, whereas the phase varies from 0° to -180° in case of a “vibrating absorber.” In this case, a mono-directional vibration along a line was assumed, leading to the clear phase differences seen in ► Fig. 13. In reality, the situation is even more complicated since the vibration is usually a two-dimensional random walk, but still similar conclusions can be drawn regarding the type of the noise source. Once the type of the source is decided, a simple model of the noise source can be set up, which can be used to elaborate an algorithm for the determination of the position of the source (“localization”).

4.1.1 Localization of Absorbers of Variable Strength

Although the terminology here refers to absorbers, these types of noise sources encompass all kinds of cross sections, that is, absorption, fission, and scattering. Absorbers of variable strengths can be represented as fluctuations in the macroscopic absorption cross sections at a given fixed location \mathbf{r}_0 and the corresponding noise source expressed as

$$\delta\Sigma_a(\mathbf{r}, \omega) = \gamma(\omega)\delta(\mathbf{r} - \mathbf{r}_0) \quad (239)$$

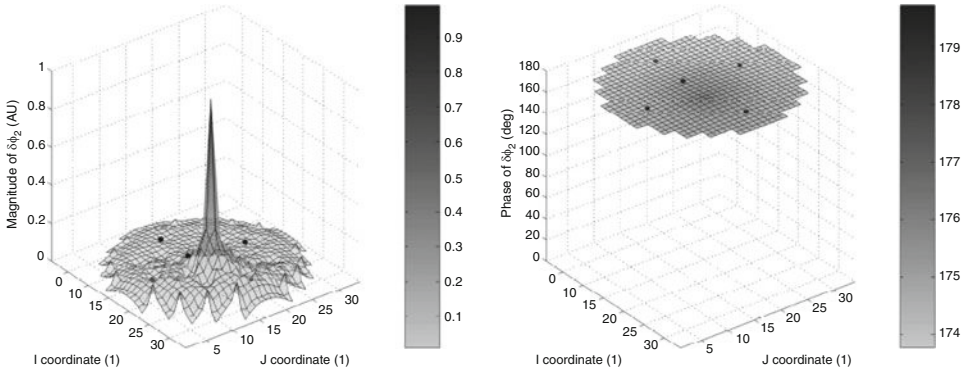


Figure 12
 Calculated (surface plot) and simulated measured (black dots) values of the neutron noise induced by a central (localized) “absorber of variable strength” in the thermal group at a frequency of 1 Hz

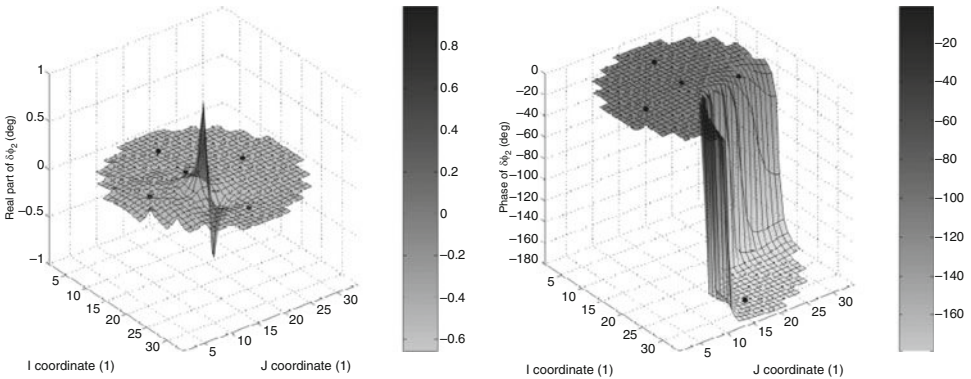


Figure 13
 Calculated (surface plot) and simulated measured (black dots) values of the neutron noise induced by a central “vibrating absorber” in the thermal group at a frequency of 1 Hz

where $\gamma(\omega)$ is the noise source strength, which might be frequency-dependent in the most general case.

The neutron noise induced by such a noise source can be formally expressed as

$$\delta\phi(\mathbf{r}, \omega) = \int G(\mathbf{r}, \mathbf{r}', \omega) \delta\Sigma_a(\mathbf{r}', \omega) \phi_0(\mathbf{r}') d\mathbf{r}' \tag{240}$$

which, due to (239), becomes

$$\delta\phi(\mathbf{r}, \omega) = \gamma(\omega) G(\mathbf{r}, \mathbf{r}_0, \omega) \phi_0(\mathbf{r}_0) \tag{241}$$

If one now assumes that the neutron noise is measured at two locations \mathbf{r}_A and \mathbf{r}_B within the core, then taking the ratio between the two neutron noise signals allows eliminating the noise

source strength $\gamma(\omega)$. That is, one has

$$\frac{\delta\phi(\mathbf{r}_A, \omega)}{\delta\phi(\mathbf{r}_B, \omega)} = \frac{G(\mathbf{r}_A, \mathbf{r}_0, \omega)}{G(\mathbf{r}_B, \mathbf{r}_0, \omega)} \quad (242)$$

The left-hand side of (242) can be obtained from measurements. The right-hand side contains the unknown of the problem, namely the location \mathbf{r}_0 as an unknown argument of a known function, since the transfer function can be calculated. Scanning all possible values for \mathbf{r}_0 thus offers the possibility of constructing a localization procedure, aiming at determining the actual location of the noise source. When there is equality between the left-hand side and the right-hand side, that is, between the measured quantity and the calculated one, the noise source has been correctly located.

In a two-dimensional case, which is what one encounters in practice since due to the core geometry, usually only the radial position of a fuel assembly or a control rod is searched, two detectors are not sufficient for the localization since there will be a whole set of \mathbf{r}_0 values, lying on a line, which will satisfy (242). At least three detectors are needed, or more. If one has access to several detectors, the following quantity can be evaluated for each detector combination (A, B):

$$\Delta_{A,B}(\mathbf{r}) = \frac{\delta\phi(\mathbf{r}_A, \omega)}{\delta\phi(\mathbf{r}_B, \omega)} - \frac{G(\mathbf{r}_A, \mathbf{r}, \omega)}{G(\mathbf{r}_B, \mathbf{r}, \omega)} \quad (243)$$

so that the minimum of the following function should correspond to the location \mathbf{r}_0 of the noise source:

$$\Delta(\mathbf{r}) = \sum_{A,B} \Delta_{A,B}^2(\mathbf{r}) \quad (244)$$


Since it is common practice to use the auto- and cross-power spectral densities (APSDs and CPSDs respectively) of the measured signals instead of their Fourier transform, (243)–(244) have to be written as follows:

$$\Delta_{A,B,C,D}(\mathbf{r}) = \frac{CPSD(\mathbf{r}_A, \mathbf{r}_B, \omega)}{CPSD(\mathbf{r}_C, \mathbf{r}_D, \omega)} - \frac{G(\mathbf{r}_A, \mathbf{r}, \omega) \times G^*(\mathbf{r}_B, \mathbf{r}, \omega)}{G(\mathbf{r}_C, \mathbf{r}, \omega) \times G^*(\mathbf{r}_D, \mathbf{r}, \omega)} \quad (245)$$


and

$$\Delta(\mathbf{r}) = \sum_{A,B,C,D} \Delta_{A,B,C,D}^2(\mathbf{r}) \quad (246)$$

Despite the apparent high number of possible detector combinations, the number of detectors quadruplets that need to be taken into account can be significantly reduced if the redundant combinations are discarded. The location of the perturbation is then found at the value of \mathbf{r} for which the right-hand side of (246) yields a minimum.

As mentioned earlier, if the system behaves in a point-kinetic manner, the space-dependence of the induced neutron noise is given by the static neutron flux, and thus does not depend on the location of the noise source. In such a case, the localization algorithm cannot be applied. As mentioned earlier, and as is seen in  Fig. 12, large systems significantly deviate from point kinetics for large enough frequencies (above 0.1 Hz), so that the localization algorithm can be used for such frequencies.

The localization algorithm was first developed using an analytical Green's function corresponding to a homogeneous reactor in one-group diffusion theory (see Kitamura et al. 1999) and later using a numerical Green's function corresponding to a heterogeneous reactor in two-group diffusion theory, that is, using the neutron noise simulator (Demazière 2006). The algorithm was also tested on real plant data, namely the Forsmark-1 channel instability event in 1996/1997 in Sweden (see Kitamura et al. 1999; Demazière 2006). In 1996, during the start-up tests of the Forsmark-1 BWR for the fuel cycle 16, local instabilities were detected at reduced power and reduced core flow. As it was clarified later, the instability was due to local density wave oscillation (DWO) in a fuel assembly, which was not properly seated on the bottom plate ("unseated" assembly). The task of the localization was to identify the unseated assembly.

During this stability measurement, the lower plane of the core was rather well equipped with local power range monitors (LPRMs) (27 of the 36 available detector strings were actually recorded). A closer look at the phase of the measured flux noise indicated that the neutron noise was driven by a local noise source, similar to the effect of an absorber of variable strength (reactor oscillator), rather than a moving absorber, such as a vibrating control rod. The localization algorithm presented above was thus applied to these measurement data in a two-dimensional representation of the core and the results are shown in  Fig. 14. The noise source pointed out by the localization algorithm is very close to a fuel assembly, which was discovered to be

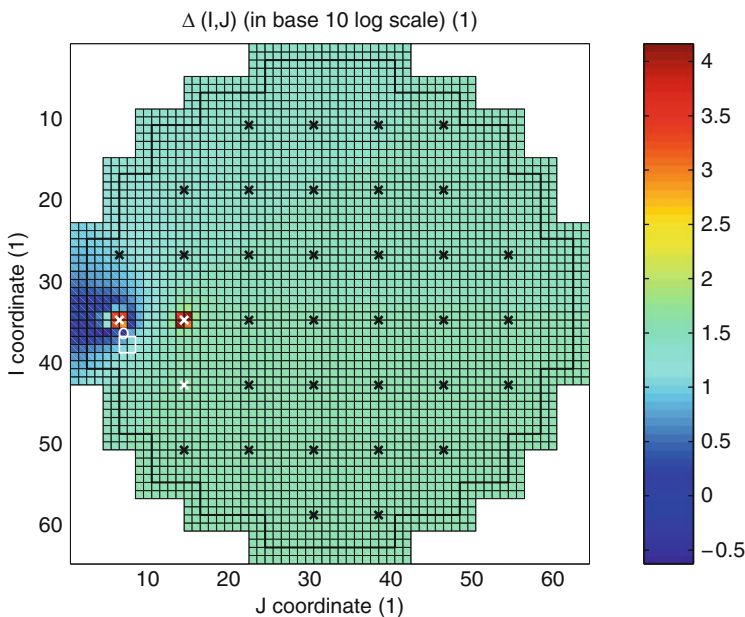


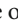
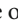
 Figure 14


Result of the localization algorithm in the Forsmark-1 case (local instability event). The unseated fuel element is marked with a square, and the noise source identified by the localization algorithm with a circle; the detectors that were used in the localization search are marked by white crosses, whereas the detectors that were not used are marked by black crosses

unseated during the fuel outage following the fuel cycle 16. Hence, the localization procedure worked rather well for this case.

4.1.2 Localization of Vibrating Control Rods

The fact that a vibrating control rod leads to detectable neutron noise is known from the ORR and HFIR reactors (Fry 1971). This meant that at least the occurrence of stronger than normal vibrations could be detected by neutron noise measurements. Later it turned out that control rod vibrations can occur even in power reactors. Since excessive vibration is always a sign of beginning malfunction, detecting and locating vibrations by neutron noise methods became an interesting task.

Compared to the absorber of variable strength, the vibrating absorber represents a very different perturbation and the neutron noise it generates, and hence also the expressions to be inverted, are also very different from that of the absorber of variable strength. The difference in the noise source can be seen by comparing (239) with (211), whereas the difference in the space-dependence of the noise is seen by comparing  Fig. 12 with  Fig. 13. Not surprisingly, also the localization algorithm will be rather different.

As already described in  3.3.2, the perturbation represented by a thin vibrating rod in two dimensions can be represented by the fluctuation of the absorption cross sections as

$$\delta\Sigma_a(\mathbf{r}, t) = \gamma [\delta(\mathbf{r} - \mathbf{r}_p - \underline{\varepsilon}(t)) - \delta(\mathbf{r} - \mathbf{r}_p)] \quad (247)$$

where \mathbf{r}_p is the equilibrium position to be determined by the diagnostics, and $\underline{\varepsilon}(t)$ is the two-dimensional displacement from the equilibrium position. As it was also shown, the neutron noise induced by such a noise source is given as


$$\begin{aligned} \delta\phi(\mathbf{r}, \omega) &= \gamma \cdot \underline{\varepsilon}(\omega) \cdot \nabla_{\mathbf{r}_p} \{G(\mathbf{r}, \mathbf{r}_p, \omega) \cdot \phi_0(\mathbf{r}_p)\} \\ &= \gamma \{\varepsilon_x(\omega)G_x(\mathbf{r}, \mathbf{r}_p, \omega) + \varepsilon_y(\omega)G_y(\mathbf{r}, \mathbf{r}_p, \omega)\} \end{aligned} \quad (248)$$

where

$$G_x(\mathbf{r}, \mathbf{r}_p, \omega) = \frac{\partial}{\partial x_p} \{G(\mathbf{r}, \mathbf{r}_p, \omega) \cdot \phi_0(\mathbf{r}_p)\}, \quad (249)$$

and similarly for $G_y(\mathbf{r}, \mathbf{r}_p, \omega)$.

Equation (248) shows that the vibration components ε_x and ε_y , which are of no direct interest, appear explicitly in the noise expression, whereas the rod position \mathbf{r}_p , the main interest of the diagnostics, is contained implicitly. It is also seen that merely taking the ratios of detector signals will eliminate the unknown rod strength γ , but will not eliminate the displacement components. To determine \mathbf{r}_p , a more involved procedure is necessary in which the unknown vibration components are eliminated.

Such a localization procedure can be constructed as follows. One selects three detectors at positions \mathbf{r}_i , $i = 1, 2, 3$, possibly with an azimuthally evenly spread arrangement as in  Fig. 15. Denoting the detector signals of the three detectors as $\phi(\mathbf{r}_i, \omega) \equiv \phi_i(\omega)$, $i = 1, 2, 3$, one has

$$\delta\phi_i(\omega) = \gamma \{\varepsilon_x(\omega)G_{i,x}(\mathbf{r}_p, \omega) + \varepsilon_y(\omega)G_{i,y}(\mathbf{r}_p, \omega)\}, \quad (250)$$

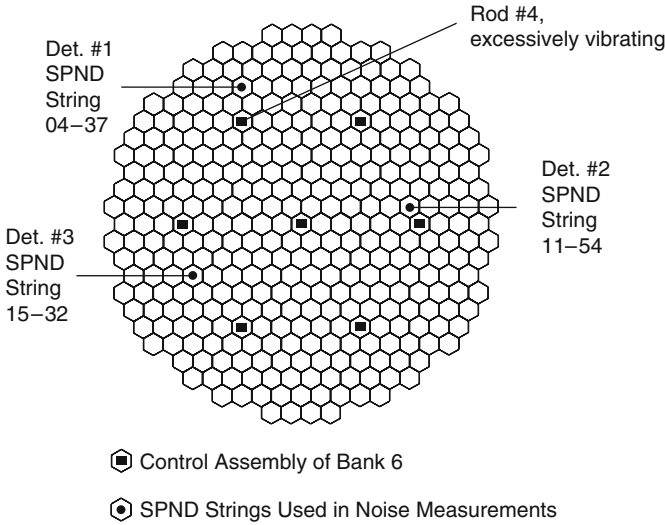


Figure 15
Core layout of the Hungarian Paks-2 PWR with the locations of neutron detectors and control rods

for all three signals, with

$$G_{i,\alpha}(\mathbf{r}_p, \omega) \equiv G_\alpha(\mathbf{r}_i, \mathbf{r}_p, \omega); \quad \alpha = \{x, y\}. \tag{251}$$

Using two equations of the type (250) to express the displacement components in terms of the measured noise and the transfer functions $G_{i,\alpha}(\mathbf{r}_p, \omega)$, and substituting these in the third equation results in an expression of the form

$$F_1(\mathbf{r}_p, \omega)\delta\phi_1(\omega) + F_2(\mathbf{r}_p, \omega)\delta\phi_2(\omega) + F_3(\mathbf{r}_p, \omega)\delta\phi_3(\omega) = 0. \tag{252}$$

Here,

$$F_1(\mathbf{r}_p, \omega) = G_{2x}G_{3y} - G_{2y}G_{3x}, \tag{253}$$

and similarly for $F_2(\mathbf{r}_p, \omega)$ and $F_3(\mathbf{r}_p, \omega)$.

Equation (252) constitutes the formal solution of the localization problem. Its use is similar to that of (243) and (244): the $\phi_i(\omega)$ are taken from the measurements, and the functional form of the $F_i(\mathbf{r}_p, \omega)$ is known from theory. In this equation, all quantities are known except the argument \mathbf{r}_p , that is, the searched rod position. The equation is only fulfilled if \mathbf{r}_p has the correct value, this parameter is thus determined as a root of the equation. The localization in a given case is thus performed as finding the root of the complex equation (252).

In practice, however, it is not the Fourier transforms of the signals that are used, rather the auto- and cross-spectra of the $\delta\phi_i$, that is, $APSD_{\delta\phi_i}(\omega)$ and $CPSD_{\delta\phi_i\delta\phi_j}(\omega)$, respectively, are used. Likewise, instead of $\varepsilon_x(\omega)$ and $\varepsilon_y(\omega)$, the auto- and cross-spectra, $S_{xx}(\omega)$, $S_{yy}(\omega)$, and $S_{xy}(\omega)$ of the displacement components need to be used as input source. With the application

of the Wiener–Khinchin theorem, the auto- and cross-spectra of the detector signals can be expressed from (250) as

$$APSD_{ii}(\omega) = APSD_{\delta\phi_i}(\omega) = \gamma^2 \{G_{ix}^2 S_{xx} + G_{iy}^2 S_{yy} + 2G_{ix}G_{iy}G_{xy}\}, \quad (254)$$

$$CPSD_{ij}(\omega) = CPSD_{\delta\phi_i, \delta\phi_j}(\omega) = \gamma^2 \{G_{ix}G_{jy}S_{xx} + G_{iy}G_{jy}S_{yy} + (G_{ix}G_{jy} + G_{jx}G_{iy})S_{xy}\}, \quad (255)$$

In the above form, for simplicity, it was assumed that we are on the plateau frequency region and can assume Green's function and the vibration displacement cross-spectra as real. The latter is the consequence of the decoupled character of the vibrations along two main axes.

In this form, the localization procedure now requires eliminating the vibration spectra $S_{xx}(\omega)$, etc., and deriving an equation similar to (252) in which only the transfer functions and the neutron noise spectra are present. Such an equation can be formally written down with the help of the spectral and transfer matrices in the form

$$\mathbf{G}_{12}^{-1}(\mathbf{r}_p)\mathbf{S}_{12}\mathbf{G}_{12}^{+1}(\mathbf{r}_p) = \mathbf{G}_{23}^{-1}(\mathbf{r}_p)\mathbf{S}_{23}\mathbf{G}_{23}^{+1}(\mathbf{r}_p) = \mathbf{G}_{13}^{-1}(\mathbf{r}_p)\mathbf{S}_{13}\mathbf{G}_{13}^{+1}(\mathbf{r}_p), \quad (256)$$

where

$$\mathbf{S}_{ij} \equiv \begin{bmatrix} APSD_{ii}(\omega) & APSD_{ji}(\omega) \\ CPSD_{ij}(\omega) & APSD_{jj}(\omega) \end{bmatrix}; \quad i, j = 1, 2, 3, \quad (257)$$

is the neutron noise spectral matrix, and

$$\mathbf{G}_{ij} = \begin{bmatrix} \mathbf{G}_{ix} & \mathbf{G}_{jx} \\ \mathbf{G}_{iy} & \mathbf{G}_{jy} \end{bmatrix}, \quad (258)$$

is the transfer function matrix. The rod position \mathbf{r}_p is still given as the root of (256). For finding its root, the equation has to be split up into scalar equations, and the simultaneous root of the several equations has to be found.

It is seen that, in contrast to locating a variable strength absorber, this method is much more complicated. Despite these difficulties, the method was applied with success to the localization of an excessively vibrating control rod in the Hungarian Paks-2 PWR (Pázsit and Glöckler 1988).

As an alternative to the above complicated algorithmic procedure, another method based on artificial neural networks (ANNs) may be used (Pázsit et al. 1996). ANNs are being increasingly used in all kinds of diagnostics that require the solution of inverse tasks (Pázsit and Kitamura 1996). Their principle of operation is that they need a certain number of training samples, in this case sets of neutron noise and rod position data that belong together. Such data are generated by model calculations, using the same transfer functions as in the algorithmic method.

To this end a model of the two-dimensional vibrations, or rather a model for the noise source spectral matrix with elements $S_{\alpha\beta}$ with $\alpha, \beta = x, y$, for example, $S_{xx} = APSD_{\varepsilon_x}(\omega)$, etc. is needed. In the simplest nontrivial random model the two-dimensional vibrations can be parametrized by two variables, an ellipticity (anisotropy) parameter $k \in [0, 1]$ and the preferred

direction of the vibration $\alpha \in [0, \pi]$ as

$$S_{xx} \propto 1 + k \cos 2\alpha, \quad (259)$$

$$S_{yy} \propto 1 - k \cos 2\alpha, \quad (260)$$

$$S_{xy} = S_{yx} \propto k \sin 2\alpha. \quad (261)$$

Then, a large number of training data are generated, and the ANN is trained to recognize the correct control rod position. When the training is finished, the ANN is ready to take measured data as its input, and it will designate one of the rods as the vibrating one.

Both the algorithmic and the ANN-based method were tested in a real measurement. This concrete application concerns the excessive vibration of a control rod in the Hungarian Paks-2 PWR in 1985. Details of the event are described in Pázsit and Glöckler (1988). Both the algorithmic and the ANN-based methods were tested, and they both pointed out correctly rod #4, which was the vibrating one. It is interesting to note that detector #1 (SPND string 04-37) (see [► Fig. 15](#)), being much closer to the vibrating rod #4 as the other two detectors, gave a slightly smaller vibration peak in its APSD as the other two detectors. This is due to the interplay of the point-kinetic and space-dependent terms of the vibration-induced noise, as shown earlier. This fact also shows that localization of a vibrating rod cannot be based on simple intuition.

4.1.3 Flow Velocity Estimations

Being able to monitor in-core coolant velocity as well as two-phase flow is of prime importance in order to detect at a very early stage any flow blockage/reduction inside the core due to debris, formation of crud, etc., before it leads to fuel damage. Western-type light water reactors are usually not equipped with in-core flow meters allowing the determination of the coolant velocity within the fuel assemblies. Nevertheless, the core is usually instrumented with in-core neutron detectors and in some cases in-core temperature detectors. If pairs of such detectors are located in the same fuel assembly, any fluctuation in the coolant flow will be registered by each of the two detectors within the same fuel assembly with some time delay. The measurement of this time delay allows estimating the coolant flow, knowing the axial separation distance between the detectors. Such methods and their applications will be described below.

Flow Velocity Estimations in BWRs from the Neutron Noise

It was noted in the early 1970s that neutron detectors in the same instrument tube in a BWR can measure the transport time of two-phase flow between two detectors from the phase of the cross-spectrum (Wach and Kosály 1974). The perturbation in this case is represented by the density fluctuations in the coolant, in form of a two-phase flow with a random spatial structure (propagating bubbles). To explain the measurements, first the existence of the local component of the induced noise was postulated (Wach and Kosály 1974), then the local component was derived by the use of two-group diffusion theory (Kosály 1975). The appearance of the local and global components of the noise in the Green's function was outlined in [► Subsect. 3.3.3](#).

It is important that in the case of BWR in-core noise, these two components give a comparable contribution to the detector signal, that is, none of them suppresses the other completely. Rather, their joint occurrence leads to interference effects as described below.

In a simplified picture, for the local component one can assume that

$$G(\mathbf{r}, \mathbf{r}', \omega) \approx \delta(\mathbf{r} - \mathbf{r}'), \quad (262)$$

that is,

$$\delta\phi_L(\mathbf{r}, t) \approx \delta\Sigma(\mathbf{r}, t)\phi_0(\mathbf{r}) \quad (263)$$

where the subscript L indicates that this refers to the local component only. If only this component existed, then the signal of two detectors placed along an axial line at a distance $z_2 - z_1$ to each other would have signals similar to each other but with a time delay

$$\tau = \frac{z_2 - z_1}{v} \quad (264)$$

where v is the propagation velocity. That is,

$$\delta\phi_L(z_2, t) = \delta\phi_L(z_1, t - \tau). \quad (265)$$

In the frequency domain, this leads to

$$\delta\phi_L(z_2, \omega) = \exp(-i\omega\tau)\delta\phi_L(z_1, \omega) \quad (266)$$

Applying the Wiener–Khinchin theorem and using (266), the cross-spectrum between the two detectors can be expressed by the auto-spectrum of one of the signals as

$$\begin{aligned} \text{CPSD}_{\phi_L}(z_1, z_2, \omega) &\cong \delta\phi_L(z_2, \omega)\delta\phi_L^*(z_1, \omega) = \delta\phi_L(z_1, \omega)\delta\phi_L^*(z_1, \omega) \times \exp(-i\omega\tau) \\ &= \text{APSD}_{\phi_L}(z_1, \omega) \times \exp(-i\omega\tau) \end{aligned} \quad (267)$$

According to (267), the phase of the cross-spectrum is a linear function of ω

$$\varphi(\omega) = -\omega\tau \quad (268)$$

from which the transit time τ of the propagation of the perturbation can be determined, and its mean velocity can then be inferred from (264).

Since the boiling process itself, to a good approximation, is usually a white noise, $\text{APSD}_{\phi}(z, \omega)$ and thus $|\text{CPSD}_{\phi}(z_1, z_2, \omega)|$ are constants in the frequency range of interest, usually between 0.1 and 10–15 Hz in a typical BWR. If (265) holds, that is the two signals are identical except for a time delay, then the coherence equals unity:

$$\text{Coh} \equiv \frac{|\text{CPSD}_{\phi_L}(z_1, z_2, \omega)|}{[\text{APSD}_{\phi_L}(z_1, \omega) \times \text{APSD}_{\phi_L}(z_2, \omega)]^{1/2}} = 1 \quad (269)$$

In reality, however, the two signals will not be identical due to generation, collapse, and coagulation of the bubbles between z_1 and z_2 , and there are always other, independent noise sources in the core. For all these reasons the coherence will be less than unity. Another, more significant fact is that in all reactors there is a so-called reactivity noise or global noise present, which is

in-phase in the signal of the two detectors. This reactivity noise is generated, for example, by the collective movement, generation, and collapse of all bubbles inside the whole reactor. This component can be described, for the present purposes, as their time-dependence being equal in the two detector signals. This can also be expressed in the frequency domain as

$$\delta\phi_G(z_1, \omega) = \delta\phi_G(z_2, \omega) = C \cdot A(\omega) \quad (270)$$

where, for simplicity, we assumed that the amplitude of the two components are equal. The total signal measured by the detectors at z_1 and z_2 are then given as

$$\delta\phi(z_1, \omega) = \delta\phi_L(z_1, \omega) + C \cdot A(\omega) \quad (271)$$

and

$$\delta\phi(z_2, \omega) = \delta\phi_L(z_1, \omega) \exp(-i\omega\tau) + C \cdot A(\omega) \quad (272)$$

Assuming that the local and global components are uncorrelated, that is, their cross-power spectrum is zero, and assuming the frequency-dependence of both the local component and the global component as constants, a simple algebra yields the result that the coherence of the total noise as measured at z_1 and z_2 as well as the CPSD will have an oscillating structure. They will have maxima at

$$\omega\tau = 2n\pi \quad \text{for } n = 0, 1, 2, \dots \quad (273)$$

and minima at

$$\omega\tau = (2n+1)\pi \quad \text{for } n = 0, 1, 2, \dots \quad (274)$$

Likewise, the phase will also deviate from the linear dependence on ω , which is shown in (268). Rather, it will slightly oscillate around the linear dependence with the same periodicity as the coherence in (273), crossing the true linear phase value periodically. Such an effect is clearly seen in some measurements (Wach and Kosály 1974).

For the sake of illustration, some measurements are shown here from the Swedish BWR Barsebäck-2 in ► Fig. 16. The slopes of the straight lines, representing the phase of the CPSD, are suitable to determine the transit time of bubbles between two axially placed detectors. It is also seen, from the change of the slope of the phase, that the transit time decreases with increasing axial height of the detectors, due to higher steam velocity in the upper part of the core. The coherence shows a behavior completely consistent with (273) and (274); that is, it has maxima at the zero-crossings and minima at the π -crossings of the phase. This way the void transit time between two detectors can be determined, and a modest axial resolution of this quantity (in the three consecutive pairs of the four detectors) can be obtained.

Flow velocity Estimations in PWRs from Temperature and Neutron Noise

Historically, first the possibility of using temperature fluctuations for the measurement of water flow in a pipe, such as the feedwater flow of a PWR, was investigated (Kosály and Meskó 1972a). A number of cross-correlation methods, using temperature, N-16 and ultrasound signals have been developed for measuring the feedwater flow, but these will not be discussed here. The

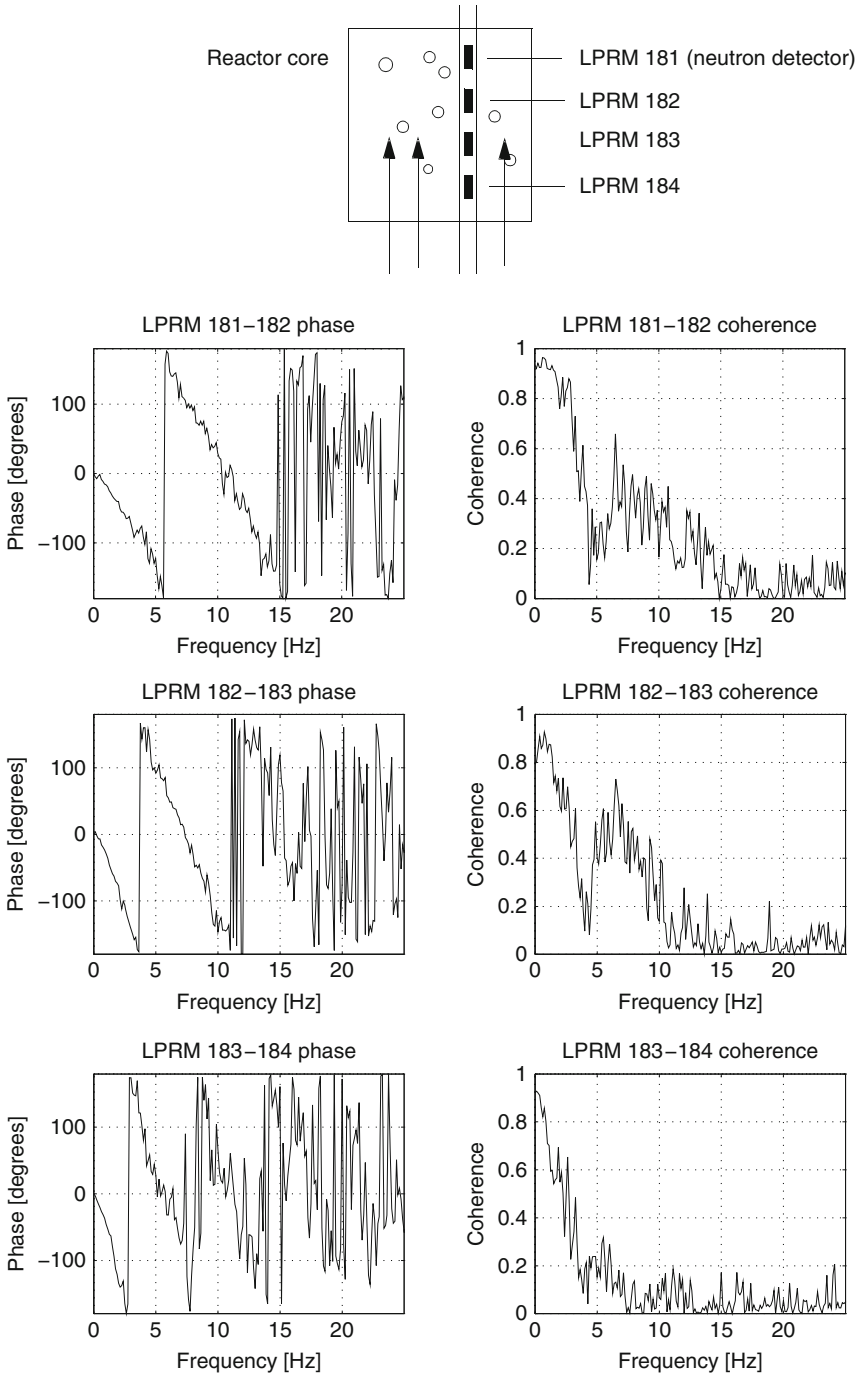


Figure 16
Phase and coherence between detectors in a detector string of the Swedish BWR Barsebäck-2

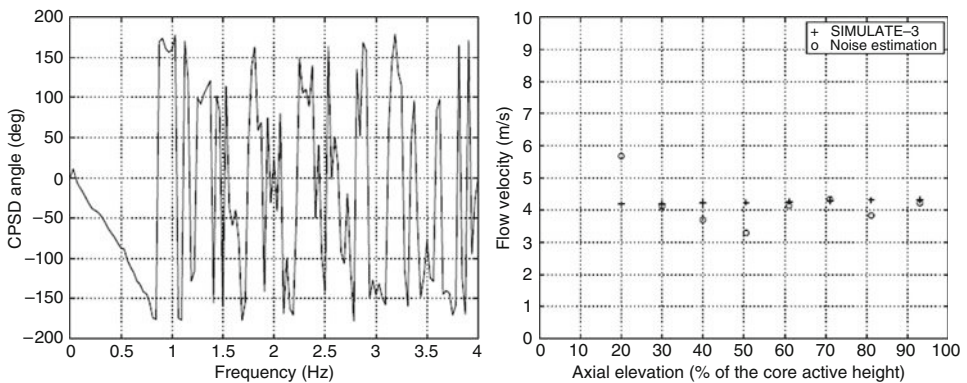
method of temperature fluctuations is taken up here partly because it can be used for measuring the core flow as well, and because it gives a background to the neutron noise-based methods of measuring coolant flow velocity in the core.

Measurements of temperature fluctuations in the coolant are local; hence such a method is equivalent to using only the local component mentioned earlier in this subsection. The measurement would lead to a linear phase whose slope yields the transit time. Alternatively, the maximum of the cross-correlation function (CCF), and a number of more refined methods, can be used. If the temperature pattern in the coolant changes when passing from one thermocouple to another, due to thermal convection, turbulence, etc., then the phase will deviate from strictly linear, and the cross-correlation function gets asymmetric.

Coolant flow measurements based on in-core temperature in PWRs are not common, due to lack of instrumentation. One example is given here for illustration, from measurements taken in the Swedish Ringhals-2 PWR. This reactor was equipped with 108 gamma-thermometers (GTs) installed permanently in the core. These detectors were distributed in 12 detector strings, each of them containing 9 GTs located at different axial levels and covering the whole core active height (► Fig. 21). Although these detectors are meant primarily to detect the gamma flux, in the frequency range 0.1–1 Hz they measure the coolant temperature fluctuations.

An illustrative example of the phase delay observed between two GTs within the same fuel assembly is given in ► Fig. 17, as well as the flow velocity estimated from the phase delay between several combinations of pairs of GTs within the same fuel assembly. The flow velocity estimations are also compared to values computed by the static core simulator SIMULATE-3. The inaccuracy observed in the estimated flow compared to the SIMULATE-3 values is due to possible differences in time constants of the cold junction of the GTs. Cross-correlation techniques are further complicated by the fact that they usually require expert knowledge and expert opinion, which prevents from applying them in an automated manner. More details can be found in Demazière and Pázsit (2002).

From the point of instrumentation, a better choice is to use in-core LPRMs or fission chambers, since many reactor types are equipped with such detectors. These can detect the effect of



■ Figure 17


Phase of the cross-power spectral density (CPSD) between a pair of gamma-thermometers (GTs) located at different axial locations (*left*) and flow velocity estimations (*right*) in the Ringhals-2 PWR

propagating temperature fluctuations on the neutron field. However, the influence of the minute temperature fluctuations on the neutron field is several orders of magnitude smaller than the effect of the two-phase flow. Hence in such measurements the global component, in form of general background noise, or even the global effect of temperature fluctuations, dominates totally. Indeed, in the early days one investigated only the reactivity effect of coolant inlet temperature fluctuations (Kosály and Meskó 1972b). Dominance of the global term results in a close to zero phase of the cross-correlation function, and on the first sight the task of measuring the velocity may appear impossible. In fact, in the first attempts to measure coolant flow velocity by in-core neutron detectors, the oscillation of the phase around zero was used to estimate the velocity (Pór 1981).

However, there is a possibility to largely eliminate the effect of the global component and enhance the information content of the cross-correlation measurement. The trick is to use, instead of the cross-correlation function (CCF) the inverse Fourier transform of the cross-spectrum divided by the auto-spectrum of one of the detectors, also called impulse response function (ICF):

$$IMP_{21}(t) = FFT^{-1} \left\{ \frac{CPSD_{21}(\omega)}{APSD_1(\omega)} \right\} \quad (275)$$




This procedure largely eliminates the contribution from the global component, and the impulse response function so determined is amenable to extract the flow velocity in PWR in-core noise measurements (Adorján et al. 2000; Pór et al. 2003).

Such measurements clarified in the Hungarian PWR Paks-2 that the reason for core power asymmetry laid in the asymmetric flow velocities in the core, due to crud building on the lowest spacers. A graphical representation of the velocity distribution over a horizontal cross section of the core of Paks-2 is shown in  Fig. 18. Such measurements are occasionally performed at other plants.

4.1.4 Miscellaneous Other Applications

Two further methods will be described briefly in which neutron noise is used to identify and quantify core processes with the aim of detecting deterioration of the core integrity. These are core-barrel vibrations and vibrations and impacting of BWR in-core detector tubes. In both cases, there is no core dynamics involved, the detectors act merely as displacement sensors, even if with an unknown scaling. These methods are described here only for sake of completeness.

Diagnostics of Core-Barrel Vibrations in PWRs

In PWRs, the core barrel is a structure hanging vertically inside the reactor pressure vessel from its top. A layout of the reactor internals for a typical PWR is given in  Fig. 19. The core barrel is exposed to pressure fluctuations of the turbulent flow in the downcomer and in the core, hence it executes small vibrations in the deep submillimeter range. Several modes of oscillations of the core barrel are usually encountered. The two most common ones are the pendular or beam-mode vibration, and the shell-mode vibration, as illustrated in  Fig. 20. Since the downcomer is in between the core and the detectors, the vibrations of the core lead to changes in the water thickness between the core and the detectors, hence to a changed attenuation. Due to this, for small vibrations, the detectors act as displacement sensors of the corresponding components of the motion, as can be inferred from  Fig. 20. The eigenfrequency of the beam-mode is around

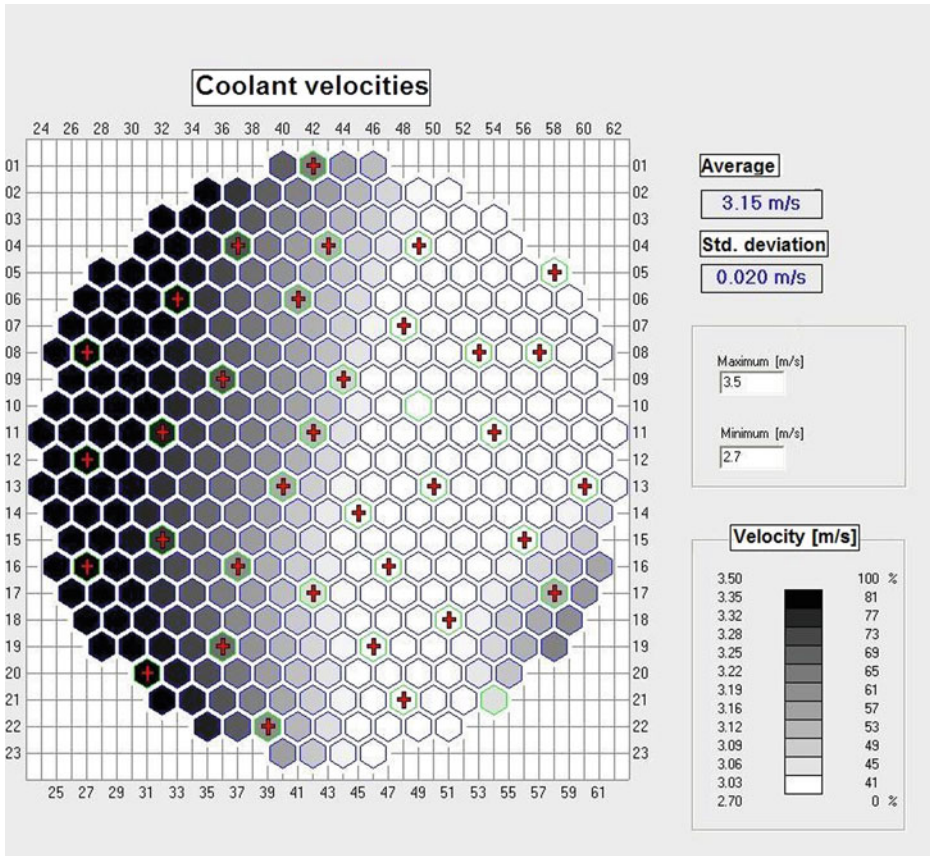


Figure 18 Asymmetric velocity profile in the core of Paks-2 (From Adorján et al. 2000)

8 Hz, whereas for the shell-mode vibration the eigenfrequency is about 20 Hz. These vibrations can be measured by accelerometers, and even by pressure sensors, but these are usually not available at operating plants, only during the preoperational tests. The core-barrel vibrations are most commonly detected by ex-core neutron detectors. Figure 21 shows the arrangement of the eight ex-core detectors, four detectors placed with equal spacing azimuthally around the core at two different axial elevations.

Monitoring of the beam-mode/shell-mode vibrations is performed by using the signals from the ex-core and/or in-core neutron detectors and analyzing the information in the amplitude of the peaks corresponding to the vibration modes of interest, mostly the beam-mode vibrations, and the phase relationships between the detectors. Taking into account the symmetry of the various vibration modes, with various combinations of the four ex-core detectors, the effect of a selected mode can be enhanced and the others suppressed. The details of this procedure will not be described here, the interested reader is referred to Pázsit and Glöckler (1998) for more details. An illustration of the separation of the modes and the resulting spectra are shown in Fig. 22.

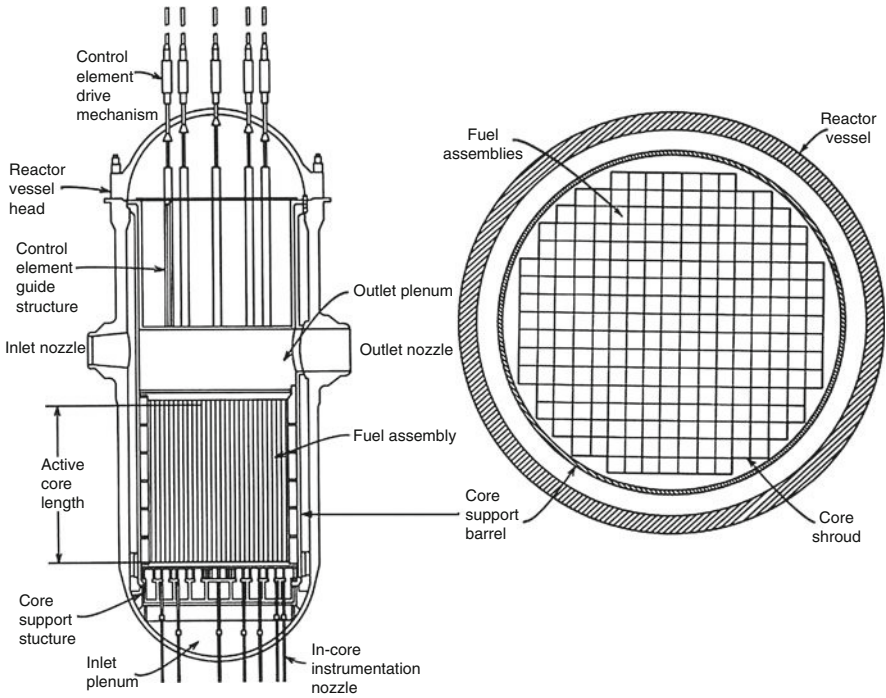


Figure 19
 Layout of the reactor internals of a pressurized water reactor (PWR) (vertical and horizontal cross sections on the left and right-hand sides, respectively) (From Graves, 1979)

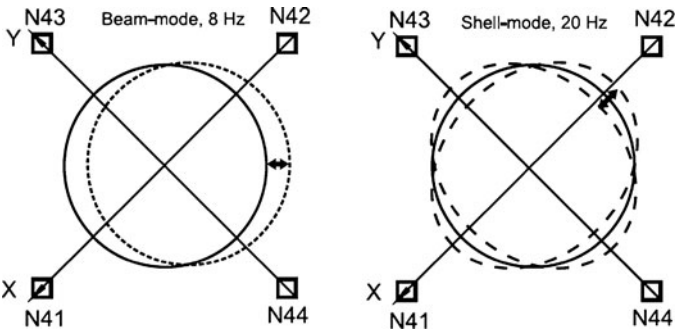


Figure 20
 Illustration of the beam- and shell-mode core-barrel vibrations (the ex-core detectors are shown as squares with the numbering N4X, X = 1..4)

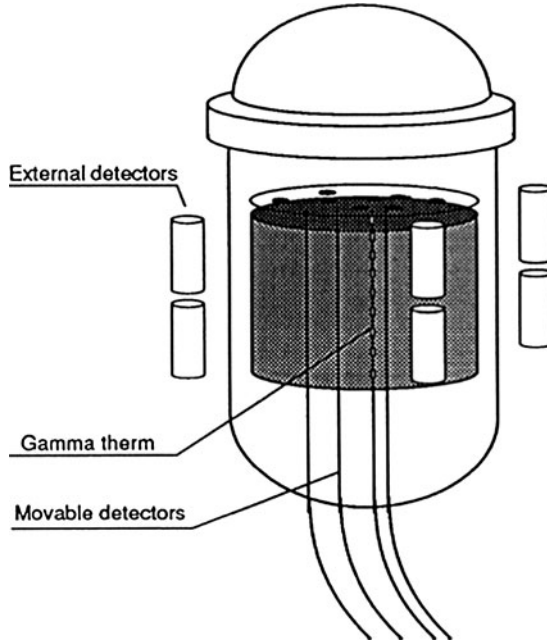


Figure 21

A schematic view of the core together with the gamma-thermometer (GT) strings, showing also the positions of the ex-core ion chambers in a PWR

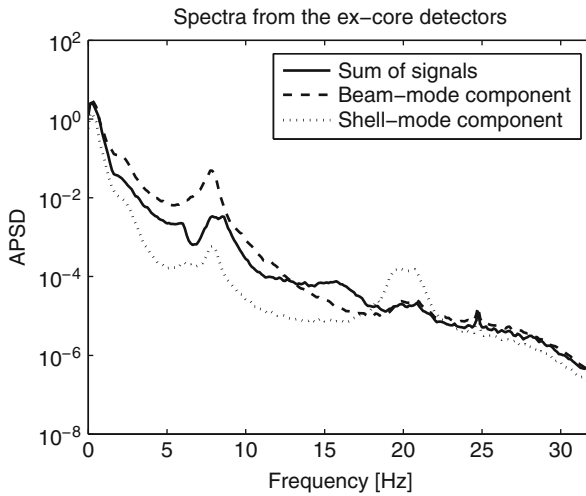


Figure 22

Spectra from ex-core detector signals from a measurement made at the Swedish Ringhals-3 PWR (the beam-mode and shell-mode components are shown separately)

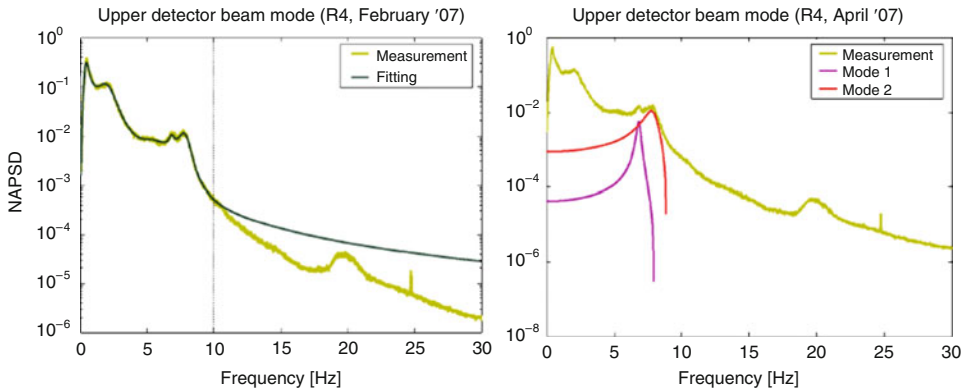


Figure 23

Auto-power spectral density (APSD) of the separated beam-mode component, and the results of a curve-fitting procedure using an analytical expression of the peaks (left), and the separation of the individual peaks in the curve-fitting procedure (right)

In order to obtain the amplitude of the peaks more objectively, and in order to resolve closely lying peaks, the vibration peaks in the beam-mode/shell-mode spectra can be fitted to an analytical expression of the peak, from which the amplitude of the peaks, the peak frequencies, and the widths of the peaks can be determined by curve fitting. Following these parameters during the life of a nuclear reactor allows characterizing the evolution of the amplitude of the beam-mode/shell-mode vibrations, from which early material degradation can be detected. A curve fitting to one of the recent measurements in Ringhals-4 is shown in [▶ Fig. 23](#) (left figure). The right figure illustrates the decomposition of closely lying vibration peaks into individual components, to enhance the determination of the magnitude of the beam-mode components in an accurate way (Pázsit et al. 2008). In [▶ Fig. 24](#), the long-term evolution of the vibration amplitudes is shown for the Ringhals reactors during the period 1991–1998 (Karlsson and Pázsit 1998).

It has to be noted that this type of analysis is hampered by the fact that the individual vibrations of fuel assemblies in the core give a contribution to the signal of the closest detector, which disturbs the symmetry of the detector signals arising from the symmetries of the various core-barrel vibration modes, hence it interferes with the mode decoupling procedure. Further, it also disturbs a precise determination of the amplitudes of the core-barrel vibrations.

Detection of Impacting Detector Strings in BWRs

Flow-induced vibrations of the detector tubes in BWRs are a possible safety concern when the vibration amplitude is such that the detector tubes impact with the neighboring fuel boxes. Impacting can damage the fuel boxes, which may also cause damage to the fuel cladding. The vibrations arise from the strong flow of cooling water in the reactor and the fact that the detector tubes, which are roughly four meters long, are fixed only in their ends. [▶ Figure 25](#) shows the configuration of a detector tube together with the surrounding fuel assemblies.

The principle of the detection is based on the signal of the vibrating detector itself. Apart from the effect of other noise sources and general background, vibration of a detector in a flux

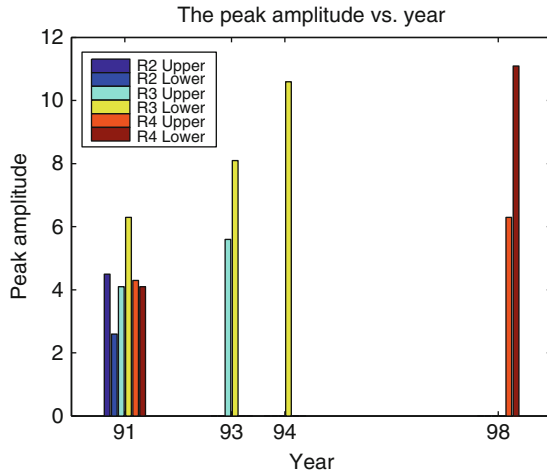


Figure 24 Trend behavior of the vibration amplitudes in some of the Swedish Ringhals PWRs during 1991–1998

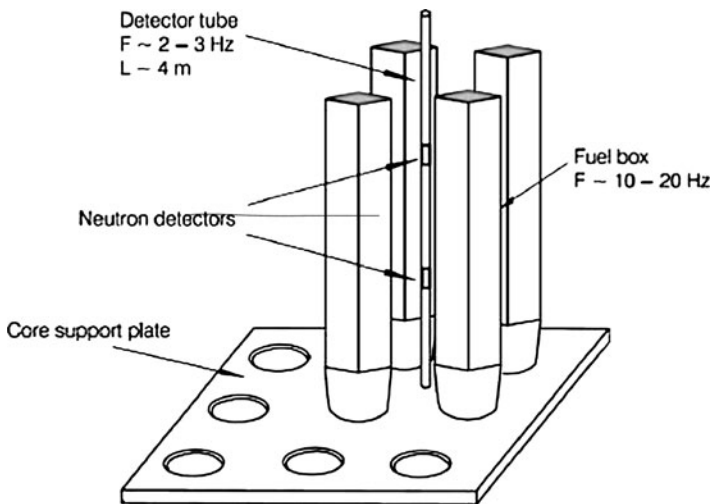
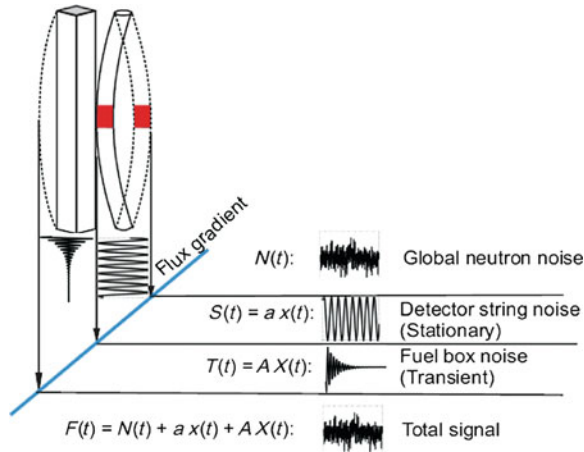


Figure 25 Illustration of a detector tube in a boiling water reactor (BWR) core with four surrounding fuel assemblies

gradient will lead to a signal proportional to the displacement of the detector, as indicated in Fig. 26. A direct scaling of the detector current to absolute displacements is though not possible, since usually neither the flux gradient, nor the direction of the vibrations (or the vibration trajectory) is known.



■ Figure 26




Illustration of the origin of the different components of the detector signal, arising from the vibration in a flux gradient, background noise, and impacting on a fuel assembly

As **►** Fig. 26 shows, it is assumed that when impacting occurs, a short-lived, transient (intermittent) vibration of the fuel assembly takes place, which is also detected by the neutron detector.

The methods used to detect impacting can be divided into two categories: traditional or spectral analysis-based methods, utilizing the stationary part of the signal, and transient analysis methods, utilizing the intermittent part of the signal. These latter methods are based on time-frequency analysis methods, such as short-term Fourier transform, wavelet analysis, and wavelet filtering. These methods will not be discussed here. The methods based on traditional signal analysis are more subjective and intuitive, and they are not absolute. The main difficulty is not the detection of the vibrations themselves, since this can be done with a spectral analysis similar to that made in the core-barrel vibration analysis; rather, to find out when impacting starts to occur. Namely, the spectral properties change only very mildly when impacting occurs, compared to the impacting-free cases.

It turns out that the most effective way of discovering strong vibrations and suspecting impacting is to use, in addition to the analysis of the peaks in the detector APSD, also the fact that there is a rather characteristic pattern of phase and coherence behavior in detectors in the same string in a BWR in the impact-free case. The observation is that this pattern changes appreciably in a characteristic way when vibrations occur, and the severity of the vibrations can also be qualitatively extracted, giving an estimate of the likelihood of impacting.

The principles of the impact-free structure of the detector spectra were explained earlier in **►** Subsect. 4.1.3. In the absence of vibrations, the APSD (auto-spectrum) of the LPRMs, that is, the individual detectors, is a smooth function of the frequency, and the coherence and phase between any two detectors in the same string follow a pattern characteristic for propagating perturbations in the presence of a local noise component (in-core BWR noise). The phase is linear up to 10 Hz, and the coherence shows a periodic peak-sink structure, whose maxima and minima coincide with the zero- and π -crossings of the phase. Such a case is shown in **►** Fig. 16.

When the detector string starts to vibrate strongly, the linear phase, and to a lesser extent also the sink structure of the coherence, gets distorted with increasing vibrations. Since the lateral vibration occurs synchronously for all four detectors, the vibrations appear as strong “global” (in-phase) components in all detector signals. Thus, over the frequency range of vibrations, the phase will tend to zero instead of being a linear function with a nonzero slope. At the same time, the sink and peak structure of the coherence, which was discussed earlier, is also changed compared to the vibration-free case (the maxima and minima do not coincide with the zero- and π -crossings of the phase). The detector signals of an excessively vibrating detector tube are given in  Fig. 27 as an illustrative example. Compared to  Fig. 16, one can clearly conclude from the measured signals that the detector string was excessively vibrating. The most visible is the distortion of the phase around the vibration frequency; with increasing strength of the vibrations, the phase tends to be zero over an increasing frequency region around the vibration frequency, owing to the simultaneous movement of the two detectors. The case shown in  Fig. 27 indicates a large likelihood of impacting, which was confirmed through visible damage to the detector and the surrounding fuel assemblies after the cycle, during refueling.

More details on this particular case and on the method in general can be found in Pázsit and Glöckler (1994). This method has been used routinely in several Swedish power plants for diagnosing detector tube impacting.

5 Special Noise Techniques: Determination of Core Global Dynamical Parameters

In this subsection, the use of noise analysis for determining core global dynamical parameters is discussed. Such determinations are carried out without disturbing reactor operation and thus represent a unique opportunity to monitor some of the most important safety parameters of nuclear reactors on-line. Two applications are dealt with hereafter: the determination of the decay ratio (DR) in BWRs and the determination of the moderator temperature coefficient of reactivity (MTC) in PWRs.

5.1 Determination of the Decay Ratio in BWRs

The instability of BWRs, which is manifested by self-sustained power oscillations in the core, has been observed at the very early days of reactor operation, and the possibility of BWR instability was predicted by Thie (1959). Such instabilities are usually encountered during start-up conditions, that is, at reduced core flow and relatively high-power level. Calculations are thus performed via adequate coupled neutronic/thermal-hydraulic codes to verify under which conditions the reactor becomes unstable. This defines an exclusion zone, that is, a set of operating conditions on the power-flow map, which the reactor operator should always avoid. During the start-up tests of the reactor, measurements of the in-core neutron noise are usually performed. The goal of these measurements is to verify that there is a good agreement with the calculations.

Monitoring the stability with measurements, as well as determining the margins to instability requires the existence of a reliable quantitative stability indicator. Such a parameter should be an integral, global parameter of the core, similar to the reactivity. However, as will be clear from the discussion below, the situation is more involved because, unlike with the definition of the

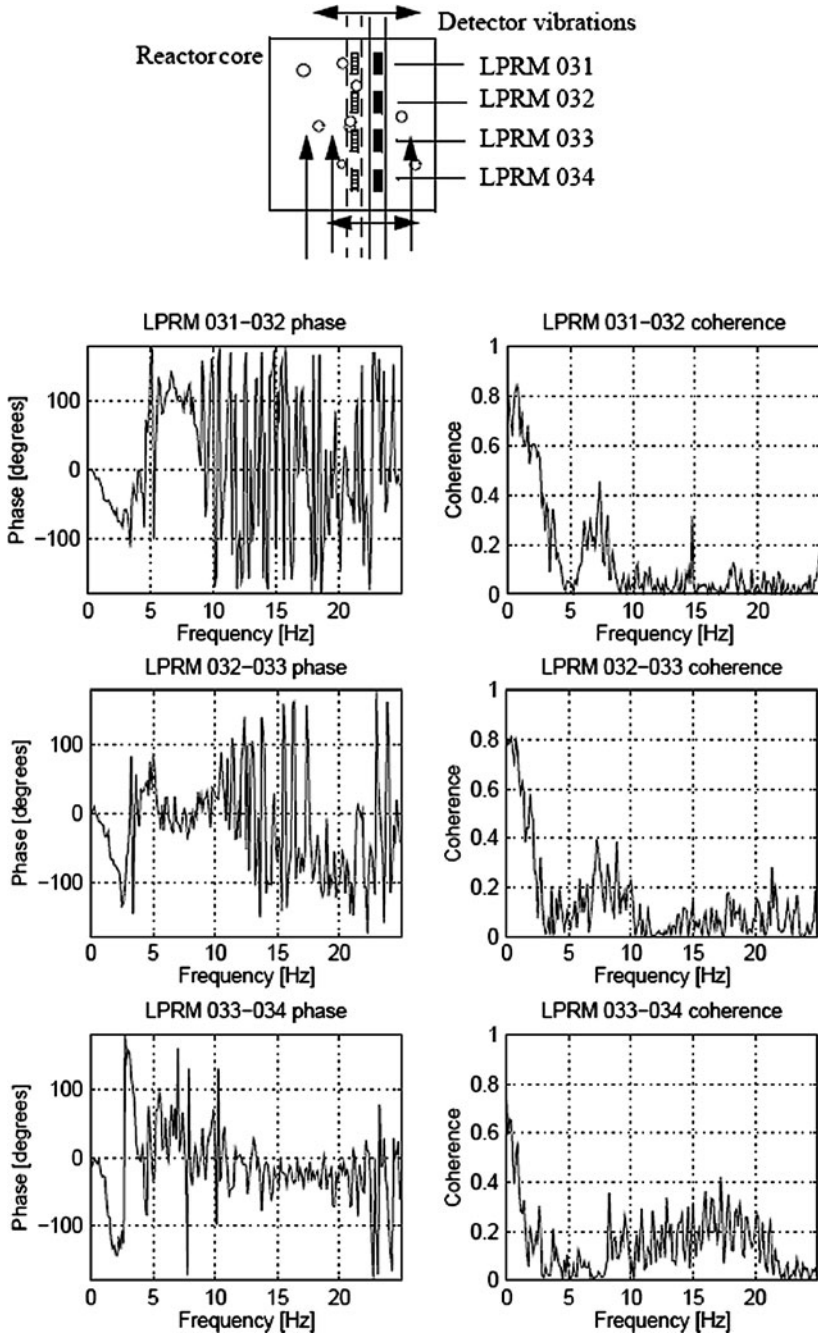


Figure 27

Abnormal phase and coherence between detectors in an impacting detector string of a BWR

reactivity, the stability cannot be characterized only with quantities belonging to the fundamental eigenvalue and fundamental eigenmode. Also, there are several possibilities for choosing a stability parameter, of which we will only discuss the most common one, the decay ratio.

BWR instability is an intriguing subject far from being fully understood, and accordingly it has a vast literature (for a review see D'Auria et al. 1997). To illustrate the point we list here a number of references, still far from being complete, to give a flavor of the diversity and vibrant character of the research in the field: van der Hagen et al. (1994), Takeuchi et al. (1994), Hennig (1999), Hotta et al. (1997), Oguma (1997), Verdú et al. (1998); Kitamura et al. (1999), Miro et al. (2000), Ginestar et al. (1992), Munoz-Cobo et al. (2004), Demazière and Pázsit (2005), and Zinzani et al. (2008).

We note here also that in this section we only consider stability analysis in the linear regime. As already mentioned, fully developed unstable oscillations are nonlinear and ways of characterizing and understanding nonlinear aspects and developing nonlinear diagnostics methods is under strong development (March-Leuba et al. 1983, 1984, 1986a, b; Cacuci et al. 1986; Cacuci 1993; Ginestar et al. 2006; Konno et al. 1999).

5.1.1 Stability Indicator

The most commonly used stability indicator is the so-called decay ratio (DR). One of the basic assumptions in the use of the DR is that the system dynamics can be modeled by a second-order oscillator, that is, any fluctuation $\delta\Psi(t)$ related to BWR instabilities obeys the following equation:


$$\delta\ddot{\Psi}(t) + 2\xi\omega_0\delta\dot{\Psi}(t) + \omega_0^2\delta\Psi(t) = f(t) \quad (276)$$

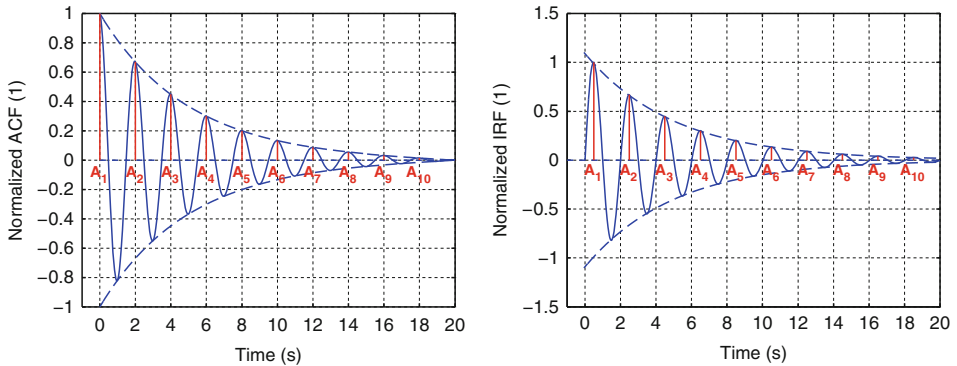
where $f(t)$ represents the driving force of the oscillation, usually assumed to be a white noise, ω_0 is the resonance frequency, and ξ characterizes the damping of the system. The general solution to this equation is given by

$$\delta\Psi(t) = A \exp(-\xi\omega_0 t) \cos\left[\omega_0 \left(\sqrt{1-\xi^2}\right) t + \varphi\right] \quad (277)$$

The DR gives a measurement of the damping of the system and is defined as the ratio between two consecutive maxima of the signal form given above and found to be given, in the case of a second-order system, as

$$DR = \exp\left(\frac{-2\pi\xi}{\sqrt{1-\xi^2}}\right) \quad (278)$$

In practice, it is not the signal itself, but the auto-correlation function (ACF) of the normalized neutron density, or alternatively the impulse response function (IRF) as calculated by using an autoregressive moving-average (ARMA) or an autoregressive model (AR) that are used. In case of a white noise driving force, these functions all have the same oscillatory and decaying properties as the deterministic solution (277). Hence, the DR is usually determined from the ratio between two consecutive maxima A_i and A_{i+1} of any of these two functions. The ACF and IRF obtained in the case of a second-order system are represented in  Fig. 28. The DR



■ Figure 28

Auto-correlation function (ACF) and impulse response function (IRF) of a second-order system (on the left-and right-hand sides, respectively)

gives therefore a measure of the inherent damping properties of the system. Using each detector separately allows estimating the decay ratio (DR) according to the following standard method (for a review, see D'Auria et al. 1997)

$$DR = \frac{A_{i+1}}{A_i}, \quad \forall i \quad (279)$$

If the dynamics of the system does not correspond to a pure second-order system, the above formula gives different results depending on which consecutive peaks of the ACF or of the IRF one considers.

5.1.2 Stability Mechanism of a BWR

Nuclear reactors must be designed such that they have a negative feedback mechanism, that is, any perturbation leading to off-normal conditions should be counteracted by some feedback, which thus brings the system back to steady-state conditions. Instabilities can arise from the fact that in a dynamic case, such feedback mechanisms act with some time delay. If the feedback was always exactly counteracting the original perturbation without time delay, the phase shift between the perturbation and the feedback should be -180° (i.e., out-of-phase). Nevertheless, in most cases, the phase shift differs from -180° . As a result, the feedback reinforces the original perturbation instead of damping it during some parts of a period.

Several physical mechanisms are responsible for the feedback in a BWR. The ones that might give rise to instabilities are the channel thermal-hydraulics (density wave oscillation, DWO) and the void-reactivity feedback. In the following, these two mechanisms are detailed. How these processes are driving instabilities will be explained in the next subsection.

A DWO corresponds to a change of the density of the coolant within one or several fuel assemblies. For illustration purposes, one can consider a perturbation induced by an inlet flow perturbation to a fuel assembly. Such an inlet perturbation will create a modification of the single-phase pressure drop in the single-phase region of the heated channel. This perturbation

will travel upward with the flow and will itself generate a modification of the two-phase pressure drop in the two-phase region of the heated channel.

The void-reactivity feedback comes from the fact that any modification of the density of the coolant affects the neutron moderation. More specifically, any decrease in the moderator density leads to a worsening of the neutron moderation. Such an effect is typically represented by the void coefficient of reactivity, that is,

$$\alpha_v = \frac{\partial \rho}{\partial v} \quad (280)$$

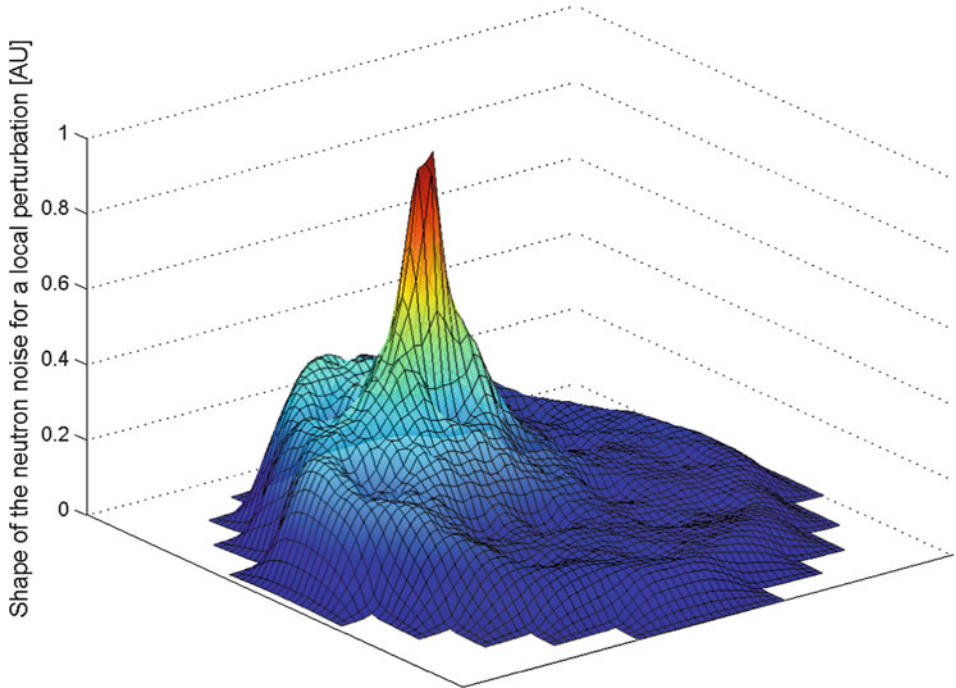
where $\delta \rho$ represents the change of reactivity of the system due to a change δv of the void fraction, with the void fraction being defined as the relative volume of vapor contained in a specific volume. Such a reactivity coefficient is strongly negative for BWRs.

Any perturbation of the reactivity of the system will lead to a perturbation of the reactor power and of the produced heat, which in turn will create a modification of the fuel temperature and of the void fraction. Because of the Doppler fuel temperature effect and of the void-reactivity feedback, such perturbations will affect the reactivity of the system. This feedback loop is called the direct loop. Further, a so-called recirculation loop is connected to the downcomer of a BWR. Such a loop has its own dynamical properties. As a consequence, any perturbation of the core outlet pressure will give rise to perturbation of the core-inlet flow via the recirculation loop dynamics. Such a feedback loop is called the indirect loop. Finally, each fuel channel has its own dynamical properties from a thermal-hydraulic point of view. Any perturbation to the channel thermal-hydraulics will give rise to DWOs, and this corresponds to the so-called DWO loop in the stability mechanism of a BWR.

5.1.3 Types of BWR Instabilities

Three types of instabilities are usually encountered in forced-circulation BWRs: pure DWOs or local oscillations, global (or in-phase) oscillations, and regional (or out-of-phase) oscillations. Whereas the global and regional oscillations also involve DWOs in the core, the instabilities are driven by the void-reactivity feedback, as will be explained in the following.

Instabilities due to pure DWOs might occur when the boundary conditions of the heated channel(s) are imposed, as is the case for the pressure drop between the inlet and outlet of the channels. Such instabilities are usually referred to as pure DWO or local oscillations. Due to this imposed boundary condition, the two-phase pressure drop in the perturbed fuel channel will create a feedback pressure perturbation of the opposite sign in the single-phase region, either reinforcing or damping the initial perturbation (see Yadigaroglu and Bergles 1972). This pressure drop oscillation can also be translated into a perturbation of the coolant density (explaining the name of DWO for this kind of perturbation). The typical frequency at which such oscillations are encountered is around 0.5 Hz, which is related to the transit time of perturbations from the inlet to the outlet of the fuel assemblies. This type of oscillation typically occurs when a fuel assembly is unseated, that is, does not sit properly of the lower fuel tie plate of the core (such a case was described in [Sect. 4.1.1](#)). Since each fuel assembly in a BWR is contained in a fuel box, the fuel channels are independent from each other. Therefore, in case of an unseated fuel assembly, some of the coolant bypasses the fuel channel. This reduces the single-phase pressure drop at the inlet of the channel, and destabilizes it. Radially, this perturbation is equivalent to



■ Figure 29

Space-dependence of the neutron noise induced by a local oscillation as calculated by the neutron noise simulator

a local noise source, or a so-called absorber of variable strength-type of noise source and can be modeled by the neutron noise simulator described in [Sect. 3.3.3](#) (Demazière 2004). An example of the results of such a modeling is shown in [Fig. 29](#). The induced neutron noise has thus its largest amplitude at the position of the noise source, and has a fast spatial decay away from it.

Instabilities due to the void-reactivity feedback may also occur in a BWR. The mechanism driving this kind of oscillation is mainly the time delay between a given power perturbation and the corresponding reactivity response due to the void/pressure coefficient. In some cases, the initial perturbation can be reinforced by the void/pressure feedback if the phase of this delayed response coincides with the phase of the power perturbation. It has to be emphasized that these instabilities also involve density waves through the core, but such waves alone are not responsible for the oscillations. Two types of instabilities involving such a coupling between the neutron kinetics and the thermal-hydraulics are usually encountered: in-phase (or global) oscillations, and out-of-phase (or regional) oscillations. In order to better understand the spatial dependence of such oscillations, the neutron flux can be expanded on the eigenfunctions of the system as

$$\phi(\mathbf{r}, t) = \sum_n a_n(t) \phi_n(\mathbf{r}) \quad (281)$$

where $\phi_n(\mathbf{r})$ represents the eigenfunction of the system of order n . For the sake of simplicity, assuming one group of delayed neutrons, a homogeneous reactor, and one-group diffusion theory, one could demonstrate that (the interested reader is referred to Lamarsh (2002) for the derivation of the following equations)

$$a_n(t) = A_n \exp(\omega_n t) \quad (282)$$

where A_n is a constant, and ω_n fulfills the following “in-hour” equation:

$$\rho_n = \frac{\omega t_n}{1 + \omega t_n} + \frac{\omega}{1 + \omega t_n} \cdot \frac{\beta}{\omega + \lambda} \quad (283)$$

with


$$t_n = \frac{1}{\nu(\Sigma_a + B_n^2 D)} \quad (284)$$


and B_n^2 is the geometrical buckling corresponding to the eigenmode n . One can easily show that

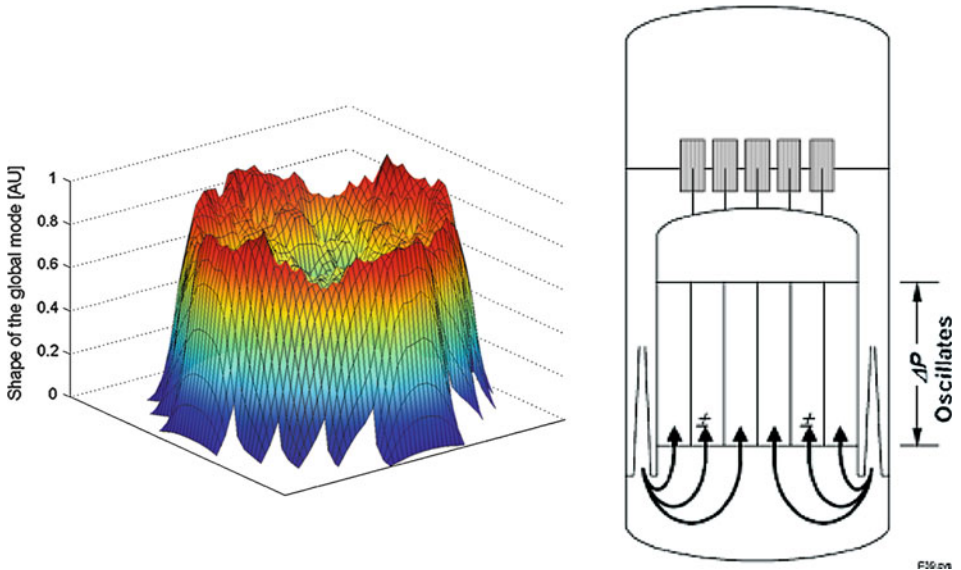
$$\omega_1 < \omega_0 \quad (285)$$

$$\dots \omega_2 < \omega_1 < 0 \quad (286)$$

and ω_0 is the only of the ω_n that can be positive.

For the global (in-phase) oscillation, the flux is oscillating over the whole core at a typical frequency of 0.5 Hz, and only the first neutronic mode (fundamental mode), that is, $n = 0$, is excited. This is explained by the fact that the reactivity ρ_0 of the fundamental mode is the only one that can be larger than zero and correspondingly ω_0 can be positive. The space-dependence of the flux is thus following the first neutronic mode. Due to the global character of the perturbation, the flow oscillations induced by the void/pressure oscillations are damped by the friction in the recirculation loop, and the recirculation loop dynamics has a stabilizing effect. The neutron noise induced by such an instability can be modeled by the neutron noise simulator, since the different eigenfunctions can be estimated by this tool. An example of the results of such a modeling is presented in  Fig. 30.

For the out-of-phase (regional) oscillation, the second and third neutronic mode (first and second azimuthal modes), that is, $n = 1$ and 2, are excited. Such modes are subcritical and should decay in time in an exponential manner. Nevertheless, the excitation of such modes leads to positive flow rate perturbations in one half of the core counterbalanced by negative flow rate perturbations in the other half of the core at any time in such a way that the boundary conditions imposed by the recirculation loop are always fulfilled. As a consequence, such oscillations are self-sustained by the thermal-hydraulics. The neutron noise induced by such an instability can also be modeled by the neutron noise simulator. An example of the results of such a modeling is presented in  Fig. 31. One characteristic of the regional oscillation is that several higher modes can be excited, compared to only one for the in-phase oscillation. Typically, the second and third modes, that is, first and second azimuthal modes, respectively, are excited. Even if these modes are subcritical, the thermal-hydraulics might self-sustain the oscillations. The oscillation frequency of these two modes, although typically close to 0.5 Hz, might be slightly different from each other. Thus, the resulting oscillation, which is the sum of these two modes, might exhibit a rotating neutral line, with the neutral line being defined as the line separating the positive



■ Figure 30

Space-dependence of the neutron noise induced by a global oscillation as calculated by the neutron noise simulator (on the left-hand side) and conceptual illustration of the in-phase behavior of the flow and power oscillations (on the right-hand side) (From Shiralkar, 2005)

and the negative lobes of the oscillation. An equivalent formulation is to say that there exists a phase shift between the first and second azimuthal modes, and that this phase shift is time-dependent, as illustrated in ► Fig. 32. Very often, a fourth mode, that is, the first axial mode, can also be excited. The regional or out-of-phase oscillation is thus a complicated oscillation due to its spatial intermittence, that is, the neutral line might be stable or it might rotate.

5.1.4 Combined Types of Oscillations

When instability events occur at nuclear power plants, several types of oscillations are usually excited simultaneously, even if typically only one is predominant. This complicates significantly the estimation of the DR, since as explained earlier, the DR is based on the assumption that only one type of oscillation exists. Furthermore, it is customary to estimate the DR from the LPRMs, that is, a value of the DR is estimated for each LPRM. One direct consequence of using local measurements for estimating a global parameter such as the DR is that the estimations might exhibit a space-dependence.

If only one mode type of oscillation is excited, then the DR is the same throughout the core. If several types are excited, the DR might become space-dependent. This can be demonstrated by assuming that the oscillations of the neutron flux can be written as a sum of the contributions of two oscillating modes, due to two different noise sources i ($i = 1, 2$), each of them being factorized into a temporal part only and spatial part only ($\varphi_i(\mathbf{r})$). In such a case, the DR, defined

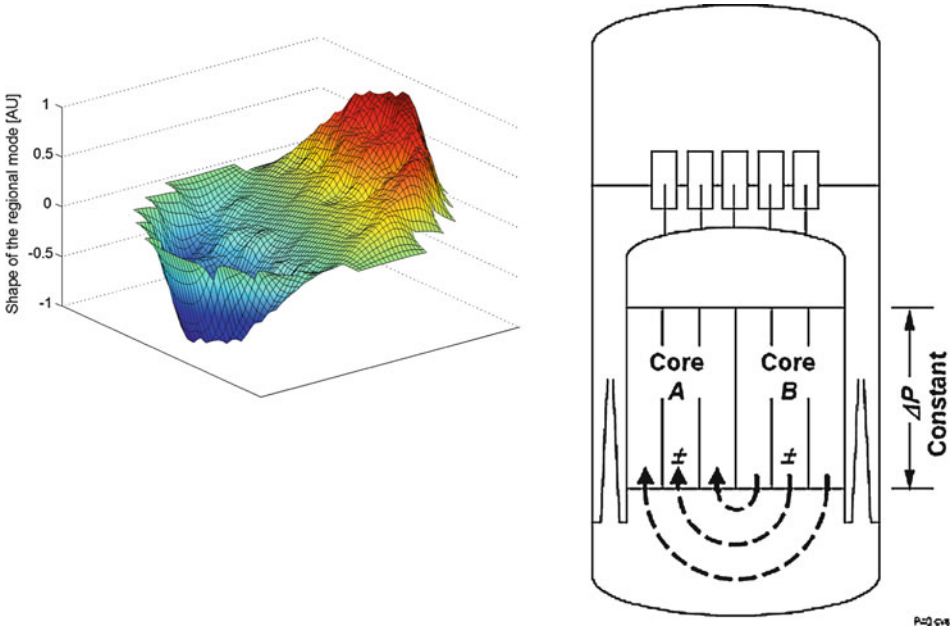


Figure 31 Space-dependence of the neutron noise induced by a regional oscillation as calculated by the neutron noise simulator (on the left-hand side) and conceptual illustration of the out-of-phase behavior of the flow and power oscillations (on the right-hand side) (From Shiralkar, 2005)

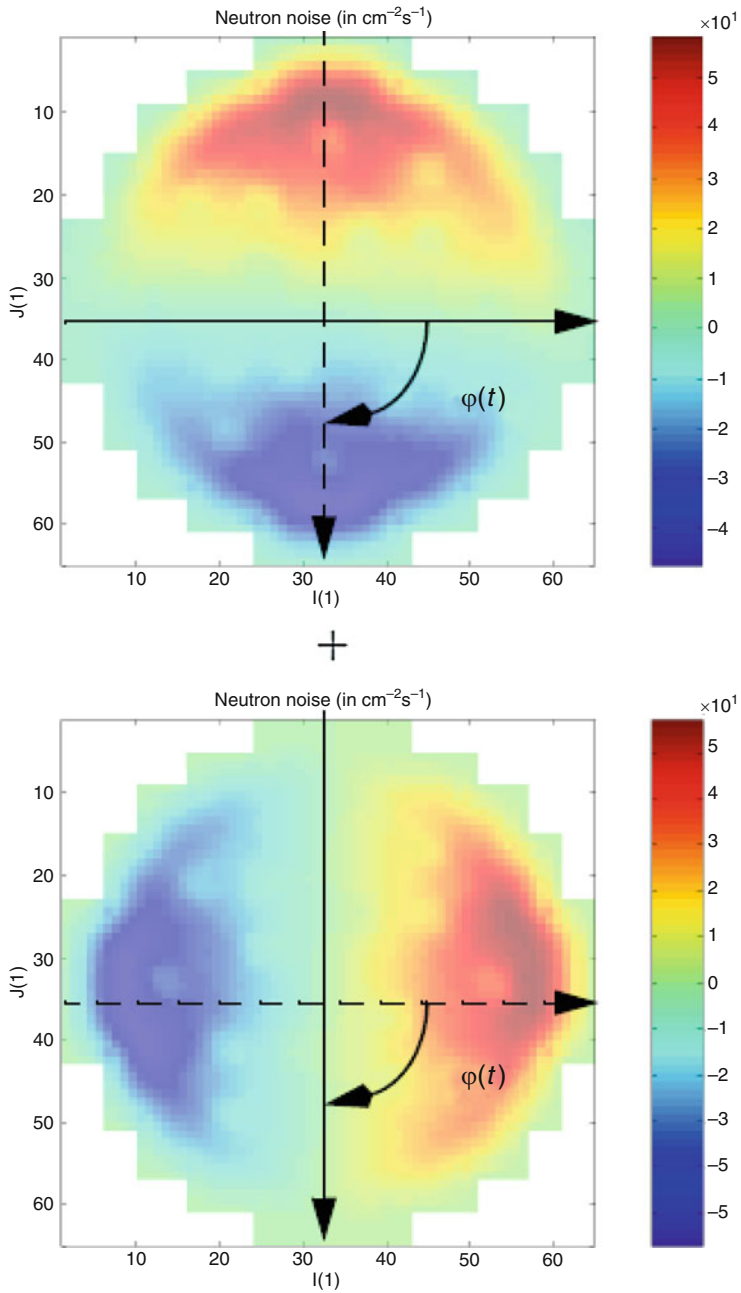
as the ratio of the first and the second maxima of the ACF, is given by (Pázsit 1995)

$$DR(\mathbf{r}) = \sum_{i=1}^2 c_i(\mathbf{r}) \cdot DR_i \tag{287}$$

with

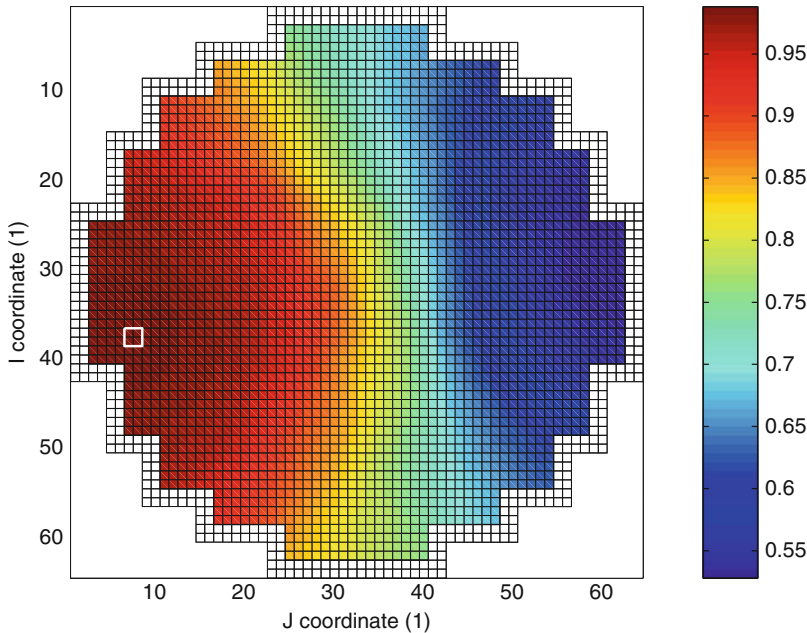
$$c_i(\mathbf{r}) = \frac{1}{1 + C \cdot \frac{\varphi_j(\mathbf{r})}{\varphi_i(\mathbf{r})} \cdot \frac{\ln(DR_i)}{\ln(DR_j)}}, \quad i \neq j \tag{288}$$

This expression was obtained assuming that each oscillation mode i has the same resonance frequency but different stability properties, that is, DRs. Furthermore, it was supposed that the CPSD between the two noise sources is negligible, and that the DR of any of the two noise sources was larger than 0.4. $\varphi_i(\mathbf{r})$ represents the radial space-dependence of the neutron noise induced by the noise source i . This spatial dependence can be estimated by the neutron noise simulator for all types of BWR instabilities (global, regional, or local oscillations). The coefficient C represents the ratio between the strength of the noise sources and is a normalization coefficient. The DR exhibits a strong radial space-dependence only when there are at least two types or sources of instabilities in the core with different stability properties, and at least one of those correspond to a local oscillation.



■ Figure 32

Definition of the time-dependent phase shift $\varphi(t)$ between the first and second azimuthal modes



■ Figure 33

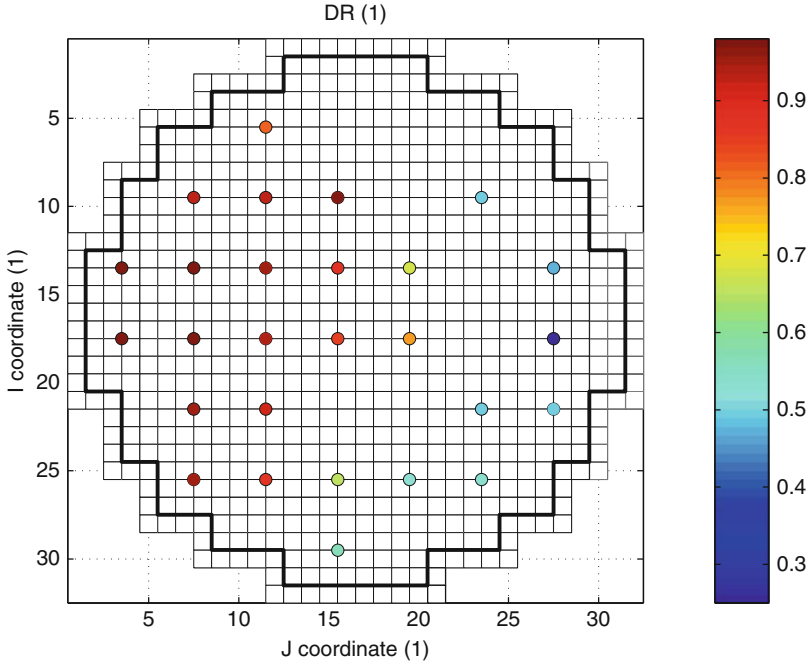
Simulated radial space-dependence of the decay ratio (DR) in case of a local noise source and a global noise source (the white square represents the location of the local noise source)

The case of a local oscillation coexisting with a global oscillation is shown in [Fig. 33](#). The reason of the sharp boundary between the two stability regions when at least one local noise source exists is the fast spatial decay of the amplitude of the local oscillations. Such a pattern for the spatial dependence of the DR was actually noticed at the Forsmark-1 BWR, as can be seen in [Fig. 34](#), during the channel instability event already mentioned in [Sects. 4.1.1](#) and [5.1.3](#) (the interested reader is referred to Oguma 1997). [Equations \(287\) and \(288\)](#) allow explaining the space-dependence of the DR in the Forsmark case, since a local oscillation could be triggered by an unseated fuel assembly.

In order to correctly estimate the stability properties of a BWR, it is thus essential to separate the different types of oscillations from each other. Thereafter, the stability of each mode can be characterized by a DR per oscillation mode. Different techniques have been elaborated for monitoring the stability of BWRs and for separating the different modes of oscillations.

While the global oscillations can be properly detected by the average-power range monitors (APRMs), the LPRMs are necessary to characterize the regional oscillations. The monitoring techniques that are capable of detecting different types of oscillations can basically be classified into three categories, which are briefly explained in the following in increasing order of sophistication.

The first class of techniques aims at monitoring the phase difference between pairs of symmetrically located LPRM detectors. A phase shift approaching 180° indicates out-of-phase oscillations, whereas a negligible phase shift indicates in-phase oscillations. The drawback of these techniques is the difficulty in monitoring combined modes of oscillations.



■ Figure 34

Radial space-dependence of the DR determined at the Forsmark-1 BWR during the 1996/1997 channel instability (Derived from Oguma, 1997)

The second category of techniques is based on the determination of the part of the LPRM signals related to the in-phase oscillations, using for instance the property of orthogonality between the fluctuations of the shape function of the neutron noise and the static flux (see (191) and (192)). This leads to

$$\frac{\delta P(t)}{P_0} = \frac{\delta \phi^{pk}(\mathbf{r}, t)}{\phi_0(\mathbf{r})} = \frac{\int \delta \phi(\mathbf{r}, t) \phi_0(\mathbf{r}) d\mathbf{r}}{\int \phi_0^2(\mathbf{r}) d\mathbf{r}} \quad (289)$$

Subtracting this in-phase component to each of the LPRM signals also allows detecting possible out-of-phase oscillations.

The last class of techniques is based on modal decomposition of the neutron noise. In this procedure, the neutron flux is expanded in the eigenfunctions of the system as

$$\bar{\phi}(t) = \sum_n a_n(t) \bar{\phi}_n \quad (290)$$

with

$$a_n(t) = \frac{\langle \bar{\phi}_n^\dagger, \bar{F} \times \bar{\phi}(t) \rangle}{\langle \bar{\phi}_n^\dagger, \bar{F} \times \bar{\phi}_n \rangle} \quad (291)$$

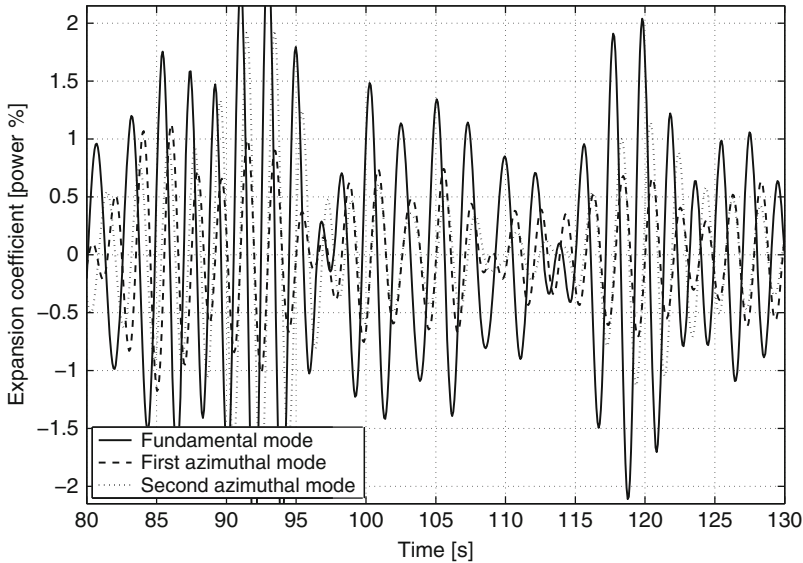


Figure 35

Time-dependence of the expansion coefficients for the three first modes applied to the local power range monitor (LPRM) signals during a stability test at the Ringhals-1 BWR

In these equations, the vector $\vec{\phi}(t)$ represents the space- and time-dependent neutron flux (where each element of the vector represents the value of the time-dependent flux at a spatial point in the system), $\vec{\phi}_n$ represents the space-dependent eigenfunction of mode n , $\vec{\phi}_n^\dagger$ is its adjoint, and \bar{F} is the fission operator. This decomposition can be performed either with the prior determination of the different modes of the static neutron flux or without it. An example of such a modal decomposition applied to a stability test performed at the Swedish Ringhals-1 BWR is represented in Fig. 35. As can be seen in this figure, both the global and the regional oscillation patterns are excited in the analyzed stability test. It is interesting to notice that both the global and regional oscillations are clearly intermittent, and that they sometimes exhibit growing amplitudes over a couple of periods. Furthermore, it can also be seen that the phase shift between the first and second azimuthal modes is varying with time. As a consequence, the regional oscillation, which is a combination of these two azimuthal modes, will be characterized by a rotating neutral (nodal) line.

5.2 Determination of the Moderator Temperature Coefficient of Reactivity in PWRs

5.2.1 Definition of the MTC

According to the newest American Standard, the MTC is defined as the partial derivative of the reactivity ρ with respect to the core-averaged moderator temperature T_m^{ave} as follows:

$$MTC = \frac{\partial \rho}{\partial T_m^{ave}} \quad (292)$$

For a small change in the average moderator temperature, the reactivity change would be

$$\delta\rho(t) = MTC \times \delta T_m^{ave}(t) \quad (293)$$

where the core-averaged moderator temperature change is defined using a proper weighting function $w(\mathbf{r})$ as

$$\delta T_m^{ave}(t) = \frac{\int \delta T_m(\mathbf{r}, t) w(\mathbf{r}) d\mathbf{r}}{\int w(\mathbf{r}) d\mathbf{r}} \quad (294)$$

The determination of the weighting function will be discussed later on.

The fact that the temperature coefficient is defined through a partial derivative means that the MTC only accounts for changes in reactivity when the temperature of the coolant is changed, but the fuel temperature does not change. Therefore, in the traditional way of measuring the MTC by the so-called boron dilution method, when the temperature of the core is raised in an adiabatic manner and the excess reactivity to keep the core critical by diluting the boron content, the contributions to the reactivity change by changed fuel temperature, through the Doppler coefficient, has to be subtracted by calculations. Hence, the traditional method is both costly and is not a pure experimental method, rather a combination of calculations and measurement.

5.2.2 Derivation of the MTC Noise Estimate

It is therefore attractive to elaborate a noise-based method, which does not interfere with the operation and which is capable to measure the true MTC without corrections based on calculations. This can be achieved with a cross-correlation between the reactivity noise, deduced from neutron noise measurements, and from measurement of the temperature noise in the core or at the core exit. Such measurements can be performed with the required accuracy since temperature measurements have a large absolute accuracy, whereas from the neutron detectors only a normalized (by the mean value) signal is needed.

The starting point of consideration is as follows. If the reactivity depends on the stationary ergodic processes $s_i(t)$, $i = 1, \dots, N$, expanding the reactivity variation around the stationary value and assuming linear theory will lead to

$$\delta\rho(t) \approx MTC \times \delta T_m^{ave}(t) + \sum_{i=1, s_i \neq T_m^{ave}}^N \frac{\partial \rho}{\partial s_i} \times \delta s_i(t) \quad (295)$$

in which the MTC effect is separated from the other effects. In (295), all the time-dependent parameters are defined as their variations compared to the mean values.

The idea of using noise analysis to monitor the MTC in PWRs was probably first introduced by Thie in 1977, who suggested to use the root-mean-square values of the temperature noise and of the reactivity noise, which can be determined from the relative neutron noise under some assumptions, to evaluate the MTC:

$$MTC = \frac{\sigma_{\delta\rho}}{\sigma_{\delta T_m^{ave}}} \quad (296)$$

From (295), one can see that the MTC evaluated by (296) is biased due to the contamination of the neutron noise from noise sources other than the moderator temperature noise.

Later Pór et al. (1985) suggested that the contribution of the other noise sources can be removed if spectral analysis of the signals is used, as explained in the following. Multiplying (295) by $T_m^{ave}(t + \tau)$ and taking the average gives

$$CCF_{\delta\rho, \delta T_m^{ave}}(\tau) = MTC \times ACF_{\delta s_i, T_m^{ave}}(\tau) + \sum_{i=1, s_i \neq T_m^{ave}}^N \frac{\partial \rho}{\partial S_i} \times CCF_{\delta s_i, \delta T_m^{ave}}(\tau) \quad (297)$$

where ACF and CCF stand for the auto-correlation function and the cross-correlation function, respectively:

$$CCF_{\delta\rho, \delta T_m^{ave}}(\tau) = \langle \delta\rho(t) \delta T_m^{ave}(t + \tau) \rangle \quad (298)$$

$$CCF_{\delta s_i, \delta T_m^{ave}}(\tau) = \langle \delta s_i(t) \delta T_m^{ave}(t + \tau) \rangle \quad (299)$$

$$ACF_{\delta T_m^{ave}}(\tau) = \langle \delta T_m^{ave}(t) T_m^{ave}(t + \tau) \rangle \quad (300)$$

If it can be assumed that the fluctuations of the different s_i parameters ($S_i \neq T_m^{ave}$) are statistically independent of moderator temperature fluctuations, then their cross-correlation vanishes

$$CCF_{\delta s_i, \delta T_m^{ave}}(\tau) = 0 \quad (301)$$

It can be shown that this assumption is valid within a certain frequency region. Then one has

$$MTC = \frac{CCF_{\delta\rho, \delta T_m^{ave}}(\tau)}{ACF_{\delta T_m^{ave}}(\tau)} \quad (302)$$

Alternatively, the MTC can also be derived by multiplying (295) by $\delta\rho(t + \tau)$ and taking the average

$$MTC = \frac{ACF_{\delta\rho}(\tau)}{CCF_{\delta T_m^{ave}, \delta\rho}(\tau)} \quad (303)$$

Equation (302) or (303) represents the MTC noise estimator that should be used in noise analysis in order to get the correct value of the MTC.

5.2.3 Measurement by Noise Analysis Technique

Although (302) and (303) are written in the time domain, it is much more common (and practical) to perform the MTC estimation in the frequency domain. This reads as

$$MTC = \frac{CPSD_{\delta\rho, \delta T_m^{ave}}(\omega)}{APSD_{\delta T_m^{ave}}(\omega)} \quad (304)$$

or

$$MTC = \frac{APSD_{\delta\rho}(\omega)}{CPSD_{\delta T_m^{ave}, \delta\rho}(\omega)} \quad (305)$$

where the APSD and CPSD stand for the auto-power spectral density and cross-power spectral density, respectively.

Nevertheless, neither the at-power reactivity noise nor the average coolant temperature noise can be measured in practice in PWRs. Only the neutron flux (either via the ex-core neutron detectors or via the in-core neutron detectors, when they are present in the core) and the core-inlet/outlet temperatures are measurable quantities in PWRs. Simply speaking, the MTC should be estimated by using global parameters, such as the reactivity and the average moderator temperature, whereas only local quantities (flux and temperature) can be measured.

The reactivity noise can, under some assumptions, be inferred from the flux noise, as explained in [Sect. 3.3.2](#). Namely, the flux noise in the frequency domain can be approximated by (second-order terms neglected)

$$\delta\phi(\mathbf{r}, \omega) = \delta\phi^{pk}(\mathbf{r}, \omega) + \delta\Psi(\mathbf{r}, \omega), \quad (306)$$

where

$$\delta\phi^{pk}(\mathbf{r}, \omega) = \phi_0(\mathbf{r}) \frac{\delta P(\omega)}{P_0} \quad (307)$$

is the point-kinetic component of the flux noise. The amplitude function itself satisfies the point-kinetic equations that can be written in the frequency domain

$$\frac{\delta P(\omega)}{P_0} = \delta\rho(\omega) G_0(\omega) \quad (308)$$

In this equation, $G_0(\omega)$ is the usual zero power reactor transfer function, in which no feedback effects between the reactor power and the coolant temperature, or between the reactor power and reactivity, are accounted for. Due to the relatively large time constant of the heat transfer dynamics from fuel to coolant, feedback effects will only occur at low frequencies, typically below 0.1 Hz. [Equation \(308\)](#) is therefore valid for frequencies higher than about 0.1 Hz. Hence one has

$$\delta\rho(\omega) = \frac{1}{G_0(\omega)} \frac{\delta\phi^{pk}(\mathbf{r}, \omega)}{\phi_0(\mathbf{r})} \quad (309)$$

In-core neutron detectors do not measure solely the point-kinetic component of the neutron noise, but the total flux noise, as defined by [\(306\)](#). Consequently, the reactivity noise can be calculated from the flux noise only if $\delta\phi^{pk}(\mathbf{r}, \omega)$ is overwhelmingly large compared to $\delta\psi(\mathbf{r}, \omega)$, that is, the reactor behaves in a point-kinetic way. As was shown in previous parts of this section, large power reactors do not respond to localized perturbations in a point-kinetic way. However, the response of the core to distributed perturbations is much more point-kinetic-like, even if the perturbations in the different spatial points are loosely coupled to each other (which is the case of temperature fluctuations over a radial cross section of the core, due to loose thermohydraulic

coupling between the fuel channels). This was proven in simulations using the noise simulator. Hence, the approximation of the reactivity noise from a single in-core neutron detector is a permissible one:

$$\delta\rho^{approx}(\mathbf{r}, \omega) = \frac{1}{G_0(\omega)} \frac{\delta\phi(\mathbf{r}, \omega)}{\phi_0(\mathbf{r})} \cong \delta\rho(\mathbf{r}, \omega) \quad (310)$$

Regarding the temperature noise, only the local temperature noise can be measured in a PWR, usually at the top of only a few fuel assemblies. For a long time, in the noise-based method of determining the MTC, only a single core-exit thermocouple was used, whereas there is no reason to believe that the moderator temperature noise is homogeneous in the core:

$$\delta T_m(\mathbf{r}, \omega) \neq \delta T_m^{ave}(\omega) = \frac{\int \delta T_m(\mathbf{r}, \omega) w(\mathbf{r}) d\mathbf{r}}{\int w(\mathbf{r}) d\mathbf{r}} \quad (311)$$

Another, final problem is represented by the separation distance between the in-core neutron detector and the core-exit thermocouple, used in the measurement. The MTC can only be accurately determined if no temperature noise is generated between the neutron and the temperature detectors. Furthermore, due to the time constant of the detectors, the overwhelmingly large background noise at high frequencies, and the separation distance between the two detectors, the moderator temperature noise recorded by the core-exit thermocouple is damped, compared with the one recorded by the in-core neutron detector. There is nevertheless a large enough coherence for frequencies lower than 1 Hz between two in-core thermocouples located within the same fuel assembly to prove that the axial damping is not crucial for such frequencies.

Consequently, the MTC has to be evaluated using frequencies smaller than 1 Hz (because of the temperature noise), and frequencies larger than 0.1 Hz (because of the unknown closed-loop reactor transfer function that has to be replaced by the known open-loop reactor transfer function). Another advantage of using the frequency band 0.1–1.0 Hz is that the open-loop transfer function, as demonstrated in [▶ Sect. 3.3.2, equation \(198\)](#) further simplifies into

$$G_0(\omega) \approx G_0^{plateau} = \frac{1}{\beta}, \quad (312)$$

which is called the plateau approximation.

Hence, the traditional MTC noise estimator that can be used in practice in the frequency range 0.1 to 1.0 Hz is defined as the H_1^{biased} estimator:

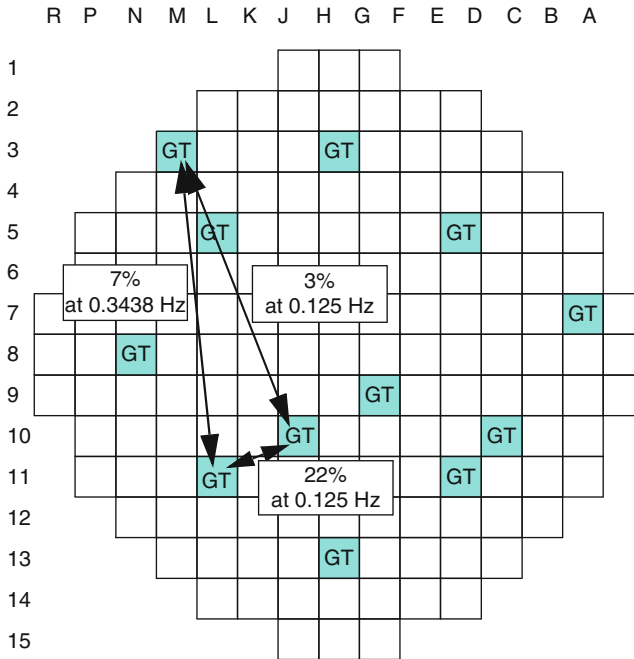
$$H_1^{biased}(\mathbf{r}, \omega) = \frac{1}{G_0(\omega)} \frac{CPSD_{\delta\phi/\phi_0, \delta T_m}(\mathbf{r}, \omega)}{APSD_{\delta T_m}(\mathbf{r}, \omega)} \quad (313)$$

or the H_2^{biased} estimator:

$$H_2^{biased}(\mathbf{r}, \omega) = \frac{1}{G_0(\omega)} \frac{APSD_{\delta\phi/\phi_0}(\mathbf{r}, \omega)}{CPSD_{\delta T_m, \delta\phi/\phi_0}(\mathbf{r}, \omega)} \quad (314)$$

depending on whether (304) or (305) is used.

The estimators (313) and (314) have been used numerous times in the past by several groups, but they did not have the expected accuracy. All results showed the same tendency: the MTC noise estimate was systematically underestimated by a factor of 2 to 5.



■ Figure 36

Maximum of the coherence between GT signals measured in Ringhals-2, cycle 24 (detectors located in the lower part of the core)

5.2.4 Elaboration of a Correct MTC Noise Estimator

The reason of the MTC underestimation by noise analysis was understood recently (Demazière 2004). Namely, the traditional noise estimator implicitly assumes that the moderator temperature noise is radially homogeneous in the core, and hence the measurement of the temperature fluctuations in one point is sufficient to estimate the driving force. However, if the temperature fluctuations are incoherent, such that they may be out-of-phase with each other at various radial points of the core, then the average temperature fluctuation is much smaller than the locally measured one, and the measurement based on the signal of a single thermocouple indeed severely underestimates the MTC.

This hypothesis was proven both in measurements and in calculations with the noise simulator. A noise measurement performed in the Swedish Ringhals-2 PWR during the fuel cycle 24 and summarized in ► Fig. 36 actually allowed mapping the radial distribution of the moderator temperature noise throughout the core via the use of gamma-thermometers (GTs), which as explained earlier, are working as ordinary thermocouples in the frequency range 0.1–1.0 Hz. It was then noticed that the moderator temperature noise was radially heterogeneous and loosely coupled.

In the simulations, spatially random temperature fluctuations with an exponentially decaying correlation were assumed as the driving source, and the neutronic response of the core was calculated with the noise simulator. The calculations proved that for such a distributed

perturbation the core response is very closely point kinetic, even if the correlation length of the perturbation is short, but for correlation lengths much smaller than the core diameter, the traditional MTC estimators significantly underestimate the true MTC.

A new MTC noise estimator, based on the radial average of the moderator temperature noise via the use of a proper weighting function, was thus derived to cope with the radially loosely coupled character of the temperature fluctuations (Demazière 2004). This new estimator assumes that the moderator temperature noise can be measured throughout the core, so that the core-averaged moderator noise can be evaluated according to (294). As a result, this new noise estimator is defined as

$$\tilde{H}_1^{\text{biased}}(\mathbf{r}, \omega) = \frac{1}{G_0(\omega)} \frac{\text{CPSD}_{\delta\phi/\phi_0, \delta T_m^{\text{ave}}}(\mathbf{r}, \omega)}{\text{APSD}_{\delta T_m^{\text{ave}}}(\omega)} \quad (315)$$

This new MTC noise estimator is still biased since, compared to the ideal MTC noise estimator given by (304), the total flux noise is used instead of its point-kinetic component for evaluating the reactivity noise. However, this bias is in general very small. The accuracy of the estimator (315) was also assessed and found rather satisfactory with the same tools, via the noise simulator and the earlier mentioned model of the temperature fluctuations, which were used to show the inaccuracy of the traditional method.

The new MTC noise estimator was tested at the Swedish Ringhals-2 PWR, where the gamma-thermometers (GTs) were used for mapping the moderator temperature noise throughout the core (► Fig. 37). Such evaluations are presented in ► Figs. 38 and ► 39 for two neutron detectors (neutron detector located in the fuel assembly L04 and in the fuel assembly H11, respectively). The MTC was also estimated using SIMULATE-3 and was found to be equal to $-51 \text{ pcm}/^\circ\text{C}$ for this core layout and burnup. In these figures, the points used for the final MTC evaluation are circled in bold and represent the frequencies for which the coherence between the neutron noise and the core-averaged moderator temperature noise is high enough to provide reliable MTC evaluations. In these estimations, the so-called w_2 weighting function was used to evaluate the core-averaged moderator temperature noise. Such a weighting function is defined as

$$w_2(\mathbf{r}) = \phi_0^2(\mathbf{r}) \quad (316)$$

since it can be proven using first-order perturbation theory (in one-group diffusion approximation) and assuming proportionality between the moderator temperature noise and the corresponding macroscopic cross section noise that the weighting function that needs to be used to evaluate the core-averaged moderator temperature noise should be equal to the square of the static flux. Furthermore, the w_2 weighting function uses the square of the mean value of the GT signals as neutron signals, since in static mode the GTs measure the gamma flux, which is proportional to the neutron flux.

The main conclusion from this MTC noise measurement is that using the new MTC noise estimator $\tilde{H}_1^{\text{biased}}$ gives an MTC value that is very close to the reference value, if one takes the confidence intervals into account. The fact that the results using the core average moderator temperature noise do not depend strongly on the radial position of the neutron detector used in the MTC evaluation and give the actual MTC value suggests that the deviation of the reactor response from point kinetics does not play a significant role on the MTC estimation by noise analysis.

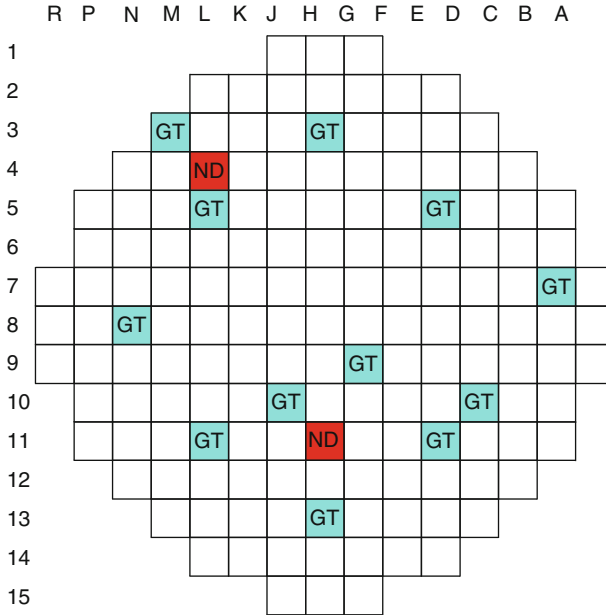


Figure 37
 Radial location of the detectors for the moderator temperature coefficient of reactivity (MTC) noise measurement in Ringhals-2, cycle 26 (GT and ND stand for gamma-thermometer and neutron detector, respectively)

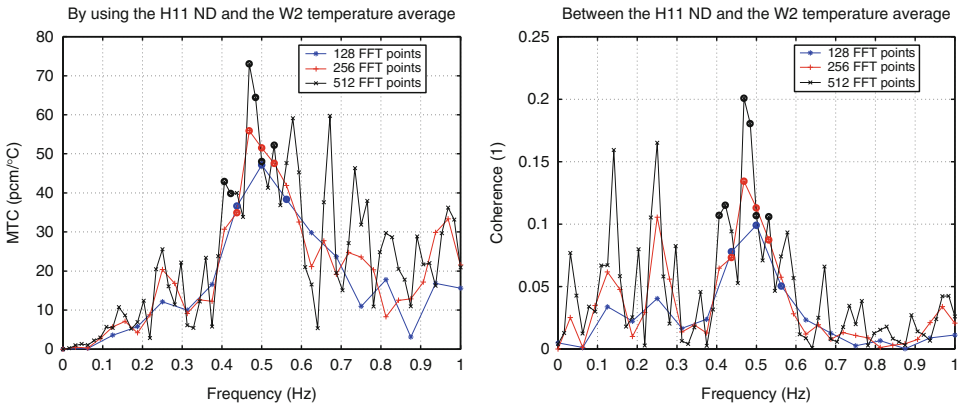


Figure 38
 MTC noise estimation using the new MTC noise estimator at Ringhals-2, cycle 26 (with the neutron noise measured in the H11 fuel assembly)

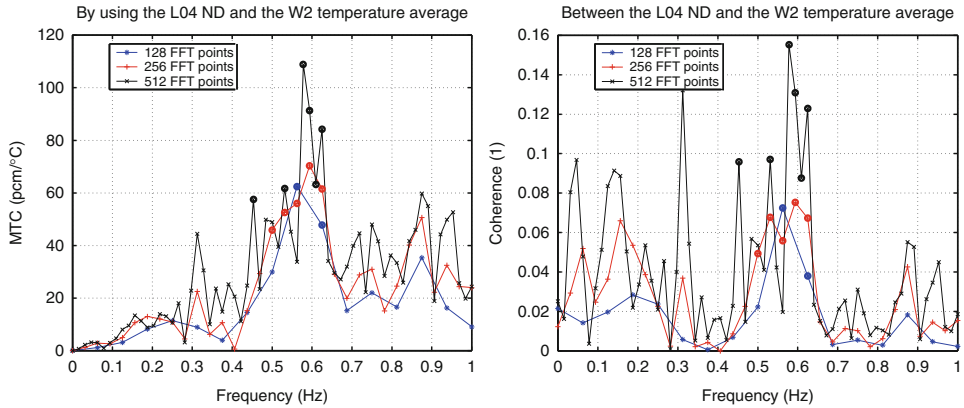


Figure 39

MTC noise estimation using the new MTC noise estimator at Ringhals-2, cycle 26 (with the neutron noise measured in the L04 fuel assembly)

The new MTC noise estimator was also proven to correctly estimate the actual value of the MTC in a subsequent measurement performed at the Ringhals-2 PWR, fuel cycle 27 (Demazière et al. 2003), as well as at the Paks-3 VVER in Hungary (Makai et al. 2007). As verified by the measurements and as predicted by the use of the neutron noise simulator, the new MTC noise estimator allows to accurately estimate the MTC. In the measurement performed at the Paks reactor, a correction for the Doppler effect had nevertheless to be applied, since the MTC evaluations were performed at rather low frequencies, that is, frequencies for which the fuel temperature feedback is of significance.

6 Conclusions and Open Issues

Neutron fluctuations in zero power systems and power reactors have been studied and used for diagnostics of nuclear systems for a long time. What regards zero power systems (branching processes in constant material), the basic theory has been elaborated many decades ago, but new application areas appeared that made it necessary to develop the theory further. One area is accelerator-driven systems (ADSs) where the source is nonstationary and non-Poissonian. In pulsed experiments, correlations may occur in the generation times of neutrons within a pulse. Advances have been made in the theoretical description of such processes, but the present experimental knowledge on the statistics of source neutrons in a pulse is not complete. The number distribution of spallation neutrons has been investigated, but the temporal correlations as well as the energy correlations of the source neutrons are not known. More experimental data are needed in these questions.

Particle fluctuations in a fusion plasma are, as a rule, not related to a branching process, and hence have not been considered in this context. However, the secondary generation of runaway electrons is a branching process (through collisions of energetic electrons with low-energy electrons), which opens an interesting new research area. Although energy conservation in the

individual collisions would keep the total energy in a cascade constant, leading to a sub-Poisson variance, energy is fed to the cascade continuously through the electric field, counteracting the conservation relation and hence leading to significant fluctuations.

It has also to be mentioned that in this chapter, we only considered temporal fluctuations of the neutron number in a static, deterministic material. A completely different type of fluctuations in particle transport arises when the multiplying material cannot be given deterministically, rather only through probability distributions. Similar to the case of a temporally randomly varying material, this is another case of a doubly stochastic process through the spatially random distributions of the reaction cross sections (Sanchez 1989; Sanchez and Pomraning 1991). Several of the planned advanced reactor types, pebble bed reactor, molten salt reactor (MSR), the supercritical water reactor (SCWR), the fluidized bed reactor, will have a spatially random composition due to the redistribution of the fuel and/or the moderator, and some fuel types, such as the MOX fuel and the fuel of a pebble bed reactor, are inherently random. The theoretical treatment of such problems is described in ► Chap. 5, “General Principles of Neutron Transport” of this Handbook by Prinja and Larsen.

In the safeguards field, the main challenge for the near future appears to be the treatment of the dead-time effect on the higher moments of the distribution of detected neutrons and photons (Degweker 1998, 1999; Croft and Bourva 2000). Recently, the dead-time problem has been only treated at the level of the first moment, whereas there are only empirical estimates or Monte Carlo simulation available to estimate the effect of dead-time on the higher moments (and hence the multiplicity detection rates). In addition, new measurement methods (coupled neutron-gamma statistics; novel uses of pulsed neutron generators) as well as new data processing methods (for unfolding of the highly nonlinear relations between the measured multiplicity rates and the searched sample parameters) are under elaboration.

In the field of power reactor diagnostics, there are challenges and open issues regarding the diagnostics of both present generation reactors as well as that of the next generation nuclear power plants. On the computational side, the emphasis was shifted from using simple models, in which analytical solutions can be obtained for the direct task, that is, an analytical expression for the noise induced by a model perturbation, to using numerical methods for the calculation of the noise in real heterogeneous systems. One significance of the analytical solution of the direct task was the potential possibility of devising an analytical, or at least algorithmic inversion procedure to express parameters of the noise source. However, in the meantime, powerful nonparametric inversion algorithms have been taken into use, such as artificial neural networks (ANN) and fuzzy logic systems. These only require a numerical training set, provided by numerical solution of the direct task, to be trained such that they can handle the inverse task.

What regards the development of such noise simulators that can be used to calculate the induced noise numerically in real heterogeneous systems, similarly to the static and dynamic safety calculations, the development points toward multi-physics calculations, that is, coupled core physics – thermal-hydraulics calculations, which take into account the feedback paths between fluid flow, heat transfer, and neutronics. Such simulators are able to handle the nonlinearity in the relevant processes.

Although, in a realistic case, such solutions can only be obtained by complete numerical simulations, the parallel work of understanding of nonlinear processes via simplified models remains an important task. The nonlinearity of the BWR instability and the use of nonlinear analysis methods for diagnostics and stability analysis of BWRs is a field under strong development.

Regarding the signal analysis part, in addition to nonlinearities, an increased attention is given to the fact that real systems, especially when they have nonlinear features, do not behave in a stationary manner. A prominent example is BWR oscillations in an unstable case, which behave clearly in an intermittent manner. It is important to both understand the physical reasons for intermittence and be able to extract maximum information from the nonstationary signals, which cannot be processed by traditional spectral analysis methods. Short-term Fourier transform and wavelet transform are two powerful methods, which started to be used for such analysis, and work is going on in this direction.

Turning into new reactors and new fuel constructions, they will raise new questions and there will be a need for developing both new core physics and diagnostic methods. Even the use of MOX fuel in Generation III and III+ reactors will pose new requests for diagnostics: it is anticipated that at the beginning of cycle the MTC will be allowed to be positive, although smaller than the Doppler effect and other negative reactivity coefficients, in order to avoid a too large negative MTC at the end of the fuel cycle. Monitoring of the MTC, and access to a reliable measurement method will gain importance.

Regarding Gen-IV reactors, and other advanced reactor concepts such as ADS, several of them have properties very much different from the reactors up to Gen-III+ (van Dam 2000; Lathouwers et al. 2003). This means that new types of anomalies may occur, necessitating new noise source models, and new methods of solving both the direct and the inverse task will be necessary to develop. In reactors, like in a subcritical ADS, or a core with circulating liquid fuel, new reactor theory is necessary even to define the kinetic approximations, the role and use of adjoint methods, etc.

Last, but not least, noise diagnostic methods used in fission reactors will be interesting to transfer to fusion reactors, as they approach more stable regimes of operation, and research in fusion and fission reactors might find synergy effects such as hybrid reactors. Such a work has already been started (Karlsson et al. 1997; Pokol et al. 2007). However, fusion plasma processes are highly nonstationary and nonlinear, which will push the development of such analysis methods further.

Acknowledgments

The first author (I.P.) is much indebted to many colleagues with whom he had a very useful and pleasant collaboration in the field of reactor diagnostics from which he benefited very much. He was introduced to the field by his PhD advisor, the late G. Kosály. Special thanks go to M.M.R. Williams of Queen Mary College and Imperial College, from whom he learnt immensely in all aspects of neutron fluctuations and reactor noise. H. van Dam is acknowledged for many enjoyable discussions and for his inspiration. The author's interest in neutron fluctuations in zero power systems stems from the pioneering work of L Pál, his former professor and once the chairman of his PhD exam. He is privileged for the opportunity to start a joint work with L. Pál at a later stage, one result of which is a recent monograph they coauthored on neutron fluctuations. The first part of this chapter is largely based on their book.

The authors wish to thank Maria Pázsit for the typesetting of the second part of this chapter, which was originally prepared with a different word processor, without which this material would not have a chance to be ready in time.

References

- Adorján F, Czibók T, Kiss S, Krinisz K, Végh J (2000) Core asymmetry evolution using static measurements and neutron noise analysis. *Ann Nucl Energy* 27(7):649–658
- Baeten P (2004) Heuristic derivation of the Rossi-alpha formula for a pulsed neutron source. *Ann Nucl Energy* 31:43–53
- Baeten P, Lafuente A, Janssens J, Kochetkov A, Pázsit I, Van Grieken G and Van den Eynde G (2010) Subcriticality determination using the ^{252}Cf source-detector method. *Ann Nucl Energy* 37(5):672–680
- Ballester D, Munoz-Cobo JL (2005) Feynman-Y function for a subcritical assembly with intrinsic spontaneous fissions driven by external pulsed sources. *Ann Nucl Energy* 32(5):493–519
- Behringer K, Kosály G, Pázsit I (1979) Linear response of the neutron field to a propagating perturbation of moderator density (two-group theory of BWR noise). *Nucl Sci Eng* 72:304
- Bell GI (1965) On the stochastic theory of neutron transport. *Nucl Sci Eng* 21:390–401
- Bell GI, Glasstone S (1970) Nuclear reactor theory. Van Nostrand Reinhold Company, New York
- Bennett EF (1981) An experimental method for reactor-noise measurements of effective beta. ANL-81-72
- Blakeman ED (2009) Summary description of the ^{252}Cf -source-driven noise analysis method for measurement of subcriticality. Oak Ridge National Laboratory internal report ORNL/TM-2008/187
- Böhnel K (1985) The effect of multiplication on the quantitative determination of spontaneous fissioning isotopes by neutron correlation analysis. *Nucl Sci Eng* 90:75
- Cacuci DG (1993) On chaotic dynamics in nuclear engineering systems. *Nucl Technol* 103: 303–309
- Cacuci DG, March-Leuba J, Perez RB (1986) Limit cycles and bifurcations in nuclear systems. *Trans Am Nucl Soc* 53:239
- Cifarelli D, Hage W (1986) Models for a three-parameter analysis of neutron signal correlation measurements for fissile material assay. *Nucl Instrum Methods* 251 (3):550–563
- Croft S, Bourva LC-A (2000) The measurement of passive neutron multiplicity counter gate utilisation factors and comparisons with theory. *Nucl Instrum Methods* 453 (3):553–568
- Czibók T, Kiss G, Kiss S, Krinisz K, Végh J (2003) Regular neutron noise diagnostics measurements at the Hungarian Paks NPP. *Prog Nucl Energy* 43:67–74
- D'Auria F et al (1997) State of the art report on boiling water reactor stability – appendix B: methods for evaluating decay ratio. NEA report NEA/CSNI/R(96) 21, pp 333–341
- Degweker SB (1998) Simple formulae for interpretation of the dead time alpha (first moment) method of reactor noise. *Ann Nucl Energy* 26(15):1267–1273
- Degweker SB (1999) An exact solution for a non-extending dead time problem in passive neutron assay. *Ann Nucl Energy* 25(15):387–401
- Degweker SB (2000) Some variants of the Feynman alpha method in critical and accelerator driven sub critical systems. *Ann Nucl Energy* 27(14):1245–1257
- Degweker SB (2003) Reactor noise in accelerator driven systems. *Ann Nucl Energy* 30:223
- Degweker SB, Rana YS (2007) Reactor noise in accelerator driven system – II. *Ann Nucl Energy* 34:463–482
- Demazière C (2004) Development of a 2-D 2-group neutron noise simulator. *Ann Nucl Energy* 19:647–680
- Demazière C (2006) Analysis methods for the determination of possible unseated fuel assemblies in BWRs. *Int J Nucl Energy Sci Technol* 2(3):167–188
- Demazière C, Pázsit I (2002) Online determination of the MTC (moderator temperature coefficient) by neutron noise and gamma-thermometer signals. In: Ruan D, Fantoni PF (eds) Power plant surveillance and diagnostics – modern approaches and advanced applications, Physica Verlag/Springer, Heidelberg, pp 135–157, ISBN 3–540–43247–7
- Demazière C, Pázsit I (2004) Development of a method for measuring the MTC by noise analysis and its experimental verification in Ringhals-2. *Nucl Sci Eng* 148 (1):1–29
- Demazière C, Pázsit I (2005) On the possibility of the space-dependence of the stability indicator (decay ratio) of a BWR. *Ann Nucl Energy* 32(12):1305–1322
- Demazière C, Pázsit I (2008) Numerical tools applied to power reactor noise analysis. *Prog Nucl Energy* 51:67–81
- Demazière C, Sunde C, Arzhanov V, Pázsit I (2003) Final report on the research project Ringhals diagnostics and monitoring, Stage 8. Chalmers report CTH-RF-177/RR-10, Chalmers University of Technology, Göteborg

- Enqvist A, Pázsit I, Pozzi SA (2006) The number distribution of neutrons and gamma photons generated in a multiplying sample. *Nucl Instrum Methods* 566:598–608
- Enqvist A, Pázsit I, Avdic S (2010) Sample characterization using both neutron and gamma multiplicities. *Nucl Instrum Methods A* 615: 62–69
- Ensslin N, Harker WC, Krick MS, Langner DG, Pickrell MM, Stewart JE (1998) Application guide to neutron multiplicity counting. Los Alamos report LA-13422-M
- Fry DN (1971) Experience in reactor malfunction diagnosis using on-line noise analysis. *Nucl Technol* 10(3):273–282
- Fry DN, Kryter RC, Robinson JC (1974) Analysis of neutron-density oscillations resulting from core barrel motion in the Palisades nuclear power plant. Oak Ridge National Laboratory internal report ORNL-TM-4570
- Ginestar D, Miró R, Verdú G, Hennig D (2002) A transient modal analysis of a BWR instability event. *J Nucl Sci Technol* 39(5):554–563
- Ginestar D, Verdú G, Miro R (2006) Singular system analysis of the local power range monitor (LPRM) readings of a boiling water reactor (BWR) in an unstable event. *Int J Nucl Energy Sci Technol* 2(3):253–265.
- Graves HW Jr (1979) Nuclear fuel management. Wiley, New York
- Hage W, Cifarelli D (1985) On the factorial moments of the neutron multiplicity distribution of fission cascades. *Nucl Instrum Methods* 236(1): 165–177
- Harris DR (1964) Naval reactor physics handbook, vol I. United States Atomic Energy Commission, Washington, pp 1010–1142
- Hennig D (1999) A study on boiling water reactor stability behaviour. *Nucl Technol* 126(1):10–31
- Henry AF (1958) The application of reactor kinetics to the analysis of experiments. *Nucl Sci Eng* 3:52–70
- Henry AF (1975) Nuclear-reactor analysis. The MIT Press, Cambridge
- Hotta A, Suzawa Y, Takeuchi H (1997) Development of BWR regional instability model and verification based on Ringhals 1 test. *Ann Nucl Energy* 24(17):1403–1427
- Karlsson JK-H, Pázsit I, Gill RD (1997) Spectral and correlation analysis of soft X-ray signals from the Joint European Torus tokamak. *Fusion Eng Des* 34–35:175–178
- Karlsson JK-H, Pázsit I (1998) Analysis of core barrel vibration in Ringhals2, 3 and 4 for several fuel cycles. Chalmers internal report CTH-RF-135/RR-5
- Karlsson JK-H, Pázsit I (1999) Localisation of a channel instability in the Forsmark-1 boiling water reactor. *Ann Nucl Energy* 26(13):1183–1204
- Kitamura Y, Pázsit I, Wright J, Yamamoto A, Yamane Y (2005) Derivation of pulsed Feynman- and Rossi-alpha formulae including delayed neutrons. *Ann Nucl Energy* 32:671–692
- Kitamura Y, Taguchi K, Misawa T, Pázsit I, Yamamoto A, Yamane Y, Ichihara C, Nakamura H, Oigawa H (2006) Calculation of the stochastic pulsed Rossi-alpha formula and its experimental verification. *Prog Nucl Energy* 48:37–50
- Kleiss E, van Dam H (1978) Analysis of neutron detector response to bubbles in a water moderated reactor. *Ann Nucl Energy* 6(7–8):385–398
- Konno H, Kanemoto S, Takeuchi Y (1999) Parametric stochastic stability and decay ratio for a stochastic non-linear BWR model below the Hopf bifurcation. *Ann Nucl Energy* 26:1465
- Kosály G (1975) Investigation of the local component of power-reactor noise via diffusion theory. KFKI report, KFKI-75–27
- Kosály G (1980) Noise investigations in boiling-water and pressurized-water reactors. *Prog Nucl Energy* 5:145–199
- Kosály G, Meskó L (1972a) Remarks on the transfer function relating inlet temperature fluctuations to neutron noise. *Atomkernenergie* 20:33–36
- Kosály G, Meskó L (1972b) Investigation of the cross correlation of coolant temperature fluctuations via the axial dependent two point model of heat transfer. *Atomkernenergie* 20:91–94
- Kuang ZF, Pázsit I (1999) The general backward theory of neutron fluctuations in subcritical systems with multiple emission sources. *Il Nuovo Cimento* 112 A:1067–1092
- Kuang ZF, Pázsit I (2002) The generalised theory of neutron noise in a random medium. *Proc R Soc A* 458:232–252
- Lamarsh JR (2002) Introduction to nuclear reactor theory. American Nuclear Society, LaGrange Park
- Larsson V, Demazière C (2009) Comparative study of 2-group P1 and diffusion theories for the calculation of the neutron noise in 1D 2-region system. *Ann Nucl Energy* 36(10):1574–1587
- Lathouwers D, Agung A, van der Hagen THJJ, van Dam H, Pain CC, De Oliveira CRE, Goddard AJH (2003) Dynamics modeling and stability analysis of a fluidized bed nuclear reactor. *Prog Nucl Energy* 43(1–4):437–443
- Makai M, Kalya Z, Nemes I, Pos I, Pór G (2007) Evaluating new methods for direct measurement of the moderator temperature coefficient in nuclear power plants during normal operation. In: Proceedings of the 17th symposium of AER

- on VVER reactor physics and reactor safety, Yalta, September 24–29, 2007
- March-Leuba J, Cacuci DG, Perez RB (1983) Non-linear dynamics of boiling water reactors. *Trans Am Nucl Soc* 45:725
- March-Leuba J, Cacuci DG, Perez RB (1984) Universality and aperiodic behavior of nuclear reactors. *Nucl Sci Eng* 86:401–404
- March-Leuba J, Cacuci DG, Perez RB (1986a) Non-linear dynamics and stability of boiling water reactors, I: qualitative analysis. *Nucl Sci Eng* 93:111–123
- March-Leuba J, Cacuci DG, Perez RB (1986b) Non-linear dynamics and stability of Boiling Water Reactors, II: quantitative Analysis. *Nucl Sci Eng* 93:124–136
- Mellier F (Co-ordinator) (2005) The MUSE experiments for sub critical neutronics validation. Final report of the EU-supported project MUSE, Contract No: FIKW-CT-2000-00063
- Mihalcz JT et al (1990) Dynamic subcriticality measurements using the 252Cf-source-driven neutron noise method. *Nucl Sci Eng* 104:314–338
- Miro R, Ginestar D, Hennig D, Verdu G (2000) On the regional oscillation phenomenon in BWRs. *Prog Nucl Energy* 36(2):189–229
- Mogilner AI, Zolotukhin VG (1961) *Atomnaya Energiya* 10:377
- Munoz-Cobo JL, Perez RB, Verdú G (1987) Stochastic neutron transport theory: neutron counting statistics in nuclear assemblies. *Nucl Sci Eng* 95(2):83–105
- Munoz-Cobo JL, Chiva S, Sekhri A (2004) A reduced order model of BWR dynamics with subcooled boiling and modal kinetics: application to out of phase oscillations. *Ann Nucl Energy* 31(10):1135–1162
- Munoz-Cobo JL, Pena J, Gonzalez E (2008) Rossi-alpha and Feynmann Y functions for non-Poissonian pulsed sources of neutrons in the stochastic pulsing method: application to subcriticality monitoring in ADS and comparison with the results of Poissonian pulsed neutron sources. *Ann Nucl Energy* 35(12): 2375–2386
- OECD (2002) Reactor surveillance and diagnostics. In: Proceedings of the SMORN conferences. <http://www.nea.fr/html/science/rsd/>
- Oguma R (1997) Application of noise analysis for the study of core local instability at Forsmark 1. SKI report 97:42, Statens Kärnkraftinspektion (Swedish Nuclear Power Inspectorate), Stockholm
- Ott KO, Neuhold RJ (1985) Introductory nuclear reactor dynamics. American Nuclear Society, La Grange Park
- Pacilio N (1970) Reactor-noise analysis in the time domain. United States Atomic Energy Commission, Washington
- Pál L (1958) On the theory of stochastic processes in nuclear reactors. *Nuovo Cimento, Supplemento* 7:25–42
- Pál L, Pázsit I (2006) Neutron fluctuations in a multiplying medium randomly varying in time. *Phys Scripta* 74(1):62–70
- Pál L, Pázsit I (2007) Theory of neutron noise in a temporally fluctuating multiplying medium. *Nucl Sci Eng* 155(3):425–440
- Pázsit I (1992) Dynamic transfer function calculations for core diagnostics. *Ann Nucl Energy* 19:303–312
- Pázsit I (1995) Determination of reactor stability in case of dual oscillations. *Ann Nucl Energy* 22:377–387
- Pázsit I (2002) Neutron noise theory in the P1 approximation. *Prog Nucl Energy* 40:217–236
- Pázsit I (2003) Hugo van Dam and the dynamic adjoint function. *Ann Nucl Energy* 30:1757–1775
- Pázsit I, Glöckler O (1988) On the neutron noise diagnostics of PWR control vibrations, III: application at a power plant. *Nucl Sci Eng* 99(4):313–328
- Pázsit I, Garis NS, Glöckler O (1994) BWR instrument tube vibrations: interpretation of measurements and simulations. *Ann Nucl Energy* 21(12): 759–786
- Pázsit I, Glöckler O (1996) On the neutron noise diagnostics of PWR control vibrations, IV: application of neural networks. *Nucl Sci Eng* 124(1):167–177
- Pázsit I, Kitamura M (1996) The role of neural networks in reactor diagnostics and control. *Adv Nucl Sci Technol* 24:95–130
- Pázsit I, Pál L (2008) Neutron fluctuations – a treatise on the physics of branching processes. Elsevier Ltd., London/New York/Tokyo
- Pázsit I, Pozzi SA (2005) Calculation of gamma multiplicities in a multiplying sample for the assay of nuclear materials. *Nucl Instrum Methods A* 555: 340–346
- Pázsit I, Karlsson JK-H, Garis NS (1998) Some developments in core-barrel vibration diagnostics. *Ann Nucl Energy* 25(13):1079–1093
- Pázsit I, Kuang ZF, Prinja AK (2002) A unified theory of zero power and power reactor noise via backward master equations. *Ann Nucl Energy* 29(2):169–192
- Pázsit I, Demazière C, Sunde C, Bernitt C, Hernández-Soliz A (2008) Final report on the research project ringhals diagnostics and monitoring stage 12. Chalmers internal report CTH-NT-220/RR-14

- Pokol G, Pór G, Zoletnik S, The W7-AS Team (2007) Application of a bandpower correlation method to the statistical analysis of MHD bursts in quiescent Wendelstein-7 AS stellarator plasmas. *Plasma Phys Control Fusion* 49: 1391-1408
- Pór G (1981) Investigations on the phase at low frequencies of the CPSD between detectors in the Borssele PWR power plant. ECN -81-131 report
- Pór G, Izsák E, Valkó J (1985) Some results of noise measurements in a PWR NPP. *Prog Nucl Energy* 15:387-393
- Pór G, Berta M, Csúvár M (2003) Measurement of the coolant flow rate using correlation of temperature fluctuations. *Prog Nucl Energy* 43:281-288
- Saito K (1979) Source papers in reactor noise. *Prog Nucl Energy* 3(3):157-218
- Sanchez R (1989) Linear kinetic theory in stochastic media. *J Math Phys* 30:2498-2511
- Sanchez R, Pomraning GC (1991) A statistical analysis of the double heterogeneity problem. *Ann Nucl Energy* 18(7):371-395
- Shiralkar B (2005) BWR stability analysis - phenomena and requirements. Talk given at the workshop on status and perspectives of coupled code analysis for BWRs, Royal Institute of Technology, Stockholm, June 27-28, 2005
- Sjöstrand NG (1956) Measurements on a subcritical reactor using a pulsed neutron source. *Arkiv för Fysik* 11:233-246
- Stacey WM Jr (1969) *Space-time nuclear reactor kinetics*. Academic, New York
- Takeuchi Y, Takigawa Y, Uematsu H (1994) A study on boiling water reactor regional stability from the viewpoint of higher harmonics. *Nucl Technol* 106 (3):300-314
- Thie JA (1959) *Dynamic behavior of boiling reactors*. ANL-5849, Argonne National Laboratory
- Thie JA (1963) *Reactor noise*. Rowman & Littlefield, New York
- Thie JA (1977) Neutron noise sources in PWRs. *Prog Nucl Energy* 1(2-4):283-292
- Thie JA (1981) *Power reactor noise*. American Nuclear Society, La Grange Park
- Uhrig RE (ed) (1966) *Proceedings of the symposium on neutron noise, waves and pulse propagation*, Gainesville
- Uhrig RE (1970) *Random noise in nuclear reactor systems*. Ronald Press, New York
- van Dam H (1975) A perturbation method for analysis of detector response to parametric fluctuations in reactors. *Atomkernenergie* 25:70
- van Dam H (1976) Neutron noise in boiling water reactors. *Atomkernenergie* 27:8
- van Dam H (2000) Self-stabilizing criticality waves. *Ann Nucl Energy* 27(16):1505-1521
- van der Hagen THJJ, Hoogenboom JE, van Dam H (1992) A multi dimensional multigroup diffusion model for the determination of the frequency-dependent field of view of a neutron detector. *Nucl Sci Eng* 110:237-253
- van der Hagen THJJ, Pázsit I, Thomson O, Melkerson B (1994) Methods for the determination of the in-phase and out-of-phase stability characteristics of a boiling water reactor. *Nucl Technol* 107(2):193-214
- Verdú G, Ginestar D, Vidal V, Miró R (1998) Modal decomposition method for BWR stability analysis. *J Nucl Sci Technol* 35(8):538-546
- Wach D, Kosály G (1974) Investigation of the joint effect of local and global driving sources in in-core neutron noise measurements. *Atomkernenergie* 23(4):244-250
- Watson HW, Galton F (1873) *Educational Times* 19:103
- Weinberg AM, Schweinler HC (1948) Theory of oscillating absorber in a chain reactor. *Phys Rev* 74:851-863
- Williams MMR (1974) *Random processes in nuclear reactors*. Pergamon Press, Oxford
- Yadigaroglu G, Bergles AE (1972) Fundamental and higher-mode density wave oscillations in two-phase flow. *Trans ASME J Heat Transfer* 94(2):189-195
- Yamane Y, Pázsit I (1998) Heuristic derivation of Rossi-alpha formula with delayed neutrons and correlated source. *Ann Nucl Energy* 25:1373-1382
- Yamane Y, Takemoto Y, Imai T (1999) Effective delayed neutron fraction measurements in FCA-XIX cores by using modified Bennett method. *Prog Nucl Energy* 35(2):183-194
- Yamane Y, Kitamura Y, Kataoka H, Ishitani K, Shiroya S (2002) Application of variance-to-mean method to accelerator-driven subcritical system. In: *PHYSOR-2002 international conference on the new frontiers of nuclear technology: reactor physics, safety and high-performance computing*, Seoul, October 7-10, 2002
- Zinzani F, Demazière C, Sunde C (2008) Calculation of the eigenfunctions of the two-group neutron diffusion equation and application to modal decomposition of BWR instabilities. *Ann Nucl Energy* 35(11):2109-2125



15 Deterministic and Probabilistic Safety Analysis

Mohammad Modarres¹ · Inn Seock Kim²

¹Department of Mechanical Engineering, University of Maryland, Martin Hall, College Park, MD, USA

modarres@umd.edu

²ISSA Technology, Inc., Germantown, MD, USA

innseockkim@gmail.com

I	<i>Origin and Methodological Framework of Deterministic Safety Analysis</i>	1742
1.1	Origin of Nuclear Power Safety and Regulation	1742
1.1.1	First Implementation of Nuclear Safety in the USA	1742
1.1.2	Reactor Design Safety by Du Pont Engineers	1742
1.1.3	US Atomic Energy Commission	1743
1.1.4	International Atomic Energy Agency (IAEA)	1744
1.2	Evolution of Methods for Safety Assurance	1744
1.3	Defense-in-Depth	1745
1.4	Design Basis Accidents	1748
1.5	Single Failure Criterion	1748
1.6	Accident Types	1749
1.6.1	Loss of Coolant Accidents	1749
1.6.2	Transient Events	1750
1.7	General Design Criteria	1751
1.7.1	Quality Control Criterion	1751
1.7.2	Design Bases for Protection against Natural Phenomena	1752
1.7.3	Fire Protection	1752
1.7.4	Environmental and Dynamic Effects Design Bases	1752
1.7.5	Sharing of SSCs	1753
1.7.6	Proven Engineering Practices	1753
1.7.7	Quality Assurance	1753
1.7.8	Self-Assessment	1753
1.7.9	Peer Reviews	1753
1.7.10	Human Factors	1754
1.7.11	Safety Assessment and Verification	1754
1.7.12	Radiation Protection	1754
1.7.13	Operating Experience and Safety Research	1754
1.7.14	Defense against Severe Accidents	1755

1.8	Requirements and Standards for Nuclear Safety	1755
1.8.1	American National Standard Nuclear Safety Criteria	1755
1.9	US Regulatory Requirements for Deterministic Safety Analyses	1757
1.10	Safety Features for Future Nuclear Plants	1758
2	<i>Evolution of Probabilistic Safety Assessment and Applications</i>	1760
2.1	Safety Issues in Nuclear and Aerospace Industries	1760
2.1.1	Safety Issues in Nuclear Industry.....	1760
2.1.2	Safety Issues in Aerospace Industry.....	1761
2.2	Reactor Safety Study (WASH-1400)	1762
2.2.1	Motivation – ECCS Issue and Loss of Fluid Tests.....	1762
2.2.2	RSS Staff	1763
2.2.3	Fault Trees and Event Trees	1763
2.2.4	Initiating Events	1763
2.2.5	Failure Data	1764
2.2.6	Uncertainty Analysis.....	1764
2.2.7	Sensitivity Analysis.....	1765
2.2.8	Consequence Analysis	1765
2.2.9	Release Categories.....	1766
2.2.10	Comparison with Other Risks	1767
2.2.11	RSS Results	1767
2.2.12	APS Review	1767
2.3	Post-RSS Review and the Three Mile Island Accident	1768
2.4	Post-TMI Accident and Revival of the Use of PSA	1769
2.5	Safety Goals	1770
2.6	NUREG-1150 Studies	1771
2.7	IPE and IPEEE	1771
2.8	NRC'S PRA Policy Statement.....	1772
2.9	EPRI's PSA Applications Guide	1773
2.10	Guidelines for Risk-Informed Regulation	1774
2.11	Reactor Oversight Process	1777
2.12	Maintenance Rule	1779
2.13	Risk-Informed Improvement to Technical Specifications	1781
2.14	Risk-Informed Licensing Structure for Design Safety.....	1782
3	<i>Probabilistic Safety Assessment</i>	1784
3.1	Strength of PSA.....	1785
3.2	Steps in Conducting a Probabilistic Safety Assessment	1785
3.2.1	Objectives and Methodology	1786
3.2.2	Familiarization and Information Assembly.....	1787
3.2.3	Identification of Initiating Events	1787
3.2.4	Sequence or Scenario Development	1789
3.2.5	Logic Modeling	1790
3.2.6	Failure Data Collection, Analysis and Performance Assessment	1791
3.2.7	Quantification and Integration	1792
3.2.8	Uncertainty Analysis.....	1793
3.2.9	Sensitivity Analysis.....	1794
3.2.10	Risk Ranking and Importance Analysis.....	1795

3.2.11	Interpretation of Results.....	1797
3.3	A Simple Example of PSA.....	1797
3.4	Future Outlook of Safety Analysis and Research Needs	1805
	<i>References</i>	1808

Abstract: The main theme of this chapter is the process and evolution of deterministic and probabilistic safety analyses that have played a backbone role in assuring public health and safety in the peaceful uses of nuclear power. The chapter begins with a discussion of the origin of nuclear power safety analysis together with the overall perspectives of both deterministic and probabilistic approaches that are still prevalent, although there is an increasing trend in application of probabilistic safety analysis in safety-related decision making. Deterministic approaches, such as the defense-in-depth or safety margin, are regarded as a means to cope with uncertainties associated with adequacy of safety features. As probabilistic methods and applications gain maturity and acceptance, the uncertainties associated with safety features are measured and described probabilistically. The chapter concludes with a detailed discussion of the probabilistic safety assessment and its uses in nuclear power safety analysis.

1 Origin and Methodological Framework of Deterministic Safety Analysis

The safety analysis of nuclear power plants to protect public health and safety from radiation exposure hazards (The word “hazard” in this chapter mainly refers to exposure of workers and the public to radiation from a nuclear plant.) is largely deterministic, although methods of probabilistic safety assessment are being increasingly used. This section discusses the origin and methodological framework of the deterministic safety analysis.

1.1 Origin of Nuclear Power Safety and Regulation

1.1.1 First Implementation of Nuclear Safety in the USA

During the pioneering experiment of a controlled nuclear fission chain reaction at the University of Chicago in 1942, the concept of safety was first implemented by the scientists led by Enrico Fermi. Contemplating the possibility of a failure in the experimental facilities, they designed multiple safeguards into the experiment to prepare for the unknown.

The first safeguard consisted of two sets of safety control rods including an emergency safety rod that played a role of “Safety Control Rod Axe Man (scram)” to cope with the failure of another set. In addition, a cadmium-salt solution was also prepared as a sort of “liquid-control squad” to allow it to pour over the experiment in the case where all the mechanical safety features fail. In fact, these multiple safeguards represent an implementation of the so-called “defense-in-depth” (DID) philosophy design in designing safety features for nuclear plants, although this terminology was not established then.

1.1.2 Reactor Design Safety by Du Pont Engineers

The Manhattan Project in the USA during the World War II included several separate disciplines: experimental and theoretical physics, chemical engineering, mechanical engineering, and electrical engineering. Each group brought different methods of design and construction

to the project. The chemical engineers of the Du Pont Corporation led the effort to build several nuclear reactors in the town of Hanford in the state of Washington. Using their background in chemical processes, the Du Pont engineers broke the reactor design into smaller, relatively independent subsystems, whose design would be frozen early, so that any dependent system could be designed as well (Rhodes 1986).

This created the concept of functional and structural independence and later gave rise to a major safety philosophy extensively applied in nuclear power arena, i.e., “defense-in-depth.” Originating from military strategy, the defense-in-depth (DID) requires a defender deploy resources such as fortifications, field works, and military units at and well behind the front line, so as to slowdown the momentum of the attacker over a period of time rather than defeating an attacker with a single strong defense line. The same philosophy in the nuclear power system design promotes use of layers of redundant and diverse independent barriers (The word “barrier” in this chapter is used to refer to those structures, systems, components, and software and human interventions that can detect, prevent, protect, and mitigate radiation exposure hazards and consequences of such hazards.) to prevent and mitigate the likelihood of release of highly radioactive fission products into the environment.

Because the Du Pont engineers lacked a track record with the nuclear technology, they incorporated several safety features to overcome the uncertainties in characterizing the performance and effectiveness of the barriers including redundancy, diversity, large safety margins, and safety systems designed to limit the release of radioactive effluents, which would contaminate the environment.

1.1.3 US Atomic Energy Commission

Shortly following the World War II, there was significant interest in the peaceful uses of nuclear power and there arose the necessity of regulating nuclear power applications. Nuclear regulation was the responsibility of the US Atomic Energy Commission (AEC), a five-member Commission that the U S Congress established as part of the Atomic Energy Act of 1946 to maintain strict control over atomic technology and to exploit it further for military applications. The 1946 Act, passed while the USA–Soviet Union relationship was strained with the start of the Cold War, tacitly acknowledged the potential peaceful benefits of atomic power. It highlighted the military aspects of nuclear energy and the need for secrecy. The 1946 law excluded commercial applications of atomic energy and rested the ownership of the nuclear knowledge with the US government.

Influenced by President Eisenhower’s “Atom for Peace” initiative in 1953, the US Congress later replaced the 1946 Act with the Atomic Energy Act of 1954, which made the commercial development of nuclear power possible. The 1954 Act ended the government’s monopoly on technical data and made the need for commercial nuclear power an urgent national goal to promote the peaceful uses of atomic energy, provided a reasonable assurance that such uses would not result in undue risks to the health and safety of the public, exists. The 1954 Act directed the AEC “to encourage widespread participation in the development and utilization of atomic energy for peaceful purposes.”

At the same time, it required the AEC to regulate the anticipated nuclear industry to protect public health and safety from radiation hazards. The AEC’s fundamental objective in drafting regulations was to ensure that public health and safety were protected without imposing overly

burdensome requirements that would impede industrial growth (NUREG-BR-0175). However, the inherent difficulty the AEC faced in distinguishing between essential and excessive safety regulations was soon compounded by technical uncertainties and limited operating experience with power reactors. The technical and safety issues that arose during this period included the effect of radiation on the properties of reactor materials; the durability of steel and other metals under stress in a reactor; the ways in which water reacted with uranium, thorium, aluminum, and other elements in a reactor; and the measures needed to minimize radiation exposure in the event of a large accident.

1.1.4 International Atomic Energy Agency (IAEA)

In 1953, US President Dwight Eisenhower delivered a speech entitled “Atoms for Peace” before the United Nations General Assembly with a vision to create an international body to control and develop the use of atomic energy. The IAEA was subsequently created in 1957, with the following dual purposes, by a twelve-nation group: (1) promote the peaceful uses of nuclear energy, and (2) ensure that nuclear power would not be used to further any military purpose (Fischer 1997). The IAEA Statute completed at a 1957 conference contains three pillars of nuclear verification and security, safety, and technology transfer. In 1986, in response to the Chernobyl disaster, IAEA expanded its nuclear safety efforts.

Since 1974, the IAEA has provided a series of safety standards as well as international cooperation to ensure that high safety performance would be attained in all nuclear facilities of the member countries. The IAEA safety standards cover diverse areas of nuclear safety, radiation protection, radioactive waste management, the transport of radioactive materials, the safety of nuclear fuel cycle facilities, and quality assurance. For example, see <http://www-pub.iaea.org/mtcd/publications/publications.asp>. They are not regulations but recommendations. However, the basic principles set forth by these documents were well received by the member countries especially in developing safety regulations by the regulatory bodies.

1.2 Evolution of Methods for Safety Assurance

Over the past 60 years, the process of assuring safety has evolved into three ways of designing against accidents: rule-based, deterministic, and probabilistic methods. The last two look for identifying potential incidents and accident scenarios, which the designer must first try to *prevent* (i.e., avoid their occurrence). The designer must also provide *protection* against such scenarios (i.e., halt their progress) and finally provide *mitigation* (i.e., reduce their effects should they occur).

The rule-based approach prescribes specific design (or good practices) for selection of systems and components and requires maintaining them properly. This approach is not widely practiced in safety design and analysis of nuclear power plants, but is commonly used in designing reactor pressure vessels.

Deterministic analysis is largely experiential and requires the designer, regardless of the likelihood of such events and accident scenarios, to provide protection/mitigation for them. It uses conservative analysis techniques to assess adequacy and performance of safety systems designed to attain the DID objectives. The key terms “prevention,” “protection,” and “mitigation”

are also another way to express the “DID” design philosophy, which states simply that plant safety should not depend on only one physical barrier or system.

Probabilistic safety analysis, on the other hand, develops a big list of possible accident scenarios in a systematic way, and selects those exceeding certain criteria such as the yearly frequency of occurrence to identify and assess adequacy of safety-significant protection/mitigation features.

In the early safety assessments in the USA, due to the lack of information about the effectiveness and performance of the safety barriers, for avoiding the need to calculate best estimate uncertainties about the performance of nuclear plant safety features, safety engineers exclusively used deterministic analysis through conservative assumptions and calculations. They devised the concept of design basis accidents (DBAs) to measure the effectiveness of the physical barriers and safety systems. Safety was, therefore, defined as the ability of the nuclear reactor to withstand a fixed set of prescribed accident scenarios judged by the regulators as the most significant adverse events in a nuclear power plant that must be designed against. The premise was that if the plant can handle the DBAs, it could handle any other accidents – an attempt to eliminate the possibility of reactor failure from fundamental design flaws and worst possible accidents. Accordingly, accidents would be credible if their occurrence is caused by one single equipment failure or operational error following certain initiating events, with some considerations of the probability of such accidents. However, consideration of “incredible events” such as the catastrophic failure of the reactor pressure vessel or multiple independent failure events was excluded.


The Three Mile Island (TMI) accident (Kemeny et al. 1979; NSAC 1979; Rogovin and Framp-ton 1980) showed that the exclusion of multiple failures in assessing safety is not justified, and such events may happen and pose consequences worse than the DBAs. In particular, this lesson from the TMI accident gave rise to sustained use of probabilistic methods in safety and regulatory decisions as a means of identifying and evaluating accident scenarios involving multiple failures. The probabilistic methods are also increasingly used in most other countries as a means to support decision making to further enhance nuclear safety.

1.3 Defense-in-Depth

As noted earlier, DID is an element of the safety philosophy that employs successive compensatory measures to prevent accidents or mitigate damage if a malfunction or accident occurs at a nuclear facility (USNRC 1998). The DID philosophy ensures that safety will not be wholly dependent on any single element of the design, construction, maintenance, or operation of a nuclear facility. The net effect of incorporating DID into design, construction, maintenance, and operation is that the nuclear facility or system in question tends to be more resilient to failures and external challenges.

For example, consider the emergency core cooling system (ECCS) designed to protect the reactor core against the DBAs such as the large loss of coolant accident (LOCA). According to the DID design philosophy, the designers should first try to prevent such an accident, e.g., by designing the piping based on high quality standards with a means to detect leak before break. But, should it occur, there should be features available to prevent the reactor core from potential melting. If a melting occurs, the release of the radioactive inventories from the melted core outside of the reactor coolant system (RCS) or the containment should be prevented

or minimized. Finally, the design should have additional features to mitigate (minimize) any radioactive release to the environment.

Another very important, but subtle objective of the DID was to manage all sorts of uncertainties about the capabilities of safety features, the concept took the view that the nuclear regulation must apply it to design, construction, and operation to assure that normal operation, plant protection, radioisotope containment, and emergency preparedness goals were present, adequate (i.e., with large extra margins) and assured. This philosophy is discussed in IAEA document INSAG-10 (IAEA 1996), in terms of five levels of protection together with the essential means of achieving them in existing plants as shown in  [Table 1](#).

If one level of defense (i.e., a barrier) is not realized, the subsequent level is to be used, and so on. Clearly, of particular interest would be the hazards that could potentially degrade or fail several levels of defense, such as fire, flooding, or earthquakes (the so-called common mode failures). Human aspects of defense are also brought into play to protect the integrity of the barriers, such as quality assurance, administrative controls, safety reviews, operating limits, operating staff qualification and training, and safety culture.

Safety system designers should ensure to the extent achievable that the different safety systems act as or protect barriers against radioactive materials, and are functionally independent under the accident conditions such as the DBAs considered. Each physical barrier should be designed to meet its objectives conservatively, and its quality should be checked to ensure that the large margins against failure exist and are retained at all times. Severe accidents in the past have been invariably due to deficiencies in multiple components of the DID that should not have been permitted.

System design according to a conservative/deterministic approach to DID includes process control as well as feedback to withstand any failures, which might otherwise allow incipient faults or abnormal conditions to lead to accidents. These controls protect the physical barriers

 **Table 1**

Levels of defense-in-depth (DID) (IAEA 1996)

Levels of DID	Objective	Essential means
Level 1	Prevention of abnormal operation and failures	Conservative design and high quality in construction and operation
Level 2	Control of abnormal operation and detection of failures	Control, limiting and protection systems and other surveillance features
Level 3	Control of accidents within the design basis	Engineered safety features and accident procedures
Level 4	Control of severe plant conditions, including prevention of accident progression and mitigation of the consequences of severe accidents	Complementary measures and accident management
Level 5	Mitigation of radiological consequences of significant releases of radioactive materials	Off-site emergency response

by keeping the plant in a well defined region of operating parameters where barriers will not be jeopardized.

As a way to confirm whether a nuclear reactor has been designed in accordance with the DID philosophy, a reactor system is considered “safe” if it can tolerate a fixed set of prescribed accident scenarios judged to be important – the so-called DBAs. The early regulators argued that if plants could handle the DBAs, they could also handle any other accidents – an attempt to eliminate the possibility of plant failures from fundamental design flaws and worst possible accidents.

Due to the fact that the deterministic safety analysis relies on DBAs and misses possibly important multiple failure events, more recently the DID concept is supplemented by probabilistic safety information (Fleming and Silady 2002). These best-estimate (rather than conservative) and probabilistic (rather than deterministic) assessments identify potential accident scenarios that could adversely contribute to safety. Specific DID-guided measures can then be taken to reduce safety risks (Delaney et al. 2005). This systematic approach relies on proven engineering, quality assurance, and reliability methods; fundamental safety principles; safety assessment and verification; operating experience; and safety research.

In summary, the concept of DID has evolved into a set of regulatory design and safety principles, which primarily includes:

1. Use of multiple active and/or passive engineered barriers to rule out any single failure leading to the release of radioactive materials.
2. Incorporation of large design margins to overcome any lack of the precise knowledge (epistemic uncertainty) about capacity of barriers and magnitude of challenges imposed by normal or accident conditions.
3. Application of quality assurance in design and manufacture.
4. Operation within predetermined safe design limits.
5. Continuous testing, inspections, and maintenance to preserve original design margins.

The first design and safety principle described above, i.e., multiple barriers, is the essence of DID philosophy, which typically consists of:

- Fuel cladding
- Reactor coolant system
- Containment

In light water reactors, nuclear fuel is generally fabricated in the form of ceramic pellets and put in metal cladding, and hence, the fuel cladding plays a role of the first physical barrier against release of radioactive material from the fuel.

The second physical barrier is the reactor coolant system RCS, which consists of reactor vessel and piping. The components that constitute the RCS pressure boundary are designed, fabricated, constructed, and maintained to protect the public, during any plant transient or natural phenomena such as earthquakes, tornadoes, flooding conditions, winds, ice, etc. Special consideration is given to static and dynamic loads, temperature, and irradiation effects to which the components might be exposed during their lifetime. Included in the design specifications for the components are requirements for safety margins to protect against unexpected internal loadings, undetected internal flaws, changes in material properties, and most importantly uncertainty posed by unknown-unknowns.

The third level of physical DID is the inclusion of physical barriers for the containment or confinement of the source terms (i.e., fission products available for release to the environment)

produced from accidents in the event that the first two levels of defense fail. These multiple barriers protect humans and the environment in a wide range of abnormal conditions by guarding against the possibility of radioactive release.

In addition to the physical barriers, DID principle is also implemented in nuclear power plants in terms of protection systems and engineered safety features (ESF). The protection systems, such as the reactor protection system (RPS), help to keep an off-normal event from escalating into a significant event threatening reactor safety. The design requirements for these protection systems are based on a spectrum of events that could lead to off-normal operations. In the case of the RPS, redundant and independent instrument channels, once activated through processing of signals, automatically initiate a protective action to suppress conditions that could result in exceeding acceptable fuel limits. The operational reliability of the RPS is attributable to its redundancy and thoughtful safety engineering. On the other hand, the ESF are automatically brought into operation in general when their activation thresholds in terms of process parameters are reached as a consequence of failures of other equipment or physical barriers in order to minimize the adverse effect from or suppress the progression of the plant anomaly. These protection systems and ESFs add further margins to the DID concept by postulating, for design purposes, the occurrence of hypothetical accidents that progress beyond what may be considered normal occurrences.

1.4 Design Basis Accidents

DBAs are the set of postulated accidents for which the designer is required to include explicit provisions (defenses in the plant), while remembering that more severe or peculiar accidents can still occur, and ensuring that the plant design has sufficient capability to cope with them. The DBAs are often defined as those conditions that the regulatory bodies require the plant owners/operators to analyze. Clearly, DBAs are postulated accidents and resulting conditions against which the structures, systems, and equipment of a nuclear facility must be assessed. These postulated or anticipated accidents are assumed to cause the most severe consequences within the design boundary (i.e., excluding those events the occurrence of which is highly unlikely), and the estimated consequences are then compared with the permissible dose exposure to an individual at the site boundary. DBAs are discussed in greater details later.

1.5 Single Failure Criterion

A single failure means an occurrence that results in the loss of capability of a component to perform its intended safety functions. Multiple failures resulting from a single occurrence are considered to be a single failure. Fluid and electrical systems are designed against an assumed single failure if neither (1) a single failure of any active component (assuming passive components function properly) nor (2) a single failure of a passive structure, system and, component (SSC) results in a loss of the capability of the system to perform its safety function (assuming active components function properly).

For example, consider a reactor that must receive a given minimum coolant flow rate to prevent its core to experience any damage following certain accident scenario initiators such as a LOCA. The plant cooling systems will be successful if they provide the minimum required flow when needed. This is the injection success criterion for such accident scenarios. The plant

systems can satisfy the single failure criterion (SFC) if the required flow can be provided in spite of the failure of any single component to perform its intended function. This can be achieved through the use of two diverse systems (or one system with two trains), provided that each system (or train or a single system) alone is capable of delivering the required flow on demand.

The two systems (or trains) are said to be redundant if they contain essentially identical components; for example, each train might contain a motor driven pump and several motor operated valves. The trains would be diverse, or partially diverse, if they rely on different energy sources; for example, one train might contain a steam driven pump rather than a motor driven pump.

The notion of SFC was embodied in the US Code of Federal Regulations (CFR) during the early days of the nuclear power industry (USNRC 1977; USNRC 1978; USNRC 2005a). The SFC exists in two major contexts: (1) system design requirements, largely associated with the general design criteria (GDC) of 10 CFR Part 50 Appendix A (USNRC 1999a) which require designing safety-related systems to perform safety functions to mitigate DBA initiating events, assuming a single failure; and (2) guidance on DBA analysis in ► Sect. 15 of Regulatory Guide 1.70 (now updated to Regulatory Guide 1.206 (USNRC 2007)) and of the standard review plan (SRP) (USNRC 2007b). The SFC is required to be applied in safety analysis in order to promote the high reliability of safety functions that are important to safety, and to help ensure that in the event of a single failure the intended safety function can still be performed. Several regulations, guidelines, and programs, including quality assurance requirements, technical specifications, testing-, inspection-, and maintenance-requirements, act in concert with the SFC to promote high system reliability.

However, the SFC has not always led to the design of safety systems whose reliabilities were judged commensurate with the frequency of safety challenges to the plant. The SFC approach also includes other important elements to address phenomena, such as common cause failure whose impacts on plant safety are not mitigated by redundancy in the design of safety functions. Some additional measures to supplement the SFC include the Reactor Oversight Process tracking of safety system availability (USNRC 2006; USNRC 2005b).

1.6 Accident Types

In the safety analysis of nuclear power plants (specifically water-cooled reactors), the potential accidents are typically divided into two types: loss of coolant accidents and transients. Each is further discussed in the following section.

1.6.1 Loss of Coolant Accidents

For many water-cooled reactors, the design basis event that results in the largest potential radiological consequences to the public is a catastrophic break of the largest pipe entering the reactor pressure vessel. Such a break is postulated in spite of the extensive measures taken in the design, construction, testing and inspection, and operation and maintenance of the plant to assure that such breaks will not occur. Given the break, the reactor coolant would discharge freely from both ends of the severed pipe. This type of break is referred to as a “double-ended guillotine break” and usually leads to the most severe calculated consequences.

Because the RCS operates under high pressure, a reactor coolant pipe break would result in rapid discharge of most of the reactor coolant into containment. In PWR containments, cold-water sprays and/or ice racks are provided to condense the steam resulting from this expulsion while in BWRs, the steam would be condensed in the water-filled pressure-suppression pool. Condensing the steam limits containment pressure, which is the driving force for outward leakage. At the end of the “blowdown” (rapid discharge) period, the primary system consists entirely of saturated steam at the same pressure as that of the containment. In fact, a large-break LOCA or main steam-line break usually determines the peak internal pressure that the containment should be designed to accommodate.

In a large-break LOCA, the reactor would immediately go subcritical due to the substantial and rapid loss of reactor coolant and the subsequent reduction in neutron moderation. Successful actuation of the (RPS), which generates a trip signal, would make the reactor subcritical when reflooded with emergency coolant. However, there would still be considerable thermal energy generated in the fuel from the decay of radioactive fission products. Immediately after shutdown, the generation rate of this “decay heat” is about 7% of the thermal power during normal operation. For example, a 1,000 MWe nuclear plant generates about 3,100 MWt during full power operation, but still generates about 225 MWt immediately after shutdown. The decay heat generation rate decreases rapidly, but will take a few days until it reaches a reasonably low level. However, if emergency cooling water were not supplied to remove heat from the core following the pipe break, core temperature would increase to the point where energetic chemical reactions would occur between hot cladding and residual water-steam in the reactor pressure vessel. Given a prolonged failure to cool the core, large quantities of hydrogen could be generated, portions of the core would melt, and fission products would be released to the containment and possibly to the environment.

In order to limit the consequences of a LOCA, each LWR is provided with an ECCS. An automatic control system senses the occurrence of a LOCA and actuates and coordinates the operation of the different parts of the ECCS as they are needed. The function of the ECCS is to supply water to the core (via spray and/or flooding systems) to cool and limit the temperature increase of the cladding, thus preventing significant core damage and release of radionuclides from the fuel rods.

The US regulations (and similar requirements exist in IAEA guidelines), according to 10 CFR 50.46 and Appendix K of 10 CFR 50 (USNRC 2003a; USNRC 1999a), require that the ECCS of light water reactors satisfy the following acceptance criteria:

- Peak cladding temperature up to 2,200 °F (1,204 °C).
- Oxidation level up to 17% of the cladding thickness.
- Hydrogen generation from hot cladding-steam less than 1% of the total available.
- The core geometry must remain coolable.
- Long-term cooling must be provided.

In a deterministic safety analysis, approved codes and methods are used to show that the safety systems meet the above requirements under conservative assumptions during the analysis.

1.6.2 Transient Events

Transient events are referred to those events that result in a reactor trip but keep the reactor-coolant boundary intact, as opposed to the LOCAs. Transients could occur from a variety of

causes, such as equipment failure or human error. The three principal areas of interest for transients are instances where the reactor power increases, the coolant flow decreases, or the coolant pressure increases. Each of these three instances could lead to a core melt or a breach of the RCS.

Transients are of two broad categories – anticipated transients, such as loss of off-site power or loss of feedwater transients, and unanticipated transients such as turbine missiles or station blackout. The assessment of the frequencies and consequences of these transients typically indicate that the potential contribution of the unanticipated transients to the overall risk is small compared to the anticipated transients. The majority of the analyses show that the most important transients in terms of their risk impact involved the loss of offsite power and the loss of plant heat removal systems.

1.7 General Design Criteria

In the US nuclear plant safety analyses, until 1965 there were no written criteria against which the various designs could be compared, and there was essentially no review of the detailed design approach, which actually determines the levels of safety achieved. As the number of new plant applications increased, there was a strong desire to restructure the licensing review process. In the spring of 1965, in response to anticipated recommendations of an outside review panel, the AEC staff began drafting what would later become the GDC, discussed in Appendix A of 10 CFR 50 (USNRC 1999a).

The GDC established minimum requirements for the principal design criteria, which an application for a construction permit must include for the proposed facility. The principal design criteria establish the necessary design, fabrication, construction, testing, and performance requirements for structures, systems, and components important to safety so as to provide reasonable assurance that the facility can be operated without undue risk to the health and safety of the public. The GDC codified in the US regulation do not provide specific or quantitative bases for establishing the safety adequacy of the proposed facility. The detailed design and its acceptability were deliberately left to the “engineering judgment” of the designer and the regulator, respectively.

The GDC addresses 64 broad issues in six major categories:

1. Overall requirements
2. Protection by multiple fission product barriers
3. Protection and reactivity control systems
4. Fluid systems
5. Reactor containment
6. Fuel and reactivity control

Several core criteria included in the first category earlier, i.e., “overall requirements,” are discussed in the following section, since these are particularly important and impact many aspects of reactor safety.

1.7.1 Quality Control Criterion

Structures, systems, and components important to safety must be designed, fabricated, erected, and tested to quality standards commensurate with the importance of the safety functions they

perform. A quality assurance program must be established and implemented in order to provide adequate assurance that these SSCs will satisfactorily perform their safety functions. Appropriate records of design, fabrication, erection, and testing of SSCs important to safety must be maintained by or under the control of the nuclear power unit licensee throughout the life of the plant.

1.7.2 Design Bases for Protection against Natural Phenomena

Structures, systems, and components important to safety must be designed to withstand the effects of natural phenomena such as earthquakes, tornadoes, hurricanes, floods, tsunami, and seiches without loss of capability to perform their safety functions. The design bases for these SSCs are required to reflect:

1. Appropriate consideration of the most severe of the natural phenomena that have been historically reported for the site and surrounding area with sufficient margin for the limited accuracy, quantity, and period of time in which the historical data have been accumulated.
2. Appropriate combinations of the effects of normal and accident conditions with the effects of the natural phenomena.
3. The importance of the safety functions to be performed.

1.7.3 Fire Protection

Structures, systems, and components important to safety must be designed and located to minimize, consistent with other safety requirements, the probability and effect of fires and explosions.

In 1980, the US NRC formally proposed Appendix R to 10CFR50 to state the minimum acceptable level of fire protection for power plants. Appendix R contains four general requirements to (1) establish a fire protection program, (2) perform a fire hazard analysis, (3) to incorporate fire prevention features, and (4) to provide alternative or dedicated shutdown capability.

1.7.4 Environmental and Dynamic Effects Design Bases

Reactor accidents may lead to harsh environmental conditions that may challenge the operation of components and systems or threaten the integrity of structures. Examples of environmental conditions that can occur include high-temperature steam, high pressure, radiation, missiles, and pipe whip.

For safety systems to function during an accident, they must be designed to withstand the expected environments. Therefore, this criterion states: "Structures, systems, and components important to safety must be designed to accommodate the effects of and to be compatible with the environmental conditions associated with normal operation, maintenance, testing, and postulated accidents, including loss-of-coolant accidents."

1.7.5 Sharing of SSCs

This criterion is intended to address features of a multiunit site that could allow problems to propagate from one unit to another. The criterion states: “Structures, systems, and components important to safety shall not be shared among nuclear power units unless it can be shown that such sharing will not significantly impair their ability to perform their safety functions, including, in the event of an accident at one unit, an orderly shutdown and cooldown of the remaining units.”

Similar to the US requirements, there are several main technical principles that are essential to the successful realization of safety technology for nuclear power plants. These principles used by IAEA are briefly discussed in ► [Sects. 1.7.6–1.7.14](#).

1.7.6 Proven Engineering Practices

Nuclear power technology should utilize engineering practices that are proven by testing and experience, and which are reflected in approved codes and standards. The design and construction of advanced power plants should rely as much as possible on experience from older operating plants or on the results of research programs, large integral facilities and prototypes. Standardization can offer economic payoff and indirect safety advantages by focusing on the resources of designers, regulators, and manufacturers on specific design and fabrication methods.

1.7.7 Quality Assurance

Quality assurance is applied to ensure with high confidence that all SCCs, services, and tasks performed meet specified requirements. High quality in equipment and human performance (HP) is most central to nuclear plant safety. The goal is to ensure that the equipment functions and individuals perform in a satisfactory way. These practices apply to the entire range of activities in design, construction, installation, and to the control of procedures in plant testing, commissioning, operation, and maintenance.

1.7.8 Self-Assessment

Self-assessment for critical activities at a nuclear plant ensures the involvement of plant staff performing line functions in detecting problems concerning safety and performance and solving them.

1.7.9 Peer Reviews

Independent peer reviews make practices and programs employed at plants performing well accessible and allow their implementation to improve safety. International organizations typically performing operational peer reviews are the World Association of Nuclear Operators (WANO) and the IAEA through their Operational Safety Review Teams.

1.7.10 Human Factors

Plant staff occupied in safety-related activities are trained and qualified to perform their respective duties. Reduction of human error in nuclear power plants may be achieved by assisting operators in making correct decisions and minimizing incorrect decisions, and by providing means for detecting and correcting or compensating for error. “Human factor improvements” are necessary in plant hardware (e.g., in ergonomic layout), plant procedures, training, and other areas to help prevent or mitigate human error. To keep the plant within the boundaries of a domain of safe operation, approved procedures for operation should be followed. To ensure this, staff training and retraining receive strong emphasis, with classroom, simulator, and plant-based studies.

1.7.11 Safety Assessment and Verification

As noted earlier two methods of analysis are possible: deterministic and probabilistic. In the deterministic method, design basis events are chosen to encompass a range of related possible initiating events that could challenge the safety of the plant. Analysis is used to show that the response of the plant and its safety systems to design basis events satisfies predetermined specifications for both the performance of the plant itself and meeting safety criteria.

Probabilistic analysis is used to evaluate the likelihood of any particular sequence and its consequences. This evaluation may take into account the effects of mitigation measures inside and outside the plant. Probabilistic analysis is used to estimate risk and especially to identify the importance of any possible weak link in design. The probabilistic method can be used to aid in the selection of events requiring deterministic analysis and the other way around.

1.7.12 Radiation Protection

A system of radiation protection practices is followed in the design, commissioning, operational, and decommissioning phases of nuclear power plants. Measures are then taken to protect workers and the public against the harmful effects of radiation in normal operation, anticipated operational occurrences and accidents.

1.7.13 Operating Experience and Safety Research

Operating experience and the results of safety-related research are exchanged, reviewed, and analyzed. The nuclear power plant owner/operator maintains an effective system for collecting and interpreting operating experiences, and sharing safety significant information rapidly among the plant staff. The root causes of accidents are reanalyzed, and events regarded as precursors of severe accidents are identified and actions are taken to prevent any recurrence.

1.7.14 Defense against Severe Accidents

Some highly unlikely plant accidents that are Beyond Design Basis Accidents (BDBA) may arise due to multiple failures of safety systems leading to significant core degradation that may jeopardize the integrity of many or all of the barriers to the release of radioactive material. These event sequences are called severe accidents.

Consideration is given to these severe accident sequences, using a combination of engineering judgment and deterministic analyses. Acceptable measures need not necessarily involve conservative engineering practices used in evaluating DBAs, but rather should be primarily based upon realistic or best estimate assumptions, methods, and analytical criteria. On the basis of operational experience, relevant safety analysis, and results from safety research, design activities for addressing severe accidents shall take into account important accident scenario events that may lead to a severe accident through a combination of probabilistic methods, deterministic methods, and sound engineering judgment.

1.8 Requirements and Standards for Nuclear Safety

1.8.1 American National Standard Nuclear Safety Criteria

In late 1965, around the time when the AEC was ready to publish the first version of their GDC, the industry prepared supplementary criteria to complement and implement the GDC. Objectives included: simplifying and streamlining the licensing procedures, providing a means to obtain industry-wide agreement on objectives, providing a means to uniformly judge the protection afforded the public, and avoiding the necessity of government articulation of such requirements in the form of rulemaking.

A series of drafts was produced and the final version, known as ANSI N18.2–1973 (ANS 1973), was eventually approved. This ANSI Standard was developed to amplify the guidance provided by the GDC. The criteria contained therein were aimed at providing a degree of assurance that PWR facilities would be designed, constructed, and can be operated without undue risk to the health and safety of the public. However, the focus of these criteria was placed on design requirements. Operating, maintenance, and testing requirements other than those affecting design, although of great safety significance, were not included.

It is notable that the ANSI N18.2–1973 Standard duly cautioned that: (1) simple adherence to the criteria might not suffice for satisfying the requirement of assuring public health and safety; and (2) an owner or designer of the facility has a responsibility, even at the design state that goes beyond the degree of safety afforded by the criteria. As such, in addition to considering these criteria and other guidance such as the GDC, the following requirements were made.

1. Identify all safety design criteria for the proposed facility and ensure that they incorporate all features for structures, systems, and components required to protect public health and safety
2. Ensure by analysis, experiment, comparison to accepted design, or experience that the fulfillment of all these safety design criteria can and will be realized.

As opposed to the GDC, the ANSI N18.2–1973 Criteria were presented in a format to provide maximum usefulness in system design, encompassing:

- Categorization of plant conditions to be considered in design
- Safety classifications of reactor containment and components
- Barrier integrity criteria
- Plant safety analysis
- Specific system design criteria

The full spectra of plant conditions were identified in accordance with their anticipated frequency of occurrence as follows:

1. Condition I: Normal Operation
2. Condition II: Incidents of Moderate Frequency
3. Condition III: Infrequent Incidents
4. Condition IV: Limiting Faults

Condition I occurrences are operations that are expected frequently or regularly in the course of power operation, refueling, maintenance, or maneuvering of the plant. Condition II occurrences include incidents that may occur during a calendar year for a particular plant. Condition III occurrences include incidents, any one of which may occur during the lifetime of a particular plant. Condition IV occurrences are faults that are not expected to occur, but are postulated because their consequences would include the potential for the release of significant amounts of radioactive material. Condition IV faults are the most drastic to be designed against, and thus represent the limiting design case. Note that large fleets of operating plants were licensed according to this categorization of plant conditions defined in ANSI N18.2–1973, although it was later replaced by ANSI/ANS-51.1–1983 (ANS 1983).

The basic principle applied in the ANSI N18.2–1973 Standard was that the plant should be designed such that the most frequent occurrences yield little or no adverse consequence to the public and such that the improbable extreme situations, having the potential for the greatest adverse consequence to the public, shall have a low probability of occurrence. Protection system and engineered safety feature functioning was required, where applicable, in fulfilling this principle.

In order to facilitate the design process, the following design requirements were specified for each plant condition in the ANSI N18.2–1973 Standard:

1. Design Requirement for Condition I: Condition I occurrences shall be accommodated with margin between any plant parameter and the value of the parameter which would require either automatic or manual protective action.
2. Design Requirement for Condition II: Condition II occurrences shall be accommodated with, at most, a shutdown of the reactor with the plant capable of returning to operation after corrective action. Any release of radioactive materials in effluents to unrestricted areas shall be in conformance with 10 CFR Part 20, “Standards for Protection Against Radiation.” By itself, a Condition II incident shall not lead to a more serious incident of the Condition III or IV type, without other incidents occurring independently. A single Condition II incident shall not cause consequential loss of function of any barrier to the escape of radioactive products.
3. Design Requirement for Condition III: Condition III incidents shall not cause more than a small fraction of the fuel elements in the reactor to be damaged. The release of

radioactive material due to Condition III incidents may exceed guidelines of 10 CFR 20, but shall not be sufficient to interrupt or restrict public use of those areas beyond the exclusion radius. A Condition III incident shall not, by itself, generate a Condition IV fault or result in a consequential loss of function of the RCS or reactor containment barriers.

4. Design Requirement for Condition IV: Condition IV faults shall not cause a release of radioactive material that results in an undue risk to public health and safety exceeding the guidelines of 10 CFR 100, "Reactor Site Criteria." A single Condition IV fault shall not cause consequential loss of required functions of systems needed to cope with the fault including those of the RCS and the reactor containment system.

1.9 US Regulatory Requirements for Deterministic Safety Analyses

The Code of Federal Regulations (CFR) of the US is a codification of the general and permanent rules published in the Federal Register by the Executive departments and agencies of the Federal Government. The Code is divided into 50 titles which represent broad areas subject to federal regulation. Nuclear regulations are contained in Title 10 – Energy (USNRC 1956).

Of the many parts in 10 CFR, the following four parts are especially relevant to safety analysis of nuclear power plants.

1. 10 CFR 20 – Standards for protection against radiation
2. 10 CFR 50 – Domestic licensing of production and utilization facilities
3. 10 CFR 52 – Licenses, certifications, and approvals for nuclear power plants
4. 10 CFR 100 – Reactor site criteria

Title 10, Code of Federal Regulations, Part 50, i.e., 10 CFR 50, has been used as a major compilation of regulations with respect to design, construction, and operation of commercial nuclear power plants. 10 CFR Part 52 was recently published for the issuance of combined licenses (COLs) for nuclear power plants. In order to guide COL applications, Regulatory Guide 1.206 (USNRC 2007a) was published in 2007 and information in this regulatory guide is reflected in NUREG-0800 (USNRC 2007b), "Standard Review Plan for the Review of Safety Analysis Reports for Nuclear Power Plants." This standard review plan (SRP) is used by the US NRC in reviewing applications for early site permits, standard design certifications, COLs, and other activities addressed by 10 CFR Part 52.

Of these regulations, the key principle of nuclear reactor regulation in the USA with regard to prospective safety analysis is reflected in the following statement that is included in 10 CFR 50.34, Contents of Applications; Technical Information: "It is expected that reactors will reflect through their design, construction and operation an extremely low probability for accidents that could result in the release of significant quantities of radioactive fission products." For the sake of demonstration of such expectations, the applicants for a construction permit, a design certification, or combined license are required to perform a safety assessment of the site and a safety assessment of the facility.

These safety assessments must determine that:

1. An individual located at any point on the boundary of the exclusion area for any 2 h period following the onset of the postulated fission product release, would not receive a radiation dose in excess of 25 rem total effective dose equivalent (TEDE).

2. An individual located at any point on the outer boundary of the low population zone, who is exposed to the radioactive cloud resulting from the postulated fission product release (during the entire period of its passage), would not receive a radiation dose in excess of 25 rem TEDE.

The whole body dose of 25 rem has been stated in the US regulation to correspond numerically to the once in a lifetime accidental or emergency dose for radiation workers which, according to NCRP recommendations at the time, could be disregarded in the determination of their radiation exposure status. However, its use is not intended to imply that this number constitutes an acceptable limit for an emergency dose to the public under accident conditions. Rather, this dose value has been set forth as a reference value, which can be used in the evaluation of plant design features with respect to postulated reactor accidents, in order to assure that such designs provide assurance of low risk of public exposure to radiation, in the event of such accidents.

➤ **Sect. 15**, “Accident Analyses,” contained in Revision 3 of Regulatory Guide 1.70, “Standard Format and Content of Safety Analysis Reports for Nuclear Power Plants – LWR Edition,” and had been used by the US NRC as a primary guidance of how applicants of a nuclear power plant should evaluate the safety of the plant (USNRC 1978). This regulatory guide issued in 1978 has been updated in 2007 into Regulatory Guide 1.206 (USNRC 2007a) to reflect current information requirements for COL applications.

As opposed to the four categories of plant conditions discussed in the ANSI/ANS N18.2–1973 Standard, each initiating event for safety analysis is classified in ➤ **Sect. 15** of NUREG-0800 (USNRC 2007b), so called the SRP, as either an anticipated operating occurrence (AOO) or a postulated accident. In both Appendix A to 10 CFR 50 and ➤ **Sect. 15** of the SRP, AOOs are defined as those conditions of normal operation that are expected to occur one or more times during the life of the nuclear power unit and include but are not limited to loss of power to all recirculation pumps, tripping of the turbine generator set, isolation of the main condenser, and loss of all offsite power. The SRP indicates that AOOs are also known as Condition II and III events. On the other hand, the SRP defines postulated accidents as unanticipated conditions of operation (i.e., not expected to occur during the life of the nuclear power unit). It also indicates that postulated accidents are alternatively known as Condition IV events. In ➤ **Sect. 15** of the SRP, various requirements for safety analysis are specified as to how to identify the limiting events that will be analyzed in detail, how to determine the specific accident sequences (e.g., consideration of single failure and coincident occurrence of a loss of offsite power), what acceptance criteria to apply for specific events or event sequences, and so on.

1.10 Safety Features for Future Nuclear Plants

Future plants continue to improve the DID safety features. Prevention of accidents remains the highest priority, but controlling the course of accidents and mitigating their consequences, if they happen, are also very important.

An important advantage of future plants is their ability to incorporate corrections to deficiencies identified in the past. The use of a deterministic checklist for such problem areas and their proposed resolution will ensure that no significant past difficulty is overlooked. Future plants have another advantage, because they can implement the results of research and

development programs, including those relating to new materials, improved coolant chemistry, methods of making best estimate predictions of operating margins and their uncertainties, and the findings from a large number of other safety analyses and research work. But it is important that features incorporated into future plants be fully proven through adequate tests and, preferably, demonstration in operating plants.

Reducing the frequency of equipment failures and the number of human errors enhances accident prevention. For equipment failure, the reduction in the likelihood of occurrences is achieved by simplifying the design and reducing the number of active components, such as pumps, which can fail to operate when demanded. Another approach is to increase the tolerance to equipment failure, thereby reducing the potential adverse impact of transients on the plant. Further capability of accident prevention may be achieved by improving human-machine interfaces or taking advantage of proven information and digital technology. When computer systems are utilized for safety functions, sufficient precautions must be taken against potential common-cause failures of their constituents comprising hardware, firmware, and software. The quality and reliability of these systems and additional measures such as an appropriate degree of diversity must be considered. In addition, the production process must include integral testing of software and hardware systems and good practices for software verification and validation.

Another opportunity to improve accident prevention is to assess the measures taken at different levels of defense in depth and, where practical, to eliminate dependence between systems. Finally, adequate provisions in terms of space and installation are necessary to improve the performance and quality of nondestructive inspections and maintenance work. Plant designers and owners/operators may provide additional margins in as many areas as appropriate for investment protection, operational flexibility, and increased safety assurance.

Accident mitigation capability should be enhanced to the extent practically achievable to reduce the consequences of radioactive releases. For future nuclear power plants, the design features related to the prevention and mitigation of accidents, including severe accidents, will be determined not only on the basis of deterministic analysis, but also best estimate probabilistic considerations as well as the application of numerical safety targets and engineering judgment. Notably, the practical elimination of accident sequences, which could lead to large, early radioactive releases, is based, as far as necessary, on detailed deterministic and/or probabilistic studies.

The role of deterministic safety analysis would be paramount, but probabilistic safety assessments (PSAs) play a critical role at the design stage as a useful tool for in-depth analysis of the contributions of the different accident sequences to the risk. This is the topic of the remaining sections of this chapter. Reaching a final decision about features to be incorporated in future nuclear power plants is an iterative process, with initial judgments made by the designers based on experience and research results and with the help of PSAs. This is followed by a review by plant owners/operators and regulators to confirm that an appropriate decision has been made. This process of careful evaluation and decision making leads to a consistent and robust set of design features.

The risks associated with future nuclear power plants will become very low, due to the reduction in both the frequency of occurrence of potential accident scenarios and the radiological consequences resulting from the accidents. However, this statement supposes that careful attention will be paid to the possibilities of common-mode failures and the uncertainties still prevalent in the understanding of severe accident phenomena. For these reasons, engineering judgment will be important in evaluating new design features.

2 Evolution of Probabilistic Safety Assessment and Applications

As was stated in [Sect. 1](#), the primary means for assuring safety in nuclear power plants has been deterministic methods. This concept while being strong has shown to be insufficient by itself in ensuring nuclear safety, and as a result, probabilistic methods would be needed to fill such shortcomings.

A comprehensive evaluation of reactor safety was performed in early 1970s using probabilistic methodologies to the feasible extent in an AEC study called the reactor safety study (RSS) or WASH-1400. This RSS was the major milestone in the history of probabilistic safety analysis because it not only established the basic methodology but also spurred a large number of similar studies throughout the international nuclear power community. After a brief introduction to safety issues in nuclear and aerospace industries, this section discusses the RSS as well as the historical perspectives of probabilistic safety analysis following the RSS. Also included herein is a description of various PSA applications that are conducted to enhance safety of nuclear power plants and improve efficiency in the plant operation and the regulatory activities.

2.1 Safety Issues in Nuclear and Aerospace Industries

2.1.1 Safety Issues in Nuclear Industry

While formal consideration of risk and reliability was not a concern of the Atomic Energy Commission (AEC), it acknowledged, however, that it could not eliminate all risks through its DID principle and design-basis accident methods. The Advisory Committee on Reactor Safeguards (ACRS) of the AEC informed the Congress in 1956 that because of technical uncertainties and limited operating experience, “the determination that the hazard is acceptably low is a matter of competent judgment.”

In 1957, WASH-740 (USAEC 1957), the first comprehensive look at the consequences of a large nuclear accident, was published by the AEC. The purpose was to help focus Congressional deliberation of the Price–Anderson Act on the potential harms from reactor accidents. The Price–Anderson Act was being considered to provide supplemental government insurance for private nuclear reactors. WASH-740 originally looked only at the 200 MW class of reactors then in operation and predicted potential damage due to an accident in the \$7 billion range. WASH-740 estimated the risk for a serious reactor accident as 1×10^{-6} per reactor-year of operation, a value still within the range of probabilities being estimated today for an occurrence of a large early release of radiation due to reactor accidents. But the Price–Anderson Act arbitrarily used a \$500-million of insurance figure, above the commercial insurance of \$60-million provided by private insurance companies. After it was revised in 1964–1965, when larger reactors were designed, the worst-case nuclear accident cost rose to \$17-billion (Wood 1983). The WASH-740 study focused on the dangers of large LOCAs as the leading source of worst radiation release into the environment.

As the reactor safety systems continued to grow in size and complexity, a new method of analysis was needed to produce reasonably more accurate risk estimates. At the urging of the ACRS, which first troubled about the so-called China syndrome, the AEC established a special task force to investigate the core-melt problem in 1966. The task force report that was published

in 1967 offered assurances about the improbability of a core meltdown and the reliability of emergency core cooling designs, but it also acknowledged that a LOCA could cause a breach of containment if the ECCS failed to operate. From this point on, the containment could no longer be regarded as an unbreakable final barrier of radioactivity. This represented a key milestone as it modified the fundamental approach to reactor safety. Once the AEC realized that under some circumstances the containment building could fail, the key to protecting the health and safety of the public shifted to preventing accidents severe enough to threaten containment.

In the late 1960s, two papers that brought PSA to the forefront of nuclear engineering thought was published. The first was a 1967 paper presented at IAEA's Vienna conference by F.R. Farmer entitled "Reactor Safety and Siting: A Proposed Risk Criterion" (Farmer 1967). This paper included the now famous Farmer Curves and concentrated on the effects of iodine-131. Another paper was a 1969 Science article "Social Benefit versus Technological Risk" by Chauncey Starr, which further elaborated on risk perception, and many of Farmer's points (Starr 1969). In the meantime, in 1966, the AEC asked General Electric, the contractor at Hanford, and Du Pont, the contractor at Savannah River, to perform calculations on the safety of the plutonium production plants that they operated. Partly influenced by Farmer's paper, General Electric showed, using a very simplistic probabilistic model, that the N-Reactor had a one-in-a-million chance per year for a catastrophic failure because each of the three major subsystems would only fail once-in-one-hundred per year (Carlisle 1997). General Electric and Douglas United Nuclear, the subcontractor that assumed operational control of the N-Reactor in 1967 then claimed that such a low probability meant that for all practical purposes, the chance of a catastrophic failure was zero, a conclusion that the AEC and others disputed (USAEC 1966).

To address the issues of safety, AEC concluded that the complexities associated with the design and operation of the reactors operating at that time exhibited so many technical challenges that a quantified risk assessment would be impossible to produce. One reason for this was that the probabilistic methodologies lacked sophistication and rigor, and the information required was not fully available (Ford 1977).

By 1971, nuclear critics were expressing resentment to the AEC because of the licensing of several reactors under review and its conflicting mission of both regulating and promoting nuclear power. However, in 1974, the AEC's regulatory programs came under such strong attacks that the Congress decided to abolish the agency. Supporters and critics of nuclear power agreed that the promotional and regulatory duties of the AEC are in conflict and should be assigned to separate agencies. The Energy Reorganization Act of 1974 created the Nuclear Regulatory Commission (NRC), which assumed the responsibility for civilian nuclear power regulation and assuring the protection of the health and safety of the public.

2.1.2 Safety Issues in Aerospace Industry

Another industry in which issues of safety and risk were of paramount importance was the aerospace industry. The Boeing Company, in conjunction with Bell Laboratories, pioneered the use of fault tree analysis during the design of the Minuteman missile for the Air Force during the 1960s to prevent inadvertent launches. In 1966, Pan Am Airlines placed an order with the Boeing Company to build the Boeing-747. Because the Boeing-747 would be the largest commercial jet in operation, boeing engineers felt that it would be important to look at the

safety systems of the plane in a different manner than they had in previous aircraft designs. The method they chose was fault tree analysis, which provided a deductive, systematic, and holistic assessment of the airplane and highlighted among the faults modeled, the critical ones and effects of such faults on the plane. This allowed the designers to appreciate how and why the failure of one system or component would affect other systems (Ericson 1999).

National Aeronautics and Space Administration (NASA) began to use probabilistic risk assessment methods in 1967, following the disastrous fire on Apollo 1. Engineers from the Boeing Company helped complete a fault tree analysis for the entire Apollo system. They relied on highly conservative measures and data and estimated failure probabilities for Apollo missions to range 0.1–0.8 per mission; a range that was higher than the actual experience, and subsequently led to a distrust of probabilistic risk assessment results. However, following the Challenger explosion in 1986, probabilistic risk assessment at NASA was revived, and the Columbia break-up in 2003 reiterated the need for such analyses. NASA used risk assessment and a combination of fault and event trees methods borrowed from the nuclear industry to model possible accident scenarios for the shuttle and International Space Station (ISS) programs. One risk study performed by the US Air Force in 1983 calculated the chances of a space shuttle solid rocket booster failing during operation to be about 1 in 35, a number disputed by NASA management (Colglazier and Weatheras 1986).

Risk assessment methods in the nuclear industry benefitted from the experience of the aerospace industry in the early 1970s. However, in the late 1980s when the need for systematic safety assessment became apparent in the space industry, it was the aerospace industry that turned to and relied primarily on the experience of the nuclear industry.

2.2 Reactor Safety Study (WASH-1400)

2.2.1 Motivation – ECCS Issue and Loss of Fluid Tests

Often bitter debates over the reliability of ECCSs, reactor pressure vessel integrity, and the likelihood of large accidents consumed the AEC, the Congress, the nuclear industry, environmentalists, and the media. In the late 1940s and most of the 1950s, public attitudes toward the technology were highly favorable as the opinion polls on the subject revealed. In the late 1950s and early 1960s, however, the public became more aware and worried about the hazards of radiation, largely as more was learned about radioactive fallout from nuclear weapons testing. Throughout the 1960s, there was a desire and interest among the public to know whether or not nuclear plants were safe. This desire for safety assurance became more urgent in the late 1960s and early 1970s, as the organized opposition to nuclear power grew and characterized AEC's safety criteria used for licensing nuclear plants as inadequate and inconsistent with respect to the apparent safety significance of various systems, structures, and components of the plants.

Of the many issues that arose these years, the most critical issue that led to an integrated assessment of safety, i.e., the RSS, was the concern about a LOCA that might lead to a core melt if the ECCS fails. A special task force established by the AEC to look into the problem of core melting indicated that the containment could no longer be regarded as an inviolable barrier to the escape of radioactivity since a LOCA could cause a breach of the containment if the ECCS failed to perform.

Therefore, the AEC performed a series of experiments at the Reactor Test Facility in Idaho using a small-scale reactor mockup. The loss of fluid tests (LOFT) suggested that the ECCS might not work as well as planned as steam build-up could prevent injection of water into the core and lead to core damage (Kouts 1998). As a result of Congressional requests coupled with concerns over the LOFT results, the AEC asked Professor Norman Rasmussen of MIT for his help to initiate and run a study of the assessment of safety of the nuclear plants in the United States.

2.2.2 RSS Staff

The staff of the RSS, or oftentimes called WASH-1400 (USNRC 1975), consisted of about 40 scientists and engineers, drawn from industry, academia, and government service. In addition to Saul Levine, seven full-time participants were the employees of AEC. Many were experts in particular reactor safety systems and some were experts in risk assessment. Also, several outside experts worked in consequence analysis – modeling the release and health effects of radiation in the environment, in which Rasmussen showed a keen interest.

2.2.3 Fault Trees and Event Trees

The RSS initially used fault trees as the basis for reactor risk calculations. The prototype fault trees for both the BWR (Peach Bottom Atomic Power Station, Unit 2) and PWR (Surry Power Station, Unit 1) designs were developed. Although fault trees were developed for almost all of the major safety-related systems, the team realized that integrating the overall fault tree analysis for the entire nuclear power plant was too complex of an undertaking for the RSS, given constraints in time and resources.

This led to the development of the event tree concept to model the approximate timeline of the possible accident scenarios. Originally borrowed from the decision analysis, the study proposed the event tree method. Event tree methodology remedied the constraints in time and resources associated with relying on fault tree analysis alone. Later the event tree approach became a predominant force in PSAs.

The event trees looked at two separate areas. The first covered failures in major systems, such as the engineered safety systems. The second investigated the ability of a nuclear power plant's containment system to prevent the spread of radiation in the case of an accident. Event trees start with an initiating event that causes the plant to enter a transient from its steady state operating condition.

2.2.4 Initiating Events

Initiating events, usually a breach in the coolant system integrity or a reactor transient, covered several possibilities that the AEC did not consider at that time. These potential problems included the possibility of reactor vessel failure and steam generator failures which had been treated by the AEC as events with negligibly small likelihoods due to the stringent quality requirements for the components. The use of event trees was a pivotal decision that made PSA a practical reality.

In connection with the aforementioned concerns over the ECCS performance, it may be noted here that these concerns from the LOFT experiments did not translate into full-scale power reactor safety systems due to scaling issues. Six specific LOCAs were analyzed in detail as initiating events that might occur in a PWR by the RSS:

- Large pipe breaks (larger than 6 in. diameter)
- Intermediate pipe breaks (2–6 in. diameter)
- Small pipe breaks (less than 2 in diameter)
- Large disruptive reactor vessel ruptures
- Gross steam generator ruptures
- Ruptures in systems that interface with the RCS

After a LOCA occurs, the ESF of a power plant are used to reduce or minimize the amount of radioactive material that reaches the environment. One key system of the ESF is the ECCS. Examples of ESFs include an airtight containment building and large tanks of water and pumps to ensure water flows into the reactor vessel in case of a leak. The goal of the event tree was to decompose any possible process, which could occur following an initiating event that results in the release of radiation, into a set of discrete failure events such that the probabilities of such events can be estimated. Fault trees were used to model the probability of the events included in the event tree. Therefore, each event tree traced the initiating event all the way through to the eventual failure of containment, and determined the probability of the containment failure.

Besides LOCAs, the RSS team investigated several types of reactor transients as possible initiating events for reactor system failure. In the study, a transient was defined as any significant deviation from the normal operating value of any of the key reactor operating parameters – including all non-LOCA situations that could lead to fuel heat imbalances.

2.2.5 Failure Data

By narrowing down the possible initiating events that could cause a radiation release, the event trees allowed the RSS team to reduce the particular fault trees that needed to be investigated. One problem with the method proved to be lack of data to estimate the probability of failure for many of the components involved – a fact noted both in the RSS itself, and in the various criticisms of it. The RSS used generic data derived primarily from similar basic components (pumps, valves, etc.) used by related industries or the military. Additional analyses into both common-cause failures addressing interdependencies within the systems, and human errors addressing external factors had to be performed.

Using fault trees, very complex systems could be broken down into constituent parts and failure probabilities could be assigned to each segment. The failure probabilities took into account the human and common-cause failures mentioned above. For the RSS, fault trees were developed for essentially all of the major individual systems included in the event trees.

2.2.6 Uncertainty Analysis

The accuracy of the study was undoubtedly the best when real-world data based on the same type of equipment used in the reactors was available. Often, other industrial data had to be used – with component failure rates and uncertainties increased, in some places substantially,

due to the unique operating environment of a nuclear reactor, especially during an accident, where exposure to high-temperature steam and radiation could cause component failure. In addition judgment from the experts in the field was used. To account for uncertainties due to limited data, failure probabilities of the events modeled were represented by lognormal distributions instead of point estimates. Because the typical probability of failure for the complete system was so small, even a factor of 100 alteration in the failure probability of most components would not produce much overall change in the system failure probabilities or consequently in the reactor safety calculations. Some system components carried more weights through the process and their associated uncertainties would produce a greater uncertainty for the entire system, but typically these systems had a much smaller uncertainty associated with their failure probabilities.

Most of the failure rates and probabilities used in the study had uncertainties on the order of a factor of 10–100; in some cases – for very low failure rates – the error factor was as much as 1,000. The study used a Monte Carlo method to calculate the overall uncertainty associated with estimated risks, assigning a lognormal distribution to the probability of failure of components and events.

2.2.7 Sensitivity Analysis

Within both the fault trees and event trees, there was no guarantee that all of the various modes leading to significant reactor failure were captured in the study, but it must be noted that the team had significant modeling experience as well as reactor operation and safety experience. All the systems associated with the primary and secondary core cooling loops and the safety systems were analyzed. The level of detail used in the fault tree could also be questioned, but the study used sensitivity tests to determine whether the fault trees had gone into more details than was needed, and determined that the level of detail was adequate.

2.2.8 Consequence Analysis

Following the attempts to model what would happen in the reactor during an accident, required the corresponding calculations of potential radiation releases from the reactor into the containment and ultimately into the environment. After the amount of radiation release was known, the consequences (expected human, economic, and environmental losses) could be estimated. The consequence section of the study was in some ways the most surprising. Before the RSS was released, the general feeling in the nuclear industry was that the consequences of a severe reactor accident would automatically be massive, but the RSS showed that most accidents that led to radiation release would only have small consequences.

The most important element of the consequence analysis was estimation of human exposures and subsequent fatalities and health effects due to any radiation released to the environment. Using the known meteorological and demographic data for each of the existing or planned 68 sites for nuclear reactors in 1974, the RSS was able to calculate the expected radiation pathways and the effects on the nearby residents. The goal was to estimate the most “realistic” radiation effects, by relying on best estimate values and avoiding, as much

as possible, any use of conservative assumptions. Doses from five potential exposure modes were used.

1. The external dose from the passing cloud (plume).
2. The dose from internally deposited radionuclides which are inhaled from the passing cloud.
3. The external dose from the radioactive material which is deposited on the ground.
4. The dose from internally deposited radionuclides which are inhaled after resuspension.
5. The dose from internally deposited radionuclides that are ingested after ground contamination.

Three kinds of effects of radiation were calculated from the total human population dose – early fatalities (within 1 year of exposure), early illnesses (people needing medical treatment), and long-term health effects (additional cancers occurring after a few years). The RSS investigated more than a thousand core-melt scenarios for the PWRs, which were sorted into 38 categories of sequences.

2.2.9 Release Categories

After running a computer code, specially developed to calculate the amount of various radioisotopes released (the CORRAL code) for each of the 38 sequences, the results were sorted into one of nine broad release categories. Similarly, for the BWR, the RSS created five broad release categories. A brief description of each broad category can be found below:

- PWR Category 1 - Steam explosion in the reactor vessel with failure of the containment.
- PWR Category 2 - Core melt with failure of the radioactive removal system.
- PWR Category 3 - Core melt with partial success of the radioactive removal system.
- PWR Category 4 - Core melt with the containment not fully isolated and failure of the radioactive removal system.
- PWR Category 5 - Core melt, similar to Category 4, with partial success of the radioactive removal system.
- PWR Category 6 - Core melt through reactor vessel with success of the radioactivity removal system.
- PWR Category 7 - Core melt through reactor vessel with failure of the radioactivity removal system failure.
- PWR Category 8 - Fuel failure with isolation failure of the containment.
- PWR Category 9 - Fuel failure with the containment integrity maintained.
- BWR Category 1 - Steam explosion in the reactor vessel with failure of the containment.
- BWR Category 2 - Core melt after containment rupture with no or little internal deposition.
- BWR Category 3 - Overpressure rupture of containment with significant deposition.
- BWR Category 4 - Containment isolation failure with no rupture.
- BWR Category 5 - Fuel failure with radioactive release through the stack.

Of significance was Category 7 for PWRs, which was largely an unknown scenario in the nuclear industry. Aside from the LOCA and transient initiating events, the RSS attempted to estimate the general magnitude of risk associated with earthquakes, floods, tornadoes, accidental aircraft impact (note the effect of a deliberate crash on a nuclear power plant was not addressed), and turbine missiles. Failure associated with each of the external events was small compared to the

overall calculated risk. During the preparation of the report, the Browns Ferry fire occurred in 1975, and was commented upon as requiring further study. The RSS also noted that straightforward measures to improve fire prevention and fire fighting capabilities could significantly reduce the risk of reactor failure from a fire.

2.2.10 Comparison with Other Risks

Possibly the most controversial part of the RSS was the comparison of risks from nuclear power plant failures to other more common or extremely remote risks encountered by the general public. Among the risks used to illustrate the issue were automobile accidents, hurricanes, tornadoes, earthquakes, meteorites, airplane crashes, explosions, dam failures, fires, and industrial accidents leading to hazardous chemical releases. For chemical releases, the RSS used a generic chlorine release on a major rail line in Ohio. The closest in risk to 100 operating nuclear power plants of any of the examples illustrated in the RSS was the risk of a large meteorite impact estimated to be about 1×10^{-4} (or a 1-in-10,000 chance) that ten people being killed and about 1×10^{-7} that 10,000 people being killed.

2.2.11 RSS Results

The RSS calculated the frequency of core melt for a PWR to be 6×10^{-5} per reactor year and for a BWR to be 3×10^{-5} per reactor year. The major change in the failure frequency for PWRs from early studies (usually about 1×10^{-6}) is that prior estimates tended to ignore or downplay the small LOCAs' contribution to core melt, whereas the RSS determined that small LOCAs had the highest contribution to the overall risk. The RSS determined that the two largest contributors to BWR frequency of core melt were the failure to rapidly shut down the reactor when needed and the failure of the decay heat removal system after transient-caused shutdowns. Previous calculations and estimates had also concentrated on worst-case scenarios when determining the consequence of reactor accidents. The RSS showed that the majority of core-melt accidents would produce modest consequences, with only very small portions of the core-melt scenarios causing catastrophic offsite damage as envisioned in WASH-740 (USAEC 1957).

The RSS found that the conditional probability of containment failing, given occurrence of an accident sequence that releases radiation into the containment atmosphere, was higher than originally believed, although often with much of the radioactive material being deposited inside the containment building before the containment failure. The RSS modeling effort succeeded in producing an accurate and far more realistic result, compared to the previous efforts, by using event and fault trees; looking at the interaction of a molten core with the containment system; investigating common-cause and human failures; understanding the safety significance of support and other "non-safety" systems and structures; and determining possible problems in operation, test, and maintenance.

2.2.12 APS Review

One panel of scientists, organized by the American Physical Society (APS), criticized much of the report; especially the fatality estimates that considered only fatalities from radiation

absorbed in the first 24 h after an accident. The APS considered radioactive cesium and strontium (both with half-lives near 30 years) to be major contributors to any radioactive exposure of the population.

Other reviewers within the APS group also criticized the treatment of the ECCS in the RSS. Other groups contributed extensive comments to the RSS team as well, although the technical sophistication of some of the groups was low (Lewis et al. 1975).

When the NRC was finally established in 1975 and took the ownership of the draft RSS report, it published the report in October of 1975 in final form. The one section of the report that was most commonly read was the Executive Summary, which had two sections – a section summarizing the results and another comparing the risk associated with nuclear reactor failures with risks from other man-made events and natural occurrences along with frequently asked questions.

Using a few diagrams, the RSS effectively communicated that the risk associated with the operation of 100 nuclear power plants is much lower than the risk associated with automobiles, airplane crashes, or hurricanes. Unfortunately for the report, the Executive Summary became a controversial issue later.

The APS review recommended staying away from point estimates, but instead recommended using bounds to account for uncertainties based as much as possible on actual operating data, which was admittedly lacking during the RSS calculations. Possibly the biggest problem that APS review had with the RSS was the way that the RSS identified and carried uncertainties through the calculations. The committee identified several areas where the RSS did not address uncertainties well, including the use of models, variations between reactors, propagation of errors where assumptions were used rather than experimental data or models, assignment of uncertainties to the assumptions, and how the overall uncertainties were calculated.

2.3 Post-RSS Review and the Three Mile Island Accident

Following the RSS reviews in September 1978, the NRC withdrew its support of the RSS results and disavowed the Executive Summary, but the Commission tried to get the NRC staff to use PSA techniques in general.

While the RSS had considered a similar sequence of events for a reactor other than the Three Mile Island (TMI) nuclear power reactor, and showed that this sequence was not among the risk-significant contributors for that reactor design, the TMI accident confirmed a major RSS insight that small LOCAs are more risk-significant than large LOCAs that the NRC used as a design basis accident for worst-case LOCAs in licensing reactors. Also, the RSS pointed out the potential role of human error, which later was found to be a highly significant factor in the TMI accident when operators turned off the ECCS (despite the fact that this particular error was not considered by the RSS). As a result, the NRC had a change of heart and made the decision in part because one of the accident sequences studied in the RSS – where the pressurizer relief valve failed to close – was very similar to what actually occurred at the TMI accident, when adjusted for the differences in the reactors. That particular sequence had not been identified as a potential problem before the RSS. Subsequently, the NRC placed much greater emphasis on operator training and “human factors” in plant performance, investigating severe accidents.

The TMI reviews suggested that future reactor safety research should be consistent with priorities determined by their relative risk contributions, and should look not only at LOCAs, but also at transients. Only the RSS provided much information about relative risk contributions of accident scenarios. The TMI underlined the need to be cognizant of the fact that operators were running the nuclear power plant, and that a “mindset” down-playing the role of humans in the safety process existed.

2.4 Post-TMI Accident and Revival of the Use of PSA

The NRC also initiated research on steam explosions under various conditions, possible interactions between a molten core and the underlying concrete, and study of the basic processes involved with release of radioactive materials from molten fuel.

During the period of 1979–1982, the NRC undertook two sets of follow-up PSA studies. The Reactor Safety Study Methodology Application Program (RSSMAP) to apply the RSS methodology to additional reactor designs and the Interim Reliability Evaluation Program (IREP) were a planned multi-plant reliability evaluation program to develop and standardize the reliability methodology involved in performing reliability and safety studies. The IREP conceived by the NRC in accordance with the action plan developed as a result of the TMI-2 accident (USNRC 1980a) was a pilot study with a scaled-up evaluation of an additional six plants. Recognizing the lack of any formal guiding documents to perform PSAs, an effort to develop such documents was proposed by the American Nuclear Society (ANS) and the Institute for Electrical and Electronics Engineers (IEEE) to the NRC and initiated in 1983. The subsequent efforts resulted in the publication of a monumental guidebook for the performance of PSA, i.e., NUREG/CR-2300 (USNRC 1983).

In the early 1980s, the NRC relied on PSA techniques in addressing a few of its unresolved safety issues involving beyond DBAs. The most notable were the Anticipated Transients Without Scram (ATWS) and Station Blackout rules. The so-called backfit rule, which attempted to remedy some of the safety concerns that surfaced following the TMI accident, was also addressed with the help of the PSA techniques.

In addition, the risk significance of incidents reported to the NRC by the plant owners in the so-called Licensee Event Reports (LERs) was analyzed using the PSA method under the Accident Sequence Precursor (ASP) program. In this study the conditional probability of core melt due to the occurrence of these incidents was estimated by viewing them as “precursors” to severe accidents. The early precursor studies received a lot of negative publicities because they predicted rather higher conditional probability of core melt than was anticipated. The controversy diminished as the methods for accounting for these precursor events improved in the subsequent studies.

Parallel to the NRC’s efforts related to PSAs, during the early- and mid-1980s, several plant owners completed PSAs of their own to facilitate technical upgrades or characterize risk to local populations. When the PSAs for Zion and Indian Point 2 and 3 were published in 1981 and 1982, they showed the risk associated with earthquakes and fires was not negligible, as was concluded in the RSS, but quite significant requiring further study. However, all the industry-supported studies confirmed the general insights of the RSS. Furthermore, the studies focused on more advanced methodologies to determine the uncertainties more systematically than the RSS’s approach. In the meantime, the nuclear industry continued to improve PSA techniques

(for example, in modeling common cause failures), and undertook additional PSAs in support of their licensing efforts (e.g., the Seabrook Station PSA effort in 1982–1983).

2.5 Safety Goals

Subsequent to the TMI accident and the Kemeny Commission's report (Kemeny et al. 1979), the ACRS of the US NRC started an extensive debate, public workshops, and meetings, which led to the release of the NRC's policy statement establishing qualitative safety goals and associated quantitative health objectives to be used for measuring the attainment of these goals (USNRC 1986). The policy statement published in 1986 was intended to come to grips with the integration of the quantitative assessment of risk into the regulatory system. During the deliberations by the ACRS, the RSS methodology was the clearest approach to measure the quantitative safety goals proposed. The primary issue for the NRC in developing safety goals was how to use the PSA techniques to help articulate a level of acceptable risk, in other words, to define "how safe is safe enough."

The policy statement proposed two safety goals and associated Quantitative Health Objectives (QHOs) to articulate levels of acceptable risk, which later served as the de facto guidelines for using PSA results in regulation. The goals provided indices for the level of "public protection which nuclear plant designers and operators should strive to achieve." The goals meant to provide additional guidance to the NRC staff for regulatory decision-making.

Two safety goals introduced by the NRC were stated in terms of public health risk – one addressing individual risk and the other addressing societal risk. The risk to an individual is based on the potential for death resulting directly from a reactor accident – that is, a prompt fatality. The societal risk is stated in terms of nuclear power plant operations as opposed to accidents alone, and addresses the long-term impact on those living near the plant. The goals were expressed in qualitative terms, perhaps, so that the philosophy could be understood. The NRC also expressed the qualitative goals for the safety of nuclear power plants in terms of individual and societal "quantitative health objectives." The quantitative goals indirectly impacted the NRC's regulations, as the goals provided indices as to the level of "public protection which nuclear plant designers and operators should strive to achieve." They were also meant to provide additional guidance to the NRC staff as part of their regulatory decision-making process. While the safety goals provided a metric to address the question of "how safe is safe enough," practical implementation of the NRC's guidance proved to be difficult because of the large uncertainties involved in the calculation of risk (Meserve 2001).

Therefore, the NRC observed that implementation of the safety goals using subsidiary objectives that achieve the same intent as the quantitative health objectives, but do not involve as much complexity, can be useful in making regulatory decisions (USNRC 2001). These subsidiary objectives anchor, or provide guidance, on an appropriate DID philosophy that balances accident prevention and mitigation. In this light, it is indicated that a core damage frequency (CDF) of less than 1 in 10,000 per year of reactor operation is a very useful subsidiary benchmark in making judgments about that portion of regulations that are directed to accident prevention. Similarly, a large early release frequency (LERF) of less than 1 in 100,000 years is a useful subsidiary benchmark to help ensure a proper balance between prevention and mitigation. These considerations later evolved into the "benchmark" values of 1×10^{-4} /year for CDF and 1×10^{-6} /year for large release frequency (LRF) (USNRC 2007d). In addition, the design is

required by the NRC to meet a containment performance goal, which includes: (1) a deterministic goal that containment integrity be maintained for approximately 24 h following the onset of core damage for the more likely severe accident challenges and (2) a probabilistic goal that the conditional containment failure probability (CCFP) be less than approximately 0.1 for the composite of all core damage sequences assessed in the PSA.

2.6 NUREG-1150 Studies

In 1986, the NRC started work on what would become NUREG-1150, “Severe Accident Risks: An Assessment for Five US Nuclear Power Plants,” (USNRC 1980b) which was essentially an update of the RSS, with 10 more years’ additional operating experience, PSA knowledge, and methods gained following the RSS release (USNRC 1980b).

NUREG-1150 was published in final form in December 1990, following a long and extensive review process, both internally within the NRC, and also by the ANS and the IAEA. This study was the most important step forward in using probabilistic techniques in safety assessments following the release of the RSS; several areas of safety, such as mechanisms of failure and potential large loads, were investigated.

NUREG-1150 showed that the risks of severe accidents were lower than those calculated in the RSS, primarily through the use of a larger database and more sophisticated models. Furthermore, the estimation of the lower risks in NUREG-1150 as compared to the RSS results from the implementation of hardware modifications and procedural improvements at some of the plants during the period of about 15 years since the RSS.

2.7 IPE and IPEEE

To make the risk technology and methods available to the industry, the NRC issued Generic Letter 88–20 (USNRC 1988), “Individual Plant Examination for Severe Accident Vulnerabilities,” in November 1988. This letter acknowledged that each nuclear power plant is unique and may have plant-specific vulnerabilities. The NRC required each plant owner:

1. To develop an appreciation of severe accident behavior.
2. To understand the most likely severe accident sequences that could occur at its plant.
3. To gain a better quantitative understanding of the overall probabilities of core damage and fission product releases.
4. If necessary, to reduce the overall frequency of core damage and fission product releases by modifying, where appropriate, hardware and procedures that would help prevent or mitigate severe accidents.

The individual plant examination (IPE) laid out the process for each plant owner to gain experience with PSA by using its own staff as much as possible to perform the examination. Furthermore, the Generic Letter gave several additional benefits for performing PSAs – support for licensing actions, license renewals, risk management, and integrated safety assessment.

In Generic Letter 88–20, the NRC discussed what a PSA was and how the industry could use it in the future. As a result of the Generic Letter, 74 PSAs with varying degrees of detail, representing 106 US nuclear power plants were completed by 1992. Each of the PSAs looked at the reactor core damage frequency and the large early release frequency, giving the utilities

appreciation for PSA methods and a method of tracking the improvements made on the reactors in terms of risk abatement and cost-effectiveness.

In June 1991 when the IPE program was near completion, the NRC issued Supplement 4 to Generic Letter 88-20 (USNRC 1991), “Individual Plant Examination of External Events (IPEEE) for Severe Accident Vulnerabilities.” This supplement was published to require the nuclear industry to look into potential vulnerabilities to severe accidents due to externally initiated events, including seismic events, internal fires, high winds, floods, and other events involving those related to transportation and nearby facilities. The NRC received 70 IPEEE submittals covering all operating US nuclear reactors.

Similar to the IPE program, many useful perspectives were obtained from the IPEEE program especially with respect to the plant-specific vulnerabilities and capabilities in connection with externally initiated events. Although these perspectives were primarily qualitative, quantitative results such as fire area CDFs were also produced from the program (USNRC 2002a).

2.8 NRC’S PRA Policy Statement

As a direct outcome of the nuclear industry’s knowledge of PSA methods, results and uses gained through their IPE studies, some industry leaders began to lobby the NRC commissioners and staff in 1992–1993 to base some of their regulatory and enforcement efforts on PSA results, tools, and techniques. In the mean time, a law called the “Government Performance and Results Act” (GPRA) was passed by the US Congress in 1993. One objective of that law is to “improve federal program effectiveness and public accountability by promoting a new focus on results, service quality, and customer satisfaction.”

In response to the GPRA, federal agencies, including the NRC, developed strategies and plans for achieving that objective. In its Strategic Plan, the NRC is committed to move toward risk-informed and performance-based regulation. As a result, when the NRC proposes a new regulation, the alternatives considered must include a performance-based alternative that enhances the focus on the effectiveness of the agency’s regulatory programs.

The “PRA Policy Statement” (USNRC 1995) formalized the Commission’s commitment to risk-informed regulation (RIR) through the expanded use of PSA, which included among others:

The use of PRA technology should be increased in all regulatory matters to the extent supported by the state of the art in PRA methods and data, and in a manner that complements the NRC’s deterministic approach and supports the NRC’s traditional DID philosophy.

The policy statement also encouraged:

- Use of sensitivity studies, uncertainty analyses, and importance measures associated with PSA.
- Realistic evaluations of PSA as practicable.
- Availability of data used in the PSA for public review.
- Appropriate consideration of uncertainties in making regulatory judgments especially in connection with the safety goals and subsidiary numerical objectives.

This policy statement affirmed the NRC’s belief that PSA methods can be used to derive useful insights, perspectives, and general conclusions as a result of an integrated and comprehensive

examination of the design of nuclear facilities, facility response to initiating events, and also the expected interactions among facility structures, systems, and components and between the facility and its operating staff.

2.9 EPRI's PSA Applications Guide

In the side of industry, the Electric Power Research Institute published “PSA Applications Guide” in 1995 to help the industry formalize decision-making processes using PSAs (EPRI 1995). The EPRI guide developed by a group of industry experts at the request of the Nuclear Energy Institute (NEI) provided a tool to the utilities to help focus resources more effectively on subjects of true safety significance. Thus the guide represented opportunities to utilities for enhancing safety in a cost-effective manner and provided the basis for modifying plant configurations, operation, or maintenance practices in order to reduce operation and maintenance (O&M) costs without compromising safety.

In the EPRI guide the PSA applications were grouped into two broad categories: evaluation of risk significance and risk-based prioritization or ranking. The first application category primarily based on the evaluation of risk significance includes:

- Technical specification improvements
- Backfit evaluations
- Plant change assessments
- In-service test and inspection improvements
- Design option studies
- Significant event evaluations
- Justifications for continued operation
- Evaluation of inspection findings
- Evaluation of equipment out-of-service
- Evaluation of nonroutine maintenance at power
- Generic issue evaluations

On the other hand, the second category where the decision making is mostly based on the risk-based prioritization or ranking includes:

- Prioritization of plant changes
- Prioritization of test requirements
- Identification of risk significant SSCs
- Risk-based inspection and testing guidance
- Maintenance prioritization
- Procedure/training improvement programs

The EPRI guide also provided quantitative criteria to be used along with the results of qualitative review for an integrated decision making. The quantitative criteria consisted of screening criteria for permanent changes in licensing basis (e.g., plant hardware or procedural modification) and criteria for overall risk significance determination. The screening criteria for permanent changes represented a kind of industry consensus until the risk acceptance criteria were developed by the NRC as part of Regulatory Guide 1.174 discussed below.

■ **Table 2**

Criteria for Risk Significance Determination (EPRI 1995)

Risk importance measure	Criteria
Risk Reduction Worth (RRW)	
System level	>1.05
Component level	>1.005
Fussell-Vesely Importance (FV)	
System level	>0.05
Component level	>0.005
Risk Achievement Worth (RAW) (Component/train level)	>2

➤ *Table 2* shows the criteria for risk significance determination recommended in the EPRI guide. The risk significance is measured in terms of importance measures consisting of Fussell-Vesely Importance (FV), Risk Achievement Worth (RAW), and Risk Reduction Worth (RRW) (Modarres 1993). The quantitative criteria in terms of these importance measures are still widely used for various PSA applications that require assessment of the degree of risk significance (i.e., importance) with respect to components, systems, or structures independent of any changes to the plant.

2.10 Guidelines for Risk-Informed Regulation

The move toward Risk Informed Regulation (RIR) was a significant transition at the NRC fueled by the premise that a reduction in unneeded expenditure of resources on matters that are not safety significant is required to make nuclear power safer. The industry welcomed RIR because it also observed that nuclear plants can be run more effectively and economically. The challenge, however, has been to accomplish this transition while maintaining the basic objectives of adequate protection of the health and safety of the public (Ahearn et al. 2001).

The key events that had a significant impact on utility decisions to make significant investments in their PSAs during this period were the issuance of Regulatory Guide 1.174 (USNRC 2002b) and associated application specific regulatory guides. Prior to these guides, industry attempts to present risk-based or risk-informed arguments to get relief from a regulation were very difficult to develop and for the NRC staff to review, due to lack of criteria for judging “how safe is safe enough,” and lack of standards for PSA quality (Fleming 2003). These factors yielded long and costly Requests for Additional Information (RAIs), RAI responses, and associated staff reviews and a high level of inconsistency in acceptance criteria. For the first time in these regulatory guides, the NRC provided clear criteria for the review of risk-informed changes to the licensing basis including quantitative risk acceptance guidelines discussed below.

The application specific regulatory guides initially published in 1988 include:

- RG 1.175 for in-service testing (USNRC 1998b)
- RG 1.176 for graded quality assurance (withdrawn in 2002)
- RG 1.177 for technical specifications (USNRC 1998c)
- RG 1.178 for in-service inspection of piping (USNRC 2003b)

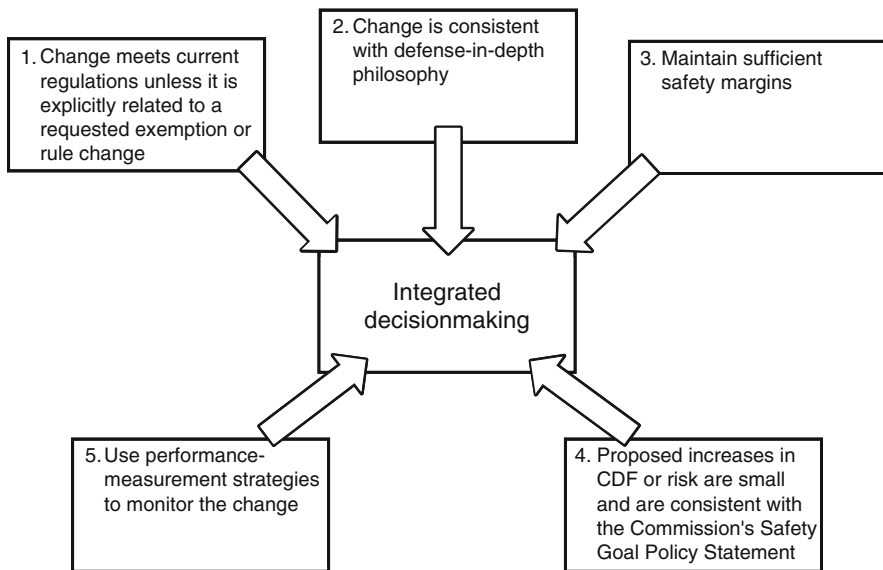
RG 1.174 (USNRC 2002b) is the basic guideline for risk-informed decision making, and as such, is supposed to be used along with the regulatory guide specifically tailored to a given application.

The request for risk-informed changes in licensing basis by a utility will be evaluated in accordance with the following principles of RG 1.174 (► Fig. 1):

1. The proposed change meets the current regulations.
2. The proposed change is consistent with the DID philosophy.
3. The proposed change maintains sufficient safety margins.
4. When proposed changes result in an increase in core damage frequency or risk, the increases should be small and consistent with the intent of the Commission's Safety Goal Policy Statement.
5. The impact of the proposed change should be monitored using performance measurement strategies.

Principle 1 requires that current regulations be met. Principles 2 and 3 represent deterministic evaluation of DID and safety margins. Principle 4 represents risk evaluation of the proposed changes where risk acceptance criteria defined in RG 1.174 are used in lieu of the safety goals. Principle 5 ensures that no adverse safety degradation occurs because of the changes to the licensing basis.

To facilitate the risk evaluation in connection with the fourth principle above, RG 1.174 provided risk-acceptance guidelines in terms of changes in the risk metrics of CDF and LERF

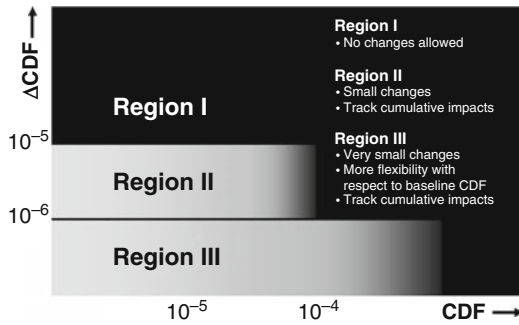


■ Figure 1

Principles of risk-informed integrated decision making for licensee-initiated request for risk-informed changes in licensing basis (USNRC 2002b)

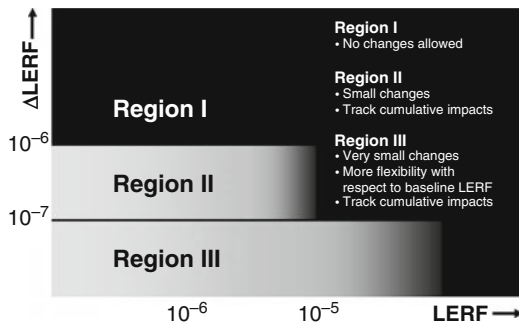
resulting from the proposed change in licensing basis as depicted in [▶ Figs. 2](#) and [▶ 3](#), respectively. PSA results are used in this decision-making process in two ways – to assess the overall baseline CDF/LERF of the plant and to assess the CDF/LERF impact of the proposed change.

It should be noted herein that risk insights will be used as one of the inputs for the integrated decision making process. Other inputs include the results of deterministic evaluation as to the maintenance of DID principle and sufficient safety margins. Furthermore, RG 1.174 requires the applicant to develop and implement a performance-monitoring



■ Figure 2

Acceptance guidelines for core damage frequency (CDF) (USNRC 2002b). The analysis will be subject to increased technical review as indicated by the darkness of the shading of the figure. In the context of the integrated decision making, the boundaries between the regions should not be interpreted as being definitive; the numerical values associated with defining the regions in the figure are to be interpreted as indicative values only



■ Figure 3

Acceptance guidelines for large early release frequency (LERF) (USNRC 2002b). The analysis will be subject to increased technical review as indicated by the darkness of the shading of the figure. In the context of the integrated decision making, the boundaries between the regions should not be interpreted as being definitive; the numerical values associated with defining the regions in the figure are to be interpreted as indicative values only

program to ensure that no adverse safety degradation occurs because of the changes to the licensing basis.

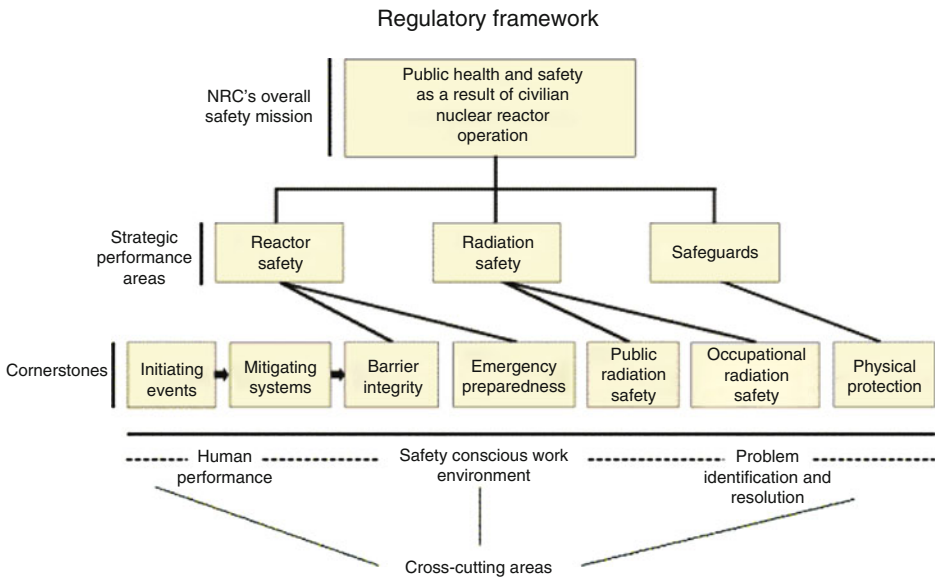
In addition, also notable is that possibly the greatest benefit that the NRC has found in the use of PSAs by utilities is that it has required the utilities to write down all the assumptions involved in reactor operation and safety systems. Prior to PSAs, many of the assumptions would never be explicitly stated in technical specifications (TS) or other design documents. By stating the assumptions explicitly, the utility could gain a better understanding of the function of the reactor and its safety systems.

2.11 Reactor Oversight Process

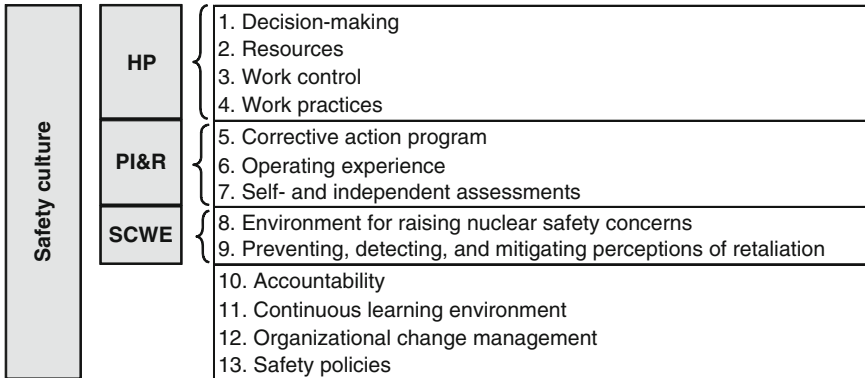
Continuous evaluation of the operational safety of nuclear power plants is the responsibility of both the nuclear industry and the regulatory authority. In the USA, the regulatory process of overseeing the safety performance of operating plants is called Reactor Oversight Process (ROP). The ROP revamped its inspection, assessment, and enforcement programs for nuclear power plants, and the new process was implemented in April 2000.

➤ *Figure 4* shows the US regulatory framework to provide a basis from which to develop the new ROP. The regulatory framework for reactor oversight consists of three key strategic performance areas:

- Reactor safety
- Radiation safety
- Safeguards



■ **Figure 4**
NRC regulatory framework for reactor oversight (USNRC 2006)



■ Figure 5

Safety culture and crosscutting issues defined in connection with the NRC regulatory framework (Kim 2008). The three crosscutting issues (i.e., human performance, problem identification and resolution, and safety conscious work environment) are included as part of the safety culture

Within each strategic performance area are cornerstones that reflect the essential safety aspects of facility operation. These seven cornerstones of safety include:

1. Initiating events
2. Mitigating systems
3. Barrier integrity
4. Emergency preparedness
5. Public radiation safety
6. Occupational radiation safety
7. Physical protection

Satisfactory licensee performance in the cornerstones provides reasonable assurance of safe facility operation and that the NRC's safety mission is being accomplished. Each cornerstone contains inspection procedures and Performance Indicators (PIs) to ensure that their objectives are being met. The safety significance of inspection findings is evaluated by Significance Determination Process (SDP) consisting of three phases, and the performance indicator data are evaluated and integrated with the SDP results to perform an integrated risk-informed assessment of plant performance.

Also notable in the regulatory framework of the NRC are the following three crosscutting areas or issues that have been identified as “cross-cutting” and potentially impacting more than one safety cornerstone (► Fig. 5):

- Human Performance (HP)
- Safety-Conscious Work Environment (SCWE)
- Problem Identification and Resolution (P&IR) programs

Satisfactory licensee performance in the seven cornerstones of safety defined in the three key strategic performance areas provides reasonable assurance of safe facility operation such that

the NRC's safety mission is being accomplished. Also notable in the framework are the three cross-cutting areas or issues that can potentially impact more than one safety cornerstone. All these cross-cutting areas are considered as constituting "safety culture" since this term is interpreted as having very wide connotations.

These aspects of licensee performance, although not identified as specific cornerstones, generally manifest themselves as the root cause of performance problems, and therefore, are very important to meeting the NRC's safety mission. The plant performance in these cross-cutting areas is assessed either explicitly in each cornerstone area or inferred through cornerstone performance results from both PIs and inspection results.

The term "safety culture," initially coined by the International Nuclear Safety Advisory Group (INSAG) of the IAEA in INSAG-4 (IAEA 1991), used to be interpreted as having the same meaning as the SCWS. However, after a further deliberation among experts in this area, it is now used in a very wide sense as encompassing all the three cross-cutting issues and beyond. As shown in ► Fig. 5, safety culture has been characterized by the NRC as consisting of not only the nine components associated with the three cross-cutting issues, but other four components as well (USNRC 2007f).

On the other hand, note that safety culture was initially defined by INSAG-4 (IAEA 1991) as follows:

Safety culture is that assembly of characteristics and attitudes in organizations and individuals which establishes that, as an overriding priority, nuclear plant safety issues receive the attention warranted by their significance.

With this definition, safety culture is regarded by the IAEA as comprising two general components. The first is the necessary framework within an organization and is the responsibility of the management hierarchy. The second is the attitude of staff at all levels in responding to and benefiting from the framework. Therefore, we can understand that the concept of safety culture has been further expanded by the NRC as compared to the original definition by the IAEA.

2.12 Maintenance Rule

In the 1980s, the NRC became concerned about the number of transients and scrams initiated as a result of problems with balance of plant systems and components. Since most of this equipment was not addressed under existing regulations, a maintenance rule (MR) was necessary. In particular, as a result of the maintenance team inspections, the NRC decided that the need for such a rule existed (USNRC 1997a). This decision rested primarily on the conclusion that proper maintenance is essential to plant safety, and that there is a clear link between effective maintenance and safety as it relates to such factors as the number of transients and challenges to safety systems and the associated need for operability, availability, and reliability of safety equipment. In addition, good maintenance is also important in providing assurance that failures of SSCs that could initiate a plant transient are minimized. On the basis of these conclusions, a risk-informed, performance-based MR was developed addressing both safety-related and certain non-safety-related SSCs.

The MR, US 10 CFR 50.65, "Requirements for monitoring the effectiveness of maintenance at nuclear power plants," was issued in July 1991 and became effective in July 1996 following a

pilot program at nine voluntary sites to verify and validate the MR inspection procedure. The text of the rule is brief, containing the basic requirements for the activities that licensees need to accomplish to monitor maintenance effectiveness. Implementation guidance was developed by the Nuclear Management and Resources Council (NUMARC), now the Nuclear Energy Institute (NEI) (NUMARC 1993). The NRC endorsed this guideline with clarifications in Regulatory Guide 1.160 (USNRC 1997b).

The purpose of the MR is to have the utilities continuously monitor the effectiveness of maintenance to ensure:

1. Safety-related and certain non-safety-related SSCs are capable of performing their intended functions.
2. For non-safety-related equipment, failures will not occur that prevent the fulfillment of safety-related functions, and failures resulting in scrams and unnecessary actuations of safety-related systems are minimized.

In light of this purpose of the MR, it is worth noting that the TMI accident was actually initiated by a scram caused by failure in the non-safety-related secondary system. More specifically, the accident investigation team identified the following maintenance problems in the non-safety-related system (Kemeny et al. 1979; Rogovin and Frampton 1980).

- The condensate polisher effluent valves closed at the beginning of the accident on March 28, 1979. These valves had closed unexpectedly twice before under similar surveillance procedures, and again later under a related condition. The postaccident investigation indicated that valve closure was triggered by water accumulating in the control air line.
- The polisher bypass valve, if appropriately designed, could provide substantial operational margin. However, it failed to open by remote control during the accident, as it had at least once before; corrective action had not been accomplished.
- In spite of the chronic problem with resin removal from a polisher and the previous failure of opening the polisher bypass valve, a serious safety problem associated with the persistent trial of removing clogged resin from the condensate polishing system was not identified by the plant personnel.
- The maintenance work package for the condensate polishing system did not properly address the contingency measure for water intrusion into the instrument air system.
- The condensate polisher, although vital to the operation of the plant, did not receive appropriate attention in design and from assurance function, engineering, management, and management review groups.

Therefore, one can understand how vital it is to perform maintenance adequately even for non-safety-related systems. A recent study (Reason and Hobbs 2003) also pointed out that maintenance errors have been among the principal causes of several major accidents in a wide range of technologies, including the Apollo 13 oxygen tank blow-out in 1970 and the crash of a Japan Air Lines B747 into the side of Mount Osutaka in 1985 as well as the TMI accident in 1979.

The initial MR was modified in July 1999 to establish requirements for the assessment and management of risk associated with maintenance activities during both power operation and shutdown; the revised rule was implemented in November 2000. The intent of this requirement is to have the configuration risk resulting from loss of function associated with unavailable equipment be appropriately controlled from a risk management perspective.

The implementation of this configuration risk management has led to day-to-day use of plant PSA model. As a result, more emphasis is now placed on requiring the PSA model to represent the as-built, as-operated plant (at least to the extent needed to support the application) (USNRC 2007e). The configuration risk management also has something to do with the requirements of technical specifications, especially limited conditions for operation, as will be discussed later. Finally, note that the implementation of the risk-informed and performance-based MR led the US nuclear industry to make considerable improvement in the plant performance as evidenced by the reduction in the number of reactor scrams and the enhanced plant availability factor, among others.

2.13 Risk-Informed Improvement to Technical Specifications

Technical Specifications (TSs) for a nuclear power plant define limits and conditions to assure that the plant is operated in a manner that is consistent with the analyses and evaluations in the plant's Safety Analysis Report. The TSs typically comprise the following major sections: (1) safety limits, (2) limiting conditions for operation (LCOs), which include allowed outage times (AOTs) for required actions, and surveillance requirements (SRs), (3) design features, and (4) administrative controls.

As the discipline of probabilistic safety assessment matures, and the computerized PSA models, such as event trees and fault trees, become available for many nuclear plants, the PSA has been increasingly used worldwide as a tool to evaluate the risk impact associated with the TS. The recent trend to move towards RIR also encourages the use of PSA. The risk evaluation of TS requirements is primarily aimed at relaxing the unnecessarily too restrictive requirements and thereby optimizing the TS requirements. Along this line, it should also be noted that some TS requirements (e.g., surveillance tests) may have adverse impact on safety, because of their potential undesirable effects, such as occurrence of test-caused reactor trips or equipment wearout resulting from too frequent tests (Kim et al. 1994; Kim 1996). In light of the recognition of such weaknesses with the traditional TS requirements, and through the results summarized in NUREG/CR-6141 (Samanta et al. 1994), RG 1.177 (USNRC 1998c) was developed to provide guidance for a risk-informed approach to licensee-initiated TS changes.

In July 1993, the NRC issued a final policy statement on TS improvements which specifically addressed the usefulness of PSA information in strengthening the technical basis of TSs (USNRC 1993). The industry and the NRC have been since pursuing increased use of PSA in developing improvements to technical specifications. At the same time great efforts were made to facilitate the license amendment process through the Technical Specification Task Force (TSTF) Travelers, the Consolidated Line Item Improvements Process (CLIIP), and the model Safety Evaluation Report (SER) (USNRC 2000b).

On behalf of the US nuclear industry the NEI is also actively pursuing Risk-Informed Technical Specifications (RITS) initiatives for fundamental improvement to the Standard Technical Specifications (STS). Some RITS initiatives represent considerable changes to the critical elements of TS requirements, i.e., AOTs and SRs. For example, the AOT for failure of a diesel generator is allowed to be temporarily extended from 7 days up 30 days, provided the configuration risk is properly managed. On the other hand, the utilities are allowed to change STIs without going through the burdensome license amendment process, if they follow the NEI guidelines already approved by the NRC (NEI 2006; NEI 2007). These initiatives have been actually implemented in several nuclear power plants of the USA.

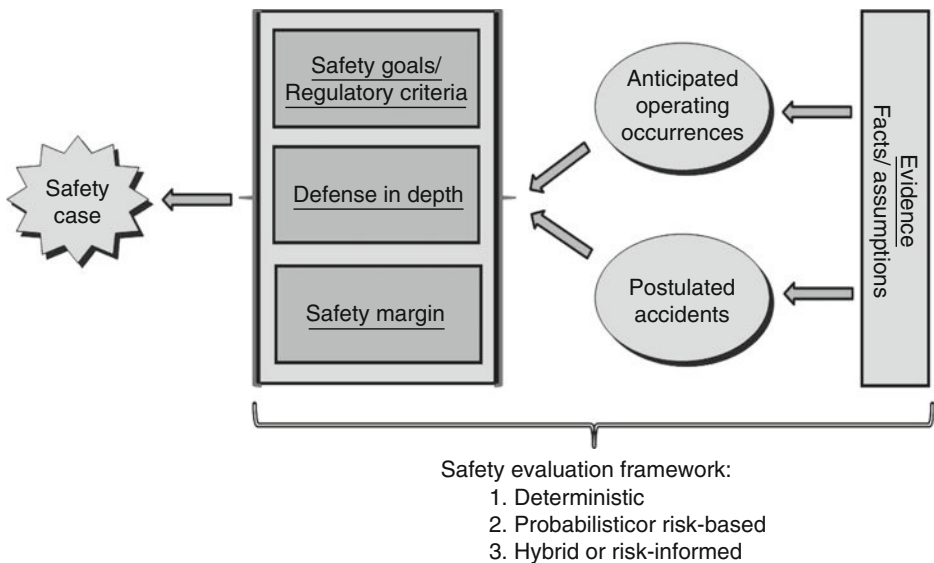
2.14 Risk-Informed Licensing Structure for Design Safety

As there is an increasing interest in constructing or developing new nuclear power plants including advanced LWRs and non-LWRs, such as Very High Temperature Reactor (VHTR) or Sodium-Cooled Fast Reactor (SFR), sometimes called Generation-IV reactors, a question arises regarding how to ensure the design safety of these new plants. Before addressing this question, let us first look back to clearly understand what kind of method has been used thus far to ensure design safety of operating nuclear plants.

➤ *Figure 6* shows a general safety evaluation framework that has been applied in order to assure design safety of operating nuclear reactors, in other words to implement a safety case for the plants. A safety case is a documented body of evidence that provides a convincing and valid argument that the plant is safe. Such safety cases for nuclear power plants are typically included in ➤ Chap. 15 of Safety Analysis Reports (SARs). The basic concept of this high-level framework for design safety could be also applied to advanced nuclear plants like Generation-IV reactors.

A safety case is made through design basis analyses documented in SARs. The basic principle applied is that the plant should be designed such that the most frequent occurrences yield little or no adverse consequence to the public, and the improbable extreme situations, having the potential for the greatest adverse consequence to the public, shall have a low probability of occurrence.

In order to make a safety case, the applicants for design certification should first select a set of design basis events (DBEs) including AOOs and postulated accidents. Then, they have to show that even if such events occur at the plant, all the safety requirements imposed by the




■ **Figure 6**

General safety evaluation framework for a nuclear power plant (Ahn et al. 2010; Kim et al. 2010)

industry consensus standards (e.g., ANSI N18.2–1973 Standard (ANS 1973)) or the regulatory body (such as safety goals, regulatory criteria, DID, or safety margins) would be satisfied with sufficient margins.

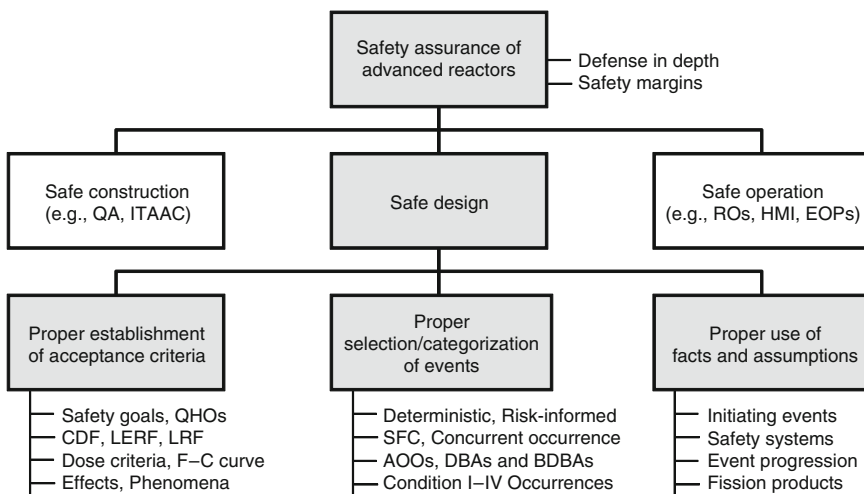
The safety of reactor designs has been typically evaluated within a deterministic framework; for example, selection of DBAs based on deterministic arguments or engineering judgments with subsequent deterministic analysis of their effects on the plant and the public. However, due to lack of specific quantitative requirements the safety-related decisions oftentimes had to be made without clear ramifications or basis.

The probabilistic or risk-informed approach can overcome the weaknesses of the deterministic approach. However, it is generally viewed that making a decision based only on probabilistic analyses is not desirable especially due to significant uncertainties associated with such analyses. Therefore, there is a worldwide interest in developing a risk-informed licensing structure to ensure design safety of new nuclear power plants.

A simplified logic tree is presented in  Fig. 7, which was developed to identify the attributes needed to ensure safety of advanced reactors. The top goal of “Safety Assurance of Advanced Reactors” can be satisfied if the three goals, i.e., “safe design,” “safe construction,” and “safe operation” are met.

For “Safe construction,” quality assurance program and programs such as Inspections, Tests, Analyses, And Acceptance Criteria (ITAAC) should be properly established. For “Safe Operation,” the plant should have competent reactor operators (ROs), appropriate human-machine interface (HMI), and emergency operating procedures (EOPs), and so on.

To assure safety of advanced reactors, they should be safely designed, constructed, and operated. Safe design can be ensured by making a safety case such that: (1) design basis events are properly selected and categorized so that a wide spectrum of events can be analyzed in details; (2) facts applicable to the reactors and design basis assumptions are properly made for event evaluation; and (3) acceptance criteria for the final decision making, deterministic and/or risk-based, are properly established.



 **Figure 7**

Logic tree for safety assurance of advanced reactors (Ahn et al. 2010; Kim et al. 2010)

Finally, the sub-goal of “Safe design” is directly related to the design safety, the focus of the present discussion. For this, the following three sub-goals should be satisfied:

1. **Proper Selection and Categorization of Events:** As indicated earlier in connection with the general safety evaluation framework, one has to select an appropriate set of events that will be used to make the safety case. Either deterministic or risk-informed methods may be used for event selection and categorization. SFC and concurrent occurrence of loss of offsite power may be applied in developing Design Basis Events (DBEs). Examples of typical event categories include: (1) AOOs, DBAs, and BDBAs; and (2) Condition I to IV occurrences.
2. **Proper Establishment of Acceptance Criteria:** Once the impacts or consequences of the selected events on the plant and the public are analyzed using deterministic or risk-informed methods, the analysis results should be compared to a certain set of acceptance criteria. The acceptance criteria may include: (1) safety goals, Quantitative Health Objectives (QHOs), surrogate objectives in terms of Core Damage Frequency (CDF), LERF, LRF, or Conditional Containment Failure Probability (CCFP); (2) dose criteria or frequency-consequence (F–C) curve; or (3) criteria on the effects of events on key plant parameters, or criteria on the special plant phenomena such as hydrogen generation or pressurized thermal shock, etc.
3. **Proper Use of Facts and Assumptions:** As mentioned earlier, facts and assumptions will be used as evidence in making the safety case. Based on the facts applicable to the plant, the expected frequencies of initiating events and the unavailabilities of safety systems for specific situations should be analyzed together with the expected progression of the assumed events in the plant, and the expected production and behavior of the fission products once a serious accident occurs. In this regard, one can note the usefulness of PSA technique that provides a systematic procedure for detailed event sequence identification and quantification. In addition, the safety classification of SSCs also should be performed under this sub-goal as part of the assumptions.

► *Figure 7* also points out that the basic principles of DID and safety margins will continue to play a very important role in assuring design safety even for advanced nuclear plants such as Generation-IV reactors, whatever methodology is applied for safety analysis.

3 Probabilistic Safety Assessment

Probabilistic Safety Assessment (PSA) (in the US regulatory applications it is mainly referred to as Probabilistic Risk Assessment (PRA)) is a systematic procedure for investigating safety of complex systems including nuclear power plants. It is used as part of design, construction and operation. The PSAs model how human, software, and hardware elements of the plant interact with each other, assess the most significant contributors to the plant safety, and also estimates the degree or probability of loss. A formal definition proposed by Kaplan and Garrick (Kaplan and Garrick 1981) provides a simple and useful description of the elements of PSA based on risk assessment that involves addressing three basic questions:

- What can go wrong that could lead to exposure of hazards?
- How likely is this to happen?
- If it happens, what consequences are expected?

The PSA procedure involves quantitative application of the above triplets in which probabilities (or frequencies) of scenarios of events leading to exposure of hazards (such as radioactive materials from the core of the reactor) are estimated, and the corresponding magnitude of health, safety, environmental, and economic consequences for each scenario are predicted. The risk value (i.e., expected loss) of each scenario is often measured as the product of the scenario frequency and its consequences. The main result of the PSA is not the actual value of the risk computed (the so-called bottom-line number); rather it is the determination of the plant elements that substantially contribute to the risks of the nuclear plant, uncertainties associated with such estimates, and effectiveness of various risk reduction strategies available. That is, the primary value of a PSA is to highlight the plant's design and operational deficiencies and optimize resources that can be invested on improving the design and operation of the plant.

In the remainder of this section, some strengths of PSA will be presented first, and subsequently major elements of PSA will be discussed with an example PSA for a simple fire protection system.

3.1 Strength of PSA

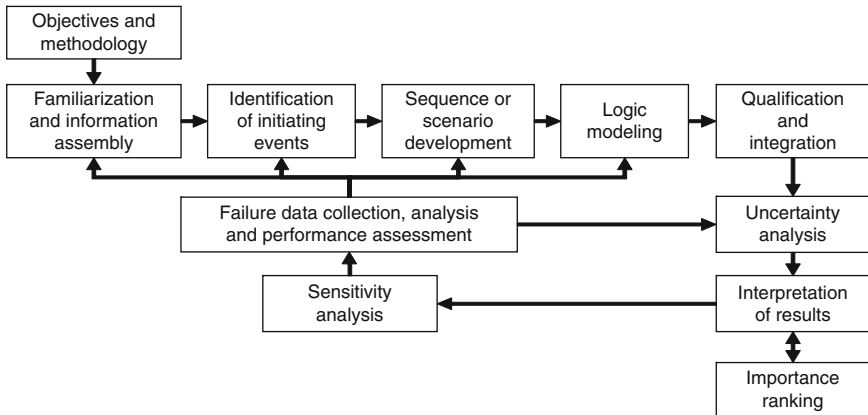
As the formal engineering approach to safety assessment, a PSA:

1. Provides an integrated and systematic examination of a broad set of design and operational features of the nuclear power plant.
2. Incorporates the influence of plant interactions and human-system interfaces.
3. Provides a model for incorporating operating experience with the nuclear power plant and updating risk estimates.
4. Provides a process for the explicit consideration of uncertainties.
5. Permits the analysis of competing risks (e.g., of one design vs. another or of possible modifications to a plant).
6. Permits the analysis of issues associated with assumptions or data via sensitivity studies.
7. Provides a measure of the absolute or relative importance of plant's systems and components to the calculated risk value.
8. Provides a quantitative measure of overall level of health and safety for the nuclear plant.

Major errors may result from weak or absent models, or associated data of potentially important factors in the risk of the plant, including cases where: (1) initiating events with very low frequencies of occurrence, human performance models and interactions with the system are highly uncertain, and (2) common cause failures resulting from an extreme operating environment are difficult to identify and model.

3.2 Steps in Conducting a Probabilistic Safety Assessment

The following subsections provide a discussion of essential components of PSA as well as the steps that must be performed in a PSA analysis (see [▶ Fig. 8](#)). The NASA PSA Procedures Guide (NASA 2002) also describes the components of the PSA. Each component of a PSA shown in [▶ Fig. 8](#) is discussed below.



■ Figure 8

Components of the overall probabilistic safety assessment (PSA) process (Source: based on NASA 2002)

3.2.1 Objectives and Methodology

Preparing for a PSA begins with a review of the objectives of the analysis. Among many objectives that are possible the most common ones include design improvement, risk acceptability, decision support, regulatory oversight support, and operations and life management. An example of a set of PSA objectives may be as follows:

1. Meet a surrogate goal of less than 1×10^{-4} /year (1×10^{-5} /year based on IAEA) for core damage frequency (CDF) and a surrogate goal of less than 1×10^{-6} /year for large (radioactive) release frequency (LRF).
2. Show that containment integrity is maintained for 24 h following the onset of core damage.
3. Prove that the conditional containment frequency is 0.1 or less for the aggregate of all dominant core damage sequences.
4. Identify potential design improvement for safety-significant scenarios.
5. Determine effectiveness of various human error prevention techniques.
6. Demonstrate feasibility of defenses against common cause failures.
7. Confirm defenses against human errors.
8. Determine needed safety margins to address uncertainty.
9. Demonstrate conformance with single failure criteria.
10. List the components with the highest contribution to plant risk and safety.

Once the objectives are clarified an inventory of possible techniques for the desired analyses should be developed. The available techniques range from required computer codes to system experts and analytical experts. This, in essence, provides a road map for the analysis. The resources required for each analytical method should be evaluated, and the most effective option selected. The basis for the selection should be documented, and the selection process reviewed to ensure that the objectives of the analysis will be adequately met. See Modarres (1993) and Kumamoto and Henley (1996) for the inventory of methodological approaches to PSA.

3.2.2 Familiarization and Information Assembly

A general knowledge of the physical layout of the overall nuclear power plant, administrative controls, maintenance and test procedures, as well as barriers and subsystems, whose job is to protect, prevent, or mitigate radioactive exposure, is necessary to begin the PSA. All subsystems, structures, locations, and activities expected to play a role in the initiation, propagation, or mitigation of a hazard exposure condition must be understood in sufficient details to construct the models necessary to capture all possible scenarios. A detailed inspection of the nuclear power plant must be performed in the areas expected to be of interest and importance to the analysis. The following items should be performed in this step:

1. Major critical barriers, structures, emergency safety systems, and human interventions should be identified.
2. Physical interactions among all major subsystems (or parts of the system) should be identified and explicitly described. The result should be summarized in a dependency matrix.
3. Past major failures and abnormal events that have been observed in the plant should be noted and studied. Such information would help ensure inclusion of important applicable scenarios.
4. Consistent documentation is critical to ensure the quality of the PSA. Therefore, a good filing system must be created at the outset, and maintained throughout the study.

With the help of the designers, operators, and owners, the analysts should determine the ground rules for the analysis, the scope of the analysis, and the configuration and phases of the operation of the nuclear plant or facility to be analyzed. One should also determine the faults and conditions to be included or excluded; the operating modes of concern and the hardware configuration on the design freeze date (i.e., the date after which no additional changes in the plant, system design and configuration will be modeled). Therefore, the results of the PSA are only applicable to the plant at the freeze date.

3.2.3 Identification of Initiating Events

This task involves identifying those events (abnormal events or conditions) that could, if not correctly and timely responded to, result in hazard exposure. In a full-power plant PSA, the initiating events are typically defined as those events causing a reactor trip, automatic or manual (if the nature of the initiating event is such that it will introduce negative reactivity that stops the chain reaction in the core). The first step involves identifying sources of hazard (mostly radioactive materials) and barriers around these hazards (cladding, reactor vessel, containment as well as safety systems). The next step involves identifying events that can lead to a direct threat to the integrity of the barriers.

A nuclear power plant may operate either at power (full power or low power), or in a shutdown mode of operation (hot standby, hot shutdown, cold shutdown, or refueling). In each operational mode, specific functions are performed. Each function is directly realized by one or more safety systems by making certain actions and behaviors. These systems, in turn, are composed of more basic units (e.g., subsystems, components, hardware) that accomplish the objective of the system. As long as a system is operating within its design parameter tolerances, there is little chance of challenging the system boundaries in such a way that hazards will escape those boundaries. These operational modes are called normal operation modes.

During a normal operation mode, loss of certain functions or systems will cause the process to enter an off-normal (transient) state transition. Once in this transition, there are two possibilities. First, the state of the plant could be such that no other function is required to maintain the process in a safe condition (the term “safe” refers to a mode where the chance of core damage or radioactive release beyond the plant boundaries is negligible.) The second possibility is a state wherein other functions (and thus systems) are required to prevent exposing hazards beyond the plant boundaries. For this second possibility, the loss of the function or the system is considered an initiating event. Since such an event is related to the normally operating equipment, it is called an operational initiating event.

Operational initiating events can also apply to various modes of the plant. The terminology remains the same since, for each mode, certain equipment, people or software must be functioning. For example, an operational initiating event found during the PSA of a test nuclear reactor was Low Primary Coolant System Flow. Flow is required to transfer heat produced in the reactor to heat exchanges and ultimately to the cooling towers and the outside environment. If this coolant flow function is reduced to the point where an insufficient amount of heat is transferred, core damage could result (thus the possibility of exposing radioactive materials – the main source of hazard in this case). Therefore, another system must operate to remove the heat produced by the reactor (i.e., a protective barrier). By definition, then, Low Primary Coolant System Flow is an operational initiating event.

One method for determining the operational initiating events begins with first drawing a functional block diagram of the plant. From the functional block diagram, a hierarchical relationship is produced, with the process objective being successful completion of the desired system. Each function can then be decomposed into its subsystems and components, and can be combined in a logical manner to represent operations needed for the success of that function.

Potential initiating events are events that result in failures of particular functions, subsystems, or components, the occurrence of which causes core damage or large radioactive release into the environment. These potential initiating events are “grouped” such that members of a group require similar subsystem responses to cope with the initiating event. These groupings are the operational initiator categories.

An alternative to the use of functional hierarchy for identifying initiating events is the use of Failure Modes and Effects Analysis (FMEA) (Stamatis 2003). The difference between these two methods is noticeable; namely, the functional hierarchies are deductively and systematically constructed, whereas FMEA is an inductive and experiential technique. The use of FMEA for identifying initiating events consists of identifying failure events (modes of failures of equipment, software and human) whose effect is a threat to the integrity and availability of the hazard barriers of the system. In both of the above methods, one can always supplement the set of initiating events with generic initiating events (if known). For example, see Sattison et al. (1990) for these initiating events for nuclear reactors, and NASA PSA Procedures Guide (NASA 2002) for space vehicles.

To simplify the process, after identifying all initiating events, it is necessary to combine those initiating events that pose the same threat to barriers and require the same mitigating functions of the process to prevent hazard exposure. The following inductive procedures should be followed when grouping initiating events:

1. Combine the initiating events that directly break all barriers.
2. Combine the initiating events that break the same hazard barriers (not necessarily all).

3. Combine the initiating events that require the same group of mitigating human or automatic actions following their occurrence.
4. Combine the initiating events that simultaneously disable the normal operation as well as some of the available mitigating human, software, or automatic actions.

Events that cause transients and require other systems to operate so as to maintain hazards within their desired boundaries, but are not directly related to a hazard mitigation, protection or prevention function, are nonoperational initiating events. These nonoperational initiating events are identified with the same methods used to identify operational events. One class of such events of interest is those that are primarily external to the plant or facility. These so-called “external events” will be discussed later in more details. The following procedures should be followed in this step of the PSA:

1. Select a method for identifying specific operational and nonoperational initiating events. Two representative methods are functional hierarchy and FMEA. If a generic list of initiating events is available, it can be used as a supplement.
2. Using the method selected, identify a set of initiating events.
3. Group the initiating events having the same effect on the system; for example, those requiring the same mitigating functions to prevent hazard exposure are grouped together.

3.2.4 Sequence or Scenario Development

The goal of scenario development is to derive a complete set of scenarios that encompasses all of the potential exposure propagation paths that can lead to loss of containment or confinement of the radioactive source term (hazard), following the occurrence of an initiating event. To describe the cause and effect relationship between initiating events and their subsequent event progression, it is necessary to identify those functions (e.g., safety functions) that must be maintained to prevent loss of barriers. The scenarios that describe the functional response of the process to the initiating events are frequently displayed by event trees.

Event trees order and depict (in an approximately chronological manner) the success or failure of key mitigating actions (e.g., human actions or mitigative hardware actions) that are required to act in response to an initiating event. In PSA, two types of event trees can be developed: functional and systemic. The functional event tree uses mitigating functions as its heading. The main purpose of the functional tree is to better understand the potential scenarios of events at an abstract level, following the occurrence of an initiating event. The functional tree also guides the PSA analyst in the development of a more detailed systemic event tree. The systemic event tree reflects the scenarios of specific events (specific human actions, protective or mitigative subsystem operations or failures) that lead to a hazard exposure. That is, the functional event tree can be further decomposed to show failure of specific hardware, software or human actions that perform the functions described in the functional event tree. Therefore, a systemic event tree fully delineates the plant or nuclear facility response to an initiating event and serves as the main tool for further analyses in the PSA. For detailed discussion on specific tools and techniques used for this purpose, see (Modarres 2006).

There are two kinds of external events. First kind refers to events that originate from within the plant or nuclear facility (but outside of the physical boundary of the plant or nuclear facility), which are called internal events external to the process of the system. Events that adversely

affect the plant or overall system and occur external to its physical boundaries, but can still be considered as part of the system, are defined as internal events external to the system. Typical internal events external to the system are internal conditions such as fires from cables and other flammable items within a plant, or floods occurred due to rupture of pipes and tanks, which are part of the plant. The effects of these events should be modeled with event trees to show all possible scenarios.

The second kind of external events are those that originate outside of the plant or facility, and are called external events. Examples of external events are fires and floods that originate from outside of the system. Examples include seismic events, extreme heat, extreme drought, transportation events, volcanic events, high-wind events, terrorism, and sabotage. Again, this classification can be used in developing and grouping the event tree scenarios.

The following procedures should be followed in this step of the PSA:

1. Identify the mitigating functions for each initiating event (or group of events).
2. Identify the corresponding human actions, systems or hardware operations associated with each function, along with their necessary conditions for success.
3. Develop a functional event tree for each initiating event (or group of events).
4. Develop a systemic event tree for each initiating event, delineating the success conditions, initiating event progression phenomena, and end effect of each scenario.

3.2.5 Logic Modeling

Event trees commonly involve branch points at which a given subsystem (or event) either works (or happens) or does not work (or does not happen). Sometimes, failure of these subsystems (or events) is rare and there may not be an adequate record of observed failure events to provide a historical basis for estimating frequency of their failure. In such cases, other logic-based analysis methods such as fault trees or master logic diagrams (MLDs) may be used, depending on the accuracy desired. The most common method used in PSA to calculate the probability of subsystem failure is fault tree analysis. This analysis involves developing a logic model in which the subsystem is broken down into its basic components or segments for which adequate data exist. For more details about how a fault tree can be developed to represent the event headings of an event tree, see Modarres et al. (1999).

Different event tree modeling approaches imply variations in the complexity of the logic models that may be required. If only main functions or systems are included as event-tree headings, the fault trees become more complex and must accommodate all dependencies among the main and support functions (or subsystems) within the fault tree. If support functions (or systems) are explicitly included as event tree headings, more complex event trees and less complex fault trees will result. For more discussions on methods and techniques used for logic modeling see Modarres (2006).

The following procedures should be followed as a part of developing the fault tree:

1. Develop a fault tree for each event in the event tree heading for which actual historical failure data does not exist.
2. Explicitly model dependencies of a subsystem on other subsystems and intercomponent dependencies (e.g., common cause failures). For common cause failures, see Mosleh et al. (1988).

3. Include all potential reasonable and probabilistically quantifiable causes of failure, such as hardware, software, test and maintenance, and human errors, in the fault tree.

The following steps should be followed in the dependent failure analysis:

1. Identify the hardware, software and human elements that are similar and could cause dependent or common cause failures. For example, similar pumps, motor-operated valves, air-operated valves, human actions, software routines, diesel generators, and batteries are major components in process plants, and are considered important sources of common cause failures.
2. Items that are potentially susceptible to common cause failure should be explicitly incorporated into the corresponding fault trees and event trees of the PSA where applicable.
3. Functional dependencies should be identified and explicitly modeled in the fault trees and event trees.

3.2.6 Failure Data Collection, Analysis and Performance Assessment

A critical building block in assessing nuclear power plants risk and safety is accessibility of the reliability and availability data of the barriers which contain the radioactive source term. In particular, the best resources for predicting future availability are past field experiences and tests. Hardware, software and human reliability data are inputs to assess performance of hazard barriers, and the validity of the results depends highly on the quality of the input information. It must be recognized, however, that historical data have predictive value only to the extent that the conditions under which the data were generated remain applicable. Collection of the various failure data consists fundamentally of the following steps: collecting generic data, assessing generic data, statistically evaluating plant, facility- or system-specific data, and developing failure probability distributions using test and/or plant-specific and system-specific data. Three types of events identified during the risk scenario definition and system modeling must be quantified for the event trees and fault trees to estimate the frequency of occurrence of sequences: initiating events, component failures and human errors.

The quantification of frequencies of initiating events as well as failure probabilities of safety systems and components involve two separate activities. First, the probabilistic failure model for each barrier or component failure event must be established; then the parameters of the model must be estimated. Typically the necessary data include time of failures, repair times, test frequencies, test downtimes, common-cause failure events. Further uncertainties associated with such data must also be characterized. Kapur and Lamberson (1977), Modarres et al. (1999), and Nelson (1990) discuss available methods for analyzing data to obtain the probability of failure or the probability of occurrence of equipment failure. Also, Crow (1990) and Ascher and Feingold (1984) discuss analysis of data relevant to repairable systems. Finally, Mosleh et al. (1988) discuss analysis of data for dependent failures, Poucet (1988) reviews human reliability issues, and Smidts (1996) examines software reliability models. Establishment of the database to be used will generally involve collection of some facility-specific or system-specific data combined with the use of generic performance data when specific data are absent or sparse. For example, Refs. (IEEE 1984; DOD 1995) describe generic data for electrical, electronic, and mechanical equipment.

To attain the very low levels of risk, the systems and hardware that comprise the barriers to radioactive exposure must have very high levels of performance. This high performance is typically achieved through the use of well-designed systems with adequate margin of safety considering uncertainties, redundancy and/or diversity in hardware, which provides multiple success paths. The problem then becomes one of ensuring the independence of the paths, since there is always some degree of coupling between agents of failures such as those activated by failure mechanisms, either through the operating environment (events external to the system) or through functional and spatial dependencies. Treatment of dependencies should be carefully included in both event tree and fault tree development in the PSA. As the reliability of individual subsystems increases due to redundancy, the contribution from dependent failures becomes more important; in certain cases, dependent failures may dominate the value of overall reliability. Including the effects of dependent failures in the reliability models used in the PSA is a difficult process and requires some sophisticated, fully integrated models be developed and used to account for unique failure combinations that lead to failure of subsystems and ultimately exposure of hazards. The treatment of dependent failures is not a single step performed during the PSA; it must be considered throughout the analysis (e.g., in event trees, fault trees, and human reliability analyses).

The following procedures should be followed as part of the data analysis task:

1. Determine generic values of material strength or endurance, load or damage agents, failure times, failure occurrence rates and failures on demand for each item (hardware, human action, or software) identified in the PSA models. This can be obtained either from plant-specific or system-specific experiences, from generic sources of data, or both.
2. Gather data on hazard barrier tests, repair, and maintenance data primarily from experience, if available. Otherwise use generic performance data.
3. Assess the frequency of initiating events and other probability of failure events from experience, expert judgment, or generic sources.
4. Determine the dependent or common cause failure probabilities for similar items, primarily from generic values. However, when significant specific data are available, they should be primarily used.

3.2.7 Quantification and Integration

Fault trees and event trees are integrated and their events are quantified to determine the frequencies of scenarios and associated uncertainties in the calculation of the final risk values. This integration depends somewhat on the manner in which system dependencies have been handled. We will describe the more complex situation, in which the fault trees are dependent, i.e., there are physical dependencies (e.g., through support units of the main safety systems such as those providing motive power, proper working environment and control functions). Normally, the quantification will use a Boolean reduction process to arrive at a Boolean representation for each scenario.

Starting with fault tree models for the various systems or event headings in the event trees, and using probabilistic estimates for each of the events modeled in the event trees and fault trees, the probability of each event tree heading (often representing failure of a hazard barrier such as a safety system) is calculated (if the heading is independent of other headings). The fault trees for the main subsystems and support units (e.g., lubricating and cooling units, power units) are

merged where needed, and the equivalent Boolean expression representing each event in the event tree model is calculated. The Boolean expressions are reduced to arrive at the smallest combination of basic failures events (the so-called minimal cut-sets) that lead to exposure of the radioactive hazards. These minimal cut-sets for each of the main subsystems (that act as barriers) – that are often identified as headings on the event trees – are also obtained.

The minimal cut-sets for the event tree event headings are then appropriately combined to determine the cut-sets for the event-tree scenarios. If possible, all minimal cut-sets must be generated and retained during this process; unfortunately in nuclear power plants this leads to an unmanageably large collection of terms and a combinatorial outburst. Therefore, the collection of cut-sets are often truncated (i.e., probabilistically small and insignificant cut-sets are discarded based on the number of terms in a cut-set or on the probability of the cut-set). This is usually a practical necessity because of the overwhelming number of cut-sets that can result from the combination of a large number of failures, even though the probability of any of these combinations may be vanishingly small. The truncation process does not disturb the effort to determine the dominant scenarios since we are discarding scenarios that are extremely unlikely.

Even though the individual cut-sets discarded may be several orders of magnitude less probable than the average of those retained, the large number of them discarded may sum to a significant part of the risk. The actual risk might thus be larger than what the PSA results indicate. This can be discussed as part of the modeling uncertainty characterization. Detailed examination of a few PSA studies of nuclear power plants shows that cut-set truncation will not introduce any significant error in the total risk assessment results (Dezfuli and Modarres 1984).

Other methods for evaluating scenarios also exist that directly estimate the frequency of scenarios without specifying cut-sets. This is often done in highly dynamic systems whose configuration changes as a function of time leading to dynamic event trees and fault trees. These dynamic systems are discussed in greater details elsewhere (Chang et al. 2003; NASA 2002; Dugan et al. 1993). Employing advanced computer programming concepts, one may directly simulate the operation of parts to mimic the real system for reliability and risk analysis (Azarkhail and Modarres 2006). The following procedures should be followed as part of the quantification and integration step in the PSA:

1. Merge corresponding fault trees associated with each failure or success event modeled in the event tree scenarios (i.e., combine them in a Boolean form). Develop a reduced Boolean function for each scenario (i.e., truncated minimal cut-sets).
2. Calculate the total frequency of each sequence, using the frequency of initiating events, the probability of barrier failure including contributions from test and maintenance frequency (outage), common cause failure probability, and human error probability.
3. Use the minimal cut-sets of each sequence for the quantification process. If needed, simplify the process by truncating based on the number of terms in a cut-set or on the probability of the cut-set.
4. Calculate the total frequency for each scenario.
5. Calculate the total frequency for all scenarios included in all the event trees.

3.2.8 Uncertainty Analysis

Uncertainties are part of any assessment, modeling, and estimation. In engineering calculations we routinely ignore the estimation of uncertainties associated with failure models and

parameters, because the uncertainties are very small and more often analyses are done conservatively (e.g., by using high safety factor, design margin). Since PSAs are primarily used for decision-making and management of risk, it is critical to incorporate uncertainties in all facets of the PSA.

Also, risk management decisions that consider PSA results, must consider estimated uncertainties. In PSAs uncertainties are primarily shown in form of probability distributions. For example the probability of failure of a subsystem (e.g., a hazard barrier) may be represented by a probability distribution showing the range and likelihood of risk values.

The process involves characterization of the uncertainties associated with frequencies of initiating events, probabilities of failure of subsystems (barriers), probabilities of all event tree headings, strength or endurance of barriers, applied load or incurred damage by the barriers, amounts of source terms, consequences of exposures to radioactivity, and sustained total amounts of losses. Other sources of uncertainties are in the models used. For example the fault tree and event tree models, stress-strength and damage-endurance models used to estimate failure or capability of some barriers, probabilistic failure models of hardware, software and human, correlation between the amount of hazard exposure and the consequence, exposure models and pathways, and models to treat inter- and intra-barrier failure dependencies. Another important source of uncertainty is incompleteness of the risk models and other failure models used in the PSAs. For example, the level of detail used in decomposing subsystems using fault tree models, scope of the PSA, and lack of consideration of certain scenarios in the event tree just because they are not known or experienced before.

Once uncertainties associated with hazard barriers have been estimated and assigned to models and parameters, they must be “propagated” through the PSA model to find the uncertainties associated with the results of the PSA; primarily with the bottom-line risk calculations, and with the list of risk significant elements of the system. Propagation is done using one of several techniques, but the most popular method used is Monte Carlo simulation. The results are then shown and plotted in form of probability distributions. Steps in uncertainty analysis include:

1. Identify models and parameters that are uncertain and the method of uncertainty estimation to be used for each.
2. Describe the scope of the PSA and significance and contribution of elements that are not modeled or considered.
3. Estimate and assign probability distributions depicting model and parameter uncertainties in the PSA.
4. Propagate uncertainties associated with the hazard barrier models and parameters to find the uncertainty associated with the risk value.
5. Present the uncertainties associated with risks and contributors to risk in an easy way to understand and visually straightforward to grasp.

3.2.9 Sensitivity Analysis

Sensitivity analysis is the method of determining the significance of choice of a model or its parameters, assumptions for including or not including a safety system, physical barrier, phenomenon or hazard, performance of specific barriers, intensity of hazards, and significance of any highly uncertain input parameter or variable to the final risk value calculated. The process

of sensitivity analysis is straightforward. The effects of the input variables and assumptions in the PSA are measured by modifying them by several folds, factors or even one or more orders of magnitude one at a time, and measure relative changes observed in the PSA's risk results. Those models, variables and assumptions whose change leads to the highest change in the final risk values are determined as "sensitive." In such a case, revised assumptions, models, additional failure data, and more mechanisms of failure may be needed to reduce the uncertainties associated with sensitive elements of the PSA.

Sensitivity analysis helps focus resources and attentions to those elements of the PSA that need better attention and characterization. A good sensitivity analysis strengthens the quality and validity of the PSA results. Usually elements of the PSA that could exhibit multiple impacts on the final results, such as certain phenomena (e.g., pitting corrosion, fatigue cracking and common cause failures) and uncertain assumptions are usually good candidates for sensitivity analysis. The steps involved in the sensitivity analysis are:

1. Identify the elements of the PSA (including assumptions, failure probabilities, models, and parameters) that analysts believe might be sensitive to the final risk results.
2. Change the contribution or value of each sensitive item in either direction by several factors in the range of 2–100. Note that certain changes in the assumptions may require multiple changes of the input variables. For example a change in failure rate of similar equipments requires changing of the failure rates of all these equipments in the PSA model.
3. Calculate the impact of the changes in step 2 one-at-a-time and list the elements that are most sensitive.
4. Based on the results in step 3 propose additional data, any changes in the assumptions, use of alternative models, modification of the scope of the PSA analysis.

3.2.10 Risk Ranking and Importance Analysis

Ranking the elements of the system with respect to their risk or safety significance is one of the most important outcomes of a PSA. Ranking is simply arranging the elements of the plant based on their increasing or decreasing contribution to the final risk values. Importance measures rank hazard barrier, subsystems or more basic elements of them usually based on their contribution to the total risk of the plant or facility. The ranking process should be done with much care. In particular, during the interpretation of the results, since formal importance measures are context dependent and their meaning varies depending on the intended application of the risk results, the choice of the ranking method is important.

There are several unique importance measures in PSAs. For example, Fussell-Vesely, Risk Reduction Worth (RRW), and Risk Achievement Worth (RAW) (Modarres et al. 1999) are identified as appropriate measures for use in PSAs, and all are representative of the level of contribution of various elements of the plant as modeled in the PSA and enter in the calculation of the total risk. For example, Birnbaum importance measure represents changes in total plant risk as a function of changes in the basic event probability of one component at a time (Birnbaum 1969). If simultaneous changes in the basic event probabilities are being considered, a more complex representation would be needed.

Importance measures can be classified based on their mathematical definitions. Some measures have fractional type definitions and show changes (in the number of folds or factors) in the system total risk under certain conditions with respect to the normal operating or use condition (e.g., as is the case in RRW and RAW measures). Some measures calculate the changes in the system total risk as failure probability of hazard barriers and other elements of the system or conditions under which the plant operates change. This difference can be normalized with respect to the total risk of the plant or even expressed in a percentage change form. There are other types of measures, which account for the rate of changes in the system risk with respect to changes in the failure probability of the elements of the plant. These measures can be interpreted mathematically as partial derivative of the risk with respect to the failure probability of its elements (barriers, components, human actions, phenomena, initiating events, etc.). For example, the Birnbaum measure falls under this category.

Another important set of importance measures focus on ranking the elements of the plant based on the contributions to the total uncertainty of the risk results obtained from PSAs. This process is called “uncertainty ranking” and is different than component, subsystem, and barrier ranking. In this importance ranking the analyst is only interested to know which of the system elements drive the final risk uncertainties, so that resources can be focused on reducing important uncertainties.

There is another classification for importance measures in which they can be divided into two major categories of absolute and relative. Absolute measures are representative of fixed importance of one element of the system, independent of the importance of other elements, while relative importance expresses significance of one element with respect to weight of importance of other elements. Absolute importance can be used to estimate the impact of component performance on the system regardless of how important other elements are, while relative importance estimates the significance of the risk-impact of the component in comparison to the effect or contribution of others.

Absolute measures are useful when we speculate on improving actions, since they directly show the impact on the total risk of the system. Relative measures are preferred when resources or actions to improve or prevent failures are taken in a global and distributed manner. The risk ranking methods and their implications in failure and success domains are discussed in greater details elsewhere (Azarkhail and Modarres 2004). Applications of importance measures may be categorized into the following areas:

1. (Re)Design: To support decisions of the plant, system design or redesign by adding or removing elements (barriers, subsystems, human interactions, etc.).
2. Test and maintenance: To address questions related to the plant performance by changing the test and maintenance strategy for a given design.
3. Configuration and control: To measure the significance or the effect of failure of a component on risk or safety or temporarily taking a component out of service.
4. Reduce uncertainties in the input variables of the PSA.

The following are the major steps of importance ranking:

1. Determine the purpose of the ranking and select an appropriate ranking importance measure that has consistent interpretation for the use of the ranked results.
2. Perform risk ranking and uncertainty ranking, as needed.
3. Identify the most critical and important elements of the system with respect to the total risk values and total uncertainty associated with the calculated risk values.

3.2.11 Interpretation of Results

When the risk values are calculated, they must be interpreted to determine whether any revisions are necessary to refine the results and the conclusions. There are two main elements involved in the interpretation process. The first is to understand whether or not the final values and details of the scenarios are logically and quantitatively meaningful. This step verifies the adequacy of the PSA model and the scope of analysis. The second is to characterize the role of each element of the system in the final results. This step defines additional analyses, failure data and information that would be needed to make the risk results more useful.

The interpretation process heavily relies on the details of the analysis to see whether the scenarios are logically meaningful (for example by examining the minimal cut-sets of the scenarios), whether certain assumptions are significant and greatly control the risk results (using the sensitivity analysis results), and whether the absolute risk values are consistent with any historical data or expert opinions, if available. Based on the results of the interpretation, the details of the PSA logic, its assumptions and scope may be modified to update the results into more realistic and dependable values.


The ranking and sensitivity analysis results may also be used to identify areas where gathering more information and performing better analysis (for example by using more accurate models) is warranted. The primary aim of the process is to reduce uncertainties in the risk results.

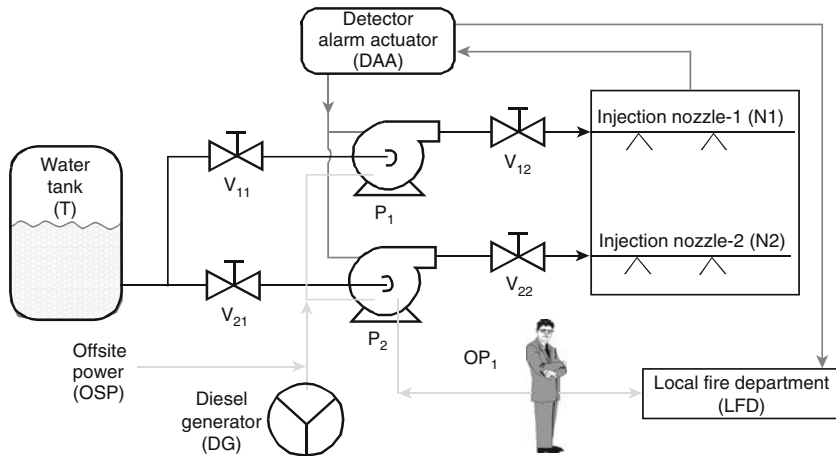
The interpretation step is a continuous process while developing the PSA. For example it continues receiving information from the quantification, sensitivity, uncertainty, and importance analysis results and assures that such results are accurate, proper, and sufficient. The process continues until the final results can be best interpreted and used in the subsequent risk management steps.

The basic steps of the PSA results interpretation include:

1. Determine accuracy of the logic models and scenario structures, assumptions, and scope of the PSA.
2. Identify system elements for which better information would be needed to reduce uncertainties in failure probabilities and models used to calculate performance.
3. Revise the PSA and reinterpret the results until attaining stable and accurate results.

3.3 A Simple Example of PSA

Consider the fire protection system shown in  Fig. 9. This system is designed to extinguish all possible fires in a plant with toxic chemicals. Two physically independent water extinguishing nozzles are designed such that each is capable of controlling all types of fires in the plant. Extinguishing (fire suppression) nozzle 1 is the primary method of injection. Upon receiving a signal from the detector/alarm/actuator device, pump-1 starts automatically, drawing water from the reservoir tank and injecting it into the fire area in the plant. If this pump injection path is not actuated, plant operators can start a second injection path manually. If the second path is not available, the operators will call for help from the local fire department (fire brigade), although the detector also sends a signal directly to the fire department. However, due to the delay in the arrival of the fire brigade, the magnitude of damage would be higher than it would be if the local fire suppression nozzles were available to extinguish the fire.



■ **Figure 9**
A fire protection system

This system is designed to extinguish all possible fires in a plant with toxic chemicals. Two physically independent water extinguishing nozzles are designed such that each is capable of controlling all types of fires in the plant. Extinguishing (fire suppression) nozzle 1 is the primary method of injection. Upon receiving a signal from the detector/alarm/actuator device, pump-1 starts automatically, drawing water from the reservoir tank and injecting it into the fire area in the plant. If this pump injection path is not actuated, plant operators can start a second injection path manually. If the second path is not available, the operators will call for help from the local fire department (fire brigade), although the detector also sends a signal directly to the fire department. However, due to the delay in the arrival of the fire brigade, the magnitude of damage would be higher than it would be if the local fire suppression nozzles were available to extinguish the fire.

Under all conditions, if the normal off-site power is not available due to the fire or other reasons, a local generator would provide electric (AC) power to the pumps. The power to the detector/alarm/actuator system is provided through the batteries, which are constantly charged by the off-site power. Even if the AC power is not available, the DC power provided through the battery is expected to be available at all times. The manual valves on the two sides of pump-1 and pump-2 are normally open, and only remain closed when they are being repaired. The entire fire system and generator are located outside of the fire compartment, and are not affected by an internal fire. Assuming all the preliminary steps of familiarization and choice of the PSA methodology have been accomplished, the remaining steps of the PSA for this situation can be performed as explained below:

Identification of Initiating Events

In this step, all equipment (e.g., cables, electric and control cabinets, pumps, ventilation system) and events (e.g., transient materials and fuel subject to ignition, hot works, and human error) that could cause fire in the reactor compartment (room), must be identified. These should include equipment malfunctions, human errors, and facility conditions. The frequency of each

event should be estimated. There are a number of sources of data that can be used to estimate the frequency of fire, e.g., NUREG/CR-6850 (EPRI 2005). Assuming that all events would lead to the same magnitude of fire, the ultimate initiating event would be occurrence of a fire, the frequency of which is the sum of the frequencies of the individual fire-causing events. Assume in this example the frequency of fire is estimated at 1×10^{-6} per year. Since fire is the only challenge to the plant in this example, we end up with only one initiating event. However, in more complex situations, a large set of initiating events can be identified, each posing a different challenge to the plant.

Scenario Development

In this step, we should explain the cause and effect relationship between the fire and the progression of events following the occurrence of fire. We use the event-tree method to depict this relationship. Generally, this is done inductively, and the level of detail considered in the event tree is somewhat dependent on the analyst. Two protective measures as hazard barriers have been considered in the event tree shown in **Fig. 10**: on-site protective measures (on-site pumps, tanks, etc.), and off-site fire department measures. The selection of these protective barriers is based on the fact that availability or unavailability of the on-site or off-site measures would lead to different damage states.

Logic Modeling

In this step, we should identify all failures (equipment or human) that lead to failure of the event-tree headings (on-site or off-site protective measures). For example, **Fig. 11** shows the fault tree developed for the On-Site Fire Protection System. In this fault tree, all basic events that lead to the failure of the two independent paths are described. Note that the detector alarm actuator (DAA), the electric power to the pumps, and the water tank are shared by the two paths. Clearly these are considered as physical dependencies. This is taken into account in the quantification step of the PSA. In this tree, all external event failures and passive failures are neglected. This tree is simple because it only includes all failures not leading to an on-time response from the local fire department. Similarly an off-site fault tree model can be developed as shown in **Fig. 12**.

It is also possible to use a master logic diagram (MLD) for system analysis. An example of the MLD for this problem is shown in **Fig. 13**. However, for this example only the fault trees are used in the PSA, although the MLD can also be used.

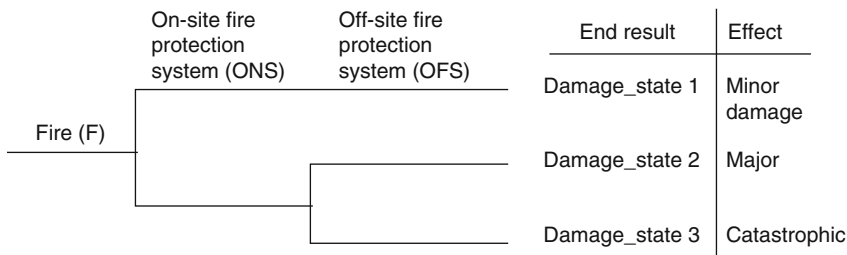


Figure 10
Scenarios of events following a fire using the event-tree methods

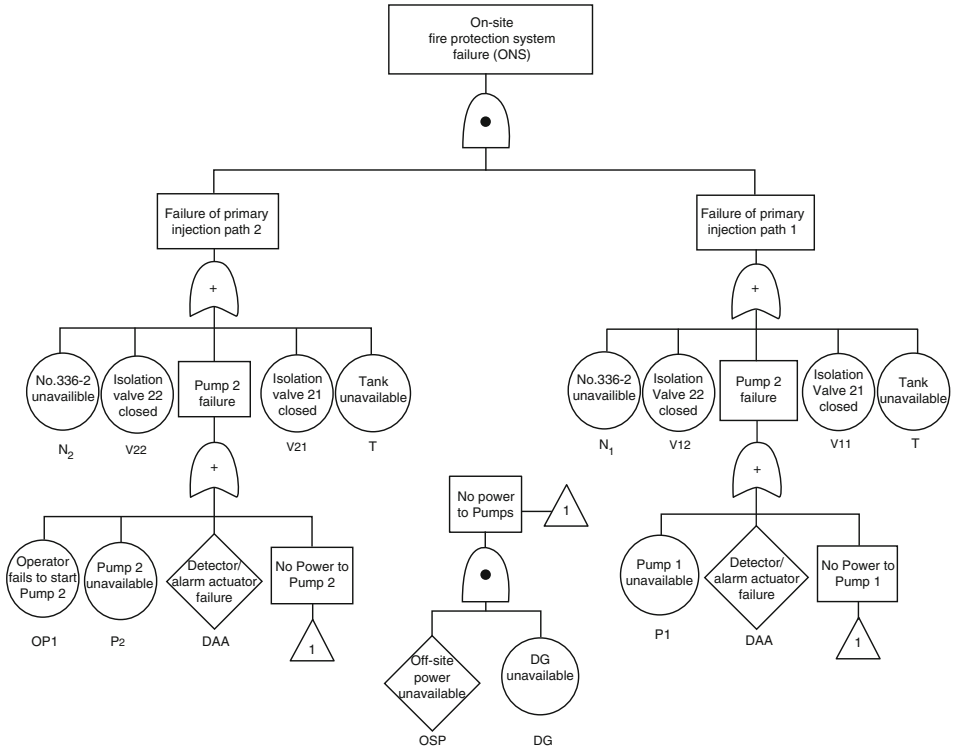


Figure 11
Fault tree for the on-site fire protection system failure

Failure Data Analysis

It is important at this point to calculate the probabilities of the basic failure events described in the event trees and fault trees. As indicated earlier, this can be done by using system-specific data, generic data, or expert judgment. [Table 3](#) describes the data used and their sources. It is assumed that at least 10 h of operation is needed for the fire to be completely under control.

Quantification

To calculate the frequency of each scenario defined in [Fig. 10](#), we must first determine the cut-sets of the two fault trees shown in [Figs. 11](#) and [12](#). From this, the cut-sets of each scenario are determined, followed by calculation of the probabilities of each scenario based on the occurrence of one of its cut-sets.

These steps are described below.

1. The cut-sets of the On-Site Fire Protection System Failure can be obtained by representing the fault tree of [Fig. 11](#) in terms of a Boolean equation for the top event, i.e., ONS, and then, reducing it by Boolean algebra (Modarres et al. 1999). These cut-sets are listed in [Table 4](#). Although several different types of common cause failure (e.g., among multiple valves or between the two pumps) can be considered, it is assumed that the potential for common cause failure exists only between the two pumps for simplicity. Cut-set number 24 represents the common cause failure of pumps 1 and 2.

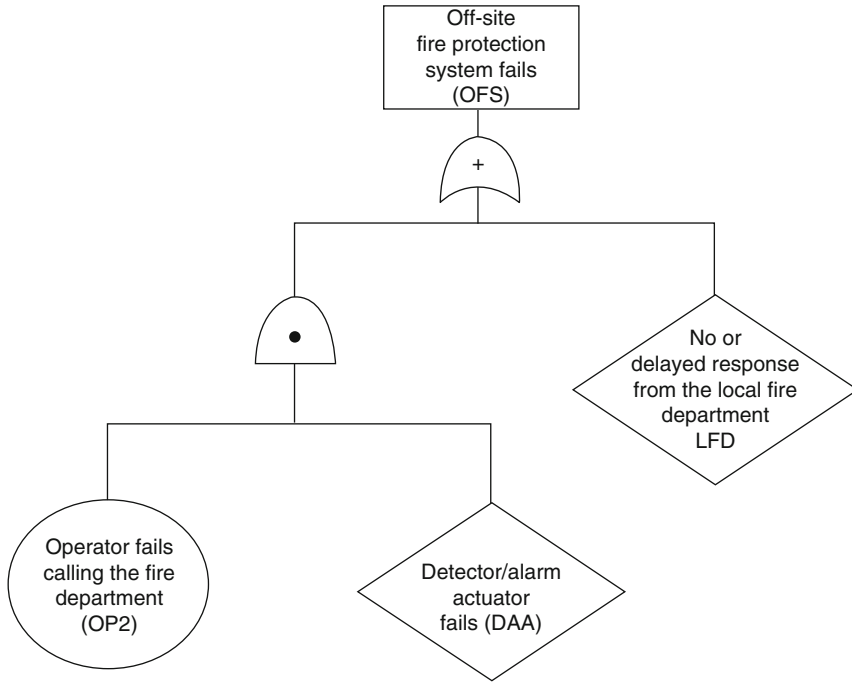


Figure 12
 Fault tree for the off-site fire protection system failure

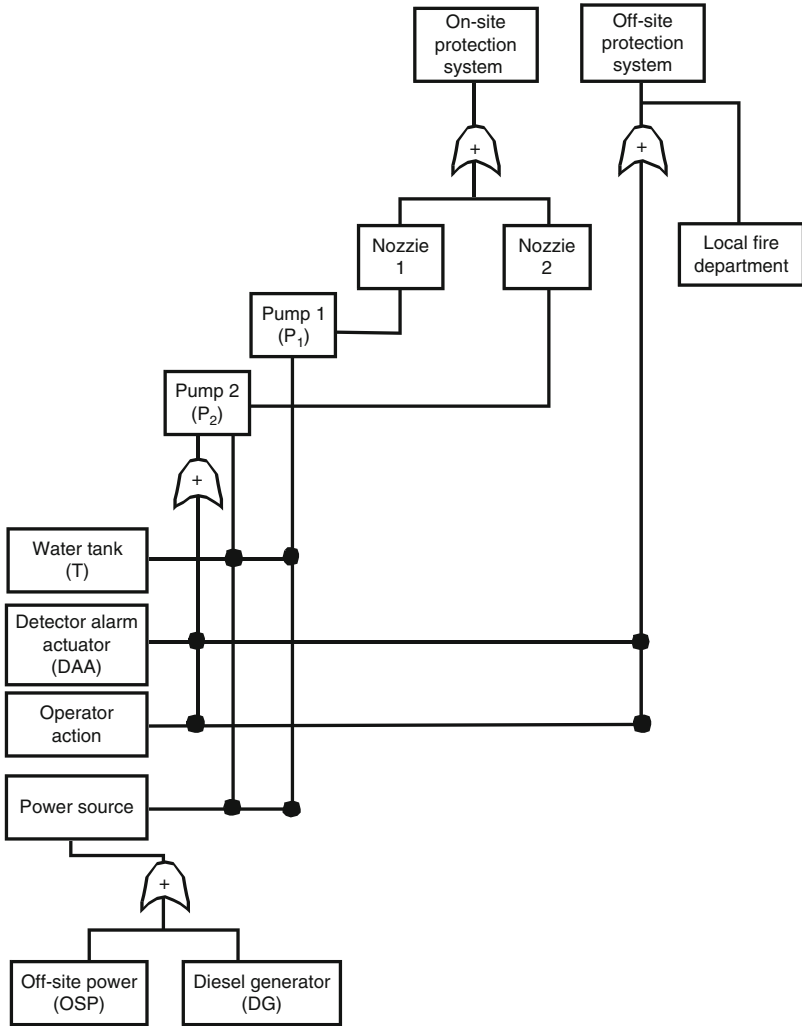
2. The cut-sets of the Off-Site Fire Protection System Failure are similarly obtained and listed in [Table 5](#).
3. The cut-sets of the three scenarios are obtained using the following Boolean equations representing each scenario:

$$\text{Scenario-1} = F \cdot \overline{\text{ONS}}$$

$$\text{Scenario-2} = F \cdot \text{ONS} \cdot \overline{\text{OFS}}$$

$$\text{Scenario-3} = F \cdot \text{ONS} \cdot \text{OFS}$$

4. The frequency of each scenario is obtained using data listed in [Table 3](#). These frequencies are shown in [Table 6](#).
5. The total frequency of each scenario is calculated using the rare event approximation. These are also shown in [Table 6](#).
6. Consequences. In the scenario development and quantification tasks, we identified three distinct scenarios of interest, each with different outcomes and frequencies. The consequences associated with each scenario should be specified in terms of both economic and/or human losses. This part of the analysis is one of the most difficult for several reasons.
 - Each scenario poses different hazards and methods of hazard exposure, and requires careful monitoring. In this case, the model should include the ways the fire can spread through the plant, how people can be exposed, evacuation procedures, the availability of protective clothing, etc.



■ Figure 13

Mater logic diagram for the entire fire protection system

- The outcome of the scenario can be measured in terms of human losses. It can also be measured in terms of financial losses, i.e., the total cost associated with the scenario. This involves assigning a dollar value to human life or casualties, which is a source of controversy.

Suppose a careful analysis of the spread of fire and fire exposure is performed, with consideration of the above issues, and ultimately results in damages measured only in terms of economic losses to the local fire compartment and beyond. These results are shown in

➤ [Table 7.](#)

Table 3
Sources of data and failure probabilities

Failure event	Plant-specific experience	Generic data	Probability used	Comments
Fire initiation frequency	No such experience in 10 years of operation	Five fires in similar plants. There are 70,000 plant-years of experience	$F = 5/70,000 = 7.1 \times 10^{-4}/\text{year}$	Use generic data
Pump 1 and Pump 2 failure	Four failures of two pumps to start in a single year were observed. Each pump has an average of ten demands (tests) per month. Repair time takes about 2.5 h. No experience of failure to run	Failure to run = $1 \times 10^{-5}/\text{h}$	$\frac{4}{2(12)(10)} = 1.7 \times 10^{-2}/\text{demand}$ Unavailability = $1.7 \times 10^{-2} + \frac{2.5(4)}{8760} = 1.8 \times 10^{-2}/\text{demand}$ $P_1 = P_2 = 1.8 \times 10^{-2}$	Failure to start is facility-specific. For failure to run, use generic data
Common cause failure between Pump 1 and Pump 2	No such experience	Using the β -factor method, $\beta = 0.1$ for failure of pumps to start	Unavailability due to common cause failure: $\text{CCF} = 0.1 \times 1.8 \times 10^{-2} = 1.8 \times 10^{-3}/\text{demand}$	Assume no significant common cause failure exists between valves and nozzles
Failure of isolation valves	Two failure to leave the valve in open position following Ten pump tests in 1 year	Not used	$V_{11} = V_{12} = V_{21} = V_{22} = \frac{2}{10(12)(4)} = 4.2 \times 10^{-3}/\text{demand}$	Facility-specific data used
Failure of nozzles	No-such experience	$1 \times 10^{-5}/\text{demand}$	$N_1 = N_2 = 1.0 \times 10^{-5}/\text{demand}$	Generic data used
Diesel generator failure	Three failures in tests. 40 h of repair per year	3.0×10^{-2} demand $3.0 \times 10^{-3}/\text{h}$	Failure on demand = $\frac{3}{12(10)}$ Failure on demand = $2.5 \times 10^{-2}/\text{demand}$ Failure on run = $3.0 \times 10^{-3}/\text{h}$ Total failure of DG = $2.5 \times 10^{-2} + 3.0 \times 10^{-3} = 5.5 \times 10^{-2}$	Facility-specific data used for demand failure
Loss of off-site power	No experience	0.1/year	OSP = $0.1 \times \frac{10}{8760} = 1.1 \times 10^{-4}/\text{demand}$	Assume 10 h of operation for fire extinguisher and use generic data

Table 3 (continued)

Failure event	Plant-specific experience	Generic data	Probability used	Comments
Failure of detector alarm actuator (DAA)	No experience	No data available	DAA = 1×10^{-4} /demand	This estimate is based on expert judgment
Failure of operator to start Pump 2	No such experience	Using THERP	OP1 = 1×10^{-2} /demand	The THERP method is discussed in (Swain and Guttman 1983)
Failure of operator to call the fire department	No such experience	1×10^{-3}	OP2 = 1×10^{-3} /demand	This is based on experience from no response to similar situations. Generic probability is used
No or delayed response from fire department	No such experience	1×10^{-4}	LFD = 1×10^{-4} /demand	This is based on response to similar cases from the fire department. Delayed/no arrival is due to accidents, traffic, communication problems, etc.
Tank failure	No such experience	1×10^{-5}	T = 1×10^{-5} /demand	This is based on data obtained from rupture of the tank or insufficient water content

7. Risk Calculation and Evaluation. Using values from Table 7, we can calculate the risk associated with each scenario. These risks are shown in Table 8. Since this analysis shows that the mean risk due to fire is rather low, uncertainty analysis is not very important. However, a certain method like Monte Carlo simulation could be used to estimate the uncertainty associated with models and parameters (e.g., failure rates) of each component and the fire-initiating event if necessary. The uncertainties should be propagated through the cut-sets of each scenario to obtain the uncertainty associated with the frequency estimation of each scenario. The uncertainty associated with the consequence estimates can also be obtained. When the uncertainties associated with the consequence

■ **Table 4**
Cut-sets of the on-site fire protection system failure

Cut-set no.	Cut-set	Probability (% contribution to the total probability)
1	T	1.0×10^{-5} (0.35)
2	DAA	1.0×10^{-4} (3.5)
3	OSP · DG	6.0×10^{-6} (0.21)
4	$N_2 \cdot N_1$	1.0×10^{-10} (~0)
5	$N_2 \cdot V_{12}$	4.2×10^{-8} (~0)
6	$N_2 \cdot P_1$	1.7×10^{-7} (~0)
7	$N_2 \cdot V_{11}$	4.2×10^{-8} (~0)
8	$V_{22} \cdot N_1$	4.2×10^{-8} (~0)
9	$V_{22} \cdot V_{12}$	1.8×10^{-5} (0.64)
10	$V_{22} \cdot P_1$	7.1×10^{-5} (2.5)
11	$V_{22} \cdot V_{11}$	1.8×10^{-5} (0.64)
12	$V_{21} \cdot N_1$	4.2×10^{-8} (~0)
13	$V_{21} \cdot V_{12}$	1.8×10^{-5} (0.35)
14	$V_{22} \cdot P_1$	7.1×10^{-5} (2.5)
15	$V_{21} \cdot V_{11}$	1.8×10^{-5} (0.64)
16	$OP_1 \cdot N_1$	1.0×10^{-7} (~0)
17	$OP_1 \cdot V_{12}$	4.2×10^{-5} (1.5)
18	$OP_1 \cdot P_1$	1.7×10^{-4} (6.0)
19	$OP_1 \cdot V_{11}$	4.2×10^{-5} (1.5)
20	$P_2 \cdot N_1$	1.7×10^{-7} (~0)
21	$P_2 \cdot V_{12}$	7.1×10^{-5} (2.5)
22	$P_2 \cdot P_1$	2.9×10^{-4} (0.3)
23	$P_2 \cdot V_{11}$	7.1×10^{-5} (2.5)
24	CCF	1.8×10^{-3} (63.8)

values are combined with the scenario frequencies and their uncertainties, the uncertainty associated with the estimated risk can be calculated. ➤ *Fig. 14* shows the risk profile based on the values of ➤ *Table 8*.

3.4 Future Outlook of Safety Analysis and Research Needs

Adequate performance of safety analysis of nuclear power plants is essential to protecting public health and safety from radiation exposure hazards. Although the safety analysis has been

■ **Table 5**
Cut-sets of the off-site fire protection system

Cut-set no.	Cut-set	Probability (% contribution to the total probability)
1	LFD	1×10^{-4} (100)
2	$OP_2 \cdot DAA$	1×10^{-7} (~ 0)
Total $Pr^{(OFF)} \approx 1 \times 10^{-4}$		

■ **Table 6**
Dominant minimal cut-sets of the scenarios

Scenario no.	Cut-sets	Frequency	Comment
1	$F \cdot \overline{ON}$	$7.1 \times 10^{-4} (1 - 2.8 \times 10^{-2})$ $= 7.1 \times 10^{-4}$	Since the probability can be directly evaluated for \overline{ON} without evaluating the need to generate cut-sets, only the probability is calculated.
2	$F \cdot DAA \cdot LFD \cdot OP_2$ $F \cdot V_{22} \cdot P_1 \cdot \overline{LFD} \cdot \overline{OP_2}$ $F \cdot V_{22} \cdot P_1 \cdot \overline{LFD} \cdot DAA$ $F \cdot V_{21} \cdot P_1 \cdot \overline{LFD} \cdot \overline{OP_2}$ $F \cdot V_{22} \cdot P_1 \cdot \overline{LFD} \cdot DAA$ $F \cdot OP_1 \cdot V_{12} \cdot \overline{LFD} \cdot \overline{OP_2}$ $F \cdot OP_1 \cdot V_{12} \cdot \overline{LFD} \cdot DAA$ $F \cdot OP_1 \cdot P_1 \cdot \overline{LFD} \cdot \overline{OP_2}$ $F \cdot OP_1 \cdot P_1 \cdot \overline{LFD} \cdot DAA$ $F \cdot OP_1 \cdot V_{11} \cdot \overline{LFD} \cdot \overline{OP_2}$ $F \cdot OP_1 \cdot V_{11} \cdot \overline{LFD} \cdot DAA$ $F \cdot P_2 \cdot V_{12} \cdot \overline{LFD} \cdot \overline{OP_2}$ $F \cdot P_2 \cdot V_{12} \cdot \overline{LFD} \cdot DAA$ $F \cdot P_2 \cdot P_1 \cdot \overline{LFD} \cdot \overline{OP_2}$ $F \cdot P_2 \cdot P_1 \cdot \overline{LFD} \cdot DAA$ $F \cdot P_2 \cdot V_{11} \cdot \overline{LFD} \cdot \overline{OP_2}$ $F \cdot P_2 \cdot V_{11} \cdot \overline{LFD} \cdot DAA$ $F \cdot CCP \cdot \overline{LFD} \cdot \overline{OP_2}$ $F \cdot CCP \cdot \overline{LFD} \cdot DAA$	7.0×10^{-8} 5.0×10^{-8} 5.0×10^{-8} 5.0×10^{-8} 5.0×10^{-8} 2.9×10^{-9} 2.9×10^{-9} 1.1×10^{-7} 1.1×10^{-7} 2.9×10^{-9} 2.9×10^{-9} 5.0×10^{-8} 5.0×10^{-8} 5.0×10^{-8} 2.0×10^{-7} 2.0×10^{-7} 5.0×10^{-8} 5.0×10^{-8} 1.3×10^{-6}	Only cut-sets from Table 4 that have a contribution greater than 1% are shown. Cut-set $F \cdot DAA \cdot \overline{LFD} \cdot DAA$ is eliminated since $DAA \cdot DAA = \phi$.
		$\Sigma_1 = 2.5 \times 10^{-6}$	
3	$F \cdot DAA \cdot LFD$ $F \cdot V_{22} \cdot P_1 \cdot LFD$ $F \cdot V_{21} \cdot P_1 \cdot LFD$ $F \cdot OP_1 \cdot V_{12} \cdot LFD$ $F \cdot OP_1 \cdot P_1 \cdot LFD$ $F \cdot OP_1 \cdot V_{11} \cdot LFD$ $F \cdot P_2 \cdot P_{12} \cdot LFD$ $F \cdot P_2 \cdot P_1 \cdot LFD$ $F \cdot P_2 \cdot V_{11} \cdot LFD$ $F \cdot CCP \cdot LFD$	7.1×10^{-12} 5.0×10^{-12} 5.0×10^{-12} 2.9×10^{-12} 2.8×10^{-12} 2.9×10^{-12} 5.0×10^{-12} 2.0×10^{-11} 5.0×10^{-12} 3.0×10^{-11}	Only cut-sets from Tables 4 and 5 that have contribution to the scenario are shown.
		$\Sigma_1 = 8.6 \times 10^{-11}$	

Table 7
Economic consequences of fire scenarios

Scenario number	Economic consequence (\$)
1	1,000,000
2	92,000,000
3	210,000,000

Table 8
Risk associated with each scenario

Scenario number	Economic consequence (expected loss)
1	$(7.1 \times 10^{-4})(\$1,000,000) = \710.000
2	$(2.5 \times 10^{-6})(\$92,000,000) = \230.000
3	$(8.6 \times 10^{-11})(\$210,000,000) = \0.018

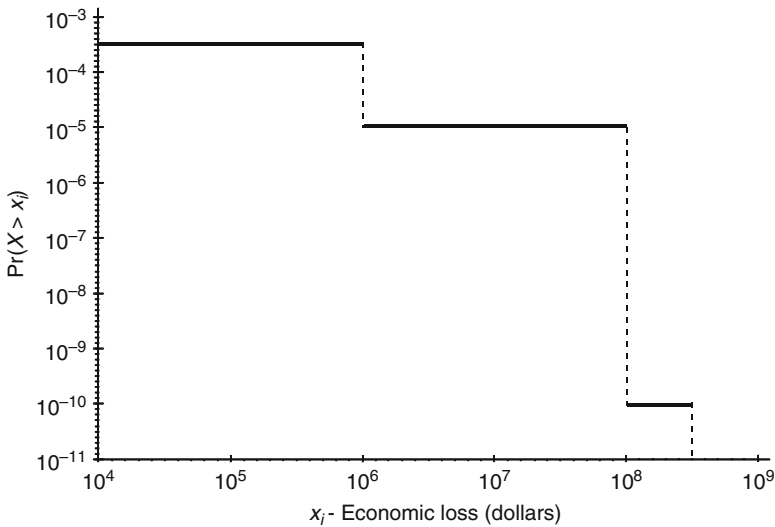


Figure 14
Risk profile of the fire protection system

largely deterministic, it is expected that PSA methods will be increasingly and more widely used to support decision making for safety along with key deterministic philosophies such as DID or safety margin. The hybrid approach of deterministic and probabilistic safety analysis methods are applied for various purposes, including: certifying nuclear plant design, preparing and evaluating requests for construction/operation permits or license amendments, assessing operational events that occur at power or during plant shutdown, reducing unnecessary operational burden, addressing security issues, etc.

The PSA methods have been considerably improved since the landmark WASH-1400 study (USNRC 1975). However, the following issues in particular should be addressed in the future to corroborate the usefulness of the probabilistic methods (USNRC 2003c; Fleming 2003):

- Model-to-plant fidelity issues including multi-unit site modeling issues, digital-systems modeling issues, and lack of detailed review by plant personnel to ensure fidelity with plant systems, operator actions, etc.
- PSA scope issues, i.e., use of limited-scope PSAs in risk-informed applications without sufficient justification.
- Lack of completeness within the specified scope, e.g., missing consideration of system interactions or particular accident scenarios.
- Lack of, or inadequate, treatment of uncertainties.
- Quantification issues (e.g., error due to cut-set truncation).
- Lack of treatment of aging effects.
- Issues with the use and interpretation of risk metrics or importance measures.
- Lack of incorporation of operating experience in PSAs.
- Inadequate treatment of common-cause failures.
- Lack of coherence between probabilistic and deterministic safety approaches.

Finally, it is also notable that a number of works have been performed to enhance the event tree/fault tree methodology generally employed in the PSAs by developing “dynamic methodologies” to treat various time-dependent interactions; namely, time-dependent interactions between plant physical processes (e.g., heatup, pressurization) and triggered or random logical events (e.g., valve openings, pump startups) as an accident evolves, or the time-dependent interactions between the plant and its human operators (Aldemir and Siu 1996). Progress is being made in the area of dynamic process system reliability, and safety analysis, although key problems still remain, for example, in: (1) creating realistic representations of overall system behavior, such as the treatment of human operators (individuals and teams) and software control systems; (2) establishing criteria to specify when exactly dynamic analyses should be employed, since such analyses require significantly more resources than conventional, static analyses.

References

-
- Ahearne J et al (2001) The regulatory process for the nuclear power reactors: a review. Report of the CSIS Nuclear Regulatory Process Review Steering Committee
- Ahn SK, Kim IS, Oh KM (2010) Deterministic and risk-informed approaches for safety analysis of advanced reactors: part I, deterministic approaches. To appear, *Reliab Eng Syst Safety*
- AICHE (1989) Guidelines for process equipment data. Center for Chemical Process Safety, American Institute of Chemical Engineers, New York
- Aldemir T, Siu N (1996) Reliability and safety analysis of dynamic process systems. *Reliab Eng Syst Safety* (Special Issue) 52:181–337
- ANS (1973) Nuclear safety criteria for the design of stationary pressurized water reactor plants, ANSI N18.2-1973. American National Standards Institute, American Nuclear Society, Hinsdale
- ANS (1983) Nuclear safety criteria for the design of stationary pressurized water reactor plants, ANSI/ANS-51.1-1983. American National Standards Institute, American Nuclear Society, La Grange Park
- Ascher H, Feingold H (1984) Repairable systems reliability: modeling and inference, misconception and their causes. Marcel Dekker, New York
- Azarkhail M (2007) Agent autonomy approach to physics based reliability modeling of structures

- and mechanical systems. Ph.d. Dissertation, University of Maryland, College Park
- Azarkhail M, Modarres M (2004) A Study of implications of using importance measures in risk-informed decisions. In: PSAM-7, ESREL 04 Joint Conference, Berlin, Germany, 2004
- Azarkhail M, Modarres M (2006) An intelligent-agent-oriented approach to risk analysis of complex dynamic systems with applications in planetary missions. In: Proceedings of the 8th international conference on probabilistic safety assessment and management, PSAM8, New Orleans, USA, 2006
- Birnbaum ZW (1969) On the importance of different components in a multicomponent system. In: Krishnaiah PR (ed) *Multivariate analysis II*. Academic Press, New York
- Carlisle R (1997) Probabilistic risk assessment in nuclear reactors: engineering success, public relations failure. *Technol Culture* 38:920–941
- Chang YH, Mosleh A, Dang V (2003) Dynamic probabilistic risk assessment: framework, tool, and application. In: Proceedings of the society for risk analysis annual meeting, Baltimore, 2003
- Colglazier E, Weatherwas R (1986) Failure estimates for the space shuttle. In: Abstracts of the Society for Risk Analysis Annual Meeting, Boston, 1986
- Crow LH (1990) Evaluating the reliability of repairable systems. In: *IEEE Proceedings of the annual reliability and maintainability symposium*, pp. 275–279
- Delaney MJ, Apostolakis GE, Driscoll MJ (2005) Risk-informed design guidance for future reactor systems. *Nuc Eng Des* 235:1537–1556
- Dezfuli H, Modarres M (1984) A truncation methodology for evaluation of large fault trees. *IEEE Trans Reliab R-33*:325–328
- DOD (1995) *Military handbook, reliability prediction of electronic equipment*. MIL-HDBK-217F, Department of Defense
- Dugan J, Bavuso S, Boyd M (1993) Dynamic fault tree models for fault tolerant computer systems. *IEEE Trans Reliab* 40(3):363
- EPRI (1995) *PSA applications guide*. Electric Power Research Institute, TR-105396, Palo Alto
- EPRI (2005) *EPRI/NRC-RES fire PRA methodology for nuclear power facilities*. EPRI 1011989, NUREG/CR-6850, Palo Alto, US Nuclear Regulatory Commission, Washington DC
- Ericson C (1999) *Fault tree analysis – A history*. In: Proceedings of the 17th international system safety conference, Orlando, 1999
- Farmer FR (1967) *Reactor safety and siting: A proposed risk criterion*. *Nucl Safety* 8:539–548
- Fischer, D (1997) *History of the international atomic energy agency: The first forty years*. International Atomic Energy Agency
- Fleming KN (2003) *Issues and recommendations for advancement of pra technology in risk-informed decision making*, NUREG/CR-6813. US Nuclear Regulatory Commission, Washington, DC
- Fleming KN, Silady FA (2002) *A risk informed defense-in-depth framework for existing and advanced reactors*. *Reliab Eng Syst Safety* 78:205–225
- Ford D (1977) *A history of Federal nuclear safety assessments: From WASH 740 through the reactor safety study*. Union of Concerned Scientists, Washington
- Frankel E (2002) *Systems reliability and risk analysis*, 2nd edn. Kluwer Academic Publishers, Boston
- Fussell J (1975) How to hand calculate system reliability and safety characteristics. *IEEE Trans Reliab* 24(3):169–174
- Green A, Bourne A (1972) *Reliability technology*. Wiley, London
- Hu YS, Modarres M (1999) Evaluating system behavior through dynamic master logic diagram (DMLD) modeling. *Reliab Eng Syst Safety* 64:241–269
- Hunt RN, Modarres M (1984) Integrated economic risk management in a nuclear power plant. In: *Proceedings of the Annual Meeting of the Society for Risk Analysis*, Knoxville, TN, October, 1984; published in *Risk Abstracts*, Vol. 2, No. 2.
- IAEA (1991) *Safety culture. 75-INSAG-4, A report by the international nuclear safety advisory group*, International Atomic Energy Agency
- IAEA (1996) *Defense in depth in nuclear safety. INSAG-10, A report by the international nuclear safety advisory group*, International Atomic Energy Agency
- IEEE (1984) *IEEE guide to the collection and presentation of electrical, electronic, sensing component, and mechanical equipment reliability data for nuclear-power generating stations*, IEEE Std 500–1984. Institute of Electrical and Electronics Engineers, New York
- Kaplan S, Garrick J (1981) On the quantitative definition of risk. *Risk Anal* 1:11–28
- Kapur KC, Lamberson LR (1977) *Reliability in engineering design*. Wiley, New York
- Kemeny JG, Babbitt B, Haggerty PE, Lewis C et al (1979) *Staff reports to the President's commission on the accident at three mile island*. Reports of the Technical Assessment Task Force, Washington, DC

- Kim IS (1996) Improving technical specifications from a risk perspective. *Reliab Eng Syst Safety* 54:83–87
- Kim IS (2008) Feasibility study for development of human error pattern analysis methodology for operational experience feedback. Korea Institute of Nuclear Safety, Republic of Korea
- Kim IS, Modarres M (1987) Application of goal tree-success tree model as the knowledge base of operator advisory systems. *Nucl Eng Des* 104: 67–81
- Kim IS, Martorell S, Vesely WE, Samanta PK (1994) Risk analysis of surveillance requirements including their adverse effects. *Reliab Eng Syst Safety* 45:225–234
- Kim IS, Ahn SK, Hong SJ, Lee HJ (2008) New insights on risk-informed performance-based approaches to technology-neutral regulatory framework for generation IV reactors. In: Proceedings of the 9th international probabilistic safety assessment and management conference, PSAM9, Hong Kong, 2008
- Kim IS, Ahn SK, Oh KM (2010) Deterministic and risk-informed approaches for safety analysis of advanced reactors: part II, risk-informed approaches. To appear, *Reliab Eng Syst Safety*
- Kouts H (1998) History of safety research programs and some lessons to be drawn from it. In: 26th water reactor safety information meeting, Bethesda, 1998
- Kumamoto H, Henley EJ (1996) Probabilistic risk assessment for engineers and scientists. IEEE Press, New York
- Lewis H et al (1975) American physical society reactor study review group. Report on WASH-1400
- Meserve R (2001) The evolution of safety goals and their connection to safety culture. Speech at the American Nuclear Society topical meeting on safety goals and safety culture, Milwaukee, 2001
- Modarres M (1993) What every engineer should know about reliability and risk analysis. Marcel Dekker, New York
- Modarres M (2006) Risk analysis in engineering, techniques, tools and trends. CRC Press, Boca Raton
- Modarres M (2009) Advanced nuclear power plant regulation using risk-informed and performance-based methods. *Reliab Eng Syst Safety* 94:211–217
- Modarres M, Kaminskiy M, Krivtsov V (1999) Reliability engineering and risk analysis: A practical guide. Marcel Dekker, New York
- Mosleh A, Fleming KN, Parry GW, Paula HM et al (1988) Procedure for treating common cause failures in safety and reliability studies, NUREG/CR-4780, US Nuclear Regulatory Commission, Washington, DC
- Stamatelatos M, Apostolakis G, Dezfuli H, Everline C et al (2002) Probabilistic risk assessment procedures guide for NASA managers and practitioners, Vers. 1.1. National Aeronautics and Space Administration, Washington, DC
- NEI (2006) Risk-informed technical specifications initiative 4b, Risk-managed technical specifications (RMTS) guidelines, NEI-06-09, Rev. 0. Nuclear Energy Institute, Washington, DC
- NEI (2007) Risk-informed technical specifications initiative 5b, risk-informed method for control of surveillance frequencies, NEI-04-10, Rev. 1. Nuclear Energy Institute, Washington, DC
- Nelson W (1990) Accelerated testing: statistical models, test plans and data analyses. Wiley, New York
- NSAC (1979) Analysis of three mile island – unit 2 accident. Nuclear Safety Analysis Center, NSAC-1
- NUMARC (1993) Industry guideline for monitoring the effectiveness of maintenance at nuclear power plants, NUMARC 93-01. Nuclear Management and Resources Council
- Poucet A (1988) Survey of methods used to assess human reliability in the human factors reliability benchmark exercise. *Reliab Eng Syst Safety* 22:257–268
- Reason J, Hobbs A (2003) Managing maintenance error. Ashgate, England
- Rhodes R (1986) The making of the atomic bomb. Simon and Schuster, New York
- Rogovin M, Frampton GT Jr. (1980) Three mile island – A report to the commissioners and to the public. Nuclear Regulatory Commission Special Inquiry Group, NUREG/CR-1250, US Nuclear Regulatory Commission, Washington, DC
- Samanta PK, Kim IS, Mankamo T, Vesely WE (1994) Handbook of methods for risk-based analyses of technical specifications. NUREG/CR-6141, US Nuclear Regulatory Commission, Washington, DC
- Sattison MB et al (1990) Analysis of core damage frequency: zion, unit 1 internal events. NUREG/CR-4550, Vol. 7, Rev. 1, US Nuclear Regulatory Commission, Washington, DC
- Smids C (1996) Software reliability. In: Whitaker JC (ed) The electronics handbook. CRC Press, Boca Raton
- Sorensen J, Apostolakis G, Kress T, Powers D (1999) On the role of defense-in-depth in risk-informed regulation. In: Proceedings of the probabilistic safety assessment PSA'99, Washington,

- DC., American Nuclear Society, La Grange Park, IL
- Stamatis DH (2003) Failure mode and effect analysis: FMEA from theory to execution, 2nd edn. ASQ Quality Press, Wisconsin, USA
- Starr C (1969) Social Benefit versus technological risk. *Science* 19:1232–1238
- Swain AD, Guttman HE (1983) Handbook of human reliability analysis with emphasis on nuclear power plant applications, NUREG/CR-1278, US Nuclear Regulatory Commission (USNRC), Washington DC
- USAEC (1957) WASH-740, Theoretical possibilities and consequences of major accidents in large nuclear power plants. US Atomic Energy Commission, AKA The Brookhaven Report
- USAEC (1966) Minutes of the AEC general advisory committee. US Atomic Energy Commission
- USNRC (1956) Domestic licensing of production and utilization facilities, Title 10. Code of Federal Regulations, Part 50, 21FR355
- USNRC (1975) Reactor safety study – an assessment of accident risks in US commercial nuclear power plants. WASH-1400 (NUREG-75/014, US Nuclear Regulatory Commission, Washington, DC)
- USNRC (1977) Single failure criterion. SECY-77-439
- USNRC (1978) Standard format and content of safety analysis reports for nuclear power plants – LWR edition. Regulatory Guide 1.70, Revision 3
- USNRC (1980a) NRC action plan developed as a result of the TMI-2 accident. NUREG-0660, Rev. 1, US Nuclear Regulatory Commission, Washington, DC
- USNRC (1980b) Severe accident risks: An assessment for five US Nuclear Power Plants. NUREG-1150, US Nuclear Regulatory Commission, Washington, DC
- USNRC (1983) PRA procedures guide: a guide to the performance of probabilistic risk assessments for nuclear power plants. NUREG/CR-2300, US Nuclear Regulatory Commission, Washington, DC
- USNRC (1986) Safety goals for the operation of nuclear power plants; policy statement. 51 FR 30028
- USNRC (1988) Individual plant examination for severe accident vulnerabilities – 10 CFR 50.54(f). Generic Lett 1:88–20
- USNRC (1991) Individual plant examination of external events (ipeee) for severe accident vulnerabilities – 10 CFR 50.54(f). Generic Lett 4: 88–20
- USNRC (1993) Final policy statement on technical specifications improvements for nuclear power plants. 58FR39132
- USNRC (1995) Use of probabilistic risk assessment methods in nuclear regulatory activities; final policy statement. 60FR42622
- USNRC (1997a) Maintenance rule status, results, and lessons learned. SECY-97-055
- USNRC (1997b) Monitoring the effectiveness of maintenance at nuclear power plants. Regulatory Guide 1.160
- USNRC (1998a) White paper on risk-informed and performance-based regulation. SECY-98-144
- USNRC (1998b) An approach for plant-specific, risk-informed decisionmaking: inservice testing. Regulatory Guide 1.175
- USNRC (1998c) An approach for plant-specific, risk-informed decisionmaking: technical specifications. Regulatory Guide 1.177
- USNRC (1999a) General design criteria for nuclear power plants, Appendix A of 10 CFR 50
- USNRC (1999b) General requirements for monitoring the effectiveness of maintenance at nuclear power plants, Title 10, Code of Federal Regulations, Part 65. 64FR72001
- USNRC (1999c) Staff Briefing on reactor inspection, enforcement and assessment
- USNRC (2000) Consolidated line item improvement process for adopting standard technical specifications changes for power reactors. Regulatory Issue Summary (RIS) 2000–06
- USNRC (2001) Modified reactor safety goal policy statement. SECY-01-0009
- USNRC (2002a) Perspectives gained from the individual plant examination of external events (IPEEE) program. NUREG-1742, US Nuclear Regulatory Commission, Washington, DC
- USNRC (2002b) An approach for using probabilistic risk assessment in risk-informed decisions on plant-specific changes to the licensing basis. Regulatory Guide 1.174, Rev. 1
- USNRC (2003a) Acceptance criteria for emergency core cooling systems for light-water nuclear power reactors, Title 10, Code of Federal Regulations. Part 46, 68FR54142
- USNRC (2003b) An approach for plant-specific risk-informed decisionmaking for inservice inspection of piping. Regulatory Guide 1.178, Rev. 1
- USNRC (2003c) NUREG-CR-6813, Issues and recommendations for advancement of PRA technology in risk-informed decision making. Letter of ACRS Chairman M.V. Bonaca to EDO Director W.D. Travers, ACRSR-2034, US Nuclear Regulatory Commission, Washington, DC

- USNRC (2004) An approach for estimating the frequencies of various containment failure modes and bypass events. NUREG/CR-6595, Rev.1, US Nuclear Regulatory Commission, Washington, DC
- USNRC (2005a) Technical work to support evaluation of a broader change to the single-failure criterion. Technical report
- USNRC (2005b) Independent verification of the mitigating systems performance index (MSPI) results for the pilot plants. NUREG-1816, US Nuclear Regulatory Commission, Washington, DC
- USNRC (2006) Reactor oversight process. NUREG-1649, Rev. 4, US Nuclear Regulatory Commission, Washington, DC
- USNRC (2007a) Combined license applications for nuclear power plants (LWR edition). Regulatory Guide 1.206
- USNRC (2007b) Standard review plan for the review of safety analysis reports for nuclear power plants. NUREG-0800, US Nuclear Regulatory Commission, Washington, DC
- USNRC (2007c) Feasibility study for a risk-informed and performance-based regulatory structure for future plant licensing. NUREG-1860, US Nuclear Regulatory Commission, Washington, DC
- USNRC (2007d) 19.0 Probabilistic risk assessment and severe accident evaluation for new reactors. In: Standard review plan for the review of safety analysis reports for nuclear power plants. NUREG-0800, US Nuclear Regulatory Commission, Washington, DC
- USNRC (2007e) An approach for determining the technical adequacy of probabilistic risk assessment results for risk-informed activities. Regulatory guide 1.200, Rev. 1
- USNRC (2007f) Operating reactor assessment program, inspection manual chapter 0305
- Wood W (1983) Nuclear safety, risks and regulation. American Enterprise Institute – Public Policy Research

16 Multiphase Flows: Compressible Multi-Hydrodynamics

Part I: Effective Field Formulation of Multiphase Flows

*Daniel Lhuillier*¹ · *Theo G. Theofanous*²

Part II: Computation with Effective-Field Models of Multiphase Flows

*Meng-Sing Liou*³ · *Theo G. Theofanous*²

¹Institut Jean le Rond d'Alembert, CNRS and University Paris, Paris, France
daniel.lhuillier@upmc.fr

²Department of Chemical Engineering,
Department of Mechanical Engineering, Center for Risk Studies and Safety,
University of California, Santa Barbara, CA, USA
theo@theofanous.net; theo@engineering.ucsb.edu

³NASA Glenn Research Center, Cleveland, OH, USA
meng-sing.liou@nasa.gov

PART I: EFFECTIVE FIELD FORMULATION OF MULTIPHASE FLOWS	1818
1 Introduction and Scope I	1818
2 Basics of Coarse-Graining	1819
2.1 The Two-Fluid Model	1819
2.2 The Kinetic Theory Model	1820
2.3 The Hybrid (Symmetry-Breaking) Model	1821
3 A General Formulation	1823
4 Non-Dissipative Model	1826
4.1 Rigid Particles	1826
4.1.1 Rigid Particles, No Velocity Fluctuations	1826
4.1.2 Rigid Particles with Added-Mass Velocity Fluctuations	1827
4.2 Compressible Particles	1830
5 Dissipative Model	1832
5.1 Noncompressible Particles: Solid Grains or Drops	1833
5.1.1 The Dissipation Rate	1833
5.1.2 The Constitutive Laws	1834
5.2 Compressible Particles: Bubbles	1836
5.2.1 The Dissipation Rate	1836
5.2.2 The Constitutive Laws	1838
5.3 Final Form of the Model	1838

6	<i>Summary of Key Results</i>	1839
6.1	Hybrid Approach for Dispersed Mixtures	1839
6.2	Supplementary Equations	1840
6.2.1	Pseudo-Turbulent Kinetic Energies	1841
6.2.2	Volume Fraction Transport	1841
6.2.3	Interfacial Energy Transport	1842
6.2.4	Particle Deformation and Dynamics of Interfaces.....	1842
6.3	Hyperbolicity	1843
6.4	Nuclear Reactor (Design) Systems Codes.....	1844
	<i>APPENDIX A: Rigid Spheres in a Nonviscous Fluid</i>	1845
	<i>APPENDIX B: Hyperbolicity Aspects of the Effective Field Model</i>	1847
	<i>APPENDIX C: Including Surface Tension</i>	1854
	<i>PART II: COMPUTATION WITH EFFECTIVE-FIELD MODELS OF MULTIPHASE FLOWS</i>	1858
7	<i>Introduction and Scope II</i>	1858
8	<i>Strategy for Computing Compressible Multi-Hydrodynamics</i>	1859
9	<i>Basics: The Riemann Problem and the Godunov Method</i>	1862
9.1	The Riemann Problem	1863
9.2	The Godunov Method	1865
10	<i>Approximate Flux “Splitting” Schemes for Single Phase Flows</i>	1867
10.1	Characteristics-Based Flux Splitting.....	1867
10.2	Direct Flux Splitting.....	1871
10.3	Advection Upstream Splitting	1875
11	<i>Advection Upstream Splitting for the Effective Field Model</i>	1880
11.1	Recasting the System of Equations in Quasi-Conservative Form	1880
11.2	Numerical Discretization.....	1883
11.3	Time Integration.....	1886
12	<i>Numerical Testing in the ARMS Code</i>	1888
12.1	Uniformly Translating Body-and-Fluid System.....	1889
12.2	The Faucet Problem	1890
12.3	Fitt’s Problem	1891
12.4	Shock Tube Problems	1892
12.5	Particle Cloud Dynamics in Gaseous Shocks.....	1893
13	<i>Conclusions and Outlook</i>	1897
	<i>APPENDIX D: Sample Computational Results</i>	1900
	<i>References</i>	1908

Abstract: Effective field modeling of two-phase flow has provided a critical part of the foundation upon which light water (power) reactor technology was made to rest some 20-30 years ago. We can envision a similarly significant role in the future as simulation capabilities are poised to meet new kinds of practical demands at the interplay between economics, safety assurance, and regulatory needs. These new demands will require better predictive reliability for larger departures from past practices, and this in turn will require strengthening of the scientific component along with translating past empiricism into more and more fundamental terms. In this perspective, the mathematical formulation of the effective field model, as well as the numerical implementation of this formulation needs to be revisited and reassessed. Helping respond to this need is the purpose of this chapter.

We delineate a conceptual framework for addressing prediction of multiphase flows at the three-dimensional, phase distribution level. This is in terms of a local, disperse system description (bubbles/drops in a continuous liquid/vapor phase). The requirement that follows is a well-posed formulation and a high-fidelity numerical treatment that allows capturing of shocks and contact discontinuities over all (relative) flow speeds, consistently with what is physically allowable according to the density ratios involved — in particular, high relative Mach numbers for droplet/particle flows. The importance of inviscid interactions (between the phases) in this context is highlighted.

The scope is for disperse-phase volume fractions up to about 20% as pertinent to fluid-fluid systems. This provides the basis for addressing phase transitions through coalescence as this process becomes significant at still higher volume fractions. The theoretical framework provides also the basis for extensions (outlined only in general terms here) to the high-volume fractions pertinent to dense solid-particle systems. The computational approach is readily applicable to both these extensions.

A general disperse system formulation is derived by means of a new, “hybrid” method that incorporates features of a statistical approach and reveals more clearly the nature of phase interactions at the individual particle scale. Moreover in this manner the formulation lends itself to elaboration of the constitutive treatment by means of numerical simulations (based on the direct solution of the Navier-Stokes equations) resolved at the particle scale. The formulation is exemplified by successive applications to various increasingly complex situations, starting with non-dissipative systems, where one or the other phase may be incompressible. At each step we examine the hyperbolic character of the system of equations, and we include consideration of high (relative) Mach numbers. The basic constitutive treatment concerns pseudo-turbulent fluctuations of the continuous phase, and the resulting systems of equations are fully closed and hyperbolic even in their non-dissipative form (ready for computation), except for a non-hyperbolic corridor around the transonic region. Results obtained are discussed in relation to formulations that form the basis of current numerical tools (codes) employed in nuclear reactor design and safety analyses (mostly addressing bubbly flows), as well as formulations found in other contexts.

This mathematical formulation is pursued further to its numerical implementation. With an emphasis on flow compressibility, we focus on capturing shocks and contact discontinuities robustly for all flow speeds and at arbitrarily high spatial resolutions. As we learn from relatively recent progress in single-phase flows, the key role is that of “up-winding” applied on the basis of a scheme that emphasizes conservative discretization. This background is briefly reviewed, culminating with a rather detailed exposition of the most recent advance in this line of development: the Advection Upstream Splitting Method (AUSM). The essential and new step here is to extend the basic ideas of the AUSM to the compressible multi-hydrodynamics

problems of interest here, and the above-mentioned EFM in particular. We also include calculations illustrative of numerical performance.

The presentation is arranged into two autonomous parts: Part I addresses the formulation of the EFM and Part II deals with the numerical implementation and testing. An overall summarization of where we stand at the completion of this work and what we see as needed future developments is provided in the following.

One basic objective was to address inviscid interactions by means of a coherent theoretical formulation and through to computational testing. In particular, we wanted to access high-fidelity simulations of the type needed to address flow regimes at all flow speeds; especially at the high relative Mach numbers pertinent to disperse particle/droplet flows. This requires that the system of equations be hyperbolic, and we wanted to achieve a solid foundation rather than adopting any of the several ad hoc constitutive models as post facto “remedying” the problem.

On theory, we begin with entropy rather than energy transport equations and we derive, consistently with thermodynamics and the momentum equations, a condition for satisfying conservation of total energy. This condition is of utmost importance showing the tight link between the conservation laws employed, and the transport equations of volume fraction and of pseudo-turbulent kinetic energies of the continuous (included) and disperse (not yet included in the derivation) phases. On this basis we demonstrate a systematic way to deduce closed systems of equations for non-dilute disperse flows, and thusly we arrive at an EFM that is hyperbolic except for a “corridor” around the transonic region. The key is a function of the disperse phase volume fraction $E(\alpha_d)$. It enters as a coefficient of the disperse phase pseudo-turbulent kinetic energy. Awaiting further definition as a function of the Mach number, by means of the type of direct simulations noted above, it is employed here throughout in its zero-Mach form. A much needed extension would also involve the pseudo-turbulent kinetic energy of the disperse phase, along with physics of dense dispersions (collisions etc.).

While terms such as those proposed previously for “interfacial pressure” and “added mass” phenomena can be identified, the complete formulation is not reducible to any of those ad hoc models. Notably, the disperse phase pressure appears nowhere in the momentum equations. Also we find that the claimed as hyperbolic, Baer-Nunziato model involves a volume fraction transport equation, which is not physically tenable for dispersions, or is it an appropriate means to dealing with ill-posedness. On the other hand, we find perfect agreement with the formulations obtained at the incompressible limit by Geurst (1985), employing a complex variational approach, and by Wallis (1989), employing a rather involved development based on potential flow theory.

On computations our objective is to capture shocks and contact discontinuities, for conditions that are within the hyperbolic regions in the Mach number space, and to explore (1) behaviors within the non-hyperbolic corridor, and (2) means of stabilization as necessary. Given the EFM development needs expressed above, it is understood that this testing in the Mach number space is strictly provisional. We begin with an adaptive mesh refinement infrastructure, and the Advection Upstream Splitting Method (AUSM), currently the method of choice for single-phase compressible flows. A key point of adaptation to our EFM is treating the pseudo-turbulent stresses within the pressure flux splitting, and ensuring that the discretization of the nonconservative terms is done in a way that satisfies propagation of contact discontinuities in uniform steady flow without disturbing the pressure field. Our approach is readily extendable to any equation of state and to adding any number of equations (volume fraction transport, multiple equations for the disperse phase for tracking multiple length scales

as may be found when the disperse phase is subject to fragmentation). The testing performed for this work was done on 1D problems only. Extending this testing to 2D and 3D problems is underway.

Testing was carried out independently with two computer codes: ARMS (all-regime multiphase simulation) and MuSiC-ARMS (Multi-scale Simulation Code-ARMS). The ARMS was built on an open access platform, the structured adaptive mesh refinement infrastructure (SAM-RAI) developed at Lawrence Livermore National Laboratory. The MuSiC-ARMS was built, more recently, on the MuSiC platform, our own specialized code, using irregular grids to “fit” areas of highest refinement (shocks, interfaces, etc.), which are embedded in a multilevel (adaptive) Cartesian mesh. This platform is also used for a DNS code, the MuSiC-SIM, and a pseudo-compressible (incompressible) code, the MuSiC-ISIM. We focus on dispersed being the heavy phase (droplet/particle flows) so as to access realistically high Mach numbers, and significant inviscid interactions.

The test cases were selected to include various kinds of Riemann problems with discontinuities in (a) Mach number only (Fitt’s problems) and (b) pressure, or pressure and disperse phase volume fraction (shock tube problems). In the Fitt’s problem case, we include parametric studies on the value of C that appears in function $E(\alpha_d)$. In addition, we consider shock wave “impact” problems on particle clouds that are either with sharp or smooth (in particle volume fraction) outer boundaries, and as part of this class also the case of dilute clouds for which we have the analytic solution for comparison. Finally, we considered the capturing of contact discontinuities in “mild” situations such as the so-called Faucet problem and the simple convection of a coherent second phase by uniform flow. The Faucet problem is well known to be failed under grid refinement in all published tests to date. The convection problem is important check of the pressure non-disturbing condition, a requirement that is hard to meet due to the non-conservative terms found in all effective field models.

The emphasis being on stability and convergence under grid refinement, all problems were carried out in the inviscid limit (no interfacial drag), and all cases passed the test except for the high pressure ratio shock tube problems where instabilities developed within the expansion wave. However, these cases were stabilized with a minimal amount of dissipation effected by adding a small amount of interfacial drag (roughly one tenth of the normal amount). These numerical results render support to the idea that, notwithstanding the “mild” non-hyperbolic corridor found in the analysis of Part I, the present effective field model is hyperbolic, and along with the numerical treatment employed they provide access to rather extreme two-phase flow conditions in a robust and accurate manner.

In an overall perspective of computational fluid dynamics, the presently offered capability is complementary to that already available through the “standard”, non-hyperbolic two-fluid model as already found in the computational frameworks of the ICE (Harlow and Amsden 1968) and SIMPLE (Patankar and Spalding 1972) methods. The special purposes aimed here are to overcome limitations in grid refinement and to approach flows where the phasic-relative velocities are high enough to introduce significant compressibility effects. Rapid advancement in hardware makes computational analysis of complex multiphase flows, even direct numerical simulations, increasingly more practical and reliable. High-fidelity/resolution techniques such as those employed here can address problems of varying time and length scales and this paves the way for actual simulations of multiphase physics at the effective field level, and even allowing a seamless analysis transitioning across regimes of multiphase flows.

PART I: EFFECTIVE FIELD FORMULATION OF MULTIPHASE FLOWS

1 Introduction and Scope I

The essence of multiphase flows is in the space-time distribution of phases and their length scales. Hence the need for an elaborated description of the Flow Regime or Flow Pattern, a topic of inquiry that began from the very first engineering efforts on the subject nearly a century ago, yet a topic of inquiry that remains largely unfulfilled (Theofanous and Hanraty 2003). Once the flow pattern is known everything else follows in a basic way. In fact all key behaviors of multiphase systems depend on the relevant flow regimes at the appropriate scale(s); for example, the limits to coolability (critical heat flux) are to be found in the microscopic flow pattern in the immediate vicinity of the heating surface, at a scale much smaller than realized previously (Theofanous et al. 2002). The fact that the design of safety systems in light water reactors has reached maturity, notwithstanding the absence of such a foundation, is owed to a large extent to a huge, comprehensively defined set of experiments over several scales up to prototypic that served to (empirically) anchor the numerical simulation tools (so-called systems codes) developed in this era (RELAP5, TRAC-BWR, and the CATHARE code that followed). Conversely, none of this would have been possible if not for the organizing principle provided by the mathematical framework (the so-called two-fluid model) at the basis of these computational tools. Indeed, it was the synergism thus created and fed by an international, enormous in scope and resources R&D effort under the leadership (and the major financial support) of the US Nuclear Regulatory Commission (Office of Nuclear Reactor Regulatory Research) that made possible to meeting the great practical need: assuring and demonstrating the safety of nuclear power reactors. Moreover, it was this juncture in the 1970s and 1980s that afforded the first quantum leap in the scientific development of the subject, and provided the basis for the further developments that were to follow in the intervening 20 years; notably in addressing steam explosions as part of severe accident management in the 1990s (Fletcher and Theofanous 1997) and in spinoffs driven by other practical needs such as the chemical process, oil and gas, and manufacturing industries (catalytic crackers, internal combustion engines, etc).

In these intervening 20 years, at the other extreme of the detailed local level, major strides have been made in the direct solution of the Navier-Stokes equations (DNS), addressing both turbulence and interfacial dynamics. The scope of such simulations is ever enlarging, in pace with ingredients of high-performance computing: machine performance, adaptive mesh platforms, and massively parallelizable schemes. On this basis and with a renewed interest in nuclear power, the “old” systems tools are poised to meet and leverage with these new developments and capabilities toward multi-scale treatments that gain in generality and predictive power as the next generation nuclear power design and safety analysis tools (the CATHARE-NEPTUNE program in France, and the RELAP7 program in the USA). If successful these efforts, both in very early stages of development, are likely to provide the next quantum leap in numerical simulation of multiphase flows. It is in this context that this chapter has been written.

The focus being, as noted above, on the numerical simulation of Flow Regimes, the basic requirements are a 3D representation and a demarcation between regions of space with topologically similar character. For example, in a gas-liquid flow we seek the demarcation between domains of bubbles dispersed in liquid, and domains of drops dispersed in gas. We call these demarcations, as large-scale discontinuities or LSDs (Theofanous and Dinh 2003). In this way

all macroscopic two-phase flows may be seen as interacting assemblages (collective effects of bubbly or droplet flow regions) of disperse flows, and the flow regime identification depends upon the spatial-temporal positioning and multiplicity of the LSDs. As a consequence, coarse-graining or the derivation of effective field (interpenetrating continua) transport equations need only address disperse media, and this focusing is important in eliminating ambiguities inherent with the coarse-graining of internal scales much larger than those of the underlying disperse flows. Moreover, based on typical regime stability requirements the region of interest is over disperse phase volume fractions of less than about 30%. As another key consequence, the numerical solution of the effective field equations must be amenable to grid refinement, so as to capture shocks, contact discontinuities, and the LSDs at arbitrarily sharp focus, and this means, besides the numerical scheme being nondiffusive, that the system of equations be well posed. A further aim in the formulation is to define the phase interaction terms clearly enough as to support the development of closures (a task of renewed potential under DNS) on a physically sound basis. Finally, emerging areas of application require the consideration of supersonic and transonic flows, areas with their own particular demands (Theofanous et al. 2004).

At this basic level of treatment the major attention is given to the dynamics of (inertial or) inviscid interactions between the dispersed and continuous phases (with due account for the so-called pseudo-turbulent fluctuations). These underlie the mathematical character of the system of conservation laws. The incorporation of turbulent stresses and of breakup/coalescence phenomena can be added according to need, for example, in the manner developed by Lahey's and Ishii's teams respectively. Some remarks on the formulation and implications of current systems codes are integrated in [▶ Sect. 6](#).

Accordingly, in Part I we are particularly interested in a *continuum-mechanical description of mixtures made of many particles dispersed in a carrier fluid*. We will present the *two* coarse-grained models relevant to the description of dispersed mixtures in [▶ Sect. 2](#). We will insist on the difficulties inherent to the modeling of the interphase force of the two-fluid model before presenting in [▶ Sect. 3](#) a special form of the two-fluid model dedicated to the description of dispersions. The non-dissipative version of that model is presented in [▶ Sect. 4](#) with special emphasis on the role of pseudo-turbulent velocity fluctuations. The dissipative counterpart is presented in [▶ Sect. 5](#), while some extensions (concerning the role of surface tension in particular) and the main results are recapitulated in [▶ Sect. 6](#). Emphasis is placed in delivering complete systems of equations that can be taken directly to numerical solution, and as such Part I provides the starting point for Part II. We also aim for clarity on the interfacial momentum transfers — a subject of prolonged, and often confusing debates. Their meaning is not readily open to intuition, while their importance is critical to the well-posedness of the mathematical system that constitutes the effective field model.

2 Basics of Coarse-Graining

2.1 The Two-Fluid Model

The most well-known coarse-grained model is certainly the *two-fluid or two-phase model* (Nigmatulin 1991; Drew and Passman 1998; Ishii and Hibiki 2006) whose exclusive specificity

to disperse systems has been acknowledged only implicitly. In its standard form, the two-fluid model is obtained as a combination of three ingredients:

- The (microscale) conservation equations for mass, momentum, and energy in each of the two phases*
- The function of presence χ_k of phase k in the mixture with $\chi_c + \chi_d = 1$ where the indices c and d stand for the carrier fluid and the dispersed particles respectively*
- A statistical (e.g., ensemble, time, or volume) averaging denoted by $\langle \dots \rangle$*

For example, the microscale momentum balance of phase k is

$$\rho_k^0 \left[\frac{\partial v_k^0}{\partial t} + (v_k^0 \cdot \nabla) v_k^0 \right] = \nabla \cdot \sigma_k^0 + \rho_k^0 g$$

where ρ_k^0 , v_k^0 and σ_k^0 are the microscale mass density, velocity, and stress-tensor. From that microscale conservation equation one deduces the macroscale momentum balances (with no mass exchange between phases, for simplicity here) (Nigmatulin 1991; Drew and Passman 1998; Ishii and Hibiki 2006)

$$\alpha_c \rho_c \frac{d_c u_c}{dt} + \nabla \cdot \langle \chi_c \rho_c^0 v_c' v_c' \rangle = \nabla \cdot \langle \chi_c \sigma_c^0 \rangle - \langle \sigma_c^0 \cdot n_d \delta_I \rangle + \alpha_c \rho_c g, \quad (1)$$

$$\alpha_d \rho_d \frac{d_d u_d}{dt} + \nabla \cdot \langle \chi_d \rho_d^0 v_d' v_d' \rangle = \nabla \cdot \langle \chi_d \sigma_d^0 \rangle + \langle \sigma_c^0 \cdot n_d \delta_I \rangle + \alpha_d \rho_d g. \quad (2)$$

Here δ_I is the function of presence of the interfaces between the two phases and n_d is the normal to those interfaces pointing outwards phase d . Moreover, $v_k' = v_k^0 - u_k$ is the velocity fluctuation relative to the mean velocity u_k , $\alpha_k = \langle \chi_k \rangle$ is the volume fraction or probability of presence of phase k , and $d_k/dt = \partial/\partial t + u_k \cdot \nabla$ is a convected time-derivative. These macroscale equations are perfectly symmetric relative to the two phases, i.e., there is no apparent distinction between the continuous and the dispersed phase.

2.2 The Kinetic Theory Model

Concerning the dispersed (particulate) phase there exists a second coarse-grained model, the *kinetic theory model* which is built on the basis of three ingredients:

- The balance equations for the mass momentum and energy of a single particle*
- The microscale number density δ_d of the particles*
- A statistical averaging based on a probability distribution function and denoted by the same symbol $\langle \dots \rangle$ as in the two-fluid approach*

For example, the equation of motion for a single particle is

$$m^0 \frac{dw^0}{dt} = \oint \sigma_c^0 \cdot n_d ds + m^0 g,$$

where m^0 and w^0 are the mass and velocity of a particle. From this equation one deduces the momentum balance of the particulate phase (Buyevich et al. 1978; Lhuillier 1992; Zhang and

Prosperetti 1994; Jackson 1997)

$$nm \left[\frac{\partial w}{\partial t} + (w \cdot \nabla) w \right] + \nabla \cdot [nm \langle w' \otimes w' \rangle] = n \langle \oint \sigma_c^0 \cdot n_d ds \rangle + nmg, \quad (3)$$

where w is the mean translational velocity of the particles, $w' = w^0 - w$ is the fluctuation relative to that mean value, m is the mean mass per particle, and $n = \langle \delta_d \rangle$ is the mean number density of the particles.

This momentum balance is rather similar to that written in the two-phase model except for two remarkable differences: (a) the particle stress which is present in (2) is absent from (3), and (b) the force exerted by the fluid is simply the mean force per particle times the particle number density. The particle stress is not present in the momentum balance but it has not completely disappeared. In fact it is taken into account in a different equation, the *equation for the moment of momentum of the particles* which writes (Lhuillier 1992)

$$\begin{aligned} \langle \delta_d \frac{d}{dt} \int \rho_d^0 r \otimes u d\tau \rangle - n \langle \int \rho_d^0 u \otimes u d\tau \rangle \\ = n \langle \oint r \otimes (\sigma_c^0 \cdot n_d) ds \rangle - n \langle \int \sigma_d^0 d\tau \rangle, \end{aligned} \quad (4)$$

where u is the particle-internal motion (a pure rotation for a rigid particle) and r is the vector joining the center of a particle to a point of its surface. The antisymmetric part of the above equation is nothing but the angular momentum balance of the particulate phase. And the symmetric part can be inverted so as to give an explicit expression for the particle stress. When the role of inertia in internal motion can be neglected one recovers Batchelor's expression (Batchelor 1970)

$$\langle \int \sigma_d^0 d\tau \rangle = \frac{1}{2} \langle \oint [r \otimes (\sigma_c^0 \cdot n_d) + (\sigma_c^0 \cdot n_d) \otimes r] ds \rangle. \quad (5)$$

2.3 The Hybrid (Symmetry-Breaking) Model

The main advantage of the kinetic theory model is that it introduces quantities (e.g., the mean force $n \langle \oint \sigma_c^0 \cdot n_d ds \rangle$ acting on the particulate phase), which have a far more intuitive meaning than the corresponding quantity for the two-fluid model (where the interphase force is written as $\langle \sigma_c^0 \cdot n_d \delta_I \rangle$). It would be nice therefore if we could express some two-phase quantities like the mean particle stress or the mean interphase force in terms of quantities pertaining to the kinetic theory approach. This transformation between two-phase and kinetic quantities is in fact well known in electrodynamics of continuous media. One makes such a transformation when writing the mean charge per unit volume as the density of true particle charges minus the divergence of the mean density of particle dipoles, etc. For two-phase flows the corresponding transformations were derived in Buyevich et al.(1978), Lhuillier (1992), Zhang and Prosperetti (1994), and Jackson (1997) with the following general results that apply to any quantity A defined on the interfaces and B defined inside the particles

$$\langle A \delta_I \rangle = n \langle \oint A ds \rangle - \nabla \cdot [n \langle \oint rA ds \rangle] + \dots \quad (6)$$

$$\langle B \chi_d \rangle = n \langle \int B d\tau \rangle - \nabla \cdot [n \langle \int rB d\tau \rangle] + \dots, \quad (7)$$

where the integrals span over the particle surface and the particle volume respectively, and the dots stand for a development in series of higher and higher moments of A and B . When B stands for the small-scale charge density one verifies the well-known result mentioned above and the dots stand for the contributions of particle quadrupoles and higher multipoles. For the modeling of suspensions of particles, A will be the local force exerted by the continuous phase and B will be the local stress inside a particle for which the above transformation rules will be written as

$$\langle \sigma_c^0 \cdot n_d \delta_I \rangle \approx n \langle \oint \sigma_c^0 \cdot n_d ds \rangle - \nabla \cdot [n \langle \oint r \otimes (\sigma_c^0 \cdot n_d) ds \rangle] \quad (8)$$

$$\langle \chi_d \sigma_d^0 \rangle \approx n \langle \int \sigma_d^0 d\tau \rangle \quad (9)$$

One can be surprised that the simplest transformation rule is applied to the particle stress while a more complete one is necessary for the interphase force. The reason is that the particle stress appears with its divergence in the momentum balance. If we limit the interphase force to the first term of the transformation rule we miss a stress term, while if we limit the particle stress to the first term, we only miss higher-order terms comparable to the terms we neglected in the interphase force.

The next step is to introduce the mean pressure p_c of the continuous phase defined as

$$\langle \chi_c \sigma_c^0 \rangle = -\alpha_c p_c I + \langle \chi_c \tau_c^0 \rangle \quad (10)$$

where τ_c^0 is the microscale fluid viscous stress. With the continuous phase pressure and the transformation rules (8) and (9) the two-phase momentum balances, (1) and (2), now appear in a special (hybrid) form

$$\alpha_c \rho_c \frac{d_c u_c}{dt} + \nabla \cdot \sigma_c + \alpha_c \nabla p_c = -F + \alpha_c \rho_c g \quad (11)$$

$$\alpha_d \rho_d \frac{d_d u_d}{dt} + \nabla \cdot \sigma_d + \alpha_d \nabla p_c = F + \alpha_d \rho_d g \quad (12)$$

with the definitions

$$F = n \langle \oint (\sigma_c^0 + p_c I) \cdot n_d ds \rangle \quad (13)$$

$$\sigma_c = \langle \chi_c \rho_c^0 v'_c \otimes v'_c \rangle - \langle \chi_c \tau_c^0 \rangle - n \langle \oint r \otimes (\sigma_c^0 + p_c I) \cdot n_d ds \rangle \quad (14)$$

$$\sigma_d = \langle \chi_d \rho_d^0 v'_d \otimes v'_d \rangle - n \langle \int \rho_d^0 u \otimes u d\tau \rangle + \langle \delta_d \frac{d}{dt} \int \rho_d^0 u \otimes r d\tau \rangle \quad (15)$$

The expression of the dispersed phase stress σ_d was obtained with the help of (4) and (9). The carrier fluid does not play any role in that stress, which vanishes for massless particles. Whenever collisions (or direct inter-particle forces) must be taken into account a collision stress (or an inter-particle stress) is to be added to the right-hand side of (15). In what follows we will use (11) and (12) as the starting point for the two-phase description of suspensions of particles.

It is remarkable that *the dispersed phase pressure nowhere appears in the two momentum equations*, a feature which is specific to dispersed mixtures. We will see however that the pressure difference $p_c - p_d$ is hidden in the stress σ_d and also that it plays a role in the energy equations as

well as in the transport equation for the volume fraction; so that the models we have to present are two-pressure models actually.

The entropy balance equations of the hybrid model are obtained in a similar way. If one neglects the interfacial entropy (linked to surface tension) as well as any entropy production at the interfaces, then the mean specific entropies s_k evolve in time as

$$\alpha_d \rho_d \frac{d_d s_d}{dt} + \nabla \cdot h_d = \Delta_d + \Sigma \quad (16)$$

$$\alpha_c \rho_c \frac{d_c s_c}{dt} + \nabla \cdot h_c = \Delta_c - \Sigma \quad (17)$$

where Δ_k and h_k are the entropy production rate and entropy flux in phase k while Σ is the interphase entropy exchange. These quantities are defined as

$$\Sigma = -n \left\langle \oint \frac{q_c^0}{T_c^0} \cdot n_d \, ds \right\rangle, \quad (18)$$

$$h_c = \left\langle \chi_c \rho_c^0 s'_c v'_c \right\rangle + \left\langle \chi_c \frac{q_c^0}{T_c^0} \right\rangle + n \left\langle \oint r \left(\frac{q_c^0}{T_c^0} \cdot n_d \right) ds \right\rangle, \quad (19)$$

$$h_d = \left\langle \chi_d \rho_d^0 s'_d v'_d \right\rangle - n \left\langle \int \rho_d^0 s_d^0 u \, d\tau \right\rangle + \left\langle \delta_d \frac{d}{dt} \int \rho_d^0 s_d^0 r \, d\tau \right\rangle, \quad (20)$$

where q_c^0/T_c^0 is the microscale entropy flux of the continuous phase. There is an evident similarity with the corresponding definitions for the momentum balances.

3 A General Formulation

The main equations describing a two-phase mixture are the six balance equations for mass, energy, and momentum. The way these equations are obtained is well documented in many textbooks (Nigmatulin 1991; Drew and Passman 1998; Ishii and Hibiki 2006). Here we prefer an entropy balance instead of the energy balance and we will use the hybrid form of the momentum equations as stressed in the previous section. Thus accounting also for phase change, the six main balance equations are written as

$$\frac{\partial}{\partial t} (\alpha_d \rho_d) + \nabla \cdot (\alpha_d \rho_d u_d) = \Gamma \quad (21)$$

$$\frac{\partial}{\partial t} (\alpha_c \rho_c) + \nabla \cdot (\alpha_c \rho_c u_c) = -\Gamma \quad (22)$$

$$\alpha_d \rho_d \frac{d_d s_d}{dt} + \nabla \cdot h_d = \Delta_d + \Sigma + \Gamma (s^* - s_d) \quad (23)$$

$$\alpha_c \rho_c \frac{d_c s_c}{dt} + \nabla \cdot h_c = \Delta_c - \Sigma - \Gamma (s^* - s_c) \quad (24)$$

$$\alpha_d \rho_d \frac{d_d u_d}{dt} + \nabla \cdot \sigma_d + \alpha_d \nabla p_c = F + \Gamma (u^* - u_d) + \alpha_d \rho_d g \quad (25)$$

$$\alpha_c \rho_c \frac{d_c u_c}{dt} + \nabla \cdot \sigma_c + \alpha_c \nabla p_c = -F - \Gamma (u^* - u_c) + \alpha_c \rho_c g. \quad (26)$$

In these equations appear the mass density ρ_k , the entropy density s_k , the volume fraction α_k , and the velocity u_k of phase k ($k = c, d$) together with the mean pressure p_c of the continuous

phase. Besides the entropy production rate $\Delta_k \geq 0$ inside phase k , are defined the intra-phase entropy flux h_k and the stress tensors σ_k together with the exchanges between phases, Γ for the mass exchange, $\Sigma + \Gamma s^*$ for the entropy exchange and $F + \Gamma u^*$ for the momentum exchange. Our aim is to close these equations, i.e., to find by all means (DNS, exact analytical results, phenomenology, etc.) explicit expressions of all averaged quantities (like the stresses σ_c , σ_d and the inter-phase force F but also s^* and u^*) in terms of the basic variables such as the mean velocities and the volume fractions.

To achieve that goal, an important step will be to assume that *the thermodynamic properties of each phase in the mixture are the same as those at work for a pure phase*. This means that the equations of state, which hold when written with local quantities are assumed to hold when written with the mean values of these quantities. In other words, one denies any role to the fluctuations around the mean pressure p_k and the mean temperature T_k inside phase k . But one acknowledges a possible difference between T_c and T_d as well as between p_c and p_d . For example the Gibbs relation of phase k in the mixture will be supposed to be

$$de_k = T_k ds_k - p_k d(1/\rho_k), \quad (27)$$

where e_k is the mean internal energy per unit mass of phase k . For convenience that Gibbs relation is rewritten as

$$\alpha_k \rho_k \frac{d_k e_k}{dt} = T_k \alpha_k \rho_k \frac{d_k s_k}{dt} + \frac{p_k}{\rho_k} \frac{d_k (\alpha_k \rho_k)}{dt} - p_k \frac{d_k \alpha_k}{dt},$$

where $d_k/dt = \partial/\partial t + u_k \cdot \nabla$ is the convected time-derivative of phase k . The evolution equations of the internal energies are then *deduced* from the above evolution equations of entropy and mass per unit volume

$$\begin{aligned} \frac{\partial}{\partial t} (\alpha_d \rho_d e_d) + \nabla \cdot (\alpha_d \rho_d e_d u_d + T_d h_d) &= T_d \Delta_d + T_d \Sigma + h_d \cdot \nabla T_d \\ + \Gamma [e_d + T_d (s^* - s_d)] - p_d \left(\frac{\partial \alpha_d}{\partial t} + \nabla \cdot (\alpha_d u_d) - \frac{\Gamma}{\rho_d} \right) & \end{aligned} \quad (28)$$

$$\begin{aligned} \frac{\partial}{\partial t} (\alpha_c \rho_c e_c) + \nabla \cdot (\alpha_c \rho_c e_c u_c + T_c h_c) &= T_c \Delta_c - T_c \Sigma + h_c \cdot \nabla T_c \\ - \Gamma [e_c + T_c (s^* - s_c)] - p_c \left(\frac{\partial \alpha_c}{\partial t} + \nabla \cdot (\alpha_c u_c) + \frac{\Gamma}{\rho_c} \right) & \end{aligned} \quad (29)$$

Note the first appearance of the dispersed phase pressure and the work of pressure forces in the volume exchange between phases. The balances of the kinetic energies are deduced from the momentum balances

$$\begin{aligned} \frac{\partial}{\partial t} \left(\alpha_d \rho_d \frac{u_d^2}{2} \right) + \nabla \cdot \left(\alpha_d \rho_d \frac{u_d^2}{2} u_d + u_d \cdot \sigma_d + \alpha_d p_c u_d \right) \\ = u_d \cdot F + \sigma_d : \nabla u_d + \Gamma \left(u_d \cdot u^* - \frac{u_d^2}{2} \right) + p_c \nabla \cdot (\alpha_d u_d) + \alpha_d \rho_d u_d \cdot g \end{aligned} \quad (30)$$

$$\begin{aligned} \frac{\partial}{\partial t} \left(\alpha_c \rho_c \frac{u_c^2}{2} \right) + \nabla \cdot \left(\alpha_c \rho_c \frac{u_c^2}{2} u_c + u_c \cdot \sigma_c + \alpha_c p_c u_c \right) \\ = -u_c \cdot F + \sigma_c : \nabla u_c - \Gamma \left(u_c \cdot u^* - \frac{u_c^2}{2} \right) + p_c \nabla \cdot (\alpha_c u_c) + \alpha_c \rho_c u_c \cdot g. \end{aligned} \quad (31)$$

The total phasic energy per unit mass is written as

$$E_k = e_k(\rho_k, s_k) + \frac{u_k^2}{2} + K_k. \quad (32)$$

where K_k is the pseudo-turbulent kinetic energy related to the velocity fluctuations around u_k . It is to be stressed that in a fluid-particles mixture those velocity fluctuations are created by the shear motion of the particles, by the relative motion between the fluid and the particles or by a change in volume or shape of the particles. They disappear as soon as the shear motion, the relative motion, or the particle deformation stops. They are thus quite different from the velocity fluctuations generated by Brownian motion or by turbulence.

After adding the balance of kinetic energy to the balances of internal energy one obtains the following evolution equations for the total energy

$$\begin{aligned} \frac{\partial}{\partial t}(\alpha_d \rho_d E_d) + \nabla \cdot (\alpha_d \rho_d E_d u_d + \alpha_d p_c u_d + u_d \cdot \sigma_d + T_d h_d) = -p_c \frac{\partial \alpha_d}{\partial t} + T_d \Delta_d \\ + \sigma_d : \nabla u_d + h_d \cdot \nabla T_d + T_d \Sigma + u_d \cdot F + \Gamma(\mu_d + T_d s^* + u_d \cdot u^* - u_d^2/2) \\ + (p_c - p_d) \left[\frac{\partial \alpha_d}{\partial t} + \nabla \cdot (\alpha_d u_d) \right] + \frac{\partial}{\partial t}(\alpha_d \rho_d K_d) + \nabla \cdot (\alpha_d \rho_d K_d u_d) + \alpha_d \rho_d u_d \cdot g \end{aligned} \quad (33)$$

$$\begin{aligned} \frac{\partial}{\partial t}(\alpha_c \rho_c E_c) + \nabla \cdot (\alpha_c \rho_c E_c u_c + \alpha_c p_c u_c + u_c \cdot \sigma_c + T_c h_c) = -p_c \frac{\partial \alpha_c}{\partial t} + T_c \Delta_c \\ + \sigma_c : \nabla u_c + h_c \cdot \nabla T_c - T_c \Sigma - u_c \cdot F - \Gamma(\mu_c + T_c s^* + u_c \cdot u^* - u_c^2/2) \\ + \frac{\partial}{\partial t}(\alpha_c \rho_c K_c) + \nabla \cdot (\alpha_c \rho_c K_c u_c) + \alpha_c \rho_c u_c \cdot g. \end{aligned} \quad (34)$$

In these equations $\mu_k = \epsilon_k + p_k/\rho_k - T_k s_k$ is the chemical potential or Gibbs free-energy per unit mass of phase k . Note the asymmetry concerning the work of the pressure difference $p_d - p_c$, which appears in the equation for the particulate phase only.

We will neglect surface tension and any interfacial energy so that the right-hand sides of the two above equations (apart from the work of external gravity forces) represent the exchange of energy between the two phases and their sum must vanish or must be equal to the divergence of some Galilean-invariant energy flux Q . Hence the *necessary condition* to be fulfilled for the total energy $E = \alpha_d \rho_d E_d + \alpha_c \rho_c E_c$ to be conserved is

$$\begin{aligned} T_d \Delta_d + T_c \Delta_c + (T_d - T_c) \Sigma + (u_d - u_c) \cdot F - (p_d - p_c) \left[\frac{\partial \alpha_d}{\partial t} + \nabla \cdot (\alpha_d u_d) \right] \\ + \Gamma[\mu_d - \mu_c + (T_d - T_c) s^* + (u_c - u^*)^2/2 - (u_d - u^*)^2/2] \\ + \sum_{k=c,d} \left[\frac{\partial}{\partial t}(\alpha_k \rho_k K_k) + \nabla \cdot (\alpha_k \rho_k K_k u_k) + \sigma_k : \nabla u_k + h_k \cdot \nabla T_k \right] + \nabla \cdot Q = 0. \end{aligned} \quad (35)$$

The above equality will play a role of utmost importance for dispersed mixtures and it holds in all cases, whether the carrier fluid is compressible or not, whether the particles are rigid or not. It must be considered as a necessary condition to be satisfied between the (yet unknown) transport equations for α_d , K_d , and K_c and the six main balance equations (21)–(26). Its significance will appear more clearly if we deal first with non-dissipative mixtures and then with dissipative ones.

4 Non-Dissipative Model

When all dissipative phenomena are discarded, condition (35) simplifies to

$$(u_d - u_c) \cdot F^R - (p_d - p_c) \left(\frac{\partial \alpha_d}{\partial t} + \nabla \cdot (\alpha_d u_d) \right) + \sum_{k=c,d} \left[\alpha_k \rho_k \frac{d_k K_k}{dt} + \sigma_k^R : \nabla u_k \right] + \nabla \cdot Q^R = 0. \quad (36)$$

stating the link to be verified between the non-dissipative form of the transport equations for α_d , K_d , and K_c and the non-dissipative parts (with superscript R) of the phasic stresses and the interphase force. We consider the consequences of that equality for cases of increasing complexity.

4.1 Rigid Particles

4.1.1 Rigid Particles, No Velocity Fluctuations

When the particles are rigid and the role of velocity fluctuations is neglected, condition (36) simplifies to $(u_d - u_c) \cdot F^R + \sigma_c^R : \nabla u_c + \sigma_d^R : \nabla u_d + \nabla \cdot Q^R = 0$ and there is apparently no other solution than $F^R = \sigma_c^R = \sigma_d^R = Q^R = 0$. This result holds for compressible as well as incompressible fluid surrounding the (compressible or incompressible) particles. The equations describing that simple non-dissipative case are

$$\frac{\partial \alpha_d}{\partial t} + \nabla \cdot (\alpha_d u_d) = 0 \quad (37)$$

$$\frac{\partial}{\partial t} (\alpha_c \rho_c) + \nabla \cdot (\alpha_c \rho_c u_c) = 0 \quad (38)$$

$$\frac{d_k s_k}{dt} = 0 \quad (39)$$

$$\alpha_k \rho_k \frac{d_k u_k}{dt} + \alpha_k \nabla p_c = \alpha_k \rho_k g. \quad (40)$$

When the carrier fluid is incompressible (38) is replaced by $\nabla \cdot u = 0$ where $u = \alpha_c u_c + \alpha_d u_d$ is the volume-weighted mean velocity of the mixture and the remaining equations are left unchanged. In all cases (rigid particles in a compressible or incompressible carrier fluid but with negligible velocity fluctuations) the balances of total energy are given by

$$\alpha_k \rho_k \frac{d_k E_k}{dt} + \nabla \cdot (\alpha_k p_c u_k) + p_c \frac{\partial \alpha_k}{\partial t} = \alpha_k \rho_k u_k \cdot g. \quad (41)$$

It is known since long (Gidaspow 1974; Stuhmiller 1977; Jones and Prosperetti 1985) that the above set of non-dissipative equations is not hyperbolic.

4.1.2 Rigid Particles with Added-Mass Velocity Fluctuations

When the carrier fluid is incompressible and its flow is *nonviscous and potential* the two momentum equations (11) and (12) can be written as (see Appendix A):

$$\alpha_c \rho_c \frac{d_c u_c}{dt} + \nabla \cdot \sigma_c^K + \alpha_c \nabla p_c = -F^K + \alpha_c \rho_c g \quad (42)$$

$$\alpha_d \rho_d \frac{d_d u_d}{dt} + \nabla \cdot \sigma_d^K + \alpha_d \nabla p_c = F^K + \alpha_d \rho_d g, \quad (43)$$

with

$$F^K = -\frac{\partial J}{\partial t} - \nabla \cdot (u_d \otimes J) - (J \cdot \nabla) u_c - \alpha_c \rho_c \nabla K_c - J \times (\nabla \times u_c) \quad (44)$$

$$\sigma_c^K = (u_d - u_c) \otimes J \quad (45)$$

where J is the (Kelvin) fluid impulse (defined in (A-8)) and K_c is the fluctuational kinetic energy of the fluid. Note that so far no expression is given for the particle stress σ_d^K . Some general definition exists for this stress tensor (Sangani and Didwania 1993; Bulthuis et al. 1995) but a closed expression in terms of the fluid impulse and other main variables has been difficult to obtain. However, some insight concerning σ_d^K can be provided by condition (36) as developed below.

When particles move relative to the fluid they drag part of the fluid mass with them and they confer the fluid a supplementary kinetic energy. *Neglecting the particles velocity fluctuations* ($K_d = 0$) results in a well-known simplified expression for the fluid pseudo-turbulent (particle-induced) kinetic energy (Geurst 1985; Wallis 1991)

$$K_c = \frac{1}{2} E (\alpha_d) (u_d - u_c)^2, \quad (46)$$

where E is a scalar depending on the particle volume fraction, which behaves like $\alpha_d/2$ for dilute suspensions. There is no real transport equation for K_c but it is possible to deduce from (46)

$$\begin{aligned} \alpha_c \rho_c \frac{d_c K_c}{dt} &= \alpha_c \rho_c \left[E (u_d - u_c) \cdot \frac{d_c}{dt} (u_d - u_c) + \frac{(u_d - u_c)^2}{2} \frac{d_c E}{dt} \right] \\ &= (u_d - u_c) \cdot \left[\frac{\partial J}{\partial t} + \nabla \cdot (u_c \otimes J) \right] - \alpha_c \rho_c \frac{(u_d - u_c)^2}{2} \frac{d_c E}{dt} \end{aligned} \quad (47)$$

where

$$J = \alpha_c \rho_c E (\alpha_d) (u_d - u_c). \quad (48)$$

With F^K and σ_c^K given by the exact results (44) and (45), and noticing that $d_d \alpha_d / dt = -\alpha_d \nabla \cdot u_d$ for rigid particles, the above (pseudo-)transport equation for K_c is finally written as

$$\alpha_c \rho_c \frac{d_c K_c}{dt} = -F^K \cdot (u_d - u_c) - \sigma_c^K : \nabla u_c - \alpha_d P^K \nabla \cdot u_d - \nabla \cdot Q^K. \quad (49)$$

with the pressure P^K and the energy flux Q^K defined as

$$P^K = -\alpha_c \rho_c \frac{\partial K_c}{\partial \alpha_d}, \quad (50)$$

$$Q^K = 2\alpha_c \rho_c K_c (u_d - u_c). \quad (51)$$

When compared to the transport equation for a turbulent kinetic energy, it is worthy to note that (49) exhibits three production terms and one flux (but no dissipation term). Taking (49) into account, relation (36) is satisfied with

$$F^R = F^K, \quad \sigma_c^R = \sigma_c^K, \quad \sigma_d^R = \alpha_d P^K I, \quad Q^R = Q^K. \quad (52)$$

We have thus obtained explicit expressions for the fluid impulse and for the particle stress, which are consistent with assumption (46). It is remarkable that the same scalar $E(\alpha_d)$ appears in the pseudo-turbulent kinetic energy (46) and in the Kelvin impulse (48). This is not true in general as was emphasized by Biesheuvel and Spoolstra (1989) but is a consequence of our neglect of the velocity fluctuations of the particles, as is clear when comparing with the general result (A-13) in Appendix A.

All these results hold for rigid spheres moving in an incompressible carrier fluid. Their extension to a compressible fluid is far from obvious. The velocity disturbances created in the fluid by the particle motion do not propagate instantaneously but with the speed of sound and they are accompanied by mass density disturbances. The simplest approximation is to consider that expression (46) is approximately correct in a compressible carrier fluid. Then it can be shown that identity (49) still holds and consequently, to describe the flow of rigid particles moving in a fluid with added-mass velocity fluctuations described by (46) one needs the following set of six non-dissipative equations

$$\frac{\partial \alpha_d}{\partial t} + \nabla \cdot (\alpha_d u_d) = 0 \quad (53)$$

$$\frac{\partial}{\partial t} (\alpha_c \rho_c) + \nabla \cdot (\alpha_c \rho_c u_c) = 0 \quad (54)$$

$$\frac{d_d s_d}{dt} = 0, \quad \frac{d_c s_c}{dt} = 0 \quad (55)$$

$$\alpha_c \rho_c \frac{d_c u_c}{dt} + \nabla \cdot \sigma_c^K + \alpha_c \nabla p_c = -F^K + \alpha_c \rho_c g \quad (56)$$

$$\alpha_d \rho_d \frac{d_d u_d}{dt} + \nabla (\alpha_d P^K) + \alpha_d \nabla p_c = F^K + \alpha_d \rho_d g. \quad (57)$$

The corresponding balances of total energies are deduced from (33) and (34) as

$$\alpha_c \rho_c \frac{d_c E_c}{dt} + \nabla \cdot (\alpha_c p_c u_c + u_c \cdot \sigma_c^K + Q^K) + p_c \frac{\partial \alpha_c}{\partial t} = -W^K + \alpha_c \rho_c u_c \cdot g \quad (58)$$

$$\alpha_d \rho_d \frac{d_d E_d}{dt} + \nabla \cdot [\alpha_d (p_c + P^K) u_d] + p_c \frac{\partial \alpha_d}{\partial t} = W^K + \alpha_d \rho_d u_d \cdot g \quad (59)$$

with the inter-phase energy exchange defined as

$$W^K = u_d \cdot F^K + \alpha_d P^K \nabla \cdot u_d. \quad (60)$$

When all terms associated with added-mass kinetic energy vanish we find back the results of **► Sect. 4.1.1**. Note that from (59) the sum $p_c + P^K$ can be considered as the particle pressure.

The mathematical character of the above set of mass and momentum equations has been investigated in Sushchikh and Chang (2009) (summarized in **Appendix B**) and, in case of an *incompressible* fluid, it was found that its hyperbolicity requires the function $E(\alpha_d)/\alpha_d$ and its first and second derivatives with respect to α_d (denoted by a prime and a double prime) to satisfy the inequality

$$\left[\alpha_d - \alpha_c \frac{\rho_d}{\rho_c} + (1 - 2\alpha_c) \frac{E}{\alpha_d} + 2\alpha_c \alpha_d \left(\frac{E}{\alpha_d} \right)' \right]^2 \geq \left[\alpha_d + \alpha_c \frac{\rho_d}{\rho_c} + \frac{E}{\alpha_d} \right] \times \left[\alpha_d + \alpha_c \frac{\rho_d}{\rho_c} + \frac{E}{\alpha_d} + 2\alpha_c^2 \alpha_d^2 \left(\frac{E}{\alpha_d} \right)'' \right]. \quad (61)$$

It is interesting to note that this inequality is *independent of the relative velocity* and cannot be satisfied when $E = 0$, that is to say when one neglects the added-mass kinetic energy of the carrier phase.

We looked for expressions of $E(\alpha_d)$ for which the above inequality is satisfied whatever the value of ρ_d/ρ_c . We found that the quadratic expression $E = (\alpha_d/2)(1 + C\alpha_d)$ (hence $(E/\alpha_d)'' = 0$) assures hyperbolicity *for any value of the density ratio provided* $C \leq -3$. Since $E(\alpha_d)$ must be positive, the choice of a particular value for C defines the range in volume fraction over which hyperbolicity can be assured on physical grounds. For example, with $C = -3$ we have

$$E(\alpha_d) = \frac{\alpha_d}{2}(1 - 3\alpha_d) \quad (62)$$

and hyperbolicity is assured up to $\alpha_d = 1/3$. That special value of C was already pointed out by Geurst (1985) who remarked that it is a sound choice in case of bubbly fluids for which a flow regime transition is expected close to $\alpha_d \approx 0.3$. This choice of C is also supported by theoretical arguments (Wallis 1989, 1991). On the other hand, it must be noted that the physical validity of this second-order expansion, beyond the value of α_d that corresponds to the maximum in E , would appear to require closer examination.

While in bubbly flows the relative velocity is always small and the simplified incompressible analysis is quite adequate, this is not the case for solid particles or drops dispersed in a compressible phase. A complete analysis for this case (Sushchikh and Chang 2009) (**Appendix B**) shows that there is a non-hyperbolic corridor around the transonic region that depends weakly on the volume fraction. Clearly, if one demands hyperbolicity for any volume fraction and any Mach number, then new physics must be introduced, involving in particular a description of *particle velocity fluctuations*, either fluid-induced or resulting from collisions. As a consequence (46) would be replaced by a more elaborated expression like

$$K_c = \frac{1}{2}E(\alpha_d, M^*)(u_d - u_c)^2 + F(\alpha_d)K_d. \quad (63)$$

Although the two scalar functions E and F behave as $\alpha_d/2$ in the dilute limit (Zhang and Prosperetti 1994) we cannot take for sure that they are equal for all concentrations. The point is that no closed expression exists for K_d itself or for its transport equation. However if (63) is accepted it is clear that the density $\alpha_d \rho_d + \alpha_c \rho_c F(\alpha_d)$ will play a main role in the transport equation for K_d as well as in the modified form of inequality (61). This is left for later studies.

4.2 Compressible Particles

In dispersed liquid-vapour mixtures the bubbles are highly compressible and the carrier fluid is generally considered as incompressible. To simplify the issue the bubble shape will be assumed to stay spherical and only monodisperse collection of bubbles with a radius $a(x, t)$ will be considered. The bubble radius changes with time and position and a relevant quantity is the convective time-derivative $d_d a/dt$. When mass exchange occurs between the bubbles and the carrier fluid $d_d a/dt$ is different from w_c the mean radial velocity of the fluid at the boundary with the bubbles. In the present section we neglect mass exchanges (a dissipative process) and take $d_d a/dt = w_c$ but to be consistent with the next section dealing with dissipative phenomena, we will consider w_c as the fundamental velocity to describe the non-dissipative radial motion of the bubbles.

The velocity w_c is responsible for a supplementary kinetic energy of the liquid, which adds to the virtual mass kinetic energy. The expression of the pseudo-turbulent kinetic energy K_c becomes

$$K_c = \frac{1}{2}E(\alpha_d)(u_d - u_c)^2 + \frac{1}{2}Q(\alpha_d)w_c^2 \quad (64)$$

where Q is a function of the volume fraction, which behaves like $3\alpha_d$ in the dilute limit. Because of the small mass density of the bubbles it is usual to assume that their kinetic energy of pulsation vanishes and we let $K_d = 0$ in what follows. To describe the motion of the bubble fluid the momentum equations are completed by two more (non-dissipative) equations (Nigmatulin 1991), the first one being the transport equation for the volume fraction with due account for the bubble expansion rate

$$\frac{\partial \alpha_d}{\partial t} + \nabla \cdot (\alpha_d u_d) = 3\alpha_d \frac{w_c}{a} \quad (65)$$

and the second one being a generalization to finite volume fractions of the single particle Rayleigh-Lamb equation

$$a d_d w_c/dt + (3/2)w_c^2 - (1/4)(u_d - u_c)^2 = (p_d - p_c)/\rho_c.$$

There is also a second quantity that must be properly generalized to finite volume fractions, the total (non-dissipative) stress, which is well known (Nigmatulin 1991) for dilute mixtures

$$\sigma_c^R + \sigma_d^R = \frac{\alpha_d}{2}\rho_c(u_d - u_c) \otimes (u_d - u_c) + \alpha_d(p_d - p_c)I + \alpha_d\rho_c w_c^2 I$$

The two generalizations we are looking for can be deduced from constraint (36).

We insist again that there is no true transport equation for K_c but, because of its dependence on the bubble volume fraction, on the relative velocity and on the bubble expansion rate, one can derive from (64) the identity

$$\begin{aligned} \alpha_c \rho_c \frac{d_c K_c}{dt} \equiv & -(u_d - u_c) \cdot \left(F^K + \frac{R^K}{3\alpha_c} \nabla \alpha_d \right) + \frac{w_c}{a} \left(\frac{R^K}{\alpha_c} + 3\alpha_d P^K - \frac{w_c}{a} M \right) \\ & - \left(\sigma_c^K + \frac{R^K}{3} I \right) : \nabla u_c - \alpha_d \left(P^K + \frac{R^K}{3\alpha_c} \right) \nabla \cdot u_d - \nabla \cdot Q^K. \end{aligned} \quad (66)$$

The Kelvin impulse J is still given by (48) and the quantities F^K , σ_c^K , P^K , and Q^K are still defined by (44), (45), (50), and (51) respectively, but with K_c now given by (64). The only new quantity is R^K which is defined as

$$R^K \equiv \frac{\partial M}{\partial t} + \nabla \cdot (Mu_d), \quad (67)$$

where M is the *scalar* Kelvin impulse of the liquid defined as

$$M = \alpha_c \rho_c Q(\alpha_d) a w_c. \quad (68)$$

The scalar M is playing for the radial motion the same role as the vector J for the relative motion. Taking (65) and (66) into account, relation (36) is satisfied with $Q^R = Q^K$ and

$$F^R = F^K + \frac{R^K}{3\alpha_c} \nabla \alpha_d, \quad \sigma_c^R = \sigma_c^K + \frac{R^K}{3} I, \quad \sigma_d^R = \alpha_d (P^K + \frac{R^K}{3\alpha_c}) I.$$

The generalized Rayleigh-Lamb equation simply appears as

$$\frac{R^K}{\alpha_c} + 3\alpha_d P^K - \frac{w_c}{a} M = 3\alpha_d (p_d - p_c).$$

while the generalized total stress is

$$\sigma_c^R + \sigma_d^R = \sigma_c^K + \alpha_d (p_d - p_c) I + w_c \frac{M}{3a} I.$$

We now gather the above results to obtain the non-dissipative equations for a suspension of spherical bubbles moving in a non-compressible fluid with a pseudo-turbulent kinetic energy given by (64),

$$\frac{\partial \alpha_d}{\partial t} + \nabla \cdot (\alpha_d u_d) = 3\alpha_d \frac{w_c}{a} \quad (69)$$

$$\frac{\partial \alpha_c}{\partial t} + \nabla \cdot (\alpha_c u_c) = 0 \quad (70)$$

$$\frac{\partial \alpha_d \rho_d}{\partial t} + \nabla \cdot (\alpha_d \rho_d u_d) = 0 \quad (71)$$

$$\frac{d_c s_c}{dt} = 0, \quad \frac{d_d s_d}{dt} = 0 \quad (72)$$

$$\alpha_c \rho_c \frac{d_c u_c}{dt} + \nabla \cdot \sigma_c^K + \alpha_c \nabla \left(\frac{R^K}{3\alpha_c} \right) + \alpha_c \nabla p_c = -F^K + \alpha_c \rho_c g \quad (73)$$

$$\alpha_d \rho_d \frac{d_d u_d}{dt} + \nabla (\alpha_d P^K) + \alpha_d \nabla \left(\frac{R^K}{3\alpha_c} \right) + \alpha_d \nabla p_c = F^K + \alpha_d \rho_d g \quad (74)$$

$$\frac{\partial M}{\partial t} + \nabla \cdot (Mu_d) - \alpha_c \frac{w_c}{a} M = 3\alpha_d \alpha_c (p_d - p_c - P^K). \quad (75)$$

These eight equations reduce to six (see \blacktriangleright Sect. 3.1.2) when the particles are incompressible : this is because (71) is redundant with (69), and (75) reduces to $p_d = p_c + P^K$. Note that this

justifies the statement made in \blacktriangleright Sect. 4.1.2 that $p_c + P^K$ represents the particle pressure in case of rigid particles.

It is sometimes interesting to have the transport equations for the total energy. The result is an extension of (58) and (59)

$$\begin{aligned} \alpha_c \rho_c \frac{d_c E_c}{dt} + \nabla \cdot \left(\alpha_c p_c u_c + u_c \cdot \sigma_c^K + (\alpha_d u_d + \alpha_c u_c) \frac{R^K}{3\alpha_c} + Q^K \right) \\ + p_c \frac{\partial \alpha_c}{\partial t} = -W^K + \alpha_c \rho_c u_c \cdot g \end{aligned} \quad (76)$$

$$\alpha_d \rho_d \frac{d_d E_d}{dt} + \nabla \cdot [\alpha_d (p_c + P^K) u_d] + p_c \frac{\partial \alpha_d}{\partial t} = W^K + \alpha_d \rho_d u_d \cdot g. \quad (77)$$

with the inter-phase energy exchange given by

$$W^K = u_d \cdot \left[F^K - \alpha_d \nabla \cdot \left(\frac{R^K}{3\alpha_c} \right) \right] + \alpha_d P^K \nabla \cdot u_d - 3\alpha_d (p_d - p_c) \frac{w_c}{a}. \quad (78)$$

The transport equation (65) for the particle volume fraction holds whether the fluid around the bubbles is compressible or not. In case of a compressible fluid the Rayleigh-Lamb equation (75) is modified (Keller and Miksis 1980). We showed with (68) that the Rayleigh-Lamb equation is intimately related to the fluid fluctuational kinetic energy and a possible way to represent the fluid compressibility is to start from a modified expression like

$$K_c = \frac{1}{2} E(\alpha_d, M^*) (u_d - u_c)^2 + \frac{1}{2} Q \left(\alpha_d, \frac{w_c}{c_c} \right) w_c^2 \quad (79)$$

where c_c is the isentropic sound speed of the carrier fluid. Deducing $\alpha_c \rho_c d_c K_c / dt$ and following the same route as above one can derive the new Rayleigh-Lamb equation in a compressible fluid. The main advantage of the method is that a lot of complex results can be deduced from rather simple expressions for the pseudo-turbulent kinetic energies. It is clear however that we supposed the particles to be spheres of variable radius. This is tenable in so far as the bubbles are not distorted by the mean flow or by the presence of neighbor particles. This simplistic description of the particle internal motion is certainly not the most general one but is the one that prevails at not too high particle volume fraction and for not too large bubbles.

5 Dissipative Model

This section will consider dissipative processes in dispersed mixtures. For condition (35) to be satisfied the first issue is to propose complete transport equations for α_d , K_d , and K_c . These transport equations are very different depending upon whether the particles are compressible or not and we will consider the two cases separately.

5.1 Noncompressible Particles: Solid Grains or Drops

5.1.1 The Dissipation Rate

Because the issue of particle velocity fluctuations has not yet been solved we assume for simplicity that $K_d = 0$ while K_c is given by the added-mass expression (46). Since we now deal with dissipative phenomena we must take mass exchanges (phase transitions) into account and the transport equation for the fluid pseudo-turbulent energy writes (compare with the former expression (49))

$$\begin{aligned} \frac{\partial}{\partial t}(\alpha_c \rho_c K_c) + \nabla \cdot (\alpha_c \rho_c K_c u_c) &= -F^K \cdot (u_d - u_c) - \sigma_c^K : \nabla u_c \\ - \alpha_d P^K \nabla \cdot u_d - \nabla \cdot Q^K + P^K \left(\frac{\partial \alpha_d}{\partial t} + \nabla \cdot (\alpha_d u_d) \right) &+ \Gamma K_c . \end{aligned} \quad (80)$$

As seen in [Sect. 4.1.2](#), the pressure difference for rigid particles results from a Bernoulli effect expressed as

$$p_d - p_c = P^K . \quad (81)$$

Hence the transport equation for the volume fraction disappears from the condition for energy conservation (35), which is transformed into an expression for the total dissipation rate

$$\begin{aligned} T_d \Delta_d + T_c \Delta_c &= -(T_d - T_c) \Sigma - (u_d - u_c) \cdot (F - F^K) - h_c \cdot \nabla T_c - h_d \cdot \nabla T_d \\ &- \Gamma [\mu_d - \mu_c + (T_d - T_c) s^* + (u_c - u^*)^2 / 2 - (u_d - u^*)^2 / 2 + K_c] \\ &- (\sigma_c - \sigma_c^K) : \nabla u_c - (\sigma_d - \alpha_d P^K I) : \nabla u_d - \nabla \cdot (Q - Q^K) . \end{aligned}$$

This expression is not yet fully satisfactory: For a dispersed mixture a dissipation rate involving ∇u_d or ∇T_d holds when the particles are in permanent contact or display frequent collisions. At variance the particulate stress originating from the viscosity of the carrier fluid and the entropy flux originating from its heat conductivity must be described differently. These fluid-induced stresses and heat fluxes will be represented in what follows by τ and h and one expects them to give rise to a dissipation rate $\tau \cdot \nabla u + h \cdot \nabla T$ (Batchelor 1970; Prosperetti et al. 1998; Lhuillier 2003) where

$$u = \alpha_d u_d + \alpha_c u_c , \quad T = \alpha_d T_d + \alpha_c T_c , \quad (82)$$

are the mean velocity and mean temperature of the whole suspension. The simplest way to obtain the desired result is to adopt the definitions

$$\begin{aligned} F &= F^K + f - \alpha_d \nabla \cdot \tau , \\ \sigma_c &= \sigma_c^K + \tau , \\ \sigma_d &= \alpha_d P^K I , \\ Q &= Q^K + (T - T_c) h + (u - u_c) \cdot \tau , \\ h_d &= 0 , \\ h_c &= h , \\ \Sigma &= H - \alpha_d \nabla \cdot h . \end{aligned}$$

With these definitions the initial equations (21)–(26) are transformed into

$$\frac{\partial \alpha_d}{\partial t} + \nabla \cdot (\alpha_d u_d) = \frac{\Gamma}{\rho_d} \quad (83)$$

$$\frac{\partial}{\partial t} (\alpha_c \rho_c) + \nabla \cdot (\alpha_c \rho_c u_c) = -\Gamma \quad (84)$$

$$\alpha_d \rho_d \frac{d_d s_d}{dt} + \alpha_d \nabla \cdot h = \Delta_d + H + \Gamma (s^* - s_d) \quad (85)$$

$$\alpha_c \rho_c \frac{d_c s_c}{dt} + \alpha_c \nabla \cdot h = \Delta_c - H - \Gamma (s^* - s_c) \quad (86)$$

$$\alpha_d \rho_d \frac{d_d u_d}{dt} + \nabla \cdot (\alpha_d P^K) + \alpha_d \nabla \cdot \tau + \alpha_d \nabla p_c = F^K + f + \Gamma (u^* - u_d) + \alpha_d \rho_d g \quad (87)$$

$$\alpha_c \rho_c \frac{d_c u_c}{dt} + \nabla \cdot \sigma_c^K + \alpha_c \nabla \cdot \tau + \alpha_c \nabla p_c = -F^K - f - \Gamma (u^* - u_c) + \alpha_c \rho_c g. \quad (88)$$

Note that, at variance with most two-fluid models, there is a single viscous stress and a single heat flux and that $\nabla \cdot \tau$ and $\nabla \cdot h$ are shared in proportion to the volume fractions. With the above definitions the total dissipation rate becomes

$$T_d \Delta_d + T_c \Delta_c = -(T_d - T_c)H - (u_d - u_c) \cdot f - h \cdot \nabla T - \tau \cdot \nabla u \\ - \Gamma [\mu_d - \mu_c + (T_d - T_c)s^* + (u_c - u^*)^2/2 - (u_d - u^*)^2/2 + K_c]. \quad (89)$$

Expression (89) plays a very important role for dissipative phenomena, similar to the role played by (36) for non-dissipative ones. The quantity $T_d \Delta_d + T_c \Delta_c$ is slightly different from the total entropy production rate $\Delta_d + \Delta_c$ but it represents a closely related quantity, the total energy dissipation rate in the mixture. And instead of the usual thermodynamic inequalities $\Delta_d \geq 0$ and $\Delta_c \geq 0$ we will rely on the related inequality $T_d \Delta_d + T_c \Delta_c \geq 0$. Hence the right-hand side of (89) must be positive in all circumstances.

5.1.2 The Constitutive Laws

According to (89) there are five different sources of dissipation corresponding to the the heat, momentum, and mass exchanges at interfaces together with the heat and momentum transport through the bulk of the mixture. The thermodynamic forces associated with these five kinds of dissipation have the intuitively expected form except for the one linked to mass exchange, which is associated with a disequilibrium involving u^* and s^* . Since the mass exchange (phase transition rate) is expected to be driven by thermodynamic quantities mainly, with a limited influence of the relative velocity, the best choice for u^* is apparently

$$u^* = \frac{u_c + u_d}{2}. \quad (90)$$

That special value for u^* was adopted by several authors (Baer and Nunziato 1986; Young 1995) but a different one ($u^* = u_d$) was preferred by Marble (1969) who supposed that no thrust force could act on the particles due to mass exchange. At variance (90) implies that the same thrust force acts on the two phases of the mixture. In other words, with choice (90) there is no “rocket

effect” due to mass exchange. Concerning the specific entropy s^* Marble (1969) suggested (for liquid droplets surrounded by their vapor) to choose

$$s^* = s_c \quad (91)$$

because all the latent heat of the phase transitions are provided by (or given to) the droplets. If we adopt Marble’s choice, the driving force for mass exchange between a noncompressible particle and its vapor is

$$\mu_c - \mu_d + s_c(T_c - T_d) \simeq (s_c - s_d)(T_{sat}(p_c) - T_d),$$

with $T_{sat}(p_c)$ the saturation temperature at the continuous phase pressure. The dissipation rate is now rewritten in the final form

$$\begin{aligned} T_d \Delta_d + T_c \Delta_c &= (T_c - T_d)H + (u_c - u_d) \cdot f - \tau \cdot \nabla u - h \cdot \nabla T \\ &+ \Gamma[(s_c - s_d)(T_{sat}(p_c) - T_d) - K_c] \geq 0. \end{aligned} \quad (92)$$

Concerning the exchanges at interfaces a positive dissipation is guaranteed with the constitutive laws

$$H = \kappa(T_c - T_d), \quad (93)$$

$$f = \zeta(u_c - u_d), \quad (94)$$

$$\Gamma = \gamma[(s_c - s_d)(T_{sat}(p_c) - T_d) - K_c] \quad (95)$$

where ζ , κ , and γ are three positive transport coefficients. The above expressions are the simplest ones with no coupling at all between the dissipative exchanges. Concerning the viscous and heat transport through the bulk of the mixture the constitutive laws are in their simplest form

$$\sigma = -\eta \nabla u \quad (96)$$

$$h = -\lambda \nabla T \quad (97)$$

where η and λ are the effective viscosity and effective heat conductivity of the mixture and are positive transport coefficients that depend on the particle volume fraction. More complicated non-Newtonian constitutive relations are possibly obeyed by σ and non-Fourier ones by h . Whatever the chosen expressions they must satisfy the thermodynamic constraint expressed by inequality (92).

Once the expression of the total dissipation rate $T_d \Delta_d + T_c \Delta_c$ has been obtained, one must decide the way it is shared between its phasic components $T_d \Delta_d$ and $T_c \Delta_c$. Baer and Nunziato (1986) proposed that the dissipation from compaction is apportioned to the dispersed phase and the dissipation from drag to the continuous phase (nothing is said concerning the thermal dissipation and mass exchange dissipation). Then it was shown in Bdzil et al. (1999) that many other choices are possible, involving up to four sharing coefficients, one for each type of interfacial dissipation. Marble (1969) proposed to give the whole dissipation to the continuous phase and this is obviously the simplest solution that we here adopt because the internal velocity field and internal temperature field inside a particle is not likely to give rise to a heat source that can compete with the heat exchanged through interfaces. We thus assume

$$\Delta_d = 0. \quad (98)$$


We acknowledge that this is a crude assumption but the use of sharing coefficients would be a source of complication for the model without any guaranty of improvement.

5.2 Compressible Particles: Bubbles

5.2.1 The Dissipation Rate

We neglect the pseudo-turbulent kinetic energy of the particles ($K_d = 0$) and assume that the pseudo-turbulent kinetic energy of the carrier fluid is given by (64) from which is deduced the pseudo-transport equation

$$\begin{aligned} \frac{\partial}{\partial t}(\alpha_c \rho_c K_c) + \nabla \cdot (\alpha_c \rho_c K_c u_c) &= -(u_d - u_c) \cdot F^K - \sigma_c^K : \nabla u_c - \alpha_d P^K \nabla \cdot u_d \\ &+ \frac{w_c}{a} \left(R^K - \frac{\dot{a}}{a} M \right) + P^K \left(\frac{\partial \alpha_d}{\partial t} + \nabla \cdot (\alpha_d u_d) \right) - \nabla \cdot Q^K + \Gamma K_c, \end{aligned} \quad (99)$$

where $\dot{a} = d_d a / dt$ and all other quantities are defined in  Sect. 4.2. Concerning the transport of the particle volume fraction we now take mass exchange into account and (65) is transformed into its dissipative counterpart

$$\frac{\partial \alpha_d}{\partial t} + \nabla \cdot (\alpha_d u_d) = 3\alpha_d \frac{w_c}{a} + \frac{\Gamma}{\rho_c}. \quad (100)$$

a result obtained from the boundary condition for radial velocities at interfaces

$$\frac{3\alpha_d}{a} w_c + \frac{\Gamma}{\rho_c} = \frac{3\alpha_d}{a} w_d + \frac{\Gamma}{\rho_d}. \quad (101)$$

With the two above transport equations, condition (35) for energy conservation now turns into

$$\begin{aligned} T_d \Delta_d + T_c \Delta_c + (T_d - T_c) \Sigma + (u_d - u_c) \cdot (F - F^K - \Delta P \nabla \alpha_d) + \Gamma [\mu_d - \mu_c + (T_d - T_c) s^* \\ - (p_d - p_c - P^K) / \rho_c + (u_c - u^*)^2 / 2 - (u_d - u^*)^2 / 2 + K_c] \\ + (\sigma_c - \sigma_c^K - \alpha_c \Delta P I) : \nabla u_c + (\sigma_d - \alpha_d P^K I - \alpha_d \Delta P I) : \nabla u_d \\ + (w_c / a) (R^K - 3\alpha_c \Delta P) + h_c \cdot \nabla T_c + h_d \cdot \nabla T_d + \nabla \cdot (Q - Q^K) = 0 \end{aligned} \quad (102)$$

where the generalized pressure difference ΔP is defined by

$$\Delta P = \alpha_d (p_d - p_c - P^K) + \frac{\dot{a}}{a} \frac{M}{3}. \quad (103)$$

We now follow the same strategy as for incompressible particles and introduce the definitions

$$\begin{aligned}
 F &= F^K + \Delta P \nabla \alpha_d + f - \alpha_d \nabla \cdot \tau, \\
 \sigma_c &= \sigma_c^K + \alpha_c \Delta P I + \tau, \\
 \sigma_d &= \alpha_d P^K I + \alpha_d \Delta P I, \\
 Q &= Q^K + (T - T_c)h + (u - u_c) \cdot \tau, \\
 h_d &= 0, \\
 h_c &= h, \\
 \Sigma &= H - \alpha_d \nabla \cdot h.
 \end{aligned}$$

To these definitions we add the generalized Rayleigh-Lamb equation written as

$$R^K + 12\alpha_d \alpha_c \eta_c \frac{w_c}{a} = 3\alpha_c \Delta P, \quad (104)$$

where η_c is the viscosity of the carrier fluid. Hence the final set of equations can be written as

$$\frac{\partial \alpha_d}{\partial t} + \nabla \cdot (\alpha_d u_d) = 3\alpha_d \frac{w_c}{a} + \frac{\Gamma}{\rho_c} \quad (105)$$

$$\frac{\partial \alpha_d \rho_d}{\partial t} + \nabla \cdot (\alpha_d \rho_d u_d) = \Gamma \quad (106)$$

$$\frac{\partial \alpha_c \rho_c}{\partial t} + \nabla \cdot (\alpha_c \rho_c u_c) = -\Gamma \quad (107)$$

$$\alpha_d \rho_d \frac{d_d s_d}{dt} + \alpha_d \nabla \cdot h = \Delta_d + H + \Gamma(s^* - s_d) \quad (108)$$

$$\alpha_c \rho_c \frac{d_c s_c}{dt} + \alpha_c \nabla \cdot h = \Delta_c - H - \Gamma(s^* - s_c) \quad (109)$$

$$\begin{aligned}
 \alpha_c \rho_c \frac{d_c u_c}{dt} + \nabla \cdot \sigma_c^K + \alpha_c \nabla \cdot \tau + \alpha_c \nabla \cdot (p_c + \Delta P) \\
 = -F^K - f - \Gamma(u^* - u_c) + \alpha_c \rho_c g
 \end{aligned} \quad (110)$$

$$\begin{aligned}
 \alpha_d \rho_d \frac{d_d u_d}{dt} + \nabla \cdot (\alpha_d P^K) + \alpha_d \nabla \cdot \tau + \alpha_d \nabla \cdot (p_c + \Delta P) \\
 = F^K + f + \Gamma(u^* - u_d) + \alpha_d \rho_d g
 \end{aligned} \quad (111)$$

$$\frac{R^K}{3\alpha_c} + 4\alpha_d \eta_c \frac{w_c}{a} = \Delta P, \quad (112)$$

while the total dissipation rate becomes

$$\begin{aligned}
 T_d \Delta_d + T_c \Delta_c = -(T_d - T_c)H - (u_d - u_c) \cdot f - h \cdot \nabla T - \tau \cdot \nabla u + 12\alpha_d \alpha_c \eta_c \left(\frac{w_c}{a} \right)^2 \\
 - \Gamma[\mu_d - \mu_c + (T_d - T_c)s^* - (p_d - p_c - P^K)/\rho_c + K_c],
 \end{aligned} \quad (113)$$

where the special value of u^* given in (90) was used. The main difference with the case of incompressible particles is the existence of a new source of dissipation linked to the radial motion and a new term involving the pressure difference in the thermodynamic force driving the mass exchange.

5.2.2 The Constitutive Laws

Most of the constitutive laws (those for H , f , h , τ , and u^*), as well as the assumption $\Delta_d = 0$, are unchanged compared to the case of incompressible particles. There are however two remarkable differences, the value of s^* and the constitutive law for Γ . The gas bubbles can hardly provide or receive the latent heat associated with mass exchange while the liquid around them is a good candidate for that role. Hence it is likely that

$$s^* = s_d \quad (114)$$

so that the entropy balance of the bubbles (85) is independent of the mass exchange. The driving force for mass exchange between a bubble and the surrounding liquid is then

$$\mu_c - \mu_d + s_d(T_c - T_d) - \frac{1}{\rho_c}(p_c - p_d) \simeq (s_d - s_c)(T_c - T_{sat}(p_d)),$$

and the mass exchange at interfaces is given by

$$\Gamma = \gamma[(s_d - s_c)(T_c - T_{sat}(p_d)) - K_c - P^K/\rho_c] \quad (115)$$

The role of the two terms related to velocity fluctuations is presumably negligible.

5.3 Final Form of the Model

The above analysis of two special cases (incompressible particles and highly compressible ones) suggests that $\Delta_d = 0$ and u^* is given by (90). As a consequence the initial equations (21)-(26) are conveniently replaced for *any dispersed mixture* by

$$\frac{\partial}{\partial t}(\alpha_d \rho_d) + \nabla \cdot (\alpha_d \rho_d u_d) = \Gamma \quad (116)$$

$$\frac{\partial}{\partial t}(\alpha_c \rho_c) + \nabla \cdot (\alpha_c \rho_c u_c) = -\Gamma \quad (117)$$

$$\alpha_d \rho_d \frac{d_d s_d}{dt} + \alpha_d \nabla \cdot h = H + \Gamma(s^* - s_d) \quad (118)$$

$$\alpha_c \rho_c \frac{d_c s_c}{dt} + \alpha_c \nabla \cdot h = \Delta_c - H - \Gamma(s^* - s_c) \quad (119)$$

$$\begin{aligned} \alpha_d \rho_d \frac{d_d u_d}{dt} + \nabla \cdot \sigma_d^R + \alpha_d \nabla \cdot \sigma + \alpha_d \nabla p_c \\ = F^R + f + \Gamma(u_c - u_d)/2 + \alpha_d \rho_d g \end{aligned} \quad (120)$$

$$\begin{aligned} \alpha_c \rho_c \frac{d_c u_c}{dt} + \nabla \cdot \sigma_c^R + \alpha_c \nabla \cdot \sigma + \alpha_c \nabla p_c \\ = -F^R - f + \Gamma(u_c - u_d)/2 + \alpha_c \rho_c g, \end{aligned} \quad (121)$$

The resulting balance equations for internal energy are

$$\begin{aligned} \frac{\partial}{\partial t}(\alpha_d \rho_d e_d) + \nabla \cdot (\alpha_d \rho_d e_d u_d) &= T_d(H - \alpha_d \nabla \cdot h) + \Gamma[e_d + T_d(s^* - s_d)] \\ &- p_d \left(\frac{\partial \alpha_d}{\partial t} + \nabla \cdot (\alpha_d u_d) - \frac{\Gamma}{\rho_d} \right) \end{aligned} \quad (122)$$

$$\begin{aligned} \frac{\partial}{\partial t}(\alpha_c \rho_c e_c) + \nabla \cdot (\alpha_c \rho_c e_c u_c + Th) &= T_c \Delta_c + (T_d - T_c)H + h \cdot \nabla T \\ &- T_d(H - \alpha_d \nabla \cdot h) - \Gamma[e_c + T_c(s^* - s_c)] - p_c \left(\frac{\partial \alpha_c}{\partial t} + \nabla \cdot (\alpha_c u_c) + \frac{\Gamma}{\rho_c} \right). \end{aligned} \quad (123)$$

while the conservation of total energy requires

$$\begin{aligned} T_c \Delta_c &= -(T_d - T_c)H - (u_d - u_c) \cdot (f + F^R) - h \cdot \nabla T - \sigma : \nabla u \\ &- \Gamma[\mu_d - \mu_c + (T_d - T_c)s^*] + (p_d - p_c)[\partial \alpha_d / \partial t + \nabla \cdot (\alpha_d u_d)] \\ &- \sum_{k=c,d} \left[\frac{\partial}{\partial t}(\alpha_k \rho_k K_k) + \nabla \cdot (\alpha_k \rho_k K_k u_k) + \sigma_k^R : \nabla u_k \right] - \nabla \cdot (Q^R). \end{aligned}$$

Hence transport equations are needed for α_d , K_d , and K_c in order to deduce the final form of the entropy production rate Δ_c . In principle, if one of the two phases is incompressible the transport equation for the volume fraction is no longer independent since it stems from the mass balance. The transport equations for the pseudo-turbulent kinetic energies will provide explicit expressions for the non-dissipative stresses σ_c^R , σ_d^R and the non-dissipative force F^R . Conversely, these three quantities are likely to disappear in case one denies any role to the velocity fluctuations. The entropy flux h is fully dissipative while σ is the sum of a viscous stress (noted τ in [Sect. 5.1](#) and [5.2](#)) and a second part representing all phenomena (depicted by ΔP in [Sect. 5.2](#)), which play a role in the pressure difference.

When collisions between particles are relevant they are taken into account with a stress tensor σ^{coll} and an entropy flux h^{coll} . A force $\nabla \cdot \sigma^{coll}$ is to be added on the left-hand side of the momentum balance (120) of the particulate phase and similarly $\nabla \cdot h^{coll}$ is to be added to the left-hand side of (118). Any physically admissible closure for σ^{coll} and h^{coll} must verify the positivity of the energy production rate $-(\sigma^{coll} : \nabla u_d + h^{coll} \cdot \nabla T_d)$.

6 Summary of Key Results

6.1 Hybrid Approach for Dispersed Mixtures

The two-phase model (built on the characteristic function of presence χ_k) is capable, formally at least, to describe any kind of mixture. In case of dispersed mixtures with particles suspended in a carrier fluid its main drawback is the lack of reference to what happens to one particle and this has important implications on the closure problem. This is an old issue and an early example was given by Batchelor (1970) who expressed (see (9) and (5)) the dispersed stress $\langle \chi_d \sigma_d^0 \rangle$ of the two-phase model in terms of the so-called particle stresslet, which is the first moment of the fluid force exerted on the particle surface $n < \oint r \otimes (\sigma_c^0 \cdot n_d) ds >$.

The presence of the small-scale number density δ_d is typical of a kinetic theory approach of the particulate phase and it happens that we know the general rules that allow to transform two-phase quantities into quantities pertaining to the kinetic theory approach. With these transformation rules elaborated in Buyevich and Schelchkova (1978), Lhuillier (1992), Zhang and Prosperetti (1994), and Jackson (1997) not only we can generalize Batchelor's result for the dispersed phase stress (see results (9) and (4)), but we also obtain a relation between the inter-phase forces of the two models (see result (8)). The later relation is remarkable and shows that the inter-phase force of the two-phase model is not only the mean force per particle times the particle number density, but that it also involves the particle stresslet. A first consequence is that the particle stresslet appears in the momentum balance of the fluid phase exclusively. A second consequence is that the two-phase momentum balances are to be written as (25) and (26) for a dispersed mixture. In these two equations nowhere appears the pressure of the dispersed phase, but only the continuous phase pressure involved in some Archimedes force apportioned to the volume fractions.

This does not mean that the dispersed phase pressure can be discarded. The models that were described above are clearly "two-pressure" models, which show that in case of compressible particles the dispersed phase pressure is involved in the compression work appearing in the energy balance equations, not to mention its influence in the transport equation for the volume fraction. Conversely, whenever the energy equations decouple from the other equations (a widely spread but debatable assumption), the only pressure that remains is that of the continuous phase and a one-pressure model is enough to describe the flow. Note also that we refrained introducing a "mean interfacial pressure" p_I as is done currently in many two-phase models and the reason is clear : we decided at the outset to work with the two mean pressures only and, to be consistent, we had no possibility for introducing a third pressure. Some forces however were deduced that look like $p_I \nabla \alpha_d$ or $(p_I - p_c) \nabla \alpha_d$. But such forces never occur alone and are part of a more general force such as $\nabla(\alpha_d P^K)$ in the case of added-mass phenomena. Focusing the efforts on a $p_I \nabla \alpha_d$ or $(p_I - p_c) \nabla \alpha_d$ type of force is thus too restrictive, it is part of the truth only.

Both in this philosophy of approaching inviscid interaction and in the final results we find agreement with Wallis (1991) and Geurst (1985). Having been derived independently and with completely different methodologies (let alone nomenclatures) these three formulations may appear completely different, however, we have verified that they are completely equivalent. In the case of Geurst, one must understand that what he calls the hydrodynamic pressure is nothing but the mean pressure $p = \alpha_c p_c + \alpha_d p_d$. In the case of Wallis, one must understand that he adopts a slightly different definition of the interphase force, which amounts to $F^K + \nabla \cdot \sigma_c^K$ and consequently the kinetic stress $(u_d - u_c) \otimes J$ is assigned to the particulate phase instead of the fluid phase.

6.2 Supplementary Equations

The standard two-fluid model is made of six equations, representing the balances of mass, momentum, and energy for each of the two phases. Do we need more equations? The answer depends on a delicate balance between precision and efficiency. Using more equations means needing more closure relations and facing more difficulties with the numerical simulations. New equations are needed for mainly two reasons: A better description of the

physics and a better description of the geometry of the interfaces (and sometimes a mixture of the two).

6.2.1 Pseudo-Turbulent Kinetic Energies

Flow-induced velocity fluctuations are at the origin of a rather formidable problem sometimes coined as “pseudo-turbulence.” Much like what happens for the true turbulence one is led to introduce new equations giving the evolution in time (and coupling with the mean flow) of quantities like the pseudo-turbulent kinetic energies or the pseudo-turbulent kinetic stresses. Such supplementary equations are of common use for the description of collision-induced velocity fluctuations of particles moving in a gas but they are still in their infancy for particles moving in a liquid of almost matching density. In the above presentation of the two-phase model we have not taken collisions into account (the divergence of a collision stress must, in some cases, be added to the right-hand side of (15)) and we were not able to propose a general form for the time evolution of the pseudo-turbulent kinetic energy or kinetic stresses. But we have insisted on two particular kinds of flow-induced velocity fluctuations, those associated with the relative fluid-particle motion and those associated with the pulsating motion of particles. These two special cases are relatively simple in so far as the related pseudo-turbulent kinetic energies are given by analytical expressions like (46) or (64) and instead of new equations we have just derived the pseudo-equations (49) and (66). But these pseudo-equations give a flavor of what the two extra equations for K_d and K_c may look like, while the constraint (35) details the way these new equations should be coupled to the six two-phase equations.

6.2.2 Volume Fraction Transport

The volume fraction is a parameter that is of crucial significance to the two-phase model. Is it necessary to write an extra equation for one of the two volume fractions? Obviously not when the particles are assumed to be incompressible because the transport equation for volume is then a mere consequence of the transport equation for mass, and this is independent of the compressibility of the continuous phase. For compressible particles new physics must be introduced, and the answer is readily obtained provided one makes simplifying assumptions concerning the particle deformation. The simplest answer is obtained with (100) after supposing that all the particles are monodispersed spheres. This introduces an extra geometric variable, the radial velocity w_c at interfaces, which is coupled to the mean flow by the Rayleigh-Lamb equation (112). Hence this is not one but two coupled extra equations that are needed in case of compressible particles. The only exception is the case of a *slow radius change* because the inertia of the liquid in the radial motion can be neglected, the Rayleigh-Lamb equation then reduces to $4\eta_c(w_c/a) = p_d - p_c$ and the transport equation for the volume fraction appears as

$$\frac{\partial \alpha_d}{\partial t} + \nabla \cdot (\alpha_d u_d) = \frac{3\alpha_d}{4\eta_c} (p_d - p_c) + \frac{\Gamma}{\rho_c}. \quad (124)$$

We thus need an eight-equation model or a seven-equation model depending whether the inertia of the continuous phase is important or not for the radial motion of the particles. Moreover,

when phase changes occur at sufficiently slow rates to assure thermodynamic equilibrium, then (124) is replaced by the fluid equation of state, thus reverting back to the six-equation model.

A seven-equation model was proposed by Baer and Nunziato (1986) but with a transport equation for the volume fraction that markedly differs from (124) since the left-hand side of (124) is replaced by a convective time-derivative $\partial\alpha_d/\partial t + V_I \cdot \nabla\alpha_d$ where V_I is sometimes called the mean interfacial velocity. That convective time-derivative was taken for granted in many subsequent works (Bdzil et al. 1999; Kapila et al. 2001; Abgrall and Saurel 2003). However, while a transport equation with a convective time-derivative is correct for separated flows averaged over a cross section (Ransom 1984/1988), its use cannot be extended to the dispersed mixtures we have considered here and for which (124), or more generally (100), is the correct answer.

6.2.3 Interfacial Energy Transport

Besides the volume fraction the density of interfacial area a_I defined as

$$a_I = \langle \delta_I \rangle \quad (125)$$

is also an important parameter for the inter-phase exchanges. The volume fraction and the interfacial area density are connected to each other via the mean particle radius $3\alpha_d/a_I$. For a monodisperse suspension of spheres one then obtains the transport equation

$$\frac{\partial a_I}{\partial t} + \nabla \cdot (a_I u_d) = \frac{2a_I}{3\alpha_d} \left(\frac{\partial \alpha_d}{\partial t} + \nabla \cdot (\alpha_d u_d) \right). \quad (126)$$

The interfacial energy of the mixture is γa_I where γ is the surface tension. Requiring the total energy $\alpha_d \rho_d E_d + \alpha_c \rho_c E_c + \gamma a_I$ to be conserved leads to a dissipation rate similar to (113) but with p_d replaced everywhere by $p_d - 2\gamma a_I/3\alpha_d$ with the consequence that $p_d = p_c + 2\gamma a_I/3\alpha_d$ at equilibrium. The above transport equation is very simple but it requires the particles to keep a spherical shape and it neglects the coalescence, break-up, and nucleation phenomena. When these phenomena occur, new terms appear in the right-hand side and an example is given below concerning the particle deformation. Concerning coalescence and break-up the main issue is to select the relevant physical phenomena (turbulence of the carrier phase, relative motion of the two phases, etc.) and the way the polydispersity of the particles modifies the intensity of the processes.

6.2.4 Particle Deformation and Dynamics of Interfaces

When the particles are deformable and depart from a spherical shape, another quantity (a tensor in general) will be needed to depict the deformations of the interfaces and their coupling to the ambient flow. Introducing a tensor as a new variable brings a lot of difficulties but it provides a way to explain part (and only part) of the lateral drift experienced by deformable particles (drops or bubbles) in a pipe flow. Usually deformable particles move toward places where they are deformed less. In a pipe flow the region of smallest deformation is the pipe axis where the

shear vanishes. Since the particle deformability depends on their size (and more generally on the capillary number) the larger particles will drift and accumulate close to the pipe axis while the smaller ones will be less sensitive to that drift and will have a more homogeneous distribution over the pipe cross section.

Other effects due to the particle deformability are known to exist such as non-Newtonian behavior of the mixture with difference of normal stresses and shear-dependent viscosity. Doi and Ohta (1991) proposed to describe the interfacial microstructure with two quantities, the interfacial area density and the anisotropy tensor $q_{ij} = \langle (n_i n_j - \delta_{ij}/3) \delta_I \rangle$, where n is the unit vector normal to the interfaces, and they derived two coupled evolution equations for q_{ij} and a_I . Their model, however was restricted to a very special flow with $\alpha_d \approx 0.5$ and equal viscosities of the two phases. Many subsequent works tried to go beyond that special case and are presented in Tucker and Moldenaers (2002).

It is possible to use the above-defined anisotropy tensor for a dispersed mixture with $\alpha_d < 0.5$. But it is much more convenient to use $C_{ij} = q_{ij}/a_I$ as the anisotropy tensor with

$$C_{ij} = \frac{\langle (n_i n_j - \frac{\delta_{ij}}{3}) \delta_I \rangle}{\langle \delta_I \rangle}. \quad (127)$$

As an example we give below the two coupled equations for an emulsion of two immiscible and incompressible phases where the interfaces are those of (slightly) deformed spheres and viscous effects are dominant. With $p = \eta_d/\eta_c$ the ratio of the droplet viscosity to the carrier viscosity, α_d the droplet volume fraction, and $\sigma + \sigma_I$ the emulsion viscoelastic stress (see Appendix C for the definition (C4) of the interfacial stress σ_I) one obtains (Lhuillier 2003)

$$\frac{\partial a_I}{\partial t} + \nabla \cdot (a_I u_d) = -a_I \mathbf{C} : \left(\frac{F}{H} \mathbf{D} + \frac{1}{2H} \frac{\gamma a_I}{\alpha_d \eta_c} \mathbf{C} \right) \quad (128)$$

$$\frac{\partial \mathbf{C}}{\partial t} + (u_d \cdot \nabla) \mathbf{C} + \mathbf{C} \cdot \Omega - \Omega \cdot \mathbf{C} = -\frac{8}{15} \left[\frac{F}{H} \mathbf{D} + \left(\frac{1}{2H} + \frac{3}{19p+16} \right) \frac{\gamma a_I}{\alpha_d \eta_c} \mathbf{C} \right] \quad (129)$$

$$\sigma + \sigma_I = -2\eta_c \left[1 + \alpha_d(p-1) \frac{F}{H} \right] \mathbf{D} + \frac{F}{H} \gamma a_I \mathbf{C} \quad (130)$$

where D and Ω are the strain rate and rotation rate of the suspension mean velocity $u = \alpha_d u_d + \alpha_c u_c$. Moreover, $H(p, \alpha_d) = p - 1 + F(\alpha_d)$ while $F(\alpha_d)$ is related to the effective viscosity of a suspension of hard spheres, with $F(\alpha_d) = 5/2(1 - \alpha_d)$ as one of the simplest possible expressions (Palierne 1990). In the two above transport equations for C_{ij} and a_I one clearly distinguishes the two main phenomena: the shear-induced deformation and the retraction due to surface tension. But the breakup and coalescence phenomena are not represented and must be taken into account by extra terms. The above three equations were written for incompressible particles. The compressibility of particles has a role in the transport equation for a_I only, the right-hand side of which is then the sum of the two right-hand sides of (126) and (128).

6.3 Hyperbolicity

Ill-posedness has been a major issue in regards to the formulation of the two-phase model since the very early efforts on behalf of nuclear reactor safety in the early 1970s (Gidaspow 1974),

and all along the way to the most recent renditions (Drew and Passman 1998; Prosperetti and Satrape 1990; RELAP5/MOD3.3 Code Manual 2001). Inviscid interactions between the phases were anticipated as the cause, and a number of empirical or ad hoc additions have been made as constitutive descriptions mainly under the names of “added mass” e.g., (Park et al. 1998) and “interfacial pressure” e.g., (Stuhmiller 1977), but the overall subject seems to still lack in clarity and definiteness. On the other hand, the unified treatments of these interactions in Wallis (1991) and independently in Geurst (1985) seemed to have gone unnoticed. These results are recovered completely independently in the present development, and so is a generalization of the requirement for hyperbolicity found in Geurst (1985) for incompressible flows (low Mach number limit in the present work) equation (62). This result is completely adequate for disperse systems as its applicability, which coincides with the natural range of disperse phase volume fractions being under about 30%. At still higher concentrations particle collisions have to be taken into account, as indeed the role of particle fluctuation adding to the kinetic energy as explained by (63). On the other hand, for highly compressible flows the function E in (46) must be redefined to include the effect of flow Mach number, and this further (and hopefully final) development of the subject will be an important task for the future. For the time being, in practical terms we have found that the present formulation is sufficient to obtain robust numerical solutions at all flow speeds (Part II).

The approach of Baer and Nunziato (1986) must be mentioned in this context. These authors proposed, for dense particulate systems, one of the rare models to be hyperbolic. Why are we skeptical concerning the potentialities of that model for dispersed mixtures? We pointed out above a strong discrepancy concerning the transport equation for the volume fraction. Another important discrepancy concerns the two momentum balances which, in the BN model, appear as

$$\alpha_c \rho_c \frac{d_c u_c}{dt} + \nabla(\alpha_c p_c) = -f - \Gamma(u^* - u_c) + \alpha_c \rho_c g \quad (131)$$

$$\alpha_d \rho_d \frac{d_d u_d}{dt} + \nabla(\alpha_d p_d) = f + \Gamma(u^* - u_d) + \alpha_d \rho_d g \quad (132)$$

These equations are different from (26) and (25). The gradient of the dispersed phase pressure is assumed to drive the motion of the dispersed phase while we claimed that the gradient of p_c is the only driving force for both the carrier fluid and the dispersed phase. It is true that the special way the momentum and volume fraction equations were written was enough to ensure hyperbolicity. But the paradox is that hyperbolicity is obtained with a set of equations that is definitely not suitable for particulate systems.

6.4 Nuclear Reactor (Design) Systems Codes

Here we specifically refer to the RELAP5 developed in the USA during the 1970s and the French code CATHARE that followed; they are the main representatives of the genre. They are based on the premise that flow and transport of heat/mass can be captured generally for all flow regimes by one and the same set of effective field equations (a system of six equations plus the equations of state of the fluids involved). These equations were written in 1D, as (channel) cross-sectional averages, and augmented by volume sources and/or sinks that represent the wall transfers. The later are determined by a logic that reflects the estimated flow pattern on the basis of vapor and liquid flow rates and other pertinent quantities. The RELAP5 code is well documented in a

comprehensive set of volumes that is openly available (RELAP5/MOD3.3 Code Manual 2001). For CATHARE the main reference is a journal paper by Bestion (1990). The comments below are based on these sources, and we focus on the momentum equations as they are the critical link to hyperbolicity, and thus to the numerical performance of these computer codes.

For RELAP5, the afore-mentioned equations are formally the same as the 1D version of (42) and (43), except for the following: (a) The phases are assumed to be at the same pressure, so in the gradient term instead of p_c write p ; (b) both phasic stresses are absent; (c) from the added-mass force only the component $\partial(u_d - u_c)/\partial t$ is retained; and (d) there are source terms to express wall transfers as noted above. For CATHARE, the spatial derivatives of the added mass term are retained and the Stuhmiller (1977) treatment of interfacial pressure is added to “render the system hyperbolic.” It is known that with an appropriate selection of the coefficient in this expression the system becomes hyperbolic for incompressible flows, but there is no consideration of the effect of Mach number. For sensitive problems the results can depend on the value of this coefficient. The RELAP5 system of equations is ill-posed and solutions are obtained by controlling the growth of oscillations. In particular, damping is affected by means of added artificial viscosity terms, and by keeping the size of the (numerical grid) nodes sufficiently large. An interesting part of the RELAP5 numerical stability analysis (RELAP5/MOD3.3 Code Manual 2001) is that the drag terms stabilize the solution down to sufficiently small wavenumbers as to render solutions for nuclear reactor scale systems practicable.

Much of the utility of these codes rests upon the dominance of phase-change effects present in applications, which these codes were intended for to begin with (nuclear reactor loss of coolant accidents). In a way this, along with conservation, provides an attractor strong enough to be a basis for tuning by means of experiments.

Acknowledgments

This work was supported by the Joint Science and Technology Office, Defense Threat Reduction Agency (JSTO/DTRA), and the National Ground Intelligence Center (NGIC) of the US Army (Dr. Richard Babarsky). Dr. S. Sushchikh and Dr. C.-H. Chang (CRSS / UCSB) participated with many helpful discussions and derivations concerning the hyperbolicity issue and comparison to other formulations. Lively discussions with (and useful comments from) Dr. C. Morel (CEA Grenoble) and Professor R. Saurel (IUSTI Marseille) are gratefully acknowledged.

Appendix A: Rigid Spheres in a Nonviscous Fluid

Our aim is to give a brief derivation of the fluid momentum balance (42) with definitions (44) and (45). We consider many rigid spheres dispersed in a nonviscous and noncompressible fluid. The momentum balances of the two phases are expressed by the general equations (11) and (12) but definitions (13)–(15) simplify to

$$F = \langle \delta_d \oint (p_c - p) n_d ds \rangle \quad (\text{A-1})$$

$$\sigma_c = \rho_c \langle \chi_c v'_c \otimes v'_c \rangle - \langle \delta_d \oint (p_c - p) r \otimes n_d ds \rangle \quad (\text{A-2})$$

$$\sigma_d = \rho_d \langle \chi_d v'_d \otimes v'_d \rangle \quad (\text{A-3})$$

where p is the microscale fluid pressure and p_c is its mean value. Note that we neglected the kinetic contribution to σ_d because the internal motion u is reduced to a rotation in case of rigid particles and the angular velocity is a constant when the rigid particles have a spherical shape. Hence the inter-phase force is linked to the pressure fluctuations on the surfaces of the particles while the phasic stresses depend on both the pressure and velocity fluctuations. To make some progress we must be able to calculate the various terms on the right-hand sides of definitions (A-1) to (A-3). This can be done if we further suppose that the nonviscous fluid has a microscale velocity v deriving from the potential ϕ . In that case the microscale equations of motion are

$$v = \nabla\phi, \quad \nabla^2\phi = 0, \quad (\text{A-4})$$

$$\frac{\partial\phi}{\partial t} + \frac{v^2}{2} + \frac{p}{\rho_c} - g \cdot x = 0. \quad (\text{A-5})$$

The fluid velocity is split into a mean value u_c and a fluctuation v'

$$v = u_c + v', \quad \langle \chi_c v \rangle = \alpha_c u_c, \quad \langle \chi_c v' \rangle = 0. \quad (\text{A-6})$$

With Wallis (1991) we split the velocity potential into an averaged value Φ and a fluctuation ϕ' defined by

$$\phi = \Phi + \phi', \quad \langle \chi_c \phi \rangle = \alpha_c \Phi, \quad \langle \chi_c \phi' \rangle = 0. \quad (\text{A-7})$$

A quantity that will prove of utmost importance is the mean fluid impulse J defined by

$$J = \rho_c \langle \chi_c \nabla\phi' \rangle = -\rho_c \langle \phi' n_d \delta_I \rangle. \quad (\text{A-8})$$

J is a Galilean-invariant momentum, which plays a role in both the mean velocity and the velocity fluctuations

$$v' = \nabla\phi' - \frac{J}{\alpha_c \rho_c}, \quad u_c = \nabla\Phi + \frac{J}{\alpha_c \rho_c}, \quad \nabla \times \left(u_c - \frac{J}{\alpha_c \rho_c} \right) = 0. \quad (\text{A-9})$$

It is now rather easy to deduce the momentum balance of the fluid phase. The microscale Bernoulli equation (A-5) is multiplied by the fluid characteristic function χ_c and one performs the statistical average noted by brackets $\langle \dots \rangle$. The result is the averaged Bernoulli equation

$$\alpha_c \frac{\partial\Phi}{\partial t} + \langle \chi_c \frac{\partial\phi'}{\partial t} \rangle + \langle \chi_c \frac{v^2}{2} \rangle + \frac{\alpha_c p_c}{\rho_c} - \alpha_c g \cdot x = 0. \quad (\text{A-10})$$

Taking the gradient of that equation and eliminating $\nabla\Phi$ with the help of (A-9) one obtains

$$\frac{\partial}{\partial t} \left(u_c - \frac{J}{\alpha_c \rho_c} \right) + \frac{1}{2} \nabla \left(u_c - \frac{J}{\alpha_c \rho_c} \right)^2 - \nabla K^* + \frac{\nabla p_c}{\rho_c} = g, \quad (\text{A-11})$$

where K^* is a specific kinetic energy related to the fluid impulse J and to the pseudo-turbulent fluid kinetic energy $K_c = \langle \chi_c v'^2 \rangle / 2\alpha_c$ by

$$2\alpha_c K^* = 2\alpha_c K_c + \alpha_c \left(\frac{J}{\alpha_c \rho_c} \right)^2 - 2\nabla \cdot \langle \chi_c \phi' \nabla\phi' \rangle. \quad (\text{A-12})$$

Moreover, the pseudo-turbulent kinetic energy of the fluid is itself related to the Kelvin impulse by

$$2\alpha_c K_c = (u_d - u_c) \cdot \frac{J}{\rho_c} - \langle \phi' (v - u_d) \cdot n_d \delta_I \rangle + \nabla \cdot \langle \chi_c \phi' \nabla \phi' \rangle. \quad (\text{A-13})$$

Equation (A-11) can be transformed into a momentum balance similar to (11) with

$$-F - \nabla \cdot \sigma_c = \frac{\partial J}{\partial t} + \nabla \cdot (u_c \otimes J) + (J \cdot \nabla)(u_c - \frac{J}{\alpha_c \rho_c}) + \alpha_c \rho_c \nabla K^* \quad (\text{A-14})$$

The main conclusion at this point is that *the dynamics of the fluid phase depends on two quantities only*, the mean fluid impulse J and the kinetic energy K^* . We can simplify the above result (A-14) if we assume the last term of (A-12) to be negligible. Then, the non-dissipative force acting on the fluid phase becomes

$$-F - \nabla \cdot \sigma_c = \frac{\partial J}{\partial t} + \nabla \cdot (u_c \otimes J) + (J \cdot \nabla)u_c + \alpha_c \rho_c \nabla K_c + J \times (\nabla \times u_c) \quad (\text{A-15})$$

where, according to (A-9), $\nabla \times u_c$ in the last term can be replaced by $\nabla \times (J/\alpha_c \rho_c)$ at will. It is clear that the above equation of motion is equivalent to (42) with definitions (44) and (45). Note however that our splitting into a force F^K and a stress σ_c^K is somehow arbitrary in so far as only the sum $F^K + \nabla \cdot \sigma_c^K$ can be deduced unambiguously from expression (A-15).

Appendix B: Hyperbolicity Aspects of the Effective Field Model with S. Sushchikh and C.-H. Chang

Here our aim is to study the mathematical character of the system (53)–(57), and as is common practice we do so in one space dimension. While the procedures are standard, the derivations are rather laborious and results for the fully compressible case (high Mach numbers) are presented here for the first time. These results are of essential use in Part II.

The system of equations is:

$$\frac{\partial}{\partial t}(\alpha_c \rho_c) + \frac{\partial}{\partial x}(\alpha_c \rho_c u_c) = 0 \quad (\text{B-1a})$$

$$\frac{\partial}{\partial t}(\alpha_d \rho_d) + \frac{\partial}{\partial x}(\alpha_d \rho_d u_d) = 0 \quad (\text{B-1b})$$

$$\frac{\partial}{\partial t}(\alpha_c \rho_c u_c) + \frac{\partial}{\partial x}[\alpha_c \rho_c u_c^2 + \alpha_c \rho_c E (u_d - u_c)^2] + \alpha_c \frac{\partial p_c}{\partial x} = -F^K \quad (\text{B-1c})$$

$$\frac{\partial}{\partial t}(\alpha_d \rho_d u_d) + \frac{\partial}{\partial x}[\alpha_d \rho_d u_d^2 + \alpha_d P^K] + \alpha_d \frac{\partial p_c}{\partial x} = F^K \quad (\text{B-1d})$$

With

$$\begin{aligned}
 F^K &= -\frac{\partial J}{\partial t} - \frac{\partial}{\partial x}(u_d J) - J \frac{\partial u_c}{\partial x} - \alpha_c \rho_c \frac{\partial K_c}{\partial x} \\
 J &= \alpha_c \rho_c E(\alpha_d)(u_d - u_c) \\
 K_c &= \frac{1}{2} E(\alpha_d)(u_d - u_c)^2 \\
 P^K &= -\alpha_c \rho_c \frac{\partial K_c}{\partial \alpha_d} \\
 &= p_d - p_c
 \end{aligned}$$

Equation of state information is introduced by defining the isentropic speeds of sound for each field:

$$a_c^2 = \frac{\partial p_c}{\partial \rho_c} \quad \text{and} \quad a_d^2 = \frac{\partial p_d}{\partial \rho_d}$$

We will cast this system in characteristic form and will determine the eigenvalues, first analytically, in the incompressible approximation, and then numerically for any Mach number flow.

In the standard wave equation form the above system becomes:

$$\mathbf{A} \frac{\partial Q}{\partial t} + \mathbf{B} \frac{\partial Q}{\partial x} = 0 \quad (\text{B-2})$$

where $Q = (\alpha_d, u_d, u_c, p_c)^T$ is the vector of primitive variables, and matrixes \mathbf{A} and \mathbf{B} are:

$$\mathbf{A} = \begin{pmatrix} A_{11} & A_{12} & A_{13} & A_{14} \\ -\rho_c & 0 & 0 & \alpha_c / a_c^2 \\ \alpha_c \rho_c E'(u_d - u_c) & \alpha_d \rho_d + \alpha_c \rho_c E & -\alpha_c \rho_c E & 0 \\ -\alpha_c \rho_c E'(u_d - u_c) & -\alpha_c \rho_c E & \alpha_c \rho_c + \alpha_c \rho_c E & 0 \end{pmatrix} \quad (\text{B-3})$$

$$\mathbf{B} = \begin{pmatrix} u_d A_{11} & \alpha_d \rho_d + u_d A_{12} & u_d A_{13} & u_d A_{14} \\ -\rho_c u_c & 0 & \alpha_c \rho_c & \alpha_c u_c / a_c^2 \\ B_{31} & B_{32} & B_{33} & B_{34} \\ B_{41} & -\alpha_c \rho_c u_d E & \alpha_c \rho_c (1 + E) u_c & \alpha_c \end{pmatrix} \quad (\text{B-4})$$

with:

$$\begin{aligned}
 A_{11} &= \rho_d - \frac{\alpha_d \rho_c (\alpha_c E'' - E') (u_c - u_d)^2}{2 a_d^2} & A_{12} &= -A_{13} = -\alpha_c \alpha_d \rho_c E' (u_d - u_c) / a_d^2 \\
 A_{14} &= \frac{\alpha_d}{a_d^2} - \frac{\alpha_c \alpha_d E' (u_c - u_d)^2}{2 a_d^2 a_c^2}
 \end{aligned}$$

And:

$$\begin{aligned}
 B_{31} &= 1/2\rho_c(u_d - u_c)^2(\alpha_d E' - 2E - \alpha_c \alpha_d E'') + \alpha_c \rho_c E' u_d (u_d - u_c) \\
 B_{41} &= -1/2\alpha_c \rho_c E' (u_d - u_c)(u_d + u_c) \\
 B_{32} &= \alpha_d \rho_d u_d - \alpha_c \alpha_d \rho_c E' (u_d - u_c) + 2\alpha_c \rho_c E (u_d - u_c) + \alpha_c \rho_c u_d E \\
 B_{33} &= -\alpha_c \rho_c E u_c + \alpha_c \rho_c (u_d - u_c)(\alpha_d E' - 2E) \\
 B_{34} &= \alpha_d + 1/2\alpha_c (2E - \alpha_d E') \frac{(u_d - u_c)^2}{a_c^2}
 \end{aligned}$$

The eigenvalues of (B-2) can be calculated by solving: $|\mathbf{B} - \lambda\mathbf{A}| = 0$ or letting $\mathbf{D} = \mathbf{B} - \lambda\mathbf{A}$, we have to solve:

$$|\mathbf{D}| = \begin{vmatrix} (u_d - \lambda)A_{11} & \alpha_d \rho_d + (u_d - \lambda)A_{12} & (u_d - \lambda)A_{13} & (u_d - \lambda)A_{14} \\ -\rho_c(u_c - \lambda) & 0 & \alpha_c \rho_c & \alpha_c(u_c - \lambda)/a_c^2 \\ D_{31} & D_{32} & D_{33} & D_{34} \\ D_{41} & -\rho_c E(u_d - \lambda) & \rho_c(1 + E)(u_c - \lambda) & 1 \end{vmatrix} = 0 \quad (\text{B-5})$$

Where:

$$\begin{aligned}
 D_{31} &= \alpha_c \rho_c E' (u_d - u_c)(u_d - \lambda) + \rho_c/2(\alpha_d E' - 2E - \alpha_c \alpha_d E'')(u_d - u_c)^2 \\
 D_{32} &= (\alpha_d \rho_d + \alpha_c \rho_c E)(u_d - \lambda) + \alpha_c \rho_c (2E - \alpha_d E')(u_d - u_c) \\
 D_{33} &= \alpha_c \rho_c E(\lambda - u_c) - \alpha_c \rho_c (2E - \alpha_d E')(u_d - u_c) \\
 D_{34} &= \alpha_d + \frac{\alpha_c (2E - \alpha_d E')}{2a_c^2} (u_c - u_d)^2 \\
 D_{41} &= \rho_c E' (u_d - u_c) (\lambda - 1/2(u_d + u_c))
 \end{aligned}$$

Equation (B-5) will lead to a fourth-order polynomial equation (quartic equation) whose roots (eigenvalues) will be examined analytically; first in the low Mach number approximation (B-1), and then numerically for the general case (B-2). We seek conditions for which all four roots are real for this is a necessary and sufficient requirement for our system to be hyperbolic.

B.1 Low Mach Number Approximation

Under the conditions (Hancox et al. 1980):

$$\begin{aligned}
 (u_c - \lambda) &\ll a_k \\
 (u_d - \lambda) &\ll a_k \quad k = c, d \\
 (u_d - u_c) &\ll a_k
 \end{aligned}$$

equation (B-5) simplifies to:

$$\begin{vmatrix} (u_d - \lambda) & \alpha_d & 0 & 0 \\ -(u_c - \lambda) & 0 & \alpha_c & 0 \\ D_{31} & D_{32} & D_{33} & \alpha_d \\ D_{41} & -\rho_c E(u_d - \lambda) & \rho_c(1 + E)(u_c - \lambda) & 1 \end{vmatrix} = 0 \quad (\text{B-6})$$

which under the transformation $X = \lambda - \frac{u_d + u_c}{2}$, can be written as:

$$K_2 X^2 + K_1 X + K_0 = 0 \quad (\text{B-7})$$

with

$$\begin{aligned} K_2 &= \alpha_d (\alpha_c \rho_d + \alpha_d \rho_c) + \rho_c E \\ K_1 &= (u_d - u_c) \left[\alpha_d (\alpha_d \rho_c - \alpha_c \rho_d) + (1 - 4\alpha_c) \rho_c E + 2\alpha_c \alpha_d \rho_c E' \right] \\ K_0 &= \frac{(u_d - u_c)^2}{4} \left[\alpha_d (\alpha_d \rho_c + \alpha_c \rho_d) + \rho_c E + 2\alpha_c^2 \rho_c (2E - 2\alpha_d E' + \alpha_d^2 E'') \right] \end{aligned} \quad (\text{B-8})$$

Thus, as a condition for real roots we must have $K_1^2 \geq 4K_2K_0$ and accordingly:

$$\begin{aligned} \left(\alpha_d - \alpha_c \bar{\rho} + (1 - 4\alpha_c) \frac{E}{\alpha_d} + 2\alpha_c E' \right)^2 &\geq \\ \left(\alpha_d + \alpha_c \bar{\rho} + \frac{E}{\alpha_d} \right) \cdot \left(\alpha_d + \alpha_c \bar{\rho} + \frac{E}{\alpha_d} + 4\alpha_c^2 \left[\frac{E}{\alpha_d} - E' + \frac{\alpha_d}{2} E'' \right] \right) & \end{aligned} \quad (\text{B-9})$$

where the density ratio is $\bar{\rho} = \rho_d / \rho_c$.

For example, if we write $E(\alpha_d) = C_1 \alpha_d + C_2 \alpha_d^2$, the hyperbolicity condition becomes:

$$4\alpha_c \alpha_d (\bar{\rho} + C_1) (1 + C_1 + C_2) \leq 0 \quad (\text{B-10})$$

Coefficients C_1 and C_2 also have to satisfy that $E(\alpha_d) > 0$. The choice made by Geurst (1985), $C_1 = 1/2$ and $C_2 = -3/2$, satisfies these conditions, although (B-10) provides considerably more latitude. We also know that the $C_1 = 1/2$ provides the correct asymptotic limit as $\alpha_d \rightarrow 0$, although remarkably, the second term is still needed for hyperbolicity. While there is some theoretical basis for the $C = C_2/C_1 \sim -3$ value, the function $E(\alpha_d)$ needs better understanding and elaboration for dense systems.

The eigenvalues, actually the “eigenspeeds” of our system, are the roots of (B-7):

$$\lambda_{1,2} = u_d - \left(\frac{\alpha_d (1 + C_1 + C_2) \mp \sqrt{-\alpha_c \alpha_d (\bar{\rho} + C_1) (1 + C_1 + C_2)}}{\alpha_d + \alpha_c \bar{\rho} + C_1 + C_2 \alpha_d} \right) (u_d - u_c) \quad (\text{B-11})$$

Now for bubbly ($\bar{\rho} \ll 1$) and droplet ($\bar{\rho} \gg 1$) flows (B-11) simplifies to:

$$\text{droplet: } \lambda_{1,2} = u_d \pm \sqrt{\frac{\alpha_d}{\alpha_c}} \sqrt{-(1 + C_1 + C_2)} \frac{(u_d - u_c)}{\sqrt{\bar{\rho}}} \approx u_d \quad (\text{B-11a})$$

$$\text{bubbly: } \lambda_{1,2} = u_d \pm \sqrt{-\alpha_d \alpha_c (1 + C_1 + C_2) / C_1} (u_d - u_c) \quad (\text{B-11b})$$

and we note that the “eigenspeeds” behave quite differently in the two cases. On the other hand, and for either case, with the Geurst choice we have exactly $\lambda_{1,2} = u_d$.

For bubbly flows the above analysis is quite sufficient since the attainment of high relative velocities in practice is severely limited by interfacial breakup (which tends to homogenize the flow). For droplet or particle flows on the other hand, high relative velocities are not only realizable, they are of the greatest interest in practice. For such flows the low Mach number analysis is a point of departure for the more general treatment provided in the following.

B.2 A General Treatment

Allowing for compressibility of the continuous phase (droplet, or particle flows in gas) the matrix of interest becomes:

$$\mathbf{D} = \begin{pmatrix} u_d - \lambda & \alpha_d & 0 & 0 \\ -\rho_c(u_c - \lambda) & 0 & \alpha_c \rho_c & \alpha_c(u_c - \lambda)/a_c^2 \\ D_{31} & D_{32} & D_{33} & D_{34} \\ D_{41} & -\rho_c E(u_d - \lambda) & \rho_c(1 + E)(u_c - \lambda) & 1 \end{pmatrix} \quad (\text{B-12})$$

The appropriate nondimensional treatment involves two characteristic Mach numbers: one based on the average velocity of the mixture, M^* , and the other on the relative velocity of the phases, \hat{M} , where:

$$M^* = \frac{(u_d + u_c)}{2a_c} \quad (\text{B-13})$$

$$\hat{M} = \frac{(u_d - u_c)}{2a_c} \quad (\text{B-14})$$

Accordingly, the Mach numbers for each of the “eigenspeeds” are $\lambda_i^* = \lambda_i/a_c$, and with $Y = \lambda^* - M^*$ equation (B-5) yields:

$$\begin{aligned} & (Y + \hat{M})^2(Y - \hat{M})^2 + K_2^*(Y - \hat{M})^2(Y + \hat{M}) + K_3^*(Y - \hat{M})(Y + \hat{M})^2 + K_4^*(Y - \hat{M})^2 \\ & + K_5^*(Y + \hat{M})^2 + K_6^*(Y - \hat{M})(Y + \hat{M}) + K_7^*(Y - \hat{M}) + K_8^*(Y + \hat{M}) + K_9^* = 0 \end{aligned} \quad (\text{B-15})$$

where:

$$K_2^* = \frac{2\hat{M}(1 - \alpha_d)E(\alpha_d E' - 2E)}{E(1 - \alpha_d) + \alpha_d \bar{\rho}(1 + E)}; \quad K_3^* = -\frac{2\hat{M}(1 - \alpha_d)(\alpha_d E'(2 + E) - 2E(1 + E))}{E(1 - \alpha_d) + \alpha_d \bar{\rho}(1 + E)};$$

$$K_4^* = \frac{4\hat{M}^2(1 - \alpha_d)E(\alpha_d E' - E)}{E(1 - \alpha_d) + \alpha_d \bar{\rho}(1 + E)} - \frac{(1 - \alpha_d)E + \alpha_d \bar{\rho}}{E(1 - \alpha_d) + \alpha_d \bar{\rho}(1 + E)};$$

$$K_5^* = \frac{2\hat{M}^2 \alpha_d^2(1 - \alpha_d)E''(1 + E)}{E(1 - \alpha_d) + \alpha_d \bar{\rho}(1 + E)} - \frac{\alpha_d^2(1 + E)}{(1 - \alpha_d)(E(1 - \alpha_d) + \alpha_d \bar{\rho}(1 + E))};$$

$$K_6^* = -\frac{4\hat{M}^2 \alpha_d(1 - \alpha_d)E'(\alpha_d E' - E)}{E(1 - \alpha_d) + \alpha_d \bar{\rho}(1 + E)} - \frac{2\alpha_d E}{E(1 - \alpha_d) + \alpha_d \bar{\rho}(1 + E)};$$

$$K_7^* = -\frac{4\hat{M}(E - \alpha_d E') + 2\alpha_d^2 \hat{M} E' + 4\alpha_d^2 (E')^2 \hat{M}^3}{E(1 - \alpha_d) + \alpha_d \bar{\rho}(1 + E)};$$

$$K_8^* = \frac{2\alpha_d^2 \hat{M} E'(1 + 2(1 - \alpha_d)\hat{M}^2 E')}{E(1 - \alpha_d) + \alpha_d \bar{\rho}(1 + E)}; \quad K_9^* = -\frac{2\alpha_d^2(1 - \alpha_d)\hat{M}^2(E'' - 2(E')^2 \hat{M}^2)}{E(1 - \alpha_d) + \alpha_d \bar{\rho}(1 + E)}.$$

As shown by Bronshtein et al. (2007), the roots of this quartic can be analyzed in terms of a resolvent cubic equation. The key steps are summarized in the following.

Rendered in the form:

$$Y^4 + p_3 Y^3 + p_2 Y^2 + p_1 Y + p_0 = 0 \quad (\text{B-16})$$

the original quartic is transformed to:

$$Y^4 + aY^2 + bY + c = 0, \quad (\text{B-17})$$

according to $a = -\frac{3}{8}p_3^2 + p_2$, $b = \frac{1}{8}p_3^3 - \frac{p_2p_3}{2} + p_1$ and $c = -\frac{3}{256}p_3^4 + \frac{p_2p_3^2}{16} - \frac{p_1p_3}{4} + p_0$. Then corresponding to (B-17) resolvent cubic equation is:

$$T^3 + rT^2 + sT + t = 0 \quad (\text{B-18})$$

with $r = 2a$, $s = a^2 - 4c$ and $t = b^2$. The quartic equation has four real roots if and only if corresponding resolvent has three real positive roots.

The roots of cubic equation are examined in terms of $Z = T + r/3$ so that (B-18) becomes:

$$Z^3 + pZ + q = 0 \quad (\text{B-19})$$

with $p = (3s - r^2)/3$; $q = 2r^3/27 - rs/3 + t$.

and for three real positive roots we must have:

$$D = \left(\frac{p}{3}\right)^3 + \left(\frac{q}{2}\right)^2 \leq 0 \quad \text{and} \quad (\text{B-20a})$$

$$T_k = Z_k - (r/3) > 0. \quad (\text{B-20b})$$

Here Z_k are obtained by


$$\begin{aligned} Z_1 &= 2\sqrt[3]{\omega} \cos\left(\frac{\phi}{3}\right); \\ Z_2 &= 2\sqrt[3]{\omega} \cos\left(\frac{\phi}{3} + \frac{2\pi}{3}\right); \\ Z_3 &= 2\sqrt[3]{\omega} \cos\left(\frac{\phi}{3} + \frac{4\pi}{3}\right). \end{aligned}$$

where $\omega = \sqrt{\frac{-p^3}{27}}$ and $\phi = \cos^{-1}\left(\frac{-q}{2\omega}\right)$.

Once functional form of $E(\alpha_d)$ is provided, the hyperbolicity boundaries can be found by numerically scanning the domain of parameter space $\hat{M}, \alpha_d, \bar{\rho}$. For the particular example considered here, we remain with the form taken for the low Mach number analysis above, with $C_1 = 1/2$ so that

$$E(\alpha_d) = \frac{1}{2}\alpha_d(1 + C\alpha_d) \quad (\text{B-21})$$

where C is now introduced as an additional parameter. As long as $\bar{\rho} \gg 1$ the results are insensitive to the actual value (10^3 is the value for which results are shown here). Also, as expected, and in contradistinction to bubbly flows, the hyperbolicity boundaries are insensitive to the presence of the added mass term, although the term is included for the results shown here.

Representative results of this type of analysis are summarized in  Fig. B1, and we can see that they correctly recover the low Mach number analysis presented above. Notable is also the increase of accessible Mach numbers within the hyperbolic domain (so that $E(\alpha_d)$ remains positive) with decreasing disperse phase volume fraction.

Perhaps more important is the finding that *in all cases* the non-hyperbolic corridor is characterized by exceedingly small but positive values (typically of order 10^{-12}) of the discriminant

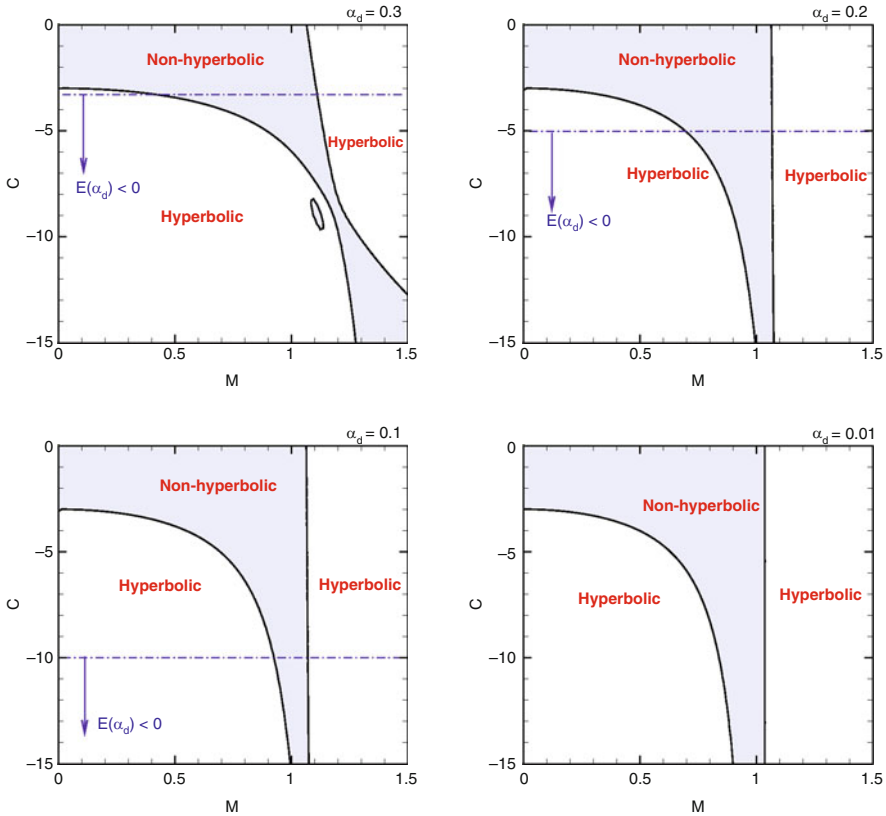


Figure B1
 Representative sample of hyperbicity maps of our effective field model employed for droplet (or particles in gas) flows. The Mach number(M) here is without the factor of 1/2 found in (B-14)

D, which can be thought of as a symptom of “mild” non-hyperbolicity. Support for such a view derives from the implied roots with very small imaginary parts, as discussed further below.

B.3 Discussion

To further explore the potential significance of the finding that failure to meet condition (B-20a) was consistently by an exceedingly small margin, we computed directly the eigenvalues (using MATHEMATICA (2008)), for a number of cases, an example of which is provided in **Table B1**. Such results allow us to generalize as follows:

- $\text{Re}(\lambda_1^*) \approx M^* + \hat{M}$ for $\hat{M} < 0.5$; $\text{Re}(\lambda_1^*) \approx M^* - \hat{M} + 1$ for $\hat{M} > 0.5$
- $\text{Re}(\lambda_2^*) \approx M^* + \hat{M}$ for all \hat{M} .
- $\lambda_3^* \approx M^* - \hat{M} - 1$ for all \hat{M} .
- $\lambda_4^* \approx M^* - \hat{M} + 1$ for $\hat{M} < 0.5$; $\lambda_4^* \approx M^* + \hat{M}$ for $\hat{M} > 0.5$

■ **Table B1**

A set of sample solutions of (B-15) with : $C = -3.3$, $\alpha_d = 0.1$, $\bar{\rho} = 1,000$

\hat{M}	M^*	λ_1^*	λ_2^*	λ_3^*	λ_4^*
0.1	0.38	0.48	0.48	-0.71	1.26
0.2	0.48	$0.68 + 0.001i$	$0.68 - 0.001i$	-0.71	1.26
0.3	0.58	$0.88 + 0.005i$	$0.88 - 0.005i$	-0.71	1.26
0.4	0.68	$1.10 + 0.012i$	$1.10 - 0.012i$	-0.71	1.26
0.5	0.78	$1.25 + 0.030i$	$1.25 - 0.030i$	-0.71	1.31
0.6	0.88	1.26	1.45	-0.71	1.50
0.7	0.98	1.26	1.65	-0.71	1.70

- The imaginary parts are always **at least** two orders of magnitude smaller than the real parts.

Moreover, using the definitions, we have the corresponding relations to the real speeds as follows:

$$M^* - \hat{M} - 1 = \frac{u_c - a_c}{a_c}, \quad M^* + \hat{M} = \frac{u_d}{a_c}, \quad \text{and} \quad M^* - \hat{M} + 1 = \frac{u_c + a_c}{a_c}.$$

In particular, when $\hat{M} \ll 0.5$ eigenvalues $\lambda_{1,2}$ are equal to u_d , recovering the result of the low Mach number analysis presented in [▶ Sect. B.1](#).

From the last bullet above, it is clear that the exceedingly small value of the discriminant can be associated with eigenvalues whose imaginary parts are very small in relation to their real parts. This in turn can be related to the stability character of our wave system (B-2), by recognizing that the unstable modes (those associated with the negative imaginary parts of the eigenvalues) grow with a characteristic time of $\tau_G = \chi/2\pi\lambda_i$ while the characteristic time for propagation is $\tau_P = \chi/2\pi\lambda_r$, where λ_i/λ_r are the imaginary/real parts of the corresponding eigenvalue, and χ is the wave length of the disturbance. Thus we have a measure of the “mild” non-hyperbolicity mentioned above as instability growth rates being slower than one-hundredth of disturbance propagation rates through our system. This, along with the fact in actual simulations the non-hyperbolic corridor would be traversed rather rapidly, suggest that our two-fluid model is effectively hyperbolic.

Appendix C: Including Surface Tension

Taking surface tension into account means upgrading the interfaces to the status of a third phase. As a consequence the interfaces have their own balance equations and they exchange mass, momentum, and energy with the two neighbor phases. Usually that third phase is supposed to have no mass and the surface tension γ is then a free energy depending on the mean temperature T_I of the interfaces. As a consequence the interfaces are endowed with an entropy

and an internal energy which, per unit volume of the mixture, are written as

$$S_I = -a_I \frac{d\gamma}{dT_I}, \quad U_I = a_I \left(\gamma - T_I \frac{d\gamma}{dT_I} \right) \quad (\text{C-1})$$

where a_I is the density of interfacial area defined in (125). The thermodynamics of interfaces is made of the above definitions for energy and entropy together with the Gibbs relation

$$dU_I = T_I dS_I + \gamma da_I. \quad (\text{C-2})$$

It is also usual to introduce a mean transport velocity V_I of the interfaces. That mean velocity is somehow arbitrary but whatever it is the above Gibbs relation can be transformed into a relation between transport equations that writes

$$\frac{\partial U_I}{\partial t} + \nabla \cdot (U_I V_I) = T_I \left[\frac{\partial S_I}{\partial t} + \nabla \cdot (S_I V_I) \right] + \gamma \left[\frac{\partial a_I}{\partial t} + \nabla \cdot (a_I V_I) \right]. \quad (\text{C-3})$$

To simplify the issue the interfaces are supposed to have no momentum and no kinetic energy. Moreover, heat transport as well as viscous phenomena are neglected in that third phase. But the forces associated with surface tension are taken into account with an interfacial stress tensor

$$\sigma_I = - \langle \gamma (I - nn) \delta_I \rangle = a_I \gamma \left(C_{ij} - \frac{2}{3} I \right) \quad (\text{C-4})$$

where the anisotropy tensor C_{ij} is defined in (127).

The main modification brought by surface tension to the two-fluid equations concerns the exchanges between the two phases. Except for mass exchanges they no longer mutually cancel. The sum of the two entropy exchanges is transformed into interfacial entropy and the sum of the two momentum exchanges is transformed into interfacial forces (interfacial stress in fact). But how the interfacial entropy and the interfacial stress are to be shared between the two phases? Let us solve that issue with the following trick: Instead of writing the balance equations for a quantity X in the form

$$\frac{dX_d}{dt} = x_d, \quad \frac{dX_c}{dt} = x_c, \quad \frac{dX_I}{dt} = -x_d - x_c \quad (\text{C-5})$$

we incorporate the third equation into the first two with a “sharing” coefficient a and write

$$\frac{dX_d}{dt} = x - a \frac{dX_I}{dt}, \quad \frac{dX_c}{dt} = -x - (1 - a) \frac{dX_I}{dt} \quad (\text{C-6})$$

Doing so we can forget the third equation and obtain a set of equations very close to the one in the main text. In fact with two sharing coefficients a_s and a_u the two-fluid equations for entropy and momentum are modified into

$$\alpha_d \rho_d \frac{d_d s_d}{dt} + \alpha_d \nabla \cdot h = \Delta_d + \Sigma + \Gamma (s^* - s_d) - a_s \left[\frac{\partial S_I}{\partial t} + \nabla \cdot (S_I V_I) \right] \quad (\text{C-7})$$

$$\alpha_c \rho_c \frac{d_c s_c}{dt} + \alpha_c \nabla \cdot h = \Delta_c - \Sigma - \Gamma (s^* - s_c) - (1 - a_s) \left[\frac{\partial S_I}{\partial t} + \nabla \cdot (S_I V_I) \right] \quad (\text{C-8})$$

$$\alpha_d \rho_d \frac{d_d u_d}{dt} + \alpha_d \nabla \cdot \sigma + \alpha_d \nabla p_c = F + \Gamma (u^* - u_d) - a_u \nabla \cdot \sigma_I + \alpha_d \rho_d g \quad (\text{C-9})$$

$$\alpha_c \rho_c \frac{d_c u_c}{dt} + \alpha_c \nabla \cdot \sigma + \alpha_c \nabla p_c = -F - \Gamma (u^* - u_c) - (1 - a_u) \nabla \cdot \sigma_I + \alpha_c \rho_c g. \quad (\text{C-10})$$

Note that we neglected the interfacial entropy production like we did in the main text. Moreover, because they have no role in surface tension phenomena we simplified the issue by discarding all forces and stresses bound to velocity fluctuations but they can be restored without any problem. And we did not write the mass balances because they are not modified by massless interfaces. Repeating the procedure detailed in [Sect. 3](#) we deduce from the above equations the transport equation for the total energy and we find

$$\begin{aligned} & \frac{\partial}{\partial t} (\alpha_d \rho_d E_d + \alpha_c \rho_c E_c) + \nabla \cdot (\alpha_d \rho_d E_d u_d + \alpha_c \rho_c E_c u_c + p_c u + u \cdot \sigma + Th) \\ &= (\alpha_d \rho_d u_d + \alpha_c \rho_c u_c) \cdot g + T_d \Delta_d + T_c \Delta_c + (T_d - T_c) \Sigma + (u_d - u_c) \cdot F \\ &+ \sigma : \nabla u + h \cdot \nabla T + \Gamma [\mu_d - \mu_c + (T_d - T_c) s^* + (u^* - u_c)^2/2 - (u^* - u_d)^2/2] \\ &+ (p_c - p_d) (\partial \alpha_d / \partial t + \nabla \cdot (\alpha_d u_d)) - T_I [\partial S_I / \partial t + \nabla \cdot (S_I V_I)] - W_I \cdot (\nabla \cdot \sigma_I) \end{aligned} \quad (\text{C-11})$$

where

$$T_I = a_s T_d + (1 - a_s) T_c \quad (\text{C-12})$$

$$W_I = a_u u_d + (1 - a_u) u_c. \quad (\text{C-13})$$

Hence the mean interfacial temperature is connected to the sharing coefficient a_s and a mean interfacial velocity W_I can be defined, which is connected to the sharing coefficient a_u . That second interfacial velocity is bound to the power developed by interfacial forces and there is no reason for that velocity to be equal to the mean transport velocity V_I . The total energy is conserved and this imposes a very specific form for its evolution equation, which can be obtained with due account for (C-3) and which writes

$$\begin{aligned} & \frac{\partial}{\partial t} (\alpha_d \rho_d E_d + \alpha_c \rho_c E_c + U_I) + \nabla \cdot (\alpha_d \rho_d E_d u_d + \alpha_c \rho_c E_c u_c + U_I V_I) \\ &+ \nabla \cdot (p_c u + u \cdot \sigma + W_I \cdot \sigma_I + Th) = (\alpha_d \rho_d u_d + \alpha_c \rho_c u_c) \cdot g. \end{aligned} \quad (\text{C-14})$$

As a consequence the total dissipation rate is

$$\begin{aligned} T_d \Delta_d + T_c \Delta_c &= (T_c - T_d) \Sigma + (u_c - u_d) \cdot F - h \cdot \nabla T + \Gamma [\mu_c - \mu_d \\ &+ (T_c - T_d) s^* - (u^* - u_c)^2/2 + (u^* - u_d)^2/2] - \sigma : \nabla u - \sigma_I : \nabla W_I \\ &+ (p_d - p_c) [\partial \alpha_d / \partial t + \nabla \cdot (\alpha_d u_d)] - \gamma [\partial a_I / \partial t + \nabla \cdot (a_I V_I)]. \end{aligned} \quad (\text{C-15})$$

For dispersed mixtures plausible values for V_I and W_I are

$$V_I = u_d, \quad W_I = u, \quad (\text{C-16})$$

meaning that the interfacial area is transported with the dispersed phase velocity and that the work of interfacial forces involves the volume-weighted velocity defined in (82), with the consequence that $a_u = \alpha_d$.

The two closures (C-16) have important consequences. The total stress of the suspension is $\sigma + \sigma_I + p_c I$. While σ_I is entirely proportional to the surface tension, a part of σ is also proportional to γ while the remaining part is a viscous stress τ^D . One is thus inclined to write

$$\sigma + \sigma_I = \alpha_d \left(p_d - p_c - \frac{2\gamma a_I}{3\alpha_d} \right) I - \tau^D - \tau^\gamma. \quad (\text{C-17})$$

Closures for τ^D and τ^y are given in (130) for the case of an emulsion. It is clear that τ^y is different from the anisotropic part $a_I \gamma C_{ij}$ of σ_I . The last four terms of the dissipation rate (C-15) are then transformed into

$$\begin{aligned} & -(\sigma + \sigma_I) : \nabla u + (p_d - p_c) \left[\frac{\partial \alpha_d}{\partial t} + \nabla \cdot (\alpha_d u_d) \right] - \gamma \left[\frac{\partial a_I}{\partial t} + \nabla \cdot (a_I u_d) \right] \\ & = \tau^D : D + \left(p_d - p_c - \frac{2\gamma a_I}{3\alpha_d} \right) \left[\frac{\partial \alpha_d}{\partial t} + \nabla \cdot (\alpha_d u_d) - \alpha_d \nabla \cdot u \right] \\ & \quad - \gamma \left[\frac{\partial a_I}{\partial t} + \nabla \cdot (a_I u_d) - \frac{2a_I}{3\alpha_d} \left(\frac{\partial \alpha_d}{\partial t} + \nabla \cdot (\alpha_d u_d) \right) - \frac{\tau^y}{\gamma} : D \right] \end{aligned} \quad (\text{C-18})$$

where $D = (1/2)(\nabla u + \nabla u^T)$ is the suspension strain rate. The total dissipation rate is thus connected to the way one writes the transport equations for the volume fraction and the transport equation for the density of interfacial area.

Let us begin with the equation for α_d and the special case of bubbles moving in a noncompressible fluid. The starting point is

$$\begin{aligned} \frac{\partial \alpha_d}{\partial t} + \nabla \cdot (\alpha_d u_d) &= 3\alpha_d \frac{w_d}{a} + \frac{\Gamma}{\rho_d} \\ \frac{\partial \alpha_c}{\partial t} + \nabla \cdot (\alpha_c u_c) &= -\frac{\Gamma}{\rho_c}, \end{aligned} \quad (\text{C-19})$$

where w_d is the radial velocity inside the bubble and close to its surface. w_d is related to the radial velocity w_c in the liquid close to the interface by the boundary condition (101) and we deduce from the two above equations $\nabla \cdot u = 3\alpha_d(w_c/a)$. Consequently

$$\frac{\partial \alpha_d}{\partial t} + \nabla \cdot (\alpha_d u_d) - \alpha_d \nabla \cdot u = 3\alpha_d \alpha_c \frac{w_c}{a} + \frac{\Gamma}{\rho_c}, \quad (\text{C-20})$$

a result equivalent to (100). That result also confirms that w_c is a much more convenient quantity to handle than w_d and that the transport equation for the volume fraction is more conveniently expressed as in (100) rather than in its more classical counterpart (C-19).

Concerning the density of interfacial area the above expression of the dissipation rate suggests to write its transport equation as

$$\frac{\partial a_I}{\partial t} + \nabla \cdot (a_I u_d) = \frac{2a_I}{3\alpha_d} \left(\frac{\partial \alpha_d}{\partial t} + \nabla \cdot (\alpha_d u_d) \right) + \frac{\tau^y}{\gamma} : D - \Phi_\gamma, \quad (\text{C-21})$$

where Φ_γ is a *positive* scalar reflecting the tendency of surface tension to decrease the total amount of interface. In (128) the $C : C$ term is a contribution to Φ_γ depicting the return to isotropic shapes. The coalescence phenomenon is represented by another contribution to Φ_γ . And the final expression of the dissipation rate is

$$\begin{aligned} T_d \Delta_d + T_c \Delta_c &= (T_c - T_d) \Sigma + (u_c - u_d) \cdot F - h \cdot \nabla T + \tau^D : D + \Gamma [\mu_c - \mu_d \\ & \quad + (T_c - T_d) s^* + (p_d - p_c - 2\gamma a_I / 3\alpha_d) / \rho_c - (u^* - u_c)^2 / 2 \\ & \quad + (u^* - u_d)^2 / 2] + 3\alpha_d \alpha_c (w_c / a) (p_d - p_c - 2\gamma a_I / 3\alpha_d) + \gamma \Phi_\gamma \end{aligned} \quad (\text{C-22})$$

a result to be compared with (113).

PART II: COMPUTATION WITH EFFECTIVE-FIELD MODELS OF MULTIPHASE FLOWS

7 Introduction and Scope II

In Part II we pursue the EFM developed in Part I to its numerical implementation. To recapitulate, the principal desiderata are: robust and high-fidelity simulations of disperse systems at all flow speeds, and this implies, sharp capturing of pressure and flow discontinuities (shock waves), as well as highly resolved material (or contact) “interfaces.” Besides a well-founded numerical scheme, these aims require an ability to refine the grid (thereby requiring stability under reduced numerical dissipation), as well as the means to do so for problems involving large spatial dimensions, which in turn translates into a requirement for adaptive mesh refinement. The cornerstone to all these is a hyperbolic system of equations, which was shown to have been effectively achieved for all conditions of interest here (Part I). This allows for a focused treatment that is based on the extensive theoretical foundation of hyperbolic conservation laws (single-phase gas dynamics, Euler’s equations), as well as ample practical experience in aerospace science and engineering. Our main challenge then will be to extend these concepts and practice to the case where the flow field is occupied simultaneously (in the sense of interpenetrating continua) by more than one phase.

As we have seen in Part I, inviscid interactions (between the phases) play a critical role in securing the hyperbolic character of our system, and accordingly we can expect that the numerical treatment of these terms will be of central importance in adapting from the single-phase methods just mentioned. To further define the scope, it is sufficient for purposes of illustration (➤ Sect. 12) to consider disperse systems with continuous to disperse density ratios much less than unity (i.e., droplet or particle flows). This is because such flows: (a) make accessible large slip between the phases, and thusly supersonic regimes that are of great interest to our aims here, and (b) can exhibit inviscid interactions that are realistically and quantitatively significant. Notably, slip is rather small in bubbly flows, even under forced accelerations; for example, in converging/diverging channels breakup due to interfacial instabilities leads to decreased length scales and thus closely followed near-equilibrium. On the other hand, recall (Part I) that for bubbly flows we need to also include (to the system considered here) equations that describe radial inertia and volume fraction transport ((69)-(75) in Part I). The extension of the present treatment to such situations is rather straightforward. Other terms in the equations that describe dissipative phenomena due to viscosity, heat transfer between phases, phase change, and breakup/coalescence can be readily added as source terms in the equations – they are indicated in Part I at the basic level, and they do not affect the numerical treatment discussed here. In other words, they concern fidelity of a simulation in a particular venue rather than robustness of the numerical scheme.

Beyond this short introduction and the statement of our problem in (➤ Sect. 8), the presentation is arranged in three parts. The first part provides the foundations from single-phase flow as mentioned already – it is separated into two sections: (➤ Sect. 9) deals with theory and exact results, and (➤ Sect. 10) that leverages these essentially exact results to the most important approximate methods that address practical utility. The second part (➤ Sect. 11) provides the extension of these methods and ideas to the treatment of the EFM; that is to the development of the AUSM-ARMS scheme specifically tailored to our present needs. The third part (➤ Sect. 12) is on sample calculations that illustrate numerical performance. Throughout, we focus on

high-speed flows where the timescales are already limited by phenomena at the acoustic timescales and accordingly we limit our consideration to explicit schemes.

Our present focus provides the complement to moderate speed and incompressible flows already well known via the methods belonging to the ICE and SIMPLE families. Indeed, they are at the genesis of the CFD era, the Implicit Continuous-Fluid Eulerian (ICE) method by Harlow and Amsden (1968), at Los Alamos Scientific Laboratory, and the Semi-implicit Method for Pressure-Linked Equations (SIMPLE) by Patankar and Spalding (1972) at the Imperial College, UK (see also Harlow and Welch 1965). The former was the first method to overcome the Courant-Friedrichs-Lax (CFL) stability criteria, thus allowing practical simulations of large systems at all flow speeds (it formed the basis for all nuclear systems codes in existence to date – RELAP5, TRAC, CATHARE, etc.). The later is arguably one of the most popular methods for low/moderate Mach number flows, especially in commercial software packages. Other well-known multiphase flow codes that are based on the ICE method include KACHINA (Amsden and Harlow 1975), K-FIX (Rivard and Torrey 1997), and MF-ICE/MAC (Kashiwa and Rauenzahn 1994). The first CFD type codes used to assess steam explosion energetics in severe nuclear reactor accidents, PM-ALPHA-3D and ESPROSE-3D (Theofanous et al. 1998a,b), were based on the K-FIX solver. Commercial code packages that are based on SIMPLE include PHOENICS (Concentration Heat and Momentum Ltd.), FLUENT (Fluent Inc. joins ANSYS Inc.), and CFX (ANSYS Inc.).

8 Strategy for Computing Compressible Multi-Hydrodynamics

On the impetus of abounding gas dynamics problems, most notably from aerospace science and engineering, the numerical solution of hyperbolic conservation laws is well founded in theory (Lax 1954; Smoller 1983), and fully endowed in practice (Roe 1986; LeVeque 1990; Toro 1997), yet the supposedly similar path with multiphase systems has been filled with confusing retours and tangents. Starting with the first serious attempt at numerical simulation of nuclear reactor (loss of coolant) accidents, it was realized that coarse-graining of two-phase flows can be much more detrimental than that of turbulent flows – while they both share the issue of closure, re-incorporation of fine-scale physics lost in averaging, the mathematical character of the two-phase system was found to have lost the hyperbolic property. First pointed out by Gidaspow (1974), this “ill-posedness” implies that numerical solutions are inherently susceptible to catastrophic instability and much of the efforts since have been focused on:

- (a) Finding numerical schemes that improve resiliency – numerical dissipation being a leading method to such an end
- (b) Aiming to show that such instabilities, moderated by nonlinear effects and by dissipative (algebraic) “source terms” would not significantly contaminate the numerical results
- (c) Adding “by hand” closure terms that would restore hyperbolicity

On the other hand, and somewhat more severely, as a result of ill-posedness, there has been left some doubt on the basic correctness of the effective field model in any of the many shapes or forms that it has appeared in the literature (Drew and Passman 1999; Prosperetti and Satrape 1990; Prosperetti 1999).


On approaches (a) and (b) the major developments were made long ago and on behalf of the RELAP5 code – they have been invaluable for nuclear system simulations and are well documented in the open literature (RELAP5-3D Manuals 2006). The main ideas are that spatial discretizations normally employed in reactor system simulations introduce a sufficient amount of numerical dissipation to stabilize the solution, and that there is a “natural” cutoff on the unstable wave-numbers that is consistent with practical system discretization requirements (at least in terms of computer hardware available at the time). Furthermore, this dissipation role was shown to be aided by the drag terms in the momentum equations.

On item (c) the efforts have been of more widespread and diverse origins. The idea was to “constitute” the phase interaction terms that appear in the averaged momentum equations in a manner that includes the “added mass” and “interfacial pressure” mechanisms (collectively called inviscid interactions herein and in Part I). More specifically, these are to address the two pairs of terms involving stresses in (1) and (2) – the first and second terms on the RHS, where the χ and δ are the phase-indicator and interface-indicator functions respectively (see (1) and (2) of Part I).

$$\alpha_c \rho_c \frac{d_c \mathbf{u}_c}{dt} + \nabla \cdot \langle \chi_c \rho_c^0 \mathbf{v}'_c \otimes \mathbf{v}'_c \rangle = \nabla \cdot \langle \chi_c \boldsymbol{\sigma}_c^0 \rangle - \langle \boldsymbol{\sigma}_c^0 \cdot \mathbf{n}_d \delta_I \rangle + \alpha_c \rho_c \mathbf{g} \quad (133)$$

$$\alpha_d \rho_d \frac{d_d \mathbf{u}_d}{dt} + \nabla \cdot \langle \chi_d \rho_d^0 \mathbf{v}'_d \otimes \mathbf{v}'_d \rangle = \nabla \cdot \langle \chi_d \boldsymbol{\sigma}_d^0 \rangle + \langle \boldsymbol{\sigma}_c^0 \cdot \mathbf{n}_d \delta_I \rangle + \alpha_d \rho_d \mathbf{g} \quad (134)$$

In these equations subscripts c/d indicate continuous/disperse phases, respectively, $\boldsymbol{\sigma}$'s are phasic stresses, \mathbf{u} 's are velocities, ρ 's are densities, α 's are volume fractions, \mathbf{v}' 's are the pseudo-turbulent velocity fluctuations, and \mathbf{n}_d is the unit vector normal to interface. The added mass, first introduced by Drew et al. (1979), is to account for accelerations of one phase relative to the other. The interfacial pressure, first introduced by Stuhmiller (1977), was visualized as a Bernoulli effect due to the continuous phase flowing “around” the individual elements of the dispersion. Stuhmiller’s approach was found to be effective in rendering the system hyperbolic in incompressible, low-speed flows, and in fact it has been incorporated in the French nuclear code CATHARE (Bestion et al. 1999) (a descendant of RELAP5). Many followed with combinations and/or variations of these two “fixes,” however, this practical path did not appear to intersect with theory to an adequate degree, therefore lacking in definitiveness of treatment (Toumi et al. 1999). In particular, no definitive treatment can be found that is fully integrated with rigorous and complete developments of the effective field model, even though two such developments have become available long ago (Geurst 1985; Wallis 1991).

These two works (Geurst 1985; Wallis 1991) share with Part I the philosophy that rather than ad hoc and separate closures for added mass and interfacial pressure, inviscid interaction terms arise naturally and together with only minimal assumptions about the role of (pseudo-turbulent) velocity fluctuations. Perhaps more importantly, the results, which can be shown (Part I,  Sect. 6.1) to be in complete agreement among these three derivations, (135)–(140) below, include terms other than those that have come to be recognized as added mass and interfacial pressure. The impact of these terms on hyperbolicity is provided in Appendix B of Part I. Notably, the methodologies employed in these three independent derivations are completely different, and thus we believe that there is a high degree of reliability in the result.

Accordingly, this system is the starting point of our numerical treatment; (53)–(60) of Part I, with the gravity terms omitted without loss of generality, and allowing for compressibility of the

disperse phase:

$$\frac{\partial \alpha_c \rho_c}{\partial t} + \nabla \cdot (\alpha_c \rho_c \mathbf{u}_c) = 0 \quad (135)$$

$$\frac{\partial \alpha_d \rho_d}{\partial t} + \nabla \cdot (\alpha_d \rho_d \mathbf{u}_d) = 0 \quad (136)$$

$$\alpha_c \rho_c \frac{d_c \mathbf{u}_c}{d t} + \nabla \cdot \boldsymbol{\sigma}_c^K + \alpha_c \nabla p_c = -\mathbf{F}^K \quad (137)$$

$$\alpha_d \rho_d \frac{d_d \mathbf{u}_d}{d t} + \nabla \cdot (\alpha_d P^K) + \alpha_d \nabla p_c = \mathbf{F}^K \quad (138)$$

$$\alpha_c \rho_c \frac{d_c E_c}{d t} + \nabla \cdot (\alpha_c p_c \mathbf{u}_c + \mathbf{u}_d \cdot \boldsymbol{\sigma}_c^K) + p_c \frac{\partial \alpha_c}{\partial t} = -W^K \quad (139)$$

$$\alpha_d \rho_d \frac{d_d E_d}{d t} + \nabla \cdot (\alpha_d (p_c + P^K) \mathbf{u}_d) + p_c \frac{\partial \alpha_d}{\partial t} = W^K \quad (140)$$

Where:

$$E_c = e_c + \frac{1}{2} \mathbf{u}_c^2 + K_c; \quad K_c = \frac{1}{2} E(\alpha_d) (\mathbf{u}_d - \mathbf{u}_c)^2;$$

$$P^K = -\alpha_c \rho_c \frac{\partial K_c}{\partial \alpha_d}; \quad p_c = f(e_c, \rho_c); \quad \mathbf{J} = \alpha_c \rho_c E(\alpha_d) (\mathbf{u}_d - \mathbf{u}_c);$$

$$\mathbf{F}^K = -\frac{\partial \mathbf{J}}{\partial t} - \nabla \cdot (\mathbf{u}_d \otimes \mathbf{J}) - (\mathbf{J} \cdot \nabla) \mathbf{u}_c - \alpha_c \rho_c \nabla K_c - \mathbf{J} \times (\nabla \times \mathbf{u}_c)$$

$$E(\alpha_d) = \frac{1}{2} \alpha_d (1 + C \alpha_d); \quad W^K = \mathbf{u}_d \cdot \mathbf{F}^K + \alpha_d P^K \nabla \cdot \mathbf{u}_d; \quad \boldsymbol{\sigma}_c^K = (\mathbf{u}_d - \mathbf{u}_c) \otimes \mathbf{J}$$

where p_c is the continuous phase pressure along with the definitions of other quantities as given above. The hyperbolicity analysis for this system will be used (► Sect. II) in setting the finite volume rendition of this system and in the construction of our numerical scheme.

As established by the landmark papers of Lax (1954) and Courant et al. (1952) and summarized in an excellent review article by Roe (1986), “shock-capturing methods have attained mathematical respectability, partly through reinterpretation of the numerical equations as expressions of integral rather than differential laws, and partly through the incorporation of ideas drawn from the theory of characteristics.” The former refers to expressing spatial derivatives in complete divergence form, and by use of Gauss’ theorem to manifest these terms as flux differences at the boundaries of finite volumes (used to discretize our flow domain) – an overall effect of conservation is quite obvious. The later refers to estimating these fluxes so that “state information” is propagated correctly from the upstream and/or the downstream directions, according to the characteristic speeds of our flowing two-phase mixture (as we will see below, these involve both the flow speeds of the phases and their sound speeds) – this we call generically “**upwinding**.” In particular this opens up access to “**weak solutions**” (Lax, 1954), that is, it allows the existence of discontinuities such as shock waves or contact discontinuities, and the numerical challenge is to accomplish this robustly and without oscillations in the solution. This is expressed as the monotonicity preserving constraint, which however according to a theorem due to Godunov (1959) it is bound to be violated for any second- or higher-order accurate **linear** scheme. On the other hand, Godunov showed that first-order upwinding (see next section) is monotonicity preserving with the least truncation error, and this formed the

basis of a general strategy, namely to adding (carefully) EOS complexity and efficiency in computation. This strategy is also the foundation of our efforts in addressing the EFM. Accordingly, [▶ Sects. 9](#) and [▶ 10](#) are dedicated to setting up this foundation.

Now in the same vein we note that our system of equations cannot be set in a fully conservative form ([▶ Sect. 11](#)). The “offending” terms are those involving the pressure gradient in the momentum equations as well as some of the terms representing inviscid interactions. More revealingly, the pressure gradient terms can be rewritten so that what is left outside the divergence sum are terms involving gradients in volume fractions – this is the real effect of “flow area” change for each of the phases, and in the extreme, it would represent a contact discontinuity (e.g., a gas flow entering a particle bed).

9 Basics: The Riemann Problem and the Godunov Method

Consider the motion of an (ideal) inviscid, compressible fluid in one space dimension. The “state” of fluid/motion at any point and time instant is described by the triplet [density, velocity, internal energy] = $[\rho, u, e]$, and the evolution from any initial state (a prescribed spatial distribution of these quantities) is governed by the conservation laws of mass, momentum, and energy – the latter follows from the requirement that, in the absence of shocks (these require special treatment), the entropy of such an ideal flow must remain constant. These are the Euler equations, which along with the fluid (thermodynamic) equation of state (EOS) write:

$$\frac{\partial \mathbf{U}}{\partial t} + \frac{\partial \mathbf{F}(\mathbf{U})}{\partial x} = 0, \quad t > 0, \quad -\infty < x < \infty, \quad E = e + 1/2 u^2, \quad e = e(\rho, p) \quad (141)$$

$$\mathbf{U} = (\rho, \rho u, \rho E)^T \text{ and } \mathbf{F}(\mathbf{U}) = [\rho u, \rho u^2 + p, (\rho E + p)u]^T$$

It can be seen that our EFM in the previous section reduces to the Euler equations when we let the disperse phase vanish. We will refer to the original triplet as “primitive” variables, while \mathbf{U} expresses a vector of “conserved” variables. The idea of conservation derives from the recognition that by use of Gauss’ theorem the divergence of the fluxes, $\mathbf{F}(\mathbf{U})$, can be written as the net (signed) flux crossing the boundaries of our system (by convection and pressure forces). In numerical implementation this crucial property can be assured at the discrete level by simply defining quantities \mathbf{U} as averages over finite (cell) volumes, and the quantities $\mathbf{F}(\mathbf{U})$ as some appropriately averaged fluxes over the cell boundaries.

For example, in one space dimension we can have our domain, say from $x = a$ to $x = b$, discretized by setting cell boundaries at $x_{j+1/2}$ ($j = 0, \dots, N$)

$$a = x_{1/2} < x_{3/2} < \dots < x_{N-1/2} < x_{N+1/2} = b \quad (142)$$

Accordingly we have cells (C_j), cell centers (x_j), and cell “volumes” (Δx_j), respectively as:

$$C_j \equiv [x_{j-1/2}, x_{j+1/2}], \quad x_j = \frac{1}{2} (x_{j-1/2} + x_{j+1/2}), \quad \Delta x_j = x_{j+1/2} - x_{j-1/2}. \quad (143)$$

On the time domain, we define

$$\mathcal{T}_n \equiv [t_n, t_{n+1}], \quad \Delta t \equiv t_{n+1} - t_n \quad (144)$$

Integration of (141) over $C_j \times \mathcal{T}_n$ gives

$$\int_{t_n}^{t_{n+1}} \frac{\partial}{\partial t} \left(\int_{x_{j-1/2}}^{x_{j+1/2}} \mathbf{U}(x, t) dx \right) dt + \int_{t_n}^{t_{n+1}} \int_{x_{j-1/2}}^{x_{j+1/2}} \frac{\partial \mathbf{F}(\mathbf{U}(x, t))}{\partial x} dx dt = 0 \tag{145}$$

which along with the definition for space and time averages:

$$\mathbf{u}_j^n \equiv \frac{1}{\Delta x_j} \int_{x_{j-1/2}}^{x_{j+1/2}} \mathbf{U}(x, t_n) dx \tag{146}$$

$$\mathbf{f}(x_{j+1/2}; t_n, t_{n+1}) \equiv \frac{1}{\Delta t} \int_{t_n}^{t_{n+1}} \mathbf{F}(\mathbf{U}(x_{j+1/2}, t)) dt \tag{147}$$

yields:

$$\Delta x_j \int_{t_n}^{t_{n+1}} \left(\frac{\partial}{\partial t} \mathbf{u}_j^n \right) dt + \int_{t_n}^{t_{n+1}} (\mathbf{F}(\mathbf{U}(x_{j+1/2}, t)) - \mathbf{F}(\mathbf{U}(x_{j-1/2}, t))) dt = 0 \tag{148}$$


If the fluxes in the above integral are evaluated at time t_{n+1} we have an implicit scheme. For our purposes it is sufficient to focus on explicit treatment, so then by dropping the t_n as well we finally have the discrete conservation law in terms of the approximate “numerical fluxes” at cell boundaries:

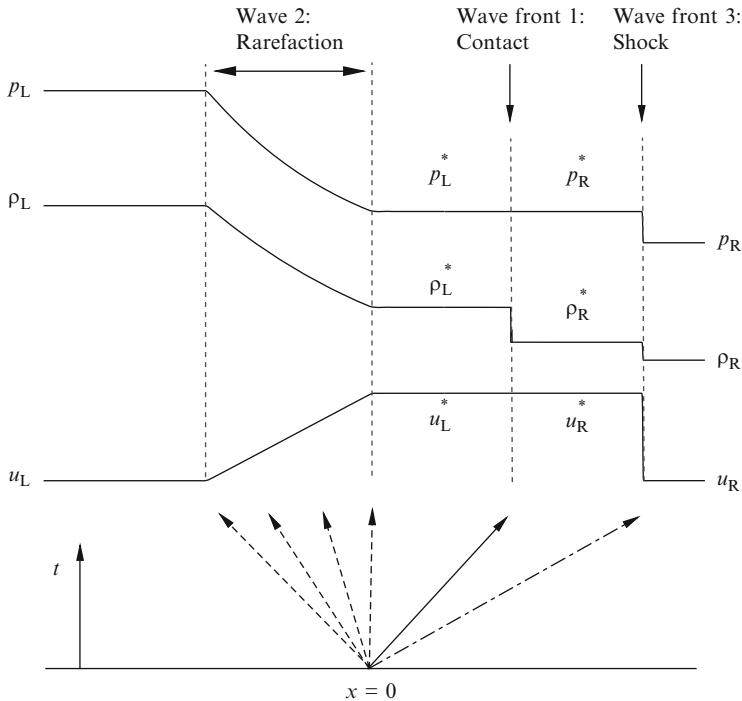
$$\mathbf{u}_j^{n+1} = \mathbf{u}_j^n - \frac{\Delta t}{\Delta x_j} (\mathbf{f}(x_{j+1/2}) - \mathbf{f}(x_{j-1/2})) \tag{149}$$

At this point it should be clear that the whole question is on how to deal with these approximate numerical fluxes so as to preserve the basic natural behavior of our system with maximum efficiency and fidelity. In particular, since the existence of weak (non-differentiable) solutions has been established theoretically, of special interest is to obtain such fluxes in the presence of discontinuities in state variables.

9.1 The Riemann Problem

Focusing on the problem of dealing with discontinuities, as introduced above, let us then consider the simplest case first, that of an infinite flow domain initially separated into two uniform states – we denote them by superscripts (or subscripts when it is more convenient) L/R (for the state on the left/right). Moreover, for illustration let us focus on a particular example of this general class of Riemann problems; the one exemplified by a shock tube allowing by release of a diaphragm to instantaneously contact two initially *stationary* states of a fluid found at two different pressure levels. Our object is to find the structure of the solution, and more specifically to determine the flux vector at the position of the diaphragm; taken at the origin, $x = 0$. With the notation introduced above, this flux vector is denoted as $\mathbf{f}(x = 0)$.

As illustrated in  Fig. 1, the solution consists of three principal wave fronts – they correspond to the three eigenvalues and propagate at constant rates that are related to the three characteristic speeds of our system, so in the $x-t$ plane the front positions of these waves can be found for any future time as shown in the figure. The central wave indicated as “contact,” provides the material displacement from the original position of the diaphragm. Both pressures and velocities across this wave are continuous, but there is a density jump on account



■ Figure 1

Illustration of the solution structure to a Riemann (shock tube) problem. The solution is a constant on any “ray” (characteristics) emanating from the origin with a constant slope of x/t . The slopes of the characteristics that trace the wave fronts correspond to the eigenvalues

that on the left the fluid expands, while on the right it is compressed. This “material” characteristic speed is written as $\lambda_1 = u_R^* = u_L^* \equiv u^*$. The wave front on the left, marked as “rarefaction” propagates with the speed $\lambda_2 = u_L^* - a^*$, where a^* is the speed of sound in the compressed state. The situation of the wave front on the right marked as “shock,” is a little more complicated. If its amplitude is sufficiently small, it propagates with the characteristic speed $\lambda_3 = u_R^* + a^*$, otherwise such acoustic waves (as their speed increases with amplitude) would “pile up” into a shock, a singularity in pressure across which energy/entropy conservation cease to be observed – accordingly the speed of such a shock needs to be determined by simultaneous consideration of the mass, momentum, and energy conservation equations (the so-called Rankine-Hugoniot (R-H) relations). The details are readily available and beyond our specific purposes here, but suffice to note that:

1. The characteristic speeds introduced above, the λ 's, are called the eigenvalues. For their explicit connection to (141) and ► Fig. 1, and their further utility in our task it is best to wait until ► 10.1.
2. The nonlinearity (increasing/decreasing sound speed with state of compression/expansion) that steepens the compression front to a shock is responsible for “flattening” (with time)

the rarefaction (at the other end) through a fan of wave “fronts” all emanating from the origin.

3. The R-H conditions on the shock and an isentropic expansion on the rarefaction allow starred quantities to be related to the initial L/R states, $\mathbf{U}_L; \mathbf{U}_R$, and these relationships along with the requirement that pressures and velocities are continuous across the contact discontinuity (note also the possibility of two different fluids involved in the use of EOS), yield an algebraic system to be solved (for the starred quantities) as the actual quantitative solution. This is the exact solution to the Riemann problem under consideration.
4. Once this solution is known, the sought-after flux at the origin is obtained simply as:

$$\mathbf{f}(x = 0, t) = \begin{cases} \mathbf{f}(\mathbf{U}_L^*; \mathbf{U}_R^*) = \mathbf{f}(\mathbf{U}_L^*) & \text{if } u^* \geq 0 \\ \mathbf{f}(\mathbf{U}_L^*; \mathbf{U}_R^*) = \mathbf{f}(\mathbf{U}_R^*) & \text{if } u^* < 0 \end{cases} \quad (150)$$

where the notation $\mathbf{f}(\mathbf{U}_L^*; \mathbf{U}_R^*)$ is to express the flux at the origin (the position of the diaphragm). As is to be seen in [▶ 9.2](#), this is a major result in motivating the concept of “upwinding.”

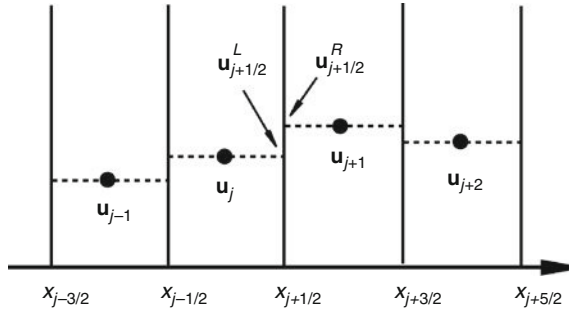
It is important to note that in general the initial state of a Riemann problem will involve nonzero velocities – they would enter in the determination of the starred quantities, and in particular in the upwinding criterion (150) – in the particular shock tube example given above $u^* > 0$ obviously, but this is not to be so in general. Also note that since there is no characteristic length or time scales imposed, the solution to our problem depends solely on the combination x/t . Lines of constant x/t are called characteristics and the solution remains constant along a characteristic. Accordingly, the space between wave fronts is described by uniform states, except in the case of an expansion, where the “front” broadens out with time ([▶ Fig. 1](#)).

Godunov (1959) capitalized on these simple ideas to propose a general numerical scheme capable of predicting evolutions from any initial state $\mathbf{U}_0(x)$, even when this initial distribution contains singularities. Moreover, even though the exact Riemann solution is not available for flows in higher dimensions, this numerical concept could be extended to provide robust and accurate results as summarized in [▶ 9.2](#) and [▶ 10.3](#). In turn these provide the cornerstone for our own developments in regards to the EFM ([▶ Sect. 11](#)).

9.2 The Godunov Method

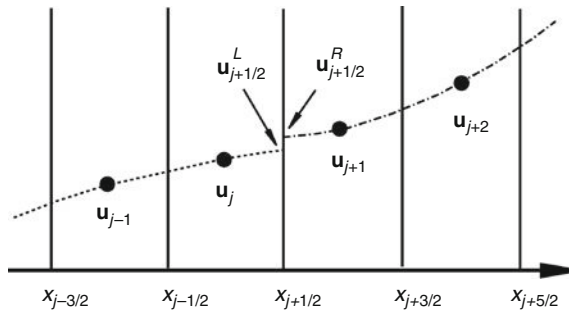
Godunov’s brilliant and path-breaking idea was to provide the exact solution to an *approximation* of the initial fluid state “decomposed” in such a manner as to conform to a series of Riemann problems as illustrated in [▶ Fig. 2](#) – in the simplest, first-order approximation, the decomposition is in terms of piece-wise constant values. Now according to notation introduced already, the \mathbf{u}_j^n ’s represent cell-average values of the “initial” state function in positions j at time cycle n , and the fluxes based on the Riemann problem across any two cells say $[j, j+1]$ are then denoted by $\mathbf{f}(x_{j+1/2}) = \mathbf{f}(\mathbf{u}_{j+1/2}^L, \mathbf{u}_{j+1/2}^R)$. Thus, the average values at each cell in the next time increment Δt can be simply written out according to (149) as:

$$\begin{aligned} \mathbf{u}_j^{n+1} &= \mathbf{u}_j^n - \frac{\Delta t}{\Delta x_j} \left(\mathbf{f}(\mathbf{u}_{j+1/2}^L, \mathbf{u}_{j+1/2}^R) - \mathbf{f}(\mathbf{u}_{j-1/2}^L, \mathbf{u}_{j-1/2}^R) \right) \\ &\equiv \mathbf{u}_j^n - \frac{\Delta t}{\Delta x_j} \left(\mathbf{f}(\mathbf{u}_j, \mathbf{u}_{j+1}) - \mathbf{f}(\mathbf{u}_{j-1}, \mathbf{u}_j) \right) \end{aligned} \quad (151)$$



■ Figure 2

Illustration of the reduction of a general Euler governed problem to the solution of a series of Riemann problems – first-order approximation



■ Figure 3

Illustration of the Godunov reduction in terms of higher-order approximations to a series of Riemann problems

For higher-order approximation the Riemann problems are defined in terms of states extrapolated from “sided” interpolations as illustrated in [Fig. 3](#).

In two or three dimensions, the procedures are very similar, as boundary fluxes are composed from appropriately defined, one-dimensional Riemann problems at each of the cell boundaries. Details on practical implementation of the Godunov method can be found in van Leer (1979), Colella and Glaz (1985), LeVeque (1990), and Toro (1997).

A recent example of the fundamental and broad reach of the Riemann solution is a particular implementation at the interface between two different fluids with high acoustic impedance mismatch – it brings the accuracy and robustness of front-tracking approach into the fast local level set front-capturing implementation of the characteristics-based matching (CBM) method (Nourgaliev et al. 2006), and further on to ab initio capturing of interfacial instabilities by the Sharp Interface Method (SIM) (Nourgaliev and Theofanous 2007; Nourgaliev et al. 2008; Chang et al. 2010b).

What remains to be done is to overcome the issues of inefficiency inherent in the method: the solution of a nonlinear set of algebraic equations by iteration methods, which is further

aggravated in the case of complex EOS (nonideal, stiffened gas, etc.). However, the Godunov method remains the “gold standard” in testing such other approaches.

10 Approximate Flux “Splitting” Schemes for Single Phase Flows



Three critical approaches in “translating” Godunov’s idea to practicality are outlined here. All three involve some sort of flux splitting aimed to “mimic” the characteristics-inspired “upwinding” discussed above but *without* solving the exact Riemann problem. In the first approach (flux difference splitting, or FDS), due to Roe (1981), this is accomplished by recasting the exact mathematical statement of the Riemann (eigenvalue) problem involved into an approximate (linearized) one whose solution can be obtained in a form convenient for numerical implementation. In the second approach (flux vector splitting, or FVS), due to van Leer (1982), the eigenvalue problem is bypassed altogether by means of a Mach-based flux splitting that provides exact upwinding for supersonic conditions and an approximate interpolation for the intermediate subsonic region. The third approach (advection upstream splitting method, or AUSM), due to Liou and Steffen (1993) and Liou (1996), is a hybrid that combines the following specific features inherent to the first two: (1) property of FVS that selects only entropy satisfying approximate solutions (it can distinguish between expansions and shocks), and (2) decisive ability of some FDS methods to exactly capture stationary contact discontinuities and shocks. Indeed, the role of the convection cannot be overstated – it is the process that embodies the nonlinear effects of Euler equations, which can turn initially smooth profiles sharper and eventually into discontinuities (shocks). Along with a summary description of each of these approaches below we provide the successive improvements achieved.

The figures of merit in this evaluation can be listed as follows:

- Discontinuity (shocks, contacts, expansions) capturing, stationary or moving, at all flow speeds
- Monotonicity preserving (not prone to spurious oscillations near discontinuities)
- Positivity preserving (thermodynamic and material parameters remaining nonnegative)

Clearly the aim is to achieve simultaneously all of the above in the most efficient computational manner and with maximum scope of application (generality). Maintaining conservation and satisfying appropriate entropy criteria are not to be sacrificed while trying to meet these ends. At a more philosophical level, the success of Godunov’s idea of using an exact solution to an approximation of the actual problem compels to further approximations in solving this Riemann problem itself.

10.1 Characteristics-Based Flux Splitting

Consider a Riemann problem, as the one in  Fig. 1, but now let us suppose that we “resolve” the discontinuities in the manner illustrated in  Fig. 4; that is, the fluxes associated with each of the three waves are thought to be decomposed into a series of infinitesimal fluxes, $\delta \mathbf{f}_k$, $k = 1, 2$ or 3 each associated with an incremental (infinitesimal) wave amplitude. In terms of our

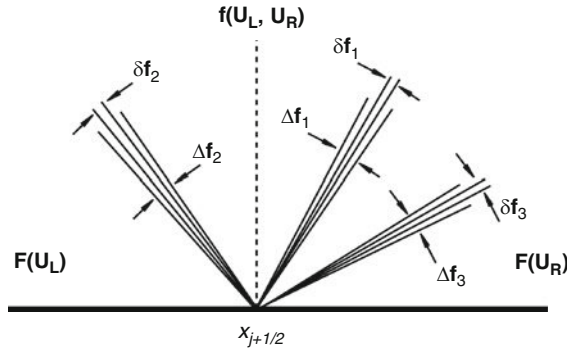


Figure 4
Illustration of Roe’s flux difference-based splitting

Jacobian matrix (\mathbf{A}), the three eigenvalues ($\lambda_1, \lambda_2, \lambda_3$) arranged along the diagonal of Λ , and the eigenmatrix \mathbf{R} and its inverse matrix $\mathbf{L} \equiv \mathbf{R}^{-1}$, the decomposition can be written as:

$$\begin{aligned} \delta \mathbf{F} &= \frac{\partial \mathbf{F}}{\partial \mathbf{U}} \delta \mathbf{U} = \mathbf{A} \delta \mathbf{U} = \mathbf{R} \Lambda \mathbf{L} \delta \mathbf{U} \\ &= \mathbf{R} \begin{pmatrix} \lambda_1 & 0 & 0 \\ 0 & 0 & 0 \\ 0 & 0 & 0 \end{pmatrix} \mathbf{L} \delta \mathbf{U} + \mathbf{R} \begin{pmatrix} 0 & 0 & 0 \\ 0 & \lambda_2 & 0 \\ 0 & 0 & 0 \end{pmatrix} \mathbf{L} \delta \mathbf{U} + \mathbf{R} \begin{pmatrix} 0 & 0 & 0 \\ 0 & 0 & 0 \\ 0 & 0 & \lambda_3 \end{pmatrix} \mathbf{L} \delta \mathbf{U} \\ &= \mathbf{R} \Lambda_1 \mathbf{L} \delta \mathbf{U} + \mathbf{R} \Lambda_2 \mathbf{L} \delta \mathbf{U} + \mathbf{R} \Lambda_3 \mathbf{L} \delta \mathbf{U} \equiv \delta \mathbf{f}_1 + \delta \mathbf{f}_2 + \delta \mathbf{f}_3 \end{aligned} \tag{152}$$

So the fluxes evaluated at the right and left states differ by:

$$\begin{aligned} \mathbf{F}(\mathbf{U}_R) - \mathbf{F}(\mathbf{U}_L) &= \int_{\mathbf{U}_L}^{\mathbf{U}_R} \mathbf{A} d\mathbf{U} \\ &= \int_{\mathbf{U}_L}^{\mathbf{U}_R} \mathbf{R} \Lambda_1 \mathbf{L} d\mathbf{U} + \int_{\mathbf{U}_L}^{\mathbf{U}_R} \mathbf{R} \Lambda_2 \mathbf{L} d\mathbf{U} + \int_{\mathbf{U}_L}^{\mathbf{U}_R} \mathbf{R} \Lambda_3 \mathbf{L} d\mathbf{U} \\ &\equiv \Delta \mathbf{f}_1 + \Delta \mathbf{f}_2 + \Delta \mathbf{f}_3 \end{aligned} \tag{153}$$

which also shows that the sign of each λ_k carries over to the sign of $\Delta \mathbf{f}_k$:

$$(\Delta \mathbf{f}_k)^\pm = \frac{1}{2} \int_{\mathbf{U}_L}^{\mathbf{U}_R} \mathbf{R} (\Lambda_k \pm |\Lambda_k|) \mathbf{L} d\mathbf{U} \tag{154}$$

Moreover, (153) provides the path to smoothly connect the fluxes across the two neighboring cells by means of the three incremental *characteristic* fluxes. In particular, using upwinding the Riemann flux at the cell boundary can be expressed by any of the three forms

(see also  Fig. 4):

$$\begin{aligned}
 \mathbf{F}(\mathbf{U}_L, \mathbf{U}_R) &= \mathbf{F}(\mathbf{U}_L) + \sum_k (\Delta \mathbf{f}_k)^- \\
 &= \mathbf{F}(\mathbf{U}_R) - \sum_k (\Delta \mathbf{f}_k)^+ \\
 &= \frac{1}{2} \left[\mathbf{F}(\mathbf{U}_L) + \mathbf{F}(\mathbf{U}_R) + \sum_k (\Delta \mathbf{f}_k)^- - \sum_k (\Delta \mathbf{f}_k)^+ \right]
 \end{aligned}
 \tag{155}$$

So far these formal results are exact and not of much help in computation since the integrations in (153) are over a continuously changing eigensystem. Roe’s idea was to replace the whole series of \mathbf{A} ’s seen in the above derivation as one traverses from state \mathbf{U}_L or \mathbf{U}_R toward the common cell boundary, by one effective \mathbf{A} . This he accomplished by evaluating \mathbf{A} at some appropriately chosen “intermediate” state, $\tilde{\mathbf{U}} = \tilde{\mathbf{U}}(\mathbf{U}_L, \mathbf{U}_R)$, so that $\tilde{\mathbf{A}}(\mathbf{U}_L, \mathbf{U}_R) = \mathbf{A}(\tilde{\mathbf{U}}(\mathbf{U}_L, \mathbf{U}_R))$ satisfies the following:

1. Matrix $\tilde{\mathbf{A}}$ has real eigenvalues and a complete set of eigenvectors (hyperbolicity)
2. $\mathbf{F}(\mathbf{U}_R) - \mathbf{F}(\mathbf{U}_L) = \tilde{\mathbf{A}}(\mathbf{U}_L, \mathbf{U}_R) (\mathbf{U}_R - \mathbf{U}_L)$ so that conservation can be ensured
3. $\tilde{\mathbf{A}}(\mathbf{U}, \mathbf{U}) = \mathbf{A}(\mathbf{U})$ for consistency

So now in place of (153) and (155) we have, respectively:

$$\begin{aligned}
 \mathbf{F}(\mathbf{U}_R) - \mathbf{F}(\mathbf{U}_L) &= \tilde{\mathbf{A}} \Delta \mathbf{U} \\
 &= \tilde{\mathbf{R}} \tilde{\Lambda}_1 \tilde{\mathbf{L}} \Delta \mathbf{U} + \tilde{\mathbf{R}} \tilde{\Lambda}_2 \tilde{\mathbf{L}} \Delta \mathbf{U} + \tilde{\mathbf{R}} \tilde{\Lambda}_3 \tilde{\mathbf{L}} \Delta \mathbf{U} \\
 &= \Delta \mathbf{f}_1 + \Delta \mathbf{f}_2 + \Delta \mathbf{f}_3
 \end{aligned}
 \tag{156}$$

$$\begin{aligned}
 \mathbf{F}(\mathbf{U}_L, \mathbf{U}_R) &= \mathbf{F}(\mathbf{U}_L) + \tilde{\mathbf{A}}^- (\mathbf{U}_R - \mathbf{U}_L) \\
 &= \mathbf{F}(\mathbf{U}_R) - \tilde{\mathbf{A}}^+ (\mathbf{U}_R - \mathbf{U}_L) \\
 &= \frac{1}{2} [\mathbf{F}(\mathbf{U}_L) + \mathbf{F}(\mathbf{U}_R) - |\tilde{\mathbf{A}}| (\mathbf{U}_R - \mathbf{U}_L)]
 \end{aligned}
 \tag{157}$$

where $|\tilde{\mathbf{A}}| = \tilde{\mathbf{A}}^+ - \tilde{\mathbf{A}}^-$ is a quantity related to the numerical dissipation. Due to the form of these equations Roe’s method is referred as Flux Difference Splitting (FDS).

To illustrate, for an ideal gas, the flux Jacobian matrix is (with γ being the ratio of specific heats):

$$\mathbf{A} = \begin{pmatrix} 0 & 1 & 0 \\ -(3-\gamma)\frac{u^2}{2} & (3-\gamma)u & \gamma-1 \\ (\gamma-1)u^3 - \gamma u E & \gamma E - \frac{3}{2}(\gamma-1)u^2 & \gamma u \end{pmatrix}
 \tag{158}$$

The eigenvalues and eigenvectors can be obtained analytically as:

$$\Lambda = \begin{pmatrix} u & 0 & 0 \\ 0 & u-a & 0 \\ 0 & 0 & u+a \end{pmatrix}
 \tag{159}$$

$$\mathbf{R} = \begin{pmatrix} 1 & -\frac{\rho}{2a} & \frac{\rho}{2a} \\ u & -\frac{\rho}{2a}(u-a) & \frac{\rho}{2a}(u+a) \\ \frac{u^2}{2} & -\frac{\rho}{2a}\left(\frac{u^2}{2} - ua + \frac{a^2}{\gamma-1}\right) & \frac{\rho}{2a}\left(\frac{u^2}{2} + ua + \frac{a^2}{\gamma-1}\right) \end{pmatrix} \quad (160)$$

$$\mathbf{L} = \begin{pmatrix} 1 - \frac{\gamma-1}{2} \frac{u^2}{a^2} & (\gamma-1) \frac{u}{a^2} & -\frac{\gamma-1}{a^2} \\ -\frac{1}{\rho a} \left(\frac{\gamma-1}{2} u^2 + ua \right) & \frac{1}{\rho a} (a + (\gamma-1)u) & -\frac{\gamma-1}{\rho a} \\ \frac{1}{\rho a} \left(\frac{\gamma-1}{2} u^2 - ua \right) & \frac{1}{\rho a} (a - (\gamma-1)u) & \frac{\gamma-1}{\rho a} \end{pmatrix} \quad (161)$$

Then from the condition 2 the Roe-“average” state $\tilde{\mathbf{U}}$ can be found analytically:

$$\tilde{\rho} = \sqrt{\rho_L \rho_R}, \tilde{u} = \frac{u_L \sqrt{\rho_L} + u_R \sqrt{\rho_R}}{\sqrt{\rho_L} + \sqrt{\rho_R}}, \tilde{H} = \frac{H_L \sqrt{\rho_L} + H_R \sqrt{\rho_R}}{\sqrt{\rho_L} + \sqrt{\rho_R}}, H = E + \frac{p}{\rho} \quad (162)$$

Finally, the numerical flux for Roe’s approximate Riemann solver can be calculated by (157).

Remarks on performance:

1. Condition (2) also ensures that the Rankine-Hugoniot conditions, relating the speed s of a single discontinuity (contact or shock) to the jump across it, is satisfied, namely:

$$\mathbf{F}(\mathbf{U}_R) - \mathbf{F}(\mathbf{U}_L) = s (\mathbf{U}_R - \mathbf{U}_L)$$

This together with condition (2) gives:

$$\tilde{\mathbf{A}} (\mathbf{U}_R - \mathbf{U}_L) = s (\mathbf{U}_R - \mathbf{U}_L) \quad \text{Or} \quad \tilde{\mathbf{A}} - s \mathbf{I} = 0$$

which shows that s is an eigenvalue of the Roe matrix $\tilde{\mathbf{A}}$; namely that $s = \tilde{u} + \tilde{a}$ ($\tilde{u} > 0$) or $s = \tilde{u}$. Clearly therefore, any two states that are “connected” by the Rankine-Hugoniot condition can be resolved by Roe’s approximate Riemann solver exactly (provided the grid moves along with the discontinuity), and stationary discontinuities can be captured in principle exactly. In practice however, the scheme is known to fail for super strong shocks (both in 1D and 2D) even if stationary (Kitamura et al. 2007), and also performance deteriorates (oscillations) in slow-moving shocks. Moving contact discontinuities can in principle be captured exactly at the CFL = 1 limit (► 10.2), but this is not useful for practice, and the scheme is diffusive.

2. The downside of this exact property of Roe splitting is that it cannot distinguish between a shock and an expansion wave – that is, the splitting does not satisfy the entropy condition, a difficulty that leads to nonphysical jump within the expansion wave, known as “expansion shock.” This occurs because one of the eigenvalues decreases toward a zero value and concomitantly the numerical dissipation gradually disappears too. To remedy the problem, one needs to impose a lower limitation on the absolute magnitude of the eigenvalue. This procedure generally known as “entropy fix” was first suggested by Harten and Hyman (1983) and has several variants now.

3. For nonideal gas the eigenvalues are the same (with the speed of sound obtained from the applicable EOS), but the eigenvectors are not, and the Roe-“average” is not unique (Liou et al. 1990; Shuen et al. 1990).
4. Finally the method is susceptible to the so-called carbuncle instability – a transverse instability in 2D or 3D shocks that will be illustrated in [10.3](#).

10.2 Direct Flux Splitting

Direct flux splitting began with Steger and Warming’s (1981) idea that, for the Euler system, the flux vector $\mathbf{F}(\mathbf{U})$ is a linearly homogenous function of degree one in \mathbf{U} and accordingly:

$$\mathbf{F} = \frac{\partial \mathbf{F}(\mathbf{U})}{\partial \mathbf{U}} \mathbf{U} \equiv \mathbf{A} \mathbf{U} \tag{163}$$

Thus following the same diagonalization procedure as applied previously to $\delta \mathbf{F}$ (Roe), we can now split \mathbf{F} directly into components associated respectively with the positive and negative eigenvalues:

$$\mathbf{F} = \mathbf{R} \Lambda \mathbf{L} \mathbf{U} \equiv \mathbf{R} (\Lambda^+ + \Lambda^-) \mathbf{L} \mathbf{U} \equiv (\mathbf{A}^+ + \mathbf{A}^-) \mathbf{U} \equiv \mathbf{F}^+ + \mathbf{F}^- \tag{164}$$

Thus, the numerical flux at the cell boundary can be expressed as:

$$\mathbf{F}(\mathbf{U}_L, \mathbf{U}_R) = \mathbf{F}^+(\mathbf{U}_L) + \mathbf{F}^-(\mathbf{U}_R) \tag{165}$$

which automatically gives the exact flux at supersonic conditions:

1. If $M_L > 1$ and $M_R > 1$, then $\mathbf{F}^+(\mathbf{U}_L) = \mathbf{F}(\mathbf{U}_L)$ and $\mathbf{F}^-(\mathbf{U}_R) = 0$;
If $M_L < -1$ and $M_R < -1$, then $\mathbf{F}^-(\mathbf{U}_R) = \mathbf{F}(\mathbf{U}_R)$ and $\mathbf{F}^+(\mathbf{U}_L) = 0$.
2. All the eigenvalues of matrices $\frac{\partial \mathbf{F}^+(\mathbf{U})}{\partial \mathbf{U}} / \frac{\partial \mathbf{F}^-(\mathbf{U})}{\partial \mathbf{U}}$ are nonnegative/nonpositive.
3. $\mathbf{F}(\mathbf{U}, \mathbf{U}) = \mathbf{F}^+(\mathbf{U}) + \mathbf{F}^-(\mathbf{U})$ for consistency.

The problem with this procedure is that the eigenvalues of \mathbf{A} do not carry over individually to the splitted Jacobians; that is:

$$\mathbf{A} \equiv \frac{\partial \mathbf{F}}{\partial \mathbf{U}} \equiv \frac{\partial \mathbf{F}^+}{\partial \mathbf{U}} + \frac{\partial \mathbf{F}^-}{\partial \mathbf{U}} \equiv \mathbf{A}^+ + \mathbf{A}^- \text{ does } \textit{not} \text{ imply } \frac{\partial \mathbf{F}^+}{\partial \mathbf{U}} = \mathbf{A}^+ \text{ and } \frac{\partial \mathbf{F}^-}{\partial \mathbf{U}} = \mathbf{A}^-$$

and the consequence in practical terms is that the zero eigenvalues expected in the splitting of \mathbf{A} may now become small positive/negative values, thereby “contaminating” upwinding, which can become particularly problematic in subsonic flow. Moreover, while the splitting in (164) yields automatically proper fully one-sided upwinding at the sonic points $|u| = a$, the switching is not differentiable, thereby resulting in glitches there, even in a smooth acceleration from subsonic to supersonic speeds. The discontinuous switching also adds more dissipation at shock points than other flux schemes such as presented in this article.

Independent work by van Leer (1982) anticipated this switching difficulty and specifically required that the Jacobians of split fluxes be differentiable at sonic point. In addition, he sought to have one eigenvalue vanish identically so that the shock is captured in two cells. To achieve this he proposed to interpolate the splitting between the two extremes (upwinding) specified

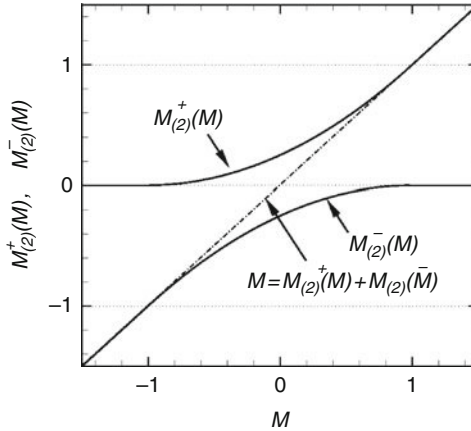


Figure 5

The interpolation of Mach split function used in van Leer's approach to subsonic flow

above for supersonic flow. More specifically, as indicated in Fig. 5, in the intermediate subsonic region one operates with a combination of both nonlinear fields characterized by $u + a > 0$ and $u - a < 0$, namely $M = \mathcal{M}^+(M) + \mathcal{M}^-(M)$. Formally, the additional conditions imposed are:

4. $\frac{\partial \mathbf{F}^{\pm}}{\partial U}$ must be continuous and have one zero eigenvalue if $|M| < 1$.
5. The $\mathbf{F}^+ / \mathbf{F}^-$ must be symmetric in M ; $\mathbf{F}^+(M) = \mathbf{F}^-(-M)$; $\mathbf{F}^-(M) = \mathbf{F}^+(-M)$.

We will build, according to van Leer, the vector \mathbf{f} for this subsonic region from its components (f_1, f_2, f_3) corresponding to the conserved variables (mass, momentum, energy), considered one by one separately. Moreover, we will use this as a way to anticipate and to bridge with AUSM – accordingly the derivation acknowledges AUSM's key physics-based idea of separating out (and treating accordingly) convective from pressure contributions to the flux vector.

From the continuity equation we have:

$$\begin{aligned} f_1 &= \rho u = \rho a M \\ &\equiv \rho a (\mathcal{M}^+(M) + \mathcal{M}^-(M)). \\ &\equiv f_1^+ + f_1^- \end{aligned} \quad (166)$$

When $M > 1$, we have $f_1^+ = f_1$ and $f_1^- = 0$, giving that $\mathcal{M}^+(M) = M$ and $\mathcal{M}^-(M) = 0$. Similarly, when $M < -1$, we have $\mathcal{M}^+(M) = 0$ and $\mathcal{M}^-(M) = M$. For the interpolation van Leer used:

$$\mathcal{M}_{(2)}^{\pm}(M) = \pm \frac{1}{4} (M \pm 1)^2 \quad (167)$$

where subscript “(2)” is to indicate the order of the polynomial employed. The numerical mass flux can then be written as:

$$(f_1)_{1/2} = \rho_L a_L \mathcal{M}_{(2)}^+(M_L) + \rho_R a_R \mathcal{M}_{(2)}^-(M_R) \quad (168)$$

For the momentum equation similarly, with the incorporation of splitting, we have:

$$\begin{aligned}
 f_2 &= \rho u^2 + p \\
 &= \rho a^2 \left(M^2 + \frac{1}{\gamma} \right) \\
 &= \frac{1}{4} \rho a^2 (M+1)^2 \left(M + \frac{1}{\gamma} (2-M) \right) + \frac{1}{4} \rho a^2 (M-1)^2 \left(-M + \frac{1}{\gamma} (2+M) \right) \\
 &\equiv f_2^+ + f_2^-
 \end{aligned}
 \tag{169}$$

Which accordingly can be seen in more familiar terms to be:

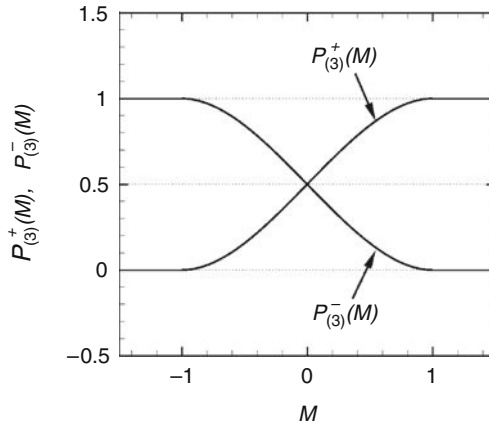
$$\begin{aligned}
 f_2^\pm &= \pm (\rho u) a \cdot \frac{1}{4} (M \pm 1)^2 + p \cdot \frac{1}{4} (M \pm 1)^2 (2 \mp M) \\
 &= (\rho u) a \cdot \mathcal{M}_{(2)}^\pm(M) + p \cdot \mathcal{P}_{(3)}^\pm(M)
 \end{aligned}
 \tag{170}$$

with the interpolated pressure split function (illustrated in  Fig. 6):

$$\mathcal{P}_{(3)}^\pm(M) = \frac{1}{4} (M \pm 1)^2 (2 \mp M)
 \tag{171}$$

Lastly, by combination of the above we obtain the splitting for energy flux:

$$\begin{aligned}
 f_3^\pm &= \frac{\gamma^2}{2(\gamma^2 - 1)} \frac{(f_2^\pm)^2}{f_1^\pm} \\
 &= \pm \frac{\rho a}{4} (M \pm 1)^2 \cdot \frac{2a^2}{\gamma^2 - 1} \left(1 \pm \frac{\gamma - 1}{2} M \right)^2 \\
 &= f_1^\pm (H - m (u \mp a))
 \end{aligned}
 \tag{172}$$



 **Figure 6**
The interpolation of pressure split function used in van Leer’s approach to subsonic flow

with

$$m = \frac{h}{a^2 + 2h} \quad (173)$$

so that the square bracket in the energy flux can be factored into a perfect square for an ideal gas. This results in a nice property that one eigenvalue of the split-flux Jacobians vanishes, thus leading to reduced numerical dissipation and sharper resolution of shocks (van Leer 1982). This property however is hard to maintain for a general gas.

To summarize, the splitted flux vector can be written so as to visualize not only the upwinding, but also the splitting between the convection and pressure components:

$$\mathbf{f}^\pm = a \mathcal{M}_{(2)}^\pm(M) \begin{pmatrix} \rho \\ \rho u \\ \rho H - \rho m(u \mp a) \end{pmatrix} + \begin{pmatrix} 0 \\ p \mathcal{P}_{(3)}^\pm(M) \\ 0 \end{pmatrix} \quad (174)$$

In this form van Leer's method is not able to maintain constant total enthalpy along a streamline. One simple "fix" derived independently in Hänel et al. (1987) and Shuen et al. (1990), is to drop the term $\rho m(u \mp a)$. Thus in final form the recommended van Leer splitting of the Riemann flux is:

$$\begin{aligned} \mathbf{f}_{1/2}(\mathbf{U}_L, \mathbf{U}_R) &= a_L \mathcal{M}_{(2)}^+(M_L) \Phi_L + a_R \mathcal{M}_{(2)}^-(M_R) \Phi_R \\ &+ \begin{pmatrix} 0 \\ p_L \mathcal{P}_{(3)}^+(M_L) + p_R \mathcal{P}_{(3)}^-(M_R) \\ 0 \end{pmatrix} \end{aligned} \quad (175)$$

with $\Phi = (\rho, \rho u, \rho H)^\top$.

It is observed that the whole splitting hinges on the split Mach numbers \mathcal{M}^\pm , which defines the mass and pressure fluxes, which in turn affects the momentum and energy fluxes.

Remarks on Performance

1. It turns out that this flux vector splitting is significantly easier to implement in comparison to Roe's scheme of building numerical fluxes, and surprisingly, it possesses a good capability of capturing shocks.
2. In addition to the advantage of being smooth at the transition points where eigenvalues change signs, this splitting does not involve differentiation of flux functions with respect to \mathbf{U} (it does not involve the Jacobian). Instead, the imprint of the EOS appears covertly (via the speed of sound), the key parameter is the Mach number, and the form of split fluxes remains the same for all types of EOS. This point becomes a tremendous advantage in computing multiphase flows. Moreover, this splitting, being in terms of mass fluxes only, allows any additional conservation laws to be easily added making extensions to other kinds of systems rather straightforward.
3. As pointed out by van Leer himself, the dispensing with the eigensystem undermines the scheme's performance in regards to contact discontinuities as can be seen in the following: Consider a moving contact discontinuity defined as:

$$\rho_j = \begin{cases} \rho_1 & \text{for } j < k \\ \rho_2 & \text{for } j \geq k + 1 \end{cases} \quad u_j = u^* \geq 0, p_j = p^*$$

From \blacktriangleright 10.1, (157), we can readily see that Roe's numerical flux is:

$$\begin{aligned} \mathbf{F}_{1/2}(\mathbf{U}_L, \mathbf{U}_R) &= \frac{1}{2} [\mathbf{F}(\mathbf{U}_L) + \mathbf{F}(\mathbf{U}_R) - |\tilde{\mathbf{A}}| (\mathbf{U}_R - \mathbf{U}_L)] \\ &= \frac{1}{2} [\mathbf{F}(\mathbf{U}_L) + \mathbf{F}(\mathbf{U}_R) - |u^*| (\mathbf{U}_R - \mathbf{U}_L)] \\ &= u^* \mathbf{U}_{L/R} + \begin{pmatrix} 0 \\ p^* \\ u^* p^* \end{pmatrix} \end{aligned} \quad (176)$$

Here the relevant velocity for upwinding is u^* , so

$$\mathbf{U}_{L/R} = \begin{cases} \mathbf{U}_L & \text{if } u^* \geq 0; \\ \mathbf{U}_R & \text{if } u^* < 0. \end{cases} \quad (177)$$

and by substitution into the discretized equations, we have:

$$\frac{\partial \mathbf{U}}{\partial t} + \mathbf{F}_{j+1/2}(\mathbf{U}_j, \mathbf{U}_{j+1}) - \mathbf{F}_{j-1/2}(\mathbf{U}_{j-1}, \mathbf{U}_j) = 0$$

(178)

or

$$\frac{\partial \mathbf{U}}{\partial t} + \frac{1}{\Delta x} [(u^* \mathbf{U})_j - (u^* \mathbf{U})_{j-1}] = 0$$

We can see that when $\frac{u^* \Delta t}{\Delta x} = 1$, Roe's scheme is able to capture the contact continuity exactly. On the other hand, for van Leer's scheme, (175), we get:

$$\frac{\partial \mathbf{U}}{\partial t} + \frac{1}{\Delta x} [(a \mathcal{M}_{(2)}^- \Phi)_{j+1} - (a (\mathcal{M}_{(2)}^+ - \mathcal{M}_{(2)}^-) \Phi)_j + (a \mathcal{M}_{(2)}^+ \Phi)_{j-1}] = 0 \quad (179)$$

and it is quite clear that when $|M_{j+1}| < 1$ we have $\mathcal{M}_{(2)}^- \neq 0$, and a flux representing downwind properties enters the calculation – destroying upwinding and leading to false updating in the presence of stationary or moving contact discontinuities.

10.3 Advection Upstream Splitting

As we have seen above the basic ideas of Roe and van Leer have much to complement each other relative to mutual shortcomings in addressing the Riemann problem (and thereby the implementation of the Godunov idea). In the Advection Upstream Splitting Method (AUSM) (Liou and Steffen 1993; Liou 1996) a synthesis (of these two approaches) is made that retains the positive attributes while canceling the negative ones. The bases are to recognize and observe the physical correctness of the pressure-convection separating of van Leer (175). As we will see (\blacktriangleright Sect. 11) this is a crucial point in the implementation of the method to the effective field model of two-phase flow. Moreover, on this basis, it retains the advantages of bypassing the need for an eigensystem. This, besides efficiency in computation offers the means to addressing complex equations of state as well as problems that may be mildly non-hyperbolic – as is the

case in certain regions of the (relative) Mach number space in the multiphase flow model recommended and utilized herein. On the other hand, the method needs to incorporate the means of resolving the contact discontinuity issue explained above.

Recalling the convective component of (175):

$$\mathbf{f}^{(c)} = a_L \mathcal{M}_{(2)}^+(M_L) \Phi_L + a_R \mathcal{M}_{(2)}^-(M_R) \Phi_R \quad (180)$$

and that the contact discontinuity issue arises from using two separate convective speeds, here we use only one convective speed comprising contributions from both “L” and “R” states and write instead:

$$\mathbf{f}^{(c)} = u_{1/2} \Phi_{L/R} = a_{1/2} M_{1/2} \Phi_{L/R} \quad (181)$$

where $M_{1/2}$ is split according to van Leer:

$$M_{1/2} = \mathcal{M}^+(M_L) + \mathcal{M}^-(M_R) \quad (182)$$

and the sound speed $a_{1/2}$ is designed to satisfy certain discontinuity capturing properties as explained further below. It turns out that this has Roe’s (FDS) contact capturing quality we were also aiming for. The pressure splitting of (175) is maintained and likewise for the energy equation we use the total enthalpy H , while the interpolations involved are extended to still higher order.

We thus have the AUSM⁺ (Liou 1996) as:

$$\mathbf{F}_{1/2} = a_{1/2} M_{1/2} \Phi_{L/R} + \begin{pmatrix} 0 \\ p_{1/2} \\ 0 \end{pmatrix} \quad (183)$$

where $M_{1/2}$ and $p_{1/2}$ are defined as:

$$M_{1/2} \equiv \mathcal{M}_{(4)}^+(M_L) + \mathcal{M}_{(4)}^-(M_R), \quad M_{L/R} = u_{L/R}/a_{1/2} \quad (184)$$

$$p_{1/2} \equiv \mathcal{P}_{(5)}^+(M_L) p_L + \mathcal{P}_{(5)}^-(M_R) p_R \quad (185)$$

With

$$\mathcal{M}_{(4)}^\pm(M) = \begin{cases} \frac{1}{2} (M \pm |M|) & \text{if } |M| \geq 1, \\ \pm \frac{1}{2} (M \pm 1)^2 \pm \frac{1}{8} (M^2 - 1)^2 & \text{Otherwise.} \end{cases} \quad (186)$$

and

$$\mathcal{P}_{(5)}^\pm(M) = \begin{cases} \frac{1}{2} \left(1 \pm \frac{|M|}{M} \right) & \text{if } |M| \geq 1, \\ \frac{1}{4} (M \pm 1)^2 (2 \mp M) \pm \frac{3}{16} M (M^2 - 1)^2 & \text{Otherwise.} \end{cases} \quad (187)$$

The $a_{1/2}$ is a “numerical” speed of sound, and its specification is done so as to assure that a stationary shock is captured by satisfying the Rankine-Hugoniot condition exactly. Once the

average state has been so fixed there is no more control; we will use this result even for moving shocks as experience shows that performance is still very good. Consider the two fluid states \mathbf{U}_L and \mathbf{U}_R separated by a stationary shock and such that $u_L > u_R > 0$. According to Rankine-Hugoniot condition, numerical fluxes $\mathbf{F}_{1/2}$ must satisfy $\mathbf{F}_L = \mathbf{F}_{1/2} = \mathbf{F}_R$, which with the incorporation of the above convection specification yields:

$$\mathbf{F}_L = \begin{pmatrix} \rho_L u_L \\ \rho_L u_L^2 + p_L \\ \rho_L u_L H_L \end{pmatrix} = \begin{pmatrix} u_{1/2} \rho_L \\ u_{1/2} \rho_L u_L + p_{1/2} \\ u_{1/2} \rho_L H_L \end{pmatrix} = \mathbf{F}_{1/2} \quad (188)$$

Now from (186), if $M_L = \frac{u_L}{a_{1/2}} > 1$, we get $\mathcal{M}_{(4)}^+(M_L) = M_L$ and

$$\begin{aligned} u_{1/2} &= a_{1/2} \left(M_L - \frac{1}{2}(M_R - 1)^2 - \frac{1}{8}(M_R^2 - 1)^2 \right) \\ &= u_L - (u_R - a_{1/2}) \left(\frac{1}{2}(M_R - 1) + \frac{1}{8}(M_R + 1)^2 \right) \end{aligned} \quad (189)$$

Thus we can choose $a_{1/2} = u_R$, and it follows $u_{1/2} = u_L$, which leads to $p_{1/2} = p_L$ and, hence, satisfy the Rankine-Hugoniot condition.

The sound speed can be written in a more general form, which involves only “upwinding” states. From Prandtl’s relation across a stationary shock wave, we have

$$(a_L^*)^2 = (a_R^*)^2 = u_L u_R, \quad (190)$$

Thus we get

$$a_{1/2} = \frac{(a_L^*)^2}{u_L} \quad (191)$$

where a^* is the critical (sonic point) speed of sound. For ideal gas, it is expressed as:

$$(a^*)^2 = \frac{2(\gamma - 1)}{\gamma + 1} H \quad (192)$$

By extending the above analysis to cover other conditions, as $u_R < -a_R$ or in subsonic flows, we have:

$$a_{1/2} = \min(\tilde{a}_L, \tilde{a}_R) \quad \text{with} \quad \tilde{a} = \frac{(a^*)^2}{\max(a^*, |u|)} \quad (193)$$

By virtue of its derivation, (193) is only applicable to the capturing stationary shocks – it does not satisfy the Rankine-Hugoniot across a moving shock exactly. Still, based on a wide range of numerical tests we can state that this drawback is only in effecting a slight amount of numerical dissipation resulting only to a minimal smearing of the shock. In fact, even the rather simple choice

$$a_{1/2} = \frac{1}{2}(a_L + a_R) \quad (194)$$

is quite satisfactory, again at the cost of smearing in the shock profile. In all cases both amplitudes and positions are captured accurately, a manifestation of satisfying conservation properties.

In a further development, the AUSM⁺ scheme was extended to addressing all-speed situations (Liou 2006). This is done by adding properly-scaled dissipation terms to the convection and pressure fluxes to enhance the coupling between pressure and velocity fields, which is especially important for multiphase flow (Chang and Liou 2003, 2007) as we may be facing great disparities in fluid properties and flow speeds. The AUSM⁺-up scheme is written as

$$\mathbf{F}_{1/2} = \left(a_{1/2} M_{1/2} \rho_{L/R} + D^{(p)} \right) \Psi_{L/R} + \begin{pmatrix} 0 \\ p_{1/2} + D^{(u)} \\ 0 \end{pmatrix} \quad (195)$$

With

$$\Psi = (1, u, H)^T \quad (196)$$

$$D^{(p)} = \kappa_p \frac{\Delta M \max(1 - \bar{M}^2, 0) (p_L - p_R)}{\bar{a}} \quad (197)$$

$$D^{(u)} = \kappa_u \mathcal{P}_{(5)}^+(\bar{M}) \mathcal{P}_{(5)}^-(\bar{M}) \bar{\rho} \bar{a} (u_L - u_R) \quad (198)$$

And

$$\Delta M = \mathcal{M}_{(4)}^+(\bar{M}_L) - \mathcal{M}_{(1)}^+(\bar{M}_L) - \mathcal{M}_{(4)}^-(\bar{M}_R) + \mathcal{M}_{(1)}^-(\bar{M}_R) \quad (199)$$

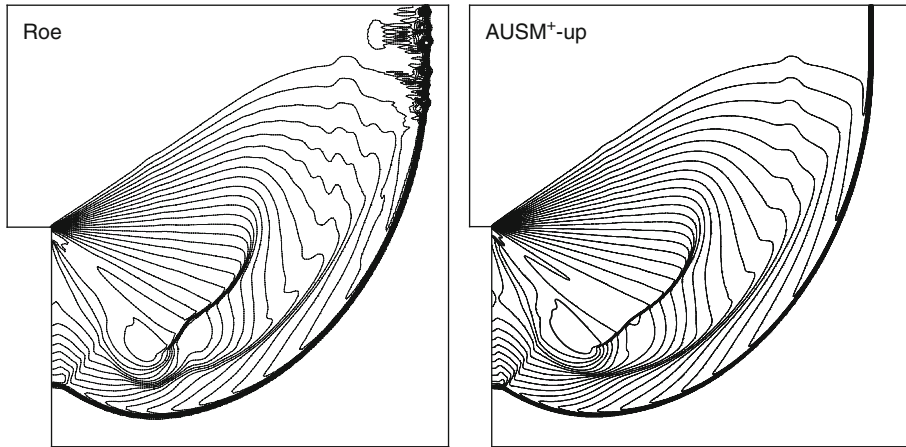
The parameters $\bar{\rho}$, \bar{a} , and \bar{M} are obtained as the arithmetic means of “L” and “R” states, and usually the coefficients $\kappa_p = \kappa_u = 1$ are sufficient to suppress numerical oscillation in both the gas and liquid fields.

Remarks on Performance

1. Discontinuity Capturing. This of course is the most crucial issue in respect to robustness as well as accuracy. For both contacts and shocks the greatest the jumps in flow and state variables involved the greatest the “stress” in the numerical scheme. Another stress is due to unsteady/nonstationary discontinuities, and unfortunately, theoretical results are available only for the stationary case: one is looking for sharp (nondiffusive) capturing. While this provides some sense of what could be expected in general for unsteady cases, as for example the development of a shock wave in an explosion (e.g., starting with ignition and run up to detonation), much of the performance characterization has to rely on empirical evidence; namely analysis of actual calculations and comparison to known solutions (like the Chapman-Jouget self-similar limit in 1D detonations) and/or experiments. On **stationary discontinuities** the situation can be summarized as follows:

- (a) For a contact AUSM⁺ automatically captures exactly the discontinuity since the mass flux is zero. In other words $\rho u = 0$, $M_L = M_R = 0$, $p_L = p_R$. As shown already the FDS also satisfies this requirement, while the FVS fails it.
- (b) For a stationary shock, AUSM⁺ with the choice of numerical speed of sound in (193) captures the discontinuity exactly (Liou 1996). Due to the design for possessing the Rankine-Hugoniot property, AUSM⁺, like Roe, cannot distinguish whether the discontinuity is a shock or an expansion – this can be remedied (Liou 2006) by the following redefinitions in (193):

$$\bar{a}_L = a^{*2} / \max(a^*, u_L), \quad \bar{a}_R = a^{*2} / \max(a^*, -u_R). \quad (200)$$



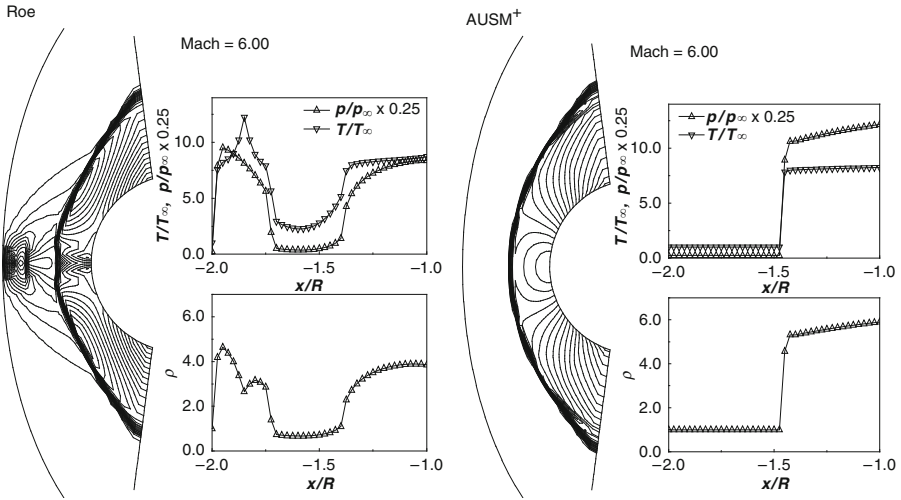
■ Figure 7

Supersonic flow past a sudden expansion (corner). The Roe method with entropy fix produces instability. The AUSM⁺ calculation (CFL=0.4 on a 400 x 400 grid) employed a MUSCL-type linear interpolation of primitive variables along with the van Albada limiter (van Albada et al. 1982) to control monotonicity

In ► Sect. 12, and in more detail in the Appendix, we illustrate these trends also for the case of multiphase flow, and also for the case of nonstationary discontinuities.

2. Positivity Preserving. Sudden expansions can lead to negative values of certain variables such as pressure, density, or volume fraction, which would terminate the calculation, thus, positivity preserving is an essential attribute of robustness of a numerical scheme. In an 1D situation violation of positivity can arise in the case of a Riemann problem with the two states set to move in opposite directions with velocities that exceed some critical value. In 2D the same can arise in a supersonic flow moving past a sharp, 90° expansion (corner) as illustrated in ► Fig. 7. In contrast to documented failings of several prominent flux schemes (Einfeldt 1991), AUSM⁺ exhibits a robust shock capturing capability typical of what is seen in ► Fig. 7. As another example, for the 1D Riemann problem $\{(-u, p, \rho)_L; (u, p, \rho)_R\}$ it has been shown (Liou and Edwards 1999) that AUSM⁺ guarantees positivity as long as: $u^{\Delta t/\Delta x} < 1$ and $u^{\Delta t/\Delta x} < 1/\gamma$ for pressure and density, respectively. For the linear case this condition coincides with the total variation diminish (TVD) condition of Harten (1983).

3. Transverse Shock Instability (Carbuncle Phenomenon). This sort of problem can arise in multidimensional situations, such as the one illustrated in ► Fig. 8, and it is due to spurious transverse waves that can amplify to a point that destroy the calculation. More specifically it has been suggested (Wada and Liou 1997) that this transverse action is originated by the few (unphysical) intermediate points of the profile approximating the shock, and their lateral influences, which in turn affect the shock in a multidimensional manner. A “shock fix” has been proposed, and it is effective but at the additional complication of the “if-then” check involved.



■ Figure 8

Density contours in steady supersonic flow past a blunt body positioned at right angles. Inset profiles are along the stagnation streamlines

As in the case for Roe (1981) (shown) also the Osher and Solomon (1982) method, as do most others fail. On the other hand, as is the case of $AUSM^+$ (shown) so is the van Leer VFS scheme not subject to this deficiency.

4. Efficiency, Generality. Unlike Roe's FDS, the numerical dissipation in $AUSM^+$ is merely a scalar, not of matrix type. As a result, the system is decoupled and hence requires only $\mathcal{O}(n)$ operations, n being the number of unknowns (and equations). Moreover, the same formula is easily extendable to include other conservation laws, or to fluids with general EOS, as is the case in multiphase flow. As in van Leer's VFS, the $AUSM^+$ does not require differentiation, or the flux Jacobian matrix; and the flux splitting always involves only the common mass-flux term for any additional conservation laws.

11 Advection Upstream Splitting for the Effective Field Model

11.1 Recasting the System of Equations in Quasi-Conservative Form

As made clear in the previous section, we need to begin the task of extending $AUSM$ to the effective field model by recasting the system of equations, (135)-(140), in conservation form. Unfortunately, this cannot be done in a complete manner – terms like $p\nabla\alpha$ and other similar terms remain, and as we shall see shortly these “nonconservative” terms create a new type of numerical challenge of significant proportions. The recasting then also aims to consolidate and

simplify these terms to the extent possible. The result is:

$$\frac{\partial}{\partial t}(\alpha_c \rho_c) + \nabla \cdot (\alpha_c \rho_c \mathbf{u}_c) = 0 \quad (201)$$

$$\frac{\partial}{\partial t}(\alpha_d \rho_d) + \nabla \cdot (\alpha_d \rho_d \mathbf{u}_d) = 0 \quad (202)$$

$$\frac{\partial}{\partial t}(\alpha_c \rho_c \mathbf{u}_c) + \nabla \cdot [\alpha_c (\rho_c \mathbf{u}_c \otimes \mathbf{u}_c + p_c \mathbf{I} + \rho_c E \mathbf{w} \otimes \mathbf{w})] = p_d \nabla \alpha_c + \Phi^K \quad (203)$$

$$\frac{\partial}{\partial t}(\alpha_d \rho_d \mathbf{u}_d) + \nabla \cdot [\alpha_d (\rho_d \mathbf{u}_d \otimes \mathbf{u}_d + p_d \mathbf{I})] = p_d \nabla \alpha_d - \Phi^K \quad (204)$$

$$\frac{\partial}{\partial t}(\alpha_c \rho_c E_c) + p_d \frac{\partial \alpha_c}{\partial t} + \nabla \cdot [\alpha_c (\rho_c E_c \mathbf{u}_c + p_c \mathbf{u}_c + \rho_c E (\mathbf{u}_d \cdot \mathbf{w}) \mathbf{w})] = \mathbf{u}_d \cdot \Phi^K \quad (205)$$

$$\frac{\partial}{\partial t}(\alpha_d \rho_d E_d) + p_d \frac{\partial \alpha_d}{\partial t} + \nabla \cdot [\alpha_d (\rho_d E_d \mathbf{u}_d + p_d \mathbf{u}_d)] = -\mathbf{u}_d \cdot \Phi^K \quad (206)$$

with $\mathbf{w} = \mathbf{u}_d - \mathbf{u}_c$ and $\Phi^K = \frac{\partial \mathbf{J}}{\partial t} + \nabla \cdot (\mathbf{u}_d \otimes \mathbf{J}) + (\mathbf{J} \cdot \nabla) \mathbf{u}_d + \mathbf{J} \times (\nabla \times \mathbf{u}_d)$.

Note: In one-dimensional flow the last term of Φ^K is identically zero, while in general it is convenient to combine the last two terms and use as:

$$\begin{aligned} & (\mathbf{J} \cdot \nabla) \mathbf{u}_d + \mathbf{J} \times (\nabla \times \mathbf{u}_d) \\ &= \alpha_c \rho_c E(\alpha_d) \left((u_d - u_c) \frac{\partial u_d}{\partial x} + (v_d - v_c) \frac{\partial v_d}{\partial x} + (w_d - w_c) \frac{\partial w_d}{\partial x} \right) \bar{\mathbf{e}}_1 \\ &+ \alpha_c \rho_c E(\alpha_d) \left((u_d - u_c) \frac{\partial u_d}{\partial y} + (v_d - v_c) \frac{\partial v_d}{\partial y} + (w_d - w_c) \frac{\partial w_d}{\partial y} \right) \bar{\mathbf{e}}_2 \\ &+ \alpha_c \rho_c E(\alpha_d) \left((u_d - u_c) \frac{\partial u_d}{\partial z} + (v_d - v_c) \frac{\partial v_d}{\partial z} + (w_d - w_c) \frac{\partial w_d}{\partial z} \right) \bar{\mathbf{e}}_3 \end{aligned} \quad (207)$$

We will demonstrate the numerics in one space dimension, and based on the above our system is:

$$\frac{\partial}{\partial t}(\alpha_c \rho_c) + \frac{\partial}{\partial x}(\alpha_c \rho_c u_c) = 0 \quad (208)$$

$$\frac{\partial}{\partial t}(\alpha_d \rho_d) + \frac{\partial}{\partial x}(\alpha_d \rho_d u_d) = 0 \quad (209)$$

$$\begin{aligned} & \frac{\partial}{\partial t}(\alpha_c \rho_c (1 + E(\alpha_d)) u_c) - \frac{\partial}{\partial t}(\alpha_c \rho_c E(\alpha_d) u_d) + \frac{\partial}{\partial x}(\alpha_c \rho_c u_c^2) \\ &+ \frac{\partial}{\partial x}[\alpha_c (p_c + \rho_c E(\alpha_d) (u_d - u_c)^2)] = p_d \frac{\partial \alpha_c}{\partial x} + \frac{\partial}{\partial x}(\alpha_c \rho_c E(\alpha_d) u_d (u_d - u_c)) + J \frac{\partial u_d}{\partial x} \end{aligned} \quad (210)$$

$$\begin{aligned} & - \frac{\partial}{\partial t}(\alpha_c \rho_c E(\alpha_d) u_c) + \frac{\partial}{\partial t}((\alpha_d \rho_d + \alpha_c \rho_c E(\alpha_d)) u_d) + \frac{\partial}{\partial x}(\alpha_d \rho_d u_d^2) \\ &+ \frac{\partial}{\partial x}(\alpha_d p_d) = -p_d \frac{\partial \alpha_c}{\partial x} - \frac{\partial}{\partial x}(\alpha_c \rho_c E(\alpha_d) u_d (u_d - u_c)) - J \frac{\partial u_d}{\partial x} \end{aligned} \quad (211)$$

$$\frac{\partial}{\partial t}(\alpha_c \rho_c E_c) + p_d \frac{\partial \alpha_c}{\partial t} + \frac{\partial}{\partial x}[\alpha_c (\rho_c H_c u_c + \rho_c E(\alpha_d) u_d (u_d - u_c)^2)] = u_d \Phi^K \quad (212)$$

$$\frac{\partial}{\partial t}(\alpha_d \rho_d E_d) + p_d \frac{\partial \alpha_d}{\partial t} + \frac{\partial}{\partial x}[\alpha_d \rho_d H_d u_d] = -u_d \Phi^K \quad (213)$$

With

$$H_d = E_d + \frac{p_d}{\rho_d} = e_d + \frac{1}{2}u_d^2 + \frac{p_d}{\rho_d}; \quad H_c = E_c + \frac{p_c}{\rho_c} = e_c + \frac{1}{2}u_c^2 + \frac{1}{2}E(\alpha_d)(u_d - u_c)^2 + \frac{p_c}{\rho_c};$$

$$\Phi^K = \frac{\partial J}{\partial t} + \frac{\partial}{\partial x}(u_d J) + J \frac{\partial u_d}{\partial x}$$

In final vector form with the convection terms collected in the manner suggested by AUSM is:

$$\frac{\partial \tilde{\mathbf{Q}}}{\partial t} + p_d \frac{\partial \mathbf{T}}{\partial t} + \frac{\partial}{\partial x}(\mathbf{F}^{(u_c)}) + \frac{\partial}{\partial x}(\mathbf{F}^{(u_d)}) + \frac{\partial}{\partial x}(\mathbf{F}^{(p)}) = p_d \frac{\partial \mathbf{G}}{\partial x} + \frac{\partial \mathbf{H}}{\partial x} + \mathbf{S} \quad (214)$$

Where:

$$\tilde{\mathbf{Q}} = \begin{pmatrix} \alpha_c \rho_c \\ \alpha_d \rho_d \\ \alpha_c \rho_c (1 + E(\alpha_d)) u_c - \alpha_c \rho_c E(\alpha_d) u_d \\ -\alpha_c \rho_c E(\alpha_d) u_c + (\alpha_d \rho_d + \alpha_c \rho_c E(\alpha_d)) u_d \\ \alpha_c \rho_c E_c \\ \alpha_d \rho_d E_d \end{pmatrix}; \quad \mathbf{T} = \begin{pmatrix} 0 \\ 0 \\ 0 \\ 0 \\ \alpha_c \\ \alpha_d \end{pmatrix} \quad (215)$$

$$\mathbf{F}^{(u_c)} = \begin{pmatrix} \alpha_c \rho_c u_c \\ 0 \\ \alpha_c \rho_c u_c^2 \\ 0 \\ \alpha_c \rho_c H_c u_c \\ 0 \end{pmatrix}; \quad \mathbf{F}^{(u_d)} = \begin{pmatrix} 0 \\ \alpha_d \rho_d u_d \\ 0 \\ \alpha_d \rho_d u_d^2 \\ \alpha_c \rho_c E(\alpha_d) (u_c - u_d)^2 u_d \\ \alpha_d \rho_d H_d u_d \end{pmatrix}; \quad (216)$$

$$\mathbf{F}^{(p)} = \begin{pmatrix} 0 \\ 0 \\ \alpha_c (p_c + \rho_c E(\alpha_d) (u_d - u_c)^2) \\ \alpha_d p_d \\ 0 \\ 0 \end{pmatrix}; \quad \mathbf{G} = \begin{pmatrix} 0 \\ 0 \\ \alpha_c \\ \alpha_d \\ 0 \\ 0 \end{pmatrix}, \quad (217)$$

$$\mathbf{H} = \begin{pmatrix} 0 \\ 0 \\ \alpha_c \rho_c E(\alpha_d) u_d (u_d - u_c) \\ -\alpha_c \rho_c E(\alpha_d) u_d (u_d - u_c) \\ 0 \\ 0 \end{pmatrix}; \quad \mathbf{S} = \begin{pmatrix} 0 \\ 0 \\ J \frac{\partial u_d}{\partial x} \\ -J \frac{\partial u_d}{\partial x} \\ u_d \Phi^K \\ -u_d \Phi^K \end{pmatrix}. \quad (218)$$

Note that the term due to velocity fluctuations in the continuous phase momentum equation is interpreted as a pressure modifier and it is split accordingly (along with pressure, rather than being treated together with the convection terms). In 2D or 3D this dyadic will have off-diagonal terms, and these interpreted as “stress” could be treated by simple central difference, or could be split as pressure.

11.2 Numerical Discretization

The convection and pressure splitting carry over directly from [10.3](#), and for the case that the volume fractions are basically continuous we have:

$$\begin{aligned} & \frac{1}{\Delta t} (\bar{\mathbf{q}}_j^{n+1} - \bar{\mathbf{q}}_j^n) + \frac{(p_d)^n}{\Delta t} (\mathbf{t}_j^{n+1} - \mathbf{t}_j^n) + \frac{1}{\Delta x} \left[(\mathbf{f}_{j+1/2}^{(u_c)})^n - (\mathbf{f}_{j-1/2}^{(u_c)})^n \right] \\ & + \frac{1}{\Delta x} \left[(\mathbf{f}_{j+1/2}^{(u_d)})^n - (\mathbf{f}_{j-1/2}^{(u_d)})^n \right] + \frac{1}{\Delta x} \left[(\mathbf{f}_{j+1/2}^{(p)})^n - (\mathbf{f}_{j-1/2}^{(p)})^n \right] \\ & = \frac{(p_d)^n}{\Delta x} [\mathbf{g}_{j+1/2}^n - \mathbf{g}_{j-1/2}^n] + \frac{1}{\Delta x} [\mathbf{h}_{j+1/2}^n - \mathbf{h}_{j-1/2}^n] + \mathbf{s}^* \end{aligned} \quad (219)$$

$$\mathbf{f}_{1/2}^{(u_c)} = \left[a_{1/2} (M_c)_{1/2} (\rho_c)_{L/R} + D_c^{(p)} \right] \begin{pmatrix} \alpha_c \\ 0 \\ \alpha_c u_c \\ 0 \\ \alpha_c H_c \\ 0 \end{pmatrix}_{L/R}; \quad (220)$$

$$\mathbf{f}_{1/2}^{(u_d)} = \left[a_{1/2} (M_d)_{1/2} (\rho_d)_{L/R} + D_d^{(p)} \right] \begin{pmatrix} 0 \\ \alpha_d \\ 0 \\ \alpha_d u_d \\ \alpha_c \left(\frac{\rho_c}{\rho_d} \right) E(\alpha_d) (u_c - u_d)^2 \\ \alpha_d H_d \end{pmatrix}_{L/R}; \quad (221)$$

$$\mathbf{f}_{1/2}^{(p)} = \begin{pmatrix} 0 \\ 0 \\ \alpha_c (p'_c)_{1/2} \\ \alpha_d (p'_d)_{1/2} \\ 0 \\ 0 \end{pmatrix} = \begin{pmatrix} 0 \\ 0 \\ \alpha_c \left(\mathcal{P}_{(5)}^+ (M_{c,L}) p'_{c,L} + \mathcal{P}_{(5)}^- (M_{c,R}) p'_{c,R} + D_c^{(u)} \right) \\ \alpha_d \left(\mathcal{P}_{(5)}^+ (M_{c,L}) p_{d,L} + \mathcal{P}_{(5)}^- (M_{c,R}) p_{d,R} + D_d^{(u)} \right) \\ 0 \\ 0 \end{pmatrix}; \quad (222)$$

where the $(M_c)_{1/2}$ is also split to account for volume fraction variation across the cell interface:

$$\begin{aligned} (M_k)_{1/2} &= \frac{1}{(\alpha_k)_{\max}} \left[\max((\alpha_k)_L - (\alpha_k)_R, 0) (M_k)_L \right. \\ & \quad \left. + \max((\alpha_k)_R - (\alpha_k)_L, 0) (M_k)_R \right] \\ & + \frac{(\alpha_k)_{\min}}{(\alpha_k)_{\max}} \left[\mathcal{M}_{(4)}^+ ((M_k)_L) + \mathcal{M}_{(4)}^- ((M_k)_R) \right] \end{aligned} \quad (223)$$

with

$$\begin{aligned} (\alpha_k)_{\min} &= \min((\alpha_k)_L, (\alpha_k)_R) \\ (\alpha_k)_{\max} &= \max((\alpha_k)_L, (\alpha_k)_R) \end{aligned}$$

In the above

$$p'_c = p_c + \rho_c E(\alpha_d) (u_d - u_c)^2 \quad (224)$$

and the numerical dissipation terms $D_k^{(p)}$, $D_k^{(u)}$ are given in (197) and (198). For numerical speed of sound $a_{1/2}$, we employ the sound speed of the continuous phase. The same speed of sound is applied to both phases simultaneously.


For inter-phasic terms, we have:

$$\frac{(p_d)_j}{\Delta x} [\mathbf{g}_{j+1/2} - \mathbf{g}_{j-1/2}] = \frac{(p_d)_j}{\Delta x} \begin{pmatrix} 0 \\ 0 \\ ((\alpha_c)_{L,j+1/2} - (\alpha_c)_{R,j-1/2}) \\ -((\alpha_c)_{L,j+1/2} - (\alpha_c)_{R,j-1/2}) \\ 0 \\ 0 \end{pmatrix}; \quad (225)$$

$$\mathbf{h}_{1/2} = [a_{1/2}(M_d)_{1/2}] \begin{pmatrix} 0 \\ 0 \\ \alpha_c \rho_c E(\alpha_d) (u_d - u_c) \\ -\alpha_c \rho_c E(\alpha_d) (u_d - u_c) \\ 0 \\ 0 \end{pmatrix}_{L/R}; \quad (226)$$

$$\mathbf{s}^* = \begin{pmatrix} 0 \\ 0 \\ \frac{J_j}{\Delta x} \Delta x (u_d) \\ -\frac{J_j}{\Delta x} \Delta x (u_d) \\ (u_d)_j \Phi_j^K \\ -(u_d)_j \Phi_j^K \end{pmatrix} \quad \text{with } \Delta x (\cdot) = \begin{cases} (\cdot)_j - (\cdot)_{j-1} & \text{if } J_j \geq 0; \\ (\cdot)_{j+1} - (\cdot)_j & \text{Otherwise.} \end{cases} \quad (227)$$

The forces expressed by the inter-phasic terms (\mathbf{H} and \mathbf{s}^*) locally must cancel, and this is assured by discretizations (226) and (227).

As we have seen already above, with the AUSM numerical speed of sound, we should be able to handle shocks and expansion waves. However, in the presence of contact discontinuities, such as jumps in volume fractions, special consideration is needed. The issue arises because the discontinuity in α would cause the nonconservative terms in (203) and (204) to create nonphysical imbalances of pressure forces if discretization is done in the standard way of using common intermediate values of α_k and pressure at cell interface, and if the $\nabla \alpha_k$ term is discretized by central difference. The problem can be addressed by allowing the discontinuities to smear but this would defeat the purpose of a high-fidelity numerical scheme. Instead, we use (228) which with the help of  Fig. 9 can be seen to assure the balance of pressure force across each cell. Recall that by conservation treatment of convection terms, momentum fluxes are automatically balanced.

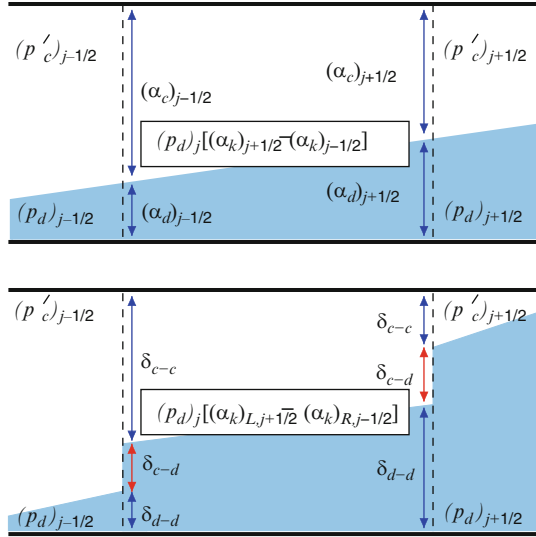


Figure 9

Illustration of pressure force applied on subcells of different fluids. (a) with continuous α_k ; (b) with noncontinuous α_k

$$\mathbf{f}_{j+1/2}^p = \begin{pmatrix} 0 \\ 0 \\ \delta_{c-c}(p_c)_{1/2} + \delta_{c-d}(p_d)_{1/2} \\ \delta_{d-d}(p_d)_{1/2} + \delta_{d-c}(p_d)_{1/2} \\ 0 \\ 0 \end{pmatrix}_{j+1/2} ; \tag{228}$$

$$\mathbf{f}_{j-1/2}^p = \begin{pmatrix} 0 \\ 0 \\ \delta_{c-c}(p_c)_{1/2} + \delta_{d-c}(p_d)_{1/2} \\ \delta_{d-d}(p_d)_{1/2} + \delta_{c-d}(p_d)_{1/2} \\ 0 \\ 0 \end{pmatrix}_{j-1/2}$$

δ_{c-c} , δ_{d-d} , δ_{c-d} , and δ_{d-c} are effective areas for fluid interface on cell boundary.

$$\delta_{c-c} = \min((\alpha_c)_L, (\alpha_c)_R) \tag{229}$$

$$\delta_{d-d} = \min((\alpha_d)_L, (\alpha_d)_R) \tag{230}$$

$$\delta_{c-d} = \max(0, \Delta\alpha_d) = \max(0, -\Delta\alpha_c) \tag{231}$$

$$\delta_{d-c} = \max(0, \Delta\alpha_c) = \max(0, -\Delta\alpha_d) \tag{232}$$

$$\Delta\alpha_k = (\alpha_k)_R - (\alpha_k)_L \tag{233}$$

In code implementation, we use a MUSCL type third-order scheme with Osher-Chakravarthy TVD limiter (Chakravarthy and Osher 1983) to determine fluid states on cell boundary. This allows us to sharply capture the shock wave and contact discontinuity while avoiding the numerical oscillation effectively.

11.3 Time Integration

For time integration, we use the Runge-Kutta time integration method (Jameson 1983). Supposing the system:

$$\frac{\partial \mathbf{Q}}{\partial t} + \mathbf{R}(\mathbf{Q}) = 0 \quad (234)$$

its time integration can be calculated by:

$$\begin{aligned} \mathbf{Q}^{(1)} &= \mathbf{Q}^n - \omega_1 \cdot \Delta t \cdot \mathbf{R}(\mathbf{Q}^n) \\ \mathbf{Q}^{(2)} &= \mathbf{Q}^n - \omega_2 \cdot \Delta t \cdot \mathbf{R}(\mathbf{Q}^{(1)}) \\ &\vdots \\ \mathbf{Q}^{(s-1)} &= \mathbf{Q}^n - \omega_{s-1} \cdot \Delta t \cdot \mathbf{R}(\mathbf{Q}^{(s-2)}) \\ \mathbf{Q}^{n+1} &= \mathbf{Q}^n - \omega_s \cdot \Delta t \cdot \mathbf{R}(\mathbf{Q}^{(s-1)}) \end{aligned} \quad (235)$$

For a four-stage Runge-Kutta, the coefficients are $(\omega_1, \omega_2, \omega_3, \omega_4) = (\frac{1}{4}, \frac{1}{3}, \frac{1}{2}, 1)$. Applying to our system of equations (214)-(218):

$$\frac{\partial}{\partial t} [\tilde{\mathbf{Q}}] + p_d [\mathbf{T}] + [\mathbf{R}] = 0 \quad (236)$$

we have:

$$\frac{1}{\Delta t} ([\tilde{\mathbf{Q}}]^{s+1} - [\tilde{\mathbf{Q}}]^n) + \frac{p_d^s}{\Delta t} \begin{pmatrix} 0 \\ 0 \\ 0 \\ 0 \\ \alpha_c^s - \alpha_c^n \\ \alpha_d^s - \alpha_d^n \end{pmatrix} + \omega_{s+1} [\mathbf{R}]^s = 0 \quad (237)$$

with

$$[\tilde{\mathbf{Q}}]^{s+1} + p_d^s \begin{pmatrix} 0 \\ 0 \\ 0 \\ 0 \\ \alpha_c^s \\ \alpha_d^s \end{pmatrix} = [\tilde{\mathbf{Q}}]^n + p_d^s \begin{pmatrix} 0 \\ 0 \\ 0 \\ 0 \\ \alpha_c^n \\ \alpha_d^n \end{pmatrix} - \omega_{s+1} \Delta t \begin{pmatrix} R_1^s \\ R_2^s \\ R_3^s \\ R_4^s \\ R_5^s \\ R_6^s \end{pmatrix} \equiv \begin{pmatrix} \tilde{W}_c \\ \tilde{W}_d \\ \tilde{M}_c \\ \tilde{M}_d \\ \tilde{E}_c \\ \tilde{E}_d \end{pmatrix} \quad (238)$$

Here $[\mathbf{R}]$ is the collection of all the spatial discretization and source terms. The specific implementation is as follows:

From the continuity equations we can update for the products $\alpha\rho$:

$$\alpha_c^{s+1} \rho_c^{s+1} = \alpha_c^n \rho_c^n - \bar{\omega}_{s+1} \Delta t R_1^s \equiv \tilde{W}_c \quad (239)$$

$$\alpha_d^{s+1} \rho_d^{s+1} = \alpha_d^n \rho_d^n - \bar{\omega}_{s+1} \Delta t R_2^s \equiv \tilde{W}_d \quad (240)$$

Then from the momentum equations we can update the velocities:

$$\begin{aligned} & \alpha_c^{s+1} \rho_c^{s+1} (1 + E^s) u_c^{s+1} - \alpha_c^{s+1} \rho_c^{s+1} E^s u_d^{s+1} \\ & = \alpha_c^n \rho_c^n (1 + E^n) u_c^n - \alpha_c^n \rho_c^n E^n u_d^n - \bar{\omega}_{s+1} \Delta t R_3^s \equiv \tilde{M}_c \end{aligned} \quad (241)$$

$$\begin{aligned} & -\alpha_c^{s+1} \rho_c^{s+1} E^s u_c^{s+1} + (\alpha_d^{s+1} \rho_d^{s+1} + \alpha_c^{s+1} \rho_c^{s+1} E^s) u_d^{s+1} \\ & = -\alpha_c^n \rho_c^n E^n u_c^n + (\alpha_d^n \rho_d^n + \alpha_c^n \rho_c^n E^n) u_d^n - \bar{\omega}_{s+1} \Delta t R_4^s \equiv \tilde{M}_d \end{aligned} \quad (242)$$

which provide the linear system:

$$\begin{pmatrix} \alpha_c^{s+1} \rho_c^{s+1} (1 + E^s) & -\alpha_c^{s+1} \rho_c^{s+1} E^s \\ -\alpha_c^{s+1} \rho_c^{s+1} E^s & \alpha_d^{s+1} \rho_d^{s+1} + \alpha_c^{s+1} \rho_c^{s+1} E^s \end{pmatrix} \begin{pmatrix} u_c^{s+1} \\ u_d^{s+1} \end{pmatrix} = \begin{pmatrix} \tilde{M}_c \\ \tilde{M}_d \end{pmatrix} \quad (243)$$

Note that instead of $E^s(\alpha_d^s)$, we could use $E^{s+1}(\alpha_d^{s+1})$ and obtain the solution by iteration.

To decode so as to obtain primitive variables (α, ρ, p) we need to involve the EOS and the energy equations.

$$\alpha_c^{s+1} \rho_c^{s+1} E_c^{s+1} + p_d^s \alpha_c^{s+1} = \alpha_c^n \rho_c^n E_c^n + p_d^s \alpha_c^n - \bar{\omega}_{s+1} \Delta t R_5^s = \tilde{E}_c \quad (244)$$

$$\alpha_d^{s+1} \rho_d^{s+1} E_d^{s+1} + p_d^s \alpha_d^{s+1} = \alpha_d^n \rho_d^n E_d^n + p_d^s \alpha_d^n - \bar{\omega}_{s+1} \Delta t R_6^s = \tilde{E}_d \quad (245)$$

We employ a stiffened gas EOS to relate internal energy (e) to the gas pressure and density:

$$e = (p_c + \gamma_c P_{\infty, c}) / \rho_c (\gamma_c - 1) \quad (246)$$

and the Newton iteration method to solve for ρ_c^{s+1} and α_c^{s+1} . To this end, the residuals Γ are:

$$\begin{aligned} \Gamma &= \begin{pmatrix} \Gamma_1 \\ \Gamma_2 \end{pmatrix} = \begin{pmatrix} \alpha_c^k \rho_c^k E_c^k + p_d^s \alpha_c^k - \tilde{E}_c \\ \alpha_d^k \rho_d^k E_d^k + p_d^s \alpha_d^k - \tilde{E}_d \end{pmatrix}; \Omega^k = \begin{pmatrix} p_c^k \\ \alpha_c^k \end{pmatrix} \\ \Gamma_1 &= \frac{\alpha_c^k}{\gamma_c - 1} (p_c^k + \gamma_c P_{\infty, c}) + \frac{1}{2} (\alpha_c^k \rho_c^k) \left((u_c^{s+1})^2 + E(\alpha_d^k) (u_d^{s+1} - u_c^{s+1})^2 \right) + p_d^s \alpha_c^k - \tilde{E}_c \\ \Gamma_2 &= \frac{\alpha_d^k}{\gamma_d - 1} (p_d^k + \gamma_d P_{\infty, d}) + \frac{1}{2} (\alpha_d^{s+1} \rho_d^{s+1}) (u_d^{s+1})^2 + p_d^s \alpha_d^k - \tilde{E}_d \\ &= \frac{\alpha_d^k}{\gamma_d - 1} \left(p_c^k - \frac{1}{2} (\alpha_c^{s+1} \rho_c^{s+1}) E'(\alpha_d^k) (u_d^{s+1} - u_c^{s+1})^2 + \gamma_d P_{\infty, d} \right) \\ &\quad + \frac{1}{2} (\alpha_d^{s+1} \rho_d^{s+1}) (u_d^{s+1})^2 + p_d^s \alpha_d^k - \tilde{E}_d \end{aligned}$$

where k is the index for iteration. The updated states after each iteration are

$$\Omega^{k+1} = \Omega^k - \left[\frac{\partial \Gamma}{\partial \Omega} \right]^{-1} [\Gamma] \quad (247)$$

With

$$\left[\frac{\partial \Gamma}{\partial \Omega} \right]_{11} = \frac{\partial \Gamma_1}{\partial p_c^k} = \frac{\alpha_c^k}{\gamma_c - 1}$$

$$\left[\frac{\partial \Gamma}{\partial \Omega} \right]_{12} = \frac{\partial \Gamma_1}{\partial \alpha_c^k} = \frac{p_c^k + \gamma_c P_{\infty,c}}{\gamma_c - 1} - \frac{1}{2} (\alpha_c^{s+1} \rho_c^{s+1}) E'(\alpha_d^k) (u_d - u_c)^2 + p_d^s$$

$$\left[\frac{\partial \Gamma}{\partial \Omega} \right]_{21} = \frac{\partial \Gamma_2}{\partial p_c^k} = \frac{\alpha_d^k}{\gamma_d - 1}$$

$$\left[\frac{\partial \Gamma}{\partial \Omega} \right]_{22} = \frac{\partial \Gamma_2}{\partial \alpha_c^k} = -\frac{p_d^k + \gamma_d P_{\infty,d}}{\gamma_d - 1} + \frac{\alpha_d^k}{2(\gamma_d - 1)} (\alpha_c^{s+1} \rho_c^{s+1}) E''(\alpha_d^k) (u_d - u_c)^2 - p_d^s$$

At convergence, we have $p_c^{s+1} = p_c^k$ and $\alpha_c^{s+1} = \alpha_c^k$.

When the volume fraction of the disperse phase becomes vanishingly small (typically a value of 10^{-5} or 10^{-6}) rather than solving for it we take it at the specified limiting value and assume that it comes to instantaneous equilibrium with the continuous phase. The error associated with this treatment is negligibly small unless we try to resolve detailed motions of very dilute clouds, which then requires special treatment (► Sect. 12.5).

12 Numerical Testing in the ARMS Code

Computations were carried out with the computer code ARMS (All-Regime Multiphase Simulation) (Chang et al. 2009), and they were independently verified with the new code MuSiC-ARMS (Chang et al. 2010a). The original ARMS was built on a public-domain platform (SAMRAI, structured adaptive mesh refinement infrastructure), while MuSiC-ARMS is our own specialised tool based on irregular grids embedded in a multi-level Cartesian mesh. This same platform supports also the MuSiC-SIM code for compressible multi-hydrodynamics at the DNS level (sharp mobile interfaces coupling Navier-Stokes solvers for each phase) based on the sharp interface method (Nourgaliev et al. 2008; Chang et al. 2010b). An early task with this code will be to build the function $E(\alpha_d)$, as it appears in B-21 of Part I, from first principles.

In all computations presented here, continuous and disperse phase thermodynamics were modeled by ideal and stiffened (246) gas equations of state, respectively. The function $E(\alpha_d)$ was fitted with a fourth-order polynomial so that it reduces smoothly to zero rather than be

allowed to take on negative values when α_d exceeds the value that renders it zero:

$$E(\alpha_d) = \begin{cases} \frac{1}{2}\alpha_d [1 + 2C\alpha_d + 5C^2\alpha_d^2 + 8C^3\alpha_d^3 + 4C^4\alpha_d^4] & \text{if } (1 + C\alpha_d) \geq 0; \\ 0 & \text{Otherwise.} \end{cases} \quad (248)$$

All computations shown here were repeated with effective grid resolutions that spanned a factor of 8, typically 500 to 4,000 cells over a 10-m long computational domain. Unless otherwise noted the CFL number was set to 0.4. The base value of the parameter C in (248) was taken as -3.1 . Sample parametric calculations for values of 0 and -4.8 are also shown.

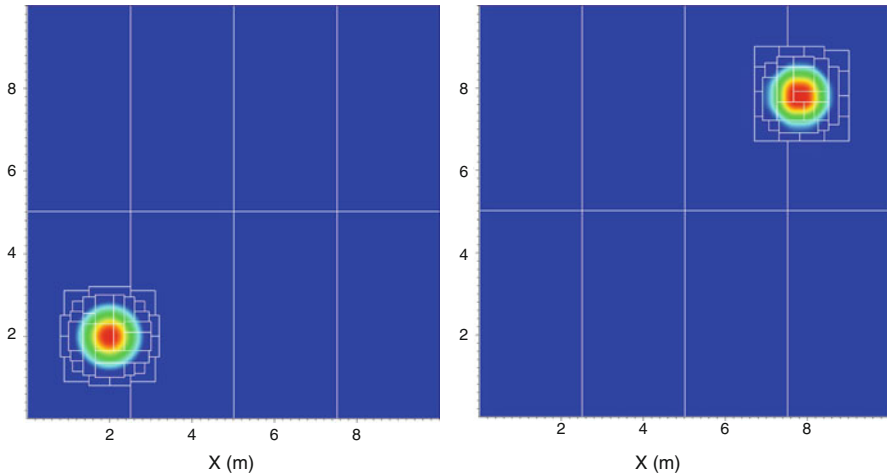
In these very basic series of tests we are concerned with the “bare” code: the inviscid constitutive treatment embodied in the EFM and computational performance of the numerical scheme to capture shocks and contact discontinuities sharply, stably, and without oscillations, even as numerical dissipation is severely reduced (grid refinement). The five series of computations and respective attributes of testing are as follows:

1. Uniformly-Translating Body-and-Fluid System. Ensuring that translation occurs without pressure disturbances, while maintaining any contact discontinuities present initially.
2. The Faucet Problem (Ransom 1987). Capturing the contact discontinuity of an abruptly initiated, at the inlet boundary of a computational domain, disperse stream that is subject to the acceleration of gravity.
3. Fitt’s Problem (1989). Capturing all wave forms and contacts in Riemann problems specified with initial discontinuities in Mach number and disperse phase volume fraction distributions. Test performance in relation to the hyperbolicity map of the EFM employed (Appendix B of Part I).
4. Shock Tube Problems. Capturing all wave forms and contacts in Riemann problems specified with initial discontinuities in pressure and disperse phase volume fraction distributions. Test performance in relation to the hyperbolicity map of the EFM employed (Appendix B of Part I). Test the role of drag to stabilize cases that are in the non-hyperbolic corridor.
5. Particle cloud dynamics in gaseous shocks. Capturing the acceleration and relaxation time of particles with and without drag. Compare to exact analytical results. Test performance in relation to the hyperbolicity map of the EFM employed (Appendix B of Part I). Test the role of drag to stabilize cases that are in the non-hyperbolic corridor.

As detailed below this initial, and far from comprehensive, testing shows sufficient promise to motivate continuing efforts in 2D and 3D geometries, and eventually quantitative comparisons with experimental data. It must be emphasized, however, that the use of function $E(\alpha_d)$ in compressible flows ($M \neq 0$) is strictly tentative until the kinds of extensions noted above have been completed.

12.1 Uniformly Translating Body-and-Fluid System

The ARMS solver is applied over a rectangular domain filled mostly with gas (liquid fraction 10^{-6}) and containing (a diffusely connected with its surroundings) circular liquid “blob” (gas



■ Figure 10

Snapshot of liquid “blob” motion in a uniformly convecting flow. Colors indicate disperse phase volume fractions. Left: $t = 0.0$; Right: $t = 0.06$ s

fraction 10^{-6}), all moving with the same velocity, which is maintained by a uniform/steady, diagonal (gas) inflow at the left and bottom boundaries, and a continuous outflow boundary condition at the other two boundaries of the domain. Obviously, there are no accelerations involved, and we expect that the solver will capture the interface without significant distortion due to motion, while the pressure remains smooth and uniform throughout within a very strict tolerance.

The computation shown in [Fig. 10](#) is for a 10×10 m domain, the flow velocity vector has components of 100 m/s in each direction, and the code was programmed to refine the grid around the boundary by three levels of AMR with a refinement ratio of 2. Thus we have an effective field resolution of 400×400 grids. The pressure remained uniform throughout the computation to within 10^{-3} Pa, and the shape of the phase boundary remained without significant additional smearing.

12.2 The Faucet Problem

The ARMS solver is applied to compute the evolution of volume fraction distributions of a uniformly supplied disperse-phase stream ($\rho_d = 10^3 \text{ kg/m}^3$) at the top boundary of the computational domain as it accelerates under gravity. For the ideal problem, with no phase interactions, there is an exact analytical solution, a snapshot of which is shown in [Fig. 11](#). Due to acceleration the disperse phase volume fraction decreases (that of the continuous phase increases) along the travel path. Also distinct is the sharp contact discontinuity formed by the sudden appearance of the inlet flow (at the “faucet”) upon initiation of the transient. The object

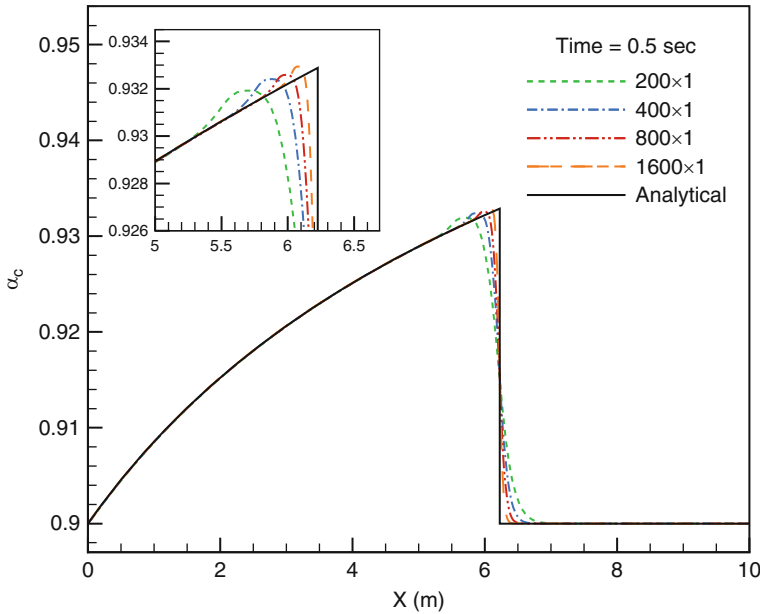


Figure 11
 ARMS performance on the Faucet problem

of the computation is to capture the front stably, sharply, and without oscillations. It is known that non-hyperbolic formulations fail this task, unless they are gridded coarsely enough, which causes excessive smearing, and severe distortion of the waveform.

In [Fig. 11](#) we can see that with increasing resolution the computations converge to the exact discontinuous result, uniformly (around the front) and without oscillations.

12.3 Fitt's Problem

The ARMS solver is applied to a set of Riemann problems with discontinuity in Mach number designed to attain various “positions” in the hyperbolicity diagram ([Appendix B](#) of Part I) as shown in [Fig. 12](#). Each case is also considered with a discontinuity in disperse phase volume fraction (marked by superscript D). The specification of the various calculations performed, in terms of the $\{\alpha_d, p, u, T\}^L$ and $\{\alpha_d, p, u, T\}^R$ employed, is given in [Table D.1](#). The Mach number values are selected by specifying appropriate values of the gas temperatures (speeds of sound) as indicated in the table. As density of the disperse phase we use 10^4 kg/m^3 .

Fitt (1989) originally used this test problem to demonstrate the failure of numerical computations with an “ill-posed” EFM formulation, and we are not aware of any subsequent elaborations with other models.

All results obtained with ARMS are summarized in [Fig. D.1](#). We can see that all cases are stable, even those that are found inside the non-hyperbolic corridor. As noted in [Appendix](#)

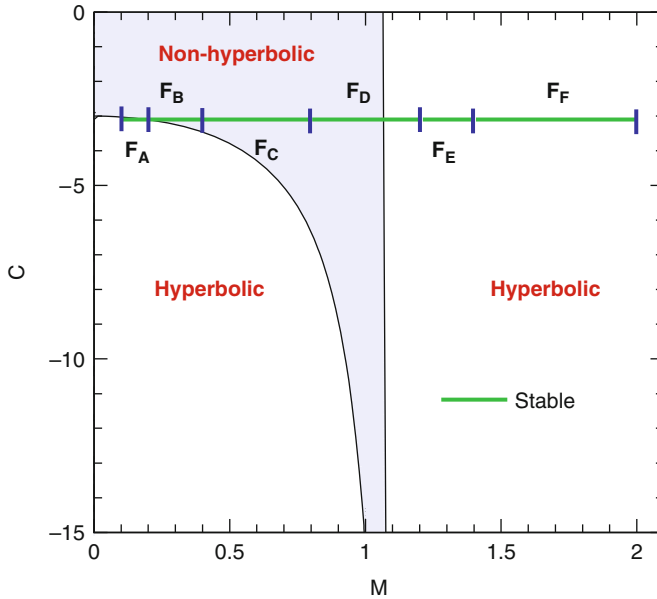


Figure 12

Locations of the various Fitt's problem computational cases on the hyperbolicity map

B of Part I this is perhaps to be expected because of the “mild” non-hyperbolicity explained therein. Nevertheless, transonic conditions can become sensitive, as for example initially supersonic D cases that lead to transonic conditions due to wave reflections.

Characteristic velocities for the various waves can be obtained as illustrated in [Fig. 13](#). The results are “paired” with those obtained from the hyperbolicity analysis ([Appendix B](#) of Part I) in [Table 1](#). Note that the nomenclature (on the various λ s) in this table is not kept the same, and that a fourth eigenvalue is now present (u_c); this is due to inclusion of the energy equation in the computation. A couple of sample results illustrating grid convergence are shown in [Fig. 14](#).

Finally, a number of parametrics on the value of C are shown in [Fig. 15](#), along with their positions on the hyperbolicity map in [Fig. 16](#). In addition to further supporting the conclusions reached above, these results also demonstrate that there is a considerable tolerance on the value of C .

12.4 Shock Tube Problems

The ARMS solver is applied to a series of Riemann problems with discontinuity in pressures and volume fractions of the disperse phase, whose density is taken as that of water. Two tests are with single phase, air or water, set at extremely high pressure ratio, and these are in excellent agreement with exact results. The rest of the cases involve two-phase conditions under varying pressure ratio so as to cover wide ranges on the hyperbolicity map as shown in [Fig. 17](#). They

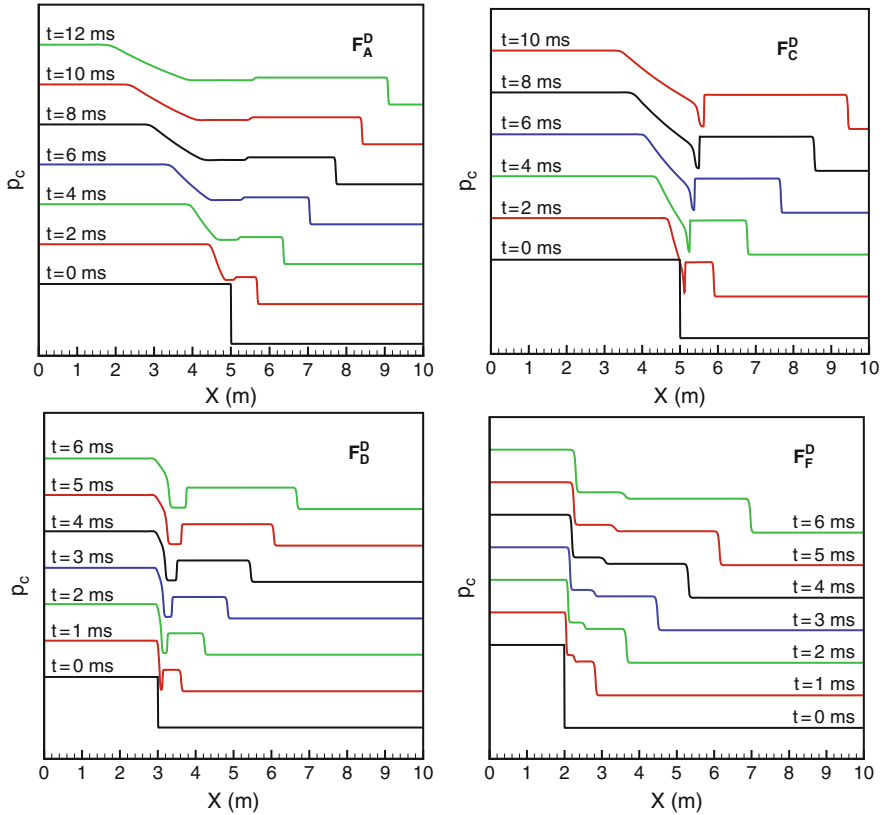


Figure 13
Propagation of characteristic waves in sample subsonic (top) and supersonic (bottom) cases. All these cases were run on 1,000 cells grid

are denoted as the S cases. All cases are specified in [Table D.2](#) in terms of the applicable $\{\alpha_d, p, u, T\}^L$ and $\{\alpha_d, p, u, T\}^R$. As indicated in the table each case was run both with a uniformly distributed disperse phase as well as with a jump at the location of the diaphragm. To maximize the computational challenge all cases were run with zero drag.

The results are summarized in Appendix, [Fig. D.2](#). We can see that instabilities develop (seen better yet in Mach number plots as in [Fig. 18](#)), however they can be effectively controlled by a small amount of dissipation, as is the case for the Cloud Dynamics problems discussed below.

12.5 Particle Cloud Dynamics in Gaseous Shocks

The ARMS solver is applied to a shock tube configuration driven by single-phase gas, and various kinds of particle clouds (water density, particle diameter 2 mm) in the expansion

Table 1

Comparison of the characteristic wave speeds from ARMS with those from the rule of thumb found in Appendix B of Part I. Of the two numerical entries the one on the *left* corresponds to the eigenvalues according to the rule developed in Appendix B of Part I, and the one on the *right* is the value found in the ARMS computation. The later case the speed of sound is found from the local computed temperature

Case	$\lambda_1; u_c + a_c$	$\lambda_2; u_c$	$\lambda_3; u_d$	$\lambda_4; u_c - a_c$
F_A^D (subsonic)	340.7; 337.1 1%	225.3; 199.2 13 %	64.7; 50 22 %	-277.3; -280.0 1 %
F_C^D (transonic)	439.0; 442.5 -1%	341.0; 301.9 11 %	69.0; 50 27 %	-150.0; -172.0 -15%
F_E^D (supersonic)	826.0; 781.7 5%	675.7; 497.1 26 %	46.3; 50 -8 %	260.0; 185.0 29%

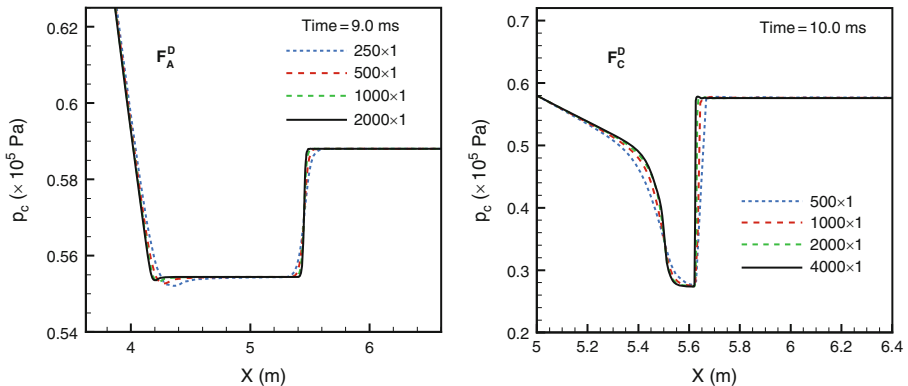


Figure 14

Illustration of ARMS performance under grid refinement for Fitt's problem

section as specified in Table D.3. To explore the effect of initial discontinuity each C case was run with a smooth (Gaussian) as well as with a top hat profile (subscripts S and T respectively). To explore the effect of drag to stabilize an unstable computation, each case was run with zero drag (subscript zero) as well as a constant drag coefficient of 0.41 (no subscript). However it should be noted that even one-tenth of this value is sufficient to stabilize these cases. Finally, to test against the exact result for a single particle accelerated in a shock, we have also case D (for dilute cloud) with particle density $\rho_d = 100 \text{ kg/m}^3$.

The positions of the various cases on the hyperbolicity map are indicated in Fig. 19. The results are summarized in Fig. D.3a for the C cases and Fig. D.3b for the D case. A key

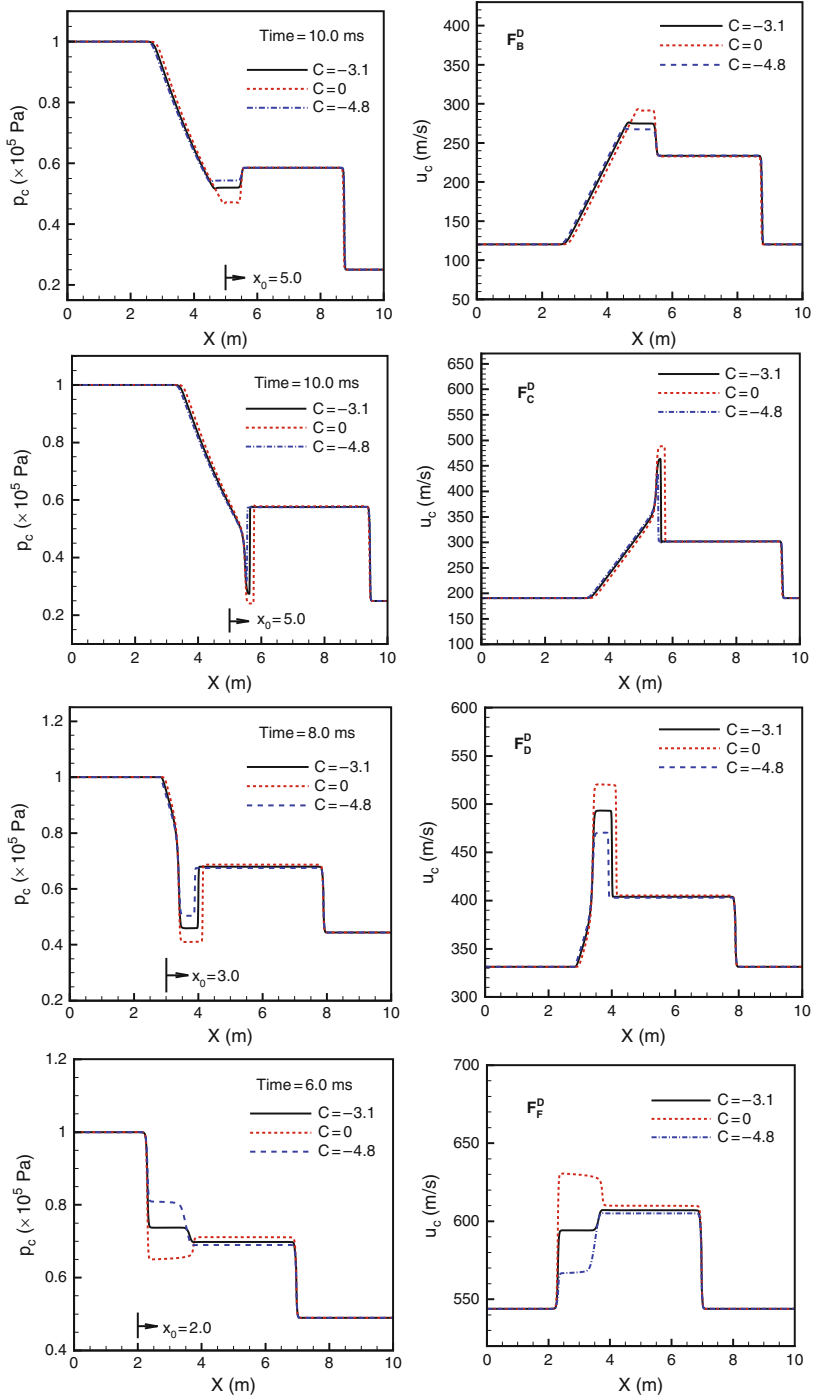


Figure 15

Parametric study on C on selected Fitt's cases. All these cases were run on 1,000 cells grid

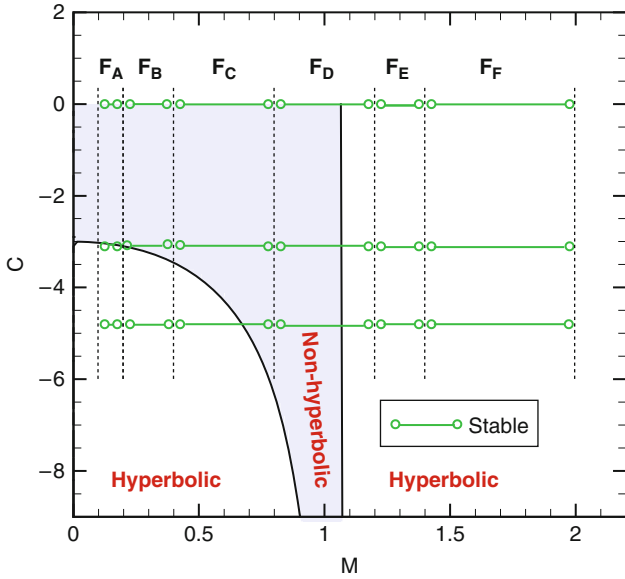


Figure 16

Locations of the various Fitt's problem C-parametrics on the hyperbolicity map. All cases are stable on 4000 cells grid

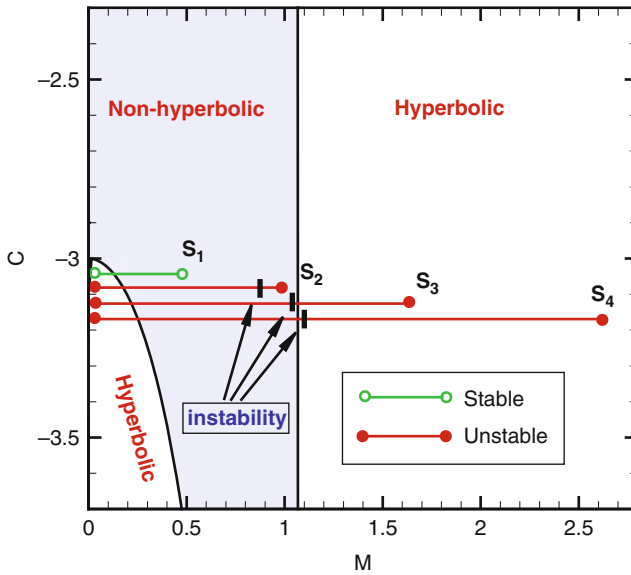


Figure 17

Ranges on the hyperbolicity map covered in each of the Shock tube problem computations

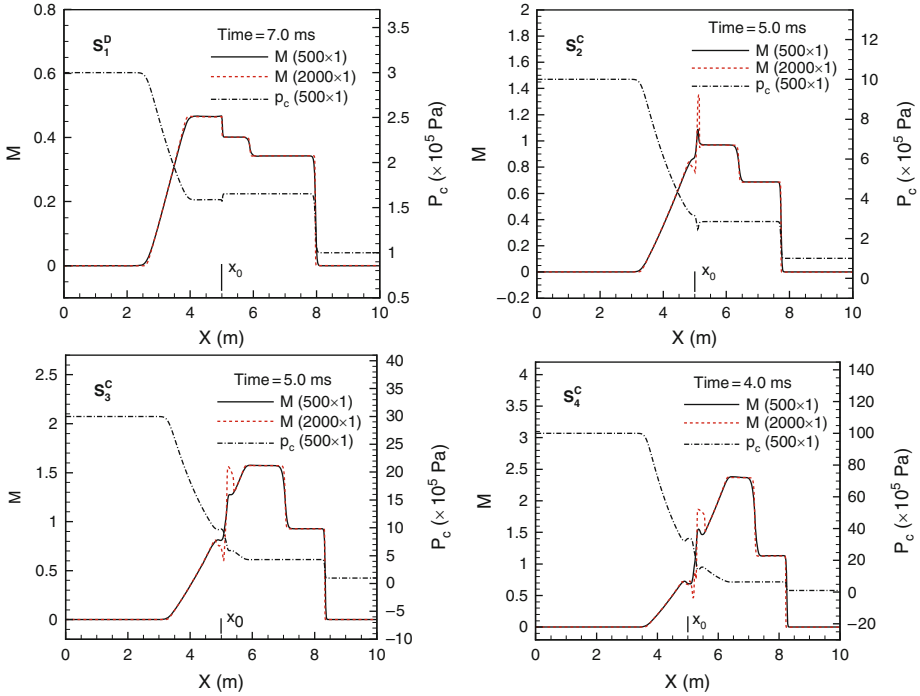


Figure 18 Illustrative snapshots of the shock tube problem computations showing stable calculations and cases with incipient instability

result is the recovery (Fig. 20) of the exact analytical result for displacement as a function of time:

$$x(t) = u_c t - \frac{4\rho_d d_d}{3\rho_c C_d} \ln \left(\frac{3\rho_c C_d u_c t}{4\rho_d d_d} + 1 \right) \tag{249}$$

Another key result is that normal drag cases are stable even though they encroach well into the non-hyperbolic zone. For those cases that are unstable the inception is around $M \sim 1$ a result already seen in the S cases above.

13 Conclusions and Outlook

In Part II, we have addressed computations in compressible multi-hydrodynamics with a heavy disperse phase (Piltch et al. 1996; Theofanous et al. 2006; Theofanous and Dinh 2008). Such flows are the counterpart of bubbly flows (found extensively in past work), and a necessary

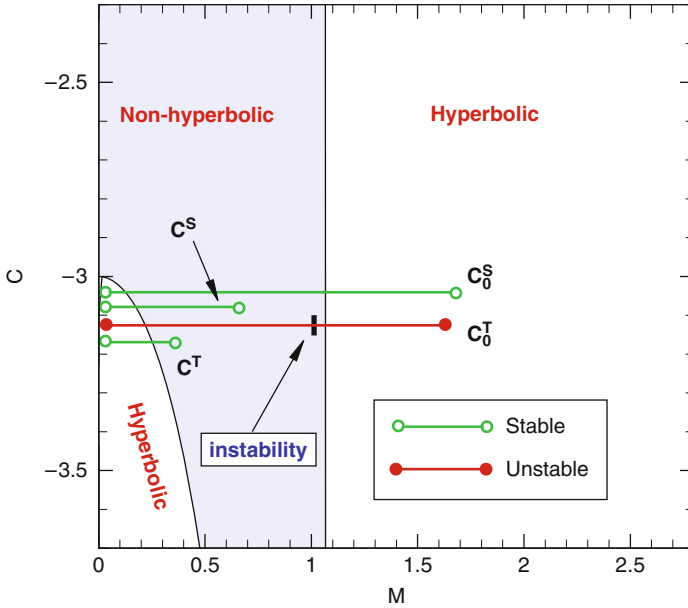


Figure 19

Locations of the cloud dynamics problem computations on the hyperbolicity map

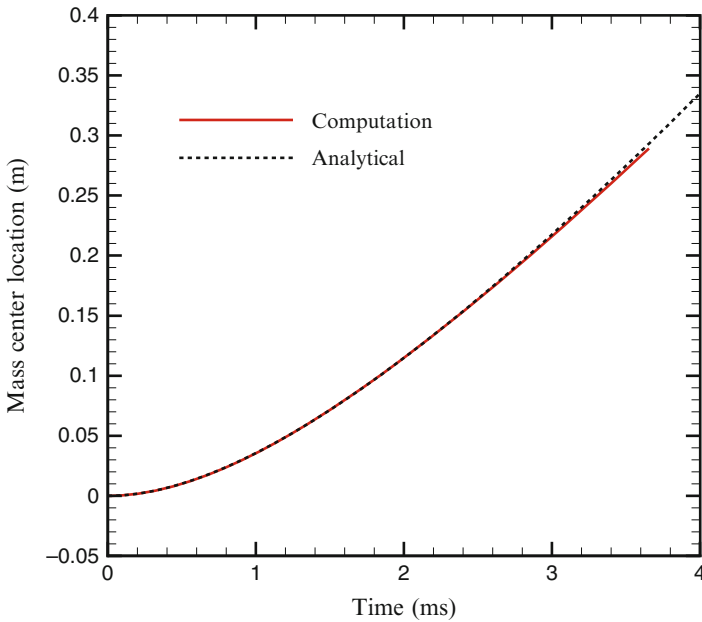


Figure 20

Recovery of exact analytical results for “single” particle displacement under a constant gas flow and drag coefficient (0.41)

complement in the understanding of disperse systems. The principal new ingredient is accessibility of high relative velocities. This is a consequence of large disperse-to-continuous density ratios, which yields strong inviscid interactions and associated inertia coupling effects. On the other hand, and in a broader context of applicability, we have also addressed high-fidelity capturing of shocks and contact discontinuities as pertinent to ab initio simulation of multiphase flow regimes and of steam explosion phenomena (Theofanous et al. 1998a,b, 1999; Yuen and Theofanous 1999).

We have shown that the EFM of Part I, with its essentially hyperbolic character as endowed by a closure that captures inviscid interactions, in combination with a numerical treatment that is based on the AUSM scheme, make available a framework for high-fidelity computation of shocks, expansion waves, and contact discontinuities in high-speed flows. In particular, by accounting for the fundamentally distinct physics between convective momentum transfer and pressure forces, we could deal with discretization of the terms that arise from inviscid interactions as well as of the nonconservative terms involving the volume fraction gradient. Inviscid computations applied to a series of highly sensitive test problems showed that stable solutions can be obtained with effectively unlimited grid resolution. Certain extreme cases, such as strong shock wave interacting with step change in disperse phase volume fraction can lead to mild instability, which however can be eliminated by a small amount of drag.

The pursuit of this framework to practical simulations, for example, shock-induced fluidization of particulated solid or liquid masses, requires developments in three main directions of further constitutive treatment. One would be toward an extension of the function $E(\alpha_d)$ into the Mach number space; that is, the definition of function $E(\alpha_d, M)$, while at the same time extending it to dense systems ($\alpha_d > 0.3$). The second direction would be toward accounting for mechanisms of direct particle to particle momentum transfers, such as pressure wave propagation via contacts in the fully packed regime, and collisions during the early stages of dispersal (dense regime). Some approach on this subject can be initially gained with reference to granular flows. The third direction, necessary for shock-induced fluidization of liquid masses, would require inclusion of the interfacial area transport, a modified version of (65) in Part I, supplemented by a constitutive treatment for interfacial breakup (and perhaps coalescence) appearing as a source term on the right-hand side. Alternatively, the numerical framework presented here could be adapted to accommodate multi-length scale particulate matter, each scale with own continuity and momentum equations, along with appropriate source/sink terms to account for breakup and coalescence phenomena. In all three directions well-instrumented experiments and direct numerical simulations will provide the building blocks for which the present foundation is beckoning.

Acknowledgment

This work was supported by the Joint Science and Technology Office, Defense Threat Reduction Agency (JSTO/DTRA), and the National Ground Intelligence Center (NGIC) of the US Army (Dr. Richard Babarsky). Dr. C.-H. Chang (CRSS / UCSB) is the ARMS and MuSiC-ARMS codes lead developer.

Appendix D: Sample Computational Results with C.-H. Chang and S. Sushchikh

D.1 Fitt's Tests

We compute the Riemann problems listed in [Table D.1](#). The results in [Fig. D.1a-c](#) are cross-referenced to the codes assigned to each case on the table. Superscripts *C/D* refer to continuous/discontinuous initial volume fraction distributions (these can also be seen in the plots). Other specifications and discussion can be found in [Sect. 12.3](#).

Table D.1
Specification of Fitt's tests

	U_L	U_R
F_A	$p_c = 1.0 \times 10^5$ Pa $u_d = 50.0$; $u_c = 85.2$ m/s $T_d = T_c = 308.0$ K $\Delta M = 0.1$	$p_c = 2.5 \times 10^4$ Pa $u_d = 50.0$; $u_c = 85.2$ m/s $T_d = 308.0$; $T_c = 77.0$ K $\Delta M = 0.2$
F_B	$p_c = 1.0 \times 10^5$ Pa $u_d = 50.0$; $u_c = 120.4$ m/s $T_d = T_c = 308.0$ K $\Delta M = 0.2$	$p_c = 2.5 \times 10^4$ Pa $u_d = 50.0$; $u_c = 120.4$ m/s $T_d = 308.0$; $T_c = 77.0$ K $\Delta M = 0.4$
F_C	$p_c = 1.0 \times 10^5$ Pa $u_d = 50.0$; $u_c = 190.8$ m/s $T_d = T_c = 308.0$ K $\Delta M = 0.4$	$p_c = 2.5 \times 10^4$ Pa $u_d = 50.0$; $u_c = 190.8$ m/s $T_d = 308.0$; $T_c = 77$ K $\Delta M = 0.8$
F_D	$p_c = 1.0 \times 10^5$ Pa $u_d = 50.0$; $u_c = 331.5$ m/s $T_d = T_c = 308.0$ K $\Delta M = 0.8$	$p_c = 4.44 \times 10^4$ Pa $u_d = 50.0$; $u_c = 331.5$ m/s $T_d = 308.0$; $T_c = 136.9$ K $\Delta M = 1.2$
F_E	$p_c = 1.0 \times 10^5$ Pa $u_d = 50.0$; $u_c = 472.3$ m/s $T_d = T_c = 308.0$ K $\Delta M = 1.2$	$p_c = 7.35 \times 10^4$ Pa $u_d = 50.0$; $u_c = 472.3$ m/s $T_d = 308.0$; $T_c = 226.3$ K $\Delta M = 1.4$
F_F	$p_c = 1.0 \times 10^5$ Pa $u_d = 50.0$; $u_c = 542.6$ m/s $T_d = T_c = 308.0$ K $\Delta M = 1.4$	$p_c = 4.9 \times 10^4$ Pa $u_d = 50.0$; $u_c = 542.6$ m/s $T_d = 308.0$; $T_c = 150.9$ K $\Delta M = 2.0$

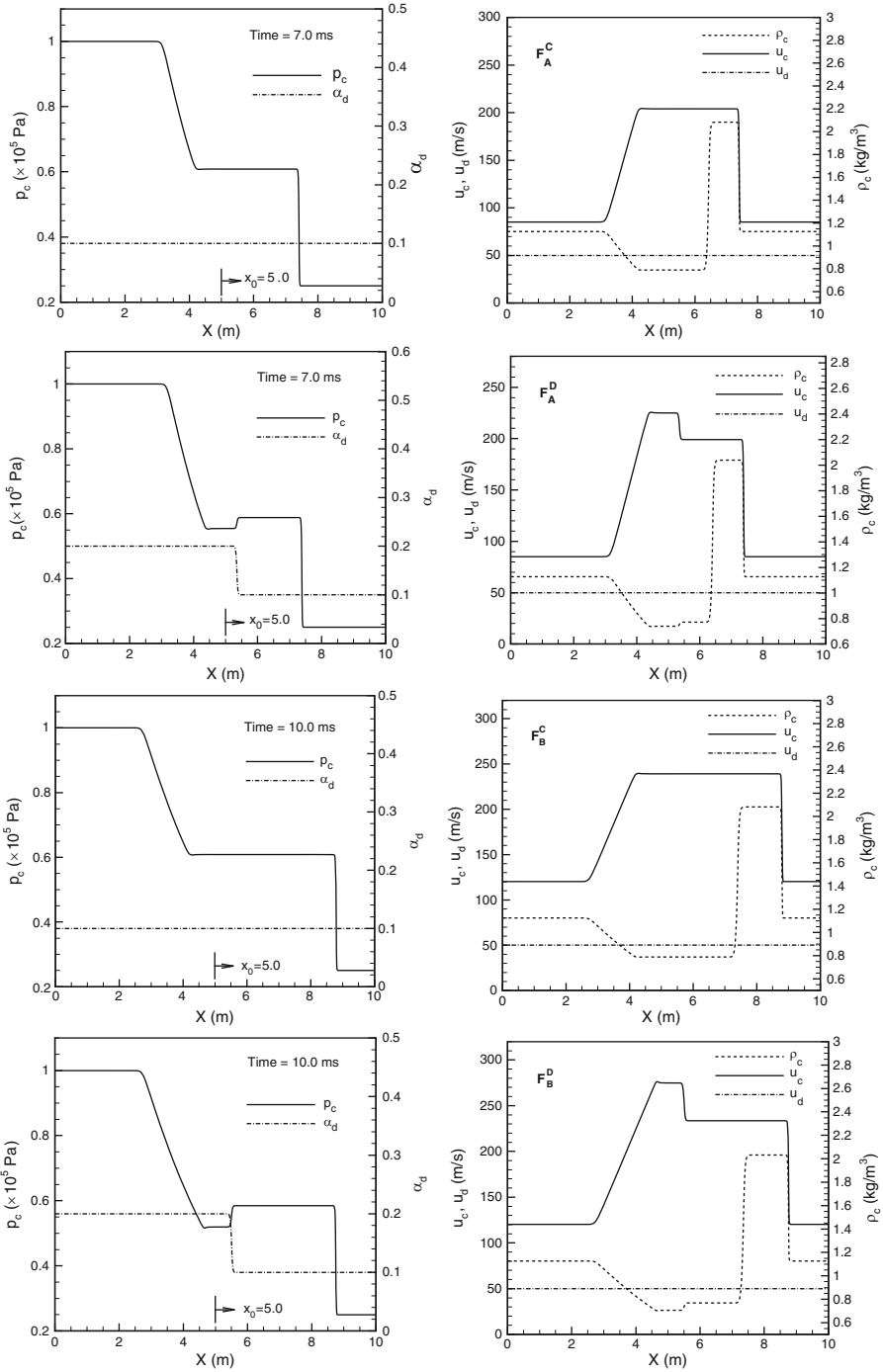


Figure D.1a

Computational results of Riemann problems defined in Table 1

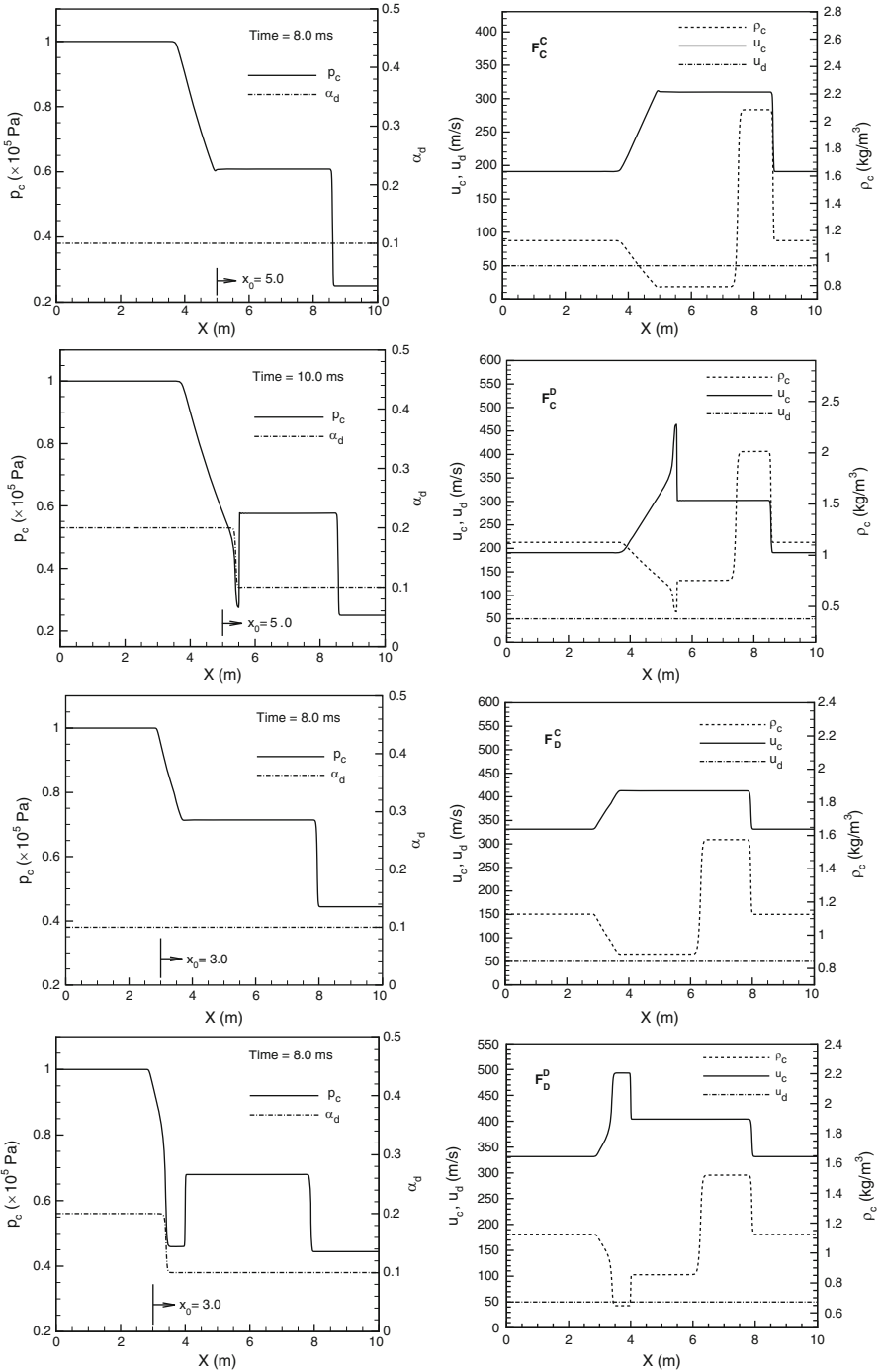


Figure D.1b

Computational results of Riemann problems defined in [Table 1](#)

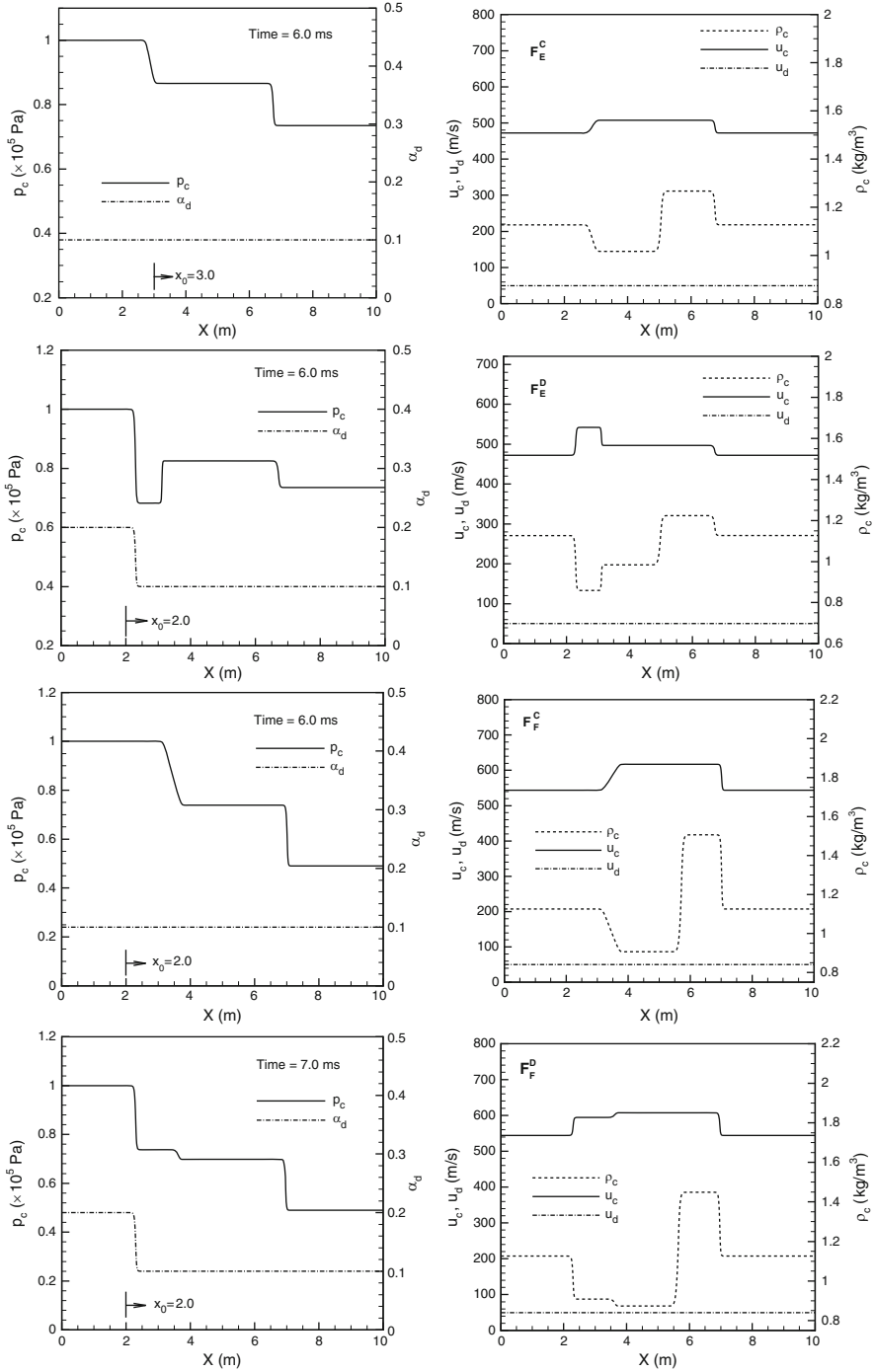


Figure D.1c

Computational results of Riemann problems defined in [Table 1](#)

D.2 Shock Tube Tests

We solve the Riemann problems listed in [▶ Table D.2](#). The results in [▶ Fig. D.2a](#) and [b](#) are cross-referenced to the codes assigned to each case on the table. Superscripts *C/D* refer to continuous/discontinuous volume fraction distributions (these can also be seen in the plots). The pure phase results (not shown) are in excellent agreement with exact solutions. Other specifications and discussion can be found in [▶ Sect. 12.4](#).

■ Table D.2

Specification of the Shock Tube Tests ($\varepsilon = 1.0 \times 10^{-6}$)

	U_L	U_R
Air	$p_c = 1.0 \times 10^8$ Pa $\alpha_d = \varepsilon$ $u_d = u_c = 0.0$ m/s $T_d = T_c = 293.15$ K	$p_c = 1.0 \times 10^5$ Pa $\alpha_d = \varepsilon$ $u_d = u_c = 0.0$ m/s $T_d = T_c = 293.15$ K
Water	$p_c = 1.0 \times 10^8$ Pa $\alpha_d = 1.0 - \varepsilon$ $u_d = u_c = 0.0$ m/s $T_d = T_c = 293.15$ K	$p_c = 1.0 \times 10^5$ Pa $\alpha_d = 1.0 - \varepsilon$ $u_d = u_c = 0.0$ m/s $T_d = T_c = 293.15$ K
S₁	$p_c = 3.0 \times 10^5$ Pa $\alpha_d = 0.1$ or 0.2 $u_d = u_c = 0.0$ m/s $T_d = T_c = 293.15$ K	$p_c = 1.0 \times 10^5$ Pa $\alpha_d = 0.1$ $u_d = u_c = 0.0$ m/s $T_d = T_c = 293.15$ K
S₂	$p_c = 1.0 \times 10^6$ Pa $\alpha_d = 0.1$ or 0.2 $u_d = u_c = 0.0$ m/s $T_d = T_c = 293.15$ K	$p_c = 1.0 \times 10^5$ Pa $\alpha_d = 0.1$ $u_d = u_c = 0.0$ m/s $T_d = T_c = 293.15$ K
S₃	$p_c = 3.0 \times 10^6$ Pa $\alpha_d = 0.1$ or 0.2 $u_d = u_c = 0.0$ m/s $T_d = T_c = 293.15$ K	$p_c = 1.0 \times 10^5$ Pa $\alpha_d = 0.1$ $u_d = u_c = 0.0$ m/s $T_d = T_c = 293.15$ K
S₄	$p_c = 1.0 \times 10^7$ Pa $\alpha_d = 0.1$ or 0.2 $u_d = u_c = 0.0$ m/s $T_d = T_c = 293.15$ K	$p_c = 1.0 \times 10^5$ Pa $\alpha_d = 0.1$ $u_d = u_c = 0.0$ m/s $T_d = T_c = 293.15$ K

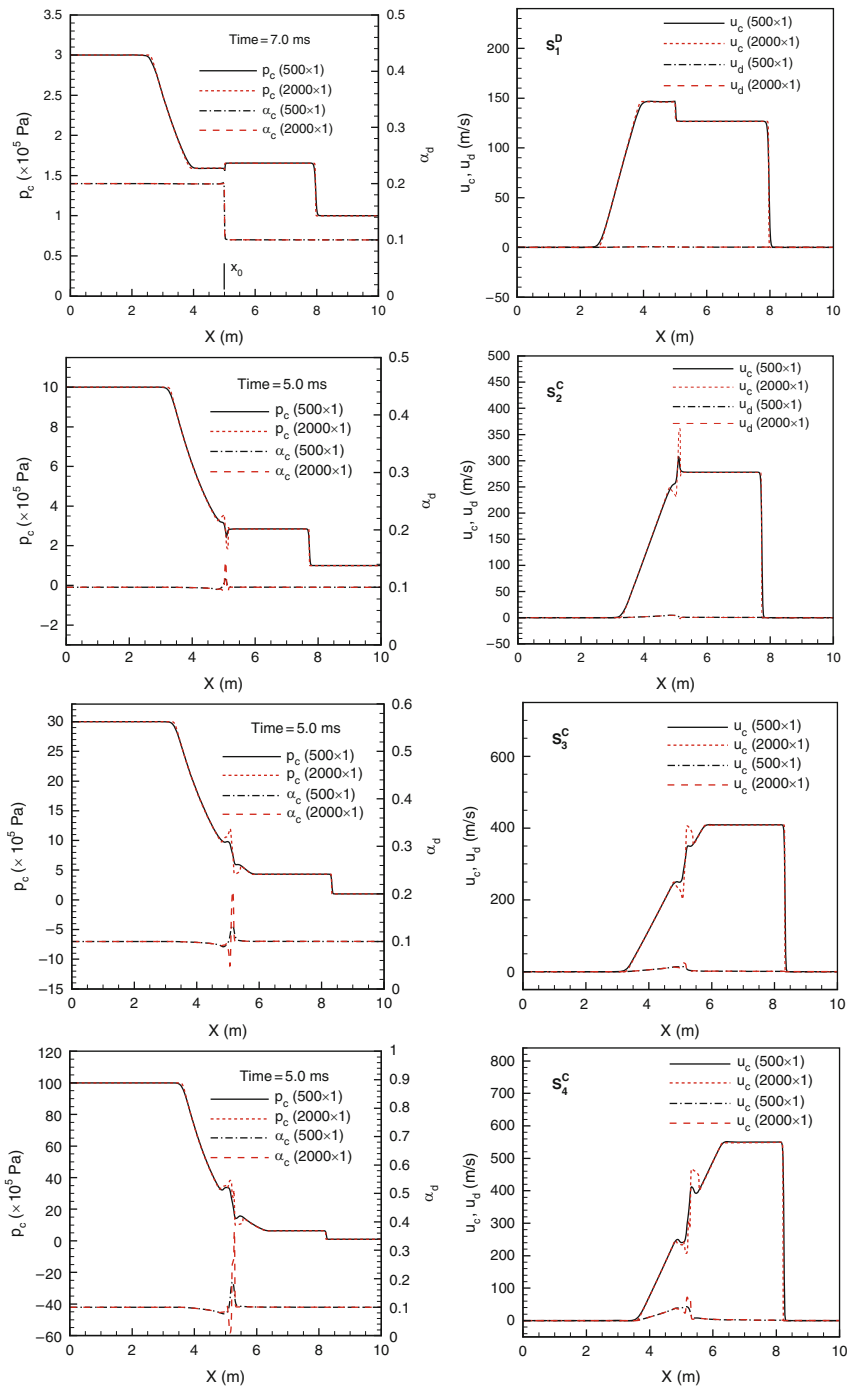


Figure D.2 Computational results of Riemann problems defined in Table 2

D.3 Shock-Induced Dispersal of Dilute Clouds in 1D

We solve the Riemann problems listed in [▶ Table D.3](#). The results in [▶ Fig. D.3a](#) and [b](#) are cross-referenced to the codes assigned to each case on the table. In all cases we have 2 mm particle diameter, and the initial cloud dimensions span 10 cm. Cases **C** were run with particle clouds initially stationary at position 5.5 m. Superscripts *S/T* stand for smooth (Gaussian)/Top-Hat volume fraction distributions, respectively. The drag coefficient was set to 0.41 in all cases except those noted by subscript 0 – for these drag was set to zero. Case **D** is for a dilute cloud to approximate single particle response (density 100 kg/m³, diameter 2 mm). Other specifications and discussion can be found in [▶ Sect. 12.5](#).

■ Table D.3

Specification of the Cloud Dynamics Tests ($\varepsilon = 1 \times 10^{-6}$)

	U_L	U_R
C₀^S	$p_c = 1.0 \times 10^6$ Pa $\alpha_d = \varepsilon$ $u_d = u_c = 0.0$ m/s $T_c = 300.0$ K $T_d = 293.15$ K	$p_c = 1.0 \times 10^5$ Pa $\alpha_{d,\max} = 0.1$ $u_d = u_c = 0.0$ m/s $T_c = 300.0$ K $T_d = 293.15$ K
C^S	$p_c = 1.0 \times 10^6$ Pa $\alpha_d = \varepsilon$ $u_d = u_c = 0.0$ m/s $T_c = 300.0$ K $T_d = 293.15$ K	$p_c = 1.0 \times 10^5$ Pa $\alpha_{d,\max} = 0.1$ $u_d = u_c = 0.0$ m/s $T_c = 300.0$ K $T_d = 293.15$ K
C₀^T	$p_c = 1.0 \times 10^6$ Pa $\alpha_d = \varepsilon$ $u_d = u_c = 0.0$ m/s $T_c = 300.0$ K $T_d = 293.15$ K	$p_c = 1.0 \times 10^5$ Pa $\alpha_{d,\max} = 0.1$ $u_d = u_c = 0.0$ m/s $T_c = 300.0$ K $T_d = 293.15$ K
C^T	$p_c = 1.0 \times 10^6$ Pa $\alpha_d = \varepsilon$ $u_d = u_c = 0.0$ m/s $T_c = 300.0$ K $T_d = 293.15$ K	$p_c = 1.0 \times 10^5$ Pa $\alpha_{d,\max} = 0.1$ $u_d = u_c = 0.0$ m/s $T_c = 300.0$ K $T_d = 293.15$ K
D	$p_c = 2.0 \times 10^5$ Pa $\alpha_d = \varepsilon$ $u_c = 181.55$ m/s $T_c = 385.77$ K	$p_c = 1.0 \times 10^5$ Pa $\alpha_{d,\max} = 0.001$ $u_d = u_c = 0.0$ m/s $T_d = T_c = 293.15$ K

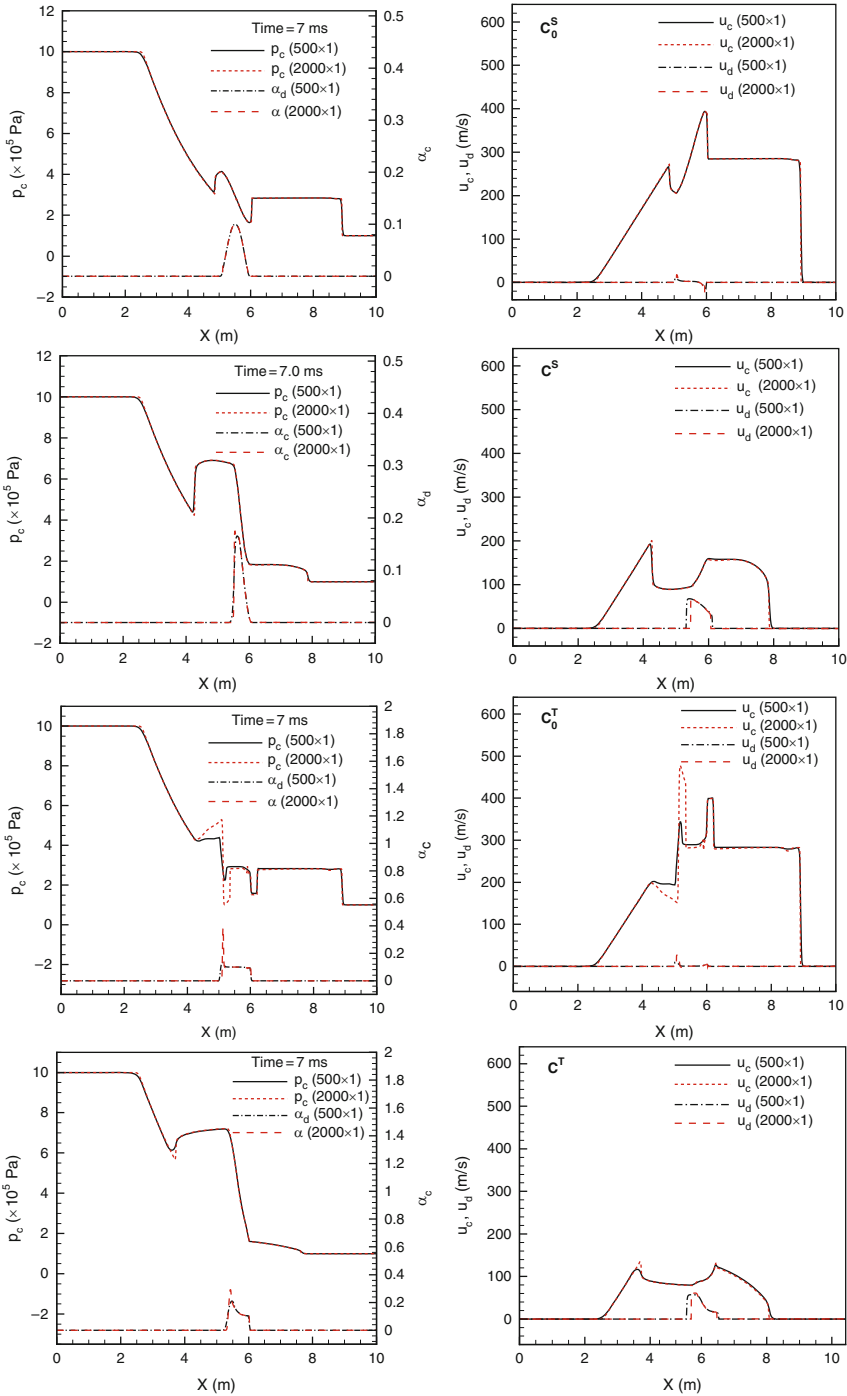
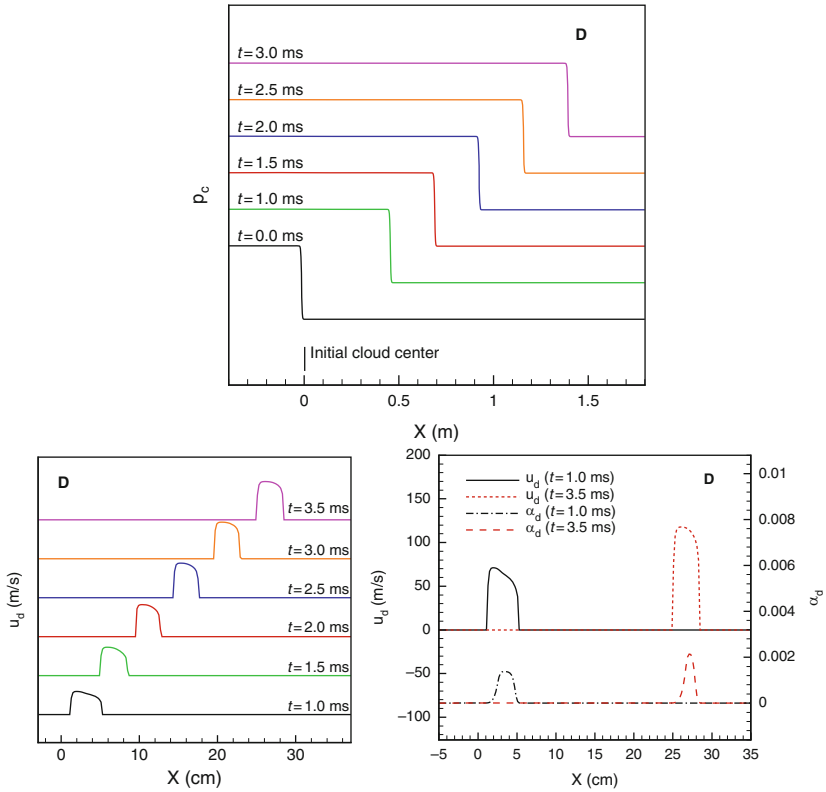


Figure D.3a
 Computational results of Riemann problems defined in Table 3



■ Figure D.3b

Computational results of Riemann problems defined in ► Table 3

References

Part I

- Abgrall R, Saurel R (2003) Discrete equations for physical and numerical compressible multiphase mixtures. *J Comput Phys* 186:361–396
- Baer MR, Nunziato JW (1986) A two-phase mixture theory for the deflagration-to-detonation transition (DDT) in reactive granular materials. *Int J Multiphase Flow* 12:861–889
- Batchelor GK (1970) The stress system in a suspension of force-free particles. *J Fluid Mech* 41:545–570
- Bdzil J, Menikoff R, Son S, Kapila A, Steward D (1999) Two-phase modeling of a deflagration-to-detonation transition in granular materials: a critical examination of modeling issues. *Phys Fluids* 11:378–402
- Bestion D (1990) The physical closure laws in the CATHARE code. *Nucl Eng Design* 124:229–245
- Biesheuvel A, Spoelstra S (1989) The added-mass coefficient of a dispersion of spherical gas bubbles in liquid. *Int J Multiphase Flow* 15:911–924
- Bronshtein IN, Semendyayev KA, Musiol G, Muehlig H (2007) *Handbook of mathematics*, 5th edn. Springer, Berlin
- Bulthuis HF, Prosperetti A, Sangani AS (1995) Particle stress in disperse two-phase potential flow. *J Fluid Mech* 294:1–16
- Buyevich YuA, Shchelchkova IN (1978) Flow of dense suspensions. *Prog Aerospace Sci* 18:121–150
- Doi M, Ohta T (1991) Dynamics and rheology of complex interfaces. *J Chem Phys* 95:1242–1248
- Drew DA, Passman SL (1998) *Theory of multicomponents fluids*. Springer-Verlag, New-York

- Fletcher DF, Theofanous TG (1997) Heat transfer and fluid-dynamics aspects of explosive melt-water interactions. *Adv Heat Transfer* 29:129–156 and 157–213
- Geurst JA (1985) Virtual mass in two-phase bubbly flow. *Physica* 129A:233–261
- Gidaspow D (1974) Modeling of two-phase flow, round table discussions. In *Proceeding of the 5th International Heat Transfer Conference*, Tokyo, Japan
- Hancox WT, Frech RL, Liu WS, Niemann RE (1980) One-dimensional models for transient gas-liquid flows in ducts. *Int J Multiphase Flow* 6: 25–40
- Ishii M, Hibiki T (2006) *Thermo-fluid dynamics of two-phase flow*. Springer, New York
- Jackson R (1997) Locally averaged equations of motion for a mixture of identical spherical particles and a Newtonian fluid. *Chem Engng Sci* 52:2457–2469
- Jones AV, Prosperetti A (1985) On the suitability of first-order differential models for two-phase flow predictions. *Int J Multiphase Flow* 11:133–148
- Kapila AK, Menikoff R, Bdzil JB, Son SF, Stewart DS (2001) Two-phase modeling of deflagration-to-detonation transition in granular materials: reduced equations. *Phys Fluids* 13:3002–3024
- Keller J, Miksis M (1980) Bubble oscillations of large amplitude. *J Acoust Soc Am* 68:628–633
- Lhuillier D (1992) Ensemble averaging in slightly non-uniform suspensions. *Eur J Mech B/Fluids* 11:649–661
- Lhuillier D (2003a) A mean-field description of two-phase flows with phase changes. *Int J Multiphase Flows* 29:511–525
- Lhuillier D (2003) Dynamics of interfaces and rheology of immiscible liquid-liquid mixtures. *CR Mecanique* 331:113–118
- Marble FE (1969) Some gas dynamic problems in the flow of condensing vapors. *Astronaut Acta* 14:585–614
- MATHEMATICA (2008) Wolfram Research, Inc., Version 7.0, Champaign, IL
- Nigmatulin RI (1991) *Dynamics of multiphase media*, vols 1 and 2. Hemisphere Publishing, New York
- Palierne JF (1990) Linear rheology of viscoelastic emulsions with interfacial tension. *Rheol Acta* 29:204–214
- Park JW, Drew DA, Lahey RT (1998) The analysis of void wave propagation in adiabatic monodispersed bubbly two-phase flows using an ensemble averaged two-flow model. *Int J Multiphase Flow* 24:1205–1244
- Prosperetti A, Satrape JV (1990) Stability of two-phase flow models. In: Joseph DD, Schaeffer DG (eds) *Two phase flows and waves*. Springer, pp 98–117
- Prosperetti A, Marchioro M, Tanksley M (1998) Closure of averaged equations for non-uniform disperse flows by direct numerical simulations, presented at ICMF'98, Lyon, France
- Ransom VH, Hicks DL (1984) Hyperbolic two-pressure models for two phase flows. *J Comput Phys* 53:124–151 and 75:498–504 (1988)
- RELAP5/MOD3.3 Code Manual Volume 1: Code structure, system models and solution methods (2001)
- Sangani AS, Didwania AK (1993) Dispersed-phase stress tensor in flows of bubbly liquids at large Reynolds numbers. *J Fluid Mech* 248:27–54
- Stuhmiller JH (1977) The influence of interfacial pressure forces on the character of two-phase flow model equations. *Int J Multiphase Flow* 3:551–560
- Sushchikh S, Chang C-H (2009) Hyperbolicity analysis and numerical stability of a fully compressible effective field model, Internal Report CRSS/UCSB, October 2009
- Theofanous TG, Dinh TN (2003) On the prediction of flow patterns as a principal scientific issue in multifluid flow: contribution to the task group on flow regimes. *Multiphase Sci Technol* 15(1–4):57–76
- Theofanous TG, Hanratty TJ (2003) Appendix 1: report of study group on flow regimes in multifluid flow. *Int J Multiphase Flow* 29(7): 1061–1068
- Theofanous TG, Dinh TN, Tu JP, Dinh AT (2002) The boiling crisis phenomenon Part 1: nucleation and nucleate boiling heat transfer, V.26 (6–7), pp 775–792. Part 2: Dryout dynamics and burnout. *J Exp Thermal Fluid Sci* 26(6–7):793–810
- Theofanous TG, Nourgaliev RR, Dinh TN (2004) Compressible multi-hydrodynamics: emergent needs, approaches and status, IUTAM Symposium Computational Approaches to Disperse Multiphase Flow. ANL Oct. 2004. In: Prosperetti A, Balachandar S (eds) *Computational approaches to disperse multiphase flow*. Springer Verlag, Heidelberg
- Tucker CL, Moldenaers P (2002) Microstructural evolution in polymer blends. *Ann Rev Fluid Mech* 34:177–210
- Wallis GB (1989) Inertial coupling in two-phase flow: macroscopic properties of suspensions in an inviscid fluid. *Multiphase Sci Technol* 5: 239–361
- Wallis GB (1991) The averaged Bernoulli equation and macroscopic equations of motion for the potential flow of a two-phase dispersion. *Int J Multiphase Flow* 17:638–695

- Young JB (1995) The fundamental equations of gas-droplet multiphase flow. *Int J Multiphase Flow* 21:175–191
- Zhang DZ, Prosperetti A (1994) Averaged equations for inviscid disperse two-phase flow. *J Fluid Mech* 267:185–219

Part II

- Amsden AA, Harlow FH (1975) KACHINA: an Eulerian computer program for multifield fluid flows, Tech. rep. la-5680, Scientific Laboratory, Los Alamos
- ANSYS Inc., <http://www.ansys.com/products/fluid-dynamics/cfx>
- Bestion D, Barre F, Faydide B (1999) Methodology, status and plans for development and assessment of CATHARE code, in Proceedings of the International Conference of OECD/CSNI. Annapolis, USA
- Chakravarthy SR, Osher S (1983) High resolution applications of the Osher upwind scheme for the Euler equations, AIAA Paper 83–1943
- Chang C-H, Liou M-S (2003) A new approach to the simulation of compressible multifluid flows with AUSM⁺ scheme, AIAA paper 03–4170
- Chang C-H, Liou M-S (2007) A robust and accurate approach to computing compressible multiphase flow: stratified flow model and AUSM⁺-up scheme. *J Comput Phys* 225:840–873.
- Chang C-H, Liou M-S, Loc N, Sushchikh S, Wilkin L, Theofanous TG (2009) The all regime multiphase simulation (ARMS) code: formulation, numerics, verification and user's manual, ver. 3.0, Report CRSS-09–1, Center for Risk Studies and Safety, University of California, Santa Barbara
- Chang C-H, Deng X, Sushchikh S, Liou M-S, Theofanous TG (2010a) A multi-scale simulation code for compressible multi-hydrodynamics (MuSiC-ARMS): formulation, numerics, verification and user's manual, ver. 1.0, Report CRSS-10–2, Center for Risk Studies and Safety, University of California, Santa Barbara
- Chang C-H, Deng X, Theofanous TG (2010b) Numerical prediction of interfacial instabilities. Part II: the SIM extended to high speed flows. *J Comput Phys* (Submitted)
- Colella P, Glaz HM (1985) Efficient solution algorithm for the Riemann problem for real gases. *J Comput Phys* 59:264–289
- Concentration Heat and Momentum Ltd., <http://www.cham.co.uk>
- Courant R, Issacson E, Rees M (1952) On the solution of nonlinear hyperbolic differential equations by finite differences. *Commun Pure Appl Math* 5:243–255
- Drew DA, Passman SL (1999) Theory of multicomponent fluids, Springer-Verlag, Berlin
- Drew D, Cheng L, Lahey RT (1979) Analysis of virtual mass effects in two-phase flow. *Int J Multiphase Flow* 5:233–242
- Einfeldt B, Munz CC, Roe PL, Sjogreen B (1991) On Godunov-type methods near low densities. *J Comput Phys* 92:273–295
- Fitt AD (1989) The numerical and analytical solution of ill-posed systems of conservation laws. *Appl Math Modelling* 13:618–631
- Fluent Inc. Joins ANSYS Inc, <http://www.fluent.com>
- Geurst JA (1985) Virtual mass in two-phase bubbly flow. *Physica* 129A:233–261
- Gidaspow D (1974) Modeling of two-phase flow, round table discussions, In 5th International Heat Transfer Conference, Tokyo, Japan
- Godunov SK (1959) A difference method for the numerical calculation of discontinuous solutions of hydrodynamic equations. *Mat Sb* 47:271–306
- Hänel D, Schwane R, Seider G (1987) On the accuracy of upwind schemes for the solution of the Navier-Stokes equations, In 8th AIAA CFD Conference AIAA Paper 87–1105-CP
- Hancox W, Ferch R, Liu W, Nieman R (1980) One-dimensional models for transient gas-liquid flows inducts. *Int J Multiphase Flow* 6:25–40
- Harlow FH, Amsden AA (1968) Numerical calculation of almost incompressible flows. *J Comput Phys* 3(80) (LA-DC-9496)
- Harlow FH, Welch JE (1965) Numerical calculation of time-dependent viscous incompressible flow of fluid with free surface, *Phys Fluids* 8: 2182–2189
- Harten A (1983) High resolution schemes for hyperbolic conservation laws. *J Comput Phys* 49:357–393
- Harten A, Hyman JM (1983) Self-adjusting grid methods for one dimensional hyperbolic conservation laws. *J Comput Phys* 50:235–269
- Jameson A (1983) Solution of the Euler equation for two dimensional transonic flow by a multigrid method. *Appl Math Comput* 13:327–355
- Kashiwa BA, Rauenzahn RM (1994) A cell-centered ICE method for multiphase flow simulations, Tech. rep. la-ur-93–3922, Los Alamos National Laboratory
- Kitamura K, Roe P, Ismail F (2007) An evaluation of Euler fluxes for hypersonic flow computations, 18th AIAA Computational Fluid Dynamics Conference, AIAA 2007–4465
- Lax PD (1954) Weak solutions of nonlinear hyperbolic equations and their numerical computation. *Commun Pure Appl Math* 7:159–193

- LeVeque RJ (1990) Numerical Methods for Conservation Laws. Birkhauser Verlag, Basel
- Liou M-S (1996) A sequel to AUSM: AUSM⁺. *J Comput Phys* 129:364–382
- Liou M-S (2006) A sequel to AUSM, Part II: AUSM⁺-up for all speeds. *J Comput Phys* 214: 137–170
- Liou M-S, Edwards JR (1999) AUSM schemes and extensions for low Mach and multiphase flows, Lecture Series 1999–03, Von Karman Institute, Belgium, March 8–12, 1999
- Liou M-S, Steffen CJ (1993) A new flux splitting scheme. *J Comput Phys* 107:23–39
- Liou M-S, van Leer B, Shuen J-S (1990) Splitting of inviscid fluxes for real gases. *J Comput Phys* 87:1–24
- Nourgaliev RR, Theofanous TG (2007) High-fidelity interface tracking in compressible flows: unlimited anchored adaptive level set. *J Comput Phys* 224:836–866
- Nourgaliev RR, Dinh TN, Theofanous TG (2006) Adaptive characteristics-based matching for compressible multifluid dynamics. *J Comput Phys* 213:500–529
- Nourgaliev RR, Liou M-S, Theofanous TG (2008) Numerical prediction of interfacial instabilities. Part I: sharp interface method (SIM). *J Comput Phys* 227:3940–3970
- Osher S, Solomon F (1982) Upwind difference schemes for hyperbolic systems of conservation laws. *Math Comput* 38(158):339–374
- Patankar SV, Spalding DB (1972) A calculation procedure for heat, mass and momentum transfer in three-dimensional parabolic flows. *Int J Heat Mass Transf* 15:1787–1806
- Piltch MM, Yan H, Theofanous TG (1994) The probability of containment failure by direct containment heating in Zion, NUREG/CR-6075, SAND93–1535; also appeared in *Nucl Eng Design* 164:1–36 (1996)
- Prosperetti A (1999) Some consideration on the modeling of disperse multiphase flows by averaged equation, *JSME International Journal. Series B* 42:573–585
- Prosperetti A, Satripe JV (1990) Stability of two-phase flow models. In: Joseph DD, Schaeffer DG (eds) *Two phase flows and waves*, Springer-Verlag
- Ransom VH (1987) Numerical benchmark tests. In: Hewitt GF, Delhay JM, Zuber N (eds) *Multiphase science and technology*, vol 3. Hemisphere Publishing, Washington, DC
- RELAP5-3D Manuals, Idaho National Laboratory (2006), <http://www.inl.gov/relap>
- Rivard W, Torrey M (1977) K-FIX: a computer program for transient, two dimensional, two-fluid flow. Tech. rep, Los Alamos Scientific Laboratory
- Roe PL (1981) Approximate Riemann solvers, parameter vectors, and difference scheme. *J Comput Phys* 43:357–372
- Roe PL (1986) Characteristic-based schemes for the Euler equations. *Ann Rev Fluid Mech* 18:337–365
- SAMRAI: Structured Adaptive Mesh Refinement Application Infrastructure, <http://www.llnl.gov/CASC/SAMRAI>
- Shuen J-S, Liou M-S, van Leer B (1990) Inviscid flux-splitting algorithms for real gases with nonequilibrium chemistry. *J Comput Phys* 90: 371–395
- Smoller J (1983) Shock waves and reaction-diffusion equations. Springer-Verlag, New York
- Steger JL, Warming RW (1981) Flux vector splitting of the inviscid gas dynamic equations with applications to finite-difference methods. *J Comput Phys* 40:263–293
- Stuhmiller JH (1977) The influence of interfacial pressure forces on the character of two-phase flow model equations. *Int J Multiphase Flow* 3:551–560
- Theofanous TG, Dinh TN (2008) Integration of multiphase science and technology with risk management in nuclear power reactors. *Multiphase Sci Technol* 20
- Theofanous TG, Yuen WW, Angelini S (1998a) Pre-mixing of steam explosions: PM-ALPHA verification studies, DOE/ID-10504; also in *Nucl Eng Design* 189:59–102 (1999)
- Theofanous TG, Yuen WW, Freeman K, Chen X (1998b) Escalation and propagation of steam explosions: ESPOSE.m verification studies, DOE/ID-10503; also in *Nucl Eng Design* 189:103–138 (1999)
- Theofanous TG, Yuen WW, Angelini S, Sienicki JJ, Freeman K, Chen X, Salmassi T (1999) Lower head integrity under steam explosion loads. *Nucl Eng Design* 189:7–57
- Theofanous TG, Nourgaliev R, Li G, Dinh TN (2006) Compressible multihydrodynamics(CMH): breakup, mixing and dispersal of liquids/solids in high speed flows. In: Prosperetti A, Balachandrar S (eds) *Computational approaches to disperse multiphase flow*. Springer Verlag, Heidelberg
- Toro EF (1997) Riemann solvers and numerical methods for fluid dynamics: a practical introduction. Springer-Verlag, Heidelberg
- Toumi I, Kumbaro A, Paillere H (1999) Approximate Riemann solvers and flux vector splitting schemes for two-phase flow, VKI Lecture Series 1999–03(von Karman Institute for Fluid Dynamics. Rhode Saint Genese, Belgium

- van Albada GD, van Leer B, Roberts WW (1982) A comparative study of computational methods in cosmic gas dynamics. *Astron Astrophys* 108: 76–84
- van Leer B (1979) Towards the ultimate conservation difference scheme V. A second order sequel to Godunov's method. *J Comput Phys* 32 (1979) 101–136
- van Leer B (1982) Flux vector splitting for the Euler equations. *Lecture Notes Phys* 170: 507–512
- Wada Y, Liou M-S (1997) An accurate and robust flux splitting scheme for shock and contact discontinuities. *SIAM J Sci Stat Comput* 18: 633–657
- Wallis GB (1991) The averaged Bernoulli equation and macroscopic equations of motion for the potential flow of a two-phase dispersion. *Int J Multiphase Flow* 17:638–695
- Yuen WW, Theofanous TG (1999) On the existence of multiphase thermal detonations. *Int J Multiphase Flow* 25:1505–1519

17 Sensitivity and Uncertainty Analysis, Data Assimilation, and Predictive Best-Estimate Model Calibration

Dan Gabriel Cacuci¹ · Mihaela Ionescu-Bujor²

¹Institute for Nuclear Technology and Reactor Safety,
Karlsruher Institut für Technologie, Karlsruhe,
Germany

dan.cacuci@kit.edu

²Fusion Program, Karlsruher Institut für Technologie,
Karlsruhe, Germany
mihaela.ionescu-bujor@kit.edu

1	<i>Introduction</i>	1916
2	<i>Measurement Uncertainties</i>	1926
2.1	Basic Concepts	1926
2.2	Classification of Measurement Errors	1929
2.3	Probabilities and Relative Frequencies: Random and Systematic Errors	1931
2.4	Direct Measurements	1933
2.5	Indirect Measurements: Propagation of Errors	1935
2.6	Glossary.....	1938
3	<i>Statistical Methods for Sensitivity and Uncertainty Analysis</i>	1940
3.1	Reliability Algorithms: FORM and SORM	1941
3.2	Design of Experiments and Screening Design Methods	1942
3.3	Sampling-Based Methods	1945
3.4	Variance-Based Methods	1951
4	<i>Deterministic Computation of Response Sensitivities to Parameters Using Adjoint Operators</i>	1954
4.1	Introduction.....	1954
4.2	Sensitivity Analysis of Nonlinear and Linear Systems with Feedback and Operator-Type Responses	1958
4.2.1	The Forward Sensitivity Analysis Procedure (FSAP).....	1960
4.2.2	Adjoint (Local) Sensitivity Analysis Procedure (ASAP)	1960
4.3	Sensitivity Analysis of Augmented Systems with Feedback	1964
4.3.1	The Forward Sensitivity Analysis Procedure (FSAP).....	1966
4.3.2	The Adjoint Sensitivity Analysis Procedure (ASAP)	1967

4.4	Illustrative Application of ASAP: Adjoint Sensitivity Analysis of Markov Dynamic Reliability Models	1972
4.5	Global Optimization and Sensitivity Analysis.....	1983
4.5.1	Critical Points and Global Optimization.....	1985
4.5.2	Sensitivity Analysis.....	1987
4.5.3	Global Computation of Fixed Points	1989
5	<i>Probability Theory and Uncertainty Information</i>	1994
5.1	Assigning Priors under Incomplete Knowledge: Group Theory and Entropy Maximization.....	1994
5.2	Recommending Nominal Values and Uncertainties: Decision Theory	2001
6	<i>Model Calibration Through Data Assimilation for Best-Estimate Predictions</i>	2002
6.1	Introduction.....	2002
6.2	Mathematical Formalism.....	2003
6.3	Data Consistency and Rejection Criteria	2013
6.4	Illustrative Application to Model Calibration for a Benchmark Blowdown Experiment	2017
7	<i>Model Validation and Calibration: Concluding Remarks and Open Issues</i>	2043
	<i>References</i>	2048

Abstract: In practice, the results of experiments seldom coincide with the computational results obtained from the mathematical models of the respective experiments. Discrepancies between experimental and computational results stem from both experimental and computational uncertainties. Such discrepancies motivate the activities of model verification, validation, and predictive estimation. Following a brief review of the classification and origins of experimental uncertainties, this chapter presents widely used statistical and deterministic methods for computing response sensitivities to model parameters, highlighting, in particular, the novel *adjoint sensitivity analysis procedure (ASAP)* for augmented nonlinear large-scale systems with feedback. The practical use of *ASAP* is illustrated by a large-scale application for analyzing the dynamic reliability of an accelerator system design for the International Fusion Materials Irradiation Facility (IFMIF).

Response sensitivities to parameters and the corresponding uncertainties are the fundamental ingredients for *predictive estimation (PE)*, which aims at providing a probabilistic description of possible future outcomes based on all recognized errors and uncertainties. The key *PE*-activity is *model calibration*, which uses *data adjustment* and *data assimilation* procedures for addressing the integration of experimental data for updating (calibrating or adjusting) parameters in the simulation model. This chapter also presents a state-of-the-art mathematical framework for time-dependent data assimilation and model calibration, using sensitivities and covariance matrices. The basic premise underlying this mathematical framework is that only means and covariance matrices are a priori available, which is the usual situation when analyzing large-scale systems. Under this premise, the maximum entropy principle of statistical mechanics is employed in conjunction with information theory to construct a Gaussian prior distribution that takes all of the available information into account while minimizing (in the sense of quadratic loss) the introduction of spurious information. This prior distribution also comprises correlations among model parameters and responses, thus generalizing the state-of-the-art data assimilation algorithms used in geosciences.

The posterior distribution for the best-estimate calibrated model parameters and responses is constructed by using Bayes' theorem. The best-estimate predicted mean values and reduced covariances, which are customarily needed when employing decision theory under "quadratic loss," are computed by extracting the bulk contributions via the saddle-point method. The minimum value of the quadratic form appearing in the exponent of the Gaussian posterior distribution can be used as an indicator of the agreement between the computed and experimentally measured responses. When all information is consistent, the posterior probability density function yields reduced best-estimate uncertainties for the best-estimate model parameters and responses. This fact is illustrated in this chapter for a time-dependent thermal-hydraulic system that can serve as a benchmark for validating and calibrating thermal-hydraulic codes. The novel features of the data assimilation and model calibration methodology presented in this chapter include: (1) treatment of systems involving correlated parameters and responses; (2) simultaneous calibration of all parameters and responses; and (3) simultaneous calibration over *all* time intervals; this includes the usual two-step time advancement procedures used in geophysical sciences.

Open issues (e.g., explicit treatment of modeling errors, reducing the computational burden, removing the current restriction to Gaussian distributions) are addressed in the concluding section of this chapter. Since predictive "best-estimate" numerical simulation models are essential for designing new technologies and facilities, particularly when the new systems cannot be readily tested experimentally, the only path to progress is to reduce drastically the uncertainties associated with such simulation tools while enlarging the respective validation domains.

1 Introduction

In practice, the results of experiments seldom coincide with the computational results obtained from the mathematical models of the respective experiments. Discrepancies between experimental and computational results are due to both experimental and computational uncertainties. The experimental uncertainties are traditionally classified as *random* and *systematic errors*; both types will be discussed in [Sect. 2](#). Models of complex physical systems are usually subject to *stochastic uncertainties* and *subjective or epistemic uncertainties*. Stochastic uncertainties arise because the system under investigation can behave in many different ways. Subjective or epistemic uncertainties arise from the inability to specify an exact value for a parameter that is assumed to have a constant value in the respective investigation. Epistemic (or subjective) uncertainties characterize a degree of belief regarding the location of the appropriate value of each parameter. In turn, these subjective uncertainties lead to subjective uncertainties of the response, thus reflecting a corresponding degree of belief regarding the location of the appropriate response values as the outcome of analyzing the model under consideration. A typical example of a complex system that involves both stochastic and epistemic uncertainties is a nuclear reactor power plant: in a typical risk analysis of a nuclear power plant, stochastic uncertainty arises due to the *hypothetical* accident scenarios which are considered in the respective risk analysis, while epistemic uncertainties arise because of uncertain parameters that underlie the estimation of the probabilities and consequences of the respective hypothetical accident scenarios.

Discrepancies between experimental and computational results actually provide the basic motivation for performing quantitative model verification, validation, and predictive estimation. *Model verification* is the process of determining that a model implementation accurately represents the developer's conceptual description of the model and the solution to the model; loosely speaking, "verification" means "are you solving the mathematical model correctly?" Model verification comprises two major activities: (1) hierarchical *numerical algorithm verification* (NAV), including numerical error estimation and (2) *software quality assurance* (SQA). Software quality assurance includes static analysis and dynamic testing (including nonregression, black box, and glass box testing). NAV includes testing the respective algorithm against analytic and manufactured solutions, ODE and PDE benchmark solutions, symmetry and conservation tests, and iterative convergence tests. The goal of NAV is to determine the observed (demonstrated) order of accuracy of models, by using a priori and *a posteriori* methods (e.g., Richardson's extrapolation, adaptive grid refinement, grid convergence index). Often the observed accuracy is less than the formal accuracy of the respective numerical method, because of singularities, discontinuities, grid clustering, under-resolved grids, boundary condition effects, non-asymptotic convergence, inadequate iterations, coupling of numerical errors to appearance of new time- and spatial-scales, etc. The responsibility of NAV rests with the code development team.

Model validation is the process of determining the degree to which a model is an accurate representation of the real world from the perspective of the intended uses of the model. In short, "model validation" means "does the model represent reality?" Ideally, model validation involves comparing system responses from multiple realizations of an experiment or multiple experiments with computational results that are characterized by probability distributions. However, model validation needs to be performed not only when strong experimental evidence exists (e.g., in the form of confirmatory mockups) but also for novel designs, when only elementary

experimental evidence may be available. Verification and predictive validation must be based on a well-established set of scientific approaches that will allow the a priori announcement of computational uncertainties with a quantified level of confidence. Model verification and validation can be done only by selected benchmarking, while taking into account systematically, by using sensitivities, all of the uncertainties (computational, experimental, etc) affecting the respective model.

The goal of *predictive estimation (PE)* is to provide a probabilistic description of possible future outcomes based on all recognized errors and uncertainties. Predictive estimation comprises three key elements: model calibration, model extrapolation, and estimation of the validation domain. *Model calibration* addresses the integration of experimental data for the purpose of updating the data of the computer model. Model calibration commences with the identification and characterization of errors or uncertainties from all steps in the sequence of modeling and simulation processes needed for a computational model prediction. This includes (1) data error or uncertainty (input data such as cross sections, model parameters such as reaction-rate coefficients, initial conditions, boundary conditions, and forcing functions such as external loading), (2) numerical discretization error, and (3) uncertainty (e.g., lack of knowledge) in physics processes being modeled. Important components include the estimation of discrepancies in the data and, more importantly, estimation of the biases between model predictions and experimental data. The mathematical framework for model calibration is provided by the *data adjustment and data assimilation* procedures (see, e.g., Cacuci et al. 2010). The state of the art of calibration of models is fairly well developed, but current methods are still hampered in practice by the significant computational effort required, especially for computing sensitivities of responses to parameters in large-scale systems. Methods for reducing the computational effort are of great interest, and methods based on adjoint models (Cacuci 2003; Cacuci et al. 2005) show great promise in this regard.

Model extrapolation addresses the prediction uncertainty in new environments or conditions of interest, including both untested parts of the parameter space and higher levels of system complexity in the validation hierarchy. Extrapolation of models and the resulting increase of uncertainty are poorly understood, particularly the estimation of uncertainty that results from nonlinear coupling of two or more physical phenomena that were not coupled in the existing validation database.

The *estimation of the validation domain* of the physics underlying the models of interest requires estimation of contours of constant uncertainty in the high-dimensional space that characterizes the application of interest. In practice, this involves the identification of areas where the predictive estimation of uncertainty meets specified requirements for the performance, reliability, or safety of the system of interest. The state of the art in the estimation of the validation domain is still in an early stage in both the conceptual and mathematical development. For example, when coupled phenomena occur, in particular for safety analyses, validation is restricted to either mockup or component-level experimental comparison, with little predictive capability.

Developing predictive, experimentally validated, “best-estimate” numerical models is particularly important for designing new technologies and facilities based on novel processes while striving to avoid, as much as possible, the costly and lengthy procedures of building representative mock-up experiments which might confirm – but would not necessarily explain – the predictions of simulation tools. For example, the performance of fuels and materials, in particular fuel irradiation behavior, is dominated by the coupled effects of several phenomena. The

corresponding confirmatory mock-up experiments have traditionally been very expensive and time-consuming (e.g., multiyear irradiations), with little or no predictive capability; improvements in this regard carry a very high potential payoff. Systems-level analysis tools, for example, are used typically for predicting properties of systems to be constructed.

The essential roles played by sensitivities and uncertainties in quantifying the degree of reliability of predicted results can be readily illustrated by considering an example from the field of reactor physics. This field was arguably the first scientific field in which sensitivity and uncertainty analysis, followed by data assimilation and adjustment of parameters (cross sections), was initiated based on mathematically and physically well-founded systematic procedures for benchmarking both nuclear data libraries as well as the corresponding computations. Consider, as an example, the comparisons (Mosteller 2007) of experimental and computational results for several critical assemblies reproduced in the Table 1.

In Table 1, the names of the various assemblies are listed in the first column; the *experimentally measured* multiplication factors, k_{eE} , of the respective assemblies are listed in the second column; the *computed* multiplication factors, $(k_{eff})_c$, obtained by using the Monte Carlo Code MCNP are given in columns three, four, five, and six, corresponding, respectively, to the widely used cross section libraries ENDF/B-VII.0, ENDF/B-VI, JEFF-3.1, and JENDL-3.3.

To begin with, note that the experimental results of an experiment devised to measure a physical parameter x are reported in the form “ $x = \mu \pm \sigma$.” The computational results are listed in a similar form. The conventional interpretation of such statements is that “ μ is the most probable value of the parameter x ,” and “ σ is the standard deviation” characterizing the range of uncertainty for the true but unknown exact value of x . More precisely, the implication of the statement “ $x = \mu \pm \sigma$ ” is that, if the measurement of x were to be repeated (on the same experimental facility), the *a priori* probability of a result within the range dx at any value x would be given by the Gaussian (or normal) distribution

$$P(x) dx = \frac{1}{\sqrt{2\pi\sigma^2}} \exp\left[-1/2\left(\frac{x-\mu}{\sigma}\right)^2\right] dx. \quad (1)$$

■ Table 1
MCNPS results for criticality safety validation set

Benchmark Assembly	Measured Benchmark k_{eE}	Calculated $(k_{eff})_c$			
		ENDF/B-VII.0	ENDF/B-VI	JEFF-3.1	JENDL-3.3
Jezebel-233	1.000 ± 0.0010	0.9996 ± 0.0003	0.9926 ± 0.0003	1.0038 ± 0.0003	1.0041 ± 0.0003
Flattop-23	1.000 ± 0.0014	0.9996 ± 0.0003	1.0003 ± 0.0003	1.0062 ± 0.0003	0.9985 ± 0.0003
U233-MF-05 (2)	1.000 ± 0.0030	0.9926 ± 0.0003	0.9972 ± 0.0003	1.0004 ± 0.0003	1.0019 ± 0.0003
Falstaff (1)	1.000 ± 0.0083	0.9845 ± 0.0005	0.9895 ± 0.0005	0.9841 ± 0.0005	0.9879 ± 0.0005
SB - 2 ¹ / ₂	1.000 ± 0.0024	1.0038 ± 0.0004	0.9964 ± 0.0004	0.9971 ± 0.0004	0.9979 ± 0.0005
ORNL-11	1.006 ± 0.0029	1.0015 ± 0.0002	0.9974 ± 0.0002	0.9975 ± 0.0002	0.9989 ± 0.0002
Godiva	1.000 ± 0.0010	1.0000 ± 0.0003	0.9963 ± 0.0003	0.9965 ± 0.0003	1.0033 ± 0.0003

It is important to note that even though the actual value of the physical parameter x is not known, that value is not random but fixed (at a definite but unknown value). To emphasize this fact, variables (such as x) associated with a distribution are commonly referred to as *variates*, rather than random variables. More formally, it may be argued that it is more sensible to consider the probabilities of the statement that *the value of x is μ* is correct for different values of μ . In practice, experimental facilities are never “ideal measuring instruments”; hence, when measurements are repeated, the resulting values are never absolutely identical. Rather, the measured values follow a pattern, that is, they manifest a distribution. Furthermore, most distributions arising in practice are sufficiently narrow to be approximated by a normal (Gaussian) distribution. Thus, any experimental facility designed to measure a parameter x may be considered to function as a generator of random numbers drawn from the normal distribution of mean μ and standard deviation σ . In this sense, it is justified to treat a possible result of a measurement as a random variable and the actual experimental data as a sample drawn from a distribution. Informally, standard deviations are often referred to as “uncertainties.” The meaning of statements about measurements and their properties (e.g., “accuracy,” “uncertainties”) will be discussed in [▶ Sect. 2](#), in the sequel.

If x is a variate, then $\delta x \equiv x - \mu$ is also a variate, with mean $\langle \delta x \rangle = 0$. The *variance* (the standard deviation squared) of x is, by definition, the mean of the square of δx , that is, $\text{var}(x) = \langle (\delta x)^2 \rangle$. The sum (and difference) $x = x_1 \pm x_2$ of two variates x_1 and x_2 is also a variate. Since $\delta x = \delta x_1 \pm \delta x_2$, it follows that

$$\text{var}(x) = \langle (\delta x_1 \pm \delta x_2)^2 \rangle = \langle (\delta x_1)^2 \rangle \pm 2 \langle \delta x_1 \delta x_2 \rangle + \langle (\delta x_2)^2 \rangle. \quad (2)$$

The cross term $\langle \delta x_1 \delta x_2 \rangle$ is called the *covariance* of x_1 and x_2 ; it vanishes if the variates x_1 and x_2 vary independently of each other. Note that the reciprocal statement (i.e., the statement “if $\text{cov}(x_1, x_2) = 0$ then x_1 and x_2 are independent of each other”) is not necessarily true. A note of caution: there is no generally accepted notation to distinguish between absolute and relative variances and covariances; therefore, the use of absolute or relative variances and covariances must be inferred from the context.

Comparing, for each assembly, the experimental results (shown in the first column of the above table) with the computational results indicates that they do not coincide; in most cases, both the respective “means” (also called “nominal values”) and uncertainties (i.e., standard deviations) quoted for the effective multiplication factors differ from the corresponding computational results. Moreover, the very small “uncertainties,” of the order of $O(10^{-4})$, quoted for the computational results seem to indicate that the computations are somehow *inconsistent* with the measurements. Is this truly the case?

The computed results represent the Monte Carlo solution of the steady-state neutron transport equation, which, for the purposes of this discussion, can be written in the form

$$\Omega \cdot \nabla \psi + \Sigma \psi = \frac{1}{k_{\text{eff}}} S_f [\psi] + S_s [\psi]. \quad (3)$$

In the above equation, ψ denotes the neutron angular flux; $\Omega \cdot \nabla \psi$ denotes the streaming operator accounting for the rate of change of the neutron angular flux along the streaming path in the direction of particle motion Ω ; the term $\Sigma \psi$ accounts for the rate at which neutrons are lost due to collisions of any kind with the nuclei comprising the medium; the term $S_s [\psi]$ denotes the “fission source” accounting for the rate at which neutrons are born in the

medium due to fissions; and the term $S_f[\psi]$ denotes the scattering source accounting for the rate at which neutrons are produced as a result of particle interactions with nuclei other than interactions leading to fissions. For the critical assemblies listed in the above table, the boundary conditions customarily used for the computation of the neutron angular flux ψ are the so-called “free-surface” or “vacuum” boundary conditions, which stipulate that neutrons leaving the external surface of the assembly will not reenter it. Although such boundary conditions represent a mathematical idealization, they are sufficiently representative of physical reality if the neutrons have a negligible probability of returning. Since both the neutron transport equation and the free-surface boundary conditions are homogeneous in ψ , it follows that (3) must be solved as an *eigenvalue problem* to determine the angular neutron flux ψ . For the specific form displayed in (3), the eigenvalue of the neutron transport equation is the so-called “effective neutron multiplication factor,” k_{eff} . “Criticality” is attained, by definition, when $k_{eff} = 1$, exactly.

Uncertainties in computational results arise from several distinct causes, most often stemming from:

1. The adequacy or inadequacy of the mathematical equations to model the actual phenomenon, which may give rise to modeling uncertainties;
2. The numerical methods use to solve the model’s equation, which also give rise to modeling uncertainties;
3. The data and parameters in a model (e.g., cross sections), which give rise to parameter uncertainties.

Other sources of uncertainties may occur in nonlinear models, but these sources are not relevant to the present discussion, since the neutron transport equation is linear in the flux ψ . Since the neutron transport equation is known to model the physical phenomena occurring in the benchmark assemblies to an extremely high degree of accuracy (i.e., up to the omission of neutron–neutron collisions), it follows that the uncertainties in $(k_{eff})_c$ can only stem from the numerical method used to solve the transport equation and from uncertainties in the cross section that enter as parameters in the respective computation. In the present case, the geometrical modeling of the various assemblies is also extremely accurate, so uncertainties due to geometrical modeling can also be neglected.

To quantify the uncertainties that could stem from cross section uncertainties, it is convenient to rearrange (3) in the form

$$\Omega \cdot \nabla \psi + \Sigma \psi = \frac{1}{\gamma} \{S_s[\psi] + S_f[\psi]\}.$$

The eigenvalue γ of the above homogeneous equation can be written explicitly in the form $\gamma = c P(\Sigma R)$, where $P(\Sigma R)$ denotes the average next-collision probability, and

$$c \equiv \frac{\bar{\nu} \sigma_f + 2\sigma_{n,2n} + 3\sigma_{n,3n} + \cdots + \sigma_s}{\sigma_{tot}}, \quad (4)$$

where $\bar{\nu}$ denotes the average number of neutrons emitted per fission, σ_f denotes the fission cross section, σ_s denotes the scattering cross section, $\sigma_{n,2n}$, $\sigma_{n,3n}$, \dots denote the neutron multiplication cross sections; σ_a denotes the absorption cross section; and $\sigma_{tot} = \sigma_a + \sigma_s + \sigma_f + \sigma_{n,2n} + \dots$ denotes the total cross section. The order-of-magnitude uncertainties in c can be assessed, step by step, by commencing, for example, with the contribution from the fission neutrons, $\bar{\nu} \sigma_f$. As

(4) indicates, the relative uncertainty in c must be proportional to the relative uncertainty in the fission cross section, that is,

$$\frac{\delta c}{c} \sim \frac{\delta \sigma_f}{\sigma_f} \rightarrow \text{var}(c) \sim \text{var}(\sigma_f). \quad (5)$$

Examining various cross section libraries (e.g., ENDF/B-VII.0, ENDF/B-VI, JEFF-3.1, and JENDL-3.3, available from the OECD/NEA Data Bank) reveals that the relative standard deviation in the fission cross section of ^{235}U is of the order of 2%. This implies that $\delta c/c \sim \delta \sigma_f/\sigma_f \sim O(10^{-2})$.

The next step in this qualitative reasoning is to note that c is proportional not only to σ_f but also to $\bar{\nu}$; hence, a more accurate estimate of the relative uncertainty $\delta c/c$ is

$$\frac{\delta c}{c} \simeq \frac{\delta \bar{\nu}}{\bar{\nu}} + \frac{\delta \sigma_f}{\sigma_f} \rightarrow \text{var}(c) \simeq \text{var}(\bar{\nu}) + \text{var}(\sigma_f), \quad (6)$$

since σ_f and $\bar{\nu}$ are uncorrelated. Since the relative standard deviation in $\bar{\nu}$ for ^{235}U is ca. 6%, it follows that the relative standard deviation in c for GODIVA would be approximately $\sqrt{(0.02^2 + 0.06^2)} = 0.063$, which is greater than the uncertainty in either σ_f or $\bar{\nu}$. This result confirms the expectation that the more uncorrelated variates are considered as contributing to the final uncertainty in a result, the larger the resulting uncertainty in the respective result.

A further step for improving the estimation of the uncertainty in c can be taken by considering also the uncertainty in the absorption cross section. Ignoring (for simplicity) the relative uncertainties contributed by the other cross sections to the relative uncertainty in σ_t , it follows from (4) that

$$\frac{\delta c}{c} \simeq \frac{\delta \bar{\nu}}{\bar{\nu}} + \frac{\delta \sigma_f}{\sigma_f} - \frac{\delta \sigma_a}{\sigma_a}. \quad (7)$$

since σ_a and σ_f are correlated to each other but $\bar{\nu}$ is independent of the various cross sections, it follows from (7) that

$$\text{var}(c) \simeq \text{var}(\bar{\nu}) + \text{var}(\sigma_f) + \text{var}(\sigma_a) - 2 \text{cov}(\sigma_f, \sigma_a). \quad (8)$$

Neglecting, once again, the relative uncertainty in the capture cross section σ_c , one readily obtains the relations

$$\text{var}(\sigma_a) = (\sigma_f/\sigma_a)^2 \text{var}(\sigma_f) \quad (9)$$

and

$$\text{cov}(\sigma_f, \sigma_a) = (\sigma_f/\sigma_a) \text{var}(\sigma_f). \quad (10)$$

Introducing (9) and (10) into (8) reduces the latter relation to

$$\text{var}(c) \simeq \text{var}(\bar{\nu}) + (1 - \sigma_f/\sigma_a)^2 \text{var}(\sigma_f). \quad (11)$$

Relations (5), (6), and (11) illustrate the effect of adding information to the dependence of c on various parameters. Thus, relations (5) and (6) indicate that $\text{var}(c)$ increases when adding

increasingly more *independent* variates (on which c depends). On the other hand, relation (11) shows that when *correlated* (i.e., mutually dependent) variates are introduced, the total uncertainty, $\text{var}(c)$, could either increase or decrease, which underscores the fact that covariances play a significant role, and disregarding them can lead to erroneous results. As will be detailed in Sect. 2, most quantities of interest are not measured directly, but are inferred, in so-called *indirect measurements*, by means of mathematical relations involving quantities measured directly. In other words, the parameters of interest are certain combinations of the actually measured quantities. Therefore, when determining the uncertainties in the values of the parameters of interest, it is essential to take into account both the variances of the directly measured quantities, as well as the possible correlations between each pair of these directly measured quantities. Hence, caution must be exercised if results for indirectly measured quantities omit reporting correlations among the measured parameters, since if such correlations are disregarded, then even the reported resulting variances may be incorrect. The usefulness of such incomplete experimental data would be seriously limited for subsequent uses, since (for example) any computations using such incomplete data could not correctly determine the uncertainties in the respective computations.

The foregoing assessment of the relative uncertainties contributed by nuclear data indicates that these are of the order of $O(10^{-2})$. Comparing this order-of-magnitude with the uncertainties quoted in Table 1 for the experimentally measured multiplication factors, k_{eE} , which are of the order of $O(10^{-3})$, or with the uncertainties quoted for the “calculated multiplication factor,” $(k_{eff})_c$, which are of the order of $O(10^{-4})$, the following conclusions become apparent:

1. The quoted uncertainty of $O(10^{-4})$ for the “calculated multiplication factor,” $(k_{eff})_c$, must have originated solely from the convergence of the numerical Monte Carlo method;
2. The accuracy of the Monte Carlo numerical method is considerably higher than the accuracy of the corresponding measurements;
3. The uncertainties due to the nuclear data are a factor of 10 larger than the experimental uncertainties, and a factor of 10^2 larger than the convergence accuracy of the Monte Carlo method;
4. The uncertainties due to the nuclear data, which enter as parameters in the Monte Carlo computations, must have not been accounted for in the uncertainties quoted for the computational results in the above table;
5. The Monte Carlo method is sufficiently accurate for the purposes of these benchmark computations, so that the uncertainties due to the “numerical methods” can be neglected in subsequent discussion of these results;
6. The computations are not necessarily inconsistent with the corresponding measurements;
7. The nuclear data in the libraries could perhaps be improved by judiciously taking into account some, if not all, of experimentally measured results, since the experimental uncertainties are considerably smaller than the uncertainties to be expected when propagating the cross-section uncertainties through the neutronics computations.

In practice, the uncertainty arising in the computed effective multiplication factor $(k_{eff})_c$ due to uncertainties in the nuclear data is *not* determined in the simple-minded way used above for illustrating the role and order-of-magnitude played by cross section uncertainties. As indicated by (3), $(k_{eff})_c$ is numerically determined as the (largest) eigenvalue of the neutron transport equation. In mathematical terminology, $(k_{eff})_c$ is an implicit *functional* of the neutron flux which, in turn, depends on various partial cross sections of the isotopes contained in the

respective critical assembly. In turn, these cross sections are functions of the neutron energy. Formally, the functional dependence of $(k_{eff})_c$ can be written in the form $(k_{eff})_c = k_{eff}(\boldsymbol{\alpha})$, where the subscript c (denoting “computed”) has been dropped to simplify the notation, and where $\boldsymbol{\alpha} = (\alpha_1, \dots, \alpha_N)$, denotes the N -component vector of *system parameters* (cross sections, number densities, etc.) that characterize the problem under consideration. Expanding $k_{eff}(p)$ in a Taylor series around the nominal parameter values (i.e., around the nominal values for the various cross sections) and retaining only the first-order terms yield the expression

$$\delta k_{eff} = \sum_{n=1}^N (\partial k_{eff} / \partial \alpha_n)^0 \delta \alpha_n, \quad \delta \alpha_n \equiv \alpha_n - \alpha_n^0. \quad (12)$$

The partial derivatives $s_n \equiv (\partial k_{eff} / \partial \alpha_n)^0$, where the superscript “zero” denotes that the respective quantity is evaluated at nominal parameter values, are called the *sensitivities* of $k_{eff}(\boldsymbol{\alpha})$ to (each of) the parameters α_n .

Denoting the covariance matrix of the parameters $\boldsymbol{\alpha}$ by $\mathbf{C}_\alpha \equiv \langle \delta \boldsymbol{\alpha} \delta \boldsymbol{\alpha}^T \rangle$, denoting by $\mathbf{S} \equiv \{(\partial k_{eff} / \partial \alpha_1)^0, \dots, (\partial k_{eff} / \partial \alpha_N)^0\}$ the N -component vector of sensitivities, and integrating formally the square of (12) over the (unknown) joint probability distribution of all system parameters leads to the following expression for $\text{var}(k_{eff})$:

$$\text{var}(k_{eff}) = \langle (\delta k_{eff})^2 \rangle = \mathbf{S} \langle \delta \boldsymbol{\alpha} \delta \boldsymbol{\alpha}^T \rangle \mathbf{S}^T = \mathbf{S} \mathbf{C}_\alpha \mathbf{S}^T. \quad (13)$$

The superscript “ T ” in (13) denotes “transposition,” a notation that will be used throughout this chapter. The relation (13) is colloquially known as the “*sandwich rule*” for propagating parameter uncertainties, and will also be derived in [► Sect. 2](#). The “sandwich rule” clearly highlights the fundamental role – as weighting functions – played by the sensitivities of the response of interest to the system’s parameters in determining the total uncertainty in the response (i.e., result) of interest. Hence, the accurate determination of these sensitivities is essential for computing the response uncertainties. In principle, the sensitivities could be estimated by recomputations using slightly perturbed parameter values in conjunction with the finite-difference approximation

$$s_n \equiv (\partial k_{eff} / \partial \alpha_n)^0 \simeq [k_{eff}(\alpha_1^0, \dots, \alpha_{n-1}^0, \alpha_n^0 + \delta \alpha_n, \alpha_{n+1}^0, \dots, \alpha_N^0) - k_{eff}(\boldsymbol{\alpha}^0)] / \delta \alpha_n. \quad (14)$$

However, for large-scale problems involving many [$N \sim O(10^2)$ or more] parameters, the finite-difference approximation in (14) is neither practical (since it would require unrealistic computational resources) nor sufficiently accurate. There are, in principle, two classes of methods for computing sensitivities, namely *statistical methods*, which will be reviewed in [► Sect. 3](#), and *deterministic methods*, particularly the very efficient ASAP, which will be reviewed in [► Sect. 4](#). Notably, a global optimization and sensitivity analysis algorithm, which determines with probability one of the systems’ critical points (maxima, minima, or bifurcations) is presented in [► Sect. 4.5](#).

As can be surmised from the discussion thus far, the following types of information can be obtained in practice: (1) a mathematical simulation model for the physical problem at hand, relating the model parameters $\boldsymbol{\alpha}$, with nominal values (i.e., “means”) $\boldsymbol{\alpha}^0$ and covariances \mathbf{C}_α ,

to the computed responses, $\mathbf{r}(\boldsymbol{\alpha})$; (2) relevant experiments for obtaining, in addition, “experimentally measured” responses, with mean values \mathbf{r}_m and experimentally measured covariance matrices \mathbf{C}_m . In many cases, (some of) the measured responses may not be independent of, but could be correlated to (some of) the parameters; such correlations are generally characterized by symmetric response-parameter covariance matrices $\mathbf{C}_{r\alpha} = \mathbf{C}_{\alpha r}$. The goal is to use all of the available information, that is, the input parameters (occasionally called also the “differential” data), the measured responses (occasionally called the “integral” data), including their respective uncertainties (covariance matrices), and the computed responses and their sensitivities to parameters, to obtain “best-estimate” adjusted (calibrated) values $\boldsymbol{\alpha}^{be}$ for the parameters, and the corresponding “best-estimate” adjusted (calibrated) values \mathbf{r}^{be} for the responses. The optimal combination of such information falls within the scope of *data assimilation and adjustment (calibration) procedures*, and the end products of these procedures are *best-estimate values for parameters and responses, as well as reduced uncertainties (i.e., “smaller” values for the variance-covariance matrices) for the best-estimate adjusted parameters and responses*.

Included within the scope of data assimilation and best-estimate adjustment procedures is also the important subject of *consistency* among experiments and computations. Thus, whenever experimental results are compared with corresponding computations or with independently measured similar results, the essential issue is to quantify the extent to which the respective sets of data agree with each other. Often, “reasonable agreement” is claimed on grounds of vague arguments and impressions, without substantial objective justifications. Consistency, however, must be indicated by a well-defined quantitative parameter which precisely determines the degree of agreement (or disagreement). Such a consistency indicator must reflect the underlying uncertainties and sensitivities, and also certain probability distributions. Unless all of the computations and experiments considered are reasonably consistent, the data assimilation and best-estimate adjustment (calibration) will yield questionable, if not altogether meaningless, end results.

As will be discussed in [► Sect. 5](#), the concept of prior probability distribution can be used to characterize the existing knowledge (or degree of belief) regarding each system parameter. The experiments and/or observations of the system responses provide additional knowledge about the system. The additional information introduced by drawing inferences from the observational data should improve the knowledge about the system. Combining *new information with prior knowledge* is customarily called “*data assimilation*.” Modern data assimilation is performed using *Bayesian inference* techniques. Furthermore, *the added knowledge, contained in the posterior probability density function, should lead to a reduction of uncertainties in both the responses and the system parameters, via the “best-estimate” adjustment procedure*.

The procedures for data assimilation and best-estimate adjustment of parameters are presented in [► Sect. 6](#). Under the assumptions discussed in [► Sect. 5](#), the Bayesian inference procedure leads to best-estimate adjusted (calibrated) parameter and responses, with reduced uncertainties, having the following expressions:

$$\boldsymbol{\alpha}^{be} = \boldsymbol{\alpha}^0 + (\mathbf{C}_{\alpha r} - \mathbf{C}_{\alpha} \mathbf{S}^T) \mathbf{C}_d^{-1} \mathbf{d}, \quad \mathbf{d} \equiv \mathbf{r}(\boldsymbol{\alpha}^0) - \mathbf{r}_m, \quad (15)$$

$$\mathbf{r}^{be} = \mathbf{r}_m + (\mathbf{C}_m - \mathbf{C}_{r\alpha} \mathbf{S}^T) \mathbf{C}_d^{-1} \mathbf{d}, \quad (16)$$

where $\mathbf{d} \equiv \mathbf{r}(\boldsymbol{\alpha}^0) - \mathbf{r}_m$ represents the vector of “deviations” between the computed and experimentally measured responses. Furthermore, the data assimilation and adjustment procedure

also yields best-estimate adjusted covariance matrices for the best-estimate adjusted parameter and responses, as follows:

$$\mathbf{C}_\alpha^{be} = \mathbf{C}_\alpha - \left(\mathbf{C}_{\alpha r} - \mathbf{C}_\alpha \mathbf{S}^T \right) \mathbf{C}_d^{-1} \left(\mathbf{C}_{r\alpha} - \mathbf{S} \mathbf{C}_\alpha \right), \quad (17)$$

$$\mathbf{C}_r^{be} = \mathbf{C}_m - \left(\mathbf{C}_m - \mathbf{C}_{r\alpha} \mathbf{S}^T \right) \mathbf{C}_d^{-1} \left(\mathbf{C}_m - \mathbf{S} \mathbf{C}_{\alpha r} \right), \quad (18)$$

$$\mathbf{C}_{\alpha r}^{be} = \mathbf{C}_{\alpha r} - \left(\mathbf{C}_{\alpha r} - \mathbf{C}_\alpha \mathbf{S}^T \right) \mathbf{C}_d^{-1} \left(\mathbf{C}_m - \mathbf{S} \mathbf{C}_{\alpha r} \right), \quad (19)$$

where

$$\mathbf{C}_d \equiv \left\langle \mathbf{d} \mathbf{d}^T \right\rangle = \mathbf{S} \mathbf{C}_\alpha \mathbf{S}^T - \mathbf{S} \mathbf{C}_{\alpha r} - \mathbf{C}_{r\alpha} \mathbf{S}^T + \mathbf{C}_m. \quad (20)$$

As indicated by the relations (17–19), the best estimate adjusted uncertainties are smaller than the original ones, since, in each case, one subtracts a positive definite matrix from the corresponding original covariance matrix. It will be shown in [Sect. 6](#) that the quantity $\chi^2 = \mathbf{d}^T \mathbf{C}_d^{-1} \mathbf{d}$ provides an overall *consistency indicator*. This quantity is actually the “chi-square” for the distribution of the M parameters (M may be equal to or less than the number of model parameters N) included in the adjustment. If $\chi^2/M \approx 1$, then the data sets in the adjustment are consistent; otherwise, particularly if $\chi^2/M \gg 1$, the respective data is inconsistent and must be rejected. Other useful “rejection gauges” are the individual “deviations” d_i , the “individual chi-square” indicator $\chi_{dia}^2 = d_i^2 (\mathbf{C}_{d_{ii}})^{-1}$, the “diagonal chi-square” indicator $\chi_{dia}^2 = d_i^2 (\mathbf{C}_d^{-1})_{ii}$, and various iterative schemes.

The implications of relations (17–19) can be readily examined for the simplest case, involving: (1) one parameter α , with nominally measured value α^0 and uncertainty $C_\alpha = \sigma_\alpha^2$; and (2) one experimentally measured response r , with the nominally measured value r_m and uncertainty $C_m = \sigma_m^2$, which is also correlated to α through the parameter-response correlation “matrix” $C_{\alpha r} = C_{r\alpha} = \rho \sigma_\alpha \sigma_m$, where $\rho \in [-1, 1]$ is the respective correlation factor. Consider that the nominal value of the computed result is r_c ; hence, the deviation between the computed and measured responses is simply $d \equiv (r_c - r_m)$. Note that the Greek letter σ is used in this example to denote “standard deviations” rather than “microscopic cross sections.”

For this simple case (i.e., one parameter and one measured response), the relation (20) reduces to

$$C_d = S^2 \sigma_\alpha^2 - 2S \rho \sigma_\alpha \sigma_m + \sigma_m^2, \quad (21)$$

where S is the sensitivity of the computed response to the parameter α . In this simple case, the matrix-valued expressions in (15–19) are reduced, respectively, to the following algebraic expressions:

$$\alpha^{be} = \alpha^0 + (\rho \sigma_m - \sigma_\alpha S) \sigma_\alpha C_d^{-1} d, \quad (22)$$


$$r^{be} = r_m + (\sigma_m - \rho \sigma_\alpha S) \sigma_m C_d^{-1} d, \quad (23)$$

$$\left(\sigma_\alpha^{be} \right)^2 = (1 - \rho^2) \sigma_\alpha^2 \sigma_m^2 C_d^{-1}, \quad (24)$$

$$\left(\sigma_r^{be} \right)^2 = S^2 \left(\sigma_\alpha^{be} \right)^2 = S^2 (1 - \rho^2) \sigma_\alpha^2 \sigma_m^2 C_d^{-1}, \quad (25)$$

$$\rho^{be} = 1. \quad (26)$$

If the response-parameter correlation were unknown, its effect on the adjusted (calibrated) best-estimate values can be quantified by considering ρ to vary within the interval $[-1, 1]$, and determining the value of ρ that is least favorable for the resulting best-estimate values. The worst-case value for ρ would maximize the value of the best-estimate calibrated uncertainty $(\sigma_r^{be})^2$. Such a worst-case adjustment would occur for that value of ρ which would cause the first-derivative of $(\sigma_r^{be})^2$, with respect to ρ , to vanish in the interval $[-1, 1]$. Taking the first derivative with respect to ρ in (25) and setting it to zero yields $\sigma_m - \rho\sigma_\alpha S = 0$; using this result in relations (22–25) leads to the following best-estimate calibrated values: $\alpha^{be} = \alpha^0 - (r_c - r_m)/S$, $(\sigma_\alpha^{be})^2 = \sigma_m^2/S^2$, $r^{be} = r_m$, and $(\sigma_r^{be})^2 = \sigma_m^2$.

Since the uncertainty in the experimentally measured response is usually less than the uncertainty in the computed response (i.e., $\sigma_m < S\sigma_\alpha$), it follows that $\sigma_\alpha^{be} < \sigma_\alpha$, which indicates that the best-estimate uncertainty for the best-estimate adjusted parameter is *reduced* (i.e., becomes smaller) even when the adjustment is made using a single consistently measured response. In addition, the best-estimate adjusted uncertainty for the best-estimate adjusted response, that is, σ_r^{be} is also reduced (in the worst-case, it is reduced to the value of σ_m). This simple example illustrates two of the most important points regarding data assimilation and best-estimate adjustment, in general: (1) the assimilation of consistent experimental data reduces uncertainties in the resulting best-estimate adjusted parameters and responses; and (2) even when the correlations between parameters and responses are neglected because they might be unknown, the assimilation and adjustment procedure is still worthwhile. Thus, consistent data assimilation and best-estimate adjustment is expected not only to improve agreement between calculation and measurement, but is also specifically expected to reduce uncertainties in calculated responses. To summarize: any additional consistent information reduces uncertainties. When relatively accurate experimental data is used, this reduction is very significant, indeed. In essence, all efforts should be aimed at using all available data to the fullest, ultimately generating the best possible “libraries,” comprising best-estimate parameter values for subsequent, predictive computations. Open issues and important avenues for further research aimed at alleviating the current shortcomings of data assimilation and best-estimate calibration procedures are presented in  Sect. 7.

2 Measurement Uncertainties

2.1 Basic Concepts

The theory of measurement errors is a branch of metrology – the science of measurements. A *measurable quantity* is a property of phenomena, bodies, or substances that can be defined qualitatively and expressed quantitatively. Measurable quantities are also called *physical quantities*. A *measurement* is the process of finding the value of a physical quantity experimentally with the help of special devices called *measuring instruments*. The *result of a measurement* is a numerical value, together with a corresponding unit, for a physical quantity. Note that a measurement has three features:

1. The result of a measurement must always be a number expressed in sanctioned units of measurements. The purpose of a measurement is to represent a property of an object by a number;

2. A measurement is always performed with the help of some measuring instrument; measurement is impossible without measuring instruments;
3. A measurement is always an experimental procedure.

The *true value* of a measurable quantity is the value of the measured physical quantity, which, if it were known, would ideally reflect, both qualitatively and quantitatively, the corresponding property of the object. The theory of measurement relies on the following postulates:

1. The true value of the measurable quantity exists;
2. The true value of the measurable quantity is constant (relative to the conditions of the measurement); and
3. The true value cannot be found.

Since measuring instruments are imperfect, and since every measurement is an experimental procedure, the results of measurements cannot be absolutely accurate. This unavoidable imperfection of measurements is generally expressed as measurement inaccuracy, and is quantitatively characterized by measurement errors. Thus, the result of any measurement always contains an error, which is reflected by the deviation of the result of measurement from the true value of the measurable quantity. The measurement error can be expressed in absolute or relative form.

The *absolute measurement error*, δ , of an indication instrument is defined as the difference between the true value of the measured quantity, Q_t , and the measured value indicated by the instrument, Q_m , i.e., $\delta \equiv Q_t - Q_m$. The absolute error is a physical quantity that has the same units as the measurable quantity. Furthermore, the absolute error may be positive, negative, or be expressed as an interval that contains the measured value. The absolute error should not be confused with the absolute value of the (absolute) error; while the former may be positive or negative, the latter is always positive. Since absolute errors have units and depend, in general, on the value of the measured quantity, they are awkward to use as a quantitative characteristic of measurement accuracy. In practice, therefore, the error is usually expressed as a fraction (usually percent or per thousand) of the true value of the measurable quantity, by using the *relative measurement error*, ε , defined as $\varepsilon \equiv \delta/Q_t$.

Knowledge of measurement errors would allow statements about measurement accuracy, which is the most important quality of a measurement: the smaller the underlying measurement errors, the more accurate the respective measurement. The accuracy of a measurement can be characterized quantitatively by the inverse of the absolute value of relative error; for example, if the relative error of a measurement is $\pm 0.2\%$, then the accuracy of this measurement is 500. The accuracy of any particular measurement is determined not only by the accuracy of the measuring instruments employed, but also by the method of measurement employed and by the skill of the experimenter. However, since the true value of a measurable quantity is always unknown, the errors of measurements must be estimated theoretically, by computations, using a variety of methods, each with its own degree of accuracy.

Occasionally, measurement errors can be estimated before performing the actual measurement. Such measurements are called measurements with ante-measurement or *a priori estimation* of errors. On the other hand, measurements whose errors are estimated after the measurement are called measurements with post-measurement or *a posteriori estimation* of errors. When a physical quantity is measured repeatedly, the measuring instrument will not yield identical indications; rather, the indications will differ from one another, in a random manner. This random component of instrument error is referred to as the *repeatability* error

of a measuring instrument. For example, instruments with moving parts have repeatability errors caused by friction in support of the movable parts and by hysteresis phenomena. The length of the range of possible values of the random component of instrument error is called the *dead band*. In other words, the dead band is the maximum interval through which a stimulus may be changed in either direction without producing a change in the response of the measuring instrument. Since instruments are constructed in order to introduce regular relations and certainty into the phenomena under consideration, it is important to reduce the random errors of instruments to levels that are either negligibly small compared with other errors or are within prescribed limits of admissible errors for the respective type of measuring devices.

The properties of measuring instruments may change in time (e.g., because of component aging and environmental influences). Such time-dependent changes in any property of the measuring instrument are characterized by the instrument's instability and drift. Instrument instability can be standardized either by prescribing the value of the limits of permissible variations of the error over a definite period of time or by prescribing different error limits to different "lifetimes" of the instrument, after it is calibrated. On the other hand, the drift of an instrument is defined as the change (always in the same direction) that may occur in the output signal over a period of time that is significantly longer than the measurement time. The drift and instability of an instrument do not depend on the input signal but they can depend on external conditions. For this reason, the drift is usually determined in the absence of an input signal.

Measuring instruments are also characterized by their sensitivity, discrimination threshold, and resolution. Thus, the *sensitivity of an instrument* is defined as the ratio of the variation in the measured quantity at the output of the measuring instrument to variation of the input value of the quantity that causes the output value to change. The *discrimination threshold* is defined as the minimum variation in the input signal that causes an appreciable variation in the output signal. Finally, the *resolution of an instrument* is the smallest interval between two distinguishable neighboring discrete values of the output signal.

Measurements are customarily categorized as direct, indirect, and combined measurements. In *direct measurements*, the quantity to be measured interacts directly with the measuring instrument, and the value of the measured quantity is read from the instrument's indications. In *indirect measurements*, the value of the physical quantity is found by using a known dependence between the quantity and its basic properties which are themselves measured by means of direct, indirect, or combined measurements. For example, the density of a homogeneous solid body is inferred from an indirect measurement, which would consist of three steps: the first two steps would involve measuring directly the body's mass and volume, respectively, while the third step would involve taking the ratio of the measurements obtained in the first two steps.

Measurements performed with single observations are called *single measurements*, while measurements performed with repeated observations are called *multiple measurements*. Customarily, an indirect measurement is regarded as a single measurement if the value of each of the components of the indirectly measured quantity is found as a result of a single measurement. Thus, the indirect measurement of the density of a solid body (performed as mentioned in the previous example) would be considered a single measurement. Combined measurements can also be regarded as single measurements, if the number of measurements is equal to the number of unknowns, so that each unknown is determined uniquely from the system of equations obtained after performing the respective measurements.

2.2 Classification of Measurement Errors

As has been previously mentioned, the absolute measurement error $\delta \equiv Q_t - Q_m$ is defined as the difference between the true value, Q_t , of the quantity being measured and the measured value, Q_m , indicated by the instrument. This equation cannot be used directly to find the error of a measurement, however, since the true value of the measurable quantity is always unknown. (If the true value were known, then there would be no need for a measurement, of course.) Therefore, measurement errors must be estimated by using indirect data. For this purpose, measurement errors are traditionally classified according to their sources and their properties.

The basic sources of measurement errors are: errors arising from the method of measurement, errors due to the measuring instrument, and personal errors committed by the person performing the experiment. These errors are considered to be additive, so that the general form for the absolute measurement error δ is $\delta = \delta_m + \delta_i + \delta_p$, here δ_m , δ_i , and δ_p represent, respectively, the methodological error, the instrumental error, and the personal error. *Methodological errors* are caused by unavoidable discrepancies between the actual quantity to be measured and its model used in the measurement. Most commonly, such discrepancies arise from inadequate theoretical knowledge of the phenomena on which the measurement is based, and also from inaccurate and/or incomplete relations employed to find an estimate of the measurable quantity. *Instrumental measurement errors* are caused by imperfections of measuring instruments. The individual characteristics of the person performing the measurement may give rise to *personal errors*.

If the results of separate measurements of the same quantity differ from one another, and the respective differences cannot be predicted individually, then the error stemming from this scatter of the results is called *random error*. Random errors can be identified by repeatedly measuring the same quantity under the same conditions. On the other hand, a measurement error that remains constant or changes in a regular fashion when the measurements of that quantity are repeated is called a *systematic error*. Systematic errors can be discovered experimentally either by using a more accurate measuring instrument or by comparing a given result with a measurement of the same quantity, but performed by a different method. In addition, systematic errors are estimated by theoretical analysis of the measurement conditions, based on the known properties of the measuring instruments and the quantity being measured. Although the estimated systematic error can be reduced by introducing corrections, it is impossible to eliminate completely systematic errors from experiments. Ultimately, a residual error will always remain, and this residual error will then constitute the systematic component of the measurement error.

The quality of measurements that reflects the closeness of the results of measurements of the same quantity performed under the same conditions is called the *repeatability of measurements*. Good repeatability indicates that the random errors are small. On the other hand, the quality of measurements that reflects the closeness of the results of measurements of the same quantity performed under different conditions, that is, in different laboratories, at different locations, and/or using different equipment, is called the *reproducibility of measurements*. Good reproducibility indicates that both the random and systematic errors are small.

It is also customary to distinguish between gross or outlying errors and blunders. An error is *gross* or *outlying*, if it significantly exceeds the error justifiable by the conditions of the measurements, the properties of the measuring instrument employed, the method of measurement, and the qualification of the experimenter. For example, if the grid voltage affects the measurements

under consideration, then a sharp brief change in the grid voltage can produce an outlying error in a single experiment. Outlying errors in multiple measurements can be discovered by statistical methods and are usually eliminated from the final error analysis. On the other hand, *blunders* occur as a result of errors made by the experimenter. Examples of blunders are a slip of the pen when writing up the results of observations, an incorrect reading of the indications of an instrument, and so on. Blunders must be discovered by nonstatistical methods, and they must always be eliminated from the final results.

As has already been mentioned, a measurement error cannot be found directly by using its definition as an algorithm, since the true value of the measured quantity is unknown. The measurement error must be found by identifying its underlying sources and reasons, and by performing calculations based on the estimates of all components of the respective measurement inaccuracy. The smallest of the measurement errors are customarily referred to as *elementary errors* (of a measurement), and are defined as those components of the overall measurement error that are associated with a single source of inaccuracy for the respective measurement. The total measurement error is calculated, in turn, by using the estimates of the component elementary errors. Since a measurement error can only be calculated indirectly, based on models and experimental data, it is important to identify and classify the underlying elementary errors. This identification and classification is subsequently used to develop mathematical models for the respective elementary errors. Finally, the resulting (overall) measurement error is obtained by synthesizing the mathematical models of the underlying elementary errors. Even though it is sometimes possible to correct, partially, certain elementary errors (e.g., systematic ones), no amount or combination of corrections can produce an absolutely accurate measurement result; there always remains a residual error. In particular, the corrections themselves cannot be absolutely accurate, and, even after they are implemented, there remain residuals of the corresponding errors which cannot be eliminated and which later assume the role of elementary errors.

In the course of developing mathematical models for elementary errors, it has become customary to distinguish four types of elementary errors, namely, absolutely constant errors, conditionally constant errors, purely random errors, and quasi-random errors. Thus, *absolutely constant errors* are defined as elementary errors that remain the same (i.e., are constant) in repeated measurements performed under the same conditions, for all measuring instruments of the same type. For example, an absolutely constant error arises from inaccuracies in the formula used to determine the quantity being measured, once the limits of the respective inaccuracies have been established. Typical situations of this kind arise in indirect measurements of quantities determined by linearized or truncated simplifications of nonlinear formulas (e.g., analog/digital instruments where the effects of electro-motive forces are linearized). Based on their properties, *absolutely constant elementary errors are purely systematic errors*, since each such error has a constant value in every measurement, but this constant is nevertheless unknown. Only the limits of these errors are known. Therefore, *absolutely constant errors are modeled mathematically by a determinate (as opposed to random) quantity whose magnitude lies within an interval of known limits*.

Conditionally constant errors are, by definition, elementary errors that have definite limits (just like the absolutely constant errors) but (as opposed to the absolutely constant errors) such errors can vary within their limits due both to the nonrepeatability and the nonreproducibility of the results. A typical example of such an error is the measurement error due to the intrinsic error of the measuring instrument, which can vary randomly between fixed limits. Usually, *the conditionally constant error is mathematically modeled by a random quantity with a uniform*

probability distribution within prescribed limits. This mathematical model is chosen because the uniform distribution has the highest uncertainty (in the sense of information theory) among distributions with fixed limits. Note, in this regard, that the round-off error also has known limits, and this error has traditionally been regarded in mathematics as a random quantity with a uniform probability distribution.

Purely random errors appear in measurements due to noise or other random errors produced by the measuring device. The form of the distribution function for random errors can, in principle, be found using data from each multiple measurement. In practice, however, the number of measurements performed in each experiment is insufficient for determining the actual form of the distribution function. Therefore, *a purely random error is usually modeled mathematically by using a normal distribution characterized by a standard deviation that is computed from the experimental data.*

Quasi-random errors occur when measuring a quantity defined as the average of nonrandom quantities that differ from one another such that their aggregate behavior can be regarded as a collection of random quantities. In contrast to the case of purely random errors, though, the parameters of the probability distribution for quasi-random errors cannot be unequivocally determined from experimental data. Therefore, *a quasi-random error is modeled by a probability distribution with parameters (e.g., standard deviation) determined by expert opinion.*

Measurements must be reproducible; otherwise they lose their objective character and become useless. As has been discussed in the foregoing, the limits imposed by errors represent a measure of the irreproducibility of the respective measurement. It is therefore very important to strive to minimize measurement errors, which implies that they should be estimated as accurately as possible. The smaller the relative error, ε , of a given experiment, the more accurate (and, in this sense, the better) the measurement.

2.3 Probabilities and Relative Frequencies: Random and Systematic Errors

Although probabilities are not relative frequencies, the two concepts are certainly related. This relationship can be highlighted by considering n measurements of some quantity x , with discrete possible outcomes (such as faces of a die or channels of an analogue-to-digital converter). Thus, consider that the measurements (trials) are labeled $k = (1, 2, \dots, n)$, the observable outcomes x_v are labeled $\mu_l (R)$, ($l = 1, \dots, 4$), and the result of the k th trial is denoted by $R(\alpha_1, \dots, \alpha_k)$. Furthermore, the probabilities $\mu_k(\alpha_i)$, ($i = 1, \dots, k; k = 1, \dots, 4$) for all N^n possible outcomes of n trials are given and properly normalized such that $(\alpha_1, \dots, \alpha_k)$.

The relative frequency with which the result v occurs within the sequence $\{v_1, \dots, v_n\}$ can be written with the Kronecker δ symbol as $f_v = (1/n) \sum_{k=1}^n \delta_{vv_k}$.

Without any frequency data, inferences must be based on the given probabilities; consequently f_v can only be estimated from its expected value

$$\langle f_v \rangle = \frac{1}{n} \sum_{k=1}^n \left[\sum_{v_1} \dots \sum_{v_n} P(v_1, \dots, v_n) \delta_{vv_k} \right] \equiv \frac{1}{n} \sum_{k=1}^n P(kv)$$

and its uncertainty (covariance matrix)

$$\langle f_{\mu} f_{\nu} \rangle = \frac{1}{n^2} \sum_{j=1}^n \sum_{k=1}^n \left[\sum_{\nu_1} \cdots \sum_{\nu_n} P(\nu_1, \dots, \nu_n) \delta_{\mu\nu_j} \delta_{\nu\nu_k} \right] \equiv \frac{1}{n^2} \sum_{j=1}^n \sum_{k=1}^n P(j\mu, k\nu),$$

where $P(k\nu)$ is the probability that the k th trial yields ν , and $P(j\mu, k\nu)$ is the joint probability that the j th trial yields μ and the k th trial yields ν . Thus, although relative frequencies are not probabilities, their expectation values can be calculated from probabilities as will be shown next. The special case $j = k$ describes one and the same measurement; hence, μ cannot differ from ν , implying that $P(k\mu, k\nu) = \delta_{\mu\nu} P(k\nu)$. The (co)variances of the estimated frequencies can therefore be written in the form

$$m \langle f_{\mu} f_{\nu} \rangle - \langle f_{\mu} \rangle \langle f_{\nu} \rangle = \frac{1}{n} (\delta_{\mu\nu} P_{\nu} - P_{\mu} P_{\nu}) + \left(1 - \frac{1}{n}\right) (P_{\mu\nu} - P_{\mu} P_{\nu}),$$

where $P_{\nu} \equiv (1/n) \sum_j P(j\nu)$ denotes the probability of observing the value x_{ν} in some unspecified single trial, and $P_{\mu\nu} \equiv (1/n(n-1)) \sum_j \sum_{k \neq j} P(j\mu, k\nu)$ denotes the probability of observing the values x_{μ} and x_{ν} in some unspecified pair of distinct trials, with $\sum_{\nu} P_{\nu} = 1$ and $\sum_{\mu, \nu} P_{\mu\nu} = 1$.

Note that the variances do not vanish in the limit of very many trials ("good statistics," $n \rightarrow \infty$) unless $P_{\nu\nu} = P_{\nu}^2$. The central limit theorem is valid only for completely independent, equivalent trials. For correlated trials, $P_{\mu\nu} \neq P_{\mu} P_{\nu}$, the variances cannot become smaller than $P_{\nu\nu} - P_{\nu}^2$ even for arbitrarily good statistics. This means that any correlation poses an irreducible limit on the accuracy with which frequencies can be predicted from probabilities. Note also that for uncorrelated measurements (i.e., when $P_{\mu\nu} = P_{\mu} P_{\nu}$), the relative frequencies are anticorrelated, since $\text{cov}(f_{\mu}, f_{\nu}) = -P_{\mu} P_{\nu} / n$ (unless $n \rightarrow \infty$). This is, of course, a consequence of the normalization condition: if one frequency varies in a certain sense, the others must be varied in the opposite sense in order to keep their normalized sum unaffected, $\sum_{\nu} f_{\nu} = 1$. The foregoing considerations underscore the fact that probabilities are not frequencies, but they enable us to predict frequencies and to assess the accuracy of the predictions.

To apply the relationship between frequencies and probabilities to a measured quantity x , consider that each measurement yields one of the N possible values x_{ν} (discretized by the electronics, for example, and differing from the true value because of errors). The sample mean $\bar{x} \equiv \sum_{\nu} f_{\nu} x_{\nu}$ is computed from observed frequencies f_{ν} for the values x_{ν} . Without additional observations, the expectation value of \bar{x} and the corresponding uncertainty $\langle \bar{x}^2 \rangle$ are given by $\langle \bar{x} \rangle = \sum_{\nu} \langle f_{\nu} \rangle x_{\nu}$ and $\langle \bar{x}^2 \rangle = \sum_{\mu, \nu} \langle f_{\mu} f_{\nu} \rangle x_{\mu} x_{\nu}$, respectively. Using the previously obtained expressions for $\langle f_{\nu} \rangle$ and $\langle f_{\mu} f_{\nu} \rangle$ leads to the following expressions for the estimated mean $\langle \bar{x} \rangle$ and variance $\text{var}(\bar{x})$:

$$\langle \bar{x} \rangle = \langle x \rangle, \text{var}(\bar{x}) \equiv \langle \bar{x}^2 \rangle - \langle \bar{x} \rangle^2 = \frac{1}{n} (\langle x^2 \rangle - \langle x \rangle^2) + \left(1 - \frac{1}{n}\right) (\langle x, x \rangle - \langle x \rangle^2),$$

where $\langle x \rangle = \sum_{\nu} P_{\nu} x_{\nu}$ and $\langle x^2 \rangle = \sum_{\nu} P_{\nu} x_{\nu}^2$ are expectation values for a single unspecified measurement, whereas $\langle x, x \rangle = \sum_{\mu, \nu} P_{\mu\nu} x_{\mu} x_{\nu}$ arises from an unspecified pair of distinct, possibly correlated measurements. Thus, the variance of the sample average is the sum of two contributions, one from uncorrelated (statistical) errors of single measurements and the other one

from correlated (systematic) errors of pairs of measurements. Correlations are usually due to common errors such as errors in standards, detector calibration, electronic settings, and so forth. The foregoing derivation shows that the total error is obtained (correctly) by adding the statistical and the systematic (root-mean-square) errors (in quadrature).

In the special case when all n measurements are equivalent (“exchangeable measurements” in statistical jargon), the probabilities $P(k\nu)$, $P(j\mu, k\nu)$ must be the same for all trials and all pairs of trials: $P(k\nu) = P_\nu$, $P(j\mu, k\nu) = P_{\mu\nu}$ for $j \neq k$. When the various measurements are completely uncorrelated (which implies that all common and/or systematic errors are excluded), the relation $P_{\mu\nu} = P_\mu P_\nu$ holds, and therefore $\text{var } \bar{x} = (1/n) \text{var } x \rightarrow 0$, for $n \rightarrow \infty$. Thus, *for independent measurements, better statistics means more accuracy.*

On the other hand, if all measurements are fully correlated, all errors being common or systematic, the result x_ν of the first trial implies the same result for all following trials; this implies, in turn, that $P_{\mu\nu} = \delta_{\mu\nu} P_\nu$, leading to the result $\text{var } \bar{x} = \text{var } x$, for all n . In this case, *repetition of the measurement does not help at all. The uncertainty after any number of trials remains the same as it was after the first trial, because the unknown errors are always the same.*

In practice, both independent and correlated errors are usually present. The correlated errors constitute a “residual core” of uncertainty that remains undiminished no matter how often the measurement is repeated. The only way to reduce this residual error is to remeasure the quantity of interest by means of other techniques, with different instrumentation, geometry, perhaps even staff, in order to obtain systematic errors as different and as independent as possible from those of the other measurements. Eventually, the effect of several remeasurements with different techniques on the overall (systematic) uncertainty will be similar to the effect that a comparable number of repetitions with the same technique has on the uncorrelated (statistical) uncertainty.

2.4 Direct Measurements

When measuring a quantity *directly*, it is useful to distinguish between single and multiple measurements of the respective quantity. The *single direct measurement* is regarded as the basic form of measurement while *multiple direct measurements* can be regarded as being derived from single measurements. A priori, the error for a single measurement can be both systematic and random; however, after the measurement has been performed, the measurement error becomes a systematic error for that measurement. This is because the result of a measurement has a definite numerical value, and the difference between the measurement result and the true value of the measured quantity is a constant. Even if the entire error in a measurement were random, the error seemingly freezes after the measurement result is obtained; thus, the error loses its random character and becomes systematic. Each of the three components of the measurement, namely, the method of measurement, the measuring instrument, and the experimenter can be sources of systematic errors. Correspondingly, methodological, instrumental, and personal systematic errors are customarily distinguished from each other.

A systematic error that remains constant and is therefore repeated in each observation or measurement is called a *constant systematic error*; for example, such an error will be present in measurements performed using balances, resistors, or similar instruments. The personal errors made by experienced experimenters can also be classified as constant (personal errors made by inexperienced experimenters, however, are considered random). Errors which increase (or

decrease) throughout the measurement time are called *progressing errors*. Errors that vary with a definite period are called *periodic errors*.

It is very difficult to identify systematic errors; for example, variable systematic errors can be identified by using statistical methods, correlation, and regression analysis. Systematic errors can also be identified by measuring the same quantity using two different instruments (methods) or by measuring periodically a known (instead of an unknown) quantity. If a systematic error has been identified, then it can usually be estimated and eliminated. However, making rational estimates of the magnitude of the residual systematic errors and, in particular, assigning consistent levels of confidence to these residual errors is an extremely difficult task. In practice, therefore, *residual systematic errors are assumed to follow a continuous uniform distribution, within ranges that are conservatively estimated based on experience and expert judgment.*

Multiple direct measurements are usually needed for measuring the average value of some parameter; for reducing the effects of random errors associated with the measuring instruments; for investigating a new phenomenon (to determine relationships between the quantities characterizing the respective phenomenon and connections to other physical quantities); and for developing new measuring instruments. Under certain restrictions on the measurement data, the methods of mathematical statistics provide means for analyzing observations and estimating measurement errors from multiple measurements. Thus, direct multiple measurements that are free of systematic errors (i.e., in which only random errors occur) can be analyzed by statistical methods directly, without additional considerations. In many practical situations, though, the mathematical restrictions required by mathematical statistics are not entirely fulfilled; hence, it is often necessary to develop practical methods for analyzing such situations individually, case by case.

When the *random character of the observational results is caused by measurement errors, the respective observations are assumed to have a normal distribution.* This assumption rests on two premises, namely: (1) since measurement errors consist of many components, the central limit theorem implies a normal distribution for such errors; and (2) measurements are performed under controlled conditions, so that the distribution function of their error is actually bounded. Hence, approximating a bounded distribution by a normal distribution (for which the random quantity can take any real value) is a conservative procedure since such an approximation leads to larger confidence intervals than would be obtained if the true bounded distribution were known. Nevertheless, the hypothesis that the distribution of the observations is normal must be verified, since the measured results do not always correspond to a normal distribution. For example, *when the measured quantity is an average value, the distribution of the observations can have any form.*

In general, both the systematic and random components of the error must be estimated. Although repeating the measurements yields information about the random components of the error, information about the systematic component cannot be extracted from the measurements themselves. Hence, the systematic errors are estimated from information about the properties of the measuring instruments employed, the method of measurement, and the conditions under which the measurements are performed. Although the random error can only be estimated *a posteriori*, the systematic error can also be estimated *a priori*. Note that the random components of all conditionally constant errors become *a posteriori* part of the random error of the respective measurement. Thus, the remaining parts of conditionally constant errors in multiple measurements become purely systematic errors. However, the values of these errors can vary in repeated measurements of the same quantity, even if the measurements are performed by the same method.

2.5 Indirect Measurements: Propagation of Errors

An *indirect measurement* is a measurement in which the value of the unknown quantity is calculated by using matched measurements of other quantities, called measured arguments or (briefly) *arguments*, which are related through a known relation to the measured quantity. From the perspective of conducting a measurement, the indirect measurements can also be divided into two classes, namely, *single indirect measurements* (in which all arguments are measured once only) and *multiple indirect measurements* (in which all arguments are measured several times).

In an indirect measurement, the *true but unknown value of the measured quantity* or *response*, denoted by R , is related to the *true but unknown values of arguments*, denoted as $(\alpha_1, \dots, \alpha_k)$, by a *known relationship* (i.e., *function*) f . This relationship is called the *measurement equation*, and can be generally represented in the form

$$R = f(\alpha_1, \dots, \alpha_k). \quad (27)$$

The specific forms of measurement equations can be considered as mathematical models of specific indirect measurements. It is very important to note here that the measurement equation can be interpreted to represent not only results of indirect measurements but also *results of computations*. In this interpretation, $(\alpha_1, \dots, \alpha_k)$ are considered to be the parameters underlying the respective computation, R is considered to represent the result or response of the computation, while f represents not only the explicit relationships between parameters and response but also represents implicitly the relationships among the parameters and the independent and dependent variables comprising the respective mathematical model.

In practice, the *nominal parameter values*, $(\alpha_1^0, \dots, \alpha_k^0)$, are known together with their *uncertainties* or *errors*, $(\delta\alpha_1, \dots, \delta\alpha_k)$. The nominal parameter values are given by their respective *expectations*, while the associated errors and/or uncertainties are given by their respective *standard deviations*. Processing the experimental data obtained in an indirect measurement is performed with the same objectives as for direct measurements, namely, to calculate the expected value, $E(R)$, of the measured response R , and to calculate the error and/or uncertainty, including confidence intervals, associated with $E(R)$. Calculating the expected value, $E(R)$, of the measured and/or calculated response R , and calculating the various higher-order moments of the distribution of R (variances and covariances, skewness, kurtosis), together with confidence intervals associated with $E(R)$, are the objectives of a procedure called the method of *propagation of moments* or *propagation of errors*, which will be presented in the sequel.

As indicated by the measurement equation, the measured (or calculated) system response R (i.e., the result of an indirect measurement or the result of a calculation) is considered to be a real-valued function of k system parameters, denoted as $(\alpha_1, \dots, \alpha_k)$; without loss of generality, these parameters can be considered to be real scalars. As discussed in the previous section, the *true values* of the parameters $(\alpha_1, \dots, \alpha_k)$ are *not* known; only their *nominal values*, $(\alpha_1^0, \dots, \alpha_k^0)$, and corresponding *uncertainties* or *errors*, $(\delta\alpha_1, \dots, \delta\alpha_k)$, are known. Usually, the nominal parameter values are taken to be the expected parameter values, while the associated errors and/or uncertainties are given by their respective standard deviations. The relative uncertainties $\delta\alpha_i/\alpha_i^0$ are usually symmetrical around α_i^0 , and smaller than unity. Therefore, the measurement equation (or computational model) can be written in the form

$$R = R(\alpha_1, \dots, \alpha_k) = R(\alpha_1^0 + \delta\alpha_1, \dots, \alpha_k^0 + \delta\alpha_k). \quad (28)$$

In the functional relation above, R is used in the dual role of both a (random) function and the numerical realization of this function. Expanding $R(\alpha_1^0 + \delta\alpha_1, \dots, \alpha_k^0 + \delta\alpha_k)$ in a Taylor series around the nominal values $\alpha^0 = (\alpha_1^0, \dots, \alpha_k^0)$ and retaining the terms up to the n th order in the variations $\delta\alpha_i \equiv (\alpha_i - \alpha_i^0)$ around α_i^0 gives:

$$\begin{aligned}
 R(\alpha_1, \dots, \alpha_k) &\equiv R(\alpha_1^0 + \delta\alpha_1, \dots, \alpha_k^0 + \delta\alpha_k) \\
 &= R(\alpha^0) + \sum_{i=1}^k \left(\frac{\partial R}{\partial \alpha_i} \right)_{\alpha^0} \delta\alpha_i + \frac{1}{2} \sum_{i_1, i_2=1}^k \left(\frac{\partial^2 R}{\partial \alpha_{i_1} \partial \alpha_{i_2}} \right)_{\alpha^0} \delta\alpha_{i_1} \delta\alpha_{i_2} \\
 &\quad + \frac{1}{3!} \sum_{i_1, i_2, i_3=1}^k \left(\frac{\partial^3 R}{\partial \alpha_{i_1} \partial \alpha_{i_2} \partial \alpha_{i_3}} \right)_{\alpha^0} \delta\alpha_{i_1} \delta\alpha_{i_2} \delta\alpha_{i_3} + \dots \\
 &\quad + \frac{1}{n!} \sum_{i_1, i_2, \dots, i_n=1}^k \left(\frac{\partial^n R}{\partial \alpha_{i_1} \partial \alpha_{i_2} \dots \partial \alpha_{i_n}} \right)_{\alpha^0} \delta\alpha_{i_1} \dots \delta\alpha_{i_n} + \dots.
 \end{aligned} \tag{29}$$

Using the above Taylor-series expansion, the various moments of the random variable $R(\alpha_1, \dots, \alpha_k)$, namely, its mean, variance, skewness, and kurtosis, are calculated by considering that the system parameters $(\alpha_1, \dots, \alpha_k)$ are random variables distributed according to a joint (albeit unknown) probability density function $p(\alpha_1, \dots, \alpha_k)$. The parameters' means (expectation values), variances, and covariances are as follows:

$$E(\alpha_i) = \alpha_i^0, \tag{30}$$

$$\text{var}(\alpha_i, \alpha_i) \equiv \sigma_i^2 \equiv \int_{S_\alpha} (\alpha_i - \alpha_i^0)^2 p(\alpha_1, \dots, \alpha_k) d\alpha_1 d\alpha_2 \dots d\alpha_k, \tag{31}$$

$$\text{cov}(\alpha_i, \alpha_j) \equiv \int_{S_\alpha} (\alpha_i - \alpha_i^0)(\alpha_j - \alpha_j^0) p(\alpha_1, \dots, \alpha_k) d\alpha_1 d\alpha_2 \dots d\alpha_k. \tag{32}$$

The procedure outlined above is called the *method of propagation of errors* or *propagation of moments*, and the resulting equations for the various moments of $R(\alpha_1, \dots, \alpha_k)$ are called the *moment propagation equations*.

For large complex systems, with many parameters, it is often impractical to consider the nonlinear terms in the Taylor expansion of the response. In such cases, response $R(\alpha_1, \dots, \alpha_k)$ is taken to be a *linear function of the parameters* $(\alpha_1, \dots, \alpha_k)$, that is,

$$R(\alpha_1, \dots, \alpha_k) = R(\alpha^0) + \sum_{i=1}^k \left(\frac{\partial R}{\partial \alpha_i} \right)_{\alpha^0} \delta\alpha_i = R^0 + \sum_{i=1}^k S_i \delta\alpha_i, \tag{33}$$

where $R^0 \equiv R(\alpha^0)$, while $S_i \equiv (\partial R / \partial \alpha_i)_{\alpha^0}$ denotes the *sensitivity of the response* $R(\alpha_1, \dots, \alpha_k)$ to the parameter α_i . The *mean value* of $R(\alpha_1, \dots, \alpha_k)$ is obtained from (33) as

$$\begin{aligned}
 E(R) &\equiv \int_{S_\alpha} \left(\sum_{i=1}^k S_i \delta\alpha_i \right) p(\alpha_1, \dots, \alpha_k) d\alpha_1 d\alpha_2 \dots d\alpha_k + R^0 \\
 &= \sum_{i=1}^k S_i \int_{S_\alpha} (\alpha_i - \alpha_i^0) p(\alpha_1, \dots, \alpha_k) d\alpha_1 d\alpha_2 \dots d\alpha_k + R^0 \\
 &= R^0.
 \end{aligned} \tag{34}$$

The various moments of $R(\alpha_1, \dots, \alpha_k)$ can be calculated by using (33) and (34); thus, the l th central moment $\mu_l(R)$ of $R(\alpha_1, \dots, \alpha_k)$ is obtained as the following k -fold integral over the domain S_α of the parameters α :

$$\mu_l(R) \equiv E\left((R - E(R))^l\right) = \int_{S_\alpha} \left(\sum_{i=1}^k S_i \delta \alpha_i\right)^l p(\alpha_1, \dots, \alpha_k) d\alpha_1 d\alpha_2 \dots d\alpha_k. \quad (35)$$

The variance of $R(\alpha_1, \dots, \alpha_k)$ is calculated by setting $l = 2$ in (35) and by using the result obtained (34), as follows:

$$\begin{aligned} \mu_2(R) \equiv \text{var}(R) &\equiv E\left((R - R^0)^2\right) \\ &= \sum_{i=1}^k S_i^2 \text{var}(\alpha_i) + 2 \sum_{i \neq j=1}^k S_i S_j \text{cov}(\alpha_i, \alpha_j) \\ &= S V_\alpha S^T, \end{aligned} \quad (36)$$

where the superscript “ T ” denotes transposition, the column vector $\mathbf{S} = (S_1, \dots, S_k)$, with components $S_i = (\partial R / \partial \alpha_i)_{\alpha^0}$, denotes the *sensitivity vector*, and V_α denotes the *covariance matrix* for the parameters $(\alpha_1, \dots, \alpha_k)$, with elements defined as

$$(V_\alpha)_{ij} = \begin{cases} \text{cov}(\alpha_i, \alpha_j) = \rho_{ij} \sigma_i \sigma_j, & i \neq j, \\ \text{var}(\alpha_i) = \sigma_i^2, & i = j. \end{cases} \quad \rho_{ij} \equiv \text{correlation coefficient}$$

The last line in the relation (36) is colloquially known as the *sandwich rule*. If the system parameters are uncorrelated, the relation (27) takes on the simpler form

$$\text{var}(R) = \sum_{i=1}^k S_i^2 \text{var}(\alpha_i) = \sum_{i=1}^k S_i^2 \sigma_i^2. \quad (37)$$

The above concepts can be readily extended from a single response to n responses that are functions of the parameters $(\alpha_1, \dots, \alpha_k)$. In vector notation, the n responses are represented as the column vector $\mathbf{R} = (R_1, \dots, R_n)$. In this case, the vector-form equivalent of relation (33) is the following linear, first-order Taylor expansion of $\mathbf{R}(\alpha)$:

$$\mathbf{R}(\alpha^0 + \delta \alpha) = \mathbf{R}(\alpha^0) + \delta \mathbf{R} \cong \mathbf{R}(\alpha^0) + \mathbf{S} \delta \alpha, \quad (38)$$

where \mathbf{S} is a rectangular matrix of order $n \times k$ with elements $(S)_{ji} = \partial R_j / \partial \alpha_i$ representing the sensitivity of the j th response to the i th system parameter.

The expectation $E(\mathbf{R})$ of \mathbf{R} is obtained by following the same procedure as that leading to (34), to obtain

$$E(\mathbf{R}) = \mathbf{R}^0. \quad (39)$$

The covariance matrix V_R for \mathbf{R} is obtained by following the same procedure as that leading to (36), to obtain

$$V_R = E\left(\mathbf{S} \delta \alpha (\mathbf{S} \delta \alpha)^T\right) = \mathbf{S} E\left(\delta \alpha \delta \alpha^T\right) \mathbf{S}^T = \mathbf{S} V_\alpha \mathbf{S}^T. \quad (40)$$

Note that the relation (40) has the same “sandwich” form as (36) for a single response.

The equations for the propagation of higher-order moments become increasingly complex and are seldom used in practice. For example, for a single response $R(\alpha_1, \dots, \alpha_k)$ and *uncorrelated parameters* $(\alpha_1, \dots, \alpha_k)$, the respective propagation of moments equations can be obtained from (29), after a considerable amount of algebra, as follows:

$$E(R) = R(\alpha_1^0, \dots, \alpha_k^0) + \frac{1}{2} \sum_{i=1}^k \left\{ \frac{\partial^2 R}{\partial \alpha_i^2} \right\}_{\alpha^0} \mu_2(\alpha_i) + \frac{1}{6} \sum_{i=1}^k \left\{ \frac{\partial^3 R}{\partial \alpha_i^3} \right\}_{\alpha^0} \mu_3(\alpha_i) \\ + \frac{1}{24} \sum_{i=1}^k \left\{ \frac{\partial^4 R}{\partial \alpha_i^4} \right\}_{\alpha^0} \mu_4(\alpha_i) + \frac{1}{24} \sum_{i=1}^{k-1} \sum_{j=i+1}^k \left\{ \frac{\partial^4 R}{\partial \alpha_i^2 \partial \alpha_j^2} \right\}_{\alpha^0} \mu_2(\alpha_i) \mu_2(\alpha_j); \quad (41)$$

$$\mu_2(R) = \sum_{i=1}^k \left\{ \left(\frac{\partial R}{\partial \alpha_i} \right)^2 \right\}_{\alpha^0} \mu_2(\alpha_i) + \sum_{i=1}^k \left\{ \frac{\partial R}{\partial \alpha_i} \frac{\partial^2 R}{\partial \alpha_i^2} \right\}_{\alpha^0} \mu_3(\alpha_i) + \frac{1}{3} \sum_{i=1}^k \left\{ \frac{\partial R}{\partial \alpha_i} \frac{\partial^3 R}{\partial \alpha_i^3} \right\}_{\alpha^0} \mu_4(\alpha_i) \\ + \frac{1}{4} \sum_{i=1}^k \left\{ \left(\frac{\partial^2 R}{\partial \alpha_i^2} \right)^2 \right\}_{\alpha^0} [\mu_4(\alpha_i) - (\mu_2(\alpha_i))^2]; \quad (42)$$

$$\mu_3(R) = \sum_{i=1}^k \left\{ \left(\frac{\partial R}{\partial \alpha_i} \right)^3 \right\}_{\alpha^0} \mu_3(\alpha_i) + \frac{3}{2} \sum_{i=1}^k \left\{ \left(\frac{\partial R}{\partial \alpha_i} \right)^2 \frac{\partial^2 R}{\partial \alpha_i^2} \right\}_{\alpha^0} [\mu_4(\alpha_i) - (\mu_2(\alpha_i))^2]; \quad (43)$$

$$\mu_4(R) = \sum_{i=1}^k \left\{ \left(\frac{\partial R}{\partial \alpha_i} \right)^4 \right\}_{\alpha^0} [\mu_4(\alpha_i) - 3(\mu_2(\alpha_i))^2] + 3[\mu_2(R)]^2. \quad (44)$$

In the relations (41–44), the quantities $\mu_l(R)$, ($l = 1, \dots, 4$), denote the respective *central moments* of the response $R(\alpha_1, \dots, \alpha_k)$, while the quantities $\mu_k(\alpha_i)$, ($i = 1, \dots, k$; $k = 1, \dots, 4$) denote the respective central moments of the parameters $(\alpha_1, \dots, \alpha_k)$. Note that $E(R) \neq R^0$ when the response $R(\alpha_1, \dots, \alpha_k)$ is a nonlinear function of the parameters $(\alpha_1, \dots, \alpha_k)$. As has been already emphasized, the relations (41–44) are valid only for uncorrelated parameters.

It is important to emphasize that the “propagation of moments” equations are used not only for processing experimental data obtained from indirect measurements, but are also used for performing statistical analysis of computational models. In the latter case, the “propagation of errors” equations provide a systematic way of obtaining the uncertainties in computed results, arising not only from uncertainties in the parameters that enter the respective computational model but also from the numerical approximations themselves. The computation of sensitivities and, subsequently, uncertainties in results produced by various models (algebraic, differential, integrals, etc.) are the objectives of [Sects. 3](#) and [4](#).

2.6 Glossary

Absolute error (of a measuring instrument): The difference between the value of the measured quantity obtained by using a measuring instrument and the true (but unknown) value of the measured quantity.

Absolutely constant elementary error: An elementary error that retains the same value in repeated measurements performed under the same conditions. The value of an absolutely constant error is unknown but its limits can be estimated.

Accuracy of measurement: A qualitative expression of the closeness of the result of a measurement to the true value of the measured quantity.

Accuracy of a measuring instrument: The ability of a measuring instrument to produce measurements whose results are close to the true value of the measured quantity.

Combined measurement: Measurement of several quantities of the same kind, using results from (and/or combinations of) direct measurements.

Conditionally constant elementary error (of a measurement): An elementary error, having definite limits, which varies in repeated measurements performed under the same conditions or with different measuring instruments of the same type. These limits can be calculated or estimated.

Dead band: Maximum interval through which a stimulus may be changed in either direction without producing a change in the response of a measuring instrument.

Drift: A slow variation in time of the output of a measuring instrument, independently of the respective stimulus.

Elementary error (of a measurement): A component of error or uncertainty of a measurement associated with a single source of inaccuracy of the measurement.

Error (of a measurement): The deviation of the result of a measurement from the true value of the measured quantity; the error is expressed in absolute or relative form.

Inaccuracy (of a measurement): A qualitative characteristic of the deviation of a measurement result from the true value of the measured quantity. Quantitatively, inaccuracy can be characterized either as a measurement error or as a measurement uncertainty.

Indirect measurement: A measurement in which the value of the measured quantity is calculated by using measurements of other quantities that are connected to the measured quantity by a known relation.

Intrinsic error: The error of a measuring instrument, determined under reference conditions.

Measurement: The set of experimental operations that are performed using technical products (measuring instruments) for the purpose of finding the value of a physical quantity.

Measuring instrument: A technical product with standardized metrological characteristics.

Measuring standard: A measuring instrument intended to materialize and/or conserve a unit of a physical quantity in order to transmit its value to other measuring instruments.

Metrology: Science of measurement: an applied science that includes knowledge of measurements of physical quantities.

Normal operating conditions: Conditions within which a measuring instrument is designed to operate so that its metrological characteristics lie within specified limits.

Primary standard: A measuring standard that has the highest accuracy (in a country).

Random error (of a measurement): A component of the inaccuracy of a measurement that varies in an unpredictable way in the course of repeated measurements of the same measured quantity under the same conditions.

Relative error: Absolute error divided by the true value of the measured quantity. In practice, the true (but unknown) value is replaced by the measurement result.

Repeatability of a measurement: The closeness of agreement among several consecutive measurements of the same quantity, performed under the same operating conditions with the same measuring instruments, over a short period of time.

Reproducibility of a measurement: The closeness of agreement among repeated measurements for the same measured quantities performed in different locations, under different operating conditions, or over a long period of time.

Resolution: The smallest, still distinguishable interval between two adjacent values of the output signal of a measuring instrument.

Result of measurement: The value obtained by measurement of a quantity. The measurement result is expressed as a product of a numerical value and a proper unit.

Sensitivity of a measuring instrument: The change in the response of a measuring instrument divided by the corresponding change in the stimulus.

Systematic error (of measurement): A component of the inaccuracy of measurement that remains constant or varies in a predictable way in the course of repeated measurements of the same measured quantity.

True value: The value of a measured quantity that (if it were known) would ideally reflect, qualitatively and quantitatively, the respective property of the quantity of interest.

Uncertainty of measurement: An interval within which the true value of a measured quantity would lie with a given probability. Uncertainty is defined with its limits and corresponding confidence probability, and can be expressed in absolute or relative form.

3 Statistical Methods for Sensitivity and Uncertainty Analysis

The purpose of this section is to review the salient features, highlighting relative strengths and weaknesses, of the most popular screening and statistical methods for sensitivity and uncertainty analysis. These statistical procedures can be classified as follows: first- and second-order reliability algorithms (*FORM* and *SORM*, respectively); screening design methods (classical one-at-a-time experiments, global one-at-a-time design methods, systematic fractional replicate designs, and sequential bifurcation designs); sampling-based methods (random sampling, stratified importance sampling, and Latin Hypercube sampling); and variance-based methods (correlation ratio-based methods, the Fourier amplitude sensitivity test, and Sobol's method).

The salient features of the first- and second-order *reliability algorithms* (*FORM* and *SORM*, respectively) are briefly reviewed in [▶ Sect. 3.1](#). [▶ Section 3.2](#) reviews representative *screening design methods*; these methods refer to preliminary numerical experiments designed to identify the parameters that have the largest influence on a particular model response. The objective of screening is to arrive at a *short list* of important factors, based on the assumption that the number of parameters that are truly important to the model response is small by comparison to the total number of parameters underlying the model. Falling within the simplest class of screening designs are the so-called *one-at-a-time* (*OAT*) experiments, in which the impact of changing the values of each parameter is evaluated in turn. However, the results of a classical *OAT* experiment are meaningful only if the model's input–output relation can be adequately represented by a first-order polynomial in the model's parameters. If the model is affected by nonlinearities, as is often the case in practice, then parameter changes around the “control” scenario could provide drastically different “sensitivities,” depending on the chosen “control” scenario. Several alternative designs have been proposed to alleviate this severe limitation of classical *OAT* designs; among the most popular alternatives are the *systematic fractional replicate design* (*SFRD*), the *global OAT* design methods, and the *sequential bifurcation* (*SB*) design. All of these methods are computationally very intensive, which severely limits the amount of reliable information that can be extracted from a screening design. Most importantly, since the importance of parameters is not obvious a priori (and may often be counterintuitive) in

large-scale, complex models, screening design methods may be a priori inadequate to identify correctly the truly important parameters.

The salient features of the most popular *sampling-based methods*, namely *random sampling*, *stratified importance sampling*, and *Latin Hypercube sampling*, are reviewed in ▶ Sect. 3.3. In particular, Latin Hypercube sampling provides a compromise importance sampling when a priori knowledge of the relationships between the sampled parameters and predicted responses is not available. The very first step in all sampling-based uncertainty and sensitivity analysis methods is crucial to the final results produced by these methods, since this initial step defines, via “expert opinions,” the distributions used to characterize the subjective uncertainty. Hence, the proper assignment of these distributions is essential for avoiding spurious results.

Finally, three of the most popular *variance-based methods* for statistical uncertainty and sensitivity analysis, namely *the correlation ratio-based methods*, the *Fourier Amplitude Sensitivity Test (FAST)*, and *Sobol’s method*, are discussed in ▶ Sect. 3.4. In particular, it is noted that the correlation ratio, the FAST, and Sobol’s methods do *not* make the *a priori* assumption that the input model parameters are linearly related to the model’s response; this is in contradistinction to the sampling-based methods reviewed in ▶ Sect. 3.3.

It is important to note that all statistical uncertainty and sensitivity analysis methods first commence with the “uncertainty analysis” stage, and only subsequently proceed to the “sensitivity analysis” stage; this procedural path is the reverse of the procedural (and conceptual) path underlying the deterministic methods of sensitivity and uncertainty analysis, where the sensitivities are determined prior to using them for uncertainty analysis. Furthermore, the actual response sensitivities to parameters cannot be computed exactly by using statistical methods; this can be done only by using *deterministic methods*, which will be reviewed in ▶ Sect. 4.

3.1 Reliability Algorithms: FORM and SORM

In many practical problems, the primary interest of the analyst may be focused on a particular mode of failure of the system under consideration, while the detailed spectrum of probabilistic outcomes may be of secondary concern. For such problems, the so-called reliability algorithms provide relatively fast and economical answers regarding the particular mode of failure of the system under consideration. The typical problems that can be analyzed by using reliability algorithms must be characterized by a mathematical model (whose solution can be obtained analytically or numerically), by input parameters that can be treated as being affected by subjective (epistemic) uncertainties, and by a threshold level that specifies mathematically the concept of “failure.” The reliability algorithms most often used are known as the first-order reliability methods (*FORM*) and second-order reliability methods (*SORM*), respectively. Both of these methods use optimization algorithms based on the mathematical model and the response functional that defines failure to seek “the most likely failure point” in the space of uncertain parameters. Once this most likely failure point, referred to as the “design point,” has been determined, the probability of failure is approximately evaluated by fitting a first- (or second-) order surface at that point. As with many optimization algorithms, the *FORM* and *SORM* algorithms are susceptible to non-convergence or to convergence to an erroneous design point, particularly when the failure probability approaches the extreme values of 0.0 or 1.0. Therefore, the numerical optimization algorithm and convergence tolerances should be tailored, whenever possible, to the specific problem under investigation.

3.2 Design of Experiments and Screening Design Methods

Design of Experiments was introduced by Fischer (1935), and calls for selecting those combinations of parameter values, called *design points*, which will provide the most information on the input–output relationship embodied by a model in the presence of parameter variations. However, the basic question underlying this selection is often a circular one: if the response function were known, then it would be easy to select the optimal design points, but the response is actually the object of the investigation, to begin with. Often used in practice is the so-called *Factorial Design (FD)*, which aims at measuring the additive and interactive effects of input parameters on the response. A *FD* simulates all possible combinations of assigned values, l_i , called *levels*, to each (uncertain) system parameter α_i . Thus, even though a *FD* can account for interactions among parameters, the computational cost required by a *FD* is $l_1 l_2 \dots l_I$, where I denotes the total number of parameters in the model; such a computational effort is prohibitively high for large-scale systems. A useful alternative is the *Fractional Factorial Design (FFD)* introduced by Box and Draper (1987), which assumes a priori that higher-order interactions between parameters are unimportant.

Screening design methods refer to preliminary numerical experiments designed to identify the parameters that have the largest influence on a particular model response. The objective of screening is to arrive at a *short list* of important factors. In turn, this objective can only be achieved if the underlying numerical experiments are judiciously designed. An assumption often used as a working hypothesis in screening design is the assumption that the number of parameters that are truly important to the model response is small by comparison to the total number of parameters underlying the model. This assumption is based on the idea that the influence of parameters in models follows Pareto's law of income distribution within nations, characterized by a few, very important parameters and a majority on noninfluential ones. Since screening designs are organized to deal with models containing very many parameters, they should be computationally economical. There is an inevitable tradeoff, however, between computational costs and information extracted from a screening design. Thus, computationally economical methods often provide only qualitative, rather than quantitative information, in that they provide a parameter importance ranking rather than a quantification of how much a given parameter is more important than another.

Falling within the simplest class of screening designs are the so-called *one-at-a-time (OAT)* experiments (Daniel 1973), in which the impact of changing the values of each parameter is evaluated in turn. The *standard OAT* experiment is defined as the experiment that uses standard or nominal values for each of the I parameters underlying the model. The combination of nominal values for the I parameters is called the *control experiment* (or *scenario*). Two extreme values are then selected to represent the range of each of the I parameters. The nominal values are customarily selected at the midway between the two extremes. The magnitudes of the *residuals*, defined as the difference between the perturbed and nominal response (output) values, are then compared to assess which factors are most significant in affecting the response.

Although the strategy described above is often used in practice, it is not the only one; *OAT* designs can be classified (Daniel 1973) into five categories, as follows: (1) *standard OAT* designs, which vary one factor from a standard condition; (2) *strict OAT* designs, which vary one factor from the condition of the last preceding experimental run; (3) *paired OAT* designs, which produce two observations and, therefore, one simple comparison at a time; (4) *free OAT* designs, which make each new computation under new conditions; and (5) *curved OAT* designs, which

produce a subset of results by varying only one parameter that is easy to vary. In general, the number of model evaluation required for an *OAT* design is of the order of $(2I + 1)$ model computations. Refinements, such as proposed in Kleijnen (1998), require only roughly half as many computations, while providing arguably more accurate estimators of the main effects.

Since classical *OAT* cannot provide information about interactions between parameters, the model's behavior can only be assessed in a relatively small interval around the "control" scenario. In other words, the classical *OAT* experiments yield information only about the system's response *local* behavior. Therefore, the results of a classical *OAT* experiment are meaningful only if the model's input-output relation can be adequately represented by a first order polynomial in the model's parameters. If the model is affected by nonlinearities (as is often the case in practice), then parameter changes around the "control" scenario would provide drastically different "sensitivities," depending on the chosen "control" scenario.

To address this severe limitation of the classical *OAT* designs, a *global OAT* design method has been proposed in Morris (1991), by covering the entire space in which the parameters may vary, independently of the specific initial "control" scenario one may commence the experiment with. A *global OAT* design assumes that the model is characterized by a large number of parameters and/or is computationally expensive (regarding computational time and computational resources) to run. The range of variation of each component of the vector α of parameters is standardized to the unit interval, and each component is then considered to take on p values in the set $\{0, (p - 1)^{-1}, 2(p - 1)^{-1}, \dots, 1\}$, so that the region of experimentation becomes an I -dimensional p -level grid. An *elementary effect* of the i th-parameter at a point α is then defined as $d_i(\alpha) \equiv [\mathbf{R}(\alpha_1, \dots, \alpha_{i-1}, \alpha_i + \Delta, \alpha_{i+1}, \dots, \alpha_I) - \mathbf{R}(\alpha)]/\Delta$, where Δ is a predetermined multiple of $1/(1 - p)$, such that $\alpha_i + \Delta$ is still within the region of experimentation. A finite distribution F_i of elementary effects for the i th-parameter is obtained by sampling α from within the region of experimentation. The number of elements for each F_i is $p^{k-1} [p - \Delta(p - 1)]$. The distribution F_i is then characterized by its mean and standard deviation. A high mean indicates a parameter with an important overall influence on the response; a high standard deviation indicates either a parameter interacting with other parameters or a parameter whose effect is nonlinear.

In its simplest form, the total computational effort required for a random sample of r values from each distribution F_i is $n = 2rI$; each elementary effect requires the evaluation of the response $\mathbf{R}(\alpha)$ *twice*. For large-scale models, therefore, the *global OAT* design requires a relatively high computational effort, and can only provide a qualitative (but not quantitative) indication of the interactions of a parameter with the rest of the model. *OAT* cannot provide specific information about the identity of the interactions, and individual interactions among parameters cannot be estimated.

The *systematic fractional replicate design (SFRD)*, proposed in Cotter (1979), does not require any prior assumptions about interactions. For a model with I parameters, a *SFRD* involves the following steps: (1) one model computation with all parameters at their low levels; (2) I model computations with each parameter, in turn, at its upper level, while the remaining $(I - 1)$ parameters remain at their low levels; (3) I model computations with each parameter, in turn, at its low level, while the remaining $(I - 1)$ parameters remain at their upper levels; (4) one model computation with all parameters at their upper levels. Thus, a *SFRD* requires $2(I + 1)$ computations. Denoting by $(R_0, R_1, \dots, R_I, R_{I+1}, \dots, R_{2I}, R_{2I+1})$ the values of the responses computed in steps (1)–(4), the measures $M(j) \equiv |C_e(j)| + |C_o(j)|$, with $|C_e(j)| \equiv [|(R_{2I+1} - R_{I+j}) - (R_j - R_0)|]/4$ and $|C_o(j)| \equiv [(R_{2I+1} - R_{I+j}) + (R_j - R_0)]/4$, are used to estimate the order of importance of the I parameters α_i .

It is apparent from the above definitions that the measures $M(j)$ may fail when a parameter induces cancellation effects on the response, so that such a parameter would remain undetected by a *SFRD*. Worse yet, it is not possible to protect oneself a priori against such occurrences. Furthermore, a *SFRD* is not sufficiently precise, since the above definitions imply that, for one replicate, the variances would be $\text{var}[C_o(j)] = \text{var}[C_e(j)] = \sigma^2/4$, whereas a fractional replicate with n -computations would allow the estimations of parameter effects (on the response) with variances σ^2/n .

In addition to screening designs that consider each parameter individually, the (originally) individual parameters can be clustered into *groups* that are subsequently treated by *group screening designs*. Perhaps the most efficient modern group screening designs techniques are the *iterated fractional factorial design (IFFD)* proposed in Andres and Hajas (1993) and the *sequential bifurcation (SB)* technique proposed in Bettonvil (1990). In principle, the *IFFD* requires fewer model computations, n , than there are parameters, I . To identify an influential parameter, an *IFFD* investigates the groups through a fractional factorial design; the procedure is then repeated with different random groupings. Influential parameters are then sought at the intersection of influential groups. The *IFFD* samples three levels per parameter, designated low, middle, and high, while ensuring that the sampling is balanced: different combinations of values for two or three parameters appear with equal frequency. Hence, *IFFD* can be considered as a composite design consisting of multiple iterations of a basic *FFD*.

The *sequential bifurcation (SB)* design combines two design techniques, namely: (1) the *sequential design*, in which the parameter combinations are selected based on the results of preceding computations, and (2) *bifurcation*, in which each group that seems to include one or more important parameters is split into two subgroups of the same size. However, the *SB* design must *a priori* assume that the analyst knows the *signs* of the effects of the individual parameter, in order to ensure that effects of parameters assigned to the same group do not cancel out. Furthermore, the sequential nature of *SB* implies a more cumbersome data handling and analysis process than other screening design methods. To assess the effects of interactions between parameters, the number of *SB* computations becomes the double of the number of computations required to estimate solely the “main effects”; in particular, quadratic effects cannot be currently analyzed with the *SB* design technique, because of prohibitive computational requirements.

The screening designs surveyed in the foregoing are the most representative and the widest used methods aimed at identifying at the outset, in the initial phase of sensitivity and uncertainty analysis, the (hopefully not too many!) important parameters in a model. Each type of design has its own advantages and disadvantages, which can be summarized as follows: the advantages of *OAT* designs are: (1) no assumption of a monotonic input–output relation; (2) no assumption that the model contains only “a few” important parameters; and (3) the computational cost increases linearly with the number of parameters. The major disadvantage of *OAT* designs is the neglect of parameter interactions. Although such an assumption drastically simplifies the analysis of the model, it can rarely be accepted in practice. This simplifying assumption is absent in the *global OAT* design, which aims at determining the parameters that have (1) negligible effects, (2) linear and additive effects, and (3) nonlinear or interaction effects. Although the *global OAT* is easy to implement, it requires a high computational effort for large-scale models, and provides only a qualitative (but not quantitative) indication of the interactions of a parameter with the rest of the model; the *global OAT* cannot provide specific information about the identity of individual parameter interactions.

The *SFRD* does not require *a priori* assumptions about parameter interactions and/or about which few parameters are important. Although the *SFRD* is relatively efficient computationally,

it lacks precision and cannot detect parameters whose effects cancel each other out. The *IFFD* estimates the main and quadratic effects, and two-parameter interactions between the most influential parameters. Although the *IFFD* requires fewer computations than the total number of model parameters, the *IFFD* gives good results only if the model's response is actually influenced by only a few truly important parameters. The *SB* design is simple and relatively cost effective (computationally), but assumes that (1) the signs of the main effects are *a priori* known, and (2) the model under consideration is adequately described by two-parameter interactions.

3.3 Sampling-Based Methods

Consider that α denotes a vector of model parameters. If the uncertainty associated with α were known unambiguously, then the uncertainty in the response $\mathbf{R}(\mathbf{u}, \alpha)$ could also be assessed unambiguously. In practice, however, the uncertainty in α can rarely be specified unambiguously; most often, many possible values of α , of varying levels of plausibility, could be considered. Such uncertainties can be characterized by assigning a distribution of plausible values (D_1, D_2, \dots, D_I) to each component $\alpha_i(\mathbf{x})$ of α . Correlations and other restrictions can also be considered to affect the parameters $\alpha_i(\mathbf{x})$. Uncertainties characterized by such distributions are called *epistemic* or *subjective uncertainties*, and characterize a degree of belief regarding the location of the appropriate value of each $\alpha_i(\mathbf{x})$. In turn, these subjective uncertainties for the parameters $\alpha_i(\mathbf{x})$ lead to subjective uncertainties for the response $\mathbf{R}(\mathbf{u}, \alpha)$, which reflect a corresponding degree of belief regarding the location of the appropriate response values as the outcome of analyzing the model under consideration.

Sampling-based methods for sensitivity and uncertainty analysis are based on a sample

$$\alpha_k = [\alpha_{k1}, \alpha_{k2}, \dots, \alpha_{kI}], \quad (k = 1, 2, \dots, n_S), \quad (45)$$

of size n_S taken from the possible values of α as characterized by the distributions (D_1, D_2, \dots, D_I). The response evaluations corresponding to the sample α_k defined in (45) can be represented in vector form as

$$\mathbf{R}(\alpha_k) = [R_1(\alpha_k), R_2(\alpha_k), \dots, R_J(\alpha_k)], \quad (k = 1, 2, \dots, n_S), \quad (46)$$

where the subscript J denotes the number of components of the response \mathbf{R} . The pairs

$$[\alpha_k, \mathbf{R}(\alpha_k)], \quad (k = 1, 2, \dots, n_S), \quad (47)$$

represent a mapping of the uncertain "inputs" α_k to the corresponding uncertain "outputs" $\mathbf{R}(\alpha_k)$, which result from the "sampling-based uncertainty analysis." Subsequent examination and post-processing (e.g., scatter plots, regression analysis, partial correlation analysis) of the mapping represented by (47) constitute procedures for "sampling-based sensitivity analysis," in that such procedures provide means of investigating the effects of the elements of α on the elements of $\mathbf{R}(\mathbf{u}, \alpha)$. Thus, *the "sampling-based uncertainty and sensitivity analysis" first commences with the "uncertainty analysis" stage, and only subsequently proceeds to the "sensitivity-analysis" stage*, which is the exact reverse of the conceptual path underlying the methods of deterministic sensitivity and uncertainty analysis.

Specifically, a “sampling-based uncertainty and sensitivity analysis” involves five steps, as follows:

1. Define the subjective distributions (D_1, D_2, \dots, D_I) for characterizing the uncertain input parameters;
2. Use the above distributions to generate the sample α_k described in (45);
3. Use each of the elements of the sample α_k in order to perform model recalculations, which then generate the responses $R(\alpha_k)$ described in (46);
4. Perform “uncertainty analysis” of the response $R(u, \alpha)$, by generating displays of the uncertainty in $R(u, \alpha)$ using the results for $R(\alpha_k)$ obtained above, in step 3;
5. Perform “sensitivity analysis” of the response $R(u, \alpha)$ to the parameters α , by exploring (using scatter plots, regression analysis, partial correlation analysis, etc.) the mappings represented by (47), to assess the effects of the components of α on the components of $R(u, \alpha)$.

Step 1: Of all of the above steps, the most important is the very first one, namely the definition of the distributions used to characterize subjective uncertainty. Because of its fundamental importance, the characterization of subjective uncertainty has been widely studied, for example, Berger (1985), Hora and Iman (1989), Bonano and Apostolakis (1991). In practice, this step invariably involves formal expert review processes. Although formal statistical procedures can be occasionally used for constructing subjective distributions, practical experience has shown that it is more useful to specify selected quantile (minimum, median, maximum, etc.) values, rather than attempt to specify a particular type of distribution (e.g., normal, beta, etc.) and its associated parameters. This is because the respective experts are more likely to be able to justify the selection of specific quantile values rather than the selection of a particular form of distribution with specific parameters. When distributions from several expert opinions are combined, it is practically very difficult to assign weights to the respective opinions; these difficulties are discussed, for example, in Clement and Winkler (1999).

Once a subjective distribution D_i has been assigned to each element $\alpha_i(x)$ of α , the collection of subjective distributions (D_1, D_2, \dots, D_I) defines a probability space (S, E, p) , which is a formal structure where: (1) S denotes the sample space (containing everything that could occur in the particular universe under consideration; the elements of S are elementary events); (2) E denotes an appropriately restricted subspace of S , for which probabilities are defined; and (3) p denotes a probability measure.

Step 2: This step is to sample the probability space. The widest used sampling procedures are: random sampling, importance sampling, and Latin Hypercube sampling; the salient features of these procedures will be summarized briefly in the following. Thus, random sampling involves selection of the observations

$$\alpha_k = [\alpha_{k1}, \alpha_{k2}, \dots, \alpha_{kI}], \quad (k = 1, 2, \dots, n_{RS}), \quad (48)$$

where n_{RS} represents the sample size, according to the joint probability distribution for the elements of α as defined by (S, E, p) . A point from a specific region of S occurs as dictated by the probability of occurrence of the respective region. Moreover, each sample point is selected independently of all other sample points. Note, however, that there is no guarantee that points will be sampled from any given subregion of S . Furthermore, if sampled values fall closely

together, the sampling of S is quite inefficient. To address and alleviate these shortcomings, the so-called *importance sampling* procedure has been developed by dividing S exhaustively into several nonoverlapping subregions, referred to as *strata* S_i , ($i = 1, 2, \dots, n_S$). Thus, n_{S_i} values for α are sampled randomly from S_i , and the resultant vectors

$$\alpha_k = [\alpha_{k1}, \alpha_{k2}, \dots, \alpha_{kI}], \quad \left(k = 1, 2, \dots, \sum_{i=1}^{n_S} n_{S_i} \right), \quad (49)$$

form a sample obtained by importance-sampling, since the strata S_i are defined on the basis of how important the parameters $\alpha \in S_i$ (i.e., parameters that are contained in the strata) are to the final outcome of the analysis. Typically, only one value is sampled from each S_i , in which case (49) reduces to (45). Importance sampling is used to ensure that specified regions in the sample space are fully covered, thereby ensuring, in particular, that parameters which have low occurrence probabilities but high consequences are included in the analysis. The idea of fully covering the range of each parameter is further extended in the *Latin Hypercube sampling* procedure (see, for example, McKay et al. 1979). In this procedure, the range of each parameter α_i is divided into n_{LH} intervals of equal probability, and one value is randomly selected from each interval. The n_{LH} values thus obtained for the first parameter, α_1 , are then randomly paired, without replacement, with the n_{LH} values obtained for α_2 . In turn, these pairs are combined randomly, without replacement, with the n_{LH} values for α_3 to form n_{LH} triples. This process is continued until a set of $n_{LH}I$ -tuples are obtained, of the form

$$\alpha_k = [\alpha_{k1}, \alpha_{k2}, \dots, \alpha_{kI}], \quad (k = 1, 2, \dots, n_{LH}), \quad (50)$$

which is called a Latin Hypercube sample. This method is suited for uncorrelated parameters only; if the parameters are correlated, then the respective correlation structure must be incorporated into the sample, for otherwise the ensuing uncertainty/sensitivity analysis would yield false results. To incorporate parameter correlations into the sample, a restricted pairing technique for generating Latin Hypercubes was proposed (Iman and Conover 1982) based on rank correlations (i.e., correlations between rank-transformed parameters) rather than sample correlations (i.e., correlations between the original, untransformed, parameters).

Since random sampling is easy to implement and provides unbiased estimates for the means, variances, and distribution functions, it is the preferred statistical technique in practice, if large samples are available. However, a sufficiently “large sample,” for producing meaningful results by random sampling, cannot be generated for complex models (with many parameters) and/or for estimating extremely high quantiles (e.g., the 0.99999 quantile), since the computation of the required sample becomes prohibitively expensive and impractical. In such cases, the random sampling method of choice becomes the stratified sampling method. The main difficulty for implementing stratified sampling lies with defining the strata and for calculating the probabilities for the respective strata, unless considerable *a priori* knowledge is already available for this purpose. For example, the fault and event trees used in risk assessment studies of nuclear power plants and other complex engineering facilities can be used as algorithms for defining stratified sampling procedures. Latin Hypercube sampling is used when very high quantiles need not be estimated, but the calculations needed for generating the “large sample” required for random sampling still remain prohibitively demanding computationally. This is often the case in practice when assessing the effects of subjective uncertainty in medium-sized problems (e.g., ca. 30 parameters), for which a 0.9–0.95 quantile would be adequate for indicating the location

of a likely outcome. For such problems, random sampling is still unfeasible computationally, but the unbiased means and distribution functions provided by the full stratification (i.e., each parameter is treated equally) of the Latin Hypercube sampling makes it the preferred alternative over the importance sampling, where the unequal strata probabilities produce results that are difficult to interpret (particularly for subsequent sensitivity analysis). In this sense, Latin Hypercube sampling provides a compromise importance sampling when *a priori* knowledge of the relationships between the sampled parameters and predicted responses is not available.

Step 3: Once the sample has been generated, its elements must be used to perform model recalculations, which then generate the responses $\mathbf{R}(\boldsymbol{\alpha}_k)$ described by (46). These model recalculations can become the most expensive computational part of the entire uncertainty and sensitivity analysis and, if the model is complex, the model recalculations may severely limit the sample size and the other aspects of the overall analysis.

Step 4: It is customary to display the estimated expected value and the estimated variance of the response (as estimated from the sample size). However, these quantities may not be the most useful indicators about the response because information is always lost in the calculations of means and variances. In particular, the mean and variance are less useful for summarizing information about the distribution of subjective uncertainties; often, quantiles associated with the respective distribution provide a more meaningful locator for the quantity under consideration. Distribution functions (e.g., cumulative and/or complementary distribution functions, density functions) would, of course, provide the complete information that could be extracted from the sample under consideration.

Step 5: In the context of sampling-based methods, statistical sensitivity analysis (as opposed to deterministic sensitivity analysis) involves the exploration of the mapping represented by (47) to assess the effects of some, but not all, of the individual components of $\boldsymbol{\alpha}$ on the response $\mathbf{R}(\boldsymbol{\alpha})$. This exploration includes examination of scatter plots, regression and stepwise regression analysis, correlation and partial correlation analysis, rank transformation, identification of nonmonotonic patterns, and identification of nonrandom patterns. The starting point of statistical sensitivity analysis is the generation of scatter plots, which are obtained by plotting the points

$$(\alpha_{kj}, R_k), \quad (k = 1, \dots, n_S), \quad (51)$$

for each element α_j of $\boldsymbol{\alpha}$ for $(j = 1, \dots, I)$. The resulting I scatter plots are then examined to find possible relations between the response $\mathbf{R}(\boldsymbol{\alpha})$ and the elements α_j of $\boldsymbol{\alpha}$.

A more formal analysis of the parameter-to-response mapping represented by (47) is to perform regression analysis on a linear model between the predicted responses, $R_{\text{predicted}}$, and the input parameters α_j , of the form

$$R_{\text{predicted}} = b_0 + \sum_{j=1}^I b_j \alpha_j. \quad (52)$$

The calculated responses, R_k , are also formally expressed in terms of the actual parameter values, α_{kj} , used in the analysis, by means of a linear relationship of the form

$$R_k = b_0 + \sum_{j=1}^I b_j \alpha_{kj} + \varepsilon_k, \quad (k = 1, \dots, M), \quad (53)$$

where M denotes the actual number of calculations, and where $\varepsilon \equiv R_k - R_{\text{predicted}}$ denotes the error between the calculated and predicted value of the corresponding element of the response. The regression analysis commences by assuming that the unknown regression coefficients b_j can be determined by minimizing the sums of the squared errors $\sum_k (R_k - R_{\text{predicted}})^2 \equiv \sum_k \varepsilon^2$. The regression coefficients b_j can be used, along with other indicators computed during the regression analysis, to assess the importance of the individual parameters α_j with respect to the uncertainty in the response components. A measure of the extent to which the regression model can match the observed data is provided by the so-called *coefficient of multiple determination*, C^2 , defined by the following ratio:

$$C^2 \equiv S_{\text{reg}}/S_{\text{tot}}, \quad S_{\text{reg}} \equiv \sum_{k=1}^M (R_{k,\text{est}} - R_{\text{ave}})^2, \quad S_{\text{tot}} \equiv \sum_{k=1}^M (R_k - R_{\text{ave}})^2, \quad (54)$$

where $R_{k,\text{est}}$ denotes the estimate of R_k obtained from the regression model, while R_{ave} denotes the mean of the R_k 's. A value of C^2 close to unity indicates that the regression model accounts well for most of the uncertainties in the quantities R_k 's; conversely, a value of C^2 close to zero indicates that the regression model accounts poorly for the uncertainties in the R_k 's. In the important particular case when the sampling design matrix α_κ is orthogonal, each coefficient b_j can be determined by means of the formula

$$b_j = \left(\sum_{k=1}^M \alpha_{kj} R_k \right) / \left(\sum_{k=1}^M \alpha_{kj}^2 \right), \quad (55)$$

which indicates that the addition or deletion of model parameters will not change the regression coefficients for the remaining parameters. Furthermore, when the sampling design matrix α_κ is orthogonal, then the coefficient of multiple determinations (54) decomposes into the additive form $C^2 = \sum_{k=1}^M C_k^2$, where C_k^2 denotes the value of C^2 when regressing R solely on α_k . In other words, when the sampling design matrix α_κ is orthogonal, C_k^2 represents the contribution of α_k to C^2 .

Other useful concepts in sampling-based uncertainty/sensitivity analysis are the sample correlation and partial correlation coefficients. The *sample correlation coefficient*, $\text{Corr}(\alpha, R)$, between a parameter α and R for a sequence of observations (α_k, R_k) , ($k = 1, \dots, M$), is defined as

$$\text{Corr}(\alpha, R) \equiv \frac{\sum_{k=1}^M (\alpha_k - \alpha_{\text{ave}}) (R_k - R_{\text{ave}})}{\left[\sum_{k=1}^M (\alpha_k - \alpha_{\text{ave}})^2 \right]^{1/2} \left[\sum_{k=1}^M (R_k - R_{\text{ave}})^2 \right]^{1/2}}, \quad (56)$$

where α_{ave} and R_{ave} denote the corresponding sample average values. Thus, the correlation coefficient, $\text{Corr}(\alpha, R)$, provides a measure of the linear relationship between the elements α_j of α , and the response(s) $R(\alpha)$.

It is important to note that correlated variables introduce unstable regression coefficients b_j , in that the values of b_j become sensitive to the specific variables introduced into the regression model. In such situations, the regression coefficients of a regression model that includes all

of the parameters are likely to give misleading indications of parameter importance. If several input parameters are suspected (or known) to be highly correlated, it is usually recommended to transform the respective parameters so as to remove the correlations or, if this is not possible, to analyze the full model by using a sequence of regression models with all but one of the parameters removed, in turn. Furthermore, if the regression model is used to match the predictions associated with individual sample parameters rather than to match the trend displayed by the collective sample, then over-fitting of data may arise if parameters are arbitrarily forced into the regression model.

Stepwise regression analysis, which involves the use of a sequence of regression models, is often used when the model under investigation contains many parameters and a regression analysis involving all the variables simultaneously is impractical. The *first step* in a stepwise regression analysis is to use a regression model that includes the single specific parameter that has the largest correlation with the response. The *second step* is to use a regression model that involves two parameters, namely: (1) the single parameter from step 1, and (2) a second parameter, chosen to be that parameter, among the remaining ones, that has the largest impact on the uncertainty that has remained unaccounted for in step 1 (i.e., the parameter that has the largest correlation with the residual uncertainty in the response R). The *third step* is to use a regression model involving three parameters, namely, (1) the two parameters from step 2, and (2) a third parameter, chosen to be that parameter, among the remaining ones, that has the largest impact on the uncertainty that has remained unaccounted for in step 2 (i.e., the parameter that has the largest correlation with the residual uncertainty in the response R , after the impact of the most important two parameters has been accounted for). This stepwise process of constructing successively more comprehensive regression models by adding additional parameters, in the order of their importance in contributing to the uncertainty in the response, is continued until the addition of further parameters can no longer account meaningfully for the residual uncertainty in the response. Note that correlations among parameters may cause an already selected parameter to be dropped out from the next-level regression model, if the respective parameter fails to have a significant impact on the residual uncertainty in the response.

In a stepwise regression analysis, it is important to guard against over-fitting the data; this danger occurs if the individual observations rather than the overall trend are fitted. For example, it is possible to fit the data apparently “better” by using a higher-order polynomial than the order indicated by the overall trend, in which case a spurious regression model would be constructed, leading to poor subsequent predictions. To protect against over-fitting, the predicted error sum of squares is usually used as a measure of the adequacy of the regression model, and also as a criterion for stopping the step-wise construction of the hierarchical regression models. Furthermore, F -tests or t -tests are used to determine when a variable is no longer needed and can therefore be dropped from the regression model.

Since the regression relationships discussed so far are based on linear representations of the impact of parameters on the response, these regression models will perform poorly when the relationships between the parameters and the response are nonlinear. In such cases, the *rank transformation* may be used to improve the construction of the respective regression model. The conceptual framework underlying rank transformation involves simply replacing the parameters by their respective ranks, and then performing the customary regression analysis on the ranks rather than the corresponding parameters (Iman and Conover 1982; Saltelli and Sobol’ 1995). In such an analysis, if the number of observations is M , then the smallest value of each parameter is assigned rank 1, the next largest value is assigned rank 2, etc., until the largest value, which is assigned rank M ; if several parameters have the same values, then they are assigned

an averaged rank. The regression analysis is then performed by using the ranks as input/output parameters, as replacements for the actual parameter/response values. This replacement has the effect of replacing the linearized parameter/response relationships by rank-transformed monotonic input/output relationships in an otherwise conventional regression analysis. In practice, a regression analysis using the rank-transformed (instead of raw) data may yield better results, but only as long as the relationships between parameters and responses are monotonically non-linear. Otherwise, the rank transformation does not improve significantly the quality of the results produced by regression analysis.

Departures from monotonic trends can be sometimes identified by using F -tests for detecting common means, χ^2 -tests for detecting common medians, and the Kruskal–Wallis test for common locations (Kleijnen and Helton 1999); all of these tests are performed using scatter plots. Scatter plots can also be used to identify nonrandom patterns, by using χ^2 -tests for detecting statistical independence between parameters. However, if the parameters are not independent but are statistically correlated, then the magnitudes and even the signs of the regression coefficients b_j associated with the respective parameters may be erroneous, and therefore indicate incorrectly the effects of such parameters on the response.

3.4 Variance-Based Methods

Sampling-based methods use variance, among other indicators, as a measure of the importance of a parameter in contributing to the overall uncertainty in the response. The concept of variance as a measure of the importance of a parameter also underlies the conceptual foundation of three further methods for statistical uncertainty and sensitivity analysis, namely, the *correlation-ratio method* (including variants thereof), the *Fourier Amplitude Sensitivity Test (FAST)*, and *Sobol's method*. It is important to note that, in contrast to the sampling-based methods discussed in the previous section, the correlation-ratio, the *FAST*, and Sobol's methods do not make the a priori assumption that the input model parameters are linearly related to the model's response.

The importance of an input parameter α in contributing to the predictive uncertainty in a response R (output) can be assessed by considering the marginal probability distribution, $p_R(R)$, of R , which can be written in terms of the conditional probability distribution, $p_{R|\alpha}(R|\alpha)$, of R conditioned on α , as follows:

$$p_R(R) = \int p_{R|\alpha}(R|\alpha) p_\alpha(\alpha) d\alpha. \quad (57)$$

The above relation can be intuitively interpreted as follows: a parameter α is important if fixing its value would substantially reduce the conditional prediction variance relative to the marginal prediction variance. This interpretation indicates that various conditional variance ratios may be used as indicators of importance. Specifically, the methods based on correlation-ratios assume that the model simulating the system under investigation is of the form

$$R = E(R|\alpha) + \epsilon, \quad (58)$$

where α represents, as before, the set of I model parameters, and ϵ represents a vector of errors with the properties that $E(\epsilon) = 0$ and $\text{Var}[E(R|\alpha), \epsilon] = \text{known}$. Note, however, that ϵ is not taken into consideration in numerical experiments.

Recall that in a standard regression analysis, the expectation $E(R|\alpha)$ is a priori assumed to have the linear form $\sum_{k=1}^M \alpha_k b_k$, where the quantities b_k are the regression coefficients, determined by least-square fitting. By contrast, there are no assumptions in (58) regarding the specific mathematical form of the conditional expectation $E(R|\alpha)$.

Based on the model defined by (58), the prediction variance, $\text{Var}(R)$, of R can be written in the form

$$\text{Var}(R) = \text{Var}_\alpha [E(R|\alpha)] + E_\alpha (\text{Var}[R|\alpha]), \quad (59)$$

where

$$\begin{aligned} E(R|\alpha) &\equiv \int p_{R|\alpha}(R) R \, dR, \\ \text{Var}_\alpha [E(R|\alpha)] &\equiv \int [E(R|\alpha) - E(R)]^2 p_\alpha(\alpha) \, d\alpha, \\ E_\alpha (\text{Var}[R|\alpha]) &\equiv \int [R - E(R|\alpha)]^2 [p_{R|\alpha}(R) \, dR] p_\alpha(\alpha) \, d\alpha. \end{aligned}$$

The quantity $\text{Var}_\alpha [E(R|\alpha)]$ is the variance of the conditional expectation of R conditioned on α ; this quantity measures the importance of α , since it indicates how the constituent parts of $\text{Var}(R)$, given by (59), relate to α . More specifically, $\text{Var}_\alpha [E(R|\alpha)]$ measures the total variation in R in the sense that, as α varies, the variation in R would match the variation in $E(R|\alpha)$, if the second term in (59), that is, $E_\alpha (\text{Var}[R|\alpha])$, were small. Actually, the term $E_\alpha (\text{Var}[R|\alpha])$ is a residual term that measures the remaining variability in R due to other unobserved inputs or other unknown sources of variation when α is fixed.

The additive decomposition in (59) can be used to define “variance-based first-order sensitivity indices,” S_i and a “variance-based correlation ratio,” η^2 , as follows

$$S_i \equiv \frac{\text{Var}_\alpha [E(R|\alpha_i)]}{\text{Var}(R)} \quad \text{and} \quad \eta^2 \equiv \frac{\text{Var}_\alpha [E(R|\alpha)]}{\text{Var}(R)}. \quad (60)$$

Note that η^2 represents a measure of the magnitude of the variance of the conditional expectation relative to the prediction variance $\text{Var}(R)$, and can be evaluated (McKay 1995) using a Latin Hypercube sampling of size m with r replicates. However, such an evaluation is computationally very expensive, requiring $rm \times (I + 1)$ model evaluations, where I represents the number of parameters in α . A somewhat more economical method for evaluating η^2 is the resampling-based method presented in Saltelli et al. (1993), which requires $n(I + 1)$ model evaluations, where n represents the sample size for evaluating $E(R|\alpha_i)$ for a specified value of α_i , and where I represents the number of parameters in α .

The FAST procedure, originally proposed in Cukier et al. (1973), uses the following Fourier transformation of the parameters α_i :

$$\alpha_i = F_i \sin(\omega_i z), \quad i = 1, \dots, I, \quad (61)$$

where $\{\omega_i\}$ is a set of integer frequencies, while $z \in (-\pi, \pi)$ is a scalar variable. The expectation $E(R)$ and variance of the response R can be approximated as follows

$$E(R) = \frac{1}{2\pi} \int_{-\pi}^{\pi} f(z) \, dz, \quad \text{Var}(R) \cong 2 \sum_{j=1}^{\infty} (A_j^2 + B_j^2),$$

where

$$f(z) \equiv f[F_1 \sin(\omega_1 z), F_2 \sin(\omega_2 z), \dots, F_I \sin(\omega_I z)],$$

$$A_j \equiv \frac{1}{2\pi} \int_{-\pi}^{\pi} f(z) \cos(jz) dz, \quad B_j \equiv \frac{1}{2\pi} \int_{-\pi}^{\pi} f(z) \sin(jz) dz.$$

The transformation shown in (61) should provide, for each parameter α_i , a uniformly distributed sample in the unit I -dimensional cube. As $z \in (-\pi, \pi)$ varies for a given transformation, all parameters change simultaneously; however, their respective ranges of uncertainty is systematically and exhaustively explored (i.e., the search curve is space-filling) if and only if the set of frequencies $\{\omega_i\}$ is incommensurate (i.e., if none of the frequencies ω_i may be obtained as a linear combination, with integer coefficients, of the remaining frequencies).

The first-order sensitivity indices are computed by evaluating the coefficients A_j and B_j for the fundamental frequencies $\{\omega_i\}$ and their higher harmonics, $p\omega_i$ ($p = 1, 2, \dots$). If the frequencies $\{\omega_i\}$ are integers, the contribution to the total variance $\text{Var}(R)$ coming from the variance D_i corresponding to parameter α_i is approximately obtained as $D_i \cong 2 \sum_{p=1}^M (A_{p\omega_i}^2 + B_{p\omega_i}^2)$, where M is the maximum harmonic taken into consideration (usually $M \leq 6$). The ratio of the partial variance D_i to the total variance $\text{Var}(R)$ provides the so-called first-order sensitivity index. The minimum sample size required to compute D_i is $(2M\omega_{\max} + 1)$, where ω_{\max} is the maximum frequency in the set $\{\omega_i\}$. Furthermore, the frequencies that do not belong to the set $\{p_1\omega_1, p_2\omega_2, \dots, p_I\omega_I\}$ for ($p_i = 1, 2, \dots, \infty$), and for any ($i = 1, 2, \dots, I$), contain information about the residual variance $[\text{Var}(R) - D_i]$ that is not accounted for by the first-order indices. This residual variance can be computed in $(I \times N_S)$ computations, where N_S is the respective sample size.

A related class of variance-based methods has its roots in a theorem by Kolmogorov that states that any multivariate function, $f(x_1, x_2, \dots, x_n)$, defined in the unit n -dimensional cube $[0, 1]^n$, can be written as a linear superposition of univariate functions, $h_j(x_i)$, of the form

$$f(\mathbf{x}) \equiv f(x_1, x_2, \dots, x_n) = \sum_{j=1}^{2n+1} g[a_1 h_j(x_1) + a_2 h_j(x_2) + \dots + a_n h_j(x_n)], \quad (62)$$

where the functions $h_j(x_i)$ are continuous (but highly non-smooth). Although Kolmogorov's expansion shown in (62) is seldom used in practice for interpolation and/or approximation of multivariate functions, it has inspired the development of several (somewhat) more practical algorithms for representing multivariate functions, such as the projection pursuit algorithms (Stone 1985), multilayer perceptrons (Parker 1985), Sobol's method (Sobol' 1993), and ANOVA-like decompositions (Archer et al. 1997), which can also be used for uncertainty and sensitivity analysis.

Perhaps the most practical of the methods mentioned above is a method due to Sobol' (1993), in which the multivariate function $f(x_1, x_2, \dots, x_n)$ is decomposed into summands of increasing dimensionality of the form

$$f(x_1, x_2, \dots, x_n) = f_0 + \sum_{i=1}^n f_i(x_i) + \sum_{1 \leq i < j \leq n} f_{ij}(x_i, x_j) + \dots + f_{12\dots n}(x_1, x_2, \dots, x_n). \quad (63)$$

The decomposition in (63) is unique if the variables are uncorrelated, and has the following properties:

1. The integrals of any summand over any of its own variables is zero, that is,

$$\int_0^1 f_{i_1 i_2 \dots i_n} (x_{i_1}, x_{i_2}, \dots, x_{i_n}) dx_{i_m} = 0, \quad \text{if } 1 \leq m \leq n,$$

2. The summands are orthogonal, that is,

$$\int_{[0,1]^n} f_{i_1 i_2 \dots i_n} f_{j_1 j_2 \dots j_m} dx = 0 \quad \text{if } (i_1, i_2, \dots, i_n) \neq (j_1, j_2, \dots, j_m);$$

3. f_0 is a constant, that is, $f_0 = \int_{[0,1]^n} f(x) dx$.

By squaring (63) and integrating the resulting expression over the unit cube $[0,1]^n$, the following relation is obtained for the total variance D of $f(x)$:

$$D \equiv \int_{[0,1]^n} f^2(x) dx - f_0^2 = \sum_{i=1}^n D_i + \sum_{1 \leq i < j \leq n} D_{ij} + \dots + D_{12\dots n}, \quad (64)$$

where the partial variances of $f(x)$ are defined as

$$D_{i_1 i_2 \dots i_m} = \int_0^1 \dots \int_0^1 f_{i_1 i_2 \dots i_m} (x_{i_1}, x_{i_2}, \dots, x_{i_m}) dx_{i_1} \dots dx_{i_m}, \quad (65)$$

for $1 \leq i_1 < \dots < i_m \leq n, m = 1, \dots, n$.

The sensitivity indices are defined as

$$S_{i_1 i_2 \dots i_m} \equiv D_{i_1 i_2 \dots i_m} / D, \quad \text{for } 1 \leq i_1 < \dots < i_m \leq n, m = 1, \dots, n. \quad (66)$$

The *first-order sensitivity index*, S_i , for the parameter x_i indicates the fractional contribution of x_i to the variance D of $f(x)$; the *second-order sensitivity index*, S_{ij} , ($i \neq j$), measures the part of the variation in $f(x)$ due to x_i and x_j that cannot be explained by the sum of the individual effects of x_i and x_j ; and so on. Note also that (65) and (66) imply that

$$\sum_{i=1}^n S_i + \sum_{i < j \leq n} S_{ij} + \dots + S_{12\dots n} = 1. \quad (67)$$

4 Deterministic Computation of Response Sensitivities to Parameters Using Adjoint Operators

4.1 Introduction

The mathematical model of a physical system usually comprises: (1) linear and/or nonlinear equations that relate the system's independent variables and parameters to the system's state (i.e.,

dependent) variables, (2) probability distributions and/or constraints that define the domains and properties of the system's parameters, and (3) one or several quantities, customarily referred to as system responses (or objective functions, or indices of performance) that are to be analyzed as the parameters vary over their respective domains.

In large-scale, complex models, the importance of parameters is not a priori obvious, and may often be counterintuitive. To analyze such complex models, information about the slopes of the model's response at a given set of nominal parameter values in parameter space is of paramount importance. The exact slopes are provided by the local partial functional derivatives $\partial R/\partial\alpha_i$ of the response R with respect to the model parameters α_i . These local partial functional derivatives are called the *local sensitivities* of the model's response to parameter variations. The objective of *local sensitivity analysis* is to analyze the behavior of the system responses locally around a chosen point or trajectory in the combined phase space of parameters and state variables. On the other hand, the objective of *global sensitivity analysis* is to determine all of the system's critical points (bifurcations, turning points, response extrema) in the combined phase space formed by the parameters, state variables, and adjoint variables, and subsequently analyze these critical points by local sensitivity analysis.

The simplest way of estimating local sensitivities is by *recalculations* of the model's response, using parameter values that deviate by small amounts, $\delta\alpha_i$, of the order of 1%, from their nominal values α_i^0 . The sensitivities are then estimated by using a finite difference approximation to $\partial R/\partial\alpha_i$ of the form

$$\left\{ \frac{\partial R}{\partial\alpha_i} \right\}_{\alpha^0} = \frac{R(\alpha_1^0, \dots, \alpha_i^0 + \delta\alpha_i, \dots, \alpha_I^0) - R(\alpha_i^0)}{\delta\alpha_i}, \quad (i = 1, \dots, I).$$

This procedure, occasionally called the “*brute-force method*,” requires $(I + 1)$ model computations; if central differences are used, the number of model computations could increase up to a total of $2I$. Although this method is conceptually simple to use and requires no additional model development, it is slow, relatively expensive computationally, and involves a trial-and-error process when selecting the parameter perturbations $\delta\alpha_i$. Note that *erroneous sensitivities will be obtained if*: (1) $\delta\alpha_i$ is chosen to be too small, in which case the computational round-off errors may overwhelm the correct values, and (2) *the parameter dependence is nonlinear and $\delta\alpha_i$ is chosen too large*, in which case the assumption of local linearity is violated.

Local sensitivities can be computed exactly only by using deterministic methods that involve some form of differentiation of the system under investigation. The (comparatively few) deterministic methods for calculating sensitivities exactly are as follows: the *direct method* (including its *decoupled direct method* variant), the *Green's function method*, the *forward sensitivity analysis procedure (FSAP)*, and the *adjoint sensitivity analysis procedure (ASAP)*. The so-called *direct method* has been applied predominantly to systems involving differential and/or algebraic equations describing chemical kinetics (including combustion kinetics) and molecular dynamics. This method involves differentiation of the system of equations underlying the model with respect to each parameter in the model. The sensitivity to each parameter is then computed by solving the respective differentiated system. The most advanced and computationally economical version of the direct method is the *decoupled direct method (DDM)*, introduced in Dunker (1984), in which the Jacobian matrix needed to solve the original system at a given time-step is also used to solve the sensitivity equations at the respective time-step, before proceeding to

solve both the original and sensitivity systems at the next time-step. Note that the computational effort increases linearly with the number of parameters.

Another method occasionally used for computing sensitivities for models governed by first-order derivatives in time is the *Green function method (GFM)*. This method commences by differentiating the underlying model with respect to its initial conditions to obtain a Green's function, which is subsequently convoluted with the matrix of parameter derivatives, and is finally integrated in time to obtain the respective time-dependent sensitivities. There are several variants of the *GFM*; the integrated Magnus version (*GFM/AIM*) proposed in Kramer et al. (1981) appears to be, the most efficient *GFM* computationally. In practice, though, the *GFM* is seldom used, since it is computationally more expensive and considerably more difficult to implement than the *DDM*.

As introduced in Cacuci (1981a, b), the most general and comprehensive way of defining *local* sensitivities for general operators (in the sense of nonlinear functional analysis) is in terms of the first *Gâteaux-differential* of the system's response, computed at the respective nominal value of the system's dependent variables and parameters. Two procedures have been developed in Cacuci (1981a, b) based on the concept of *Gâteaux-differentials*, for computing the local sensitivities for any type of response, namely: the *forward sensitivity analysis procedure (FSAP)* and the *adjoint sensitivity analysis procedure (ASAP)*. The *FSAP* constitutes a generalization of the *decoupled direct method (DDM)*, since the concept of *Gâteaux-differential* (which underlies the *FSAP*) constitutes the generalization of the concept of total-differential in the calculus sense, which underlies the *DDM*. Notably, the *Gâteaux-differential* exists for operators and generalized functions (e.g., distributions) that are not continuous in the ordinary calculus-sense, and therefore do not admit the “nice” derivatives required for using the *DDM*. As expected, the *FSAP* reduces to the *DDM*, whenever the continuity assumptions required by the *DDM* are satisfied. Finally, even though the *FSAP* represents a generalization of the *DDM*, the *FSAP* requires the *same* computational and programming effort to develop and implement as the *DDM*. Hence, just as the *DDM*, the *FSAP* is advantageous to employ only if the number of different responses of interest for the problem under consideration exceeds the number of system parameters and/or parameter variations to be considered. Otherwise, the use of either the *FSAP* or the *DDM* becomes impractical for large systems with many parameters, because of the very large demand on computational resources.

For large-scale systems, in which the number of system parameters and/or parameter variations to be considered exceeds the number of responses of interest, the *ASAP* is, by far, the most advantageous method to employ, even though it can only be implemented if an appropriately constructed adjoint sensitivity system is already available. The remarkable efficiency of the *ASAP* stems from the fact that the adjoint sensitivity system is linear in the adjoint function, and is independent of any parameter variations. Hence, the adjoint sensitivity equation needs to be solved only once, for each response, in order to obtain the adjoint function. In particular, if the original model is linear in the state (i.e., dependent) variables, then the adjoint sensitivity equation can be solved independently of the original model. In turn, once the adjoint function has been calculated, it is used to obtain the sensitivities to all system parameters, by simple quadratures, without needing to solve repeatedly differential and/or integral equations. Thus, for the large-scale systems, with many parameters, as usually encountered in practice, the *ASAP* is the most efficient method to use for sensitivity analysis. The general mathematical framework for deriving both the *FSAP* and *ASAP* for nonlinear systems with feedback and operator-type responses will be presented in ➤ Sect. 4.2, in the sequel.

Since the operations of discretization and Gâteaux-differentiation do not commute, there are two distinct paths that can be pursued for computing sensitivities, namely:

- (a) first apply the *FSAP* and *ASAP* to differential and/or integral equations, then discretize the resulting Forward and/or Adjoint Sensitivity Equations, and finally solve the resulting algebraic equations numerically; or
- (b) first discretize the original (linear and/or nonlinear) differential and/or integral equations, then apply the *FSAP* and *ASAP* to the resulting linear and/or nonlinear algebraic equations, and finally solve the resulting algebraic equations numerically. These procedures were first developed in Cacuci (2003) and Cacuci et al. (2005) under the names *discrete forward sensitivity analysis procedure (DFSAP)* and *discrete adjoint sensitivity analysis procedure (DASAP)*, respectively.

The algebraic equations resulting from following path (a) will be different from the algebraic equations resulting from path (b), because the two paths will, in general, produce different truncation errors. Thus, it is very useful, both theoretically and in practice, to distinguish between the procedures underlying path (a) and those underlying path (b), respectively. Of course, it is paramount to ensure that both paths yield consistent discretizations, since they both should constitute discretization of the same adjoint sensitivity equations. These important issues are discussed in detail in Cacuci (2003) and Cacuci et al. (2005).

As mentioned in [▶ Sect. 3](#), the exact local sensitivities obtained by using deterministic methods can be used for the following purposes: (1) understand the system by highlighting important data; (2) eliminate unimportant data; (3) determine effects of parameter variations on system behavior; (4) design and optimize the system (e.g., maximize availability/minimize maintenance); (5) reduce over-design; (6) prioritize the improvements effected in the respective system; (7) prioritize introduction of data uncertainties; and (8) perform local uncertainty analysis by using the “propagation of errors” method.

Large-scale simulation models have been historically developed without simultaneously implementing the corresponding adjoint sensitivity models. Implementing *a posteriori* the *ASAP* for large-scale simulation codes is not a trivial task, and the development and implementation of the adjoint sensitivity model for an entire large-scale code system can seldom be executed all at once. Hence, the recommended strategy for building the adjoint sensitivity system for a large-scale simulation code is a module-by-module implementation of the *ASAP* to each simulation module. In the final step of such a “modular” implementation of the *ASAP*, the adjoint sensitivity systems for each of the respective modules is “augmented,” without redundant effort and/or loss of information, until all adjoint modules are judiciously connected together, accounting for all of the requisite feedbacks and liaisons between the respective adjoint modules. [▶ Section 4.3](#) presents the theoretical foundation for the modular implementation of the *ASAP* for a complex simulation system, by starting with a selected code module, and then augmenting the size of the adjoint sensitivity system, module by module, until completing the entire system under consideration. This presentation closely follows the original derivations in Cacuci and Ionescu-Bujor (2005) and Ionescu-Bujor et al. (2005).

As an illustrative application of the *ASAP* to a large scale system, [▶ Sect. 4.4](#) presents a paradigm adjoint sensitivity analysis of dynamic reliability models based on Markov chains, following the novel work presented in Cacuci and Ionescu-Bujor (2008) and Cacuci et al. (2008). This novel application of the *ASAP* is relatively easy to follow, and has large applicability since Markov chains are used extensively to analyze and predict system reliability and availability in many branches of industry (e.g., cell phones, computers, communication and networks,

health equipment, aviation and aerospace, automotive engineering, chemical processing, military application, nuclear engineering), economic/econometric models, population forecasting, biology, and even financial planning. Other applications of ASAP can be found in the references listed at the end of this chapter.

The earliest attempts at extending the region of validity of local sensitivities beyond first-order were focused on computing second- and higher-order response derivatives with respect to the system's parameters. However, the number of equations that would need to be solved for obtaining the second- (and higher-) order derivatives of the response is very large, and depends on the number of parameter variations. For this reason, none of the deterministic techniques (proposed in the literature thus far) for computing second- and higher-order response derivatives with respect to the system's parameters has proven routinely practicable for large-scale problems. In particular, the computation of the second-order derivatives of the response and system's equations is already as difficult as undertaking the complete task of computing the exact value of perturbed response. Furthermore, since the Taylor series is a local concept, valid within some radius of convergence of the respective series around the nominal parameter values, it follows that even if the response derivatives were available to all orders, they would still merely provide local, but not global, information. Thus, they would yield little, if any, information about the important global features of the physical system, namely, the critical points of the response and the bifurcation branches and/or turning points of the system's state variables.

Instead of computing higher order response derivatives, the so-called *feature sensitivity analysis* for nonlinear probing of a larger region in the parameter-space has been proposed in Kramer et al. (1984), but the applications thus far have been limited to illustrative applications. A genuinely global deterministic method for sensitivity analysis, called the *global adjoint sensitivity analysis procedure* (GASAP), has been developed in Cacuci (1990). The GASAP uses both the forward and the adjoint sensitivity system to explore, exhaustively and efficiently, the entire phase-space of system parameters and dependent variables, in order to obtain complete information about the critical points of the response and the bifurcation branches and/or turning points of the system's state variables. The GASAP and the "feature sensitivity analysis" methods will be discussed in [▶ Sect. 4.5](#).

4.2 Sensitivity Analysis of Nonlinear and Linear Systems with Feedback and Operator-Type Responses

The physical system considered in this chapter is modeled mathematically by means of K coupled nonlinear equations represented in operator form as

$$N[\mathbf{u}(\mathbf{x}), \boldsymbol{\alpha}(\mathbf{x})] = \mathbf{Q}[\boldsymbol{\alpha}(\mathbf{x})], \quad \mathbf{x} \in \Omega, \quad (68)$$

where

1. $\mathbf{x} = (x_1, \dots, x_j)$ denotes the phase-space position vector; $\mathbf{x} \in \Omega \subset \mathbb{R}^J$, where Ω is a subset of the J -dimensional real vector space \mathbb{R}^J ;
2. $\mathbf{u}(\mathbf{x}) = [u_1(\mathbf{x}), \dots, u_K(\mathbf{x})]$ denotes the vector of dependent (i.e., state) variables; $\mathbf{u}(\mathbf{x}) \in E_u$, where E_u is a normed linear space over the scalar field F of real numbers;
3. $\boldsymbol{\alpha}(\mathbf{x}) = [\alpha_1(\mathbf{x}), \dots, \alpha_I(\mathbf{x})]$ denotes the vector of system parameters; $\boldsymbol{\alpha} \in E_\alpha$, where E_α is also a normed linear space; in usual applications, E_α may be one of the Hilbert spaces L_2

or l_2 ; occasionally, the components of α may simply be a set of real scalars, in which case E_α is \mathbb{R}^I ;

4. $\mathbf{Q}[\alpha(\mathbf{x})] = [\mathbf{Q}_1(\alpha), \dots, \mathbf{Q}_K(\alpha)]$ denotes a (column) vector whose elements represent inhomogeneous source terms that depend either linearly or nonlinearly on α ; $\mathbf{Q} \in E_Q$, where E_Q is again a normed linear space; the components of \mathbf{Q} may be operators (rather than just functions) acting on $\alpha(\mathbf{x})$ and \mathbf{x} ;
5. $\mathbf{N} \equiv [N_1(\mathbf{u}, \alpha), \dots, N_K(\mathbf{u}, \alpha)]$ is a K -component column vector whose components are, in general, *nonlinear* operators (including differential, difference, integral, distributions, and/or infinite matrices) of \mathbf{u} and α .

In view of the definitions given above, \mathbf{N} represents the mapping $\mathbf{N} : D \subset E \rightarrow E_Q$, where $D = D_u \times D_\alpha$, $D_u \subset E_u$, $D_\alpha \subset E_\alpha$, and $E = E_u \times E_\alpha$. Note that an arbitrary element $e \in E$ is of the form $e = (\mathbf{u}, \alpha)$. Even though in most practical applications E and E_Q will be Hilbert spaces (e.g., the space L_2 , the Sobolev spaces H^m), this restriction is not imposed at this stage for the sake of generality. If differential operators appear in (68), then a corresponding set of boundary and/or initial conditions (which are essential to define D) must also be given. The respective boundary conditions are represented as

$$[\mathbf{B}(\mathbf{u}, \alpha) - \mathbf{A}(\alpha)]_{\partial\Omega} = 0, \quad x \in \partial\Omega, \quad (69)$$

where \mathbf{A} and \mathbf{B} are nonlinear operators while $\partial\Omega$ is the boundary of Ω .

The vector-valued function $\mathbf{u}(\mathbf{x})$ is considered to be the unique nontrivial solution of the physical problem described by (68) and (69). The system response (i.e., performance parameter) $\mathbf{R}(\mathbf{u}, \alpha)$ associated with the problem modeled by (68) and (69) is a phase-space dependent mapping that acts nonlinearly on the system's state vector \mathbf{u} and parameters α , and is represented in operator form as

$$\mathbf{R}(e) : D_R \subset E \rightarrow E_R, \quad (70)$$

where E_R is a normed vector space.

The nominal parameter values $\alpha^0(\mathbf{x})$ are used in (68) and (69) to obtain the nominal solution $\mathbf{u}^0(\mathbf{x})$ by solving

$$\mathbf{N}(\mathbf{u}^0, \alpha^0) = \mathbf{Q}(\alpha^0), \quad x \in \Omega, \quad (71)$$

$$\mathbf{B}(\mathbf{u}^0, \alpha^0) = \mathbf{A}(\alpha^0), \quad x \in \partial\Omega. \quad (72)$$

Once the nominal values $\mathbf{u}^0(\mathbf{x})$ have been obtained by solving the above equations, they are used together with the nominal parameter values $\alpha^0(\mathbf{x})$ in (70) to obtain the nominal response value $\mathbf{R}(\mathbf{u}^0, \alpha^0)$.

Feedback is introduced into the model by allowing some (or all) of the parameters α to depend on some (or all) of the components of \mathbf{u} . Without loss of generality, a feedback mechanism can be specified by adding an operator, $F(\mathbf{u})$, to the nominal parameter values α^0 . Thus, in the presence of feedback, the values of the parameters become $\alpha^0 + F(\mathbf{u})$; correspondingly, the solution \mathbf{u}^f of the system with feedback will satisfy the equations

$$\mathbf{N}[\mathbf{u}^f, \alpha^0 + F(\mathbf{u}^f)] = \mathbf{Q}[\alpha^0 + F(\mathbf{u}^f)], \quad x \in \Omega, \quad (73)$$

$$\mathbf{B}[\mathbf{u}^f, \alpha^0 + F(\mathbf{u}^f)] = \mathbf{A}[\alpha^0 + F(\mathbf{u}^f)], \quad x \in \partial\Omega. \quad (74)$$

The system response with feedback becomes $\mathbf{R}[\mathbf{u}^f, \boldsymbol{\alpha}^0 + \mathbf{F}(\mathbf{u}^f)]$. The difference

$$\mathbf{R}[\mathbf{u}^f, \boldsymbol{\alpha}^0 + \mathbf{F}(\mathbf{u}^f)] - \mathbf{R}(\mathbf{u}^0, \boldsymbol{\alpha}^0), \quad \mathbf{x} \in R, \quad (75)$$

gives the actual effect of the feedback \mathbf{F} on the response $\mathbf{R}(\mathbf{u}^0, \boldsymbol{\alpha}^0)$, and can be calculated exactly only by solving (73) and (74) anew for each \mathbf{F} , and then using the respective solution \mathbf{u}^f to evaluate $\mathbf{R}[\mathbf{u}^f, \boldsymbol{\alpha}^0 + \mathbf{F}(\mathbf{u}^f)]$.

The sensitivity, DR_F , of the response with feedback, $\mathbf{R}[\mathbf{u}^f, \boldsymbol{\alpha}^0 + \mathbf{F}(\mathbf{u}^f)]$, to parameters and feedback variations around the nominal response value $\mathbf{R}(\mathbf{u}^0, \boldsymbol{\alpha}^0)$ is given by the Gâteaux-differential

$$DR_F \equiv \left\{ \frac{d}{d\varepsilon} \mathbf{R}[\mathbf{u}^0 + \varepsilon \mathbf{h}, \boldsymbol{\alpha}^0 + \varepsilon \mathbf{F}(\mathbf{u}^0 + \varepsilon \mathbf{h})] \right\}_{\varepsilon=0}, \quad (76)$$

where $\mathbf{h} \equiv \mathbf{u}^f - \mathbf{u}$. For most practical applications, performing the operations indicated in (76) gives

$$DR_F = \mathbf{R}'_1(\mathbf{u}^0, \boldsymbol{\alpha}^0) \mathbf{h} + \mathbf{R}'_2(\mathbf{u}^0, \boldsymbol{\alpha}^0) \mathbf{F}(\mathbf{u}^0), \quad \mathbf{x} \in \Omega_R, \quad (77)$$

where \mathbf{R}'_1 and \mathbf{R}'_2 denote, respectively, the Gâteaux-derivatives of $\mathbf{R}(\mathbf{u}, \boldsymbol{\alpha})$ with respect to its first and second arguments. Customarily, the second term on the right-side of (77) can be calculated directly, with little effort, since it does not depend on \mathbf{h} ; therefore, this term is usually called the “*direct effect*” term. However, the first term on the right-side of (77) can only be computed after having determined the variational vector on \mathbf{h} ; hence, this term is called the “*indirect-effect*” term, since it contributes to the sensitivity DR_F through \mathbf{h} .

4.2.1 The Forward Sensitivity Analysis Procedure (FSAP)

The vector of variations, $\mathbf{h} \equiv \mathbf{u}^f - \mathbf{u}$, is needed in order to compute the sensitivity DR_F obtained in (77) above. To first order variations in the feedback and/or parameters, the variations $\mathbf{h} \equiv \mathbf{u}^f - \mathbf{u}$ are obtained by solving the equations obtained by taking the Gâteaux-differentials of (73) and (76) at $(\mathbf{u}^0, \boldsymbol{\alpha}^0)$, namely

$$\mathbf{N}'_1(\mathbf{u}^0, \boldsymbol{\alpha}^0) \mathbf{h} = [\mathbf{Q}'(\boldsymbol{\alpha}^0) - \mathbf{N}'_2(\mathbf{u}^0, \boldsymbol{\alpha}^0)] \mathbf{F}(\mathbf{u}^0), \quad \mathbf{x} \in \Omega, \quad (78)$$

$$\mathbf{B}'_1(\mathbf{u}^0, \boldsymbol{\alpha}^0) \mathbf{h} = [\mathbf{A}'(\boldsymbol{\alpha}^0) - \mathbf{B}'_2(\mathbf{u}^0, \boldsymbol{\alpha}^0)] \mathbf{F}(\mathbf{u}^0), \quad \mathbf{x} \in \partial\Omega. \quad (79)$$

Equations (78) and (79) are called the *forward sensitivity equations*, or the *forward variational tangent model*. In principle, the sensitivity DR_F can be evaluated once (78) and (79) have been solved to determine \mathbf{h} . However, these equations would have to be solved anew for each \mathbf{F} , and this becomes prohibitively expensive if many effects of all possible feedback and parameter variations are to be analyzed.

4.2.2 Adjoint (Local) Sensitivity Analysis Procedure (ASAP)

The *Adjoint Sensitivity Analysis Procedure* (ASAP) is the alternative method for calculating the sensitivity DR_F , and the ASAP circumvents the need for repeatedly solving (78) and (79). To

begin with, we note that the second term on the right-side of (77) can be calculated directly, with little effort, since it does not depend on \mathbf{h} (this is the so-called “direct effect” term). To calculate the first term on the right-side of (77), that is, the “indirect-effect” term, the spaces E_u , E_Q , and E_R are henceforth considered to be Hilbert spaces and denoted as $H_u(\Omega)$, $H_Q(\Omega)$, and $H_R(\Omega_R)$, respectively. The elements of $H_u(\Omega)$ and $H_Q(\Omega)$ are, as before, vector functions defined on the open set $\Omega \subset \mathbb{R}^J$, with a smooth boundary $\partial\Omega$. The elements of $H_R(\Omega_R)$ are vector- or scalar-valued functions defined on the open set $\Omega_R \subset \mathbb{R}^m$, $1 \leq m \leq J$, with a smooth boundary $\partial\Omega_R$. Of course, if $J = 1$, then $\partial\Omega$ merely consists of two endpoints; similarly, if $m = 1$, then $\partial\Omega_R$ consists of two endpoints only. The inner products on $H_u(\Omega)$, $H_Q(\Omega)$, and $H_R(\Omega_R)$ are denoted by $\langle \bullet, \bullet \rangle_u$, $\langle \bullet, \bullet \rangle_Q$, and $\langle \bullet, \bullet \rangle_R$, respectively.

Since $\mathbf{R}'_1(\mathbf{u}^0, \boldsymbol{\alpha}^0) \mathbf{h} \in H_R(\Omega_R)$, it follows that

$$\mathbf{R}'_1(\mathbf{u}^0, \boldsymbol{\alpha}^0) \mathbf{h} = \sum_{s \in S} \langle \mathbf{p}_s, \mathbf{R}'_1 \mathbf{h} \rangle_R \mathbf{p}_s, \quad (80)$$

where \mathbf{p}_s is an orthonormal basis for $H_R(\Omega_R)$, $\langle \cdot, \cdot \rangle_R$ denotes the inner product in H_R , and the series $\sum_{s \in S}$ converges unconditionally over the nonzero elements in S (which could be infinitely many).

The functionals $\langle \mathbf{p}_s, \mathbf{R}'_1 \mathbf{h} \rangle_R$ are the Fourier coefficients of $\mathbf{R}'_1 \mathbf{h}$ with respect to the basis \mathbf{p}_s . In practice, the basis \mathbf{p}_s is often chosen to be a set of orthogonal polynomials, particularly Chebyshev polynomials. Note that since the operator $\mathbf{R}'_1 \mathbf{h}$ is linear in \mathbf{h} , the functionals $\langle \mathbf{p}_s, \mathbf{R}'_1 \mathbf{h} \rangle_R$ are also linear in \mathbf{h} . Furthermore, since $\mathbf{R}'_1 \mathbf{h} \in L(H_u(\Omega), H_R(\Omega_R))$ and since Hilbert spaces are self-dual, it follows that $\mathbf{R}'_1(\mathbf{u}^0, \boldsymbol{\alpha}^0)$ admits a unique adjoint operator, denoted here as the linear operator $\mathbf{M}(\mathbf{u}^0, \boldsymbol{\alpha}^0) \in L(H_R(\Omega_R), H_u(\Omega))$, and defined, as customary, in terms of inner products by means of the relationship:

$$\langle \mathbf{p}_s, \mathbf{R}'_1(\mathbf{u}^0, \boldsymbol{\alpha}^0) \mathbf{h} \rangle_R = \langle \mathbf{M}(\mathbf{u}^0, \boldsymbol{\alpha}^0) \mathbf{p}_s, \mathbf{h} \rangle_u, \quad \text{for every } s \in S. \quad (81)$$

Equations (78) and (79) reveal that the Gâteaux-derivatives $\mathbf{N}'_1 \mathbf{h}$ and $\mathbf{B}'_1 \mathbf{h}$ are linear in \mathbf{h} . It is therefore possible to introduce, for every vector $\boldsymbol{\psi}_s \in H_Q(\Omega)$, the operator adjoint to $\mathbf{N}'_1 \mathbf{h}$, by means of the relation

$$\langle \boldsymbol{\psi}_s, \mathbf{N}'_1(\mathbf{u}^0, \boldsymbol{\alpha}^0) \mathbf{h} \rangle_Q = \langle \mathbf{L}^+(\mathbf{u}^0, \boldsymbol{\alpha}^0) \boldsymbol{\psi}_s, \mathbf{h} \rangle_u + \{ \mathbf{P}(\mathbf{h}, \boldsymbol{\psi}_s) \}_{\partial\Omega}, \quad s \in S, \quad (82)$$

where the $K \times K$ matrix $\mathbf{L}^+ = [L^+_{ij}]$, ($i, j = 1, \dots, K$), obtained by transposing the formal adjoints L^+_{ij} of the operators $(\mathbf{N}'_1)_{ij}$, is the formal adjoint of $\mathbf{N}'_1(\mathbf{u}^0, \boldsymbol{\alpha}^0)$, while $\{ \mathbf{P}(\mathbf{h}, \boldsymbol{\psi}_s) \}_{\partial\Omega}$ represents the associated bilinear form (concomitant) evaluated on $\partial\Omega$. The domain of \mathbf{L}^+ is determined by selecting adjoint boundary conditions, represented here in operator form as

$$\{ \mathbf{B}^+(\mathbf{u}^0, \boldsymbol{\alpha}^0; \boldsymbol{\psi}_s) - \mathbf{A}^+(\boldsymbol{\alpha}^0) \}_{\partial\Omega} = 0, \quad s \in S. \quad (83)$$

The above adjoint boundary conditions are determined by requiring that: (1) the relation (83) must be independent of \mathbf{h} and \mathbf{F} , and (2) substitution of (83) and (79) into $\{ \mathbf{P}(\mathbf{h}, \boldsymbol{\psi}_s) \}_{\partial\Omega}$ must cause all terms containing unknown values of \mathbf{h} to vanish. This selection of the adjoint boundary conditions reduces $\{ \mathbf{P}(\mathbf{h}, \boldsymbol{\psi}_s) \}_{\partial\Omega}$, to a quantity, denoted here as $\hat{\mathbf{P}}(\mathbf{F}, \boldsymbol{\psi}_s, \mathbf{u}^0, \boldsymbol{\alpha}^0)$, that contains

only known values of F , ψ_s , \mathbf{u}^0 , and α^0 . In particular, \hat{P} may vanish as a result of this selection of B^+ and A^+ . Furthermore, this selection of B^+ and A^+ , and the subsequent reduction of $\{P(\mathbf{h}, \psi_s)\}_{\partial\Omega}$ to $\hat{P}(F, \psi_s, \mathbf{u}^0, \alpha^0)$ reduces (82) to

$$\langle \psi_s, N'_1(\mathbf{u}^0, \alpha^0) \mathbf{h} \rangle_Q - \hat{P}(F, \psi_s, \mathbf{u}^0, \alpha^0) = \langle L^+(\mathbf{u}^0, \alpha^0) \psi_s, \mathbf{h} \rangle_u, \quad s \in S. \tag{84}$$

Requiring now that the first terms on the right-sides of (84) and (79), respectively, represent the same functional of \mathbf{h} yields the relation

$$L^+(\mathbf{u}^0, \alpha^0) \psi_s = M(\mathbf{u}^0, \alpha^0) \mathbf{p}_s, \quad s \in S, \mathbf{x} \in S, \tag{85}$$

which holds uniquely by virtue of the Riesz representation theorem. The system represented by (85) is the adjoint sensitivity system. Furthermore, using (84) and (85) in (81) reduces the latter to

$$\langle \mathbf{p}_s, R'_1 \mathbf{h} \rangle_R = \langle \psi_s, N'_1 \mathbf{h} \rangle_Q - \hat{P}(F, \psi_s, \mathbf{u}^0, \alpha^0), \quad s \in S. \tag{86}$$

Replacing now $N'_1 \mathbf{h}$ in (86) by the expression on the right-side of (78), substituting the resulting expression into the right-side of (80), and using (77) yields the following expression for the local sensitivity $DR_F(\mathbf{u}^0, \alpha^0, F)$ of the response R to the feedback F :

$$DR_F = R'_2(\mathbf{u}^0, \alpha^0) F(\mathbf{u}^0) + \sum_{s \in S} \left\{ \langle \psi_s, [Q'(\alpha^0) - N'_2(\mathbf{u}^0, \alpha^0)] F(\mathbf{u}^0) \rangle_Q - \hat{P}(F, \psi_s, \mathbf{u}^0, \alpha^0) \right\} \mathbf{p}_s. \tag{87}$$

It is important to note that the unknown (forward) functions \mathbf{h} do not appear in the above expression for the local sensitivity DR_F , which means that the need to solve (78) and (79) has been eliminated. Instead, it is necessary to compute as many adjoint functions ψ_s by solving (85) subject to the adjoint boundary conditions represented by (83) as there are nonzero terms retained in the summation representation in (87). In practice, this number of nonzero terms (and hence the number of required adjoint functions) is dictated by accuracy considerations, and varies from application to application. *Minimizing the number of terms in this summation falls within the objective of research activities known as “reduced-order modeling,”* but a detailed description of these activities is beyond the scope of this chapter.

Note that an expression similar to (87) holds also for systems without feedback. For such systems, the parameter variations are independent of the state variables \mathbf{u} and hence do not induce feedback via \mathbf{u}^f . The feedback operator $F(\mathbf{u}^0)$ reduces, in such cases, simply to parameter variations, that is, $F(\mathbf{u}^0) = \alpha - \alpha^0 \equiv \mathbf{h}_\alpha$. Consequently, the expression (87) giving the sensitivity of responses to parameters in systems without feedback reduces to

$$DR_F = R'_\alpha(\mathbf{u}^0, \alpha^0) \mathbf{h}_\alpha + \sum_{s \in S} \left\{ \langle \psi_s, [Q'(\alpha^0) - N'_\alpha(\mathbf{u}^0, \alpha^0)] \mathbf{h}_\alpha \rangle_Q - \hat{P}(F, \psi_s, \mathbf{u}^0, \alpha^0) \right\} \mathbf{p}_s, \tag{88}$$

where $\mathbf{h}_\alpha \equiv \alpha - \alpha^0$ denotes the I -component (column) vector of parameter variations around the nominal values α^0 . As before, when R is a functional of \mathbf{u} and α , then the summation in (88) reduces to a single term, and only a single adjoint function would need to be calculated for obtaining DR_F .

The customary applications of DR_F as given by (87) are for:

1. Ranking the importance of feedbacks or parameter variations in affecting the response \mathbf{R} ;
2. Uncertainty analysis (deterministic, response surface, Monte Carlo, etc.);
3. System improvements and/or design;
4. Inclusion of experimental information (e.g., via data adjustment procedures) to obtain best estimate codes;
5. Reduction of uncertainties in models;
6. Assessing the first-order local variations in \mathbf{R} caused by feedback and/or parameter changes \mathbf{F} by means of the functional Taylor expansion

$$\mathbf{R}[\mathbf{u}^f, \boldsymbol{\alpha}^0 + \mathbf{F}(\mathbf{u}^f)] - \mathbf{R}(\mathbf{u}^0, \boldsymbol{\alpha}^0) = DR_F(\mathbf{u}^0, \boldsymbol{\alpha}^0, \mathbf{F}) + H.O.T(\mathbf{h}, \mathbf{F}), \quad (89)$$

where $H.O.T(\mathbf{h}, \mathbf{F})$ denotes higher (than first-) order terms in $\|\mathbf{h}\|$ and $\|\mathbf{F}\|$.

For *linear systems*, the representation (68) and (69) reduce, respectively, to

$$\mathbf{L}(\boldsymbol{\alpha}) \mathbf{u} = \mathbf{Q}[\boldsymbol{\alpha}(\mathbf{x})], \quad \mathbf{x} \in \Omega, \quad (90)$$

$$[\mathbf{B}(\boldsymbol{\alpha}) \mathbf{u} - \mathbf{A}(\boldsymbol{\alpha})]_{\partial\Omega} = \mathbf{0}, \quad \mathbf{x} \in \partial\Omega. \quad (91)$$

Consequently, the *forward sensitivity system* defined by (78) and (79) reduces to

$$\mathbf{L}(\boldsymbol{\alpha}^0) \mathbf{h}_u + [\mathbf{L}'_{\alpha}(\boldsymbol{\alpha}^0) \mathbf{u}^0] \mathbf{h}_{\alpha} - \delta\mathbf{Q}(\boldsymbol{\alpha}^0; \mathbf{h}_{\alpha}) = \mathbf{0}, \quad \mathbf{x} \in \Omega, \quad (92)$$

$$\{\mathbf{B}(\boldsymbol{\alpha}^0) \mathbf{h}_u + [\mathbf{B}'_{\alpha}(\boldsymbol{\alpha}^0) \mathbf{u}^0] \mathbf{h}_{\alpha} - \delta\mathbf{A}(\boldsymbol{\alpha}^0; \mathbf{h}_{\alpha})\}_{\partial\Omega} = \mathbf{0}, \quad \mathbf{x} \in \partial\Omega, \quad (93)$$

where $\mathbf{L}'_{\alpha}(\boldsymbol{\alpha}^0)$ and $\mathbf{B}'_{\alpha}(\boldsymbol{\alpha}^0)$ denote, respectively, the partial G-derivatives at $\boldsymbol{\alpha}^0$ of \mathbf{L} and \mathbf{B} with respect to $\boldsymbol{\alpha}$. The adjoint sensitivity system, cf. (85) and (83) becomes

$$\mathbf{L}^+(\boldsymbol{\alpha}^0) \boldsymbol{\psi}_s = \mathbf{M}(\boldsymbol{\alpha}^0) \mathbf{p}_s, \quad s \in \mathbf{S}, \mathbf{x} \in \Omega, \quad (94)$$

subject to the adjoint boundary conditions

$$\{\mathbf{B}^+(\boldsymbol{\psi}_s; \boldsymbol{\alpha}^0) - \mathbf{A}^+(\boldsymbol{\alpha}^0)\}_{\partial\Omega} = \mathbf{0}, \quad s \in \mathbf{S}, \mathbf{x} \in \partial\Omega. \quad (95)$$

It is important to note that the adjoint sensitivity system, consisting of (94) and (95) is independent of the nominal solution \mathbf{u}^0 . This means that for *linear systems*, the ensuing adjoint sensitivity system can be solved independently of the solution \mathbf{u}^0 of the original equations. This fact simplifies considerably the choice of numerical methods for solving the adjoint system.

The derivations that yielded relation (88) remain formally unchanged in the case of linear systems, giving the following expression for the sensitivity $DR(\mathbf{e}^0; \mathbf{h})$ of $\mathbf{R}(\mathbf{e})$ at \mathbf{e}^0 :

$$DR(\mathbf{e}^0; \mathbf{h}) = \mathbf{R}'_{\alpha}(\mathbf{e}^0) \mathbf{h}_{\alpha} + \sum_{s \in \mathbf{S}} \left[(\boldsymbol{\psi}_s, \delta\mathbf{Q}(\boldsymbol{\alpha}^0; \mathbf{h}_{\alpha}) - [\mathbf{L}'_{\alpha}(\boldsymbol{\alpha}^0) \mathbf{u}^0] \mathbf{h}_{\alpha})_{\mathbf{Q}} - \hat{\mathbf{P}}(\mathbf{h}_{\alpha}, \boldsymbol{\psi}_s; \boldsymbol{\alpha}^0) \right] \mathbf{p}_s. \quad (96)$$

4.3 Sensitivity Analysis of Augmented Systems with Feedback

Consider now that the primary (original, nonaugmented) nonlinear system, represented by (68) and (69), is augmented by additional equations, containing additional independent variables, additional dependent variables, and additional parameters. A general way to represent mathematically such an augmentation process is as follows:

1. The augmented system may depend on more independent variables than the original system. To reflect this possibility, the original phase-space position vector, $\mathbf{x} = (x_1, \dots, x_{J_x})$, $\mathbf{x} \in \Omega_x \subset \mathbb{R}^{J_x}$, is augmented by the additional phase-space position vector $\mathbf{y} \equiv [y_1, \dots, y_{J_y}]$; $\mathbf{y} \in \Omega_y \subset \mathbb{R}^{J_y}$, where Ω_y is a subset of the J_y -dimensional real vector space \mathbb{R}^{J_y} . Thus, the phase-space position vector for the (entire) augmented system will be denoted as $\mathbf{z} \equiv (\mathbf{x}, \mathbf{y})$; $J \equiv J_x + J_y$; $\mathbf{z} \in \Omega \equiv \Omega_x \cup \Omega_y \subset \mathbb{R}^J$.
2. The augmented system may comprise more dependent variables than the original system. To reflect this possibility, the original vector of dependent (i.e., state) variables, $\mathbf{u}(\mathbf{x}) = [u_1(\mathbf{x}), \dots, u_{K_u}(\mathbf{x})]$, $\mathbf{u}(\mathbf{x}) \in E_u$, is augmented by the vector of additional dependent variables $\mathbf{v}(\mathbf{z}) = [v_1(\mathbf{z}), \dots, v_{K_v}(\mathbf{z})]$, $\mathbf{v}(\mathbf{z}) \in E_v$ where E_v is a normed linear space over the scalar field F of real numbers, and where K_v denotes the total number of additional state (i.e., dependent) variables appearing in the augmented system.
3. The augmented system may depend on more parameters than the original system; furthermore, components of the original vector of system parameters, $\boldsymbol{\alpha}(\mathbf{x}) = [\alpha_1(\mathbf{x}), \dots, \alpha_I(\mathbf{x})]$, $\boldsymbol{\alpha} \in E_\alpha$, can become functions of additional parameters, $\mathbf{b}(\mathbf{z}) = [b_1(\mathbf{z}), \dots, b_{I_b}(\mathbf{z})]$, $\mathbf{b} \in E_b$, where E_b is a normed linear space. In addition, feedback may be introduced in the augmented system, if some (or all) of the parameters $\boldsymbol{\alpha}$ become dependent on some (or all) of the components of $\mathbf{u}(\mathbf{x}) \in E_u$ and/or the components of $\mathbf{v}(\mathbf{z}) \in E_v$. Finally, a subset $\boldsymbol{\beta}(\mathbf{x}) = [\beta_1(\mathbf{x}), \dots, \beta_{I_\beta}(\mathbf{x})]$, $\boldsymbol{\beta} \in E_\beta$, where E_β is also a normed linear space, of the original parameters may remain unaffected by the transition from the original to the enlarged, augmented system. In a very general manner, therefore, the transition from the original system to the enlarged, augmented system can be described mathematically by the mapping $\boldsymbol{\alpha} \rightarrow \mathbf{a}[\boldsymbol{\beta}(\mathbf{x}), \mathbf{b}(\mathbf{z}); \mathbf{u}(\mathbf{x}), \mathbf{v}(\mathbf{z})]$, $\mathbf{a} \in E_a$. Note that the normed linear space E_a for the augmented system will generally differ from the normed linear space E_α to which the parameters of the original (unaugmented) system belonged.
4. In view of the extensions described above in items 1–3, the operators appearing in (68) will undergo the following transformations:

$$\begin{aligned} N(\mathbf{u}, \boldsymbol{\alpha}) &\rightarrow N[\mathbf{u}, \mathbf{a}(\boldsymbol{\beta}(\mathbf{x}), \mathbf{b}(\mathbf{z}); \mathbf{u}(\mathbf{x}), \mathbf{v}(\mathbf{z}))] \\ &\equiv [N_1(\mathbf{u}, \mathbf{a}(\boldsymbol{\beta}, \mathbf{b}; \mathbf{u}, \mathbf{v})), \dots, N_{K_u}(\mathbf{u}, \mathbf{a}(\boldsymbol{\beta}, \mathbf{b}; \mathbf{u}, \mathbf{v}))] \\ Q[\boldsymbol{\alpha}(\mathbf{x})] &\rightarrow Q[\mathbf{a}(\boldsymbol{\beta}(\mathbf{x}), \mathbf{b}(\mathbf{z}); \mathbf{u}(\mathbf{x}), \mathbf{v}(\mathbf{z}))] \\ &\equiv [Q_1[\mathbf{a}(\boldsymbol{\beta}, \mathbf{b}; \mathbf{u}, \mathbf{v})], \dots, Q_{K_u}[\mathbf{a}(\boldsymbol{\beta}, \mathbf{b}; \mathbf{u}, \mathbf{v})]]. \end{aligned}$$

Note also that, for the augmented system, $\mathbf{Q} \in E_q$, where E_q is a normed linear space that differs from the original normed linear space E_Q . Similarly, the boundary operators appearing in (69) will undergo the transformations $\mathbf{A}(\boldsymbol{\alpha}) \rightarrow \mathbf{A}[\mathbf{a}(\boldsymbol{\beta}, \mathbf{b}; \mathbf{u}, \mathbf{v})]$ and $\mathbf{B}(\mathbf{u}, \boldsymbol{\alpha}) \rightarrow \mathbf{B}[\mathbf{u}(\mathbf{x}); \mathbf{a}(\boldsymbol{\beta}, \mathbf{b}; \mathbf{u}, \mathbf{v})]$,

respectively. Therefore, (68) and (69) will be mapped into the following forms within the augmented system:

$$N[\mathbf{u}, \mathbf{a}(\boldsymbol{\beta}, \mathbf{b}; \mathbf{u}, \mathbf{v})] = \mathbf{Q}[\mathbf{a}(\boldsymbol{\beta}, \mathbf{b}; \mathbf{u}, \mathbf{v})], \quad \mathbf{z} \in \Omega, \quad (97)$$

$$\mathbf{B}[\mathbf{u}, \mathbf{a}(\boldsymbol{\beta}, \mathbf{b}; \mathbf{u}, \mathbf{v})] = \mathbf{A}[\mathbf{a}(\boldsymbol{\beta}, \mathbf{b}; \mathbf{u}, \mathbf{v})], \quad \mathbf{z} \in \partial\Omega. \quad (98)$$

In addition to the relations (97) and (98), the augmented system will also contain further equations and corresponding boundary and/or initial conditions, as needed to balance the total number of state (i.e., dependent) variables (\mathbf{u}, \mathbf{v}) with the total number of equations, in order to have a well-posed augmented system. These additional equations can be written in operator form as

$$\mathbf{M}[\mathbf{u}(\mathbf{x}), \mathbf{v}(\mathbf{z}), \mathbf{b}(\mathbf{z})] = \mathbf{S}(\mathbf{b}), \quad \mathbf{z} \in \Omega, \quad (99)$$

with corresponding boundary and/or initial conditions written in operator form as

$$\mathbf{C}[\mathbf{u}(\mathbf{x}), \mathbf{v}(\mathbf{z}), \mathbf{b}(\mathbf{z})] = \mathbf{D}(\mathbf{b}), \quad \mathbf{z} \in \partial\Omega. \quad (100)$$

Each of the vector-valued operators appearing in (99) comprise K_v -components of the form

$$\begin{aligned} \mathbf{M}[\mathbf{u}(\mathbf{x}), \mathbf{v}(\mathbf{z}), \mathbf{b}(\mathbf{z})] &\equiv [M_1(\mathbf{u}, \mathbf{v}, \mathbf{b}), \dots, M_{K_v}(\mathbf{u}, \mathbf{v}, \mathbf{b})], \\ \mathbf{S}[\mathbf{u}(\mathbf{x}), \mathbf{v}(\mathbf{z}), \mathbf{b}(\mathbf{z})] &\equiv [S_1(\mathbf{u}, \mathbf{v}, \mathbf{b}), \dots, S_{K_v}(\mathbf{u}, \mathbf{v}, \mathbf{b})], \quad \mathbf{S} \in E_S. \end{aligned}$$

In view of the definitions given above, the augmented vector of operators (\mathbf{N}, \mathbf{M}) represents the mapping $(\mathbf{N}, \mathbf{M}) : D_{\text{aug}} \subset E_{\text{aug}} \rightarrow E_q \times E_S$, where $D_{\text{aug}} = D_u \times D_v \times D_a$, $D_u \subset E_u$, $D_v \subset E_v$, $D_a \subset E_a$, and $E_{\text{aug}} = E_u \times E_v \times E_a$. The subscript ‘‘aug’’ denotes ‘‘augmented space.’’ Note that a generic element $\mathbf{f} \in E_{\text{aug}}$ is of the form $\mathbf{f} \equiv [\mathbf{u}, \mathbf{v}, \mathbf{a}(\boldsymbol{\beta}, \mathbf{b}; \mathbf{u}, \mathbf{v})]$. The vector-valued function $[\mathbf{u}(\mathbf{x}), \mathbf{v}(\mathbf{z})]$ is considered to be the unique nontrivial solution of the physical problem described by (97) through (99).

The system response (i.e., performance parameter) associated with the augmented system modeled by (97–100) will be denoted in the sequel as $\Theta(\mathbf{f})$, and is considered to be an operator that acts nonlinearly on the augmented system’s state vector $[\mathbf{u}(\mathbf{x}), \mathbf{v}(\mathbf{z})]$ and parameters $\mathbf{a}(\boldsymbol{\beta}, \mathbf{b}; \mathbf{u}, \mathbf{v})$; $\Theta(\mathbf{f})$ can be represented in operator form as the mapping $\Theta(\mathbf{f}) : D_{R_{\text{aug}}} \subset E_{\text{aug}} \rightarrow E_{R_{\text{aug}}}$, where $E_{R_{\text{aug}}}$ is another normed vector space.

In practice, the exact values of the parameters $\boldsymbol{\alpha}$, $\boldsymbol{\beta}$, and \mathbf{b} are not known exactly; only their nominal (mean) values, $\boldsymbol{\alpha}^0$, $\boldsymbol{\beta}^0$, and \mathbf{b}^0 , and their associated uncertainties are usually available. The nominal parameter values \mathbf{a}^0 are used in (97–100) to obtain the nominal solution $[\mathbf{u}^0(\mathbf{x}), \mathbf{v}^0(\mathbf{z})]$, by solving the ‘‘base-case’’ augmented system

$$N[\mathbf{u}^0, \mathbf{a}^0(\boldsymbol{\beta}^0, \mathbf{b}^0; \mathbf{u}^0, \mathbf{v}^0)] = \mathbf{Q}[\mathbf{a}^0(\boldsymbol{\beta}^0, \mathbf{b}^0; \mathbf{u}^0, \mathbf{v}^0)], \quad \mathbf{z} \in \Omega, \quad (101)$$

$$\mathbf{B}[\mathbf{u}^0, \mathbf{a}^0(\boldsymbol{\beta}^0, \mathbf{b}^0; \mathbf{u}^0, \mathbf{v}^0)] = \mathbf{A}[\mathbf{a}^0(\boldsymbol{\beta}^0, \mathbf{b}^0; \mathbf{u}^0, \mathbf{v}^0)], \quad \mathbf{z} \in \partial\Omega, \quad (102)$$

$$\mathbf{M}[\mathbf{u}^0(\mathbf{x}), \mathbf{v}^0(\mathbf{z}), \mathbf{b}^0(\mathbf{z})] = \mathbf{S}(\mathbf{b}^0), \quad \mathbf{z} \in \Omega, \quad (103)$$

$$\mathbf{C}[\mathbf{u}^0(\mathbf{x}), \mathbf{v}^0(\mathbf{z}), \mathbf{b}^0(\mathbf{z})] = \mathbf{D}(\mathbf{b}^0), \quad \mathbf{z} \in \partial\Omega. \quad (104)$$

Using the base-case solution of the augmented system obtained by solving (101–104) yields the base-case value, $\Theta(\mathbf{f}^0)$, $\mathbf{f}^0 \equiv [\mathbf{u}^0, \mathbf{v}^0, \mathbf{a}^0(\boldsymbol{\beta}^0, \mathbf{b}^0; \mathbf{u}^0, \mathbf{v}^0)]$, of the response for the augmented system.

The sensitivity of the response, $\Theta(\mathbf{f})$, at $\mathbf{f}^0 \equiv [\mathbf{u}^0, \mathbf{v}^0, \mathbf{a}^0(\boldsymbol{\beta}^0, \mathbf{b}^0; \mathbf{u}^0, \mathbf{v}^0)]$ to variations $\mathbf{h} \equiv [\mathbf{h}_u, \mathbf{h}_v, \mathbf{h}_\beta, \mathbf{h}_b]$ in the augmented system's parameters is the Gâteaux-(G)-differential, $\delta\Theta(\mathbf{f}^0; \mathbf{h})$, defined as

$$\delta\Theta(\mathbf{f}^0; \mathbf{h}) \equiv \left\{ \frac{d}{dt} [\Theta(\mathbf{f}^0 + t\mathbf{h})] \right\}_{t=0} = \lim_{t \rightarrow 0} \frac{\Theta(\mathbf{f}^0 + t\mathbf{h}) - \Theta(\mathbf{f}^0)}{t}, \quad (105)$$

for $t \in \mathbb{F}$, and all (i.e., arbitrary) vectors $\mathbf{f} \in \mathbb{E}_{\text{aug}}$.

4.3.1 The Forward Sensitivity Analysis Procedure (FSAP)

Just as for the original system, the augmented system's state vector $[\mathbf{u}(\mathbf{x}), \mathbf{v}(\mathbf{z})]$ and parameters $(\boldsymbol{\beta}, \mathbf{b})$ are related to each other through the relations (97–100). Hence, it follows that the vector of variations $(\mathbf{h}_u, \mathbf{h}_v)$ around the nominal values $[\mathbf{u}^0(\mathbf{x}), \mathbf{v}^0(\mathbf{z})]$ of the state functions $[\mathbf{u}(\mathbf{x}), \mathbf{v}(\mathbf{z})]$ is also related to the vector of parameter variations $(\mathbf{h}_\beta, \mathbf{h}_b)$ around the nominal values $(\boldsymbol{\beta}^0, \mathbf{b}^0)$. Therefore, the sensitivity $\delta\Theta(\mathbf{f}^0; \mathbf{h})$ of $\Theta(\mathbf{f})$ at \mathbf{f}^0 can only be evaluated after determining the variations $(\mathbf{h}_u, \mathbf{h}_v)$ in terms of the vector of parameter variations $(\mathbf{h}_\beta, \mathbf{h}_b)$. The first-order relationship between $(\mathbf{h}_u, \mathbf{h}_v)$ and $(\mathbf{h}_\beta, \mathbf{h}_b)$ is obtained by taking the G-differentials of (101–104), to obtain the relations

$$\begin{aligned} & \begin{pmatrix} N'_u(\mathbf{f}^0) + [N'_a(\mathbf{f}^0) - Q'_a(\mathbf{f}^0)] a'_u(\mathbf{f}^0) & [N'_a(\mathbf{f}^0) - Q'_a(\mathbf{f}^0)] a'_v(\mathbf{f}^0) \\ M'_u(\mathbf{f}^0) & M'_v(\mathbf{f}^0) \end{pmatrix} \begin{pmatrix} \mathbf{h}_u \\ \mathbf{h}_v \end{pmatrix} \\ & = \begin{pmatrix} [Q'_a(\mathbf{f}^0) - N'_a(\mathbf{f}^0)] a'_\beta(\mathbf{f}^0) & [Q'_a(\mathbf{f}^0) - N'_a(\mathbf{f}^0)] a'_b(\mathbf{f}^0) \\ 0 & S'_b(\mathbf{b}^0) - M'_b(\mathbf{f}^0) \end{pmatrix} \begin{pmatrix} \mathbf{h}_\beta \\ \mathbf{h}_b \end{pmatrix} \end{aligned} \quad (106)$$

together with the G-differentiated boundary/initial conditions

$$\begin{aligned} & B'_u(\mathbf{f}^0) \mathbf{h}_u + [B'_a(\mathbf{f}^0) - A'_a(\mathbf{f}^0)] [a'_u(\mathbf{f}^0) \mathbf{h}_u + a'_v(\mathbf{f}^0) \mathbf{h}_v] \\ & = [A'_a(\mathbf{f}^0) - B'_a(\mathbf{f}^0)] \times [a'_\beta(\mathbf{f}^0) \mathbf{h}_\beta + a'_b(\mathbf{f}^0) \mathbf{h}_b], \quad \mathbf{z} \in \partial\Omega, \end{aligned} \quad (107)$$

$$C'_u(\mathbf{f}^0) \mathbf{h}_u + C'_v(\mathbf{f}^0) \mathbf{h}_v = \delta D(\mathbf{b}^0; \mathbf{h}_b) - C'_b(\mathbf{f}^0) \mathbf{h}_b, \quad \mathbf{z} \in \partial\Omega. \quad (108)$$

Note that the left-side of (4.39) represents a block-matrix-valued linear operator, $L_a(\mathbf{f}^0)$, defined as

$$\begin{aligned} L_a(\mathbf{f}^0) & \equiv \begin{pmatrix} L_{11}(\mathbf{f}^0) & L_{12}(\mathbf{f}^0) \\ L_{21}(\mathbf{f}^0) & L_{22}(\mathbf{f}^0) \end{pmatrix} \\ & \equiv \begin{pmatrix} N'_u(\mathbf{f}^0) + [N'_a(\mathbf{f}^0) - Q'_a(\mathbf{f}^0)] a'_u(\mathbf{f}^0) & [N'_a(\mathbf{f}^0) - Q'_a(\mathbf{f}^0)] a'_v(\mathbf{f}^0) \\ M'_u(\mathbf{f}^0) & M'_v(\mathbf{f}^0) \end{pmatrix}. \end{aligned} \quad (109)$$

In the above expressions, the subscript “a” denotes “augmented.” For a given vector of parameter variations $(\mathbf{h}_\beta, \mathbf{h}_b)$, the system of equations (106–108) can be solved to obtain, to first-order, the vector of variations $(\mathbf{h}_u, \mathbf{h}_v)$. In turn, the variations $(\mathbf{h}_u, \mathbf{h}_v)$ and $(\mathbf{h}_\beta, \mathbf{h}_b)$ are used in (105) to calculate the sensitivity $\delta\Theta(\mathbf{f}^0; \mathbf{h})$ of $\Theta(\mathbf{f})$ at \mathbf{f}^0 , for given parameter variations $(\mathbf{h}_\beta, \mathbf{h}_b)$. Equations (106–108) represent the “forward sensitivity equations (FSE),” [also called the “tangent

linear model (TLM)"]. The forward sensitivity analysis procedure (FSAP) would proceed with the direct calculation of the response sensitivity $\delta\Theta(\mathbf{f}^0; \mathbf{h})$ by using the $(\mathbf{h}_\beta, \mathbf{h}_b)$ -dependent solution of the forward sensitivity equations. From the standpoint of computational costs and effort, the FSAP is advantageous to employ only if, in the problem under consideration, the number of different responses of interest exceeds the number of system parameters and/or parameter variations to be considered.

4.3.2 The Adjoint Sensitivity Analysis Procedure (ASAP)

The practical motivation underlying the development of an alternative method for sensitivity analysis is to avoid the need for repeatedly solving the FSE represented by (106–108). This goal was achieved for the original (unaugmented) system by constructing an adjoint system that was (1) uniquely defined, (2) independent of the vectors \mathbf{h}_u and \mathbf{h}_α , and (3) such that its solution can be used to eliminate all unknown values of \mathbf{h}_u from the expression of $\delta\Theta(\mathbf{f}^0; \mathbf{h})$. A similar path will also be followed for the augmented system. For this purpose, the spaces E_u , E_v , E_S , and E_q will henceforth be considered to be real Hilbert spaces denoted by H_u , H_v , H_q , and H_S , respectively. The inner products on $H_u \times H_v$ and $H_q \times H_S$ will be denoted by $(\bullet, \bullet)_{u \times v}$ and $(\bullet, \bullet)_{q \times S}$, respectively.

To define the formal adjoint $L_a^+(\mathbf{f}^0)$ of $L_a(\mathbf{f}^0)$, we recall from the geometry of Hilbert spaces $H_u \times H_v$ and $H_q \times H_S$ that the following relationship holds for a (column) vector $(\psi_u, \psi_v)^T \in H_q \times H_S$, where the superscript “ T ” denotes “transposition”:

$$\begin{aligned} & \left\langle \left(\begin{array}{c} \psi_u \\ \psi_v \end{array} \right)^T, \left(\begin{array}{cc} L_{11}(\mathbf{f}^0) & L_{12}(\mathbf{f}^0) \\ L_{21}(\mathbf{f}^0) & L_{22}(\mathbf{f}^0) \end{array} \right) \left(\begin{array}{c} \mathbf{h}_u \\ \mathbf{h}_v \end{array} \right) \right\rangle_{q \times S} \\ &= \left\langle \left(\begin{array}{c} \mathbf{h}_u \\ \mathbf{h}_v \end{array} \right)^T, L_a^+(\mathbf{f}^0) \left(\begin{array}{c} \psi_u \\ \psi_v \end{array} \right) \right\rangle_{u \times v} + \{P(\mathbf{f}^0; \psi_u, \psi_v; \mathbf{h}_u, \mathbf{h}_v)\}_{\partial\Omega}. \end{aligned} \quad (110)$$

The quantity $\{P(\mathbf{f}^0; \psi_u, \psi_v; \mathbf{h}_u, \mathbf{h}_v)\}_{\partial\Omega}$ in the above equation denotes the associated bilinear form (the “bilinear concomitant”) evaluated on $\partial\Omega$.

Replacing (109) on the left-side of (110) and carrying out the operations indicated by the respective inner products shows that the explicit form for the formal adjoint operator $L_a^+(\mathbf{f}^0)$ is the following 2×2 block-matrix:

$$\begin{aligned} L_a^+(\mathbf{f}^0) &\equiv \begin{pmatrix} L_{11}^+(\mathbf{f}^0) & L_{12}^+(\mathbf{f}^0) \\ L_{21}^+(\mathbf{f}^0) & L_{22}^+(\mathbf{f}^0) \end{pmatrix} \\ &\equiv \begin{pmatrix} [N'_u(\mathbf{f}^0)]^+ + \{[N'_a(\mathbf{f}^0) - Q'_a(\mathbf{f}^0)]\mathbf{a}'_u(\mathbf{f}^0)\}^+ & [M'_u(\mathbf{f}^0)]^+ \\ \{[N'_a(\mathbf{f}^0) - Q'_a(\mathbf{f}^0)]\mathbf{a}'_v(\mathbf{f}^0)\}^+ & [M'_v(\mathbf{f}^0)]^+ \end{pmatrix}, \end{aligned} \quad (111)$$

where the quantities $[N'_u(\mathbf{f}^0)]^+$, $\{[N'_a(\mathbf{f}^0) - Q'_a(\mathbf{f}^0)]\mathbf{a}'_u(\mathbf{f}^0)\}^+$, $[M'_u(\mathbf{f}^0)]^+$, $\{[N'_a(\mathbf{f}^0) - Q'_a(\mathbf{f}^0)]\mathbf{a}'_v(\mathbf{f}^0)\}^+$, and $[M'_v(\mathbf{f}^0)]^+$, denote the formal adjoint operators corresponding to $N'_u(\mathbf{f}^0)$, $[N'_a(\mathbf{f}^0) - Q'_a(\mathbf{f}^0)]\mathbf{a}'_u(\mathbf{f}^0)$, $M'_u(\mathbf{f}^0)$, $[N'_a(\mathbf{f}^0) - Q'_a(\mathbf{f}^0)]\mathbf{a}'_v(\mathbf{f}^0)$, and $M'_v(\mathbf{f}^0)$, respectively.

The boundary conditions for the adjoint operator $L_a^+(f^0)$, which define its domain, must be determined next. They are represented here in operator form as

$$\{\Gamma_1^+(f^0; \psi_u, \psi_v) - \Gamma_2^+(f^0)\}_{\partial\Omega} = 0, \quad \mathbf{z} \in \partial\Omega, \quad (112)$$

and are determined by requiring that (1) they must be independent of $(\mathbf{h}_u, \mathbf{h}_v)$ and $(\mathbf{h}_\beta, \mathbf{h}_b)$, and G-derivatives with respect to β and \mathbf{b} ; (2) they must cause all terms containing unknown values of $(\mathbf{h}_u, \mathbf{h}_v)$ to vanish when substituted together with (107) and (108) into the expression of $\{P(f^0; \psi_u, \psi_v; \mathbf{h}_u, \mathbf{h}_v)\}_{\partial\Omega}$.

Thus, when the conditions (112) for $L_a^+(f^0)$ are substituted together with (107) and (108) into the expression of $\{P(f^0; \psi_u, \psi_v; \mathbf{h}_u, \mathbf{h}_v)\}_{\partial\Omega}$, this bilinear concomitant will be reduced to a quantity that contains boundary terms involving solely known values of $(\mathbf{h}_\beta, \mathbf{h}_b)$, (ψ_u, ψ_v) , and, possibly, f^0 ; this quantity will be denoted in the sequel by $\hat{P}(f^0; \psi_u, \psi_v; \mathbf{h}_\beta, \mathbf{h}_b)$. In general, $\hat{P}(f^0; \psi_u, \psi_v; \mathbf{h}_\beta, \mathbf{h}_b)$ does not automatically vanish as a result of these manipulations, although it may do so in particular instances. In practice, $\hat{P}(f^0; \psi_u, \psi_v; \mathbf{h}_\beta, \mathbf{h}_b)$ will ultimately appear as a readily computable quantity in the expression of the response sensitivity $\delta\Theta(f^0; \mathbf{h})$.

Replacing now (107) and (108) together with the adjoint boundary conditions, given in (112) for $L_a^+(f^0)$, into (110) reduces the latter equation to

$$\begin{aligned} & \left\langle \left(\begin{array}{c} \psi_u \\ \psi_v \end{array} \right)^T, \left(\begin{array}{cc} L_{11}(f^0) & L_{12}(f^0) \\ L_{21}(f^0) & L_{22}(f^0) \end{array} \right) \left(\begin{array}{c} \mathbf{h}_u \\ \mathbf{h}_v \end{array} \right) \right\rangle_{q \times S} \\ & = \left\langle \left(\begin{array}{c} \mathbf{h}_u \\ \mathbf{h}_v \end{array} \right)^T, L_a^+(f^0) \left(\begin{array}{c} \psi_u \\ \psi_v \end{array} \right) \right\rangle_{u \times v} + \hat{P}(f^0; \psi_u, \psi_v; \mathbf{h}_\beta, \mathbf{h}_b). \end{aligned} \quad (113)$$

Replacing the quantity $\left(\begin{array}{cc} L_{11}(f^0) & L_{12}(f^0) \\ L_{21}(f^0) & L_{22}(f^0) \end{array} \right) \left(\begin{array}{c} \mathbf{h}_u \\ \mathbf{h}_v \end{array} \right)$ by the quantity $\left(\begin{array}{cc} [Q'_a(f^0) - N'_a(f^0)] \mathbf{a}'_\beta(f^0) & [Q'_a(f^0) - N'_a(f^0)] \mathbf{a}'_b(f^0) \\ 0 & S'_b(\mathbf{b}^0) - M'_b(f^0) \end{array} \right) \left(\begin{array}{c} \mathbf{h}_\beta \\ \mathbf{h}_b \end{array} \right)$ in the relation (113) transforms the latter into the form

$$\begin{aligned} & \left\langle \left(\begin{array}{c} \mathbf{h}_u \\ \mathbf{h}_v \end{array} \right)^T, L_a^+(f^0) \left(\begin{array}{c} \psi_u \\ \psi_v \end{array} \right) \right\rangle_{u \times v} = -\hat{P}(f^0; \psi_u, \psi_v; \mathbf{h}_\beta, \mathbf{h}_b) \\ & + \left\langle \left(\begin{array}{c} \psi_u \\ \psi_v \end{array} \right)^T, \left(\begin{array}{cc} [Q'_a(f^0) - N'_a(f^0)] \mathbf{a}'_\beta(f^0) & [Q'_a(f^0) - N'_a(f^0)] \mathbf{a}'_b(f^0) \\ 0 & S'_b(\mathbf{b}^0) - M'_b(f^0) \end{array} \right) \left(\begin{array}{c} \mathbf{h}_\beta \\ \mathbf{h}_b \end{array} \right) \right\rangle_{q \times S} \end{aligned} \quad (114)$$

To complete the ASAP, the left-side of the above equation needs to be related to the sensitivity $\delta\Theta(f^0; \mathbf{h})$ defined by (105). This can be done only when $\Theta(f)$ satisfies a weak Lipschitz condition at f^0 , and also satisfies the relation

$$\Theta(f^0 + t\mathbf{h}_1 + t\mathbf{h}_2) - \Theta(f^0 + t\mathbf{h}_1) - \Theta(f^0 + t\mathbf{h}_2) + \Theta(f^0) = o(t) \quad (115)$$

for two arbitrary vectors of increments \mathbf{h}_1 and \mathbf{h}_2 that have the same form (and the same number of components) as \mathbf{h} . In such cases, the response sensitivity $\delta\Theta(f^0; \mathbf{h})$ is linear in

$\mathbf{h} \equiv [\mathbf{h}_u, \mathbf{h}_v, \mathbf{h}_\beta, \mathbf{h}_b]$, and therefore becomes the total G-derivative $D\Theta(\mathbf{f}^0; \mathbf{h})$ of $\Theta(\mathbf{f})$ at \mathbf{f}^0 , of the form

$$\begin{aligned} D\Theta(\mathbf{f}^0; \mathbf{h}) &= \Theta'_u(\mathbf{f}^0) \mathbf{h}_u + [\Theta'_v(\mathbf{f}^0) + \Theta'_a(\mathbf{f}^0) \mathbf{a}'_v(\mathbf{f}^0)] \mathbf{h}_v \\ &\quad + \Theta'_a(\mathbf{f}^0) [\mathbf{a}'_\beta(\mathbf{f}^0) \mathbf{h}_\beta + \mathbf{a}'_b(\mathbf{f}^0) \mathbf{h}_b]. \end{aligned} \quad (116)$$

In the above expression, the quantities $\Theta'_u(\mathbf{f}^0)$, $\Theta'_v(\mathbf{f}^0)$, and $\Theta'_a(\mathbf{f}^0)$, denote the respective partial G-derivatives of $\Theta(\mathbf{f})$ at \mathbf{f}^0 , while $\mathbf{a}'_v(\mathbf{f}^0)$, $\mathbf{a}'_\beta(\mathbf{f}^0)$, and $\mathbf{a}'_b(\mathbf{f}^0)$ denote the respective partial G-derivatives of $\mathbf{a}(\mathbf{f})$ at \mathbf{f}^0 .

As indicated by (116), the $(\mathbf{h}_u, \mathbf{h}_v)$ -dependence in $D\Theta(\mathbf{f}^0; \mathbf{h})$ is separated from the $(\mathbf{h}_\beta, \mathbf{h}_b)$ -dependence. Furthermore, the 2-component column block-vector $[\Theta'_u(\mathbf{f}^0), \Theta'_v(\mathbf{f}^0) + \Theta'_a(\mathbf{f}^0) \mathbf{a}'_v(\mathbf{f}^0)]^T$ operates linearly on the vector $(\mathbf{h}_u, \mathbf{h}_v)^T$, which implies that

$$[\Theta'_u(\mathbf{f}^0), \Theta'_v(\mathbf{f}^0) + \Theta'_a(\mathbf{f}^0) \mathbf{a}'_v(\mathbf{f}^0)]^T \in L(H_u \times H_v, H_{\text{Raug}}(\Omega_{\text{Raug}}))$$

The *direct effect term* $\Theta'_a(\mathbf{f}^0) [\mathbf{a}'_\beta(\mathbf{f}^0) \mathbf{h}_\beta + \mathbf{a}'_b(\mathbf{f}^0) \mathbf{h}_b]$ can be calculated directly at this stage. On the other hand, the quantity $\Theta'_u(\mathbf{f}^0) \mathbf{h}_u + [\Theta'_v(\mathbf{f}^0) + \Theta'_a(\mathbf{f}^0) \mathbf{a}'_v(\mathbf{f}^0)] \mathbf{h}_v$ cannot be evaluated directly at this stage, since it depends on the unknown vector-valued function $(\mathbf{h}_u, \mathbf{h}_v)^T$, and is therefore called the *indirect effect term*.

To proceed with the evaluation of the indirect effect term $\{\Theta'_u(\mathbf{f}^0) \mathbf{h}_u + [\Theta'_v(\mathbf{f}^0) + \Theta'_a(\mathbf{f}^0) \mathbf{a}'_v(\mathbf{f}^0)] \mathbf{h}_v\} \in H_{\text{Raug}}(\Omega_{\text{Raug}})$, we consider that the orthonormal set $\{\theta_s\}_{s \in S}$, where s runs through an index set S , is an orthonormal basis of $H_{\text{Raug}}(\Omega_{\text{Raug}})$. Therefore, the indirect effect term $\Theta'_u(\mathbf{f}^0) \mathbf{h}_u + [\Theta'_v(\mathbf{f}^0) + \Theta'_a(\mathbf{f}^0) \mathbf{a}'_v(\mathbf{f}^0)] \mathbf{h}_v$ can be represented as the Fourier series

$$\begin{aligned} &\Theta'_u(\mathbf{f}^0) \mathbf{h}_u + [\Theta'_v(\mathbf{f}^0) + \Theta'_a(\mathbf{f}^0) \mathbf{a}'_v(\mathbf{f}^0)] \mathbf{h}_v \\ &= \sum_{s \in S} \langle \Theta'_u(\mathbf{f}^0) \mathbf{h}_u + [\Theta'_v(\mathbf{f}^0) + \Theta'_a(\mathbf{f}^0) \mathbf{a}'_v(\mathbf{f}^0)] \mathbf{h}_v, \theta_s \rangle_{\text{Raug}} \theta_s. \end{aligned} \quad (117)$$

The notation $\sum_{s \in S}$ is used to signify that in the above sum only an at most countable number of elements are different from zero, and the series extended upon the nonzero elements converges unconditionally. According to customary terminology, the functionals $\langle \Theta'_u(\mathbf{f}^0) \mathbf{h}_u + [\Theta'_v(\mathbf{f}^0) + \Theta'_a(\mathbf{f}^0) \mathbf{a}'_v(\mathbf{f}^0)] \mathbf{h}_v, \theta_s \rangle_{\text{Raug}}$ are called the Fourier coefficients with respect to the basis $\{\theta_s\}$, and are linear functionals in $(\mathbf{h}_u, \mathbf{h}_v)^T$.

The next step is to express each of the functionals $\langle \Theta'_u(\mathbf{f}^0) \mathbf{h}_u + [\Theta'_v(\mathbf{f}^0) + \Theta'_a(\mathbf{f}^0) \mathbf{a}'_v(\mathbf{f}^0)] \mathbf{h}_v, \theta_s \rangle_{\text{Raug}}$ as an inner product of $(\mathbf{h}_u, \mathbf{h}_v)^T$ with a uniquely defined vector in $H_u \times H_v$, which remains to be determined. Recalling that $[\Theta'_u(\mathbf{f}^0), \Theta'_v(\mathbf{f}^0) + \Theta'_a(\mathbf{f}^0) \mathbf{a}'_v(\mathbf{f}^0)]^T \in L(H_u \times H_v, H_{\text{Raug}}(\Omega_{\text{Raug}}))$, it follows that we can define the linear operator $\Pi(\mathbf{f}^0) \in L(H_{\text{Raug}}(\Omega_{\text{Raug}}), H_u \times H_v)$ to be the adjoint of $[\Theta'_u(\mathbf{f}^0), \Theta'_v(\mathbf{f}^0) + \Theta'_a(\mathbf{f}^0) \mathbf{a}'_v(\mathbf{f}^0)]^T \in L(H_u \times H_v, H_{\text{Raug}}(\Omega_{\text{Raug}}))$, by means of the relationship

$$\left\langle [\Theta'_u(\mathbf{f}^0) \Theta'_v(\mathbf{f}^0) + \Theta'_a(\mathbf{f}^0) \mathbf{a}'_v(\mathbf{f}^0)] \begin{pmatrix} \mathbf{h}_u \\ \mathbf{h}_v \end{pmatrix}, \theta_s \right\rangle_R = \left\langle \Pi(\mathbf{f}^0) \theta_s, \begin{pmatrix} \mathbf{h}_u \\ \mathbf{h}_v \end{pmatrix} \right\rangle_{u \times v}, \quad s \in S. \quad (118)$$

The operator $\Pi(\mathbf{e}^0)$ is actually a two-component operator (with components of dimensions equal to the vectors \mathbf{h}_u and \mathbf{h}_v , respectively), and is unique if

$\Theta'_u(\mathbf{f}^0)\mathbf{h}_u + [\Theta'_v(\mathbf{f}^0) + \Theta'_a(\mathbf{f}^0)\mathbf{a}'_v(\mathbf{f}^0)]\mathbf{h}_v$ is densely defined. The right-side of (118) can now be required to represent the same functional as the left-side of (114); this requirement yields the adjoint sensitivity system

$$L_a^+(\mathbf{f}^0) \begin{pmatrix} \psi_u^s \\ \psi_v^s \end{pmatrix} \equiv \begin{pmatrix} L_{11}^+(\mathbf{f}^0) & L_{12}^+(\mathbf{f}^0) \\ L_{21}^+(\mathbf{f}^0) & L_{22}^+(\mathbf{f}^0) \end{pmatrix} \begin{pmatrix} \psi_u^s \\ \psi_v^s \end{pmatrix} = \Pi(\mathbf{f}^0) \boldsymbol{\theta}_s, \quad s \in S, \quad (119)$$

which holds uniquely in view of the Riesz representation theorem. Note that the superscript s has been used to indicate the particular adjoint functions that are solutions of (119). This last step completes the construction of the *adjoint sensitivity system*, which consists of (119) and boundary conditions given in (112) for the adjoint function $(\psi_u^s, \psi_v^s)^T$. Furthermore, the relation (114) together with the relations (116–118) can now be used to obtain the following expression for the sensitivity $D\Theta(\mathbf{f}^0; \mathbf{h})$ of $\Theta(\mathbf{f})$ at \mathbf{f}^0 :

$$D\Theta(\mathbf{f}^0; \mathbf{h}) = \Theta'_a(\mathbf{f}^0) [\mathbf{a}'_\beta(\mathbf{f}^0) \mathbf{h}_\beta + \mathbf{a}'_b(\mathbf{f}^0) \mathbf{h}_b] + \sum_{s \in S} \boldsymbol{\theta}_s [-\hat{\mathbf{P}}(\mathbf{f}^0; \psi_u^s, \psi_v^s; \mathbf{h}_\beta, \mathbf{h}_b) + \left(\begin{pmatrix} \psi_u^s \\ \psi_v^s \end{pmatrix}^T, \begin{pmatrix} [Q'_a(\mathbf{f}^0) - N'_a(\mathbf{f}^0)] \mathbf{a}'_\beta(\mathbf{f}^0) & [Q'_a(\mathbf{f}^0) - N'_a(\mathbf{f}^0)] \mathbf{a}'_b(\mathbf{f}^0) \\ 0 & S'_b(\mathbf{b}^0) - M'_b(\mathbf{f}^0) \end{pmatrix} \begin{pmatrix} \mathbf{h}_\beta \\ \mathbf{h}_b \end{pmatrix} \right)_{q \times S} \right)]. \quad (120)$$

As (120) indicates, the desired elimination of all unknown values of $(\mathbf{h}_u, \mathbf{h}_v)^T$ from the expression of the sensitivity $D\Theta(\mathbf{f}^0; \mathbf{h})$ of $\Theta(\mathbf{f})$ at \mathbf{f}^0 has thus been accomplished. To evaluate the sensitivity $D\Theta(\mathbf{f}^0; \mathbf{h})$ by means of (120), one needs to compute as many adjoint functions $(\psi_u^s, \psi_v^s)^T$, ($s = 1, 2, \dots$), using (119) and (112) as there are nonzero terms in the representation of $\Theta'_u(\mathbf{f}^0)\mathbf{h}_u + [\Theta'_v(\mathbf{f}^0) + \Theta'_a(\mathbf{f}^0)\mathbf{a}'_v(\mathbf{f}^0)]\mathbf{h}_v$ given in (117). Although the linear combination of basis elements \mathbf{p}_s given in (117) may, in principle, contain infinitely many terms, only a finite number of the corresponding adjoint functions $(\psi_u^s, \psi_v^s)^T$ can be calculated in practice. Therefore, special attention is required to select the Hilbert space $H_{\text{Raug}}(\Omega_{\text{Raug}})$, the orthonormal basis $\{\boldsymbol{\theta}_s\}_{s \in S}$ for this space, and a notion of convergence for the representation given in (117) to best suit the problem at hand. This selection is guided by the need to represent the indirect effect term $\Theta'_u(\mathbf{f}^0)\mathbf{h}_u + [\Theta'_v(\mathbf{f}^0) + \Theta'_a(\mathbf{f}^0)\mathbf{a}'_v(\mathbf{f}^0)]\mathbf{h}_v$ as accurately as possible with the smallest number of basis elements; a related consideration is the viability of deriving bounds and/or asymptotic expressions for the remainder after truncating (117) to the first few terms. *Minimizing the number of terms in this summation falls within the objective of research activities known as “reduced-order modeling,”* but a detailed description of these activities is beyond the scope of this chapter.

In the important practical case when the *system response is a nonlinear functional* of the form $\Theta(\mathbf{f}) : D_{\text{Raug}} \subset E_{\text{aug}} \rightarrow F$, the space E_{Raug} is the underlying scalar field F of real numbers, and the sensitivity $\delta\Theta(\mathbf{f}^0; \mathbf{h})$ also becomes a functional that takes values in F . Furthermore, it will be assumed that the response $\Theta(\mathbf{e})$ satisfies a weak Lipschitz condition at \mathbf{f}^0 and also satisfies the relation shown in (115), so that the linear (in \mathbf{h}) G-differential $D\Theta(\mathbf{f}^0; \mathbf{h})$ exists. In this case, the summation $\sum_{s \in S}$ shown in (117) for the indirect effect term $\Theta'_u(\mathbf{f}^0)\mathbf{h}_u + [\Theta'_v(\mathbf{f}^0) + \Theta'_a(\mathbf{f}^0)\mathbf{a}'_v(\mathbf{f}^0)]\mathbf{h}_v$ reduces to a single term ($s = 1$); the subscript s can therefore be omitted in the sequel. Furthermore, the Riesz representation theorem ensures that there exists a unique 2-component vector $[\nabla_u \Theta(\mathbf{f}^0), \nabla_v \Theta(\mathbf{f}^0)]^T \in H_u \times H_v$, where the

respective components are defined via the relationship

$$\begin{aligned} \Theta'_u(\mathbf{f}^0) \mathbf{h}_u + [\Theta'_v(\mathbf{f}^0) + \Theta'_a(\mathbf{f}^0) \mathbf{a}'_v(\mathbf{f}^0)] \mathbf{h}_v \\ = \left[[\nabla_u R(\mathbf{f}^0) \nabla_u R(\mathbf{f}^0)], \left(\begin{array}{c} \mathbf{h}_u \\ \mathbf{h}_v \end{array} \right) \right]_{u \times v}, \quad \mathbf{h}_u \in H_u, \mathbf{h}_v \in H_v \\ \nabla_u \Theta(\mathbf{f}^0) \equiv [\Theta'_u(\mathbf{f}^0)]^T \in H_u, \\ \nabla_v \Theta(\mathbf{f}^0) \equiv [[\Theta'_v(\mathbf{f}^0) + \Theta'_a(\mathbf{f}^0) \mathbf{a}'_v(\mathbf{f}^0)]]^T \in H_v. \end{aligned} \quad (121)$$

Comparison of (122) and (118) reveals that (119) becomes

$$\mathbf{L}_a^+(\mathbf{f}^0) \left(\begin{array}{c} \psi_u \\ \psi_v \end{array} \right) \equiv \left(\begin{array}{cc} \mathbf{L}_{11}^+(\mathbf{f}^0) & \mathbf{L}_{12}^+(\mathbf{f}^0) \\ \mathbf{L}_{21}^+(\mathbf{f}^0) & \mathbf{L}_{22}^+(\mathbf{f}^0) \end{array} \right) \left(\begin{array}{c} \psi_u \\ \psi_v \end{array} \right) = \left(\begin{array}{c} \nabla_u R(\mathbf{f}^0) \\ \nabla_v R(\mathbf{f}^0) \end{array} \right). \quad (122)$$

Furthermore, the expression for response sensitivity $D\Theta(\mathbf{f}^0; \mathbf{h})$, cf. (120) reduces to

$$\begin{aligned} D\Theta(\mathbf{f}^0; \mathbf{h}) = \Theta'_a(\mathbf{f}^0) [\mathbf{a}'_\beta(\mathbf{f}^0) \mathbf{h}_\beta + \mathbf{a}'_b(\mathbf{f}^0) \mathbf{h}_b] - \hat{\mathbf{P}}(\mathbf{f}^0; \psi_u, \psi_v; \mathbf{h}_\beta, \mathbf{h}_b) \\ + \left\langle \left(\begin{array}{c} \psi_u \\ \psi_v \end{array} \right)^T, \left(\begin{array}{cc} [\mathbf{Q}'_a(\mathbf{f}^0) - \mathbf{N}'_a(\mathbf{f}^0)] \mathbf{a}'_\beta(\mathbf{f}^0) & [\mathbf{Q}'_a(\mathbf{f}^0) - \mathbf{N}'_a(\mathbf{f}^0)] \mathbf{a}'_b(\mathbf{f}^0) \\ 0 & \mathbf{S}'_b(\mathbf{b}^0) - \mathbf{M}'_b(\mathbf{f}^0) \end{array} \right) \left(\begin{array}{c} \mathbf{h}_\beta \\ \mathbf{h}_b \end{array} \right) \right\rangle_{q \times s}. \end{aligned} \quad (123)$$

Thus, once the single calculation to determine the adjoint function $(\psi_u, \psi_v)^T$ from (122) and (112) has been carried out, the adjoint function $(\psi_u, \psi_v)^T$ can be used in (123) to obtain efficiently the sensitivity $D\Theta(\mathbf{f}^0; \mathbf{h})$ of $\Theta(\mathbf{f})$.

In practice, when the ASAP is applied successively to the various component modules of a complex code system, the practitioner first develops an adjoint sensitivity model of the form described by (85) and then augments the adjoint operator $\mathbf{L}^+(\mathbf{e}^0)$ to construct the augmented adjoint operator $\mathbf{L}_a^+(\mathbf{f}^0)$ defined in (111). From a programmer's point of view, the adjoint operator $\mathbf{L}_{11}^+(\mathbf{f}^0) \equiv [\mathbf{N}'_u(\mathbf{f}^0)]^+ + \{[\mathbf{N}'_a(\mathbf{f}^0) - \mathbf{Q}'_a(\mathbf{f}^0)] \mathbf{a}'_u(\mathbf{f}^0)\}^+$ can be formally constructed by starting from the adjoint operator $\mathbf{L}^+(\mathbf{e}^0) \equiv [\mathbf{N}'_u(\mathbf{u}^0, \boldsymbol{\alpha}^0)]^+$ of the original (nonaugmented) system, and then adding the operator $\{[\mathbf{N}'_a(\mathbf{f}^0) - \mathbf{Q}'_a(\mathbf{f}^0)] \mathbf{a}'_u(\mathbf{f}^0)\}^+$. This is because the numerical representation of the operator $[\mathbf{N}'_u(\mathbf{f}^0)]^+$ is the same as that of $[\mathbf{N}'_u(\mathbf{u}^0, \boldsymbol{\alpha}^0)]^+$. The fact that these two operators are then evaluated at distinct nominal parameter values clearly plays an important role in the solution evaluation, but not in the initial construction and programming of $\mathbf{L}_{11}^+(\mathbf{f}^0)$. Of course, the adjoint operators $\mathbf{L}_{12}^+(\mathbf{f}^0)$, $\mathbf{L}_{21}^+(\mathbf{f}^0)$, and $\mathbf{L}_{22}^+(\mathbf{f}^0)$ are specific to the augmented system, and must therefore be constructed/programmed *ab initio*.

Often, the adjoint sensitivity system for the augmented system can be solved by using the same numerical methods as used for solving the non-augmented adjoint system, particularly when the numerical representation of the matrix operator $\mathbf{L}_a^+(\mathbf{f}^0)$ can be inverted by partitioning. Of course, if the off-diagonal operators $\mathbf{L}_{12}^+(\mathbf{f}^0)$ and/or $\mathbf{L}_{21}^+(\mathbf{f}^0)$ vanish, then the inversion of $\mathbf{L}_a^+(\mathbf{f}^0)$ becomes significantly simpler.

The inverse route, namely, going from the augmented system to the non-augmented one is accomplished by simply setting the operators $\mathbf{L}_{12}^+(\mathbf{f}^0)$, $\mathbf{L}_{21}^+(\mathbf{f}^0)$, and $\mathbf{L}_{22}^+(\mathbf{f}^0)$ to zero. In this case, (120) also reduces to (87), as would be expected.

4.4 Illustrative Application of ASAP: Adjoint Sensitivity Analysis of Markov Dynamic Reliability Models

Markov chains are extensively used to analyze and predict system reliability and availability in many branches of industry (e.g., cell phones, computers, communication and networks, health equipment, aviation and aerospace, automotive engineering, chemical processing, military application, nuclear engineering), economic/econometric models, population forecasting, biology, and financial planning (see, e.g., Henley and Kumamoto 1992; Norris 1997). A Markov chain typically models the respective physical system as a set of states in which the system can find itself during its life period, together with the transitions that can occur between these states, accounting for statistical dependences among failures and/or repairs. A state is a unique configuration of failed and operational components or subsystems. The states and transitions for a Markov chain with $I = \{1, 2, \dots, n\}$ states are modeled by a system of ordinary differential (Kolmogorov's) equations, including the corresponding initial probability distribution, and can be written in matrix form as follows:

$$\begin{cases} \frac{d\Pi(t)}{dt} = [\mathbf{Q}(t)] \Pi(t), & t \geq t_0 \\ \Pi(t_0) = \Pi_0, \end{cases} \quad (124)$$

where the column vector $\Pi(t)$ represents the state probability vector

$$\Pi(t) = [\pi_1(t), \pi_2(t), \dots, \pi_n(t)]^T, \quad (125)$$

and the column vector Π_0 represents the initial state probability vector at initial time t_0 , $0 \leq t_0 < t$. If, in particular, the analysis commences from an initial time in which the system is in a state with all components operational, then the initial state probability vector is $\Pi_0 = [1, 0, \dots, 0]^T$.

The transition rate matrix $\mathbf{Q}(t) = [q_{ij}(t)]_{n \times n}$, $i, j \in I$, in (124) is a square matrix of order n , with the property that all of its off-diagonal components are positive and the component on the main diagonal is negative and equal with minus sum of all other elements on column, that is, $q_{ii}(t) = -\sum_{i \neq j} q_{ji}(t)$. The elements $q_{ij}(t)$ are considered to depend on the system's parameters $\alpha_k(t)$. The true values of these parameters are not known precisely in practice, but may vary according to some known distribution or (if this is unknown) within some limiting values (finite or infinite) that reflect the corresponding incomplete knowledge or uncertainty. The Kolmogorov system (124) becomes at steady state ($t \rightarrow t_\infty$)

$$\mathbf{Q}(t_\infty) \Pi(t_\infty) = 0, \quad (126)$$

where $\Pi(t_\infty) \equiv [\pi_1(t_\infty), \pi_2(t_\infty), \dots, \pi_n(t_\infty)]^T$ represents the steady state probability vector at equilibrium (steady state) satisfying the relation $\sum_{i \in I} \pi_i = 1$ (conservation of probability).

Reliability of a component is defined as the probability that the component survives until some time t , considering that at a time t_0 the component was operating properly, $0 \leq t_0 \leq t \leq \infty$. Extended to a system, the *reliability* $R(t)$ of a physical system is the probability that the system is functional until a time t given that the system was operating correctly at an initial time t_0 . The definition of reliability implies that the system was not under repair until time t . In Markov

analysis for reliability quantification, the failure states of the system are considered absorbing states (defined as a state which the system never leaves after entering it), while the other states are considered to be transient states (defined as a state in which the system enters, exits, and never returns to it during its evolution) or recurrent states (defined as a state to which the system can return during its evolution.). The complementary function of reliability is called *unreliability*, $\overline{R}(t)$, of the system and is defined as $\overline{R}(t) \equiv 1 - R(t)$. The *availability*, $A(t)$, of a physical system is the probability that the system is operating correctly at a requested time t . The complementary function of availability is called *unavailability*, $\overline{A}(t)$, of the system and is defined as $\overline{A}(t) \equiv 1 - A(t)$. When computing the unavailability of a system, the failure states in the underlying Markov chain need not necessarily be absorbing states, since the system could have been repaired or components replaced during the time period from t_0 to t ; in such a case, the operational states could be either transient or recurrent states. Taking in account the properties of the states in Markov chain, the availability and reliability are computed in similar ways. Thus, if the states $I = \{1, 2, \dots\}$ of a Markov chain consists of a set of states in which the system is failed $\{Down\}$ and operational $\{Up\}$, then the transient solution of Kolmogorov equations gives the reliability/availability of the system as

$$R(t) = \sum_{i \in Up} \pi_i(t), \quad (127)$$

while the complementary function, the unreliability, is obtained as

$$\overline{R}(t) = \sum_{i \in Down} \pi_i(t) = 1 - R(t). \quad (128)$$

Recall that the instantaneous or point availability $A(t)$ of a component or a system is defined as the probability that the component or system is properly functioning at time t . In the absence of a repair or a replacement, the availability $A(t)$ is simply equal to the reliability $R(t)$ for a component. The instantaneous availability is always greater than or equal to the reliability. For a component, the instantaneous availability is

$$A(t) = \pi_i(t), \quad i \in \{Up\}. \quad (129)$$

The limiting or steady state availability is the limiting value of $A(t)$ as t approaches infinity, that is, $A = \lim_{t \rightarrow \infty} A(t) \neq 0$; this measure is usually nonzero, in contrast to limiting reliability which is always zero, that is, $R = \lim_{t \rightarrow \infty} R(t) = 0$. The average or interval availability represents the expected fraction of time the system is up in a given interval of time $[t_0, t]$, $0 \leq t_0 < t \leq \infty$, that is,

$$A_I \equiv \frac{1}{t_f} \int_{t_0}^{t_f} A(t) dt. \quad (130)$$

The repairing or replacing of a system component is characterized mathematically through transitions between states in the Markov chain representing the respective system. The failure behavior of components is determined statistically, and is consequently described by statistical distributions. The *failure (or hazard) rate* $\lambda(t)$ describes the expected number of failures in a given time period. The concepts of *mean time to failure (MTTF)*, *mean time to repair (MTTR)*, and *mean time between failures (MTBF \equiv MTTF + MTTR)* are also used for components and

systems. The mean time to repair is obtained from statistical considerations, but the mean time to failure can be computed in terms of the system's reliability as

$$MTTF = \int_{t_0}^{t_f} R(t) dt, \quad 0 \leq t_0 < t \leq \infty. \quad (131)$$

All of the system responses (i.e., reliability measures) defined in (127–131) are functionals of the transient probabilities $\pi_i(t)$, $i = 1, \dots, n$, and the elements $q_{ij}(t)$ of the transition rate matrix, which can in turn depend on external parameters, denoted in the sequel as $\alpha_k(t)$, that is, $q_{ij}(t) = f(\alpha_k(t))$, for $i, j = 1, \dots, n$; $k = 1, \dots, m$. Thus, all of these responses can be represented mathematically in the general form

$$R(\Pi(t), \alpha) \equiv \int_{t_0}^{t_f} F(\Pi(t), \alpha) dt, \quad 0 \leq t_0 < t, \quad (132)$$

where n denotes the number of states in Markov chain, m denotes the number of system parameters, t_0 and t_f represent the initial and, respectively, the final time under consideration, and $F(\pi_i; \alpha_k; t)$ represents a (possibly nonlinear) function of the indicated arguments.

As previously mentioned, the true values of the parameters α are not known in practice; usually, only their nominal (mean) values $\alpha^0 = (\alpha_1^0(t), \dots, \alpha_m^0(t))$ and their uncertainties $\delta\alpha \equiv (\delta\alpha_1, \dots, \delta\alpha_m)$ (variation intervals, bounds, or variance-covariances) are known. Hence, the Kolmogorov equations (124) can be solved using the nominal values $\{\alpha_1^0(t), \dots, \alpha_m^0(t)\}$ together with the nominal initial probability vector, $\Pi^0(t_0) = [\pi_1^0(t_0), \dots, \pi_n^0(t_0)]^T$, to obtain the nominal solution $\Pi^0(t)$ which is used, in turn, to obtain the base case response value $R^0(\Pi^0, \alpha^0)$. Note that the superscript “zero” is used throughout this work to denote base-case (i.e., nominal) values.

The typical deterministic approach for computing sensitivities for Markov chains is to solve the original system for the base case together with a larger set of differential equations for the respective sensitivities (see, e.g., Cao and Wan 1998; Ou and Dugan 2003). This set can be represented compact in matrix form as follows:

$$\left\{ \begin{aligned} & \left[\frac{d}{dt} [\Pi^0(t)]_{n \times 1}, \frac{\partial}{\partial \alpha_k} \left(\frac{d}{dt} [\Pi^0(t)]_{n \times 1} \right) \right] \\ & = \begin{bmatrix} [\mathbf{Q}^0(t)]_{n \times n} & [0]_{n \times n} \\ \frac{\partial}{\partial \alpha_k} [\mathbf{Q}^0(t)]_{n \times n} & [\mathbf{Q}^0(t)]_{n \times n} \end{bmatrix} \begin{bmatrix} [\Pi^0(t)]_{n \times 1} \\ \frac{\partial}{\partial \alpha_k} [\Pi^0(t)]_{n \times 1} \end{bmatrix} \\ & \left[[\Pi^0(t_0)]_{n \times 1}, \frac{\partial}{\partial \alpha_k} [\Pi^0(t_0)]_{n \times 1} \right] = \left[[\Pi_0]_{n \times 1}, \frac{\partial}{\partial \alpha_k} [\Pi_0]_{n \times 1} \right], \quad k = 1, \dots, m, \end{aligned} \right. \quad (133)$$

where the vector/matrix subscripts indicate the sizes of the respective vectors and matrices. In principle, the above equations can be solved repeatedly to obtain the functions $(\partial/\partial\alpha_k)[\Pi^0(t)]_{n \times 1}$. Subsequently, these functions can be used to compute the first-order effects of parameter variations $\delta\alpha_k$ on the response R . Since the set of differential equations need to be solved anew for each parameter variation $\delta\alpha_k$, this procedure is just as expensive as recalculating the perturbed response $R(\Pi^0 + \Phi, \alpha^0 + \delta\alpha^0)$ after having repeatedly solved the Kolmogorov system (124).

The need for solving repeatedly the system (133) can be avoided by applying the ASAP to the Kolmogorov system (124) and response (132), as generally shown in \blacktriangleright Sect. 4.3. The first step to compute the G-differential of the response (132) to obtain

$$\begin{aligned} DR(\Pi^0, \alpha^0; \Phi, \delta\alpha) &\equiv \frac{d}{d\varepsilon} \left\{ \int_{t_0}^{t_f} F(\Pi^0 + \varepsilon\Phi, \alpha^0 + \varepsilon\delta\alpha) \right\}_{\varepsilon=0} \\ &= \sum_{k=1}^m \int_{t_0}^{t_f} \left(\frac{\partial F}{\partial \alpha_k} \right)_{(\Pi^0, \alpha^0)} \delta\alpha_k dt + \int_{t_0}^{t_f} \left(\frac{\partial F}{\partial \Pi} \right)_{(\Pi^0, \alpha^0)}^T \Phi(t) dt \\ &\triangleq R'_\alpha(\Pi^0, \alpha^0) \delta\alpha + R'_\Pi(\Pi^0, \alpha^0) \Phi, \end{aligned} \quad (134)$$

where Φ denotes the vector of variations in Π (due to parameter variations $\delta\alpha$), $\partial F/\partial \Pi \equiv (\partial F/\partial \pi_1, \dots, \partial F/\partial \pi_n)^T$, and where

$$R'_\alpha(\Pi^0, \alpha^0) \delta\alpha \equiv \sum_{k=1}^m \int_{t_0}^{t_f} \left(\frac{\partial F}{\partial \alpha_k} \right)_{(\Pi^0, \alpha^0)} \delta\alpha_k dt \quad (135)$$

is the so-called “direct effect” term, while

$$R'_\Pi(\Pi^0, \alpha^0) \Phi \equiv \sum_{k=1}^m \int_{t_0}^{t_f} \left(\frac{\partial F}{\partial \Pi} \right)_{(\Pi^0, \alpha^0)}^T \Phi(t) dt \quad (136)$$

is the so-called “indirect effect” term, which can only be computed after having determined the functions $\Phi(t)$. Recall that

$$R(\Pi^0 + \Phi; \alpha^0 + \delta\alpha) = R(\Pi^0, \alpha^0) + DR(\Pi^0, \alpha^0; \Phi, \delta\alpha) + O(\|\Phi\|^2 + \|\delta\alpha\|^2),$$

indicating that the exact value of the perturbed response using recalculations is predicted by the sensitivity $DR(\Pi^0, \alpha^0; \Phi, \delta\alpha)$ to first-order accuracy in $\|\Phi\|^2$ and $\|\delta\alpha\|^2$, respectively.

The next step is to derive the forward sensitivity system [cf. (78) and (79)] by computing the G-differential to the Kolmogorov equations (124), to obtain

$$\begin{cases} L\Phi(t) = [\delta Q] \Pi^0(t); & L \equiv \frac{d}{dt} I - Q^0(t) \\ \Phi(t_0) = \Phi_0. \end{cases} \quad (137)$$

The final step is to construct the system adjoint to (137), by following the general procedure that lead to (85). For the particular case of (137), the required inner product between two vector valued functions $f(x) \equiv [f_1(x), \dots, f_n(x)]^T$, $g(x) \equiv [g_1(x), \dots, g_n(x)]^T$ is

$$\langle f(t), g(t) \rangle \equiv \sum_{i=1}^n \int_{t_0}^{t_f} [f(x)]^T [g(x)] dx. \quad (138)$$

Forming thus the inner product of (137) with a vector $\Psi(t) \equiv [\psi_1(t), \dots, \psi_n(t)]^T$ yields

$$\int_{t_0}^{t_f} \Psi^T(t) \left(\frac{d}{dt} I - Q^0 \right) \Phi(t) dt = \int_{t_0}^{t_f} \Psi^T(t) [\delta Q] \Pi^0(t) dt. \quad (139)$$

Performing the integration by parts on the left side of the above equation in order to transfer all the differentiation operations from the vector $\Phi(t)$ to the vector $\Psi(t)$ gives

$$\int_{t_0}^{t_f} \Psi^T(t) \left(\frac{d}{dt} I - Q^0 \right) \Phi(t) dt = \langle L^* \Psi, \Phi \rangle + \Psi^T(t_f) \Phi(t_f) - \Psi^T(t_0) \Phi(t_0), \quad (140)$$

where

$$L^*(\cdot) = \left(-\frac{d}{dt} I - [Q^0(t)]^T \right) (\cdot) \quad (141)$$

is the operator formally adjoint to the operator L . The construction of the adjoint sensitivity system can now be completed in two steps, as follows: (1) requiring that the first term on the right side of (140) represent the same functional as the “indirect-effect term” (136); and (2) eliminating the unknown value $\Phi(t_f)$ by requiring that $\Psi^T(t_f) = 0$. Following these two steps yields the adjoint sensitivity system

$$\left(-\frac{d}{dt} I - [Q^0(t)]^T \right) \Psi(t) = \left(\frac{\partial F}{\partial \Pi} \right)_{(\Pi^0, \alpha^0)}; \quad \Psi(t_f) = 0, \quad (142)$$

and the following alternative expression for the response sensitivities in terms of the adjoint function $\Phi(t)$:

$$\begin{aligned} DR(\Pi^0, \alpha^0; \Phi, \delta\alpha) &= \int_{t_0}^{t_f} \Psi^T(t) [\delta Q] \Pi^0(t) dt + \Psi^T(t_0) \Phi(t_0) \\ &+ \sum_{k=1}^m \int_{t_0}^{t_f} \left(\frac{\partial F}{\partial \alpha_k} \right)_{(\Pi^0, \alpha^0)} \delta\alpha_k dt. \end{aligned} \quad (143)$$

Note that the adjoint sensitivity system (142) is linear in the adjoint function Ψ , depending on the response R , and is independent of parameter variations $\delta\alpha$. Hence, this system needs to be solved only once per response to obtain the adjoint function Ψ . In turn, Ψ is used in the integrand in (143) for computing efficiently the response sensitivities to all system parameters. Since the Kolmogorov system (124) are linear in Π , the adjoint sensitivity system can be solved independently of the base-case solution Π^0 , as expected.

The Kolmogorov system (124), the forward sensitivity system (137), and the adjoint sensitivity system (142) are all linear systems of ordinary differential equation which can be written generically in the form

$$\frac{dy_i}{dt} = f_i(t, y_1, \dots, y_n); \quad y_i(t_0) = y_{i_0}, \quad i = 1, \dots, n, \quad (144)$$

and can therefore be solved efficiently and accurately using, for example, the VODPK solver developed in Brown et al. (1989) and Brown and Hindmarsh (1989) together with incomplete LU-factorization for preconditioning (Rauzy 2004).

The implementation of the ASAP for sensitivity analysis of dynamic reliability of systems modeled by Markov chains comprises the following steps:

1. Abstraction of the physical system to construct fault tree diagrams;
2. Qualitative analysis of these fault trees for determining the generic fault states and minimal cut-sets;
3. Use of fault trees to construct the corresponding Markov chain;

4. Construction of the adjoint sensitivity system;
5. Solution of the resulting Kolmogorov differential equations, and of the adjoint system;
6. Use of adjoint functions to compute sensitivities of reliability measures to parameters;
7. Use of sensitivities.

The above steps have been implemented (Cacuci et al. 2008) in a computer software package comprising three interconnected modules, called QUEFT (qualitative evaluator for fault tree), MARKOMAG-S (Markov chain matrix generator and solver), and MCADJSEN (Markov chain adjoint sensitivity module). This computer software package has been used to perform a sensitivity and uncertainty analysis of the dynamic reliability of the international fusion material irradiation facility (IFMIF). This facility is projected (IFMIF-CDA Team; Martone 1996) to provide the necessary irradiation field for testing new materials and for generating a database for the behavior of materials under irradiation by 14-MeV neutron-fields, as would be expected during the operation of future fusion power reactors. The IFMIF facility comprises five main subsystems: test facilities, target facilities, accelerator facilities, conventional facilities, and the central control and common instrumentation subsystem, respectively. Reliability studies (IFMIF-CDA Team; Martone 1996) have indicated that these subsystems would need to fulfill a minimum total availability of 80.7% for the overall IFMIF. Furthermore, these studies have also indicated that, of all five IFMIF-subsystems, the IFMIF-accelerator system has the lowest availability, namely 88%. This accelerator-system for IFMIF has not been built yet, so the availability value of 88% was computed (IFMIF-CDA Team; Martone 1996) using fault-tree methods for the main accelerator subsystems. The data for the various components comprising the accelerator system were obtained from components of existing accelerator facilities, for a mission time of 168 h (7 days), which is considered to be the period of time between two scheduled maintenance operations. Furthermore, the availability value of 88% was obtained without taking into account any uncertainties. Since time-dependent changes are likely to occur (e.g., due to maintenance, repair, or replacement considerations in order to minimize the expenses for building and operating the accelerator facility) before commencing the actual construction of the accelerator facility, sensitivities and uncertainty studies must be performed in order to assess the influence of reliabilities of the various components on the overall accelerator system availability and reliability.

A simplified representation (Piaszczyk 1996) of the accelerator system is presented in [▶ Fig. 1](#), while [▶ Fig. 2](#) depicts the fault tree of (only) the first level of the accelerator system. The associated Markov chain comprises 32 coupled differential equations corresponding to the transitions shown in [▶ Fig. 3](#). The corresponding transition rate matrix is sparse, containing just 193 nonzero elements; its structure is shown in [▶ Fig. 4](#).

[▶ Table 2](#) presents results for the sensitivities of the average (or interval) availability response to the initial state probability vector, while [▶ Table 3](#) presents sensitivities of the same response to the system parameters (failure and repair rates), for the first-level fault tree of the accelerator system. The average (or interval) availability response is represented mathematically as the integral $R = (1/t_f) \int_{t_0}^{t_f} \pi_1(t) dt$; this type of response produces a source term of form $\partial F / \partial \Pi = [1, 0, \dots, 0]^T$ in adjoint sensitivity system, for all time steps until the final mission time at $t_f = 168$ h [cf. (142)]. The results presented in [▶ Table 2](#) show that the response depends linearly on the initial conditions, and the ASAP computes the respective sensitivities very accurately. On the other hand, the comparisons between the exact recalculations and the corresponding ASAP results presented in [▶ Table 3](#) indicate that the response depends nonlinearly on the respective failure and repair rates.

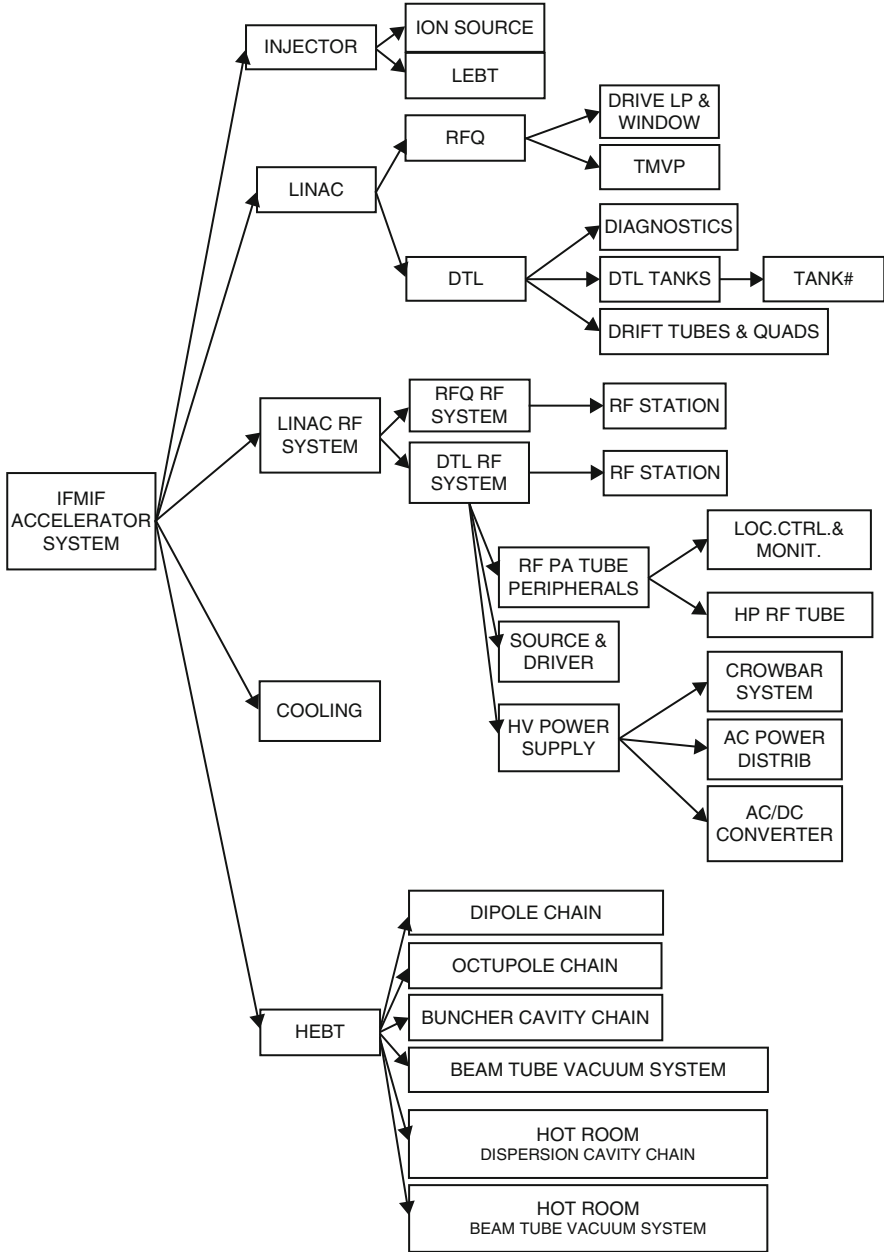


Figure 1 The main subsystems of the IFMIF-accelerator design

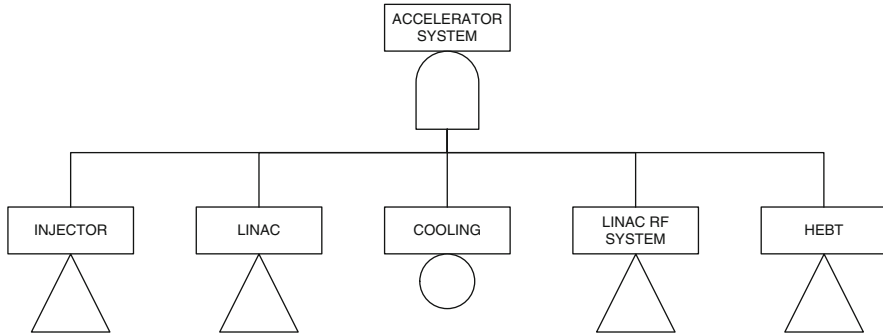


Figure 2
The first level of the fault-tree for the accelerator system

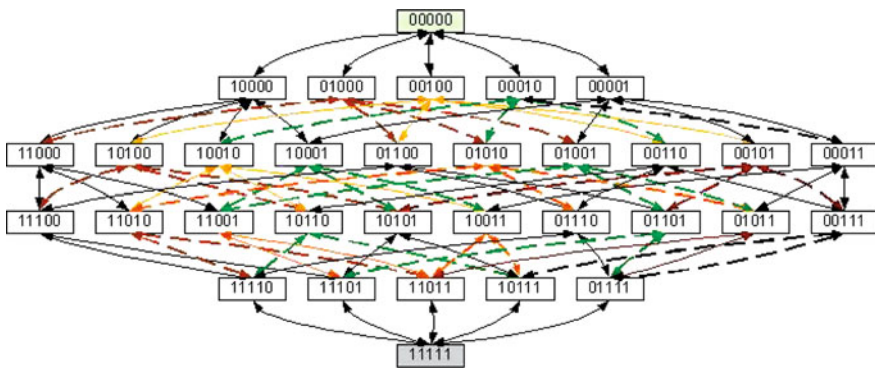


Figure 3
The Markov chain transitions for the first level of the accelerator system

The magnitudes of the relative sensitivities of the average availability $R = (1/t_f) \int_{t_0}^{t_f} \pi_1(t) dt$ to the *MTTFs* and *MTTRs* of over 180 components of the IFMIF accelerator system are presented in Cacuci et al. (2008). The importance ranking of these components for the average availability response is depicted in Fig. 5, which indicates that the highest sensitivities of the average availability of the IFMIF accelerator systems are, in order, to the LINAC-RF-parameters, followed by the LINAC-parameters, HEBT-parameters, INJECTOR-parameters, and the COOLING-system parameters.

Another important response for the IFMIF accelerator system facilities is the system's availability at the final mission time of $t_f = 168$ h (7 days). In this case, the mathematical representation of the system response is $R = \int_{t_0}^{t_f} \pi_1(t) \delta(t - t_f) dt = \pi_1(t_f)$, where the symbol δ represents the Dirac-delta functional, and where the initial time has been taken as $t_0 = 0$. This response gives rise to a source term in the adjoint sensitivity equations [cf. (142)] of the form $\partial F / \partial \Pi = [1, 0, \dots, 0]^T$ at the end of mission time $t_f = 168$ h, and $\partial F / \partial \Pi = [0, 0, \dots, 0]^T$ for all other time steps. The results of the sensitivity analysis for this response are summarized pictorially in Fig. 6, which presents the importance ranking of the IFMIF accelerator system

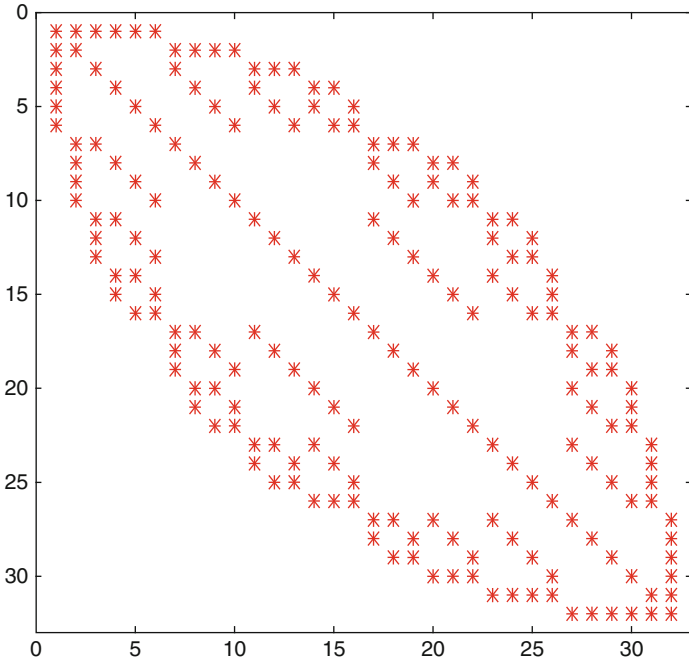


Figure 4
The structure of the transition rate matrix for the first level of the accelerator system

Table 2
Sensitivities of the average (or interval) availability to the initial state probability vector

Pert.in initial cond.	Trans. duration (h)/ no. of time steps	Nom. value R^0	Rel. sens $\frac{\Delta R}{\Delta \alpha_i} \cdot \frac{\alpha_i^0}{R^0}$	ASAP $R_{pred} - R^0$	Exact recal. $R_{recalc} - R^0$
-10% of $\pi_1(t_0)$	1/100	.9920	1.000	-.0992	-.0992
	12/1200	.9452	.9197	-.0869	-.0869
10% of $\pi_{32}(t_0)$	168/16800	.8882	.1425	-.0127	-.0127

components based on the sensitivities of the *final-time availability* response to the components' *MTTFs* and *MTTRs*. The results show that, although the importance ranking is generally the same (within the subsystems) as it was for the “average availability” response, the overall importance of the subsystems to the accelerator facility is changed, in that the LINAC and RF system have changed places, with the LINAC-sensitivities now displaying the largest absolute values. In other words, the reliability of the LINAC-components is the most important factor for the final-time availability of the overall IFMIF-accelerator, but the reliability of the RF-components is the most important factor for the average reliability of the overall IFMIF-accelerator. The complete sensitivity analysis, including numerical results for the sensitivities of

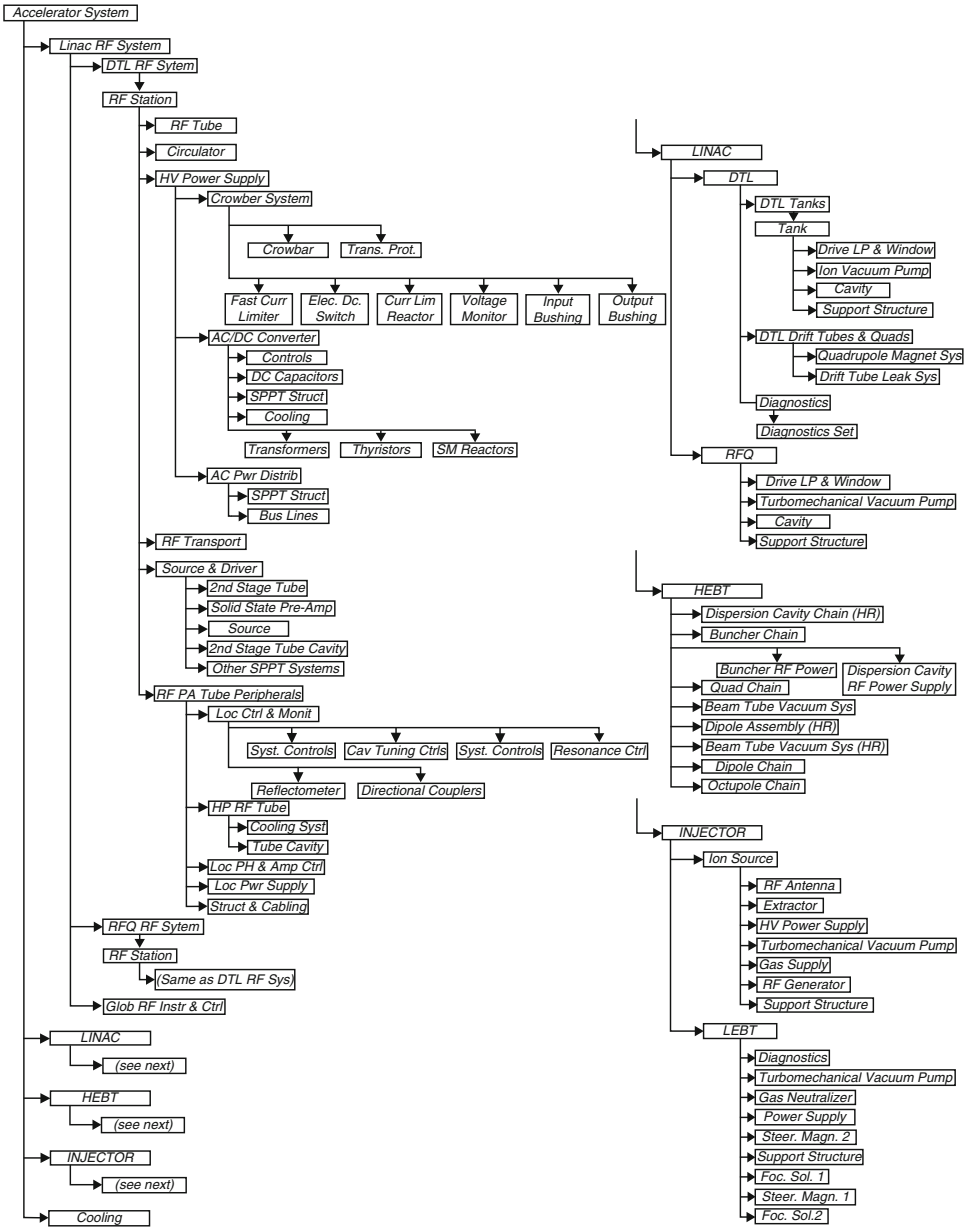


Figure 5 Importance ranking of the IFMIF accelerator system components based on the sensitivities of the average availability response to the components' MTTFs and MTTRs

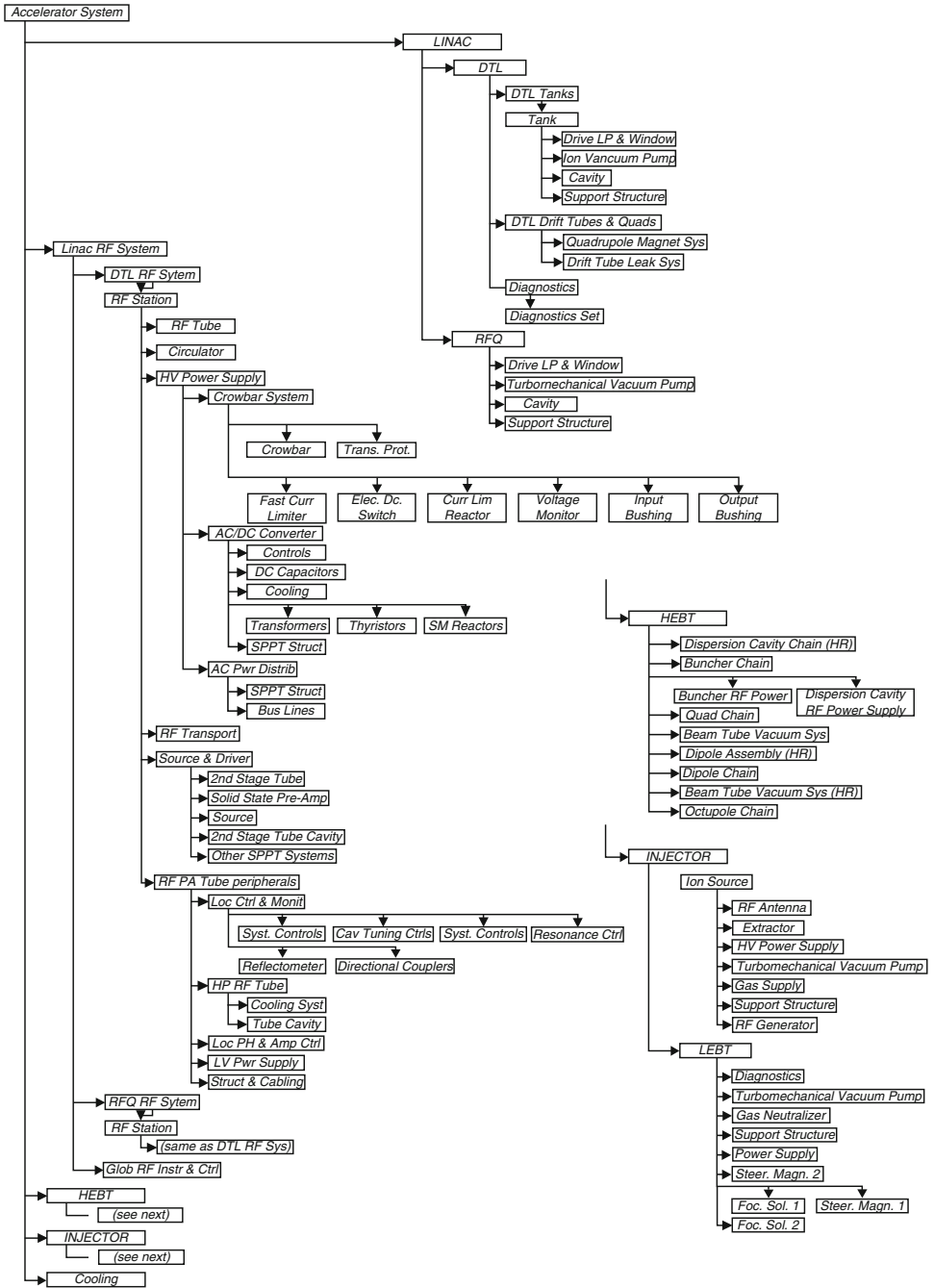


Figure 6 Importance ranking of the IFMIF accelerator system components based on the sensitivities of the final-time availability response to the components' MTTFs and MTTRs

■ Table 3

Sensitivities of the average (or interval) availability to the failure and repair rates of the first-level fault-tree of the accelerator system ($t_f = 168$ h)

Param. α_j	$\frac{\Delta \alpha_j}{\alpha_j^0}$	Nom. value R^0	Rel. sens. $\frac{\Delta R}{\Delta \alpha_j} \cdot \frac{\alpha_j^0}{R^0}$	ASAP $R_{pred} - R^0$	Exact recal. $R_{recalc} - R^0$
$\lambda_{INJECTOR}$	-10%	.8882	-.0136	.12E-02	.12E-02
$\mu_{INJECTOR}$	10%		.0135	.12E-02	.12E-02
λ_{LINAC}	-10%		-.0349	.31E-02	.312E-02
μ_{LINAC}	10%		.0305	.27E-02	.25E-02
$\lambda_{COOLING}$	-10%		-.78E-05	.7E-06	.7E-06
$\mu_{COOLING}$	10%		.76E-05	.7E-06	.7E-06
λ_{RFSys}	-10%		-.0363	.32E-02	.32E-02
μ_{RFSys}	10%		.0342	.30E-02	.29E-02
λ_{HEBT}	-10%		-.0316	.28E-02	.28E-02
μ_{HEBT}	10%		.0301	.2670E-02	.2446E-02

the “final-time availability” response to the over 180 IFMIF-system parameters are presented in Cacuci et al. (2008).

4.5 Global Optimization and Sensitivity Analysis

As discussed in Sect. 4.4, the scope of local sensitivity analysis is to calculate exactly and efficiently the sensitivities of the system’s response to variations in the system’s parameters, around their nominal values. As has also been shown in those chapters, the sensitivities are given by the first Gâteaux-differential of the system’s response, calculated at the nominal value of the system’s dependent variables (i.e., state functions) and parameters. Two procedures were presented for calculating the local sensitivities exactly, namely, the *forward sensitivity analysis procedure* (FSAP) and the *adjoint sensitivity analysis procedure* (ASAP). Among other uses, these sensitivities provide the first-order changes in the response due to parameter variations. However, the contributions from the higher-order terms in $\|\delta \alpha\|$ would require knowledge of the higher-order Gâteaux-differentials of the response and of the operator equations underlying the mathematical description of the physical system under investigation, since, as is well known, the Taylor series of a general operator reads

$$\begin{aligned}
 F(x_0 + h) = & F(x_0) + \delta F(x_0; h) + \frac{1}{2} \delta^2 F(x_0; h) + \dots + \frac{1}{(n-1)!} \delta^{n-1} F(x_0; h) \\
 & + \int_0^1 \frac{(1-t)^{n-1}}{(n-1)!} \delta^n F(x_0 + th; h) dt,
 \end{aligned}
 \tag{145}$$

Although several techniques have been proposed (see, e.g., IFMIF-CDA Team; Martone 1996) for calculating the higher-order response derivatives with respect to the system’s parameters, none has proven routinely practicable for large-scale problems. This is because the systems

of equations that need to be solved for obtaining the second (and higher) order Gâteaux-differentials of the response and system's operator equations are very large and depend on the perturbation $\delta\alpha$. Thus, even the calculation of the second-order Gâteaux-differentials of the response and system's operator equations is just as difficult as undertaking the complete task of computing the exact value of perturbed response $R(\alpha_1^0 + \delta\alpha_1, \dots, \alpha_k^0 + \delta\alpha_k)$.

As is well known, *the Taylor series is a local concept, valid within some radius of convergence of the series around the base-case value x_0* . This means that even if the Gâteaux-differentials of the response $R(\alpha)$ around α^0 were, in theory, available to all orders, they would still merely provide local, but not global, information. They would yield little, if any, information about the important global features of the physical system, namely, the critical points of $R(\alpha)$ and the bifurcation branches and/or turning points of the system's state variables. In practice, of course, it is very difficult, if not impossible, to calculate the requisite higher-order Gâteaux-differentials for large-scale systems with many parameters.

As mentioned in [Sect. 4](#), an alternative to computing higher order response derivatives has been presented in Kramer et al. (1984), which proposed the so-called *feature sensitivity analysis* method for nonlinearly probing a larger region in the parameter-space. This method considers that the response $R(r, t; \alpha)$ can be written in the equivalent form $R(r, t; \alpha + \Delta\alpha) \equiv P[r, t; \beta(\alpha + \Delta\alpha)]$, where $\beta(\alpha) \equiv (\beta_1, \beta_2, \dots)$ is a vector whose components are the "feature" parameters, and where the form of $P[r, t; \beta(\alpha + \Delta\alpha)]$ is assumed to be explicitly known. In such a case, it is possible to consider the linear expansion $\beta(\alpha + \Delta\alpha) \cong \beta(\alpha) + \Delta\alpha \partial\beta/\partial\alpha$, which can be substituted in the expression of $R(r, t; \alpha + \Delta\alpha)$ to obtain a nonlinear scaling expression with respect to the parameters $\Delta\alpha$. This way, it is possible to enlarge (somewhat) the investigation of the response to a larger neighborhood of the nominal parameter values α_k^0 . Nevertheless, the feature sensitivity analysis method is not a genuinely global method, since it cannot compute critical points (e.g., bifurcations, extrema) globally.

A genuinely global method has been proposed in the original work (Cacuci 1990) for determining, with probability one, all of the system's critical points (bifurcations, turning points, response extrema) in the combined phase space formed by the parameters, state variables, and adjoint variables, and subsequently analyze these critical points by local sensitivity analysis. The salient features of this global method will be presented in the sequel, by considering that the mathematical model of the physical system and associated responses has been discretized as would be required prior to numerical computations. This description in terms of algebraic (as opposed to differential and/or integral) operators in finite dimensional vector spaces simplifies considerably the mathematical manipulations to follow without detracting from the conceptual generality and applicability of the underlying methodology. In the sequel, all vectors are considered to be column vectors, while the superscript T will be used to denote transposition.

The canonical discretized mathematical representation of the physical system under consideration comprises:

1. m linear and/or nonlinear equations represented in operator form as:

$$N(\varphi, \alpha) = 0, \quad N \equiv [N_1(\varphi, \alpha), \dots, N_m(\varphi, \alpha)] : D_N \subset D_\varphi \times \mathbb{R}^i \rightarrow \mathbb{R}^m, \quad (146)$$

where each algebraic operator component $N_m(\varphi, \alpha)$ is considered to act nonlinearly on the vector of system parameters $\alpha \equiv (\alpha_1, \dots, \alpha_i)$, $\alpha \in \mathbb{R}^i$, and on the vector of state functions $\varphi \equiv (\varphi_1, \dots, \varphi_m)$, $\varphi : D_\varphi \subset \mathbb{R}^m$. Note that the components of both α and φ are considered here to be scalar quantities, taking on values in the real Euclidean spaces \mathbb{R}^i and \mathbb{R}^m , respectively. Since (146) is a canonical representation for problems that have been fully discretized in

preparation for a numerical solution, it automatically comprises all initial and/or boundary conditions which may have appeared in the originally continuous-variable description of the physical problem.

2. k inequality and/or equality constraints:

$$g(\boldsymbol{\alpha}) \leq 0, \quad g(\boldsymbol{\alpha}) \equiv [g_1(\boldsymbol{\alpha}), \dots, g_k(\boldsymbol{\alpha})] : D_g \subset \mathbb{R}^i \rightarrow \mathbb{R}^k, \quad (147)$$

where $\mathbf{g}(\boldsymbol{\alpha}) \equiv [g_1(\boldsymbol{\alpha}), \dots, g_k(\boldsymbol{\alpha})]$ is a k -component column vector, defined on a domain D_g that delimits, directly or indirectly, the range of the parameters α_i .

3. A system response, $R(\boldsymbol{\varphi}, \boldsymbol{\alpha})$, considered to be a real-valued functional of $\boldsymbol{\varphi}$ and $\boldsymbol{\alpha}$, defined on a domain D_P and having its range in \mathbb{R}^1 , that is,

$$R(\boldsymbol{\varphi}, \boldsymbol{\alpha}), \quad R(\boldsymbol{\varphi}, \boldsymbol{\alpha}) : D_P \subset D_\varphi \times \mathbb{R}^i \rightarrow \mathbb{R}^1. \quad (148)$$

4.5.1 Critical Points and Global Optimization

The fundamental problem of global optimization is to find the points that minimize or maximize the system response $R(\boldsymbol{\varphi}, \boldsymbol{\alpha})$ subject to the equality and inequality constraints represented by (146) and (147). This problem is typically handled by introducing the Lagrange functional, $L(\boldsymbol{\varphi}, \mathbf{y}, \boldsymbol{\alpha}, \mathbf{z})$, defined as

$$L(\boldsymbol{\varphi}, \mathbf{y}, \boldsymbol{\alpha}, \mathbf{z}) \equiv R(\boldsymbol{\varphi}, \boldsymbol{\alpha}) + \langle \mathbf{y}, \mathbf{N}(\boldsymbol{\varphi}, \boldsymbol{\alpha}) \rangle_m + \langle \mathbf{z}, \mathbf{g}(\boldsymbol{\alpha}) \rangle_k, \quad (149)$$

where the angular brackets denote inner products in \mathbb{R}^m and \mathbb{R}^k , respectively; that is,

$$\langle a, b \rangle_n = a \bullet b = \sum_{i=1}^n a_i b_i; \quad a, b \in \mathbb{R}^n; \quad (n = m \text{ or } k), \quad (150)$$

while $\mathbf{y} = (y_1, \dots, y_m)$ and $\mathbf{z} = (z_1, \dots, z_k)$ are column vectors of Lagrange multipliers. The critical points (i.e., extrema) of R are found among the points that cause the first Gâteaux-variation δL of L to vanish for arbitrary variations $\delta\boldsymbol{\varphi}$, $\delta\mathbf{y}$, $\delta\mathbf{z}$, and $\delta\boldsymbol{\alpha}$.

From (149), δL is obtained as

$$\delta L(\boldsymbol{\varphi}, \mathbf{y}, \boldsymbol{\alpha}, \mathbf{z}) = \langle \delta\boldsymbol{\varphi}, \mathbf{N}^+(\boldsymbol{\varphi}, \mathbf{y}, \boldsymbol{\alpha}) \rangle + \langle \delta\mathbf{y}, \mathbf{N}(\boldsymbol{\varphi}, \boldsymbol{\alpha}) \rangle + \langle \delta\mathbf{z}, \mathbf{g}(\boldsymbol{\alpha}) \rangle + \langle \delta\boldsymbol{\alpha}, \mathbf{S}(\boldsymbol{\varphi}, \mathbf{y}, \boldsymbol{\alpha}, \mathbf{z}) \rangle, \quad (151)$$

where the column vectors \mathbf{N}^+ and \mathbf{S} are defined as

$$\mathbf{N}^+(\boldsymbol{\varphi}, \mathbf{y}, \boldsymbol{\alpha}) \equiv \nabla_\varphi R + (\nabla_\varphi \mathbf{N}) \mathbf{y}, \quad (152)$$

$$\mathbf{S}(\boldsymbol{\varphi}, \mathbf{y}, \boldsymbol{\alpha}, \mathbf{z}) \equiv \nabla_\alpha R + (\nabla_\alpha \mathbf{N}) \mathbf{y} + (\nabla_\alpha \mathbf{g}) \mathbf{z}. \quad (153)$$

The gradient vectors and matrices appearing in (152) and (153) are defined as follows:

$$\nabla_\varphi R \equiv \left(\partial R / \partial \varphi_p \right)_{m \times 1}, \quad \nabla_\alpha R \equiv (\partial R / \partial \alpha_q)_{i \times 1}, \quad (154)$$

$$\nabla_\varphi \mathbf{N} \equiv \left(\partial N_r / \partial \varphi_p \right)_{m \times m}, \quad \nabla_\alpha \mathbf{N} \equiv (\partial N_r / \partial \alpha_q)_{i \times m}, \quad (155)$$

$$\nabla \mathbf{g} \equiv (\partial g_s / \partial \alpha_q)_{i \times k}. \quad (156)$$

The requirements that the first Gâteaux-variation δL of L vanish, for arbitrary $\delta\varphi$, δy , δz , and $\delta\alpha$, together with the constraints $g \leq 0$, lead to the following necessary conditions:

$$\begin{aligned} N^+(\varphi, y, \alpha) &= \mathbf{0}, & S(\varphi, y, \alpha, z) &= \mathbf{0}, \\ N(\varphi, \alpha) &= \mathbf{0}, \langle z, \mathbf{g} \rangle &= \mathbf{0}, & \mathbf{g} \leq \mathbf{0}, \quad z \geq \mathbf{0}, \end{aligned} \quad (157)$$

for the minima of $R(\varphi, \alpha)$ and similar conditions (except that $z \leq \mathbf{0}$) for the maxima of $R(\varphi, \alpha)$. The inequalities in (157) imply a lack of global differentiability, so a direct solution is usually hampered by computational difficulties. Such computational difficulties can be mitigated by recasting the last three conditions in (157) into the following equivalent form which involves equalities only:

$$K \equiv (K_1, \dots, K_k) = 0, \quad K_i \equiv (g_i + z_i)^2 + g_i |g_i| - z_i |z_i|. \quad (158)$$

Using (158) in (157) makes it possible to recast the latter into the equivalent form

$$F(\mathbf{u}) \equiv [N^+(\mathbf{u}), N(\mathbf{u}), S(\mathbf{u}), K(\mathbf{u})] = 0, \quad \mathbf{u} \equiv (\varphi, y, \alpha, z), \quad \mathbf{u} \in \mathbb{R}^{2m+i+k}, \quad (159)$$

where the components of the column vector \mathbf{u} are, respectively: the dependent variables, φ ; their corresponding Lagrange multipliers, y ; the parameters, α ; and the Lagrange multipliers, z , corresponding to the inequalities constraints, \mathbf{g} .

As will be shown in the sequel, choosing the above structure of F allows considerable simplifications in the global numerical procedure to be devised for finding the roots and critical points of (159). It is important to note that F is globally differentiable if R , N , and \mathbf{g} are differentiable twice globally. The Jacobian matrix $F'(\mathbf{u})$ of $F(\mathbf{u})$ has the block matrix structure

$$F'(\mathbf{u}) = \begin{bmatrix} \nabla_{\varphi} N^+ & \nabla_{\varphi} N & \nabla_{\varphi} S & \mathbf{0} & \mathbf{0} \\ (\nabla_{\varphi} N)^T & \mathbf{0} & (\nabla_{\alpha} N)^T & \mathbf{0} & \mathbf{0} \\ (\nabla_{\varphi} S)^T & \nabla_{\alpha} N & \nabla_{\alpha} S & \nabla \mathbf{g}_A & \nabla \mathbf{g}_I \\ \mathbf{0} & \mathbf{0} & 2Z_A (\nabla \mathbf{g}_A)^T & \mathbf{0} & \mathbf{0} \\ \mathbf{0} & \mathbf{0} & \mathbf{0} & \mathbf{0} & 2C_I \end{bmatrix}, \quad (160)$$

where $A \equiv \{j|g_j = 0\}$ and $I \equiv \{j|g_j < 0\}$ denote the set of indices corresponding to the active and inactive constraints, respectively, while the remaining quantities are defined as follows:

$$\nabla_{\varphi} N^+ \equiv \left[\partial^2 R / \partial \varphi_p \partial \varphi_r + \langle y, \partial^2 N / \partial \varphi_p \partial \varphi_r \rangle_m \right]_{m \times m}, \quad (161)$$

$$\nabla_{\varphi} S \equiv \left[\partial^2 R / \partial \varphi_p \partial \alpha_q + \langle y, \partial^2 N / \partial \varphi_p \partial \alpha_q \rangle_m \right]_{m \times i}, \quad (162)$$

$$\nabla_{\alpha} S \equiv \left[\partial^2 R / \partial \alpha_q \partial \alpha_r + \langle y, \partial^2 N / \partial \alpha_q \partial \alpha_r \rangle_m + \langle z, \partial^2 g / \partial \alpha_q \partial \alpha_r \rangle_k \right]_{i \times i}, \quad (163)$$

$$\nabla \mathbf{g}_A \equiv (\partial g_j / \partial \alpha_q)_{(j \in A) \times i}, \quad Z_A \equiv \text{diag}(z_j)_{j \in A}, \quad (164)$$

$$\nabla \mathbf{g}_I \equiv (\partial g_j / \partial \alpha_q)_{(j \in I) \times i}, \quad C_I \equiv \text{diag}(g_j)_{j \in I}. \quad (165)$$

By introducing the equivalence (157) \Leftrightarrow (159), all inequalities have disappeared from $F(\mathbf{u}) = 0$. Furthermore, the Jacobian $F'(\mathbf{u})$ is nonsingular at the zeros of $F(\mathbf{u})$, so efficient numerical methods, such as locally superlinearly convergent quasi-Newton methods, can be used to find

these zeros. Note that in the two extreme situations when the constraints are either all inactive or all active, the matrices $\nabla \mathbf{g}_A$ and $2Z_A (\nabla \mathbf{g}_A)^T$ or the matrices $\nabla \mathbf{g}$ and C_I disappear, respectively, from the structure of $F'(\mathbf{u})$. The Jacobian $F'(\mathbf{u})$ vanishes, though, at the bifurcation and limit and/or turning points present in our system. Such critical points need to be located by using global methods (as will be presented in [▶ Sect. 4.5.3](#)) that are capable of avoiding local non-convergence problems.

4.5.2 Sensitivity Analysis

The fundamental problem in sensitivity analysis is to determine the effects caused by variations $\delta \alpha$ around nominal parameter values α^0 in the response $R(\varphi, \alpha)$, subject to the constraints represented by (146) and (147). Within the framework of sensitivity analysis, therefore, both α^0 and $\delta \alpha$ are known, at the outset, and variations $\delta \alpha$ around α^0 induce variations in the response that can be computed, to first order, from the Taylor series

$$\begin{aligned} \Delta R(\varphi^0, \alpha^0) &\equiv R(\varphi, \alpha) - R(\varphi^0, \alpha^0) \\ &= \left\langle \delta \alpha, \{\nabla_{\alpha} R\}_{(\varphi^0, \alpha^0)} \right\rangle + \left\langle \delta \varphi, \{\nabla_{\varphi} R\}_{(\varphi^0, \alpha^0)} \right\rangle + O(\|\Delta \alpha\|^2, \|\Delta \varphi\|^2). \end{aligned} \quad (166)$$

The above expression explicitly indicates the important fact that the respective gradients are to be evaluated at the nominal values α^0 and $\varphi^0 = \varphi(\alpha^0)$, obtained from the solution of $N(\varphi^0, \alpha^0) = \mathbf{0}$. As shown in [▶ Sect. 4.4](#), the variations $\delta \varphi$ and $\delta \alpha$ in (166) are not independent, but are related to each other through the relationship

$$\begin{bmatrix} \left\{ \left\{ (\nabla_{\varphi} N)^T \right\}_{(\varphi^0, \alpha^0)} \right\} & \left\{ (\nabla_{\alpha} N)^T \right\}_{(\varphi^0, \alpha^0)} \\ 0 & \left\{ (\nabla_{\alpha} \mathbf{g})^T \right\}_{(\varphi^0, \alpha^0)} \end{bmatrix} \begin{pmatrix} \delta \varphi \\ \delta \alpha \end{pmatrix} = O(\|\Delta \alpha\|^2, \|\Delta \varphi\|^2), \quad (167)$$

which are obtained by taking Gâteaux-differentials of (146) and (147), respectively. Forming the inner product of (167) with the partitioned vector (\mathbf{y}, \mathbf{z}) , and transposing the resulting expression (which corresponds to determining the respective adjoint operators and functions in the continuous-variable case) yields

$$\left\langle \delta \varphi, \{\nabla_{\varphi} N\}_{(\varphi^0, \alpha^0)} \mathbf{y} \right\rangle + \left\langle \delta \alpha, \{\nabla_{\alpha} N\}_{(\varphi^0, \alpha^0)} \mathbf{y} + \{\nabla_{\alpha} \mathbf{g}\}_{(\varphi^0, \alpha^0)} \mathbf{z} \right\rangle = O(\|\Delta \alpha\|^2, \|\Delta \varphi\|^2). \quad (168)$$

Requiring next that the Lagrange multipliers (which are actually the adjoint functions) \mathbf{y}^0 be the solutions of the adjoint equations,

$$\{\nabla_{\varphi} N\}_{(\varphi^0, \alpha^0)} \mathbf{y}^0 + \{\nabla_{\varphi} R\}_{(\varphi^0, \alpha^0)} = \mathbf{0}, \quad (169)$$

and using their resulting expressions in (168) gives

$$\left\langle \delta \varphi, \{\nabla_{\varphi} R\}_{(\varphi^0, \alpha^0)} \right\rangle = \left\langle \delta \alpha, \{\nabla_{\alpha} N\}_{(\varphi^0, \alpha^0)} \mathbf{y}^0 + \{\nabla_{\alpha} \mathbf{g}\}_{(\varphi^0, \alpha^0)} \mathbf{z}^0 \right\rangle + O(\|\Delta \alpha\|^2, \|\Delta \varphi\|^2). \quad (170)$$

Finally, replacing (4.103) in (4.99) gives

$$\Delta R(\varphi^0, \alpha^0) = \delta \alpha \bullet \mathbf{S}(\varphi^0, \mathbf{y}^0, \alpha^0, \mathbf{z}^0) + O(\|\Delta \alpha\|^2, \|\Delta \varphi\|^2), \quad (171)$$

where the components of the vector $\mathbf{S}(\boldsymbol{\varphi}^0, \mathbf{y}^0, \boldsymbol{\alpha}^0, \mathbf{z}^0)$, defined as

$$\mathbf{S}(\boldsymbol{\varphi}^0, \mathbf{y}^0, \boldsymbol{\alpha}^0, \mathbf{z}^0) \equiv \{\nabla_{\boldsymbol{\alpha}} R\}_{(\boldsymbol{\varphi}^0, \boldsymbol{\alpha}^0)} + \{\nabla_{\boldsymbol{\alpha}} \mathbf{N}\}_{(\boldsymbol{\varphi}^0, \boldsymbol{\alpha}^0)} \mathbf{y}^0 + \{\nabla_{\boldsymbol{\alpha}} \mathbf{g}\}_{(\boldsymbol{\varphi}^0, \boldsymbol{\alpha}^0)} \mathbf{z}^0, \quad (172)$$

contain the first-order sensitivities at $\boldsymbol{\alpha}^0$ of $R(\boldsymbol{\varphi}^0, \boldsymbol{\alpha}^0)$ to variations $\delta\boldsymbol{\alpha}$, and where the adjoint variables \mathbf{y}^0 are the solutions of (169) while the Lagrange multipliers \mathbf{z} are chosen such as to enforce the linear independence of the constraints, that is, $\langle \mathbf{z}, \mathbf{g} \rangle = 0$; note that the adjoint system is occasionally defined with $(-\mathbf{y}^0)$ replacing \mathbf{y}^0 in (169).


On the other hand, adopting a variational point of view, the sensitivity expression given by (172) can also be obtained by using the same Lagrange functional, L , as used in (149); recall that its first Gâteaux-variation, δL , has the form given in (151), which is repeated below for convenience:

$$\begin{aligned} \delta L(\boldsymbol{\varphi}, \mathbf{y}, \boldsymbol{\alpha}, \mathbf{z}) &= \langle \delta\boldsymbol{\varphi}, \nabla_{\boldsymbol{\varphi}} R + (\nabla_{\boldsymbol{\varphi}} \mathbf{N}) \mathbf{y} \rangle + \langle \delta\mathbf{y}, \mathbf{N}(\boldsymbol{\varphi}, \boldsymbol{\alpha}) \rangle \\ &\quad + \langle \delta\mathbf{z}, \mathbf{g}(\boldsymbol{\alpha}) \rangle + \langle \delta\boldsymbol{\alpha}, \nabla_{\boldsymbol{\alpha}} R + (\nabla_{\boldsymbol{\alpha}} \mathbf{N}) \mathbf{y} + (\nabla_{\boldsymbol{\alpha}} \mathbf{g}) \mathbf{z} \rangle. \end{aligned} \quad (151)$$

At this stage, it is important to note that, in contradistinction to the optimization framework, the parameter variations $\delta\boldsymbol{\alpha}$ are not arbitrary in sensitivity analysis, but are prescribed at the outset. Hence, imposing now the requirement that δL be stationary at $(\boldsymbol{\varphi}^0, \boldsymbol{\alpha}^0)$ with respect to arbitrary variations $\delta\boldsymbol{\varphi}$, $\delta\mathbf{y}$, $\delta\mathbf{z}$ (but not with respect to $\delta\boldsymbol{\alpha}$, since these variations are not arbitrary!) has the following consequences:

- A stationary δL at $\boldsymbol{\alpha}^0$ with respect to $\delta\mathbf{y}$ implies that $\mathbf{N}(\boldsymbol{\varphi}^0, \boldsymbol{\alpha}^0) = \mathbf{0}$, thereby fixing the nominal values $\boldsymbol{\varphi}^0$;
- A stationary δL at $(\boldsymbol{\varphi}^0, \boldsymbol{\alpha}^0)$ with respect to $\delta\boldsymbol{\varphi}$ implies that the adjoint variables \mathbf{y}^0 must satisfy the adjoint Eq. (169) at $(\boldsymbol{\varphi}^0, \boldsymbol{\alpha}^0)$;
- A stationary δL at $(\boldsymbol{\varphi}^0, \boldsymbol{\alpha}^0)$ with respect to $\delta\mathbf{z}$ ensures that the constraints $\mathbf{g}(\boldsymbol{\alpha}^0)$ are satisfied while fixing the values \mathbf{z}^0 of the Lagrange multipliers \mathbf{z} , and

$$\begin{aligned} \delta L(\boldsymbol{\varphi}^0, \mathbf{y}^0, \boldsymbol{\alpha}^0, \mathbf{z}^0) &= \left\langle \delta\boldsymbol{\alpha}, \{\nabla_{\boldsymbol{\alpha}} R\}_{(\boldsymbol{\varphi}^0, \boldsymbol{\alpha}^0)} + \{\nabla_{\boldsymbol{\alpha}} \mathbf{N}\}_{(\boldsymbol{\varphi}^0, \boldsymbol{\alpha}^0)} \mathbf{y}^0 + \{\nabla_{\boldsymbol{\alpha}} \mathbf{g}\}_{(\boldsymbol{\varphi}^0, \boldsymbol{\alpha}^0)} \mathbf{z}^0 \right\rangle \\ &= \delta\boldsymbol{\alpha} \bullet \mathbf{S}(\boldsymbol{\varphi}^0, \mathbf{y}^0, \boldsymbol{\alpha}^0, \mathbf{z}^0) \\ &= \Delta R(\boldsymbol{\varphi}^0, \boldsymbol{\alpha}^0) + O(\|\Delta\boldsymbol{\alpha}\|^2, \|\Delta\boldsymbol{\varphi}\|^2), \end{aligned} \quad (173)$$

which is the same expression for the sensitivity ΔR of R at $(\boldsymbol{\varphi}^0, \boldsymbol{\alpha}^0)$ as was obtained in (171) via the Gateaux-differential approach of  Sect. 4.4 (as opposed to the variational approach in this section).

Even though both the optimization and sensitivity analysis frameworks use the first Gâteaux-variation $\delta L(\boldsymbol{\varphi}, \mathbf{y}, \boldsymbol{\alpha}, \mathbf{z})$ of the same formal Lagrangian functional $L(\boldsymbol{\varphi}, \mathbf{y}, \boldsymbol{\alpha}, \mathbf{z})$, there are fundamental conceptual differences between them. On the one hand, the sensitivity analysis framework revolves fundamentally around the *a priori known* nominal point $\boldsymbol{\alpha}^0$, and imposes on $\delta L(\boldsymbol{\varphi}, \mathbf{y}, \boldsymbol{\alpha}, \mathbf{z})$ the requirements that it be stationary at $(\boldsymbol{\varphi}^0, \boldsymbol{\alpha}^0)$ with respect to arbitrary variations $\delta\boldsymbol{\varphi}$, $\delta\mathbf{y}$, $\delta\mathbf{z}$, but not with respect to $\delta\boldsymbol{\alpha}$, since these variations are not arbitrary, as has been previously noted. On the other hand, the optimization theory framework for finding the critical points of $R(\boldsymbol{\varphi}, \boldsymbol{\alpha})$ imposes the requirements that (1) δL be stationary with respect to

δy , implying that $N(\boldsymbol{\varphi}^*, \boldsymbol{\alpha}^*) = \mathbf{0}$ at the *yet unknown critical point* $(\boldsymbol{\varphi}^*, \boldsymbol{\alpha}^*)$; (2) δL be stationary with respect to $\delta \boldsymbol{\varphi}$, implying that \mathbf{y}^* must satisfy at $(\boldsymbol{\varphi}^*, \boldsymbol{\alpha}^*)$ the adjoint equation $N^+(\boldsymbol{\varphi}^*, \mathbf{y}^*, \boldsymbol{\alpha}^*) \equiv \{\nabla_{\boldsymbol{\varphi}} N\}_{(\boldsymbol{\varphi}^*, \boldsymbol{\alpha}^*)} \mathbf{y}^* + \{\nabla_{\boldsymbol{\varphi}} R\}_{(\boldsymbol{\varphi}^*, \boldsymbol{\alpha}^*)} = \mathbf{0}$; (3) δL be stationary with respect to $\delta \mathbf{z}$, implying that the respective constraints must be satisfied at the yet unknown critical point $(\boldsymbol{\varphi}^*, \boldsymbol{\alpha}^*)$; and, *in contradistinction to the sensitivity analysis framework*, the requirement that (4) δL be stationary with respect to $\delta \boldsymbol{\alpha}$, implying that

$$S(\boldsymbol{\varphi}^*, \mathbf{y}^*, \boldsymbol{\alpha}^*, \mathbf{z}^*) \equiv \{\nabla_{\boldsymbol{\alpha}} P\}_{(\boldsymbol{\varphi}^*, \boldsymbol{\alpha}^*)} + \{\nabla_{\boldsymbol{\alpha}} N\}_{(\boldsymbol{\varphi}^*, \boldsymbol{\alpha}^*)} \mathbf{y}^* + \{\nabla_{\boldsymbol{\alpha}} \mathbf{g}\}_{(\boldsymbol{\varphi}^*, \boldsymbol{\alpha}^*)} \mathbf{z}^* = \mathbf{0} \quad (174)$$

at the critical point $(\boldsymbol{\varphi}^*, \boldsymbol{\alpha}^*)$. Note that the critical point $(\boldsymbol{\varphi}^*, \boldsymbol{\alpha}^*)$ is not *a priori* known, but is to be determined from the solution of (159). In other words, the foregoing conditions (1)–(4) constitute a system of $2m + i + k$ equations whose simultaneous solution yields the regular critical points $(\boldsymbol{\varphi}^*, \boldsymbol{\alpha}^*)$ of $R(\boldsymbol{\varphi}^*, \boldsymbol{\alpha}^*)$ together with the respective values \mathbf{y}^* and \mathbf{z}^* of the Lagrange multipliers. *Note the important fact that condition (4) above cannot be imposed within the framework of sensitivity analysis, since δL cannot be required to vanish for known variations $\delta \boldsymbol{\alpha}$ around a fixed, a priori known point $(\boldsymbol{\varphi}^0, \boldsymbol{\alpha}^0)$; δL will vanish for variations $\delta \boldsymbol{\alpha}$ only if the respective point $(\boldsymbol{\varphi}^0, \boldsymbol{\alpha}^0)$ happens to coincide with a regular critical point $(\boldsymbol{\varphi}^*, \boldsymbol{\alpha}^*)$.*

4.5.3 Global Computation of Fixed Points

The vector $\mathbf{F}(\mathbf{u})$ defined in (159) contains all the features necessary for performing both global optimization and sensitivity analysis. Setting to zero all *four* components of $\mathbf{F}(\mathbf{u})$, namely: $N(\mathbf{u})$, $N^+(\mathbf{u})$, $\mathbf{K}(\mathbf{u})$, and $\mathbf{S}(\mathbf{u})$, yields the respective critical points \mathbf{u}^* that optimize the system response. On the other hand, setting only *three* components of $\mathbf{F}(\mathbf{u})$, that is, $N(\mathbf{u})$, $N^+(\mathbf{u})$, and $\mathbf{K}(\mathbf{u})$, to zero at *any* point \mathbf{u}^0 and calculating its fourth component $\mathbf{S}(\mathbf{u}^0)$ yields the first-order local sensitivities at \mathbf{u}^0 . Of course, $\mathbf{S}(\mathbf{u}^0)$ would vanish if \mathbf{u}^0 happened to coincide with a critical point \mathbf{u}^* of $R(\boldsymbol{\varphi}, \boldsymbol{\alpha})$. Devising a computational algorithm that could determine the features mentioned in the foregoing, over the global space of allowed parameter variations, would extend the scopes of both optimization and sensitivity analysis while unifying their underlying computational methodologies. Such a computational algorithm will be briefly described in the remainder of this section.

The initial information available in practical problems comprises the nominal design values $\boldsymbol{\alpha}^0$ of the problem's parameters $\boldsymbol{\alpha}$, and the ranges over which the respective parameters can vary, as expressed mathematically by the constraints in (147). As the parameters $\boldsymbol{\alpha}$ vary over their respective ranges, the state variables $\boldsymbol{\varphi}$ and the response R vary in phase space. The objective of the computational algorithm, therefore, is to determine all of the critical points where the solution path $\boldsymbol{\varphi}$ bifurcates (i.e., splits in two or more branches) and where the response R attains maxima, minima, and/or saddle points. The bifurcation points occur at the zeros of the determinant of the Jacobian matrix $\mathbf{F}'(\mathbf{u})$, denoted as $\text{Det}[\mathbf{F}'(\mathbf{u})]$, while the maxima, minima, and/or saddle points of R occur at the zeros of $\mathbf{F}(\mathbf{u})$, respectively.

To determine all the zeros of both $\mathbf{F}(\mathbf{u})$ and $\text{Det}[\mathbf{F}'(\mathbf{u})]$, it is essential to use an algorithm that embodies the following properties:

- (a) Efficiently avoids non-convergence problems at the singularities of $\mathbf{F}'(\mathbf{u})$;
- (b) Avoids getting bogged down (as many local methods do) at the first zero of $\mathbf{F}(\mathbf{u})$ that it may happen to find; and

- (c) Finds all the fixed points \mathbf{u}_i^* of $\mathbf{F}(\mathbf{u})$ regardless of the starting point \mathbf{u}_0 . It is apparent that local computational methods would not satisfy all these requirements; a global method would need to be devised for this purpose.

Perhaps the most powerful mathematical techniques for obtaining global results are the homotopy theory-based continuation methods. Typically, these methods compute the solution \mathbf{u}^* of a fixed-point equation such as (159) by embedding it into a one-parameter family of equations of the form $\mathbf{G}(\mathbf{u}, \lambda) = \mathbf{0}$, where $\lambda \in \mathbb{R}^1$ is a real scalar. Most of the direct procedures to follow the path $\mathbf{u}(\lambda)$ typically encounter difficulties (slow convergence, small steps, or even failure) at points where the Fréchet-derivative $\mathbf{G}'_{\mathbf{u}}$ does not have a bounded inverse. Such difficulties can be efficiently circumvented by the “pseudo-arc-length” (i.e., distance along a local tangent) continuation methods, which employ a scalar constraint in addition to the homotopy $\mathbf{G}(\mathbf{u}, \lambda) = \mathbf{0}$, thus “inflating” the original problem into one of higher dimension.

To determine the roots of $\mathbf{F}(\mathbf{u}) = \mathbf{0}$ and $\mathbf{F}'(\mathbf{u}) = \mathbf{0}$ by means of the pseudo-arc-length continuation method, the homotopy $\mathbf{G}(\mathbf{u}, \lambda) = \mathbf{0}$ is specified to be of the form

$$\mathbf{G}(\mathbf{u}, \lambda) \equiv \mathbf{F}[\mathbf{u}(s)] - \lambda(s) \mathbf{F}(\mathbf{u}_0) = \mathbf{0}. \quad (175)$$

where $\mathbf{F}[\mathbf{u}(s)]$ is as defined in (159), while \mathbf{u}_0 denotes a fixed (e.g., starting) value of \mathbf{u} . Note that (175) implies that $\mathbf{u}(s)$ must satisfy the differential equation obtained by setting to zero its first Gâteaux-derivative with respect to s , namely,

$$\mathbf{F}'(\mathbf{u}) \mathbf{w}(s) + \mu(s) \mathbf{F}(\mathbf{u}_0) = \mathbf{0}. \quad (176)$$

In addition to the above homotopy, we impose the additional condition that

$$\|\mathbf{w}(s)\|^2 + \mu(s) = 1, \quad \mathbf{w}(s) \equiv \frac{d}{ds} \mathbf{u}(s), \quad \mu(s) \equiv \frac{d}{ds} \lambda(s), \quad (177)$$

where $s \in \mathbb{R}^1$ is a real-valued parameter and $\lambda(s) \in \mathbb{R}^1$ is a function of s , thereby making s the arc-length parameter along the path $[\mathbf{u}(s), \lambda(s)]$ in the inflated space $\mathbb{R}^{2m+i+k+1}$. As (175) and (176) imply the values of s for which $\lambda(s)$ vanishes determine the zeros of \mathbf{F} (and, consequently, the extrema of R), while the values of s for which $\mu(s)$ vanishes determine the zeros of \mathbf{F}' (and, consequently, the bifurcation, limit, and turning points in the problem under consideration). The Jacobian matrix $\mathbf{F}'(\mathbf{u})$ appearing in (176) has, of course, the same block matrix structure as given in (160).

The numerical solution of (175–177) is computed as follows. Suppose that $(\mathbf{u}_0, \lambda_0)$ is a known solution point of (175). Then, corresponding to this point, there is the pseudo-arc-length parameter point $s_0 \in \mathbb{R}^1$. The starting point is thus set to be $[\mathbf{u}(s_0), \lambda(s_0)] \equiv (\mathbf{u}_0, \lambda_0)$. The direction of the tangent along the solution path at $(\mathbf{u}_0, \lambda_0)$ is given by $[\mathbf{w}(s_0), \mu(s_0)]$, which is obtained by solving (176) and (177) at $s = s_0$. The next point $[\mathbf{u}(s), \lambda(s)]$ on the solution path, for $s \neq s_0$ (but s near s_0), is obtained by solving the following system of equations:

$$\mathbf{G}[\mathbf{u}(s), \lambda(s)] \equiv \mathbf{F}[\mathbf{u}(s)] - \lambda(s) \mathbf{F}[\mathbf{u}(s_0)] = \mathbf{0} \quad (178)$$

and

$$\begin{aligned} \mathbf{M}[\mathbf{u}(s), \lambda(s), s] \equiv & \mathbf{w}(s_0) \bullet [\mathbf{u}(s) - \mathbf{u}(s_0)] \\ & + \mu(s_0) \bullet [\lambda(s) - \lambda(s_0)] - (s - s_0) = \mathbf{0}. \end{aligned} \quad (179)$$

When $(\mathbf{u}_0, \lambda_0)$ is a regular or a simple limit point of $\mathbf{G}(\mathbf{u}, \lambda)$, the Jacobian

$$J \equiv \begin{bmatrix} \mathbf{F}'(\mathbf{u}) & -\mathbf{F}(\mathbf{u}_0) \\ (\mathbf{w}_0)^T & \mu_0 \end{bmatrix}$$

of (178) and (179) is nonsingular. Furthermore, while the bifurcations in (178) and (179) are identical to those of $\mathbf{F}(\mathbf{u})$, the structure of (178) and (179) at a bifurcation point possesses distinctly advantageous convergence properties over that of $\mathbf{F}(\mathbf{u})$.

To compute $[\mathbf{u}(s), \lambda(s)]$ from (178) and (179), it is advantageous to use Newton's method because of its simplicity and superior convergence properties (quadratic or, at worst, superlinear at bifurcation points). Applying Newton's method to (178) and (179) and rearranging the resulting expressions yield the iterations

$$\Delta \mathbf{u}^v \equiv \mathbf{u}^{v+1} - \mathbf{u}^v, \quad \Delta \lambda^v \equiv \lambda^{v+1} - \lambda^v; \quad (v = 0, 1, \dots), \quad (180)$$

where

$$\Delta \lambda^v = [\mathbf{u}(s_0) \bullet \mathbf{b} - \mathbf{M}(\mathbf{u}^v, \lambda^v, s)] / [\mathbf{w}(s_0) \bullet \mathbf{a} + \mu(s_0)] \quad (181)$$

and

$$\Delta \mathbf{u}^v = (\Delta \lambda^v) \mathbf{a} - \mathbf{b}. \quad (182)$$

In the above equations, the vectors \mathbf{a} and \mathbf{b} denote, respectively, the solutions of

$$\mathbf{F}'(\mathbf{u}^v) \bullet \mathbf{a} = \mathbf{F}(\mathbf{u}_0) \quad (183)$$

and

$$\mathbf{F}'(\mathbf{u}^v) \bullet \mathbf{b} = \mathbf{G}(\mathbf{u}^v, \lambda^v). \quad (184)$$

The initial point $\mathbf{u}_0 = (\boldsymbol{\varphi}_0, \mathbf{y}_0, \boldsymbol{\alpha}_0, \mathbf{z}_0)$ for the Newton iteration is chosen as follows: initially, only the nominal values $\boldsymbol{\alpha}_0$ of the system parameters $\boldsymbol{\alpha}$ are specified, usually as part of the definition of the physical system under consideration. If any of the constraints $\mathbf{g}(\boldsymbol{\alpha})$ are to remain strict equalities over the entire range of variations of the parameters $\boldsymbol{\alpha}$, then we include them in the definition of $N(\boldsymbol{\varphi}, \boldsymbol{\alpha})$, thereby redefining (1) the parameters $\boldsymbol{\alpha}$ that are to be considered as independent variables, and (2) the corresponding structure of the vector $\boldsymbol{\varphi}$ of dependent variables. The corresponding nominal values $\boldsymbol{\varphi}_0$ of the state variables $\boldsymbol{\varphi}$ are then obtained by solving the equation $N(\boldsymbol{\varphi}_0, \boldsymbol{\alpha}_0) = \mathbf{0}$. The nominal values \mathbf{y}_0 are obtained as the solutions of the adjoint equations

$$N^+(\boldsymbol{\varphi}_0, \boldsymbol{\alpha}_0, \mathbf{y}) \equiv \nabla_{\boldsymbol{\varphi}} R(\boldsymbol{\varphi}_0, \boldsymbol{\alpha}_0) + [\nabla_{\boldsymbol{\varphi}} N(\boldsymbol{\varphi}_0, \boldsymbol{\alpha}_0)] \mathbf{y}_0 = \mathbf{0}. \quad (185)$$

Furthermore, the inequality constraints $g_j(\boldsymbol{\alpha})$ are arranged to be inactive at $\boldsymbol{\alpha}_0$, so that the inequalities $g_j(\boldsymbol{\alpha}_0) < 0$ are satisfied. This is always possible by appropriately defining the respective functions g_j . Consequently, the initial values for the respective Lagrange multipliers \mathbf{z} are $\mathbf{z}_0 = \mathbf{0}$. Finally, having obtained all the components of \mathbf{u}_0 as $\mathbf{u}_0 = (\boldsymbol{\varphi}_0, \mathbf{y}_0, \boldsymbol{\alpha}_0, \mathbf{0})$, we

compute the (first-order) sensitivities at $\mathbf{u}_0 = (\boldsymbol{\varphi}_0, \mathbf{y}_0, \boldsymbol{\alpha}_0, \mathbf{0})$, namely, $\mathbf{S}(\mathbf{u}_0) = \nabla_{\boldsymbol{\alpha}} P(\boldsymbol{\varphi}_0, \boldsymbol{\alpha}_0) + [\nabla_{\boldsymbol{\alpha}} \mathbf{N}(\boldsymbol{\varphi}_0, \boldsymbol{\alpha}_0)] \mathbf{y}_0$. This also completes the calculation for the starting value $\mathbf{F}(\mathbf{u}_0)$, whose components are thus $\mathbf{F}(\mathbf{u}_0) = [\mathbf{0}, \mathbf{0}, \mathbf{S}(\mathbf{u}_0), \mathbf{0}]$.

Having obtained \mathbf{u}_0 , we select the starting value $\lambda_0 = \lambda(s_0)$ by noting that the point $(\mathbf{u}_0, \lambda_0 = 1)$ satisfies (175); the initial directions (\mathbf{w}_0, μ_0) are then obtained by solving (176) and (177) at $(\mathbf{u}_0, 1)$. The initial guess for the Newton method is provided by a single Euler step

$$\mathbf{u}^0 = \mathbf{u}_0 + (s - s_0) \mathbf{w}_0, \quad \text{for } v = 0, \quad (186)$$

and

$$\lambda^0 = \lambda_0 + (s - s_0) \mu_0, \quad \text{for } v = 0, \quad (187)$$

where $s - s_0$ can be estimated from convergence theorems for Newton-like methods within a ball of radius $|s - s_0|$ around s_0 .

It is advantageous to use the largest step-length $|s - s_0|$ that still assures convergence of the iterative process. For the illustrative examples to be presented in the next section, the step-length $|s - s_0|$ was estimated from the expression

$$|s - s_0| = \left\{ \|\mathbf{F}(\mathbf{u}_0 + \Delta \mathbf{w}_0) - 2\mathbf{F}(\mathbf{u}_0) + \mathbf{F}(\mathbf{u}_0 - \Delta \mathbf{w}_0)\| \Delta^{-2} \gamma(J) \right\}^{-1/2}, \quad (188)$$

where $\gamma(J)$ is the condition number of the Jacobian J of (178) and (179), and Δ is a small increment. The expression for $|s - s_0|$ given in (188) is obtained by using the Kantorovich method as sufficient condition for the convergence of the Newton method in a ball around s_0 , by neglecting all terms of order higher than two in $|s - s_0|$, and approximating the Hessian $\mathbf{F}''(\mathbf{u}_0)$ by finite differences. While this procedure is useful for many practical applications, it may not always be optimal; therefore, alternative means of obtaining an optimal maximum step length $|s - s_0|$ remain of interest.

Calculating the Newton iterates $\Delta \lambda^v$ and $\Delta \mathbf{u}^v$ from (181) and (182), respectively, requires solving (183) and (184) to obtain the vectors \mathbf{a} and \mathbf{b} , respectively. For large-scale problems, $\mathbf{F}'(\mathbf{u})$ is a very large matrix, so a direct solution of (183) and (184) would be impractical. Note, though, that the special structure of $\mathbf{F}'(\mathbf{u})$ was deliberately created by the structural arrangements in the definitions of $\mathbf{F}(\mathbf{u})$ and \mathbf{u} in order to simplify the subsequent task of solving Eqs. (183) and (184), by exploiting the positioning of the zero submatrices and the easy invertibility of the diagonal matrices \mathbf{Z}_A and \mathbf{C}_I . By partitioning the vector \mathbf{a} in the form

$$\mathbf{a} = (\mathbf{a}_\varphi, \mathbf{a}_y, \mathbf{a}_\alpha, \mathbf{a}_A, \mathbf{a}_I), \quad (189)$$

with components having the same dimensions as those of $\boldsymbol{\varphi}, \mathbf{y}, \boldsymbol{\alpha}, A$ (i.e., number of active constraints), and I (i.e., number of inactive constraints), respectively, the task solving (183) is reduced to solving the following matrix equations:

1. When all constraints are inactive, the set A is empty; it then follows from (183) that $\mathbf{a}_A = \mathbf{0}$ and $\mathbf{a}_I = \mathbf{0}$. Hence, (183) is reduced to solving

$$\mathbf{F}_1(\mathbf{u}^v) \begin{pmatrix} \mathbf{a}_\varphi \\ \mathbf{a}_y \\ \mathbf{a}_\alpha \end{pmatrix} = \begin{pmatrix} \mathbf{0} \\ \mathbf{0} \\ \mathbf{S}(\mathbf{u}_0) \end{pmatrix}, \quad (190)$$

where $F_1(\mathbf{u})$ is the symmetric matrix defined as

$$F_1(\mathbf{u}) \equiv \begin{bmatrix} \nabla_{\varphi} N^+ & \nabla_{\varphi} N & \nabla_{\varphi} S \\ (\nabla_{\varphi} N)^T & \mathbf{0} & (\nabla_{\alpha} N)^T \\ (\nabla_{\varphi} S)^T & \nabla_{\alpha} N & \nabla_{\alpha} S \end{bmatrix}. \quad (191)$$

2. When some constraints are active, then \mathbf{A} is not empty but (183) still implies that $\mathbf{a}_I = \mathbf{0}$; in this case, (183) is reduced to solving

$$F_2(\mathbf{u}^v) \begin{pmatrix} \mathbf{a}_{\varphi} \\ \mathbf{a}_y \\ \mathbf{a}_{\alpha} \\ \mathbf{a}_A \end{pmatrix} = \begin{pmatrix} \mathbf{0} \\ \mathbf{0} \\ S(\mathbf{u}_0) \\ \mathbf{0} \end{pmatrix}, \quad (192)$$

where $F_2(\mathbf{u})$ is the symmetric matrix defined as

$$F_2(\mathbf{u}) = \begin{bmatrix} & & \vdots & \mathbf{0} \\ & F_1(\mathbf{u}) & \vdots & \mathbf{0} \\ \dots & \dots & \vdots & \nabla \mathbf{g}_A \\ \mathbf{0} & \mathbf{0} & (\nabla \mathbf{g}_A)^T & \mathbf{0} \end{bmatrix}. \quad (193)$$

In preparation for solving (184), the vectors \mathbf{b} and \mathbf{G} are partitioned as follows:

$$\mathbf{b} = (\mathbf{b}_{\varphi}, \mathbf{b}_y, \mathbf{b}_{\alpha}, \mathbf{b}_A, \mathbf{b}_I) \quad (194)$$

and

$$\mathbf{G} = (\mathbf{G}_{\varphi}, \mathbf{G}_y, \mathbf{G}_{\alpha}, \mathbf{G}_A, G_I), \quad (195)$$

respectively. This way, (184) is reduced to solving one or the other of the following matrix equations:

1. When all constraints are inactive, it follows from (184) that

$$\mathbf{b}_A = \mathbf{0}, \quad \mathbf{b}_I = \frac{1}{2} [\mathbf{C}_I(\boldsymbol{\alpha}^v, \mathbf{z}^v)]^{-1} \mathbf{K}(\boldsymbol{\alpha}^v, \mathbf{z}^v). \quad (196)$$

Hence, the remaining components of \mathbf{b} are obtained by solving

$$F_1(\mathbf{u}^v) \begin{pmatrix} \mathbf{b}_{\varphi} \\ \mathbf{b}_y \\ \mathbf{b}_{\alpha} \end{pmatrix} = \begin{pmatrix} \mathbf{G}_{\varphi} \\ \mathbf{G}_y \\ \mathbf{G}_{\alpha} - [\nabla \mathbf{g}(\boldsymbol{\alpha}^v, \mathbf{z}^v)] \mathbf{b}_I \end{pmatrix}. \quad (197)$$

2. When some constraints are active, then \mathbf{b}_I is still given by (196), while solving (184) is reduced to solving the system

$$F_2(\mathbf{u}^v) \begin{pmatrix} \mathbf{b}_{\varphi} \\ \mathbf{b}_y \\ \mathbf{b}_{\alpha} \\ \mathbf{b}_A \end{pmatrix} = \begin{pmatrix} \mathbf{G}_{\varphi} \\ \mathbf{G}_y \\ \mathbf{G}_{\alpha} - [\nabla \mathbf{g}_I(\boldsymbol{\alpha}^v, \mathbf{z}^v)] \mathbf{b}_I \\ \frac{1}{2} [\mathbf{Z}_A(\mathbf{z}^v)]^{-1} \mathbf{K}_A(\boldsymbol{\alpha}^v, \mathbf{z}^v) \end{pmatrix}. \quad (198)$$

The matrix $F'(\mathbf{u})$ and, equivalently, the matrix F_1 (or F_2) become singular at the bifurcation points. It is therefore essential to determine correctly the rank of F_1 or F_2 when solving the equations involving these matrices. In actual computations, singular value decomposition procedures are recommended to determine the null vectors of F_1 (or, respectively, F_2); these null vectors play an essential role for continuing the solution through a bifurcation point.

The Newton algorithm described in the foregoing generates a sequence of points $[\mathbf{u}(s_j), \lambda(s_j)]$ and corresponding tangent directions $[\mathbf{w}(s_j), \mu(s_j)]$, starting at $j = 0$ and continuing until the algorithm terminates at some point j_{final} . When $\lambda(s)$ changes sign between two points, $[\mathbf{u}(s_{r-1}), \lambda(s_{r-1})]$ and $[\mathbf{u}(s_r), \lambda(s_r)]$ on the solution path, then a root $\mathbf{u}^* \equiv \mathbf{u}(s^*)$ of $F(\mathbf{u})$ must correspond to the root $\lambda(s^*) = 0$ that occurs at $s^* \in (s_{r-1}, s_r)$. On the other hand, the points $\mathbf{u}^{**} \equiv \mathbf{u}(s^{**})$ where the determinant of $F'(\mathbf{u})$ vanishes correspond to the points where $\mu(s^{**}) = 0$. These points are found analogously to those where $\lambda(s^*) = 0$, but by monitoring the sign changes in $\mu(s)$ instead of those in $\lambda(s)$. To find the precise locations of the roots $\lambda(s^*) = 0$ and $\mu(s^{**}) = 0$, it is useful to switch, in the respective interval (s_{r-1}, s_r) , from the Newton marching algorithm to the secant method coupled with *regula falsi*, to ensure rapid convergence.

5 Probability Theory and Uncertainty Information

5.1 Assigning Priors under Incomplete Knowledge: Group Theory and Entropy Maximization

Repeated measurements of the same physical quantity yield values that differ from each other, as well as from the true but unknown value of that quantity. This variation in results is due to experimental errors, imperfect instruments, and imperfectly known calibration standards. Hence, around any reported experimental value, there always exists a range of values that may also be plausibly representative of the true value. In turn, this means that all inferences, predictions, engineering computations, and other applications of measured data are necessarily founded on weighted averages over all the possibly true values, with weights indicating the degree of plausibility of each value. These weights and weighted averages are what we call probabilities and expectation values. The interpretation of probabilities as *degrees of plausibility or rational expectation*, on a numerical scale ranging from 0 (impossibility) to 1 (certainty), dates back at least to Bernoulli (1713) and Laplace (1812). Probabilities encode incomplete information, in that persons possessing different information or knowledge would assign different probabilities, and would update the respective probabilities whenever new information became available. Since the true value of physical quantities cannot be measured exactly, nominally measured values are insufficient, by themselves, for applications; the quantitative uncertainties accompanying the measurements are also needed, along with the respective nominal values. Combination of data from different sources involves a weighted propagation (e.g., using sensitivities) of various uncertainties, requiring reasoning from incomplete information for extracting “best” values together with “best” uncertainties from often sparse, incomplete, error-afflicted, and occasionally discrepant experimental data. A wide range of probability-theory concepts and tools are employed in data evaluation and assimilation, from deductive statistics involving mainly frequencies and sample tallies to inductive inference for assimilating non-frequency data and a priori knowledge.

The interpretation of probability as a *relative frequency* is straightforward when studying physical laws, since such laws are assumed to act the same way in repeated experiments, implying that the validity of the assigned probability values can be tested experimentally. However, the concept of probability as a relative frequency becomes questionable when attempting to assign probabilities for very rare (or even uniquely occurring) phenomena such as a core meltdown in a nuclear reactor or the big bang. In such cases, probability must be considered to be a mental construct for expressing a degree of belief about events; this mental construct provides the premises of the Bayesian (or subjective) interpretation of probability. In this interpretation, the underlying sample space is formed of elements that correspond to hypotheses or propositions, that is, statements that are either true or false. Then, the probability associated with a cause or hypothesis A is interpreted as a measure of degree of belief, namely:

$$P(A) \equiv \text{a priori measure of the rational degree of belief} \\ \text{that } A \text{ is the correct cause or hypothesis.}$$

Since a statement like “a measurement will yield a given outcome for a certain fraction of the time” can be regarded as a hypothesis, it follows that the framework of subjective probability includes the interpretation of probability as a relative frequency. In particular, a subjective probability can be associated with the value of an unknown constant; this association reflects one’s confidence that the value of the respective probability is contained within a certain fixed interval.

The elementary conditions for logical consistency imply two fundamental rules, namely, the *sum* and the *product rules*, from which all other mathematical relationships between probabilities can be derived (see, e.g., Cox 1946). These rules can be written in the form

$$P(A|B) + P(\bar{A}|B) = 1; P(A|BC) P(B|C) = P(B|AC) P(A|C), \quad (199)$$

where A , B , and C represent propositions (e.g., “the cross section is larger than 10 barn”). The product AB indicates that “both A and B are true,” \bar{A} indicates “ A is false,” while $P(A|B)$ denotes the probability of A given B . The above notation indicates that all probability assignments are conditional, based on either empirical or theoretical information or on assumptions. The sum rule indicates that, under all circumstances B , the more probable A is the less probable \bar{A} , the unit sum of both probabilities representing the certainty that one of these alternatives must be true. The product rule says that, under all circumstances C , the probability that both A and B are true is equal to the probability of A given B , times the probability that, in fact, B is true; note that A and B enter symmetrically in the product rule, so their respective roles are interchangeable. As shown in Cox (1946) and Renyi (1954), the sum and product rules are the only rules that are consistent with the arithmetic of logic (Boolean algebra), under the very general assumptions that $P(\bar{A}|B)$ somehow depends on $P(A|B)$, and that $P(AB|C)$ somehow depends on $P(A|BC)$ and $P(B|C)$, where the P ’s represent degrees of plausibility between 0 and 1.

An immediate consequence of the product rule is *Bayes’ theorem* (Bayes 1763) which, in its simplest form, can be expressed as

$$P(A|BC) = \frac{P(B|AC) P(A|C)}{P(B|C)}. \quad (200)$$

When evaluating scientific data, B usually denotes data that depend on the value of an unknown physical quantity A and on other circumstances C . The (so-called) likelihood function $P(B|AC)$

usually represents a statistical model that indicates how likely the data B would be under the circumstances C , if the unknown quantity were in fact A . Finally, if the “*a priori*” probability, or “*prior*,” for short, $P(A|C)$ is also available, then the “*a posteriori*” probability, or the updated “*posterior*” $P(A|BC)$ is proportional to the product $P(B|AC)P(A|C)$. The prior summarizes what was known about A before the data became available, the likelihood function conveys the impact of the data, and the posterior contains the complete information available for further inference and prediction.

The generalization of (200) to several distinct and mutually exclusive alternatives A_v was obtained in Laplace (1812) in the form

$$P(A_v|BC) = \frac{P(B|A_vC) P(A_v|C)}{\sum_v P(B|A_vC) P(A_v|C)}, \quad v = 1, 2, \dots, N. \quad (201)$$

The above probability is normalized to unity as demanded by the sum rule. For continuous variates A and B , the finite probabilities $P(A|C)$, $P(B|AC)$, etc., are replaced by infinitesimal probabilities $p(A|C)dA$, $P(B|AC)dB$, etc., with probability densities $p(A|C)$, $p(B|AC)$, etc., while the sum over all alternatives is replaced by an integral. Hence, for continuous variates, (201) takes the form

$$p(A|BC) dA = \frac{p(B|AC) p(A|C) dA}{\int p(B|AC) p(A|C) dA}, \quad A_{\min} \leq A \leq A_{\max}. \quad (202)$$

The above forms of Bayes’ theorem provide the cornerstone for data evaluation, assimilation, and calibration (adjustment), indicating how prior knowledge (e.g., a data file) is to be updated with new evidence (new data). The customary way to express Bayes theorem in words is “posterior \propto likelihood \times prior,” where the “prior” distribution summarizes the knowledge extant prior to observing the (new) data, the “likelihood” distribution conveys the impact of the new information brought by the (new) data, while the “posterior” distribution contains the full information available for further inference, prediction, and decision making. Thus, Bayes’ theorem is a formal model for updating, or learning, from observations. Note that the terms “posterior” and “prior” have logical rather than temporal connotations, implying “with” and, respectively, “without” the assimilation of new data. Once a prior probability has been assigned, Bayesian statistics indicates how one’s degree of belief should change after obtaining additional information (e.g., experimental data). Since the prior probability for the data, $P(\text{data})$, does not appear explicitly, the relation

$$\text{“posterior} \propto \text{likelihood} \times \text{prior”}$$

expresses a proportionality rather than an equality.

However, Bayesian statistics provides no fundamental rule for assigning the prior probability to a theory. The choice of the “most appropriate” prior distribution is essential for applying Bayes’ theorem to practical problems, and has caused considerable debates over the years. Thus, when the prior information related to the problem under consideration can be expressed in the form of a probability distribution, this information should certainly be used; in such cases, the repeated application of Bayes’ theorem will serve to refine the knowledge about the respective problem. Ultimately, the proper repeated use of Bayes’ theorem ensures that the impact of the choice of priors on the finally recommended results diminishes as additional information (e.g., measurements) containing consistent data is successively incorporated.

In the absence of any prior information, the principle of insufficient reason works well for coins, dice, playing cards, and other similar cases characterized by discrete alternatives. However, this principle appears to lead to difficulties for continuous alternatives characterized by infinitesimal probabilities, $p(x)dx$, because a continuous uniform distribution, taken to describe equal probabilities, becomes nonuniform under change of variables. For example, when estimating the decay constant λ of a radionuclide, if all decay constants are equally probable a priori, the prior distribution would be $p(\lambda)d\lambda \sim d\lambda$. On the other hand, if all mean lives $\tau = 1/\lambda$ were considered to be equally probable a priori, the prior distribution would be $p(\tau)d\tau \sim d\tau \sim d\lambda/\lambda^2$. In the past, such apparent arbitrariness regarding priors for continuous random quantities had hampered the use of priors and hence the use of Bayes' theorem. However, while establishing *decision theory*, Wald (1950) proved that the optimal strategy for making decisions (i.e., recommending a value for some uncertain quantity, for instance) is based on Bayes' theorem, which renewed the interest in searching logically well-founded prescriptions for assigning priors. A breakthrough in this regard was achieved by Jaynes (1983), who demonstrated that in some very important practical cases, the invariance properties of the problem under investigation uniquely determine the "least informative" prior that describes initial ignorance about numerical values. Thus, if a *location parameter* is to be estimated (e.g., the center μ of a Gaussian), the form of the prior must be invariant under an arbitrary shift of location, for otherwise, some locations would be preferred to others, which would be contrary to the assumption of total ignorance. This invariance implies that $p(\mu)d\mu = p(\mu + c)d(\mu + c)$, which is a functional equation that is satisfied by the uniform distribution, that is,

$$p(\mu) d\mu \sim d\mu, \quad -\infty < \mu < \infty. \quad (203)$$

For a *scale parameter* (e.g., the standard deviation σ of a Gaussian), the form of the prior must be invariant under an arbitrary rescaling, implying that $p(\sigma)d\sigma = p(c\sigma)d(c\sigma)$. The solution of this functional equation is

$$p(\sigma) d\sigma \sim \frac{d\sigma}{\sigma}, \quad 0 < \sigma < \infty. \quad (204)$$

The above prior was introduced for scale parameters by Jeffreys (1939), and is therefore called Jeffreys' prior. Although the least informative priors given in (200) and (201) are not normalizable, they may be considered as limits of very broad, normalizable distributions in the same way as Dirac's delta function may be considered as the limit of normalizable distributions that are extremely broad or extremely narrow, respectively, compared to the distributions with which they are convoluted.

For Bernoulli trials with probability of success θ , the requirement of *invariance under change of evidence* yields the prior

$$p(\theta) d\theta \sim \theta^{-1} (1 - \theta)^{-1} d\theta, \quad 0 \leq \theta \leq 1, \quad (205)$$

if $\theta = 0$ (only failures) and $\theta = 1$ (only successes) cannot be excluded a priori. The posterior probability, obtained with the familiar binomial likelihood function for Bernoulli trials, remains concentrated overwhelmingly on the values $\theta = 1$ (or $\theta = 0$) as long as only successes (or failures) occur. If, on the other hand, exactly one success and one failure was observed, then the posterior is uniform, that is, $p(\theta)d\theta = d\theta$, $0 < \theta < 1$.

In the language of group theory, a least informative prior that describes invariance under a group of continuous transformations is equivalent to the right invariant Haar measure, that is, to the weight function that ensures invariance of integrals over the whole group. More specifically, the right Haar measure is related to the prior by a change of variables, from transformation labels to possible parameters (e.g., the additive group is associated with location parameters, while the multiplicative group is associated with scale parameters).

Although the least informative priors in (203–205) are not normalizable, they may be considered as limits of extremely broad, normalizable distributions, on a linear scale ($d\mu$) or on a logarithmic scale ($d\sigma/\sigma = d(\ln \sigma)$), etc., in the same way as Dirac's delta function may be considered as the limit of extremely narrow, normalizable distributions.

While establishing information theory, Shannon (1948) proved that the lack of information implied by a discrete probability distribution, p_n , with mutually exclusive alternatives can be expressed quantitatively (up to a constant) by its *information entropy*,

$$S = - \sum_{n=1}^N p_n \ln p_n. \quad (206a)$$

Shannon proved that S is the only measure of indeterminacy that satisfies the following three requirements:

1. S is a smooth function of the p_i ;
2. If there are N alternatives, all equally probable, then the indeterminacy, and hence S must grow monotonically as N increases; and
3. Grouping of alternatives leaves S unchanged (i.e., adding the entropy quantifying ignorance about the true group, and the suitably weighted entropies quantifying ignorance about the true member within each group must yield the same overall entropy S as for ungrouped alternatives).

For continuous distributions with probability density, $p(x)$, the expression for its information entropy becomes

$$S = - \int dx p(x) \ln \frac{p(x)}{m(x)}, \quad (206b)$$

where $m(x)$ is a prior density that ensures form invariance under change of variable.

When the underlying distribution $p(x)$ is unknown and needs to be determined from incomplete information, the principle of maximum entropy provides optimal compatibility with the available information, while simultaneously ensuring minimal spurious information content. An important application of the principle of maximal entropy is to the optimal determination of an unknown distribution $p(x)$ when the only available information comprises the (possibly noninformative) prior $m(x)$ and “*integral data*” in the form of moments of several known functions $F_k(x)$ over the unknown distribution $p(x)$, namely,

$$\langle F_k \rangle = \int dx p(x) F_k(x), \quad k = 1, 2, \dots, K. \quad (207)$$

According to the *principle of maximum entropy*, the probability density $p(x)$ would satisfy the “available information” [i.e., would comply with the constraints expressed in (207)] without

implying any spurious information or hidden assumptions, if $p(x)$ maximized the information entropy defined by (206) subject to the known constraints given in (207). This variational problem can be solved by using Lagrange multipliers, λ_k , to obtain the following expression:

$$p(x) = \frac{1}{Z} m(x) \exp \left[- \sum_{k=1}^K \lambda_k F_k(x) \right]. \quad (208)$$

The normalization constant Z in (208) is defined as

$$Z \equiv \int dx m(x) \exp \left[- \sum_{k=1}^K \lambda_k F_k(x) \right]. \quad (209)$$

In statistical mechanics, the normalization constant Z is called the partition function (or sum over states), and carries the entire information available about the possible states of the system. The moments, $\langle F_k \rangle$, representing in practice the “expected integral data,” are obtained by differentiating Z with respect to the respective Lagrange multiplier, that is,

$$\langle F_k \rangle = - \frac{\partial}{\partial \lambda_k} \ln Z, \quad k = 1, 2, \dots, K. \quad (210)$$

In the case of discrete distributions, when the integral data $\langle F_k \rangle$ are not yet known, then $m(x) = 1$, and the maximum entropy algorithm described above yields the uniform distribution, as would be required by the principle of insufficient reason. Therefore, the principle of maximum entropy provides a generalization of the principle of insufficient reason, and can be applied to both discrete and continuous distributions, ranging from problems in which only information about discrete alternatives is available, to problems in which global or macroscopic information is available.

Scientific data is usually reported in the form $\langle x \rangle \pm \Delta x$, with $\Delta x \equiv \sqrt{\text{var } x}$. This information implies the availability of the first and second moments, $\langle x \rangle$ and $\langle x^2 \rangle = \langle x \rangle^2 + (\Delta x)^2$, respectively, of the underlying unknown distribution. In such cases, the maximum entropy algorithm above can be used with $K = 2$, and (208) can be readily used to obtain the form $p(x) \sim \exp(-\lambda_1 x - \lambda_2 x^2)$ as the most objective probability density for further inference. In terms of the known moments $\langle x \rangle$ and $\langle x^2 \rangle$, $p(x)$ would be a Gaussian having the following specific form:

$$p(x | \langle x \rangle, \Delta x) dx = \frac{\exp \left[-\frac{1}{2} \left(\frac{x - \langle x \rangle}{\Delta x} \right)^2 \right]}{[2\pi (\Delta x)^2]^{1/2}} dx, \quad -\infty < x < \infty. \quad (211)$$

When several observables x_i , $i = 1, 2, \dots, n$, are simultaneously measured, the respective results are customarily reported in the form of “best values,” $\langle x_i \rangle$, together with covariance matrix elements $c_{ij} \equiv \langle \varepsilon_i \varepsilon_j \rangle \hat{=} \text{cov}(x_j, x_k) = c_{ji}$, $c_{jj} \hat{=} \text{var } x_j$, where the errors are defined through the relation $\varepsilon_j \equiv (x_j - \langle x_j \rangle)$. In this case, (208) takes on the form

$$p(\boldsymbol{\varepsilon} | \mathbf{C}) d\boldsymbol{\varepsilon} = \frac{1}{Z} \exp \left(- \sum_{i,j} \varepsilon_i \lambda_{ij} \varepsilon_j \right) d\boldsymbol{\varepsilon} = \frac{1}{Z} \exp \left(- \frac{1}{2} \boldsymbol{\varepsilon}^\dagger \boldsymbol{\Lambda} \boldsymbol{\varepsilon} \right) d\boldsymbol{\varepsilon}, \quad (212)$$

where the Lagrange multiplier λ_{ij} corresponds to c_{ij} ; the normalization constant is defined as $Z \equiv \int d\boldsymbol{\varepsilon} \exp(-(1/2)\boldsymbol{\varepsilon}^\dagger \boldsymbol{\Lambda} \boldsymbol{\varepsilon})$; $\boldsymbol{\varepsilon} = (\varepsilon_1, \dots, \varepsilon_n)$ denotes the n -component vector of errors; $\mathbf{C} \hat{=} (c_{ij})_{n \times n}$ is the $n \times n$ covariance matrix for the observables x_i , $i = 1, 2, \dots, n$; and $\boldsymbol{\Lambda} = (\lambda_{ij})_{n \times n}$ denotes the $n \times n$ matrix of Lagrange multipliers. The explicit form of the normalization constant Z in (212) is obtained by performing the respective integrations to obtain

$$Z = \sqrt{\frac{\pi^n}{\det(\boldsymbol{\Lambda})}}. \quad (213)$$

The relationship between the Lagrange multiplier λ_{ij} and the covariance c_{ij} is obtained by differentiating $\ln Z$ with respect to the respective Lagrange multiplier, cf. (210), to obtain

$$c_{ij} = -\frac{\partial}{\partial \lambda_{ij}} \ln Z = \frac{1}{2} (\boldsymbol{\Lambda}^{-1})_{ij} \quad (214)$$

since differentiation of the determinant $\det(\boldsymbol{\Lambda})$ with respect to an element of $\boldsymbol{\Lambda}$ yields the cofactor for this element (which, for a nonsingular matrix, is equal to the corresponding element of the inverse matrix times the determinant). Replacing (213) and (214) in (212) transforms the latter into the form

$$p(\boldsymbol{\varepsilon}|\mathbf{C}) d^n \boldsymbol{\varepsilon} = \frac{\exp\left(-\frac{1}{2}\boldsymbol{\varepsilon}^\dagger \mathbf{C}^{-1} \boldsymbol{\varepsilon}\right)}{\sqrt{\det(2\pi\mathbf{C})}} d^n \boldsymbol{\varepsilon}, \quad -\infty < \varepsilon_i < \infty, \quad (215)$$

with $\langle \boldsymbol{\varepsilon} \rangle = \mathbf{0}$, $\langle \boldsymbol{\varepsilon} \boldsymbol{\varepsilon}^\dagger \rangle = \mathbf{C}$, which is an n -variate Gaussian centered at the origin. In terms of the expected values $\langle x_i \rangle$, the above expression becomes

$$p(\mathbf{x}|\langle \mathbf{x} \rangle, \mathbf{C}) d\mathbf{x} = \frac{\exp\left[-\frac{1}{2}(\mathbf{x} - \langle \mathbf{x} \rangle)^\dagger \mathbf{C}^{-1}(\mathbf{x} - \langle \mathbf{x} \rangle)\right] d\mathbf{x}}{\sqrt{\det(2\pi\mathbf{C})}}, \quad -\infty < x_j < \infty. \quad (216)$$

Thus, the foregoing considerations show that, when only mean values and covariances are known, the maximum entropy algorithm yields the Gaussian probability distribution in (216) as the most objective probability distribution, where \mathbf{x} is the data vector with coordinates x_j ; \mathbf{C} is the covariance matrix with elements C_{jk} ; $d\mathbf{x} \hat{=} \prod_j dx_j$ is the volume element in the data space, and the dagger denotes transposition.

Often in practice the variances c_{ii} are known (or can be estimated reasonably well) but the covariances c_{ij} are not, in which case the covariance matrix \mathbf{C} would a priori be diagonal. In such a case, only the Lagrange parameters λ_{ii} would appear in (212), so that the matrix $\boldsymbol{\Lambda}$ would also be a priori diagonal. In other words, in the absence of information about correlations, the maximum entropy algorithm indicates that unknown covariances can be taken to be zero. This is another example of a general property of maximum entropy distributions: all moments vanish unless the constraints demand otherwise. The above results and considerations also provide a justification for the use of the well-known “least squares approximation” method.

Gaussian distributions are often considered appropriate only if many independent random deviations act in concert such that the central limit theorem is applicable. Nevertheless, if only

“best values” and their (co)variances are available, the maximum entropy principle indicates that the corresponding Gaussian is the best choice for all further inferences, regardless of the actual form of the unknown true distribution. Furthermore, in contrast to the central limit theorem, the maximum entropy principle is also valid for correlated data. The maximum entropy principle can also be employed to work with systematic errors when their possible magnitudes can be (at least vaguely) inferred but their signs are not known. The maximum entropy principle indicates that such errors should be described by a Gaussian distribution with zero mean and a width corresponding to the (vaguely) known magnitude, rather than by a rectangular distribution. Although the above results have been derived for observables x_j that vary in the interval for $-\infty < x_j < \infty$, these results can also be used for positive observable x_j ($0 < x_j < \infty$) by considering a logarithmic scale (or lognormal distributions on the original scale). The foregoing considerations underscore the fact that the maximum entropy principle is a powerful tool for the assignment of prior (or any other) probabilities, in the presence of incomplete information.

5.2 Recommending Nominal Values and Uncertainties: Decision Theory

Since probabilities cannot be measured directly, they are either inferred from the results of observations or they are postulated and (partially) verified through accumulated experience. In practice, though, certain random vectors tend to be more probable, so that probability distributions tend to be nonuniform. Therefore, the most important features of probability functions of practical interest are the measures of location and of dispersion, which are provided by the expectation and moments of the respective probability function. If the probability function is known, these moments can be calculated directly, through (a process called) statistical deduction. Otherwise, if the probability function is not known, the respective moments must be estimated from experiments, through (a process called) statistical inference. Since measurements rarely yield true values, it is necessary to introduce surrogate parameters to measure location and dispersion for the observed results. Practice indicates that *location* is best described by the *mean value*, while the *dispersion* of observed results appears to be best described by the *variance*, which is a second-order moment. In particular, the mean value can be interpreted as a locator of the center of gravity, while the variance is analogous to the moment of inertia (which linearly relates applied torque to induced angular acceleration in mechanics). For multivariate probability distributions involving n random variables, all second-order moments are collected in an $n \times n$ matrix called the variance–covariance matrix, or, simply, the covariance matrix.

Ideally, knowledge of scientific and technological data should be described in terms of complete probability distributions. In practice, though, such distributions are seldom available; furthermore, users are often interested only in practical “recommended values” and “error bars.” Prescriptions for recommending rigorously founded “best values” and “error bars” are provided by decision theory, which demonstrates that a disadvantage or penalty arises for any estimate, x_{est} , of an uncertain (unknown) parameter x . This penalty can be described by a *loss function* that vanishes at the unknown true value x but grows as the deviation $|x_{est} - x|$ increases. Near the true value, x , any reasonably smooth loss function can be taken to be proportional to the squared deviation, $(x_{est} - x)^2$, since the Taylor expansion of such a function about zero error

begins with the quadratic term. For a set of given probabilities, P_n , for the various alternatives n , the expected loss function

$$\sum_n P_n (x_{est} - x_n)^2 = \min, \quad (217)$$

is minimized when $x_{est} = \langle x \rangle$; hence $x_{est} = \langle x \rangle$ would be “the recommended value.” For a continuous random quantity with probability density, $p(x)$, the expected loss function is minimized in a similar way, that is,

$$\int dx p(x) (x_{est} - x)^2 = \min, \quad (218)$$

when $x_{est} = \langle x \rangle$. The above considerations indicate that the expected squared error is minimal when $x_{est} = \langle x \rangle$, and is equal, at the minimum, to the variance of the probability distribution. This argument justifies the choice of “mean” and “variance” as the “best indicators” for a distribution under quadratic loss: the “mean” is the optimal estimate of the (always unknown) true value, and the standard deviation (square root of the variance, also called dispersion, standard error, or “ 1σ ” uncertainty) is the best, in the sense of *quadratic loss*, indication of its uncertainty. Hence, parameter estimates should be presented in the form $\langle x \rangle \pm \Delta x$, where $\Delta x = \sqrt{\text{var } x}$. Although other types of loss functions may be preferable for some very specific applications, the quadratic loss is employed as the optimal choice in general, particularly when errors are small and data applications are not specified.

The generalization of the foregoing arguments to several uncertain quantities is accomplished by replacing the scalar observable x with a vector \mathbf{x} whose components are the respective observables. The “*estimate under quadratic loss*” is then described by the vector $\langle \mathbf{x} \rangle$ of mean values, and by the covariance matrix $\langle (\mathbf{x} - \langle \mathbf{x} \rangle) (\mathbf{x} - \langle \mathbf{x} \rangle)^\dagger \rangle$, with the dagger indicating “transposition” (since all components of the respective vectors and matrices are real numbers). Note that the expectation values $\langle \mathbf{x} \rangle$ are averages over the joint distribution of all the coordinates of the vector of observables, and the covariance matrix contains both the respective variances and correlations.

6 Model Calibration Through Data Assimilation for Best-Estimate Predictions

6.1 Introduction

The probabilistic description of possible future computational and experimental outcomes, based on all recognized errors and uncertainties, is the aim of *predictive estimation*. Predictive estimation comprises three key elements: model calibration, model extrapolation, and estimation of the validation domain. *Model calibration* involves the integration (assimilation) of new data for updating (i.e., “calibrating” or “adjusting”) the parameters characterizing a computational model. The procedures for model calibration must encompass the propagation of all relevant uncertainties, including:

1. Data uncertainties (input data, model parameters, initial and boundary conditions, forcing functions, etc);

2. Numerical discretization errors;
3. Discrepancies within the experimental data and/or discrepancies between data and model predictions; and
4. Uncertainties in the physics of the modeled processes (e.g., due to incomplete knowledge).

The results of model validation are best-estimated values for parameters and predicted responses, as well as best-estimate reduced uncertainties (i.e., “smaller” values for the variance–covariance matrices) for the predicted best-estimate parameters and responses, provided all elements involved in the calibration process are consistent with each other. *Quantitative model extrapolation* addresses the prediction of uncertainty in new environments or conditions of interest, including both untested parts of the parameter space and higher levels of system complexity in the validation hierarchy. *Estimation of the validation domain* addresses the estimation of contours of constant uncertainty in the high-dimensional space that characterizes the application of interest.

This section presents a rigorous mathematical methodology for predictive estimation through data assimilation and simultaneous calibration of model parameters and responses for a generic time-dependent physical system, generalizing and setting on a rigorous basis the pioneering work originally presented in Barhen et al. (1980, 1982), as well as the data assimilation methodologies currently used in geophysical sciences [see, e.g., Kalnay 2003; Lewis et al. 2006]. This methodology also provides quantitative indicators, based on uncertainties and sensitivities, for determining the degree of agreement or disagreement relevant to the assimilation and best-estimate adjustment of computational and experimental parameters and responses.

This section is structured as follows: ➤ Sect. 6.2 introduces the mathematical and physical bases for assigning prior probability distributions under incomplete information. ➤ Section 6.3 presents the mathematical framework for data assimilation and simultaneous calibration of model parameters and responses for a generic time-dependent physical system; of course, time-independent systems are included as a particular case within this framework. Furthermore, this framework also encompasses the basic elements for quantitative model extrapolation (i.e., prediction of uncertainty in new environments or conditions of interest, including both untested parts of the parameter space and higher levels of system complexity in the validation hierarchy) and estimation of the validation domain. The data assimilation and best-estimate model calibration methodology presented in ➤ Sect. 6.3 also includes quantitative indicators (based on uncertainties and sensitivities) for data consistency and rejection criteria, in order to determine the degree of agreement (or disagreement) relevant to the assimilation and best-estimate adjustment of parameters and responses, of computations and experiments. The applicability of the methodology presented in ➤ Sect. 6.2 is illustrated in ➤ Sect. 6.4 by performing data assimilation and model calibration for a paradigm transient thermal-hydraulics system of benchmark quality for reactor safety codes.

6.2 Mathematical Formalism

The time-dependent generic physical system to be analyzed in the sequel is considered to comprise N_α^v model parameters and N_r^v distinct responses, respectively, at every time node $v = 1, 2, \dots, N_t$. Hence, at every time node v , the (column) vector α^v of J_α^v system parameters,

and the (column) vector \mathbf{r}^v of J_r^v measured responses can be represented in component form as

$$\boldsymbol{\alpha}^v = \{ \alpha_n^v \mid n = 1, \dots, N_\alpha^v \}, \quad \mathbf{r}^v = \{ r_i^v \mid i = 1, \dots, N_r^v \}, \quad v = 1, \dots, N_t. \quad (219)$$

At any time node v , the system parameters are considered to be variates with mean values $(\boldsymbol{\alpha}^0)^v$. Furthermore, the correlations between two parameters α_i^v and α_j^μ , at two time nodes μ and v , have the general form

$$c_{\alpha_i, j}^{v\mu} \equiv \left\langle \left[\alpha_i^v - (\alpha_i^v)^0 \right] \left[\alpha_j^\mu - (\alpha_j^\mu)^0 \right] \right\rangle. \quad (220)$$

The above covariances constitute the elements of symmetric covariance matrices of the form

$$\mathbf{C}_\alpha^{\mu v} \triangleq \left\langle (\boldsymbol{\alpha} - \boldsymbol{\alpha}^0)^\mu \left[(\boldsymbol{\alpha} - \boldsymbol{\alpha}^0)^v \right]^\dagger \right\rangle = (\mathbf{C}_\alpha^{\mu v})^\dagger = \mathbf{C}_\alpha^{v\mu} = (\mathbf{C}_\alpha^{v\mu})^\dagger. \quad (221)$$

Similarly, the *measured* responses are characterized by mean values $(\mathbf{r}_m)^v$ at a time node v , and by symmetric covariance matrices between two time nodes μ and v defined as

$$\mathbf{C}_m^{\mu v} \triangleq \left\langle (\mathbf{r} - \mathbf{r}_m)^\mu \left[(\mathbf{r} - \mathbf{r}_m)^v \right]^\dagger \right\rangle = (\mathbf{C}_m^{\mu v})^\dagger = \mathbf{C}_m^{v\mu} = (\mathbf{C}_m^{v\mu})^\dagger. \quad (222)$$

In the most general case, the measured responses may be correlated to the parameters through symmetric *response parameter uncertainty* matrices of the form

$$\mathbf{C}_{r\alpha}^{\mu v} \triangleq \left\langle (\mathbf{r} - \mathbf{r}_m)^\mu \left[(\boldsymbol{\alpha} - \boldsymbol{\alpha}^0)^v \right]^\dagger \right\rangle = (\mathbf{C}_{r\alpha}^{\mu v})^\dagger = \mathbf{C}_{r\alpha}^{v\mu} = (\mathbf{C}_{r\alpha}^{v\mu})^\dagger. \quad (223)$$

Note that the matrices $\mathbf{C}_{r\alpha}^{\mu v}$ are *not* bona fide variance–covariance matrices, in that they are not necessarily square positive matrices (often, they are rectangular), and the elements on their respective main diagonals (if they happen to be square) are also covariances (or correlations) rather than variances.

At any given time node v , a response r_i^v can be a function of not only the system parameters at time node v , but also of the system parameters at all previous time nodes μ , $1 \leq \mu \leq v$; this means that $\mathbf{r}^v = \mathbf{R}^v(\mathbf{p}^v)$, where the vector $\mathbf{p}^v \triangleq (\boldsymbol{\alpha}^1, \dots, \boldsymbol{\alpha}^\mu, \dots, \boldsymbol{\alpha}^v)$ has been introduced for notational convenience. In general, the response computed using the model depends nonlinearly and implicitly (in an analytically intractable form) on the model parameters. Furthermore, the uncertainties in parameters and modeling induce uncertainties in the computed responses, and can be computed either by means of statistical methods (for relatively simple models with few parameters) or deterministically, by using the *propagation of moments (errors)* method (see, e.g., Cacuci 2003). In this method, the computed response is linearized via a functional Taylor-series expansion around the nominal values, $\mathbf{p}_0^v \triangleq ((\boldsymbol{\alpha}^0)^1, \dots, (\boldsymbol{\alpha}^0)^\mu, \dots, (\boldsymbol{\alpha}^0)^v)$, of the parameters \mathbf{p}^v , as follows:

$$\mathbf{r}^v = \mathbf{R}^v(\mathbf{p}^v) = \mathbf{R}^v(\mathbf{p}_0^v) + \sum_{\mu=1}^v \mathbf{S}^{v\mu}(\mathbf{p}_0^\mu) \left[\boldsymbol{\alpha}^\mu - (\boldsymbol{\alpha}^0)^\mu \right] + \dots, \quad v = 1, \dots, N_t, \quad (224)$$

where $\mathbf{R}^v(\mathbf{p}_0^v)$ denotes the vector of computed responses at a time node v , at the nominal parameter values \mathbf{p}_0^v , while $\mathbf{S}^{v\mu}(\mathbf{p}_0^\mu)$, $1 \leq \mu \leq v$, represents the $(J_r^v \times J_\alpha^\mu)$ -dimensional matrix containing the first Gateaux-derivatives of the computed responses with respect to the parameters, defined as

$$\mathbf{S}^{v\mu}(\mathbf{p}_0^\mu) \triangleq \begin{pmatrix} s_{11}^{v\mu} & \cdots & s_{1N}^{v\mu} \\ \vdots & s_{in}^{v\mu} & \vdots \\ s_{l1}^{v\mu} & \cdots & s_{lN}^{v\mu} \end{pmatrix} \triangleq \begin{pmatrix} \frac{\partial R_1^v(\mathbf{p}_0^\mu)}{\partial \alpha_1^\mu} & \cdots & \frac{\partial R_1^v(\mathbf{p}_0^\mu)}{\partial \alpha_N^\mu} \\ \vdots & \frac{\partial R_l^v(\mathbf{p}_0^\mu)}{\partial \alpha_n^\mu} & \vdots \\ \frac{\partial R_l^v(\mathbf{p}_0^\mu)}{\partial \alpha_1^\mu} & \cdots & \frac{\partial R_l^v(\mathbf{p}_0^\mu)}{\partial \alpha_N^\mu} \end{pmatrix}, \quad 1 \leq \mu \leq v. \quad (225)$$

Since the response $\mathbf{R}^v(\mathbf{p}_0^v)$ at time node v can depend only on parameters $(\boldsymbol{\alpha}^0)^\mu$ which appear up to the current time node v , it follows that $\mathbf{S}^{v\mu} = \mathbf{0}$ when $\mu > v$, and hence nonzero terms in the expansion shown in (224) can only occur in the range $1 \leq \mu \leq v$. It is important to note that discretization parameters are also included among the components of $\boldsymbol{\alpha}$, and the sensitivities of responses to such discretization parameters can be computed as described in Cacuci (2003) and Cacuci et al. (2005).

By introducing the block matrix

$$\mathbf{S} \triangleq \begin{pmatrix} \mathbf{S}^{11} & \cdots & \mathbf{0} \\ \vdots & \ddots & \vdots \\ \mathbf{S}^{N_t,1} & \cdots & \mathbf{S}^{N_t,N_t} \end{pmatrix}, \quad (226)$$

and the (block) column vectors

$$\boldsymbol{\alpha} \triangleq (\boldsymbol{\alpha}^1, \dots, \boldsymbol{\alpha}^\mu, \dots, \boldsymbol{\alpha}^{N_t}), \quad \mathbf{r} \triangleq (\mathbf{r}^1, \dots, \mathbf{r}^\mu, \dots, \mathbf{r}^{N_t}), \\ \mathbf{R}(\boldsymbol{\alpha}^0) \triangleq (\mathbf{R}^1, \dots, \mathbf{R}^\mu, \dots, \mathbf{R}^{N_t}), \quad (227)$$

the system shown in (224) can be written in the form

$$\mathbf{r} = \mathbf{R}(\boldsymbol{\alpha}^0) + \mathbf{S}(\boldsymbol{\alpha} - \boldsymbol{\alpha}^0) + \text{higher order terms} \quad (228)$$

Applying the propagation of errors method (see, e.g., Cacuci 2003), which involves the formal integration of (228) over the unknown joint distribution of the parameters $\boldsymbol{\alpha}$, yields the following expressions for the expectation value, $\langle \mathbf{r} \rangle$, of the response \mathbf{r} , and the corresponding covariance matrix, $C_{rc}(\boldsymbol{\alpha}^0)$, of the computed responses: that is,

$$\langle \mathbf{r} \rangle = \mathbf{R}(\boldsymbol{\alpha}^0), \quad (229)$$

and

$$C_{rc}(\boldsymbol{\alpha}^0) \triangleq \langle \delta \mathbf{r} \delta \mathbf{r}^\dagger \rangle = [\mathbf{S}(\boldsymbol{\alpha}^0)] \langle \delta \boldsymbol{\alpha} \delta \boldsymbol{\alpha}^\dagger \rangle [\mathbf{S}(\boldsymbol{\alpha}^0)]^\dagger = [\mathbf{S}(\boldsymbol{\alpha}^0)] \mathbf{C}_\alpha [\mathbf{S}(\boldsymbol{\alpha}^0)]^\dagger. \quad (230)$$

The covariance matrix of the computed responses, \mathbf{C}_{rc} , has the symmetric structure

$$\mathbf{C}_{rc} \triangleq \begin{pmatrix} \mathbf{C}_{rc}^{11} & \cdots & \mathbf{C}_{rc}^{1N_t} \\ \vdots & \ddots & \vdots \\ \mathbf{C}_{rc}^{N_t 1} & \cdots & \mathbf{C}_{rc}^{N_t N_t} \end{pmatrix}, \text{ with components defined as}$$

$$\mathbf{C}_{rc}^{v\mu} = \sum_{\eta=1}^v \sum_{\rho=1}^{\mu} \mathbf{S}^{v\eta} \mathbf{C}_{\alpha}^{\eta\rho} (\mathbf{S}^{\mu\rho})^{\dagger} = (\mathbf{C}_{rc}^{\mu v})^{\dagger}; \quad v, \mu = 1, \dots, N_t. \quad (231)$$

As indicated by (229), the expectation value of the computed responses for linearized models in which the numerical errors are neglected is given by the value of the response computed at the nominal parameter values.

Applying now the maximum entropy algorithm described in [Sect. 5.1](#) [cf. (216)] to the computational and experimental information described in (219–231) indicates that the most objective probability distribution for this information is a multivariate Gaussian of the form

$$p(\mathbf{z}|\mathbf{C}) d(\mathbf{z}) = \frac{\exp[-(1/2) \mathbf{Q}(\mathbf{z})]}{\det(2\pi\mathbf{C})^{1/2}} d(\mathbf{z}), \quad \mathbf{Q}(\mathbf{z}) \equiv \mathbf{z}^{\dagger} \mathbf{C}^{-1} \mathbf{z}, \quad -\infty < z_j < \infty, \quad (232)$$

where

$$\mathbf{z} \equiv \begin{pmatrix} \boldsymbol{\alpha} - \boldsymbol{\alpha}^0 \\ \mathbf{r} - \mathbf{r}_m \end{pmatrix}, \quad \boldsymbol{\alpha}^0 \triangleq ((\boldsymbol{\alpha}^0)^1, \dots, (\boldsymbol{\alpha}^0)^{\mu}, \dots, (\boldsymbol{\alpha}^0)^{N_t}), \quad (233)$$

$$\mathbf{C} \equiv \begin{pmatrix} \mathbf{C}_{\alpha} & \mathbf{C}_{\alpha r} \\ \mathbf{C}_{r\alpha} & \mathbf{C}_m \end{pmatrix}, \quad (234)$$

with

$$\mathbf{C}_{\alpha} = \begin{pmatrix} \mathbf{C}_{\alpha}^{11} & \mathbf{C}_{\alpha}^{12} & \cdots & \cdots \\ \mathbf{C}_{\alpha}^{21} & \mathbf{C}_{\alpha}^{22} & \cdots & \cdots \\ \cdots & \cdots & \cdots & \cdots \\ \cdots & \cdots & \cdots & \mathbf{C}_{\alpha}^{N_t N_t} \end{pmatrix}, \quad \mathbf{C}_{\alpha r} = \begin{pmatrix} \mathbf{C}_{\alpha r}^{11} & \mathbf{C}_{\alpha r}^{12} & \cdots & \cdots \\ \mathbf{C}_{\alpha r}^{21} & \mathbf{C}_{\alpha r}^{22} & \cdots & \cdots \\ \cdots & \cdots & \cdots & \cdots \\ \cdots & \cdots & \cdots & \mathbf{C}_{\alpha r}^{N_t N_t} \end{pmatrix}, \quad \text{and}$$

$$\mathbf{C}_m = \begin{pmatrix} \mathbf{C}_m^{11} & \mathbf{C}_m^{12} & \cdots & \cdots \\ \mathbf{C}_m^{21} & \mathbf{C}_m^{22} & \cdots & \cdots \\ \cdots & \cdots & \cdots & \cdots \\ \cdots & \cdots & \cdots & \mathbf{C}_m^{N_t N_t} \end{pmatrix}$$

The posterior information, which is contained in (232) and (228), can now be condensed into a recommended best-estimate value $(\mathbf{z}^{be})^v$ at a time node v for the parameters $\boldsymbol{\alpha}^v$ and responses \mathbf{r}^v , together with corresponding best-estimate recommended uncertainties for these quantities. If a loss function is given, decision theory indicates how these best-estimate quantities are to be computed. If no specific loss function is provided, the recommended best-estimate updated posterior mean vector $(\mathbf{z}^{be})^v$ and its respective best-estimate posterior covariance matrix are usually evaluated by assuming “quadratic loss.” In such a case, the bulk of the contribution to the distribution $p(\mathbf{z}|\mathbf{C})$ in (232) is extracted by computing it at the point in phase space where the respective exponent attains its minimum, subject to (228). Subsequent computations are facilitated by recasting (228) in the form

$$\mathbf{Z}(\boldsymbol{\alpha}^0) \mathbf{z} + \mathbf{d} = 0, \quad \mathbf{d} \triangleq \mathbf{R}(\boldsymbol{\alpha}^0) - \mathbf{r}_m, \quad (235)$$

where $\mathbf{r}_m \triangleq (\mathbf{r}_m^1, \dots, \mathbf{r}_m^\mu, \dots, \mathbf{r}_m^{N_t})$ is the vector comprising all of the experimentally measured responses, $\mathbf{d} \triangleq \mathbf{R}(\boldsymbol{\alpha}^0) - \mathbf{r}_m$ is a vector of “deviations” reflecting the discrepancies between the nominal computations and the nominally measured responses, while \mathbf{Z} denotes the partitioned matrix

$$\mathbf{Z} \triangleq (\mathbf{S} \quad \mathbf{U}); \quad \mathbf{U} \triangleq \begin{pmatrix} -\mathbf{I}^{11} & \dots & \mathbf{0} \\ \vdots & \ddots & \vdots \\ \mathbf{0} & \dots & -\mathbf{I}^{N_t N_t} \end{pmatrix}, \quad (236)$$

where $\mathbf{I}^{\nu\nu}$, $\nu = 1, \dots, N_t$, denotes the identity matrix of the corresponding dimensions.

Computing the stationary point of $Q(\mathbf{z})$ subject to (235) poses a constrained minimization problem which can be solved by introducing Lagrange multipliers, $\boldsymbol{\lambda}$, to construct the augmented Lagrangian functional $P(\mathbf{z}, \boldsymbol{\lambda})$ defined as

$$P(\mathbf{z}, \boldsymbol{\lambda}) \equiv Q(\mathbf{z}) + 2\boldsymbol{\lambda}^\dagger [\mathbf{Z}(\boldsymbol{\alpha}^0)\mathbf{z} + \mathbf{d}] = \min, \quad \text{at } \mathbf{z} = \mathbf{z}^{be} \equiv \begin{pmatrix} \boldsymbol{\alpha}^{be} - \boldsymbol{\alpha}^0 \\ \mathbf{r}^{be} - \mathbf{r}_m \end{pmatrix}. \quad (237)$$

where $\boldsymbol{\lambda} = (\boldsymbol{\lambda}^1, \dots, \boldsymbol{\lambda}^\nu, \dots, \boldsymbol{\lambda}^{N_t})$ denotes the corresponding vector of the Lagrange multipliers. In the above expression, the superscript “be” denotes “best-estimated values,” and the factor “2” was introduced for convenience in front of $\boldsymbol{\lambda}$ in order to simplify the subsequent algebraic derivations. The point \mathbf{z}^{be} where the functional $P(\mathbf{z}, \boldsymbol{\lambda})$ attains its extremum (minimum) is defined implicitly through the conditions

$$\nabla_{\mathbf{z}} P(\mathbf{z}, \boldsymbol{\lambda}) = \mathbf{0}, \quad \nabla_{\boldsymbol{\lambda}} P(\mathbf{z}, \boldsymbol{\lambda}) = \mathbf{0}, \quad \text{at } \mathbf{z} = \mathbf{z}^{be}. \quad (238)$$

The solution to the above constrained minimization problem is detailed in Cacuci and Ionescu-Bujor (2010). The final results (Cacuci and Ionescu-Bujor 2010) for the predictive best-estimate parameters– responses, and their corresponding reduced uncertainties (covariance matrices) are as follows:

1. The best-estimate predicted nominal values for the calibrated (adjusted) parameters:

$$\boldsymbol{\alpha}^{be} = \boldsymbol{\alpha}^0 + \left(\mathbf{C}_{\alpha r} - \mathbf{C}_\alpha [\mathbf{S}(\boldsymbol{\alpha}^0)]^\dagger \right) [\mathbf{C}_d(\boldsymbol{\alpha}^0)]^{-1} \mathbf{d}. \quad (239)$$

In component form, the above expression for the calibrated best-estimate parameter values becomes

$$\left(\boldsymbol{\alpha}^{be} \right)^v = \left(\boldsymbol{\alpha}^0 \right)^v + \sum_{\mu=1}^{N_t} \left\{ \left[\mathbf{C}_{\alpha r}^{\nu\mu} - \sum_{\rho=1}^{\mu} \mathbf{C}_{\alpha}^{\nu\rho} \left(\mathbf{S}^\dagger \right)^{\mu\rho} \right] \left[\sum_{\eta=1}^{N_t} \mathbf{K}_d^{\mu\eta} \mathbf{d}^\eta \right] \right\}, \quad v = 1, \dots, N_t, \quad (240)$$

where $\mathbf{K}_d^{\nu\eta}$ denotes the corresponding (ν, η) -element of the block-matrix \mathbf{C}_d^{-1} , with the block-matrix $\mathbf{C}_d(\boldsymbol{\alpha}^0)$ defined as follows:

$$\begin{aligned} \mathbf{C}_d(\boldsymbol{\alpha}^0) &\triangleq \langle \mathbf{d} \mathbf{d}^\dagger \rangle = \left\langle \left(\delta \mathbf{r} - \mathbf{S}(\boldsymbol{\alpha}^0) \delta \boldsymbol{\alpha} \right) \left(\delta \mathbf{r}^\dagger - \delta \boldsymbol{\alpha}^\dagger [\mathbf{S}(\boldsymbol{\alpha}^0)]^\dagger \right) \right\rangle \\ &= \mathbf{C}_{rc}(\boldsymbol{\alpha}^0) - \mathbf{C}_{r\alpha} [\mathbf{S}(\boldsymbol{\alpha}^0)]^\dagger - [\mathbf{S}(\boldsymbol{\alpha}^0)] \mathbf{C}_{\alpha r} + \mathbf{C}_m \end{aligned} \quad (241)$$

In component form, the matrix C_d is expressed as

$$C_d \triangleq \begin{pmatrix} C_d^{11} & \cdots & C_d^{1N_t} \\ \vdots & \ddots & \vdots \\ C_d^{N_t 1} & \cdots & C_d^{N_t N_t} \end{pmatrix} = \begin{pmatrix} C_{rc}^{11} + C_m^{11} & \cdots & C_{rc}^{1N_t} + C_m^{1N_t} \\ \vdots & \ddots & \vdots \\ C_{rc}^{N_t 1} + C_m^{N_t 1} & \cdots & C_{rc}^{N_t N_t} + C_m^{N_t N_t} \end{pmatrix} \\ - \begin{pmatrix} C_{r\alpha}^{11} (\mathbf{S}^\dagger)^{11} + \mathbf{S}^{11} C_{\alpha r}^{11} & \cdots & \mathbf{S}^{11} C_{\alpha r}^{1N_t} + \sum_{\rho=1}^{N_t} C_{r\alpha}^{1\rho} (\mathbf{S}^\dagger)^{N_t \rho} \\ \vdots & \ddots & \vdots \\ C_{r\alpha}^{N_t 1} (\mathbf{S}^\dagger)^{11} + \sum_{\rho=1}^{N_t} \mathbf{S}^{N_t \rho} C_{\alpha r}^{\rho 1} & \cdots & \sum_{\rho=1}^{N_t} [C_{r\alpha}^{N_t \rho} (\mathbf{S}^\dagger)^{N_t \rho} + \mathbf{S}^{N_t \rho} C_{\alpha r}^{\rho N_t}] \end{pmatrix}. \quad (242)$$

2. The best-estimate predicted nominal values for the calibrated (adjusted) responses:

$$\mathbf{r}(\boldsymbol{\alpha}^{be}) = \mathbf{r}_m + \left(C_m - C_{r\alpha} [\mathbf{S}(\boldsymbol{\alpha}^0)]^\dagger \right) [C_d(\boldsymbol{\alpha}^0)]^{-1} \mathbf{d}. \quad (243)$$

At a specific time node v , each component $(\mathbf{r}^{be})^v$ of $\mathbf{r}(\boldsymbol{\alpha}^{be})$ has the explicit form

$$(\mathbf{r}^{be})^v = (\mathbf{r}_m)^v + \sum_{\mu=1}^{N_t} \left\{ \left[C_m^{v\mu} - \sum_{\rho=1}^{\mu} C_{r\alpha}^{v\rho} (\mathbf{S}^\dagger)^{\mu\rho} \right] \left[\sum_{\eta=1}^{N_t} \mathbf{K}_d^{\mu\eta} \mathbf{d}^\eta \right] \right\}, \quad v = 1, \dots, N_t. \quad (244)$$

3. The expressions for the best-estimate predicted covariances C_α^{be} and C_r^{be} , corresponding to the best-estimate parameters $\boldsymbol{\alpha}^{be}$ and responses $\mathbf{r}(\boldsymbol{\alpha}^{be})$, together with the predicted best-estimate parameter–response covariance matrix $C_{\alpha r}^{be}$ are as follows:

$$C_\alpha^{be} \triangleq \left\langle \left(\boldsymbol{\alpha} - \boldsymbol{\alpha}^{be} \right) \left(\boldsymbol{\alpha} - \boldsymbol{\alpha}^{be} \right)^\dagger \right\rangle = C_\alpha - [C_{\alpha d}(\boldsymbol{\alpha}^0)] [C_d(\boldsymbol{\alpha}^0)]^{-1} [C_{\alpha d}(\boldsymbol{\alpha}^0)]^\dagger, \quad (245)$$

$$C_r^{be} \triangleq \left\langle \left(\mathbf{r} - \mathbf{r}(\boldsymbol{\alpha}^{be}) \right) \left(\mathbf{r} - \mathbf{r}(\boldsymbol{\alpha}^{be}) \right)^\dagger \right\rangle = C_m - [C_{rd}(\boldsymbol{\alpha}^0)] [C_d(\boldsymbol{\alpha}^0)]^{-1} [C_{rd}(\boldsymbol{\alpha}^0)]^\dagger, \quad (246)$$

$$C_{\alpha r}^{be} = C_{\alpha r}^{be} \triangleq \left\langle \left(\boldsymbol{\alpha} - \boldsymbol{\alpha}^{be} \right) \left(\mathbf{r} - \mathbf{r}(\boldsymbol{\alpha}^{be}) \right)^\dagger \right\rangle = C_{\alpha r} - [C_{rd}(\boldsymbol{\alpha}^0)] [C_d(\boldsymbol{\alpha}^0)]^{-1} [C_{\alpha d}(\boldsymbol{\alpha}^0)]^\dagger, \quad (247)$$

where

$$C_{rd}(\boldsymbol{\alpha}^0) \triangleq \left\langle \left(\mathbf{r} - \mathbf{r}_m \right) \mathbf{d}^\dagger \right\rangle = \left(C_m - C_{r\alpha} [\mathbf{S}(\boldsymbol{\alpha}^0)]^\dagger \right), \quad (248)$$

$$C_{\alpha d}(\boldsymbol{\alpha}^0) \triangleq \left\langle \left(\boldsymbol{\alpha} - \boldsymbol{\alpha}^0 \right) \mathbf{d}^\dagger \right\rangle = \left(C_{\alpha r} - C_\alpha [\mathbf{S}(\boldsymbol{\alpha}^0)]^\dagger \right), \quad (249)$$

For completeness, the block-matrix components, which correlate two (distinct or not) time nodes of the above calibrated best-estimate covariance matrices are given below:

$$\left(\mathbf{C}_\alpha^{be}\right)^{v\mu} = \mathbf{C}_\alpha^{v\mu} - \sum_{\eta=1}^{N_t} \sum_{\rho=1}^{N_t} \left[\mathbf{C}_{\alpha r}^{v\rho} - \sum_{\pi=1}^{\rho} \mathbf{C}_{r\alpha}^{v\pi} \left(\mathbf{S}^\dagger\right)^{\rho\pi} \right] \mathbf{K}_d^{\rho\eta} \left[\mathbf{C}_{r\alpha}^{\eta\mu} - \sum_{\pi=1}^{\eta} \mathbf{S}^{\eta\pi} \mathbf{C}_\alpha^{\pi\mu} \right], \quad (250)$$

$$\left(\mathbf{C}_r^{be}\right)^{v\mu} = \mathbf{C}_m^{v\mu} - \sum_{\eta=1}^{N_t} \sum_{\rho=1}^{N_t} \left[\mathbf{C}_m^{v\rho} - \sum_{\pi=1}^{\rho} \mathbf{C}_{r\alpha}^{v\pi} \left(\mathbf{S}^\dagger\right)^{\rho\pi} \right] \mathbf{K}_d^{\rho\eta} \left[\mathbf{C}_m^{\eta\mu} - \sum_{\pi=1}^{\eta} \mathbf{S}^{\eta\pi} \mathbf{C}_{\alpha r}^{\pi\mu} \right], \quad (251)$$

$$\left(\mathbf{C}_{r\alpha}^{be}\right)^{v\mu} = \mathbf{C}_{r\alpha}^{v\mu} - \sum_{\eta=1}^{N_t} \sum_{\rho=1}^{N_t} \left[\mathbf{C}_m^{v\rho} - \sum_{\pi=1}^{\rho} \mathbf{C}_{r\alpha}^{v\pi} \left(\mathbf{S}^\dagger\right)^{\rho\pi} \right] \mathbf{K}_d^{\rho\eta} \left[\mathbf{C}_{\alpha r}^{\eta\mu} - \sum_{\pi=1}^{\eta} \mathbf{S}^{\eta\pi} \mathbf{C}_\alpha^{\pi\mu} \right], \quad (252)$$

Note in (245) that a symmetric positive matrix is subtracted from the initial parameter covariance matrix \mathbf{C}_α ; hence, in this sense, *the best-estimate predicted parameter uncertainty matrix \mathbf{C}_α^{be} has been reduced by the calibration (adjustment) procedure, through the introduction of new information from experiments*. Similarly, a symmetric positive matrix is subtracted in (246) from the initial covariance matrix \mathbf{C}_m of the experimental responses; hence, *the best-estimate predicted response covariance matrix \mathbf{C}_r^{be} has been improved (reduced) through the introduction of new experimental information*. Furthermore, Eq. (247) indicates that the calibration (adjustment) procedure will introduce correlations between the calibrated (adjusted) parameters and responses even if the parameters and response were initially uncorrelated, since $\mathbf{C}_{r\alpha}^{be} \neq 0$ even if $\mathbf{C}_{r\alpha} = 0$, that is,

$$\mathbf{C}_{r\alpha}^{be} = \mathbf{C}_m \left[\mathbf{C}_{rc}(\boldsymbol{\alpha}^0) + \mathbf{C}_m \right]^{-1} \left[\mathbf{S}(\boldsymbol{\alpha}^0) \right] \mathbf{C}_\alpha, \quad \text{when } \mathbf{C}_{r\alpha} = 0. \quad (253)$$

As the above expression indicates, the adjustment (calibration) modifies the correlations among the parameters through couplings introduced by the sensitivities of the participating responses. In the calibration procedure, the sensitivities play the role of weighting functions for propagating the initial parameter covariances and experimental-response covariances to the adjusted best-estimate predicted quantities. Thus, as indicated by (245–247), the incorporation of additional (experimental) information in the adjustment (calibration) process reduces the variances of the adjusted parameters and responses while also modifying their correlations.

Note that, Eq. (246) expresses the best-estimate response covariance matrix, \mathbf{C}_r^{be} in terms of the initial covariance matrix, \mathbf{C}_m , of the experimental responses. Alternatively, it is of interest to derive the expression of the computed best-estimate response covariance matrix, \mathbf{C}_{rc}^{be} , directly from the model (the subscript “rc” denotes “computed response,” to distinguish it from the covariance \mathbf{C}_r^{be} , which is obtained directly from the calibration/adjustment process). The starting point for computing \mathbf{C}_{rc}^{be} is the linearization of the model, similar to that shown in (228), but around $\boldsymbol{\alpha}^{be}$, instead of $\boldsymbol{\alpha}^0$, that is,

$$\mathbf{r} = \mathbf{R}(\boldsymbol{\alpha}^{be}) + \mathbf{S}(\boldsymbol{\alpha}^{be}) \left(\boldsymbol{\alpha} - \boldsymbol{\alpha}^{be} \right) + \text{higher order terms.} \quad (254)$$

It follows from (254) that

$$\begin{aligned}
 \mathbf{C}_{rc}^{be} &= \left\langle \left(\mathbf{r} - \mathbf{R}(\boldsymbol{\alpha}^{be}) \right) \left(\mathbf{r} - \mathbf{R}(\boldsymbol{\alpha}^{be}) \right)^\dagger \right\rangle \triangleq \left[\mathbf{S}(\boldsymbol{\alpha}^{be}) \right] \left\langle \left(\boldsymbol{\alpha} - \boldsymbol{\alpha}^{be} \right) \left(\boldsymbol{\alpha} - \boldsymbol{\alpha}^{be} \right)^\dagger \right\rangle \left[\mathbf{S}(\boldsymbol{\alpha}^{be}) \right]^\dagger \\
 &= \left[\mathbf{S}(\boldsymbol{\alpha}^{be}) \right] \mathbf{C}_\alpha^{be} \left[\mathbf{S}(\boldsymbol{\alpha}^{be}) \right]^\dagger \\
 &= \left[\mathbf{S}(\boldsymbol{\alpha}^{be}) \right] \left[\mathbf{C}_\alpha - \left(\mathbf{C}_{\alpha r} - \mathbf{C}_\alpha \left[\mathbf{S}(\boldsymbol{\alpha}^0) \right]^\dagger \right) \left[\mathbf{C}_d(\boldsymbol{\alpha}^0) \right]^{-1} \left(\mathbf{C}_{\alpha r} - \left[\mathbf{S}(\boldsymbol{\alpha}^0) \right] \mathbf{C}_\alpha \right) \right] \left[\mathbf{S}(\boldsymbol{\alpha}^{be}) \right]^\dagger
 \end{aligned} \tag{255}$$

Comparing (255) to (246) reveals that, in general, $\mathbf{C}_{rc}^{be} \neq \mathbf{C}_r^{be}$ since $\mathbf{S}(\boldsymbol{\alpha}^{be}) \neq \mathbf{S}(\boldsymbol{\alpha}^0)$. Nevertheless, when the model is “perfect” (i.e., free of higher-order numerical errors) and exactly linear, then the sensitivity matrix \mathbf{S} is independent of the parameter values $\boldsymbol{\alpha}$, that is,

$$\mathbf{S}(\boldsymbol{\alpha}^{be}) = \mathbf{S}(\boldsymbol{\alpha}^0) = \mathbf{S}, \quad \text{for “perfect” and linear models,} \tag{256}$$

Using (256) in (255) reduces the later expression to

$$\begin{aligned}
 \mathbf{C}_{rc}^{be} &= \mathbf{S} \left[\mathbf{C}_\alpha - \left(\mathbf{C}_{\alpha r} - \mathbf{C}_\alpha \mathbf{S}^\dagger \right) \mathbf{C}_d^{-1} \left(\mathbf{C}_{\alpha r} - \mathbf{S} \mathbf{C}_\alpha \right) \right] \mathbf{S}^\dagger \\
 &= \mathbf{C}_{rc} - \left(\mathbf{C}_{rc} - \mathbf{S} \mathbf{C}_{\alpha r} \right) \left[\mathbf{C}_{rc} + \mathbf{C}_e - \mathbf{C}_{r\alpha} \mathbf{S}^\dagger - \mathbf{S} \mathbf{C}_{\alpha r} \right]^{-1} \left(\mathbf{C}_{rc} - \mathbf{C}_{\alpha r} \mathbf{S}^\dagger \right) \\
 &= \mathbf{C}_r^{be}, \quad \text{for “perfect” linear models.}
 \end{aligned} \tag{257}$$

It is important to note that the computation of the best-estimate parameter and response values, together with their corresponding best-estimate uncertainties, cf., (239), (243), and (245–247) require the inversion of a single matrix, namely, the matrix $\mathbf{C}_d(\boldsymbol{\alpha}^0)$ defined in (242). This is usually advantageous in practice, since the order of the matrix $\mathbf{C}_d(\boldsymbol{\alpha}^0)$ is given by the number of measured (or computed) responses, which are most often considerably smaller than the number of model parameters under consideration.

On the other hand, when the number of parameter exceeds the number of responses, it is possible to derive alternative expressions for the best-estimate calibrated parameters and their corresponding best-estimate covariances, by performing all derivations in the “parameter space” rather than in “response space.” This entails using (228) to eliminate the response (variables) \mathbf{r} at the outset, and carrying out the minimization procedure solely for the parameters (variables), $\boldsymbol{\alpha}$. Equivalently, as shown in (Cacuci et al. 2010), the Sherman–Morrison–Woodbury extension can be employed to obtain the alternative expression

$$\begin{aligned}
 \mathbf{C}_d^{-1} &\triangleq \left(\mathbf{C}_{rc} - \mathbf{C}_{r\alpha} \mathbf{S}^\dagger - \mathbf{S} \mathbf{C}_{\alpha r} + \mathbf{C}_m \right)^{-1} \\
 &= \mathbf{A}^{-1} - \mathbf{A}^{-1} \mathbf{S} \left(\mathbf{C}_\alpha^{-1} + \mathbf{S}^\dagger \mathbf{A}^{-1} \mathbf{S} \right)^{-1} \mathbf{S}^\dagger \mathbf{A}^{-1}; \quad \mathbf{A} \triangleq \mathbf{C}_m - \mathbf{C}_{r\alpha} \mathbf{S}^\dagger - \mathbf{S} \mathbf{C}_{\alpha r}.
 \end{aligned} \tag{258}$$

The above expression provides the bridge between the “response-space” and “parameter-space” formulations. This expression also highlights the fact that the response-space formulation

requires a single inversion of a square symmetric matrix (namely, the matrix, C_d) of the same dimensions as the number of responses. In contradistinction, the “parameter space” formulation requires the inversion of three symmetric matrices, two of which have dimensions equal to the number of parameters and one of dimensions equal to the number of responses. Hence, from a computational standpoint, the “response-space” formulations should be used whenever possible.

As highlighted by the expression of C_d in (242), it is essential to note that the inverse matrix, C_d^{-1} , incorporates simultaneously all of the available information about the system parameters and responses, at all time nodes [i.e., $\nu = 1, 2, \dots, N_t$]. Specifically, at any time node, ν , C_d^{-1} incorporates information not only from time nodes prior in time to ν (i.e., information regarding the “past” and “present” states of the system) but also from time nodes posterior in time to ν (i.e., information about the “future” states of the system). Through the matrix C_d^{-1} , at any specified time node ν , the calibrated best-estimates parameters $(\mathbf{a}^{be})^\nu$ and responses $\mathbf{r}(\mathbf{a}^{be}) \triangleq \mathbf{r}^{be}$, together with the corresponding calibrated best-estimate covariance matrices $(C_\alpha^{be})^{\nu\mu}$, $(C_r^{be})^{\nu\mu}$, and $(C_{\alpha r}^{be})^{\nu\mu}$ will also incorporate automatically all of the available information about the system parameters and responses at all time nodes [i.e., $\nu = 1, 2, \dots, N_t$].

In this respect, the methodology presented in this section is conceptually related to the “fore-sight” aspects encountered in decision analysis. It is also important to note that, in practice, the application of the methodology developed in this section involves two distinct computational stages. A complete sensitivity data base (i.e., sensitivities $s_{ni}^{\nu\mu}$ at all times nodes, $\nu, \mu = 1, \dots, N_t$) needs to be generated “off-line” prior to performing the “data assimilation” and “model calibration” (or data adjustment) stages. All sensitivities are subsequently combined with appropriate covariance matrices to compute calibrated best-estimate responses, parameters, and best-estimate covariance matrices.

Because of the “foresight” and “off-line” characteristics, the methodology presented in this section can be called the “off-line with foresight” data assimilation and adjustment (model calibration) methodology, underscoring that all sensitivities are generated separately, prior to performing the uncertainty analysis, and that foresight characteristics are included in the calibration procedure. Since the incorporation of foresight effects involves the inversion of the matrix, C_d , this methodology is best suited for problems involving relatively few time nodes. For large-scale highly nonlinear problems involving many time nodes, the matrix C_d becomes very large, requiring large amounts of computer storage; the inversion of C_d may become prohibitively expensive in such cases. These difficulties can be reduced at the expense of using less than the complete information available at any specific time node. For example, even in time-dependent problems in which the entire time history is known (e.g., transient behavior of reactor systems), one may nevertheless choose to use only information up to the current time index, and disregard the information about “future” system states.

On the other hand, in dynamical problems such as climate or weather prediction, in which the time variable advances continuously and states beyond the current time are not known, information about future states cannot be reliably accounted for anyway. Thus, the most common way of reducing the dimensionality of the data assimilation and model calibration problem is to disregard information about future states and limit the amount of information assimilated about “past states.” Data assimilation and model calibration procedure using such a limited amount of information can be performed either off-line or on-line, assimilating the new data as the time index advances.

The simplest case of dynamic data assimilation and model calibration is when these operations are performed by using information on-line from only two successive time steps. In this particular case, the expressions given by (240), (244), and (250–252) for the best-estimate predicted calibrated quantities reduce (see Cacuci et al. (2010) for details) to the following explicit formulas:

1. The components $(\mathbf{a}^{be})^k$, representing the calibrated best-estimates for the system parameters at time node, k , can be written in a particular form of (240), as follows:

$$(\mathbf{a}^{be})^k = (\boldsymbol{\alpha}^0)^k + \sum_{\mu=k-1}^k \left\{ \left[\mathbf{C}_{\alpha r}^{k\mu} - \sum_{\rho=k-1}^{\mu} \mathbf{C}_{\alpha}^{k\rho} (\mathbf{s}^\dagger)^{\mu\rho} \right] \left[\sum_{\eta=k-1}^k \mathbf{K}_d^{\mu\eta} \mathbf{d}^\eta \right] \right\}, \quad k = 1, 2, \dots, N_t. \quad (259)$$

2. The vector $(\mathbf{r}^{be})^k$, representing the best-estimates predicted values for the system parameters at a time node, k , take on the following particular form of (244):

$$(\mathbf{r}^{be})^k = (\mathbf{r}_m)^k + \sum_{\mu=k-1}^k \left\{ \left[\mathbf{C}_m^{k\mu} - \sum_{\rho=k-1}^{\mu} \mathbf{C}_{r\alpha}^{k\rho} (\mathbf{s}^\dagger)^{\mu\rho} \right] \left[\sum_{\eta=k-1}^k \mathbf{K}_d^{\mu\eta} \mathbf{d}^\eta \right] \right\}, \quad k = 1, 2, \dots, N_t. \quad (260)$$

3. The components $(\mathbf{C}_{\alpha}^{be})^{v\mu}$, $(v, \mu = k-1, k)$, of the calibrated best-estimate covariance matrix, \mathbf{C}_{α}^{be} , for the calibrated best-estimates system parameters is obtained by particularizing (250) to two consecutive time nodes $(k-1, k)$, $k = 1, 2, \dots, N_t$, leading to

$$(\mathbf{C}_{\alpha}^{be})^{v\mu} = \mathbf{C}_{\alpha}^{v\mu} - \sum_{\eta=k-1}^k \sum_{\rho=k-1}^k \left[\mathbf{C}_{\alpha r}^{v\rho} - \sum_{\pi=k-1}^{\rho} \mathbf{C}_{\alpha}^{v\pi} (\mathbf{s}^\dagger)^{\rho\pi} \right] \mathbf{K}_d^{\rho\eta} \left[\mathbf{C}_{r\alpha}^{\eta\mu} - \sum_{\pi=k-1}^{\eta} \mathbf{s}^{\eta\pi} \mathbf{C}_{\alpha}^{\pi\mu} \right],$$

for $v = k-1, k$; and $\mu = k-1, k$; $k = 1, 2, \dots, N_t$. (261)

4. The components $(\mathbf{C}_r^{be})^{v\mu}$, $(v, \mu = k-1, k)$, of the calibrated best-estimate covariance matrix \mathbf{C}_r^{be} , for the best-estimate responses takes on the following particular form of (251):

$$(\mathbf{C}_r^{be})^{v\mu} = \mathbf{C}_m^{v\mu} - \sum_{\eta=k-1}^k \sum_{\rho=k-1}^k \left[\mathbf{C}_m^{v\rho} - \sum_{\pi=k-1}^{\rho} \mathbf{C}_{r\alpha}^{v\pi} (\mathbf{s}^\dagger)^{\rho\pi} \right] \mathbf{K}_d^{\rho\eta} \left[\mathbf{C}_m^{\eta\mu} - \sum_{\pi=k-1}^{\eta} \mathbf{s}^{\eta\pi} \mathbf{C}_{\alpha r}^{\pi\mu} \right],$$

for $v = k-1, k$; and $\mu = k-1, k$; $k = 1, 2, \dots, N_t$. (262)

5. The components $(\mathbf{C}_{\alpha r}^{be})^{v\mu}$, $(v, \mu = k-1, k)$, of the best-estimate response–parameter covariance matrix $\mathbf{C}_{\alpha r}^{be}$ take on the following particular form of (252):

$$(\mathbf{C}_{\alpha r}^{be})^{v\mu} = \mathbf{C}_{r\alpha}^{v\mu} - \sum_{\eta=k-1}^k \sum_{\rho=k-1}^k \left[\mathbf{C}_m^{v\rho} - \sum_{\pi=k-1}^{\rho} \mathbf{C}_{r\alpha}^{v\pi} (\mathbf{s}^\dagger)^{\rho\pi} \right] \mathbf{K}_d^{\rho\eta} \left[\mathbf{C}_{r\alpha}^{\eta\mu} - \sum_{\pi=k-1}^{\eta} \mathbf{s}^{\eta\pi} \mathbf{C}_{\alpha}^{\pi\mu} \right]$$

for $v = k-1, k$; and $\mu = k-1, k$; $k = 1, 2, \dots, N_t$. (263)

For each time node, $k = 1, 2, \dots, N_t$, the quantities $\mathbf{K}_d^{v\eta}$ which appear in (259–263) have the following expressions:

$$\mathbf{K}_d^{k-1,k-1} = \left[\mathbf{C}_d^{k-1,k-1} - \mathbf{C}_d^{k-1,k} \left(\mathbf{C}_d^{k,k} \right)^{-1} \mathbf{C}_d^{k,k-1} \right]^{-1} \quad (264)$$

$$= \left(\mathbf{C}_d^{k-1,k-1} \right)^{-1} + \left(\mathbf{C}_d^{k-1,k} \right)^{-1} \mathbf{C}_d^{k-1,k} \mathbf{K}_d^{k,k} \mathbf{C}_d^{k,k-1} \left(\mathbf{C}_d^{k-1,k-1} \right)^{-1}$$

$$\mathbf{K}_d^{k-1,k} = - \left(\mathbf{C}_d^{k-1,k-1} \right)^{-1} \mathbf{C}_d^{k-1,k} \left[\mathbf{C}_d^{k,k} - \mathbf{C}_d^{k,k-1} \left(\mathbf{C}_d^{k-1,k-1} \right)^{-1} \mathbf{C}_d^{k-1,k} \right]^{-1} \quad (265)$$

$$= - \left(\mathbf{C}_d^{k-1,k-1} \right)^{-1} \mathbf{C}_d^{k-1,k} \mathbf{K}_d^{k,k}$$

$$\mathbf{K}_d^{k,k} = \left[\mathbf{C}_d^{k,k} - \mathbf{C}_d^{k,k-1} \left(\mathbf{C}_d^{k-1,k-1} \right)^{-1} \mathbf{C}_d^{k-1,k} \right]^{-1} \quad (266)$$

$$= \left(\mathbf{C}_d^{k,k} \right)^{-1} + \left(\mathbf{C}_d^{k,k-1} \right)^{-1} \mathbf{C}_d^{k,k-1} \mathbf{K}_d^{k-1,k-1} \mathbf{C}_d^{k-1,k} \left(\mathbf{C}_d^{k,k} \right)^{-1}$$

$$\mathbf{K}_d^{k,k-1} = - \left(\mathbf{C}_d^{k,k} \right)^{-1} \mathbf{C}_d^{k,k-1} \left[\mathbf{C}_d^{k-1,k-1} - \mathbf{C}_d^{k-1,k} \left(\mathbf{C}_d^{k,k} \right)^{-1} \mathbf{C}_d^{k,k-1} \right]^{-1} \quad (267)$$

$$= - \left(\mathbf{C}_d^{k,k} \right)^{-1} \mathbf{C}_d^{k,k-1} \mathbf{K}_d^{k-1,k-1}$$

For *time-independent* problems, the (time-dependent) results derived in (259–263) reduce to expressions that are formally identical to (239), (243), and (245–247). Hence, the later expressions can be used directly to obtain the best-estimate predicted values for parameters, responses, and their respective covariances. Recall that modeling errors can be treated in a manner similar to parameter uncertainties, by including the discretization intervals among the components of the vector α of model parameters, as detailed in Cacuci (2003) and Cacuci et al. (2005).

Finally, it is important to emphasize that the explicit formulas presented in this section are based on the linearized relationship between responses and parameters that customarily underlies the “propagation of moments” method, that is, (228), without considering nonlinearities explicitly. Nevertheless, this limitation is not as severe as it may appear at first glance, since nonlinear relations between computed responses and model parameters can be treated by considering (228) iteratively, starting with the known nominal values of the quantities involved. The first iteration (in such an iterative procedure) would yield all of the major explicit results derived in (239), (243), and (245–247). The subsequent iteration would be the results of (239), (243), and (245–247) as the “prior information” in a second application of these formulas, and compute the new (“second iteration”) best-estimate quantities by using once again these formulas. This iterative procedure would be continued until the best-estimated values would converge within a small, user-specified convergence criterion.

6.3 Data Consistency and Rejection Criteria

The actual application of the model calibration (adjustment) algorithms, cf. (239), (243), and (245–247), to a physical system is straightforward in principle, although it can become computationally very demanding in terms of data handling and computational speed requirements. It is also important to note that the indiscriminate incorporation of all (seemingly relevant)

experimental-response data could produce a set of calibrated (adjusted) parameter values that might differ unreasonably much from the corresponding original nominal values. Worse yet, the indiscriminate use of information might even fail to improve the agreement between the calculated and measured values of some of the very responses by which the library was calibrated (adjusted).

When calibrating (adjusting) a library of model parameters, it is tacitly assumed that the given parameters are basically “correct,” except that they are not sufficiently accurate for the objective at hand. The calibration procedure uses additional data (e.g., experimental responses) for improving the parameter values while reducing their uncertainties. Although such additional information induces modifications of the original parameter values, the adjusted parameters are still generally expected to remain consistent with their original nominal values, within the range of their original uncertainties. As just mentioned, however, indiscriminate calibration of model parameters by experimental responses that significantly deviate from their respective computed values would significantly modify the resulting adjusted parameters.

On the other hand, calibrating a parameter library by using measured responses that are very close to their respective computed values would cause minimal parameter modifications and a nearly perfect reproduction of the given responses by the adjusted library (as would be expected). In such a case, the given responses would be considered as being consistent with the parameter library, in contradistinction to adjustment by inconsistent experimental information, in which case the adjustment could fail because of inconsistencies. These considerations clearly underscore the need for using a quantitative indicator to measure the mutual and joint consistency of the information available for model calibration.

As shown in Cacuci et al. (2010), the minimum value, $Q_{\min} \equiv Q(\mathbf{z}^{be})$, of $Q(\mathbf{z})$ takes on the following expression:

$$Q_{\min} \equiv Q(\mathbf{z}^{be}) = \mathbf{d}^\dagger [\mathbf{C}_d(\boldsymbol{\alpha}^0)]^{-1} \mathbf{d}, \quad \mathbf{d} \triangleq \mathbf{R}(\boldsymbol{\alpha}^0) - \mathbf{r}_x. \quad (268)$$

As the above expression indicates, $Q_{\min} \equiv Q(\mathbf{z}^{be})$ represents the square of the length of the vector \mathbf{d} , measuring (in the corresponding metric) the deviations between the experimental and nominally computed responses. Note that $Q_{\min} \equiv Q(\mathbf{z}^{be})$ can be evaluated directly from the given data (i.e., given parameters and responses, together with their original uncertainties) after having inverted the deviation-vector uncertainty matrix $\mathbf{C}_d(\boldsymbol{\alpha}^0)$. It is also very important to note that $Q_{\min} \equiv Q(\mathbf{z}^{be})$ is independent of calibrating (or adjusting) the original data. As the dimension of \mathbf{d} indicates, the number of degrees of freedom characteristic of the calibration under consideration is equal to the number of experimental responses. In the extreme case of absence of experimental responses, no actual calibration takes place, since $\mathbf{d} = \mathbf{R}(\boldsymbol{\alpha}^0)$, so that the best-estimate parameter values are just the original nominal values, that is, $(\boldsymbol{\alpha}^{be})^k = (\boldsymbol{\alpha}^0)^k$; an actual adjustment occurs only when at least one experimental response is included.

Replacing (268) in (232) shows that the bulk of the contribution to the joint posterior probability distribution, which comes from the point $\mathbf{z} = \mathbf{z}^{be}$, takes on the form of the following multivariate Gaussian distribution:

$$p(\mathbf{z}^{be} | \mathbf{C}) \sim \exp \left[-\frac{1}{2} Q(\mathbf{z}^{be}) \right] = \exp \left\{ -\frac{1}{2} [\mathbf{r}_x - \mathbf{R}(\boldsymbol{\alpha}^0)]^\dagger [\mathbf{C}_d(\boldsymbol{\alpha}^0)]^{-1} [\mathbf{r}_x - \mathbf{R}(\boldsymbol{\alpha}^0)] \right\}. \quad (269)$$

The above relation indicates that experimental responses can be considered as random variables approximately described by a multivariate Gaussian distribution with means located at the nominal values of the computed responses, and with a covariance matrix $\mathbf{C}_d(\boldsymbol{\alpha}^0)$. In turn, the random variable, $Q_{\min} \equiv Q(\mathbf{z}^{be})$, obeys a χ^2 -distribution with n degrees of freedom, where n denotes the total number of experimental responses considered in the calibration (adjustment) procedure. Since $Q_{\min} \equiv Q(\mathbf{z}^{be})$ is the “ χ^2 of the calibration (adjustment) at hand,” it can be used as an indicator of the agreement between the computed and experimental responses, measuring essentially the consistency of the experimental responses with the model parameters. Recall that the χ^2 (chi-square) distribution with n degrees of freedom of the continuous variable x , $0 \leq x < \infty$, is defined as

$$P(x < \chi^2 < x + dx) \triangleq k_n(x) dx \\ = \frac{1}{2^{n/2} \Gamma(n/2)} x^{n/2-1} e^{-x/2} dx, \quad x > 0, (n = 1, 2, \dots). \quad (270)$$

The χ^2 -distribution is a measure of the deviation of a “true distribution” (in this case: the distribution of experimental responses) from the hypothetical one (in this case: a Gaussian). The mean and variance of x are $\langle x \rangle = n$ and $\text{var}(x) = 2n$. Further, practically useful asymptotic properties of the χ^2 -distribution for $n \rightarrow \infty$ are as follows: (1) x is asymptotically normal with mean n and variance $2n$; (2) x/n is asymptotically normal with mean 1 and variance $2/n$; (3) $\sqrt{2x}$ is asymptotically normal with mean $\sqrt{2n-1}$ and variance 1. Although the χ^2 -distribution is extensively tabulated, the notation is not uniform in the literature for the various derived quantities (in particular, for the corresponding cumulative distribution functions and fractiles). The cumulative distributions, denoted here by $P_n(\chi^2)$ and $Q_n(\chi^2)$, are defined as

$$P_n(\chi_0^2) \triangleq P(\chi^2 \leq \chi_0^2) \triangleq \int_0^{\chi_0^2} k_n(t) dt; \quad Q_n(\chi_0^2) \\ \triangleq P(\chi^2 \geq \chi_0^2) \triangleq \int_{\chi_0^2}^{\infty} k_n(t) dt = 1 - P_n(\chi_0^2) \quad (271)$$

In practice, one rejects a hypothesis using the χ^2 -distribution when, for a given significance level α and number of degrees of freedom n , the value of $Q_{\min} \equiv \chi^2$ exceeds a chosen critical fractile value $\chi_{\alpha}^2(n)$. Published tables often show $\chi_{1-\alpha}^2(n)$ versus α . When the number of degrees of freedom is large ($n > 30$), a useful asymptotic approximation is $\chi_{\alpha}^2(n) \approx (1/2)(\sqrt{2n-1+z_{2\alpha}})^2$, with $z_{2\alpha}$ denoting the corresponding fractile of the standard normal distribution $\Phi_0(z)$, computed by solving the equation $2\Phi_0(z_{2\alpha}) = 1 - 2\alpha$, using the tabulated tables for $\Phi_0(z)$. For large or small values of α , a more accurate approximation is $\chi_{\alpha}^2(n) \approx n(1 - (2/9m) + z_{2\alpha}\sqrt{(2/9m)})^3$. It may be often more convenient to transform χ^2 to the variate $t = \chi^2/n$ (i.e., “ χ^2 per degree of freedom”), in which case the transformed distribution, $g_n(t)$, becomes $g_n(t) = nk_n(nt)$, with mean value $\langle t \rangle = 1$ and variance $2/n$.

For *model calibration* (adjustment), it is important to assess if: (1) *the response and data measurements are free of gross errors* (blunders such as wrong settings, mistaken readings, etc.), and (2) *the measurements are consistent with the assumptions regarding the respective means, variances, and covariances*. For example if $\chi^2/n \approx 1$, then the measurements are very likely to be both, free of gross errors and consistent with the assumptions. However, if $\chi^2/n \gg 1$ or $\chi^2/n \ll 1$, the measurements (or at least some measurements), the assumptions, or both are

suspect. In particular, unusually large values $\chi^2/n \gg 1$ could be obtained when the original variances are underestimated; increasing them beyond their assumed nominal values would cause the adjusted values of χ^2/n and $P_n(\chi^2)$ to decrease accordingly. The reverse argument would apply if the *a priori* values of χ^2/n and $P_n(\chi^2)$ were unusually small (e.g., $\chi^2/n \ll 1$, $P_n(\chi^2) \sim 10^{-4}$), which could be the result of *a priori* overestimated variances. A practical quantitative criterion for the “acceptance” or “rejection” of experimental results in conjunction with a given “theoretical” model (i.e., in conjunction with the assumptions regarding the variates underlying the model) is to accept the value of χ^2/n whenever $0.15 < P_n(\chi^2) < 0.85$, in analogy to the “1 σ ” range of normal distributions. Note that, when setting an acceptance criterion for χ^2/n of the general form

$$\alpha < P_n(\chi^2) < 1 - \alpha \quad (272)$$

the exact value of α is not essential and is subject to personal judgment. This is because the probability $P_n(\chi^2)$ is still sensitive to the value of χ^2/n due to the fact that $\chi^2/n \simeq 1 \pm \sqrt{(2/n)}$ (except for few degrees of freedom, e.g., for $n \leq 5$), so the acceptable range of χ^2/n narrows as $1/\sqrt{n}$ (see also the previously noted asymptotic forms for χ^2/n). In other words, moderate changes in χ^2/n lead to significant relative changes in $P_n(\chi^2)$. For example, the central 50%-range of $\chi^2/20$ is (0.77, 1.19), and the corresponding 90%-range is (0.54, 1.57), implying that values of $\chi^2/20$ below $\simeq 0.4$ or above $\simeq 2.0$ would be definitely unacceptable.

In addition to measuring the overall consistency of a given set of parameters and responses, the quantity χ^2/n also measures the consistency among the measured responses. Hence, an entire data set (model parameters and/or experimental responses) should not be indiscriminately disqualified because of a “too high” or “too low” value of χ^2/n , since even a single “outlying” response could significantly degrade the set’s overall consistency. Note that a simple-minded assessment and ranking of “questionable responses” according to the values of the “individual consistencies” (i.e., the values of χ^2 obtained for each response as if it were the only response available for calibrating the entire set of parameters), would be very likely misleading. This is because the sum of the respective “individual consistencies” [which would numerically be obtained by dividing the squares of the deviations, d_i^2 , through the sum of the respective variances of the computed and measured responses $\text{var}(r_i^{\text{comp}}) + \text{var}(r_i^{\text{exp}})$], would not be equal to the “joint consistency” (i.e., the joint χ^2) of the entire set of experimental responses. This is because the deviation-vector uncertainty matrix $C_d(\alpha^0) \triangleq C_{rc}(\alpha^0) - C_{r\alpha}[\mathbf{S}(\alpha^0)]^\dagger - [\mathbf{S}(\alpha^0)]C_{\alpha r} + C_x$ is generally non-diagonal, even if both $C_{rc}(\alpha^0)$ and C_x are diagonal. On the other hand, verifying the consistency of all partial sets of the array of n responses with respect to their consistency with the given library is usually impractical, since the number of partial sets of an array of n responses is $2^n - 1$; hence, such a verification would be practically feasible only when the number of measured responses is very small.

A procedure that has been successfully used to identify successively the responses which are least consistent with a given library of parameters is based on leaving out one response at a time and evaluating $\chi_{n-1}^2(1)$ for the remaining $n - 1$ responses. The response left out is subsequently returned to the response set, another response (response “two”) is eliminated, and the corresponding $\chi_{n-1}^2(2)$ is evaluated. This procedure is continued until all remaining $\chi_{n-1}^2(i)$, $i = 3, \dots, n$, are successively evaluated. The response that yields the lowest χ_{n-1}^2 when eliminated is considered to be “the least consistent,” and is thus ranked “last” in the consistency sequence, and eliminated from further consideration. The evaluation procedure is then repeated

for the remaining $n - 1$ (“more consistent”) responses, to identify the “second least consistent response,” which is then ranked next-to-last. The procedure is then repeatedly applied to the successive, fewer and fewer partial response sets until establishing the complete consistency sequence. Establishing such a consistency sequence requires only $n(n + 1)/2$ computations of χ^2 , as compared to $(2^n - 1)$ calculations needed to assign χ^2 values to all possible partial sets of n responses.

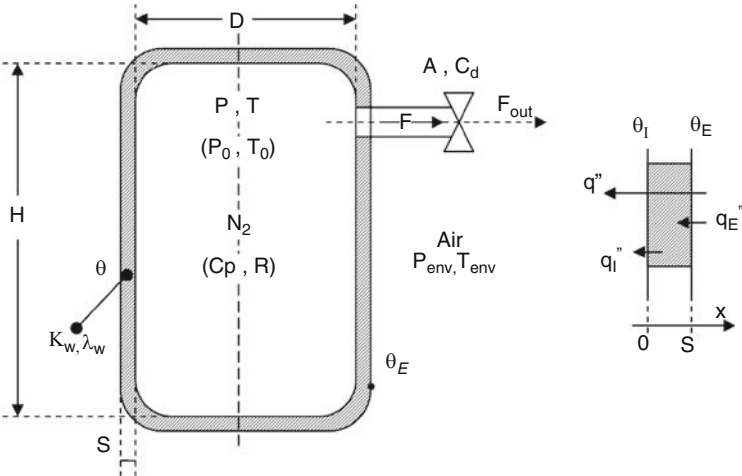
The quantity χ^2/n measures the consistency of any set of n experimentally measured responses with a given library of model parameters, in the sense that if χ_1^2 refers to a specific set of n experimental responses and χ_2^2 to another set of n responses, then $\chi_1^2 < \chi_2^2$ means that the first set is more consistent with the library than the second. On the other hand, when varying the number of responses, it is not *a priori* obvious whether the set yielding a smaller χ^2/n is also necessarily the most consistent with the given parameters. As an example, consider the value $P_n(\chi^2) = 0.85$, which can correspond to both $\chi^2/5 = 1.623$ and also to $\chi^2/10 = 1.453$. If, for example, one set of five responses would give a computed value $\chi^2/5 = 1.6$, and second set of ten responses would give $\chi^2/10 = 1.5$, the first set would be considered to be the “more consistent set,” for it falls within the “central 70% range,” whereas the second set does not. In such situations, it is preferable to use the quantity $Q_n(\chi^2) = 1 - P_n(\chi^2)$, as an additional measure of consistency.

Quite generally, therefore, the calibration (adjustment) of a set of model parameters and experimental responses must include the verification of their mutual consistency, which is performed by first generating the consistency sequence, and then determining the probabilities $Q_i(\chi^2)$, when $i = 1, 2, \dots, n$, while generating the sequence. The less consistent responses will show up at the end of the sequence, and the probabilities $Q_i(\chi^2)$ will generally decrease as i approaches the total number of responses, n . Such an analysis would identify the significantly less-consistent responses, and would also indicate the level of consistency of all response subsets along the consistency sequence.

In parallel, the irregular model parameters, if any, must also be identified. This can be done by computing not only χ^2 for any response subset, but also computing from (239) the corresponding best-estimate parameters $\alpha^{be} = \alpha^0 + (C_{\alpha r} - C_{\alpha} [S(\alpha^0)]^{\dagger}) [C_d(\alpha^0)]^{-1} d$. This way, the actual individual parameter adjustments induced by the respective response subset are also examined while proceeding step-by-step along the consistency sequence, noting which parameters vary more than others, and by how much. Usually, the parameter adjustments induced by the more consistent subsets of responses tend to be marginal. The less consistent responses and the questionable parameters would tend to undergo larger adjustments, requiring specific further examinations.

6.4 Illustrative Application to Model Calibration for a Benchmark Blowdown Experiment

The best-estimate model calibration methodology presented in the foregoing sections will be applied in this section to perform a predictive best-estimate analysis of benchmark blowdown experiment ICl (Haque et al. 1992a, b; Petrucci 2008), which was performed at London’s Imperial College. This benchmark experiment involves the rapid depressurization (blowdown) of a

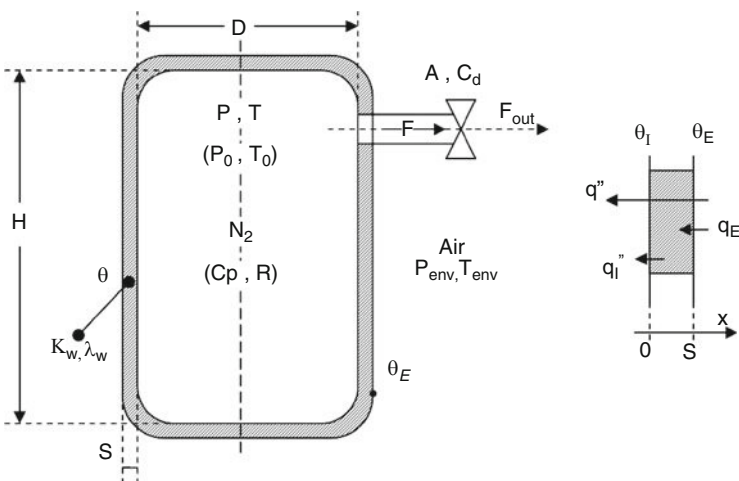
vertical cylindrical vessel with flat ends, containing nitrogen. The geometry of the vessel and the system diagram are depicted in  Fig. 7, below.

The geometry of the vessel is characterized by the vessel's internal diameter D , height H , wall thickness S , volume V , and surface area A_s . Since the vessel's wall is thin, the internal and external wall surface areas of the vessel can both be considered to be equal to A_s . Furthermore, the heat transfer coefficients (between nitrogen and the internal wall, and between air and the external wall) through the horizontal surfaces of the flat ends of the vessel are computed using the same correlations as for the heat transfer coefficients through the vertical cylindrical surface. The vessel wall is made of stainless steel, with thermal conductivity K_w and thermal diffusivity λ_w . The gas outside the vessel is air at stagnant conditions, characterized by the pressure P_{env} and temperature T_{env} .

Initially, the vessel contains M_0 kilograms of pressurized nitrogen gas at temperature T_0 and pressure P_0 , and the vessel wall is at the uniform temperature $\theta(x, t) = T_0$. The transient depressurization process is initiated at $t = t_0$ by releasing the gas through a valve with a discharge flow rate, F_{out} . The nitrogen gas is considered to behave as a perfect gas that is characterized by the heat capacity at constant pressure, C_p , and the specific gas constant, R . These fundamental properties yield the following derived properties for some specified pressure, P , and temperature, T : the heat capacity at constant volume, $C_v = C_p - R$; the ratio between the heat capacities at constant pressure and volume, $k = C_p/C_v$; the gas specific volume, $\nu = RT/P$; the gas enthalpy, $h = C_p T$; the gas internal energy, $u = C_v T$.

Denoting the temperature within the vessel's wall by $\theta(x, t)$, the gas pressure in the vessel by $P(t)$, and the gas temperature by $T(t)$, the equations describing the corresponding energy and mass balances, subject to a rigid volume constraint and gas-state relations, can be conveniently represented in operator form as follows (Petruzzi et al. 2010):

$$N[\mathbf{u}(t), \boldsymbol{\alpha}] = \mathbf{0}, \quad t > 0, \quad (273)$$



 **Figure 7**
Transient thermal-hydraulics (blowdown) system diagram

subject to the initial conditions

$$\begin{cases} P(t=0) = P_0, \\ T(t=0) = T_0, \\ \theta_j(t=0) = \theta_{j,0} = T_0 = T_{env}, \quad j = 0, \dots, J. \end{cases} \quad (274)$$

where $\alpha \triangleq (\alpha_i)$, $i = 1, \dots, I \triangleq 281 + 2 + 1 = 284$, denotes the vector of system parameters (including the two initial conditions, P_0 and T_0 , as well as the discretization parameter Δx), with the following components, in order:

$$\alpha = \left\{ \begin{array}{l} D, H, S, A, C_d, T_{env}, P_{env}, a, b, c, d, k, R, \lambda_w, K_w, g, \rho_{N,P_r,T_s}, C\rho_{N,P_r,T_s}, \dots \\ \dots, k_{N,P_r,T_s}, \mu_{N,P_r,T_s}, \beta_{N,P_r,T_s}, \rho_{A,T_k}, C\rho_{A,T_k}, k_{A,T_k}, \mu_{A,T_k}, \beta_{A,T_k}, P_0, T_0, \Delta x \end{array} \right\} \quad (275)$$

$$\mathbf{u}(t) \triangleq [P(t), T(t), \theta_j(t)] \quad (276)$$

denotes the column vector of $J + 3$ state variables, where $\theta_j(t) \triangleq \theta(x_j, t)$; and $\Delta x \triangleq S/J$; $x_j \triangleq j \cdot \Delta x$; for $j = 1, \dots, J - 1$;

$N[\mathbf{u}(t), \alpha]$ denotes the following $J + 3$ -component column vector:

$$N[\mathbf{u}(t), \alpha] \triangleq \left\{ \begin{array}{l} \frac{dP}{dt} - N_1 \\ \frac{dT}{dt} - N_2 \\ N_3 \\ \vdots \\ \frac{\partial \theta_j(t)}{\partial t} - N_{3+j} \\ \vdots \\ N_{J+3} \end{array} \right\} \quad (277)$$

where

$$N_1 \triangleq \frac{1}{V} \cdot \{ (k-1) \cdot [h_N(T, \theta_0, P; \alpha) \cdot (\theta_0(t) - T(t)) \cdot A_S] - F_{out}(P, T, \alpha) \cdot k \cdot R \cdot T(t) \};$$

$$N_2 \triangleq \frac{k-1}{V} \cdot \left[\frac{[h_N(T, \theta_0, P; \alpha) \cdot (\theta_0(t) - T(t)) \cdot A_S] \cdot T(t)}{P(t)} - F_{out}(P, T, \alpha) \cdot \frac{R \cdot T(t)^2}{P(t)} \right];$$

$$N_3 \triangleq -K_w \cdot \frac{\theta_1(t) - \theta_0(t)}{\Delta x} + h_N(T, \theta_0, P; \alpha) \cdot (\theta_0(t) - T(t));$$

$$N_{3+j} \triangleq \lambda_w \cdot \frac{\theta_{j+1}(t) - 2 \cdot \theta_j(t) + \theta_{j-1}(t)}{(\Delta x)^2}; \quad j = 1, \dots, J - 1;$$

$$N_{3+J} \triangleq K_w \cdot \frac{\theta_J(t) - \theta_{J-1}(t)}{\Delta x} + h_A(\theta_J; \alpha) \cdot (\theta_J(t) - T_{env}).$$

The time dependence in (273) is discretized using the forward Euler method for the equations containing the time derivatives of P and T , and using the backward Euler method for the remaining equations. This discretization yields the following system of nonlinear algebraic equations:

$$\mathbf{A}(\mathbf{X}^n) \mathbf{X}^{n+1} = \mathbf{B}(\mathbf{X}^n) \quad (278)$$

where \mathbf{X}^{n+1} denotes the vector of unknown state variables at the new time step ($n+1$), \mathbf{B} denotes a vector of quantities known from the previous time step n , while \mathbf{A} denotes a sparse matrix of coefficients. The explicit form of these quantities is given below:

$$\mathbf{X}^{n+1} = \begin{pmatrix} P^{n+1} \\ T^{n+1} \\ \theta_0^{n+1} \\ \vdots \\ \theta_j^{n+1} \\ \vdots \\ \theta_J^{n+1} \end{pmatrix}; \quad \mathbf{B} = \begin{pmatrix} P^n + \Delta t \cdot \left\{ \frac{1}{V} \cdot [(k-1) \cdot (h_N^n \cdot (\theta_0^n - T^n) \cdot A_S) - F_{out}^n \cdot k \cdot R \cdot T^n] \right\} \\ T^n + \Delta t \cdot \left\{ \frac{k-1}{V} \cdot \left[\frac{(h_N^n \cdot (\theta_0^n - T^n) \cdot A_S) \cdot T^n}{P^n} - F_{out}^n \cdot \frac{R \cdot (T^n)^2}{P^n} \right] \right\} \\ \theta_0^n \\ \vdots \\ \theta_j^n \\ \vdots \\ \theta_J^n + 2 \cdot F_o \cdot h_A^n \cdot \frac{\Delta x}{K_w} \cdot T_{env} \end{pmatrix}$$

$$\mathbf{A} = \begin{pmatrix} 1 & 0 & 0 & 0 & 0 & \dots & 0 \\ 0 & 1 & 0 & 0 & 0 & \dots & 0 \\ 0 & -2F_o h_N^n \frac{\Delta x}{K_w} & 1 + 2F_o \left(1 + h_N^n \frac{\Delta x}{K_w} \right) & -2F_o & 0 & \dots & 0 \\ 0 & 0 & 0 & 0 & \vdots & \dots & \vdots \\ \vdots & \vdots & \vdots & 1 + 2F_o & -F_o & 0 & \vdots \\ 0 & 0 & \vdots & -F_o & 1 + 2F_o & -F_o & \vdots \\ \vdots & \vdots & \vdots & 0 & -F_o & 1 + 2F_o & \vdots \\ \vdots & \vdots & \vdots & \vdots & \vdots & \ddots & \vdots \\ 0 & 0 & \dots & \dots & 0 & -2F_o & 1 + 2F_o \left(1 + h_A^n \frac{\Delta x}{K_w} \right) \end{pmatrix}$$

where: $F_o \hat{=} \lambda_w \cdot \Delta t / \Delta x^2$; $x_j \hat{=} j \cdot \Delta x$; $t^n \hat{=} n \cdot \Delta t$; $\theta_j^n \hat{=} \theta(x_j, t^n)$; $P^n \hat{=} P(t^n)$; $T^n \hat{=} T(t^n)$.
Note also that:

1. $F_{out}^n \hat{=} F_{out}(P^n, T^n; \boldsymbol{\alpha}) = F_{break}^n$, with

$$F_{break}^n = \begin{cases} F_{choke}^n = C_d \cdot A \cdot \sqrt{k \cdot \frac{(P^n)^2}{R \cdot T^n} \cdot \left(\frac{2}{k+1} \right)^{\frac{k+1}{k-1}}}; & r^n \hat{=} \frac{P_{env}}{P^n} \leq r_c \\ F_{choke}^n \cdot \frac{\sqrt{(r^n)^{\frac{2}{k}} - (r^n)^{\frac{k+1}{k}}}}{\sqrt{r_c^{\frac{2}{k}} - r_c^{\frac{k+1}{k}}}}; & r_c < r^n \leq 1 \\ 0 & r^n > 1 \end{cases};$$

2. $h_N^n \hat{=} h_N(T^n, \theta_0^n, P^n; \boldsymbol{\alpha}) = \frac{k_N^n \cdot \overline{Nu}_N^n}{H}$; with

$$\overline{Nu}_N^n = \begin{cases} a \cdot (Gr_N^n \cdot Pr_N^n)^c, & \text{for } Gr_N^n \cdot Pr_N^n \leq 10^9; \text{ laminar} \\ c \cdot (Gr_N^n \cdot Pr_N^n)^d, & \text{for } Gr_N^n \cdot Pr_N^n \leq 10^9; \text{ turbulent} \end{cases}$$

$$Gr_N^n \hat{=} \frac{g \cdot \beta_N^n \cdot (\rho_N^n)^2}{(\mu_N^n)^2} \cdot H^3 \cdot (\theta_0^n - T^n); \quad Pr_N^n \hat{=} \frac{C p_N^n \cdot \mu_N^n}{k_N^n}$$

In the above expressions, the physical properties of nitrogen (i.e., k_N , β_N , ρ_N , μ_N , Cp_N) is denoted by γ_N , and is obtained by double interpolation (Petruzzi et al. 2010), as follows

$$\begin{aligned}\gamma_N^n &= \left(\gamma_N^{P_r}\right)^n + \frac{\left(\gamma_N^{P_{r+1}}\right)^n - \left(\gamma_N^{P_r}\right)^n}{P_{r+1} - P_r} \cdot (P^n - P_r); \quad P_r \leq P^n < P_{r+1}; \\ \left(\gamma_N^{P_i}\right)^n &= \gamma_N^{P_r, T_s} + \frac{\gamma_N^{P_r, T_{s+1}} - \gamma_N^{P_r, T_s}}{T_{s+1} - T_s} \cdot (\overline{T_N}^n - T_s); \quad T_s \leq \overline{T_N}^n < T_{s+1}; \\ \overline{T_N}^n &= \frac{T^n + \theta_0^n}{2}; \\ \gamma_N^{P_r, T_s} &= \gamma_N(\overline{T_N} = T_s, P = P_r)\end{aligned}$$

3. $h_A^n \triangleq h_A(\theta_j^n; \alpha) = \frac{k_A^n \cdot \overline{Nu}_A^n}{H}$; with

$$\begin{aligned}\overline{Nu}_A^n &= \begin{cases} a \cdot (Gr_A^n \cdot Pr_A^n)^b, & \text{for } Gr_A^n \cdot Pr_A^n \leq 10^9; \quad \text{laminar} \\ c \cdot (Gr_A^n \cdot Pr_A^n)^d, & \text{for } Gr_A^n \cdot Pr_A^n > 10^9; \quad \text{turbulent} \end{cases} \\ Gr_A^n &= \frac{g \cdot \beta_A^n \cdot (\rho_A^n)^2}{(\mu_A^n)^2} \cdot H^3 \cdot (T_{env} - \theta_j^n); \quad Pr_A^n = \frac{Cp_A^n \cdot \mu_A^n}{k_A^n};\end{aligned}$$

where the respective physical property of air (i.e., k_A , β_A , ρ_A , μ_A , Cp_A) is denoted by γ_A , and is obtained by linear interpolation (Petruzzi et al. 2010), as follows:

$$\begin{aligned}\gamma_A^n &= \gamma_A^{T_k} + \frac{\gamma_A^{T_{k+1}} - \gamma_A^{T_k}}{T_{k+1} - T_k} \cdot (\overline{T_A}^n - T_k); \quad T_k \leq \overline{T_A}^n < T_{k+1}; \quad \overline{T_A}^n = \frac{\theta_j^n + T_{env}}{2}; \\ \gamma_A^{T_k} &= \gamma_A(\overline{T_A} = T_k).\end{aligned}$$

The above discretized system can be conveniently solved by determining at the outset the gas pressure P^{n+1} and the gas temperature T^{n+1} from the first and second equations. Then, the remaining system becomes tridiagonal (Petruzzi et al. 2010), and is easily solvable for the unknown vector, θ_j^{n+1} , by a standard two-sweep method.

Typical measurements performed for the benchmark blowdown experiment ICI (Haque et al. 1992a, b; Petruzzi 2008) involve pressures and temperatures at given locations and instances in time. In order to use such measurements for calibrating the various system parameters, the responses (or results) computed by means of the mathematical model presented in the forgoing must correspond to the respective measurements. The most general mathematical representation of such a response is a functional of the system's parameters and state variables, of the form

$$R = \int_{t=0}^{t=t_f} F(P, T, \theta_0, \dots, \theta_j; \alpha) dt \quad (279)$$

where $F(P, T, \theta_0, \dots, \theta_j; \alpha)$ is a suitably defined function of the state variables \mathbf{u} and of the system parameters α , while t_f denotes the time at which the simulated transient ends. For example, if the response of interest is the gas temperature, $T(\bar{t})$, at some point in time, \bar{t} , then $F(P, T, \theta_0, \dots, \theta_j; \alpha) \equiv T(t) \cdot \delta(t - \bar{t})$ where $\delta(t - \bar{t})$ is the Dirac-delta function.

Applying the general theory presented in Cacuci (2003) and Cacuci et al. (2005), the sensitivities of the response, R , to the model parameters, α , are given by the Gateaux-derivative, DR, along the (284-component) variational vector $\delta\alpha$ and the $(J+3)$ -component variational vector $\delta\mathbf{u} \hat{=} \mathbf{h} \hat{=} (h_p, h_T, h_{\theta_0}, \dots, h_{\theta_j})$. For the response defined in (279), the respective Gateaux-derivative, DR, is obtained as

$$\begin{aligned} DR &= \int_0^{t_f} \left[\left(\frac{\partial F}{\partial P} \right)^0 h_p + \left(\frac{\partial F}{\partial T} \right)^0 h_T + \left(\frac{\partial F}{\partial \theta_0} \right)^0 h_{\theta_0} + \dots + \left(\frac{\partial F}{\partial \theta_j} \right)^0 h_{\theta_j} \right] dt \\ &+ \int_0^{t_f} \left[\sum_{i=1}^{284} \left(\frac{\partial F}{\partial \alpha_i} \right)^0 \delta\alpha_i \right] dt = \int_0^{t_f} [(\tilde{N}_u F)^0 \mathbf{h}] dt + \int_0^{t_f} [(\tilde{N}_\alpha F)^0 (\delta\alpha)] dt \\ &\hat{=} DR_i + DR_d \end{aligned} \quad (280)$$

The so-called “direct-effect” term, DR_d , is independent of the variations \mathbf{h} and can be computed readily. However, the so-called “indirect-effect” term, DR_i , can be computed only after having determined the variational vector \mathbf{h} . This vector is the solution of the “forward sensitivity system” (also called “variational tangent model”) obtained by taking the Gateaux-derivatives of (273), computed at the nominal parameter values, along the variational vectors $\delta\alpha$ and $\delta\mathbf{u} \hat{=} \mathbf{h} \hat{=} (h_p, h_T, h_{\theta_0}, \dots, h_{\theta_j})$. Applying the general theory presented in Cacuci (2003) and Cacuci et al. (2005), the Gateaux-derivative of (273) yields the following forward sensitivity system:

$$\begin{aligned} \frac{dh_p}{dt} - \left(\frac{\partial N_1}{\partial P} \right)^0 h_p - \left(\frac{\partial N_1}{\partial T} \right)^0 h_T - \left(\frac{\partial N_1}{\partial \theta_0} \right)^0 h_{\theta_0} - \left(\frac{\partial N_1}{\partial \theta_j} \right)^0 h_{\theta_j} &= \sum_{i=1}^{284} \left(\frac{\partial N_1}{\partial \alpha_i} \right)^0 (\delta\alpha_i) \equiv q_1; \\ \frac{dh_T}{dt} - \left(\frac{\partial N_2}{\partial P} \right)^0 h_p - \left(\frac{\partial N_2}{\partial T} \right)^0 h_T - \left(\frac{\partial N_2}{\partial \theta_0} \right)^0 h_{\theta_0} - \left(\frac{\partial N_2}{\partial \theta_j} \right)^0 h_{\theta_j} &= \sum_{i=1}^{284} \left(\frac{\partial N_2}{\partial \alpha_i} \right)^0 (\delta\alpha_i) \equiv q_2; \\ -\frac{K_W}{\Delta x} (h_{\theta_1} - h_{\theta_0}) + \left[\left(\frac{\partial h_N}{\partial P} \right)^0 h_p + \left(\frac{\partial h_N}{\partial T} \right)^0 h_T + \left(\frac{\partial h_N}{\partial \theta_0} \right)^0 h_{\theta_0} \right] &(\theta_0^0 - T^0) + (h_{\theta_0} - h_T) h_N^0 \\ &= \left[\frac{\delta K_W}{\Delta x} - \frac{K_W}{(\Delta x)^2} \delta(\Delta x) \right] (\theta_1^0 - \theta_0^0) - (\theta_0^0 - T^0) \sum_{i=1}^{284} \left(\frac{\partial h_N}{\partial \alpha_i} \right)^0 (\delta\alpha_i) \equiv q_3; \\ \frac{dh_{\theta_j}}{dt} - \frac{\lambda_w}{(\Delta x)^2} (h_{\theta_{j+1}} - 2h_{\theta_j} + h_{\theta_{j-1}}) & \\ &= (\theta_{j+1}^0 - 2\theta_j^0 + \theta_{j-1}^0) \left[\frac{\delta \lambda_w}{(\Delta x)^2} - \frac{2\lambda_w \delta(\Delta x)}{(\Delta x)^3} \right] \equiv q_{j+3}; \quad j = 1, \dots, J-1; \\ \frac{K_W}{\Delta x} (h_{\theta_j} - h_{\theta_{j-1}}) + \left(\frac{\partial h_A}{\partial \theta_j} \right)^0 (\theta_j^0 - T_{env}^0) h_{\theta_j} + h_A^0 h_{\theta_j} & \\ &= -(\theta_j^0 - \theta_{j-1}^0) \left[\frac{\delta K_W}{\Delta x} - \frac{K_W \delta(\Delta x)}{(\Delta x)^2} \right] - (\theta_j^0 - T_{env}^0) \sum_{i=1}^{284} \left(\frac{\partial h_A}{\partial \alpha_i} \right)^0 (\delta\alpha_i) + (\delta T_{env}) h_A^0 \equiv q_{J+3}; \end{aligned}$$

The above system is linear in \mathbf{h} and can therefore be written in matrix form as

$$\mathbf{A}\mathbf{h} = \mathbf{q} \quad (281)$$

where the coefficients of the matrix \mathbf{A} are operators containing Gateaux-derivatives with respect to the state variables \mathbf{u} , while the components of the vector \mathbf{q} comprise operators containing Gateaux-derivatives with respect to the system parameters $\boldsymbol{\alpha}$. The explicit expressions of these Gateaux-derivatives are listed in Petruzzi et al. (2010). All of these quantities are evaluated at the nominal solution of the original system, $N(\mathbf{u}^0, \boldsymbol{\alpha}^0) = \mathbf{0}$, as indicated by the superscript “zero” attached to the respective quantities.

The initial conditions for (281) are obtained by taking the Gateaux-derivatives of (274), yielding:

$$h_p(0) = \delta P_0; \quad h_T(0) = \delta T_0; \quad h_{\theta_j}(0) = \delta T_{env} = \delta T_0; \quad j = 1, \dots, J-1. \quad (282)$$

The time-dependent profiles of the sensitivities of the system’s state variables to each of the $I = 284$ parameters α_i can be obtained by repeatedly solving (281) and (282), for each parameter variation, $\delta\alpha_i$, to obtain the corresponding vector \mathbf{h} . In turn, \mathbf{h} is used in (280) to compute the corresponding sensitivity DR . This procedure is customarily called the *forward sensitivity analysis procedure (FSAP)*. Alternatively, the need to calculate \mathbf{h} for each parameter variation $\delta\alpha_i$ can be circumvented by using the *adjoint sensitivity analysis procedure (ASAP)* (Cacuci 2003; Cacuci et al. 2005) to express the indirect-effect term in (280) in terms of an appropriately defined adjoint function $\mathbf{u}^* \triangleq (P^*(t), T^*(t), \theta_0^*(t), \dots, \theta_J^*(t))$, such that

$$DR_i = \int_0^{t_f} (\mathbf{u}^* \cdot \mathbf{q}) dt - \left[\int_0^{t_f} (\mathbf{u}^* \cdot \mathbf{A}\mathbf{h} - \mathbf{h} \cdot \mathbf{A}^* \mathbf{u}^*) dt \right] \quad (283)$$

where \mathbf{A}^* is the adjoint of the matrix-valued operator \mathbf{A} , and the adjoint function \mathbf{u}^* is the solution of the operator equation

$$\mathbf{A}^* \mathbf{u}^* = \nabla_{\mathbf{u}} F \quad (284)$$

subject to the final time conditions

$$P^*(t_f) = 0; \quad T^*(t_f) = 0; \quad \theta_j^*(t_f) = 0; \quad j = 1, \dots, J-1. \quad (285)$$

Evaluating the second integral in (283) leads to the following for the indirect term DR_i :

$$DR_i = \int_0^{t_f} \left[P^* q_1 + T^* q_2 + \sum_{j=0}^J \theta_j^* q_{3+j} \right] dt + P^*(0) \delta P_0 + T^*(0) \delta T_0 + \sum_{j=1}^{J-1} \theta_j^*(0) \delta T_{env}. \quad (286)$$

It is convenient to change independent variables in (284) from t to $\tau \triangleq t_f - t$, thereby transforming that final-time value problem into the following initial-value problem in τ :

$$\begin{aligned}
 \frac{dP^*}{d\tau} &= \left(\frac{\partial F}{\partial P} \right)_\tau^0 + \left(\frac{\partial N_1}{\partial P} \right)_\tau^0 P^*(\tau) + \left(\frac{\partial N_2}{\partial P} \right)_\tau^0 T^*(\tau) - \left(\frac{\partial h_N}{\partial P} \right)_\tau^0 (\theta_0^* - T^0)_\tau \theta_0^*(\tau) \\
 \frac{dT^*}{d\tau} &= \left(\frac{\partial F}{\partial T} \right)_\tau^0 + \left(\frac{\partial N_2}{\partial T} \right)_\tau^0 T^*(\tau) + \left(\frac{\partial N_1}{\partial T} \right)_\tau^0 P^*(\tau) - \left[\left(\frac{\partial h_N}{\partial T} \right)_\tau^0 (\theta_0^* - T^0)_\tau - h_N^0(\tau) \right] \theta_0^*(\tau) \\
 0 &= \left(\frac{\partial F}{\partial \theta_0} \right)_\tau^0 + \left(\frac{\partial N_1}{\partial \theta_0} \right)_\tau^0 P^*(\tau) + \left(\frac{\partial N_2}{\partial \theta_0} \right)_\tau^0 T^*(\tau) \\
 &\quad - \left[\left(\frac{\partial h_N}{\partial \theta_0} \right)_\tau^0 (\theta_0^0 - T^0)_\tau + h_N^0(\tau) + \frac{K_W}{\Delta x} \right] \theta_0^*(\tau) + \frac{\lambda_w}{(\Delta x)^2} \theta_1^*(\tau); \\
 \frac{d\theta_1^*}{d\tau} &= \left(\frac{\partial F}{\partial \theta_1} \right)_\tau^0 + \frac{K_W}{\Delta x} \theta_0^*(\tau) - \frac{2\lambda_w}{(\Delta x)^2} \theta_1^*(\tau) + \frac{\lambda_w}{(\Delta x)^2} \theta_2^*(\tau) \\
 \frac{d\theta_j^*}{d\tau} &= \left(\frac{\partial F}{\partial \theta_j} \right)_\tau^0 + \frac{\lambda_w}{(\Delta x)^2} \theta_{j-1}^*(\tau) - \frac{2\lambda_w}{(\Delta x)^2} \theta_j^*(\tau) + \frac{\lambda_w}{(\Delta x)^2} \theta_{j+1}^*(\tau); \quad j = 2, \dots, J-2; \\
 \frac{d\theta_{J-1}^*}{d\tau} &= \left(\frac{\partial F}{\partial \theta_{J-1}} \right)_\tau^0 + \frac{\lambda_w}{(\Delta x)^2} \theta_{J-2}^*(\tau) - 2 \frac{\lambda_w}{(\Delta x)^2} \theta_{J-1}^*(\tau) + \frac{K_W}{\Delta x} \theta_J^*(\tau) \\
 0 &= \left(\frac{\partial F}{\partial \theta_J} \right)_\tau^0 + \left(\frac{\partial N_1}{\partial \theta_J} \right)_\tau^0 P^*(\tau) + \left(\frac{\partial N_2}{\partial \theta_J} \right)_\tau^0 T^*(\tau) + \frac{\lambda_w}{(\Delta x)^2} \theta_{J-1}^*(\tau) \\
 &\quad - \left[\frac{K_W}{\Delta x} + \left(\frac{\partial h_A}{\partial \theta_J} \right)_\tau^0 (\theta_J^0 - T_{env}^0)_\tau + h_A^0(\tau) \right] \theta_J^*(\tau) \\
 P^*(0) &= 0; \quad T^*(0) = 0; \quad \theta_j^*(0) = 0 \quad j = 1, \dots, J-1
 \end{aligned}$$

Note that the adjoint sensitivity system is independent of any parameter variations $\delta\alpha_i$. Therefore, it needs to be solved only once for every response considered, thereby reducing significantly the computational costs, when the number of responses of interest is smaller than the number of parameters α_i . Note that the variation $DR_{j,i}$ of the generic response R_j to the variation $\delta\alpha_i$ of the parameter α_i yields the absolute respective sensitivity; the corresponding relative sensitivity is defined as:

$$s_{j,i} = \frac{\alpha_i}{R_j} \cdot \frac{DR_{j,i}}{\delta\alpha_i} \quad (287)$$

The experiment IC1 was performed using 100 mole-% of nitrogen (at the nominal parameter values listed in [Table 4](#)), in a vertical cylinder with flat ends having the following dimensions: length = 1.524 m, inside diameter = 0.273 m, and wall thickness = 25 mm. Starting from an initial pressure of 150 bar and initial temperature of 290 K, the nitrogen was released from the top through a choke of equivalent diameter 6.35 mm. The blowdown time was ca. 100 s, and there was no liquid formation by condensation from the gas. The experiment was conducted in a bunker; the air surrounding the experiment was stagnant at 1.01 bars and 290 K. Several thermocouples for measuring the fluid and the wall temperatures during the blowdown transient were located at various spatial positions; the corresponding experimental error bands, at several instants in time, are listed in [Table 5](#).

Table 4

Nominal parameter values for experiment IC1

#	Component		Description	ID	Value	Unit
1	Vessel	Input	Height	H	152.4	cm
2			Internal diameter	D	27.3	cm
3			Wall thickness	S	2.5	cm
4			Wall thermal cond.	K_w	14.42	W/m·K
5			Wall thermal diff.	λ_w	4.50×10^{-6}	m ² /s
6		Derived	Volume	V	89207.25	cm ³
7			Vessel surface area	A_s	14839.83	cm ²
8	Break orifice		Break orifice equivalent area	A	0.31669	cm ²
9			Orifice discharge coefficient	C_d	0.8	–
10	Internal gas	Input	Heat capacity at constant pressure	C_p	1140.67	J/kg·K
11			Specific gas constant	R	296.79	J/kg·K
12		Derived	Heat capacity at constant volume	C_v	743.88	J/kg·K
13			Ratio between C_p and C_v	k	1.3990	–
14	External Environment		Air pressure	P_{env}	1.01	bar
15			Air temperature	$T_{env} = T_o$	290	K
16	Initial Conditions		Gas initial pressure	P_o	150	bar
17			Gas initial temp.*	$T_o = T_{env}$	290	K
18			Vessel wall temp. distribution *	$\theta_0(\mathbf{x}) = T_{env}$	290	K
19	Correlations		Laminar multiplicative factor	a	0.555	–
20			Laminar exponential factor	b	1/4	–
21			Turbulent (multiplicative factor)	c	0.130	–
22			Turbulent (exponential factor)	d	1/3	–
23	Numerical parameters		Time step	Δt	0.1	s
24			Mesh size	Δx	0.25	cm

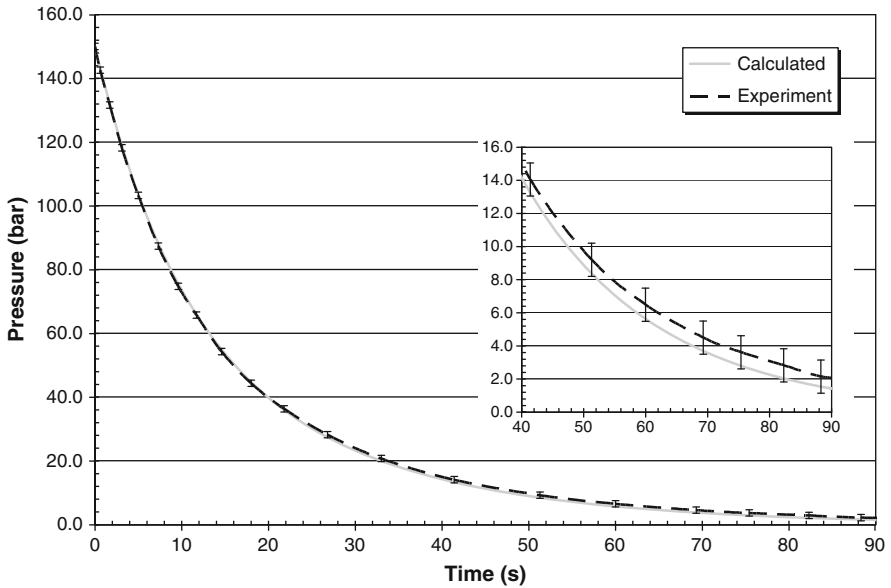
*: The initial system conditions are assumed to be stationary.

The benchmark blowdown experiment IC1 was simulated numerically for the nominal parameter values shown in Table 4, using the discretized mathematical model (278). Figure 8 presents comparisons between the experimental and computational results for the gas pressure, while Fig. 9 presents the comparison between computational and experimental results for the gas and vessel wall temperatures, including the respective experimental uncertainty bands. As depicted in Fig. 8, the computed results for the gas pressure are practically indistinguishable from the experimental results for the first 20 s but display a slight deviation from the experimental data after 20 s. The computed evolution of the vessel's surface temperature in contact with the gas (internal vessel wall) also shows excellent agreement with the experimental data, practically coinciding with the upper experimental curve, as shown

■ **Table 5**
Error bands for gas pressure and gas/wall temperatures

Time (s)	Experimental error bands (upper-lower)		
	Gas pressure (bar)	Gas temperature (K)	Wall temperature (K)
0		1	1
10		6	3
20		16	5
30		16	6
40	2.0*	20	6
60		23	6
80		28	6
100		27	5

* ± 1 bar has been assumed due to the digitalization process by which the experimental values of the gas pressure have been derived.



■ **Figure 8**
Benchmark experiment IC1: measured and computed pressure

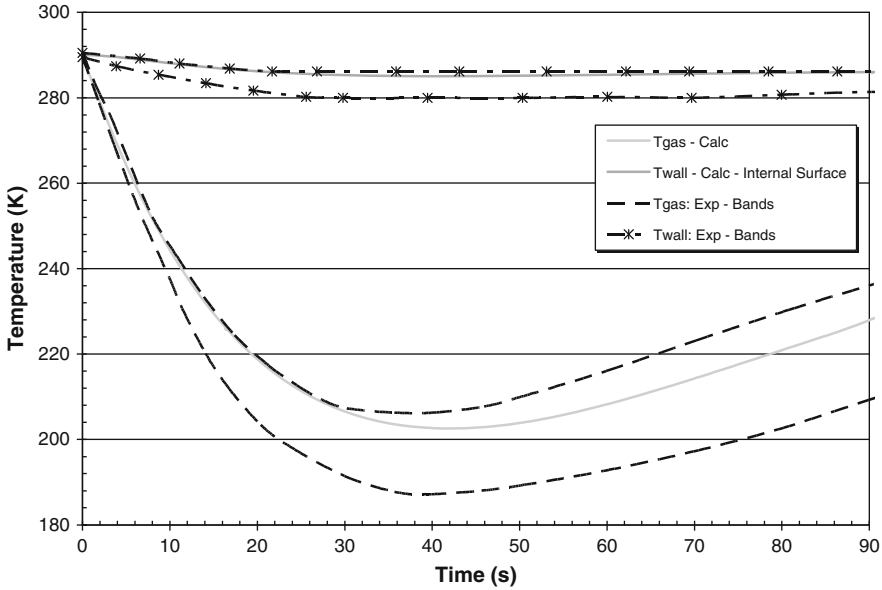


Figure 9
Benchmark experiment IC1: measured and computed temperature

in Fig. 9. This figure also shows that the computed gas temperature lies within the region spanned by the two experimental curves, even though the computed results tend toward the upper (experimental) uncertainty band during the time span between 15 and 30 s. These comparisons provide credible evidence in support of both the verification and validation of the numerical model (278).

Since the vessel walls are very thin, the discretization parameter Δx need not be considered as uncertain, so that the total number of uncertain parameters is $N_\alpha = 281 + 2 = 283$ (where the '+2' is referring to the two initial boundary conditions for the gas pressure P_0 and gas temperature T_0 model parameters), as follows:

$$\alpha = \left\{ \begin{array}{l} D, H, S, A, C_d, T_{env}, P_{env}, a, b, c, d, k, R, \lambda_w, K_w, g, \rho_{N,P_r,T_s}, Cp_{N,P_r,T_s}, \dots \\ \dots, k_{N,P_r,T_s}, \mu_{N,P_r,T_s}, \beta_{N,P_r,T_s}, \rho_{A,T_k}, Cp_{A,T_k}, k_{A,T_k}, \mu_{A,T_k}, \beta_{A,T_k}, P_0, T_0 \end{array} \right\}$$

Response sensitivities to parameters were computed using both the forward sensitivity (“variational tangent”) model and the adjoint sensitivity model, and the complete results are presented in Petruzzi et al. (2010). In particular, Figs. 10 and 11 depict time-dependent sensitivity profiles of the gas pressure and temperature, respectively, to the most important parameters. As shown in these figures, the gas pressure is most sensitive initially to internal diameter of the vessel, D , followed by the sensitivities to the vessel’s height H , the orifice discharge coefficient, C_d , and the initial conditions (P_0 and T_0). On the other hand, the gas temperature is initially (for ca. 20 s) most sensitive to T_0 , but the sensitivity to the coefficient d in the Nusselt correlation becomes dominant later. The various time-dependent graphs in Figs. 10 and 11 highlight clearly the fact that several important sensitivities change sign during the transient.

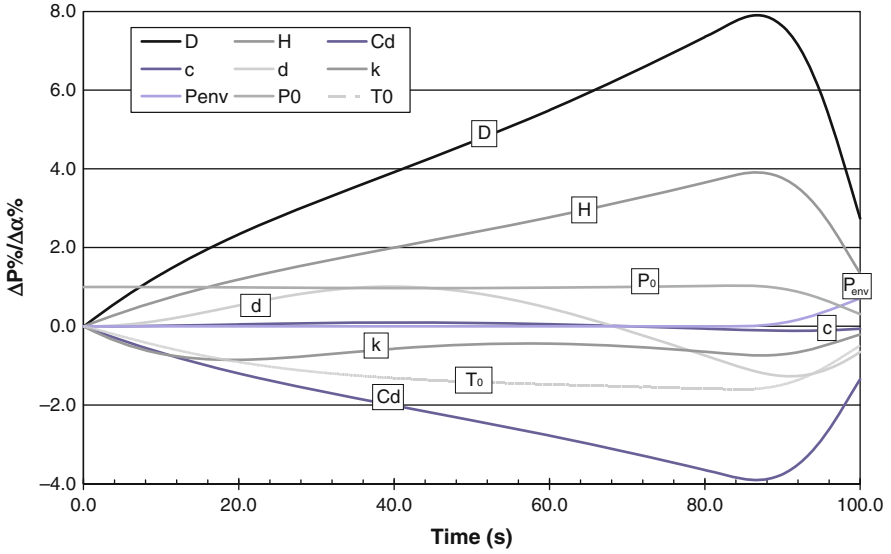


Figure 10 Time-dependent profiles of largest sensitivities for gas pressure

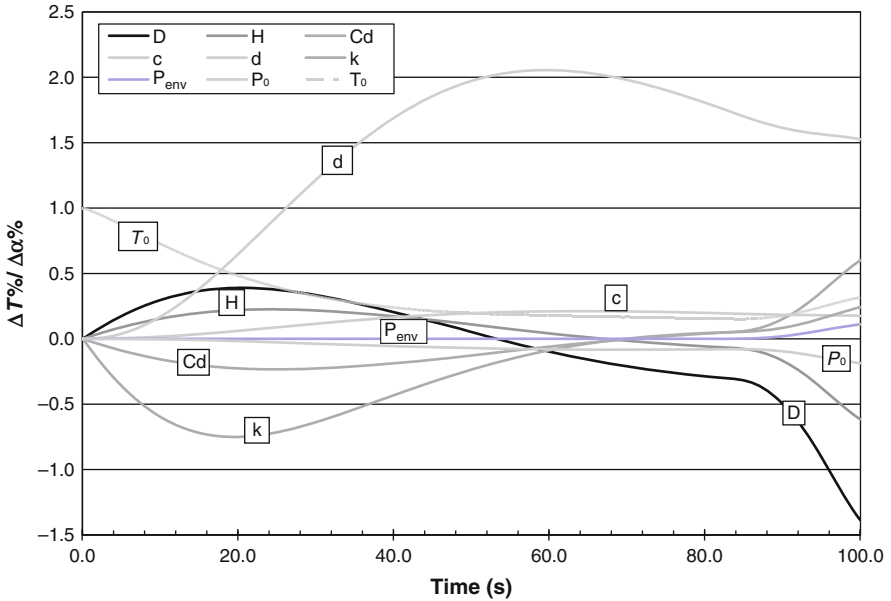


Figure 11 Time-dependent profiles of largest sensitivities for gas temperature

In addition to verifying and validating the software modules for computing the state variables (pressures and temperatures), both the forward sensitivity and the adjoint sensitivity models were verified by using the first-order Taylor expansion

$$\left[R(\mathbf{u}^0 + \mathbf{h}; \alpha_i^0 + \delta\alpha_i) - R(\mathbf{u}^0; \alpha_i^0) \right] / \delta\alpha_i = DR(\mathbf{u}^0, \boldsymbol{\alpha}^0; \mathbf{h}, \delta\alpha_i) + O[(\delta\alpha_i)^2] \quad (288)$$

The left side of the above expression was obtained by recomputations using the nonlinear model, by varying the parameters α_i , one at a time, by 1% around their nominal values listed in [Table 4](#). The sensitivities on the right side of (288) were computed by using both the forward and the adjoint sensitivity models. For such small (1%) parameter variations, the response varies linearly with the respective parameter variations. Therefore, the agreement (or disagreement) between the left- and right-sides of (288) provides a verification that the respective numerical procedures have been implemented correctly (or not) in both the forward and adjoint sensitivity models for computing sensitivities. [Figure 12a–d](#) depict comparisons between recomputations and sensitivities calculated using the forward and adjoint sensitivity models, for the parameter k . Such good agreements were typical for this experiment, thus lending support to “model verification,” indicating that the numerical procedures for computing sensitivities were correctly implemented in both the forward and adjoint sensitivity models. Typical nonlinear effects are displayed in [Fig. 12d](#), where the sensitivities computed by the forward and the adjoint methods agree with one another, but both deviate (by roughly 0.1%) from recomputations at times beyond ca. 70 s.

For this benchmark experiment, all parameters are uncorrelated constants, assumed to be normally distributed, with standard deviations (taken as the respective 95%-probability values) as shown in [Table 6](#). Therefore, the parameter covariance matrix will initially

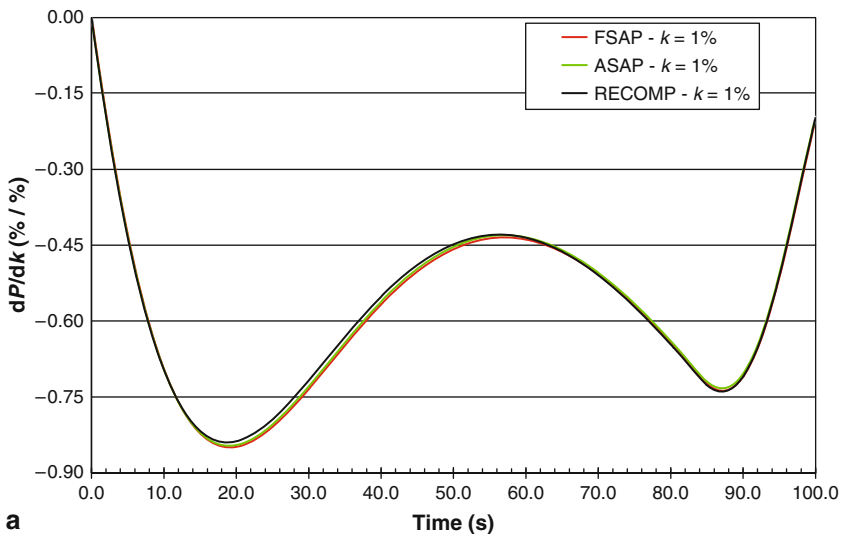


Figure 12a
Gas pressure variations induced by 1% variation in the parameter k

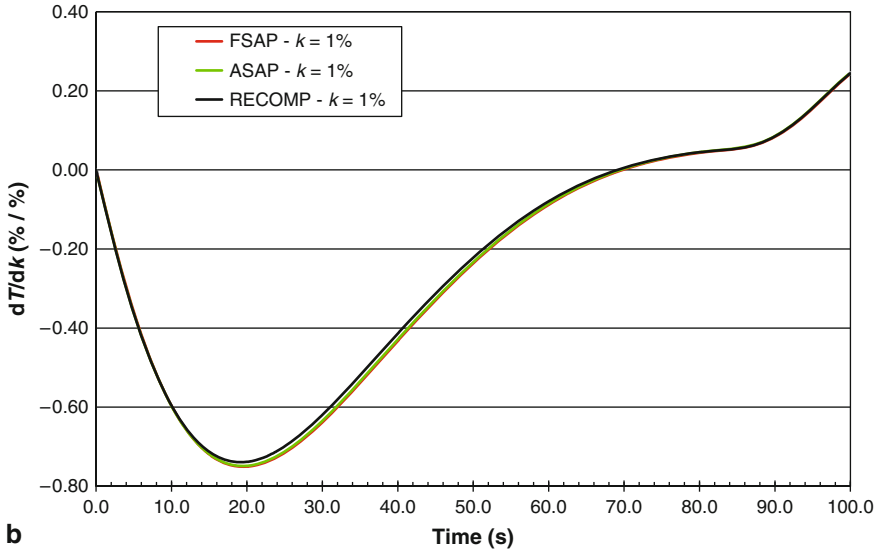


Figure 12b

Gas temperature variations induced by 1% variation in the parameter k

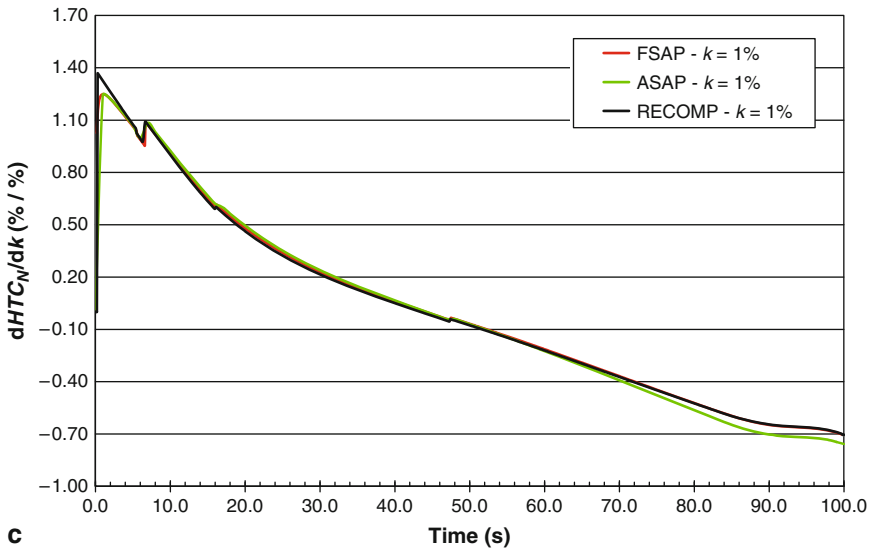


Figure 12c

Variations in the nitrogen heat transfer coefficient induced by 1% variation in the parameter k

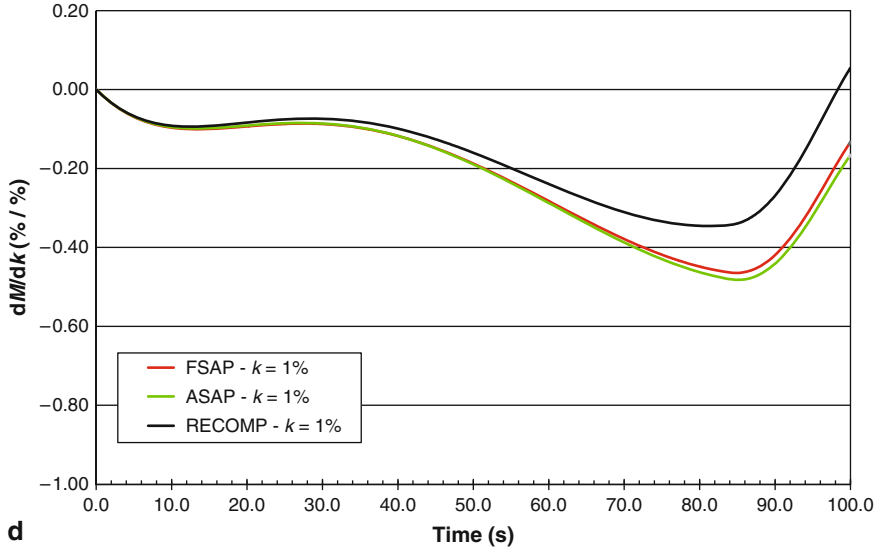


Figure 12d
Variations mass inventory induced by 1% variation in the parameter k

Table 6
Parameter standard deviations (95% probability)

Description	Parameters	Uncertainty (%)
Geometrical parameters, linear	D, H, S	0.1
Geometrical parameters, area	A	0.2
Discharge coefficient	C_d	10.0
Gas and wall temperatures	T_o, T_{env}	0.17
Gas pressures	P, P_{env}	0.13
Code correlations (HTC)	a, b, c, d	2.0
Wall properties	λ_w, K_w	2.0
Nitrogen and air density	$\rho_{N,P,T_s}, \rho_{A,T_k}$	0.02
Nitrogen and air heat capacity	$C_{p_{N,P,T_s}}, C_{p_{A,T_k}}$	0.3
Nitrogen and air thermal conductivity	k_{N,P,T_s}, k_{A,T_k}	2.0
Nitrogen and air viscosity	$\mu_{N,P,T_s}, \mu_{A,T_k}$	2.0
Nitrogen and air expansion coefficient	$\beta_{N,P,T_s}, \beta_{A,T_{ks}}$	2.0

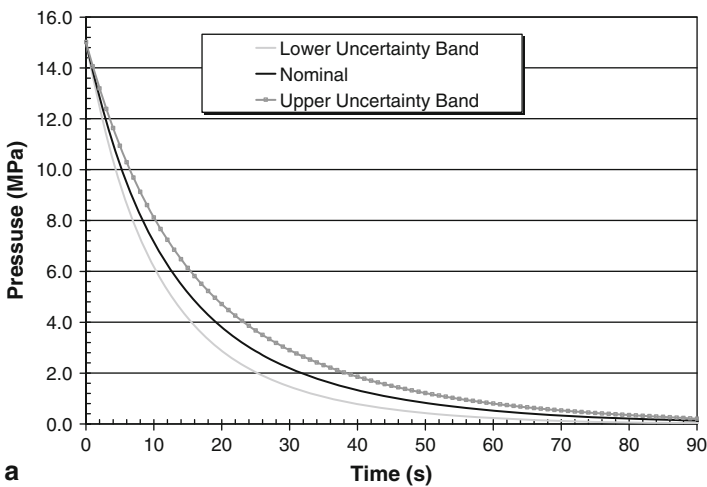
(i.e., at time $t = 0$) be time-independent, with the following structure:

$$\mathbf{C}_\alpha = \begin{pmatrix} \bar{C}_\alpha & \bar{C}_\alpha & \cdots & \bar{C}_\alpha \\ \bar{C}_\alpha & \bar{C}_\alpha & \cdots & \bar{C}_\alpha \\ \vdots & \vdots & \ddots & \vdots \\ \bar{C}_\alpha & \bar{C}_\alpha & \cdots & \bar{C}_\alpha \end{pmatrix}; \quad \bar{C}_\alpha \triangleq \text{diag}[\text{var}(\alpha_i)].$$

The covariance matrix for the computed responses, $\mathbf{C}_{rc}(\boldsymbol{\alpha}^0)$, is obtained by combining the above parameter covariance matrix with the parameter sensitivities according to the “sandwich formula” (230), repeated below for convenience:

$$\mathbf{C}_{rc}(\boldsymbol{\alpha}^0) \triangleq \langle \delta r \delta r^\dagger \rangle = [\mathbf{S}(\boldsymbol{\alpha}^0)] \langle \delta \alpha \delta \alpha^\dagger \rangle [\mathbf{S}(\boldsymbol{\alpha}^0)]^\dagger = [\mathbf{S}(\boldsymbol{\alpha}^0)] \mathbf{C}_\alpha [\mathbf{S}(\boldsymbol{\alpha}^0)]^\dagger. \quad (230)$$

► *Figures 13a–15* present results that illustrate the wealth of information contained in the final form of the response covariance matrix. For example, ► *Fig. 13a–f* display time-dependent standard deviations for several computed responses (gas pressure and temperature, mass inventory, internal wall temperature, and internal and external heat transfer coefficients, respectively). Noteworthy in ► *Fig. 13f* is the jump-discontinuity in the nominal value and computed uncertainties in the heat transfer coefficient to the external wall; this discontinuity is due to the transition from laminar to turbulent regime. ► *Figure 14a–d* depict time evolution of correlations between several responses (i.e., gas pressure, gas and wall temperatures, mass flow rate, etc.) at various time instants (10 s, 50 s, 70 s, and 90 s). These snapshots show that the responses, which are uncorrelated at the initial time, become weakly correlated as time progresses, except for the heat transfer coefficients and break area, which become somewhat stronger correlated beyond ca. 70 s. These time correlations arise due to the time-dependent sensitivities that appear



■ **Figure 13a**

Time-dependent variance of computed gas pressure, due to parameter uncertainties

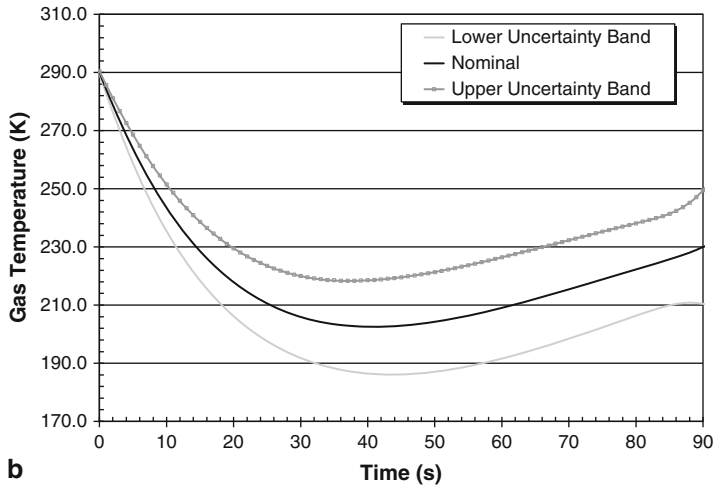


Figure 13b

Time-dependent variance of computed gas temperature, due to parameter uncertainties

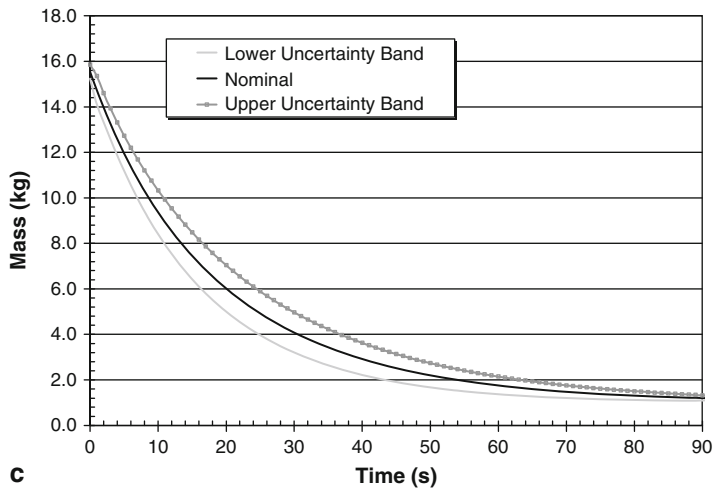


Figure 13c

Time-dependent variance of mass inventory, due to parameter uncertainties

as the weighting functions in the “sandwich formula” given by (230). [Figures 15a–d](#) depict the time evolution of correlations between selected pairs of responses, indicating that:

The gas temperature is anti-correlated with the mass flow rate at the beginning and end of the transient, but is positively correlated during the time interval between ca. 20 and 60 s;

The gas pressure is positively correlated with the gas temperature trough almost all of the transient becoming anti-correlated at the very the end of the transient; and

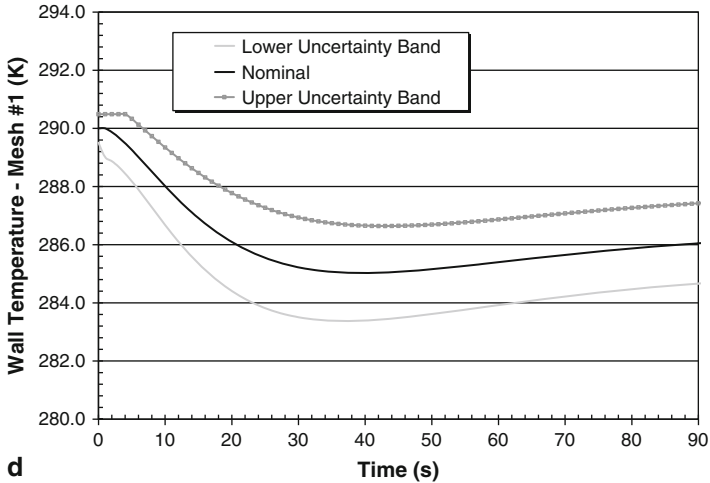


Figure 13d

Time-dependent variance of internal vessel wall temperature, due to parameter uncertainties

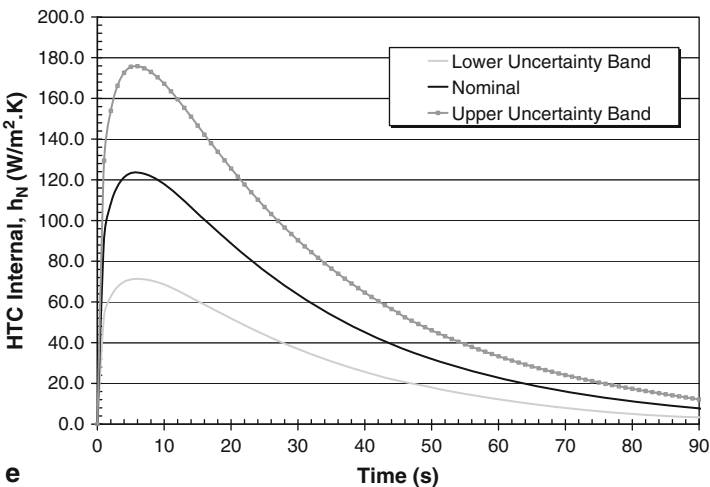


Figure 13e

Time-dependent variance of internal heat transfer coefficient, due to parameter uncertainties

The gas pressure is time-wise correlated and time-wise anti-correlated with the mass inventory and mass flow rate, respectively.

The assimilation of experimental data from the blowdown experiment in ICI for obtaining best-estimate predicted parameters, responses, and corresponding reduced uncertainties were performed by using the “two-step” “on-line” formulas derived in (259–263). Furthermore, since the model parameters are uncorrelated to the measured responses in the blowdown experiment

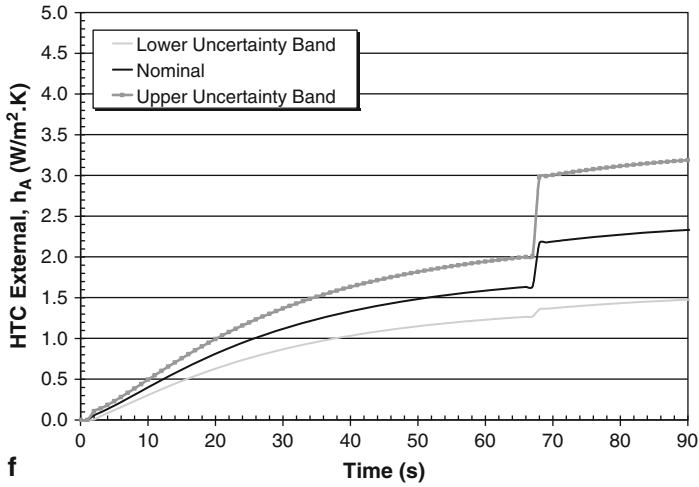


Figure 13f Time-dependent variance of external heat transfer coefficient, due to parameter uncertainties

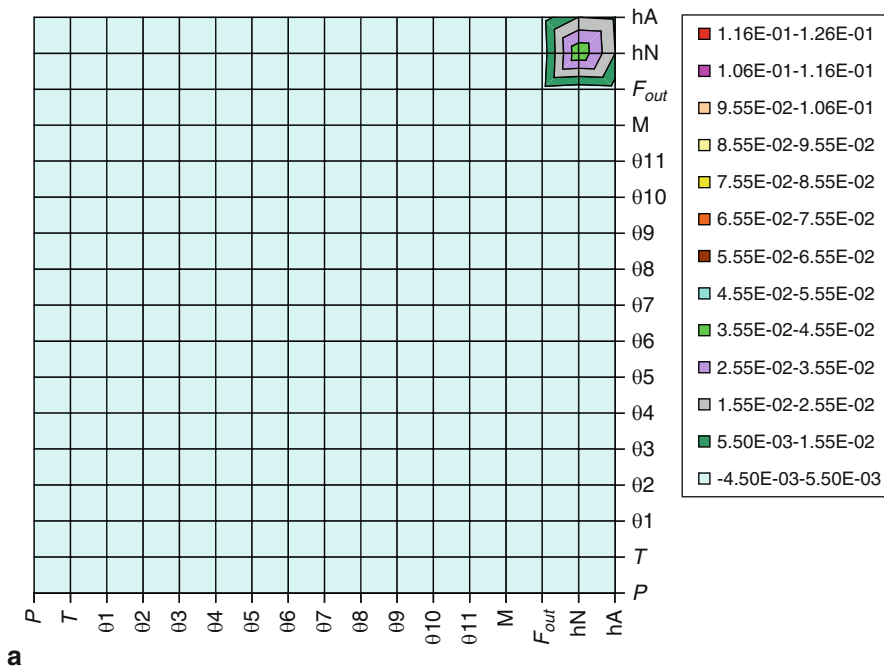


Figure 14a Computed responses relative covariances at 10 s

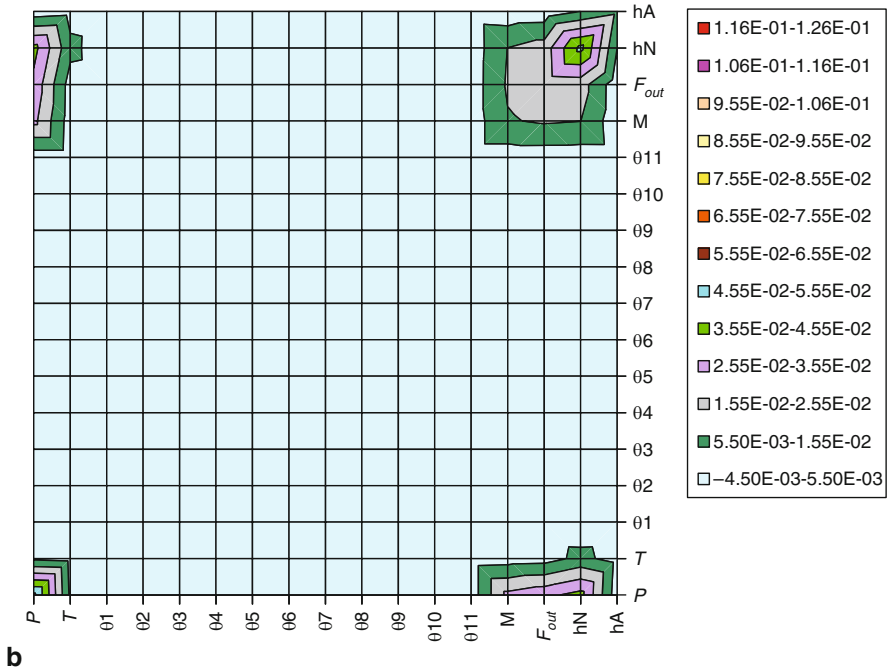


Figure 14b
Computed responses relative covariances at 50 s

in IC1, these general formulas become significantly simpler by setting $C_{r\alpha}^{v\mu} = 0$. Thus, the specific formulas used for the data assimilation/predictive estimation for the experiment IC1 are as given below:

Best-estimate values for model parameters:

$$\left(\alpha^{be}\right)^k = \left(\alpha^0\right)^k - \sum_{\mu=k-1}^k \left\{ \left[\sum_{\rho=k-1}^{\mu} C_{\alpha}^{k\rho} \left(\mathbf{s}^{\dagger}\right)^{\mu\rho} \right] \left[\sum_{\eta=k-1}^k \mathbf{K}_d^{\mu\eta} \mathbf{d}^{\eta} \right] \right\}, \quad k = 1, 2, \dots, N_t. \quad (289)$$

Best-estimate values for responses:

$$\left(\mathbf{r}^{be}\right)^k = \left(\mathbf{r}_m\right)^k + \sum_{\mu=k-1}^k \left\{ \left[C_m^{k\mu} \right] \left[\sum_{\eta=k-1}^k \mathbf{K}_d^{\mu\eta} \mathbf{d}^{\eta} \right] \right\}, \quad k = 1, 2, \dots, N_t. \quad (290)$$

Best-estimate parameter covariances:

$$\left(C_{\alpha}^{be}\right)^{v\mu} = C_{\alpha}^{v\mu} - \sum_{\eta=k-1}^k \sum_{\rho=k-1}^k \left[\sum_{\pi=k-1}^{\rho} C_{\alpha}^{v\pi} \left(\mathbf{s}^{\dagger}\right)^{\rho\pi} \right] \mathbf{K}_d^{\rho\eta} \left[\sum_{\pi=k-1}^{\eta} \mathbf{s}^{\eta\pi} C_{\alpha}^{\pi\mu} \right] \quad (291)$$

for $v = k - 1, k$; and $\mu = k - 1, k$; $k = 1, 2, \dots, N_t$.

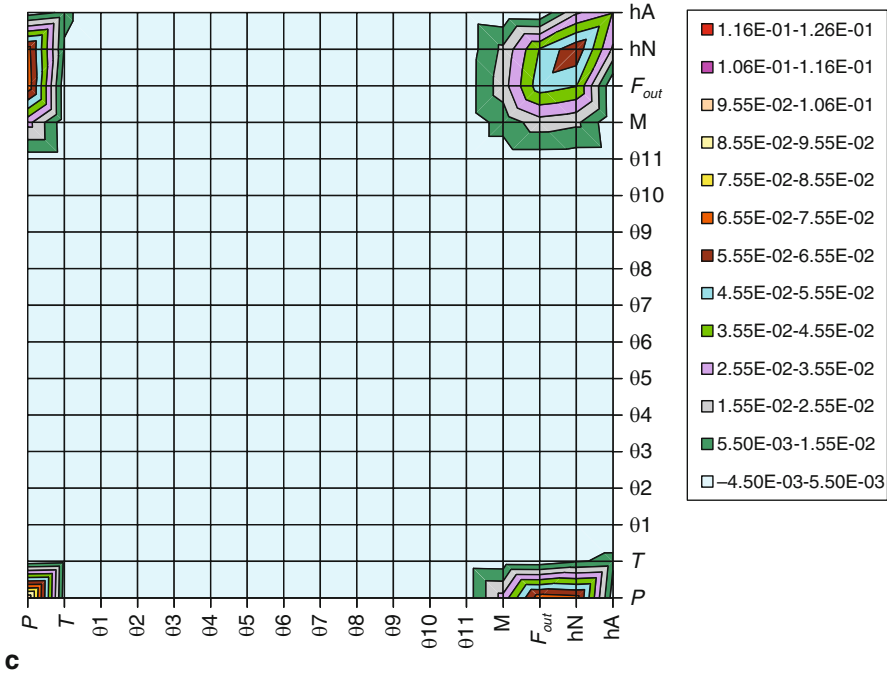


Figure 14c
Computed responses relative covariances at 70 s

Best-estimate response covariances:

$$\left(\mathbf{C}_\alpha^{be}\right)^{v\mu} = \mathbf{C}_\alpha^{v\mu} - \sum_{\eta=k-1}^k \sum_{\rho=k-1}^k \left[\sum_{\pi=k-1}^{\rho} \mathbf{C}_\alpha^{v\pi} \left(\mathbf{s}^\dagger\right)^{\rho\pi} \right] \mathbf{K}_d^{\rho\eta} \left[\sum_{\pi=k-1}^{\eta} \mathbf{S}^{\eta\pi} \mathbf{C}_\alpha^{\pi\mu} \right]$$

for $v = k - 1, k;$ and $\mu = k - 1, k;$ $k = 1, 2, \dots, N_t.$ (292)

Best-estimate parameter–response covariances:

$$\left(\mathbf{C}_{r\alpha}^{be}\right)^{v\mu} = \sum_{\eta=k-1}^k \sum_{\rho=k-1}^k \mathbf{C}_m^{v\rho} \mathbf{K}_d^{\rho\eta} \sum_{\pi=k-1}^{\eta} \mathbf{S}^{\eta\pi} \mathbf{C}_\alpha^{\pi\mu}$$

for $v = k - 1, k;$ and $\mu = k - 1, k;$ $k = 1, 2, \dots, N_t.$ (293)

Typical best-estimate values and uncertainty bands are presented in [Fig. 16a, b](#) for the gas pressure and temperature responses, respectively. These results were obtained following the assimilation of 20 experimental measurements taken at the time steps indicated in the respective figures. The value of “ χ^2 per degree of freedom” was close to unity for both of these data assimilation applications, thus indicating consistency among the parameters and the respective measured and computed responses. As depicted in [Fig. 16a, b](#), the calibration procedure

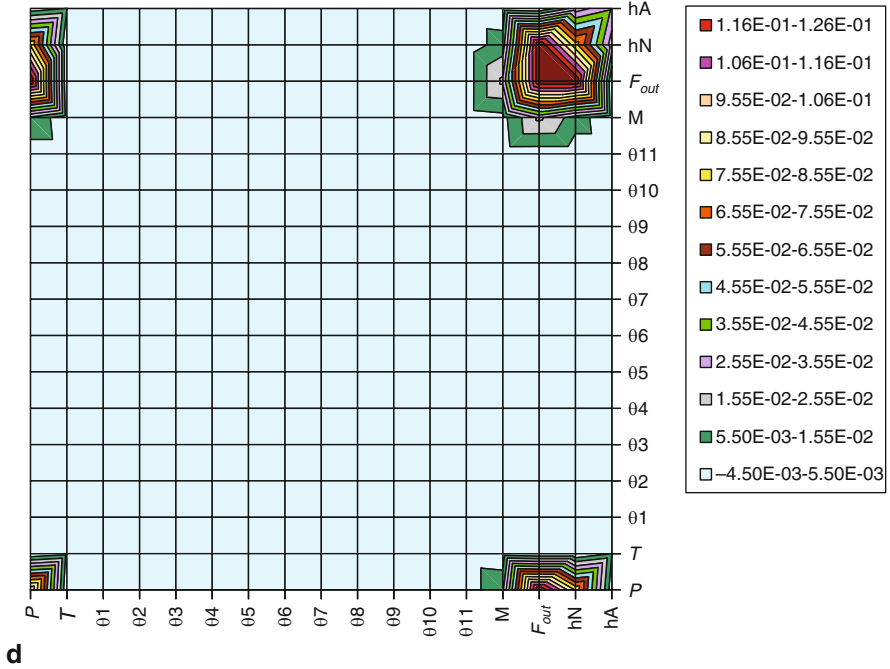


Figure 14d
Computed responses relative covariances at 90 s

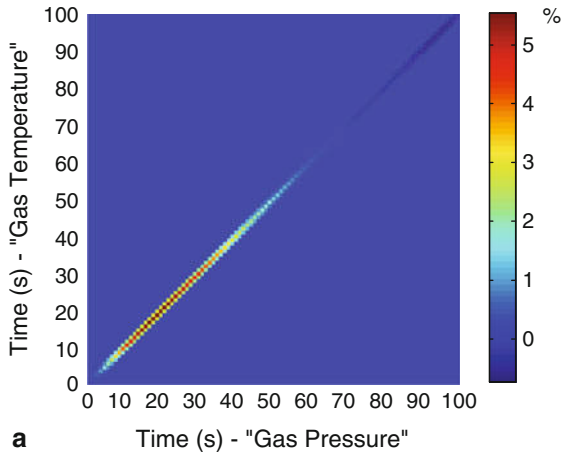
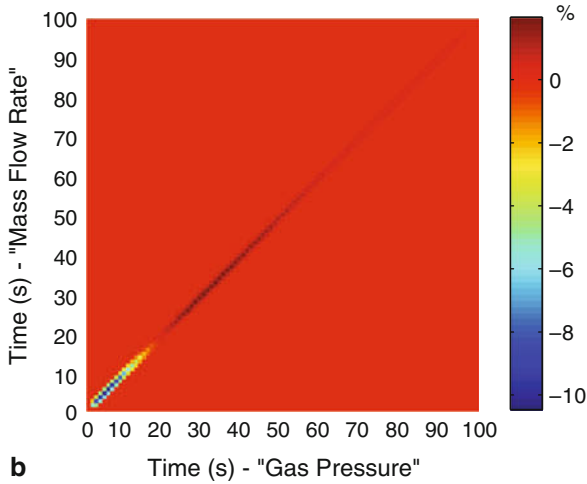
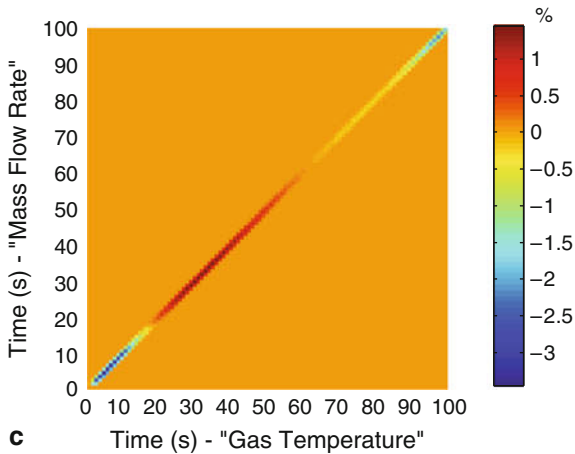


Figure 15a
Time evolution of relative covariances (normalized respect to response value at time 0) between the gas pressure and gas temperature responses



■ Figure 15b

Time evolution of relative covariances (normalized respect to response value at time 0) between the gas pressure and mass flow rate responses



■ Figure 15c

Time evolution of relative covariances (normalized respect to response value at time 0) between the gas temperature and mass flow rate responses

moves the values of the best-estimate responses (blue curves) toward the measured values, as would be expected for this benchmark experiment, which has measurement uncertainties smaller than the computed response uncertainties (due to parameter uncertainties). Furthermore, the calibration procedure clearly reduces best-estimate upper and, respectively lower uncertainty bands for both the gas pressure and temperature responses, in agreement with the reduction of variance values (i.e., the diagonal elements) from the matrix C_m to C_r^{be} , as

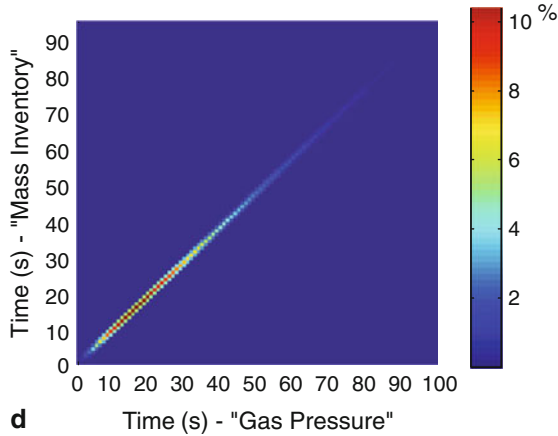


Figure 15d

Time evolution of relative covariances (normalized respect to response value at time 0) between the gas pressure and mass inventory responses

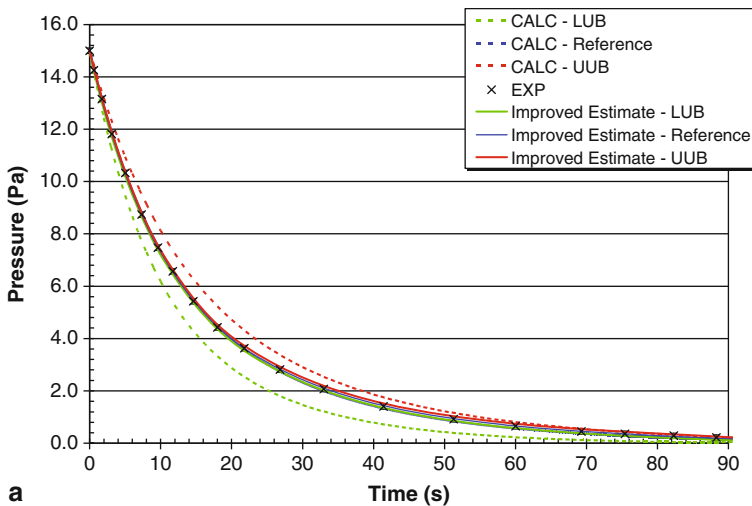


Figure 16a

Best-estimate calibrated values and uncertainty bands for the gas pressure following data assimilation/model calibration

expressed by (292). The reduction in the best-estimate predicted uncertainties is much larger for the gas pressure (since the measurement uncertainties for this quantity are very small) than for the gas temperature (for which the experimental uncertainties are comparatively larger). The largest variations in time experienced by the best-estimate calibrated parameters and their corresponding calibrated variances are presented in Figure 17a, b, illustrating typical

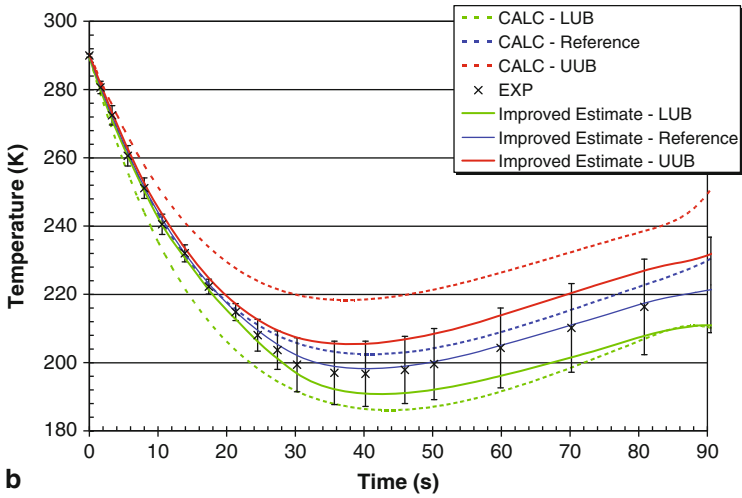


Figure 16b

Best-estimate calibrated values and uncertainty bands for the gas temperature following data assimilation/model calibration

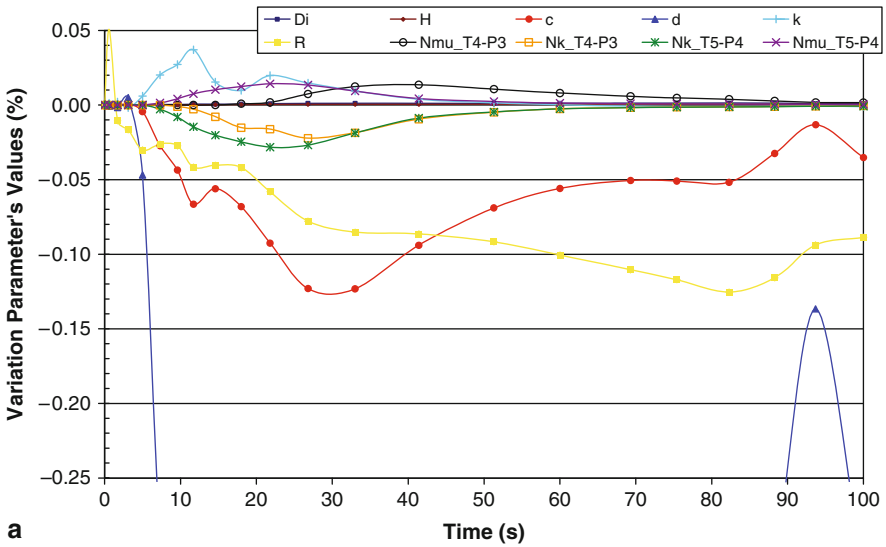


Figure 17a

Largest time variations of predicted best-estimate parameter values following data assimilation/model calibration

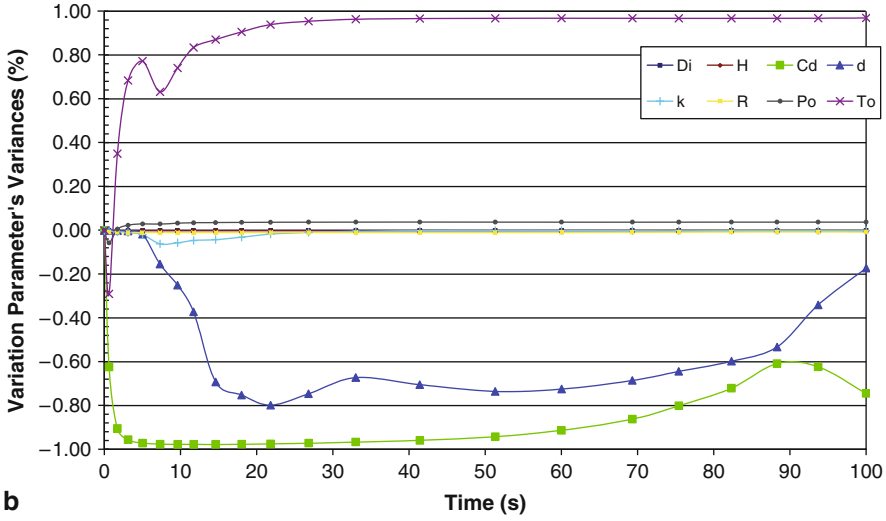


Figure 17b

Largest time variations of predicted best-estimate parameter variances following data assimilation/model calibration

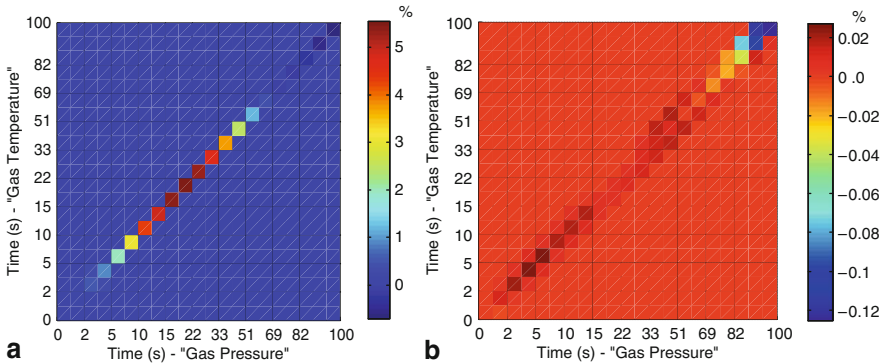


Figure 18

Illustrative uncertainty reduction: comparison of the time-dependent relative covariances (normalized respect to response value at initial time) between the gas pressure and temperature, before and after data assimilation/model calibration

results obtained by consistent data assimilation. The reduction in the best-estimate uncertainty obtained after consistent data assimilation is illustrated in [Fig. 18](#) for the gas pressure, which highlights the significant reduction in the magnitudes of the uncertainties on the anti-diagonal of the respective relative covariance matrices.

7 Model Validation and Calibration: Concluding Remarks and Open Issues

As has been discussed throughout this chapter, the results of experiments seldom coincide in practice with the computational results obtained from the mathematical models of the respective experiments. Such discrepancies between experimental and computational results provide the basic motivation for performing quantitative *model verification, validation, qualification, and predictive estimation*. The need for the evaluation of uncertainty associated with the prediction of computer codes in nuclear reactor safety technology is mandatory when using the so-called “*best estimate codes*” in the licensing process and for *safety analyses* (see, e.g., U. S. Nuclear Regulatory Commission 2005; International Atomic Energy Agency 2008). Several international activities addressing the current state-of-the-art methods for evaluating and predicting uncertainties in reactor thermal hydraulics and safety have been completed or are ongoing (Wickett et al. 1998; OECD/NEA 2007; Chauliac et al. 2009). The robustness of the traditional method for propagating model input errors to obtain errors in the model’s outputs, typified by the CSAU (Code Scaling and Applicability Uncertainty) method (Boyack et al. 1990), has been improved (Hofer 1993) by using Wilks’ statistical results (Wilks 1941). Nevertheless, coupling between system codes (e.g., thermal hydraulics and three-dimensional neutron kinetics codes) provides additional challenges to uncertainty analysis methods, as illustrated by the ongoing international assessment within the OECD/NEA UAM (Uncertainty Assessment Method) project (OECD/NEA 2007).

Although the above-mentioned methods have been continually improved from a computational standpoint, the incomplete and user-dependent (Aksan et al. 1995) results obtained by using them in practice provide a strong motivation for developing alternative methods that are mathematically more rigorous and, hence, less prone to subjective application and interpretation. Such methods must comprise the following activities: model verification, model validation and qualification, and predictive estimation. Loosely speaking, “*model verification*” means “are you solving the mathematical model correctly?” Model verification involves activities that are related to software quality assurance (SQA) practices and to activities directed toward finding and removing deficiencies in numerical algorithms used to solve partial differential equations (PDEs). SQA procedures are needed during software development and modification, as well as during production computing. SQA procedures are well developed in general, but areas of improvement are needed with regard to software operating on massively parallel computer systems. *Numerical algorithm verification (NAV)* addresses the software reliability of the implementation of all the numerical algorithms that affect the numerical accuracy of solutions produced by the code. Numerical algorithm verification is conducted by comparing computational solutions with benchmark solutions: analytical solutions, manufactured solutions, and highly accurate numerical solutions. Solution verification, also called *numerical error estimation*, deals with the quantitative estimation of the numerical accuracy obtained when PDEs are solved using discretization methods. The primary goal in solution verification is the estimation of the numerical accuracy of all of the solution quantities of interest in a given simulation. Solution verification is related to the topic of *adaptive mesh refinement (AMR)*, although the goals of AMR are more restrictive than those of solution verification. The discretization errors must be quantified in order to separate them, in principle, from other error and uncertainty sources, such as physics modeling errors and variability in physical properties. Two major shortcomings affect current verification methods, namely: (1) estimating discretization errors using solutions

on multiple mesh resolutions is a computationally expensive process, and (2) current methods for complex physics simulations are not robust.

Model validation means “does the model represent reality?” Specifically, model validation emphasizes the quantitative assessment of computational model accuracy by comparison with high-quality *validation experiments* – that is, experiments that are well characterized in terms of measurement and documentation of all the input quantities needed for the computational model, including carefully estimated and documented experimental measurement uncertainties. These validation experiments can be conducted on hardware that represents any level of simplification or disassembly of the actual, or complete, system of interest (for example, even experiments conducted on simple geometries with only one element of physics occurring). The state-of-the-art in model validation addresses issues of: (1) assessing model accuracy when several system response quantities have been measured and compared, and (b) comparing system response quantities from multiple realizations of the experiment with computational results that are characterized by probability distributions. Model validation emphasizes assessing the accuracy of physics-based models in blind comparisons with experimental data, a goal that is complementary to the goal of predictive capability in modeling and simulation.

Model qualification means certifying that a proposed simulation/design methodology/system satisfies all performance and safety specifications. Validation and qualification can be done only by selected benchmarking, taking into account systematically (i.e., using sensitivities) all of the uncertainties (computational, experimental, etc.). Verification and predictive validation must be based on a well-established set of scientific approaches that will allow the *a priori* announcement of quantified computational uncertainties. Model validation encompasses issues of quantifying model accuracy when several system response quantities have been measured and compared, and comparing system response quantities from multiple realizations of the experiment with computational results that are characterized by probability distributions. For this purpose, it is essential to construct a *parameter importance ranking table (PIRT)* which ranks, hierarchically, the importance of parameters, physical processes, and interactions of processes for all tiers and faces of the validation process, from single-effects benchmarks to system-level comparisons. The availability of response sensitivities, in addition to uncertainties, is paramount for constructing the *PIRT*.

Implementation of validation procedures for computations and experiments needed for model verification and validation is neither inexpensive nor easy. However, the quality of the verification and validation processes will be improved with each included step, resulting in increased confidence in the modeling and simulation capability. It is important to note that *verification and validation* is a process, *not a product*.

For improving the verification and validation processes, it is useful to attempt to define what ideal processes should be and assess practical difficulties in reaching these, as exemplified in the following:

Ideally, the application domain for the modeling and simulation capability under consideration would be well defined, with known accuracy requirements. Often, however, only some parts of the application domain are understood and some of the accuracy requirements are known.

Ideally, the validation tier hierarchy (from single-effect benchmarks to coupled system-level benchmarks) would be well established. Often, however, the validation hierarchy is known for individual subsystems or components, but the interactions between subsystems remain to be analyzed.

Ideally, the *PIRT* (*parameter importance ranking table*) has been constructed (quantitatively using all of the required sensitivities and uncertainties) and employed to rank the importance of physical processes and interactions of processes for all tiers of the validation hierarchy.

Ideally, the results of the *PIRT* would be used to define and prioritize code verification and validation activities, including corresponding schedules and needed resources. Often, however, the available resources rather than the *PIRT* dictate the schedule and priorities of code verification and validation, eliminating many possible verification and validation activities.

Ideally, the *SQA* procedures would have been defined, implemented, and documented. Often, however, *SQA* procedures are incompletely defined, partially implemented, adhered to just before a new code release, and informally documented.

Ideally, highly converged numerical solutions, in both space and time, would be obtained for every validation experiment conducted. Often, however, quantitative numerical error estimates are computed for some validation experiments, but some complex-system experiments only have qualitative error estimates.

Ideally, validation-experiment data would be well characterized, and a large number of experimental realizations would be available for estimating random and systematic (bias) errors. Often, however, only a few experimental realizations are available, and the respective experimental data is incompletely characterized.

Ideally, the validation metrics would be precisely defined (using statistical data for both computational and experimental results) and clearly connected to the modeling and simulation requirements for the respective application domain. Often, however, validation metrics and requirements are incompletely characterized, even for high-level system responses, and are lacking for low-level-tier physical response.

Ideally, the results and lessons learned from all of the validation activities would be clearly formulated, documented, and broadly communicated. Often, however, the results and lessons learned are documented only for “successful” validation experiments.

Predictive estimation (PE) comprises three key elements: *model calibration*, *model extrapolation*, and *estimation of the validation domain*. The result of the PE analysis is a probabilistic description of possible future outcomes based on all recognized errors and uncertainties. *Model calibration* addresses the integration of experimental data for the purpose of updating the data of the computational model. *Model extrapolation* addresses the prediction uncertainty in new environments or conditions of interest, including both untested parts of the parameter space and higher levels of system complexity in the validation hierarchy. Extrapolation of models and the resulting increase of uncertainty are poorly understood, particularly the estimation of uncertainty that results from nonlinear coupling of two or more physical phenomena that were not coupled in the existing validation database.

The *estimation of the validation domain* of the physics underlying the models of interest requires estimation of contours of constant uncertainty in the high-dimensional space that characterizes the application of interest. In practice, this involves the identification of areas where the predictive estimation of uncertainty meets specified requirements for the performance, reliability, or safety of the system of interest. The state-of-the-art in estimation of the validation domain is very early in both the conceptual and mathematical development. Developing predictive experimentally validated “best-estimate” numerical models is particularly important for designing new technologies and facilities based on novel processes, while striving to avoid, as much as possible, the costly and lengthy procedures of building representative mock-up experiments which might confirm – but would not necessarily explain – the predictions of

simulation tools. For example, the performance of fuels and materials, in particular fuel irradiation behavior, is dominated by the coupled effects of several phenomena and relies uniquely on very expensive and time-consuming confirmatory mockup experiments (e.g., multiyear irradiations), with little or no predictive capability; improvements in this regard have very high potential payoff. Also, systems-level analysis tools are, by nature, primarily predictive because they are evaluating systems that typically do not exist. When coupled phenomena occur, in particular for safety analyses, validation has been restricted to either mockup or component-level experimental comparison, with little predictive capability.

The most important activity in predictive estimation (PE) is *model calibration*, since the other two ingredients of PE could not be performed without the availability of a consistently calibrated model (in this context, “model” refers to the largest set of codes under consideration). The model calibration activity commences by identifying and characterizing errors and/or uncertainties from all steps in the sequence of modeling and simulation processes involved in a computational model prediction, including at least the following:

Data error or uncertainty (input data such as cross sections, model parameters such as reaction-rate coefficients, initial conditions, boundary conditions, and forcing functions such as external loading);

Model uncertainties: correlations, numerical discretization errors stemming from solution schemes, model options, incomplete modeling, simplified assumptions and approximations, uncertainty stemming from lack of knowledge about the physical processes being modeled;

Representation uncertainties: imperfect representation of facility geometry, higher dimensional (3D) effects, control, and system simplifications;

Scaling uncertainties: prototypes typically characterized by different geometric dimensions and materials (including working fluids), ranges of variation for thermal-hydraulic quantities usually differ (in prototypes) from full-scale plants;

Plant data uncertainties: unavailability of some plant parameters, instrument errors, and uncertainty in instrument response;

User effects, which are often implicitly present in all of the above-mentioned broad classes of uncertainties.

The mathematical framework for model calibration is provided by the *data adjustment and data assimilation* procedure. A state-of-the-art mathematical framework for data assimilation and model calibration for a generic time-dependent system was presented in ► Sect. 6. The basic premise underlying this mathematical framework is that only first- and second-order information (i.e., means and covariance matrices) is *a priori* available, which is actually the case in most practical situations, particularly when large-scale systems are involved. When only first and second moments of model parameters and experimental responses are available, the maximum entropy principle of statistical mechanics was employed in conjunction with information theory to construct a Gaussian prior distribution that takes all of the available information into account while minimizing (in the sense of quadratic loss) the introduction of spurious information. This prior distribution comprises also any correlations among model parameters and responses, thus generalizing the state-of-the-art data assimilation algorithms used in the geosciences (Kalnay 2003; Lewis et al. 2006).

The posterior distribution for the best-estimate calibrated model parameters and responses was constructed by using Bayes’ theorem. The best-estimate predicted mean values and reduced covariances, which are customarily needed when employing decision theory under “quadratic loss,” were computed by extracting the bulk contributions via the saddle-point method. In particular, this procedure yields the same Gaussian posterior distribution as would be obtained by

using the maximum likelihood method. The minimum value of the quadratic form appearing in the exponent of the Gaussian posterior distribution also provides the “ χ^2 of the calibration (adjustment) at hand.” This quadratic form can therefore be used as an indicator of the agreement between the computed and experimentally measured responses, indicating essentially the consistency of the measured responses with the model parameters. When all information is consistent, the posterior probability density function yields reduced best-estimate uncertainties for the best-estimate model parameters and responses, as illustrated for the paradigm benchmark time-dependent thermal-hydraulic system described in [Sect. 6.4](#).

The model calibration methodology presented in this work provides a rigorous mathematical foundation for similar methodologies used in geophysical sciences (Kalnay 2003; Lewis et al. 2006), while extending these methodologies in the following directions:

- Treatment of systems involving correlated parameters and responses (as opposed to no parameter–response correlations, e.g., in geophysical sciences);

- Simultaneous calibration of all parameters and responses (as opposed to just initial conditions, as usually performed in geophysical sciences);

- Simultaneous calibration over all time intervals; the usual two-step time advancement procedures used in geophysical sciences simply becomes a consequence, as a particular case, of the general methodology presented in this work.

From a computational point of view, the most intensive aspect of the data assimilation and model calibration methodology (cf. [Sect. 6](#)) is the computation of the sensitivities of responses to model parameters; these sensitivities play a fundamental role as weighting functions in all of the expressions for the best-estimated predicted values for parameters, responses, and their associated best-estimated reduced uncertainties. For large-scale systems, the most efficient method for computing these sensitivities is the *adjoint sensitivity procedure* (ASAP), as detailed in Cacuci et al. (2005, 2010) and Cacuci (2003). Note though, that the development of the adjoint sensitivity models underlying ASAP is far from trivial, and, as generally discussed in Cacuci et al. (2005) and Cacuci (2003), could benefit significantly from further theoretical and computational advances, including the class of methods collectively known under the name of *reduced-order modeling*. The other computationally intensive aspect in the assimilation and calibration methodology (cf. [Sect. 6](#)) is the inversion of the covariance matrix $C_d(\alpha^0)$ associated with the vector $\mathbf{d} \triangleq \mathbf{R}(\alpha^0) - \mathbf{r}_x$, which measures the deviations between the respective computed and experimentally measured responses. Methods for efficiently inverting this matrix, as well as for reducing its dimension through “reduced-order modeling” using proper orthogonal decomposition methods are of substantial interest.

The best-estimate calibrated values for model parameters obtained through the application of the mathematical framework presented in [Sect. 6](#) can also be used to estimate quantitatively the validation domain of the model under consideration, by computing *contours of constant best-estimate uncertainties in the high-dimensional parameter-space*. The best-estimate calibrated values can also be used to perform “model extrapolation,” by predicting uncertainties in new environments or conditions of interest. Extrapolation of large-scale models would address both untested parts of the parameter space and higher levels of system complexity in the validation hierarchy.

The explicit formulas presented in [Sect. 6](#) are based on the linearized relationship between responses and parameters that customarily underlies the “propagation of moments” method, without explicitly considering nonlinearities and modeling errors. Nevertheless, neither of these limitations is as severe as it may appear at first glance, since: (1) modeling errors

can be treated in a manner similar to parameter uncertainties, as shown in Cacuci et al. (2005) and Cacuci (2003), by including the discretization intervals in the vector of model parameters; and (2) nonlinear relations between computed responses and model parameters can be treated iteratively, and hence by considering (224), all of the major results derived explicitly in [▶ Sects. 3](#) and [▶ 4](#), as the first step in an iterative procedure, which starts with the known nominal values of the quantities involved. The subsequent step of such an iterative procedure would be to use the formulas for the best-estimate mean values and covariances for the parameters and responses obtained ([▶ Sect. 6.2](#)) as the “prior information,” and compute the new (“second-generation”) best-estimate quantities by using once again the formulas ([▶ Sect. 6.2](#)). This iterative procedure would be repeated until the best-estimated values would not change any longer, thereby indicating convergence of the nonlinear iterative procedure.

Ongoing research is currently devoted to the explicit treatment of modeling errors, and to extending the results ([▶ Sect. 6.2](#)) by including not only the sensitivities (i.e., first-order information) but also the Hessians (i.e., second-order information) of the responses. Additional work is also ongoing to remove the current restriction to Gaussian distributions. Actually, the de-facto limitation to Gaussian distribution is characteristic of all of the state-of-the-art procedures for data assimilation and model calibration, as evidenced by the scientific literature published thus far. Removing these limitations would contribute significantly to understanding the validation of coupled nonlinear multi-physics models (e.g., of two or more physical phenomena that were not coupled in the initial validation database), particularly the accompanying increase of uncertainty. Developing predictive experimentally validated “best-estimate” numerical models is particularly important for designing new technologies and facilities based on novel processes, while striving to avoid, as much as possible, the costly and lengthy procedures of building representative mock-up experiments, which might confirm – but would not necessarily explain – the predictions of simulation tools.

It may be argued that the costs of “validation, verification, and model calibration through data assimilation” activities could exceed their value added. It is conceivable that such an argument could be correct under certain circumstances. However, the costs of “validation, verification, and model calibration through data assimilation” must be weighed against the costs of incorrect or improper decisions based on possibly faulty computational modeling and simulation. Analogous to probabilistic risk assessment activities, *risk* is typically defined as the product of the probability of the occurrence of the event and the consequence of the event. If erroneous conclusions based on modeling and simulations are made on high-consequence events, decision makers could place their constituency at extreme risk. This is especially true for systems that cannot be tested. For such systems, the only path to progress is to improve drastically the confidence and understanding of computational simulations, while continually relaxing their limitations and enlarging their validation domains.

References

-
- Aksan SN, D'Auria F, Staedtke H (January 1995) User effect on the transient system code calculations. OECD/CSNI Report, NEA/CSNI/R(94)35, Paris
- Andres TH, Hajas WC (1993) Using iterated fractional factorial design to screen parameters in sensitivity analysis of a probabilistic risk assessment model. In: Proceedings of the joint international conference on mathematical methods and supercomputing in nuclear applications, vol. 2, 19–23 April 1993. Karlsruhe, Germany, p. 328

- Archer G, Saltelli A, Sobol' IM (1997) Sensitivity measures, ANOVA like techniques and the use of bootstrap. *J Statist Comput Simul* 58:99
- Barhen J, Cacuci DG, Wagschal JJ, Bjerke MA, Mullins CB (1982) Uncertainty analysis of time-dependent nonlinear systems: theory and application to transient thermal-hydraulics. *Nucl Sci Eng* 81:23–44
- Barhen J, Cacuci DG, Wagschal JJ, Mullins CB (1980) A systematic methodology for the reduction of uncertainties in transient thermal-hydraulics by using in-bundle measurement data. In: ANS topical conference 1980 advances in reactor physics and shielding, Sun Valley, Idaho, 14–17 September 1980, ANS/70048, pp. 156–168
- Bayes T (1763) An essay toward solving a problem in the doctrine of chances. *Philos Trans Roy Soc* 53:370. (Repr. Pearson ES, Kendall MG (1970) *Studies in the history of statistics and probability*. Hafner, Darien)
- Berger J (1985) *Statistical decision theory and Bayesian analysis*, 2nd edn. Springer, New York
- Bernoulli J (1713) *Ars Conjectandi*, Thurnisiorum. Basel (Repr. Die Werke von Jakob Bernoulli. Birkhäuser, Basel, 1975)
- Bettonvil B (1990) *Detection of important factors by sequential bifurcation*. Tilburg University Press, Tilburg
- Bonano EJ, Apostolakis GE (1991) Theoretical foundations and practical issues for using expert judgments in uncertainty analysis of high-level radioactive waste disposal. *Radioact Waste Manag Nucl Fuel Cycle* 16:137
- Box GEP, Draper NR (1987) *Empirical model-building and response surfaces*. Wiley, New York
- Boyack BE, Catton I, Duffey RB, Griffith P, Katsma KR, Lellouche GS, Levy S, Rohatgi US, Wilson GE, Wulff W, Zuber N (1990) An overview of the code scaling, applicability and uncertainty evaluation methodology. *J Nucl Eng Des* 119(1):1–16. (See also other papers in the same issue of the Journal)
- Brown PN, Byrne GD, Hindmarsh AC (1989) VODE, a variable-coefficient ODE solver. *SIAM J Sci Statist Comput* 10:1038–1051
- Brown PN, Hindmarsh AC (1989) Reduced storage matrix methods in stiff ODE systems. *J Appl Math Comput Sci* 31:40–91
- Cacuci DG (1981) Sensitivity theory for nonlinear systems. I. Nonlinear functional analysis approach. *J Math Phys* 22:2794
- Cacuci DG (1981) Sensitivity theory for nonlinear systems. II. Extensions to additional classes of responses. *J Math Phys* 22:2803
- Cacuci DG (1990) Global optimization and sensitivity analysis. *Nucl Sci Eng* 104:78
- Cacuci DG (2003) *Sensitivity and uncertainty analysis: theory*, vol 1. Chapman & Hall/CRC Press, Boca Raton
- Cacuci DG, Balan I, Ionescu-Bujor M (2008) Adjoint sensitivity analysis of dynamic reliability models based on Markov Chains: application to a model of the international fusion materials irradiation facility. *Nucl Sci Eng* 158:114–153
- Cacuci DG, Ionescu-Bujor M (2005) Deterministic local sensitivity analysis of augmented systems. I. Theory. *Nucl Sci Eng* 151:55–66
- Cacuci DG, Ionescu-Bujor M (2008) Adjoint sensitivity analysis of dynamic reliability models based on Markov Chains: theory. *Nucl Sci Eng* 158:97–113
- Cacuci DG, Ionescu-Bujor M (2010) Best-estimate model calibration and prediction through experimental data assimilation: theory. *Nucl Sci Eng* 165:18–44
- Cacuci DG, Ionescu-Bujor M, Navon MI (2005) *Sensitivity and uncertainty analysis: applications to large scale systems*, vol 2. Chapman & Hall/CRC Press, Boca Raton
- Cacuci DG, Navon MI, Ionescu-Bujor M (2010) *Computational methods for data evaluation and assimilation*. Chapman & Hall/CRC Press, Boca Raton
- Cao X-R, Wan Y-W (1998) Algorithms for sensitivity analysis of Markov systems through potentials and perturbation realization. *IEEE Trans Control Syst Technol* 6(4):482–494
- Chauliac C, Aragonés JM, Bestion D, Cacuci DG, Crouzet N, Weiss F-P, Zimmermann MA (2009) NURESIM – a European simulation platform for nuclear reactor safety: multi-scale and multi-physics calculations, sensitivity and uncertainty analysis. In: FISA, 22–25 June 2009, Prague
- Clement RT, Winkler RL (1999) Combining probability distributions from experts in risk analysis. *Risk Anal* 19:187
- Cotter SC (1979) A screening design for factorial experiments with interactions. *Biometrika* 66:317
- Cox RT (1946) Probability. Frequency, and reasonable expectation. *Am J Phys* 14:1
- Cukier RI et al (1973) Study of the sensitivity of coupled reaction systems to uncertainties in rate coefficients. I. Theory. *J Chem Phys* 59:3873
- Daniel C (1973) One-at-a-time-plans. *J Am Statist Assoc* 68:353
- Dunker AM (1984) The decoupled direct method for calculating sensitivity coefficients in chemical kinetics. *J Chem Phys* 81:2385
- Fischer RA (1935) *The design of experiments*. Oliver & Boyd, Edinburgh

- Haque MA, Richardson SM, Saville G (1992) Blowdown of pressure vessels. I. Computer model. *Trans I Chem E* 70(Part B):3-9
- Haque MA, Richardson SM, Saville G et al (1992) Blowdown of pressure vessels. II. Experimental validation of computer model and case studies. *Trans I Chem E* 70(Part B):10-17
- Henley EJ, Kumamoto H (1992) Probabilistic risk assessment: reliability engineering, design and analysis, 2nd edn. IEEE Press, The Institute of Electrical and Electronics Engineers, Inc., New York
- Hofer E (January 1993) Probabilistische Unsicherheitsanalyse von Ergebnissen umfangreicher Rechenmodelle. GRS-A-2002
- Hora SC, Iman RL (1989) Expert opinion in risk analysis: the NUREG-1150 methodology. *Nucl Sci Eng* 102:323
- IFMIF-CDA Team, Martone M (eds) (December 1996) IFMIF - International Fusion Materials Irradiation Facility, Conceptual Design Activity, Final Report. ENEA Frascati Report RT/ERG/FUS/96/11
- Iman RL, Conover WJ (1982) A distribution-free approach to inducing rank correlation among input variables. *Commun Statist Simul Comput B* 11:311
- International Atomic Energy Agency (2008) Best estimate safety analysis for nuclear power plants: uncertainty evaluation. IAEA safety reports series, vol 52. Vienna, Austria, pp 1-162
- Ionescu-Bujor M, Jin X, Cacuci DG (2005) Deterministic local sensitivity analysis of augmented systems. II. Applications to the QUENCH-04 experiment using the RELAP5/MOD3.2 code system. *Nucl Sci Eng* 151:67-81
- Jaynes ET (1893) In: Rosencrantz RD (ed) *Papers on probability, statistics, and statistical physics*. Reidel, Dordrecht
- Jeffreys H (1939) *Theory of probability*. Clarendon Press, Oxford
- Kalnay E (2003) *Atmospheric modeling, data assimilation and predictability*. Cambridge University Press, Cambridge
- Kalnay E (2003) *Atmospheric modeling, data assimilation and predictability*. Cambridge University Press, Cambridge
- Kleijnen JPC (1998) Experimental design for sensitivity analysis, optimization and validation of simulation models. In: Banks J (ed) *Handbook of simulation - principles, methodology, advances, applications, and practice*. Wiley, New York
- Kleijnen JPC, Helton JC (1999) Statistical analyses of scatterplots to identify important factors in large-scale simulations. 1. Review and comparison of techniques. *Reliab Eng Syst Saf* 65:147 (See also: Kleijnen JPC, Helton JC (1999) Statistical analyses of scatterplots to identify important factors in large-scale simulations. 2. Robustness of techniques. *Reliab Eng Syst Saf* 65:187)
- Kramer MA et al (1981) An improved computational method for sensitivity analysis: Green's function method with AIM. *Appl Math Model* 5:432
- Kramer MA et al (1984) Parameter scaling of mathematical models. *Appl Math Model* 8:341
- Laplace PS (1812) *Théorie analytique des probabilités*. Courcier, Paris. (Repr. *Oeuvres complètes*. Gauthiers-Villars, Paris, 1878-1912)
- Lewis JM, Lakshminarayanan S, Dhall SK (2006) Dynamic data assimilation: a least square approach. Cambridge University Press, Cambridge
- McKay MD (1995) Evaluating prediction uncertainty. Technical Report NUREG/CR-6311. US Nuclear Regulatory Commission and Los Alamos National Laboratories
- McKay MD et al (1979) A comparison of three methods of selecting values of input variables in the analysis of output from a computer code. *Technometrics* 21:239
- Morris MD (1991) Factorial sampling plans for preliminary computational experiments. *Technometrics* 33:161
- Mosteller RD (June 2007) Comparisons of results for the MCNP criticality validation suite using ENDF/B-VII.0 and other nuclear data libraries. Los Alamos Report LA-UR-07-0362
- Norris JR (1997) *Markov Chains*. Cambridge University Press, Cambridge
- OECD/NEA (2007) Technology relevance of the uncertainty analysis in modelling project for nuclear reactor safety. NEA/NSC/DOC (2007)15
- OECD/NEA (October 2007) Bemuse phase III report, uncertainty and sensitivity analysis of the LOFT L2-5 test. OECD/NEA/CSNI/R(2007)4. Nuclear Energy Agency, Issy-les-Moulineaux
- Ou Y, Dugan JB (2003) Approximate sensitivity analysis for acyclic Markov reliability models. *IEEE Trans Reliab* 52(2):127
- Parker D (1985) *Learning logic*. Working paper 47. Center for Computational Research in Economics and Management Science, MIT Press
- Petruzzi A (2008) Development and application of methodologies for sensitivity analysis and uncertainty evaluation of the results of the best estimate system codes applied in nuclear technology. PhD thesis, University of Pisa
- Petruzzi A, Cacuci DG, D'Auria F (2010) Best-estimate model calibration and prediction through experimental data assimilation: theory. *Nucl Sci Eng* 165:45-100

- Piaszczyk CM (1996) IFMIF – reliability, availability & maintainability – accelerator. In: Presentation at IFMIF design integration meeting, Tokai, Ibaraki, Japan, 25–26 May 1996
- Rauzy A (2004) An experimental study on iterative methods to compute transient solutions of large Markov models. *Reliab Eng Syst Saf* 86: 105–115
- Renyi A (1954) Valoszinűségsszámítás (“Probability Calculus”). Budapest. (Presented in slightly generalized form by: Aczel J (1964) Lectures on functional equations and their applications. sec 7.1.4. Academic Press, New York)
- Saltelli A et al (1993) Sensitivity analysis of model output: an investigation of new techniques. *Comput Statist Data Anal* 15:211
- Saltelli A, Sobol’ IM (1995) About the use of rank transformation in sensitivity analysis of model output. *Reliab Eng Syst Saf* 50:225
- Shannon CE (1948) *Bell Syst Tech J* 27:379 and 623. (See also: Shannon CE, Weaver W (1949) The mathematical theory of communication. University of Illinois Press, Urbana)
- Sobol’ IM (1993) Sensitivity analysis for non-linear mathematical models. *Math Model Comput Exp* 1:407
- Stone CJ (1985) Additive regression and other non-parametric models. *Ann Statist* 13:689
- U. S. Nuclear Regulatory Commission (December 2005) Regulatory guide 1.203, transient and accident analysis methods. US NRC
- Wald A (1950) Statistical decision functions. Wiley, New York
- Wickett T et al (June 1998) Report of the uncertainty method study for advanced best estimate thermalhydraulic code applications, vols. I and II. OECD/NEA/CSNI R (97) 35
- Wilks SS (1941) Determination of sample sizes for setting tolerance limits. *Ann Math Statist* 12:91–96



18 Reactor Physics Experiments on Zero Power Reactors

Gilles Bignan · Philippe Fougeras · Patrick Blaise ·

Jean-Pascal Hudelot · Frédéric Mellier

French Atomic Energy Commission, Reactor Studies

Department, Cadarache Research Center, Saint Paul Lez

Durance, France

gilles.bignan@cea.fr

philippe.fougeras@cea.fr

patrick.blaise@cea.fr

jean-pascal.hudelot@cea.fr

1	<i>The Contribution of CEA Critical Mock-Ups in Nuclear Reactor Simulation</i>	2057
2	<i>Description of the EOLE Mock-Up</i>	2059
3	<i>Experimental Programs on the EOLE Mock-Up</i>	2063
3.1	The EPICURE Program	2064
3.2	The MISTRAL Program	2065
3.3	The BASALA Program	2068
3.4	The ADAPh Program	2069
3.5	The FUBILA Program	2070
3.6	The FLUOLE Program	2071
3.6.1	Reason for the Program	2071
3.6.2	Characteristics of the FLUOLE Program	2072
3.7	The PERLE Program	2073
3.7.1	Reason for the Program	2073
3.7.2	PERLE Program Characteristics	2074
3.8	The AMMON Program and the Jules Horowitz Reactor	2077
3.9	MOX Powder Criticality Requirements	2080
3.10	Criticality at Loading	2080
3.11	Plutonium and High Combustion Rate Control. EPR Support	2081
3.12	Support Program for CELESTIN Reactors	2083
3.13	An Experimental Platform	2083
3.14	Support for Generation IV Reactor Concepts	2084
3.15	Conclusions	2084
4	<i>Description of the MINERVE Reactor</i>	2084
4.1	General Description	2084
4.1.1	The Cavity	2085
4.1.2	Driver Zone Fuel Elements	2085

4.1.3	The External Reflector	2085
4.1.4	The Central Cavity	2087
4.1.5	Control-Command	2087
4.2	Advantages of the MINERVE Reactor	2087
4.3	Coupled Assemblies.....	2088
4.3.1	MELODIE Assembly Representative of Pressurized Water Lattices	2090
4.3.2	MORGANE Assembly for Lattices Representative of Under-Moderated Reactors (RSM)	2093
4.3.3	ERMINE Assembly for Fast Neutron Multiplier Lattices	2095
4.3.4	ELOISE Assembly for Heavy Water Moderated Lattices	2096
5	<i>Experimental Programs in the MINERVE Reactor</i>	2096
5.1	Main Programs Achieved Between 1959 and 1990	2098
5.2	The CREDIT BURN UP Program (From 1993 to 2001).....	2100
5.3	The CERES Program (From 1992 to 1995)	2101
5.4	The High Burn-Up (HTC) Program (From 2003 to 2004)	2102
5.5	The VALMONT Program (2003–2004)	2103
5.6	The ADAPh Program (2005)	2104
5.7	The OSMOSE Program	2104
5.8	The OCEAN Program	2105
5.9	Training Activities.....	2105
5.9.1	EDF Training.....	2105
5.9.2	INSTN Training	2105
5.9.3	Other Training	2106
5.10	The Gas Fast Reactor (GFR) Program	2106
5.11	The HTR Program.....	2106
5.12	HTC Program Supplement	2107
5.13	Program on Structure Materials and Moderators.....	2107
5.14	FP and Absorber Supplementary Program	2107
5.15	Program in Support of JHR for Qualification of HORUS3D for U_3Si_2	2108
5.16	Cadmium Measurements	2108
5.17	Other Programs	2108
5.18	Conclusion	2109
6	<i>Description of the MASURCA Reactor</i>	2109
6.1	Core Building Principles	2111
6.2	Simulation Materials.....	2114
7	<i>Experimental Programs in MASURCA</i>	2116
7.1	The RZ and PLUTO Programs (1969–1975)	2118
7.2	The PECORE Program (1975)	2118
7.3	The PRE RACINE and RACINE Programs (1976–1984).....	2118
7.4	The BALZAC Program (1985–1988)	2121
7.5	The CONRAD Program (1989–1992).....	2121
7.6	The BERENICE Program (1993)	2121
7.7	The CIRANO Program (1994–1997)	2121
7.8	The COSMO Program (1998–1999).....	2122
7.9	The MUSE Program (2000–2004)	2122

7.10	The Facility Refurbishment Project	2123
7.11	A Program in Support of SFR and the 2020 Prototype: GENESIS	2124
7.12	A Program in Support of GFR: ENIGMA	2125
7.13	A “FBR Large Cores” Generic Study Program	2125
7.14	A “Reflector and Shield” Program	2126
7.15	A “Deteriorated and Accidental Configuration” Program	2126
8	<i>Experimental Methods Used and Being Developed on These Critical Mock-Ups</i>	2126
8.1	The Main Measuring Techniques Used	2126
8.1.1	Measurements by Miniature Fission Chambers	2127
8.1.2	Measurements by γ Spectrometry	2127
8.2	Classification	2127
8.3	Measurement Electronics at EOLE/MINERVE	2127
8.3.1	γ Spectrometry Benches	2128
8.3.2	Automatic Changer	2129
8.3.3	Use of DSP	2129
8.4	Fission Chambers	2130
8.5	Gamma Ionization Chambers	2133
8.6	Fissile and Activation Detectors	2135
8.7	Procedures Linked to the Oscillation Technique	2136
8.7.1	Oscillator	2136
8.7.2	The Automatic Pilot Rod	2136
8.7.3	Acquisition and Online Processing System for Oscillation Measurements	2138
8.7.4	Active Sample Handling Equipment	2138
8.7.5	Oscillation Samples	2138
9	<i>Integral Parameter Determination Through Experiment</i>	2141
9.1	Critical Size	2142
9.1.1	Application of Critical Size Determination	2144
9.2	Reactivity Effect Measurements	2145
9.2.1	Reactivity Worth Measurement by Inverse Kinetics	2145
9.2.2	Reactivity Effects by Subcritical Measurements	2147
9.2.3	Principle of Subcritical Measurements	2147
9.2.4	Amplified Source Method (ASM)	2147
9.2.5	Modified Source Multiplication (MSM) Method	2149
9.2.6	Practical Implementation of ASM and MSM Subcritical Measurements	2151
9.2.7	Associated Uncertainties	2152
9.2.8	Example: Isothermal Temperature Coefficient (ITC)	2153
9.2.9	Reactivity Effect Measurements by Sample Oscillation	2154
9.3	Measurement of Fission Rate Distributions	2159
9.3.1	Distributions by Fission Chambers	2160
9.3.2	Distributions by Integral Gamma Spectrometry	2161
9.3.3	Particular Use of Fission Rate Distributions: The Buckling Estimation	2164
9.3.4	Determination of the Reflector Saving	2165
9.3.5	Adjustment of Fission Maps by Particular Peaks	2165
9.4	Spectral Indexes	2168
9.4.1	Basic Principle	2169

9.4.2	Modified Conversion Factor	2170
9.5	γ Heating Measurements	2173
9.5.1	Principle	2173
9.5.2	γ Dose Calculation	2174
9.5.3	The Different Types of TLDs Used	2175
9.6	Neutron Noise Measurements	2175
9.6.1	The Power Spectral Density (PSD) Method	2176
9.6.2	Experimental Principle	2177
10	Conclusion	2178
	References	2178

Abstract: The CEA (Commissariat à l'Énergie Atomique) is strongly involved in R&D research programs concerning the use of nuclear energy as a clean and reliable source of energy and consequently is working on the present and future generations of reactors on various topics such as ageing plant management, optimisation of the plutonium stockpile, waste management and innovative systems exploration. Core physics studies are an essential part of this comprehensive R&D effort. In particular, the Zero Power Reactors (ZPR) of CEA: EOLE, MINERVE and MASURCA play an important role in the validation of neutron physics calculation tools (codes and nuclear data).

Most recent programs notably contributed to:

- Obtain a very large and accurate experimental database for nuclides arising in plutonium and waste management (heavy nuclides and long lived fission products).
- Explore long-lived nuclides transmutation.
- Support the present French PWR fleet and the future reactors such as EPR.
- Explore innovative systems and new concepts in terms of new materials and fuels (ABWR, new MTR such as the Jules Horowitz Reactor under construction in Cadarache).
- Improve the physics of hybrid systems, involving a sub-critical reactor coupled with an external accelerator (ADS). A vast majority of these programs are carried out within the frame of international collaboration.

The Zero Power Reactors are also essential tools in the activities of teaching various topics related to experimental reactor physics. In particular, practical work on the operation and control of reactors and the associated methods of experimentation is done by the students enrolled in the “Génie Atomique” French nuclear engineering school.

The experimental programs defined in the EOLE, MINERVE and MASURCA facilities aim at improving the calculation routes by reducing the uncertainties of the experimental databases. They also provide accurate data on innovative systems in terms of new materials (moderating and decoupling materials) and new concepts (ADS, ABWR, GEN IV) involving new fuels, absorbers and coolant materials.

After a description of the previous experimental programs, an overview of the future experimentation is given in this chapter.

1 The Contribution of CEA Critical Mock-Ups in Nuclear Reactor Simulation

From the beginning of history of the nuclear reactor, the example of Zoé, the first French reactor, demonstrates that there is no development of nuclear concepts and techniques without an experimental portion conducted on critical mock-ups. Of course, neutronics relies on equations that are perfectly representative of the phenomena. However, the amplitude of energy fields at stake, the diversity of materials and their characteristics, and the complexity of assembly geometry means that it involves qualifying all physical data and calculation models with precision, making experimentation on such mock-ups a necessity. It will remain in the future within the context of developing digital simulation to enable adjustments and the qualification of simulation methods and tools.

CEA contributes to the study of reactor physics by designing and performing integral experiments for the qualification of neutron calculation forms, protection (gamma and neutron

attenuation in materials), and basic nuclear data on three critical mock-ups at Cadarache: EOLE (PWR and BWR spectra), MINERVE (all types of spectra), and MASURCA (“fast” and accelerator-driven lattice (ADS) spectra).

These critical mock-ups are reactors which use very low powers. Their neutronic behaviors can be directly extrapolated with physical phenomena encountered in power reactors (to a *close representativity factor*). In EOLE, the experiments conducted have always been designed in such a way that the C/E (calculation/experimentation) deviation highlighted is directly the calculation error that would be obtained in the industrial application (representativity factor mock-up $r = 1$ as it uses the same fuel and the same geometry as PWR and BWR assemblies).

These mock-ups are very flexible, adaptable, easy to access and easy to instrument while still being reliable.

Designing integral experiments consists in using a sequence of sensitivity calculations and uncertainty calculation models and should enable verification of the adequacy of the experiment with the expressed qualification requirement.

Conducting neutronic experimental programs is based on determining and measuring main parameters or phenomena of interest to qualify calculation tools and nuclear data “libraries.” Two types of main integral experiments can be identified: fundamental type aimed at qualifying basic nuclear data by measuring parameters which are themselves fundamental such as k_{eff} , spectral indexes, integral cross sections, ^{238}U conversion rates, temperature coefficient, or β_{eff} and mock-up type aimed at qualifying calculation methods through project parameters such as reaction rate distributions, soluble boron efficiency, efficiency of absorber rod clusters, or drainage coefficients.

Determining these parameters relies on the use of numerous and different experimental techniques that can be classified into three main families depending on whether the measurements are used to determine.

- Measuring techniques to determine the “absolute” (reactivity scale) or “relative” reactivity (difference between two levels of reactivity).
- Measuring techniques to determine the distribution of “in core” or “postirradiation” reaction and flux rates.
- Measuring techniques for gamma or neutron dose determination.

Experimental parameter values must be accompanied by controlled uncertainty values. Therefore, for a given parameter, the simultaneous use of several measuring techniques allows the systematic uncertainty term to be lowered. Conducting several series of measurements with a single experimental technique allows this aim to be achieved.

Within the framework of simulation development and with the aim to improve calculation scheme predictions by improving mathematic models and databases used in neutron forms, this naturally leads to the development of new measurement methods and related acquisition channels or improvements of existing experimental techniques.

Thus, determining experimental uncertainty is associated with the implementation, maintenance, and evolution of these techniques, as well as with the development of new measuring techniques. For example, the recent development of a measuring channel of the capture cross-section of U^{238} directly on fuel rod during the MISTRAL program in EOLE and that of a dynamic reactivity measuring channel using a pulsated neutron generator can be quoted.

The improvement of these methods also requires advanced instrumentation expertise. To closely measure local parameters of cores with more precision, very small-sized fission chamber

type neutron flux detectors had to be developed associated with an acquisition electronic system and signal processing to allow satisfactory analysis of measurements.

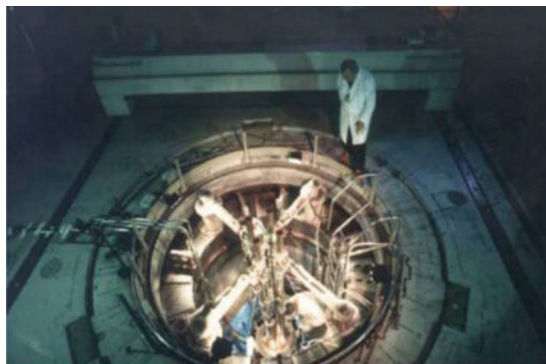
2 Description of the EOLE Mock-Up

The EOLE experimental reactor (➤ *Fig. 1*), with very low power, is a support structure comprising a reactor block offering biological shielding for operation with a flux level up to $10^9 \text{ n cm}^{-2} \text{ s}^{-1}$ in the core. The regulatory limit is currently 100 W whereas in the building order the limit was at 10 kW.

In this structure, an aluminum (AG3) tank of approximately 2.3 m in diameter and 3 m high was built to receive 12 tons of heavy water from the first experimental programs (➤ *Fig. 2*).



■ Figure 1
View of reactor block



■ Figure 2
View of the EOLE tank from above

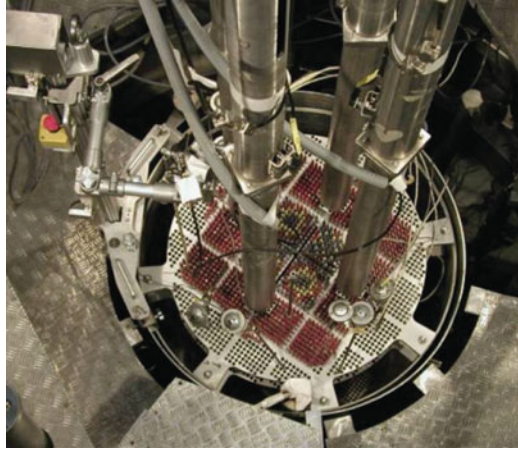


Figure 3
View of EPICURE tank

In the center of this tank (called EOLE), there is another smaller tank (EPICURE tank: $h = 1,200$ mm, inner diameter = 984 mm, outside diameter = 992 mm). A shell inside this tank ($h = 1,122$ mm, inner diameter = 944 mm, outside diameter = 956 mm) allows it to receive any type of water reactor lattice thanks to a set of interchangeable grids (► Fig. 3).

For the requirements of the FUBILA program, this internal tank was replaced by another slightly larger one (FUBILA tank: $h = 1,194$ mm, inner diameter = 1,188 mm, outside diameter = 1,200 mm). The FUBILA shell inside this tank has the following dimensions: $h = 1,093$ mm, inner diameter = 1,148 mm, outside diameter = 1,160 mm.

Four safety rods, attached to hoists above the shell, for which the structure (plate or rods), position, and composition, depending on the cores studied, allow the reactivity to be controlled at any times. Its rods drop very quickly through a launcher and gravity.

Likewise, a pilot rod for which the structure, position, and composition can be chosen allows divergence to be carried out and power to be stabilized between 0 and 100 W (maximum power authorized). This pilot rod has a reactivity weight lower than $\beta/2$.

Fuel rods are identical in height (80 cm fissile height) to those of lattices used in power reactors (uranium oxide or mixed uranium and plutonium oxide).

Several types of fuel (MOX, PWR, and BWR type UO_2) have been used in the facility and some of them are still available for future programs:

225	MOX EPICURE 8.7% rods
1,604	MOX EPICURE 7% rods
202	MOX EPICURE 4.3% rods
23	MOX BASALA 3% rods
20	MOX FUBILA 3% rods
36	MOX FUBILA 5% rods
120	MOX FUBILA 8% rods
264	MOX FUBILA 11.5% rods
1,600	UO_2 EPICURE 3.7% rods

As an example, the core loaded with the most MOX fuel (MISTRAL-2) contained approximately 44 kg of Pu.

However, it should be noted, that the facility is unable to use and store irradiated fuel that limits EOLE to lattice characterizations at “Zero time,” without the ability to qualify changing codes.

Numerous absorber materials, burnable or structure poisons (natural and enriched B_4C , AIC, Hf, $UO_2-Gd_2O_3$, $UO_2-Er_2O_3$, pyrex, Zy-2, steel, etc.) can be used.

In 1995, a thermostation was set up with water systems enabling filling, drainage, and the introduction of boron in the moderator able to get the moderator’s temperature to be selected from 5 to 80°C with $\pm 0.1^\circ C$ precision (➤ Fig. 4).

In 1997, the installation of a small chemical laboratory enabling precise measurement of the soluble boron concentration of the moderator can also be noted (➤ Fig. 5).

In 1990, the reactor’s instrumentation and control system was entirely refurbished with, in particular, neutron signal digital processing, the use of programable controllers, and the visual display of reactor status (➤ Fig. 6). In 2003, neutron control racks and the supervisor were updated (➤ Fig. 7).

Searching for the critical status of the reactor is carried out by the rise of the moderator solution (borated or not) in the reactor tank, then, when the moderator solution circulates in the thermo-control system at the desired temperature (by overflow between the tank and the shell) by the gradual rise of the control rods.

The reactor must be slightly subcritical with the four control rods in raised position, pilot rod fully inserted in the core and slightly supercritical with the pilot rod in raised position



■ Figure 4
View of the thermostation



■ Figure 5
View of the small chemistry laboratory



■ Figure 6
View of the control room (1990)

(there are therefore no longer any absorbers in the core). Criticality is sought with the pilot rod partially inserted in the core.

Core reactivity is adjusted through iteration on one of the following two parameters:

- Moderator concentration in soluble boron (light water)
- The fuel mass by adding or removing some peripheral fuel rods

These two parameters are called *critical parameters*.



■ **Figure 7**
View of the control room (2005)

3 Experimental Programs on the EOLE Mock-Up

The Building Order for EOLE dated 23 June 1965 was signed by Prime Minister Georges POMPIDOU and the Secretary of State for the first Minister responsible for Scientific, Atomic, and Space Research, Yvon BOURGES. The EOLE nuclear reactor, which was built to study CELESTIN lattices, replaces the AQUILON reactor (D_2O natural and enriched uranium at Saclay 1956) and constitutes a flexible critical experiment for the physics of cores and has a D_2O reference thermo-column. The maximum operating power was 10 kW.

After 2 years of work (1964–1965), the first divergence took place on 2 December 1965.

1965: Natural uranium and heavy water Thermo-Column calibration with respect to Aquilon reactor.

1966: Study of CELESTIN lattices notably with a plutonium and heavy water lattice.

1968: The FOEHN experiment was a critical mock-up of the RHF high flux reactor at the Laüe-Langevin Institute in Grenoble.

1969: Validation of calculation codes for EL4 type lattices.

1970: Lattice EL3 experiment with enriched U annubis tubular fuel (93%).

1970: Marks the end of the use of heavy water in EOLE.

1971: Critical experiment for a thermoelectronic direct conversion reactor, with ceramic fuel – molybdenum enriched uranium metal and tungsten electron conductor.

1972: Critical mock-up of safety test reactors with the CABRIOLE program for CABRI, the PHEBEE program for PHEBUS and SCARABEE.

1978: The CRISTO I program for the study of the criticality of pressurized water reactor large pitch fuel storages. An additional CRISTO-Mist configuration simulated the density of optimum hydrogen (fire or mist/smoke lance in dry storage) through expanded polystyrene blocks in which fuel rods were inserted.

1979: The CREOLE program for the study of temperature coefficients for UOX and MOX fuels. 200 MOX rods were placed in a loop (temperature at approximately 300°C pressurized

at 120 bars. This experiment allowed, for example, a precise form of the ^{235}U η factor to be obtained).

1980: The CRISTO II program for the study of PWR assembly large pitch fuel compact storages for pressurized water reactors.

1982: The CAMELEON program was dedicated notably to the qualification of calculation schemes for neutron absorbers (hafnium, boron, gadolinium with different supports, co-milled or grain) in UO_2 PWR type cores.

1985: The ERASME program studied closed MOX lattices, under-moderated for cores for ^{238}U - ^{239}Pu convertor.

Since 1989, EOLE has been mainly dedicated to plutonium recycling studies in light water reactors (PWR and BWR).

3.1 The EPICURE Program

The EPICURE program (between 1989 and 1994) was jointly agreed upon in 1988 by the three partners EDF, FRAMATOME, and CEA and was to examine uncertain margins related to neutron quantities associated in PWR with plutonium recycling and propose actions needed for their reduction in such a way as to not penalize the operation of plant units concerned, by ensuring the required level of safety.

It also had the objective of qualifying calculation schemes of PWR cores loaded to 30% of MOX assemblies (➔ Fig. 8).

EPICURE therefore enabled reduction of the calculation uncertainty of the multiplication factor of PWR lattices by a factor of 2. Furthermore, it returned the precision of MOX lattice parameters to the level of that of UO_2 lattices.

Particular attention had to be paid to problems linked to the interface between MOX and UO_2 assemblies. A statistical analysis allowed a distribution map to be created for fission rates with an experimental uncertainty of $\pm 0.6\%$ (at 1σ) for UO_2 rods and $\pm 0.9\%$ (at 1σ) for main assembly MOX rods (the uncertainties for existing MOX experiments are approximately $\pm 1.5\%$). Uncertainty on the power peak was able to be decreased by more than half to arrive at 1%.

The diagram below summarizes the configurations and different measurements studied: The EPICURE program also enabled:

- Through its representativity, qualification of the MOX/ UO_2 interface calculation and zoning, as well as qualification of the P/A factor (assembly average power divided by the activity of the fission chamber placed in the center of the assembly)
- Qualification of calculations of various types of absorber rods, as well as the obtaining of an experimental basis for the validation of absorbers in UO_2 and MOX PWR assemblies
- Power distributions and reactivity effects in the case of local drainage as well as for rod bowing effects to be obtained
- Qualification of the APOLLO-2 code and basic data, notably the CEA93 library. Furthermore, interpretation of the PWR type configuration recycling plutonium, enabled a reference calculation scheme based on the APOLLO-2 Sn 2D module to be developed.

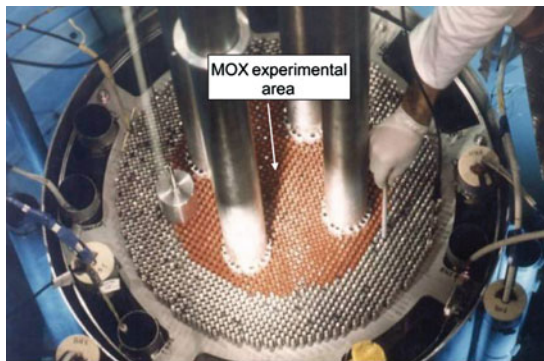
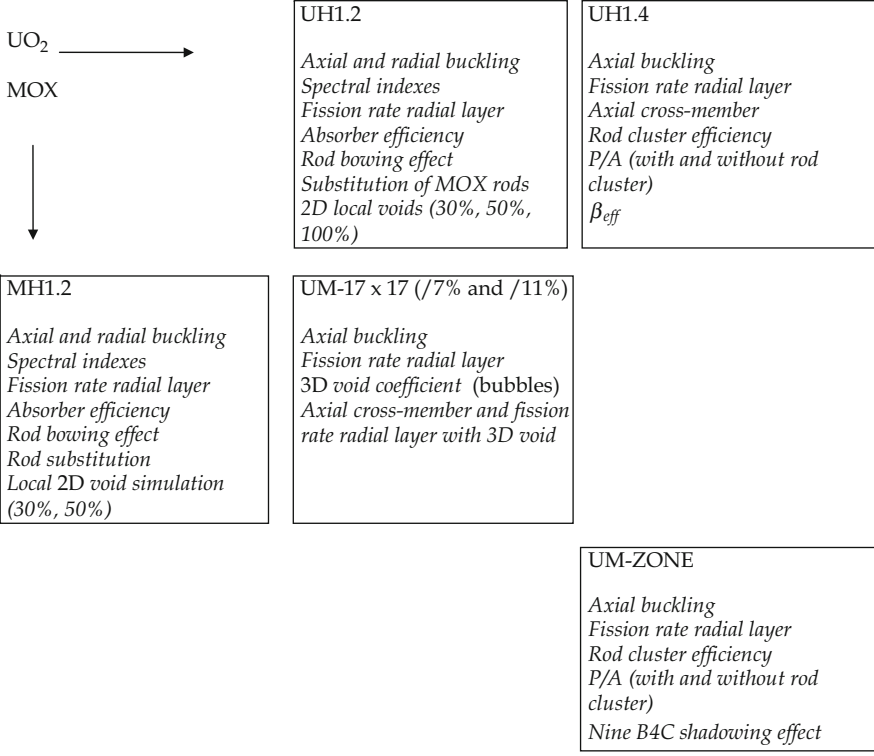


Figure 8
View of the EPICURE MH1.2 configuration

3.2 The MISTRAL Program

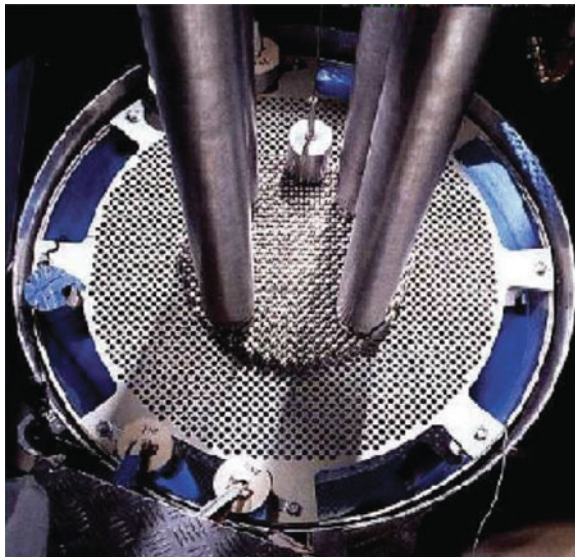
The MISTRAL program (between 1995 and 2000) in collaboration with the Japanese organization “NUPEC” (Japan) and the French industrial partners EDF and FRAMATOME, accompanied Japanese and French studies on MOX 100% loaded cores with increases of the moderating ratio $H/HM = 4-6$ in four different configurations including one mock-up type.

The experimental program was centered around four experimental cores in which the majority of neutronic parameters of Advanced water reactors loaded at MOX-100% were measured, and for which the moderating ratio is increased with respect to that of standard PWR currently in operation in France. The cores were the following:

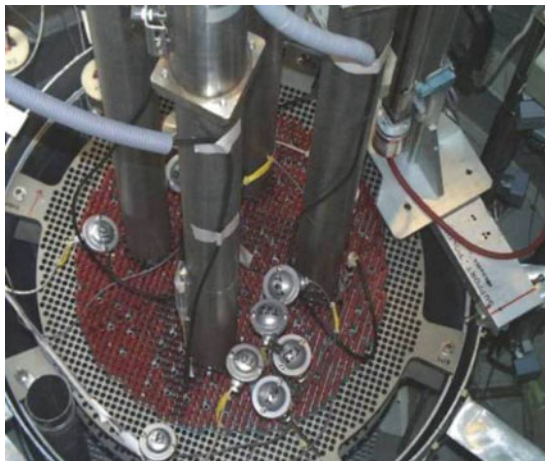
- MISTRAL-1: This involved a core with a moderating ratio of approximately 1.8 (H/HM ratio ~ 5.0) loaded with UO_2 rods with 3.7% ^{235}U . This core was used as a reference for cores at 100% MOX (► *Fig. 9*).
- MISTRAL-2: This involved a core with a moderating ratio of approximately 1.8 (H/HM ratio ~ 5.0) loaded with MOX rods at 7%.
- MISTRAL-3: This involved a core with a moderating ratio of approximately 2.2 (H/HM ratio ~ 6.0) loaded with MOX rods at 7%.
- MISTRAL-4: This involved a mock-up core in which a certain number of advanced PWR assemblies were simulated. The lattice pitch was set at 1.32 cm so as to increase the moderating ratio with respect to a standard PWR and thus approach the design of advanced PWRs able to recycle 100% of MOX fuel. The moderating ratio for this core was approximately 2.1 (volume) (► *Fig. 10*).

The MISTRAL program allowed experimental results, never conducted so far, to be obtained. Their analysis through calculation allowed trends on nuclear data libraries to be obtained and calculations to be modeled.

The implementation and improvement of the measuring technique proposed by Nakajima (JAERI) helped obtain the conversion rate modified in MOX and UO_2 rods in fundamental mode at better than $\pm 2\%$. The ^{238}U capture rate shows a slight overestimation in JEF2.2, which seems to increase with the moderating ratio.



■ **Figure 9**
View of the MISTRAL-1 configuration



■ **Figure 10**
View of the MISTRAL-4 configuration

The measurement of the bucking parameter in the MISTRAL allowed it to be confirmed that the UO_2 multiplication factor was overestimated (problem with the ^{235}U capture section in the resonance range in JEF2.2) and also overestimated in the MOX.

The installation of a thermoregulation lattice on the EOLE reactor enabled measurement of the isotherm temperature coefficient between 10 and 80°C in the MOX and UO_2 lattices with very good precision. The measured temperature coefficient allowed it to be concluded that in UO_2 , the calculation perfectly reproduces the measurement and the entire temperature range as well as the 10–40°C range for MOX. However, between 40 and 80°C, underestimation is observed in the MOX lattices.

The differential worth of the soluble boron was measured around the critical value at $\pm 5\%$. The full worth was also measured in a critical CB Boron concentration at critical CB + 600 ppm. Measurements show that this worth is almost linear with the quantity of boron.

The fraction of delayed neutrons was measured with the neutron noise method at better than $\pm 3\%$ in the MOX and UO_2 lattices. The fraction of delayed neutrons is well reproduced in the MOX by APOLLO-2 and the CEA93 library with a tendency for slight overestimation in UOX.

MISTRAL enabled distinct improvement of precision on central absorber rod reactivity effects ($\text{UO}_2\text{-Gd}_2\text{O}_3$, AIC, natural B_4C and enriched B_4C representative of PWR) as well as related fission rate distributions with respect to measurements carried out in EPICURE.

In the same respect, the MISTRAL-1 lattice was taken advantage of to conduct a short program (MIRTE) to study the negative reactivity of erbium within the wider scope of the EROINE program.

Due to a relatively large lattice pitch, the MISTRAL-3 core enabled simulation of a zone drained at 100% in a 100% MOX lattice to be carried out. The reactivity effects and distribution of radial and axial fission were carried out with very high precision. The drainage effects

in MISTRAL-3 are reproduced very well by APOLLO-2 (reactivity effect and power distributions). As for APOLLO-2, calculations showed some deficiencies linked to the lack of aluminum self-shielding and weaknesses linked to the implementation of condensation/homogenization techniques.

The MISTRAL-4 core allowed for simulation of an advanced PWR with increased moderation and loading to 100% MOX. In particular, a systematic study of rod assemblies representative of 24 absorbers was undertaken (natural hafnium, Ag-In-Cd, natural B₄C and enriched B₄C rods). Thus, it was possible to assess their relative and absolute worth as well as related fission rate distributions.

The enriched B₄C 24 rod cluster (90% ¹⁰B and 70% theoretical density) was studied both in a 100% MOX assembly and in a UO₂ assembly. This experiment allowed comparison of worths and related power distribution map.

3.3 The BASALA Program

The international BASALA program, conducted between 2000 and 2002 in collaboration with the Japanese organization NUPEC, and the COGEMA was accompanied by Japanese studies on cores loaded at 100% MOX in boiling water reactors (9 × 9 rod assemblies). Two cores in particular were studied:

- The BASALA H core representative of a 100% MOX advanced boiling water reactors (ABWRs) core in hot operating conditions (190°C, 75 bars, 42% average void fraction).
- The BASALA C core representative of a 100% MOX cold ABWR core (0% void fraction and T = 20°C).

Each core was the subject of several configurations allowing neutron parameters representative of a nuclear reactor to be studied, for 100% MOX BWR assemblies:

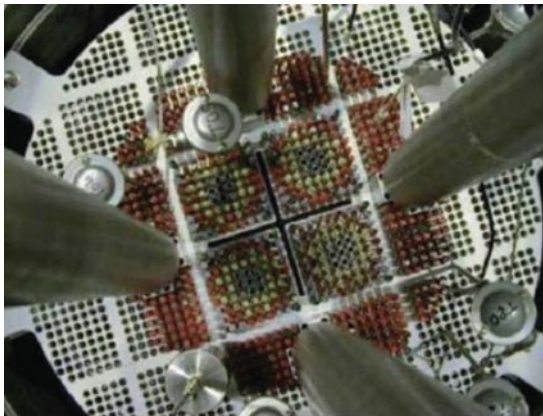
- In reference conditions
- In the presence of burnable poisons
- In conditions simulating strong drainage rates
- In presence of absorber control cross (B₄C and/or Hf) with fuel substitutions

The objectives in terms of target uncertainties were reached and calculation results also generally reproduce the experiment well. Thus, it can be noted that:

- BASALA cores were perfectly characterized in terms of reactivity: reactivity effects of heterogeneities were assessed at better than 6% (1σ) and Monte Carlo calculations reproduce these various effects very well.
- More than 1,200 rods were the subject of gamma spectrometry measurements with an experimental uncertainty of ±1.0% to ±1.7% (1σ) both in reference cores and disturbed cores: Monte Carlo codes reproduce power distribution maps measured at better than ±1.4%.
- The reactivity effect of metal Hf and natural B₄C control crosses was measured in the BASALA-C configuration and are of the same order of magnitude (therefore in cold conditions).
- The temperature coefficient in BASALA-C without absorbers is positive till 30°C.



■ Figure 11
View of the BASALA-H/REF configuration



■ Figure 12
View of the BASALA-C/REF configuration

- The full reactivity effect of soluble boron is almost linear between 0 and 600 ppm in the reference BASALA core (➤ [Figs. 11](#) and ➤ [12](#)).

3.4 The ADAPh Program

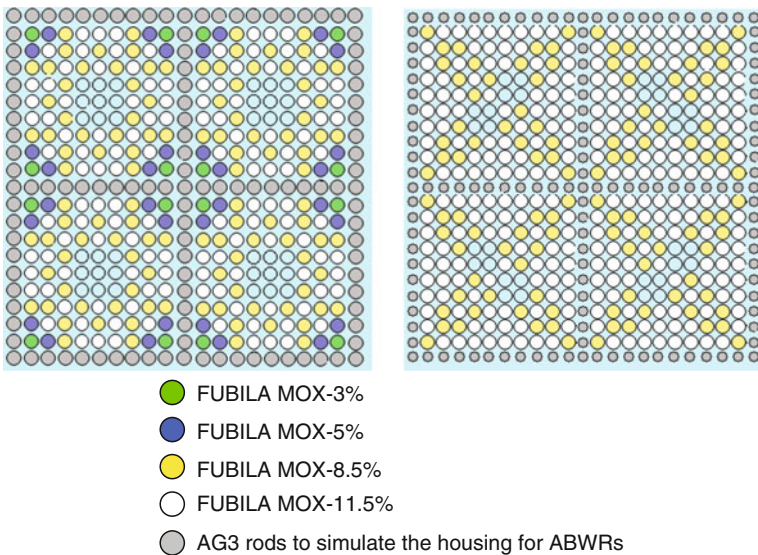
In 2004, from January to April, the ADAPh program (*Amélioration des Données de bAse Photonique – Photonics Basic Data Improvement*) was used to support qualification of the HORUS-3D-P tool intended to calculate photon heating of Jules Horowitz's Reactor systems. It will be used as a support element during presentation of the Preliminary Safety Report (PSR) closer to 2008.

However above all, the objective of the ADAPh program was the qualification of the thermoluminescence technique for the future AMMON experimental program. The targeted objective, which is quite ambitious, is to ensure approximately 15% (2σ) precision on heating calculations. Currently, precision linked to basic data is estimated at 30% (2σ). Precisions obtained on gamma dose rates in measured positions are approximately 7% (at 1σ). The techniques used are explained in the chapter on gamma heating measurements.

3.5 The FUBILA Program

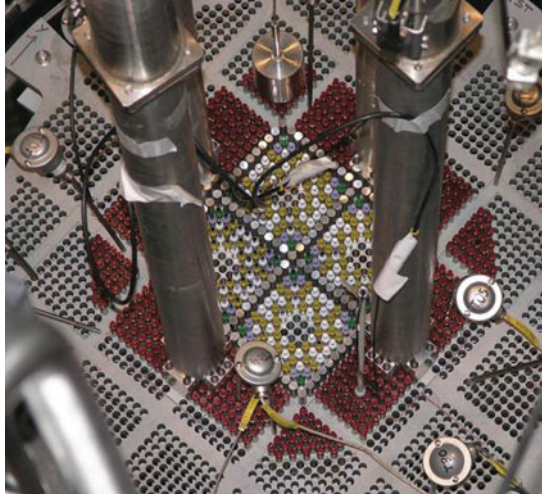
The main objective of the FUBILA experimental program is an experimental database to accompany the validation of codes related to the design of high combustion rate ABWRs, recycling plutonium. Its main characteristic is the increased representativity allowed by the implementation of BWR geometry rods (larger diameter than PWR) and higher plutonium contents.

The FUBILA program is dedicated to the study of 9×9 and 10×10 100% MOX assemblies with high combustion rates and increasing void fractions: 0, 40, and 70%. The void is modeled through the addition of aluminum cylinders inserted between fuel rods or through an AG3 solid block in which rods are inserted (🔍 [Fig. 13](#)).



🔍 **Figure 13**

Central patterns of REF (0% void – on the left) and 10×10 (40% void – on the right) experimental zones: FUBILA MOX-3%, FUBILA MOX-5%, FUBILA MOX-8.5%, FUBILA MOX-11.5%, and AG3 rods to simulate the housing for advanced boiling water reactor (ABWRs)



■ **Figure 14**
FUBILA/REF core

This program, which was centered around eight main cores, was carried out in EOLE between January 2005 and September 2006 (► [Fig. 14](#)).

3.6 The FLUOLE Program

3.6.1 Reason for the Program

In current PWRs, peripheral assemblies comprise an approximately 2-cm thick steel baffle located between the fuel rods and the barrel (a relatively thick moderator zone is also present between the baffle and the barrel).

If a water reflector slows down the neutrons directly through elastic scattering on hydrogen atoms, the baffle's steel behaves more like a spectrum adaptation zone by slowing down fast neutrons into epithermal neutrons, through inelastic scattering on the steel's constituents. These inelastic sections are not known very well and the energy field concerned has been studied little in water reactors as main reaction rates are produced in the thermal (fissions) and epithermal (captures in resonances) field.

Thus, the calculation of these inelastic slowing phenomena and consequently the calculation of the reflector gain is marred by high uncertainties for which CEA does not have experimental results in representative situations in order to qualify both the calculation tools and basic data libraries.

The fluence and damages suffered by the reactor tank are limiting factors for the service life of nuclear power plants and they should be evaluated. In this perspective, there are a certain number of capsules containing specific irradiated materials in a zone near the PWR tank (depending on the type of bearing). The analysis of detectors arranged in these capsules allows the fluence received by the capsule to be determined using neutronic calculation results; then, the calculation allows fluences and damages on the tank to be estimated.

As indicated above, several types of materials are located between the core assemblies and the reactor tank. These include the steel baffle (22.2-mm thick), a water area, the reactor barrel (approximately 5 cm), another water area, the thermal shield, a third water area, and finally the detector holder, which contains capsules in a water area, then the tank.

Furthermore, the thermal shield and the detector holder are not present on the entire periphery of the core and the peripheral part of the core is not cylinder-shaped. Consequently, the tank does not undergo the same fluence everywhere and capsules are not necessarily representative of the whole.

Analysis through the calculation of capsule detector reaction rates indicates deviations ranging between 10 and 15% depending on the type of reaction in question. Consequently, the fluence undergone by the tank is marred by a relatively high bias.

- The source of neutrons in the fuel itself (distribution, fission spectrum)
- The cross-sections of the various materials located between the fuel and the tank
- The cross-sections of detectors
- The model used in the calculation

In order to determine the contribution of each parameter to the bias and be able to draw leads to reduce such bias more accurately, the decision was made to define a targeted experimental program implementing several “steel/water” sandwiches located at various distances from the core and to measure the reaction rates provided by the detectors at activation covering the same energy field as those used in the irradiation capsules.

This FLUOLE program provides significant information for the validation of the TRIPOLI 4 (Monte Carlo Transport Code) scheme for the tank fluence of PWR 1,300s, for which there is currently no experimental data, as the water-steel distributions are different than those for PWR 900s. This scheme should be in use when the Safety Authorities assess files which EDF (French Nuclear Operator) will present to obtain the authorization to extend the service life of PWR 1,300s beyond 40 years. At this time EDF will no longer have any (or very little) margins on fluences with respect to those of design. The scheme must therefore be perfectly validated in terms of centered values hence the potential determination of bias by comparison of calculations/measurements and uncertainties.

3.6.2 Characteristics of the FLUOLE Program

One of the characteristics of this experiment is the possibility of simulating several azimuths around the EOLE core and of obtaining precise measurements for different neutron energy levels through specific instrumentation depending on water and steel thicknesses. They will also be conducted through fission chambers and through dosimetry per activation. The latter is adapted to obtain maximum information on the neutron spectrum and its distortion in water-steel leafing.

Collaboration with the CEA laboratories specialized in measuring very low activities will allow results obtained through dosimetry in these high attenuation neutron fields to be compiled. In addition, measurements taken through gamma spectrometry on EOLE rods will allow precise characterization of sources for the calculation.

It led to introduce into EOLE a 29×29 cell PWR type square core containing 3.7% ^{235}U enriched UO_2 fuel rods with Zy-4 cladding and placed under AG3 double-cladding in order to



■ **Figure 15**
Core structures during mounting and adjustment

obtain a moderating ratio representative of PWRs on the spot (identically to EPICURE where the over-cladding was 0.5-mm thick).

Four control/safety rods are placed in the corners of this square and a pilot rod is required to control the reactivity around the criticality. This is obtained by boric acid dilution in the moderator.

The water-steel leafing encountered in PWR between the core and the tank (baffle, barrel, and thermal shield) is simulated by a 22.2-mm thick stainless steel baffle (identical to that of PWRs) one part in stainless steel with a 1/2 cylinder shape and another part in stainless steel with a 1/2 cylinder shape with a different radius.

A schematic diagram of this configuration is shown in ➤ [Fig. 15](#).

Measurements were specifically dedicated to measure the flux using activation detectors such as ^{115}In (fast flux > 1.3 MeV), ^{64}Zn (fast flux > 2.8 MeV), ^{27}Al (fast flux > 7.3 MeV), ^{197}Au , and ^{55}Mn (thermal and epithermal flux). Reaction rates were carried out on representative cross-members (for example the two diagonals) in all the core materials (fuel, reflector, baffle, barrel, and thermal shield). Miniature fission chambers enabling access to the fission rate of specific isotopes (for example, ^{237}Np , fast flux representative of DPAs; ^{235}U , thermal flux) were also implemented.

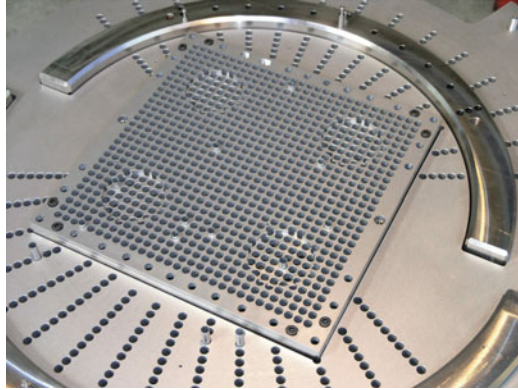
The FLUOLE program took place on EOLE between October 2006 and June 2007 (➤ [Fig. 16](#)).

3.7 The PERLE Program

3.7.1 Reason for the Program

Currently, all experimental programs conducted at CEA, and particularly at EOLE, have only implemented cores with moderator at their periphery (borated water reflector or not).

Current design studies for the EPR reactor use a thick stainless steel reflector, generally called “heavy reflector,” instead of the standard baffle and the water located between the baffle and barrel, in order to limit the fluence suffered by the tank and to improve the reflection of fast neutrons.



■ **Figure 16**
FLUOLE Upper grid with core mini-grid mounted

This concept emphasizes even more the inelastic diffusion phenomena mentioned above and leads to quite different reflector gains than those obtained with a water moderator. A targeted experimental study will help obtain necessary information on reflector gains and neutron attenuation in the heavy baffle. Effects on the power distribution map (switches) should also be assessed.


In addition to the “neutronic” effects, all the materials located between the assemblies of the core and the tank undergo a very high rate of irradiation through gamma rays, which contributes notably to their heating through energy deposit. This phenomenon is predominant for heavy reflectors for which there are currently water channels for cooling. The quantity, dimension, and location of cooling channels are strongly tied to the amount of γ radiation deposited. An in situ measurement is required to validate the design calculations.

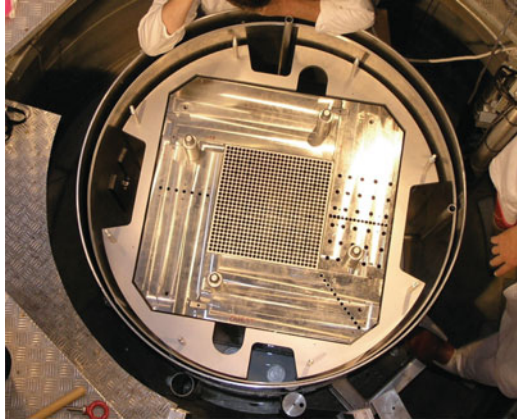
The PERLE program (*Programme d’Etude de Réflecteur Lourde dans Eole* – Heavy Reflector in Eole Study Program) is intended for the qualification of calculation tools used for the EPR reactor and specifically to assess the calculation errors linked to the presence of the steel reflector around a PWR rod zone.

3.7.2 PERLE Program Characteristics

In order to maintain certain consistency with FLUOLE, it was considered of interest to define the common lattice (pitch, size of the over-cladding). Thus, it will involve introducing into EOLE a 27×27 cell (instead of 29×29 in the FLUOLE program) PWR type square core containing 3.7% ^{235}U enriched UO_2 fuel rods with Zy-4 cladding and placed under AG3 double-cladding in order to obtain a moderating ratio representative of PWRs on the spot.

Likewise, the four control/safety rods will be placed in the corners of this square and a pilot rod will be required to control the reactivity around the criticality. This will be obtained by diluting boric acid in the moderator.

A schematic diagram of this configuration is shown in  [Fig. 17](#).



■ **Figure 17**
Schematic diagram of the PERLE configuration

The experimental program took place in two phases of approximately 5 and 3 months during which the physics phenomena linked to the presence of the steel heavy reflector is investigated in detail (determining the reflector gain, neutron propagation within the reflector, gamma heating, etc.) with the aim of reducing uncertainties on cross-sections of steel constituents. The program is structured around two different core configurations.

The Homogeneous Configuration

The PWR regular lattice core with homogeneous reflector constitutes a first step in generating an experimental database related to the qualification of the steel reflector concept. This core will enable:

- Qualification of the reflector gain calculation
- Qualification of the core/reflector interface calculation
- Qualification of the neutron flux with intermediary energies in the reflector
- Assessment of the induced gamma heating in the steel
- Reduction of uncertainties on nuclear data and quantification through a TRIPOLI-4 standard calculation
- The feed-back return on the JEFF-3.1 data library assessment

Configuration with “EPR Type Reflector”

The final step, based on the parametric approach that is used for years in designing a full qualification program, comes after an intermediary step where, *a minima*, local heterogeneities of the heavy reflector must be reproduced in a representative manner, which can be easily done. For this reason, the reflector was redesigned in order to take into account the presence of water channels on one side of the core. Thirty-five holes with 13-mm diameters (● [Fig. 17](#)) are drilled into the block and plugged with steel mandrels to ensure sealing and homogeneity of the matter during the “homogeneous steel reflector” phase. When switching onto the configuration with



■ Figure 18

View of the block with water channels, plugged by steel mandrels (homogeneous configuration)

water channels, these mandrels are removed allowing the water to penetrate into the heavy baffle (► Fig. 18).

The scientific interest of this type of configuration is different from the configuration with a homogeneous reflector. Here it involves directly measuring the neutronics parameters impacted by the presence of said water channels, which locally generate over-moderation that is unfavorable to the reflector gain (increased thermalization of neutrons in the steel followed by absorption).

Here, the predominant measurements, other than the critical size, which will give macroscopic information on the reactivity effect of water channels compared to the homogeneous case, will be the neutron flux and gamma heating cross-members coupled with measurements by different threshold fission chambers.

The effects of water channels on the critical size and also on the local distribution of fine rod/rod power are significant. The last design calculations carried out using TRIPOLI-4, showed the following effects:

- The effect on the k_{eff} is 300 pcm, measurable with excellent accuracy through the adjustment of the configuration's boron concentration. This effect is equal to a reduction of the boron concentration by approximately 27 ppm, measured with 0.1 ppm (0.5%) precision.
- The effect of flux distribution in the heavy baffle at the mid-height plane of the core is clearly visible in intermediary regions ($E_n > 100$ keV) and in the thermal field ($E_n < 1$ eV). The disturbance generated is approximately several tens of percents in the zones where the water holes are concentrated, much higher than measurement precisions by fission chambers (1%) or by dosimeters (2–3%)
- The effect on flux distribution in the first rows of fuel is between 5% for the first row and approximately 2% at the fifth row, much higher than the precision of measurements by γ -scanning (1%).

In addition to the points previously mentioned for the configuration with homogeneous reflector, this configuration will enable:

- Qualification of local heterogeneity effects in the calculation of the reflector gain, in terms of reactivity but also in terms of neutron and photon spectrum disturbance, as shown in the previous figures
- Determination of the reflector's gamma heating with channels
- Calibration of a reference deterministic model for this simplified case with water channels
- Recommend new industrial calculation schemes and methods and deduction of methodological biases

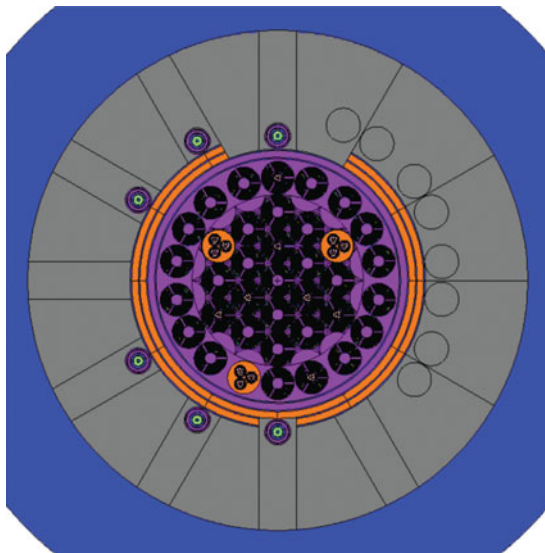
The PERLE program took place between July 2007 and June 2008.

3.8 The AMMON Program and the Jules Horowitz Reactor

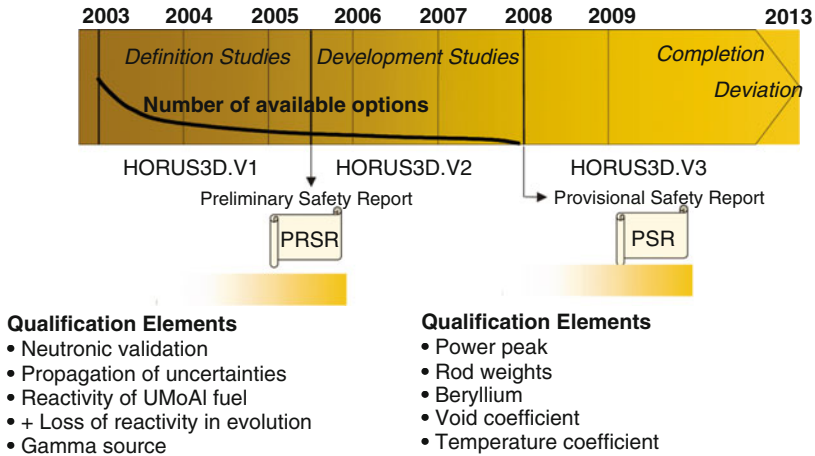
EOLE provides experimental qualification information as part of the design of the Jules Horowitz reactor (JHR) and the development of the *HORUS3D* form (🔗 *Fig. 19*).

In particular, qualification of the UMoAl type fuel intended for the JHR led to:

- A test program conducted on MINERVE in 2003 to specify the UMoAl basic neutron data (reactivity, reaction rate): *VALMONT* program.
- A more in-depth program to qualify all the neutronic characteristics of the JHR core, on EOLE: *AMMON* program. This last program on EOLE should provide a set of calculation tools needed to design the JHR.



📌 **Figure 19**
Radial cross-section of the Jules Horowitz reactor (JHR) core



■ Figure 20

JHR definition and development process procedure, associated with safety and qualification deadlines

Qualification of the HORUS3D neutronic form must accompany the requirements related to the basic design of JHR, separated into two phases: definition and development (► Fig. 20).

The elementary qualification experimental requirements for the preliminary safety report (PRSR) are covered by the following experimental programs: VALMONT, ADAPh, and IRIS- γ . Specific qualification elements are required to draft the Preliminary Safety Report (PSR).

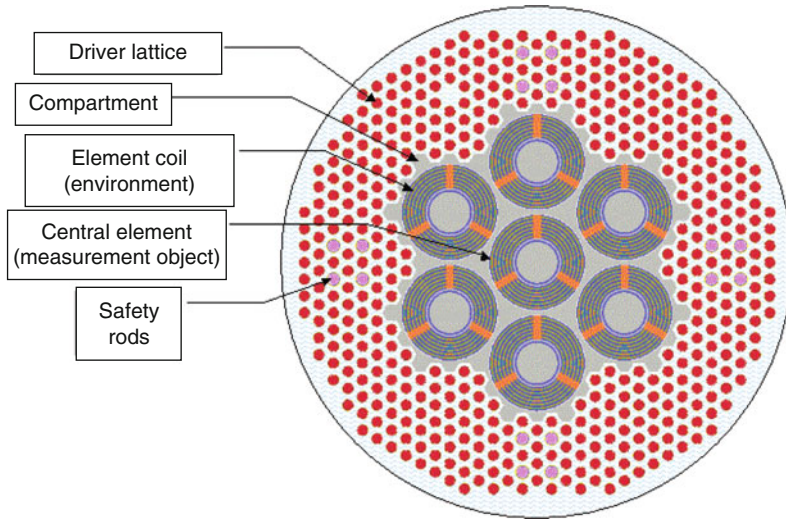
The measurements for this program first aim at demonstrating the control of significant safety aspects. Therefore, the experimental objectives involve:

- The reactivity of a JHR assembly
- The fine distribution of power in the assembly
- The reactivity effect of absorbers (Hf control rod, borated stiffeners)
- The effect of experimental systems in reactivity and in terms of power distribution
- The reactivity effect of the Beryllium reflector and the spectrum in and near the reflector
- The void and temperature reactivity coefficients

The reference configuration for the AMMON experiment comprises seven JHR type assemblies, arranged in a hexagonal lattice inside an aluminum compartment. This housing is surrounded by a hexagonal lattice with diameter 19.2 cm, comprising approximately 415 EPICURE type UO₂ rods (3.7% mass enrichment). The pitch for this lattice is 1.40 cm in order to create a full subdivision of the hexagonal pitch for JHR assemblies and then facilitate the adaptation of the two geometries.

The schematic diagram for the reference configuration is shown in ► Fig. 21.

During the feasibility phase for the JHR project, the decision was made for the structuring option not to create a critical mock-up of the core for the JHR facility identical to the ISIS mock-up for the OSIRIS reactor. Within this framework, an operating mode for the JHR (“low power



■ Figure 21
Schematic diagram for AMMON configuration

mode”) was simply maintained, open on the cavity, for which the low power can be evacuated through natural convection.

The inconveniences of this mode are that it does not allow all the functions accessible on a core mock-up such as ISIS to be recreated, and that it is also used to the detriment of the operation of the powered core (reduced availability of the facility for neutron production).

The low power operating mode for JHR (“mock-up mode”) is, by definition, representative of the core + reflector geometry. It allows irradiated fuels to be measured, rods to be weighed or other objects inserted into the core to be measured. However, use of this mode has the following limitations:

- The use of soluble poisons in the primary coolant is not foreseeable; consequently, all the positions of regulating and shim rods are not accessible in the core
- At this point in studies, the possibilities of core fine instrumentation in mock-up mode have not been checked; given the presence of other internal core structures, instrumentation could be less flexible with respect to the case of a critical mock-up
- This mode is used to the detriment of the core’s power operation

The interest of EOLE for the JHR lies in the possibility of conducting full semi-analytical experiments (representative of a given pattern) in critical mock-up, in order to qualify HORUS 3D calculation forms in neutron or photon mode.

This activity is of significant interest from the start of the design phase and is worth being developed during the operation of the JHR: improvement of calculation reconstruction accuracy, ability to experimentally test or check (transparently with respect to the operating load of the JHR), local layouts which are difficult to understand through calculation alone, etc.

3.9 MOX Powder Criticality Requirements

An important meeting of experts organized by OCDE/NEA took place in April 2004. This meeting pinpointed the international lack of full critical experiments as being representative of highly under-moderated MOX powders. This problem is particularly raised for the safety-criticality file for various stations at MELOX (100% PuO₂ jars, UO₂-PuO₂ master batch at 30% Pu, final MOX and pellets up to 12.5% Pu).

In EOLE, it is possible to build homogeneous cores using enough MOX 27% Pu rods to reach the criticality of the support block (approximately 2,500 rods).

Two cores are foreseeable with moderating ratios (V_m/V_{comb}) of 0.3 (MOX master powder simulation at 30% Pu) and 0.6 (MOX 12% Pu final mixture simulation), respectively.

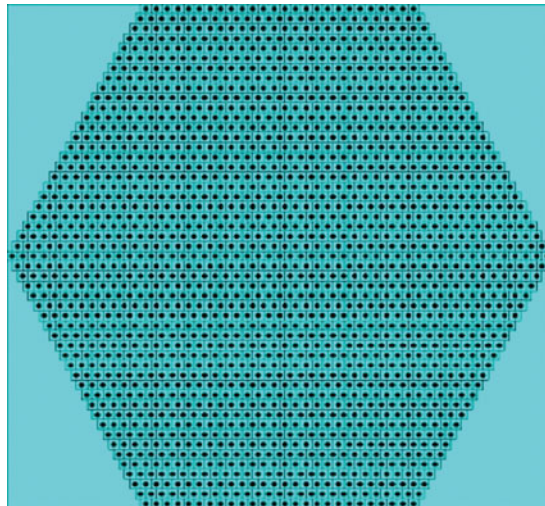
The following would be measured in both the configurations:

- The critical size
- The fission rate axial and radial cross-members
- The spectral indexes
- The temperature coefficient of the moderator between 10 and 80°C

These experiments would allow the uncertainty on the k_{eff} of primary and final powders to be greatly reduced through a breakdown of the various terms in the neutron balance (► [Fig. 22](#)).

3.10 Criticality at Loading

In 2001, an “incident” occurred at the Dampierre plant during the new assembly loading phase. The mistake of loading a specific assembly led to the introduction of several new



■ Figure 22
Schematic diagram of a POWDER configuration

assemblies in the same zone of the core and thus the approach to the criticality. This phenomenon was only detected by a small part of ex-core chambers and only at the end of the phase.

At the request of EDF, several simulation calculations for this loading phase were carried out at CEA to determine the subcriticality level of the core and the response rate of ex-core detectors depending on the time to see if there was the possibility of detecting earlier that there was a loading error.

Beyond the analysis of the Dampierre incident itself, it was observed that the responses provided by ex-core detectors of a power reactor depend greatly on the source of neutrons and therefore on the combustion rate of each core assembly and their position in relation to detectors.

Each situation is therefore very specific and consequently difficult to “model” through an experiment in EOLE. It seems that it would be much more sensible to first correctly assess the neutron source of the core for each loading step through calculation.

Next, ex-core detector responses must be modeled through calculation.

The EOLE reactor could contribute to providing a qualification basis for these models thanks to the “Multiplication of Neutron Sources” type measurement method in subcritical status, provided that:

- The subcriticality level of a core can be easily measured by the MSM method (this requires first calibrating the reactivity scale with respect to a well-known effect, for example, the pilot rod). A core containing MOX rods would be implemented in order for there to be an inherent source in the core.
- Several types of reactivity disturbances can therefore be simulated by the drop of one or several control rods, removal or addition of a sufficient number of different types of rods simulating one or several assemblies inserted or removed from the core in various areas of the core in order to vary the reactivity and/or source of neutrons. Furthermore, the soluble boron in the moderator may be used as a standard of reactivity introduced or removed from the core.

Interpretation of experimental results will allow qualification of models capable of both predicting the variation of the multiplication factor at almost constant source and at modified source as well as the detector responses in various situations. It should however be emphasized that this experiment would not be fully representative of the loading phase for a PWR.

3.11 Plutonium and High Combustion Rate Control. EPR Support

In France, plutonium control is aimed at maintaining the plutonium in the fuel's cycle and stabilizing the total inventory associated with operating the fleet over time. Plutonium mono-recycling practiced currently in the form of cores at 30% MOX fuel in PWR-900s could end up being insufficient to stabilize the inventory. Furthermore, the decision to remove irradiated MOX fuel would initially pave the way for multi-recycling in water reactors.

A need was identified for experimental programs to ensure qualification coverage of calculation tools beyond the current limit and to respond in part to new concepts.

Mock-up experiments in EOLE with highly enriched UO_2 fuel with 4.95% ^{235}U and MOX 12% fuel cores (high Pu load, multi-recycling and deteriorated Pu) could provide answers.

17×17 PWR type assembly simulations with UO_2 fuel enriched at 4.95% ^{235}U or MOX fuel enriched at 12% Pu with a 1.26 cm lattice pitch could be carried out in an EPI-CURE UH1.4 configuration type concept. The square critical contour will allow the size of the core to be increased by increasing the radial leaks. Measurements carried out using experimental techniques will be directly influenced by the key parameters of these new concepts:

- Reactivity of the core and the MOX lattice (k_{eff} , buckling).
- Fraction of delayed neutrons, life of prompt neutrons.
- Efficiency of B_4C , AIC, enriched B_4C , Hf control clusters.
- Efficiency of Pyrex, $\text{UO}_2\text{-Er}_2\text{O}_3$ burnable poisons.
- Efficiency of $\text{UO}_2\text{-Gd}_2\text{O}_3$ burnable poisons (with more Gadolinium enrichment on an enriched ^{235}U support for long campaigns).
- Soluble Boron differential worth.
- Moderator temperature coefficient (isotherm).
- 2D and 3D and total drainage void coefficient.

These programs would be associated with recent needs of utilities to launch a high burn-up (Haut Taux de Combustion, HTC) program to broaden the qualification of neutron calculation tools (60 GWj/t UO_2 and MOX parity) in order to introduce HTC fuels during future decennial inspections. The ALLIANCE program can be alluded to along with the study of EPR assembly with burn up above 60 GWj/t.

Likewise, mixed loading cores covering the 50% MOX situation planned in EPRs should probably also be built.

Naturally, it is true that EOLE can be used to support the qualification of deteriorated Pu recycling and standard geometry type assemblies (17×17 CORAIL design), comprising standard geometry rods (^{235}U enriched UOX rods at the center and MOX rods on the periphery of the assembly with a proportion of approximately 30% per assembly). From a design very close to the current standard, it is ready to be industrialized.

The short-term implementation prospects for multiple recycling of plutonium in reactors of the fleet in operation, therefore, rely on quick industrial qualification of CORAIL for introduction into reactors of the current fleet.

If CORAIL can be brought to mind for the relatively short term, in the long term the Advanced Plutonium Assembly (APA) and DUPLEX (standard geometry APA variant) concepts, which would allow the plutonium stock to be reduced if necessary, would themselves also require that related calculation schemes be qualified on a representative experimental basis. Linked to these assembly and rod concepts (The small crosses of APA-PC can notably be brought to mind), Inert Matrix fuels represent interesting solutions in terms of innovation. Several inert materials are being studied to be used as a matrix; the choice of CERMET metal matrix fuels was selected. However, the lack of uranium leads to very penalizing control parameters and notably strong deterioration of the void coefficient, the effective fraction of delayed neutrons, as well as a loss of traditional control efficiency for which we will undoubtedly be asked for precisions.

Obviously, when evoking fuel irradiated fuel or even irradiated assemblies can also be studied even if the feasibility for using this type of fuel in EOLE must currently be obtained.

3.12 Support Program for CELESTIN Reactors

Ideas for an experimental support program for CELESTIN reactors were evoked in the following topics:

- The up-grade of neutron calculation codes
- Actions to support requests of the 2002 Safety commission linked to the refurbishment of the reactors and to maintain them in operation

A need to improve knowledge on the core reactivity of reactors should allow the management of fuel assemblies to be refined through reactivity measurements on EOLE.

3.13 An Experimental Platform

CEA-Research Reactors Division has renowned expertise in the area of reactor nuclear instrumentation (flux measurement, spectral index measurement, characterization of rods after irradiation, etc.). Fundamental work is underway on the expertise of measurement methods implemented and on the management and reduction of related uncertainties:

- Measurement of fundamental neutronic parameters such as: β_{eff} – fraction of delayed neutrons, Λ – neutron life, ρ – reactivity).
- Dynamic measurement techniques (frequential methods) based on Dating systems (real time neutron dating).
- Gamma spectrometry method (prospective search for more interesting peaks, capture study for certain actinides, and digital counting channel enabling work at high counting rates).
- Design of new fission chamber type sensor, back to back, new reference detector for absolute measurements (this item is part of dosimetry).

The aim of this action plan to control experimental uncertainties includes:

- Exhaustively taking into account sources of uncertainties
- Eventually achieving reduced and controlled uncertainties
- Reliably predicting uncertainties related to the physical parameters of an experiment

Furthermore, this instrumentation improvement project could be associated with an *instrumentation platform* where EOLE would be the core for developing new experimental techniques, which is currently a solution to overcome an important step in qualifying calculation schemes: it is also important to make an effort on experimentation as part of an effort to perpetuate and improve instrumentation and optimize the management of uncertainties.

Obviously, at the center of this experimental platform will be the X-MODE project, which is a true instrumentation and physical measurement system. Its aim is the development of this innovative measuring channel by implementing an instrumentation platform and active participation in the development of data acquisition, reduction, and analysis algorithms.

3.14 Support for Generation IV Reactor Concepts

A final line of research could be the qualification of calculation schemes supporting the generation IV reactor concept and notably HTRs (GT-MHR), hence the need for a neutron calculation tool qualified with the specificity of HTRs whose physics are completely different from those of water reactors.

A final line of research could be the study of light water supercritical reactors, again within the framework of the Generation IV forum.

3.15 Conclusions

Since its first criticality in 1965, EOLE has provided high-quality experimental programs recognized by all “customers” requesting experimental data to qualify their calculation schemes or to check the feasibility of new reactor concepts.

Conducting experimental programs for 20 years with the Under-Moderated Reactor-ERASME, PWR-EPICURE, RMA MISTRAL, and BWR programs with BASALA and FUBILA, in addition to selling experimental results, have enabled the facility to be profitable, allowed for continuous maintenance to uphold deadlines, and have maintained operating and safety teams, and especially reactor physicists at a high level of expertise.

These programs also enabled the upgrading and improvement of instrumentation and experimental measuring methods which make the facility competitive and of high quality.

Today, EOLE can offer new programs such as PERLE and FLUOLE in support of the EPR heavy reflector and the fluence of PWR tanks and sees a promising future; other programs of interest for industrial companies and CEA are on the horizon.

4 Description of the MINERVE Reactor

4.1 General Description

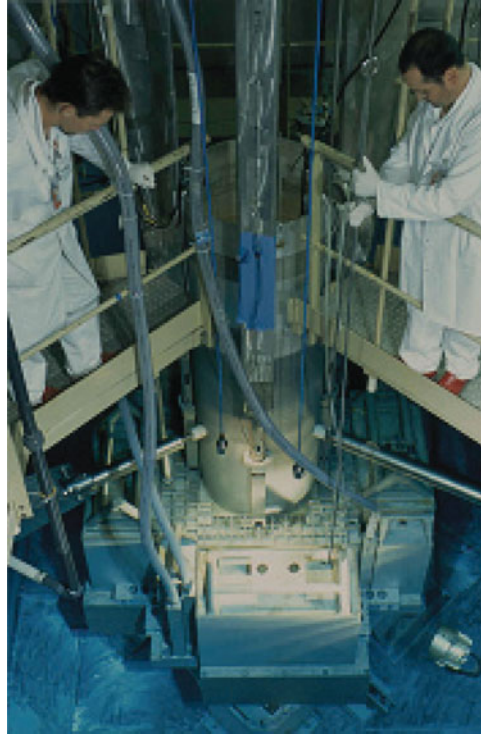
The reactor is built in a 120 m^3 rhomb-shaped stainless steel cavity. The moderator is ordinary demineralized water purified in filters and ion exchange resins. The core is submerged under 3 m of water and is cooled through natural convection. The maximum power is 100 W, which corresponds to a thermal flux of $10^9 \text{ n cm}^{-2} \text{ s}^{-1}$.

The core is divided into two zones:

- The driver zone comprises material testing reactor (MTR) type aluminum/uranium alloy plate assemblies, 3 m below water. It is surrounded by a graphite reflector
- The measuring zone receives experimental lattices introduced into a $70 \times 70 \text{ cm}^2$ cavity in the center of the driver zone. This experimental zone reproduces characteristic neutron spectra with light water lattices (MELODIE), fast RSMs (MORGANE-S and MORGANE-R), with sodium coolant (ERMINE), even heavy water (ELOISE)

The reactor is controlled using four hafnium rods operating both in control or safety mode.

The entire instrumentation and control system and the reactor control room, were renovated in 2002 (► [Figs. 23–25](#)).



■ Figure 23
Overall view of the MINERVE reactor

4.1.1 The Cavity

The reactor is built in a 4×5 m, and 6 m deep stainless steel rhomb-shaped cavity.

4.1.2 Driver Zone Fuel Elements

This involves MTR type fuel elements made up of 90 or 93% ^{235}U enriched aluminum-uranium alloy plates. These plates are aluminum plated and assembled in elements containing 9, 12 or 18 plates each.

4.1.3 The External Reflector

This comprises aluminum-plated graphite blocks. It allows the critical mass of the core to be reduced.

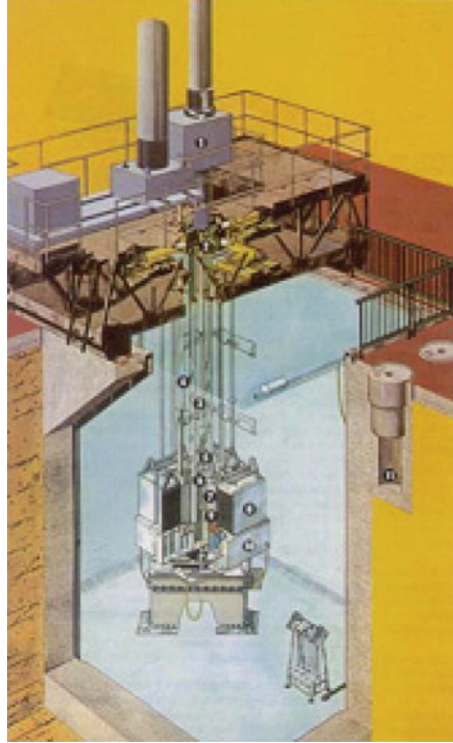
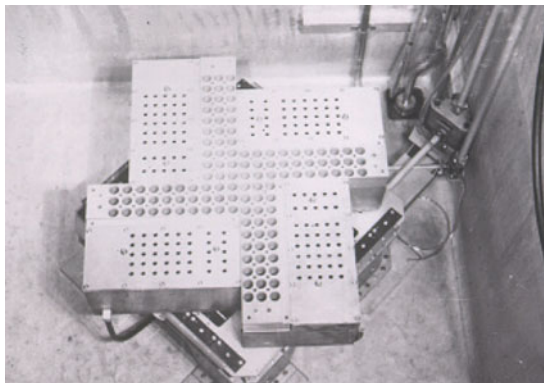


Figure 24
MINERVE artist drawing



Figure 25
MINERVE reactor control room



■ Figure 26
MINERVE reactor lower table and grids

4.1.4 The Central Cavity

The fuel elements and external reflector elements are distributed between four grids which can move simultaneously on the table supporting them along the two diagonals, by freeing a square at the center with sides which can vary between 0 and 900 mm (🔍 Fig. 26).

4.1.5 Control-Command

Neutron control is performed by two start-up channels and two high-level channels equipped with boron-lined fission chambers.

Command is provided by four identical control and safety rods, comprising two stainless steel plated natural hafnium plates, which slide to the center of a 93% ^{235}U enriched aluminum-uranium 12 plate fuel element.

The rods are coupled with the raising–descending mechanisms using electromagnets, which allow a drop through gravity to take place.

4.2 Advantages of the MINERVE Reactor

The main advantages of the MINERVE reactor lie in:

- *The precision of measurements* carried out through the oscillation technique with the aim of determining the reactivity weight of samples containing studied materials (dopant isotopes, alloys, irradiated fuels). The measurements guarantee reproducibility of approximately 1%, or an absolute uncertainty of approximately 0.1 pcm on samples with a reactivity weight of approximately 10 pcm. Eventually, after interpreting experiments, taking into account the uncertainty of measurement reproducibility ($\sim 1\%$), the uncertainty linked to the material balance of samples ($\sim 2\%$), and the uncertainty of modeling ($\sim 2\%$), an uncertainty of approximately 3% is obtained on the absolute reactivity weight of samples.

Currently, the oscillation technique alone allows reactivities to be determined with such precision. However, the CEA Valduc B equipment can also be mentioned as another experimental tool which allows reactivity measurements to be taken with excellent precision. This apparatus allows the reactivity of samples (liquid or solid) placed in the center to be determined through the rising water subcritical approach technique. The uncertainty on experiments, at approximately 100 pcm, however requires the use of samples corresponding to several thousand pcm, therefore containing large quantities of dopants. The result obtained is therefore no longer related only to the isotope studied in infinite dilution, and only isotopes available in large quantities can thus be used. Therefore, measurements carried out in the B equipment are complementary to those carried out in MINERVE: they represent industrial configuration geometries and do not constitute fundamental experiments.

It should be noted that MINERVE is the last reactor in the world in which oscillation experiments are carried out further to the shutdown of the UKAEA DIMPLE reactor. In the past, oscillation measurements were also carried out in the MARIUS, CESAR, and MASURCA reactors at CEA Cadarache. Furthermore, MINERVE is unique in that it carries out constant power oscillations, i.e., by maintaining the reactor critical through an automatic pilot rod. This technique is more precise and differs from that traditionally used, for example, in DIMPLE, which consists in monitoring and allowing the reactor to evolve (successive divergences and convergences) during oscillations, then in tracing the reactivity through occasional kinetic equations.

- *The flexibility in terms of neutron spectra:* It is possible to cover the full range of neutron spectra, from a very thermalized spectrum representative of a dissolver to a fast spectrum, passing PWR, PWR-MOX, BWR or epithermal type spectra. It is obviously possible to create experimental lattices adapted to future concepts (RCG, HTR) at the MINERVE plant.
- *The low cost of experiments:* Experiments are generally conducted in already existing core configurations, or which do not require the supply of new fuel, hence a low cost for experiments. The main cost stems from manufacturing oscillation samples which contain, due to the reactivity effect targeted at roughly 10 pcm, small quantities of materials and/or dopants (approximately 50 and 0.01 g give or take a few grams, respectively depending on the isotope) and therefore remain relatively inexpensive. These small quantities of dopants to be used often facilitate the feasibility of the experiment given the rareness of some of them, and allow selective integral information to be obtained with respect to the isotopes studied.

It can also be noted that a new safety calculation scheme was created in 2004. It relies on recent and qualified calculation codes: TRIPOLI4, APOLLO-2, and MCNP4C.

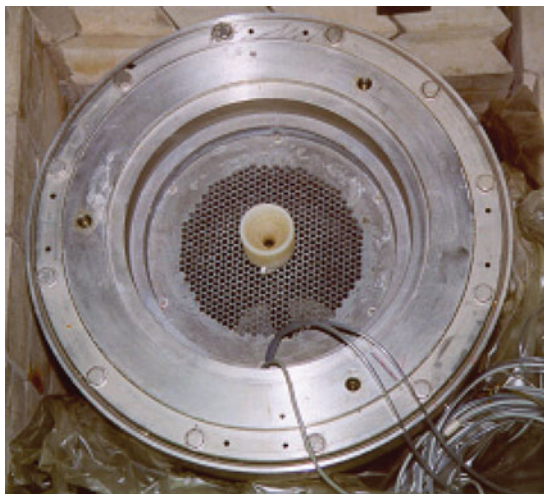
4.3 Coupled Assemblies

In order to obtain the most exhaustive possible qualification base for calculation forms, a wide range of neutron spectra can be used in MINERVE. The following experimental lattices have been designed using MELODIE (➤ Fig. 27), MORGANE (➤ Fig. 28), and ERMINE assemblies (➤ Table 1).

The moderating ratios and slowing down densities at the cut-off (at 2.77 keV) of the various light water experimental lattices are given in (➤ Table 2).



■ Figure 27
MELODIE assembly



■ Figure 28
MORGANE assembly in MORGANE-R configuration

■ Table 1

List of assemblies and configurations currently possible in MINERVE

Assembly	Experimental lattices	Neutron spectrum
MELODIE	R2-UO ₂	Dissolver spectrum
MELODIE	R1-UO ₂	UO ₂ PWR spectrum
MELODIE	R1-MOX	MOX PWR spectrum
MELODIE	BWR	BWR spectrum
MORGANE	MORGANE-R	RCVS type epithermal spectrum
MORGANE	MORGANE-S ^a	Closed RSM type epithermal spectrum
ERMINE	ERMINE ^a	Fast spectrum

^a Additional studies must be conducted for these configurations, concerning the adaptation zone between the driver zone and the center of the experimental lattice

■ Table 2

Moderating ratio and slowing down current ($E_c = 2.77$ keV) of light water lattices in MINERVE

Experimental lattice	V_m/V_f	q
R2-UO ₂	1.4	0.80
R1-UO ₂	1.4	0.60
R1-MOX	1.4	0.55
MORGANE R	0.9	0.35
MORGANE S	0.5	0.32

4.3.1 MELODIE Assembly Representative of Pressurized Water Lattices

General Description

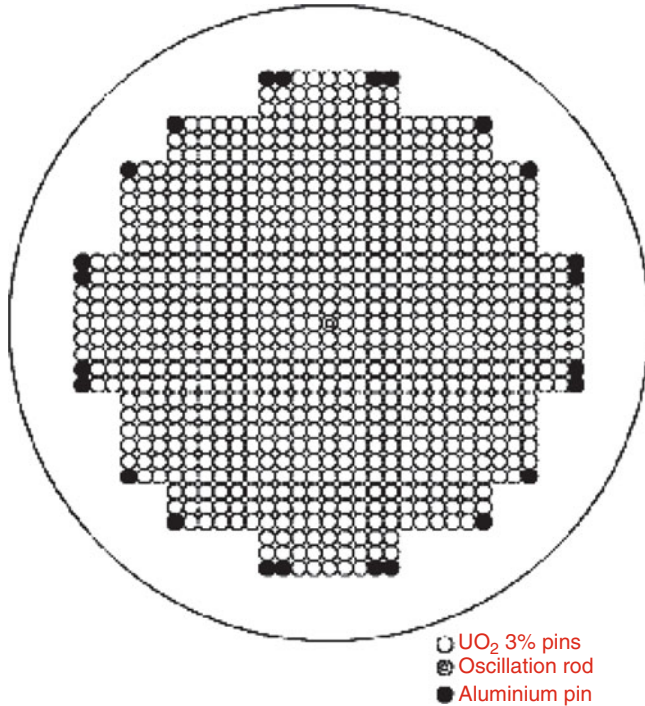
The MELODIE assembly (see ► Fig. 27) is a 71.2 cm diameter cylinder.

The center of the MELODIE internal structure comprises a lower grid and an upper grid made of aluminum, drilled with 801 holes with a pitch of 1.26 cm, connected by aluminum tubes ($\varnothing 0.970 \times 1.10$ cm) which are used as an over-shield for the fuel. This zone forms a cylinder with a diameter of approximately 40 cm.

On a stainless steel bottom plate, aluminum blocks are arranged sideways which, on the inside, follow the contour of the grids, and on the outside are turned to a diameter of 71.2 cm.

R1-UO₂ Lattice Representative of a UO₂-PWR Spectrum

The MELODIE R1-UO₂ lattice is representative of UO₂-PWRs. It was optimized to have the spectrum of a PWR in normal operating conditions at the center of the oscillation channel, but also on a wide area around the channel.



■ **Figure 29**
R1-UO₂ experimental lattice

In this configuration (see ► [Fig. 29](#)):

- Seven hundred and seventy-six cells contain a MINERVE II type ²³⁵U 3% enriched UO₂ rod (second manufacturing series of MELODIE rods)
- Twenty-four cells placed on the periphery of the lattice contain aluminum rods
- The central cell receives the oscillation rod

Numerous experiments have been conducted in this lattice. They showed the adequacy of the lattice for representation of a UO₂-PWR spectrum.

R1-MOX Lattice Representative of a MOX-PWR Spectrum

The R1-MOX experimental configuration (see ► [Fig. 30](#)) was optimized to represent a UO₂-PuO₂ fuel PWR lattice, allowing oscillation measurements to be taken in a MOX spectrum.

In this configuration, at the center of a lattice of MINERVE II type ²³⁵U 3% enriched UO₂ rods (584 rods), a 13 × 13 cell UO₂-PuO₂ assembly is formed including:

- One-hundred and twenty four central cells containing MINERVE III type UO₂-PuO₂ rods (third manufacturing series of MELODIE rods loaded with 4% Pu

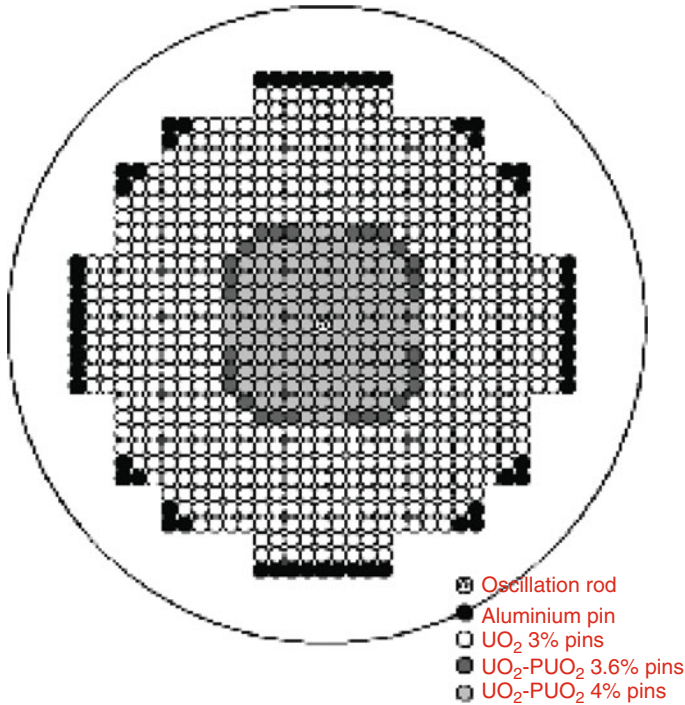


Figure 30
R1-MOX experimental lattice

- Twenty-eight cells around the periphery of the latter, containing MINERVE III type UO₂-PuO₂ rods loaded with 3.6% Pu and placed near the corners (simulation of MOX assembly zoning)
- One central cell for the oscillation rod

Previous experimentations conducted in this lattice proved the adequacy of the R1-MOX configuration to take measurements in a MOX PWR spectrum.

R2-UO₂ Lattice Representative of a Dissolver Spectrum

The MELODIE R2-UO₂ experimental lattice was optimized in order to represent the prevailing spectrum in a dissolver in the oscillation channel.

This configuration (see [Fig. 31](#)) is in the same form as R1-UO₂, with the exception of a 3 × 3 cell central water hole which allows the well-heated desired spectrum to be obtained in the oscillation channel. Seven hundred and sixty eight cells contain a MINERVE II type ²³⁵U 3% enriched UO₂ rod.

R2-UO₂ was used in 1996 and 1997 for burn up credit studies applied to a Reprocessing Plant dissolver and therefore proved its capability for taking measurements in a dissolver spectrum.

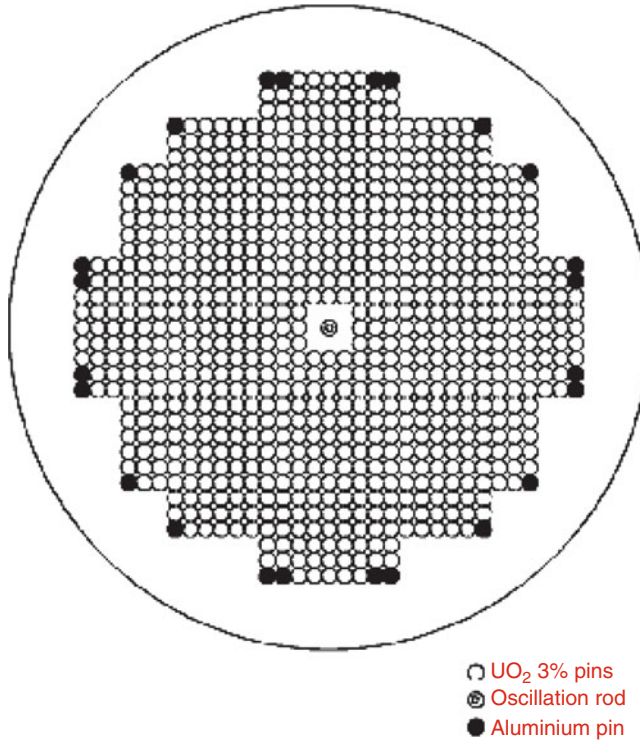


Figure 31
R2-UO₂ experimental lattice

BWR Lattice

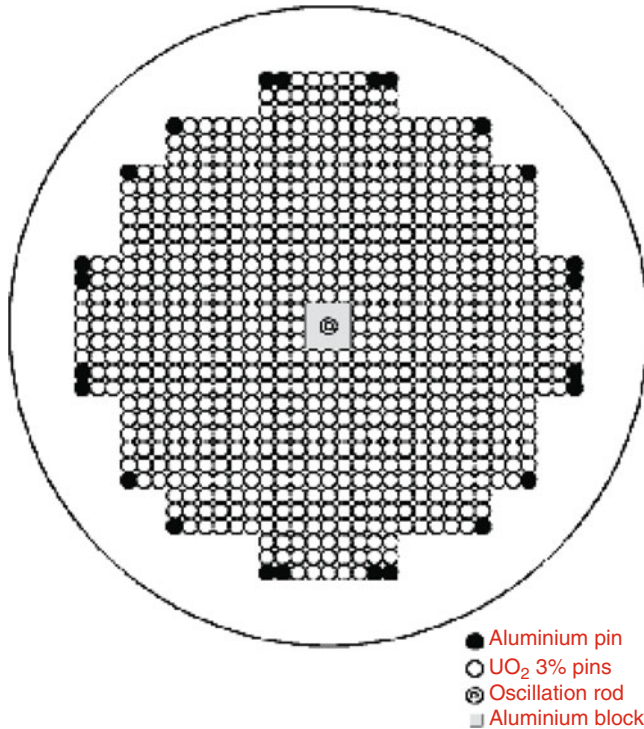
The BWR lattice (see ► Fig. 32) is identical to R2-UO₂, with the exception of its center comprising an $11.34 \times 11.34 \text{ cm}^2$ aluminum block (or equivalent to nine cells), drilled in the center with a 15.5-mm diameter channel.

The BWR lattice was used in 2000 and 2001 for burn up credit studies in the BWRs and therefore proved its capability for taking measurements in a BWR spectrum.

4.3.2 MORGANE Assembly for Lattices Representative of Under-Moderated Reactors (RSM)

General Description

MORGANE S and R lattices were optimized in order to conduct reactivity loss studies by cycle in Closed type (MORGANE S) and realistic MORGANE R type under-moderated lattices, corresponding to studies on RSMVS (spectrum variation and high conversion rate reactor) concepts.



■ Figure 32
BWR experimental lattice

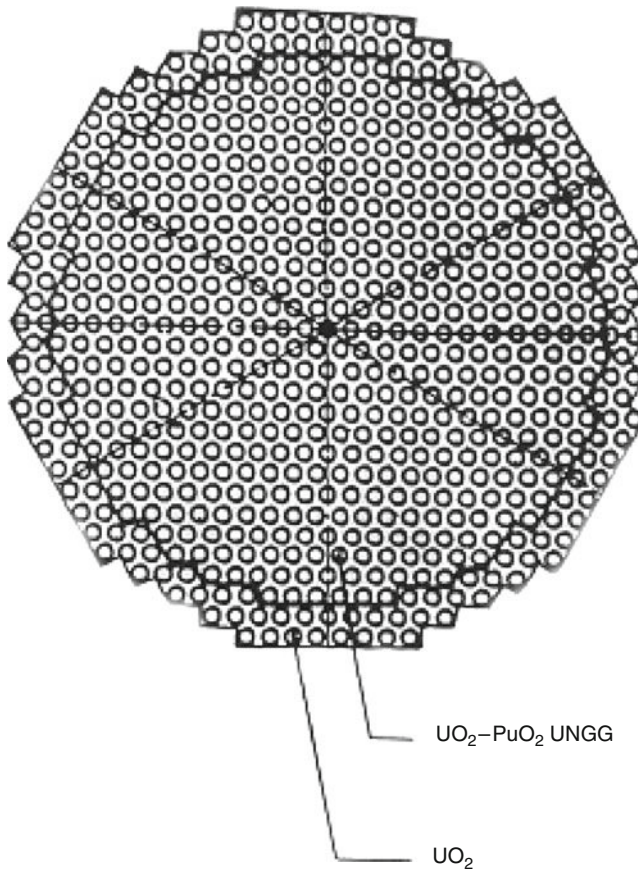
The experiments conducted on these lattices showed the adequacy of these blocks in representing epithermal spectra.

MORGANE-R Lattice

MORGANE R comprises a triangular “realistic” RSM lattice with a pitch of 10.35 mm (moderating ratio $V_m/V_c = 0.9$). In the center, it includes 499 $\text{UO}_2\text{-PuO}_2$ rods of graphite-gas natural uranium (UNGG) origin with 8.5% fissile plutonium, and 162 UO_2 rods enriched with 3.5% ^{235}U used as an adaptation zone (see ▶ [Figs. 28](#) and ▶ [33](#)). The experimental lattice (661 rods in total) is installed inside the structure of the ERMINE block. The space between the lattice and the structure is filled with AG 4.5 sections (see ▶ [Fig. 28](#)).

MORGANE-S Lattice

MORGANE S comprises a triangular “closed” RSM lattice with a pitch of 9.45 mm (moderating ratio $V_m/V_c = 0.5$). At the center, it includes 721 $\text{UO}_2\text{-PuO}_2$ rods with 8.5% fissile plutonium of UNGG origin (499 rods) and of PWR origin (222 rods), and 528 UO_2 rods enriched with 3.5% ^{235}U used as the adaptation zone (see ▶ [Fig. 34](#)). The experimental lattice (1,249 rods in total) is installed inside the structure of the ERMINE block. The space between the lattice and the structure is filled with AG 4.5 sections (see ▶ [Fig. 28](#)).



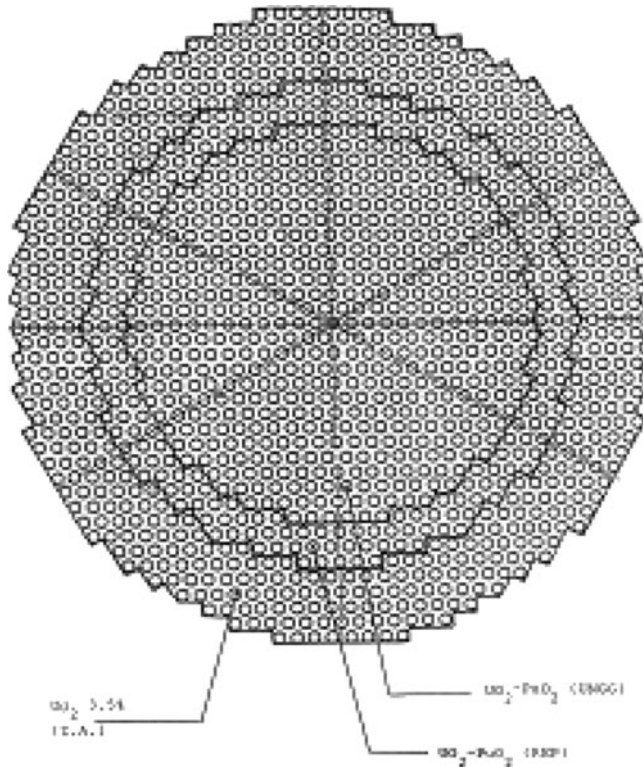
■ Figure 33
MORGANE-R lattice

4.3.3 ERMINE Assembly for Fast Neutron Multiplier Lattices

In the current version (ERMINE 5), the measuring zone is placed in a sealed chimney with a 735 mm diameter cylinder-shaped tube rising above the water level. The constituent elements of the studied lattice are assembled in a block that is then installed in the chimney. These elements include fuel, generally in the form of oxide mandrels, containing approximately 50 kg of plutonium or ^{235}U , sodium and steel (► Fig. 35).

The ERMINE block is an experimental block that can hold several experimental lattices representative of fast spectra. Several lattices (see ► Table 3) have previously been created and experimented in MINERVE. It should be noted that the fuel used comes from the MASURCA reactor.

The interpretations made on this lattice showed, however, that it is necessary to refine the adaptation and filtering of the spectrum between the experimental zone ZONA1 and the driver zone of MINERVE (thermal neutron/fast spectrum coupling established in a wide zone around



■ Figure 34
MORGANE-S lattice

the oscillation channel). Moreover, creating other assemblies representative of future fast neutron reactor concepts is foreseeable in the future: gas fast reactor (GFR) for example, or “fast moderated” type assembly for incineration, located between MORGANE S’s pure fast and hard epithermal spectrum (► [Fig. 36](#)).

4.3.4 ELOISE Assembly for Heavy Water Moderated Lattices

The measuring zone placed at the center has a tight aluminum container filled with heavy water and crossed by vertical channels in which natural uranium or slightly enriched fuel elements are placed.

5 Experimental Programs in the MINERVE Reactor

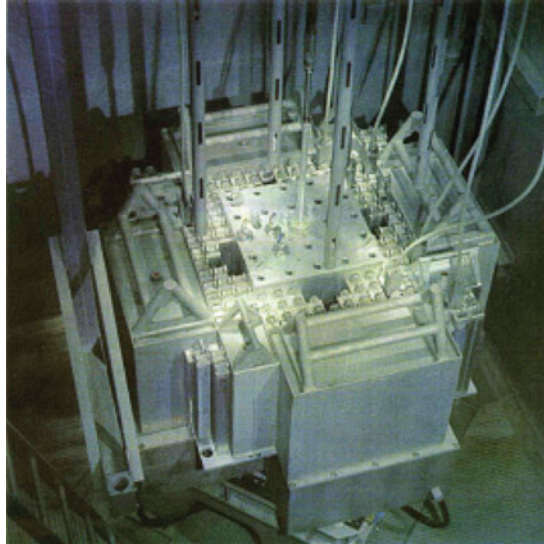
The reactor went critical on 29 September 1959 at CEA Fontenay-aux-Roses. The main experimental programs carried out since 1959 are detailed below.



Figure 35
ERMINE assembly

Table 3
Characteristics of the ERMINE-5 lattice

ERMINE lattice (740-mm diameter)	Fuel		Thinner	Observations
	Nature	Average enrichment (%)		
OU 10	UO ₂	7	SS	Uranium at 27% ²³⁵ U Small proportion of thinner
OP 40	UO ₂ -PuO ₂	10	SS	Plutonium at 45% ²⁴⁰ Pu Small proportion of thinner
OP 20	UO ₂ -PuO ₂	7	SS	SNEAK plutonium: grid strap lattice Small proportion of thinner
OP 11	UO ₂ -PuO ₂	7	SS Na	Plutonium at 8% ²⁴⁰ Pu
R 3	Metal U	15	SS Na	Uranium at 30% ²³⁵ U
RONA 3	UO ₂	13.5	SS Na	Uranium at 27% ²³⁵ U
ZONA 3	UO ₂ -PuO ₂	13.5	SS Na	Plutonium at 18% ²⁴⁰ Pu
ZONA 1	UO ₂ -PuO ₂	20	SS Na	Plutonium at 18% ²⁴⁰ Pu



■ Figure 36
ELOISE assembly

5.1 Main Programs Achieved Between 1959 and 1990

Up to 1966

MINERVE was first used mainly for thermal cross section and resonance integral measurements, and for studies on recycling plutonium in natural uranium systems.

- Neutron studies
 - Measurement of complete and incomplete fuel element reactivity weights
 - Measurement of spectra through activation of detectors and fission chambers
- Measurements of absorption resonance integrals in a 45×45 mm cavity: Mn-Fe-Co-Ni-Zr-Mo
- Measurements on cells simulating a heavy water system core

Two types of cells were simulated in the MINERVE cavity.

They were used:

1. To develop the local signal technique
2. To study the neutron characteristics of plutonium for a known spectrum with samples of uranium containing small amounts of plutonium or boron
3. To measure the overall capture of fission products with samples of uranium at 1.6% irradiated in EL3 (ELOISE lattice)

The results were to be used to validate calculation forms for worn fuel elements.

From 1966

In 1966, the first thermal-fast critical assembly of the ERMINE series (Expérience Rapide MINerve – Minerve Fast Experiment) was conducted in MINERVE, which comprised the driver zone, the transition zone, and the experimental zone.

At the time, MINERVE was dedicated to studies for the fast neutron reactor field conducted by placing much more subcritical volumes of different fast neutron multiplier lattices in MINERVE's central cavity (ERMINE).

Up to September 1967 – ERMINE 1

Measurements of reactivity coefficients, through the oscillation method, for a certain number of materials.

Measurements of spectral indexes.

Source oscillations.

Comparison of U8/U5 indexes with those measured in HUG (HARMONIE reactor).

From October 1967 – ERMINE 2

Metal uranium–plutonium fuel.

U1-P1-U2-P2 cores.

Doppler effect measurements on uranium-238.

From March 1969 – ERMINE 3

Metal uranium–plutonium fuel

Cores at $k_{\infty} = 1$ -KP1-KP2-KU-UK1-UK5 (European collaboration)

Heterogeneity studies

- Grid strap fuel – HP
- Terminal block fuel – H1–H2

Qualification of calculations on heterogeneity studies

HO cores – terminal block fuel

Experiments with measurement of the local signal and overall signal; measurement of the capture ratio on Pu-239 fission

From November 1971

Alternate creation of ERMINE 4 and ERMINE 5 “fast” cores and MELODIE cores (light water).

In particular, the following were carried out:

In ERMINE 5 (oxide fuel) the following configurations:

OP 10–OP 20–OP 40–OP 41–OP 50–OP 51 at $k_{\infty} = 1$, measurements taken as part of the PLUTO program, between MASURCA and MINERVE, for the qualification of plutonium (oxide) fuel cores.

ZONA 1–ZONA 2–RONA 3, for the qualification of codes involving the capture of fission products in fast neutron reactors.

In MELODIE 1–2–3 cores, UO₂ VENUS rods:

- First qualification of light water fuel lattices.
- Measurement of the capture of fission products on the SENA plant fuel.

In *MELODIE 4*, 17×17 PWR type – UO_2 rods:

- Qualification of the 17×17 type PWR lattice.

On 30 April 1976, the *MINERVE* reactor operated for the last time at Fontenay-aux-Roses

Its transfer and reinstallation at Cadarache took place in 1976 and 1977, as part of decentralization measures aimed at grouping the majority of CEA critical experiments outside the Paris region.

From September 1977, the light water and fast configurations were installed alternately in *MINERVE*.

In *MELODIE 4* the following were carried out:

- An initial qualification of gadolinium based burnable poisons
- The EURATOM program on recycling PWR plutonium and qualification of French tools as part of the system becoming French
- Doppler effect studies
- Studies on the capture section of gadolinium, used as burnable poison

In *ERMINE 5* the following were created or carried out:

- RONA 3–ZONA 1–ZONA 3 cores, for the study of fission product capture
- OA 10 and ON 10 cores for the study of the absorption section of steel and nickel
- Heterogeneity studies between grid strap and terminal block fuels (four cores)
- A degraded spectrum core. Qualification of the CARNAVAL code
- The ZOCA 13 core (plutonium). Measurement of the Doppler effect
- The ROCA one core (uranium). Study of the absorption section of structure materials

From the second quarter of 1986, *MORGANE* experiments to study under-moderated type light water lattices (RSM) were conducted in *MINERVE* (UO_2 – PuO_2 fuel). The aim was to measure the overall capture of fission products through oscillation of irradiated fuels. The following lattices were therefore studied:

- *MORGANE-S*: Closed pitch ($V_m/V_f = 0.5$)
- *MORGANE-R*: Realistic intermediary pitch ($V_m/V_f = 0.9$)

In 1987–1988, the P/A experiment (Assembly power/Internal instrumentation activity) was conducted in the *MELODIE* PWR block. This experiment established an experimental basis for qualification of the use of internal instrumentation of a PWR in the case of mixed loading with MOX assemblies, particularly useful for the start-up of PWR 900 moxing in Saint Laurent B1.

5.2 The CREDIT BURN UP Program (From 1993 to 2001)

The CREDIT BURN UP experimental program stems from the growing interest for the consideration of fuel wearing in criticality–safety. Between 1993 and 2001 it was the subject of a joint program between CEA and COGEMA.

The aim was to optimize the various facilities of the cycle with respect to criticality–safety constraints, more specifically, the consideration of minor actinides and stable and non-gaseous absorber PFs, enabling significant improvement of the dimensioning of facilities for the storage, transport, or reprocessing of fuels.

The following experiments were carried out as part of this program:

- Reactivity measurements in the MINERVE reactor in order to take into account the negative reactivity of products formed with the wearing of the fuel (fission products, and major and minor actinides)
- The poisoning effect of each of the 15 Fission Products PFs selected for credit burn up, with the oscillation of UO_2 samples doped with a separate isotope
- The analysis of the main absorber (and non gaseous) FPs in irradiated samples to qualify the calculation of inventory

In a more detailed manner, the program in MINERVE enabled the qualification of absorption cross-sections for 13 credit burn up fission products: ^{147}Sm , ^{149}Sm , ^{152}Sm , and Sm nat , ^{143}Nd , ^{145}Nd , and Nd nat , ^{155}Gd , ^{153}Eu , ^{103}Rh , ^{95}Mo , ^{99}Tc , ^{133}Cs , ^{109}Ag and Ag nat , Ru nat . The reactivity loss with mass combustion was also studied through measurements on sections of fuels with various combustion rates: PWR-UOX irradiated from 20 to 60 GWj/t (Bugey-3, Fessenheim-2, Gravelines-3), fresh MOX and BWR-UOX irradiated up to 45 GWj/t (Gundremmingen).

These measurements took place in four types of spectra corresponding to the following four different experimental lattices: R1- UO_2 (standard PWR spectrum), R2- UO_2 (spectrum representative of a dissolver), R1-MOX (PWR-MOX spectrum), and BWR (boiling reactor spectrum).

5.3 The CERES Program (From 1992 to 1995)

The CERES program stems from collaboration between the research centers at Winfrith and Cadarache, as part of official CEA/UKAEA collaboration on water reactors. Its objective was to provide an experimental benchmark for the validation of nuclear data (in particular JEF2.2) on actinides and on fission products used to calculate fuel burn-up and for criticality studies. The WIMS calculation code was used at AEA, and APOLLO-2 at CEA, as well as the CRIBLE criticality form.

For this, experiments conducted in the DIMPLE reactor at Winfrith and MINERVE reactor at Cadarache were conducted based on common samples manufactured at Cadarache. In addition to the measurements, the material balance of samples was analyzed at CEA Cadarache.

In 1993, phase I of the CERES program consisted in measuring reactivity for the following fuels: fresh UO_2 (from 0.25 to 5.1% U-235 enrichment), fresh $\text{UO}_2\text{-PuO}_2$ (from 0.4 to 9.56% Pu content) and irradiated UO_2 (Fessenheim and Bugey) from 20 to 60 GWj/t. In DIMPLE, the reactivity effects were obtained by measuring doubling time in three different spectra:

- Assembly I: spectrum thermalized by ordinary water
- Assembly II: “hard” PWR spectrum: lattice of UO_2 rods enriched with 7% U-235
- Assembly III: maxwellian spectrum: heavy water tank at the center of DIMPLE

In MINERVE, the measurements were taken within the framework of the CREDIT BURN UP program in the R1- UO_2 core configuration (see  Sect. 5.2).

In 1994, phase II was dedicated to measuring samples containing separated or natural fission products, diluted either in a nat UO_2 matrix, or in an aluminum-silicate matrix, or in solution in nitric acid. The experiments were carried out in assemblies II and III of DIMPLE, and in MINERVE/R1- UO_2 (for nat UO_2 samples + fission products).

Phase III of the program was the subject of wider collaboration between CEA, UKAEA, BNFL and Sandia. The CEA samples provided were of fresh MOX, irradiated MOX ($\sim 25 \text{ GWj/t}$) and nat UO_2 + fission product type. AEA/Sandia samples were of irradiated PWR and irradiated BWR type. The measurements were carried out in assembly I of DIMPLE and in MINERVE/R1- UO_2 .

5.4 The High Burn-Up (HTC) Program (From 2003 to 2004)

The HTC program (Haut Taux de Combustion – High Burn Up) is part of an R&D program in partnership with EDF and FRAMATOME.

It is split into two parts. The first is dedicated to chemical and isotopic analysis of irradiated fuels. The second consists of oscillation experiments on irradiated fuel sections in the MINERVE reactor. The objective is to improve knowledge on the loss of reactivity of the UOX and MOX fuel during irradiation.

The HTC program on MINERVE deals within the framework of increasing the time the fuel spends in the cores of French electronuclear reactors and the increased use of MOX fuel and the need to qualify changing neutron calculation schemes.

The program has been divided in two phases:

- PWR-MOX for MOX fuels irradiated (Dampierre-2) from 1 to 5 cycles (from 10 to 55 GWj/t) in 2003
- PWR- UO_2 for UO_2 fuels irradiated (Cruas-2 and Gravelines-5) from 1 to 6 cycles (from 50 to 70 GWj/t) in 2004

Spectral index, conversion and capture rate and axial and radial reaction rate distribution measurements were also carried out in order to refine neutron characterization of the lattices studied.

For light water reactors the HTC program contributed:

- To studies on high burn up rates and on increasing the time the fuel spends in the core of electronuclear reactors
 - The evolution of fuel should be controlled over time for high irradiation rates. The interpretation of experiments now contributes to the qualification of the APOLLO-2 code, notably the R2 extended qualification report
 - To studies on credit burn up by extending the qualification range to high burn up of UOX and MOX assemblies
 - More generally, in association with isotopic analysis experiments on irradiated fuels, the program enables studies on storage, warehousing, transportation, and reprocessing to be completed
- To the improvement of basic nuclear data on constituent isotopes of irradiated fuel samples.

5.5 The VALMONT Program (2003–2004)

Within the framework of JHR definition studies and the elaboration of the preliminary safety report for the latter, the VALMONT program (Validation of uranium Molybdenum Aluminum fuel for Neutronics – Validation du combustible ALuminum MOlybdène uranium pour la Neu-Tronique) was carried out in late 2003 and early 2004 in the MINERVE reactor, in order to improve precision on the reactivity and reaction rates of the new UAlMo fuel.

It was aimed at qualifying, from a neutronics standpoint, a set of tools needed to design the JHR, called HORUS3D (HOrowitz Reactor simulation Unified Lattice). The issues of the program address the wider issues of the HORUS3D form, that is to say:

- Controlling neutron calculation within the framework of safety studies
- Quality: qualification enables exact assessment of results uncertainties and contributes therefore to correct assessment of performances to be reached
- Savings, in the sense that insufficient control of uncertainties and limits of a form lead to significant and therefore expensive design margins

VALMONT is split into two distinct parts:

- The study of UAlMo fuel reactivity effects through oscillation of samples.

The VALMONT oscillation samples (see [▶ Table 4](#)) were manufactured at CERCA Romans. They contain variable concentrations of aluminum, molybdenum and uranium, which enabled the study of differential effects linked to the density of the fuel, the ^{235}U enrichment, the molybdenum content, and the nature of the base.

- The study of production and neutron absorption effects, through measurements using a dedicated fuel rod containing UMo/Al enriched with 19.75% ^{235}U .

The reaction rate axial and radial profiles as well as the ^{238}U modified conversion rate measurements were carried out through gamma spectrometry near the UMo/Al rod.

■ Table 4

Samples for the VALMONT program

Sample	Characteristics
APur	Pure Al_2O_3 , used as a reference
UappAl	UAl_x containing low-density depleted uranium (2.2 g U cm^{-3}), to assess the effect of the ^{238}U
UAl20	Low-density UAl_x enriched with 19.75% uranium, to measure the influence of the enrichment
UMo/Al 2.2	Low-density UMo/Al enriched with 19.75% uranium, to measure the influence of the molybdenum
UMo/Al 8	High-density JHR reference fuel, enriched with 19.75% uranium (8 g cm^{-3}), to assess the impact of density

5.6 The ADAPh Program (2005)

As part of designing the JHR (“Jules Horowitz Reactor”) irradiation reactor, significant work was dedicated to the elaboration and qualification of a recommended neutron/thermo hydraulic coupled calculation scheme, called HORUS-3D (Jules HORowitz Reactor Unified System).

The ADAPh program (Improvement of Basic Photon Data) in MINERVE has been used as a support for qualification of the HORUS-3D-P tool intended to calculate the photon heating of JHR reactor devices. It was a support element during presentation of the preliminary safety report (PSR) around 2008.

It is part of the continuation of the ADAPh program carried out in the EOLE reactor in 2004. It aims at both reducing calculation-experiment deviations and if possible, decreasing uncertainties on experiments. The other objective is to obtain measurements in a UO₂ neutron spectrum which is more representative of the JHR spectrum than the MOX spectrum of the BASALA program.

The first phase of the program took place in January 2005 and used thermo-luminescent detectors (TLD), inserted, after calibration, in the center of the MINERVE reactor in R1-UO₂ configuration (neutron spectrum representative of a PWR-UO₂).

The second phase of the program (May 2005) was dedicated to measurements by gamma ionization chamber. These, on the one hand, helped obtain measurements separate from those given by the TLDs, and on the other hand, helped assess the contribution of delayed photons more accurately through a pulsed recording on line.

5.7 The OSMOSE Program

The OSMOSE (Oscillations of Isotopes in Eupractic Spectra in Minerve–Oscillations dans Minerve d’isotopes dans des Spectres Eupraxiques) experimental program was designed within the framework of CEA/EDF joint work. It has also been the subject of I-NERI collaboration between DOE and CEA since 2001.

The program took place between 2005 and 2008.

The aim of OSMOSE is to gain more knowledge on basic nuclear data on heavy isotopes. The goal is both to improve calculation forms and for LWR, FBR and hybrid reactors, to back up studies on reactor physics, plutonium multi-recycling, incineration and the transmutation of actinides, storage and warehousing, and credit burn-up through heavy nuclei and fission products. This program significantly contributes to the JEFF3 project, for the qualification of actinide nuclear data.

It complements the CREDIT BURN-UP program, which it follows on the facility, and which involves absorber PFs.

More specifically, the OSMOSE program aims at providing specific experimental data (absorption cross-sections) on heavy nuclei: ²³²Th, ²³³U, ²³⁴U, ²³⁵U, ²³⁶U, ²³⁸U, ²³⁷Np, ²³⁸Pu, ²³⁹Pu, ²⁴⁰Pu, ²⁴¹Pu, ²⁴²Pu, ²⁴¹Am, ²⁴³Am, ²⁴⁴Cm, and ²⁴⁵Cm.

The study using the nuclei oscillation technique took place on a wide range of neutron spectra (PWR-UO₂, PWR-MOX, dissolver, RSM type epithermal) corresponding to various experimental lattices.

The samples consisted in the homogeneous integration of a dopant actinide into a sintered nat UO₂ matrix. They are manufactured in ATALANTE at CEA Marcoule. The 8.1-mm diameter

and 95-mm high pellet column is inserted into a Zircaloy4 welded and tight double cladding, with a diameter and height of 10.6 and 103.5 mm, respectively.

5.8 The OCEAN Program

The OCEAN (Oscillation en Coeur d'Echantillons d'Absorbants – Core Oscillation of Neutron Absorber Samples) experimental program was supported by EDF and CEA. It took place from 2005 to 2008.

On the one hand, OCEAN is aimed at improving knowledge on absorber isotope basic nuclear data, and on the other hand, qualifying neutron calculation codes for burnable poisons and new absorbers for light water reactors. The goal is both to improve calculation forms and to study the feasibility of new fuel cycle options.

This program contributes significantly to the qualification of JEFF3 assessments. In particular, it addresses the need to conduct new experiments to improve knowledge of resonance integrals of hafnium isotopes.

More specifically, the OCEAN program aims at providing specific experimental data (capture cross-sections) on the following isotopes: Gd-155, Gd-157, Gd-nat, Hf-177, Hf-178, Hf-179, Hf-180, Er-166, Er-167, Er-168, Er-170, Dy-160, Dy-161, Dy-162, Dy-163, Dy-164, Eu-151, Eu-nat, Eu-153.

The study using the nuclei oscillation technique took place on a wide range of neutron spectra (dissolver, PWR-UO₂, PWR-MOX, epithermal (RSM type)) corresponding to various experimental lattices.

The samples consist of an absorber dopant mixed homogeneously in a sintered nat UO₂ matrix. They are manufactured at the Fuel Research Department at CEA Cadarache. The 8.1-mm diameter and 95-mm high pellet column is inserted into a Zircaloy4 welded and tight double cladding, with a diameter and height of 10.6 and 103.5, mm respectively.

Spectral index, conversion and capture rate, and reaction rate axial and radial distribution measurements were also carried out in order to refine the neutron characterization of studied lattices.

5.9 Training Activities

5.9.1 EDF Training

Since 2004, the MINERVE reactor has been used to support training for future EDF operators. This activity takes up approximately 1 month/year, and should remain the same or be slightly less in the future.

5.9.2 INSTN Training

Since 1998, MINERVE has also been used within the framework of practical work for Atomic Engineering training for the INSTN Cadarache. From time to time, practical work for radio-protection *Brevets de Techniciens* (BT and BTS – technician diploma) of the INSTN Cadarache have also been carried out in the past. It is used for 1 week/year.

5.9.3 Other Training

The extension of training activities to other engineering schools, master's programs or university activities is however foreseeable in the future.

5.10 The Gas Fast Reactor (GFR) Program

CEA and US-DOE have shown strong interest for an oscillation program in an GFR type core configuration within the framework of the GENERATION IV forum. Such a program would be complementary to the ENIGMA program planned in MASURCA, as it would provide experimental measurements on basic nuclear data.

This program could be carried out based on existing OSMOSE, OCEAN and CBU samples if their reactivity weight is sufficient. If this is not the case, other samples would need to be manufactured.

A feasibility study would also need to be carried out on one or several GFR configurations in MINERVE (representativity of the neutron spectrum for samples, adequacy with the maximum available space in the center of the driver zone and compliance with safety criteria).

It would also be interesting to add a Doppler study to these programs. It involves studying a sample heat-up system, which could fulfill the same functions as the one that existed in the early 1980s (HF heating). Emphasis must be placed on controlling the temperature of samples, the temperature axial profile which must be as flat as possible, and compliance with safety criteria.

Finally, reinterpretation of the PROFIL and PROFIL-2 experiments held in PHENIX Fast Reactor revealed lacks in fast spectrum in the assessment of certain fission products of the JEFF3.0 library of the ERANOS-2.0 code system. New measurements would therefore be necessary on the following PFs: Mo-95, Mo-97, Ru-101, Pd-105, Pd-106, Pd-107, Cs-133, Cs-134, Nd-143, Nd-144, Nd-145, Sm-147, Sm-148, Sm-149, Sm-150, Sm-151, Eu-151, Eu-153, and Eu-154. The feasibility of manufacturing samples containing these separate isotopes with a sufficient isotopic purity with respect to target uncertainties would therefore be interesting to study.

5.11 The HTR Program

The idea is to oscillate burn up fuel rods (or any other form of fuel representative of the HTR fuel) and/or fuel rods of different natures at the center of the configurations (to be designed) of the core, representative of HTR spectra. An experimental lattice which can be adjusted (the same way as MELODIE can be changed to R2-UO₂, R1-UO₂ and R1-MOX) can be of interest to have several points in the spectrum.

The oscillation of existing samples (OSMOSE, OCEAN and CREDIT BURN UP) would also be carried out if their reactivity weight is sufficient (~10 pcm in the thermal/epithermal spectra studied).

Carrying out a Doppler study is also foreseeable.

5.12 HTC Program Supplement

It must be reminded that the oscillation of the ALIX 75 GWj/t fuel was postponed due to the fact that this fuel was unavailable at the time of the HTC-UOX program. This oscillation remains interesting and can still be carried out.

It is reminded that the interpretation of radiochemical analyses for UOX fuels irradiated at 60 GWj/t in CRUAS2 NPP highlighted an inconsistency between the errors on the fuel inventory (high overestimation of the Pu-239 concentration) and the reactivity effect of corresponding oscillation samples (overestimation of the reactivity loss with the burn up fraction).

It would also be interesting to oscillate HBU samples in highly thermalized (R2-UO₂) and epithermal (MORGANE-R) spectra.

5.13 Program on Structure Materials and Moderators

This program is part of the issues surrounding basic nuclear data.

It involves steel, Al, Pb, Cu, Cr, Ni, and Fe type structure materials, activation products from Co-59 or Cl-35, or Be, C, H₂O, CH₂ type moderator materials. The list of materials remains open.

The required qualification of basic nuclear data was particularly highlighted during qualification studies for the CRISTAL VI form and within the framework of an ISTC international project.

The idea would be to compare the signal of these samples with that of a vacuum filled sample.

We can also consider studying the reactivity variation of these samples according to temperature, particularly in the case of moderator materials for the study of $S(\alpha, \beta)$ treatments, linked to the crystalline structure of the material, which is involved in the neutron thermalization process.

5.14 FP and Absorber Supplementary Program

Interpretation problems due to the volatility of metallic FPs during sintering, then due to dissolution difficulties were observed during the CBU program, particularly for Ag-109, Rh-103, and Tc-99, as well as for Cs-133 due to its strong volatility. Two solutions can be selected to solve this problem:

- Carry out a destructive analysis on existing samples. This solution must however take into account the fact that current dissolutions of metallic FPs are still not fully developed. Furthermore, CBU samples in question would no longer be available for other experiments.
- Have other samples containing these PFs manufactured in a compacted nat UO₂ matrix, which would avoid the need for analyses as there is no loss of PF during compacting (as opposed to the case of sintering), then re-oscillate them in core configurations of interest. It would also be interesting to have an Sm-147 sample containing less Sm-149 “pollutant” manufactured.

Moreover, some interesting absorbers such as Gd-154, Gd-156, and Gd-158, were not selected for the OCEAN program for financial and/or insufficient isotopic purity reasons. However, the interest of manufacturing such samples is justified by the following elements:

- These pair isotopes are responsible for the residual penalty of gadoliated burnable poisons
- The problem of isotopic purity is reduced in an epithermal spectrum such as that for MORGANE-R, or all the more in a fast spectrum. There is a possibility (to be studied) of measuring these samples through oscillation with correct uncertainty. It is also possible to cut the spectrum's thermal component using a Cadmium filter, in which case the isotopic purity is no longer a problem

5.15 Program in Support of JHR for Qualification of HORUS3D for U_3Si_2

There is the possibility, if needed, of carrying out an oscillation program of approximately 3 months, of the same type as VALMONT but for U_3Si_2 (back-up fuel candidate for JHR).

5.16 Cadmium Measurements

For all programs, it would be interesting to carry out oscillations measurements on samples with Cadmium, in addition to measurements without Cadmium. This would enable:

- Elimination of thermal components from highly capturing impurities, and thus improve the uncertainties linked to the interpretation of measurements. For example, Gd-155 and Gd-157 impurities in Gd-154 and Gd-156.
- The origin of any deviations between calculations and experiments to be targeted by having information on the thermal part and on the epithermal/fast part of the signal.

This solution will be studied by CEA. It involves integrating the Cadmium into the oscillation rod, all while complying with facility safety criteria (particularly reactivity effect lower than $\beta/2$).

5.17 Other Programs

In addition to the aforementioned programs, other oscillation experiments can be planned for the future in MINERVE, within the framework of:

- Support for the French electronuclear fleet. There is the possibility of testing new fuel options in the future, or as already mentioned in [▶ Sect. 5.12](#), of studying increasingly higher burn ups
- International collaborations. There is the possibility of carrying out benchmarks of the same type as the CERES program in the future
- Studies on under-moderated reactors (RSM), with the possibility of creating experimental lattices other than MORGANE R and S, corresponding to intermediary neutron spectra
- The opening up towards fields other than reactor physics, such as the needs in basic nuclear data for astrophysics
- Studies on materials for the ITER project
- Support for JHR

5.18 Conclusion

Since its first divergence in 1959, the various experimental programs carried out in MINERVE helped determine integral nuclear data with high precision in various neutron spectra (thermal, epithermal, and fast).

Updating the instrumentation and control system and the oscillator further to the CREDIT BURN UP program allowed the HTC, VALMONT, OCEAN, and OSMOSE programs to be carried out with increased quality of results and an optimum level of safety starting in 2003.

These experimental programs are also based on the upgrading and development of instrumentation and experimental measurement techniques, which improve the competitiveness and quality of experiments.

In the near future, the OSMOSE and OCEAN programs will be completed between now and late 2008 in various light water lattices.

After Safety Reassessment of the Eole and Minerve facilities planned for 2010–2011, other experimental programs are being studied, to support future reactor concepts (GFR and HTR, with Doppler effect study), the current fleet (HBU supplement, structure materials, supplement to fission products and absorbers), the JHR (U_3Si_2 fuel study), or more generally to improve basic nuclear data (cadmium measurements, various needs in reactor physics or astrophysics).

6 Description of the MASURCA Reactor

The MASURCA reactor is one of the critical mock-ups from the “zero power” class, operated by CEA on the Cadarache site (Bouches du Rhône). Built between 1964 and 1965 (🕒 *Fig. 37*), this reactor went critical for the first time on 14 December 1966. It was authorized to operate at a maximum neutron power of 5 kW in 1969 and since then has been used mainly to study fast neutron reactors.

The MASURCA facility is located at the South-East end of the Cadarache Research Centre near the RAPSODIE reactor and the zone of the old HARMONIE reactor. The MASURCA zone comprises of four main buildings that are connected to each other through underground



📷 Figure 37
Construction of MASURCA



Figure 38
Aerial view of the MASURCA zone in the early 1970s

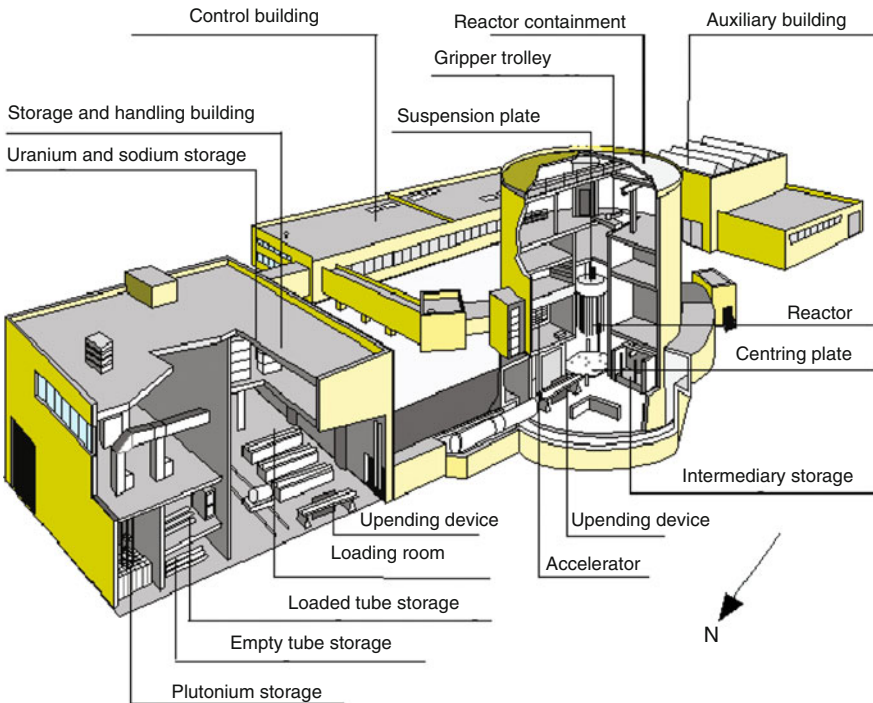


Figure 39
MASURCA platform

galleries or covered passages on the surface (► Fig. 38). This approximately 6,000-m² platform is included in a zone with a total surface area of approximately three hectares surrounded by a double fence. These four buildings are (► Fig. 39):

- The reactor containment
- The control building containing control and monitoring equipment, the reactor's Control room as well as the measurement room used by researchers



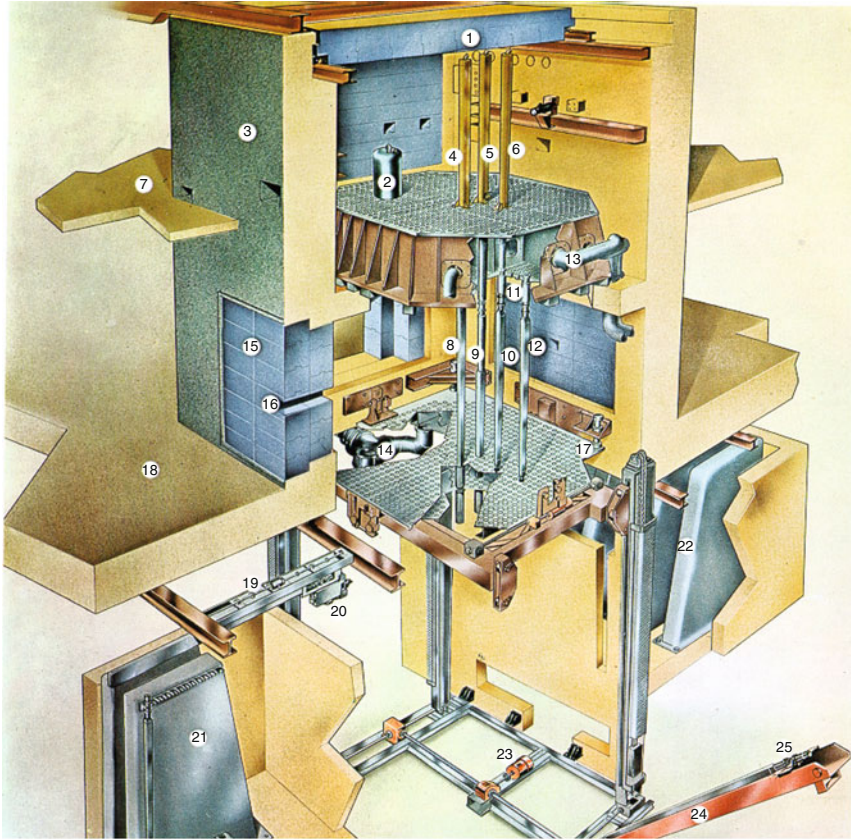
▣ Figure 40
View of MASURCA reactor containment

- The storage and handling building where simulation elements are stored
- The auxiliary building

The reactor building, partly buried, has a total height of 26 m (🕒 Fig. 40). It comprises a circular metal shell topped with a dome and resting on a circular base slab made of 1 m thick concrete. It comprises the reactor core supported by massive reinforced concrete inner structures, the main equipment which is used for experimentation, a vertical storage area for loading tubes as well as various handling means to allow the loading or unloading of various loading tubes in the reactor core. It also houses part of the ventilation system organs dedicated to dynamic containment of the structure and cooling the core (🕒 Fig. 41).

6.1 Core Building Principles

The cores studied in MASURCA comprise a lattice of stainless steel assemblies (tubes) called “loading tubes,” which can be removed, loaded with simulation elements and attached at the upper part to rhomb shaped vessel, set with corners cut, comprising two assembled base plates. The lower base plate is drilled with bore holes to receive seals in which the tube heads are locked. The tube legs fit into bore holes on a second plate, the centering plate, ensuring the safety of the attachment, the centering of tubes and the closure of the cooling system. The centering plate is mobile and can also occupy:



- | | |
|---------------------------------|---------------------------------|
| 1: Rolling slabs | 14: Core output ventilation |
| 2: Start-up source | 15: Removable biological shield |
| 3: Biological shield | 16: Radial channel |
| 4: Type 1 control rod mechanism | 17: Centring plate |
| 5: Type 2 control rod mechanism | 18: Level +0.00 m |
| 6: Pilot rod mechanism | 19: XY East handling arm |
| 7: Level +4.94 m | 20: XY trolley |
| 8: Type 1 rod | 21: East vertical storage |
| 9: Type 2 rod | 22: West vertical storage |
| 10: Pilot rod | 23: Centring plate mechanism |
| 11: Suspension nozzle | 24: Upending device |
| 12: Tube | 25: Tube head |
| 13: Core input ventilation | |

■ Figure 41

Artist's view of the inside of the reactor containment: (1) rolling slabs, (2) start-up source, (3) biological shield, (4) Type 1 control rod mechanism, (5) Type 2 control rod mechanism, (6) pilot rod mechanism, (7) level + 4.94 m, (8) Type 1 rod, (9) Type 2 rod, (10) pilot rod, (11) suspension nozzle, (12) tube, (13) core input ventilation, (14) core output ventilation, (15) removable biological shield, (16) radial channel, (17) centering plate, (18) level + 0.00 m, (19) XY east handling arm, (20) XY trolley, (21) east vertical storage, (22) west vertical storage, (23) centering plate mechanism, (24) upending device, and (25) tube head

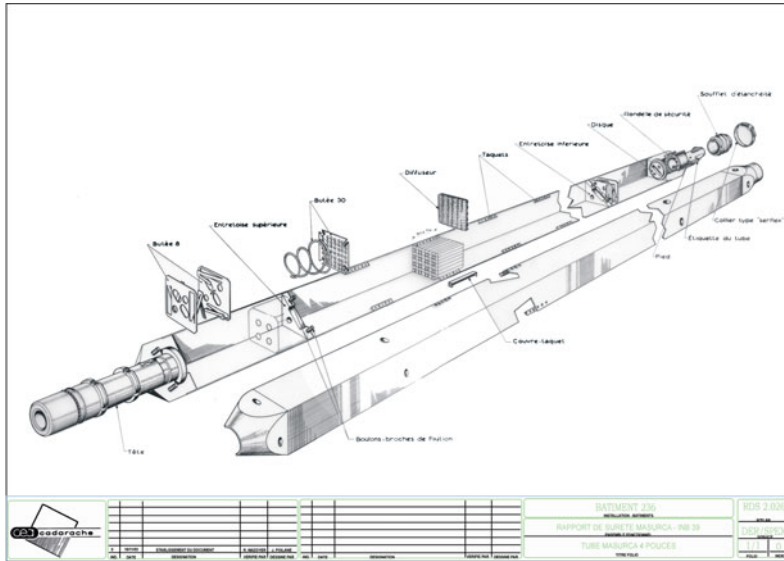


Figure 42
Diagram of a MASURCA tube

- An intermediary position for handling tubes
- A lower position for handling safety rods

A maximum of 1,100 tubes can be installed, allowing simulation of cores able to reach a total diameter of approximately 3.8 m.

In practice, two types of tubes are mainly used:

- The MASURCA tube (► Fig. 42), comprising two stainless steel sheet metal half casings with an overall dimension of $104.9 \times 104.9 \text{ mm}^2$ for a casing sheet thickness of 1.45 mm and a total length of 3.80 m (tube head and leg included). These tubes are used to hold simulation elements in the form of terminal blocks
- The 4/4 tube (► Fig. 43) comprising four $2 \times 2''$ (Most dimensions typical of tubes or simulation elements are expressed in inches. This results from a historical desire to facilitate communication with other European and international critical mock-ups.) tubes connected at the head and leg in order to recreate the overall geometry similar to that of MASURCA tubes. Each $2''$ tube has the shape of a prismatic box, with a square base (of $52.5 \times 52.5 \text{ mm}$ overall, for a tube sheet thickness of 0.725 mm) with a total length equal to that of MASURCA tubes (tube head and leg included). The use of these tubes allows better flexibility when several elementary patterns must be installed in one tube. They are also often used to ensure correct roundness of various zones of the core

The control bodies associated with the core are:

- Safety rods (SR) which ensure safety of the reactor during operation and handling
- The pilot rod (PR) is used to regulate the reactor

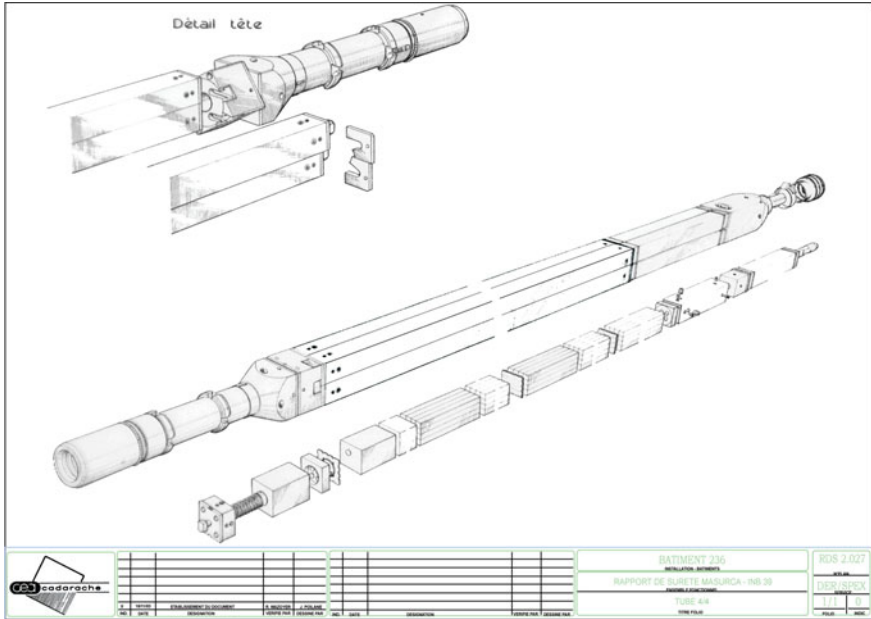


Figure 43
Diagram of a 4/4 tube

The core includes a variable number of safety rods (between 4 and 8) depending on the characteristics and the size of cores. These safety rods are composed with absorber material (B_4C blocks or bars) in the upper part and fissile materials in the lower part with the same pattern as in the core. In normal operating, since these rods are always positioned in raised position, the homogeneity of the core is preserved (► Fig. 44).

To reach the criticality and obtain the power required for the experiments, a Pilot rod (PR) with reactivity worth less than half a dollar, is used. In order to reduce the disturbances created by such a lattice, it is composed of a fuel tube containing a mobile part made of a ^{235}U enriched rod surrounded by stainless steel in the upper part and moderator material in the lower part (► Fig. 45). Tuning the position of this Pilot rod, the criticality is obtained by moderator effect.

To carry out the measurements, special channels can be opened throughout the MASURCA tubes to introduce different measurement devices (fission chambers, monitors, foils, neutron sources): two horizontal channels at 90° around the mid-plane (radial channels) and as many axial channels as necessary (an axial channel can be arranged in any sub-assembly).

6.2 Simulation Materials

The simulation elements (fissile, fertile, reflector, inert, or absorber materials) are in the form of 1/2 in. (12.7×12.7 mm (Some fissile materials are also available in the form of 1/4 in. diameter (6.35 mm) terminal blocks.)) or diameter square or circular section terminal blocks, with a



Figure 44
View of suspension table and safety rods mechanisms

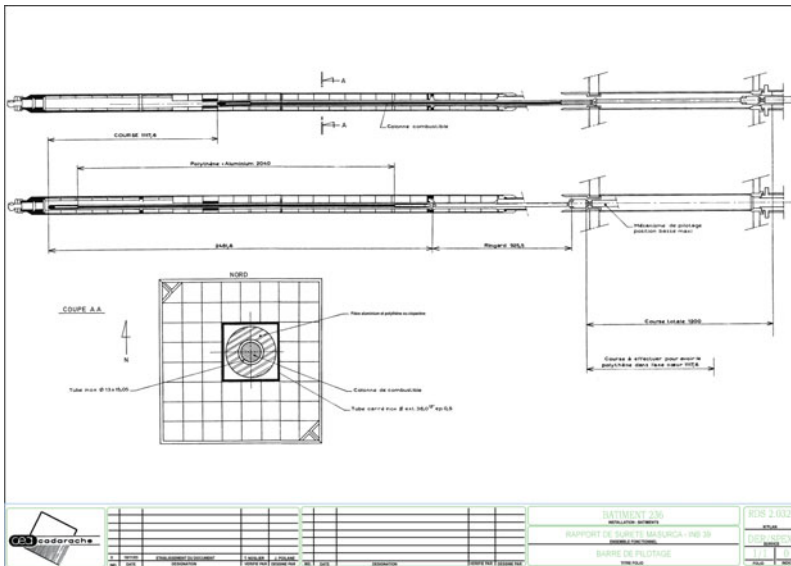


Figure 45
Diagram of the pilot rod



■ Figure 46

View of a few fissile elements (U^{235} enriched metal uranium terminal blocks)

height of 4–24 in. They are grouped together so as to form elementary patterns (generally made up of 4–8 terminal blocks) which are reproduced inside tubes. These elementary patterns (cells) allow simulation of core characteristics to be studied (volume percentage of different materials, enrichment).

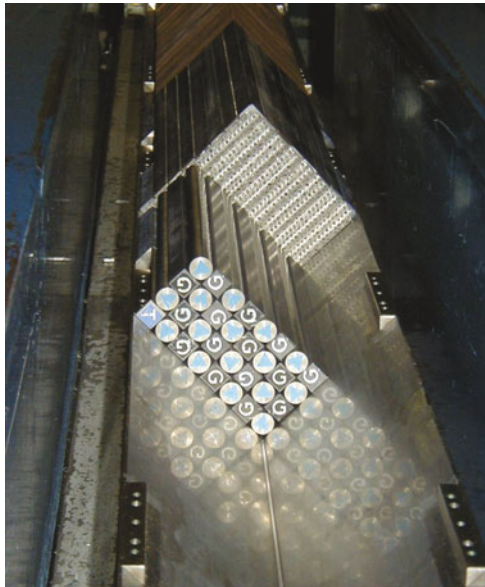
The list of nuclear materials that are currently used at MASURCA includes oxide of thorium, metallic uranium with up to 35% ^{235}U , uranium oxides (depleted and enriched with 30% ^{235}U), metallic plutonium, plutonium oxide and mixed plutonium and uranium oxides with various ^{240}Pu contents (8–44%). Several types of inert materials – sodium, stainless steel, graphite, lead – are also set-up to simulate the coolant, the reflector parts, and the structure materials. The amounts available allow cores with varying fissile zone volumes to be built: the smallest core loaded was 140 l (annex x) when the largest was 3,400 l in comparison to the volume of the PHENIX core (around 1,500 l) (► Figs. 46–48).

7 Experimental Programs in MASURCA

MASURCA went critical for the first time on 14 December 1966 with a UPuFe/graphite core. After a period dedicated to studying the behavior of the facility and the development of the first experimental measurement techniques (1967–1969), the programs were first tied to basic studies as fissile materials became available (RZ and PLUTO programs). From 1976, after the industrial commissioning of the PHENIX reactor 2 years earlier, the experiments were oriented towards support for the start-up of SUPERPHENIX (PRE-RACINE, RACINE and BALZAC



▣ Figure 47
Building of a fissile tube



▣ Figure 48
View of a tube

programs), and the investigation of questions linked to the SPX2 and EFR – European Fast Reactor – (CONRAD program) projects. In a third period, at the instigation of the law dated 30 December 1991 on the management of long life radioactive waste, three major programs were led within the framework of axis 1 (separation–transmutation) of the law:

- From 1994 to 1997, the CIRANO program enabled the study of cores burning plutonium within the framework of the CAPRA project (Increased Plutonium Consumption in Advanced Reactors)
- From 1998 to 1999, motivated by the introduction of ECRIX experiments in PHENIX, the COSMO program examined the effects of minor actinide transmutation in heterogeneous mode in moderated targets placed in an RNR
- Finally, from 2000 to 2004, subcritical systems coupled with an external neutron source which were studied extensively during MUSE-4 experiments

A summary of the objectives and major events for each of the programs led is given in the following section.

7.1 The RZ and PLUTO Programs (1969–1975)

The main objective of the RZ program was to study material buckling according to enrichment for Uranium (R) and Plutonium (Z) cores (➤ [Table 5](#)). The analysis and interpretation of this program led to the development of the CARNAVAL III calculation form that enabled the characteristics of cores containing a Pu fuel with low ^{240}Pu and ^{241}Pu content to be predicted. The PLUTO program, carried out at the same time in MASURCA and MINERVE (ERMINE configurations) was aimed at improving knowledge on plutonium superior isotopes. These experiments led to the creation and qualification of the CARNAVAL IV form.

7.2 The PECORE Program (1975)

This program was conducted within the framework of collaboration with the CNEN (Italian Committee for nuclear energy) for the PEC irradiation reactor project. Two core configurations were investigated:

- The PECORE 1 configuration with an internal zone loaded with UPuO_2 fuel and external zone loaded with the R2 cell. It simulated the actual environment of the PEC reactor.
- The PECORE 2 configuration with an internal zone loaded with the R2 cell and an external zone loaded with UPuO_2 fuel (ZONA 2 cell). This configuration was put in place to study the system of PEC reactor control rods.

7.3 The PRE RACINE and RACINE Programs (1976–1984)

The RACINE program is one of the most important conducted at MASURCA in terms of its duration as well as its objectives and stakes. The objective of the program was to validate the calculation tools and schemes used for SUPERPHENIX studies and to explore, to a certain

■ Table 5

Characteristics of cores studied during the RZ and PLUTO programs

Program	Core	Year	Fissile cell	Fuel nature	Comments
RZ	2A	1969	Z2	Metal (UPuFe)	
	2B	1969, 1970	R2	Metal (enriched U)	Two cores studied: A first core with a 60-cm high fissile zone A second with a 90-cm high fissile zone First "sodium" core First measurements of the reactivity effect in the event of sodium drainage
	3B	1970, 1971	R1	Metal (enriched U)	Several axial blankets studied (depleted uranium, steel/sodium, UO ₂ /sodium)
	4B	1971	R3	Metal (enriched U)	
	4A	1971	Z3	Metal (UPuFe)	
	4B'	1972, 1973	R3	Metal (enriched U)	"Absorber rod at center" program Measurement of radial and axial "sodium" void
	PLUTO	7A	1974	ZONA3	Oxide (UPuO ₂)
6A'		1975	ZOCO1	Oxide (UPuO ₂)	Smallest core ever created Approximately 27 cm critical radius
PECORE 2		1975	ZONA2	Oxide (UPuO ₂)	CEA/CNEN collaboration for the PEC reactor

degree, the physical characteristics and problems of large cores. The RACINE experiments thus enabled:

- The in-depth study of the "radial composite core" concept (RACINE 1A, 1B, 1C, and 1F)
- The question of calculating the efficiency of control rods and interaction problems between rods (RACINE 1D and 1E) to be treated
- Investigation of certain questions concerning SUPERPHENIX neutron control (simulation of neutron guides)
- Examination of calculation tool performances and the experimental technique used for the "checkerboard pattern" subcritical approach selected for loading SUPERPHENIX

The measurements carried out during this program are summarized in [🔗 Table 6](#).

■ **Table 6**
Measurement carried-out during RACINE program

Parameter	Program phase	Comments
Reaction rate distribution	RACINE 1A	Different fertile ring positions but with the same volume
	RACINE 1B	
	RACINE 1C	Increased ring volume
	RACINE 1F	Measurements close to control rod singularities
	RACINE 1E	IRMA experiment – international benchmark for reaction rate technique inter-comparison
	RACINE 1I	
γ -Heating	RACINE 1A	Multi-laboratories inter-comparison of techniques
Control rod worth	RACINE 1D	A reference core and a configuration with a single rod at core center
	RACINE 1E	Multiple rod configurations
	RACINE 1F	Inter-comparison of rod drop analysis method (CEA/France, ANL/US, GKAE/Russia) for inserted reactivities in the range [0.25\$; 1.2\$]
Criticality approach and neutron control lattice issue	RACINE 1S	
Sodium void	RACINE 1F	

The RACINE 1A, 1B, 1C configurations were aimed at studying different configurations each with a central island and an external fertile ring. In these three configurations, the external ring was positioned differently but its volume remained the same.

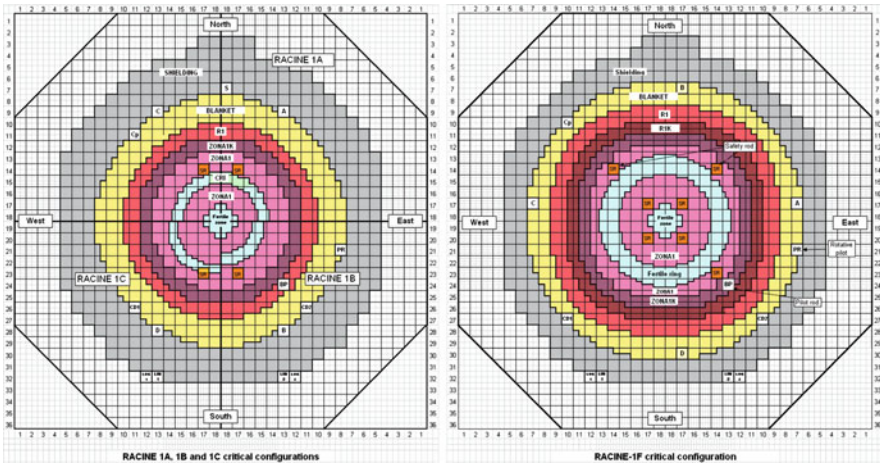
RACINE 1F was aimed at studying the effects produced by a larger volume fertile ring. This core is one of the largest cores ever built at MASURCA. The external diameter of the fissile zone was approximately 2.2 m.

Two distinct experiments were interested in the calculation and measurement of the reactivity weight of control rods:

- The RACINE 1D experiment that had two configurations: a “clean” reference critical configuration and one with an absorber rod simulated in the core’s center.
- The RACINE 1E experiment for which the goal was to study the problems of interaction between rods. This experiment was an initial approach to problems raised by large cores though the separation ratio of eigenvalues is much lower than the desired values.

The main objective of the RACINE 1S program was to study the checkerboard pattern loading method selected for the start-up of SUPERPHENIX.

- Creation of two critical configurations comprising a significant number of thinner assemblies (75% steel, 25% sodium)



■ Figure 49

RACINE 1A, 1B and 1C critical configurations.
RACINE, 1F critical configuration

- Simulation of the “neutron guide” system implemented at SUPERPHENIX

7.4 The BALZAC Program (1985–1988)

Additional studies to calculate the worth of control rods and the effect of the design (heterogeneity effect). Fine simulation of rods used at SUPERPHENIX to explain the calculation-experiment deviations observed during start-up tests.

7.5 The CONRAD Program (1989–1992)

Study of the axial heterogeneous concept but with a “decoupled large core” phase (separation parameter of eigenvalues above 15) was never carried out.

7.6 The BERENICE Program (1993)

This was the international Benchmark on measuring the effective fraction of delayed neutrons (beta effective) on two different cores:

- A uranium core, loaded with the R2 cell, similar to the 2B core studied in 1969
- A plutonium core loaded with the ZONA2 cell

7.7 The CIRANO Program (1994–1997)

This program included three main phases. The first one, devoted to the study of the replacement of fertile blanket by a steel/sodium reflector, included three different configurations:

- ZONA2-A: reference core with uranium/sodium (50/50) blanket

- ZONA2-A3: change of the radial Uranium/Sodium blankets with a steel/sodium reflector (75/25)
- ZONA2-B: change of the axial Uranium/Sodium blankets with a SS/sodium reflector (75/25)

The second phase addressed the internal assembly storage zone issue. It also included three different configurations:

- ZONA2-B SI-Ref: reference configuration with an extended steel-sodium reflector
- ZONA2-B-SII: set-up of a row of fissile tubes in the storage zone
- ZONA2-B-SI2: set-up of a row of absorber tubes between the storage zone and the core

The last phase of the CIRANO program aimed to load, in the central zone of the ZONA2B configuration, some tubes with a high Pu content and various Pu isotopic compositions. Pu content varied in the [25%; 48%]. Pu240 content varied from 8 to 33%. The objective was to carry out characterization measurements with a central zone with features intermediate between SUPERPHENIX and CAPRA (Consommation Accrue de Plutonium dans les Réacteurs Avancées – Increased Burn Up of Plutonium in Advanced Reactors).

7.8 The COSMO Program (1998–1999)

From 1998 to 1999, the COSMO program aimed to study the Physics of the irradiation of long lived fission products targets in moderated sub-assembly at the periphery of fast neutron reactors. The effects of various moderators, $^{11}\text{B}_4\text{C}$, CaH_2 , ZrH_2 , have been investigated. This program helped in particular, to prepare the ECRIX experiments that were loaded in the PHENIX reactor in 2003.

7.9 The MUSE Program (2000–2004)

Neutronic experiments, studies and the associated calculation tools have mainly been achieved in the past for *critical* reactors. Experimental techniques have also been developed, directly applied to power critical operating lattices. The same approach for studying neutronics of subcritical lattices driven by an external source is based on the decoupling of the validation of the subcritical multiplying medium behavior from the validation of the external source characteristics.

Following this roadmap, the MUSE experiment series at MASURCA constituted the first phase at zero power. From 1995, the MUSE-1 experiments then the MUSE-2 experiments, performed with a ^{252}Cf source located at the center of the MASURCA core, aimed to demonstrate that experimental measurement techniques used for critical cores could be also used for subcritical configurations. In 1998, the MUSE-3 experiments constituted the first important parametric study with the loading of several configurations with increasing subcriticality levels. Based on the use of a commercial neutron generator, once more located at the center of the core, these experiments helped, following the problems encountered in the interpretation of measurements, to define the conditions to carry out a MUSE-4 program and to specify the characteristics of a more intense and more suitable neutron source for the envisaged measurements.

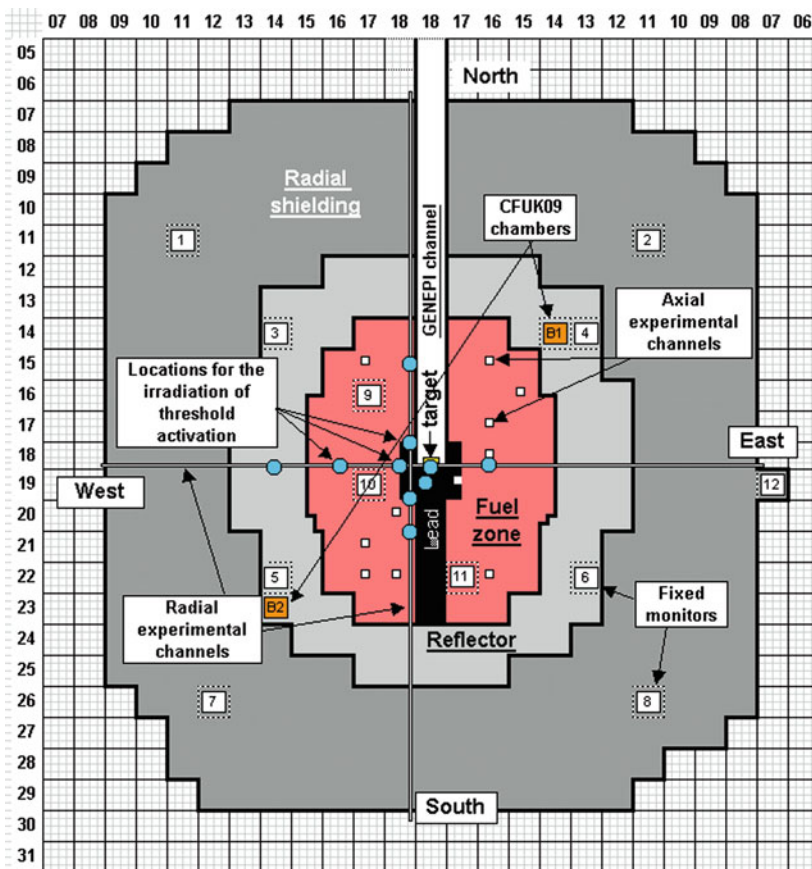
The objectives of the MUSE-4 program were (1) to operate a fast subcritical core coupled with an external neutron source simulating the spallation source of an ADS without feedback effect, (2) to characterize such a lattice providing experimental data for calculation tool

validation and (3) to investigate techniques and analysis methods for subcritical measurement and monitoring.

All the configurations, representative of a fast burner reactor, were loaded with MOX fuel and sodium as a coolant. The core was surrounded, axially and radially, with a reflector composed of sodium and stainless steel. The simulation of the spallation target and the neutron source (the GENEPI neutron generator consisted of a 250 keV deuteron beam horizontally guided on a target (either TiD or TiT) located at the center of the core and surrounded by a lead buffer. To compensate the spatial effect due to the presence of the GENEPI guide in the north part of the loading, the south symmetrical part was loaded with pure lead (99.99% of Pb) simulating the Pb circulation of the target.

7.10 The Facility Refurbishment Project

Before new experimental programs within the framework of the GEN-IV forum are launched, important work will be conducted at MASURCA in order to extend its service life. This



■ Figure 50
The MUSE-4 Program: radical critical configuration

renovation program will mainly impact the electric power supplies, the back-up lattices, the handling machine, the core cooling circuits, and fire prevention. Seismic reinforcement work and the complete modification of the control room will be also carried out. This “new” facility should start by 2015–2017. Outlines of experiments in support of SFR (GENESIS program) and GFR (ENIGMA program) have already been investigated. This work is being pursued.

7.11 A Program in Support of SFR and the 2020 Prototype: GENESIS

For oxide fuel FBRs, an experimental program can be built based on the ZONA3F* or ZONA3M* cells. It is, however, observed that the cells are not very reactive: $k^* \sim 1.05$ and 1.09. Therefore, in practice, it will be difficult to build a homogeneous core exclusively made up of these patterns. To maintain reasonable experimental volumes (outer diameter of the fissile zone < 1.4 m), we will have to radially create cores with two fissile zones (at least) to reach criticality: the inner zone made up of ZONA3F* cells or ZONA3M* cells, will be surrounded by a peripheral zone supplying the additional neutrons. The inner zone should be large enough for the fundamental mode to be established in the central region. The outer zone will be made up of enriched uranium-based cells, asymptotically equivalent to the inner cells.

For carbide fuel FBRs, a cell similar to ZONA3F* or ZONA3M*, but U-Pu-C fuel based, is to be created using graphite terminal blocks. The tests conducted are similar to those proposed for oxide cores.

The cores thus created will be surrounded by a radially compact zone of reflectors-shields and axially topped with a sodium plenum.

The GENESIS program, for GENERation of Experiments for Sodium-cooled Innovative Systems, will include:

- A *full neutron characterization* of the core (fundamental mode at center): reactivity, spectral index measurements at the center, material buckling, reaction rate cross-members, important cross-members, β_{eff} , etc.
- A parametric study of *sodium drainage* effects on variable height zones
- Partially or fully “drained plenum” configurations
- Study configurations for softening of the neutron spectrum in the core
- Studies of variations by *substitutions* of the following materials *at the center* of the core:
 - Deteriorated plutonium zone (+ effect of local drainage)
 - Absorbers
 - Zone made up of another fuel (carbide, metal) + effect of local drainage
 - Samples of various materials
- *Gamma heating* measurements
- Characterization measurements of core-reflector (➤ Sect. 6.2.4) and core-plenum *interface zones*

Study of the plenum drainage and drainage in the core could be limited to a central zone of approximately 20–30 tubes. In doing so, the time needed to conduct these experiments is approximately 1 and a half years: 8 months for loading and characterization of the initial configuration, 6 months to create different “drained plenum” configurations (subcritical and critical measurements), 4 months for sodium drainage experiments in the core (subcritical measurements only).

Creating these configurations, based on a single ZONA3M* type fissile cell (no peripheral driver zone), would require a complement on the stock of Pu-based fuel. Configurations implementing different patterns, from the core's center towards the periphery, can nevertheless be created with PuO₂-UO₂ fuel, currently in stock, and an addition of enriched metal uranium terminal blocks.

7.12 A Program in Support of GFR: ENIGMA

The ENIGMA program, Experimental Neutronics Investigation of Gas-cooled configurations in MASURCA, is devoted to GFR system generic phenomena in an initial phased of approximately 2 years. This initial phase relies on the use of current fuel stock.

Like GENESIS, this program will include a set of *physical characterization* measurements of a reference core, which will be based on the ZOGA1 cell. *Substitutions* in a central zone will be used to study the effects of streaming, the softening of the spectrum by introducing graphite, deteriorated plutonium vector fuels, the effects caused by the presence of innovative structure materials (Si, Zr), etc.

A second phase will be dedicated to studying control means. This could be accomplished by introducing an absorber rod for which the drawing would be changed, into the core's center. This study could then be conducted by moving the same rod away from the core's center to be in real conditions of a rod in a power reactor.

Finally, in a third phase, over a period of 2 years, more specific problems will be looked into, highlighted by design studies conducted within the frameworks of GEN-IV and REDT (Réacteur Expérimental et de Démonstration Technologique – Experimental and Technological Demonstration Reactor). It could be carried out with a core partially loaded with fuel (U,Pu)C (several batches with different Pu vectors) for which the supply will have been launched long enough in advance to follow through with safety studies as well as the updating of the safety report. For this reason, it can be noted that MASURCA originally had UPuFe (two different fabrications with 4 and 8% Pu240 respectively) for simulation of both oxide and carbide fuels (where the oxide oxygen was provided by Iron oxide simulation elements – Fe₂O₃ – and the carbide carbon provided by graphite simulation elements). This fuel was eliminated in the early 1970s following handling problems encountered.

7.13 A “FBR Large Cores” Generic Study Program

This program is aimed at studying particular specific phenomena for FBR large cores: decoupling between the various zones, questions related to distortion of the power distribution map, interactions between absorber rods, instrumentation and detection problems in the event of incidents and/or accidents (for example, issue of handling error).

To facilitate carrying out this type of experiment, there would be a need to add to the stock of materials available at MASURCA. As a reminder, although the CONRAD-DC program (never carried out) was supposed to use all the stock (ZEBRA Pu metal included), the amplification factors of the various configurations remained nevertheless below typical values for envisaged power cores.

Due to the lack of enough fissile material to create a large volume block, this core could be created based on the ZOCO3* cell, which particularly allows the migration area of neutrons to

be diminished, and therefore neutronic conditions equivalent to those of a large core in a small block to be created. Measurements will involve the study of radial decoupling. The problem of optimal positioning of control rod curtains will be studied.

Such a program could *last* for approximately 2 years: loading and characterization of the reference configuration (10 months), characterization of decoupling effects between zones (8 months), simulation of accidental configurations (handling error, rod riser) (6 months). The study of “large core instrumentation” issues could be conducted in parallel, during the various phases of the characterization program.

7.14 A “Reflector and Shield” Program

This program is of interest for all future FBR systems, implementing various reflector and shield concepts: homogeneous reflectors of various natures like steel, SiC, ZrC, Zr₃Si₂, heterogeneous reflectors which may contain absorber materials, more or less compact protection zones.

In order to simplify things, it is suggested that these studies be conducted on axial reflectors (30 cm high minimum) and on a radius zone limited to twenty assemblies. This solution, if acceptable (insignificant disturbances along the measuring axis), would allow procurements and the time required to change from one solution to another to be limited. A 1-year program would probably allow 4–5 different concepts to be studied.

7.15 A “Deteriorated and Accidental Configuration” Program

The purpose of this program would be to create benchmarks to check the quality of calculation predictions on configurations very different from those normally processed. This program could cover aspects such as fusion of the structure tube, fuel collapse, fuel compacting, as well as configurations with other distributions of materials.

For this type of experiment, only reactivity effects would be measured and depending on the expected variation, they could even be limited to subcritical measurements. A program of this type could therefore be carried out relatively quickly if the number of MASURCA tubes to be remodeled remains limited.

8 Experimental Methods Used and Being Developed on These Critical Mock-Ups

8.1 The Main Measuring Techniques Used

Mainly two types of measurements can be identified, which can be associated with a large number of experimental techniques:

- So-called “online” measurements, that is to say mainly monitoring fission chamber counting rates (in critical or subcritical)
- Postirradiation measurements, carried out directly on fuel rods (γ -scanning), after irradiation in the core

8.1.1 Measurements by Miniature Fission Chambers

Measurements by fission chambers can be separated into two categories, depending on the desired integral quantity to be obtained:

- *Kinetic* measurements, mainly doubling time and rod drop measurements
- *Quasi-static* measurements, where the counting rate of chambers is analyzed. They provide information on the criticality level of the core or on fission rate distributions or information on the local spectrum in the lattice

8.1.2 Measurements by γ Spectrometry

Gamma spectrometry measurements (γ -scanning) are postirradiation: they provide information on the reaction rates generated in the core. The main rates measured are fission (locally or its distribution) and radiative capture, by measurement of the total gamma activity of the fuel rod in question or that of specific isotopes (fission products or capture products). In this way, it is complementary to the measurement of distribution by fission chambers. Gamma spectrometry can be split into two complementary techniques:

- *The integral gamma scanning technique*, used for axial and radial distribution measurements in fuel rods with the same or a similar nature. It provides an averaged value in energy on the neutron spectrum. It is used to validate calculation models of assemblies, or 2D core calculation models, even 3D if an axial heterogeneity is present.
- *The specific peak technique*, also called “peak check” where the activity of a specific isotope is measured. It is used in power calibrating two integral γ -scanning maps carried out on rods of different natures, or to determine specific spectral indexes, such as the modified conversion rate.

8.2 Classification

It is not easy to process critical mock-up measurements as several approaches can be chosen:

- Classification according to measurement techniques (fission chambers or γ -scanning)
- Classification according to integral variables of interest

We have chosen the latter approach in this document. This allows information provided by measurements in terms of qualification of calculation codes to be detailed.

8.3 Measurement Electronics at EOLE/MINERVE

Measurement electronics at EOLE are used for both in core measurements, that is to say by fission chambers, and postirradiation measurements (gamma spectrometry). Measuring channels are based on a similar principle. Each channel is equipped with:

- A detector (fission chamber or diode), which enables the collection of loads associated with a specific reaction (neutron for the fission chamber, or photon in the case of spectrometry)
- High voltage (HV), connected to the detector
- A preamplifier and a load amplifier, to formulate impulses emitted by the detector

- A discriminator
- A coder
- A signal processing interface

Here, particular attention will be paid to the electronics associated with spectrometry.

8.3.1 γ Spectrometry Benches

Several γ -scanning benches are used in the facility. They measure fuel rod gamma activity. There are five of them.

- BASILIC, used for integral γ -scanning axial and radial distributions and specific peak measurements
- BANEX, DECROISSANT, and PIC LA for decay measurements during integral γ -scanning and specific peak measurements
- Capture U8, with respect to measuring the modified conversion rate

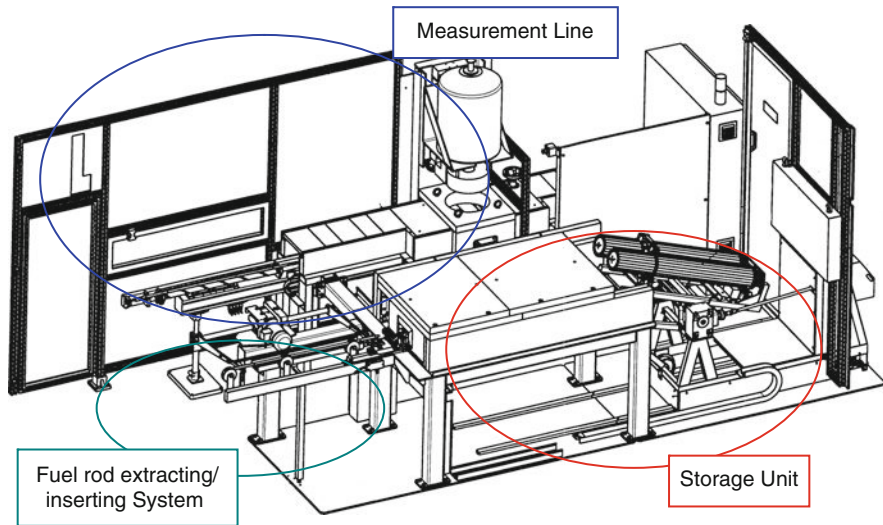
The detectors used are hyper pure Germanium diodes (HP-Ge), cooled with liquid nitrogen. These detectors enable fine resolution of peaks emitted by fission products.

Each bench has its own electronics, calibrated, steered, and qualified separately. However, these electronics are identical, in order to homogenize experimental tools (► [Fig. 51](#)).



■ Figure 51

View of gamma spectrometry benches used at EOLE and MINERVE



■ **Figure 52**
Schematic diagram of automatic changer

8.3.2 Automatic Changer

One of the large improvement works performed over the last few years was the creation of an automatic fuel rod changer called BASILIC, to replace the old system where rods were placed one by one under the measurement diode. It has numerous advantages which include the following:

- Fewer human risks during measurements.
- Risks of rod drops avoided.
- Time gained between two measurements.
- Minimized contact between researchers and fuel rods (reduced dosimetry).
- Optimized precision for the position of rods under the diode (► [Fig. 52](#)).

The changer comprises three main parts, shown in (► [Fig. 53](#)).

1. The rod storage unit, made up of two storage drums which can hold 20 rods each, placed on a tilting trolley to store rods in a reinforced tunnel
2. The rod extracting/inserting system, made up of a grappler arm and a conveyor to carry rods to the measurement line
3. The actual measurement line made up of a sideways moving trolley, the diode and γ shielding/collimation materials

8.3.3 Use of DSP

In the approach for improvement, control, and reduction of uncertainties and experimental optimization, the old analog measurement channels dedicated to gamma spectrometry were



■ Figure 53

View of the automatic changer

fully renovated to switch to the use of a digital channel. The Digital Signal Processor (DSP) stage replaces the amplifier-coder pair in the analog channel. It allows systematic errors linked to electronics downtime to be highly minimized thanks to certain advanced functions of the digital coder part, particularly the ability to take into account stacks during acquisition. At DSP output, two AIM multichannel analyzers allow the DSPs to be connected two at a time in the NIM racks and to connect them directly to the acquisition PC through an Ethernet connection (or USB), which greatly facilitates the synchronized control of the five measurement benches. They also help avoid compatibility problems with ISA buses, which are more and more frequent with new PCs.

The use of these DSPs on the five spectrometry channels either increases counting rates all while enabling correction of downtime to ensure measurement quality (the statistical uncertainty linked to counting itself is therefore highly diminished in the final result), or reduces measurement times thanks to its ability to process the strongest signal (► Fig. 54).

8.4 Fission Chambers

One of the historical activities of CEA/Cadarache is to design and manufacture neutron detectors called fission chambers (FC). These fission chambers are manufactured in a dedicated laboratory then used in nuclear reactor cores in France or abroad, with the aim to locally characterize the neutronic field (fluence rate, spectral indexes, etc.). This laboratory, which is one of a kind in Europe or even worldwide, has the ability to provide physicists with special detectors unavailable on the market, notably due to the nature of sensitive deposits made available (thorium, uranium, neptunium, plutonium, etc.). For example, the only one French manufacturer of fission chambers can only provide U^{235} detectors in its catalog.

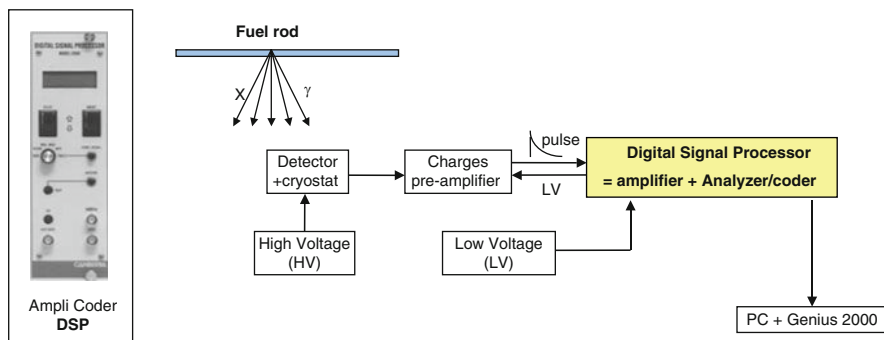


Figure 54
Measurement system

These small detectors have the interest of obtaining local neutron flux measurements with precise positioning and a signal obtained and processed by the measurement channel, mainly due to neutrons.

Fission chambers are gas detectors where one of the two cylindrical electrodes is covered with a thin layer of fissile matter. In a neutron field, the nuclei of this deposit can “fission” and thus emit two very energetic fission products (160 MeV overall). They are emitted at 180° from one to the other: one of the two fission products is stopped in the deposit itself (or its base) and the other will ionize the gas (usually argon) contained in the detector. Charges are collected through the electrical field generated by the high voltage applied to the two electrodes.

The general characteristics of a fission chamber are:

- Bias voltage
- Gas pressure: 50–500 V, 5–20 bar
- Lining thickness $< 1 \text{ mg cm}^{-2}$

We therefore measure either pulses or a constant current if the number of fissions is high. This current increases with the bias voltage up to a V_{\min} value where all electrons produced have been collected (before any recombination in the gas). This phenomenon, called chamber saturation, exists up to another voltage V_{\max} at which point sufficiently energetic primary electrons will in turn ionize the gas. This saturation range (or saturation plateau) corresponds to the main operating zone of the sensor.

These fission chambers are generally manufactured in a glove box as shown in [Fig. 55](#).

The process used to assemble fission chambers is tungsten inert gas (TIG) or laser welding. Welding is performed in an argon atmosphere stabilized by a few rods in a sealed chamber placed in a glove box used for welding ([Fig. 56](#)).

The standard models of assembled sensors are miniature cylindrical fission chambers with an outside diameter of 8, 4, and 1.5 mm. CEA can also design prototypes to meet a specific requirement ([Figs. 57–59](#)).

It is therefore a live “in-core” measurement which requires the presence of a measurement channel (instrumentation tube to allow passage of the measuring rod). This fission chamber is connected to an electronic channel with a pre-amplifier, amplifier, and multichannel analyzer to obtain a pulse spectrum which is then processed ([Fig. 60](#)).



■ Figure 55
Glove box holding electrodepositions



■ Figure 56
Glove box holding electrodepositions



■ Figure 57
Eight millimeter fission chambers



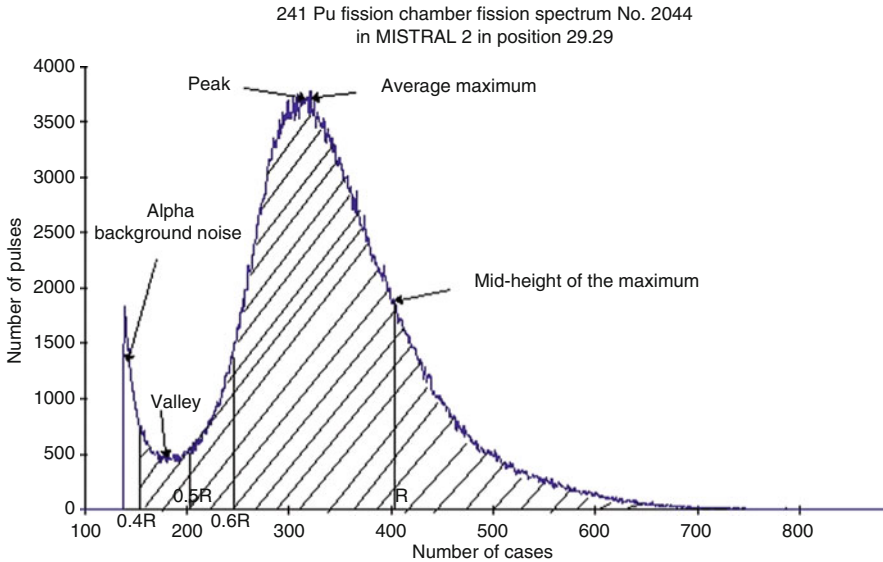
■ Figure 58
Four millimeter fission chambers



■ Figure 59
1.5 mm fission chambers

8.5 Gamma Ionization Chambers

The gamma ionization chamber is associated with a 7-mm diameter cable, an electrometer with a PC outlet, and an acquisition software program for online recording.



■ Figure 60

Example of measurements obtained with these fission chambers. Fission spectrum of a ²⁴¹Pu-lined fission chamber



■ Figure 61

Gamma ionization chamber

These ionization chambers must be calibrated beforehand using a reference gamma source.

The chamber can be introduced into the reactor either in fixed or movable position through an automatic linear axial positioning device (positioner).

The gamma ionization chamber used is of 0.3 cm³ PTW semiflex type. Its outside diameter is 6.9 mm. Its sensitivity limit is 1.2 mGy min⁻¹ (☛ Fig. 61).

This ionization chamber was implemented during the ADAPH program in MINERVE in 2005 (see ☛ Sect. 5.6). It particularly enables the evolution of the delayed gamma population to be followed after a power transient.

8.6 Fissile and Activation Detectors

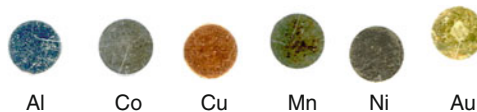
A case of ten activation detectors covering a wide range of use is available in the measurement room of the EOLE/MINERVE facility (► Fig. 62).

It allowed characterization of the flux by power unit ($2.5 \times 10^6 \text{ n cm}^{-2} \text{ s}^{-1} \text{ W}^{-1}$) and the neutron spectrum of the thermal thimble (measurement channel located in a graphite assembly, outside the driver zone) of MINERVE using the Cadmium ratio measurement ($R_{Cd} \approx 3$).

It is planned that this irradiation channel will be used to take capture cross-section measurements on actinides of interest, in particular, ^{238}U and ^{237}Np . The idea is to determine the Cadmium ratio of an isotope of interest, in relation to that of a reference isotope with a well-controlled section. An additional study carried out using other detectors, notably manganese, gold, aluminum-gold (0.1%), copper, tantalum, and cobalt helped assess those most well adapted to this type of study.

A device for centering and positioning dosimeters and calibration sources was also manufactured in order to reduce the uncertainty on the ability to reproduce the measurement (► Fig. 63).

Further to these preliminary studies, Cu-Mn (80%) and Al-Au (0.1%) “monitor” dosimeters in the form of 0.762 and 1 mm wires will be used, along with ^{238}U and ^{237}Np fissile detectors, in the form of encapsulated balls in a Vanadium capsule. It will first involve showing the feasibility of the thermal ($\sigma_{2,200}$) and epithermal (I_0) ^{238}U capture cross-section measurement, with an uncertainty below 5%. This measurement can then be extended to ^{237}Np and more generally, to any other isotope of interest (fissile or not) in the future.



■ Figure 62

Examples of leaf type dosimeters of the EOLE/MINERVE facility Al, Co, Cu, Mn, Ni, Au



■ Figure 63

Dosimeter centring and positioning devices

8.7 Procedures Linked to the Oscillation Technique

8.7.1 Oscillator

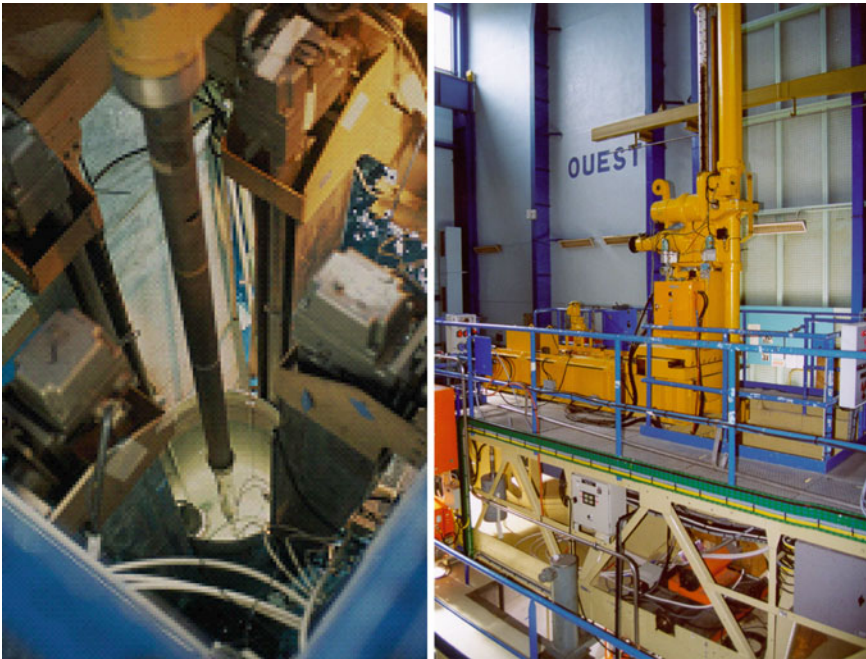
It is a vertical electromechanical oscillator, controlled by a position servomechanism with the following main characteristics:

- Sinusoidal, square, or pseudo-square movement
- 0–900 mm course with selection of the average position
- Sinusoidal period: from 10 to 120 s
- Square or pseudo-square period: from 20 to 120 s
- Square transit time: 1 s
- Pseudo-square transit time: 5 s

It is controlled by a time base with a clock, which issues synchronization signals sent to the acquisition system (👉 [Fig. 64](#)).

8.7.2 The Automatic Pilot Rod

The MINERVE automatic pilot rod (see 👉 [Fig. 65](#)) is made up of a rotor and a stator covered with cadmium sections. Its total worth is several dozen pcm, and its differential worth is from



📷 Figure 64
View of the MINERVE oscillator

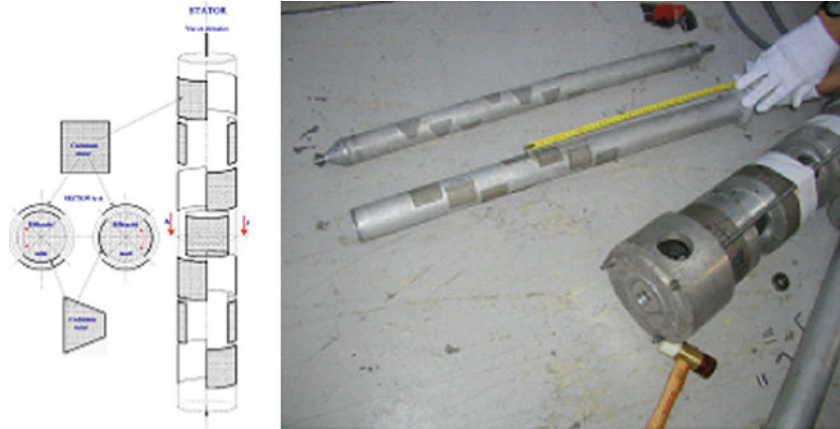


Figure 65
MINERVE reactor automatic pilot rod with cadmium sections

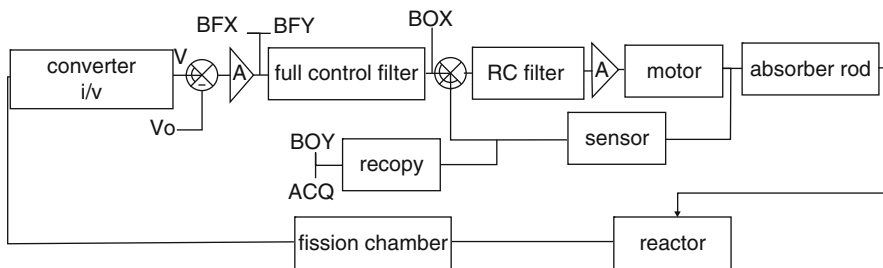


Figure 66
Closed loop control between the pilot chamber and the automatic pilot rod

0.3 to 1 pcm per degree depending on the layout of absorbers and the position in the reflector. A capacitive sensor allows the rotor's rotation angle to be recorded (i.e., the coverage of cadmium sectors) in the form of analog voltage.

It is coupled with a CC5 type boron lined ionization chamber (“pilot chamber”) placed in the reflector through a closed loop control channel (see Fig. 66) controlled by neutron flow variations.

This measurement assembly has a wide pass band (of approximately 10 Hz) and high performance in order to compensate for reactivity variations generated by the oscillation of samples. It allows reactivity variations to be measured with $10^{-8} \Delta k/k$ precision for a measurement period of approximately 1 h. It also ensures the criticality of the core by compensating for the slight reactivity disturbances caused by the oscillations.

The pilot rod underwent maintenance in 2002 (installation of a ball bearing and replacement of the rod). The pilot chamber connector technology was also reworked in 2003. It must however be noted that in order to extend programs, the pilot chamber and closed loop control channel will eventually need to be replaced by more modern systems.

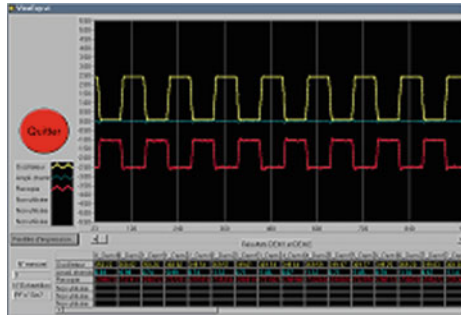


Figure 67

Example of an acquisition signal during an oscillation measurement

8.7.3 Acquisition and Online Processing System for Oscillation Measurements

Oscillation experiments require the analysis of periodic signals presented in the form of analog voltages, images of phenomena.

Information (see Fig. 67) on the pilot chamber signal (in blue), the rotation angle of the pilot (in red), and the position of the oscillator (in yellow), are synchronized on the clock which controls the oscillator and are processed in real time by an acquisition system comprising a micro-computer and an acquisition card with analog-digital converters.

8.7.4 Active Sample Handling Equipment

Ventilated enclosure: A ventilated enclosure (see Fig. 68) is associated with the MINERVE and EOLE reactors. It contains:

- Two glove boxes for handling samples containing plutonium
- One shielded cell for handling fissile samples irradiated in power reactors, or more generally, active samples

It should be noted that the MINERVE facility currently does not have a neutron shielded cell.

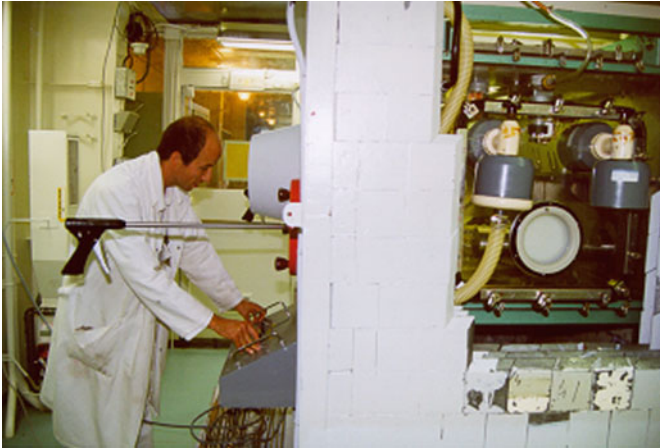
The transfer container or “milk can”: A “milk can” container (see Fig. 69) is used to transfer irradiated or active samples from the shielded cell to the chimney of the MINERVE reactor.

A neutron shielded milk can is currently being studied in order to transfer Curium samples for the OSMOSE program (see Sect. 5.7) to the reactor.

8.7.5 Oscillation Samples

Sample Origin and Manufacturing

In general, samples studied until now in MINERVE can be classified according to two categories: irradiated (or fresh) fuel samples, and samples containing a specific dopant isotope.



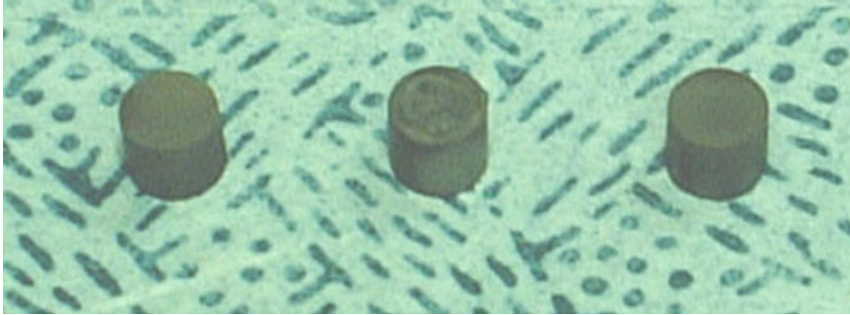
■ Figure 68
Shielded cell for handling active samples



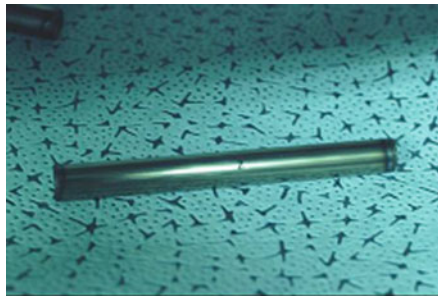
■ Figure 69
"Milk can" for transferring samples from the cell to the MINERVE reactor chimney

The general characteristics of previous and current samples are listed below. However, there is the possibility of changing these characteristics in the future, for example, to adapt to new types of fuels (HTR fuel rods for example).

- *Irradiated samples* are made up of a length of irradiated fuel rod from a light water power reactor (LWR) assembly, generally cut at the Cadarache Department of Fuel Studies. This length therefore includes both the irradiated fuel and the original cladding of the rod. It is approximately 95 mm long.
Two sealed Zircaloy four sheaths make up the outer casing of the sample. Their dimensions are adapted to those of the length of fuel.
The material balance of the irradiated fuel is known by dissolution of an adjacent length.



■ **Figure 70**
Example of fuel pellets for the OSMOSE program



■ **Figure 71**
OSMOSE oscillation sample

- *Samples containing a dopant isotope* are made up of fuel pellets containing the studied dopant isotopes, and two sealed Zircaloy four sheaths.

Fuel pellets (see example in ► [Fig. 70](#)) are manufactured by homogeneously mixing the dopant isotope in a matrix which can be either fissile (usually natural or depleted UO_2) or inert (Al_2O_3). The pellet column is approximately 95 mm long, and has a standard PWR diameter of approximately 8.1 mm. Pellet centering is generally favored in the case of a UO_2 matrix due to mechanical resistance, lack of humidity and mixture homogeneity. The dopant mass is determined using determining design calculations, and optimized so as to correspond with the linear operating range of the automatic pilot rod ($\sim \pm 10$ pcm). It should be noted that it is possible to create annular pellets to reduce the sample's reactivity if necessary.

In order to control the fuel's material balance, at least three control pellets are manufactured. Two of them are intended for analyses after dissolution. The third is preserved in case of inconsistency between the analyses of the first two.

The Zircaloy four sheaths generally have diameters of $\varnothing 8.36 \times 9.56$ mm, and $\varnothing 10.2 \times 10.6$ mm. The overall length of samples (see ► [Fig. 71](#)) is approximately 103.5 mm.

The sample manufacturer differs depending on the nature of the dopant isotope. An inert dopant can be used in a simple fume chamber or glove box, a radioactive isotope may require the much more cumbersome use of a shielded cell.

Sample Transport and Transfer

Transporting active samples (irradiated or containing gamma emitter actinides or neutrons for example) from their manufacturing location to the MINERVE, then from it to the MINERVE reactor, *has become a major issue* during recent experimental programs (HTC, CREDIT BURN UP, OSMOSE). It involves adapting to regulations in force and their changes, to available means, effective authorizations, regular maintenance and to the various constraints of the facilities involved.

Currently, the kinematics of samples is as follows:

$$\begin{array}{l} \text{manufacturer} \xrightarrow{\text{ad hoc flask}} \text{COMIR(CHICADA)} \xrightarrow{\text{IL30}} \text{INB MINERVE} \\ \xrightarrow{\text{milk can}} \text{MINERVE reactor.} \end{array}$$

To control the non-contamination and to transport active samples from their manufacturing location to COMIR hot laboratory (eventually replaced by CHICADE) requires a durable transport flask approved for the content of the samples. The RD15IIB should meet this requirement. An authorization extension is however required for any new types of content (for example, for all actinides containing OSMOSE samples).

Transporting samples from COMIR (CHICADE) to the MINERVE shielded cell requires:

- A durable transport flask approved for the content of samples
- That the shielded cell be equipped with docking compatible with the transport flask
- Zero contamination of samples (therefore, particularly a clean transport container)

Currently, the IL30 is used for transport between COMIR and MINERVE. This aging flask is currently the last existing able to adapt to the docking of the MINERVE shielded cell, however it will not last forever (it should also be noted that it cannot leave the Cadarache site). In addition, switching to PADIRAC type docking (adapted to the RD15IIB or equivalent) on the MINERVE shielded cell seems necessary in the long run.

Transferring the shielded cell to the MINERVE reactor plant is carried out using a “milk can.” It must be adapted to the type of radiation emitted by the sample (beta-gamma or neutrons).

9 Integral Parameter Determination Through Experiment

The physical measurements taken in a core modeled by a critical mock-up are used to qualify all or part of the core codes which will then be used in production. A full program is built according to the expectations in terms of qualification requirements, but also in terms of significant advances in measuring techniques (related precision and uncertainties). The variables of interest are called *integral parameters* (as opposed to differential measurements such as cross-sections), simply due to the fact that they are expressed as variables represented (mathematically) by integrals (on all or part of the space coordinates of the phases, notably energy).

The main parameters measured during an experimental campaign are the following:

- *The critical size* (through measuring the doubling time).
- *The reactivity effects*, that is to say the modification of the neutron balance in a particular configuration, due to inserting a particular heterogeneity (presence of absorbers, modification

of the geometry, aging of the fuel). When the reactivity variation is carried-out to another variation, it is referred to as *reactivity coefficients* (temperature coefficient, boron coefficient, etc.).

- *The axial and radial fission rate distributions* using the gamma scanning technique or using miniature fission chambers. In regular lattices, these measurements provide the material buckling.
- *Power renormalization* by specific peaks.
- *The spectral indexes* either by γ -scanning (for example, the modified conversion factor) or by using fission chambers.
- *The gamma doses*, which are a first step in determining gamma heating itself.
- *The delayed neutron fraction*, using neutron noise techniques.

For each type of measurement, the associated techniques are now generally outlined.


9.1 Critical Size

Critical size determination enables validation of different parts of a core calculation route:

- On a homogeneous lattice (one speaks about “regular” lattice), critical size gives information mainly either on nuclear data used by the code, the core (lattice) modeling being simplified, or on the self-shielding and leakage models for deterministic codes
- On a heterogeneous lattice (one speaks about “mock-up”), critical size enables validation of the calculation scheme in its totality, i.e., both nuclear data libraries and the numerical treatment of the Boltzman equation in the case of deterministic codes (self-shielding treatment, flux calculation by more sophisticated methods as Method of Characteristics, interface current in multicell, equivalence, etc.)

The critical size is fully characterized by:

- The number of rods loaded in the core
- The number of guide-tubes
- The temperature of the moderator
- The soluble boron concentration (if necessary)
- The residual reactivity of the core obtained by divergence and measurement of the doubling time
- The critical dimension of the pilot rod inserted into the core, in order to maintain power at a certain value
- The divergence date (mainly for MOX cores, due to the aging Pu)

The doubling time is systematically measured on EOLE during each approach. It is based on the monitoring of the neutron population of the core through the evolution of the counting rate of a calibrated fission chamber in the core. This monitoring is shown in  [Figs. 72–74](#).

The power increase is directly proportional to the neutron population increase, in such a way that the following can be written: $P(t) = P_0 \exp(\omega t)$ with $\omega \equiv \ln 2/T_d$, T_d being the doubling time of the critical configuration in question.

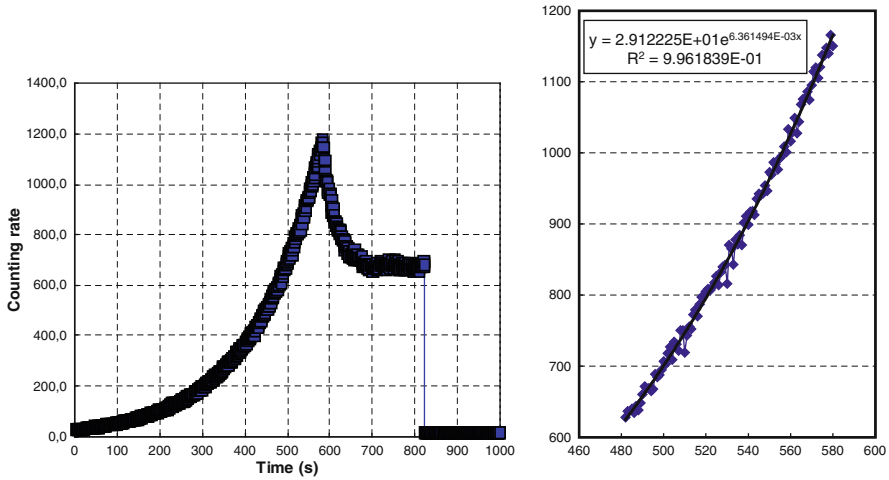


Figure 72 Measurement of the counting rate rise during divergence and extraction of the doubling time

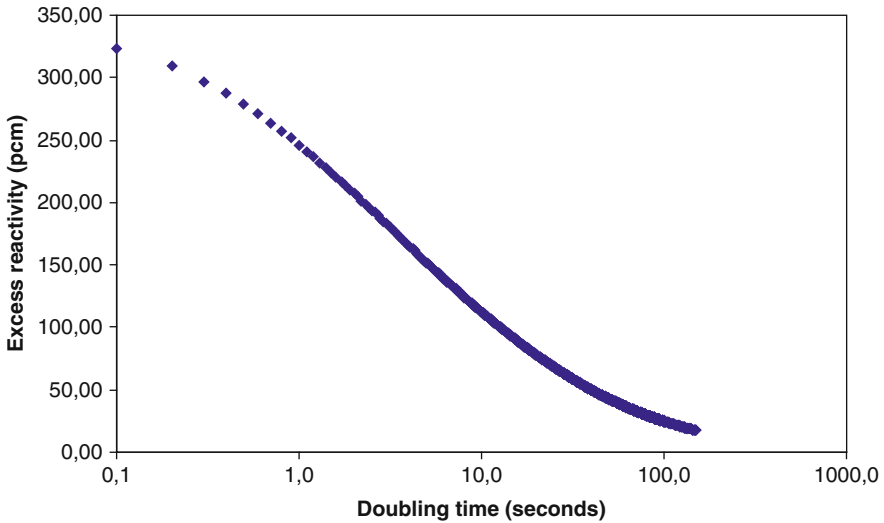
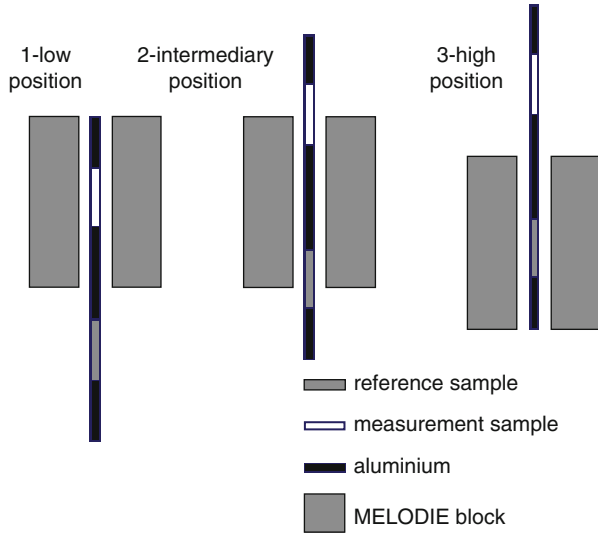


Figure 73 Example of Nordheim curve

The doubling time thus obtained is then inserted into the core's Nordheim equation, which provides the excess reactivity value (in delayed neutron fraction units – the pcm).

$$\rho_{excess} = \ell\omega + \beta - \sum_i \beta_i \frac{\lambda_i}{\omega + \lambda_i}, \tag{1}$$



■ **Figure 74**
Movement of samples during oscillations in MINERVE

where

- ℓ is the neutron generation time
- β is the effective fraction of delayed neutrons
- The λ_i and β_i are the partial decay and fraction constants of delayed neutrons in the delayed neutron i groups

The following figure shows the graphic representation of this evolution: (FUBILA/REF core).

9.1.1 Application of Critical Size Determination

This paragraph would formally belong to [Sect. 9.2](#). We will show how to use the critical parameters to deduce reactivity effects between to critical configurations. As we just mentioned, each critical configuration is fully determined by: the number and type of fuel rods and guide-tubes loaded, the boron concentration (if any), the temperature of the moderator and the excess reactivity ρ_{excess} deduced from the doubling time measurement by using the ad hoc Nordheim curve (for MOX core, one will add the date as complementary information). We will take the case of the isothermal temperature coefficient (ITC) for the sake of simplicity.

The ITC is formerly defined by the reactivity variation versus temperature between one (critical) state “ i ” and another denoted “ j ,” through the relationship: $\alpha = (\Delta\rho/\Delta T)_{i,j}$.

The reactivity variation can be covered by an increase or decrease of boron in the moderator, so that the ITC is expressed as

$$\alpha = \left(\frac{\Delta\rho}{\Delta T} \right)_{i,j} = \frac{\rho_{excess,i}(T_i, B_i) - \rho_{excess,j}(T_j, B_j)}{T_i - T_j} + \frac{C_{B,i} - C_{B,j}}{T_i - T_j} \left(\frac{\Delta\rho}{\Delta C_B} \right)_{i,j} \quad (2)$$

and becomes, without boron:

$$\alpha = \left(\frac{\Delta \rho}{\Delta T} \right)_{i,j} = \frac{\rho_{excess,i}(T_i) - \rho_{excess,j}(T_j)}{T_i - T_j}. \quad (3)$$

As one can see, the divergence approach needs to keep the configuration parameters (except temperature) constant in order to deduce a consistent coefficient. The difficulty arising in this approach is to recover a wide range of temperature variations by using the same critical size, in particular in the presence of boron or if the ITC value is high between two temperatures. The subcritical approach to this measurement is developed in [Sect. 9.2.8](#).

9.2 Reactivity Effect Measurements

Reactivity effect measurements are one of the most important parameters measured in the experimental reactors. Their precision involves many parameters and as many different techniques.

Various common techniques are described hereafter to measure reactivity effect measurements in critical to slightly subcritical lattices. The problem of ADS subcriticality determination, that is an absolute measure, will not be described here.

One will focus on three main techniques used:

- Inverse kinetics, for dynamic measurements
- Amplified and/or modified source methods (ASM and MSM) for quasi static measurements
- Sample oscillation technique

The first one is an absolute measurement, as the two other ones are relative measurements. They are based on the use of miniature fission chambers whose count rate is analyzed to unfold the reactivity effect.

9.2.1 Reactivity Worth Measurement by Inverse Kinetics

Reactivity effect measurement by inverse kinetics is a dynamic method based on online monitoring of counting during the experiment. It can be applied to a wide range of reactivity measurements without significant restrictions. On the one hand, it uses gross rod drop measurements of various rods and on the other hand, the time analysis of these files using an equation resolution Point Reactor approximation kinetics program. As a reminder, this equation is given by the following expression (1):

$$\begin{aligned} \frac{\rho(t)}{\beta} = & \frac{\Lambda}{\beta} \frac{\dot{C}(t)}{C(t)} + 1 - \frac{C_0}{C(t)} \sum_k \alpha_k \exp(-\lambda_k t) - \frac{\varepsilon}{\beta C(t)} \sum_k \zeta_{0k} \exp(-\lambda_k t) \\ & - \frac{1}{C(t)} \sum_k \alpha_k \lambda_k \int_0^t C(t') \exp(-\lambda_k(t-t')) dt' - \frac{s\varepsilon}{\beta C(t)}, \end{aligned} \quad (4)$$

where notations are standard. In particular, ε represents the fission chamber detection efficiency. This last equation is discretized for numerical resolution. Three major contributions can be pointed out:

- Prompt neutrons:

$$\frac{\Lambda \dot{C}(t)}{\beta C(t)}. \quad (5a)$$

- The source term

$$\frac{s\varepsilon}{\beta C(t)}. \quad (5b)$$

- Delayed neutrons

$$1 - \frac{C_0}{C(t)} \sum_k \alpha_k \exp(-\lambda_k t) - \frac{\varepsilon}{\beta C(t)} \sum_k \zeta_{0k} \exp(-\lambda_k t) - \frac{1}{C(t)} \sum_k \alpha_k \lambda_k \int_0^t C(t') \exp(-\lambda_k(t-t')) dt'. \quad (5c)$$

The discretized form of (4) is the following:

$$\rho_s(n) = 1 + \frac{\Lambda}{\beta\theta} \times \frac{W_{n+1} - W_n}{W_n} - \frac{1}{W_n} \times \sum_{j=1}^6 \alpha_j W_0 \exp(-\lambda_j t_n) - \sum_{j=1}^6 \alpha_j (1 - \exp(-\lambda_j \theta)) \sum_{p=1}^{n-1} \frac{W_p}{W_n} \exp(\lambda_j(t_p - t_n)) - \frac{\Lambda S_e}{\beta W_n}, \quad (6)$$

where

- $\rho_s(n)$ is the reactivity at time step “ n ”
- θ is the sampling time (typically 0.4 s)
- n is the current time (step)
- W_n is the power at time step “ n ”
- S_e is the intrinsic effective source seen by the detector
- The other notations have their usual significations

This statistical uncertainty increases with “ n ” because the counting decreases with time and because the reactivity at n depends on all reactivity measured at previous times. One evaluates this statistical uncertainty to range between ± 0.5 and 1.0%.

However, one must take into account the systematic uncertainties due to the kinetics parameters themselves which are calculated values. One evaluates the systematic uncertainty on the pilot rod reactivity due to each parameter to be:

- ℓ (Prompt neutron generation time): $< \pm 0.5\%$
- β : $< \pm 0.2\%$
- (α_j, λ_j) : $\sim \pm 5\%$

The associated statistical uncertainty on the reactivity measured by rod drop is small (less than 1%). The method is very sensitive to the effective source term S_e which must be determined with special care; the reactivity does not depend strongly on the prompt neutron lifetime and on the β_{eff} . The precision on (α_j, λ_j) is the dominant source of uncertainty.

The rod drop technique can be used with confidence for reactivity worths up to few delayed neutron fractions.

9.2.2 Reactivity Effects by Subcritical Measurements

9.2.3 Principle of Subcritical Measurements

The interest of subcritical measurements is to provide an additional value of a reactivity effect or reactivity coefficient by avoiding an analysis of two critical states for which either the number of rods or the soluble boron variation between the two states are to be taken into account as a bias in the calculation.

They help determine the reactivity effect of a local or overall disturbance (of any kind) using a critically measured reactivity standard (generally, the reactivity weight of the pilot rod measured with the rod drop technique). Just as for determining the critical size, these subcritical measurements of a reactivity effect allow libraries and/or calculation schemes of the pattern in question (regular or mock-up) to be qualified. These measurements apply just as well to the effects of an isolated absorber or a cluster of absorbers as to a temperature or soluble boron concentration variation. They are used to obtain an effect value in addition to that obtained by critical size measurement. They require counting rates of fission chambers arranged in the core.

The reactivity effects of a disturbance of any kind (absorber, solution boron, fuel substitution or temperature coefficient, etc.) are determined from counts carried out subcritically in a so-called disturbed configuration, and then compared with counts carried out in a so-called "reference" configuration. The subcritical measurements are carried out using fission chambers ($\varnothing = 8$ mm, with a high fissile mass content) arranged in several areas of the core at the mid-height plane. This determination of the reactivity is a relative method requiring the knowledge of a reactivity standard, which is generally the reactivity weight of the pilot rod, also measured, generally using the rod drop technique described in [Sect. 9.2.1](#).

9.2.4 Amplified Source Method (ASM)

The ASM method is based on the use of the occasional kinetic model, for which the steady state caused by a source (effective or external) is established. The equations, given irrespective of time, governing the system are the following:

$$\begin{cases} 0 = \frac{(\rho - \beta_{eff})}{\Lambda} \bar{N} + \sum_{i=1}^6 \lambda_i \bar{C}_i + S_{eff}, \\ 0 = \frac{\beta_{i,eff}}{\Lambda} \bar{N} + \lambda_i \bar{C}_i, \quad i = 1, \dots, 6 \end{cases} \quad (7a)$$

with \bar{N} the effective population of neutrons in the core

$$\bar{N} = \left\langle \phi^*, \frac{1}{\nu} \Phi \right\rangle \quad (7b)$$

\bar{C}_i the effective concentration of the i family of precursors

S_{eff} the effective outside source

λ_i the decay constant of the i family of precursors

ρ the core's reactivity

Λ the prompt neutron generation time

$$\Lambda = \frac{\langle \phi^*, \frac{1}{v} \Phi \rangle}{\langle \phi^*, F\Phi \rangle}. \quad (7c)$$

In steady-state operating conditions, time is not a factor; the average \bar{N} population of the core depends only on the source used and the negative reactivity inserted. Therefore,

$$\rho = -\frac{\Lambda S_{eff}}{\bar{N}}. \quad (8)$$

By inserting the reaction rate in the detector, defined by $R = \langle \Sigma_d, \Phi \rangle$, the following is obtained by multiplying the top and bottom of (8) with the previous notations (7b) and (7c):

$$\rho = -\frac{S_{eff} \langle \Sigma_d, \Phi \rangle}{R \langle \phi^*, F\Phi \rangle}, \quad (9)$$

where

S_{eff} is the effective outside source,

R is the reaction rate

Σ_d is the diffusion factor

Φ represents the flux (subcritical) in the reactor

ϕ^* is the adjoint flux in the critical reactor associated with the real reactor (it is a function of weighting, chosen as being the adjoint for the sake of convenience)

F is the multiplication operator by fission

With the approximations of the monokinetic point reactor, where the flux can be broken down into a function of time only $n(t)$ and a function of the other space coordinates of the phases $\psi(\mathbf{r}, E)$, the latter relationship is, more generally, written as follows:

$$\rho = -\frac{\varepsilon S_{eff}}{R}, \quad (10)$$

where

$$\varepsilon = \frac{\langle \Sigma_d, \Psi \rangle}{\langle \phi^*, F\Psi \rangle}, \quad (11)$$

where ψ is the shape factor of the subcritical flux, depending on \vec{r} and E , and stemming from the decomposition of the flux (depending on time) as in $\Phi(t, \vec{r}, E) = n(t) \Psi(\vec{r}, E)$. When the system is stationary, the subcritical flux is identified with the shape factor: $\Phi(\vec{r}, E) = \Psi(\vec{r}, E)$.

The relationships (10) and (11) show that the negative reactivity of a configuration is inversely proportional to the counting rate R of the detector if one assumes that ε and S_{eff} are constant. As the latter variables cannot be measured (only calculated), it is difficult, or even impossible, to associate them with any uncertainties. Therefore, the absolute measurement of reactivity is not possible with this method. However, it is possible to use it through another method using a reactivity taken as a reference standard.

If one knows the negative reactivity ρ_0 of a reference state which corresponds to a reaction rate measured in the detector R_0 , ρ_1 is deduced corresponding to the reaction rate R_1 through the following simple relationship:

$$\rho_1 = \frac{R_0}{R_1} \rho_0. \quad (12)$$

The negative reactivity measured through the ASM method is simply deduced from the relationship of two reaction rates (which in practice is reduced to two counting rates).

The validity assumptions of the kinetic-point model expressed (ϵ and S_{eff} considered as constants) require however, that the reactivity measured be low enough for the shape factor $\Psi(\vec{r}, E)$ to not only be modified locally, and for the detector to be considered as located outside the disturbed area.

When the reactivity variation due to a disturbance is too high to avoid spatial and energetic effects at the detector, a calculation correction is required. This correction is called MSM, which is described in the following section.

9.2.5 Modified Source Multiplication (MSM) Method

The corrective parameters to be applied to the detector's response stem from calculations of disturbances carried out on the various configurations of the studied core.

The starting equation is the source inhomogeneous transport equation

$$(F - L)\Phi = S, \quad (13)$$

where

F is the fission production operator

L is the decay operator (transfers, leaks, various absorptions, etc.)

S is the source term

This equation corresponds with two other sourceless relationships (direct and adjoint) without source corresponding to the related critical system:

$$\begin{cases} (\lambda F - L)\phi(\vec{r}, E) = 0, \\ (\lambda F^* - L^*)\phi^*(\vec{r}, E) = 0, \end{cases} \quad (14)$$

where $\lambda - 1/k_{eff}$, $\phi(\vec{r}, E)$ and $\phi^*(\vec{r}, E)$ are respectively the direct and adjoint fluxes of the critical state, F^* and L^* are respectively the adjoint operators of F and L .

Scalar products are used to write the following by multiplying (13) by $\phi^*(\vec{r}, E)$ and by integrating on the space of the phases:

$$\rho = -\frac{\langle \phi^*, S \rangle}{\langle \phi^*, F\Phi \rangle}. \quad (15)$$

By inserting the detector's response into the latter relationship, the following expression is obtained:

$$\begin{aligned} \rho &= -\frac{\langle \phi^*, S \rangle}{\langle \phi^*, F\Phi \rangle} \times \frac{R}{R} = -\langle \phi^*, S \rangle \frac{\langle \Sigma_d, \Phi \rangle}{\langle \phi^*, F\Phi \rangle} \times \frac{1}{\langle \Sigma_d, \Phi \rangle} \\ &= -\epsilon \frac{S_{eff}}{R}, \end{aligned} \quad (16)$$

where

$$\epsilon \equiv \frac{\langle \Sigma_d, \Phi \rangle}{\langle \phi^*, F\Phi \rangle} \quad (17)$$

and

$$S_{eff} = \langle \phi^*, S \rangle. \quad (18)$$

The definition of the detector's worth shows that it depends on both the position of the detector in the core (in relation to the disturbance) and, of course, the nature of the detector through the intermediary of Σ_d . The worth takes into account the disturbances induced near the detector through the shape factor $\Phi(\vec{r}, E)$.

In addition, the effective source depends mainly on the critical adjoint flux $\varphi^*(\vec{r}, E)$ and on the type of source used, S .

The reactivity can only give reactivity variation relative values, for the same reasons as the ASM method. For a reactivity standard (in "0" state), (16) is rewritten as:

$$\rho_1 = \underbrace{\frac{R_0}{R_1} \rho_0}_{\text{"ASM" value}} \times \underbrace{\frac{\varepsilon_1 S_{eff,1}}{\varepsilon_0 S_{eff,0}}}_{\text{MSM correction}} \quad (19)$$

the term $(\varepsilon_1/\varepsilon_0) (S_{eff,1}/S_{eff,0})$ takes into account the variation of the detector's worth and the effective source between the two compared states. These variables are calculated through the transport code.

The corrections used should allow any reactivity variation to be determined, regardless of its amplitude or the position of the detector. The corrective factor can be broken down into several terms.

Either the index m corresponding to the *measurement* (reaction rates in the detectors), or the c index corresponding to the *calculation* (detector worths and the source term)

Equation (19) can be rewritten

$$\frac{\rho_1(\vec{r})}{\rho_0(\vec{r})} = \frac{R_{m,0}(\vec{r})}{R_{m,1}(\vec{r})} \times \frac{\varepsilon_1(\vec{r}) S_{eff,1}}{\varepsilon_0(\vec{r}) S_{eff,0}}, \quad (20)$$

where

$$\varepsilon_i(\vec{r}) = \frac{\langle \Sigma_d, \Phi_i \rangle}{\langle \phi_i^*, F \Phi_i \rangle} = \frac{R_{c,i}(\vec{r})}{I_{F,i}} \quad i = 0, 1 \quad (21)$$

with $I_{F,i} \equiv \langle \varphi^*, F \Phi_i \rangle$ the fission normalization integral (for the i configuration)

This therefore gives,

$$\frac{\rho_1(\vec{r})}{\rho_0(\vec{r})} = f_{MSM}(\vec{r}) \times \frac{R_{m,0}(\vec{r})}{R_{m,1}(\vec{r})} \quad (22)$$

with

$$f_{MSM}(\vec{r}) \equiv \left(\frac{S_{eff,1}}{\langle \phi_1^*, F \Phi_1 \rangle} \right) / \left(\frac{S_{eff,0}}{\langle \phi_0^*, F \Phi_0 \rangle} \right) \times \frac{R_{c,1}(\vec{r})}{R_{c,0}(\vec{r})}. \quad (23)$$

This MSM corrective factor appears as a correlation factor between the detector's position and the inferred reactivity value, knowing the standard. When the MSM factor is equal to the unit, determination of the reactivity becomes independent from the position of the fission chamber. The flux's shape factor remains constant between the two states (low disturbance, the asymptotic rate is quickly established), as well as the effective source, and the kinetic point model applies. The results from the ASM technique are found.

9.2.6 Practical Implementation of ASM and MSM Subcritical Measurements

The subcritical measurement technique, based on amplification of the source, is based on the premise that the counting rates of fission chambers arranged in and around the core are proportional in terms of subcriticality in the core, according to the following relationship:

$$C = \frac{RCaFa}{\rho} \times \varepsilon_{MSM}, \quad (24)$$

where

- C is the counting rate in the chamber
- ρ is the subcriticality level
- $RCaFa$ is a proportionality factor (*Reactivity Calibration Factor*)
- ε_{MSM} is the “MSM” factor described in the previous paragraph

The $RcaFa$ factor is obtained by using the reactivity value of the pilot rod measured by inverse kinetics (rod drop). This factor is given by the following relationship:

$$RCaFa = \frac{\Delta\rho^{PR}}{\left(\frac{\varepsilon}{C_{PRd}} - \frac{1}{C_{PRu}}\right)} \quad (25)$$

with

$\Delta\rho^{PR}$ being the pilot rod efficiency, measured by rod drop,

$1/C$ is the inverse of the count rate

PRu corresponds to the pilot rod in raised position (out from the core)

PRd corresponds to the pilot rod in lowered position (down)

ε is the MSM factor between PRu and PRd configuration (generally equal to 1 since the PR worth is about several tens of β_{eff})

The overall reactivity effect is calculated as:

$$\Delta\rho = \underbrace{\left(\frac{\varepsilon_{MSM}}{C_{Pert.}} - \frac{1}{C_{Ref.}}\right)}_{\text{direct term}} \times RCaFa + \underbrace{\frac{\delta\rho}{\delta T} \cdot (T^{Ref.} - T^{Pert.}) + \frac{\delta\rho}{\delta t} \cdot (t^{Ref.} - t^{Pert.}) + \frac{\delta\rho}{\delta CB} \cdot (CB^{Ref.} - CB^{Pert.})}_{\text{correction terms}} \quad (26)$$

relationship where

$1/C$ is the inverse of the count rate

Ref. represents the reference condition

Pert. represents the disturbed condition

$RCaFa$ is a calibration factor of the count rate on the pilot rod worth (*Reactivity Calibration factor*)

T is the temperature

t is the date of the measurement. This must be taken into account in the case of MOX cores where Pu aging cannot be negligible)

$\delta\rho/\delta T$ is the ITC

$\delta\rho/\delta t$ is the plutonium aging

$\delta\rho/\delta CB$ is the boron worth coefficient

ε_{MSM} is what is called modified source multiplication (MSM) factor between the reference configuration and the disturbed one

9.2.7 Associated Uncertainties

The uncertainty on the ASM reactivity coefficient is deduced from the error propagation law.

$$\sigma(\Delta\rho)^2 = \sum_i \left(\frac{\partial\Delta\rho}{\partial x_i} \right) \sigma(x_i)^2 + 2 \sum_{i=1}^{n-1} \sum_{j=i+1}^n \left(\frac{\partial\Delta\rho}{\partial x_i} \right) \left(\frac{\partial\Delta\rho}{\partial x_j} \right) \text{cov}(x_i, x_j), \quad (27)$$

where the x_i are all the variables contained in (26).

For the general purpose, we will consider that all the variables are independent, so the correlation term in (27) can be neglected.

After some trivial algebra, the final variance of the reactivity worth in subcritical measurement is given by the expression:

$$\begin{aligned} & \left[\frac{\sigma(\Delta\rho)}{\Delta\rho} \right]^2 \\ &= \underbrace{\left[\frac{RCaFa \times \left(\frac{\varepsilon_{MSM}}{C_{pert}} - \frac{1}{C_{ref}} \right)}{\Delta\rho} \right]^2 \times \left[\left(\frac{\sigma(RCaFa)}{RCaFa} \right)^2 + \frac{\left(\frac{\sigma(\varepsilon_{MSM})}{C_{pert}} \right)^2 + \left(\frac{\varepsilon_{MSM}\sigma(C_{pert})}{C_{pert}^2} \right)^2 + \left(\frac{\sigma(C_{ref})}{C_{ref}^2} \right)^2}{\left[\frac{1}{C_{ref}} - \frac{\varepsilon}{C_{pert}} \right]^2} \right]}_{\text{countings}} \\ &+ \underbrace{\left[\frac{\frac{\delta\rho}{\delta T} \times (T^{ref} - T^{pert})}{\Delta\rho} \right]^2 \times \left[\left(\frac{\sigma(\delta\rho/\delta T)}{\delta\rho/\delta T} \right)^2 + \frac{\sigma(T^{ref})^2 + \sigma(T^{pert})^2}{(T^{ref} - T^{pert})^2} \right]}_{\text{temperature}} \\ &+ \underbrace{\left[\frac{\frac{\delta\rho}{\delta t} \times (t^{ref} - t^{pert})}{\Delta\rho} \right]^2 \times \left[\left(\frac{\sigma(\delta\rho/\delta t)}{\delta\rho/\delta t} \right)^2 + \frac{\sigma(t^{ref})^2 + \sigma(t^{pert})^2}{(t^{ref} - t^{pert})^2} \right]}_{\text{Pu decay}} \\ &+ \underbrace{\left[\frac{\frac{\delta\rho}{\delta CB} \times (CB^{ref} - CB^{pert})}{\Delta\rho} \right]^2 \times \left[\left(\frac{\sigma(\delta\rho/\delta CB)}{\delta\rho/\delta CB} \right)^2 + \frac{\sigma(CB^{ref})^2 + \sigma(CB^{pert})^2}{(CB^{ref} - CB^{pert})^2} \right]}_{\text{boron concentration}}, \quad (28a) \end{aligned}$$

where

$$\left[\frac{\sigma(RCaFa)}{RCaFa} \right]^2 = \left[\left(\frac{\sigma(\Delta\rho_{RodDrop})}{\Delta\rho_{RodDrop}} \right)^2 + \frac{\left(\frac{\sigma(\varepsilon_{MSM})}{C_{PRd}} \right)^2 + \left(\frac{\varepsilon_{MSM}\sigma(C_{PRd})}{C_{PRd}^2} \right)^2 + \left(\frac{\sigma(C_{PRUp})}{C_{PRUp}^2} \right)^2}{\left[\frac{\varepsilon_{MSM}}{C_{PRd}} - \frac{1}{C_{PRUp}} \right]^2} \right]. \quad (28b)$$

In the particular case where no MSM correction is taken into account, $\epsilon_{MSM} = 1$ (the reactivity effect is small enough to neglect the local flux disturbance), the two last expressions can be rewritten as, remembering that $\sigma(C) = \sqrt{C}$

$$\begin{aligned} \left[\frac{\sigma(\Delta\rho)}{\Delta\rho} \right]^2 &= \left[\frac{RCaFa \times \left(\frac{1}{C_{pert}} - \frac{1}{C_{ref}} \right)}{\Delta\rho} \right]^2 \times \left[\left(\frac{\sigma(RCaFa)}{RCaFa} \right)^2 + \frac{\left(\frac{1}{C_{pert}} \right)^3 + \left(\frac{1}{C_{ref}} \right)^3}{\left[\frac{1}{C_{ref}} - \frac{1}{C_{pert}} \right]^2} \right] \\ &+ \left[\frac{\frac{\delta\rho}{\delta T} \times (T^{ref} - T^{pert})}{\Delta\rho} \right]^2 \times \left[\left(\frac{\sigma(\delta\rho/\delta T)}{\delta\rho/\delta T} \right)^2 + \frac{\sigma(T^{ref})^2 - \sigma(T^{pert})^2}{(T^{ref} - T^{pert})} \right] \\ &+ \left[\frac{\frac{\delta\rho}{\delta t} \times (t^{ref} - t^{pert})}{\Delta\rho} \right]^2 \times \left[\left(\frac{\sigma(\delta\rho/\delta t)}{\delta\rho/\delta t} \right)^2 + \frac{\sigma(t^{ref})^2 - \sigma(t^{pert})^2}{(t^{ref} - t^{pert})} \right] \\ &+ \left[\frac{\frac{\delta\rho}{\delta CB} \times (CB^{ref} - CB^{pert})}{\Delta\rho} \right]^2 \times \left[\left(\frac{\sigma(\delta\rho/\delta CB)}{\delta\rho/\delta CB} \right)^2 + \frac{\sigma(CB^{ref})^2 - \sigma(CB^{pert})^2}{(CB^{ref} - CB^{pert})} \right] \end{aligned} \quad (29a)$$

with

$$\left[\frac{\sigma(RCaFa)}{RCaFa} \right]^2 = \left[\left(\frac{\sigma(\Delta\rho_{RodDrop})}{\Delta\rho_{RodDrop}} \right)^2 + \frac{\left(\frac{1}{C_{PRd}} \right)^3 + \left(\frac{1}{C_{PRUp}} \right)^3}{\left[\frac{1}{C_{PRd}} - \frac{1}{C_{PRUp}} \right]^2} \right]. \quad (29b)$$

In general $\sigma(\Delta\rho_{RodDrop}) \sim 5.1\%$ is the dominant term of the uncertainty formula. Since it arises from the nuclear data used for the rod drop analysis, it is not reducible and represents the lower uncertainty value attainable with this method.

9.2.8 Example: Isothermal Temperature Coefficient (ITC)

The temperature coefficient will be given by the expression $(\Delta\rho/\Delta T)_{i,j} = \Delta\rho_{ASM}/T_i - T_j$ where $\Delta\rho_{ASM}$ does not contain the temperature dependence, as in (26) (since it is the coefficient we look for).


The uncertainty of the reactivity worth in subcritical measurement is found by propagating the individual variances through error propagation law. The final variance is given by the expression:

$$\delta^2 \left(\frac{\Delta\rho}{\Delta T_{i,j}} \right)_{ASM} = \frac{1}{(T_i - T_j)^2} \left[\delta^2(\Delta\rho_{ASM}) + \frac{2(\Delta\rho_{ASM})^2}{(T_i - T_j)^2} \delta^2(T_i) \right], \quad (30)$$

where

$$\left[\frac{\sigma(\Delta\rho_{ASM})}{\Delta\rho_{ASM}} \right]^2$$

$$\begin{aligned}
&= \underbrace{\left[\frac{RCaFa \times \left(\frac{\epsilon_{MSM}}{C_{pert}} - \frac{1}{C_{ref}} \right)}{\Delta\rho_{ASM}} \right]^2 \times \left[\left(\frac{\sigma(RCaFa)}{RCaFa} \right)^2 + \frac{\left(\frac{\sigma(\epsilon_{MSM})}{C_{pert}} \right)^2 + \left(\frac{\epsilon_{MSM}\sigma(C_{pert})}{C_{pert}^2} \right)^2 + \left(\frac{\sigma(C_{ref})}{C_{ref}} \right)^2}{\left[\frac{1}{C_{ref}} - \frac{\epsilon}{C_{pert}} \right]^2} \right]}_{\text{countings}} \\
&+ \underbrace{\left[\frac{\frac{\delta\rho}{\delta t} \times (t^{ref} - t^{pert})}{\Delta\rho_{ASM}} \right]^2 \times \left[\left(\frac{\sigma(\delta\rho/\delta t)}{\delta\rho/\delta t} \right)^2 + \frac{\sigma(t^{ref})^2 + \sigma(t^{pert})^2}{(t^{ref} - t^{pert})^2} \right]}_{\text{Pu decay}} \\
&+ \underbrace{\left[\frac{\frac{\delta\rho}{\delta CB} \times (CB^{ref} - CB^{pert})}{\Delta\rho_{ASM}} \right]^2 \times \left[\left(\frac{\sigma(\delta\rho/\delta CB)}{\delta\rho/\delta CB} \right)^2 + \frac{\sigma(CB^{ref})^2 + \sigma(CB^{pert})^2}{(CB^{ref} - CB^{pert})^2} \right]}_{\text{boron concentration}}. \tag{31}
\end{aligned}$$

These equations can be used, for example, in parallel to equations of  Sect. 9.1 for the critical determination of the reactivity coefficient.

9.2.9 Reactivity Effect Measurements by Sample Oscillation

Principle

The experimental oscillation technique is used to measure small reactivity variations. The interest of oscillations stems from the fact that neutron measurements can be carried out using very small quantities of materials, for example, a single fuel element or a small sample of a few grams of the body or isotope studied.

When a small zone at the center of a reactor is made to undergo a periodic disturbance, for example, capture or fission type, the neutron density disturbance can be separated into two components.

The first, irrespective of the position, is called overall disturbance, and is expressed in the following way:

$$\frac{dn}{dt} = H \frac{dk}{k}, \tag{32}$$

where H is the reactor's transfer function and dk/k is the reactivity variation.

The second component, in phase with the disturbance, quickly diminishes when one moves away from the disturbed zone and is called local disturbance. This measurement is used for experiments based on the method of the equivalent sample; the signal is therefore obtained by fission chambers surrounding the oscillation rod. It can be shown that by disregarding the terms due to transfers, the overall disturbance can be expressed as follows:

$$\frac{dn}{dt} = AH\delta\Sigma_a + BH\delta\Sigma_f, \tag{33}$$

where $A\delta\Sigma_a + B\delta\Sigma_f$ represents the reactivity variation.

The overall signal can be measured anywhere in the reactor far enough away from the disturbance. Rather than measure the neutron density variation (as was the case on the UKAEA DIMPLE reactor), for MINERVE, it is preferred that the reactivity effect of the studied sample

be compensated using an automatic pilot rod (see [Sect. 8.7.2](#)) especially designed to respond quickly to small reactivity variations (~ 10 pcm). In the past, other reactors (MARIUS, CESAR, and MASURCA) were also equipped with such a system.

Practical Implementation

The technique consists in oscillating studied samples at the center of the experimental lattice, with the aim of measuring the reactivity variation associated with an uncertainty linked to the less than 1% reproducibility of the experiment. Each sample is placed in an oscillation rod and is moved vertically from time to time between two positions located in the mid-height plane and outside the experimental zone (see [Fig. 62](#)).

The signal of the upper axle (containing the studied sample) is compared with the signal of the lower axle (containing a reference sample) of the oscillation rod (see [Fig. 62](#)). The reactivity effect difference of the two samples then allows the effect of the upper and lower axles to be avoided. Each sample is measured five times in order to identify any systematic biases and to reduce the standard deviation on the measurement average. One measurement consists of 20 oscillations lasting 60 s each, or ten oscillations lasting 120 s each.

The flux variation resulting from the oscillation is detected by a boron-lined fission chamber called pilot chamber, placed outside the driver zone and connected to an automatic pilot rod made up of a stator and rotor covered with cadmium sections: the relatively significant covering provokes a reactivity variation which can reach approximately ± 20 pcm. The connection between the rotation angle of the rod and the reactivity is determined experimentally using calibration samples with various ^{235}U enrichments and various ^{10}B contents, whose reactivity is known at better than 1% through deterministic calculations.

By quadratically accumulating the uncertainties linked to the reproducibility of measurements ($\sim 1\%$), to the material balance of samples ($\sim 1\text{--}2\%$) and to the calibration of the automatic pilot rod ($\sim 2\%$), the final uncertainty on reactivity is approximately 3% at 1σ .

The average amplitude of the automatic pilot rod's signal is determined for each oscillation cycle. The comparison of amplitudes of each cycle for a single measurement gives information on the repeatability of the experiment. The comparison of the average amplitude of five measurements of a single sample gives information on the reproducibility of measurements. The average amplitude for all the measurements of a single sample is therefore compared with that of calibration samples in order to determine the reactivity effect of the studied sample.

The experimental values are generally interpreted through an exact disturbance calculation. The reactivity effects of studied samples are generally used in the calculation for the reactivity effect of ^{235}U and boron through calibration samples.

Calibration of the Automatic Pilot Rod

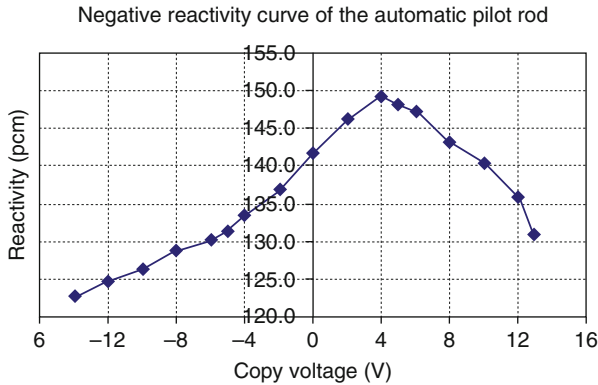
Calibration of the automatic pilot rod (see description in [Sect. 8.7.2](#)) takes place in two phases:

- Determination of the pilot rod's negative reactivity curve
- Determination of the pilot rod's differential calibration curve

1. Negative reactivity curve of the automatic pilot rod

This phase has the following objectives:

- To check the correct operating and proper centering of the automatic pilot rod. It involves making sure that the overlapping of cadmium sections does in fact vary when the pilot rod's rotation angle is influenced from the control rack, and therefore that



■ **Figure 75**
Pilot rod negative reactivity curve during HTC-MOX program in R1-MOX

the position control operates properly and that the rotor's movement is not restricted (mechanical seizure for example).

- To make sure that the automatic pilot rod is capable of compensating reactivity variations ranging between $[-10 \text{ pcm}; +10 \text{ pcm}]$.
By designing oscillation samples, the reactivity variation caused by oscillation is in absolute value, less than or equal to 10 pcm.
- To define an operating range on which the issued signal/negative reactivity relationship is bijective.

Indeed, two signals can potentially correspond to a single deployed cadmium surface and therefore the same negative reactivity, as shown in ► [Fig. 63](#).

In practice, the measurement is carried out in the following way:

- Positioning of the rotor at a given angle (i.e., a given signal (*copy voltage*))
- Divergence of the reactor all rods raised and determination of the core's excess reactivity using the measurement of the doubling time and the Nordheim curve

The example of the negative reactivity curve of the automatic pilot rod obtained during the HTC-MOX program in the R1-MOX configuration of the MINERVE reactor is shown in ► [Fig. 75](#).

The rotor was taken to its maximum rotation angles, corresponding to the copy voltages -14 V and $+13 \text{ V}$. Beyond these extremes, the automatic pilot rod is no longer able to compensate: this is referred to as pilot rod stalling.

It is observed that a bijective relationship between the copy voltage and negative reactivity is only possible on the range $[-14 \text{ V}; +4 \text{ V}]$ or on the range $[+4 \text{ V}; +13 \text{ V}]$ and that only the first range guarantees the ability to compensate reactivity effects of $\pm 10 \text{ pcm}$.

2. Differential worth curve of the automatic pilot rod

(a) Principle

The purpose of the differential worth curve is to determine an operating point within the operating range chosen in accordance with *point 1*.

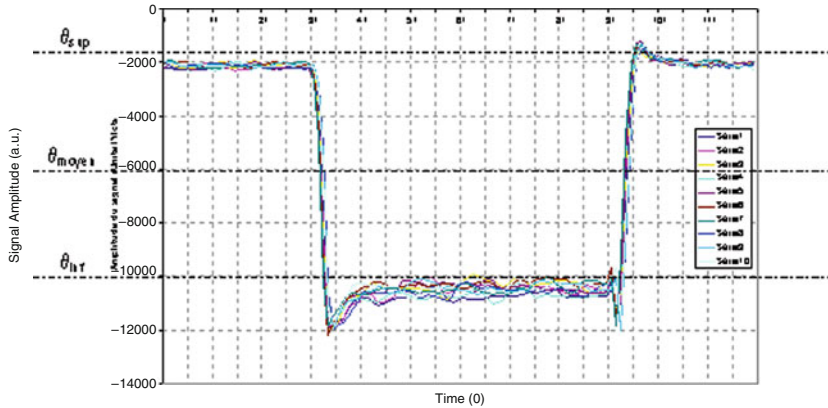


Figure 76
Illustration of the reference angle on a standard oscillation signal

This operating point corresponds to a given copy voltage and therefore to a reference rotation angle which will be noted θ_0 . In practice, it will represent the average ideal value of the signal obtained during sample oscillation. ▶ Figure 76 depicts this point.

With

θ_{raised} = average maximum angle obtained during oscillation of a given sample, corresponding to a given position of the oscillator (raised or lowered to a stop)

θ_{low} = average minimum angle obtained during oscillation of a given sample, corresponding to the other given position of the oscillator (lowered or lowered to a stop)

θ_{avg} = average angle = $(\theta_{\text{raised}} + 2\theta_{\text{low}})/2$. $\theta_{\text{avg}} \neq \theta_0$ must be followed

It is recalled that the purpose of oscillation measurements is to compare amplitudes ($\theta_{\text{raised}} - \theta_{\text{low}}$) obtained using various studied samples.

(b) Experimental implementation

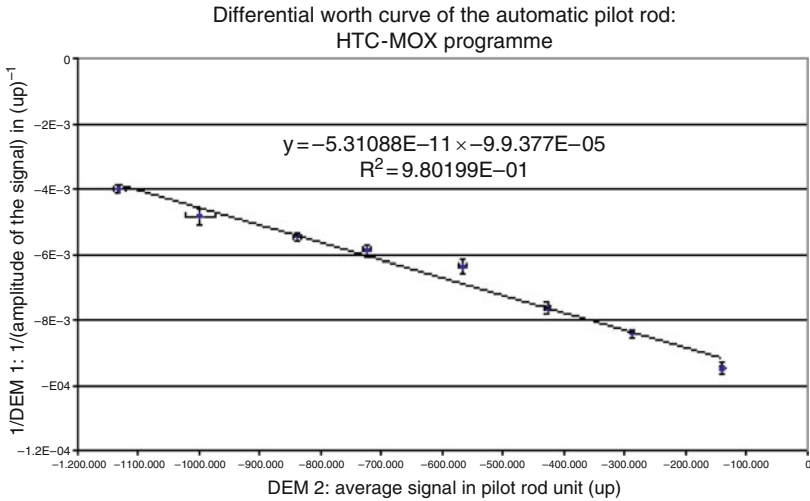
Experimentally, the measurement is carried out by positioning the automatic pilot rod at various angles, i.e., at various copy voltages, in the determined operating range using the negative reactivity curve (see *point 1*).

For each copy voltage, at the *BFX* point of the closed loop control (see ▶ Sect. 8.7.2) (that is to say downstream of the pilot chamber and upstream of the automatic pilot rod), an outside test signal (simulating a neutron flux disturbance) is inserted in the form of low amplitude voltage (at approximately 0.1 V in absolute value), and in each case the signal's amplitude and average position is recorded.

The differential calibration curve of the automatic pilot rod is therefore recreated, as given in the example in ▶ Fig. 77.

It can be shown that on a certain operating range, this curve can be written in the following way:

$$f = f(\theta) = \frac{1}{\alpha\theta + \beta} \quad (34)$$



■ **Figure 77**

Example of the differential calibration curve

or otherwise written as

$$f(\theta_0) = f(\theta) \times (1 - C_B \times (\theta - \theta_0)) \quad (35)$$

with

θ_0 = the reference angle to be determined and which will be worked around for all oscillations

θ = average angle for a given measurement, such as $\theta \neq \theta_0$

$f(\theta)$ = experimentally obtained amplitude for a given measurement

$f(\theta_0)$ = the amplitude which would have been obtained if it had been possible to perfectly experimentally adjust θ such as $\theta = \theta_0$

θ_0 is therefore chosen toward the middle of this range, while making sure that a reactivity variation of ± 10 pcm around this position is possible without stalling the pilot rod and so that θ_0 is part of the operating range determined in [▶ Sect. 3.1](#).

C_B is directly deduced from the value of α , β , and θ_0 through the relationship $C_B = -1/\theta_0 + \beta/\alpha$.

Statistical processing through linear regression enables the uncertainty on coefficients on the right, and therefore on C_B to be determined, while taking into accounts both uncertainties on the average signal and on the amplitude.

Signal Calibration

Once the automatic pilot rod is calibrated, the signal issued by the pilot rod must be calibrated. To do so, two series of calibration samples are used. One consists of UO_2 samples with various

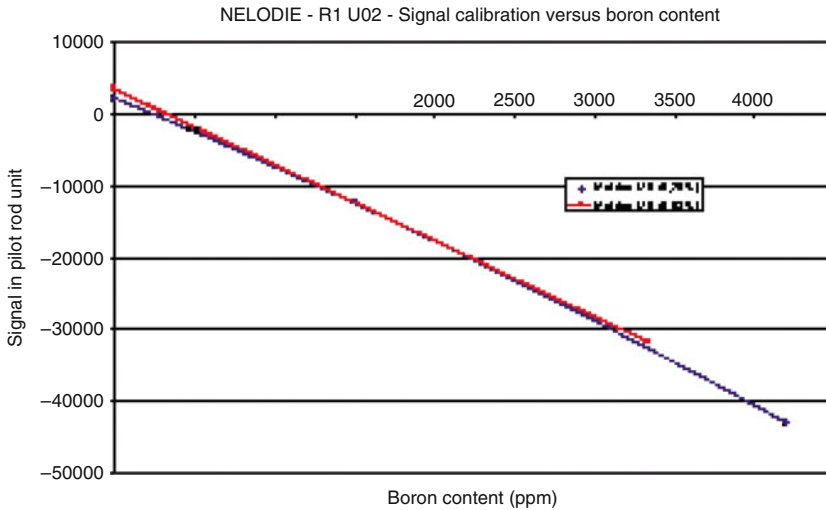


Figure 78
Calibration curve with borated samples

^{235}U enrichments (0.25, 0.5, 0.72, 1, 2, 3, 4, and 4.95%). The other is made up of UO_2 matrix samples mixed with boron with various contents (0, 60, 100, 150, 200, 333, 400, 419, 500, and 1,062 ppm). ➤ [Figures 78](#) and ➤ [79](#) give examples of calibration curves obtained in R1- UO_2 during the HTC program.

The reactivity of these samples is also calculated using deterministic calculation codes, with an uncertainty, linked to the knowledge of nuclear data on ^{235}U and boron, of approximately 1% (1σ). Thus, the reactivity of any samples oscillated in MINERVE can be determined by simple comparison of its response to that of calibration samples.

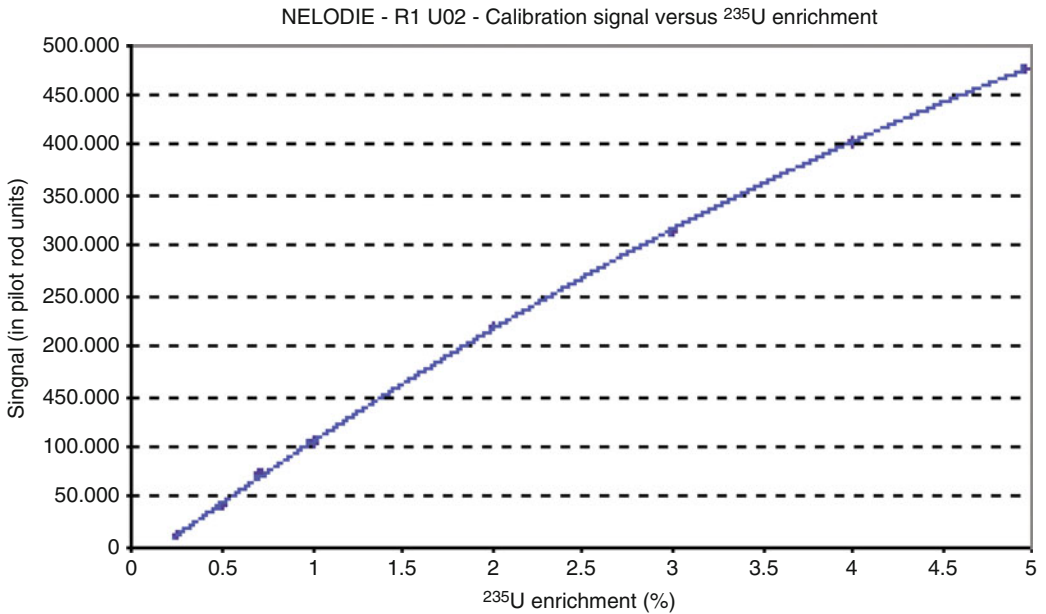
The total uncertainty on calibration measurements, taking into account uncertainties on the material balance of samples, the reproducibility of measurements, and the uncertainty on their calculated reactivity weights, is approximately 2% (1σ).

9.3 Measurement of Fission Rate Distributions

Fission rate distributions are measured using two complementary techniques: fission chambers and integral gamma spectrometry.

They have several advantages: for regular cores (axially and/or radially), the distribution of fission rates allows the flux curve to be determined and thus identify the “fundamental” parameters such as the material buckling. This material buckling is then used either as input data to qualify the calculation of the cell in an infinite environment, or compared with the buckling calculated for the cell at $k_{eff} = 1$. Axially, it also allows the core calculation scheme to be qualified (regular or mock-up lattice) by imposing axial leaks, radially, it conditions the critical size calculation.

In “homogeneous” cores, the axial and radial distributions also enable the *reflector gain* calculation to be qualified. This will be developed further on.



■ Figure 79

Calibration curve with U-235 samples

9.3.1 Distributions by Fission Chambers

Distributions by fission chambers are accomplished by inserting a miniature fission chamber ($\varnothing 4$ mm) into a sealed over-cladding, in replacement of a fuel rod. Measurements are taken in critical conditions.

As opposed to gamma spectrometry, they help highlight the spectrum effects in distributions using fission chambers of different types:

- Fissile isotopes for the thermal field
- Fertile isotopes for the highest energies

These spectrum effects, characterized by “spectral indexes,” are covered in [▶ Sect. 9.4](#).

Radial Measurements

Radial measurements are carried out in the core’s mid-height plane in order to avoid the axial curve of the fission rate distribution. The counting rates for the chamber are renormalized on a chamber calibrated in the core, which follows the power variation during measurement. When the measurement is completed, the chamber is moved to another position.

Axial Measurements

Axial measurements are carried out using the linear positioner allowing the chamber in question to be inserted at various heights in the core. The counting rate of the chamber is renormalized in the same way as for the radial measurement.

As opposed to gamma spectrometry measurements, distribution measurement by fission chambers allows us to go beyond the fissile column, in the reflector, and to validate the reflector gain calculation.

The uncertainties on axial and radial distributions by fission chambers are less than or around 1% at 1σ .

9.3.2 Distributions by Integral Gamma Spectrometry

Integral spectrometry is based on the measurement of the total gamma activity of a fuel rod after irradiation. This measurement allows the total fission rate in the rod to be traced. For the same type of fuel (MOX or UO_2), the total activity is directly proportional to the fission rate, through emitter fission products. Measurement of this γ activity is carried out between 550 keV (beyond the Compton front) and up to 2,500–3,000 keV.

As the activity depends greatly on fission products and their lifetime, it must be normalized at a decay “standard,” which is a fuel of the same nature, measured continuously.

The integral γ spectrometry technique is used for:

- Radial measurements
- Axial measurements

These two measurements are slightly different in the way the final result is normalized, however the renormalization principle for decay is identical (► [Figs. 80](#) and ► [81](#)).

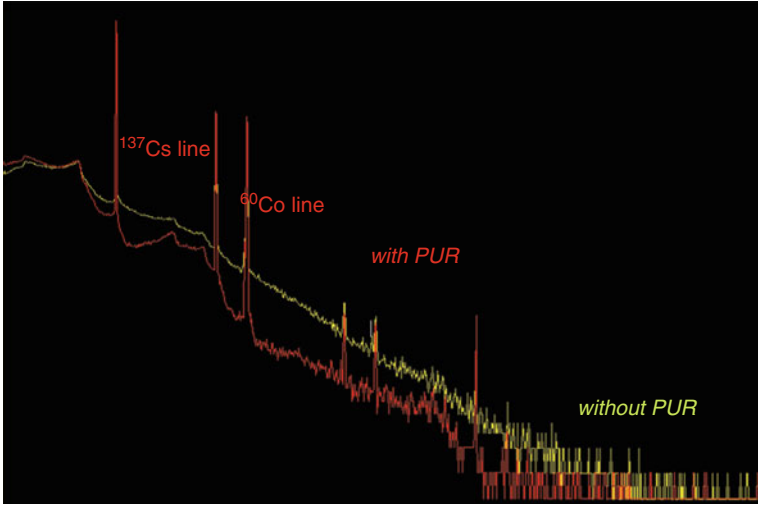
Radial Measurements

For radial measurements, counts are carried out at the core’s mid-height plane, where the fission rate axial distribution is the most level, which allows any curve correction whatsoever to be avoided. The advantage of the γ -scanning technique is completely clear here: it is possible to create fission rate maps on a large number of rods in a minimum amount of time. The number of



■ Figure 80

Gamma spectrometry measurement on EOLE/MINERVE critical mock-ups. Insertion of UO_2 or MOX fuel rods under a germanium diode



■ Figure 81

Gamma spectrometry measurement on EOLE/MINERVE critical mock-ups. Example of taking into account the dead time on fission product spectrums

rods generally measured is often around a hundred, broken down into several individual maps with twenty rods. Each individual map is the subject of a dedicated measurement.

Rods are counted several times (runs) on the measurement channel in order to reduce the associated statistical uncertainty. The analysis is carried out as follows.

Where $T_{i,k}$ is the count rate γ of an individual rod i at k run, the renormalized fission rate is given by:

$$T_{i,k} = \frac{C_{i,k} - R_i}{C_{M,k} - R_M}, \quad (36)$$

where

$C_{i,k}$ is the count rate of the rod i at k run

R_i is the measurement of the residual activity of the rod i (counted once)

$C_{M,k}$ is the count rate of the monitor rod M at k passage

R_M is the residual activity of the same monitor M

The statistical uncertainty on this count rate is given by the well-known propagation law, and leads to:

$$\begin{aligned} (\Delta T_{i,k})^2 = & \left(\frac{\partial T_{i,k}}{\partial C_{i,k}} \right)^2 (\Delta C_{i,k})^2 + \left(\frac{\partial T_{i,k}}{\partial R_i} \right)^2 (\Delta R_i)^2 + \left(\frac{\partial T_{i,k}}{\partial C_{M,k}} \right)^2 (\Delta C_{M,k})^2 \\ & + \left(\frac{\partial T_{i,k}}{\partial R_M} \right)^2 (\Delta R_M)^2 \end{aligned} \quad (37)$$

with

$$(\Delta C_{i,k})^2 = C_{i,k},$$

$$(\Delta R_i)^2 = R_i,$$

$$(\Delta C_{M,k})^2 = C_{M,k}, \quad (38a)$$

$$(\Delta R_M)^2 = R_M,$$

$$\left(\frac{\partial T_{i,k}}{\partial C_{i,k}}\right)^2 = \left(\frac{\partial T_{i,k}}{\partial R_i}\right)^2 = \frac{1}{(C_{M,k} - R_M)^2}, \quad (38b)$$

$$\left(\frac{\partial T_{i,k}}{\partial C_{M,k}}\right)^2 = \left(\frac{\partial T_{i,k}}{\partial R_M}\right)^2 = \frac{(C_{i,k} - R_i)^2}{(C_{M,k} - R_M)^4}. \quad (38c)$$

We suppose here that the counts are independent from each other so that there is no correlation between the runs or the rods.

Performing some algebra and reorganizing leads to the following relationship, in terms of relative uncertainties:

$$\left(\frac{\Delta T_{i,k}}{T_{i,k}}\right)^2 \equiv \delta T_{i,k}^2 = \frac{C_{i,k} + D_{i,k}}{(C_{i,k} - D_{i,k})^2} + \frac{C_M + D_M}{(C_M - D_M)^2}. \quad (39)$$

The average value of each individual rod after the three runs is then the combination of these individual uncertainties. So, the following is obtained:

$$\bar{T}_i = \frac{\sum_k T_{i,k} / (\delta T_{i,k})^2}{\sum_k 1 / (\delta T_{i,k})^2} \quad (40)$$

with a relative statistical uncertainty given by

$$\delta \bar{T}_i = \sqrt{\frac{1}{\sum_k 1 / (\delta T_{i,k})^2}}. \quad (41)$$

As usual, the more the number of measurements is, the less the associated uncertainty on the average value will be.

Once the individual uncertainties are calculated for each run, an average value is calculated as the weighted average of the chosen fuel rods. Once individual counts are completed, each fission rate is then renormalized on a set value (generally the average value of the fission rate of a few fuel rods). This allows a full γ -scanning map to be created by mixing several separate normalized measurements on the same fuel rods.

The average A is calculated as

$$A = \frac{1}{N} \sum_{i=1}^N T_i, \quad (42)$$

where N is the number of weighting fuel rods. The associated uncertainty is given by

$$\delta A = \frac{1}{N} \sqrt{\sum_{i=1}^N (T_i)^2}. \quad (43)$$

Each new fuel rod now has the value

$$\tilde{T}_i = \bar{T}_i / A. \quad (44)$$

The associated uncertainty will be the quadratic combination of both statistical and weighting terms:

$$\delta \tilde{T}_i = \sqrt{(\delta \bar{T}_i)^2 + (\delta A)^2}. \quad (45)$$

Axial Measurements

Axial γ -scanning is very similar to the radial γ -scanning process. It differs among other things by the opening of the measurement window in order to integrate the γ activity on a smaller part of the fuel. Here, the axial variation of the curve must be highlighted. The fissile height is subdivided into units measured from the bottom of the rod up to the top of the rod. Once the measurements are completed, the curve obtained over the maximum is renormalized.

Uncertainties on axial or radial distributions by γ -scanning are approximately 1–1.5% (at 1σ).

9.3.3 Particular Use of Fission Rate Distributions: The Buckling Estimation

The buckling can be deduced from axial and radial distributions, in the case of homogeneous cores, with both fission chambers and integral gamma spectrometry. The processing of the buckling is based on a fit of the fission rates using a cosine or Bessel function of the first kind which is the eigenfunction of the axial or radial Helmholtz equation respectively.

For an axial fit for example, the function $a \cos(\sqrt{B^2 z + c})$ is adjusted on the set of experimental points using a descending Newton algorithm. Several calculations are carried out using various z value thresholds in order to estimate the best z range fitting the data (to avoid discrepancies due to thermal flux increases in the upper and in the lower part of the core).

The uncertainty on the three adjusted parameters (a, B^2, c) comes from error propagation using the Monte Carlo method. The convergence of the standard deviation for a set of points is checked by looking at its variation and figure of merit (FOM) versus history number (generally 1,000 history per threshold value is enough). Standard deviations of the fission rate at each z coordinate are estimated using error propagation on measured and monitor rods and then fission rates are sampled until calculation convergence.

The B^2 value to be retained (matching a given z threshold) is a compromise between a reduced chi-square χ_R^2 per degree of freedom as close to one as possible (checked to be less than a unilateral 5% risk threshold) and an uncertainty on B^2 as low as possible. The first criterion tends to reduce the z data range whereas the second tends to enlarge this range.

The statistical weighted average and the reduced uncertainty are obtained using the following formulae.

$$\bar{B}_z^2 = \frac{\sum_{i=1}^n (B_z^2)_i / \sigma_i^2}{\sum_{i=1}^n 1 / \sigma_i^2} \quad \text{and} \quad \bar{\sigma}_z^2 = \frac{1}{\sum_{i=1}^n 1 / \sigma_i^2}. \quad (46)$$

9.3.4 Determination of the Reflector Saving

The buckling values obtained enable one to extract the axial reflector saving δ_z of the core; for example. Knowing that, for a cylindrical core, the axial buckling is defined by

$$B_z^2 = \left(\frac{\pi}{H_{ext}} \right)^2 = \left(\frac{\pi}{H + 2\delta_z} \right)^2 \quad (47)$$

with H being the core fissile height, considered in first approximation without uncertainty.

The uncertainties are calculated as:

$$\Delta H_{ext} = \left(\frac{\pi}{B_z^2} \right) \Delta B_z \quad \text{or} \quad \Delta \delta_z = \frac{1}{2} \left(\frac{\pi}{B_z^2} \right) \Delta B_z. \quad (48)$$

9.3.5 Adjustment of Fission Maps by Particular Peaks

The renormalization of fission rate distributions between fuel rods of different types is of great interest for the physics of advanced cores where we mix both UO₂ and MOX assemblies, or between fuels of the same type but with very different fissile vectors. This adjustment is due to the normalization technique for integral γ -scanning maps on a decaying rod. The latter has a pseudo decay period that makes it impossible to mix two rods of different types on one map. Therefore, an absolute standard must be used, which is the formation rate of a fission product common to both types. Its contribution to the qualification of the calculation scheme is not direct; it is only done through the total renormalized fission rate distribution map.

Principle of Peak Check Technique

The purpose of the adjustment is to determine the relationship [(Fuel₁ fission rate)/(Fuel₂ fission rate)] It is carried out as follows:

$$\left[\frac{F_{Fuel_1}}{F_{Fuel_2}} \right]_{Exp} = \left[\frac{FP_{Fuel_1}}{FP_{Fuel_2}} \right]_{Exp} \times \left[\frac{r_{Fuel_2}}{r_{Fuel_1}} \right]_{Cal}, \quad (49)$$

where

- F_{Fuel_1} and F_{Fuel_2} are the fission rates measured in rods 1 and 2, respectively
- FP_{Fuel_1} and FP_{Fuel_2} are the quantities measured for a particular fission product of interest
- r_{Fuel_1} and r_{Fuel_2} are calculated correction factors (average fission yields)

The latter are expressed as:

$$r_i^{Fuel_1} = \sum_{k=1}^L (\tau_k \times y_k^i)_{fast}^{Fuel_1} + (\tau_k \times y_k^i)_{thermal}^{Fuel_1} \quad \text{is the average fission yield in the type 1 rod} \quad (50a)$$

and

$$r_i^{Fuel_2} = \sum_{k=1}^L (\tau_k \times y_k^i)_{fast}^{Fuel_2} + (\tau_k \times y_k^i)_{thermal}^{Fuel_2} \quad \text{is the average fission yield in the type 2 rod} \quad (50b)$$

with

$$\sum_{k=1}^L (\tau_k)_{fast}^{Fuel_1} + (\tau_k)_{thermal}^{Fuel_1} = \sum_{k=1}^L (\tau_k)_{fast}^{Fuel_2} + (\tau_k)_{thermal}^{Fuel_2} = 1, \quad (50c)$$

where

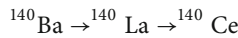
- y_k^i is the cumulated fission yield of the fission product i for the fissile isotope k
- τ_k is the fission rate of the fissile isotope k
- L is the number of fissile nuclei contained in the fuel

with a gap between the thermal and fast ranges in order to properly take into account the fission yields.

The commonly used fission product is ^{140}Ba , even though other FPs can also be analyzed, as for example ^{92}Sr . ^{140}Ba is a fission product with a very high cumulated fission yield whose direct descendent, ^{140}La , has several particularities which make it a good candidate for the particular peak measurement:

- High intensity and high energy (1,596 keV) γ line, not disturbed by the Compton front
- A relatively long decay period enabling low residual activity postirradiation measurements

The formation reaction of ^{140}La is as follows:



It can be shown that the total fission rate emitted in the fuel rod is given by the following expression:

$$F = \left\langle \frac{F_{La}}{Y_{Ba}} \right\rangle = \frac{C_{La}(\lambda_{La} - \lambda E)}{I_\gamma Y_{La} f_{La} \times \left[\frac{\lambda_{La}}{\lambda_{Ba}} e^{-\lambda_{Ba} T_0} (1 - e^{-\lambda_{Ba} I}) (1 - e^{-\lambda_{Ba} T_c}) - \frac{\lambda_{Ba}}{\lambda_{La}} e^{-\lambda_{La} T_0} (1 - e^{-\lambda_{La} I}) (1 - e^{-\lambda_{La} T_c}) \right]} \times \frac{T_c}{T_a}, \quad (51)$$

where

- $Y_{Ba} = \sum_j (Y_{j,th} \tau_{j,th} + Y_{j,F} \tau_{j,F})_{Ba}$
- $Y_{j,th}$ is the thermal fission yield of the ^{140}Ba (^{140}La) for the isotope j
- $\tau_{j,th}$ is the thermal fission relationship of the isotope j in the fuel at the total fission rate
- $Y_{j,F}$ is the fast fission yield of the ^{140}Ba (^{140}La) for the isotope j
- $\tau_{j,F}$ is the fast fission relationship of the isotope j in the fuel at the total fission rate
- F is the overall fission rate in the fuel

- F_{Ba} is the production rate of the ^{140}Ba $F_{Ba} = F \times Y_{Ba}$
- C_{La} is the integral of the peak at 1,596 keV of the ^{140}La
- I is the irradiation time
- T_0 is the cooling time for the rod, that is to say the amount of time between the end of irradiation and the start of the measurement
- T_c corresponds to the measuring time
- f_{La} is the self-absorption factor of the gamma in the fuel, that is to say its probability of being detected without being absorbed. It is deduced from a photonic propagation calculation using the Monte-Carlo MCNP code precisely modeling the fuel rod and the measuring bench with the associated detectors
- I_γ is the intensity of the gamma line detected

$\lambda_{Ba}(\ln(2)/T_{Ba} = 6.2971 \times 10^{-7} \text{ s}^{-1}$, with $T_{Ba} = 12.74j(\pm 1.2 \text{ h i.e., } 0.39\%)$ for the ^{140}Ba and $\lambda_{La}(\ln(2)/T_{La} = 4.7812 \times 10^{-6} \text{ s}^{-1}$, with $T_{La} = 40.27 \text{ h } (\pm 25.2 \text{ s i.e., } 0.02\%)$ for the ^{140}La are the decay constants of the two fission products.

Associated Uncertainties

The wide majority of uncertainty on the readjustment factor stems from the calculation of average yields. This uncertainty has two distinct sources:

- Basic nuclear data (fission yields), for which the uncertainties are known through assessed datasheets
- The calculated values (fission rates), for which the uncertainties are generally estimated. Firstly, they are considered equal to uncertainties a priori of fission integrals of isotopes taken into account in the calculation

One can consider that irradiation time, cooling time and count time are error free with regard to other sources of uncertainties. Usually, one postulates that dead time correction of a multi-channel analyzer should be perfect if dead time does not exceed 30–40%. With the new electronics (DSP, Digital Signal Processing) and associated research and investigation on its behavior versus dead time, one can precisely estimate the numerical correction brought by the lattice. Measurements show that the lattice is capable of reproducing integral and particular peak count rates at less than 1% precision up to dead times exceeding 50%. The uncertainty on this parameter will be considered as negligible with respect to the others sources. They are:

- Standard error on the net peak area C , equal to \sqrt{C} if we assume that the count rates follow a Poisson law and that the background count rate under the peak remains negligible.
- Precision on nuclear data (decay constants, cumulated fission yields, etc.).
- Precision on calculated data used for the data unfolding (mainly the fission rates and the γ self-absorption factor).

The propagated uncertainty on the fission rate is directly connected to the error propagation law, taking into account the previous parameters. Two different partial derivatives will appear in the equations. The application of the error-propagation law leads to:

$$\left(\frac{\Delta F}{F}\right)_{La} = \sqrt{\left(\frac{\Delta C_{La}}{C_{La}}\right)^2 + \left(\frac{\Delta Y_{Ba}}{Y_{Ba}}\right)^2 + \left(\frac{\Delta f_{La}}{f_{La}}\right)^2 + \chi_{La}^2 (\Delta \lambda_{La})^2 + \chi_{Ba}^2 (\Delta \lambda_{Ba})^2} \quad (52)$$

with

$$\frac{\Delta C_{La}}{C_{La}} = \frac{1}{\sqrt{C_{La}}} \quad (53a)$$

$(\Delta f_{La}/f_{La})^2$ is the propagated uncertainty on the self-absorption factor, $(\Delta Y_{Ba}/Y_{Ba})^2$ is the uncertainty due to nuclear data (yield) and

$$\chi_{La}^2 = \left(\frac{1}{F} \frac{\partial F}{\partial \lambda_{La}} \right)^2 \quad \text{and} \quad \chi_{Ba}^2 = \left(\frac{1}{F} \frac{\partial F}{\partial \lambda_{Ba}} \right)^2. \quad (53b,c)$$

Performing some algebra leads to the following relationships:

$$\chi_{La}^2 = \left\{ \frac{1}{\lambda_{La} - \lambda_{Ba}} - \left[\begin{array}{l} \frac{e^{-\lambda_{Ba} T_0}}{\lambda_{Ba}} (1 - e^{-\lambda_{Ba} I}) (1 - e^{-\lambda_{Ba} T_c}) \\ + \frac{\lambda_{Ba}}{\lambda_{La}} \left(T_0 + \frac{1}{\lambda_{La}} \right) e^{-\lambda_{La} T_0} (1 - e^{-\lambda_{La} I}) (1 - e^{-\lambda_{La} T_c}) \\ - \frac{\lambda_{Ba} I}{\lambda_{La}} e^{-\lambda_{La} T_0} e^{-\lambda_{La} I} (1 - e^{-\lambda_{La} T_c}) \\ - \frac{\lambda_{Ba} T_c}{\lambda_{La}} e^{-\lambda_{La} T_0} e^{-\lambda_{La} T_c} (1 - e^{-\lambda_{La} I}) \end{array} \right] \right\} \left/ \left[\frac{C_{La} (\lambda_{La} - \lambda_{Ba}) T_c}{F \times Y_{Ba} \times f_{La} \times T_a} \right] \right\}^2 \quad (54)$$

for the derivation versus the ^{140}La variables
and

$$\chi_{Ba}^2 = \left\{ \frac{1}{\lambda_{La} - \lambda_{Ba}} - \left[\begin{array}{l} \frac{e^{-\lambda_{La} T_0}}{\lambda_{La}} (1 - e^{-\lambda_{La} I}) (1 - e^{-\lambda_{La} T_c}) \\ + \frac{\lambda_{La}}{\lambda_{Ba}} \left(T_0 + \frac{1}{\lambda_{Ba}} \right) e^{-\lambda_{Ba} T_0} (1 - e^{-\lambda_{Ba} I}) (1 - e^{-\lambda_{Ba} T_c}) \\ - \frac{\lambda_{La} I}{\lambda_{Ba}} e^{-\lambda_{Ba} T_0} e^{-\lambda_{Ba} I} (1 - e^{-\lambda_{Ba} T_c}) \\ - \frac{\lambda_{La} T_c}{\lambda_{Ba}} e^{-\lambda_{Ba} T_0} e^{-\lambda_{Ba} T_c} (1 - e^{-\lambda_{Ba} I}) \end{array} \right] \right\} \left/ \left[\frac{C_{La} (\lambda_{La} - \lambda_{Ba}) T_c}{F \times Y_{Ba} \times f_{La} \times T_a} \right] \right\}^2 \quad (55)$$

for the derivation versus the ^{140}Ba variables.

Classically, the count integral C is higher than 40,000 counts, leading to a statistical uncertainty of less than 0.5%. The self-absorption factor can be obtained with an uncertainty of less than 0.3% if an adequate convergence criterion (statistical – Monte Carlo – uncertainty on the tally in the detector) is selected. On the basis of an irradiation time of 1 h, and a cooling time of several days, with count rates of about 1–2 h, the relative uncertainty due to the $\chi_{La \times \Delta \lambda_{La}}$ term is lower than 0.001% and lower than 0.02% for the $\chi_{Ba \times \Delta \lambda_{Ba}}$ term.

The propagation of all sources of uncertainty generates an overall uncertainty on the adjustment factor of the ^{140}La of approximately 1.5%, which, combined with the overall uncertainty on radial maps by integral γ -scanning, gives an uncertainty on the renormalized map of approximately 2–2.5% (at 1σ).

9.4 Spectral Indexes

The spectral indexes allow the characterization of an energetic distribution of neutrons in the core. They are mainly measured in very well characterized spectrums such as regular lattices,

though they can also be measured in mock-up type configurations. Calculation of a spectral index in simplified geometry enables *qualification of nuclear data* associated with the calculation scheme in a given energetic range.

The standard measurement is carried out using miniature fission chambers (with a diameter of 4 mm) inserted into the core in mid-height position, although the use of activation foils allowed good results to be obtained in UOX configurations with removable rods in previous programs. These detectors are planned for future programs.

Roughly, one hundred fission chambers of various types (fissile or fertile, with a diameter of \varnothing 1.5, 4, 8 or 10 mm) are available at EOLE, which can be used to characterize the spectrum at an area in the core.

By taking the five following chambers as examples:

- ^{235}U
- ^{238}U
- ^{239}Pu
- ^{242}Pu
- ^{237}Np

the following spectral indexes, among other things, can be deduced:

- $\sigma f^{238}\text{U}/\sigma f^{235}\text{U}$
- $\sigma f^{239}\text{Pu}/\sigma f^{235}\text{U}$
- $\sigma f^{237}\text{Np}/\sigma f^{239}\text{Pu}$
- $\sigma f^{242}\text{Pu}/\sigma f^{239}\text{Pu}$

and all the other possible variants.

9.4.1 Basic Principle

The general expression of a spectral index of an isotope “a” as compared to an isotope “r” is:

$$\frac{\bar{\sigma}_a}{\bar{\sigma}_r} = \frac{C_a/C_r}{(C_a/C_r)_c} \left(\frac{N_a^c \sigma_a^c}{N_a \sigma_r^c} + \sum_{i \neq a} \frac{N_i^c \sigma_i^c}{N_a \sigma_r^c} \right) - \sum_{i \neq a} \frac{N_i \bar{\sigma}_i}{N_a \bar{\sigma}_r}, \quad (56)$$

where

- C_a/C_r is the relationship of count rates of the chamber “a” as compared to chamber “r”
- $(C_a/C_r)_c$ is the same relationship in a reference spectrum (for example, in a thermal column)
- N_a^c/N_a represents the case where the isotope “a” decreased since the measurement in the reference spectrum (particularly Pu-238 and Pu-241),
- σ_a^c/σ_r^c is the relationship of cross-sections averaged in the reference spectrum
- $\sum_{i \neq a} (N_i^c/N_a) (\sigma_i^c/\sigma_r^c)$ represents the contributions of impurities in the reference spectrum
- $\sum_{i \neq a} (N_i/N_a) (\bar{\sigma}_i/\bar{\sigma}_r)$ represents the contributions of impurities during measurement

By using the expressions $S = (\bar{\sigma}_a/\bar{\sigma}_r)\sigma_{a,c} = (\sigma_a^c/\sigma_r^c)\sigma_{i,c} = (\sigma_i^c/\sigma_r^c)\sigma_i = \bar{\sigma}_i/\bar{\sigma}_r$ and $C = (C_a/C_r)/(C_a/C_r)\varepsilon_a = (N_a^c/N_a)\varepsilon_{i,c} = (N_i^c/N_a)\varepsilon_i = N_i/N_a$ the spectral index, S, is re-written:

$$S = C(\varepsilon_a\sigma_{a,c} + \varepsilon_{i,c}\sigma_{i,c}) - \varepsilon_i\sigma_i. \quad (57)$$

The associated uncertainties depend greatly on the type of chamber used. They vary from 2% to nearly 10% for fertile fission chambers (^{238}Pu or ^{242}Pu lined).

Some Examples

1. Pu-239/U-235 spectral index

Pu-239/U-235 becomes the simplest case with both chambers assumed to be isotopically pure. In this case, the general expression reduces to:

$$\frac{\bar{\sigma}_9}{\bar{\sigma}_5} = \frac{C_9/C_5}{(C_9/C_5)_c} \frac{\sigma_9^c}{\sigma_5^c}. \quad (58)$$

Defining the spectral index as $S = \bar{\sigma}_9/\bar{\sigma}_5$ and $C = (C_9/C_5)/(C_9/C_5)_c$ and the ratio of the cross-sections as $\sigma = \sigma_9^c/\sigma_5^c$, the uncertainties in this case are expressed as:

$$\left(\frac{\Delta S}{S}\right)^2 = \left(\frac{\Delta C}{C}\right)^2 + \left(\frac{\Delta \sigma}{\sigma}\right)^2. \quad (59)$$

2. Np-237/Pu-239

In the Np-237 chamber, there can be no thermal column calibration, so the spectral index must be derived from calibrations in a fast spectrum. In this case, the count-rate ratio in the spectrum of interest is:

$$\frac{C_a}{C_r} = \frac{k_a \left(N_a \bar{\sigma}_a + \sum_{i \neq a} N_i \bar{\sigma}_i \right)}{k_r N_r \bar{\sigma}_r}, \quad (60)$$

where k is the efficiency of the chambers.

Replacing the kN products by the effective masses yields the following relationship for the general spectral index

$$\frac{\bar{\sigma}_a}{\bar{\sigma}_r} = \frac{M_r}{M_a} x \frac{A_a}{A_r} (C_a/C_r) - \sum_{i \neq a} \frac{N_i}{N_a} \frac{\bar{\sigma}_i}{\bar{\sigma}_r}. \quad (61)$$

For the Np-237 chamber, $N_i = 0$, therefore:

$$\frac{\bar{\sigma}_a}{\bar{\sigma}_r} = \frac{M_r}{M_a} x \frac{A_a}{A_r} x \frac{C_a}{C_r}, \quad (62)$$

where M_r , M_a are the effective masses and A_r , A_a are the atomic masses (239 and 237, respectively).

The uncertainty is simply calculated from the following:

$$\left(\frac{\Delta S}{S}\right)^2 = \left(\frac{\Delta C}{C}\right)^2 + \left(\frac{\Delta m}{m}\right)^2. \quad (63)$$

9.4.2 Modified Conversion Factor

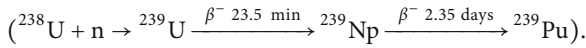
The modified conversion factor is a spectral index, but is particular in the sense that it does not use fission chambers but relies on the particular peak spectrometry technique.

The modified conversion factor is defined as the ratio of ^{238}U radiative captures on total fission rate in the fuel rod. It is mainly used in the MOX fuel rods.

$$\text{Modified conversion factor} = \frac{^{238}\text{U captures}}{\text{total fissions}} = \frac{C8}{F_{total}}. \quad (64)$$

This definition is broader than that found in an all UO_2 core where the denominator is mainly the ^{235}U fission rate. This measurement is a postirradiation measurement directly on fuel rods.

The measurement is based on the detection of gamma peaks of two fission products: ^{143}Ce at 293.27 keV and ^{140}Ba at 537.31 keV, as well as ^{239}Np at 277.60 keV which characterizes the capture rate of the ^{238}U through the reaction



This measurement requires the detection of low energy gamma rays, which requires the use of a high efficiency diode. The ^{140}La peak at 1,596 keV is used as power normalization. It is shown that the modified conversion rate is given by the following expressions:

$$C8 = \frac{(\lambda_{\text{U9}} - \lambda_{\text{Np}}) \times N_{\text{Np}}}{g_{\text{Np}} \times \eta_{\text{Np}} \times f_{\text{Np}} \times \frac{\lambda_{\text{U9}}}{\lambda_{\text{Np}}} \times (1 - e^{-\lambda_{\text{Np}} t_e}) \times e^{-\lambda_{\text{Np}} t_c} \times (1 - e^{-\lambda_{\text{Np}} t_m})}, \quad (65)$$

for capture

$$F = \frac{\lambda_p \times C_{FP}}{Y_{FP} \times I_{FP} \times \eta_{FP} \times f_{FP} \times (1 - e^{-\lambda_p t_e}) \times e^{-\lambda_p t_c} \times (1 - e^{-\lambda_p t_m})} \quad (66)$$

for fission, which gives the final relationship for the modified conversion rate:

$$\frac{C8}{F} = \frac{\lambda_{\text{U9}} - \lambda_{\text{Np}}}{\lambda_p} \times \frac{\lambda_{\text{Np}}}{\lambda_{\text{U9}}} \times \frac{C_{\text{Np}}}{C_{\text{FP}}} \times Y_{\text{FP}} \times \frac{I_{\text{FP}}}{I_{\text{Np}}} \times \frac{\eta_{\text{FP}}}{\eta_{\text{Np}}} \times \frac{f_{\text{FP}}}{f_{\text{Np}}} \times \frac{(1 - e^{-\lambda_p t_e}) \times e^{-\lambda_p t_c} \times (1 - e^{-\lambda_p t_m})}{(1 - e^{-\lambda_{\text{Np}} t_e}) \times e^{-\lambda_{\text{Np}} t_c} \times (1 - e^{-\lambda_{\text{Np}} t_m})}, \quad (67)$$

where the notations are similar to the particular peak:

- F_p is the analyzed fission product
- λ_i is the decay constant of the nuclide i
- C is the integral count of the gamma peak of interest
- I_i is the probability of emission of the nuclide i gamma line
- f_i is the self-absorption factor of the gamma line
- η_i is the worth of the detector used
- t_e, t_c, t_m the irradiation, cooling and counting time

and $Y_{FP} = \sum_i (Y_{iT} \times \alpha_{iT} + Y_{iF} \times \alpha_{iF})$ is the effective fission yield of the fission product, calculated as for the peak check.

The self-absorption of gamma in the fuel is calculated in the same way as in the case of the measurement of the particular peak. The uncertainty associated with the modified conversion rate measured is approximately 2% (at 1 σ).

These two last equations is rewritten in a slightly different form as:

$$C_8 = \frac{A(E_c)}{I_\gamma(E_c)R^P(E_c)T(E_c)}, \quad (68)$$

$$F = \frac{A(E_f)}{YI_\gamma(E_f)R^P(E_f)T(E_f)}, \quad (69)$$

where

$I_\gamma(E)$ is γ -ray emission probability of the reaction product with the energy E

$R^P(E)$ is the detection efficiency for a point source with the energy E

$T(E)$ is the efficiency transfer correction

Y is the average fission yield over all fissionable isotopes

$A(E)$ is the saturated count rate of the gamma-ray with the energy E

The saturated count rate $A(E)$ is obtained from net peak area measurements using the following relationship:

$$A(E) = \frac{N(E)}{t_r} C_\theta C_{dec} \quad (70)$$

with:

$N(E)$ is the net area of the photopeak with the energy E , unfolded with the spectrum software

t_r is the real time of measurement

C_θ is the dead time correction factor

C_{dec} is the decay correction factor

Then the spectral indexes, which describe the capture rate on ^{238}U per unit of fission, are given by:

$$\frac{C_8}{F} = Y \frac{A(E_c)}{A(E_f)} \frac{I_\gamma(E_f)}{I_\gamma(E_c)} \frac{R^P(E_f)}{R^P(E_c)} \frac{T(E_f)}{T(E_c)}. \quad (71)$$

The saturated count rates and the detection efficiencies are obtained from measurements. Some nuclear data is also required: fission yields, radioactive periods and gamma-ray emission probabilities. They can be extracted from the JEF2.2, JEFF3.1, or ENDF/B-VI.8 nuclear data libraries. Finally, relative reaction rate calculations must be performed to estimate average fission yields and efficiency transfer corrections. They will be described in the next section.

The overall uncertainty on this particular spectral index is simply obtained from the variance propagation relationship, given at the first order by:

$$\frac{u^2\left(\frac{C_8}{F}\right)}{\left(\frac{C_8}{F}\right)^2} = \frac{u^2(Y)}{Y^2} + \frac{u^2\left(\frac{A(E_c)}{A(E_f)}\right)}{\left(\frac{A(E_c)}{A(E_f)}\right)^2} + \frac{u^2\left(\frac{I_\gamma(E_f)}{I_\gamma(E_c)}\right)}{\left(\frac{I_\gamma(E_f)}{I_\gamma(E_c)}\right)^2} + \frac{u^2\left(\frac{R^P(E_f)}{R^P(E_c)}\right)}{\left(\frac{R^P(E_f)}{R^P(E_c)}\right)^2} + \frac{u^2\left(\frac{T(E_f)}{T(E_c)}\right)}{\left(\frac{T(E_f)}{T(E_c)}\right)^2}. \quad (72)$$

9.5 γ Heating Measurements

9.5.1 Principle

The gamma dose measurement is an important integral parameter in several situations where the heating due to energetic photons takes on some problems. This particularly applies for the heating in experimental devices inserted into irradiation cores. This dose can be measured using ionization chambers or using TLD. This thermo-luminescence is caused by irradiation beforehand by ionizing radiation. TL is only observed on non-metallic materials and mainly on crystallized ion composites. We consider a band gap insulating material, typically of a few eV. The impurities and effects caused by doping the material create the following electronic levels in the band gap:

- Confined levels (CL), generally close to the conduction band (CB) or the valence band (VB). They “capture,” trap electrons during irradiation and “free” them when sufficient thermal energy is provided.
- Recombination centers (RC), deeper in the gap, are where the electron/hole radiative exchange (emission of a visible photon) takes place when an electron is released from a confined level.

As these materials are insulators, an electron has a very short lifetime in the CB.

During irradiation by ionizing radiation (► Fig. 82), ionization of a certain number of atoms occurs; VB electrons are freed into the CB (1) in which they move freely whereas the holes created move into the VB. During this transitional phenomenon, two events may occur:

- The electron recombines with a hole (annihilation). If the recombination is radiative, the emission of fluorescence is observed. However, this band to band recombination is unlikely.

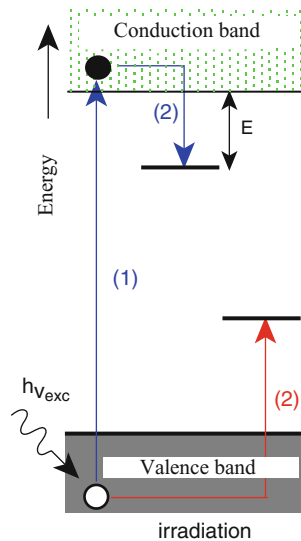
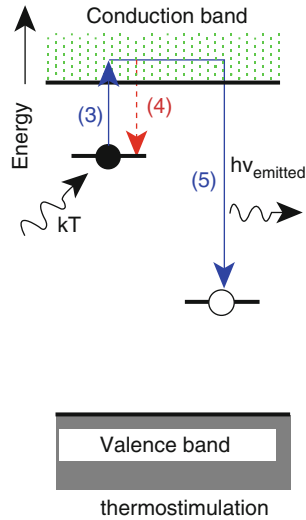


Figure 82
Irradiation



■ **Figure 83**

Thermal stimulation process

- The charges are trapped (2 and 2'). As the confined levels are metastable levels, the electrons can only be freed if they are provided with energy E required to make them pass into the CB from which the recombination step is possible.

Energy E can be supplied by a gradual increase of the crystal's temperature: this thermal excitation is called thermo-stimulation (➤ Fig. 83).

The electron will be unconfined (3) at a specific temperature of the defect with which the confinement is associated.

Once the electron is released, two events may occur:

- The electron is trapped again (4), however it will immediately “leave” as the temperature is too high
- It recombines with a hole (5). If the recombination is radiative, *emission of thermoluminescence* is observed, in the visible photonic and/or UV spectrum, the emission spectrum depends on the depth of the trap

If E is low (shallow trap for the temperature in question), the ambient thermal agitation is enough to provoke the release. The emission which can be observed is called phosphorescence. It takes place at ambient temperature.

9.5.2 γ Dose Calculation

Measurement of the gamma dose in mixed neutron – gamma field (n, γ), particularly in a hydrogenated environment, creates serious problems due to the sensitivity of most TLDs to neutrons with different energies. The signal emitted by the TLD can be interpreted as resulting from the sum of three terms, corresponding respectively to the following.

- The total gamma dose to be measured
- The parasite contribution of thermal and epithermal neutrons
- The fast neutron dose

In these conditions, the measured dose (D_{mes}) can be broken down according to the following relationship:

$$D_{mes} = hD_{tot} + k_{th}\Phi_{th} + h_{rap}D_{rap}, \quad (73)$$

where

h attributed to the total gamma dose depends on the spectral response of the TLD. It is given the same value if the spectrum of the photon component of the radiation field does not have energies which are too low (< 100 keV or too high > 10 MeV) with respect to the calibration radiation of cobalt-60. Prior knowledge of the predominant photon spectrum in the core is therefore necessary.

k_{th} [$\text{Gy}/(10^{12} \text{ n cm}^{-2})$], corresponding to the fluence of thermal neutrons Φ_{nth} , depends on the nature of the TLD and the neutron energy spectrum: it expresses the sensitivity of thermo-luminescent materials to thermal neutrons as the parasite response is mainly due to the latter.

h_{rap} [per neutron: Gy cm^{-2}] is minor in a fission field. This contribution is not currently taken into account, however some information can be found in literature.

Obtaining the γ dose of TLDs requires several preliminary TLD and calibration individual characterization steps. These steps then allow a gamma dose to be deduced from thermo-luminescent emissions, at the end of final irradiation in the reactor, after adjustment on the reactor's power.

9.5.3 The Different Types of TLDs Used

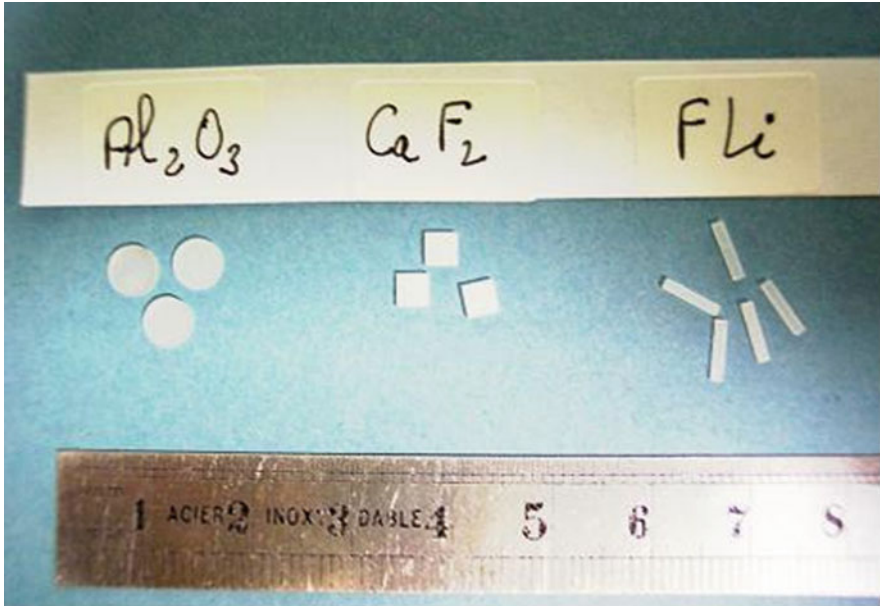
The different TL materials which are used are:

- $\text{CaF}_2:\text{Mn}$
- $\text{Fl}i^7:\text{Mg,Ti}$ (TLD700 and MTS-7)
- $\text{Al}_2\text{O}_3:\text{C}$
- $\text{Al}_2\text{O}_3:\text{Na}$ (powder) (► [Fig. 84](#))

9.6 Neutron Noise Measurements

Measurement of the delayed neutron fraction falls under the category of so-called “neutron noise” measurements. Neutron fluctuation measurements are based on stable or transitional macroscopic statuses generated in low power reactors, for example, fissions or neutron sources, etc. Several methods exist and are applied in the critical mock-ups. They are classified into two categories:

- Pulsed methods: Feynman- α and Rossi- α
- Frequential methods: power spectral density (PSD), ^{252}Cf source



■ Figure 84

Example of TLDs used at EOLE, MINERVE and MASURCA

All these methods have been tested and their validation range estimated on MASURCA, as part of determination measurements for the reactivity of subcritical systems (MUSE program).

Here, the PSD method, implemented in EOLE, is of particular interest.

9.6.1 The Power Spectral Density (PSD) Method

This is a so-called “correlation” technique based on the study of correlations between detections at an instant t and $t + T$. It is based on the measurement of the reactor’s transfer function, given by the standard expression

$$|H(\omega)|^2 = \frac{\eta_0^2}{\left(\beta_{\text{eff}} - \rho - \sum_j \frac{\lambda_j^2 \beta_j}{\lambda_j^2 + \omega^2}\right)^2 + \omega^2 \left(1 + \sum_j \frac{\lambda_j^2 \beta_j}{\lambda_j^2 + \omega^2}\right)} \quad (74)$$

with the following approximations.

- Spatial effect not considered (point reactor approximation)
- Stable state: no reliance on time
- Low power, no counter-reaction effects

The most frequently used approximations are $\ell \gg \sum_j \lambda_j^2 \beta_j / \lambda_j^2 + \omega^2 \ll \beta_{\text{eff}} - \rho$ and the previous expression becomes:

$$|H(\omega)|^2 = \frac{\eta_0^2}{(\beta_{\text{eff}} - \rho)^2 + \omega^2 \ell^2}. \quad (75)$$

It involves a first rate filter for which the plateau is given by:

$$\omega \ll \frac{\beta_{\text{eff}} - \rho}{\ell} \quad \text{and} \quad |H(\omega)|_{\text{plateau}}^2 = \frac{\eta_0^2}{(\beta_{\text{eff}} - \rho)^2} \quad (76)$$

and the cut-off frequency is expressed as,

$$\omega_c = \frac{\beta_{\text{eff}} - \rho}{\ell} \quad \text{or} \quad f_c = \frac{\beta_{\text{eff}} - \rho}{2\pi\ell}. \quad (77)$$

The statistical nature of the reactor noise helps determine the average level of the neutron population. It can be shown that the spectral density of the equivalent noise source is given by

$$\langle |S|^2 \rangle = 2 \left(\frac{\eta_0}{\ell} \right)^2 \frac{D}{F}, \quad (78)$$

where

$$D = \frac{\overline{v(v-1)}}{\overline{v}^2} \text{ is the Diven factor,} \quad (79a)$$

$$F = \frac{1}{v} \frac{\eta_0}{\ell} F \text{ is the total number of fissions in the core per time unit.} \quad (79b)$$

It represents the distribution of power on the frequency axis.

9.6.2 Experimental Principle

Measurement of the transfer function and the PSD is carried out using specific fission chambers, highly loaded, operating in standard mode and placed around the core, as close as possible to the fuel. They are positioned symmetrically in order to increase the probability of detecting correlated events. The signal coming from these chambers is then filtered of its continuous component, seen as white noise. It is shown that the final expression allowing the PSD to be linked with the delayed neutron ratio is given by:

$$\frac{DSPI}{V_1 V_2} = \frac{2D}{F} \times \frac{1}{(\beta_{\text{eff}} - \rho)^2}, \quad (80)$$

where V_1 and V_2 are the voltages of fission chambers placed in the core.

The fraction of delayed neutrons is obtained from this relationship

$$\beta_{\text{eff}}^2 = \frac{2D}{F(1 + \rho)^2} \times \frac{V_1 V_2}{DSPI}. \quad (81)$$

The Diven factor is calculated. It depends relatively little on the case in question and its value is often close to $0.800 \pm 2\%$ (1σ). The other sizes are determined experimentally.

The fission integral measurement, in particular, is obtained using $F = P/F_N$ where P is the core's power (Watt)

$F_N = 3.2 \times 10^{-11}$ W/fission s is the average energy released by fission.

The power is measured using a calibrated fission chamber, placed at the center of the core. The power is then expressed as:

$$P = f \times \frac{C}{m_5} \quad (82)$$

with

$$f = M_5 \times \frac{\sigma_{f5}^{core}}{\sigma_{f5}^{chamber}} \times \frac{1}{\alpha\beta} \times \frac{I_{fT}}{I_{f5}} \times F_N, \quad (83)$$

where C is the count rate of the chamber, m_5 is the ^{235}U mass in the chamber, M_5 is the ^{235}U mass in the core, σ_{f5} is the fission cross-section of the ^{235}U , α is the axial shape factor, β is the radial shape factor, and I_f is the fission integral (core or chamber).

The total uncertainty on the value of the delayed neutron fraction is approximately 1.6%, without taking into account the uncertainty stemming from the Diven factor which contributes 3% at 1σ on the β_{eff}^2 .

10 Conclusion

This chapter indicates the key-role of the Zero Power Reactors for the development of a sustainable nuclear energy.

It has shown that whatever the progress of simulation tools, a complementary experimental program for qualification and validation is often necessary.

During these last decades, the ZPR help the various entities working in the nuclear energy domain (utilities, technical support to regulatory bodies, research Institutes, etc.) to improve their knowledge on reactor physic and nuclear data (reduction of target uncertainties, better estimation of fundamental parameter such as k_{eff} , beta effectif, power map, etc.).

As a positive feedback, we can quote the improvement of Nuclear Power Plant competitiveness (Higher Burn-up, new fuel design, new core design, etc.), life time extension (fluence dosimetry on reactor vessel and internals, etc.) safety (neutron absorber, reactivity coefficient, etc.) and the proposal of new data libraries based on fundamental nuclear data.

Moreover, these ZPR are also important for the design of new generation of MTR for qualification of new fuel and associated calculation tools.

Last but not least, these ZPR have been and will stay of particular importance for training of young scientists and Engineers and operating teams working in the field of nuclear reactors (research reactors or power reactors).

References

Generalities

Darrouzet M, Salvatores M (1988) Reactor physics activities in France. In: Proceedings of the international reactor physics conference, vol I, p 1, ANS, Jackson Hole, 18–22 Sept 1988

Fougeras P, Chauvin JP, Cabrillat JC, Martini M (1996) The use of the CEA critical facilities for the assessment of the physics. In: ENS class1 topical meeting on research facilities for the future of nuclear energy, Brussels, 4–6 June 1996

- Bignan G, Rippert D, Fougeras P (2001) The key role of critical mock-up facilities for neutron-physic assessment of advanced reactors: an overview of CEA/CADARACHE tolls. In: ARWIF 2001, Chester, 23–26 Oct 2001
- Bignan G, Zaetta A, Fougeras P, Jacqmin R, Bosq JC, Klein JC, Lyoussi A, Mellier F, Blaise P, Chabre A, Sacristan P (2008) Experimental reactor physic perspective in France. In: PHYSOR2008 international conference on the physics of reactor, Interlaken, 14–19 Sept 2008
- Fougeras P, Porracchia A (2006) Les maquettes critiques du CEA. RGN No. 2, March–April 2006
- Fougeras P, Hudelot JP, Antony M, Mellier F, Destouches C, Cathalau S, Blaise P, Thiollay N (2005a) EOLE, MINERVE and MASURCA facilities and their associated neutron experimental programmes. In: 13th international conference on nuclear engineering ICONE13, Beijing, 16–20 May 2005
- Fougeras P, Chabre A, Mergui C (2005b) The place of EOLE, MINERVE and MASURCA facilities in the R&D activities of the CEA. In: IGORR 10: international group on research reactors, Gaithersburg, 12–16 Sept 2005
- Fougeras P, Hudelot JP, Rippert D, Mellier F, Blaise P, Antony M, Huot N (2007) The place of EOLE, MINERVE and MASURCA facilities in the R&D Activities of the CEA. In: PHYTRA 2007, GMTR, Marrakech, 14–16 March 2007
- International Handbook of Evaluated Reactor Physics Benchmark Experiments. Nuclear Energy Agency, NEA/NSC/DOC(2006)1, March 2007
- IRPhE – An International Reactor Physics Benchmark Experiments Database. <http://www.inel.gov/energy/nuclear/irpheap/>
- Soule R, Fougeras P, Assal W, Blaise P, Bompas CA, Cathalau S, Chaussonnet P, Chauvin JP, Granget G, Hudelot JP, Laurens JM, Laval V, Lebrat JF, Martini M, Philibert H, Flamenbaum G, Salvatores M (1999) Neutron integral experiments in support to the Pu utilization and waste incineration. In: Global'99 international conference on the future nuclear systems, Jackson Hole, 29 Aug–3 Sept 1999
- Programmes in EOLE**
- Blaise P, Fougeras P, Philibert H, Laval V, Perret G (2002) Preliminary analysis of the BASALA-H experimental programme. In: ICONE10, Arlington, 14–18 April 2002
- Blaise P, Fougeras P, Santamarina A, Cathalau S (2004) Integral needs for MOX powders: state-of-the-art at CEA\Cadarache on MOX fuel experiments. In: OECD/NEA workshop on MOX powders, Paris, 13–14 April 2004
- Blaise P, Thiollay N, Fougeras P, Pont T, Destouches C, Beretz D, Lee Y-K, Chiron M, Janski S (2006) Neutron vessel fluence assessment in the 1300MWe NPP French Fleet: the FLUOLE program in EOLE. In: ICAPP'06 international congress on advances in nuclear power plants, Reno, 4–8 June 2006
- Blaise P, Thiollay N, Fougeras P, Huot N, Laval V, Roche A (2007) Full MOX ABWR neutron characterization with void increase: the FUBILA program M&C + SNA 2007: joint international topical meeting on mathematics and computation, supercomputing in nuclear applications, Monterey, 15–19 April 2007
- Blaise P, Vidal JF, Santamarina A (2009a) Validation of the REL2005 code package on poisoned PWR type assemblies through the CAMELEON experimental program. In: ICAPP 09, Tokyo, 10–14 May 2009
- Blaise P, Vaglio-Gaudard C, Vidal JF, Ruggieri JM (2009b) Deterministic modeling of 100% MOX ABWR lattices with increasing void fraction: validation of the REL2005 code package on FUBILA experimental program. In: ICAPP 09, international congress on advances in nuclear power plants, Tokyo, 10–14 May 2009
- Blaise P, Thiollay N, Fougeras P (2010) Monte Carlo modelling of increasing void fraction in 100% MOX ABWR lessons drawn from the FUBILA program. *J Nucl Sci Technol*
- Blaise P, Thiollay N, Huot N, Santamarina A, Fougeras P (2010) High-burn up 10×10 100% MOX ABWR FUBILA experimental program analysis with APOLLO2.8 and TRIPOLI-4 codes. *Ann Nucl Energy*
- Blaise P, Litaize O, Vidal J-F, Santamarina A (2010) Qualification of the French APOLLO2.8/CEA2005V4 code package on absorber clusters in 17×17 PWR type lattices through the CAMELEON program. In: PHYSOR2010, Pittsburgh, 9–14 May 2010
- Cathalau S (1988) Qualification des propriétés neutroniques des réacteurs sous modéré à l'eau légère. PhD thesis, Orsay, 19 June 1988
- Cathalau S, Chauvin JP, Maghnoouj A, Fougeras P (1996a) Calculation of 2D and 3D local void effects in MOX reactors: the EPICURE results. In: International conference on the physics of reactors PHYSOR'96, p C-11, Mito, Japan 16–20 Sept 1996
- Cathalau S, Cabrillat JC, Chauvin JP, Finck PJ, Fougeras P, Flamenbaum G, Matsu-Ura H, Ueji M, Yamamoto T (1996b) MISTRAL: an experimental programme in the EOLE

- facility devoted to MOX core physics. In: International conference on the physics of reactors PHYSOR'96, p H-84, Mito, Japan 16–20 Sept 1996
- Cathalau S, Fougeras P, Santamarina A (1998) First validation of neutronic lattice parameters of overmoderated 100% MOX fueled PWR cores on the basis of the MISTRAL experiment. In: International conference on the physics of nuclear science and technology. Future nuclear systems, p 393, ANS, Long Island, 5–8 Oct 1998
- Cathalau S, Fougeras P, Blaise P, Thiollay N, Santamarina A, Litaize O, Chabert C, Yamamoto T, Iwata Y, Umamo T, Kanda R, Girieud P, Biron D, Tatsumi M, Kan T, Ando Y, Ishii K (2002) Full MOX recycling in ALWR: lessons drawn through the MISTRAL program. In: PHYSOR 2002, Seoul, 7–10 Oct 2002
- Cathalau S, Fougeras P, Blaise P, Thiollay N, Santamarina A, Litaize O, Yamamoto T, Umamo T, Nigon JL (2004) Advanced BWRs fully loaded with MOX fuel: the BASALA experimental program. In: PHYSOR 2004, Chicago, 25–29 April 2004
- Cerdan C (1984) Qualification du calcul des réseaux modérés à l'eau légère et empoisonnés au Gadolinium. PhD thesis, Orsay, 25 Oct 1984
- Chauvin JP, Granget G, Martini M, Mondot J, Lefebvre JC, Vallee A (1992) Validation of the experimental methods used in the EPICURE programme and their associated uncertainties. In: ANS topical meeting on advances in reactor physics CHARLESTON 1992
- Chauvin JP, Cabrillat JC, Fougeras P, Cathalau S, Finck PJ (1996) EPICURE: an experimental program devoted to the validation of the calculation scheme for the pressurized water reactor recycling MOX Fuel. In: International conference on the physics of reactors PHYSOR'96, p E-133, Mito, 16–20 Sept 1996
- Doutriaux D, Martin-Deidier L, Roshd M, Santamarina A (1983) CRISTO I et II. Expériences de qualification des calculs de criticité des stockages pour des assemblages REP. In: ICNC'83, Dijon, 19–22 Sept 1983
- Erradi L, Santamarina A, Litaize O (2003) The reactivity temperature coefficient analysis in light water moderated UO_2 and UO_2 - PuO_2 lattices. Nucl Sci Eng 144:47–74
- Fougeras P (1992) Qualification des schémas de calcul pour le recyclage du Plutonium dans les Réacteurs à Eau sous Pression. Expérience EPICURE. PhD thesis No. 2309, Orsay, 10 Nov 1992
- Fougeras P, Cathalau S, Mondot J, Klenov P (1995) Optimization of a calculation scheme for the treatment of Pu recycling in PWRs. Nucl Sci Eng 121:32–40
- Fougeras P, Cathalau S, Finck PJ, Klenov P (1996a) Improved calculational scheme for absorber clusters in 30% MOX fueled PWRs. In: International conference on the physics of reactors PHYSOR'96, p A-258, Mito, 16–20 Sept 1996
- Fougeras P, Garzenne C, Stankovski Z, Aigle R (1996b) Generalised geometry analysis of the EPICURE measurements of the effects of the radial displacement of a MOX or UO_2 Fuel pin. In: International conference on the physics of reactors PHYSOR'96, p E-124, Mito, 16–20 Sept 1996
- Fougeras P, Blaise P, Cathalau S, Philibert H, Laval V, Chauvin JP, Girieud R, Santamarina A, Yamamoto T, Iwata Y, Ueji M (1999) MISTRAL-4: an experimental mockup in the EOLE facility devoted to high moderation 100% MOX core physics. In: Global'99 international conference on the future nuclear systems, Jackson Hole, 29 Aug–3 Sept 1999
- Klein JC, Thiollay N, Di Salvo J, Bignan G, Bosq JC, Sireta P, Wieryszkov JP, Alexandre P, Garnier D (2009) AMMON: an experimental program in the EOLE Critical facility for the validation of the JHR neutron and photon HORUS3D calculation scheme. In: IGORR12, Beijing, Oct 2009
- Litaize O, Santamarina A, Hervault M, Cathalau S, Fougeras P, Blaise P, Yamamoto T, Kanda R, Sasgawa M, Kikushi T (2004) Monte Carlo analysis of high moderation 100% MOX BWR cores using JEF2 and JENDL3 nuclear data. In: PHYSOR 2004, Chicago, 25–29 April 2004
- Martin-Deidier L, Santamarina A (1984) CAMELEON: a benchmark experiment of absorbers and burnable poisons in PWR assemblies. Trans Amer Nucl Soc, vol 1, 46–755
- Martin-Deidier L, Santamarina A, Cathalau S, Gomit JM, Chauvin JP (1986) ERASME: an extensive experiment for LWHCR design qualification. In: Topical meeting on reactor physics, Saratoga, Sept 1986
- Martin-Deidier L, Santamarina A, Cathalau S, Gomit JM, Chauvin JP (1987) Undermoderated PWR neutronic qualification through the ERASME experiments. In: Conf Int sur le développement en Physique des Réacteurs et méthodes de calcul, Paris, April 1987
- Mondot J, Gauthier JC, Chauchepat P, Chauvin JP, Lefebvre JC, Vallee A (1990) EPICURE: an experimental programme devoted to the validation of the calculational schemes for plutonium recycling in PWRs. In: International conference on physics of reactor operation, design and computation (PHYSOR'90), vol 1, p VI-53, Marseille, 23–26 April 1990

- Porta J, Baldi S, Chauvin JP, Fougeras P (2001) Qualification of the neutronic efficiency of erbium at zero burnup. *Nuclear Energy*, vol 38, no. 3-4, February 2001
- Santamarina (1995) A Storage array of 3% LWR assemblies. The CRISTO II experiments in the EOLE reactor. NEA/NSC/DOC(95)03, LEU-COMB-THERM
- Santamarina A (1987) Temperature effects analysis in light water reactor lattices. Thermal cross-sections shapes and qualification through French integral experiments. In: IAEA-TEC-DOC-491 proceedings of an IAEA advisory group meeting, Vienna, 7-10 Dec 1987
- Santamarina A, Martin-Deidier L (1982) Experimental qualification of the calculated subcriticality in high density fuel storage. In: Meet on advances in reactor physics and core thermal hydraulics, Kiamesha Lake, Sept 1982
- Santamarina A, Golinelli C, Erradi L (1984) Temperature effects analysis in light water reactor lattices. In: ANS topical meeting on reactor physics and shielding, Chicago, Sept 1984
- Santamarina A, Venard C, Blaise P, Rippert D, Fouillaud P, Girault E, Duhamel I, Rouyer V (2004) Critical experiments for criticality code validation on low-moderated MOX media with Appareillage-B and EOLE. In: WPNCs-MOX experiment meeting, Prague, 31 August 2004
- Santamarina A, Vaglio-Gaudard C, Blaise P, Huot N, Litaize O, Thiollay N, Vidal J-F (2008) The PERLE experiment for the qualification of heavy reflector. In: PHYSOR 2008, Interlaken, 14-19 Sept 2008
- Vidal J-F, Blaise P, Huot N, Guillot G, Litaize O, Santamarina A, Vaglio-Gaudard C (2008) Analysis of the FLUOLE experiment for the APOLLO2 validation of PWR core reflector. In: PHYSOR 2008, Interlaken, 14-19 Sept 2008
- Yamamoto T, Matsu-Ura H, Ueji M, Cathalau S, Cabrillat JC, Chauvin JP, Finck PJ, Fougeras P, Flamenbaum G (1997) Core physics experiment of 100% MOX core: MISTRAL. In: International conference on future nuclear systems'97 GLOBAL, p 395, Yokohama, 5-10 Oct 1997
- Yamamoto T, Iwata Y, Ueji M, Cathalau S, Fougeras P, Blaise P, Chauvin JP, Santamarina A (2000) BASALA: advanced BWR MOX core physics experiments. In: 2000 ANS international meeting on advances in reactor physics and mathematics and computation into the next millennium PHYSOR2000, Pittsburg, 7-12 May 2000
- Yamamoto T, Iwata Y, Umano T, Kanda R, Cathalau S, Fougeras P, Thiollay N, Blaise P, Santamarina A, Nigon JL (2002) BWR MOX core physics experiments and preliminary analysis. In: PHYSOR 2002, Seoul, 7-10 Oct 2002

Programmes in MINERVE

- Anno J, Barreau A, Hudelot JP, Girault E, Fouillaud P, Toubon H (2003) French fission products experiments performed in Cadarache and Valduc. In: Results comparison ICNC 2003 conference, Tokai-Mura, Oct 2003
- Antony M, Pepino A, Di Salvo J, Lyoussi A, Bosq JC, Hudelot JP, Leconte P, Bernard D (2009) Oscillation experiments techniques in CEA MINERVE pool experimental reactor. In: ANIMMA, Marseille, 7-10 June 2009
- Bernard D, Santamarina A (2003) Doppler calculation challenge in MOX lattices. Qualification on MINERVE oscillation experiment. In: Nuclear mathematical and computational sciences conference, Gatlinburg, 6-11 April 2003
- Bernard D, Santamarina A, Sargeni A, Antony M, Hudelot JP (2006) Experimental validation of the LWR reactivity loss with burn up: analysis of spent fuel oscillation experiments. In: PHYSOR 2006 advances in nuclear analysis and simulation, Vancouver, 10-14 Sept 2006
- Chauchepret P, Mondot J (1988) MORGANE S fission product capture measurement in a HCLWR high lattice. In: ANS topical meeting, Jackson Hole, Sept 1988
- Chauchepret P, Santamarina A, Bioux P, Perrutel JP (1986) Mixed loading calculation scheme FOR Pu recycling in PWRs. Qualification of the Pu MINERVE experiment. In: International conference on reactor physics, Saratoga Springs, Sept 1986
- Darrouzet M (1969) Mesure du rapport capture sur fission du ^{239}Pu dans l'assemblage critique thermique-rapide ERMINE. PhD thesis, Orsay, 1969
- Gruel A (2009) Interpretation of in-pile oscillation experiments in the minerve facility for the improvement of fission product cross sections. In: ANIMMA international conference on advancements in nuclear instrumentation, measurement methods and their applications, Marseille, 7-10 June 2009
- Hudelot JP, Chauvin JP, Thiollay N, Cathalau S, Fougeras P, Santamarina A, Toubon H (2000) The credit burn up program on the MINERVE facility. In: 2000 ANS annual meeting, San Diego, 4-8 June 2000
- Hudelot JP, Chabert C, Chauvin JP, Fougeras P, Perret G, Genin X, Leorier C, Moulinier JM (2001)

The OSMOSE experimental program for the qualification of the integral cross sections of actinides. In: 2001 nuclear data, Tsukuba, 7–12 Oct 2001

- Hudelot JP, Chabert C, Chauvin JP, Fougeras P, Perret G, Genin X, Leorier C, Moulinier JM (2002) The OSMOSE experimental program for the qualification of the integral cross sections of actinides. *J Nucl Sci Technol* 2:1007–1080
- Hudelot JP, Klann R, Fougeras P, Genin X, Drin N, Donnet L (2004) OSMOSE: An experimental program for the qualification of integral cross sections of actinides. In: *PHYSOR 2004*, Chicago, 25–29 April 2004
- Hudelot JP, Döderlein C, Antony M, Girard JM, Laval V, Fougeras P, Willermoz G, Leconte P (2005) The VALMONT program: accurate experimental techniques to support the neutronics qualification of UMo/Al. In: 9th international topical meeting on research reactor fuel management (RRFM) RRFM 2005, Budapest, 10–13 April 2005
- Hudelot JP, Antony M, Testaniere S, Fougeras P (2006a) OCEAN: an ambitious experimental program for the qualification of integral capture cross sections of neutron absorbers. In: *PHYSOR 2006 advances in nuclear analysis and simulation*, Vancouver, 10–14 Sept 2006
- Hudelot JP, Klann R, Antony M, Testaniere S, Fougeras P, Jorion F, Drin N, Donnet L, Leorier C (2006b) The OSMOSE program for the qualification of integral cross sections of actinides: preliminary experimental results in a PWR-UOX spectrum. In: *PHYSOR 2006 advances in nuclear analysis and simulation*, Vancouver, 10–14 Sept 2006
- Laponche B (1970) Méthode de l'échantillon équivalent pour interpréter les expériences d'oscillations d'échantillons fissiles dans une pile à neutrons thermiques. PhD thesis, Orsay, 1970
- Martin-Deidier L (1979) Mesure intégrale de la capture des produits de fission dans les réacteurs à neutrons rapides. PhD thesis, Orsay, 1979 ORSAY University, Paris XI
- Mondot J (1990) Synthesis of experimental validation of global fission product capture for PWR's and advanced reactor lattices. In: Topical meeting ANS Physor'90, Marseille, 23–27 April 1990
- Santamarina A (1978) Calcul des assemblages PWR. Qualification du système NEPTUNE par les expériences MELODIE dans MINERVE. In: Conférence sur les méthodes d'homogénéisation en Physique des Réacteurs, IAEA TECDOC-231, Lugano, Nov 1978

Programmes in MASURCA

- Assal W, Bosq JC, Mellier F (2009) Experimental measurements at the MASURCA facility. In: ANIMMA, Marseille, 7–10 June 2009
- Barre JY, Boyer J, Mougnot JC, Sicard B (1972) Reactor physics and fast power breeders: MASURCA CORE RZ program. In: Meeting on new developments in reactor physics, Kiamesha Lake
- Bertrand P (1996) BERENICE – inter laboratory comparison of β eff measurement techniques at MASURCA. In: Proceedings of the international conference on *PHYSOR'96*, vol 2, pp E190–E199, Mito, Sept 1996
- Bouget YH, Cosimi M, Hammer P, Humbert G, Lyon F, Martini M (1979) Physics performances of a heterogeneous fast reactor core concept in MASURCA. *Nucl Technol* 44:61–75
- Destouches C, Fruneau M, Belmont JL, Do Pinhal J, Albrand S, Carreta JM, Chaussonnet P, De Conto JM, Fontenille A, Fougeras P, Garrigue A, Guisset M, Laurens JM, Loiseaux JM, Marchand D, Micoud R, Mellier F, Perbet E, Planet M, Ravel JC, Richaud JP (2006) The GENEPI accelerator operation feedback at the MASURCA reactor facility. *Nucl Instrum Meth Phys Res A* 562:601–609
- D'orval CC, Engelmann P, Helm F, Jourdan G, Meyer-Heine A, Pilate S, Schmidt AP, Tretiakoff O, Vidal R, Wittek G (1970) Joint experiments on MASURCA, ERMINE and SNEAK in support of fast breeder projects Phenix and SNR. *Trans Am Nucl Soc* 13:292–293
- Finck PJ, Cabrillat JC, Martini M, Soule R, Rimpault G, Jacqmin R (1996) The CIRANO experimental programme in support of advanced fast reactor physics. In: Proceedings of the international conference on the physics of reactors *PHYSOR'96*, Mito, 16–20 Sept 1996
- Giese H, Caravec C, Granget G, Palmiotti G (1986) The RACINE-1E critical experiments for control rod method and data calculation. Experimental and calculation results. In: Proceedings of the topical management advances in reactor physics and safety, Saratoga Springs, 17–19 Sept 1986
- Humbert G, Kappler F, Martini M, Norvez G, Rimpault G, Ruelle B, Scholtyssek W, Stanculescu A (1984) Parametric studies on heterogeneous cores for fast breeder reactors: the pre-racine and racine experimental programs. *Nucl Sci Eng* 87:233–251
- Improvements of the predicted characteristics for fast power reactor from integral experiments: Cadarache Version III multigroup cross section

- set. In: International fast reactor physics symposium, Tokyo, 16–19 Oct 1973
- Integral experiments performed at CEA to improve the Pu higher isotope nuclear data: “PLUTO programme”. In: Specialists meeting on the nuclear data of higher plutonium and americium isotopes for reactor applications, Brookhaven, 20–22 Nov 1978
- Lebrat JF, Aliberti G, D’Angelo A, Billebaud A, Brissot R, Brockmann H, Carta M, Destouches C, Gabrielli F, Gonzalez E, Hogenbirk A, Klein-Meulenkamp R, Le Brun C, Liatard E, Mellier F, Messaoudi N, Peluso V, Plaschy M, Thomas M, Villamarin D, Vollaie J (2008) Global results from deterministic and stochastic analysis of the MUSE-4 experiments on the neutronics of ADS. *Nucl Sci Eng* 158(1):49
- Lyon F, Martini M, Rimpault G (1979) Etude de l’effet vidange sodium dans des milieux représentatifs des centrales à neutrons rapides de type classique ou hétérogène – expériences faites au cours du programme Pré-Racine sur Masurca. In: Proceedings of the international conference on fast reactor physics, Aix, 24–28/09/1979, IAEA-SM-244/23, vol 2, IAEA
- MASURCA (1963) Maquette critique à neutrons rapides – description fonctionnelle et objectifs. In: Proceedings of the symposium on “Exponential and Critical Experiments” held by the IAEA in Amsterdam, Netherlands, vol I, pp 135–155, 2–6 Sept 1963
- Mellier F, Billebaud A, Brissot R, Destouches C, Fougeras P, Le Brun C, Liatard E, Jammes C (2006) Conclusions and perspectives after the achievement of the MUSE4 programme at the MASURCA facility. In: 9th IEM on actinide and fission product partitioning and transmutation, Nimes, 25–29 Sept 2006
- Perret G, Destouches C, Fougeras P, Soule R, Hudelot JP, Jammes C, Assal W, Chaussonnet P, Laurens JM, Bignan G (2002) Determination of reactivity by revised rod-drop technique in the MUSE-4 programme. In: Comparison with dynamic measurements. Actinide and fission product partitioning & transmutation, Jeju, 14–16 Oct 2002
- Rimpault G, Jacqmin R, Matini M, Soule R, Smith P, Ohki S (1998) The CIRANO experimental programme for the characterisation of highly enriched plutonium oxide fuel in fast reactors. In: Proceedings of the international conference on PHYSOR’98, Long Island
- Soule R, Salvatores M, Bignan G, Jammes C, Destouches C, Fougeras Ph, Lebrat JF, Billebaud A, Brissot R, Fruneau M, Giorni A, Le Brun C, Loiseaux JM, Merle E, Wachtarczyk Ph, Villamarin D, Plaschy M, Seltborg P, Imel G (2001) Experimental validation of the neutronic characteristics of the sub-critical multiplying medium of an ADS: the MUSE programme. In: AccApp’01 & ADTTA’01 nuclear applications in the new millennium, Reno, 11–15 Nov 2001
- Soule R, Salvatores M The Experimental Balzac Program at Masurca in Support of the design of Super Phenix 2. In: Proceedings of the topical meeting on reactor physics and safety, Saratoga Springs, 17–19 Sept 1986
- Vaglio-Gaudard C, Lebrat JF, Pénéliou Y, Ruggieri JM, Sublet JC, Tommasi J, Vidal JF, Lyoussi A (2010) Analysis of the gas benchmark in MASURCA facility for the calculation of the steel reflector in fast reactors. *Nucl Sci Eng*
- Villamarin D, Perret G, Gonzalez E, Soule R, Jammes C, Imel G, Destouches C, Chaussonnet P, Laurens JM, Thomas GM, Fougeras P, Bignan G (2002) First measurements of the kinetic response of the MUSE-4 fast ADS mock-up to fast neutron pulse. In: Actinide and fission product partitioning & transmutation, Jeju, 14–16 Oct 2002

Experimental Techniques and Methods

- Amharrak H, Di-Salvo J, Thiollay N, Lyoussi A, Bosq J-C, Bignan G (2009) In core measurements using thermo-luminescent detectors (TLD). In: ANIMMA, Marseille, 7–10 June 2009
- Blaise P, Fougeras P, Cathalau S (2000) New developments in representativity approach to study advanced assembly concepts in the EOLE critical facility. In: 2000 ANS international meeting on advances in reactor physics and mathematics and computation into the next millennium PHYSOR2000, Pittsburg, 7–12 May 2000
- Blaise P, Cathalau S, Thiollay N, Fougeras P, Laval V, Philibert H, Girard JM, Hudelot JP (2004) Fission products particular peak measurement for UO_2 - Gd_2O_3 -MOX γ -scanning renormalization in 100% MOX ABWR mock up cores. In: 12th international conference on nuclear engineering (ICONE 12), Arlington, 25–29 April 2004
- Blaise P, Serviere H, Roche A, Fougeras P, Blanchet D, Huot N (2005a) Recent advances in gamma heating measurement in full MOX cores by using TLD technique: the ADAPh program. In: GLOBAL 2005, Tsukuba, 9–13 Oct 2005
- Blaise P, Fougeras P, Cathalau S, Laval V, Philibert H, Girard JM, Yamamoto T (2005b) Experimental investigation of isothermal temperature coefficient in ALWR type UOX and full MOX cores. In: GLOBAL 2005, Tsukuba, 9–13 Oct 2005
- Blaise P, Mellier F, Fougeras P (2009) Application of the modified source multiplication (MSM)

- technique to subcritical worth measurements in thermal and fast reactors systems. In: ANIMMA international conference on advancements in nuclear instrumentation, measurement methods and their applications, Marseille, 7–10 June 2009
- Blanc de Lanaute N, Mellier F, Lyoussi A, Chaussonnet P, Bosq JC (2009) Reduction of uncertainties concerning fission chambers measurements through a better understanding of the calibration process and the dead time phenomenon. In: ANIMMA, Marseille, 7–10 June 2009
- Cabrillat J-C, Martini M (1990) Power and neutron flux distributions in the core and shielding. *Nucl Sci Eng* 106:37–46
- Chauvin JP, Cabrillat JC (1995) Validation of one axial γ scanning measurement bench for the determination of the axial fission rate directly on the core pin from the EOLE or MINERVE facilities. In: Annual meeting on nuclear technology 95, Meistersingerhalle Nurnberg, 16–18 May 1995
- Gauthier J-C, Cabrillat J-C, Palmiotti G, Salvatore M, Giese M, Carta M, West J-P (1990) Measurement and predictions of control rod worth. *Nucl Sci Eng* 106:18–29
- Geslot B, Jammes C, Nolibe G, Fougeras P (2005) Multimode acquisition system dedicated to experimental neutronic physics. In: IMTC 2005 – instrumentation and measurement technology conference, Ottawa, 17–19 May 2005
- Girard JM, Philibert H, Domergue Ch, Beretz D (2009) The MADERE radio-activity measurement Platform: developments for a better address of the experimental needs. In: IGORR12, Beijing, Oct 2009
- Hudelot J-P (1998) Développement, Amélioration et calibration des mesures de taux de réaction neutroniques: élaboration d'une base de techniques standards. PhD thesis, June 1998
- Hudelot JP, Girard JM (2009) An innovating active neutronics interrogation and time-dependent method for calibrating fission chambers in the dedicated celina facility using a pulsed neutron generator. In: ANIMMA, Marseille, 7–10 June 2009
- Hudelot JP, Fougeras P, Cathalau S (2002) Measurement of the modified conversion ratio of ^{238}U by gamma-ray spectrometry on irradiated fuel pin. In: 11th international symposium on capture γ -ray spectroscopy and related topics, Pruhonice, 2–6 Sept 2002
- Jammes C, Geslot B, Rosa R, Imel G, Fougeras P (2005) Comparison of reactivity estimations obtained from rod drop and pulsed neutron source experiments. *Ann Nucl Energy* 32:1131–1145
- Jammes Ch, Filliatre P, Geslot B, Oriol L, Berhouet F, Villard J-F (2009) Research activities in fission chamber modeling in support of the nuclear energy industry ANIMMA, Marseille, 7–10 June 2009
- Leconte P (2006) Optimisation et développement de techniques de mesure par spectrométrie g sur combustible irradié. Maîtrise et réduction des incertitudes. PhD thesis, Oct 2006
- Leconte P, Hudelot JP, Antony M, Bernard D (2006a) An innovating gamma-spectroscopy experimental technique for measuring the integral capture cross section of actinides. In: PHYSOR 2006 advances in nuclear analysis and simulation, Vancouver, 10–14 Sept 2006
- Leconte P, Hudelot JP, Antony M (2006b) Integral capture rate measurements of neutron poisons and minor actinides by g-ray spectrometry on specific fuel samples. In: IYNC international youth nuclear congress, Stockholm, 18–23 June 2006
- Lüthi A, Chawla R, Rimpault G (2001) Improved gamma-heating calculational methods for fast reactors and their validation for plutonium-burning configurations. *Nucl Sci Eng* 138:233–255
- Pang H (1995) Development of stochastic and deterministic techniques for the determination of delayed neutron yields and β effective. PhD thesis, no. 3634, Orsay, 28 March 1995
- Perret G (2003) Amélioration et développement des méthodes de détermination de la réactivité –Maîtrise des incertitudes associées. PhD thesis, Orsay, 2003
- Plaschy M, Destouches C, Chawla R, Beretz D, Mellier F, Serviere H, Fougeras P, Chaussonnet P, Domergue C, Laurens JM, Philibert H (2005) Determination of adjusted neutron spectra in different MUSE configurations by unfolding techniques ISRD12, Gatlinburg, 8–13 May 2005

19 Pressurized LWRs and HWRs in the Republic of Korea

Nam Zin Cho¹ · Han Gon Kim²

¹Department of Nuclear and Quantum Engineering,
Korea Advanced Institute of Science and Technology,
Daejeon, Korea
nzcho@kaist.ac.kr

²Advanced Plant Development Office, Korea Hydro and
Nuclear Power Co., Ltd, Daejeon, Korea
kimhangon@khnp.co.kr

1	<i>New Pressurized LWRs Built (or To Be Built) in the Republic of Korea</i>	2187
1.1	Introduction	2187
1.2	OPR1000 (Optimized Power Reactor 1000)	2188
1.2.1	Design Description	2189
1.2.2	Major Safety Design Features	2199
1.3	APR1400 (Advanced Power Reactor 1400)	2201
1.3.1	Design Description	2201
1.3.2	Major Safety Design Features	2219
1.4	Operation and Construction	2226
1.4.1	Status of Operation	2226
1.4.2	Construction	2227
2	<i>CANDU Reactors in the Republic of Korea</i>	2230
2.1	Introduction	2230
2.2	System Description	2231
2.2.1	CANDU Reactor Model	2231
2.2.2	Primary Heat Transport System (PHTS)	2233
2.2.3	Moderator System	2234
2.2.4	Emergency Core Cooling System (ECCS)	2236
2.2.5	Shutdown System	2239
2.2.6	Containment System	2239
2.3	Major Safety Design Features	2241
2.3.1	Defense in Depth	2242
2.3.2	Availability	2244
2.4	Status of Operation	2244
2.5	Spent Fuel Storage Facility	2244
2.5.1	Wet Storage of Spent CANDU Fuel	2245

2.5.2	Dry Storage of Spent CANDU Fuel.....	2245
3	<i>Conclusions</i>	2245
	<i>References</i>	2247

Abstract: This chapter describes Korean experiences and accomplishments in construction, operation, and design development of nuclear power plants. Recognizing domestic energy-resource scarcity, Korea has steadily constructed, operated, and improved nuclear power plants based on self-reliant technologies and accumulated experiences. This chapter describes specifically i) two pressurized light water reactor models (OPR1000 and APRI400) currently being built and to be built in the future, and ii) experience with the pressurized heavy water reactors (CANDUs) built and in operation, in the Republic of Korea.

1 New Pressurized LWRs Built (or To Be Built) in the Republic of Korea

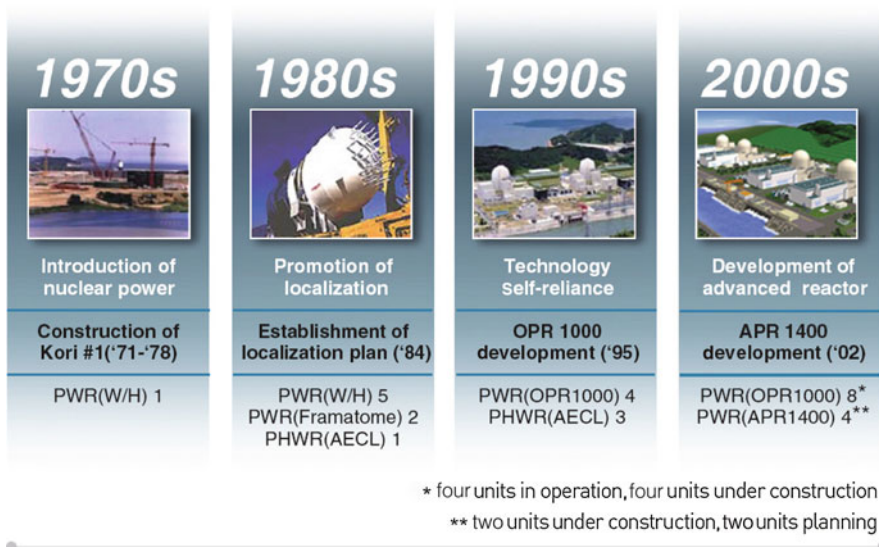
1.1 Introduction

Since 1978, when Kori Unit 1 nuclear power plant had commenced commercial operation, Korea has successfully constructed and operated nuclear reactors. As of 2006, 20 nuclear power plants are in operation, which cover about 40% of total electricity generation in Korea. As a subsidiary of Korea Electric Power Corporation (KEPCO), Korea Hydro and Nuclear Power (KHNP) as the nuclear power utility of Korea has operated several types of qualified nuclear reactors, which include Westinghouse- and CE-designed PWRs, Framatome-designed PWRs, and Canadian PHWR CANDU reactors. In spite of various operating reactors, KHNP showed outstanding operation capability. The average annual capacity factor in 2005 for the 20 operating nuclear units was 95.5% and they have achieved over 90% continuous annual average capacity factor since 2000.

➤ *Figure 1* shows a history of nuclear power plant introduction in Korea. The 1970s was a period of introduction of the first nuclear power plant in Korea. This period started with the construction of Kori Unit 1 nuclear power plant (Westinghouse PWR) with a turnkey contract. One unit was built during this period. The 1980s was a period of induction of domestic companies to participate in the construction with an individualized separate contract for each company. During this period, seven PWR units had been constructed with partially acquired foreign nuclear technology. Through the Nuclear Power Plant Standardization Program, which began in 1984 and continued for over 10 years, KHNP developed Optimized Power Reactor 1000 (OPR1000), as a Korean standard model, based on operational experiences as well as construction and maintenance experiences. In particular, the Yonggwang #3&4 (Combustion Engineering PWR) project provided valuable experience in OPR1000 development. The OPR1000 design aimed at maximizing operational efficiency and minimizing inadvertent effects on operators and environment.

In continuation, the 1990s was a period of technological self-reliance. Self-reliance in terms of nuclear technology was the main theme of this period by designing the OPR1000 without relying on foreign companies. Six units began construction during this period, and it was completed by 2005 (Ulchin Unit 3 is the first OPR1000 nuclear power plant that has been in commercial operation since 1998). Four additional OPR1000 units are currently under construction.

The 2000s is a period of development of an advanced nuclear reactor. The repeated constructions and the operation experiences of OPR1000 brought forth internationally competitive construction technology and outstanding operation and maintenance capabilities. By adopting advanced design features based on the self-reliant technologies, Korea developed the Advanced



■ Figure 1

History of Korean nuclear technology development (Courtesy of Korea Hydro and Nuclear Power Co., Ltd.)

Power Reactor 1400 (APR1400) next to meet Korean Utility Requirement Document (KURD) that reflects the ALWR design requirements developed by Electric Power Research Institute (EPRI), European Utilities Organization, and others. The APR1400 design evolved from the accumulated experience of nuclear power plant construction and development for 3 decades in Korea.

Korea is a unique country that has steadily constructed and updated nuclear power plants since the 1980s. Based on self-reliant technologies and experiences from the design, construction, operation, and maintenance of OPR1000, the APR1400 has been developed by adopting advanced design features to enhance plant safety and economical efficiency. The APR1400 is an embedment of all these experiences and technologies for the past 30 years in Korea.

The APR1400 obtained its design certification (DC) from Korean nuclear regulatory body in May 2002. The construction of Shinkori #3&4 commenced as the first APR1400 plants in 2007, and they are planned to start commercial operation in 2013 and 2014, respectively. Two units of Shin-Ulchin #1&2 are planned as the second construction project of the APR1400.

The first CANDU began operation in 1983, and three additional units in 1997, 1998, and 1999.

1.2 OPR1000 (Optimized Power Reactor 1000)

OPR1000 is a PWR model, developed as a result of the plant standardization program and incorporating construction and operating experience in Korea. Six units are currently in operation and four units are under construction (expected to be completed during 2009–2011) (☛ Fig. 2).

OPR1000 Development process

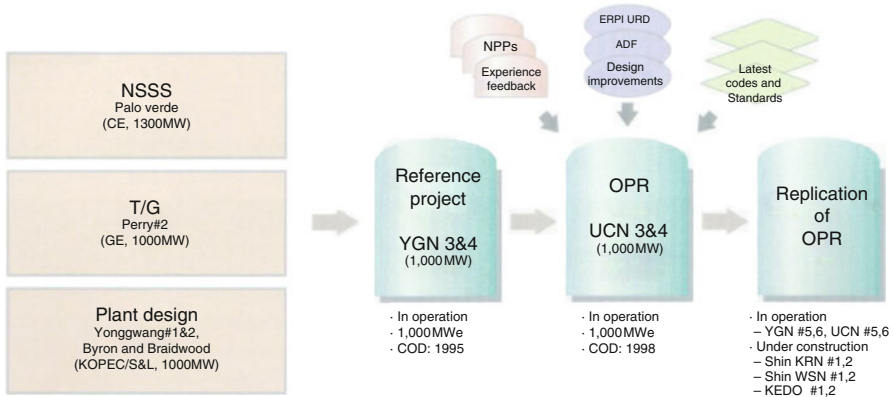


Figure 2 OPR1000 development process (Courtesy of Korea Hydro and Nuclear Power Co., Ltd.)

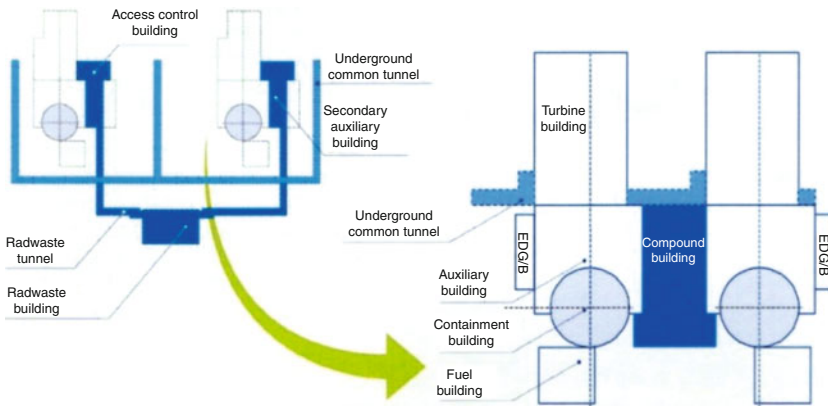


Figure 3 Building arrangement improvement (Courtesy of Korea Hydro and Nuclear Power Co., Ltd.)

1.2.1 Design Description

Building and Structure

The general arrangement of OPR1000 is based on the twin-unit concept with a slide-along arrangement of one Compound Building for two units, which comprise common facilities such as the Secondary Auxiliary Building, Access Control Building, and Radwaste Building (Fig. 3 and Table 1). The merits of improved design are:

1. Elimination of Radwaste Tunnel
2. Minimization of the length of underground common tunnel
3. Reduction of building volume and occupational radiation exposures

■ **Table 1**
Reactor containment building design values

Parameter	Design value
Leak rate (%/day)	0.2 (for 24 h), 0.1 (after 24 h)
Design pressure (psig)	57
Free volume (ft ³)	2.727×10^6
Height (ft)	216
Diameter (ft)	144

Sources: Data compiled from Ulchin Unit 5, 6 Final Safety Analysis Report and Shinkori Unit 3, 4 Preliminary Safety Report.

Primary System

Reactor Coolant System The reactor coolant system (RCS) consists of two heat-transfer loops forming a barrier to release radioactive materials from reactor core to secondary system and containment atmosphere. The main components are a reactor vessel, two steam generators, and four reactor coolant pumps that are symmetrically located on opposite sides of the reactor vessel with a pressurizer on one side; all these components are located in the Containment Building and connected through pipe assemblies. The pressure-retaining components for the reactor coolant pressure boundary are fabricated in accordance with the ASME Boiler and Pressure Vessel Code, Section III.

Reactor Core The reactor core consists of 177 fuel assemblies, which include 73 control element assemblies (CEAs) and 45 in-core instrument (ICI) assemblies.

The core is now fueled with PLUS7 advanced fuel assemblies with maximum discharge rod burnup of 60,000 MWD/MTU (➤ [Table 2](#)) (PLUS7 Fuel Design 2006). The refueling cycle length is 18 months with gadolinia burnable absorber. PLUS7 is a new fuel design, replacing GUARDIAN (Fuel Design Report 1995). More detailed description for PLUS7 is provided in ➤ [Sect. 1.3.1](#).

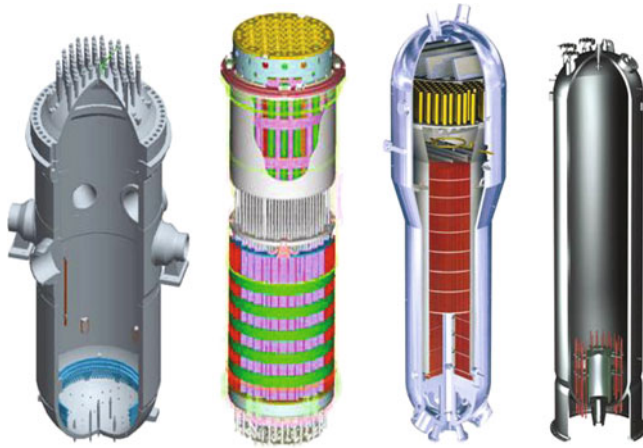
Reactor Vessel The reactor vessel (RV) is fabricated by ring-forged shells. These ring-forged shells eliminate the need for longitudinal seam welds, thereby reducing the production and inspection time. The material for reactor vessel head penetration nozzles is Alloy 690 to get better resistance against many corrosive aqueous media at high-temperature environment. To adopt R/C inspection camera robot for the periodical inspection of reactor vessel head penetration area, reactor vessel head insulation has been designed to have clearance between reactor vessel head and insulation and changed from fixed type to removal type. The weld preparations for head penetration nozzles are optimized to get better welding and minimum weld-deposited metal (➤ [Fig. 4](#) and ➤ [Table 3](#)).

Reactor Vessel Internals The OPR1000 reactor vessel internals (RVI) design contains very limited number of bolts to eliminate the possibility of loose parts during operations. Upper guide structure (UGS) lower flange and support plate have been designed as integral type, which increases the structural integrity of RVI and minimizes the possibility of deformation from related weld work. Concerning the flow-induced vibration, the integrity of RVI had been verified through the comprehensive vibration assessment program (➤ [Fig. 5](#)).

■ **Table 2**
RCS main design values

Parameter	Design value
Power (MW _{th})	2,815
Hot leg diameter (in.)	42
Cold leg diameter (in.)	30
Operating pressure (psia)	2,250
Reactor inlet temperature (°F)	564.5
Reactor outlet temperature (°F)	621.2
Design pressure (psia)	2,500
Design temperature (°F)	650
Hydrostatic test pressure (psia)	3,125
Total reactor coolant volume (ft ³)	10,023
Total RCS minimum design flow (gal/min)	330,000
Number of RCP	4
Rated head (ft)	337
Pump speed (rpm)	1,190
Design pressure (psia)	2,500
Design temperature (°F)	650
Number of fuel assemblies	177
Maximum fuel rod burnup (MWD/MTU)	60,000
Number of refueled fuel at equilibrium cycle	64
Fuel assembly type	16 × 16
Number of fuel rods in fuel assembly	236
Total number of fuel rods in core	41,772
Number of CEA guide tube in fuel assembly	4
Number of ICI guide tube in fuel assembly	1
Fuel pellet material	UO ₂
Fuel clad material	Zircaloy-4
Burnable absorber material	Gd ₂ O ₃ -UO ₂
Fuel pellet diameter (in.)	0.325
Fuel pellet length (in.)	0.39
Fuel rod outer diameter (in.)	0.382
Fuel rod clad thickness (in.)	0.025
Active fuel height (in.)	150
Core equivalent diameter (in.)	123

Sources: Data compiled from Ulchin Unit 5, 6 Final safety analysis report and Shinkori Unit 3, 4 Preliminary Safety Report.



■ Figure 4

RV structure, internal assembly, steam generator, and pressurizer (Courtesy of Korea Hydro and Nuclear Power Co., Ltd.)

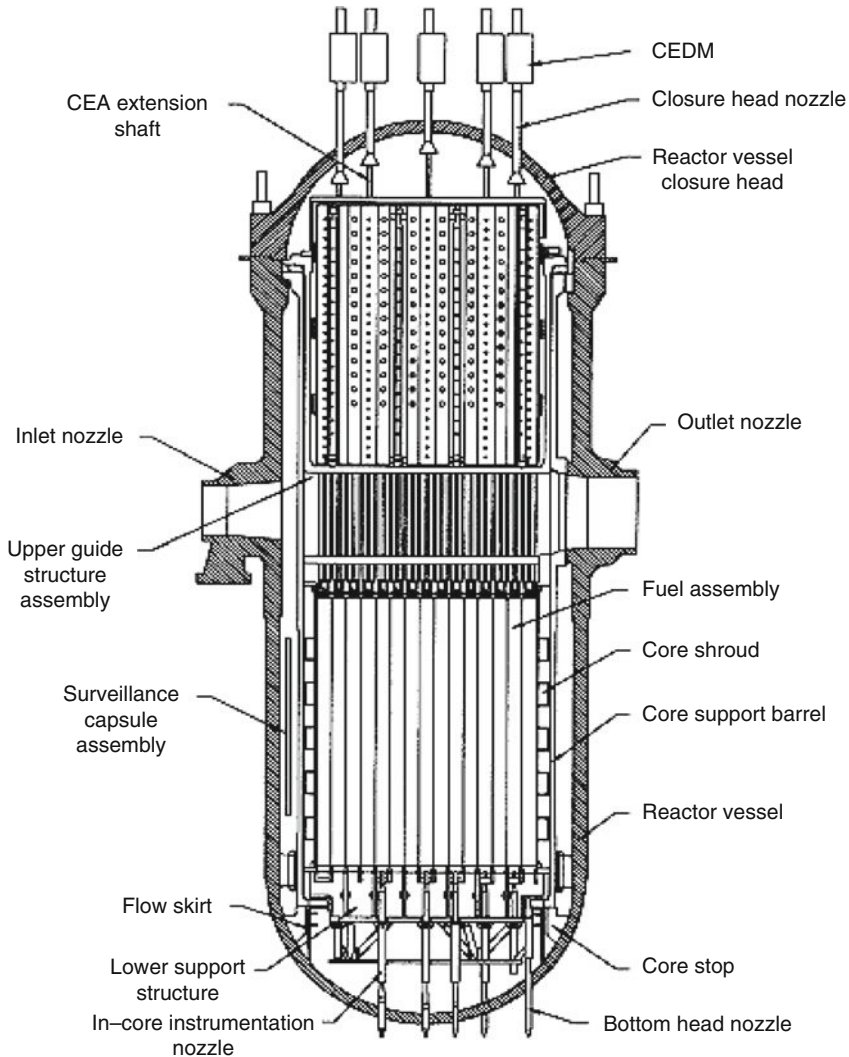
■ Table 3

Reactor vessel main design values

Parameter	Design value
Design pressure (psia)	2,500
Design temperature (°F)	650
Inside diameter at shell (in.)	172
Overall height of vessel and enclosure (ft-in.)	4 11-3/4
Minimum cladding thickness (in.)	1/8

Sources: Data compiled from Ulchin Unit 5, 6 Final safety analysis report and Shinkori Unit 3, 4 Preliminary Safety Report.

Steam Generator OPR1000 has two steam generators. Each steam generator includes U-tube bundle, evaporator with integral economizer, double main feed lines and single auxiliary feed line, double steam lines with integral flow restrictors, high-capacity moisture separators, and high-efficiency dryers. It is designed to have an 8% tube plugging margin to ensure a longer full power life. A major improved feature incorporated into the steam generator design is the use of thermally treated corrosion-resistant material in U-tubes, namely Inconel-690 instead of previous Inconel-600. To support the tubes, vertical and horizontal strips are added at the inner and upper side of the tube bundle and reducing the tube wear caused by flow induced and low frequency vibrations. Feedwater is shared between the economizer and downcomer region of the steam generator for improving feedwater recirculation. This results in a reduction of water hammer in the feedwater system, and increases the thermal efficiency (► [Table 4](#)).



■ Figure 5
 Reactor vessel (Courtesy of Korea Hydro and Nuclear Power Co., Ltd.)

Pressurizer The pressurizer design adopts the EPRI's requirements for advanced light water reactor (ALWR). The pressurizer volume is about 30% larger than the volume of System 80 Plants. This improves plant response capability at transient and accident conditions.

Sufficient RCS depressurization and overpressure protection capabilities are provided by reactor coolant gas vent system, safety depressurization system and three pressurizer safety valves installed at the top of the pressurizer. Replaceable 36 heaters with total 1,800 kW capacity at the bottom head control the system from under-pressurization. To resist

■ **Table 4**
S/G main design values

Parameter	Design value
Number of SG	2
Number of tube per SG	8,214
Tube metal	Alloy 690
Tube-side operating pressure (psia)	2,250
Shell-side maximum operating pressure (psia)	1,170
Steam pressure at full power (psia)	1,070
Steam temperature at full power (°F)	552.9
Steam flow per SG at full power (lb/h)	6.36×10^6
Maximum moisture at outlet at full power (w/o)	0.25

Sources: Data compiled from Ulchin Unit 5, 6 Final safety analysis report and Shinkori Unit 3, 4 Preliminary Safety Report.

■ **Table 5**
Pressurizer main design values

Parameter	Design value
Design pressure (psia)	2,500
Design temperature (°F)	700
Operating pressure (psia)	2,250
Operating temperature (°F)	652.7
Free volume (ft ³)	1,800
Heater capacity (kW)	1,800

Sources: Data compiled from Ulchin Unit 5, 6 Final safety analysis report and Shinkori Unit 3, 4 Preliminary Safety Report.

high-temperature/pressure transient during operation, Inconel-690 is used for heater support and spray head support in accordance with the ASME section NB requirement (● [Table 5](#)).

Control Element Drive Mechanism The control element drive mechanism (CEDM) is an electromechanical device that provides controlled linear motion to CEA through an extension shaft assembly (ESA) in response to operating signals received from CEDM control system. CEA motion occurs when power is sequentially applied to the series of electrical coils located outside of the primary water pressure housing. In an emergency shutdown, the CEAs are inserted into the core by gravity upon initiation of a scram signal. As an advanced design feature, the seismic support system has been incorporated into the CEDM to transmit seismic load from CEDMs and integrated head assembly (IHA) to refueling pool wall through the seismic restraint. The seismic caps are installed to each CEDM top-side and connected to seismic ring beam, which

■ **Table 6**
CEA design values

Parameter	Design value
Material (full/part length)	B4C/Inconel-625
Number of control assembly (full/part length)	76/17
Clad material	Inconel-625

Sources: Data compiled from Ulchin Unit 5, 6 Final safety analysis report and Shinkori Unit 3, 4 Preliminary Safety Report.

is connected to seismic restraint. The addition of these seismic support systems contributes to reduction of the seismic loads from the CEDM cable. Also, CEDMs are operable for cumulative 100,000 ft travel length as minimum, move 30 in./min at normal operating condition, and are lubricated by primary coolant (➤ [Table 6](#)).

Containment Spray System The containment spray (CS) system as an engineered safety feature (ESF) reduces containment pressure and temperature following a postulated loss of coolant accident (LOCA) or main steam-line break (MSLB) inside containment. It also removes radioactive fission products from the containment atmosphere, and mixes containment atmosphere to prevent local accumulation of combustible gases following a postulated LOCA.

The CS heat exchanger of OPR1000 was eliminated by sharing the shutdown cooling heat exchanger for cooling sprayed water. This technical improvement results in significant cost reduction.

Secondary System

Main Steam System The main steam system is designed to maintain functionality during and following a safe shutdown earthquake (SSE). The main steam system contains safety valves to prevent system pressure from exceeding preset limits imposed by code requirements. Also, the main steam system contains main steam atmospheric dump valve on each of the four main steam lines to allow controlled cooldown capability for steam generator when main steam isolation valves (MSIVs) are closed.

The main steam system can deliver steam to the turbine bypass system to discharge steam to the condenser and to the atmosphere to permit load rejection of any magnitude including turbine trip from full power without reactor trip or opening pressurizer safety valve and/or main steam safety valve. The turbine bypass system can provide controlled plant cooldown capability after reactor trip by diverting steam directly to the condenser and/or to the atmosphere (➤ [Table 7](#)).

Main Feedwater System The feedwater system consists of three 55% capacity variable speed turbine-driven pumps, three 55% capacity motor-driven booster pumps, and three stages of feedwater heaters. Six closed-type high-pressure feedwater heaters consist of two 75% capacity parallel trains as three heaters in each train. Three turbine-driven pumps and three motor-driven booster pumps are operated in normal plant operation. When one of the three operating feedwater pump trips, the remaining two pumps can supply enough feedwater to

■ **Table 7**

Main steam system main design values

Parameter	Design value
Total steam flow (lb/h)	12.72×10^6
Steam generator exit pressure (psia)	1,070
Steam generator temperature (°F)	552.9

Sources: Data compiled from Ulchin Unit 5, 6 Final safety analysis report and Shinkori Unit 3, 4 Preliminary Safety Report.

■ **Table 8**

Pump design values of main feedwater system

Parameter	Design value
Main feedwater pump	2 × 55%, TBN driven (TD) 1 × 55%, MTR driven (MD)
Boost pump	3 × 55%, MD
Start-up pump	1 × 5%, MD

Sources: Data compiled from Ulchin Unit 5, 6 Final safety analysis report and Shinkori Unit 3, 4 Preliminary Safety Report.

steam generators at the maximum of 110% rated flow against steam generator pressure without reactor trip. The low–low net positive suction head (NPSH) trip interlocks for feedwater pumps/feedwater booster pumps are provided for the low–low NPSH protection of the feedwater pumps/feedwater booster pumps. Appropriate time delays and two out of three logic for the NPSH trip signal are provided to avoid immediate trips. The feedwater system includes one 5% capacity motor-driven start-up feedwater pump to be used during start-up, shutdown, and hot standby operation. This standby feedwater pump can prevent reactor scrams caused by feedwater shortage (➤ [Table 8](#)).

Turbine The turbine of OPR100 is thermodynamically designed to obtaining high efficiency and economical steam-path arrangement. OPR100 has one double-flow high-pressure turbine and three double-flow low-pressure turbines. The turbine of OPR1000 is six-flow tandem-compound type with rated speed 1,800 rpm. Especially, mono-block rotor design is applied to remove stress corrosion cracking at shrunk-on region, crack initiation at contact surface of disk and shaft, and poor dynamic stability. With the fast developed forging technology, the turbine manufacturer applied mono-block-type rotor to OPR1000, and it could fully make up for the disadvantage of existing shrunk-on type rotor. Also, mono-block completed rotor package from the manufacturing shop makes large reduction of site construction period (➤ [Table 9](#)).

Generator The generator system of OPR1000 consists of the generator itself and auxiliary systems such as stator cooling water system, gas control system, and hydrogen seal oil system. Stator of the generator takes highly reliable F-class Micapal II insulation system and brazing technology. Rotor also takes highly reliable F-class insulation system and radial flow cooling method (➤ [Table 10](#)).

■ **Table 9**
Turbine characteristics

Parameter	Design value
Number	1 double-flow HP TBN, 3 double-flow LP TBN
Type	Tandem-compound, 6 flow
Speed (rpm)	1,800
Rated output (MW)	1,050
Last stage bucket size (in.)	43

Sources: Data compiled from Ulchin Unit 5, 6 Final safety analysis report and Shinkori Unit 3, 4 Preliminary Safety Report.

■ **Table 10**
Generator characteristics

Parameter	Design value
Number	1
Type	Direct driven (water cooled)
Capacity (kV A)	1,219,600 @ 0.9 pf and 75 psig of H ₂
Rated voltage	22 kV, 3 phase

Sources: Data compiled from Ulchin Unit 5, 6 Final safety analysis report and Shinkori Unit 3, 4 Preliminary Safety Report.

Moisture Separator Reheater (MSR) The moisture of wet steam expanded at high-pressure turbine (HP TBN) is separated and reheated through moisture separator reheater (MSR) to protect the corrosion of the LP TBN blades. Therefore, the enhanced performance of MSR increases the cycle efficiency and the lifetime of the turbine.

Application of Plate-Type Heat Exchanger The plate-type heat exchangers are adopted in the component cooling water system and the spent fuel pool cooling and cleanup system instead of shell-tube-type heat exchanger. The plate-type heat exchangers have greater heat-transfer efficiency than shell-tube-type heat exchangers. Small size and low weight reduce initial installation cost, while high heat-transfer efficiency makes low operating costs. With larger free space, easy maintenance is available. The number and specifications of the plates can simply be increased, reduced, or altered as required.

Enhanced Intake and Discharge System Intake channel design for the circulating water system is enhanced by reducing the number of traveling screens and pumps. It improves the operability of pumps and traveling screens. OPR1000 apply submerged intake and discharge system with multi-velocity cap and diffuser. It reduces temperature rise of seawater from discharged cooling water and minimizes the effect on environment and recirculation rate of thermal discharge.

Control and Electrical Systems

Station Power System The switchyard is a 345 kV full gas insulated substation with a breaker-and-a-half configuration. The Station Power System consists of the main power (MP), auxiliary

power (AP), DC & IP, emergency diesel generator, and alternative alternate current diesel generator (AAC DG). The normal power source for class 1E and nonclass 1E loads is the off-site power source and the generator. If the normal power source is not available, class 1E and nonclass 1E loads are covered by the standby off-site power source via the standby auxiliary transformers as an alternative source.

Electric power necessary for the class 1E systems is supplied through four alternative ways as follows:

1. Normal off-site power and the in-house generation (PPS-1)
2. Off-site power connected through the standby auxiliary transformers (PPS-2)
3. Two class 1E emergency diesel generators (EDG)
4. Alternate AC diesel generator (AAC DG)

The on-site emergency power supply is ensured by two independent-class 1E diesel generators connected to each 4.16 kV class 1E bus. The alternate AC source adds more redundancy to the electric power supply, although it is not a safety-grade system. The nonclass 1E alternate AC is to cope with station blackout (SBO) condition where there is a high potential of transients progressing to severe accidents.

Plant Control System (PCS) The balance of plant (BOP) plant control system (PCS) remotely controls and monitors most of the safety-related and non-safety-related plant equipment including engineered safety feature actuation system (ESFAS) from the main control board or remote shutdown panel. PCS is divided into safety-related and non-safety-related subsystems. Each subsystem consists of control cabinets that have on-off control and analog control function, communication devices, human-machine interface (HMI), and other auxiliary devices. In addition, the PCS interfaces with the T/G control system and radiation monitoring system to provide the operating status of various equipment and trend information of diverse process variables to operators and the plant monitoring and annunciator system (PMAS).

PCS for OPR1000 uses the distributed control system (DCS) that incorporates the state-of-the-art digital technology. It uses the multi-loop control concept where one controller executes the control logic for several equipments. In order to improve the reliability and safety of the system, the power, communication devices, and controllers are designed by redundant concept. Also, the control system for radwaste system is designed as screen-based control instead of using conventional control board to improve the operational convenience. In order to secure the safety of the system, PCS-adopted stringent design criteria such as environmental requirement for seismic and electromagnetic interference/radio frequency interference (EMI/RFI).

Main Control Room (MCR) To enhance the operational convenience and reliability, human factors engineering (HFE) technology is adopted systematically (🔍 Fig. 6). The design of OPR1000 embodies human-centered man-machine interface (MMI) technology that meets latest licensing requirements, by developing and applying systematic HFE program that incorporates:

1. Review of operating experience
2. Functional requirement analysis (FRA) and functional allocation (FA)
3. Task analysis (TA)
4. HFE verification and validation (V&V)



■ Figure 6

Main control room (Courtesy of Korea Hydro and Nuclear Power Co., Ltd.)

1.2.2 Major Safety Design Features

Safety

Safety Enhancement Probability safety assessment (PSA) has been employed during the design of each OPR1000 power plant. As a measure of the plant safety, core damage frequency (CDF) for internal initiating events during at-power operation was used. Based on the PSA results of the original design, several design changes to improve the plant safety were adopted:

1. Add safety depressurization system (SDS) for feed and bleed operation for total loss of feedwater event.
2. Add alternative AC power source for station blackout.
3. Change the design of auxiliary feedwater system to improve reliability.

Defense in Depth The safety concept of OPR1000 is based on the principle of defense-in-depth concept by providing the following multiple, diverse principles for accident prevention and mitigation of the consequences:

1. High-quality process systems to accommodate plant transient and to minimize the likelihood of the accident.
2. Reliable safety systems for reactor shutdown, emergency core cooling, decay heat removal, and containment heat removal.
3. Reliable safety support systems to provide services to the safety systems and other mitigating systems.
4. Passive heat sink to increase resistance against both design basis events and severe accidents.
5. Application of multiple barrier concept consisting of
 - a. Fuel pellet and cladding
 - b. Reactor coolant pressure boundary
 - c. Steel-lined prestressed concrete containment
 - d. Exclusion area

The design of the safety systems follows the principles of separation, diversity, and reliability. High degrees of redundancy concept are adopted in the system design to ensure that the safety functions can be carried out, even when systems or components are impaired. Protections against seismic, flooding, and fire events are also provided to ensure highly reliable and effective mitigation of postulated events, including shutdown and severe accidents.

ALARA Concept As low as reasonably achievable (ALARA) philosophy is applied from the initial design of OPR1000 and implemented and documented via internal design reviews. These reviews are conducted and documented in conformance to the Korean Atomic Energy Act (KAEA). It also satisfies the ICRP60 recommendation. The plant design is reviewed, updated, and modified continuously during the design and construction phases. This includes plant layout, shielding, ventilation, and monitoring system design with traffic control, security, access control, maintenance, in-service inspection, and radiation protection aspects to ensure that the overall design results of radiation exposure will achieve the ALARA philosophy. ALARA design improvements of OPR1000 include the use of low cobalt materials for steam generator tubes and valve hard facing material and adoption of an extended fuel cycle length that reduces the frequency of extensive maintenance work. These improvements are expected to result in an annual occupational radiation dose (man-Sv) that would be less than the dose for conventional PWRs. Since Yonggwang (YGN) 3&4, OPR1000's annual occupational radiation dose was gradually reduced. The annual occupational dose for latest OPR1000 is expected to be about 1.07 man-Sv per unit (Ulchin Unit 5, 6 FSAR 2003).

Severe Accident

The design principle of OPR1000 is to prevent and mitigate severe accident events and minimize their consequences. The systems and features of OPR1000 for this purpose ensure the public safety by maintaining the integrity of the containment and limiting the release of radioactive materials within the allowable limits (Ulchin Unit 5, 6 FSAR 2003).

Reactor Cavity Design The reactor cavity structure of the OPR1000 is designed to suppress the release of corium debris into the containment atmosphere to preclude high-pressure melt ejection (HPME) and direct containment heating (DCH) and to prohibit melt-through of the reactor cavity floor concrete.

Corium Debris Collection Chamber When the reactor vessel breaches under high pressure conditions, the molten corium ejected into the reactor cavity is released into the containment atmosphere through the ICI cavity – ICI guide tube passway. The collection chamber is designed to confine and to suppress the release of corium debris to the containment atmosphere.

Flow Restrictor A flow restrictor is used to block the release of corium debris to ICI guide tube exit. The flow restrictor can mitigate the DCH phenomenon by restricting the flow of high-pressure corium as much as possible.

Reactor Cavity Floor Radioactive materials can be released due to melt-through of the reactor cavity floor during molten core–concrete interaction (MCCI). To prevent melt-through of the concrete floor, the cavity floor thickness is modified.

Mitigation System Reactor Cavity Flooding System (RCFS)

During a postulated severe accident, MCCI may threaten the integrity of the containment. To prevent MCCI, reactor cavity flooding system (RCFS) is installed in OPR1000, which injects cooling water into the reactor cavity. For this purpose, flanged branch connection is provided to supply cooling water into the reactor cavity from the fire protection system.

Hydrogen Control OPR1000 adopted passive autocatalytic recombiners (PARs) instead of conventional active thermal hydrogen recombiner for the hydrogen control in the reactor containment to improve the safety following DBA LOCA. Although the PAR system is basically intended for design basis hydrogen control for OPR1000, it is also expected to function during severe accidents as the passive characteristics for hydrogen removal. The capacity and the number of PARs are determined to limit the hydrogen concentration below the flammable limit following a DBA LOCA.

Characteristics of PARs are:

1. Hydrogen control during all design basis accidents
2. Total prevention of combustion and exclusion of combustion loads during DBA
3. Simple passive design without moving parts
4. No external power supply
5. Self-starting and self-feeding operation
6. Easy installation and in-service inspection

Besides, OPR1000 adopted hydrogen ignition system (HIS) to maintain the hydrogen concentration within design limit. The HIS consists of 20 thermal plug-type hydrogen igniters located throughout containment and is capable of igniting the hydrogen to facilitate controlled burning. The hydrogen igniters are powered by electrically isolated Class 1E power bus.

Containment Filtered Vent System (CFVS) During a postulated severe accident, generation of large amount of steam or noncondensable gas can cause over-pressurization of the containment. To prevent the over-pressurization, containment penetration of OPR1000 is exclusively assigned in conjunction with the containment-filtered vent system (CFVS). And for future use, a dedicated 3 ft diameter containment penetration and the space are provided.

1.3 APR1400 (Advanced Power Reactor 1400)

APRI400 stands for advanced power reactor, which is a 1,400 MW pressurized water reactor developed in Korea. Based on the self-reliance technologies and experiences from the design, construction, operation, and maintenance of OPR1000, APRI400 adopts advanced design features to further enhance plant safety, economical efficiency, and convenience of operation and maintenance (➤ Fig. 7).

1.3.1 Design Description

Building and Structure

The general arrangement of APRI400 has been developed based on the twin-unit and slide-along concepts. The layout of APRI400 can be divided into Nuclear Island (NI) and Turbine

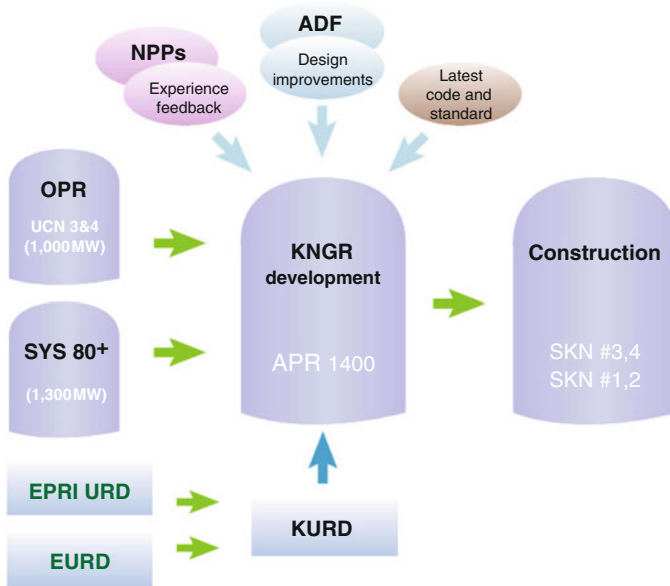


Figure 7

Flow diagram of APR1400 development (Courtesy of Korea Hydro and Nuclear Power Co., Ltd.)

Island (TI). The NI consists of Reactor Containment Building (RCB), Auxiliary Building (AB), and Compound Building (CB). The CB includes access control area, radwaste treatment area, and hot machine shop as common facilities for both units. The TI is composed of Turbine Building (TB) and Switchgear Building (SB). The RCB is located at the center of the NI and is placed on a common basemat with the AB, which houses EDGs and fuel handling area (FHA). The layout of NI improves the structural safety margin against external events such as a seismic event. The layout of AB, particularly for the physically separated arrangement of safety equipment, is designed to enhance plant safety. As examples, four-train safety injection systems (SISs) and two set of EDGs are arranged in such a way that each one is placed in the physically separated division of AB. This configuration prevents propagation of system damage by internal and external events such as flood, fire, security threat, and sabotage. Other internal structures are also arranged to improve maintainability, accessibility, and convenience of equipment replacement (➤ Fig. 8).

Reactor Containment Building The RCB is a prestressed concrete structure in the shape of a cylinder with a hemispherical dome as seismic category I and is founded on a common basemat with the AB. The inner surface of RCB is steel-lined for leak-tightness and a protective layer of concrete covers the portion of the liner over the foundation slab. The in-containment refueling water storage tank (IRWST) is located in the RCB, in an annular-shaped configuration between the secondary shield wall and the containment wall. Therefore, the safety injection pumps (SIPs) always take water from the IRWST without switching its suction from the IRWST to the containment sump for the long-term cooling following a LOCA. As measures to mitigate the consequences of severe accidents, the reactor vessel cavity is designed for heat-transfer area

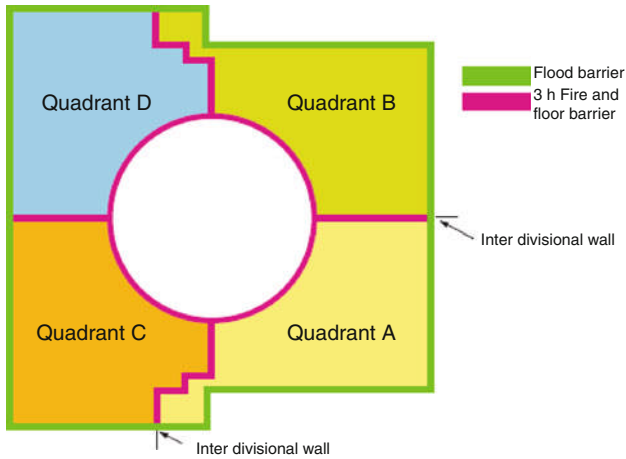


Figure 8

Quadrant arrangement of auxiliary building (Courtesy of Korea Hydro and Nuclear Power Co., Ltd.)

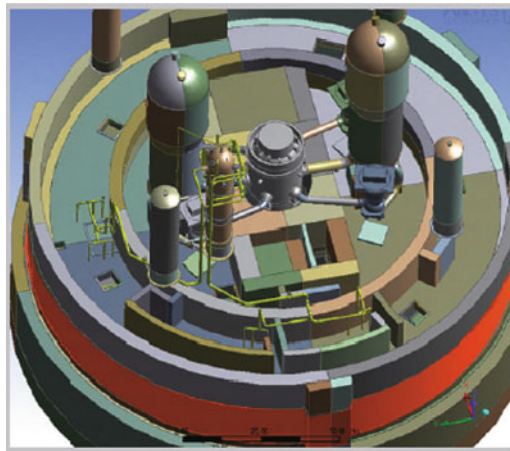


Figure 9

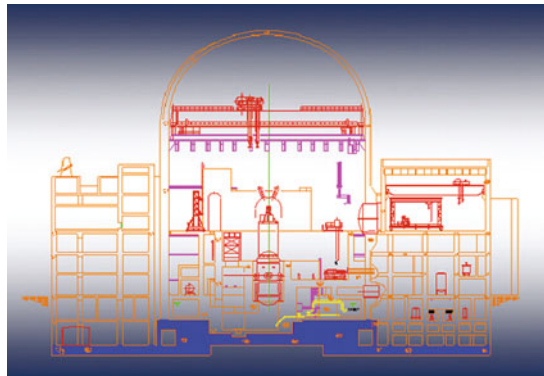
IRWST structure (Courtesy of Korea Hydro and Nuclear Power Co.,Ltd.)

of corium to be not less than $0.02 \text{ m}^2/\text{MW}$, such that it is cooled and solidified on the cavity floor. Also, the convoluted vent path of the reactor vessel cavity prevents the molten-core debris from being released into the containment atmosphere. In order to improve the convenience of maintenance, the equipment hatch, the arrangement of the structures, and the polar bridge crane are designed for a steam generator to be replaced in one piece. Also, work platforms are installed to enhance the convenience of in-service inspection (ISI) for steam generators and maintenance of reactor coolant pumps (RCPs) (► Fig. 9 and ► Table 11).

■ **Table 11**
Reactor containment design characteristics

Parameter	Design
Leak rate (%/day)	0.15 (for 24 h), 0.075 (after 24 h)
Design pressure (psig)	60
Free volume (ft ³)	3.194×10^6
Height (ft)	250.5
Diameter (ft)	150

Source: Data compiled from Shinkori Unit 3, 4 Preliminary Safety Report.



■ **Figure 10**
Common basemat of containment building and auxiliary building (Courtesy of Korea Hydro and Nuclear Power Co., Ltd.)

Auxiliary Building The AB is designed with reinforced concrete structure as seismic category I and placed on a common basemat with the RCB. It wraps around the RCB with a quadrant arrangement. The AB houses the MCR, EDGs room, FHA, and the safety-related components such as SIS. The systems and internal structures in the AB are arranged to provide physical separation for minimizing the hazard from internal and external events such as flood, fire, security problem, and sabotage without adversely affecting accessibility. The safety equipment is spatially separated to enhance its actuation reliability. Each train of SIS, which consists of four trains, is located in each separate division. The EDGs are also spatially separated on opposite sides. In order to improve the convenience of operation and maintenance, the internal layout of the AB is designed to provide sufficient space and lifting rig for replacing heat exchangers and replace a generator of EDG without removing the outer wall. The technical support center (TSC) is located adjacent to the MCR to improve communication between operators and technical crews during abnormal plant situations. The passages are designed for visitors and plant crews not to interfere with each other in the FHA, the MCR, and turbine-operating floor. And the internal arrangement of components is divided into the radiation area and clean area to reduce the occupational exposure dose (➤ Fig. 10).

Compound Building As a common facility for both units, the Compound Building (CB) is designed with reinforced concrete structure as seismic category II. This building houses an access control area, a radwaste treatment area, primary and secondary sampling laboratories, and a hot machine shop. This arrangement makes access from each unit more convenient and reduces the size of the power block by making it more compact.

Turbine Building The TI consists of the TB and SB arranged in the radial direction to the NI. Both buildings are situated on a common basemat and designed with steel structure and reinforced concrete turbine pedestal as seismic category II. The TB encloses the components that constitute heat cycle and produce electricity. The SB houses the electrical distribution equipment. The conventional construction method for outdoor underground facilities delays the construction because of repeated digging and filling for the installation of various underground equipments. To reduce the construction schedule, the underground common tunnel is designed to accommodate all underground facilities in the base floor of the TB. In addition, for the effective maintenance, the whole demineralizers in the plant are located at the same level.

Primary System

Reactor Coolant System The core outlet temperature is lowered to increase the core thermal margin. This contributes to the decreased unplanned reactor trips during normal operation and the enhancement of the operational flexibility. In addition, the reduction of the core outlet temperature relieves the degradation of the steam generator tube due to the stress corrosion by adopting Inconel-690 as the steam generator tube material, which is known to be more resistant to the stress corrosion cracking than Inconel-600 of the conventional plants. The pressurizer volume is designed to be larger than those of the conventional plants. This design makes the APRI400 accommodate transients without power-operated relief valves (PORVs) and minimizes unplanned reactor trips during the transients. The pilot-operated safety relief valves (POSRVs) are used to perform the functions of pressurizer safety valves (PSVs) and safety depressurization valves (SDVs). This change ensures reliable valve operation without chattering and leakage for any type of discharge flow condition and allows remote manual operation of valves under postaccident conditions. The POSRVs perform the function of pressure relief for RCS overpressure transients and RCS depressurization for the feed and bleed operation. Moreover, during severe accidents (SAs), these valves relieve the RCS pressure rapidly to prevent the high-pressure ejection of molten core that may induce direct containment heating (► [Fig. 11](#)).

To reduce unplanned reactor trips, the core thermal margin is increased by more than 10% (compared to OPR1000) by lowering the core outlet temperature and increasing the RCS coolant flow. In addition, the pressurizer volume relative to power is enlarged to enhance the capability of coping with the transients (► [Table 12](#)).

Reactor Vessel and Internals The reactor vessel consists of a vertically mounted cylindrical vessel welded with a hemispherical lower head and a removable hemispherical upper closure head (► [Fig. 12](#) and ► [Table 13](#)). The internal surfaces that are in contact with the RCS coolant are clad with austenitic stainless steel to prevent corrosion. The reactor vessel is manufactured with three shell sections, a vessel flange, and a hemispherical bottom head. The three shell sections, bottom head forging, and vessel flange forging are welded together, along with four inlet nozzle forgings, two outlet nozzle forgings, four direct vessel injection (DVI) nozzle forgings, and 61 ICI nozzles. The upper closure head is fabricated separately and is bolted to the reactor vessel. The dome and flange are welded together to form the upper closure head, on which the CEDM



Figure 11
Reactor coolant system (Courtesy of Korea Hydro and Nuclear Power Co., Ltd.)

nozzles are welded. The nil ductility reference temperature (RTNDT) of the reactor vessel is lowered from 10°F of the conventional reactor vessel to -10°F by using low carbon steel, which has lower contents of Cu, Ni, P, and S than those of the conventional reactor. This material improvement extends the lifetime of the reactor vessel to 60 years. In addition, the Cobalt (Co) content in the reactor vessel material is lowered to reduce the occupational exposure dose. The reactor vessel internals of the conventional plant are fabricated into three parts of upper guide structure, core support barrel, and lower support structure. This compares with the reactor vessel internals of the APRI400, which are manufactured into two parts by integrating the core support barrel and lower support structure. This improvement contributes to the shortening of the construction schedule (Shinkori Unit 3, 4 PSAR 2008).

Reactor Core The reactor core consists of 241 fuel assemblies, which include 93 CEAs and 61 ICI assemblies. The core is designed for the refueling cycle to be greater than 18 months, with maximum discharge rod burnup of 60,000 MWD/MTU, and the thermal margin to be increased by more than 10%. This core design leads to the improvement of the economical efficiency and safety by increasing the plant availability factor with a longer refueling cycle and the reduction of unplanned reactor trips.

APRI400 uses the advanced fuel assembly, named PLUS7 (Fig. 13) (PLUS7 Fuel Design 2006). PLUS7 is a new fuel design, enhanced in thermal hydraulic and nuclear performance and structural integrity compared with conventional fuel assemblies. The mixing vanes with high thermal performance, which induce a relatively small pressure loss, are adopted in all mid-grids to increase the thermal margin by more than 10% (than GUARDIAN). This

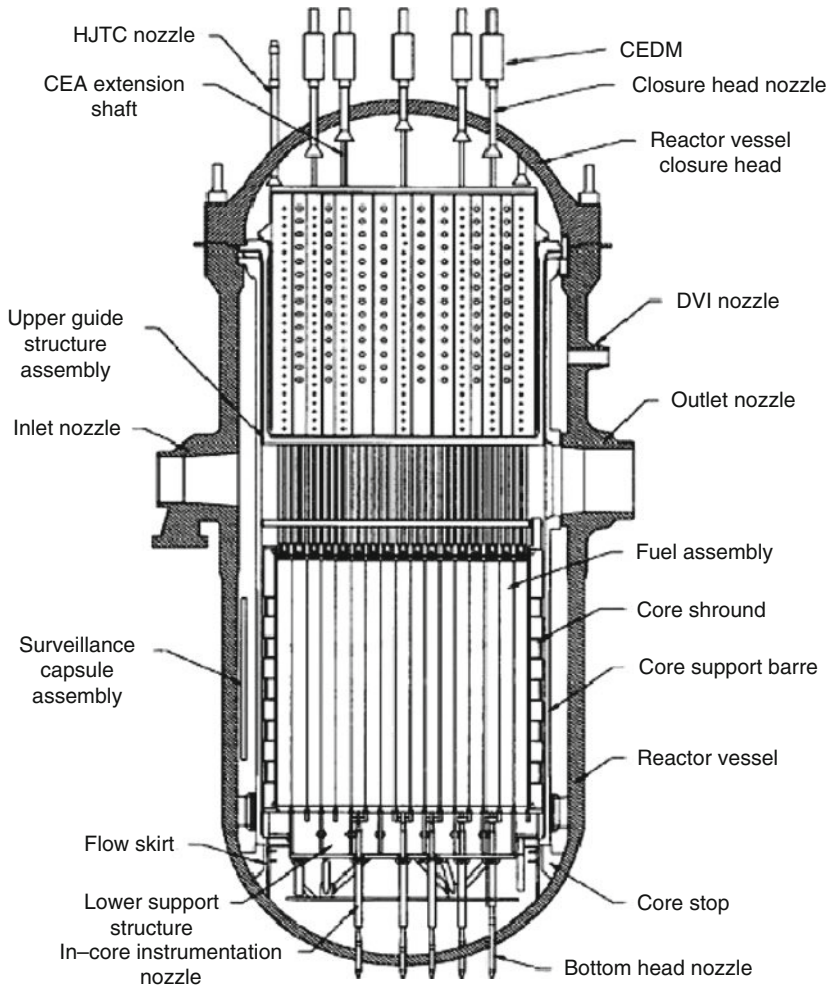
■ **Table 12**
RCS main design values

Parameter	Design value
Power (MW _{th})	3,983
Hot leg diameter (in.)	42
Cold leg diameter (in.)	30
Operating pressure (psia)	2,250
Reactor inlet temperature (°F)	555
Reactor outlet temperature (°F)	615
Design pressure (psia)	2,500
Design temperature (°F)	650
Hydrostatic test pressure (psia)	3,125
Total reactor coolant volume (ft ³)	16,020
Total RCS minimum design flow (gal/min)	446,300
Number of RCP	4
Rated flow rate (gpm)	121,600
Rated head (ft)	360
Pump speed (rpm)	1,190
Design pressure (psia)	2,500
Design temperature (°F)	650

Source: Data compiled from Shinkori Unit 3, 4 Preliminary Safety Report.

has been confirmed in critical heat flux (CHF) test. The batch average burnup is increased to 55,000 MWD/MTU by optimizing the fuel assembly and fuel rod dimensions and adopting an advanced Zirlo alloy as fuel clad. The neutron economy is improved with the introduction of the axial blankets at both ends of the pellet region and the optimization of the fuel rod diameter. The mid-grid buckling strength has been increased using straight grid straps and optimizing grid height. These design improvements increase the seismic resistance for the fuel assembly to maintain its integrity even under severe seismic-related accidents. The conformal type contact geometry between the mid-grid spring and fuel rod increases the in-between contact area to improve the resistance capacity for fretting wear. The debris-filter bottom nozzle (DFBN) is adopted to trap most debris before they enter the fuel assembly. This increases the debris-filtering efficiency and reduces fretting wear-induced fuel failures (► [Tables 14](#) and ► [15](#)) (Ulchin Unit 3, 4 RTSR 2005).

Control Element Assembly The CEA is composed of 12 fingers full strength, 4 fingers full strength, and 4 fingers part strength CEAs (► [Table 16](#)). Neutron-absorbing material is contained within a cylindrical sealed metal tube. The absorber material used for full strength control rod is boron carbide (B4C) pellets. Inconel-625 is used as the absorber material for the part-strength control rods.



■ **Figure 12**
Reactor vessel (Courtesy of Korea Hydro and Nuclear Power Co., Ltd.)

Integrated Head Assembly The reactor vessel upper closure head area of the conventional plant consists of CEDM cooling system, cooling shroud assembly, heat junction thermocouples, missile-shielding structure, and head lift rig (► *Fig. 14*). These components are usually disassembled, separately stored, and reassembled during every refueling outage. The IHA is applied to simplify the structure configuration on the reactor vessel upper closure head region and to improve the convenience of maintenance. All components on the head region are handled as single unit to reduce the occupational exposure dose of the maintenance personnel, the space required for equipment storage, and to shorten the overhaul duration (Shinkori Unit 3, 4 PSAR 2008).

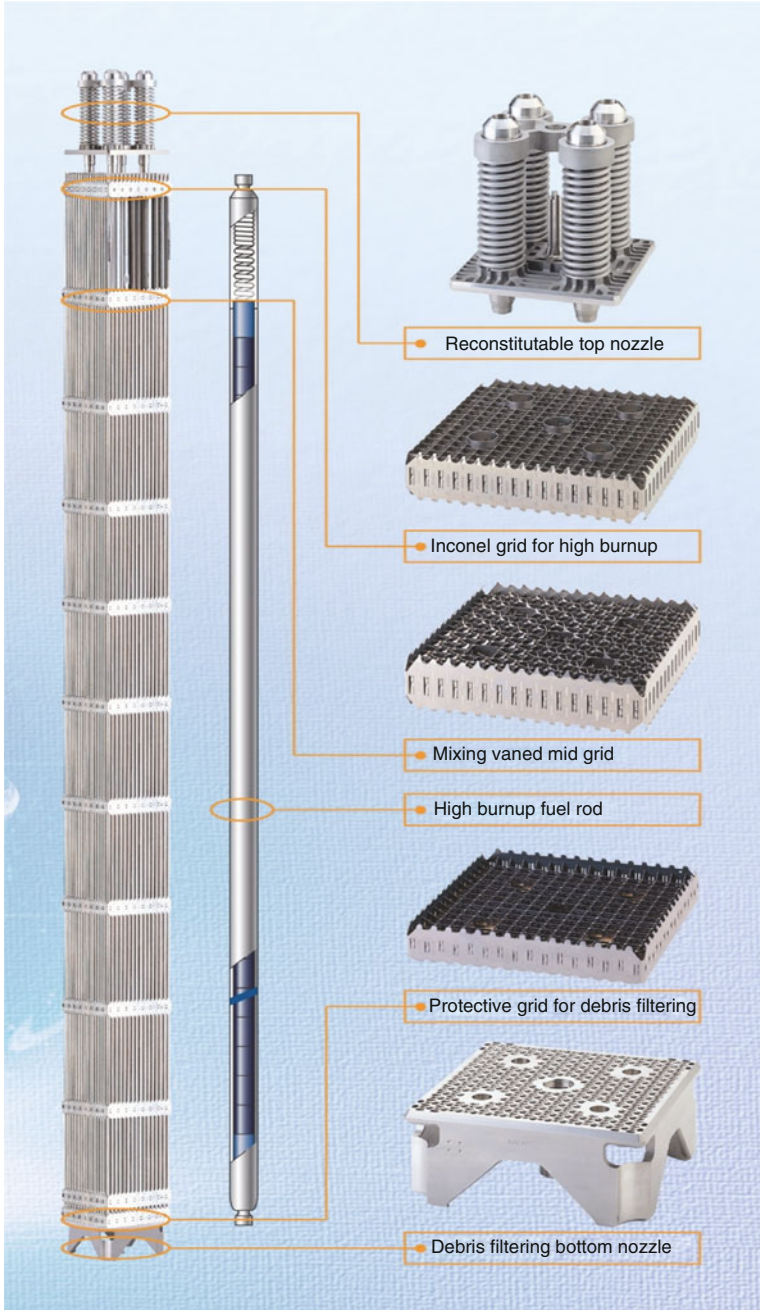


Figure 13
PLUS7 fuel assembly (Courtesy of Korea Nuclear Fuel Co., Ltd.)

■ **Table 13**
Reactor vessel main design values

Parameter	Design value
Design pressure (psia)	2,500
Design temperature (°F)	650
Inside diameter at shell (in.)	182-1/4
Overall height of vessel and enclosure (ft-in.)	48 7-7/8
Minimum cladding thickness (in.)	1/8

Source: Data compiled from Shinkori Unit 3, 4 Preliminary Safety Report.

Pressurizer The pressurizer is a vertically mounted cylindrical pressure vessel. Replaceable direct immersion electric heaters are vertically mounted in the bottom head (► [Table 17](#)). The pressurizer is furnished with nozzles for the spray, surge, POSRVs, and pressure and level instrumentation. A manway is provided in the top head for access for inspection of the pressurizer internals. The pressurizer surge line is connected to one of the reactor coolant hot legs and the spray lines are connected to two of the cold legs at the reactor coolant pump discharge. The pressurizer maintains RCS pressure within specified limits in conjunction with the chemical and volume control system (CVCS) against all normal and upset conditions without reactor trip. The pressurizer volume relative to power is increased to enhance the transient response of the RCS to reduce unplanned reactor trips. Four POSRVs are adopted instead of two SDS valves and three PSVs of the conventional plants, including OPR1000. POSRVs perform the overpressure protection for the RCS, depressurize the RCS for the initiation of a feed and bleed operation in the event of a total loss of feedwater (TLOFW), and allow remote manual operation under postaccident conditions to prevent high-pressure ejection of molten core. The outlet lines from the POSRVs connect directly to the ring-shaped section of the pressurizer discharge header, which transfers the steam/water discharge to the IRWST. This design prevents the contamination of containment by RCS coolant discharge and ensures reliable valve operation without chattering and leakage for any type of discharge flow condition (Shinkori Unit 3, 4 PSAR 2008).

Steam Generator The steam generator (SG) is a vertically inverse U-tube heat exchanger with an integral economizer, which operates with the RCS coolant in the tube side and secondary coolant in the shell side. The two SGs are designed to transfer the heat of 3,983 MWth from the RCS to the secondary system. The secondary system produces steam to drive the turbine-generator, which generates 1,400 MW of electrical power. Moisture separators and steam dryers in the shell side limit the moisture content of the exit steam to less than 0.25 w/o during normal full power operation. An integral flow restrictor has been provided in each SG steam nozzle to restrict the discharge flow in the event of a steam-line break. For the inspection and maintenance of the primary side, a 21 in. primary manway is provided in the cold leg and hot leg side of the primary head, respectively. For the secondary shell side, two 21 in. secondary manways allow access to separator, dryer area, and internal hatch over the top of the tube bundle, and two 8 in. handholes are provided for sludge lancing on the top of tube-sheet. To improve the integrity of SG tubes, the SG tubes are made of Inconel-690, which has high resistance to corrosion. The loose parts trapping feature inside of the feedwater nozzle is adopted to prevent damage to the internals and tubes of the SG by foreign materials originating from the

■ **Table 14**
Benefits of PLUS7 fuel

	Benefits	Features	
		PLUS7™	Conventional fuel
1	Increased thermal margin as much as 12.8%	Mixing vane mid-grid	No mixing vane mid-grid
2	High burnup capability (batch average 43 → 55 GWD/MTU)	ZIRLO™ cladding Optimized fuel dimension	Zry-4 cladding
3	Superior neutron economy (save fuel cycle cost \$1 million/cycle)	0.374" rod diameter Axial blankets	0.382" rod diameter No axial blankets
4	High seismic capability (mid-grid dynamic buckling strength 3,400 → 4,900 lb)	High-strength straight grid strip Increased load bearing length	Low-strength straight wavy grid strip
5	Improved fuel rod fretting resistance	Large contact area with conformal surface spring and dimple Inconel top and bottom grids with optimized spring rate	Normal contact area with cantilever spring and arched dimple Zry-4 top grid and Inconel bottom grid
6	Improved debris-filtering capability	Small hole and slot bottom nozzle Protective grid with long end plug	Standard large hole bottom nozzle GUARDIAN™ grid with long end plug
7	High manufacturing productivity	Standardized fuel rod size and manufacturing process Spot welded guide tube-to-grid structure	TIG welded guide tube-to-grid structure

connected secondary system. The upper tube support bar and plate are designed to prevent the SG tube from flow-induced vibration. The SG tube plugging margin is increased by 10% (compared to OPR1000). This increases the SG tube heat-transfer area, which increases steam flow. This design improvement accommodates increased core power and compensates for the lower operating temperature of the secondary side, which is induced from the reduced core exit temperature. This design also enhances the resistance of the SG tube to stress corrosion and extends the lifetime of the SG. The water volume of the SG secondary side is enlarged to increase the dry-out time up to 20 min in the event of TLOFW. This design enhances the capability of alleviating the transients during normal operation and reduces the potential for unplanned reactor trips and enhances plant safety and operational flexibility. To improve operability, the angle of the primary outlet nozzles is modified to enhance the stability of mid-loop operation, and the SG water-level control system is designed such that the water level is controlled automatically over the entire operating range (➤ [Table 18](#)) (Shinkori Unit 3, 4 PSAR 2008).

Secondary System

The secondary system consists of the main steam, turbine generator, condensate, feedwater, extraction steam, and auxiliary systems. The heat balance of the secondary system is determined through optimization studies considering system operability, reliability, and economy. The secondary system is designed to be capable of operating at 3–6% house load for a period of at least

■ **Table 15**
PLUS7 fuel assembly main design values

Parameter	Design value
Number of fuel assemblies	241
Maximum fuel rod burnup (MWD/MTU)	60,000
Number of refueled fuel at equilibrium cycle	100
Fuel assembly type	16 × 16
Number of fuel rods in fuel assembly	236
Total number of fuel rods in core	56,876
Number of CEA guide tube in fuel assembly	4
Number of ICI guide tube in fuel assembly	1
Fuel pellet material	UO ₂
Fuel clad material	Zirlo
Burnable absorber material	Gd ₂ O ₃ -UO ₂
Fuel pellet diameter (in.)	0.3225
Fuel pellet length (in.)	0.387
Fuel rod outer diameter (in.)	0.374
Fuel rod clad thickness (in.)	0.0225
Active fuel height (in.)	150
Core equivalent diameter (in.)	143.6

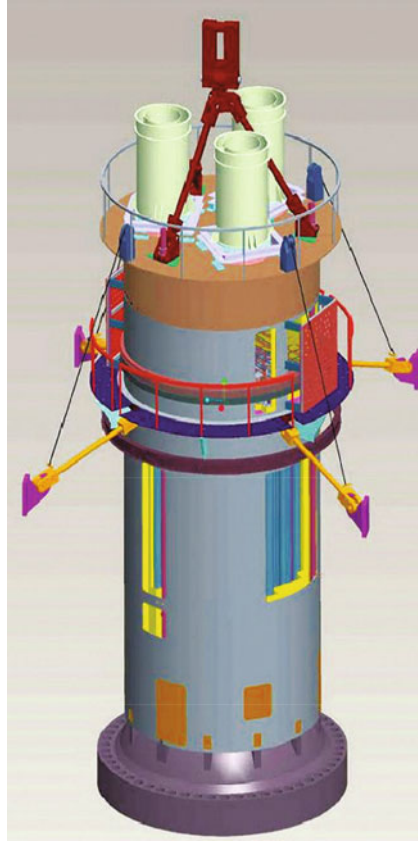
Source: Data compiled from Shinkori Unit 3, 4 Preliminary Safety Report.

■ **Table 16**
CEA characteristics

Parameter	Design value
Material (full/part length)	B4C/Inconel-625
Number of control assembly (full/part length)	76/17
Clad material	Inconel-625

Source: Data compiled from Shinkori Unit 3, 4 Preliminary Safety Report.

4 h without any detrimental effects on the systems and increasing the plant condition from a cold condition to full power within 200 min, excluding rotor preheating. The main steam supply system (MSSS) transports the steam from the steam generators to the power-conversion system and removes the heat from the RCS. The steam flow is directed from the SGs to the high-pressure (HP) turbine, of which the inlet steam pressure is maintained at 962 psia during full power. The turbine generator consists of a double-flow HP turbine and three double-flow low-pressure (LP) turbines driving a direct-coupled generator. The LP turbine rotors are of mono-block type. The material used for the LP rotors is Ni-Cr-Mo-V alloy steel and is treated to obtain enough toughness. The 52 in. last stage buckets of the LP turbine are designed to have low stress and



■ Figure 14
Integrated head assembly (Courtesy of Korea Hydro and Nuclear Power Co., Ltd.)

increased stiffness. The turbine rotor is manufactured as one piece by forging to reduce the susceptibility of stress corrosion cracks (SCCs). The turbine control system is improved to enhance the reliability and maintainability by the redundant design of controllers and the strengthening of the diagnostic functions. The vibration monitoring functions are improved by strengthening the self-diagnostic functions of the detectors and multidirectional measurements. In addition, earthquake-proof structures are installed to prevent a turbine trip caused by high vibration.

The generator system consists of the generator itself and auxiliary systems such as a stator cooling water system, gas control system, and seal oil system. The stator of the generator takes a highly reliable F-class Micapal II insulation system and a highly reliable brazing technology. The rotor of the generator also adopts the highly reliable insulation system and radial flow cooling method. Static excitation type is adopted to reduce mechanical wearing. The auto-voltage regulator (AVR) is placed in a dedicated room to minimize its malfunction by protecting it from heat and humidity. Also, the filtration abilities of the stator cooling water pipelines are strengthened to not heat up by the reduced coolant flow.

■ **Table 17**
Pressurizer main design values

Parameter	Design value
Design pressure (psia)	2,500
Design temperature (°F)	700
Operating pressure (psia)	2,250
Operating temperature (°F)	652.7
Free volume (ft ³)	2,400
Coolant volume at full power (ft ³)	1,110
Heater capacity (kW)	2,400

Source: Data compiled from Shinkori Unit 3, 4 Preliminary Safety Report.

■ **Table 18**
Steam generator main design values

Parameter	Design value
Number of SG	2
Number of tube per SG	13,102
Tube metal	Alloy 690
Heat transfer area (ft ²)	163.67
Tube side operating pressure (psia)	2,250
Shell side maximum operating pressure (psia)	1,100
Steam pressure at full power (psia)	1,000
Steam temperature at full power (°F)	545
Steam flow per SG at full power (lb/h)	8.975×10^6
Maximum moisture at outlet at full power (w/o)	0.25
Total steam flow (lb/h)	17.95×10^6
Steam generator exit pressure (psia)	1,000
Steam generator temperature (°F)	544.6

Source: Data compiled from Shinkori Unit 3, 4 Preliminary Safety Report.

The condensate and feedwater systems transfer condensate from the main condenser hotwells to the SGs, while the feedwater heaters raise the condensate temperature by using the extraction steam, and the deaerator removes the entrained oxygen and noncondensable gases. The feedwater heaters are installed in six stages and arranged horizontally for easy maintenance and reliability. The feedwater flow control system is designed to control the feedwater flow automatically over the full operation range and to operate three turbine-driven main feedwater pumps during normal power operation. When one main feedwater pump is tripped during the full power condition, the other two main feedwater pumps would be able to provide the total

Table 19
Turbine generator and feedwater pumps

	Parameter	Design value
Turbine	Number	1 double-flow HP TBN, 3 double-flow LP TBN
	Type	Tandem-compound, 6 flow
	Speed (rpm)	1,800 rpm
	Rated output (MW)	1,455
	Last stage bucket size (in.)	52
Generator	Number	1
	Type	Direct driven (water cooled)
	Capacity (kV A)	1,690,000 @ 0.9 pf and 75 psig of H ₂
	Rated voltage	24 kV, 3 phase
	Frequency (Hz)	6
FW pump	Main feedwater pump	3 × 55%, TBN driven (TD)
	Boost pump	3 × 55%, MD
	Start-up pump	1 × 5%, MD

Source: Data compiled from Shinkori Unit 3, 4 Preliminary Safety Report.

feedwater flow to the full power condition. This design reduces unnecessary power cutback and unplanned turbine trip.

The configuration of the main feed water pump (MFWP) is designed to be 3×55% to allow more reliable operation. Even if one MFWP is tripped during full power condition with three MFWPs operating, the other two MFWPs could recover the total feedwater flow to the nominal value of the full power condition and the plant is restored to the full power condition. This design reduces unnecessary power cutbacks and unplanned turbine trips. The auxiliary feedwater system (AFWS) supplies feedwater to the SGs for events resulting in loss of normal feedwater and requiring heat removal through the SGs. The AFWS is actuated by an auxiliary feedwater actuation signal (AFAS) from the ESFAS or the diverse protection system (DPS). The ESF-component control system (ESFCCS) includes logic to close the flow-control valves when the SG water level has risen above a high-level set point and to reopen this valve when the SG water level drops below a low-level set point. Different from the conventional plant, the AFW storage tank is installed in the auxiliary building separated from the condensate tank to enhance the system reliability in transients (➤ [Table 19](#)).

MMIS and Electrical System

I&C System In order to come up with high performance and maintainability, I&C systems including control and monitoring systems are based on proven, diverse, and commercial off-the-shelf hardware, network, and software platforms such as DCS and programmable logic controller (PLC) with operating experience of more than 3,000 years. The I&C architecture consists of two platforms. One is a safety grade PLC platform, which is comprised of core protection



■ Figure 15

Main control room (Courtesy of Korea Hydro and Nuclear Power Co., Ltd.)

calculator (CPC), plant protection system (PPS), and ESF-component control system (ESF-CCS). These safety systems are designed to meet the licensing requirements for independence, defense-in-depth, diversity analysis, failure mode analysis, and environmental qualification. The fail-safe concept is implemented such that the system is allowed to operate safely. The other is a non-safety-grade DCS platform, which consists of PCS, NSSS process control system (NPCS), process-component control system (P-CCS), DPS, and information processing system (IPS). The DCS with multi-loop controllers is adopted for these non-safety I&C systems. The number of I&C platform is minimized to increase the cost-effectiveness and to decrease operator's maintenance burden. Defense against the common mode failure (CMF) of digital plant protection systems is one of the key requirements in designing digital I&C systems. The DPS is designed to be diverse from the PPS against the CMF of the digital plant protection system. Diverse manual ESF actuation is also designed to keep the plant safety against severe situations due to a simultaneous digital system failure of the PPS and the DPS. The open architecture concept is applied to the configuration of the I&C system for high reliability and maintainability. In addition, the stringent software and hardware qualification process is established and followed for the life cycle.

Main Control Room The computerized MCR of APR1400 adopts compact workstations (➤ Fig. 15). These workstations are integrated with operator support systems with a human-centered automation concept. The MCR provides operating crews with an information-oriented operational environment that enables fast situational awareness of plant status. The design goal of the advanced MCR is to enhance the plant safety by extending operator coping time against accidents and to reduce human errors by improving the operational readiness. The following advanced technologies and design concepts are being incorporated to achieve the design goal. In addition, a safety console is provided in the MCR as a backup facility for safe operation against a total failure of workstations.

Compact Workstation The MCR contains workstations, a large display panel (LDP), and a safety console. The workstations are identical and reconfigurable so that an operator has a backup workstation to cope with the situation when different types of workstation failures are encountered. The workstations are placed near one another in a fixed location to improve communication among the operators. A unified computer-based MMI design is applied for all the major plant systems for operator's convenience. The compact workstation with a computer-based MMI reduces the interface management tasks using the two-click access and format chaining. The MMI design adopts the system- and function-based displays as well as the diverse information displays for operation. The enhanced display includes dynamic logic display, P&ID, video data from CCTVs, and design data. In addition, the compact workstation is designed to provide all operational means, including the computerized operator support functions, such as critical function monitoring, success path monitoring, signal validation, and computerized procedures. This integrated compact workstation design is expected to reduce workload of the operating crew.

Large Display Panel The LDP is large enough to be viewed from anywhere in the MCR. It presents the plant-level indications and alarms, which enable the operating crews to assess the plant situation related to the critical safety and the power production functions. The LDP displays are developed to have a simplified and fixed format with the 'dark board' concept. A 'dark board' concept means that no alarm indicates the normal state of plant. This allows operating crews quickly and easily to assess the plant status at a glance. The LDP is designed to quickly direct the operators' attention to the exact trouble source and to allow them to diagnose the severity of the plant incidents. The LDP provides sufficient information for emergency operations. The LDP also continuously displays the critical function performance and the success path availability.

Safety Console The safety console is provided as a backup for safe operation against a total DCS failure. The safety console indications are designed to provide qualified information and alarms in a similar format to the LDP display to enhance familiarity of the display.

Computerized Procedure System The computerized procedure system (CPS) provides an integrated presentation of procedural instructions and related process information needed to execute applicable procedures by both an operator and the operating crews. The CPS also monitors the plant condition and supports the recovery actions for inadvertent errors committed by operators. The CPS is designed to monitor continuously applied steps and nonsequential steps. The CPS supports the multiple procedure execution as well as the multiuser execution. The CPS is capable of accessing information displays and alarm systems and evaluating the instruction logic of a procedure.

Human Factors Engineering The extensive HFE program is incorporated to reduce the possibility of a human error in the MCR. In the conceptual and basic design at the R&D stage as well as during the construction phase of the plants, the MMI design has been analyzed and evaluated in an iteratively expanding manner with participation of more than 100 licensed operators and human factors specialists to optimize the design. During the APRI400 development, the evaluation for the MMI design has been performed seven times with full-scope dynamic mockups and an APRI400-specific dynamic mockup. The evaluation verified that the MMI are suitable

for the human factor principles and guidelines. The new MCR design was also validated to support the normal and emergency operations appropriately.

Electrical System The plant electrical system consists of the generator, the generator circuit breaker, the main transformer (MT), the unit auxiliary transformers (UATs), and the standby auxiliary transformers (SATs). The normal power sources for non-safety loads are the off-site power through the main transformer and the on-site power through the UATs from the generator. The electric power for the safety-related systems is supplied from the following four alternative ways: (1) the normal power source of the normal off-site power through the MT or the on-site power through UATs generated by the in-house generator, (2) the standby off-site power connected through the SATs with the grid, (3) the on-site standby power supply from two EDGs, and (4) an alternative alternate current (AAC) source from a backup diesel generator. During normal operation, the electric power for the safety-related systems is supplied from the normal power source of the normal off-site power through the MT or the on-site power through the UATs. If the normal power source is not available, the safety loads are covered with the off-site power source via the SATs. Then, if the off-site power source to the safety-related systems is interrupted, the safety loads are backed up by two independent Class 1E EDG sets. Each of them is located in a separated room of the auxiliary building and is connected to two 4.16 kV safety buses. The nonclass 1E AAC source adds more redundancy to the electric power supply for safety systems. It is provided to cope with SBO situation, which has a high potential of transients to severe accidents. The AAC source has sufficient capacity to accommodate loads on the safety (► Fig. 16).

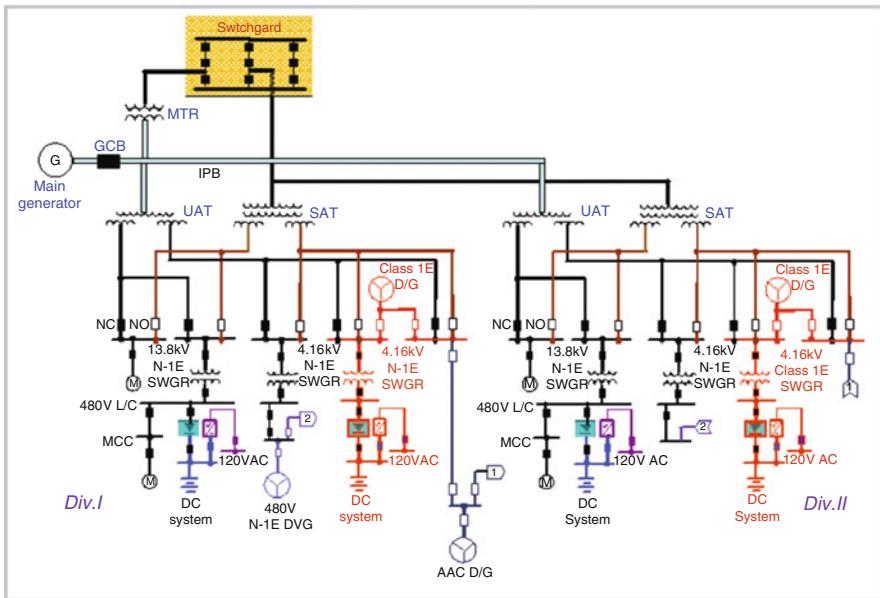


Figure 16

One line diagram of station power block (Courtesy of Korea Hydro and Nuclear Power Co., Ltd.)

1.3.2 Major Safety Design Features

Safety

Goals and Design Philosophy One of the APRI400 development policies is to dramatically increase the level of safety (APRI400 SSAR 2002). The following safety goals are established to improve the plant safety level by ten times. The APRI400 design has been made to meet these safety goals with securing an additional margin of safety to protect the owner's investment as well as public health (Kim et al. 2005).

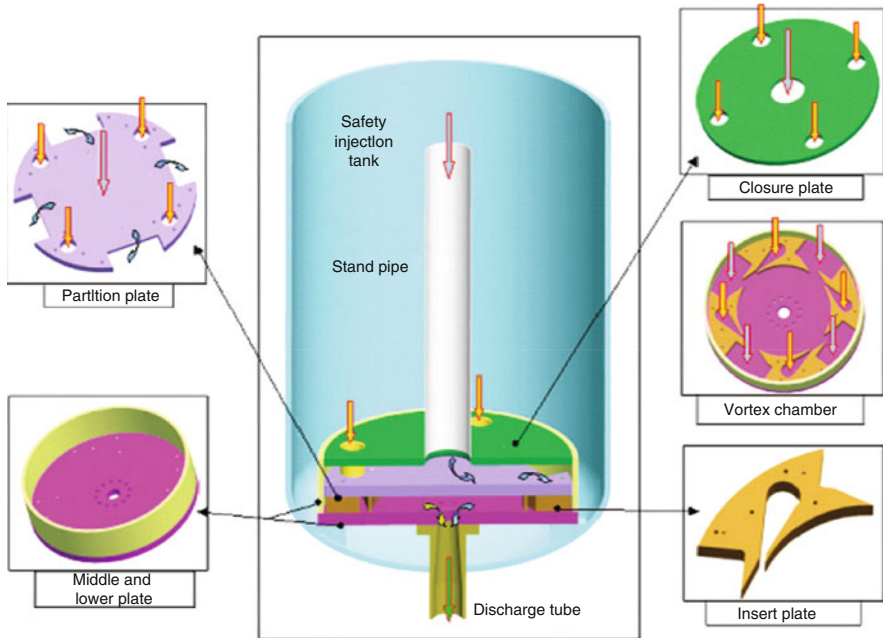
The major safety goals of APRI400 (KURD 1998) are as follows:

1. The total CDF shall not exceed 10⁻⁵/RY for both internal and external initiating events and 10⁻⁶/RY for a single event and an incident occurring in a high-pressure condition.
2. The containment failure frequency shall be less than 10⁻⁶/RY.
3. The whole body dose at the site boundary shall not exceed 0.01 Sv (1 rem) for 24 h after the initiation of core damage with a containment failure.

Safety Systems and Features The safety systems consist of SIS, IRWST, safety depressurization and vent system (SDVS), containment spray system (CSS), and AFWS (► Fig. 17). The main design concept of the SIS is simplification and redundancy to achieve higher reliability and better performance than the conventional plant. The SIS is comprised of four independent mechanical trains without a tie line among the injection paths and two electrical divisions. Each train has one active SIP and one passive safety injection tank (SIT) equipped with a fluidic device (FD). For simplicity and independence of SIS, the common header installed in the SIS lines of the conventional plant is eliminated (Kim et al. 2000).

This design separates the functions of SIS and shutdown cooling system (SCS) (► Fig. 18). The passive flow regulator, that is, the FD is installed in the SIT. The basic concept of the FD is vortex flow resistance. When water flows through the stand pipe, which is installed in a rectangular direction with the exit nozzle, it creates low vortex resistance and a high flow rate. When the water level is below the top of the stand pipe, inlet flow is switched to the control ports that are installed in a tangential direction with the exit nozzle, and it makes a high vortex resistance and low flow rate. Thereby, the SIT discharges a large amount of water to fill the reactor vessel lower plenum rapidly when water level is above the stand pipe. However, when the water level is below the stand pipe, the SIT injects a relatively small amount of water for a long time. The FD installed in SIT substitutes for the low-pressure SIPs such that the low-pressure SIP is eliminated.

The IRWST is located inside the containment and the arrangement is made in such a way that the injected emergency cooling water returns to the IRWST. This design removes the operator action of switching the suction of SIP from the IRWST to the containment recirculation sump, required in the conventional plant. This new design lowers the susceptibility of IRWST to external hazards. The IRWST provides the following functions: storing refueling water, a water source for the SIS, shutdown cooling system, and containment spray system, a heat sink to condense steam discharged from the pressurizer for rapid depressurization if necessary. This prevents high-pressure molten corium ejection and enables feed and bleed operation. This also allows supplying coolant to the cavity-flooding system, which mitigates molten corium concrete interaction in severe accidents. By adopting the advanced features of the FD in SIT and the IRWST, the high-pressure injection, low-pressure injection, and recirculation modes of the conventional SIS are merged into one operational mode of safety injection. The SIS is designed



■ Figure 17

Fluidic device (Courtesy of Korea Hydro and Nuclear Power Co., Ltd.)

for safety water to be injected directly into the reactor vessel so that the discharge of injected flow through the broken cold leg is eliminated. The SDVS is a dedicated safety system designed to provide a safety grade means to depressurize the RCS in the event that the pressurizer spray is unavailable during plant cooldown to cold shutdown and to rapidly depressurize the RCS to initiate the feed and bleed method of plant cooldown subsequent to the total loss of feedwater event (Kwon et al. 1997). The POSRVs are employed for feed and bleed operation. This system establishes a flow path from the pressurizer steam space to the IRWST. The CSS consists of two trains and takes the suction of its pump from the IRWST to reduce the containment temperature and pressure during accidents occurring in the containment. The CSS is interconnected with the SCS, which is also comprised of two trains. The pumps of these systems are designed to have the same type and capacity. This design makes the CSS have a higher reliability compared with the conventional plant. The AFWS consists of two divisions and four train systems and supplies feedwater to the SGs for RCS heat removal in the case of loss of main feedwater. In addition, the AFWS refills the SGs following a LOCA to minimize leakage through preexisting tube leaks. The reliability of AFWS has been increased by the use of two 100% motor-driven pumps, two 100% turbine-driven pumps, and two independent safety-related emergency feedwater storage tanks located in the auxiliary building instead of a condensate storage tank of the conventional plant.

Seismic Design The buildings and structures are designed with the application of the SSE criterion of 0.3 g as a design basis earthquake (DBE) to increase their ductility against earthquakes.

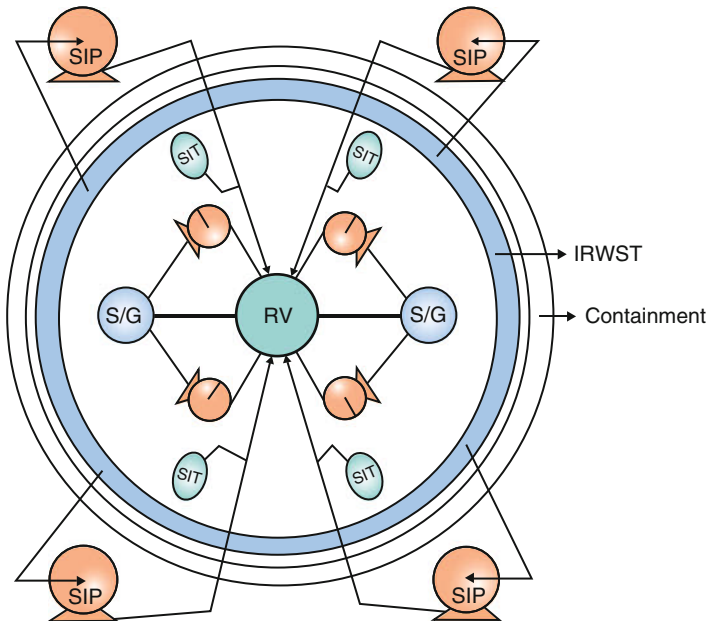


Figure 18
Safety injection system (Courtesy of Korea Hydro and Nuclear Power Co., Ltd.)

The seismic input motion enforced in the high frequency range is applied to envelope the design ground response spectrum of the Regulatory Guide 1.60 standard spectrum. The design load of operating base earthquake (OBE) is eliminated to improve design and verification according to 10 CFR 50 Appendix S. Since the seismic evaluation is performed with the inclusion of the effects of soil–structure interaction on soil sites, the APRI400 can be constructed on rock bed sites as well as on soil sites (KURD 1998).

Severe Accident

Reactor Containment Building Design In order to maintain the integrity of the RCB and to prevent the leakage of radioactive materials during SAs, the RCB is designed to have free volume large enough so that the structural load is maintained below the ASME Section III Service Level C for 24 h after SAs. This also helps keep hydrogen concentration under 13% in case of 75% oxidation of fuel clad steam. Another design feature to prevent leakage is installation of the 0.25 in. steel liner plate on the inboard side of the RCB. In addition, the RCB is constructed with the prestressed concrete having the high compressive strength of 6,000 psi after 91 days of curing. The reactor vessel cavity is designed such that molten core materials spread out for its heat transferable area to be not less than $0.02 \text{ m}^2/\text{MW}$ and is cooled to solidify on the cavity floor. Also, the convoluted vent path of the reactor vessel cavity prevents the molten core debris from releasing to the containment atmosphere.

Mitigation Systems The SAs management system prevents and mitigates SAs, and maintains containment integrity. It is designed to meet the procedural requirements and criteria of US NRC regulations, including the post Three Mile Island (TMI) requirements for new plants as reflected in 10 CFR 50.34 (f) and SECY-93-087. This system includes a large dry prestressed concrete containment, hydrogen management system (HMS), large reactor cavity and core debris chamber, cavity flooding system (CFS), In-vessel corium retention through external reactor vessel cooling system (IVR-ERVCS), SDVS, emergency containment spray backup system (ECSBS), and severe accidents management procedure (SAMP) (KURD 1998).

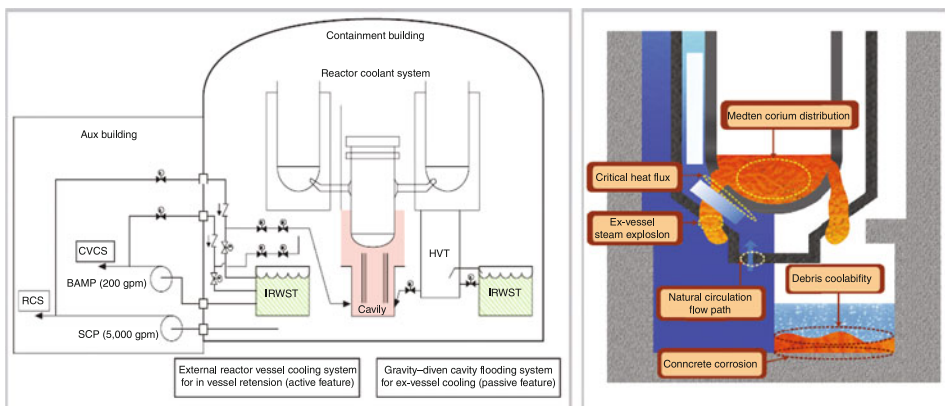
Hydrogen Mitigation System The HMS consists of 26 PARs and 10 glow plug igniters. The capacity of the HMS is designed to accommodate the hydrogen production from 100% metal–water reaction of fuel cladding and to limit the average hydrogen concentration in containment below 10% in accordance with 10 CFR 50.34 (f) for a degraded core accident.

Reactor Cavity Design The reactor cavity adopts a core debris chamber, which is designed to have heat transfer area of corium more than $0.02 \text{ m}^2/\text{MWth}$. The flow path of the reactor cavity is convoluted to hinder the transfer of core debris to the upper containment. This design prevents DCH due to core debris.

Cavity Flooding System The APRI400 has two strategies for cooling the molten core: ex-vessel cooling (EVC) and in-vessel retention (IVR). The CFS supplies the coolant for ex-vessel cooling. It consists of two trains connected with IRWST and two isolation valves that are installed in each line. When the two isolation valves are open during the SAs, the cavity cooling water is supplied from the IRWST to the reactor cavity by the gravity. It cools down the core debris in the reactor cavity, scrubs fission product releases, and mitigates the MCCI (Kim et al. 1992).

In-Vessel Corium Retention through External Reactor Vessel Cooling System

IVR-ERVCS retains molten core in the reactor vessel by cooling the external surface of the reactor vessel (► Fig. 19). This system submerges the reactor vessel bottom head before molten core relocates to the bottom head. Cooling water is supplied from the IRWST by a shutdown



■ Figure 19

Cavity flooding system and IVR-ERVCS (Courtesy of Korea Hydro and Nuclear Power Co., Ltd.)

cooling pump (SCP) and a boric acid makeup pump (BAMP). This system maintains the reactor vessel integrity and reduces the threat of containment integrity.

Emergency Containment Spray Backup System The ECSBS provides long-term coolability by supplying spray water to containment for 48 h so that the containment temperature and pressure are reduced during the SAs. This system consists of spray nozzle, piping, and containment penetration. Spray water is supplied by external pump from temporary external water source. The ECSBS contributes to relieving the threat of containment integrity.

Proven and Evolutionary Technology

In order to enhance safety, operational convenience, and maintainability, the APRI400 was developed by adopting advanced design features. These advanced design features are based on the proven nuclear power plant design technology gained through many years of repeated constructions and extensive operation experiences of the OPRI1000 (see [Fig. 1.2](#)). The new design features have been successfully evaluated to ensure that they enhance the performance and safety of the APRI400. The following relevant experimental studies have been conducted over the several years by Korea Atomic Energy Research Institute (KAERI) in support of the APRI400 design.

Safety Injection Performance Test for Direct Vessel Injection

The safety injection (SI) nozzles in the APRI400 are located in the upper part of the reactor pressure vessel (RPV) downcomer. Due to this design feature, in a LOCA, the thermal-hydraulic phenomena in the RPV downcomer differ from those in the case of cold leg injection (CLI) design, and this difference is believed to govern a large break loss-of-coolant accident (LBLOCA) reflood phase (Cha and Jun 1994, Cho 1997).

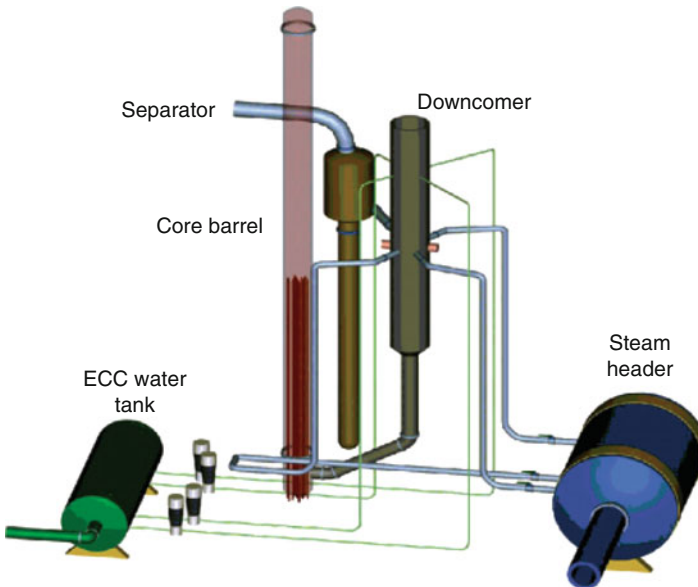
In order to evaluate the emergency core coolant (ECC) bypass during the reflood phase of a postulated LBLOCA and to assess the contribution of the new SI system to safety enhancement, the performance of the SI system was examined by using the multidimensional investigation in downcomer annulus simulation (MIDAS) facility ([Figs. 20](#) and [21](#)). The MIDAS facility was designed to be one-fifth length scale of the APRI400 and to use steam and water as test fluids at 190 psia and 572°F as design conditions (Kim 1994).

Performance Test for Fluidic Device in Safety Injection Tank

The APRI400 uses an FD that is installed inside a SIT as a passive design feature to ensure effective use of the SIT water. This design feature enables the APRI400 to achieve the goals of minimizing the ECC bypass during a blowdown, and of preventing a spillage of excess ECC water during the refill and reflood phases of a LBLOCA. The FD provides a high discharge flow rate of SI water when the FD starts to operate, which is required during the refill phase of a LBLOCA. When the refill phase is terminated, the discharge flow rate of the SI water drops sharply but is still large enough to remove any decay heat during the reflood phase. Because of the strong vortex motion in the FD, the pressure-loss coefficient of the low flow rate period is almost ten times higher than that of the high flow rate period. The difference in the pressure drop helps extend the total duration of the SI and also allows the low-pressure safety injection pump to be removed from the SI system. In order to confirm the performance of the FD designs, full-scale performance tests were carried out in the valve performance evaluation rig (VAPER) facility, which was designed with the same size and operating conditions as those



■ Figure 20
MIDAS facility (Courtesy of Korea Atomic Energy Research Institute)



■ Figure 21
Schematic diagram of MIDAS facility (Courtesy of Korea Atomic Energy Research Institute)



■ **Figure 22**
VAPER facility (Courtesy of Korea Atomic Energy Research Institute)

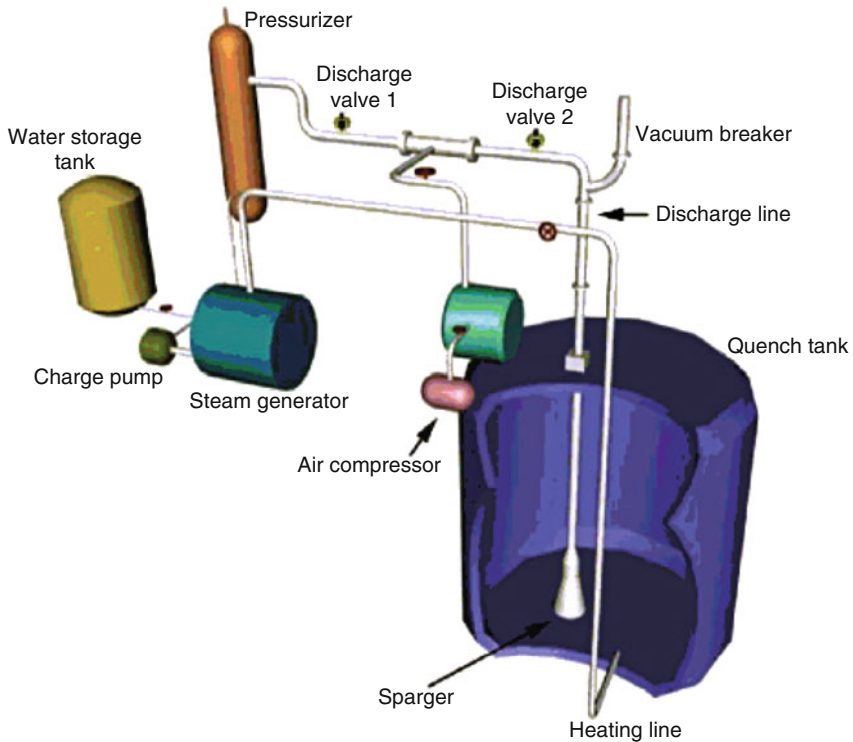
of the APRI400 SIT. It was verified from these full-scale tests that the performance of the FD satisfies the standard design requirements of the APRI400 (► [Fig. 22](#)) (Kim et al. 2000).

Performance Test for IRWST Sparger To cope with transients such as a RCS overpressure, the SDVS, which enables feed and bleed operation, and the SIS are incorporated in the APRI400 to maintain the integrity of the RCS and the core. Actuation of POSRVs results in a transient discharge flow of air, steam, or a two-phase mixture to the IRWST through the spargers (IRWST T/H Load Analysis 1996).

The discharge of these fluids induces complicated thermal-hydraulic phenomena such as water jet, air clearing, and steam condensation (► [Figs. 23](#) and ► [24](#)). These phenomena impose hydrodynamic forces on the IRWST structure and the components of the SDVS. These structures shall be designed so as to withstand these hydrodynamic loads and to maintain their structural integrity as well as the safety functions of the engineered safety features systems. The hydrodynamic loads on the IRWST wall and the components of SDVS are induced by air clearing and steam jet discharge through a prototype sparger of the APRI400. The relevant tests of these loads were conducted at the blowdown and condensation (B&C) facility.

Advanced Thermal Hydraulic Test Loop for Accident Simulation

The advanced thermal hydraulic test loop for accident simulation (ATLAS) (► [Figs. 25](#) and ► [26](#)) is a thermal hydraulic integral effect test facility constructed at Korea Atomic Energy Research Institute (Baek et al. 2005). It was used for simulations of various transients and accident conditions of the APRI400 and the OPR1000. It simulates various accident scenarios at actual pressure and temperature conditions of the APRI400. The integrated safety of the APRI400 with new design features has been verified through accident simulation in the ATLAS (Baek et al. 2009). The major accident scenarios are reflood phase of the LBLOCA, small-break LOCA scenarios including the DVI line breaks, steam generator tube ruptures, main steam line breaks, feedwater line breaks, mid-loop operation, and other transient conditions.



▣ Figure 23

Schematic diagram of B&C facility (Courtesy of Korea Atomic Energy Research Institute)



▣ Figure 24

IRWST sparger (Courtesy of Korea Atomic Energy Research Institute)

1.4 Operation and Construction

1.4.1 Status of Operation

KHNP is the largest of the six power-generation subsidiaries created from Korea Electric Power Corporation (KEPCO) in April 2001. In terms of installed capacity and gross power generation, nuclear power in Korea constituted 27% and 39%, respectively, as of 2006. This high attribution ratio of nuclear power generation results from the fact that nuclear power plants are base load plants in Korea, which maintain high capacity factor.

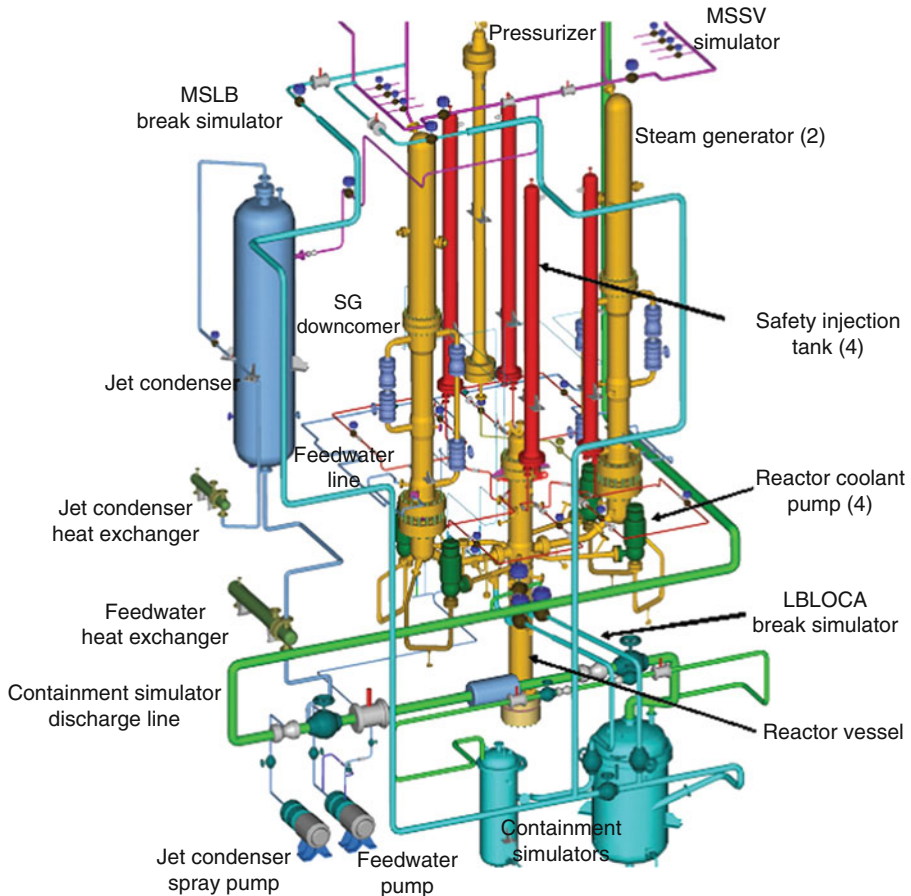


Figure 25
Schematic diagram of ATLAS (Courtesy of Korea Atomic Energy Research Institute)

KHNP has made great strides in achieving capacity factor over 90% (as high as 100% for Yonggwang Unit 3 in 2005) and one cycle trouble free (OCTF) operation (as long as 482 days for Ulchin Unit 3). The outstanding performance exceeding the global average could be attributed to the excellent operation and maintenance techniques accumulated for the last 30 years (► Fig. 27).

Due to the high operability and maintainability that come from the operational characteristics and design improvements of OPR1000, OPR1000 units have shown excellent operational performances: high capacity factor, short maintenance period, reduced reactor scram, high thermal efficiency, and reduced radiation exposure and radwaste (► Tables 20–22).

1.4.2 Construction

A new construction schedule and constructability-enhancement methods were developed based on the experience gained from repeated OPR1000 constructions. The power block



Figure 26
ATLAS facility (Courtesy of Korea Atomic Energy Research Institute.)

foundation of APRI400 is seismically enhanced with the application of 0.3 g SSE criterion as a DBE. The RCB and the AB are built on a common basemat. This design requires a highly increased mat size and the amount of concrete. Thus, the construction method for this massive concrete structure is reviewed to meet the target duration. The common basemat foundation is simplified as a flat type so that it may benefit the concrete works. Modularization has been introduced to reduce the construction period and the cost. There are three types of modules: the structural, mechanical equipment, and composite modules. To expand the modular construction, the research is being done for the steel-plate concrete (SC) structure module, the mechanical equipment, and the composite module. If the composite module is applied to all buildings in the nuclear power plant, the construction time will be dramatically reduced to less than 40 months through prefabrication at both the factory and the site (▶ [Table 23](#)).

Reactor Containment Building Work

There are two ways to bring big components such as steam generators into the RCB and to place them in the proper locations. One is the over-the-top method (OTM), in which massive equipment is placed into its proper position through the top of the RCB by a large capacity crane. The other is the conventional side method (SM), in which major components are brought into the RCB through an equipment hatch and positioned with a polar crane in containment. Since

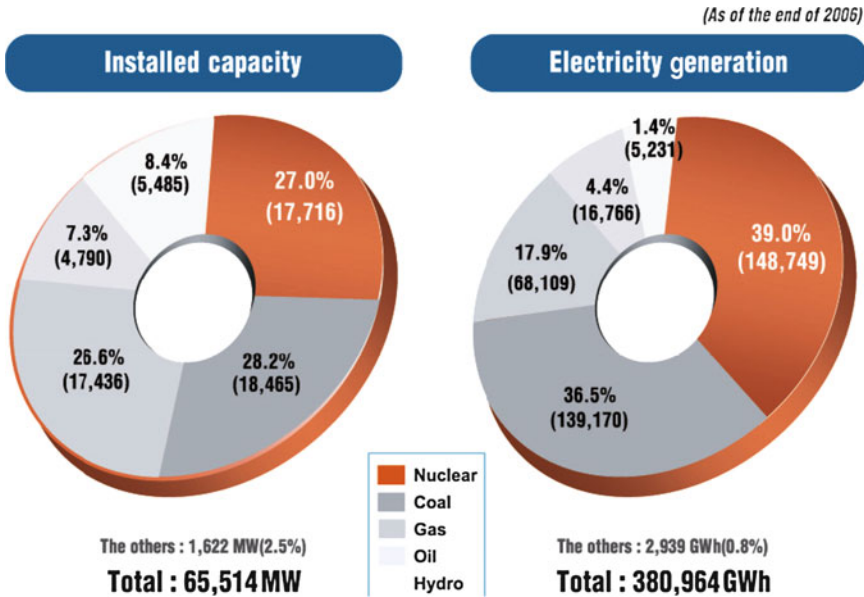


Figure 27 Supply mix (Courtesy of Korea Hydro and Nuclear Power Co., Ltd.)

the SM requires two steps, it takes longer. Since the RCB is wrapped around the AB and has bigger and heavier components than those of conventional nuclear power plants, the OTM is favorable for the installation of major components. To reduce the construction time, the OTM has been adopted after a comparative study and assessment. The detailed installation procedure has been verified through simulation by using three-dimensional computer-aided design (3-D CAD) models to confirm its feasibility (► Fig. 28).

Modularization

To reduce the construction time, fabrication work at the factory for mechanical and electrical equipment needs to be increased. Approximately 80 items of the APRI400, including auxiliary and containment building water chillers and pumps, feedwater pumps and turbine drives, charging pumps, turbine building component cooling water heat exchangers, and condensers, have been identified to be suitable for modularization. Reactor internal assembly is manufactured into three pieces in the conventional plant: core support barrel (CSB), the lower support structure (LSS) with core shroud, and the UGS. The assembling of reactor internals at the construction site takes a long time and is on the critical path of the construction schedule. Reactor internals of the APRI400 are fabricated into two parts by integrating the CSB, LSS, and CS. This modularization of reactor internals is estimated to reduce the construction time by approximately 3 months. In the condenser modularization, three shells and transitions are assembled in the factory, and the low-pressure feedwater heaters and the water boxes are assembled at the construction site.

■ Table 20

Capacity factors^a of OPR1000 in 2001–2007

Unit	Year							Commercial operation date
	2001	2002	2003	2004	2005	2006	2007	
Yonggwang Unit 3	103.6	92.1	93.9	91.8	104.1	87.5	89.5	1995.3.31
Yonggwang Unit 4	87.1	92.1	102.9	91.5	93.3	99.9	88.1	1996.1.1
Yonggwang Unit 5	-	103.3	91.1	66.9	93.6	88.9	99.5	2002.5.21
Yonggwang Unit 6	-	105.3	92.5	76.6	94.0	91.8	90.6	2002.12.24
Ulchin Unit 3	94.9	93.0	104.4	94.8	92.2	96.8	90.8	1998.8.11
Ulchin Unit 4	93.1	88.1	95.4	103.3	96.1	90.7	91.2	1999.12.31
Ulchin Unit 5	-	-	-	102.8	88.3	90.6	92.2	2004.7.29
Ulchin Unit 6	-	-	-	-	103.7	85.2	91.0	2005.4.22
Average	94.7	95.7	96.7	89.7	95.7	91.4	91.6	

$${}^a \text{Capacity factor} = \begin{cases} \frac{\text{Total MWh gross}}{\text{Capacity MW gross} \times 8,760 \text{ h}} \times 100 \% & \text{for } 2001\text{--}2005 \\ \frac{\text{Total MWh gross}}{\text{Recent three years average generation output MW} \times 8,760 \text{ h}} \times 100 (\%) & \text{for } 2006\text{--}2007 \end{cases}$$

APR1400 Construction Schedule

Along with the many new construction methods, the modularization technologies of reactor internals and the mechanical and structural composites have been applied to the construction of APR1400. The OTM allows the major components in the containment to be manufactured as large modules and installed in the early phase of construction. The modular construction method is applied to the containment liner plate (CLP) and stainless steel liner plate (SSLP) to reinforce the steel and the structural steel module. This method is also applied to the fabrication of equipment such as the reactor internals and the condenser. The deck plate construction method is applied to the construction and the installation of mechanical and electrical equipment to be carried out simultaneously in the auxiliary building and compound building. The first two units in APR1400 fleet (Shinkori 3&4) commenced construction in 2007. It is estimated that Shinkori 3&4 will be constructed in less than 51 months for the first unit and 45 months for the second unit. The succeeding units are expected to be constructed in 40 months (🔗 Fig. 29).

2 CANDU Reactors in the Republic of Korea

2.1 Introduction

In addition to the main fleet of light water pressurized water reactors (PWRs), Korea has installed Canadian pressurized heavy water reactor (PHWR) CANDU6's as a complementary reactor type. Korea Hydro and Nuclear Power (KHNP) began to operate the first CANDU

■ **Table 21**

One Cycle Trouble Free (OCTF) operation records of OPR1000

Unit	Cycle duration	Days	Commercial operation date
Yonggwang Unit 3	1997.3.31 to 1998.3.31	366	1995.3.31
	2000.11.19 to 2002.3.8	475	
	2002.4.15 to 2003.5.26	407	
	2004.11.10 to 2006.1.5	422	
Yonggwang Unit 4	1997.12.3 to 1998.12.24	387	1996.1.1
	2000.4.3 to 2001.5.3	396	
	2001.6.28 to 2002.10.14	474	
	2004.6.28 to 2005.8.25	468	
	2005.9.29 to 2007.1.4	463	
Yonggwang Unit 6	2002.12.24 to 2003.11.19	331	2002.12.24
	2000.7.8 to 2001.6.30	358	
Ulchin Unit 3	2001.7.30 to 2002.11.23	482	1998.8.11
	2003.1.1 to 2004.4.10	466	
Ulchin Unit 4	2005.2.5 to 2006.5.22	472	1999.12.31
Ulchin Unit 5	2005.8.7 to 2006.9.10	400	2004.7.29

unit (Wolsong 1) in 1983, and three additional units (Wolsong 2, 3, 4) in 1997, 1998, and 1999, respectively. ➤ [Table 24](#) provides a list of Canadian design nuclear power plants. ➤ [Table 25](#) shows the construction and operation phases of CANDU reactors in Korea (Wolsong Unit 3, 4 FSAR, 2003).

2.2 System Description

2.2.1 CANDU Reactor Model

Among the several types of heavy water reactors considered worldwide, the dominant type is the heavy water cooled, heavy water moderated pressure tube reactor developed in Canada (Heavy Water Reactors, 2002). This type of reactor is designed to use natural uranium, but it can also use slightly enriched uranium or a variety of other fuels. Typically, the reactor core is contained in a cylindrical stainless steel tank (calandria), which holds the heavy water moderator at low temperatures ($<80^{\circ}\text{C}$) and low pressure (~ 0.1 MPa).

➤ [Figure 30](#) shows a schematic of CANDU6 reactor. ➤ [Figure 31](#) shows a cross-section of CANDU6 calandria. The calandria houses fuel channels that span horizontally and it also houses reactivity mechanisms that span vertically. The calandria shell is a horizontal, single-walled cylinder made of austenitic stainless steel. The ends of the calandria shell are enclosed

■ Table 22

NPPs in operation: 20 units (17,716 MW)

Unit		Reactor type	Capacity (MW)	NSSS supplier	Plant A/E	Commercial operation	Remarks
Kori	#1	PWR	587	W/H	Gilbert	April 1978	
	#2	PWR	650	W/H	Gilbert	July 1983	
	#3	PWR	950	W/H	Bechtel/KOPEC	September 1985	
	#4	PWR	950	W/H	Bechtel/KOPEC	April 1986	
Wolsong	#1	PHWR	679	AECL	AECL	April 1983	
	#2	PHWR	700	AECL/DOOSAN	AECL/KOPEC	July 1997	
	#3	PHWR	700	AECL/DOOSAN	AECL/KOPEC	July 1998	
	#4	PHWR	700	AECL/DOOSAN	AECL/KOPEC	October 1999	
Yonggwang	#1	PWR	950	W/H	Bechtel/KOPEC	August 1986	
	#2	PWR	950	W/H	Bechtel/KOPEC	June 1987	
	#3	PWR	1,000	DOOSAN	KOPEC	March 1995	OPR1000
	#4	PWR	1,000	DOOSAN	KOPEC	January 1996	OPR1000
	#5	PWR	1,000	DOOSAN	KOPEC	May 2002	OPR1000
	#6	PWR	1,000	DOOSAN	KOPEC	December 2002	OPR1000
Ulchin	#1	PWR	950	Framatome	Framatome	September 1988	
	#2	PWR	950	Framatome	Framatome	September 1989	
	#3	PWR	1,000	DOOSAN	KOPEC	August 1998	OPR1000
	#4	PWR	1,000	DOOSAN	KOPEC	December 1999	OPR1000
	#5	PWR	1,000	DOOSAN	KOPEC	July 2004	OPR1000
	#6	PWR	1,000	DOOSAN	KOPEC	April 2005	OPR1000

by stainless steel tube-sheets, which form a common boundary between the calandria and the end-shields.

The heavy water moderator in the calandria is a unique feature in CANDU reactors, which provides a passive heat sink for some accident scenarios. A cover gas system maintains a pressure of less than 27.6 kPa (4 psia) above the moderator.


The CANDU6 reactor core has 380 fuel channels. Each fuel channel consists of a zirconium/niobium alloy pressure tube surrounded by a zircaloy-2 calandria tube with CO₂ gap (annulus gap) in between. Inside each pressure tube, the heavy water coolant (separated from the heavy water in calandria) flows through the fuel channel to remove the heat produced by fission of the natural uranium fuel. Each fuel channel contains 12 fuel bundles. The fuel bundles are made up of 37 Zircaloy-4 tubes containing natural UO₂ pellets.  Figure 31 also shows a fuel bundle.

Table 23

NPPs under construction/planning: 8 units (9,600 MW)

Unit		Reactor type	Capacity (MW)	Plant model	Expected commercial operation	Remarks
Shinkori	#1	PWR	1,000	OPR1000	December 2010	Construction
	#2	PWR	1,000	OPR1000	December 2011	Construction
	#3	PWR	1,400	APR1400	September 2013	Construction
	#4	PWR	1,400	APR1400	September 2014	Construction
Shin-Wolsong	#1	PWR	1,000	OPR1000	March 2012	Construction
	#2	PWR	1,000	OPR1000	January 2013	Construction
Shin-Ulchin	#1	PWR	1,400	APR1400	December 2015	Planning
	#2	PWR	1,400	APR1400	December 2015	Planning

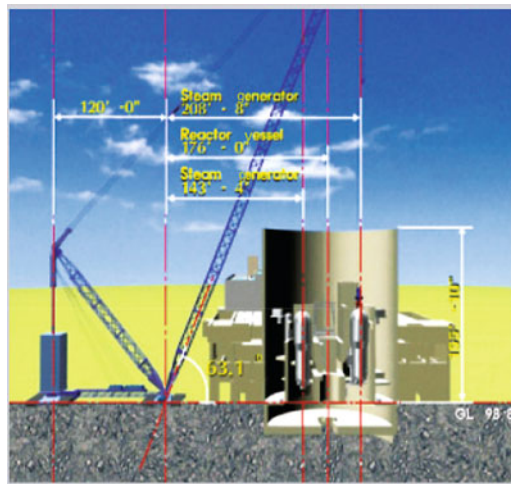
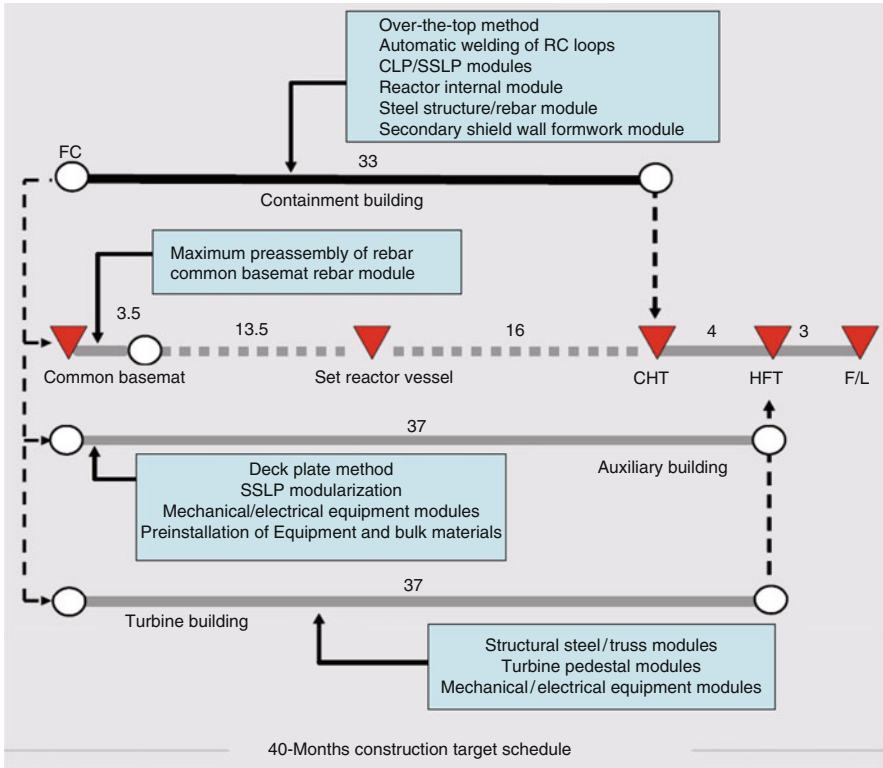


Figure 28

Over-the-top method (Courtesy of Korea Hydro and Nuclear Power Co., Ltd.)

2.2.2 Primary Heat Transport System (PHTS)

The primary heat transport system is comprised of two loops. Each loop serves 190 of the 380 reactor fuel channels. Each loop contains two pumps, two steam generators, two inlet headers, and two outlet headers in a “figure-of-eight” arrangement (Fig. 32). Feeders connect the inlet and outlet ends of the fuel channels to the inlet and outlet headers, respectively. Pressurized heavy water circulates through the reactor fuel channels to remove the heat produced by fission. The heat is transported by the reactor coolant to steam generators where it is transferred to light water to generate steam, which subsequently drives the turbine generators. The steam



■ Figure 29

APRI400 construction schedule (Courtesy of Korea Hydro and Nuclear Power Co., Ltd.)

generators, PHTS pumps, and headers are located above the reactor, permitting the heat transport system coolant to be drained to the head elevation for maintenance of the PHTS pumps and steam generators, and also facilitating thermosyphoning (natural circulation) when the PHTS pumps are unavailable and the reactor is shut down.

The two closed loops are generally interconnected with isolation valves. An automatic loop isolation reduces the rate of reactor coolant loss in the event of a loss of coolant accident. The isolating valves are automatically closed when the PHTS pressure drops to below certain set-point pressure whether or not a loss of coolant accident (LOCA) has occurred and whether or not the emergency core cooling system (ECCS) is actuated. The reactor outlet headers at one end of the reactor are connected to a common pressurizer. The pressurizer is the principal component for pressure control of the heat transport system.

2.2.3 Moderator System

The heavy water moderator in the calandria is used to thermalize fast neutrons produced by fission. The heavy water moderator is circulated through the calandria and moderator heat

■ **Table 24**
Canadian design nuclear power plants

Plant	Owner	MW(e) (net)	Year of Start-up
1. NPDP	Ontario Hydro/AECL	22.0	1962
2. Douglas Point	AECL	206.0	1968
3. Pickering "A"	Ontario Hydro	4 × 515.0 = 2,060.0	1971–1973
Pickering "B"	Ontario Hydro	4 × 516.0 = 2,064.0	1983–1984
4. Gentilly 1	AECL	250.0	1972
5. KANUPP	Pakistan	125.0	1971
6. RAPP	India	2 × 200.0 = 400.0	1972–1975
7. Bruce "A"	Ontario Hydro	4 × 740.0 = 2,960.0	1977–1979
Bruce "B"	Ontario Hydro	4 × 750.0 = 3,000.0	1983–1987
8. Gentilly 2	Hydro-Quebec	638.0	1983
9. Cordoba	CNEA, Argentina	600.0	1983
10. Point Lepreau (Unit 1)	NBEPCC, New Brunswick	1 × 635.0 = 635.0	1982
11. Wolsong 1	KEPCO, Korea	628.0	1983
12. Darlington	Ontario Hydro	4 × 881.0 = 3,524.0	1990–1993
13. Cernavoda (Unit 1 of 5)	Romania	1 × 628.6 = 628.6	1995
14. Wolsong 2	KEPCO, Korea	1 × 664.9 = 664.9	1997
Wolsong 3	KEPCO, Korea	1 × 664.9 = 664.9	1998
Wolsong 4	KEPCO, Korea	1 × 664.9 = 664.9	1999
		19,735.1	

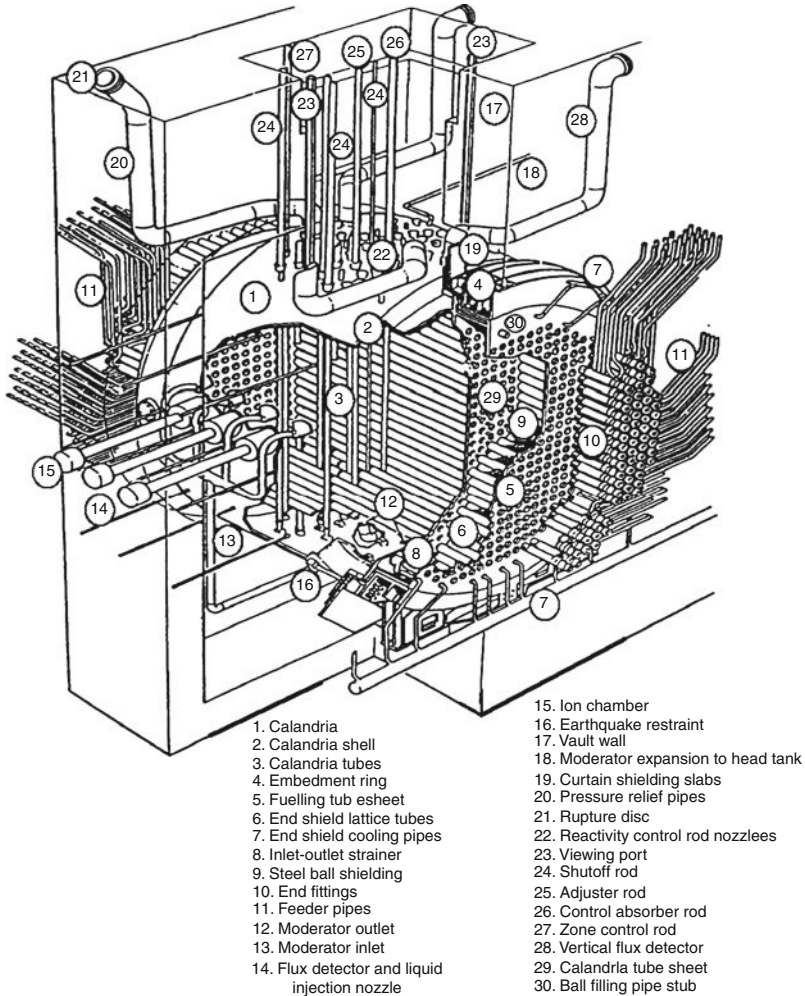
Source: Data from Wolsong 3, 4 final safety analysis report.

■ **Table 25**
Construction and operation phases of CANDU reactors in Korea

Plant	Date of commencement of:		Date of start-up/ connection to grid	Current generation capacity (MWe)
	Design	Construction		
Wolsong 1	1973	1977	1983	678
Wolsong 2	1987	1990	1997	700
Wolsong 3	1990	1991	1998	700
Wolsong 4	1990	1991	1999	700

exchangers to remove the heat generated in the moderator during reactor operation. The moderator heat is in turn rejected to the recirculated cooling water system. The operating pressure at the moderator free surface is slightly above atmospheric.

The moderator system is fully independent of the primary heat transport system (► Fig. 33). The moderator system includes two 100% pumps and two 100% tube and shell heat exchangers.



■ Figure 30

A Schematic of a CANDU6 PHWR (Courtesy of Korea Hydro and Nuclear Power Co., Ltd.)

The moderator system head tank maintains the moderator level in the calandria within the required range by accommodating moderator swell and shrink resulting from temperature fluctuations. The heavy water in the calandria functions as a heat sink in the unlikely event of a loss of coolant accident coincident with failure of the ECCS. The capability of this heat sink is assured by controlling the heavy water temperature in the calandria within specified limits.

2.2.4 Emergency Core Cooling System (ECCS)

The function of the ECCS is to provide an alternate means of cooling the reactor fuel, in the event of a LOCA, which depletes the normal coolant inventory in the PHTS to an extent that fuel cooling is not assured.

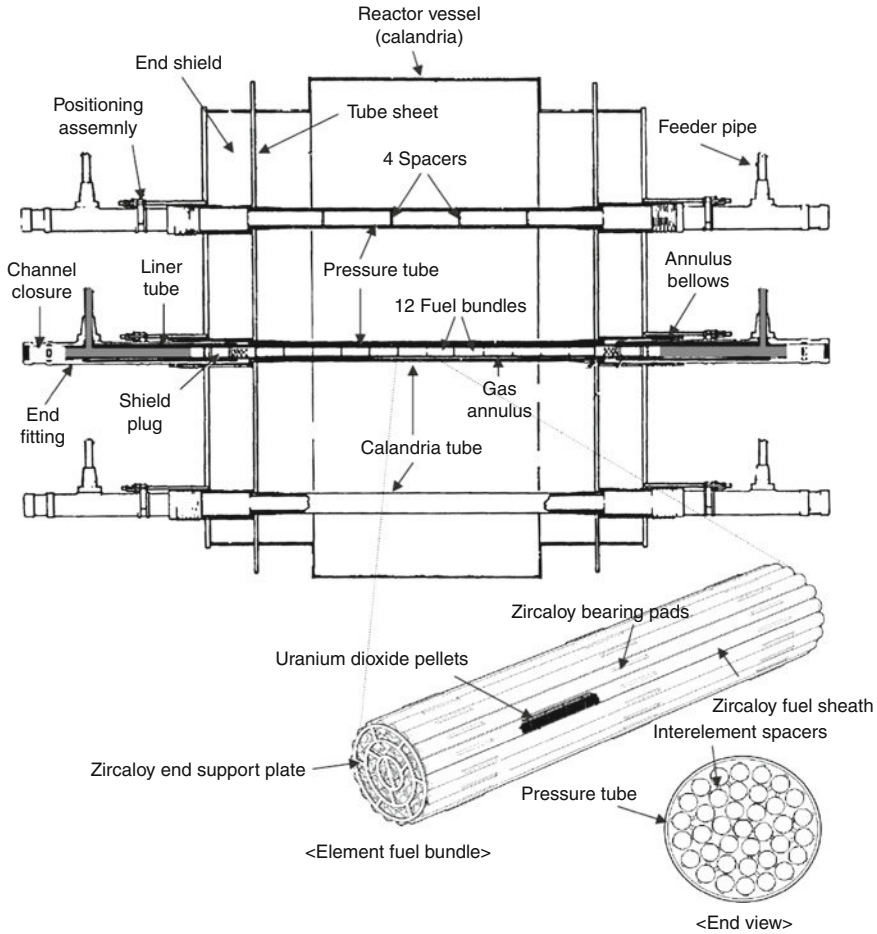


Figure 31
Cross-section of CANDU6 calandria (Courtesy of Korea Hydro and Nuclear Power Co., Ltd.)

There are three stages of ECCS operation according to the operating pressure: high, medium, and low pressure. As soon as the PHTS header pressure drops to below 4.04 MPa(g) (586 psig), water flows from the high-pressure ECCS tanks into headers of the failed loop. Although the flow rate from the water tanks depends on the break size, the high-pressure injection lasts for a minimum of 2.5 min for a 100% header break size.

The medium pressure injection valves open when the low high-pressure ECC water tank levels signal on. The ECC pump injects water from the dousing tank to all reactor headers when the pump discharge pressure is higher than the reactor header pressure. The medium pressure injection lasts for a minimum of 12.5 min for a 100% header break size.

As the dousing tank water depletes, the medium pressure injection is automatically terminated and low-pressure injection starts. Long-term low-pressure injection is provided by collecting the mixture of H₂O and D₂O from the reactor building sump and recirculating it

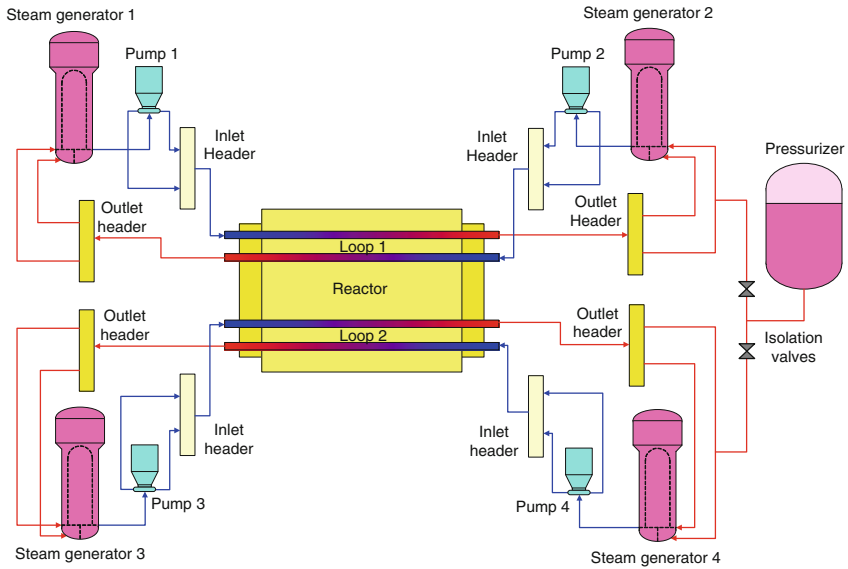


Figure 32
Two loop primary heat transport system (PHTS) in a CANDU6 PHWR

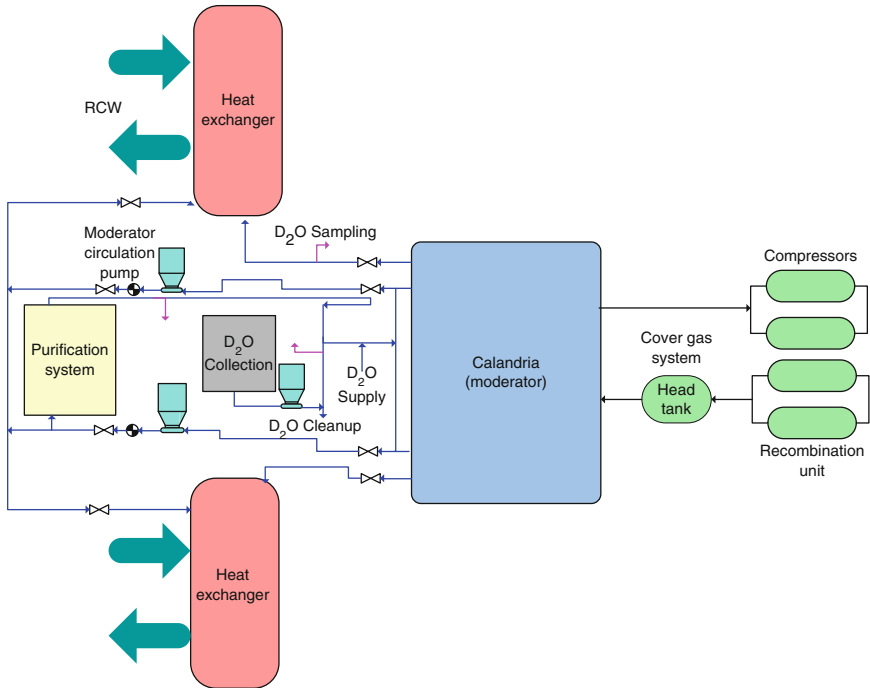


Figure 33
Schematic diagram of the moderator system

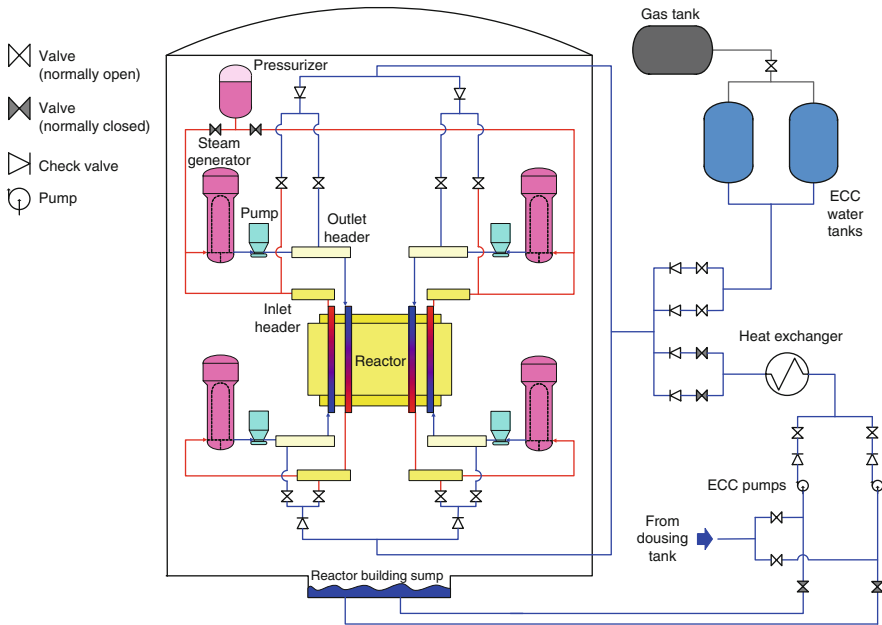


Figure 34
Emergency core cooling system (ECCS) of a CANDU6

into the PHTS via the emergency cooling system heat exchangers. The low-pressure ECCS circuit is designed to operate at least 3 months following a LOCA. **Figure 34** shows a simplified diagram of the ECCS. For large breaks, the ECCS recovery heat exchanger is the main heat sink. For small breaks, the steam generator continues to be the main heat sink.

2.2.5 Shutdown System

The CANDU6 reactor uses two diverse, passive, shutdown systems that are independent of each other and from the reactor regulating system. Each shutdown system is capable of tripping the reactor and has sufficient negative reactivity to maintain it in a shutdown state. Especially even if any class of electrical power fails, shutdown system has no effect in tripping the reactor.

Shutdown system No.1 consists of mechanical shutdown rods, which drop into the core when a trip signal de-energizes clutches that hold them out of the core (**Fig. 35**). Shutdown system No.2 injects a concentrated solution of gadolinium nitrate into the low-pressure moderator to quickly render the core subcritical. The injection is initiated by opening fast acting valves to pressurize the individual poison tanks associated with each of the injection nozzles with helium.

2.2.6 Containment System

The major function of the containment system is to confine the release of fission products into the environment during accident to within the acceptable limits. The containment system

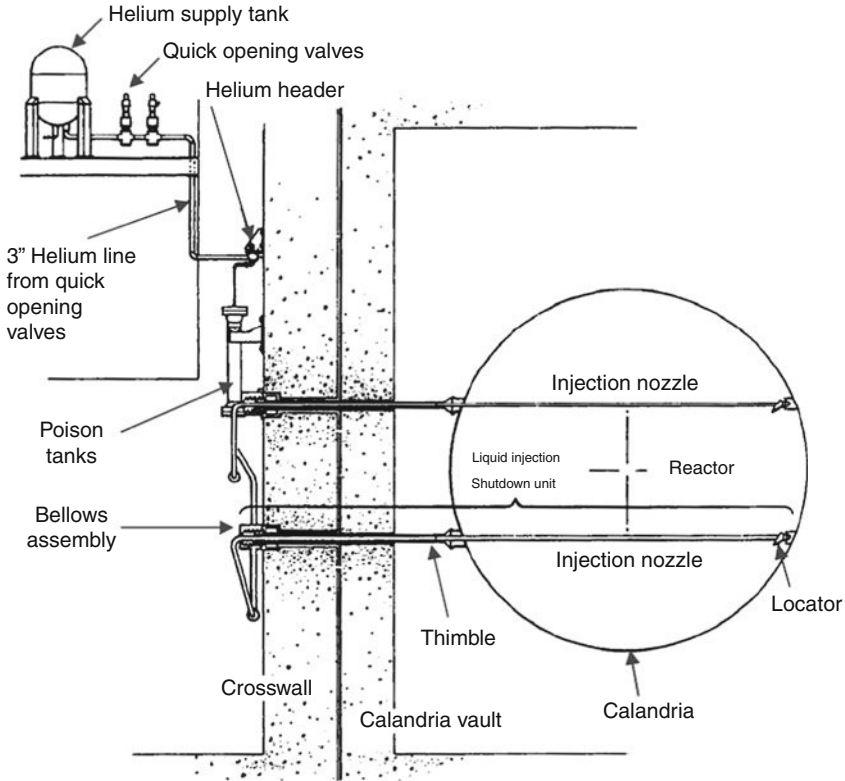


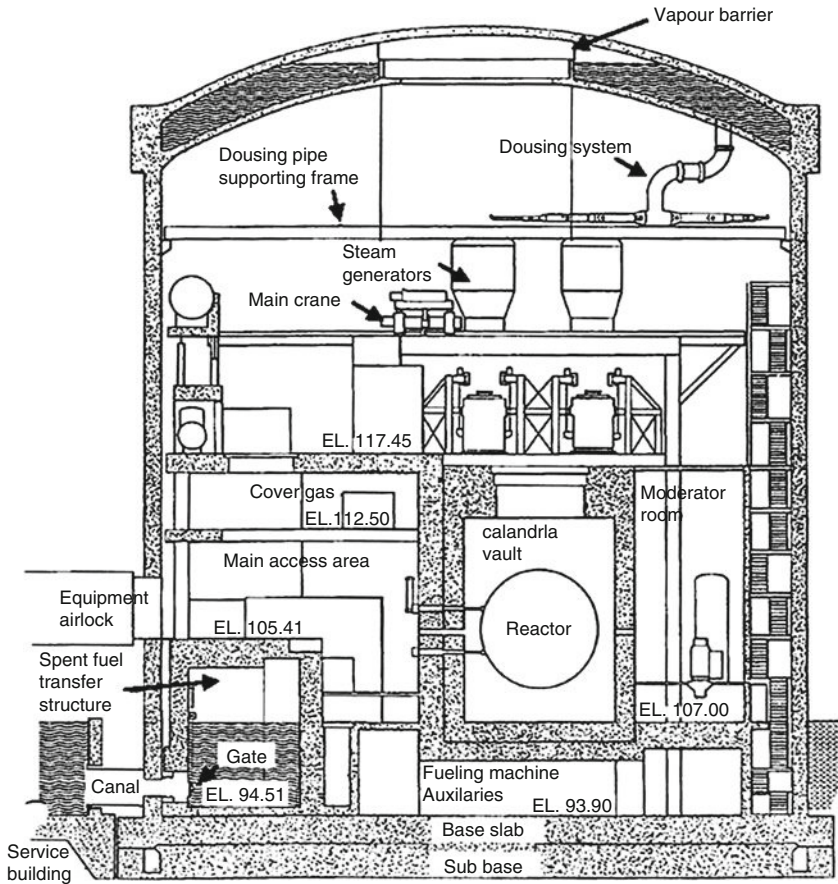
Figure 35
Shutdown system (Courtesy of Korea Hydro and Nuclear Power Co., Ltd.)

consists of a leaktight envelope around the reactor and associated nuclear systems, and includes containment isolation systems, containment atmosphere energy removal systems, and cleanup systems.

The CANDU6 single unit containment is a prestressed concrete building consisting of three principal structural components: a base slab, a cylindrical wall, and a spherical segmental dome. The concrete provides strength and shielding. The inner surface of the reactor building is lined with an epoxy coating, instead of steel plate, to improve leaktightness (🔗 [Fig. 36](#)).

The spray dousing system is designed to limit the magnitude and duration of containment overpressure caused by a LOCA or a main steam line break inside the reactor building. The system is automatically initiated when the containment pressure exceeds 14 kPa (2 psig). The flow rate is designed to limit the maximum building pressure to less than the design pressure following a guillotine rupture of the heat transport system header. When containment pressure decreases to 7 kPa(g) (1 psig), the dousing valves close in 7 s. According to the size of the break, there is a continuous or cyclic operation of dousing valves. Manual operation of the dousing system is possible from either control center.

In recent CANDU6 plants such as Wolsong 2, 3, and 4, a network of hydrogen igniters is provided to burn any local concentrations of hydrogen formed in the long-term post-LOCA and



■ **Figure 36**
Single unit containment (Courtesy of Korea Hydro and Nuclear Power Co., Ltd.)

in dual failures (LOCA plus loss of ECCS), preventing hydrogen from reaching deflagration or detonation levels by using controlled ignition as soon as the hydrogen concentration reaches flammable limits.

2.3 Major Safety Design Features

The inherent safety features available in the CANDU concept are provided by various engineered safety features built into the design. This section discusses the principles followed for the design of engineered safety features in CANDUs and provides a description of some of the salient features. In the engineering of the systems, well-established safety design principles and guidelines are followed, some of which are uniquely applied to CANDUs. These are highlighted below.

2.3.1 Defense in Depth

The defense in depth principle is, of course, not unique to CANDUs. In following the principles of defense in depth, emphasis is placed on minimizing the challenges to the lower echelons. Accident prevention is similar to that employed for other reactor types and, with one exception, will not be described in detail here. In fact, many of the events of moderate frequency can be handled by normal operating or process systems without needing to invoke any of the safety systems; for example, many deviations and transients can be safely handled by the reactor set back that reduces reactor power at a predetermined rate through the reactor regulating system. Small leaks from the HTS, such as those from breaks in instrument tubing, which are within the capacity of the D₂O feed pumps, can be handled by operator actions to shut down the reactor and actuate the small leak handling system.

One particular aspect of defense in depth in pressure tube CANDUs is the application of “leak before break” to the pressure boundary of the core (the pressure tubes). The critical crack length is well above the crack length at which leaks occur; such leaks are detected through an annulus gas system that monitors the gas between the calandria tube and the pressure tube in each fuel channel. The operator can then shut down and depressurize the reactor long before a rupture occurs.

Leak before break can be prevented by the occurrence of excessive local zirconium hydride concentrations in the pressure tube, resulting from, for example, pressure tube/calandria tube contact. Zirconium–niobium does not hydride as fast as Zircaloy-2, but separation must still be maintained between the pressure tube and the calandria tube. In current CANDUs, the pressure tube/calandria tube gap and pressure tube hydride concentration are carefully monitored to ensure that all known pressure tube failures would be signaled beforehand by a leak.

Two Group Concept

In order to protect the plant against common mode incidents such as fires and missiles, the safety systems have been divided into two groups that are functionally and physically independent of each other and which use diverse and independent support systems such as electrical power and service water. Each group has the capability to

- Shut down the reactor,
- Remove decay heat from the fuel,
- Minimize the escape of radioactivity,
- Monitor the safety status of the plant.

Group 1 comprises

- Normal plant operating systems, including the reactor regulating system, all process systems (except for the moderator cooling) and the main control room
- SDS 1 and the ECCS.

Group 2 comprises

- An emergency power supply,
- An Emergency Water Supply (EWS),
- SDS2 and containment systems,

■ **Table 26**
Required safety functions of Groups 1 and 2

Required safety function	Mechanism employed	
	Group 1	Group 2
	SDS 1	SDS 2
Shutdown of the reactor	Steam generator cooling or shutdown cooling or ECCS	Cooling by EWS or firewater through the steam generator and moderator cooling
Removal of decay heat		
Minimization of radioactivity release	Decay heat removal via the steam generators or shutdown cooling or ECCS	Containment system
		Hydrogen ignition system (on recent HWRs)
Monitoring of the safety status of the plant	Main control room	Secondary control area and local panels/controls

This allocation of systems to groups is typical of most CANDUs. However, in the CANDU9 design, the ECCS is Group 2 system and containment systems are Group 1, allowing for a simplified layout.

- Emergency moderator cooling and circulation,
- A secondary control area or supplementary control room.

The EWS is plant dependent; in most CANDUs it consists of a portion of the dousing tank water and/or an external water reservoir, with pumps powered by the emergency power supply. The required safety functions and the systems in each of the two groups to satisfy these functions are shown in [▶ Table 26](#).

Redundancy

In line with the usual practice for nuclear power plants, adequate redundancy is provided in safety systems such that the minimum safety functions can be performed even in the event of failure of any single active component in the system. Over and above this “single failure criterion,” safety systems in CANDUs are also required to meet specified unavailability targets, the evaluation of which takes into account the maximum permissible downtime of the equipment (specified in station technical specifications for operation) due to maintenance, etc.

Separation

Physical and functional separation is ensured between each safety system and any process system, so that a failure in a process system does not impair the safety systems that are intended to protect against it or to mitigate it. As far as is practicable, this separation is also provided between different safety systems, as well as between redundant components within a safety

system. These features ensure that a single local event (i.e., fire, missile impact, pipe failure) will not result in multiple component or system failures, and that the functions required for the safety of the reactor will not be impaired.

Fail-Safe Feature

In order to minimize the probability of unsafe failures, wherever possible, the logic and instrumentation circuits are designed to fail in the safe direction. The limitations of this concept are due to not always being possible to define a unique fail-safe position (e.g., HTS liquid relief valves) and also because a system that requires powered operation cannot be fail-safe on loss of power. Thus, systems that are mostly passive, such as the shutdown systems and the containment isolation systems, are fail-safe on loss of control power, but the ECCS pumps rely on electrical power to operate.

2.3.2 Availability

The four CANDU safety systems, sometimes termed special safety systems (i.e., SDS1, SDS2, ECCS, and containment), are designed to meet numerical availability targets, typically 0.999 for the most recent CANDUs. This availability must be demonstrated during plant operation by periodic testing. The safety systems must be designed to permit such testing without negative impact on operations.

2.4 Status of Operation

In Korea, Wolsong Unit 1, which is the first heavy water CANDU reactor with 678MW of generation capacity was constructed with a turnkey contract in 1983. Wolsong Unit 2, 3, and 4, with 700 MW of generation capacity were constructed and started commercial operation respectively in 1997, 1998, and 1999. In the year of 2008, these heavy water CANDU reactors generated 23,006,763 MWh electricity in total. ➤ [Table 27](#) shows statistics on capacity and availability factors of CANDU reactors in operation in Korea (Nuclear Power Generation White Paper, 2009).

2.5 Spent Fuel Storage Facility

The simple fuel design of CANDU offers many benefits in spent fuel handling, storage, and disposal. Over 20 years of experience gained in the development and application of medium-term storage have resulted in technology that is well proven and economical, and which has a high degree of public and environmental protection. In fact, both the short-term (water pool) storage and medium-term (dry canister) storage of spent HWR fuel are lower in terms of cost per unit of energy than for other reactor types.

Table 27
Capacity/availability factors (%) of CANDUs in Korea

Year Unit	2003	2004	2005	2006	2007	2008
Wolsong #1	89.5/88.2	90.3/87.4	77.7/82.9	91.4/91.3	89.8/90.8	93.0/95.5
Wolsong #2	95.3/91.5	94.9/89.8	98.1/94.1	99.7/99.4	90.9/90.7	92.2/92.0
Wolsong #3	97.3/93.3	96.4/91.2	104.5/100.0	94.0/93.7	94.3/94.1	93.0/92.5
Wolsong #4	98.2/94.3	97.4/92.8	98.4/94.2	100.4/100.0	93.2/93.1	94.5/94.2

2.5.1 Wet Storage of Spent CANDU Fuel

After a natural uranium fuel bundle is discharged from the CANDU reactor, having spent about 1 year of irradiation, it is removed to a pool system for interim storage. The water in the pool removes the residual heat produced by the spent fuel and provides radiation shielding for workers. The compact design of the CANDU fuel bundle and the impossibility of criticality occurring for CANDU natural uranium spent fuel bundles under storage conditions in water pools make for extremely simple pool storage.

To ensure protection of the environment and public health, the spent fuel pool in CANDU reactors is provided with double concrete walls, designed such that any leakage through the inner wall would enter drains located between the walls and would flow to the cleanup system. The water acts to shield personnel from the radiation emitted by the spent fuel, and the heat generated by the radioactive decay is transferred to the water. The water is cooled by circulating it through heat exchangers and is purified by passing it through filters and ion exchange systems that remove any dissolved and suspended radionuclides.

2.5.2 Dry Storage of Spent CANDU Fuel

Besides wet storage of spent fuel, the method of dry storage for spent CANDU fuel is currently used (🔍 [Fig. 37](#)). Spent fuel that has already been cooled in the spent fuel pool is surrounded by inert gas inside a large cask. These casks are typically steel cylinders that are either welded or bolted closed. Each cylinder is surrounded by additional steel, concrete, or other material to provide radiation shielding to workers and members of the public. There are various dry storage cask system designs. With some designs, the steel cylinders containing the fuel are placed vertically in a concrete vault; other designs orient the cylinders horizontally. The concrete vaults provide the radiation shielding. In Korea, dry storage facilities which are vertical type of concrete vaults with air cooling have been constructed respectively in 1992, 1998, 2002, and 2006 (🔍 [Table 28](#)).

3 Conclusions

Since Korea introduced a Westinghouse-designed pressurized light water reactor (PWR) in 1978 and an Atomic Energy of Canada Limited (AECL)-designed pressurized heavy water reactor



■ Figure 37

Dry storage facility of Wolsong NPP in Korea (Courtesy of Korea Hydro and Nuclear Power Co., Ltd.)

■ Table 28

Capacity of spent fuel storage in Korea

Facility	Storage type	Capacity (MTU)
Wolsong #1	Wet storage	801
Wolsong #2	Wet storage	706
Wolsong #3	Wet storage	706
Wolsong #4	Wet storage	706
Dry storage	Dry storage	3,061

(CANDU) in 1983 as turnkey projects, she has steadily constructed, operated, and improved nuclear power plants with self-reliant technologies. Sixteen PWRs and four CANDUs are in operation and eight additional PWRs are under construction at the time of this writing. In terms of installed capacity and gross power generation, the current nuclear power portion amounts to 27 and 39% (as of 2006), respectively, of total electricity generation in Korea.

Following the national policy of maintaining PWRs as main reactor type and CANDUs as complementary, Korea focused on and developed PWR technology through the Nuclear Power Plant Standardization Program, which began in 1984 and continued for over 10 years. This effort resulted in the Optimized Power Reactor 1000 (OPR1000) model, that aimed at maximizing operational efficiency and minimizing inadvertent effects on operators and environment by incorporating construction and operating experiences in Korea. Six units of this model are currently in operation and four units are under construction. The core is fueled with PLUS7, a new fuel assembly design with enhanced thermal-hydraulic and nuclear performance and structural integrity. The refueling cycle length is 18 months with gadolinia burnable absorber, achieving maximum discharge rod burnup of 60,000 MWD/MTU.

In the 1990s and 2000s, Korea next developed the Advanced Power Reactor 1400 (APR1400) model. APR1400 is designed to meet the Korean Utility Requirement Document that reflects the ALWR design requirements developed by Electric Power Research Institute (EPRI), European Utilities Organization, and others. Based on the self-reliant technologies and experiences

from the design, construction, operation, and maintenance of OPR1000, the APRI400 model has adopted advanced design features to enhance plant safety and economical efficiency. The advanced design features include a pilot-operated safety relief valve (POSRV), a four-train safety injection system with direct vessel injection (DVI), a fluidic device (FD) in the safety injection tank, an in-containment refueling water storage tank (IRWST), a cavity flooding system for ex-vessel cooling and in-vessel retention, and an external reactor vessel cooling system. Four units of this model are currently under construction in Korea.

The four CANDU reactors in Korea will continue to operate to their design lives with potential life extension. However, no additional new units are expected to be introduced due, in part, to the burden of establishing and maintaining infrastructure related to the unique CANDU technology.

References

- APRI400 Standard Safety Analysis Report (2002) Korea Hydro and Nuclear Power Co., Ltd, Korea
- Baek WP, Song CH, Yun BJ, Kwon TS, Moon SK, Lee SJ (2005) KAERI integral effect test program and the ATLAS design. *Nuclear Technol* 152:183–195
- Baek WP, Kim YS, Choi KY (2009) LBLOCA and DVI line break tests with the ATLAS integral facility. *Nuclear Eng Technol* 41:775–784
- Cha JH, Jun HG (March 1994) An investigation of fluid mixing with direct vessel injection. *J Korean Nucl Soc* 1(1):63–77
- Cho BH (May 1997) Analysis of fluid mixing characteristics in reactor vessel downcomer using Theofanous and Wallis' Mixing Model-DVI Case. Korea Atomic Energy Research Institute, Korea. Internal Technical Report
- Fuel Design Report for UCN 3&4 Nuclear Fuel (September 1995) Korea Atomic Energy Research Institute, Korea. KAERI/TR-547/95
- IRWST T/H Load Analysis (1996) The Korea Power Engineering Company, Korea
- Heavy Water Reactors (2002) Status and projected development. International Atomic Energy Agency, Technical Reports Series No. 407
- Kim YS (December 1994) DVI design development for R&D for KNGR. Korea Atomic Energy Research Institute, Korea. Internal Technical Report
- Kim MH, Chung CY, Kim HD, Kim SB (1992) Experimental study on direct containment heating phenomena. In: 1st Korea–Japan joint workshop on PSA, Seoul, November 30–December 2
- Kim HG et al (2000) The development of passive design features for Korean next generation reactor. *Nucl Eng Des* 201(2–3):259–271
- Kim HG et al (2005) Advancing reactors -APRI400-. *Nucl Eng Int* 50(615):16–19
- Korea Utility Requirement Document (1998) Korea Hydro and Nuclear Power Co., Ltd, Korea
- Kwon YM et al (June 1997) Safety depressurization system for Korean next generation reactor. In: 2nd international conference on advanced reactor safety, Orlando, Florida, pp 1294–1301
- Nuclear Power Generation White Paper (2009) Ministry of Knowledge Economy and Korea Hydro and Nuclear Power Co., Ltd
- PLUS7 Fuel Design and Safety Evaluation for Korean Standard Nuclear Power Plants (2006) Korea Nuclear Fuel Co., Ltd, Korea. KNF-TR-DMR-04001/N/A Rev.0
- Shinkori Unit 3, 4 Preliminary Safety Analysis Report (2008) Korea Hydro and Nuclear Power Co., Ltd, Korea
- Ulchin Unit 5, 6 Final Safety Analysis Report (2003) Korea Hydro and Nuclear Power Co., Ltd, Korea
- Ulchin Unit 3, 4 Reload Transition Safety Analysis Report (2005) Korea Hydro and Nuclear Power Co., Ltd, Korea
- Wolsong Unit 3, 4, Final Safety Analysis Report (2003) Korea Hydro and Nuclear Power Co. Ltd



20 VVER-Type Reactors of Russian Design

Sergei B. Ryzhov^{1,4} · Victor A. Mokhov^{1,4} · Mikhail P. Nikitenko^{1,4} ·
George G. Bessalov^{1,4} · Alexander K. Podshibyakin^{1,4} ·
Dmitry A. Anufriev^{1,4} · János Gadó^{2,4}

Chapter Editors: János Gadó^{2,4} · Ulrich Rohde³

¹OKB “GIDROPRESS”

²KfKI, Atomic Energy Research Institute of the Hungarian
Academy of Sciences, Budapest, Hungary
gado@sunserv.kfki.hu

³Institute of Safety Research, Research Center
Dresden-Rossendorf, Germany
u.rohde@fzd.de

⁴Joint Stock Company, State Atomic Energy Corporation
“Rosatom”, Podolsk, Moscow Region, Russia

1	Introduction	2253
2	VVER-440 Reactors	2256
2.1	Design Description	2256
2.1.1	Buildings and Structures	2256
2.1.2	Systems of the Primary Circuit	2263
2.1.3	Systems of the Secondary Circuit	2277
2.1.4	Instrumentation and Electrical Systems	2280
2.2	Basic Safety Properties	2282
2.2.1	Safety Philosophy	2282
2.2.2	Safety Systems and Properties	2283
2.2.3	Maximum Design Basis Accident	2285
2.2.4	Severe Accidents	2285
2.2.5	Seismic Design	2286
2.3	Operational Experience and Decommissioning	2287
2.3.1	Operational Experience	2287
2.3.2	Life-Time Extension	2288
3	VVER-1000 Reactors	2289
3.1	Design Description	2289
3.1.1	Buildings and Structures	2290
3.1.2	Systems of Primary Circuit	2295
3.1.3	Secondary-Side Systems	2307
3.1.4	I&C and Electrical Systems	2309
3.2	Main Aspects of VVER-1000 Safety	2312

3.2.1	Safety Philosophy.....	2312
3.2.2	Safety Systems and Distinctive Features.....	2313
3.2.3	Maximum Design Basis Accident.....	2317
3.2.4	Severe Accidents.....	2317
3.2.5	Seismic Design.....	2318
3.3	Operational Experience	2318
4	Conclusion	2319

Abstract: This chapter contains detailed description of the design and technical layout of Russian VVER-type reactors. Both the VVER-440 and the VVER-1000 reactor types are described. VVER reactors are a special design of Pressurized Water Reactors with some particular design features listed in the introduction. The most important of them are:

- A hexagonal geometry of the fuel assemblies (FA) with arrangement of the fuel rods in a triangular grid
- Zirconium-niobium alloy as fuel rod claddings material
- Possibility to transport all large-sized equipment by railway to enable a complete manufacturing process under factory conditions (resulting in a limitation of the outer diameter of the reactor pressure vessel)
- An original design of horizontal type steam generators with a tube sheet in the form of two cylindrical heads

VVER reactors are the most frequently built reactor type in the world. Presently, there are 23 units of VVER-440 and 28 units of VVER-1000 worldwide in operation (see tables in [▶ Sects. 2.3](#) and [▶ 3.3](#)).

In the introduction, a historical overview on the design of VVER-440 and VVER-1000 reactors is given. First units with predecessors of VVER-440 type reactors were erected at the Novovoronezh NPP site in 1972 and 1973. The second step in the development of VVER-440 type reactors was the V-230 design, where the number of mechanical control rods was reduced from 73 to 37 due to introduction of boron as a moderator. In the period from 1973 to 1982, all 14 units were constructed with the V-230 design. The third step in VVER-440 development was V-213 reactor design referred to as the second generation of the standard VVER-440 reactors; their design basis included a double-ended instantaneous guillotine break of the maximum diameter primary pipeline.

The development of VVER-1000 reactors was started by OKB Gidropress in 1966. The first reactor with an electrical power of 1,000 MW was commissioned at Novovoronezh NPP Unit 5 in 1980. In the design, the traditional engineering solutions of VVER were used with the appropriate modernization from the experience obtained in the design, manufacture, and operation of the VVER prototypes. The design concept was oriented to an increase in economic efficiency of the nuclear power plant (NPP) construction and operation, ensuring safety in accordance with the regulatory documents that were valid at the time. An instantaneous double-ended guillotine break of the main coolant pipeline was considered as the maximum design basis accident. The reactor plant was placed into a containment of prestressed concrete.

Further on, the design modifications ended up in elaboration of V-302 Project implemented at the South-Ukraine NPP Unit 1 and V-338 Project implemented at the South-Ukraine NPP Unit 2 and the Kalinin NPP Units 1 and 2. Elaboration of these projects classified as small series designs and their realization was under way from 1976 to 1987.

All the power units of VVER-1000 NPPs, beginning with 1985, were constructed to a standard design that contains the V-320 reactor plant, capable of being sited in seismic areas with earthquakes up to magnitude 9 (SSE), the reactor of small series; D nom 850 circulation loops without gate valves; wet reloading of internals; PGV-1000 horizontal steam generators; and GTsN-195M reactor coolant pumps (large series).

The main feature of the enhanced standard VVER-1000 reactor is the application of jacket-free fuel assemblies (their quantity increased from 151 pcs. to 163 pcs. and the reduction of control rods from 109 to 61 [up to 49 at the South-Ukraine NPP Unit 1]) and the application of ShEM drives in reactor trip system.

The large series designs have been realized since 1978 up to now. Twenty-eight Generation II power units with VVER-1000 have been constructed and are in operation at NPPs.

The accidents at TMI-2 and Chernobyl-4 NPPs have shown that it is necessary to take into consideration the beyond design basis accidents (BDBA) during their design and operation. In 1988 a new V-1000 design was launched (V-392 Project), which focused on safety improvements in response to new requirements of regulatory documents in order to prevent occurrence of BDBAs and to mitigate their consequences in the case that they happened.

The idea was implemented in the RP design of V-392 Project incorporated into NPP-92 design. The main RP equipment of the V-392 design, including the reactor, was implemented in a set of RP V-428 at “Tianwan” NPP. The information on this NPP design was incorporated into the chapter on VVER-1000 reactors. The modifications to V-392 RP design can be found in the design of RP V-412, which are being implemented now at “Kudankulam” NPP. Designs of Units with RP V-392, V-428, and V-412 are referred to Generation III reactors. In both VVER-440 and VVER-1000 sections of the chapter, first, the main design parameters of these reactors are given. Second, the buildings and structures are described that house the reactor plant and auxiliary systems. As a special feature of VVER-440, two power units of this reactor type are incorporated into one main building of the NPP. Further, a tower, being a part of the reactor building with V-213 reactor plant, houses the vacuum-bubbler passive system to reduce pressure in the containment.

Quite comprehensive sections are devoted to the primary circuit systems and equipment. The reactor coolant system, reactor, main circulation pumps, pressurizer, steam generators, and chemical and volume control systems are described. While the VVER-440 reactors dispose of six primary circuit loops, the VVER-1000 has four loops.

Special attention is paid to the core and fuel design. Special features of the VVER-440 core design are the fuel assemblies with housings and control assemblies, which consist of two parts: an absorber part and a fuel follower. When the absorber part is withdrawn from the reactor core, the fuel follower is inserted into the core. In VVER-440, profiled fuel assemblies with Gd_2O_3 burnable absorber are used to decrease the power peaking factor in the core. The control elements for VVER-1000 reactors are of the cluster type, similar to western PWR designs. Typically, 18 absorber rods are placed in a control assembly.

In subsequent sections, the secondary circuit components (Main Steam Line System, Main Feedwater System, Turbine, Generator, and Moisture Separator Reheater) are described. The power units with VVER-440 are equipped with two turbines and generators of 220 MW electrical power and the power units with VVER-1000 have one 1,000-MW-turbine driving one generator.

Further I&C as well as electrical systems are briefly described. The instrumentation and control systems of some of the VVER-440 units have been recently updated. The refurbishments were mainly aimed at the introduction of advanced features for data processing, transmission, and archiving.

In ▶ Sects. 2.2 and ▶ 3.2, the safety philosophy and safety systems of VVER-440 and VVER-1000 are described. The applied concept of safety assurance for power units of Generations II and III is outlined. For the Generation III VVER designs, significant improvements were implemented in accordance with the up-to-date international requirements for NPP safety assurance.

The data on the VVER reactors under construction, operation, and decommissioning are presented in ▶ Sects. 2.3 and ▶ 3.3.

1 Introduction

VVER-type reactor development was started by OKB “GIDROPRESS” in 1955. The first reactor of 210 MW (el.) power was commissioned at Unit I of Novovoronezh NPP (NV NPP) in 1964. A number of basic engineering solutions developed for the first VVER were of original character and most of them became traditional features for subsequent VVER generations. Such solutions included the following:

- A hexagonal grid for the arrangement of fuel assemblies (FAs) in the reactor core and accordingly the shape of fuel assemblies is hexahedral; the fuel rods in fuel assembly are arranged in triangular grid,
- Zirconium–niobium alloy is used as the material for fuel rod claddings,
- Possibility to transport all large-sized equipment by railway to enable a complete manufacturing process under factory conditions,
- High-strength alloyed carbon steel, which is serviceable in high neutron radiation fluxes, is used as the reactor vessel material,
- The bottom part of reactor vessel, which has no nozzles or any other holes, contains the core,
- The reactor vessel is manufactured of solid-forged shells without longitudinal welds,
- CPS (control and protection system) drives, outlets of temperature and power control systems are arranged on the removable upper head unit of the reactor,
- An original design of horizontal type steam generators with a tube sheet in the form of two cylindrical heads,
- Austenitic stainless steel is used as the material of steam generator HX tubes.

The first VVER core had an equivalent diameter of 2.9 m, a height of 2.5 m, and a thermal power output of 760 MW without any special measures being provided in the design for neutron flux equalization. The resultant operation of the core showed that the capabilities of this design specification were still not exhausted. Using this experience, a reactor with a power of 365 MW (el.), which had a similar core size was designed for Novovoronezh NPP, Unit 2. The design considered measures for the equalization of the neutron flux. This Unit was commissioned in 1969.

The first VVER reactors were designed for a service life of 20 years and were decommissioned in 1984 and 1990, respectively.

The development of VVER-440 reactor started simultaneously with the design of Unit 2 of Novovoronezh NPP. It was assumed as the “standard” version for the construction of a number of NPPs with VVER. The core sizes and design were mainly similar to the VVER-365

reactor. The increase in the electrical power output of the units was mainly due to enhancements of the NPP efficiency relating to modifications to parameters associated with the primary coolant and steam, respectively. This was achieved by the application of other power equipment and some changes to the equipment used in reactor coolant system. The first VVER-440 (B-179) reactors were commissioned at Units 3 and 4 of Novovoronezh NPP in 1971 and 1972, respectively.

The second step in development of VVER-440 type reactors was the V-230 design, where the number of mechanical control rods was reduced from 73 to 37 due to introduction of boron as a moderator. From 1973 to 1982, in all 14 Units were constructed with the V-230 design.

Reactors V-179 and V-230 are referred to as the first generation of the standard VVER-440 reactors. The specifications of these plants provide a high quality of pipelines, equipment, and other reactor plant components that allowed the prevention of significant damage and thus the avoidance of the possibility of breaks in the large diameter primary pipelines. Accordingly, the safety systems of the reactors were designed for a limited size of leak in the primary circuit.

The third step in VVER-440 development was V-213 reactor design referred to as the second generation of the standard VVER-440 reactors; their design basis included a double-ended instantaneous guillotine break of the maximum diameter primary pipeline. The first two Units of this series were constructed at NPP “Loviisa” in Finland in 1977 and 1980, respectively. The containment of these Units presented a shell with ice condensers. The original vacuum-relief system where the building is directly connected to a sealed box of the reactor coolant system is used at other NPPs with V-213 reactor. At present, 16 of such Units are in operation.

The development of VVER-1000 reactors by OKB Gidropress was started in 1966. The first reactor with an electrical power of 1,000 MW (V-187 Project) was commissioned at Novovoronezh NPP Unit 5 in 1980. In the design, the traditional engineering solutions of VVER (see ► Chap. 1.4.A) were used with the appropriate modernization from the experience obtained in the design, manufacture, and operation of the VVER prototypes. The design concept was oriented to an increase in economic efficiency of the NPP construction and operation ensuring safety in accordance with the regulatory documents that were valid at the time. An instantaneous double-ended guillotine break of the main coolant pipeline was considered as the maximum design basis accident, similar to Project V-213. The reactor plant was placed into a containment of prestressed concrete.

Further design modifications resulted in the development of V-302 Reactor Plant, which was implemented at the South-Ukraine NPP, Unit 1, and the V-338 Reactor Plant was implemented at the South-Ukraine NPP, Unit 2, and Kalinin NPP, Units 1 and 2. The development of these projects was classified as “small series” designs and their realization took place between 1976 and 1987.

Since 1985, all Units operated with VVER-1000 have been constructed to a standard design. This included the standard V-320 reactor plant, which could be sited in seismic areas with earthquakes of up to magnitude 9 (SSE), and the standard modernized reactors constructed with the “small series” modifications. The design comprised D_{nom} 850 circulation loops without gate valves; “wet” reloading of internals, horizontal steam generators of Unit 5 of NV NPP; reactor coolant pumps GCN-195M (“large series”).

The main feature of the modernized standard VVER-1000 reactor is the application of jacket-free fuel assemblies with an increase in their number from 151 pieces to 163 pieces. There was also a decrease in the number of control rods from 109 pieces to 61 pieces (to 49 pcs. at South-Ukraine NPP, Unit 1) with CPS pitch electromagnetic drives applied to the control rods.

The “large series” designs have been realized since 1978. On the whole, 28 Units with VVER-1000 reactors have been constructed and they are currently in operation at NPPs. All these Units are referred to as VVER of Generation II.

The accidents at TMI-2 and Chernobyl-4 NPPs have shown that it is necessary to take into consideration the beyond design basis accidents (BDBAs) during their design and operation. This is despite the low probability of such accidents. Appropriate requirements were introduced into the new revisions of the regulatory documents on NPP safety assurance.

In 1988, a new V-1000 design was launched (V-392 Project), which focused on safety improvements in response to new requirements of regulatory documents in order to prevent occurrence of BDBAs and to mitigate their consequences in case they happened.

The idea that was implemented in V-392 Project and incorporated into NPP-92 design was given a EUR certificate. The design modification provided for an engineering embodiment of the safety systems andbdba management systems that conceptually differ through the different ratios of passive and active systems, which are applied for accident management.

The main RP equipment of the V-392 design, including the reactor, is now implemented in a set of RP V-428 at “Tianwan” NPP. Information on this NPP design is incorporated into the chapter on VVER-1000 reactors. The latest modifications to V-392 RP design can be found in the design of RP V-412, which are being implemented now at “Kudankulam” NPP. Units 1 and 2 of “Tianwan” NPP were constructed and commissioned in 2007.

Designs of Units with RP V-392, V-428, and V-412 are referred to as Generation III reactors. Data on the VVER reactors under construction, operation, and decommissioning are presented in [▶ Sects. 2.3](#) and [▶ 3.3](#).

In preparing the given information, the following sources were used:

Sidorenko V.A. (ed). History of nuclear power engineering in the USSR and Russia. Moscow: IzdAT Publishing House, 2001.

Denisov V.P., Dragunov Yu.G. VVER reactors for nuclear power plants. Moscow: IzdAT Publishing House, 2002.

Bessalov G.G., Denisov V.P., Melnikov N.F., Dragunov Yu.G. VVER reactors for medium power NPPs. Moscow: IKC “Akademkniga,” 2004.

Logvinov S.A., Bezrukov Yu.A., Dragunov Yu.G. Experimental verification of thermo-hydraulic reliability of VVER reactors. Moscow: IKC “Akademkniga,” 2004.

Dranchenko B.N., Dragunov Yu.G., Portnov B.B., Seleznev A.V. Experimental studies of stressed state and strength of VVER equipment. Moscow: IKC “Akademkniga,” 2004.

Podshibyakin A.K., Nikitenko M.P., Berkovich V.M. Designing ofbdba management systems at NPPs with VVER reactor. Article in Collection of papers of the 3rd Scientific and Technical Conference Safety Assurance of NPPs with VVER, Podolsk, May 26–30, 2003.

2 VVER-440 Reactors

2.1 Design Description

2.1.1 Buildings and Structures

Reactor Building

Two power units of the type VVER-440 are incorporated into the main building of the NPP. The layout of the reactor compartment contains power units, which are reflected through the general transport corridor (➤ [Figs. 1](#) and ➤ [2](#); ➤ [Table 1](#)).

The main NPP building comprises of the reactor compartment, which includes a system of sealed rooms containing both power units, the turbine hall, a longitudinal stack of electric devices with forced ventilation equipment, two transverse stacks of electrotechnical devices, a stack of special ventilation, and two underground emergency boron inventory tanks. The main building is connected with an auxiliary building by a covered trestle. The trestle is adjoined to the reinforced-concrete ventilation duct of 120 m height. The total length of the reactor compartment comprising two Units with common facilities is 126 m (➤ [Fig. 3](#)).

All rooms of the main building are separated into two categories: restricted and free access areas according to radiation exposure standards. The rooms of reactor compartment, ventilation stack, and boron emergency inventory tank are defined as restricted areas. The turbine hall, the longitudinal and transverse stacks of electrotechnical devices are the free access areas. The reactor compartment includes the systems of sealed rooms in which both units are contained and between which common-unit rooms are located.

The attended reactor hall is common for both power units. The fresh fuel unit, the spent fuel pool, reactor units unloading, and inspection locations with other equipment for each unit are located in the reactor hall. The spent fuel and handling pool is not included in the system of sealed rooms. However, the outer walls of the pool and bottom floor including the facing on the side of SG box are included in the set of enclosure structures of the sealed rooms. The reactor hall is connected to the transport corridor via the system of removable floors.

The system of sealed rooms of a single unit includes the steam generators box, the reactor concrete cavity, the reactor coolant pump (RCP) and main gate valve(MGV) drives room, the inventory tank of emergency boron solution, and other rooms.

The base with rails for the fuel-handling machine is arranged above the upper part of the reactor concrete cavity and spent fuel pool. The fuel-handling machine is used for both reactor units. Equipment is transferred with the use of traveling cranes that is also common to both reactor units.

A VVER-440 reactor and the associated primary equipment are arranged in each set of sealed rooms in the reactor compartment. The sealed rooms are formed by airtight reinforced-concrete walls with a thickness of 1,500 mm, which are sealed by the covering of metal sheets. A protective bonnet hermetically seals reactor concrete cavity from the reactor hall. The upper part of the reactor unit protrudes into the reactor hall.

The equipment is mounted in the reactor concrete cavity that is intended for biological shielding against core radiation, reactor safe fastening, and thermal insulation. The concrete cavity is separated into top and bottom parts by an annular console. The upper part is connected with spent fuel pool by the transport corridor and is flooded with water during refueling. The upper part of the concrete cavity is isolated from the lower part by concrete truss with

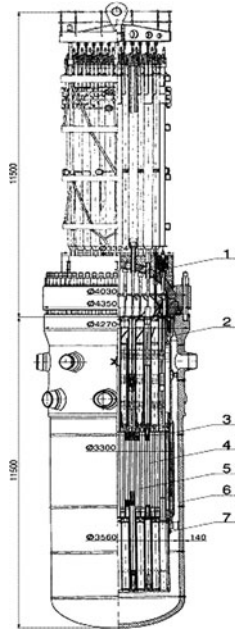


Figure 1

Reactor V-230. 1 – Top head, 2 – Protective tube unit, 3 – Core barrel, 4 – ERC assembly, 5 – Working assembly, 6 – Vessel, 7 – Core barrel bottom

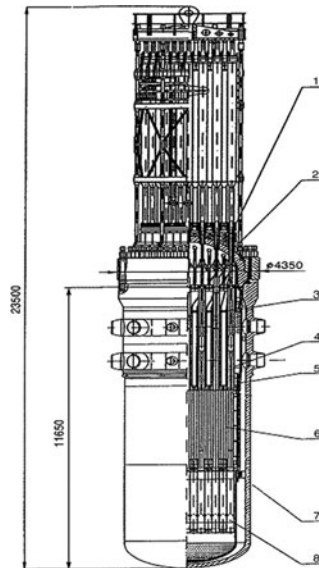


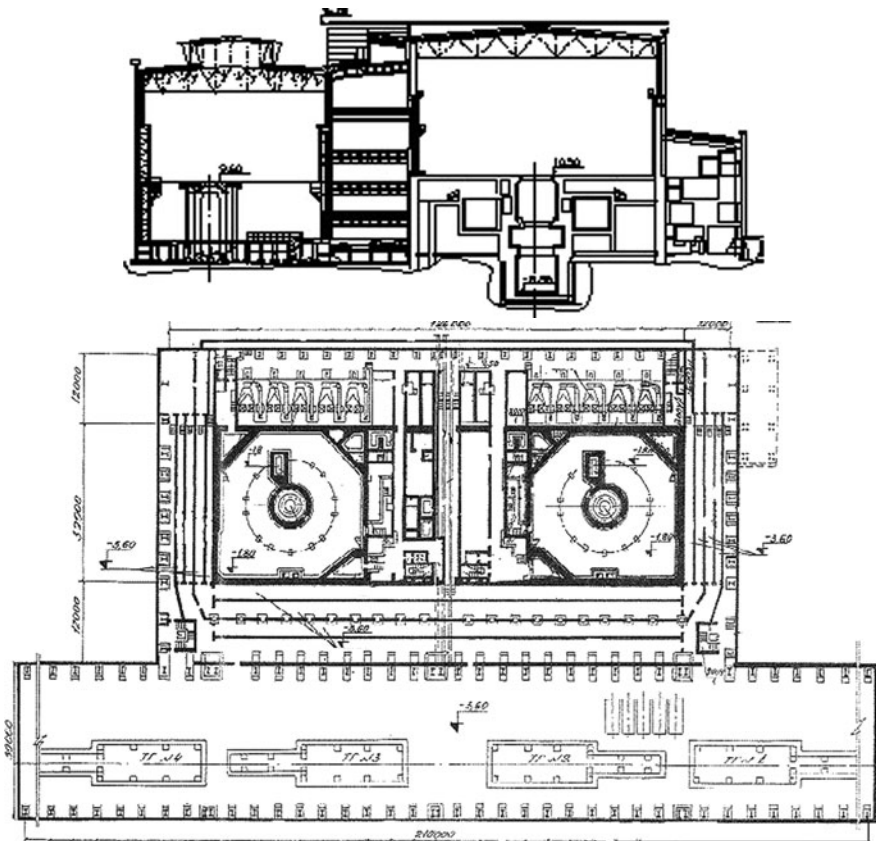
Figure 2

Reactor V-213. 1 – ERC drive, 2 – Top head unit, 3 – Protective tube unit, 4 – Intermediate rod, 5 – Core barrel, 6 – Reactor core, 7 – Reactor vessel, 8 – Core barrel bottom

■ Table 1
Main design parameters of the VVER-440

Thermal power, nominal, MW	1,375
Primary pressure, MPa	12.26
Steam generator vessel pressure, MPa	4.6
Reactor coolant flow, m ³ /h	41,000
Reactor outlet temperature, °C	300
Number of fuel assemblies, pcs.	312
Number of CPS assemblies, pcs.	37
Uranium loading, t	41.5
Fuel enrichment in isotope U-235, %	3.6 ^a

^aFuel average enrichment is increased to 4.87% in the course of FA design improvement.



■ Figure 3
Main building of V-230 reactor plant

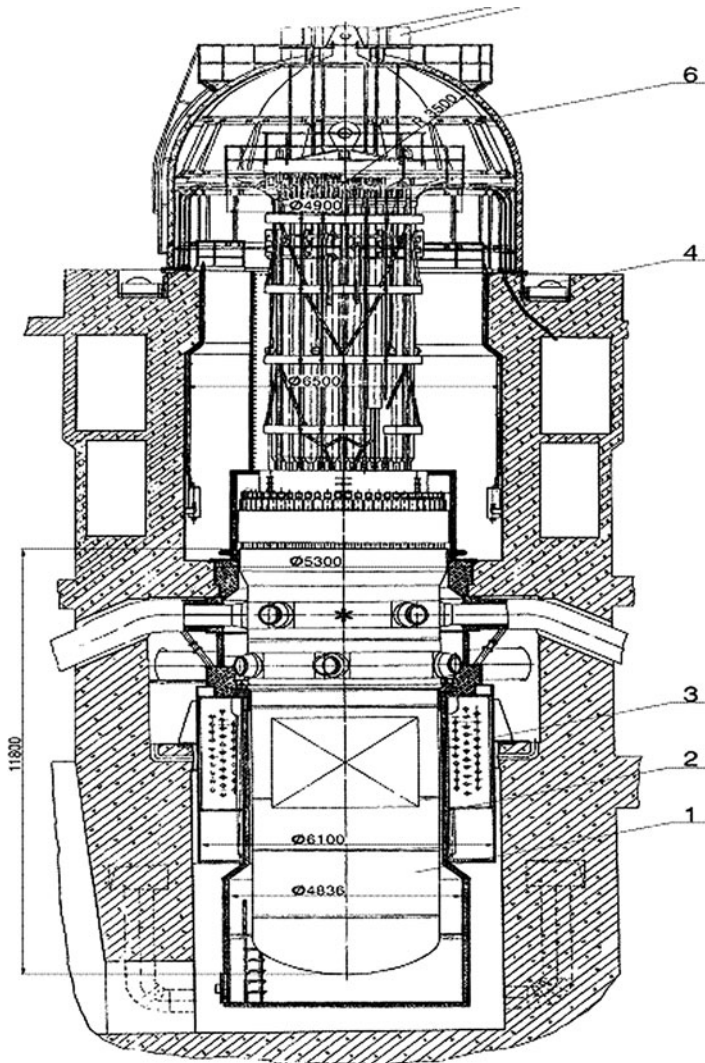
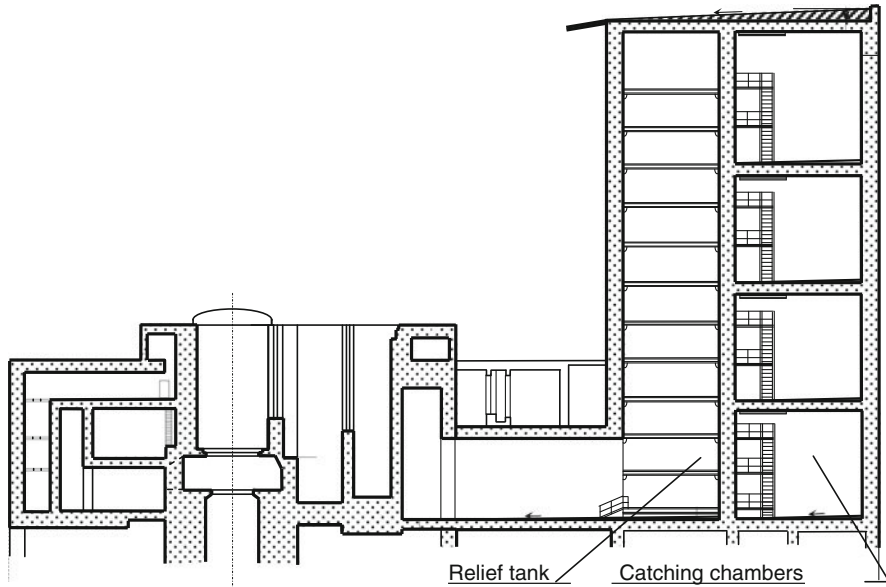


Figure 4
 Reactor plant V-230. 1 – Reactor, 2 – Thermal insulation, 3 – Annular tank, 4 – Bonnet

metal bellows. The refueling transport corridor is sealed with a special partition during reactor operation.

In a V-230 reactor plant (Fig. 4), an annular tank filled with water is used as a reactor vessel support and for the radiation protection of external structures. The tank water volume is 90 m^3 ; the annular thickness is about 1 m. Cooling of the lower part of the concrete cavity and the annular tank is provided with an airflow rate of $50,000 \text{ m}^3/\text{h}$.

As the containment of RP V-230 in the building of the two units arrangement was not designed for the pressure experienced under maximum design basis accident ($D_{\text{nom}} 500$ break), a system of depressurization was introduced into the containment for V-213 reactor plants. This



■ **Figure 5**
Containment of V-213 reactor plant

comprises of an active sprinkler system and passive vacuum–relief system. The vacuum–relief system is located in a special tower for pressure relief (► [Fig. 5](#)).

The V-213 reactor vessel support is a supporting truss, which was designed for the loading conditions it would have received under a break of D_{nom} 500 pipeline. External structural protection against core radiation is provided by the dry shielding made in the form of circular metalwork filled with serpentine concrete.

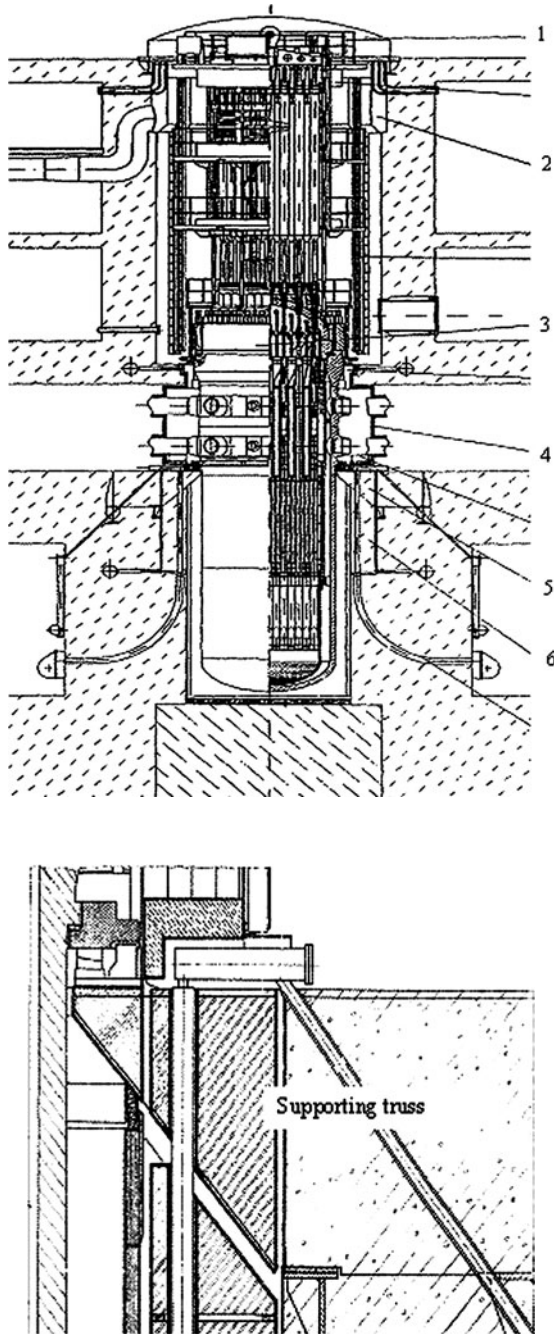
Unlike the V-230 reactor plant, ducts are provided for emergency steam discharge from the upper part of the reactor concrete cavity into SG box. Gaps can be enlarged in the thermal insulation for performing inspections of the reactor vessel. These gaps are located at the nozzle, the vessel bottom, and the lower part of the vessel (► [Fig. 6](#)).

Pressure Relief Tower

The vacuum–relief system comprises of a relief tank and catching chambers arranged in an independent construction (i.e., the pressure relief tower). The tower dimensions are 39×21.5 m² with a height of 41.9 m. The tower is connected with the sealed rooms of reactor compartment with a channel of cross section 11.5×6.2 m and length of 15 m. The tower with sealed rooms presents a compact closed structure.

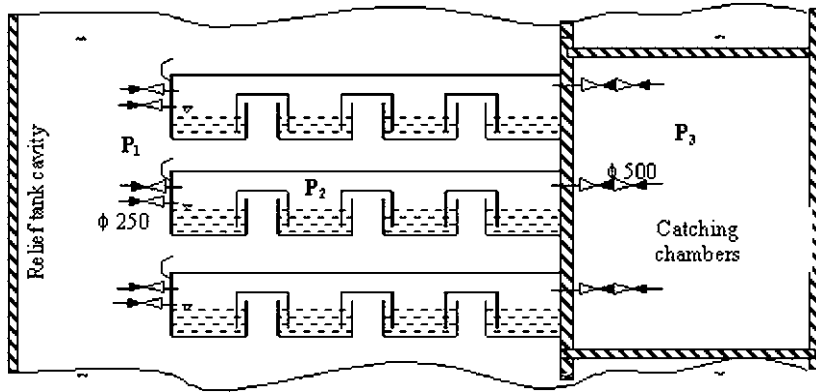
The pressure relief tower is a reinforced-concrete structure with a wall and ceiling thickness of 1,500 mm. The tower is separated by a wall axially into the relief tank room, which is 39×8.55 m² and rooms of four catching chambers with dimensions of 39×11.45 m².

The relief tank room has a total volume of 13,970 m³ and the total volume of the catching chambers is 16,465 m³. The inner walls of the relief tank are covered with metal sheets fixed



■ Figure 6

Reactor plant V-213. 1 – Protective bonnet, 2 – Steam emergency discharge ducts, 3 – Reactor, 4 – Nozzle area thermal insulation, 5 – Supporting truss, 6 – Dry shielding



■ Figure 7

Vacuum-relief operating pattern

on structural reinforcement. All inner walls, ceilings, and floors of catching chambers are also covered with metal sheets providing maximum impermeability of the structure.

The vacuum-relief system (☉ Fig. 7) is a passive system of pressure relief in the containment area, which works in coordination with the sprinkler system when accidents with large leaks of primary and secondary coolant into the containment ensue. Under accident situations, which originate in the SG box, the pressure increase in the vacuum-relief system provides for the following:

- The containment pressure relief by steam condensation in bubbling chutes,
- Localization of non-condensable gases in catching chambers,
- Capture of radioactive fission materials in bubbling chutes.

The system dimensions were selected for the suppression of the pressure increase that could occur under maximum design basis event. This was determined to be a double-ended break with primary coolant leak through two cross sections of D_{nom} 500 mm into the sealed rooms. Such a passive operation system should provide the capability to withstand dynamic impacts of jets of steam-water mixtures. It must absorb a considerable portion of the thermal energy that is released by the break. The associated pressure increase must also be automatically decreased. The intention of the system is to prevent the loss of leak-tightness of the sealed room and, consequently, reduce the possibility of a release of radioactive materials outside the containment with any deterioration of radiation situation.

The vacuum-relief system must be in a state of permanent readiness for operation (i.e., bubbling chutes should be filled with boric acid solution) during NPP normal operation.

The load-bearing structure for placing the inventory of water required for steam condensation and for supporting 12 floors of bubbling chutes is installed in the relief tank building. Each relief tank floor has one independent outlet of air and non-condensable gases into the capture chamber via double check valve (D_{nom} 500) that is equipped with a guiding inlet nozzle on the side of relief tank. There is one common capture chamber for every three adjacent floors of the relief tank.

The space above the chutes is also connected with the relief tank cavity by two relief valves ($D_{\text{nom}} 250$) that remain in a closed position when the pressure in the relief tank cavity exceeds 165 kPa. When the pressure decreases below this value, the valves are unlocked and pressure above the chutes level is equalized with the pressure in the relief tank cavity.

Auxiliary Building

The auxiliary building is intended for arrangement of the equipment for the preparation, cleaning, and treatment of the water used in the reactor coolant and interrelated systems and for radioactive waste storage. The building is divided into two parts: specific water treatment and radioactive waste storage. The building size is 102×36 m. The building is a rigid box-shaped structure of solid reinforced concrete from the base plate to the ceiling top.

The tanks for the storage of radioactive liquids are made in the form of metal tanks installed in the rooms with enclosure structures of solid reinforced concrete with metal facings. This approach uses the principle “tank in tank” with the purpose of monitoring occasional leaks of the main tank and preventing ingress of radioactive liquids into concrete. The thickness of walls and ceilings is determined to satisfy the requirements of biological shielding.

The auxiliary building is connected to the main building by a two-tier trestle. An air duct connects the upper tier of the auxiliary building to the ventilation channel at an elevation of +10.500 m. Trestle lower tier is separated into “clean” and “contaminated” areas. The “clean” area is intended to provide for access of operators into the auxiliary building. The pipeline is a connection between main and special buildings, which is provided via “contaminated” area. The thickness of structures in this trestle part is governed by the requirements of biological shielding.

Turbine Building

The turbine hall is referred to as a nonrestricted access area of the main building. The length of turbine hall for two reactor units is 246 m. The span of the turbine hall is 39 m. The turbine hall is equipped with three bridge electrical cranes of load carrying capacity 125/20 t each, with a span of 36.5 m.

The longitudinal stack of electrotechnical devices, above which the secondary pipelines (steam lines, feedwater lines) are arranged, is located between the reactor and the turbine hall.

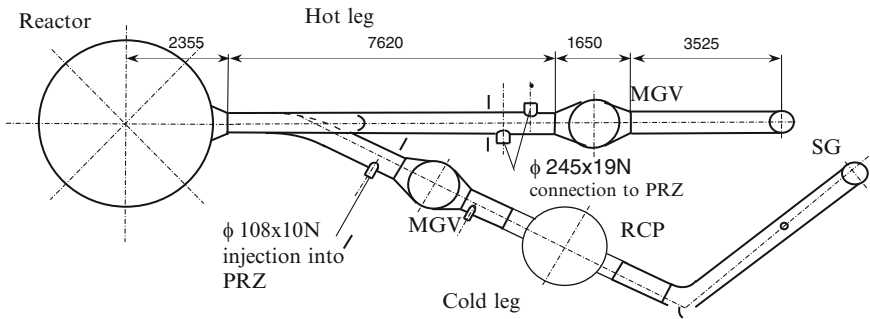
The turbine generators are oriented axially along the length of the turbine hall.

2.1.2 Systems of the Primary Circuit

Reactor Coolant System

Under normal operating conditions both V-230 and V-213 reactor types are cooled by six circulation loops of the main coolant pipeline (MCP). The pipelines are located in an airtight compartment around reactor concrete cavity. Each circulation loop is welded to the inlet and outlet nozzles of reactor vessel. The pipelines contain a reactor coolant pump (RCP) and a steam generator connected by $D_{\text{nom}} 500$ pipelines. The pipelines are made of stainless steel (08Kh18N19T).

➤ *Figure 8* above shows the circulation loop with the pressurizer to be attached; the other loops are of similar size and layout.



■ **Figure 8**
Circulation loop 1 of reactor V-213

The cold and hot legs of the circulation loops are equipped with main gate valves (MGVs) (► Fig. 9) to isolate the loop from the circulation circuit or to limit the reverse flow of coolant in the case of a tripped RCP.

The time required for the opening and closure of an MGv is as follows:

- Manual – 280 s,
- Automatic – 80 s.

Coolant inventory in the hot leg is 2.75 m^3 . Coolant inventory in the cold leg (without RCP) is 3.25 m^3 .

In VVER-440 reactors, all the line-to-MCP joints are equipped with primary leak restriction devices in case of pipeline breaks.

Reactor Vessel and Internals

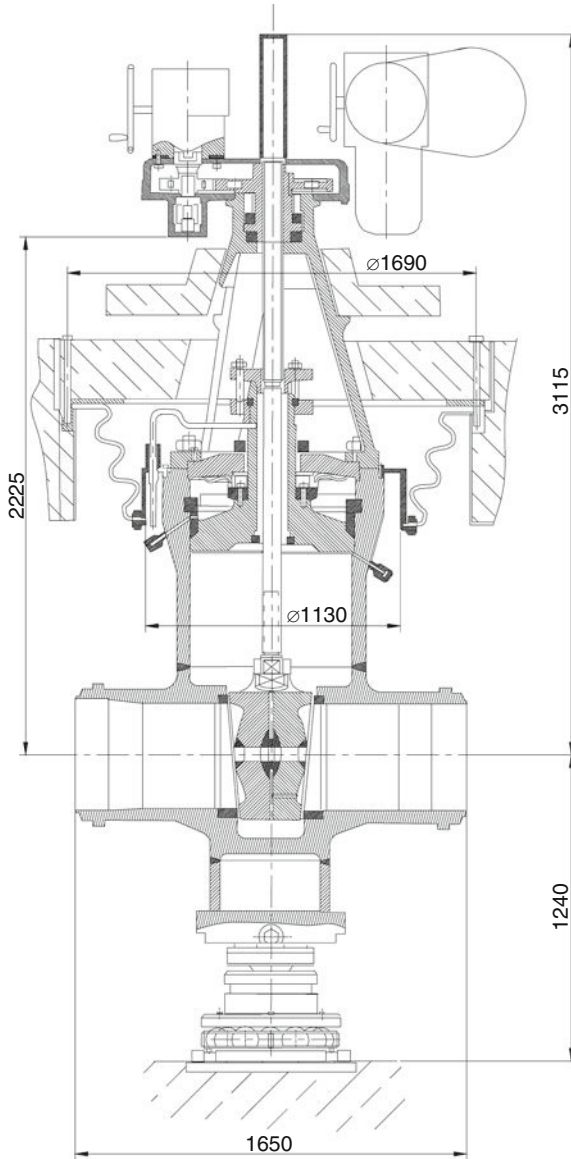
The VVER-440 reactor vessel design is based on meeting the following requirements:

- Proven materials and structures,
- Complete manufacture of the vessel with workshop testing included,
- Possibility of vessel transport by railway,
- Possibility of vessel in-service inspection.

The vessel is made of heat-resistant chromium–molybdenum steel of Grade 15Kh2MFA. The steel and the welding materials were chosen from the results of numerous analyses of mechanical properties, the absence of susceptibility to brittle fracture, the absence of thermal embrittlement, durability, and irradiation resistance. The steel was proven in manufacturing and it has been used in the fabrication of all VVER-440 reactor vessels.

The upper cylindrical part of V-230 reactor vessel has 6 inlet and 6 outlet D_{nom} 500 nozzles for coolant to flow and one D_{nom} 100 nozzle for pressure-measurement pulse tubes and level gauge. The D_{nom} 500 nozzles are located in two rows away from the area of maximum neutron irradiation.

Four D_{nom} 250 nozzles were additionally included in the design for the V-213 reactor vessel for the application of the emergency core cooling system (ECCS). Two nozzles of this diameter are placed in each row of D_{nom} 500 nozzles.



■ Figure 9
Main gate valve

There is an annular shoulder on the internal surface of the vessel, which is located between the rows of nozzles that separate the inlet and outlet coolant flows. The shoulder allows the alignment of the core barrel with respect to the vessel. Corrosion-resistant cladding of internal surface was only applied to the area of vessel-to-top head joint in the first V-230 reactor vessels (6 vessels). All other vessels were covered with corrosion-resistant cladding all over the internal surface.

The support shoulder on the external surface of the vessel is below the lower row of the nozzles and it serves as the flange upon which the vessel is installed on the support ring that is fastened to the support structure in the concrete cavity.

The reactor vessel and top head are sealed through a pressure ring with 60 M140 studs. The vessel-to-top head joint is sealed with two nickel-wire gaskets, which are 5 mm in diameter. Spherical top head of reactor vessel is part of the upper unit. Thirty seven housings for ERC (emergency reactor control) drives are installed on the top head as well as the nozzles for temperature monitoring sensor and neutron flux measuring channel installation and associated seals. ERC drive cooling systems and systems for air removal at reactor filling up are also mounted on the top head.


Electrical-mechanical ERC drives of rack-and-pinion type are used in VVER-440 reactors. In the drive, the rotational motion of electric motor rotor is converted with a reducer into the translational motion of the rack. The ERC drives of V-230 reactor are equipped with the electric motor installed down and induction linear position indicator. The ERC drive for VVER-213 reactors is equipped with a low-speed electric motor placed in the upper position and linear position indicator installed on the electric motor flange. The design has simplified the kinematic diagram of the drive and the drive-to-ERC assembly engagement and disengagement procedures. Both drives provide the normal motion of the ERC assembly at a velocity of 20 mm/s and an emergency drop rate of the rack with FA of 200–300 mm/s. The time required to accelerate the rack to a velocity of 200 mm/s after the drive de-energization at a scram does not exceed 0.7 s.

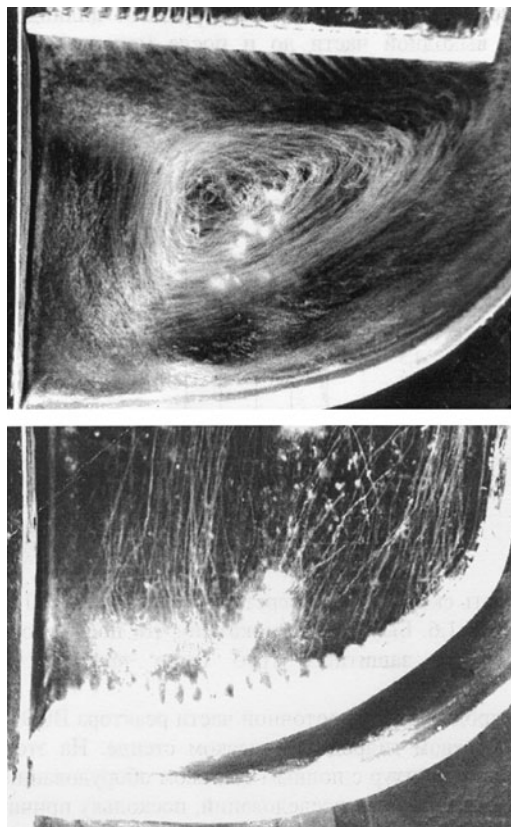
The reactor internals comprise the following:

- Reactor core barrel with the bottom that defines coolant flow arrangement inside reactor and supports,
- The basket that houses the core,
- A protective tube unit (PTU) that serves to fix the fuel assemblies in the core and protect the extension shafts, drives, and ERC fuel assemblies from the action of the coolant flow.

The design of internals and their mutual and in-pile fastening make it possible to extract all the units to examine the internal surface and vessel metal inspection. The material for all the internals is stainless steel Grade 0Kh18N10T.

The separation area for inlet and outlet coolant flow is sealed due to the difference between the temperature expansion of stainless steel and carbon steel vessel. The upper part of the core barrel between the flange and flow separator has many perforations for the coolant velocity field leveling upstream of reactor vessel outlet nozzles. The lower part of the core barrel is aligned and fastened to reactor vessel with eight keys fixed to the vessel. Unlike the V-230 reactor, the V-213 core barrel is provided with channels to install reactor vessel metal surveillance specimens.

The core barrel bottom contains the top and bottom grids linked with a shell and 37 tubes to install the ERC assemblies. Hydraulic snubbers reduce the impact of the dropping fuel assemblies. Unlike the V-230 reactor, the core barrel of V-213 reactor has an elliptical perforated bottom that levels coolant flow profiles as it turns out of the downcomer.  *Figure 10* illustrates the observed structures of coolant flow in reactor lower plenum. The images were obtained with the hydrodynamic model without the elliptic bottom (top) and with the elliptic bottom (bottom). In the flat bottom design, major vortices arise at the inlet to the core bottom, which lead to unsteady coolant flow. The perforated elliptic bottom eliminates these vortices and equalizes the coolant velocities over the core radius. The elliptical bottom also reduces the effect of the vibration load on the structure.



■ **Figure 10**
Picture of coolant flow in the reactor lower plenum

A removable basket is installed on the core barrel bottom to house the core fuel assemblies. The lower plate of the basket has perforations to install the working assemblies and hexahedral openings for ERC assemblies to pass. A faceted belt with a core baffle over the entire height of working assemblies is welded over the core perimeter on the internal surface of the basket.

A protective tube unit is installed on the faceted belt of the basket and it is pressed with reactor upper unit through the spring units placed in the upper unit top part. Housings for coolant temperature monitoring thermocouples at the working assembly outlets and the axial channels, which are used in the measurement of core power, are routed among the protective tubes. There are 12 channels of this type in V-230 reactor and their number is increased to 36 in V-213 reactor. All the housings and channels are assembled and fastened in bundles that have sealed outlets. They are located in the corresponding nozzles of reactor top head unit.

Reactor Core

The VVER-440 reactor core (🔍 [Fig. 11](#)) contains 349 fuel assemblies, of which 312 are working assemblies (WAs) (➤ [Fig. 12](#)), and 🔍 37 are ERC assemblies (➤ [Fig. 13](#)).

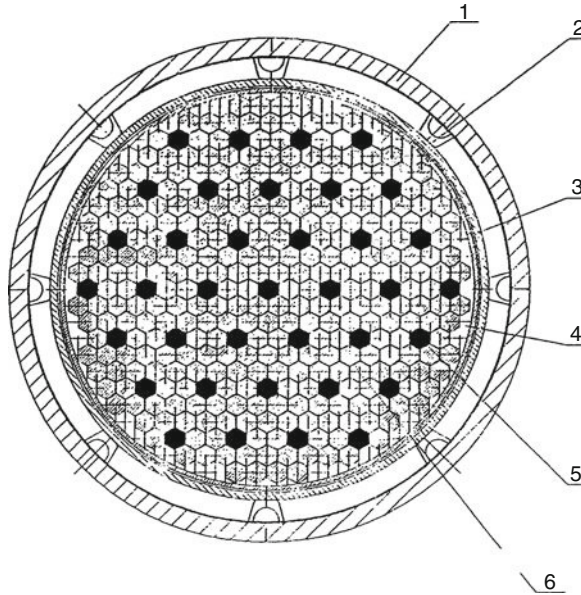


Figure 11
 Reactor core arrangement. 1 – Vessel, 2 – Fixing of Core Barrel, 3 – Core barrel, 4 – Basket, 5 – ERC assembly, 6 – Working assembly

An ERC assembly is the actuating component of reactor control and protection system. The ERC assembly performs the following main functions:

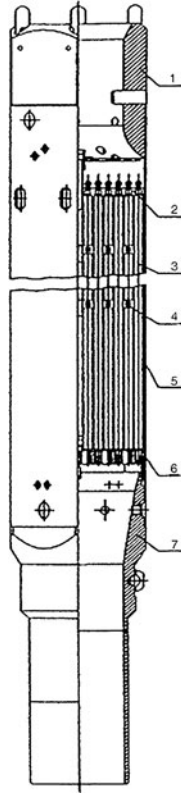
- Ensures a quick termination of chain fission reaction by quick insertion of a neutron absorber into the core with a simultaneous withdrawal of assembly fuel-containing portion out of the core,
- Participates in automatic control of maintaining reactor power at the assigned level and its changeover from level to level,
- Compensates for quick reactivity changes (temperature, power effects, poisoning, etc.).

The WA and ERC are positioned in a hexagonal grid with a spacing of 147 mm.

All the fuel assemblies are hexahedral and the fuel rods are placed in the assembly in a triangular grid pattern. The fuel rod bundle of the assembly is enclosed in a hexahedral jacket with the width across the flats equal to 144 mm.

As the core is assembled, the working assemblies are installed into the holes in reactor basket plates. The ERC fuel assemblies pass through the hexahedral holes of the basket and they are installed in protective tubes at the core barrel bottom.

The ERC assemblies are divided into six groups. In the working position, the first five groups of six assemblies are withdrawn to the outermost upper level and are used to perform the scram function. The sixth group containing seven assemblies is left in an intermediate position and is used to control the reactor power. The time an ERC assembly takes to drop from the upper position is from 8 to 13 s.



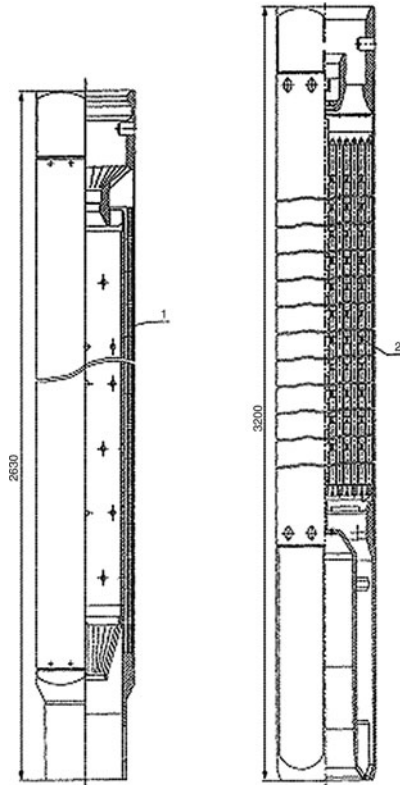
■ Figure 12

Working assembly. 1 – Top nozzle, 2 – Upper grid, 3 – Fuel rod, 4 – Spacer grid, 5 – Jacket, 6 – Lower grid, 7 – Bottom nozzle

The working assembly contains a top nozzle, a bottom nozzle, jacketed tube, and fuel rod bundle. The top nozzle has fingers for fuel handling via machine grips and spring-loaded dowels that keep the working assembly from lifting up and therefore compensate for the effects of thermal expansion and the process tolerances of reactor internals. The working assembly is installed into the basket bottom seat with the bottom nozzle, which is a spherical surface that is supported by a seat cone.

The fuel rods are located in the bundle in a triangular grid pattern with a pitch of 12.2 mm. Spacer grids of the cell type are mechanically fastened onto the central tube and the fuel rods are slotted into the gaps in the grid. The lower support grid is welded to the bottom nozzle. The upper spacer grid has a wide rim in order to center the bundle in the top part of the tube jacket. The protrusions are specially intended for this purpose in the hexahedral tube. It eliminates the effect of upper grid deformation in case of nonuniform fuel rod radiation growth in the bundle.

The fuel rod claddings and spacer grids are made of the E110 zirconium alloy (Zr + 1% Nb), while the jacket tubes of the WA and FA are made of the E125 zirconium alloy (Zr + 2.5% Nb).



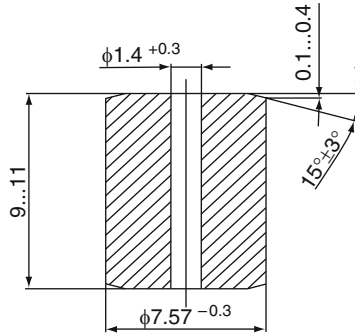
■ **Figure 13**
ERC assembly. 1 – Absorber follower, 2 – Fuel assembly

The ERC assembly consists of two parts: an absorber follower and a fuel assembly. The ERC assembly is moved with the ERC drive via the intermediate rod engaged with the gripping device located at the FA top nozzle. The intermediate rod passes through the alignment sleeves of the follower, which is installed on the FA top nozzle. The intermediate rod-to-FA top nozzle engagement is of a bayonet type, which interlocks to prevent rotation and disengagement.

The design and fastening of the fuel rod bundle in the FA found in the ERC assembly are the same as those of the working assembly. There is a thimble in the FA bottom nozzle that together with the dowel in the core barrel protective bottom provides the hydraulic damping of the assembly in case it drops in an intermediate rod break accident.

Hafnium plates are placed on the inside surface of the top part of the jacket tube to limit power ramps in the working assembly fuel rods that surround the ERC working group when it is located in an intermediate position along the core axis.

The absorber follower is a welded hexahedral stainless steel structure that houses hexahedral insertions of boronized steel. The insertion is a hexahedral tube 7.1 mm thick and 102 mm high with the width across the flats equal to 137 mm. The boronized steel insertions are based on chromium–nickel stainless steel with 1.6–2.0% of natural boron added to the mass.



■ **Figure 14**
Fuel pellet

Each fuel rod is a cylindrical shell plugged on the edges with Thomson welding. The outside diameter of cladding is 9.1 mm, the inside diameter is 7.73 mm. The cladding houses a fuel column assembled of uranium dioxide pellets. The fuel column is fixed with a spring-type lock, which protects the fuel pellets (➤ [Fig. 14](#)) from displacement during transportation and installation.

The rods are filled with helium at a pressure of 0.5–0.7 MPa. The fuel pellet density is 10.4–10.7 g/cm³. The total length of each fuel rod is 2,536 mm.

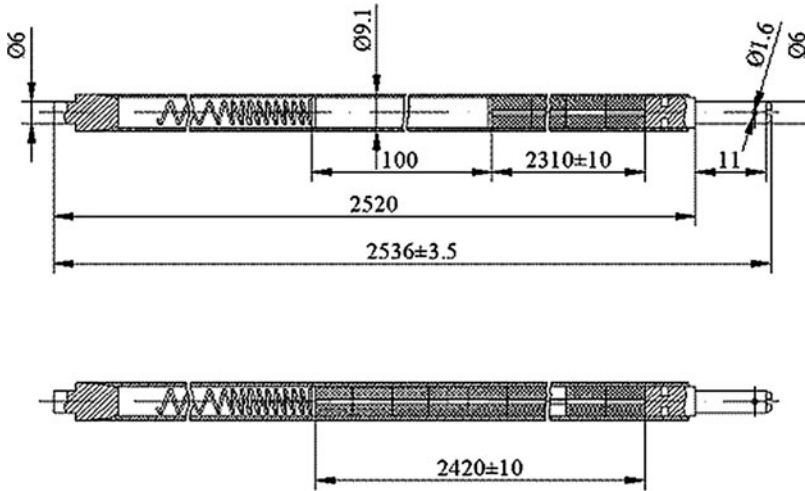
The operating experience of VVER-440 reactor cores has shown that the neutron–physical and thermal–hydraulic characteristics are such that the actual (calculated and measured) power peaking factors of assemblies and fuel rods are, as a rule, less than the design values. The design of Generation II fuel assemblies was developed to improve the efficiency of operation that possesses the following features:

- The number of fuel pellets inside the fuel rod was increased,
- The water–uranium ratio was optimized due to an increase in the pitch of fuel rod location in the bundle from 12.2 to 12.3 mm,
- Harmful neutron absorbance was reduced by reductions of the hafnium content of the zirconium cladding from 0.05 to 0.01%,
- FA jacket thickness in the ERC assembly (➤ [Fig. 15](#)) was reduced to 1.5 mm.

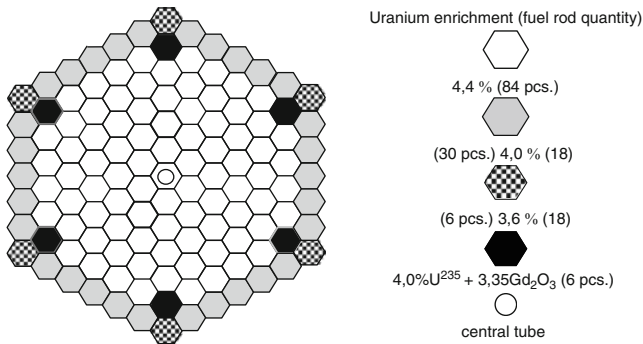
A decrease in the power peaking factor in the core is reached by the use of profiled fuel assemblies. A Gd₂O₃ absorber is integrated with a content of 3.35% into a number of fuel assemblies to aid fuel profiling.

The development of the Generation II fuel assemblies enables the switch over to a new fuel cycle with fuel assemblies capable of operating for 5 years. The fuel rod bundles in the assemblies used over the fuel cycle are composed of 120 rods of which 6 fuel rods contain Gadolinium that give the profiled enrichment. The average enrichment of a WA fuel bundle is 4.25% (➤ [Fig. 16](#)). The average enrichment of an ERC assembly fuel bundle is 3.84% (➤ [Fig. 17](#)).

A parallel task was to increase the vibration resistance of the fuel assembly. The introduction of the method of fuel rod installation in the support grid with an elastic tip and the change in the unit of jacket-to-bottom nozzle fastening in the WA provides a possibility to disassemble the fuel assembly of the given design.



■ Figure 15
Dimensions of ERC assembly fuel rod (up) and working assembly (down)



■ Figure 16
Profiling diagram for fuel rod bundle of 4.25% average enrichment

The results of the trial operation of the new fuel show that the operational limits of the standard fuel are not exceeded at its introduction, which corroborates the compatibility of the new and standard fuel.

Another step in the development of the Generation II fuel is a transfer to a higher fuel enrichment in the WA and FA. It is here that the application of the Generation III fuel rods differs in principle from Generation II fuel rods, which is most promising. The Generation III fuel rods allow an increased fuel loading by removing the centerline hole in the fuel pellet and increasing the pellet diameter.

An alternative option for the development of fuel for VVER-440 NPP is the creation and introduction of Generation III fuel assemblies (➤ Fig. 18) that use an angled skeleton instead of hexahedral jacket.

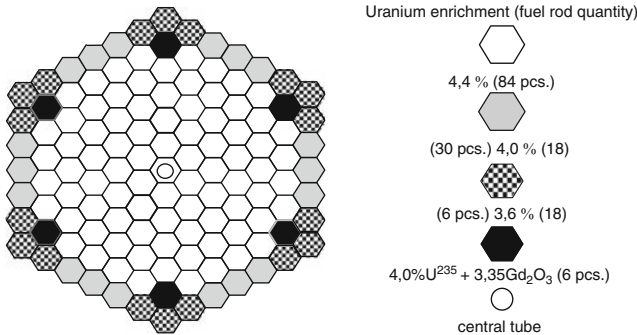


Figure 17
Profiling diagram for fuel rod bundle of 3.84% average enrichment

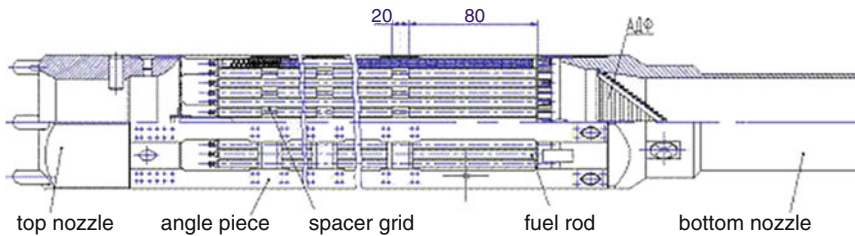


Figure 18
Generation III working assembly

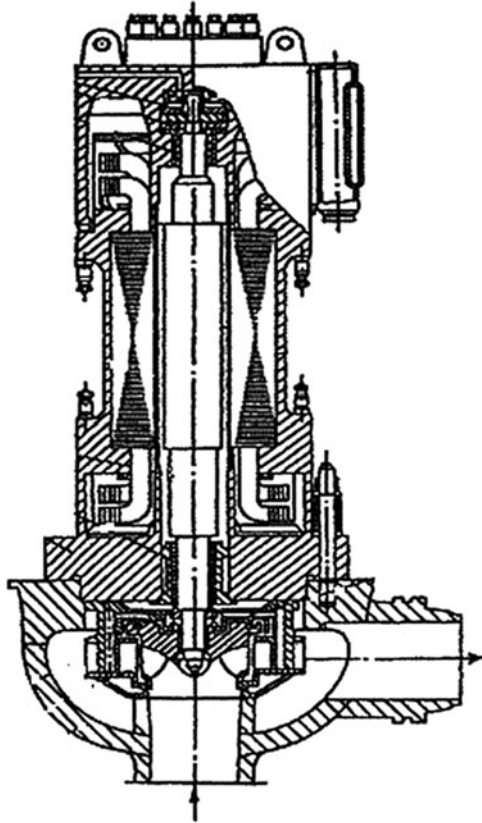
Reactor Coolant Pump

Reactor plants of the V-230 type are featured with centrifugal one-stage vertical pumps of the packless type with an integrated electric drive of type GCN-310. The pumps (RCP) (Fig. 19) are used in the primary coolant circuit. Such leakproof pumps have been proved to be highly reliable with no leaks of radioactive primary water and they are simple in operation. Disadvantages of these pumps include low efficiency due to the high electromagnetic losses on sealing metal partition of electric motor and a small inertia coastdown in the case of the loss of power. Note that with reactor plants of the type V-230, the coastdown of four RCPs in case of loss of power together with coastdown of the turbine generators, power supply to these RCPs is provided by the terminals of the station service generator located on one shaft with the main generator (Tables 2 and 3).

Reactor plant V-213 is featured with pumps of GCN-317 (Fig. 20) having mechanical sealing of the shaft, equipped with flywheels. The pump of GCN-317 is equipped with antireversing mechanism.

Pressurizer

VVER-440 reactor plants are provided with steam pressurizers. The pressurizer is connected to a non-isolated part of the hot leg of one of the primary recirculation loops. Controlled injections of coolant are provided into the pressurizer steam space from a non-isolated part of cold leg of



■ Figure 19
GCN-310

■ Table 2
Basic performances of GCN-310

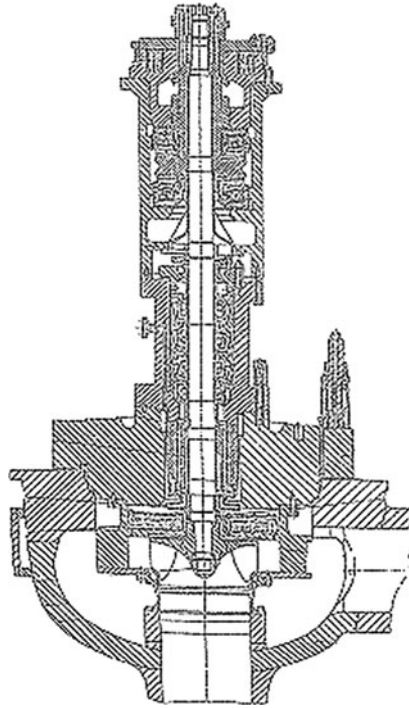
Capacity, m ³ /h	6,500
Pressure head, kg/cm ²	5.3
Rotational speed, rpm	1,500
Power, kW	2,000
Efficiency, %	56

the same loop. The electric heaters for generating steam pressure are arranged in the lower part of the pressurizer.

The internal volume of the pressurizer on a V-230 reactor plant is 38 m³ of which 18 m³ is occupied by steam under nominal conditions. Electric heaters are organized into two start-up groups with a power of 540 kW each, two operating groups with a power of 90 kW each, and two control groups with a power of 45 kW each.

■ **Table 3**
Basic performances of GCN-317

Capacity, m ³ /h	7,100
Pressure head, kg/cm ²	5.9
Rotational speed, rev./min	1,500
Power, kW	1,400
Coastdown period, min	2–3



■ **Figure 20**
GCN-317

The internal volume of the pressurizer is larger on a V-213 reactor plant with a volume of 44 m³, while the steam volume is smaller with 16 m³ under nominal conditions. Electric heaters are broken down into five groups: two groups with a power of 180 kW each, two groups with power of a 360 kW, and one group with a power of 540 kW.

The pressurizer is equipped with two pilot-operated relief valves with the main purpose of providing overpressure protection in the primary circuit. Some pressurizers of the V-213 reactor plants have one more relief valve in addition to the safety valves that also serve as an overpressure protection for the reactor vessel when it is in a cold state.

Steam dumping from safety devices is provided into a dedicated relief tank whose total volume amounts to 15 m³, of which a volume of 11 m³ is water. The water inventory is cooled by an intermediate circuit that provides an operational temperature within the range of 25–50 °C.

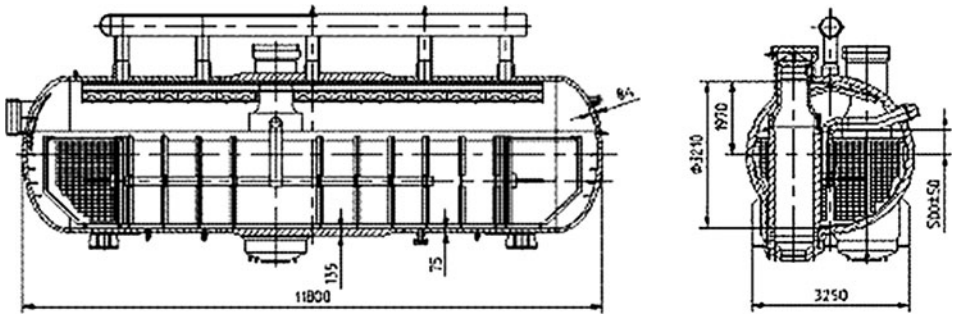


Figure 21
Steam generator PGV-4

Table 4
Steam generator performances

Steam capacity, t/h	452
Feedwater temperature, nominal, °C	223
Feedwater temperature with high pressure heater (HPH) switched off, °C	164
Steam pressure (abs.), MPa	4.71
Steam temperature, °C	260
Feedwater flowrate, t/h	453
Steam humidity at SG outlet (maximum), %	0.25

Steam Generator

The basic structural feature of VVER steam generators (Fig. 21) is the horizontal arrangement of the cylindrical vessel, the submerged heating tube bundle, the cylindrical vertical collectors of the tubes, natural circulation of the boiler water, and an integrated steam separation system.

Tube bundle consists of 5,146 stainless tubes with the outer diameter of 16 mm and wall thickness of 1.4 mm. The entire heat exchange surface is equal to 2,570 m².

The important advantage of horizontal steam generators is that there is a large water inventory in the secondary circuit. This large water volume provides favorable inertial characteristics for the whole of the reactor plant under transient and accident processes, thereby essentially enhancing its safety (Table 4).

Chemical and Volume Control System

The chemical and volume control system is intended for

- Compensation of the identified and non-identified leaks from the primary circuit;
- Compensation of reactivity changes by supply of boric concentrate or pure condensate into the primary circuit;
- Arranging the primary coolant cleaning;
- Filling, draining, and hydrotests of the primary circuit;

- Pressurizer level maintenance under reactor power variation;
- Pressurizer cooling down.

Operational reliability of the system is ensured by twofold redundancy of the equipment for deaeration and cooling of makeup water, equipment for blowdown and pipeline routes.

The basic technical data of the chemical and volume control system for a V-213 reactor plant is

Makeup pump	
Maximum flowrate	60 m ³ /h
Suction pressure, nominal	0.67–0.70 MPa
Pressure head, max	14.7 MPa
Blowdown pump	
Flowrate	50 m ³ /h
Maximum permissible suction pressure	1 MPa
Pressure head	0.6 MPa

2.1.3 Systems of the Secondary Circuit

Main Steam Line System

The main steam line system comprises of six steam lines with dimensions of $\phi 456 \times 16$ mm. The steam is transported through the steam lines from six steam generators of the primary system to the main steam header (MSH), which has dimensions of $\phi 521 \times 16$ mm and operates with a maximum pressure of 4.4 MPa. The steam lines from the odd numbered steam generators are connected to one half of MSH, while steam lines from the even numbered steam generators are attached to the other half of MSH. The steam lines from 1, 3 and 2, 4 steam generators are extended as supply pipelines of dimensions $\phi 521 \times 16$ mm to the stop and control gate valve units of two turbine generators.

Each steam line of the relevant steam generator is equipped with pilot-operated relief valves that act against excessive pressure. Thus, in the case of a pressure increase above the permissible limit, steam is dumped to the atmosphere via a common discharge pipeline, which has outlets on the building roof.

The SG steam lines are furnished with quick-acting valves that are controlled by high-pressure air. The main steam gate valves with bypasses are initiated when it is necessary to disconnect the relevant steam generator from MSH.

The main steam header is separated with three quick-acting isolation valves, which are controlled by high-pressure air. Each half of MSH is arranged with one steam dump valve to atmosphere (BRU-A) via a discharge pipeline of dimensions $\phi 530 \times 8$ mm, where the outlets are located on the building roof. Note that the BRU-A of the last units built of the V-213 type are placed on each SG steam line near to the safety valves.

The main steam headers of the neighboring units are isolated from each other by electric gate valves.

Main Feedwater System

The main feedwater system consists of five feedwater pumps (FWPs) with connecting pipelines. Four pumps meet the full power of the reactor unit; the fifth pump provides backup cover. The feedwater inventory is stored in two feedwater tanks per reactor unit. The feedwater is transferred from each tank via a $\phi 630 \times 8$ mm pipeline into the suction collector, which is separated into two halves by two electric valves. Collector has a $\phi 426 \times 8$ mm branch for each FWP.

The discharge pipelines are connected to the common discharge collector, which has dimensions of $\phi 457 \times 20$. All FWPs have a minimum bypass that provides safe operation of the FWP when there is a reduction in the amount of feedwater fed or when an FWP is operated with a closed valve. The feedwater is transferred from discharge collector for high-pressure regeneration of both TGs. After heating, it flows to the main feedwater collector, which has dimensions of $\phi 457 \times 20$ mm.

The feedwater is supplied from the main feedwater collector to the steam generators via D_{nom} 250 pipelines through six big control valves or via D_{nom} 100 pipelines through six small control valves. There are quick-acting valves and check valves between the valves and the SG. The control valves are used to maintain a constant level in the SG under different operating conditions.

Basic performances of feedwater pump	
Operational range of flowrate	150–900 t/h
Suction pressure	0.84 MPa
Pressure head	6.6 MPa
Pump rotational speed	2,975 rpm

Turbine

Each VVER-440 Unit has two turbine plants. Each turbine plant includes a turbine, a condenser, regeneration system, separator–superheaters, and other auxiliary equipment.

A K-220-44-3 type steam turbine is a single-shaft three-cylinder set involving a high-pressure cylinder (HPC) and two low-pressure two-flow cylinders (LPCs) with four steam outlets in two condensers. Between the HPC and the LPC, there are separator–superheaters, wherein a two-stage steam superheating occurs.

The turbine operates with dry saturated steam at a pressure of 4.3 MPa upstream of the stop valves and there are eight noncontrolled steam outlets intended for feedwater heating and for other NPP auxiliaries.

Basic performance of the steam turbine	
Nominal power, on generator terminals	220 MW
Nominal steam flowrate	1,322 t/h
Nominal steam pressure upstream of StV	4.3 MPa
Pressure at HPC outlet	0.4 MPa
Nominal steam pressure upstream of LPC valves	0.37 MPa
Nominal steam temperature upstream of LPC valves	216.5 °C
Nominal revolutions	3,000 rpm

Generator

The output of the electric generators is 220 MW as alternating current. The generators have an end face design where the bearings are located in the stator faces. It has a combined cooling system with hydrogen and water used as the coolants. The rotor of the generator is connected to the rotor of low-pressure cylinder of the steam turbine with a rigid coupling. The stator has internal and external frames, due to access required for mounting and repair.

The cooling water is applied to stator winding while hydrogen coolant is used in the other parts of the generator. The stator winding is directly cooled by condensate from the turbine circuit. Some conductors are made in the form of copper rectangular tubes where cooling water is transferred.

The parts other than the stator winding, which are cooled by pressurized hydrogen, include a rotor, stator metal, and frontal parts of the stator. The rotor winding is made from hollow conductors, where hydrogen is fed into conductors and released into the gas gap in the middle part of the device. The stator metal is cooled by an axial hydrogen flow. The condensate flows via hydrogen cooler.

Basic performances of generator	
Nominal active power	220,000 kW
Nominal $\cos \varphi$	0.85
Nominal voltage	$15,750 \pm 5\% V$
Nominal phase current of stator	9,500 A
Nominal frequency	50 Hz
Maximum hydrogen temperature	40 °C
Condensate flowrate for hydrogen coolant	250 m ³ /h
Condensate flowrate for stator winding cooling	120 m ³ /h

Moisture Separator–Reheater

The moisture separator–reheater (MSR) is intended to remove moisture and to reheat the incoming steam from the high-pressure cylinder of the turbine. Each MSR consists of two vertical vessels with 3.4 m diameter and 14 m height that are connected in parallel to heating and heated steam. The main components of the separator are corrugated stainless steel plates with a thickness of 1 mm. The plates are arranged in the upper part of vessel.

The heating is performed over two stages. The first stage is heated by steam from the seventh outlet and the second stage is heated from the eighth outlet. Both stages of the heater are made from steel tubes with longitudinal ribs welded-on. The heating is driven by the condensation of steam on the inside of the tubes.

The separated moisture is bled into low-pressure heater. The steam condensate from the hot side of the first stage is transferred into the feed tank and the steam condensate from the hot side of the second stage is passed to the feedwater high-pressure heater.

The MSR includes a separated moisture tank, a pump for separated moisture delivery, and a tank for collecting condensate from the first and second heating stages.

2.1.4 Instrumentation and Electrical Systems

Instrumentation and Control Systems

Instrumentation and control systems (I& C) provide plant data acquisition, its transformation, distribution, processing, displaying to operating personnel, logging and archiving, as well as automatic and remote control of systems in all modes of operation. Automation of protective actions has priority over the operator's commands.

The following belongs to the main instrumentation and control systems:

- Reactor trip system (emergency protection);
- Reactor power limitation system;
- Unit power control system;
- Safety assurance system;
- Engineered safety feature actuation systems (ESFASs) of the unit equipment;
- Systems for pressure and level control in individual equipment of the unit.

Signals of reactor trip and safety assurance systems are generated independently in two self-supporting protection networks. The signals of the same value come into both networks but from different, mutually independent measurement circuits. For scram and activation of safety systems, it is significant that at least one of the two networks would generate an emergency signal. The reliability of signal generation is ensured via the "two out of three" principle.

The core neutron power is measured with the help of ionization chambers placed in 24 channels outside the reactor vessel. The in-core instrumentation system (ICIS) includes neutron flux sensors that are mounted in the central tubes of the working assemblies (36 at reactor V-213) and 216 temperature sensors for coolant temperature measurement at the outlet of the working assemblies.

Core power is controlled with the help of an automatic power controller (APC) and a power governor (PG).

The instrumentation and control systems of some of the VVER-440 Units have been recently refurbished. The "Siemens" and "Areva" companies were involved in the refurbishments, which were mainly related to introduction of advanced features for data processing, transmission, and archiving.

Main Control Room

The monitoring of reactor plant state, control of reactor plant, as well as monitoring and control of associated engineered systems of the unit under normal operating conditions, anticipated operational occurrences, and accidents is performed from main control room (MCR).

All the required information is displayed in MCR; this information provides reliable control of safety systems, normal operation systems important to safety, as well as the normal operation systems that provide the generation of electric power.

The control of power unit is a man-machine system wherein the man plays an important part from the viewpoint of safety. The MCR is a central element of this man-machine system,

it is designed to create reliable instrumentation and control system, to provide easy work of operator, and to decrease the probability of an erroneous action of the operator. This is achieved due to improvement of control automation level, as well as displaying the information in easy and concentrated form.

The composition and architecture of the MCR equipment used at various NPPs of the VVER-440 type is different from one another, as development and upgrading of the instrumentation and control system has been implemented by different companies.

There is an emergency control room (ECR) at each NPP in the event that the MCR should become unavailable.

Electrical Systems

The output of electrical power generated in the turbine generators of the unit to the electrical system as well as the supply of electrical power from the electrical system to the auxiliaries systems in the unit is performed by the transformers, which convert the 15.75 kV electric power produced in generators to the voltage of electrical system.

Two units of generator–transformer are united on the high-voltage side. A generator breaker is mounted between the generator and the transformer. An auxiliary transformer is connected between the generator breaker and the unit transformer. A provision is made for a standby transformer connected to the outdoor switchgear, which can be used as a source for standby power supply to the auxiliaries.

The essential energy-consuming systems that ensure the nuclear safety of the unit are fed from reliable category I power supply systems. In the case of the loss of the working power supply, a standby source of storage batteries supplies the energy-consuming systems when the power supply interrupted. This mode is limited by the storage battery capacity, which is sufficient to provide power demand to the corresponding systems for at least 2 h. Automatic insertion of rectifiers and charging of storage batteries occurs after recovery of the working power supply.

The reliable supply of power of the category I classification consists of equivalent three independent structures and procedures, which belong to the safety systems.

The usage of inertial RCP with a coastdown is sufficient for the changeover to natural circulation at V-213 type plants, which makes it possible to consider the system as a power consumer; thus, this allows the imposition of less stringent requirements on its uninterrupted power supply. These RCPs are connected to the sections of auxiliary transformers. At V-230 type plants with inertialess RCPs, four of the RCPs are connected to the turbine generator terminals. Coastdown of these RCPs is implemented together with the coastdown of the turbine generator.

The reliable power supply system of the category II classification also consists of three equivalent independent systems, which belong to safety systems. A power supply source of each category II system is a diesel generator (DG), which is started up in response to signals that indicate the loss of normal power supply to the unit. The time required from signal initiation for the reliable supply of power from the DG is at the most 15 s. A stepwise start-up automatically connects the consumers temporarily to the switchgears of category II system after changeover to power supply from DG in order to avoid prohibitive overloading of DG. It therefore avoids any subsequent shutdown by the system protections or from any damage. Power supply to the safety system equipment is immediately provided.

2.2 Basic Safety Properties

2.2.1 Safety Philosophy

One of the most important trends related to nuclear power engineering safety is to neutralize the potential danger of the uncontrolled distribution of radioactive substances that are generated inside the nuclear reactor.

In the evolution of the NPP safety concept in Russia, three specific periods may be singled out. The first one refers to the initial stage of the development of nuclear power engineering, when it was supposed that because of the high quality of the reactor plant equipment, pipelines, and other components, it might be possible to avoid significant damage, thereby, excluding the possibility of severe accidents.

At the initial stage, a high emphasis in the domestic nuclear engineering industry was placed on a special technical regulation, which was based on the enhanced requirements for equipment and systems quality. This included the development of new techniques. It was ultimately aimed at reaching a high-level of reliability. In using these specifications, it was possible to determine that the increase in the quality and reliability indices was many times that compared to the traditional heat-and-power engineering. As a result of this, the first VVER-type reactor designs considered the ultimate size of the coolant leak as the maximum design basis accident and, respectively, the requirements for the accident localization system were restricted.

The second period of safety concept evolution is characterized by formation of a comprehensive approach to the NPP as an enhanced hazard that demands development and application of the special measures for safety assurance. During this period, the specifications of the emergency cooling systems and accident localization systems for the calculated instantaneous break of main coolant pipeline were created.

The third period is related to a new safety concept that covered beyond design basis accidents and possible severe core damages.

For a choice of technical solutions and parameters of nuclear power installations both a conservative approach, and the use of significant margins to dangerous design parameters, were identified as of great importance. Such a status was accepted for designing the VVER-440 reactor. The reactor features related to the design and operational safety basis are as follows:

- Reduced core power density;
- Significant heat-engineering margins to the limiting values;
- Spatial power distribution stability;
- Negative reactivity coefficients for the operational parameters;
- Steady natural coolant circulation without falling outside the design parameters to 10% of thermal power;
- High redundancy of the capital equipment (6 reactor cooling loops) with the possible long-term operation at the decreased power (to 3 loops);
- Large water inventory above the core and in the circulation circuit that facilitates the running of the emergency loss-of-coolant processes;
- Horizontal steam generators with a large water inventory that ensures residual heat removal within about 4–5 h without makeup in the case of a complete loss of NPP power;
- Reactor vessel is made of steel of improved radiation strength without longitudinal welds;
- Vessel lower part does not have insertions in the form of nozzles;
- Primary circuit pipelines are made of stainless steel that allows the realization of the “leak-before-break” concept.

2.2.2 Safety Systems and Properties

- a. The V-230 reactor plant was designed during the first period of safety concept development. The break of the main coolant pipeline made of stainless steel not being subject to brittle fracture was not considered in the project. The accident localization system consisted of the leak-tight rooms was designed for excess pressure in case of limited leak and the sprinkling system was intended for condensation of steam released during the accident.

During loss-of-coolant accident (LOCA) in the V-230 reactor plant, the emergency core cooling system in the primary circuit is brought into operation. This system includes three channels each consisting of two emergency makeup pumps and a delivery pipeline D_{nom} 100, which supply borated water into the non-disconnected part of the first, third, and fifth circulation loops, respectively. Each of the process emergency makeup channels is connected to the respective individual channel of reliable electrical power supply, control, and monitoring.

The emergency makeup pump characteristics are as follows:

- Capacity of $48 \text{ m}^3/\text{h}$;
- Pressure head not less than 110 kgf/cm^2 ,
- Pumped liquid temperature not more than 75°C .

The suction pipelines of the emergency makeup pumps are connected to the emergency boron solution tank, which is a part of the leak-tight volume and connected to the primary circuit box through the box floor draining sumps.

The emergency primary circuit makeup system is automatically connected in response to one of three signals, which characterize the loss-of-coolant accident:

- Primary pressure $\leq 90 \text{ kgf/cm}^2$,
- Simultaneous primary pressure decrease ($\leq 110 \text{ kgf/cm}^2$) and a pressurizer level 2.56 m below the nominal level,
- Decrease in the pressurizer level to -2.7 m of the nominal.

By the activation of the emergency signals in each channel, two pumps are connected with prohibition of their disconnection.

- b. The V-213 reactor plant was designed during the second period of safety concept development.

In this reactor plant, the project provides for emergency core cooling system (ECCS) that consists of

- A passive system of two individual and functionally similar subsystems (100% redundancy). Each subsystem consists of two hydraulic accumulators (HAs), one of which supplies water into the reactor volume above the core and the other supplies the volume under the core. The passive emergency core cooling system is brought into operation without the initiating signals and power supply. When the reactor pressure decreases below the HA pressure, the working medium is displaced due to expansion of the compressed nitrogen from HA into the reactor. To prevent the nitrogen from getting into the reactor, the HAs are provided with a ball-floating valve (➤ [Table 5](#)).
- Two active high- and low-pressure systems, each having three individual and functionally similar subsystems (200% redundancy) (➤ [Table 6](#)).

Table 5
Technical characteristics of hydraulic accumulators (HAs)

Nominal pressure, MPa	3.5
Working solution volume, m ³	40–43.5
Nominal temperature, °C	55–60
Boric acid concentration, g/kg	12
Nitrogen volume, m ³	30

Table 6
Technical characteristics of the high-pressure emergency core cooling system (ECCS) pump

Flowrate, m ³ /h	65 under backpressure of 12.7 MPa 115 under backpressure of 9.4 MPa
Pressure under delivery side, MPa	Min. 9.17; Max. 14.3
Medium temperature, °C	Max. 70

Table 7
Technical characteristics of low-pressure emergency core cooling system (ECCS) pump

Flowrate, m ³ /h	280 under backpressure of 0.71 MPa 360 under backpressure of 0.63 MPa
Medium temperature, °C	Max. 90

The pump pressure head is connected to the non-disconnected parts of cold legs in the relevant circulation loops. The pumps are connected in response to a “LB LOCA” signal, a “SB LOCA” signal, or a “MSH rupture” signal and simultaneously the quick-acting valves open in response to these signals. The time required from the pump start-up to supply the whole coolant amount into the primary circuit is 10.5 s. The minimum concentration of H₃BO₃ in the emergency tanks is 39 g/kg (🔍 [Table 7](#)).

The pump pressure head is connected to the reactor vessel above and under the core and separated from the reactor by a set of check valves. The pumps are connected in response to a “LB LOCA” signal, a “SG compartment pressure” signal, or a “medium size leak” signal and simultaneously the quick-acting valves open in response to these signals. The time required from the pump start-up to supply the whole coolant amount into the primary circuit under

primary pressure of 0.75 MPa is 10.5 s. The minimum concentration of H_3BO_3 in the emergency tanks is 12 g/kg.

- SG super-emergency feedwater system (EFWP) consists of the working and backup pumps connected by the “feedwater loss” signal and supplying demineralized water at a temperature of about 20°C from three tanks with a volume of $1,000\text{ m}^3$. The super-emergency feedwater pipelines are not connected to the SG main and emergency feedwater. The cold water is supplied into the steam generators through a special nozzle (➔ [Table 8](#)).
- A system of emergency gas removal from the primary circuit that allows for the gas blanket in the emergency cases to be efficiently removed from the reactor and SG collectors into the pressurizer system through the special tubes connected to the air vents. The signal appearing on the level indicator of the reactor is generated by the special indicators, which are the part of the ICIS.

2.2.3 Maximum Design Basis Accident

The maximum design basis accident of a V-230 reactor plant had as the proceeding from the supporting structures, the possibility of a primary coolant blowdown being equivalent to 32 mm diameter. Thus, all the main coolant pipeline insertions were provided with devices limiting the leak from the primary circuit up to this value.

An instantaneous double-ended guillotine break of the main coolant pipeline $D_{\text{nom}} 500$ was assumed as the maximum design basis accident in the V-213 reactor plants.

2.2.4 Severe Accidents

In the VVER-440 reactor plant design, the severe accidents with fuel melting were not considered because of the features of these plants specified in ➔ [Sect. 1](#) that make the accidents of such kind improbable. The conservative safety analyses that were made showed an absence of core damage beyond the safety criteria. This included an analysis of a reactor scram failure.

However, in connection with introduction of the new requirements that prescribe the consideration of severe accidents at some VVER-440 Units, the possibility that reactor vessel cooling from outside is considered for the case of an improbable severe accident.

The long-term and efficient reactor vessel cooling implemented at the units in operation is a very difficult problem. This is because any such operation should be performed in the restricted space of the reactor concrete cavity in the presence of the irradiated equipment.

■ **Table 8**

Technical characteristics of pump (EFWR)

Flowrate, m^3/h	60.0
Pressure at the pressure head, MPa	5.5

A similar design was supposed to be realized at “Mochovce” NPP, Units 3, 4 in Slovakia. According to this design, the following measures that ensure that the flooding of the reactor concrete cavity during the severe accident as intended:

- Configuration changes in the pipeline for air supply to cool the reactor concrete cavity (this pipeline is designed to be mounted inside the concrete structures) and the additional valves on this pipeline with their control and signaling that restricts water getting into the ventilation post;
- Reconstruction of thermal insulation of the reactor vessel bottom head to ensure the gap required;
- New structural decision on thermal insulation in the reactor vessel nozzle area to ensure a free steam discharge from the reactor concrete cavity;
- Reconstruction of the penetrations in the reactor concrete cavity and modification of the doors entering the concrete cavity;
- Sufficiently low-pressure loss for coolant flow;
- Reconstruction of drainage line from the reactor concrete cavity and control of its closing before the onset of flooding.

Modifications were also proposed to the chute drainage set of the bubbler–vacuum system to control drainage of the water from the chutes onto the box floor. A further system of additional coolant tanks and pumps that are common to both operating units were constructed in order to feed the coolant into the containment area through the sprinkling system.

2.2.5 Seismic Design

The seismic stability of a VVER-440 reactor plant is justified both by calculations using the response spectra and floor-response accelerograms, and by a set of experimental studies of the small-scale models and at full-scale equipment. The full-scale studies make it possible to determine the main modes and frequencies of vibrations and the quantitative values of the factors (mounting gaps, nonlinearities, etc.), which influence the overload caused by seismic impacts. The results of full-scale studies at various NPPs enabled the statistically validated data to be used in the calculations of reactor plant equipment and pipelines for seismic impacts. The calculation to check the strength of the equipment and the pipelines is performed by considering the combined effect of operational and seismic loads.

Experimental studies to justify the earthquake resistance of the primary equipment for VVER-440 NPP were performed with small-scale and large-scale metal models. A 1:20 scale reactor model and a 1:25 scale model of the circulation loop were studied.

The results of calculations and the experimental activities showed that the additional fastening of the reactor internals was required to reduce their displacement with respect to each other. The supports of tube bundle in steam generator were also strengthened due to these studies. Fastenings that reduced the effect of seismic impacts were introduced for circulation loop equipment (MGV, RCP, SG), where snubbers were used to also prevent buckling through the thermal expansion of a loop.

The scram signal is introduced in case of operating basis earthquake (OBE).

2.3 Operational Experience and Decommissioning

2.3.1 Operational Experience

NPP	Unit and reactor type	Electric power, MW	Commissioning	Decommissioning	Gross generation till 2009, GW h
Novovoronezh, Russia	Unit 3, V-179	385	29.06.1972	–	87,502
	Unit 4, V-179	385	24.03.1973	–	93,751
Kola, Russia	Unit 1, V-230	412	28.12.1973	–	82,569
	Unit 2, V-230	411	21.12.1975	–	80,932
	Unit 3, V-213	411	03.12.1982	–	68,877
	Unit 4, V-213	411	06.12.1984	–	61,942
Nord, GDR	Unit 1, V-230	408	12.07.1974	14.02.1990	35,452
	Unit 2, V-230	408	16.04.1975	14.02.1990	36,569
	Unit 3, V-230	408	01.05.1978	28.02.1990	33,271
	Unit 4, V-230	408	01.11.1979	22.07.1990	28,920
Kozloduy, Bulgaria	Unit 1, V-230	408	28.10.1974	31.12.2002	61,070
	Unit 2, V-230	408	19.11.1975	31.12.2002	62,819
	Unit 3, V-230	408	20.11.1981	31.12.2006	62,817
	Unit 4, V-230	408	17.05.1982	31.12.2006	60,991
Bohunice, Slovakia	Unit 1, V-230	408	01.04.1980	31.12.2006	71,567
	Unit 2, V-230	408	01.01.1981	–	76,957
	Unit 3, V-213	408	14.02.1985	–	66,102
	Unit 4, V-213	408	18.12.1985	–	64,808
Rovno, Ukraine	Unit 1, V-213	363	21.09.1981	–	71,557
	Unit 2, V-213	377	30.07.1982	–	70,879
Loviisa, Finland	Unit 1, V-213	488	09.05.1977	–	179,290
	Unit 2, V-213	488	05.01.1981	–	100,392
Dukovany, Czech Republic	Unit 1, V-213	412	03.11.1985	–	71,426
	Unit 2, V-213	412	21.09.1986	–	69,334
	Unit 3, V-213	412	20.07.1987	–	67,698
	Unit 4, V-213	412	19.01.1988	–	66,798
Paks, Hungary	Unit 1, V-213	430	10.08.1983	–	83,223
	Unit 2, V-213	433	14.11.1984	–	73,007
	Unit 3, V-213	433	01.12.1986	–	72,915
	Unit 4, V-213	433	01.11.1987	–	72,366
Mohovce, Slovakia	Unit 1, V-213	388	29.10.1998	–	29,528
	Unit 2, V-213	388	11.04.2000	–	14,789

Nowadays the increase in power of VVER-440 Units is a high-priority task. In transition to the operation at increased power, it is reasonable to use the fuel assemblies with an extended height of fuel column (second-generation assemblies). The results of a pilot study on the viability of the new fuel configuration show that during the implementation of the second-generation fuel, the operational limits for the standard fuel are not violated. This confirms the compatibility of new and standard fuel assemblies.

Numerous experimental studies, performed for the fuel with burnup of (50–60) MW·day/kg-U under transient and accident conditions, as well as post-reactor studies of assemblies, the fuel rods, and the fuel pellets of 5-years operation, confirm a high reliability of fuel, availability of high margins for the state of fuel column that promotes operation of the reactor at increased power.

At present, Units 1, 2, 4 of Kola NPP and Unit 2 of Rovno NPP have experience in operating reactors under increased power. The Units of “Loviisa” NPP are operated at 109% power.

By the beginning of 2009, the second-generation fuel had been implemented at a number of NPP Units with VVER-440. The safety justification of operation at the increased power has been made for the reactor cores of the following NPPs: NPP B2 “Bohunice” (Units 3 & 4), NPP “Mohovce” (Units 1 & 2), NPP “Dukovany” (Units 1–4), NPP “Kola” (Units 3 & 4).

2.3.2 Life-Time Extension

The design service life of the VVER-440 reactors is 30 years. In 2000, a set of regulatory and guiding documents was established in Russia wherein the basic criteria and requirements are stated for evaluation of a possible service life extension, as well as safety measures to be taken during the period of extended operation.

According to these requirements, the following shall be done for each power Unit:

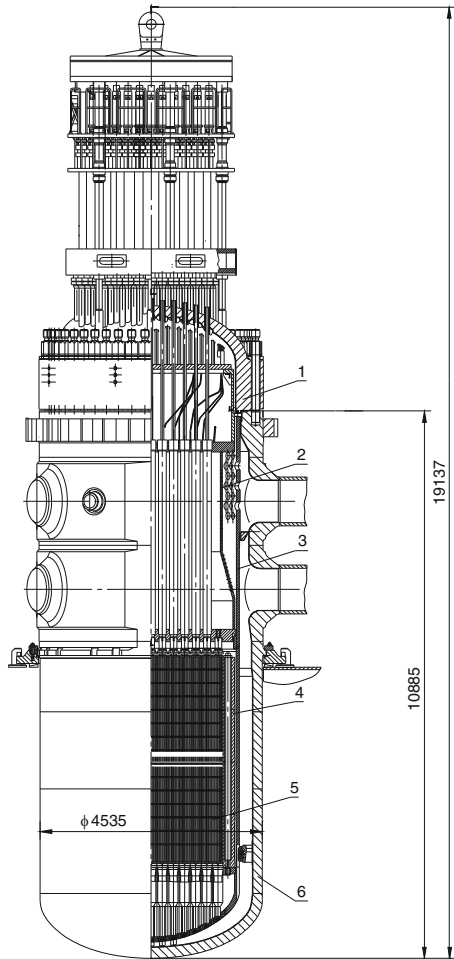
- The studies shall be performed to determine the residual life of non-recoverable components of a Unit and the measures shall be taken on the extension of the residual life of these components;
- The reports shall be prepared on the in-depth safety assessment considering all measures implemented on modernization including deterministic safety analysis, probabilistic safety assessment (PSA) of level one, and an analysis of the operating history.

Such complex activities were performed for Units 3 & 4 of Novovoronezh NPP and Units 1 & 2 of Kola NPP where the design life expired between 2002 and 2005. The license was obtained for an extension of their respective service life for further 15 years.

At present, the appropriate activities are conducted at NPPs with V-213. Their service life is planned to be extended for 25–30 years.

3 VVER-1000 Reactors

3.1 Design Description



■ Figure 22

V-320 RP reactor. 1 – Upper unit, 2 – Protective tube unit, 3 – Core barrel, 4 – Core baffle, 5 – Core, 6 – Reactor pressure vessel

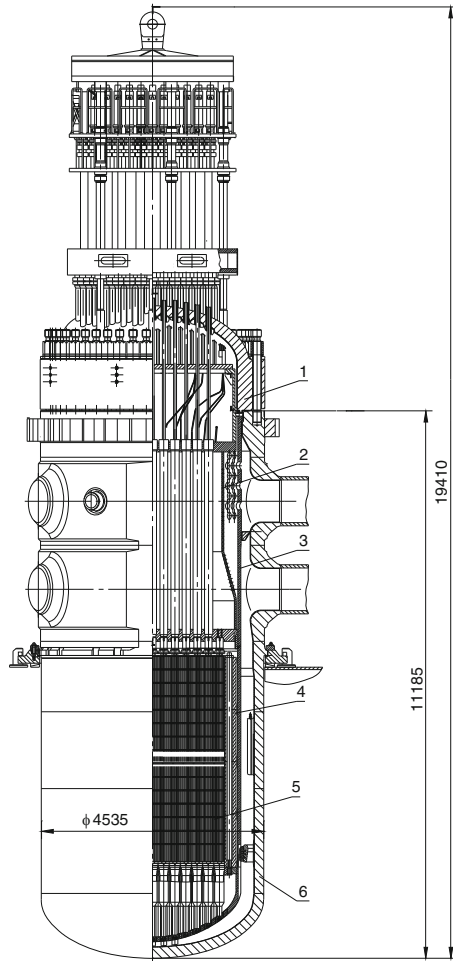


Figure 23

V-428 RP reactor. 1 – Upper unit, 2 – Protective tube unit, 3 – Core barrel, 4 – Core baffle, 5 – Core, 6 – Reactor pressure vessel

3.1.1 Buildings and Structures

The building layout of the Tianwan NPP Unit is presented in [Figs. 24](#) and [25](#).

The key building that determines the power unit layout is the reactor building ([Figs. 22](#) and [23](#); [Table 9](#)).

Safety-related buildings are located around reactor building: the steam cell, the safety building, and the control building. The emergency diesel power station is sited behind the safety building and it is aligned across reactor axis.

■ **Table 9**

Main design characteristics of V-320 and V-428 reactor plants

Parameter	Value	
Reactor plant type	V-320	V-428
Thermal power (nom.), MW	3,000	
Primary pressure, MPa	15.7	
Secondary pressure, MPa	6.27	
Coolant flowrate through reactor, m ³ /h	84,800	86,000
Coolant temperature at reactor outlet, °C	320	321
Quantity of fuel assemblies, pcs.	163	
Quantity of control rod drives, pcs.	61	121
Uranium loading, t	80	
Fuel enrichment with isotope U-235, %	4.4	
RP service life, years	30	40

The auxiliary system building, the fresh fuel storage, the solid radioactive waste storage, and the nuclear service building are located in the sector, which borders on the control building, the reactor building, and the safety building.

The turbine building is sited behind the steam cell.

The NPP Unit also comprises a vent tube, a treated water storage tank, and a separate water tank to store water for the extinguishing of fire, transformers, and underground structures.

The architecture of Units at NPPs with V-428 and V-320 Project designs is almost identical.

Reactor Building

The reactor building is the main construction of the NPP around which the other buildings are sited. It houses the nuclear steam supply station and all the emergency systems required to cool down the reactor.

Apart from the load bearing and enclosure functions, the structures of the reactor building simultaneously perform protective and isolation functions. The building is a spacious construction combining two protective envelopes, internal and external. The structures inside the building are used to hold the equipment. The foundation slab must support the erected envelopes and internal structures.

A single-envelope containment made of prestressed concrete is used in the NPPs with V-320 reactor. The double-envelope containment minimizes the release of emergency radioactivity into the environment. The external envelope serves for physical protection of the internal confinement and the equipment it houses from all external impacts. The internal confinement provides airtightness of the space inside containment under all the conditions of NPP operation, including accidents.

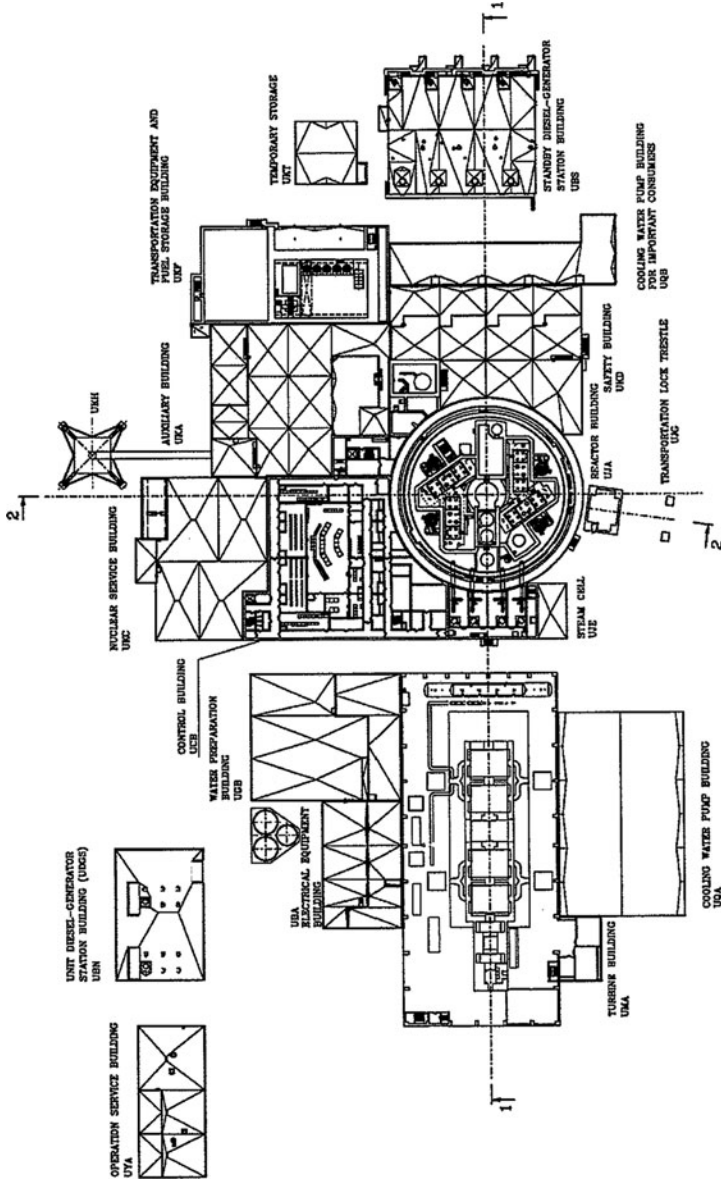


Figure 24
 Layout of the Unit buildings at the elevation mark +20.4

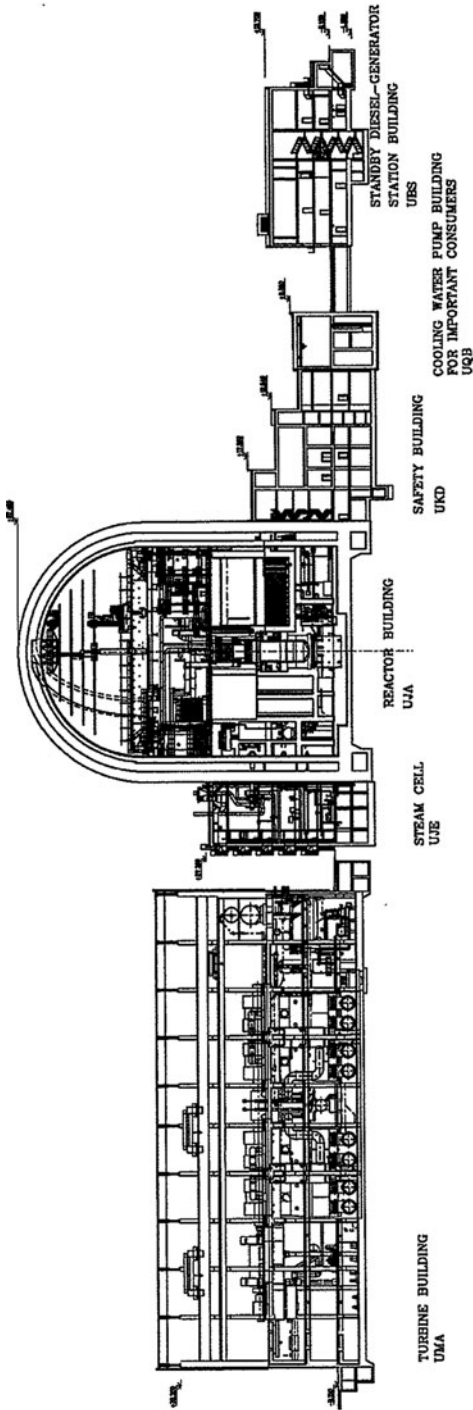
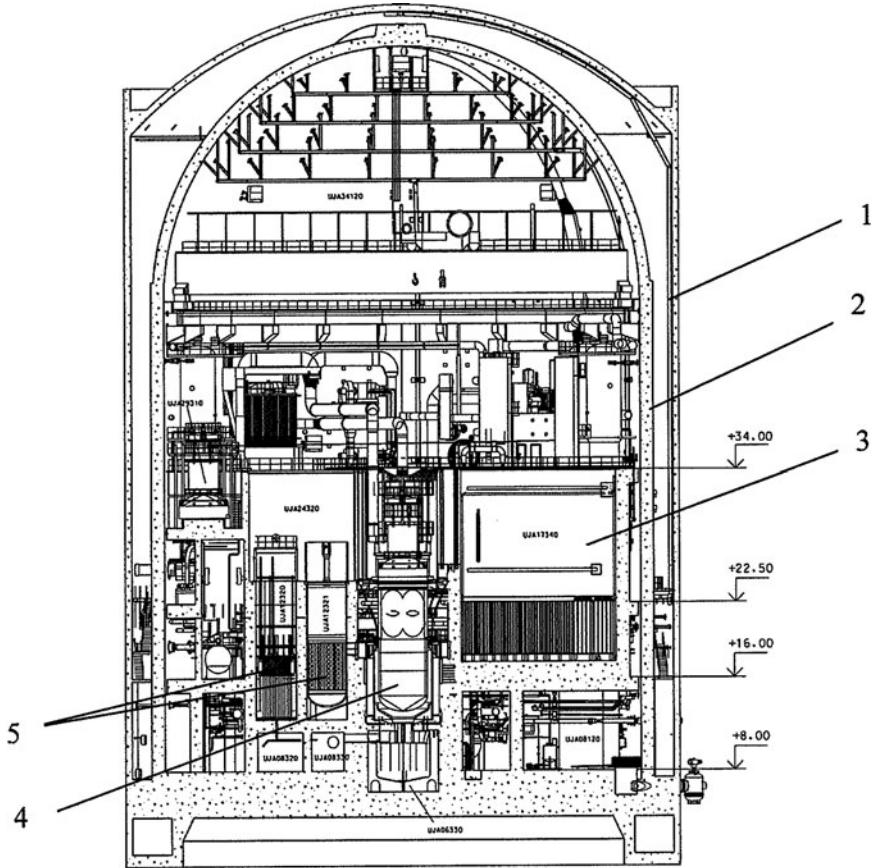


Figure 25
Cross section of the Unit buildings. Section 1-1



■ Figure 26

Reactor building. 1 – External envelope, 2 – Confinement, 3 – Spent fuel and refueling pond, 4 – Reactor, 5 – Inspection wells of upper unit and internals

The internal envelope is a prestressed concrete structure in the form of a cylinder with a semispherical dome. The internal surface of the envelope is covered with 6-mm carbon steel to provide airtightness.


The containment rests on the foundation plate. Both the internal confinement and the foundation contribute to the hermetically sealed space with its integrity assured for a maximum design basis loss-of-coolant accident.

The external envelope physically protects the prestressed concrete confinement from outside impacts and ensures the reduction of emergency release into the environment by the creation of an envelope-to-envelope gap to localize any emergency leaks through the internal confinement barrier.

The external envelope is made of monolithic reinforced concrete. The envelope consists of a cylinder with a gently sloped dome. The annular gap between the inside and outside envelopes is 1,800 mm wide in the cylindrical part. In the dome, the gap width varies owing to differences between the internal and external dome configurations.

The external envelope is separated from the adjacent buildings with an aseismic seam, which includes the safety building, the control building, the steam cell, and the auxiliary building.

The containment houses all the equipment of reactor plant. The reactor is installed in the concrete cavity on a support truss. Annular metalwork filled with serpentine concrete forms the dry shielding to protect the structures against irradiation. The core catcher is located in the bottom part of the concrete cavity. A core catcher was not included in the NPP design with the V-320 reactor plant.

The general layout of the containment with the equipment of V-320 RP design and main rooms it houses is shown in  Fig. 26.

Auxiliary Building

The auxiliary building is located in the central part of the station. It is adjacent to the control building, the nuclear service center, the safety building, the solid radioactive waste storage, and fresh fuel storage.



The building houses the primary-side auxiliary systems, water purification systems, liquid radioactive waste collection and storage systems, and equipment of venting systems of the limited access area.

Turbine Building


The turbine building belongs to the free access area. It houses a turbine, a generator, and their auxiliary systems, such as separation and intermediate superheating, condensate purification, the high- and low-pressure regeneration systems, the feedwater system, the station auxiliaries steam collector, and the oil systems for the turbine and generator.

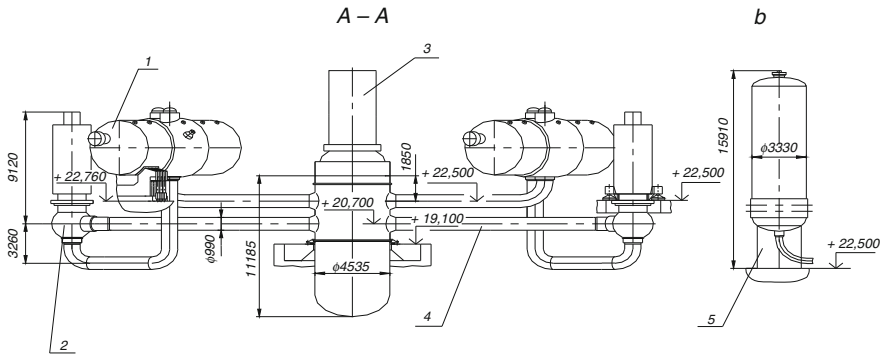
3.1.2 Systems of Primary Circuit

Reactor Coolant System

The system of reactor cooling for the V-428 and V-320 reactor plants under normal operating conditions (primary side) consists of four circulation loops ( Figs. 27 and  28). Each circulation loop comprises a reactor coolant pump (RCP) and a steam generator. Each loop has two pipeline sections defined as hot and cold legs. The pipe section from the reactor outlet nozzle-to-steam generator collector is the hot leg. The pipe sections from the steam generator outlet nozzle-to-RCP inlet (suction) nozzle and the RCP outlet (discharge) nozzle-to-reactor inlet nozzle make the cold leg.

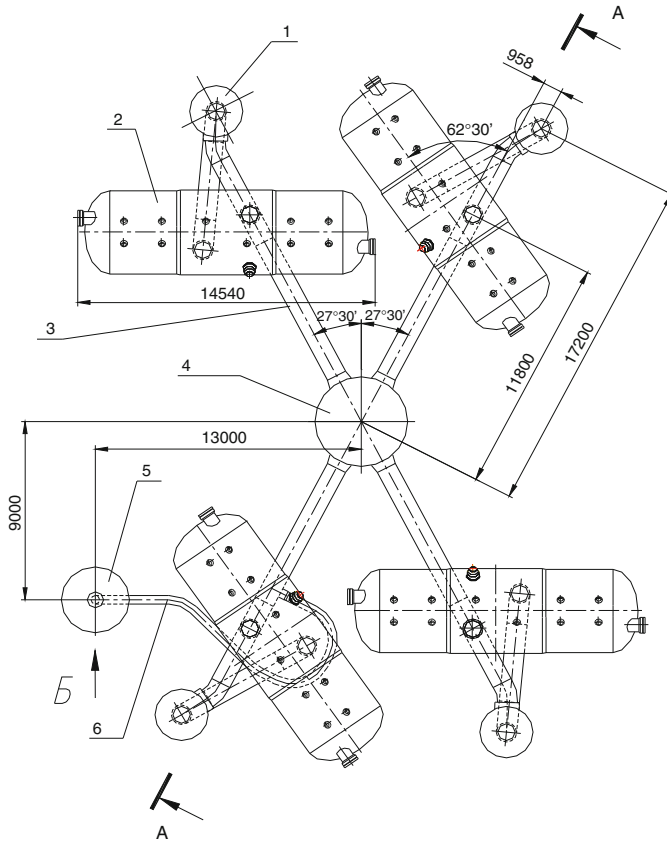
A 426 × 40-mm surge line connects the hot leg of the fourth circulation loop to the pressurizer. A 219 × 20 mm line connects the hot leg of the third circulation loop to the pressurizer and it is an injection line.

The MCP ( Table 10) is made of 10GN2MFA alloy structural steel. The internal pipe surface is clad with corrosion-resistant 04X20N10G2B stainless steel not susceptible to intergranular corrosion by the coolant.



■ Figure 27

Primary circuit layout. 1 – Steam generator, 2 – Reactor coolant pump, 3 – Reactor, 4 – Main coolant pipeline, 5 – Pressurizer



■ Figure 28

Primary circuit layout. 1 – Reactor coolant pump, 2 – Steam generator, 3 – Main coolant pipeline, 4 – Reactor, 5 – Pressurizer, 6 – Surge line

■ **Table 10**
Main coolant pipeline (MCP) performance

Parameter	Value
Inside diameter of hot leg/cold leg, mm/mm	850
Wall thickness, mm	70
Coolant flowrate in the loop, m ³ /h	21,500
Hot leg length, m	10
Cold leg length, m	26

Reactor Vessel and Internals

A reactor is a vertical pressurized vessel that houses a core barrel with the baffle, protective tube unit, fuel assemblies, reactor trip system control assemblies that are engaged with extension shafts of the drive motion units and detectors for the in-core instrumentation system.

The reactor flange supports top head of the reactor, which has the housings and electro-magnet units attached to outside to allow for axial movement of the reactor control assemblies (RCCAs) in the core.

The VVER-1000 reactor vessel design is based on meeting the following requirements:

- Proven manufacturing process and structural materials;
- Complete in-shop manufacture of the vessel, tests included;
- Possibility of vessel transport by railway and by sea;
- Possibility of periodic in-service inspection of vessel state.

The reactor vessel consists of several forged shells welded to each other, an elliptic bottom head, and a flange. The reactor is sealed with bar gaskets and tightened with 54 M170 studs.

Two of the vessel shells each have four D_{nom} 850 nozzles, which are connected to the main coolant pipeline of reactor coolant system. Thus, the vessel shells make outer surface of the inlet and outlet chambers for the reactor coolant.

A ring welded to the vessel internal surface clad from austenitic steel serves to separate the inlet and outlet chambers. Barrel-mated keys are used to keep the ring from undergoing radial displacements. Hermetically sealed casks are installed on hangers to hold the vessel steel surveillance specimens.

The reactor vessel is made of heat-resistant alloy steel Grade 15Kh2NMFA. The reactor vessel steel and welding materials were chosen on the basis of mechanical property analysis, the lack of susceptibility to brittle fracture, its durability, and its irradiation stability.

The core barrel is a welded cylindrical shell with a supporting bottom and a flange, which supports the barrel at the vessel shoulder. The perforated elliptical bottom of the core barrel, 163 perforated support tubes, and the support grid contribute to the structures that support and space the FAs.

A core baffle is placed next to the barrel at the core level. It is approximately the distance of the structural gap of an FA from the periphery row. The baffle serves as a displacer and as a protective screen. The core baffle is made of several massive rings that are mechanically attached to each other and to the bottom of the core barrel.

The longitudinal channels are used to ensure that the flowing coolant can effectively decrease any swelling of the metal in the core barrel metal. The swelling is caused by the working temperature range and the accumulated neutron fluence over the service life of the vessel.

A protective tube unit (PTU) is installed on the top of the core. It is pressed against the core barrel flange with the force of the elastic element installed between the PTU and the top head of the vessel. The PTU and elastic element are compressed as reactor main joint is sealed.

The perforated shell of the PTU with plates and protective tubes make a rigid support structure that spaces the FAs and prevents them from lifting up. The protective tubes house RCCAs, in-core instrumentation detectors (ICID), and in-core instrumentation system detectors.

The internals are made of corrosion-resistant steels of the austenitic grade.

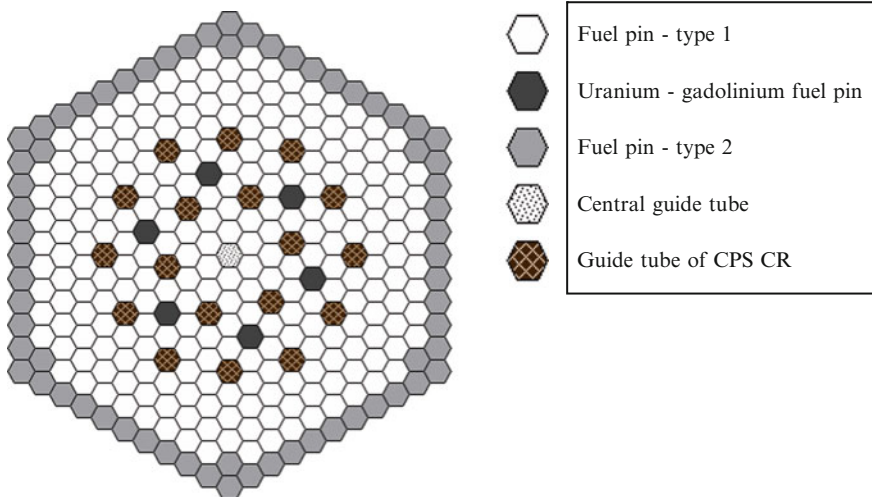
The upper unit structurally integrates an elliptical head with a flange. Nozzles are inserted for RCCA drives, metalworks, and crosspieces.

The pitch electromagnetic drive of the ShEM-3 type moves the control rods at a rate of 2 cm/s.

The quantity of drives installed in the upper unit for a V-428 reactor can be varied from 85 to 121 pcs., the amount of which is dependent on the fuel loading. For V-320 type reactors the number of drives is fixed at 61 pcs. The core is made of 163 FAs that are identical in structure but different in fuel enrichment.

Reactor Core

The VVER-1000 reactor cores contain 163 hexagonal fuel assemblies (FAs). The lattice pitch is 23.6 cm. The fuel rods are arranged in a hexagonal structure inside FA. Note that the FAs are jacket-free. A welded skeleton is formed from the spacer grids, control rod guide tubes, angle-pieces, and other smaller parts that make the assembly rigid. One important aim of FA development was the improvement of the skeleton for ensuring the long-term reliability. Bowing problems that were experienced in the first years of their use were eliminated by such



■ Figure 29

Enrichment pattern in the FA

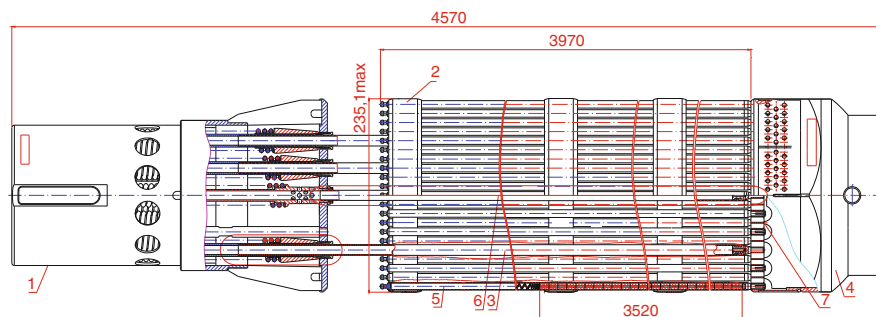


Figure 30 Fuel assembly. 1 – Top nozzle, 2 – Spacer grid, 3 – Guide channel, 4 – Bottom nozzle, 5 – Fuel rod, 6 – Central tube, 7 – Bottom grid

Table 11

Main stages of VVER-1000 fuel evolution

Commissioning/year	Before 1997	1998–2000	Since 2003/2003	Since 2006
FA type	TVS (TVS-M)	UTVS	TVSA/TVS-2	TVSA-ALFA/TVS-2M
Bundle type	Blocked absorber	U-Gd	U-Gd	U-Gd
Reload batch average enrichment [% ^{235}U]	4.31	3.74	~ 4.26	4.83/4.88
Spacer grid pitch (mm)	1.275	1.275	1.275	1.275

developments. The FAs contain 331 rod positions. In the currently typical case, the central position is a tube with water, one position is used for in-core measurements, guide tubes of movable control rods are placed into 18 positions, and the 312 positions are filled with fuel rods. Six of the fuel rods can contain burnable absorbers. The pattern is profiled as shown in Fig. 29.

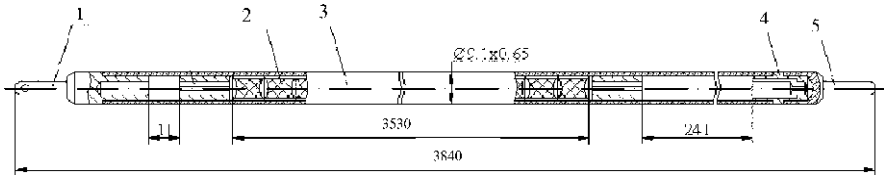
The control rods can move in the guide tubes. They are fully inserted into the core when the reactor is in the shutdown state, while for power operation they can be pulled upward out of the core.

Burnable absorbers must be included in VVER-1000 reactors, since the excess reactivity of the initial core design without burnable absorbers could not be adequately compensated by diluted boric acid. This enabled a negative reactivity feedback coefficient. Removable boron rods were chosen as the blocked burnable absorbers. They were placed into the guide tubes of control rods and were removed after 1 year of operation. In order to improve neutron economics, stainless steel FA components were replaced with components made from zirconium alloy. Switching the component materials enabled a decrease in the enrichment of the fuel rod. Therefore, blocks of burnable absorber rods were no longer required. The rods that contain burnable absorber in the form of gadolinium could be placed into optimum positions within the fuel assembly.

A general view of fuel assembly is provided in Fig. 30.

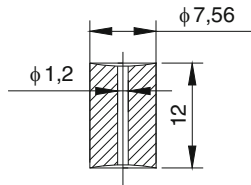
The main stages of VVER-1000 fuel development are shown in Table 11.

Alternative fuel assembly (AFA) advance fuel assemblies are used in RP V-428 design. All types of fuel are used in V-320 design.



■ Figure 31

VVER-1000 fuel rod. 1 – Lower plug, 2 – Fuel pellet, 3 – Cladding, 4 – Gas space, 5 – Upper plug



■ Figure 32

VVER-1000 pellet

Fuel Rods The fuel rods are closed cylinders with an outer diameter of 9.1 mm and an inner diameter of 7.73 mm. The length of the fuel rods is 3,840 mm. The length of the fuel stack is 3,530 mm. The fuel rods are filled with helium at a pressure of 2.0–2.5 MPa. ➤ *Figure 31* shows the fuel rod.


The fuel pellets are made of sintered UO_2 with or without a central hole. The outer diameter is 7.56 mm. The height of the pellet is 12 mm. The UO_2 density is not less than 10.2 g/cm. The configuration of the rod can be seen in ➤ *Fig. 32*. Fuel rods with various uranium enrichments are available. The fuel enrichment, which is typically used has values of 1.6%, 2.4%, 3.3%, 3.7%, and 4.1%. FAs with fuel of 1.6 and 2.4% enrichment are not profiled and they are used mostly in the first cycles. FAs with fuel of 3.7 and 4.1% enrichment are profiled with the placing of fuel rods that have 3.3 and 3.7% enrichment, respectively, into the outermost row of the FA and into the first neighbor position in the corners.

VVER-1000 fuel cladding is made of the E110 zirconium alloy (with a niobium content of 0.9–1.1%). This material is well known because of its very low hydrogen uptake during normal operating conditions, which leads to a high reliability concerning their long-term operation and in respect to reactivity-induced accidents.

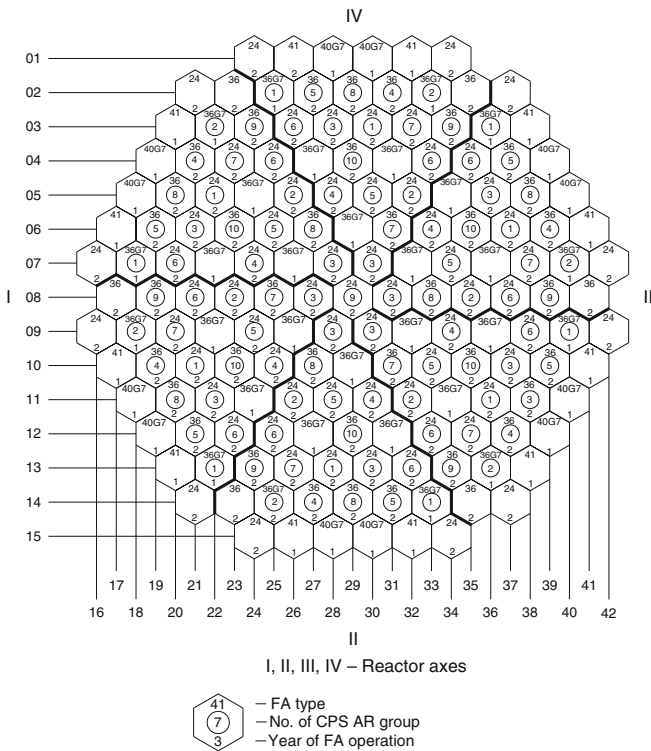
Burnable Absorbers The 18 guide tubes in the FA can be used to load burnable absorbers into the core for a given cycle. In the case of using blocked burnable absorbers, 42 FAs are typically loaded with them in the first cycle. The number of burnable absorbers is later reduced to 18 FAs. The blocked burnable absorber is chromium diboride (CrB_2) in matrix of aluminum alloy with three different natural boron contents (0.020 g/cc, 0.036 g/cc, 0.050 g/cc). The higher the enrichment in the FA the greater the amount of boron loaded into the FAs.

Rods containing Gd absorber have the same dimensions as those of the usual fuel rods. The Gd content in the burnable absorber rods is 8 wt%, while the uranium enrichment is 3.6 wt%.

Control Rod Clusters Boron carbide (B_4C) powder is used to manufacture the control rods for VVER-1000 reactors. This material is used in the top of the rods with a pellet length of 320 mm. The bottom part, which is 30 cm long, is made of dysprosium titanate. In the first phase of developing VVER-1000 reactors, other materials (e.g., europium oxide [Eu_2O_3]) were also used as absorbers.

The 18 control rods in a FA form a cluster. Control rod clusters are typically placed in 103 FAs. Note that 85 FAs are used in the first cycle. These numbers have been varied with time and NPP unit. The control rod clusters are grouped into 10 groups, which move together. Each of them contains 6–12 clusters. Reactor power and power distribution are controlled with the help of a group of clusters partly inserted into the core. The other groups are fully withdrawn during power operation. Typical core pattern for RP V-428 reactor is shown in  Fig. 33.

The time taken for a control rod drop at reactor scram does not exceed 4 s.



FA type	Average enrichment in U_{235} , % mass
24	2, 40
41	4, 10
36	3, 62
36G7	3, 61
40G7	4, 00

 **Figure 33**
The first fuel cycle of RP V-428 reactor

■ **Table 12**
Main performance

Parameter	Value
Capacity, m ³ /h	22,000
Nominal supply pressure head, MPa	0.588
Rotational speed (synchronous), rev./min	1,000
Nominal power, kW	5,000
Rotor moment of inertia, kg/m ²	7,600

Reactor Coolant Pump

The RCP is a one-stage centrifugal pump, which is aligned vertically (➤ [Table 12](#)). The RCP consists of a pump casing, an electric motor, a sealed drive shaft and gears, a flywheel, top and bottom insertions, supports, and auxiliary systems.

The electric motor is of the vertical asynchronous double-speed type. To prevent the reverse rotation of the rotor, the RCP is provided with a cam-and-ratchet mechanism. RCP is also supplied with a flywheel to provide inertia coastdown.

General view of RCP is provided in ➤ [Fig. 34](#).

GTsN-195M pumps are used in the V-320 RP design, while GTsN-1391 pumps are used in the V-428 RP design.

The GTsN-1391 pump is a further evolution of GTsN-195M design and its enhancements are described as follows:

- Main thrust bearing is water-cooled and water-lubricated;
- Application of double-speed electric motor decreases grid loading at pump start-up;
- The applied shaft sealing ensures cold and hot standby with an unlimited outage on condition of intermediate circuit locking and sealing water is supplied also on the condition that the outage following an NPP blackout (loss of cooling) under coolant nominal parameters is for not less than 24 h providing leaks through the sealing are not above 50 l/h.

Pressurizer

The steam pressurizer that is installed at V-428 and V-320 reactor plants is a vertical vessel with electrical heaters to increase primary pressure (➤ [Table 13](#)).

The pressurizer vessel is made of carbon steel with corrosion-resistant austenitic cladding of the internal surfaces.

Two independent nozzles with spray devices are installed in the upper part of the pressurizer in V-428 design while a single nozzle was employed in the V-320 design. They ensured the water injection into steam space from the following sources:

- The RCP discharge line under normal operating conditions and under anticipated operational occurrences;
- The discharge line of the high-pressure emergency injection pumps under design-basis and beyond-design basis accidents.

The pressurizer is connected to the hot leg of the main coolant pipeline through the lower nozzle of D_{nom} 350 surge line.

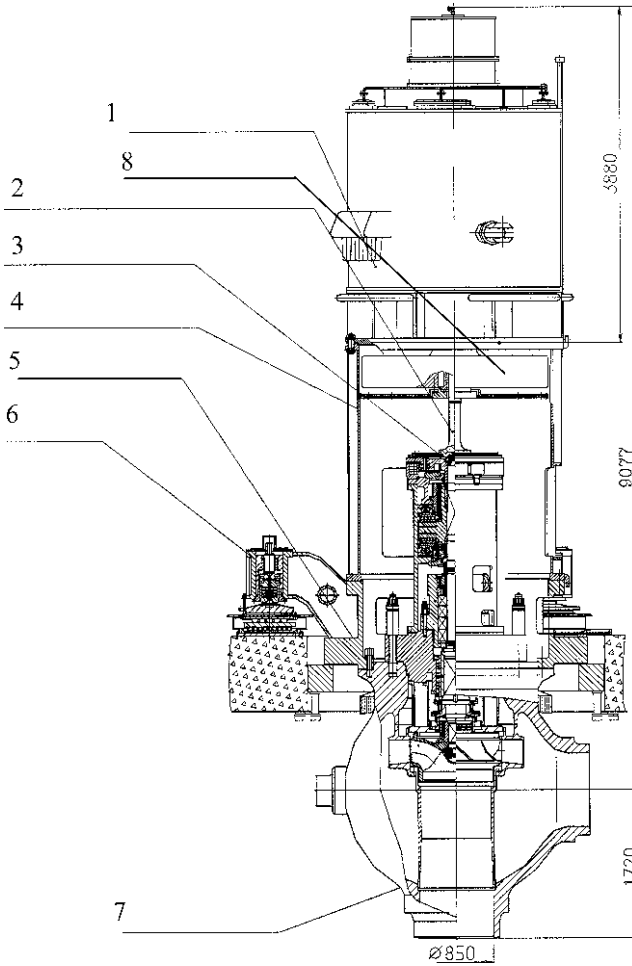


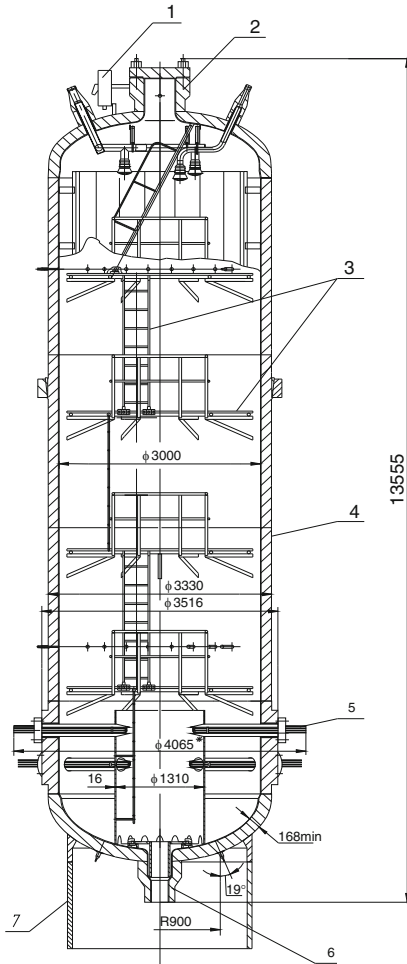
Figure 34

Reactor coolant pump. 1 – Electric motor, 2 – Laminated coupling torsion bar, 3 – Internals, 4 – Top insertion, 5 – Bottom insertion, 6 – Support, 7 – Pump casing, 8 – Flywheel

Table 13

Pressurizer performance

Parameter	Value
Pressure, MPa	15.7
Capacity (full volume), m ³	79
Water inventory under nominal conditions, m ³	55
Power of electric heaters (total), kW	2,520
Quantity of electric heaters, pcs.	28
Diameter of supply tubes (surge line), mm	426 × 40



■ Figure 35

Pressurizer. 1 – Surge bottle, 2 – Neck, 3 – Internals, 4 – Vessel, 5 – Tubular electric heater unit, 6 – Nozzle, 7 – Support

There is a nozzle in the top section of the pressurizer to attach the overpressure protection system that consists of three pilot-operated relieve valves.

A general view of the pressurizer is given in ➤ [Fig. 35](#).

Steam Generator

The steam generators employed in the both V-320 and V-428 Projects are of the PGV-1000M type. It is a single-vessel recuperative heat exchanger, which is aligned horizontally, what ensures that the heat transfer surfaces are submerged. A general view of steam generator is presented in

➤ [Fig. 36](#).

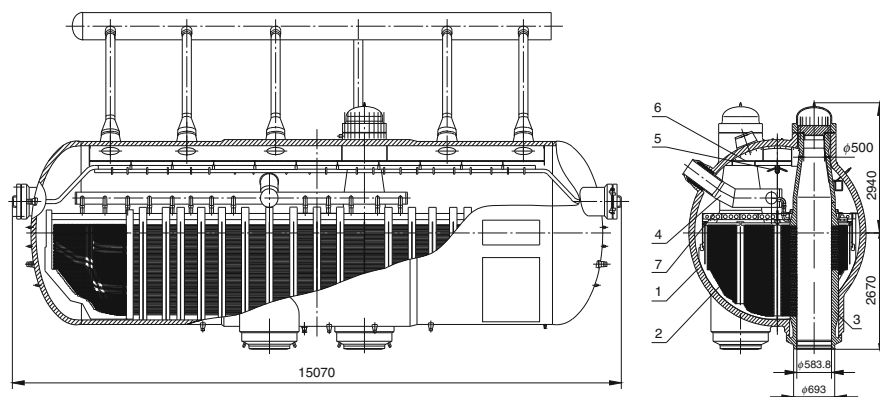


Figure 36

General view of APGV-1000M steam generator. 1 – Vessel, 2 – Heat transfer surface, 3 – Primary-side collectors, 4 – Main feedwater distribution devices, 5 – Emergency feedwater distribution devices, 6 – Steam-receiving perforated plate, 7 – Submerged perforated plate

Table 14

PGV-1000M steam generator nominal operation performance

Parameter	Value
Steam capacity, t/h	1,470
Steam pressure in SG vessel, MPa	6.39
Steam pressure at SG outlet, MPa	6.28
Primary coolant temperature at the SG inlet, °C	321
Primary coolant temperature at the SG outlet, °C	291
Feedwater temperature, °C	220
Feedwater temperature with high-pressure heaters switched off, °C	164
Steam moisture at SG outlet, %, not above	0.20

The steam generator is designed to house the heat transfer surface, which contacts the primary coolant with the secondary coolant. Its vessel consists of forged shells, stamped elliptic bottoms, and forged nozzles that are joined by welding. The vessel design provides easy access to examine the internal structures from the secondary side.

The heat transfer surface comprises of 10,978 U-tubes 16×1.5 mm in diameter that are arranged in coils and positioned horizontally in a staggered order. The coils are connected to primary-side collectors. The U-tube ends are hydraulically expanded over the collector wall thickness and are argon-arc welded onto the inside surface of the collectors. Austenitic steel is used as the material of the tubes.

The primary-side collectors are designed to distribute the coolant in the heat exchange tubes, collect, and evacuate it.

The internal surface of the collector has two layers of corrosion-resistant cladding.

The steam-receiving perforated plate is installed in the top section of the vessel.

The steam load is leveled with the perforated plate positioned under the SG water level.

Any water that has an increased salt concentration and fouling is accumulated inside the SG close to one of the bottoms (in the so-called salt pocket). This is due to an appropriate arrangement of feedwater and SG blowdown.

A large inventory of water is the merit of PGV-1000 steam generator. It provides favorable dynamic characteristics of all the reactor plants in the case of a loss-of-feedwater accident (☛ [Table 14](#)).

Chemical and Volume Control System

The chemical and volume control system comprises of

- Two high-capacity pumps;
- Three low-capacity pumps;
- Regenerative heat exchanger of blowdown steam;
- Pipelines and related valves;
- A makeup deaerator.

The low-capacity pumps are not applied in NPPs where V-320 reactors are operated.

The blowdown pipelines are connected to the cold legs of circulation loops 1 and 4 on the discharge side of reactor coolant pumps.

Makeup pumps are connected to the cold legs of all four loops at RCP suction nozzle (☛ [Tables 15–17](#)).

■ **Table 15**
High-capacity pump performance

Type	Centrifugal
Pressure head, MPa	18.5
Temperature of pumped medium, °C	70
Capacity, m ³ /h	60

■ **Table 16**
Low-capacity pump performance

Type	Piston
Pressure head, MPa	16
Temperature of pumped medium, °C	104
Capacity, m ³ /h	6.3

■ **Table 17**
Deaerator performance

Deaerator working pressure, MPa (gauge pressure)	0.02
Operating capacity of accumulator, m ³	19

3.1.3 Secondary-Side Systems

Main Steam Line System

Steam from the main pipelines enters the turbine via four 630×25 mm nozzles.

The main steam header (MSH) equalizes the steam pressure upstream of the turbine. Steam is tapped for station auxiliaries by a dedicated steam dump device, to the turbine bypass system, a separation, and intermediate superheating system.

The main parameters of main steam are	
Steam pressure at steam generator outlet, MPa	6.27
Steam temperature at steam generator outlet, °C	278.5
Steam pressure upstream of the stop valves, MPa	5.88
Steam temperature upstream of the stop valves, °C	274.3
SG capacity, t/h	1,470

The valves of the steam generator in the Tianwan NPP are installed in the following sequence on each steam line:

- Main steam valve unit, shut-off valves on the main steam isolation valve (MSIV) bypass;
- Isolation valves;
- Main steam gate valve;
- Valves on the main steam gate valve bypass.

The main steam valve unit comprises of the MSIV, the steam generator safety valves, the steam dump valve to the atmosphere, and the shut-off valve upstream of it.

For NPP with V-320 reactors, the main steam isolation valve, the steam generator safety valves, and the steam dump valve are treated as separate equipment.

Main Feedwater System

The main feedwater system comprises of the following unit operations:

- Main electric feedwater pumps;
- Deaerator plant;
- Pipelines and valves (shut-off, control, safety).

Feedwater is supplied to steam generators via the deaerator plant, where the condensate from turbine is also supplied.

Five feedwater pumps are connected to the deaerator plant.

Each pump is equipped with a recirculation line to deaerator that provides pump testing and a possibility of its operation under pump transient operation with low flows.

Feedwater is supplied from the pressure collector of feedwater pumps through two $D_{\text{nom}} 500$ lines to the high-pressure heaters on the turbine. Downstream of the high-pressure heaters, the feedwater is supplied to $D_{\text{nom}} 500$ collectors and then passed on to the steam generators along four $D_{\text{nom}} 400$ pipelines.

The control valves are installed outside the containment on the lines of feedwater supply to each steam generator to maintain the nominal level in the SGs at power operation.

Five electric feedwater pumps (four in operation, one in standby) are installed at NPPs operated with V-428 reactors.

Two turbine-driven feedwater pumps are installed at NPPs operated with V-320 reactors, their capacity being 3,000 m³/h each.

Electric feedwater pumps are designed to supply feedwater to steam generators under normal operating conditions.

The pumps are of the centrifugal type. They are aligned horizontally with two casings. The pumps have four stages.

The main performance of feedwater pump	
Capacity, m ³ /h	1,650
Pressure head, MPa	9.1
Pumped liquid temperature	172

Deaerator is designed to remove corrosive gases and to heat up the turbine condensate under nominal, start-up, and transient conditions of operation.

Deaerator performance	
Capacity, t/h	6,000
Working pressure, MPa, abs.	0.824
Working temperature, °C	172
Material	Carbon steel
Geometrical volume of accumulator, m ³	400
Accumulator useful capacity, m ³	250

Turbine

At all NPP Units operated with V-320 reactors both low-speed K-1000-60/1500 and high-speed K-1000-60/3000 turbines are installed. At the NPP Units with V-428 K-1000-60/3000 steam turbines are installed. It is a condensation type turbine, with one-shaft, five cylinders (2 low-pressure cylinders + 1 high-pressure cylinder + 2 low-pressure cylinders), intermediate separation, and steam superheating. The turbines have a nominal power of 1,000 MW with a rotational speed of 50 Hz or 3,000 rev./min. The energy of the steam supplied to the turbine is used to drive a TVV-1000-2 AC generator directly. The generator is mounted on the same foundation as the turbine.

The scheme of the turbine has 2 LPCs + 1 HPC + 2 LPCs.

Steam is supplied from the HPC along four D_{nom} 1,600 steam lines to four separator-superheaters (SSHs). The separation and steam superheating are performed in one stage. Downstream of the SSH steam is supplied to each of the four low-pressure cylinders. The

Main parameters of the turbine plant	
Nominal power at generator terminals, MW	1,000
Steam flowrate through turbine, t/h	5,870
Steam pressure upstream of HPC valves, MPa	5.88
Steam pressure upstream of LPC, MPa	0.516
Steam temperature upstream of the LPC	250.0
Nominal revolutions, rev./min	3,000

butterfly gates installed in this path perform the functions of stop valves and regulating valves.

Steam is dumped out of each LPC to a dedicated condenser. The condensers are of the surface type. They are basement-positioned, two-flow, and subdivided for pressure. The steam-receiving devices are built-in into the condenser and they accept the SG steam dumped to condenser via steam dump station under start-up and transient operating conditions.

The turbine is also equipped with a regenerative plant to heat up the condensate and feedwater with separator–heaters. Uncontrolled steam extractions can be performed to the regeneration systems, heaters, and to the station auxiliaries.

Generator

The TVV-1000-2UZ generator is installed at each power unit with a nominal power of 1,000 MW, $\cos \varphi$ 0.9, voltage 24 kV.

Separator–Superheater

The K-1000-60/3000 turbine is equipped with a special system of intermediate separation and superheating of the steam after it leaves the HPC and before the steam enters the LPC. The task of the separator–superheater is to separate and evacuate moisture. Moisture is separated in the upstream separators wall moisture built-in into crossover steam lines that supply each SSH. Moisture is also separated in speed separators that collect the suspended moisture, which contacts the SSH casing. Main steam extracted from the lines upstream of the turbine is heated up to 250 °C in order for it to be supplied to LPC. The separated water is pumped out of the sump shared by the four SSH to the main condensate path. Heating obtained from steam condensate in the condensate sump, which is shared with the SSH, is supplied to feedwater path downstream of the high-pressure heater.

3.1.4 I&C and Electrical Systems

I&C System

The I&C system comprises of all the systems, hardware, and actions that are required to measure the process parameters, signal processing, the generation of emergency signals and messages on the state of closed and open control circuits, and limiting conditions of operation, as well as implementation of protective actions and provision of appropriate power supply.

I&C incorporates the following main systems:

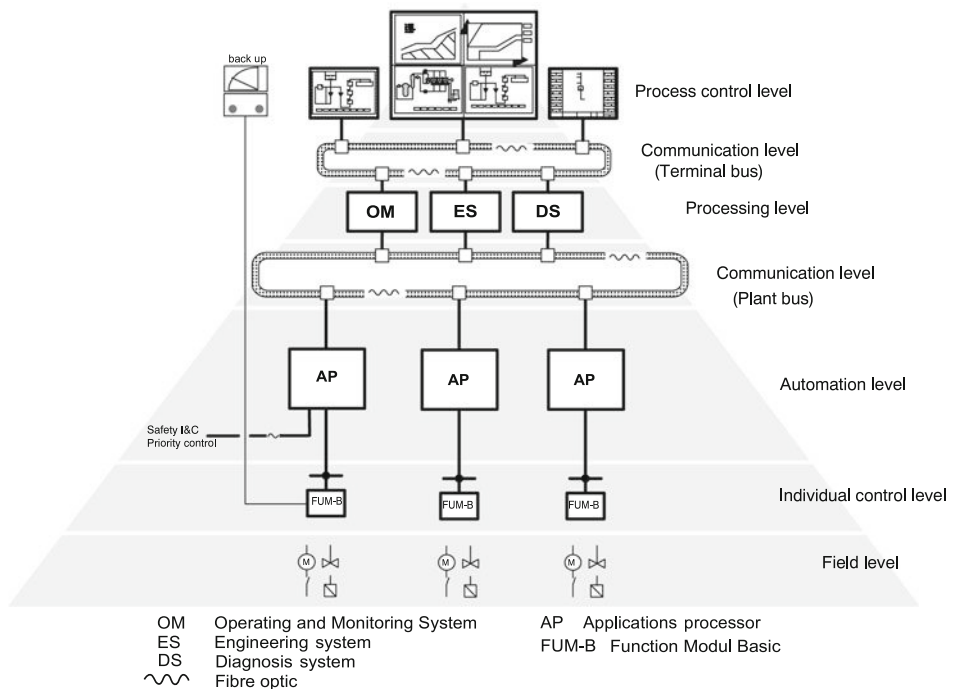
- Reactor trip system (reactor scram);
- Reactor power limitation system;
- Reactor and unit power control system;
- Monitoring, control, and diagnostics system;
- I&C safety system;
- Engineered safety feature actuation system (ESFAS);
- Level and pressure control systems in individual unit equipment.

A simplified structure of the I&C system is presented in ► Fig. 37.

Two system families TELEPERM XP (TXP) and TELEPERM XS (TXS) provide the basis of the general architecture of RP V-428 I&C systems.

TXS is mainly used to perform the functions of the reactor trip system (reactor scram and actuation of engineered safety features). It is given the highest safety qualification and integrity requirements. It is also used for such specific nuclear functions as the systems of reactor power operation including the automatic power controller.

TXP is an automated system for all other applications of the NPP that require control by automation processors and functional modules dealing with data acquisition and processing, drive actuation, and drive control. These functions cover the safety-related I&C area and normal operation I&C, which includes control of the turbine and some independent control



■ Figure 37

Simplified structure of I&C system engineered features

systems. The system performs automated functions such as consequent control, regulation, signal processing, drive monitoring, and control.

The system also actuates the Operation Monitoring (OM) I&C system to monitor the process on visual display units. The system consists of a set of processors that process signals dealing with the man-machine interface and short-time data recording. The server saves data for the OM and a number of operator stations are designed to display all the monitored functions in the VDUs. Each monitor is capable of performing all the I&C functions (control, emergency signal presentation, information display, archiving, and digital registration). The terminal bus provides communication between the processors and the operator terminals.

The traditional equipment of the man-machine interface (Mosaic panels) is used for control in case of a postulated failure of the OM system.

The I&C in the V-320 design differs from the features given below:

Before 2000, the I&C safety systems for the NPP operated with V-320 reactor were created on the basis of hardwired logic and the application of information systems only at the top level of the unit. After 2000, the structures, hardware, and software of the I&C systems are similar to V-428 design:

- Two of four logic with four sensors is applied in the I&C safety systems of V-428 design;
- Two of three logic with three sensors in each safety train is applied in the I&C safety systems of V-320 design.
- There are two sets of reactor trip system.

Main Control Room

For the operator, the main control room is the center of units' control and process monitoring via the I&C systems. It is sited in the control building.

The main control room is divided into several working areas. It gives a possibility of strict separation between the process control panels and the panels of other functions needed for NPP operation.

The operators and shift chief engineer monitor all the events on the displays. There is a possibility to overview all the system control consoles and panels in the main control area.

In case of a postulated OM system failure, the required and safety-related information is displayed in the control panels. Based on the information given, the operator can maintain the station in steady-state operating conditions for a certain period of time or shut the reactor down and bring it to a safe state. Control panels are mainly used to perform this task. The system provides the operator with all the information to monitor the systems that are important for safety and manual process control. In the case that it is impossible to realize monitoring with the OM system, the mosaic panels provide basic information to exercise control with the traditional hardware interface in the main control room with indicators, recorders, signaling system elements, and control keys. The amount of information displayed in the mosaic panel is sufficient to implement the safety functions, as a minimum.

The principles of the main control room architecture are similar for NPPs operated with both V-428 and V-320 reactor plant designs.

Electrical Systems

The electrical systems of the plant include the electric power generation, the supply system, and the power supply for the station service system.

■ **Table 18**
Electrical system performance

Parameter	Value
<i>Generator and transformer system</i>	
Main generators	
Quantity, pcs.	1
Power, MV A	1,178
Quantity of main transformers, pcs.	1
<i>Station power supply systems</i>	
Quantity and power of emergency diesel-generators, pcs. × MW	4 × 5.5
Quantity and power of station diesel-generators, pcs. × MW	2 × 5.0

NPP power output is realized at a voltage of 500 kV. NPP 500 kV switchgear is connected to the electricity grid with three 500 kV transmission lines.

The power supply redundancy of NPP station service consumers is obtained from the external power grid at a voltage of 220 kV.

The electric power generation and supply system for each NPP unit includes a turbine generator of the type TVV-1000-2UZ and a unit step-up transformer, which is connected to it.

The power supply system of the station service consists of three systems:

- Normal operation power supply system;
- Reliable normal operation power supply system;
- Emergency power supply system.

The power supply system for the reliable normal operation of the station service of each unit is broken down into two channels with similar basic components and similar functions that must be fulfilled. Each channel of the power supply system for reliable normal operation includes a diesel generator plant, storage batteries, uninterrupted power supply devices, low-voltage transformers, 6.3 kV switchgears, and AC and DC low-voltage switchgears.

The emergency power supply system of each NPP unit is broken down into four identical channels. Each channel of the emergency power supply system includes a diesel generator plant, storage batteries, uninterrupted power supply devices, low-voltage transformers, 6.3 kV switchgears, and AC and DC low-voltage switchgears (🔗 [Table 18](#)).

3.2 Main Aspects of VVER-1000 Safety

3.2.1 Safety Philosophy

In accordance with the conceptual approach to safety assurance covered in 🔗 [Sect. 2](#), throughout its development, the VVER-1000 reactor design can be attributed to the second and third Generations of nuclear reactor technology. This involved the application of the defense-in-depth principle that assigns top priority to the prevention of unfavorable events and the

mitigation of the consequences in the case of a failure to prevent them. The principle is realized through engineering and organizational measures that are specified in the regulatory documents for each of the five levels of defense-in-depth.

The tasks stated for Level 1 (prevention of anticipated operational occurrences) and Level 2 (prevention of design basis accidents) were to increase the reliability of the equipment and the systems of normal operation. These Levels were devised to improve the operational characteristics of the VVER-1000. This included an increase in the parameters that characterized the plant in comparison to VVER-440 plants.

The task stated for Level 3 (prevention of beyond-design basis accidents by safety systems) was to justify and ensure the efficiency of safety systems in coping with design basis accidents, while maintaining the single failure criterion as the basic principle of designing these systems.

The task stated for Level 4 (beyond-design basis accident management) was to justify and ensure the efficiency of the applied systems and engineering features of BDBA management. The principle of single failure criterion is not applied to BDBA, but considerations of the requirements, which stem from common-cause failures, are made.

For the Generation III designs, the task was solved through using passive systems, which were not previously applied in Generation II designs. An example of such a system is a core catcher for corium outside reactor vessel. The core catcher and other BDBA management systems were not envisaged in Generation II designs and the procedures of BDBA management are based on the application of engineering features envisaged in the design.

A conservative approach was used to justify the design solutions for their application within the normal operating conditions and the anticipated operational occurrences as before, except for DBDA/BDBA where the realistic approach was used.

The main differences in Generation II and Generation III VVER-1000 designs are described as follows:

- Application of the main equipment of reactor plant that had been improved on the basis of new regulatory and technical documents;
- Application of improved, a more economic and reliable core that eliminates any positive reactivity effects because of parameter feedback;
- Improvement of the active safety systems and the application of new passive systems of BDBA management;
- Application of new enhanced automated process control systems and diagnostics systems;
- Application of leak-before-break concept for primary pipelines larger than D_{nom} 200 mm;
- Application of spent fuel pond with compact fuel storage and improved refueling system;
- Applications of a containment system with two envelopes and a core catcher to retain corium melt.

3.2.2 Safety Systems and Distinctive Features

Protective, localizing, supporting, and control safety systems are provided for the prevention or the limitation of reactor plant damage and the localization of radioactive substances within NPP. Technical data of these systems for “Tianwan” NPP design with V-428 RP are given below. The V-320 design differs from the V-428 design, both in number of channels and in technical characteristics. The V-320 design assumes a three-channel concept of safety systems.

Protective Systems

Emergency core cooling system (ECCS) is intended to provide reactor core cooling under loss-of-coolant accidents. ECCS consists of the following subsystems:

- High-pressure emergency cooling system;
- Passive emergency core cooling system;
- Low-pressure emergency cooling system;

The ECCS consists of four similar channels being completely independent of each other.

High-pressure emergency cooling system is intended for the supply of borated water to the primary circuit under LOCAs conditions in the primary circuit and leaks from the secondary circuit. The pumps on pressure head side are connected to the cold legs of circulation loops. The start-up of pumps is realized by a control safety system (CSS) initiating system, which responds to Primary in secondary (PRISE) leak signals.

Characteristics of high-pressure emergency injection pump	
Nominal capacity, t/h	150
Pressure head at nominal supply, MPa	6.5
Maximum capacity, t/h	260
Pressure at maximum capacity, MPa	3.5
Boric acid concentration, g/kg	16
Operating temperature of medium, °C	70–95

Characteristics of low-pressure emergency boron injection pump	
Nominal capacity, t/h	800
Pressure head at nominal supply, MPa	1.5
Maximum capacity, t/h	900
Pressure head at maximum capacity, MPa	1.2
Operating temperature, °C	70–95

Passive ECCS provides a quick supply of boric acid solution into the reactor for core cooling and its flooding under loss-of-coolant accidents when primary pressure drops below 5.9 MPa.

Passive part consists of four hydroaccumulators and pipelines with valves (two check valves and two quick-acting shut-off valves in each line). Two of the hydroaccumulators are connected to the reactor vessel to supply water for core bottom flooding and the other two hydroaccumulators are used for core top flooding. The system is based on a passive principle of action. When the pressure in the reactor decreases below that in hydroaccumulator, then the check valves open and a working medium is pressed out into the reactor due to the pressure of nitrogen blanket. Nitrogen injection into the reactor is prevented by the isolation of hydroaccumulator with quick-acting valves when the level drops below the permissible value.

Technical characteristics of hydroaccumulator	
Nominal pressure, MPa	5.9
Total volume, m ³	60
Water volume in the tank, m ³	50
Boric acid concentration in water, g/kg	16
Water temperature in tank, °C	55–60

Low-pressure emergency cooling system provides supply of borated water to the primary circuit for reactor core cooling undergoing loss-of-coolant accidents after the primary pressure has decreased to 2.5 MPa.

Each channel is featured with a pump and pipelines with valves. The system consists of 4 × 100% channels. Start-up of the system is realized from a CSS initiating part and by a stepwise start-up program when there is a loss of power to the plant.

Each channel is connected to the storage tanks of borated water having 16 g/kg boric acid concentration with a volume of 1,200 m³ as well as to the containment sump.

All channels are connected to the reactor coolant system in such a way that they uniformly distribute the cooling water supply to the core top and bottom due to the following reasons:

- Two channels are connected to RCS loops so that one half of the flowrate is directed to the cold leg and the other one to the hot leg;
- Two channels are connected between two check valves, which are located on the pipelines from the hydroaccumulators. There are two hydroaccumulators per channel for core top and bottom flooding.

Emergency boron injection system is intended for injection of borated water into the pressurizer under a PRISE leak signal and for the fast transition of the reactor plant into a subcritical state under the conditions with anticipated operational occurrences that are accompanied with a failure of the reactor scram. In the latter case, the boron solution injection is provided in the cold leg of the main coolant pipeline.

The system consists of four similar and completely independent channels. Each channel of the system is connected using a pipeline connected to one out of two storage tanks with 150 m³ of borated water in each tank that has a concentration 40 g H₃BO₃/kg H₂O.

The discharge pipelines of each channel are connected to the cold legs of the main circulation loops and to the steam space of pressurizer. The connection of the system to Pressurizer (PRZ) injection line is provided automatically or manually.

Characteristics of emergency boron injection pump	
Number of pumps, pcs.	4
Type of the pump	Piston
Flowrate, m ³ /h	145
Operating temperature, °C	70
Boric acid concentration of the pumped boron solution, g/kg	40

Characteristics of the emergency feedwater pump	
Nominal capacity, m ³ /h	150
Pressure head at nominal supply, MPa	9.0
Maximum capacity, m ³ /h	275
Pressure head at maximum capacity, MPa	3.71

Emergency feedwater system is intended for providing the steam generators with feedwater under anticipated operational occurrences and design basis accidents when the feedwater supply from the main and auxiliary systems is impossible.

The system consists of four similar and completely independent channels.

Each channel is provided with an emergency feedwater pump, associated valves, and pipelines.

Each channel is connected to a storage tank of demineralized water with a volume 700 m³. The assigned temperature of demineralized water in the tanks is maintained between 25 and 35 °C.

Emergency gas removal system is intended for the removal of steam–gas mixture from the primary circuit and to decrease the pressure below the beyond design basis conditions.

The system consists of a set of valves, pipelines connected to the primary circuit equipment. With various combinations of open valves, there is a possibility of online removal of gas blanket from the reactor and the steam generator collectors into the pressurizing system and from the reactor, pressurizer, and the steam generator collectors into the relief tank. The signal on occurrence of emergency level in the reactor is generated by special indicators.

There are also overpressure protection systems installed on the primary and secondary circuit.

Localizing Systems

The localizing systems are intended to prevent or limit the spread of radioactive substances that might be released during accidents inside the NPP and into the environment.

The reactor containment is double in structure. The design value of a leak into the space between the confinement wall and the external envelope after a postulated accident amounts to 0.2% of the air mass in the building for 24 h. The design pressure of the confinement amounts to 0.50 MPa and the design temperature is 150 °C.

The sprinkler system fulfills the following functions:

- Pressure decrease in the mode of injection and recirculation after the design basis accident with the aim of maintaining the pressure in the containment at values below the design pressure;
- Post-accident decay heat removal from the containment;
- Removal of radioactive aerosols and iodines from the containment atmosphere thereby reducing their release into the environment due to the leaks through any breaches in the double containment;
- Control of water temperature in the containment sump under accident conditions with a primary coolant leak.

The system of hydrogen removal from the containment is intended to decrease the hydrogen content of the containment atmosphere after loss-of-coolant accident, which includes severe accidents. The aim of hydrogen removal is to prevent an uncontrolled hydrogen ignition, which can be the cause of loss of containment integrity.

Supporting Systems

The supporting systems are intended for the provision of safety systems with power, a working medium, and the conditions for their operation.

The basic supporting systems involve the following:

An intermediate cooling circuit system of essential consumers provides cooling of the reactor plant equipment, its auxiliary and safety systems under normal operating conditions, anticipated operational occurrences, and design basis accidents. The system provides a barrier between the auxiliary systems of the reactor plant, containing radioactive media, and service water system.

- Service water system for essential consumers removes heat from intermediate cooling circuit system of essential consumers to the ultimate heat sink under all NPP operating conditions;
- Emergency power supply system; and
- Others.

Control Systems

Control systems include

- Engineered safety feature actuation system;
- Reactor trip system.

3.2.3 Maximum Design Basis Accident

A double-ended instantaneous guillotine break of a cold leg of a circulation loop with a diameter of D_{nom} 850 mm is assumed as maximum design basis accident. (This term is not applied in the latest revisions of the Russian regulatory documents). Justification of NPP safety and the determination of design characteristics of the safety systems were realized both for this initiating event and for the others specified in regulatory documents (RDs) and the technical requirements of the operating organizations.

The leak before break (LBB) concept for the pipeline $\geq D_{\text{nom}}$ 200 is applied in the V-428 design unlike the V-320 design.

3.2.4 Severe Accidents

With the justification of meeting current regulatory documents (RD) requirements, a device for corium localization is provided in the design of NPP “Tianwan”. It is regarded as an engineered feature (measure), which is intended for the management of severe accidents where corium spreads beyond the boundaries of the reactor vessel.

The device for corium localization confines the corium and any solid fragments of the destroyed core, parts of reactor vessel, and other internals. Localization and cooling of the

corium is realized within the boundaries of the under-reactor space of the concrete cavity. During the first 24 h after the accident under NPP blackout, localization and cooling of the corium is provided without the additional makeup of cooling water from outside the containment. To provide subsequent corium confinement in the device for corium localization, replenishment of the water inventory is necessary.

For severe accident management the following systems are also provided:

- Primary circuit pressure suppression system with the help of PRZ pilot operated relieve valve (PORV);
- Emergency gas removal system from the primary equipment.

3.2.5 Seismic Design

The RP V-428 design for “Tianwan” NPP is realized with regard for the seismic loads at safe shutdown earthquake (SSE) of magnitude 8 by scale of seismic impact classification (MSK) scale and the operating basis earthquake (OBE) of magnitude 7. In the SSE case, ground horizontal acceleration amounts to -0.2 g and vertical acceleration is 0.1 g. For an operating basis earthquake, the acceleration limits are assumed two times lower than the SSE limit. RP V-320 design is realized for SSE up to magnitude 9.

The justification of the seismic stability of the reactor plant equipment of the VVER-1000 type was performed using calculation procedures and the results of experimental studies that are based on applying floor-response spectra and accelerograms. The strength calculations to check the equipment and pipeline viability are performed by considering the combination of the operational, accident, and seismic loads.

3.3 Operational Experience

As of 30.09.2009, there are 28 NPPs with VVER-1000 reactors in operation and a total operational experience of over 480 reactor-years has been accumulated.

A list of NPPs with VVER-1000 reactors is given in [▶ Table 19](#).

Nowadays, studies are under way to justify the power uprating of operating units, which are equipped with V-320 RP.

More detailed information on the design of reactor plants for NPP with VVER reactor is found in the following publications (in Russian):

Sidorenko V.A. (ed). History of nuclear power engineering in Soviet Union and Russia. Moscow: Izdat, 2001

Denisov V.P., Dragunov Yu.G. VVER reactor plants for nuclear power stations. Moscow: Izdat, 2002.

Bessalov G.G., Denisov V.P., Melnikov N.F., Dragunov Yu.G. VVER reactors for medium power NPPs. Moscow: IKC “Akademkniga,” 2004.

Logvinov S.A., Bezrukov Yu.A., Dragunov Yu.G. Experimental verification of thermo-hydraulic reliability of VVER reactors. Moscow: IKC “Akademkniga,” 2004.

Dranchenko B.N., Dragunov Yu.G., Portnov B.B., Seleznev A.V. Experimental studies of stressed state and strength of VVER equipment. Moscow: IKC “Akademkniga,” 2004.

■ **Table 19**
NPPs with VVER-1000 reactors in operation

NPP	Unit and reactor type	Electric power, MW	Commissioning	Gross generation till 2009, GW h
Volgodonsk, Russia	Unit 1, B-320	10,000	03.2001	51,093.87
Balakovo, Russia	Unit 1, B-320	1,000	12.1985	113,280
	Unit 2, B-320	1,000	09.1987	113,280
	Unit 3, B-320	1,000	12.1988	114,344
	Unit 4, B-320	1,000	03.1993	96,155
Kalinin, Russia	Unit 1, B-338	1,000	04.1984	145,900
	Unit 2, B-338	1,000	12.1986	134,572
	Unit 3, B-320	1,000	12.2004	25,386
Novovoronezh, Russia	Unit 5, B-187	1,000	05.1980	147,222
Zaporozhe, Ukraine	Unit 1, B-320	1,000	12.1984	124,507
	Unit 2, B-320	1,000	10.1985	127,965
	Unit 3, B-320	1,000	12.1986	125,828
	Unit 4, B-320	1,000	12.1987	127,163
	Unit 5, B-320	1,000	08.1989	118,303
	Unit 6, B-320	1,000	10.1995	84,119
Rovno, Ukraine	Unit 3, B-320	1,000	10.1986	125,565
	Unit 4, B-320	1,000	10.2004	20,116
Khmelnitsky, Ukraine	Unit 1, B-320	1,000	11.1987	125,671
	Unit 2, B-320	1,000	08.2004	24,920
South Ukraine, Ukraine	Unit 3, B-320	1,000	09.1989	111,782
	Unit 2, B-338	1,000	01.1985	126,311
	Unit 1, B-302	1,000	12.1982	142,493
Kozloduy, Bulgaria	Unit 5, B-320	1,000	11.1987	93,946
	Unit 6, B-320	1,000	05.1991	84,787
Temelin, Czech Republic	Unit 1, B-320	1,000	12.2000	38,382
	Unit 2, B-320	1,000	05.2002	36,290
Tianwan, China	Unit 1, B-428	1,000	05.2006	12,662
	Unit 2, B-428	1,000	05.2007	10,977

4 Conclusion

VVER reactors are pressurized water reactors developed in the Soviet Union and the Russian Federation. Because of certain peculiarities (hexagonal reactor grid, horizontal steam generators, etc.) and historical reasons they are distinguished from Western PWRs. The development

of VVER reactors was started already in 1955 and the first VVER reactor of 210 MW power was commissioned at Novovoronezh in 1964. Since then, two generations of VVER-440 reactors and the family of VVER-1000 reactors were developed. In Russia and in several other countries, 32 VVER-440 units and 28 VVER-1000 units were put into operation and until now only some of them were decommissioned. Safety philosophy of VVER reactors has been gradually refined and by applying new solutions for the new reactors and also by the safety enhancement of the existing reactors the present safety level of VVER reactors is widely accepted.

Mainly due to the special alloy of fuel rod claddings, the VVER fuel has an extremely good reputation. The conservative power density of VVER-440 reactors allow for power uprating whenever appropriate fuel (higher enrichment, burnable absorber) is introduced. Selection of structural materials and the applied water chemistry generally ensure the long-term operation of the VVER units.

Application of horizontal steam generators is a further specific feature of VVER-type reactors. They ensure very acceptable conditions even in complex cases. On the other hand, the horizontal arrangement of steam generators leads to a large containment.

21 Sodium Fast Reactor Design: Fuels, Neutronics, Thermal-Hydraulics, Structural Mechanics and Safety

*Jacques Rouault¹ · P. Chellapandi² · Baldev Raj² · Philippe Dufour³ ·
Christian Latge¹ · Laurent Paret¹ · Pierre Lo Pinto¹ · Gilles H. Rodriguez¹ ·
Guy-Marie Gautier¹ · Gian-Luigi Fiorini¹ · Michel Pelletier¹ ·
Dominique Gosset¹ · Stéphane Bourganel⁴ · Gerard Mignot¹ ·
Frédéric Varaine¹ · Bernard Valentin¹ · Patrick Masoni¹ ·
Philippe Martin¹ · Jean-Claude Queval¹ · Daniel Broc¹ ·
Nicolas Devictor¹*

¹French Atomic Energy Commission (CEA), France

jacques.rouault@cea.fr
christian.latge@cea.fr
laurent.paret@cea.fr
pierre.lopinto@cea.fr
gilles.rodriguez@cea.fr
guy-marie.gautier@cea.fr
gian-luigi.fiorini@cea.fr
michel.pelletier@cea.fr
dominique.gosset@cea.fr
gerard.mignot@cea.fr
frederic.varaine@cea.fr
bernard.valentin@cea.fr
patrick.masoni@cea.fr
philippe.martin@drncad.cea.fr
jean-claude.queval@cea.fr
daniel.broc@cea.fr
nicolas.devictor@cea.fr

²Indira Gandhi Center for Atomic Research, India

pcp@igcar.gov.in
dir@igcar.gov.in

³Chargé demission RNA-Na, CEA/DEN/CAD/DER/SESI

French Atomic Energy Commission (CEA), France

philippe.dufour@cea.fr

⁴CEA Saclay, Centre d'Etudes Nucléaires de Saclay, France

stephane.bourganel@cea.fr

1	<i>Motivations for Fast Neutron Systems</i>	2328
1.1	Basic Principles and Consequences.....	2328
1.1.1	Conditions for Breeding.....	2328
1.1.2	Simplified Neutronic Balance in a PWR.....	2329
1.1.3	Simplified Neutronic Balance in a FBR.....	2330
1.1.4	Balances Comparison.....	2330
1.2	Effective Utilization of Resources.....	2331
1.2.1	Uranium Resources and Breeding.....	2332
1.3	Flexible Use of Actinides.....	2333
1.4	Waste Minimization.....	2333
2	<i>SFR History and Current Projects</i>	2335
2.1	Overview.....	2335
2.2	USA.....	2337
2.3	Russia.....	2338
2.4	Europe.....	2338
2.4.1	France.....	2338
2.4.2	UK.....	2339
2.4.3	Germany.....	2339
2.4.4	Italy.....	2340
2.4.5	Belgium, Netherland.....	2340
2.4.6	Multinational Project: EFR.....	2340
2.5	Japan.....	2341
2.5.1	Joyo.....	2341
2.5.2	Monju.....	2341
2.5.3	Rapid-L.....	2342
2.5.4	L-4S “Nuclear Battery”.....	2342
2.5.5	Commercial Fast Reactor Development Program.....	2343
2.6	India.....	2343
2.6.1	FBTR.....	2347
2.6.2	PFBR.....	2347
2.7	China.....	2348
2.8	Korea.....	2351
3	<i>Basic Design Choices</i>	2352
3.1	Sodium as Coolant.....	2352
3.1.1	Physical Properties.....	2353
3.1.2	Chemical Properties.....	2357
3.1.3	Neutronic Properties.....	2361
3.2	Fuel Design.....	2361
3.2.1	Fuel Element.....	2361
3.2.2	Fuel Subassembly.....	2362
3.3	Pool/Loop and Modular Design.....	2364
3.3.1	Features of the Primary Circuit Concepts.....	2364
3.3.2	Pool Concept: Motivation and Challenges.....	2365
3.3.3	Loop Concept: Motivation and Challenges.....	2366

3.3.4	Modular Concept: Motivation and Challenges	2366
3.4	Main Components and Systems	2367
3.4.1	Description of Heat Transport Circuits and Components	2368
3.4.2	Primary Component Layout on the Top Shield	2368
3.4.3	Reactor Assembly Support Options	2372
3.4.4	Basic Design Options of Primary Circuit Components	2374
3.4.5	Design Improvements for Future SFRs	2392
3.4.6	Intermediate Circuits and Steam Generator	2393
3.4.7	Summary	2417
3.5	Fuel Handling	2417
3.5.1	Function	2418
3.5.2	Classification	2418
3.5.3	On-Line Versus Off-Line Refuelling	2419
3.5.4	Fresh Subassembly Handling	2419
3.5.5	Spent Subassembly Handling	2420
3.5.6	In-Vessel/Ex-Vessel Storage to Reduce Decay Heat of Subassembly	2421
3.5.7	Design Validation	2425
3.5.8	Innovative Fuel Handling Concepts	2428
3.6	Recent Evolution	2429
3.6.1	Intermediate Coupling Fluid	2430
3.6.2	Advanced Energy Conversion System	2436
3.6.3	Plant Layout	2451
4	<i>Safety Principles</i>	2453
4.1	Introduction	2453
4.2	Safety Features Associated with Sodium	2454
4.2.1	Physical Properties	2454
4.2.2	Nuclear Properties	2455
4.2.3	Chemical Reactions	2455
4.2.4	Thermalhydraulics and Structural Mechanics Considerations	2457
4.3	Safety Objectives and Principles Applicable for Future Reactors	2457
4.4	The Defense in Depth Principle	2458
4.4.1	The Levels of the Defense in Depth	2458
4.4.2	Objectives and Scope of Defense in Depth	2459
4.5	Safety Approach for the SFR to Address the Severe Plant Conditions	2460
4.6	SFR: Safety Demonstration vis-à-vis of the Whole Core Melting	2461
4.6.1	Prevention of Whole Core Melting Situations	2463
4.6.2	Whole Core Melt Situations: Consequences' Control and Mitigation	2464
4.6.3	Initiating Events, Sequences, and Situations "Practically Eliminated"	2465
4.6.4	Control and Management of the Safety Functions	2466
4.6.5	Other Specific Risks	2468
4.6.6	Hazards	2468
4.7	R&D Organization	2468
4.8	Conclusions	2469
5	<i>The Materials</i>	2470
5.1	Fuel Materials	2470
5.1.1	Oxide	2470

5.1.2	Metal	2479
5.1.3	Properties of Metal Fuel for Design	2481
5.1.4	Carbide and Nitride	2489
5.2	Structural Materials	2499
5.3	Absorber Materials	2499
5.3.1	Introduction	2499
5.3.2	Boron Carbide	2501
5.3.3	Absorber Pins	2506
5.3.4	Developments	2507
5.4	Shield Materials	2508
5.4.1	Vessel Shielding	2508
5.4.2	Sodium Activation	2509
6	<i>Core Design</i>	2510
6.1	Performances Objectives and Design Criteria	2510
6.1.1	Safety Objectives	2510
6.1.2	Flexibility SFR Cores	2510
6.1.3	Core Competitiveness	2511
6.1.4	Design Criteria	2511
6.1.5	Core Shape Design	2513
6.2	Core Neutronics	2513
6.2.1	Elementary Physical Analysis	2513
6.2.2	Predesign Studies	2514
6.2.3	Detailed Design Studies	2515
6.2.4	Calculation Tool for Neutronic Core Design	2517
6.3	Core Thermalhydraulics	2518
6.3.1	Core Flow Distribution	2518
6.3.2	Calculation of Fuel Assembly Thermalhydraulics	2520
6.3.3	Assessment of Hexcan Temperatures	2522
6.4	Core Mechanics	2524
6.4.1	Subassemblies Distortions	2524
6.4.2	Operating Considerations	2524
6.4.3	Modeling of the SFR Core Static Mechanical Behavior	2525
6.4.4	Experimental Validation	2526
6.4.5	Conclusion	2529
6.5	Reactivity Effects	2529
6.5.1	Description of the Feedback Effects	2529
6.5.2	Calculation Method	2533
6.5.3	Return to a Temperature Variation	2534
6.5.4	Validity of These Coefficients	2536
7	<i>Specific Thermalhydraulics Issues</i>	2536
7.1	Thermal Stratification	2536
7.1.1	Phenomena	2536
7.1.2	Locations Prone to Stratification	2537
7.1.3	Effect of Stratification	2538
7.1.4	Numerical Simulation of Stratification	2538
7.1.5	Experimental Simulation of Stratification	2539

7.1.6	Design Guidelines for Stratification	2540
7.2	Thermal Striping.....	2542
7.2.1	Phenomenon of Striping	2542
7.2.2	Locations Prone to Thermal Striping	2542
7.2.3	Effect of Striping.....	2543
7.2.4	Prediction of Thermal Striping	2543
7.2.5	Design Guidelines for Striping	2546
7.3	Free Level Fluctuations	2549
7.3.1	Phenomenon	2549
7.3.2	Locations of Concern	2550
7.3.3	Methods for Prediction of Level Fluctuations	2551
7.4	Cellular Convection.....	2551
7.4.1	Phenomenon	2551
7.4.2	Location of Cellular Convection	2553
7.4.3	Effects of Cellular Convection	2554
7.4.4	Methods for Prediction of Cellular Convection.....	2554
7.4.5	Managing Cellular Convection	2555
7.5	Gas Entrainment	2556
7.5.1	Phenomenon	2556
7.5.2	Potential Areas for Gas Entrainment	2559
7.5.3	Effect of Gas Entrainment.....	2559
7.5.4	Prediction of Gas Entrainment	2560
7.5.5	Design Provisions Against Gas Entrainment and Other Remarks	2562
7.6	Thermalhydraulic Design Criteria and Analysis Methods	2563
7.6.1	Temperature Asymmetry in Cold Pool.....	2563
7.6.2	Free Level Fluctuation	2563
7.6.3	Free Surface Velocity in the Pool	2564
7.6.4	High-Cycle Temperature Fluctuation	2564
7.6.5	Heat Loss to Top Shield.....	2564
7.6.6	Analysis Methods	2564
8	<i>Specific Structural Mechanics Issues</i>	2566
8.1	Introduction.....	2566
8.2	High Cycle Thermal Fatigue: Thermal Striping and Stratification Instabilities	2566
8.2.1	Experimental Evidence of Thermal Striping.....	2567
8.2.2	Assessment of Potential Damage by Thermal Striping at the Design Stage.....	2570
8.2.3	Conclusion, Future Prospects	2571
8.3	Free Level, Stratification Level Fluctuations	2572
8.3.1	The Free Level Issues.....	2572
8.3.2	In Sodium Stratification Issues	2577
8.3.3	Conclusion	2577
8.4	Seismic-Induced Forces and Their Effects	2577
8.4.1	Geologic Phenomena	2577
8.4.2	Seismic Risk	2578
8.4.3	Site Effects of Seismic Forces	2578

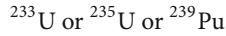
8.4.4	Effects of Seismic Forces on Structures.....	2579
8.4.5	Seismic Piping Behavior and Design Criteria.....	2581
8.5	Fluid Structure Interaction in the Fast Reactor Cores.....	2584
8.5.1	Short Description of the Structures of the Reactor.....	2584
8.5.2	Methods to Take into Account FSI.....	2584
8.5.3	Seismic Behavior of the Fast Reactor Cores.....	2586
8.5.4	Design Model for the Seismic Behavior of the Core.....	2586
8.5.5	Overflow Instabilities.....	2587
8.5.6	New Fluid Structure Interaction Phenomena to be Investigated.....	2587
8.6	Buckling of Thin Shells.....	2587
8.6.1	Buckling Design Approach.....	2591
8.6.2	Simplified Analysis Method for Buckling of Shells Under Seismic Loadings.....	2591
8.6.3	Thermal Buckling Due to Stationary Temperature Gradient.....	2596
8.6.4	Progressive Buckling Due to Moving Temperature Gradients.....	2598
8.6.5	Creep Buckling.....	2599
8.6.6	An Integrated Buckling Analysis of Thin Vessels of Reactor Assembly.....	2601
8.6.7	Investigation of Buckling of Safety Vessel Subjected to Seismic Loading ...	2610
8.6.8	Investigation of Buckling of Top Shield Plates under CDA Loading.....	2613
8.6.9	Experimental Validations of Computer Codes.....	2615
8.6.10	Summary.....	2619
8.7	Design Criteria and Analysis Method.....	2620
8.7.1	Loadings.....	2622
8.7.2	Design Limits.....	2623
8.7.3	Analysis Methods.....	2625
8.7.4	Buckling Design.....	2626
9	<i>Plant Dynamics</i>	2630
9.1	About the Design Basis Conditions, the Design Extension Conditions and the Residual Risk.....	2632
9.2	Safety Criteria.....	2635
9.3	Analysis Methods.....	2638
9.3.1	Rules for the Different Conditions.....	2639
9.3.2	Line of Protection Analysis.....	2641
9.3.3	Method for Safety Classification of Reactor Components.....	2643
9.3.4	Probabilistic Safety Assessment.....	2644
9.4	Illustration of SFRs Behavior in Typical Transient Situations.....	2644
9.5	Anticipated Transients Without SCRAM.....	2649
10	<i>Severe Accidents</i>	2651
10.1	Introduction.....	2651
10.2	History.....	2653
10.2.1	Instances of Severe Accidents in Fast Reactors.....	2654
10.3	Defense in Depth.....	2655
10.3.1	Physical Barriers.....	2656
10.4	CDA: Phenomenology.....	2657
10.4.1	Different Phases of a CDA.....	2658
10.5	Analysis for Mechanical Consequences.....	2659

10.5.1	Idealization of Molten Core Expansion Behavior	2659
10.5.2	Analysis for Vessel and Roof Mechanical Loading	2661
10.6	Post Accident Phase	2673
10.6.1	Scenarios	2673
10.6.2	Core Debris Accommodation	2676
10.6.3	In-Vessel Debris Accommodation	2677
10.6.4	Ex-Vessel Debris Accommodation	2679
10.7	Computer Codes and Validation	2680
10.7.1	Validation of Codes: A Case Study	2681
10.8	Innovations Toward Enhanced Safety	2681
10.8.1	Core	2681
10.8.2	Sodium Fire and Sodium–Water Reactions	2682
10.8.3	Reliable and Diverse Shutdown Systems	2682
10.8.4	Decay Heat Removal Systems	2683
10.8.5	Core Catcher	2683
10.8.6	Breakthroughs for Future SFR	2683
10.9	Summary	2684
11	<i>French Licensing Experience on SFR</i>	2684
11.1	Phenix	2684
11.2	SPX-1	2686
11.3	SPX-2	2687
12	<i>Innovative Design Evolutions</i>	2687
12.1	In India	2687
12.1.1	Pool Type Concept	2687
12.1.2	Reactor Power	2688
12.1.3	Core	2688
12.1.4	Shutdown Systems	2689
12.1.5	Main Heat Transport System	2690
12.1.6	DHR System	2692
12.1.7	Main Structural Materials	2693
12.1.8	Operating Temperatures	2693
12.1.9	Reactor Assembly	2694
12.1.10	Component Handling	2694
12.1.11	Plant Layout	2696
12.2	In France	2697
12.2.1	A Core with Improved Safety Performances	2697
12.2.2	A Better Resistance to Severe Accidents and External Hazards	2698
12.2.3	An Optimized Energy Conversion System Optimized to Reduce or Exclude the Risk of Sodium–Water Reaction	2698
12.2.4	A Reexamination of the Reactor and Its Components Design	2699
12.2.5	ASTRID Program	2699
	<i>References</i>	2700

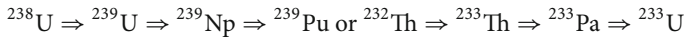
1 Motivations for Fast Neutron Systems

1.1 Basic Principles and Consequences

In any nuclear reactor, there is both fissile material destroyed (FD)



and produced by conversion of the fertile material (FP):



The degree of conversion that occurs in a reactor is denoted by the general term of conversion ratio, CR, which is defined as $\text{CR} = \text{FP}/\text{FD}$. If this conversion ratio is greater than 1, it is called breeding ratio, **BR**.

1.1.1 Conditions for Breeding

A nuclear reactor can be a breeder in broad neutron energy spectrum, but adequate breeding ratios can be achieved only by selecting the appropriate fertile and fissile isotopes for that spectrum.

Starting from the fission process, if

- ν is the number of neutrons produced per fission
- η is the number of neutrons produced per neutron absorbed
- α is the ratio capture/fission (σ_c/σ_f),

these parameters are related by $\eta = \nu/(1 + \alpha)$.

The necessary condition for breeding is $\eta > 2$:

- One neutron for a new fission
- One neutron for a new conversion
- x for leakages or parasitic captures

► *Figure 1* shows that for U–Pu fuel, a sufficient value of η can be obtained only with a fast neutron spectrum.

One notices that the condition for breeding is well fulfilled in fast spectrum reactor in particular for ^{239}Pu for which the value of η averaged is about 2.3.

The ► *Table 1* below provides for U5 and Pu9 compared parameters in thermal and fast spectrum.

In a fast neutron reactor, the neutrons available for conversion are 1.3 or more. In such a reactor, there is net production of fissile material that can be used to fuel another reactor. This is “breeding,” fundamental characteristic of fast neutron reactors. To understand how breeding is possible in a FR and not in a PWR, it is worthwhile to compare the balance sheet neutron as depicted in ► *Fig. 2*.

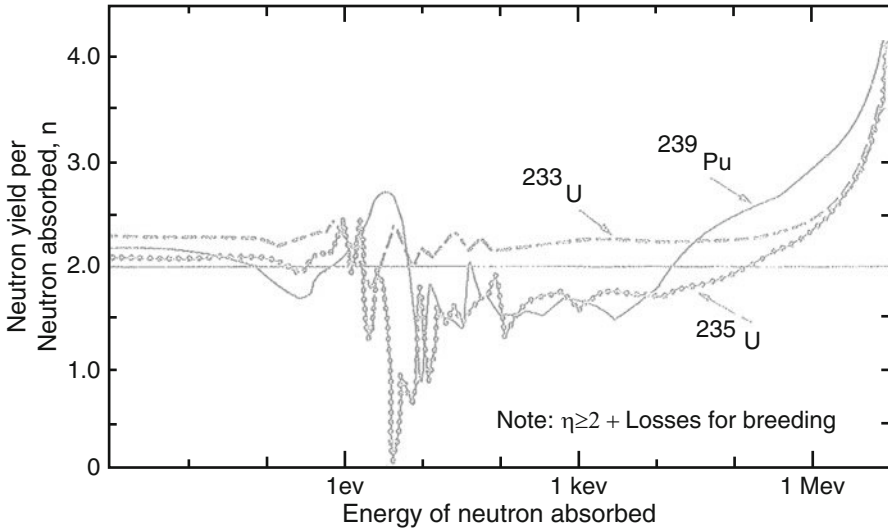


Figure 1
Neutron yield (From Waltar and Reynolds)

Table 1
Fissile isotopes comparison

Isotope Spectrum	^{235}U		^{239}Pu	
	Thermal	Fast	Thermal	Fast
α	0.17	0.29	0.36	0.26
ν	2.42	2.43	2.87	2.94
η	2.07	1.88	2.11	2.33

Source: Traité de neutronique, Bussac, Reuss

1.1.2 Simplified Neutronic Balance in a PWR

This assessment is presented very schematically in Fig. 2 for a conventional PWR of about 1,000 MWe, assuming that the only fissile material is ^{235}U . The numbers given must be understood as orders of magnitude. One hundred fissions of ^{235}U release about 240 neutrons, and these neutrons give rise to the following reactions:

- 100 neutrons cause 100 new fissions, maintaining the chain reaction and consuming 100 fissile nuclei,
- 70 neutrons are absorbed by capture in fertile material (^{238}U), converting them into fissile nuclei (^{239}Pu),
- 45 neutrons are absorbed by sterile capture, of which 17 are by fissile nuclei,
- 60 neutrons leaking outside the core (and will be captured by the neutron shielding).

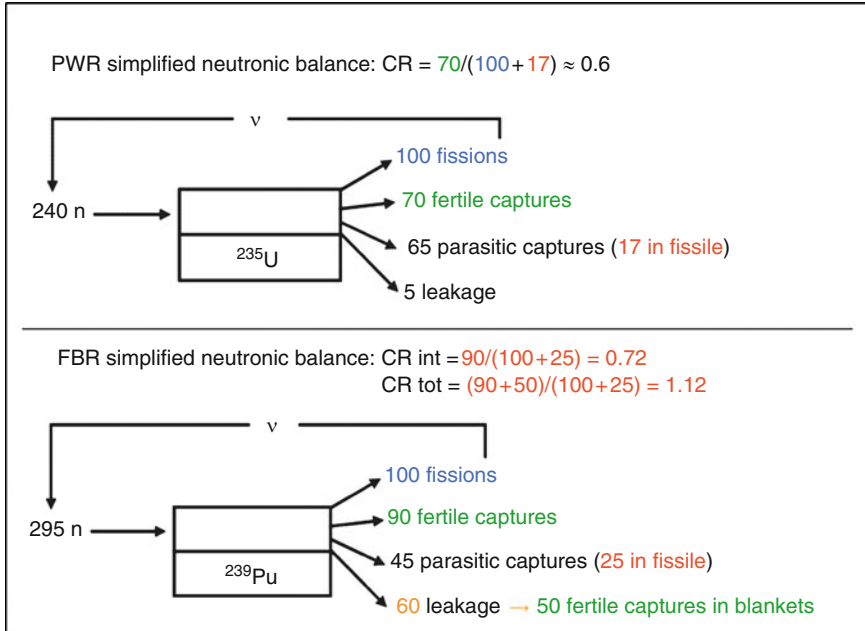


Figure 2

Comparison of neutron balance between PWR and FBR systems

1.1.3 Simplified Neutronic Balance in a FBR

This assessment is presented very schematically in [Fig. 2](#) for a FBR having power close to 1,000 MWe, very schematic, assuming that the only fissile material is ^{239}Pu .

One hundred fissions of ^{239}Pu release nearly 300 neutrons. These neutrons will yield the following reactions:

- 100 neutrons cause 100 new fissions, maintaining the chain reaction and consuming 100 fissile nuclei of ^{239}Pu
- 90 neutrons are absorbed by capture in fertile material (^{238}U) in the core of the reactor, converting them into fissile nuclei (^{239}Pu)
- 45 neutrons are absorbed by sterile capture, 25 of which are by fissile nuclei
- 60 neutrons leaking outside the core itself to the blankets, where they are, for the most part (~ 50 neutrons), absorbed by capture in fertile material (^{238}U), converting them into fissile nuclei (^{239}Pu); other neutrons (~ 10) are absorbed by sterile capture in blankets or in the neutron shielding.

1.1.4 Balances Comparison

It is in the large number of neutrons leaking out of the core to be captured by the nuclei of ^{238}U in the blankets that we find the possibility of breeding in the FBR.

That is demonstrated by calculating the conversion rate (or regeneration) in the two preceding examples which, despite their schematic nature, are sufficiently representative of orders of magnitude.

It is easy to find

- $CR = 70/(100 + 17) \approx 0.6$ in PWR
- $CR \text{ (internal)} = 90/(100 + 25) = 0.72$ in FBR core only
- $CR \text{ (total)} = (90 + 50)/(100 + 25) = 1.12$ in FBR core and blankets

We may therefore conclude that

- The rate of regeneration of the core itself a FR is certainly higher than the conversion ratio of a PWR of equivalent power but it remains less than 1 in this example.
- It is thanks to the blankets that a FR can breed.

In relation to these conclusions, two points must be underlined:

- Surrounding the core of a PWR with a blanket does not significantly change its conversion ratio due to the low number of neutrons leaking out of the core.
- It is relatively easy to modulate the breeding ratio of a FBR, for example, by changing the thickness of the blankets and therefore, the number of neutrons that are captured, to modulate the breeding ratio of a FBR.

1.2 Effective Utilization of Resources

The Nuclear Energy Agency has published the state of reserves and resources of uranium with different levels of cost and certainty (► [Table 2](#)). However, there is a slight confusion on the quantity of reserves (some resources) and resources (which are assumed or very possible). However, the “proven” reserves announced by the NEA can increase or decrease substantially depending on the year.

■ **Table 2**

State of reserves and resources of uranium

Reserves and resources in 2006	Uranium cost	Uranium quantity (kt U)	Amount (kt U)
RAR: Resources reasonably assured (reserves)	<40 \$/kg U	1,947	1,947
	40–80 \$/kg U	696	2,643
	80–130 \$/kg U	654	3,297
Inferred resources	<40 \$/kg U	799	4,096
	40–80 \$/kg U	362	4,458
	80–130 \$/kg U	285	4,743
To discover, predicted	<80 \$/kg U	1,700	6,443
	80–130 \$/kg U	819	7,262
To discover, speculative	<130 \$/kg U	4,557	11,819
	Unknown cost	2,979	14,798

Uranium world reserves (3.3 Mt) and resources (11.5 Mt) are estimated to be about 15 Mt or about 150 Gtoe. At the rate of current global consumption (0.6 Gtoe/year) and assuming the use of water reactor cycles opened, reserves and resources represent about 250 years of production.

The major trend that emerges by 2050 in terms of primary energy needs is a strong growth in primary energy needs that could rise from 9.8 Gtoe in 2000 to almost 15 Gtoe in 2020. Afterward, there is more uncertainty, but then, it might rise from 18 to 40 Gtoe in 2050 (which would mean doubling or quadrupling).

A possible scenario of the contribution of various energy sources to world consumption of commercial primary energy fits in perfectly with the WEC 98 projections for the years of 2000/2100, corresponding to the median doubling of world commercial energy consumption (~20 Gtep). The assumption was made that

- Growth in energy demand will be linear between 2010 and 2050.
- Nuclear power should contribute to the adjustment in the application, leading to increased production of nuclear power from 0.6 to 4 Gtoe/years between 2000 and 2050.

In this context, the pressure resulting from a growing demand and linked to strong constraints on fossil fuels (USA and China's heavy dependence on coal; USA and Europe's dependence on oil and gas) should lead to the relaunching of nuclear plant construction in countries possessing nuclear technology and to the development of this same technology in others.

The unavoidable steady reduction of economically exploitable resources of natural uranium will contribute to reliance on nuclear energy for sustainable development and cause nuclear energy to play a heightened role in the future, a point of view which is feasible on a more or less long-term basis. Only through the exploitation of fertile material and, therefore, through the use of fast neutron reactors can this be implemented. With fast neutron reactors, the only reserves ^{238}U , currently stored as tails (tails represent the depleted ^{238}U , which remains after completion of the enrichment process) from enrichment plants, allows for increased energy reserves up to a factor of about 50 in comparison to the current light water reactor technology. Therefore, fast reactors are the key to an efficient use of uranium resources.

1.2.1 Uranium Resources and Breeding

While these long-term considerations are rather clear, the near-term considerations that govern the timing for the introduction of a commercial FBR and the ensuing strategies are more complex for the transition to that FBR or to an FBR-LWR mix. Since fast reactors have to be loaded initially with plutonium produced by light water reactors of current technology, the availability of plutonium determines the maximum rate at which fast reactors can be introduced and the nuclear energy that can be provided.

An initial assessment of energy production has been formulated with the following assumptions:

- All uranium is used in LWRs
- LWRs have a lifespan of 60 years,
- Plutonium produced by LWRs is used in FBRs

To maximize the nuclear contribution, the use of FBRs is necessary. For example, an assessment with the optimistic assumption of a breeding gain of 0.2 and a doubling time of 50 years would lead to a power greater than 6 Gtoe/year in 2050.

1.3 Flexible Use of Actinides

Fast reactors play a unique role in the actinide management mission because they operate with high energy neutrons that are more effective in fissioning transuranic actinides. In contrast, thermal reactors extract energy primarily from fissile isotopes; a thermal spectrum also leads to the generation of higher actinides that complicate subsequent recycling. Fast reactors can operate in three distinct fuel cycle roles. A conversion ratio (the conversion ratio is defined as the ratio of the transuranics production rate to the transuranics destruction rate, whereas the breeding ratio is a similar ratio for the fissile material) less than 1 (“transmuter” mode) means that there is a net consumption of transuranics. Here, “transmute” means to convert transuranics into shorter-lived isotopes in order to reduce long-term waste management burdens. A conversion ratio close to 1 (“converter mode”) provides a balance in transuranic production and consumption. This mode results in low reactivity loss rates with associated control benefits. A conversion ratio greater than 1 (“breeder mode”) means that there is a net creation of transuranics. This approach allows the creation of additional fissile materials, but requires the inclusion of extra uranium in the SFR and fuel cycle. An appropriately designed fast reactor has the flexibility to shift between these operating modes and the desired actinide management strategy will depend on a balance of waste management and resource extension considerations.

1.4 Waste Minimization

Owing to their high level of neutron flux (10 times higher than that of a PWR) and to the ratios of capture cross sections on fission cross sections of major actinides more favorable in the fast spectrum (by a factor of 10), FBRs are the best tool for the transmutation of actinides in reactor.

Two modes of waste incineration have been considered:

- The homogeneous mode wherein actinides to be transmuted (Np, Am, Cm) are mixed with standard fuel in limited quantities (a few percent), thereby “diluting” the impact on the reactor and the fuel cycle facilities.
- The mixed mode in which the elements are separated from the fuel and placed in a limited number of devices is known as “targets.” The impact on all posts in the fuel cycle is then increased substantially but for a reduced flow of materials.

In order to establish the scientific feasibility of these different modes, radiation experiments are now being carried out in France in the PHENIX reactor. In conjunction with the actinide management, the SFR technology offers the means to reduce waste generation by features such as improved thermal efficiency, greater use of fuel resources, and the development of superior waste forms for the SFR closed fuel cycle. It is also obvious that SFR nuclear power contributes to the reduction of the greenhouse effect (CO₂ emissions) compared to electricity generation using fossil fuels. Efforts will also be made to achieve reductions in the amount of waste generated from the operations and maintenance and the decommissioning of system facilities and the amount of waste migrating into the environment.

There are potential benefits of a closed fuel cycle based on fast reactors for waste management. It is easier to transmute TRU or MA in a fast reactor core, and there is less impact on the fuel cycle (e.g., at fuel fabrication). It is then possible to have a sustainable close cycle, with reduced burden on a deep geological storage (🔍 Fig. 3). Certain elements (plutonium, americium, cesium, strontium, and curium) are primarily responsible for the decay heat that can cause repository temperature limits to be reached. Large gains in repository space are possible

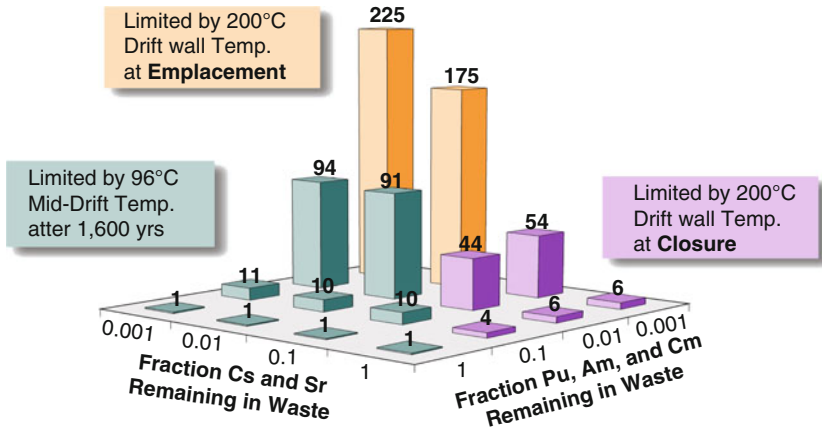


Figure 3
Repository space requirements

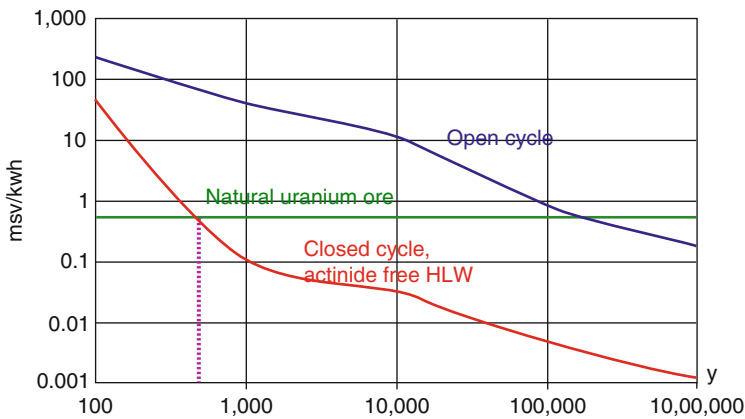


Figure 4
Benefits of closed fuel cycle

by processing spent nuclear fuel to remove those elements (► Fig. 4). Related to treatment of recovered elements, cesium and strontium can be stored separately for 200–300 years and plutonium, americium, and curium can be recycled for transmutation and/or fission by irradiation in fast reactors. These advantages had been envisaged as early as in 1946 by Enrico Fermi, who demonstrated the breeding principle and stated that “the people who will develop SFR technology will lead the world in the future.” Further, in 1951, the world’s first nuclear-generated electricity is EBR-1. In 1964, at the third Geneva Conference, it was stated that “full-sized SFR stations will probably be commissioned in the early 1970s.” Against this backdrop, it is an unfortunate scenario that the SFR development has gone to standstill for many years. It is comforting now that the importance of SFRs is being felt by various countries and systematic plan of actions for the future growth have been formulated.

2 SFR History and Current Projects

2.1 Overview

Ever since the early research on nuclear energy in the 1940s and the 1950s, thermal neutron reactors and fast neutron reactors were studied and experimented at the same time. The first electricity generation produced by a nuclear reactor occurred in 1951 and it was achieved by EBR1, a fast neutron reactor. Even as far back as these times, scientists (In 1945 Enrico Fermi said, “The country that first develops a breeder reactor will have a great competitive advantage in atomic energy.) and even politicians understood that breeding could provide humanity, at least partially, with a solution to the energy problem, a solution that now in the perspective of the Generation IV reactor, we call “sustainable.”

FBRs have been built and operated in USA, UK, France, the former USSR, India, and Japan. An experimental FBR in Germany was built but never operated. As of now, three SFRs are under construction in China, one in India, and one in Russia.

But even if, as we have seen, research on fast neutron reactors and on thermal neutron reactors started at the same time, it must be pointed out that only a dozen fast neutron reactors have been built in the world as compared to hundreds of thermal neutron reactors. This is due, of course, to the fact that the long-term benefit of FBRs associated with the economy of resources is counterbalanced by the short-term additional costs involved in the use of a sodium coolant, which requires a more robust technology.

The development of FBRs could be considered only through different stages: first, the attainment of purely technical targets (the mastery of plutonium and sodium) and afterward, the validation of design options that will lead to industrial and economic solutions. The same steps have been observed in the various countries involved in the development of FBRs. Basically, they can be summarized in the following sequence:

- A preliminary step aimed at demonstrating its physical feasibility.
- A stage involving the building of experimental reactors to solve basic technical problems.
- A stage consisting of the construction of a demonstration reactor for testing designs.
- A final stage involving the creation of prototype power reactors.

The preliminary step includes the Clementine reactor in USA and BR2 in USSR, both are very low power and mercury-cooled and then, the first piles representing the technology of fast neutron reactors: the EBR1 in USA in 1951 and the BR5 in USSR in 1958. The next step, that of experimental reactors of significant size, included a set of achievements that runs from the DFR (70 MW) begun in 1959 in UK to the CEFR in China whose divergence is scheduled for 2010. ➤ [Table 3](#) below lists these existing reactors in the world.

These reactors had essentially twofold aims: On the one hand, their purpose was to provide experience in the operation of sodium-cooled reactors on a sufficient scale, and on the other, they were designed to allow the development of a fuel element capable of withstanding high burnup.

The next phase is that of demonstration reactors. These reactors are electricity generators with a power ranging between 100 and 600 MWe, and their purpose is to prepare for the introduction of high-power reactors by validating their concepts. ➤ [Table 4](#) lists these types of reactors in the world.

■ Table 3

Small reactor in the world

	Name	Thermal power (MW)	Criticality	Country	Status
Prelim.	Clementine	0.02	1946	USA	Stopped 1952
	EBR-I	1.4	1951	USA	Stopped 1963
	BR 1		1955	Russia	
	BR 2	0.2	1956	Russia	Stopped 1957
	BR 5–BR 10	5/10	1958/1973	Russia	Stopped 2002
	LAMPRE	1	1961	USA	Stopped 1965
Experimental	DFR	75	1959	UK	Stopped 1977
	EBR-II	60	1963	USA	Stopped 1993
	EFFBR	200	1963	USA	Stopped 1972
	RAPSODIE	24/40	1967/1970	France	Stopped 1983
	BOR 60	60	1968	Russia	Running
	SEFOR	20	1969	USA	Stopped 1972
	KNK1–KNK2	60	1972/1977	Germany	Stopped 1991
	JOYO	50	1977	Japan	Running
	FFTF	400	1980	USA	Stopped 1992
	FBTR	40	1985	India	Running
	PEC	120		Italy	Given up
	CEFR	60	2010	China	Under construction

■ Table 4

Medium size reactors in the world

Name	Electrical power (MWe)	Criticality	Country	Status
EFFBR	100	1963	USA	Stopped 1972
BN 350	150	1972	Kazakhstan	Stopped 1993
Phenix	250	1973	France	Stopped 2009
PFR	250	1974	UK	Stopped 1994
BN 600	600	1980	Russia	Running
SNR 300	300		Germany	Given up
Monju	280	1992	Japan	To restart
CRBR	350		USA	Given up
PFBR	500	2011	India	Under construction

The last phase involves the construction of high-power prototype reactors, between 750 and 1,500 MW, in order to achieve economic competitiveness. The first such project was the Super-Phenix reactor designed and built by a European consortium composed of France, Germany, and Italy. The reactor was connected to the grid in 1985 and shut down in 1998; the operation history of this reactor is detailed in the specific paragraph pertaining to Europe.

Other projects undertaken include the DFBR in Japan, the ALMR in USA, the SNR2 in Germany, the CDFR in UK, and then the EFR again within the framework of a European consortium, but these projects have all been abandoned. The reasons for that are not technical, but they are mainly due to a rise of hostility to nuclear energy rise in western nations and a lack of economic competitiveness demanding the development of fast reactor technology.

Today only the BN800, in Russia, is under construction but in recent years we have witnessed a renewed interest in nuclear reactors for the sake of saving natural resources. This corresponds to the launching of the Generation-4 International Forum. Such an event has led several countries to boost research on fast reactors, not only in USA, Japan, and France but also in Europe under the aegis of the European Commission, in Korea, and in China. It should be noted that in India, this technology has never been abandoned.

2.2 USA

On December 20, 1951, the fast reactor, EBR-I (Experimental Breeder Reactor-1) at the Idaho National Laboratory in Idaho Falls, produced enough electricity to power four light bulbs and the next day it produced enough power to run the entire EBR-I building. This was a milestone in the development of nuclear power reactors. The next generation experimental breeder was EBR-II (Experimental Breeder Reactor-2), which went into operation in 1964 and operated until 1994. It was designed to be an “integral” nuclear plant, equipped to handle fuel recycling onsite. It typically operated at 20 MW out of its 62.5 MW maximum design power and provided the bulk of heat and electricity to the surrounding facilities. The world’s first commercial LMFBR and the only one ever built in USA was the 94 MW Unit 1 at the Enrico Fermi Nuclear Generating Station. It was designed by Dow Chemical and Detroit Edison in a joint effort as part of the Atomic Power Development Association consortium. Groundbreaking began in Lagoona Beach, Michigan (near Monroe, Michigan) in 1956. The plant went into operation in 1963. However, it was shut down on October 5, 1966 due to high temperatures caused by a loose piece of zirconium that was blocking the molten sodium coolant nozzles. Partial melting damage to six subassemblies within the core was eventually found. (This incident provided the basis for a controversial book written by investigative reporter John G. Fuller entitled *We Almost Lost Detroit.*) The zirconium blockage was removed in April 1968, and the plant was ready to resume operation by May 1970, but a sodium coolant fire delayed its restart until July. It subsequently ran until August 1972 when its operating license renewal was denied.

The Clinch River Breeder Reactor Project was announced in January 1972. A government/business cooperative effort, construction proceeded fitfully. Funding for this project was halted by Congress on October 26, 1983. The Fast Flux Test Facility, first critical in 1980, is not a breeder but is a sodium-cooled fast reactor, which is in cold standby, with the possibility of restarting it for use in an international framework, currently under discussion (GNEP, GEN-IV).

2.3 Russia

The Soviet Union built a series of fast reactors, the first being mercury-cooled and fuelled with plutonium metal. Later plants were sodium cooled and fuelled with plutonium oxide.

BR-1 (1955) in Obninsk was 100 W (thermal) and fuelled with plutonium metal. It was upgraded in 1956 and renamed BR-2 at 100 kW. BR-2 was then replaced by BR-5 (5 MW) which attained criticality in 1958. It was the first reactor in the world to be fuelled with plutonium oxide. This reactor was operated until 1964 and then reloaded with a uranium carbide core. In 1972 the reactor was upgraded again and renamed BR-10 as 10 MW reactor fuelled with plutonium oxide. This reactor was shutdown in 2002.

BOR-60 (first criticality 1969) was a 60 MW reactor and its construction started in 1965 in Dimitrovgrad. This reactor was initially built as a Material Test reactor (MTR), but steam generators were added in 1970 and 1973 in order to provide 12 MW of electric power.

BN-350 (1973) was the first full-scale Soviet FBR. Constructed in Chevtchenko on the Mangyshlak Peninsula in Kazakhstan and on the shores of the Caspian Sea, it supplied 130 MW of electricity plus 80,000 tons/day of desalinated fresh water to the city of Aktau. Its total output was regarded as the equivalent of 350 MW, hence the designation. This loop-type reactor was fuelled with UO_2 .

The construction of the pool-type reactor BN-600 was completed in 1979 and criticality was achieved in 1980. This is a 1,470/600 MW reactor with a uranium core that is still in operation today.

Today, a larger plant, BN-800 (800 MW) is under construction at Beloyarsk.

2.4 Europe

2.4.1 France

In France, the first chapter in the history of fast reactors was the construction of the “Rapsodie” reactor (1962–1966) that used sodium as a coolant and mixed oxide fuel. The operation of Rapsodie was excellent from 1967 to 1978 (initially at 24 MW, it was upgraded to 40 MW in 1971). Rapsodie was an outstanding irradiation tool, allowing the demonstration of oxide fuel capabilities and an initial screening of the core structural material. However, from 1978 to 1982, the detection of primary sodium aerosols in areas surrounding the primary circuit hampered its operation. The reactor was finally shut down in April 1983, after several end-of-life tests; since 1983, the reactor has been undergoing decommissioning. The present strategy, defined in 2004 consists of two main steps: a cleansing period from 2004 to 2008 followed by a dismantling period lasting from 2008 to 2013.

The prototype fast reactor, Phenix (a pool-type reactor, 250 MW) went into commercial operation in 1974. Fifty one cycles were run, and more than 20 billion kWh were produced. Since the initial design life of the reactor was 20 years, the reactor should have been shut down in 1994, but in the mid-1990s, the role of the reactor changed: it was to be used as an irradiation tool acting as a support to the R&D transmutation programme of the CEA within the framework of the 1991 French law relating to long-lived radioactive waste management. This new objective required an extension of the planned reactor lifetime. A large refurbishment programme was defined and carried out in two phases within 6 years: the first phase lasting from 1994 to 1997

and the second from 1999 to 2003. These two phases were separated by one operating cycle and the plant resumed power at the end of 2003 and operated at its nominal power throughout 2004 and 2005. Five operating cycles (representing 600 EFPD) have been scheduled to carry out the experimental irradiation programme until the final shutdown of the plant in 2009. Preliminary studies on one end-of-life test and expertise programmes were performed and proposed to the international scientific community in the prospect of SFR development.

Construction of the SuperPhenix plant, in cooperation with Germany and Italy, lasted from 1977 to 1985. Full power was reached in 1986 and until the end of 1996, the plant operated for 4.5 years at different levels of power, with scheduled periods of maintenance and tests. It remained shutdown for 4.5 years, although still in an operational state, due to administrative procedures underway and a little more than 2 years went by following technical incidents and repairs. The last operating year was remarkable; the complete programme of overall qualification by successive stages of 30%, 60%, and 90% nominal power progressed without difficulty. After an interruption of activity of more than 5 years, all the parameters were found to be normal. Following the declaration made to the French National Assembly on June 19, 1997, the French government decided on February 2, 1998, to shut down the SuperPhenix plant permanently. The decree of December 31, 1998 finalized the immediate and permanent shutdown of the plant.

2.4.2 UK

The UK fast reactor programme was conducted at Dounreay, Scotland from 1957 until the programme was cancelled in 1994. Two fast reactors were built along with fabrication and reprocessing facilities for fuel, also collocated. The Dounreay Fast Reactor (DFR) achieved its first criticality in 1959 with uranium metal fuel. It used NaK coolant and produced 14 MW of electricity. This was followed by the sodium-cooled 250 MWe Prototype Fast Reactor (PFR) in the 1970s. The PFR, which was the first reactor with a $\text{UO}_2\text{-PuO}_2$ core, was shut down in 1994 as the British government withdrew major financial support for nuclear energy development.

2.4.3 Germany

Germany built two FBRs, but both were closed in 1991 without the larger of the two ever having achieved criticality. The KNK-II was converted from a thermal reactor, called KNK-I, which had been used to study aspects related to technology of sodium cooling. KNK-II first achieved criticality as a fast reactor in 1977 and produced 20 MWe. The outer driver core was uranium oxide, and the central test section was loaded with mixed oxide fuel.

Construction of the prototype plant 300 MWe SNR-300 at Kalkar in North Rhine-Westphalia was completed in 1985, but owing to political pressure, it was never operated. The plant was maintained and staffed until a decision to close it was finally made in 1990. It has since been decommissioned. Today, it houses an amusement park (Wunderland Kalkar).

SNR2 was a power reactor project of 1,300 MWe, which, of course, was abandoned as was the case of SNR-300.

2.4.4 Italy

In Italy, the PEC reactor (“Prova Elementi di Combustibile,” i.e., Fuel Element Test Facility) was an experimental, sodium-cooled fast reactor specially designed to study the behavior of fuel elements under thermal and neutronic conditions comparable to those expected in commercial power plants. The plant was erected at Brasimone, an ENEA (Since 1983, CNEN changed its name in ENEA.) research center located about 60 km from the city of Bologna. The first design studies, which began in 1964, were performed by the CNEN (Comitato Nazionale dell’Energia Nucleare). In 1973, the project progressed considerably, thanks to different agreements (Agreement between the CEA and CNEN on fast reactor R&D; the setting up of the NERSA Company with the participation of ENEL, the public Italian Utility; an agreement between NOVATOME and NIRA for the design and construction of SPX1, etc.). However, after the Chernobyl incident, the development of the PEC reactor was dropped, even if the state of the work was equal to 70% completion with an investment of about 1.5 billion euros. At the same time, Italy was working in fast reactor component development under a cooperative agreement signed with France and Germany for the SuperPhenix design and construction.

2.4.5 Belgium, Netherland

Belgium and the Netherlands have joined with Germany in a series of FBR development projects, namely, the SNR-300 and the SNR-2.

2.4.6 Multinational Project: EFR

In Europe, the construction of fast reactors of increasing size under the national development programs in France, Germany, and the UK secured a solid foundation on which to base the development of the combined European expertise on fast reactor technology.

The EFR program was based on the solid expertise in Europe on fast reactor technology and on the wide knowledge developed by the associated R&D. The main milestones concerning the fast reactors development and construction in Europe are recalled:

- Experimental reactors: DFR in the UK, Rapsodie in France, KNK II in Germany
- Prototype power plants (250–300 Mwe): Phénix in France, PFR in the UK, SNR 300 in Germany
- Industrial power plant (1,200 Mwe): Superphénix

The initial major objectives for initiating a new industrial concept were based on:

- An up-to-date safety level comparable with that of future LWR, leading to make easier licensability without significant design changes
- Potentially competitive electricity, generating costs compared to future LWR

Taking into account on one hand, the high flexibility of fast reactors regarding to the fuel utilization (breeding, self-sustaining, transmutation, or incinerating) and on the other hand, the important feedback (safety and economics) of the Superphénix operating experience, three

other objectives were added in order to furthermore enhance competitiveness as regard to nuclear acceptance and proliferation risk minimization:

- Demonstration that a high load factor and increased lifetime (60 years) could be achieved with up-to-date operating and safety standards, notably as regard to severe accidents
- Progress concerning the capabilities for In-Service Inspection and Repair
- Flexibility related to the fuel cycle and notably possible integration of Plutonium burner core designs or high-level radioactive wastes incineration

The whole project was spread in three phases over 10 years: conceptual (technical and economical) design, concept validation (design support by R&D, leading to improvements for safety or economics), and design consolidation (consistent design).

2.5 Japan

Nuclear power accounts for about 30% of the electricity generated. From 1961 to 1994, there was a strong commitment to FBRs, but in 1994, the FBR commercial deployment was set out to 2030, and presently, commercial FBRs are envisaged by 2050.

2.5.1 Joyo

Japan's first experimental FBR, Joyo is located at Japan Atomic Energy Agency's O-arai Research and Development Centre. It became critical in 1977 with the MK-I breeder core. The objective of the reactor is to conduct irradiation tests on fuel and materials, carry out experiments, gain operating experience, and validation of innovative technology for development of future FBR. The Joyo has been supporting the development of sodium-cooled fast reactors by providing valuable irradiation testing of advanced fuels and materials, and improvements in fast reactor safety and operation. The first major upgrade of Joyo to the 100 MWt MK-II irradiation test bed was successfully operated from 1982 to 2000. Work began in 2000 on the 140 MWt MK-III program, which was the second major upgrade to improve the irradiation capability of Joyo. Start-up test of the MK-III core was conducted from June to October 2003. The rated power operational cycle of MK-III core was started in May 2004. The Joyo MK-III core is going to serve as a powerful irradiation test facility for the fast reactor development needs of Japan and the world.

2.5.2 Monju

Monju is a prototype reactor designed to generate 280 MWe (714 MWt), fueled with Pu-U mixed oxide and cooled by liquid sodium (3 loops), with a rated capacity of 714 MWt/280 MWe. It is located in Tsuruga, Fukui Prefecture. The core of Monju and its sodium equipments were designed based on experience in Joyo as well as R&D results which had been obtained mainly at the O-arai Research and Development Center. The objectives of the development of Monju are to demonstrate the performance, reliability, and safety of an FR power plant; to establish the sodium handling technology during its design, fabrication, construction, operation, and

maintenance of the plant; and to contribute to technology development for commercialized FR cycle systems in Japan and world-wide. Monju successfully achieved its first criticality in April 1994 and supplied electricity to the grid initially in August 1995. However, the preoperational test of the plant was abruptly interrupted by a sodium leak accident in the secondary heat transport system in December 1995 during a 40% power operation test. After carrying out the investigation and the comprehensive safety review for 2 years and the necessary licensing procedure, the permit for plant modification (countermeasure against potential sodium leak, etc.) was issued in December 2002 by the Ministry of Economy, Trade, and Industry (METI). JAEA have started preparatory work for modification, after given prior approval by the local governor of Fukui in February 2005, and the main modification work is in progress since September 2005. The function test for modified systems has been in progress since December 2006. Sequentially the comprehensive system function test, considering the long period of plant shutdown, is scheduled in the near future. The restart (criticality) is expected to be achieved in 2010.

2.5.3 Rapid-L

A small-scale design developed by Toshiba Corporation in cooperation with Japan's Central Research Institute of Electric Power Industry (CRIEPI) and funded by the Japan Atomic Energy Research Institute (JAERI) is the 5 MWe, 200 kWe Rapid-L, using lithium-6 (a liquid neutron poison) as control medium. It has 2,700 fuel pins of 40–50% enriched uranium nitride integrated into a disposable cartridge. The reactivity control system is passive, using lithium expansion modules (LEM), which give burnup compensation, partial load operation, as well as negative reactivity feedback. As the reactor temperature rises, the lithium expands into the core, displacing an inert gas. Other kinds of lithium modules are also integrated into the fuel cartridge, to facilitate shut down and start up of the reactor. Cooling is by molten sodium, and with the LEM control system, reactor power is proportional to primary coolant flow rate. Refuelling would be carried out every 10 years in an inert gas environment. Operation would require no skill, due to the inherent safety design features.



2.5.4 L-4S “Nuclear Battery”

The Super-Safe, Small & Simple – 4S “nuclear battery” system is being developed by Toshiba and CRIEPI in Japan in collaboration with STAR work in USA. It is Pb–Bi cooled version of 4S conceived under GEN IV systems. It uses sodium as coolant (with electromagnetic pumps) and has passive safety features, notably negative temperature and void reactivity. The whole unit would be factory-built, transported to site, installed below ground level, and would drive a steam cycle. It is capable of 3 decades of continuous operation without refuelling. Metallic fuel (169 pins, 10 mm diameter) is uranium–zirconium or U–Pu–Zr alloy enriched to less than 20%. Steady power output over the core lifetime is achieved by progressively moving upward an annular reflector around the slender core (0.68 m diameter, 2 m high). After 14 years, a neutron absorber at the center of the core is removed and the reflector repeats its slow movement up the core for 16 more years. In the event of power loss, the reflector falls to the bottom of the reactor vessel, slowing the reaction, and external air circulation gives decay heat removal. Both 10 and 50 MWe versions of 4S are designed to automatically maintain an outlet coolant temperature of


510 °C – suitable for power generation with high temperature electrolytic hydrogen production. The design has gained considerable support in Alaska and toward the end of 2004, the town of Galena granted initial approval for Toshiba to build a 4S reactor in that remote location. A pre-application NRC review is being sought with a view to a demonstration unit operating by 2012.

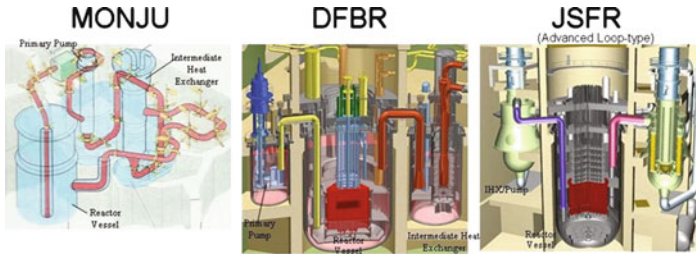
2.5.5 Commercial Fast Reactor Development Program

The feasibility study on commercialized fast reactor (FR) cycle systems was initiated in July, 1999 with an initial two-year period of study (Phase I), and followed by a five-year period of study (Phase II). The Phase II final report was compiled in March, 2006, and the feasibility study was finalized at the end of March, 2006. A wide range of technical options have been evaluated to select several promising concepts as candidates for the commercialization. JAEA focuses on the R&D for commercialization as “Fast Reactor Cycle Technology Development” (FaCT) project and accelerate the R&D of FBR Cycle. According to current knowledge, sodium-cooled fast breeder reactor (MOX fuel) + advanced aqueous reprocessing + simplified pelletizing fuel fabrication were considered as the main concept to be implemented in the future because these were the most viable for commercialization facility. The sodium-cooled fast breeder reactor (metallic fuel) + metal electrorefining reprocessing + injection casting fuel fabrication were secondary concept because these were viable for commercialization facility but relatively uncertain in terms of social and technical aspects. JAEA aims at getting the conceptual design to meet the development goal and design requirement by concretizing conceptual design to judge the viability of the innovative technology of main concept by 2015.

In order to satisfy the high design requirements mentioned above, JSFR of 1,500 MWe with advanced loop type MOX fueled core has been conceived. Totally 13 innovative technologies were identified and included in the current design. The roadmaps of their R&D have been developed. They are categorized into three areas: for economic competitiveness, enhancement of reliability, and enhancement of safety. Advanced loop type design has a higher potential for drastic reduction of the plant materials compared with pool-type design. The 10 m diameter reactor vessel with 1,500 MWe core and simple and large capacity two-loop heat transport system are considered as major contributors for the reduction of the material amount. R&D items unique to the advanced loop type design are four: two-loop piping system, high chromium ferritic steel, pump-integrated IHX, and hot vessel. Technical feasibility has been already obtained for these items and activities related to validation of the technologies are in progress. The current and future SFRs in the Japanese program are shown in  Fig. 5 and technical data are given in  Table 5.

2.6 India

A survey by the Department of Atomic Energy forecasts electricity growth rate of 6.3%/y till the year 2020 and about 4.0%/y from 2020 to 2050. Nuclear share is planned to be about 25% by 2050. The growing energy demand would have to be met through fast breeder reactors and thorium fuelled reactors, in combination with other energy resources, taking into account sustainability and environmental issues. To achieve this, three stage programme is being followed ( Fig. 6). In the first stage, Pressurized Heavy Water Reactors (PHWRs) are employed which



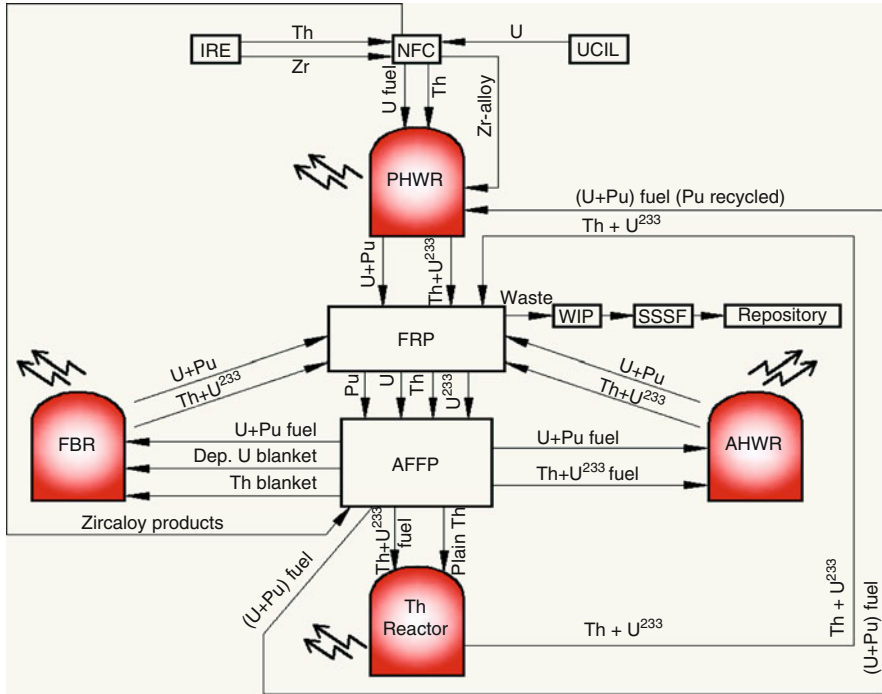
■ **Figure 5**
Fast reactor in Japanese program

■ **Table 5**
Technical data on the current and future SFRs in Japan

	Monju	DFBR	JSFR
Output power	280 MWe/714 MWt	670 MWe/1,600 MWt	1,500 MWe/3,570 MWt
Number of loops	3	3	2
Primary coolant temperature (°C)	529/397	550/395	550/395
Secondary coolant temperature (°C)	505/325	520/335	520/335
Main steam temperature/pressure (°C/MPa)	483/12	495/17	495/19
Core fuel	MOX	MOX	MOX
Burn up (driver fuel discharge average) (GWd/t)	80	90	150
Breeding ratio	1.2	1.05–1.2	1.03–1.1
Cycle length (months)	6	15	26

will use natural uranium resource. PHWR is currently in commercial phase with 17 PHWRs in operation including 2 Boiling Water Reactors (BWRs), generating 4,120 MWe. Five reactors are under construction, which includes 2 VVERs. Liquid sodium cooled fast breeder reactors (FBRs) form the second stage of the nuclear power programme. Plutonium (Pu) generated from PHWRs would be used as the fuel with a closed fuel cycle programme. Subsequently, thorium resource will be utilized in the third stage reactors which will be either thermal or fast breeders.

The seed for fast reactor programme in India was sown through the establishment of a research center (then called Reactor Research Centre) in 1972 dedicated to the development of fast reactor technology and the decision to construct Fast Breeder Test Reactor (FBTR) at Kalpakkam. The experience gained in the construction, commissioning, and operation of FBTR as well as 390 reactor-years worldwide FBR operational experience, rich experience with



FBR : Fast breeder reactor
 IRE : Indian rare earth ltd.
 NFC : Nuclear fuel complex
 UCIL : Uranium corp. of India ltd.
 WIP : Waste immobilisation plant

PHWR : Pressurised heavy water reactor
 FRP : Fuel reprocessing plants
 AFFP : Advanced fuel fabrication plants
 AHWR : Advanced heavy water reactor
 SSSF : Solid storage surveillance facility

■ **Figure 6**
Roadmap for Indian Nuclear Programme

MOX fuel, 30 years of focused R&D programme involving extensive testing and validation, material and manufacturing technology development and demonstration, peer reviews, and synergism among DAE, R&D Institutions and Industries, have provided the necessary confidence to launch a Prototype FBR of 500 MW capacity (PFBR). The reactor construction was started in 2003 and the reactor is scheduled to be commissioned by 2010. As a follow-up to PFBR, it is planned to construct two twin units of 500 MW reactors, with improved economy and safety during 2010–2020. Various elements of reactor design are being carefully analyzed with the aim of introducing innovative features toward further reduction in unit energy cost and enhancing safety in these reactors. Clear strategies have been identified to simplify the design, reduce construction time, enhance the burnup and close the fuel cycle with minimum cooling, and out-of-pile inventory, without sacrificing over all safety during entire process. It is targeted to bring down the unit energy cost by ~25%. Further, with advanced structural materials for clad and wrapper, a burnup of 25 at.% is envisaged for mixed oxide fuels.

It has been realized that for enhanced growth of fast reactors in the country, it is imperative to develop metallic fuelled FBRs, which promise a much higher breeding. A comprehensive

programme on development of metal fuelled reactor and its fuel cycle has been undertaken with the aim of introducing metal fuel in commercial FBRs by 2020. Fabrication of test fuels for irradiation in FBTR and pilot plant for pyrochemical reprocessing are the firm action plans under implementation. Directed research to develop metallic fuels for achieving high breeding ratio (1.45) and high burn up of ~25 at % is the target; based on which a spectrum of activities with synergism have been undertaken in the Department of Atomic Energy.

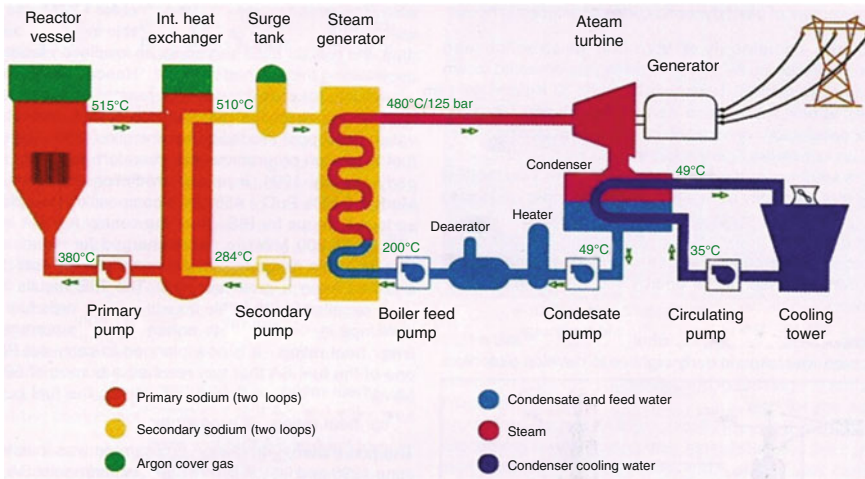


Figure 7
FBTR flowsheet

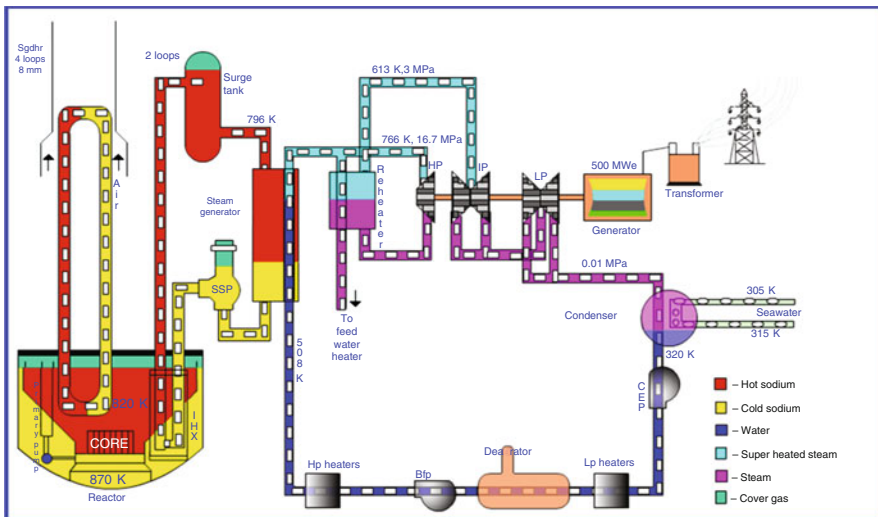




Figure 8
PFBR flowsheet

2.6.1 FBTR

FBTR is a sodium cooled loop type 40 MWt/13.2 MWe experimental reactor operating at Kalpakkam. FBTR has two primary and two secondary sodium loops and each secondary loop has two once-through, serpentine type Steam Generators (SG). The schematic sketch is shown in  Fig. 7. All the four SG modules are connected to a common steam–water circuit having a Turbo-Generator (TG) and a 100% steam Dump Condenser (DC). The first criticality was achieved in October 1985 with a small core of 22 fuel subassemblies (SA) of MK-I composition (70% PuC + 30% UC), with a design power of 10.6 MWt and peak linear heat rating (LHR) of 250 W/cm. Progressively, the core was expanded by adding subassemblies at peripheral locations. Toward increasing the core size and hence the reactor power, carbide fuel of MK-II composition (55% PuC + 45% UC) was inducted in the peripheral locations in 1996. MK-I carbide fuel has so far seen a burnup of 165 GWd/t without any pin failure. TG was synchronized to the grid for the first time in July 1997. The reactor has so far been operated up to a power level of 17.4 MWt by raising the LHR of MK-I fuel to 400 W/cm in 2002. During the recent campaign, Delayed Neutron Detector calibration experiments were carried out. Also, experiments are under way for mapping of flux at the grid plate location, accelerated irradiation of grid plate material as a part of its residual life assessment, short-term irradiation of a single pin of PFBR fuel for studying the initial restructuring and irradiation of core structural materials. PFBR test fuel irradiation would be continued to attain its target burn-up. Further, the reactor life is to be extended by 20 years to serve as an irradiation facility for the development of future fuels and core.

2.6.2 PFBR

Toward techno-economic demonstration of fast breeder reactor technology, based on the experiences gained with international FBRs, including FBTR, and comprehensive research and technology development programme in collaboration with a large number of academic and industrial organizations, a 500 MWe capacity Prototype Fast Breeder reactor (PFBR) is being established at Kalpakkam. It is a pool type reactor with two primary and two secondary loops with four steam generators per loop ( Fig. 8). It uses mixed oxide fuel with two enrichment zones (21% and 28% PuO₂), with a target burnup of 100 GWd/t, which is aimed to be increased to 150 GWd/t subsequently. Twenty percent cold worked D9 material (15% Cr–15% Ni with nano size TiC precipitates) is used for the core. SS 316 LN is the major structural material for the sodium components and modified 9 Cr–1 Mo is the material for steam generators. The sodium temperatures are 820 and 670 K for hot and cold pools, respectively. The design plant life is 40 years, with at least 75% load factor to be successively enhanced to 85%. The construction of PFBR in Kalpakkam has been started, and the reactor is planned to be commissioned in 2011. All the nuclear steam supply system components are being manufactured by the Indian Industries, based on the technology development, including in-sodium testing of relevant components over the last 2 decades.

In order to ensure comprehensive performance assessment of the components, an elaborate technology development program was carried out in which critical components such as absorber rod drive mechanisms, steam generator, and transfer arm were manufactured on a full

scale and tested in sodium. Few important reactor assembly components went through a manufacturing technology development program. The technology for the production of enriched boron carbide for use in control rods, as well as the MOX fuel has been established.

To close the fuel cycle of PFBR, a dedicated Fast Reactor Fuel Cycle Facility (FRFCF) is also being established at Kalpakkam. This facility would be operational by 2012 and will comprise a fuel fabrication plant, a fuel reprocessing plant, a waste management plant, as well as a plant for processing reprocessed uranium oxide. The colocation of these facilities with sharing of common facilities is a significant step toward the reduction of the fuel cycle cost for PFBR.

It is planned to construct a series of 500 MWe reactors similar to PFBR with improved economy and safety during 2010–2020. From the point of view of economy and experience gained/to be gained in construction and operation, it is planned to go in for a larger reactor (500, 1,000 MWe), rather than smaller sized modular type reactors. The next four reactors to be constructed after PFBR would also use mixed oxide as the fuel. Sodium will be used as the coolant. These reactors would be designed in such a way as to enable introduction of metallic fuels in a part of the core. Two of these reactors would be constructed at Kalpakkam site and the remaining at a suitable alternate site. The reactors to be built subsequently will use metallic fuel. The choice of metallic fuel is based on its good breeding characteristics and the possibility of realizing a fuel cycle based on pyrochemical reprocessing of the fuel, which would ensure reprocessing of fuel after a high burn-up and with short cooling. Thus, the choice of metallic fuel is an essential ingredient of the plans for the rapid growth of fast reactors in India. Beyond 2020, a series of large size reactors (1,000 MWe) with metallic fuel will be constructed. Emphasis would be placed on innovation, scientific break throughs, development of quality human resources, and robust technologies through academy–research–industry synergy.

Thorium would be irradiated in the second stage FBRs with the objective of generating U-233 which will form the fuel for the third stage reactors. Toward this direction, Advanced Heavy Water Reactors (AHWRs) are planned to demonstrate the technology of innovative thorium-based reactors and fuel cycle, and the design is under regulatory review presently. Clearance for construction is expected in a few years.

2.7 China

China began work in fast neutron breeder reactors in the late 1960s. During the initial period from 1965 to 1987, the works were focused on fast reactor physics, thermodynamics, sodium technology, and development of small sodium facilities. Further, about 12 experimental setups were established, and one sodium loop was constructed. This included a 50 kg U-235 zero-power neutron setup, which achieved criticality in June 1970. The engineering goal for the applied research phase program (1987–1993) was to construct a 65 MWt (25 MWe) experimental fast reactor. Further developments were made in sodium technology, fuel and materials, fast reactor safety, and reactor design. A preliminary foundation for a fast reactor design was established, and approximately 20 experimental setups and sodium loops were built. Currently, the experimental validation phase focuses on sodium loop technology. Two sodium loops were imported from Italy: ESPRESSO (sodium flow rate $110 \text{ m}^3/\text{h}$, maximum sodium temperature 650°C) and CEDI (sodium flow rate $320 \text{ m}^3/\text{h}$, maximum sodium temperature 650°C). The primary conceptual design was completed in 1992 and the final design was completed in 1994. To test the concept of the design, a zero-power simulation experiment was conducted at the

Physics and Dynamics Engineering Institute in Russia. It was not until January 1998 that construction work began on the country's first fast neutron reactor. The China Institute of Atomic Energy (CIAE), in cooperation with the Beijing Institute of Nuclear Engineering, is constructing the FBR with Russian technical assistance.

The strategy of fast reactor development is divided into three steps of experimental, prototype, and demonstration stages as outlined in [Table 6](#).

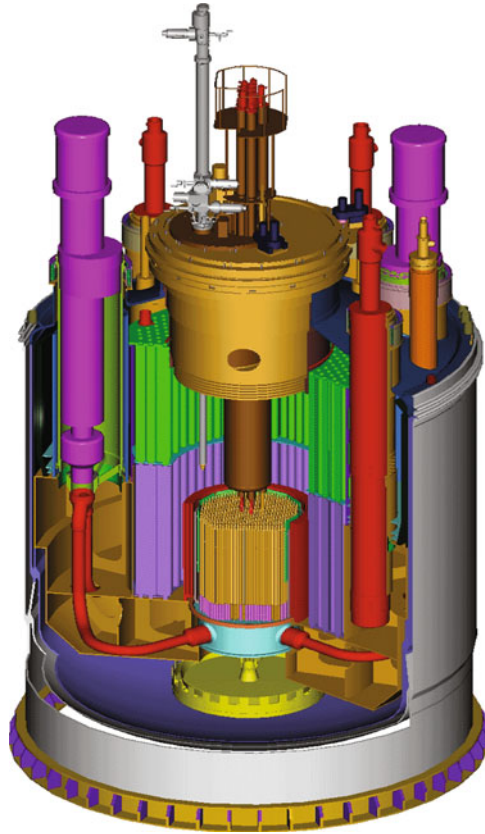
In the framework of the National High-Tech Program, China Experimental Fast Reactor (CEFR) project has been executed since 1990. The power tests including electricity generation test is planned in 2009. The CEFR is a sodium cooled 65 MWt experimental fast reactor with (Pu,U)O₂ as fuel, but UO₂ as the first loading, Cr–Ni austenitic stainless steel as fuel cladding and reactor block structure material, bottom supported pool type, two main pumps, and two loops for primary and secondary circuits, respectively. The water–steam tertiary circuit is also two loops, but the superheat steam is incorporated into one pipe, which is connected with a turbine. Design work was started in 1990 and preliminary safety analysis report review was carried out during 1998–2000.

The CEFR block shown in [Fig. 9](#) is composed of main vessel and guard vessel supported from bottom on the floor of reactor pit with the diameter 10 m and height 12 m. The reactor core is composed of 81 fuel subassemblies and is supported on lower internal structures. Three safety subassemblies, three compensation subassemblies and two regulation subassemblies, then 336 stainless steel reflector subassemblies, and 230 shielding subassemblies and in addition 56 positions for primary storage of spent fuel subassemblies are included. Two main pumps and four intermediate heat exchangers are supported on upper internal structures. These two structures are mounted on the main vessel. Two DHR heat exchangers are hung from the shoulder of main vessel. The double rotating plugs on which control rod driving mechanisms, fuel handling machine and some instrumentation structures are mounted, are supported on the main vessel top.

CEFR right now is under installation. About 450 bigger components have been pre-installed and 80% non-sodium system and 30% sodium systems have been installed. Main vessel installation was started in August 2005. Preoperation testing of auxiliary systems is under way. Eighty five tons of nuclear grade sodium has been stored in the storage tanks. In order to validate the design, a number of demonstration loops and facilities were built during 1995–2006, such as sodium component cleaning, sodium purification system, sodium fire testing lab, fixed expansion graphite extinguishing facility, sodium fire detection system, sodium sol–gel purification

Table 6
China FBR development strategy

Reactor	Power (MWe)	Beginning of design	Commissioning schedule
CEFR	20	1990	2008
CPFR	600	2009	2020
CMFR	$n \times 300$	If needed	
CDFR	1,000–1,500	2015	2025
CCFR	1,000–1,500	2020	2030–2035



■ Figure 9
CEFR reactor block

and filtration facility, sodium testing loop, water testing loop, reactor vessel water natural convection simulation, sodium siphon testing facility, over-pressure protection test facility, sodium valve testing loop, fuel handling system summing-up demonstration.

The government also proposes design and development of China prototype fast reactor (CPFR), during the Eleventh Five Year Plan (2006–2010) with the target to complete its construction in 2020. After CPFR, two possibilities are foreseen: (1) CPFR could be deployed in a manner of one-site multi-reactors (CMFR-B) around 2030, which should be still as a breeder in case the uranium resource is not sufficient to support PWRs development and (2) to deploy fast burners of 600 MWe size around 2030 in the same manner as breeder reactors if experience is enough on the partitioning technology, Minor Actinides (MAs) fuel fabrication and transmutation in fast reactor for MAs and long lived fission products (LLFP). In order to shorten the fast reactor engineering development period from CEFR to China demonstration fast reactor (CDFR) and to decrease technical-economic risks and for their follow-up, maximum continuity will be emphasized in the main technical selections for these reactors, such as coolant, primary circuit structure, decay heat removal system, fuel handling systems, etc.

2.8 Korea

A draft long-term SFR development action plan has been prepared with milestones of standard design approval by 2020 and construction of demonstration SFR by 2028 as shown in [Fig. 10](#). Process for the finalization of the draft action plan is in-progress.

Korea Atomic Energy Research Institute (KAERI) is developing 600 MWe capacity liquid metal fast reactor KALIMER-600, which can satisfy the Gen-IV technology goals of sustainability, safety and reliability, and economics and proliferation resistance. With a strong emphasis on proliferation resistance, the core design of KALIMER-600 is evolved to have a single enrichment zone without any blanket. KALIMER-600 is a pool-type sodium-cooled reactor with a fast spectrum neutron reactor core. The passive safety mechanism with an inherent safety is highly emphasized to realize the KALIMER-600 design targets. A reliable decay heat removal system is also employed as a passive safety-grade decay heat removal method. The investment protection and the achievement of a high plant performance are the other important aspects of the KALIMER-600 design. The net plant efficiency of 39.4% is much higher than that of the nuclear plants currently under operation in Korea. This high efficiency would enable us to utilize the nuclear fuel more effectively and mitigate the thermal load on the environment. The design life time is set to 60 years which is evaluated to be long enough to provide the role imposed on it without any degradation of the plant efficiency. The heat transport system of KALIMER-600 consists of primary heat transport system (PHTS), intermediate heat transport system (IHTS), residual heat removal system (RHRS), and steam generating system (SGS). They are configured in series and located on a bed seismically from the ground.

The PHTS of KALIMER-600 is constructed in a large sodium pool. This design feature eliminates the possibility of a coolant loss by a pipe break and it also provides a large thermal damping of the system which yields a slower transient, longer grace time at an accident condition, and eventually increases plant safety. The IHTS consists of two identical loops and this feature contributes to the flexibility of the plant operation and increases the reliability of the decay heat removal by the normal procedures. KALIMER-600 has 3-layered RHRS such as PDRC (passive decay-heat removal circuit), intermediate reactor auxiliary cooling system

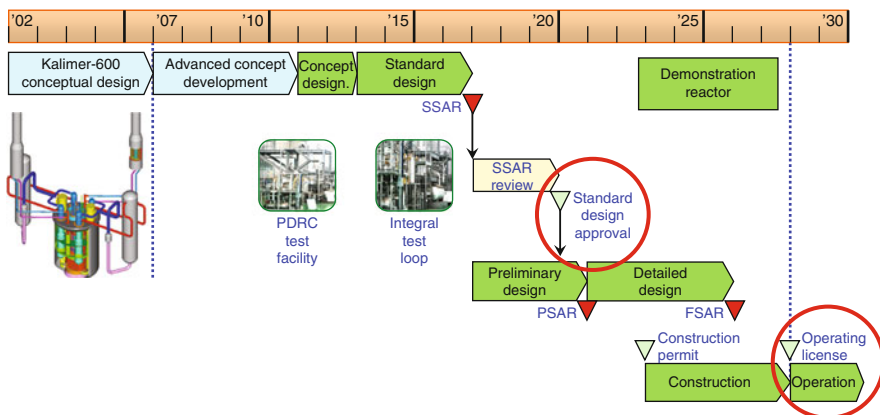


Figure 10
Draft action plan for SFR development in Korea

■ **Table 7**
Candidate concepts for an advanced SFR system

		KALIMER-600	Candidate concepts	Advanced concept
Reactor	Power (MWe)	600	600/900/1,200	To be decided
	Conversion ratio	1.0	0.5–0.8, 1.0	0.5–0.8, 1.0
	Core exit T (°C)	545	510–550	To be decided
	Cladding material	Mod.HT9	Mod.HT9/FMS	To be decided
	Fuel type	U-TRU-Zr	U-TRU-Zr	U-TRU-Zr
NSSS	No. of loops	2	2, 3	To be decided

(IRACS), and steam/feed water system to enhance the safety of the system. The PDRC is a pure passive system without any operator action and active components. The heat removal by PDRC relies exclusively on a natural convection heat transfer. The PDRC system comprises of two independent heat removal loops, and each loop is equipped with single sodium–sodium decay heat exchanger (DHX), one sodium–air heat exchanger (AHX) and the heat removing sodium piping connecting DHX with AHX.

Based upon the experiences gained during the development of the conceptual designs for KALIMER, KAERI is developing key SFR technologies. There are three categories of activities under way: (1) advanced concept design studies, (2) development of advanced SFR technologies necessary for its commercialization, and (3) development of basic technologies. For advanced concept design studies, various candidate concepts and options are under consideration and feasibilities of these concepts are being studied. ▶ [Table 7](#) shows a comparison of KALIMER-600 and candidate concepts.

3 Basic Design Choices

3.1 Sodium as Coolant

The sodium fast reactor (SFR) is a very promising candidate for the development of fast neutron reactors. It is well known owing to its wide development since the 1950s, throughout all countries involved in the development of nuclear power plants. The development of sodium-cooled fast neutron reactors is possible, thanks to the very attractive nuclear, physical, and even some of chemical properties of sodium. Sodium is the most common of the alkali metals. It is widespread in nature but only in the form of compounds (sea salt, rock salt, carbonates, nitrates), and it is the sixth most abundant element in the earth's crust (about 2.8% of terrestrial rock and present in great quantities in sea water as sodium chloride).

Sodium has been known since the early antiquity. The etymology of the word “sodium” and the symbol “Na” stretches back across history. The word “neter” is found in the bible, the word “natrium” is found in Latin, and the word “natron” in ancient Egyptian, where it was used to designate sodium carbonate decahydrate, a compound used to conserve mummies. Moreover, the word “natron” persisted into the middle ages; the word “natrium” is still used to designate

sodium in German, and in the present day, we still use the chemical symbol Na to designate sodium.

Sodium in its metallic form can be used to refine some reactive metals, such as zirconium and potassium, from their compounds. Other uses are for medicine, sodium vapor lamps, and chemistry as a reducing agent (i.e., styrene purification, methylate preparation. . .) and as a coolant in sodium fast reactors or in previous solar plants.

Sodium is a soft, silvery white alkali metal. A sodium atom has the symbol ${}_{11}^{23}\text{Na}$, which signifies that it consists of the following:

- A nucleus with 11 protons and 12 neutrons,
- Surrounded by 11 electrons distributed according to the formula $1s^2 2s^2 2p^6 3s^1$, which can also be written $(\text{Ne}) 3s^1$, which makes explicit reference to neon, the rare gas whose electron structure is most similar to sodium.

The atomic mass of sodium, for which the only naturally occurring isotope is ${}_{11}^{23}\text{Na}$, is 22.99 g. Like all the other alkali metals, sodium is a very reactive element (reducer), which easily loses its outer electron (singlet). In the majority of its compounds, it is found in the form of the cation Na^+ , which is clearly its most stable configuration.

Because of its very high reactivity, sodium does not exist in nature as a pure metallic element. Sodium salts are the most commonly used mineral salts due to their high solubility and their moderate price. Some exist in nature. Most of the others, including sodium hydroxide, the principle chemical base, can be prepared without returning to the metallic state. The metal itself, which is a strong reducer, is very difficult to obtain by chemical means; indeed, Humphrey Davy, the British chemist and physicist, first isolated it in 1807 by electrolysis of molten sodium hydroxide. Sodium is now produced commercially through the electrolysis of liquid sodium chloride: it is prepared in an electrolysis cell in which the NaCl (40%) is mixed with calcium chloride (60%) to lower the melting point down to 580 °C. The Na^+ ions are attracted to the cathode, and sodium is formed there. As calcium is less electropositive than sodium, no calcium will be formed at the anode.

3.1.1 Physical Properties

For the heat transfer calculations and thermalhydraulic analysis, the sodium properties are essential input data. Some of the important properties are given below. For each physical property, the references, from which the physical properties of liquid sodium have been taken, are given. There is not, in the thermodynamic sense, a coherent database for sodium within SFR community. By “reference database,” we mean a database having been the subject of a coherent internal thermodynamic study. We recommend that this activity be carried out within the framework of an International Organization (IAEA, OECD-NEA. . .).

Due to difference of structure and inter-atomic distances, most of the characteristics of sodium exhibit a discontinuity when passing from the solid to the liquid state; thus we give some different equations for each state, that is, solid and liquid, but clearly the characteristics of the liquid are of greater relevance to SFR.

At the atmospheric pressure, sodium is a liquid from its melting point, 371 K, to its boiling point, 1,156 K (➔ Sect. 3.1). This important range in the liquid state at atmospheric pressure is crucial when compared to the thermal inertia of the whole system for safety.

The critical temperature is relatively high which varies between 2,846 and 3,006 K (➤ Sect. 3.2).

The density of sodium decreases as the temperature increases (➤ Sect. 3.3):

$$\rho = 950.0483 - 0.2298 (T - 273.15) - 14.6045 \times 10^{-6} (T - 273.15)^2 + 5.6377 \times 10^{-9} (T - 273.15)^3 \quad (1)$$

with ρ in kg/m^3 , T in Kelvin.

It is always less than that of water. It has a value of around 850 kg/m^3 at 673 K. The density of liquid phase is higher than the solid phase's one (volume expansion is about 2.7%): due to this characteristic, it is necessary to foresee specific procedures for melting sodium in storage tanks or any other containment.

The viscosity of sodium at 673 K (➤ Sect. 3.3) is of the same order as the viscosity of water at 373 K, that is, 310 and 280 Pa s respectively.

$$\log_{10} \mu = -2.4892 + \frac{220.65}{T} - 0.4925 \log_{10} T \quad (2)$$

with μ in Pa s, T in Kelvin

Due to the similitude between sodium and water density and viscosity, it is possible to carry out some experimental thermohydraulic studies and code validation with water.

Wettability of structural material depends in a complex way on temperature, on the purity of the sodium, on the nature of the solid and on its surface state, as well as the possible presence of adsorbed gas and oxides, which are inevitably present on the surface, and which considerably modify the boundary conditions between sodium and the surface. Hence, the wetting characteristics of sodium on steel change as we go to temperatures higher than around 573 K, which corresponds to the dissolution of metallic oxides, inducing a very good contact between the sodium bulk and the structural material, which remains, after a period at raised temperatures (let us say around 24 h at 573 K), at lower temperatures, that is, 453 K.

Thermal conductivity of sodium is very high (➤ Sect. 3.3): about $76.6 \text{ W m}^{-1} \text{ K}^{-1}$ at 573.15 K. Comparatively, the conductivity of water varies from $0.6 \text{ W m}^{-1} \text{ K}^{-1}$ at 297 K to $0.465 \text{ W m}^{-1} \text{ K}^{-1}$ at 633 K (at a pressure of 150 bars), whereas the conductivity of sodium is between 100 and 150 times higher (and this of course at atmospheric pressure).

For solid sodium:

$$\lambda = 135.6 - 0.167 (T - 273.15) \quad (3)$$

For liquid sodium:

$$\lambda = 92.951 - 5.8087 \times 10^{-2} (T - 273.15) + 11.7274 \times 10^{-6} (T - 273.15)^2 \quad (4)$$

with λ in $\text{W m}^{-1} \text{ K}^{-1}$, T in Kelvin

Heat capacity of sodium is very attractive (➤ Sect. 3.3): at 673 K, that is, 1, 25 103 $\text{J kg}^{-1} \text{ K}^{-1}$ (water at 293 K: 4.18 103 $\text{J kg}^{-1} \text{ K}^{-1}$)

For solid sodium:

$$C_p = 1,199 + 6,491 \times 10^{-4} (T - 273.15) + 1,052.9 \times 10^{-5} (T - 273.15)^2 \quad (5)$$

For liquid sodium:

$$C_p = 1,436.715 - 0.5805 (T - 273.15) + 4.6273 \times 10^{-4} (T - 273.15)^2 \quad (6)$$

with C_p in $\text{J kg}^{-1} \text{K}^{-1}$, T in Kelvin

The fact that sodium has a very high boiling point (the boiling point is by definition the temperature at which the saturated vapor pressure is equal to the atmospheric pressure) leads one to expect that sodium is not very volatile.

The saturation vapor pressure is given by the following equation:

$$\ln P_s = 23.99 - 12,580 T^{-1} - 0.2241 \ln T + 1.712 \times 10^{-22} T^6 \quad (7)$$

with P_s in Pa and $371 < T < 2,573 \text{ K}$

The fact that sodium is not very volatile has several consequences:

- In normal operation, evaporation rapidly attains an equilibrium level (condensation = vaporization). Consequently, in the various gas plenums, and more particularly in the primary vessel, the mass transfer toward the colder roof of the slab is rather limited, particularly in the presence of argon, due to its low thermal conductivity. Nevertheless, the SFR operational feedback shows that there is a possibility of observing some sodium aerosols deposited in the upper structures or narrow gaps, and it is necessary to foresee vapor and aerosol traps in cover gas, to prevent any related issues.
- Vacuum distillation is not a very efficient cleaning technique, prior to inspection or repair. It should be pointed out, however, that evaporation, which depends only on the partial vapor pressure of the sodium, can occur at conditions away from boiling, for example, by flushing with hot gas.
- Due to this low volatility, the sodium flames are very short and the heat produced by the fire is rather low: thus, it is possible to extinguish the fire by spreading a powder, mixture of Na carbonate, Li carbonate, and graphite.

Sodium, like all metals, has a very low electrical resistivity:

$$\rho_e = 6.1405 \times 10^{-8} + 3.5047 \times 10^{-10} (T - 273.15) + 5.6885 \times 10^{-14} (T - 273.15)^2 + 1.66797 \times 10^{-17} (T - 273.15)^3 \quad (8)$$

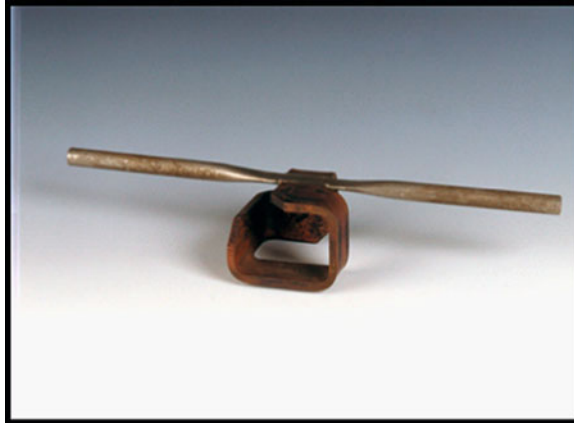
with ρ_e in $\Omega \text{ m}$, T in Kelvin

These attractive conduction properties are widely used in sodium technology: instrumentation, level probes, flow measurements, electromagnetic pumps (➤ [Fig. 11](#)), and leak-detection (➤ [Fig. 12](#)).

The speed of sound in sodium varies little with temperature. It can be given by the relationship (➤ [Sect. 3.4](#)):

$$C = 2577.2 - 0.5234 (T - 273.15) \quad 373.15 < T < 643.15 \text{ K} \quad (9)$$

with C in m s^{-1} , T in Kelvin



■ Figure 11
Electro-magnetic pump (conduction pump-single phase current)



■ Figure 12
Insulated "sandwich" leak detection system (Courtesy of CEA)

This formula can be extrapolated up to 1,673 K.

Sound waves, therefore, propagate faster in sodium. This property is widely used in all the metrology and visualization techniques in sodium, and compensates the opacity in sodium for in service inspection operations (► [Fig. 13](#)). The influence of temperature remains weak; nevertheless, the temperature could also be deduced from the sound velocity in sodium. In order not to affect the accuracy of measurements and to avoid parasite echoes, it is necessary to make sure that the particulates and gas content in sodium are extremely low.

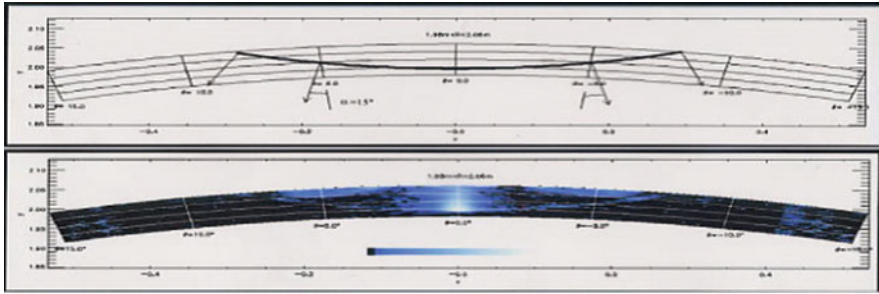


Figure 13
Under sodium viewing

3.1.2 Chemical Properties

Since sodium has a tendency to lose its external electron, it will have very significant reducing characteristics, as do all the alkali metals. It reacts exothermically with water, and potentially with violence, as a function of local conditions. The reaction with water produces sodium hydroxide and hydrogen gas, inducing hazards to be analyzed when the sodium is used for chemistry or as a coolant. This reaction is strongly exothermic (162 kJ/mol Na) and extremely fast. For these reasons, sodium–water interaction which can occur in the Steam Generator Units is considered as an important issue and safety means are developed and implemented to mitigate this event.

Nevertheless, this reactivity with water is commonly used for the development of cleaning processes for structural material wetted with sodium, during handling operations and moreover for the conversion of the large amounts of sodium into sodium hydroxide, at the end of the reactor operation, during the decommissioning phase. Solid sodium quickly oxidizes in air and liquid sodium burns in air over melting point, that is, 370 K if it is spread out in air, and over 413 K, in other cases; it forms sodium peroxide Na_2O_2 , or with limited oxygen, the oxide Na_2O . If burned in oxygen under pressure, sodium super oxide NaO_2 will also be produced. Because of this high chemical reactivity, extreme care is required in handling elemental/metallic liquid or solid sodium: it must be stored or used in liquid phase in an inert (oxygen and moisture free) atmosphere such as nitrogen or argon. Specific means have been developed to reduce the occurrence of sodium leaks; for example, specific detection systems, based on insulated electrical wire: in case of sodium leak, sodium is put in contact with this wire inside the pipe and therefore generates a warning (🔍 Fig. 12).

For sodium fires, several approaches have been developed, based generally on the limitation of oxygen available for the combustion: specific catchers, dedicated volume portioning. Specific extinguishing powders have also been developed among the so-called “Marcalina” powder, made of sodium and lithium carbonate, mixed with graphite, spread out over the fire (🔍 Fig. 14) to insulate it from air.

Despite high care, with regard to the contact with air and water, thanks to protection devices and confinement, sodium contains various nonradioactive impurities either present from the start or introduced during operation.



■ **Figure 14**

Sodium fire extinguishing operation (Courtesy of Na School in CEA – Cadarache)

In the primary circuit, there is essentially

- One source of discontinuous contamination by oxygen and hydrogen at the start of the cycle and at the end of the handling of the assemblies
- One continuous source of hydrogen coming by permeation from the secondary circuit.

On the intermediate loops, there are essentially:

- One continuous source of hydrogen, mainly due to aqueous corrosion in Steam Generator Units, which produces magnetite Fe_3O_4 and native hydrogen.

In the event of a sodium–water reaction, there is one discontinuous source of hydrogen, sodium hydroxide, which is potentially decomposed over 593 K and produces Na_2O and NaH crystallized products, which dissolve if the sodium temperature is over its saturation temperatures, given by the respective solubility laws of oxygen and hydrogen in liquid sodium (see below). This is also the case after a contamination by air and moisture, following a handling operation.

Thus, oxygen and hydrogen constitute the major contaminants.

The respective solubilities of oxygen and hydrogen are very low; the solubility reaches a value around nul, near the melting temperature, that is, 371 K (this is property specific to sodium, in comparison with other liquid metals, used as coolants).

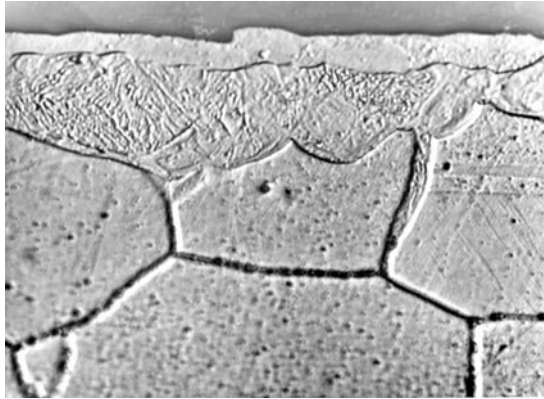
For oxygen, Noden law (➤ Sect. 3.5)

$$\log_{10} [\text{O}(\text{ppm})] = 6.250 - \frac{2,444.5}{T(\text{K})} \quad (10)$$

For hydrogen, Wittingham law (➤ Sect. 3.6)

$$\log_{10} [\text{H}(\text{ppm})] = 6.467 - \frac{3,023}{T(\text{K})} \quad (11)$$

Oxygen contributes to corrosion of steel (➤ Fig. 15), and the corroded activation products are transported from the core toward the components and mainly to the intermediate heat exchangers, leading to their contamination. All the elements that go to constitute steel (iron, Cr, Ni, Mn, C . . .)



■ **Figure 15**
General corrosion: formation of a ferrite film at the surface of sound austenite

are susceptible to being dissolved in sodium. Nevertheless, this phenomenon, which depends on diffusion near the interfaces, remains very weak because the diffusion coefficients of the components of steel are very low (► Sect. 3.9). General corrosion kinetics is a function of sodium physical parameters (temperature and flow rate) and sodium chemistry (mainly oxygen activity), and corrosion models have been established. Even if it is generally considered that corrosion is only significant for temperatures higher than 817 K and for oxygen contents of order 10 ppm, it is generally considered that a SFR requires to be operated with an oxygen content below 3 ppm, in normal operation, to limit the corrosion, consequently the contamination and associated dosimetry during handling or repair operations.

Some stress corrosion cracking phenomena can occur in the presence of aqueous soda, when the component, wetted by a residual film of sodium, is filled with air and moisture, which reacts with the film of sodium. Over 353 K for ferritic steels and over 383 K for austenitic steels, trans-granular cracking can occur. When preheating the facilities, prior to filling with sodium, such temperatures can be obtained. Therefore, it is necessary to avoid any presence of residual aqueous soda on components, gaps, by appropriate rinsing and drying processes.

Because steels tend to exchange nonmetallic elements such as carbon and nitrogen with the liquid metal, the effects of these elements have to be taken into account not only for the evaluation of the corrosion behavior of steels in liquid sodium and for mass transfer calculations but also for potential evolution of mechanical properties. At high temperatures, the diffusion rate of carbon in steel is fast enough to cause changes of carbon concentrations in cladding materials for instance. These evolutions have generally marginal effects on the corrosion behavior of steels at 873 K, but could be much more important at higher temperatures.

In the intermediate loops, hydrogen content has to be maintained as low as possible (<0.1 ppm), in order to allow a fast detection of water ingress. Moreover, some detrimental effects due to material embrittlement should be avoided, thanks to an efficient sodium purification campaign, after a sodium–water interaction, inducing a very high hydrogen content. The detection can be carried out with hydrogen-meters, diffusion type with Ni membrane (► Fig. 16), used in various countries and mass spectrometer or electrochemical cell, developed by IGCAR (India), implemented on PFBR.



■ **Figure 16**
Hydrogen-meter based on Ni diffusion

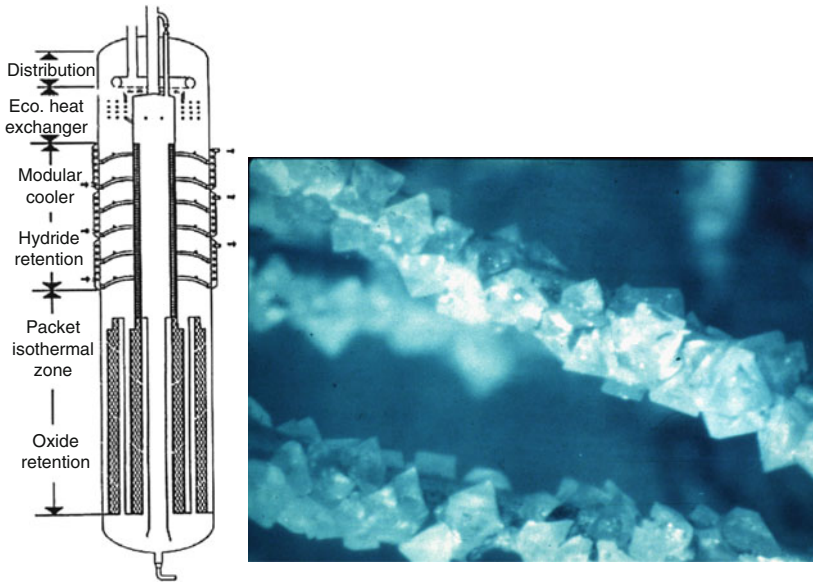
Two main sodium purification processes have been developed with regard to oxygen and hydrogen control:

- Cold trapping (➤ Sect. 3.7) by crystallization of Na_2O and NaH , by lowering the sodium temperature below the saturation temperature and thus creating the optimal conditions for Na_2O and/or NaH nucleation and growth on a steel packing distributed in an auxiliary cooled vessel. Cold trapping (➤ Fig. 17) is the process used worldwide for sodium purification in the sodium fast reactors, due to its undeniable advantages: the trapping of oxygen and hydrogen, which are the two most important impurities to trap in an SFR, in the same component, the easy reachability of lowest oxygen and hydrogen concentration due to the respective solubility laws, the highest efficiency and capacity obtained with optimized designs of cold traps, and the ability for the cold trap to be regenerated by extracting solely the packing or by *in situ* appropriate chemical process.
- Hot trapping or “getter” operation (➤ Sect. 3.8) based on the capacity of the chosen material (i.e., zirconium–titanium alloy for oxygen) to oxidize when it is placed in the presence of sodium containing some amount of oxygen. This last process is generally chosen for small sodium volumes to be purified and when the risk of Na_2O dissolution by loss of cooling function in the cold trap is unacceptable. As example, the $\text{Zr}_{0.87}\text{-Ti}_{0.13}$ alloy has been qualified for hot trapping in an irradiation loop for Phenix: kinetics and optimized operating conditions have been established for further use:

$$V = 41.26 \times 10^{-3} \times \exp(-40.3 \times 10^3 RT) [\text{O}] \text{ kg (O) h}^{-1} \text{ m}^{-2} \quad (12)$$

where V is the rate of oxygen trapping (mol h^{-1}), T designates the hot trap temperature (K), R is the Boltzman’s constant ($\text{J mol}^{-1} \text{ K}^{-1}$), and $[\text{O}]$ is the oxygen content in ppm.

For hydrogen trapping, “hydride” traps (i.e., yttrium) could also be set-up but, due to their very low potential capacity and reversibility, their application for large sodium volumes has never been foreseen. The monitoring of sodium quality can be performed by numerous on-line (plugging-meters, hydrogen-meter, and oxygen-meter) or off-line (sampling by dip sampler then analysis in laboratory: atomic absorption, distillation. . .).



■ **Figure 17**
Intermediate cold trap for SuperPhenix with NaH

3.1.3 Neutronic Properties

Sodium has only one stable isotope, namely, $^{23}_{11}\text{Na}$. The neutron flux leads to formation of radioactive isotopes: two other isotopes, with significant half life, are created: ^{24}Na (half life 14.98 h), inducing the necessity to wait for decay before some interventions on primary circuits and ^{22}Na (half life: 2.6 years), to be taken into account during decommissioning and sodium treatment. This low activation is also a very attractive property of sodium for nuclear use in SFR.

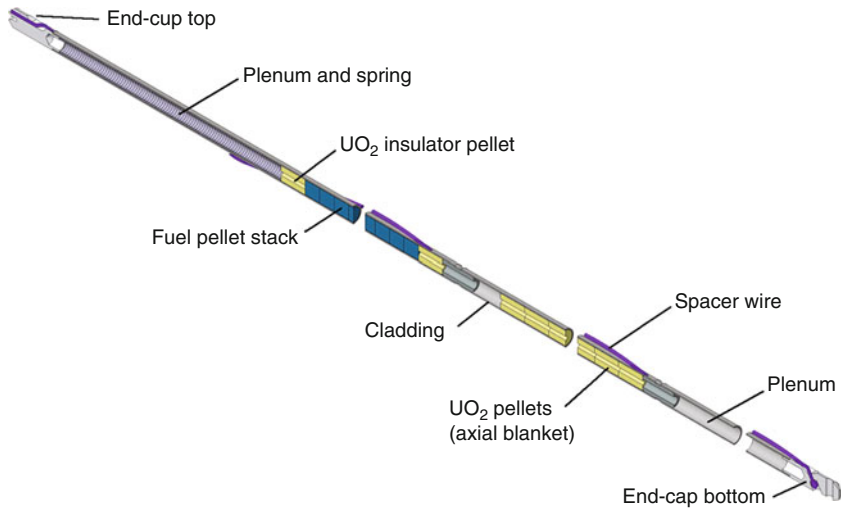
3.2 Fuel Design

3.2.1 Fuel Element

In most cases, the fuel element is a cylindrical solid of revolution. A circular section is the most adapted to allow the cladding to withstand the primary pressure stresses: for SFR application, the internal pressure of the fission gases released in operation outside the fuel.

Typical fuel element is shown in ► [Fig. 18](#). The fuel pin is mainly made up of the cladding containing the fuel pellets or rods and is closed by two welded end plugs, which results in a gastight assembly. In the top part of the pin, there is generally a spring, which maintains the fuel column in place and creates a gap (plenum) for fission gas expansion and fuel elongation. If the volume of fission gases released is very high, a large area at the bottom of the pin is also left.

Disks made of refractory materials (natural or depleted uranium oxide, alumina. . .) can be placed at the top and bottom parts of the fuel to insulate it from the metallic parts (plugs, spring. . .). The SFR fuel pin can include columns made of fertile material making up the axial blankets.



■ **Figure 18**

Illustration of fuel element: Phenix case

To improve heat transfer between fuel and cladding, the fuel element is filled with helium at atmospheric pressure. In the case of a fuel material that swells (metal alloy, carbide, nitride), a large gap is needed, and the thermal gradient increases in the gap. To reduce it, one can fill the pin with sodium (possible because of the good compatibility between these materials), in order to obtain very good heat transfer between fuel and cladding and thus take full advantage of the good thermal conductivity of the fuel. In this case, an alternative solution would be to have a fuel element with a vent, an opening equipped with a filter allowing the fission gases to be continuously released from the pin. We thus abandon the concept of a “clean reactor.” But the vented fuel has never really been used, except in the DFR experimental fast neutron reactor of Dounreay (UK).

A spacer wire, made of steel of the same nature as that of the cladding, is helically wrapped around each pin and attached to the end plugs. This solution

- Ensures regular spacing of the pins over the whole length
- Minimizes vibrations
- Ensures sodium mixing
- Allows some straining (by irradiation effect) of the pin cluster compared to the wrapper tube without any cooling perturbation

3.2.2 Fuel Subassembly

For the purpose of illustration, a typical fuel subassembly is shown in [Fig. 19](#). Fuel subassembly design, as far as the number, diameter, and arrangement of fuel elements is concerned, is mainly guided by thermomechanical, hydraulic, and neutronic considerations:

For a given power density (W/cm^3) to be evacuated, the temperature at the center of the fuel increases with its diameter (increase of the linear heat rate), which leads to fraction the fuel into several elements of small diameters so as to avoid reaching, at the center of the fuel, a

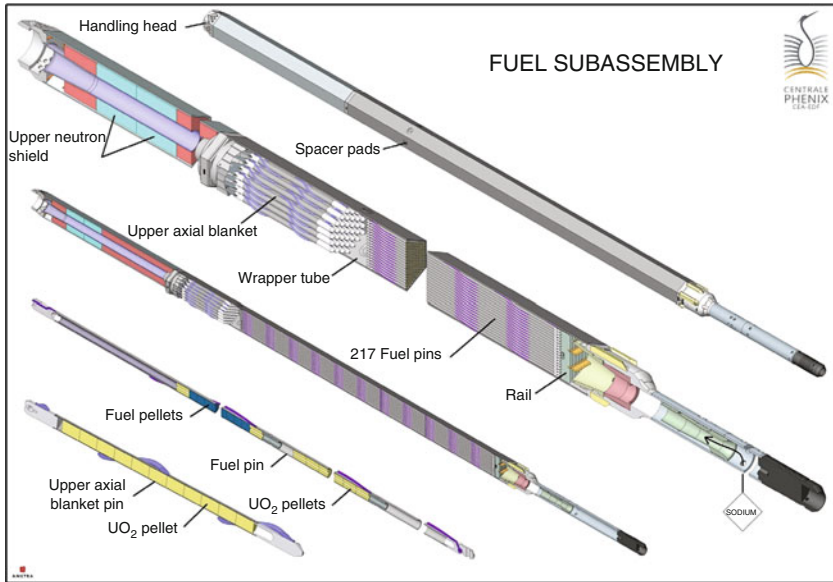


Figure 19
Illustration of fuel subassembly: Phenix case

temperature that would be incompatible with its limits of use (margin to fuel melting, thermal stability, chemical interactions. . .)

Another limit is given by the maximum surface heat flux (in W/cm^2), which the coolant is capable of extracting. For a given power density released by a fuel element, the surface heat flux decreases when the exchange surface increases, and therefore, when the diameter increases.

The bottom nozzle of the subassembly allows it to be positioned in a diagrid which is a cold sodium collector and supplies it with sodium several radial openings. It includes a pressure drop device used to adjust the sodium flow rate, as the fuel subassemblies are distributed over several flow rate areas, varying according to the radial (and axial) power distribution.

The median part includes the fuel pins contained in a steel hexagonal wrapper tube which has two functions: it forms the cooling channel, allowing sodium flow to be adjusted, and makes up, with the top and bottom nozzles to which it is connected by welding and crimping, the mechanical structure of the subassembly.

At about the same level as the top of the fuel, the wrapper tube includes spacer pads, which are dimples impressed on each face of the tube, with a small gap under cold conditions between two neighboring subassemblies, in order to obtain a compact core in normal operation under effect of thermal expansion.

The top nozzle, consisting of a steel hexagonal block with a circular central hole allowing circulation of sodium leaving the subassembly, is used both as neutron protection of the top components of the reactor and as the gripper head of the assembly for handling.

The FR fuel subassembly is characterized by:

- A high plutonium content (from 15 to 30% for example for the French FR)
- A fuel in the shape of solid or annular pellets of $(U,Pu)O_2$, $(U,Pu)N$, $(U,Pu)C$ or in the shape of rod of U–Pu–Zr metallic alloy

- Large plena (bottom and top)
- A spacing made by a wire helically wound around each of pins (even though different solutions, such as grid spacing have been tested)
- An hexagonal wrapper tube
- The use of austenitic, ferritic–martensitic steels or nickel alloys as materials for structural components

The previous paragraphs are a general description of the fuel element and the subassembly designed for the SFR and the Phenix design is chosen as an illustration.

The precise design of the subassembly (Fuel pin included) can continuously evolve because it depends on the objectives set and the state of knowledge achieved and can be changed during the life time of reactor. The cycle facilities have to be built to accept these evolutions (certainly very complicated if the nature of the fissile compound has to change). In the subassembly design of FR for new objectives such as Pu balance or minor actinides transmutation, different solutions can be taken into account, both during the study of new projects and during the definition of new reloads for operating reactors.

3.3 Pool/Loop and Modular Design

3.3.1 Features of the Primary Circuit Concepts

The primary circuit of the existing SFRs is based on two concepts:

- The pool concept
- The loop concept

The Pool concept is featured by nearly all the primary sodium coolant inside the reactor vessel. Therefore, this main reactor vessel encloses the primary pumps (PP) and intermediate heat exchangers (IHXs), in addition to the internal structures surrounding the core and devoted either to its feeding and supporting or separation of the various hydraulic plenums.

As opposed to the pool primary system, the loop concept is characterized by some major primary components outside the reactor vessel. Several variants of the loop concept exist. In the earlier existing loop-type SFRs, the primary pumps and the IHXs, without grouping, are located adjacent to reactor vessel and are connected together by inlet and outlet pipes through nozzles. Less conventional variants try to cope with the loop-type drawbacks, whereas the loop-type benefits are kept, and for this purpose:

- The nozzles, especially at the bottom part of the reactor vessel, are eliminated. The top-entry concept is typically a kind of solution with penetrations of the primary pipes through the reactor roof (either U-shape or L-shape pipes)
- Shortened primary pipes reducing the number of bends. This trend is illustrated by the Japanese reactor designs where the number and the length of primary pipes are strongly reduced.
- Primary pumps and IHXs can be located into dedicated component vessels or gathered in a single PP-IHX component.

In addition, some innovative conceptual designs try to combine the features of the pool and loop concepts in order to sum their own benefits and to remove their respective drawbacks. These variants can be considered as hybrid designs, but strictly speaking, they are variants of either pool or loop concept.

A detailed analysis of pool and loop concepts shows that the reactor unit power level can influence the choice of design variants. The possibility of components manufacturing in factory, and not on site, is considered by designers as an attractive option. In this respect, the modular plant concept characterized by several reactor power units coupled to a same power block (i.e., same balance of plant), complying with a commercial-size of power supply, is preferable. On the contrary, if the power units for the plant site are separated, in case of the large-size nuclear plant units, then, only possible size effects are preferred, but without common equipments for a given power block.

Generally speaking, modular concept can be applied to any component; for example, modular steam generator can be implemented on large-size power unit. The meaning of modular concept in the present case is particular to the reactor primary system.

An intermediate sodium system is usually added between the primary circuit and the energy conversion system for either pool or loop primary circuit concept (ECS), to prevent primary sodium–water interaction by means of two physical barriers (IHX and SG tubes). For the loop concept, the number of intermediate circuits has to be compatible with the number of primary loops, whereas for the pool concept the number of intermediate circuits is quite an open design option; it is based on reactor size.

Tentative of elimination of the intermediate system existed in the past from economic point of view, and it is considered again recently when alternative conversion systems (ECS without water–steam cycle) were proposed as concerns the sodium–water interaction risk. Feasibility of SFR without intermediate system is not yet demonstrated, but tentative designs are only based on loop concept (more suitable than the pool concept).

The advantages and drawbacks of each concept depend in practice on the design variants. However, one can notice some general trends allocated to each main concept but to be considered carefully based on the previous discussions. Some general trends are mentioned in the following paragraphs.

3.3.2 Pool Concept: Motivation and Challenges

The topics of motivation for a pool-type primary circuit can be perceived as opposed to the loop concept:

- There is no relevant accident scenario of loss of primary coolant. The primary sodium inventory is managed by safety provisions (e.g., guard vessel)
- The large thermal inertia of the reactor block contributes to slow down any transient loss of heat sink
- There is no risk to break the hydraulic loop from the core outlet toward the core inlet
- A very efficient natural circulation of the primary circuit is expected, as a flow backup at reactor shutdown state, in case of loss of the forced flow mode (e.g., pumps trip)
- There exists a cold sodium plenum at the pumps suction upstream, which acts as buffer against either thermal chocks or gas entrainment toward the core
- In practice, there is no risk of radioactive sodium fire, except for limiting events leading to a hypothetical core disruptive accident (HCDA)

- Good mechanical behavior of the primary containment against energetic HCDA
- Ease of radiation protection in normal operation.

On the other hand, matters on competitiveness and on flexible operational conditions remain as challenges:

- Limited access for inspection and repair of the under-sodium internal equipments
- Seismic behavior of sodium free-level and large structures
- Reactor-block compactness limitation due to integrated large components

3.3.3 Loop Concept: Motivation and Challenges

In the same way, motivation for loop concept and challenge as opposed to the pool concept can be perceived:

- Ease of access for maintenance and repair of those of the primary components located outside the reactor-block (e.g., IHX)
- Compactness of the reactor-block (e.g., vessel diameter) and reduction of the primary loops number
- Potential for further construction cost reduction and for innovative change of primary and intermediate equipment (e.g., pump design, integrated components, intermediate circuit change. . .)
- Any rotating pump-shaft is away from the core vicinity

In return, the designer has to solve some issues about:

- Prevention of loss of the primary coolant (e.g., pipe integrity) and provisions to keep a hydraulic loop through the core whatever the abnormal operating conditions are
- Potential consequences of a LOCA, inside (e.g., gas entrainment) and outside the primary circuit (e.g., active sodium fire)
- Provision against asymmetric operating faults (e.g., trip of one of the pumps leading to reverse flow)
- Suitable implementation of several decay heat removal (DHR) systems in order to cope with different accidental configurations of the primary circuit
- Additional provisions regarding the radiological protection

3.3.4 Modular Concept: Motivation and Challenges

The primary circuit of a reactor unit of the modular plant concept is equally a pool-type or a loop-type concept, and then the generic positive and negative features mentioned above remain applicable. Whatever the choice of primary circuit concept is (i.e., pool or loop), the search of variants is driven by size effect considerations. Therefore, topics of consideration depend on design variants. Some such topics connected to size effects are listed below:

- Improvement of the DHR safety function through a complete diversification of the redundant means, in particular with one of the means being a reactor vault auxiliary cooling system (RVACS), efficiency of which depending on size effects
- The largest components (internal structures, roof, core-support bottom structures, vessels. . .) *made in factory* which changes the fabrication modes and then the quality

(need of inspection in operation. . .); but this involves some limitations on the component dimensions for transport reason

- Potential for better availability rate as regards the electric power supply, in that only one reactor module is at shutdown state for some configurations
- Ease of safety demonstration, in particular to account for hypothetical core severe accidents and their consequences on the containment
- Validation at full scale for one first-of-kind seems sufficient, instead of validation (a demonstrator and a prototype) for the conventional high power reactor system
- Potential for easier repair (e.g., IHX handling) and end-of-life dismantling conditions

But generally speaking, the cost balance being more favorable when increasing the reactor power, the main challenge for the modular concept is then to reach competitiveness in terms of cost by a different way than the unit power. For this aim, the designer has to find technological thresholds in the reactor module design, thanks to size effects (e.g., use of electro-magnetic pump), in addition to the other saving items in the cost breakdown: production in series, reduced delay of the plant under construction, sharing of equipment (sized for one module scale) between the power units. . .


3.4 Main Components and Systems


The choice of design option is crucial at the start of conceptual design stage in order to meet the requirements for achieving safety and economy, concurrently. Hence, the concepts selected should be simple, mature, and robust and should be based on operating experiences, availability of relevant design criteria, analysis capability, operating experiences, international trends, availability of materials and constructability including transportation. Newer materials and concepts should be introduced carefully after detailed analysis and thorough validations for meeting both functional and safety requirements. Standard and proven concepts should be adopted wherever possible. The functions of each component should be defined comprehensively. The operating conditions, environments, safety classifications, design requirements and interfaces constraints should be identified clearly. While selecting the SFR components, whose design is largely governed by neutronics, complex pool hydraulics, structural mechanics, seismic design requirements, shielding requirements, etc., it is preferable to introduce judicious mix of flexibility and rigidity. From the point of long and reliable operation of the plant, needless redundancy and rigid geometrical constraints should be avoided. The geometrical features should be selected as far as possible to have complete access for inspection and to achieve reliable technology. The synergy and interplay of various governing performances need to be understood in a scientific manner with due regards to constraints in realization of technology.

In this part of the chapter, the important components in the heat transport circuits are introduced. The heat transport system of SFR, addressed in this chapter, has an intermediate circuit. Designs without intermediate circuits are found in literature, which are not covered. Accordingly, this chapter covers description of main heat transport system components, such as main vessel, grid plate, core support structure, inner vessel, primary sodium pump, control plug, and top shield, which belong to primary sodium circuit. Further main components of intermediate heat transport circuits such as intermediate heat exchangers, secondary sodium pump, and steam generators are covered subsequently. Finally, the components in the decay heat removal circuit are described. To start with, the overall heat transport circuit is briefly introduced. The major design choice for the reactor is the selection of number of primary and secondary loops and components, which is dealt in a comprehensive manner. The types of support arrangement

for the reactor block, also termed as reactor assembly, which is also an important design consideration, are brought out. Subsequently, design choices for each component are described in detail. While describing the design choices, the main functions and concepts adopted in various SFRs are brought out with schematic sketches. In this context, the international SFRs, mainly Fast Breeder Test Reactor (FBTR), Rapsodie, Phenix, SuperPhenix (SPX1), Prototype Fast Reactor (PFR), BN-350, BN-600, Monju, prototype fast breeder reactor (PFBR), BN-800, European Fast Reactor (EFR) and Commercial Demonstration fast reactor (CDFR) are referred. At the end of this chapter, certain innovative designs being conceived in advanced and future SFRs are also highlighted. For quantifying certain design parameters, where necessary, a typical 500 MWe pool type fast breeder (PFBR) is used as the reference case.

3.4.1 Description of Heat Transport Circuits and Components

The heat transport system consists of primary, secondary, and steam–water circuits. The purpose of primary circuit is to transport the heat energy, generated in the core to the intermediate heat exchangers (IHX), from which the heat is transported to the secondary circuit. The secondary circuit, in turn transfers the heat to the water circulating in steam generators, to generate steam. The steam–water circuit is the conventional electricity generating system, called as balance of plant (BoP). The main components in the primary circuit are main vessel (MV), also called reactor vessel (RV), which houses the core and contains the coolant, grid plate, primary sodium pumps (PSP), and top shield. The grid plate supports the core and facilitates circulating the sodium to the core subassemblies to remove the nuclear heat. The main vessel contains primary sodium and supports the grid plate. Primary pumps provide required pressure head to the sodium to flow through the core subassemblies. In the pool-type concept, there is a need of a vessel called inner vessel which separates the hot and cold sodium in the main vessel which houses the entire radioactive primary sodium circuit. Thus inner vessel ensures desired flow through IHX and targeted design temperatures in the hot and cold pools. The absence of inner vessel or a large leak in the inner vessel will result in higher stabilized overall temperatures of pool (which will exceed the structural temperature limits) in the process of heat removal by intermediate heat exchangers (IHX) from the mixed pool. The IHX, steam generators (SG), and secondary sodium pumps (SSP) are the main components in the secondary circuit. The heat transport circuit components of typical pool- and loop-type reactors are shown in  Fig. 20.

Apart from the above mentioned circuits, decay heat circuit consisting of dedicated heat exchangers immersed in hot pool (in the case of pool concept) and air heat exchangers to transport the heat to the atmosphere (ultimate heat sink) during decay heat removal operations are important systems from point of view of safety. Depending upon the system, this circuit consists of decay heat exchangers (DHR) and pumps. Compared to thermal reactors, SFR system operates with high operating temperature.  Table 8 provides the core outlet and steam temperatures in a few SFR power plants.

In view of higher steam temperatures, thermodynamic efficiency is around 40%, which implies less thermal pollution and less loss of nuclear heat. This is one of the main advantages of SFR power plants, compared to water reactors.

3.4.2 Primary Component Layout on the Top Shield

The layout of equipment depends upon the concept of the reactor system, namely, loop or pool type. In loop-type reactor system, the equipment such as primary coolant circulation pump,

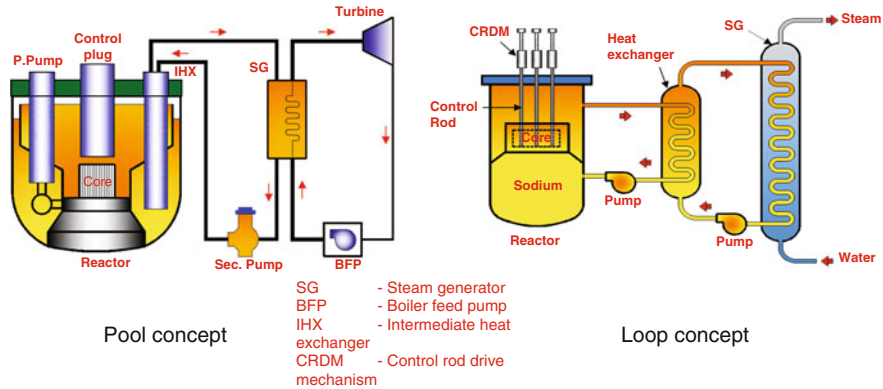


Figure 20
 Heat transport circuits of SFR power plant

Table 8
 Operating temperatures of FR power plants

Reactor	Thermal power (MW)	Electric power (MW)	Core outlet temperature – K (°C)	Steam temperature – K (°C)
BOR-60	55	12	803 (530)	703 (430)
FBTR	40	13	788 (515)	753 (480)
EBR-II	62.5	20	646 (473)	706 (433)
KNK-II	58	21	798 (525)	758 (485)
Phenix	563	250	833 (560)	785 (512)
PFR	650	270	833 (560)	788 (515)
Monju	714	280	802 (529)	756 (483)
BN 350	750	350	710 (437)	678 (405)
PFBR	1,250	500	820 (547)	766 (493)
BN 600	1,470	600	823 (550)	778 (505)
BN-800	2,000	800	820 (547)	763 (490)
SPX-1	3,000	1,240	818 (545)	763 (490)

intermediate heat exchanger, etc., are spread out and distinctly located outside reactor vault and hence does not influence the reactor block dimensions. On the other hand, in pool-type configuration, all these equipments are located within a single vessel, leading to close interplay of many parameters. This is broadly discussed in the following paragraphs.

As the reactor vessel in pool-type reactor is designed without any penetrations to assure highest reliability for the coolant boundary, all the equipment of primary coolant circuit, reactor control, and safety systems, etc., pass through the penetrations in the top cover of reactor vessel known as top shield. This brings the crucial issue of their layout over the top shield,

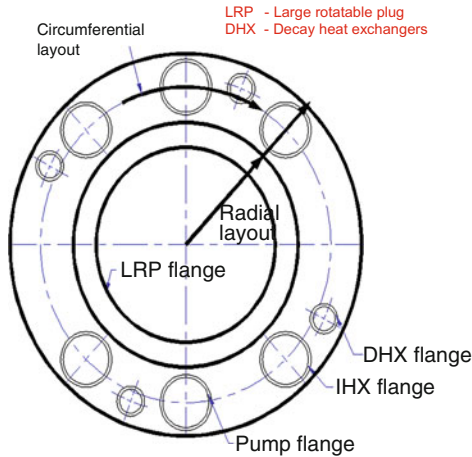


Figure 21
Radial/circumferential spaces in layout

which is one of the important factors in optimizing the overall dimensions of the reactor block. The overall dimension is governed by space requirements either in radial or circumferential directions (► Fig. 21). The core diameter and height are also governed by reactor physics considerations. The heat transport system components, such as primary pumps and IHXs should be positioned around the core. With more number of primary and secondary sodium loops (>2), the pitch circle diameter (PCD) of the component's layout on the top shield would be decided by the circumferential spacing. This is because of the large number of equipment to be arranged over the top shield, leading to a limiting value for the PCD beyond which it cannot be reduced. For lesser number of components, say for a typical two loop concept, PCD would be governed by radial spacing. These aspects are however linked to the size of the reactor. Generally, larger size reactors (say >600 MWe) are designed with more than two secondary sodium loops. On the other hand, medium size reactors (~500 MWe) are designed with two loops as it generally leads to optimum reactor block dimensions. However, for reactors with relatively lower number of loops, the reactor block dimensions are governed by radial considerations decided by the size of the equipment.

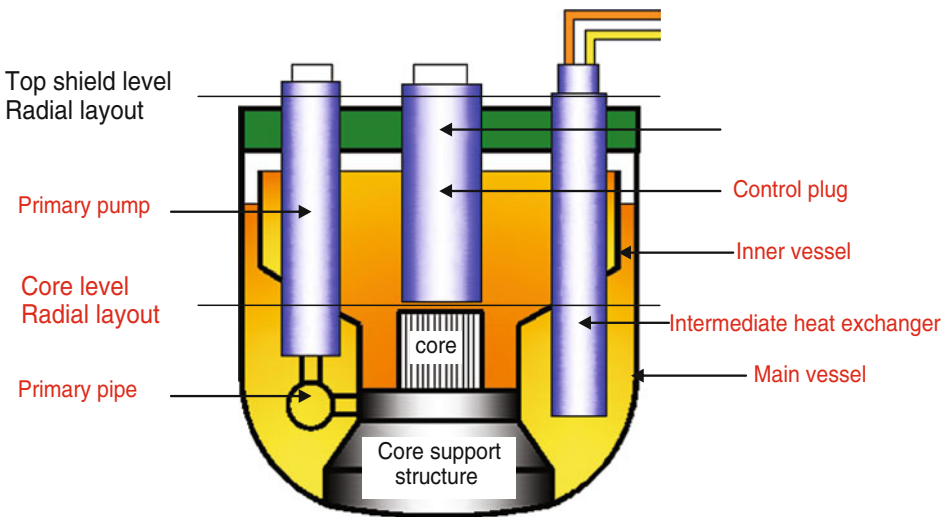
It is to be noted that the size of the pump and numbers would be decided with considerations of single/double suction option, flow, and temperature requirements based on the reactor power. Further, reducing their number beyond a value would not be practical from practical considerations. This is because, for removing the required amount of heat, certain minimum mass flow rate (m) is required as per equation: $Q = m C_p \Delta T$. The mass flow rate is decided by the number of pumps, which would increase in case the numbers are minimized. Further, safety considerations would demand minimum number of pumps to be not less than two.

Generally, in pool-type reactors, the ratio of the number of primary pumps to IHXs is maintained as 1:2. This is to take care of the loose coupling effect between the pump and IHX in pool-type configuration unlike in the loop-type configuration, where direct linkage is present between the pump and corresponding IHX. The ratio of 1 in a pool-type reactor ensures that if the situation so warrants, some flexibility for making finer adjustments in the outlet temperature

of IHXs is built into the system. This flexibility arises from the arrangement of one pump surrounded by IHX of the same secondary loop on either side. For a pool type, the basis for arriving at typical layout of equipment over the top shield based on various numbers of secondary loops and corresponding number of equipment is indicated in the following paragraphs, with reference to a typical 500 MWe pool-type fast reactor.

Estimation of Main Vessel and Top Shield Diameter: An Illustrative Example

The number of primary/secondary loops is varied from two to four. Accordingly, the number of pumps is varied from two to four, and IHX number is varied from four to eight, maintaining 1:2 ratios. The diameters of the pumps and IHX are assumed to respect the process requirements. With these assumptions, the main vessel/top shield diameter is calculated based on layout verification at core level and top shield level (👉 Fig. 22), both in radial and circumferential directions. In the radial direction, the diameter of the core, gap between core and inner vessel, stand pipe dimensions, radial clearances between various shells, and thickness of various shells decide the radius of main vessel at the core level. At the top shield level, diameters of various plugs and components and their layout, shielding and handling aspects would also control the radius of the main vessel. In the axial direction, core height, heat exchanger/pump heights, cover gas height, submergence requirements for inlet windows and pump impellers, and gap between the core top and bottom of above core structure would decide the height of the main vessel. This apart, the thickness of the top shield, the support skirt height should be added with main vessel height for arriving at the overall height of the reactor assembly. The diameter and height of the reactor assembly thus arrived at should be optimized through several iterations which is mainly due to diameter to height ratios of the intermediate heat exchanger and primary pump.



■ Figure 22

Reference levels in pool type SFR

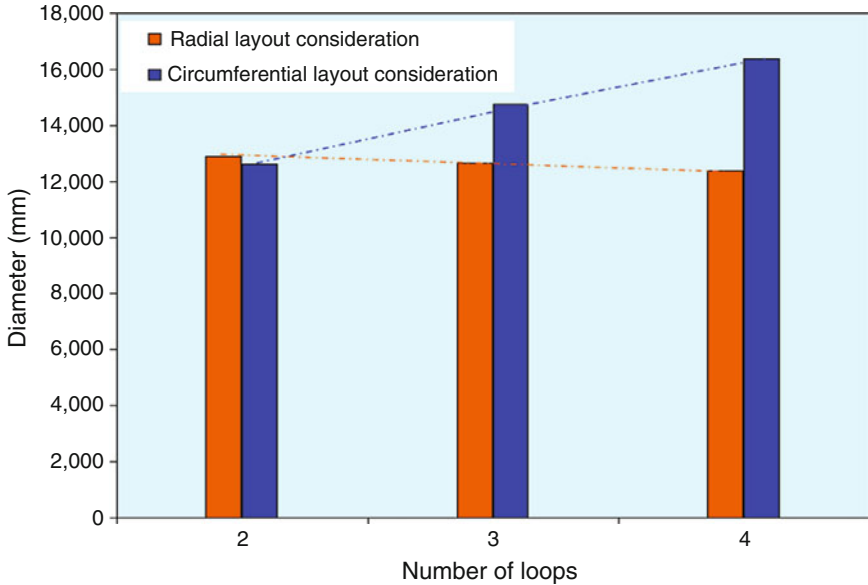


Figure 23

Main vessel/top shield diameter vs. number of loops

Results for a Typical 500 MWe SFR

The diameter of main vessel/top shield is influenced by the number of equipment located over the top shield, which in turn depends on the number of loops and the size of primary loop components, which once again depends on the number of loops. Toward this, a study on minimum top shield/main vessel diameter with reference to the number of loops was made taking 500 MWe SFR design as a reference. The study indicates that for a typical 500 MWe reactor with two loops, the radial layout of equipment at both core/top shield level governs the size of main vessel/top shield where as the circumferential layout consideration governs the main vessel/top shield size, if the number of loops is increased. This is depicted in [Figure 23](#). Further, it can also be observed that the two loop design gives the optimum main vessel/top shield diameter. However, as indicated above, the diameter is also a strong function of primary loop equipment size, and hence, for reactors of different rating, similar study needs to be carried out. [Figure 24](#) shows the component layout over the top shield for the two, three, and four loop concepts.

3.4.3 Reactor Assembly Support Options

The other important decision is the option of supporting the reactor assembly either at the top or bottom. [Figures 25](#) and [26](#) show a few typical support arrangements adopted in the international loop and pool-type SFRs, respectively.

Both top support and bottom support arrangements have relative merits and demerits that require careful consideration. The top supported vessel is free to expand both in radial (except at the support location) and axial directions, leading to lower stress levels of thermal origin.

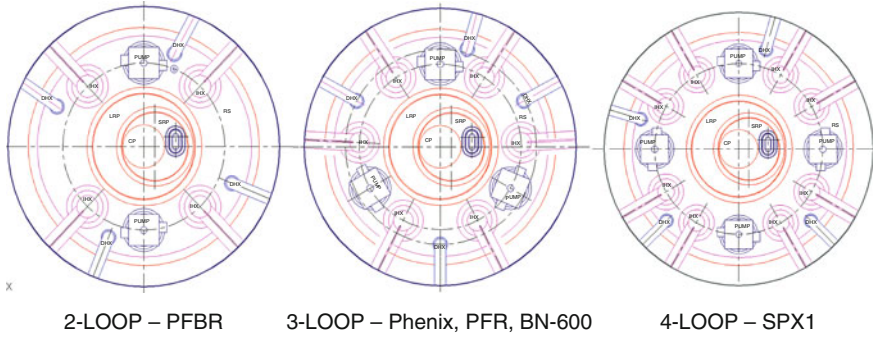


Figure 24
Component layout on the top shield vs. number of loops

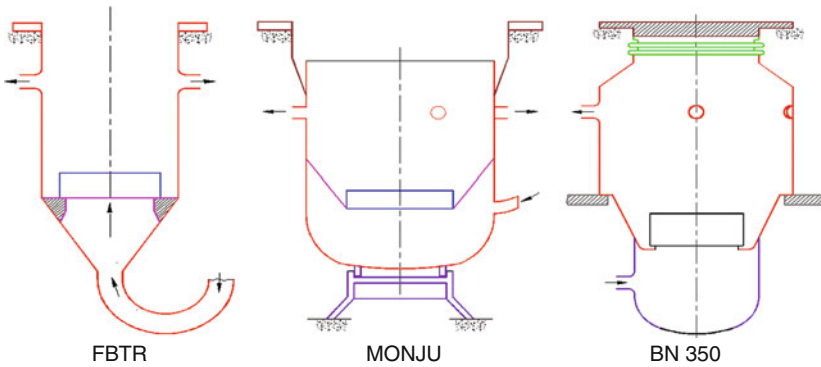


Figure 25
Reactor assembly support arrangements for loop type reactors

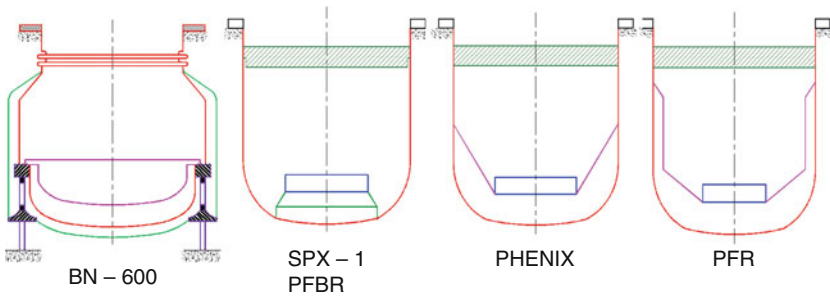


Figure 26
Reactor assembly support arrangements for pool type reactors

On the other hand, the loss of this advantage, together with requirement of large diameter below for accommodating the axial thermal expansion between the support and the top cover, might weigh against the option of bottom supported vessel, especially, for larger power (>500–800 MWe) stations. However, the advantages of bottom supported vessel for seismic-induced loading is obvious in view of the possibility of bringing the support elevation in line with the mass center of the reactor assembly, and the overall weight of top shield could be reduced by transferring loads of the pumps and heat exchangers in the vicinity of the bottom support. In the bottom supported vessel design, the diameter of the top cover can be reduced (e.g., BN 600) by supporting the primary sodium equipment over the extended cantilever portion of reactor vault, thereby relieving the reactor vessel of such a function. In the loop-type design built so far, the top supported vessel designs have been predominantly favored except in BN 350, wherein a support closer to core level has been chosen. Generally, for both loop and pool designs, bottom supported option has been largely favored in Russian designs.

3.4.4 Basic Design Options of Primary Circuit Components

Reactor Vessel (Main Vessel)

The reactor vessel is one of the important components of reactor assembly as it forms a boundary for radioactive primary sodium and argon cover gas and is a part of core support path. In pool type, the vessel is generally made of a cylindrical shell with bottom dished head. The designs of various reactors vary in the kind of supports: bottom or top supports as discussed in [▶ Sect. 3.4.3](#), shape of the bottom dished head, and top shield arrangements ([▶ Figures 25 and 26](#)). The basic parameter that has high impact on the economy is the size of the vessel, that is, diameter and height. The vessel diameter of the main vessel for the pool-type concept has to be studied in a detailed manner. The basis of selecting diameter is dealt in [▶ Sect. 3.4.2](#). Owing to its size requirements and design loadings, the optimization of vessel geometry leads to a large diameter thin shell structure, whose design is largely governed by buckling considerations under seismic loading.

Apart from process parameters including core diameter, the main vessel cooling requirement and the form tolerances of the various vessels, such as main vessel, inner vessel, and thermal baffles, positioned coaxially, have high influence on the main vessel diameter: Experiences indicate that it is easier to achieve tight tolerances with smaller diameter, and large tolerances need to be specified relatively for the large dimensioned vessel. This calls for larger radial gaps between the shells to meet the functional requirements, which in turn results in larger diameter of the main vessel, due to the cascading effects. For example, the form tolerance targeted for Indian PFBR, whose main vessel diameter is 12.9 m, is less than its thickness in order to minimize the above effects. This has been achieved with considerable efforts put forth by the industry. An alternate could be machined main vessel, by which the vessel can have perfect geometrical shape that has high buckling resistance, which is one of proposals for the European Fast Reactor (EFR). Another aspect is main vessel cooling. The main vessel is designed with cooling by “cold sodium” (e.g., PFBR, BN 600, Phenix, SPX-1, etc.) to enhance the structural integrity by lowering the vessel temperature so as to minimize the formation of undesirable carbides and sigma phases in the austenitic stainless steel material and to maintain its temperature and temperature gradients (axial and circumferential) within acceptable limits (from creep and creep-fatigue aspects) during all operating conditions so that the dimensional limits for the

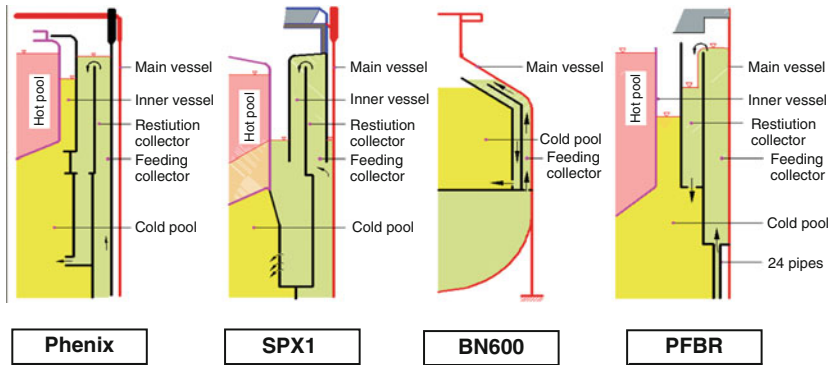


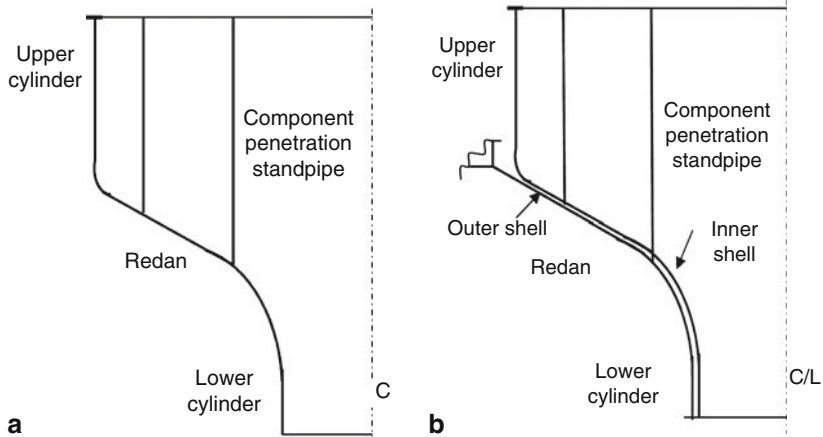
Figure 27
Main vessel cooling arrangements

main vessel are met over the design life. Figure 27 shows the cooling arrangements for a few international SFRs. The kind of cooling circuit concept adopted in these designs incorporates a weir shell over which cold sodium flows to cool the adjacent main vessel. The circuit generally consists of feeding collector (plenum adjacent to the main vessel), restitutions collector (plenum adjacent to feeding collector). The sodium after passing through these two collectors joins back to the cold pool. Apart from this, it also eliminates the possibility of sodium level and temperature fluctuations (responsible for thermal ratchetting and fatigue) on the surface of the main vessel. Hence, practically the vessel is subjected to insignificant creep-fatigue damage and ratchetting. In view of high incentive to design the vessel without cooling in terms of significant reduction of vessel diameter, it is worth putting efforts to eliminate the vessel without sacrificing the structural integrity and reliability requirements. This of course calls for many challenges to be addressed. However, with confidence gained through operating SFR and the advances in material development of high temperature design rules, it is possible to succeed in future reactors, which is one of means to make SFRs economically competitive.

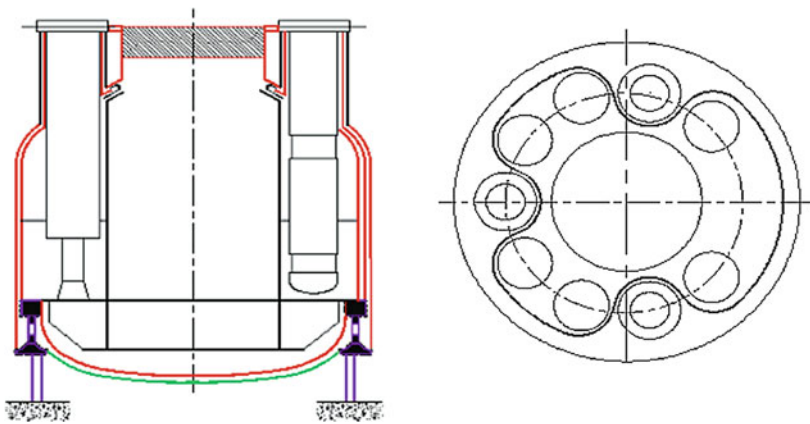
Inner Vessel

The inner vessel is incorporated in pooltype reactors as a barrier between hot and cold pools of primary coolant. On the other hand, loop-type reactors do not require inner vessel. The geometry of inner vessel is designed with penetrations permitting passage of components passing through the vessels. Either single wall or double wall concept is adopted in the international SFRs. The single wall concept (Figure 28a) is generally a selfstanding vessel that carries both mechanical and thermal loads in an optimum way. On the contrary, in the double wall concept (Figure 28b), mechanical and thermal loads are separated out. In SPX1, the inner vessel, which is in contact with hot pool, absorbs thermal gradients in view of its flexibility and outer vessel, which is in contact with cold pool, carries the mechanical load due to the sodium pressure head and self weight including stand pipe. In BN series of reactors, the pumps are kept outside the inner vessel which is feasible for bottom support designs (Figure 29).

The other choice for the inner vessel is the kind of sealing system to be provided at the IHX stand pipes to minimize the leakage of hot sodium to cold sodium. In SPX1, an innovative system using argon pocket is employed. Though it has many advantages in terms of



■ Figure 28
(a) Single wall concept; (b) Double wall concept



■ Figure 29
Lobe type inner vessel concept adopted for BN-600

good leak tightness, construction simplicity, and ease of disassembly and assembly of IHX for maintenance, gradual loss of argon due to diffusion into the hot liquid sodium and consequent fear of argon entry into the core has led not to use this option for future reactors. Alternatively, mechanical seals are preferred, which can be designed to minimize the sodium leakage to insignificant level. ● Figure 30 shows argon and mechanical seal arrangements. Mechanical seals are employed in BN600 and PFBR.

The overall shape of the component is largely influenced by thermalhydraulics and structural mechanics considerations. Minimization of through-wall temperature gradients and thermal stratification in the hot pool are the main thermalhydraulics issues to be addressed.

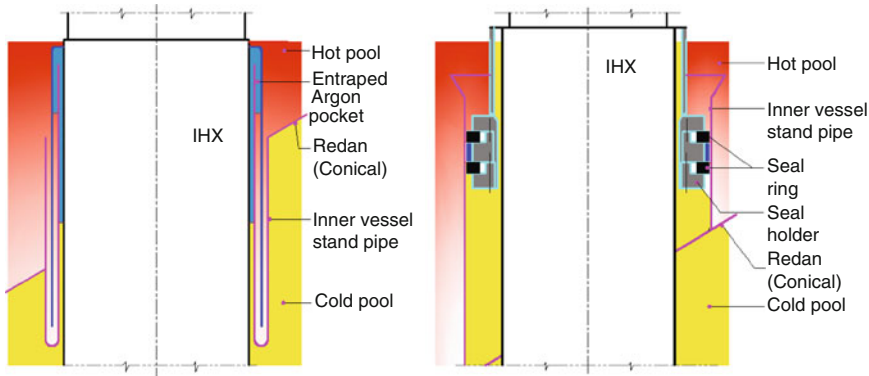


Figure 30
Sealing arrangements used in inner vessel

From the structural mechanics point of view, buckling of torus portion of the vessel under mechanical loads combined with seismic-induced dynamic pressure, thermal gradients is the critical issue to confirm the shape of the vessel and thickness. Details of thermalhydraulics and structural analyses will be presented in the later chapters.

Grid Plate (Diagrid)

The grid plate supports the core subassemblies and acts as plenum for sodium coolant to pass through the core subassemblies. The coolant entry into grid plate is achieved through pipes. The salient features of grid plate: box-type structures with vertical sleeves connecting the top and bottom plates. The sleeves, apart from facilitating required flow to the various subassemblies, contribute to the rigidity of the structure. The grid plate should be very rigid so that the verticality of subassemblies will be ensured under all operating conditions including seismic events. Grid plate is generally supported on the strong back, which is also called the core support structure. Figure 31 shows the various possible support arrangements for the bottom of the grid plate. The support of grid plate can be through a peripheral ring (Figure 31a) or through multiple intermediate supports (Figure 31b). Generally, a combination of both is preferred (Figure 31c), as the ring provides sealing boundary at the periphery, and the multiple intermediate supports structurally connect both strong back and grid plate, which are beneficial for supporting the core with minimum deflection in grid plate. This also provides adequate rigidity under seismic loading.

Next issue is the connection of primary pipes, which delivers the coolant to the grid plate. A few potential layouts of pipes are depicted schematically in Figure 32. Conventionally, the pipes are connected to the grid plate so that there will be radial entry as in PFBR and SPX1. The plan of pipes can be in the horizontal or vertical plane. The entry can be axial for coolant as in CDFR (Figure 32c). The axial entry concept leads to larger diameter of grid plate compared to radial entry, wherein the nozzle size influences the height of the grid plate. It is desirable to keep the height of grid plate as minimum as possible as it affects the height of main vessel. Design with circular header, which provides multiple radial entries to the grid plate is also possible

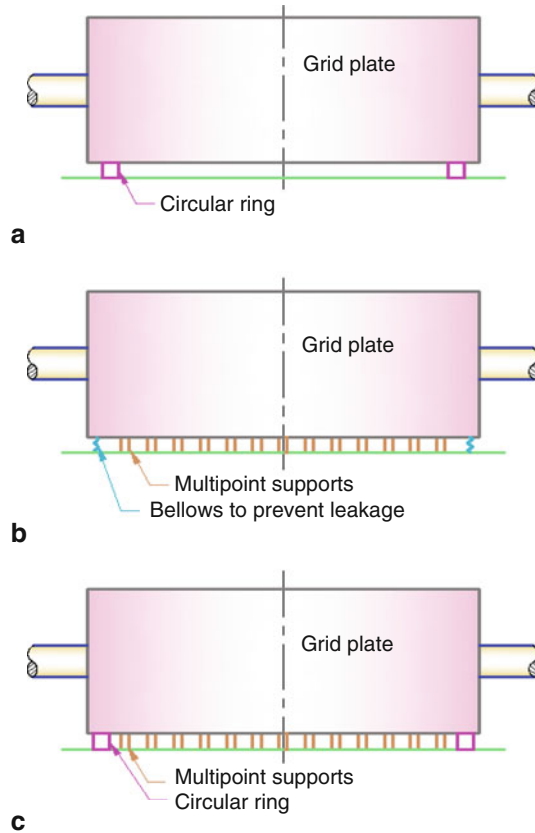


Figure 31

Various support arrangements for grid plate

as shown in ► [Fig. 32d](#). Any particular design selected should be based on available space, flexibility, nozzle junction stress considerations.

Another feature that requires careful evaluation is the type of construction of the grid plate, that is, bolted or welded. ► [Figure 33](#) shows the schematics of these options. The decision of choosing a particular option largely depends on the manufacturing capability. While bolted option is favorable from relatively ease of manufacture, welded option is preferable from totally avoiding coolant leakage from pressure plenum and significant economy.

Core Support Structure (Strong Back)

In pool-type reactors, the strong backup is structurally rigid passive structure providing support for grid plate and finally transmitting the loads to reactor vessel. The important functional requirement for core support structure (CSS) is to provide adequate rigidity to the grid plate. This should be achieved with possibly minimum weight. Hence, stiffened box-type structure is selected. The selection of stiffener configuration is an important design choice, which should be arrived at through comprehensive structural optimization studies. For EFR and PFBR, the

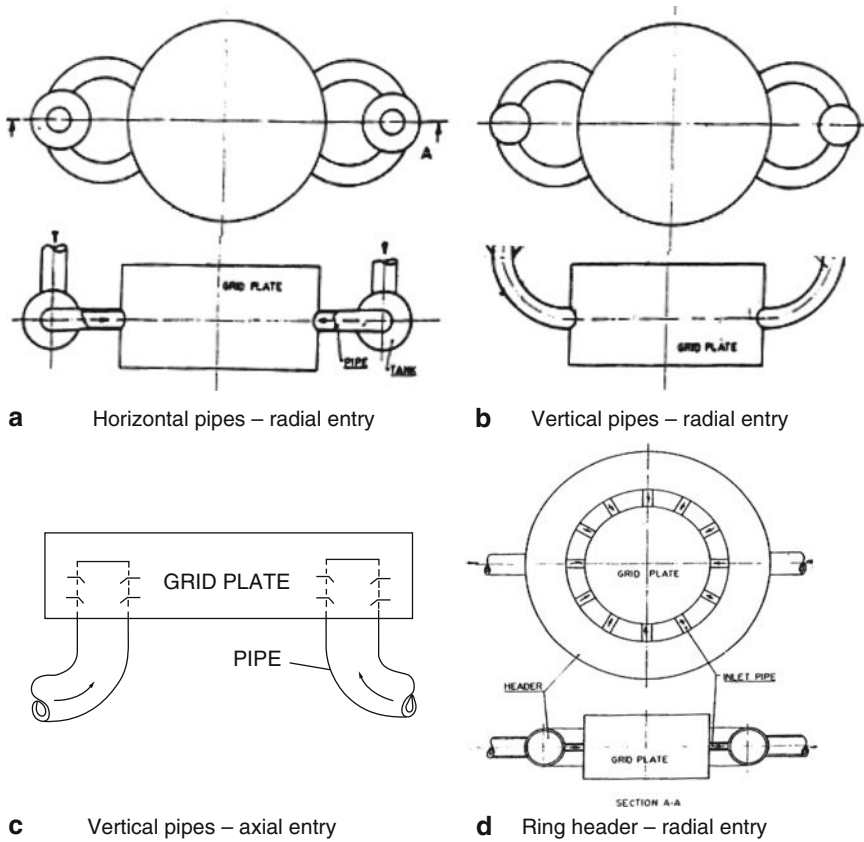


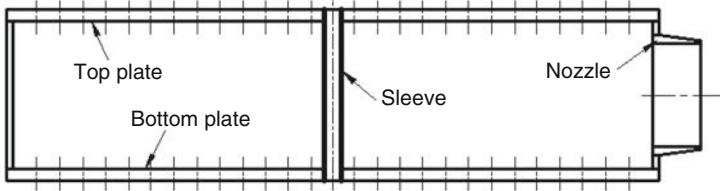
Figure 32
Primary pipe connections to grid plate

stiffener layout consists of a square grid pattern in the central zone with the radial stiffener at the periphery (► [Fig. 34](#)). This arrangement provides nearly uniform stiffness for the plate over the fuel subassembly zone, which minimizes “compaction” and “flowering” mode of core displacements, particularly during seismic events.

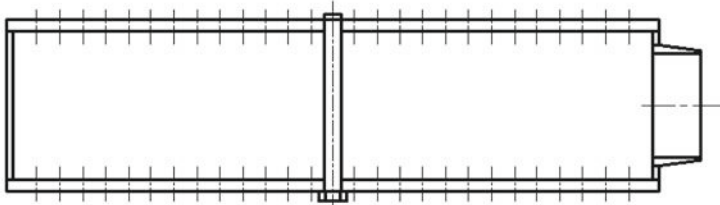
The CSS concepts adopted in SFRs are shown in ► [Figs. 35](#) and ► [36](#). The CSS adopted for CDFR has a unique feature that it is an integral with grid plate as shown in ► [Fig. 35](#). This would be advantageous for the spherical dished end concept adopted for CDFR. For the tori-spherical heads, this may not be an economical option from space utilization considerations. Concepts adopted for SPX1 and EFR (► [Fig. 36](#)) are preferred from structural reliability considerations.

Control Plug

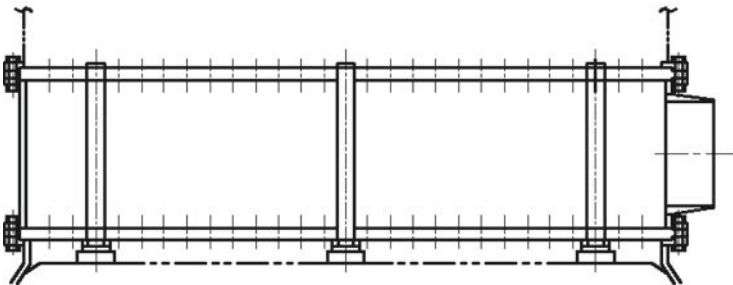
Control plug is a part of top shield of reactor assembly and is in-line with reactor core. It accommodates the components/equipments related to safety of the reactor, such as absorber rod drive mechanisms (ARDMs), core monitoring thermocouples, neutron detectors, and failed fuel location systems. It is partially immersed in hot pool sodium. It promotes mixing of sodium



a Fully welded: Sleeves as well as shell, nozzle & plates are welded



b Partly welded: Sleeves bolted and shell, nozzle & plates are welded



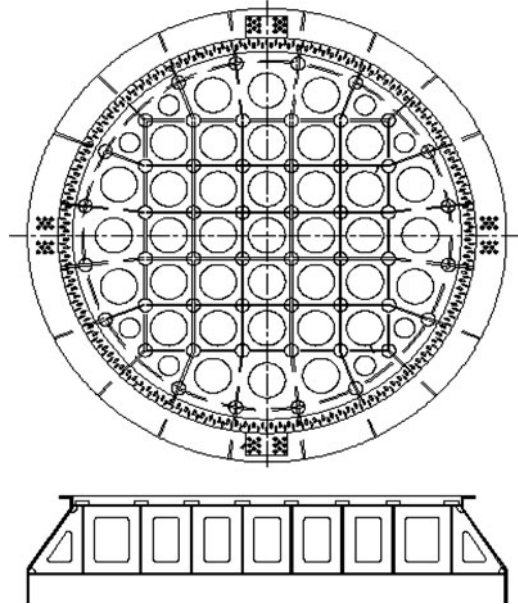
c Fully bolted: Sleeves, shell, nozzle & plates are bolted

■ **Figure 33**

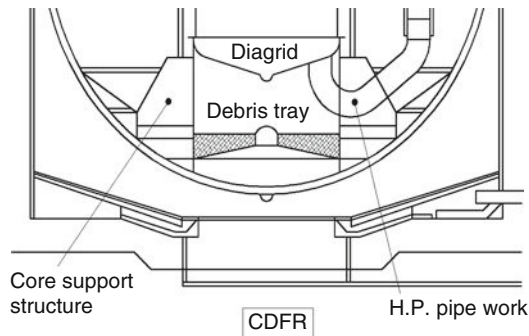
Various support arrangements for grid plate

exiting from the fuel subassemblies and reduces perturbation of sodium free level so as to prevent gas entrainment. As a part of top shield, it acts as biological and thermal shields. It absorbs significant mechanical energy release under core disruptive accident. The control plug forms a leak-tight barrier between RCB and reactor internals.

Generic Geometric and Design Features Control plug consists of many vertical tubes to provide passages for and to accommodate ARDMs, thermocouple sleeves, sodium sampling tubes, etc., which are positioned properly within a skirt assembly. The skirt assembly consists of perforated lattice plate, core cover plate, stay plates, etc. The diameter of the control plug is decided by the number of core (fuel/blanket) subassemblies, which are under temperature monitoring and would be roughly equal to the core diameter. ● *Figure 37* shows 3-D views of a typical control plug part. The height is decided by the level difference between the top shield and the top end of core subassemblies. The geometrical shape of the core cover plate, the gap between

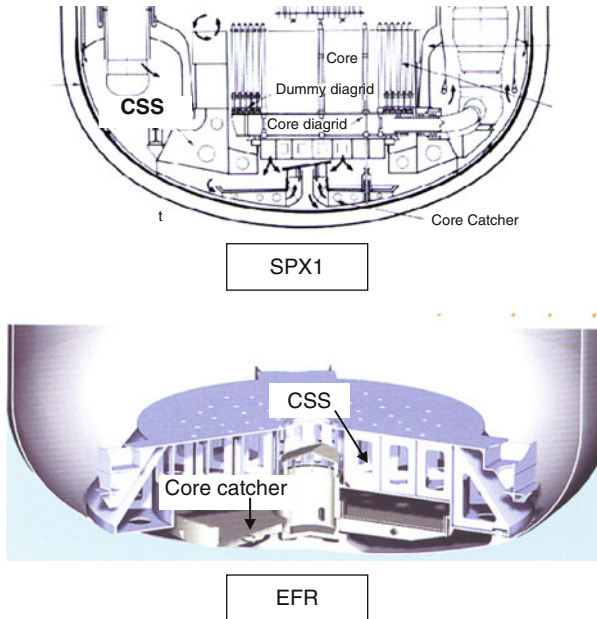


■ Figure 34
Square & radial grid stiffener configuration



■ Figure 35
Integral CSS and grid plate concept for CDFR

the core cover plate and the top end of core subassemblies, perforations in the skirt shell and perforations in the shroud tubes influence the hot pool hydraulics significantly. Thermal stratification in the hot pool, gas entrainment in the vicinity of sodium free level, and thermal loadings on the inner vessel are decided by control plug. The flow through control plug is a critical parameter. While higher flow is preferred to minimize thermal gradients in various parts of control plug under thermal transients, lower flow is better from flow induced-vibration and gas entrainment points of view. Hence, the flow into control plug should be optimized through detailed thermalhydraulics analysis supported by experimental validations to ensure



■ Figure 36
Isolated CSS concept of SPX1 and EFR

that thermal transient effects, gas entrainment, and flow-induced vibration risks are minimum and acceptable. Further, optimum gap has to be provided between the thermowells of core monitoring thermocouples and the head of subassemblies, so that free rotation of the plugs is possible during fuel handling operation.

The important design requirement is the slope at the support locations of absorber rod drive mechanisms due to self weight, and other loads should be minimum for ensuring smooth operation of ARDMs. Further its structural integrity should be ensured under all operating conditions. In view of its position just above the core, the bottom portion of the control plug is subjected to all thermal transients of core. The bottom end of skirt assembly experiences thermal striping because of differential temperature of sodium exiting from various core subassemblies. The skirt assembly in the vicinity of sodium free level is subjected to level fluctuations, thereby high cycle fatigue. The parts immersed in sodium may also be subjected to flow-induced vibrations. The perforated lattice plate provides guided passage for thermocouple tube sheath to avoid flow-induced vibration. The control plug is one of the critical components in the reactor assembly, which decides the design life of the reactor plant.

Many features are added to enhance the reliability of the plug. Stay plates provide structural rigidity to the shell and support the shroud tubes for absorber rod drive mechanisms. Thermal shields at the bottom of plug protect the core cover plate from thermal striping. The thickness of the shell and the plates are optimized by the detailed thermomechanical analysis during normal operation and seismic condition including fluid–structure interaction effects. Welding is avoided in the highly stressed locations and in the shell near the sodium free level.

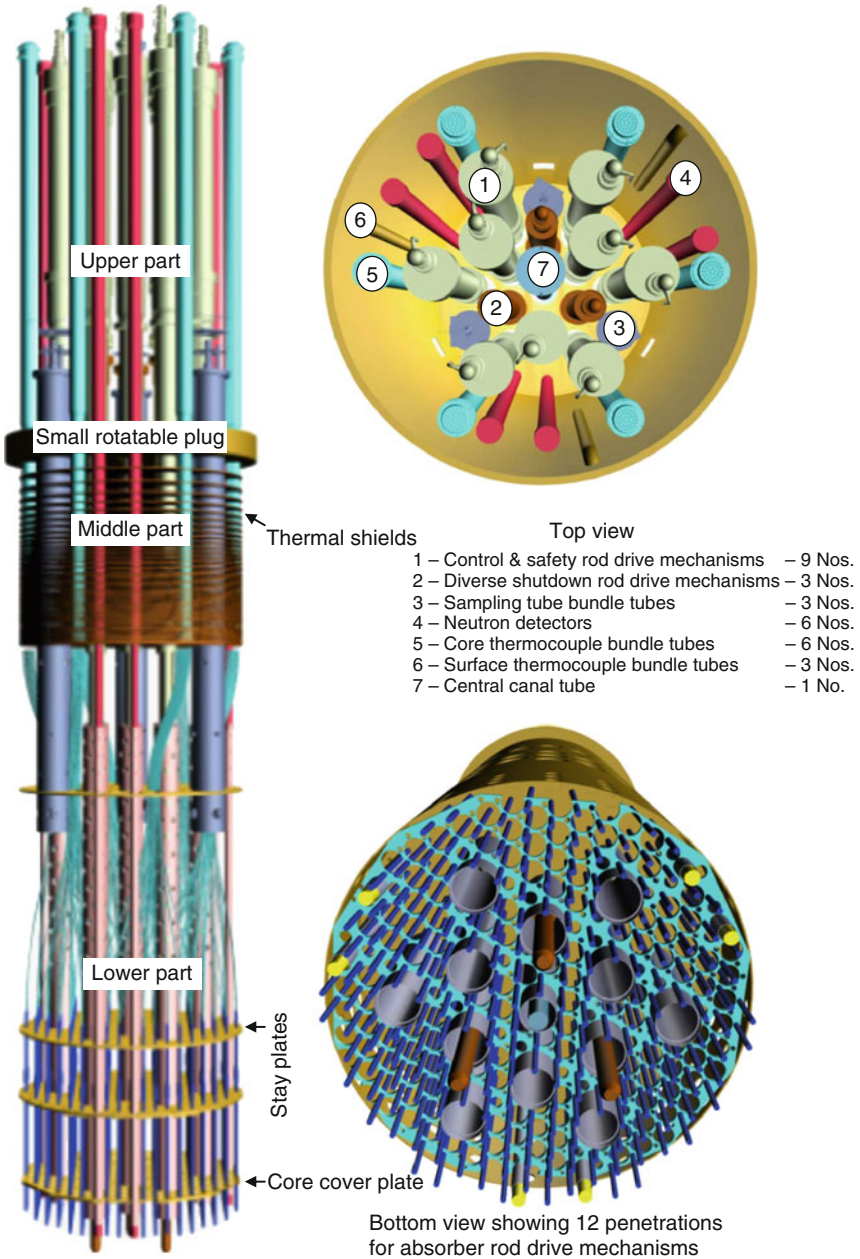
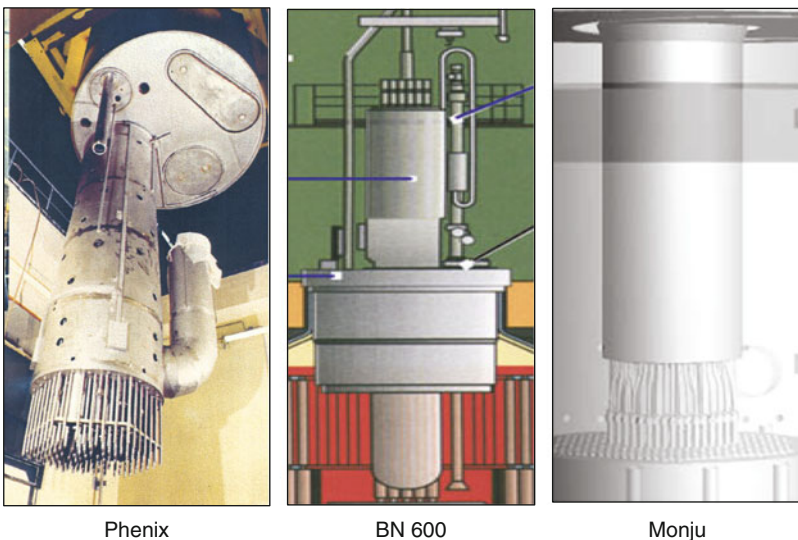


Figure 37
 Three-dimensional view of typical control plug parts

The middle assembly acts as thermal and biological shield. The purpose of shielding is to limit the radiation level over the control plug. Concrete is not considered as a shielding material, since the operating temperature is high. The possible alternatives are graphite, steel balls, and steel plates. It may be a single thick plate or multiple plates of same total thickness distributed over the plug height. The cellular convection in the annular gap between the middle assembly region of the shell and the housing shell produces circumferential temperature dissymmetry and may lead to shifting of core monitoring thermocouples due to tilting of the control plug. The Mechanism box assembly covers all the components, which are supported on the control plug.

Design Options/Trends ➤ *Figure 38* shows a few typical control plugs adopted in the international reactors. The control plug may be a separate or an integral part of the rotatable plug. Separate control plug is used in SPX-1 and PFBR and considered for SPX-2 and SNR-2, whereas PFR, SNR-300, and Phenix have integrated control plug with rotatable plug. The shape of the plug may be cylindrical or conical with tapering in or tapering out from top to bottom. A few variations of geometrical shapes of control plug is illustrated in ➤ *Fig. 39*, which are mainly in the shape, sizes, and perforations of the outer shell and shape of the bottom portion. Tapered shapes conceived for EFR and CDFR, curved shapes of the core cover plate (CCP) used in Russian reactors and Monju and cylindrical shapes with perforations used in SPX1, PFBR and PFR can be seen in ➤ *Fig. 39*.

All FBRs use a core cover plate. The shape of the core cover plate may be flat or curved. CRBRP uses a separate mixing chamber below the core cover plate. Other reactors do not use mixing chamber but allow sodium to mix in the pool. Core cover plate encompasses all the fuel subassemblies in most cases. BN-1600 has core cover plate size less than core size. Outlet temperature monitoring of individual fuel subassembly is done in all SFRs except in Russian reactors. Thermocouples are used in all the reactors. Monju, FFTF, and SNR-300 use miniature



Phenix

BN 600

Monju

■ **Figure 38**
Typical control plugs in SFRs

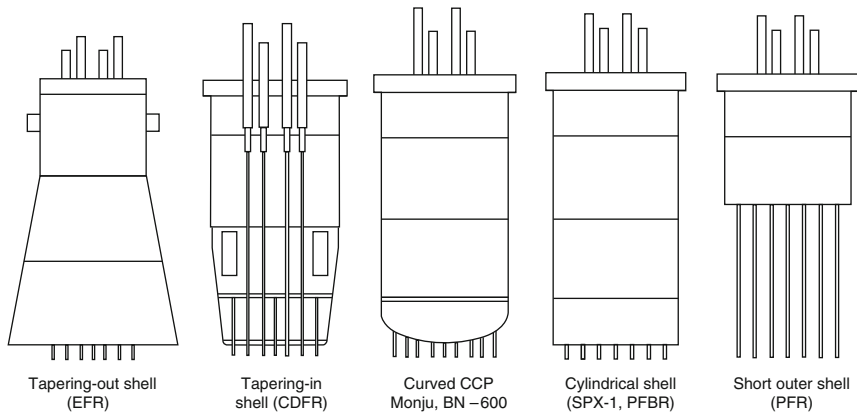


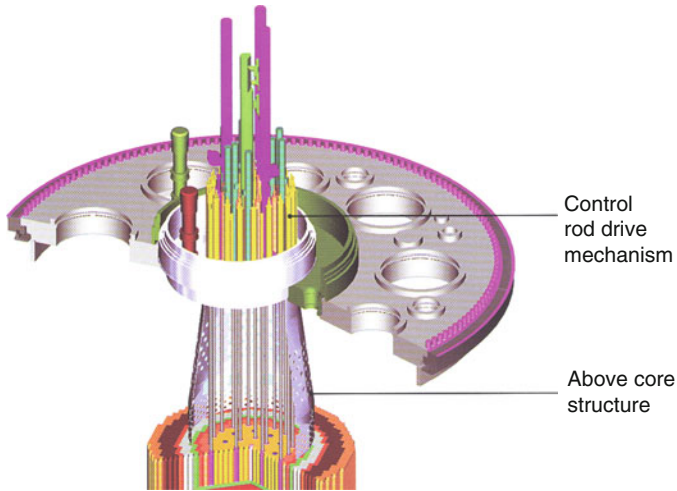
Figure 39
Geometrical variations of bottom portion of control plugs in SFRs

flow meters for each fuel subassembly. Acoustic detectors or wave guides are also used to detect boiling or acoustic noise in PFR, Phenix, and SPX-1. The location of core cover plate varies. PFR and SNR-300 provide this plate very near to free level of sodium. PFBR, SPX-1, SPX-2, and CDFR have indicated this about 1–1.5 m above the subassembly heads. PFR, SPX1, and PFBR have thermocouple tube sheaths located at about 100 mm over fuel subassemblies. In Rapsodie and FBTR, mobile core cover plate is used, and in other reactors, it is stationary. SS plates as insulation and shielding have been used in Phenix and SPX-1. Shroud tubes are provided around absorber rod drive mechanisms in all LMFBRs. Top plate temperature of SPX-1 control plug is 323 K and it is not cooled within and it is 383 K in PFBR.

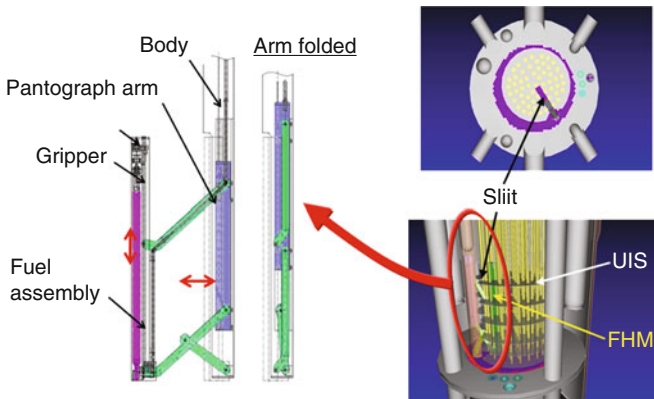
In the recent innovative type of design of SFRs, control plug integral with small rotating plug (Fig. 40) and control plug with a slit to accommodate in-vessel fuel handling machine have been conceived (Fig. 41) for EFR and JSFR (Japanese concept), respectively. With the integral control plug adopted in EFR, the main vessel diameter can be reduced significantly. The option of split control plug as shown in Fig. 41 is being studied for JSFR to have compact reactor assembly by having the provision to lift the control plug above top shield during fuel handling operation to facilitate free access for the fuel transfer machine to handle the core subassemblies below the control plug region.

Top Shield

The top shield provides biological and thermal shielding in the top axial direction of the reactor and provides a leak tight barrier between cover gas and reactor containment building. It consists of stationary part (roof slab) and rotatable plugs. In the pool-type design, the stationary part supports the components, such as IHXs and primary sodium pumps. In the loop type, it forms the interface between the rotatable portion and reactor vessel. Depending upon the design concepts, there can be single or multiple rotatable plugs, which houses the mechanisms for the absorber rod drives and fuel handling machines. The components hanging from the top shield are generally very long, and thus, a small rotation of top shield parts would get amplified, resulting in large lateral displacements at the bottom locations, which



■ Figure 40
Integral control plug with small rotating plug (EFR)



■ Figure 41
Slit type control plug with in-vessel transfer machine (JSFR)

should be restricted so that the absorber rods, pumps, and IHX can be moved up and down without much mechanical constraints. This calls for very rigid design concepts (e.g., box-type design). The components, mounted on the top shield, penetrate it to enter the reactor and thus, annular spaces are unavoidable. Freezing of sodium in these annular spaces causes major problems during fuel handling and removal/replacement of the components for maintenance. To avoid freezing of sodium aerosols in the narrow annular gaps, it is preferred that the temperature of the top shield is maintained above sodium freezing point. To facilitate the plug rotations during fuel handling operations without any unacceptable leaks of radioactive cover gas to reactor containment building, proper seals should be provided. Thus, designing for high

rigidity, managing the sodium freezing problems, and sealing are the major challenges in the design and construction of top shield.

Regarding loadings, self weight along with the component weights supported on it are the main loads, under normal operation. Inertial forces generated during seismic events, weights of shielded flasks used for removal of components for maintenance, and transient forces due to sodium slug impact under core disruptive accident add additional major loads to the component, which decide the basic thickness requirements. It is preferable to keep the top shield temperatures low so that personnel access is possible for various maintenance operations. However, sodium freezing concern does not allow this, and hence minimum temperature of about 100 °C is always maintained. This is called warm roof concept. However, it is possible to maintain the structure at low temperature, by providing proper insulation, which is called “cold roof concept.” Thus, there are three types, namely, cold roof ($T = 40\text{--}60\text{ }^{\circ}\text{C}$), warm roof ($T = 100\text{--}120\text{ }^{\circ}\text{C}$), and hot roof ($T = 200\text{ }^{\circ}\text{C}$). US reactors have adopted the hot roof concept while French reactors initially adopted the cold roof and later switched over to warm roof. In cold roof, special insulation (as in SPX-1) is provided to keep the bottom and penetration inner surfaces hot to avoid sodium deposition. However, this is a very costly option. Among these three, warm roof concept is preferred in view of concerns of sodium freezing at the narrow annular penetrations. Further, irrespective of the concepts chosen, the temperature gradients across the height/thickness should be limited so that the tilting of components hanging from it would be within the acceptable values.

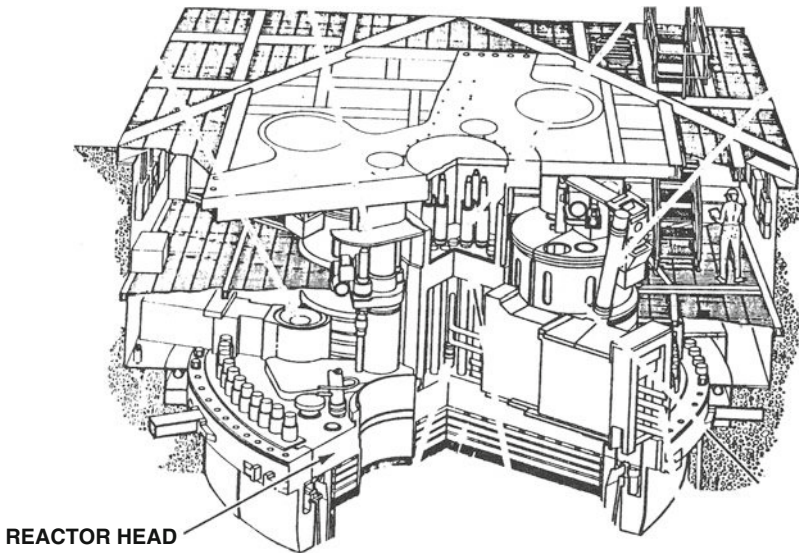
There are various options in the conceptual design of roof slab, which may be categorized based on (1) temperature of operation, (2) type of construction, (3) type of support, and (4) location of rotatable plugs. The roof slab can be constructed in different ways, namely, box type with radial/circumferential stiffeners and shielding material within the box structure or using thick plate. The box-type construction is a welded construction using plates and required structural strength is achieved by choosing proper combinations of height and number of radial and circumferential stiffeners. Concrete is generally filled as the shielding material within the box structure. Alternatively, top shield can be constructed by welding of thick plates and shielding is achieved by choosing appropriate plate thickness. Thus, the chosen plate thickness should meet both shielding as well as structural requirements. Cooling circuit can be embedded within the box structure to enable cooling of the structure and thus the absolute temperature as well as gradient can be controlled. In case of thick plate construction, adequate insulation should be provided at the bottom surface to ensure minimum heat transfer to the slab. The roof slab is connected to the reactor vessel by using a stepped construction at periphery. Generally, carbon steel is chosen as the structural material from economic reasons, there should be a dissimilar weld between reactor vessel and roof slab. The roof slab along with all the components is to be supported over the reactor vault. It can rest through either of rollers, screw jack, or welded skirt. The support should accommodate thermal expansion of the roof slab. The load distribution in the vault as well as roof slab shall be as uniform as possible. It should provide leak tightness between the concrete vault and the RCB atmosphere. The rotatable plugs facilitate the fuel handling operation and the location of the same can be concentric or eccentric with the core based on fuel handling option selected. The layout options of the components on the top shield are dealt in [Sect. 3.4.2](#).

A few typical concepts used in other SFRs are highlighted here. FFTF, CRBRP, and EBR-II have adopted a hot roof concept. In FFTF, thick plate concept is used and a combination of passive insulation system plus active head heating and cooling system is provided to maintain the temperature ([Fig. 42a](#)). The CRBRP reactor conceives a design similar to FFTF

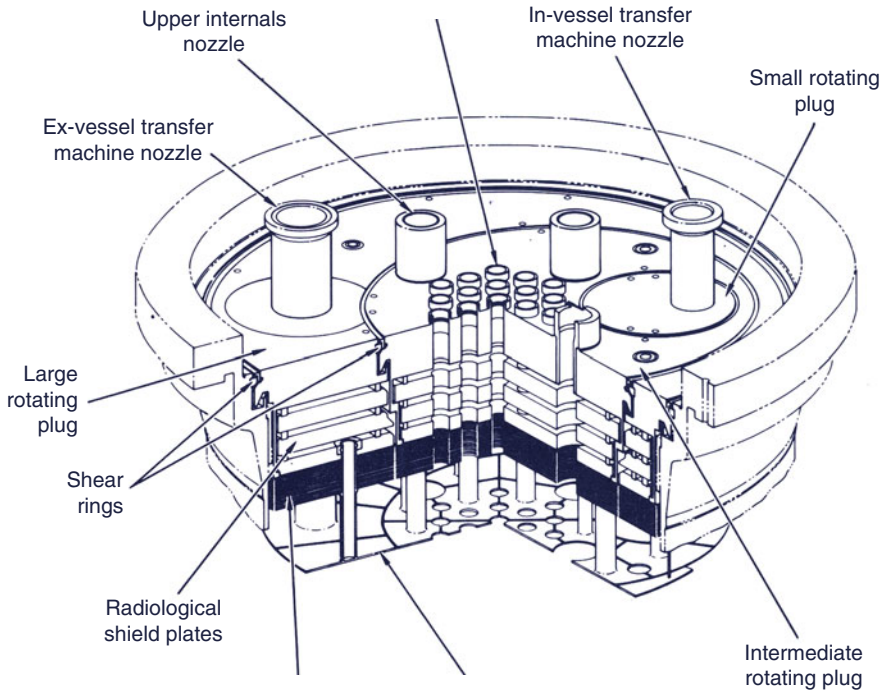
(➤ *Fig. 42b*). In EBR-II, box-type construction filled with steel shots with provision of insulation and electrical heaters on top of the roof slab is used with no cooling provision (➤ *Fig. 42c* and ➤ *Figure 43*).

Features of Shaft The shaft transmits the torque from the drive motor to the impeller. The shaft of vertical sodium pumps are generally lengthy especially for pool-type reactors because of the submergence of the impeller, traverse of the reactor cover gas space, and radiation shielding requirements. To meet the simultaneous requirement of the torque and critical speed, it is made of composite construction with a hollow middle portion welded on either side to solid ends. A shaft based on critical speed alone would be uniformly hollow. However, in order to provide shielding against radiation, shaft is made solid at the top and bottom from hydraulic considerations. The diameters at the various sections are fixed based on torque and critical speed considerations. An important feature of the shaft fabrication is the stress relieving heat treatment to be carried out after the welding of the hollow and solid ends in a vertical furnace (to avoid the sagging of the long shaft) to remove the residual stress. If residual stresses are not removed, the shaft may distort during operation. The shaft is evacuated after the heat treatment to eliminate the convection currents inside the shaft. Precision manufacture and balancing of the pump assembly especially the rotor part should be done to have vibration characteristic to the desired level as problems of shaft vibration have been reported in BN-600.

Bearings in Sodium In order to avoid over hang in long shaft, bottom bearing is generally located underneath free sodium level closer to the impeller. Therefore, it becomes necessary



■ **Figure 42a**
Hot roof concept of FFTF (Thick plate)



■ **Figure 42b**
Hot roof concept of CRBRP (Thick plate)

that the bottom bearing be lubricated by sodium. Because of the rather low kinematic viscosity of the sodium at the operating temperature and the fact that maximum rotational speed is limited, the bearing used for this purpose is of hydrostatic type. These bearings get the sodium feed from the pump discharge itself. There is some flexibility in selecting the clearance for a hydrostatic bearing (hydrostatic bearing can permit more clearance). Higher clearance is required for sodium operated pumps to avoid any blocking due to impurities as compared to a hydrodynamic bearing, the only limitation being the permissible leakage flow. The top bearing is conventional as it is not immersed in sodium.

Seals Mechanical seals are used for sealing between the rotating shaft and the stationary parts of the pump to prevent escape of radioactive cover gas on the one hand and entry of air into the main vessel on the other hand. Stuffing box-type seals are not employed because of its leaking characteristic.

Materials The material selected should have (1) compatibility with liquid sodium, (2) good weldability, (3) good formability, (4) high temperature strength, etc. Based on these requirements, SS 304 LN is widely used as principal material for sodium pumps. Wherever metal to metal contact is inevitable, the surfaces are hard faced. The materials used for the major parts of the pumps operating at cold temperatures are listed in ► [Table 9](#).

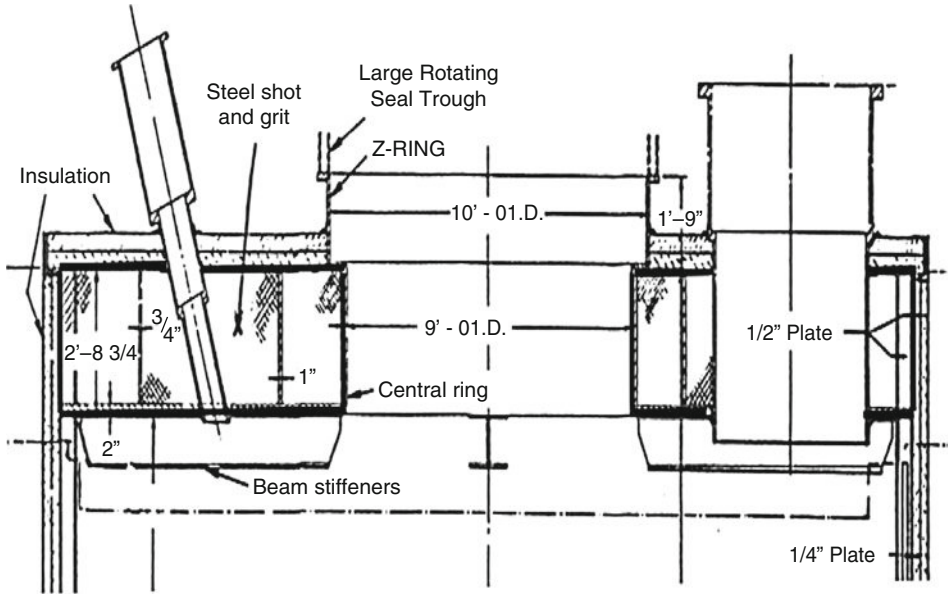


Figure 42c
Hot roof concept of EBR II (Box type)

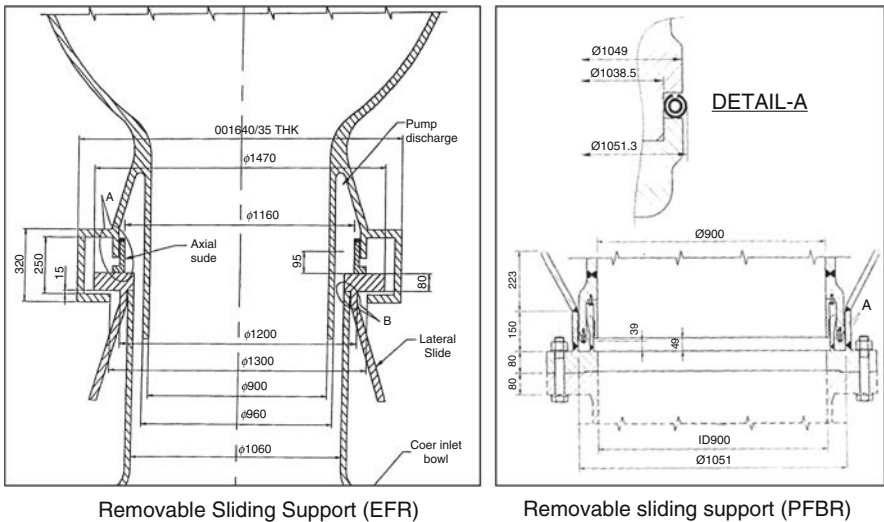
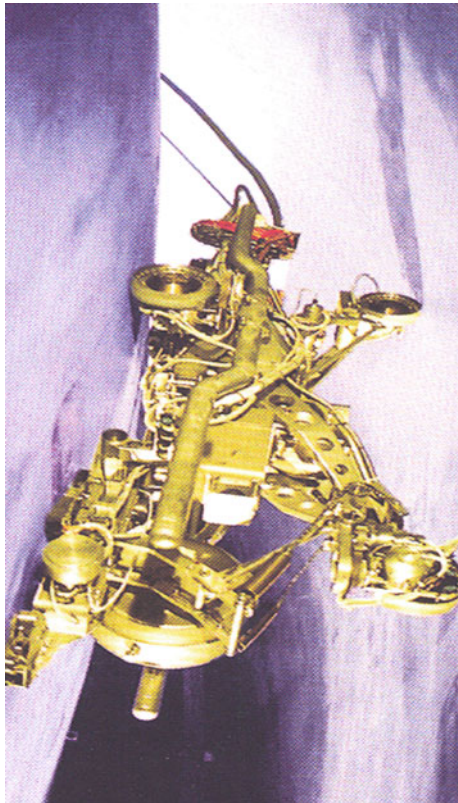


Figure 43
Pump to pipe connections in various PSPs

Safety Vessel The sodium leakage in the main vessel can be a cause of great concern to safety because of the loss of coolant to remove the decay heat. Hence, to avoid any unacceptable loss

■ **Table 9**
PSP materials (typical)

Component	Material (typical)
Hydraulic parts (impeller, diffuser, suction and discharge casing)	SS 304 L
Shaft, flanges, journal	SS 304 LN forging
Bolts for sodium service	SA 453 grade 660 class B
Bolts for non sodium service	A 193 Grade B7
Fly wheel	SA-508 Grade 2 (carbon steel forging)
Hard facing	Colomoney (nickel base alloy)



■ **Figure 44**
ISI device in annular gap between MV and SV (SPX1)

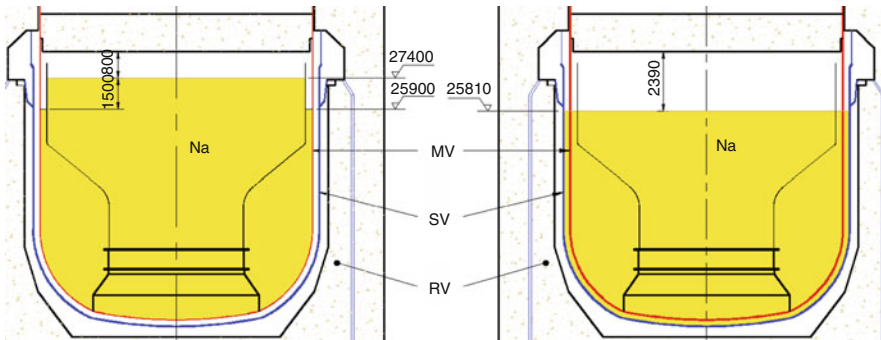


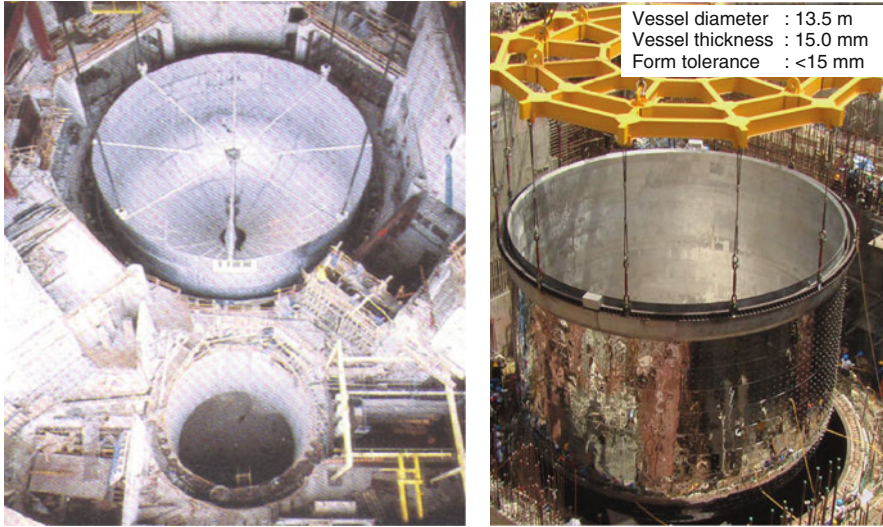
Figure 45
Fall of sodium levels due to postulated leak in the main vessel

of coolant from the main vessel, a safety vessel is provided surrounding the main vessel with optimum annular nominal gap so that the sodium level in the main vessel does not fall below the inlet windows of decay heat exchangers. Further, with the minimum gap between main vessel and safety vessel (MV–SV) selected, it should be possible to have full access for the periodic inspection of main vessel outer surface (➤ *Fig. 44*), after accounting for the possible deformations of vessel due to thermal ratchetting in particular. The gap is filled generally with nitrogen and is monitored for any sodium leak from the main vessel. The weight of the reactor internals including the core does not act on the safety vessel, even under an unlikely event of main vessel leak; only hydrostatic pressure of sodium would act on the safety vessel. Hence, the minimum nominal radial gap selected is 300 mm for PFBR and 700 mm for SPX1. Hence, the thickness of the vessel can be selected lower than that of the main vessel. The choice of the material can either be austenitic stainless steel 304 LN or even carbon steel for economic considerations. ➤ *Figure 45* shows the sodium level variations when main vessel leaks in case of a typical 500 MWe PFBR.

There is a need to minimize the heat loss from the hot pool and thereby reduce the heat load for the reactor vault cooling circuit. For achieving this, it is not preferred to mount thermal insulation on the main vessel surface, to avoid any difficulty of inspection. Alternatively, the outer surface of the safety vessel can be used for supporting thermal insulation panels. Thermal insulation panels should function reliably over the entire plant life of the reactor. Based on thorough analysis, thermal insulation panels constituted with specified numbers of thin polished stainless steel sheets arranged in parallel is found to be suitable for this important function. However, development, manufacture, and erection of such panels involve many challenges to be addressed. This has been successfully resolved for Indian PFBR. The safety vessel has been erected in the reactor pit precisely with the insulation panels mounted on it. ➤ *Figure 46* shows the vessel just before its introduction in to its location in the reactor pit for SPX1 and PFBR.

3.4.5 Design Improvements for Future SFRs

There are certain areas where we can apply new ideas from safety as well as from the economy point of view. This includes development of double suction pumps, which will reduce the size



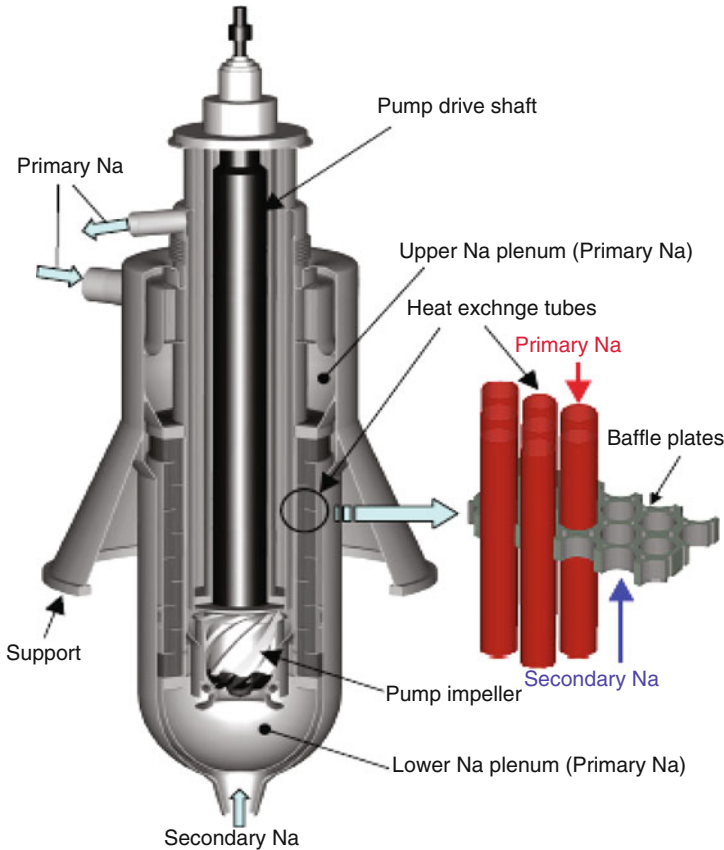
■ **Figure 46**
Safety vessels of SPX1 and PFBR at the time of lowering into reactor pit

of the pump. Integration of intermediate heat exchangers with primary pump is an option to consider reducing the size of the reactor block. Leakage of oil from mechanical seals to primary system was reported in two reactors (PFR, BOR 60). Therefore, usage of oilless seals and bearings is being explored. Integration of the primary pump and IHX is another innovative design approach considered for Japanese SFR (JSFR). By integrating the primary pump and IHX, the primary heat transport system is remarkably simplified (➤ *Fig. 47*). The middle leg piping that connects IHX and pump is not necessary, and also the number of components is reduced by this design. In this design, a mechanical pump is selected. This is because the technological base accumulated through the development of the mechanical pumps for Joyo and Monju is available. Development of bearings for stabilization of the shaft and reduction of the vibration transfer to IHX tubes are major R&D issues.

The broad background on design options and other relevant details required for selection of the pump and also for carrying out detailed design has been highlighted in this chapter. Also, the design features of various PSPs of international SFRs are summarized in ➤ *Fig. 48* for information.

3.4.6 Intermediate Circuits and Steam Generator

The intermediate circuit is interposed between primary sodium circuit and tertiary steam–water system from considerations of reactor safety, in the sense that the primary sodium systems would be free from mechanical and chemical effects of sodium–water reaction, if it



■ **Figure 47**
Pump-integrated IHX (JSFR)

occurs in steam generator (SG). The overall reactor design incorporates provisions, for example, in vessel shielding around core, and the like, to render the secondary sodium circuit to be of nonradioactive type, thus making its components generally amenable for maintenance with adequate care. Provisions such as surge tanks/cover gas in SG are incorporated in the circuit to absorb the pressure surges during inadvertent sodium–water reaction. Apart from piping, the important components of the circuit are IHX, secondary sodium pump (SSP), and SG (● *Fig. 49*). From an economic consideration, there is incentive to minimize the overall length of piping and optimize the location of various equipments, thereby leading to compact circuit layout. Further, a detailed study is desirable to arrive at the number of loops in secondary sodium circuit. The operating experience of SFR worldwide has demonstrated the reliable operation of sodium pumps and IHXs (except in Phenix) as compared to steam generators, wherein maintenance operations on account of sodium–water reactions have led to prolonged shutdown of the respective plants. Therefore, plant availability considerations would desire incorporation of many SG modules, and hence, a

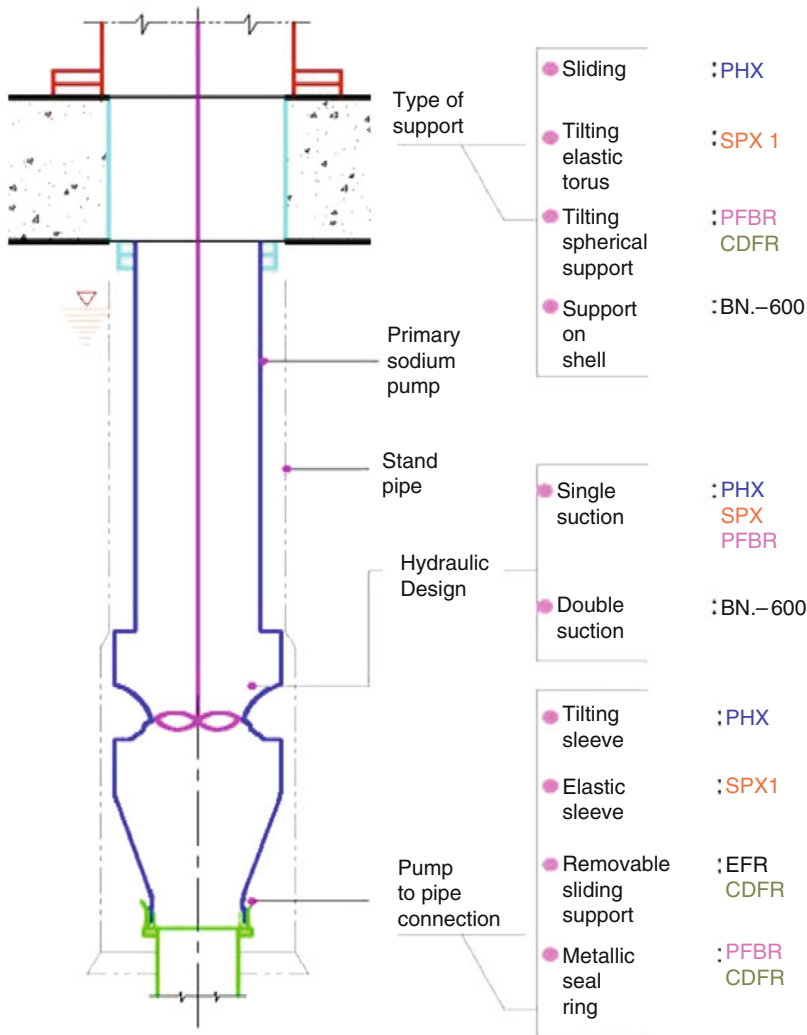
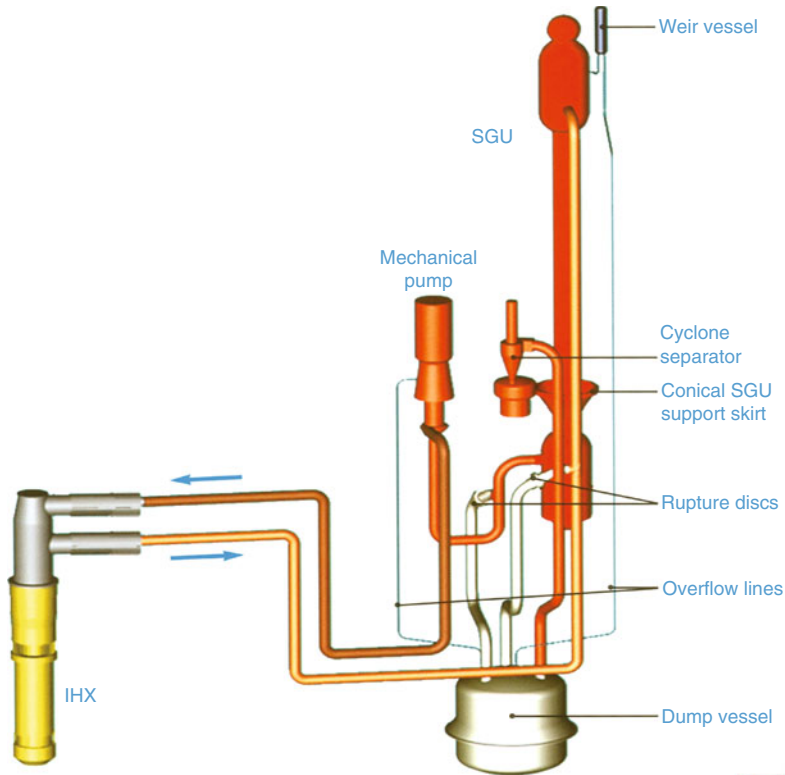


Figure 48
Summary of design features of various PSPs

detailed risk economic trade-off studies is to be carried out with due consideration to manufacturing and other infrastructure capabilities. A brief description and the salient features of important secondary sodium circuit components are highlighted in the following paragraphs.

Secondary Sodium Pump

In the case of pool-type reactors, the primary sodium pumps are always located in the cold pool. However, the secondary sodium pumps of both pool and loop-type reactors can be located in either the hot leg or the cold leg. Table 10 shows a number of PSPs and SSPs in the various



■ Figure 49
Schematic sketch of intermediate circuit

■ Table 10
Number of sodium pumps in various SFRs

	Rapsodie, KNK-II, PFBR	FFTF, Monju, PFR, Phenix, BN 600, BN 800	SPX-1, CDFR	EBR-II	EFR
No. of PSP	2	3	4	2	3
No. of SSP	2	3	4	1	6

reactors. It can be seen in the table that the numbers of PSPs and SSPs are generally equal. In EFR, more number of SSPs is adopted for having operational flexibility with nonavailability of SG module.

The secondary sodium pumps of all operating fast power reactors and most experimental reactors in the world are located in the cold leg at a higher elevation with respect to the steam generator. The design of secondary sodium pump is generally similar to that of primary sodium pump. The major differences are shorter shaft, absence of radiation shielding, and absence of the need for accommodating differential expansion. As the cover gas pressure in the secondary circuit can be higher than the primary circuit, the speed of operation of the

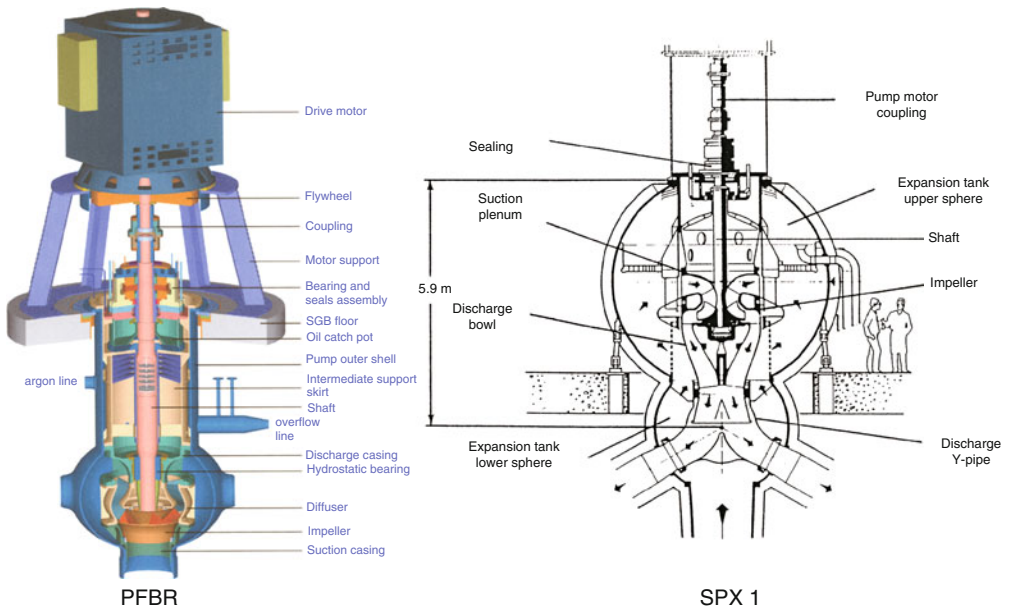


Figure 50
Typical secondary sodium pumps

secondary sodium pump (900–1,000 rpm) is more than PSP (500–700 rpm), thereby making the SSP more compact. Figure 50 shows two typical SSPs of PFBR and SPX1.

Steam Generators

Steam generator availability is recognized as the major factor for achieving good load factor, thereby commercial success of the SFR power plant. The reliability results not only from good design and fabrication practices but also from a proper selection of the structural material. A worldwide survey of fast reactor steam generators (SGs) in operation or under development shows considerable diversity in design and selection of materials. Many factors that are often difficult to quantify are involved, and considerable amount of judgment is required in assessing a steam generator design. The operating conditions of fast reactor SG are not severe compared to that of fossil fueled power plants; however, the tube leakage leading to severe sodium–water reaction affects the availability of the plant. No satisfactory design, which will ensure complete protection against the tube leakage, has been evolved. Due to this reason, no standard steam generator concept is available. Countries such as US, France, UK, Japan, and India have adopted diverse design for their fast reactor program.

The two different concepts generally followed for the steam generator design (Fig. 51) are

- Recirculation type
- Once-through type

The recirculation type consists of two units, namely, evaporator and super heater, which are connected through a steam drum. The water in the evaporator gets heated up to a certain quality

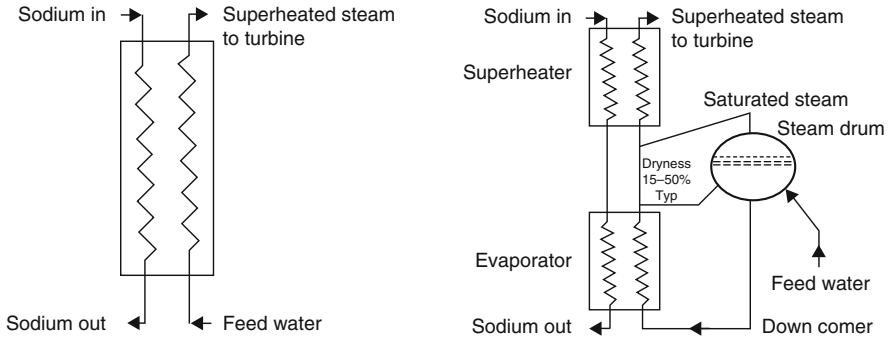


Figure 51
Once through and recirculation types of SG

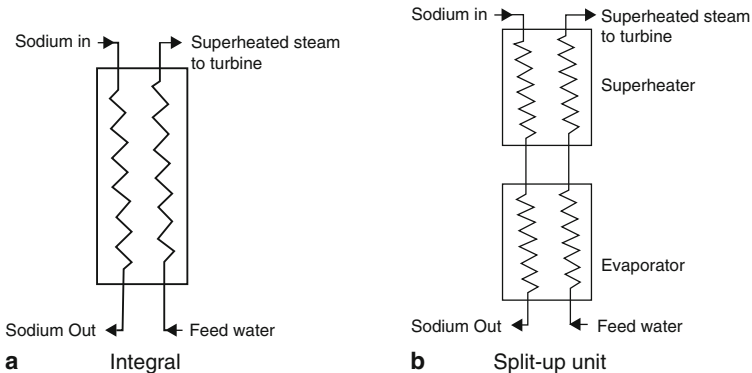


Figure 52
Types of once-through SG

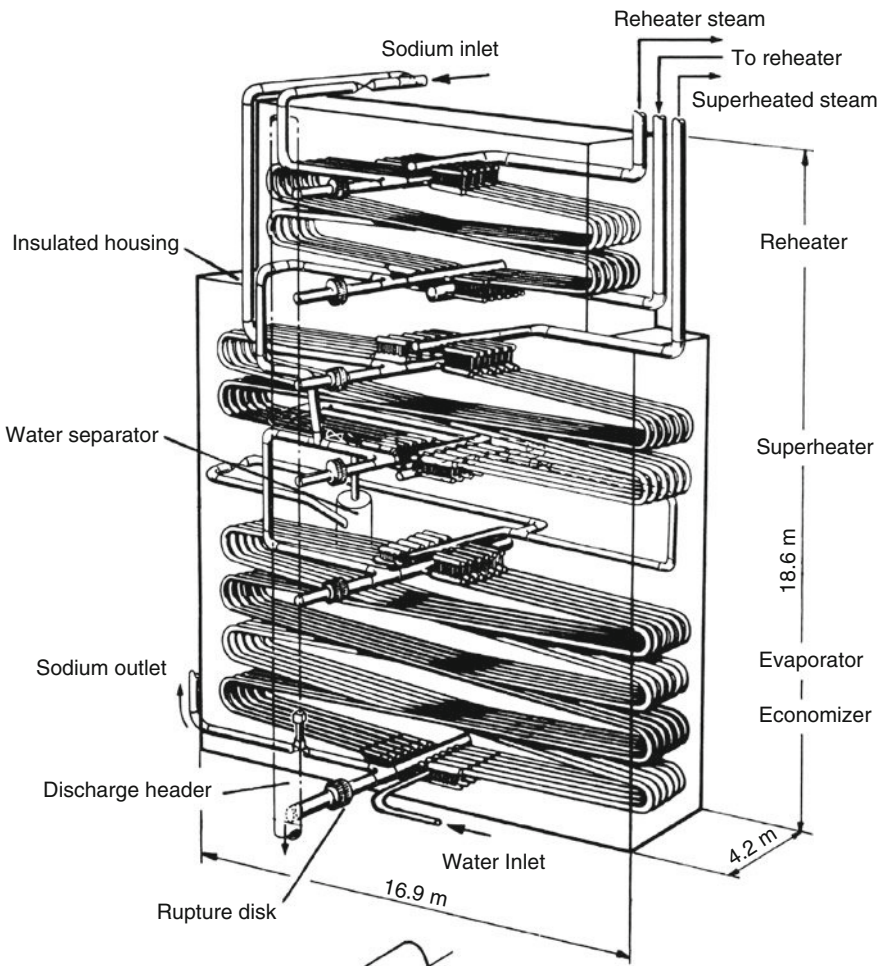
and then the water–steam mixture gets discharged into steam drum. In the drum, the steam separators separate steam from the two phase mixture, and the steam goes to the super heater for super heating. In once-through type, the drum is absent, and the water entering the steam generator gets heated up to the super heat temperature passing through all heat transfer regimes. Once-through type steam generators have two variants, namely, integrated type and split up unit. In the integrated type, the evaporator and super heater are integrated in one unit, and water enters to the SG and come out as the super heated stem (Fig. 52a). In the split up type (Fig. 52b), the evaporator and super heater are separate units, and these two units are connected in series. Water enters to the evaporator and comes out as saturated steam, which enters to the super heater and come out as the super heated steam.

PFR, BN-350, EBR-I, EBR-II, and CRBRP have adopted the concept of recirculation type, while reactors such as Phenix, SPX1, Monju, and PFBR have once-through type SGs. All the new generation reactors have high power capacity and are now adopting once-through type SGs.

Design Options The SGs are shell and tube type, and different designs exist due to the different configurations of shell and tubes. Tube and shell configurations should be such that it must be able to accommodate the differential thermal expansion of the tube bundle and shell. The selection of the configuration is influenced by the following factors:

- Good tube bundle accessibility for inspection, maintenance and repair
- Relative freedom from sodium stratification
- Performance sensitivity with plugged tubes
- Ability to limit damage in the event of a sodium–water reaction

Based on the above requirements, different designs are evolved in different countries in which tube configuration may be either straight tube, helical, serpentine, or U tube. Tube may be either



■ Figure 53
Phenix SG

single wall tube or duplex wall tube. Among various choices available, each country adopted different designs in the early stages of the LMFBR reactor program.

Serpentine Type SGs of Phenix and FBTR fall under this category. The schematic of PHENIX steam generator (once-through integrated type) is shown in [Fig. 53](#). Similar type of SG is used in FBTR.

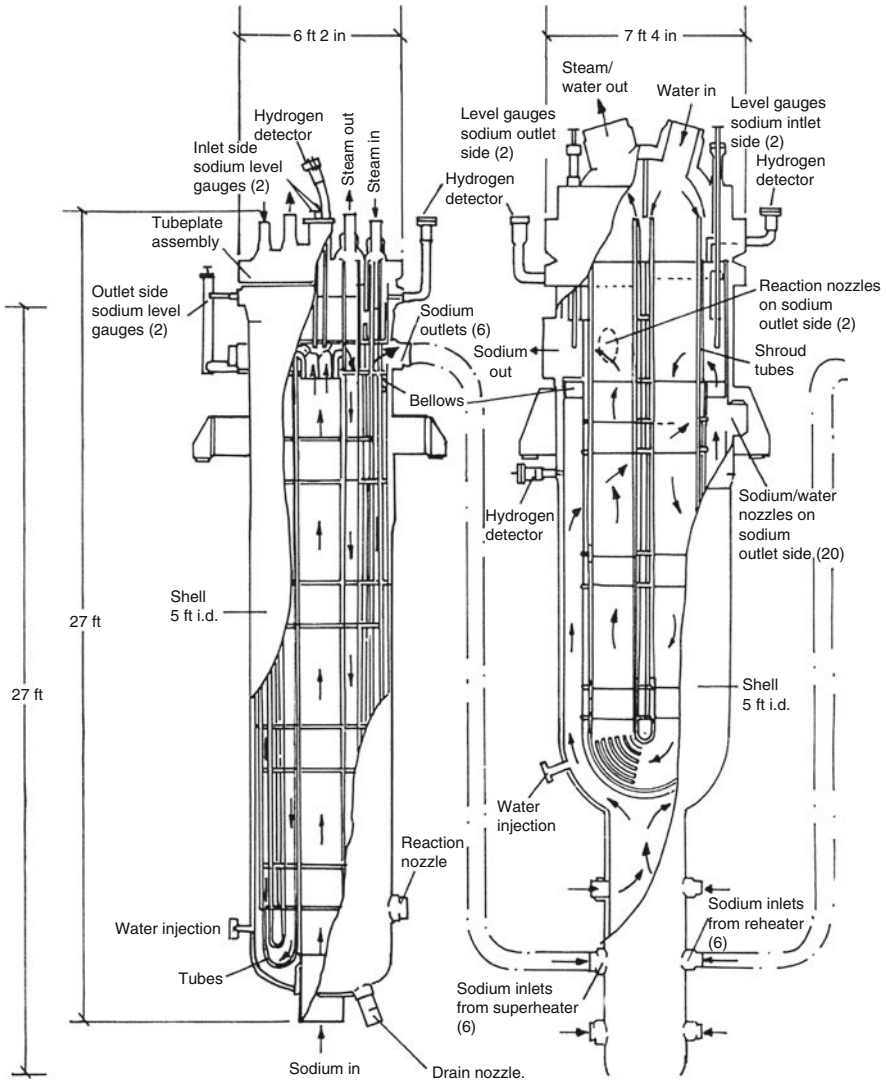
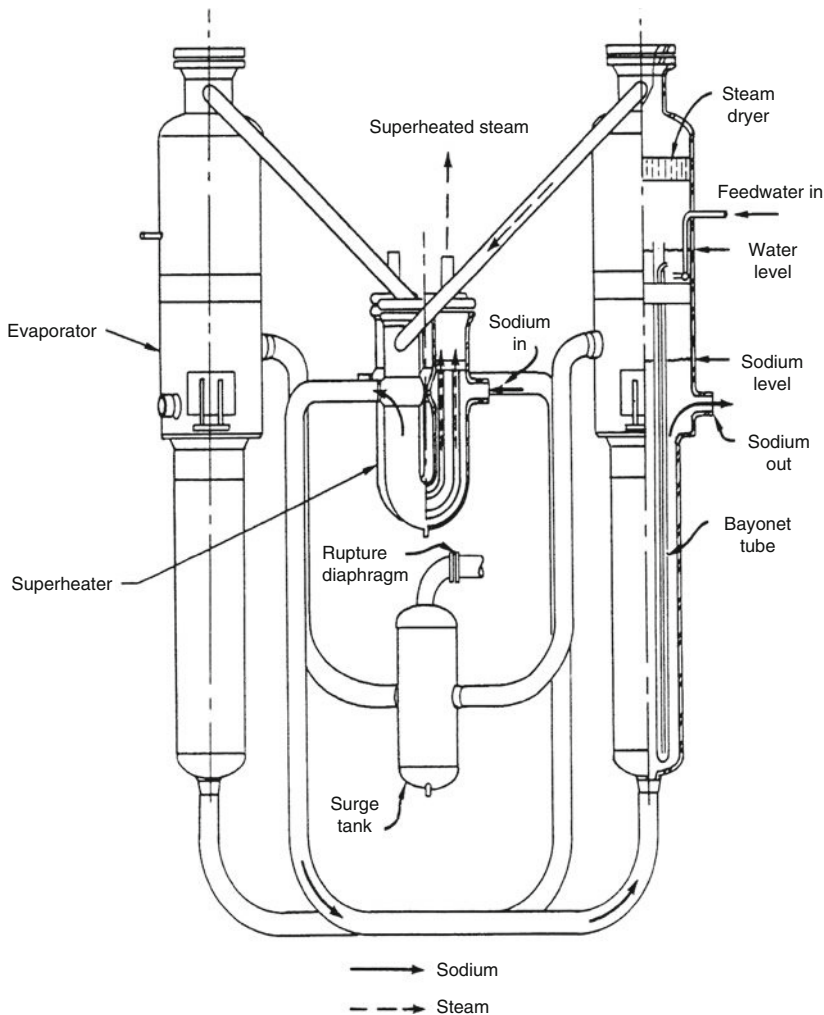


Figure 54
PFR SG

U Tube Type This design is adopted by older generation breeder reactors. This configuration provides reduced overall height and simplifies transportation and installation. The differential expansion between shell and tube bundle can be easily accommodated in this configuration. One of the examples of this design is the SG in PFR, UK, which was commissioned in 1975. PFR SG is a recirculation type with water in the tube and sodium in shell side (● Fig. 54). The tube bundle is removable. The evaporator, super heater, and reheater are using rigid shell with U-tubes. The SG in BN-350, which is a recirculating type, uses a bayonet tube for boiler–evaporator that is closed at bottom end (● Fig. 55). The evaporator is a shell and tube heat exchanger with U-tubes.



■ Figure 55
BN-350 SG

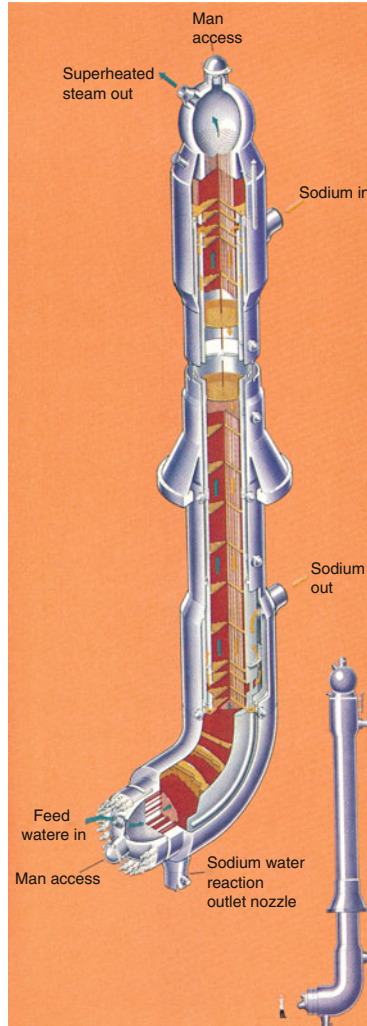
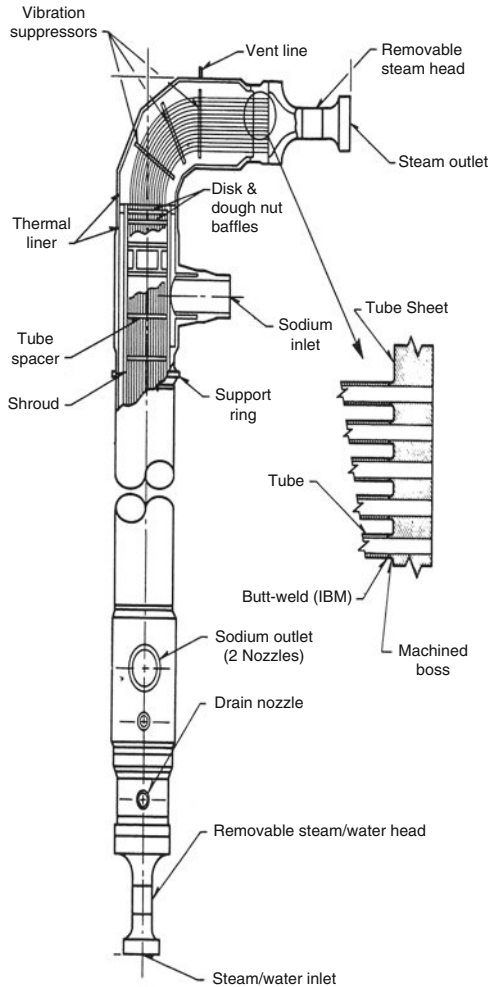


Figure 56
UK design CDFR

Hockey Stick or J-Tube Steam Generators This type of design evolved in the early 1970s for large plant applications. Development of these types of SG is taken up in USA for CRBRP and in UK for the CDFR. This type of design provides enough flexibility for high temperature operation due the bend in the tubes as well as in the shell. In this type of design, the horizontal leg can be either at the inlet or at the outlet of the SG. The UK design has the horizontal leg at the water inlet (► Fig. 56), while the US design for CRBRP has the horizontal leg at the steam outlet (► Fig. 57).

Helical Tube Type Helical coil SGs provide a compact unit thus simplifying transport and installation. This configuration is also good to take care of differential expansion between shell

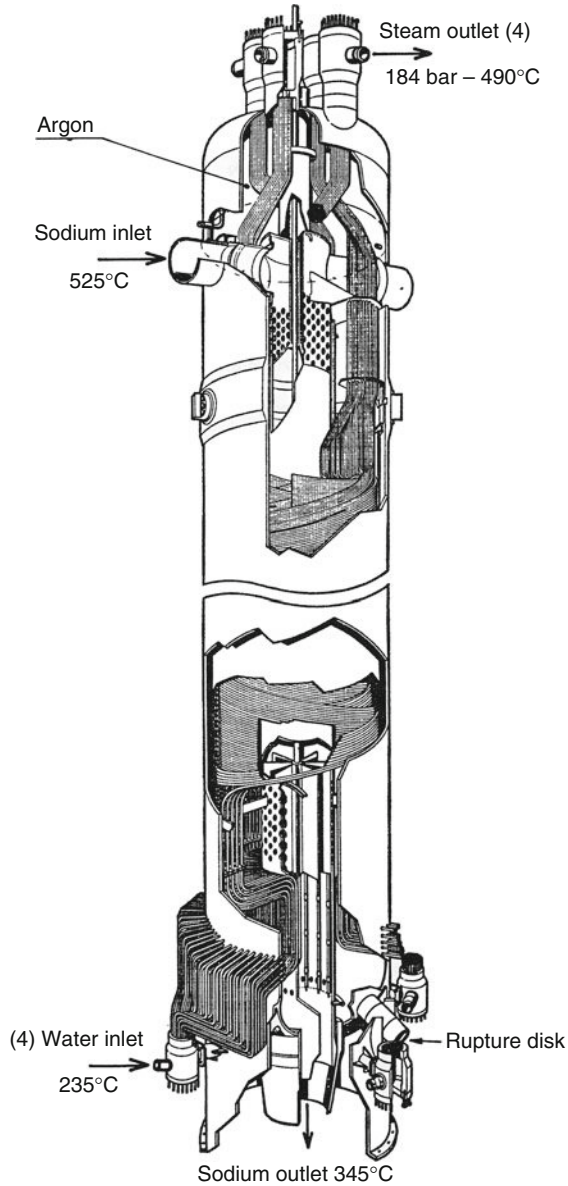


■ Figure 57
US design CRBRP

and tube bundles and amongst the tubes. Helical tube design is adopted for SPX1 and Monju Reactors. The SG for SPX1 is shown in ► Fig. 58 and that of Monju, Japan, is shown in ► Fig. 59.

Straight Tube Designs Straight tube with bellows is used for BN-600 (► Fig. 60a) and EFR (► Fig. 60b), while shell and tubes with bend are used for PFBR SG (► Fig. 61). In the case of EBR-II, straight double walled tube with cold springing shell (shell was thermally elongated during the tube to tube sheet welding so that tubes were in compression at room temperature and hence relaxed stress state was achieved under operating conditions) (► Fig. 62).

Materials for Steam Generators Selection of good structural material for SG is an important step in the SG design. Material generally used for fast reactor steam generators are austenitic and



■ Figure 58
SPX1 SG

ferritic steels with exception of alloy-800 in SuperPhenix-1. The primary criteria for the selection of materials for SG are fabricability and resistance to stress corrosion cracking. The trend in first generation heat exchangers was to use austenitic stainless steel of type 321 or 316 for super heater and reheater and ferritic steel for evaporators. In PFR the material for evaporator was 2.25 Cr-1



Figure 59
Monju SG

Mo, and austenitic steel of type 316 for super heater and reheater. In the case of PHENIX reactor steam generator the evaporator is 2.25 Cr-1 Mo and the super heater and reheater are made of austenitic steel of type 321. Subsequent to severe damage in PFR reheater, no design has favored austenitic stainless steel for any portion. However, in BN 800, sodium/steam temperature has been lowered to mitigate the problem. The second generation breeder reactors in USA such as EBR-II, CRBRP Fermi, and HNPf used ferritic steels of 2.25 Cr-1 Mo for the SGs. Super-Phenix reactor in France used alloy-800 for tube and stainless steel of type 316 for shell. In UK, different materials were used for super heater and evaporator of PFR; but the same material ferritic 9 Cr-1 Mo was used in CDFR for both shell and tubes. The material used for PFBR steam generator which is an integrated type is modified 9 Cr-1 Mo for both shell and tubes. The first power generating fast reactor in Japan Monju has used 2.25 Cr-1 Mo for evaporator and material of SS-321 for super heater. ▶ [Table 11](#) gives the summary of SG designs used in various international SFRs.

Innovative Design for Future Reactors Elimination of intermediate piping is one of the steps to achieve economy. With this objective, French conceives a design, as shown in ▶ [Fig. 63](#), in

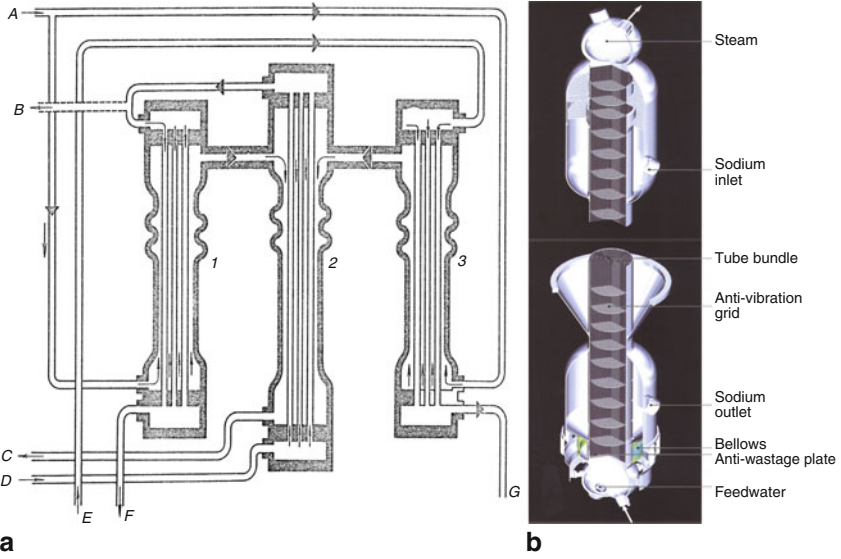


Figure 60
Straight tube SG with bend in shell

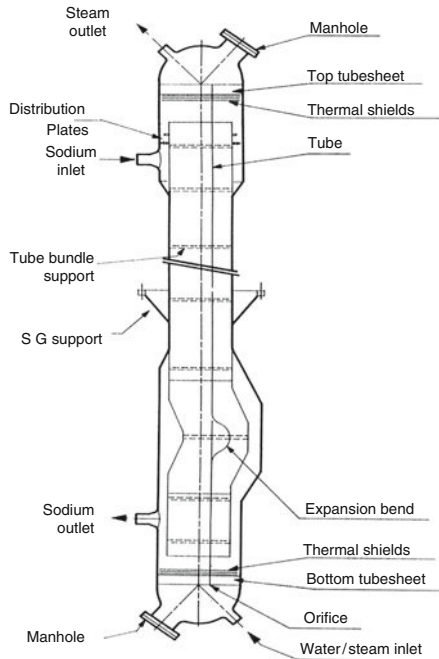


Figure 61
PFBR SG

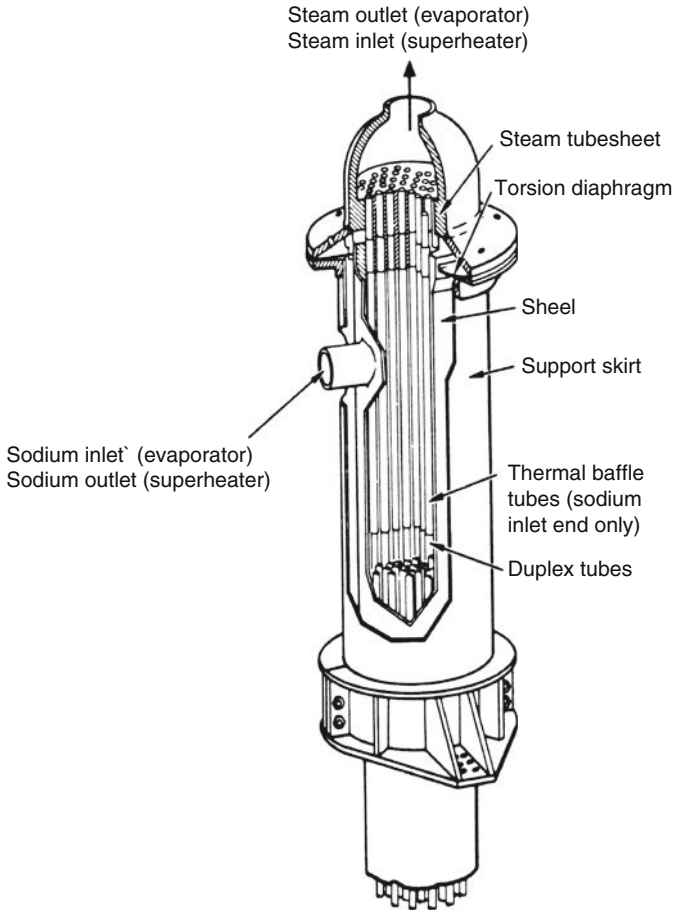


Figure 62
EBR-II SG

which IHX and SG are combined. The primary sodium will enter through the top header and flow down through the tubes. The coupling fluid, which passes through the shell side, takes away heat from the primary sodium and transfers it to the water passing through the coils surrounding the shell side generating steam. This design the main problem facing the steam generator design, that is, the sodium–water reaction due the presence of the coupling fluid and reduce the heat loss due to the transport from IHX to steam generator.

JSFR conceives another concept, which uses a duplex straight tube concept with bellows in the shell side to take care of the differential thermal expansion (➤ Fig. 64). The SG uses a spherical tube sheet which enables different tube length reducing the differential expansion among the tubes. For the SGs, for future FBRs in India (CFBR), less number of SG modules, that is, the four/loop used in PFBR reduced to three with longer tube length of 30 m, is conceived to improve economy as well as enhance reliability through reduction of the number of welds (➤ Fig. 65).

■ **Table 11**
Details of SG designs in various international SFRs

Reactor	SG type	Configuration	Material
Phenix	One trough split type	Serpentine	2.25 Cr-1 Mo for evaporator and SS-TYPE 321 for super heater and evaporator
FBTR	One trough split type	Serpentine	2.25 Cr-1 Mo stabilized
PFR	Recirculation type	U tube	21/4 Cr-1 Mo for evaporator and SS-316 for super heater and evaporator
BN-350	Recirculation type	Bayonet tube for evaporator	2 Cr-1 Mo
EBR-1	Falling film type	Shell tube type with below in the outer shell	Tube of composite assembly of inner nickel middle copper and outer nickel and SS shell
EBR-II	Recirculation type, duplex tube	Straight tube with cold springing shell	21/4 Cr-1 Mo
SPX1	One through integrated	Helical coil tube	Alloy 800 for tube and SS-316 or 304 for shell
CRBRP	Recirculation type	Hockey stick	2.25 Cr-1 Mo
Monju	One trough split type	Helical coil tube	2.25 Cr-1 Mo for evaporator and SUS-321 for super heater
PFBR	Once through integrated	Shell and tube with bend	Modified 9 Cr-1 Mo
CDFR	Once through	J tube	9 Cr-1 Mo
EFR	Once through integrated	Straight tube with bellows in shell	Modified 9 Cr-1 Mo
BN-600	Once through	Straight tube with bellows in shell	2.25 Cr-1 Mo for evaporator & 304 SS for super heater
BN-800	Once through	Straight tube with bellows in shell	2.25 Cr-1 Mo for evaporator and super heater

Intermediate Heat Exchanger (IHX)

IHX transfers thermal energy from radioactive sodium on primary side to the nonradioactive sodium on the secondary side. IHX along with the steam-water circuit will be the normal decay heat removal path. In case of an on-site or off-site power failure, safety grade decay heat removal system is used to remove decay heat of the core. IHX is a shell and tube-type heat exchanger. In a loop-type fast reactor, the primary coolant is circulated through IHX external to the reactor tank (but within the biological shield owing to the presence of radioactive sodium-24 in the primary coolant). In a pool type fast reactor, IHX is immersed in the reactor tank.

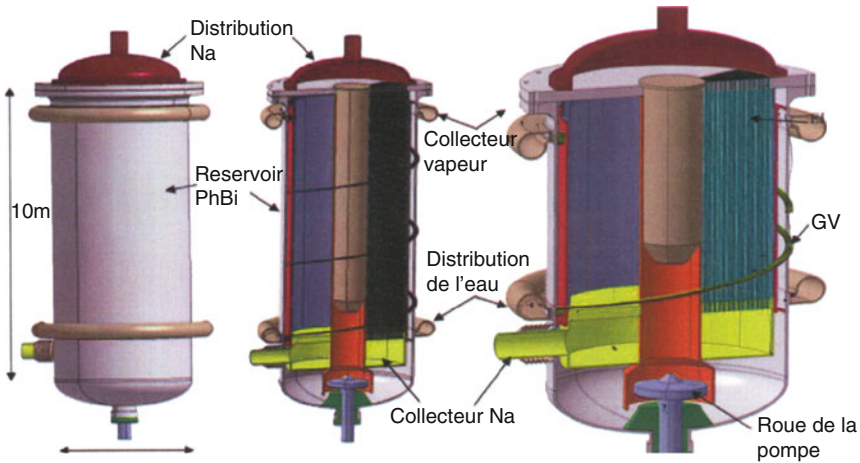


Figure 63
Combined IHX and SG with a coupling fluid

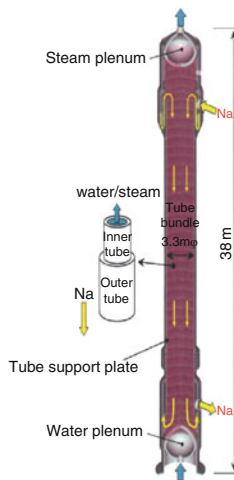


Figure 64
SG for JSFR

Design Options For pool-type reactors, two IHXs per pump are preferred per secondary loop in order to better pool hydraulics with compactness. Moreover, same handling flask can be used for both primary sodium pump and IHX. However, in loop-type reactors, since this constraint does not exist, one IHX per loop is generally preferred though exceptions might exist. Figure 66 depicts the design options of a few typical loop-type SFRs. The IHX of BN 350 has a few unique features, namely, single shell accommodating three tube bundles (Figure 67), compared to other loop-type reactors, as depicted in Figure 66.

Figure 68 shows IHX concepts of a few typical pool-type SFRs. PFR, Phenix, BN-600, SuperPhenix, SNR-2, CDFR, PFBR, and PRISM have two IHXs per secondary loop. Of the

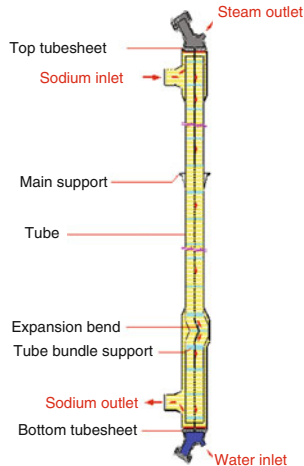


Figure 65
SG for CFBR

loop-type reactors, Monju, CRBRP, FFTF, and FBTR have one IHX per secondary loop though SNR-300 has three IHXs per secondary loop. The IHX thermal center is to be located above that of the core so as to promote natural circulation for ease of decay heat removal.

One of the options available for IHX is choosing the shell side sodium. Secondary sodium has been selected for the shell side in PFR, CDFR, and EPRI. In other reactors (Phenix, SPX-1, SPX-2, SNR-2, BN-600, PRISM, PFBR, FBTR, FFTF, CRBRP, Monju, SNR-300), primary sodium is put in the shell side. This issue is not of much concern in loop-type reactors where pressure drop restriction on the shell side is not a strong design parameter. Generally, the countries continued with the same option for the subsequent reactors.

In IHX tube bundle tubes can be either straight or with an expansion bend. Tube bundle with straight tubes has the advantages of lesser tube sheet thickness, ease of manufacture, less pressure drop, and low FIV due to the absence of bend. In some reactors (FBTR, PFR, BN-600, FFTF), tubes are provided with expansion bend to take care of differential thermal expansion among tubes, plugged tubes and other tubes, between central down-comer shell and tube bundle. The difference in temperature between the outer and inner rows of tubes due to the cross flow effects at inlet and outlet can be overcome by varying the secondary sodium flow with more flow in the outer rows by using a flow distribution plate at the bottom of the tube-sheet. By elimination of tube plugging, disadvantages of straight tube design can be further minimized.

The primary requirement of tube to tube-sheet joint is that it should be leak-tight and it should withstand pressure and temperature under various loading conditions. There are basically four options: internal bore welding (FFTF, PFR, and SNR), electron beam welding (alternative studies for Phenix), explosive welding (candidate choice for CDFR), and conventional rolled and welded (FBTR, Phenix). Internal bore welded joint offers advantage of crevice free joint and better inspectability, but it is more expensive. It has been reported and also can be interpreted from the operating experiences of Rapsodie and Phenix that crevice free joint is not a must for IHX. For CRBRP the front face fillet and explosively rolled weld was proposed instead of internal bore weld design of FFTF from economy consideration. Electron beam welding offers advantage of elimination of groove machining on tube-sheet and provided

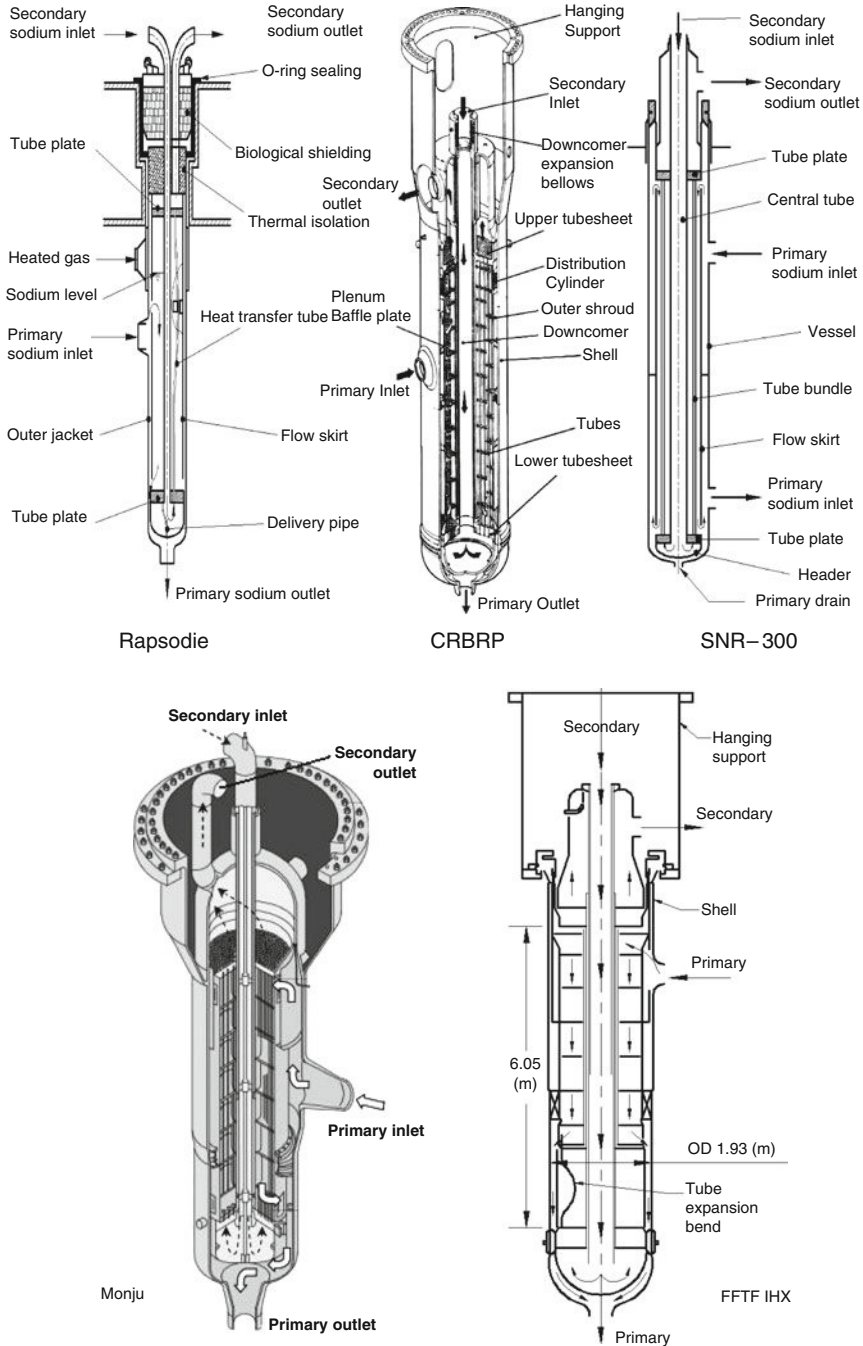
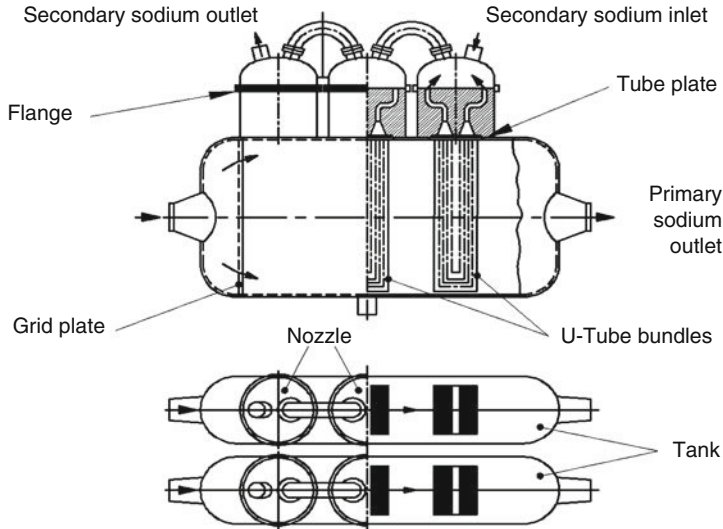


Figure 66
IHX options for typical loop type SFRs



■ **Figure 67**
IHX of BN-350

better penetration. This technique calls for greater development and incidentally has not been reported to have utilized for any IHX. Explosive welding provides a potential for cost reduction. However, this welding technique is at an infancy stage in India. Good amount of knowledge has been generated on rolled and welded joint during the course of manufacture of FBTR IHX. Hence, the preferred choice for tube to tube-sheet joint is mechanically rolled and pulse TIG welded without filler wire.

The design of tube bundle support arrangement is important for the performance of any heat exchanger. Serious leaks have occurred in many heat exchangers due to fatigue failure caused by tube vibration or stress concentration by welded support arrangement. Tube bundle support arrangement choice is difficult because of conflicting requirements. Welded support arrangement is rejected as it is difficult for a closely spaced tube arrangement. No LMFBR IHX has adopted this design. The use of non-welded-type arrangement means that the risk of fretting under sodium has to be considered and such designs would need to be substantiated by experiments or adopted from proven designs. Hence, the preferred choice is tubes held by ferrules and anti-vibration belt. Such a design is used for Rapsodie, FBTR, Phenix, and SPX-1. Rapsodie IHXs had given satisfactory performance, and no problems have been reported yet on Phenix and FBTR because of tube bundle support design. 🔗 *Figure 69* shows a few options for tube bundle support, commonly used in SFR IHXs.

All intermediate heat exchangers in pool-type reactors admit fluid on the shell side through circumferential openings in the shell, called windows. Windows should provide minimum obstruction to flow. Since primary sodium pressure drop is very important from the perspective of main vessel and inner vessel sizes and as a result cost of the reactor, it is paramount to ensure minimal pressure drop through IHX. Various different options for window configurations are available. The shell of the heat exchanger can be rolled to full length and windows of required dimensions at appropriate elevations can be cut off. Perforations in the rolled shell at

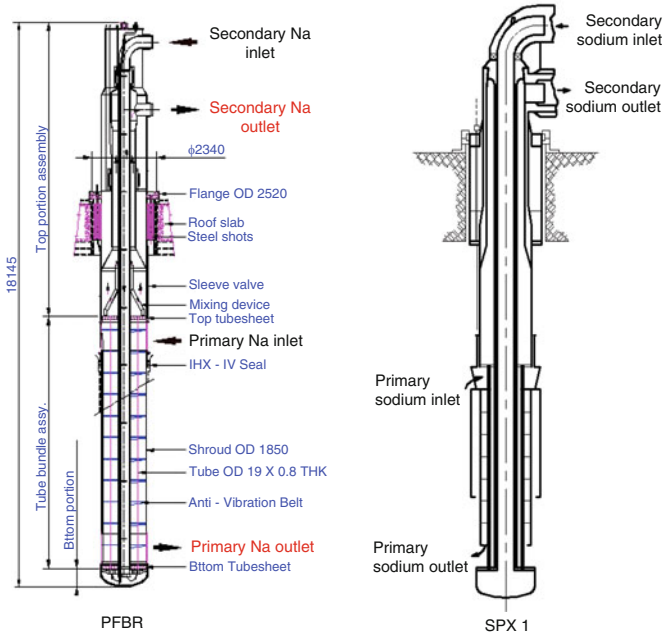
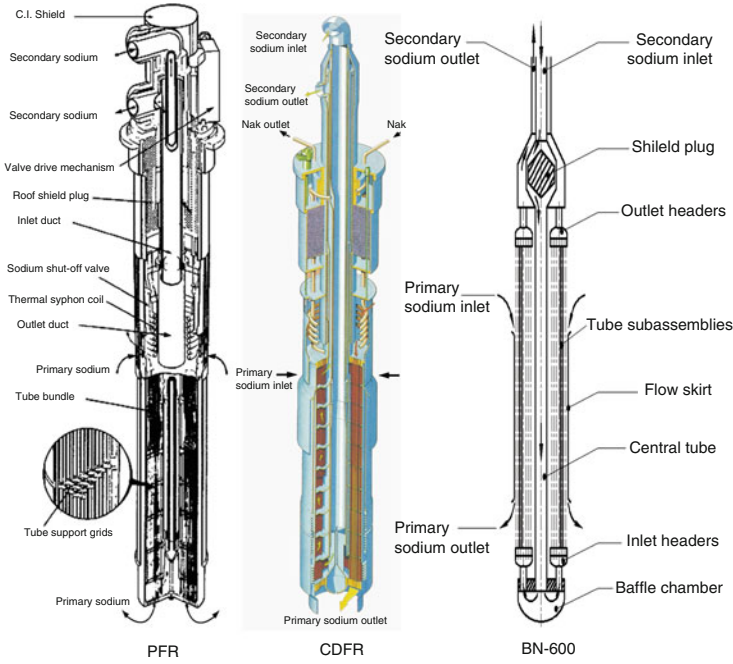
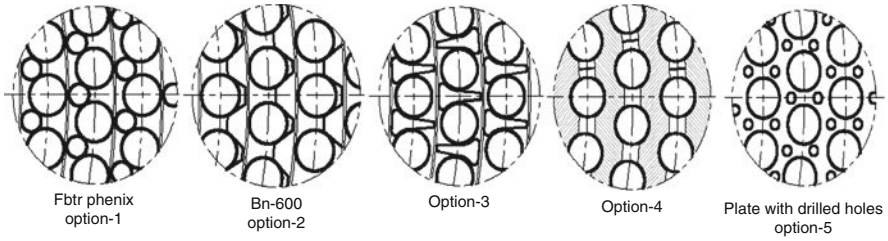
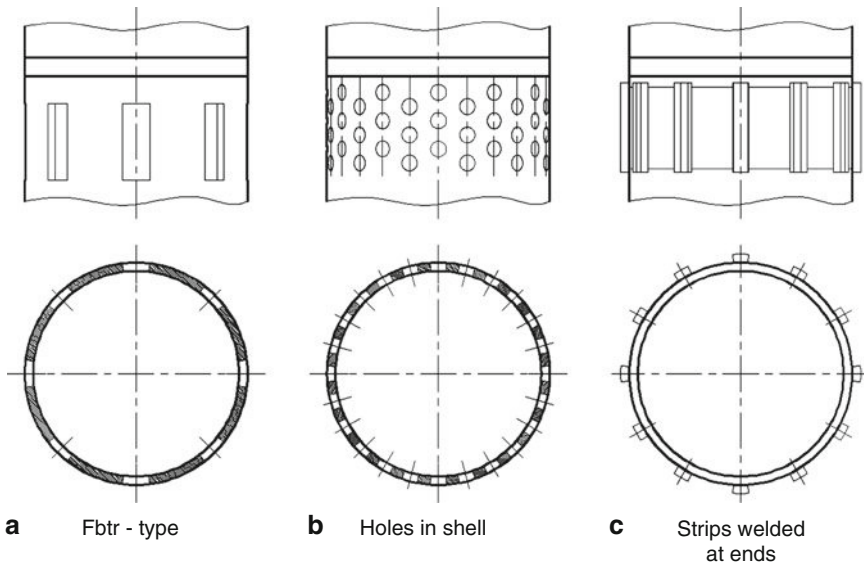


Figure 68
Design options used in typical pool type SFRs



■ Figure 69

Various options for the tube bundle supports



■ Figure 70

Options for primary sodium inlet/outlet windows

the inlet and outlet positions can also serve the purpose. Another option includes providing shells excluding the window locations and connecting them using small strips running across the height of the window.

The IHX principal support should allow easy removal of component for easy maintenance. At the same time, it should be sufficiently rigid to resist seismic loading and at the same time facilitating sufficient hold down force to prevent ejection of component during DBA. Its thermal expansion should not be constrained, and it should be easy to manufacture. In pool-type reactors the differential expansion between the IHX and the roof slab is accommodated by having adequately sized openings in the inner vessel where it penetrates.

For IHX biological shielding design, iron shots and stacked stainless steel (SS) plates are two options exercised in many reactors around the world. FBTR (India) uses iron shots for

shielding. However, the use of SS sheets is preferred and is used in most other reactors because it leads to a reduction of temperature differences between thermo siphon hot and cold legs. The annular space between secondary sodium outlet header and supporting shell is filled with thermal insulation to minimize heat loss from the sodium. Annular stainless steel plates are stacked enveloping the supporting shell.

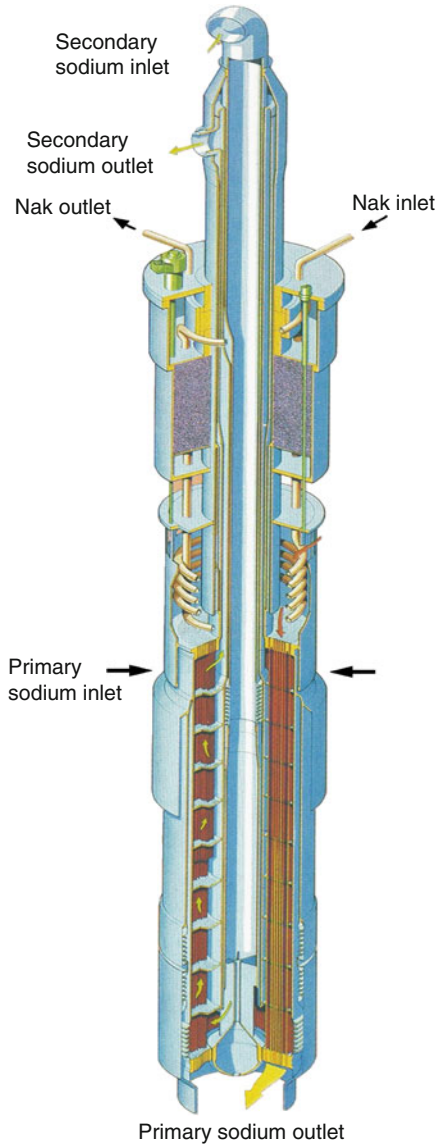


Figure 71
CDFR IHX

Some IHX windows have isolation valves installed (SNR-2, CDFR, PFBR). They are often manually operated sleeve valves. These valves are provided in case the reactor has to be operated with a reduced number of loops. Most of the existing IHXs in the world are vertical in orientation, counter flow, shell, and tube heat exchangers. The tubes are basically straight, though expansion bends are provided in many models. However, there exists an important exception to this configuration. The primary side of IHX of Russian BN 350 fast reactor (Fig. 70) is horizontally oriented, its cross section being rectangular. Each of the horizontal IHXs are provided with three openings at the top through which U-tube bundles with rectangular cross sections are inserted, which serves as the secondary side. The tubes end in flat tube plates. Secondary sodium flows in series in the three tube bundles. Primary sodium enters in the horizontal shell from one side and exits from the other side. This configuration makes it a cross flow heat exchanger.

Materials Austenitic stainless steels are the principal materials preferred as structural material for IHX, owing to its superior high temperature behavior. SS316 and SS304 are the most preferred stainless steels. Variants of these steels obtained through small modifications with their constitution such as L, LN, etc. are often used for specific requirements. In some reactor, IHX SS321 was also used. SS316 is the principal material of construction in IHXs of FBTR, Phenix,

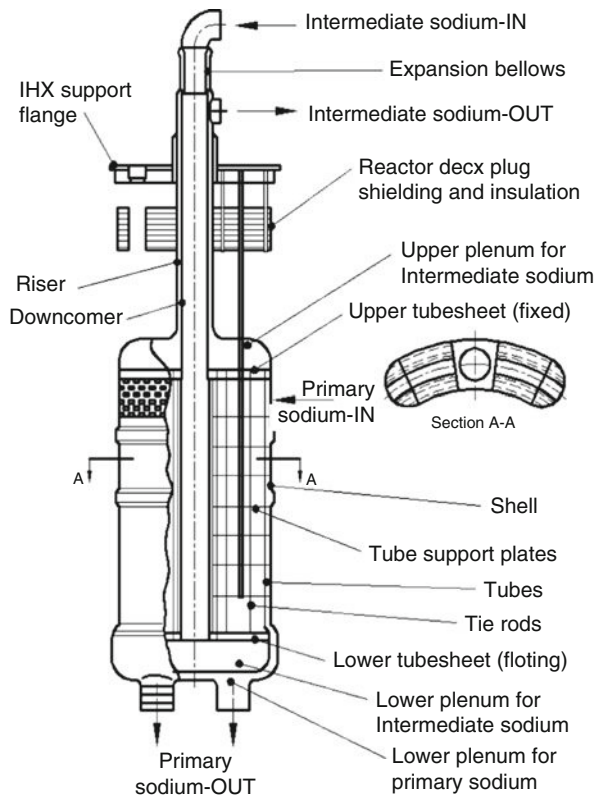


Figure 72
Kidney shaped IHX for PRISM

SNR 2, as also for primary inlet nozzle of CRBRP. PFR IHX uses SS 321 while SS 316L is used for Phenix IHX tubes as well as tubes of SuperPhenix. SS 304 is the chief structural material for FFTF, CRBRP, and PRISM. SPX1 uses SS 316LN.

Innovative Designs CDFR (United Kingdom), a pool-type reactor is one of the few reactors that has primary sodium on the tube side and the higher pressure secondary sodium on the shell side (also PFR). This particular feature allows easy integration of decay heat removal system with the IHX. Thus, in CDFR, DHX and IHX are integrated (➤ Fig. 71). PRISM (USA-GE) is another reactor with some novel features. Its IHX is noncircular in cross section (➤ Fig. 72). The shell of the IHX is kidney shaped, while the parts seeing secondary sodium are circular tubes. Also, the IHX is fitted with baffles on alternative sides. These baffles are perforated with the holes serving the purpose of holding tubes and for allowing some flow through. The flow hole sizes are controlled in order to control cross flow velocity.

3.4.7 Summary

Design options adopted for the primary components in various SFRs and innovative features are highlighted. The concepts are addressed with simple schematic sketches to bring out the convergence and variants among the designs. This background would certainly help to conceive new and innovative design options for future SFRs.

3.5 Fuel Handling

The term “fuel handling” refers to the operating sequences related to refuelling of the reactor. In SFRs, these operations are generally carried out in shutdown condition of the reactor. In this section, the functions of fuel handling system, its classification, reasons for performing fuel handling during reactor shut down, basic fuel handling scheme, safety/design requirements during handling, and basic design choices related to fuel handling are discussed. The choice of refuelling interval is linked to physics of core management. A batch of subassemblies is replaced at the end of each operational campaign fixed in terms of effective full power days (EFPD). The batch size may vary depending on number of replacement cycles of a full core. Additionally, a proportion of blanket subassemblies and control rods are also replaced depending on their cycle life.

The sodium temperature and cover gas pressure during fuel handling influence the design. The temperature of sodium is reduced to 423–553 K during fuel handling in order to reduce the influence of sodium aerosols on operation of fuel handling mechanisms. In this temperature range, the formation of sodium aerosols is very less and hence, this will lead to less deposition problems during rotation of rotatable plugs and movement of fuel handling machines. The temperature selected is also sufficiently high to avoid freezing of sodium at stagnant locations within the sodium pool. The pressure of cover gas during normal reactor operation is 10–50 kPa with respect to reactor containment building pressure. During fuel handling, it is reduced to few mbar with respect to reactor containment building pressure in order to reduce leakage through the dynamic seals of rotatable plugs.

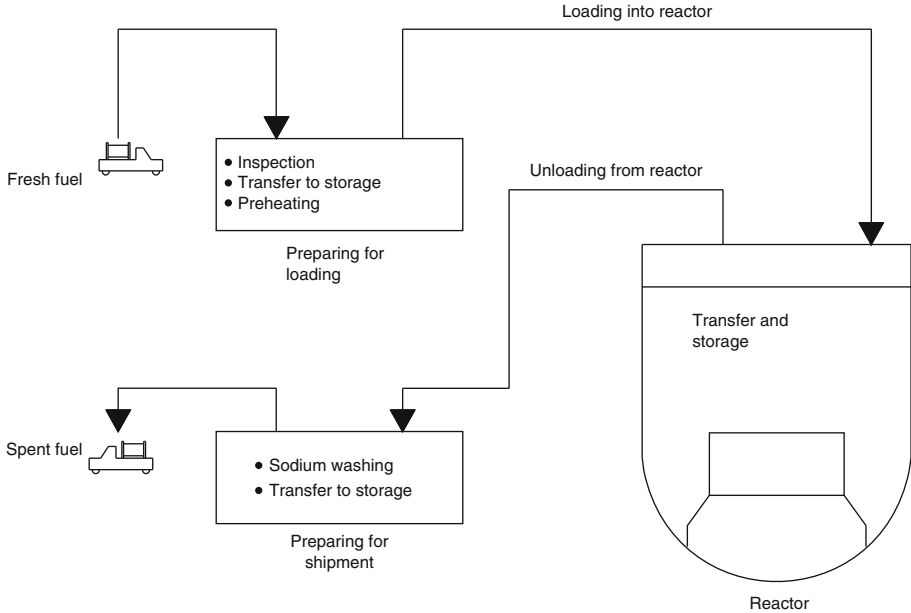


Figure 73
Functions of Fuel Handling System

3.5.1 Function

The functions of fuel handling system are:

- Receipt of fresh fuel from the fuel fabrication plant into the reactor plant
- Preparation of fresh fuel before loading into the reactor, which includes inspection, transfer to storage locations, and preheating prior to loading
- Transfer of fresh fuel into the reactor, shuffling of fresh/spent fuel within the reactor vessel, and transfer of spent fuel out of the reactor
- Storage of spent fuel to reduce the decay heat (in-vessel/ex-vessel)
- Washing of spent fuel to clean the sodium sticking to the fuel and storage of fuel for shipment to reprocessing plant
- Shipment of spent fuel to the reprocessing plant

The functions of fuel handling system are schematically shown in [Fig. 73](#)

3.5.2 Classification

The fuel handling is broadly classified as indicated below:

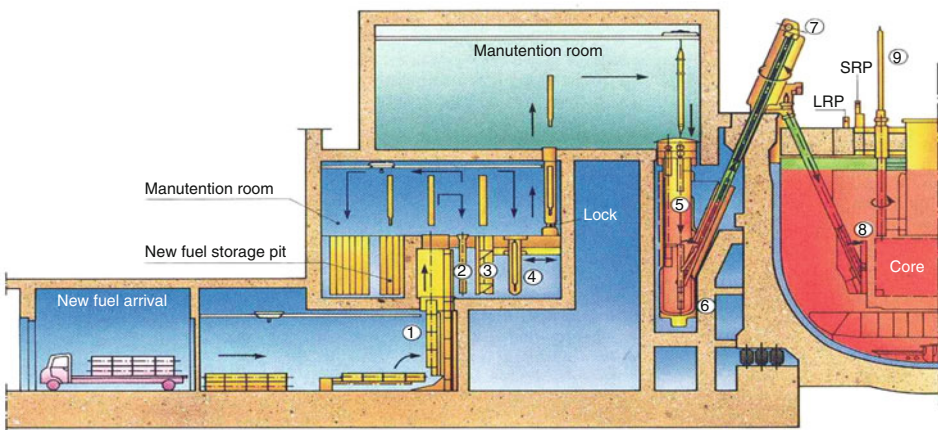
- State of reactor during refuelling: on-line and off-line refuelling
- Type of subassemblies being handled: fresh and spent subassembly handling
- Associativity with respect to reactor vessel: in-vessel and ex-vessel handling

3.5.3 On-Line Versus Off-Line Refuelling

SFR is characterized by a reactor core with high power density (~ 500 kW/L) and liquid sodium as the coolant with high heat transfer capability. The power density is obtained by a closely packed array of fissile material provided in the form of hexagonal subassemblies. The amount of reactivity associated with a single subassembly is considerable and reactivity changes due to subassembly loading/unloading, while the reactor is in power, would result in unsatisfactory reactor operation. SFR is generally refuelled in the shutdown condition of the reactor when all the control rods are fully inserted into the core and the core has sufficient negative reactivity. In addition, generally SFR has a vertical configuration of the reactor with the control rods along with their drive mechanisms housed in a control plug located above the core. The core is supported from the bottom of the reactor vessel. Since it is difficult to provide direct sealing for the high temperature and radioactive sodium present within the reactor vessel, an argon cover gas is used above the sodium level to provide an inert gas blanket for the sodium and to enable provision of sealing for the radioactive cover gas. Hence, the configuration of the reactor is such that, to gain access to the core subassemblies directly below the control plug, it becomes necessary to move the control plug away from the centerline of the core during fuel handling. This requires the control rods to be detached from their drive mechanisms resulting in need for reactor to be shut down. The time required for fuel handling more or less matches with the shutdown time required for other planned maintenance activities of the reactor and hence does not influence the availability of the reactor. Hence, off-line refuelling has been the choice in all SFRs.

3.5.4 Fresh Subassembly Handling

► *Figure 74* shows a typical fresh subassembly handling scheme as in SPX-2 reactor.



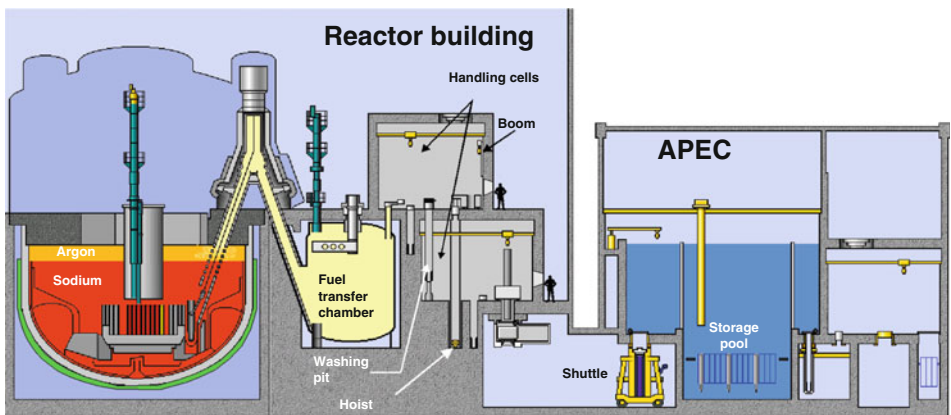
■ **Figure 74**
Fresh subassembly Handling scheme in SPX-2

The new or fresh subassemblies are brought to the reactor plant from the fuel fabrication plant inside a fuel transport cask. The new fuel has radioactivity due to gamma activity from residual fission products, low energy gamma rays from plutonium, and americium and neutron emissions largely from the (α,n) reactions from the oxide fuel. Hence, the fresh fuel subassembly requires moderate shielding. From the cask, the subassembly is transported to an inspection facility for checking of subassembly identification number, enrichment level, dimensional check, visual check, subassembly flow zone identification, and flow blockage test. After successful inspection, the subassembly is stored in a storage bay designed with adequate spacing to prevent criticality. Rejected subassembly, if any, is stored separately and returned back to the fuel fabrication plant. All the above operations are carried out with the subassembly in air. During a fuel handling campaign, the subassembly is loaded into the reactor which has argon as the cover gas. Hence, there is a need for change of contact of the medium in contact with the subassembly to an inert gas before loading into the reactor. This can be effected by transferring the subassembly through an inert gas filled cell and loading into the reactor through ex-vessel handling machine.

3.5.5 Spent Subassembly Handling

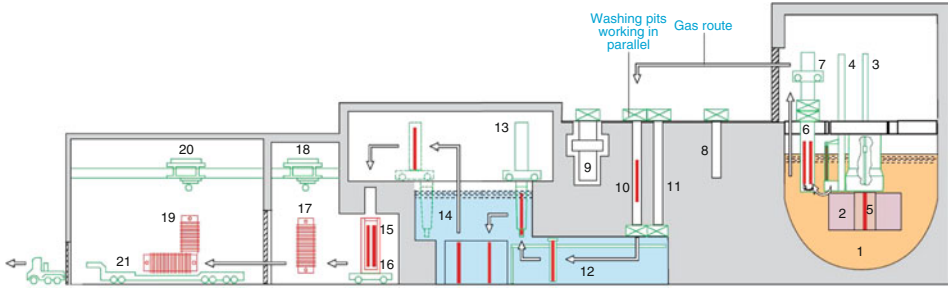
- *Figure 75* shows a typical spent subassembly handling scheme as in SPX-1 reactor.
- *Figure 76* shows the scheme adopted in EFR.

The main challenge in handling of a spent subassembly is its high decay heat shortly after reactor shut down and its high radioactivity. The decay heat is strongly dependent on the specific power (kW/kg of U+Pu) and cooling time (days after discharge from reactor) and is less dependent on burnup (MWd/t). This is illustrated in ➤ *Table 12* from published data (Noraiki Takahashi et al. 1989). The high decay heat leads to an increase in temperature of the fuel clad and if adequate heat sink is not provided during handling, it may lead to loss of integrity of the clad with resultant release of radioactivity into the working environment. While handling under



■ **Figure 75**

Spent subassembly Handling scheme in SPX-1



■ **Figure 76**
Spent subassembly handling scheme in EFR

■ **Table 12**
Decay heat in kW for 100 kg fuel (U+Pu)

Sl. No	Fuel Burnup (MWd/t)	Specific Power (kW/kg)	Days after discharge from reactor		
			10	40	100
1	100,000	400	77	41	21
2	50,000	400	67	31	15
3	100,000	100	23	12	6
4	50,000	100	21	11	5.5

sodium, decay heats upto ~ 90 kW can be dissipated without loss of integrity of the clad (Blanks 1985). However, the spent subassembly has to be handled in an inert gas environment prior to its washing to remove the sodium sticking to SA.

This calls for storage of the spent subassembly either within the reactor vessel (in-vessel storage) or outside the reactor vessel (ex-vessel storage) in order to reduce its decay heat to a level compatible with handling in gaseous medium. The subassembly is then washed in washing pits to remove the sodium sticking to the SA. This is done to avoid the load of subassembly cleaning on the reprocessing plant. After sodium cleaning, the subassembly is stored temporarily to bring the decay heat to a level compatible with reprocessing plant requirements. The subassembly is then shipped to the reprocessing plant using a shipping cask.

3.5.6 In-Vessel/Ex-Vessel Storage to Reduce Decay Heat of Subassembly

In the case of in-vessel storage, the spent subassembly with high decay heat is stored in internal storage locations located on the periphery of the core. The subassembly is stored for one or more campaigns till the decay heat is reduced to a level suitable for subsequent handling. Initially, dummy subassembly is provided in these storage locations, which are progressively replaced with spent subassembly during successive fuel handling campaigns. In-vessel storage is provided in Phenix, PFBR, Superphenix-2, and EFR.

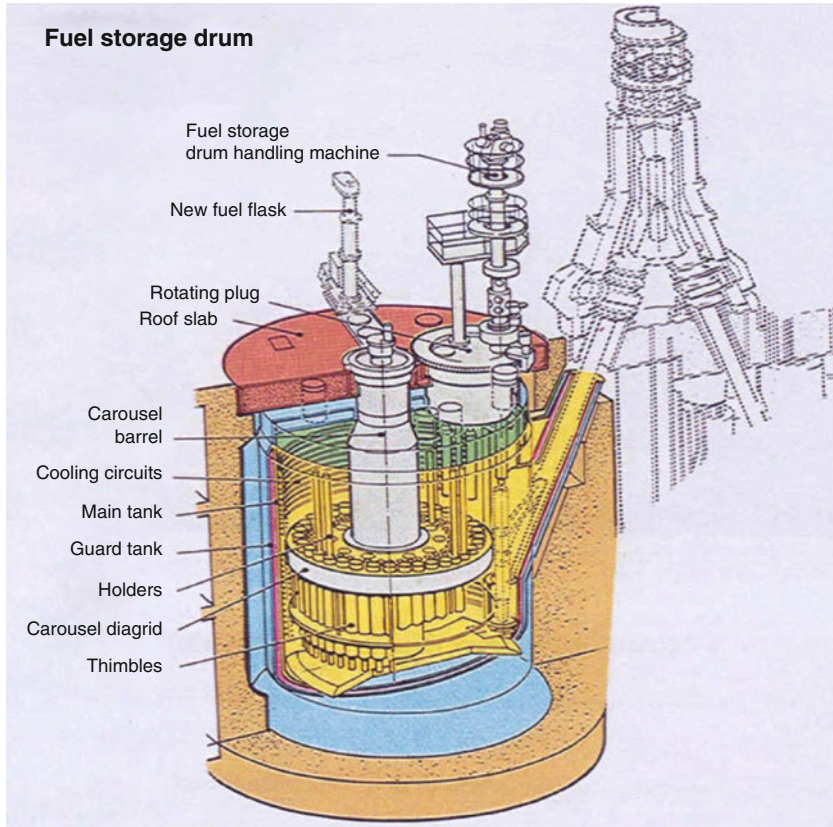


Figure 77
Storage drum in Phenix

Alternatively, the spent subassembly can be transferred for storage outside the reactor vessel and this is known as ex-vessel storage. This can be in the form of a vessel filled with sodium and with provisions to store subassembly vertically. Figure 77 shows the ex-vessel sodium storage drum in Phenix reactor. The vessel has provision for cooling to remove the decay heat transferred from the subassembly and a dedicated purification system to maintain purity of the sodium. The transfer of subassembly between the reactor and ex-vessel storage takes place in a sodium filled pot. By this method, subassembly having a large decay heat ($\sim 25\text{--}35$ kW) can be transferred out of the reactor vessel. Adequate number of storage locations are provided in the storage vessel to store fresh assemblies also prior to a fuel handling campaign. During a handling campaign, the spent subassembly is exchanged with a fresh subassembly between the reactor vessel and the storage vessel. The advantage of ex-vessel storage is shorter fuel handling time (subsequent transfers from the storage vessel to outside is done in parallel with reactor operation), capability to remove subassembly with large decay heats, and shortest time required for full core unloading, whenever the need arises. The disadvantages are that the storage vessel is a replica of reactor vessel with its own associated cover gas/cooling and purification systems,

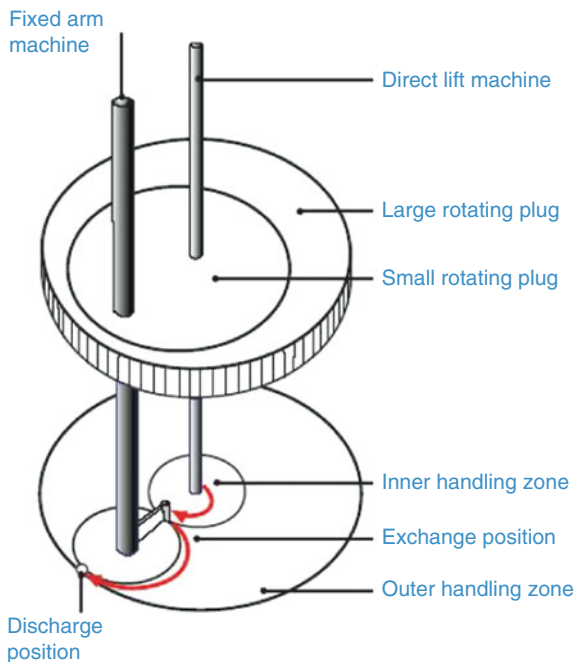
large sodium inventory, and additional machines to transfer the fuel within the storage vessel resulting in high overall cost.

Ex-vessel storage in a large sodium vessel is adopted for Phenix and Superphenix-1. In Superphenix-1, there was a sodium leak due to failure in the welds of the storage vessel and ultimately, the sodium storage option was deleted. From economic considerations, the sodium vessel storage concept is not preferred though it offers great flexibility in fuel handling.

In-Vessel Handling

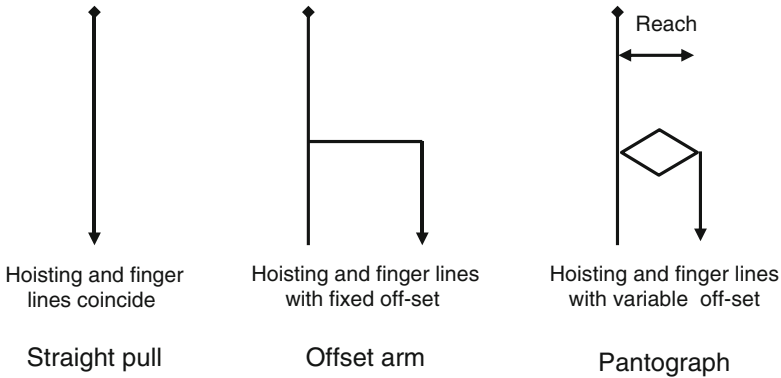
In-vessel handling or transfer of fuel within the reactor vessel is carried out using combined rotation of one or more rotatable plugs and using one or more in-vessel handling machines (IVHM). The principle of EFR in-vessel handling scheme using two rotatable plugs and two in-vessel handling machines is illustrated in [▶ Fig. 78](#). There are mainly three types of in-vessel handling machines: (i) straight pull, (ii) offset arm, and (iii) pantograph type. The three types of in-vessel handling machines differ in the location of gripper finger axis with respect to machine hoisting axis. For straight pull type, both the axes are coincident. For offset arm type, the hoisting axis is offset by a fixed distance from the gripper axis. In the pantograph type, the hoisting axis is offset but variable from the gripper axis. This is illustrated in [▶ Fig. 79](#).

[▶ Figure 80](#) shows three types of IVHM. FBTR, Superphenix –1, EFR, Joyo, DFBR, BN-350, BN-600, FFTF, and CRBRP have adopted the straight pull type; Phenix, PFBR, SPX-2,



■ Figure 78

In-vessel handling scheme in EFR



■ **Figure 79**
Working Principles of various types of IVHM

and Monju have adopted the offset arm type; and PFR, DFBR, and JSFR have adopted the pantograph type.

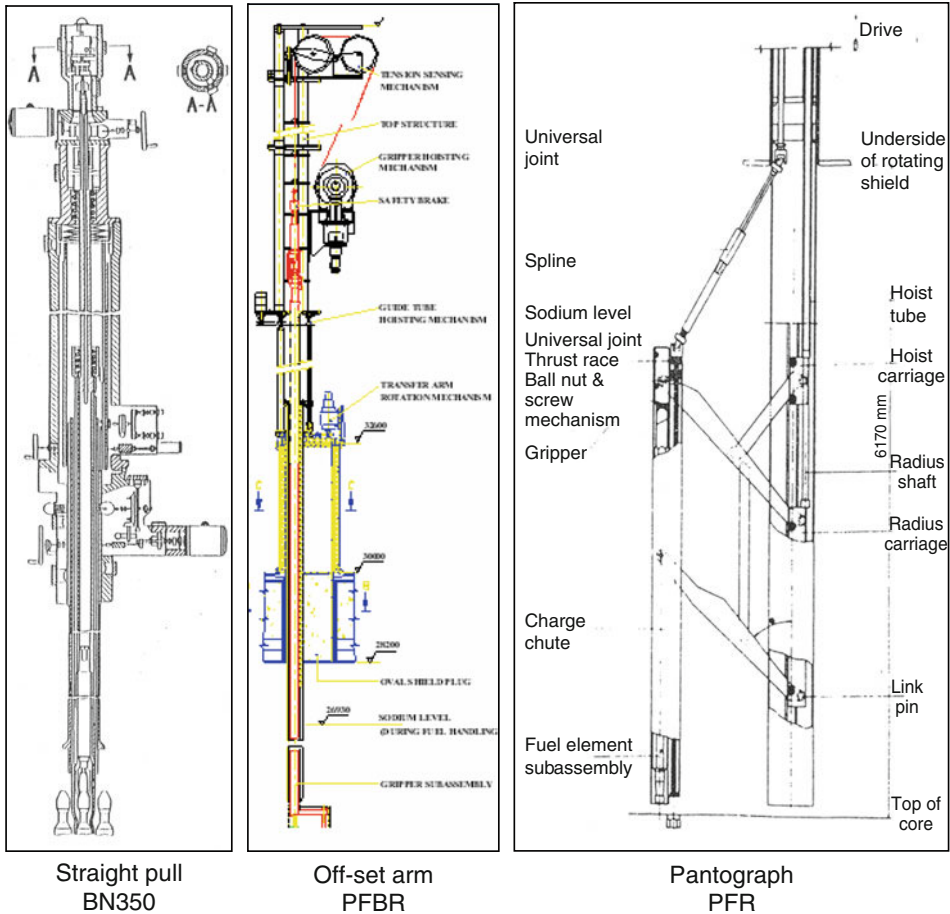
Straight pull type is the simplest and offers simplicity in design and operation. Offset arm and pantograph types have relatively complex loading due to eccentric application of load on gripper with respect to the hoisting function of the machine. However, all the three options have been designed and used in various reactors as indicated above and hence are technically feasible. Pantograph machine is the most complex among the three types but give great economical advantage of use of single rotatable plug and smallest LRP flange diameter as seen in recent innovative designs in Japanese reactors (JSFR).

Ex-Vessel Handling

Ex-vessel handling refers to the transfer of subassembly from IVTP (within the reactor vessel) to a location outside the reactor from where the subassembly is subsequently transferred by other machines for subsequent sodium cleaning and storage. The ex-vessel handling schemes is of two types namely, flask transfer and cell transfer.

The method of flask transfer is illustrated in ► [Fig. 81](#). In flask transfer, a leaktight argon filled flask is connected to a canal in the roof above IVTP and the subassembly is gripped and hoisted up into the flask. Leaktight valves, one on the roof and another on the flask, are provided. The valves are kept open for subassembly movement and are closed during transfer of subassembly to the washing pit. Before opening the flask and canal valves, the interspace between the valves is flushed with argon. The flask is handled by the building crane or moved on dedicated rails. The drawback of flask transfer is that it is a time-consuming process and leads to longer fuel handling time. There is also a limit to cooling during handling and subassembly with high decay heats cannot be handled.

In cell transfer, a dedicated cell is provided linking the canal in the reactor roof and a transfer location outside the reactor. The cell is filled with argon. The subassembly is transferred through the inert gas filled cell using a crane or a transfer machine. ► [Figure 82](#) shows the method of cell transfer. In another variant, a rotating transfer lock is provided between the reactor and outside. The lock has two inclined ramps through which the subassembly is hoisted up. The



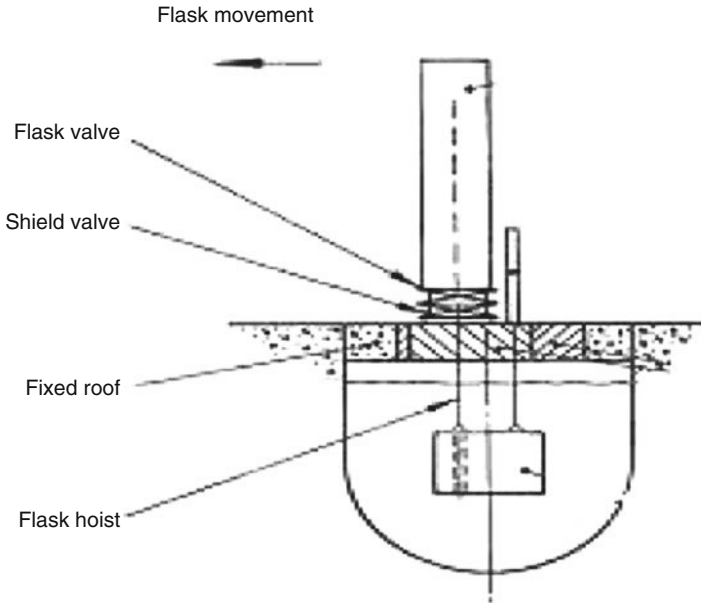
■ **Figure 80**
Various types of in-vessel fuel handling machines

subassembly, after it is hoisted up, is either transferred to the other side of the ramp either by rotation or by swinging. This concept is adopted in PFBR, Phenix, Superphenix-1, and EFR. The cell transfer method is preferred due to reduction in fuel handling time and capability to transfer subassembly with larger decay heats.

The design choices adopted for fuel handling systems in various international SFRs are summarized in ► [Table 13](#).

3.5.7 Design Validation

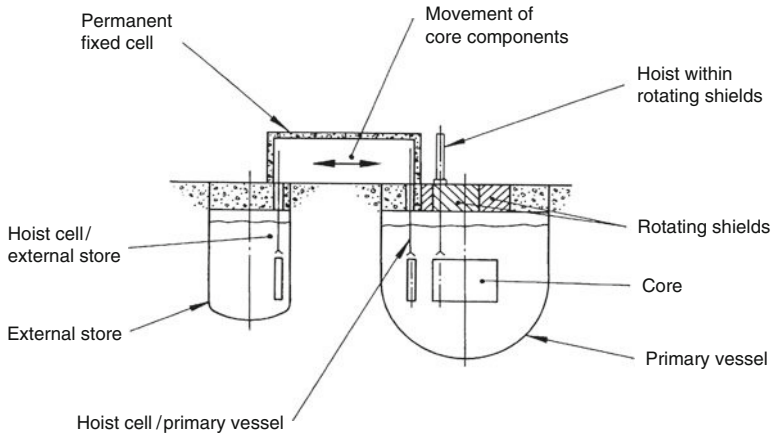
The fuel handling machines have to be highly reliable to ensure higher reactor availability (due to off-line refuelling employed in fast reactors) and also to ensure safety during handling. In the



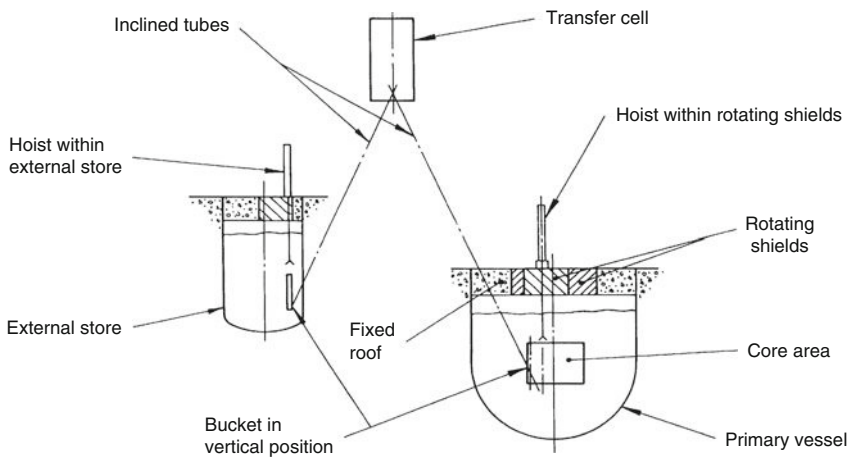
■ **Figure 81**
Flask Transfer Concept

design stage, higher reliability of the machine is achieved by providing a simple design, providing a high factor of safety in the design, adoption of single failure proof features in the load path to avoid load fall, and by extensive design validation by testing. To ensure reliability during operation, redundant and diverse instrumentation are provided with adequate interlocks between the various operations based on the feedback from the instruments provided. Extensive use of computers is used to assist the operator during fuel handling operations. A systematic maintenance schedule is also implemented in order to ensure smooth and trouble free operational performance of the machines.

The design of the critical in-vessel fuel handling machines is validated by extensive performance testing both in air and sodium. Generally, full-scale prototypes of the machines are manufactured and are performance tested with test cycles simulating the actual operations carried out. Testing is carried out first in air to study the behavior of the various moving parts and to take remedial action required, if any. Subsequent to this, testing is carried out in hot argon (few cycles) and in sodium under conditions identical to that in the reactor. Since it is difficult to simulate and maintain the required temperature distributions during hot argon testing, the number of cycles is kept limited. Sodium testing is carried out under conditions similar to both reactor operation and fuel handling simulated alternately as in the reactor. The effect of higher friction in sodium, sodium aerosol deposition in the annular gaps, behavior of material and material pairs in sodium, choice of hardfacing materials, and their behavior under actual loading in sodium are some of the key parameters which get qualified by testing in sodium. The fuel handling machines of Phenix, PFR, and Superphenix-1



a Using fixed cell



b Using rotating transfer lock

Figure 82
Cell transfer concepts

were qualified by testing in air/hot argon/sodium and similar approach is followed in PFBR also.

In addition, dedicated experimental setups/facilities were made to verify certain major influencing parameters/validation of computational codes. These include insertion/extraction forces of subassemblies using core mechanics experiments, experimental verification of decay heat of subassemblies, syphoning time of sodium from the sodium filled pot used in IFTM, time for sodium dripping from subassemblies prior to handling, efficiency of sodium cleaning

Table 13

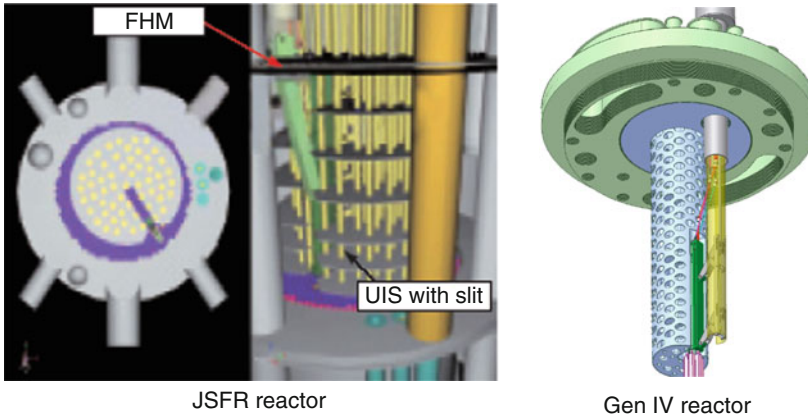
Design choices of fuel handling system adopted in various reactors

Sl. No	Reactor	In-vessel handling scheme	Ex-vessel handling scheme	Storage for decay heat reduction	Handling temperature (°C)
1	Phenix	1 RP + 1 OA	Cell (A-frame)	Ex-vessel sodium	250
2	SPX-1	2 RP + 2 SP	Cell (A-frame)	Ex-vessel Sodium	180
3	SPX-2	2 RP + 1 OA	Cell (A-frame)	In-vessel	
4	EFR	2 RP + SP + 1 OA	Cell (A-frame)	In-vessel	
5	DFR	2 RP + 1 SP	Flask		
6	PFR	1 RP + 1 PM	Flask		250
7	FBTR	2 RP + 2 SP	Flask		150
8	PFBR	2 RP + 1 OA	Cell (A-frame)	In-vessel	200
9	Joyo	2 RP + 1 SP	Flask	In-vessel	
10	Monju	1 RP + 1 OA	Flask	In-vessel	280
11	DFBR	2 RP + 1 SP + 1 PM	Cell (Transfer rotor)	Ex-vessel Sodium	
12	JSFR	1 RP + 1 PM	Flask		
13	BOR-60	2 RP + 1 SP	Flask		
14	BN-350	2 RP + 1 SP	Cell (Elevator)	Ex-vessel NaK	
15	BN-600	2 RP + 2 SP	Cell (Elevator)	Ex-vessel Sodium	260
16	FFTF	3 RP + 3 SP	Flask	Ex-vessel Sodium	230
17	CRBRP	3 RP + 1 SP	Flask		
18	ALMR	2 RP + 2 PM	Flask		

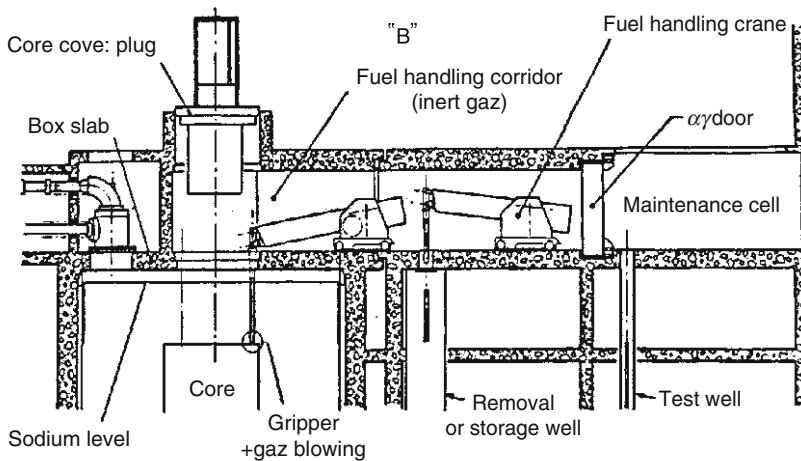
process for subassemblies, dimensional inspection of spent subassemblies after irradiation to high burnups, and inspection of fresh subassemblies prior to loading into the core.

3.5.8 Innovative Fuel Handling Concepts

With the accumulated experience of fuel handling system, it is recognized that scope exists for design simplification and use of innovative designs in order to reduce the cost of fuel handling system. This includes the provision of slit in control plug (or upper internal structure) along with use of a pantograph machine which will result in a compact rotatable plug arrangement thus leading to main vessel diameter reduction. This scheme is illustrated in [Fig. 83](#) as in JSFR and Gen IV sodium cooled fast reactor designs. Also a design which eliminates use of rotatable plug and which makes use of a fuel handling mobile crane for refuelling is shown in [Fig. 84](#). An inert cell is provided above the reactor into which the control plug is lifted to make way for the use of crane for refuelling. The objective is to achieve cost reduction of fuel handling system to have an overall economic design.



■ **Figure 83**
Arrangement of Slit in Control Plug & Pantograph machine



■ **Figure 84**
Crane type Fuel handling machine concept

3.6 Recent Evolution

For the Generation IV sodium fast reactor (SFR) systems, improvements are researched on safety approach and capital cost reduction. One of the main drawbacks to be solved by the standard SFR design is the proper management of the risk of leakage between the intermediate circuit filled with sodium and the energy conversion system using a water Rankine cycle. The limitation or reduction of this risk requires notably an early detection of water leakage to prevent a water–sodium reaction propagation and damages (i.e., to other tubes). Two innovative and alternative solutions to this problem can be proposed. They consist in the replacement of the sodium in the secondary loops by an alternative liquid fluid, less (or no) reactive with water,

either to the replacement of water to another nonreactive fluid (i.e., inert gas with a Brayton cycle). These two technological options are presented in the following sections.

3.6.1 Intermediate Coupling Fluid

This alternative fluid (AF) might also allow innovative designs, for example, intermediate heat exchanger (IHX) and steam generator (SG) grouped in the same component. For economical reasons, this fluid must be a liquid if a Rankine cycle is chosen. Many coolants have been tried or proposed in the past for fast reactors, but mostly for the primary circuit. The aim is now to evaluate the most interesting ones for the intermediate loop through a multi-criteria analysis in order to select the one or two most promising candidates which could be more thoroughly studied and envisaged as sodium substitute.

Fluid Preselection

The fluid must be compatible with a classical sodium reactor with a Rankine cycle. The temperature in the hot branch of the primary system is about 550°C and the one of the cold branch about 400°C. No fluid was selected or rejected a priori, but according to the following criteria:

- Melting point lower than 250°C (for easy cold trap operations)
- Boiling or complete decomposition point above 650°C
- Low corrosion rate allowing long-term use of the components
- Simple mixture (limited to ternary compounds) with consistent composition of each compound (more than 5 molar %) for chemistry control sake
- Compounds of reasonable cost and availability
- Reactivity with water and air significantly lower than sodium

The fluids were researched using simple elements and their mixtures, molten salts and hydroxides, and organic fluids. At the end, only six fluids fulfilled these preliminary required criteria. They are binary or ternary mixtures at eutectic composition. Their composition and melting point are given in [▶ Table 14](#).

Pb-Bi is well known as a fluid worldwide studied for the accelerator driven systems (ADS) and it has been experienced as a primary coolant in alpha class submarines. Two other bismuth alloys containing cadmium could be of interest due to their low melting point. Nitrate salts are of particular interest in solar application. The NaNO₃-KNO₃ mixture selected was used as coolant in the Solar2 Project. The hydroxides received the most attention in the 1950s, when they were tested as primary coolants for aeronautics applications.

Evaluation Method

It was decided to evaluate each of the selected fluids through a multi-criteria analysis known as “Kepner-Tregoe type” decision-making structured methodology. Eleven major criteria were defined and weighted according to their importance for the intermediary circuits (see [▶ Table 15](#)). The weights range from 10 (less important) to 50 (most important). For each of the nine first major criteria, sub-criteria with relative weights were also defined. Then a list of technical questions was established for each sub-criterion in order to rationalize the evaluation of the fluids through a consensual notation by experts ranging from 0 (very bad) to 40 (very good).

The two other major criteria, “confidence” and “availability and manageability of the reactor” are evaluated through the other nine major criteria, by giving also a notation for these criteria when the sub-criteria are evaluated. The analysis was applied to the six selected fluids of ► [Table 15](#). The sodium was also evaluated for sake of comparison. When all notations are completed, a weighted summation of the different criteria yields the final evaluation of the fluid (given as percentage of the maximum note). It was also thought that the best fluids should present equilibrate notation for each criterion: weak points should not be hindered by a good global note. It was decided to evaluate this quantitatively by calculating the average of the notation of major criteria dividing by the standard deviation between the notations. Practically, it yields an “equilibrium note” between 1 (bad unbalanced fluid) and about 10 (very good and balanced fluid).

Thermal Properties The ability of the fluid to transport and transfer the heat will directly impact the cost of investment by determining the size of the circuits and the exchangers surface.

Interaction with Structures The interactions between fluid and material lead to specific material choices. This item includes general corrosion (oxidation or dissolution), localized corrosion (grain boundary corrosion, liquid metal embrittlement, etc.), mass transfer (plugging, fouling), mechanical properties, and long-term behavior.

Interaction with Other Fluids The intermediate fluids can react with sodium, water, air, or other materials or fluids like concrete or oil (in case of abnormal situations). Thermodynamics, kinetics, and by-products of these reactions and their effects (corrosion, erosion, plugging, toxicity, etc.) must be considered to be compared with the case of sodium.

Chemistry Control, Operating Range Coolant can be operated in ranges of temperature, pressure, and chemistry (of the fluid or the gas phase) that have to be specified. The consequences

■ **Table 14**

Selected fluids for evaluation at SFR intermediate loops, molar composition, and melting point

Fluid	Pb-Bi	Bi-Cd	Pb-Bi-Cd	NaNO ₃ -KNO ₃	NaNO ₃ -LiNO ₃ -KNO ₃	NaOH-KOH
Composition (mol%)	Pb 45% Bi 55%	Cd 60% Bi 40%	Pb 38% Bi 48% Cd 14%	NaNO ₃ 64% KNO ₃ 36%	NaNO ₃ 17% LiNO ₃ 37% KNO ₃ 46%	NaOH 49% KOH 51%
Melting point	124°C	144°C	92°C	235°C	120°C	170°C

■ **Table 15**

Major criteria and their relative weight (10 – less important, 50 – most important)

Major criteria	Thermal properties	Interactions with structure	Interactions with fluids	Chemistry control	Safety, security environment	
Weight	30	50	50	30	50	
Major criteria	ISIR	Components and circuits	Cost	Level of use	Level of confidence	Availability and manageability
Weight	30	20	20	10	30	30

of out-of-range operation (temperature sudden rise, impurity ingress, etc.) must be evaluated. Measurement and control systems are evaluated through their reliability, sensibility, accuracy, robustness, efficiency, etc.

Safety, Security, and Environment Consequences of different types of leaks and reaction between fluids must be evaluated, by taking into account the risks of core plugging, gas bubbles in the core, exothermicity of reactions, risks of fire, etc.


In Service Inspection and Repair (ISIR) In operation, the following physical properties of the fluid must be measured: temperature, flow rate, and pressure. Leak of one fluid in another must also be detected. Maintenance of the components and the circuits is a periodical operation, while repair operations are not. But the related problems are globally the same: components must be cleaned (and decontaminated for the IHX) and requalified and strict procedures of start-up of the reactor must be followed. Experimental feedback from sodium fast reactors has revealed that difficulties arose mainly during start-up of the reactor after maintenance operations.


Components and Circuits The fabricability (including weldability) and approximate cost of the following components and circuits were evaluated: HX, SG, pumps, valves, main circuit, auxiliary circuit, chemistry control circuit, instrumentation.

Experience A fluid can be most confidently chosen if it has been already experienced as a coolant, especially in a nuclear context.

Cost The cost of a fluid (with purity specification) was estimated, as well as the availability of the component and the cost during operation.

Results

The final results of the evaluation are given in  [Fig. 85](#). The final notation of the fluid is given as a percentage of the maximum note, first (blue) bars. The “equilibrium notes” are the second (red) bars ($\times 10$ for easier comparison in the graph). The note of sodium is given for sake of comparison. The best note is obtained by Pb-Bi, 64%. It corresponds to a note between “average” and “good.” Pb-Bi is also the fluid with the best “equilibrium note”: 6.6. Another fluid has also good notes but its equilibrium note is much lower NaOH-KOH: 2.2. It is worth noting that a sensitivity analysis to the ponderations for the major criteria (in particular by giving less weight for the interaction with structure and a higher one to components and structure) has pointed out that the results stay globally unchanged in a reasonable extent.

In  [Fig. 86](#), a radar graph represents the notes of the major criteria for the most promising fluids: Pb-Bi. It can be seen that Pb-Bi does not suffer any weak point but at once does not present any good notation. NaOH-KOH has very good, but bad notes too, mainly in corrosion that disqualify it. In final today only Pb-Bi alloy can be considered as an alternative to sodium with a relative good maturity for nuclear application envisaged for a Gen IV reactor. Therefore, the major information regarding Pb-Bi alloy in this evaluation will be presented.

Key features for the Pb-Bi alloy

Thermal Properties Globally all fluids have good final notes for this criterion. Trivially liquid metals are good coolants.

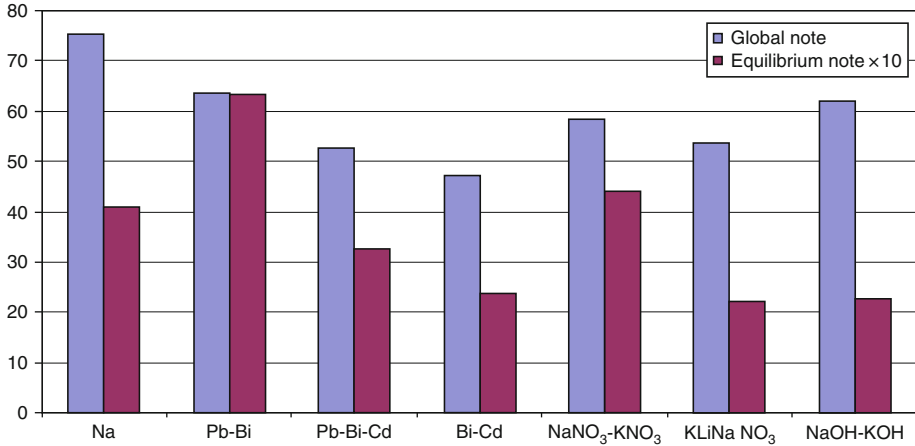


Figure 85

Global (first bars) and equilibrium (second bars) notations of alternative fluids for the intermediate circuits of SFR

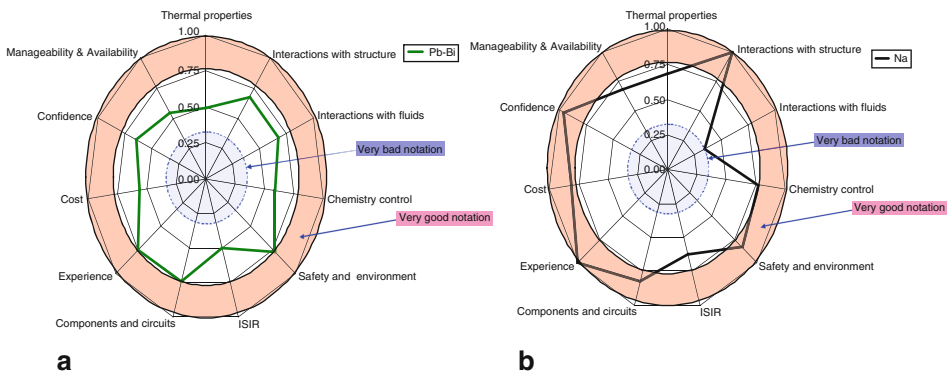


Figure 86

Radar graph of the evaluations of major criteria for (a) Pb-Bi and (b) sodium

Interactions with Structure It was calculated for Pb-Bi by using an oxidation model that T91 steel at 520°C and at the lowest acceptable level of oxygen (about 10^{-3} ppm) would develop an oxide layer of about 40 μm in 20 years. Mass transfer due to magnetite layer (half of the mixed chromium iron oxide layer) removal could be observed. For heavy liquid metal, significant gains could be obtained by operating at lower temperature or by using corrosion resistant steels (forming alumina or silica protective layers). Embrittlement by lead-bismuth is mostly observed in non-oxidizing conditions but would remain very low.

Interactions with Other Fluids HLM will react with Na above 400°C and forms solid phases as BiNa₃ and BiNa. The BiNa₃ formation is exothermic: $190 \text{ kJ}\cdot\text{mol}^{-1}$ from pure components.

Heavy BiNa_3 particles might settle and only those which diameter is smaller than $1 \mu\text{m}$ are transported by the sodium. Pb-Bi slightly reacts with air, the reaction being exothermic.

Chemistry Control, Operating Range Pb-Bi has a large liquid range ($125\text{--}1,670^\circ\text{C}$), a low vapor pressure (around 10^{-5} times lower than sodium at 520°C) but suffers from oxygen contamination. Oxygen content must be kept between two extreme values on the operating range: the upper limit corresponds to PbO formation (risk of plugging) and the lower value to the formation of protective oxide layers (Fe_3O_4) necessary for the protection against corrosion. Practically, the oxygen content should be fixed between $5 \cdot 10^{-4}$ and 10^{-2} ppm.

Safety and Environment For HLM, leaks in primary sodium could lead to safety hazards if the reaction products (BiNa_3 , etc.) has a probability to plug the assemblies.

ISIR The detection of HLM reactions with sodium could be performed by using two complementary methods: ultrasonic (US) measurement for BiNa_3 particles, and Laser Induced Breakdown Spectroscopy (LIBS) for elements dissolved in sodium (as Bi, Pb with a detection limit postulated to be around 1 ppm).

Components and Circuits For HLM, the materials should be T91 type (9 Cr) steels. Due to the high density of the liquids, short circuits are preferred (for seismic resistance purposes, etc.).

Experience Lead-bismuth is the only fluid that benefits from an experience as a coolant in nuclear facilities and international experimental facilities, in the framework of the ADS programs. But it should be underlined that the facilities do not address all problems arising when using these fluids in an SFR (in particular interaction with sodium).

Cost Lead and bismuth are rather low cost elements (maximum $10\$/\text{kg}$ for Bi), but the cost of the pure mixture could be one order of magnitude higher. This has to be compared to the estimated price of nuclear sodium, about $10 \$/\text{kg}$.

Availability and Manageability The notes of the fluid for this criterion are rather low, in particular in comparison with sodium, although it was expected that the elimination of the reactions with air and water would greatly improve this point. This is mostly due to the corrosion impact and the risks of the reaction with the primary sodium itself, and the instrumentation and safety approach which have to be implemented to detect it or prevent it.

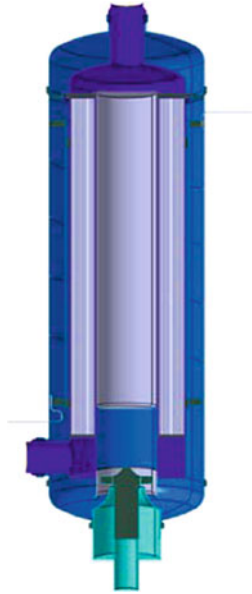
Impact on Design

Some preliminary design calculations have been realized to validate these options using Pb-Bi as coupling fluid. The main parameters were the following:

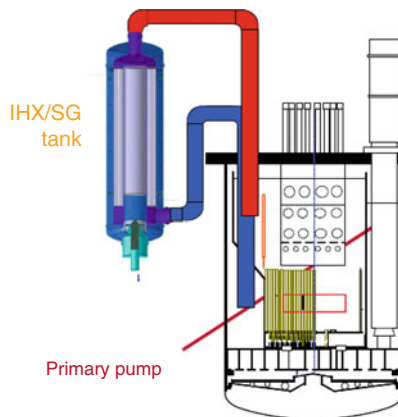
- Selection of a loop type or hybrid SFR concept.
- Intermediate heat exchanger (IHX) and steam generator units (SGU) are in the same tank, thermally coupled with Pb-Bi coolant.

IHX/SGU component integration in a lead/bismuth filled tank is achieved with:

- A peripheral helical SGU
- A central straight tubes IHX
- A mechanical Pb/Bi circulating pump

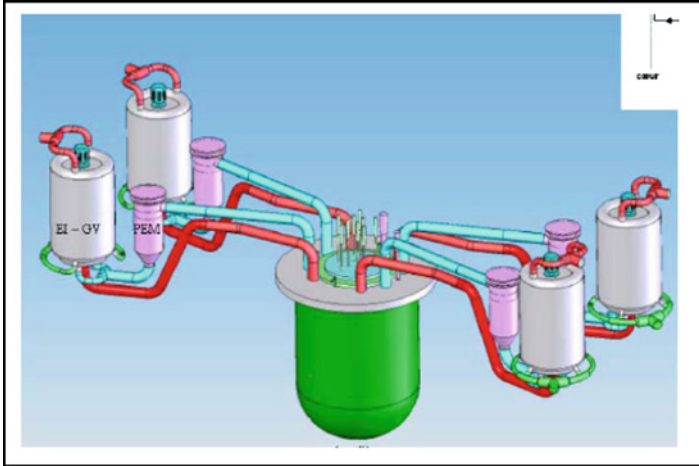


■ Figure 87
IHX/SGU with Pb/Bi coupling



■ Figure 88
SFR hybrid concept with IHX/SGU option

The 600 MWth component is shown in [Fig. 87](#). The overall dimensions for 600 MWth components are a diameter of around 4 m and of height of 17 m. These components could be associated with a hybrid reactor block in which the primary pumps are installed in the reactor vessel ([Fig. 88](#)) or with a classical loop type reactor ([Fig. 89](#)).



■ Figure 89

SFR IHX/SGU option: four loops and four electromagnetic pumps (tertiary circuit is not represented)

Conclusions

Only one fluid seems to require attention considering its global notes: Pb-Bi. Indeed, Pb-Bi is a fluid with no major drawbacks (good equilibration note) and gets large benefits from an international research. Nevertheless this choice would imply heavy consequences and several technological breakthroughs remain to be solved. The gains in selecting Pb-Bi are mainly the suppression of the sodium/water reaction and the sodium fire hazards. But the Kepner Tregoe matrix has revealed that these gains are almost annulled (or compensated) by the existence of new specific risks: Na/Pb-Bi interactions, oxygen accurate monitoring, corrosion on metals, and long-term behavior. The replacement of Na by Pb-Bi in the intermediate loop is still an option under development that requires a complete rethinking of the SFR design and its safety approach in comparison with the existing and operating ones (i.e., such as Phenix). Thus, the difficult issue of the balance between advantages and drawbacks in the change of sodium to Pb-Bi is not completely settled. R&D improvement in the future will help to clear the debate. This is also the reason why today this option for GEN IV innovative SFR is not unique and an alternative approach remains the use of gas energy conversion system instead of water (see ► Sect. 3.6.2).

3.6.2 Advanced Energy Conversion System

Introduction

SFRs have traditionally employed a Rankine steam cycle for power conversion. For instance, the Superphenix plant was based on a Rankine steam cycle for power conversion allowing a 40% net efficiency with 545°C for the core outlet temperature. Although the Rankine cycle is a well-developed technology, the design and licensing safety evaluation must deal with the

sodium–water reaction and the secondary sodium fire issues. Potential sodium–water reactions which result in formation of combustible hydrogen gas and exothermic energy release can be eliminated by adopting a gas-based energy conversion system (ECS). Moreover, the interest for other cycles or architectures to extract power can be argued by costs reduction (efficiency improvement with the same core temperature, ECS design simplification, operability and maintenance and the potential of suppression or simplification of the intermediate loop).

Evaluations of an alternative power conversion system have to be carried out in three steps:

- The first step is the examination and assessment of the application to the SFR concept of such a cycle using a gas-based ECS. The thermodynamic efficiency of each cycle is investigated. The analysis considers parametrical studies. The cycle's efficiencies are compared to Rankine cycle.
- In a second step, the safety concerns related to each cycle must be investigated. Among the transients that must be considered, some must be assessed and the consequences have to be evaluated, for example, the depressurisation of the gas circuit.
- In a third step, the development of the main components must be considered, particularly the intermediate heat exchanger (IHX) design, taking into account Na–gas interaction risks and their consequences as well as monitoring and in-service inspection and reparability (ISIR) aspects.

This chapter will deal only with the first step. The first section describes numerical tools, in particular the Cyclop code. In the second section, design considerations for Brayton cycle will be presented and the main input data and the assumptions for the involved components will be provided (compressors, turbine, heat exchangers, etc.). Then, we will present the study done by the expert group from the viewpoints of thermodynamic analyses and cycle efficiency optimization for various types of gas and for indirect and indirect/combined cycles.

Design Consideration for Brayton Cycle

The Brayton cycle consists of an intermediate heat exchanger, a low pressure compressor, a high pressure compressor, a turbine, a pre-cooler, an intercooler, a recuperator, pipes, and a generator. Gas at relatively low pressure and temperature is brought by a low pressure compressor to an intermediate pressure; then it is cooled by the intercooler and brought by a high pressure compressor to a higher pressure; it is preheated by the recuperator before entering the intermediate heat exchanger. Downstream of the intermediate heat exchanger, the hot gas is expanded in a turbine to another state point. The turbine drives the two compressors and the three components are coupled on a single shaft. Downstream of the turbine, the gas is cooled in a recuperator which is a gas-to-gas heat exchanger after which it is further cooled in a pre-cooler: a gas-to-water heat exchanger.

➤ *Figure 90* illustrates a closed-cycle gas turbine applied to SFR and ➤ *Fig. 91* shows a schematic of the corresponding enthalpy–isentropy diagram.

The principal system parameters under the designers control are including:

- Turbine inlet temperature, T_3
- Recuperator effectiveness, ϵ
- Turbine and compressors efficiencies (low pressure compressor: LPC and high pressure compressor: HPC), $\eta_T, \eta_{LPC}, \eta_{HPC}$
- System pressure, P_x
- System $\Delta P/P_x$, where ΔP is the system pressure drop

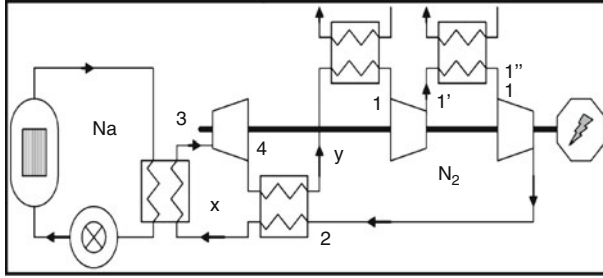


Figure 90
Brayton cycle applied to SFR

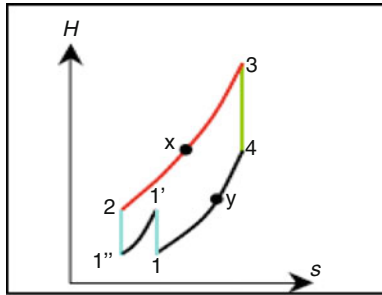


Figure 91
Typical enthalpy-isentropy plot

The theoretical cycle efficiency is based on next expression:

$$\eta_{cycle} = \frac{w_{cycle}}{q_{cycle}} \tag{13}$$

where w_{cycle} is the work received by the turbine shaft and q_{cycle} is the heat energy exchanged through the IHX.

The turbine, compressors, and the generator components are coupled to a single shaft. The work received by the turbine shaft is:

$$w_{cycle} = w_T - w_{LPC} - w_{HPC} \tag{14}$$

The above equation can also be written using enthalpies H_i :

$$w_{cycle} = (H_3 - H_4) - (H_{1'} - H_1) - (H_2 - H_{1''}) \tag{15}$$

The heat exchanged by the IHX is given by:

$$q_{cycle} = (H_3 - H_x) \quad (16)$$

Turbine and compressors efficiencies are based on the following expressions:

$$\eta_T = \frac{(H_3 - H_4)}{(H_3 - H_{4,is})} \quad (17)$$

$$\eta_{LPC} = \frac{(H_{V,is} - H_1)}{(H_{V'} - H_1)} \quad (18)$$

$$\eta_{HPC} = \frac{(H_{2,is} - H_{V''})}{(H_2 - H_{V''})} \quad (19)$$

The recuperator effectiveness is given by the following expression:

$$\varepsilon = \max \left[\frac{(H_x - H_2)}{(H_4 - H_2)}; \frac{(H_4 - H_y)}{(H_4 - H_2)} \right] \quad (20)$$

Finally, the theoretical cycle efficiency is:

$$\eta_{cycle} = \frac{(H_3 - H_4) - (H_{V'} - H_1) - (H_2 - H_{V''})}{(H_3 - H_x)} \quad (21)$$

The IHX inlet temperature (T_x) is a dependent variable that is determined by optimization of the turbine pressure ratio. However, in practical systems, T_x can be constrained by material considerations. Concerning the overall pressure ratio, this parameter can be constrained by manufacturing considerations. For instance, if the gas is helium, because of the high-specific heat, helium compressors and turbines have a relatively low adiabatic head per stage, hence a large number of stages. Consideration of the number of stages can limit the optimization range of the overall pressure ratio. Selection of each of the parameter values is constrained by cost and material considerations. It is assumed that the ECS cost optimization will be driven by efficiency gains on each ECS components. Thus, we can assume that ECS component designs are limited mainly by technology. ➤ [Table 16](#) shows the current values of each power cycle system parameter.

The individual effect of these parameters on system performance and the cumulative effect is illustrated in the next section. Quite clearly, changing the core outlet temperature has the major effect on variations of the overall global cycle. Changing the other parameters within the stated range is playing a lesser but still significant role. In the future, a compromise will be found between high values of components efficiency and technological options.

Classical Indirect Gas ECS

The model consists of a closed-loop primary circuit with sodium as liquid metal coolant (see ➤ [Fig. 92](#)). The intermediate circuit also uses sodium as coolant. The Brayton cycle consists of a closed-loop circuit with gas as coolant and two open-loop coolant circuit for the pre-cooler and the intercooler (water). The gas average pressure ranges between 30 and 250 bar.

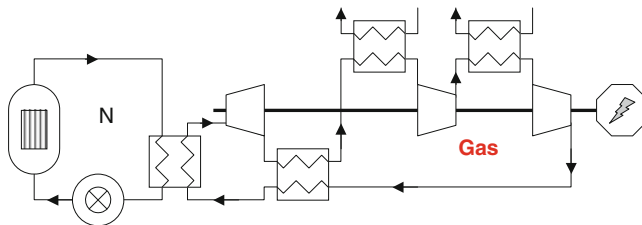
Many sensitivity tests were performed on various parameters (gases, cycle arrangement, gas pressure, recuperator effectiveness, turbine and compressor efficiencies, core outlet temperature, IHX pinch point, cycle cold point) in order to analyze previous assumptions and conceptual choices. The overall cycle efficiency is currently used to compare cycles. Later on, a compromise between high values of overall cycle efficiency and economical/technological issues will have to be found.

Gases Various types of gas are considered (helium, nitrogen, argon, separately or mixed, air, sub or supercritical carbon dioxide). The interest of the mixture He–N₂ is a gas density near air which allows using existing turbo-machines technology jointly with a good thermal exchange efficiency. These Cyclop calculations are performed using 550°C for the core outlet temperature (520°C for the turbine temperature inlet: $TIT = T_3$) and 50 bar for the turbine pressure inlet. Cycle cold point (gas compressor inlet temperature) is taken to 21°C in this assessment.

■ Table 16

Main input data

Gas secondary circuit components	Reference value
Pressure: P_3	30–250 bar
<i>Turbines</i>	
Isentropic efficiency: η_T	91–93% in gas
<i>Compressors</i>	
Isentropic efficiency: η_{LPC}, η_{HPC}	87–88% (HPC) 88–89% (LPC)
<i>Heat exchangers</i>	
IHX pinch point	15–30 K for Na–Na 15–30 K for Na–gas
Recuperator effectiveness : ε	90–95%
<i>Generator</i>	
Electrical losses	2%
<i>Shaft</i>	
Mechanical losses	1.3%



■ Figure 92

Schematic layout of indirect cycle

■ **Table 17**

Gases (core outlet temperature: 550°C, TIT: 520°C, 50 bar, cycle cold point: 21°C, with intermediate loop)

Gas	$T_{in, core}$ (°C)	Π_T	Net η (%)
He	390	1.7	35.5
He-N ₂ (He mass percent: 20%)	392	1.9	36.1
N ₂	393	2.1	36.6
Air	394	2.1	36.3
Ar	381	1.7	34.7
subcritical CO ₂	403	2.8	37.4

By assumption, pressure drops first evaluations are 1.4 bar for IHX1 and IHX2 (sodium side), 0.4 bar for each exchanger of the secondary circuit (IHX2, recuperator, coolers), and 5 bar for the core (Superphenix value).

Previous values are then refined using an iterative optimization process.

Components pre-sizing is undertaken with Copernic tool. Pressure drop and heat transfer correlations are based on the geometrical and thermal hydraulic characteristics of each component. Then, a new Cyclop optimization is performed taking into account calculated pressure drops.

According to these Cyclop calculations (see ► [Table 17](#)), sub-critical CO₂ as coolant is the most efficient gas. But nitrogen at high pressure is also considered as a promising candidate; following coolants are, in order, air and He–N₂ mixture. Concerning sub critical CO₂, a test has been performed at 65 bar (pressure lower than critical pressure: 73.77 bar) at TIT = 530°C and without intermediate loop: the net plant efficiency is 38.5%; in this case, the analysis must be pursued with a chemical evaluation to achieve compromise between thermodynamic properties and chemical specificities.

Cycle Arrangement Right now, sodium drawbacks make necessary to use an intermediate loop in the reactor system between the core cooling and the power conversion (► [Fig. 93](#)). An intermediate circuit leads to eliminate potential introduction of Na–gas reaction products into the primary system, and the potential for gas transport to the core. The elimination of the intermediate loop leads to a gain of 1% in plant efficiency and to the removal of one pump. The elimination of the intermediate loop is promising for future SFR; nevertheless, consequences of the gas circuit depressurisation as well as IHX tube failure have to be evaluated.

Gas Pressure In this assessment, the influence of gas pressure has been performed using nitrogen as coolant, in a wide range: 30 < pressure < 250 bar. The net plant efficiency becomes constant between 180 and 250 bar (► [Fig. 94](#)).

This high pressure (250 bar) may lead to significant technical challenges for critical components (turbo-machine, heat exchangers) and strongly encourages to turn to a lower pressure at the turbine inlet. With intermediate loop, at 100 bar, the net plant efficiency is around 38%; this level of efficiency is very close to the value obtained at 180 bar:38.5%.

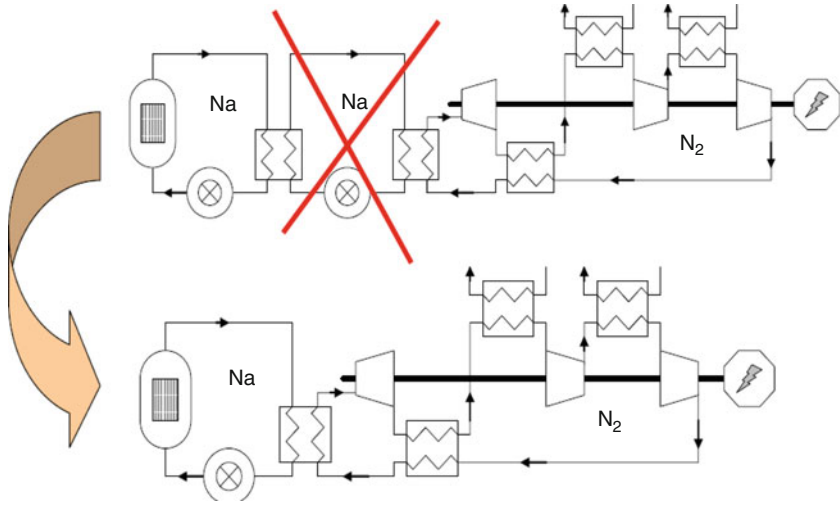


Figure 93
Cycles with and without intermediate loop

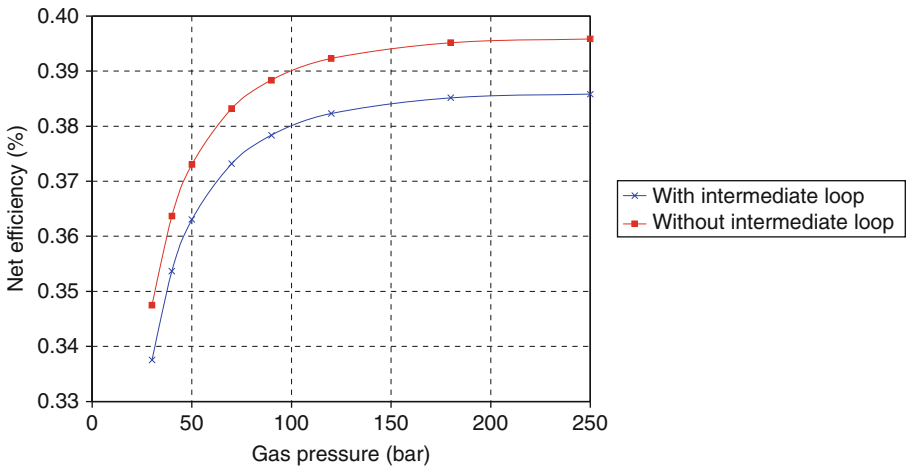


Figure 94
Overall cycle efficiency as a function of gas pressure (nitrogen, core outlet temperature: 550°C, TIT: 520°C, cycle cold point: 21°C, with intermediate loop)

Nitrogen cycle at high pressure (180 bar) and without intermediate loop appears very promising for SFR, with a potential of high net plant efficiency (39.5%). At the time of writing, cycle definition is in progress and gas pressure must be optimized to achieve compromise between technical challenges for critical components and plant efficiency.

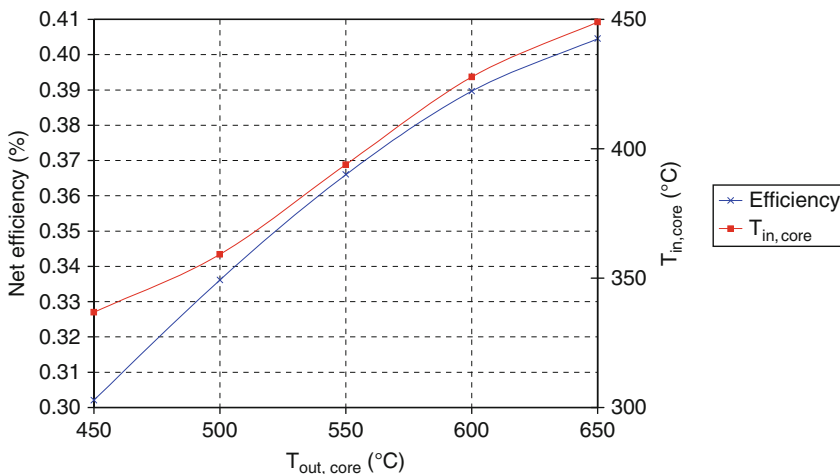
Components Efficiency Sensitivity tests were performed on recuperator effectiveness and on compressors and turbine efficiencies:

- 2% on recuperator effectiveness leads to -1.6% on η_{cycle}
- 2% on compressors efficiency leads to -1% on η_{cycle}
- 2% on turbine efficiency leads to -1.1% on η_{cycle}

The heat exchanger effectiveness is a function of the heat exchange area and of the overall heat transfer coefficient and is therefore a design choice. Since the price of the recuperator increases with area, an efficiency of 95% seems to be a good compromise between performance and cost. This level of efficiency seems to be a maximal value; this key parameter will be assessed in the future. Concerning the turbo-machine, axial solution for turbine and compressors is privileged. According to experts, a value of 93% for the turbine, 89% for the low pressure compressor efficiency, and 88% for the high pressure compressor efficiency are maximal values for helium turbo-machines. In this assessment, the same values are taken for nitrogen turbo-machines.

Core Outlet Temperature With an increase of 25°C (550–575°C) at the core outlet, the net plant efficiency can be increased of 1.2% (see [Fig. 95](#)). This level of temperature should be assessed.

IHX Hot End Temperature Difference The cycle and plant efficiencies can be improved by increasing the turbine inlet temperature through the enhancing of IHX performance. Several technical solutions have been considered for the IHX: finned plates, printed circuit heat



■ Figure 95

Overall cycle efficiency as a function of core inlet and outlet temperature (nitrogen, 50 bar, cycle cold point: 21°C, with intermediate loop)

■ **Table 18**

Efficiency versus core outlet temperature (tertiary pressure: 180 bar)

Secondary pressure (bar)	$T_{out, core}$ (°C)	$T_{in, core}$ (°C)	$\eta_{secondary\ loop}$ (%)	Net η (%)
50	550	277	5	35.7
50	650	287	20	40
180	550	287	8,4	36.3

exchangers (PCHes). Heat exchangers evaluations and designs definition should be done for each specific cycle. IHX failure consequences have to be further studied on the safety point of view; in particular, in case of gas leakage into sodium, the separation of gas from liquid will be required (see Sect. VI.D. b).

The core outlet temperature is deliberately restricted to 545°C and a conservative IHX design is selected having a pinch point (primary sodium inlet temperature minus intermediate sodium outlet temperature) of 15°C. Decreasing the pinch point raises the cycle efficiency by decreasing the difference between the core outlet and TIT: 30°C \diamond net η = 38.7% and 15°C \diamond net η = 39.5%. Nevertheless, a pinch point of 15°C is considered as a weak value. In the future, this parameter must be optimized.

Cycle Cold Operating Point Cycle efficiency dependency upon temperature at the main compressor inlet is investigated. Decreasing the cycle cold point raises the cycle efficiency: 21°C \diamond net η = 39.5% and 27°C \diamond net η = 38.7%. Nevertheless, a cold point of 21°C is considered as a weak value. For future work, this parameter, depending on site location and cooling system technology, which is a key factor affecting the Brayton cycle efficiency should be known precisely.

Balance A compromise between a high overall cycle efficiency, technological, and chemical views leads to use nitrogen as the working fluid in an indirect Brayton cycle. The optimization iterative process, associated with 530°C and 180 bar respectively for the turbine inlet temperature and pressure, leads to a net plant efficiency of 39.5% for the nitrogen indirect Brayton cycle, without sodium intermediate loop. This evaluation considers maximal values for nitrogen turbo-machine and recuperator efficiencies and a low cycle cold operating point (21°C). The plant efficiency can be increased by increasing the core outlet temperature; in this case, significant material challenges for critical components will be necessary.

Indirect/Combined ECS

An alternative to the previous indirect cycle consists to use an indirect/combined cycle. The model consists of a closed-loop primary circuit with sodium as coolant. The second circuit uses helium–nitrogen mixture (He mass percent: 20%). The third circuit is a Rankine steam cycle for power conversion (see \blacktriangleright Fig. 96). The net plant efficiency is around 36.3%, at 180 bar for the secondary pressure. Sensitivity tests were performed on core outlet temperature and on the secondary pressure (\blacktriangleright Table 18). The secondary loop does not lead to a significant gain, in comparison with the Na–Na–H₂O cycle. According to this preliminary evaluation, indirect/combined cycle does not appear promising for SFR.

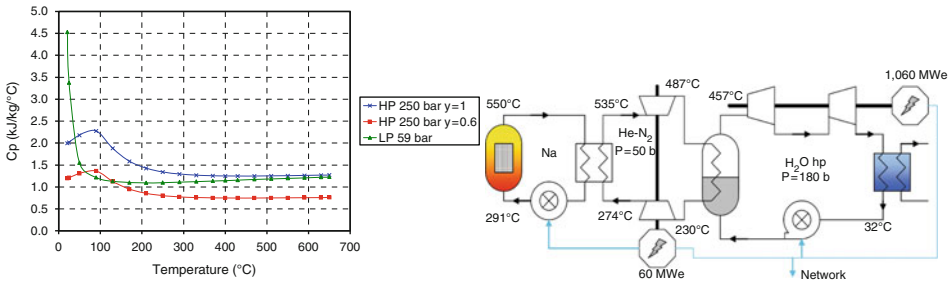


Figure 96
Schematic layout of indirect/combined cycle, with example of data

Supercritical Carbon Dioxide Indirect ECS

The supercritical carbon dioxide (S-CO₂) cycle was selected as the reference energy converter for the advanced burner test reactor (ABTR) pre-conceptual design developed at Argonne National Laboratory (ANL). The cycle is also under development for several years mainly in Japan, Korea, and France, because of:

1. The potential to reach high net plant efficiency
2. The elimination of potential sodium-water reactions
3. The potential for reduction in ECS costs from small turbo-machines having reduced costs

Supercritical CO₂ Properties S-CO₂ power conversion benefits rely on high supercritical CO₂ density and low work to compress S-CO₂ immediately above the critical point ($P_{crit} = 73.77$ bar, $T_{crit} = 30.98^\circ\text{C}$). S-CO₂ thermophysical properties exhibit strong variations, particularly in the vicinity of the CO₂ critical point. Rapid variation in thermophysical properties impacts cycle layout (flow split between heat rejection and direct recompression), compressor design, recuperator design, and cooler design. In this system, a partial cooling cycle is employed to compensate a difference in heat capacity for the high temperature-low pressure side and low temperature-high pressure side of the recuperators to achieve high cycle thermal efficiency (🔍 Fig. 97).

The thermal balance between low and high pressure legs can be written:

$$y \int C_p(T, HP) dT = \int C_p(T, LP) dT \quad (22)$$

where y is the part of the flow rate entering the main compressor, LP is the low pressure, and HP is the high pressure.

Cycle Description The preliminary reference S-CO₂ cycle is a recompression cycle with the turbine, compressors, and generator on a single shaft incorporating separate high temperature recuperator (HTR) and low temperature recuperator (LTR).

The flow from the low temperature recuperator is split such that $(1-y)\%$ of the CO₂ optimally rejects heat in the cooler and then enters the main compressor at a nominal inlet temperature; the remaining $y\%$ enters the by-pass recompressing compressor and is directly recompressed. Then, CO₂ enters the LTR, the HTR, and Na-to-CO₂ heat exchanger (see 🔍 Fig. 98).

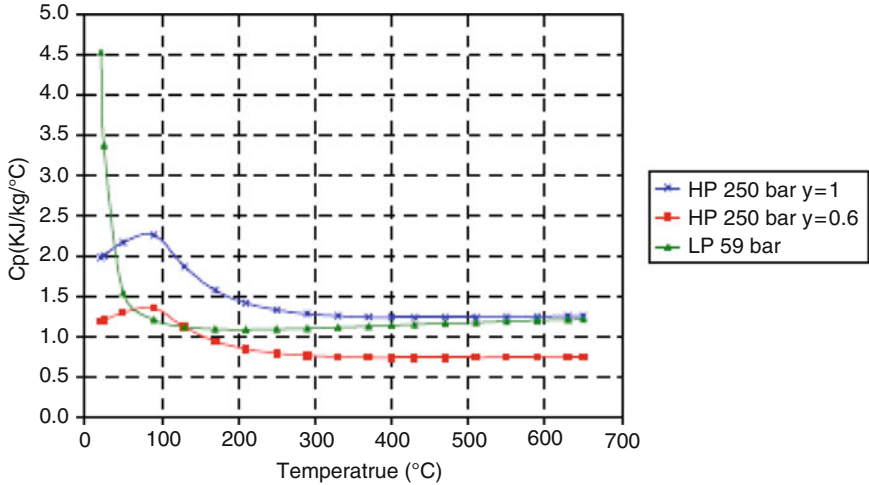


Figure 97
Heat capacity versus temperature

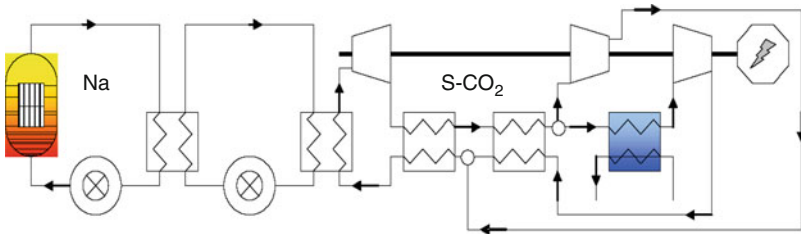


Figure 98
Schematic layout of S-CO₂ ECS

Sensitivity Tests Tests were performed on various parameters (cycle arrangement, turbine inlet temperature, pressure losses and components efficiencies and cycle cold point) in order to analyze conceptual choices.

(a) **Cycle Arrangement** The preliminary adopted configuration consists of elimination of the intermediate circuit (► [Fig. 99](#)). The elimination of the intermediate loop leads to a gain of 1% in plant efficiency and the removal of one pump.

(b) **Turbine Inlet Temperature** ► [Figure 100](#) shows a comparison of cycle efficiency versus turbine inlet temperature for S-CO₂ cycle Brayton cycle and helium ideal gas Brayton cycle [6], [7]. Over the temperature range of interest to the SFR, the S-CO₂ cycle clearly provides a significantly greater efficiency.

(c) **Pressure Losses and Components Efficiencies** Sensitivity tests were performed on heat exchangers effectiveness and pressure losses (► [Table 19](#)). A cycle efficiency of 45.4% and a net plant efficiency of 43.6% can be obtained.

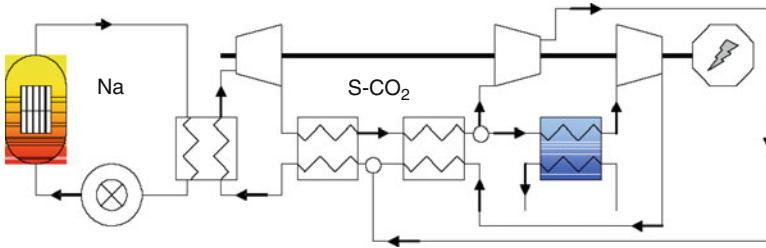


Figure 99
Schematic layout of S-CO₂ ECS without intermediate circuit

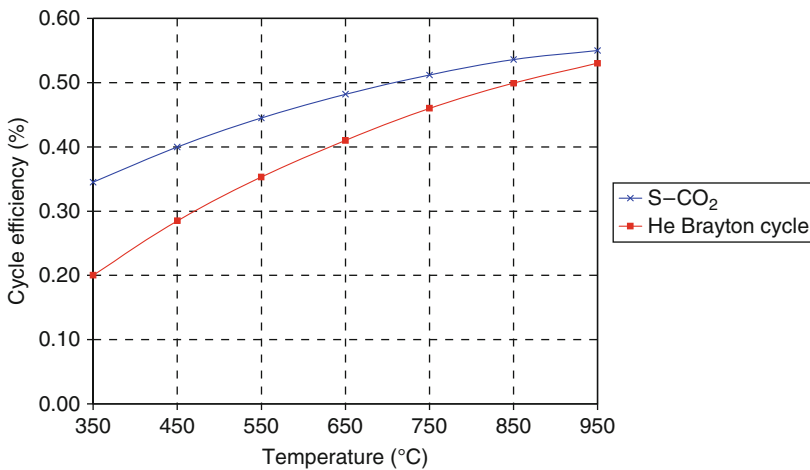


Figure 100
Efficiencies versus turbine inlet temperature for S-CO₂ Brayton cycle and traditional Helium Brayton cycle, without sodium intermediate loop

Table 19
Overall cycle efficiency (core inlet/outlet temperatures: 395°C/545°C, 250 bar, cycle cold point: 32°C, IHX pinch point: 15°C, without intermediate loop)

IHX pinch point (°C)	ε IHX (%)	ε HTR (%)	ε LTR (%)	ΔP IHX (bar)	ΔP HTR (bar)	ΔP LTR (bar)	ΔP cooler (bar)	net η (%)
30	85.7	88.2	90.1	1.4/1	0.4/0.4	0.4/0.4	0.4	42.2
15	92.2	92.5	92.5	0.2/1	0.5/0.5	0.5/0.5	0.5	44
15	92.2	92.5	92.5	0.2/1	1/1	1/1	0.5	43.6

(d) Cycle Cold Point There is incentive to cool carbon dioxide to as near the critical temperature as feasible. However, operation of the main compressor must remain stable over a sufficiently wide operating range near the critical point. Compressor work decreases when operating near the critical point. The low work of the compressor is the essential feature of the cycle that contributes to its improved efficiency over traditional gas Brayton cycles. In part, this is due to the high density of carbon dioxide immediately above the critical point ($P_{crit} = 73.77$ bar, $T_{crit} = 30.98^\circ\text{C}$).

32°C \diamond main compressor work: 77.47 MW, net $\eta = 43.6\%$

35°C \diamond main compressor work: 92.3 MW, net $\eta = 42.6\%$

Complementary Studies

(a) Sodium–Carbon Dioxide Interaction The supercritical carbon dioxide Brayton cycle option for the energy conversion has been considered because of its high thermodynamic efficiency and its potential compactness. Nevertheless, it assumes that the supercritical carbon dioxide–sodium interaction has less serious consequences than the water–sodium reaction or may be mitigated easily. Studies of the chemical interaction between sodium and CO_2 via calorimetric methods have been performed [8]; such methods are able to point out exothermic phenomena and to measure heat of chemical reactions. The view of reaction scheme is the following:

$T < 500^\circ\text{C}$

Complex scenario.

Kinetically controlled.

Carbonate and oxalate formation.

Na / oxalate and oxalate decomposition (CO release).

Na / CO reaction (induction time).

By-products: CO / Na_2CO_3 / $\text{Na}_2\text{C}_2\text{O}_4$ / C / Na_2O / NaCO / $\text{Na}_2\text{C}_6\text{O}_6$.


$T > 500^\circ\text{C}$

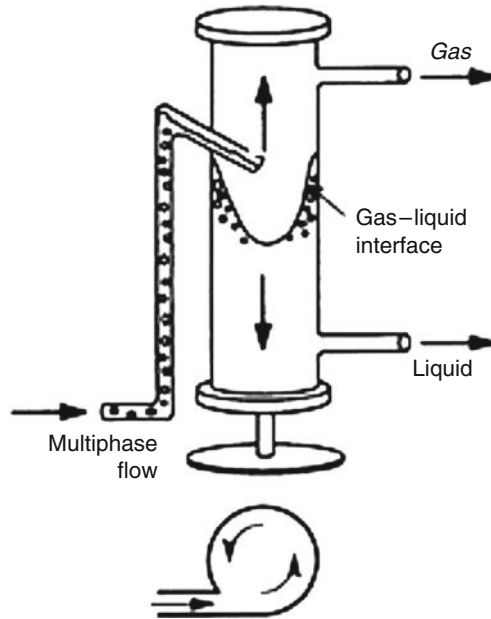
No more induction.

Fast global reaction: $2\text{Na} + 1.5\text{CO}_2 \diamond \text{Na}_2\text{CO}_3 + 0.5\text{C}$ (a)

From experiments, it seems that the interaction reactions Na- CO_2 and Na-CO are slow and become faster at high temperature ($>500^\circ\text{C}$). The kinetics would depend heavily on the contact mode between the sodium and the carbon dioxide and has to be extensively studied in view to control the global reactivity.

(b) Separation of Gas from Liquid The safety concerns related to gas cycle must be assessed and the consequences of some transients have to be evaluated, for instance the depressurisation of the gas circuit. In case of gas leakage into sodium, the separation of gas from liquid is required. The separator would be required for any Brayton cycle without intermediate loop (Sect. IV. B).

A schematic layout of a gas–liquid separator is proposed in  Fig. 101 as a preliminary solution. The fluid enters an inclined tangential inlet nozzle, sized to deliver a preconditioned flow stream into the separator vessel. The fluid momentum combined with the tangential inlet gener-



■ **Figure 101**
Schematic layout of a separator gas – liquid

ates a rotating liquid vortex with sufficient forces (centrifugal, gravity) to promote the separation of the dispersed gas from the carrying liquid. Finally, the gas exits at the top of the separator while the liquid exits at the bottom of the vessel. The separator is inserted in the sodium primary circuit between the IHX outlet and the pump.

Synthesis and Future Prospects of Advanced ECS

The gas Brayton cycle offers many solutions for nuclear power systems, in particular nitrogen at high pressure (between 100 and 180 bar). A net plant efficiency of 39.5% can be obtained with maximal values for cycle components efficiencies and with 395°C and 545°C respectively for the core temperature inlet and outlet. The individual effect of system parameters on performance has been investigated and reported in this paper. Quite clearly, increasing the core temperature has the major effect on increasing the overall global cycle.

An alternative Brayton cycle that offers higher efficiency at a lower reactor coolant outlet temperature is the Brayton cycle using super-critical CO₂. The main reason of the high thermal efficiency is attributed to a reduced compressor work at the vicinity of critical point. The use of a supercritical carbon dioxide Brayton cycle would potentially reach a net plant efficiency of 43.6% with a peak coolant temperature of 545°C and for a compressor inlet temperature of 32°C.

The main future R&D works on gas-based ECS concerns: gas insertion in the core in the case of suppression of the sodium intermediate loop, components technology, cycle operation, and sodium–gas interaction. For gas insertion in the core, the use of an efficient separator must be investigated as a countermeasure system against leakage of gas into sodium.

Supercritical carbon dioxide cycle components technology is less well developed than that for the Rankine cycle. The main concern is compressor efficiency due to its very small blades. The determination of the most adapted compressor type must be investigated, in particular the relevance of a radial compressor instead of an axial. Moreover, in the near critical regime, the values of properties such as heat capacity, density, etc. vary sharply and nonlinearly dependent on pressure and temperature. To our knowledge, there was no such turbo-machine used in a critical regime. Then, turbo-machine experimental data are strongly needed. For supercritical carbon dioxide cycle operation, stability concern due to significant variations of physical properties close to critical point needs a dynamic code to be investigated.

Gas cycle is a credible alternative to the steam cycles if the safety demonstration can be obtained with a design remaining competitive. Problems related to safety are mainly linked to the gas ingress into the core in case of leak. Concerning sodium–CO₂ interaction, future R&D actions are still necessary mainly to get a better knowledge of:

- The interaction in more representative conditions
- The particles issue (carbonate): dissolution or trapping
- The reaction detection systems: efficiency and reliability

Nomenclature

C_p	Heat capacity (J/kg/K)
ρ	Density (kg/m ³)
H	Enthalpy (J/kg)
P	Pressure (bar)
ΔP	System pressure drop (bar)
T	Temperature (K)
η	Turbomachine isentropic efficiency (-)
Π	Pressure ratio (-)
ε	Recuperator effectiveness (-)
q_{cycle}	Heat exchanged through the IHX (J/kg)
w_{cycle}	Work received by the turbine shaft (J/kg)
ABTR	Advanced Burner Test Reactor
ANL	Argonne National Laboratory
ECS	Energy Conversion System
HP	High Pressure
HPC	High Pressure Compressor
HTR	High Temperature Recuperator
IHX	Intermediate Heat exchanger
ISIR	In-Service Inspection and Reparability
LP	Low Pressure
LPC	Low Pressure Compressor
LTR	Low Temperature Recuperator
PCHE	Printed Circuit Heat Exchangers
SFR	Sodium Fast Reactor
TIT	Turbine Inlet Temperature

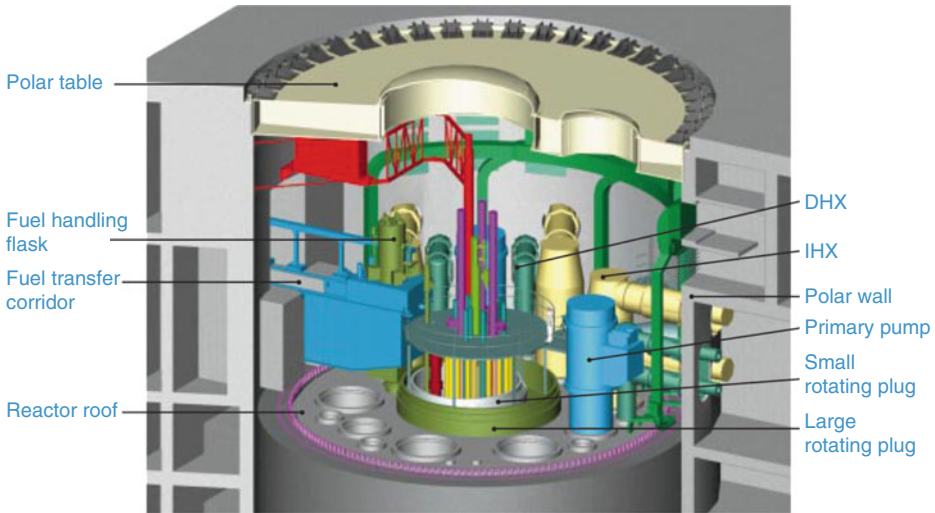


Figure 102
Above the roof area

3.6.3 Plant Layout

Reactor Building

The reactor building is designed to accommodate the reactor and its associated auxiliary systems, along with the fuel and component handling equipment, fuel decontamination facilities and stores for new and spent fuel. Other major features for sizing the reactor building are the provision for flasking of reactor components above the polar table using the reactor building crane and provision for protection against aircraft crash. A rectangular shape has been adopted for the reactor building, which is constructed of unlined reinforced concrete and forms, together with part of the polar wall, the containment boundary. It is designed to prevent the release of radioactivity and to provide radiological shielding. It is also designed to withstand the pressure resulting from a sodium fire on the reactor roof, for which it is assisted by the polar table, which provides a partial (non-leaktight) closure of the above roof area (► Fig. 102).

This has the dual function of limiting the oxygen supply to the sodium fire and attenuating the pressure rise in the crane hall. It consists of a rotatable circular steel slab with two holes, one central and one offset, which allow access for reactor component handling. The holes have steel covers which are only removed for component handling operations. The reactor building together with the adjacent steam generator buildings, switchgear buildings, and auxiliary building are all on a common raft with bearing pads for effective isolation of horizontal earthquake-induced loads. The reactor vault is additionally separated from the raft by springs to reduce the vertical seismic loads. However, this last feature is optional and required only in sites of very high earthquake activity, which are not likely in Europe. The isolation assures an essentially common seismic resistant design for a range of site conditions. It is

possible to save the cost of the isolators where this is justified by the site conditions without jeopardising the common design concept. The reactor building is subdivided into four main areas.

Crane Hall

This is the volume occupied from the building roof level to the polar table level. This area is served by an overhead bridge crane equipped with a selection of component handling flasks which allow reactor components to be removed and posted into transfer flasks inside the reactor building. The components can then be transferred out of the reactor building, via an airlock, and into the maintenance building (6) using special transporters.

Above Roof Area

The volume above the reactor roof is bounded by a cylindrical, steel lined concrete polar wall, of similar diameter to the reactor vault, and the polar table. This area contains all the components which interface with the primary circuit through the reactor roof in addition to roof and component cooling systems, i.e., primary pumps, IHXs, DHXs, the secondary and DHR sodium pipework, primary sodium purification and cover gas circuit pipework, the rotating plugs and their associated equipment and penetrations plus the cable support system.

Reactor Service Area

This is the volume surrounding the reactor and vault to the ground level. It contains cooling and auxiliary plant rooms, for example, the cover gas systems, the primary sodium purification system, vault cooling, and roof cooling. The air conditioning and recirculation systems are also housed within this area.

Fuel and Component Handling Area

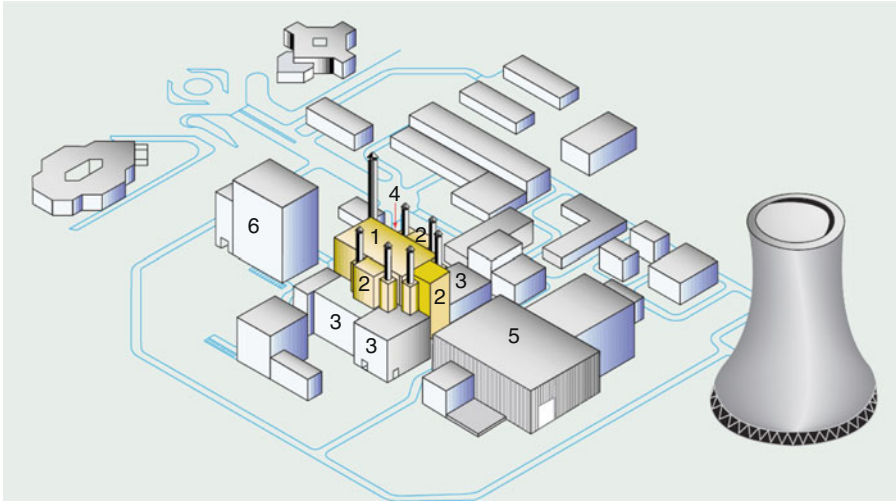
This occupies about half of the reactor building below the crane hall, and comprises: fuel handling facilities, new and spent fuel stores, fuel cask and component handling flask servicing facilities, an area for posting of components into transfer flasks, a large airlock for transfer of components into and out of the reactor building.

Steam Generator and DHR Buildings

The three steam generator buildings are arranged on three sides of the reactor building. The location of the steam generator buildings is dictated by the position of the reactor in the reactor building and the component arrangement on the reactor roof (IHX, DHX). Each steam generator building is separated into two steam generator compartments. Each steam generator compartment comprises one secondary loop, one direct reactor cooling (DRC) loop, and parts of one feedwater/steam piping system with their auxiliaries/ancillaries.

Plant Layout

The reactor building is a component of the plant layout. The general site is based on a river site with a cooling tower, or near the sea. Here, we show an example of general layout based on a river site (► [Fig. 103](#)). The center of the Nuclear Island is formed by the rectangular reactor building



■ **Figure 103**
General plant layout

(1). Adjacent to the reactor building are the three steam generator buildings (2). In addition the nuclear island incorporates the switchgear buildings (3) which house the essential and non-essential electrics, and the auxiliary building (4) housing the nuclear island component cooling system and the reactor building HVAC system. The turbine generator building (5) is connected to the steam generator buildings by feed water and main steam lines. Tunnels are used for cables and pipes to connect the different buildings.

4 Safety Principles

4.1 Introduction

This chapter proposes safety orientations for future sodium cooled fast neutron reactors (SFR). It is established based essentially on the position that is expressed by the French Advisory Group on Safety (GCFS 2007) to start the process that has to lead to the definition of the safety approach and then to the selection of the corresponding safety options for these reactors (GCFS). The content is also coherent with the position of the GIF (Generation IV International Forum)-Risk and safety Working Group (RSWG 2008).

➤ **Section 4.2** indicates the specificities due to the use of sodium as coolant.

As a preamble, the chapter exposes, within ➤ **Sect. 4.3**, the safety objectives and the general principles suggested for all the future reactors, for example, those studied within the framework of the GIF. These objectives and principles apply for an industrial SFR.

➤ **Section 4.4** briefly reminds the objectives and scope of the defense in depth.

➤ **Section 4.5** addresses the general principles for the treatment of severe accidents or, more generally, “severe plant conditions.” It considers the possibility of developing a concept allowing excluding the occurrence of generalized core degradation by limiting the considered

severe accident to limited core degradation but, waiting for the results of the engaged R&D, which hopefully will support this strategy, the contents of the section remain focused on the treatment of the situations with whole core melting.

➤ **Section 4.6** examines the themes for the safety improvement and its demonstration; its content is based on the feedback experience acquired by the design, the operation and the safety analysis of the Creys-Malville (SPX1) power plant and of the more recent projects: SPX2 and EFR (European Fast Reactor), as well as by their examination by the European and French safety Authorities. The section deals, in particular, with the consideration of severe plant conditions and with the need to take into account their consequences within the design.

➤ **Section 4.7** presents briefly the review of the needed R&D actions.

It has to be noted that aspects related to the proliferation resistance and physical protection, and those connected to the safety of the fuel cycle, are not addressed hereafter.

4.2 Safety Features Associated with Sodium

In view of high heat removal capability, light weight, excellent compatibility with structural materials once purity is maintained and good neutronic behavior, and vast experience accumulated over the years through test loops, experimental, and prototype reactors, sodium has been a universal choice for the coolant for SFR. However, there is a need to address a few disadvantages of sodium, mainly due to its violent chemical interactions with air and water. These aspects are addressed in this portion.

4.2.1 Physical Properties

Salient physical properties of sodium are given in ➤ **Table 20**, and corresponding properties of water are also given for comparison. Melting point of sodium is approximately 2 K below the boiling point of water, and the melting is accompanied by a volume increase of 2.17%. Molten sodium appears like mercury but is actually lighter than water. Because of its high boiling point, sodium has a large liquidus range (1,057 K), which is next only to that of lithium among other alkali metals. Its thermal conductivity (0.84 *J/cm/s/K*) is approximately two orders higher than

■ **Table 20**

Physical properties of sodium and water

Property	Sodium	Water
Melting point	370.8 K	273 K
Boiling point	1,155.9 K	373 K
Density	0.904 g/cm ³ at 473 K	0.99 g/cm ³ at 323 K
Latent heat of fusion	0.113 kJ/g	0.334 kJ/g
Latent heat of vaporization	4.31 kJ/g	2.28 kJ/g
Specific heat	1,383 J/kg K at 371 K	3,275 J/kg K at 371 K
Thermal conductivity	0.84 J/cm/s/°C at 473 K	0.0067 at 323 K
Viscosity	0.45 cps at 473 K	0.55 cps at 323 K
Vapor pressure	2 Pa at 573 K	101,325 Pa at 373 K

that of water, and its specific heat ($1,383 \text{ kJ/kgK}$) is 2.5 times less than that of water. As seen from the table, viscosities of sodium and water are not very different. Hence, operations such as pouring, mechanical pumping, stirring, and other general laboratory manipulations of molten sodium are very similar to those of water. Electrical resistivity of sodium is very low (in fact, among alkali metals, it has the lowest electrical resistivity), and this enables it to be efficiently pumped by electromagnetic principles.

4.2.2 Nuclear Properties

Liquid sodium has very low absorption cross section for fast neutrons. The absorption cross section of ^{23}Na is 0.87 mb for fast neutrons. The (n, γ) activation product is ^{24}Na , which is a strong beta-gamma emitter. Fortunately, it has a short half-life of 15 h. It is possible to approach the radioactive sodium coolant circuit for maintenance and repair after about ten half-life periods from reactor shutdown. However, during reactor operation, the activity level is in mCi/cm^3 . The other activation product of ^{23}Na is ^{22}Na by $(n, 2n)$ reaction. This has a rather long enough half-life of 2.7 years. However, it has a high absorption cross section for thermal neutron, which prevents it from building up above a few mCi/cm^3 levels. The (n, p) reaction product of ^{23}Na is ^{23}Ne , which has a very short half-life of 38 s. This is quantitatively released to the cover gas space. Sodium is sufficiently non-moderating and can preserve the hardness of the neutron spectrum. It has a moderating ratio of only 0.89 compared to 62 for water. One nuclear property of the coolant that is important for reactor safety is its reactivity coefficient for both sodium temperature and void.

The temperature and power coefficients of reactivity of any reactor should be negative so that temperature and power transients are self-limiting. Further, the time constant associated with them should be small so that the reactivity feedbacks are available promptly and the system is stable. Upon temperature rise in the sodium coolant, larger leakage of neutrons occurs, leading to negative reactivity changes. Increased fast fission from fertile materials leads to positive reactivity changes. Increase in " η ," (neutrons emitted per neutron absorbed) leads to positive reactivity changes. Loss in density of sodium leads to reduction in absorption of neutrons and hence the positive reactivity effect. However, this effect is negligibly small. Calculations that have been confirmed experimentally indicate that for small size reactors such as FBTR, the net coolant reactivity coefficient is negative, while for medium and large sized reactors such as SuperPhenix, it is positive. In case of PFBR, though coolant reactivity coefficients (both temperature and power) are positive, the net reactivity coefficient constituted by fuel, clad, and coolant is negative. The contribution of coolant temperature reactivity coefficient is only 20% of the total. In power coefficient, only 4% contribution comes from positive reactivity coefficient of sodium and the rest is from the fuel. Thus, any under-cooling transient or reactivity-initiated incidents are mainly arrested by fuel reactivity coefficient not by coolant reactivity coefficient. Also, the time constant associated with the fuel and coolant reactivity coefficients are small and so pose no stability problem.

4.2.3 Chemical Reactions

Being an alkali metal, sodium metal is highly reactive. On exposure to dry air, solid sodium first reacts with oxygen to form voluminous sodium oxide layer, which retards the rate of further reaction. Sodium does not react with nitrogen and does not form any stable nitride. It reacts

with humid air very fast, and the major reaction product is sodium hydroxide, which subsequently reacts with carbon dioxide in air to yield sodium carbonate. Since these reaction products are highly hygroscopic, uncontrolled exposure of sodium to moist air can lead the metal coming into contact with water (or water rich phases), resulting in explosive sodium–water reaction. Liquid sodium reacts instantaneously with gaseous oxygen. It burns in air to yield sodium oxide. Under oxygen deficient conditions, the product formed is sodium monoxide, Na_2O . When oxygen supply is unlimited and temperature is low, the product formed would be sodium peroxide, Na_2O_2 . Liquid sodium reacts with gaseous hydrogen and forms its hydride, NaH . Reaction rate with gaseous hydrogen is slow at temperatures below 523 K and is very fast at temperatures above 673 K. Na_2O and NaH dissolve in liquid sodium before precipitating as a separate phase. Solubility of these compounds in sodium increases with increase in temperature.

Liquid sodium is generally contained in austenitic and ferritic steel circuits. Sodium is quite compatible with them under pure conditions. Solubility of the steel constituents, namely, iron, chromium, nickel, manganese, molybdenum, etc., in sodium is low and is in ppm ranges only. However, higher oxygen contents in sodium (>5 ppm) would lead to enhanced corrosion and mass transport phenomenon. Carbon is an important interstitial alloying element in structural steels, and sodium can act as a medium for its transfer from one section of structural component to another. This can arise because of to the presence of temperature gradient in a sodium circuit with structural components made of single alloy and/or presence of multi-alloy components in that circuit. Carbon transport is kinetically slow at temperatures below 673 K and can become very significant above 873 K.


Reaction of sodium with water–steam is of special importance. Heat from secondary sodium is transferred to water across a ferritic steel tube wall in the steam generator of a fast reactor. In case of a steam leak into sodium circuit, sodium reacts instantaneously with steam–water forming sodium hydroxide and hydrogen. The exothermic nature of the sodium–water reaction and the caustic nature of the product can lead to tube material wastage and cause the steam leak to expand rapidly. In case, these leaks are not detected in time and remedial action not taken, the growing flame can cut the adjoining steam carrying tubes and lead to sodium–water explosions. Such a blowout in PFR resulted in the destruction of 40 steam tubes, and the one at BN-350 resulted in a long shutdown. However, these incidents did not lead to any catastrophe or nuclear release, and the events were completely manageable. Sodium hydroxide is stable in sodium only above 693 K. Sodium hydroxide in excess sodium decomposes to yield Na_2O and NaH below this temperature. Hydrogen formed in the sodium–water reaction can dissolve further in sodium, the slow kinetics of which has been mentioned earlier.

In the Creys-Malville plant and for the EFR, these risks are mostly minimized by secondary loops placed between the primary system and the steam generators. The consequences of sodium–water reactions are also minimized by measures put in place to detect and limit loads (detection of hydrogen in the sodium, acoustic detection, and ruptured membranes). One possible way of increasing safety is to find measures that would intrinsically limit loads, thereby limiting the sensitivity of the safety case to the way the accident in question is defined in terms of number of ruptured tubes. An example of how this could be achieved could be to limit the size of the steam generators (modular design).

Eliminating water by using another cycle (e.g., gas) would remove this problem. However, other specific risks would then have to be considered (potential source of gas injection into the core or shaking of the core).


4.2.4 Thermalhydraulics and Structural Mechanics Considerations

Being a liquid metal, it is an efficient coolant, having high heat transfer properties and high boiling point, by which it is possible to have large margin between operating temperature ($\sim 550^\circ\text{C}$) and boiling point of coolant (980°C). Hence, there is no need to pressurize the system, and all the disadvantages associated with the unforeseen depressurization of coolant are absent in FBR. High thermal conductivity, low viscosity, and large difference between the hot sodium and air coupled with significant variation of sodium density with temperature permit decay heat removal through natural convection modes. Sodium provides high thermal inertia, and hence, more time is available for the operator to act in case of exigencies without fear of any temperature rise followed by thermal transients, exceeding acceptable limits.

High thermal conductivity of sodium ($70\text{ W/m}\cdot\text{K}$ at 700 K) enhances its heat transfer property, which is not favorable from structural mechanics point of view, particularly under thermal transients. Any transient temperature change in the sodium following thermal transients (reactor scram, for example) would be transmitted to the adjoining structural wall surface without any attenuation, causing high skin stress. This is the main structural mechanics problem, particularly when the austenitic stainless steel is the structural material, which has low thermal conductivity and high thermal expansion coefficient. Some issues to be addressed are illustrated in  Sect. 8.

4.3 Safety Objectives and Principles Applicable for Future Reactors

As for the safety objectives applicable to future reactors, and especially to the SFR, it is considered that those applicable for the European pressurized reactor (EPR) are already very ambitious and guarantee a very high level of protection. Further, prescriptive reduction of the risk with regard to this level of safety, in particular in terms of probability, is not justified and could even be counterproductive. (Within the range of very low frequencies of occurrence, the quantitative level of safety is difficult to measure because of the uncertainties [due to, e.g., the not recognizable common modes]. This level can be used to compare the nuclear risks with the other risks in human activities, but it should not be used as an absolute value for the design and the safety demonstration. Actually, the strengthening of the safety objectives for highly improbable events would have a marginal impact on the safety, or even could go against this last one, for example, by increasing the complexity of the installation.) That is why analogous objectives are retained for all the future reactors. Safety improvements will nevertheless be looked for, especially in terms of qualitative safety and robustness of the safety demonstration. This can be achieved taking into account safety requirements since the early phases of the design, that is, achieving a safety “built in” rather than “added on.”

This ambitious level of safety is achieved for the EPR through, among others, a design domain that addresses the treatment of severe plant conditions, both from the viewpoint of the prevention and from that of the consequences’ management and minimization. For the EPR, the reference for the severe accident remains the whole core melting. For the future SFR, it is not excluded that design innovations will allow to practically eliminate the situations with generalized core damage by limiting the severe accident domain to limited core degradations. The search for such innovations represents a key subject of the current R&D effort  Sect. 4.4).

An essential contribution to the safety improvement will come via the capability to realize a robust safety demonstration. For that purpose, the approach has to be based on the feedback experience as well as on design options and R&D programs which will contribute to the reduction and the mastery of the uncertainties, the introduction of adequate margins and the rejection of any possible cliff edge effect.

The design approach will remain essentially deterministic, based on the defense in depth (🔍 Sect. 4.4) and conventional rules as, for example, the single failure criteria (when justified), and will take advantage of insights brought by probabilistic studies. In these conditions, the safety objectives will integrate acceptability criteria, both deterministic and probabilistic.

4.4 The Defense in Depth Principle

The safety approach remains based on the prevention and the mitigation of the abnormal situations, the objective being to make acceptable the risks for all the events susceptible to arise in the installation. For that purpose, the approach leans on the full implementation of the concept of defense in depth (DiD).

4.4.1 The Levels of the Defense in Depth

Following the IAEA/INSAG 10, measures relative to defense in depth are generally ranked in five levels of defense. The first four levels are oriented toward the protection of barriers and mitigation of releases; the last level relates to off-site emergency measures to protect the public in the event of a significant release.

Level 1: Prevention of abnormal operation and failures

Measures at Level 1 include a broad range of conservative provisions in design, from siting through to the end of plant life, aimed at confining radioactive material and minimizing deviations from normal operating conditions (including transient conditions and plant shutdown states). The safety provisions at Level 1 are taken through the choice of site, design, manufacturing, construction, commissioning, operating, and maintenance requirements.

Furthermore, Level 1 provides the initial basis for protection against external and internal hazards, even though some additional protection may be required at higher levels of defense.

Level 2: Control of abnormal operation and detection of failures

Level 2 incorporates inherent plant features, such as core stability and thermal inertia, and systems to control abnormal operation (anticipated operational occurrences), with account taken of phenomena capable of causing further deterioration in the plant status. The systems to mitigate the consequences of such operating occurrences are designed according to specific criteria (such as redundancy, layout, and qualification). The objective is to bring the plant back to normal operating conditions as soon as possible.

Level 3: Control of accidents within the design basis

In spite of provisions for prevention, accident conditions may occur. Engineered safety features and protection systems are provided to prevent evolution toward severe plant conditions and also to confine radioactive materials within the containment system. The measures taken at this level are aimed at preventing core damage in particular.

To ensure a high reliability of the engineered safety systems, design principles are adhered to such as: redundancy; prevention of common mode failure by physical or spatial separation, and

structural protection, by diversity or functional redundancy; automation to reduce vulnerability to human failure; testability to provide clear evidence of system availability and performance; qualification of systems, components, and structures for specific environmental conditions that may result from an accident or an external hazard.

Level 4: Control of severe conditions including prevention of accident progression and mitigation of the consequences of a severe accident

For the concept of defense in depth as applied to currently operating plants, it is assumed that the measures considered at the first three levels will ensure maintenance of the structural integrity of the core and limit potential radiation hazards for members of the public. Nevertheless, additional efforts are made in order to further reduce the risks. The broad aim of the fourth level of defense is to ensure that the likelihood of an accident entailing severe core damage, and the magnitude of radioactive releases in the unlikely event that a severe plant condition occur, are both kept as low as reasonably achievable, economic and social factors being taken into account.

The most important objective for mitigation of the consequences of an accident in Level 4 is the protection of the confinement.

It has to be pointed out that accident management may not be used to excuse design deficiencies at prior levels.

Level 5: Mitigation of the radiological consequences of significant external releases of radioactive materials

Even if the efforts described in the foregoing are expected to be effective in limiting the consequences of severe accidents, it would be inconsistent with defense in depth to dismiss off-site emergency plans. These plans cover the functions of collecting and assessing information about the levels of exposures expected to occur in such very unlikely conditions, and the short- and long-term protective actions that constitute intervention. The responsible authorities take the corresponding actions on the advice of the operating organization and the regulatory body.

4.4.2 Objectives and Scope of Defense in Depth

Defense in depth is a rational response to uncertainties associated with the design construction and operation of a nuclear power plant.

Since nuclear power plant accidents are extremely rare events, empirical uncertainties exist about how the plant and its safety architecture will actually respond to certain challenges. In part, because of those uncertainties, overlapping levels of safety intentionally provide margin in addition to that which is likely to be needed to respond to a plant upset. In some respects, Generation IV designs will present significant new uncertainties that, from both a design and a regulatory point of view, will require defense in depth that will be set up in ways that have not been seen before.

In this context, one specific challenge for Generation IV systems is to develop an approach to defense in depth that is both consistent with the successful practices that have been used in operating reactors and that makes use of the improved analytical methods that have come to be available, the objective being the identification and the sizing of design provisions in such a way as to cost-effectively optimize the value of that defense in depth. For Generation IV systems, the goal will be to apply defense in depth in a manner that explicitly takes into consideration uncertainties based on their systematic assessment. The ideal outcome will be a design that optimizes both capital costs and safety by applying defense in depth where it will have the desired effect, but not to “over-design” in a way that adds cost but not safety.

The deterministic and probabilistic considerations have to be integrated into the comprehensive implementation of defense in depth. The notions of “deterministic success criteria” and “probabilistic success criteria” are suggested to help in correctly designing the provisions while fulfilling the requested missions for each DiD level. The performances of these provisions have to be defined in terms of physical performances and required reliability; following these requested performances the provisions have to be – if needed/justified – adequately safety classified. The final goal of this process is the optimization of the whole safety architecture in terms of performances, reliability, and costs.

Other complementary and essential characteristics that help improving the whole safety level, ensuring the effectiveness of the defense-in-depth concept, optimizing the risk-informed implementation, and easing the safety demonstration are as follows:

- An exhaustive defense, that is, the identification of the risks, which leans on the fundamental safety functions, should look for exhaustiveness; the identification of the corresponding scenarios to be retained to design and size of the safety architecture provisions must be as exhaustive as possible.
- A graduated, progressive defense; without that, “short” sequences can happen for which, downstream from the initiator, the failure of a particular provision entails a major increase, in terms of consequences, without any possibility of restoring safe conditions at an intermediate stage. (It is worth noting that graduate and progressive defense is an efficient means for investment protection.)
- A tolerant defense: no small deviation of the physical parameters outside the expected ranges can lead to severe consequences (i.e., rejection of “cliff edge effects”).
- A forgiving defense, which guarantee the availability of a sufficient grace period and the possibility of repair during accidental situations.
- A balanced or homogeneous defense, that is, no sequence participates in an excessive and unbalanced manner to the global frequency of the damaged plant states.

The application of these principles has to lead to an architecture leaning, as much as possible, on a “simple” design and uncomplicated conditions of exploitation (operation and maintenance) in normal and accidental situations.

4.5 Safety Approach for the SFR to Address the Severe Plant Conditions

Coherently, with the requirements related, in general, to the defense in depth and, in particular, to the fourth level of the DiD, this section addresses the consideration of the severe plant conditions, for this has a major impact on the reactor design. In these conditions, two safety strategies are possible to address the treatment of these conditions:

- The first strategy tries to use and develop the favorable characteristics of the SFR (e.g., large thermal inertia) to “practically eliminate” the occurrence of scenarios leading to the generalized core melting. For that purpose, it is necessary to provide a robust demonstration of such elimination. This demonstration should allow balancing the lack of feedback experience by the rigorous consideration of the principles of defense in depth with, in particular and nevertheless, the consideration of severe plant conditions characterized by situations with core degradation of lower amplitude.

- If it is impossible to develop a design allowing to eliminate all the situations that can lead to the generalized core damage, coherently with the fourth level of the defense in depth, a certain number of representative sequences leading to degraded states that can go until generalized core melting will be identified to design, size, and implement provisions allowing to master and mitigate the consequences.

The design studies and the current R&D are realized according to these two strategies (including the search for cores design with intrinsically favorable safety characteristics). Their results will allow determining which strategy is the best adapted and compatible with the implementation of the envisaged technical solutions.

It is indeed necessary to consider, from the early phases of the reactor design, if the SFR has to be conceived by taking into account the consequences of situations with whole core degradation, or if it is feasible to envisage a design allowing not having to consider the consequences of such whole core melting situations.

It is worth noting that the second strategy, with the consideration of whole core degradation, is coherent with the fundamental principles which have been the base of the safety approach retained for the EPR; the design of the latter, as a supplement to a substantial effort for the prevention of the accidental situations, takes conventionally into account severe plant conditions with the whole core melting. The strategy is also coherent with the feedback experience of the SPX2 project, for which the improvement of the prevention effort did not allow not to have to consider such situations.

Having said that, one can conclude that the success of the first strategy (i.e., practical elimination of the whole core melting) supposes an effort of prevention larger than those implemented for the SPX2 and EFR (and formally, higher of the one implemented for the EPR), and this as well as regards the selection of technical options, and as regards the robustness of the demonstrations that validate the implementation of these options.

For the moment, awaiting the results of the engaged R&D, it is the strategy that supposes the generalized core melting, which is retained and developed hereafter.

Besides, independent of the selected strategy (i.e., taken into account or not the situations of whole core melting), for a limited number of initiating events, sequences, or situations, whose consequences cannot realistically be covered by the design, the demonstration of their “practical elimination” will be brought by a specific method, appropriate to each single selected situation (➤ Sect. 4.5.3).

4.6 SFR: Safety Demonstration vis-à-vis of the Whole Core Melting

This section addresses the details of the strategy that consider the whole core melting.

The approach to address such accident leans on both the robustness of the prevention, the management, and the mitigation of its consequences, and especially on the efficiency of the confinement of dangerous materials. It is useless to say that the consequences’ management and mitigation rest on the mastery of complex phenomena in particular for the first phases of the accident.

The improvement of the safety demonstration with regard to the SFR of the previous generation (Creys-Malville and EFR essentially) is thus based on:

- The consideration of the feedback experience from the previous SFR, for example, for the identification of significant initiators and sequences, and from the improvements already achieved on other types of reactor, notably on the EPR.

- A significant effort to reinforce the prevention of the occurrence of whole core melting situations. The approach adopted for the EFR (e.g., third level of shutdown) is kept for the SFR with ways of progress detailed in ➤ Sect. 4.5.1.
- The consideration, coherently with the defense in depth, of severe plant conditions with generalized core degradation. The important way of progress with regard to the EFR is an improved mastery of the consequences through the development of a design aiming simultaneously at the decrease of the mechanical energy released during the accident and favoring the control of the uncertainties associated with the complex phenomenology which characterize the accident progression (➤ Sect. 4.5.2).
- The practical elimination of initiators, sequences, or situations by means of an adequate design and demonstration (➤ Sect. 4.5.3).

The safety demonstration for the SFR will benefit from positive aspects of the technology such as the capability to evacuate the produced heat by natural convection, the significant margin with regard to the sodium boiling, the favorable character of the concept toward the radioprotection concerns, the low pressure within the primary circuit and, in particular for the concept of pool reactor, the important thermal inertia, etc.

The selection of innovative options will have to take into account the specific issues related to the fast reactor technology in general or specifically related to the use of sodium as primary coolant. According to the feedback experience, several issues deserve a particular attention:

- The core is not in its most reactive geometry.
- The draining of primary coolant from the core (i.e., the sodium voiding) can lead to the introduction of positive reactivity (it is the same in case of disappearance of the core structural materials).
- Some safety characteristics are degraded if the fuel is strongly loaded with minor actinides.
- The power density could be high.
- The core is sensitive to certain types of external hazards (shakings).
- The sodium reacts with the water and the air; the reaction leads to releases of energy which can be violent, as well as a production of hydrogen during the reaction with the water. Besides, in case of fire, the created sodium aerosols present a risk of chemical toxicity and can make difficult the interventions (loss of visibility).
- The opaqueness and the temperature of the liquid sodium make difficult the inspection of the internal structures.
- Although for certain components the design can anticipate and ease the maintenance/repair intervention (for example, certain components can be drained away), the interventions or the palliatives measures on sodium circuits and components in postaccidental situation remain difficult,
- The duration of the fuel subassemblies downloading is longer than on a LWR, and this can have an impact on the management of certain accidental situations.

These specificities have to be considered for both the pool and the loop reactor types.

The human factor will be considered so as to minimize by design its possible impact, as well from the viewpoint of the risks of initiating an accident and during the accident progression.

4.6.1 Prevention of Whole Core Melting Situations

The objective is to set up a set of provisions to assure a very high level of prevention of sequences susceptible to degenerate into situation of whole core melting. The application of the principles of the defense in depth drives the approach for the definition and the implementation of these provisions. Probability studies will come to confirm the meeting of the requested level of prevention.

Quantitative Probability Objectives

For the SFR, within the framework of the strategy with consideration of the whole core melting, the objective for the core melt frequency (CMF) is roughly 10^{-6} (x reactor year) for the risks related to the internal events (same objective as for the EFR project).

Implementation of the Provisions for the Accident Prevention

Each of the sequences which can lead to a situation of whole core melting shall be made extremely unlikely. Besides, one should look for a level of balanced risk, reducing and equilibrating the worth of the dominant sequences.

Beyond the necessary measures, to meet the probability objective (10^{-6} x reactor year, for internal events), additional measures should be looked for and selected, based on an objective of reasonable and homogeneous minimization of the risk (ALARP).

To complete the demonstration of prevention, and according to the practices of the safety analysis, a set of envelope situations will be considered, independent of their expected frequency of occurrence.

Among these envelope situations, for example, for the EFR, there is the total loss of the offsite power, some unprotected sequences for which the failure of the shutdown system is arbitrarily postulated, the subassembly melting (resulting, for example, from a blockage) and the sodium leakages, even if they are prevented by specific design options (as, for example, the double envelope design).

This has to be translated into requirements and criteria in terms of allowable kinetics and amplitude for the transients and phenomena susceptible to tackle the safety functions, which have to be considered.

Axes of Improvement

With regard to the EFR, the possibilities of improving the prevention has to be examined, in particular as regards: the covered domain, which has to be as exhaustive as reasonably feasible, the improvement in mastering the uncertainties, the check of the existence of sufficient margins toward cliff edge effects, and the minimization of potential for common modes.

The evaluation of the options selected for the prevention has to systematically consider their global impact on the installation. In particular the designer has to privilege

- The solutions that would be independent, as much as feasible, from the scenarios.
- The forgiving solutions, in particular, those favoring the design which offers grace periods for possible corrective actions and which leave possibilities of repair.

4.6.2 Whole Core Melt Situations: Consequences' Control and Mitigation

A limited number of situations with whole core melting are considered to conceive and size the provisions needed to control and mitigate the corresponding consequences.

Implementation of Provisions Allowing Mastering the Consequences of the Whole Core Accident

With regard to the previous SFR, the important way of progress, resulting from the improvement of the knowledge and the experience feedback, lies on the implementation of provisions allowing to better control and mitigate the consequences of selected situations with generalized core degradation, and to provide a robust safety demonstration of their effectiveness. The innovation in this domain could go up to the partial or total suppression of some of the unfavorable characteristics of the SFR cores.

For that purpose, the designer should identify, as exhaustively as feasible, the sequences which can lead to the core degradation and the corresponding phenomena. Once the sequences are identified, adequate provisions have to be set up to guarantee that the corresponding consequences are correctly controlled and mitigated. For these situations, the designer should try to reduce the possible release of mechanical energy, on one hand, by reducing the risk of sharp insertion of reactivity and, on the other hand, by improving the control and the management – as far as feasible – of the interaction between the liquid-sodium and the melted fuel.

The structures which guarantee the confinement of dangerous materials, and the specific systems which achieve the safety functions during the selected situations, will be sized not only to cope with the loads inferred by these situations, but also for more severe loads, searching for possible threshold effects and trying to identify and correct – as far as feasible – residual weakness.

The approach consists then in:

- Identifying the phenomena involved by the accidents (in particular, those who are going to affect the amplitude and the kinetics of the reactivity effects/insertions) and to adapt the design so that, in an intrinsic way, their consequences are minimized and any cliff edge effects avoided.
- Acquire a detailed knowledge of the scenarios and the involved phenomena. This will, in particular, allow to control and minimize the mechanical energy susceptible to be released.
- Conceive the confinement by making it as robust as feasible and by identifying and correcting the weak points (notion of “homogeneous confinement”).
- Set up provisions allowing guaranteeing the long-term confinement and cooling of the melted core.

Main Phenomena Which Can Lead the Release of Mechanical Energy

The release of mechanical energy, the consequences of which should be minimized, result from phenomena susceptible to sharply insert positive reactivity, namely

- The draining of the sodium from the core region (sodium voiding). This insertion of positive reactivity is compensated during the accident by other effects: thermal counter reactions (for example, the Doppler effect linked to the fuel temperature increase, the expansion of the structures, etc.) followed, if the fuel melt happens (linked to the kinetics and the amplitude of the reactivity insertion) by the counter reaction related to the fuel dispersal.
- The movements of the fuel when it begins to melt. According to the scenario of the accident, these movements can occur inside and/or outside the fuel elements, before and/or after the

clad rupture/melting. The fuel design has to look for the reduction of the risk of centripetal movements of the fuel leading to its compaction and, on the contrary, has to favor the fuel dispersal.

- The movements of the melted steel from the core structures away from the core region. This effect (positive reactivity insertion), which can be very important and significantly higher than the sodium voiding effect, happen during the accident. The core and fuel element's design has to favor the heterogeneous behavior of the melted structures both from spatial and temporal point of view in order to "dilute" the reactivity injection
- The gravitational compaction of the melted core. As recommended for the management of the melted steel movements, the core and fuel element design has to favor a heterogeneous behavior and movements of the melted core both from spatial and temporal point of view. More generally, the designer should look for provisions allowing guaranteeing the quick and controlled core relocation and the achievement and the preservation of subcritical configurations for the melted core.

As already indicated, during the accident progression, a mechanical energy release can also result from the interaction between the liquid sodium and the melted fuel.

A particular attention has to be paid for the case of core bearing minor actinides for which some parameters which have an impact on the progress of the accident could be degraded.

Radiological Consequences

For the whole core melt situations, the objective for the SFR should at least be equivalent to that of the EPR for which, for these situations, *"the associated maximal conceivable releases require only protective measures of the populations very limited in terms of affected area and of duration."*

4.6.3 Initiating Events, Sequences, and Situations "Practically Eliminated"

When the risk associated to an initiating event, a sequence, or a situation is considered as unacceptable, provisions have to be implemented to make this risk acceptable. This is realized:

- First and foremost, by the implementation of provisions allowing to handle the initiator, the sequence, or the situation coherently with the design requirements and to guarantee the consequences management and mitigation (i.e., bringing the initiator, the sequence, or the situation within the extended design domain).
- If this is not feasible and if it is considered that it is not reasonable to look for the consequences management and mitigation, the designer should implement provisions for which the requirements are defined on a case by case basis, and which shall allow guaranteeing their "practical elimination." The demonstration of the "practical elimination" of the initiator, the sequence, or the situation shall be sufficiently robust to justify the fact that their consequences management and mitigation are not addressed by the design. The approach justification can lean on strategies similar to those used for the EPR, in comparable cases

Among the situations not covered by those retained by the design, and for which the experience feedback allows to envisage their "practical elimination," one can find, for example, the collapse of the core support structures, the sharp core draining due to the passage of a large bubble of gas of large volume, and the excessive compaction of the core. For these situations, the justification "practical elimination" will lean first and foremost on particular measures of prevention taken in the design (including the necessary measures for the plant operation).

These initiators, sequences, and situations will be identified as exhaustively as feasible since the early phases of the design and the corresponding measures to guarantee their “practical elimination,” immediately defined.

4.6.4 Control and Management of the Safety Functions

Below, some guidelines are given to exploit at best the experience feedback from previous studies and realizations. These guidelines should allow to define the technical options to be selected to realize the main safety functions, on one hand to prevent the occurrence of situations of whole core melting and, on the other hand, to control and mitigate the consequences.

Reactivity Control

Among the means allowing guaranteeing the reactivity control, one can quote:

- Shutdown systems. These systems will be conceived so as to assure their mission, with the due reliability, without requiring any source of power. In particular, in case of confirmed loss of power (some seconds), the shutdown of the reactor will be achieved in an intrinsic way by gravitational insertion of the absorber elements.
- Globally negative coefficients of counter reaction.
- Provisions allowing the “practical elimination” of initiating events, sequences, or situations that will lead reactivity insertion, for which the shutdown systems, and/or the counter reaction coefficients, would be insufficient to avoid unbearable releases of mechanical energy vis-à-vis of the confinement barriers.

In the Creys-Malville plant and for the EFR, two redundant and diversified shutdown systems were set up. Whenever an emergency shutdown was necessary, it was generally initiated by the detection of two distinct characteristics that typify the feared event (e.g., in the event of an LOF, a reduction of primary coolant flow and an increase in sodium temperature at the fuel assembly outlet). Further diversification was also provided by passive measures (or active measures if these are effective, yet diversified and reliable) that amplify natural counterreactions (e.g., for the EFR, measures identified as part of the “third-level shutdown” concept, such as those conducive to control rod expansion, etc.).

Further reinforcement is possible at this level, essentially to improve the reliability of the measures used to detect abnormal states. This should be achieved by finding systems that are capable of detecting variations in parameters that typify damage to the installation, rather than variations in parameters related to a given accident scenario. For example, one need to find a reliable and high-performance system that can detect sodium boiling, should it occur.

In the event of core meltdown, reactivity is controlled by fuel dispersion and relocation and a core geometry that keeps it subcritical. This implies that the structure that will receive the molten core in the long term is designed to ensure it remains subcritical (sufficient spreading and dilution of the molten core catcher). It is also essential that the entire route taken by the fuel, from the initial position to the final position, does not enable it to reach any critical status that might lead to a major release of mechanical energy.

Decay Heat Removal

The decay heat removal has to be assured in all the plant conditions, to avoid the occurrence of situations of core melting and, if this happen, to guarantee the cooling and the stabilization of

the degraded core. This mission has to be guaranteed over a lapse of time compatible with the needs to preserve safe configurations.

The accidents that could lead to the prolonged total loss of this function should be “practically eliminated.” This will lean in particular on the capability of circuits, including primary circuit, to evacuate the residual power in natural convection, as well as on the minimization of the risk of common mode failure of the provisions which realize the function.

In large-scale reactors such as that of the Creys-Malville plant and the EFR, decay heat is essentially removed by way of sodium loops. Despite the wide range of systems, their high level of redundancy and their capacity to operate in natural convection mode, improvements remain possible especially considering that:

- Few corrective actions can be carried out to counter any failure or human error – the systems are difficult to repair in accident situations and there are few ways of limiting damage other than those repairing faulty systems and refilling with sodium.
- There is a potential for common mode failure, given the fact that the systems lead into the vessel and exit it via the slab to release heat into the atmosphere. Therefore, any fault in the slab may have a knock-on effect to the systems. In the same way, a core meltdown accident could damage all of those parts of the various systems that pass through the reactor vessel.

Improvements that would address these items will make the function more robust and the corresponding safety case, therefore, more convincing, for example, by developing decay heat removal systems that use a fluid that is easier to handle than sodium and that minimize the risks of common modes in certain areas. (Finding an alternative fluid to sodium to evacuate residual power is particularly important, given how long the corresponding systems are in operation for (several months in the case of the EFR). The objective is to significantly increase the reliability of the system, with greater scope for repairs.)

The possibility must also be examined of setting up an entirely diversified system for the long-term cooling of a molten core.

The efficiency of the provisions will also be verified for minor actinides bearing cores which have a higher residual power.

Confinement of Radioactive and Harmful Materials

The confinement of the radioactive materials, and more generally harmful materials, is assured during all the normal and accidental situations, considering the possible failure of the implemented barriers.

Concerning the guidelines for the confinement (limitation, control of the radiological releases, protection of the safety functions against internal and external hazards), the strategy is to retain the same objectives as for the EPR. Accident sequences involving core damage and spurious containment bypass must be “practically eliminated.”

In order to avoid weaknesses, the possibility must be examined of setting up a double containment barrier system, whereby the second barrier would catch any leaks from the first barrier in the event of a core meltdown accident. Such a system would be all the more appreciable given that the first of the two barriers could, in an accident scenario, be exposed to high loads.

For the situations with whole core melting, measures of confinement will allow to avoid unacceptable radiological releases in order to guarantee the need for “*protective measures of the populations very limited in terms of affected area and duration.*”

4.6.5 Other Specific Risks

Sodium Fires

The risks of sodium leakages and the consecutive fires shall be taken into account in the design.

The risks, in case of sodium leakage, concern mainly the aggression of the confinement: pressure and temperature increase due to the fire and production of hydrogen in the presence of water (steam released by the concrete). The risk of aggression for the systems which achieve the other safety functions should also be considered; the consequences' control and mitigation will be guaranteed by the redundancy and the physical separation of the concerned systems.

In the Creys-Malville plant and for the EFR, minor fires in the sodium primary coolant are avoided by systematically using a second shroud containing an inert gas. For more severe accidents, sodium fires on the base slab are taken into account. Secondary cooling systems, however, are surrounded by a simple air shroud.

One possible way of improving safety would be to eliminate these risks by design, in all areas where they might affect safety functions, for example, by placing all critical systems in gas atmospheres that are inert in the presence of sodium, protecting the concrete and ruling out the presence of water in these areas. Having these systems in inert gas atmospheres would also make them harder to access during operation, thereby also minimizing the risk of malicious acts.

Finally, the sodium aerosols released during the fire could degrade the safety functions, in particular by making difficult post-accidental actions. They potentially represent an aggression for the operators, the environment, and the population. Provisions shall be implemented to minimize their impact.

4.6.6 Hazards

The main risks, in case of hazards, are the initiation of accidents and the unacceptable degradation of the provisions implemented to achieve the safety functions; the design of the reactor and the selection and sizing of these provisions should minimize their sensitivity vis-à-vis of these hazards.

The hazards will be defined and characterized according to an approach similar to that adopted for the EPR. The specific risks for the sodium technology (e.g., the potential for core compaction and the possible wave's effects at the free surfaces of sodium) shall be addressed.

4.7 R&D Organization

Given the analysis developed in the previous paragraphs, it is suggested that there be three main lines of R&D:

- Identification of the measures enabling integration of experience feedback on SFRs, with specific actions laid out for the various safety functions and acknowledgment of the risks inherent in sodium.
- Actions to strengthen core meltdown prevention, including the identification of measures that could make each sequence leading to this scenario highly unlikely. In particular, the aim

of these actions is to “practically eliminate” accidents that could lead to consequences that are difficult or impossible to control using the selected measures.

- Actions that give a stronger demonstration of the capacity to manage deteriorated core situations, and show robust containment as regards typical accidents (UTOP, ULOF) and their associated phenomena:
 - Identification of measures to “practically eliminate” those accident phases likely to lead to major releases of mechanical energy.
 - Simplify the safety case and improve robustness where necessary by suitable means (e.g., core and internals design, including the core catcher).
 - Check that the consequences of interaction between sodium and the molten fuel remain tolerable.
 - Optimize the design of those reactor structures that contribute to safety functions in degraded situations, finding and eliminating the potential weaknesses as regards mechanical energy releases and radioactive product containment.

4.8 Conclusions

The objective of this chapter is to set out the principles and objectives in terms of nuclear safety that would apply to a SFR of fourth generation.

The principles and the general objectives established for the EPR and the adoption and the application of the principle of the defense in depth guarantee a very high level of protection and are thus retained for the SFR.

The principles and objectives are set out focusing and dealing, as a matter of priority, with severe plant conditions which, coherently with the defense in depth, have to be considered by the design.

The chapter considers the possibility of developing a concept that practically allows eliminating the occurrence of a generalized core degradation by limiting the severe accident considered within the design to a limited core degradation, but, waiting for the results of the engaged R&D, its contents focus on the treatment of the whole core accident situations.

As for the safety demonstration, it will lean on the following:

- The consideration of the specificities related to sodium cooled fast neutrons reactor (taking into account the experience feedback and the risks specific to the technology).
- The prevention of occurrences such as the situations of whole core melting: the design will make highly improbable all the identified sequences that can lead to it.
- If the design innovations allow it: the elimination of the risk of severe and generalized core damage.
- Otherwise, the control and the mitigation of the consequences of initiators, sequences, or situations that lead to the whole core melting, and the implementation of a robust and homogeneous confinement. In this context, the designer should look for the possibility of designing innovative core with safety characteristics more favorable compared to those of the previous SFR.
- The “practical elimination” of initiators, sequences, or situations, the consequences of which are considered unacceptable.

The integration of these items within the SFR design effort is going to allow identifying and organizing the corresponding R&D effort.

5 The Materials

5.1 Fuel Materials

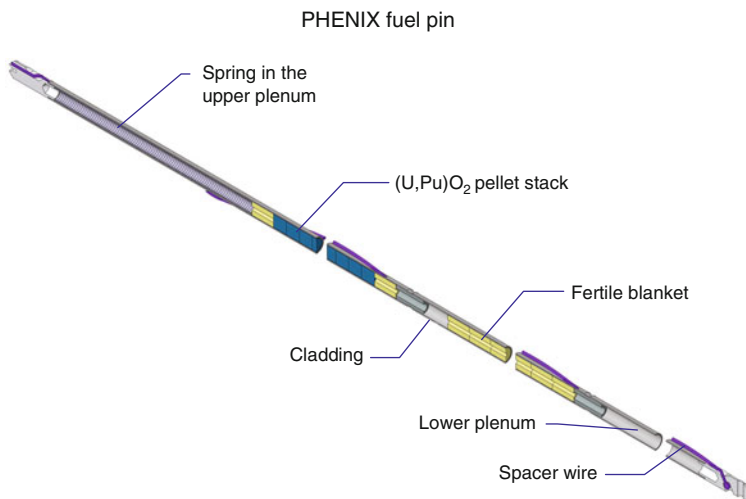
5.1.1 Oxide

Fuel Element Characteristics

The Fuel pin of a SFR is composed of several elements (► [Fig. 104](#)):

- A cylindrical cladding, closed at both ends by welded plugs, prevents direct contact between fissile material and sodium coolant. The cladding serves as a first safety barrier and was designed to keep its integrity in nominal and off-normal operations.
- A fissile column consists of a stack of fuel pellets whose outer diameter is chosen to provide an initial gap (a few hundreds of microns) between the fuel and the internal diameter of the cladding. The most widely used fuel is the mixed uranium–plutonium oxide: $(U, Pu)O_2$. Depending on the irradiation conditions, pellets are designed without initial central hole (case of Phénix) or as annular pellets (case of SuperPhénix).
- One or two axial fertile blankets are fabricated with depleted or natural uranium oxide UO_2 .
- Two free volumes (gas plenum) are located on both sides of the column and initially contain helium gas under 1 bar pressure. The main purpose of gas plena is to accumulate fission-gas products released during irradiation and limit the internal pressure below a few dozen bars,
- Other internal structures are added such as braces to support the fissile columns and a spring located in the upper plenum to keep the pellet in place before and early in the irradiation.

The main characteristics for Phénix and SPX1 fuel pins are provided in the following (► [Table 21](#)).



■ **Figure 104**
Typical SFR Fuel Pin

■ Table 21

Main characteristics for Phénix and SPX1 fuel pins

	Phénix (standard)	SuperPhénix
Outer cladding diameter (mm)	6.55	8.50
Cladding thickness (mm)	0.45	0.565
Cladding material	CW 15-15 Ti	CW 15-15 Ti
Outer pellet diameter (mm)	5.42	7.14
Inner pellet diameter (mm)	–	2
Plutonium enrichment: Pu/(U + Pu) (%)	20–28*	15–22*
O/M (M = U + Pu)	1.97 ± 0.02	≥1.96 < 2.00
Fuel fabrication density (%TD)	95.5	95.5
Fuel smear density (%TD)	88.1	82.5
Fissile column length (mm)	850	1,000
Lower fertile column length (mm)	300	300
Upper fertile column length (mm)	–	300
Fuel pin length (mm)	1,793	2,700

* Orders of magnitude for internal and external core.

TD: theoretical density.

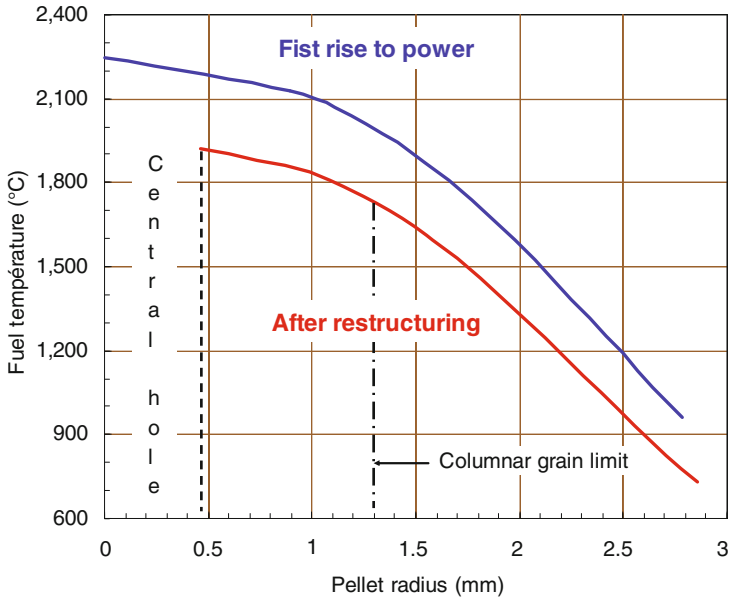
Irradiation Conditions in Nominal Operation

The SFR core is characterized by a rather low height over diameter ratio (H/D) compared to PWR. Therefore, the axial profile for neutron flux, power density, and linear heat rate (LHR) is well pronounced with a $\Phi_{\max.}/\Phi_{\text{mean}}$ ratio of about 1.2–1.3.

The LHR depends on the radial position of the fuel subassembly in the core but also on the depletion of fissile material with the burnup. In standard SFR core, the fuel power roughly decreases continuously at constant neutron flux, with a rate depending on the initial plutonium enrichment. The cladding nominal temperature, on the top of the fissile column is between 893 and 923 K for an inlet sodium temperature in the assembly of about 663 K.

Temperatures in the Fuel Element

Thermal Conductivity of Mixed Oxide Fuel The thermal conductivity is a crucial property of a nuclear fuel and determines the temperatures when the linear heat rate and the surface temperature are known. Uranium–plutonium mixed oxide fuel, like most oxides ceramic, features a low thermal conductivity. Most of measurements carried out on mixed oxide with plutonium content between 15 and 30% do not exhibit a significant plutonium content dependence. In contrast, the thermal conductivity depends markedly on oxygen content O/M: a slight deviation from the stoichiometric composition (O/M = 2.00) leads to a major thermal conductivity decrease. Under irradiation, the evolution of fuel microstructure (cracks formation, porosity change, restructuring process, formation of a central hole, etc.) also tends to reduce the thermal conductivity. Accumulation of soluble fission products (in metallic or oxide phases) during irradiation affects thermal performance at high burnup.



■ **Figure 105**
Fuel temperatures prediction in a PHENIX fuel pin

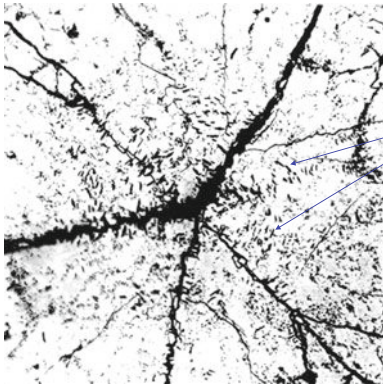
Heat Transfers into the Fuel Element Heat generated in the oxide fuel by the slowing down of fission fragment is transferred by conduction in the fuel itself, by conduction and radiation in the fuel pellet/cladding gap and by conduction in the cladding thickness to be finally evacuated by the sodium coolant. ▶ *Figure 105* shows an example of radial temperature distribution in a PHENIX fuel element at the beginning of life (start-up – blue curve) and after fuel restructuring (after a few days – red curve). The importance of the thermal barrier constituted by the fuel pellet/cladding gap should be noted: at start-up, the temperature jump in the open gap filled with helium, can reach about 673 K.

Beginning of Life Phenomena

Phenomena Occurring During the First Rise to Power $(U, Pu)O_2$ ceramic has a brittle mechanical behavior at low temperature ($T < 0.5 T_{\text{melting}}$, i.e., up to 1,473–1,573 K) but becomes viscoplastic at higher temperature. Consequently, during the first power rise, axial and radial cracks are rapidly formed because of the strong temperature gradient.

Very quickly, equiaxed grains (size: $\sim 10 \mu\text{m}$) grow in the fuel area where the temperature is higher than $\sim 1,573$ K. In addition, it is observed a migration of the intragranular porosity and a coalescence of this porosity at grain boundaries. The resulting fuel swelling leads to a macroscopic expansion of the pellet fragments and contributes to reduce the fuel/cladding gap.

The most striking phenomenon in a SFR oxide fuel is the formation of elongated grains (columnar grains), which move toward the center of the fuel pin by the so-called sublimation–condensation process and form a large central hole. This mechanism occurs in the region where temperature exceeds $\sim 2,173$ K. Above that temperature, high values of vapor pressures of uranium and plutonium compounds play a major role in this restructuring process (▶ *Fig. 106*).



Lenticular pores will develop from the manufactured porosity but also from the voids created into the central area of the pellet by its initial cracking.

These lenticular pores, by migrating toward the centre, “sweep up” the porosity and leave behind elongated grains denser than the original ones.

■ Figure 106

Beginning of fuel restructuring – migration of the porosity toward the pellet centre

Lenticular pores will develop not only from the manufactured porosity but also from the voids created into the central area of the pellet by its initial cracking.

These lenticular pores, by migrating toward the center “sweep up” the porosity and leave behind elongated grains denser than the original ones.

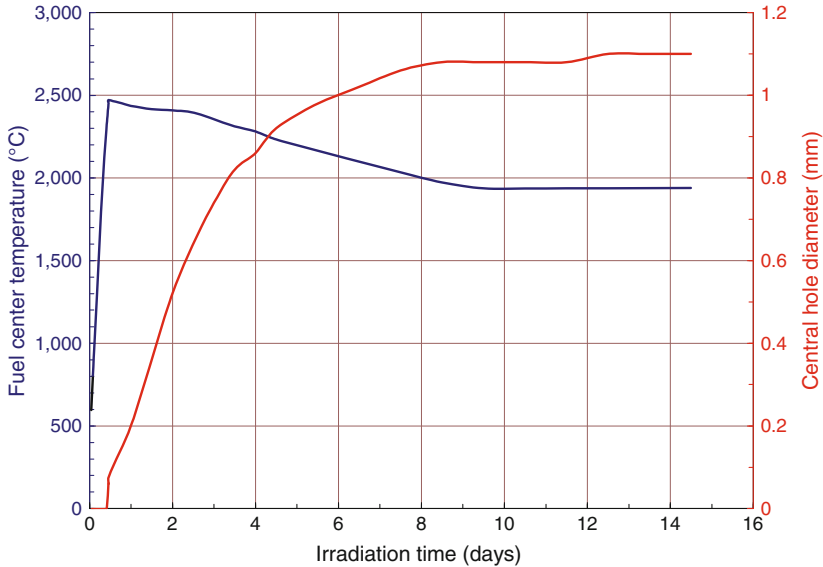
Consequences of These Structural Changes In addition to the fuel microstructure modification, a radial redistribution of oxygen, uranium, and plutonium occurs.

- Oxygen, by thermodiffusion in solid and gas phases, is rapidly transferred from the hot center of the pellet to the cold periphery. Oxygen migration creates a radial distribution in the local oxygen potential and, of course, locally influences the thermal conductivity.
- At high temperature, a mixed oxide fuel with an O/M ratio greater than 1.92 is characterized by a gas phase more enriched in uranium (UO_3) than plutonium. As previously mentioned, the sublimation–condensation process in the enriched uranium vapor is responsible for the motion of lenticular pores. This process probably combined with a diffusion mechanism in the solid phase also contributes to significant plutonium enrichment in the hot part of the pellet, near the central void.

In the case of annular fuel (SuperPhénix manufacturing for example), the same mechanisms may occur. However, at comparable LHR, the maximum temperature in an annular fuel is smaller by 200–300 °C than in a solid fuel pellet. Thus, restructuring processes in an annular fuel is usually less pronounced and only cause a small increase of the initial hole radius.

The second effect of this fuel transformation is the fuel/cladding gap closure. The kinetics of this phenomenon is faster when the local power is high. Thus, the gap closure occurs in the first place at the axial position where the LHR is maximal and then gradually extends to both ends of the fissile column.

The main consequence of the previous mechanisms is an overall decrease of the fuel temperature; gap closure lowers the surface temperature of the fuel by roughly 200–300 °C, while fuel restructuring and associated geometric changes contribute to decrease the fuel center temperature and increase the margin to fuel melting (► [Fig. 107](#)).



■ Figure 107

Calculation, with the GERMINAL code, of the beginning of life fuel centre temperature and the central hole opening for a mixed oxide fuel for a PHENIX fuel element

Phenomena Occurring During the Life in Reactor

Generation of Fission Products The continuous accumulation of fission products (FPs) in a fast reactor fuel affects its physical and chemical properties. These are essentially the FP considered as stable throughout the duration of irradiation which will play an important role on the fuel behavior.

These FPs are customarily classified into five different families according to their chemical state:

- The noble gases (Kr and Xe) with a production yield of about 0.25 atom/fission in a fast reactor spectrum. They are chemically inert, thermodynamically not soluble in mixed oxide and thus, contribute to the fuel swelling
- The metallic inclusion (noble metals such as Ru, Pd, Rh, Tc. . .) which tends to accumulate in grain boundaries. Their total fission yield is about 0.5 atom/fission
- The oxide inclusions (Ba, Zr, Sr) with a production yield of about 0.1 atom/fission
- The fission product in solid solution (mainly the rare earth: Nd, Pm, Ce. . .) with a yield of about 0.5 atom/fission
- The so-called “volatile” FP such as Cs, Te, or I (0.27 atom/fission). During normal fuel pin operation, volatile FP can easily migrate under thermal radial and axial temperature gradients.

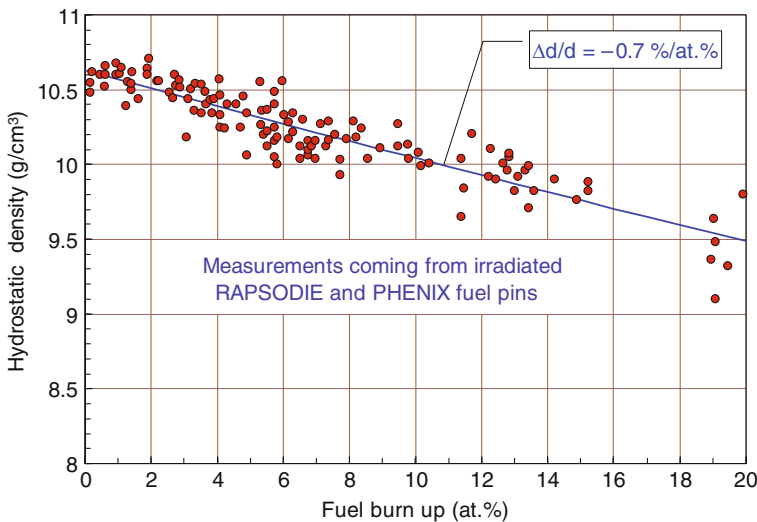
Chemical state of fission products primarily depends on the oxygen potential (ΔGO_2) imposed by the mixed oxide which increases during irradiation. The chemical state of molybdenum, for instance (0.21 atom Mo/fission), changes during irradiation: at low burn up, Mo is mostly transformed into metallic precipitates with ruthenium and palladium, while at high burn up (>10 at.%), it can be found in oxidized compounds such as caesium molybdate Cs_2MoO_4 .

The main effects of irradiation and fission-product accumulation on the fuel properties are the following:

- The melting temperature slightly decreases
- The thermal conductivity also decreases by the combined effects of composition change of the fuel and the accumulation of radiation damage in the lattice
- The oxygen potential tends to increase as demonstrated by measurements made on PHENIX irradiated fuels. This trend is related to the oxidative nature of plutonium fission. The O/M ratio also increases by nearly 0.003/at.%
- The fuel volume increases due to the solid and gaseous swelling

Fuel Swelling The fuel swelling rate versus burnup depends on the physical and chemical FP state. The SFR fuel, because of its very high thermal regime, releases a large proportion of fission gas into the pin free volumes. Fission gas atoms left in the fuel and closed pores are mainly located in the outer part of pellets and contribute to the total swelling. Fission products in oxide phases having usually a smaller density than the mixed oxide will also lower the average density. Thus, measurements on samples from irradiated fuel pins (► Fig. 108) show a regular decrease of the hydrostatic density with an average slope of 0.7/at.%.

Creep mechanisms can accommodate the fuel swelling as long as voids exist in the fuel section (fuel/cladding gap, cracks, porosity, central hole), even if the cladding deforms by swelling and irradiation creep. During operation at full power, mechanical interaction with the cladding (pellet-cladding mechanical interaction PCMI) is often negligible compared to the stress from the fission gas pressure (some MPa). Only in the case of fast power transients, the cladding can experience significant strain level. Experiments showed that the level of cladding stress rarely leads to a permanent plastic strain or a cladding failure.



■ Figure 108

Fuel density change with the burn up of some SFR mixed oxide fuels

Fission Gas Release The behavior of fission gas (FG) is complex. Given their very low solubility in mixed oxide fuel, fission gas atoms will tend to diffuse within the grains and precipitate as intragranular bubbles on structural defects. Then FG will accumulate at grain boundaries to form intergranular bubbles which will gradually interconnect and initiate a release in the open porosities. In nominal operating conditions, the average fuel temperature being high, a large majority of fission gas atoms will be quickly released (see Sect. Fuel Swelling).

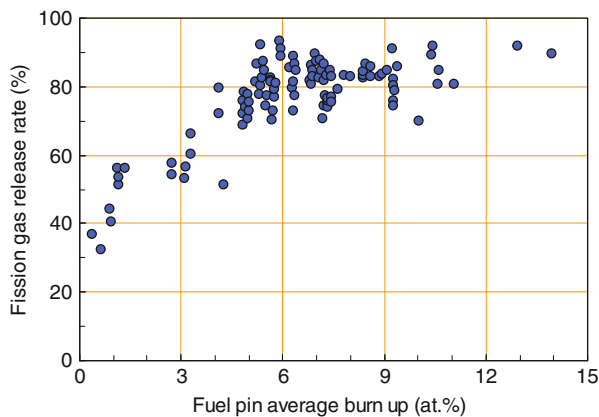
The FG release rate (► Fig. 109) ranges from 30 to 50% at low burn up (<1–2 at.%) and commonly reaches 80–90% at high burnup. Up to about 6–8 at.%, the fuel temperature is the most sensitive parameter. At higher burnup (>8 at.%), the cold part of the pellet, which has accumulated large amount of fission gases, will experience a structural process similar to the high burn up structure (HBS) observed in PWR: the decrease of grain size will favor a thermal release. FG-retention measurements, performed by fuel sublimations and quantitative microprobe analysis in the burnup range 4–12 at.%, have highlighted this FG behavior occurring in the coldest part of the fuel.

Volatile Fission Products Behavior The high temperature of SFR fuel enhances the mobility of volatile fission products such as Cs, Rb, Te, Se, I, or Br. Like fission gases, volatile fission products usually leave the center of the restructured zone and condense in the colder outer area.

At low burnup (<7 at.%), the volatile FP compounds such as CsI, Cs₂Te, and Cs₂(U, Pu)O₄ (caesium-uranoplutonate) species are predominant. At higher burnup, with the increase of oxygen potential, caesium will gradually form caesium molybdate (Cs₂MoO₄).

O/M Ratio and Fuel Oxygen Potential Oxide fuel is chosen slightly under stoichiometric (O/M₀ ~1.97) to control the oxygen potential. However, during irradiation, with the oxidizing effect of fission products, the oxygen potential and O/M increase almost linearly to a value close to stoichiometry at a burnup between 5 and 8 at.%, depending on the initial O/M value.

At low burnup, the fission-product Mo is in metallic form, but, since the free energy of formation of MoO₂ is close to the oxygen potential of a stoichiometric fuel, Mo will gradually oxidize to MoO₂ and stabilize the O/M ratio to a nearly stoichiometric value. The evolution of



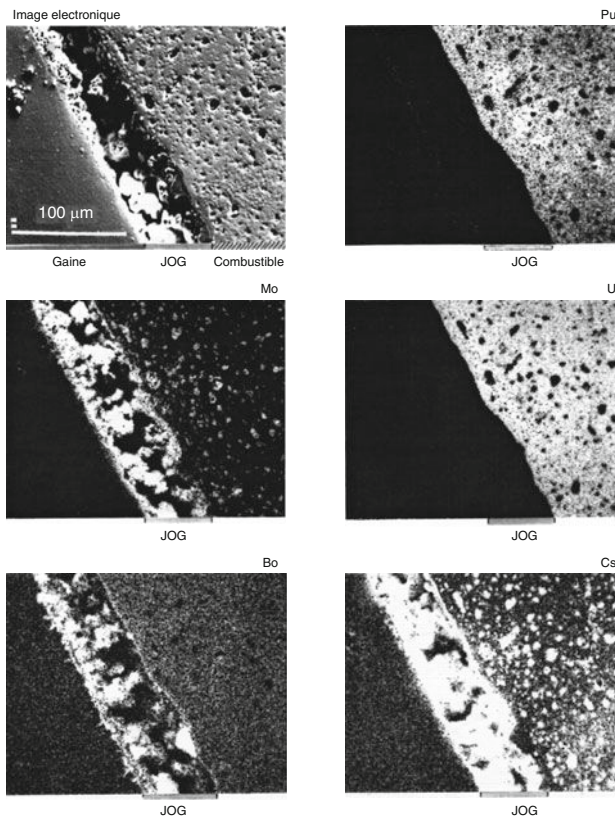
■ Figure 109

Fission gas release rate of standard PHENIX fuel pins according to average fuel burn up

O/M and oxygen potential plays a key role in two important phenomena encountered in the SFR irradiated pins at burnup (>68 at.%): the formation of a joint oxide gain in French (JOG) and the chemical reactions of the fuel with the cladding.

Joint Oxide Gain (JOG) Formation As said before, the high temperature of the SFR fuel favors the migration of volatile fission products such as cesium and tellurium not only from the hot central region of the fuel pellets to the periphery but also to the lower and upper ends of the fissile column. Postirradiation examinations with optical metallographic observations and more precise investigations with SEM and EPMA technique of fuel pins with burnup >7 at.% have identified between the periphery of the fuel pellet and the inner wall of the cladding a layer containing oxidized fission products such as Cs, Mo, Pd, Te, and Ba (➤ Fig. 110). The thickness of this layer, known as JOG, increases with burnup.

Inner Corrosion of the Cladding Most cladding materials tested in the SFR belongs to the family of “austenitic stainless steels” (AISI316 for instance) and nickel alloys. These alloys are characterized by chromium content greater than 12% to provide a chemical protective layer made of chromium oxide.



■ Figure 110
Microprobe analysis of JOG of PHENIX pin irradiated at 14 at.%

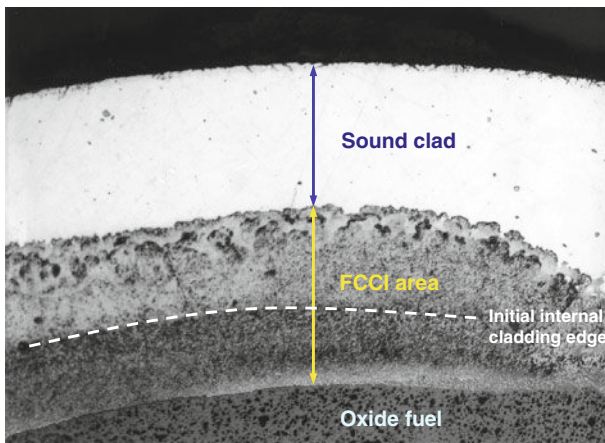
The increase of oxygen potential and the change in the chemical balance of fission product will favor chemical reactions of some FP such as caesium with chromium oxide. Simultaneously, other FP as volatile tellurium and iodine, made free by the association of caesium with chromium or molybdenum (see JOG Formation) can chemically react with the major components (Fe, Cr, Ni) of the cladding.

Fuel cladding chemical interaction (FCCI) usually takes place in the upper half of the column fissile where favorable thermodynamic conditions exist: high temperature and low cladding strain. This FCCI is seen as a localized attack (a few tens of millimeters in height) and affect a fraction or the entire inner wall of the cladding (➤ Fig. III). In other circumstances, FCCI can affect the cladding at the junction between the column fissile and fertile blanket. In these corroded areas, the sound cladding thickness can be significantly reduced (30–40%), and it constitutes an “Achilles’ heel” for the mechanical strength of the fuel pin in normal and accidental operations.

Behavior Under Irradiation of the Cladding The materials for subassembly structures and cladding for fuel pins experience two main kinds of damage during irradiation:

- The temperatures conditions between 673 and 923 K can lead to structural changes such as formation of destabilizing phases, producing a structural tightening with loss of ductility and toughness
- The important fast flux ($E > 0.1$ MeV) causes damages (dpa) in the atomic lattice of metallic materials. In the early stage of irradiation ($< \sim 10$ dpa), damages favor hardening effects (increase in yield strength) with significant losses of initial ductility. At high dose of irradiation (~ 100 dpa), a volume swelling due to the formation of stable cavities may lead to a complete embrittlement of the material (fracture toughness reduced to a few $\text{MPa}\sqrt{\text{m}}$).

The most frequently used cladding materials are the austenitic stainless steels, which have a very good structural stability in the operating range but are characterized by a fast swelling rate after an incubation period (which depends on the grade considered). The titanium stabilized cold



■ Figure 111
FCCI of PHENIX pin irradiated at a very high burn up (16 at.%)

worked steel such as the “CW 15-15 Ti” grade is today the reference cladding material in order to reach maximum doses of about 120–130 dpa with a swelling below 6%.

To reach higher doses and higher fuel burnup, investigations are focused on cubic-centered materials such as ferritic–martensitic steels reinforced by a dispersion of nano-oxides (oxide dispersion strengthened steels). They have a low sensitivity to swelling as it was demonstrated up to 130 dpa for a classical ferritic–martensitic steel (EM12 grade) in the PHENIX reactor. However, some grades may be weakened in the range of low temperatures, resulting in a too high increase of their ductile–fragile transition temperature (DBTT).

To prevent the risk of a cladding brittle fracture, the material needs to avoid excessive embrittlement by the combined effects of temperature and neutron dose, but it is also important to use design methodology that takes into account the evolution under irradiation of mechanical and all the loads that the cladding will experience in normal operating and incidental conditions. These considerations are reflected in the French design rules methodology, which is applied to embrittled materials by irradiation (RAMSES II).

Interaction with Sodium Fuel pins are designed to keep the probability of cladding failure as low as possible. The example of PHENIX reactor is therefore instructive, as the rate of failures requiring the unloading of the failed subassembly is only $5 \times 10^{-5}/(\text{pin} \cdot \text{year})$ despite the presence of many experimental subassemblies and capsules.

Nevertheless, cladding failures have to be properly managed because mixed oxide and sodium are not chemically compatible in a wide range of temperature and stoichiometry. Kinetics of reaction depends on many parameters such as sodium flow rate, oxygen diffusion, and burnup. The sodium-uranoplutonium compound has a lower density by almost a factor of 2 and a lower thermal conductivity compared to mixed oxide (factor of 4). These features are in favor of changing the initial cladding crack into a large breach, which has to be avoided.

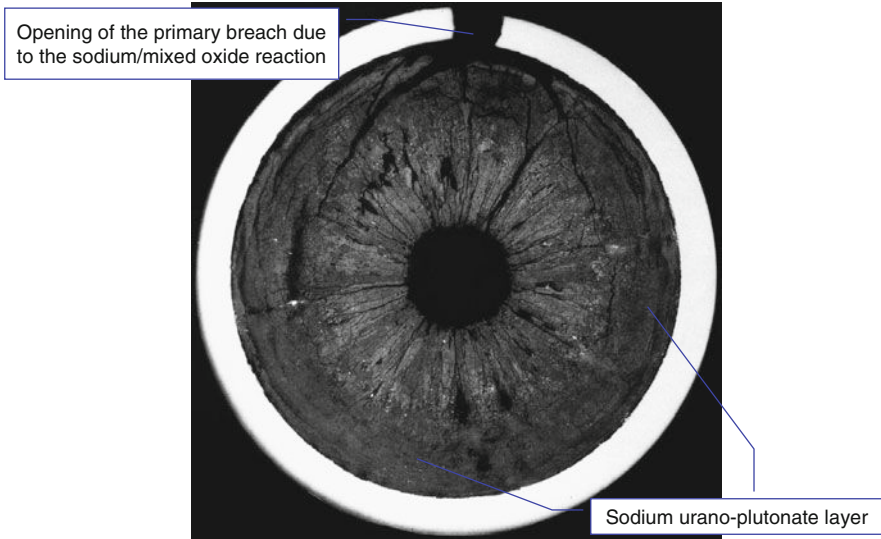
In general, a cladding failure starts with a “primary failure” corresponding to a loss of sealing, which leads to a release of the fission gas under high pressure. This initial phase may be followed by a secondary one due to the development of the chemical reaction between the mixed oxide and the sodium (➤ *Fig. 112*). This second phase must be properly handled by means of gas and DDN (detection of delayed neutrons) detection systems because it would lead to FP and actinides severe pollution of the primary circuit.

Kinetics of formation of primary and secondary failures can be highly variable: from a few minutes to hundred days. However, the main factor that favors a rapid evolution of the breach is the embrittlement of the cladding material by an excessive void swelling or by an intrinsic weakening of the microstructure such as certain Ni alloys (Inconel 706).

Conclusion The numerous irradiation experiments carried out during 4 decades in the French sodium fast reactors Rapsodie and Phénix have significantly contributed to a better understanding of the mixed uranium–plutonium oxide fuel pin behavior in normal operating condition and in case of cladding failure. Despite some negative aspects, oxide fuels still remain the reference fuel for the Gen-IV sodium fast reactor.

5.1.2 Metal

Metal fuel is considered for future SFRs due to its high breeding potential owing to its high metal atom density and hard spectrum and ease of fuel fabrication. Metallic fuels are also amenable for



■ **Figure 112**
Macrograph of a failed fuel pin after the beginning of the second phase

■ **Table 22**
Salient properties of fuel materials

Fuel	Thermal conductivity (W/m-K)	Mass density (kg/m ³)	Breeding potential
Oxide	2–4	10,000–11,000	~1.1
Carbide	12–16	13,500–13,800	~1.2
Nitride	12–16	13,600–14,000	~1.3
Metal	30–35	19,000–20,000	~1.6

advanced reprocessing methods like pyrochemical reprocessing. Compared to oxide, carbide, and nitride fuels, metallic fuels have high mass density, high thermal conductivity, and breeding potential at typical operating conditions (► [Table 22](#)).

Generally, the composition of metallic fuel is a binary alloy of uranium metal and plutonium, the exact composition being decided by the reactor size. However, the melting point of such a binary alloy is lower and also it forms eutectic compounds with clad material at a lower temperature. To overcome this difficulty, normally Zr is added in small quantities either in the fuel matrix (U–Pu–Zr) or as a sacrificial liner around the fuel. The effects of Zr addition in a typical binary alloy are depicted in ► [Fig. 113](#). Also, zirconium improves the chemical compatibility between fuel and the austenitic stainless steel cladding material by suppressing the inter-diffusion of fuel and cladding components.

However, Zr addition reduces the breeding ratio marginally (◉ [Fig. 114](#)). The choice of binary (U–Pu) or ternary (U–Pu–Zr) or binary with a liner (U – Pu + Zr) depends upon the operating temperatures, linear power, and breeding requirements.

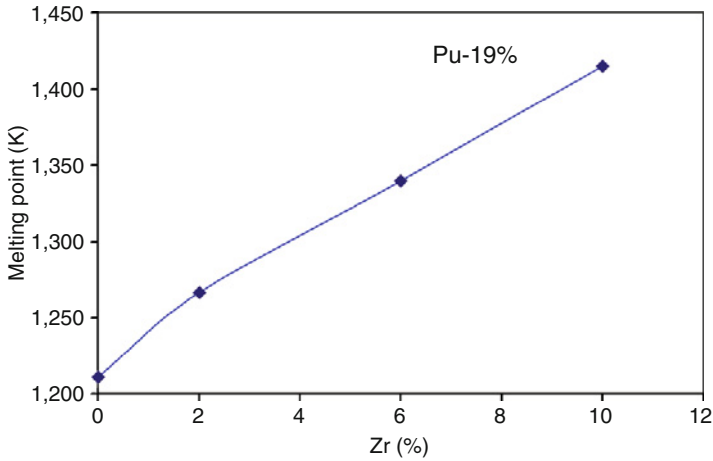


Figure 113
Melting point variation with Zr content

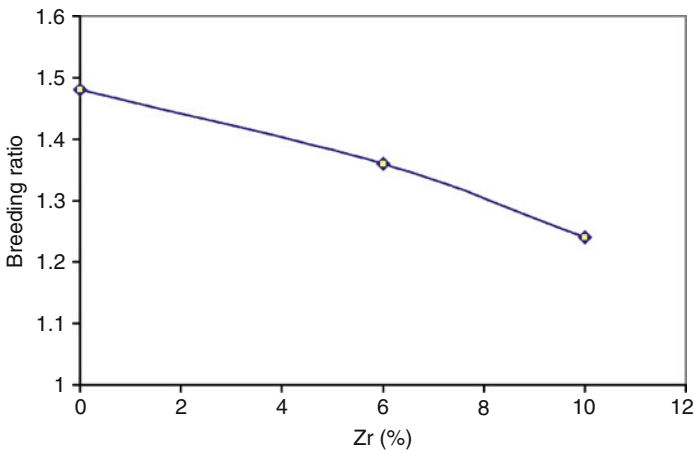
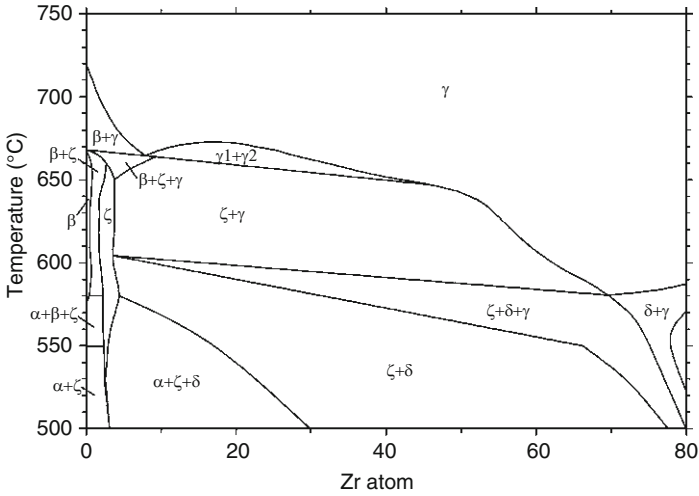


Figure 114
Breeding ratio as a function of Zr content

5.1.3 Properties of Metal Fuel for Design

Phase Diagram

The phase diagram of the U–Pu–Zr metallic fuel is given in [Fig. 115](#) as a function of Zr atom percent constituent. This will be useful in determining the various phase while deciding the fuel composition and their implications during its operating condition.



■ Figure 115
Binary (U-Pu)-Zr phase diagram (Pu at 19 wt%)

Density

Element	Density (ρ), g/cc	Atom fraction
U	19.1	$X_U = 1 - X_{Pu} - X_{Zr}$
Pu	19.816	X_{Pu}
Zr	6.5	X_{Zr}

Density of U-Pu-Zr = $X_U \cdot \rho_{U_r} + X_{Pu} \cdot \rho_{Pu} + X_{Zr} \cdot \rho_{Zr}$.

Thermal Conductivity of Fuel

Fig. 5.1.12 Binary (U-Pu)-Zr phase Diagram (Pu at 19 wt%)

Thermal conductivity of fuel for the calculation of fuel temperature is taken from the literature and is given below.

$$K(T) = a + bT + cT^2, \text{ W/m-K}$$

where

$$a = 17.5 \cdot ((1 - 2.23 \cdot W_{Zr}) / (1 + 1.61 \cdot W_{Zr}) - 2.62 \cdot W_{Pu})$$

$$b = 0.0154 \cdot ((1 + 0.061 \cdot W_{Zr}) / (1 + 1.61 \cdot W_{Zr}) + 0.9 \cdot W_{Pu})$$

$$c = 9.38 \cdot 10^{-6} \cdot (1 - 2.7 \cdot W_{Pu})$$

W_{Zr} , W_{Pu} , W_U are weight fractions of Zr, Pu, and U, respectively.

For U-15% Pu-6% Zr system,

$$K(T) = 6.945681 + 0.016174 T + 5.58 \times 10^{-6} T^2, \text{ W/m-K}$$

where T is in Kelvin.

For fuel with pores, porosity effect is considered in the fuel. Correction factor for porosity is, $f_{\text{pore}} = (1 - P)/(1 + 2.5P)$ where P is the porosity of the fuel.

$$K(T, P) = f_{\text{pore}} \times K(T, 100\% \text{ TD}).$$

Thermal Conductivity of Fuel with Burnup

With burnup, fuel swells which results in increase of pores and consequently in the reduction of thermal conductivity of fuel. Metallic fuel thermal conductivity comes down till a porosity of 0.23 is attained and from then onward sodium infiltrates into the porosity due to release of fission gases and thereby increasing the thermal conductivity of fuel. The factor, X, that minimizes thermal conductivity for an irradiated fuel has been evolved and is given by the equation

$$X = (1 - P_{\text{min}})^{(3/2)\epsilon}$$

where $P_{\text{min}} = 0.23$, $\epsilon = 1.75$ for metal fuel gas filled pores.

$$\text{Accordingly, } X = (1 - 0.23)^{1.5\epsilon} = 0.51$$

Thermal conductivity of metal fuel before sodium infiltration is $0.51 \times K_{\text{fuel}}$.

After this, fuel porosities become interconnected and sodium infiltrates into the pores, thereby improving the fuel thermal conductivity to the original value.

Coefficient of Thermal Expansion of Fuel

Coefficient of thermal expansion is given by the expression

$$\alpha_{\text{fuel}} \times 10^6 = 19.41 + 12.67 * C_{\text{Pu}} - 13.37 * C_{\text{Zr}} \text{ mm/mm-K}$$

where C_{Pu} and C_{Zr} are concentration of Pu and Zr in atom fraction, respectively.

Fission Gas Release

The fractional release rate, F_g , is dependent on burnup (Bu in at. %), porosity (P), temperature (T), and fuel swelling strain (ϵ_s) due to gas bubbles according to

$$F_g = [1 - \exp(-\alpha \text{Bu})] [1 + C_g (P - 0.1)P^{2/3}] R_g \exp(-Q_g/RT) + f(\epsilon_s - \epsilon_{s1}), s^{-1}$$

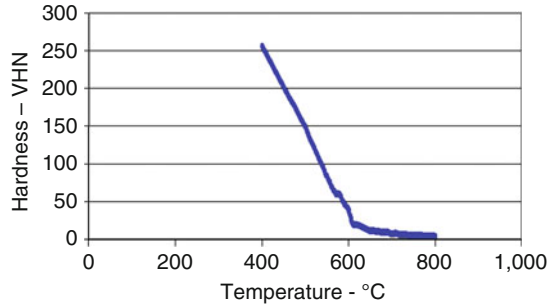
where $(P - 0.1) > 0$, $(\epsilon_s - \epsilon_{s1}) > 0$, and α , C_g , R_g , Q_g , f , and ϵ_{s1} are empirical parameters to be determined from in-reactor data. For example, the parameters used for U-Zr and U-Pu-Zr fuels are $\alpha = 1.0$, $C_g = 7.0$, $R_g = 1.14 \times 10^{-5}$, $Q_g/R = 5.6 \times 10^3 \text{ K}$, $f = 1 \times 10^{-2}$, and $\epsilon_{s1} = 0.3$. For $\epsilon_s > 0.3$, the second term is orders of magnitude larger than the first term in 8, giving rapid gas release for fuel regions with gas bubble swelling $>30\%$.

Hardness of Material – U-15 Wt% Pu-6.8 Wt% Zr

Hardness of material (VHN) is defined as follows for a typical load of 200 g:

$$\text{VHN} = 2e - 12Xt^6 - 8e - 9Xt^5 + 1.05e - 5Xt^4 - 0.0091Xt^3 + 3.9422Xt^2 - 898.5Xt + 84,536$$

where $t = T - 273$, T is temperature in Kelvin. ➤ [Figure 116](#) shows the variation of hardness.



■ Figure 116
Hardness variation with temperature

Melting Point

Fuel composition	Solidus	Liquidus
U-15 wt% Pu-6.8 wt% Zr	1,105 + 10 °C	1,240 + 20 °C
U-15wt% Pu-13.5 wt% Zr	1,195 + 10 °C	1,425 + 20 °C
U-15% Pu	976 + 40 °C	

$$\Delta T_{\text{Melting point}} = 13\text{ }^{\circ}\text{C}/\text{wt}\% \text{ of Zr.}$$

Other Properties

Property	U	U-5Fs	U-10Zr	U-8Pu-10Zr	U-19Pu-10Zr
Enthalpy, J/g (relative to 25 °C)	83.5	93.9	95.0	96.6	98.7
	(±2%)	–	(±5%)	(±5%)	(±5%)
Young's modulus, 10 ⁵ MPa	1.26	1.19	1.13	1.03	0.89
	(±10%)	(±10%)	(±10%)	(±20%)	(±20%)
Poisson's ratio	0.30	0.32	0.34	0.34	0.34
	(±5%)	(±10%)	(±10%)	(±10%)	(±10%)
Ultimate tensile strength, MPa	79.2	200	690	474	41.4
	(±30%)	(±30%)	(±30%)	(±50%)	(±50%)
Brittle-to-ductile transition temp., °C	<25	<25	<25	<350	>350

Behavior under Irradiation

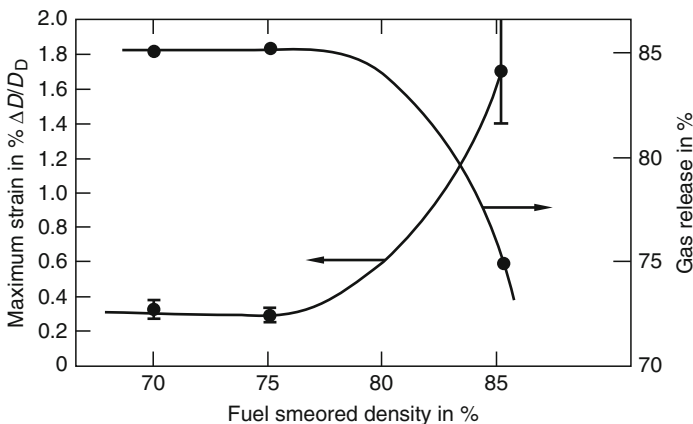
Importance of Smeared Density Under irradiation, the major concern is its high swelling. When metal fuel swells due to accumulation of fission gases, the fuel slug diameter and length increase

but the swelling is not isotropic. The length increase is consistently less than would be predicted from isotropic swelling. This difference was attributed to the difference in swelling behavior between the hotter center of the fuel and the colder periphery. The low smeared density (effective fuel cross section area/clad inside area) allows the fuel to swell to certain extent to enable the interconnection of pores which in turn facilitates the release of fission gases. If adequate free expansion is not allowed, the fuel slug creates strong fuel clad mechanical interaction (FCMI) forces, resulting in unacceptable stains. Many failures were reported in the earlier design of metallic fuel pins with high smear density due to high swelling and FCMI. Hence, a lower smeared density is essential for accommodating swelling. The smeared density effects are shown in **► Fig. 117**. The interconnection of porosities is reported to happen at $\sim 25\%$ volumetric swelling.

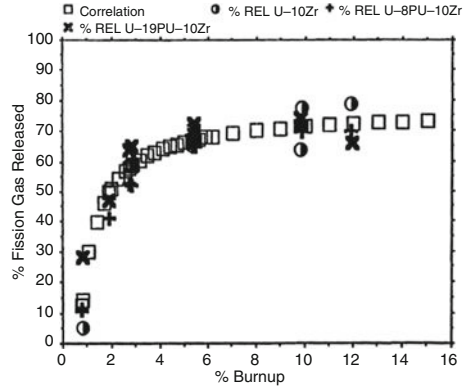
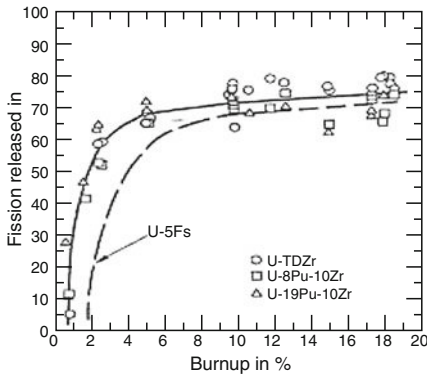
Fission Gas Release There is a need to provide adequate gas plenum at the top of the pin to accommodate the accumulated fission gas releases. The fission gas release is not a strong function of fuel composition and gets saturated at about 80%, as seen in **► Fig. 118**.

Radial Swelling Behavior **► Figure 119a** shows radial averaged swelling of 85% smeared density with U-19% Pu-10% Zr fuel plotted against burnup at the middle of the core. It is observed from **► Fig. 120a** that in the case of 85% smeared density, swelling due to the open pores is only $\sim 5\%$ at ~ 1 at. % burnup when the initial slug-cladding gap is filled with swollen slug. At a latter stage of irradiation, the open pore volume is replaced by the solid fission product (FP) swelling and cannot accommodate the solid FP swelling. FCMI stress continues to grow as seen from the **► Fig. 119b** for the same fuel composition and smeared density.

In the case of lower density fuel (75% smeared density), the open pore swelling amounts to about 20% and serves as a buffer to the solid FP swelling as seen from **► Fig. 120a**. As a result, there is no FCMI stress even at 2 at. % burnup as evident from **► Fig. 120b**. It is observed that fuel contacts with the clad around 3 at. % burnup and 75% smeared density fuel

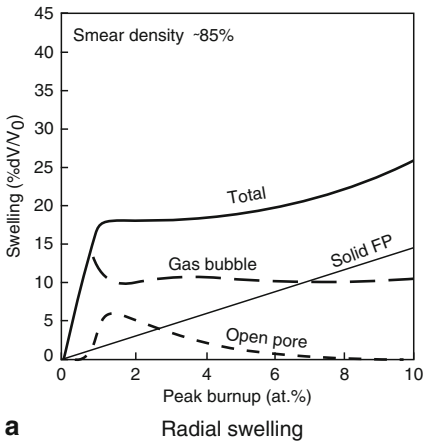


► Figure 117
Influence of metallic fuel smeared density



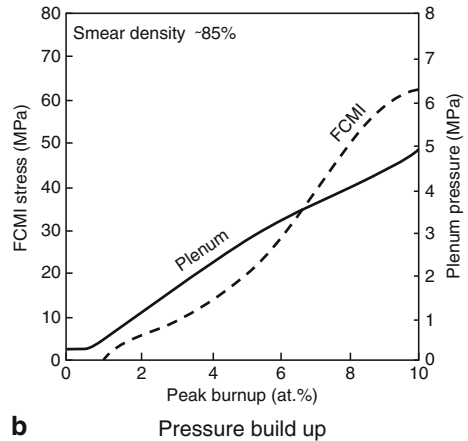
■ Figure 118

Fission gas release for different metal alloy composition



a

Radial swelling



b

Pressure buildup

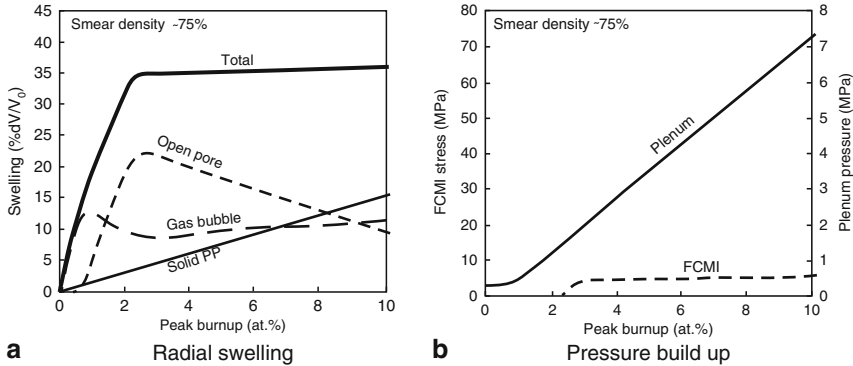
■ Figure 119

Swelling and pressure buildup with U-19%, Pu-10%, Zr (85% TD)

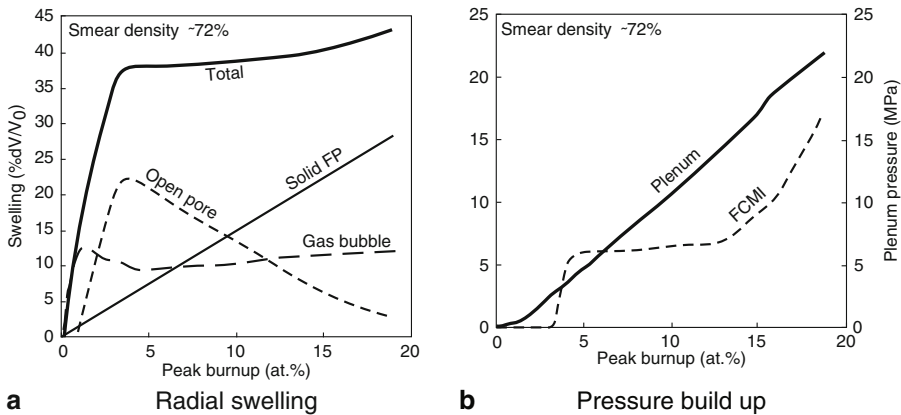
can accommodate about 35% swelling before it contacts the clad and remains constant beyond 3 at. % burnup. When the burnup becomes very high, significant FCMI can occur for even lower smeared density fuel slog, as seen from [Fig. 120a](#), because of the accumulation of the solid FP.

When the burnup becomes very high, significant FCMI can occur for even lower smeared density fuel slog, as seen from [Fig. 121a](#), due to the accumulation of the solid FP.

In this case, although the decrease in the open pore volume accommodates solid FP swelling until ~13 at. % burnup, the remaining volume of the open pores becomes too small at the higher burnup. It leads to significant increase in the FCMI stress as indicated in [Fig. 121b](#).



■ **Figure 120**
Swelling and pressure buildup with U-19%, Pu-10%, Zr (75% TD)

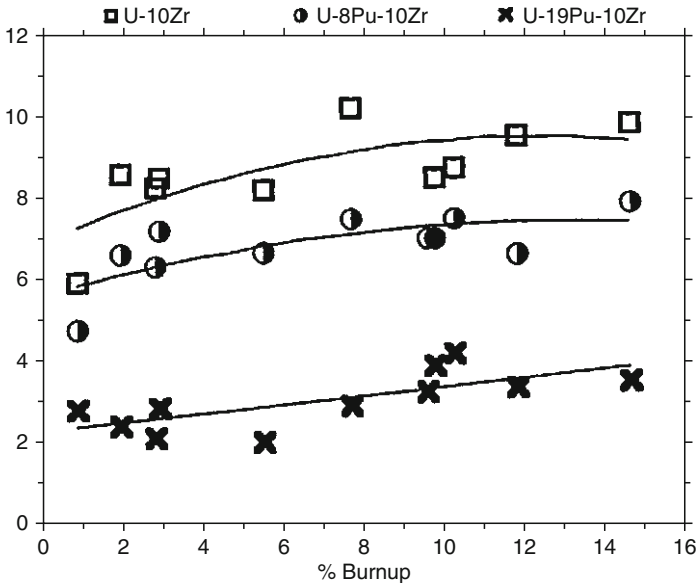


■ **Figure 121**
Swelling and pressure buildup with U-19%, Pu-10%, Zr (72% TD)

Based on the above discussions, it can be stated that swelling of fuel depends on the smeared density chosen for the fuel and burnup target.

Axial Swelling Behavior The axial fuel growth due to fission gas retention is expected to be around 2–4% as shown in the ► [Fig. 122](#) and is expected to be completed within 1–2 at. % burnup.

Safety Issues in Metallic Fuel Advantageous safety features of metal fuel are its high thermal conductivity, which results in less temperature, less temperature coefficient of reactivity and consequently less burnup reactivity swing, higher fuel axial expansion coefficient, and high negative reactivity feedback. However, sodium void worth is higher in metal fuelled core. Safety arising from low fuel temperature and strong axial expansion reactivity feedbacks make the metal fuelled core safe even though the sodium void worth is higher. Also, core reactivity does



■ Figure 122
Axial swelling for typical fuel compositions

not fall with burnup in such a core. Hence, the core size becomes more important in the physics design, and higher sodium void worth up to \$7 is permissible from the safety point of view. Low operating temperature, even though not favorable from the point of view of thermodynamic efficiency, leads to higher margin for sodium voiding. Other design measures that could be thought of toward minimizing the sodium void reactivity effect are use of sodium plenum in place of axial blanket and reduction of sodium volume fraction in the core.

One of the important safety issues to be addressed is redistribution of fuel constituents. Owing to interdiffusion of U, Pu and Zr within the fuel, Zr-depleted radial zones are created with lower solidus temperatures locally. Although it is not reported to be life limiting, it becomes important during transients as operational limits under incident conditions have to be determined. Another issue is fuel clad chemical interaction. When the metal fuel comes in contact with the cladding a situation involving multi-component diffusion transpires. In addition to fuel elements redistribution according to the phase relationships due to temperature gradient, the solid fission products participate in this radial diffusion process. So also the cladding elements. Three issues arise due to this complex interdiffusion process enhanced by the presence of lanthanide fission products with increased burnup. The effective cladding thickness could be uniformly thinned due to wastage. The cladding could be weakened due to grain boundary embrittlement. The combination of fuel and cladding elements could lead to an undesirable low melting alloy adjacent to the cladding. This may affect the clad integrity. In summary, low melting eutectic formation is one of the major issues in the case of metallic fuels.

High swelling and its non-isotropic characteristics have significant influence in design, especially while aiming for higher burnup, which would have to be handled by suitable design measures, choosing appropriate selection of smeared density, for example.

5.1.4 Carbide and Nitride

It has been demonstrated that mixed oxide behavior is satisfactory up to high burnup (15–20 at.%), and during the various steps in the fuel cycle (fabrication, storage, and reprocessing). Nevertheless, it has important drawbacks: a low heavy-atom density, a low thermal conductivity, and poor sodium compatibility. To overcome those current shortcomings, R&D organizations (CEA in particular) investigate potentially more effective fuels such as carbide and nitride ceramics as well as metal alloys (see ▶ Sect. 5.2 and ▶ Table 22).

Among these alternative fuels, most studies around the world have been focused on carbide, carbonitride, and nitride ceramics.

In the early days, the main reason for using dense uranium and plutonium fuel ceramics was to get a low doubling time (~15 years). Today, their main interests are the following:

- A good thermal conductivity leads to a low operating temperature at nominal power. Carbide and nitride can be considered as “cold” fuels with an important margin to fuel melting. This behavior improves core reactivity feedback coefficients. The Na-coolant Doppler ratio is also more favorable and provides a more satisfactory dynamic behavior and a good passive safety;
- High heavy atoms density favors a better breeding gain and therefore a smaller loss of core reactivity. Thus, longer irradiation cycles and/or a reduction of the number of control and shutdown (CSD) rods are possible;
- A very good chemical compatibility of these dense ceramics with liquid sodium enables, in case of clad failure, to continue the reactor operation with a broken fuel element until the next scheduled stop.

However, the design of carbide or nitride fuel element must take into account high swelling rates to ensure that the stress level in the cladding due to fuel cladding mechanical interaction (FCMI) remains acceptable at high burnup. Swelling behavior is certainly the most important drawback of these alternative fuels and will be discussed in the second part.

Properties of Dense Ceramic Fuels

This chapter examines not only the key physical properties of carbide and nitride fuels but also the most significant features concerning their behavior under irradiation.

A number of properties of (U,Pu)C and (U,Pu)N fuels, compared to oxide fuel (U, Pu)O₂ are provided in ▶ Table 23.

Chemical Properties Concerning the chemical properties of mixed carbide fuels, the phase diagram exhibits a very narrow C/M range for mono-uranium and plutonium carbide. After carbothermic manufacturing from mixed oxides, the monocarbide coexists with either a metallic phase or a higher carbide phase of type M₂C₃. The presence of a metallic phase should be avoided because it melts at low temperature (< 1,200 °C) and is chemically reactive with the cladding (eutectic phase formation).

Accordingly, manufactured carbides have usually a hyperstoichiometric composition with a major phase (U,Pu)C and a second phase (U, Pu)₂C₃. However, to avoid a chemical reaction of fuel with cladding steel (formation of Cr₂₃C₆ at grain boundaries of austenitic steel grades), the amount of M₂C₃ needs to be restricted to less than 15%.

For nitride fuel, manufacturing studies have shown that it was easier to control the amount of M₂N₃ by an adequate thermochemical treatment.

■ Table 23

Comparison of some properties of various ceramic fuels for FR (Pu/M = 20%)

	(U,Pu)O ₂	(U,Pu)C	(U,Pu)N
Theoretical density (TD) (kg/m ³)	11,000	13,600	14,300
Heavy atoms density (kg/m ³)	9,700	12,900	13,500
Density ratio (reference is oxide)	1	1.33	1.39
Heavy atoms density for a fixed smeared density (SD) (kg/m ³)	8,051 (SD = 83% TD)	9,675 (SD = 75% TD)	10,125 (SD = 75% TD)
Smeared density ratio (reference is oxide)	1	1.2	1.26
Thermal conductivity at 1,000 °C (W/m-K)*	2.0	12.0	13.2
Thermal expansion coefficient (20 ⇒ 1,000 °C)(10 ⁻⁶ /K)	11.5	12.1	9.5
Melting temperature (solidus) (°C)	2,740	2,325	2,720**
Compatibility with sodium	Poor	Good	Good
Compatibility with air	Good	Poor	Good
Compatibility with water	Good	Poor	Average

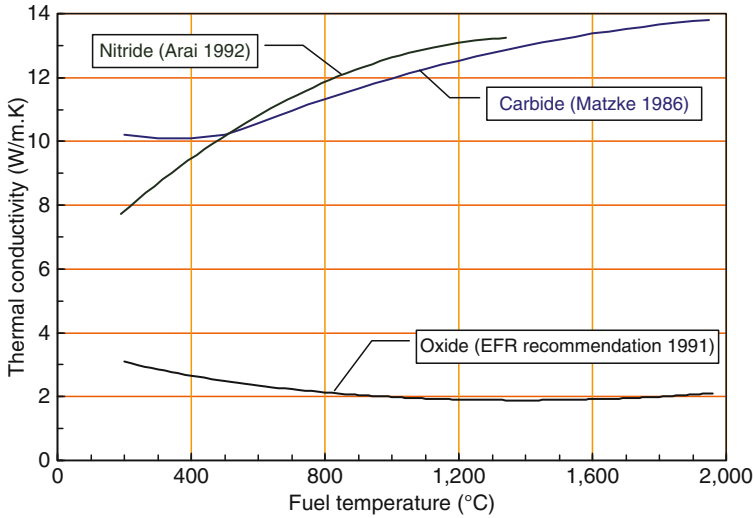
* For an hypostoichiometric oxide (O/M = 1.97) and a fabrication porosity respectively of 4% for the oxide and 17.5% for the dense ceramics.

** Above 2,000 K (1,723 °C), under helium atmosphere, a metallic phase (uranium and plutonium alloy) is formed by dissociation of mixed nitride: (U,Pu) N (s) ⇒ U (liq.) + Pu (liq.) + ½N₂ (g)

Nuclear Properties Nuclear reaction on carbon is not a serious issue for neutronics performance. A major problem during nitride-fuel irradiation is the formation of carbon-14 by (*n, p*) reaction on ¹⁴N and the production of ⁴He by (*n, α*) reaction. The occurrence of these nuclear reactions has three major impacts:

- It provides an additional gas production (He) estimated to at least 10% of the fission-gas production
- The production and release of ¹⁴CO₂ during reprocessing operations and during waste storage (the radioactive period of ¹⁴C is 5,600 years) needs to be handled
- The neutronics penalty can be balanced by an increase of the fuel plutonium enrichment with the negative effect of a reduction of the internal breeding gain

To limit ¹⁴C and He productions in nitride fuel, technical and economical feasibility of ¹⁵N enrichment have been assessed. At least two chemical processes could be developed: the NITROX and the chromatographic processes. The price range of the ¹⁵N produced by both techniques is about 8.2–12.2€/g, increasing the cost of the fuel assembly by about 10%. This additional cost could be, however, reduced if the ¹⁵N is recycled during the reprocessing stage.



■ Figure 123

Comparison of thermal conductivities of mixed oxide fuel (O/M = 1.97, P = 4%) and mixed carbide and nitride fuels (P = 17.5%)

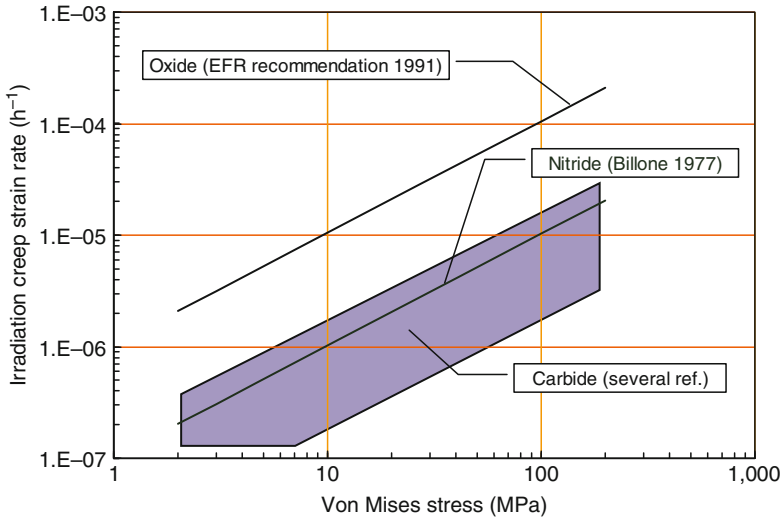
Thermal Conductivity Carbide and nitride fuels have a higher thermal conductivity than the oxide fuel (see ► Table 22 and ► Fig. 123). Although these fuels need a strong manufacturing porosity (15–20%), which greatly penalizes thermal performance, the thermal conductivity of carbide and nitride remains much higher by a factor of 3–6 than oxide.

Mechanical Properties Among the various mechanical properties required to understand the fuel behavior under irradiation, creep properties are important for a reliable assessment of FCMI. In case of mechanical interaction between fuel and cladding, it is mainly the contribution of irradiation creep that allows the accommodation. Despite large scattered experimental data (see ► Fig. 124), carbide and nitride fuels have a similar irradiation-creep rate (ICR), which is an order of magnitude lower than oxide. This reduced irradiation creep for carbide and nitride fuels is a counterpart of their better thermal conductivity.

Fuel Swelling The main disadvantage of dense ceramic fuels is a high swelling rate under irradiation. Most of the experimental data have been obtained on carbide rather than nitride fuel. However, there is a general agreement in the open literature that nitride fuel does not swell as much as carbide (see ► Fig. 124).

Correlations drawn from fuel pin deformations (diameter deformation and elongation of the fissile column) as well as more accurate data such as density-pellets measurements or more rarely some image analysis on SEM or TEM led to the following conclusions:

- Below a critical temperature, athermal swelling occurs driven by the inclusion of solid-fission products (FPs) (typical value of ~0.5/at.%) and by fission-gas atoms in the crystal lattice or in nano-bubbles (<30 nm). The swelling rate is roughly a linear function of burnup: ~1.5–1.6/at.%,



■ Figure 124

Comparison of carbide, nitride and oxide irradiation creep rates

- Beyond this critical temperature, observations show that these nano-bubbles rapidly grow (30–400 nm) and increase the gaseous swelling. As shown in [Fig. 125](#), the critical temperature decreases with the increasing burnup. For a carbide fuel, the critical temperature is evaluated to 1,100 °C at the irradiation start-up, but only to 800 °C at 5 at.% burnup. [Fig. 125](#) illustrates the differences in the critical temperature between carbide and nitride and the influence of nitrogen content in carbonitrides. These data confirm the U.S. gas-swelling results obtained by density measurements (integrated swelling within the pellet fuel) showing a critical temperature of nitride higher by about 150 °C than carbide.

At high burnup, two effects limit the macroscopic fuel swelling:

- Saturation of gas swelling occurs through the interconnection of intergranular bubbles and interaction of this bubble population with the fuel microstructure: fabrication porosity and grain boundaries (it is estimated that the gaseous swelling cannot exceed 30–40%)
- When the fuel comes into mechanical interaction with the cladding (FCMI), effect of hydrostatic pressure on bubble behavior will limit the gas swelling

In conclusion, dense fuels tend to swell significantly at the beginning of life when the fuel/cladding gap is open (He-bonded concept) and when the pellets are above the critical temperature. Then, under the combined effects of gap closure, a possible power decrease and the FCMI, the swelling rate will decrease and stabilize at a level depending on various manufacturing and irradiation parameters.

Current swelling models ([Fig. 126](#)) for carbide and nitride in fuel behavior codes are usually simplified and include only few parameters such as fabrication porosity, irradiation temperature, and burnup.

A better description of situations encountered by a carbide or a nitride fuel during its normal irradiation and power transients will be possible if models include

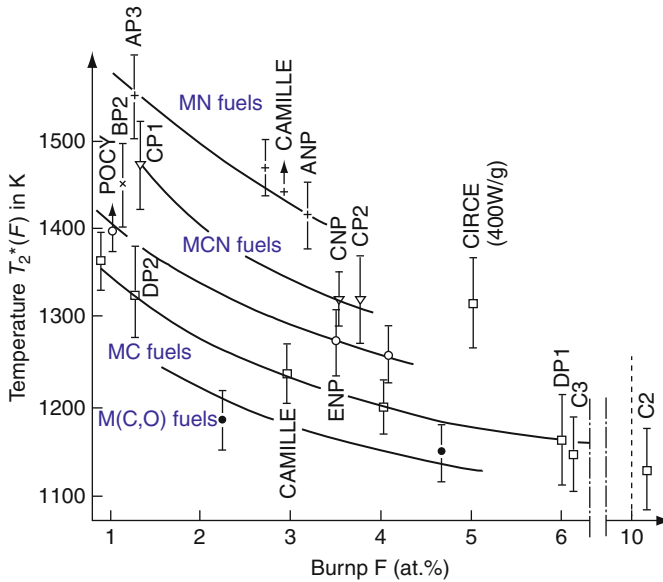


Figure 125

Variation of critical temperature with fuel composition (From Ronchi et al., 1984)

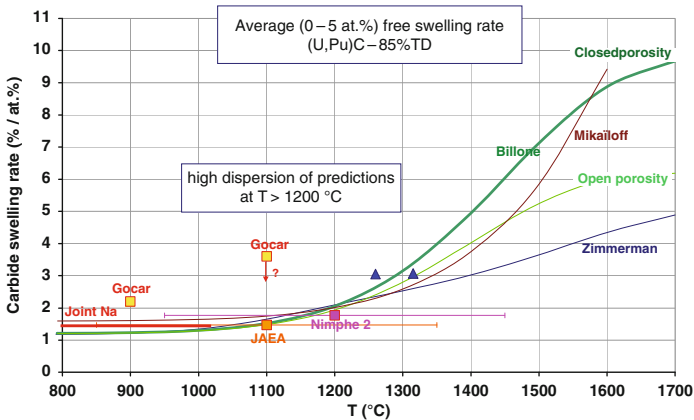


Figure 126

Comparison of some empirical correlations for carbide fuel swelling

- Manufacturing parameters: porosity (open and close porosity and their repartition between grain and grain boundary), M_2C_3 content, oxygen content, grain size
- Irradiation parameters: time, BU, temperature, and mechanical loading history
- The development of such model requires a large and reliable experimental database for the selection of important physical mechanisms and for validation purpose.

Fission Gas Release The release of fission gas strongly depends on the fuel thermal regime but also on some fabrication parameters such as the nature of porosity: open and/or closed.

As previously said, the (n, α) reactions on nitrogen-14 lead to an extra production of gas (He) causing additional release (more important for nitride than carbide).

The results on helium-bonded carbide or nitride pins fabricated with a large amount of open porosity show that the fission-gas release remains always lower than in oxide fuel (irradiated in the same conditions) but still can reach values greater than 50% at high burnup.

Chemical Stability The chemical stability of (U,Pu)C and (U,Pu)N compounds depends on the temperature and on the gas confinement.

In carbide, the vapor pressure of plutonium in equilibrium with solid (U,Pu)C contributes almost exclusively to the total pressure. This strongly incongruent evaporation has consequences for fuel fabrication (possibility of plutonium losses) and performance when high level of temperature is reached ($> 1,650^\circ\text{C}$). The result is a plutonium enrichment observed in the peripheral region of the pellets and along the radial cracks.

In nitride:

- In helium atmosphere and above 2,000 K, loss of plutonium and nitrogen can be encountered. However, the rate of dissociation is rather slow; consequently, a brief temperature rise might not have a severe penalty on the fuel behavior in transients.
- Under nitrogen atmosphere, until 2,700 K, the decomposition of (U,Pu)N should not happen. However, recent investigations of nitride irradiations, carried out in the PHENIX and Joyo (Japan) fast reactors, have confirmed that nitride could exhibit signs of dissociation, with precipitation of plutonium-enriched metallic phase in the gap between fuel and cladding.
- In case of clad failure (open system), nitride could be dissociated for temperature as low as 2,000 K.

Physical Stability Drastic pellet geometric changes as observed in oxide fuel (columnar grains and central hole formation) are not possible for dense fuels in most situations.

However, given their high manufacturing porosity, these fuels may be subject to an in-pile densification if the operating temperature is close to the sintering temperature. A significant in-pile densification can increase the fuel/cladding gap and cause a fuel overheating. In addition, the fabrication porosity is chosen to accommodate the fuel swelling and its partial removal would have undesirable effects on FCMI.

Studies for optimizing a fuel manufacture with high-porosity content, thermally stable under irradiation, were carried out at CEA and at other research organization such as the *European Institute for Transuranium Elements* (ITU) and *Japan Atomic Energy Agency* (JAEA). All these processes use the carbothermic reduction from a mixture of oxides and graphite but differ in methods to obtain the thermally stable porosity:

- The thermal stable fuel proposed by JAEA involves the use of pore former and Ni powder additions as a sintering aid, leading to a high proportion of closed porosity.
- The method of direct pressing (DP method) proposed by ITU does not use any additives but achieves the carbothermic reduction stage on cylindrical clinkers directly into the required “green” pellets shape for sintering. A variant is the “granules” (G method) in which carbothermic reduction stage is performed on 0.5–1.25 mm granules of mixture ($\text{UO}_2 + \text{PuO}_2 + \text{C}$), which are directly pressed and sintered. These methods lead to a fuel with large proportion of open porosity.

Both ways provide a good thermal stability for dense fuel but, according to the nature of porosity: closed (JAEA) or open (ITU), irradiation phenomena such as fission gas release, gaseous swelling, and its accommodation can greatly differ.

Behavior of Fission Products For sake of simplicity, three categories of fission products (FPs) in irradiated carbide and nitride fuels can be considered:

- Rare earth FP (La. . .)
- Noble metal FP (Ru. . .)
- Volatile and gaseous FP (Cs, Xe. . .)

Regarding the first category, lanthanides are much more soluble in nitride than in carbide. For example, La and Nd are soluble in MN but only partially soluble in MC. According to Kleycamp, they can also form sesquicarbides such as La_2C_3 and Nd_2C_3 or dicarbides (LaC_2 and NdC_2).

In the second category, $\text{UFP}_3\text{C}_{1-x}$ carbide types have been observed by MET examinations. Intermetallic compounds, such as MFP_3 , are observed in nitride. Molybdenum also behaves differently in the two fuels: it tends to form MoC and Mo_2C in carbide.

Volatile FPs (Cs, Br, I, Te) behave chemically in the same manner in carbide, nitride, and oxide fuel. The solubility of rare gases is very low, forming an intragranular nano-bubbles network in the U, Pu matrix.

As a consequence, the C/M ratio will decrease during irradiation (existence of many FP carbides), while the N/M ratio tends to increase due to the strong solubility of lanthanides. These trends could be changed, especially for carbide fuel by the presence of a greater amount of residual oxygen after manufacture. In this case, FP such as Ba and Sr will preferentially oxidize rather than forming carbide compound and will slow down the C/M decrease.

Corrosion of the Cladding During irradiation, cladding austenitic steel carburization can occur through transfer of carbon coming from the M_2C_3 phase decomposition, which is less chemically stable than the chromium carbide (Cr_{23}C_6). A similar risk of nitriding exists for nitride fuel.

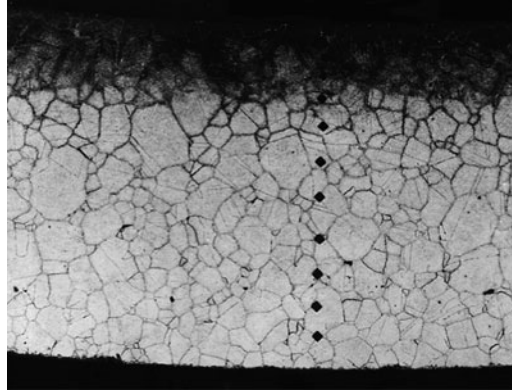
The kinetics of the process depends on factors such as the nature of fuel/cladding bonding (sodium or helium), the M_2C_3 content in carbide fuel, the linear heat rate (LHR), and of course the irradiation duration. It is generally for Na-bonded carbide fuel pins (► [Fig. 127](#)) that the highest carbon concentrations have been measured with values ranging from 0.4 (low LHR) to ~2 w% (high LHR > 1,000 W/cm). The extension of carburization can affect up to 2/3 of the initial clad thickness. However, carburization of He-bonded fuel elements may be also significant, because, after the closing of the fuel/cladding gap, a direct transfer of carbon by intergranular diffusion, with a kinetic similar to the Na-bonded concept, can take place.

The major outcome of this clad carburization is a significant embrittlement of the austenitic steel in the carburized region with the presence of numerous radial cracks. However, in most cases, cracks are confined in this zone without causing clad failure.

Design of Dense Ceramic Fuel Pins

Choice of Dense Fuel In the previous chapters, we have seen that carbide and nitride fuels had many things in common. Advantages and drawbacks can be compared on the following aspects: core performance, safety, fuel cycle, manufacturing, and past experience.

Previous considerations demonstrate that the carbide achieves the best performance, especially in terms of core volume and fissile material optimization. To get an equivalent level of



■ Figure 127

Carburization of the inner wall of an austenitic-steel cladding for a Na-bonded fuel pin irradiated at 3 at. %

performance, nitride would require nitrogen-15 enrichment to at least 50%. Without enrichment, helium generation from (n, α) reactions on ^{14}N has a direct consequence on decreasing the discharge burnup.

Another negative point for nitride is a worse chemical stability at high temperature during a core disruptive accident where the low partial pressure of nitrogen favors substantial nitride fuel dissociation.

Carbide, because of its instability in the presence of oxygen or water, has a much lower ignition threshold. For the same reasons, it is difficult to produce a carbide fuel without impurities, which may have a negative impact on in-reactor behavior. Handling carbide fuel, during the fuel fabrication stages, requires a perfect control of experimental conditions, which may be extremely difficult to achieve in an industrial context. In this respect, nitride would exhibit a greater tolerance.

Compared to existing fabrication processes, a technological gap is required. In the carbide case, the pyrophoricity and impurity issues must be overcome. For nitride fuel, technological improvements are also essential to attain adequate ^{15}N enrichment at a reasonable cost or to remove the ^{14}C from fuel.

The choice between carbide and nitride is not that obvious; it depends on the relative importance of key criteria (safety, manufacturing, irradiation performance. . .). Nevertheless, carbide, with a larger experimental feedback, a safer behavior in accidental situation, and despite a more complex manufacturing process, appears to be the best option at this time.

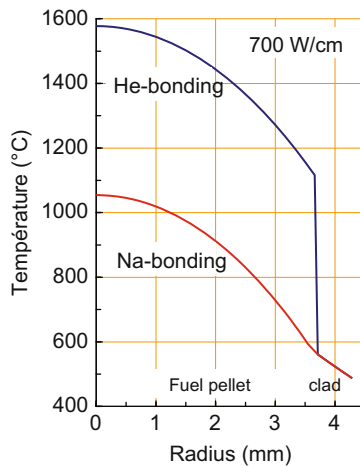
Choice of Fuel-Pin Concept Two different fuel-pin designs were investigated in detail: the sodium and the helium-bonded fuel/cladding gap. ▶ [Table 24](#) summarizes the positive and negative points for both types of fuel elements.

As ▶ [Table 24](#) shows, the main interest of Na-bonded concept is a relatively low-level operating fuel temperature (usually $< 1,000\text{ }^\circ\text{C}$), which remains constant during irradiation. This low-temperature regime causes a moderate fuel swelling rate and prevents the FCMI risk if the fuel/cladding Na gap is large enough. In addition, it guarantees a large margin to melting and a good safety Doppler coefficient.

■ Table 24

Comparison of dense fuel pin concepts

	Main advantages	Major drawbacks
Sodium-bonded fuel/cladding gap	Lower fuel temperature: Gain for Doppler coefficient, Rather low swelling rate, In principle, no severe FCMI	Fabrication and reprocessing, High risk of clad carburization, Risk in case of defective Na bonding in fabrication or during in-pile irradiation
Helium-bonded fuel/cladding gap	Conventional manufacturing, Lesser risk of clad carburization	Risk of thermal instability and high swelling rate before fuel cladding-gap closure, FCMI \Rightarrow difficulty to design fuel element for high BU rate



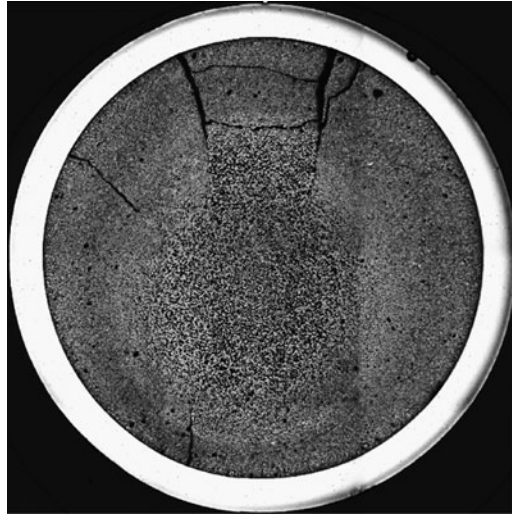
■ Figure 128

Comparison of temperature profiles for both Na and He-bonded concepts at 700 W/cm

Unfortunately, international experience pointed out serious flaws regarding the Na-concept:

- The fabrication at an industrial scale is difficult
- A large amount of contaminated sodium during reprocessing operations has to be handled

For He-bonded concept (► Fig. 128), we can observe a very different thermomechanical behavior. The necessity of having a large amount of preexisting voids (fabrication pores and fuel/cladding gap) leads to a poor heat transfer and implies that the fuel will perform at high temperatures. Thus, the fuel will swell significantly, leading to rapid closure of the fuel/cladding gap and to FCMI.



■ Figure 129

Macrograph of a He-bonded carbide fuel pin irradiated to 6 at.% in PHENIX reactor

FCMI can occur at the burnup of a few at.% as shown by numerous carbide and nitride fuel irradiations (see ► Fig. 129). Despite this predictable mechanical interaction, experiments carried out in various countries and involving He-bonded fuel elements have demonstrated that a well-suited design can handle FCMI situation without severe damage.

Nowadays, the choice for a dense fuel element clearly leans in favor of the He-bonded concept.

Optimized Design of a Carbide Fuel Element The performance of a carbide fuel pin depends on its design which has to ensure that the FCMI effects remain always acceptable in normal and incidental situations.

The first criterion is the choice of the smeared density (SD, see ► Table 23). It is a compromise between a better internal breeding gain and a limitation of the FCMI consequences. French and American experiences demonstrate the need to set the smeared density around 75–78% TD to reach a burnup of 15 at.%.

The voids in the fuel pin for a given smeared density may come from

- Fuel fabrication porosity
- Choice of a hollow pellet
- Fuel pellet/cladding gap

The balance between these contributions aims at maximizing the efficiency to accommodate the fuel swelling and minimize the cladding-stress level due to FCMI.

A central hole does not seem to be an efficient solution to accommodate the fuel swelling.

The use of a rather high fuel fabrication porosity (15–20%) associated with a reasonable fuel/cladding gap size is a good compromise to regulate the temperature level during the gap closure period and is more efficient to reduce the “constraint” swelling rate. In addition, experiments have shown that a too large gap may cause an important unrestrained relocation

of fuel fragments, leading to major cladding ovalizations. Thus, a good value of gap/diameter ratio seems to be around 3–4%.

Finally, the cladding material has also an essential role in the design of a dense fuel element. Most irradiation results on carbide fuel pins were obtained with conventional cladding materials such as austenitic stainless steels. These materials provide satisfactory mechanical properties at irradiated state (residual ductility and thermal creep behavior) and a good resistance to sodium corrosion. Its main weakness is a high swelling rate leading to significant cladding macroscopic deformations for neutron dose >130 dpa for the best grades.

There are only few experiments with materials resistant to swelling such as Nickel alloys or ferritic–martensitic steel grades. Nevertheless, the better dimensional stability of these alloys at high dose rate and a possibly worse ability to creep, could lead to additional difficulties for carbide fuel pin design.

Conclusion

This review of physical properties and design approach of carbide and nitride summarizes its strengths and weaknesses for use in SFRs. Today, the He-bonded concept of carbide fuel pin with an adequately smeared density of about 75–78% TD seems to be the best compromise to compete with the oxide reference. Nevertheless an experimental large-scale demonstration in a power reactor is still missing to validate this conclusion.

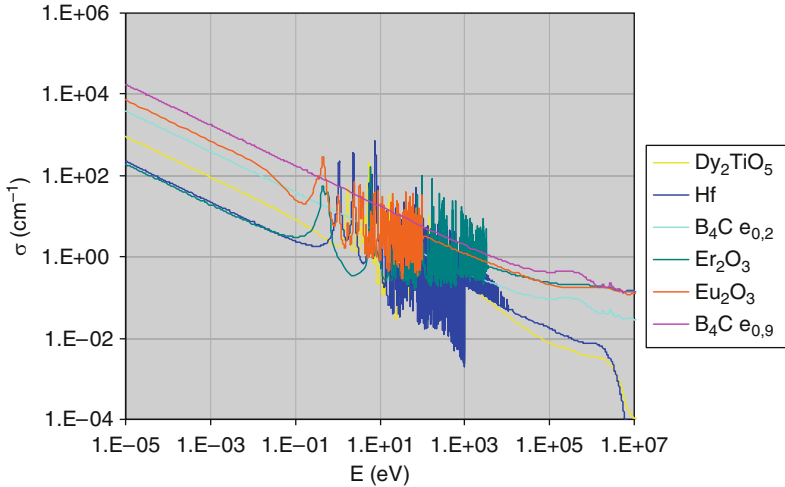
5.2 Structural Materials

5.3 Absorber Materials

5.3.1 Introduction

Most of the data presented here are obtained from IAEA reports (fast reactor data retrieval and knowledge preservation initiative) (IAEA-TECDOC-884 1996; IAEA-TECDOC-1083 1999). All the present or planned fast neutron reactors use boron carbide as a neutron absorber, which then appears as the reference material. This is due to the relatively good absorption cross section of ^{10}B in the fast neutron energy range, a smooth $\sigma(E)$ curve (no resonances) allowing easy efficiency calculations (➤ Fig. 130), nearly no long life wastes (except ^3H and impurities). However, most of the concepts require high ^{10}B enrichment, from the natural one (19.8 at.%) up to 90%. This leads to high elaboration costs. This drawback has been tentatively addressed by considering more complex absorber elements allowing a local moderation of the neutron spectrum. As a result, lower enriched boron carbide or even other material (hafnium) could be reconsidered. $^{11}\text{B}_4\text{C}$ has also been considered as a moderator, although with a lower efficiency than the hydrides.

The main features of the behaviour of boron carbide under neutron irradiation in a fast neutron reactor environment have been identified in the 1970s: cracking due to thermal gradients and swelling due to helium retention in highly pressurized bubbles (IAEA-TECDOC-1083 1999). Behavior laws have then been tentatively developed by most of the involved countries (mainly USA, GB, France, Japan, and USSR). However, the more recent available data have mainly been obtained in Japan, Russia, and France. Some of the most salient results are reported here. We then present a summary of the results obtained on boron carbide.



■ Figure 130

Macroscopic neutron absorption cross sections for some materials (90% density for B_4C), as deduced from the corresponding microscopic cross sections, from ENDF data base

Russia

The first design of B_4C control rods was sealed pins. They unfortunately have a too short lifetime (2–3 months) due to helium release and internal pressure increase leading to a quick recourse to vented pins. Costs reduction is obtained by reuse of irradiated boron carbide. Two processes are considered. First, non-damaged pellets can be directly reused in new rods. Second, damaged pellets are ground to powder then sintered to obtain new pellets. In both cases, a relatively low γ -activity is required.

BN-600 (Russia) and BN-350 (Kazakhstan) cumulate more than 20 years of operation. At the moment, the lifetime of the control rods (BN600) is around 500 epfd with a burnup around 19%.

Tests in BOR-60 in 1972–1973 of CrB_2 –Ta composites showed good radiation stability but too low efficiency as compared to B_4C . The most serious alternative to B_4C is Eu_2O_3 : this material shows a higher efficiency, no swelling, no gas release. The major drawback is the residual activity. Owing to the cost of highly enriched boron carbide, new designs have been tested to obtain better yields. A promising one consists in composite rods (so-called rod-traps) containing an absorber (Eu_2O_3 , B_4C) and a moderator (ZrH_2). Eu_2O_3/ZrH_2 rods are somewhat less efficient than B_4C/ZrH_2 ones. Different designs were tested in BN-350 and BN-600, for as long as 450 epfd. Other materials such as hafnium can then be considered leading to an improved use of B_4C .

France

Boron carbide was the only used neutron absorber in the French fast neutron reactors. From neutron economy considerations, it was soon considered that high density, high ^{10}B enriched materials were required. The first control rods used large pellets, resulting in very short lifetimes (clad cracking, recrystallization of the center of the B_4C pellets). Many improvements were then

successively introduced: lowering the pellets diameter, reducing the enrichment at the feet of the rods, introducing a contention shroud. As a result, a good overall behavior was obtained in the last experimental rods (SuperPhenix design), with high operating conditions (650 efpd, burnup up to $2.5 \times 10^{22} \text{ }^{10}\text{B/cm}^3$).

Further improvement routes were considered in the 1990s on an experimental level: further reducing the pellet diameter (thermal cracking reduction) and lowering the density instead of the enrichment (swelling reduction).

Japan

Experimental pins were irradiated in Joyo. A maximum burnup of $2.3 \times 10^{22}/\text{cm}^3$ was achieved, leading to one of the most comprehensive available data bases (IAEA-TECDOC-1083 1999). Swelling is determined at low burnups from volume measurements on non-cracked pellets and picnometry for the higher burnups. Helium release increases with temperature and appears close to the formation rate at the highest burnups and temperatures.

B_4C -Cu composites have been elaborated. As compared to similar French materials elaborated in the 1970s, a better Cu- B_4C bonding is obtained (IAEA-TECDOC-1083 1999). Control rods made of hafnium hydride are presently considered in which hydrogen is used as moderator to improve the absorption efficiency of hafnium (Basmajian et al. 1972).

Main Control Rods Characteristics

Some characteristics of the control rods of experimental or commercial reactors are reported in [Table 25](#). It appears that most of the absorber pins are now based on a double-vented concept, allowing efficient cooling of B_4C by sodium and helium release. Sealed pins have been developed, however leading to too short life-time (internal pressure increase due to helium release). Diving-bell concepts have also been considered (USA, China) with the major drawback that the B_4C temperature cannot be controlled due to high fluctuations of the internal sodium level related to helium bursts release.

5.3.2 Boron Carbide

Properties

Boron carbide is a light, brittle, very hard, refractory ceramic. It is most often obtained by carbothermal reduction at high temperature of purified boron oxide. The material has then to be ground to powder. In France, a magnesothermal process was used leading directly to micronic powders. In both cases, the powders are hot-pressed to obtain the cylindrical pellets constituting the absorber pins. In actual materials, the grain size usually ranges from 5 to 20 μm , and the density is around 80–95%. Industrial materials all have a composition very close to B_4C . Because of the bad behavior of graphite under irradiation (swelling, sodium intercalation), materials with as low as possible free carbon contents are required.

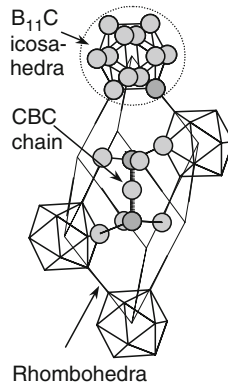
The thermal conductivity is mainly phonon-like, with a $1/T$ variation (for a 95% dense material, around 27 W/m-K at RT and ~ 12 W/m-K at 1,000 °C). The mechanical behaviour is purely brittle up to 1500 °C (for a 90% dense material at RT, $K_{1C} \sim 2.5 \text{ MPa}\sqrt{\text{m}}$, Young modulus ~ 250 GPa, yields ~ 400 MPa). Those properties decrease as the porosity increases.

Boron carbide has a complex crystal structure ([Fig. 131](#)) constituted of nearly regular icosahedra (mean composition B_{11}C) interconnected according a rhombohedral network. The

Table 25
Main characteristics of absorber elements in different reactors

Reactor	Country	Dates of operation	Cooling	Diameter pin/absorber (mm)	Absorber*	Density (%)	efpd''	Max. reported burnup ($10^{20}/\text{cm}^3$)
Rapsodie	France	1967–1982	Na	45/	BC90			
KNK-II	Germany	1983–1991	Na	10.3/	BC93		275	45
FBTR	India	1985	Na		BC90			
PEC	Italy	No author	Na	17.7/	BC90			
Joyo	Japan	1977	Na		BC90			230
DFR	UK	1959–1977	Na	23/	Fuel			
BOR-60	Russia	1973	Na	12/	BC80/Eu ₂ O ₃			
EBR-II	USA	1963–1994	Na		Fuel + BC			
Fermi	USA	1962–1972	Na	15.9/	BC			
FFTF	USA	1980–1992	Na	12/	B20			
BRS-10	Russia.	1958	Na					
CEFR	China	Under constr.	Na	14.9/12.2	BC20, BC91	92	P 400	
Phénix	France	1973–2009	Na	28/	BC48		N 240 E 650	240
SNR-300	Germany	No author	Na	15.5/	BC47			
PFBR	India	Under constr.	Na	21.4/	BC65			
Monju	Japan	1993–1995	Na	17/	BC39			
PFR	UK	1974–1994	Na	22/	BC20			75
BN-350	Kazakhstan	1973–1999	Na	23/	BC60			
BN-600	Russia fed.	1980	Na	23/19.6	BC20, BC90		N 365 E 550	180
BN-800	Russia fed.	Under constr.	Na					
ALMR	USA	Design	Na		BC92			
Kalimer-150	Rep. Korea	Design	Na		BC			

* BC%: B₄C, ¹⁰B enrichment; ''N (nominal), E (experimental), P (projected).



■ **Figure 131**
B₄C crystal structure

center of the cells is filled with a C–B–C chain allowing additional tight bondings between the icosahedra. It is then isostructural to some borides (e.g., B₆Si), mainly differing by the composition of the central element. Depending on the actual composition of the cell elements, boron carbide exists in a large composition range, from B₄C to approximately B₁₀C. Interatomic bondings are mainly covalent, this conferring its mechanical and thermal properties.

Behavior under Neutron Irradiation

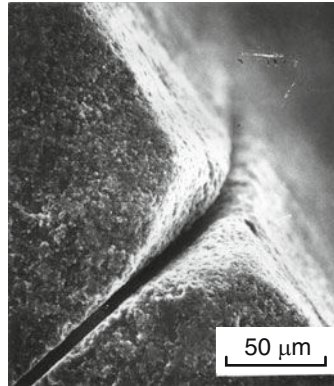
Most of the damages observed in boron carbide directly flow from the main neutron absorption reaction:



Depending on the control rods' design and use, very high operation parameters can be reached, for example, a resulting volume power up to 400 W/cm³ and helium production up to 0.05 mol/cm³.

No clear effect of Li has ever been observed, but from diffusion coefficients as measured on B₄C irradiated in experimental reactor, it can be deduced that a high fraction of lithium is released in the temperature range in the absorber pins (IAEA-TECDOC-1083 1999). Even at the highest burnups (up to 2.5×10^{22} ¹⁰B/cm³, i.e., ~25% of total boron), the crystal structure is not modified. This can flow from the capacity of the structure of those borides to accommodate very large composition variations but also from very efficient (although unidentified) mechanisms for the healing of point defects. As compared to the stoichiometry limit formula “B₄C,” large excess carbon is produced during irradiation: no available study mentions the possible consequences of this composition variation. No reaction with sodium has been observed: the main effect seems to be a tearing of the surface grains due to the grain boundaries damage (► Fig. 132).

The first damage mechanism results from the high radial thermal gradients (up to 1,000 °C/cm) arising from the conjunction of the capture reaction energy and the low thermal conductivity of B₄C. This leads to thermal stresses, which exceed the yield of the material. This results in radial cracks at the very beginning of life in the most demanded parts of the control rods (feet of rods, high enrichment zones). This mechanism remains active as burnup increases, since the thermal conductivity of irradiated B₄C strongly decreases (► Fig. 134).



■ Figure 132

Tearing of B_4C grains (Phenix experimental control rod, $2.5 \times 10^{21}/cm^3$, 55 efpd)

Most of produced helium remains in B_4C at low burnups and low temperature. At the beginning of life, the retention rate is over 80% (► Fig. 133) with slight temperature dependence. This results in the second damage mechanism. In the grains, helium accumulates in a high density network (10^{15} – $10^{16}/cm^3$) of lenticular bubbles under high pressure (>5 GPa, IAEA-TECDOC-1083 1999) inducing high internal stresses. These bubbles are parallel to the (111) plane of the rhombohedral structure, inducing very anisotropic swelling and stresses (IAEA-TECDOC-1083 1999) and then high shear stresses between adjacent grains. Close to the grain boundaries, helium migrates and accumulates also in lenticular bubbles, here parallel to the boundaries. This results in depleted zones without helium bubbles at the periphery of the grains (thickness around 100–300 nm). Both mechanisms (shear stresses and grain boundary damage) induce intergranular cracking for burnups around 1×10^{21} $^{10}B/cm^3$. At higher burnups (threshold around 5×10^{21} $^{10}B/cm^3$), the stresses induced by the intragranular bubbles induce intragranular cracking. Both mechanisms (inter- and intra-granular cracking) induce an increase of helium release: for burnups over $1 \times 10^{22}/cm^3$ (and temperatures over 1,000 °C), Maruyama et al. (1997) have observed a helium release rate close to the formation rate. At high temperature (above 1,500 °C), the flat bubbles relax and transform to classical three-dimensional faceted ones, inducing an accelerated swelling and extensive grain boundary damage. As compared to other materials such as fuel, metals, or other borides, the intrinsic volume swelling of B_4C appears low, thanks to the high internal pressure in the bubbles. Most results show a nearly linear swelling as a function of burnup, with an apparent saturation for the highest burnups (over $1.5 \times 10^{22}/cm^3$), related to a higher release rate. The swelling values range around 0.15–0.2 volume percent for 10^{20} captures/ cm^3 . The macroscopic deformation in a given absorber rod section is somewhat different since it results from different mechanisms (swelling, cracking, and relocation of fragments). A high initial porosity leads to a lower and delayed geometric swelling. Relocation of fragments induces an anisotropic deformation (axial compaction, radial expansion). It is worth noting here that the so-called swelling is generally determined from the evolution of the density of irradiated fragments (e.g., by picnometry). As a result, it does not take into account the lithium and helium releases. The obtained values are then underestimated. Actual swelling values as determined from geometric measurements show significant discrepancy between swelling and density variation for the highest burnups (over $1.5 \times 10^{22}/cm^3$),

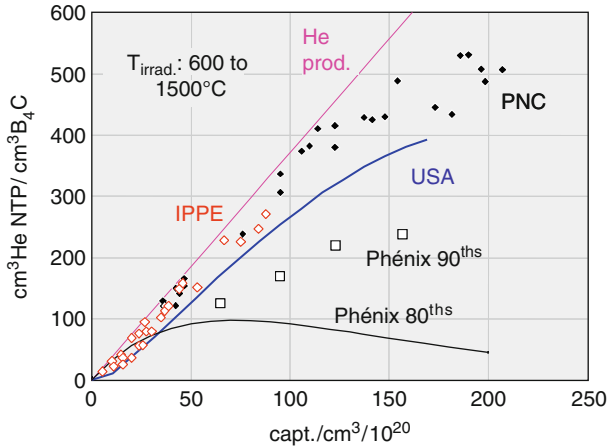


Figure 133

Helium retention as a function of burnup for some control rods. French data appear significantly different

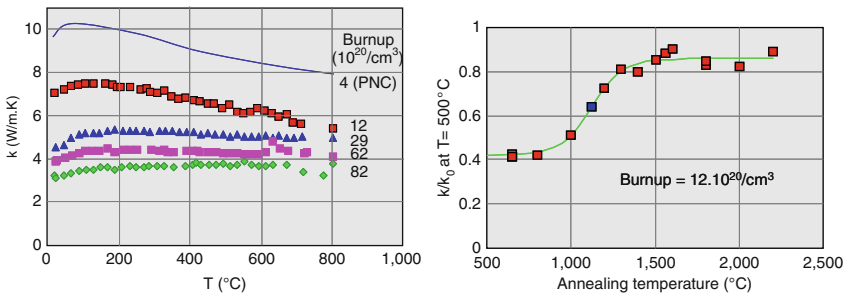


Figure 134

Left: thermal conductivity of irradiated B_4C (experimental Phenix control rod) as a function of burnup. Right: isochronal annealing ($1.2 \times 10^{21} \text{ B/cm}^3$)

evidencing a significant release of the fission products (He, Li) (Evaluated Nuclear Data File 2008).

The thermal conductivity strongly decreases during irradiation (► Fig. 134). This results from different mechanisms, helium bubbles formation, microcracking, internal stresses, and irradiation defects. Annealing above the BDT temperature allows the healing of the two latter damages but induces a strong swelling of the material due to the growth of the bubbles: the resulting conductivity is close to the one of an unirradiated material with a porosity equivalent to this swelling. Irradiation at lower temperature induces accelerated thermal conductivity damage.

Tritium is produced via a minor absorption reaction on ^{10}B with fast neutrons (depending on the actual local neutron spectrum, around $5 \text{ mCi}/10^{20} \text{ captures/cm}^3$) (► Fig. 135). The

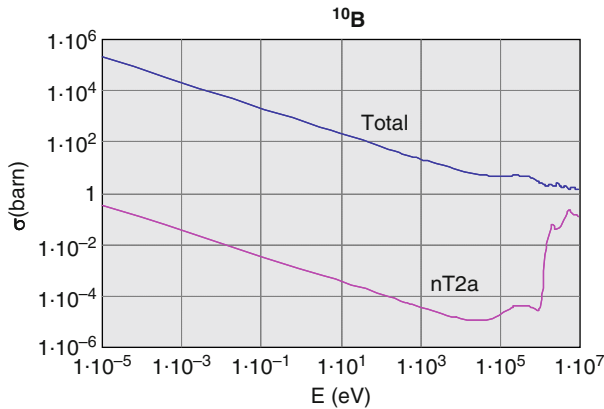


Figure 135

Microscopic cross sections for the $^{10}\text{B}(n, \alpha)^7\text{Li}$ and $^{10}\text{B}(n, 2\alpha)^3\text{H}$ reactions

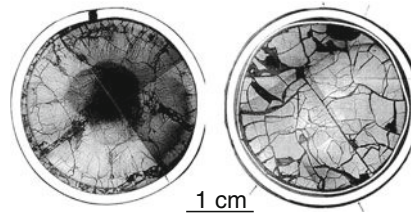
release rate is, however, high, over 50% in the hottest parts of the rod, that is, in the highest burnup sections. The use of locally moderated control rods would significantly lower this tritium formation.

On a general point of view, most data have been obtained on actual control rods or experimental pins: very few analytical results are available. As a result, the irradiation parameters are strongly dependant on the reactor operating conditions. As an example, the higher burnups are most often obtained thanks the high neutron flux at the feet of the rods, leading to the higher absorber temperatures. There is then a strong implicit coupling between temperature and burnup (Evaluated Nuclear Data File 2008); the time dependant parameters (e.g., diffusion) can then be hardly deduced.

5.3.3 Absorber Pins

The first limitation to the lifetime of the control rods is the damage of the cladding induced by interactions with the absorber. This results first from deformation induced by both the swelling of B_4C and the relocation of fragments (ACMI: absorber–clad mechanical interaction) and second from embrittlement due to chemical interaction (mainly carburization, ACCI: absorber–clad chemical interaction).

The mechanical interaction directly flows from the swelling of B_4C , higher than the metal's one. On classical rods, this interaction is anticipated due to the relocation of fragments (bevelled cracking) and filling of the gap with small ships, even with over-dimensioned clearance. Both effects limit the sodium flow in the gap, eventually allowing the formation of gas sections then inducing a strong increase of the B_4C temperature. The shrouded pins have shown an improved behavior: the shroud – even if extensively cracked – first efficiently contains the fragments and prevents their relocation and allows sodium to flow in the clad–shroud gap (Fig. 136). On the other hand, the cladding carburization is limited. This is clearly visible in Fig. 136: the absorber rod on the left shows first a clad failure but also very dense radial cracking. This may



■ Figure 136

Influence of the shroud on the absorber-cladding mechanical interaction (Phenix experimental pins). *Left:* 140 efpd, 1.4×10^{22} $^{10}\text{B}/\text{cm}^3$, $270 \text{ W}/\text{cm}^3$, showing gap filling with B_4C fragments and subsequent clad failure and extensive core damage (the hole at the center of the pellet results from post-irradiation machining). *Right:* 657 efpd, 2.5×10^{22} $^{10}\text{B}/\text{cm}^3$, $180 \text{ W}/\text{cm}^3$ showing shroud cracking but remaining gap

be attributed to clad–pellet gap closure leading to the formation of helium-filled gap sections inducing high temperatures in the core of the pellet, then an increased swelling of the core of the pellet.

Most of the postirradiation examinations (PIEs) have evidenced a strong carburization of the internal side of the clad, producing severe embrittlement. This shows that sodium is an efficient medium for carbon diffusion. A niobium coating has shown to efficiently prevent chemical interaction (Heuvel et al. 1985).

5.3.4 Developments

Major design modifications, based on numerous PIEs, have been performed, leading to strong improvements in the performances of the LMFNR absorber elements. However, the highest obtained life times, even for experimental control rods, remain lower than the fuel's one, which constitutes a major drawback for the reactor economy. Moreover, most of the behavior laws are only phenomenological ones: physically based laws are then clearly needed (e.g., fission products release).

From the results detailed here, a possible optimized (although classical) concept would have the following characteristics:

- B_4C absorber with
 - Density around 90% (optimum of mechanical properties, cheaper elaboration)
 - As small as possible (submicron) grain size (increased helium release)
- Small diameter pellets, reducing the thermal stresses
- Double ^{10}B enrichment, lower at the feet of the column (limitation of damage)
- Vented pins, allowing helium release and absorber cooling by sodium,
- Shrouded absorber column, preventing fragments relocation and sodium gap closure
- Niobium coating of the clad, limiting carburization

However, further improvements are necessary to reach the planned targets (lifetime in the range of 800–1200 efpd, corresponding to burnups around $2\text{--}3 \times 10^{22}$ captures/ cm^3). They would require the development of new concepts. In this frame, the design of moderated absorber

rods, as considered by Japan (hafnium hydride) and Russia (mixed zirconium hydride – B₄C/Hf rods), appears quite attractive.

5.4 Shield Materials

5.4.1 Vessel Shielding

This section deals with the shielding evaluation about neutron fluence and neutron dose on the SFR reactor vessel. The neutron fluence and DPA undergone by the vessel influence the plant lifetime. This evaluation is performed with TRIPOLI-4 Monte Carlo code (Lee and Hugot).

TRIPOLI-4 is a 3D Monte Carlo point-wise code developed by CEA. It is dedicated to radiation protection and shielding, criticality, and reactor core projects. It is used as a reference tool by CEA as well as its industrial or institutional partners, and in the NURESIM European project. It is available from the NEA and RSICC web sites.

The reactor is modeled from the core to the primary concrete. Assemblies, lateral reflectors, and neutron shields are homogenized. ➤ [Figure 137](#) shows a view of the reactor modeled using TRIPOLI-4 code.

Neutron sources are modeled in respect with the V2B configuration (Buiron 2009). They are homogenized for each assembly and are based on a common axial power distribution.

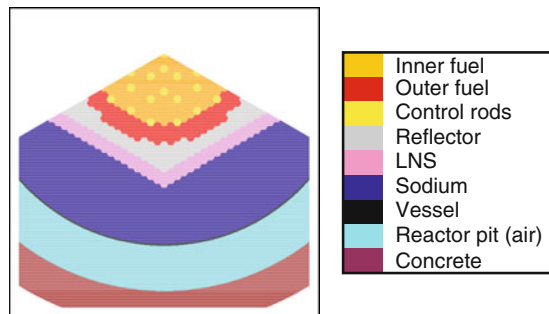
A preliminary shielding study was carried out to determine the lateral neutron shielding (LNS) thickness to respect the fluence and the DPA criterion (Bourganel).

The fluence and DPA criterion for RCGSC reactor are chosen as below:

- > 100 keV fluence criterion: $1.0 \times 10^{18} \text{ n cm}^{-2}$.
- > 1 MeV fluence criterion: $6.5 \times 10^{19} \text{ n cm}^{-2}$.
- DPA criterion: 0.1.
- The supposed load factor is 80%.

This study led to the necessity to use two LNP rows made of enriched boron carbide (B₄C).

A new reactor design is defined with a minor actinide charged blanket row (MACB) located between the reflector and the LNS, as shown in ➤ [Fig. 138](#).



■ **Figure 137**

Horizontal view of the SFR reactor

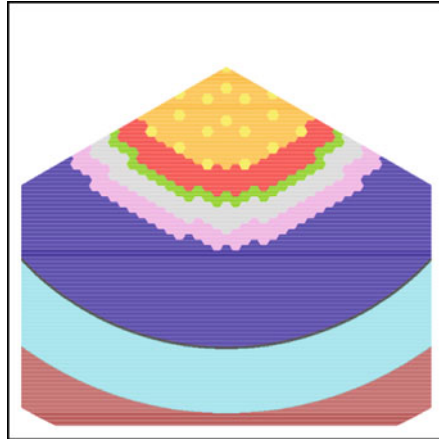


Figure 138
Horizontal view of the SFR reactor including a MACB row (green)

Table 26
MACB effect on fluence and DPA maximal values

Configurations	>1 MeV fluence	>100 keV fluence	DPA
V2B	$4.87E + 15n \times cm^{-2}$	$5.29E + 16n \times cm^{-2}$	2.96E-05
V2B with MACB	$2.86E + 15n \times cm^{-2}$	$3.75E + 16n \times cm^{-2}$	1.74E-05

The effect of this actinide row versus the fluence and DPA calculation is examined.

Table 26 gathers results.

In spite of the MACB row presence, representing an additional neutron source in the core, the fluence and DPA criterion is respected (Jasserand).

5.4.2 Sodium Activation

The sodium activation in the heat exchanger inside the reactor is calculated using a three-step calculation involving the TRIPOLI-4 code to calculate the neutron flux in the heat exchanger, the DARWIN/PEPIN2 activation/depletion code (Tsilanizara) to determine the sodium activation and the associated emitted gamma rays, and finally TRIPOLI-4 again to obtain the dose equivalent rate induced by these γ -rays around a sodium pipe outside the reactor.

Taking the French law into consideration (Arrêté 2006), the calculated dose equivalent rate when the reactor is working is low enough to allow a human presence if a special event requires it. However, a delay of 6 days after the reactor shutdown is required to reduce the dose equivalent rate corresponding to the regulated work area ($25 \mu Sv/h$).

6 Core Design

6.1 Performances Objectives and Design Criteria

The core design of sodium-cooled fast reactors is mainly driven by the enhancement of performances in terms of safety, competitiveness, and flexibility domains, compared to previous SFR projects. Performances objectives are:

- Improvement of safety features based on minimization of the burnup reactivity loss (to limit consequences of control rod withdrawal transients), a significant reduction of the sodium void effect, and a high resistance to core compaction, particularly with regard to earthquake risks. All these points aim to improve natural core behavior during transients and to exclude important mechanical energy release in case of severe core damage accidents.
- Flexible management of plutonium (optimization of uranium resources) and transmutation of minor actinides (environmental burden decrease).
- High burnup rates, high power density, low Pu core inventories.

6.1.1 Safety Objectives

According to the analysis of background of SuperPhenix reactor and EFR project, the major guidelines for core design are the following:

- Reduction of the burnup reactivity loss in order to limit consequences of control rods withdrawal accidents, in particular by reducing control rods neutronic weight. SFR cores with high internal breeding gain (internal breeding gain closed to 0) are particularly interesting because they minimize the BU reactivity loss. For instance, the BU reactivity loss by cycle is around $3\% \Delta k/kk'$, while for advanced SFR cores with $IBG = 0$, the BU reactivity loss is less than $0.5\% \Delta k/kk'$.
- Reduction of the sodium void effect in order to improve the natural core behavior during loss of flow accidents or gas core ingress accidents, limit the mechanical energy release in case of a core disruptive accident. The target for sodium void value is significantly less than \$6.
- Optimization of the Doppler Effect, knowing that increase of Doppler Effect is favorable for accidents of reactivity (such as control rod withdrawal), and decrease of the Doppler Effect is rather favorable for transient of flow.
- Reduction of the core pressure drop to facilitate the establishment of sodium natural convection during transients of loss of flow. The core ΔP was about 6 bar for EFR core; For the JSFR core, the core ΔP is about 2 bar.
- Decrease of plutonium enrichment which appears to be potentially favorable to limit consequences of CDA, in particular with regard to recriticality risks.

6.1.2 Flexibility SFR Cores

Depending on changes in the future in terms of natural resources, an important flexibility capability for plutonium management is needed for new SFR cores. It is essential for SFR cores to cover a wide range of breeding gain. The breeding gain (BG) represents the net production of

atoms of Pu (Pu-239 equivalent) by fission. The PHENIX reactor has a positive global breeding gain ($GR = +0.1$) because of the contribution of radial and axial blankets, and the internal breeding gain is clearly negative ($IBG = -0.5$). It is also the case for the EFR core, which has a slightly positive $BG = +0.02$ with blankets, with $IBG = -0.20$. It is understood that the design of SFR cores with IBG close to 0 is particularly favorable since it can reach high values of BG ($BG > 0.2$) by adding fertile blankets.

Also, new SFR cores have to recycle minor actinides (MA). Transmutation of MA is currently envisaged using two modes:

- The homogeneous mode for which minor actinides are mixed into the fuel
- The heterogeneous mode, for which minor actinides can be loaded in blankets subassemblies located in periphery of the core

Both options must be taken into account knowing that:

- Heterogeneous management of MA should not affect characteristics of the core,
- Homogeneous management of MA also should not significantly modify key physical parameters of the core (reactivity coefficients, IBG) if the quantity of MA in the fuel is not too large ($\approx 1\%$ of total heavy metal in the case of auto recycling, the limit being around 2.5–3% by mass).

6.1.3 Core Competitiveness

Reaching high fuel burnup ($BU > 100 \text{ GWd}/t_{HM}$) promotes the minimization of material fluxes in manufacturing and reprocessing plants, and therefore reduces the fuel cycle costs. To get high burnup, requirements are to have cladding materials and metallic structures, which are resistant to high neutron doses. Oxide dispersed steel are studied in many R&D programs because it could enable support of high level of neutron dose ($\approx 200 \text{ dpa}$).

For the deployment of a SFR reactors fleet, the core Pu inventory is an important parameter (with time off reactor) because it manages, for a given stock of plutonium, the total capacity of installed power. In this perspective, concepts of SFR cores which reduce plutonium inventories are interesting.

6.1.4 Design Criteria

Criteria for Fuel Design

The criteria are reported in the following [Table 27](#).

No Fuel Melting Criterion This criterion is based on an analysis of the uncertainties of calculating the fuel temperature and margins to take into account, the probability of fuel melting for each category of operation. For EFR project, the methodology for assessing the maximum linear power is based on the calculation of the no fuel melting probability considering a control rod withdrawal accident.

The maximum linear power usually varies between 350 and 450 W/cm for standard SFR cores.

No Sodium Boiling Criterion This criterion must be respected in all situations. It is usually “covered” by the criterion of no clad damage.

■ **Table 27**
Criteria for fuel design

Major criteria	Design criteria
No fuel melting	Max. linear power
	Max. fuel temperature
No sodium boiling	Clad nominal temperature
No damage on fuel cladding	Clad maximal temperature
	Maxi neutron dose
No mechanical fuel/clad at the end of life	Smeared density
	Central hole diameter of fuel pellet
Pressure strength of fuel rod	Gas expansion volume
	Clad thickness
	Limit of clad diameter deformation
	Limit of clad swelling

No Clad Material Damage Criterion This criterion indicates that for all the operating situations, the cladding material must keep intact and its structure must not be modified significantly. The maximal clad temperature corresponding to this criterion is 620 °C for stainless steel materials (type 316 Ti).

Criterion of No Mechanical Fuel–Clad Interaction

This criterion is essential to guarantee the fuel rod mechanical resistance to the end of life. The mechanical fuel–clad interaction is a result of the fuel swelling due to burnup. The initial available volumes: fuel porosity, initial gap between fuel and cladding, and presence of a central hole are gradually used by the fuel to accommodate its swelling. The background has shown that it is possible to achieve high burnup (15 at.%), with a smeared density around 88% Dth. Usually, fuel pins get a central hole with an internal diameter comprised between 1 and 2.5 mm.

Because the criterion of noninteraction is difficult to meet, it can use another criterion based on the reduction of the initial section of central hole, which appears to be a good indicator of an imminent risk of mechanical interaction, when it reaches about 50%.

Criterion of Strength for Fuel Rod Due to Internal Pressure

The increase of internal pressure due to fission gas production depends on the volumes of fission gas plena inside the fuel rod. These plena are located on both sides of the fissile column. The dimensions of the expansion volumes impact directly the primary stress and it is possible to respect criterion with adapted volumes of expansion plena.

Other Design Criteria

A limit for diameter deformation is imposed on the one hand, by the thermalhydraulics calculations that define a value beyond which the reduction of sodium channel generates excessive

temperature and the other by the mechanical behavior of the fuel bundle which does not lead to direct contacts between fuel rods. This limit is usually set to 6%.

Another limit concerns clad volumic swelling, which is used to prevent excessive weakness of the clad material. This swelling limit is set to 6% which corresponds to a clad diameter deformation of 3% (swelling + irradiation creep). It can be noticed that the limit swelling for ferritic–martensitic steels including the ODS is not known at this time.

Criteria for Wrapper Tube

The choice of thickness of the hexagonal tube and distance between assemblies must be compatible with the maximum allowable deflection of faces under creep irradiation and the maximum deformation by swelling.

The criterion of maximum deformation of the outer flat–flat wrapper tube is the absence of contact between faces of two neighbored wrapper tubes.

Moreover, the level of wrapper tube pads must be compact in normal operation: the outer flat–flat pads should be equal to the expanded pitch of wrapper tubes.

6.1.5 Core Shape Design

A reduced height for SFR cores enables to decrease the subassembly length (economic benefit), and the sodium void coefficient (safety benefit). However, it leads to a larger core radius which can be penalizing with regard to control for large cores. Usually, an active core height of 1 m is a convenient compromise and a minimum height/diameter ratio of ~ 0.2 is used for big size cores.

6.2 Core Neutronics

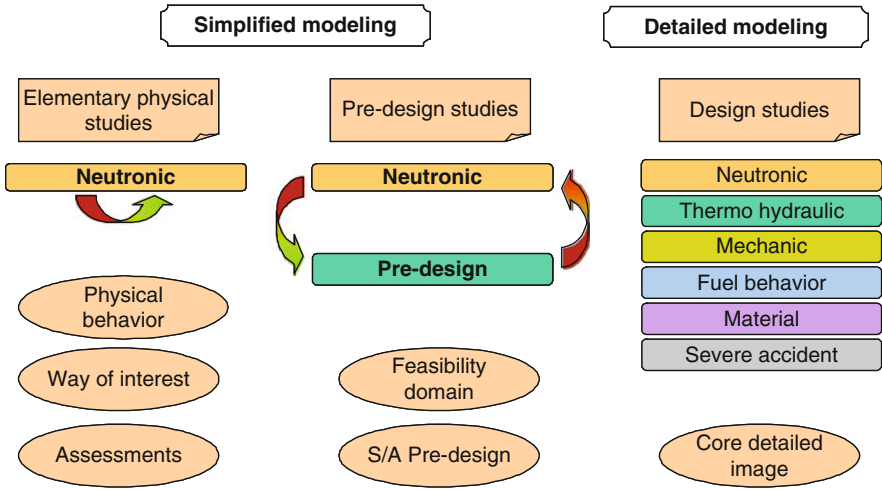
Neutronic core design studies can be grouped into three main families (➤ [Fig. 139](#)), within a classic design approach:

- Elementary physical analysis
- Pre-design studies
- Detailed design studies

In addition, analysis tools to quantify the effects, as the calculations of perturbations, and produce, in fine, high levels of uncertainty about the parameters required for full-end designers. The diagram below shows a simplified set of these studies and their purpose, as well as other scientific areas in liaison and interaction with purely neutronic studies.

6.2.1 Elementary Physical Analysis

To evaluate or design a core of a new reactor type, it is essential to master and understand the physics that governs, not only in order to master a high predictability on the system, but also to identify the first order parameters proceeding on it. Thus, it is possible to access both at the physical phenomenon and identify the way of progress and perform a first assessment. For that we need to have not only physical analysis tools, but also simplified and adaptable modeling.



■ Figure 139

Main families in neutronic core design

This type of study being strongly parametric, each elementary calculation should be done within a short time, both in the implementation and CPU time itself.

At this step of study we do not see strong linkages with other disciplines in the approach itself today. On the other side, the promising results obtained in this phase will be taken as an input for the pre-design studies.

Currently this type of evaluation is based:

Cell calculations in homogeneous description:

- Core calculation in 2D (R, Z) modeling, in diffusion approximation or in transport theory
- On sensitivity analysis based on perturbation theory

The analyzed parameters at this level are macroscopic type:

- The K_{eff}
- The average enrichment
- Core safety coefficients (Void effect, Doppler constant, delayed neutron fraction)
- The burnup
- The cycle length

For the core safety coefficient, calculation methods are given in [Sect. 6.5](#).

6.2.2 Pre-design Studies

The pre-design studies can be performed after preliminary physical analysis studies in order to evaluate a promising concept and also be used in the case of existing concepts adaptation or evaluation.

In the case of the design approach ([Figs. 140](#) and [141](#)), these studies are designed to resize a fuel element (pin for example) in the subassembly and adapt the core to reach the main objectives.

The objectives translation in term of neutronic core design could be converted in terms of area of feasibility as shown below.

This approach is iterative with other disciplines involved in subassembly design (thermohydraulic, thermomechanical, fuel physical chemistry. . .). The repetitive character of this approach requires simple models, near the one used in the previous step with robust methods, fast implementation, and short time calculations. And so, the calculation schemes are quite similar to the scheme used in the elementary physical analysis, but differ on the other hand by the type of results to be extracted here.

We need, at this stage, more comprehensive and detailed results not only for an access to new information but also to transfer data to other design disciplines involved in the holistic design approach.

The results are:

- The fissile enrichment values
- The equivalent plutonium W_i and associated W_i
- The heavy nuclide mass to reload
- The isotopic compositions of spent fuel
- The breeding gain
- Average and max burnup
- Average and max DPA
- Power and flux distribution
- The cycle length
- Average reactor safety coefficient (see drain effect, Doppler, proportion of delayed neutrons)
- An assessment of control rods total weight

The W_i value is defined by:

$$W_i = \frac{\sigma_i^+ - \sigma_{U-238}^+}{\sigma_{Pu-239}^+ - \sigma_{U-238}^+}$$

σ_i^+ is defined by:

$$\sigma_i^+ = \nu \sigma_{f,i} - \sigma_{a,i}$$

with

$\sigma_{f,i}$, equivalent fission cross section for the i nuclide (average on the core)

ν , the average number of neutrons by fission

$\sigma_{a,i}$, equivalent absorption cross section for the i nuclide (average on the core)

The total quantity of equivalent Pu-239 equivalent is defined by: $M_{Pu-239\acute{e}quiv} = \sum_i M_i W_i$.

6.2.3 Detailed Design Studies

These studies are carried out chronologically once the core design is roughly defined by previous studies. These studies are the full core design and could be corresponding to the phases of the feasibility report or detailed design of a design project. In terms of physic studies it is the maturity of the project which will see it will be in one phase or another. As against the code validation level and associated uncertainties will be refined as the project progressed and the needs of designers.

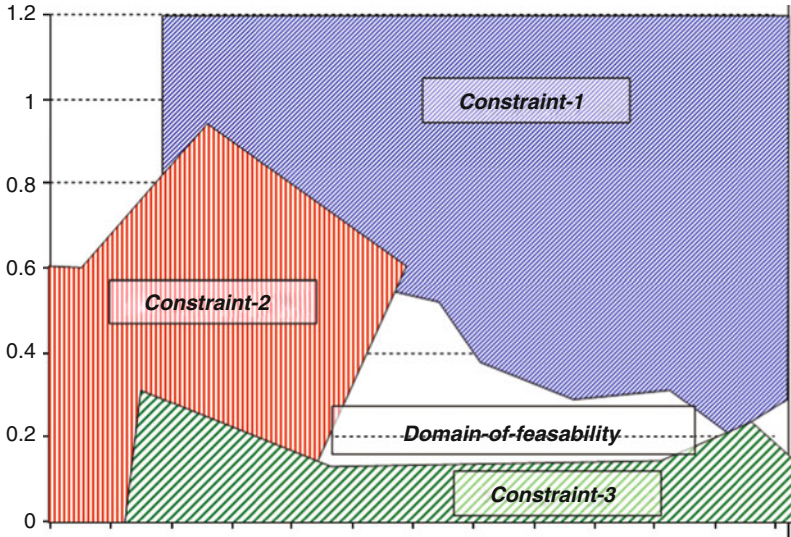


Figure 140
Example of feasibility domain

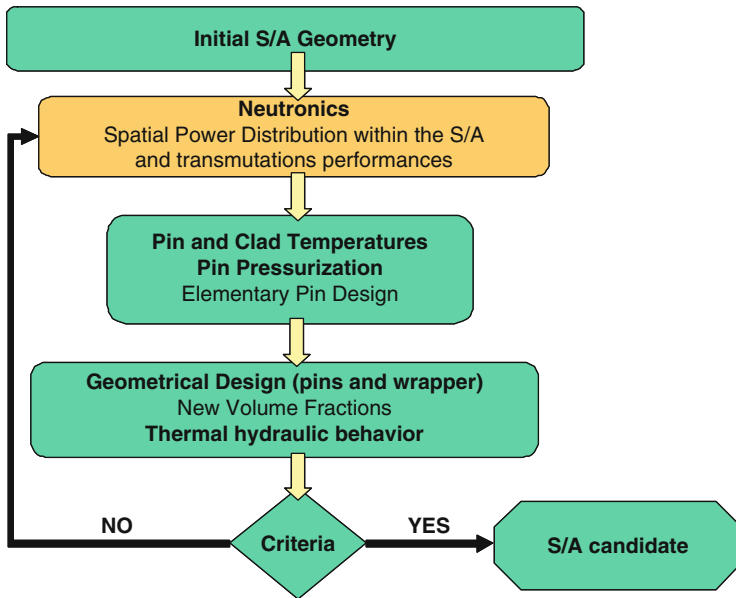
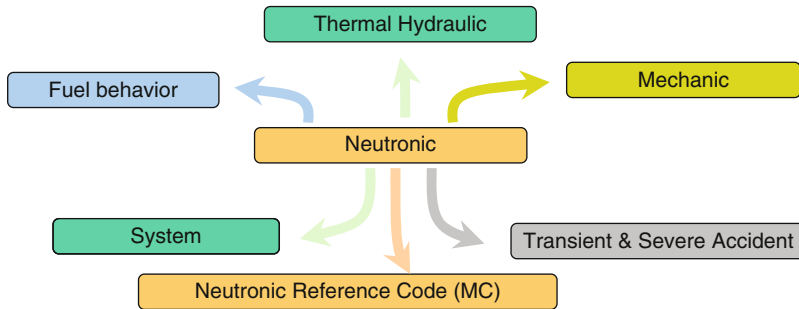


Figure 141
Design process



■ **Figure 142**
Synoptic scheme of needs between domain

For these studies, it is necessary to access on a very large number of parameters greater and more detailed than the previous stage and take into account more accurately the S/A and core geometry. The neighboring of the core will be also described as accurately as possible (fertile and/or radial reflector, radial and axial protection).

Geometric descriptions are three-dimensional and the mesh description is refined (as an example for a large core 350,000 meshes and 5,000 evolving medium. The subassemblies are axially subdivided into zones of independent evolution (10–15) and 1–19 volumes radially).

To reach the objective of an increase of the calculation accuracy it is necessary to perform best estimate calculations (with Monte Carlo Method and also with deterministic method using best validate schemes for cell and core calculations).

The needs in terms of result are quite similar to the previous step, but the uncertainty level could be associated with each result (► [Fig. 142](#)). During these detailed design studies, it is also necessary to transfer huge amounts of data to the other domain and associated codes.

6.2.4 Calculation Tool for Neutronic Core Design

The deterministic ERANOS neutronic system consists of data libraries, codes, and calculation procedures which have been developed within the European Collaboration on Fast Reactors over the past 20 years or so. The ERANOS code system was developed to answer the needs of both industrial and R&D organizations. A modular structure was adopted in ERANOS to allow the incorporation of the most recent research and development innovations.

This modular structure allows different modules to be linked together in procedures corresponding to recommended calculation routes ranging from fast running and moderately accurate “routine” procedures to slow running but highly accurate “reference” procedures.

The main features of ERANOS that are presented here are:

- Nuclear data libraries: several neutron cross section libraries, all derived from the JEFF-3.1, JENDL3.3, and ENDF/B-VII nuclear data evaluated files are available, each containing:
 - 1,968-groups library for the main resonant nuclides
 - 33-groups library for fast-spectrum applications
 - 175-groups library for shielding calculations
 - 172-groups library for thermal-spectrum applications

- The ECCO cell/lattice code prepares self-shielded cross sections and matrices by combining a slowing-down treatment in many groups (1,968 groups) with the subgroup method within each fine group and collision probabilities calculation for many types of geometries
- Core and shielding calculation codes:
 - Diffusion (1-D, 2-D, 3-D) codes
 - The BISTRO Sn transport 1-D or 2-D (X-Y, R-Z, R- θ) code
 - Variational Nodal Method transport 2-D and 3-D Cartesian and hexagonal, with “TGV/VARIANT code”

These codes solve both homogeneous and inhomogeneous (external source) equations and provide direct and adjoint solutions. A kinetics driver named KIN3D has been developed using the TGV/VARIANT module and is integrated into ERANOS.

6.3 Core Thermalhydraulics

A core design has a threefold objective:

- Guarantee the thermomechanical behavior of cladding in each subassembly (S/A) under nominal operating conditions
- Avoid the risk of compaction based on knowledge of the static mechanical equilibrium of the core
- Ensure fuel subassembly unloading

To achieve this threefold objective, it is essential to fully understand the thermal fields of the fuel (and breeder) assembly structures in the core (cladding and hexagonal wrapper tube or hex-can). The flow and temperature distributions in the coolant need to be calculated to determine these thermal fields. The temperature (structures and coolant) and flow calculations concern the field of core thermalhydraulic studies. The CEA has developed a core design method for its fast reactors, which is described below.

6.3.1 Core Flow Distribution

Objective

Calculating the core flow distribution is also a threefold process:

- The core outlet temperature must:
 - Be as high as possible to avoid affecting the reactor efficiency
 - Take into account the thermomechanical resistance of the reactor block structures
- Each subassembly (S/A) must be cooled correctly,
- The core outlet temperature map must be flattened to ensure resistance of the upper structures to temperature fluctuations (thermal stripping).

Method

The core design method involves meeting a given nominal clad temperature (NCT), defined as follows:

$$\text{NCT} = T_{\text{inlet}} + \Delta T_{\text{hsc}} + \Delta T_f + \Delta T_{1/2C}$$

where

T_{inlet} : Core inlet temperature,

ΔT_{hsc} : Heating of the hottest sub-channel,

ΔT_f : Temperature drop in the viscous sub-layer,

$\Delta T_{1/2C}$: Temperature drop in the cladding half-thickness (outside inward).

The NCT must remain below a criterion during the irradiation of the S/A in the core. It is therefore necessary to define a maximum power configuration for which the flow distribution is calculated. This envelope configuration is defined according to the maximum linear power of each S/A between the beginning and end of its residence in the reactor.

The solution chosen for the fast reactor technology involves classifying the fuel and breeder subassemblies into different flow zones. The subassemblies in the same flow zone share the same flow. This flow is determined by the subassembly with the hottest sub-channel, whereas the other subassemblies are slightly overcooled.

Once the envelope configuration has been calculated, it is necessary to determine the optimal number of:

- Flow zones, representing the first level of optimization,
- Subassemblies per flow zone, representing the second level of optimization.

Once this optimization process has been completed (by the SUPTHYL computer code), the flow of each subassembly classified into a flow zone is known. The following aspects must then be checked:

- Flattening of the core outlet temperature map
- Difference in outlet temperatures for two neighboring subassemblies at each moment of the cycle (start and end)

Mixing Coefficients

A thermohydraulic model for the subassembly is also required to obtain an optimal flow distribution in the core. This model must take into account:

- Geometry and orientation of the assembly
- Axial and radial power distribution in the bundle of pins
- Mixing effects due to the spacer wires (see chapter on “Modeling”)

The temperature map of a bundle cross section is defined by the parameter A as follows:

$$A_i = \left[\frac{T_i - T_{\text{inlet}}}{T_{\text{mean}} - T_{\text{inlet}}} \right]$$

where

T_{inlet} : Core inlet temperature

T_i : Sub-channel temperature i

T_{mean} : Mean temperature of the cross section

Axial Power Profile The parameter A is more or less independent of the axial power profile.

Radial Power Profile and Subassembly Orientation The orientation of a subassembly depends on the type of radial power gradient. There are two types of orientations:

- Side: when the most powerful pin is located in the middle of the side of a hexcan
- Angle: when the most powerful pin is located on an angle of a hexcan.

The power variation is assumed to be linear between two sides or two opposite angles. The radial power gradient depends on the (α_R , orientation) couple, with α_R being defined as such:

$$\alpha_R = \frac{P_{1 \max}}{P_{1 \min}}$$

where

$P_{1 \max}$: Maximum linear power of the most powerful pin

$P_{1 \min}$: Maximum linear power of the mean pin

Mixing Effects The effects of mixing due to the helical spacer wire are assessed with the CADET computer code on the basis of a sub-channel approach (see  Sect. 6.3.2). CADET is used to calculate two different temperature maps:

- A : A_i With mixing effects for each orientation and for different values of α_R . A is expressed as follows:

$$A(\alpha_R, \text{orientation}) = \left[\frac{T_{\text{hsc}} - T_{\text{inlet}}}{T_{\text{mean}} - T_{\text{inlet}}} \right]^{(\text{with_mixing})} = \left[\frac{\Delta T_{\text{hsc}}}{\Delta T_{\text{mean}}} \right]^{(\text{with_mixing})}$$

- F : A_i Without mixing effects for $\alpha_R = 1$. F is expressed as follows:

$$F = A(\alpha_R = 1) = \left[\frac{T_{\text{hsc}} - T_{\text{inlet}}}{T_{\text{mean}} - T_{\text{inlet}}} \right]^{(\text{no_mixing})} = \left[\frac{\Delta T_{\text{hsc}}}{\Delta T_{\text{mean}}} \right]^{(\text{no_mixing})}$$

ΔT_{hsc} : Heating of the hottest sub-channel with mixing effects (with_mixing) or without mixing (no_mixing),

ΔT_{mean} : Mean heating of the S/A in the hottest sub-channel with mixing effects (with_mixing) or no mixing (no_mixing).

The mixing coefficient C_m used for optimization purposes is defined as such:

$$C_m(\alpha_R, \text{orientation}) = \frac{A}{F\alpha_R}$$

6.3.2 Calculation of Fuel Assembly Thermalhydraulics

Introduction

The first objective of the CADET project code is to calculate the NCT, which requires both a global and local understanding of the fuel bundle thermalhydraulics. One of the main effects to be taken into account is coolant mixing due to the spacer wires. These wires impose local and global coupling in a bundle limited by a hexcan. The second objective is to calculate the above-mentioned mixing coefficients C_m .

The CADET computer code uses a sub-channel approach to achieve these objectives. Two different sub-channels are differentiated by a fictive boundary that is common to both and where thermalhydraulic coupling occurs. This approach requires physical models that are based on theoretical, analytical, and experimental data.

Thermal Balance Equation

CADET calculates the axial steps (Δz) for each sub-channel. The thermal balance for each sub-channel is as follows:

$$q_j(z) \cdot C_p \cdot [\theta_j(z + \Delta z) - \theta_j(z)] = W_j - \sum_a B_j^a [\bar{\theta}_j - \bar{\theta}_a] - B_j^r [\bar{\theta}_j - \bar{\theta}_r]$$

$$\bar{\theta} = \frac{\theta_j(z) + \theta_j(z + \Delta z)}{2}$$

where

q_j , sub-channel flow j

θ , temperature of sub-channel no. j (θ_j) or an adjacent sub-channel ($\bar{\theta}_a$) or a thermal boundary condition $\bar{\theta}_r$

B_j^a , equivalent thermal diffusivity modeling the transverse coupling between two sub-channels

B_j^r , equivalent thermal diffusivity modeling the thermal couple with a thermal limiting condition

W_j , dissipated power in the main sub-channel j

The thermal diffusivity B_j^a is equivalent to the sum of the three terms used to model the three radial thermal couplings:

- $B_j^{\prime a}$, thermal coupling due to deviated flow: $B_j^{\prime a} = q_j^a C_p \Delta z$ (Sect. Modeling Flow Deviated between Sub-Channels)
- $B_j^{\prime\prime a}$, thermal coupling by conduction in the coolant (Fourier's law)
- $B_j^{\prime\prime\prime a}$, thermal coupling due to eddy diffusion (correlation).

Bundle Flow Distribution

CADET assumes an isopressure for each planar coolant cross section of the bundle, which is a slightly conservative assumption. The flow is therefore constant per type of sub-channel.

Modeling Flow Deviated between Sub-Channels

Three types of sub-channels are defined: triangular, rectangular and corner. A by-passed flow law is required for each type of sub-channel. The incoming and outgoing flows at each mesh level are also assumed to be equivalent. The mass transfer occurs at the neck between two sub-channels in relation to the location and rotation of the spacer wire according to a sine function. This function is determined by equalizing the surface covered by the helical wire and the surface of the sine function. The by-passed flows per sub-channel type (over a half-pitch $h/2$ of the spacer wire) are expressed as follows:

- Two triangular channels (Δ):

$$q_{\Delta \rightarrow \Delta}^{(h/2)} = \text{COE1.0,6046 } d_{\text{wire}} (2D_{\text{pin}} - d_{\text{wire}}) q_{\Delta} / S_{\Delta}$$

- Two peripheral channels (\square):

$$q_{\square \rightarrow \square}^{(h)} = \text{COTRA} \pi d_{\text{neck}} (D_{\text{pin}} + d_{\text{neck}}) q_{\square} / S_{\square}$$

- A triangular sub-channel (Δ) and a rectangular sub-channel (\square):

$$q_{\Delta \rightarrow \square}^{h/2} = \text{COE2.0,6046 } d_{\text{wire}} (2D_{\text{pin}} - d_{\text{wire}}) q_{\Delta} / S_{\Delta}$$

where S represents the flow cross section; d or D are the diameters; and $COE1$, $COE2$, and $COTRA$ are coefficients adjusted according to the experimental results.

6.3.3 Assessment of Hexcan Temperatures

Safety studies require understanding the mechanical behavior of subassemblies for two main reasons: (1) verification of the level of stress on each wrapper with the reactor under nominal conditions, and (2) knowledge of strain in these same wrappers which, if too high, will prevent their unloading after reactor shutdown. These objectives necessitate:

- Understanding the irradiation conditions of subassemblies (neutron studies)
- Estimating the thermal loads of wrappers (thermohydraulic studies). These estimates are obtained by calculations.

Simplified Description of the Core Thermalhydraulics

Sodium flows into the core through the diaphragm. Most of this flow is distributed between the subassemblies in relation to their own pressure losses. This flow rises. At the core outlet, part of this flow hits the above-core structure (BCC in [Fig. 143](#)) and generates overpressure. This overpressure acts like a piston on the inter-wrapper flow which drops toward the bottom of the core and then rises to the core periphery ([Fig. 143](#)). The inter-assembly flow is also amplified by a leak in the sphere-cone bearing at the bottom part of the core ([Fig. 143](#)).

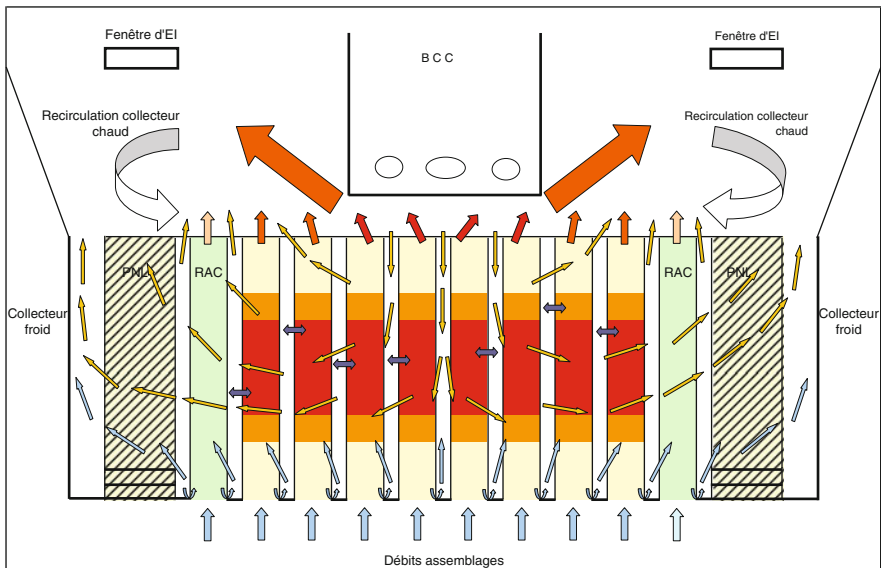


Figure 143

Simplified thermalhydraulic description

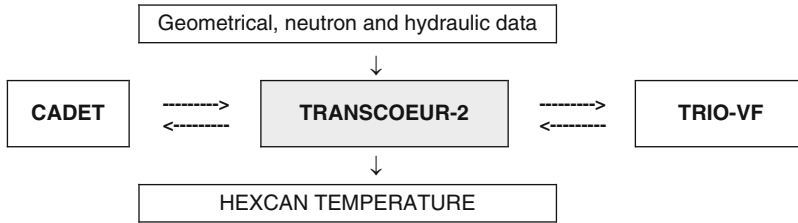


Figure 144
Schematic flow diagram

Calculation of Hexcan Temperatures

The coolant flowing into the subassemblies is heated by the full length of the pins in the bundle. This heating – for all fuel and breeder subassemblies – is calculated by the CADET computer code under thermal limiting conditions defined by the inter-wrapper flow. These thermal boundary conditions are calculated with the TRIO-VF finite-volume code. TRIO-VF predicts the thermalhydraulic behavior of the inter-wrapper flow under the thermal boundary conditions defined by the CADET calculations. At the end of the iterative calculation process, the temperatures of all six sides on each hexcan in the core are known, from the bottom to the top of the core and for different axial levels.

The TRANSCOEUR-2 code combines these calculations (► Fig. 144). This code also requires a geometrical description and a neutronic description (axial profiles and maximum linear powers) of each subassembly, as well as the core flow distribution.

TRIO-VF Thermalhydraulic Computer Code

The TRIO-VF finite-volume code can calculate complex laminar and turbulent flows under permanent or transient conditions. The fluids are assumed to be Newtonian, noncompressible and they are used to check the BOUSSINESQ approximation. The boundary conditions can be either DIRICHLET (imposed velocities or temperatures) or NEWMAN (imposed fluxes). The balance equations are averaged NAVIER–STOKES equations.

Core Modeling

The inter-wrapper space is described by an axisymmetrical geometry. The inter-wrapper flow model is based on a porous medium approach: obstacles in contact with sodium (subassemblies) are taken into account by porosity and pressure loss coefficients defined by:

- Radial porosity attributed to each ring, representing the inter-assembly distance divided by the pitch of the subassembly lattice
- Axial porosity equal to the ratio of the sum of the S/A hexagonal cross sections for the ring in question, divided by the surface of this ring

The subassemblies are classified by types (fuel, breeder, steel, neutron shielding) and integrated into the radial zones. Only the fuel and breeder zones are coupled with the internal temperature fields calculated with CADET (thermal boundary conditions). A power density can be attributed to the other subassemblies. The leak flow rate at the foot of the subassemblies and the overpressure gradient due to the above core structure are the hydraulic boundary conditions for the calculation.

6.4 Core Mechanics

Situated in a particularly hostile environment, SFR core subassemblies (S-As) undergo thermomechanical distortions, which induce S-As displacements that can be relatively large, and contacts between one another, which could be a cause of disturbance in the reactor operation.

A set of computer codes, named HARMONIE, has been created and developed by CEA in order to model the irradiated core static mechanical behavior as accurately as possible.

It is able to foresee the in-irradiation core static mechanical equilibrium evolution and to evaluate, while spending as little time and money as possible, the evolution of design changes.

6.4.1 Subassemblies Distortions

Steel wrapper tubes surrounding the fuel pins bundle are merged in the fast neutronic flux, which induces irradiation swelling and creep.

The permanent resulting distortions add to purely mechanical and thermic distortions and the total S-As distortions prove to be made up of lengthening, bowing, and cross section variation of wrapper tubes.

Broadly speaking, the core can be divided into three areas with respect to spatial distribution of neutronic flux and temperatures (► *Fig. 145*).

Almost constant in the central area where cross section variation of wrapper tubes can be observed, these fields are highly variable in the external fuel area where thermic and neutronic gradients induce centrifugal bowings.

The core external area, where small neutronic fluxes and smaller temperatures induce small distortions of the S-As wrapper tubes, generates a phenomenon of natural elastic hooping of the outward bowed S-As.

The S-As interactions mainly appear by the means of pads which are stamped on the wrapper tube, just above the axial fuel zone. By the way of thermal expansions these pads cancel the inter S-As gaps in full power reactor operation.

This resulting compact plane reduces the S-As vibrations due to the flowing sodium and plays an important part with respect to reactor safety.

6.4.2 Operating Considerations

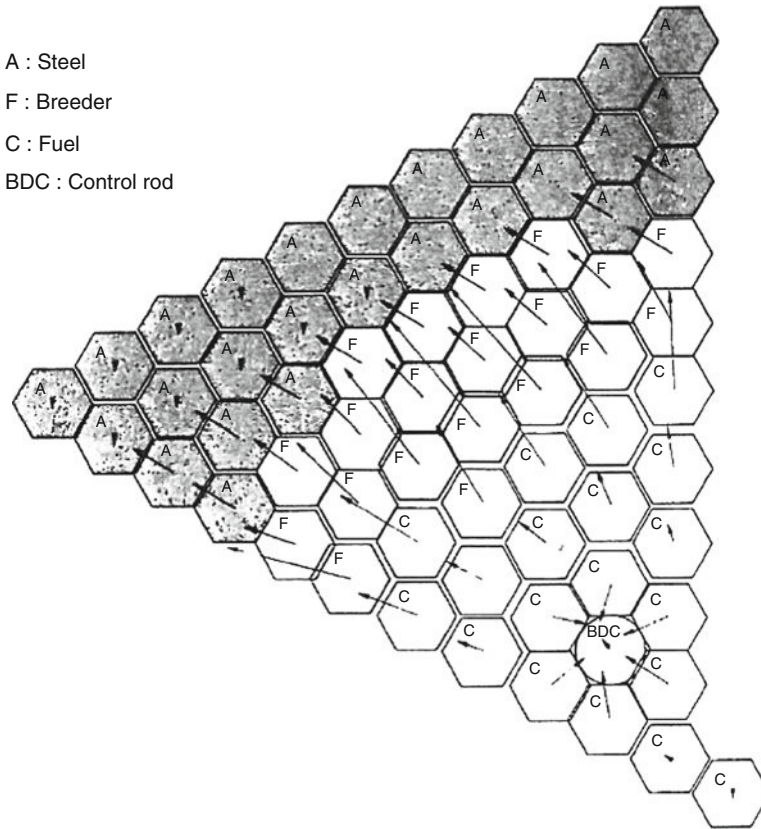
S-As Wrapper tubes large displacements could generate handling problems and difficulties in measuring exit sodium temperatures.

On the other hand, the S-As interaction forces must not be too large in order to handle and remove easily S-As in the core lattice. From this point of view the increase of the wrapper tubes cross section must not create an additional contact level in the fuel axial zone.

Safety Considerations

S-As Wrapper tubes large displacements could generate problems in operating down the in-core safety devices.

On the other hand, it is necessary to control the core reactivity evolution between two states of equilibrium. It can be a slow evolution over an operation cycle to adjust the control rods anti-reactivity. Moreover fast transient accidental situations are studied, such as the so-called “pad



■ **Figure 145**
S-As head displacement. See the control rod perturbation area

effect”: the pad temperature increase generates, by their cumulated thermal expansions, the outward expansion of the whole core, which induces a decrease of reactivity and consequently a decrease of reactor power.

In order to derive a benefit from this effect, which is favorable in consideration of safety, the core must be compact enough at the pads axial level.

Therefore, criteria with respect to main characteristic parameters are needed to operate the reactor with accuracy and safety. Meeting these requirements involves consequences concerning the core design and sizing.


For instance, the smaller the inter pad gaps are, the higher the handling friction forces are, but the tighter the bundle of core S-As is.

6.4.3 Modeling of the SFR Core Static Mechanical Behavior

The knowledge of physical phenomena occurring in the core while operating the reactor enables us to predict their evolutions through modeling, to emphasize the main parameters and determine their influence. Modifications of design are thus made possible.

HARMONIE is a set of computer programs successively describing, using precise 3D distributions of the neutronic flux and the temperature fields, the 3D distortions of each sub-assembly, the in-core interactions, the handling forces and the consequences of the whole core distortion with respect to reactivity:

- The calculation of distortions of each S-A, supposed to be alone in the core, is based upon the hypothesis, very classical with respect to the beam theory, that a cross section remains plane all through the S-A stretching. This plane is precisely the one which minimizes the internal energy of cross section distortion and its slope defines the local camber which, by integration over the height of the S-A, leads to the bend of the wrapper tube. On the other hand, at each vertical level, the expansion of the radial cross section is evaluated by means of the average value of each of the six side distortions. The increase of length is calculated by integration of the average axial distortion all over the height of the S-A. The individual history of each S-A is taken into account through the evolutions of its in-core position and orientation.
- The resulting state of mechanical equilibrium of the whole core, that is to say, the location of inter S-As contacts, the values of interaction forces, and resulting static displacements, is then determined.

The physical model consists of a bundle of beams, with an axial distribution of moments of inertia. The most probable levels of contact are selected (generally speaking pad level and S-A head level) and the elastic bending elementary matrix of the beam is only made consequently of the so-called Maxwell coefficients of the S-A, which are the horizontal displacements at each level due to a unit force put at the other one. Cross section distortions at the contact levels are taken into account through an elementary matrix of local flexibilities. Besides an elementary matrix of beam creep velocity is defined in a similar way (the evolution of creep bowings is supposed to be linear with respect to time). The bending potential energy of the bundle of S-As can be, therefore, expressed in a matricial way. The conditions of equilibrium of the core are determined by minimization of this energy with conditions of no overlapping of S-As with each other. As soon as the interaction forces are known, displacements all along the S-As can be calculated and other possible contact levels can be displayed (see  Fig. 146).

These efforts are also used to calculate stresses in the S-As wrapper tube and spike and besides, when the reactor is stopped and the core temperatures have decreased consequently, they are at last used to calculate the handling forces of the removed S-As through a friction coefficient.

It must be noticed that these handling forces can be calculated at different steps of the removal of the S-As.

Besides, a spatial distribution of neutronic coefficients describes the reactivity weight of the nuclear materials in the core. For a given state of equilibrium of the core, the reactivity variation – with respect to a reference state corresponding to a “new core in a cold state” – can be simply derived from the calculated displacements. Thus, it is possible to differentially assess the change of reactivity between any two equilibrium states, whatever.

6.4.4 Experimental Validation

In the past, three real scale experimental rigs in France, and another one in UK, have been designed and built, each of them made of a lattice equipped with a bundle of S-As (91 positions

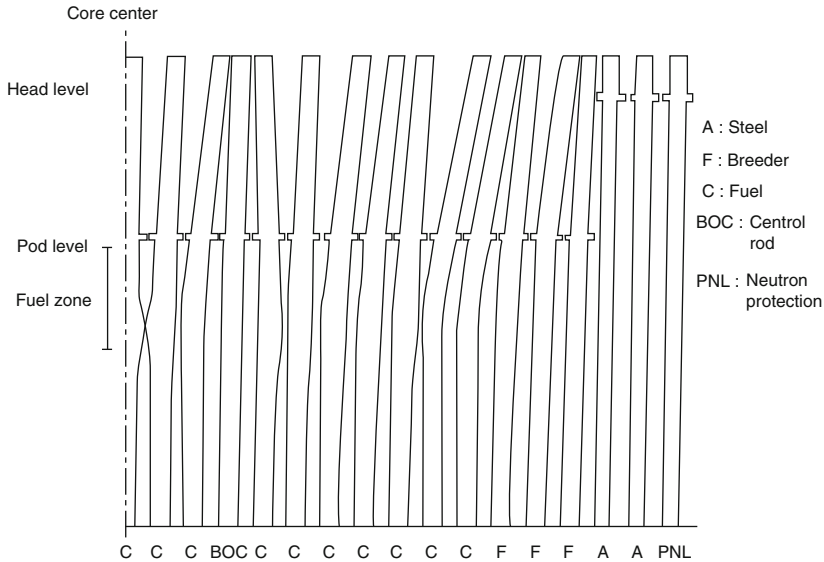


Figure 146
S-As bending and cross section expansion

for Rapsodie and Phenix simulations, and 106 positions for SuperPhenix simulations in the French rigs, 61–91 positions for EFR simulations in the UK-AEA rig).

Most part of HARMONIE validation has been realized with the 106 positions rig, operated at air temperature by the Italian ENEA and CEA (► *Fig. 147*).

A complete program consisted in distorting bundles of S-As by the use of jacks, with bent and/or expanded cross section S-As. Handling tests operating a SuperPhenix-like machine have also been made. Comparisons between measured and HARMONIE calculated results showed an almost complete consistency regarding contact positions and orientations of S-As displacements (► *Fig. 148*).

About 20% gap has been observed.

Besides, specific tests have been made to measure the pad rigidity at the air temperature or in hot temperature conditions. Transposition of these results to the real reactor operating conditions has been derived from sodium friction tests and the SuperPhenix handling machine qualification tests.

Moreover HARMONIE results have been compared to a great deal of Phenix irradiated S-As measures and handling forces measurements.

The strict HARMONIE validation is less easy in such cases because of the complex S-As managing and the great deal of experimental S-As in Phenix core. However theoretical S-As lifetime limitations have always proved to be less than the real lifetimes observed in Phenix.

This proves that HARMONIE overestimates the real physical values which are in favor of reactor operating safety.

Although the physical phenomena are very well known and correctly simulated with HARMONIE a 50% uncertainty coefficient is taken into account concerning most of the parameters,



Figure 147
Operating the CEA 106 E rig in Cadarache (handling test)

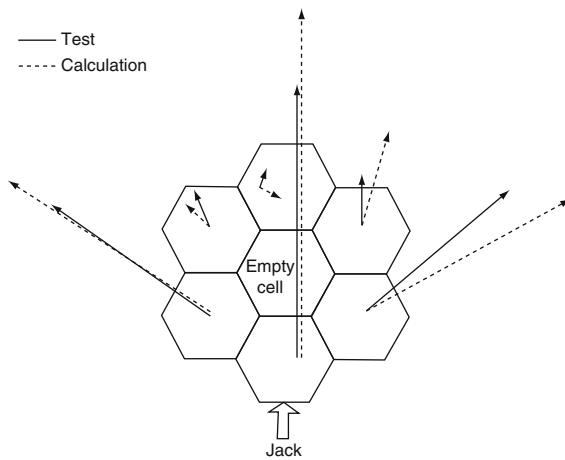


Figure 148
S-As handling has been simulated in distorted S-As bundles by the way of jacks. Qualitative consistency between tests and calculations is satisfactory

up to 95% concerning the friction handling forces. These coefficients stand for the irradiated wrapper tubes steel behavior laws and the various mathematical modelings all together.

6.4.5 Conclusion

Although mathematical models of HARMONIE be quite satisfactory, it would be of great interest to reduce uncertainties coefficients, in order to enhance SAs lifetime.

Complex phenomena such as inter-pad friction and lattice/S-As spike gaps could be therefore usefully studied.

6.5 Reactivity Effects

6.5.1 Description of the Feedback Effects

In this part, we will describe theoretically each feedback coefficient and the effect they have on the reactivity function of the temperature variation. The different effects are done for an increase of the considered temperature. The opposite effect (for a decrease of the temperature) is easily deduced.

Doppler Effect

An increase of the fuel temperature has for consequence a bigger thermal agitation provoking, for each isotope of the fuel, a broadening of the capture and fission resonances.

In fast reactors, the Doppler Effect coefficient is negative. Further, to an increase of the fuel temperature, the Doppler Effect involves a decrease of the reactivity, and conversely for a decrease of the temperature. This intrinsic effect is mainly due to the presence of the isotope U-238 and of its absorption resonances on the energy domain of 0.1–10 keV.

Sodium Expansion

The increase of the sodium temperature involves a decrease of its density, and so a decrease of the interactions between neutrons and coolant nucleus.

It involves a spectral effect (positive), an effect due to the leakages (negative) and an effect bound to the captures (positive):

- Spectral effect: due to the decrease of the coolant interactions, the spectrum becomes faster, and so in the case of a fast reactor, the reactivity increases. The increase or decrease of the reactivity depends on the fuel type; each isotope has its own distribution of cross section functions of the incoming neutrons energy.
- Effect bound to the leakages: as there are fewer interactions with the sodium, there are more available neutrons; on the other hand these are more energetic. Although the interaction and absorption probability function of the incoming neutrons energy depends on each isotope, it generally decreases with energy. And so it increases the leakages of the core.
- Capture effect: the decrease of the sodium interactions involves a decrease of the capture by the sodium and so an increase of the available neutrons. This positive effect is however weak.

The variation of the core reactivity depends on the competition between these three effects. In case of fast reactors, the global variation of the reactivity due to the sodium expansion is generally positive.

Clad Expansion

The clad expansion is subdivided into two effects.

- Axial expansion: the axial expansion of the clad involves a decrease of the steel concentration (geometry unchanged), and a decrease of the interactions between neutrons and steel nucleons. This effect is positive.
- Radial expansion: the radial expansion involves an increase of the clad volume chasing away an equivalent volume of sodium. This effect is similar to the decrease of the sodium density (previously described): it is a positive effect.

Wrapper Expansion

The wrapper expansion is subdivided into two effects like the clad expansion case: an axial and a radial expansion. This effect is positive.

Fuel Expansion

The fuel expansion is subdivided into two effects:

- Axial expansion:
 - Decrease of the fissile nucleons concentration in the fuel: negative effect on the reactivity
 - Increase of the fissile core height: positive effect
 - Increase of the sodium mass in the core due to the increase of the fissile core height. This effect corresponds to the effect of the increase of the sodium density (previously described): negative effect.
 - The axial expansion is taken as a whole negative.
- Radial expansion: the radial expansion of a cladding fuel does not change the sodium volume (unless there is a sodium gap). The radial expansion of the fuel is so without effects on the reactivity.

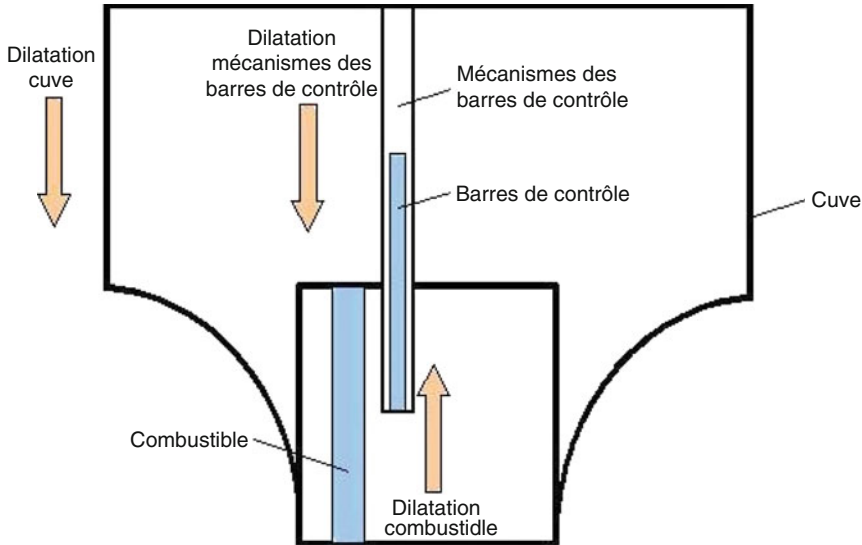
Grid Expansion

It concerns the increase of the core radius due to the grid expansion, provoked by an increase of the incoming sodium temperature. On one hand, the sodium volume inside core increases (effect previously described); on the other hand, the core volume increases (despite a constant fuel mass) and so the leakages increase. The global effect is negative.

Differential Expansion between Core, Vessel and Control Rods

This reactivity coefficient corresponds to three effects:

- An increase of the fuel temperature involves its axial expansion (it means in relative a control rod's insertion)
- An increase of the core out coming sodium temperature causes the axial expansion of the control rod's pipes, and so an insertion of these ones if their mechanism are fixed to the top of the vessel.
- An increase of the temperature of the cold sodium involves an axial expansion of the vessel to the bottom.



■ Figure 149

Differential expansion between core, vessel, and control rods in the case of an increase of the temperatures

The first two effects correspond to an insertion of the control rods in the core, and so a negative effect. It is the opposite effect for the third one. The global effect depends on the temperature variation of the incoming and out coming sodium and of the linear expansion coefficients of the different materials (vessel, fuel, control rods mechanisms). ► *Figure 149* explains this situation in the case of an increase of the temperatures compared to the nominal situation.

To notice: all these effects depend on different time constants, following the reactor conception.

The reactivity coefficient due to the grid expansion is related to the only variation of the incoming sodium and is bound to a time constant of several tens of seconds. So it does not appear in the slow transients.

The reactivity coefficient bound to the differential effect starts with the variation of the fuel height, then with the expansion of the control rod's pipes and endlessly with the vessel expansion. These last two effects are essential for the slow transients.

Pad Effect

It comes from the difference of radial expansion between the bottom of the subassemblies at the incoming sodium temperature and the top, at the pad level, at the out coming sodium temperature. But this effect is very low and will not appear in the calculation of the reactivity coefficients.

Summary of the Location of the Coefficient Calculation  [Table 28](#)

Table 28
This table sums up the location of the calculated reactivity coefficients

	Radial clad expansion	Radial wrapper expansion	Axial clad expansion	Axial wrapper expansion	Sodium expansion	Doppler constant	Axial fuel expansion	Grid expansion
Fissile	Yes	Yes	Yes	Yes	Yes	Yes	Yes ^b	Yes
Fertile ^a	Yes	Yes	Yes	Yes	Yes	Yes	Yes ^b	Yes
Bottom reflector	No	No	No	No	Yes	No	No	Yes
Plenum	No	No	No	No	Yes	No	No	Yes
Top reflector	No	No	No	No	Yes	No	No	Yes
Rod follower	No	No	No	No	No	No	No	Yes
Radial reflector	No	No	No	No	No	No	No	Yes

^a Axial and/or radial.

^b Linked or not.

Yes, if the coefficient is calculated on this region; No, if it is not.

6.5.2 Calculation Method

Main Principle

The principle is to use the perturbations method, available in the ERANOS code. The aim is to calculate the different reactivity coefficients within each region.

First, we have to generate the self-shielded cross sections and matrices of both the situations: standard and perturbed. Because of the thermal expansions, it has been chosen to decrease the concentrations of 1% to create the new cross sections. Second, equivalent temperature variations will be calculated with the corresponding expansion coefficient.

So, new cross sections, new concentrations, and new fluxes will be available for the perturbed situation at the corresponding “step.”

Cross Section Calculation Method

Doppler calculation: new cross sections have to be calculated at the new temperature: this one can be $T_{\text{standard}} + 30 \text{ K}$, or T_{fusion} , or . . .

Fuel, sodium, clad or wrapper calculation: new mediums and cross sections will be created: the density of the corresponding material will be multiplied by a constant of 0.99, simulating a decrease of the concentration of 1%.

Grid calculation:

- Homogeneous cell: the whole volume fractions change: except for sodium, each fraction is divided by a factor of $(1.01)^2$, simulating an increase of the core pitch of 1%. The sodium fraction is calculated to replace the created void by the new fractions.
- Heterogeneous cell: the cell pitch is multiplied by the 1.01 factor.

Flux and concentration calculation:

The evolution of each perturbed concentration is made with the nominal flux and in the standard geometry. At each step, nominal fluxes, adjoint fluxes of the nominal case are conserved.

For the sodium, clad, and wrapper expansions or for the Doppler Effect, perturbed flux calculations are done using perturbed cross sections and corresponding concentrations. Then, exact perturbation calculations are done to obtain a spatial decomposition of the variation:

$$\Delta\rho = \frac{\langle \Phi_1^*, (\lambda_2 \partial P_1 - \partial K_1) \Phi_2 \rangle}{\langle \Phi_1^*, P_1 \Phi_2 \rangle} \quad (24)$$

with

- Φ_1^* : standard adjoint flux
- Φ_2 : perturbed flux
- The whole terms with a subscript 1 correspond to the standard situation, the ones with a subscript 2 correspond to the perturbed situation. The associated terms correspond to the following Boltzmann equation for a critical reactor: $(\lambda P - K) \Phi = 0$ and the adjoint equation: $(\lambda P^+ - K^+) \Phi^+ = 0$.

For the grid expansion, a new geometry has to be created with the new core pitch (“standard one” $\times 1.01$). Then perturbed flux are calculated using perturbed cross sections, corresponding concentrations, and the perturbed geometry. The corresponding $\Delta\rho$ is calculated between the two direct flux calculations.

For the fuel expansion, a new geometry has to be created in order to conserve the fuel inventory of the core. The whole fissile and fertile height is increased by a factor 1.01. The perturbed

flux is calculated with the perturbed cross sections, the corresponding concentration and the “new” geometry. The corresponding $\Delta\rho$ is calculated between the two direct flux calculations.

However, to obtain a spatial decomposition of this effect, it is possible to do an exact perturbation calculation:

$$\Delta\rho = \frac{\langle \Phi_1^*, (\lambda_2 \partial P_1 - \partial K_1) \Phi_2 \rangle}{\langle \Phi_1^*, P_1 \Phi_2 \rangle} \quad (25)$$

But Φ_2 is not the perturbed flux calculated on the new geometry: the geometry has to be the same between the standard and the perturbed situation for a perturbation calculation. So, we calculate the perturbed flux with the perturbed cross sections, with the corresponding concentration but with the standard geometry. The obtained result will be normalized with the $\Delta\rho$ obtained from the direct flux calculations.

6.5.3 Return to a Temperature Variation

The last part consists in calculating the temperature variations corresponding to the expansions we made. In the whole following document, the variable i will refer to a subassembly, the variable j will refer to an axial mesh.

Sodium expansion: the equivalent temperature variation to a decrease of the sodium concentration of 1% is:

$$\Delta T_{\text{Na}} = \left[\sqrt[3]{1/0.99} - 1 \right] \cdot \frac{1}{\alpha_{\text{Na}}} \quad (26)$$

where α_{Na} is the linear expansion coefficient of the sodium at the calculation temperature of the material sodium. The corresponding coefficient is:

$$K_{\text{Na}}(i, j) = (\Delta\rho_{\text{Na}}(i, j)/\Delta T_{\text{Na}}) \text{ (pcm/K)}.$$

Axial clad and wrapper expansion: the equivalent temperature variation corresponds to a decrease of the concentration of 1%. However, this decrease can take place only on the axial direction. Then:

$$\Delta T_{\text{clad}} = \left[\frac{1}{0.99} - 1 \right] \cdot \frac{1}{\alpha_{\text{clad}}} \quad (27)$$

$$\Delta T_{\text{wrapper}} = \left[\frac{1}{0.99} - 1 \right] \cdot \frac{1}{\alpha_{\text{wrapper}}} \quad (28)$$

where α_{clad} and α_{wrapper} are the linear expansion coefficients of the clad and of the wrapper at the calculation temperature of the materials. The corresponding coefficient are: $K_{\text{clad}}^{\text{axial}}(i, j) = (\Delta\rho_{\text{clad}}(i, j)/\Delta T_{\text{clad}}) \text{ (pcm/K)}$ and $K_{\text{wrapper}}^{\text{axial}}(i, j) = (\Delta\rho_{\text{wrapper}}(i, j)/\Delta T_{\text{wrapper}}) \text{ (pcm/K)}$.

Radial clad and wrapper expansion: this coefficient does not come from a loss of the structural mass, but from a loss of the core sodium.

- Wrapper expansion: on each region of the core, we have the following coefficients $K_{\text{wrapper}}^{\text{radial}}(i, j) \text{ (pcm/K)}$, corresponding to the local variations $\Delta\rho_{\text{Na}}(i, j)$. The local reactivity coefficient is thus:

$$K_{\text{wrapper}}^{\text{radial}}(i, j) = \frac{\Delta\rho_{\text{Na}}(i, j)}{\Delta T_{\text{wrapper}}} \times 100 \times 0.02 \times \left(\frac{F_{\text{wrapper}}}{F_{\text{Na}}} \right) \text{ (pcm/K)}$$

where

- F_{wrapper} is the cell volume fraction of the wrapper
- F_{Na} is the cell volume fraction of the sodium
- $\Delta T_{\text{wrapper}}$ is calculated (18).

Clad expansion in the case of a sodium gap: just as it has been made for the radial wrapper expansion, we have the following coefficient.

$$K_{\text{clad}}^{\text{radial}}(i, j) = \frac{\Delta \rho_{\text{Na}}(i, j)}{\Delta T_{\text{clad}}} \times 100 \times 0.02 \times \left(\frac{F_{\text{clad}}}{F_{\text{Na}}} \right) \quad (\text{pcm/K})$$

where

- F_{clad} is the cell volume fraction of the clad
- F_{Na} is the cell volume fraction of the sodium
- ΔT_{clad} is calculated at (17).

The term $(1 - F_{\text{wrapper}} - F_{\text{Na}})$ corresponds to the pin volume fraction in the cell.

Fuel expansion: The temperature variation to expand the fuel in an axial direction (without a loss of fuel mass) depends if this last one is linked or not to the clad.

$$\Delta T_{\text{fuel}} = \left[\frac{1}{0.99} - 1 \right] \cdot \frac{1}{\alpha_X} \quad (29)$$

where

- $\alpha_X = \alpha_{\text{fuel}}$ if the fuel is not linked to the clad
- $\alpha_X = \alpha_{\text{clad}}$ if the fuel is linked to the clad The global effect is obtained by doing the difference between the k-effective of both the direct calculations: $\Delta \rho_{\text{fuel}}$. The spatial distribution of this reactivity coefficient depends on the values of the perturbation calculation: $\delta \rho_{\text{fuel}}(i, j)$.

$$K_{\text{fuel}}(i, j) = \frac{\Delta \rho_{\text{fuel}}}{\Delta T_{\text{fuel}}} \times \frac{\delta \rho_{\text{fuel}}(i, j)}{\sum_{i, j} \delta \rho_{\text{fuel}}(i, j)} \quad (\text{pcm/K})$$

- Doppler constant: the Doppler constant is calculated on the entire fuel zone: fissile and fertile. As their temperatures are different, it is important to separate them.

$$K_{\text{Doppler}}^{\text{fissile}} = \frac{\Delta \rho_{\text{Doppler}}^{\text{fissile}}(i, j)}{\ln \left(\frac{T_{\text{Doppler}}^{\text{fissile}}}{T_{\text{nominal}}^{\text{fissile}}} \right)} \quad (\text{pcm})$$

$$K_{\text{Doppler}}^{\text{fertile}} = \frac{\Delta \rho_{\text{Doppler}}^{\text{fertile}}(i, j)}{\ln \left(\frac{T_{\text{Doppler}}^{\text{fertile}}}{T_{\text{nominal}}^{\text{fertile}}} \right)} \quad (\text{pcm})$$

The whole temperatures are calculated in Kelvin.

- Grid expansion: both the direct flux calculations involve the reactivity variation: $\Delta \rho_{\text{grid}}$. The temperature variation is:

$$\Delta T_{\text{grid}} = \left[\frac{1}{0.99} - 1 \right] \cdot \frac{1}{\alpha_{\text{grid}}} \quad (30)$$

Thus, the reactivity coefficient is:

$$K_{\text{grid}} = \frac{\Delta \rho_{\text{grid}}}{\Delta T_{\text{grid}}} \quad (\text{pcm/K})$$

6.5.4 Validity of These Coefficients

It's important to notice that all these coefficients are calculated at a fixed temperature. Thus, it would not be discerning to apply these to the calculation of transients on the core in a very different situation: beginning of fusion of the core, for example.

Furthermore, if these coefficients are used for the calculation of transients with important variations of temperature of the considered materials, it is important to update the calculated reactivity coefficients with the correct expansion coefficient. For example, if the sodium coefficient has been calculated at the temperature T_0 and during a transient, varies between the temperature T_1 and T_2 , the correct reactivity coefficient for this phase will be:

$$K_{\text{sodium}}(\bar{T}) = K(T_0) \times \frac{\bar{\alpha}}{\alpha(T_0)},$$

with

$$\bar{\alpha} = \frac{1}{T_2 - T_1} \int_{T_1}^{T_2} \alpha(T) dT$$

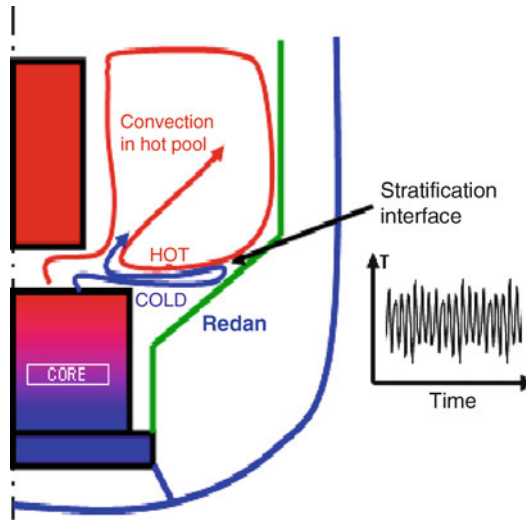
Finally, if it is not possible to do some perturbation calculations, and only direct flux calculations, it will be important to verify the uncertainties on the k -effectives, because of the small reactivity variations. If they are so important, a solution could be to increase the percentage of density variation. Consequently, the whole temperature variations would have to be changed.

7 Specific Thermalhydraulics Issues

7.1 Thermal Stratification

7.1.1 Phenomena

High boiling point implies that sodium remains in liquid state up to the temperature of 1,175 K at atmospheric pressure and excellent heat transfer characteristics bring many advantages for the sodium as coolant. Higher boiling point permits high operating temperature for the reactor, still ensuring sufficiently high margin to avoid boiling of the coolant under all the design basis events. Sodium remains in liquid state during operating conditions without calling for any pressurization and hence design pressure for components is nearly atmospheric, in turn requiring lower wall thickness for the structures. The excellent heat transfer properties provide high natural heat removal capability, particularly in the pool type concept. While pool type concept has many distinct advantages from the point of view of safety, there are certain critical structural mechanics issues, especially with the austenitic stainless steels, commonly used structural materials in view of its excellent compatibility with sodium and high strength at elevated temperatures. In the pool type concept, both hot sodium pool which is about 820 K and cold pool




■ Figure 150
Development of stratification

at about 670 K coexist, which imposes high ΔT (150 K-maximum) in sodium in the narrow transition regions of hot and cold pools, during operating as well as transient conditions. This is termed as “thermal stratification.” Further, such stratification is also caused due to different temperatures of sodium jets coming out from core subassemblies. The compact arrangement of fast reactor core comprises fuel, breeder, and internally stored spent fuel subassemblies, located in the same layout. In spite of the elaborate flow zoning provisions, the temperatures of sodium exiting from the fuel (850 K typical), breeder (750 K typical), and spent (680 K typical) subassemblies are vastly different. The lower part of the hot pool is also influenced by the presence of cold flow due to leakage from the feet of the subassemblies. The difference of temperature between the hot pool and the cold pool induces a thermal flux through the inner vessel structures. These thermal conditions prevailing in the pool coupled with large thermal expansion coefficient of sodium ($2.8 \times 10^{-4} \text{ K}^{-1}$) and large size of the reactor pool, the Richardson number in the pool is of the order of unity, indicating the inertial and buoyancy forces are of similar magnitudes. As a result of this, a stratification interface is developed as shown in ► Fig. 150.

7.1.2 Locations Prone to Stratification

In SFRs, the bottom part of the hot pool is a transition area between the hot and cold zones of the reactor. This region is annular and bounded laterally by the core periphery and the redan portion of the inner vessel. The thermal behavior of this zone is influenced by two conflicting phenomena viz. (1) cold boundary layer due to the heat flux across the redan shell and cold sodium flow from peripheral subassemblies of core which generates a stable cold layer and (2) the main sodium in hot pool which causes penetration of hot sodium into this area. This hot main sodium flow is the consequence of the recirculation created by the core outlet flow. The

equilibrium between these two effects causes mixed convection and stratified flow in this region as shown in  Fig. 150.

Stratification effects will also be observed in pools during transient conditions. The limiting transient states for a pool type reactor are emergency shutdowns or rapid shutdowns. During such transients, cold sodium jets will be injected into the hot sodium pool. The sodium temperature at the core outlet falls rapidly (reduction in the temperature of the order of 130 K at 20 K/s). During these transient conditions, depending on the operating strategy adopted for the reactor, the primary sodium flow rate may also vary. Hence, under these conditions coupled with the temperature difference effects, the flow reduction effects will add to the net buoyancy forces imposed on the main sodium flow in the hot pool. This can in turn produce considerable changes in the flow pattern in the hot plenum, and can even lead to the formation of a stratified hot layer above the inlet windows of the intermediate heat exchangers.

Similarly, stratification effects may also be caused in the cold pool during transient conditions. Changes in the flow pattern may be brought about by the influence of buoyancy forces caused due to the temperature difference between sodium streams at the outlet of intermediate heat exchanger coupled with flow changes under transient conditions. These effects can produce, depending on operating conditions, considerable changes of flow in the cold plenum and may even lead to the formation of a hot stratified layer above the lower part of the pump assembly. Apart from pool, thermal stratification can develop in sodium pipelines also, if the conditions are conducive.

7.1.3 Effect of Stratification

With the austenitic stainless steel as structural material that has low thermal conductivity and high coefficient of thermal expansion and the sodium with its inherently high heat transfer coefficient, the adjoining structural wall surface is subjected to high temperature gradient (ΔT), created in sodium without any significant film drop and time delay. This causes high thermal stress range ($\Delta\sigma$) in the structural wall. Further concern of thermal stratification is steady oscillations, relatively at lower frequencies (<1 Hz), which is one of the sources of high cycle thermal fatigue damage for the metal wall.

7.1.4 Numerical Simulation of Stratification

Thermal effects cannot be adequately represented by water model tests and the construction and operation of large size sodium experimental facilities are also prohibitively expensive and time consuming; computational fluid dynamics (CFD) analysis is an essential tool for the prediction of temperature distributions in the reactor structures. In the CFD computations, turbulence model is a critical issue, especially for stratified flow conditions. Most of the turbulence models have been developed mainly for the forced convective flows. Identification of suitable turbulence model for stratified flow (buoyancy dominated), geometrical regimes for the computation and establishing the optimum mesh (computational time, memory and desired accuracy) are challenges in the CFD analysis for SFR applications. More fundamental studies (Surle et al. 1993; Iritani et al. 1991) on thermal stratification show the capability of the computational approach to estimate the time average vertical temperature gradients and interface position

correctly, making use of classical $k-\epsilon$ turbulent models. Additionally, three-dimensional large eddy simulation modeling calculations have been shown (Surle et al. 1993) to provide simulations of turbulent fluctuations and global instabilities. In this field, more work is necessary to assess to what extent time-averaged gradient characteristics are representative of instantaneous conditions and to validate more precisely the prediction of the frequency and amplitude of temperature fluctuations.

7.1.5 Experimental Simulation of Stratification

Experimental studies play a role in the validation of the computational modeling methods and also to study certain specific problems concerning transient and multidimensional effects involved in the phenomena. In the experimental simulations of thermal stratification in the hot pool, certain nondimensional numbers should be respected between the model and prototype. The Richardson number (Ri), which represents the ratio between the buoyancy and inertia forces involved in the flow and Reynolds number to simulate the flow fluctuations are also important nondimensional numbers that need to be simulated correctly. Further, the ratio of heat transfer by convection to that by conduction should be preserved for which the Peclet number should be nearly equal. In particular, Richardson number is important for thermal process. This is justified in the following two situations, that is, steady state and transient conditions.

Under steady state conditions, there exists a critical Richardson number Ri_c , beyond which the form of the flow pattern in the hot plenum is modified in comparison with the pattern under nominal operating conditions (Tenchine et al. 1990; Roubin et al. 1988; Astegiano et al. 1981). This is illustrated in [Fig. 151](#). [Figure 151a](#) shows the flow configuration when $Ri < Ri_c$ (Ri_c is about 2.6) where the inertial effects are large compared to buoyancy effects. Hence, the sodium emerging from core is able to move upward to produce strong recirculation in the upper portion of hot pool as well as in the cavity between core and inner vessel, thus facilitating good mixing and hence there is no stratification. [Figure 151b](#) shows the flow pattern when $Ri > Ri_c$, that is, the buoyancy effects are dominant compared to inertial effects, where the cold

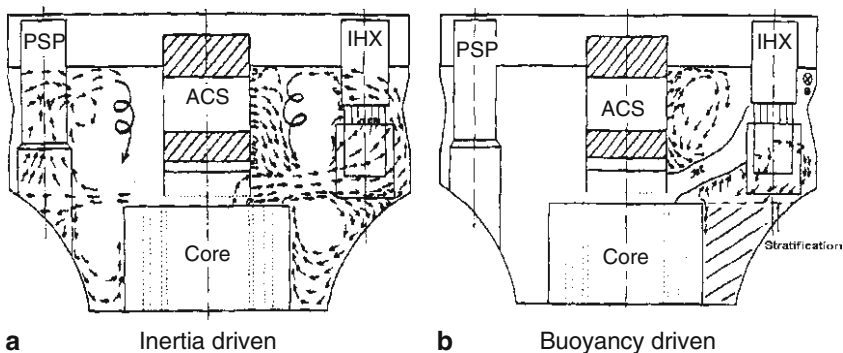
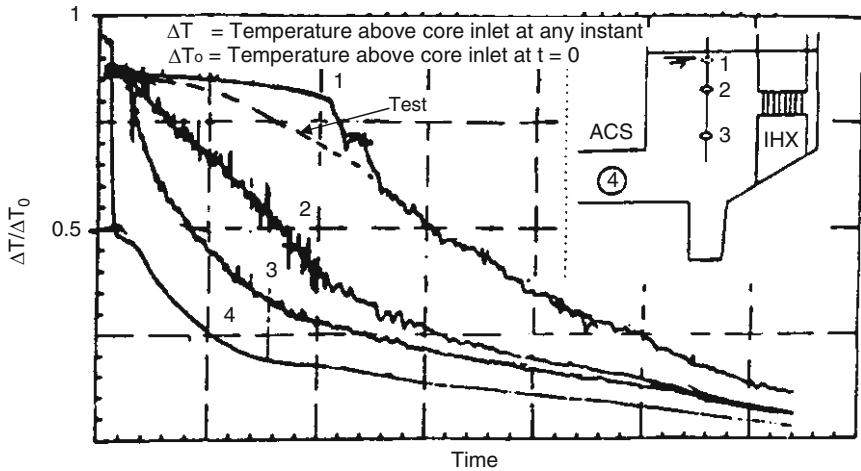


Figure 151

Stratification mechanisms in hot pool (PSP – primary sodium pump; ACS – above core structure)



■ Figure 152

Hot plenum stratification after a SCRAM at 23% nominal power in SPX1

sodium from the peripheral subassemblies separates from the hot sodium of fuel subassemblies and occupies the cavity. This leads to inadequate mixing, creating stratification.

The transient thermalhydraulic behavior of hot pool can also be characterized by means of a Richardson number (Ri). In the same way as for steady state conditions, fully turbulent flow in the model must be ensured by imposing a low Reynolds distortion. Comparative studies were performed in SPX1 geometry (🔍 Fig. 152) (Astegiano et al. 1981; Astegiano 1990) between mock-up test measurements and reactor measurements, to simulate the transient temperature evolutions at various locations in the hot pool following a reactor scram. Under this transient, the hot pool temperature in the vicinity of core top drops rapidly (location 4 in the figure) compared to the locations far from the core (location 1). This has been simulated correctly in the model studies where Richardson similitude is satisfied.

7.1.6 Design Guidelines for Stratification

The generally adopted design solution to avoid the thermal stratification effects during steady state operating conditions of the reactor is to provide some devices that are able to break the stratification interfaces. These devices offer good mixing amongst the varying temperature streams, before they reach IHX primary inlet windows in the hot pool. Detailed multidimensional CFD studies aid in arriving at the design configuration of such devices. One such device adopted in the design of PFBR, is a porous cylindrical skirt provided just below the control plug (Tenchine et al. 1990). The effect of this skirt is to increase the sodium velocity entering into the hot pool and thereby promoting good mixing and avoiding stratification as shown in 🔍 Fig. 153. However, provision of this skirt increases the pressure below the control plug bottom. This increased pressure increases the flow entering the control plug through the annular passages in the absorber rod mechanisms. Large flow in the control plug is of concern from

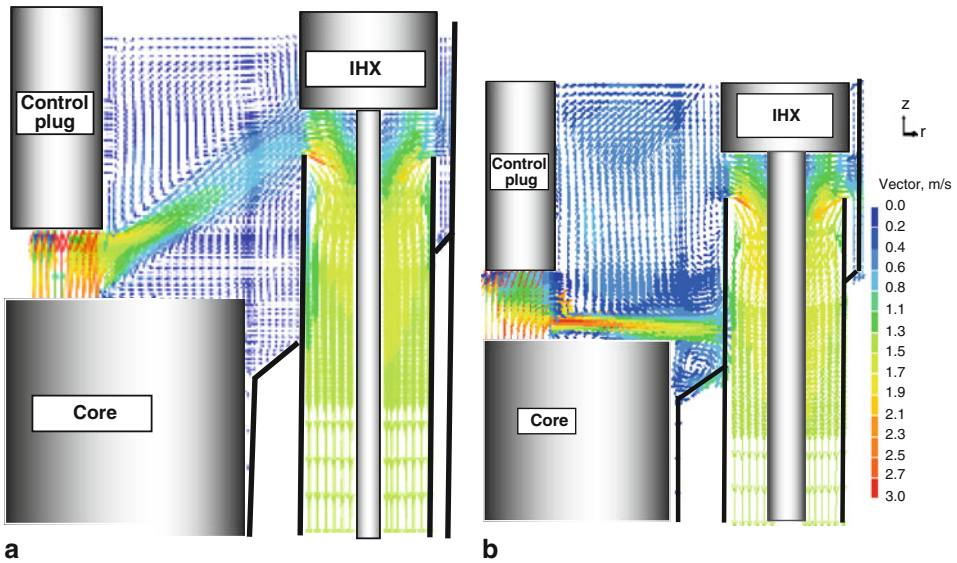


Figure 153
 (a) Stratified flow in hot pool; (b) Stratification eliminated by skirt

transient temperature (cold shock) seen by the control plug parts during a reactor SCRAM. Ideally, the flow entering the control plug has to be proportional to its volume in the hot pool. This can be achieved by choosing proper combination of annular clearances between the shroud tubes and respective absorber rods drive mechanisms and the perforations in the shroud tubes. However, care has to be exercised to ensure adequate clearances are available for facilitating smooth drop of absorber rods.

There are other detrimental effects due to the provision of the skirt. The skirt increases the radial velocity of sodium steam with which it enters the hot pool. This will result in increased velocity of sodium at the sodium free surface which can be harmful from gas entrainment considerations. The skirt diverts sodium flow exiting from various subassemblies in the radial direction. This causes the sodium streams exiting out of subassemblies located in the periphery of the core to be masked by the sodium stream from those located in the central region. Therefore, the positioning of thermocouples in the core temperature monitoring instrumentation should be very carefully decided to satisfy the subassembly plugging detection requirements. Another effect that is caused by the skirt is the nonuniform velocity profile of sodium at the entry to the intermediate heat exchangers, which is critical from flow-induced vibration of IHX tubes. Detailed experimental and theoretical studies have to be carried out in selecting the proper design configuration for the cylindrical skirt. Thus, the porosity of the skirt has to be optimized considering these factors. Typical porosity value of the skirt is 10%.

The skirt may not be effective in avoiding stratification in the pool at all power levels of operation of the reactor. If the low power operation is envisaged by reducing the flow (Q) proportionally to maintain the temperature rise across the core (ΔT), the Richardson number ($\Delta T/Q^2$) increases which promotes stratification. To avoid this, a strategy can be adopted

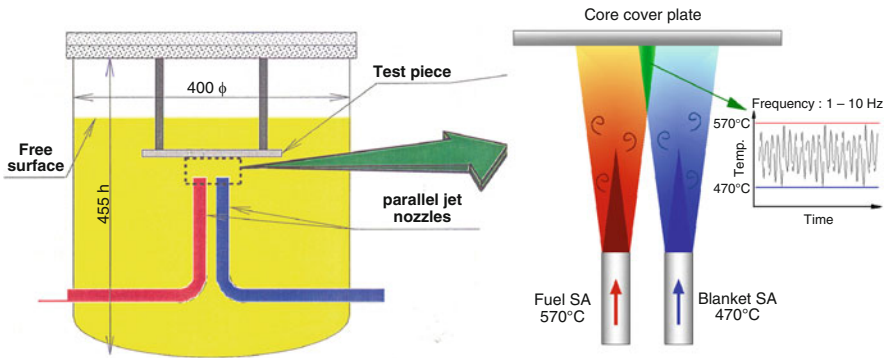


Figure 154

Thermal stripping phenomenon in the vicinity of core cover plate in SFR

wherein the flow can be reduced at the level so as to keep the Richardson number more or less unchanged; that is, the value of $(\Delta T/Q^2)$ remains nearly the same for all the power levels.

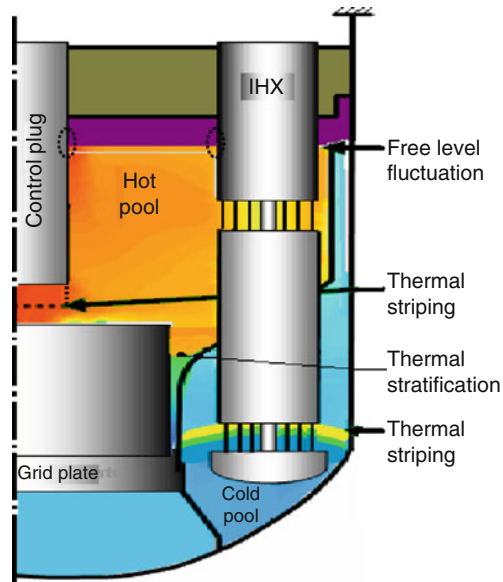
7.2 Thermal Stripping

7.2.1 Phenomenon of Stripping

Thermal stripping is a complex thermal hydraulics phenomenon, which generates random fast temperature fluctuations, originating from the incomplete mixing of hot and cold jets of fluid, sodium in the present context, in the vicinity of adjoining structural wall surface (► Fig. 154). The frequency of oscillations under thermal stripping is reported as 1–10 Hz. When the fluid temperature fluctuation amplitude and then thermal stress are large, structural integrity might be lost due to high cycle thermal fatigue. The amplitude and the frequency of the temperature fluctuations are important parameters on which the damage caused on the structures depends. The oscillating temperature phenomenon is basically caused due to the jet instability and turbulence.

7.2.2 Locations Prone to Thermal Stripping

Thermal stripping occurs at a few locations in the hot and cold sodium pools in the reactor assembly, predominantly on the core cover plate of control plug and at mixing “Tee” junctions in the secondary sodium pipelines. It is worth mentioning that apart from thermal stripping, oscillations of thermal stratification layers and sodium free level do cause temperature fluctuations in certain locations in the sodium pools. ► Figure 155 shows a few potential areas of level fluctuation, thermal stratifications, and thermal stripping. Another important location in the reactor which is prone to thermal stripping is the surge tank where, under specific transient conditions, mixing of sodium jets at different temperatures happens.



■ **Figure 155**
Zones of thermal fluctuations in SFR

The concerns of thermal fluctuations are also addressed comprehensively in Ohshime et al. (1994) and Gelineau and Sperandio (1994). There are a few reported failures, in the form of extensive cracking due to thermal striping in the operating reactors at: secondary sodium pump vessel in Phenix (Gelineau and Sperandio 1994), Tee junction of an auxiliary pipe of the secondary circuit in SPX (Gelineau and Sperandio 1994), control rod guide tube in PFR (Bettes et al. 1994), and primary cold trap in BN 600 (Sobolev and Kuzavkov 1994).

7.2.3 Effect of Striping

High thermal fatigue cycles are caused by thermal striping. The range of frequency of oscillations under thermal striping is reported as 1–10 Hz. Thermal striping occurs at a few locations in the hot and cold sodium pools in the reactor assembly, predominantly on the core cover plate of control plug and at mixing “Tee” junctions in the secondary sodium pipelines.

7.2.4 Prediction of Thermal Striping

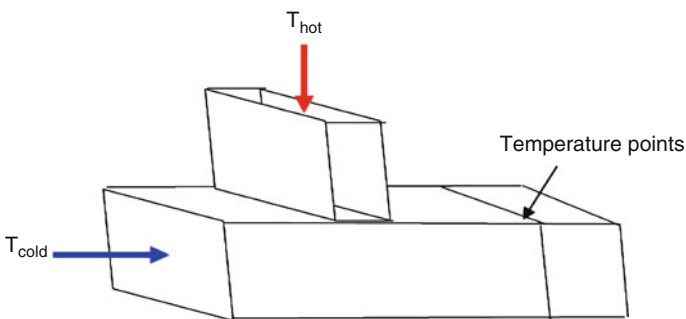
Thermallydraulics of thermal striping phenomenon is governed by many physical phenomena, with each one having its own difficulties and limitations. There are difficulties with the experimental quantification and the modeling of turbulent mixing (temporal and spatial multi-scale phenomena). Since, thermal effects are associated with this phenomena the experimental simulation calls for sodium experiments. The oscillating temperature field in sodium is caused by

jet instabilities and turbulence. The size of turbulent eddies and their life depends on the velocity and hydraulic diameter of issuing jets. Therefore, the experimental simulation needs to be carried out on equal scale models with exact simulation of flow velocity. Meanwhile, on the theoretical modeling of this phenomenon, progress has been made with the advanced turbulence models, namely, large eddy simulation (LES), very large eddy simulation (VLES), and detached eddy simulation (DES). But these are still in the development and validation stages. The qualification of these models is extremely difficult as a result of measurement difficulties and uncertainty in the validation of the numerical and experimental results. The success of the numerical simulation of thermal striping depends on how accurately the turbulent scales responsible for the oscillating flow and temperature field are modeled. These methods require fine resolution of geometry to capture the formation and movement of eddies. Enormous computational resources are required for these calculations. Performing such calculations for the entire hot plenum of an LMFBR is very difficult. In this context, a localized analysis approach is a better alternative. However, presently there is a trend toward solving large numerical models that current computers can barely handle to simulate the entire range of fluctuations. On the heat transfer aspect, there are still difficulties in measuring and modeling the heat exchange between the fluid and the wall. In addition, there are theoretical problems associated with lack of understanding of the boundary layer phenomenon. Recent computational studies (Muramatsu 1993, 1994a, 1998a,b; Hu and Kazimi 2006; Menant and Villand 1994) have shown that simulations using high order accurate numerical schemes and advanced turbulence models (LES) are giving promising results in the prediction of distributions of the intensity and frequency of temperature fluctuations in liquid metal reactor systems. Menant and Villand (1994) have predicted the temperature fluctuations in a square section duct with T-junction (➤ Fig. 156) using the TRIO-VF code employing the LES model.

➤ Figure 157 shows the computed temperature fluctuations in the duct at various locations, for the temperature difference of 45 K in the fluid streams. The computed temperature fluctuation on the metal wall is found to be 20 °C, indicating an attenuation of about 50%.

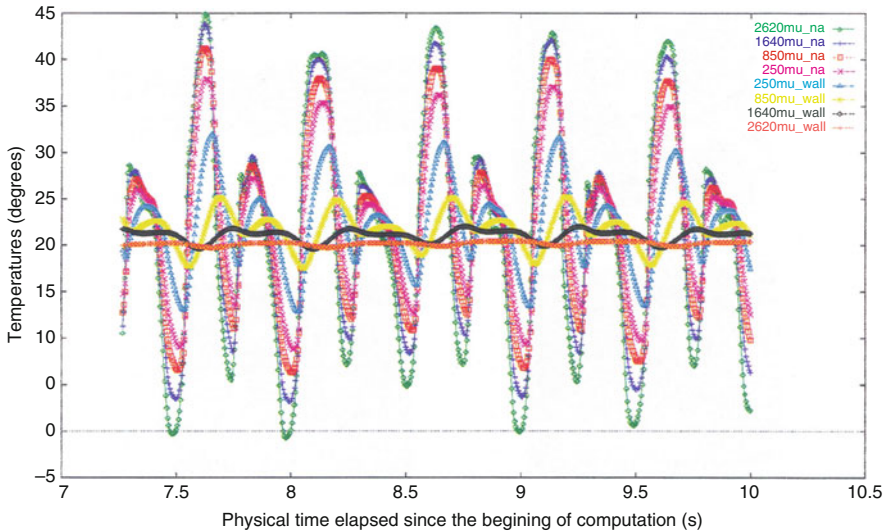
Direct numerical simulation (DNS) on simplified and approximated two-dimensional geometries have also been attempted recently (➤ Fig. 158) for the prediction of temperature fluctuation in fluid due to jet instability effects.

In view of the difficulties associated with the complete modeling of the phenomena, the usual approach followed is a combination of numerical and experimental simulations.



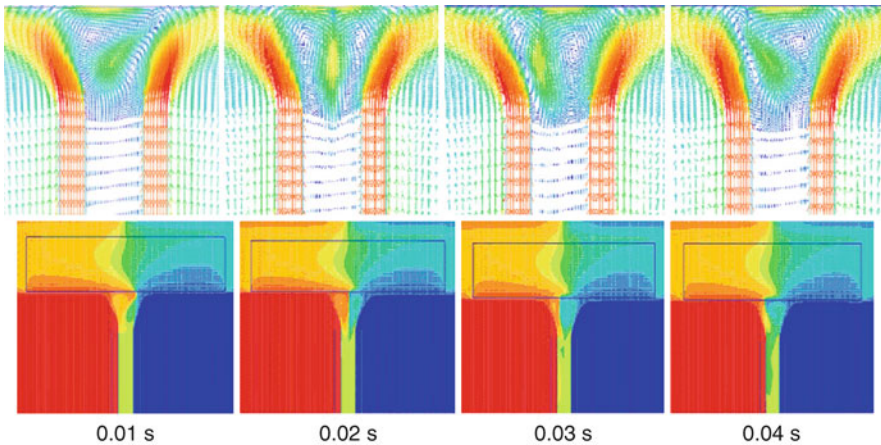
■ Figure 156

Square section with Tee junction for numerical simulation



■ Figure 157

Temperature fluctuations in a typical T-junction predicted by TRIO-VF code at various nodes located 0.7D downstream of inlet



■ Figure 158

Transient flow and temperature profiles near the plate

Thermalhydraulics studies cover basic understanding of the phenomenon (Popiel and Trass 1991; Tokuhiro and Kimura 1999), establishing experimental simulation principles and assessments based on tests with water and air (Moriya et al. 1988) and attenuation characteristics of thermal striping on the metal wall (Muramatsu 1994b; Wakamatsu et al. 1995a). Experimental studies (Wakamatsu et al. 1995b) are generally performed for the validation of numerical models. International scenario in the understanding of thermal striping is very encouraging. Owing

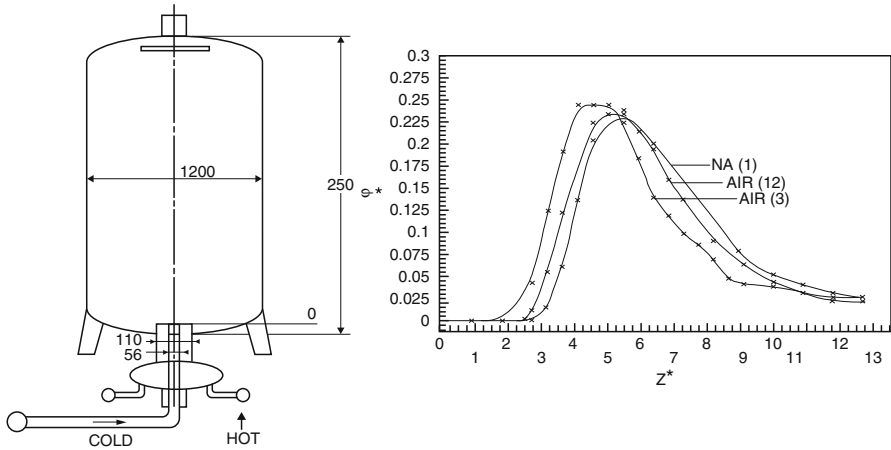


Figure 159

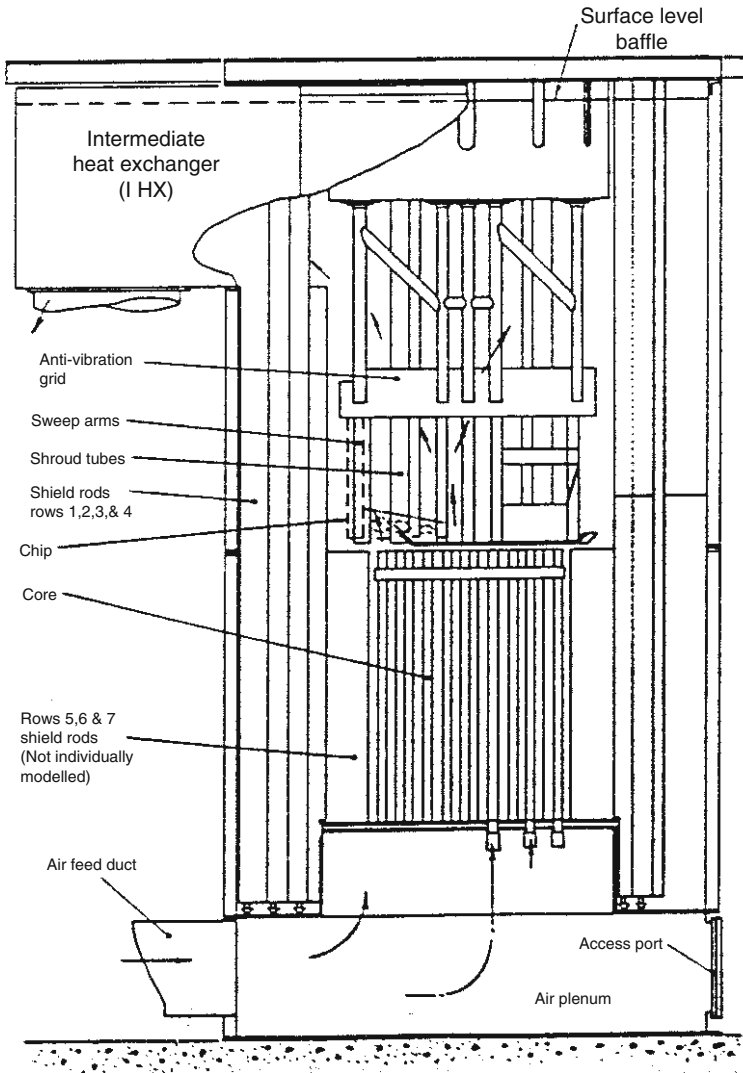
Sodium and air experiments on mixing of coaxial non-isothermal jets (left: experimental setup and right: variation of temperature fluctuation along the axis)

to vast experience gained in operation of fast reactors, France has reported many important observations related to thermal striping noticed in the operating plants, PHENIX and SPX-1 (Gelineau and Sperandio 1994). Tenchine and Moro (1999) carried out experiments in air and sodium (Fig. 159) to understand thermal striping during mixing of non-isothermal axisymmetric jets in a pool. They observed that the maximum amplitude of temperature fluctuation occurs at a nondimensional axial distance of ~ 5 .

In UK, Betts et al. (1983) carried out elaborate experimental research to understand if air or water could be used to simulate sodium in thermal striping studies. They found that air can be used to predict the temperature fluctuations in the fluid if the Reynolds number is of the order of 106 (Fig. 160). However, the boundary layer attenuation and the resulting temperature fluctuations in the structures cannot be predicted by air/water tests. This is because of the large difference in the heat transfer coefficient of sodium and air. To overcome this difficulty, Wakamatsu et al. (1995a) proposed an equivalent boundary layer model for the determination of boundary layer attenuation and the resultant temperature fluctuations in the structures (Fig. 161). Thermal striping phenomenon has been simulated in water tests through a dedicated test setup, developed at Indira Gandhi Centre for Atomic Research (IGCAR) (Fig. 162) (Chellapandi et al. in press). The setup simulates the situations of thermalhydraulics in the vicinity of core cover plate, placed on the control plug just above core. Temperatures and flow rates of hot and cold water are varied over wide ranges. A maximum ΔT of 90 K is possible in the setup. A few typical PSD generated from test data are also included in Fig. 162.

7.2.5 Design Guidelines for Striping

As the complete theoretical or experimental simulation of thermal striping phenomenon in a fast reactor system is difficult, the usual methodology followed in design is a combination of



■ Figure 160
Air model of PFR (1:5 scale)

simplified global and detailed local analysis approach. After a first step using global thermal-hydraulic models to identify the areas where thermal striping may occur, the characteristics of the fluctuation have generally been estimated from model tests using sodium as the working fluid. Based on global 3-D thermalhydraulic studies carried out for the primary sodium circuit, the localized zones prone to thermal striping identified in a pool type SFR are, namely, (1) fuel-breeder interface around the lattice plate, (2) fuel-breeder interface around the core cover plate, (3) bottom location of absorber rod drive mechanism where fuel-control subassembly sodium flows interact, and (4) main vessel near IHX outlet. These localized zones have to be further

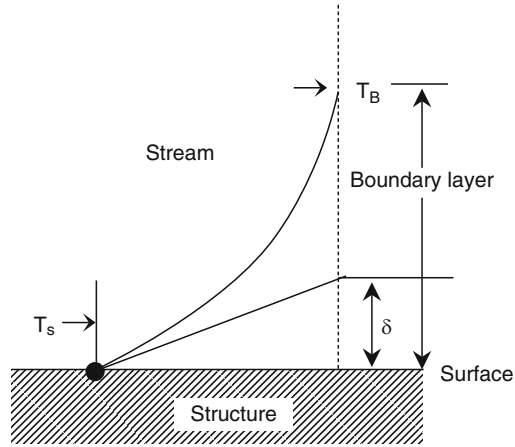


Figure 161

Model to estimate boundary layer attenuation

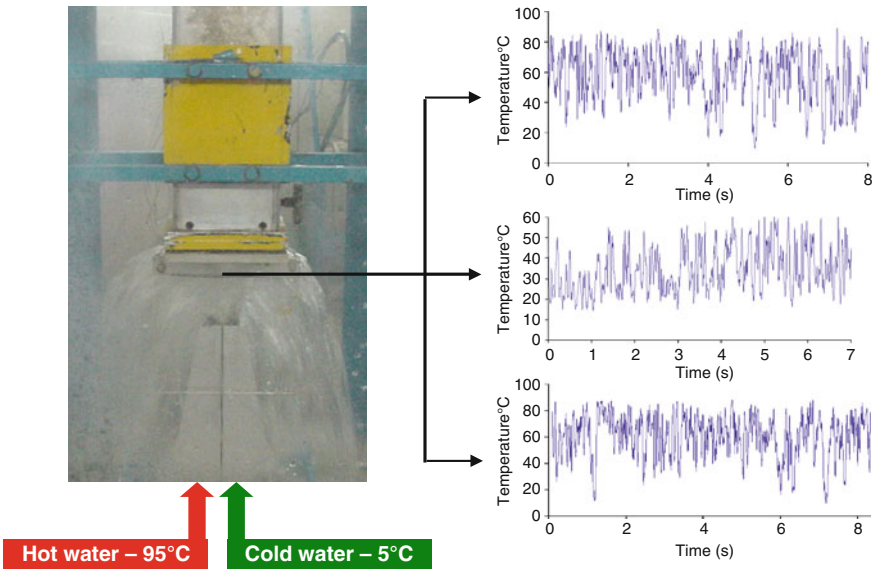


Figure 162

Water test facility to simulate thermal stripping (IGCAR)

considered for the detailed prediction of flow and temperature oscillations. With the velocity and temperature values prescribed for the jet streams, the oscillations in the mixing layer region (interface) can be predicted at different locations. For conservatism, the influence of global flow field in the domain caused by other flow sources in the circuit can be neglected. Further, for a simplified numerical prediction of the fluctuating temperature phenomena, a method can be

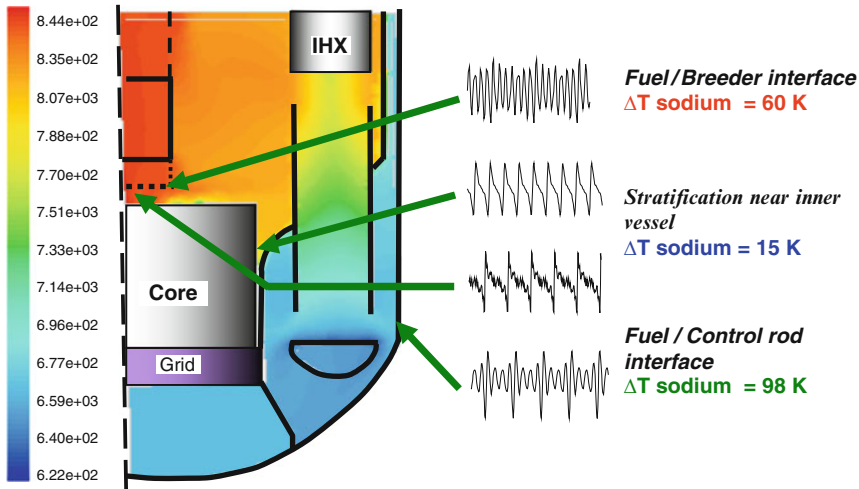


Figure 163
Regions prone to thermal stripping in primary sodium

brought out by approximating the local geometry in each case to an equivalent two-dimensional domain and direct numerical simulation (DNS) calculation can be performed (Velusamy et al. 2005). The temporal oscillations and spectral distributions for each of the locations predicted for PFBR are summarized in [Fig. 163](#). Three-dimensional simulations would definitely lead to more accurate results compared to the two-dimensional predictions. The two-dimensional simulation is a compromise for the easy handling of the large geometrical domain of hot pool regions prone to thermal striping.

7.3 Free Level Fluctuations

7.3.1 Phenomenon

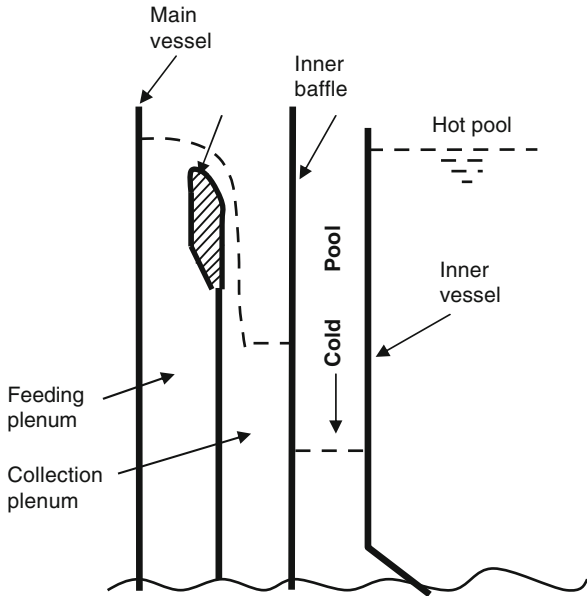
Argon cover gas is maintained above the sodium pools/tanks in the fast reactor. This is to accommodate volume changes in sodium as a result of temperature changes in sodium. The interface between the sodium top surface and argon cover gas is known as sodium free level. Some of the components in a fast reactor with sodium free levels are primary sodium hot and cold pools, surge tank, pump vessel and storage tank in the secondary sodium circuit, expansion tank in the safety grade decay heat removal (SGDHR) circuits, etc. These free levels are susceptible to fluctuations if, either the sodium has large velocities or the diameter of the vessel is large. The free level is a region of large axial temperature variation in the vessel walls as well as in structures partially immersed in sodium and partially exposed to argon. Normally, the sodium is at a higher temperature than the cover gas. The gas temperature reduces sharply from that of the sodium within a thin boundary layer of 20–30 mm over the sodium free surface. The heat transfer coefficient of sodium is very large ($\sim 104 \text{ W/m}^2\text{-K}$), due to its large thermal conductivity. Due to free level fluctuations, the components partially dipped in sodium will alternately see hot sodium and cooler argon (cover gas). These temperature fluctuations can lead to thermal

fatigue. Due to large heat transfer coefficient of sodium, the thermal attenuation in the wall boundary layer will be very low, leading to large amplitude of fluctuations in the structures.

When the amplitude of local sodium level fluctuations exceeds a critical value, it leads to entrainment of argon gas into the sodium. This entrained sodium is a source of concern, it enters the active core.

7.3.2 Locations of Concern

The level fluctuations in the expansion tank of safety grade decay heat removal (SGDHR) circuit are expected to be low, as the expected velocity levels in the tank as a result of buoyancy as well as the size of the tank are very small. In the case of storage in the secondary system, the sodium velocities are very less although the vessel diameter is significantly large. But in the case of hot pool, due to the interaction of sodium stream from the core with the free surface and cross flow-induced vortex shedding behind the immersed structures like pump, IHX, etc., the level fluctuation is critical. The components which would experience temperature fluctuation due to level fluctuations in the hot pool are inner vessel, IHX, DHX, control plug, level probes, etc.

Main vessel being the main load bearing member of the reactor assembly, in order to protect it from thermal fatigue effects due to free level fluctuations, a design that ensures constant level of sodium at free level is essential. This is achieved through the vessel cooling system designed to have an overflow weir, where sodium overflows from the feeding plenum to the collection plenum as shown in  Fig. 164.

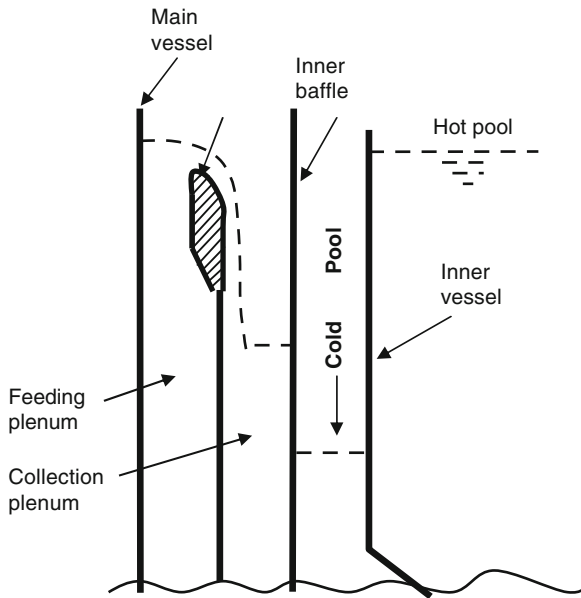


 Figure 164

Main vessel cooling circuit with overflow weir system

7.3.3 Methods for Prediction of Level Fluctuations

The phenomenon of level fluctuation in the sodium pool is governed by inertial forces of the sodium flow and the gravitational forces of the fluctuating sodium free levels. The fluctuation is a random phenomenon of local nature. Prediction of the level fluctuation by computational fluid dynamics studies calls for 3-D, transient studies coupled with complex modeling features for predicting free surface profiles. Experimental simulation is the favored option. For the numerical prediction of these types of flows with moving gas–liquid interface, numerical methods such as height function method and volume of fluid (VOF) method (Harlow and Welch 1965; Hirt and Nichols 1981) have been developed and incorporated in commercial CFD computer codes. In order to capture the free level fluctuations of frequency less than 1 Hz, the simulations also have to be carried out with smaller time steps. The domain of our interest being a large pool, the number of computational cells will be large. Solving a three-dimensional transient problem of this nature is a computational challenge.

The free level fluctuations are governed by the balance between the inertial, gravitational, and frictional forces. The appropriate nondimensional number that governs the inertial force to gravitational force is Froude number (Fr) and the number that governs the inertial force to frictional force is Reynolds number (Re). These nondimensional numbers can be respected by water models. Since no heat transfer is involved, poor thermal conductivity of water is not a constraint. The effect of Re is secondary once the flow is well in the turbulent regime, and hence distortion in the Re can be permitted. Hence, water experiments, on geometrically similar scaled down models respecting Fr number similarity, are carried out and the measured free level fluctuations are extrapolated for the reactor.

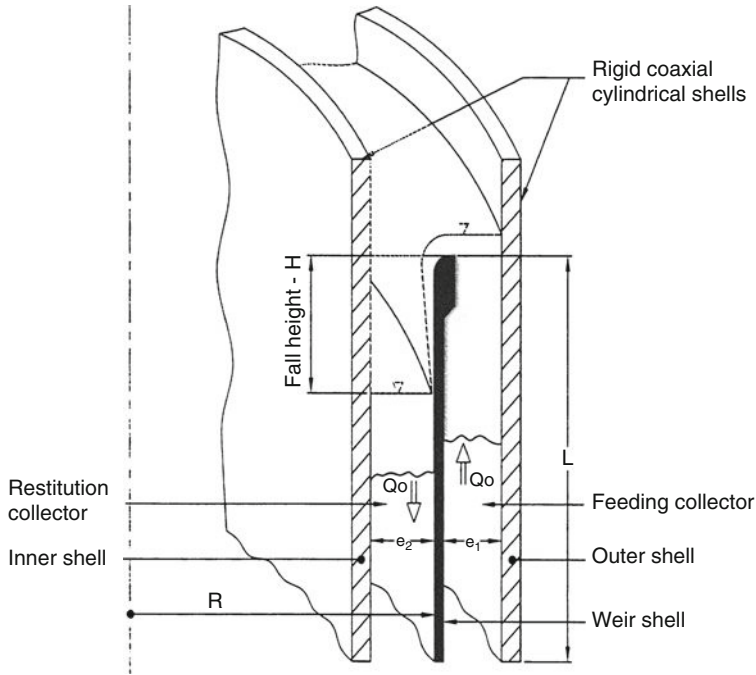
The experimental studies on a $1/4$ model (Laxman et al. 2004) reveal that the free level fluctuations are not uniform throughout the hot pool and that the ripple height and the fluctuation frequency depend on the location in the pool. For nominal flow condition the maximum amplitude is about 82 mm in the vicinity of the control plug extrapolated to prototype conditions. The predominant frequencies of fluctuations for the reactor vary between 0.25 and 1.6 Hz. Using these data of frequency and amplitude of level fluctuations, the transient temperature fluctuations in partially submerged structures are determined by solving the transient heat conduction equation. It shall be highlighted that structural temperature fluctuations cannot be predicted by water experiments.

The free level fluctuations in the pool should be quantified for choosing the margins for avoiding the gas entrainments into the heat exchangers immersed in the hot pool. This apart, the free fluctuations cause special type of structural damage called “thermal ratchetting” on thin shells in the vicinity of level fluctuations, which is described in [► Sec. 8.1](#). Since the weir ensures maintaining the constant sodium free level in the vicinity of main vessel irrespective of the sodium flow rate, there is no possibility of level fluctuations in the main vessel ([► Fig. 165](#)).

7.4 Cellular Convection

7.4.1 Phenomenon

Natural convection of gases/liquids in vertical enclosures is a normal phenomenon, where the fluid absorbs heat from hot wall during its upward travel and deposits the heat on the cold wall during its downward travel. During these upward and downward movements, boundary



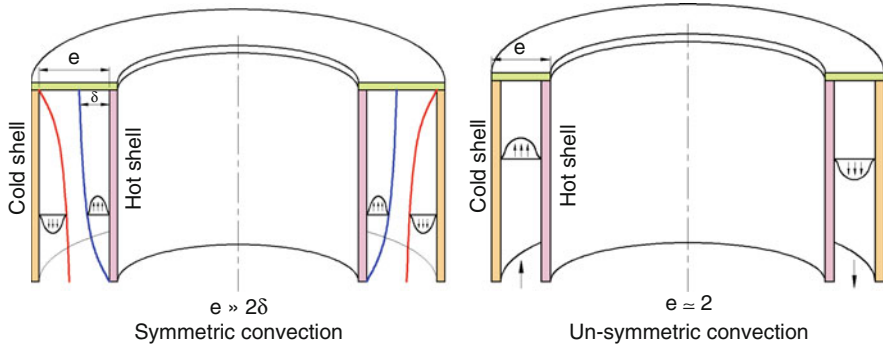
■ Figure 165

A schematic of weir flow system

layers develop over the hot and cold vertical walls. When the width of the annular space (e) reduces or the height of the enclosure (H) increases (i.e., as the aspect ratio, e/H reduces) the hot wall and cold wall boundary layers approach each other. At some specific value of aspect ratio, which depends upon the temperature for the given geometry, both the boundary layers would interact. This interaction is the condition for onset of the breakdown of symmetry in the flow structure leading to asymmetric convection. This phenomenon is termed as cellular convection (Goldstein et al. 1979). For example, the top shield penetrations face this phenomenon, which is depicted in Fig. 166. In this figure, the hot shell represents outer shell of IHX and cold shell represents the roof slab penetration shell, cooled by air. The annular space is filled with cover gas argon. In such conditions, the type of convection pattern formed in the annulus depends on many factors, namely, temperature difference between the source and sink, width of the annulus, ratio of length to height of the annulus and cooling conditions on the various boundary surfaces of the annulus.

Based on experimental studies performed, the geometric parameters of the cylindrical annuli where the convective flow turns out to be unsymmetric have been arrived. When the aspect ratio of the annulus is less than 0.21, unsymmetric pattern has been observed (Siegel and Norris 1957; Timo 1954), that is, $e/H < 0.21$. A more general relationship has been arrived at relating boundary layer thickness (δ) to the gap width as: $e/\delta < 3$.

The number of loops of convective flow formed depends on the ratio of the circumference (πd) and height of the annulus (H) (Mejane and Durin 1982). When this ratio is of the order

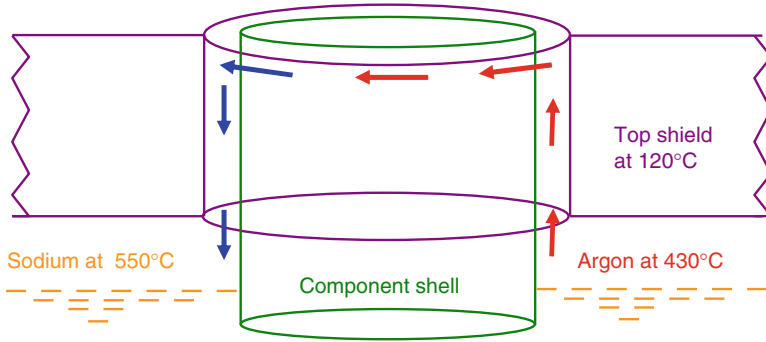


■ **Figure 166**
Condition for onset of cellular convection

of 2, the number of loops formed is one, that is, one hot leg and one cold leg. When this ratio is of the order of 4, the number of loops formed is two. However, a clear dependency relation has not yet been established. The vertical penetration depth of cellular convection depends strongly on e/H and cooling conditions. The convection is weak, if e/H is small and top shield cooling is strong.

7.4.2 Location of Cellular Convection

In an SFR, the primary sodium inside the vessel is blanketed by an inert cover gas, normally argon. The top shield forms a cover for the primary sodium pool with argon gas between its bottom and free level of sodium. Outside of the top shield is the ambient environment of the reactor containment building. The top shield has many penetrations for components like, IHX, decay heat exchanger (DHX), sodium pimps, control plug, rotating plugs, etc. These penetrations form narrow vertical cylindrical annuli open at the bottom. The temperature of sodium pool is $\sim 550^\circ\text{C}$ during nominal condition and the top shield is cooled to maintain its temperature at $\sim 120^\circ\text{C}$ (in the reactor adopting hot roof concept) and at $\sim 50^\circ\text{C}$ (in reactors adopting cold roof concept). The gap width of the annular penetrations has to be as narrow as possible to have compact top shield of small diameter and to reduce the heat load on the top shield. The height of the annular penetrations is typically 1.5–2.0 m. This large height is required from the considerations of biological shielding offered by the concrete that fills the box-type top shield. As a result of these, the bulk temperature of argon cover gas attains a value in between that of sodium and top shield. The gap width of the annular penetrations being very small ($\sim 10\text{--}25\text{ mm}$), compared to the height ($\sim 1.8\text{ m}$), the natural convection of argon taking place in the annuli is asymmetric as shown in [Fig. 167](#), because the hot argon enters the annulus at one circumferential location and leaves the gap at the opposite side. It is worth mentioning that if the gap would have been wide, both upward and downward flows occur within the annular gap resulting in symmetric flow pattern over the entire circumference.



■ Figure 167
Asymmetric convection of argon

7.4.3 Effects of Cellular Convection

Due to asymmetric nature of cellular convection, the hot argon enters the annulus at one circumferential segment of the penetration. It gets cooled along its vertical and circumferential travel in the annulus and then leaves the annulus in some other annular segment. As a result of this, the component wall becomes hot in one sector and cold in another sector. This leads to differential thermal expansion of the structures. As the components of SFR (namely, IHX, pump, control drive mechanisms, etc.) are thin and long structures (~10 m long). The long length of the structures amplifies the tilt and adverse interaction of the components with their mating parts inside the pool, as well stress. This tilt is very critical in components like control drive mechanisms.

When the number of loop is one, the maximum and minimum temperatures occur along the shell exactly at the opposite meridian lines, under which the component tilts without change of circularity (insignificant stresses). In the design maximum allowable tilting is specified for smooth functioning of mechanical seals in IHX and pump-pipe connections in the spherical header. When the number of loops is more, there would be multiple maxima and minima along the circumference, resulting changes of circular shapes (ovality), without causing significant tilting. However, the resulting ovality causes high hoop stresses, which are to be limited from thermal fatigue considerations. For very narrow annulus possible in the case of machined penetrations, flow through annulus is restricted and hence a stagnant region would be developed at the upper part of the annulus. Hence, the convective flow pattern would be restricted at the lower part of the annulus, which does not have any significance. Hence machined penetrations are preferred solution.

7.4.4 Methods for Prediction of Cellular Convection

As the cellular convection is a geometry-dependent and boundary condition-dependent phenomenon, involving radiative heat transfer in evaporation and condensation of sodium vapor and natural convection of sodium mist laden argon cover gas, the experimental studies have to be carried out on full scale models [Baldasari et al. 1984; Roux and Elie 1988; Lenoir et al. 1981]. The approach adopted in design is a combination of experimental and theoretical analyses.

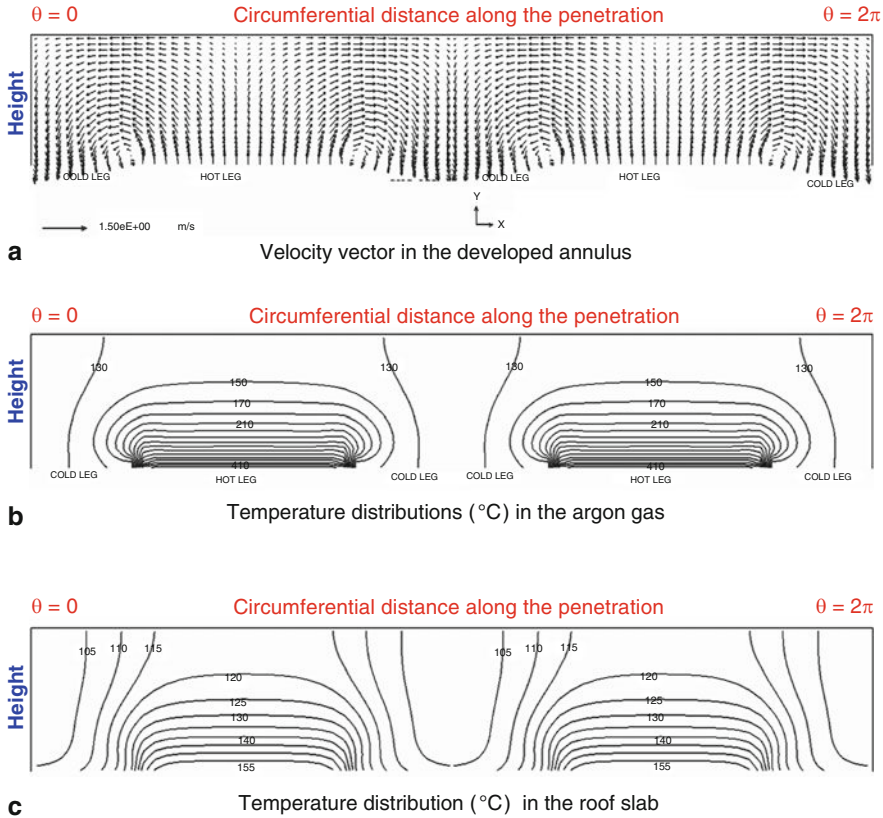


Figure 168

Important cellular convective parameters 1

Experimental studies are used for the validation of theoretical models and design predictions are made using the validated theoretical models (Yamakawa et al. 1986; Toda et al. 1990; Francois and Azarian 1989). Cellular convection in the penetrations and resulting asymmetric temperature distribution in the shells, have to be predicted by a conjugate thermalhydraulic model considering natural convection of argon, heat conduction in the multiple shells, radiative heat exchange among the shells, and forced convection cooling boundary conditions simultaneously (Silver et al.). Suitable turbulence models (depending on the Rayleigh number) with special approaches recommended for the simulation of natural convective flows have to be adopted in these predictions. The cellular convection velocity pattern and corresponding temperature pattern in the annulus predicted for a typical component penetration is shown in [Fig. 168](#).

7.4.5 Managing Cellular Convection

In FBTR, the cellular convection formed between the reactor vessel and the large rotating shield plug led to the uneven expansion and hence the tilting of reactor vessel (Vaidyanathan). In order

to overcome this problem, a comparatively lighter helium gas is being injected from the top of the penetration to suppress the cellular convection.

The tilting of components caused due to cellular convection has to be managed through proper care taken in the design. The tilting of control plug causes the thermocouples of the core temperature monitoring instrumentation to get offset with respect to the center of the sub-assembly. This needs to be considered in deciding the normal location of thermocouple with respect to the subassembly. The tilting of pump assembly due to cellular convection needs to be considered in the design of the spherical seat support. Wherever the cellular convection effects are unmanageable, proper design provisions have to be made for arresting the convection by the use of anti-convection barriers. Thus, cellular convection is an important aspect to be considered in the design to meet the functional requirements of various systems and mechanical design of various components.

7.5 Gas Entrainment

7.5.1 Phenomenon

In an SFR, argon gas blanket is maintained above the sodium free surface to accommodate volume changes of sodium as a result of its thermal expansion, due to various operating conditions of the reactor, as well as to avoid sodium–air contact through the numerous penetrations in the roof slab. Hence, a large sodium surface, which interfaces with argon, is formed as shown in [Fig. 169](#).

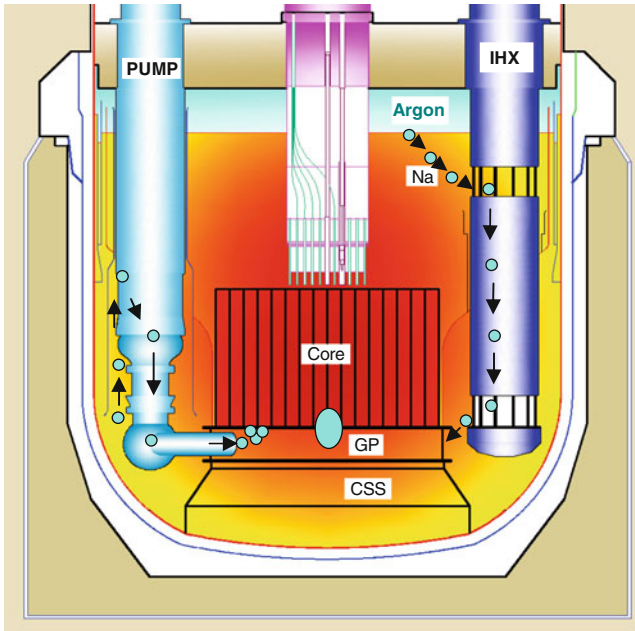
Reducing the size of the reactor vessel offers significant economic incentives. However, the reduction has a large impact on the thermohydraulics of the hot pool. One of the main problems in reducing the size of the vessel is the agitation of sodium free surface. The agitation of free surface due to large convective velocities can lead to entrapment of argon gas within high velocity sodium and its transportation to the intermediate heat exchangers (IHX). The mechanisms associated with various types of gas entrainment phenomenon are detailed below ([Fig. 170](#)):

Entrainment Due to Differential Dissolution of Argon

It may be mentioned that argon dissolves in sodium and its dissolution increases with temperature. The equilibrium concentration of argon in the hot pool, when the sodium temperature is 820 K is $\sim 7.5 \times 10^{-2} \text{ g/m}^3$ (Winterton 1972). Similarly, the equilibrium concentration of argon in the cold pool sodium, at 670 K, is $0.5 \times 10^{-2} \text{ g/m}^3$. Because of this, some quantity of argon is bound to be present in sodium. However, the dissolved argon is not expected to cause any reactivity perturbations in the core. But the argon bubbles, which are entrained by sodium that stays as separate phase has a potential to pass through the core sporadically.

Liquid Fall

One of the mechanisms, which can cause entrapment of gas in hot pool, is “liquid fall” (Kobus 1991). This is due to the fact that when the vertical velocity of liquid in the hot pool is large, the flow rises above the mean free surface forming a local hump. The flow, which rises above the free surface, falls back to the sodium surface as a liquid fall. The interaction between the falling liquid and the nearly stagnant pool causes entrainment of argon as shown in [Fig. 170a](#). The gas thus entrapped can be carried to the inlet window of intermediate heat exchangers, depending



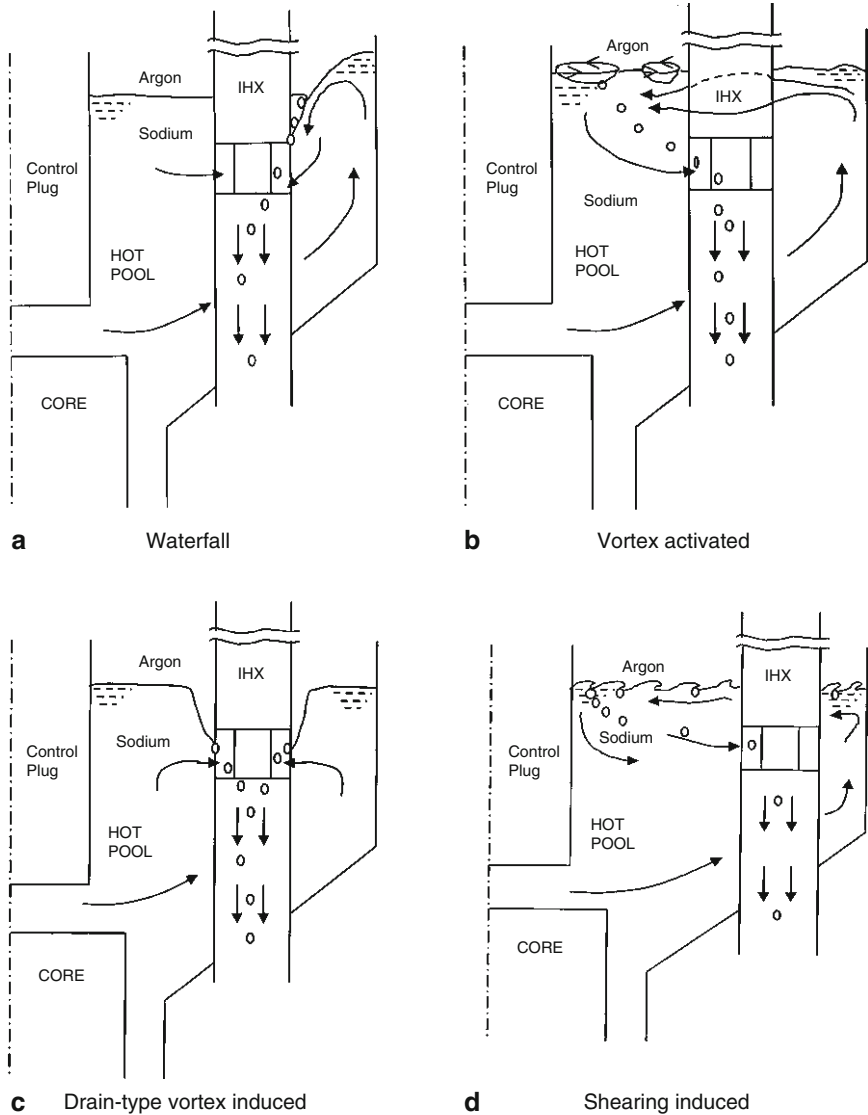
■ Figure 169

Gas entrainment in SFR (IHX – intermediate heat exchanger; GP – grid plate; CSS – core support structure)

on the size of the gas bubble and the velocity of sodium, which decides the drag force: $F_d = C_d (\pi D^2/4)(\rho_{sod} V^2/2)$. The drag coefficient (C_d) for a spherical bubble of argon varies from 0.7 to 0.4 for range of Reynolds number (Re) between 200 and 105. ρ_{sod} is the density of sodium, D is the diameter of the argon bubble, and V is the upward velocity of the bubble as a result of buoyancy in a quiescent sodium liquid. The upward buoyancy force acting on the bubble (F_b) is given by, $F_b = (\rho_{sod} - \rho_{arg}) g (\pi D^3/6)$. ρ_{arg} is the density of argon and g is the acceleration due to gravity. Equating F_b and F_d , the terminal velocity of the bubble (also known as bubble rise velocity) can be calculated to vary as $\sim 5 \times D^{1/2}$. If the downward sodium velocity were larger than the terminal velocity of the bubble, the bubble would be carried along with the sodium. On the contrary, if the sodium velocity were less than the terminal velocity, then the bubble would escape to the free surface. It is estimated from the above that the terminal velocity of a bubble of 1 mm diameter is only ~ 0.18 m/s or a downward velocity of 0.5 m/s can successfully drag a spherical argon bubble of 10 mm diameter. For identical bubble sizes, the terminal velocity of bubble is slightly more in sodium than in water, due to the lower value of sodium viscosity.

Vortex Activated Entrainment


The sodium pool consists of many objects, which are partially immersed in sodium and partially exposed to argon gas. Horizontal sodium flows at the free surface past these structures lead to formation of vortices behind the structures. These rotating vortices have dimples of gas at the center as shown in [Fig. 170b](#). The vortices thus generated, travel along the liquid. If the vortices are strong, they take longer time to dissipate their energy. But, if they encounter strong vertical downward currents before their dissipation, it can lead to entrapment of gas in sodium.




■ **Figure 170**
Gas entrainment mechanisms in hot pool

The depth of the dimple is expected to be of the order of $V^2/2g$, where V is the horizontal velocity at the free surface of the pool. Typically, for a free surface velocity of 0.5 m/s, the depth of the dimple could be of the order of 1.25 cm. Generally, these vortices are generated at the periphery of the hot pool, close to the upper shell of inner vessel and get transported toward the control plug. If the free surface velocity is less, then the transit time of the vortices increases enhancing the possibility of dissipation of the vortices.

Drain-Type Vortex

The drain-type vortex, also known as “bathtub” vortex or “standing vortex,” occurs when the submergence level of inlet window, of heat exchangers for the given entry velocity of sodium to the heat exchanger is inadequate. In this type of entrainment, a long gas core is formed around the drain location starting from the free surface, as shown in  Fig. 170c. Presence of such a vortex can lead to transportation of large quantity of argon gas in IHX. Such drain-type vortices are not expected in decay heat exchangers as the associated natural convection velocity through them is of very low magnitude.


Shearing of Gas–Liquid Interface

When the free surface velocity is large, the shearing interface between sodium and argon gas becomes unstable leading to generation of surface waves as shown in  Fig. 170d. These waves can lead to gas entrainment near the free surface.

7.5.2 Potential Areas for Gas Entrainment

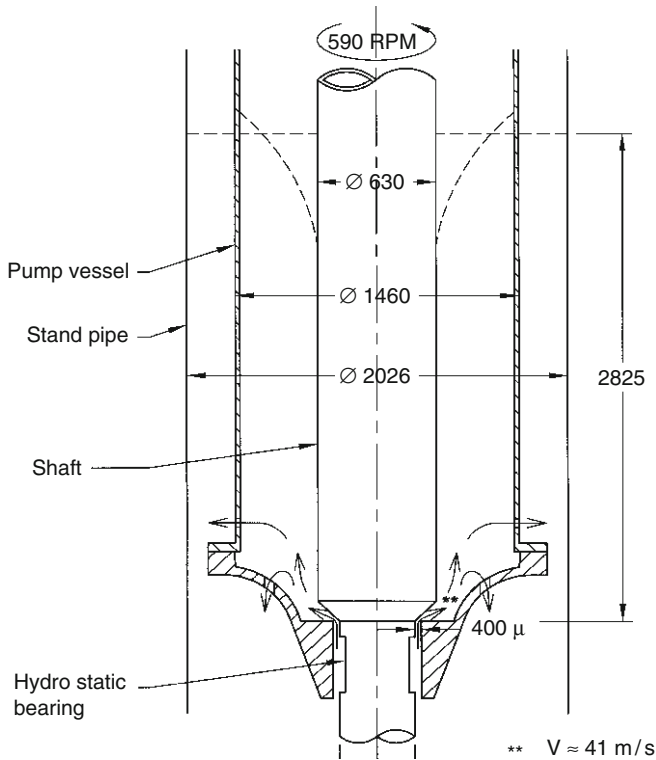
In the hot pool, IHX is the only source through with gas entrains. Other zones prone to gas entrainment risks in the primary sodium circuit are: (1) the free fall of main vessel cooling flow in the collection plenum and (2) the sodium free level around the rotating shaft of primary sodium pump. Gas entrainment is possible in the surge tanks of the secondary sodium circuit also. In the surge tank, secondary sodium from two or more IHX join and mix before branching to the steam generators, which are connected to the same secondary sodium pump. However, gas entrainment in surge tank does not pose any safety problem. Large-scale argon entrainment in surge tank is expected to affect the heat transfer in steam generators, due to poor heat transfer coefficient of argon laden sodium.

This has been explained in the previous section. In order to have a constant sodium level adjacent to the main vessel during all operating conditions of the reactor, the vessel cooling system is designed to have an overflow weir, where sodium overflows from the feeding plenum to the collection plenum. The overflowing sodium impinges on the sodium surface in the collection plenum. The impingement velocity depends on the flow rate, fall height, and shape of the weir. At the impingement point, it is possible that argon bubbles get entrained into sodium and this mechanism is the liquid fall entrainment described earlier.

The shaft of PSP is covered by a static pump vessel. Between the pump vessel and the shaft a sodium plenum is present. Due to the rotation of the shaft, the free surface of sodium between the shaft and vessel is expected to deform with a depression around the shaft as shown in  Fig. 171, similar to a drain-type vortex. The depth of this depression is a function of the rotational speed of the shaft, diameter of the shaft, and the radial gap between the shaft and the conical vessel. If the depression is very deep, argon entrainment and its passage to pump suction along with the hydro-static bearing flow are possible.

7.5.3 Effect of Gas Entrainment

The argon bubbles, thus entering the heat exchangers can reach the suction of the primary sodium pump, if they do not bubble out to the cover gas in the cold pool, which



■ Figure 171
Gas entrainment mechanism in pump vessel

depends on the velocity of sodium prevailing in the cold pool. The passage of argon through the core leads to reactivity oscillations. If the gas passes through the central part of the active core in medium/large size LMFBR, it leads to positive reactivity, while if it passes through the peripheral part of the active core, it leads to negative reactivity. Presence of large quantity of argon in sodium can lead to poor heat transfer in the core and heat exchangers.

7.5.4 Prediction of Gas Entrainment

The nondimensional numbers, which govern the flow distribution in the hot pool with undulated free surface, are the Froude number (Fr), the Reynolds number (Re), and the Weber number (We) (Guidez and Gognet 1990). The obvious choice of a simulant, which can be used to simulate sodium, is water due to the fact that it is transparent, cheap, and easy to handle. The kinematic viscosity of sodium ($3 \times 10^{-7} \text{ m}^2/\text{s}$) is half of that of the room temperature water ($6 \times 10^{-7} \text{ m}^2/\text{s}$). The surface tension force of sodium (0.16 N/m) is double that

of water (0.07 N/m). Due to these reasons, respecting all the three nondimensional numbers simultaneously is impossible in any scale size of the water model. However, the effect of Re is secondary, once the flow is in the turbulent regime, where flow pattern is not changing once $Re > 104$ and hence distortion in the Re can be permitted. Considering this, it can be shown that a scale of 0.59 is necessary to respect the Fr and We numbers exactly (Guidez and Gognet 1990). Thus the scale requirement is very large. Hence, chemicals such as sodium oleate have been proposed in literature which when added to water alter the surface tension of water. Alternatively, experiments can be carried out on a few small scale models and the results can be extrapolated for the full scale condition, based on the scale effect brought out by the study.

The mechanism of shearing gas–liquid interface depends on the horizontal velocity of sodium at the free surface. In scaled down models respecting Fr number, the velocity is always less than the prototypic value. Hence, it is essential to make sure that no entrainment takes place in the small-scale model even if the velocity is increased to the prototypic value. Based on such considerations, some researchers (Funada et al. 1991; Eguchi et al. 1994) propose equal velocity similitude (between the model and the prototype) for a conservative simulation of gas entrainment. On similar lines, Smith (1990) argues that the downward velocity level in the model should be more than the terminal velocity, if the prototypic downward velocity is more than the terminal velocity. Violation of this criterion is expected to distort the distribution of entrained bubble size. Another important aspect is that gas entrainment phenomenon is highly geometry dependent. Hence, experiments need to be carried out in models having exact geometric similarity with the prototype. The following are the major experimental findings related to gas entrainment in hot pool:

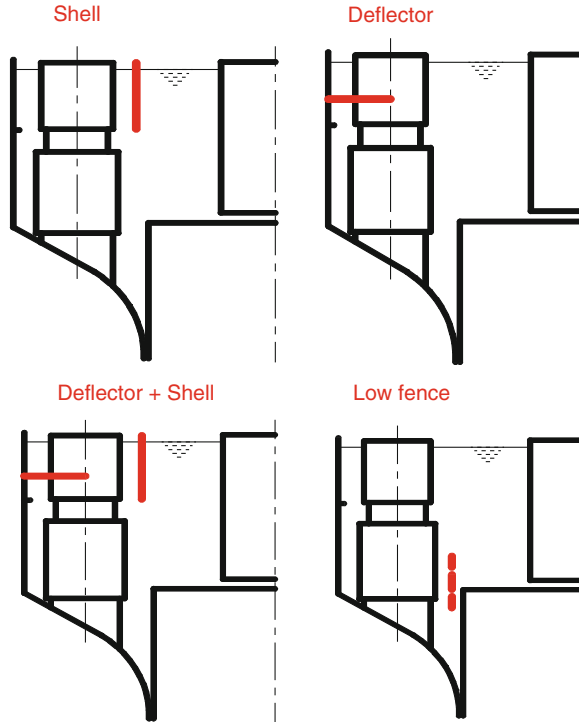
Small-scale experiments are nonconservative with respect to gas entrainment.

The nonconservatism stems from the fact that in Fr number similarity, which is normally adopted for a free surface flow, the model velocity is always less than that of the prototype. Hence, it appears that equal velocity simulation would yield realistic result.

No drain-type vortex entrainment has been observed in the model tests related to any reactor. Shearing of the interface between a liquid and gas requires large horizontal velocity at the free surface (>2 m/s) and hence this mechanism is also not expected to be present in hot pool.

Vortex-activated gas entrainment developed due to large horizontal velocities and liquid fall-induced gas entrainment developed due to large vertical velocities is the most probable mechanisms of gas entrainment in hot pool.

Established numerical methods are in vogue for the solution of Navier–Stokes equations, which govern distribution of single-phase three-dimensional flow. For the prediction of 3-D flows with deforming gas–liquid interface, numerical methods such as height function method and volume of fluid (VOF) method (Harlow and Welch 1965; Hirt and Nichols 1981) have been developed and incorporated in commercial computational fluid dynamic (CFD) computer codes. Typical diameter of spherical gas bubble, when entrainment takes place, is 0.5–10 mm. In order to capture these small gas bubbles in a computational mesh, the problem has to be solved in three-dimensions and the mesh size has to be at least one tenth of the bubble size. This results in a large number of mesh points, which is almost impossible to handle in the present day computers (Funada et al. 1991)]. To compound these difficulties, the three-dimensional numerical solution needs to be obtained in time domain to track the movement and breakup of the gas bubbles entrained. To circumvent these difficulties, the experimental approach or a combination of experimental and numerical approaches is being followed to study gas entrainment in sodium systems.



■ Figure 172

Devices to mitigate gas entrainment in hot pool

7.5.5 Design Provisions Against Gas Entrainment and Other Remarks

The free surface velocity estimated for the compact reactors SPX2, EFR, and PFBR is in the range of 0.6 m/s. Severe gas entrainment observed in the model tests of these reactors as well as that of DFBR IHX-plenum were overcome by simple solutions, like providing stiffeners and perforated plates. ➤ *Figure 172* shows a few practical options to mitigate the gas entrainments in hot pool.

The concept of purger subassemblies to vent out the gas pockets that are generated in the grid plate due to the accumulation of micro gas bubbles is well warranted to avoid the passage of the gas through the harmful regions of the core (➤ *Fig. 173*). A few purger subassemblies are positioned at the grid plate periphery, which are the preferential location for the gas segregation. After accumulation of a certain quantity, the gas escapes to the hot pool through the purger subassemblies bypassing the core. Hence, there would not be risk of reactivity effects in the core. Typically about six purger subassemblies are distributed around the outer periphery within the grid plate.

Suitable profiling of the weir-crest in the main vessel cooling system can avoid flow separation and minimizes gas entrainment.

Suitable vortex breakers have to be identified and installed in pump vessel to eliminate gas entrainment around the PSP shaft.

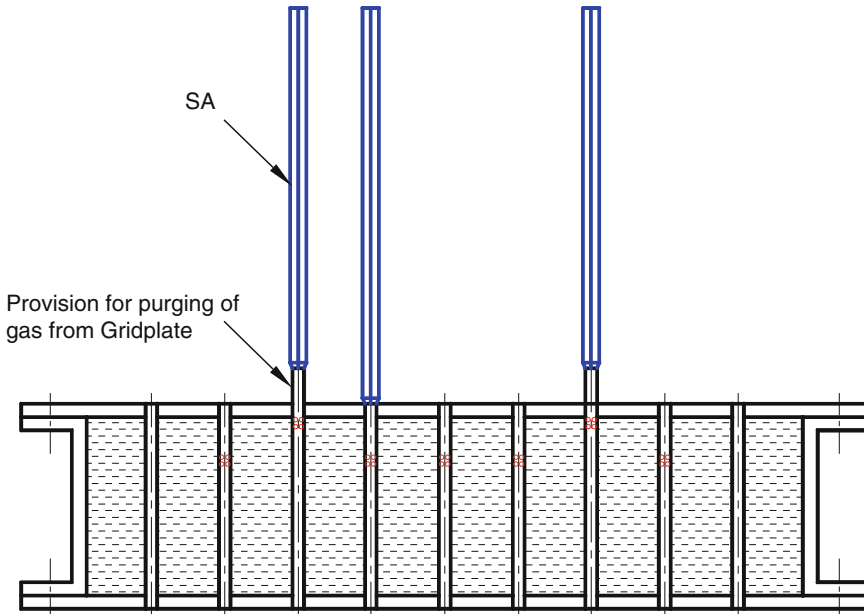


Figure 173
Purger subassembly to avoid gas entrainment problems in core

Hence, adequate care needs to be taken in the design to avoid any entrainment of argon, in terms of adequate submergence of heat exchanger primary inlet windows and lower levels of velocity close to the free surface.

7.6 Thermalhydraulic Design Criteria and Analysis Methods

7.6.1 Temperature Asymmetry in Cold Pool

During plant transients associated with one secondary loop, the temperature in the cold pool associated with the affected loop becomes hotter or colder than that of the unaffected loop. This leads to circumferential temperature difference in the cold pool structures, namely, main vessel, grid plate, etc. The flow coast down characteristics of the secondary sodium pump and cold pool capacity need to be arrived at such that the circumferential temperature difference (temperature asymmetry) is less than 30 K in the structures. Similarly, the flow in the main vessel cooling system is to be distributed to respect this temperature asymmetry limit.

7.6.2 Free Level Fluctuation

Due to large surface area ($>100 \text{ m}^2$) interfacing with argon, the hot pool free surface oscillates. The height of the inner vessel above mean hot pool sodium level should be adequate to avoid

overflow of hot pool sodium to cold pool. The amplitude of the fluctuation has to be minimum so that the height of the inner vessel can be minimum. The nominal temperature of hot pool is about 550 °C and that of argon cover gas is 430 °C. When the level fluctuates, structures partly immersed in hot pool and partly exposed to cover gas see alternating temperatures. From high cycle fatigue considerations, the amplitude of fluctuations has to be less than 50 mm.

7.6.3 Free Surface Velocity in the Pool

To avoid stratification risk in the pool, the velocity in the bottom part of the pool has to be high. At the same time, the velocity at the free surface has to be limited to 0.5 m/s to avoid gas entrainment. The entrainment of gas has to be limited to the extent that it does not cause any reactivity changes in the core. Continuous limited flow of argon through core is not any serious concern. But segregation of minute bubbles in grid plate to agglomerate into a larger bubble and its sudden movement into the core is to be avoided.

7.6.4 High-Cycle Temperature Fluctuation

The extent of stratification in the hot pool is a function of ratio of buoyancy forces to inertial forces. Stronger the inertial forces, the lower will be the axial temperature gradient. The stratification interface normally oscillates. Based on detailed structural mechanics calculations, it has been established that the gradient has to be limited to <300 K/m. From thermal striping considerations, the peak to peak temperature fluctuations on the structures has to be limited to 60 K for control plug and 40 K for main vessel and inner vessel.

7.6.5 Heat Loss to Top Shield

The heat loss to the top shield has to be minimum to minimize the heat load on the top shield cooling circuit. By the provision of thermal shield, the direct radiation heat load and argon convection heat load are reduced by ~50%. But this in turn increases the bulk temperature of argon cover gas. Increase in the bulk temperature will enhance cellular convection and the associated temperature asymmetry. The bulk cover gas temperature will also affect the axial temperature gradient in the structures. Cellular convection of argon in the narrow gap penetrations of the top shield has to be managed to have temperature asymmetry less than 30 K. The annular gap size and cooling conditions of the top shield are to be optimized to respect this limit.

7.6.6 Analysis Methods

The thermalhydraulic parameters can be predicted either by experimental simulations or by numerical simulations. Since sodium reacts in a strong manner with air and water with potential consequences, sodium experiments need to be designed with extra care for safety. Moreover, sodium is in liquid phase only above 98 °C. Hence, sodium experiments have to be performed at elevated temperatures. To compound these difficulties, sodium is opaque and hence flow visualization is difficult. Thus, large-scale experiments in sodium are costly and time consuming. Normal fluids like air and water cannot simulate sodium conditions for heat transfer, due to large difference in the values of their Prandtl numbers. But hydraulic conditions of sodium can

be nearly simulated by water models. Even for gases such as argon and nitrogen, the numerical simulation is cheaper and faster, especially when the number of parameters involved is large. But numerical models and the codes developed need to be validated by suitable experiments. For a successful design, a judicious combination of experimental and numerical approaches is a must. The method adopted in the design of SFR is based on performing many large-scale water experiments and limited sodium experiments to validate computer codes and then using these validated computer codes for numerical prediction of sodium flow and temperature distributions in the reactor.

The computational fluid dynamics-based approach calls for specific models for a particular phenomenon to be investigated. For example, for the prediction of gas entrainment in the pools, we need to adopt the VOF method, which is a 3-D transient simulation to predict the deformation of the free surface. For this simulation, we also need to take into account the surface tension effects. The number of grids or grid refinement has to match with the purpose of simulation. For example, to predict the deformation of the free surface, the grid need not be very fine. Coarser grid is adequate for the prediction of sodium level fluctuations that would be the input for thermal ratchetting phenomena. But to predict the onset of gas entrainment and tracking of the entrained gas bubble within the sodium, the grid has to be finer than the bubble size. Thermal striping arises due to jet instability. Conventional/standard turbulence models of $k-\epsilon$ family are adequate to predict the global features of turbulent flow. They cannot predict the intricacies of generation and decay of vortices around the jets. For a realistic simulation of thermal striping, direct numerical simulation (DNS) is essential. But to a large extent, the Large Eddy Simulation (LES) will be able to cater for the objective of thermal striping simulation. This is due to the fact that large eddies are associated with low frequency temperature fluctuations which are very critical in thermal striping. Fine eddies are associated with high frequency and low amplitude temperature fluctuations, which does not significantly alter the temperature of the structures. On the similar lines, the standard $k-\epsilon$ turbulence models have been developed and validated for forced convective regime. Application of this model for stratified sodium flow conditions requires detailed validation. Identification of suitable turbulence model for buoyancy dominated sodium flows is an on-going research in CFD.

Internationally, fast reactor pool hydraulics has been investigated successfully by many countries, especially, France, UK, USA, Japan, Russia, and India. All these countries have utilized a hybrid computational-cum-experimental approach. France has developed the TRIO-VF and TRIO-FE codes (Menant and Villand 1994). The former is based on finite volume method while the latter is based on finite element method. They have also developed the N3S code which is based on finite element method. These codes have been utilized for investigations of conventional pool hydraulics during steady and transient conditions and prediction of temperature history during thermal striping. Japan has developed many thermal hydraulic codes, namely, THERVIS-III (Yamakawa 1983) and AQUA (Muramatsu and Ninokata 1991) for pool thermal-hydraulics and DINUS-3 (Muramatsu 1993), which is a DNS code for the thermalhydraulic prediction of thermal striping.

UKAEA has developed the FLOW-3D code which has finally become the commercial CFX code (Presentation by AEA Technology – UK 1994) for the prediction of global thermalhydraulics of fast reactors. Simultaneously, academicians and consultants of UK have developed the two popular CFD tools, namely, PHOENICS (Cham Ltd.) (Farrar 1990) and STAR-CD (CD-Adapco). Russians have also developed many in-house CFD codes, of which TURBO-FLOW (Scherbakov 1994) is the notable one. India has also developed two CFD codes, namely, THYC-2D and THYC-3D for global thermal hydraulics of fast reactors.

8 Specific Structural Mechanics Issues

8.1 Introduction

Apart from excellent heat transfer properties, the use of sodium results in large margin between operating temperature and boiling point of coolant. Hence, there is no need to pressurize the system and all the disadvantages associated with the unforeseen depressurization of coolant are absent in SFR. High thermal conductivity, low viscosity, and large difference between the hot sodium and air coupled with significant variation of sodium density with temperature permit decayed heat removal through natural convection modes. It also provides high thermal inertia and hence, more time is available for the operator to act in case of exigencies without fear of any temperature raise exceeding acceptable limits.

Sodium has, however, certain disadvantages. It introduces challenging thermohydraulics and structural mechanics issues. High thermal stresses and thermal shocks are induced on the adjoining metal wall and also, the temperature fluctuations on the metal are to be considered due to sodium free level fluctuations. Temperature fluctuations are also created on the metal wall due to a special type of phenomenon called thermal striping which is caused due to lack of perfect mixing of sodium streams at different temperatures particularly in the sodium piping. The stainless steel parts when subjected to temperature fluctuations are subjected to high cycle fatigue damages. Seismic response analysis of thin walled vessels, pumps, and absorber rod mechanisms calls for complex numerical and experimental simulation techniques. These failure modes are presented comprehensively in [▶ Fig. 174](#).

8.2 High Cycle Thermal Fatigue: Thermal Striping and Stratification Instabilities

In the zones where hot and cold sodium flows meet, incomplete mixing (in spite of turbulent diffusion) can occur so that surrounding structures have to sustain temperature fluctuations on their surface. The consequence in fatigue damage (appearance of a network of cracks at the surface, [▶ Fig. 175](#)) is usually named as thermal striping. High frequency fluctuations of stratified zones if any result in similar consequences. The efficiency in rising stresses in the material is governed by

- Heat transfer at the surface of the structure,
- Thermal diffusion inside the wall of the structure.

Kasahara et al. (2002) have proposed analytic formulations of the bidimensional problem relying on a separation of these two effects and in the hypothesis of elasticity. They consider a sinusoidal fluctuation of the temperature of the fluid at the frequency f , applied to one side of a wall (the other side being in adiabatic conditions), of thickness L , thermal conductivity λ , and diffusivity a . This fluctuation will be transferred to the surface of the solid through a *heat transfer function* H , depending on this frequency f (or nondimensional frequency fL^2/a) and on the Biot number ($Bi = hL/\lambda$), h being the heat transfer coefficient.

The consequences in terms of stresses inside the material can be expressed as a stress function S of the nondimensional frequency fL^2/a , material data (thermal expansion factor, Young's modulus, Poisson's ratio), and a stress factor K determined from geometry and mechanical bounding conditions at the borders of the wall. It is worth noticing that the "gain" of the heat transfer function H decreases as the frequency increases and that the one of the stress function S

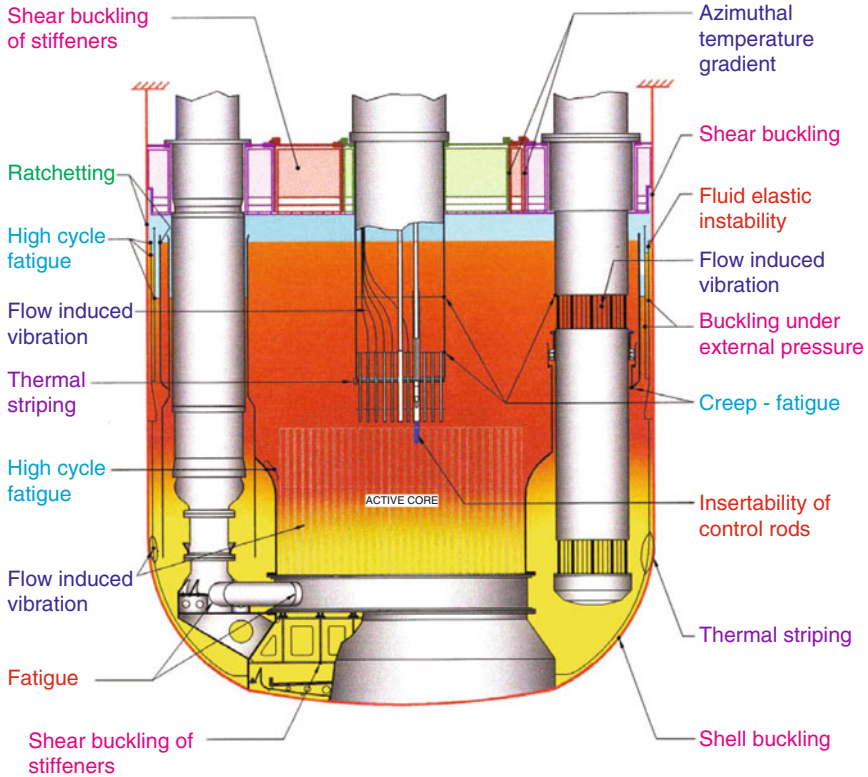


Figure 174
Failure modes for structural design

increases in the meantime. As a consequence, the resulting function $G = HS$ reflects the fact that there should exist a range of frequencies that has a maximal detrimental potential in fatigue. Figure 176 shows this effect with bending (only) constraint at the borders of the wall. A partition of the stress into different components such as membrane, bending, peak stress from this type of model was used in CEA to help fatigue analysis of complex cases (Chapuliot et al. 2005).

8.2.1 Experimental Evidence of Thermal Striping

In sodium, thermal striping has been obtained in laboratory in different dedicated loops: FAENA (Figure 177) in CEA, France, TIFSS (Figure 178) in JAEA, Japan (Lejeail and Kasahara 2005). Results are very useful for the verification of transfer functions discussed above, and check damage assessment methods discussed in Sect. 8.2.2.

FAENA used tubular (square cross section) specimens submitted to alternative hot and cold sodium injections. Mean flow rate could reach 700 l/h (velocity in the specimen 0.5 m/s), frequency range was 0.07–0.3 Hz, ΔT at the specimen inlet 398–553 K, (323–473 K at outlet), cycle numbers 10^4 to some 10^6 , surface roughness Ra 0.1–0.3 μm , and equivalent strain range at the level of the last crack initiated, 0.2–0.77%. These tests have concerned 316L and 316 LN austenitic

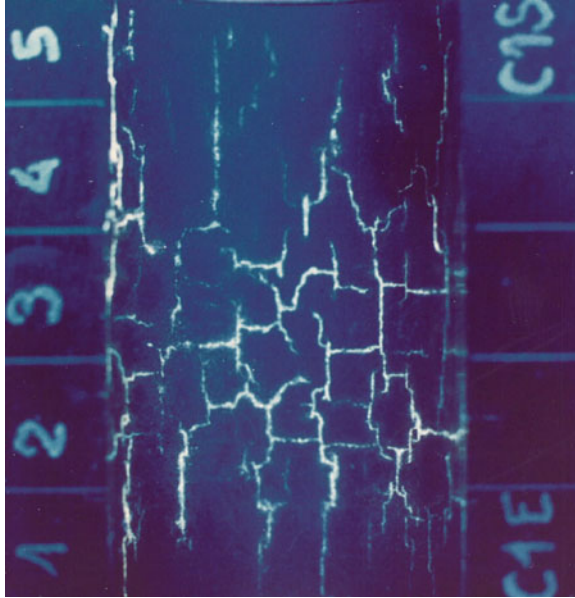


Figure 175
Thermal fatigue cracked surface

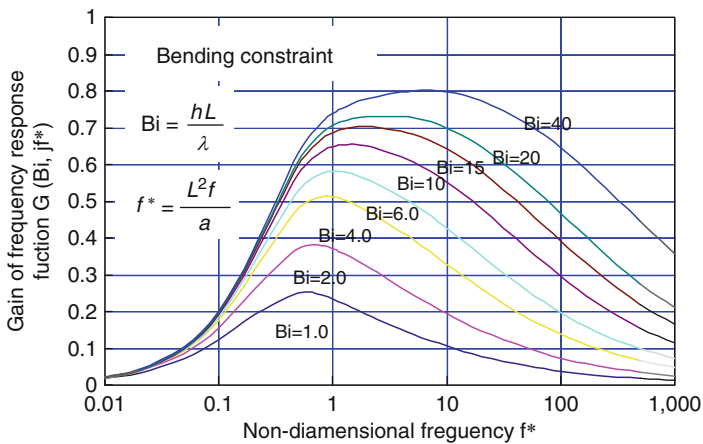
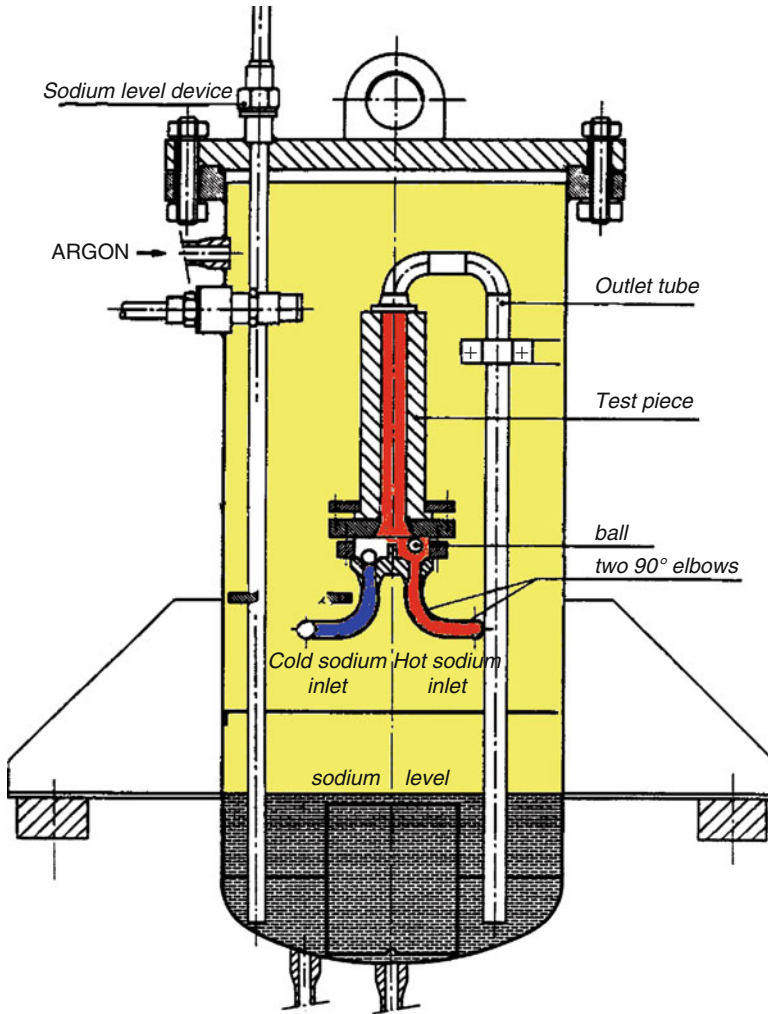


Figure 176
Thermal shock attenuation under thermal striping (From Kasahara et al. 2002)

grades and, to a smaller extent, 9Cr 1Mo mod martensitic steel. Some specimens were tested with successive different ranges in order to test damage accumulation rules.

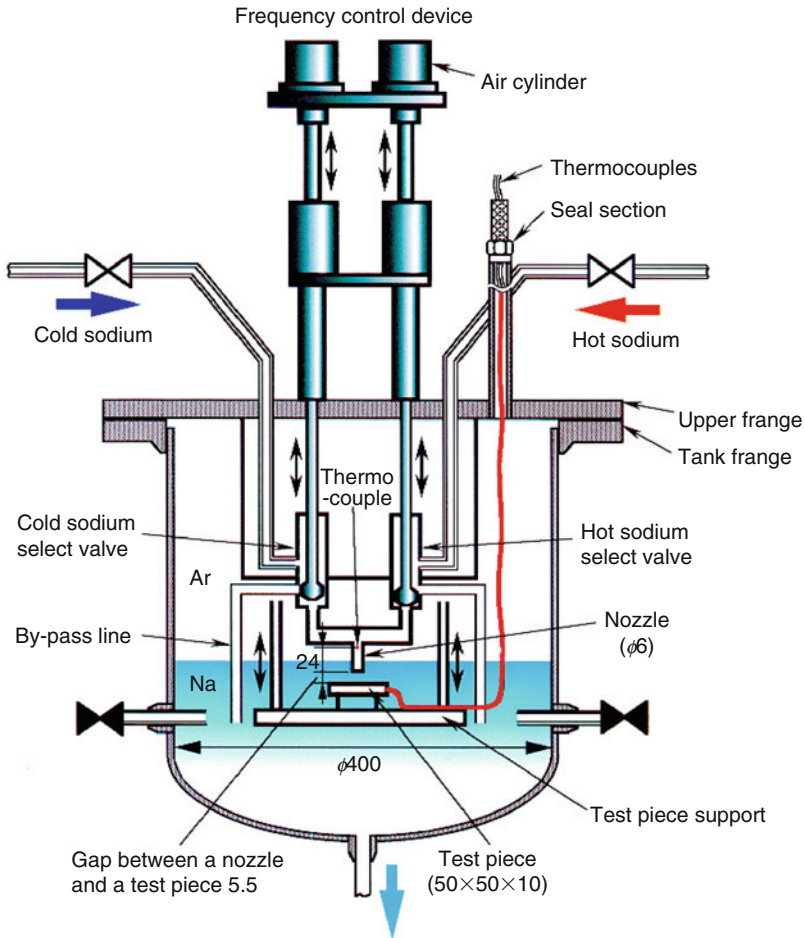
In TIFSS, hot and cold sodium is alternatively fed into a nozzle and projected on a flat specimen as a vertical jet in the middle of a sodium pool. Temperature range at the nozzle is



■ Figure 177
FAENA facility

about 235°C (741–505 K), and frequencies are in the range 0.01–0.2 Hz. Specimens are 316 FR grade. In both experiments, the test specimens are fitted with thermocouples in the thickness that allow for adjustment of the temperature data, and interpretation.

Thermal striping has also been observed in reactor circuits, for instance in the PHENIX 250 MW sodium demonstration plant in France. A Tee junction of a small pipe ($T_{\text{Na}} = 700\text{ K}$, flow rate 7 kg/s) with a larger one ($T_{\text{Na}} = 610\text{ K}$, flow rate 800 kg/s) was affected by thermal striping at a location downstream from the tee, at a weld (geometrical/material discontinuity). This case was the opportunity to make an international benchmark on predictive methods (Gelineau et al. 1999), liable to be used at the design stage. Another case of mixing tee on a PWR unit has been detected and analyzed in depth from thermohydraulics, mechanics, and material science points of view (including some crack propagation aspects). The contribution of large scale flow



■ Figure 178
TIFSS facility

instability (such as pulsing) at low frequency was established, and the question of precluding such consequences at the design stage is pointed out (Chapuliot et al. 2005).

8.2.2 Assessment of Potential Damage by Thermal Stripping at the Design Stage

If fluid temperature ranges (ΔT_{fluid}) and associated frequencies (f) are known from the thermohydraulics studies (DNS, LES, $k-\epsilon-\theta^2$ methods, see “acronyms” below, experimental mock-ups), analytical solutions (such as Kasahara et al. 2002; Kasahara and Lejeail 2002) can be used. They allow for assessment of temperature and finally surface stress fields ($\Delta \sigma$ (f)) response, provided transposition of the model to more or less a complex structure (with peculiar

boundary conditions) remains relevant. It is worth noticing that this kind of method allows also for simplification of the problem by showing the most damageable frequency domain, and provided a service period is given, makes easy to get the input of the fatigue analysis as a set of $\Delta\sigma$ (N), where N is a cycle number during the said period.

An alternative case in design is to draw directly the mechanical response at the surface of the structure by chaining mechanical finite elements calculations of stresses with thermally-hydraulics. The information in terms of frequencies (cycle numbers) and stress ranges can be then derived from analysis of a time sequence long enough by some wave counting method, such as rainflow method (AFNOR 1996).

In both routes described above, stress ranges

- Are multiaxial and usually assessed according to the elastic behavior assumption for the material (so plasticity corrections are to be introduced if necessary).
- Have to be converted in strain ranges and expressed in terms of equivalent prior to enter (uniaxial) fatigue curves of the material.

For that purpose, the procedure of RCC-MR design code (2007i) for instance, for pure thermal fatigue (Additional plasticity corrections are to be applied if there is a possibility of elastic follow-up for instance, as are amplification factors related to discontinuities, if any.) is as follows. Equivalent strain variations are determined as

$$\overline{\Delta\varepsilon_t} = \frac{2}{3} \frac{1+\nu}{E} K_{vb} \overline{\Delta\sigma_{\varepsilon t}} \quad (31)$$

K_{vb} is a coefficient, which represents the difference of triaxiality between elastic and elastoplastic behavior; it depends on the elastic equivalent stress variation $\overline{\Delta\sigma_{\varepsilon t}}$, ν is Poisson's ratio, and E Young's modulus. The evaluated strain range $\overline{\Delta\varepsilon_t}$ predicts an allowable cycle number $N_f(\overline{\Delta\varepsilon_t})$ from fatigue curves of the material at the maximum temperature. Finally, Miner's rule evaluate fatigue damage factor D_f as:

$$D_f = \sum \frac{N(\overline{\Delta\varepsilon_t})}{N_f(\overline{\Delta\varepsilon_t})} \quad (32)$$

where $N(\overline{\Delta\varepsilon_t})$ is the applied cycle number of strain range $\overline{\Delta\varepsilon_t}$ and D_f is asked to remain lesser than one. This method and the one proposed by Japanese teams and their comparison versus FAENA tests can be found in Chapuliot et al. (2005).

8.2.3 Conclusion, Future Prospects

Coupled numeric simulation of thermallyhydraulics and mechanics problems offers now interesting prospect. Nevertheless, numerical simulation to predict the behavior covering the entire plant life is still costly in terms of CPU time. Extrapolation for the service duration should rely on statistical approaches that are an open field of work. Identification of damageable frequency range by simplified solutions can help to rationalize this approach.

Procedures for damage assessment exist in codes and standards. Nevertheless, establishing a safe limitation (making thermal striping analysis not mandatory) for max ΔT in design in between flows or zones of sodium at different temperatures would result in quite low values (some few tenth of degrees), which is not yet codified.

The other open topic is related to the question of consideration of a mean stress superimposed on thermal striping cycles (especially in case of small strain ranges). Most of the data and qualification of these procedures were obtained on austenitic steels. The trend in the new design of SFR is use of ferritic–martensitic steels, which appears at a first glance as favorable because of lesser thermal expansion and higher thermal conductivity of these steels with respect to austenitics. This needs confirmation by a limited number of tests in sodium. Nevertheless, more data and an in-depth analysis are desirable with water tests. A few tests have shown adverse results, raising the question of an environment effect and other considerations.

Acronyms:

DNS: Direct Navier–Stokes method,

LES: Large Eddy Simulation method,

$k-\varepsilon-\theta'^2$: Turbulent kinetic energy/rate of turbulent kinetic energy dissipation/temperature variance method.

8.3 Free Level, Stratification Level Fluctuations

SFR designs generally include the presence of a free level of sodium in some components. An inert gas (usually argon), at low pressure (max some bars), fills the space over the free level of sodium. These provisions allow for thermal expansion of sodium during temperature transients and guaranties inert chemical conditions above sodium.

Different vessels and tanks are concerned, whatever the type of concept (loop, pool):

- The main vessel itself
- The inner primary vessel that collects the hot sodium at the outlet of the core in case of pool type design
- According to the design, different baffle rings may exist (for instance, in case of design with dedicated circuit for cooling down the main primary vessel at the temperature of core inlet)
- The main primary pipes (hot, cold) in the loop type that may cross the free level in the main vessel. . .
- The dedicated expansion tanks and/or the main steam generator vessels in the secondary circuits that transfer the heat to the energy conversion system. . .

Stratifications can take place in cases of loss of forced convection trips, for instance. In both cases, axial thermal gradients are induced on the surrounding structures.

8.3.1 The Free Level Issues

They rely on the following facts:

- The projected part of shells has high-temperature inertia when compared with the part dipped in sodium, due to the very good heat transfer in sodium compared with gas.
- In the (theoretical) case of temperature step ΔT applied on a thin ($e \ll R$) shell, and with the assumption of linear behavior of the material, for instance, the stress system exhibits an axial bending maximum $\sigma_b \sim 0.3 \times E\alpha\Delta T$, and a hoop membrane stress $\sigma_h \sim 0.5 \times E\alpha\Delta T$,

the decay length along the shell affected by significant stress level being $\sim \pi/\beta$, with $\beta^2 = [3(1 - \gamma^2)]^{1/2}/e.R$

E: Young's modulus

α : thermal expansion coefficient of the material

ΔT : temperature step amplitude


γ : Poisson's ratio

e: shell's thickness

R: shell's radius


For stainless steel, 316L grade,

$R = 10$ m, $e = 2 \times 10^{-2}$ m, $T \sim 500$ °C, $\Delta T = 100$ °C, $\pi/\beta \sim 1$ m, $\sigma_b \sim 95$ MPa, $\sigma_h \sim 160$ MPa.

Furthermore, one can expect that the temperature gradient can vary and move along the shell (at free level: due to the thermal expansion of sodium associated with the transient, and/or variation of the pump speed depending on the trip considered, or in the hypothesis of stratification, by evolution of the level) as depicted by  Fig. 179.

Potential Thermomechanical Damages Associated With Free Level Issues

Their assessment requires considering the whole set of loads applied to free level zones. Nevertheless, loadings associated with mechanical loads (the so-called “primary stresses” that are not relaxable by the strain that they can yield), typically induced by inner pressure and weight, are very low in sodium fast reactors.

Basically, the thermal stresses induced by free level issues are prevailing and look like displacement controlled stresses (“secondary” stresses type in codes & standards). They must be assessed against fatigue and creep–fatigue damages, usually in the low/mean cycles (plastic) range (high frequency components come rather under  Sect. 8.1.).

In fact, such stresses are not to be considered as fully displacement controlled. The reason is that, due to temperature variation along the axis of the shell considered, the mechanical properties of the steel vary with temperature.

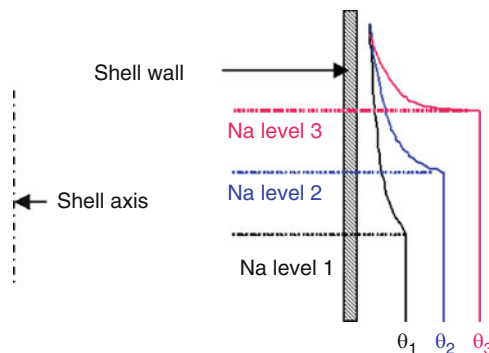


 Figure 179

Temperature gradients in the vessel near sodium free level

The “hot” zone exhibits a lesser yield stress with regard to the colder one. Furthermore, depending on the design and the component considered, the conditions can be such that they may be subjected to creep deformations.

As a result, both mechanisms will contribute to concentrate inelastic deformation in the hot part, while unloading the colder one: this situation is currently qualified as “elastic follow-up” in codes and standards. The potential consequences are as follows:

- Strain buildup at each cycle that can result in possible geometric increments (so-called ratchetting behavior) that may introduce functional disturbances (depending on the design)
- Effect on creep–fatigue damage because accumulation of strain that was shown to contribute to lifetime decreases if excessive; for this reason, accumulated strain has to be limited to a few percent, prior to entering fatigue–creep fatigue analysis
- Effect on creep–fatigue damage because of strain range enhancement by elastic follow up
- Risk of buckling associated with membrane compressive hoop stresses, and that may be emulated by geometric evolutions (interaction with geometric disturbances). Nevertheless, it is worth noticing that such a buckling would be limited because displacement is controlled.

Experimental Evidences of Damages Induced at Free Level

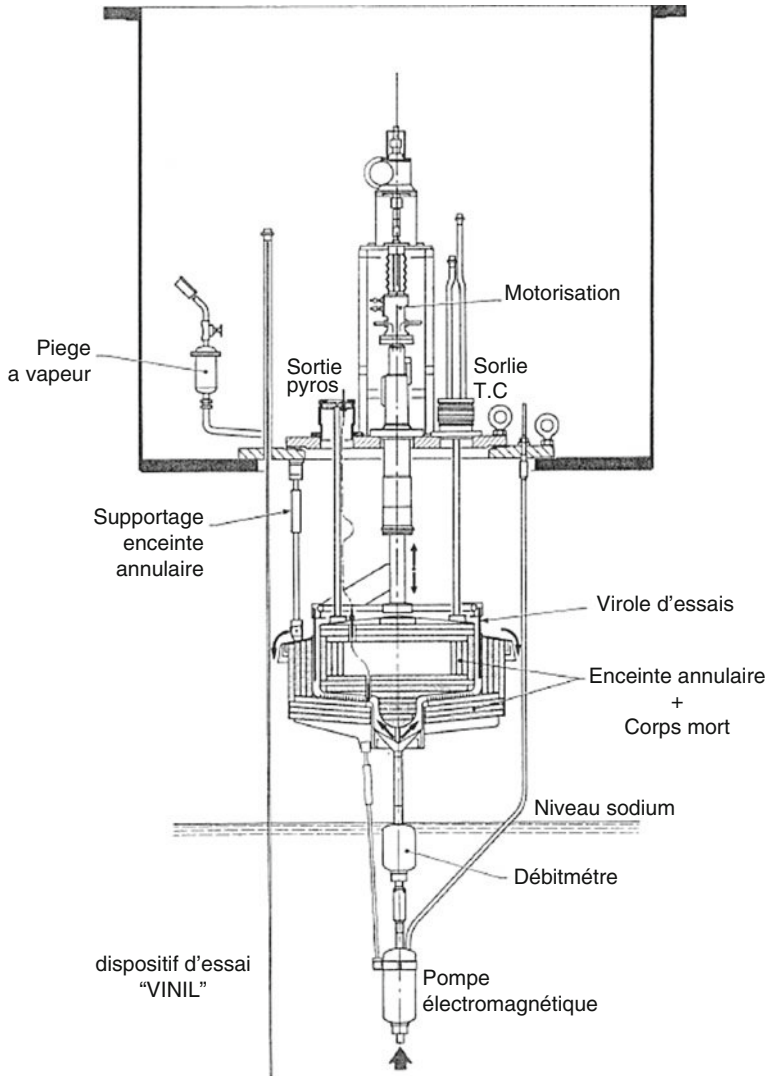
At the CEA (France), sodium experiments were made with the so-called VINIL device (➤ [Fig. 180](#)) on 316LN, on shells 800 mm in diameter, 1.2 mm in thickness, two different heights. ➤ [Figure 181](#) shows the loadings conditions and ➤ [Fig. 182](#) presents the displacements observed after 930 cycles. It is worth noticing that no buckling was observed. Other references with water devices are available (Wada et al. 1995). Japanese experiments with smaller samples (radius 76.5 mm, thickness 2 mm) on two 316 SS grades are also reported in Igari et al. (2002).

Assessment of Free level Problems at the Design Stage

Simplified Methods Early methods dedicated to this type of ratchetting (likely to occur in lack of significant primary stress, radically different of Bree type to this extent) have been proposed in Japan (Igari et al. 1993) for prediction of the strain increment by cycle. They rely on elastic/perfectly plastic material behavior, are based essentially on the membrane hoop stress, and are specific for travel of simple temperature profiles on cylinders. Refinements have been introduced later (Wada et al. 1995) for consideration of effects of axial bending stress, (low) primary stress, existence of work hardening in the material, and have been compared with small-scale water tests for 316 austenitic grades.

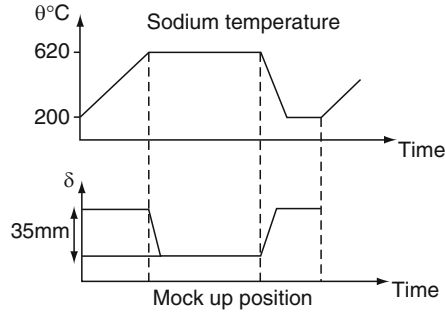
In France, following the VINIL tests, completed with COTHAA tests (double tubes with geometrical discontinuities, combination of thermal and primary loads, program undertaken in the frame of PWRs technology (Cabrilat et al. 1997)), a simplified assessment method was implemented in the French standard RCC-MR (2007a,b,c).

It consists, for those cycles that include membrane stresses (Q_m) induced by thermal effects, in considering that one part of this Q_m is to be combined with the membrane stresses induced by mechanical loads. The result of this combination is then used to determine the so-called “equivalent” primary stress (i.e., granted to yield the same strain as the whole set of loads) out of the “efficiency” diagram; the equivalent primary stress is finally used to check whether the strain limits are met or not. The application of both Japanese and French simplified methods to the VINIL experiments show quite a satisfactory result, with some conservatism.

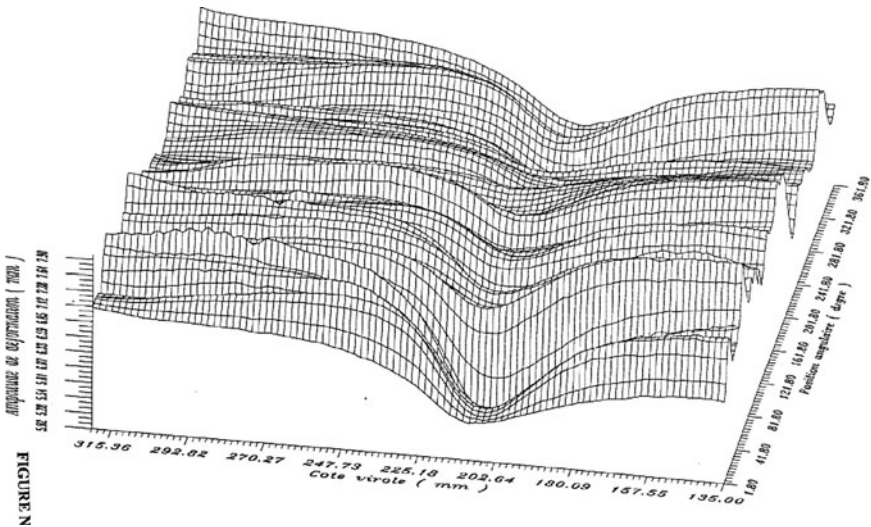


■ Figure 180
VINIL test setup

Inelastic Analysis Different advanced models (i.e., beyond the elastic/perfectly plastic, isotropic hardening, and kinematic hardening bilinear models, which are disqualified intrinsically by the excessive simplicity of their description of plasticity effects) were tested against COTHAA tests ($T < 723\text{ K}$) results, in the frame of a benchmark by different teams in France in 1997 [3]. Most of these models are based on the use of non-linear laws for the evolution of the kinematic variable(s) and were used in elastic–plastic or elastic–viscoplastic formulations. The so-called “micro–macro” model that defines constitutive equations at a microscale was also tested.



■ Figure 181
Temperature variation



■ Figure 182
Displacement pattern variation

Igari et al. (2002) deals with a Japanese study, which also includes a set of models incorporating several types of kinematic hardening rules, creep being dealt with by superposition, except for the two so-called unified constitutive models.

The state of the art in the field of assessment of ratchetting on the basis of non linear, inelastic, materials behaviour models, is not yet in a position to allow for accurate results.

8.3.2 In Sodium Stratification Issues

It is clear that in sodium stratification resulting in steep temperature axial gradient in the surrounding structure, for instance, in the case of loss of flow, can lead to very similar situations and be dealt with by the same methods as free level issues.

8.3.3 Conclusion

Ratcheting induced by free level/stratification travels with negligible mechanical stress is a new area. A classical simplified method for ratcheting has been modified satisfactorily to deal with this case, and allows for conservative designs. A method specifically dedicated to the problems of thin shells at free level (short/long travels) has been shown to perform correctly compared to the experimental cases featuring the different hypothesis considered.

Further reduction of conservatism and generalization is still a matter of R&D, due to complexity of plasticity mechanisms and interactions with structures and loadings applied. To this extent, inelastic models keep a role to play.

The choice of materials too, is relevant to this problem, as differences are revealed out of simple tests, such as uniaxial stress–strain response. For instance, low carbon, nitrogen added, 316 grade stainless steel exhibits small ratcheting as compared to some others (304 grade for instance, [lgari])

It is worth mentioning that new materials considered for fast reactors, that is, ferritic–martensitic grades that exhibit softening in cyclic test, have to be studied from the point of view of the candidates for free level components.

8.4 Seismic-Induced Forces and Their Effects

8.4.1 Geologic Phenomena

Lithospheric displacements of the plates are carried out via motions along fault planes where concentrate the tectonic forces. The faults are breaks of the rigid terrestrial lithosphere accompanied by a relative displacement of the two compartments. There are basically two types of constraints or forces tectonic, which deform the rocks: compressive stresses and those of tension. In compression, the forces converge. In tension, the forces diverge and cause the material to stretch. The fault plane between two blocks is a “rough” zone on which the slip is not carried out easily. While the two blocks want to slip length one of the other, the fault is a surface of friction, which can block the motion.

The accumulation of the constraints continues until reaching a breaking value that the rocks cannot support any more. A brutal rupture then occurs. The rocks slacken: it is the earthquake. At the end of the earthquake, the constraints accumulate again along the fault until reaching a new threshold causing a new rupture: these successions of phase of activity and lull constitute the seismic cycle.

The power of an earthquake is quantified by its magnitude (magnitude of Richter is the most known scale). The magnitude is calculated starting from the various types of seismic waves

recorded by the seismographs. Richter magnitude is logarithmic scale: to increase the magnitude of one unit is equivalent to multiplying by 30 the energy released by the rupture. This scale also makes it possible to appreciate dimensions of the activated fault.

8.4.2 Seismic Risk

The seismic risk can be defined like the possibility for an area or a site to be exposed to an earthquake of given characteristics, expressed as much as possible in the form of parameters such as macro seismic intensity, acceleration, velocity, displacement, and spectrum of the temporal signal. The risk is characterized by the probability of occurrence of a given event and the vulnerability, which expresses the gravity of the effects or the consequences of the event supposed to be able to occur.

A seismic study of risk comprises three successive stages:

The first two relate to the identification of the seismic sources and the evaluation of the regional seismic motion according to a probabilistic or deterministic approach.

The third relates to the taking into account of the modifications of the seismic vibration with the geological and local topographic conditions.

The probabilistic evaluation of the seismic risk indicates, at any point of the territory, the level magnitude or acceleration of the ground (m/s^2) likely to be reached for one period of time given.

The deterministic evaluation is founded on the one hand on a detailed analysis of the various regional seismic sources and on the constraints governing the deformation and on the other hand on a precise study of the historical seismicity.

8.4.3 Site Effects of Seismic Forces

Seismic waves of the earthquake are amplified related to the topographic or geological configuration of the site. Site effects are as function of the structure and the nature of the ground: the mechanical characteristics (density, rigidity, and compressibility) and the geometry of the formations (stacking, basic filling of valley) can accentuate the effects of the seismic motion.

The seismic motion is a nonstationary, transitional, and unpredictable signal. However, it can mainly be characterized by

- The duration (ten seconds to several minutes).
- The frequency range (1–40 Hz).

The intensity characterizes the effects and local damage caused by the earthquake in a specified area. It is measured, thanks to seismometers. It is maximum plumb with the hearth of the earthquake. The scale most used in the world to measure the intensity is MSK scale (Medvedev, Sponheuer, Karnik, 1964). But EMS 1998 tends to scale replace it. (European Macro Seismic Scale). EMS 1998 Scale is adapted to current constructions. The seismic vibration can start motions of ground such as crumbling of underground cavities, cliff collapses, falls of blocks, and landslides (🕒 *Fig. 183*). Topographic effects of site: tops of hillock, lengthened peaks, and edges of plates and cliffs induce important amplification of the seismic motion.

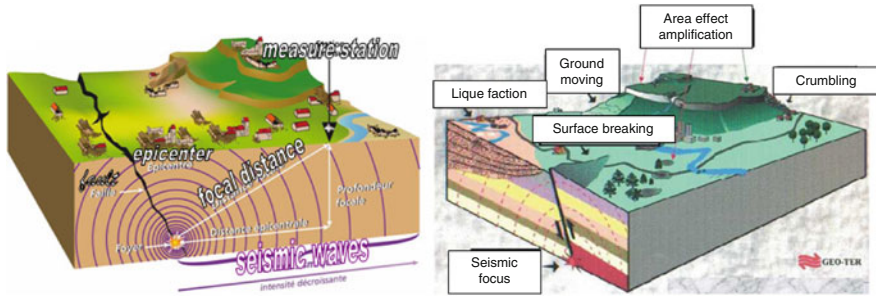


Figure 183
Generation of seismic waves and their effects

In certain cases, the rupture of the fault plane is propagated to the surface of the ground, generating a rupture surfaces, some along the fault of a few centimeters to several meters of rejection. This propagation to the surface of the ground of the fault plane having broken depends on the initial depth of the seismic hearth (place of the fault plane where the rupture began) and magnitude of the earthquake (dissipated energy).

Temporary liquefaction of granular mediums (sandy or muddy horizons) gorged with water: seismic motion can produce a fast compression of the sediments and then the water contained in the sediments will be expelled with a brutal deconsolidation of material results: it is the phenomenon of liquefaction.

8.4.4 Effects of Seismic Forces on Structures

The physical damages due to earthquakes are depicted in [Fig. 184](#). Seismic excitation can be an important load to take under account during the design of structures. In many countries, the seismic risk is high and structures have to be designed using seismic codifications. For example, Europe recently created a codification, named Eurocode 8, dealing with seismic design of structures. Structure type has to be taken under account too; power plants have not the same design as standard building. Linear or nonlinear numerical methods can be used for the design. For example, an approximation of the structure response can be deduced from the linear response spectrum:

For a given earthquake excitation, the response spectrum is defined as the maximum displacement of a simple degree of freedom (1 DOF) structure with a damping ξ , and within a range of natural periods (or frequencies).

The maximum displacement for each frequency can be found from the computed displacement of the 1 DOF at this frequency. A plot of maximum displacement versus natural period is constructed, representing the deformation (or displacement) response spectrum.

From [Fig. 185](#), we can directly read the maximum relative displacement of any structure of natural period T (and a particular value of ξ , as damping). In order to cover the damping range of interest, it is common to perform the same calculations for $\xi = 0.0, 0.02, 0.05, 0.10$, and 0.20 . It is seen in the figure that the maximum response at short period (high frequency, stiff



Figure 184
Physical damages of earthquakes

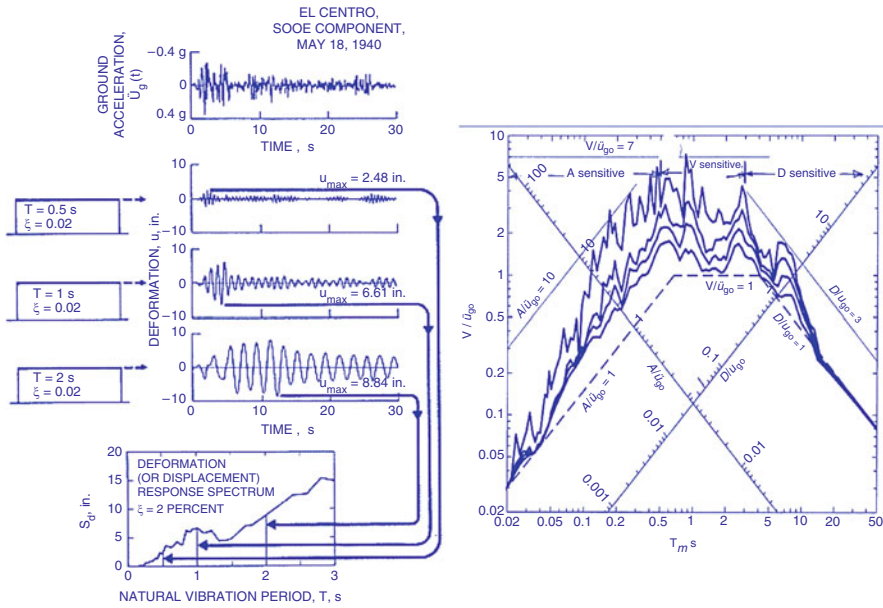


Figure 185
Dynamic responses under seismic loadings

structure) is controlled by the ground acceleration. Low frequency (long period) is controlled by the ground displacement, and intermediate period by ground velocity. Many laboratories, over the world, are working to better understand the seismic behavior of components, equipments, and structures with experimental and numerical approaches. The objective is to reduce the consequences of earthquakes with improvement of standards and diagnosis of existing facilities.

8.4.5 Seismic Piping Behavior and Design Criteria

Context and Issues

Since the beginning of the 1980s, many R&D programs have been devoted to seismic design of piping systems. The reasons why there have been such activities on that subject are manifold:

- Piping systems do have good seismic behavior, as has been noted during real earthquakes as well as during laboratory experiments.
- Present design criteria are overly conservative.
- The application of these criteria leads to additional supports, which may be harmful from an economic and a safety point of view. Indeed, by limiting the piping system deformations, these supports can be harmful in regard to in-service loadings, such as thermal loadings.

A common objective of many of these R&D programs has been to reduce the present conservatism, but different means have been proposed to reach this goal, and none of these approaches has been totally convincing (Bertrand and Devictor 2006). So R&D programs have been pursued in order to reach sounder and more justified conclusions. The CEA R&D approach is based on the difference between the real behavior (or the best estimated computed one) with the codified methods. Criteria are applied on an elastically calculated behavior that can be significantly different from the real one: the effect of plasticity may be very meaningful, even with low incursion in the plastic domain. Moreover, and particularly in piping systems, the elastic follow-up effect affects stress distribution, for both seismic and thermal loads.

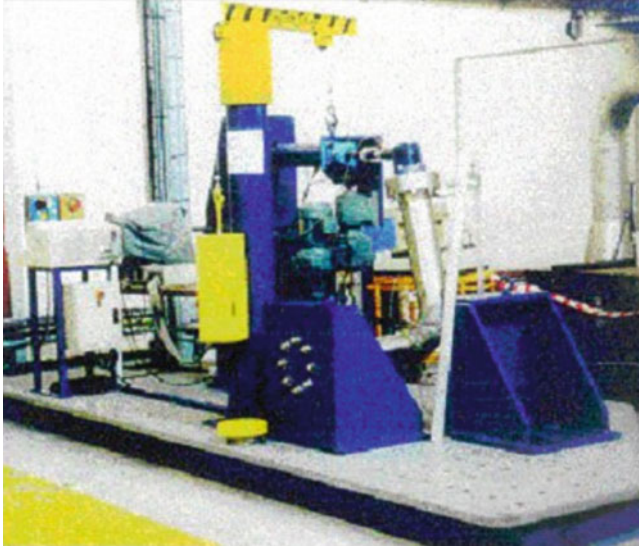
Experience feedback from seismic tests on piping has shown its ability to support very high levels of acceleration that are unacceptable under the current criterion (Farvacque et al. 2003).

Characterization of Nonlinear Behavior of Piping Systems under Seismic Loading

In piping system, the weakest parts are the elbows, where stress concentrations may be high. Under intense seismic loading, they are subjected to cyclic loads causing them to work in the plastic domain and resulting in consumption of a substantial amount of the kinetic energy of the piping. We therefore concentrated exclusively on these components to quantify the margins (the difference between the criterion and failure) inherent in the current criterion to establish a new one using the ductility of the piping.

A large number of static tests on elbows (➤ Fig. 186) and straight parts to the point of failure show that:

- Failure of elbows, under static conditions, is due to the plastic instability that appears when a certain angular threshold is reached (angle of closure).
- The limit angle depends weakly on the geometrical parameters of elbows, but more on the mode of bending of the elbow (in the plane or out of the plane), the internal pressure conditions, and the properties of the materials (tensile curve).
- A limit angle to avoid failure can be defined for a given material and a bending mode.
- Failure moment of straight parts is due to the buckling. This failure moment depends weakly on the geometrical parameters of straight parts but more on materials, and it does not depend on internal pressure conditions.



■ **Figure 186**
Actuator system for testing elbows

Seismic tests carried out on the Azalée shaking table (► [Fig. 187](#)) of the Tamaris facility (Blay et al. [1997a,b](#)) shows that:

- Pipe failure does not occur at the seismic levels that were reached during the tests (around 3 g in ZPA),
- Seismic failure is attributed to plastic instability, as under quasi-static conditions. This is not an oligocyclic fatigue problem, as around a thousand cycles would be required, which is not compatible with seismic excitation.
- The seismic response of the piping can be calculated with a linear kinematic strain hardening model for the plastic behavior.
- Calculations confirm that extremely high seismic levels are necessary for failure to occur.

The New Earthquake Design Basis Criterion

The new criterion proposed has the following form:

$$\sigma_{ref} = \left[\left(D_1 \frac{PD_e}{2h_c} \right)^2 + \sum_{i=1,2,3} \left(D_{2i} \frac{M_i}{Z} \right)^2 \right]^{1/2} \leq S_{adm} = k S_r \quad (33)$$

with

D_e , h_c , and Z geometrical parameters,

D_i stress intensity coefficients, depend on the component and the type of loading,



■ Figure 187
AZALEE shaking table

S_{adm} allowable stress taking into account margin k (corresponding of RCC-MR level) and failure stress S_r

P and M_i , the pressure and the elastic moments (response spectrum method for seismic load)

Moments M_i are elastic moments calculated in accordance with usual practice:

$$M_i = |M_i^p| + g_d \left(|M_i^d| + |M_i^{ds}| \right) + g_s |M_i^s| \quad (34)$$

M_i^p moment due to loading of the imposed force type (static accelerations, forces or weights, etc.).

M_i^d moment due to loading of the imposed displacement non-earthquake type (thermal expansion, etc.).

M_i^{ds} moment due to seismic differential displacement of the anchor points.

M_i^s moment due to the dynamic effects of the earthquake (inertial part) and other reversible dynamic loading.

g_d and g_s are reduction coefficients lower than 1 applied to elastic thermal and seismic moments.

The reduction coefficients is a way to take into account the elastoplastic behavior by Elastic Follow-Up method (extend Roche method).

8.5 Fluid Structure Interaction in the Fast Reactor Cores

The coupling between the movements of structures with fluid is called “Fluid Structure Interaction,” or “FSI.” Many different physical phenomena are concerned (Gibert 1988; Delangre 2001; Fritz 1972; www.cast3M.fr): the phenomena of interest in the Fast Reactors will only be considered here.

In the Fast Reactor cores, the fluid is the sodium. The excitation of the fluid–structure system may be an external loading (earthquake, impact) or, eventually, the fluid flow. Many different structures of the reactor are concerned. Important FSI R&D programs have been performed in the last decades, during the first generation of the Fast Reactors, for example, on the seismic behavior of the core (Buland 1995; Fontaine 1997): and to the stability of the vessels under fluid flow. The results of these programs have to be used in the Gen IV program.

It has to be noticed that, for many applications, the methods to take into account the FSI phenomena have been improved from the first studies on the Fast Reactors, in the understanding of the physical phenomena, in the numerical methods, and in the capacities of the computers. These new methods will allow, in the frame of the Gen IV program, to get a better understanding of the already studied phenomena (seismic behavior of the core, stability of the vessels), and to investigate new phenomena also. Here are presented:

- A short description of the mechanical structure of the reactor.
- Some elements on the methods to take into account FSI (modeling and numerical methods).
- Elements on the seismic behavior of the fast reactor cores: the movements of the assemblies lead to variations of the volume of the core with changes in the nuclear behavior of the core.
- Elements on possible vibrations of the vessels under the sodium fluid flow.
- Elements on new points to be investigated, using the now available FSI methods.

8.5.1 Short Description of the Structures of the Reactor

➤ *Figure 188* presents two schemes of the main vessel of a Fast Reactor: pool and loop configuration, and a mock-up of the core. In the “pool” reactors configurations, the vessels are very thin. It is necessary to control a possible buckling under thermal loading. In the analysis of the dynamic behavior, the vessel cannot be considered as a rigid boundary, and interactions could take place between the movements of the fluid and deformations of the vessel. Instabilities due to the fluid flow could take place. The core is constituted of beams (fuel assemblies, neutronic shields, etc.) immersed in the sodium. The confinement is high (thin space between two assemblies).

8.5.2 Methods to Take into Account FSI

It is necessary, in a FSI problem, to solve the coupled system constituted of the structure equations and the fluid equations (Gibert 1988; Delangre 2001; Axisa and Antunes; Fritz 1972). In the general case, the Navier–Stokes equations are used for the fluid. Depending on the

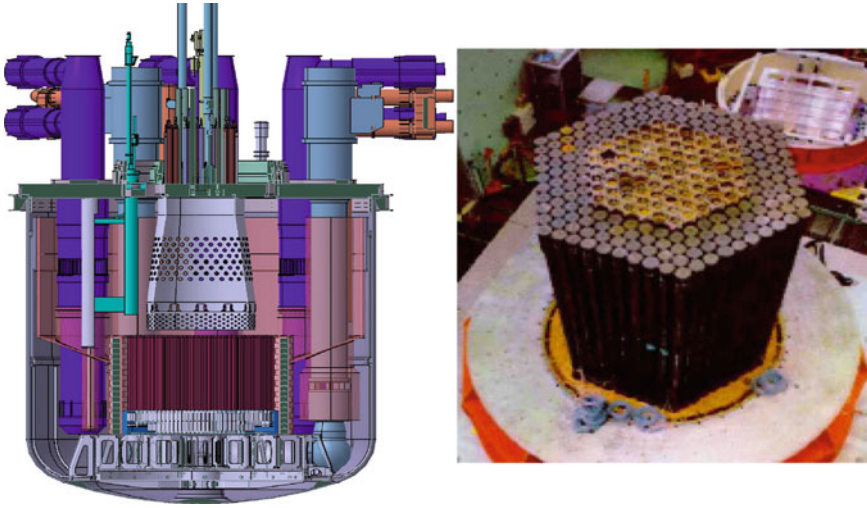


Figure 188
Fast reactor vessel, mock-up of a core

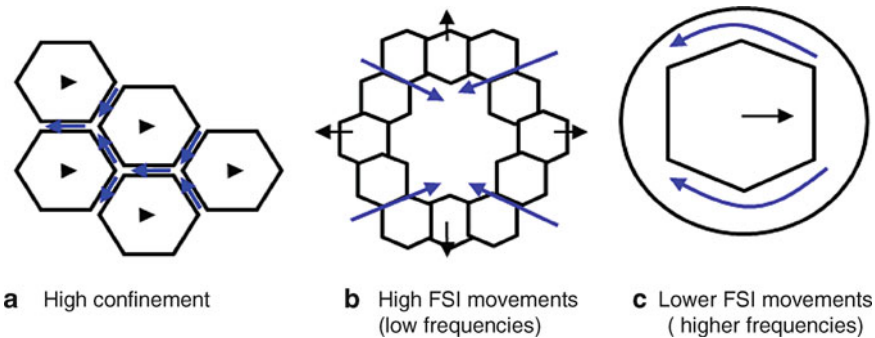
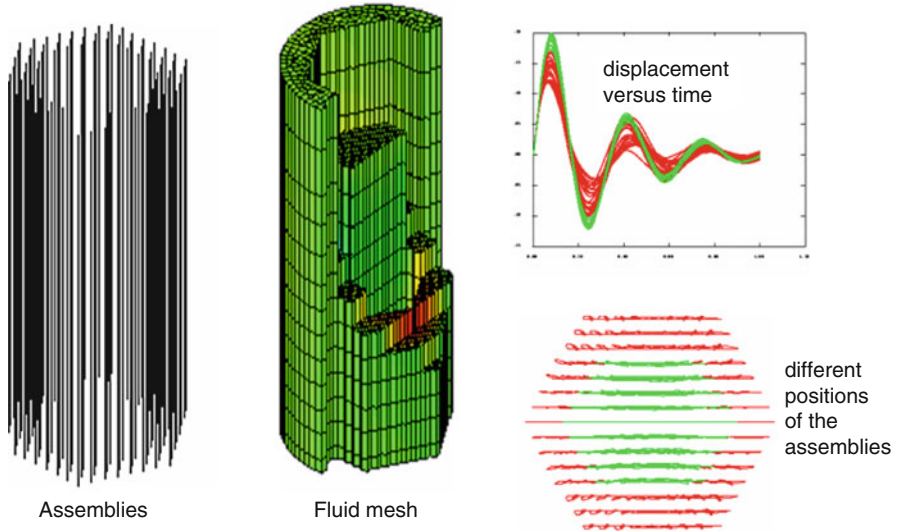


Figure 189
FSI phenomena in SFR core

conditions, simplifications can be made. In some cases, the Euler equations (more simple than the Navier–Stokes) may be used. Important improvements have been made in the methods to study FSI problems: in the understanding of the physical phenomena, in the numerical methods, and in the capacities of the computers. More accurate methods can be applied to the dynamic behavior of the Fast Reactors. For example, the use of homogenization methods for the dynamic behavior of tubes bundles immersed in a fluid will allow to perform simulations and analysis on a whole core (Sigrist and Broc 2007). The size of the mesh is strongly reduced



■ Figure 190

Three-dimensional modeling of the FSI in a fast reactor core (generic case)

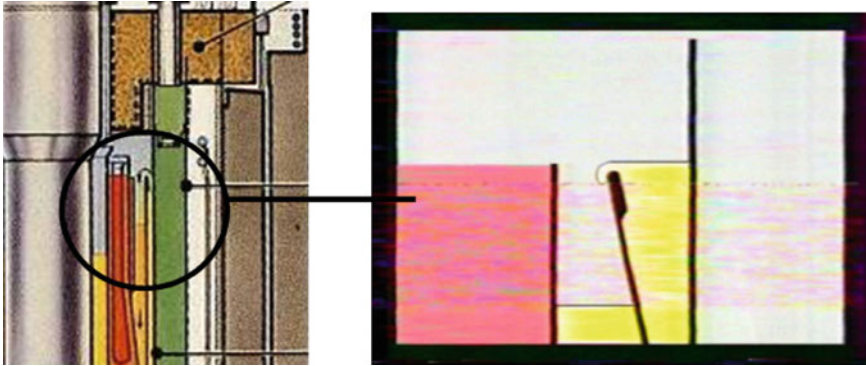
as only one fluid element is needed for one beam in 2D calculations, or 20 fluid elements for a 20 elements 3D assembly beam.

8.5.3 Seismic Behavior of the Fast Reactor Cores

The main physical FSI phenomena in a SFR core are presented in ► [Fig. 189](#): the confinement is high (a). The space between two assemblies is thin and the fluid velocity may be much higher than the structured ones (a). Important FSI will take place, with inertial effects (with lower natural frequencies) and dissipative effects also (with higher damping). FSI will be higher for “breathing” modes (b, decrease of 60% of the frequencies) and lower for global movements (c, decrease of 15% of the frequencies). ► [Figure 190](#) presents an example of the calculations, which can be made now on a whole core, by using the homogenization methods.


8.5.4 Design Model for the Seismic Behavior of the Core

The design models for the seismic behavior of the Fast Reactor cores consider that the study may be reduced to the central row of the assemblies. So, the size of the problem is lower. Research programs (Buland 1995; Fontaine 1997) have shown that this hypothesis is not valid. Interactions take place, by the fluid, between the assemblies in the whole core. It is no more possible to reduce the study to the central row. A new design model has to be built.



■ **Figure 191**
Overflow instability in the SPX fast reactor



8.5.5 Overflow Instabilities

Weir instabilities could occur, in the SPX reactor, depending on the operating conditions, which is depicted in  *Fig. 191*. Such phenomena are due to the fact that the vessels are very thin, with a low stiffness.

8.5.6 New Fluid Structure Interaction Phenomena to be Investigated

Due to actual analysis of FSI methods, it is possible to get a better understanding of the phenomena in the Fast Reactor cores. It has been seen, for example, that the “one row” design model for the seismic behavior of the core is no more valid. A new model has to be built, taking into consideration the interaction between the assemblies in the whole core. Global investigation will have to be done to identify improvements of already identified phenomena or new phenomena as well (for example, coupling by the fluid between the vessels and the core).

8.6 Buckling of Thin Shells

It is well known that large diameter thin walled shell structures are prone to buckle under compressive stresses. In SFRs, pool type concept has such vessels, namely, main vessel, inner vessel, thermal baffles, and safety vessel, which have to be checked against this failure mode ( *Fig. 192*). Further, box type structures such as top shield, grid plate, and core support structure constituted by plates have buckling risks ( *Fig. 193*).

For these vessels/plates, generally lower wall thickness is selected due to (1) low design pressure at the operating temperatures (sodium coolant can remain in liquid state up to about 950 °C); (2) requirement of adequate flexibility under various operating conditions (550 °C for hot pool and 400 °C for cold pool under steady state, isothermal temperature of 220 °C

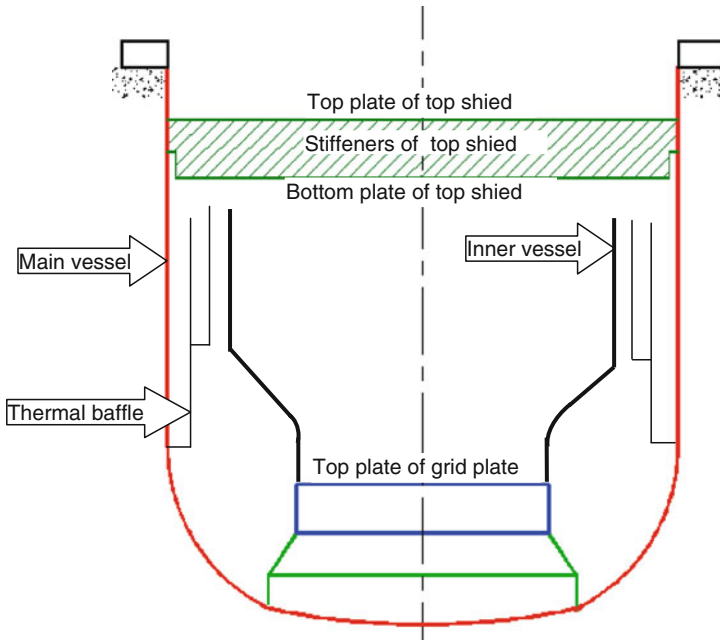


Figure 192
Thin shells/plates in SFR having risk of buckling

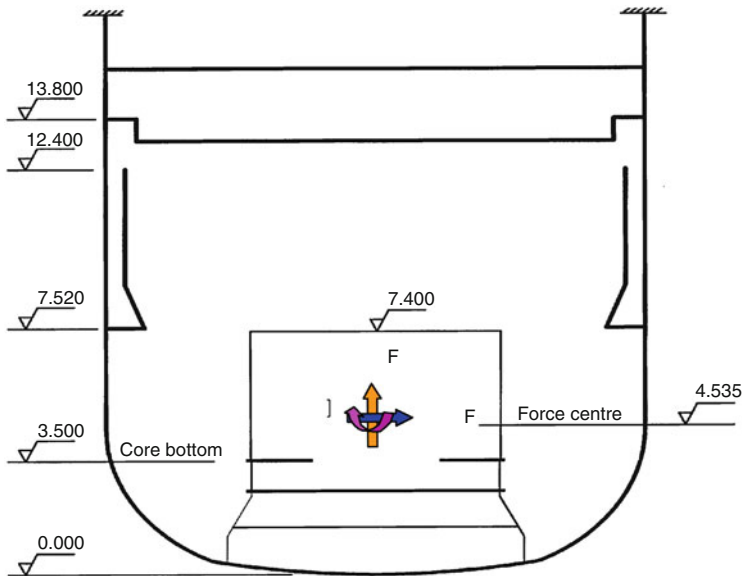


Figure 193
Integrated seismic forces concentrated at mass center

■ **Table 29**

Dimensions of main vessel and primary sodium masses of international SFRs

Parameter	Phenix	PFR	BN-600	SPX 1	PFBR	EFR
Diameter (m)	11.85	12.25	12.92	21	12.9	17.2
Thickness (mm)	15	25	30	24	25	35
Diameter/thickness	790	490	431	875	516	491
Primary Na mass (t)	800	850	770	3,200	1,150	2,200

during shutdown, and thermal transient of about 15 K/s during reactor scram); and (3) economic considerations, since the capital cost is directly linked to the steel consumption. The diameter to thickness ratios (D/h ratio) of main vessel of few international reactors is presented in ► [Table 29](#): the table indicates that D/h ratios lie in the range of 430–875; thus they are considered as slender.

The loads such as self weight, sodium pressure head, temperature, and thermal gradients are generally not critical under normal operating conditions. However, the forces generated under seismic events impose important loadings to the structures to cause buckling. The reasons for this are elaborated as follows.

The vessels, namely, main vessel, inner vessel, thermal baffles, and safety vessel are generally over hanging with “cantilever type” support arrangements as seen in ► [Fig. 192](#). For example, let us consider a top supported main vessel, carrying heavy liquid mass and dead load due to core and other internal structural mass (1,150 t of sodium with 700 t of other load acting at the vessel bottom for PFBR). This vessel would have natural frequency lying in the range 5–10 Hz where seismic force amplification is generally the maximum. Further, there exists relatively thin annulus of liquid between: (1) inner vessel to inner baffle, (2) inner baffle to outer baffle, (3) outer baffle to main vessel, and (4) main vessel to safety vessel under the event of main vessel leak. The radial annulus gap to diameter ratio lies around $\sim 1/100$ and the sodium confined in this space enhances added mass to the adjoining shells to reduce the natural frequencies, as well as generates high dynamic pressure during seismic events. The existence of large free fluid surfaces is the source of sloshing, which generates significant convective masses and forces under seismic events. Apart from seismic forces, stationary as well as cyclic loads do cause buckling, which are of different kinds in these shells. Nature of buckling of thin shells of SFR can be broadly classified as follows:

- *Shear buckling*: caused by shear stresses in plates and shells
- *Shell mode buckling*: constituted by circumferential waves caused by compressive membrane stress due to axial and bending stress in shells.
- *Localized shell mode buckling*: caused by local axial membrane compressive stress caused by axial thermal stress gradients, in shells near sodium free level.
- *Progressive buckling*: caused by combined steady axial stress of mechanical origin and cyclic variation of axial thermal stresses in shells.
- *Creep buckling*: caused by creep deformation of shells operating at high temperature.
- *Bowing mode*: created on plates subjected to compressive membrane stress.

The structural portions and associated buckling modes are presented in the ► [Table 30](#).

■ **Table 30**
Important buckling modes for various thin shells

Governing loads	Buckling mode
<i>Main vessel – cylindrical portion</i>	
Shear forces generated under seismic excitations	Shear mode
Cyclic axial temperature distribution in the vicinity of free level due to variation of levels	Progressive buckling
<i>Main vessel – bottom dished head</i>	
Combined effects of hydrostatic pressure of sodium and axial force acting at triple point under normal and seismic loading conditions	Shell mode
<i>Inner vessel – torus/redan portion</i>	
Combined mechanical and axial and through-wall temperature gradients	Creep buckling with shell mode
<i>Inner vessel – upper cylindrical portion</i>	
Cyclic axial temperature distribution in the vicinity of free level due to variation of levels	Progressive buckling
<i>Thermal baffles – top cylindrical portion</i>	
Cyclic axial temperature distribution in the vicinity of free level due to variation of levels	Progressive buckling
<i>Thermal baffles – bottom portion above the support</i>	
Combined effects of hydrostatic pressure of sodium under normal and seismic loading conditions	Shell mode
<i>Grid plate – top plate</i>	
Compressive stress developed under hot shock	Bowing
<i>Roof slab – top plate</i>	
Compressive stress developed due to self weight, weight of components mounted on it plus inertial forces generated under seismic events	Bowing
<i>Roof slab – stiffener plate</i>	
Shear force transmitted by stiffeners under normal and seismic loading conditions	Shear buckling
<i>Roof slab – bottom plate</i>	
Sodium slug impact pressure plus compressive stress developed under core disruptive accident	Bowing (concave upward)

8.6.1 Buckling Design Approach

In order to ensure that there is no risk of buckling, it is required to determine the critical loads at which buckling occurs in the first step by taking into account all the possible parameters which govern the phenomenon. The important parameters, apart from nominal geometrical and normal loading parameters, are geometrical deviations introduced during manufacturing, which are acceptable from functional point of view, elastoplastic behavior of structural material, thermal loads, seismic-induced forces, and dynamic pressure. Matured buckling design charts are presented for the standard symmetrical shells such as cylindrical, conical, spherical, and tori-spherical heads, subject to external pressure in design codes, namely, RCC-MR: Appendix A12 (RCC-MR 2007) and ASME Sec III Div 1 (2007). These aspects are not repeated here. In view of special geometrical features (mainly 3-D with stiffeners), presence of thermal loads which may be stationary or cyclic, concentrated loads at some selected locations, asymmetrical forces generated under seismic loadings, geometrical deviations to respect the functional limits and creep effects, the thin shells of reactor assembly call for special buckling analysis methods. The critical buckling loads/load combinations should be derived through detailed analysis. Simplified analysis methods are available to certain extent and presented in design code RCC-MR: Appendix A7 (2007). However, detailed analysis is inevitable in SFR design of thin shells, to determine the buckling loads realistically. Toward this, computer codes such as ABAQUS or CAST3M (CEA 2003) are used extensively. Since there are many uncertainties in buckling analysis of thin shells under the complex loading conditions, experimental validations are, however, essential to raise the confidence.

It should be ensured that the design loads specified for the components should be less than the critical buckling loads with appropriate factors of safety (FOS). Design codes specify the minimum FOS required. These factors of safety depend upon the various service loading conditions. As per the French design code RCC-MR, which is judged to be the most appropriate for FBR geometry and loading conditions, that is, for the normal, upset, and abnormal loads, categorized under “level-A loadings,” the highest FOS, equal to 2.5, is required. For emergency loading conditions, categorized under “level C loadings,” FOS specified is 2. For the faulted condition, the minimum FOS of 1.3 is sufficient. To respect these buckling design criteria, it is required to estimate the buckling loads either computed numerically or determined experimentally.


It is clear that the determination of critical buckling loads is essential for the buckling design. In SFR, thermal and seismic loadings are important to be considered. As far as thermal loads are concerned, both stationary and cyclic loadings should be seen. The seismic loadings involve combination of axial, bending, and shear forces, in association with dynamic pressure distributions on the shell surfaces. The determination of both mechanical and thermal loadings calls for detail analysis, which is not covered here. However, method of idealization of seismic forces is presented.


8.6.2 Simplified Analysis Method for Buckling of Shells Under Seismic Loadings

For applying simplified methods, the geometry and applied stresses should be idealized. The idealized geometry considered for main vessel is a cylindrical shell of mean radius R , height H , and wall thickness h , which is subjected to axial compressive stress σ_a , bending stress σ_b , and



shear stress τ . The height of vessel (H) is taken in the analysis as the sum of the actual height of the cylindrical portion and one third of the height of the dished head (RCC-MR 2007). The basic material properties are Young's modulus (E), average yield stress (S_y), and Poisson's ratio (ν).

Derivation of Idealized Stresses

Under normal operating conditions, the cylindrical portion of the main vessel sees only tensile stress due to dead loads, and hence, there is no risk of buckling. However, seismic event generates axial compression due to vertical excitations and bending moment and shear forces due to horizontal excitations. These forces are generally extracted from detailed seismic analysis of vessel and its internals including fluid–structure interaction effects, which are difficult to obtain by either hand calculations or simplified analysis.  Figure 193 depicts the peak forces and bending moment generated at the mass center of reactor assembly, which have been arrived at by integrating the appropriate stress distributions.

The distribution of various stresses as extracted from detailed analysis, do not vary uniformly in view of inertial local forces developed at the intermediate locations. Hence, for applying any simplified methodology to check the buckling strength, stresses are to be linearized, conserving the axial force, shear force, and bending moment generated, which are termed as σ_{a-cr} , σ_{b-cr} , and τ_{cr} . The distribution of various linearized stresses is depicted schematically in  Fig. 194.

Derivation of Allowable Buckling Strength for Main Vessel Straight Portion

Critical axial compressive, bending, and shear stresses (σ_{a-cr} , σ_{b-cr} , and τ_{cr}) are obtained through empirical correlations that have been recommended based on extensive testing and evaluations in Japanese design guidelines (Akiyama 1997).  Figure 195 depicts the static deformations created by these three stresses, and  Fig. 196 depicts corresponding buckled modes.

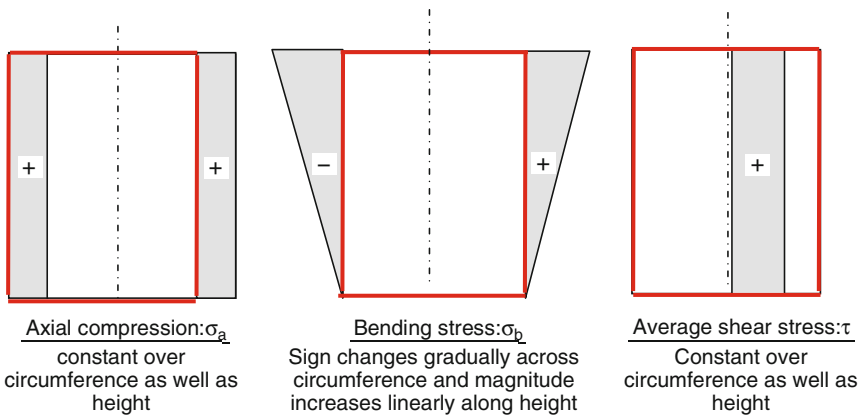
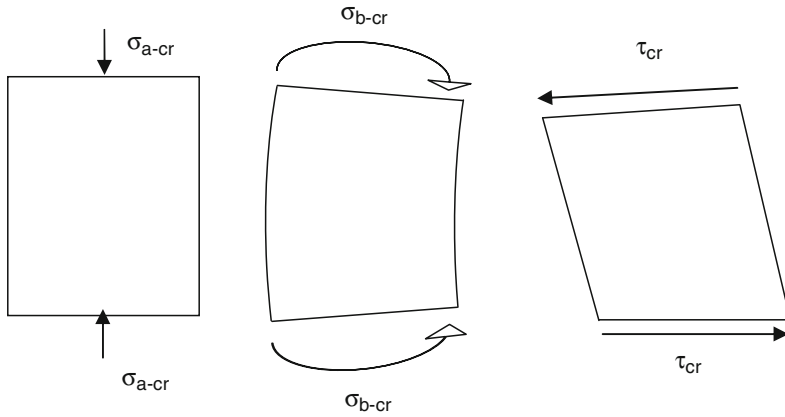
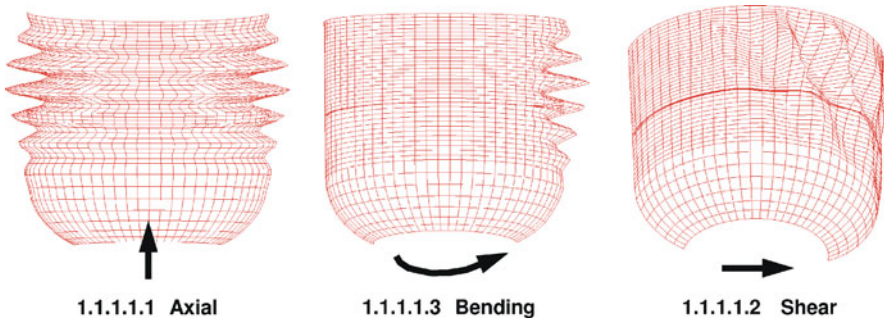


 Figure 194

Linearized stresses on the main vessel cylindrical portion



■ Figure 195
Unbuckled deformation modes created by linearized stresses



■ Figure 196
Critical buckling mode shapes

Critical axial compressive stress σ_{a-cr} :

$$\sigma_{a-cr}^e = 0.6 \times \left[1 - 0.901 \times \left\{ 1 - \exp \left(-\frac{1}{16} \sqrt{\frac{R}{h}} \right) \right\} \right] \cdot \frac{Eh}{R} \quad (35)$$

$$\sigma_{a-cr} = \sqrt{\frac{1}{(1/\sigma_{a-cr}^e)^2 + (1/S_y)^2}} \quad (36)$$

Critical bending stress σ_{b-cr} :

$$\sigma_{b-cr}^e = 0.6 \times \left[1 - 0.731 \times \left\{ 1 - \exp \left(-\frac{1}{16} \sqrt{\frac{R}{h}} \right) \right\} \right] \cdot \frac{Eh}{R} \quad (37)$$

$$\sigma_{b-cr}^p = \sqrt{\frac{1}{(1/\sigma_{b-cr}^e)^2 + (1/S_y)^2}} \quad (38)$$

Critical shear stress τ_{cr} :

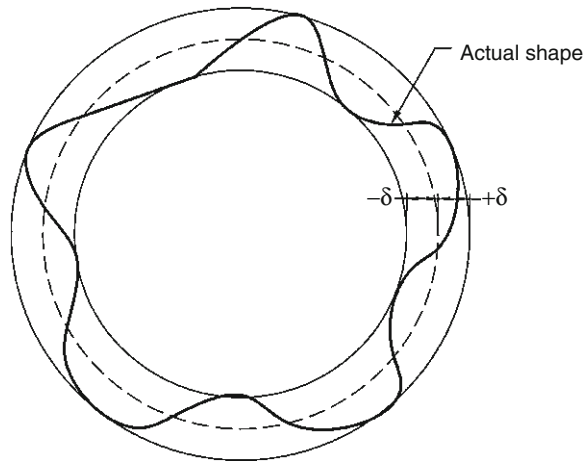
$$\tau_{cr}^e = 0.8 \frac{4.82}{(H/\sqrt{Rh})^2} \cdot \sqrt{1 + 0.0239x \left(\frac{L}{\sqrt{Rh}} \right)^3} \cdot \frac{Eh}{R} \quad (39)$$

$$\tau_{cr}^p = \sqrt{\frac{1}{(1/\tau_{cr}^e)^2 + \sqrt{(3/S_y)^2}}} \quad (40)$$

Effects of Geometrical Imperfections

The geometrical imperfections are expressed as form tolerance, which is the maximum radial deviation (δ) achieved during the manufacturing stage (► Fig. 197). The maximum δ value assumed in the above equations (25–30) is $h/2$. This reflects the possible manufacturing deviations of the practical SFR components. If such imperfections should exceed the value, that is $\delta > h/2$, then, it shall be necessary to reduce the allowable strength obtained by a correction factor, computed from the following equation.

$$\eta = \frac{1}{(1 + 0.092(X - 1)^{0.9})} \quad (41)$$



■ Figure 197
Definition of form tolerance

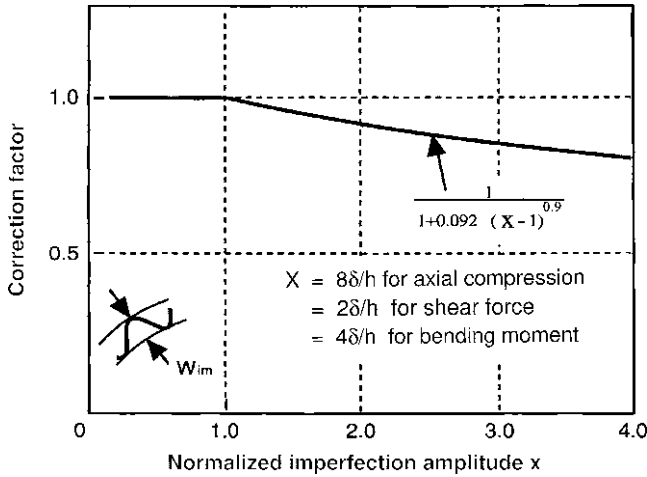


Figure 198
Buckling strength reduction factors

where X is equal to $2\delta/h$ for shear force (applicable for main vessel undergoing shear buckling) and $4\delta/h$ for bending moment (applicable for inner vessel and thermal baffles, undergoing shell type of buckling). The formula recommended in (31) has been derived based on extensive tests conducted (Fig. 198) for establishing Japanese design code (Akiyama 1997). The critical buckling stress values arrived at through application of (26, 28, and 30) are to be multiplied by appropriate η values.

Effects of Interaction among Various Buckling Modes

Seismic forces are acting simultaneously, even though peak values may not occur at the same time. Hence, it is required to consider the effects of interaction among forces and moments. For quantifying the interaction, Japanese design procedure (Akiyama 1997) is followed, which is given in the following equations.

FOS for the individual cases are computed using the following (32):

$$\begin{aligned}\lambda_{\text{axial}} &= \sigma_a / \sigma_{a\text{-cr}}^p \\ \lambda_{\text{shear}} &= \tau / \tau^p \\ \lambda_{\text{bending}} &= \sigma_b / \sigma_{b\text{-cr}}^p\end{aligned}\quad (42)$$

The effective FOS, taking into account the interaction among axial, bending, and shear buckling modes (λ_{eff}), are obtained from the following (33), which has been derived based on empirical fitting of extensive experimental data.


$$1/\lambda_{\text{eff}}^5 = 1/\lambda_{\text{axial}}^5 + 1/\lambda_{\text{shear}}^5 + 1/\lambda_{\text{bending}}^5 \quad (43)$$

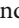
The λ_{eff} values are computed both for operating basis earthquake (OBE) as well as safe shutdown earthquake (SSE) and it should be ensured that they are higher than the appropriate minimum FOS, specified in the design code (25).



8.6.3 Thermal Buckling Due to Stationary Temperature Gradient

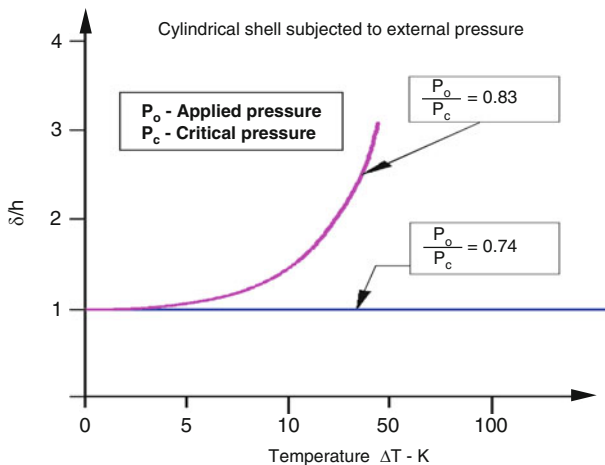
Thermal loading is defined by temperatures and temperature gradients. For the main vessel, inner vessel and thermal baffles, the locations in the vicinity of sodium free level are critical, due to high axial thermal stresses developed due to sharp temperature gradients. This apart, the inner vessel is subjected to large through-wall temperature gradient and axial temperature gradients in the redan portion. The effects of these thermal loads on the buckling behavior of shells should be seen critically.


A few experimental works are reported in Brochard et al. (1991) and the following are the experimental observations:

The tests on cylindrical shell subjected to external pressure indicate that the reduction of buckling load is marginal (<20%), which is mainly due to the reduced value of material properties, namely, Young's modulus and yield stress and also amplification of initial geometrical imperfections caused by thermal stresses. The amplification of imperfection depends upon the thermal gradients as shown in  Fig. 199 for a typical case of cylindrical shell subjected to external pressure.

Tests conducted on many thin shells (400 mm diameter and 0.8 mm thickness) with a large axial temperature gradients do not indicate any onset of buckling ( Fig. 200). Hence, it can be said that pure stationary thermal gradients do not cause buckling cause. However, thermal gradients cause large plastic strains in the form of local buckling due to thermal stresses developed in the vicinity of interfaces.

Tests on thin cylindrical shells subjected to axial tension and the axial gradient of temperature are reported in Combescure and Brochard (1991). The amplitude of the buckles is of about three or four times the thickness, when the cylinder is hot, but the residual buckle at room temperature is about one tenth of the thickness. A few experimental results are given in  Fig. 201 which shows that no buckling could be observed when there is no sufficient axial tension. Different load histories were also studied and one sees that the buckling is possible under tensile stress with the axial gradient of temperature ( Fig. 201).

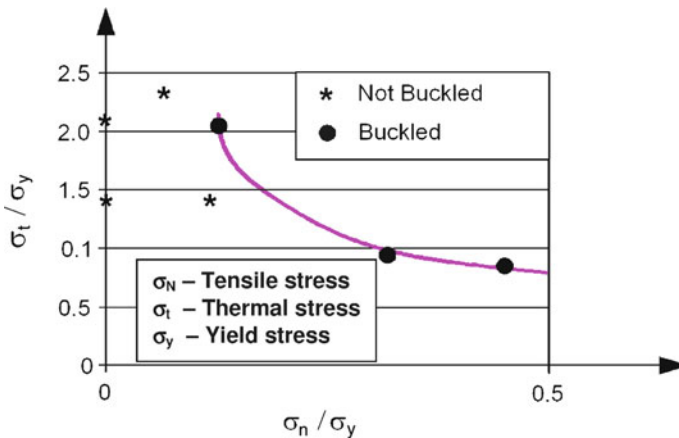


 Figure 199

Amplification of geometrical deviation versus thermal load



■ **Figure 200**
Symmetric bulging of shell subjected to sharp axial thermal gradient



■ **Figure 201**
Effect of axial tension on thermal buckling

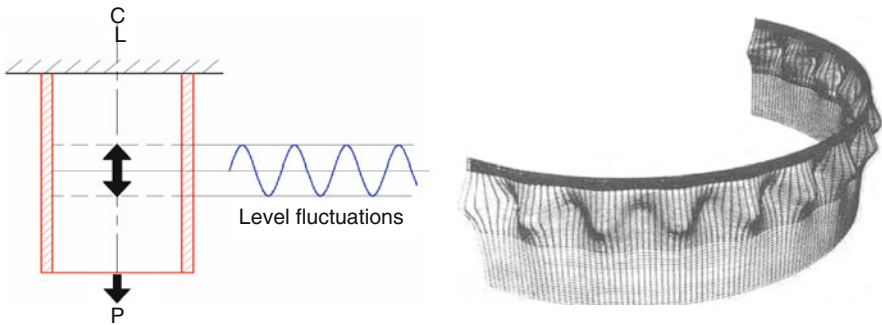
Theoretical analysis of critical buckling load under thermal loads is performed as follows (Brochard et al. 1991). First assuming that the structure is perfect, that is, there is no imperfection, elastic buckling analysis is performed with the applied mechanical and thermal loads and buckling mode is extracted. In the second phase, “large displacement elastoplastic analysis” is performed through incremental computation, introducing the geometrical deviations parallel to the buckling mode of the perfect structure, from which the ultimate load is calculated. The amplitude of deviations is chosen in two ways:

- Maximum deviation of the measured defect for 3-D buckling analysis.
- Amplitude of the measured deviation for a particular buckling mode harmonic, obtained by a Fourier decomposition of the deviations.

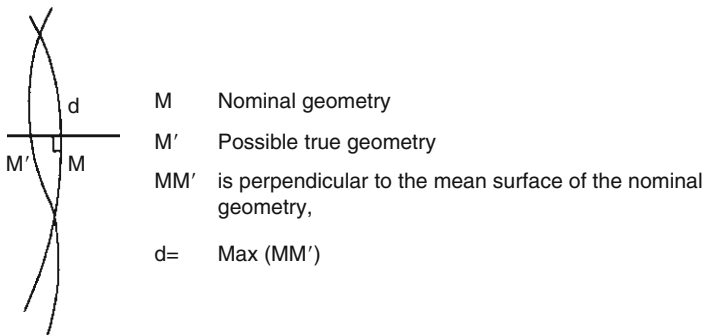
The above calculations can be performed with CAST3M, developed by CEA. A few benchmark analyses indicate that in the presence of thermal gradients, the computed critical buckling load is found to be too conservative in comparison with experimental results. In fact, it corresponds to the formation of a stable buckling mode, the amplitude of which is limited to a very small value (less than shell thickness). Hence, from an experimental point of view, it can be said that the structure does not buckle. The incremental computations on the imperfect structure give ultimate loads, which are in good agreement with the experimental results.

8.6.4 Progressive Buckling Due to Moving Temperature Gradients

When the axial temperature gradient is moving up and down along the cylindrical shell (🔍 Fig. 202), the shell develops wrinkles (indication of buckling), and the amplitude of wrinkles grows progressively as the number of thermal cycle increases. This is called progressive buckling. Typical buckled mode shape is included in 🔍 Fig. 203.



■ Figure 202
Buckled mode in the shell subjected to moving temperature gradient



■ Figure 203
Definition of "d"

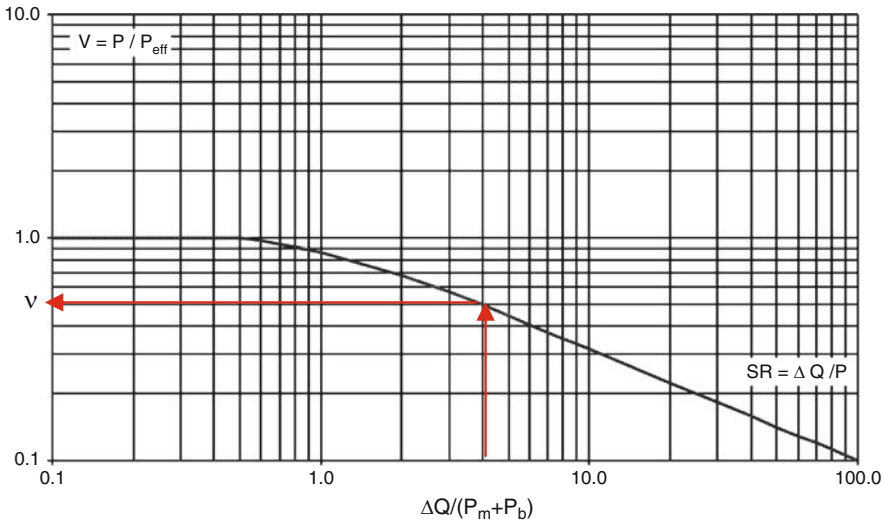


Figure 204
Efficiency index diagram (RCC-MR, 2007)

Based on extensive testing and evaluation, the design rules have been proposed in Clement and Drubay (1991), which are highlighted below:

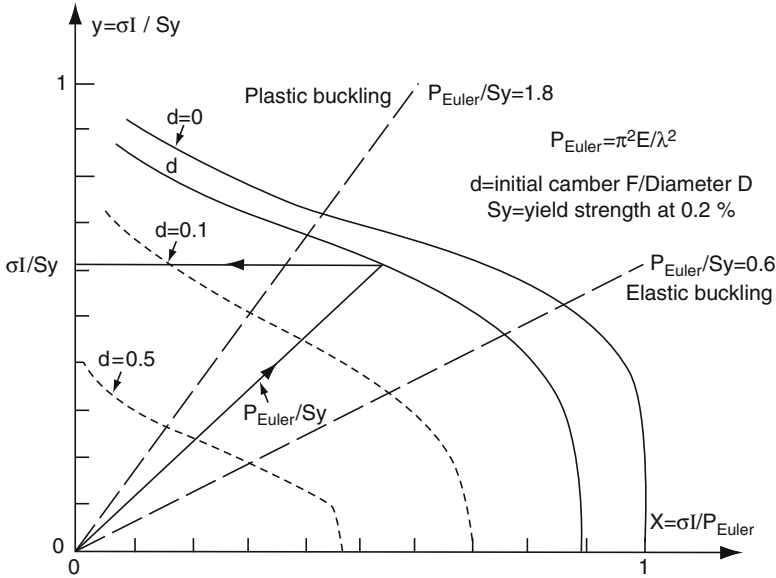
The basic parameters required are geometric deviation “ d ,” as illustrated in Fig. 203, primary membrane, and bending stress intensity ($P_m + P_b$) caused by mechanical load acting along the shell and stress intensity range created by cyclic variation of axial stress intensity (ΔQ). These apart, yield stress of material ($R_{0.2}$) is also required.

The first step is to determine the effective primary stress intensity ($P_{\text{eff}} = (P_m + P_b)/\nu$), and efficiency index “ ν ” is derived from efficiency index diagram as shown in Fig. 204, knowing the value of $\Delta Q/P_m$.

Second step is to determine the instability stress σ_I , which is derived from the interaction diagram presented in Fig. 205. Once the kind of buckling (elastic or plastic buckling) is defined and d value (here it is equal to deviation/diameter) is also known, “ x ” and “ y ” are extracted, from which σ_I (minimum value) is computed knowing S_y and P_{Euler} .

8.6.5 Creep Buckling

Creep buckling occurs on the shell, which is prone to buckle under compressive stress field, even though the applied stress is less than the critical stress, after a certain time period. The prediction of creep buckling is very difficult because of many uncertainties, particularly in the material parameters. The geometry of the structure and its deviations have to be well defined to have accurate prediction of failure loads. Hence, design rules have been developed (Combesure 1999), based on the case of shells subjected to external pressure axial compression. The instability of mechanism is the following: When the initially imperfect shell is loaded



■ Figure 205

Determination of instability stress

by the external P_0 , it undergoes a constant axial symmetric displacement (W_0), which produces a hoop membrane stress “ σ ,” as well as a circumferential mode “ m ” displacement field. The initial mode “ m ” imperfection amplitude ξ_0 increases to a value ξ_1 . If this does not lead to instantaneous failure by the formation of plastic hinge or elastic instability, then the creep buckling can take place. If a relatively high initial load is applied on a perfect structure, an elastic instability induced by evolution of the initial imperfection by creep is likely mechanism. This is also the case, when material is essentially elastic. If the initial imperfection is greater or the initial load P_0 is lower, it can be easily imagined that the instability will be of the plastic hinge type.

Design Rules for Creep Buckling as per RCC-MR (2007)

In the event of significant creep, the method described in the A75000 may be used to determine whether a structure subjected to thermomechanical loadings leading to primary stresses is prone to buckle at a lower loading level than the level that would cause instantaneous buckling, given the operating temperature and the holding time at this temperature. This method requires the calculation of both the critical Euler load and the load that causes the structure to start plastic flow. The method is limited to shells made of austenitic steel SS 316 LN. Where post bifurcation is unstable, steps shall be taken to ensure that the instantaneous critical load is virtually the same as would be obtained with the same structure if the post bifurcation was stable. The method comprises the following seven steps:

- Determine the operating temperature of the structure θ_m (maximum mean temperature in the thickness) and corresponding hold time t_m .

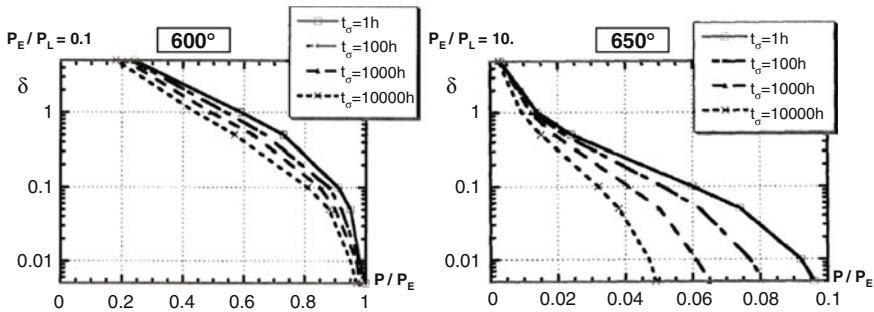


Figure 206

Typical design charts for assessing creep buckling in thin shells

- Calculate the critical Euler load at temperature θ_m ; this load P_E is obtained by an elastic buckling computation with no geometrical imperfection.
- Calculate the load at which the neutral fiber of the structure starts plastic flow. This load P_L is obtained with an elastic calculation of the structure, given the minimum yield strength $(R_{p0.2})_{\min}$ at temperature θ_m .
- Calculate the slenderness ratio for the structure P_E/P_L and select the diagram corresponding to the next largest P_E/P_L . It is also possible to select the diagrams that correspond to next largest and next smallest P_E/P_L ratios and then by linear interpolation, construct the instability curve corresponding to the instant t_m or both curves enclosing it. [Figure 206](#) shows two typical design charts.
- Calculate ratio $x = P/P_E$, where P is the nominal load multiplied by the margin coefficient for the specified condition of loading.
- Determine factor $\delta = d/h$ (ratio of geometrical imperfection over thickness).
- If point $M(x, \delta)$ lies beneath the instability curve at instant t_m , then buckling due to creep will not occur. On the selected diagram, the instability curve at instant t_m , could also be obtained by logarithmic interpolation.


8.6.6 An Integrated Buckling Analysis of Thin Vessels of Reactor Assembly

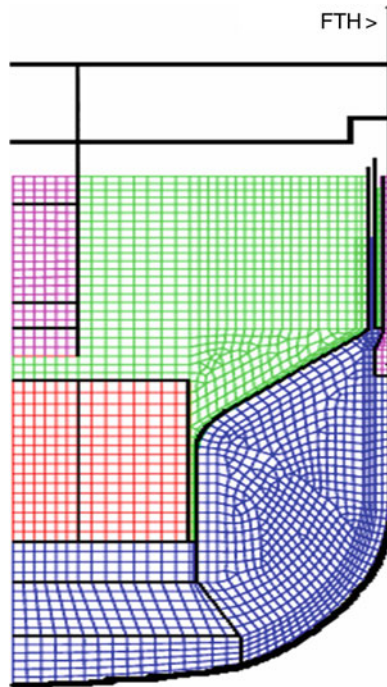
In [Sect. 8.5.3](#), simplified analysis method has been presented. In this section, detailed analysis procedure is described. The procedure consists of three broad steps: (1) natural frequency analysis, (2) seismic response analysis and (3) buckling analysis using established finite element computer codes. The natural vibration and seismic response analyses are performed for the reactor assembly components, including the essential internals and sodium. In case of axisymmetric analysis, Fourier option can be chosen, appropriately, to account for the circumferential variations of loads. Seismic analysis is to be carried out in time domain to determine the stresses at every discrete time steps involved. Subsequently elastic buckling analysis can be carried out at any time, knowing the stress distributions at the corresponding time step. Since the number of time steps required for the dynamic analysis (total duration of seismic event/minimum time steps for stable solution) is generally very large, carrying out buckling analysis at every time

step, covering the entire time steps, is computationally very expensive. Hence, it is appropriate to choose a few selected time steps, called “critical time steps” at which buckling analysis can be carried out, which provides lowest buckling loads. This should be based on a robust criterion. Critical time step is an instant during the earthquake at which the buckling load factor is possibly the minimum, for a particular vessel. The buckling load factor generally depends upon the magnitude of compressive stress field developed in the structure. In the complex structures where the compressive stress varies over the length, it is difficult to identify a particular value, which decides the buckling of the vessel. Hence, it is necessary to identify a global parameter. In this regard, the critical time steps are selected based on the integrated strain energy absorbed by the entire vessel or a few selected locations of vessel prone to buckle. As far as reactor assembly is concerned, the main vessel, inner vessel, and thermal baffles are the important shell structures, which are to be checked for buckling risks. Specifically, the cylindrical portion of the main vessel (prone to buckle under shear stress), the torus portion of the inner vessel (prone to buckle by meridional compressive stress), and the upper cylindrical portions of the thermal baffles (prone to buckle under hoop compressive stress) are the critical parts in the reactor assembly. Accordingly, the strain energies that are associated with shear, meridian, and hoop compressive stress distributions, respectively, in the critical portions of main vessel, inner vessel, and thermal baffles are computed at each time step, which forms part of seismic analysis. Subsequently, buckling analysis can be restricted only at these time steps, where strain energy is highest.

In order to account for the possible randomness on the applied support time histories, three time histories are artificially generated in each direction: (1) nominal time histories, (2) modified time histories by compressing the time scale by about 10%, and (3) modified time histories by expanding the time scale by about 10%. This implies that the above analysis should be repeated thrice and finally, the lowest buckling loads can be arrived at. More details of seismic analysis, such as generation of support time histories, idealization of geometries, boundary condition, kind of damping values to be applied, and practical application to the buckling analysis of PFBR vessels, are presented in Chellapandi et al. (2008). Some specific aspects to be applied and summary of the results are presented in the following paragraphs.

Geometrical Idealizations

The finite element model (FEM) generated with CAST3M, consists of structures (main vessel, inner vessel, outer and inner thermal baffles, CSS, grid plate, core, control plug, top shield, and support skirt), hot and cold sodium pools, sodium in the feeding and restitution collectors, sodium–shell interfaces, and sodium free level boundaries for predicting sloshing. The structures are modeled with “2-noded conical shell elements.” The sodium is modeled with “4-noded quadratic elements.” Special element called “RACC” is used for fluid–structure interaction effects at the sodium–shell interfaces. In order to simulate the sloshing behavior, five free level surfaces in (1) feeding collector, (2) restitution collector, (3) cold pool between inner vessel and inner thermal baffle, (4) hot pool, and (5) hot pool within control plug are considered. In the FEM, apart from the masses of core, grid plate, CSS, control plug, and top shield, the self-masses of main vessel (156.9 t), inner vessel (63 t), thermal baffles (68 t), and sodium (1,150 t) are automatically included. Thus, the total mass of reactor assembly including sodium (3,409.4 t) is preserved. The top edge of support skirt is fixed at which support excitations are applied. The FE mesh developed for the analysis is shown in  Fig. 207.



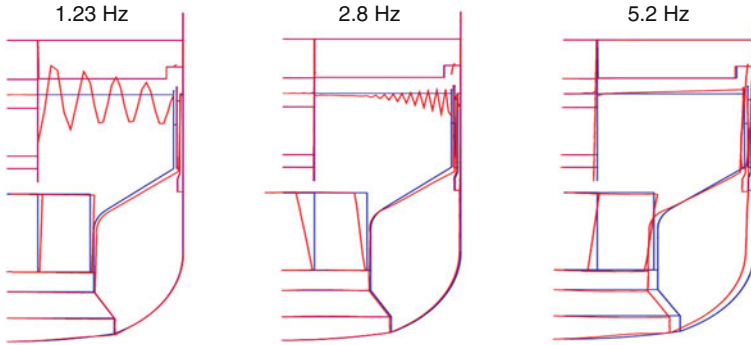
■ Figure 207
FE model

Natural Vibration Analysis

Analysis is performed to determine the natural frequencies up to 50 Hz. Three mode shapes depicting (1) rocking of inner vessel along with CSS, grid plate, and core about the triple point of the main vessel (1.23 Hz), (2) swaying of core along with inner vessel about grid plate (2.8 Hz), and (3) swaying of main vessel along with thermal baffles about the reactor assembly support (5.2 Hz) are shown in [Fig. 208](#). These modes have the dominant modal masses of 1,370 t, 534 t, and 1,785 t respectively. The modes having frequencies 1.23 Hz and 2.8 Hz can contribute significantly in generating high seismic forces on the inner vessel and the mode having 5.2 Hz has significance from the point of imposing forces on main vessel and thermal baffles, as seen from the respective modal displacements.

Seismic Response Analysis

Axisymmetric analysis is carried out for determining displacements, velocities, and accelerations with Fourier option assigning the harmonic wave number, equal to one applicable for the horizontal excitations and 4% damping value applicable for the mechanical components under safe shutdown earthquake (SSE). Totally, six analyses are carried out: three for X and three for Y directions by employing three support time histories (time scale compressed, nominal, and time scale expanded) for each direction. Analysis is carried out up to 20 s with the time step size of 0.001 s consistently for all the calculations.



■ **Figure 208**
Critical buckling mode shapes for the reactor assembly vessels

Strain Energy Distributions

The strain energies generated in the critical portions, namely, main vessel cylindrical portion due to shear stresses (U_{MV}), torus portion of inner vessel due to meridional compressive stresses (U_{IV}), and inner and outer baffles due to hoop compressive stresses (U_{IB} and U_{OB}) are computed using the following equations:

$$U_{MV} = \frac{1}{2} \sum_e \frac{\tau_e^2}{G \Delta V_e}, \quad e = 1, \quad n, \text{ number of elements in cylindrical portion} \quad (44)$$

$$U_{IV} = \frac{1}{2} \sum_e \frac{\sigma_{Ie}^2}{E \Delta V_e}, \quad e = 1, \quad n, \text{ number of elements in the toroidal portion} \quad (45)$$

$$U_{IB} = \frac{1}{2} \sum_e \frac{\sigma_{me}^2}{E \Delta V_e}, \quad e = 1, \quad n, \text{ number of elements in cylindrical portion} \quad (46)$$

$$U_{OB} = \frac{1}{2} \sum_e \frac{\sigma_{me}^2}{E \Delta V_e}, \quad e = 1, \quad n, \text{ number of elements in cylindrical portion} \quad (47)$$

where τ_e , σ_l , & σ_m are shear, meridional and hoop stresses, respectively, which are calculated from the associated stress resultants N divided by corresponding thickness, at the centroid of a particular element “e.” E and G are the Young’s modulus and shear modulus, respectively, of the structural steel of the vessels. ΔV_e is the volume of element “e” given by $2\pi R h \Delta L$ where R and h are radius and thickness at the centroid. ➤ [Figure 209](#) depicts a typical time variation of strain energy developed in the critical portion of the main vessel, which shows that the maximum strain energy is 300 kJ, which occurs at 5.3 s.

The values of strain energy are presented in ➤ [Table 31](#) for excitations X as well as Y directions including the variations considered in the time histories.

The critical time steps computed for the main vessel, inner vessel, and thermal baffles are shown in ➤ [Table 32](#).

Pressure Distributions on Vessels at Critical Time Steps

The dynamic pressure distributions generated over the vessel surfaces are responsible for buckling. The differential pressure distributions acting on the main vessel, inner vessel, and inner and

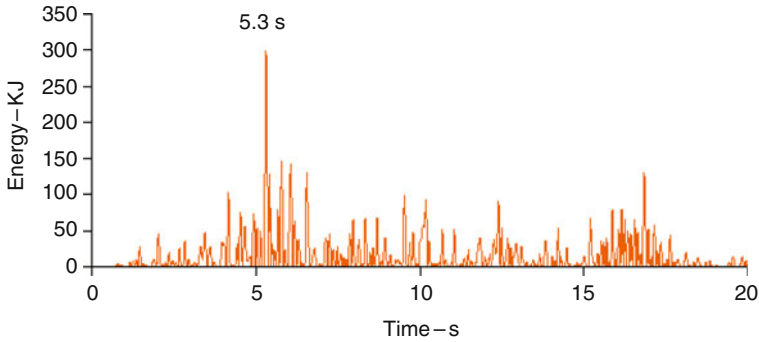


Figure 209
Strain energy distribution in cylindrical portion of main vessel

Table 31
Strain energy generated in the critical portions – kJ

Sl. no	Location	X-direction			Y-direction		
		c	n	e	c	n	e
1	Cylindrical portion of main vessel	140	173	300	177	179	207
2	Toroidal portion of inner vessel	13.5	9.6	9.4	10.9	12.3	9.6
3	Cylindrical portion of inner baffle	3.8	3.8	5.8	8.4	7.9	8.5
4	Cylindrical portion of outer baffle	4.8	3.8	5.0	12.7	5.8	7.9

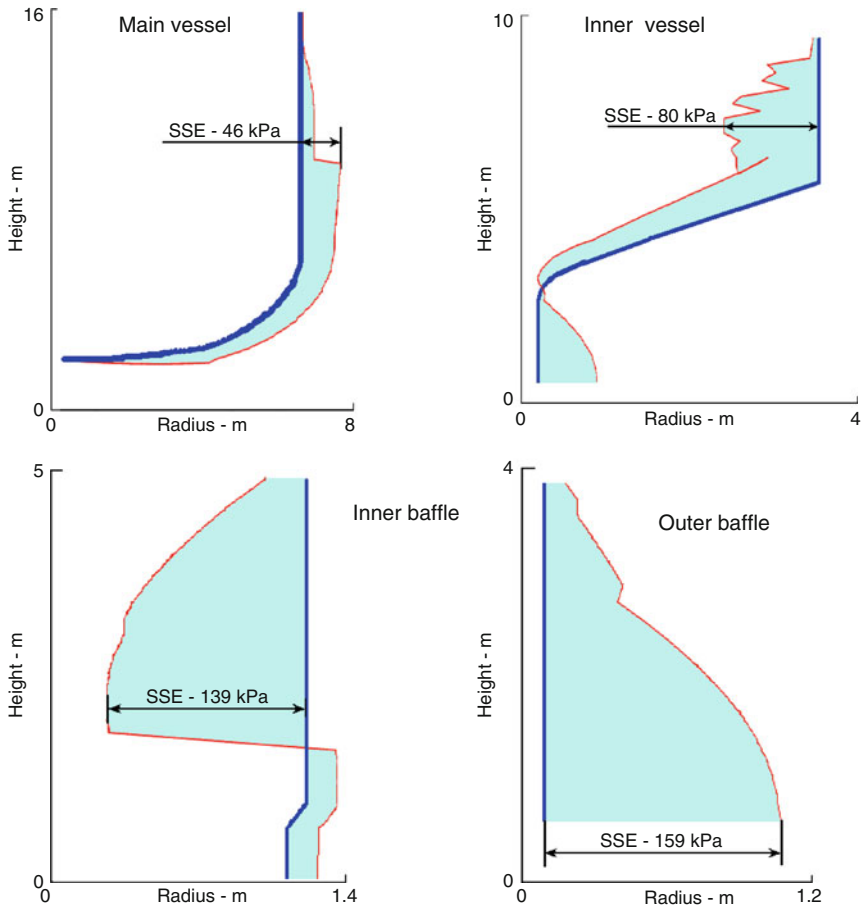
c – compressed time history, n – normal time history, and e – expanded time history.

Table 32
Strain energy-based critical time step for the various vessels – s

Sl. no	Location	X-direction			Y-direction		
		c	n	e	c	n	e
1	Cylindrical portion of main vessel	11.4	4.9	5.3	5.5	15.5	5.8
2	Toroidal portion of inner vessel	10.5	11.7	6.7	5.1	5.7	6.1
3	Cylindrical portion of inner baffle	11.5	15.0	5.7	13.3	4.8	5.4
4	Cylindrical portion of outer baffle	11.6	12.0	5.6	11.7	15.7	6.3

c – compressed time history, n – normal time history, and e – expanded time history.

outer baffles are extracted at the specified critical time steps. In order to have a feel of distributions, a few typical distributions extracted from the seismic response analysis for the expanded time histories corresponding to the excitation in the X-direction, are also shown in Fig. 210. The inner and outer baffles are subjected to high dynamic pressures due to high added mass effects of the fluid confined in the narrow annular spaces between the shells.



■ Figure 210

Pressure distributions at the respective critical time steps

D Buckling Analysis

In order to obtain the lowest critical load factor in a single analysis including 3 D geometrical features, buckling analysis is performed on 3 D geometries. Toward this, the pressure/force distributions extracted from axisymmetric analysis, at the given critical time step, are translated to corresponding 3 D geometries.

Half-symmetric geometries are generated for the main vessel, inner vessel, and integrated geometry of inner and outer thermal baffles. Since the main vessel and thermal baffles are symmetric structures, 3 D geometries are generated by 180° rotation of the respective axisymmetric elements. For the inner vessel, three standpipes, one for primary sodium pump (PSPSP) and two for intermediate heat exchangers (IHXP1 & IHXP2), are included in the finite element model. Fixed boundary conditions (arresting all the displacements and rotations) are applied at the top edge for the main vessel, the bottom edge for the inner vessel, and the edge connected with the main vessel for the thermal baffle. The symmetric boundary conditions are applied all

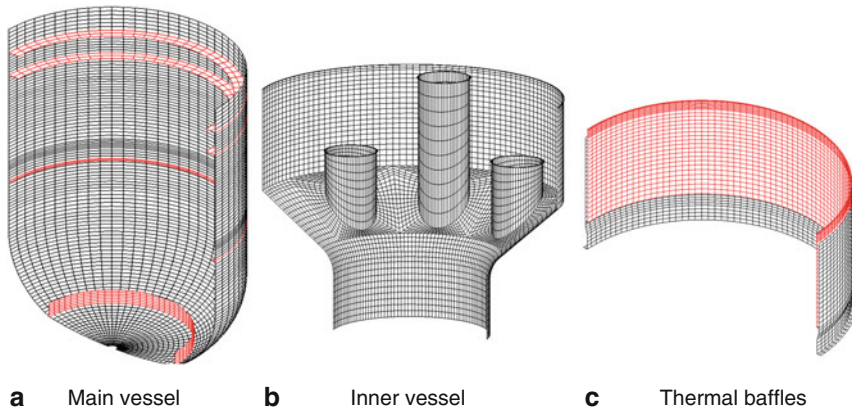


Figure 211

Three-dimensional finite element models of vessels

along the edges lying in the vertical symmetrical plane. The finite element models are shown in [Fig. 211](#).

Pressure Distributions on 3D Geometries

The hydrostatic pressure P_H acting on the surface that is in contact with sodium is symmetrically distributed. The pressure $P_{it}(\theta)$ generated in any node ‘ i ’ at the critical time step ‘ t ’ during horizontal excitation is superimposed as follows:

$$\text{Pressure : } P(\theta) = P_H + P_{it}(\theta) \quad (48)$$

$$P_H = \rho q H_i \quad \text{and} \quad P_{it}(\theta) = P_{ni}(t) \cos(\theta_i) \quad (49)$$

where ρ is density of sodium at operating temperature (880 kg/m^3), g is acceleration due to gravity (9.81 m/s^2), H_i is height of the node ‘ i ’ with reference to free level of sodium, θ_i is angle in radian of the node ‘ n ’ with respect to the X-axis, and $P_{ni}(t)$ is the pressure derived from the results of axisymmetric-Fourier analysis, at the specified time ‘ t ’ corresponding to the originating node ‘ n_i ’. The node ‘ n ’ and ‘ i ’ which lie in the same horizontal plane at the elevation H_i are indicated in [Fig. 212](#).

For the portions of inner vessel and thermal baffles which are in contact with sodium on both surfaces, $P_{ni}(t)$ is replaced by the differential pressure distribution $\Delta P_{ni}(t)$ which is derived directly from the axisymmetric analysis. However, for the main vessel which is in contact with sodium only on the inner surface and the portions of inner vessel and thermal baffles which are in contact with sodium either inner or the outer surface $P_{ni}(t)$ is directly applicable.

Force Distributions on 3D Geometries

In the FE model of main vessel, its connecting structures, namely, CSS, thermal baffles, and roof slab are not included. However, both static and seismic forces are applied appropriately along the edges at which these structures get isolated. The static and seismic forces acting on the CSS support skirt transmitted to the triple point are important for the buckling of the main vessel.

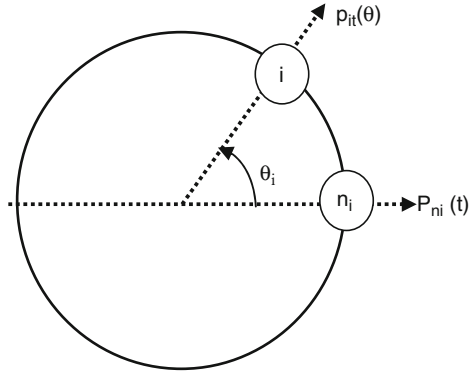


Figure 212
Position of nodes “n” and “i”

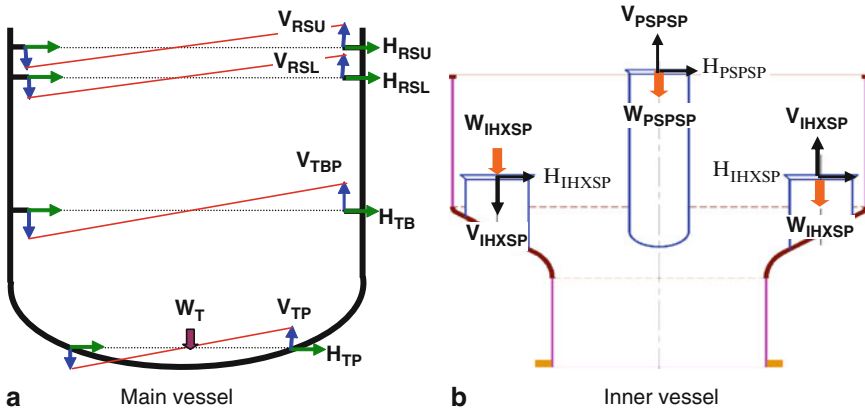


Figure 213
Distribution of forces acting on main vessel and inner vessel

The static loads applied at the triple point (W_{TP}) are 400 t for the half symmetric model. For the inner vessel, the static loads are 6.9 t on each IHX standpipe and 10.8 t for each pump standpipe, which are applied uniformly along the upper edges of standpipes. The distributions of static and seismic forces acting on the main vessel and inner vessel are indicated in [Fig. 213](#).

The seismic forces developed at triple point and standpipes are presented in [Table 33](#).

Elastoplastic Buckling Analysis

The minimum buckling factors thus obtained for various cases are summarized in [Table 34](#). The inner vessel, in virtue of high inertia imparted by the hot pool during safe shutdown earthquake (SSE) in conjunction with the pressure head, is the most critical component, that has the lowest buckling load factor of 1.9. The effect of randomness on time history is not significant on the buckling load factor of inner vessel and the effects are significant for the main vessel and

Table 33

Static and seismic forces applied on main vessel and inner vessel

Force	X-direction			Y-direction		
	c	n	e	c	n	e
$H_{TP} - t/m$	-28.0	-34.6	34.9	-32.3	66.7	33.8
$V_{TP} - t/m$	-49.4	-59.6	56.6	-49.4	72.1	67.3
$H_{IHXP} - t$	0.05	-0.08	0.6	-1.4	-1.2	0.6
$V_{IHXP} - t$	1.0	2.13	2.9	1.6	0.7	3.0
$H_{PSP} - t$	0.08	-0.13	1.0	-2.1	-1.8	0.9
$V_{PSP} - t$	1.6	3.4	4.5	2.5	1.1	4.7

Table 34

Critical buckling load factors for the vessels under SSE

(Fig. 183)

Sl. no	Component	X-direction			Y-direction		
		c	n	e	c	n	e
1	Main vessel	4.3	3.4	3.2	3.6	3.7	3.6
2	Inner vessel	1.9	2.7	2.1	2.0	1.9	1.9
3	Outer baffle	4.7	5.0	3.8	3.8	4.0	3.2
4	Inner baffle	5.6	5.8	3.8	4.4	4.2	3.0

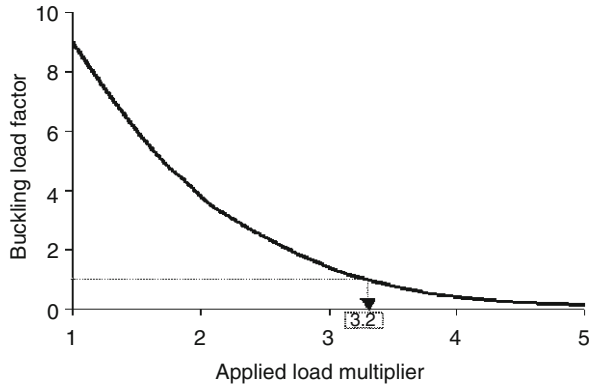
c – compressed time history, n – normal time history, and e – expanded time history.

thermal baffles. However, the load factors are higher than those seen for the inner vessel. From Table 34, the minimum buckling load factors are extracted: 3.2 for main vessel, 1.9 for inner vessel, 3.2 for inner baffle, and 3.0 for outer baffle.

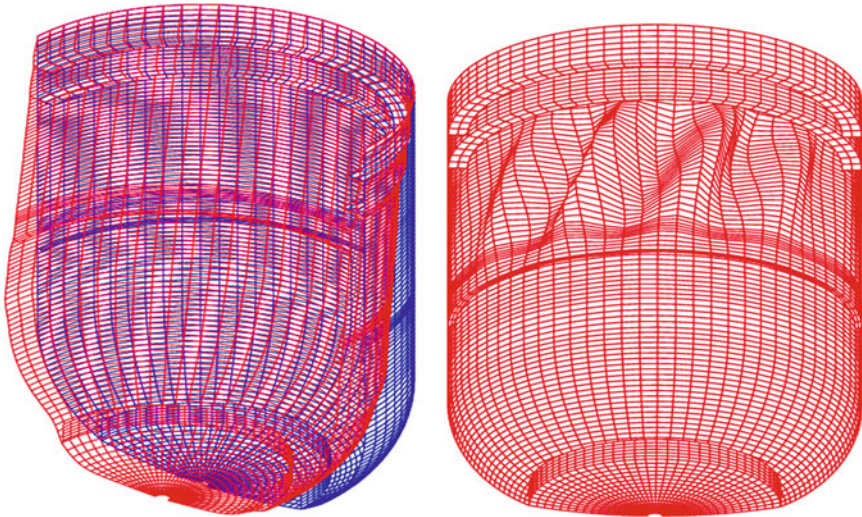
The elastoplastic deformations and the buckled mode shapes for the main vessel, inner vessel, and thermal baffles, which have yielded the possibly lowest load factors, are shown in Figs. 215–217, respectively. Shear buckling mode shape of main vessel, asymmetrical shell buckling mode shapes of inner vessel, and thermal baffle can be seen clearly in these figures.

Design Check

The design code RCC-MR (2007) specifies a requirement of minimum 1.3 factor of safety on the computed critical buckling load, for the category D loadings. SSE is categorized as level D loading. This means that the minimum critical buckling load should be more than 1.3 times the imposed load under SSE. With the minimum load factors of 2.72, 1.52, 2.56, and 2.4 computed for the main vessel, inner vessel, inner, and outer thermal baffles, respectively, it is demonstrated that the critical vessels in the reactor assembly respect the buckling design criteria of RCC-MR.



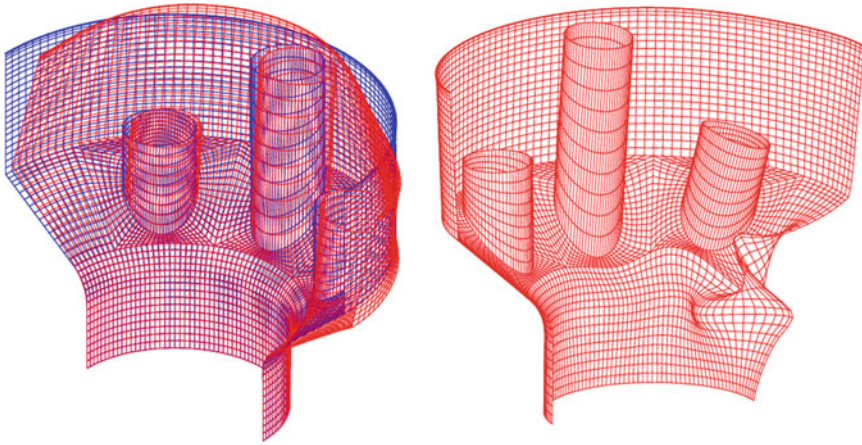
■ Figure 214
Critical buckling load factor for the main vessel



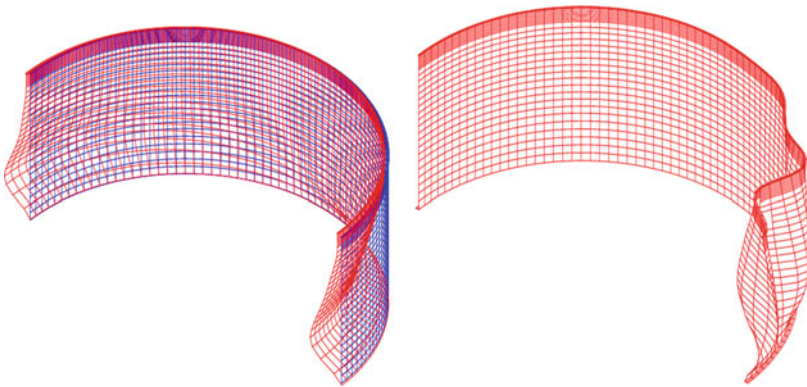
■ Figure 215
Elastoplastic deformation and buckled mode shape of main vessel

8.6.7 Investigation of Buckling of Safety Vessel Subjected to Seismic Loading

In a pool type SFR, safety vessel is incorporated in the reactor assembly surrounding the main vessel, to collect the leaked sodium from main vessel, under unlikely event of main vessel leak. The annular gap between main vessel and safety vessel is chosen such that the sodium level in the hot pool will be maintained to the extent that sufficient sodium flow will take place in the decay heat exchangers immersed in hot pool. In this respect, it is preferred to have possibly lesser gap. However, some minimum gap has to be ensured for having free access of ISI equipment



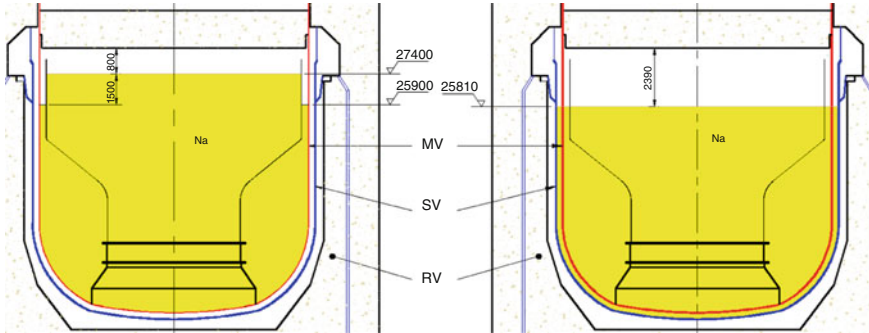
■ Figure 216
Elasto-elastic deformation and buckled mode shape of inner vessel



■ Figure 217
Elasto-elastic deformation and buckled mode shape of outer baffle

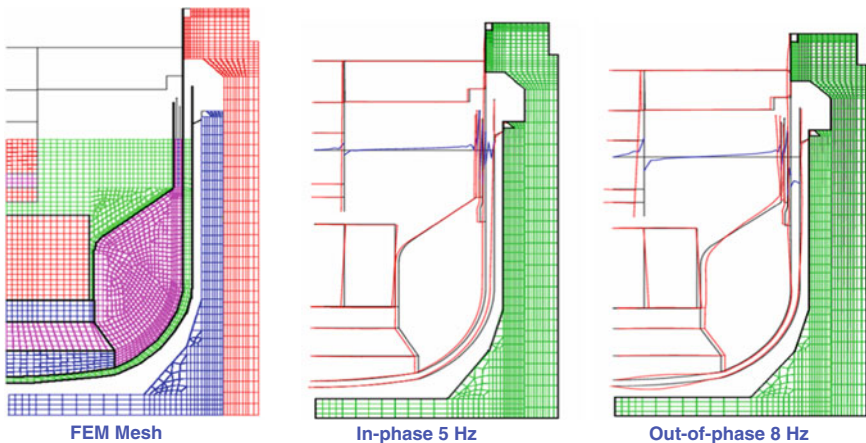
which travels in the interspace for periodic in-service inspection. In finalizing gap, allowance should be given for the possible form tolerances for the main vessel and safety vessel achieved during the manufacturing processes. Typical gaps are 700 mm for SPX1 and 300 mm for PFBR. The level fall in the case of PFBR is shown in [Fig. 218](#).

Simultaneous occurrence of main vessel leak and a seismic event is a beyond design basis event (BDBE), for which the structural integrity of main vessel and safety vessel should be demonstrated. The main loading on the vessels is the dynamic pressure developed in the sodium filled in the inter-vessel space. This pressure acts on the outer surface of the main vessel and the inner surface of the safety vessel. Since the buckling strength of the main vessel is much higher than the safety vessel, the safety vessel is critical under this condition. The analysis methodology to ensure that the safety vessel does not buckle under this extreme loading situation is illustrated with reference to PFBR situation.



■ Figure 218

Fall of sodium levels due to postulated leak in the main vessel

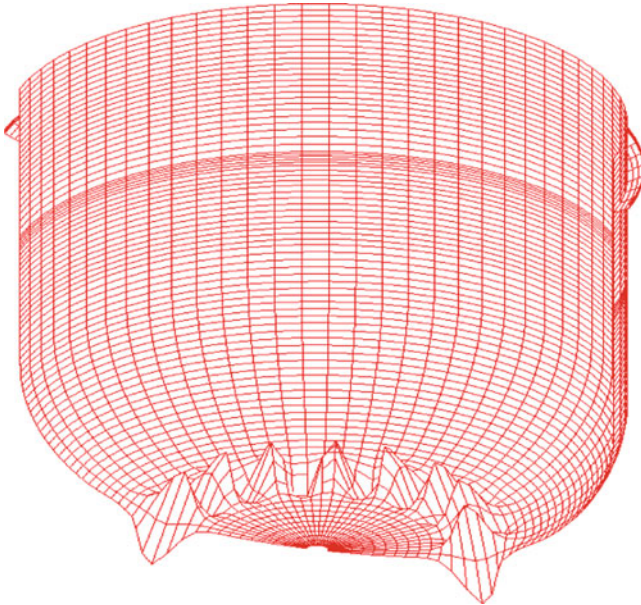


■ Figure 219

Important natural frequencies of vessels under MV leaked condition

The first step in the analysis is finite element discretization of various geometries such as reactor assembly including reactor internals and sodium, sodium free levels and fluid–structure interactions, safety vessel, and reactor vault. The finite element mesh thus developed is shown in [Fig. 219](#). The second step is the determination of natural frequencies and mode shapes up to 50 Hz wherein the seismic excitations have significant energies. The analysis should identify two important additional modes of natural vibration, namely, in-plane and out-of-plane vibration of main vessel and safety vessel coupled by liquid sodium confined in the inter-vessel space. These modes are responsible for generating high inertia forces on the inner wall during SSE. The typical natural frequency values are 4.4 Hz (in-plane) and 7.7 Hz (out-of-plane) for PFBR case. The associated mode shapes are also shown in [Fig. 219](#).

The third step is seismic analysis to determine the dynamic pressure distributions on the safety vessel inner surface. The last step is buckling analysis of safety vessel under these pressures at every time step and determination of load factors. The lowest load factor should be more than 1.3 to respect the RCC-MR buckling design criteria (25). It has been found from analysis carried



■ **Figure 220**
Buckled mode shape of safety vessel

out for safety vessel of PFBR that the torispherical head portion develops many buckles under this situation (► [Fig. 220](#)). The design meets the buckling design criteria.

8.6.8 Investigation of Buckling of Top Shield Plates under CDA Loading

The cover gas pressure rise and subsequent impact of hot pool sodium at the bottom portion of top shield are the two important mechanical consequences of a core disruptive accident (CDA) in a SFR, for which the buckling of bottom plate of top shield has to be investigated. (► [Figure 221](#) shows the results of analysis carried out for PFBR, which depicts this scenario. (► [Figure 222](#) shows the cover gas pressure rise during CDA in PFBR.

The loading scenario is well explained in Breuil et al. (1991). The highlights are given below:

During the core bubble expansion, the cover gas pressure increases monotonically. Under this condition, the bottom plate of roof slab bows upward instantaneously since the natural frequency of the bottom plate is high (~100 Hz). Due to sodium slug impact, bowing of bottom plate increases sharply followed by global bending of (upward) top shield, whose natural frequency is about 5–10 Hz. These two consequent events cause the bottom plate to buckle. The buckling analysis calls for estimation of transient pressure history at the bottom plate and subsequently large displacement elastoplastic analysis. In order to limit the deformation of bottom plate, design provisions are kept in the top shield. The buckling analysis should take into account such provisions which call for nonlinearities caused by gaps between the plate and design provisions embedded in the top shield. A few highlights of experimental investigations carried out toward SPX2 (Breuil et al. 1991) are presented below:

The plate geometry simulating the dimension of bottom plate with the appropriate gap between the rigid rods which limit the displacements, provision of axial force, and distributed

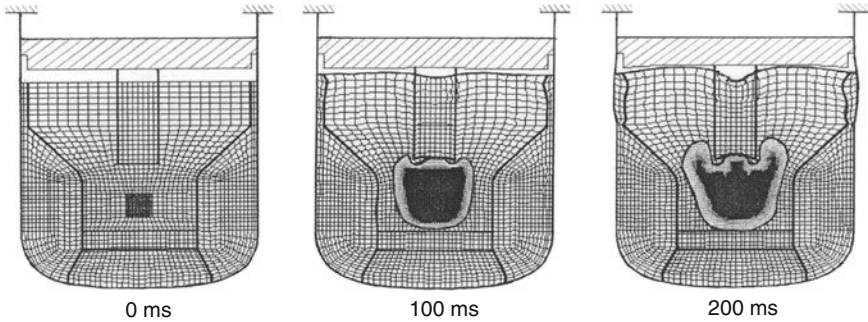


Figure 221

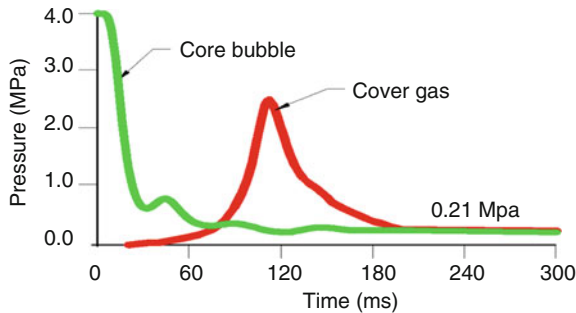


Figure 222

Typical pressure history in core bubble and cover gas under CDA

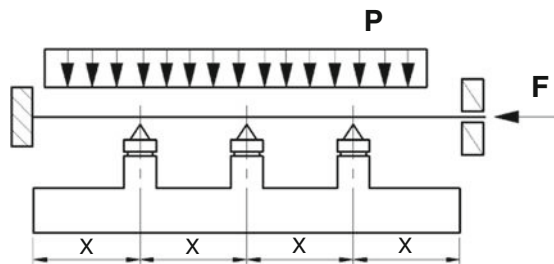
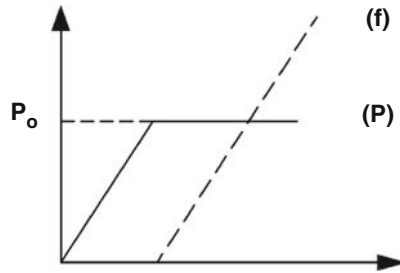


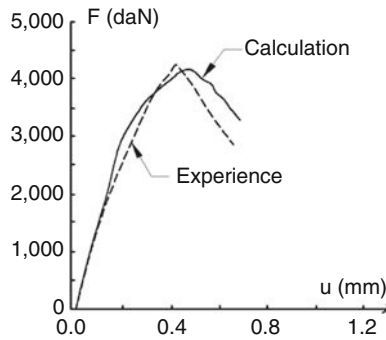
Figure 223

Specimen simulating bottom plate

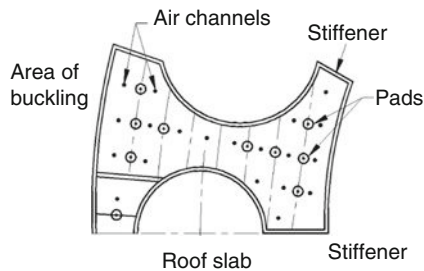
force (pressure) on the surface is considered (► Fig. 223). The pressure and in-plane forces are applied with a specified time delay as shown in ► Fig. 224. The nonlinear analysis methodology is validated with test data as seen in ► Fig. 225. After establishing the procedure and validating the computer code, optimum number of stoppers and corresponding locations are recommended as shown in ► Fig. 226.



■ Figure 224
Pressure & force history



■ Figure 225
Validation of analysis method

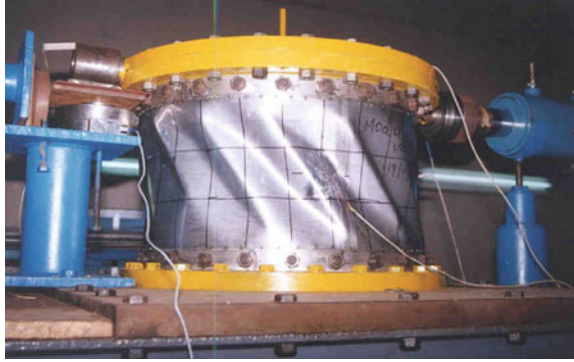


■ Figure 226
Recommended stopper locations

8.6.9 Experimental Validations of Computer Codes

Validation of CAST3M

Since the buckling is a very complex phenomenon and numerical prediction of buckling loads and mode shapes involves very sophisticated analytical techniques, a few important predictions



■ **Figure 227**
Buckled MV models under shear



■ **Figure 228**
Buckled shells (1/18th model of main vessel) vessels under shear

by CAST3M code developed by CEA, France are validated by experimental data to raise the confidence. With this objective, a series of simulated buckling tests have been conducted at IGCAR (India) on various scaled down models of main vessel and inner vessel (Athiannan 2002; Bose 2001). Buckling tests on 1/18th scaled down models of main vessel made of SS 304 were completed under shear plus bending moments. For conducting these tests, a 100 t capacity loading frame and an automatic vessel profile measurement system were specially designed and constructed at IGCAR. ➤ *Figure 227* shows test setup for shear buckling experiments.

Totally 12 tests were conducted for validating shear buckling results and buckled vessels are shown in ➤ *Fig. 228*.

In order to validate CAST3M, large displacement elastoplastic analysis has been completed based on incremental theory and results are stored at every time step. Subsequently, buckling analysis is performed at every time step. The results are presented for three thicknesses in ➤ *Fig. 229*. The results are summarized in ➤ *Table 35*, which indicates that CAST3M are able to predict the buckling loads satisfactorily. The prediction of buckled mode shape is also found to be very good (➤ *Fig. 230*).

The buckling of inner vessel under internal pressure and loads through stand pipes has been simulated on 1/13th scaled models. Six tests were conducted and the vessel buckles at the torus

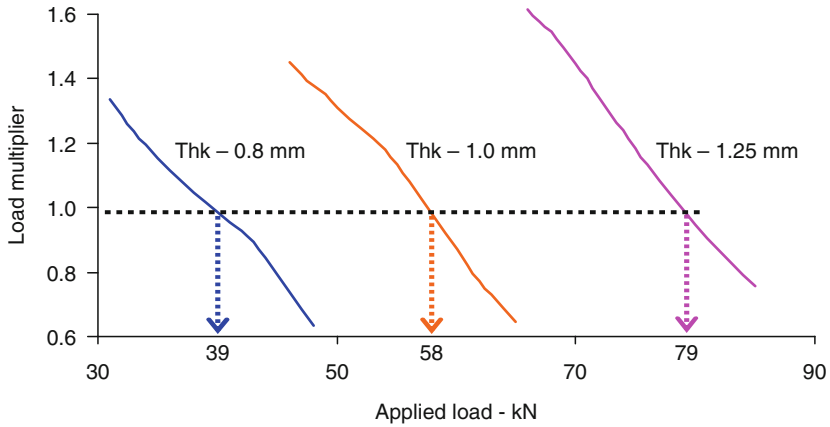


Figure 229
Determination of shear buckling loads

Table 35
Prediction of shear buckling loads by CAST3M

Thickness	No of tests	Imperfection (mm)	Buckling load (t)	
			Test	FEM
0.8	4	2.2–3.8	33–54	28–32
1.0	4	1.1–4.2	50–69	42–58
1.25	4	1.2–3.4	60–73	72–99

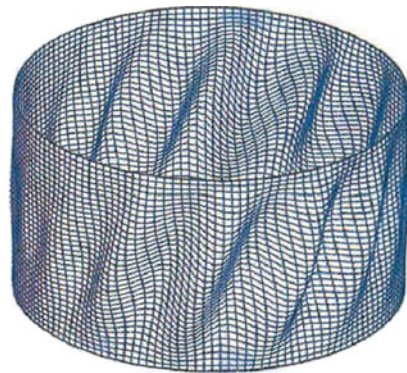


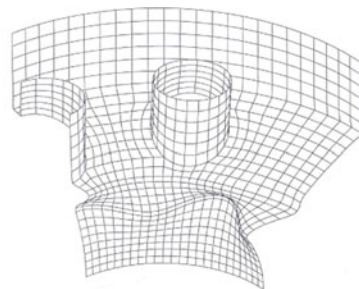
Figure 230
Prediction of buckled mode shape by CAST3M



■ Figure 231
Buckled mode shapes of inner vessel models

■ Table 36
Prediction of buckling strength of inner vessel models by CAST3M

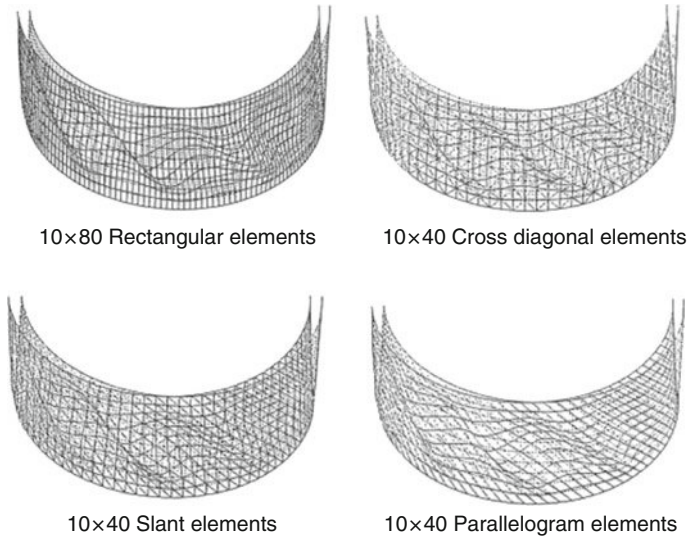
Loading	Tolerance (mm)	Test	CAST3M	Test/CAST3M
Pressure (P) (MPa)	-2.7 to 1.7	0.90	0.95	0.95
Force (F) (t)	-2.9 to 2.5	1.61	1.40	1.15
P (MPa) F = 1.18 t	-1.8 to 1.4	0.175	0.151	1.16



■ Figure 232
Prediction of buckled mode shape by CAST3M

portion as seen in [Fig. 231](#). The results are summarized in [Table 36](#), which demonstrates that the CAST3M predictions are satisfactory.

The buckled mode shape predicted by CAST3M is shown in [Fig. 232](#), which demonstrates clearly the capability of CAST3M code.



■ **Figure 233**
Prediction of buckled mode shape of shells under shear force

Validation of ABAQUS Code

Many tests have been conducted at CREPI Laboratory, Japan to validate ABAQUS code (Matsuura and Nakamura 1997). Two sets of results are presented here: one set on shear buckling and another on the buckling of shells subjected to bending moment, both are representative loads developed under seismic event. ➤ *Figure 233* depicts a few predictions of mode shape by ABAQUS code.

➤ *Figure 234* shows the comparison of predictions of shear buckling loads by ABAQUS which lies within 20% deviation.

For the case of shells subjected to bending moment, ABAQUS predicts within 20% deviations, as seen in ➤ *Fig. 235*.

From the above two benchmark exercise, it is clear that the buckling loads can be predicted by matured computer codes within 20% error.

8.6.10 Summary

In this portion of the chapter, various critical portions of reactor assembly shells, which are prone to buckle, are listed out along with respective buckling modes. Design criteria and methodologies are brought out clearly. Analysis procedures for the nonclassical buckling modes for nonstandard geometries are highlighted. This includes buckling of thin shells subjected to seismic-induced forces and moments, thermal buckling, progressive buckling, and creep buckling. An integrated analysis approach is presented with reference to investigations carried

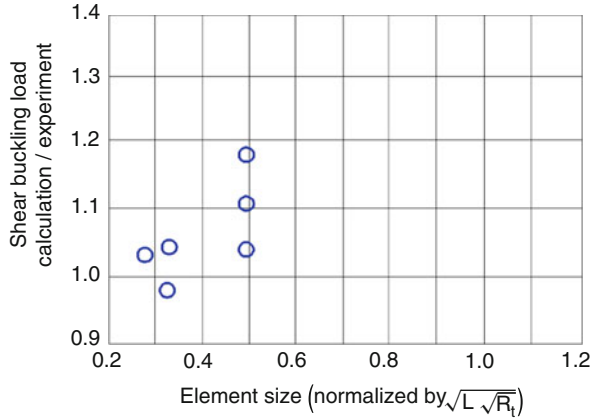


Figure 234

Prediction of shear buckling loads by ABAQUS



12 elements wrinkle

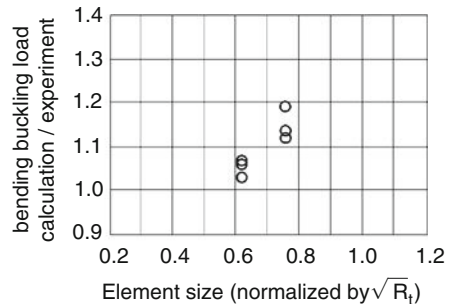


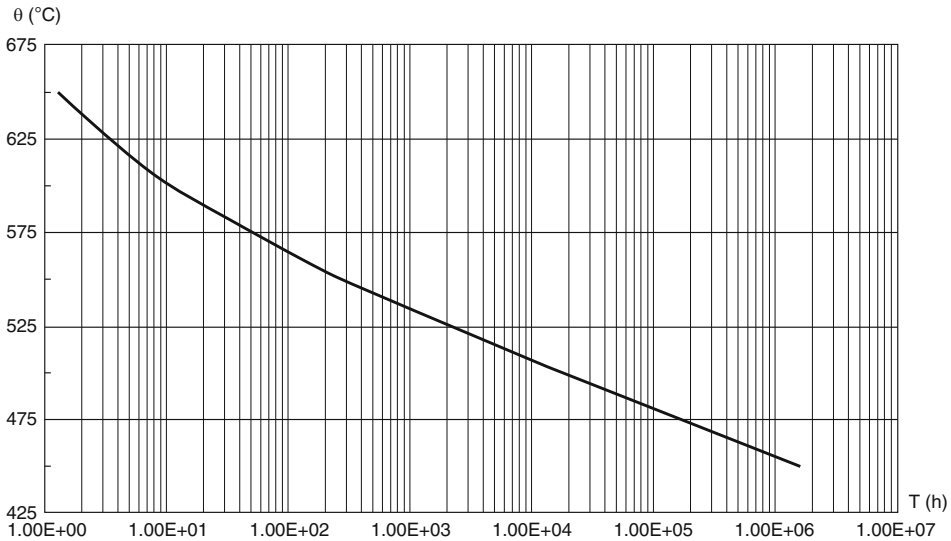
Figure 235

Prediction of buckling of shells under bending moment by ABAQUS

out for reactor assembly of typical pool type fast reactor (PFBR). As per this approach, the seismic analysis and subsequent buckling analysis are performed with careful translation of data from one stage to other stage. Experimental validation aspects of buckling of thin FBR shells are highlighted and buckling loads can be predicted within 20% error by matured codes such as CAST3M and ABAQUS. With these information and data, a design engineer can carry out the buckling design of FBR shells comprehensively.

8.7 Design Criteria and Analysis Method

Mechanical design of FBR components generally follows “design by analysis” method. American code ASME Section III, division 1 (2001) and French code RCC-MR (2002) are



■ **Figure 236**
Creep crossover curve for SS 316 LN as per RCC-MR

commonly used for the design. These codes identify the possible failure modes under creep and non-creep regimes, which depend upon the temperature and time duration that a particular component is subjected to. One broad guideline specified in ASME Section III: Subsection NB is the temperature limit, i.e., for austenitic stainless components, temperature above which creep is significant is 427°C . For ferritic steels, this value is 370°C . However, significant creep is possible at any high temperature, only if the component is exposed for sufficiently long time depending upon the temperature itself. Based on this fact, the French code RCC-MR specifies the rational criteria in the form of creep crossover curve to identify the combination of temperature and time which can cause significant creep effects. A typical creep crossover curve recommended in RCC-MR for austenitic stainless steel SS 316 LN is reproduced in

► [Fig. 236](#).

The failure modes addressed in the non-creep regime are the following:

- Gross deformation due to gross yielding
- Ductile rupture from short-term loading
- Incremental collapse and ratcheting
- Fatigue damage
- Buckling due to short-term loading

In the creep regime, the following additional failure modes are considered:

- Gross deformation due to creep deformation
- Time-dependent progressive deformation
- Creep rupture from long-term loadings
- Creep-fatigue interaction
- Creep buckling due to long-term loadings

■ **Table 37**

Permissible base materials for structures other than bolting

Material	304 SS	316 SS	Alloy 800H	2¼Cr-1Mo	9Cr-1Mo-V
Maximum temperature	815°C	815°C	760°C	650°C	650°C

While RCC-MR provided design rules concurrently, ASME provides similar rules in a dedicated subsection called “NH.” The design criteria specified in the codes are applicable for the materials specified in the code along with the maximum specified temperature. A few typical materials specified in ASME Sec. III Subsection NH are shown in ▶ [Table 37](#).

Further, specific design rules are called for the heat exchanger tubesheets, bolted joints, dished heads in the non-mandatory appendices, for example, RCC-MR Section I: Subsection Z.

8.7.1 Loadings

There are four service loadings specified in codes, namely design, Level A, Level B, Level C, and Level D. Design loadings are used to arrive at the reference thickness. Subsequently, adequacy of thickness needs to be confirmed for all the service loadings by respecting the primary stress limits specified below.

Design loadings shall equal or exceed those of the most severe combinations of coincidence pressure, temperature, and load forces specified under events, which cause service Level A loadings for the same zone of the component. Apart from these, it is required to specify the design life “*t*” in hours. For example, for a typical fast reactor, the design life is 40 years with a load factor of 75%. This yields a value for *t* equal to 2.63×10^5 h ($40 \times 0.75 \times 365 \times 24$).

Level A Service Loadings

Level A service loadings are any loadings arising from system startup, operation in the design power range, hot standby, and system shutdown, and excepting only those loadings covered by Level B, C, and D service loadings or test loading.

Level B Service Loadings

These loadings arise from the incidents of moderate frequency. These are deviations from Level A service loadings that are anticipated to occur often enough that design should include a capability to withstand the loadings without operational impairment. The events, which cause Level B service loadings, include those transients that result from any single operator error or control malfunction, transients caused by a fault in a system component requiring its isolation from the system, and transients due to loss of load or power. These events include any abnormal incidents not resulting in a forced outage and also forced outages for which the corrective action does not include any repair of mechanical damage. The estimated duration of a Level B service loading shall be included in the design specifications.

Level C Service Loadings

These loadings arise from infrequent incidents. These are deviations from Level A service loadings, which require shutdown for correction of the loadings or repair of damage in the system. The conditions have a low probability of occurrence, but are included to provide assurance that no gross loss of structural integrity will result as a concomitant effect of any damage developed in the system. The total number of postulated occurrences for such events may not exceed 25. If more than 25 are expected, then some types of events must be evaluated by the more stringent requirements of the Level B service limits. For a nuclear plant, a moderate earthquake, called operating basis earthquake (OBE), is considered under this category.

Level D Service Loadings

These loadings arise from limiting faults. These are combinations of loadings associated with extremely low probability, postulated events whose consequences are such that the integrity and operability of the nuclear energy system may be impaired to the extent that only considerations of public health and safety are involved. In the seismic design of fast reactor components, design basis earthquake, called safe shutdown earthquake (SSE), is considered under this category.

8.7.2 Design Limits

The important feature of the design codes is the classification of stresses, as primary and secondary. While primary stresses generated in the structure to maintain the equilibrium under externally applied mechanical loads such as dead loads and pressure, can cause failures (gross deformation or tensile rupture) upon single applications, secondary stresses, generated in the structures to conserve the continuity or compatibility conditions, can cause failure only after application of repeated loading cycles (e.g., ratcheting). The primary stresses are limited by appropriate stress intensities expressed in terms of “basic allowable stress intensity (S_m)” for non-creep regime and S_t for creep regime.

S_m : Smaller of the following quantities

- Two third of minimum yield stress other than austenitic stainless steels. For austenitic stainless steels, it is 90 % of minimum yield stress ($\sigma_{0.2}$) in view of its high strain hardening contribution.
- One third of minimum tensile stress.

S_t : Smaller of the following quantities

- Hundred percent of average stress required to obtain a total (elastic, plastic, primary, and secondary creep) strain of 1% at the specified time t .
- Eighty percent of minimum stress to cause initiation of tertiary creep at “ t .”
- Sixty-seven percent of the minimum stress to cause rupture at “ t .”

S_{mt} : Lower of S_m and S_t

Depending upon different loading condition, different factor of safety is used. For example, the primary membrane stress intensity is limited by S_m for Level A and Level B, $1.2S_m$ for Level C, and $2.4S_m$ for the Level D loading conditions.

The secondary stresses are controlled by limiting the accumulated strains. These apart, the component life would be limited by the accumulated creep-fatigue damages. These are illustrated in the following paragraphs.

Strain Limits

The principle strain components, namely, maximum positive membrane strain (ϵ_m), positive bending strain (ϵ_b) and positive local strain (ϵ_L) are to be limited as follows:

$$\epsilon_m \leq 1\%, \epsilon_m + \epsilon_b \leq 2\%, \text{ and } \epsilon_m + \epsilon_b + \epsilon_L \leq 5\% \text{ for base metal.}$$

For welds, 50% of these values should be applied. Since the ratcheting induces rapid strain growth, effect of ratcheting has to be considered in the computation of strains.

Creep Damage

Creep damage defined by Robinson's rule as $D_c = t/T_d$ should be less than 1. Where t is the total duration of a given stress (σ_{eff}) at maximum temperature θ . T_d is allowable time duration determined from stress-to-rupture curves for the stress (σ_{eff}) at temperature θ . The computation of σ_{eff} from the individual stress components depends upon the kind of multiaxial rule followed for creep damage estimation. Giving due consideration for the role of hydrostatic component in influencing the creep damage in addition to the Von Mises component, RCC-MR defines the effective stress as:

$$\begin{aligned} \sigma_{\text{eff}} &= 0.867\sigma_{\text{VM}} + 0.4\sigma_{\text{H}} \\ \sigma_{\text{VM}} &= 1/\sqrt{2}[(\sigma_1 - \sigma_2)^2 + (\sigma_2 - \sigma_3)^2 + (\sigma_3 - \sigma_1)^2]^{1/2} \quad \sigma_{\text{H}} = [\sigma_1 + \sigma_2 + \sigma_3]/3 \end{aligned}$$

where σ_i are the principal stresses.

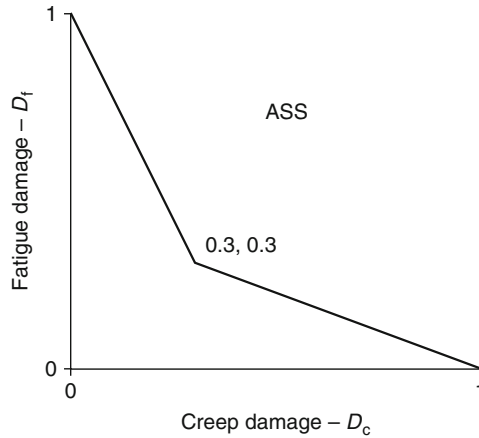
The criteria adopted in ASME-NH, which is given below:

$$\begin{aligned} \sigma_{\text{eff}} &= \bar{\sigma} \exp \left[C \left(\frac{J_1}{S_s} - 1 \right) \right] \\ J_1 &= \sigma_1 + \sigma_2 + \sigma_3 \\ S_s &= [\sigma_1^2 + \sigma_2^2 + \sigma_3^2] \\ \bar{\sigma} &= \frac{1}{\sqrt{2}} [(\sigma_1 - \sigma_2)^2 + (\sigma_2 - \sigma_3)^2 + (\sigma_3 - \sigma_1)^2] \end{aligned}$$

where σ_i are the principal stresses. The constant C is defined as follows:

- For Types 304 and 316 stainless steels, $C = 0.24$.
- For Alloy 800R, $C = 0$.
- For $2^{1/4}\text{Cr-1Mo}$ and 9Cr-1Mo-V : 0.16 if $J_1/S_s \geq 1.0$ and = 0 if $J_1/S_s < 1.0$.

There is a need to apply a factor of safety K' by dividing the σ_{eff} before entering in to creep rupture curve. K' values are 1/0.9 for ASS.



■ **Figure 237**
Creep-fatigue ine


Fatigue Damage

At any material point, fatigue crack initiation occurs if fatigue damage (D_f) defined by: $D_f = n/N_d$ exceeds unity. Where n is applied number of strain cycles with the strain range of $\Delta\epsilon$ at temperature θ . N_d is permissible number of cycles determined from design fatigue curve. The design fatigue curves were determined from completely reversed loading conditions at appropriate strain rates. These curves have a factor of safety 20 on life and 2 on strain range.

Creep-Fatigue Interaction

When both creep and fatigue damages occur together, there can be a strong interaction, which reduces the life significantly. Accordingly, the sum of creep and fatigue damages should be limited to a specified value D follows:

$$D_c + D_f \leq D$$

As shown in  Fig. 237, the values of D are expressed as a function of either D_c or D_f .

8.7.3 Analysis Methods

Simplified Methods

The primary stress intensities are computed from the results of elastic stress analysis. However, for computing the stresses and strains accurately to check the strain, creep, and fatigue damage limits, inelastic analysis methods are preferred. However, considering the complexities, requirement of high level of expertise and sophisticated material data and high computational cost involved in the inelastic analysis, the codes provide robust and conservative simplified method to evaluate inelastic stress and strains based on elastically computed stresses and

strains. However, before applying these simplified procedures, certain restrictions on accumulated strains need to be respected. Accordingly, the first step is estimation of strains based on simplified methods as described in AFCEN (2002) and Roche and Nouailhas (1989). In the computation of inelastic strains, creep strains and cumulative strains accumulated due to cyclic thermal loadings in conjunction with primary stress (ratcheting) are computed by the simplified methodologies proposed in the code. Methodology recommended in ASME-NH is based on O'Donnell and Porowski diagram and that recommended in RCC-MR is based "efficiency index diagram." These diagrams are shown in [▶ Figs. 238](#) and [▶ 239](#) respectively. Additional details and systematic procedures are provided in both RCC-MR and ASME-NH for computing strain range and sustained stresses for estimating fatigue and creep damages. These procedures call for determination of maximum stress range ($\Delta\sigma_{\max}$) from elastically calculated stresses.

Inelastic Analysis

Inelastic analysis is essential for predicting accurately the stress and strain history in the components subjected to mechanical and thermal loadings and thereby for the accurate estimation of ratcheting, creep, and fatigue damages. This calls for use of realistic material constitutive models to be employed in the numerical prediction of stress-strain history at all the critical locations. The constitutive model should be able to simulate accurately the complex material behavior caused by monotonic and cyclic, mechanical and thermal loadings at high temperature. Apart from creep and creep relaxation, the material hardening behavior by which the instantaneous yield stress and strain hardening behavior changes continuously in stress or strain cycling is an important aspect need to be modeled. ASS exhibits cyclic hardening behavior. Further, depending upon the values of primary and secondary stress ranges, the material point exhibits many complex behaviors, namely, elastic cycling, shake down, and ratcheting. Under various cyclic loading as illustrated in [▶ Fig. 240](#), there is no permanent strain at end of each elastic cycling ([▶ Fig. 240a](#)). Under shakedown, there is no accumulation of strains except strain cycling with a fixed magnitude ([▶ Fig. 240b](#)). Under very high strain cycling (ratcheting), there is a possibility of progressive growth of strain, cycle by cycle, which can lead to development of unacceptable strains after application of a few number of load cycles ([▶ Fig. 240c](#)).

The behavior model to be considered will depend on the physical phenomenon and on the collapse mode to be analyzed. [▶ Table 38](#) gives a guideline for cyclic hardening materials and this table should be used with care when dealing with cyclic softening materials. Roche and Nouailhas (1989) can be consulted for further details about the viscoplastic constitutive model commonly used for numerical simulation of austenitic stainless steels.

8.7.4 Buckling Design

Time Independent Buckling

In the non-creep temperature range for structures, buckling occurs instantaneously. The critical buckling load can be determined by stability analysis. Normally the analysis is directed against

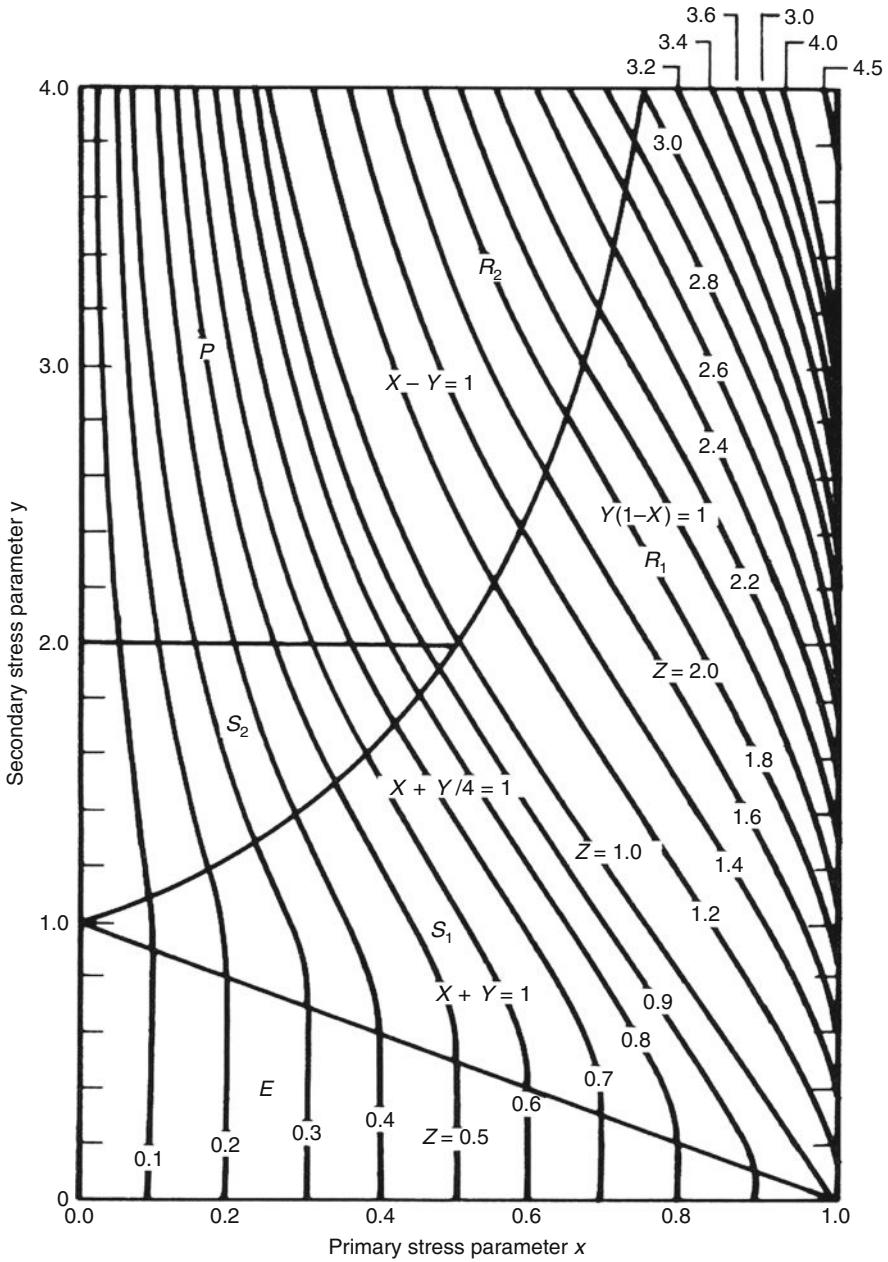


Figure 238

O'Donnell Porowski diagram – ASME-NH

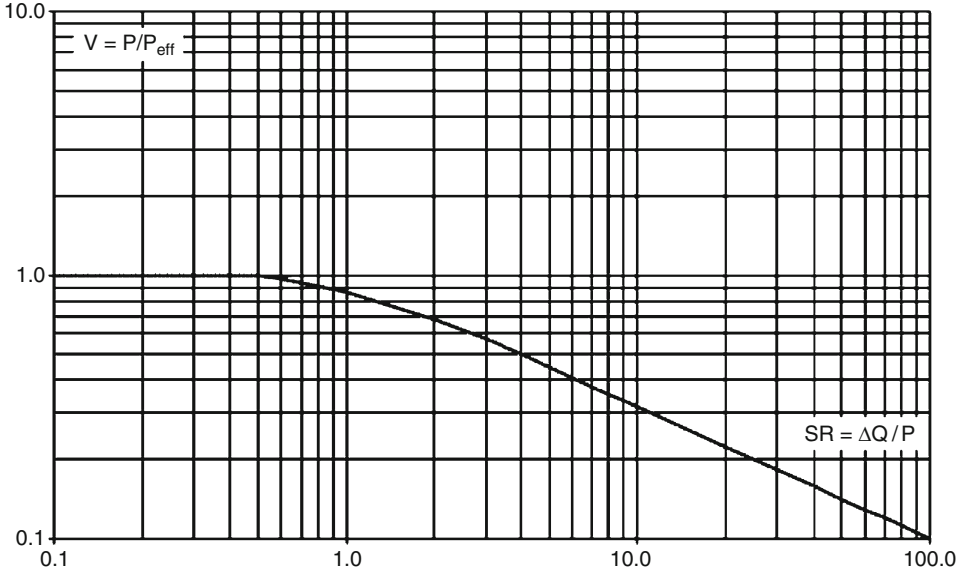


Figure 239
Efficiency index diagram – RCC-MR

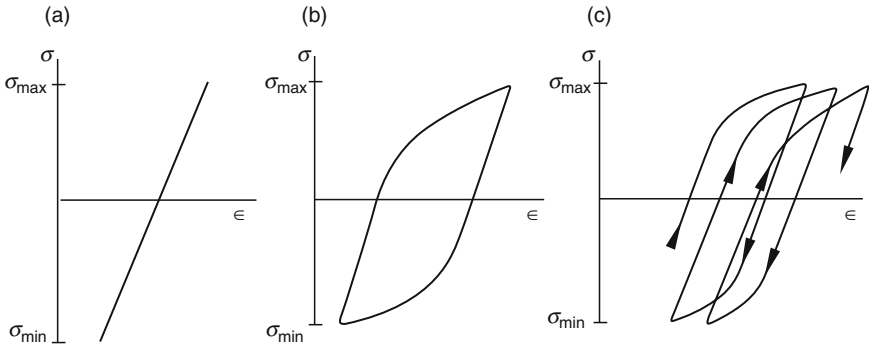














Figure 240
Various modes of cyclic loading under stress controlled

■ Table 38

Guidelines to choose appropriate material models

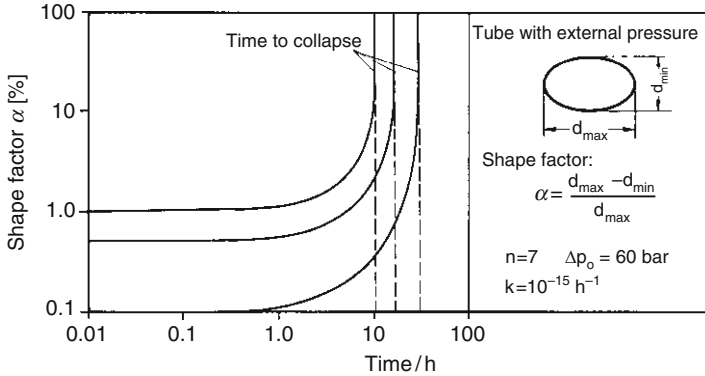
Collapse mode → Behaviour model ↓	Excessive deformation, Plastic instability	Progressive deformation	Creep-fatigue
Perfect plastic + creep rule	Suitable 	avoid 	avoid 
Isotropic strain hardening + creep rule	Suitable 	avoid 	avoid 
Linear kinematic hardening + creep rule	avoid 	Use with care 	Use with care 
Combined hardening (Chaboche viscoplastic, etc.)	Suitable 	Use with care 	Suitable 

snap-through or bifurcation instability, taking into account time-independent elastoplastic material behavior. Calculation schemes are given to design against such buckling phenomena. After determining critical buckling load (P_{cr}), the allowable buckling load is established by applying required factor of safety (FOS). In case of buckling under mechanical loads such as pressure or dead load, minimum FOS required is 3. In case buckling occurs under strain-controlled loading such as thermal loadings, minimum FOS required is 1.67. These factors are applicable for design, Level A and Level B loadings. The corresponding factors for Level C are 2.5 and 1.4 and for Level D are 1.5 and 1.1 for load-controlled buckling and strain-controlled buckling.

In the determination of buckling loads, the effects of initial geometrical imperfection (which is very critical for axial compression and external pressure) and plasticity should be included carefully. To simplify the designers work, for the cylindrical and spherical shells under external pressure and cylindrical shell under axial compression, design charts are given in NB for checking that design pressure is less than the critical buckling pressure including effects of imperfection and plasticity.

Time-Dependent Buckling Design

At high temperatures, the creep buckling is a time-dependent phenomenon. It develops mostly as follows: at first deformations occur very slowly, but they change the shape in a disadvantageous manner. So it seems that two phases exist. Firstly, a slow deformation process, and then rapid deformations determined by strongly accelerated creep processes in some



■ Figure 241
Concept of creep buckling

sensitive regions of the structure. Creep buckling phenomenon for a typical heat exchanger tube subjected to external pressure is illustrated in [Fig. 241](#).

Design charts are provided in the codes that can be used provided the temperature and time combinations lie in the non-creep regime of charts, for the cylindrical and spherical shells both in ASME and RCC-MR. For the special types of geometries, buckling analysis is to be done either using bifurcation type or large displacement elastoplastic-creep analysis. After determining the load, for which the structure becomes unstable at the end of specified design life, factor of safety is applied appropriately as 1.5 for the Level A, Level B, and Level C loadings and 1.25 for Level D loading.

9 Plant Dynamics

A comprehensive list of conditions and its classification following their frequency of occurrence is an essential basic element for design safety analyses and afterward validation of the facility project. The demonstration of the adequacy of the design with the safety objectives is made through the analysis of three kinds of conditions:

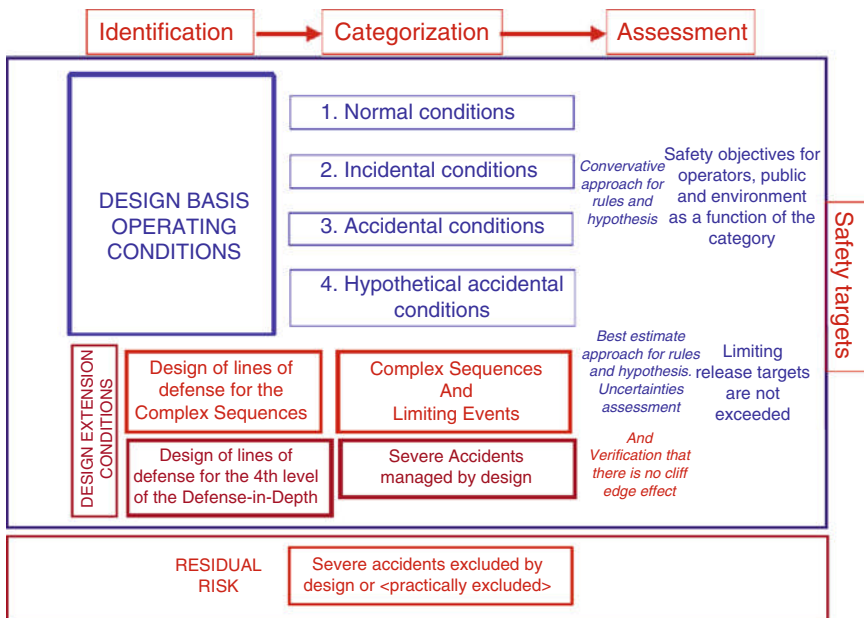
- **The design basis conditions.** The safety design of the plant mainly results from the analysis of these conditions. It must be shown that the consequences of accidents occurring in the previous situations are matching the objectives targeted in terms of radiological releases and radiation protection. Moreover, the estimated frequencies of incidents and accidents determine the acceptable consequences for each situation postulated. And it must be checked that the risk of whole core degradation initiated by the initiating events (IE) is very low.
- **Design extension conditions.** Complex sequences, limiting events, and severe accidents are evaluated despite their low occurrence frequency. The consequences of these accidents are

analyzed, and their consequences in the environment have to be demonstrated to be lower than the limiting release targets.

- **Residual risk situations.** The consequences of these situations are not analyzed. If these situations are not demonstrated to be physically impossible, the prevention measures regarding their occurrence have to be demonstrated to be sufficient to “practically eliminate” them.

► *Figure 242* describes the approach apply for a new design in order to determine and analyze its relevant operating conditions.

The objective of this chapter is to give examples of design basis events and safety criteria, then to explain analysis methods for such situation. Finally, examples of SFRs behavior in typical transient situations are described. If all this information is strongly dependent on the design (oxide or metal or carbide fuel, loop, pool or modular reactor with water or gas energy conversion system. . .), then the following information could not be considered as completed. At the end of the chapter are presented some anticipated transients without SCRAM (ATWS) as they are representative of the inherent behavior of the SFRs. Examples are given only as examples. The following references (Bertrand and Devictor 2006; GenIV GIF; IAEA 1996, 1999, 2000, 2005, 2007; Justin et al. 1985; Libman 1996; Waltar and Reynolds 1981) provide more details and examples.



■ **Figure 242**
General approach for the safety-related design and assessment

9.1 About the Design Basis Conditions, the Design Extension Conditions and the Residual Risk

A design basis condition is a plant condition resulting from the combination of a normal operating condition (category 1, see hereafter) and of an initiating event belonging to the design basis area, that is, classified from category 2 to category 4 (according to its probability, see definition hereafter). Initiating events may arise due to component failure, operator errors, internal, or external hazards. Their consequences affect the plant behavior. The design basis conditions are grouped in four categories on the basis of the expected occurrence frequency of the corresponding initiating events. Definition of the categories, referring to EFR, is as follows:

- **Normal operating conditions** are plant conditions planned and required. They include special conditions such as tests during commissioning and start-up, partial loading, shutdown states, handling states, partial unavailability for inspection, test, maintenance, and repair. The decommissioning conditions are not included in the safety analysis of the operating plant; they will be specifically analyzed in good time. Nevertheless, considerations concerning the decommissioning have to be made. The goal of the safety analysis of normal operating conditions is to verify that their consequences on the staff and the public are ALARA and in any case lower than the corresponding release criteria.
- **Category 2 operating conditions** are operating conditions not planned but expected to occur one or more times during the life of the plant (mean occurrence frequency estimated greater than 10^{-2} per year). Plant shall be able to return to power in short term after fault rectification. The goal of the safety analysis of category 2 operating conditions is to verify that their consequences on the staff and the public are ALARA and in any case lower than the corresponding release criteria.
- **Category 3 operating conditions** are operating conditions not expected to occur during the life of the plant (mean occurrence frequency between 10^{-4} per year and 10^{-2} per year) but after which plant restarting, by possible repair, is required for investment cost guarantee. The goal of the safety analysis of category 3 operating conditions is to verify that their consequences on the public are lower than the corresponding release targets.
- **Category 4 operating conditions** are operating conditions after which plant restart is not required because there is no expectation of occurrence during the plant life. The consequences of an operating condition must not exceed category 4 limits with a mean value of their frequency higher than 10^{-7} per year. The goal of the safety analysis of category 4 operating conditions is to verify that their consequences on the public are lower than the corresponding release targets.

Referring to the EFR categorization, the **Design Extension Conditions (DEC)** are not defined on the basis of their occurrence frequency, but they are postulated to be bounding cases resulting from risks specific to the design or the process. Two kinds of design extension conditions are considered: the situations for which the consequences have to be demonstrated to be limited and the severe accidents. The goal of the safety analysis of DEC is to verify that their consequences on the public are lower than the limiting release targets. In the safety approach developed in the European Utility Requirements (EUR), *complex sequences* are design extension conditions which are not covered by the safety analysis of category 2, 3, and 4 operating

conditions, but the occurrence frequency of which is not demonstrated to be sufficiently low (i.e., well below the mean value of 10^{-7} /sequence/year/plant). In the EFR safety approach, the complex sequences are complemented by limiting events defined for licensing purposes. They are bounding cases resulting from risks specific to the design or the process. The consequences of complex sequences and limiting events are investigated. This can lead to enhance the design in order to show that core damage is prevented, and then that the limiting release targets are not exceeded. *Severe accidents* are considered in order to verify that there is no “cliff edge” effect on the consequences even for very hypothetical conditions. The goal of the analysis of severe accidents is to prove the efficiency of the containment measures for limiting the consequences of core damage accidents. The radiological consequences shall be lower than the limiting release targets.

Residual Risk (RR) situations are accident conditions for which the prevention regarding their occurrence is such that the analysis of their consequences is not required by the safety demonstration. On the other hand, the adequacy of the prevention of these accident conditions has to be demonstrated. Such a demonstration may be performed using probabilistic assessment. In this case, the goal is to show that accident conditions which the consequences may exceed the limiting release targets have a mean frequency well below to a threshold, as for example 10^{-7} event/year/plant.

Hazards must be considered in order to add provisions aiming to avoid that they provoke an accident and to protect the systems permitting to control the facility conditions. The hazards to consider in the design of a plant could result from internal causes or external ones and are qualified as internal hazards and external hazards. A typical list of internal hazards to be taken into account is internal flooding, internal fire, electromagnetic perturbations (possibly externally caused, like lightning, but having an effect on control system of the plant), internal explosion, and missile projection. The following external hazards are usually considered: earthquake, extreme weather conditions, aircraft crashes, industrial environment (explosion, fire, . . .), external fire, and external flooding. For SFRs, specific hazards from the use of sodium are studied due to fire or leak, or gel of sodium.

The analysis of the causes of safety function losses by means of decoupling criteria leads to a set of typical families of initiating events: untripped or protected loss of flow (ULOF or LOF), untripped or protected loss of heat sink (ULOHS or LOHS), untripped or protected transient of power (UTOP or TOP), untripped or protected loss of power (including ULOSSP or LOSSP for the loss of station service power), loading error, local assembly fault, leak or sodium fire, sodium–water reaction or sodium–water–air reaction, internal and external hazard.

Their ranging in the previous categories depends on the design options, and then no categorization is proposed in the following sections. For some families, progressiveness in the severity is applied and the events are ranged in different categories. Examples of progressiveness are:

- The origin of a pump failure could be a speed reduction or a triggering or a jamming.
- For the sodium–water reaction, different quantities of broken tubes are considered.
- The duration of the loss of station service power affects the range, as for example for EFR project in Category 2 for a duration less than 1h, and in Category 3 for a longer duration.

The following list gives typical situations usually studied in the design basis:

- Spurious reactor trip,
- Pin failure leading to DND signal.
- Inadvertent withdrawal of an absorber rod.
- Internal and external flooding.
- Extreme weather conditions.
- Large leak (IXH secondary circuits or DRC circuits).
- Multiple faults in fuel transfer and storage systems.
- Conventional fire.
- Subassembly drop.
- Local subassembly cooling disturbances.
- Primary and secondary pump faults.
- Leakage or rupture of primary pump diaphragm connection of internal structures.
- Primary sodium vessel leak.
- Loading error.
- Large leak of cover gas.
- Abnormal passage of gas through the core.
- Large steam generator leak.
- Primary sodium circuit leakage in the secondary containment.
- Dropped loads.
- Earthquake.

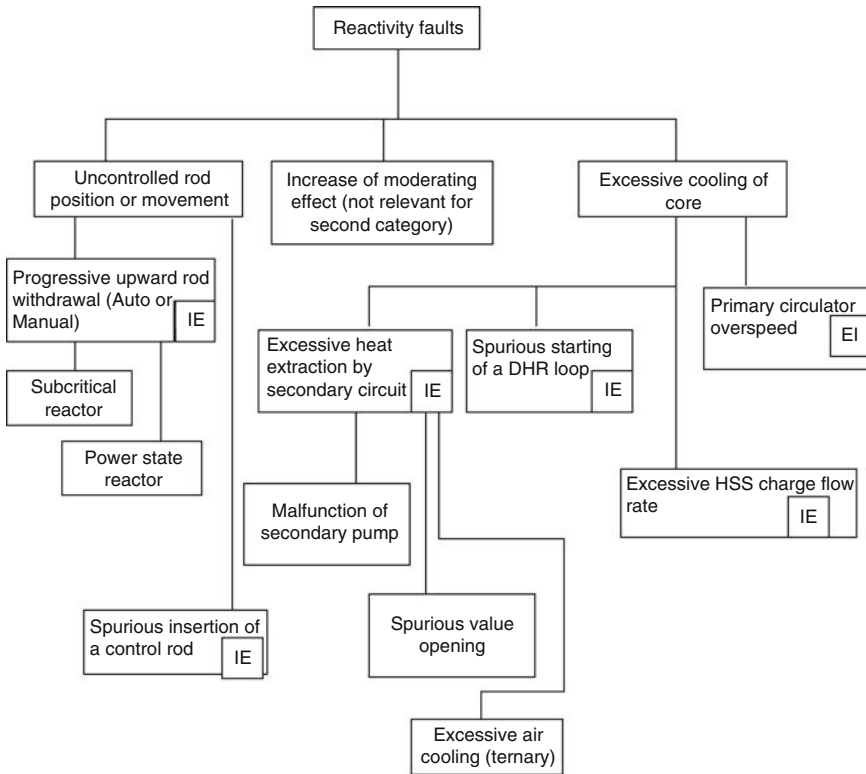
A list of typical DEC is:

- Leakage of main and safety vessels.
- Fuel subassembly meltdown.
- Sodium–water–air reaction in a steam generator building.
- Large sodium–water reaction in a steam generator (larger than design basis event).
- Large sodium leak on the reactor roof.
- Large sodium leak outside the secondary containment up to guillotine failure of a main sodium pipe.

Furthermore, in case of accidental sequences possible to quantify, probabilistic approach postulating failure of various safety systems and components could help in the identification of the sequences to consider in the DEC, thanks to a more realistic methodology than engineer judgement usually adopted. In particular, the identification of pertinent complex sequences postulating the failure of one or several mitigating means will be improved with probabilistic approach.

Some events needing the demonstration of classification as residual risk are

- Large reactivity insertion (HCDAs) due to core support failure, core compaction, voiding, large loading errors or ejection of control rod.
- Loss of all decay heat removal systems.
- Dropped large load causing failure of primary coolant system.
- Primary pump flywheel failures.
- Primary vessel buckling due to external overpressure Ingress of water into primary circuit.
- Large aircraft crash (could be classified in limiting events according to some national requirements).
- Large gas cloud explosion (could be classified in limiting events according to some national requirements).



▣ **Figure 243**
Example of a logic diagram for IEs resulting from category 2 reactivity faults

In case of innovative design, a possible approach for identifying new initiating events relies on the assessment of mechanisms to control in order to fulfil the main safety functions of the reactor. Once these mechanisms have been identified, cause–consequences diagram (inspired by Master Logic Diagram methodology, Papazoglou and Aneziris 2003) could be built in order to identify initiating events leading to induce the mechanisms presented as the top level of the diagrams. In other terms, the initiating events identification of the design basis area has been performed by looking for the physical phenomena able to disturb the physics of the reactor regarding each of the main safety function. An example of such a diagram is presented in [► Fig. 243](#).

9.2 Safety Criteria

According to the objective of progressiveness, targets of radiological dose to public are established as function of occurrence category. An illustration is given in [► Table 39](#), showing an ALARA approach from SPX to EFR. Some intermediate design criteria that ensure in particular

Table 39
Examples of plant and safety criteria

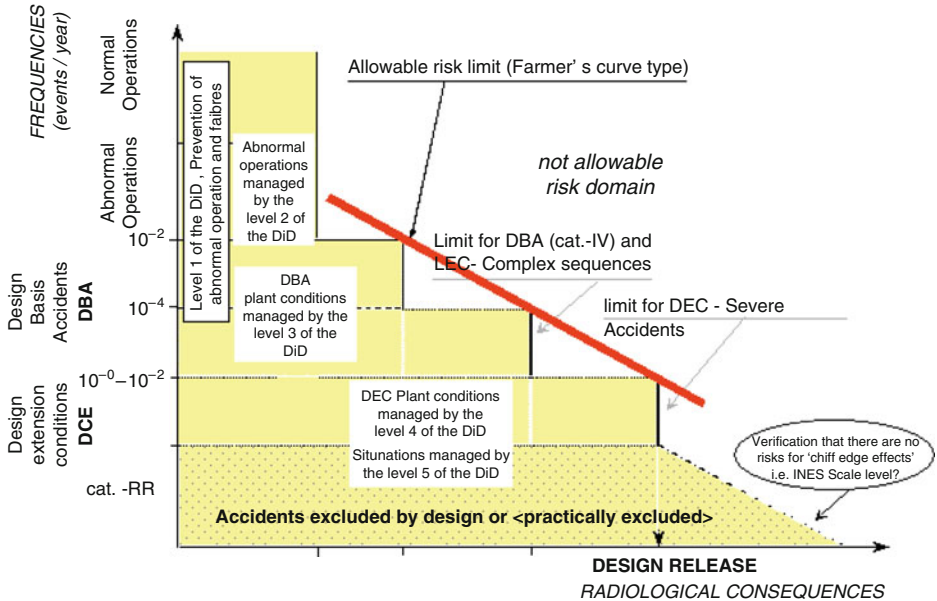
Category of conditions	Event frequency	Plant criteria	Safety criteria	Radiological criteria	
				EFR	SPX
1. Normal	$>1/\text{year}$	High availability	Radiological release ALARA	50 $\mu\text{Sv}/\text{year}$	To meet authorized release limits
2. Incidental	$>10^{-2}/\text{year}$	Able to return to power at short term after rectification	Radiological release lower than the limit	50 $\mu\text{Sv}/\text{year}$	
3. Accidental	$>10^{-4}/\text{year}$	Able to restart after inspection, repair, requalification	Radiological release lower than the limit	1 mSv/year	5 mSv/year (body)
					15 mSv/year (thyroid)
4. Hypothetical	$>10^{-6}/\text{year}$	Plant restart not required	To maintain core coolability, limited change of core geometry	50 mSv/year	150 mSv/year (at site boundary)
DEC	$>10^{-7}/\text{year}$	(Loss of plant investment)	Releases lower than the targets (no need off-site provisions)		250 mSv/event (30 days at 15 km)
Residual Risk	$<10^{-7}/\text{year}$	–	(No “cliff edge” effect)		

■ Table 40

Examples of design criteria for the core integrity, the core support, and the reactor block integrity (should be adapted to the design options)

Category of conditions	Cladding limits (MCT = maximum clad temperature for an oxide fuel)	Fuel limits	Primary boundary – cold structure	Primary boundary – hot structure
1. Normal	Non-open clad failure	No melting	Max. T° core inlet	<545 °C
	MCT < 700 °C			
2. Incidental	No clad failure, except due to random effect. MCT <700 °C and 700 °C < MCT < 740 °C during 2 h and 740 °C < MCT < 780 °C during 10 min	No melting	<520 °C	<545 °C
3. Accidental	No systematic (i.e., large number of) pin failures nor large increase of leak rate.	No melting	<530 °C	<545 °C
4. Hypothetical	“Reversible local sodium boiling” criteria.	Any predictable local fuel melting to be shown acceptable (simultaneous clad failure and fuel melting of the same pin excluded).	<630 °C	<880 °C
DEC	Coolability of damaged core; propagation of a pin bundle blockage must be prevented	Severe accident admitted complying with the containment measures; no recriticality.	<630 °C	
Residual Risk	Core collapse excluded by design	Energetic severe accident excluded by design	–	–

that the radiological limits are not exceeded are defined through the application of the defense-in-depth principle. Design criteria related to the design basis operating conditions (► [Table 39](#)) are then established as concerns the plant availability, integrity of the fuel elements, and of the mechanical reactor components(► [Table 40](#)). The safety demonstration requires not only



■ **Figure 244**
Relationship between categories and safety targets

to meet the design criteria during the transient (e.g., maximum temperature at the transient peak), but also to meet safe shutdown state criteria just after the event transient. Analysis of the scheduled shutdown states as normal operating conditions and of the transient operating conditions are both important. This analysis requires specific design criteria impacting the negative reactivity margins of each control rods system. The design criteria are generally as follows:

- To keep reactor cold state (180°C) by each shutdown system minus the most reactive rod ($n - 1$).
- To keep reactor cold state by the two shutdown systems minus one rod, in case of fuel handling mistake (one control rod replaced by one fuel assembly).
- To reach reactor hot state (330°C) by only the complementary emergency shutdown system.

➤ *Figure 244* shows the relationship between the categories described in the previous section and the safety targets.

9.3 Analysis Methods

These rules and methods depend on the conditions considered among the design basis operating conditions, the design extension conditions, and the residual risk situations.

9.3.1 Rules for the Different Conditions

For the **normal operating conditions (Category 1)**, the definition and the studies of these conditions are aimed to specify the variation range of the main physical parameters featuring the reactor operation. These parameters deal mainly with the protection of the physical barriers and also permit to check the integrity of the barriers (measurement of radio contamination, tightness of barriers. . .). These conditions include the different states of the reactors and the definition of the transients permitting to switch from one state to the other. The definition of these conditions is a starting point for the elaboration of the operating procedures (instrumentation and control system and human actions) and for the sizing of the threshold triggering the limitation actions permitting to maintain the reactor in normal operation. Moreover, the transient studies in normal operating conditions permit to assess the performance of the reactor and the sizing of the components regarding cyclic loadings. Finally, the systematic investigation of normal operating conditions permits to identify the enveloping situations to retain as an initial state to combine with an IE for the building of the operating situations. Considering each IE, the most unfavorable state must be retained.

For the **incidental and accidental operating conditions (Categories 2–4)**, the study of those conditions or, more precisely, of their representative enveloping situations is aimed to size the systems permitting their control and to avoid that they lead to nonacceptable consequences toward the facility and the surrounding. The acceptability criteria of the consequences deal with general safety objectives and more practically, they deal with the decoupling criteria. Actually, these criteria permit to uncouple and to perform separately the thermalhydraulic and neutronic transient calculations from the release calculations. Decoupling criteria will be elaborated for each category of operating situations. They deal generally with maximal admissible loadings (thermal, mechanical, power density) of the fuel and of the two first safety barriers. These criteria are defined to bring out a margin up to the physical resistance of the fuel and of the barriers or at least (for the highest category) to limited damages.

Once the various situations have been defined, the transient calculations of the sequences corresponding to the operating situations will be performed considering conservative assumptions that are supposed to lead to appropriate design margins. The deterministic approach relies on the pertinent selection of the conservative assumptions in order to cover the various uncertainties and the possible lack of exhaustivity of the analysis. Prior to applying the penalizing value on the key physical parameters in the calculation, those parameters are supposed to be identified properly. Moreover, an aggravating failure will be taken into account in the studies of the operating situations. Finally, the end of the incidental and accidental sequences investigated must correspond to a safe final state, which is either a controlled state or the safe shutdown state.

For the **Design Extension Conditions**, it should be remembered that these conditions include the complex sequences, the limiting events, and the managed severe accidents. The study of these conditions must show that the release target of the fourth category of the design basis situations is reached. These situations are built without respect with the rules applied for the definition of the design basis situations. The study of such situations relies on realistic hypothesis. More precisely,

- The initial state of the reactor is the nominal state.
- All the systems are available except those postulated unavailable due to the accident considered.
- The instrumentation and control system operates correctly.

- The physical calculations are performed with realistic hypothesis (best-estimate calculations plus uncertainties assessment).
- No additional aggravating failure is considered.

However, the uncertainties on physical parameters able to induce “cliff edge” effects will be assessed with a particular attention. The final state of the accident must correspond to a safe state insuring durably the core subcriticality, the decay heat removal, and radiological releases, fulfilling the acceptance criteria.

For the **residual risk situations**, the practical elimination of such situations must be shown according to a case-by-case analysis on the basis of the physical impossibility to obtain the situations considered, taking into account the design and safety provisions including ultimate systems, or by a combination of deterministic and probabilistic arguments.

The adequacy of the redundancy level of the systems fulfilling safety functions and more generally of the robustness of the safety design will be analyzed using when helpful.

- The aggravating failure assumption for the safety analysis of the design basis operating conditions
- The combination of initiating events according to a cause–effect reasoning
- The single failure criterion

Aggravating failure

When performing the study of design basis operating conditions, an aggravating failure on one of the system required to mitigate the IE is combined with this event. This failure must be independent of the IE causing the accident. The aim of this combination is to show that the consequences of the operating conditions remain lower than the limit allowed for the category of the initial initiating event. However, the combination of the initiating event with the aggravating failure may be classified in a higher category, thanks to a probabilistic assessment, the corresponding consequences being allowed to be larger. In order to simplify the approach and the number of combination investigated, the considered aggravating failure must induce the largest adverse effect. When the operating procedures are available, an operator error could be taken as an aggravating failure.

Examples of combination of IEs

Each design basis initiating fault must be analyzed in combination with a loss of station service power (LOSSP) of long or short duration, if it has an adverse effect. Combination with LOSSP is made at the most unfavorable time of the event. The combination of the initiating fault with LOSSP is considered to be a design basis operating condition (category 3 or 4 according to the category of the initiating event and the duration of the LOSSP). And combination of LOSSP with design extension conditions has to be examined on a case-by-case basis.

Earthquakes

Earthquakes are special initiating events because they affect at the same moment all the components of the plant and some systems outside the site, as the grid, for example, and then specific rules are used in practice. For example, for EFR project, the following rules have been proposed. Two kinds of earthquakes are defined in the design basis:

- An operational earthquake is defined in Category 3 mainly for the plant availability: the plant has to restart after such an earthquake.
- A safe shutdown earthquake is defined as an envelop of highly unlikely but most dangerous earthquake and is classified in Category 4.

Due to the possible consequences of the earthquakes (for example, multiple failures for the structures, multiple and simultaneous pin failures), an automatic trip initiated by specific seismic instrumentation is provided. The trip system response time and the absorber rod drop duration are taken into account in the analysis. These failures lead to plant transients, which are analyzed by taking into account all these consequential failures, an aggravating failure. Because the grid is not seismically qualified, these transients are combined with a consequential long-term LOSSP of 192 h.

The combination of earthquakes with initial states of the plant (part load, shutdown states, handling states, partial unavailability) depends on the estimated duration of these normal operating conditions, as for example EFR.

- In Category 3, the operational earthquake is combined with initial states which have a duration higher than 1,000 h per year.
- In Category 4, the operational earthquake is combined with initial states which have a duration higher than 1 h per year, but less than 1,000 h per year;
- In Category 4, the safe shutdown earthquake is combined with initial states which have a duration higher than 10 h per year.

Only for the safe shutdown earthquake, combinations of the failure of seismically qualified components are considered beyond the design, in DEC.

Single Failure Criterion

The single failure criterion (SFC) states that a system performing a safety function is able to fulfil its mission even if a single component of this system fails. It can be noticed that a system directly performing a safety function (reactor shutdown, decay heat removal, and containment) is usually designed according to the SFC (a safety function is indispensable to meet radiological limits imposed for any design basis operating condition). It is proposed as a design criterion for safety systems.

Basically, the single failure considered is different for passive systems (for instance, a leak) and for active systems (for instance, failure of a pump when functioning is required or spurious starting when it has an adverse effect). Regarding electric systems, all kinds of failure have to be considered. When applying SFC, the fulfilment of the mission of a system is not necessarily be obtained by the redundancy of an equipment, but can also be achieved by a functional redundancy. For instance, a DHR loop can operate in forced convection regime and in some situations in natural convection regime.

9.3.2 Line of Protection Analysis

The line of protection (LOP) method derived from the line of defense method is officially used since the RNR-1500 project has the advantage to gather the main components of the deterministic safety approach and to translate them into a single analysis method applicable for safety conceptual design as well as for safety assessments and analyses. The deterministic-based LOP method is semiquantitative, incorporating probabilistic notions. Any safety provision is conventionally agreed.

- Either as a strong line (“a”), when considering a material or system safety graded and, therefore, complying with the criteria of conception (e.g., “single failure” criterion), design (e.g., margins), fabrication (e.g., modes), surveillance, maintenance. . . ; in particular high

quality active system with internal redundancy (typical example: each shutdown system), high quality passive component or inherent behavior that allows long delays for fault rectifications could be considered as a strong line;

- Or as a medium line (“**b**”), when considering a material reliable but not safety graded or a human provision (e.g., in- or off-site procedure).

A conventional rate of reliability is assigned to each type of line of protection, based on experience (expert advice): one strong line (**a**-type) has an expected failure rate of about 10^{-3} to 10^{-4} per demand, and one medium line (**b**-type) has an expected failure rate of about 10^{-1} to 10^{-2} per demand. The respective reliabilities of successive lines of protection, implemented against a given risk, can be cumulated provided these lines are independent (common mode failures not possible). As a global objective, total loss of each main safety function must be equivalent to failures of at least two strong plus one medium lines: $2\mathbf{a}+\mathbf{b}$ (i.e., $< 10^{-7}$ /year/function). Then, from application of the LOP method, it is possible to check and justify the classification of the operating conditions and events and to classify any combination of several events, as shown in **Table 41**. The reliability of different LOP will depend on the redundancy (that provides protection against single failures), the diversity (that provides protection against common mode failures), and the independence (that provides protection against potential failure of common support systems, such as power supply).

■ **Table 41**


Theoretical relationship between LOP and operating conditions

Category of resulting event sequence	Category of initiating event or event sequence			
	2	3	4	DEC
3	b			
4	a	b		
DEC	2a	a + b	a	
Residual Risk	2a + b	2a	a + b	b

■ **Table 42**

Rule for analysis of LOP failure combined with operating situations


Initiating event	Failure of line of protection	Limits to be respected
Category 2	b	Category 3
Category 2	a	Category 4
Category 2	2a	Prevention of severe accident (DEC)
Category 3	a or b	Category 4
Category 3	a + b	Prevention of severe accident (DEC)
Category 4	a	Prevention of severe accident (DEC)


Additional LOP can be provided to minimize risk, but this should be considered based on the ALARP principle. Moreover, according to the categorization of operating conditions, combination of operating conditions with LOP failure can be analyzed following the requirements presented in the  [Table 42](#).

9.3.3 Method for Safety Classification of Reactor Components

The purpose of ranking safety functions into safety classes is to provide a basis upon which it is possible to establish adequate design and construction requirements for components performing the safety functions. Classification of the safety functions is based on the consequences of the safety function failure and the probability that the safety function would be required. The consequences are ranked by comparing with the release targets, and the probabilities are ranked by comparing the frequencies of the events requiring the safety function with the event classification used in the safety analysis.

Using these basic criteria, the method for classification of the safety functions should be in accordance with the rules defined in the selected design code. The methodology developed for the EFR project is not plant specific and could be used with simple adaptation for any plant provided it is designed using the standard European design code. On this basis, the consequences of the failure of the function are compared with the dose limits for the normal and category 2 operating conditions. If the releases are lower, the function is not safety classified, and the limiting release targets. If the consequences are higher, the function is fundamental for the protection of the public and the environment, and if the consequences are lower, the function allows minimizing the consequences.

The probability that the safety function would be required is compared with the expected occurrence frequency of the frequent events (normal and category 2 initiating faults), the infrequent events (category 3 and 4 initiating faults), the frequency of incredible events (design extension conditions). Thus, combining these comparison criteria, three safety classes can be defined as indicated in  [Table 43](#).

Components and parts of components are classified in design and construction classes in accordance with the safety functions they perform. The correspondence between the safety functions and the design and construction classes for the components is based on the class of the safety function performed by the component, and the reliability of the component to perform the safety function when required. The reliability is assessed taking into account the redundancy and the diversity with other components performing the same safety function in the same conditions, the degree of passivity of the component, and the delay before reaching unacceptable consequences after the failure of the component when required, and possibilities for corrective measures during this delay. Assuming the utilization of the European design and construction code (RCC-MR 2007), used for EFR, the correspondence between the safety functions and the design and construction classes of the mechanical components is indicated in  [Table 44](#). For electrical components, ranked as active components, the classical European codes generally consider two safety classes. The classification uses the same principle.

Additional requirements have to be considered. In order to exclude beyond the category 4 a double-ended pipe rupture, the leak-before-break approach (LBB) can be used. For this purpose, the concerned pipes and vessels have to be safety class 2 at least, independently of the safety function they perform. Concerning the earthquake, specific requirements are related to the

■ **Table 43**

Example of classification of safety functions

Safety functions	Classification
Function indispensable to meet the limiting releases in normal operating conditions or during a category 2 operating condition.	1
Function indispensable to meet the limiting releases during a category 3 or 4 operating condition.	2
Function indispensable to meet the limiting releases during a design extension condition.	3
Function allowing to meet the doses limits for normal and category 2 operating conditions.	3
Function allowing to meet the dose limits of category 2 during a category 3 or 4 operating condition (minimization).	3
Function not necessary to meet the dose limits for normal and category 2 operating conditions.	Not safety classified

components if they have to ensure their safety function during or after earthquake. Generally, components performing safety class 1 and 2 functions are seismically qualified. Components performing safety class 3 functions or non-safety functions may be seismically qualified if their failure during the earthquake leads to the failure of safety class 1 or 2 components.

9.3.4 Probabilistic Safety Assessment

The use of PSA for safety analysis and in support to design (see [Fig. 245](#)) is recognized under the framework of the risk-informed methodology. Several applications take profit of their use, as the checking of safety criteria associated to the core damage frequency or the plant damage states the definition of the design basis events and the critical SSCs (“systems, structures, and components”), and the maintenance in order to optimize the availability, and the choice among several options or among several optimizations of the architecture. . . (Bertrand and Devictor 2006; GenIV GIF; IAEA 2007; Kotake et al. 1993; Rasmussen 1975).

9.4 Illustration of SFRs Behavior in Typical Transient Situations

Reactor behavior depends on the characteristics of the core (sodium void, reactivity feedback coefficients. . .) and its inherent characteristics, for example, the quantities of sodium, the ratio of sodium quantities between the cold plenum and the hot plenum, the primary pump power supply. . . The behavior of a sodium fast cooled reactor under representative conditions is described in this chapter. The values given in the following figures are approximated results in support to the intention of the chapter, but are not related to an existing reactor. These examples have been obtained with an oxide core. The protection system of the reactor would be actuated

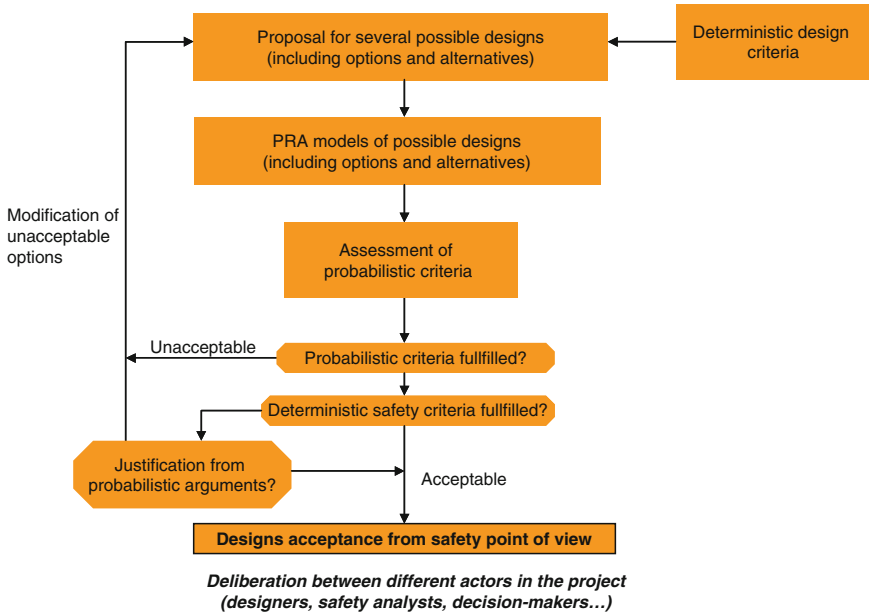
■ Table 44

Example of mechanical component classification

Classification of the function performed by the mechanical component	Characteristics of the mechanical component	Mechanical RCC-MR design and construction class
1 or 2	Active component needed before corrective measures can be implemented	1
1 or 2	Active component only needed after a delay which allows corrective measures to be implemented	2
1	Passive mechanical component with no redundancy provided	1
1	Passive mechanical component with redundancy provided	2
2	Passive mechanical component	2
3	Mechanical component	3

from protection or safety signals. A noncomprehensive list of continuously monitored signals is given thereafter: the individual subassembly outlet temperature, the core outlet temperature, the core inlet temperature, the neutron power/core flow ratio, the absolute and relative neutron flux, the delayed neutrons fraction, the primary and secondary pump speeds, the feed flows, the steam generator outlet temperature, the steam generator leak... ➤ [Table 45](#) explains their use related to some possible events.

One of the objectives of thermalhydraulic studies is to foresee the thermal loads on the internal structures during different reactor operating conditions. To obtain these thermal loads, the detailed thermalhydraulic behavior of the reactor block should be known. The different results of thermalhydraulic studies are mainly the knowledge of velocity and temperature fields in the vicinity of the reactor block structure and around the core for nominal and partial-load steady state or transient operating conditions, heat and mass transfer in the cover gas, gas entrainment at the free surface, thermal striping. A general remark is that the various thermalhydraulic problems which occur in the primary circuit are connected. Thus their analyses require the use of system codes, as for example CATHARE (Farvacque et al. 2003) or RELAP (INEEL 2001), coupled with representative mock-ups; CATHARE v2 has been used for the examples in the ➤ [Sects. 9.4](#) and ➤ [9.5](#).



■ Figure 245

Example of a risk-informed methodology for design

For the analysis of the hot plenum, representative transients are emergency shutdowns or rapid shutdowns. During these transient conditions, the sodium temperature at the core outlet falls rapidly (► Fig. 246). Moreover, depending on operating choices, the primary flow rate can also vary. When these transients occur, two problems must be examined: the evaluation of the thermal shock on the structure (the above core structure in particular) induced by the rapid change in core outlet temperature, and the evaluation of the flow changes generated by the influence of buoyancy forces (core ΔT , minimal flow rate); depending on the operating conditions, which can, in fact, produce considerable flow changes in the hot plenum, and can even lead to the formation of a stratified hot layer above the inlet windows of the intermediate exchangers.

For the cold plenum, thermalhydraulics studies are used to study the thermal stresses in the structures (in particular the main vessel and the internal vessel), and the hydraulic supply to the primary pumps to be ensured. Transients of interest are, for example, asymmetrical transients with a secondary circuit out of operation, the variation of the primary flow, according to operating options. ► Figure 247 describes an example of a drying up of a steam generator. It implies a large hot shock in the diagrid, and a convergence of the inlet and outlet temperature of the intermediate heat exchanger (IHX). The questions to be risen are to know the effect of the temperature difference at the intermediate heat exchanger outlets in the vicinity of the structures (main vessel and internal vessel), both in terms of mean temperature and fluctuations, and the influence on the cold plenum thermalhydraulics of the difference of temperature between the hot plenum and the cold plenum that will induce a thermal flux through the internal structures.

Other interesting transients representative of the inherent behavior of a plant are transients of natural convection, as for example protected loss of station service power (PLOSSP). ► Figure 248 shows the evolution of the core inlet and core outlet temperatures during this

Table 45
Detection of some design basis initiating events

Parameters	Shutdown system	Plant protection system	Clad failure	Withdrawal of one CSD rod	Coastdown of all primary pumps	Coastdown of all secondary pumps	Decrease of water flow	LOSSP	LIPOSO failure	Subassembly fault
DND	1+2		1+2							3
Individual subassembly outlet temperature	2									1
Core outlet temperature	2				3	3	3	3	2	
Subassembly outlet temperature around CSD	2			1						
Core outlet temperature	1					2	2			
Neutron power/core flow ratio	1				2	2				
Neutronic monitoring	1			2						
Neutronic power/secondary pump speed ratio		PP				1		1		
Secondary pump speed/primary pump speed ratio		PP			1					
Feed flow/secondary pump speed ratio		PP					1			
Primary pump speed difference		PP			1					
Acoustic boiling noise detection		PP	3							2

1: 1st parameter, 2: 2nd parameter, 3: 3rd parameter.

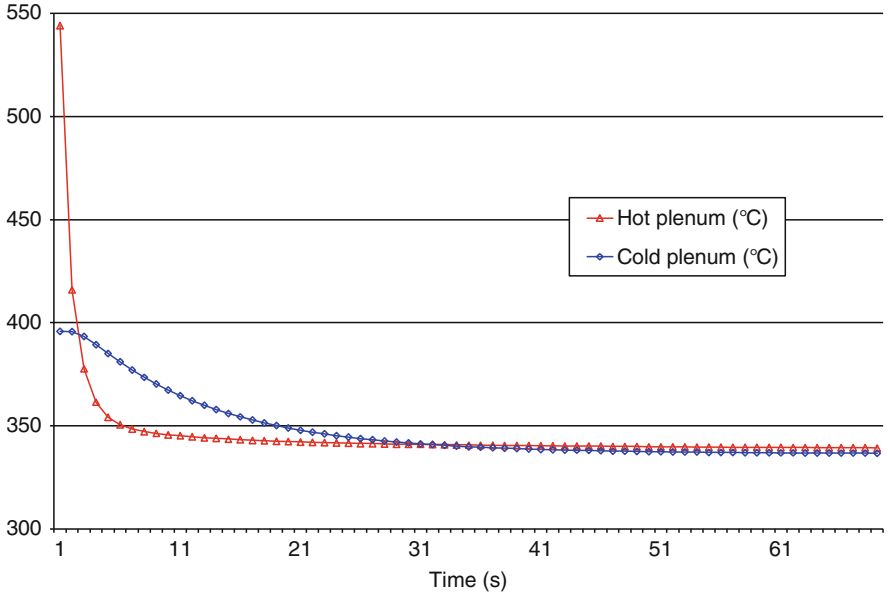


Figure 246
Evolution of the temperatures in the cold plenum and the hot plenum

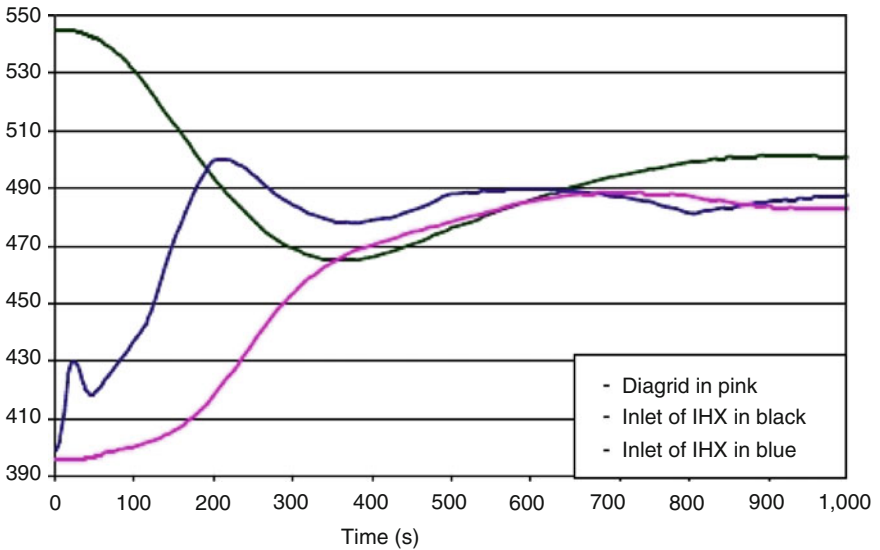
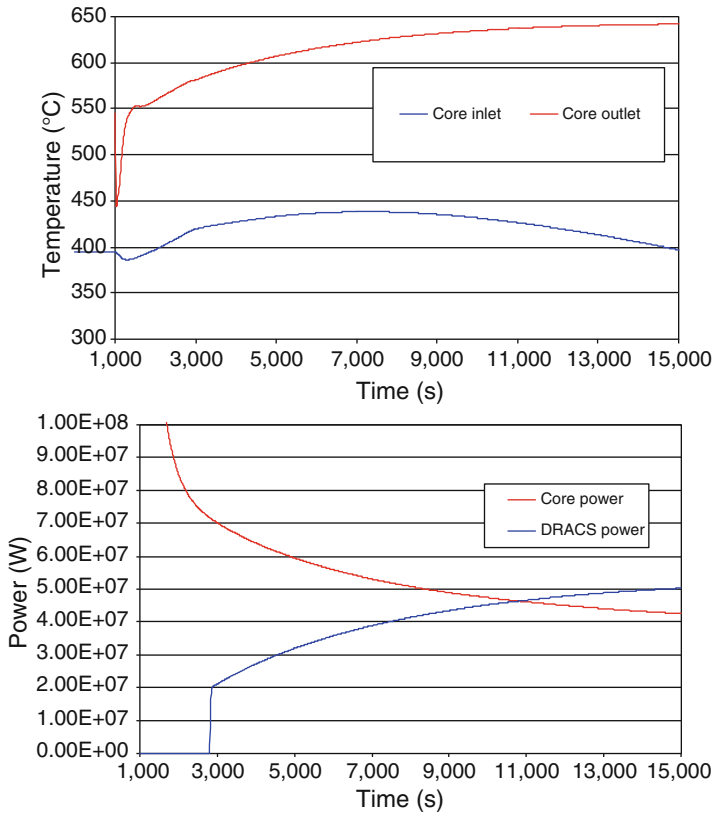


Figure 247
Evolution of the temperatures in the diagrid and in the IHX as a function of the time (s)



■ Figure 248

Evolution of the core inlet and core outlet temperatures and of the powers

transient. At 1,000s, primary and secondary pumps are fully turned off on their inertia. Shutdown system is actuated. One DRACS, which is able to remove 100% of the residual power, starts within a delay of 30 min after the triggering of the pumps. The IHX and the DRACS have been designed to fulfil a constraint on the maximal temperature in the pool ($700\text{ }^{\circ}\text{C}$); we can observe that after the starting of the DRACS the temperatures reach a maximum value below $700\text{ }^{\circ}\text{C}$ and thus decrease.

9.5 Anticipated Transients Without SCRAM

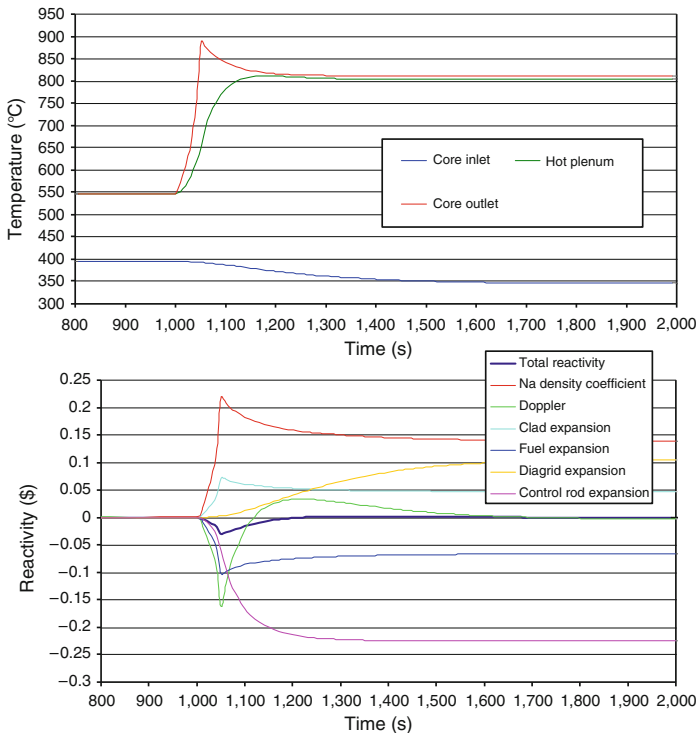
Three anticipated transients without SCRAM (ATWS) are studied in order to contribute to the assessment of the robustness of a reactor:

- Loss of coolant flow without scram, also known as untripped loss of flow (ULOF), due to a loss of power to the coolant pumps, causing a flow coastdown and a large mismatch in core power and coolant flow (P/F ratio).

- Loss of main heat sink without scram (ULOHS), characterized by the loss of the ability to reject heat at the steam generator, such as sudden loss of generator load, increasing core inlet temperature.
- Uncontrolled fast transient of overpower due, for example, to a gas passage in the core (fast transient) or to an uncontrolled withdrawal of a reactor control rod, causing a slow transient overpower condition (UTOP).

The values given in the following figures are approximated results in support of the illustrative objective of the chapter, but are not related to an existing reactor. These examples have been obtained with an oxide core.

The **untripped loss of flow (ULOF)** accident is a challenging accident if only a passively safe response is expected, due to the severity of the conditions. The accident is initiated from nominal full power steady state conditions, and at the start of the accident, all power is lost to the coolant pumps, and the scram failed. The result of this accident is a coastdown of the forced flow through the reactor, governed by the stored inertia in the pumps (typical flow-halving time of about 10 s as for EFR project or 30 s for SuperPhenix). However, since the reactor is still operating at full power, this results in a rapid heating of the coolant. Depending on the timing and magnitude of the reactivity feedback, the reduction in power could be sufficient to prevent excessive temperatures and a coolant boiling. ➤ [Figure 249](#) describes the typical behavior of the



■ **Figure 249**
Example of an ULOF

temperatures in the hot plenum and the core inlet and outlet temperatures, and the influences of the different reactivity feedback; in this example primary pump power supply is actuated at a 28% of nominal flow. The Doppler is the first reactivity feedback opposing the effect of the decrease of the sodium coolant density. After a few minutes, this Doppler reactivity feedback is positive because of the power decrease, and the reactivity feedback due to the fuel, the structures, and the control rods expansion counterbalance the sodium void and the other positive reactivity feedback. Consequently the occurrence of a coolant boiling depends on the design choice for the architecture (for example, via the inertia of the pumps. . .) and the core reactivity feedback coefficients.

The occurrence of an **untripped loss of heat sink (ULOHS)** implies a rise of the core inlet temperature that yields a negative reactivity feedback. The main challenge is to avoid high temperature for the structures over the authorized time period, in order to avoid too important thermomechanical damages.

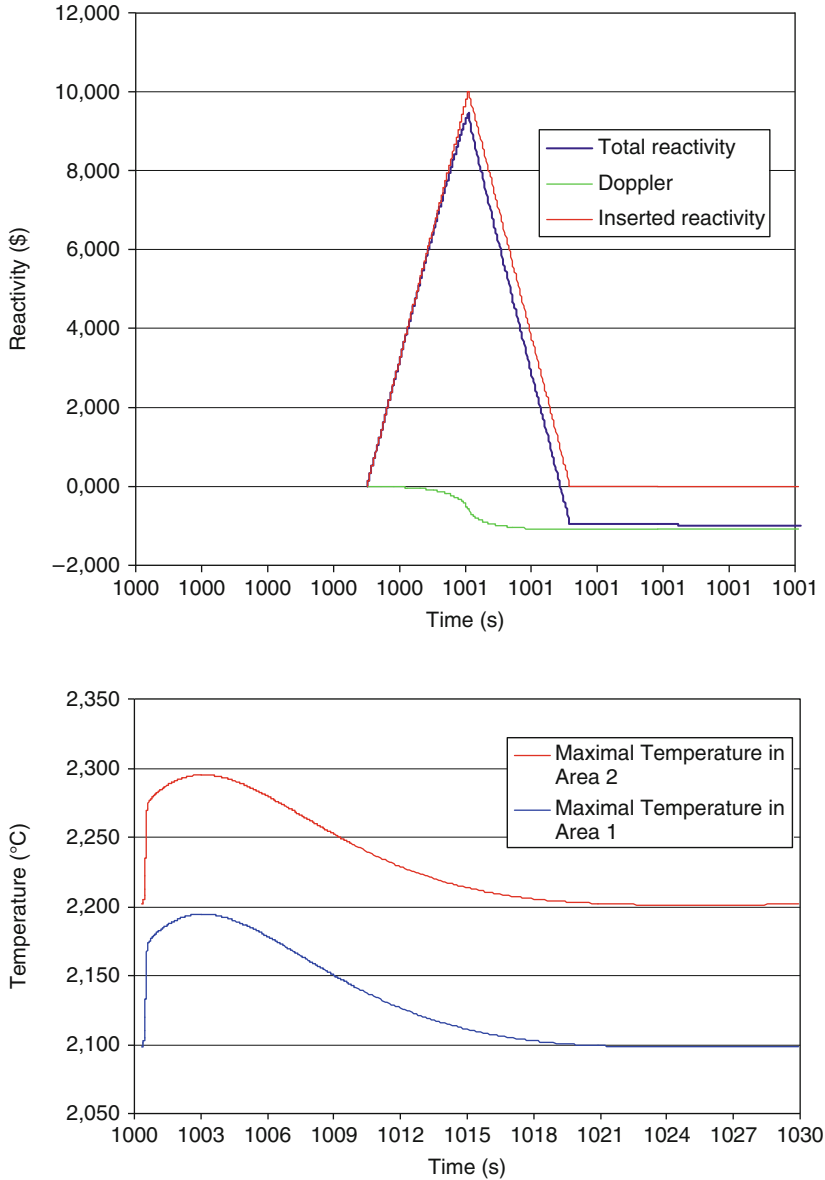
An **untripped transient of overpower (UTOP)** is a transient of a reactivity insertion, leading to power increase. For fast UTOP only the Doppler feedback could be efficient to counterbalance this insertion. ➤ *Figure 250* shows the consequence of a gas bubble leading to an insertion of 1\$ in 0.15 s then a back to normal into 0.15 s on the maximal temperatures in two areas of the studied core and the variation of the different components of the reactivity.

10 Severe Accidents

10.1 Introduction

In the water reactor, the core is in its most reactive configuration and hence, any phenomenon that results in disintegration of core makes the reactor, generally, to shutdown automatically. This is not the case with SFR. The disintegration of core in SFR (fuel slumping, for example) may lead to power excursion, resulting in an accident. The core has high density of power, which can have a positive voiding effect. The physicochemical characteristics of sodium pose sodium–water reaction and chemical toxicity challenges. There is a need for development of specific and innovative technologies for in-service inspection of the structures under sodium due to opaqueness of sodium. Repairing circuits and components in postaccidental situation call for sophisticated and specific technologies. The SFR components, i.e., large size thin walled shell structures, are also sensitive to earthquake loadings. The requirement of high breeding ratio, burning of minor actinides in suitable matrices and enhanced safety with improved economy needs advanced materials and technologies which call for extensive experimental, modeling and simulation technologies. High burnup targeted for the future reactors and near complete burning of minor actinides and long lived fission products introduce higher levels of radioactivity during fuel handling and fuel reprocessing.

Fast reactors are designed to be stable, and experiences accumulated so far have demonstrated the attainability of such behavior. Though the potential for radiation release to the atmosphere exists, there are numerous inherent and engineered safety features to inhibit such release. Robust design philosophy is commonly applied for the core and coolant circuits by way of choosing high quality materials, adopting matured design, construction and inspection



■ **Figure 250**
Example for a fast UTOP

standards, guides and methodologies, with the ultimate objective of minimizing/eliminating the initiators, which lead to partial and whole core accident. Design provisions, such as diversity in shutdown and decay heat removal systems are introduced to meet the safety limits with adequate margins for the design basis events, so as to prevent beyond design basis

accidents. Advanced design features such as recriticality in molten core, effective core catcher, and containment are introduced for the management of beyond design basis accidents.

In order to demonstrate the safety, analysis is performed by postulating various scenarios of high probability to very low probability. The events that result in the highest damage are commonly labeled beyond design basis accident (BDBA). Beyond the DBA, there lies a domain of accident consequences which are less probable and in order for such accident to take place, at least two or more low probability failures must take place in sequence, e.g., a large reactivity insertion event coupled with complete failure of the plant protection system. Those BDBA which involve degradation/melting of whole core is termed as core disruptive accident (CDA) or severe accidents.

In this chapter, the history of CDA, various phases of accident scenarios, mechanical and thermal consequences and post accident heat removal conditions, and computer codes used for the safety studies are described. Finally, various international computer codes used for the CDA analysis are highlighted.

10.2 History

From early days (1950s), the perspective on severe accident in SFR has been influenced greatly by the fact that core compaction in SFR results in increase of reactivity, in contrast to thermal reactor systems. Also, the low value of delayed neutron fraction and prompt neutron lifetime, raises concerns that a core melt down may rapidly lead to a prompt critical condition and that the power rises beyond that point could be extremely rapid. A mismatch between heat generation and heat removal in the core can lead to fuel melting and ultimately to a CDA, if the reactor shutdown system fails on demand. Although fuel vaporization, an inherent shutdown mechanism, would ultimately limit the energy generated by physically moving the core apart, the concern has been visualized that potential work energy released might be larger than practically containable (Walter and Reynold 1981). Initial analysis led to conservative and very high values of energy release in CDA, like the one proposed by Bethe and Tait, which assumes a gravity-driven collapse of the core and a hydrodynamic core disassembly. It also assumed no Doppler feedback and no delayed neutrons. During early 1960s, the safety analyses of EBR-II were performed considering reactivity feed backs and simplified but conservative core slumping models after onset of fuel melting (Graham 1971). During 1970s and 1980s, with experimental knowledge from primarily TREAT, ACRR, CABRI, and SCARABEE test reactors used for validation, safety analysis codes SAS3D and SIMMER-II were integrated for CDA analysis in 2-D. It was shown that the energy production in the initiating phase decreased drastically (Nonaka and Sato 1992). In 1990s with more experiments, the understanding of the phenomenon improved considerably and validation of SAS4A and SIMMER-III led to further reduction of energy release values (Tobita et al. 1999). During 2000s, the analysis capabilities have further improved with the development of SIMMER-IV for 3-D modeling (Yamano et al. 2008). In [Fig. 251](#) and [Table 46](#), the trend of energy release predictions from examples of various reactors is depicted, which reflects the reducing value of the ratio of CDA energy release (MJ) to reactor power (MWt). Even, near zero energy release has been computed in CDA as indicated for EFR with in-pin fuel motion with intact clad. Thermal energy release and its consequences are being studied in depth internationally.

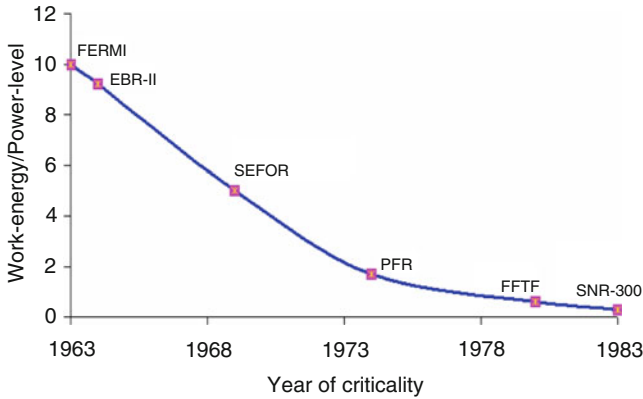


Figure 251

Trend of mechanical energy release in various reactors

Table 46

CDA energy release for reactors

Reactor	Power – P (MWt)	Mechanical energy – W (MJ)	Ratio – W/P
SPX1	3,000	800	0.270
SPX2	3,500	110	0.030
BN 800	2,100	50	0.024
DFBR	1,600	50	0.031
EFR	3,600	150	0.040
PFBR	1,250	100	0.080

10.2.1 Instances of Severe Accidents in Fast Reactors

Core melt down accidents have occurred in EBR-I and Enrico Fermi Fast Breeder Reactor. These accidents were severe accidents, though there was no whole core disruption subsequent to core melt down.

EBR-I reactor was metal fuelled (highly enriched uranium), NaK cooled low power (1 MWt) reactor. A core melt down accident occurred in EBR-I in November 1955 (Thomson and Beekery 1964). Tests were being run involving reactivity ramps at low flows. As the power neared the safety limit, a slow shutdown was initiated by mistake, instead of a scram. Temperatures at the center of the core exceeded the NaK coolant boiling point. Then the fuel also melted. The boiling NaK forced molten fuel material outward, both above and below the core. The channels were then blocked by freezing of the core material that formed a cup into which further fuel material fell. Fission products were released as gas bubbles, forming a porous fuel mass when the fuel froze. Forty to fifty percent of the fuel of the core melted before shutdown occurred. The EBR-I had a small core 20 cm in diameter. The consequences of this event are perhaps not representative of a CDA that would occur in a large core. Nevertheless, the quick progression

of the accident (less than few seconds) gave strong indication that such accidents, even when they occur in large cores, will happen within a short duration.

Enrico Fermi reactor was a 200 MWt/65 MWe, U metal fuelled, SFR. The reactor became critical in 1963. A core melt down accident occurred in October 5, 1966 (Anderson 1978). There was earlier history of unexplained subassembly outlet temperature rise ($>30^{\circ}\text{F}$) over the earlier 3 months. This was observed even after relocating the subassemblies. On the day of the incident, the absorber rods had to be withdrawn to higher level than previous values at 30 MWt. The operator got alerted and suspected unaccounted negative reactivity. The radiation detectors in containment building gave alarm from radioactivity of the cover gas and containment was isolated. Subsequently, the reactor was manually shut down by which time gamma monitors in fuel building also gave alarm. It was understood that heating and voiding of the four subassemblies due to reduced coolant flow was the source of negative reactivity, which resulted in the higher absorber rod level. Trip on rate of power reduction had been introduced earlier (6 MWt/s) against sudden insertion of negative reactivity. It was diagnosed that partial flow blockage had been caused by segments of zirconium plates relocated from above the core. Earlier noted higher subassembly outlet temperatures were due to this partial blockage. The accident caused by flow reduction of about 97%, resulted in melting in 2 subassemblies.

10.3 Defense in Depth

Application of the concept of defense in depth (INSAG-10 1996) throughout design and operation provides a graded protection against a wide variety of transients, anticipated operational occurrences and accidents, including those resulting from equipment failure or human action within the plant, and events that originate outside the plant. The following five levels of defense (inherent features, equipment, and procedures), aimed at preventing accidents and ensuring appropriate protection in the event that prevention fails, have been listed in IAEA safety standard (IAEA 2000).

Level-1

The aim of the first level of defense is to prevent deviations from normal operation, and to prevent system failures. This leads to the requirement that the plant be designed with sufficient safety margins, comprehensively addressing the possible failure modes and operating experiences, constructed and operated in accordance with high quality levels and engineering practices, such as the application of redundancy, independence, and diversity. To meet this objective, careful attention is paid to the selection of appropriate design codes and materials, and to the control of fabrication of components and of plant construction. Design options that can contribute to reducing the potential for internal hazards, e.g., controlling the response to a postulated initiating event (PIE), to reducing the consequences of a given PIE, or to reducing the likely release source term following an accident sequence, contribute at this level of defense. Attention is also paid to the robust procedures involved in the in-service inspection and maintenance. This whole process is supported by a detailed analysis, testing, validations, and peer reviews.

Level-2

The aim of the second level of defense is to detect and intercept deviations from normal operational states in order to prevent anticipated operational occurrences from escalating to accident conditions. This is in recognition of the fact that some PIEs, such as power failure and pump trips, are likely to occur over the service lifetime of a nuclear power plant, despite the care taken

to prevent them. This level necessitates the provision of specific systems as determined in the safety analysis and the definition of operating procedures to prevent or minimize damage from such PIEs.

Level-3

For the third level of defense, it is assumed that, although very unlikely, the escalation of certain anticipated operational occurrences or PIEs may not be arrested by a preceding level and a more serious event may develop. These unlikely events are anticipated in the design basis for the plant, and inherent safety features, fail-safe design, additional equipment, and procedures are provided to control their consequences and to achieve stable and acceptable plant states following such events. This leads to the requirement that engineered safety features be provided that are capable of leading the plant first to a controlled state, and subsequently to a safe shutdown state, and maintaining at least one barrier for the confinement of radioactive material.

Level-4

The aim of the fourth level of defense is to address severe accidents in which the design basis may be exceeded and to ensure that radioactive releases are kept as low as practicable. The most important objective of this level is the protection of the confinement function. This may be achieved by complementary measures and procedures to prevent accident progression, and by mitigation of the consequences of selected severe accidents, in addition to accident management procedures. The protection provided by the confinement may be demonstrated using best-estimate methods.

Level-5

The fifth and final level of defense is aimed at mitigation of the radiological consequences of potential releases of radioactive materials that may result from accident conditions. This requires the provision of an adequately equipped emergency control center, and plans for the on-site and off-site emergency response.

10.3.1 Physical Barriers

A relevant aspect of the implementation of defense in depth is the provision of a series of physical barriers to confine the radioactive material at specified locations. Three barriers exist within a reactor to physically prevent the release of fission products to the outside environment. These include (1) the fuel matrix itself, (2) the fuel pin cladding, and (3) the primary coolant system. A fourth barrier, the outer containment, represents an engineered safeguard.

The fuel matrix, normally a ceramic material, has considerable capability for retaining solid fission products, as well as gaseous fission products in the unrestrained region. Fission gas, which is released during irradiation, is normally contained in a fission gas plenum, in order to prevent contamination of coolant. However, reactors are designed to operate with a small fraction of failed fuel. All large reactors have a radioactive waste removal system built in as part of the cover gas system, and small amounts of radioactive debris in the primary sodium can be removed in a routine manner using cold traps.

To provide framework for establishing a defense-in-approach, it is necessary to recognize the relationship between the anticipated frequencies of occurrence for various accidents versus the accident severity levels, which could be accepted for each event. Such a relationship should

certainly indicate little or no damage to the reactor system for high frequency events, whereas relatively higher levels of damage could be tolerated for lower frequency events. Appropriate engineering features, such as an effective plant protection system (PPS) should be available to ensure such a characteristic.

10.4 CDA: Phenomenology

A mismatch between heat generation and heat removal in the core can occur if either heat generated is more than heat removal, or heat removal is less than heat generated. The former situation will arise if there is uncontrolled reactivity addition in the core, and corresponding power increase. The later situation will arise if there is coolant flow starvation and reduced heat removal. With an accompanying shutdown system failure, the former situation can lead to a unprotected transient overpower accident (UTOPA) and the later situation to a unprotected loss of flow accident (ULOFA). Apart from this, if there is failure in decay heat removal in shutdown reactor, it can potentially lead to protected loss of heat sink accident (PLOHSA) resembling a gradual LOFA. But probability for such an accident is still lower and this is presently considered under the category of residual risk due to the highly reliable and passive decay heat removal systems. In case of UTOPA, fuel melts initially. This results in in-pin fuel motion (Porten et al. 1981), which can act as a shutdown mechanism. If the positive reactivity excursion continues, the clad failure, Na voiding, and then core collapse are possible. In ULOFA, initially coolant voids were followed by clad failure and then, fuel slumping. Core collapse or slumping can introduce positive reactivity and produce CDA where a lot of thermal energy is released due to the neutronic power excursion. Subsequent core dispersal reduces core reactivity and terminates the highly energetic phase of the accident.

Uncontrolled reactivity addition leading to UTOPA can occur due to (1) uncontrolled withdrawal of control rods, (2) passage of large bubble in core, and (3) collapse of core support structure leading to core compaction. Uncontrolled withdrawal of control rods is a PIE, even though control rods are usually moved for a preplanned distance. If the worth of the rod is high enough or more than one rod is involved, it can lead to high reactivity addition and, consequently, large power increase. Uncontrolled reactivity addition can also occur due to passage of large gas bubble in the core. Passage of such a large gas bubble in the core is very highly unlikely, and the reactivity that can be inserted in present designs (with low coolant void reactivity effect) is low. Small gas bubbles result in very negligible reactivity addition. UTOPA can perhaps occur due to sudden structural failure of core support structure which is again considered as residual risk at present. The core support structure is a safety class 1 component with a box type structure and random failures or stiffeners do not degrade its performance. Structural vibrations caused by seismic excitations can give rise to only reactivity oscillations, which are small in magnitude (less than 0.5\$, which a peak pulse), and further there is damping due to negative reactivity feedbacks and which can be shown to result in only a small increase in reactor power (Srinivasan 2002). Hence, the uncontrolled withdrawal of control rod is the only initiator considered for UTOPA and possible CDA.

The coolant flow starvation can be initiator for ULOFA, caused by failure of primary pump or seizure of primary pump or pipe rupture or total instantaneous blockage in subassembly. The failure of primary pump due to loss of power supply can be an initiator for CDA. The loss of power supply leads to flow coastdown (with flow-halving time of about 8–10 s) and reduced heat removal, leading to mismatch in heat balance. The pipe rupture does not lead to total flow

starvation. Total instantaneous blockage is prevented by having multiple holes for coolant entry in the foot of the subassembly, and an adapter at the top of the subassembly gives an alternate flow path. Pump seizure can lead to a CDA, if it does not recover operation within a few tens of seconds. Thus, the pump seizure or stoppage of primary pump due to loss of power supply is the only main initiator for ULOFA and possible CDA.

10.4.1 Different Phases of a CDA

Analysis of CDA is carried out in a rigorous manner from early stage, starting with the initiating event, through various stages, until the estimation of mechanical energy release, and the response of the main vessel and top shield to the mechanical energy release. Different physical phenomena are dominant at various stages of the accident and also the time scales involved are different. Therefore, the accident progression is analyzed deterministically in different phases using cause and effect phenomenology and adopting a conservative approach where deterministic analysis is not possible. The phases of accident analysis are discussed below.

Pre-disassembly Phase

This phase of analysis deals with the transient response from accident initiation to the point of (1) neutronic shutdown with essentially intact geometry, (2) a gradual core melt down where the computational models needed for tracking the accident further must be significantly modified, or (3) the onset of conditions for hydrodynamic core disassembly due to generation of high internal pressures from vaporized core materials. Calculations are performed deterministically for core neutronics, reactivity feedbacks, thermohydraulics, sodium boiling, fuel pin failure, cladding and fuel slumping, and their relocation and fuel coolant interaction.


Transition Phase

At the end of the pre-disassembly phase, the reactor can become subcritical if there are sufficient negative reactivity feedbacks. Then the accident gets terminated. If the negative reactivity feedbacks are insufficient, the fuel and clad can melt and form a molten pool. This is the called transition phase, since the fuel attains gradual transition from solid to liquid phase, and since this phase is sandwiched between the pre-disassembly and disassembly phase. The core can boil and then cool – subcritical configuration could be established or criticality conditions can recur.

Disassembly Phase

Once the fuel starts dispersing, fuel displacement feedback dominates, time scales are short (of the order of milliseconds) and all other reactivity feedbacks except the Doppler can be ignored. The core loses its integrity. The core neutronics and core hydrodynamics calculations are performed for the dispersing core. This phase lasts till the reactor attains subcriticality due to fuel dispersal.

Mechanical and Thermal Consequences of CDA

The various phases of CDA are illustrated in  Fig. 252. In the pre-disassembly phase, the heat is generated due to power excursion that could melt the core, to the extent of saturated liquid state. Subsequent heating generates vapor phase, which is having high potential to do mechanical

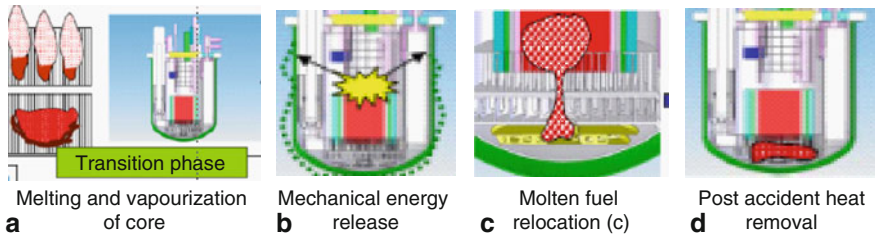


Figure 252
Mechanical and thermalhydraulics consequences of CDA

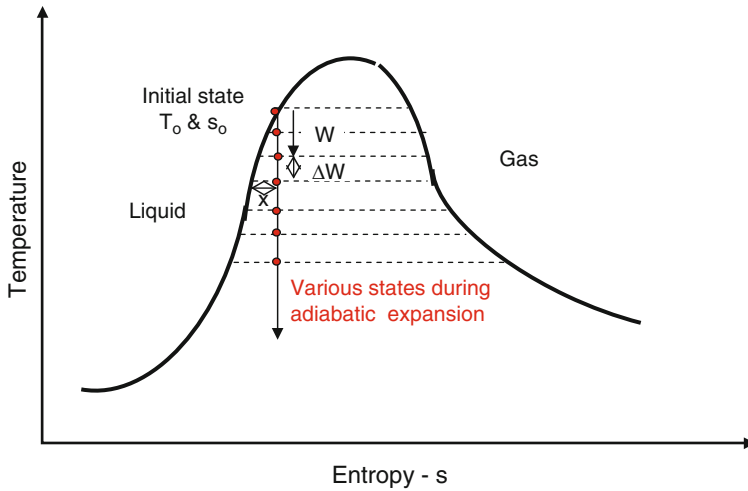
work, in view of its high temperature and high pressure (► Fig. 252a). The mechanical energy release is due to expansion of vapor phase from initial pressure (P_0) which is at saturated condition to the final pressure (P_f) equal to ambient condition prevailing in the reactor. During this rapid expansion of core bubble in the liquid sodium environment which is considered as isentropic, the pressure/shock waves are generated, which deform the shell structures surrounding the core (► Fig. 252b). Subsequent to completion of mechanical work, the vapor phase which is at $\sim 5,000$ K, condenses due to cooling of sodium pool, which is at 855 K and starts moving downward melting the support structures, such as grid plate and core support structure (► Fig. 252c). Finally, the liquid settles on the core catcher and subsequently will be cooled by natural convection (► Fig. 252d).

10.5 Analysis for Mechanical Consequences

10.5.1 Idealization of Molten Core Expansion Behavior

The mechanical consequences are described based on the energy stored in the core at the end of the neutronic event. The mechanical energy release (W) is the expansion work that can be delivered by the molten core while expanding from its initial state (high pressure and high temperature) to the state of ambient pressure (~ 1 bar). The W depends on the equation of state of molten core. The molten core would be in the form of saturated liquid and vaporizes sequentially in the process of expansion. Hence, for the analysis of mechanical consequences, equation of the state of core bubble has to be established first. Since temperatures of core are different at different locations, the integrated effect of the core bubble should be established correctly. For this, the core is divided into number of cells in the reactor physics computation. The average temperatures are extracted at the center of each cell. From the individual cell temperatures (T_i) and cell mass (M_i), the average temperature and mass of homogenized molten core are computed as: $M_o = \sum M_i$ and $T_o = \sum M_i T_i / M_o$. Further, assuming conservatively that the entire homogenized core is at its saturated liquid state, the following steps are adopted to derive the equation of state:

Knowing to, the initial state of saturated liquid is identified in the “T-s” diagram and path of the various states in the course of adiabatic expansion are shown in ► Fig. 253. Then, initial



■ Figure 253

Adiabatic expansion of core bubble

enthalpy h_0 , equal to cpT_0 and entropy s_0 from thermodynamic property tables and pressure P_0 are computed from the following equation of state (Srinivasan 2002):

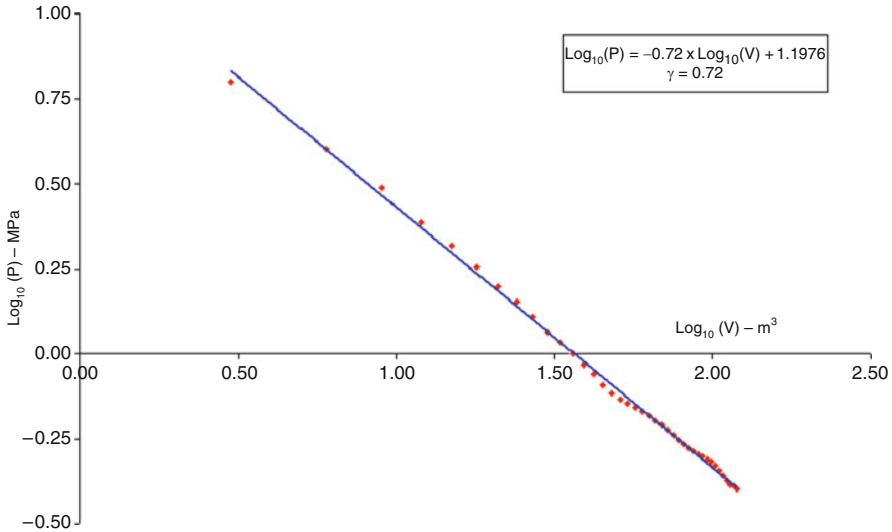
$$P_0 = e^{(A+B/T_0+C \log_e T_0)} \quad (50)$$

where $A = 68.3$; $B = -8.0541 \times 10^4$; $C = -5.641$.

Assuming a small value for V_0 in the first iteration, the starting point (P_0 and V_0) is fixed in the P versus V diagram. Subsequent points are arrived at by adopting the following steps.

- Step-1: Assume a small drop of temperature from T_0 to T
 - Step-2: From T , extract hL and hLg and sL and sLg from thermodynamic data for oxide fuel
 - Step-3: Compute vapor mass fraction: $x = M_v/M_o = (s_0 - sL)/sfg$ for the isentropic expansion
 - Step-4: Compute $h = (1 - x)hL + x hLg$
 - Step-5: Compute $\Delta W = M_o(h_0 - h)$
 - Step-6: Compute $\Delta V = \Delta W/P_0$ (assuming pressure is constant for a small volume change)
 - Step-7: Compute $V = V_0 + \Delta V$
 - Step-8: Thus the next point in P vs. V diagram is arrived at.
- The above 8 steps are repeated sequentially by updating pressure ($P_0 = P$) and volume ($V_0 = V$), till P is equal to ambient pressure P_a of 0.1 MPa.
- Step-9: Plot the $\log P$ versus $\log V$ diagram
 - Step-10: Draw the trend line and the slope of the curve is the exponent " γ " for the equation of state for homogenized core gas bubble: $PV^\gamma = \text{constant}$

Following the above methodology, the equation of state has been derived for a typical 500 MWe SFR as depicted in [Fig. 254](#), wherein the γ value is found to be 0.72, yielding 100 MJ of mechanical energy.



■ Figure 254

Determination of exponent of equation of state: $PV^\gamma = \text{constant}$

10.5.2 Analysis for Vessel and Roof Mechanical Loading

The core bubble containing highly pressured mixture vapor phase can generate pressure/shock waves. An immediate effect of such waves is plastic deformation of surrounding structures, which offers resistance for the propagation of pressure waves. Due to the presence of cover gas space above the sodium free level, there is less resistance for the movements of liquid in the upward direction and hence, a portion of sodium above the bubble is accelerated upward. Hence, a net force develops in the downward direction due to which, the main vessel is pulled down. This in turn produces compressive force on the reactor vault. This force is termed as “pull-down force.” The accelerated sodium continues to move upward for a certain period (50 ms typical) during which, there is no significant mechanical deformations, till sodium impacts on the top shield. Once the sodium impacts on the top shield, which is termed as “sodium slug impact,” the kinetic energy of the moving sodium is converted into pressure energy. Consequently, the pressure in the cover gas as well as in the sodium increases steeply, producing (1) further overall plastic deformation on the main vessel, (2) large local deformation on the main vessel near top shield junction in the form of bulging, and (3) impact force on the top shield in the upward direction. The slug impact phenomenon (from the start of impact till stabilization of vessel deformation) occurs during 100–150 ms (typical).

The two important phases of the accident, where the vault is subjected to forces, are: (1) the reactor vault is pulled down by the main vessel through support shell, due to net unbalanced pressure force acting on the bottom portion, and (2) it is subjected to upward force through top shield due to sodium slug impact. The force acting on the support shell, which in turn transmits to the reactor vault, is the net effect of these two forces. During the slug impact, the bolts of top shield components elongate and the seals in the annular gaps of the top shield may fail; as a result of this, sodium may fill the top shield penetrations. Subsequently, sodium

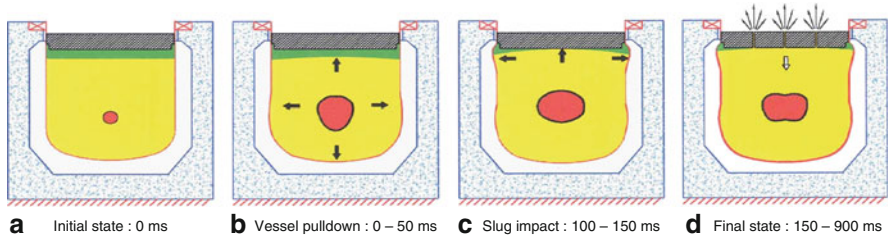


Figure 255

Mechanical consequences of CDA

leaks to reactor RCB. In the quasi-static condition when the sodium leak phenomenon occurs, the core bubble pressure drops. This is mainly due to the cooling of the bubble by the surrounding subcooled sodium, which has high heat capacity, while the volume of the core bubble remains unchanged. The quasi-static condition prevails during 150–900 ms (typical). The leaked sodium will catch fire and cause temperature and pressure rise in the reactor containment building (RCB). The RCB is designed for this pressure. Figure 255 depicts the above mentioned scenarios. Beyond 900 ms, the mechanical consequences are terminated except creep of high-temperature components, which depends upon the heat removal provisions made in the design.

Theoretical Predictions

Analysis is generally carried out using either finite element or finite difference method-based codes. These codes solve a set of governing differential equations of fluid, structure, and fluid–structure interaction dynamics, written in Lagrangian, Eulerian, or Mixed Lagrangian–Eulerian (ALE) coordinate systems. The generic form of equations is as follows:

Mass balance

$$\frac{dM}{dt} = \frac{d}{dt} \int_{V(t)} \rho dV = \oint_{S(t)} \rho \left(\overrightarrow{W} - \vec{V} \right) \cdot \vec{n} dS$$

Energy balance

$$\frac{dE}{dt} = \frac{d}{dt} \int_{V(t)} \rho e dV = \oint_{S(t)} \rho e \left(\overrightarrow{W} - \vec{V} \right) \cdot \vec{n} dS - \oint_{S(t)} p \vec{V} \cdot \vec{n} dS + \int_{V(t)} \rho \vec{g} \cdot \vec{V} dV$$

Momentum balance

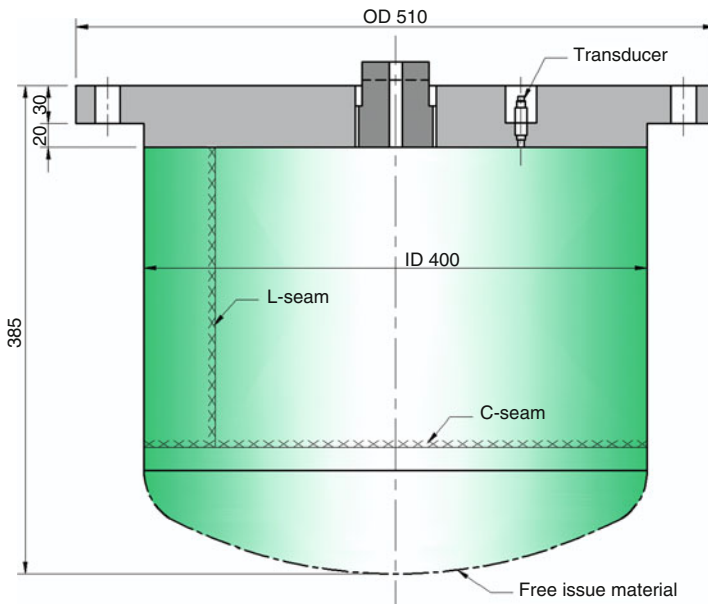
$$\frac{d\vec{Q}}{dt} = \frac{d}{dt} \int_{V(t)} \rho \vec{V} dV = \oint_{S(t)} \rho \vec{V} \left(\overrightarrow{W} - \vec{V} \right) \cdot \vec{n} dS - \int_{V(t)} \text{grad } p dV + \int_{V(t)} \rho \vec{g} dV$$

The complexities modeled in the code are large distortions in fluids, large displacements in structures, interactions of fluids with structures completely immersed as well as partly contact with fluid, treatment of solid–fluid and liquid–gas boundaries, sodium slug impact and shock wave propagation. An efficient numerical solution technique involving explicit algorithm to calculate initial values and subsequent implicit algorithm to get converged values

has to be incorporated to the resulting equations. The computer code should have an efficient automatic rezoning algorithm at the end of every time step. The code needs to be validated. REXCO (Chang and Gvildys 1975), SEURNUK (Cameron et al. 1978), EURDYN (Donea et al. 1980), PISCES (Cowler and Hancock 1979), SIRIUS (Blanchet et al. 1981), FUSTIN (Chellapandi 2000a), ICECO (Wang 1975) and Cassiopee (Graveleau and Louvet 1979) are the international codes developed for this purpose. For illustrating the numerical prediction capability of the computer codes, a few typical results obtained by FUSTIN for assessing the structural integrity assessment of the PFBR components are presented.

Experimental Validation of Computer Codes: Typical Case Study

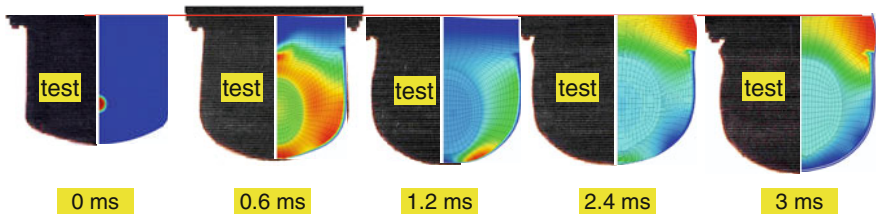
One typical experimental validation relevant to the present problem is presented in this chapter (Chellapandi et al. 2007). The test problem deals with 1/30th scaled down model of PFBR main vessel with rigid top cover, subjected to low density explosive (LDE). The vessel is filled with water leaving an empty space at the bottom. The dimensional details are shown in ► Fig. 256. The LDE is produced from the basic chemical called PTN precipitated in foam to bring down the density from ~ 0.8 to ~ 0.14 g/cc (the targeted value) and placed at the center. Three tests were carried out to ensure the repeatability. The work potential and equation of the state of the LDE charge are established simultaneously from the tests on simple cylindrical shell with rigid top and bottom covers, completely filled with water. Post processing of the test data yields values for work potential of 2.3 kJ/g and equation of state: $P = P_0 (V_0/V)^{0.75}$ (MPa), where $P_0 = 40$ MPa and $V_0 =$ parameter (m^3). The mass of charge denoted for the tests is 2.2 kg which



■ Figure 256
Geometrical details of test vessel

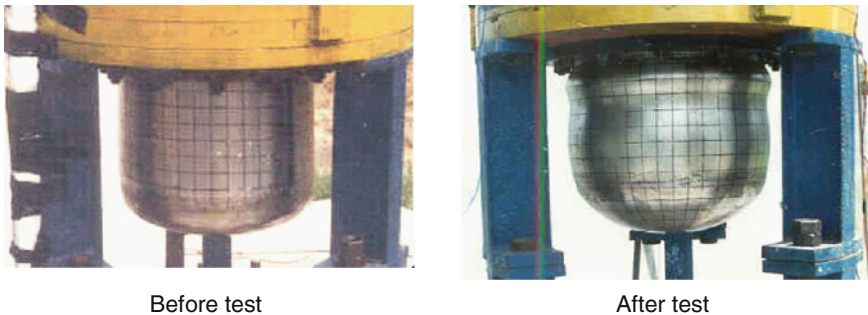
yields mechanical energy release of about 5 kJ. The evolution of vessel deformations is captured by high speed photography. ▶ *Figure 257* shows a few frames that depict the vessel deformation scenario in which the numerical prediction is the same as predicted by FUSTIN code. The transient pressure distribution in the water during the process of loading is also superimposed in ▶ *Fig. 257* to understand the sequence of loading. The vessel is highly strained in two phases. During the first phase, which lasts about 1 ms, the bottom portion of the vessel undergoes radial bulging and downward motion, and the top portion is subjected to high axial tensile stress. This is due to the impact of direct pressure waves on the bottom portion of the vessel. It is worth noticing that the top portion shrinks slightly, while the bottom portion moves down due to Poisson's effect. During the subsequent phase (1–2.5 ms) the upper portion of the vessel undergoes local radial bulging due to water slug impact on the top cover and subsequent local pressurization in water in the process of conversion of kinetic energy into pressure energy. These scenarios are clearly depicted in ▶ *Fig. 257*.

The initial and final shapes of the vessel as seen in the test setup are shown in ▶ *Fig. 258*. The transient evolution of vessel deformations at various instants is shown in ▶ *Fig. 259*. The comparison is found to be excellent.



■ **Figure 257**

Evolution of vessel deformations and internal pressure as predicted by FUSTIN



■ **Figure 258**

Undeformed and deformed shapes of the vessel in the test setup

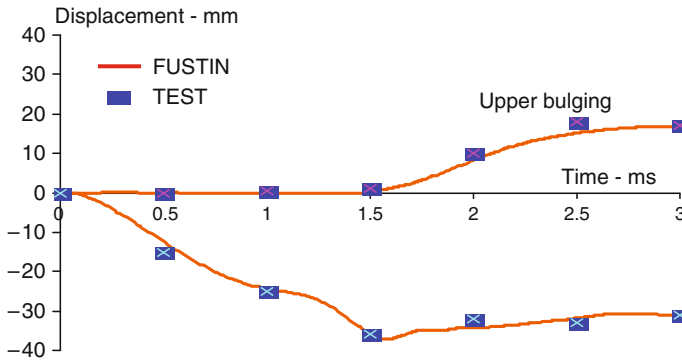
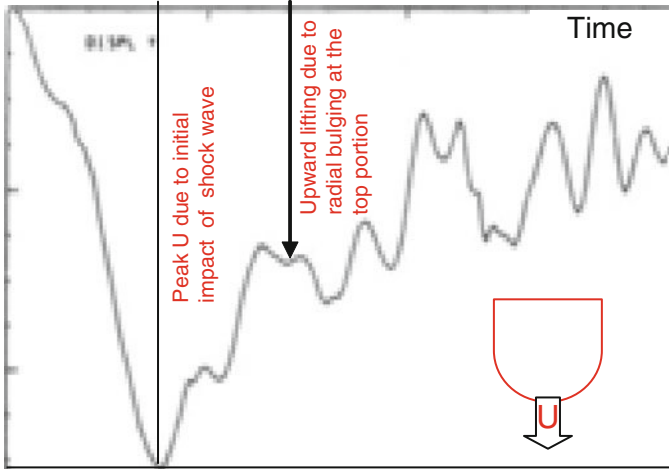


Figure 259
Prediction of vessel deformations by FUSTIN

Structural Integrity Assessment under CDA: Two Case Studies

Theoretical Investigations For SPXI, the CDA has been analyzed for mechanical consequences on internal and main vessels for the energy release of 800 MJ energy (Bour et al.). The hydrodynamic and structural aspects are coupled for the whole reactor block, except for the roof slab, which were analyzed with a structural code, gravity loads not taken into account in the hydrodynamic analysis. The fluids are modeled as compressible medium. The structural material is austenitic stainless steel SS316 LN, which is treated as elastoplastic materials and best fit properties are used in all analyses. The hydrodynamic and structural calculations were carried out by 2D explicit Lagrangian code SIRIUS, developed by CEA, which uses finite difference discretization for the fluid and the thick structures and a finite element meshing for the shell structures. Subsequently, the mechanical calculations are carried out using INCA for roof, TRICO for dome, and TEDEL for IHX and secondary loops. [Figure 260](#) shows the deformation of main vessel bottom. The important results are the maximum displacements, strains, and stresses at critical locations in the reactor block, for 800 MJ energy release. The maximum deflection calculated at the roof is 35.2 mm. The maximum strain observed in the high part of the main vessel is 4.2% in the meridian direction (bulged area). Hence, there is no risk of a shock between main and safety vessels deduced from the calculated displacements.

For PFBR, analysis is carried out using the finite element code called “FUSTIN,” which uses Arbitrary Lagrangian–Eulerian coordinate system for describing fluid motions and convected coordinate system for modeling the geometrical nonlinearity of structures (Chellapandi et al. 2000b). Further, to overcome the limitations of the algorithm to handle the complicated core boundary movements with the presence of reactor internals, particularly the control plug, a “two phase fluid element” is developed and implemented in the code. With this element, the core bubble boundary nodes need not be purely Lagrangian. The code FUSTIN has been validated against many international experimental and theoretical problems. The equation of state for sodium is: $P = a_1\mu + a_2\mu|\mu| + E(b_1 + b_2\mu)$, where $\mu = \rho/\rho_0$; $\rho_0 = 832 \text{ kg/m}^3$, $\rho =$ instantaneous density, $E =$ internal energy per unit volume, $a_1 = 4.44 \times 10^9 \text{ Pa}$, $a_2 = 4.328 \times 10^9 \text{ Pa}$, $b_1 = b_2 = 1.218$. The equation of state for argon is $PV^\gamma = \text{constant} = P_0V_0^\gamma$, where $P_0 = 0.1 \text{ MPa}$, $V_0 = 104 \text{ m}^3$, and $\gamma = 1.67$. The true stress–strain curve for structural material SS 316 LN recommended by RCC-MR (2002) at metal average temperature 773 K is used. The initial volume and pressure



■ Figure 260
SPX1 main vessel deformation (U)

of core bubble are 2.56 m^3 and 4 MPa, respectively. The core bubble is considered as a spherical ball, governed by the equation of state: $PV^{0.72} = \text{constant}$.

The main vessel, core support structure, grid plate, control plug and top shield, and support skirt are included in the geometrical model. The vessel is filled with sodium with a cover gas gap of 800 mm. The masses of thermal baffles are lumped at a junction point on the main vessel. The masses of core, grid plate, and core support structure are distributed appropriately. With these added/distributed masses, the entire mass of reactor assembly is truly conserved. The geometry consists of core bubble, sodium, cover gas, and vessels with the interfaces between core bubble and sodium, sodium and cover gas, sodium to metal surface, cover gas and metal surface, and the core bubble to metal surface (in case the bubble interacts with the inner vessel and control plug). The shell structures are modeled with “2-noded conical shell element.” The structural nodes are Lagrangian. The sodium and core bubble are modeled by “quadralateral axisymmetric solid elements.” The interface between the structures and fluids are ALE since the fluid nodes, which are attached to the specific structural nodes, move with the corresponding structural nodes. The argon space is considered as a single homogeneous medium obeying the equation of state. The finite element model of various geometries is shown in [Fig. 261a](#).

From the analysis, the overall sequence of events is depicted clearly as shown in [Fig. 261](#). The sequence of events which are depicted is: upward bowing of core cover plate of control plug and bulging of inner vessel and downward displacement of main vessel bottom portion ([Fig. 261b](#)), core bubble crossing the control plug ([Fig. 261c,d](#)), sodium slug impact on the top shield, reflection of pressure waves from top shield and downward bowing of core cover plate and downward displacements of sodium free levels ([Fig. 261e](#)). Important observations are regularities of meshes till the end of the analysis, simulation of complicated motions of core bubble around the control plug, sequential immersion of inner vessel in the sodium pools, upward and downward bowing of plates in the control plug, high local straining of main vessel due to load transmitted at the triple point, sodium impact restricted to a small zone on the top

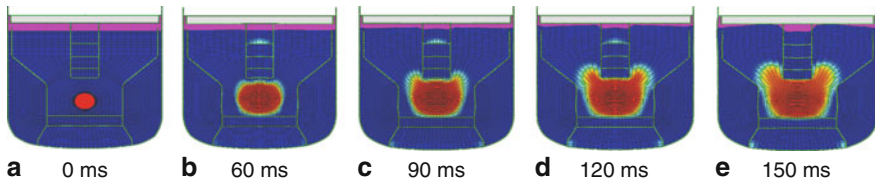


Figure 261
Evolution of core bubble behavior in PFBR reactor assembly during CDA

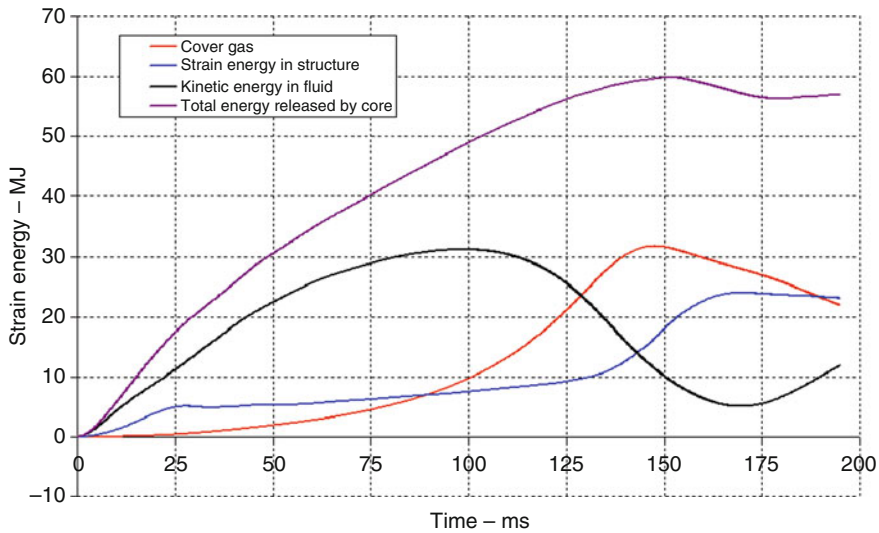
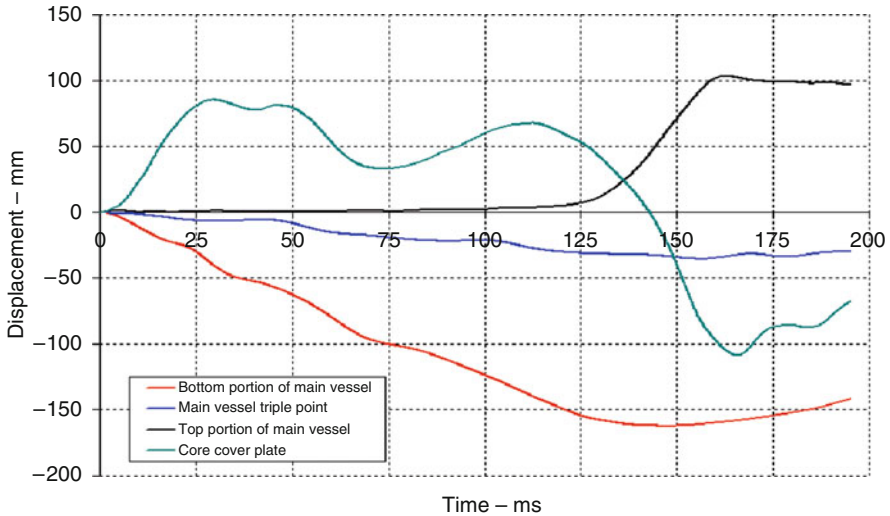


Figure 262
Evolution of energy distribution

shield around the control plug and no impact of sodium slug within the control plus on the top shield, and nearly uniform overall deformations of internals and main vessel.

The energy balance is shown in Figure 262. Due to constraints of main vessel and internals, the maximum energy released by core bubble is 60 MJ during transient condition. Under quasi-static condition when the kinetic energy is ignored, the energy released by core is fully absorbed by vessels and cover gas space. The total energy would be 45 MJ. The main vessel absorbs the energy in two phases: at about 25 ms due to initial impact of pressure waves propagated in sodium at about 25 ms subsequently, due to cover gas pressurization resulting due to sodium slug impact, which initiates at about 135 ms and completes at 145 ms. The cover gas absorbs 31 MJ (maximum) which is elastic in nature, responsible for free levels oscillations without any further staining of main vessel.

Figure 263 shows the evolution of displacements of various structures. The core cover plate oscillations, bending upward (~ 70 mm) and bowing downward (~ -110 mm) are seen clearly in the figure. The peak main vessel bottom displacement is 160 mm and the radial bulging is 103 mm. The triple point moves down by 36 mm (maximum).



■ Figure 263

Evolution of displacements of structures

The important strains are peak strains on the main vessel surface. There are two critical locations: one is triple point and another is the upper cylindrical portion above sodium free level. ▶ Figure 264 and ▶ Figure 265 show the strain evolution at these two critical locations. The peak strains are: 2.6% (longitudinal) and (−0.1% hoop) at the triple point and 1.53% (hoop) in ▶ Figure 264 and −0.1% (longitudinal) at the upper portion in ▶ Figure 265.

Experimental Approach For the early SFRs, the fraction of energy generated during disassembly that was assumed to be converted to mechanical work was based on conservative assumptions. Later research succeeded in reducing this conservatism to some extent, and there is research still underway to establish the degree to which additional physical phenomena may reduce this fraction still further. Early assessments of damage potential due to such energy release were based on equating this potentially available work energy to an equivalent charge of TNT, that is, 4.2 MJ ~ 1 kg of TNT. Hence, every MJ of work potential was assumed to represent the explosive potential of about 250 g of TNT. The principal reason for using this equivalence was that substantial experience existed. Any attempt to predict the actual mechanical response of an FBR system to a CDA excursion using the TNT energy equivalence model is ambiguous because the pressure–time characteristics of a TNT detonation are considerably different from those of a nuclear excursion. Mechanical damage from an explosion or pressure transient can be caused by both a shock wave, which is transmitted rapidly to a structure, and the more slowly expanding bubble of reaction products or vaporized material. Pressures in a TNT detonation build up on a microsecond time scale and reach the order of 5,000 MPa. Hypothesized energy releases from an HCDA excursion, on the other hand, built up over a millisecond time scale, and peak pressures are orders of magnitude lower. As a consequence, much of the damage potential of a TNT detonation to surrounding structures comes from shock wave effects, whereas longer-term bubble expansion would be the predominant damage mode for the slower time-scale pressure

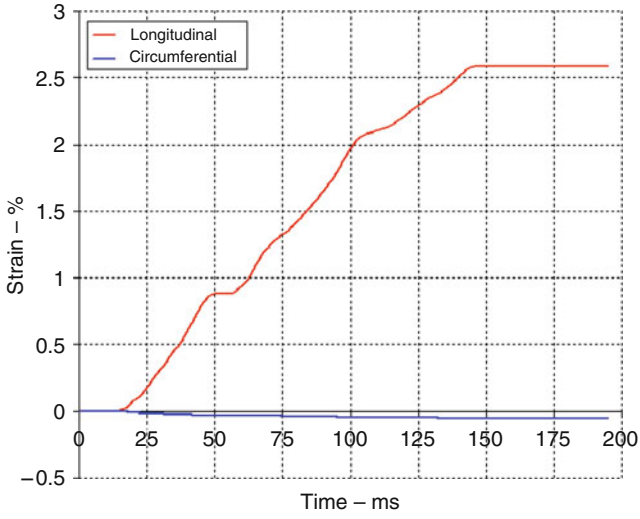


Figure 264
Strains at MV triple point

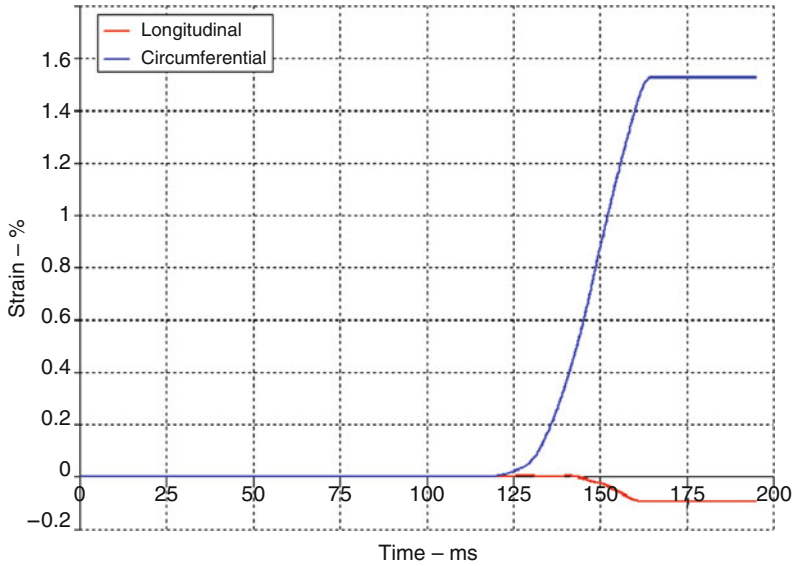


Figure 265
Strains at upper portion of MV

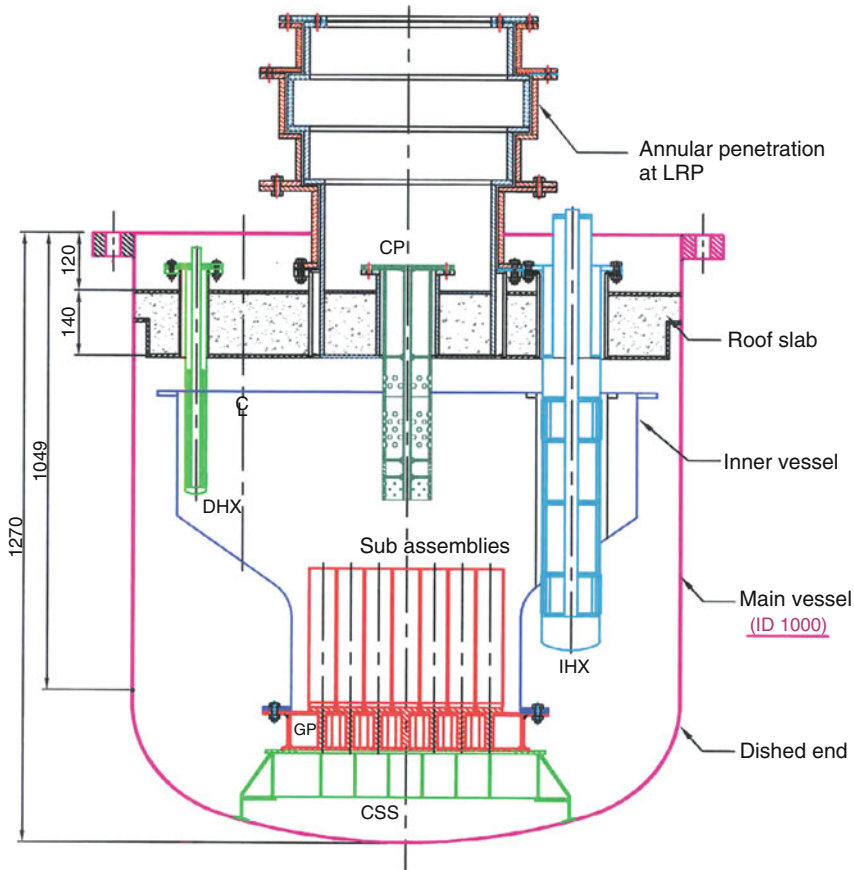
buildup of an FBR excursion. Hence, a considerable effort was expended to develop simulant explosives with a burning rate more compatible with the millisecond time frame. In addition to the vessel damage experiments referenced above, tests with simulant explosives under sodium have been conducted at Cadarache to study breach of the cover and sodium transport through the cover in an HCDA. Small scale in-pile tests involving fuel and/or sodium expansion and energy partitioning have been carried out at several transient test reactors, for example, TREAT, ACPR, and CABRI.

For SPX1, two series of experiments were carried out in the early 1980s: MARA program, based on 1/30th scale mock-up representing only the main vessel and coarsely the internal structures were undertaken in order to have accurate information about the roof and main vessel and also used for validation of SIRIUS (Louvet et al. 1987). More elaborated mock-up called MARS was built with representative inner components (1/20 scale). The most challenge in the definition of mock-up is appropriate simulation laws for loading, structural material, fluid, and explosive behavior. Water is used in place of sodium and 80 g of L54/16 explosive which can yield 800 MJ (equivalent) energy release is used for simulating nuclear excursion. The explosive has been qualified on MANON tests. Essential instrumentations were incorporated to measure the parameters related to the mechanical behavior and also to compare with calculations results. Tests indicated that there is no leakage observed, and welds were found to be safe. After transposition to the reactor scale, the maximum radial displacement in the bulge area is 240 mm and maximum deflection for the roof slab deduced is 110 mm. The main strains are 2.4% at the bulge level (hoop) and 1% at the vessel bottom (axial and hoop).

Toward assessing the structural integrity of PFBR components under CDA, the tests were carried out in three stages (Chellapandi et al. 2002). In the first stage under TRIG-I series, 17 tests were conducted in water filled cylindrical shells with rigid and fixed top and bottom plates of various dimensions to characterize the chemical charges (the energy conversion ratio, i.e., mechanical energy release per unit mass and the equation of state). In the second stage under TRIG-II series, tests were conducted in the main vessel models without any internals. Under this series, 30 tests on 1/30th scale models and 3 tests on 1/13th scale models were conducted. Sufficient data have been generated for validating the FUSTIN code and also for establishing acceptable strain limits for the vessels under simulated CDA loading conditions. In the last stage, under TRIG-III, tests were conducted on 1/13th scale mock-ups with the main purpose to demonstrate the structural integrity of IHX and DHX and also to estimate the sodium leak based on simulation principles. Totally 61 tests were completed during the period of 4 years.

► *Figure 266* shows a schematic of the mock-up. The entire core is simulated with 37 hexagonal core subassembly (CSA) models, which have matching rigidity characteristics as that of CSA in reactor. The top shield assembly consists of roof slab, rotating plugs, and control plug (CP). The roof slab is an annular box type structure having ten penetrations essentially to accommodate four pumps, two IHX, and four DHX models. The pumps are simulated by cylindrical tubes with appropriate thickness to represent the rigidity characteristics. The DHX and IHX models have all the essential parts of the prototype components including the required number of tubes. The annular leak paths in the top shield were modeled in detail incorporating all the geometrical characteristics to simulate the flow resistances. The entire mock-up is supported on the reactor vault through a cylindrical skirt. The reactor vault is represented by six steel columns embedded in the concrete, instead of continuous structure, to facilitate photography.

A low density explosive (LDE) has been specially developed which can simulate satisfactorily the rate of energy release including peak pressure, at TBRL using a technique of lowering the



■ **Figure 266**
1/13th scale mock-up of PFBR reactor assembly

density of PETN by precipitating it in the U foam, thereby reducing the charge density of PETN from ~ 0.8 to ~ 0.14 g/cc. This LDE is used for the PFBR mock-up trials. The overall dynamic displacements of main vessel, top shield, lifting of plugs, CP, DHX, and IHX are captured through two high-speed cameras: one is digital (3,000 pps) and another is conventional one (6,000 pps). Sufficient strain gauges are pasted at the critical locations in the main vessel, cylindrical support skirt, and reactor vault structures. Accelerometers are placed on the top shield to understand the inertial forces and pressure transducers are placed on the bottom of the top shield to measure the dynamic pressures due to slug impact. Five tests were conducted with 22 g LDE, which simulates 110 MJ of energy release in the reactor scale, which is the design requirement. It is noted from the tests that the main vessel, top shield, DHX, and IHX were integral with negligible deformations (🔍 Fig. 267). It is worth mentioning that the tests with increasing quantity of LDE (up to 220 g) indicate that the main vessel without internals is integral up to 1,200 MJ (🔍 Fig. 268). The maximum rupture strain is established as 30% for welded SS 316 plates at room temperature under simulated CDA loadings. However, a strain limit of 16% is considered



■ Figure 267
Removal of tested IHX



■ Figure 268
Deformed MV (1,200 MJ case)

(welded vessel) for PFBR at the operating temperature including the effects of multiaxiality, irradiation, accumulated creep–fatigue damage, etc. (Kaguchi et al. 1999).

10.6 Post Accident Phase

10.6.1 Scenarios

The capability in achieving a stable coolable material configuration following the postulated accident is demonstrated by appropriate objective of post accident heat removal (PAHR) mechanisms. The distribution of heat sources following the accident is a controlling factor in the assessment of adequacy of PAHR. Because of the substantial differences in the accident scenario, the post accident dispersion behavior also varies. The PAHR analysis should therefore be prepared to cover a range of possible fuel distribution patterns. Analysis of the UTOPIA shows that the early sweep out of fragmented fuel may limit the damage in the core to few subassemblies. However, scenario following a ULOFA may result in gross whole core melt down. In such a case, sufficient steel and fuel vapor may be generated in the core to result in fuel removal from the core, within a two phase mixture of fuel and steel, thus leading to neutronic shutdown. The exact amount of fuel that will be driven into the cold plenum of the reactor vessel cannot be predicted. Therefore, to define the pattern of fuel dispersal following a CDA in an SFR, a semi-mechanistic approach is currently being pursued.

Upward relocation of fuel and steel will depend on the ease with which the mixture can penetrate through the pin bundle above the active core region of subassemblies. Ostensen et al. (1974) were the first to consider the fuel penetration behavior in the steel cladding structures. They assumed that fuel freezing will depend on reducing the average enthalpy in the leading edge of the flow to the enthalpy of solid fuel at its melting point. This condition of freezing has become known as bulk freezing. Their analysis seemed to be supported by experiments utilizing thermite generated molten fuel. Epstein et al. (1976) proposed that the bulk freezing is in fact due to steel melting, ablation, and mixing with flowing fuel. Therefore, the voids formed during the penetration process will have large impact on the freezing behavior. Downward relocation of fuel and steel may occur by two mechanisms, namely, (1) axial melting through the lower assembly structure and (2) streaming through the coolant channels in the lower assembly structure. Streaming is a much more rapid mechanism for relocation. Molten fuel may not penetrate far in the pin cladding structure without plugging, because of the small channel flow area/cladding surface area and due to significant potential for steel melting. However, large coolant paths existing below the active core region facilitate the steaming process. Studies carried out for CRBRP have shown that coolant streaming is possible within seconds. In summary, a significant portion of core materials may be redistributed to the cold plenum in a short time following a CDA. The molten core debris ejected in the cold plenum will be quenched in the subcooled sodium and converted into particles. The debris particles will then settle on the core catcher.

Heat Source Strength

The heat generation following CDA involves (1) transient heat generation associated with the decreasing fission process (immediately after neutronic shutdown), (2) decay heat of the activated fuel nuclides, (3) decay heat of fission products, and (4) decay heat due to stainless steel activation. The transient heat generation is significant only for very short duration (~ 10 s) after


attaining subcriticality. Analytical tool commonly adopted in the estimation of the heat load is RIBD code (Bunch and O'Dell 1969). In large power plants, considerable decay heat will be generated in the radial blanket subassemblies and such heat generation should also be included in the PAHR studies.

In-Place Fuel Retention

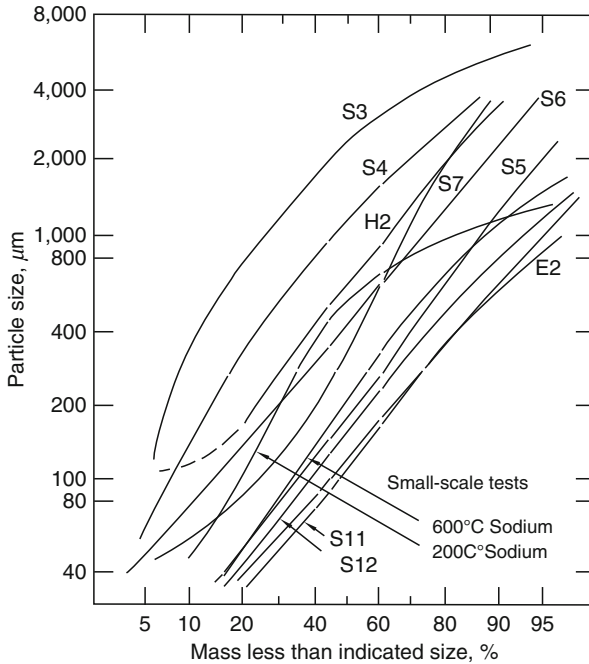
This concept involves retention of the fuel material in the core position. In the case of in-place cooling, the fuel material in the original core region is cooled by (1) cooling of the subassemblies that remain intact by liquid sodium flow, (2) survival of the partial voided assemblies due to coolant flow near the assembly walls, (3) recovery of voided assemblies due to cooling by neighboring intact assemblies, (4) cooling of particulate debris in blocked assemblies by sodium leakage through the debris, and (5) containment of the assemblies in the lower shielding section of the assemblies due to heat transfer to neighboring assemblies. Many of these mechanisms depend on the specific arrangement of core, the severity of the accident, and the resulting damage pattern.

Kazimi et al. (1977) have analyzed a specific situation for CRBR by considering the core region to be completely blocked while radial blanket and shielding assemblies remained undamaged. Part of the debris was assumed to lie in the upper and lower plena with some fraction still remaining in the core region. Considering complete loss of pumping power, they estimated coolant flow capability due to natural convection of sodium from the reactor vessel to intermediate heat exchangers. The results indicated that steady state natural convection is potentially capable of preventing gross sodium boiling in the vessel. However, if the fuel debris is localized, local sodium boiling may occur. Larger surface area available for debris cooling prevented sodium boiling. This can be achieved by selecting a large size of vessel.

Molten Fuel Relocation

Another scenario which is most probable is the formation of a particulate bed at the bottom of the reactor vessel. In the absence of adequate heat removal, the frozen core debris would remelt due to internal heat generation and may promote melting process of steel structures and move downward. It has been established from studies of fuel-coolant interactions that molten fuel and steel tend to fragment and form solid particulates upon quenching in sodium. The size distribution of these particles significantly affects the ultimate coolability of debris bed. In-pile tests in transient reactor test facility (TREAT) (Gabor et al. 1974) have shown that the particle size distribution is scattered as shown in  Fig. 269. The general indication is that the major fraction of debris (70–80%) has diameters <math><1,000\ \mu\text{m}</math>. The average fuel size of fuel particle is $\sim 200\ \mu\text{m}$ and that of steel particles is $\sim 400\ \mu\text{m}$. In all experiments, difference in appearance between metallic particles and UO_2 particles has been observed. The metal particles are generally rounded whereas UO_2 particles are irregular and of smaller size. The fragmentation is primarily due to thermal and mechanical interactions, including hydraulic forces and thermal stress cracking.

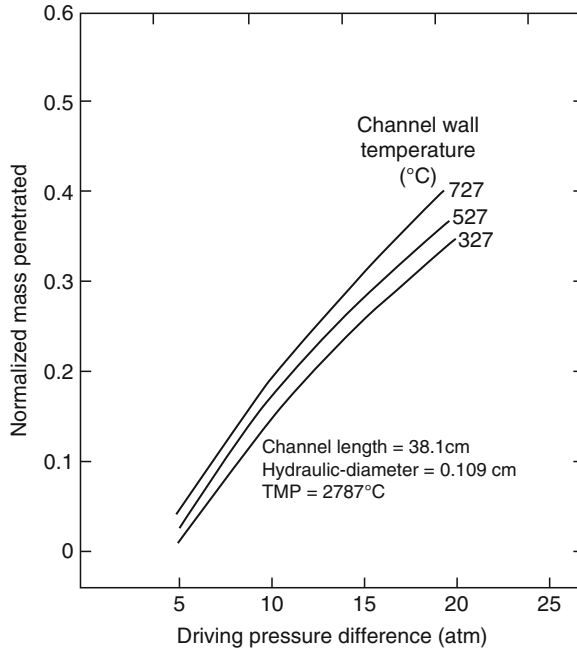
Core debris generated by quenching of molten core debris in sodium is expected to settle downward. Before the particles settle on the main vessel/core catcher, the debris has to cross lower axial blanket, grid plate, and core support structure. The debris may reach the foot of subassembly and are then collected between sleeves of the grid plate. If the mass of the debris is large enough, they might spread and deposit on the peripheral region of the grid plate. An analysis of downward streaming from the core and freezing of molten fuel/steel mixture indicated that at least one third of the fuel will reach the grid plate in a very short time period (several seconds) (Glueckler et al. 1982). This fraction would be higher if the flow through the control



■ **Figure 269**
Debris particle size distribution

rod channels is high or if the remaining fuel mass becomes critical and remelts the frozen fuel plug. A typical result of material penetration as a function of the driving pressure is shown in [Fig. 270](#). The debris could melt the lower plate of the grid plate or open a way through the sleeves of grid plate. French study (Le and Kayer 1979) for SPX-1 has indicated that if the debris is deposited on the grid plate 100 s after the accident, the time needed to melt the lower plate of grid plate would be 1,600 s. At the same time incipient sodium boiling below the grid plate is expected.

Gluekler et al. (1979) have conducted a study on the ability of the 50 mm thick lower plate of grid plate to retain the debris. In this study, the core debris was assumed to reach the inlet plenum 1 s after the neutronic shutdown and to consist of molten fuel and steel. The debris layer was assumed to have a maximum thickness of 140 mm. The time of complete melt through of the plate is shown in [Fig. 271](#). In this figure, fuel mass fraction refers to fraction of fuel, internal blanket, and steel materials in the active region plus all materials in the lower axial blanket. It has been indicated that the failure mode in most cases is expected to be by creep rupture prior to melt through. The fuel mass fractions greater than 25% would have a high probability for melt through within 100 s. This fuel mass fraction corresponds to a molten debris layer thickness greater than 70 mm. The result of this study has indicated that the grid plate has a considerable core debris retention capability even for the extremely pessimistic initial debris conditions and transport times. Once the grid plate structure fails, the core debris will be settled on the horizontal surface of the main vessel and form a core debris bed.




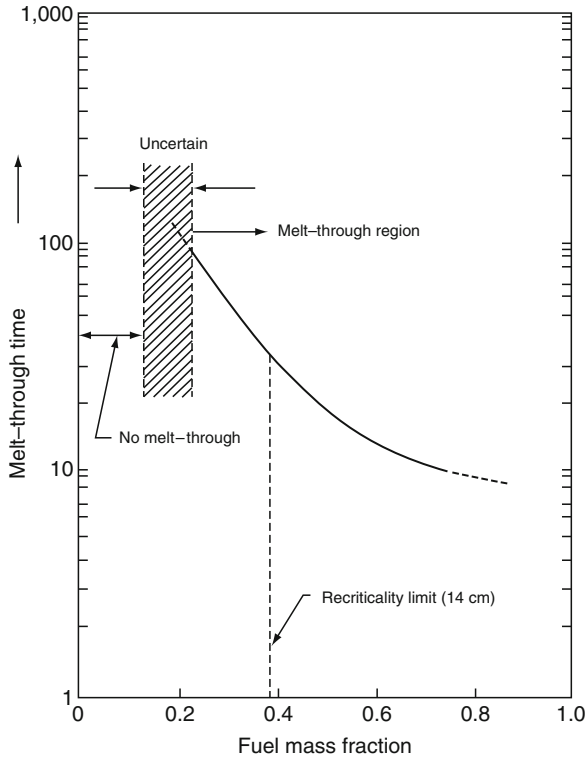
■ Figure 270

Material penetration under CDA

For the event of large accumulation of core debris (10–100%) at the bottom of main vessel, the bed would be in a molten state. If the steel and fuel separate due to density differences, then no steel boiling is expected. For a homogeneous mixture of fuel and steel, maximum layer temperature can be 3,200 K. Therefore, steel boiling may occur and this would increase upward heat transfer and sodium boiling leading to further pressurization of main vessel. The debris bed in contact with the bottom of the main vessel would penetrate through the wall. The vessel may fail due to structure melting and creep rupture. Characteristics failure time of 12–60 min have been reported for melt through failure if the heat removal from the bottom of the vessel is by thermal radiation only. High pressure exerted on the vessel would cause structural failure prior to melting. Conditions following failure of main vessel and safety vessel are very serious. It can lead to failure of liner resulting in chemical attack of concrete by core debris and sodium resulting in degradation of structure, hydrogen production, and pressurization of containment. In view of the above serious consequences, there is a need for accommodating the core debris in a safe manner.

10.6.2 Core Debris Accommodation

There are two approaches to debris accommodation. One approach is to retain the debris temporarily within the containment system followed by a controlled release, such as filtered vents. The second method is permanent retention either through inherent or engineered features. The retention may be achieved either in-vessel or ex-vessel. The concepts used various reactors for core debris accommodation is shown in  Table 47.



■ Figure 271
Grid plate melt through time


10.6.3 In-Vessel Debris Accommodation

Considerable improvement of retention capability within the main vessel can be accomplished by placing a core catcher for collection of debris in the sodium plenum under the core support structure. The core catcher with heat removal capability from the bottom could increase the coolability range to a value between 55 and 100% of the core fuel (Dufour 2007). The overall conclusion of the in-vessel retention study is that a partial core meltdown involving up to, approximately, 50% of the core can be accommodated within the main vessel provided a heat sink is available. One important advantage for a pool type SFR is that the cooling capabilities of the sodium inventories can still be used if the main vessel remains intact. The thermal capacity of the in-vessel sodium between normal operating temperature and sodium boiling point is substantial and provides a period of several hours before significant sodium boiling occurs. For a number of core melt accident sequences, the decay heat removal loop may still be functioning and this gives a scenario satisfactory mode of heat rejection. Natural convection occurs in internally heated molten pools, with hot fluid rising and colder fluid moving downward. The onset of motion in a fluid occurs when buoyancy forces caused by temperature gradients

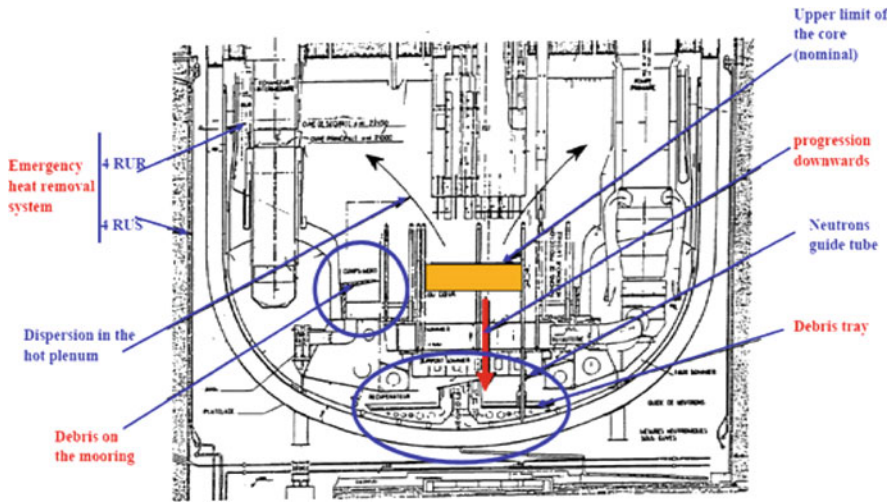
■ Table 47

Core debris retention concepts adopted in various reactors

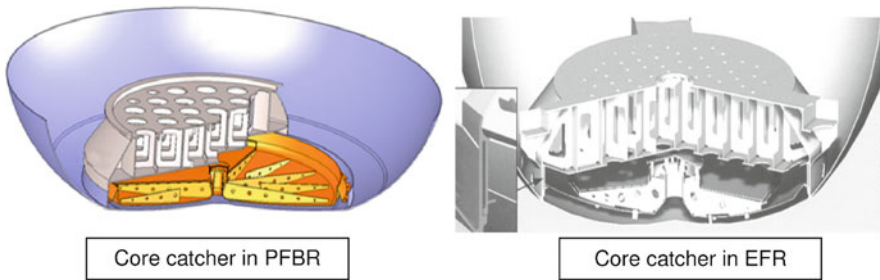
Reactor	Provisions
EBR-I & -II	None
FERMI-I	In-vessel: zirconium meltdown pan and ex-vessel: graphite crucible below vessel with primary shield tank
SEFOR	Ex-vessel: sodium catch tank 45 ft below vessel. Fuel dispersion cones below vessel and in catch tank
CRBRP	In-vessel: some small amount of debris cooling on reactor internal structures, but not special design provisions and ex-vessel: lined and insulated reactor cavity, vented pipe chase and ex-containment cooling–venting purge system
DFR	Fuel dispersion cone and melt tubes to bedrock
PFR	Single layer of trays within tank; capable of retaining seven assemblies
CDFR	Three layers of trays within tank; retention capacity for entire core
Rapsodie	None
Phenix	Externally cooled outer vessel
SPX-1	In-vessel catch trays, external cooling of safety vessel
SNR-300	In-vessel: catch trays in lower plenum

exceed the viscous forces. Inertial forces also affect the transport process after flow develops. According to the studies carried out in France for the SPX-1 on the postaccident situation, it is difficult to conceive that the non-molten subassemblies are not blocked by the debris ejected upwards (Gluekler et al. 1979). Consequently, the cooling of the non-molten subassemblies by natural convection cannot be ensured, which can lead to a slow fusion under residual power. The debris settlement behavior considered is shown in  Fig. 272.

Further PAHR study considers three different possible cases, namely, (1) the lower plenum remains closed after the passage of the debris, (2) the lower plenum is in communication with the upper plenum through a hole at the diagrid level (The total exchange coefficient between the two plena was estimated for a hole of 0.2 m diameter from the results obtained on LULU-II water mock-up.), and (3) the lower plenum is in communication with the upper plenum through a broad hole at the diagrid level (the total exchange coefficient between the two plena was assumed equal to ten times that of the case (2)). The transfers of heat by natural convection of sodium around the debris tray and under the support plate were evaluated in steady state operation from experimental correlations. LULU-II water mock-up tests were carried out to study the influence of the forms of the core catcher plate, chimney, and containment of the fluid on the heat transfer. The PAHR performance was evaluated based on the following three criteria, namely, (1) the damage on the triple point during the transient is within permissible limits, (2) the sodium temperature under the debris tray is below sodium boiling to avoid deterioration of heat transfers in the downward direction, and (3) sufficient mechanical resistance for the core catcher plates taking into account the mechanical loads and temperature reached. (at least several hundreds of seconds). Thus, the only possible evolution is the progression of molten materials



■ Figure 272
Debris settlement behavior considered for PAHR studies of SPX-1



■ Figure 273
In-vessel core catchers in international SFRs

to the bottom. The core debris penetrates the grid plate only after several thousands of seconds subsequent to the end of the power transient. Schematic sketches of in-vessel core catcher conceived in PFBR and EFR are shown in [Fig. 273](#).

10.6.4 Ex-Vessel Debris Accommodation

Broadly two concepts are adopted. The concepts under first category are designed to prevent failure of reactor containment by relying on somewhat involved engineered core retention systems. Such systems include a sacrificial bed of refractory materials, a multi-tray system cooled by natural convection and a single crucible cooled by forced convection. The concepts under second category allow for failure of reactor containment, but rely on either inherent capabilities

of the reactor building or simple solutions to sufficiently delay containment failure and hence keep radioactivity release within the regulated guidelines. The concept may include a concrete filled reactor cavity and/or special venting and filtering measures for containment.

10.7 Computer Codes and Validation

The accident propagates through various phases, namely, pre-disassembly phase, transition phase, disassembly phase, and mechanical energy release/system response phase. The computer code developments over the past 4 decades have gone through for all these phases, with thorough verifications both with in-pile and out-of-pile experiments.

For the pre-disassembly phase, the SAS series of codes were developed in the 1970s at the Argonne National Laboratory in USA. The first code in the series is SASIA (Carter et al. 1970) code. Subsequently, the SAS2A (Dunn et al. 1974), SAS2B, SAS3A (Stevenson et al. 1974), SAS3D (Cahalan et al. 1977), and SAS4A (Wider et al. 1982) were developed. The last version of the code is the SAS4A version, which was widely used in the US, Europe, and Japan. The SASIA code started with a single pin representation in a channel. The different coolant channels are not coupled thermohydraulically. It performs neutronics calculations by point kinetics model, taking into account reactivity feedbacks from Doppler, fuel and clad axial expansion feedback, coolant density feedback, and radial feedback. The sodium boiling model is a two phase slug ejection and single bubble model. An additional slumping reactivity feedback is also included. Fuel motion and clad deformation models are also included. All the calculations are done for the fresh pins only.

The next version of the SAS series code is SAS2A. This code is a multi-channel code, which can couple thermohydraulics between the different channels. Primary loop model is included in this version. The code was also improved to include transient fuel pin mechanics (fission gas pressure, effect of fission gases on clad deformation, etc.). The sodium boiling model is a two phase slip flow slug ejection multiple bubble mode. The SAS3 series of codes (SAS3A–SAS3D) were further improved to calculate fuel coolant interaction (FCI), FCI-driven fuel motion and voiding and primary and secondary loops for thermalhydraulics.

The last in the series is SAS4A version which was widely used in the recent past. In SAS4A code, new features were incorporated. A balance of force model was incorporated to calculate the fuel axial expansion. The clad motion and sodium boiling were coupled. The sodium boiling model was improved to treat a variable coolant flow cross section to couple with pin mechanics. A unified molten fuel motion model was also incorporated.

All the SAS series codes use point kinetics model for neutronics. The space time kinetics model may be required when there is a large scale fuel and clad motion. The recent SAS4A modeling includes (Cahalan and Wei 1990) extension of the boiling model to treat sudden fission gas release upon pin failure, fuel deformation to handle advanced cladding materials, and metallic fuel modeling capability to fuel relocation model.

A computer code system, KALDIS, is used for PFBR analysis (Harish 1999). For pre-disassembly phase, a computer code, PREDIS has been developed, and it forms part of KALDIS. The processes modeled in the code are: core neutronics, transient thermalhydraulics, reactivity feedbacks like Doppler, fuel and clad axial expansion, coolant expansion, spacer pad, grid plate, main vessel and differential control rod expansion, coolant boiling, and clad and fuel melting and slumping. For disassembly phase, VENUS-II code (Jackson and Nicholson 1972) developed

by ANL is commonly used. In this code, point kinetics is used for power calculations and using the 2D reactivity worth and Doppler coefficient distribution, the calculations of displacement and Doppler reactivity feedbacks are performed. Calculations are stopped once the multiplication factor of the reactor is 0.98 or 0.95 due to outward material movement of the core. The calculations of work energy potential of the thermal energy released in the disassembly phase is calculated using the straight forward methodology available for isentropic expansion of fuel vapor expansion up to one atmospheric pressure or up to the upper cover gas volume (Walter and Reynold 1981). This algorithm has been made a part of the VENUS-II code.

10.7.1 Validation of Codes: A Case Study

For ULOFA, the code is tested up to onset of boiling against BN-800 IAEA CRP Benchmark (🔗 [Table 48](#)) (Om Pal Singh and Harish 1998; Sathiyasheela et al. 1998). It is found that of boiling and its location, the sodium void reactivity, and net reactivity are predicted nearly same by all the countries, even though some differences are noted in Doppler reactivity.

10.8 Innovations Toward Enhanced Safety

10.8.1 Core

Improvement of the core behavior to achieve possibly lowest ratio of sodium void effect/Doppler effect, reduced sodium volume fraction, higher fuel volume fraction, reduction of height/diameter ratio, moderate core size, annular fuel pellet, use of metallic core, use of advanced cladding materials (15/15Ti, ODS, etc.) to gain higher margins for the cladding ruptures during transients and state-of-art core monitoring instrumentations are some of the innovations, being considered by international expert groups.

📌 **Table 48**

Results of onset of boiling

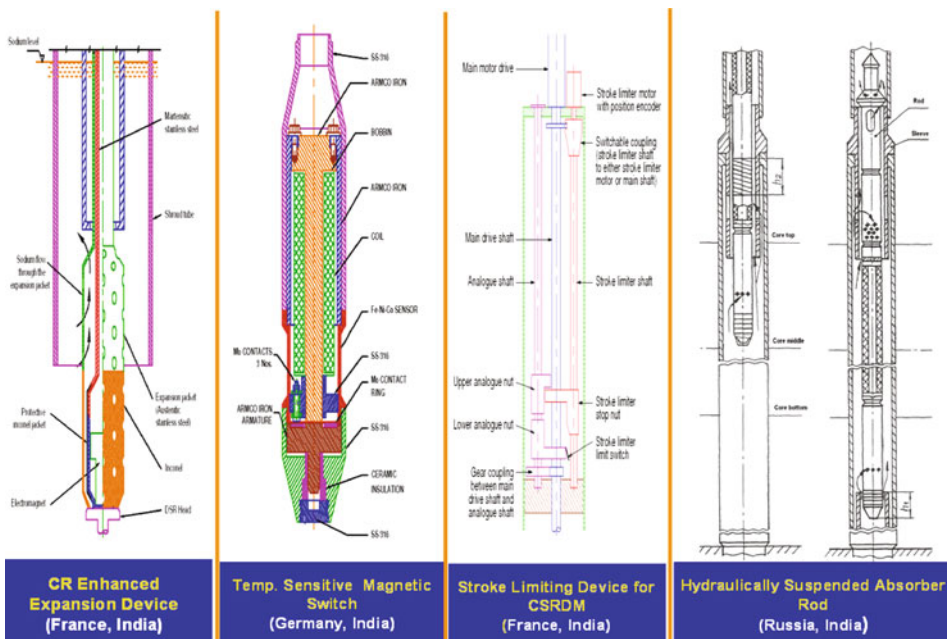
Parameter	Germany	France	Japan	Russia	India
Time (s)	17.96	18.93	18.96	16.72	17.60
Channel no.	5/1	5/1	5/1	5/1	5/1
Axial position from core bottom (cm)	84–90	95	87–94	85	84
Normalized power	0.66	0.63	0.63	0.71	0.71
Net reactivity (ρ)	-0.17	-0.183	-0.183	-0.135	-0.147
Doppler reactivity	0.026	-0.005	-0.004	+0.039	+0.027
Fuel axial expansion reactivity (ρ)	-0.003	+0.015	+0.014	+0.017	+0.020
Sodium reactivity (ρ)	-0.207	-0.205	-0.205	-0.188	-0.223

10.8.2 Sodium Fire and Sodium–Water Reactions

The main objective is to practically eliminate sodium fires and sodium–water reactions susceptible to degrade the safety functions in an unacceptable manner or to lead to unacceptable consequences in the environment. In order to achieve this, apart from the existing design features, reduction of welds in piping by reducing number of sodium loops, shortening of pipe with high chromium content, double wall piping, double wall steam generator tubes, integrated pump-IHX, and state-of-art inspection and repair systems are being considered. The passive systems for self-extinguishing of the sodium fires when sodium is leaking from the circuits: sodium discharge into a pan with hydrolock; sodium discharge into a tank blanketed by inert gas, sophisticated numerical simulation of sodium fire and sodium–water reactions coupled with extensive experimentation and validation are the few additional innovative features envisaged in the future designs.

10.8.3 Reliable and Diverse Shutdown Systems

A few innovations are introduced in the shutdown systems (► Fig. 274). In case of power excursion, automatic negative reactivity insertion devices (1) by way of enhanced expansion of the core and shutdown systems, (2) use of curie point electromagnets or magnet switches to de-energize the magnet holding the absorber rods, hydraulically suspended rods which would lower automatically into the core in case of any loss of flow due to pump seizure or primary



► Figure 274

Passive shutdown system concepts

pipe rupture, stroke limiting devices to arrest the uncontrolled withdrawal of absorber rods and self-actuating devices to shutdown the reactor directly under class 4 power supply failure, are considered for ensuring reactor shutdown. Details can be found in INPRO (2007).

10.8.4 Decay Heat Removal Systems

Pumps with high mass inertia to ensure heat removal before establishing adequate natural convection, introduction of reliable electromagnetic pumps in the decay heat removal circuit, passive decay heat removal features, like use of shape memory alloys for automatic opening of dampers, thermal valves which opens to enhance the flow paths during decay heat removal conditions are a few innovations being envisaged by the designers worldwide.

10.8.5 Core Catcher

Subsequent to partial or whole core melting of core subassemblies, the molten core (debris) would be settled at the bottom of the main vessel. This may cause the rupture of the vessel, if it is not protected. For this, the core catcher is placed with the objective of maintaining the core in stable conditions within the vessel. The core debris settled at the core catcher is called corium. Hence, the core catcher does very important safety function. The robust design of core catcher involves definition of scenarios for the core melt down relocation, settling behavior of debris within sodium, post accident heat removal of corium (pool thermalhydraulics, decay heat removal aspect) and design analysis to demonstrate integrity of the main vessel.

10.8.6 Breakthroughs for Future SFR

Certain breakthroughs are also considered for the future innovative reactors. In the core design, in order to eliminate the possibility of flow blockage and at the same time to achieve lower pressure drop, power flattening is achieved without gagging by the use of different core zones at identical Pu content with different pin sizes or adopting the design of subassemblies with perforated wrapper or without wrapper by use of advanced spacer concepts for pin bundle. Stable power shape with burnup, metal plate concept for metallic fuels in place of pellets, ultra long life core, fuel assembly design for enhancement of molten fuel discharge upon the unprotected core degradation (parallel path for molten fuel), and engineering for the stabilized sodium boiling in the upper part of the S/A without voiding the fissile part are some additional breakthrough reported. In the natural decay heat removal circuit, multiple flow paths in the pool to facilitate increased natural circulation (e.g., thermal valve in the inner vessel) are proposed.

For the shutdown system, fusible shutdown devices (FSD) are used placed above the upper fissile zone, which acts when a fusible threshold is reached. The core catcher would have features to achieve enhanced cooling of debris and to prevent recriticality. These can be achieved by incorporating enlarged coolant plenum for molten fuel quenching and pelletizing the debris, novel chimney for effective coolant circulations, multilayer debris tray debris for debris retention within limited height for cooling and subcritical state, well-defined paths for debris, sacrificial layers, etc. Alternate coolants and comprehensive ISI and repair strategy are also the breakthroughs being thought of for the future design.

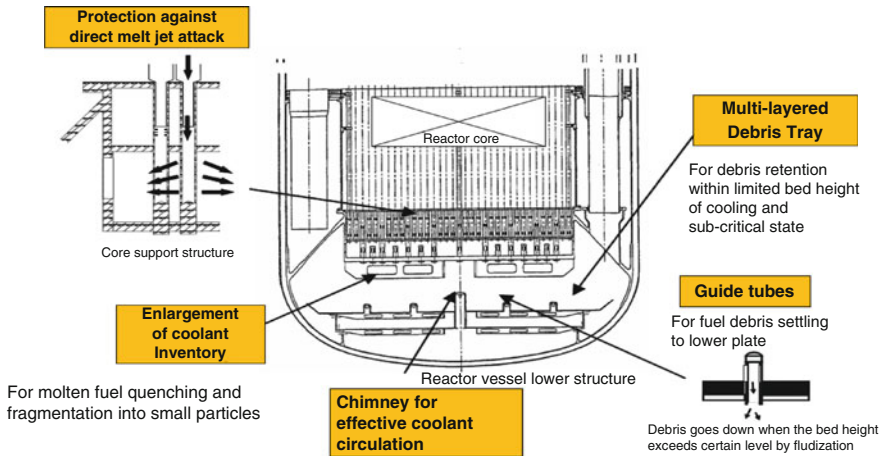


Figure 275

Post accident heat removal mechanisms: French proposal

Enhanced safety concepts are being considered for future SFRs in France (Fig. 275) and Japan (Fig. 276) (TWG-FR 2008a,b). The ultimate objective of the French proposal is to make CDA, nonenergetic, that is, the mechanical consequences, such as loadings on the vessel and top shield and sodium release need not be considered, as illustrated in Fig. 277 (INPRO).

10.9 Summary

The severe accident scenarios which lead to core disruptive accident have been analyzed thoroughly by various countries. Several dedicated safety tests such as TREAT, CABRE, and SCRABE were conducted and advanced computer programs have been developed to get excellent insight to the problems. With these, it is time to consider elimination of such severe accidents in the reactor safety studies. International experts are proposing very elaborate R&D program, which should be executed through international collaborations. In spite of these developments, numerical and experimental simulations of severe accidents are challenging and provide high impetus to the advancements in wide spectrum of subjects, both in science and technology.

11 French Licensing Experience on SFR

11.1 Phenix

- The evolution of knowledge which results in improving the reliability of safety systems:
 - Better evaluation of residual power and natural convection: this led to an operation at a reduced power
 - Improvement of the redundancy of power supplies with the ultimate energy supply

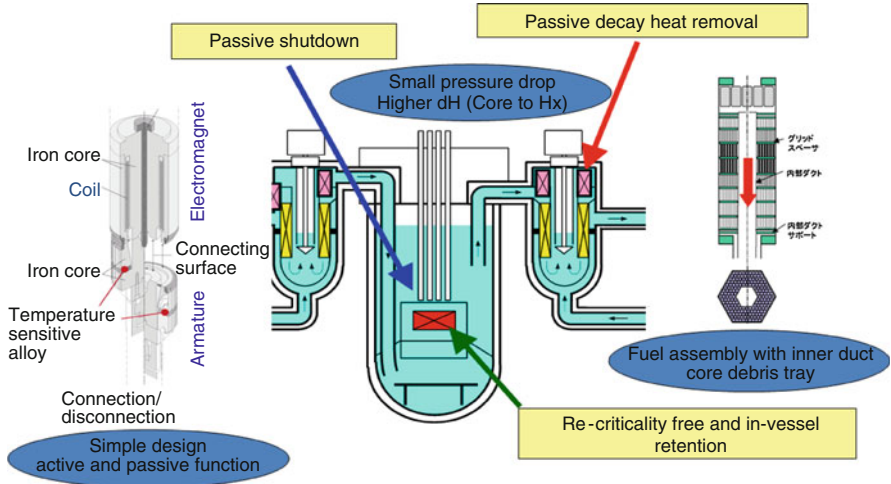


Figure 276
Enhanced safety features: Japanese proposal

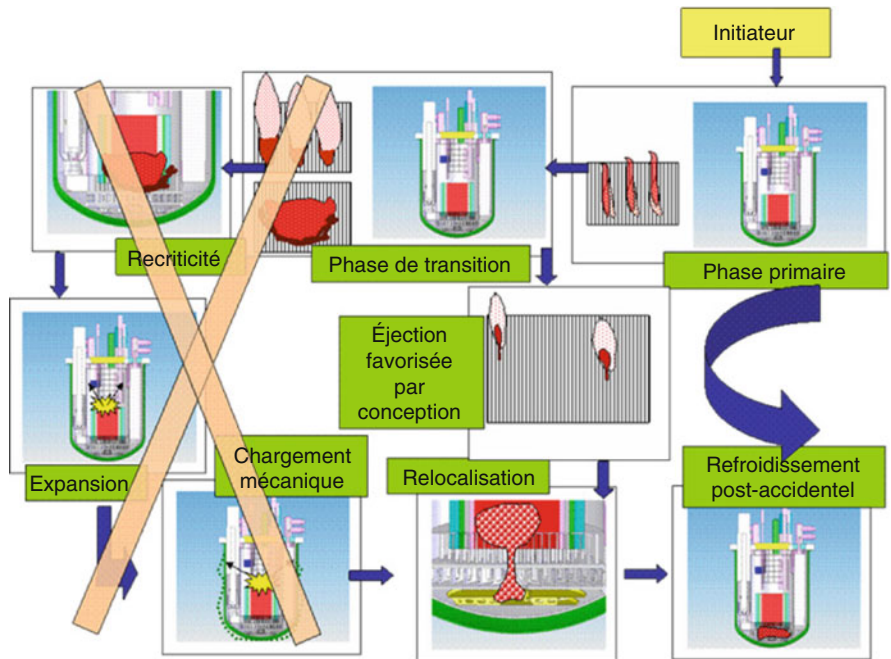


Figure 277
Elimination of mechanical consequences of CDA: French proposal

- Improvement of the diversification of reactor shutdown systems (complementary shutdown systems)
- Reevaluation of seism: reinforcement works
- Confirmation of proper behavior of the structures: extensive ISI program, including on the reactor internals
- Same as for SPX: pulverized sodium fires
- Reactor shutdown events resulting from a negative reactivity signal: the lessons learnt from a licensing point of view are that an event difficult to conceive or predict did occur and that it is thus necessary to target designs not very sensitive to specific SFR-related risks, even if one does not see a priori what would cause them
- Like in the case of SPX, one can also underline the confirmation of the favorable aspects, in particular the absence of any events due to the core (except for the RSNR) and the mastering of the water–sodium reactions

11.2 SPX-1

- The initial regulatory framework, all while reminding that there was no specific framework for the SFR, and that the standard regulatory process was applied (the same as that of the PWRs making up the fleet)
- The topic of severe accidents which resulted in a very detailed specification right from the creation decree of the reactor (definition of the core disruptive accident based on a mechanical energy level to be used for the containment design): the rationale being that the authorities fixed this energy level on the experts' judgement without awaiting the results of the studies. In parallel, studies and R&D (CABRI) were launched to demonstrate that the energy released during a CDA was below the fixed criteria. With the current EPR feedback, such an approach would turn out to be difficult today
- The SPX studies, R&D and operation showed that new situations were to be considered or to be considered differently. For example,
 - The control rod withdrawal which shows that licensing requires qualified tools to evaluate the fuel behavior
 - The external fuel storage vessel leak which highlighted the need for long-term accident management, and for fast neutron reactors, the problem of rapid core unloading and the difficulty of ISI on the internals
 - The air ingress event which shows on one hand, that situations, which seemed highly improbable, had occurred, and on the other hand that very limited effort would have been required to detect it at an early stage. The need for simple monitoring and clear procedures for the operator was also underlined
 - The taking into account of pulverized fires, which shows that it is necessary to account for, in the design, an evolution not necessarily compatible with commonly accepted and known scenarios
 - The goal is not to deal in this presentation with all the problems which occurred, but, rather, to focus on those which have had a significant impact on safety and licensing. One could also present the positive aspects of the fast neutron reactors confirmed by the SPX operation: No core incidents and no radio-protection problems were reported (the roof was a green zone); Good passive behavior (natural convection of primary and secondary circuits and of the DHR circuits), as well as negative reactivity feedbacks were demonstrated.

11.3 SPX-2

After recalling that its review by the Safety Authority was made at the time of the Chernobyl accident, and while the need for breeding in France was not topical, the presentation could focus on the failure of the severe accident exclusion strategy, the demonstration of which was based on semi-probabilistic objectives. In spite of that, the consequences of severe accidents had been taken into account based on the R&D carried out for SPX and by improving the SPX design. One could indicate that the results of SPX2 are included in the EFR project which did not undergo a licensing procedure, even if a very preliminary examination was made of it by the Safety Authority experts of the three countries involved in the project.

To help in the better understanding of the presentation, one could start with a brief description of the three reactors, at least of their safety functions.

12 Innovative Design Evolutions

12.1 In India

Selection of main options for a large FBR power plant is an important phase of the project as this gives a definite shape to the plant. The satisfactory plant operation depends on correct selection of the robust concepts. The concepts affect not only PFBR but also the future FBR program. The concepts are selected based on the energy situation in the country, economic competitiveness of the plant, design trends in other countries, operating experience of other fast reactors including FBTR, PHWR experience in India, industrial infrastructure, design and construction codes, available materials, O&M requirements, electric power grid, site characteristics, R&D requirements, safety and engineering judgment.

12.1.1 Pool Type Concept

The loop and pool concepts have been discussed qualitatively in several forums. Although many prefer pool concept, both types are in use. Pool concept is decided for PFBR due to the following advantages:

- Simple shape of reactor vessel without any nozzles, low neutron fluence and its easy in-service inspection results in high reliability.
- Large thermal inertia of the pool attenuates thermal shocks, results in slow temperature rise during decay heat removal and load throw conditions, and gives longer time for operator action.
- Capability to withstand higher work potential under core disruptive accident.
- Containment of radioactive components and fluids is easy.
- Compact primary sodium circuit layout. Russian and Japanese studies indicate that the pool type is less costly than loop type. Based on experience with loop (BN 350) and large pool (BN 600) reactors, Russians prefer pool type concept for plants with generation capacity more than 300–400 MWe.
- Preheating is simple
- Leakage in primary sodium circuit will not lead to LOCA and hence there exists high reliability of core cooling.

The pool type concept, however, calls for a few challenging aspects to be resolved successfully:

- Complex pool hydraulics: Specially developed computer codes and several scaled down water models have solved these problems successfully. Operation of EBR-II, PHENIX, PFR, BN600, and SPX has demonstrated the compliance with the predicted thermalhydraulic behavior.
- Complex seismic design of thin vessels with large mass of sodium: Robust analysis techniques developed and validated with experiments.
- There is more interdependence for overall optimization in component designs. The design of primary sodium pump, intermediate heat exchanger, inner vessel, and roof slab are closely interconnected. Few (~2–3) design iterations give good judgment for the design decisions.
- Large size of vessels need site assembly. The vessels are assembled at site workshop by welding with stringent tolerances specified.
- Difficulty in maintenance on the top of pile: Close layout of many components on reactor assembly resulting in space constraint can prolong maintenance works, thus affecting capacity factors. This has been taken care of by reducing the number of components and also making them compact. Thorough check on drawing boards toward avoiding interference and availability of adequate space for component handling and further full scale sector mock-up have been done to eliminate such problems.
- Measurement of neutron flux in start-up range and primary sodium flow require special instrumentation: Indigenous neutron flux monitoring systems have been developed.

12.1.2 Reactor Power

The following considerations lead to selection of 500 MWe capacity:

- Specific capital cost is lower for 500 MWe than for lower power, say 250 MWe (~30%).
- Medium size power is desirable for constructing more number of similar follow on plants, before a large commercial scale plant is built.
- Coal fired power plants and PHWR of 500 MWe capacities have been designed. The coal fired plants are in operation and PHWR are under construction. The conventional power equipment of this size, particularly TG set, is readily available.
- Design and development efforts for 250 and 500 MWe plants are comparable.
- Constructability of 500 MWe size components was assessed based on the experience of 220 and 500 MWe PHWR and FBTR. The Indian industries are equipped with necessary infrastructure.
- Large size pool type reactors have operated in other countries up to 1,240 MWe and basically there are no technological problems.

12.1.3 Core

Fuel

PuC-UC has been used as fuel for FBTR due to nonavailability of enriched uranium for mixed oxide option. For PFBR, enriched uranium is not required. Though carbide gives high breeding ratio, it raises safety problems in fabrication because of its pyrophorocity. Fabrication cost is also high. Fuel burnup is lower compared to oxide because of its high swelling rate. Reprocessing

on prototypic scale has not yet been done anywhere and this cost is also expected to be more. Being a large power plant, proven fuel cycle is essential. High breeding is not the objective for PFBR. As the design of the entire plant revolves around the fuel, a firm decision is essential.

Most of the large sized FBR use MOX fuel. This choice was natural since the technology of mixed oxide fuels is very similar to that of UO_2 , which is used in thermal reactors. MOX fuel has shown excellent performance in all FBR where it has been used, with respect to high burnup (up to 200,000 MWd/t on full size subassemblies) and has proven reprocessing technology. A large experimental data base with respect to satisfactory behavior under off-normal operating conditions is available. Extensive experience is also available in India from thermal reactors. Therefore, MOX is chosen as fuel for PFBR.


Core Layout

A conventional homogeneous type of layout is selected for the core and blankets. The core is provided with both radial and top and bottom axial blankets. Radial heterogeneous configuration, in spite of advantages of higher breeding ratio and reduced sodium void coefficient, is not considered due to increase in higher fissile inventory, larger core size, reduction in Doppler coefficient, requirement of increased thermal striping protection arrangements for the above core internal structures and possible difficulty in achieving optimum neutronic coupling between core zones without extensive experimental studies.

Core Height

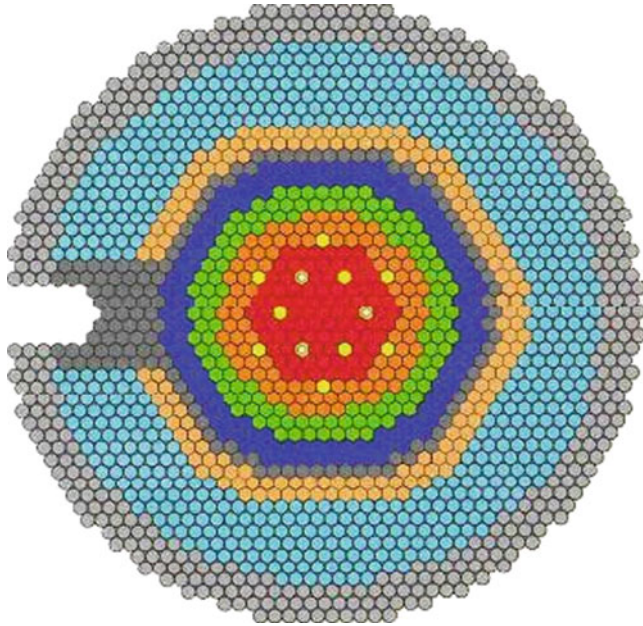
Core height has an effect on both physics and engineering design parameters. These have been studied in detail. The advantages of small core heights are increased fuel volume fraction for the same coolant pressure drop, reduced subassembly length, easier fuel fabrication, and reduced sodium void coefficient. The disadvantages are increased fissile inventory, larger number of pins, and larger core radius. Based on the parametric study to limit the penalty on fissile inventory, an active core height of 1 m with height/diameter ratio of ~ 0.5 has been selected.

Pin and Subassembly Sizes

The choice of pin diameter significantly affects the fissile inventory, fuel cycle cost, and doubling time. Parametric studies made for doubling time and fuel cycle cost considerations for oxide fuel indicate that the optimum pin diameter is 8–9 mm depending on the out-of-pile time. In order to reduce Pu inventory, a small pin diameter of 6.6 mm has been selected. Pu inventory for 6.6 mm pin is lower by $\sim 15\%$ in comparison to optimum pin diameter range. Considering factors like, subassembly worth, decay heat of spent fuel, handling loads, number of positions on grid plate, core monitoring positions, core average burnup, handling time, fabrication cost, etc., 217 fuel pins per subassembly have been selected. The active core consists of 181 fuel subassemblies of which 85 are in the inner enrichment zone and 96 are in the outer enrichment zone. The core layout is shown in  Fig. 278.

12.1.4 Shutdown Systems

For the reactor shutdown, two diverse, redundant, and independent systems, namely, control and safety rods (CSR) and diverse safety rods (DSR) have been provided to increase the reliability of shutdown. Enriched B_4C pellets are used as neutron absorbing material in both CSR and DSR.



■ Figure 278
Core layout

12.1.5 Main Heat Transport System

Main heat transport system comprises primary sodium, secondary sodium, and steam–water circuits. Sea water is the ultimate heat sink. A secondary sodium circuit is interposed between primary and steam–water circuits from the consideration of safety. It avoids entry of moderating and corrosive material into the core during sodium–water reaction in SG. Further, this avoids radioactive contamination of SG and steam–water system.

It is worth noting that the investment cost is the major contributor (~75%) of unit energy cost in comparison with 15 and 10% for O&M and fuel cycle costs, respectively. Out of 75% investment cost, ~25% is contributed by sodium heat transport systems. This indicates that the major efforts should be directed toward reducing the capital cost and construction schedule which, in turn, calls for a less number of systems and components.

A study on 2/3/4 primary and secondary sodium loops was made. Due to adoption of design improvements, the increase in size of components, when the number of loops is decreased, is not large and the increased component dimensions are within the Indian industrial capability. The reduction in the number of components helps to reduce the capital cost, construction time, and the outage time due to generic design failure/inspection/repair of components. Hence, the capacity factor is expected to be marginally higher for the case with lower number of components/loops, except for SG where more units offer higher capacity factor as failure is linked to number of tube to tube sheet welds.

Reduction in number of loops also reduces instrumentation and control, electrical systems, and the space required for layout of components. Hence, the two-loop concept has been selected

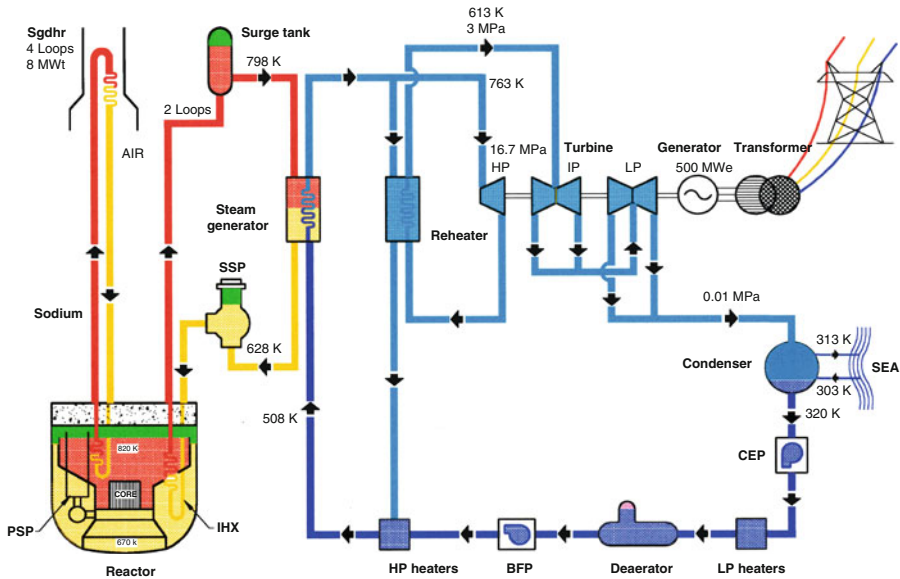


Figure 279
Main heat transport flow sheet

which results in two primary sodium pumps, four IHX, and two secondary sodium pumps. Each primary pump is flanked by two IHX as in other large pool reactors to optimize the main vessel size and economics.

Figure 279 shows the flow sheet of the main heat transport system. Liquid sodium is circulated through the core using two primary sodium pumps. The sodium enters the core at 397°C and leaves at 547°C .

The hot primary sodium is radioactive and is not used directly to produce steam. Instead, it transfers the heat to secondary sodium through four intermediate heat exchangers. The non-radioactive secondary sodium is circulated through two independent secondary loops, each having a sodium pump, two intermediate heat exchangers, and four steam generators. The choice of four steam generators per loop is based on overall optimization studies carried out considering capital cost, outage cost, and operation cost with three steam generators in the affected loop in case of a leak in one steam generator. The primary and secondary pumps are vertical, single stage, and single suction centrifugal type, with variable speed. AC drives are provided with flywheels to meet the flow coastdown requirements of 8 and 4 s, respectively. An AC pony motor of 30 kW rating is additionally provided for each of the primary pumps. The steam generator is a once through integrated type design using straight tubes and an expansion bend in each tube. The decay heat is removed using the operation grade decay heat removal system of maximum 20 MWt capacity in the steam–water system under normal conditions. In case of off-site power failure or nonavailability of steam–water system, the decay heat is removed by a passive safety grade decay heat removal circuit consisting of four independent loops. Each safety grade decay heat removal loop is rated for 8 MWt and consists of a decay heat exchanger immersed in the hot pool, one sodium/air heat exchanger, associated sodium piping, tanks, and

air dampers. Diversity is provided for decay heat exchanger, air heat exchanger, and dampers. The circulation of sodium and air is by natural convection.

Once through concept is selected for SG because of reduced water inventory, which minimizes the consequences of large sodium–water reaction and improves economics. Considering the advantages of simplification in design, manufacture, reduction in capital costs, construction schedule, operation, and availability of proven turbine, steam reheat cycle has been chosen. Most of the FBR designs use steam reheat concept to reduce the complexity. Saturation steam cycle does not permit the exploitation of higher steam temperatures possible in FBR. Hence, super heated steam cycle is adopted.

For SG, modular type concept, that is, more number of units/secondary loop, is opted, because of inherent advantages in design and construction of smaller units. In the modular concept, the tube sheet size is also relatively small. The choice of 4 SG module/loop has been arrived at based on optimization of capital cost and outage cost in case of a tube leak, with due consideration to construction schedule, while permitting $(n - 1)$ module operation. From economic considerations, integrated design, combining evaporator and superheater, is preferred over the split up units. Since steam pressure is high, the instability problem can be easily taken care of.

Finally, the combination of two PSP/four IHX/two secondary loop/four SG per loop is selected from both economic and availability considerations as compared to other combinations such as two PSP/four IHX/four secondary loop/eight SG per loop, 4 PSP/four IHX/four secondary loop/four SG module per loop, etc.

12.1.6 DHR System

Even after the reactor is shutdown, there is heat generation in the core due to radioactive decay of fission products. This heat, called decay heat, needs to be removed to prevent unacceptable temperature rise. When off-site power is available, the decay heat is removed through normal heat transfer path of primary sodium, secondary sodium, and steam–water circuits. Under loss of off-site power or nonavailability of secondary sodium circuit or steam–water circuit, the decay heat is removed through independent safety grade decay heat removal (SGDHRS).

Various options are available for SGDHRS. Main options are radiant vessel auxiliary cooling system (RVACS) wherein the heat is transferred from fuel to main vessel through natural convection and then, from main vessel by conduction, convection, and radiation (Phenix, SPX, PRISM), independent Na–air HX riding on the secondary sodium circuit with the primary and secondary sodium pumps having emergency power supply (SPX and Monju), direct reactor auxiliary cooling system (DRACS) wherein the decay heat is removed by sodium to sodium heat exchangers immersed in the hot pool, which in turn transfers the heat to sodium–air heat exchanger (SPX, EFR, DFBR, BN-600M). RVACS does not provide adequate heat transfer capabilities for the large pool type plants (>350 MWt). The function of DHR system attached with secondary sodium depends upon the availability of the latter and also requires safety grade design for the secondary sodium system. Hence, for PFBR, DRACS option is selected.

Four independent loops of 8 MWt capacity each have been selected in order to provide adequate redundancy. Even with one of these loops not being available on demand, it is possible to keep the temperatures within the acceptable values for upset conditions. Each of these loops comprises one sodium–sodium heat exchanger dipped in reactor hot pool, one sodium–air heat

exchanger, associated piping, and tanks. Except for the dampers on the air side, this system is entirely passive. In order to enhance the availability, dampers are motorized with the provision for manual operation. NaK which has low melting point is not considered as coolant in the loops of SGDHRs, because of its higher chemical affinity for air, inferior thermal properties, higher cost compared to sodium and possibility of NaK leaking into primary sodium. Sodium is used as the intermediate coolant. There is no risk of sodium freezing in SGDHRs as dampers are closed whenever the sodium temperature falls below 433 K.

12.1.7 Main Structural Materials

Twenty percent CW D9 material is selected for cladding and hexcan because of its improved resistance against swelling due to neutron irradiation, high strength at operating temperature, and good corrosion resistance against Na and fuel. Ferritic steel will be considered for hexcan of future cores. AISI 316M has been used in FBTR for sodium components except SG. There has been no problem with this material. It is decided to adopt the same grade with some improvements. SS 316 LN minimizes risk of sensitization during welding and avoids risk of IGSCC, while maintaining high-temperature strength. The embrittlement due to thermal ageing is also within acceptable limits and operating experience of other FBR has indicated satisfactory performance of this material. Hence it is selected for out-of-core sodium components. Use of SS 304 LN for cold leg is chosen except for parts where there is risk of mix up (e.g., sodium piping). Modified 9 Cr–1 Mo steel has been selected for SG because of its high mechanical strength, freedom from the risk of stress corrosion cracking (problem with stainless steels) and also decarburization (problem with 2.25 Cr–1 Mo). Based on economic considerations, A516 Gr 65/A 48 P2 (French AFNOR Std) type carbon steel is selected for top shield of the reactor because of low operating temperature, good impact strength, and compatibility with sodium vapor.

12.1.8 Operating Temperatures

High reactor outlet temperature is always preferred for achieving high thermodynamic efficiency. However, this is limited by fuel clad and component structural integrity considerations. In order to satisfy the allowable clad hotspot temperature of 973 K, the reactor outlet temperature can be as high as 833 K with 150 K ΔT across the core. As regards structural integrity of high-temperature components, with the recent advancements in high-temperature design codes and structural analyses methodology, the reactor outlet temperature is limited to 825 K. Detailed inelastic and viscoplastic analyses have been performed for control plug, inner vessel, and IHX using ORNL and Chaboche viscoplastic models. While the permissible reactor outlet temperature is about 770 K in order to satisfy the design rules of RCC-MR through “elastic” route, the viscoplastic analysis indicates that the acceptable temperature can be 825 K. Modified 9 Cr–1 Mo can permit up to 775 K steam temperature. The turbines used in conventional thermal power plants allow steam temperature of 811 K. The reactor inlet temperature and hot and cold temperatures of the sodium in the secondary sodium circuit are arrived at from overall cost optimization studies.

- Core inlet/outlet (T_{ri}/T_{ro}): 670/820 K
- Primary Na inlet/outlet to IHX: 817/667 K
- Secondary Na inlet/outlet to IHX: 628/798 K

12.1.9 Reactor Assembly

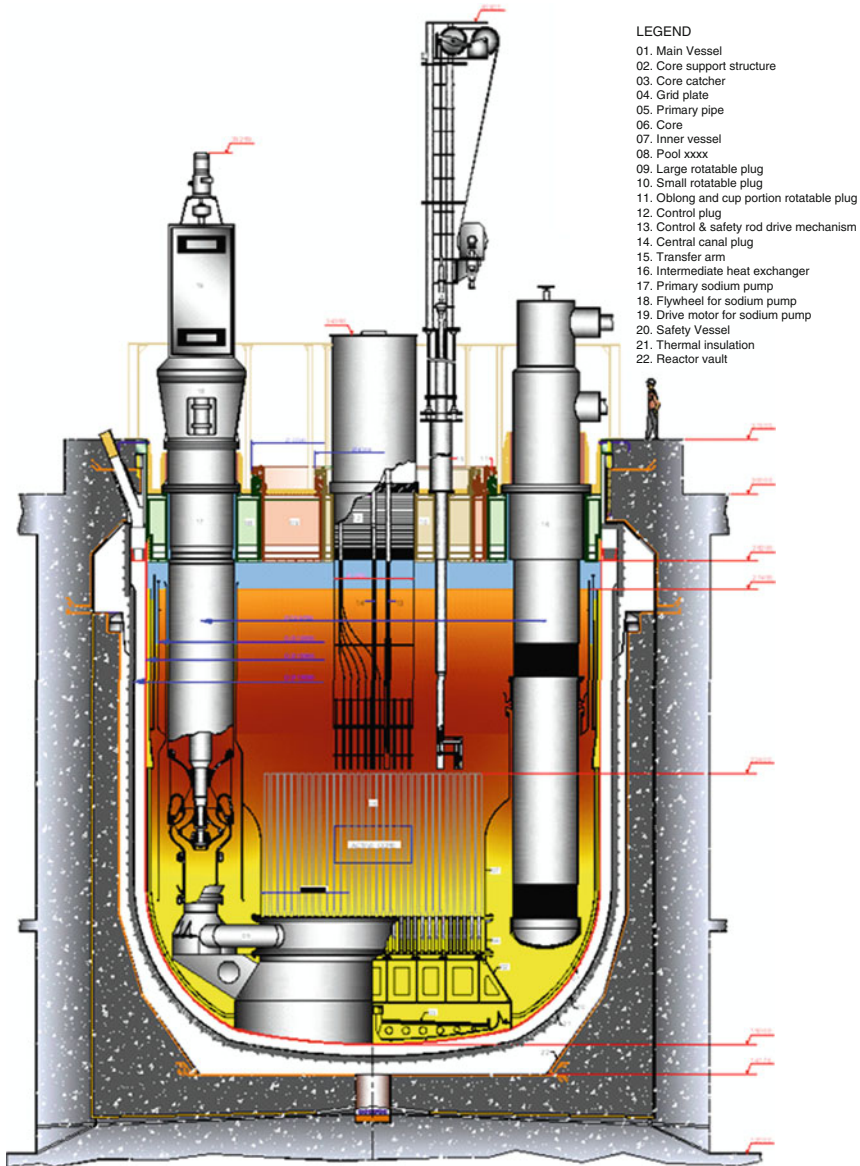
The primary sodium circuit is housed in a single vessel called main vessel (MV). This is closed at the top by top shield, which includes roof slab, large and small rotatable plugs (LRP & SRP), and control plug (CP). The roof slab supports the major components such as main vessel, rotatable plugs, two primary sodium pumps, four intermediate heat exchangers, four decay heat exchangers, eight delayed neutron detectors, etc. CP houses nine control and safety rod drive mechanisms (CSRDMs) and three diverse shutdown rod drive mechanisms (DSRDMs), core thermocouples, and three failed fuel localization modules (FFLM). The main vessel is surrounded by the safety vessel (SV) to ensure that the sodium level inside the reactor, even in the case of unlikely leak in the main vessel, will be sufficient to send the sodium into the IHX and DHX for the decay heat to get removed. To achieve this, a nominal gap of 300 mm is chosen between main vessel and safety vessel. It is ensured that the robotic ultrasonic inspection device developed for the inspection of the main and safety vessels has free access for the smooth operations.

The interspace between main and safety vessel is inerted with nitrogen. SV is supported directly on the reactor vault independent of the support for main vessel. On the outer surface of SV, metallic insulation is provided to limit the heat transfer to the vault. The core subassemblies are supported on grid plate and their combined load is transferred to main vessel through core support structure (CSS). The main vessel contains about 1,150 t of primary sodium. The sodium pool is divided into two parts, namely, hot pool and cold pool by the inner vessel. Argon is used as the cover gas above the sodium pool. The cover gas height is chosen as 0.8 m giving due considerations to thermomechanical behavior apart from other functional requirements. A core catcher is provided below the core support structure and prevents the core debris from coming in contact with the main vessel during the extremely unlikely event of CDA. Inner vessel is incorporated to separate the hot and cold pools of sodium. The assembly of main vessel and its internal and top shield along with safety vessel is called reactor assembly (► Fig. 280). The reactor vault which supports the reactor assembly consists of two walls: the inner wall supports the safety vessel and top shield carrying other components is supported on the outer wall.

The top shield is a box structure made from special carbon steel plates and is filled with heavy density concrete ($\rho = 3.500 \text{ kg/m}^3$) and provides thermal and biological shielding in the top axial direction. The principal material of construction is SS 316 LN for the vessels and boiler quality carbon steel for top shield. The biological shielding in the radial and bottom axial direction outside the main vessel is provided by the reactor vault concrete.

12.1.10 Component Handling

Fuel handling is done after 185 effective full power days with reactor in shutdown condition at a sodium temperature of 200°C . Two rotatable plugs and a transfer arm are provided for in-vessel handling of core subassemblies. For ex-vessel handling, an inclined fuel transfer machine and cell transfer machines are used. The preheated fresh subassemblies are transferred to the core using cell transfer machine and inclined fuel transfer machine. The spent fuel subassemblies are stored inside the main vessel for one campaign and then shifted to a demineralized water filled spent subassembly storage bay pool located in fuel building. Sodium sticking to subassembly is



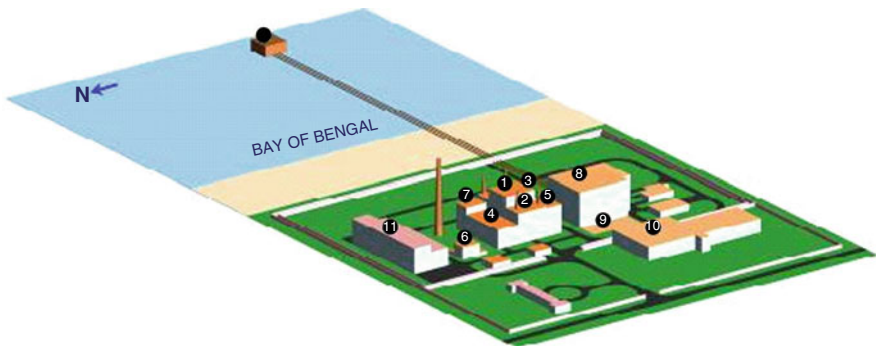
■ Figure 280
Reactor assembly

washed in spent subassembly washing facility. Leak-tight shielded flasks are provided for special handling of components like primary sodium pumps, intermediate heat exchangers, decay heat exchangers, absorber rod drive mechanisms, and transfer arm. The components are decontaminated in a separate facility provided within reactor containment building before they are

taken for maintenance. After decontamination, the above components are shifted to a separate building for maintenance purposes.

12.1.11 Plant Layout

The plant layout is evolved on the basis of a single unit. The reactor assembly, primary sodium purification, primary argon cover gas system including its tanks and cover gas purification, and decontamination facility are housed in a rectangular reactor containment building. Each of the two steam generator buildings houses four steam generators and associated components and piping. The reactor containment building, steam generator building, and fuel building are connected and laid on a common base raft (► Fig. 281). This minimizes the differential movement in piping and facilitates satisfactory working of inclined fuel transfer machine. In addition, control building, two electrical buildings, and radwaste building are also laid on the common raft and connected to form a nuclear island, to reduce the magnitude of structural response under seismic loads and length of cables. The elevation of the raft is +12 m for reactor containment building and steam generator buildings and +14 m for the other buildings of nuclear island from functional, economic, and seismic considerations (finished floor elevation is +30 m). A service building is provided to cater to the needs of plant services. The turbine building layout is selected such that the turbine missile trajectory is outside the safety-related buildings. The finished floor levels of all safety-related structures are above the design basis flood level estimated for 1,000 year return period. The finished floor levels of non-safety-related structures is based on design basis flood level of 100 year, and these structures are located 1.5 m lower than the safety-related structures from cost considerations. The diesel generators are housed in two separate safety-related buildings. A 100 m tall stack is located close to the radwaste building.



- | | |
|---------------------------------|--------------------------|
| 1. Reactor containment building | 7. RAD waste building |
| 2. Steam generator building | 8. Turbine building |
| 3. Control building | 9. Switch yard |
| 4. Fuel building | 10. Transformer yard |
| 5. Electrical building | 11. Site assembly shop |
| 6. Service building | 12. Sea water pump house |

Figure 281
Plant layout

12.2 In France

The reactor technologies deployed today use only a small part of the energetic potential of natural uranium. Internationally, the need to deploy at the appropriate time the fast reactor (FBR) that has the ability to extract about 100 times more energy from this resource is a consensus. The FBRs have also the ability to burn minor actinides, leading to a reduction in the amount and duration of life of final radioactive wastes.

In this context, the sodium-cooled fast breeder reactors (SFR) is the reference in France: It has already reached the industrial level in France and Russia. In France, more than 60 years of combined experience with Rapsodie, Phenix, and Superphenix has been accumulated. This feedback is particularly important in the field of materials (fuel, cladding and hexagonal tube, structural material of the primary circuit), the physic of the core, operation, and safety (building a very important base of experimental safety tests). However, some improvement tracks are still open:

- **Safety:** must be at least equivalent to that of GEN-III systems and be a differentiating factor compared to the past.
- **Economy:** will reduce the amount of investment and financial risk and increase availability, while reducing the operating costs. It will also extend the lifetime of the reactor to 60 years (or more).

The development of efficient techniques for in-service inspection and repair (ISIR) is a key contributor to these two areas for improvement.

The CEA and its French industrial partners, Areva and EDF, have elaborated in spring 2007 a program of work in four axes of research innovations:

- The development of an attractive and safe core, taking into account the specificities of the fast neutrons and sodium and also the ability to transmute minor actinides
- A better resistance to severe accidents and external hazards
- The search for an optimized energy conversion system, reducing the sodium risks
- The reexamination of the reactor and components design to improve the conditions of operation and the economic competitiveness

A first exploration phase of innovative options was conducted until late 2009.

12.2.1 A Core with Improved Safety Performances

This involves optimizing the core according to several criteria that are difficult to combine: improving prevention and control of accidents (reactivity insertion due to sodium voiding and minimization of the initial reactivity reserve of fuel), looking for efficient fuel, and possibility of minor actinides recycling.

An innovative core using oxide fuel was developed. It has safety features constituting a substantial step: it involves the use of large diameter fuel pins spaced by a small diameter wire, which maximizes the fuel content and thus reduces the enrichment, the reactivity margins, and the sodium voiding effect.

Such cores require a cladding material which does not swell under irradiation. Ferritic-martensitic steels strengthened by oxide dispersion (ODS) as reference, and enhanced austenitic

steels as an alternative, are candidate materials. Their development is the key of the concept. New grades of ODS have been developed in 2007 and were irradiated in the MATRIX 2 experiment in Phoenix from June 2008. A first ODS tube with the geometry considered in these new concepts of core has been successfully fabricated in late 2009.

New options for minor actinides recycling have been studied, including the heterogeneous recycling mode using blankets loaded with actinides and placed at the periphery of the core and it looks very attractive.

12.2.2 A Better Resistance to Severe Accidents and External Hazards

The R&D objectives in the field of safety are divided into two paths of study: practically eliminate by design the wool melting of core, or if not feasible, practically eliminate the accident sequences that would lead to an excessive energy release with, respect to the defense in depth, mitigation options (path, cooling, and containment melted core ["corium"]) took into account in the design of the reactor. More generally, the safety level referred to is equivalent to the EPR, with an emphasis on the robustness of the safety demonstration opposite to that of the previous SFR.

12.2.3 An Optimized Energy Conversion System Optimized to Reduce or Exclude the Risk of Sodium–Water Reaction

Various tracks have been explored to simplify the reactor design and reduce the sodium risks using a cycle of energy conversion with gas (nitrogen or carbon dioxide supercritical), development of a compact intermediate circuit using a low reactive with water and with sodium thermal coupling fluid, and design of a robust steam generator minimizing the consequences of sodium/water reactions.

For energy conversion by conventional gas, which is not the solution preferred by the industry, choosing to work with a high pressure gas is preferred to a temperature increase of sodium output. Regarding safety, the elimination of intermediate circuit seems to be not reasonable. For supercritical CO₂ option, the intermediate circuit is necessary because the fluid reacts chemically with the sodium. Attractive efficiency seems yet accessible.

For the energy conversion using a water–steam cycle, seven intermediate coupling fluids have been selected (liquid metals and molten salts) for a thorough evaluation. The Pb-Bi was finally chosen and a long-term program concerning the feasibility points of this alloy has been launched for 3 years beginning 2009. The design of an integrated intercooler/steam generator component with Pb/Bi as a coupling fluid has been studied in some depth.

Finally are proposed steam generator designs for confining the consequences of any sodium–water reaction (including limit scenarios of simultaneous failure of 100% of tubes of a SG module) that in this aim of a robust safety demonstration. SG modules with a capacity of 150 MW seem accessible. Studies on structural materials lead to consider the application of ferritic-martensitic 9% Cr steels to the steam generators, allowing a greater compactness.

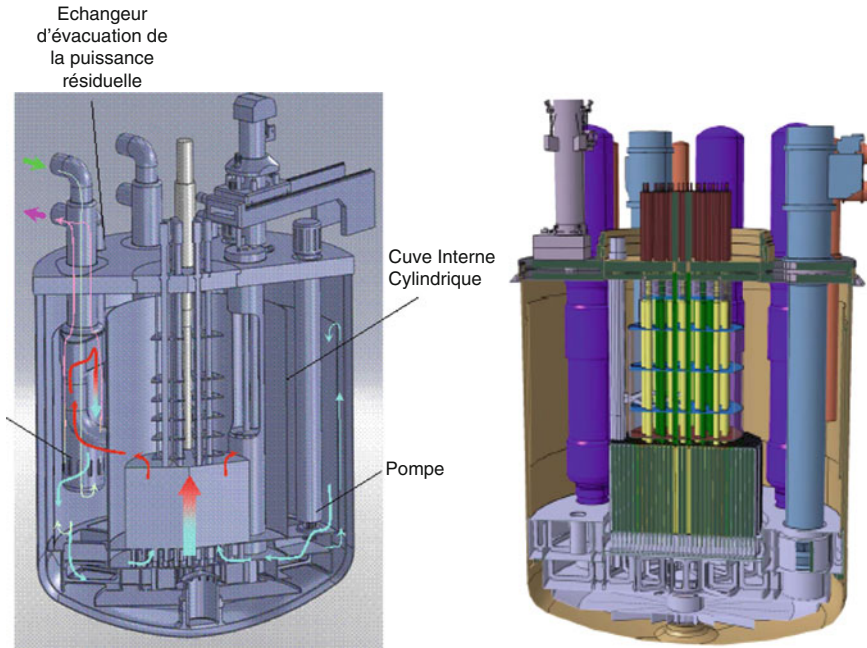


Figure 282

Examples of pool reactors with cylindrical internal vessel and simplified core support structures

12.2.4 A Reexamination of the Reactor and Its Components Design

The work on reactor sketches aims to provide a report, comparing pool and loop designs and comparing between high-power units called “monolithic” and modular concepts. Studies on the pool reactor were particularly highlighting the potential interest of concepts with:

- Cylindrical internal vessel (an example is given in [Fig. 282](#)),
- Simplified and integrated support structures of the core
- Slab cooled by air

12.2.5 ASTRID Program

The ASTRID prototype (as for Advanced Sodium Technological Reactor for Industrial Demonstration) is seen as an industrial prototype prior to the first-of-a-kind, meaning that extrapolability of the technical options and of the safety demonstration is of utmost importance. The reactor will also provide some irradiation capacities especially in order to validate the expected properties for the new fuel (big pin and ODS clad) and the ability to burn Minor Actinides in an industrial way.

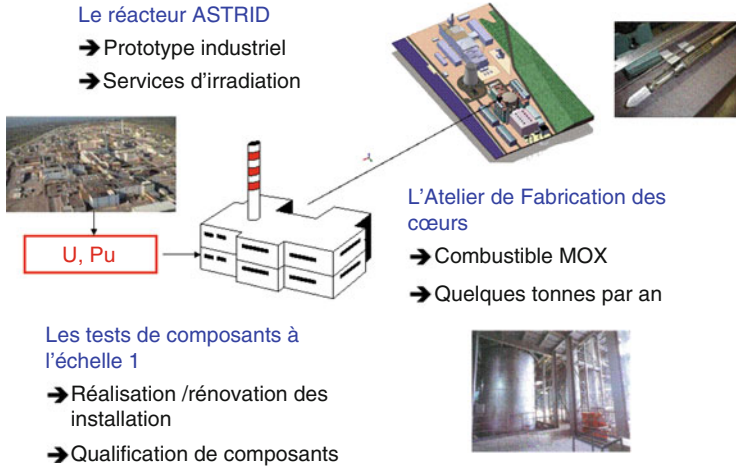


Figure 283
Components of the ASTRID program

The ASTRID program (► *Fig. 283*) defined by CEA also includes the facility to manufacture the fuel for the reactor, of limited capacity, from 5 to 10 t heavy metal per year. The refurbishment of existing testing facilities and the construction of new tools is part of the program as well.

ASTRID shall be coupled to the grid with an electrical power of about 600 MWe. It shall integrate operational feedback of past and current reactors. It is seen as a full Generation IV prototype reactor. Its safety level shall be at least as good as current third-generation reactors, with strong improvements on core- and sodium-related issues. After a learning period, the reactor shall have a high load factor (e.g., more than 80%). The reactor shall provide capability for demonstration of transmutation of minor actinides, at larger scale than previously done in Phénix. And of course, the investment costs of the prototype shall be kept to the lowest possible, with technical options compatible with later deployment on a commercial facility.

References

- A review of fast reactor program in Japan. In: Annual Meeting of the technical working group on fast reactors (TWG-FR), IAEA Vienna, 26–29 May 2008
- ABAQUS Version 6.7 Simulia Dassault Systems, USA
- Absorber materials, control rods and designs of shutdown systems for advanced LMFR. (1996). IAEA-TECDOC-884
- AFNOR 1996, A3-406, RCC-MR, RB 3261.123, 2007 issue. AFCEN, Paris
- AGT 1 sub-group 1 (AEA Windscale and Harwell, CEA Cadarache, KfK Karlsruhe, Interatom, Belgonucleaire) (ed) (1990) Catalogue Europeen des propriétés de l'oxyde mixte (U,Pu)O₂ – fast reactor data manual 1. CEA
- Anderson EP (ed) (1978) Fermi I: new age for nuclear power. ANS publication
- Anzieu P, Serpantie J-P, Verwaerde D, Dufour Ph, Martin Ph (2007) A program on innovative SFR in France. In: Proceedings of ICAPP2007, paper 7398, Nice Acropolis, France, 13–18 May 2007
- Arai Y, Suzuki Y, Iwai T, Ohmichi T (1992) Dependence of the thermal conductivity of (U,Pu)N on porosity and plutonium content. J Nucl Mater 195:37

- Arnoldov MN et al (2004) The permeability and solubility of hydrogen in a lead-bismuth melt of eutectic composition. *High Temp* 42(5):715–719
- Arrêté du 15 mai 2006 relatif aux conditions de délimitation et de signalisation des zones surveillées et contrôlées et des zones spécialement réglementées ou interdites compte tenu de l'exposition aux rayonnements ionisants, ainsi qu'aux règles d'hygiène, de sécurité et d'entretien qui y sont imposées
- ASME Sec III Div 1, Subsection NB-3133, Components under External Pressure, 2007
- Astegiano J-C (1990) Assessment of thermal-hydraulic characteristics of primary circuit. *Nucl Sci Eng* 106
- Astegiano JC et al (1981) EFR primary system thermal-hydraulics – status on R&D and design studies. In: Proceedings of the international conference on fast reactor and related fuel cycles, Kyoto, Japan
- Athiannan K (2002) Buckling of imperfect cylindrical shell. PhD thesis, IIT Madras
- Auger T et al (2008) Liquid metal embrittlement of T91 and 316L steels by heavy liquid metals: a fracture mechanics assessment. *J Nucl Mater* 377(1):253–260
- Axisa F, Antunes J Modelling of mechanical systems. Fluid Structure Interaction Hermès
- Bagley H, Harbourne B, Lennov T, Linekar G, Mignanelli M, Plitz H, Pluchery M, Rouault J (1989) Synthesis report on the understanding of failed LMFBR fuel element performance. CEA/UKAEA/KFK/PSB. Report IV 307 KL IV
- Balbaud-Célérier F et al (2001) Investigation of models to predict the corrosion of steels in flowing liquid lead alloys. *J Nucl Mater* 289(3):227–242
- Baldasari JP et al (1984) Open azimuthal thermosyphon in annular space – comparisons of experimental and numerical results. In: Liquid metal engineering and technology. BNES, London, pp 463–467
- Basmajian JA et al (1972) *Nuclear Technology* 16:238
- Benamati G et al (2002a) Mechanical and corrosion behaviour of EUROFER 97 steel exposed to Pb-17Li. *J Nucl Mater* 307–311, Part 2, 1391–1395
- Benamati G et al (2002b) Temperature effect on the corrosion mechanism of austenitic and martensitic steels in lead-bismuth. *J Nucl Mater* 301(1):23–27
- Blanks DM (1985) Fuel handling options for commercial fast breeder reactors. In: International conference on engineering developments in reactor refueling, England, 13–15 May 1985
- Bernard H (1989) Advanced fuel fabrication. *J Nucl Mater* 166:105
- Bertrand F, Devictor N (2006) Combination of deterministic and probabilistic safety analysis in support to the design of new nuclear reactor. In: Proceedings of the IAEA technical meeting on effective integration of deterministic and probabilistic safety analysis in plant safety management, Barcelona, Spain, 4–8 September 2006
- Bettes C, Judd AM, Lewis WWJ (1994) Avoiding thermal striping damage: experimentally based design procedures for high cycle thermal fatigue. IWGFR/90. In: Specialists meeting on correlation between material properties and thermohydraulics conditions in LMFBRs, Aix-en-Provence, France, 22–24 November 1994
- Betts C, Bourman C, Sheriff N (1983) Thermal striping in liquid metal cooled fast breeder reactors. In: Second international topical manufacturing on nuclear reactor thermal hydraulics, NURETH-2, Santa Barbara, California, pp 1292–1301
- Billone MC, Jankus VZ, Kramer JM, Yang CI (1977) Progress in modelling carbide and nitride fuels performance in advanced LMFBRs. In: Advanced LMFBR fuels – topical meeting proceedings, 10–13 October 1977, Tucson, Arizona, USA
- Billone et al (1986) Status of fuel element modeling codes for metallic fuels (pp. 5.77–5.91). In: Reliable fuels for liquid metal reactors, TUCSON conference, Arizona, September 1986, p. 5.77
- Blanchet Y, Oby P, Louvet J (1981) Treatment of fluid–structure interaction with the SIRIUS computer code. In: SMIRT-6, Paris, B8/8
- Blay N, Touboul F, Blanchard MT, Lebreton F (1997a) Piping seismic design criteria: experimental evaluation. In: SMIRT 14, Lyon, K15/4, pp 95–102
- Blay N, Touboul F, Blanchard MT, Lebreton F, Cara S (1997b) Piping seismic design criteria: test simulations. In: SMIRT 14, Lyon, K15/5, pp 103–110
- BN-350 reactor. (1969). *Fuel Processing Technology* 12:323–334
- Bogolovskaia GP et al (2002) Comparative assessment of thermophysical and thermohydraulic characteristics of lead, lead-bismuth and sodium coolants for fast reactors. IAEA-TECDOC-1289, Vienna
- Borstedt HU, Champeix L (1989) Corrosion in fast breeder reactors. EFC publication N°1. The Institute of Metals, Brussels, Belgium, ISBN 0-901462-73-X
- Bose MRSC, Thomas G, Palaninathan R, Damodaran SP, Chellapandi P (2001) Buckling investigations on a nuclear reactor inner vessel model. In: Experimental mechanics. SAGE publications, vol 41, no 2, pp 144–150

- Bour C, Sperandio M, Louvet J, Rieg C LMFBR's core disruptive accident mechanical study of the reactor bloc of SPX-1. In: Tenth SMIRT, Anaheim, USA
- Bourganel S Etudes de radioprotection dédiées au réacteur RNR-Na pour la configuration de cœur Valentin V2B. Rapport DM2S/SERMA/LPEC/RT/08-4602/A
- Brehm WF et al (1987) Corrosion and fission products in primary systems of liquid metal cooled reactors in the USA. In: Proceedings of fission and corrosion product behaviour in primary circuit of LMFBRs, IWGFR/64, RFA, Karlsruhe, 5–8 May 1987; Feuerstein H, Thorley AW (eds) (1987) KfK 4279, pp 75–92
- Briceno DG et al (2001) Behaviour of F82H mod. stainless steel in lead-bismuth under temperature gradient. *J Nucl Mater* 296:265–272
- Brissonneau L et al (2008) Evaluation of alternative fluids for SFR intermediate loops. In: Proceedings of ICAPP'09, Tokyo
- Brissonneau L, Simon N, Saez M, Balbaud F, Rochwarger D, Baqué F, Rodriguez G, Gerber A, Menou S, Prêle G, Capitaine A (2009) The potential use of an alternative fluid for SFR intermediate loops: selection and first design. In: Proceedings of FR'09, Kyoto, Dec 2009
- Breuil E, Sperandio M, Waackel N, Djouini C, Julien JF (1991) How to improve the post-buckling stiffness of the LMFBR roof slab's bottom plate. In: SMIRT 11 transactions, vol E, August 1991, Tokyo, Japan
- Brochard J, Combescure A, Tomassian R, Locatelli Th (1991) Thermal buckling influence on reduction of critical buckling loads. In: SMIRT 11 transactions, vol E, August 1991, Tokyo, Japan
- Buiron L (2009) (Courriel de) Données SFR 3600 pour le dimensionnement des protections. (DER/SPRC) du 11 mars 2009
- Buland P (1995) Symphony experimental mockup SMIRT
- Bunch WL, O'Dell LD (1969) Fission product inventory and decay heat associated with FTR fuel. BNWL-961
- Cabrillat et al (1997) Benchmark on a thermal ratchetting test. Comparison of different constitutive models. Transactions of the 14th conference on structural mechanics (SMIRT 14th), LW/4, Lyon, France
- Cahalan JC, Wei TYC (1990) Modeling development for the SAS4A and SASYS computer codes. In: Proceedings of international fast reactor safety meeting, Snowbird, Utah
- Cahalan JE et al (1977) A preliminary users guide to version 1.0 of the SAS 3D accident analysis code. SR-239831. ANL
- Cameron IG et al (1978) The computer code SEURENUK-2 for fast reactor containment studies. *Comp Phys Comm* 13:197
- Carter JC et al (1970) SAS1A – a computer code for the analysis of fast reactor power and flow transients. ANL-7607
- CEA internal reports
- CEA (2003) <http://www-cast3m.cea.fr/cast3m/>. CAST3M – user manual
- Chang YM, Gvildys J, REXCO-HEP (1975) A two-dimensional computer code for calculating the primary system response in fast reactors. ANL-75-19. Argonne National Laboratory
- Chang YI, Konomura M, Lo Pinto P (2007) A case of small modular fast reactor. *J Nucl Sci Technol* 44(3):264–269
- Chapuliot et al (2005) Hydro-mechanical analysis of thermal fatigue in a mixing tee. *Nucl Eng Des* 235:575–596
- Chellapandi P (2000a) FUSTIN: a code for structural analysis of primary containment under CDA: mathematical modeling. PFBR/31050/DN/1016
- Chellapandi P, Chetal SC, Bhoje SB (2000b) Effect of reactor internals on structural integrity of PFBR main vessel under CDA. ASME, PVP 403:161–172
- Chellapandi P, Chetal SC, Raj B (Aug 2008) Investigation on buckling of FBR vessels under seismic loading with fluid structure interactions. *J Nucl Eng Des* 238:3208–3217
- Chellapandi P, Chetal SC, Raj B Investigation of structural mechanics failure modes in FBR. In: Raj B et al (eds) Pressure vessels and piping: codes, standards, design and analysis. Narosa Publishing House, New Delhi (in press)
- Chellapandi P, Suresh Kumar R, Chetal SC, Raj B (2007) Numerical and experimental simulation of large elastoplastic deformations of FBR main vessel under core disruptive accident loadings. In: IMPLAST 2007, symposium on plasticity and impact mechanics, Ruhr University, Germany, 21–24 August 2007
- Chellapandi P, Velusamy K, Kannan SE, Om Pal Singh, Chetal SC, Bhoje SB (2002) Core disruptive accident analysis in prototype fast breeder reactor. In: First national conference on nuclear reactor safety, 25–27 November 2002, Mumbai, India
- Ciampichetti A et al (2008) LBE-water interaction in sub-critical reactors: first experimental and modelling results. *J Nucl Mater* 376(3): 418–423
- Clement G, Drubay B (1991) Influence of cyclic loading on buckling progressive buckling. In: SMIRT 11 transactions, vol E, August 1991, Tokyo, Japan

- Combescur A (1999) Proposition of a design for creep buckling. In: LMT-Cachan/CEA-DMT-SEMT, France, transactions of the 15th conference on SMIRT-15, Seoul, Korea, 15–20 August 1999
- Combescur A, Brochard J (1991) Recent advances on thermal buckling new results obtained at CEA. In: SMIRT 11 transactions, vol E, August 1991, Tokyo, Japan
- Conceptual design of advanced fast reactors. In: Proceedings of a technical committee meeting, Kalpakkam, 3–6 October 1995. IAEA-Tecdoc-907
- Core safety improvements in sodium fast reactors. In: INPRO meeting, CEA, Cadarache, 7 February 2007
- Courouau JL (2004) Electrochemical oxygen sensors for on-line monitoring in lead-bismuth alloys: status of development. *J Nucl Mater* 335(2):254–259
- Courouau JL (2007) Chemistry control and monitoring systems. In: Fazio C (ed) Handbook on lead-bismuth eutectic alloy and lead properties, materials compatibility, thermal-hydraulics and technologies, OECD, pp 129–177
- Cowler MS, Hancock SL (1979) Dynamic fluid-structure analysis of shells using the PISCES-2DELK computer code. In: SMIRT-5, Berlin, B1/6
- Crawford et al (2007) Fuels for sodium cooled fast reactors – US perspective. *Journal of Nuclear Materials* 371:202–231
- Crespo LS et al (2001) Short-term static corrosion tests in lead-bismuth. *J Nucl Mater* 296:273–281
- Defense in depth in nuclear safety – INSAG-10 (1996). A report of international. Nuclear Safety Advisory Group, IAEA, Vienna
- Delangre E (2001) Fluides et solides Les éditions de polytechnique
- Design of the Clinch river breeder reactor plant steam generator. (1976). *Nucl Tech* 28:305–314
- Donea J, Fasoli-Stella P, Giuliani S, Halleux JP, Jones AV (1980) The computer code EURDYN-1M for transient dynamic fluid-structure interaction. EUR 6751. Commission of the European Communities
- Dufour Ph (2007) Post accident heat removal analysis for SPX and EFR. In: CEA-IGCAR technical seminar on liquid metal fast reactor safety aspects related to severe accidents, Kalpakkam, India, February 2007
- Dunn FE et al (1974) The SAS2A LMFBR accident analysis computer code. ANL-8138
- Eguchi Y, Yamamoto K, Funada T et al (1994) Gas entrainment in the IHX vessel of top-entry loop type LMFBR. *Nuclear Engineering and Design* 146:373–381
- Eptein M, Grolmes MA, Henry RE, Fauske KK (1976) Transient freezing of a flowing ceramic fuel in a steel channel. *Nucl Sci Eng* 61:310
- Evaluated nuclear data file (2008). <http://www-nds.iaea.org/exfor/endl.htm#1>
- Experience with liquid metal fast breeder reactor steam generators – U.S design. (1981). *Nuclear Technology* 55:60–87
- Farrar B (1990) Use of the PHOENICIS CFD code to simulate the 3D thermal hydraulic behavior of a pool type LMFBR hot plenum. In: IMechE seminar on thermohydraulics of nuclear reactors, London, pp 95–105
- Farvacque M et al (2003) CATHARE 2 v2.5: a fully validated CATHARE version for various applications. In: Proceedings of NURETH-10, Séoul, Korea, 2003
- Fazio C et al (2001) Compatibility tests on steels in molten lead and lead-bismuth. *J Nucl Mater* 296(1–3):243–248
- Fazio C (2007) handbook on lead-bismuth eutectic alloy and lead properties, materials compatibility, thermal-hydraulics and technologies, vol 1. OECD, Paris
- Fink JK (2000) Zircaloy thermal conductivity. Argonne National Laboratory
- Fleitman AH et al (1971) Mercury as a nuclear coolant. *Nucl Eng Design* 16:266–278
- Foletti C et al (2008) ENEA experience in oxygen measurements. *J Nucl Mater* 376(3):386–391
- Fontaine B (1997) Seismic analysis of LMFBR reactor cores. SYMPHONY mockup SMIRT
- François G et al (2008) Sodium fast reactor concepts. In: Proceedings of ICAPP'08, Anaheim
- Francois G, Azarian G (1989) SUPER PHENIX reactor block thermohydraulic behaviour comparison between calculations and experimental results. In: Tenth international conference on structural mechanics in reactor technology, Lyon, France, pp 37–42
- French steam generator experience – Phenix and beyond. (1976). *Nuclear Technology* 28:482–488
- Fritz J (1972) The effect of liquids on the dynamic motions of immersed solids. *J Eng Ind*
- Funada T, Yamamoto K, Eguchi Y et al (1991) Gas entrainment in the IHX vessel of top-entry loop type LMFBR. In: Proceedings of NURETH-5, Salt Lake City, pp 1399–1406
- Gabor JD et al (1974) Studies and experiments on heat removal from fuel debris in sodium. In: Proceedings of fast reactor safety conference, FONF-740401, p 823

- GCFS (2007) Fondamentaux de Sûreté Nucléaire pour la conception des Réacteurs de Génération IV. Safety Approach for the design and the assessment of future nuclear systems. FRENCH ADVISORY GROUP ON SAFETY, ICAPP
- Gelineau O, Sperandio M (1994) Thermal fluctuation problems encountered in LMFBRs. IAEA-IWGFR/90. In: Specialistic meeting on correlation between material properties and thermohydraulics conditions in LMFBRs, Aix-en-Provence, France, 22–24 November 1994
- Gelineau et al (1999) Predictive methods applied to thermal striping problems and recommendations, SMIRT 15. Paper F 0/6
- GenIV GIF. Basis for the safety approach for design & assessment of generation IV nuclear systems. Report GIF/RSWG/2007/002/Rev.1
- Gessi A et al (2005) Parametric experiments on Eurofer steel corrosion by Pb-17Li; LB-A-R-022. Final report on EU Task TW2-TTBC003.D3, ENEA Brasimone
- Gessi A et al (2008) Corrosion experiments of steels in flowing Pb at 500°C and in flowing LBE at 450°C. *J Nucl Mater* 376(3):269–273
- Gibert RJ (1988) Vibration des structures. Eyrolles
- Glueckler EL, Huang TC, Josph D (1979) In-vessel retention of core debris in LMFBRs. In: Proceedings of international meeting in fast reactor safety technology, Seattle
- Glueckler EL et al (1982) Analysis of in-vessel core debris retention in large LMFBRs. In: Proceedings of the LMFBR safety topical meeting, Lyon
- Golden GH, Tokar JV (August 1967) Thermophysical properties of sodium. ANL-7323. Argonne National Laboratory, Illinois
- Goldstein S, Joly J, Vidard M (1979) Thermal analysis of the penetrations of a LMFBR. In: Fifth international conference on structural mechanics in reactor technology
- Gorse-Pomonti D et al (2007) Liquid metals for nuclear applications. *J Non-Crystalline Solids* 353:32–40, 3600–3614
- Gosset G, Simeone D, Quirion D (2000) Endommagement du carbure de bore sous irradiation neutronique : évaluation en diffraction X. *J Phys Fr IV(Pr)*, 10–55
- Gosset J, Gicquel R, Lecomte M, Queiros-Conde D (2005) Optimal design of the structure and settings of nuclear HTR thermodynamic cycles. *Int J Thermal Sci* 44(12):1169–1179
- Glasbrenner H et al (2001) Corrosion investigations of steels in flowing lead at 400°C and 550°C. *J Nucl Mater* 296(1-3):237–242
- Graham J (1971) Fast reactor safety. Academic, New York
- Graveleau JL, Louvet P (1979) Calculation of fluid-structure interaction for reactor safety with the CASSIOPEE code. In: Proceedings of the fifth international conference on structural mechanics in reactor technology, Paper B1/7, Berlin, Germany
- Gregory JN et al (1956) The static corrosion of nickel and other materials in molten caustic soda, AERE C/M 272, Harwell, Berks
- Guérin Y, Rouault J (1986) In-pile behaviour of carbide fuel elements designed for low doubling time. In: Proceedings of the international conference on reliable fuels for LMR, 7–11 September 1986, Tucson, Arizona, USA
- Guidez J, Gognet G (1990) Simulation by water-test of the argon entrainment in the sodium breeder. In: Proceedings of second international symposium on gas transfer at water surfaces, Minneapolis
- Harbur et al (1970) Studies on U–Pu–Zr alloy system for fast breeder applications. Report TID-4500
- Harish R, Sathiyasheela T, Stinivasan GS, Om Pal Singh (1999) KALDIS: a computer code system for core disruptive accident analysis of fast reactors. IGC-208
- Harlow FH, Welch JE (1965) Numerical calculation of time dependent viscous incompressible flow of fluid with free surfaces. *Physics of Fluids* 8:2182–2188
- Haubensack D, Thevenot C, Dumaz P (2004) The COPERNIC/CYCLOP computer tool: pre-conceptual design of generation 4 nuclear systems. In: 2nd international topical meeting high temperature reactor technology, HTR 2004, Beijing, China, 22–24 September 2004
- Heuvel HJ, Höller P, Donner P (1985) Absorber material cladding chemical interaction in vented FBR absorber pins. *J Nucl Mat* 130:517
- Hiroshi Akiyama. 'Seismic Resistance of FBR Components Influenced by Buckling, Kajma Institute publishing, Japan, 1997
- Hirt CW, Nichols BD (1981) Volume of fluid (VOF) method for the dynamics of free boundaries. *Journal of Computational Physics* 39: 201–225
- Hu LW, Kazimi MS (2006) LES benchmark study of high cycle temperature fluctuations caused by thermal striping in a mixing tee. *J Heat Fluid Flow*
- IAEA annual reports: status of fast reactor programmes
- IAEA (1996) Absorber materials, control rods and designs of shutdown systems for advanced liquid metal fast reactors. IAEA-TECDOC-884
- IAEA (1996) Defense-in-depth in nuclear safety. IAEA safety series no. 75. INSAG-10

- IAEA (April 1999) Status of liquid metal cooled fast reactor technology. IAEA-TECDOC-1083
- IAEA (2000) Safety of nuclear power plants: design. IAEA safety standards series NS-R-1
- IAEA (2005) Assessment of defence in depth for nuclear power plants. IAEA safety report series no. 46
- IAEA (2007) Proposal for a technology – neutral safety approach for new reactor designs. IAEA-TECDOC-1570
- IAEA INSAG10 Defence in depth in nuclear safety
- Igari et al (1993) Proposal of a new estimation method for the thermal ratchetting of a cylinder subjected to a moving temperature distribution. Nucl Eng Des 139:261–267
- Igari et al (2002) Inelastic analysis of new thermal ratchetting due to a moving temperature front. Int J Plas 18:1191–1217
- INEEL (2001) RELAP5-3D^f code manual, vol I: code structure, system models, and solution methods. Report INEEL-EXT-98-00834. Idaho National Engineering and Environmental Laboratory, Idaho Falls, Idaho
- International symposium on fast breeder reactors: experience and future trends, Lyon, France, 22–26 July 1985
- Iritani Y et al (1991) Development of advanced numerical simulation of thermal stratification by highly-accurate numerical method and experiments. In: Proceedings of the international conference on fast reactor and related fuel cycles, Kyoto, Japan
- Iwai T, Nakajima K, Arai Y, Suzuki Y (1996) Fission gas release of uranium–plutonium mixed nitride and carbide fuels. IAEA-TECDOC-970. Studies on fuels with low fission gas release
- Iwasaki T, Konashi K, (2009) Development of hydride absorber for fast reactor, Application of hafnium hydride to control rod of large fast reactor. J Nucl Sci Tech 46(8): 874–882
- Jackson JE, Nicholson RB (1972) VENUS-II; a LMFBR disassembly program. ANL-7951
- Jasserand F Etudes de radioprotection dédiées au réacteur RNR-Na pour la configuration de cœur Valentin V2B. Rapport DM2S/SERMA/LPEC/RT/09-4694/A
- Justin F, Natta M, Orzoni G (1985) Safety criteria for the future LMFBRs in France and main safety issues for the Rapide 1500 project. In: Proceedings of the international topical meeting on fast reactor safety, Knoxville
- Kaguchi H et al (1999) Strain limits for structural integrity assessment of fast reactors under CDA. In: Proceedings of ICONE-7, Tokyo, Japan
- Kasahara, Lejeail (2002) Frequency response approach for thermal fatigue induced by random fluctuation of fluid temperature. ASME, PVP
- Kasahara et al (2002) Structural response function approach for evaluation of thermal striping phenomena. Nucl Eng Des 212:281–292
- Kazimi MS, Tsai SS, Gasser RD (1977) Post accident fuel relocation and heat removal in LMFBR. BNL-50570
- Kikuchi K et al (2004) Lead-bismuth eutectic compatibility with materials in the concept of spallation target for ADS. JSME Int J Ser B Fluids Thermal Eng 47(2):332–339
- Kobus H (1991) Introduction to air–water flows. In: Wood IR (ed) Air entrainment in free surface flows. IAHR hydraulic structures design manual. A.A. Balkema, Rotterdam
- Kondo M et al (2005) Metallurgical study on erosion and corrosion behaviors of steels exposed to liquid lead-bismuth flow. J Nucl Mater 343(1–3):349–359
- Kondo M et al (2006a) Corrosion resistance of Si- and Al-rich steels in flowing lead-bismuth. J Nucl Mater 356(1–3):203–212
- Kondo M et al (2006b) Study on control of oxygen concentration in lead-bismuth flow using lead oxide particles. J Nucl Mater 357(1–3): 97–104
- Konys J et al (2004) Oxygen measurements in stagnant lead-bismuth eutectic using electrochemical sensors. J Nucl Mater 335(2): 249–253
- Kotake S et al (1993) Application of the PSA method to decay heat removal systems in large scale FBR design. In: Proceedings of the IAEA specialists' meeting on evaluation of decay heat removal by natural convection, Oarai, Japan
- Latgé PhD (October 1981) Study of the Na₂O crystallization in liquid sodium. Application to the sodium purification in SFR
- Latge S, Sellier (1993) Oxidation of zirconium–titanium alloys in liquid sodium: validation of a hot trap, determination of the kinetics. In: Borgstedt HU (ed) Material behaviour and physical chemistry in liquid metal systems, vol 2. Plenum Press, New York
- Laxman D et al (2004) Free level fluctuations study in 1/4 scale reactor assembly model of PFBR. In: NUTHOS-6, Nara, Japan, 4–8 October
- Le RC, Kayer G (1979) An internal core catcher for a pool type LMFBR and connected studies. In: Proceedings of international meeting on fast reactor safety technology, Seattle
- Lee YK, Hugot FX Validation/qualification du code Monte Carlo TRIPOLI-4.4 en

- neutronique-criticité: résultats. Rapport SERMA/LEPP/RT/05-3613/A
- Lee YK, Hugot FX Validation/qualification du code Monte Carlo TRIPOLI-4.4 en protection: résultats. Rapport SERMA/LEPP/RT/05-3621/B
- Lejeail, Kasahara (2005) Thermal fatigue evaluation of cylinders and plates submitted to fluid temperature fluctuations. *Int J Fat* 27:768–772
- Lenoir G et al (1981) Thermal hydraulics of the annular spaces in roof slab penetrations at liquid sodium cooled fast breeder reactor. In: Sixth international conference on structural mechanics in reactor technology, Paris, pp 104–118
- Libman J (1996) Elements of nuclear safety. Les Editions de Physiques
- Liquid metal cooled reactors: experience in design and operation. (2007). IAEA TECDOC – 1569
- Liquid metal fast breeder reactor steam generator design and experience in UK. (1986). *Nuclear Energy* 6:355–360
- Louvet J, Hamon P, Smith BL, Zucchini A (1987) MARA 10: an integral model experiment in support of LMFBR containment analyses. In: Ninth SMIRT, vol E
- Marth W (1988) Sodium – still the best coolant for fast breeder reactor. In: Proceedings of LIMET, SFEN, AvignonSFEN
- Martin Ph, Rouault J, Serpantie J-P, Verwaerde D French program towards a GEN IV sodium cooled fast reactor. In: ENC 2007, Brussels, Belgium, 16–20 Sept 2007
- Martin P, Pelletier M, Every D, Buckthorpe D (eds) (2008) French and United Kingdom experience of high-burnup mixed-oxide fuel in sodium-cooled fast breeder reactors. *Nucl Tech* 161:35
- Maruyama T, Onose S, Kaito T, Oriuchi H (1997) Effect of fast neutron irradiation on the properties of boron carbide pellet. *J Nucl Sci Tech* 34(10):1006
- Maruyama T, Onose S (1999) Fabrication and properties of boron carbide/copper cermet, *J Nucl Sci Tech* 36(4):380
- Matsuura S, Nakamura H (1997) Shear bending buckling analysis of fast breeder reactor main vessel. In: Seismic resistance of FBR components influenced by buckling. Kajma Institute, Japan
- Matzke Hj (1986) Science of advanced LMFBR fuels. North Holland Physics Publishing, Holland
- Mejane H, Durin M (1982) Natural convection in an open annular slot. In: Proceedings of seventh international heat transfer conference, Meichen, Germany
- Menant B, Villand M (1994) Thermal fluctuations induced in conducting wall by mixing sodium jets: an application of TRIO-VF using large eddy simulation modeling. In: IAEA specialist meeting on correlation between material properties and thermohydraulics conditions in liquid metal-cooled fast reactors (LMFRs), Aix-en-Provence, France, 22–24 November 1994
- Mineral commodity summaries 2007 US Geological Survey, Ed. Washington, 2007
- Miyahara S et al (2006) Reaction, transport and settling behavior of lead-bismuth eutectic in flowing liquid sodium. In: Proceedings of 14th international conference of nuclear engineering (ICONE), ASME, Miami
- Moriya S et al (1988) Thermal striping in coaxial jets of sodium, water and air. In: Proceedings of the fourth international conference on liquid metal engineering and technology, Avignon, France
- Müller G et al (2002) Results of steel corrosion tests in flowing liquid Pb/Bi at 420–600 °C after 2000 h. *J Nucl Mater* 301(1):40–46
- Müller G et al (2003) Control of oxygen concentration in liquid lead and lead-bismuth. *J Nucl Mater* 321(2–3):256–262
- Muramatsu T (1993a) Intensity and frequency evaluation of sodium temperature fluctuation related to thermal striping phenomena based on numerical methods. In: Proceedings of the fifth international symposium on refined flow modelling and turbulence measurements, Paris, France, 1993
- Muramatsu T (1993b) Frequency evaluation of temperature fluctuations related to thermal striping phenomena using a direct numerical simulation code DINUS-3. In: Proceedings of ASME PVP conference, Colorado, vol 253
- Muramatsu T (1994a) Development of thermohydraulics computer programs for thermal striping phenomena. In: IAEA specialist meeting on correlation between material properties and thermohydraulics conditions in liquid metal-cooled fast reactors (LMFRs), Aix-en-Provence, France, 22–24 November 1994
- Muramatsu T (1994b) Investigation on the reduction measures of coolant temperature fluctuations based on numerical methods in LMFR designs. In: IAEA specialist meeting on correlation between material properties and thermohydraulics conditions in liquid metal-cooled fast reactors (LMFRs), Aix-en-Provence, France, 22–24 November 1994
- Muramatsu T (1998a) Computer code developments and their validations for the thermal striping phenomena in PNC. In: Third research coordination meeting (RCM) of the IAEA coordinated research programme (CRP) on harmonization and validation of fast reactor thermomechanical and thermohydraulic codes and relations using experimental data, France

- Muramatsu T (1998b) Numerical analysis of non-stationary thermally response characteristics for a fluid-structure interaction system. In: ASME/JSME pressure vessels and piping conference, USA, 1998
- Muramatsu T, Ninokata H (1991) Intensity evaluation of the temperature fluctuations related to thermal striping phenomena using the algebraic stress turbulence model. In: Proceedings of ANS winter meeting, San Francisco, pp 156-162
- Nam HO et al (2008) Dissolved oxygen control and monitoring implementation in the liquid lead-bismuth eutectic loop: HELIOS. *J Nucl Mater* 376(3):381-385
- Noraiki Takahashi et al (1989) Study of an advanced fuel handling system. *Nucl Technol* 86
- Noden JN (1972) A general equation for the solubility of O₂ in liquid. Sodium British Report RB/B/N 2500
- Nonaka N, Sato I (1992) Improvement of evaluation method for initiating-phase energetics based on CABRI-1 in-pile experiments. *Nucl Tech* 98:54
- Ogata A, Yokoo A (1999) Development and validation of ALFUS: an irradiation behaviour analysis code for metallic fast reactor fuels. *Nucl Tech* 128:113-123
- Ohshime H et al (1994) Current status of studies on temperature fluctuation phenomena in LMFBRs. IAEA-IWGF/90. In: Specialists meeting on correlation between material properties and thermohydraulics conditioning in LMFBRs, Aix-en-Provence, France, 22-24 November 1994
- Olander DR (1976) Fundamental aspects of nuclear reactor fuel elements. ERDA Technical Information Center, Oak Ridge
- Old CF (1980) Liquid metal embrittlement of nuclear materials. *J Nucl Mater* 92:2-25
- Om Pal Singh, Harish R (1998) Results of transient calculations up to onset of boiling of a comparative calculation for unprotected loss of flow accident in BN-800 type reactor with near zero void reactivity coefficient. In: IAEA/EC consultancy meeting on the comparative calculations for severe accident in BN-800 reactor, Obninsk, Russia, 2-16 June 1998
- Operating experience on fast reactor. (1986). *Nucl Ene* 2:73-84
- Ostensen RW, Henry RE, Jackson JF, Goldfuss GT, Gunther WH, Parker NE (1974) Fuel flow and freezing in the upper subassembly structure following an LMFBR disassembly. *Trans Amer Nucl Soc* 18:214
- Pacheco JE (2002) Final test and evaluation results for the solar two project, SAND 2002-0120, Sandia National Laboratories, Albuquerque
- Pahl et al (1988) Experimental studies of U-Pu-Zr fast reactor fuel pins in EBR-II. Conf 8009202-2
- Papazoglou IA, Aneziris ON (2003) Master logic diagram: method for hazard and initiating event identification in progress plants. *Journal of Hazardous Material* A97:11-30
- Pascal P Nouveau traité de chimie minérale, vol II - Lithium. Sodium Edition Masson et Cie
- Petiot P, Seiler JM, CEN G (Grenoble) (1984) Physical properties of sodium: a contribution to the estimation of critical coordinates. *High Temperatures High Pressures* 16:289-293
- Popiel CO, Trass O (1991) Visualization of a free and impinging round jet. *Experimental Thermal and Fluid Science*; Elsevier Science, Elsevier, Amsterdam
- Porten DR et al (1981) Internal fuel motion as inherent shutdown mechanism. In: Proceedings of topical meeting on reactor safety aspects of fuel behaviour, Sun Valley, Idaho
- Presentation by AEA Technology - UK (1994) Thermal striping benchmark exercise: thermal hydraulic analysis of the T-junction. In: Proceedings of specialists meeting on correlations between material properties and thermohydraulics conditions in LMFR, Aix-en-Provence, France, 22-24 November 1994
- Proceeding of international conference on fast reactors and related fuel cycles (FR'91), Kyoto, 28 October-1 November 1991
- Raj B (2007) Assessment of Indian INS. In: INPRO meeting, CEA, Cadarache, 7 February 2007
- Rasmussen NC (1975) Reactor safety study: an assessment of accident risks in US commercial nuclear power plants. WASH 1400-NUREG-75/014. US DOE
- RCC-MR (2007a) Règles de Conception et de Construction des Matériaux Mécaniques des Installations Nucléaires. AFCEN editions
- RCC-MR (2007b) RB 3261.1112, out of the creep range/RB 3262.1112, in the creep range. AFCEN, Paris
- RCC-MR (2007c) RB 3261.114, out of the creep range/RB 3262.1131, in the creep range, 2007 issue. AFCEN, Paris
- RCC-MR (2007d) RB3261.115, out of the creep range/RB 3262.114, in the creep range, 2007 issue. AFCEN, Paris
- RCC-MR (2007e) Section I, Design and construction rules for mechanical components of nuclear installations. RCC-MR, Subsection Z, Appendix A12, AFCEN, Paris
- RCC-MR (2007f) Section I, Design and construction rules for mechanical components of nuclear

- installations. RCC-MR, Subsection Z, Appendix A7, AFCEN, Paris
- RCC-MR (2007g) Section I, Design and construction rules for mechanical components of nuclear installations. RCC-MR, Subsection Z, Appendix A3, AFCEN, Paris
- RCC-MR (2007h) Section I, Design and construction rules for mechanical components of nuclear installations. RCC-MR, Subsection B, AFCEN, Paris
- RCC-MR (2007i) RB3261. 123. AFCEN, Paris
- RCC-MR(2002) Design and construction rules for mechanical components for FBR nuclear islands, Section I, Subsection B, Class 1 Components, AFCEN, 2002.
- Roche JL, Nouailhas D (1989) A unified constitutive model for cyclic viscoplasticity and its applications to various stainless steels. *ASME J Eng Mater Technol* 111:424–430
- Ronchi C, Campana M, Coquerelle M, Van de Laar J (1984) Reactor performance of MC, MN, MCN and MCO: results of the comparative irradiation experiments. *European Applied Research–Nuclear Science Technology*, Gocar, vol 6, nos 1 and 2, p. 323
- Roubin P et al (1988) Thermal-hydraulic study of LMFBR hot pool with internal storage. An experimental and computational approach. In: *Proceedings of the fourth international conference on liquid metal engineering and technology*, Avignon, France
- Roux S, Elie D (1988) Comparison between measurement and computational analysis on open azimuthal thermosyphons in annular space of the Lilliput model. In: *Liquid metal engineering and technology*, pp 410_1–410_12
- RSWG (2008) Basis for the safety approach for design & assessment of generation IV nuclear systems. November 24, 2008
- Saez M et al (2007) Thermal criteria to compare fast reactors coolants for the intermediate loop. In: *Proceedings of GLOBAL 07 – advanced nuclear fuel cycles and systems*, ANS, Boise
- Safety of nuclear power plants: design (2000). IAEA safety standards series, NS-R-1. IAEA
- Sathiyasheela T, Harish R, Om Pal Singh (1998) A comparative study of ULOF for BN-800 reactor with non-zero sodium void coefficient. *RPD/SAS-101*
- Scherbakov SI (1994) Computational investigations of thermohydraulic aspects of two convergent flows at different temperatures mixed in the Tee junction area. In: *Proceedings of specialists meeting on correlations between material properties and thermohydraulics conditions in LMFR*, Aix-en-Provence, France, 22–24 November 1994
- Section III, Div 1, Subsection NH, Class 1 Components in elevated temperature service, 2001
- Seran JL, Levy V, Dubuisson P, Gilbon D, Mailard A, Fissolo A, Touron H, Cauvin R, Chalony A, Le Boulbin E (1992) Behavior under neutron irradiation of the 15-15Ti and EM10 steels used as standard materials of the Phénix fuel subassembly. In: *Proceedings of 15th international symposium: effects of radiation on materials*, p. 1209. AST International
- Shuh PY, CC Scott (December 2005) Attenuation measurements of sound and performance of ultrasonic transducers in 600 °F liquid Na. *APDA-180*
- Siegel R, Norris RH (1957) *Transactions of ASME* 79(1):663–673
- Sienicki J, Moiseyev A, Cho D, Momozaki Y, Kilsdonk D, Haglund R, Reed C, Farmer M (2007) Supercritical carbon dioxide Brayton cycle energy conversion for sodium-cooled fast reactors/advanced burner reactors. In: *GLOBAL '07 – advanced nuclear fuel cycles and systems*, Boise, 9–13 Sept 2007
- Sigrift JF, Broc D (2007) Dynamic analysis of a tube bundle with fluid structure interaction modelling using a homogenization method. *Computer Methods in Applied Mechanics and Engineering*
- Silver et al Three-dimensional finite-element analysis of the cellular convection phenomena in the Clinch River Breeder Reactor Plant prototype pump
- Simeone D, Deschanel X, Berthier B, Tessier C, (1997) Experimental evidence of lithium migration out of an irradiated boron carbide material. *J Nucl Mat* 245:27
- Simon N, Latgé C, Gicquel L (2007) Investigation of sodium – carbon dioxide interactions with calorimetric studies. In: *Proceedings of ICAPP2007*, paper 7547, Nice Acropolis, France, 13-18 May 2007
- Smith MR (1990) Techniques for the investigation of scaling criteria for gas entrainment mechanisms in liquid metal cooled fast reactors. *GEC Journal of Research* 8: 49–56
- Sobolev VA, Kuzavkov NG (1994) Identification of places with fluid temperatures in BN 600 reactor and reactor systems. IAEA-IWGFR/90. In: *Specialists meeting on correlation between material properties and thermohydraulics conditions in LMFRs*, Aix-en-Provence, France, 22–24 November 1994

- Srinivasan GS (2002) Kinetic studies of reactivity oscillations under seismic conditions. PFBR/01117/DN/1019. IGCAR report
- Status of French nuclear program. In: Meeting of the technical working group on fast reactors (TWG-FR), 26–29 May 2008
- Status of liquid metal cooled fast reactors technology. (1999). IAEA-TECDOC-1083
- Stevenson MG et al (1974) Current status and experimental basis of the SAS LMFBR accident analysis code system. In: Proceedings of international conference on fast reactor safety, Beverley Hills, California
- Subbotin VI et al (2002) Liquid metal coolants for nuclear power. Atomic Energy 92(1): 29–40
- Surle F et al (1993) Comparison between sodium stratification tests on the CORMORAN model and TRIO-VF computation. In: Proceedings of the sixth international topical meeting on nuclear reactor thermal hydraulics, Grenoble, France
- Tenchine D et al (1990) Sodium thermal-hydraulics in the pool LMFBR primary vessel. Nuclear Engineering and Design 124
- The BN-800 reactor – a new stage in fast reactor development. IAEA/SM/284. pp 209–216
- The nuclear fuel of pressurized water reactors and fast reactors – design and behaviour. (1999). In: Bailly H, Messier D, Prunier C (eds) Collection du Commissariat à l’Energie Atomique. Lavoisier
- Thomson TJ, Beekerly JG (1964) The technology of nuclear reactor safety, vol I. MIT Press
- Timo DP (1954) Free convection in narrow vertical sodium annuli. Knolls Atomic Power Laboratory Report: 1082. Schenectady
- Tobita Y et al (1999) Evaluation of CDA energetics in the prototype LMFBR with latest knowledge and tools. In: Proceedings of ICONE-7, Tokyo
- Toda et al (1990) Natural convection in a vertical narrow annular gap. In: Proceedings of ninth international heat transfer conference, Jerusalem, Israel, vol 2, pp 199–204
- Tokuhiro A, Kimura N (1999) An experimental investigation on thermal striping mixing phenomena of a vertical non-buoyant jet with two adjacent buoyant jets as measured by ultrasound Doppler velocimetry. J Nucl Eng Des
- Touboul F, Blay N, Lacire MH (1999) Experimental, analytical, and regulatory evaluation of seismic behavior of piping systems. J Pres Ves Tech 121(November):388–392
- Touboul F, Blay N, Sollogoub P, Chapuliot S (2006) Enhanced seismic criteria for piping. Nucl Eng Des 236(1):1–9. Janvier
- Tourasse M, Boidron M, Pasquet B (1992) Fission product behaviour in Phenix fuel pins at high burn up. J Nucl Mater 187:122
- Tsilanizara A, Huyhn TD, Jouanne C, Luneville L Guide d’utilisation du logiciel Darwin/Pepin2 version 2.2. Rapport DM2S/SERMA/LPEC/RT/07-4168/A
- Vaidyanathan G An overview of activities pertaining to heat and mass transfer in reactor cover gas of FBTR. In: Proceedings of specialists meeting on heat and mass transfer in cover gas, IWGFR-57, Harewell, England
- Vanavaramban S (2008) Solidus and liquidus temperatures for metallic fuels. CG
- Velusamy K et al (2005) Investigations of thermal striping in primary circuit of prototype fast breeder reactor. In: Proceedings of ICONE 13, Beijing, China
- Wada et al (1995) Mechanism-based evaluation of thermal ratchetting due to moving temperature distribution. ASME PVP 313(2):471–480
- Wakamatsu M et al (1995) Attenuation of temperature fluctuations in thermal striping. Journal of Nuclear Science and Technology 32(8)
- Wakamatsu M, Nei H, Hashiguchi K (1995) Attenuation of temperature fluctuations in thermal striping. Journal of Nuclear Science and Technology 32(8):752–762
- Walker RA et al (1970) The solubilities of bismuth and tellurium in liquid sodium. J Nucl Mater 34:165–173
- Waltar AE, Reynolds AB (1981) Fast breeder reactors. Pergamon Press
- Walter AE, Reynolds AB (1982) Fast breeder reactor. Pergamon, UK
- Walters et al (1984) Performance of metallic fuels and blankets in liquid metal breeder reactors. Nuclear Technology 65:179–231
- Walters, Reynolds Fast breeder reactors. Pergamon
- Wang CY, ICECO (December 1975) An implicit Eulerian method for calculating fluid transient in fast reactor containment. ANL-75-81
- Weeks JR (1971) Lead, bismuth, tin and their alloys as nuclear coolants. Nucl Eng Design 15:363
- Weisenburger A et al (2008) T91 cladding tubes with and without modified FeCrAlY coatings exposed in LBE at different flow, stress and temperature conditions. J Nucl Mater 376(3): 274–281
- Wider HU et al (1982) Status and validation of the SAS4A accident analysis code system. In: Proceedings of LMFBR safety topical meeting, ANS, France
- Winterton RHS (1972) Cover-gas bubbles in recirculating sodium primary coolant. Nuclear Engineering and Design 22:262–271

- Wittingham (1976) An equilibrium and kinetic study of the liquid sodium hydrogen reaction. *Journal of Nuclear Materials* 60:119
- Working Group Report – A Technology Roadmap Generation. (December 2002). GIF-007-00
- Yamakawa M (1983) Thermal hydraulic analysis in LMFBR plenum. In: International conference on numerical methods in nuclear engineering, Montreal, Canada
- Yamakawa et al (1986) Analysis of natural convection in narrow annular gaps of LMFBR. *Journal of Nuclear Science and Technology* 23(5): 451–460
- Yamano H et al (2008) Development of 3-D CDA analysis code: SIMMER-IV and its application to reactor case. *Nuclear Engineering and Design* 238:66
- Yevick JG (1966) *Fast reactor technology*. Plant design. MIT Press, USA
- Yokoo et al (August 2000) A design study on the FBR metal fuel and core for commercial applications. *Nucl Sci Tech* 37(8): 636–645
- Zimmermann H (1982) Investigation of swelling of U–Pu mixed carbide. *J Nucl Mater* 105:56
- Zuppiroli L, Lesueur D (1989) Modelling the swelling and microcracking of boron carbide under neutron irradiation. *Phil Mag* 60(5): 539

22 Gas-Cooled Reactors

Bertrand Barré

Professor Emeritus INSTN, Chaville, France

bcbarré@wanadoo.fr

1	<i>Gas Cooling</i>	2712
2	<i>Natural Uranium Fueled Reactors: Magnox and NUGG</i>	2713
2.1	The Magnox Family	2714
2.2	Natural Uranium Graphite Gas (NUGG) Reactors.....	2716
2.3	Safety of NUGG and MAGNOX Reactors	2717
3	<i>Advanced Gas-Cooled Reactor (AGR)</i>	2719
4	<i>High Temperature Reactors HTR</i>	2720
4.1	Particles, Pebbles and Prisms	2720
4.2	HTR Demos: Dragon, AVR, Peach Bottom	2721
4.2.1	Dragon	2721
4.2.2	AVR	2722
4.2.3	Peach Bottom	2724
4.3	Fort St Vrain and THTR Prototypes	2724
4.3.1	Fort St Vrain.....	2724
4.3.2	The Schmehausen HTTR.....	2725
4.4	Lessons Learned from the First HTR Units.....	2728
4.5	Recent Japanese and Chinese Demos.....	2730
4.6	GT-MHR and PBMR	2730
4.6.1	GT-MHR, Gas Turbine Modular High Temperature Reactor.....	2732
4.6.2	ESKOM PBMR Pebble Bed Modular Reactor	2732
4.6.3	PBMR Fuel Fabrication and Fuel Cycle	2736
5	<i>The NERVA Story (Simpson JW 1995)</i>	2737
6	<i>Gas Cooling in Generation IV (DEN 2006)</i>	2737
6.1	VHTR	2739
6.1.1	Electricity Production	2739
6.1.2	Hydrogen Production.....	2741
6.1.3	Water Desalination	2742
6.1.4	NGNP Project (USA)	2743
6.2	GFR.....	2744
6.2.1	Specific Problems Associated with the GFR	2746
6.2.2	The Advantages of the GFR System Have Two Main Origins	2747
7	<i>Conclusion</i>	2747
	<i>References</i>	2748

Abstract: This chapter describes the various families of reactors in which the primary fluid cooling the core is a gas, usually carbon dioxide or helium.

Early on, gas cooling was mostly used in graphite moderated reactors fueled with natural uranium, the British Magnox, and the French natural uranium graphite gas (NUGG). The availability of low enriched uranium fuel allowed the British to develop the advanced gas-cooled reactor as a successor to the Magnox.

In a world progressively dominated by the water cooled reactors, mostly PWR and BWR, gas cooling remained alive in the high temperature reactor families, prismatic, and pebble bed HTR, associated with graphite moderation. Both are based on the use of a very innovative fuel element, the coated particle.

The same fuel was used in a seldom known US program to develop nuclear propulsion for rockets: this NERVA story will be briefly recalled.

Still marginal, gas cooling is also present among the “Generation IV” concepts, through the very high temperature reactor system aimed at both electricity generation and hydrogen production and the GFR, gas cooled fast neutrons reactor.

1 Gas Cooling

If the very first man-made nuclear reactor, CP1, had no coolant at all, the second, X10, which achieved criticality in November 1943 at Oak Ridge, was cooled by a gas (air). But today, most nuclear reactors are water cooled (PWR, BWR, HWR, and RBMK, in that order).

Despite its name, the real task of a coolant is not to cool the fuel but to transport heat from the reactor core to the boilers to produce steam for electricity generation or to generate process heat. In that respect, gases exhibit interesting qualities, as described in Mc Farlane et al. (1992).

First, because the density of a gas is variable, its operating temperature can be chosen independently of the operating pressure. Thus, a high gas temperature can be used, limited only by the core and circuit materials, to give good steam conditions from the boiler and thus good conversion of heat to electrical energy through the resulting high turbine efficiency. The optimum pressure can be selected separately on considerations of safety and of the economies of pumping power and pressure circuit costs.

Gas has certain intrinsic safety advantages. It can undergo no phase change as a result of rising temperature or falling pressure, and so there cannot be any discontinuity in cooling under fault conditions, and flows and temperature can be predicted more simply and with greater confidence.

Continuity of fuel cooling for on-load refueling is more easily achieved with a gas. In addition with a gas, there is no risk of a fuel-coolant interaction of the kind that in certain circumstances could result from the dispersion of melted fuel in a liquid coolant. Finally, a gas carries a relatively low burden of activated corrosion products, gives low radiation levels for maintenance round the circuit, requires small active effluent plants, and gives rise to only low radiation doses to the operators.

Offsetting these virtues is the combination of low density and low specific heat of gases. Even with fairly high pressures, this requires comparatively large temperature differences to transfer the heat between the fuel and gas, and between the gas and the boiler surface. As a result core ratings are low and core and boilers need to be large. It also requires large volume flows to transport the heat, and therefore large circulator sizes and powers.

Table 1
Properties of some possible coolant gases

Gas	Molecular weight	Density at 1 bar (kg/m ³)	Specific heat at 1 bar (kJ/kg °C)	Absorption cross section (barn)
Air	29	0.60	1.0	1.9
Oxygen	32	0.67	1.0	0
Nitrogen	28	0.58	1.1	2.4
Hydrogen	2	0.04	14.7	0.4
Helium	4	0.08	5.2	0
CO ₂	44	0.92	1.1	0.003

The question of what gas to use is associated with the choice of moderator to slow the neutrons to thermal velocities. The first gas-cooled nuclear reactor above mentioned used graphite. The good moderating properties of graphite, combined with its low neutron capture cross-section, have led to it being used almost universally for gas-cooled reactors. Only a handful of experimental or demonstration reactors have been built with heavy water as moderator with pressure tubes containing the fuel and gas coolant, like the French 70 MWe EL4 at Brennilis. Indeed, graphite moderation has become almost synonymous with gas-cooled reactors. If gas-cooled fast breeders are developed, this couple will have to divorce.

The choice of coolant gas is influenced mainly by the thermodynamic, nuclear and chemical properties, and by its cost and supply. ▶ [Table 1](#) gives properties of some of the candidates at 300°C, a typical temperature of interest.

For good heat transfer and heat transport with low pumping power, a gas with high specific heat and high molecular weight, or density, is desirable. The coolant needs to have a low neutron absorption, to give good neutron economy and to avoid a rise in core reactivity if the reactor accidentally loses pressure. It also needs to be stable under irradiation, and preferably to have low neutron-induced radioactivity. Good chemical stability and low corrosion are obviously important. Of the many gases available the choice narrows quickly. Two gases stand out as candidates: carbon dioxide which is dense, cheap, but not chemically fully inert and helium which is inert, has a high specific heat, but is costly.

These two coolants have led to parallel lines of development in the family of gas-cooled reactors, sharing much common technology but with differing characteristics. The carbon dioxide reactors are characterized by relatively low specific core ratings, moderate temperatures, and large size – typically the natural uranium plants of the UK and France and the advanced gas-cooled reactors (AGRs). The helium reactors aim for high ratings, small size and high temperature: the family of high-temperature reactors, or HTRs.

2 Natural Uranium Fueled Reactors: Magnox and NUGG

Most “first generation” gas-cooled power plants were designed and built in the UK – the Magnox series – and in France – the NUGG. Both countries started their nuclear generation program in the early 1950s. Both had access to sufficient quantities of uranium ore, but no heavy water or

enrichment facilities, and this severely limited the choices available. Graphite has many advantages as a moderator as it absorbs few neutrons enabling the use of natural uranium as a fuel. The graphite industry was also a mature one as the material had been used for a long time in the electrochemical and electrometallurgical industries.

To use natural uranium in a graphite moderated reactor, the fuel must be in its metallic state in order to achieve a high enough density of fissile material. It must also be renewed at regular intervals to minimize the number of sterile captures by the fission products. The MAGNOX and NUGG reactors used bars of uranium clad in a magnesium alloy. These were inserted into channels in a massive graphite pile through which carbon dioxide was circulated under pressure. These reactors were built using fairly primitive technology – that available in France immediately after the war – but the poor slowing-down power of graphite meant that the size of the plants had to be large in order to achieve significant power levels, and this in turn led to a high capital cost. Their sensitivity to the xenon effect made them very inflexible in operation, but the ability to unload the fuel without having to shut down the reactor made it possible to produce almost pure ^{239}Pu for military applications by short irradiation.

Early “production” reactors, Windscale in the UK and G1 in France were cooled by air, but even before the 1957 fire of the Windscale reactor (due to the sudden release of the energy stored in the graphite by the “Wigner” effect during an attempt to anneal the pile), it was decided to turn to carbon dioxide as a coolant: This gas was readily available, cheap, and well known in industry. It has good heat transfer characteristics (for a gas) and good neutronic properties. It is also chemically compatible with the use of graphite as the moderator and with the cladding material and fuel used, provided certain precautions are observed. In addition to the series described below, two Magnox were exported by the British industry to Italy (Latina) and Japan (Tokai Mura), while a “sister ship” of the French St Laurent units was built in Spain (Vandellos).

2.1 The Magnox Family

The first nuclear electricity on the western side of the iron curtain was generated by dual purpose (weapon-grade plutonium production and power generation) Magnox plants located at Calder Hall, a station inaugurated by HM Queen Elizabeth II in October 1956. Eight 60 MWe reactors were built almost simultaneously by the UKAEA: 4 units at Calder Hall and 4 at Chapelcross, in Scotland. The Calder Hall design was simple and reliable but was not very efficient (22% thermal efficiency). The gas pressure was limited to 6.9 bar and the maximum outlet temperature was kept at 345°C. Refueling was carried out off-load at atmospheric pressure. All those units were shut down in 2003 and 2004, having operated over 45 years.

In 1955, Great Britain decided to embark on a significant program of nuclear power plants. The Magnox (magnesium non-oxidizing) alloy used to clad the uranium rods gave its name to the series. Nine commercial power stations with twin plants were eventually built in England, Scotland, and Wales, totaling 5,000 MWe (➤ [Table 2](#)).

The fuel was in form of metal rods, 28 or 29 mm diameter and between 48 and 128 cm length according to the model, clad with magnesium alloyed with a little beryllium and aluminum. The cladding is finned to improve the heat transfer to the gas. Gas outlet temperature was in the range 340–410°C and refueling was carried out on-load, to improve availability. That made it possible to unload immediately any failed fuel element without shutting the plant down.

Despite such a significant series, there was no standardization because the plants were designed and built by up to five different industrial consortia!

Table 2
UK commercial Magnox stations

Site	Operating	Shutdown	Net output MWe	Efficiency (%)	Vessel	Pressure bar
Berkeley	1962	1989	2 × 138	25	Steel	9
Bradwell	1962	2002	2 × 150	28	"	9
HunterstonA	1964	1990	2 × 160	28	"	10
HinkleyA	1965	2000	2 × 250	26	"	13
Trawsfynydd	1965	1991	2 × 250	29	"	16
DungenessA	1965	2006	2 × 275	33	"	18
SizewellA	1966	2006	2 × 290	31	"	19
Oldbury	1968		2 × 300	33	Concrete	24
Wylfa	1971		2 × 590	31	"	27

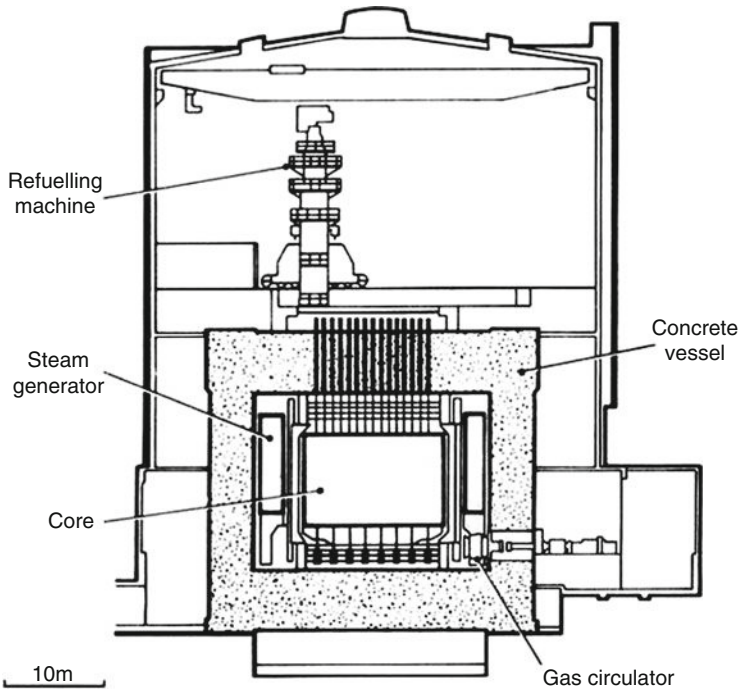


Figure 1
The 300 MWe Magnox reactor Oldbury A1 (Marshall W 1981)

The Magnox reached their peak efficiency, 33.6%, in Oldbury A (Fig. 1), the general layout of which was to inspire the following AGR series. Once-through boilers were integrated around the core in the central cavity of a prestressed concrete vessel (Table 3).

Volumic power was low and, consequently, capital costs were high but fuel costs were low enough to make the stations economically competitive during the 1970s and 1980s. Toward the

■ **Table 3**

UK commercial gas-cooled reactor (AGR) stations

Site	Operating	Net output (MWe)	Efficiency (%)	Concrete vessel type	Pressure bar
DungenessB	1980	2 × 600	41	Single cavity	32
HinkleyB	1976	"	41.5	"	42
HunterstonB	1976	"	"	"	42
Hartlepool	1983	"	"	Multiple pods	41
HeyshamI	1983	"	"	"	41
HeyshamII	1986	"	"	Single cavity	43
Torness	1986	"	"	"	43

end of the Magnox construction program, in order to reduce the corrosion of mild steel by carbon dioxide, it was decided to restrict the outlet temperature below 360°C.

2.2 Natural Uranium Graphite Gas (NUGG) Reactors

Nine NUGG reactors were built in France. The first three reactors, at Marcoule, were used almost exclusively for the production of plutonium. The electrical power generation program began with the successive commissioning of Chinon 1 (1957), Chinon 2 (1958), and Chinon 3 (1961), with power capabilities of 70,200 and 480 MWe net respectively. There was no question of waiting for these reactors to go critical, even less of waiting for the first operational results, before starting work on the next design. These three reactors were prototypes, and each very different from the others. The next reactors were built at Saint Laurent des Eaux (1963 and 1966) and Bugey (1965). The Fifth Plan (1966–1970) included plans to build a total capacity of 2,500 MWe of NUGG reactors. The construction of a new unit at Fessenheim began in 1967, but was abandoned at the end of 1968. By that time, water-cooled reactors had become the favored option.

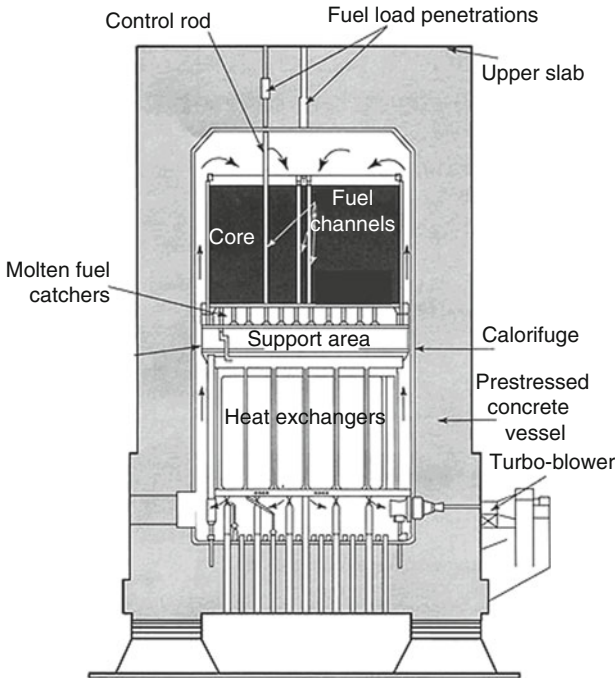
The characteristics of NUGG reactors are listed below, using Saint Laurent 2 as an example (see ► [Fig. 2](#) and ► [Table 4](#)).

The low specific power of the reactor meant that the core had to be very large. This core was enclosed in a vessel that also contained the coolant circuit and its heat exchanger. The vessel was a prestressed concrete structure, 33 m in diameter and 48 m high. The internal face of the vessel was lined with steel, 25 mm thick, in order to prevent any leakage of the CO₂ under a pressure of 29 bar.

The graphite pile in the reactor was in the form of a vertical cylinder 10.2 m high and 15.7 m in diameter. It consisted of a network of columns locked together by mortise and tenon joints. The pile weighed no less than 2,680 tons.

The four CO₂-steam heat exchangers were single tube cross circulation types. The water inlet was in the lower section, while the hot CO₂ entered the upper section. The total CO₂ flow rate was 8.6 tons/s, and the steam flow rate was 0.6 tons/s.

The fuel elements were replaced while the reactor was in operation, at a rate of around 2–3 channels per day, requiring the use of a sophisticated handling system.



■ Figure 2
St Laurent reactor layout

A system for detecting the presence of fission gasses in the coolant was used to detect and locate any breaks in the claddings.

The fuel elements used in the NUGG reactors were developed over time. In the latest versions, each element consisted of a metal tube of uranium alloyed with 0.07% aluminum and 0.03% iron, surrounding a graphite core. The borderline neutron balance of the NUGG reactors resulted in a fairly low fuel burnup rate of 6.5 GWd/tons. The maximum operating temperature of the reactor was determined by the maximum permissible temperature of the uranium. This was set at 650°C at the internal surface of the tube.

The last NUGG plant, 540 MWe Bugey 1 was shut down in 1994.

2.3 Safety of NUGG and MAGNOX Reactors

The containment of the fission products is provided by two barriers: the fuel element cladding and the prestressed concrete vessel. As the cladding is exposed to conditions close to its technological limits during operation, specific precautions must be taken in order to ensure that it remains within these limits. The core cooling is an essential factor in maintaining the integrity of the cladding. Four independent cooling systems are used.

The monitoring of the cladding integrity is also a crucial factor in maintaining the safety of NUGG and MAGNOX reactors. The monitoring system works by preventing the operation of

■ Table 4

Comparison of the characteristics of an AGR (Hinkley point B), a MAGNOX reactor (Wylfa) and a natural uranium graphite gas (NUGG) reactor (Saint Laurent 2)

	Units	AGR	MAGNOX	NUGG
Mass of U	Tons	114	395	430
Fuel		UO ₂ oxide Steel cladding	U metal Mg alloy cladding	U metal Mg alloy cladding
Power density	MW/m ³	3	~1	1
Enrichment	%	2.1–2.6%	Natural U	Natural U
Cladding		Stainless steel	Mg alloy	Mg–Zr alloy
Coolant gas pressure	Bar	41.9	27.6	29
Number of heat exchangers		12	4	4
Gas outlet temperature	°C	645	414	400
Maximum cladding temperature	°C	825	450	473
Mass of graphite pile	Tons	1,248	3,735	2,440
Net electrical power	MWe	625	590	480
Net efficiency	%	41.7	31.4	28.7
CO ₂ flow rate	tons/s	3.8	10.2	8.6
Burnup rate	GWd/tons	18	4	6.5

the reactor if any of the claddings are damaged. This is to avoid the oxidation of the metallic uranium by the CO₂ and to keep the coolant gas as clean as possible. In the event of a failure of the first barrier, the vessel is purged through filters trapping aerosols and radioactive iodides.

The Design Basis Accident for these reactors is a loss of pressure in the vessel via a fuel loading well or following a break in a gas pipe. A backup cooling system maintains the integrity of the barriers in the event of a total loss of the normal cooling systems. Studies of the radiological consequences of an accident do not indicate any major environmental risks. The addition of a further containment vessel was not considered necessary.

The only notable incidents occurring in this type of reactor were the meltdown of five fuel elements at Saint Laurent 1 and four fuel elements at Saint Laurent 2. Both had only minor consequences for the operating personnel, and the environmental impact was negligible.

The main components of the solid waste produced by these reactors are the graphite sleeves from the fuel elements. The annual volume produced by a 500 MWe NUGG or MAGNOX reactor is around 25 m³, equivalent to a mass of 45 tons.

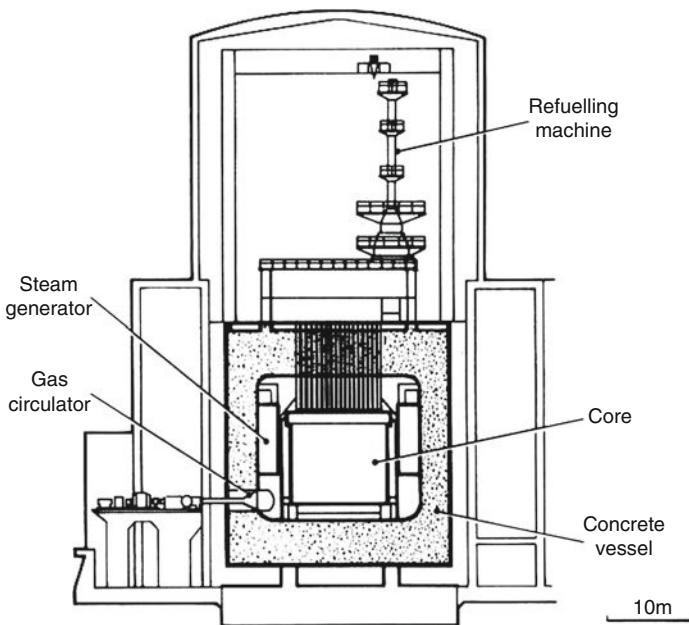
The main problem with this type of reactor was the corrosion of structural components by oxidizing radicals produced by radiolysis of the carbon dioxide gas. The power levels of MAGNOX and NUGG reactors had to be reduced slightly in order to minimize this effect. For the same reason, the gas outlet temperature was limited to a maximum of 400°C. Other problems

associated with these old graphite-moderated gas-cooled reactors include friction wear, noise, and vibration.

Contrary to spent LWR fuel assemblies, spent Magnox and NUGG fuel elements could not be stored under water for long periods of time: For this spent fuel, early reprocessing was a necessity. Furthermore, at the time, breeder reactors were expected to be developed much sooner than they actually were: plutonium was considered on short supply. Here is the main reason why both British and French chose to reprocess their commercial spent fuel, making it an industrial success where the US industry failed.

3 Advanced Gas-Cooled Reactor (AGR)

The limitations inherent to the use of natural uranium were recognized from the start. In the mid-1950s, the British started studies of an improved design, based on low enriched uranium oxide fuel, manufactured in clusters of small diameter pins, with stainless steel cladding. This design was called AGR (► Fig. 3). The AGR is a direct descendent of the MAGNOX reactor and has only been built in Great Britain. After a small demonstration 30 MWe reactor commissioned at Windscale in 1962, a commercial AGR program of seven twin 600 MWe units was started (► Table 3). The power density is four times that of a MAGNOX reactor, and the volume of the heat exchangers is smaller. The chemical compatibility of UO_2 and CO_2 and refractory nature of the oxide make operation at higher temperatures possible. The coolant is at 650°C on leaving the core, giving the AGR an excellent electrical efficiency (42%). The first reactors



■ Figure 3
Cross-section of an advanced gas-cooled reactor (AGR) with single cavity vessel (Marshall W 1981)

suffered from a number of problems, partly due to failures in industrial organization, and partly due to a failure to control corrosion. Methane was added to the coolant gas in order to reduce radiolytic corrosion by CO and the oxidizing free radicals formed by the irradiation of the CO₂. Controlling the concentration of this gas proved to be difficult.

This first generation of gas-cooled reactors has an excellent operating record, generating electrical power continuously with no major accidents. However, these old NUGG, MAGNOX, and AGR designs are now obsolete for economic reasons. Graphite-moderated gas-cooled reactor technology has gradually been abandoned in France, Italy, Spain, and Japan, and only accounted for 4% of worldwide nuclear capacity in 2008. The British AGR and MAGNOX reactors are the only types still in operation. All of them should be decommissioned by 2020.

4 High Temperature Reactors HTR

High Temperature Reactors HTR, first developed during the 1970s and 1980s in Germany and the USA, may be doing a comeback based on their high thermal efficiency and their very high degree of “intrinsic” safety. These characteristics derive from the use of helium gas as coolant (Melese and Katz 1984), graphite as moderator, and, above all, a very unusual type of fuel.

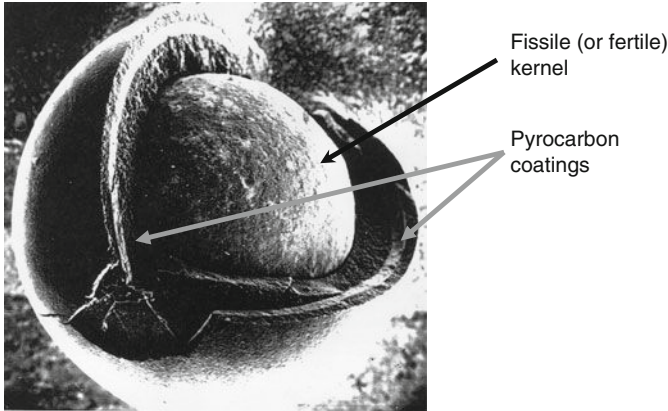
4.1 Particles, Pebbles and Prisms

What constitutes the specificity of the HTRs and gives them their qualities is their fuel. It was invented in Harwell, UK, during the mid-1950s. Wholly refractory and helium cooled, the core is made of tiny fissile particles, less than 1 mm diameter, dispersed within a graphite moderator.

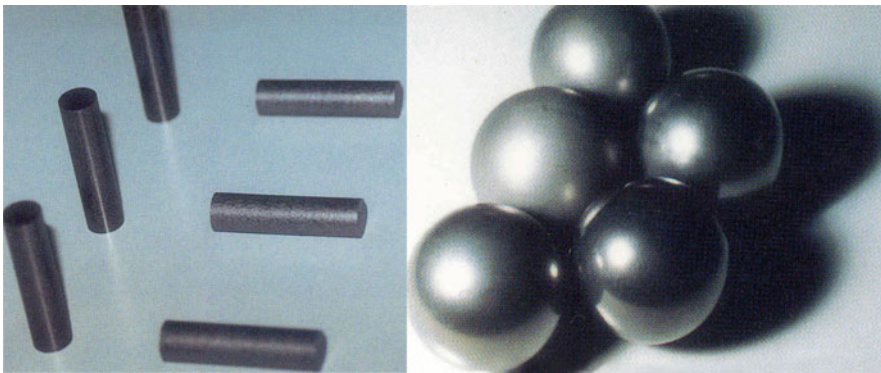
The kernel of each individual particle is coated (🔍 Fig. 4) by catalytic cracking in fluidized bed, with a number of concentric layers, like the sugar coatings of the almond in a *dragée*: inner layers of pyrocarbon which protect a layer of silicon carbide SiC from the hot kernel and outer layers of dense pyrocarbon which can withstand the pressure of fission gases up to very high burnups. The SiC layer is a leaktight barrier to contain the fission products: it plays the role of the cladding in a conventional fuel pin. The outermost carbon layer facilitates the agglomeration of the particles inside “compacts” or pebbles (🔍 Fig. 5).

Extremely divided and fully refractory, this fuel enables the reactor to operate with very high coolant temperatures (we shall see how high later) and therefore with an excellent thermal efficiency while the center of the particle remains relatively cold. The coated particle is, indeed, a very special breed of fuel element:

- There are several tens of billion particles in a reactor core. It is therefore a mass produced object, whose quality can only be assessed by statistical tools (no fewer than 10¹¹ individual claddings constitute the first barrier against radioactivity dispersal, versus the 2×10⁵ pin claddings of a PWR).
- There is an almost unlimited flexibility in the core composition. You can freely select the nature (fissile, fertile, burnable poison, mixture) and dimension (i.e., self-protection) of the kernels. You can adjust the particle concentration within the graphite matrix of the compact or pebble, as well as their distribution by size (double heterogeneity). HTRs can therefore be adapted to any fuel cycle whatsoever.



■ Figure 4
Scanning electron micrography of a coated particle



■ Figure 5
The two families of fuel elements (compacts-in-prism and pebbles)

The actual flexibility offered to the designer can be illustrated by the two types of fuel elements used in the HTR prototypes, prisms in Fort Saint Vrain and pebbles in THTR, not to mention many other types tested in Dragon (annular, teledial, etc.).

4.2 HTR Demos: Dragon, AVR, Peach Bottom

4.2.1 Dragon

It is around 1956, while the UK was launching its big Magnox program, that the Harwell discovery was developed inside the Dragon Project, an ad hoc OECD enterprise located on the UKAEA Winfrith site. A demonstration facility was built and operated at Winfrith as soon as

■ **Table 5**
Characteristics of HTR demos

Characteristics	Dragon	Peach bottom	AVR
Criticality/shutdown	1964/1975	1966/1974	1966/1988
Thermal power (MWt)	20	115	46
Net electrical power (MWe)	–	40	15
Helium pressure (absolute bars)	20	24	11
Core inlet temperature (°C)	350	340	260
Core outlet temperature (°C)	750	715	950
Core diameter (m)	1,1	2,8	3
Core height (m)	1,6	2,3	3
Power density (MW/m ³)	14	8,3	2,2
Fuel element	Prismatic	Prismatic	Pebble
Fuel cycle	Various	²³⁵ U/Th	²³⁵ U/Th

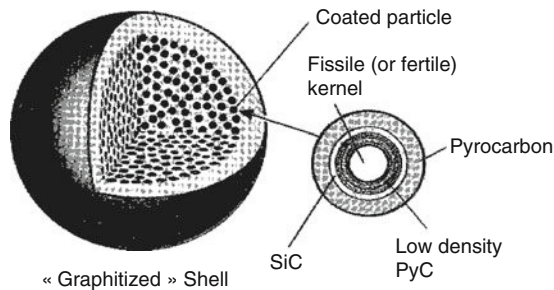
1964, and established successfully the HTR feasibility. In addition to building and operating the reactor, the 12-country Dragon team paved the way for future HTRs by exploring reactor designs and testing a number of fuel cycles (low enriched uranium LEU, thorium/²³⁵U, and plutonium, both with oxide or carbide kernels).

Being multinational, Dragon Project introduced the HTR to the whole Europe and triggered interest in the USA, then Japan (🔗 [Table 5](#)).

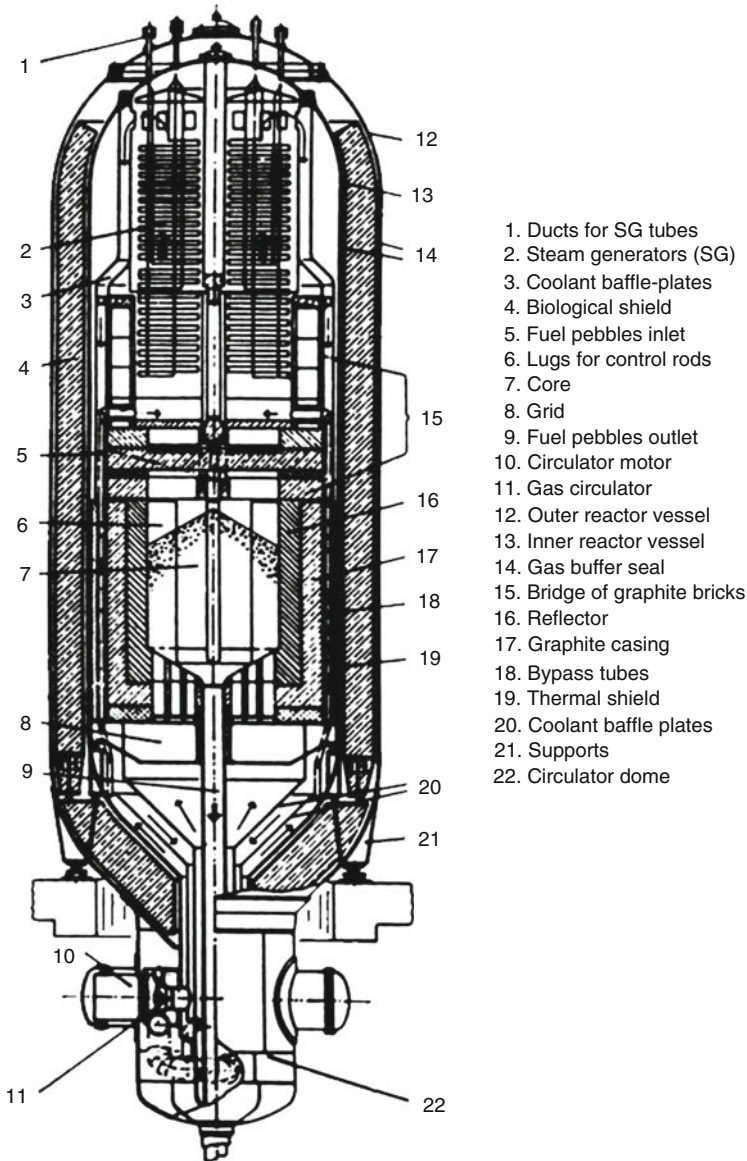
4.2.2 AVR

Dragon partner through Euratom, Germany developed HTRs as its first purely national design. As soon as 1967, the AVR, a very innovative demonstration reactor, began operation in Jülich, where it operated very successfully for more than 20 years.

Both core and steam generator were contained in a single steel double walled pressure vessel. The helium coolant was circulating upward, as its outlet temperature was increased from 750



■ **Figure 6**
HTR pebble



■ **Figure 7**
 The Jülich AVR

to 850°C , and then to 950°C during its last two years of operation. The temperature was even pushed to $1,050^{\circ}\text{C}$ in the last days before shutdown.

The main innovation of AVR was its spherical fuel element, the 6 cm diameter graphite “pebble” inside which coated particles were agglomerated (➤ [Fig. 6](#)). Hundred thousand pebbles are heaped inside a funnel shaped graphite cavity. The control rods move in channels within the graphite reflector (➤ [Fig. 7](#)).

Six hundred pebbles a day were continuously extracted from the bottom of the funnel, and tested for physical integrity and burnup. Ninety percent were recycled on top of the heap, with the required complement of fresh pebbles: an intact pebble traveled therefore ten times through the core before disposal. Each pebble contained on average 1 g of HEU and 6 g of thorium, in particles with a “BISO” all pyrocarbon coating. Burnups as high as 150 GWd/tons were routinely reached in AVR.

4.2.3 Peach Bottom

Fifty-three electricity producers, with support from the US government, very soon entered the HTR race and built a demonstration reactor at Peach Bottom (Pennsylvania), which reached its nominal 40 MWe power in 1967. The Peach Bottom fuel element is close to the Dragon design, a long hexagonal graphite prism with a pile of annular compacts inside. The core, surrounded by a graphite reflector, is located at the bottom of a steel pressure vessel. The first core was fabricated using particles with a coating still imperfect. It was soon replaced by a core with much improved fission products retention. Peach Bottom was decommissioned in 1974, just after the start-up of the Fort Saint Vrain prototype.

The very successful operation of these three demos gave great hopes concerning the future of the HTR families. Unfortunately, the performances of their immediate successors were less bright.

4.3 Fort St Vrain and THTR Prototypes

4.3.1 Fort St Vrain

In 1968, 1 year only after the start-up of Peach Bottom, general atomic started the construction on the Fort St Vrain site of a 330 MWe HTR prototype. The operator was to be Public Service of Colorado, a small utility without previous nuclear experience. Being a prototype, Fort Saint Vrain was built with federal support (👉 [Table 6](#)).

The general layout of the reactor (👉 [Fig. 8](#)) is strongly inspired by the 500 MWe St Laurent UNGG design but with a reactor cavity six times smaller.

The core is composed of 1,483 prismatic fuel elements (👉 [Fig. 9](#)) superposed on six layers. Each fuel element is a hexagonal graphite prism in which cylindrical blind channels are bored. Cylindrical compacts fill these channels, which are surrounded by coolant channels in which helium circulates downwards, under 48 bars pressure.

The compacts are fabricated by mixing two types of particles: fissile particles with a kernel of HEU dicarbide $^{235}\text{UC}_2$ with TRISO coating including one SiC layer and fertile particles ThC_2 with a BISO coating without silicon carbide. The core is axially and radially zoned, and it is reloaded by 1/6th at each annual outage.

Twelve once-through helical steam generator modules are located below the core.

Critical in 1974, Fort St Vrain was connected to the grid in 1976, to be decommissioned in 1989 with a cumulative load factor of 30%. The fuel behaved successfully, but the reactor's overall design was rather a failure.

At the very beginning of the 1970s, while Fort St Vrain was under construction and Peach Bottom still operating, a few US utilities ordered from General Atomic, then a subsidiary of

■ **Table 6**
Characteristics of HTR prototypes

Characteristics	Fort St Vrain	THTR 300
Criticality/shutdown	1974/1989	1983/1989
Thermal power (MWt)	842	750
Net electrical power (MWe)	330	300
Efficiency (%)	39	40
Active core height (m)	4, 8	6
Equivalent diameter (m)	5, 9	5, 6
Power density (MW/m ³)	6, 3	5, 1
Inlet/outlet temperatures (°C)	405/780	260/750
Helium pressure (bars)	48	40
Particles	UC ₂ TRISO/ThC ₂ BISO	UO ₂ /ThO ₂ BISO
Fuel element	Prism, 6 layers	Pebble
# Fuel elements	1,462	675,000
Average burnup (GWd/tons)	100	< 150
Fuel reload	Annual per 1/6th	Continuous

Gulf Oil (and soon of Shell as well), 8 large HTR rating 1,160 or 770 MWe, two very similar models with either three or two loops.

The general layout (➔ [Fig. 10](#)) is derived from the pods-type AGR, but with downward coolant circulation to protect the upper structures and control rod mechanisms from the hot helium. Prominent in this design stands the massive prestressed concrete reactor vessel (PCRV), with vertical tendons and circumferential wire wrappings. In the center of the PCRV, a main cavity contains the core while peripheral cavities (the “pods”) contain the helical SGs and the helium circulators. The core, extrapolated from Fort Saint Vrain, was supported by a forest of graphite pillars above a lower plenum connected to the pods by hot ducts with thermal insulation.

The 1974 oil shock triggered overnight a rash of nuclear project cancellations in the USA: latest ordered, most HTR projects were victims of this epidemic. The vendor itself canceled in 1975 the last two survivors. One must remember that there has been no surviving nuclear order in the USA since 1973.

4.3.2 The Schmehausen HTTR

In 1970, The German industry received an order for a 300 MWe prototype developed from AVR, to be built on the Schmehausen site.

The construction of THTR lasted 14 years, but the plant was operated only for four years before definitive shutdown. A number of technical difficulties, mostly due to the increase in size were met, but none appeared insolvable: the control rods had to be inserted in the stack of

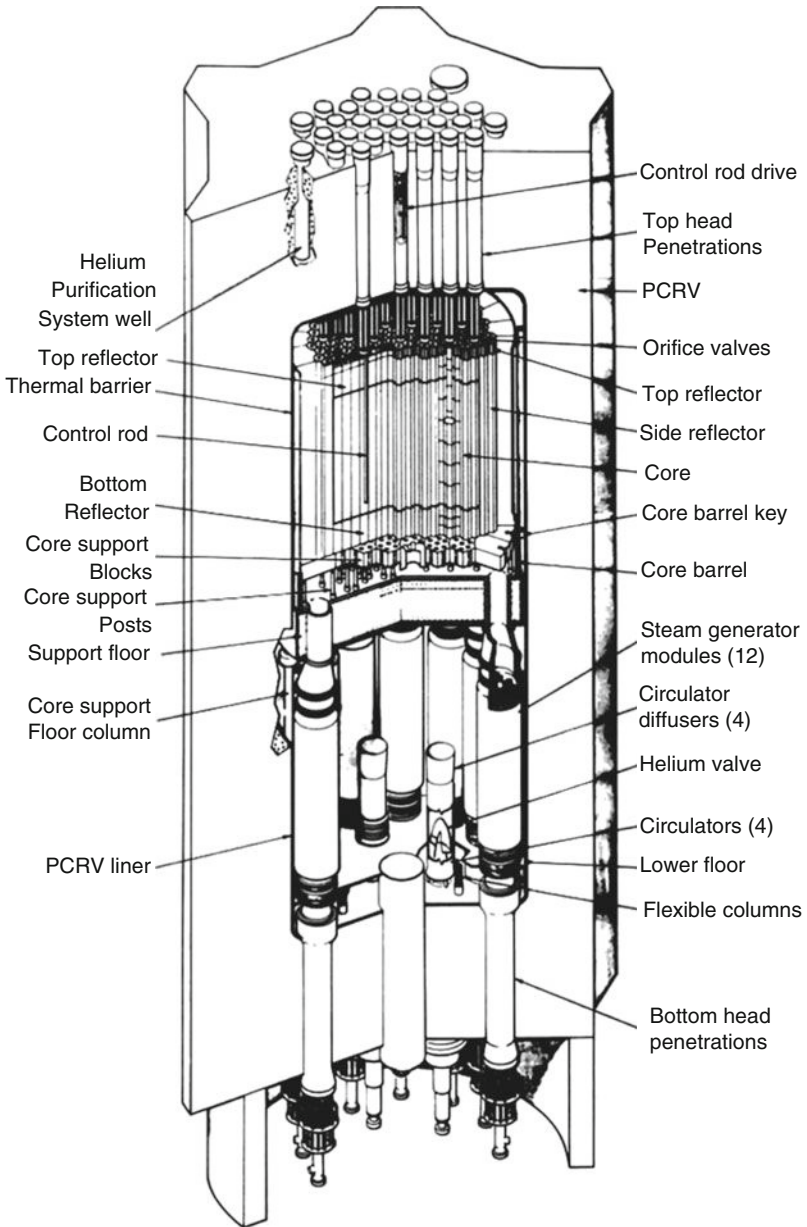


Figure 8
Fort Saint Vrain reactor layout (Melese & Katz 1982)

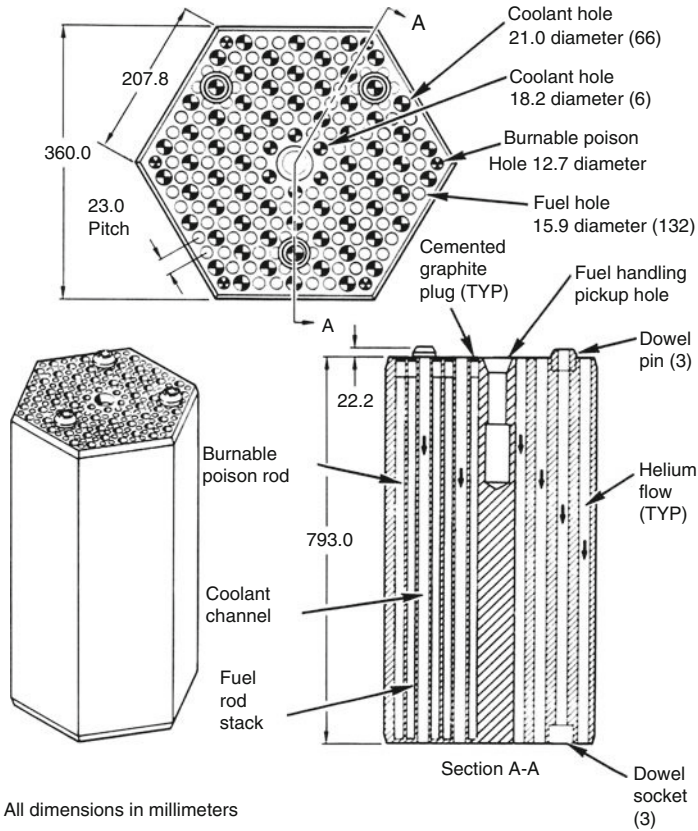
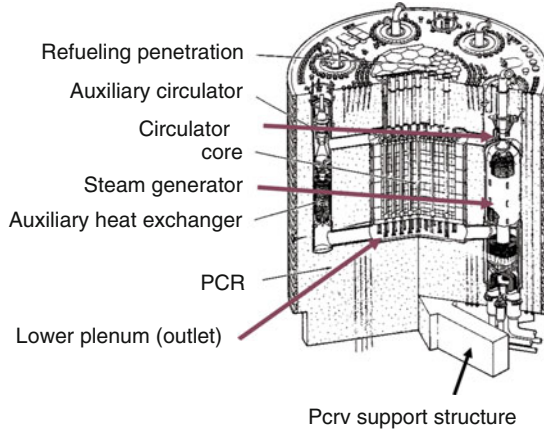


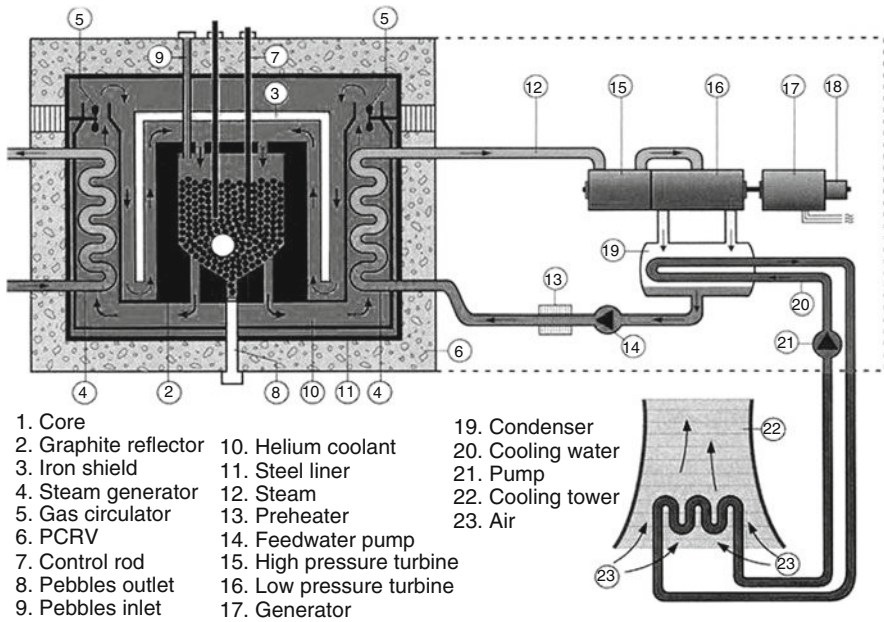
Figure 9
HTR prism

pebbles instead of in the reflector, the mass flow of helium was too big to allow counter current circulation of helium and pebbles, fixation of the graphite to the wall of the core cavity above the level of the top of the pebbles heap proved to be uneasy (Fig. 11). But the real reasons of THTR premature shutdown were the context of a German public opinion becoming antinuclear, and power struggles between the Land and the Federal government about licensing issues.

The mediocre performances of Fort St Vrain did not convince utilities from other countries to order HTR plants, but General Atomic, well introduced in the US Congress, managed to get year after year enough money on the US DOE budget to keep alive a small but highly competent team of engineers and scientists. But the thorium cycle was abandoned because it needed highly enriched uranium HEU to start the cycle and as a complement to ^{233}U because HTR are not breeders. After 1974 and the Indian explosion, the civilian use of HEU became taboo for nonproliferation reasons. Today, one would likely use plutonium to start a thorium cycle.



■ Figure 10
1160MWe HTR Project (1973) (Melese & Katz 1982)



■ Figure 11
THTR schematics

4.4 Lessons Learned from the First HTR Units

Despite the abortion of the US and German programs, the results of this first part of the HTR saga were far from negligible.

On the plus side:

- This type of reactor can reach a high thermal efficiency, as good as that of the best gas turbines
- Cold fuel, refractory core, high thermal inertia, one-phase coolant chemically inert: all these elements result in a high level of safety and forgiveness of operator mistakes
- The particle-based fuel can accommodate any possible fuel cycle
- The first small demos have proven the concept feasibility (and the rocket program described below demonstrated the existence of huge margins)
- HTR is one of the very few concepts to offer real prospects of non electrical uses of fission (together with the Gas-cooled breeder, which exists only on paper)

On the minus side:

- The low core power density means a large vessel and therefore a high capital cost
- The GA 1160 Project did not have a secondary containment
- If core meltdown is beyond credibility (though the SiC layer begins to deteriorate when the particle temperature exceeds 1,600°C), a massive water ingress in the hot core might provoke a dangerous weakening by corrosion of the core support pillars
- The core itself is quite refractory, but the long-term behavior of the materials outside the core exposed to hot helium is of concern. This includes the concrete PCR/V
- Both prototypes did not meet with great success

On the “plus or minus” side:

For all its great qualities, the HTR fuel is not easily reprocessed – and reprocessing is indispensable if one wants the advantages of the thorium cycle. The process originally developed at the laboratory scale at Idaho Falls had the following stages:

- Crushing of the prismatic blocks to free the compacts. The graphite fragments would have been incinerated, with the corresponding ^{14}C release, which would no longer be acceptable today
- Burning of the compact matrix as well as the outer pyrocarbon layers. This operation bares the BISO kernels, while the TRISO keep their SiC shell
- Dissolution of the BISO kernels in nitric acid: the remaining thorium is separated from ^{233}U by solvents extraction, PUREX type, while TRISO particles remain solid
- Crushing of the TRISO SiC shell and burning of the inner pyrocarbon
- Dissolution of the uranium kernel to recover the residual ^{235}U , contaminated with ^{236}U but still valuable

This difficulty to reprocess was considered a weakness in 1970, within a thorium cycle vision. After switching to LEU (about 8% ^{235}U enriched), and taking into account the very high burnups achievable, the residual value of the remaining fissile materials is very low. Reprocessing is all the less desirable that the spent fuel, whose graphite resists corrosion quite well at moderate temperatures, appears to constitute a quite acceptable waste form for direct disposal. The low power density of the core becomes then an asset. The fact that reprocessing is difficult and not very attractive is now advertised as an advantage in terms of non-proliferation.

In retrospect, HTRs have suffered above all from a bad timing of introduction. Their story might have been quite different if a few of the – better designed – large reactors ordered in the 1970s had actually been built. Their performance might have erased the bad memory of Fort St Vrain.

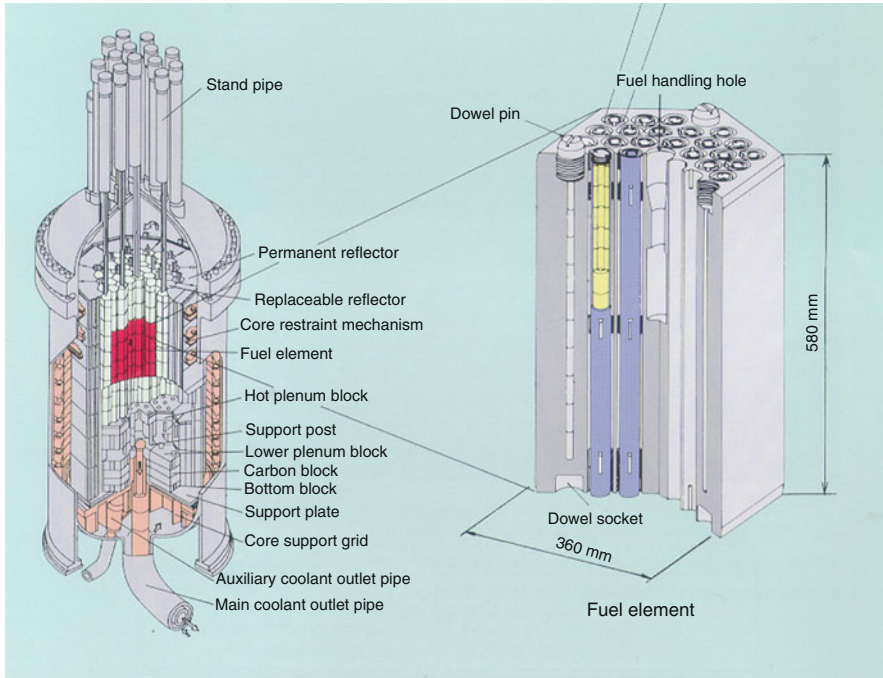


Figure 12
HTTR core and fuel element (from JAEA)

4.5 Recent Japanese and Chinese Demos

While both USA and Germany were abandoning the HTR development, it was continued along both types of HTR, but in other countries.

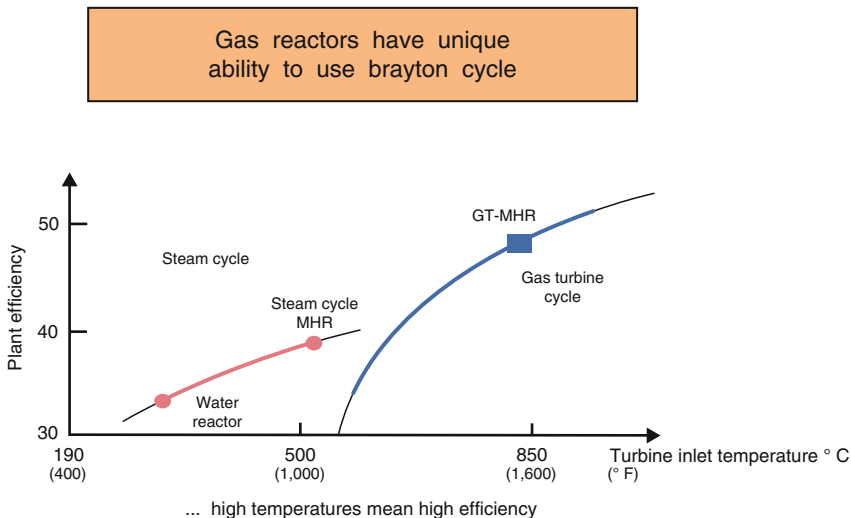
Japan built the HTTR, a 30 MWt demo HTR, whose construction by JAERI started in 1990, which has been operating since 1998. The HTTR uses prismatic blocks but the fuel design is not identical to the US: annular compacts are piled within a cylindrical graphite sleeve, located in open channels of the graphite hexagonal prism (Figure 12). Helium flows in the annulus between the sleeve and its channel. HTTR is planned to be used to demonstrate hydrogen production using nuclear heat (see Sect. 6).

The Chinese have built a small 10 MWt pebble bed demo, which went critical in December 2000. This reactor can passively evacuate its decay heat and has carried out some interesting safety experiments.

4.6 GT-MHR and PBMR

Since the 1980s, a number of evolutions have triggered a renewed interest in HTRs, even from some PWR champions like AREVA-NP (formerly Framatome) or Westinghouse (at least when it was affiliated to BNFL).

1. To overcome the formidable economic “size effect” and attempt to remain competitive with plants adapted to the needs of emerging countries, i.e., much smaller than 1,600+ MWe EPR, many reactor vendors have considered in the 1980s “modular” concepts. A modular power plant would be built progressively by adding identical units, small enough to have a high degree of prefabrication in factory and, therefore, a minimum construction – or rather assembly – time on-site. The progressiveness allows the first unit to start generating power, hence cash flow, when later units are still under construction. Taking into account the weight of interests during construction IDC in the capital cost of a plant, both prefabrication and stepwise assembly offer the prospect to balance the size penalty.
2. Below a threshold in size, it becomes possible to remove the decay heat after shutdown through purely passive means: thermal conduction and convection. Of course, the pressure vessel must be metallic. The threshold comes from the surface/volume ratio, for a given power density. If the safety authorities accept the demonstration, one can get rid of expensive emergency core cooling systems – there again, to overcome the size penalty.
3. Taking advantage from the fallouts of the aerospace developments, gas turbines have achieved spectacular improvements, both in size and efficiency. This underlined the importance of thermal efficiency, one HTR strong point (➡ Fig. 13), and lent credibility to the feasibility of high power helium turbine, hence the direct cycle HTR.
4. Nuclear weapons reduction agreements between the USA and the Russian Federation after the end of the Cold War have “freed” huge quantities of weapon-grade plutonium, which must be “disposed of.” The best way is to burn this plutonium in power plants. With their wide fuel cycle flexibility, HTRs can be optimal plutonium burners (➡ Table 7).



■ Figure 13
Achievable thermal efficiencies

4.6.1 GT-MHR, Gas Turbine Modular High Temperature Reactor

As mentioned above, during the “lean cows” years, General Atomic still carried out some HTR development, federally funded. In 1993, this development was boosted in an American-Russian framework, to design a HTR optimized for weapon-grade plutonium burning. Framatome (now AREVA-NP) joined the project in 1995, followed by Fuji Electric.

The GT-MHR nuclear island has the following characteristics:

- Steel pressure vessel without thermal insulation to allow heat removal by radiation
- Prismatic “GA type” fuel elements constituting an annular core to maximize the surface-to-volume ratio (The center columns of the core, in pure graphite, add to the overall thermal inertia)
- Cooling panels inside the walls on the underground reactor containment building, operating in natural convection

The conventional island features:

- A direct cycle helium turbine, allowing for excellent thermal efficiency and eliminating the risk of water ingress in the core
- Magnetic bearings (water ingress through the bearings was an endemic plague in Fort St Vrain)

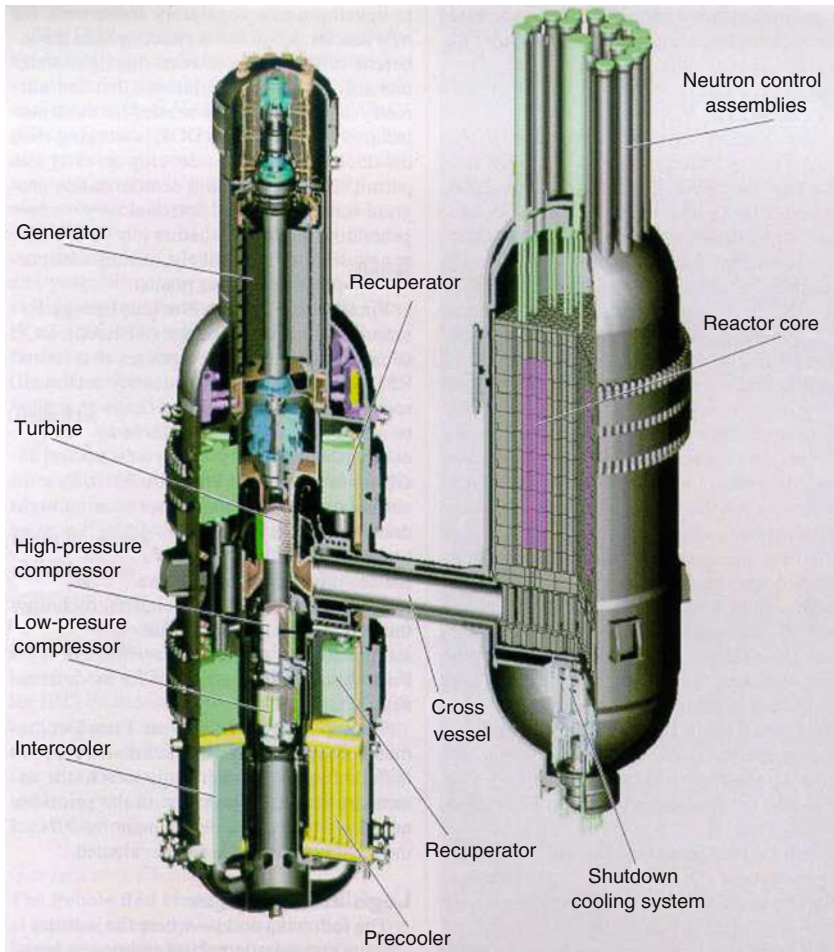
The core, on the one hand, and the single shaft turbo-alternator-compressors are located side by side in two separate steel vessels connected by a short duct. The whole layout is quite compact (► [Fig. 14](#)).

4.6.2 ESKOM PBMR Pebble Bed Modular Reactor

While GT-MHR was directly in line with the General Atomic family, PBMR, derives from the Jülich AVR, revisited by the South African utility ESKOM. Here were its original characteristics:

■ **Table 7**
PBMR and GT-MHR characteristics

Characteristics	PBMR	GT-MHR
Thermal power (MWt)	265	600
Net electric power (MWe)	116	285
Efficiency (%)	44	47,5
Core inlet/outlet temperatures (°C)	536/900	490/850
Helium mass flow (Kg/s)	140	320
Turbine inlet/outlet temperatures (°C)	751/554	850/510
Turbine inlet/outlet pressure (MPa)	7,0/4,3/2,6	7,0/2,6
Fuel element	Pebbles	Prismatic



■ Figure 14
GT-MHR's two "bottles" (from AREVA)

The PBMR is very simple and the fuel has been thoroughly qualified (but the German fabrication facilities have disappeared). On the other hand, construction time and cost initially quoted by ESKOM were not quite credible. Over the years, PBMR has increased its rating to 165 MWe and adopted an annular core design, and PBMR intends to build a high-temperature ($>1,000^{\circ}\text{C}$), high-pressure (90 bar) demonstration reactor at Koeberg. A Helium Test Facility (HTF) is already testing many components in a helium environment at Pelindaba in the North West province. The HTF has specifically been built to test helium at the very high temperatures and pressures that will be experienced in the Pebble Bed Modular Reactor. According to the PBMR website <http://www.pbmr.co.za/>, the latest design is as follows:

The PBMR essentially comprises a steel pressure vessel, which holds about 456,000 fuel spheres. The fuel consists of low enriched uranium triple-coated isotropic particles contained

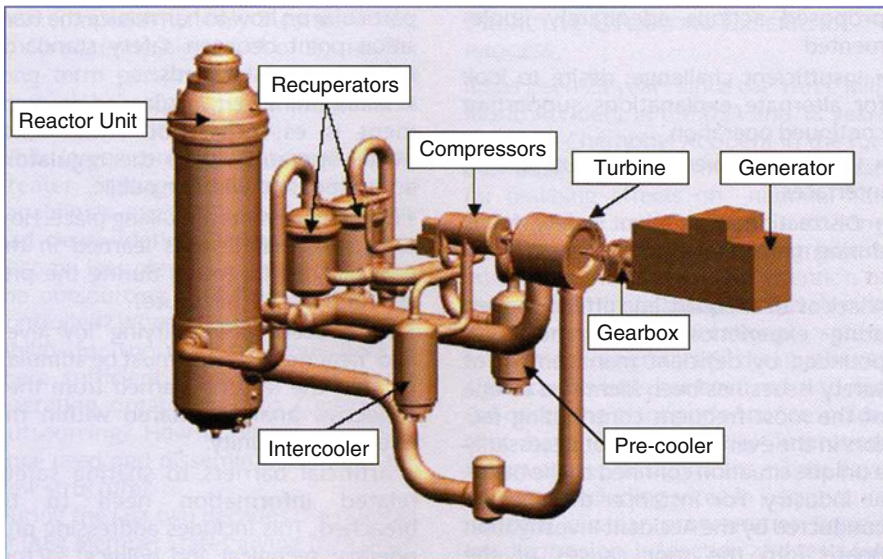
in a molded graphite sphere. A coated particle consists of a kernel of uranium dioxide coated with silicon carbide and pyrolytic carbon. The particles are encased in graphite to form a fuel sphere or pebble about the size of a tennis ball. Helium is used as the coolant and energy transfer medium, to drive a closed cycle gas turbine and generator system.

The plant comprises a module building with the reactor pressure vessel (RPV) and the power conversion unit (PCU) (► Fig. 15).

The PBMR has a 27 m high vertical steel reactor pressure vessel (RPV) with an inner diameter of about 6.2 m. The RPV contains and supports a metallic core barrel. It is lined with a 1 m thick layer of graphite bricks, which serves as an outer reflector and a passive heat transfer medium. The geometry of the fuel region is annular and located around a central graphite column. The latter serves as an additional neutron reflector. The core barrel supports the annular pebble fuel core, which is located in the space between the graphite reflectors. Vertical borings in these reflectors are provided for the reactivity control elements. Two diverse reactivity control systems are provided for shutting the reactor down. One of the systems is 24 control rods in the outer reflector, while the other consists of small absorber spheres which are dropped into eight borings in the central reflector.

To remove the heat generated by the nuclear fission reaction, helium coolant enters the reactor vessel at a temperature of about 5,000°C and a pressure of nine MPa. The gas flows down between the hot fuel spheres, after which it leaves the bottom of the vessel having been heated to a temperature of about 900°C.

The hot gas then enters the turbine, which is mechanically connected to the generator through a speed-reduction gearbox on one side and the gas compressors on the other side.



► Figure 15
PBMR nuclear island

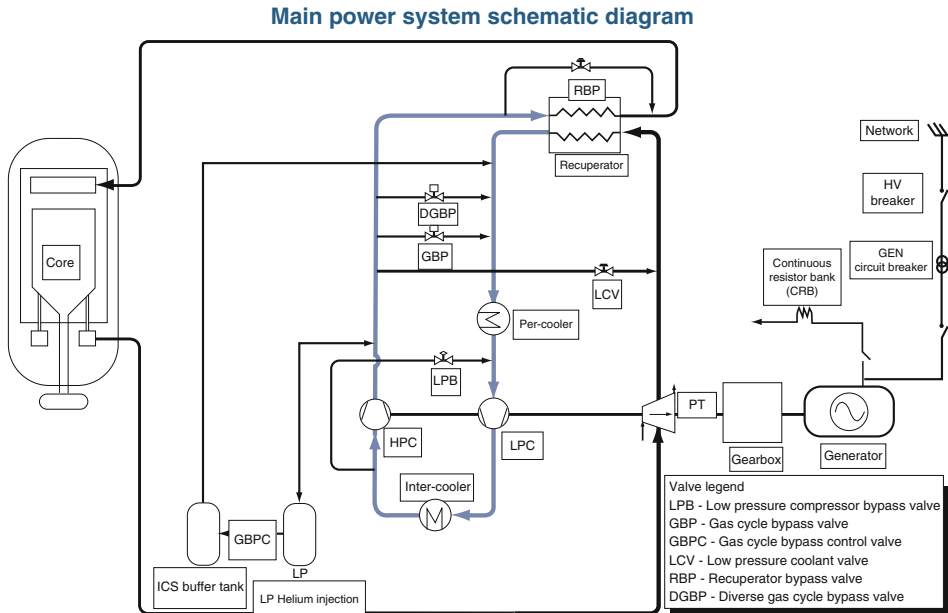


Figure 16
PBMR Flow Chart

The coolant leaves the turbine at about 500°C and 2.6 MPa, after which it is cooled, recompressed, reheated, and returned to the reactor vessel (🔍 Fig. 16).

The thermodynamic cycle used is a Brayton cycle with a water-cooled pre-cooler and inter-cooler. A high efficiency recuperator is used after the power turbine. The helium, cooled in the recuperator, is passed through the pre-cooler, low-pressure compressor, the inter-cooler, and high-pressure compressor before being returned through the recuperator to the reactor core.

The power taken up by the helium in the core and the power given off in the power turbine is proportional to the helium mass flow for the same temperatures in the system. The mass flow rate depends on the pressure, so the power can be adjusted by changing the pressure in the system. The high pressure and high temperature operation of the reactor in a relatively high thermal efficiency.

While a typical light water reactor has a thermal efficiency (electrical power output/thermal heat input) of approximately 33%, an efficiency of about 41% is anticipated in the basic PBMR design.

Online refueling is another key feature of the PBMR. Fresh fuel elements are added to the top of the reactor while used fuel is removed at the bottom while the reactor is at power. The aim is to operate uninterrupted for 6 years before the reactor is shut down for scheduled maintenance. For the demonstration module, however, a number of interim shutdowns will be required for planned evaluation of component and system performance.

Shutdown will be done by inserting the control rods. Start-up is effected by making the reactor critical, then using nuclear heat-up of the core and circulating the coolant by motoring the turbo-generator set. Heat is then removed by the pre-cooler and inter-cooler. At a specified temperature, the cycle becomes self sustaining.

4.6.3 PBMR Fuel Fabrication and Fuel Cycle

PBMR fuel is based on the proven, high-quality AVR fuel design consisting of low enriched uranium triple coated isotropic (LEU-TRISO) particles contained in a molded graphite sphere. A coated particle consists of a kernel of uranium dioxide surrounded by four coating layers. The uranium in the PBMR fuel is enriched to about 10% in ^{235}U .

In the fabrication process, a solution of uranyl nitrate is dropped from small nozzles to form microspheres, which are then gelled and calcined to produce uranium dioxide fuel “kernels.” The kernels are then run through a chemical vapor deposition (CVD) furnace in an argon environment at a temperature of $1,000^{\circ}\text{C}$, in which layers of specific chemicals can be added with extreme precision.

For PBMR fuel, the first layer deposited on the kernels is porous carbon. This is followed by a thin coating of pyrolytic carbon (a very dense form of carbon), a layer of silicon carbide (a strong refractory material), and finally, another layer of pyrolytic carbon. The porous carbon accommodates any mechanical deformation that the uranium dioxide kernel may undergo during the lifetime of the fuel, as well as gaseous fission products diffusing out of the kernel. The pyrolytic carbon and silicon carbide layers provide an impenetrable barrier designed to contain the fuel and fission products. Some 15,000 of these coated particles, now about a millimeter in diameter, are then mixed with graphite powder and a phenolic resin into 50 mm diameter spheres. A 5 mm thick layer of pure carbon is then added to form a “non-fuel” zone, and the resulting spheres are sintered and annealed to make them hard and durable. Finally, the spherical fuel “pebbles” are machined to a uniform diameter of 60 mm. Each fuel pebble contains about 9 g of uranium, i.e., ~ 1 g of ^{235}U . The total uranium in one fuel load is 4.1 metric tons, and the total mass of a fuel pebble is 210 g.

The reactor is continuously replenished with fresh or reusable fuel from the top, while used fuel is removed from the bottom. After each pass through the reactor core, the fuel pebbles are measured to determine the amount of fissionable material left. If a pebble still contains a usable amount of the fissile material, it is returned to the reactor at the top for a further cycle. Each cycle takes about 6 months. Each pebble passes through the reactor about six times and lasts about 3 years before it is spent, which means that a reactor will use 15 total fuel loads in its design lifetime of 40 years.

The PBMR fuel will be manufactured at the Necsa site at Pelindaba near Pretoria. The facility will have an initial capacity of 270,000 fuel spheres per year. A 165 MWe PBMR module will generate about 32 tons of spent fuel pebbles per annum, about 1 ton of which is uranium.

The storage of PBMR spent fuel should be easier than for fuel elements or rods from conventional nuclear reactors, as no safety graded cooling systems are needed to prevent fuel failure. The fuel is transported to the spent fuel storage facility in the reactor building by means of a pneumatic fuel handling system. The spent fuel storage consists of ten tanks, each with a diameter of 3.2 m and a height of 18 m. One tank can store 600,000 pebbles. There will be enough room for the spent fuel to be stored in dry storage tanks at the PBMR plant for the power station’s expected 40-year operational life, during which time no spent fuel will have to be removed from the site. After the plant has been shut down, the spent fuel can be safely stored on site for another 40 years before being sent to a final repository.

5 The NERVA Story (Simpson JW 1995)

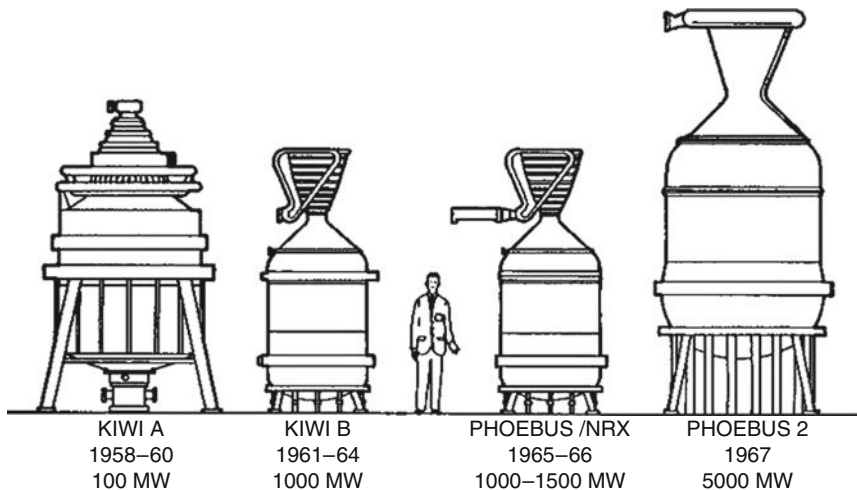
Let us forget electricity for a while, and follow the HTR adventure in the wake of the famous APOLLO space program.

In parallel with their conventional program of chemical rockets development, during 20 years or so, the US developed a project of nuclear propulsion rocket of an incredible ambition, as seen today. The objective was to heat much above $2,000^{\circ}\text{C}$ and for several tens of minutes formerly liquid hydrogen, using the heat generated by a nuclear reactor. For the sake of comparison, the Vulcain motors powering the Ariane V rocket are qualified to operate during no more than 10 min. Only the particle-based HTR fuel could let one dream of such performances.

The most surprising is that, despite incredible technical difficulties, this project met a total success (➤ *Figs. 17* and ➤ *18*). From the tiny Kiwi to the big Phoebus, from 1959 to 1972, all records were consistently broken, as shown on the (➤ *Table 8*). The project was then completely dropped, as NASA never launched the APOLLO XVIII to XX though completely built: 3 years after the first Moon landing, space was no longer a national priority. Over those years, the complete Rover/NERVA program cost amounted to a total of \$ 1.5 billion. Since 2000, NASA and DOE have somehow revived a few nuclear space propulsion projects. Whatever their future may be – and it is too early to guess – the early space attempt has demonstrated the huge margins imbedded in the HTR fuel!

6 Gas Cooling in Generation IV (DEN 2006)

Much energy has been vested in international cooperation to define goals for the nuclear energy systems of the future, and also select the key technologies for achieving them. The effort has



■ **Figure 17**
The NERVA series of reactors



Figure 18
The Phobos 2 Test, at Jackass Flats, Nevada

Table 8
A few rover/NERVA tests

Date	Test	P_{\max} (MWt)	Time at P_{\max}	Outlet T_{\max} ($^{\circ}\text{C}$)
7/1959	Kiwi 1A	70	5 min	
7/1961	Kiwi B1A	300	30 s	
9/1962	Kiwi B1B	900	a few s	
5/1964	Kiwi B4D	1,000	40 s	2,220
7/1964	Kiwi B4E	900	8 min	2,390
9/1964	NRX A2	1,100	3, 4 min	2,300
5/1965	NRX A3	1,122	13 min	2,450
6/1965	PHOEBUS	1,090	10, 5 min	2,480
6/1966	1A NRX A5	1,140	2 times 15 min	2,450
2/1967	PHOEBUS	1,500	30 min	2,445
12/1967	1B	1,100	62 min	2,550
6/1968	NRX A6	4,300	12 min	2,310
12/1968	PHOEBUS	514	12 min	2,750
7/1972	2A PEEWEE FURNACE	44	109 min, 4 tests	2,450

been made primarily through the Generation IV International Forum (GIF) that the American Department of Energy (DOE) launched during the course of 2000. In 2009, GIF participants were Argentina, Brazil, Canada, China, the European Union, France, Japan, Russia, South Africa, South Korea, Switzerland, UK, and USA.

The GIF is a major initiative to identify and organize the R&D required to develop a new generation of nuclear energy systems due to go on stream around 2040. Each of the systems

comprises a nuclear reactor, an energy conversion system and the necessary fuel cycle, fuel manufacturing, spent fuel, and final waste management equipment.

GIF participants agreed on four major goal areas: aptitude for developing sustainable energy, economic competitiveness, more robust safety and reliability, and nuclear materials proliferation resistance along with physical protection for installations.

Twenty families of nuclear systems were initially presented by nuclear engineers and scientists. A one hundred-strong international expert panel evaluated the performances of each family against 24 metrics. Final selection of the systems also brought into play considerations such as the selection's completeness in terms of diversity of technologies, deployment lead times, the possibility of staged development and the ability to meet the identified needs of electricity production, hydrogen production, fissile material regeneration, and transmutation of long-lived waste for forthcoming decades.

The following six systems deemed the most promising at the end of this evaluation exercise were called on to rally Forum cooperation on development work starting from 2004:

- VHTR – very high temperature reactor system, over 1,000°C, helium-cooled, dedicated to hydrogen production or hydrogen/electricity cogeneration
- GFR – gas-cooled fast reactor system – helium-cooled fast reactor
- SFR – sodium-cooled fast reactor system
- SCWR – super critical water-cooled reactor system
- LFR – lead-cooled fast reactor system – lead or Pb-Bi alloy-cooled fast reactor
- MSR – molten salt reactor

The first two of the six selected systems are gas-cooled. VHTR offers the strengths of economics and safety in particular. Because an open cycle is used, its aptitude for sustainability is deemed to be similar to that of a second generation reactor. Likewise, the radiotoxicity and volume of VHTR waste are characteristically high.

GFR offers a different picture: its closed fuel cycle makes both waste and its aptitude for sustainability of positive strengths. On the other hand, it meets the economics and safety criteria less satisfactorily, and would need a much longer development time.

6.1 VHTR

The VHTR is one of the six concepts selected by the GIF as a candidate model for Generation IV. With respect to the other concepts, VHTR stands apart: it offers very little improvement in terms of sustainability (fissile material utilization and waste management), but it opens to nuclear fission a wide new range of applications, the most promising of which appears to be hydrogen production.


6.1.1 Electricity Production


As seen above, HTRs were developed in the 1970s. Reactors of this type were subsequently built and operated, and numerous test facilities were also built (e.g., to test the performance of direct-cycle gas turbines, the heat resistance of refractory concretes, or the oxidation resistance of graphite).

The pursuit of increased system performance led to the idea to increase the reactor operating temperature. According to the Carnot principle, the efficiency of a reversible thermodynamic system increases with temperature as follows:

$$\eta = 1 - \frac{T_2}{T_1},$$

where T_1 and T_2 are the absolute temperatures of the hot and cold source, respectively.

If technologically possible, increasing the core outlet temperature approximately 100° improves efficiency by several points. For example, under otherwise identical conditions, the electrical production efficiency of an industrial machine operating on a direct Brayton-cycle with helium as the working fluid increases from 50.5 to 56% when T_1 increases from 850 to 1,000°C (see  Fig. 19, dotted curve).

However, the technological constraints associated with the resistance of the reactor vessel steel limit the foreseeable increase, i.e., an increase in core outlet temperature is generally accompanied by an increase in helium return temperature near the reactor vessel. The best reactor vessel material currently being developed (chrome steel) does not withstand temperatures above 490°C. With a core outlet temperature of 1,000°C and a helium return temperature of 490°C, the electrical production efficiency is only 53% ( Fig. 19, poor efficiency curve). An increase in efficiency of 2.5 points amounts to a 5% decrease in production cost. Moreover, increasing the efficiency without modifying the fuel quantity used, which is the case when switching from an HTR to a VHTR, leads to a proportional decrease in the quantity of radioactive waste created per kilowatt-hour produced.

The benefits of higher temperatures are apparent, but also the difficulty of achieving them.

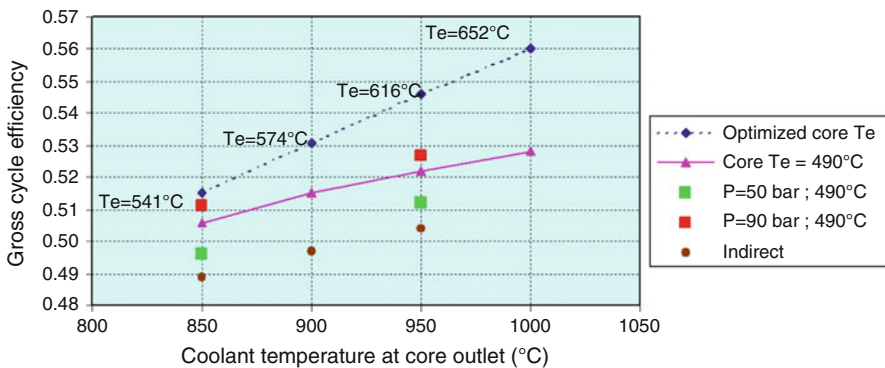
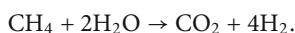


 Figure 19


Electrical production efficiency of a very high temperature reactor system (VHTR) using a direct helium cycle (Brayton), as a function of core outlet temperature and return temperature (T_e). Depending on the reactor vessel steel used, a low return temperature may be necessary to prevent embrittlement (in this case $T_e = 490^\circ\text{C}$ for chrome steel, poor efficiency curve), which produces a reduction in efficiency as compared to unconstrained conditions (dotted curve) (DEN 2006)

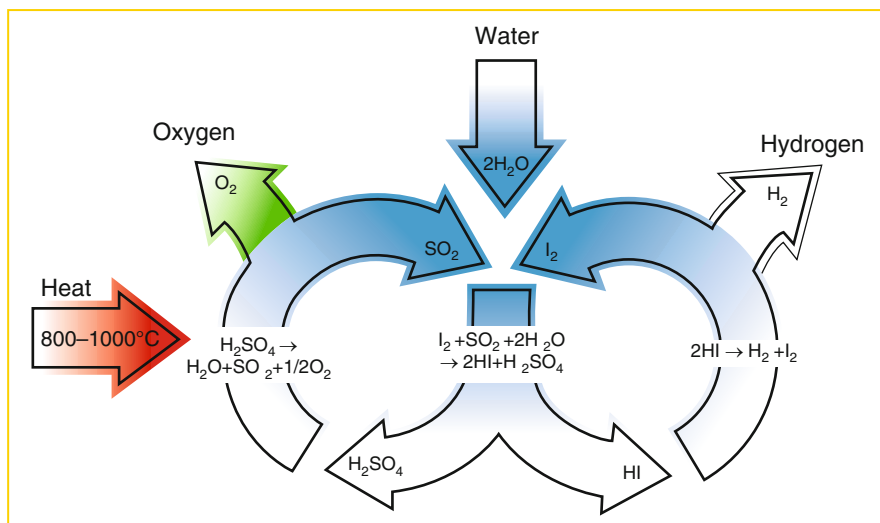
6.1.2 Hydrogen Production


Very high temperatures also allow the possibility of producing hydrogen directly via thermochemical cycles, without transforming heat into electricity. Hydrogen is a good substitute for hydrocarbon fuels because its combustion in air yields only water. It may even be more interesting as feedstock for synthetic liquid fuels, associated with coal or biomass. But hydrogen does not exist naturally in free state: it needs to be produced. Dissociating a water molecule is an attractive solution, as the water cycle (dissociation and combustion) constitutes a closed and clean cycle, but it is energetically costly. We currently know how to produce hydrogen by water electrolysis, but at a very high cost. Most of the industrial production of hydrogen is achieved by making light hydrocarbons react with high-temperature steam. For example, methane reformation with steam consists of the following reaction:

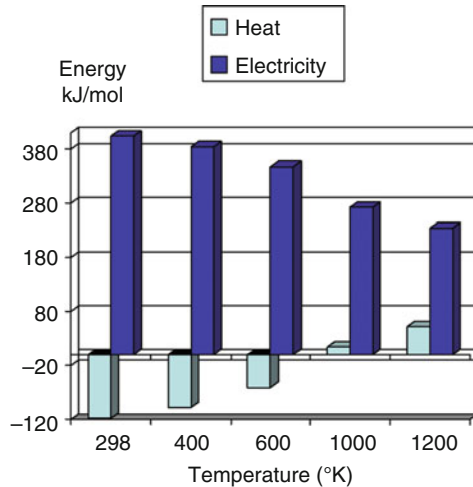


The reformation is performed at over 700°C , burning part of the methane to produce the heat required. This economic process consumes hydrocarbons and produces carbon dioxide contributing to the greenhouse effect. The concept of using nuclear heat as an energy source and water as a resource allows the possibility of industrial production without greenhouse gases.

In order to chemically dissociate a water molecule, various reaction methods can be considered. They involve intermediate steps with additional products that are recycled in the process, therefore acting as chemical catalysts. The most studied processes operate at very high temperatures, typically above 900°C , hence the interest of a heat source exceeding 950°C . For example, sulfur-based cycles use a sulfuric acid dissociation reaction that only works above 870°C and whose efficiency increases with temperature (see  Fig. 20).



 **Figure 20**
Hydrogen production by iodine-sulfur thermochemical cycle (DEN 2006)



■ Figure 21

Energy required to dissociate a water molecule by steam electrolysis, as a function of temperature. Below 600°C, electricity is partly lost heating the water. Above this temperature, the direct heating of the water reduces the electricity required (DEN 2006)

This cycle decomposes the water molecule using heat at over 870°C.

We can also dissociate a water molecule by steam electrolysis. Preheating the water vaporizes and superheats it, thereby decreasing the electrical energy required for its dissociation. The direct use of heat minimizes losses associated with the transformation of heat into electricity

(► Fig. 21).

As described above, the electrical transformation efficiency of an HTR is approximately 50% (as compared to only 30% for a PWR). Assuming an electrolyzer efficiency of 80% at 900°C, the global efficiency of the system is 40%. On the other hand, if part of the reactor's calorific energy is used to heat the electrolyzer and decrease the share of electricity required, the global efficiency can be increased by several points so as to approach 50%.

Again, as in the case of electricity production, the final criterion is the cost of the hydrogen produced, but good efficiency is essential no matter what method is used.

6.1.3 Water Desalination

Saltwater desalination at low cost is another interesting application of HTRs. The production of freshwater constitutes a major challenge for numerous countries in the years to come. Seawater desalination technologies are already available and industrially implemented throughout the world, but their cost is high. Water desalination processes require mechanical or heat energy, depending on the method used.

For example, we can vaporize saltwater and condense the steam obtained, which no longer contains salt. This process is efficient at temperatures above 120°C. HTR thermodynamic cycle optimization processes produce temperatures of 120–130°C, depending on the circuits used.

This heat is released to the exterior and it is perfectly possible to install a desalination circuit. In that case, only the cost of the desalination circuit needs to be considered. The heat is free (normally unused), thereby reducing desalination costs. Moreover, by increasing the hot temperature of a VHTR, we also increase the temperature of this heat energy by a few tens of degrees, making the desalination process even more attractive.

6.1.4 NGNP Project (USA)

Simultaneously with the international structuring of research on future reactor systems (GIF) in 2003, the US DOE announced the construction of a VHTR prototype in the near future. Referred to as the *next generation nuclear plant* (NGNP), this prototype should demonstrate high-efficiency electricity production and hydrogen production capacities.

The objective is twofold: to produce a prototype that can be marketed as such in an electronuclear fleet, and to promote associated research and development for innovation. The initial development plan was very ambitious (construction between 2011 and 2015). Subsequent innovation scheduling analyses showed the need for a transition period from recognized HTR technologies to the more ambitious VHTR technologies described above. In 2008, the NGNP was scheduled to begin operation in 2018.

The NGNP consists of a fourth generation VHTR prototype to be financed by the DOE and a consortium of US research centers and industrial partners. The NGNP will be built at the Idaho National Laboratory (INL). The main characteristics of this reactor are the following:

- Helium-cooled reactor
- Helium temperature at core outlet: 1,000°C
- Modular reactor with an output power of 300–600 MWth
- TRISO particle fuel
- Graphite core (prismatic or pebble bed)
- Hydrogen coproduction
- Attractive safety characteristics

The NGNP should produce electricity at an attractive cost. Its temperature of 1,000°C should allow for an efficiency of 50%.

Technologies suitable for operating at such temperatures will need to be developed based on the knowledge acquired in previous HTR projects. The core temperature increase of 150°C (under otherwise identical conditions) requires the confinement of fission products within multilayer particles. Metallurgists consider that the exposure of internal components and circuits to temperatures exceeding 950°C imposes a radical change in the choice of materials. Further research on energy conversion systems coupled to a direct helium cycle turbomachine will also be necessary.

Hydrogen production demonstrations will concern two processes. A high-temperature thermochemical cycle capable of directly using the heat produced will be tested using the iodine-sulfur cycle as the reference. It will be coupled to a production loop drawing 50 MWth from the NGNP. The resulting production will amount to approximately 500 kg/h of hydrogen, the equivalent of 40,000 l of gasoline per day. The second demonstration, to be conducted in parallel, will concern hydrogen production by high-temperature electrolysis with an equivalent

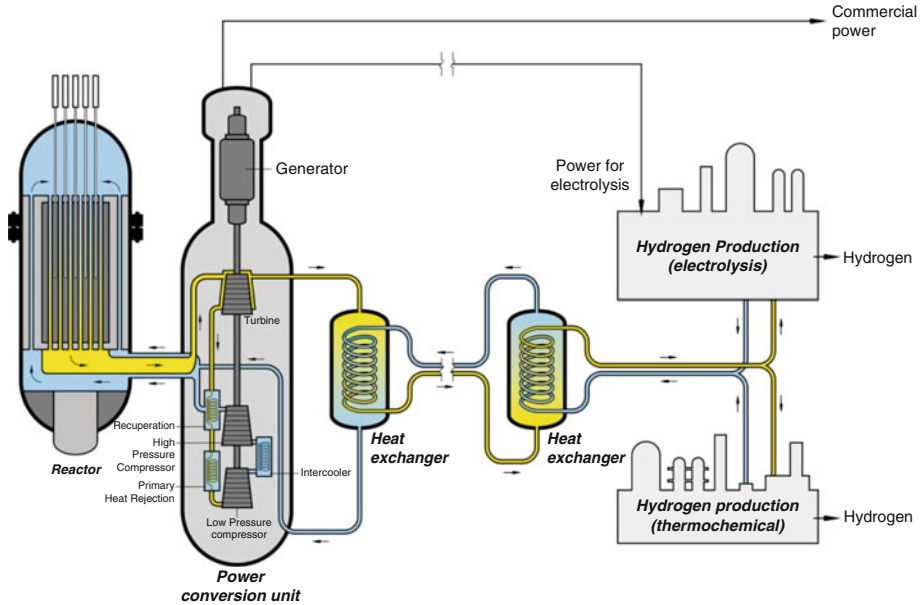


Figure 22

Basic diagram of the next generation nuclear plant (NGNP)

output power (i.e., 5 MWth and 20 MWe). A basic diagram of the NGNP concept is shown in (Fig. 22).

The choice of core type (prismatic or pebble bed) will be postponed until after the preproject phase, thus allowing the various engineering teams involved to defend their positions. The GIF is organizing R&D activities on the VHTR in support of this project.

To be in a position to answer a potential DOE bid, AREVA has developed the Antares conceptual design of a VHTR cogeneration demonstrator (Fig. 23). Leaving out the direct cycle helium turbine of the GT-MHR, judged still to be a technological uncertainty, the Antares reactor is coupled to the applications through an Intermediate gas-to-gas heat exchanger IHX. The high temperature calories can be used either to produce hydrogen or to generate electricity in a gas turbine (using an air-like mix of helium and nitrogen) and a bottoming conventional steam cycle generate additional electricity, like in a combined cycle gas turbine.

6.2 GFR

The Generation IV GFR project addresses a twofold challenge: combining high thermodynamic efficiency through high temperatures, and high neutronic efficiency (with significant economization of resources in the case of the uranium-plutonium cycle) through fast spectrum conditions. It has therefore been referred to as a “high-efficiency reactor,” constituting the second wave of modern GCRs (beyond HTRs).

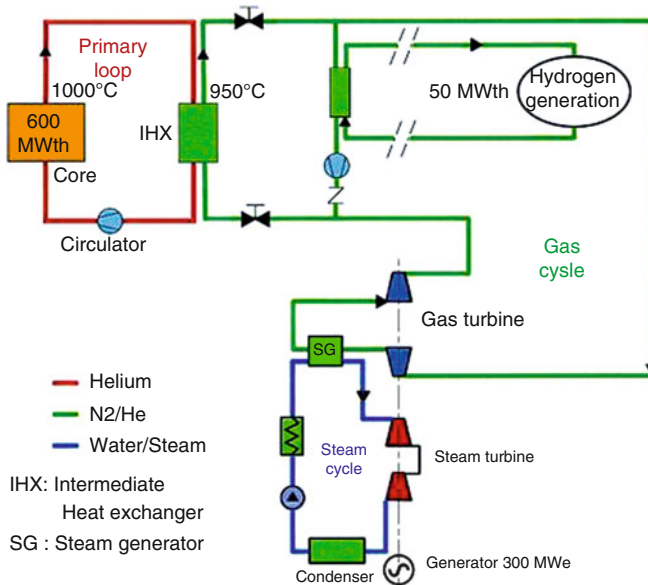


Figure 23
ANTARES flow chart (from AREVA)

The specific advantages of the GFR are the following: knowledge and operating experience acquired with GCRs, twofold concept allowing the nuclearization of high-performance modern technologies developed outside the nuclear field, and progressive transition via the HTR-type thermal GCR fleet that will precede it.

To address the twofold challenge of fast spectrum and high temperature conditions, the GFR possesses advantages inherited from modern HTR concepts, i.e., combination of a chemically inert coolant (helium) transparent to neutrons (no capture, little diffusion, no activation, even at pressures of several tens of bar) with a refractory and mechanically robust core using “cold” fuel and locally confining FPs at high temperatures.

This combination makes it possible to benefit from the decoupling of neutronics and thermal hydraulics, and thermomechanics and chemistry. The design of nuclear reactors is determined by the analysis of failure modes associated with couplings of neutronics, thermal hydraulics, material mechanics, and chemistry. The benefits of said decouplings, associated with a more efficient fuel, manifest themselves under both normal and accident operating conditions.

The helium flow path in the core can be modified beyond a minimum core volume without significant disturbance of spectrum, capture, and leak conditions. Together with the possibility of significant increases in core temperature, this property allows for reducing the pumping power under normal operating conditions and favors gas convection in decay heat evacuation situations.

The practical exclusion of recriticality accidents through the insertion of reactivity exceeding the delayed neutron fraction constitutes a significant advantage for the design of a fast neutron reactor concept subject to increased core sensitivity (namely due to the loading

dominated by plutonium, which reduces the delayed neutron fraction β_{eff} , and also due to the short lifetimes of prompt neutrons under fast spectrum conditions, i.e., approximately one microsecond). The increase in reactivity due to depressurization can be limited by design to a value less than β_{eff} .

The use of a chemically inert coolant makes it possible to benefit from the refractory and mechanical robustness qualities of the core. In severe accident situations, an additional margin of a few 100° is guaranteed beyond the fission gas containment limit (i.e., before extended core degradation leading to a loss of geometry inhibiting core cooling in the long term, or to a core collapse possibly resulting in a significant release of energy due to recriticality).

Helium is not activated under neutron flux. It is chemically inert and, if pure, does not contribute to structural corrosion or activation. This advantage has been confirmed in HTRs. Combined with the HTR fuel containment quality, it has led to very satisfactory operating experience in terms of doses. It is particularly advantageous in the hypothesis of reactors operating on a direct cycle with gas turbines.

It is therefore possible to benefit from the remarkable increases in efficiency and competitiveness achieved by fossil fuel plants over the past decades with conventional industrial coolants (gas and steam or supercritical water). This is particularly clear in the case of gas turbines.

The GFR system combines high thermodynamic and neutronic efficiency. It is a modern and competitive technology capable of following up on progress with fossil thermal systems (particularly as regards coal, a potential competitor in the long term). It guarantees a sustainable development of nuclear energy by maximizing the use of uranium resources through industrially optimized plutonium recycling.

6.2.1 Specific Problems Associated with the GFR

These problems are due to the above-mentioned twofold objective (high temperatures and fast spectra) and mainly concern the following: fuel and structural materials under flux, economic fuel reprocessing and fabrication, and evacuation of residual power under loss-of-pressure accident conditions. They can be overcome through a combination of technological innovation and optimized reactor design.

A steel-clad pellet-type fuel with large volumes of fission gas expansion outside the core, such as that developed for SFRs, can be adapted for a GFR core. However, it does not provide the second set of properties sought, characteristic of micro-confining, refractory (cold), and mechanically robust fuels such as the graphite matrix particle fuels tested up to very high burn-up fractions under thermal spectrum conditions in HTRs. Due to the damage associated with fast spectrum irradiation, and given the power density sought, these fuels are not usable as such in a GFR system.

In addition, imposing fission gas retention within the core volume leads to a diluted core and makes it more difficult to obtain a hard spectrum. Adapting such concepts, modifying the materials and ensuring competitive fuel reprocessing and fabrication is therefore one of the greatest challenges for the GFR. The same applies to the core structures and, more generally, the flux-exposed structures.

The need to evacuate residual power under loss-of-pressure accident conditions with loss of nominal forced gas convection contributes to the design of the backup systems. The combination of high specific power (aimed at minimizing the plutonium inventory required for a

given power output) and high concentration of fissile nuclei (aimed at hardening the spectrum) imposes a power density of between 50 and 100 MWth/m³. Correlatively, the thermal inertia of the core and structures (thermally coupled) is reduced as compared to HTR systems. As a result, the GFR cannot copy the solution implemented in HTR systems, which is primarily based on thermal inertia. It is necessary to use gas convection, maintaining a backup pressure capable of ensuring minimum thermal efficiency for the coolant.

In a high-power core, with moderate power density compared to that of conventional water-cooled reactors, increasing the core fraction reserved for the coolant has little impact on spectrum hardness and reactivity. We can therefore consider a “porous” core with low hydraulic resistance but still mechanically robust. Satisfactory gas convection for residual power evacuation as per admissible core outlet temperatures can be ensured for a core power of approximately one electric gigawatt through the use of backup systems pumping requiring approximately 100 kW, assisted by natural convection capable of taking over after a few hours.

6.2.2 The Advantages of the GFR System Have Two Main Origins

Firstly, the genealogy and operating experience of the series are very significant. In addition to the AGR, this particularly includes the AVR (pebble-bed HTR), which operated for approximately 20 years and sustainably achieved core outlet temperatures of 950°C. It also includes the reactors of the NERVA nuclear space propulsion program, which achieved exceptional performance in terms of hydrogen outlet temperature (2,500°C) and power density (4,000 MW/m³) due to the absence of industrial constraints regarding cost, lifetime, and safety. The most powerful reactor of the series had a total power output of 4.3 GWth, close to that of the EPR (and the largest ever built in the USA).

Secondly, significant scientific and technological progress has been achieved regarding high temperature and fluence materials, and also high-temperature mechanics. In addition, at the system level, the benefits of the twofold concept enable the exploitation of high-temperature technologies, particularly for gas turbines.

The GFR is still mostly a “paper-design,” which cannot be fairly compared to the Sodium-cooled SFR for instance. The fuel remains to be designed, even though some preliminary tests were carried out in the Phénix reactor during its very last years of operation. It is notably impossible to venture any comment about its future economics.

Its prospects will depend upon the magnitude of the so-called “Renaissance” expected to take place soon in nuclear power development, because this magnitude shall, through the fear of uranium scarcity, determine the timing of deployment of generation IV fast breeders. If this deployment starts around 2040, it will be too early for the GFR to have passed through the steps of demo plant and prototype and be ready for commercialization. If the renaissance is slower, then, maybe, the intrinsic qualities of the GFR will open opportunities for its deployment.

7 Conclusion

As we have seen, gas cooling was extensively used in the early days of nuclear power. For reasons completely independent of their technical characteristics, HTRs missed their commercial introduction in the late 1970s and are still today considered as “promising” designs. It is the

personal opinion of the author that as pure electricity producers they will not compete economically with LWRs, the dominant species in the nuclear “biotope.” Their future may be as co-generators of electricity and process heat, notably to produce hydrogen as feedstock for synthetic liquid fuels, which would provide the opportunity for nuclear power to enter significantly the transportation sector. They might, later on, share this “niche” with GFRs.

References

- DEN Monograph (2006) Gas-cooled nuclear reactors. CEA, Le Moniteur editions
- Mc Farlane H et al (1992) Controlled nuclear chain reaction, the first 50 years. ANS, La Grange Park, IL
- Marshall W (1981) Nuclear power technology – volume 1: reactor technology. Clarendon Press, Oxford
- Melese G, Katz R (1984) Thermal and flow design of helium-cooled reactors. ANS, La Grange Park, IL
- Simpson JW (1995) Nuclear power from underseas to outer space. ANS, La Grange Park, IL

23 Lead-Cooled Fast Reactor (LFR) Design: Safety, Neutronics, Thermal Hydraulics, Structural Mechanics, Fuel, Core, and Plant Design

Luciano Cinotti¹ · Craig F. Smith² · Carlo Artioli³ · Giacomo Grasso⁴ · Giovanni Corsini⁵

¹MERIVUS srl, Roma, ITALY

luciano.cinotti@gmail.com

²Naval Postgraduate School, Monterey, CA, USA

cfsmith@nps.edu

³Italian National Agency for New Technologies, Energy and Sustainable Economic Development, Bologna, ITALY

carlo.artioli@enea.it

⁴Italian National Agency for New Technologies, Energy and Sustainable Economic Development, Bologna, ITALY

giacomo.grasso@enea.it

⁵Giovanni.Corsini@tele2.it

1	<i>Lead-Cooled Fast Reactor (LFR) Development</i>	2752
1.1	Lead–Bismuth Eutectic (LBE) for Submarine Propulsion	2752
1.2	The Russian Design for Civilian Fast Reactors Cooled by HLM.....	2753
1.2.1	The BREST 300	2753
1.2.2	The SVBR-75	2754
1.3	HLM-Cooled ADS Systems.....	2754
1.4	The LFR in Generation IV	2755
1.5	The LFR and ADS Designs Considered in the Handbook.....	2758
1.5.1	SSTAR.....	2759
1.5.2	ELSY	2761
1.5.3	MYRRHA	2764
1.5.4	EFIT.....	2765
2	<i>Design Criteria and General Specifications</i>	2766
2.1	Sustainability	2769
2.1.1	Resource Utilization	2769
2.1.2	Waste Minimization and Management.....	2769

2.2	Economics	2769
2.2.1	Risk to Capital	2770
2.2.2	Other Use of Nuclear Heat	2771
2.3	Safety and Reliability	2771
2.3.1	Operation Will Excel in Safety and Reliability	2771
2.3.2	Low Likelihood and Degree of Core Damage	2774
2.3.3	Reduced Need for Offsite Emergency Response	2774
2.4	Proliferation Resistance and Physical Protection	2775
2.4.1	Unattractive Route for Diversion of Weapon-Usable Material	2775
2.4.2	Increased Physical Protection Against Acts of Terrorism	2775
3	<i>Neutronics</i>	2775
3.1	Neutronic Properties of Lead	2776
3.1.1	Moderation	2776
3.1.2	Absorption	2778
3.2	Fuel Performances in LFRs	2778
3.2.1	Fission Cross Sections	2779
3.2.2	Average Number of Fission Neutrons	2779
3.2.3	Fuel Utilization	2779
3.2.4	Spectrum Evolution with Burn-Up	2779
3.2.5	Effective Delayed Neutron Fraction and Prompt Neutrons Lifetime	2780
3.2.6	LFR Capabilities of MAs Transmutation	2780
3.3	Neutronic Performances of Typical Absorbers in an LFR	2780
3.3.1	Boron Carbide	2780
3.3.2	Indium–Cadmium Eutectic	2781
3.3.3	Europium	2781
4	<i>Lead Properties</i>	2782
4.1	Physical Properties	2782
4.2	Chemistry Control and Monitoring Systems	2786
4.2.1	The Thermodynamical Base	2786
4.2.2	Thermodynamical Data and Diagrams	2790
4.3	Thermal Hydraulics	2792
5	<i>Compatibility of Structural Materials with Lead</i>	2793
5.1	Structural Materials Corrosion in Lead	2793
5.2	Effect of Lead on Properties of Structural Materials	2794
6	<i>Core</i>	2796
6.1	Introductory Remarks for LFR Core Design	2796
6.1.1	Preliminary Evaluation of Lead and LBE Impact on Core Design	2797
6.1.2	Technological Constraints for LFR Design	2797
6.2	Conceptual Design Approach	2797
6.2.1	Critical Reactors	2798
6.2.2	Subcritical Reactors	2807
6.2.3	Adiabatic Reactors	2815
6.3	Design Diagnostics and Post-Process Feedbacks	2820
6.3.1	Overall BU Performances	2820
6.3.2	Sizing and Placement of Control Systems	2820

6.4	Reactivity Coefficients	2821
6.4.1	Lead Void Reactivity	2821
6.4.2	Doppler Effect	2822
6.4.3	Dimension and Density Reactivity Coefficients	2822
6.4.4	Feedback Reactivity Coefficients	2824
7	<i>Reactor System</i>	2825
7.1	Reactor Vessel and Safety Vessel	2825
7.2	Reactor Internal Structures	2825
7.3	Steam Generator	2827
7.4	Primary Coolant Circulation	2829
8	<i>Decay Heat Removal System</i>	2830
8.1	Reactor Vessel Air Cooling System	2830
8.2	Water Loops and Associated Dip Coolers	2830
8.3	Steam Condensers on the Steam Loops	2832
9	<i>Nuclear Island</i>	2833
10	<i>Concluding Remarks and Open Issues</i>	2835
	<i>References</i>	2839

Abstract: The lead-cooled fast reactor (LFR) has both a long history and a currency of innovation. With early work related to the mission of submarine propulsion dating to the 1950s, Russian scientists pioneered the development of reactors cooled by heavy liquid metals (HLM). More recently, there has been substantial design interest in both critical and subcritical reactors cooled by lead (Pb) or lead–bismuth eutectic (LBE), not only in Russia, but also in Europe, Asia, and the USA. This chapter reviews the historical development of the LFR and provides detailed descriptions of the recent and current initiatives to design a variety of LFR concepts with several different missions in mind: accelerator-driven subcritical (ADS) systems for nuclear materials management, small modular systems for deployment in remote locations, and central station plants for integration into developed power grids. It describes design criteria and system specifications; features particular to the LFR in terms of neutronics, coolant properties, and material compatibility issues; approaches taken to core and reactor design; and considerations related to the balance of plant and plant layout.

1 Lead-Cooled Fast Reactor (LFR) Development

The idea of developing fast spectrum reactors with molten lead (or lead alloy) as a coolant is not a new one. Although initially considered in the West, in the 1950s, such technology was not pursued to completion because of the anticipated difficulties associated with the corrosive nature of these coolant materials. However, in the Soviet Union, such technology was actively pursued during the same time frame (1950s through the 1980s) for the specialized role of submarine propulsion. More recently, there has been a renewal of interest in the West for such technology, for critical as well as for accelerator-driven subcritical (ADS) systems. Meanwhile, interest in the former Soviet Union, primarily Russia, has remained strong and has expanded well beyond the original limited mission of submarine propulsion. This section reviews the past and current status of LFR development.

1.1 Lead–Bismuth Eutectic (LBE) for Submarine Propulsion

Heavy liquid metals (HLM) such as lead (Pb) or lead–bismuth eutectic (LBE) were proposed and investigated as coolants for fast reactors as early as the 1950s (e.g., in the USA). In most cases, with breeding a primary driver, sodium became the preferred choice in the 1960s, due to the higher power density achievable with this coolant, which resulted in lower doubling times, an important objective at that time. However, major contributions in the development of lead technology were carried out by Soviet (and then Russian) scientists and industries who have actively pursued lead-cooled reactor technology for more than 50 years (Gromov 1998).

In the early 1950s in the Soviet Union, research and design of the use of lead–bismuth alloy as the coolant for nuclear reactors was initiated by academician A. I. Leipunsky at the Institute of Physics and Power Engineering (IPPE) in Obninsk. The principal objective of these efforts was the design and construction of nuclear reactors for submarine propulsion.

The first of these systems, a 70 MWth 27/VT land prototype reactor, achieved criticality and started full power operation at IPPE in 1959. In 1963, the first nuclear submarine with an HLM-cooled reactor was put into operation. It was designated “Project 645, Submarine K-27, NATO designation November class K-27 variant” and utilized two 73 MWth reactors. Beginning in 1971, two new series of nuclear powered submarines termed “Projects 705 and 705K, NATO

designation Alfa class” were put into operation. Both of these series utilized a single 155 MWth reactor. The distinction between the two was based on their steam supply systems, one type of which was designed by the Experimental Design Bureau of Machine Building (OKBM), and the second was designed by the Experimental Design Bureau “Gidropress” (OKB Gidropress). In total, seven nuclear submarines of the Project 705/705K type were constructed following the original single submarine of the “Project 645” type. In addition, a second land-based prototype designated the KM-1 and mainly supporting Project 705K was put into operation at the A. P. Aleksandrov Scientific Technical Research Institute (NITI) in Sosnovy Bor in 1978.

An extensive research and development program focusing on HLM coolant technology and materials was carried out with emphasis on the chemical control of the liquid metal to avoid the possibility of plugging due to the formation of slag and to enhance corrosion resistance of internal components made from steels specifically developed for such service.

1.2 The Russian Design for Civilian Fast Reactors Cooled by HLM

In the 1990s, there was a renewal of interest in Russia concerning lead and LBE as coolants for civilian fast reactors. The lead-cooled BREST (the Russian acronym for Pb-cooled fast reactor) (Perera 2003) concept, developed in the early 1990s, is the most widely known; in addition, the Russians have placed considerable effort in the development of the LBE-cooled SVBR (the Russian acronym for lead–bismuth fast reactor) concept.

1.2.1 The BREST 300

BREST-300 is designed as a multipurpose reactor; it produces electric power, consumes and produces plutonium, produces radioisotopes for industry and medical applications, and transmutes long-lived fission products and actinides generated in reactor operations.

The main operating mode of this reactor system is base-load power production, although operation at reduced power levels is also anticipated.

It has a semi-integrated, multi-compartment metallic vessel (with characteristics of both pool- and loop-type cooling systems). The vessel, 19 m in height, has a diameter of 5.5 m at the bottom and 11.5 m at the top. The wide upper part of the reactor vessel is separated from its narrow central part by a barrel that forms an annular chamber, outside the central part of the vessel. In this semi-integral arrangement, the steam generator (SG) and the main circulating pumps are placed in the annular chamber, outside the central part of the vessel.

The core is loaded with wrapper-less fuel assemblies of square cross section. The fuel assembly lattice has 121 square cells of which 114 are taken up by fuel rods and 7 by guide tubes. The height of the fuel pellet column in the core is 1.1 m and the cover gas plenum is 0.9 m high. The content of plutonium and minor actinides (MA) is 13 wt%.

The fuel cladding consists of a thin-walled tube of 12% chromium–ferritic–martensitic steel. It has high corrosion resistance to lead, limited swelling, and satisfactory temperature dependence of strength and creep.

The outer diameters of the tubes to be used as cladding in the central, middle, and peripheral regions of the core are 9.1, 9.6, and 10.4 mm, respectively.

1.2.2 The SVBR-75

The SVBR-75 was designed as a modular compact unit to be installed in the SG compartments of shutdown VVER-440-type reactors.

The main characteristics are as follows (Toshinsky et al. 2002):

- Pool-type reactor
- Two-loop system for decay heat removal (DHR) using natural circulation
- Guard vessel
- Fuel subassemblies without wrapper
- SG with saturated steam generation
- Low-speed gas-tight motor of less than 500 kW power for main circulating pumps
- The ability to repair and/or replace all internal components of the reactor
- Subassembly by subassembly refueling of the whole core at a time
- Multi-fuel capability (UO₂, MOX with MA, nitrides fuels) with the same reactor design

The main plant parameters are as follows:

Thermal power (nominal), MW	280
Steam capacity, t/h	580
Steam pressure (saturated), MPa	9.5
Feedwater temperature, °C	240.9
Primary coolant flow rate, kg/s	11,760
Primary coolant temperature, inlet/outlet, °C	320/482
Core dimensions: diameter/height, m	1.645/0.9
Number of fuel pins	12,114
Number of control rods	37
Mean power density in the core, MW/m ³	140
Mean linear load of the fuel element, kW/m	24.3
Refueling interval, year	8
Core charge, (UO ₂) with uranium: mass, kg/enrichment, %	9,144/16.1
Number of main circulating pumps	2
Lead–bismuth coolant volume in the reactor, m ³	18
Reactor outline dimensions: diameter/height, m	4.55/7.55

1.3 HLM-Cooled ADS Systems

The features and the associated technologies of HLM coolants inspired several projects in the emerging field of ADS, and in particular lead and LBE have been considered as both coolants and neutron spallation targets for several such energy amplification projects under development in the USA, Europe, Japan, and the Republic of Korea since the mid-1990s.

At the Korea Atomic Energy Research Institute (KAERI) and Seoul National University (SNU) in the Republic of Korea, ADS systems have been developed since 1997 in order to explore proliferation-resistant and safe transmutation technology. One such ADS named Hybrid Power Extraction Reactor (HYPER) is intended primarily for transmutation of long-lived nuclear wastes. HYPER uses LBE as both coolant and spallation target.

In Japan, at the Japan Atomic Energy Research Institute (JAERI), an ADS with the thermal power of 800 MW has been designed, where 250 kg of MA and some long-lived fission products

(LLFP) can be transmuted annually. R&D has been conducted on ADS using LBE as a spallation target and coolant.


At SCK_CEN, Belgium, since 1997, studies in the field of LBE technology have been carried out for the Multi-purpose Hybrid Research Reactor for High-tech Applications (MYRRHA) project, aimed at the development of a research subcritical reactor driven by an accelerator, where LBE is used as spallation target and coolant.

The MYRRHA design has merged since 2005 with the European project IP-EUROTRANS, which includes also the detailed design of the associated linear proton accelerator and a generic conceptual design of the European Facility for Industrial Transmutation (EFIT), in which pure lead is used as the core coolant and spallation material. EFIT is loaded with U-free transmutation-dedicated fuel.

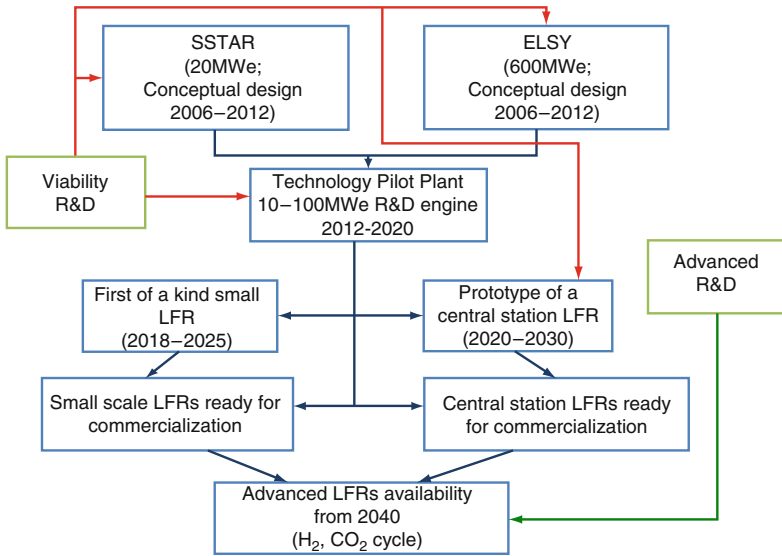
1.4 The LFR in Generation IV

The Generation IV (GEN IV) Technology Roadmap (U.S. DOE Nuclear Energy Research Advisory Committee and the Generation IV International Forum 2002), prepared by Generation IV International Forum (GIF) member countries, in 2002 identified the six most promising advanced reactor systems and related fuel cycles, and the R&D necessary to develop these concepts for potential deployment. Among the promising reactor technologies being considered by the GIF, the LFR has been recognized as a technology with great potential to meet the needs for both remote sites and central power stations.

In the GEN IV technology evaluations, the LFR system was top-ranked in sustainability because it uses a closed fuel cycle, and top-ranked in proliferation resistance and physical protection because it employs a long-life core. It was rated good in safety and economics. Safety was considered to be enhanced by the choice of a relatively inert coolant. The LFR was primarily envisioned for missions in electricity and hydrogen production and actinide management. Given its R&D needs for fuel, materials, and corrosion control, the LFR system was forecast to be deployable by 2025. The LFR system features a fast-neutron spectrum and a closed fuel cycle for efficient conversion of fertile uranium. The LFR can also be used as a burner of all actinides from reprocessed LWR spent fuel and as a burner/breeder with thorium matrices.

In 2007, the GIF LFR Provisional System Steering Committee (PSSC), after the evaluation of current international initiatives in the field, prepared a draft System Research Plan (SRP) for the LFR with molten lead as the reference coolant and lead–bismuth as a backup option.  *Figure 1* illustrates the basic approach being recommended in the LFR SRP. It portrays the dual-track viability research program with convergence to a single, combined demonstration facility (demo, also called technology pilot plant – TPP) leading to the eventual deployment of both types of systems. The dual-track approach is based on the development of the small secure transportable autonomous reactor (SSTAR) and the European Lead-cooled System (ELSY) reactor projects that represent two potential applications of the LFR.

SSTAR, whose development is performed under the US Department of Energy Generation IV Nuclear Energy Systems Initiative, is a small natural circulation fast reactor of 20 MWe/45 MWth that can be scaled up to 180 MWe/400 MWth. The key technical aspects of SSTAR are the use of lead as the coolant and a long-life sealed core in a small, modular system. The compact active core operates for a very long time (15–30 years) without refueling, and the fuel is either retained in the reactor vessel for recycle or removed as a single cassette during refueling and replaced by a fresh core.



■ Figure 1
LFR GIF-SRF conceptual framework

ELSY, whose development started in 2006 with the support of the Framework Program 6 (FP6) of Euratom, aims at demonstrating the design of a competitive and safe fast critical reactor using simple engineered technical features. The use of compact in-vessel SGs and of a simple primary circuit, with possibly all internals being removable, is among the reactor features for competitive electric-energy generation and long-term investment protection.

Besides Russia, the USA, and Europe, LFR studies are also being performed in Japan and Korea.

In Japan, the relevant activities are associated with each of the key research organizations including the Japan Atomic Energy Agency (JAEA), the Central Research Institute of the Electric Power Industry (CRIEPI), and the Tokyo Institute of Technology.

At JAEA, an LBE-cooled fast reactor design and the related fundamental corrosion experiments were carried out within the framework of the “Feasibility Study on Commercialized Fast Reactor Cycle Systems” from 1999 to 2005. Experimental studies to solve the corrosion problem have been carried out since 2001. At the early stage of this study, the maximum cladding temperature was set to 650 °C, and then changed to 570 °C based on the results of experimental studies. As a result, the core inlet and outlet coolant temperatures are 285 °C and 445 °C, respectively. The specific gravity of LBE is 12 times that of sodium. This property affects structural integrity, a particular concern for the very high seismicity in Japan. According to the feasibility study, it is estimated that the LFR plant size in Japan would be limited to less than medium-scale size of around 750 MWe, even with the adoption of 3D seismic isolation.

At CRIEPI, consideration has been given to the possibility of an LBE-cooled fast reactor as a candidate for the next generation of nuclear reactors. The interest at CRIEPI was the result of its efforts to use LBE as an intermediate coolant for a sodium-cooled fast breeder reactor. In this concept, an innovative steam generator (SG) was envisioned in which heat was transferred by direct contact between LBE and water within the intermediate loop. While an LBE-cooled

reactor based on this technology has not yet been designed, CRIEPI believes that this approach could represent a workable research direction

To evaluate the heat-transfer performance of LBE in the intermediate loop and the two-phase flow characteristics of LBE, water, and steam, the “CRIEPI Pb–Bi Test Loop on Thermal Hydraulics” was constructed in 1997. The results of the heat-transfer performance around SG tubes and the performance of gas lift pumps for LBE were tested in the loop and presented in Nishi et al. (2003).

To clarify the corrosion characteristics of LBE, the “CRIEPI Static Corrosion Test Facility” was constructed in 2001. The objective of this facility was to understand the corrosion behavior of stagnant LBE at 650 °C on high chromium martensitic stainless steel, a promising-candidate structural material for LFRs. A series of corrosion tests were performed jointly by CRIEPI and JAEA (Aoto et al. 2003).

To explore the advantages and disadvantages of lead as a coolant, an LBE-cooled 4S (the super safe, small, and simple reactor, normally a sodium-cooled system) was designed and studied by CRIEPI and TOSHIBA.

The Tokyo Institute of Technology proposed a small long-life fast reactor cooled by LBE and presented a preliminary design in 1991. Since then, the importance of the Tokyo Tech's study has become gradually widely recognized, and, as a result, programs were supported to promote LFRs in the following areas:

- Polonium (Po) behavior, treatment, cross-section measurements (FY 1998–2000)
- Corrosion (materials test, oxygen control) (FY 1999–2001)
- CANDLE burn-up (FY 2001–2003)
- Steam lift pump reactor designs and basic research (FY 2002–2004)

The Pb–Bi-cooled direct-contact boiling water fast reactor (PBWFR), the steam lift pump-type LFR (SLPLFR), and the constant axial neutron during the life of energy (CANDLE) reactor are the main recent activities in the area of reactor design.

In the PBWFR, direct contact boiling provides significantly higher heat transfer. The PBWFR electric power is 150 MW. The design limit of the cladding temperature is 650 °C. The LBE core outlet temperature is 460 °C. The LBE temperature rise across the core is 150 °C. The conditions of the secondary coolant steam are the same as those of conventional BWRs. The PBWFR plant is equipped with a reactor vessel air cooling system (RVACS) a primary reactor auxiliary cooling system (PRACS), and an auxiliary water supply tank to cope with the loss of feedwater. Hydrogen is dissolved in the feedwater at a concentration of 100–500 ppb to keep the oxygen concentration in the LBE coolant around 10^{-5} wt%.

The SLPLFR reactor concept has SGs in the reactor vessel, and subcooled water is injected into LBE above the core at a low flow rate. The resulting steam condenses in a dedicated heat exchanger, which serves also as the re-heater of the feedwater. In comparison with the PBWFR, the SLPLFR is expected to have a higher thermal efficiency with higher LBE temperature, lower pressure in the primary loop, and no Po or LBE droplet contamination in the turbines.

For the CANDLE reactor, the neutron flux shape and the nuclide and power density distributions remain constant but progresses in an axial direction during the core lifetime. The solid fuel is fixed at each position, and no movable reactivity control mechanisms are required. The change of excess reactivity during burn-up is theoretically zero for ideal equilibrium conditions. The core characteristics, such as power feedback coefficients and power peaking factors, do not change over the operational life. Since the k -infinity of replacement fuel is less than unity, the transport and storage of such fuels is easy and safe. Application of this burn-up strategy to

LFRs with metallic or nitride fuels enables the following excellent characteristics: initial fissile material is required only for the nuclear ignition region of the initial core, and only natural or depleted uranium is required for the remaining region of the initial core and for succeeding cores. The average burn-up of the spent fuel is about 40%; that is equivalent to 40% utilization of the natural uranium without reprocessing or enrichment.

The Korean LFR Program has two main objectives:

- A technology development requirement for nuclear waste transmutation
- A new electricity generation unit development requirement to match the needs of developing nations and especially remote communities without major electrical grid connections

To meet the first goal, the proliferation-resistant environment-friendly accident-tolerant continuable-energy economical reactor (PEACER) development was initiated with the objective of developing a system to transmute long-lived fission products in the spent nuclear fuel into short-lived low-intermediate-level waste.

For the second goal, Korea initiated the development of the Battery-Optimized Reactor Integral System (BORIS) that is an integral-type optimized fast reactor with an ultra-long-life core coupled with a supercritical CO₂ Brayton cycle power conversion system.

PEACER is a Pb–Bi-cooled fast reactor being developed at the Seoul National University, designed for power production and waste transmutation. PEACER incorporates a pancake-type core with a U–Pu–Zr metallic fuel with a high thermal conductivity in square lattice cooled by forced circulation by a main coolant pump (MCP), and the Rankine cycle for power generation. As with other Pb–Bi-cooled fast reactor concepts, the operating coolant temperature is low, spanning from 300 °C to ~ 400 °C to achieve corrosion-resistant conditions and a longer reactor lifetime.

PEACER provides two reactor designs of different capacity. PEACER-550 has a 1,560 MWth core, following the basic integral fast reactor design. PEACER-300 is designed to produce 850 MWth. There is no intermediate heat transport system. The steam at the turbine inlet is superheated to 633.15 K and 8 MPa. The thermal efficiency is estimated to be 35.3%.

PEACER is equipped with an active reactivity control and shutdown system (motor-driven) and a passive reactor shutdown system (gravity-driven). The active reactivity control and shutdown system consists of 28 control assemblies that are used for power control, burn-up compensation, and reactor shutdown.

BORIS is being developed as a multipurpose integral optimized fast reactor with an ultra-long-life core at the Seoul National University. BORIS aims at satisfying various energy demands, maintain inherent safety using the Pb coolant, and improved plant economics. BORIS is being designed to generate 22.2 MWth with 10 MWe for at least 20 consecutive years without refueling and to meet the Generation IV nuclear energy system goals of sustainability, safety, reliability, and economics. BORIS is conceptualized to be used as the main power and heat source for remote islands and barren lands, and also considered to be deployed for desalinization purpose. BORIS consists of modular components to enable rapid construction and easy maintenance, and incorporates an integrated heat exchanger system operated by natural circulation of Pb without pumps to realize a compact reactor.

1.5 The LFR and ADS Designs Considered in the Handbook

The renewed interest in lead technology for critical fast reactors and ADS systems has resulted in the initiation of several projects, all at preliminary stage, most of them having been briefly

described above. Their level of development, and their characteristics and objectives are in general very different and their prospects for full-scale development are uncertain at the moment of the issuance of this handbook.

In the following discussion, details will be discussed for four systems that are more developed or present a better characterization of the potential of lead coolant technology for critical and subcritical systems.

The four systems selected for further discussion are SSTAR, ELSY, MYRRHA, and EFIT.


1.5.1 SSTAR

The US LFR Program is focused on the development of a small transportable reactor system known as the SSTAR with the following objectives (Sienicki et al. 2007a):

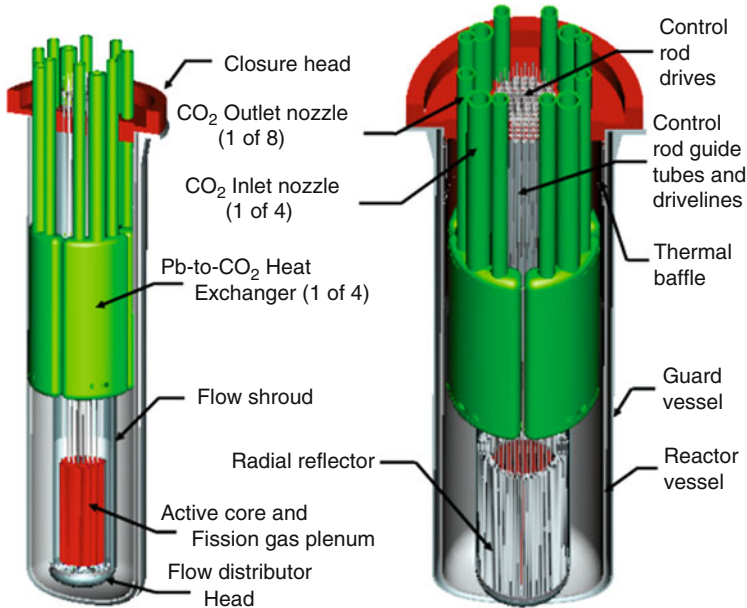
- Sealed core with no on-site refueling or whole-core cassette refueling.
- Transportability: the entire core and reactor vessel are delivered by ship or overland transport.
- Long-life core: 15–30-year core life is the target.
- Autonomous load followed by simple integrated controls: minimum operator intervention or maintenance required.
- Local and remote observability: rapid detection/response to perturbations.
- Minimum industrial infrastructure required in host location.
- Very small operational (and security) footprint.

In furtherance of the above objectives, current system development activities are being directed toward a pre-conceptual design and viability assessment for a SSTAR 20 MWe (45 MWth) natural circulation LFR for international deployment consistent with overall programmatic goals.

In addition, following the development of initial pre-conceptual designs, the LFR program was realigned to focus upon a concept for a near-term technology pilot plant to demonstrate successful reactor operation with a lead coolant at realistic system temperatures and incorporating innovative engineering that will help show the economic benefits and industrial attractiveness of Pb as a primary coolant.

A sketch of the current reference concept for the SSTAR small, modular, fast reactor is shown in  Fig. 2 (Sienicki et al. 2007b). This pre-conceptual design is a small shippable reactor (12 × 3.2 m vessel), with a 30-year open-lattice cassette core and large-diameter (2.5 cm) fuel pins held by spacer grids welded to control rod guide tubes. The design integrates three major features: primary cooling by natural circulation heat transport; lead as the coolant; and transuranic nitride fuel in a pool vessel configuration. The main mission of the 20 MWe (45 MWth) SSTAR is to provide incremental energy generation to match the needs of developing nations and remote communities without electrical grid connections, such as those that exist in Alaska or Hawaii, island nations of the Pacific Basin, and elsewhere. This may be a niche market within which costs that are higher than those for large-scale nuclear power plants can still be considered competitive. The design features of the reference SSTAR, in addition to the lead coolant, 30-year cassette core, and natural circulation cooling, include autonomous load following without control rod motion, and the use of a supercritical CO₂ (S-CO₂) Brayton cycle energy conversion system. The incorporation of inherent thermo-structural feedbacks imparts walk-away passive safety, while the long-life cartridge core life imparts strong proliferation resistance. If these technical

Small Secure Transportable Autonomous Reactor (SSTAR)



■ Figure 2
Conceptual 20 MWe (45 MWth) SSTAR system

innovations can be realized, the LFR will provide a unique and attractive nuclear energy system that meets Generation IV goals.

Some of the key design parameters of SSTAR are summarized in [Table 1](#).

The research priorities of the SSTAR program are organized to address system design and evaluation, fuel cycle, energy conversion, and material issues.

The R&D efforts required to advance the SSTAR concept are intended to address viability issues associated with the small transportable LFR and activities leading to the design and construction of a demo or pilot LFR plant. Viability will be established through focused R&D tasks in the areas outlined below and guided by formulation of a technically defensible pre-conceptual design:

- **System design and evaluation.** R&D tasks for system design and evaluation address the areas of core neutronics, system thermal hydraulics, mechanical design, passive safety evaluation, containment and building structures, in-service inspection (ISI), and assessing cost impacts. Core design is essential to establishing the necessary features of a 15–30-year life core and determining core parameters that impact feedback coefficients. R&D tasks associated with this work include further optimization of the core configuration, establishing a start-up/shutdown rod and control rod strategy, and calculating reactivity feedback coefficients.

■ **Table 1**
Key parameters of SSTAR

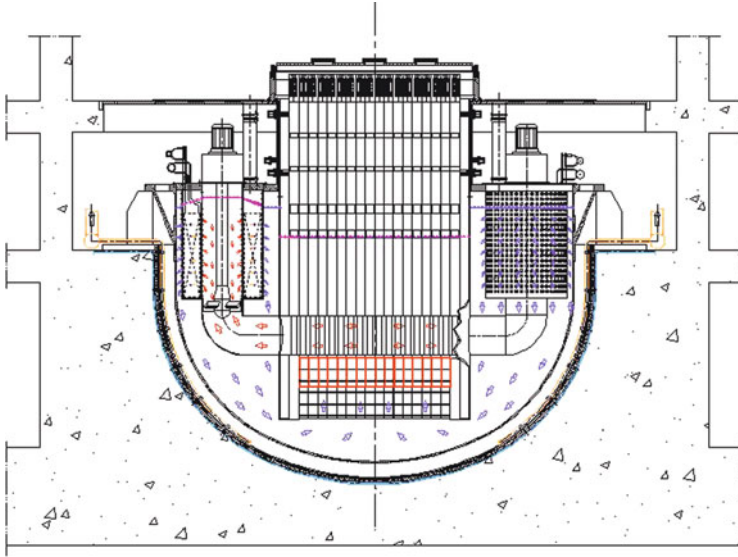
Power (MWe)	19.8
Conversion ratio	~ 1
Thermal efficiency (%)	44
Primary coolant	Lead
Primary coolant circulation (at power)	Natural
Primary coolant circulation for DHR	Natural
Core inlet temperature (°C)	420
Core outlet temperature (°C)	567
Fuel	Nitride
Fuel cladding material	Si-enhanced F/M stainless steel
Peak cladding temperature (°C)	650
Fuel-pin diameter (mm)	25
Active core height/diameter (m)	0.976/1.22
Primary pumps	None
Working fluid	Supercritical CO ₂ at 20 MPa, 552 °C
Primary/secondary heat-transfer system	N °4 Pb-to-CO ₂ HXs
Safety grade DHR	Reactor vessel air cooling system + multiple direct reactor cooling systems

- **Fuel and fuel cycle.** Viability of both nitride fuel and whole-core cassette refueling is to be addressed in the fuel and fuel-cycle R&D.
- **Energy conversion.** Use of an S-CO₂ Brayton cycle for energy conversion offers the prospect of higher thermal efficiencies with lower Pb coolant outlet temperatures and small turbo-machinery reducing the footprint and cost of the power converter.
- **Materials.** Viability of long core lifetime, passive safety, and economic performance (both capital and operating costs) of the LFR concept will depend on identifying materials with the potential to meet service requirements.

1.5.2 ELSY

ELSY – the European Lead-cooled System – is a pool-type lead-cooled 600 MWe fast reactor, developed since September 2006, within the Sixth EURATOM Framework Programme (FP6).

ELSY aims at demonstrating the possibility of designing a fast reactor using simple engineered technical features, while fully complying with the Generation IV goals of sustainability, economics, safety, proliferation resistance, and physical protection (Cinotti et al. 2006, 2007a, b; GEN IV International Forum 2008).



■ **Figure 3**
ELSY primary system arrangement and coolant flow path

ELSY is an innovative project intended to globally address several of the most important technical challenges related to the use of lead technology in general, issues that have for the most part been only partially addressed in previous projects, namely:

- How to extend the LBE experience, with LBE to pure lead as a coolant?
- How to mitigate the seismic issue?
- How to design a highly compact primary system?
- How to avoid in-vessel storage of spent fuel?
- How to cool high power spent fuel elements during refueling?
- How to design a compact SG?
- How to avoid the risk of catastrophic primary system pressurization associated with water or steam collector failure?
- How to mitigate the effect of a steam generator tube rupture (SGTR)?
- How to make the reactor internals removable?
- How to handle fuel elements while maintaining a temperature of 400 °C in lead?
- How to support the fuel elements in lead?
- How to design a simple and reliable safety-related DHR system?

The elimination of an intermediate cooling system and the development of a compact and simple primary circuit with all internal components removable are among the features needed to assure reduced capital cost and construction time, competitive electric-energy generation, and long-term investment protection.

The relatively small size of the reactor vessel results from advanced solutions adopted for the primary system that features a cylindrical inner vessel, primary pumps installed in the inner zone of innovative flat-spiral-tube SGs, and fuel elements substantially supported by buoyancy.

In addition, the heads of the fuel elements extend above the vessel fixed roof as they are provided with long stems to allow fuel handling from the above-reactor hall under full visibility.

In spite of the reduced coolant speed and of the moderate power density core, the innovative solutions adopted for ELSY allow reduced primary system dimensions (main vessel preliminary dimensions of 12.5 m diameter and 8.7 m height), which are similar to, or even smaller than, those of advanced pool-type SFRs (➤ [Fig. 3](#)).

Safety relies on the beneficial physical characteristics of lead, redundant and diverse DHR systems, and other innovative features, which make the primary system more tolerant to the effects of a SGTR accident.

➤ [Table 2](#) provides the preliminary parameters of ELSY.

■ **Table 2**

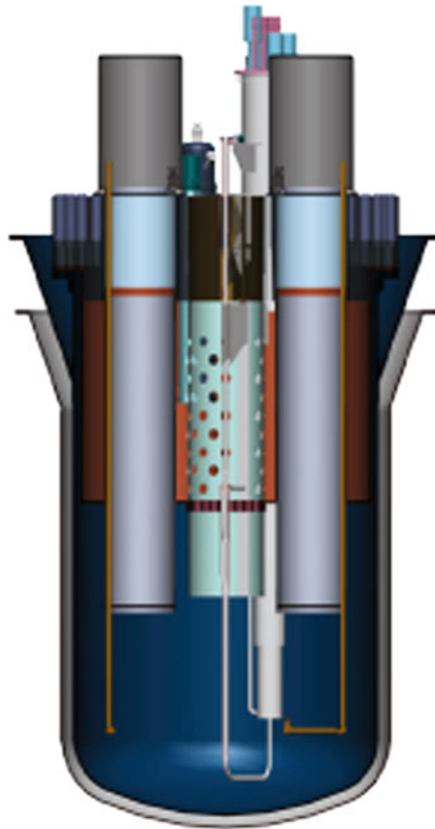
Main parameters of the ELSY plant

Power (MWe)	600
Thermal efficiency (%)	40
Primary coolant	Pure lead
Primary system	Pool type, compact
Primary coolant circulation	Forced, at power, natural circulation + Pony motors for DHR
Primary pressure loss (bar)	~ 1.5
Core inlet temperature (°C)	~ 400
Core outlet temperature (°C)	~ 480
Fuel	MOX with consideration also of nitrides and dispersed minor actinides
Fuel cladding material	T91 (aluminized)
Fuel cladding temperature (°C)	(max) ~550
Main vessel	Austenitic stainless steel, hung, short height ~9 m; diameter ~12.5 m
Safety vessel	Anchored to the reactor pit
Steam generators	N°8, integrated in the main vessel
Secondary cycle	Water-superheated steam at 180 bar, 450 °C
Primary pumps	No. 8 mechanical, integrated in the steam generators
Internals	Removable
Inner vessel	Cylindrical
Hot collector	Small volume, above the core
Cold collector	Annular, outside the inner vessel, free level higher than free level of hot collector
DHR coolers	No. 4, DRC loops + a reactor vessel air cooling system
Seismic design	2D isolators supporting the reactor building

1.5.3 MYRRHA

Following the conceptual design phase of an experimental ADS conducted during the Euratom Framework Programme 5 (FP5) project PDS-XADS (Maes 2006), a more advanced design for an Experimental Transmutation Accelerator Driven System, namely MYRRHA/XT-ADS, is being carried out within the FP6 integrated project (IP) known as EUROTRANS (Knebel et al. 2006) and is continued within the FP7 central design team (CDT) in the near-term period (i.e., through 2012). The major technological issues identified in this work are as follows:

- System and plant design
- Necessary dedicated R&D support issues
- Material qualification program
- Fuel qualification program
- High-intensity proton accelerator performances and reliability

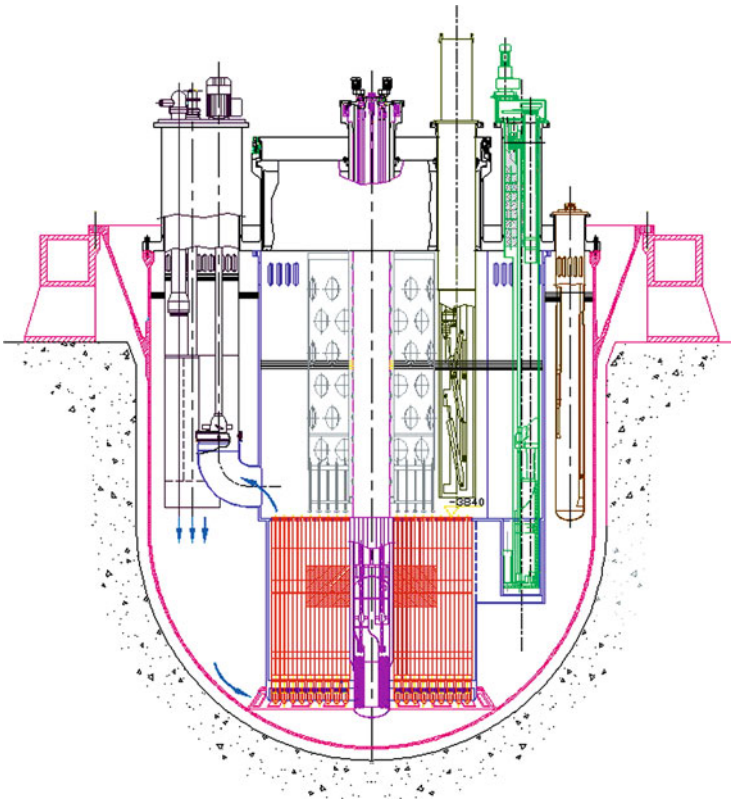


■ Figure 4
MYRRHA/XT-ADS primary system arrangement

For the medium term (i.e., to 2020), the emphasis will be on the construction of MYRRHA/XT-ADS at Mol, Belgium. For the longer term, the development and qualification of innovative fuels (especially minor actinide-bearing inert fuels) with appropriate cladding and associated reprocessing techniques is a challenging task. Having these innovative fuels is mandatory to prove the technological feasibility of transmutation. Since the development of these innovative fuels will require a long time, research on this topic has already been started, but for the viability demonstration of ADS, it is of high importance to focus on current fuel qualification efforts of the driver fuel for fast spectrum systems (➤ Fig. 4).

1.5.4 EFIT

EFIT is the conceptual design of a European Facility for Industrial Transmutation (EFIT), with a pure lead-cooled subcritical reactor of about 400 MWth with the capability for minor actinide (MA) burning and electricity generation.



■ Figure 5
EFIT primary system arrangement

EFIT will be loaded with U-free fuel containing MA, namely (Pu,Am,Cm) O_{2-x} – MgO-type fuel.

The neutronic design has confirmed the potential of EFIT to be an effective burner of MA with a net balance of -40.17 kg of MA/TWh and nearly a zero Pu balance (-1.74 kg/TWh).

MA burning, in addition to electricity generation, is an important added value of EFIT in the economic balance. However, a fraction of the electric power is used to produce the 16 MW proton beam and the accelerator and spallation target represent a significant part of the capital cost. It should be noted that the primary system volume per unit power is at least twice that of a pool-type SFR or LFR. Additional studies are necessary to understand if this penalty in the primary system dimensions is an unavoidable consequence of a subcritical system, or can be reduced by optimization.

Based on the feedback from the operation of MYRRHA/XT-ADS and further progress on system design and fuel and material research, the construction of an EFIT can be envisaged as the final goal.

2 Design Criteria and General Specifications

The requirements for the design of the LFR stem from engineering knowledge enhanced by the experience gained and the lessons learned in the field of sodium-cooled fast reactors (e.g., SPX1), in the LBE technology for use in Russian submarines and in the technological limits acquired in the frame of several international experimental activities.

These requirements aim at achieving the main design missions of the LFR, which are the demonstration of its technical feasibility for electric-energy generation and the demonstration of its capability to comply with the Generation IV goals (especially the capability of consuming MA and of good economic performance).

Most requirements, such as the MA-burning capability, are thus not absolute, however, and may undergo adjustment for optimization in the course of future design activities. It will be noted that the physical and neutronic properties of lead cannot be fully exploited simultaneously from the very beginning of the LFR design, because of technological and time constraints. The potential of burning MA from reprocessed spent fuel of LWR implies deployment of special, novel-design cores, which require qualification and testing in existing reactor systems.

On a global basis, priority is given to the demonstration of the technical feasibility of the LFR within a relatively short time frame with confirmation of structural material properties with effective oxygen control and with features such as a mixed oxide (MOX) fuel core that is self-sustaining in Pu, while being adiabatic in terms of consumption of the self-generated MA. It is expected that development of the LFR to the more ambitious goals of high-temperature operation and burning capability beyond the self-generated MA will be pursued in the future and developed as appropriate depending on R&D and design achievements, and budget.

Compliance with the guidelines of Generation IV is an integral part of the LFR requirements. The tentative main design solutions are listed by the four Generation IV goal areas and the eight Generation IV goals in the following sections. These solutions are deemed to be sufficient as starting features for a successful demonstration of the feasibility of the LFR.

The main LFR features identified in order to achieve the Generation IV goals are discussed below and summarized in [▶ Table 3](#). These features are based either on the properties of lead as a coolant or on specifically engineered designs.

■ Table 3

LFR potential performance against the four goal areas and the eight goals for Generation IV

Generation IV goal areas	Goals for Generation IV nuclear energy systems	Goals achievable via	
		Properties of lead	Specifically engineered solutions
Sustainability	Resource utilization	<ul style="list-style-type: none"> • Lead is a low moderating medium • Lead has low-absorption cross section • This enables a core with fast-neutron spectrum even with a large coolant fraction 	<ul style="list-style-type: none"> • Conversion ratio close to 1
	Waste minimization and management		<ul style="list-style-type: none"> • Great flexibility in fuel loading including homogeneously diluted MA
Economics	Life cycle cost	<ul style="list-style-type: none"> • Lead does not react with water • Lead does not burn in air • Lead has a very low vapor pressure • Lead is cheap 	<ul style="list-style-type: none"> • Reactor pool configuration • No intermediate coolant loops • Compact primary system • Simple design of the reactor internals • Superheated steam or supercritical CO₂ (high efficiency)
	Risk to capital (investment protection)		<ul style="list-style-type: none"> • Small reactor size • Potential for in-vessel replaceable components
Safety and reliability	Operation will excel in safety and reliability	Lead has (a) very high boiling point, (b) low vapor pressure, (c) high shielding capability for gamma radiation, (d) good fuel compatibility and fission product retention	<ul style="list-style-type: none"> • Primary system at atmospheric pressure • Low coolant ΔT between core inlet and outlet

■ Table 3
(continued)

Generation IV goal areas	Goals for Generation IV nuclear energy systems	Goals achievable via	
		Properties of lead	Specifically engineered solutions
	Low likelihood and degree of core damage	Lead has (a) good heat-transfer characteristics, (b) high specific heat and thermal expansion coefficient	<ul style="list-style-type: none"> • Large fuel-pin pitch • Natural circulation cooling (small system) • Decay heat removal (DHR) in natural circulation • Primary pumps in the hot collector (moderate- or large-size system) • DHR dip coolers in the cold collector
	No need for offsite emergency response	<ul style="list-style-type: none"> • Lead density is close to that of fuel (considerably reduced risk of re-criticality in case of core melt) • Lead retains released fission products 	
Proliferation resistance and physical protection	Unattractive route for diversion of weapon-usable material.	<ul style="list-style-type: none"> • Lead system neutronics enables long core life 	<ul style="list-style-type: none"> • Small system features sealed, long-life core • Use of a MOX fuel containing MA increases proliferation resistance
	Increased physical protection against acts of terrorism	<ul style="list-style-type: none"> • Primary coolant chemically compatible with air and water operating at ambient pressure 	<ul style="list-style-type: none"> • Simplicity in design • Independent, redundant, and diversified DHR loops • No use of reactive or flammable coolant materials

2.1 Sustainability

According to Generation IV, *sustainability* is the ability to meet the needs of the present generation while enhancing the ability of future generations to meet society's needs indefinitely into the future. Appropriate resource utilization and waste minimization and management are the two main aspects of the sustainability.

2.1.1 Resource Utilization

Because lead is a coolant with very low neutron absorption and energy moderation properties, it is possible to maintain a fast-neutron flux even with large amount of coolant in the core. This allows the efficient use of a variety of fuel materials, including fuels with homogeneously mixed MA. The reactor can be designed to achieve a conversion ratio of ~ 1 (without the need for a blanket), along with long core life and a high fuel burn-up. The preliminary results of the ELSY project indicate that a core with an active length of 0.9 m containing about 35 t of heavy metals (HM) is critical with 17.6 wt% Pu and has a breeding ratio of about 1. Obviously a core with the same fuel content with a longer active length or larger fuel-to-coolant ratio will result in a breeding core.

The greatest experience on the use of heavy coolant is related to LBE because of its use in Russian submarine reactors and because of the technological development for subcritical (ADS) reactors.

LBE is not considered, however, to be a sustainable coolant technology, because of the limited availability of bismuth. It is not proven that current bismuth resources will allow a large international deployment of central station reactors. Lead is much more abundant than bismuth and much less expensive, and can be considered to be always available, even in the case of deployment of a large number of LFRs.

2.1.2 Waste Minimization and Management

A fast-neutron flux significantly reduces waste generation, with Pu recycling in a closed cycle being the first condition recognized by Generation IV for waste minimization. The capability of the LFR systems to safely burn recycled MA within the fuel will add to the attractiveness of the LFR and meet another important Generation IV condition.

Preliminary results of the ELSY core indicate the possibility to reach an MA content at equilibrium of 310 kg, which corresponds to 0.9% of the fuel inventory.

Obviously loading the core with an MA content greater/lower than 310 kg will result in net MA burning/generating respectively.

2.2 Economics

According to GEN IV, the economic goals broadly consider competitive life cycle and energy production costs, reducing financial risks of nuclear energy systems. Additional use of nuclear

energy is also considered, like low-temperature heat for water desalination or district heating and high-temperature heat for hydrogen production.

The cost advantages of the LFR are expected to result from relatively low capital cost, short construction duration, and low fuel production cost.

The economic utilization of MOX fuel in a fast spectrum has been already successfully demonstrated in the case of the sodium fast reactor (SFR), and a similar conclusion can be expected for the LFR.

Because of the favorable characteristics of molten lead, it will be possible to significantly simplify the LFR systems, and hence to reduce its overnight capital cost, which is a major cost factor for the competitive generation of nuclear electrical energy.

A simple plant will be the basis for reduced capital and operating cost. A pool-type, low-pressure primary system configuration offers great potential for plant simplification.

The use of in-vessel energy conversion equipment and the consequent elimination of the need for an intermediate system is a key factor to provide competitive generation of electrical energy in the LFR. In the case of conventional steam cycle power conversion, this approach is possible because of the absence of fast chemical reactions between lead and water, although the SGTR accident (i.e., risk of important pressure waves inside the steam generator unit (SGU)) must be considered in the design.

In the case of small-size plants, such as SSTAR, the use of molten Pb to CO₂ heat exchangers with supercritical carbon dioxide Brayton cycle energy conversion system can also be envisaged.

2.2.1 Risk to Capital

The use of a new technology represents a potential risk for investors. Such risk must be overcome by innovative design features that bring about plant simplification and assurance of excellent economic performance.

Corrosion by molten lead of candidate structural steels for the primary system is a main issue in the design of an LFR. New materials are being sought for special components such as pump impellers. For near-term deployment, the use of classical materials for most of the reactor components will be made possible by limiting the core outlet temperature. In spite of this limitation, the overall system efficiency remains high because there will be no intermediate system to degrade the thermal cycle.

In-lead refueling and in-service inspection and repair (ISI& R) of the core support structures in lead are additional critical aspects of licensing and operation.

In the ELSY project, it is proposed to face these apparent drawbacks by reducing the number of components/machine operating in lead, in particular by eliminating the core support plate and the in-vessel fuel-transfer machine, which has, as yet, never been designed or tested in lead.

This is considered possible because the very low vapor pressure of molten lead should allow relaxation of the otherwise stringent requirements for gas-tightness of the reactor head and this allows the adoption of simpler solution.

In general, for small, transportable systems, a limitation to the risk to capital results from the small reactor size. With particular relevance to the central station system, a reduction in the risk to capital results from combining plant simplification with the design of removable/replaceable in-vessel components.

2.2.2 Other Use of Nuclear Heat

In a future expanded market of nuclear energy, it is expected that additional uses of nuclear energy will be sought. For example, low-temperature heat for water desalination or district heating can be readily envisioned. In this respect, an LFR can play a role similar to other nuclear power reactors and, in particular, it will favor modular applications. In the case of large hydrogen demand, LFR could provide electricity for hydrogen generation by water electrolysis. The high boiling temperature of lead is potentially exploitable for hydrogen generation by high-temperature chemical processes, but this possibility is conditioned to time-consuming development/use of new materials that are resistant to lead corrosion at higher temperatures.

2.3 Safety and Reliability

Pure lead as a coolant is chemically inert in comparison to sodium and, moreover, it is preferred to LBE in terms of safety because of its substantially lower radiological concern, especially ^{210}Po .

One of the advantages in the use of lead in a fast reactor is the fact that lead retains hazardous radionuclides like iodine and cesium, even in the event of a very severe accident involving the failure of the reactor vessel, failure of the reactor building, and exposure of the coolant to the atmosphere. This advantage is considerably reduced in the case of LBE because of the much higher production of the radiotoxic ^{210}Po . The polonium production in an LBE-cooled reactor is so high that in the 80 MW LBE-cooled ADS developed in the Fifth Framework Programme of Euratom the polonium inventory was evaluated to be 2 kg at equilibrium. This amount of Po produces a decay heat in the primary system that equals the fuel-decay power, after 5 days of cooling.

Pure lead is not exempt from polonium formation. In pure lead, ^{209}Bi is produced from ^{208}Pb , and ^{210}Po results from the further activation of ^{209}Bi ; however, the rate of Po production is less by about four orders of magnitude than in case of LBE, and its decay power is negligible in comparison to that of the fuel.

The slightly higher density (4%) of lead in comparison to LBE has a marginal negative impact on the mechanical design, but the fact that the lead density is higher than that of an oxide fuel is beneficial in the event of an hypothetical severe accident, because the high density can further reduce the risk of re-criticality following a core melt.

In-vessel fuel handling is facilitated by the use of LBE that allows operation at lower temperatures, but the ex-vessel fuel and component handling is facilitated by pure lead because of the reduced polonium inventory.

In general, pure lead's characteristics facilitate the fulfillment of Generation IV objectives.

2.3.1 Operation Will Excel in Safety and Reliability

Safety is based both on the properties of lead as well as on the engineered solutions mentioned in the specific projects to meet the safety objectives. Molten lead has the advantage of allowing operation of the primary system at low (atmospheric) pressure. A low dose to the operators can also be predicted, owing to its low vapor pressure, high capability of trapping fission products, and high shielding of gamma radiation. In the case of accidental air ingress, in particular

during refueling, any produced lead oxide can be reduced to lead by injection of hydrogen gas, and the reactor operation safely resumed. Any leaked lead would solidify without significant chemical reaction affecting the operation or performance of surrounding equipments or structures.

Due to the low moderating capability of lead, it is possible to have relatively large spacing among the fuel rods with low pressure losses in spite of the high density of lead. In ELSY and EFIT, the specified moderate core ΔT between the inlet and outlet temperatures not only minimizes the potential for material corrosion, but also the thermal stress during transients, and the relatively low core outlet temperature minimizes the creep in steels.

In ELSY, an innovative reactor layout such as primary pumps installed in the hot collector has been developed, which, besides the economic advantages, improves several safety-related aspects, such as the following:

- Moderate volume of hot collector and large volume of cold collector.
- DHR coolers immersed in the cold collector. This favors natural circulation and eliminates the interference between hot coolant streaming from the core and cold coolant from the outlet of the DHR coolers.
- Free level of the cold collector, in normal operation, higher than the free level of the hot collector. This, in case of primary pump shutdown, favors a mild transition from forced to natural circulation of the coolant and hence ensures adequate heat removal from the core during a transient.

The installation of SGs inside the vessel is the real safety challenge of a LFR design.

Preventing and mitigating provisions must be conceived to address the possibility of high-pressure water and steam release into lead. These measures will be directed toward reducing the frequency of occurrence of such releases, reducing the potential amount or rates of such releases, and mitigating the consequences.

A robust SG design and an appropriate plant operation and ISI program is necessary to reduce the frequency of release.

A typical provision to reduce large releases is the elimination of the risk of failure of the water and steam collectors inside the primary boundary by installing them outside the reactor vessel. This provision aims to eliminate by design a potential initiator of a severe accident of low probability and potentially catastrophic consequences. The associated accident scenario has never been evaluated, but the complete disruption of the primary boundary and even of the overall core cannot be excluded.

In the case of SGTR, a sensitive and reliable leak-detection system coupled with a fast SG depressurization and isolation system are the basic features to minimize the risk of damage. High reliability requires redundancy of the leak-detection system achieved by the means of (i) acoustic system, (ii) steam detection in the reactor cover gas, and (iii) pressure increase detection of the reactor cover gas. Fast depressurization from high pressure in a few seconds will be achieved by operating on both the water side as well as steam side.

Several provisions can be provided to mitigate the consequences of the SGTR accident, which typically are the pressure-wave formation and propagation inside the primary system, and the pressurization of the primary boundary.

To this end, three provisions have been conceived in ELSY:

- The first provision is the installation on each tube of a check valve close to the steam header and of a Venturi nozzle or flow blockage device close to the feedwater header. With these

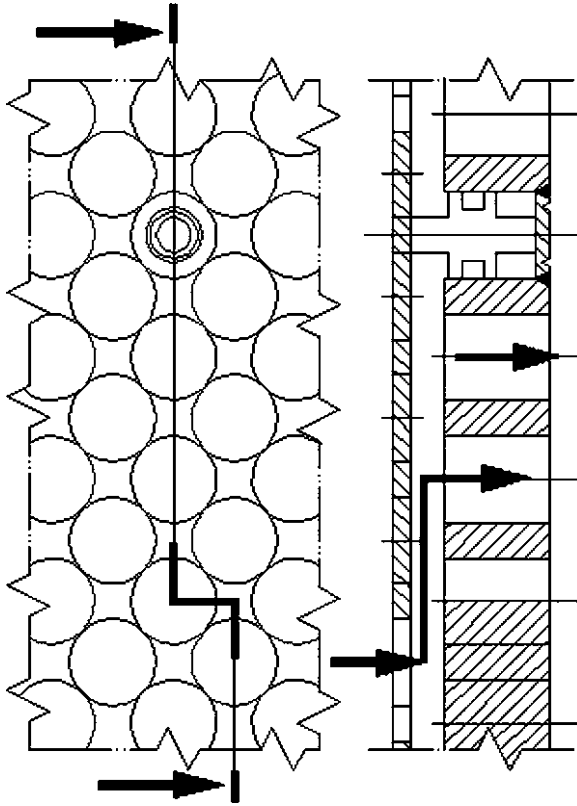


Figure 6
Double SG outer shell

devices, reverse steam flow is prevented and any leaking tube is, at least partially, promptly isolated.

- The second provision aims at ensuring that the flow of any feedwater–steam–primary-coolant mixture be redirected upward, and the risk of potentially disruptive pressure surges within the reactor vessel prevented by design. To this purpose, in the event of an SGTR, the normal radial flow is deviated upward by design features that are fully passive and are actuated by pressurization in the SG bundle. Thus, thin perforated companion inner and outer shells are placed in the annulus close to inner and outer shell, respectively, held apart to a few millimeters by spacers. The spacers are designed to collapse in the event that the inner companion shells are acted upon by a specified inner pressure. Thus, in case of an inner pressure surge, the companion shells would blow out against the inner and outer shell (Fig. 6) respectively, and since the holes of the corresponding perforations have been designed staggered and the bottom end of the annulus is closed, there will be no other exit path for the mixture, but the upward flow toward the cover gas plenum, that damps the pressure surge without risk of serious damage of the reactor internals.

- As a third provision, pressure-relieving ducts, each with two rupture discs, installed on top of each SGU, hydraulically connect the reactor cover gas plenum with the above-reactor enclosure in case of inner pressure surge, particularly brought about by the SGTR accident.

2.3.2 Low Likelihood and Degree of Core Damage

Lead allows a high level of natural circulation of the coolant; this results in less stringent requirements for the timing of operations and simplification of control and protection systems.

In case of leakage of the reactor vessel, lead is collected inside a safety vessel and the coolant is designed to maintain a minimum level that ensures the coolant circulation through, and the safe heat removal from, the core. In ELSY, a specific solution has been developed with spiral-tube SG feed from the bottom, which, without any penalty on the main vessel height, maintain a lead flow path beneath the minimum level.

For small-size reactors, since the vessel outer surface is relatively large in comparison with the reactor power, DHR, can simply be accomplished by a RVACS, which is a very reliable system. For medium- and large-size reactors, additional safety-grade systems are needed. The fact that molten lead does not react violently with air or water gives the designer some freedom in the choice of the liquid for the DHR loops, the use of air and water remaining the preferred and most simple approach.

For power control and reactor shutdown, two completely different strategies are applied in case of ADS system or critical LFRs. In the case of an ADS, power level is controlled by means of the generated proton beam current.

In case of a critical LFR diversified solutions are possible, in general, based on the control rod technology similar to SFRs, even if the use of lead as a coolant increases the spectra of the potential solutions. A control/shutdown rod can replace a fuel element in the core layout, or can be located inside a fuel element. A control rod can be moved by electrical equipment located in the gas space. A shutdown rod can be introduced from the bottom of the core by lead buoyancy, from the top through motor-driven action, by the gravity of structural masses located in gas space, or by gravity-driven action inside an evacuated tube.

At the date of issuance of this document, several solutions/proposals are under investigation, but with large uncertainties and only after an appropriate test campaign in lead it will be possible to select the most promising solutions and confirm the level of reliability and diversification that can be achieved.

2.3.3 Reduced Need for Offsite Emergency Response

In the LFR, fuel dispersion dominates over fuel compaction, thus reducing considerably the likelihood of the occurrence of severe re-criticality events in the case of core disruption. In fact, lead density, which is slightly higher than that of the fuel, and convective streams make it rather difficult to achieve scenarios leading to fuel aggregation with subsequent formation of a secondary critical mass, in the event of postulated fuel failure.

In addition, the ability of lead to trap and retain fission products, in particular iodine and cesium, and the fact that a loss of coolant accident (LOCA) will not result in significant pressurization of the containment are features of primary importance in reducing the potential consequences of severe accidents.

2.4 Proliferation Resistance and Physical Protection

The physical characteristics of lead, the selected fuel cycle, and the adopted design features can contribute to increase the proliferation resistance and physical protection (PR&PP) characteristics of an LFR. For PR, nevertheless, international safeguards for each of the major elements of the system fuel cycle remain an independent assurance against potential diversion of nuclear fuel to produce or provide materials for nuclear weapons.

2.4.1 Unattractive Route for Diversion of Weapon-Usable Material

The use of MOX fuel containing MA increases proliferation resistance (PR) because of the inherent properties of the nuclear material. Uranium enrichment is not necessary. A breeding (conversion) ratio close to 1 is achievable in a medium-size reactor without providing fertile regions in the core and hence improving PR. Fertile regions can nevertheless be necessary to maintain a breeding ratio close to 1 in small reactors or to achieve a higher level of breeding.

Moreover, the SSTAR system has been designed from the beginning to achieve nonproliferation goals by incorporating a sealed core and very long-life fuel.

High burn-up and hence a high spent fuel radiological barrier (up to about 100 GWd/tHM in the short term, up to about 200 GWd/tHM in the longer term when adequate structural material for fuel cladding has been made available) improves PR.

Other additional benefits that can result from the fuel cycle are the introduction of pyro- or advanced aqueous fuel-reprocessing methods featuring incomplete removal of fission products and MA, no separation of uranium and plutonium at any fuel-cycle stage, and inherently low decontamination factors for fuel, with the need for remote handling, which complicates operations but enhances proliferation resistance.

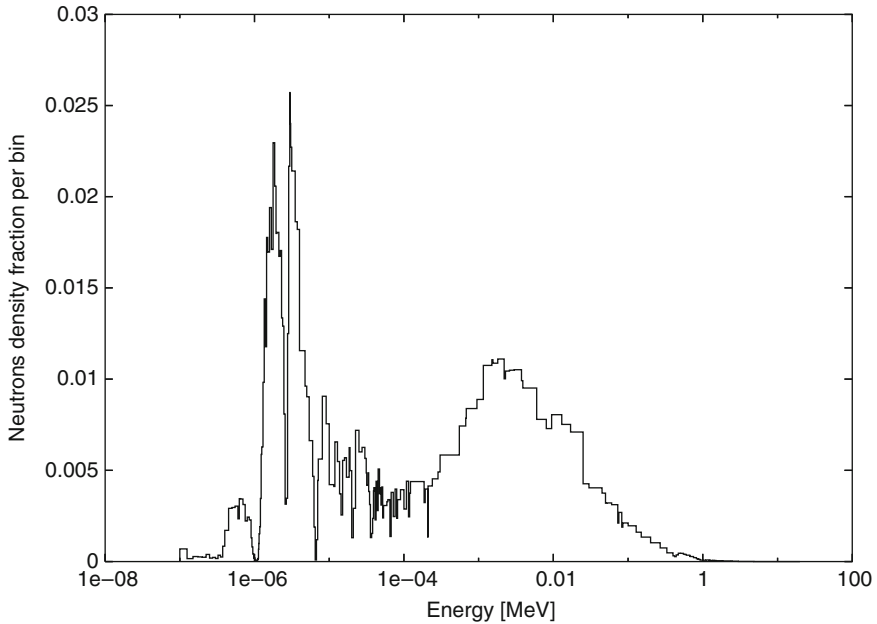
2.4.2 Increased Physical Protection Against Acts of Terrorism

The use of a coolant chemically compatible with air and water and operating at ambient pressure greatly enhances physical protection (PP). There is a reduced need for robust protection against the risk of catastrophic events, initiated by acts of sabotage because there is a little risk of fire propagation. There are no credible scenarios of significant containment pressurization. Significant PP features of the LFR systems include the following:

- System simplification, no intermediate cooling system, and consequent robustness
- Passive decay heat removal
- Compact security footprint
- Possibility of partial or full underground siting

3 Neutronics

Fast reactors cooled by HLMs such as lead or LBE rely primarily on the physics of very high-energy neutrons: the high mass number of lead (and bismuth) results in the maintenance of a very hard (high-energy) neutron spectrum.



■ Figure 7

Typical neutron spectrum in an LFR (e.g., ELSY), expressed as fraction of the neutron density per energy bin $\left(\frac{n_{\text{bin}}}{n_{\text{tot}}\Delta E_{\text{bin}}}\right)$

A typical neutron energy distribution in an LFR is shown in [Fig. 7](#) referring to ELSY. The mean neutron energy in a typical LFR lies in the range of 400–450 keV (depending also on the fuel type, i.e., oxide, nitride, or metallic).

The mean free path associated to the given spectrum, for a typical LFR, is of the order of 2–3 cm.

3.1 Neutronic Properties of Lead

In order to investigate the peculiarities of an LFR (for comparison with other reactor types), it is important to consider the range of neutronic properties of the coolant including moderation (slowing down) and absorption affinity.

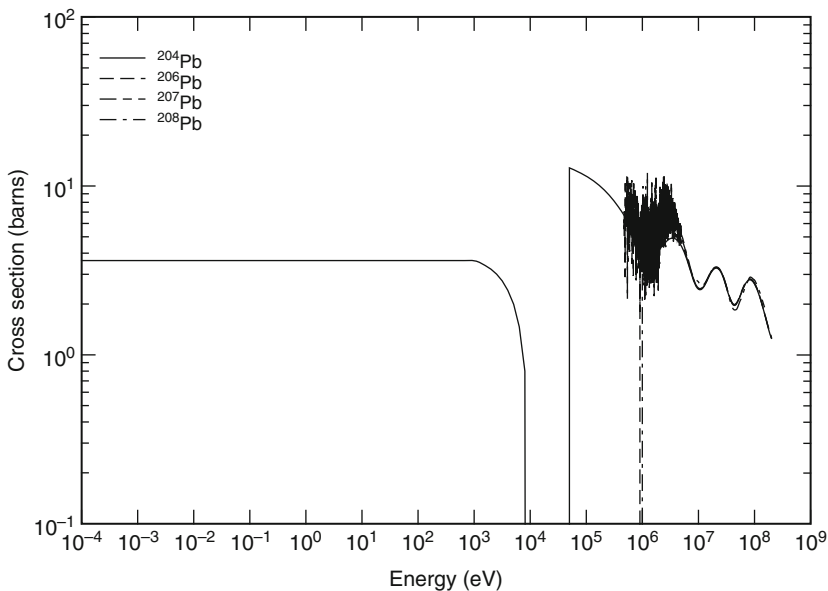
3.1.1 Moderation

The hardness of the neutron energy spectrum described in the previous section and depicted in [Fig. 7](#) can be understood by taking into account the average lethargy change per elastic collision,

$$\xi = 1 - \frac{(A-1)^2}{2A} \ln\left(\frac{A+1}{A-1}\right),$$

■ **Table 4**
Average lethargy change per elastic collision and moderating power for some typical coolants/moderators

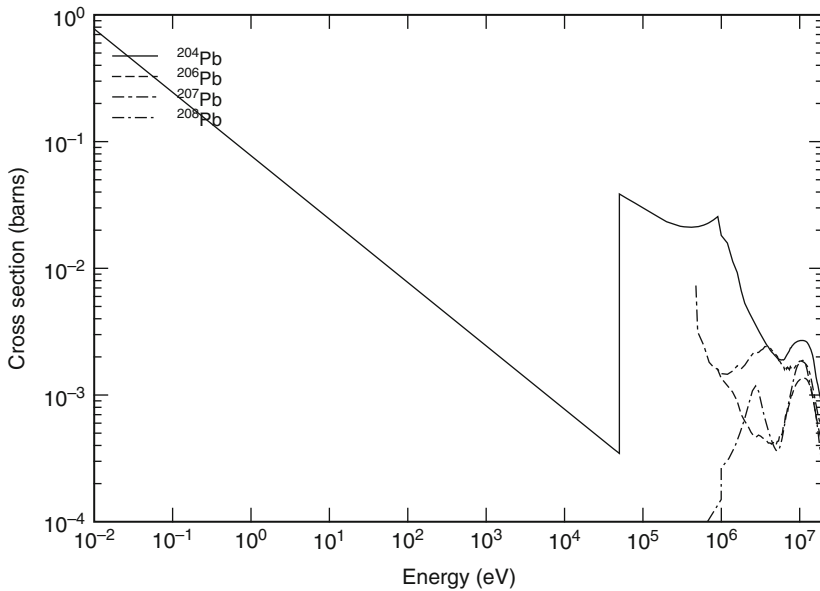
	ξ	$\xi\Sigma_s$
H ₂ O	0.920	1.425
D ₂ O	0.509	0.177
Helium	0.425	9.0e-6
Graphite	0.158	0.083
Sodium	0.0825	0.0176
Lead	0.00963	0.00284



■ **Figure 8**
Elastic cross section of naturally occurring lead isotopes (Data from ENDF/B-VII library)

where A is the mass number of the considered isotopes. ➤ [Table 4](#) resumes typical values of the average lethargy change per elastic collision and the moderating power for lead and other main coolants/moderators.

The elastic cross section of naturally occurring lead isotopes is shown in ➤ [Fig. 8](#). In the energy range of interest the elastic cross section assumes almost the same value for all isotopes.



■ Figure 9

(n,γ) absorption cross section of naturally occurring lead isotopes (Data from ENDF/B-VII library)

3.1.2 Absorption

The lead coolant is one of the main contributors to the neutron balance in the core: as a matter of fact, the captures in the coolant directly impact the reactivity of the unit cell of the system, and thus the neutronic design of the whole core (see [► Sect. 6](#)).

The (n,γ) absorption cross section of naturally occurring lead isotopes is shown in [► Fig. 9](#).

It is to be pointed out that the most highly absorbing isotope (^{204}Pb) has a natural abundance of only 1.4%, sustaining the low total absorption rate of lead.

3.2 Fuel Performances in LFRs

While a variety of fuels is accounted worldwide for LFRs (e.g., oxide in the European concept, nitride in the American one), their typical composition is a mixture of reactor-grade plutonium (referring to an isotopic vector as if extracted from the spent fuel of a typical LWR after a mean burn-up (BU) of some 50 GWd/tHM and a cooling period of 10 years) and depleted uranium (DU), eventually doped by the inclusion of some MAs. The only exception to this scheme is represented by the EFIT fuel: it is made of Pu oxide with a considerable fraction of MA oxide only (thus U-free) in an inert matrix (MgO in the preliminary hypothesis).

Besides the peculiarities of oxide versus metallic fuels (mainly influencing the thermal design of the pin, such as the fuel thermal conductivity and its melting temperature), a series of common properties can be pointed out referring to the overall performances of fissile and fertile isotopes in an LFR.

■ **Table 5**

Typical microscopic cross sections of main fuel isotopes in an LFR compared to the ones of LWRs

	Capture [barns]			Fission [barns]		
	ELSY	ENHS ^a	LWR	ELSY	ENHS	LWR
²³⁸ U	0.282	0.210	1.03	0.035	0.030	0.107
²³⁹ Pu	0.487	0.297	42.23	1.753	1.640	101.02
²⁴¹ Pu	0.475	0.313	37.89	2.501	2.110	109.17

^a The encapsulated nuclear heat source (ENHS) is a SSTAR-type reactor (see ▶ Sect. 1.5.1) candidate conceived by the University of California – Berkeley, the Lawrence Livermore National Laboratories and the Argonne National Laboratories.

3.2.1 Fission Cross Sections

An immediate drawback related to the hard neutron spectrum can be found in what concerns the fission cross sections of odd nuclides (about one to two orders of magnitude less than in thermal reactors): typical values are shown in ▶ Table 5 compared to corresponding capture cross sections. Despite the fact that an increase of the fission rates for even nuclides can be gained, resulting in a wider contribution to criticality among nuclides in the fuel inventory, the reduction of the fission cross sections implies larger inventories of fissile material to maintain criticality.

3.2.2 Average Number of Fission Neutrons

The hard spectrum represents a positive contribution in what concerns the average number of neutrons per fission, $\bar{\nu}$, which is higher (about 2.93 for almost all the systems considered in the present chapter) than in thermal reactors. The higher number of neutrons available in the system, once criticality has been achieved, can be exploited for captures in fertile material to provide a higher breeding.

3.2.3 Fuel Utilization

Supported also by the increase of $\bar{\nu}$, the fertility factor, η , (▶ Chaps. 2 or ▶ 9) increases monotonically above 100 keV: the main reason for this can be ascribed to the lower capture rate due to the higher separation of the bulk of the neutron spectrum from the absorption resonance energy range. LFRs, therefore, can rely on a more-efficient fuel utilization, allowing a higher relative arrangement of fertile material in the fuel, thus resulting in a higher conversion ratio (CR).

3.2.4 Spectrum Evolution with Burn-Up

The particularly hard spectrum of LFRs is poorly affected by the buildup of fission products (FPs) during operation. Hence, the neutronic properties of the system can be assumed to remain approximately constant during the whole-core life (e.g., the error introduced on criticality evaluation is few tens of pcm after complete irradiation of the fuel).

3.2.5 Effective Delayed Neutron Fraction and Prompt Neutrons Lifetime

In a typical LFR with iso-breeding Pu content (such as ELSY or SSTAR), the value of the effective delayed neutron fraction β_{eff} is in the range 370 (ELSY) to 420 (SSTAR) pcm. This value is smaller than that of LWRs (~ 650 pcm) because of the lower fraction of delayed neutrons per fission of a ^{239}Pu isotope than for ^{235}U . In case of MA-doped fuel (with equilibrium concentrations, i.e., some 1 at% of HM), the value of β_{eff} is further reduced to some 325 pcm because of the small delayed neutron fraction associated to the fission of MA isotopes.

The impact of more highly energetic neutrons also implies a lower prompt neutrons lifetime, λ (of the order of 10^{-6} to 10^{-7} s), in comparison with thermal reactors (about two orders of magnitude higher).

The direct drawbacks related to the values of these parameters are the narrower margin to prompt-criticality and the lower capabilities for reactor control in case of prompt-criticality accident.

3.2.6 LFR Capabilities of MAs Transmutation

Finally, the harder the spectrum, the higher the fission cross sections of MAs (triggering the highest level of threshold fission reactions among even nuclides). As far as MA transmutation is concerned, this implies that the balancing of production and removal rates for the latter (which represents the frontier between MA breeders and burners) is attained by a low content of MAs in the fuel.

The possibility of relying on a low fraction of MAs in the fuel allows more flexibility in waste transmutation for LFRs: performances being equal, the lower detriment to the total average fraction of delayed neutrons (since the low contribution associated to MAs) represents a larger operability margin to what concerns such a stringent constraint for reactor control.

3.3 Neutronic Performances of Typical Absorbers in an LFR

The choice of an effective neutron-absorbing material is fundamental in the design of a critical reactor because of the need to control and regulate its operation. In the hard spectrum of an LFR, particular care should be paid to the evaluation of the absorption cross sections of the control material candidates.

3.3.1 Boron Carbide

Boron carbide, B_4C , is the reference-absorbing material for FRs in general. Besides the availability of boron and the ease of its fabrication, therefore, the low costs related to the adoption to B_4C -based control systems, the neutronic properties of the ^{10}B isotope are excellent even in the fast spectrum because of its (n, α) reaction cross section (🔗 [Fig. 10](#)).

Since the main isotope responsible for neutron absorption is the ^{10}B , the natural abundance of which is 19.9% (the rest being ^{11}B , whose neutronic properties are practically unusable), reactor grade B_4C is usually enriched in ^{10}B (up to $\sim 90\%$).

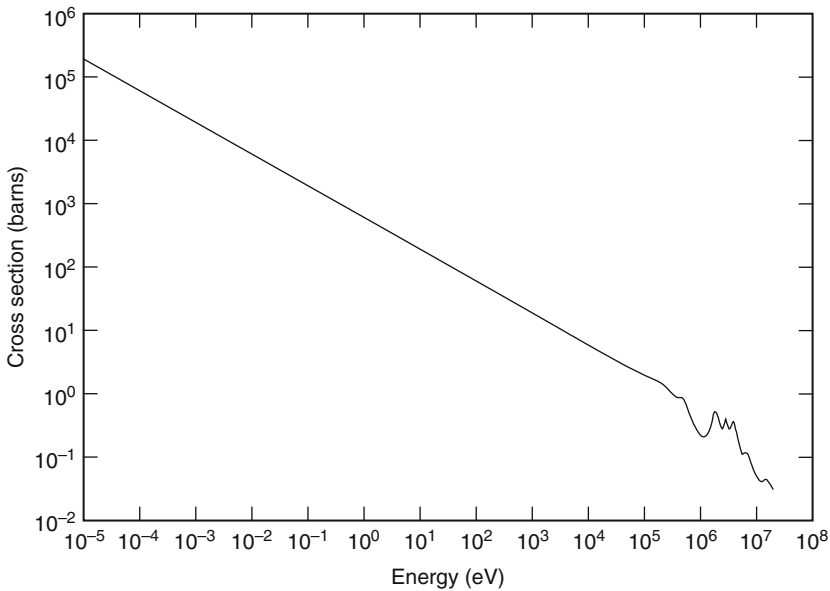


Figure 10
 ^{10}B absorption cross section (Data from ENDF/B-VII library)

3.3.2 Indium–Cadmium Eutectic

An interesting alternative to boron carbide could be represented by the indium–cadmium eutectic (75 wt% In and 25 wt% Cd): at typical LFR-operating temperatures ($>400^\circ\text{C}$), this alloy is liquid ($T_{\text{melt}} = 122.5^\circ\text{C}$); thus its operability could be assured even in case of control rod thimble guide distortion after a severe accident.

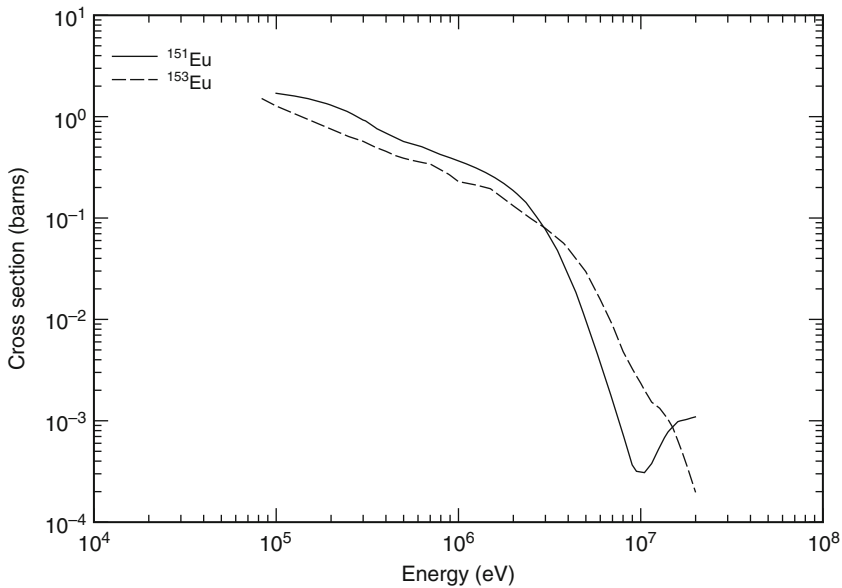
A main drawback can be ascribed to this solution taking into account the absorption effectiveness of the eutectic in the hard spectrum of LFRs. Despite the high content of indium in the mixture (the absorption effectiveness of pure cadmium being about 60% of that of pure indium), preliminary evaluations performed on an ELSY In–Cd control system, when replacing a reference 90% ^{10}B -enriched B_4C configuration, showed reactivity reduction to about 14% of the latter configuration. Based on this assessment, large volumes in the core would need to be devoted to such a control system, resulting in the practical infeasibility for this solution.

3.3.3 Europium

The last candidate absorber for LFRs is europium sesquioxide (Eu_2O_3). This material, well known in reactor physics, has high (n, γ) absorption cross sections in the fast spectrum (comparable to that of ^{10}B for both naturally occurring isotopes ^{151}Eu and ^{153}Eu , \blacktriangleright Fig. 11).

In order to decide whether to choose this material instead of B_4C it is worth taking into account the following details:

- No He is produced (since the capture mechanism is Eu radiative absorption), thus no venting is required for europium sesquioxide control rods.



■ Figure 11

Naturally occurring europium isotopes (n, γ) absorption cross section (Data from ENDF/B-VII library)

- The daughter products are also good neutron absorbers, thus the loss of anti-reactivity worth is reduced with respect to B_4C absorbers.
- The Eu self-shielding is such that the effectiveness of a Eu_2O_3 control rod, in LFRs, is about 40% of that of an equivalent one made of enriched B_4C , thus close to that of natural B_4C .

4 Lead Properties

This chapter reports data on the main physical properties of technically pure molten lead with a few complementary data of LBE acquired from the open literature. (Technically pure lead is not synonymous with nuclear-grade lead, because lead as a coolant in a fast reactor is likely to require more stringent limitations than high-purity industrial lead, in terms of concentrations of impurities, which could become activated or affect corrosion, mass transfer, and scale formation on heat-transfer surfaces. The impurity concentrations are so low, however, that the physical properties of lead of both grades are the same, for the purpose of this compilation.) It will be noted that, in some cases, these are recommended as best-fit data, because of the significant discrepancies among the values given by different sources.

4.1 Physical Properties

The properties of molten lead are given by parameter in the form of the recommended value or correlation over a temperature range, and, eventually, in the form of a table of main parameters

relevant to heat transfer, of both pure lead and the LBE over the range of more frequent use, for quick check, and comparative analysis purpose.

In general, the reliability of the recommended correlations about thermal–physical property data of molten lead is satisfactory and the correlations can be used for engineering estimates and design calculations, in spite of the uncertainty still existing on heat capacity, boiling temperature, and thermal conductivity.

For the high-temperature range, the set of thermodynamic and transport properties (thermal conductivity, viscosity, and surface tension) relevant for reactor safety analysis are not reported, but the basic properties such as the liquid density, vapor pressure, and liquid adiabatic compressibility are estimated up to the critical point using semiempirical models based on the extrapolation of low-temperature data (OECD-NEA 2007), owing to the lack of experimental data published in the open literature.

Normal Melting Point

The melting point of technically pure lead is as follows:

$$T_{melt}^{\text{Pb}} [\text{K}] = 600.6 \pm 0.1.$$

The melting point increases by 0.0792 K per 1 MPa when pressure increases from about 15 to 200 MPa.

Volume Change at Melting

Similar to the majority of metals with FCC crystal structure, lead exhibits a volume increase upon melting. At normal conditions a volume increase

$$\Delta V_m / V_m = 3.7\%$$

is the recommended value for lead of technical purity.

Latent Heat of Melting at the Normal Melting Point

The recommended heat of melting of lead at the normal melting point (the enthalpy change on melting) is

$$Q_{melt}^{\text{Pb}} [\text{kJ/kg}] = 23.8 \pm 0.7$$

Normal Boiling Point

The value of

$$T_{boil}^{\text{Pb}} [\text{K}] = 2,016 \pm 10$$

is recommended for the boiling temperature of technically pure lead at normal conditions.

Heat of Vaporization at the Normal Boiling Point

The latent heat (enthalpy) of vaporization is a measure of the cohesive energy of atoms in a liquid metal. Therefore, it correlates with surface tension and thermal expansion. The literature values are very close, with the difference between maximum and minimum values less than 1%. The mean value and the mean deviation are as follows:

$$Q_{boil}^{\text{Pb}} [\text{kJ/kg}] = 858.2 \pm 1.9.$$

Saturation Vapor Pressure

The vapor pressure of a liquid metal is an important property, which is directly related to the latent heat of evaporation (cohesive energy, ΔH). The following correlation is recommended for the saturated vapor pressure of molten lead where temperature is in kelvin:

$$p_s^{\text{Pb}} [\text{Pa}] = 6.189 \times 10^9 \times \exp(-22,216/T).$$

The above equation can provide approximate values for equilibrium vapor pressures over a wide range of temperature and is recommended from the melting point up to the normal boiling point. ΔH is included as a constant owing to the relatively small variation with temperature.

Surface Tension

The surface tension of liquid surfaces (σ) is related to tendency to minimize the surface energy. It decreases with increasing temperature and reduces to zero at the critical temperature (T_c), where difference disappears between liquid and gas phases.

The temperature dependence of surface tension is linear for most liquid metals.

The recommended correlation is the following formula where temperature is in kelvin and is conservative in the range from the melting temperature of 600.6–1,200 K (327.6–927 °C):

$$\sigma^{\text{Pb}} [\text{N/m}] = 0.519 - 1.13 \times 10^{-4} \times T.$$

Density

The temperature dependence of density provides essential information for the development of an equation of state (EOS). It is used to determine the concentration of atoms in unit volume and hydraulic parameters in reactor design. Also, the measurement or calculation of basic physical properties, e.g., viscosity, surface tension, thermal diffusivity, requires knowledge of density. The set of the selected data can be fit as follows, with linear temperature dependence, where temperature is in kelvin:

$$\rho^{\text{Pb}} [\text{kg/m}^3] = 11,367 - 1.1944 \times T.$$

Thermal Expansion

The coefficient of thermal expansion (CTE), derived from temperature dependence of density of molten lead, is as follows:

$$\beta_p^{\text{Pb}} [\text{K}^{-1}] = 1/(9,516.9 - T).$$

Sound Velocity and Compressibility

The correlation recommended for the estimation of the sound velocity in the molten lead is:

$$u_{\text{sound}}^{\text{Pb}} [\text{m/s}] = 1,951.75 - 0.3423 \times T + 7.635 \times 10^{-5} \times T^2,$$

where the temperature is in kelvin.

At normal atmospheric pressure, the temperature dependence of the elastic modulus of molten lead can be described with the help of parabolic and linear functions as follows:

$$BS^{\text{Pb}} [\text{Pa}] = (42.15 - 1.652 \times 10^{-2} \times T + 3.273 \times 10^{-6} \times T^2) \times 109.$$

Heat Capacity

Available experimental data on heat capacity of heavy liquid metals are few. The following correlation is recommended for the heat capacity of molten lead in the temperature range of T_{melt} to 1,300 K (1,027 °C), where temperature is in kelvin:

$$c_p^{Pb} \text{ [J/kg/K]} = 175.1 - 4.961 \times 10^{-2} \times T + 1.985 \times 10^{-5} \times T^2 - 2.099 \times 10^{-9} \times T^3 - 1.524 \times 10^6 \times T^{-2}.$$

Critical Constants

Critical parameters. The mean rounded values of two sources are recommended for the critical temperature, pressure, and density of lead:

$$\begin{aligned} T_c^{Pb} &= 4,870 \text{ K (4,597 °C)}, \\ p_c^{Pb} &= 100 \text{ MPa}, \\ \rho_c^{Pb} &= 2,490 \text{ kg/m}^3. \end{aligned}$$

Viscosity

The following empirical equation, obtained by fitting selected values into an Arrhenius-type equation, is recommended to describe the temperature dependence of the dynamic viscosity of molten lead:

$$\mu^{Pb} \text{ [Pa s]} = 4.55 \times 10^{-4} \times \exp(1,069/T),$$

where temperature is in kelvin. This correlation is valid in the temperature range T_{melt} to 1,470 K (1,197 °C).

Electric Resistivity

The electrical resistivity of liquid lead, as of most liquid metals, increases linearly with temperature (in the temperature region of interest). The recommended empirical equation suitable for the calculation of the electrical resistivity is as follows:

$$r^{Pb} \text{ [}\Omega \text{ m]} = 0.666 \times 10^{-6} + 4.79 \times 10^{-10} \times T,$$

which is valid in the temperature range of 601/1,273 K (328/1,000 °C). The deviation of the selected data from this correlation is less than 1%.

Thermal Conductivity and Thermal Diffusivity

Experimental determination of thermal conductivity of liquid metals is difficult because of the problems related to convection and wetting. At present, few experimental data are available, sometimes presenting discrepancies between different sets of data. The high thermal conductivity of liquid metals is mainly due to free electrons. A simple theoretical relation exists for pure metals between electrical and thermal conductivities known as Wiedemann–Franz–Lorenz law. In an effort to find a physically reasonable compromise among the experimental data sets and taking into account the relation with the electrical conductivity, the following linear correlation is recommended for the thermal conductivity of molten lead:

$$\lambda^{Pb} \text{ [W/m/K]} = 9.2 + 0.011 \times T,$$

where temperature is in kelvin. This correlation is applicable in the temperature range of T_{melt} –1,300 K (1,027 °C).

Thermal diffusivity a is defined as follows:

$$a = \lambda / (\rho \times c_p).$$

So, it can be calculated using data for thermal conductivity, density, and specific heat. Fitting the data with a linear function yields a correlation that can be of practical use for calculating the dimensionless Péclet and Prandtl numbers.

The values of main parameters and transport properties at discrete temperatures in the range 400–600 °C for lead (and LBE for comparison with pure lead) in [▶ Table 6](#).

4.2 Chemistry Control and Monitoring Systems

The chemical properties data of solubility and diffusivity of oxygen and some metallic elements, e.g., Fe, Cr, and some oxides (e.g., iron oxides, chromium oxides, etc.) in the molten lead are of paramount importance for:

- Preventing oxidation of the coolant
- The assessment of the materials corrosion rate
- The design and engineering of HLM purification systems, for the development of a corrosion protection strategy that is based on protective oxide layers on the structural materials
- The source term assessment

The accuracy of the formula that fits the solubility data of oxygen is not reported in the literature, although solubility is one of the key parameters of lead chemistry. On lack of accurate data, a larger margin against risk of reaching saturation will have to be specified, particularly at the cold temperature of the thermal cycle (1 decade from saturation, say). Diffusivity of oxygen is of lesser concern, because, although the diffusion rate in the melt of atomic oxygen is slow, the coolant flow itself will provide for uniform concentration of the dissolved oxygen wherever turbulent flow prevails at a rate that can be 1,000 times the rate of diffusion through stagnant lead.

It will be noted, at the outset, that the aim of controlled dissolved oxygen in the melt is to protect the structural steels such as stainless steels and low-alloy steels from corrosion by means of an oxide barrier and that this technique is effective up to about 500 °C.

This implies the presence of dissolved oxygen in the melt in equilibrium with oxygen gas in the cover gas plenum above the melt.

4.2.1 The Thermodynamical Base

Oxygen gas dissolves in liquid metals in atomic form. The amount of dissolved oxygen is proportional to the square root of its partial pressure above the melt (relationship known as Sievert's law), provided that its concentration is less than 1 wt% and oxide-forming elements are absent. This holds true for the oxygen concentration range in the pure lead melt of LFR, the upper limit of which is the saturation concentration with respect to lead oxide and the lower limit the saturation concentration with respect to magnetite. Thus, iron is kept fully oxidized (as magnetite) and lead fully reduced (as metallic lead).

All elements less noble than iron, if present, are a fortiori completely oxidized and all elements more noble than lead, if present, are in their metallic form. Elements that are between iron and lead are kept at low concentration either by specification of the grade of the original

Table 6
 Values of physical and transport properties of molten lead (and of lead–bismuth eutectic alloy, for comparison)

Fluid	Temperature (°C)	Density, ρ (kg/m ³)	Specific heat, c_p (J/kg/K)	Dynamic viscosity, η (10 ⁻⁴ Pa s)	Kinematic viscosity, ν (10 ⁻⁸ m ² /s)	Thermal conductivity, λ (W m/K)	Thermal diffusivity, a (10 ⁻⁶ m ² /s)	10 ⁻² Pr = ν/a	Thermal expansion, β (10 ⁻⁴ K ⁻¹)	Surface tension, σ (10 ⁻³ N/m)
Lead	400	10,563	146.7	22.3	21.1	16.6	10.7	1.86	1.12	443
	425	10,533	146.3	21.0	20.0	16.9	10.9	1.71	1.13	440
	450	10,503	145.9	20.0	19.0	17.2	11.2	1.59	1.13	437
	475	10,473	145.5	19.0	18.1	17.4	11.4	1.48	1.13	434
	500	10,444	145.1	18.1	17.4	17.7	11.7	1.38	1.13	432
	525	10,415	144.7	17.4	16.7	18.0	11.9	1.29	1.14	429
	550	10,384	144.3	16.7	16.0	18.2	12.2	1.21	1.14	426
	575	10,354	143.9	16.0	15.5	18.5	12.4	1.13	1.15	423
	600	10,324	143.5	15.5	15.0	18.8	12.7	1.07	1.15	420
	LBE	400	10,205	144	15.1	14.8	13.0	8.3	1.67	1.29
425		10,172	143	14.5	14.3	13.4	8.6	1.56	1.29	391
450		10,139	143	14.0	13.8	13.7	8.9	1.47	1.30	389
475		10,473	143	13.5	13.4	14.0	9.2	1.38	1.30	388
500		10,073	142	13.1	13.0	14.3	9.4	1.30	1.30	386
525		10,040	142	12.7	12.6	14.6	9.7	1.23	1.31	384
550	10,006	141	12.3	12.3	14.9	10.0	1.17	1.31	383	
575	9,973	141	12.0	12.0	15.2	10.3	1.11	1.32	381	
600	9,940	141	11.7	11.8	15.5	10.5	1.06	1.32	379	

lead charge (arsenic, bismuth) or by prevention from leaching out of steel into the melt (nickel) and play therefore a small to negligible role in the economy of dissolved oxygen concentration at normal operation or during tests.

Oxygen concentration changes as a consequence of changing partial pressure above the melt according to Sievert's law and/or of changing temperature of the melt. The rate of change due to changes of the partial pressure may be slow if diffusion is the only driving force or relatively fast if turbulent motion is involved. The rate of change due to local cooling (heating up) of the melt, as it occurs in the SGs or in the core depends on the formation (dissolution) rate of the metal oxides.

It will be noted that any change of oxygen concentration is related to the dissolved oxygen. The total oxygen may have remained constant, while the oxygen concentration has changed, as in the case of formation of metal oxide particles or dissolution of metal oxide particles in the bulk of the melt.

The physical-chemical principles of metal oxide formation, particularly the relationship between free energy and equilibrium constant, are treated in handbooks on thermodynamics (Perry et al. 1963; Hougen et al. 1959; Moore and Boyce 1990) and concisely summarized here below.

The general chemical equation of metal oxide formation with 1 mol of oxygen is the reference for the calculations. Thus, for lead the equation becomes



Lead oxide formation in presence of water vapor can be conveniently expressed combining (1a) and the equation of water formation



as follows



Because the Gibbs free energy change ΔG is the driving force of a chemical reaction, on the equilibrium position ΔG vanishes, i.e., an equilibrium mixture of both products and reactants is obtained when the free energy change of the system between the initial condition and the final condition has become zero (position of minimum free energy toward which the system tends). If the initial condition is taken to refer to standard conditions, the calculation of the standard free energy change ΔG_T° at any temperature T allows the calculation of the equilibrium constant K at that temperature according to (2)

$$\Delta G_T^\circ = -RT \ln K, \quad (2)$$

where:

R = Gas constant, 8.314 J/K/mol

T = Temperature, K

If Pb and PbO involved in (1a) are pure liquid and solid, respectively, their concentrations remain constant, allowing their active masses to be taken as 1, and the equilibrium constant may be written in terms of the partial pressure of oxygen only,

$$K = \frac{1}{p_{\text{O}_2}}, \quad (3a)$$

and, by substitution in (2):

$$\Delta G_T^\circ = RT \ln p_{O_2},$$

allowing the dissociation or equilibrium p_{O_2} values to be calculated. The value of p_{O_2} , which is the reciprocal of K , is the equilibrium pressure of oxygen, below which the oxide will decompose (therefore also called dissociation pressure) and above which the metal will oxidize. Low dissociation pressure favors more ready formation of the metal oxide.

In the case of the water vapor formation, (1b) the equilibrium constant is in terms of partial pressures of all involved substances,

$$K_p = \frac{p_{H_2O}^2}{p_{H_2}^2 \times p_{O_2}}. \quad (3b)$$

In the case of dissolution of a metal oxide in the melt, $M_xO_y = xM + yO$, the equilibrium constant is in terms of the molar concentration of the solved elements,

$$K_c = [M]^x \times [O]^y. \quad (3c)$$

The same reasoning as for the dissociation pressure applies considering the reaction of lead oxide formation in presence of water vapor, (1c): at any temperature T , equilibrium exists only at that value of the $\frac{p_{H_2}}{p_{H_2O}}$ partial pressures ratio that satisfies (3b), once the value of the dissociation pressure has been substituted for p_{O_2} . If the pressure ratio is kept lower than the equilibrium ratio, all lead is in the oxide form and, vice versa, all lead is in metallic form (see also [Table 6](#), where related equilibrium values for both pressures ratio and oxygen dissociation pressure can be read at 400 °C for lead oxide and magnetite).

At low partial pressure of the oxygen gas above the melt, the knowledge of the equilibrium constant of water vapor offers a means of controlling p_{O_2} according to (3b): at a given p_{H_2O} , p_{O_2} varies with $\frac{1}{p_{H_2}^2}$, the inverse of the square partial pressure of the hydrogen gas. At low p_{O_2} , the measurement of the associated hydrogen partial pressure is easy.

The standard free energy is defined in terms of enthalpy and entropy as follows:

$$\Delta G_T^\circ = \Delta H_T^\circ - T\Delta S_T^\circ, \quad (4)$$

where conventionally $\Delta G_T^\circ = \Delta G_{T,prod}^\circ - \Delta G_{T,react}^\circ$, i.e., change in the free energy referred to the moles of the reactants and products shown in (1a), at 1 atm and at a stated temperature T , with the substances in the physical state normal under these conditions. As can be seen from (4), ΔG_T° is made up of an enthalpic and of an entropic term.

The enthalpic term may be calculated as follows if the enthalpy change for the reaction at another specified temperature, usually 298 K, and molar heat capacity data are available from data books:

$$\Delta H_T^\circ = \Delta H_{298K}^\circ + \int_{298}^T \Delta C_p dT \pm \text{latent} \cdot \text{heats}. \quad (5)$$

The entropic term may be calculated with the same procedure as for the enthalpic term as follows:

$$\Delta S_T^\circ = \Delta S_{298K}^\circ + \int_{298}^T \frac{\Delta C_p}{T} dT \pm \frac{(\text{latent} \cdot \text{heats})}{T_m}. \quad (6)$$

Latent heats are subtracted if reactants transform.

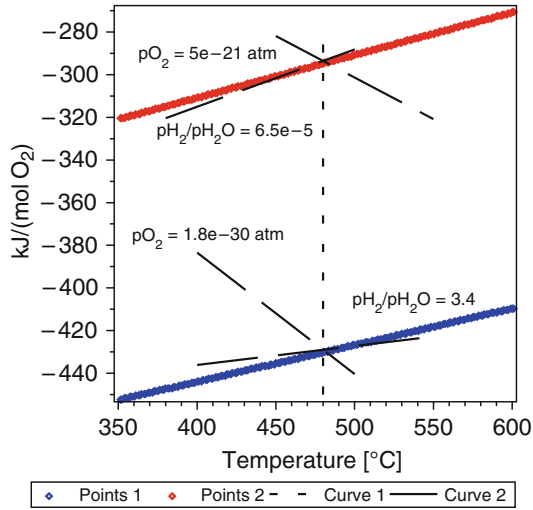


Figure 12

Standard free energy change for the formation of 2 mol of PbO (*upper line*) and half a mole of magnetite, Fe₃O₄

Table 7

Free energy change and dissociation pressures of lead oxide and magnetite at 400 °C and 480 °C

	$\Delta G^\circ_{400\text{ }^\circ\text{C}}$ (kJ/mol O ₂)	$p_{\text{O}_2,400\text{ }^\circ\text{C}}$ (atm)	$\Delta G^\circ_{480\text{ }^\circ\text{C}}$ (kJ/mol O ₂)	$p_{\text{O}_2,480\text{ }^\circ\text{C}}$ (atm)
PbO	-309.6	1.1×10^{-24}	-293.5	5.0×10^{-21}
Fe ₃ O ₄	-442.8	4.5×10^{-35}	-429.1	1.8×10^{-30}

4.2.2 Thermodynamical Data and Diagrams



Heats of formation can be read from Table 3.201 of Perry et al. (1963), absolute entropies at 298 K from Table 68 of Hougen et al. (1959), heat capacities from Table 3.173 of Perry et al. (1963) and Table 2.2 of Moore and Boyce (1990).


The following solubility at saturation – [wt%] – versus T of oxygen, (7), and of iron, (8), in molten lead has been determined experimentally within the temperature range 400–900 °C for iron (Gromov 1998):

$$\log C_{[\text{O}],s} = 3.2 - \frac{5,000}{T} \quad (7)$$

$$\log C_{[\text{Fe}],s} = 2.1 - \frac{4,380}{T}. \quad (8)$$

Change in the Standard Free Energy


The change in the standard free energy ΔG° versus T for the formation of 2 mol of PbO and half a mole of magnetite, Fe_3O_4 , calculated with the relationships written above and the thermodynamic data, is plotted on the following diagram of  Fig. 12 along with iso- $\frac{p_{\text{H}_2}}{p_{\text{H}_2\text{O}}}$ pressure ratio, and iso- p_{O_2} pressure lines of interest. Selected values at 400 °C and 480 °C are reported in .

The values of the dissociation pressures are so low that their direct measurement in the cover gas is impractical (.

The oxygen activity is defined as the ratio, at any temperature, of the actual dissolved oxygen concentration to the concentration of saturation for PbO, arbitrary chosen as standard state:

$$a[\text{O}] = \frac{C_{[\text{O}]}}{C_{[\text{O}],s}} \quad (9)$$

where $C_{[\text{O}],s}(T)$ is given by (7).

Values of $C_{[\text{O}],s}(T)$ by step of 10 K are listed in the following . They are noted as standard values, because used as reference values in (9) for calculating $a[\text{O}]$.

The activity $a[\text{O}]$ gives the measure how far (how close) the actual oxygen concentration in the melt is from the upper allowable limit, where lead oxide would start to form. Because

$$C_{[\text{O}],a} = k\sqrt{p_{\text{O}_2}}, \quad (10)$$

the smaller the $C_{[\text{O}],a}$, the smaller is the $a[\text{O}]$ value until it corresponds to the dissociation pressure of magnetite via (8) and (10).


The theoretically allowable activity ranges are listed in  at several temperatures. The ranges cannot be exploited in their full extension, however, because if the oxygen activity would be controlled at its upper limit, lead oxide precipitation would occur in the melt, and predictably on the colder heat-transfer surface of the SG tubes, while cooling down (too much dissolved oxygen) or, conversely, there would be dissolution of magnetite out of the mixed oxide film barrier of the austenitic steels, if the activity would be controlled at its lower limit (too little dissolved oxygen).

Table 8

Weight percent (wt%) of oxygen dissolved in molten lead as function of the temperature at equilibrium with the dissociation pressures of lead oxide, [O]_{sat, std}, and magnetite, [O]_{min}

Temp (°C)	Pure lead		
	[O] <i>sat, std</i> (wt%)	[O] <i>min</i> (wt%)	$-\log a[\text{O}]$
400	4.5e-5	2.94e-10	5.2
450	1.6e-4	2.03e-9	4.9
480	3.0e-4	5.74e-9	4.7
500	4.6e-4	1.10e-8	4.6
550	1.2e-3	4.86e-8	4.4
600	2.7e-3	1.82e-7	4.2

Thus, the operating activity range must be controlled between the two range limits with margin.

4.3 Thermal Hydraulics

There are two kinds of open issues in this area. The first is related to the fundamental nature of heavy liquid metals.

The Prandtl number of HLMs (Pr of lead at 400 °C is 0.019) is more than two orders of magnitude lower than that of water and air. This is because HLMs have a significantly higher thermal conductivity λ [W/mK], lower specific-heat capacity c_p [J/(kgK)], and lower kinematic viscosity.

Low Prandtl number means that the thickness of the viscous boundary layer is negligibly small compared to the thermal boundary layer. In gas or water flow, the thickness of the thermal and the viscous boundary layer are of the same order of magnitude, as Pr is ~ 1 .

With lead in laminar flow, molecular conduction of heat controls the heat transfer. Accordingly, the classical nondimensional correlations for heat transfer can be applied also to liquid metal.

Under turbulent flow conditions, however, eddy conduction of heat becomes important and heat transfer is determined by both molecular and eddy conduction in the fluid stream. While in ordinary fluids like air and water molecular conduction is only of importance near the wall, in a liquid metal the magnitude of the molecular conductivity is of the same order as that of the eddy conductivity. Thus, the molecular conduction is effective not only in the boundary layer but also to a significant extend in the bulk of the fluid stream. Therefore, relationships (or correlations) developed to determine the heat-transfer coefficients for turbulent flows in air or water cannot be used.

A further consequence of the importance of molecular conduction of thermal energy in turbulent liquid metal flow is that the concept of the hydraulic diameter cannot be used so freely to correlate heat-transfer data from systems that differ in configuration but retain a similar basic flow pattern. As an example in Pr ~ 1 fluids, basic heat-transfer data for flow through circular pipes can be used to predict Nusselt (Nu) numbers for flow parallel to a rod bundle by evaluating the hydraulic diameter of the rod bundle and using this in the nondimensional correlations for the circular pipe.

This calculation approach is invalid for liquid metal systems, and accordingly theoretical, numerical, or experimental heat-transfer relationships must be developed to deal with each specific configuration.

The second kind of issues is technological, and mostly related to the nature of the HLM-cooled system design and operation. Using coolant chemistry control and surface protective oxide formation to mitigate steel corrosion has consequences in heat-transfer performance, particular for the long-term or in abnormal situations, such as a buildup of oxides and high level of solid oxide particles. HLM-cooled nuclear reactors usually have open-lattice configurations to reduce pumping power needs and enhance passive safety. Flow circulation methods, transients, flow stability, and elimination of undesired instability are all important issues to be investigated.

It is necessary to develop and validate more suitable turbulent model(s) for computational thermal hydraulics, especially for complex geometries and critical components, such as the core.

The results of the experiments shall be used, in turn, to improve the related physical models, and to evaluate and benchmark the CFD codes.

5 Compatibility of Structural Materials with Lead

The use of lead or lead alloy as the coolant in advanced fast reactors implies high-temperature operation and requires structural steels qualified for use in these reactors. Known structural materials like the ferritic–martensitic T91 and the austenitic stainless steel 316L have been a first choice, but they can undergo severe dissolution attack.

Corrosion is, however, but one phenomenon among those relevant to the contact with the liquid metal to be investigated for the qualification of a structural material. Other important phenomena are material failure under static loading, such as brittle fracture, and failure under time-dependent loading, such as fatigue and creep.

5.1 Structural Materials Corrosion in Lead

Molten lead or lead alloy is corrosive toward structural materials. The main parameters impacting the corrosion rate of steels are the nature of the steel (material side), the temperature, the liquid metal velocity, and the dissolved oxygen concentration. A provision that can be adopted to reduce leaching out of steel-alloying elements (typically nickel, which is a component of the austenitic stainless steels and dissolves in the molten lead) is to maintain a controlled amount of oxygen dissolved in the melt. Dissolved oxygen forms a layer of metal oxide on the steel surfaces in contact with lead that protects the steel from dissolution and recovers the metal oxide layer in case of erosion by the flowing heavy metal (self-healing effect).

It has been demonstrated that, in the low-temperature range, e.g., below 450 °C, and with an adequate oxygen activity in the liquid metal, ferritic–martensitic, and austenitic steels build up an oxide layer, which behaves as a corrosion barrier.

However, in the higher-temperature range, i.e., above ~500 °C, corrosion protection through the oxide barrier seems to fail (Fazio et al. 2005). Indeed, a mixed corrosion mechanism has been observed, where both metal oxide formation and dissolution of the steel elements occur (➤ [Table 9](#)).

It has been demonstrated that, especially in the high-temperature range, the corrosion resistance of structural materials can be enhanced by FeAl alloy coating, a recent surface-coating technique developed for the purpose and shown effective for up to 600 °C.

Several exploratory experiments carried out in the past in LBE and pure lead on different type of steels did show that generally below 450 °C, and with an appropriate dissolved oxygen concentration in the liquid metal, both martensitic and austenitic steels build up an oxide layer (a barrier), which prevents leaching of alloy elements into the liquid metal and liquid metal penetration along grain boundaries. For temperatures above ~500 °C, the prevention of liquid metal–steel interaction through the oxide layer seems to fail due to the occurrence of a mixed corrosion mechanisms, where both oxidation as well as dissolution can occur. It has been demonstrated, however, that the corrosion resistance of the structural materials at temperatures above 500 °C can be enhanced by coating the steel surface with FeAl alloys. This is of paramount interest for the fuel cladding, for which coating shall be thin, in order not to significantly affect heat transfer, besides the properties of mechanical stability and adhesion to

■ **Table 9**

Protective action via controlled dissolved oxygen at increasing temperature

Effective corrosion protection	Transition zone		Additional protection needed
Compact stable oxide barrier on ferrite–martensite and austenite	Oxide formation on ferrite–martensite		Unstable metal oxide layer
	Mixed corrosion mechanism: oxidation/dissolution on austenite		Stable FeAl alloy coating
400 °C	500 °C	550 °C	600 °C

the substrate material requested to any protective oxide layers. Coating material is FeCrAlY. It contains aluminium, which forms alumina in situ. To increase the adhesion and improve the stability, such coatings can be melted or fused together with the surface of the substrate, for example, by using large-area pulsed electron beams as is done in the GESA process, developed by the Karlsruhe Institute of Technology (KIT) in Germany.

The long-term stability in flowing liquid metal of the oxide layer (for temperatures <500 °C) as well as the GESA FeAl alloy coating (for temperatures >500 °C) has not yet been proven, however.

Planned European tests (i.e., the DEMETRA program under IP-EUROTRANS) include therefore corrosion tests in flowing liquid metal (with representative parameters of the fuel cladding and in-vessel components) to estimate corrosion kinetics, and to assess the long-term stability of the protective layers. The experimental program will go along with modeling activities, which help to define the corrosion kinetics for the types of steels under investigation.

It is worthwhile to note that the limitation on the upper temperature of the thermal cycle is considered a temporary compromise solution that allows the reactor design to proceed until new high-temperature materials become available, which will allow greater exploitation of the favorable properties of heavy metal coolants; these longer-term developments are likely to hold the key of the commercial viability of advanced fast reactors to be deployed for hydrogen as well as electric-energy generation.

Thus, the present design approach for ELSY is to limit the mean core outlet temperature to less than 500 °C, and to protect the T91 steel, as the construction material of the unavoidably thermally high-loaded fuel cladding tubes, with Fe/Al alloy coating.

5.2 Effect of Lead on Properties of Structural Materials

The use of heavy liquid metals, and especially of lead-cooled or lead-alloy-cooled (primarily LBE) fast reactor (LFR) concepts of Generation IV requires an assessment of their compatibility with structural materials under the fast-neutron spectrum typical of fast reactors. Although western countries did acquire substantial experience with sodium-cooled fast reactors, the expertise on compatibility of stainless steels with sodium is not transferable to lead and lead alloys, owing to the significant differences in their physical and metallurgical properties. Thus,

the older literature dedicated to the mechanical properties of steels, from carbon steels to high Cr steels, in contact with lead and lead alloys is essentially of Russian origin.

Because the 316L austenitic stainless steel and the T91 martensitic steel have been preselected for the design of future European transmutation facilities (EFIT, XT-ADS) and eventually also for the lead-cooled ELSY, the effect of LBE or lead on the mechanical behavior of these steels is being extensively investigated in Europe and worldwide, and results are available, but they are not yet exhaustive. The effect of lead or LBE on the tensile properties of T91 is well documented, thanks to the European TECLA and MEGAPIE-TEST programs of FP5. It has been shown that under MEGAPIE-relevant conditions, (i.e., temperatures below 400 °C and very low dissolved oxygen concentration in the liquid metal, i.e., reducing conditions below the potential of iron oxide formation), not only no oxide barrier forms on the steel (i.e., direct contact between steel surface and liquid metal), but worsening of the mechanical performance of the steel also occurs, if surface cracks are present. Particularly, low cycle fatigue (LCF) tests performed on T91 samples with different pretreatments did show that strong LBE attack appreciably reduces the LCF resistance of the steel, with respect to pre-oxidized samples and to the as-received samples. These tests as well as slow strain rate and tensile tests provide evidence of the effect of the surface condition on the mechanical behavior of the T91 when in contact with LBE. The latest results of LCF tests performed on the AISI 316L steel in air and LBE have shown a fatigue lifetime reduction in LBE for higher strain ranges.

Today, and in spite of a lack of quantitative results on fatigue and fracture, based on analysis of the data collected on the tensile and fatigue tests, the question of the susceptibility to LME (embrittlement) of T91 in contact with LBE can be addressed, particularly how to proceed from the metallurgical and chemical points of view to prevent LME. Thus, there are some data available on real systems about wetting, which is one of the two main conditions for occurrence of LME, in addition to abundant theoretical literature. The knowledge of the stress level responsible for plastic deformation, even at microscopic scale, as the second main condition for occurrence of LME, would allow eventually the definition of the criteria for preventing LME failure. Environment-assisted cracking (EAC) is a phenomenon closely related to LME, which permits an interpretation of the results of some tensile tests conducted on T91 or 316L steel in lead or LBE environments.

Information on the effect of lead or LBE on the creep properties of both T91 and 316L is scarce. There is almost no information on creep strength, creep damage, and creep crack growth rates in the currently available accessible literature.

Proposed explanations consider liquid-metal-accelerated creep (LMAC), whereby liquid metals can accelerate, at the same time, creep and the nucleation growth of vacancy voids near the metal surface in traction or compression.

Creep tests were performed in Russia in the context of the BREST-OD-300 reactor system, on a chromium steel 10Kh9NSMFB (containing 1.2% Si) in flowing liquid lead under 70–100 MPa between 420 °C and 550 °C, showing an earlier transition into the third stage of creep and a decrease of the duration of the steady creep stage, explained as a consequence of the lead corrosiveness. More detailed information about the test conditions and composition and structure of the steel–lead interface would be of interest at all stages of the test. This would imply access to the Russian literature on structural materials in contact with liquid metals for nuclear applications.

Information on fracture mechanics, from fracture toughness to crack growth behavior in contact with LBE, does not exist. There is a large body of literature devoted to the fracture of structural materials, hardened and often embrittled under irradiation, covering a wide range

of experimental test conditions. This is, indeed, information of primary importance, which, for example, did allow for an estimate of the service life of the MEGAPIE target window. There is no such information available for structural materials in contact with lead. It is sometimes stated that the ductile to brittle transition temperature, which may increase by approximately 100° after irradiation, should be only little increased by contact with HLMS. If proven, this fact would be of paramount importance and hence it must be verified experimentally.

In summary, dedicated test plans will have to be set up in order to provide data, particularly in the higher-temperature range, on tensile, creep, creep-fatigue and fracture mechanics, and fatigue crack growth of steels in contact with the selected HLM, including testing of irradiated specimens. Results of similar experiments carried out in the frame of different technologies, such nuclear fusion, shall not be disregarded as they can be conveniently used as a guide for the HLM-dedicated experiments. Austenitic stainless steels ($T \leq 500^\circ\text{C}$) and ferritic-martensitic steels ($T \leq 600^\circ\text{C}$) are likely to remain the main candidate materials for the future power reactors in spite of uncertainties in the areas of irradiation-induced embrittlement at low temperatures and radiation damage from high He/dap ratio. Prospective candidate materials are the ODS martensitic steels (temperature window can be increased to 650°C), and in the longer term the ferritic ODS steels, ceramic composites, and refractory alloys for the higher temperatures.

6 Core

The LFR core design approach is here presented and discussed. An integrated neutronic-thermal-hydraulic approach is envisaged in order to address the whole process toward the most effective solution to what concerns the design goals, according to the related technological constraints.

Starting from the peculiarities of lead- or LBE-cooled systems, the overall design approach will be presented and actualized according to general typologies of reactors: critical, subcritical (i.e., ADS), and “adiabatic.” The latter typology stands for critical reactors able to operate while maintaining unaltered the inventory of “valuable” isotopes (e.g., all TransUranics, TRUs) along the cycle (in an “extended” nuclear equilibrium state), thus not exchanging with the environment (hence the term adiabatic) any bulk materials except either natural or depleted uranium as an input stream, and fission products (FPs) as output. This solution, implementing the fuel-cycle closure within the reactor itself, represents the most charming candidate for giving body to the sustainable nuclear development aimed by the Generation IV initiative.

6.1 Introductory Remarks for LFR Core Design

Besides the main changes in the neutronic performance of the system, due to the hard spectrum set up by lead (see [◆ Sect. 3](#)), several other peculiar aspects must be accounted for in approaching the core design of an LFR.

These peculiarities, mainly related to the thermal-hydraulic properties of the coolant and the specific technological constraints introduced by the choice of lead, have to be added to the list of criteria and specimens commonly considered in the standard design route of FRs, for a proper core conceptualization of such systems.

6.1.1 Preliminary Evaluation of Lead and LBE Impact on Core Design

The low (here “low” is intended with respect to sodium in SFRs) coolant flow velocity in LFRs (because of structures erosion, see ▶ Sect. 6.1.2) imposes the need of large coolant channels to ensure the proper cooling of the system, immediately leading to low power densities in the core due to the high coolant volumetric fraction in the elementary cell (as mentioned in ▶ Sect. 1.1). Despite the fact that low pressure drops can be attained in the core, a first drawback impacts the overall dimensions of the core, which – on the other hand – has to comply with the need to reduce the system volume because of seismic risk. A second drawback is related to the specular reduction of the fuel volumetric fraction in the cell, which results in the need of increasing the cell reactivity (either by increasing the number of pins – modifying as a consequence also the system power – or the fuel enrichment – hence affecting the breeding capabilities). It must be noticed that the absolute magnitude of the latter effect is limited by the low-absorption cross sections of lead (see ▶ Sect. 3.1).

6.1.2 Technological Constraints for LFR Design

The first constraint following the choice of lead as coolant is related to the high melting point (327 °C) of the latter (123.5 °C in case of LBE), resulting in a lower limit on coolant inlet temperature T_{inlet} . According to this, and considering the need to mitigate the embrittlement of ferritic–martensitic steels (FMS, preferable to austenitic stainless steels, SS, for neutronics since the lower Ni content; see ▶ Sect. 5.2) because of neutron irradiation, a typical value for the minimum allowed temperature is set to 400 °C for lead (350 °C in case of LBE).

On the other hand, the high corrosion of FMS in the lead environment (see ▶ Sect. 5.1) imposes an upper limit on coolant outlet temperature T_{outlet} and/or on the ratio between the maximum linear power q' and the fuel-pin diameter d (determining the thermal head between the clad and the coolant to evacuate the fission power from the fuel pin). Recalling ▶ Sect. 5.1, the maximum wall temperature for the clad, T_{clad} , must be kept within 500 °C to prevent corrosion unless superficial coatings are foreseen: the preliminary evaluations on several aluminization techniques seem to confirm good resistances to corrosion up to 600 °C under active oxygen control.

Structural integrity must be preserved also against erosion phenomena: an upper limit of 2 m/s on the coolant flow velocity v through the channel must be therefore taken into account. As for corrosion, surface coatings may allow for maximum coolant velocities up to 3 m/s.

Finally, the hard spectrum of LFRs imposes stringent constraints to what concerns the structural damage (the number of displacements per atoms, DpA, indeed depends mainly on the hard tail of the neutrons spectrum). According to this, the in-pile residence time for fuel assemblies (FAs) made of FMS must be set to keep the fast-neutron ($E > 0.1$ MeV) fluence below 4×10^{23} n/cm²: hence the corresponding limit on maximum irradiation in an LFR might force a reduction in the planned fuel burn-up performance.

6.2 Conceptual Design Approach

The core design aims at determining the main parameters that univocally define a reactor configuration providing the required neutronic features and complying with all the (mainly)

thermal-hydraulic constraints (among these, the ones specific to lead are listed in [Sect. 6.1.2](#)). Since there is a strong interdependence among the core parameters, it is therefore a complex task to balance the pros and cons considering any consistent combination of these parameters.

If one defines a “reactors space” as a hyper-space, where the axes represent the independent core parameters, core design can be visualized as the research for an optimal operating point in this multi-parameter diagram: the technological limits introduce boundaries narrowing the viability domain, the parameter interdependence laws define hyper-surfaces representing the relationships between degrees of freedom and constraints, and the goal features provide the criteria to orient the choice for the most suitable operating point in the design domain.

6.2.1 Critical Reactors

In order to define the viability domain in the reactor space, each single constraint must be translated into an equivalent inequality defining the actual range for the corresponding parameter. In particular, the ranges for the coolant inlet temperature and the clad wall temperature are fixed according to

$$T_{inlet} = \max \{ T_{melt}, T_{embrittlement} \} + \Delta T_{margin} \quad (11)$$

$$T_{clad} = T_{corrosion} - \Delta T_{margin}. \quad (12)$$

The coolant flow velocity must be analogously limited according to

$$v \leq v_{erosion}. \quad (13)$$

Besides the specific constraints of LFRs, the maximum fuel temperature must be accounted for to prevent (with a sufficient margin) the possibility of fuel melting. According to this, the maximum fuel temperature can be translated into an equivalent upper limit on the maximum linear power, q'_{max} , expressed by the conductivity integral relation:

$$q'_{max} \leq 4\pi \int_{T_{f-g}}^{T_0} k_f(T) dT, \quad (14)$$

where $T_0 = T_{f,melt} - \Delta T_{margin}$ is the maximum allowable temperature for the fuel (at the center of the pellet), T_{f-g} is the temperature at the pellet surface (i.e., at the fuel–gap interface) and $k_f(T)$ is the thermal conductivity of the fuel.

Once the viability domain in the reactor space has been determined, the starting point for the neutronic design of a core is represented by the thermal-hydraulic design of the fuel pin and the coolant channel: as a matter of fact, both the pin radius r and lattice pitch p depend only on the thermal-hydraulic consistency of the system. Since the system must be dimensioned to prevent out-of-range working everywhere in the core, the most peaked fuel pin is assumed as reference for the design.

The core inlet and outlet average temperatures of the coolant can be identified according to the technological constraints introduced in [Sect. 6.1.2](#), so that the maximum outlet temperature in the hottest channel can be inferred in turn by introducing the expected estimate for the radial distribution factor f_{rad} . (The “radial distribution factor” can be defined as the ratio

between the power released from the hottest pin to the average pin power in the core. It should be noticed that uneven outlet temperature distributions are usually mitigated (by gaging the inlet orifice of wrapped FAs and/or by segmenting the core into zones with differently enriched fuels or different fuel volumetric fractions to flatten the power distribution) not to damage the thermal efficiency of the system.)

A preliminary evaluation of the active height h_{fuel} can then be introduced together with the gas plenum height h_{plenum} and, according to the latter, the clad thickness s_c determined to stand the pressure of gaseous FPs corresponding to the aimed BU.

By introducing an attempt value for the axial maximum-to-average factor f_{ax} (guessed or borrowed from previous calculations or analogous systems), an estimate of the power distribution along the pin can be inferred by assuming

$$q'_{max}(z) = q'_{max} \int_0^{h_{fuel}} \cos\left(\frac{\pi}{L}\left(z - \frac{h_{fuel}}{2}\right)\right) dz. \quad (15)$$


The parameter L in (15) must be computed so that the length of the arc over which the cosine is defined provides the assumed axial distribution factor, that is

$$\int_{-\beta}^{\beta} \cos(\alpha) d\alpha = \frac{1}{f_{ax}} \rightarrow \frac{\sin(\beta)}{\beta} = \frac{1}{f_{ax}} \Rightarrow L = \frac{\pi h}{2\beta}.$$

The coolant temperature profile along the hottest channel, $T_l(z)$, can then be retrieved as

$$T_l(z) = T_{inlet} + (T_{outlet} - T_{inlet}) f_{rad} \frac{\int_0^z q'_{max}(z') dz'}{\int_0^{h_{fuel}} q'_{max}(z') dz'}. \quad (16)$$

At last, the gap thickness, s_g , can be preliminarily dimensioned to host the fuel swelling related to the aimed BU, not to incur pellet-clad mechanical interaction (PCMI).

In order to guarantee the respect of the clad wall and fuel centerline temperature limits, the dimensioning of the fuel pin (or, equivalently, of the fuel pellet since all remaining radial dimensions have been already fixed), together with the evaluation of the maximum admissible linear power, can then be carried out by taking into account the thermal fluxes through the pin. As a matter of fact, the thermal resistance of the fuel, the gap, and the clad act in series in determining the succession of temperature gains providing the necessary thermal heads to evacuate the local fission power from the fuel to the coolant, in the typical temperature profile of  Fig. 13.

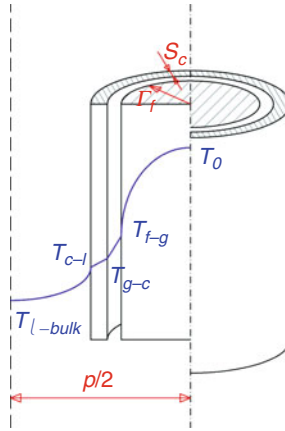
All these gains depend on the geometry and the materials of the pin only, as expressed by

$$T_0(z) - T_{f-g}(z) = \frac{q'_{max}(z)}{4\pi \langle k_f \rangle} \quad (17)$$

$$T_{f-g}(z) - T_{g-c}(z) = \frac{q'_{max}(z)}{2\pi k_g} \ln \frac{r_g}{r_f} \quad (18)$$

$$T_{g-c}(z) - T_{c-l}(z) = \frac{q'_{max}(z)}{2\pi k_c} \ln \frac{r_c}{r_g} \quad (19)$$

$$T_{c-l}(z) - T_l(z) = \frac{q'_{max}(z)}{2\pi h_l r_c}. \quad (20)$$



■ **Figure 13**
Radial temperatures profile in the elementary cell

In the previous system, single subscripts refer to materials (f for fuel, g for the gas filling the gap, c for clad, and l for the coolant), while coupled subscripts refer to materials interfaces ($f-g$ for fuel–gap interface, $g-c$ for gap–clad interface, and $c-l$ for clad–coolant interface); k_i indicates the thermal conductivity of material i , and h_l indicates the heat-transfer coefficient of the coolant.

It is therefore possible to put together (17–20) in order to obtain a single expression for the dimensioning of the pin (which can be limited to r_f):

$$T_0(z) = T_l(z) + \frac{q'_{max}(z)}{2\pi} \left(\frac{1}{2\langle k_f \rangle} + \frac{1}{h_g r_f} + \frac{1}{k_c} \ln \frac{r_f + s_g + s_c}{r_f + s_g} + \frac{1}{h_l (r_f + s_g + s_c)} \right) \quad (21a)$$

The same relation holds for hollowed fuel pins too, with minor changes: said γ_f the ratio between the hollow and pellet radii, (21a) becomes

$$T_0(z) = T_l(z) + \frac{q'_{max}(z)}{2\pi} (1 - \gamma_f^2) \left(\frac{1}{2\langle k_f \rangle} \left(1 + \frac{\gamma_f^2 \ln \gamma_f^2}{1 - \gamma_f^2} \right) + \frac{1}{h_g r_f} + \frac{1}{k_c} \ln \frac{r_f + s_g + s_c}{r_f + s_g} + \frac{1}{h_l (r_f + s_g + s_c)} \right). \quad (21b)$$

The logical process for the fuel-pin dimensioning can be represented by the dependencies scheme of ► [Fig. 14](#).

Once the fuel radius (and the eventual hollow one) has been defined, the coolant channel must be dimensioned. The pitch of the pins lattice, p , is to be chosen according to the average coolant temperature gain along the average channel. The increase of the coolant temperature in the channel is derived from the enthalpy balance equation

$$\rho_l A v c_p \Delta T = \frac{q'_{max}}{f_{rad} f_{ax}} h_{fuel}, \quad (22)$$

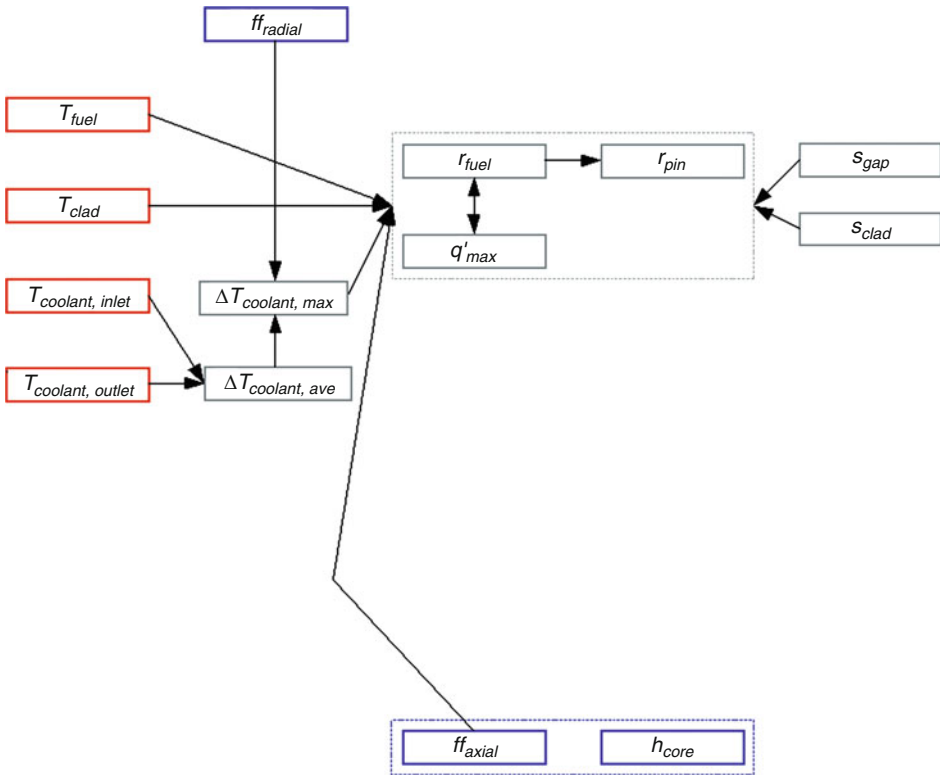


Figure 14
Scheme of core parameters dependences for fuel-pin diameter dimensioning

where ρ_l and c_p are the coolant average density in the channel and heat capacity, respectively (see Sect. 4.1) and A , the flow area of the channel, depends on the fuel-pin radius and lattice pitch according to

$$A = \begin{cases} \frac{p^2 \sqrt{3}}{2} - \pi r_c^2 & \text{hexagonal lattice} \\ p^2 - \pi r_c^2 & \text{square lattice} \end{cases} \quad (23)$$

The reference pitch value must be set by taking into account also the maximum allowed coolant velocity, (13), and the pressure drops through the channel.

The latter comes from the requirement of providing a sufficient natural circulation, in case of unprotected loss of flow (ULOF) accident, so as to guarantee nominal heat removal from the core within an acceptable temperature range ΔT_{ULOF} (ΔT_{ULOF} is the temperature gain along the channel, which is established in order to provide the required prevalence for natural circulation). According to core integrity, it is important that ΔT_{ULOF} settles so as to keep T_c below the critical clad failure temperature: as a matter of fact, the allowed temperature gain in accidental condition is higher than the normal one because the higher-temperature range is supposed to last for a limited time span (typically 30 min before human intervention), during which the clad must mechanically resist to the stresses due to the internal pressure of gaseous FPs for all surface

corrosion at the time of the accident.) According to this, the channel must be dimensioned so as to keep the pressure losses in.

The thermal head assessing in natural circulation can be easily determined as

$$\Delta p = \Delta \rho g h_{buoyancy} \cong 3\alpha \Delta T_{ULOF} \rho_{inlet} g h_{buoyancy}, \quad (24)$$

where g is the strength of the gravitational field, $h_{buoyancy}$ is the buoyancy height (i.e., the height of the primary circuit hot-leg, from core midplane to SGs midplane) and α is the linear thermal expansion coefficient of the coolant.

This forcing term must overtake the pressure drop through the whole primary circuit, expressed, separating the contribution within and outside the core, as

$$\Delta p = \Delta p_{core} + \Delta p_{system} = f \frac{h_{channel}}{D_h} \frac{\rho_l v^2}{2} + \Delta p_{system}, \quad (25)$$


where f is the effective friction term in the channel, D_h and $h_{channel}$ are, respectively, the hydraulic diameter and the length of the channel.

Putting together (24) and (25), and applying (22) to ULOF case, the following expression involving the geometry of the channel can be extracted

$$3\alpha \Delta T_{ULOF} \rho_{inlet} g h_{buoyancy} = f \frac{h_{channel}}{D_h \rho_{inlet} (2 - 3\alpha \Delta T_{ULOF})} \left(\frac{\langle q \rangle}{Ac_p \Delta T_{ULOF}} \right)^2 + \Delta p_{system} \quad (26)$$

for testing whether the temperature gain set up for coolant circulation is acceptable. In (26), the average power per fuel pin has been defined as

$$\langle q \rangle = \frac{q'_{max} h_{fuel}}{f_{rad} f_{ax}}.$$

The logical process of coolant channel dimensioning can be represented by the dependencies scheme of  Fig. 15.

Once the elementary cell has been determined, the axial and radial form factors are used to infer the average linear power in the core:

$$\langle q' \rangle = \frac{q'_{max}}{f_{rad} f_{ax}}. \quad (27)$$

This can be used in turn to calculate the total development of the fuel H needed to achieve the desired nominal power P_{th} :

$$H = \frac{P_{th}}{\langle q' \rangle}. \quad (28)$$

Combining the total development of the fuel H with the preliminary core height h_{fuel} to retrieve the number of fuel pins, n_{pins} , the radius of the core equivalent cylinder results

$$r_{core} = \sqrt{\frac{1}{\pi} n_{pins} A_{cell}} = \begin{cases} \sqrt{\frac{H}{\pi h_{fuel}} \frac{p^2 \sqrt{3}}{2}} & \text{hexagonal lattice} \\ \sqrt{\frac{H}{\pi h_{fuel}} p^2} & \text{square lattice} \end{cases}. \quad (29)$$

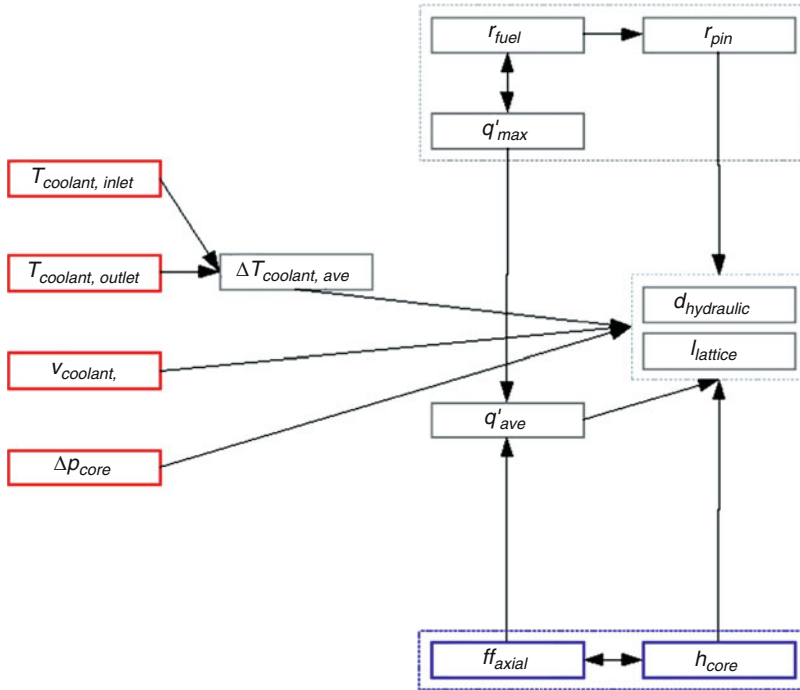


Figure 15
Scheme of core parameters dependences for coolant channel dimensioning

The aimed BU performances also allow to preliminary evaluate an in-pile residence time for the fuel. According to this, the core can be also segmented into batches for refueling, so to define the mean fuel aging at beginning of cycle (BoC) and end of cycle (EoC), averaging the in-pile residence time of the FAs belonging to different batches just before (EoC) and immediately after (BoC) the refueling. This approach leads to a one-batch approximation (which has been proven (Artioli et al. 2009) to be equivalent – in terms of criticality swing along the cycle – to the real n -batches refueling strategy) for the criticality analysis of the core.

The assessment of criticality can be performed taking into account that the overall shape of the system fixes the geometrical buckling of the reactor. Considering the system as a homogeneous volume V , the neutrons net balance, expressed as the ratio of the material buckling upon the geometrical one, can be translated into a balance between the net production in the reactor over the net leakage from the latter:

$$\frac{Prod}{Leak} = 1 \Rightarrow \frac{\int_V v \Sigma_f \phi dV - \int_V \Sigma_a \phi dV}{\int_V \nabla \cdot \vec{j} dV} = 1. \quad (30)$$

The volumes in the cells are fixed by the thermal-hydraulic analysis of the channel. The neutron spectrum is, therefore, also fixed by the volumetric fraction of the coolant, fuel, and structural materials in the cell. For criticality, neutronic calculations must be performed to assess the composition of the fuel (i.e., its enrichment), which is used as an almost free parameter to match the

required reactivity during the cycle and the power distribution flattening: as a matter of fact, the fuel must be enriched so to adjust the material buckling coherently with the geometrical one. The increase of the fuel enrichment both acts in increasing the fission term and in reducing the absorption one (i.e., the fissile is added to the detriment of the absorbing fertile).

It is clear that modifying the mutual abundances of fissile and fertile also changes the breeding capacity of the system, which could represent a design goal acting as feedback parameter in the design process; the same is valid for the eventual dispersion of MAs in the fuel. Furthermore, it is to be noticed that the enrichment also determines the flux level, according to the fixed power density in the fuel: the higher the enrichment, the lower the flux needed to achieve the same power density

$$q' \propto \phi \rho_{\text{fuel}} \sigma_f. \quad (31)$$

For instance, in designing experimental reactors, the flux level could represent a binding criterion: again, also the peak neutron flux can be used as a feedback parameter for core design.

As a matter of fact, the collection of resulting output performances due to the present core configuration should be used as feedback to adjust the core design in order to achieve completely all the aimed goals, in an iterative process.

The overall dependencies scheme for core design is shown in  Fig. 16.

Case study: ELSY

The technological constraints in ELSY design were fixed as follows:

- $\max\{T_0\} = 2,100^\circ\text{C}$ to prevent traditional MOX fuel melting
- $T_{\text{inlet}} = 400^\circ\text{C}$ for limiting structurals embrittlement

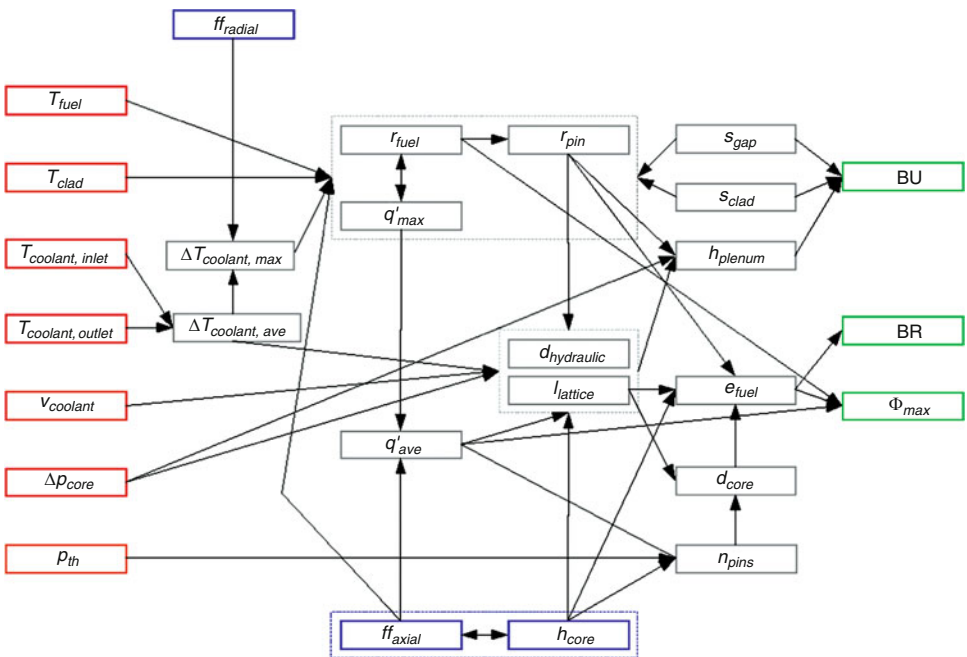


 Figure 16

General scheme of core parameters dependences

■ **Table 10**
First issue of ELSY core parameters

Parameter	Reference value
Fuel pellet (solid) radius	4.50 mm
Gap thickness	0.15 mm
Clad thickness	0.60 mm
Fuel pin radius	5.25 mm
Pins lattice pitch (square)	13.9 mm
Active height	90 cm
Coolant velocity	1.61 m/s
Maximum linear power	347 W/cm

- $\max\{T_c\} = 550^\circ\text{C}$ for limiting corrosion under active oxygen control
- $\max\{v\} = 2\text{ m/s}$ for limiting erosion

An acceptable value of the coolant outlet temperature was also set to 480°C .

Under such hypotheses, and assuming also that in case of unprotected transient due to ULOF the cladding is allowed to reach a maximum temperature of 700°C when assessing natural circulation, the iterative design process led to the assessment of the core parameters. The resulting parameters are listed in [► Table 10](#).

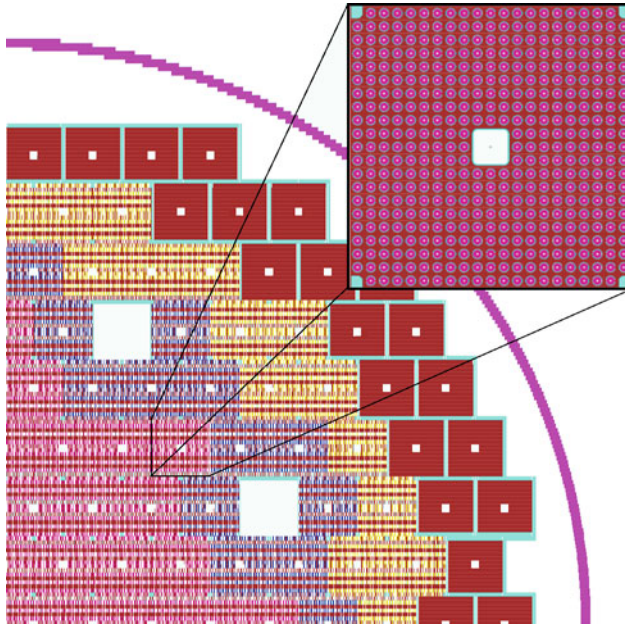
The overall core layout (Sarotto et al. 2008) resulted by arranging all the fuel pins needed to achieve the aimed thermal power (1,500 MWth) according to square 21×21 pins patterns. The resulting 162 FAs have been organized to reproduce the pseudo-cylindrical core shown in [► Fig. 17](#).

The enrichments needed to ensure both criticality and power/FA distribution flattening (with a 1.2 limit for maximum-to-average power/FA ratio) for the reference core led also a unitary breeding ratio (BR), which permits a moderate criticality swing during the cycle, limiting therefore the anti-reactivity required to compensate it. On the other hand, the smear density of the fuel within the clad (0.89) allows a maximum fuel BU of 60 GWd/tHM, which is below the aimed value (100 GWd/tHM).

Considering the BU goal priority with respect to the BR one, the smear density had to be reduced to 0.84 in order to obtain the aimed BU. The adopted solution was to hollow the fuel pellet (2 mm hole diameter) without altering any other core parameter.

The removal of part of the fuel resulted in an increase of the enrichments to maintain the criticality. In first approximation (i.e., neglecting the reactivity gain due to the fewer captures by the lower U amount), it could be thought to create the hole in the pellet by selectively removing the U only, leaving unaltered the Pu amount by increasing its content (i.e., enrichment) in the remaining fuel. Within the clad, the total fuel volume is thus reduced by a factor

$$\frac{V'_f}{V_f} = \frac{\pi(r_f^2 - r_h^2)}{\pi r_f^2} = \frac{4.5^2 - 1.0^2}{4.5^2} = 0.95, \quad (32)$$



■ Figure 17

Preliminary ELSY core scheme (1/4) surrounded by dummy elements within the barrel and FA layout

which in turn can be ascribed to an equivalent loss of U only, according to

$$\frac{V'_U}{V_U} = 1 - \frac{1 - \frac{V'_f}{V_f}}{VF_U} = 1 - \frac{0.05}{0.83} = 0.94. \quad (33)$$

The achievement of the target BU implies thus a degradation of the BR according to the same relative reduction of U amount: as expected, the BR for the new system was found to be 0.94 (Sarotto et al. 2009).

Case study: ENHS

In the ENHS design scheme all the main dependences among the core parameters have been referred to the core pitch-to-diameter (p/d) ratio, inheriting the same approach of thermal reactors design. The desirable BR is therefore achieved by adjusting the core p/d ratio; moreover, the larger is the p/d ratio, the smaller become the coolant friction losses through the core and the larger becomes the power that can be removed from the core by natural circulation.

The technological constraints in ENHS design were fixed as

- $\max\{T_0\} = 900^\circ\text{C}$ to prevent metallic fuel melting
- $T_{inlet} = 400^\circ\text{C}$ for limiting structurals embrittlement
- $\max\{T_c\} = 600^\circ\text{C}$ for limiting corrosion

An acceptable value of the coolant outlet temperature was also set to 550°C .

The natural circulation goal can be achieved, smoothing the constraints to the core design, by tuning the height of the riser in order to adjust the thermal head to the actual pressure drops.

■ **Table 11**
First issue of the ENHS core parameters

Parameter	Reference value
Fuel pellet (solid) radius	5.630 mm
Gap thickness	0.870 mm
Clad thickness	1.300 mm
Fuel pin radius	7.800 mm
Pins lattice pitch (hexagonal)	21.216 mm
Active height	125 cm
Riser height	13 m
Coolant velocity	0.44 m/s
Maximum linear power	179 W/cm

The core design process led to the following core parameters (► [Table 11](#)) (Hong and Greenspan 2005).

The overall core layout resulted by arranging all the fuel pins needed to achieve the aimed thermal power (125 MWth) according to a uniform, core-wise hexagonal lattice. No FA has been introduced in the model, because of the modularity of the core: fuel pins are therefore directly connected to the lower diagrid to reproduce the aimed pseudo-cylindrical core configuration. ► [Figure 18](#) shows the ENHS battery module layout where both the core and the coolant riser are represented as resulting from the core design.

The enrichments needed to ensure the criticality for the reference core led to an insufficient BR (0.97) with respect to the aim of $\Delta k_{\text{eff}} \sim 0$. In order to increase the BR, the p/d parameter had to be adjusted to permit a reduction of the Pu amount, thus a higher U amount and, in turn, a higher BR.

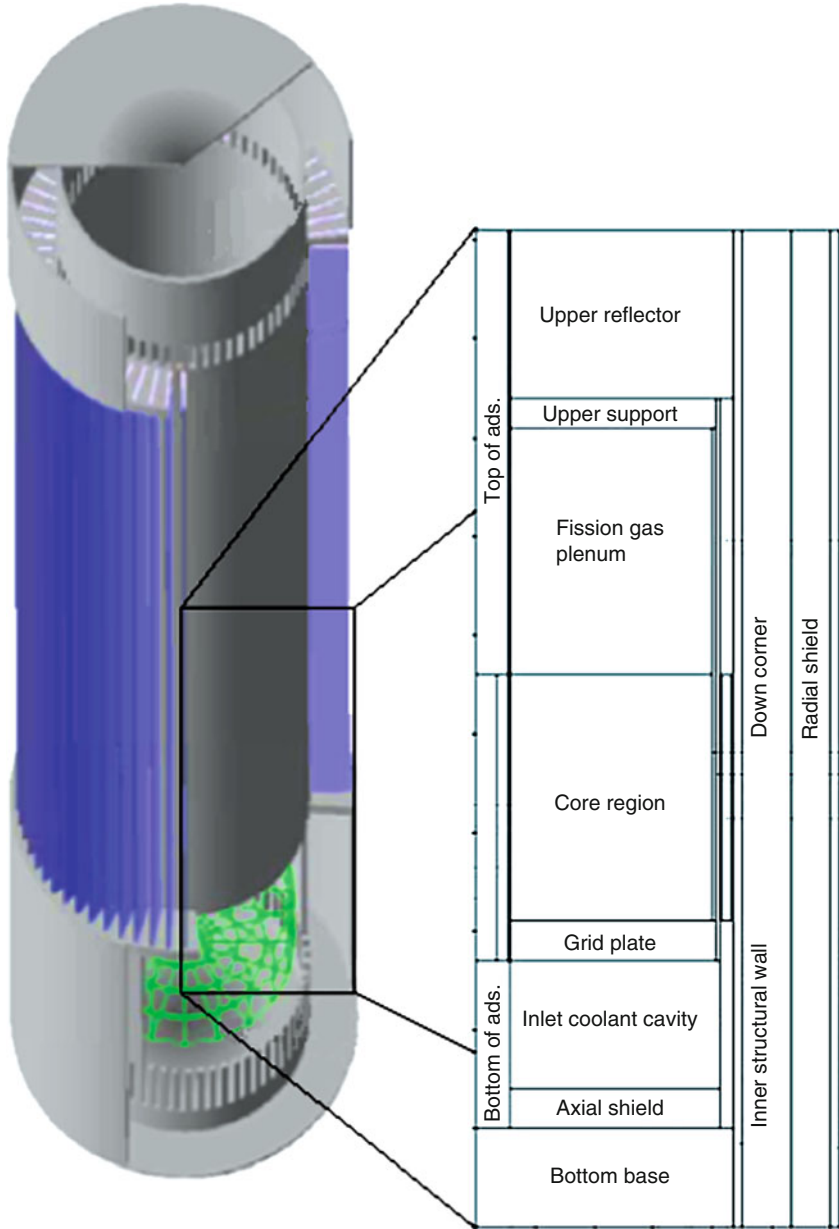
The reduction of the fissile inventory can be obtained by increasing the intrinsic reactivity of the system, i.e., by a reduction of the capture losses in the coolant.

The aimed BR (1.02) was then obtained by moving to a lower p/d ratio (reducing the pitch): the optimal p/d ratio resulted then 1.34 (Greenspan et al. 2008).

The smaller flow area in the fuel cell (thus the higher pressure drops through the core) set the coolant velocity to a lower value, necessary to increase the driving ΔT (clad wall – coolant bulk) and thus the prevalence due to the thermal head. Nevertheless, the small reduction of the pitch required to adjust the BR (from 21.216 to 20.904 mm) allows a clad temperature still below the safety limits.

6.2.2 Subcritical Reactors

The recent interest in ADS systems has been driven by the possibility of setting up power reactors able to burn considerable quantities of MAs by eliminating the safety-related drawbacks due to the inclusion of MAs in the fuel: as a matter of fact, relying on a large margin to criticality

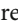


■ Figure 18
ENHS battery module layout and simplified sketch of its central region

allows to neglect the reduction of the delayed neutrons fraction of such systems, leaving room to increase the MAs content – from a neutronic point of view – at will.

The design of an ADS core must therefore take into account the two aims at optimizing the MAs-burning capabilities and producing energy: about these two main points the logics of the core design must be exploited to highlight the rationales for answering three basilar questions:

1. What exactly is meant by burn MAs “at best”?
2. How the burning capability can be optimized?
3. What about the two main goals whether they were contradictory?

A first consideration can be brought taking into account that the fuel of an ADS will be composed of a “driver” material, containing Pu, which is the main responsible for the criticality of the system, and the “target” MAs. The mutual abundances of Pu and MAs in the fuel set both fission and transmutation reaction rates: according to  Fig. 19, the higher the MAs content, the higher the reaction rates of MAs to Pu transmutation (overcoming the opposite Pu to MA transmutations).

Another important remark must be made to what concerns the normalization of the reaction rates in the system: according to the fission Q-value, for every terawatt hour (TWh) of energy produced, some 42 kg of fuel is actually fissioned, the contributions of Pu and MAs being split according to their mutual abundances. On the other hand, a different MA disappearance rate can be observed, representing the further net contribution of MAs to Pu transmutation: hence MA removal rates higher than 42 kg/TWh must be interpreted as 42 kg MAs actually fissioned, and the remaining transmuted into new Pu (the system would therefore act as a Pu breeder); vice versa, MAs removal rates lower than 42 kg/TWh imply that the complement is represented by Pu fissions, reducing the inventory of the latter (the system would also act as a Pu burner).

It is worth noticing that the rate of Pu production/removal directly impacts also the criticality swing along the cycle: according to this, and taking into account the accumulation of

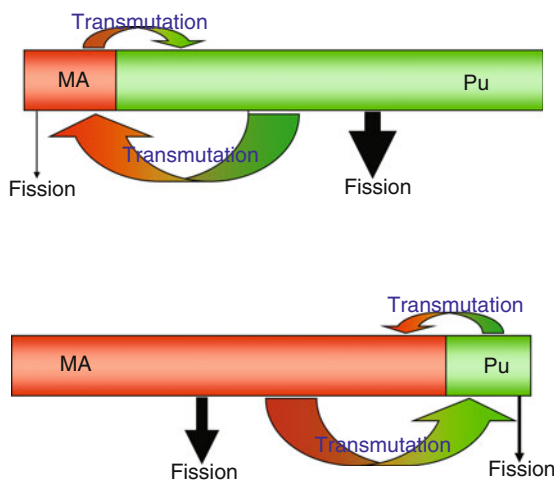
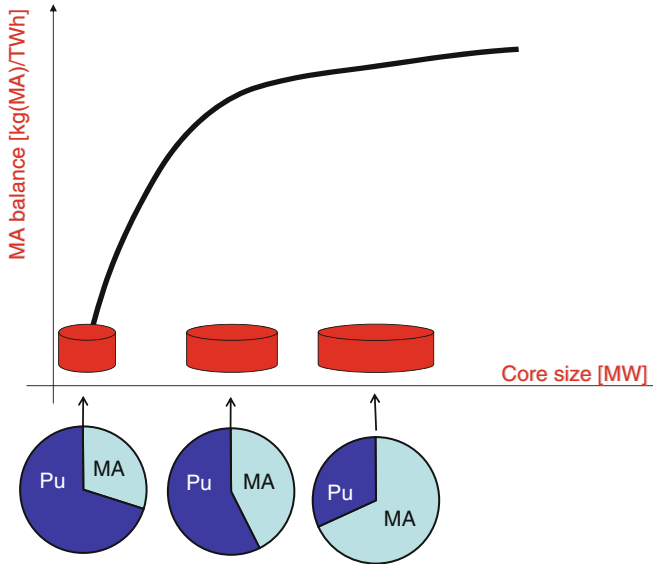


 Figure 19

Fission and transmutation rates as a function of Pu and MA mutual abundances in the fuel



■ Figure 20

Fuel enrichment as a function of core size

poisoning FPs during operation, the goal of zeroing the criticality swing points at a Pu/MAs assortment in the fuel different from the one needed to obtain an equilibrium Pu content.

The last preliminary consideration takes into account that the Pu content in the fuel is set according to the required reactivity inventory for the system: assuming that the pin lattice is almost fixed because of thermal-hydraulic design (as for critical reactors, see previous subsection), the power size of the reactor can be translated into its geometrical size. According to this, the more pins are arranged in the core, the lower is the Pu content in the fuel to provide the aimed reactivity, as shown in [Fig. 20](#).

[Fig. 20](#) also highlights a direct relationship between the core power and the MAs burning performances: bigger cores allow the arrangement of a higher relative amount of MAs in the fuel, and thus provide higher MAs removal rates.

According to these introductory remarks, the previous three main questions can be answered, providing the final design strategy for an ADS core:

- Unless precise policies for producing new Pu are envisaged, the burning of MAs at best means that no “expensive” neutrons must be used to either burn or breed Pu, thus devoting all the net fission losses to MAs (-42 kg/TWh of MAs and 0 kg/TWh Pu balances, according to the so called “42-0” approach).
- Since looking for an MAs burning performance better than -42 kg/TWh is meaningless, the optimization leads to the research of the minimum cost of the TWh or, considering the velocity of burning 42 kg/h/TWh, the minimum cost of the deployed power (which is the same optimization required for the energy production).

Exploiting these general remarks, the design approach for an ADS core immediately follows, as depicted in [Fig. 21](#).

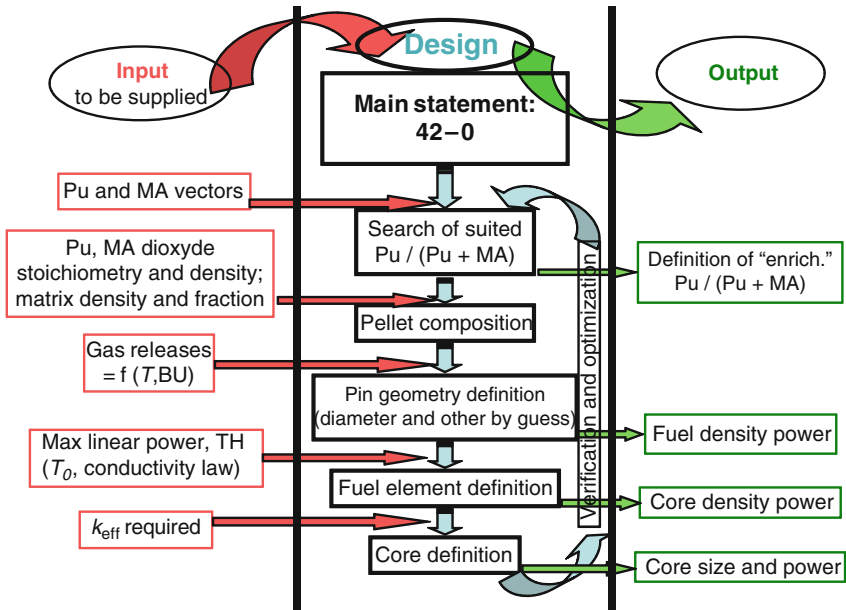


Figure 21
ADS core design scheme

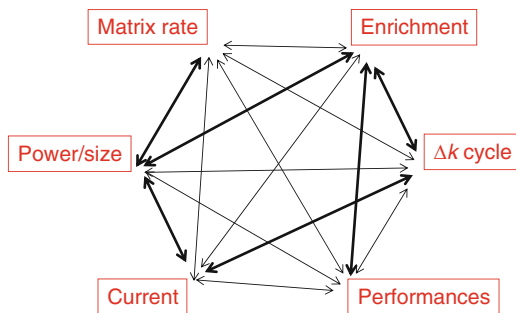


Figure 22
Mutual interdependences between main core parameters

The mutual influence between the main core parameters (roughly shown in Fig. 22, where the arrows thickness represent the strength of the corresponding interdependences) can be better visualized into a properly compiled worksheet (“A-BAQUS” (Artioli 2007)), organized according to the general logic scheme of Fig. 21.

The A-BAQUS worksheet is organized per quadrants, with multiple axes representing the main core parameters. In the first quadrant, the two axes represent the relative Pu content in the fuel (thus the fuel enrichment e) and the percentage of inert matrix in the pellet, as shown in Fig. 23.

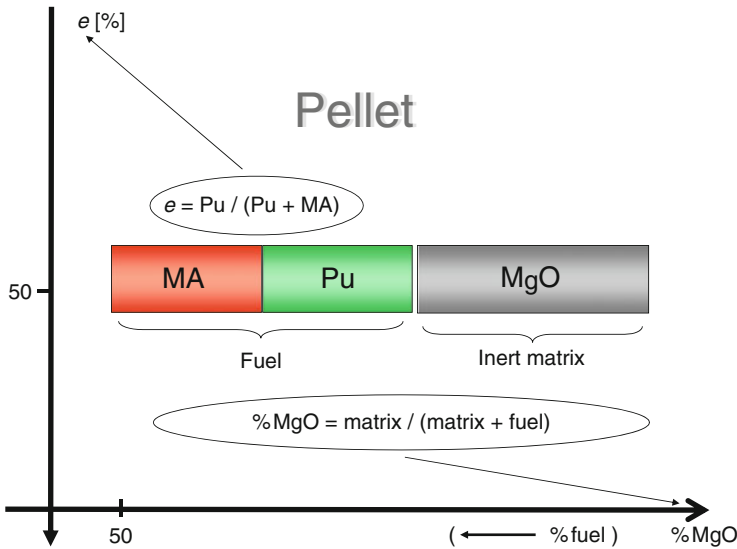


Figure 23
First quadrant of the A-BAQUS worksheet

In the same quadrant it is possible to add two more axes, relating the fuel enrichment to the MAs transmutation capabilities (● Fig. 24) and the criticality swing along the cycle (● Fig. 25) as described in the previous lines.

The fourth quadrant of the A-BAQUS worksheet (● Fig. 26) relates the fuel fraction in the pellet to the core thermal power. It is to be noticed indeed that, once the fuel pin and coolant designs are fixed, the higher the inert matrix fraction (thus the lower the fuel fraction), the more pins are needed to reestablish criticality (fuel enrichment being equal) increasing the core size and, in turn, increasing the core power.

The last (third) quadrant of the A-BAQUS worksheet relates the core power to the proton current to be provided by the accelerator module. It is known indeed that to maintain a constant power level during operation, a neutron source (by spallation from an in-core target) has to be provided, proportional to the aimed flux level in the system (thus to the core power P) and to the average number of neutrons per fission ν , and inversely proportional to both the fission Q -value and the average number of neutrons emitted by spallation per incident proton S . In order to relate the neutron source to the proton current, also the effective multiplication of the system, M_{eff} , and the specific multiplication of the neutron source, M_s , are to be accounted for. The overall law to determine the proton current i can be therefore expressed as

$$i = \frac{P\nu}{SQ} \frac{1 - k_{\text{eff}}}{\phi^* k_{\text{eff}}}, \quad (34)$$

where ϕ^* is the ratio between the source multiplication and the effective multiplication of the system:

$$\phi^* = \frac{M_s}{M_{\text{eff}}} = \frac{\frac{k_s}{1 - k_s}}{\frac{k_{\text{eff}}}{1 - k_{\text{eff}}}}.$$

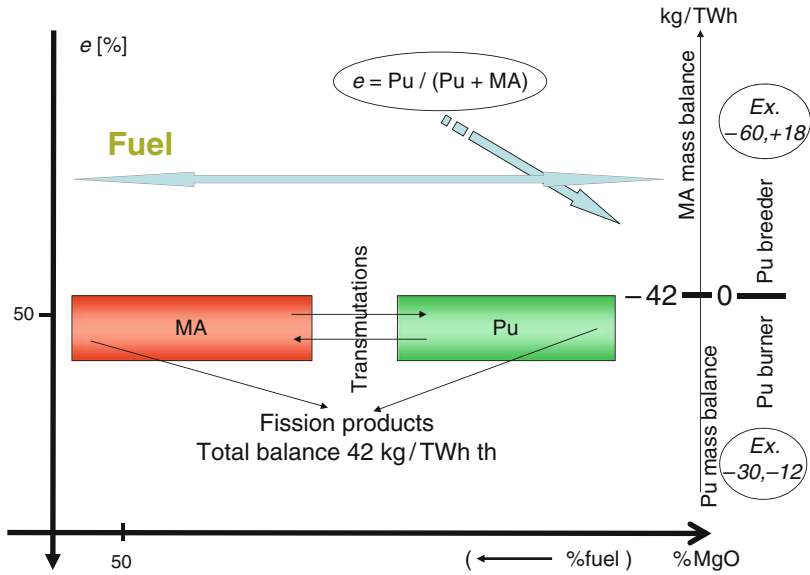


Figure 24 Additional MA transmutation performances axis in the first quadrant of the A-BAQUS worksheet

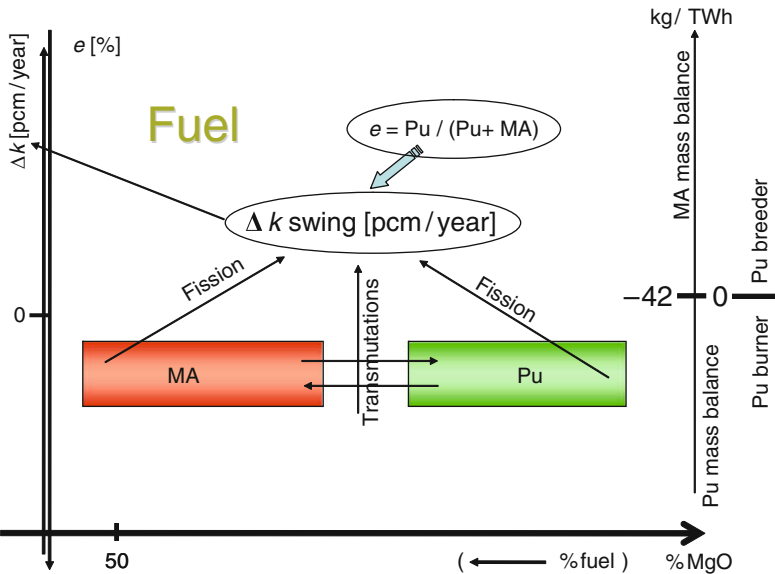
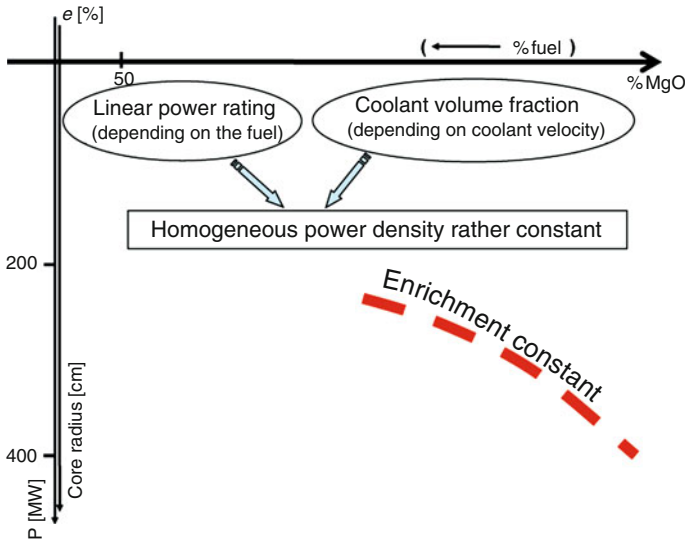


Figure 25 Additional criticality swing axis in the first quadrant of the A-BAQUS worksheet



■ **Figure 26**
Fourth quadrant of the A-BAQUS worksheet

Finally, since the criticality of the system may evolve during operation, the accelerator is required to provide a proton current range to keep the power constant along the cycle, as shown in [Fig. 27](#).

Case Study: EFIT

In order to design the EFIT ADS system, the A-BAQUS worksheet has been used to conceive the optimal configuration according to the aimed goal. Among the possible core optimizations (Δk swing = 0, high MAs transmutation rate, etc.), the 42-0 approach has been chosen as the leading criterion because of the general goal of “burning MAs at best” highlighted for the whole project (the zero-net Pu balance was also found consistent with the choice of a U-free fuel) (Artioli et al. 2008).

The technological constraints pointed out for the EFIT system are as follows:

- 50% minimum matrix volumetric fraction (VF) to ensure the thermal conductivity of a CERCER (Pu,MA) O_{2-x} -MgO (thus U-free) fuel within the pellet
- $\max \{T_0\} = 1,650 \text{ }^\circ\text{C}$ for preventing inert matrix melting/disintegration (corresponding to a $q'_{max} < 180 - 200 \text{ W/cm}$, depending on the matrix VF)
- $\max \{T_c\} = 550 \text{ }^\circ\text{C}$ for limiting corrosion
- $\max \{v\} < 1 \text{ m/s}$ for limiting erosion effects

An acceptable value of the coolant outlet temperature was also set to $480 \text{ }^\circ\text{C}$.

Starting from the design of an elementary cell respecting all the technological constraints listed above, a set of preliminary calculations have been carried out to provide the information necessary to draw the respective curves on the A-BAQUS worksheet for different core optimization strategies, as shown in [Fig. 28](#).

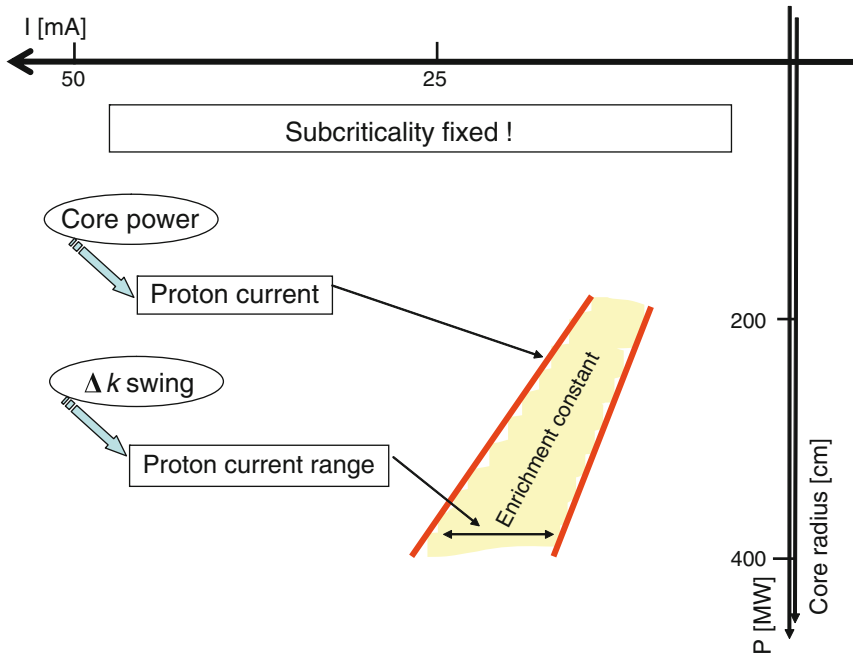


Figure 27
Third quadrant of the A-BAQUS worksheet

The core design process (Sarotto et al. 2008), targeting also a maximization of the power density to keep the core dimensions (because of seismic risk) and a power/FA distribution flattening for improving the thermal yield of the plant (aiming at a costs minimization for the produced terawatt hour), then led to the core parameters listed in Table 12.

Since the fuel enrichment must be constant to guarantee the aimed MAs transmutation performances, the core flattening task has been pursued by segmenting the core into three zones with different fuel volumetric fractions. In order to simplify the construction of different pins, in the inner zone the matrix volumetric fraction has been increased (with respect to the values in the intermediate and outer fuel), while the outer zone relies on enlarged pins (as far as possible), as sketched out in Fig. 29.

A general view of the final EFIT core, according to the 42-0 approach, is shown in Fig. 30.

6.2.3 Adiabatic Reactors

Aiming at designing adiabatic reactors, to ensure the sustainability of nuclear energy through the closure of the fuel cycle within the reactor itself, it is fundamental to clearly point out the parameters univocally defining the goal, borrowing the same approach implemented in the EFIT design (see Sect. 6.2.2).

In order to design an adiabatic reactor, as a first step the equilibrium isotopic composition of the fuel must be fixed (Artioli et al. 2010). This constraint in turn determines the intrinsic

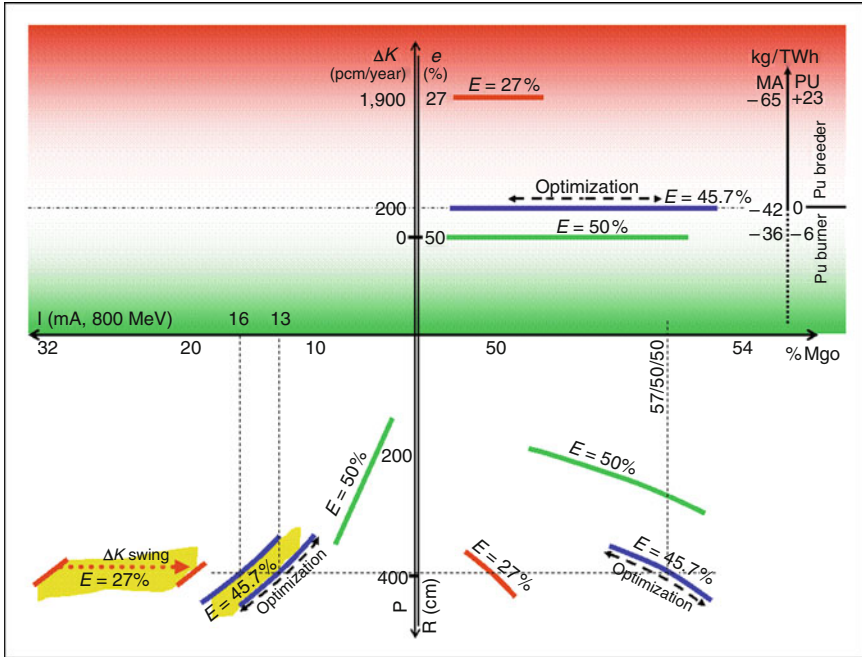


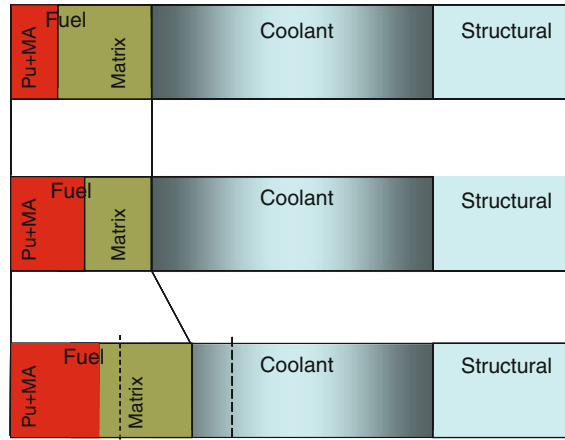
Figure 28

The A-BAQUS worksheet showing some curves correlating the core parameters under different optimization strategies

Table 12

EFIT main core parameters

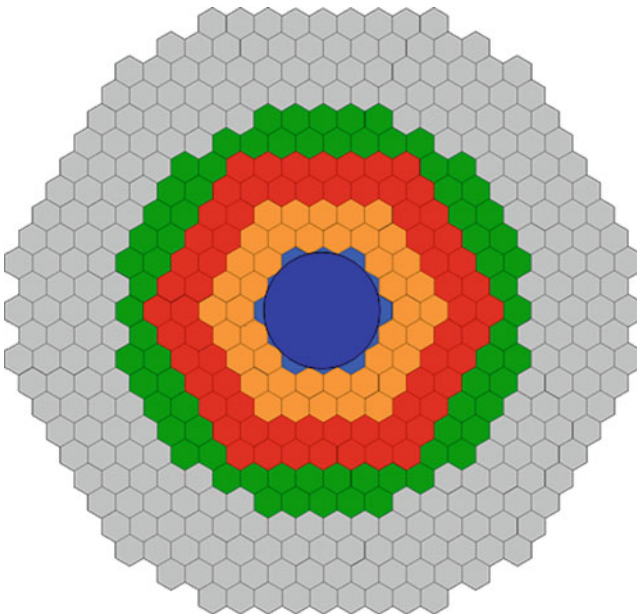
Parameter	Reference value
Fuel pellet (solid) radius	3.55/3.55/4.00 mm
Matrix volumetric fraction	57/50/50%
Gap thickness	0.16 mm
Clad thickness	0.60 mm
Fuel pin radius	4.31/4.31/4.76 mm
Pins lattice pitch (hexagonal)	13.63/13.63/13.54 mm
Active height	90 cm
Coolant velocity	1.00 m/s
k_{eff} (BoC)	0.97400
Δk swing (BoC – EoC)	500 pcm
Thermal power	400 MW
Proton current at BoC	13.2 mA



*Pin "size" to obtain the same max PD
but T_{out} should be unacceptable*

■ Figure 29

Pellet (fuel and matrix), coolant, and structural volumetric fractions in the different EFIT elementary cells

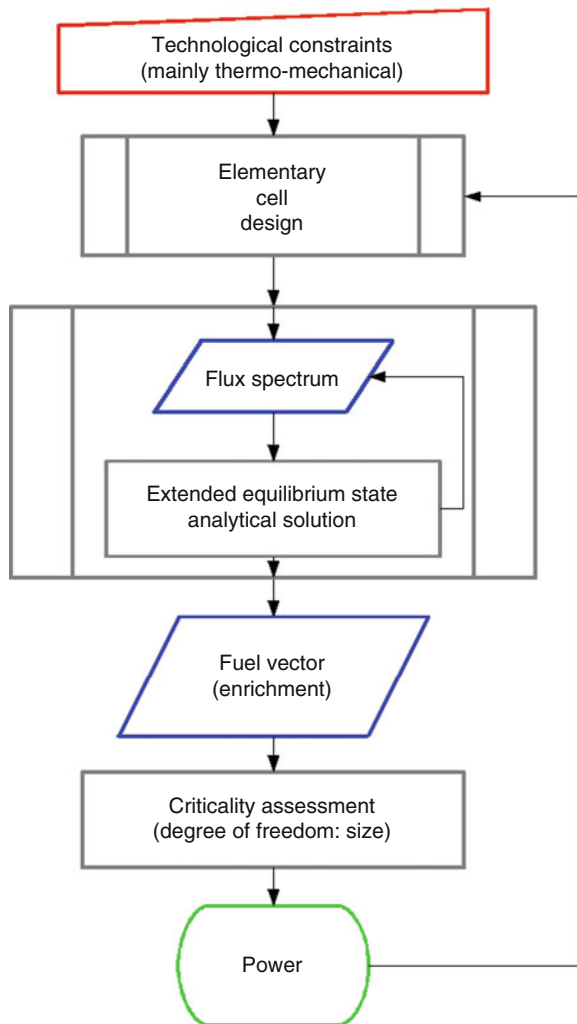


■ Figure 30

Final EFIT core scheme: different gray tones in the three innermost regions refer to inner, intermediate, and outer FAs position, arranged around the cylindrical spallation target and surrounded by four rings of dummy elements

reactivity of the fuel: hence, the core designer is not able to design nuclear reactors to achieve an aimed power by setting the core size, and consequently adjusting criticality by tuning the fissile content in the fuel (➤ Sect. 6.2.1); he must rather set up a critical arrangement for the given fuel.

According then to the thermal-hydraulic feasibility of the resulting core, and exploiting its viability, the system power will be univocally determined. This acts as – *si parva licet* – a “Copernican” revolution in the way of conceiving reactors, reversing the mental approach of subordinating the core design to its power: the whole design will be based on the fuel enrichment, fixed for the adiabaticity of the system; it will be possible then to tune the power by



■ Figure 31

Logical flowchart for adiabatic reactors design according to the new paradigm

iteratively adjusting the elementary fuel cell and the corresponding fuel vector acting on the fuel volume fraction. A logical scheme for the design of an adiabatic core, according to this new paradigm, is shown in [Fig. 31](#).

The starting point for the whole process is the definition of the equilibrium vector. In order to retrieve the volume fractions of the materials in the elementary fuel cell (which determine the neutrons spectrum), a preliminary dimensioning of the fuel pin and coolant channel, i.e., both the pin radius and lattice pitch, is needed. As described in the previous section ([Sect. 6.2.1](#)), it is possible indeed to determine those parameters a priori, by investigating the thermal-hydraulic consistency of the system according to the technological constraints represented by the allowable maximum temperatures for the coolant, the clad, and the fuel as well as the maximum allowable coolant velocity and pressure drops through the core.

Once the fuel vector has been determined, whether its reactivity (i.e., the k_{∞} of the elementary cell) is enough higher than 1, the number of pins to be arranged in the core to get the criticality of the system is univocally determined, balancing the material buckling with the geometrical one. The number of pins in turn defines the corresponding core power. According to this reverted scheme, the dependency among the core parameters can be represented by the scheme of [Fig. 32](#).

Hence, in an adiabatic core the dimensioning of the elementary cell unequivocally determines a core power. The matching between the aimed power and the criticality of the system can be set by acting on the fuel volume fraction, thus redefining from scratches the elementary cell in an iterative process (since the latter affects the neutron spectrum).

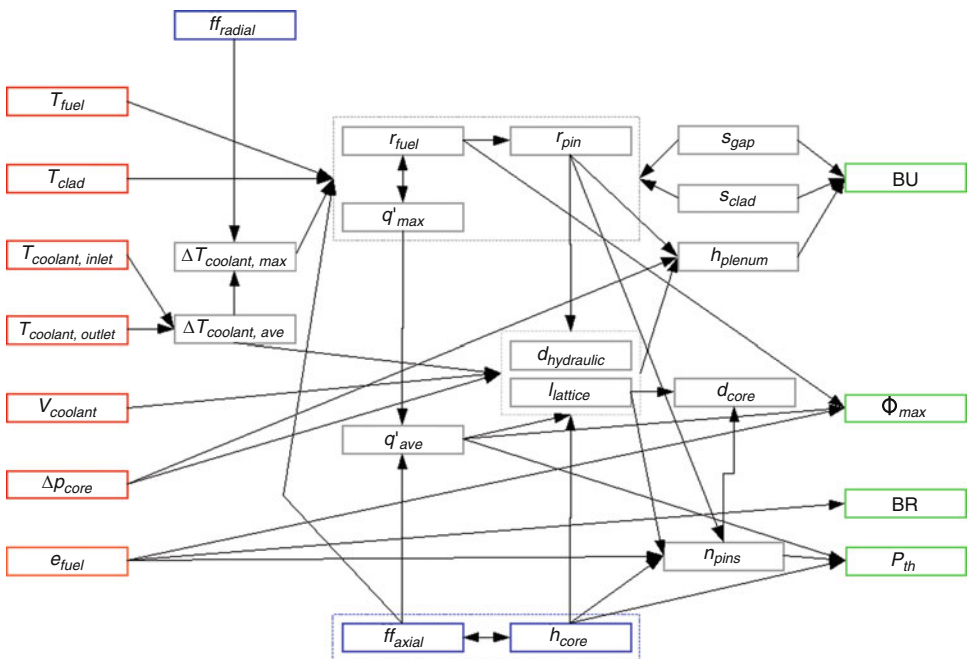


Figure 32

General scheme of adiabatic core parameters dependences in the new paradigm

6.3 Design Diagnostics and Post-Process Feedbacks

As described in the previous section, according to the technological constraints, the core design is carried out by exploiting the mutual relationships among the core properties in order to outline the most exhaustive working point with respect to the aimed performances. In general:

- At first, the design constraints are translated into a set of viability ranges for the directly implied parameters.
- Hence, axial and radial form factors are guessed (or inferred by previous analyses), corresponding to an initial hypothesis on the reactor shape.
- The remaining equations are then put together and solved, taking also into account the design goals, providing the complete set of core parameters.

After the final core configuration has been assessed, a finalization phase follows, performing detailed calculations in order to retrieve actual estimates of the core performances. Besides a careful analysis to check the consistency of both system criticality and core temperatures to the design assumptions, further information must be retrieved, to be used as feedback information for the whole design process as well as to infer the core management strategies and anti-reactivity requirements.

6.3.1 Overall BU Performances

The first feedback information comes from a detailed neutronics calculation accounting for the actual FAs refueling and reshuffling in the exact n -batches strategy to check the consistency of the one-batch approximation preliminary assumed for core design (see [Sect. 6.2.1](#)).

According to this more detailed evaluation of fuel BU performances, both the actual criticality swing and power distribution evolution in the core (as a matter of fact, a segmentation of the core into zones with different fissile content – the most common solution to achieve power/FA distribution flattening – implies differently enriched FAs breed unevenly, altering the total power contributions redistribution) during the cycle can be checked.

This detailed analysis allows the determination of whether fuel swelling due to gaseous FPs does not overcome the designed in-clad void space, originating excessive PCMI, as well as determining that the limit for the maximum DpA on cladding is not exceeded.

According to these results, the allowed in-pile residence time and fuel management strategy can be fixed.

6.3.2 Sizing and Placement of Control Systems

A last analysis must be performed to check whether the supposed control, compensation, and regulation systems are actually able to provide the required anti-reactivity for safe shutdown and cold arrest, as well as the anti-reactivity for criticality swing compensation and regulation during the cycle.

The results of this detailed analysis also provide useful information in order to resize or reposition the regulation/compensation and shutdown systems (taking also into account the required redundancy and differentiation) if needed.

6.4 Reactivity Coefficients

The evaluation of the reactivity coefficients for the system is the last-step in core design. A complete list of parameters such as the following must be computed:

- The coolant void reactivity worth
- The Doppler coefficient
- Dimension coefficients and
- Density coefficients

These parameters are computed to provide the required information for kinetic and dynamic analyses of the system: the viability of a core configuration is assessed indeed after a complete safety analysis concerning both operative and incidental transients.

The required reactivity coefficients are evaluated simulating perturbed configurations, where each parameter is singularly changed, and evaluating the criticality change for the system.

6.4.1 Lead Void Reactivity

The evaluation of the lead void reactivity coefficient is performed assuming all the coolant in the active zone is removed. Unlike SFRs, the lead boiling scenario can be assumed as unreal (the boiling temperature for lead being 1,749 °C, far from common reactor coolant operating temperatures, versus 883 °C boiling temperature for sodium): according to this, the complete voiding computation hypothesis is kept for coherence with sodium-cooled reactors rather than for realistic accidental scenarios, even assuming large coolant losses (as for LOCA, mitigated by the pool-type plant design) or strong injections of steam in the core following a massive SGTR.

Nevertheless, the evaluation of the reactivity insertion due to the complete voiding of the cooling channels leads, for present LFR designs, to the typical values reported in [Table 13](#).

It is worth noticing that different computation hypotheses are taken into account, referring to more realistic loss of coolant conditions. For instance, interesting results are obtained assuming that the core together with the upper and/or the radial reflectors is voided. Under such hypothesis, due to the high reflective power of lead, the coolant void coefficient is greatly reduced, even up to a sign change, as shown in [Table 14](#) for ELSY (Sarotto et al. 2009).

It is worth noticing that although negative void reactivity coefficient is not necessary for the safety of lead or LBE-cooled fast reactors, in any case it is possible to reconceive the core design to feature such a feedback. The main approaches for turning the positive void coefficient negative rely:

Table 13
Typical void reactivity coefficient of present LFR designs

System	Reactivity coefficient (pcm)
ELSY	+4,000
ENHS	+2,700
EFIT	+6,400
MYRRHA	-2,300

■ **Table 14**

Void reactivity coefficient of ELSY according to different voiding scenarios

Scenario	Reactivity coefficient (pcm)
Active zone	+4,042
Active zone and upper reflector	-1,232
Active zone, upper and radial reflectors	-5,251

- On an enhancement of the neutrons leakage probability, for instance by:
 - Reducing the fuel length
 - Incorporating neutron absorbers in the core boundary
 - Using a gas lift pump – that is, introducing gas bubbles throughout the coolant in the core and fission gas plenum regions
 - Incorporating neutron streaming channels in and adjacent to the core
- On the introduction into the core of materials having enhanced absorption cross section at high energy
- On the introduction into the core of materials that will keep the neutrons spectrum softer in case of coolant voiding

6.4.2 Doppler Effect

The Doppler effect, acting as a self-shielding reduction because of absorption resonances broadening, is a main issue in reactor dynamics. Its effect on reactivity, behaving almost logarithmically as a function of the fuel temperature, is usually expressed by evaluating the Doppler coefficient α , defined as

$$\frac{dk}{dT_f} = \frac{\alpha}{T_f}.$$

The Doppler coefficient is usually inferred by two criticality calculations on systems identical but for the fuel temperature. For ELSY (MOX fuel), a typical value of the Doppler coefficient results -700 pcm (Sarotto et al. 2009).

6.4.3 Dimension and Density Reactivity Coefficients

The reactivity variations of a system due to either dimensional or density perturbations provide useful information for transient analysis. The main dimension and density reactivity coefficients are expressed as

$$\frac{\partial \delta k / k}{\partial \delta p / p}, \quad (35)$$

where p represents the perturbed parameter and δp the corresponding elementary perturbation.

A typical set of elementary perturbations, singly introduced to modify the reference system, lists:

- A radial extension of the core by scaling all radial dimensions, with nominal densities
- An axial extension of the core by scaling all axial dimensions, with nominal densities (thus introducing some “slab” portion of core)
- A relative extraction of the control rods from their operative position
- A reduction of the coolant density in the active zone
- A reduction of the coolant density in the whole system
- A reduction of the fuel density
- A reduction of the steel density
- A reduction of the absorbers density

Some other coefficient may be added to the list above to complete the set of information regarding the core neutronics, such as:

- An increase of the Pu enrichments in the core
- A reduction of the U density in the fuel (maintaining the Pu density unchanged)
- A reduction of the Pu density in the fuel (maintaining the U density unchanged)

Once the set of elementary perturbations has been pointed out, some relative variations have to be assumed for each parameter in order to define the perturbed configuration to be simulated. A typical computational scheme (showing the values assumed for each elementary perturbation and the corresponding effect on criticality for ELSY (Sarotto et al. 2009)) is resumed in [Table 15](#).

By combining the computed criticality change to the relative perturbation of the corresponding parameter, the aimed dimension and density reactivity coefficients can be finally retrieved.

Table 15

ELSY computational scheme for dimension and density reactivity coefficients evaluation and corresponding reactivity effect

Perturbation	Variation	Δk_{eff} (pcm)
Radial extension of the core	$R_{\text{core}} + 2.5\%$	+239
Axial extension of the core	$H_{\text{core}} + 5\%$	+842
Partial extraction of absorbers from the core	$L_{\text{ins}} - 1 \text{ cm}$	+36
Reduction of coolant density in the core	$\rho_{\text{cool}}^{\text{core}} - 5\%$	+161
Reduction of coolant density in the whole system	$\rho_{\text{cool}}^{\text{sys}} - 5\%$	-22
Reduction of fuel density	$\rho_{\text{fuel}} - 5\%$	-1,614
Reduction of steel density	$\rho_{\text{steel}} - 5\%$	+170
Reduction of absorbers density	$\rho_{\text{abs}} - 5\%$	+13
Increase of Pu enrichments	$E_{\text{Pu}} + 1 \text{ pt}$	+3,507
Increase of U density in the fuel	$\rho_{\text{U}} + 5\%$	-1,190
Increase of Pu density in the fuel	$\rho_{\text{Pu}} + 5\%$	+2,734

6.4.4 Feedback Reactivity Coefficients

The dimension and density reactivity coefficients introduced in the previous subsection provide the elementary information to compute the feedback reactivity coefficients used for actual system transient analysis. As a matter of fact, every transient the system undergoes is the result of a complex combination of a multitude of single effects: for instance, in case of positive transient of power (TOP), every material in the core increases its temperature so that, besides the most immediate Doppler and density effects, also geometrical effects must be accounted because of the dilation of the whole system.

Therefore, in order to provide a unique combined reactivity coefficient, all the involved effects, examined in the previous step, must be related to a common parameter driving all the elementary perturbations. The most suitable parameter, which can also be identified the cause of all perturbations, is temperature. The aimed feedback reactivity coefficient will be therefore expressed as

$$\frac{\partial \delta k/k}{\partial T} = \sum_i \frac{\partial \delta k/k}{\partial \delta p_i/p_i} \frac{\partial \delta p_i/p_i}{\partial T}, \quad (36)$$

where the sum is extended over all the elementary contributions participating to the effect under investigation.

In general, also the feedback reactivity coefficients are separated to provide a more flexible input capability to security analysis tools. The most common feedback reactivity coefficients are therefore related to the diagrid-driven radial dilation of the core, and to the axial dilation of the latter.

To what concerns the diagrid-driven dilation feedback reactivity coefficient, the following expression relating the single reactivity coefficients is adopted:

$$\begin{aligned} \left. \frac{\partial \delta k/k}{\partial T} \right|_{\text{diagrid}} = & \frac{\partial R_{\text{core}}}{R_{\text{core}}} \left\{ \frac{\partial \frac{\delta k}{k}}{\partial \frac{\delta R_{\text{core}}}{R_{\text{core}}}} + \frac{\partial \frac{\delta \rho}{\rho}}{\partial \frac{\delta R_{\text{core}}}{R_{\text{core}}}} \left[\frac{\partial \frac{\delta k}{k}}{\partial \frac{\delta \rho_{\text{fuel}}}{\rho_{\text{fuel}}}} + \right. \right. \\ & \left. \left. + \frac{\partial \frac{\delta k}{k}}{\partial \frac{\delta \rho_{\text{steel}}}{\rho_{\text{steel}}}} + \frac{\partial \frac{\delta k}{k}}{\partial \frac{\delta \rho_{\text{abs}}}{\rho_{\text{abs}}}} + \left(1 - \frac{\partial \frac{\delta \rho_{\text{cool}}}{\rho_{\text{cool}}}}{\partial \frac{\delta \rho}{\rho}} \right) \frac{\partial \frac{\delta k}{k}}{\partial \frac{\delta \rho_{\text{cool}}}{\rho_{\text{cool}}}} \right] \right\}. \quad (37) \end{aligned}$$

A similar expression holds also in the case of axial dilation of the system:

$$\begin{aligned} \left. \frac{\partial \delta k/k}{\partial T} \right|_{\text{axial}} = & \frac{\partial H_{\text{core}}}{H_{\text{core}}} \left\{ \frac{\partial \frac{\delta k}{k}}{\partial \frac{\delta H_{\text{core}}}{H_{\text{core}}}} + \frac{\partial \frac{\delta \rho}{\rho}}{\partial \frac{\delta H_{\text{core}}}{H_{\text{core}}}} \left[\frac{\partial \frac{\delta k}{k}}{\partial \frac{\delta \rho_{\text{fuel}}}{\rho_{\text{fuel}}}} + \frac{\partial \frac{\delta k}{k}}{\partial \frac{\delta \rho_{\text{steel}}}{\rho_{\text{steel}}}} \right] \right\} \\ & + \frac{\partial \frac{\delta k}{k}}{\partial l_{\text{CRs insertion}}} \frac{\partial l_{\text{CRs insertion}}}{\partial T}. \end{aligned}$$

7 Reactor System

All primary system configurations proposed so far for an LFR are of the pool type (Cinotti et al. 2008, 2009; Alemberti et al. 2009; Smith et al. 2009). This is the obvious result of the cost and technical difficulties associated with a loop-type configuration. In fact at present a good design practice is to limit the lead speed to 2 m/s to reduce both pressure loss and erosion of structural material and this would result in large-diameter heavy tubes for a loop-type reactor.

Several configurations have been proposed for the primary system ranging from the natural circulation (SSTAR) solution, the enhanced circulation solution using gas injection (XT-ADS) in the riser, and the solution of forced circulation (ELSY).

Natural circulation is convenient for simplification of small reactor (tens of megawatts electrical), whereas forced circulation is necessary for compactness of large reactors (hundreds of megawatts electrical). Mechanical pumps are generally proposed because of the low efficiency of electromagnetic pumps in lead.

Because of the low allowed lead speed, the primary flow path must be simple and as short as possible to reduce the mass of lead to guarantee a successful mechanical behavior under seismic loads for which a reduced vessel length is an additional need.

7.1 Reactor Vessel and Safety Vessel

It is a classical approach in case of a liquid-metal-cooled reactor to have a reactor vessel that contains the primary system surrounded by a safety vessel that collects potential leakage of coolant from the reactor vessel.

The reactor vessel is in general shaped as a cylinder with a hemispherical bottom and a flat roof. The lead level is kept below the roof to accommodate the thermal gradient between the vessel in contact with lead and the colder roof. The reactor vessel can be supported directly by the roof as in SSTAR or by a connection below the roof to a conical shell as in ELSY. The object of the ELSY solution is to separate the mechanical load due to the lead weight from the thermal gradient of the connection to the roof.

The roof is a thick plate with penetrations for the components and the above-core structures that are laded on it.

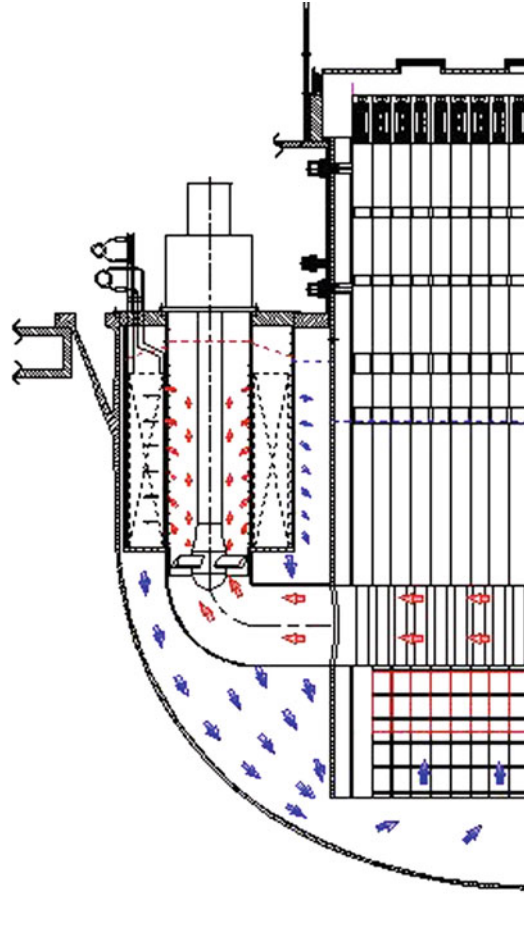
The safety vessel can be conceived as an additional steel vessel surrounding the reactor vessel or can be integrated in the reactor pit as a liner of the concrete walls. In the latter case the safety vessel is protected, reactor side, by an insulating layer and is kept cold by a reactor concrete cooling system (RCCS) consisting of water pipes located inside the reactor pit concrete.

RVACS pipes can be located outside the safety vessel in the first case and between the two vessels in the second case.

The volume above the lead free level is filled with inert gas.

7.2 Reactor Internal Structures

The cylindrical inner vessel configuration is the classical configuration adopted for LFRs in natural circulation because of its simplicity and reduced pressure loss. This configuration is characterized by a core, located centerline in the bottom part of the reactor vessel and its upper structures surrounded by a cylindrical structure that contains inside the hot lead of the riser and,



■ **Figure 33**
 Detail of the ELSY primary system arrangement and coolant flow path

with the reactor vessel, delimits an annular volume of cold lead where the main components are located, namely the SGs, the pumps, the purification units, and the dip coolers of the DHR systems (● *Fig. 33*). The differential weight of the lead inside the riser and the lead in the riser produce the driving head necessary for the natural circulation of lead of the primary system. SGs can be freely installed inside the cold collector, with the inconvenience of a thermal stratification in the cold collector and in the reactor vessel or hydraulically connected with more complicate reactors internals and additional difficulties for component replacement.

In case of forced circulation, the hydraulic connection between the SG and the riser is definitely necessary.

A particular innovative solution has been identified in ELSY to adopt an inner vessel of perfect cylindrical shape, while ducts are mechanically connected to the SGs to be fed. The cylindrical inner vessel, as usual, constitutes the lateral restraint of the core but, differently from

previous solutions, is not connected to the core support plate, which can be avoided, thanks to more advanced solutions. The core support plate constitutes in general a critical component submitted to fast-neutron flux, difficult to replace and with difficulty/impossibility of ISI and repair. A simple cylindrical inner vessel can be supported in the upper part by the roof with a releasable connection for its replacement in case of need.

A peculiar load to be considered for the seismic design of the internals of an LFR is the load associated to lead sloshing that can be only partially mitigated by the adoption of seismic isolators. In fact seismic isolators of the reactor building drastically reduce the acceleration of the reactor structures but also lower the frequencies and move them closer to the frequencies typical of the sloshing phenomena.

To be removable, the internals can be hung from and supported by the reactor roof, a metallic plate welded to the reactor vessel. The reactor roof with its sealed penetration for the components together with the reactor vessel constitute the primary containment.

7.3 Steam Generator

Several types of SG have been proposed for LFRs, the most common being the helical-tube SG for which a deep experience exists for SFR applications. An innovative SG has been introduced instead in the ELSY project looking at several advantages in terms of reactor cost, safety, reactor operability, and simplicity of the lead flow path.

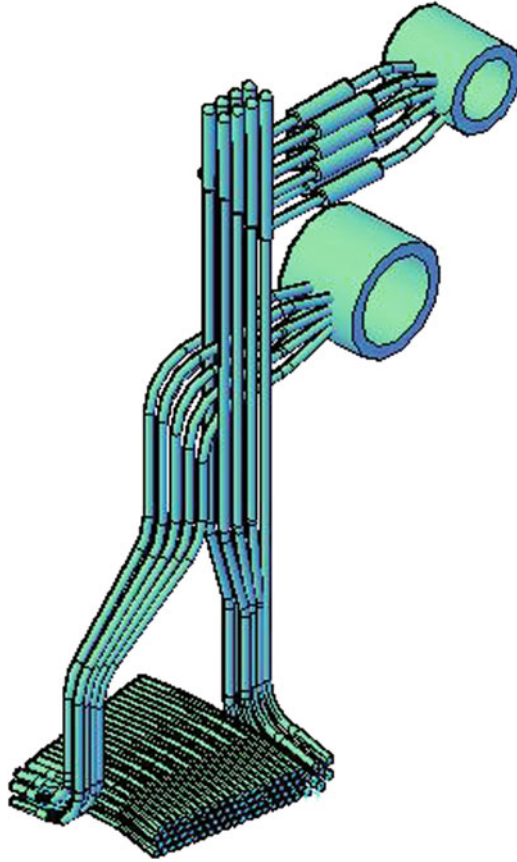
This innovative SG is composed of a stack of spiral-wound tube bundle (► Fig. 34) arranged in the bottom-closed, annular space formed by a vertical outer and an inner shells. The inlet and outlet ends of each tube are connected to the feedwater header and steam header, respectively, both arranged above the reactor roof.

The tube spirals, one spiral for each tube, two spirals per layer, are arranged one above the other and equally spaced.

The coolant flows radially through the perforated inner shell and, past the tube spirals, through the outer shell. This scheme is thermally almost equivalent to a pure countercurrent scheme because the feedwater in the tube circulates from the outer spiral to the inner spiral, while the primary coolant flows in the opposite direction from the inner to the outer shell of the SG. There is no window as primary coolant inlet port and consequently there is no constraint, typical of the classical design, to locate deep enough the bottom edge of the window to cope with the case of leaking reactor vessel, in fact the shell perforations extend below the accidental coolant free level and ensure adequate flow rate for core cooling. As a by-product, the SGU can be positioned at a higher level in the downcomer and the RV shortened, accordingly.

The suction pipe is an integral part of the SG bottom structure and extends outside the SG circular orthogonal projection to match the contour of the port cut out in the wall of the cylindrical inner vessel. The horizontal duct between the SG and the inner vessel normally constitutes a major obstacle for the replacement of the component to which is connected, namely, the SG or the inner vessel because of its interference with the smaller penetration through the reactor roof. Feeding the SG from the bottom offers the additional advantage of providing a procedure to extract the SG from the reactor vessel provided that the two geometrical condition of ► Fig. 35 are satisfied.

The first small displacement, radial, aims at disengaging the SG horizontal duct from the inner vessel taking profit of the clearance between the SG and its penetration through the reactor roof. The second displacement, vertical, brings the horizontal duct nearly in contact



■ Figure 34
Steam generator with a spiral-wound tube bundle

with the lower surface of the reactor roof. The third displacement, radial, brings the horizontal duct inside the orthogonal projection of the roof penetration. The fourth displacement, vertical, allows the complete extraction of the SG from the reactor vessel.

With removable SG's and PP's, also the cylindrical inner vessel can be designed as a removable unit, and eventually the design goal of all removable internals becomes feasible.

It should be noted that the reason in favor of the helical-tube SG, with respect to other conventional SG concepts, has always been that it copes better with high thermal loading, in spite of higher cost.

The rationale of the spiral-tube SG versus the helical-tube GV can be stated as follows:

- Tolerant to thermal loading as the helical-tube GV
- Predictable lower cost because the tube spirals are easier to assemble and require simpler supports
- Adequately fed also in case of coolant free level drop further to the reactor vessel leakage accident

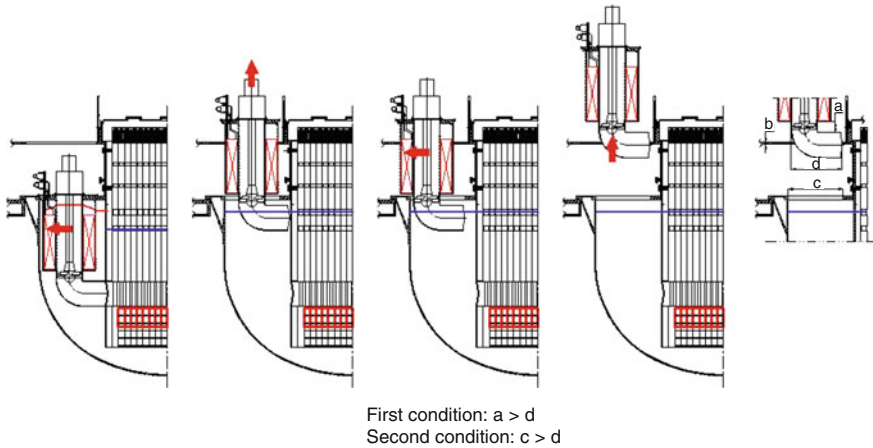


Figure 35
Geometrical conditions for the SG replacement with the connecting duct

- Less space required (tube bundle volume reduced of a factor 2 owing to the simpler-tube support system) and shell-side pressure loss reduced by about factor 2 (less tubes to flow through)

The installation of SGs inside the reactor vessel is a major challenge of an LFR design, which includes the need for a sensitive and reliable leak-detection system and a highly reliable depressurization and isolation system.

In ELSY careful attention has been given to the issue of mitigating the consequences of the SGTR accident to reduce the risk of pressurization of the primary boundary; to this end, innovative provisions have been conceived that make the primary system more tolerant of the SGTR event (see [▶ Sect. 2.3.1](#)).

7.4 Primary Coolant Circulation

Small-size reactors (e.g., SSTAR) can rely on lead natural draft, which can be of the order of 1,500 Pa for each meter of relative elevation between core and SG.

The use of airlift can deliver a draft of about 5,000 Pa for each meter of the riser length, and it can be a solution to shorten the reactor vessel of small-size reactors in comparison to the use of the natural circulation.

Forced circulation with mechanical or electromagnetic pumps is necessary to deliver a head of 1–2 bar necessary to reduce the size of large power reactors.

At present electromagnetic pumps has been disregarded by all LFR designers, presumably because of their low efficiency.

Mechanical pumps for LFRs are a suitable solution with high efficiency and great simplicity. A pump impeller placed a few meters deep in lead can guarantee the required net positive

section head (NPSH) and consequently a short shaft is sufficient to connect the pump impeller to the pump motor located on the reactor roof. No supporting bearing in lead is necessary. In case of ELSY for additional compactness, the shaft and the impeller of the pump are located in a free volume inside the spiral-tube SG.

8 Decay Heat Removal System

A LFR normally relies on the secondary system (the water-steam system, in the case of ELSY) to remove decay heat.

The water-steam system, however, is not a safety-grade system and additional, more-reliable safety-grade systems are necessary to meet the safety objectives.

A reliable system for DHR is the RVACS.

Unfortunately, the RVACS by itself can be used only in small-size reactors, the reactor vessel outer surface of which is relatively large to enable the transfer of the generated reactor decay power.

For a large power reactor it is necessary to install additional loops equipped with coolers immersed in the primary coolant, a DHR system hereinafter called the DRC (direct reactor cooling) system.

The DRC system is comprised of loops that operate with stored water (W-DHR).

The DRC loops, because of their greater complexity, will result in a lower reliability than the simple RVACS.

Stringent safety and reliability requirements of the DHR system will be achieved by redundancy and diversification. Diversification of the DHR system is provided with steam condensers on the steam loops.

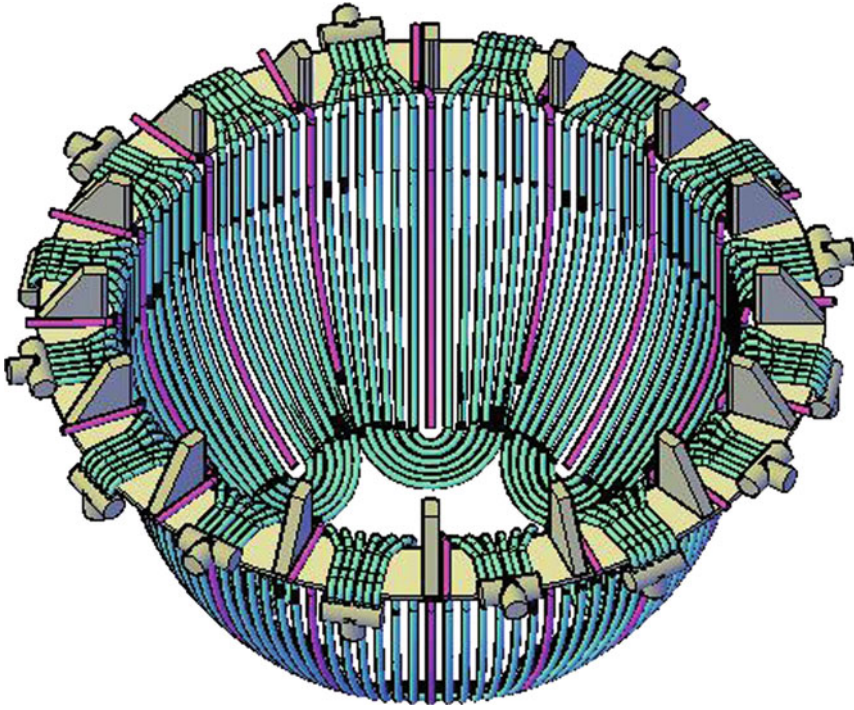
Additional cooling functions are also necessary to permanently cool the concrete of the reactor pit and to control the air temperature of the reactor pit itself during ISI of the reactor vessel.

8.1 Reactor Vessel Air Cooling System

Different RVACS configurations have been proposed for LFR based on SFR experience. The RVACS system developed for ELSY consists basically of an annular pipe bundle of U-pipes arranged between the reactor vessel and the safety vessel in a nest-type configuration with atmospheric air flowing pipe-side in natural or forced circulation (➤ *Fig. 36*). In spite of the improvements in this design relative to earlier concepts, even in ELSY, the performance is sufficient only in the long term (after about 1 month after shutdown) and additional loops are needed for short-term DHR.

8.2 Water Loops and Associated Dip Coolers

The fact that molten lead does not react violently with air or water gives the designer some freedom in the choice of the coolants to be used in the DHR loops, the use of air and water remaining the preferred approach.



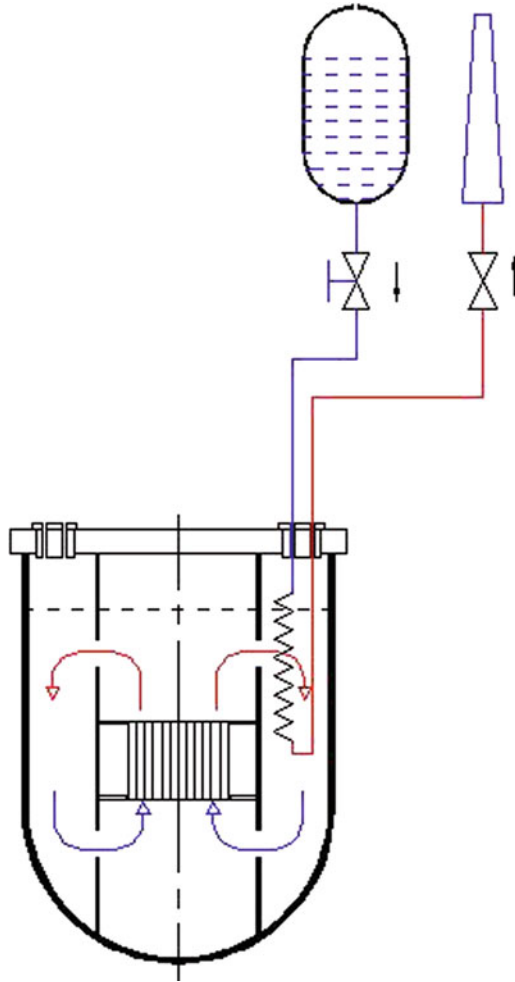
■ Figure 36
The nest configuration of the ELSY RVACS

A typical scheme of a DRC system for LFR based on water, the W-DHR loops, with coolers immersed in the primary system, is presented in ▶ Fig. 37.

Each W-DHR loop is made of a cooling water storage tank, a water–lead dip cooler, interconnecting piping, and steam vent piping to discharge steam to the atmosphere.

The dip cooler tube bundle is made of bayonet tubes (see ▶ Fig. 38). The bayonet consists of three concentric tubes, the outer two of which have the bottom end sealed. Water evaporation or air heating takes place in the annulus between inner and the intermediate tube. The annulus between the outer and intermediate tube is filled with He gas at a pressure higher than the lead pressure at the bottom end of the bundle. All annuli are interconnected to form a common He gas plenum, the pressure of which is continuously monitored. A leak from either wall of any of the outer tubes is promptly detected because of depressurization of the common gas plenum.

The proposed bayonet RC dip coolers are different with respect to classical bayonets, which consist each of only a pair of concentric tubes. The two outer tubes do not constitute a double walled tube, but are mechanically and, thermally decoupled. This configuration allows localizing the most part of the thermal gradient between lead and boiling water across the gas layer,



■ Figure 37

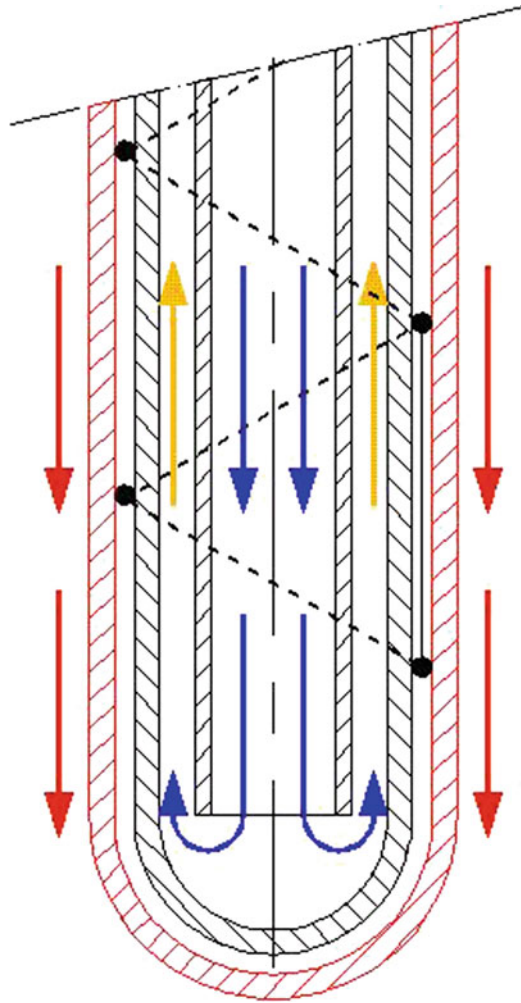
The DRC W-DHR process scheme

avoiding both risk of lead freezing and excessive thermal stresses across the tube walls during DHR steady state operation and transients.

The typical outer diameter of the outer tube is about 25 mm.

8.3 Steam Condensers on the Steam Loops

Steam condensers on the steam loops provide diversification of the DHR system. The steam condenser is immersed in a water pool and connected at the inlet to the main steamline and at the outlet to the feedwater line. When main and feed line are isolated and the isolation valve below the bottom header of the condenser is opened, the system is able to remove decay



■ Figure 38
Bayonet tubes of the DHR dip coolers

power using the SG tube bundle and by steam condensation returning the condensate to the feed line.

9 Nuclear Island

The following considerations on LFRs are based on the hypotheses of a central reprocessing and fuel fabrication plant physically separated from the reactor. This is applicable to both the small reactors (SSTAR type) and large reactors (ELSY type).

As regards to the spent fuel reprocessing and fabrication of fresh fuel, the situation of the LFR is similar to that of the SFR.

A significant difference between the two LFR systems is that SSTAR foresees the supply and replacement of the entire core, whereas ELSY foresees quite standard operational practices with periodic access to the core for fuel handling and partial replacement of the core.

It should be noted that the genesis for the SSTAR concept was the idea of developing a reactor that was, by design, low in proliferation risk and therefore deployable virtually anywhere in the world. The objectives resulting from this goal included factory fabrication (and fuelling) transportability of the reactor system to the site and installation without the requirement for handling fresh fuel or for developing a fuel supply infrastructure ultra-long core life to enable long-term operation without refueling and robustness and simplicity of design (e.g., reliance on natural convection flow for heat removal) to minimize operational complexity and maintenance requirements.

In the case of ELSY, considerable work has been carried out to define the overall plant layout.

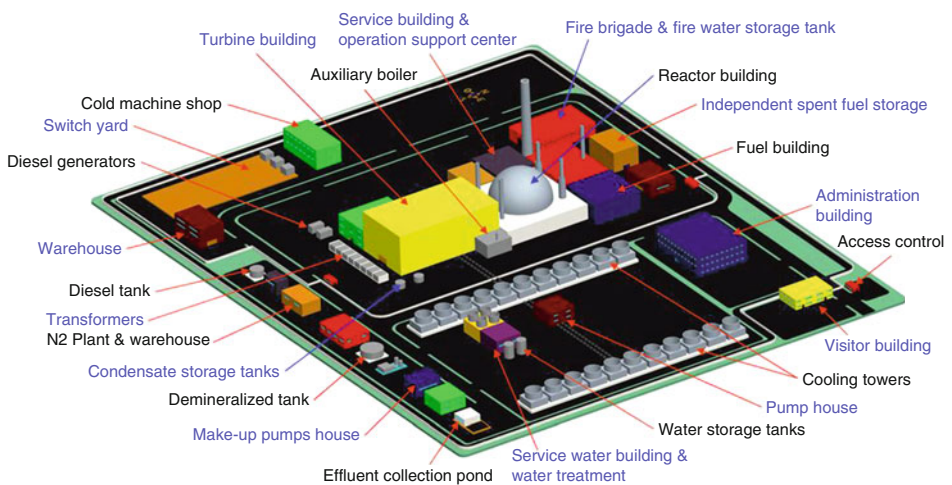
► **Figure 39** below provides an overview sketch of the current reference plant layout.

The reference design shown incorporated forced-draft cooling towers. A second option has also been studied based on natural-draft cooling towers.

The ELSY reactor building is sixstoried, two stories of which are below ground level. It is of cylindrical shape. Its base plate, located below grade, rests on seismic supports and a single foundation slab. The lowest floor is the storage area for fresh and spent fuel assemblies.

With respect to spent fuel, it is possible either (i) to store all spent fuel inside the reactor building or (ii) to provide a limited storage capacity inside the reactor building (namely, sufficient storage for a single core) with additional capacity in an auxiliary dedicated building.

The reactor building is designed to withstand anticipated earthquake stresses and it is provided with double barrier containment. The outer containment barrier is made of reinforced concrete with a steel liner on the inner surface, and is designed to withstand the double-ended rupture of one main steam manifold.



■ **Figure 39**
ELSY general layout

The ARE performs as the first containment barrier and contained work area whenever the vessel head is removed and in-vessel components and fuel assemblies are lifted from the reactor vessel by the means of large and small cranes, respectively, both cranes being arranged in the ARE.

Besides the reactor vessel, the reactor building houses water storage pools required to supply the safety-grade DRC system and the piping for the RVACS. Two additional water storage pools for the secondary loops reactor cooling system are located outside the reactor building at both sides of the steam tunnel. The three DHR systems are connected to four chimney stacks, allowing for the release of the RVACS hot air and the steam of the other systems.

The four chimneys are arranged symmetrically around the reactor building, one chimney stack in each quadrant.

The reactor building is supported by seismic isolation bearings to decouple the building from the ground, lengthening the period of the building, and lowering the response for the structures.

10 Concluding Remarks and Open Issues

The LFR systems offer great promise in terms of the potential for providing cost-effective, simple, and robust fast reactor concepts that are essential to long-term sustainability of the nuclear energy option.

Recent efforts, particularly in the development of the ELSY concept, have gone a long way toward verifying the advantages of lead-cooled systems. Clearly additional work needs to be done, but overall, the prospects continue to appear very positive.

ELSY aims at demonstrating the possibility of designing a fast reactor using simple engineered technical features, while fully complying with the Generation IV goals of sustainability, economics, safety, proliferation resistance, and physical protection.

The elimination of the intermediate cooling system and the compact and simple primary circuit with all internal components removable are among the features to assure reduced capital cost and construction time, competitive electric-energy generation, and long-term investment protection.

The design of the industrial prototypes of the central station LFR and of the SSTAR should be planned in such a way as to start construction as soon as beginning of the TPP operation at full power has given assurance of the viability of this new technology.

Molten lead has the advantage of allowing operation of the primary system at atmospheric pressure. Low doses to the operators can also be anticipated, owing to lead low vapor pressure, high capability of trapping fission products, and high gamma radiation shielding.

In case of leakage from the reactor vessel, the free level of the coolant can be designed such as to guarantee the coolant circulation through, and the safe heat removal from, the core. Any leaked lead would solidify without significant chemical reaction affecting the operation or performance of surrounding equipment or structures.

Fuel dispersion dominates over fuel compaction, thus reducing considerably the likelihood of the occurrence of severe re-criticality events in the case of core disruption. In fact the lead density, which is slightly higher than the fuel density, and convective streams make it rather difficult to imagine scenarios leading to fuel aggregation with subsequent formation of a secondary critical mass, in the event of postulated fuel failure.

The use of MOX fuel containing MA increases proliferation resistance because of the difficulties in partitioning pure Pu from this nuclear material.

Despite the high density of lead, the pressure loss can be kept pretty low (about one bar across the core for a total of about 1.5 bar across the whole primary system) because low neutron energy losses in lead allow for a larger fuel rods pitch. Moreover, lead allows a reliable natural circulation of the primary coolant, which results in a suitable grace time for operation and simplification of control and protection systems.

The use of a coolant chemically inert with air and water and operating at atmospheric pressure greatly enhances physical protection. In the case of accidental air ingress, in particular during refueling, any produced lead oxide can be reduced to lead metal by injection of hydrogen gas and the reactor operation safely resumed.

There is less need of robust protection against the risk of catastrophic events, initiated by acts of sabotage, because there is a little risk of ignition and fire propagation. There are no credible scenarios of significant containment pressurization.

The hard neutron spectrum of LFRs (because of the low moderation and neutron-absorption properties of lead) allows both an efficient use of the fuel and a high number of neutrons per fission: according to this, the core of an LFR can be easily designed to provide a unitary breeding ratio along with long core life and high fuel burn-up.

Furthermore, the hard neutron spectrum significantly reduces MA generation, a fact that is basic for the envisaged close fuel cycle. The possibility of relying on a low fraction of MAs in the equilibrium fuel allows more flexibility in exploiting LFRs for MAs burning both in critical and subcritical cores. Proper design of the critical core, for instance, can be achieved by the adiabatic core concept, i.e., a core self-sustaining in both Pu and MAs, thus being able to be fed with either natural or depleted uranium only, and producing fission fragments as the only waste to be disposed of in a geological repository. Lead-cooled ADS systems, on the other hand, can be envisaged for large-scale MA transmutation, exploiting lead properties also for the spallation target. The EFIT core design demonstrated the possibility of effective MA burning (along with a zero Pu balance) and electricity generation.

Corrosion of structural materials in lead is one of the main issues for the design of LFRs.

A larger effort has been dedicated to short- or medium-term corrosion experiments in both stagnant and flowing LBE. A few experiments have been carried out in pure Pb and knowledge is still missing on medium- or long-term corrosion behavior in flowing lead. Experiments confirm that corrosion of steels strongly depends on the operating temperature and amount of dissolved oxygen. Indeed, at low oxygen concentration and associated reducing environment, corrosion brings about dissolution of the structural steel instead of creating the oxide layer by surface oxidation. Moreover, a relationship between oxygen concentration, coolant flow velocity, temperature, and stress conditions of the structural material has been observed as well. It has been demonstrated that, generally, in the low-temperature range, e.g., below 450 °C, and with an adequate dissolved oxygen activity, ferritic–martensitic and austenitic steels build up a stable oxide layer, which behaves as a barrier against leaching of steel elements providing thereby effective corrosion protection.

Conversely, in the higher-temperature range, i.e., above ~ 500 °C, corrosion protection through the oxide barrier by dissolved oxygen only seems to fail. Indeed, a mixed corrosion mechanism has been observed, whereby both metal oxide formation and dissolution of the steel elements occur. Especially in the high-temperature range, the corrosion resistance of structural materials can be enhanced by FeAl alloy coating.

Thus, at the present status of development of the corrosion protection technology, near-term deployment of the LFR is possible only by limiting the mean core outlet temperature to around 500 °C. The possibility of operating at higher temperature offered by the high boiling point of lead will be exploited only in the longer term after successful qualification of new, high-temperature materials such as ODS steels, ceramics, and refractory metals and relevant corrosion protection techniques.

Acknowledgment

The work on LFR in GIF is supported by the European Commission through the Euratom Framework Programmes, by the US Department of Energy Generation IV Nuclear Energy System Initiative and by the Tokyo Institute of Technology. The ELSY, CDT, and IP-EUROTRANS consortia in Europe are coordinated by Ansaldo Nucleare, SCK-CEN, and KIT, respectively.

Abbreviations

4S	Super Safe, Small and Simple reactor
A-DHR	external Air Decay Heat Removal
ADS	Accelerator Driven Subcritical system
ARE	Above-Reactor Enclosure
BoC	Beginning of Cycle
BORIS	Battery Optimized Reactor Integral System
BR	Breeding Ratio
BREST	Russian acronym for Lead-cooled Fast Reactor
BU	Burn Up
CANDLE	Constant Axial Neutron During the Life of Energy reactor
CDT	FP7 Central Design Team
CR	Conversion Ratio
CRIEPI	Central Research Institute of the Electric Power Industry of Japan
CTE	Coefficient of Thermal Expansion
DHR	Decay Heat Removal
DpA	Displacement per Atom
DRC	Direct Reactor Cooling
DU	Depleted Uranium
EAC	Environment-Assisted Cracking
EFIT	European Facility for Industrial Transmutation
ELSY	European Lead-cooled SYSTEM
EoC	End of Cycle
EOS	Equation Of State
FA(s)	Fuel Assembly(ies)
FMS	Ferritic Martensitic Steel
FP(s)	Fission Product(s)
FP5 (6, 7)	Fifth (Sixth, Seventh) EURATOM Framework Programme
GIF	Generation IV International Forum

- HLM** Heavy Liquid Metals
HM(s) Heavy Metal(s)
HYPER HYbrid Power Extraction Reactor
IP Integrated Project
IPPE Institute of Physics and Power Engineering of Obninsk
ISI&R In-Service Inspection and Repair
JAEA Japan Atomic Energy Agency
JAERI Japan Atomic Energy Research Institute
KAERI Korea Atomic Energy Research Institute
LBE Lead-Bismuth Eutectic
LCF Low Cycle Fatigue
LFR Lead Fast Reactor
LLFP(s) Long-Lived Fission Product(s)
LMAC Liquid Metal Accelerated Creep
LME Liquid Metal Embrittlement
LOCA Loss Of Coolant Accident
MA(s) Minor Actinide(s)
MCP Main Coolant Pump
MOX Mixed OXide
MYRRHA Multipurpose hYbrid Research Reactor for High-tech Applications
NITI A. P. Aleksandrov Scientific Technical Research Institute of Sosnovy Bor
OKB Experimental Design Bureau
OKBM Design Bureau of Machine Building
PBWFR Pb-Bi cooled directcontact boiling Water Fast Reactor
PCMI Pellet-Clad Mechanical Interaction
PEACER Proliferation-resistant Environment-friendly Accident-tolerant Continuable-energy Economical Reactor
PP Physical Protection
PR Proliferation Resistance
PRACS Primary Reactor Auxiliary Cooling System
PR&PP Proliferation Resistance and Physical Protection
PSSC GIF LFR Provisional System Steering Committee
RCCS Reactor Concrete Cooling System
RVACS Reactor Vessel Air Cooling System
SFR Sodium-cooled Fast Reactor
SG Steam Generator
SGTR Steam Generator Tube Rupture
SLPLFR Steam Lift Pump type LFR
SNU Seoul National University
SRP System Research Plan
SSTAR Small Secure Transportable Autonomous Reactor
SVBR Russian acronym for Lead-Bismuth Fast Reactor
TOP Transient Of Power
TPP Technology Pilot Plant
ULOF Unprotected Loss Of Flow
VF Volume Fraction
W-DHR stored Water Decay Heat Removal

References

- Alemberti A, Carlsson J, Malambu E et al (2009) European Lead-Cooled Fast Reactor. Seventh European Commission conference on Euratom research and training in reactor systems (FISA 2009), Prague, Czech Republic, 22–24 June 2009
- Aoto K, Nishi Y, Furukawa T (2003) Corrosion behavior of high chromium martensitic steel in LBE. Global 2003: Atoms for Prosperity: Updating Eisenhower's Global Vision for Nuclear Energy (Global 2003), New Orleans, LA, 16–20 November 2003
- Artioli C (2007) A-BAQUS: a multi-entry graph assisting the neutronic design of an ADS. Case study: EFIT. 5th International Workshop on the Utilization and Reliability of High Power Proton Accelerator, Mol, Belgium, 6–9 May 2007
- Artioli C, Chen X, Gabrielli F et al (2008) Minor actinide transmutation in ADS: the EFIT core design. International Conference on the Physics of Reactors (PHYSOR 2008), Interlaken, Switzerland, 14–19 September 2008
- Artioli C, Grasso G, Sarotto M et al (2009) ELSY neutronic analysis by deterministic and Monte Carlo methods: an innovative concept for the control rod systems. International Congress on Advances in Nuclear Power Plants 2009 (ICAPP09), Tokyo, Japan, 10–14 May 2009
- Artioli C, Grasso G, Petrovich C (2010) A new paradigm for core design aimed at the sustainability of nuclear energy: The solution of the extended equilibrium state. doi: 10.1016/j.anucene.2010.03.016
- Cinotti L, Ait Abderrahim H, Benamati G et al (2006) Lead-Cooled Fast Reactor. Conference on Euratom Research and Training in Reactor Systems (FISA 2006), Luxembourg, 13–16 March 2006
- Cinotti L, Smith CF, Sienicki JJ et al (2007a) The potential of lead fast reactor and ELSY project. International Congress on Advances in Nuclear Power Plants 2007 (ICAPP07), Nice, France, 13–18 May 2007
- Cinotti L, Smith CF, Sienicki JJ et al (2007b) The potential of the LFR and the ELSY Project. RGN, Année 4
- Cinotti L, Locatelli G, Ait Abderrahim H et al (2008) The ELSY project. International Conference on the Physics of Reactors (PHYSOR2008), Interlaken, Switzerland, 14–19 September 2008
- Cinotti L, Smith CF, Sekimoto H (2009) Lead-Cooled Fast Reactor (LFR) overview and perspectives. Proceedings of the GIF Symposium 2009, Paris, France, 9–10 September 2009
- Fazio C, Alamo A, Almazouzi A et al (2005) Assessment of reference structural materials, heavy liquid metal technology and thermal-hydraulics for European waste transmutation ADS. GLOBAL 2005, Tsukuba, Japan, 9–13 October 2005
- GEN IV International Forum (2008) 2008 Annual Report. Technical report
- Greenspan E, Hong SG, Lee KB et al (2008) Innovations in the ENHS reactor design and fuel cycle. Prog Nucl Energy 50(2–6):129–139
- Gromov BF (ed) (1998) Designing the Reactor Installation with Lead-Bismuth Coolant for Nuclear Submarines. The Brief History. Summarized Operation Results. Proceedings of the Conference Heavy Liquid Metal Coolants in Nuclear Technology, Obninsk, Russia, 5–9 October 1998
- Hong SG, Greenspan E (2005) Power flattening options in the ENHS (encapsulated nuclear heat source) core. Prog Nucl Energy 47(1–4):178–189
- Hougen OA, Watson KM, Ragatz RA (1959) Chemical process principles, 2nd edn, part 2. Wiley, New York
- Knebel JU, Ait Abderrahim H, Cinotti L et al (2006) European Research Programme for the transmutation of high level nuclear waste in an accelerator driven system. 9th International Exchange Meeting on Partitioning & Transmutation (IEMPT9), Nimes, France, 25–29 September 2006
- Maes D (2006) Mechanical design of the small-scale experimental ADS MYRRHA. Energy Conv Manag 47:2710–2723
- Moore JJ, Boyce EA (1990) Chemical metallurgy. Butterworths, London
- Nishi Y, Kinoshita I, Nishimura S (2003) Experimental study on gas lift pump performance in lead-bismuth eutectic. International Congress on Advances in Nuclear Power Plants 2003 (ICAPP03), Cordoba, Spain, 4–7 May 2003
- OECD-NEA (2007) Handbook on lead-bismuth eutectic alloy and lead properties, materials compatibility, thermal-hydraulics and technologies, F-92130 Issy-les-Moulineaux, France, OECD-NEA 6195
- Perera J (2003) Brest is best. Nucl Eng Int 48(582):18–21
- Perry JH, Perry RH, Chilton CH et al (1963) Chemical engineers' handbook, 4th edn. McGraw-Hill, New York
- Sarotto M, Artioli C, Grasso G et al (2008) Open square Fuel Assembly design and drawings. Technical report D6 Deliverable, EURATOM

- Sarotto M, Artioli C, Grasso G et al (2009) ELSY core design static, dynamic and safety parameters with the open square FA. Technical report D8 Deliverable, EURATOM
- Sienicki JJ, Wade DC, Moisseytsev A (2007a) Role of small lead-cooled fast reactors for international deployment in worldwide sustainable nuclear energy supply. International Congress on Advances in Nuclear Power Plants 2007 (ICAPP07), Nice, France, 13–18 May 2007
- Sienicki JJ, Moisseytsev A, Wade DC et al (2007b) Status of development of the small secure transportable autonomous reactor (SSTAR) for worldwide sustainable nuclear energy supply. International Congress on Advances in Nuclear Power Plants 2007 (ICAPP07), Nice, France, 13–18 May 2007
- Smith CF, Cinotti L, Sekimoto H (2009) Lead-Cooled Fast Reactor (LFR) ongoing R&D and key issues. Proceedings of the GIF Symposium 2009, Paris, France, 9–10 September 2009
- Toshinsky GI, Grigoriev OG, Efimov EI et al (2002) Safety aspects of SVBR – 75/100 reactor. Workshop on Advanced Nuclear Reactors, Safety Issues and Research Needs, Paris, France, 18–20 February 2002
- U.S. DOE Nuclear Energy Research Advisory Committee and the Generation IV International Forum (2002) A Technology Roadmap for Generation IV Nuclear Energy Systems. Technical report GIF-002-00

24 GEM*STAR: The Alternative Reactor Technology Comprising Graphite, Molten Salt, and Accelerators

Charles D. Bowman¹ · R. Bruce Vogelaar² · Edward G. Bilpuch³ · Calvin R. Howell³ · Anton P. Tonchev³ · Werner Tornow³ · R.L. Walter³

¹ADNA Corporation, Los Pueblos, Los Alamos, NM, USA
cbowman@cybermesa.com

²Virginia Tech, Blacksburg, VA, USA

³Triangle Universities Nuclear Laboratory, Duke University, Durham, NC, USA

I	<i>Introduction</i>	2843
2	<i>Supplemental Neutrons from Accelerators</i>	2845
3	<i>Molten Salt Technology</i>	2847
4	<i>Graphite Developments</i>	2852
5	<i>Integrating Accelerators, Molten Salt, and Graphite</i>	2856
6	<i>Calculations of GEM*STAR Burn-Up Performance</i>	2859
7	<i>Corrections for MCNP5 Graphite Absorption</i>	2865
8	<i>GEM*STAR Reactor Parameters</i>	2868
9	<i>Burning LWR Spent Fuel</i>	2875
10	<i>Other Fuels</i>	2879
10.1	Thorium and Depleted Uranium Fuels.....	2879
10.2	Fueling GEM*STAR Over the Long Term.....	2882
II	<i>Other Factors Affecting GEM*STAR Success</i>	2884
11.1	Ultimate Ocean Disposal?.....	2884
11.2	GEM*STAR Comparison with Fast Breeder Reactors	2885

11.3	Fusion Neutron Sources	2885
12	<i>Nonproliferation Advantages of GEM* STAR</i>	2886
13	<i>Cost Estimation</i>	2888
13.1	GEM* STAR Accelerator Costs	2888
13.2	GEM* STAR Reactor Costs and Breakeven Electricity Price	2890
14	<i>Summary</i>	2892
	<i>References</i>	2892

Abstract: The technology of nuclear power could be quite different from today's if it had been practical in the beginning to supplement fission neutrons with accelerator-produced neutrons. The purpose of this chapter is to illustrate the possible benefits of implementing supplementary neutrons from accelerators in an optimized reactor. GEM*STAR (Green Energy Multiplier* Subcritical Technology for Alternative Reactors developed by *Accelerator Driven Neutron Applications* (ADNA Corp) is a subcritical thermal-spectrum reactor operating with molten salt fuel in a graphite matrix and in a continuous flow mode initially at $k_{\text{eff}} = 0.99$. The model described is able to use natural uranium as fuel and generate twice as much electric power as a light water reactor (LWR) generates from the same mined uranium. GEM*STAR at $k_{\text{eff}} = 0.99$ also can be fueled with unprocessed LWR spent fuel, and it can generate as much electricity as the LWR had generated from the same fuel. Because GEM*STAR uses liquid fuel, it can recycle its own fuel at $k_{\text{eff}} = 0.95$ without any operations on the fuel. This recycle can be repeated several more times, always without reprocessing, as accelerator or fusion neutron generation technology development reduces the cost of neutrons. GEM*STAR therefore increases the electricity from mined uranium many times while avoiding the serious problems of current nuclear-power technology arising from enrichment, reprocessing, fast reactor deployment, and near term high-level waste storage. GEM*STAR also offers technology for nuclear energy generation that promises reductions in nuclear electricity cost and eliminates major proliferation concerns. The technology can use a modest source of intermittent "green" electricity such as wind or solar as input power to drive an accelerator that, in effect, multiplies the green energy by a factor of about 30 with 24–7 continuity and without compromising any environmental objectives of green energy sources. This chapter is not a complete history of molten salt, graphite, and accelerator technologies, but a description of how these orphan elements of nuclear power development may be integrated for a GEM*STAR solution to the main barriers that constrain the full deployment of today's nuclear power technology.

1 Introduction

The fundamental problem for nuclear power technology has always been too few neutrons per fission. The performance of the earliest reactors was limited by the number of neutrons from fission of ^{235}U and the loss of too many of these neutrons to capture in ^{238}U . Uranium enrichment technology was therefore developed to overcome parasitic losses of neutrons. As a consequence, enrichment coupled nuclear power to nuclear weapons, and this coupling has always been a burden to nuclear power.

In addition, concerns about long-term uranium supply have been present from the beginning of the nuclear age; therefore, fast breeder reactors (FBR) were introduced to convert ^{238}U to ^{239}Pu , which could be used as a fission fuel. However, ^{239}Pu is also an excellent weapon material, and so the coupling between nuclear energy and nuclear weapons was tightened further.

Light water reactors (LWRs), which produce ^{239}Pu and consume some of it as fuel, have been the primary source of the world's nuclear energy production till the present. Both the LWR and the breeder reactor spent fuel require reprocessing to extract the plutonium for energy production and for removal of fission products that otherwise would spoil the breeder reactor neutron economy through useless neutron absorption. The scale of reprocessing necessary for nuclear to provide a substantial part of the world's energy supply requires a major international reprocessing industry and an accompanying worldwide plutonium economy. Reprocessing further binds nuclear energy to nuclear weapons.

Advocates of reprocessing make a distinction between weapons plutonium (W-Pu), with about 7% of ^{240}Pu accompanying the ^{239}Pu and commercial plutonium (C-Pu), with about 30% of ^{240}Pu . Neutrons from the spontaneous fission of ^{240}Pu cause problems in starting the chain reaction of the nuclear weapons that introduces significant uncertainties in the explosive energy release. How useful C-Pu might be for nuclear weapons is not discussed in the open literature, but US President Carter, a nuclear engineer, issued an executive order against reprocessing in the USA owing to nuclear weapons proliferation centered on C-Pu concerns that stayed in effect until the second Bush administration. The second Bush administration instead proposed a Global Nuclear Energy Partnership (GNEP) (DOE 2008) that placed strict controls on where and who would do reprocessing that obviously recognized a nuclear weapons issue from C-Pu.

It seems unlikely that the Democratic Obama administration will support either breeder reactors or reprocessing under GNEP. So the controversy over reprocessing, which has extended for 30 years, and the coupling it provides between nuclear weapons and nuclear energy seems likely to remain an issue for the foreseeable future. This concern along with others have created a widespread perspective in the USA and perhaps elsewhere that nuclear technology will not develop beyond today's LWRs, which are viewed as only an interim solution to the CO_2 problem until other "green energy" alternatives can be developed.

Another problem accompanying reprocessing is the separation of high-level nuclear waste from fission products and leak-through to the waste stream in chemical reprocessing of higher actinides including neptunium, plutonium, americium, and curium. Near-term reprocessing also requires a near term final solution for the reprocessing wastes with the present US solution being near-term repositories such as Yucca Mountain (now canceled). A fundamental flaw to a single geologic storage site for nuclear waste for a nation of the size of the USA is the obvious unfairness of forcing what much of the public feels to be the most dangerous waste on one state perceived to be politically the weakest.

The need for some form of geologic storage is advanced by those who oppose reprocessing and advocate the "once-through" approach where both the accumulated and future LWR spent fuel is sent directly to geologic storage (Bunn et al. 2003; von Hippel 2007). This viewpoint implies that the uranium resource is large enough, so that, by the time there is a need for conversion or breeding of ^{238}U into ^{239}Pu , alternative nonnuclear energy sources could take care of the world's energy needs. Repositories used in this way are also future mines of plutonium and the point has been made (Peterson 1996) that it would be much faster and much cheaper to mine plutonium from the world's many repositories instead of taking either the enrichment or the reactor approach to weapons material production. We would add here that the US Nuclear Regulatory Commission's concerns about performance of Yucca Mountain extend well beyond the 13,000 years, the time required for ^{240}Pu to decay to ^{236}U , resulting in the conversion of stored LWR plutonium from C-Pu to W-Pu. Considering the problems with geologic storage both from just the waste management perspective and as plutonium mines, any alternative nuclear technology approach should include an approach to geologic storage that addresses both nagging concerns.

The obvious problems of nuclear power summarized above including enrichment, reprocessing, fast reactors for breeder or conversion, and geologic storage should *all* be addressed by any new fuel cycle technology. There is little advantage to addressing one or two and leaving the others hanging as is the case for the several Generation IV reactor technologies. In addition, any alternative system must be at least economically competitive with today's LWRs as even new

LWRs face cost issues that move nuclear power costs uncomfortably close to other approaches for electricity production.

The Green Energy Multiplier* Subcritical Technology for Alternative Reactors (GEM* STAR) technology discussed later in this chapter appears to satisfactorily address the issues of proliferation, cost, and waste disposition. It is based on the beneficial combination of three technologies largely neglected since 1970 that substantially enhance the graphite thermal reactor neutron economy. The three technologies include (1) supplemental neutrons from accelerators, (2) liquid fuel in the form of molten salt, and (3) the selection and implementation of graphite to reduce graphite parasitic neutron capture and optimize neutron reflection. Some history on these three topics follows before the discussion of the integration of the three technologies into GEM* STAR.

2 Supplemental Neutrons from Accelerators

Cyclotrons and electrostatic accelerators played an essential and well known role in the early development of nuclear technology, and it was natural to apply them to the development of nuclear energy both in the weapons and energy realms. Thus, the first significant quantity of enriched ^{235}U was obtained from the large fleet of systems based on these technologies called Calutrons which was developed under the leadership of E.O. Lawrence of the UC Berkeley Laboratory. However, Calutron production of ^{235}U could not compete with the high production and lower costs of gaseous diffusion methods for the same purpose.


In the early 1950s, concerns about the US supply of uranium focused attention on the need to produce ^{239}Pu from neutron capture on ^{238}U . Lawrence brought much higher power accelerators into the picture as intense sources of neutrons around 1955 with the construction (Lawrence in the Cold War 2002) of Mark I of the materials test accelerator (MTA) in a hanger at an air force base in Livermore, California. The MTA was a drift tube linear accelerator (linac) designed for both high current and high energy with a diameter of 19 m and a length of 27 m, commonly referred to as “large enough to fly an airplane through.” The history of high vacuum technology annals refers to it as the most challenging vacuum project of the day. The accelerator required 18 MW of radio frequency (r.f.) power and intermittently reached unprecedented currents of 50 mA of deuterons at an energy of 10 MeV for an average power of 0.5 MW. The beam current was two million times larger than that of the Berkeley cyclotrons.

A Mark II version of the MTA was planned for another site to produce 1 A of 350 MeV deuterons with a beam power of 350 MW. The accelerator probably would have produced about ten neutrons per deuteron and ^{239}Pu at the rate of about 500 kg/year (enough for about 100 nuclear weapons per year). However, the discovery of abundant uranium in Colorado and New Mexico along with the success of plutonium production reactors at ORNL and Hanford, Washington ended the MTA initiative. The discontinuance of the MTA project in 1958 and of a major role of accelerators in large scale applied nuclear technology was a major disappointment to Lawrence, whose laboratory had discovered ^{239}Pu and also led in the development of both cyclotrons and linacs. He died the same year at the age of 57, and a major early role for accelerators in nuclear energy died as well. For the next 40 years, the advancement of accelerator technology for neutron production was driven by basic rather than applied science.

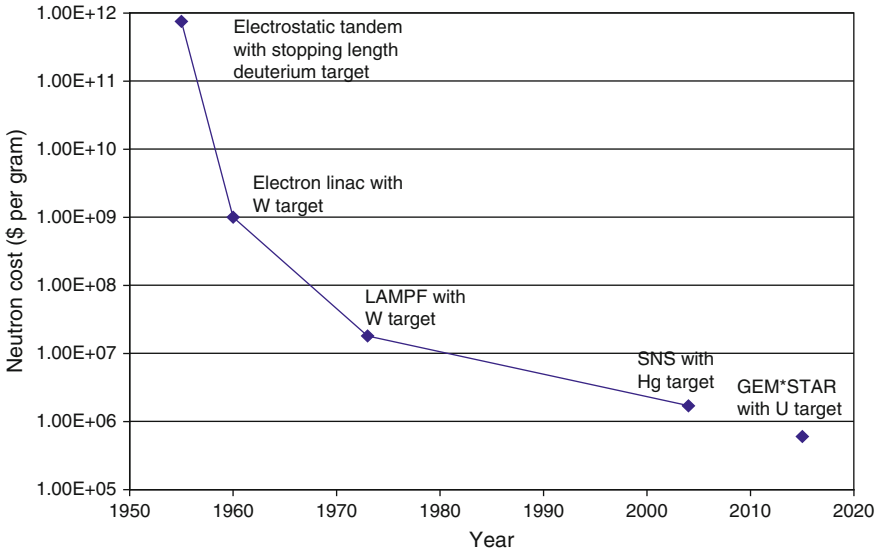
If the number of fission neutrons were about 25% lower, nuclear energy as we know it today would probably have not been possible, but almost certainly high power accelerator technology starting from the MTA would have advanced much faster, probably enabling economic

electricity production long ago from subcritical reactors anyway. The Mark II 350 MWb accelerator would have produced 250 times more beam power than the accelerator power specified later in this report for the production of 220 MW_e of electricity from the burning of natural uranium. An attempt was made in Canada to introduce accelerators into nuclear energy (Lewis 1966) with the intense neutron generator (ING) project that included an accelerator of 1 GeV protons with a current of 300 mA. The goal was to use accelerator technology to produce fissile material for reactors without enrichment, but the success of the Canadian CANDU reactor that burned natural uranium as fuel undercut the need for the ING.

The first major demonstration of a reliable high power accelerator did not occur until 1973 with the completion of the Los Alamos Meson Physics Facility (LAMPF) (Rosen 1973) that accelerated as much as 1.3 mA of protons to 800 MeV for a maximum beam power of 1 MWb. The typical LAMPF beam current was 1 mA. The next major effort for high beam power was the Los Alamos Accelerator Production of Tritium (APT) project (Lawrence et al. 1996) that included detailed design and costing for a 1.6 GeV linac with a continuous current of 100 mA at a beam power of 160 MWb. Costing was also done for powerful accelerators for a US Accelerator Transmutation of Waste (ATW) project (Smith et al. 1999) that used a pair of 1 GeV accelerators with 45 mA of beam power each producing a power of 45 MWb. Accurate costing is also available for the recently completed spallation neutron source (SNS) at ORNL with an energy of 1 GeV and a current of 1 mA. Accurate costing is also available for the continuous spallation neutron source (CSNS) designed (Shapiro et al. 2003) for BNL with a beam energy of 1.25 GeV and a current of 8 mA for an average beam power of 10 MWb. Of the four accelerators mentioned above after LAMPF, only the SNS was actually constructed.

A rough time-trend in neutron cost for linear accelerators is shown in  Fig. 1 with costs in 2008 dollars per gram (or per mole). The first point is the cost of neutrons from an electrostatic tandem accelerator used with a stopping length deuterium gas target as measured recently (Bowman et al. 2009b) with a proton energy of 15 MeV. The second point is an estimated neutron cost for the Los Alamos LAMPF accelerator, which is the first reliable proton accelerator operating near the megawatt range. The third point is for the SNS that was recently completed with firm cost numbers and a mercury target. Although the mercury target might not be practical for GEM*STAR, the solid target that replaces it will have a roughly equivalent neutron cost even if the source brightness is less than anticipated. The fourth point is estimated for GEM*STAR using a combination of six accelerators of 1.3 mA each and an energy of 0.5 GeV with costing based on the APT, ATW, SNS, and CSNS cost estimates as described later in this chapter. This lowest neutron cost is obtained by the use of a uranium target with beryllium multiplication and with a length somewhat less than the GEM*STAR graphite core dimension. Although the trend since 1970 seems to be a consistent reduction in cost by about two per decade, every technology has practical limitations and linear accelerators with spallation targets might not be reduced further by more than a factor of two or to about \$0.3 million per gram.

For a subcritical system with $k_{\text{eff}} = 0.99$, 40 g of neutrons per year is sufficient to produce about 1 GWe for 1 year. At \$0.05/kWh, this electricity can be sold for about \$450 million with the 40 g of neutrons costing \$24 million per year. Although implementing accelerator technology into nuclear power at the beginning of the nuclear age was out of the question, the million-fold reduction in neutron cost over the past 60 years strongly suggests the need to examine the economic viability for subcritical systems in 2010. GEM*STAR, with deep burning of natural uranium as fuel, promises economic competitiveness for nuclear energy and increased safety without the need for proliferation-prone enrichment, reprocessing, fast reactors, or near-term geologic storage and the associated additional costs of this burdensome infrastructure.



■ Figure 1

Approximate cost of neutrons per gram (or per mole) from high power linear proton accelerators. Although the long-term trend since 1970 is a reduction of about two per decade, the technology might be reaching its limits and further improvements below about \$0.3 million per gram might not be practical. For a subcritical system with $k_{\text{eff}} = 0.99$, 40 g of neutrons per year is sufficient to produce about 1 GWe for 1 year. At \$0.05/kWh, this electricity can be sold for about \$450 million with the 40 g of neutrons costing \$24 million per year as shown later in this report. Although implementing accelerator technology into nuclear power at the beginning of the nuclear age was out of the question, the million-fold reduction in neutron cost over the past 60 years strongly suggests economic viability for subcritical systems in 2010

The prospect for realizing this promise is boosted by the practical implementation of molten salt fuel and the use of improved graphite, both of which are described below.

3 Molten Salt Technology

Any discussion of molten salt technology must first start with the molten salt reactor experiment (MSRE) at ORNL in the 1960s described in detail in a 114 page report (Weinberg et al. 1970). The purpose of this experiment was to enable online liquid fuel reprocessing for the removal of fission products and to use other advantages of this approach to demonstrate the practicality of a thorium breeder reactor. The MRSE need not be described in detail here, but the introduction (Weinberg et al. 1970) to the record of the MSRE operation is quoted below.

The MSRE is an 8-MW_t reactor in which molten salt fluoride salt at 1,200 °F (700 °C) circulated through a core of graphite. Its purpose was to demonstrate the practicality of the key features of molten salt power reactors.

Operation with ^{235}U in the fuel salt began in June 1965 and by March 1968 nuclear operation amounted to 9,000 equivalent full-power hours. The goal of demonstrating reliability had been attained. Over the last 15 months of ^{235}U operation, the reactor had been critical 80% of the time. At the end of a 6-month run, which climaxed this demonstration, the reactor was shut down and the uranium in the fuel was removed very efficiently in an on-site fluorination facility. ^{233}U was then added to the carrier salt making the MSRE the world's first reactor to be fueled with this fissile material. Nuclear operation was resumed in October 1968 and over 2,500 equivalent full-power hours were produced with ^{233}U .

The MSRE has shown that salt handling in an operating reactor is quite practical, the salt chemistry is well behaved, there is practically no corrosion, the nuclear characteristics are very close to predictions, and the system is dynamically stable. Containment of fission products has been excellent and maintenance of radioactive components has been accomplished without unreasonable delay and with very little radiation exposure.

The conclusion of the Experiment Report (Weinberg et al. 1970) included the following:

From the months of operation and experiments a very favorable picture emerged. In properly designed equipment, handling the high-melting salt proved to be easy. Maintenance of the radioactive systems was not easy, but there were no unforeseen difficulties and control of contamination was, if anything, less difficult than expected. Fuel chemistry and materials compatibility lived up to expectations, showing no adverse effects due to the reactor environment. The noble gases, xenon and krypton, were stripped efficiently. It was found that noble metal fission products, whose behavior had hitherto been uncertain, partially plated out on metal surfaces and partially came off the salt surface as smoke, thus providing important information for future reactors. Although the operation of the MSRE showed that the design of some equipment and systems could be improved, key components performed well.

The on-site removal of the original uranium from the fuel and the loading of the ^{233}U into the stripped carrier salt extended the usefulness of the MSRE and the simplicity and efficiency of these steps illustrated one of the virtues of the fluid-fuel molten-salt systems.

The nuclear start-up experiments and operation at power confirmed the adequacy of the data and procedures used to predict the behavior. The system was quite stable and easy to control even during ^{233}U operation with a delayed neutron fraction lower than in any other reactor. Finally burn-up over an extended period at high power should yield very accurate information on ^{233}U cross section ratios in a neutron energy spectrum typical of molten salt reactors. A net result of the MSRE operation is enhanced confidence in the practicality and performance of future molten salt reactors.

In spite of the success of the MSRE summarized above, the molten salt breeder was competing with the liquid metal fast breeder reactor (LMFBR), which exhibited a higher breeding ratio. The MSR requirement of an online fuel cleansing system was viewed as a liability compared to the LMFBR solid fuel being reprocessed off site in a central location.

Another potential problem developed with the alloy used in contact with the molten salt. The metal testing and demonstration went through several stages settling first on a nickel-based alloy Hastelloy, then Hastelloy-N, and then Modified Hastelloy-N. The last alloy was a great success relative to corrosion issues, but the lifetime of the alloy in the thermal neutron flux was disappointingly and puzzlingly short. The problem was recognized early as buildup of ^4He in the pores of the alloy from the $\text{Ni}(n,\alpha)$ reaction, but the reason for a fast He buildup was not understood. The origin of the short life of the alloy was discovered after the MSRE program had suffered the loss of most of its financial support. The most abundant isotope ^{58}Ni (68%) has a substantial neutron capture cross section that yielded ^{59}Ni , which had an even larger cross

section for the (n,α) reaction. The only solution probably was the removal of ^{58}Ni by isotope separation, which would almost certainly prove economically impractical. (The required ratio of the mass difference between ^{58}Ni and ^{60}Ni divided by the nuclide mass is 1/30 whereas the same parameter for ^{235}U isotopic separation is about 1/80. There is therefore some possibility that isotopic separation of nickel might become economically practical.) The GEM*STAR system described later in this chapter does not use modified Hastelloy-N in regions where the thermal neutron flux is high.

A fully engineered conceptual design was completed for a 1,000 MW_e molten salt breeder reactor (MSBR) (Weinberg et al. 1970). This design was criticized because of the need for transport of the hot molten salt out of the reactor to external heat exchangers and back to the reactor for reheating. The salt flow rate is necessarily high between the reactor and the heat exchanger and in case of a highly damaging earthquake, much of the highly radioactive salt might spill out on the plant floor from broken piping before the pumps could be stopped. GEM*STAR uses internal heat exchangers with transfer of heat from the fuel salt to a lower melting point secondary salt so that the primary fuel salt never leaves the reactor tank.

The MSBR reactor was said to be less safe because of inferior containment arising from the use of fuel in liquid instead of solid form. Yet today's LWRs use solid fuel clad in low-melting-point zircalloy that melts almost immediately, with the fuel melting soon after, should water coolant on the surface of the fuel disappear. In this situation the cladding offers little containment, and the consequence of cladding failure is the release of all the accumulated noble gases. In contrast, liquid fuel allows for the removal of noble gases continually so that the most volatile source of dispersible radioactivity is absent should an accident occur with a molten salt system.

The MSBR also was less attractive to reactor vendors than solid fuel reactors because the MSBR reactor owners would not have to purchase manufactured solid fuel from the reactor vendors (Lamarsh 1983). The typical LWR was sold close to the cost of the manufacturer with the primary financial gain coming from spent fuel contracts that might extend over the life of the reactor.

A bitter battle was fought in the USA over breeding in the liquid fueled MSBR versus the solid fueled LMFBR with the latter having the benefit of an earlier start and a stronger funding base. In its favor, the LMFBR achieved a better breeding ratio for ^{239}Pu from uranium than the MSBR did for breeding ^{233}U from thorium. Then director of ORNL Alvin Weinberg was fired eventually for pushing for the MSBR after the decision for termination had been made. Later, perhaps partly in an attempt at compensation, the government started construction of the first US commercial scale breeder reactor called CRBR at Oak Ridge. Part way through the construction, the project lost the support from commercial nuclear industry leaders and construction was terminated. A smaller fast reactor called the fast fuel test facility (FFTF) was eventually constructed at Hanford, Washington, but support for its operation was too weak to enable a long period of operation. Nevertheless, large scale fast reactors were pursued aggressively and built in France, Russia, and Japan; although none has been economically successful. Plutonium-breeding reactors are still vigorously advanced in many countries along with the reprocessing necessary for their operation on the doubtful basis that they eventually will be required for better utilization of the uranium and thorium resources and that the FBR is the only technology that can accomplish this.

However, the success of the MSRE at ORNL attracted attention worldwide and studies of the technology were conducted in Russia in particular and also in France, Germany, and Japan. The collection of all ORNL reports relevant to molten salt reactors is available at

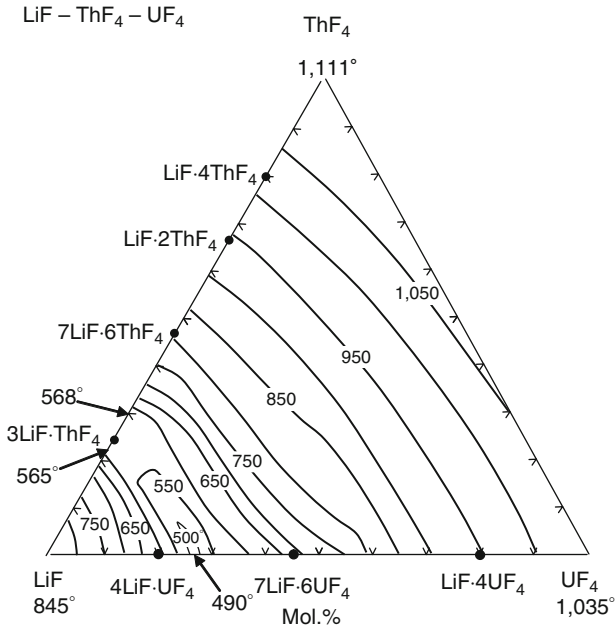


Figure 2
Phase diagram for LiF-UF₄-ThF₄

<http://www.energyfromthorium.com/pdf/>. The majority of them were generated at ORNL and many of them were devoted to measurements of the chemical and physical properties of various relevant mixtures of molten salts. The purpose of similar work conducted outside ORNL was to check the ORNL findings. Such studies were not pursued aggressively as investigators soon found that the quality of the ORNL results made such repetition unnecessary (Ignatiev 1995, personal communication).

An important example is shown in **Fig. 2**, which shows the melting point for the LiF-UF₄-ThF₄ mixture (Weinberg et al. 1970). The three corners correspond to the melting points of each of the three salts unmixed. The mid-point of one side gives the melting point for a 50–50 mixture of the materials marked at the ends of that side. So on the bottom side the melting point of a 50–50 mixture of LiF and UF₄ is about 700 °C. The lowest melting point of the mixture at 490 °C, called the eutectic mixture, is at 73:27 LiF: UF₄. Likewise, the eutectic point for LiF: ThF₄ is at 568 °C with a ratio of 70:30. Examination of the area in the lower left corner shows that almost any mixture of ThF₄ and UF₄ with 66% LiF will melt near 550 °C. The minimum temperature of the salt during normal GEM*STAR operation is 650 °C, so burning U or Th or any combination of them requires no change in reactor design or minimum operating temperature.

For about 30 years after the shut-down of the MSRE project, the interest in molten salt continued but in a relatively quiescent mode owing to an absence of significant financial support in any country. Perhaps the strongest initiative toward revival of molten salt technology was made during the origins of the accelerator transmutation of waste (ATW) (Bowman et al. 1992) project at LANL in the early 1990s. During most of the ATW project, the optimal combination of accelerator and reactor technology was taken to be a subcritical graphite-moderated reactor

with molten salt fuel. Although the LANL program stimulated a worldwide examination of the integration of accelerators into reactor technology, support in every country has always been restricted essentially to discretionary internal laboratory funding, and the accelerator-based technology never gained a firm funding foothold. The thermal spectrum approach was pursued further (Bowman 1998, 2000a) by ADNA Corporation after the LANL ATW effort ended. A patent (Bowman 2001) was granted in 2001 with the key element being the continuous flow of molten salt fuel that is part of the basis for the GEM*STAR system, described later in this chapter.

The study of molten salt reactors has regained some momentum by stepping away from the focus of the original MSR program at ORNL on optimizing the neutron economy sufficiently for thermal reactors to enable full use of the thorium and uranium fuel resource. The ORNL technology was steered toward niche activity such as weapons plutonium burning (Gat et al. 1992) and waste burning (Gat and Dodds 1993) in the early 1990s. Other means of deployment of molten salt reactors were also studied (Moir and Teller 2005) later. A more significant departure was the consideration of fast-spectrum molten-salt reactors (Furukawa et al. 1994). The fast spectrum offers some advantages including the elimination of graphite in the core and therefore concerns about the graphite lifetime, the use of NaF instead of ${}^7\text{LiF}$ in eliminating the need for isotopic separation of ${}^7\text{Li}$, the advantage of a harder neutron spectrum for transmuting non-fissile nuclides, and the claim of a neutron economy superior to the thermal spectrum. Recent papers (Forsberg et al. 2004; Merle-Lucotte et al. 2006; Forsberg 2007) provide many references to studies of fast-spectrum molten-salt reactors including the use of salt only as a coolant and not as a fuel. The latter designs are proposed for high temperature reactors capable of supplying heat at about 850 °C for hydrogen production and sometimes as small reactors for isolated regions.

In spite of 50 years of study of many reactor designs, the LWR supplies more than 90% of the world's nuclear electric power and the percentage is likely to grow higher as there are few current plans to build types other than LWRs for the foreseeable future. Today's typical advanced reactor design addresses only one problem of nuclear energy and neglects many others: the need for enrichment, reprocessing, expensive sodium-cooled fast reactors, lower cost of electricity, simple use of LWR waste as fuel, the elimination of a near term high-level waste stream requiring geologic repository storage, and weapons plutonium burn-up. One may argue that the goal for reactor development should be a single reactor design that satisfies all of these requirements and also enables the use of a significant part of the U and Th energy resource. The best option for that single design may well rest with the ORNL MSR thermal-spectrum design of 50 years, modified for subcritical operation and graphite-optimized to enhance the neutron economy.

The well-moderated thermal spectrum of a graphite-moderated molten salt reactor has a little known but notable advantage over other reactors because it has a much lower neutron loss from fission product capture than any other reactor design. The isotopes produced in fission are centered in the mass region where the p-wave neutron strength function peaks and generally away from the s-wave strength function (Mughabghab 1984). In the thermal neutron region where only s-wave neutron interaction is possible, the capture cross section therefore is *inhibited*. However, in the higher keV region of fast reactors, the angular momentum bias against p-wave capture disappears and p-wave neutron capture is *enhanced*.

Neutron resonance spacing also is an important factor when the spacing is much larger than the width of the neutron spectrum. In the well moderated molten salt reactor, nearly the entire neutron spectrum is contained in the energy band between 0.01 and 0.20 eV. The typical spacing between resonances for fission products is much larger than 0.2 eV, so fission product

resonances, where neutron capture is greatly enhanced, rarely fall in the 0.2 eV window. In the few cases where they do such as ^{151}Sm , the isotope is quickly transmuted to a much lower cross section nuclide. For ^{135}Xe , the same would be true except that volatile species can be quickly removed from liquid fuel. Taking these burn-up and removal factors into account the effective capture cross section for fission products has been calculated (Bowman 2000a) and found to be 6.0 barns for a thermal fluence of $3 \times 10^{22} \text{ n/cm}^2$ or 0.03 n/barn. (The same methodology has been applied for GEM*STAR, giving 8.6 barns at its lower fluences.) The fission cross section for ^{239}Pu at the same energy is about 100 times larger.

For a fast spectrum an abundance-weighted average of all of the fission product capture cross sections at 50 keV gives 0.145 barns (McLane et al. 1988) compared with the fission cross section of ^{239}Pu at the same energy of 1.5 barns; only 10 times larger. *The neutron loss to fission products is much larger in a fast spectrum reactor than in a well moderated molten salt reactor.*

The harder neutron spectrum of a fast reactor that enables more fission of even-even actinides than a thermal spectrum is the primary basis for the claim of a more favorable neutron economy for a fast reactor than a thermal reactor burning predominately ^{239}Pu . The inferiority of the fast spectrum with regard to neutron loss to fission product is uniformly ignored. The clinching argument added in favor of the fast spectrum is that higher actinides must be reduced as much as possible owing to the problems they cause with reprocessing. GEM*STAR does not require reprocessing. The usual arguments for superiority of a fast spectrum whether with molten salt or a solid fuel reactor are therefore not on sound footing.

Finally, it should be mentioned that the graphite-moderated molten-salt reactor will also be superior to the LWR with regard to fission-product neutron losses. An LWR is sufficiently loaded with fissile material that the neutrons are absorbed at an average energy of about 6 eV. The width of the LWR neutron spectrum is several eV rather than 0.2 eV, so the spectrum is more than ten times likely to include a neutron resonance with neutron-enhanced absorption. The LWR losses to fission products therefore might be comparable to that of fast spectrum reactors.

4 Graphite Developments

The earliest reactors were constructed of graphite and so graphite received extensive attention in the beginning years of reactor technology. General graphite studies were summarized by Nightingale (1962) and Poulter (1963). Studies of bulk graphite nuclear properties are summarized in ANL-5800 (1963) and most of the experimental methods are described by Beckurts and Wirtz (1964) and Glasstone and Edlund (1952). The high neutron absorption property of boron was always a concern and the term “reactor-grade graphite” was used to describe graphite with less than about 3 ppm by weight of boron. The investigation of the nuclear properties of graphite largely stopped in about the mid 1950s. With the widespread availability of low enriched uranium (LEU) in the nations with nuclear weapons stockpiles, uncertainties in the expected performance of new graphite reactors could be compensated simply and cheaply by adjusting the ^{235}U fraction of the LEU fuel.

With the advent of Monte Carlo codes such as MCNP5 (The MCNP5 Code, developed at the Los Alamos National Laboratory, Distributed by the Radiation Safety Information Computational Center, ORNL, www-rsicc.ornl.gov.) with capability to include complex geometry and an accuracy in neutron transport calculation limited only by the data input, more was asked and expected of neutron transport calculations. In order to perform optimally in neutron transport in the thermal neutron range, the MCNP5 code contains models for the molecular and



■ Figure 3

Apparatus for measuring the neutron diffusion and absorption of graphite. A pulsed proton beam from the Triangle Universities Nuclear Laboratory accelerator at Duke University enters the tank from the right where it strikes a target producing neutrons

crystalline structure for several materials including graphite. For graphite the model assumes a perfect crystal structure, which would be appropriate for practical calculations for natural (mined) graphite that has nearly a perfect crystal structure. Unfortunately, mined graphite contains too much boron making it impractical for use in a reactor. Therefore, manufactured graphite must be used for reactor construction and the crystal structure of manufactured graphite is much inferior to that of mined graphite. Most manufactured graphite also exhibits a significant anisotropy in properties such as thermal and electrical conductivity, strength, and also neutron transport properties.

Neither the imperfect crystal structure nor the anisotropy of manufactured graphite can be taken into account in present Monte Carlo codes like MCNP5; therefore, there is a substantial basis for doubting the reliability of such codes for neutron transport in reactor design. This doubt was confirmed by an initial series of neutron transport experiments that led to the first experimental measurement of the diffusion coefficient and boron content of manufactured graphite (Bowman et al. 2009a) in many years. The apparatus is shown in ► Fig. 3. The thin steel container was filled with granulated manufactured graphite. A hole across the diameter allowed a pulsed proton beam to enter from the right and to strike a target at the center of the tank producing a pulse of neutrons. The neutrons moderated and then died away exponentially by both neutron diffusion out of the tank and neutron absorption in the graphite. The decay time thus enabled a measurement of the combination of neutron diffusion and neutron absorption. A second experiment was performed on the same apparatus by placing a neutron source under the tank and measuring the neutron intensity as a function of position along the tank axis. The intensity decreased exponentially from the bottom to the top (aside from top and bottom corrections) owing to a combination of neutron absorption in graphite and neutron diffusion out of the side of the tank. A combination of the two experiments allowed the separation and determination of the graphite absorption and the diffusion coefficient.

The experiment was performed on granulated manufactured graphite, avoiding differences associated with the anisotropy of manufactured graphite. The diffusion coefficient was found

to be 25% larger than that calculated from MCNP5. The natural boron content was found to be less than 0.2 ppm by weight, and, therefore, much less than that is expected in reactor grade graphite. The smaller boron content reduced the neutron absorption in graphite below that which is expected from reactor grade by about 5% and taking this together with the increase in diffusion coefficient gave a total reduction in neutron absorption in graphite of 30%.

In order to pin down the origin of the difference between what MCNP5 predicted and what was measured, another experiment was done at the LANSCE facility at LANL. Very-high-resolution Bragg edges were studied (Bowman et al. 2008) by transmission on both granular and solid samples from 1 meV to 1 eV that enabled the separation of neutron diffraction from inelastic scattering. The Bragg diffraction was found to be very much reduced and the inelastic scattering correspondingly enhanced compared with the MCNP5 predictions for perfect crystalline graphite, indicating a high degree of crystalline distortion in the manufactured graphite. The distortion was even larger than that measured (Arnold et al. 1949) in older manufactured graphite and this was attributed partly to the addition of high pressure on the graphite during the last phase of the graphite manufacturing process that was not present in the early years of graphite production. By comparison with the MCNP5 calculations on perfect crystalline graphite (Bowman et al. 2008), the disorder in the manufactured graphite was found to be equivalent to that associated with the atomic vibrations from heating perfect crystalline graphite to about 1,500 °C (1,800 K) as shown in ► Fig. 4. This means that the energy-dependent ratio of diffraction to inelastic scattering measured at room temperature would be essentially the same at the reactor operating temperature of 700 °C, and that this ratio would not change significantly unless the reactor temperature approached 1,500 °C.

The measurements (Bowman et al. 2008) also showed a significant difference in the inelastic to diffraction ratio depending on the orientation of the graphite during the extrusion step (Nightingale 1962) of the manufacturing process. This implies that the optimal geometry for a graphite reactor is not necessarily a cube but perhaps a rectangular parallelepiped, depending on whether the extrusion direction is confined to the vertical direction or the extrusion direction is laid criss-cross in the horizontal direction. Also the reflective properties of graphite would be better if the graphite extrusion direction is the same direction as neutron flow into the reflector. While the effects might be small on the neutron economy from these geometric considerations, the impact on practical reactor design can still be significant (Poulter 1963) because 1% improvement in the neutron economy can translate to a 40% decrease in the reactor volume.

The next experiments planned for graphite will be performed on a cubic block of solid graphite of roughly $8 \times 8 \times 8$ ft.³ dimension that would enable an improvement in accuracy of both the diffusion coefficient and the graphite absorption by about a factor of two. This experiment will be followed by a restacking of the graphite with the extrusion direction criss-crossed in the horizontal direction and then with the extrusion direction in the vertical direction. The diffusion coefficient measured along the z-axis should differ by about 15% for the two graphite orientations. The last experiment would be to heat the cube to about 300 °C and repeat the z-axis measurement. At 300 °C the experiment should have a sufficient sensitivity to detect any significant temperature effect on the diffusion coefficient.

A larger diffusion coefficient is of no advantage for homogeneous reactors, but offers a major gain for heterogeneous reactors. This subtle point follows from consideration of the diffusion equation for a homogeneous medium without fissile material, which can be written as

$$D\Delta^2\phi - \Sigma_{ca}\phi = 0, \quad (1)$$

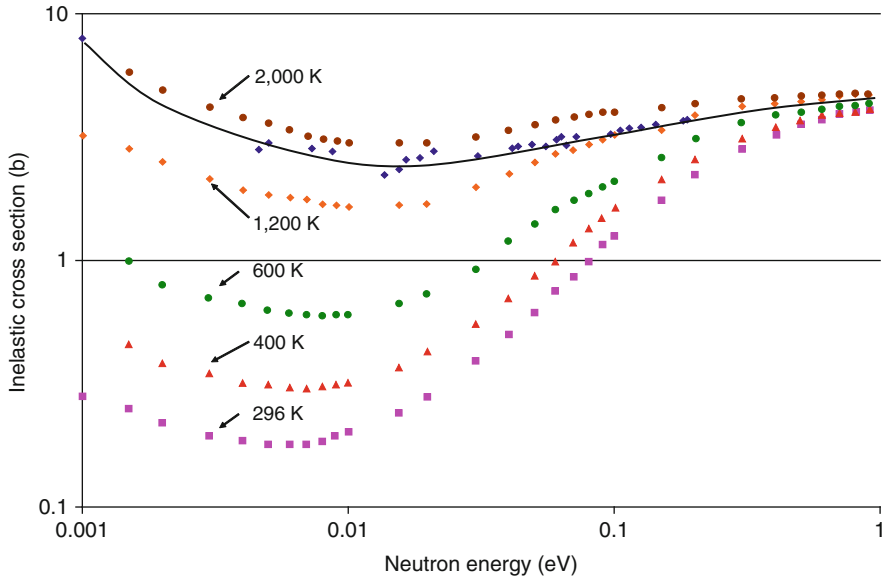


Figure 4

Inelastic scattering cross section in barns versus neutron energy. The MCNP5 calculations for the inelastic scattering from perfect crystalline graphite are shown for several temperatures. The *solid curve* is the measured (Bowman et al. 2008) inelastic scattering cross section at room temperature for graphite manufactured under high pressure. Note that, at 0.025 eV the measured inelastic scattering is 10 times higher than the MCNP5 calculation for perfect crystalline graphite and about the same as that predicted by MCNP5 for perfect crystalline graphite at 1,800 K. The MCNP5 calculation shows that the diffraction is depressed as the temperature rises, and the inelastic scattering enhanced, because the thermal motion of the atoms moves them farther from their equilibrium position in the crystals. For the manufactured graphite, the inelastic scattering is enhanced over diffraction because of the distortions in the crystal lattice introduced by manufacturing under high pressure

where D is the diffusion coefficient, ϕ is the neutron flux, and Σ_{ca} is the macroscopic neutron capture cross section defined as the carbon atom density times the carbon capture cross section. The first term is the rate of neutron entry into a differential volume element and the second is the rate of absorption in the volume element. Dividing (1) by D gives the form

$$\nabla^2 \phi - [\Sigma_{ca}/D]\phi = 0. \quad (2)$$

Clearly, the neutron loss during diffusion is reduced by the presence of a larger diffusion coefficient. However, for a homogeneous medium of carbon and uranium fissile material, (2) must be rewritten with capture and fission terms added as

$$\Delta^2 \phi - [\Sigma_{ca}/D]\phi + [(-\Sigma_{Uc} + \nu \Sigma_{Uf})/D]\phi = 0, \quad (3)$$

where ν is the number of neutrons per fission. Obviously *both* the fission term and carbon capture are reduced by a larger value for D , so there is no advantage to a larger diffusion coefficient for a homogeneous (carbon and fuel) reactor.

For a lightly loaded heterogeneous reactor in which a thermal neutron scatters many times on graphite before encountering uranium fuel, the larger diffusion coefficient of graphite reduces loss in graphite during diffusion while having no effect on the neutron absorption in fissile material. Nearly, all modern graphite reactors are effectively homogeneous reactors that cannot take advantage of the larger diffusion coefficient that can be manufactured into modern graphite. GEM*STAR is purposely a heterogeneous reactor that optimizes the neutron economy, not only with regard to the diffusion coefficient but also with regard to the ^{238}U resonance escape and fast fission factor characteristics for ^{238}U that Fermi employed (Stephenson 1954) to achieve the world's first chain reaction.

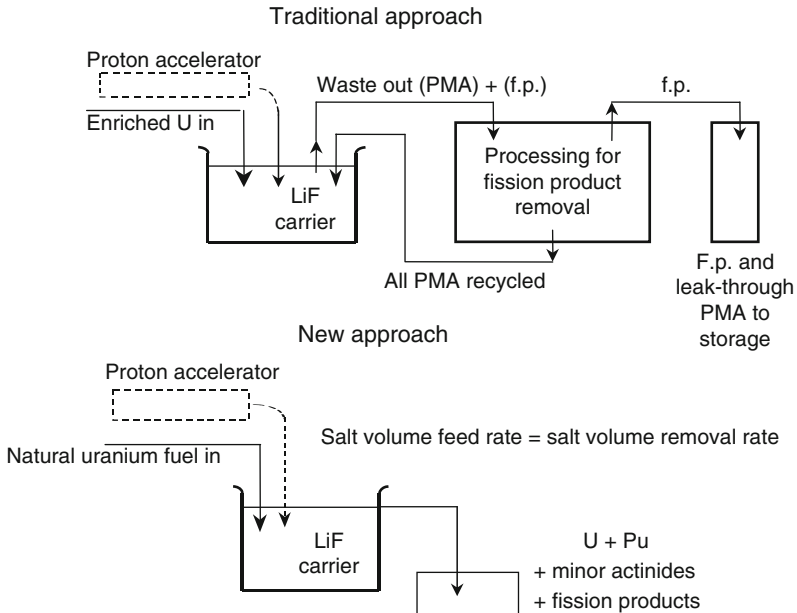
To summarize the graphite developments, modern codes for neutron transport in graphite based on a perfect crystalline structure grossly overestimate diffraction scattering and underestimate inelastic scattering. Because the distortion of the crystal structure of graphite depends on the manufacturing process, measurements instead of calculations will be required for predicting graphite reactor performance. The known anisotropies in the diffusion coefficient, which cannot be taken into account in today's codes, are likely to impact optimal reactor design and means must be found to address this issue. The boron content is much lower in some of today's manufactured graphite than traditional reactor-grade graphite. And finally, the cost of graphite today, taking inflation into account, is much lower than it was 40 years ago, so that graphite is not the significant cost factor for future reactors as it was for reactors of the past.

5 Integrating Accelerators, Molten Salt, and Graphite

The most recent serious attempt to introduce accelerators into nuclear energy technology was launched in the 1990s at Los Alamos National Laboratory (Bowman et al. 1992) as ATW and it attracted broad international attention and collaboration for several years. The technology was constrained however to *assisting* the established nuclear energy infrastructure including LWRs, breeder reactors, enrichment, reprocessing, and near-term geologic waste storage. Introducing an accelerator, which is not cost-free, to achieve modest incremental improvements into this already exceedingly complex infrastructure proved impractical, and any effort to use accelerators to simplify or eliminate any of the established elements encountered overwhelming political opposition. The ATW project did not succeed under the constraint that it was to provide little real impact on nuclear energy's problems.

GEM*STAR is an alternative nuclear power technology being developed by ADNA Corporation in the private sector using a continuous flow of liquid fuel without fission product (other than noble gases) or minor actinide removal (Bowman 1998, 2001). ➤ *Figure 5* shows the conventional molten salt approach and our new approach. The conventional approach is essentially that of the molten salt program of ORNL during the 1960s. Fissile and other actinide material flow in and irradiated fuel containing fission products flow out to an online chemistry facility that removes the fission products along with some leak-through actinides. The purified actinides and the non-fissile carrier salts are returned to the reactor. The system can achieve high burn-up of thorium without an accelerator, but it requires costly reprocessing, creates a flow of high-level waste that must be managed, and enables simple access to ^{233}U as weapons material. Subcritical operation with an accelerator would enable the system to operate on natural uranium, but would also provide access to plutonium for weapons use.

GEM*STAR operates on the system shown in the lower part of ➤ *Fig. 5* with a simple equilibrium overflow system where the volume flow in equals the volume flow out. The outflow



■ Figure 5

The *upper* part of the figure shows the system studied at ORNL using on-line reprocessing for plutonium, minor actinide (PMA), and fission product (f.p.) removal, but also with an accelerator added. The *lower* part of the figure shows the Green Energy Multiplier* Subcritical Technology for Alternative Reactors (GEM*STAR) approach with a simple equilibrium overflow system where the volume flow in equals the volume flow out. The outflow can be recycled several times using more non-fission neutrons each cycle as technology advances reduce the cost of neutrons

can be recycled several times at lower k_{eff} using ever larger fractions of non-fission neutrons – made economical as advances in technology reduce the cost of neutrons. It must be emphasized that the flow is not through a continuous tube inside the tank but that the inflow is thoroughly mixed continuously while in the tank. While any single atom might rarely come out almost immediately after entry or stay inside indefinitely, there is an average residence time and the neutron flux times the average residence time defines the average neutron fluence that the fuel coming out of the tank had experienced in the tank.

The system operates in equilibrium on the first cycle at $k_{\text{eff}} = 0.99$, but must be managed through a nonequilibrium period starting with k_{eff} less than 0.99. During the approach to equilibrium that might take several years, a protocol is followed by choice of initial fuel loading and by varying the fuel-carrier fraction, and the flow rate to eventually reach $k_{\text{eff}} = 0.99$ and stable operation. It is obvious but important to note that once equilibrium is reached, the composition of the outflow is the same as that inside the tank. Therefore, the outflow from a mother GEM*STAR can be transferred to a daughter GEM*STAR that can be immediately started *in equilibrium*. In this way, a situation similar to conventional breeding is established in which a mother might provide start-up fuel for many daughters with the daughters doing the same. The time for outflow of a full load of equilibrium fuel is typically about 5 years, roughly corresponding to a conventional breeding ratio of about 1.15. Obviously the GEM*STAR out-flow is

a financial asset particularly during the start-up and growth of GEM*STAR deployment as the outflow does not pass through any reprocessing step.

The system is subcritical initially at $k_{\text{eff}} = 0.99$ with the continuous in-out flow enabling stable operation without loss of neutrons to control rods. GEM*STAR uses a particular graphite that absorbs 30% less neutrons than ordinary reactor grade graphite as discussed earlier. The improved graphite, along with $k_{\text{eff}} = 0.99$, and avoidance of control rod loss enables an improvement in the neutron economy by about 8%. This change is the equivalent of raising the number of neutrons per fission from ^{235}U , from 2.43 to about 2.62 with significant consequences.

As shown later in this chapter, today's spent fuel presently bound for permanent geologic storage, can be burned without reprocessing in GEM*STAR. As much energy can be generated from it with $k_{\text{eff}} = 0.99$ as was generated in the LWR using fresh low-enriched uranium. Furthermore, existing accelerator technology enables the same energy to be produced at $k_{\text{eff}} = 0.95$ from recycling the GEM*STAR outflow at $k_{\text{eff}} = 0.99$ (with the required accelerator power only rising from 3 to 15%). The output can be recycled yet again at $k_{\text{eff}} = 0.90$ with the likely assumption that accelerator efficiency can be increased by two (neutron cost further reduced by two) before reaching the limits of today's understanding of accelerator design. And that is not the end. It can be shown (Bowman and Magill 2006) that long before fusion even nears practicality as a competitive energy source, it will produce neutrons more cheaply than accelerators enabling the recycling to continue much further.

But how much time would be available for developing and deploying practical fusion neutron sources? The present 100 GWe from US LWRs will result in 140,000 tons of spent fuel if their lifetime is extended from 40 to 80 years. If 100 GWe of new LWR power is brought on, the total spent fuel when both are retired will be 280,000 tons. If GEM*STAR systems start to replace the LWRs starting in 2020 and the US nuclear electricity grows to 200 GWe and continues indefinitely and GEM*STAR generates as much energy per tons of the spent fuel as the LWRs did, the GEM*STAR units can operate on LWR fuel for 80 years at $k_{\text{eff}} = 0.99$. With today's accelerator technology, another 80 years would be available from further recycle of original LWR fuel at $k_{\text{eff}} = 0.95$. With a factor of two improvement in accelerator performance beyond today's technology, recycle at $k_{\text{eff}} = 0.90$ could proceed toward the use of the original LWR fuel extensively for another 80 years, reaching about 240 years into the future. By that time, more advanced fusion neutron sources would be required to further recycle the original LWR fuel.


Three more recycles with fusion neutrons would extend the use to another 250 years. Therefore, 500 years hence the energy generation from today's LWR spent fuel would end with about 20% of the ^{238}U burned and about 20% of the mass being fission products. But that's not the end of the fission resource. We show in this chapter that natural uranium will perform as well in GEM*STAR as LWR spent fuel starting with $k_{\text{eff}} = 0.99$, so that another 500 years is added by only doubling the uranium used in the USA to date. Going even further we also show in the following section that depleted uranium can be used if we start with $k_{\text{eff}} = 0.95$, and there are about 7 tons of depleted uranium for every ton of low enriched fuel for LWRs enabling another 7×500 years. Finally, there is four times as much thorium as uranium in the earth's crust (Lide 1991), and GEM*STAR can burn thorium starting at $k_{\text{eff}} = 0.95$ for another $4 \times 8 \times 500$ years. By any measure, the fission energy resource opened up with supplemental neutrons from accelerators and from fusion and without invoking enrichment, FBR breeding, reprocessing, and near term high-level waste storage is enormous.

Since fusion neutrons help generate half of the energy in the above fission scenario, one might argue that one should instead proceed on to direct fusion energy production to open up an even more vast energy resource instead of just harnessing fusion to produce neutrons

cheaply. However, the earth's deuterium–tritium fusion energy resource is actually less than that from fission. The total of the U and Th in the earth's crust is 12.3 mg/kg (Lide 1991). Fusion energy ultimately relies on ${}^6\text{Li}$. The amount of Li is 20 mg/kg (Lide 1991) including 1.5 mg/kg amount of ${}^6\text{Li}$. Taking into account the masses, the atom ratio of U + Th to ${}^6\text{Li}$ in the earth's crust is 0.22. However, the energy per fission of U or Th is 200 MeV and that from ${}^6\text{Li}$ is about 20 MeV, so that this measure gives twice as much fission energy from the earth's crust as from fusion. With fusion energy appearing to be far into the unforeseeable future, one could make a strong case for directing some fusion research funds to the primary goal of efficient and cheap production of neutrons for fission.



At each step in the GEM*STAR recycle, there is no need for any chemical separations whatsoever on the fuel. By leaving in the higher actinides and fission products (other than noble gasses), these concurrently are transmuted to stable species instead of being separated out for attempts at special burn-up treatment as in the US DOE's current plan for the future of nuclear power (Report to congress 2006). It is shown below that the higher actinide species will be reduced by about a factor of 10/MWh produced after about six recycles. The long-lived fission products will also be transmuted because they have larger thermal capture cross sections on average than the shorter lived or stable fission products. Whenever final disposition of the GEM*STAR remnant fuel must be undertaken after at least several centuries, the mass and long-term radioactivity will be very significantly reduced from that of the current once-through process, made necessary by cost and proliferation concerns for more complex fuel cycles.

6 Calculations of GEM*STAR Burn-Up Performance

Determining the performance of a GEM*STAR system is relatively simple, due to its equilibrated state during operation. For each isotope in the feed fuel, one calculates the resulting equilibrium chain of isotopes within the system by specifying a neutron fluence and using estimates of the spectral average neutron cross sections. These chains are then combined, and the actinide fraction in the feed minus the equilibrium fraction in the full mixture, gives the burn-up fraction and the fission product fraction to add. Next, all the molten fuel components and other reactor elements are assembled in the design geometry, and MCNP is used to determine the “as-built” average cross sections. If these differ from before, the new ones are used to recalculate the equilibrium isotope distributions within each chain, the result reassembled, and MCNP run again. The process converges quickly, and k_{eff} is taken from the last iteration. Due to the larger diffusion coefficient in our graphite, a fraction of the neutron captures on carbon predicted by MCNP are redistributed among all the other reactions, weighted by their respective rates. This results in an increased k_{eff} , calculated by summing the products of fission rates times the average number of neutrons produced per fission, and dividing by the sum of neutron loss rates (see  Fig. 7). The process is then repeated for a different neutron fluence, generating points on a graph of k_{eff} and burn-up fraction versus neutron fluence for the specified isotope distribution in the feed fuel. The equilibrium equations are derived below, and then each step above is illustrated, noting any approximations or minor corrections applied.

The calculation of burn-up of a nuclide by successive neutron captures in a neutron flux with known capture and fission cross sections can be carried out using a set of coupled time-dependent differential equations first studied by Bateman (1927) that have complicated analytic solutions. For practical problems, alpha and beta decay might need to be taken into account and this is not possible with the Bateman equations. Instead the burn-up with decay can be

calculated with the ORIGEN 2 (Radiation Safety Information Computational Center (RSICC), Oak Ridge National Laboratory) code. However, even Origen 2 is not directly applicable to the in-out flow of the GEM* STAR system as it can only account for the start-to-finish isotopic evolution of a single load of fuel.

The lower part of  shows schematically the situation for burning natural uranium used as a fluoride salt. To explain in more detail, UF_4 is combined with 7LiF in a 1:2 mole concentration. This is a eutectic mixture that melts at about $520^\circ C$ compared to the melting points of $1,035$ and $848^\circ C$ for UF_4 and 7LiF , respectively as shown in . This salt is added slowly to a tank filled with the same mixture at maximum operating temperature of about $750^\circ C$. The tank also contains 93 volume percent of solid graphite with the melted salt occupying the other 7% of the tank volume. The system with the graphite and uranium is adjusted to $k_{eff} = 0.99$ and driven by supplementary neutrons so that the average thermal neutron flux in the tank is about $10^{14} \text{ n/cm}^2 \text{ s}$.

The tank is full and therefore overflows when more $UF_4 - {}^7LiF$ salt is added, for example, at the rate of about 0.80 l/h . The average atom in the tank is resident for about 4 years. In this flux for this period, considerable fission and capture take place on the uranium isotopes producing fission products and higher actinides besides uranium isotopes. The following definitions enable the writing of the differential equations that describe the time dependence for any nuclide in the tank.

V	Salt volume in the tank and internal heat exchanger
v	Volume flow rate into the tank in cm^3/s
N_i	Concentration of the nuclide i per cm^3
$\sigma_{ai} = \sigma_{ci} + \sigma_{fi}$	Absorption, capture and fission cross section of nuclide i
ϕ	Neutron flux averaged over the tank
F	Atom density of feed nuclide N_1 in atoms per cm^3

The rate of change in the tank of the total amount of the starting nuclide N_1 is

$$V \frac{dN_1}{dt} = Fv - \phi N_1 \sigma_{a1} V - N_1 v. \quad (4)$$

Neutron absorption in nuclide N_1 can lead to fission or by neutron capture (and any rapid beta decay) to nuclide N_2 . The total amount N_2 in the volume is then given by

$$V \frac{dN_2}{dt} = +\phi N_1 \sigma_{c1} V - \phi N_2 \sigma_{a2} V - N_2 v. \quad (5)$$

Similarly, the amount of the product nucleus N_3 is given by

$$V \frac{dN_3}{dt} = +\phi N_2 \sigma_{c2} V - \phi N_3 \sigma_{a3} V - N_3 v. \quad (6)$$

This set of differential equations can be solved for the time dependence of the concentration of all of the nuclides N_1 , N_2 , and N_3 , in the tank from the feed of N_1 . However, after the system has run for a while under proper controls the nuclide concentrations will equilibrate. This is the condition of most interest, and it may be calculated by setting all of the equations to zero, resulting in a set of algebraic equations instead of differential equations. Therefore, in equilibrium,

$$N_1/F = 1/[1 + \phi \sigma_{a1} (V/v)], \quad (7)$$

$$N_2/N_1 = \phi \sigma_{c1} (V/v)/[1 + \phi \sigma_{a2} (V/v)], \quad (8)$$

$$N_3/N_2 = \phi \sigma_{c2} (V/v)/[1 + \phi \sigma_{a3} (V/v)] \quad (9)$$

and similar equations for other daughters. Obviously the amounts of all daughters originating from a constant feed F will be at equilibrium as follows:

$$N_1 = F/[1 + \phi \sigma_{a1}(V/v)], \quad (10)$$

$$N_2 = N_1(N_2/N_1), \quad (11)$$

$$N_3 = N_1(N_2/N_1)(N_3/N_2). \quad (12)$$

And in general, since the ratio V/v is the average time that a nucleus stays in the flux, one can define a neutron fluence $F = \phi(V/v)$ with units n/cm^2 on an atom, giving

$$\begin{aligned} N_1 &= F/[1 + \phi \sigma_{a1}(V/v)] = F/[1 + F\sigma_{a1}], \\ N_i &= N_1 \prod_{j=2,i} (N_j/N_{j-1}) = N_1 \prod_{j=2,i} \{ \phi \sigma_{c(j-1)}(V/v) / [1 + \phi \sigma_{aj}(V/v)] \} \\ &= N_1 \prod_{j=2,i} \{ F\sigma_{c(j-1)} / [1 + F\sigma_{aj}] \} \quad i \geq 2. \end{aligned} \quad (13)$$

A simple hand calculation can be performed using (13) and starter values of flux and cross section estimates to get a distribution of isotopes from the feed of a single nucleus. If natural uranium is the feed material, it has two main isotopes ^{235}U and ^{238}U . Therefore, two separate calculations must be performed and the results added. In our calculations for uranium feed, the isotopes calculated included $^{235,236,238}\text{U}$, ^{237}Np , $^{238,239,240,241,242}\text{Pu}$, ^{243}Am , and $^{244,245,246}\text{Cm}$. The nuclides $^{241,241m}\text{Am}$ arising from the decay of ^{241}Pu were neglected owing to the ^{241}Pu decay half-life being long compared to the dwell time of a nucleus in the flux. The effect of neglecting the americium isotopes is very small on the neutron economy because the fission of ^{242m}Am yields 3.25 neutrons and the ^{242}Am decays mostly to ^{238}Pu as if the decay from ^{241}Pu to ^{241}Am had not taken place.

The calculation was done in several steps.

Step 1

In order to apply (13), one must specify a fluence. For a flux of $7.2 \times 10^{13} \text{ n/cm}^2 \text{ s}$ and an average residence time V/v of 4 years, the fluence $\phi(V/v)$ is about 0.009 n/barn or $0.009 \times 10^{24} \text{ n/cm}^2$. One then needs the capture and fission cross sections for each of the nuclides averaged over the neutron spectrum and volume of the reactor to get $\langle \sigma_{ci} \rangle$ and $\langle \sigma_{ai} \rangle$. These cross sections are not the thermal cross section because the flux extends up to the original fission neutron energy range. The flux shape to some degree depends on the isotopic composition, so the flux-averaged cross section also depends on the isotopic composition. The cross sections therefore must be obtained from MCNP5 calculations of interaction rates for all of the isotopes in an iterative process.

The average cross sections for a fluence $F = 0.009 \times 10^{24} \text{ n/cm}^2$ can be estimated from the interaction rates provided by an MCNP5 calculation which are shown in [Table 1](#). These need only be starting estimates of cross sections since they are updated by later iterations.

The abundance values are normalized for MCNP5 so that when the fractions of Li, F, and fission products are added to the sum of column 2 in [Table 1](#), the total is 1.0000. The small amount of ^4He added to the salt does not influence the spectrum but gives a means of calculating the collision rate of neutrons in the salt because the scattering cross section was set to one barn for all energies by means of a modified input library. The starred values for He in [Table 1](#) are not the capture rate but the He scattering rate and the He scattering cross section, respectively.

Table 1
Effective cross section calculation in barns

(1) Isotope	(2) Abundance	(3) Capture rate	(4) σ_c	(5) Fission rate	(6) σ_f	(7) σ_a
²³⁵ U	3.06E-4	0.0204	28.1	0.109	149	177
²³⁶ U	7.17E-5	0.00169	9.93	0	0	10.1
²³⁷ Np	3.93E-6	0.000597	64.0	0	0	64.2
²³⁸ U	1.09E-1	0.367	1.42	0.00972	0.038	1.46
²³⁹ Pu	3.19E-4	0.0891	118	0.192	253	371
²⁴⁰ Pu	1.21E-4	0.0581	203	0.000087	0.304	203
²⁴¹ Pu	4.56E-5	0.0116	108	0.0332	307	415
²⁴² Pu	3.35E-5	0.00301	37.9	0	0	38.0
⁴ He	1.31E-3	0.00315 ^a	1.00 ^a			

^aScattering rate and scattering cross section (manually set to 1 barn)

The capture rate R_{238} for ²³⁸U is given by $R_{238} = N_{238} \int \phi(E) \sigma_{c238}(E) dE$ and the scattering rate for He R_{He} is given by $R_{He} = N_{He} \sigma_{sHe} \int \phi(E) dE$. The average value for

$$\sigma_{c238} = \left[\int \phi(E) \sigma_{c238}(E) dE \right] / \left[\int \phi(E) dE \right] = [R_{238}/N_{238}] [R_{He}/N_{He} \sigma_{sHe}] \quad \text{or}$$

$$\sigma_{c238} = [N_{He} \sigma_{sHe}/R_{He}] \times [R_{238}/N_{238}] = [0.00131 \times 1.00/0.00315] \times [0.367/0.109] \quad \text{or}$$

$$\sigma_{c238} = [0.416] \times [3.37] = 1.40 \text{ barn.} \quad (14)$$

The factor 0.416 in (14) derived from the He can then be used to calculate cross sections for all of the other isotopes in Table 1 from the abundances and the reaction rates calculated from MCNP5.

Step 2

Using the cross sections above in the set of (13) enables the calculation of the burn-up for a fluence of $0.009 \times 10^{24} \text{ n/cm}^2 \text{ s}$ as shown in Table 2.

The ratios in column 6 correspond to those indicated in (13) and are derived from data in columns 4 and 5. The fractions in column 7 are successive products of the ratios in column 6 indicated in (13). For example, the value 0.375 for ²⁴⁰Pu in column 6 is found from dividing the number 1.062 for ²³⁹Pu in column 4 by the number 2.83 in column 5. The number 0.00109 in column 7 is obtained by multiplying the number 0.375 in column 6 for ²⁴⁰Pu by the number 0.00292 in column 7 for ²³⁹Pu.

The first three numbers in column 8 of Table 2 are the numbers in column 7 multiplied by the isotopic abundance 0.0072 of ²³⁵U in natural uranium. Similarly, the last five numbers are multiplied by the abundance 0.9928 of ²³⁸U in natural uranium. The sum of all of the numbers in column 8 (except for the feed) is 0.985. This number subtracted from 1.0000 gives the fission burn-up of 1.5% of the fed natural uranium. Retaining more significant digits throughout the calculations gives a burn-up of 1.19%.

■ **Table 2**

Burn-up calculations at a fluence of $F = 0.009 \times 10^{24} \text{ n/cm}^2$

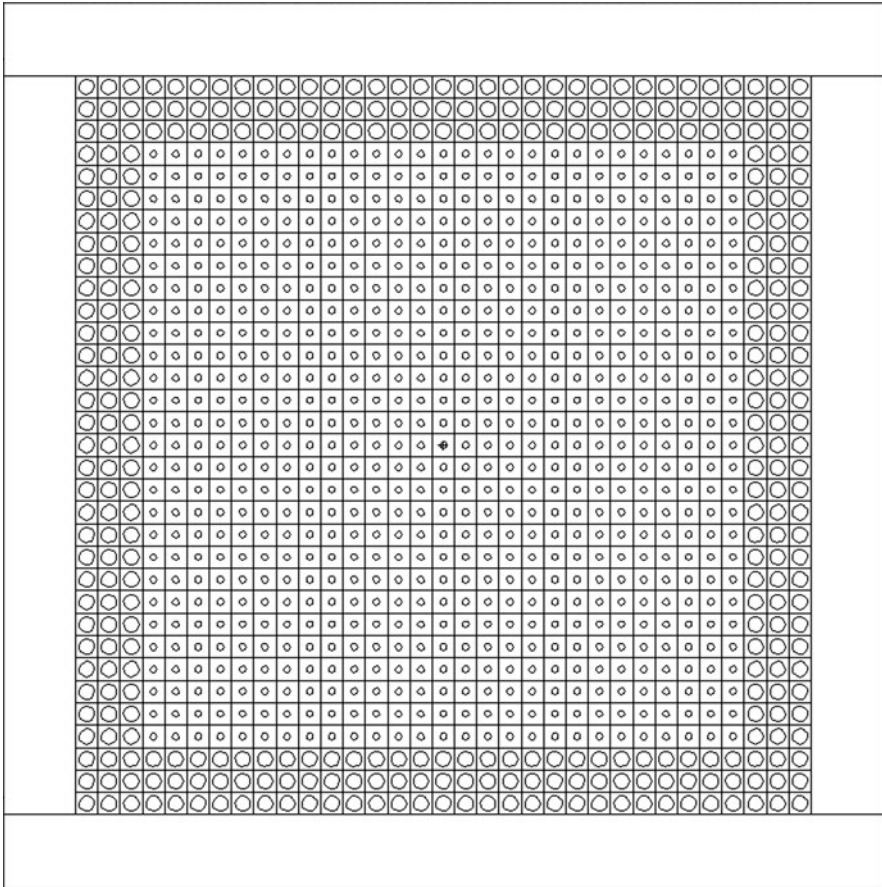
(1) Isotope	(2) σ_c	(3) σ_a	(4) $F\sigma_c$	(5) $(1 + F\sigma_a)$	(6) Ratio	(7) Fraction	(8) Normalized
F(²³⁵U)			1			1	0.0072
²³⁵ U	28.1	177	0.253	2.59	0.386	0.386	0.00278
²³⁶ U	9.93	10.1	0.0894	1.091	0.231	0.0895	0.000645
²³⁷ Np	64.0	64.2	0.576	1.58	0.0566	0.00507	0.000036
F(²³⁸U)			1			1	0.9928
²³⁸ U	1.42	1.46	0.0128	1.01	0.990	0.990	0.9800
²³⁹ Pu	118	371	1.062	4.34	0.00295	0.00292	0.00290
²⁴⁰ Pu	203	203	1.827	2.83	0.375	0.00109	0.00108
²⁴¹ Pu	108	415	0.972	4.73	0.386	0.000420	0.000418
²⁴² Pu	37.9	38.0	0.341	1.342	0.724	0.000304	0.000302

Step 3

The MCNP5 code is then used to calculate k_{eff} for the fluence of $0.009 \times 10^{24} \text{ n/cm}^2$. The graphite is included along with the code's $S(\alpha, \beta)$ distribution for room temperature graphite. The isotopic distributions in column 8 of [Table 2](#) are fed as the actinide component of the fuel along with the ^{10}B fraction and the He, ^7Li , and F fractions not shown in [Table 2](#). The ^{10}B is for the purpose explained in the next paragraph. The ^7Li and actinide (Ac) fractions in the salt are constrained by the eutectic 2:1 mole ratio of ^7LiF to AcF_4 .

The fission products present absorb neutrons and these neutron losses must be taken into account. Some of the fission product absorption cross sections are quite large so that a fission product nucleus can capture more than one neutron in one dwell period in the reactor. The average fission product neutron capture cross section can be taken into account (Bowman 2000b) including the possibility of multiple neutron capture. An average capture of 8.6 barns is found at thermal energy for a fluence $F = 0.01 \times 10^{24} \text{ n/cm}^2$. The average fission product capture cross section depends weakly on the fluence, but the effect is small compared to other uncertainties in the data for fission products. The fission product cross sections generally exhibit an inverse dependence on velocity ($1/v$). The fission products are therefore represented in the calculation by a proper amount of ^{10}B via the $^{10}\text{B}(n, \alpha)$ reaction, which also exhibits a $1/v$ dependence in the range of interest. The fission product fraction produced in the burn-up of [Table 2](#) is $2 \times 0.0119 = 0.0238$. Using ^{10}B to represent the fission products in MCNP5 as the code does not have all of the fission product capture data, we find that the ^{10}B fraction must be $0.0238 \times 8.6/3,837 = 0.0000533$ with the absorption of ^{10}B being 3,837 barns. This ^{10}B fraction probably overestimates the fission product absorption because the ^{10}B cross section averaged over the spectrum is considerably lower than the thermal value of 3,837 barns. However, owing to the uncertainty of the fission product cross sections, if the calculation errs with regard to fission product absorption, it overestimates the fission product absorption and underestimates overall GEM*STAR performance.

The calculation geometry, shown in plan view in [Fig. 6](#), is a cube surrounded by a 50-cm thick reflector. The cube is 503 cm on a side and it contains 33×33 square cylinders that



■ Figure 6


Plan view of geometry for MCNP5 burn-up calculation. The outside dimension of the cube is 603 cm on a side with a 50-cm thick graphite reflector on all six sides. The array of graphite elements is 503 cm on a side and it contains 33×33 square bars that are 503 cm long and 15.2 cm on each side running from the reactor bottom to the top. The inner set of bars running from top to bottom consisting of the central array of 27×27 cylinders is referred to here as the core. The rest of the bars nominally three cylinders thick is the blanket. The *square cylinders* of the core have a hole along the axis with 2.3 cm radius for the salt flow corresponding to a fuel volume fraction of 7.2%. The *square bars* in the blanket have a hole along the axis of radius 5.23 cm for the fuel salt and corresponding to a 37% salt volume

are 503 cm long and 15.2 cm on each side. There is an inner set of cylinders consisting of the central array of 27×27 cylinders referred to here as the core. The rest of the cylinders, nominally three cylinders, thick is the blanket. The square cylinders of the core have a hole along the axis with 2.3 cm radius for the salt flow corresponding to a fuel volume fraction of 7.2%. The square cylinders in the blanket have a hole along the axis of radius 5.23 cm for the fuel salt and corresponding to a 37% salt volume.

The Monte Carlo calculation yields $k_{\text{eff}} = 0.962$. The surface leakage fraction is 0.0083, the graphite absorption fraction is 0.0445, and the loss of neutrons to fission product absorption is 0.00984. Owing to the problems in MCNP in handling neutron transport in graphite, the value of k_{eff} calculated is too low by several percent. Corrections to this value of k_{eff} are calculated later for GEM*STAR graphite.

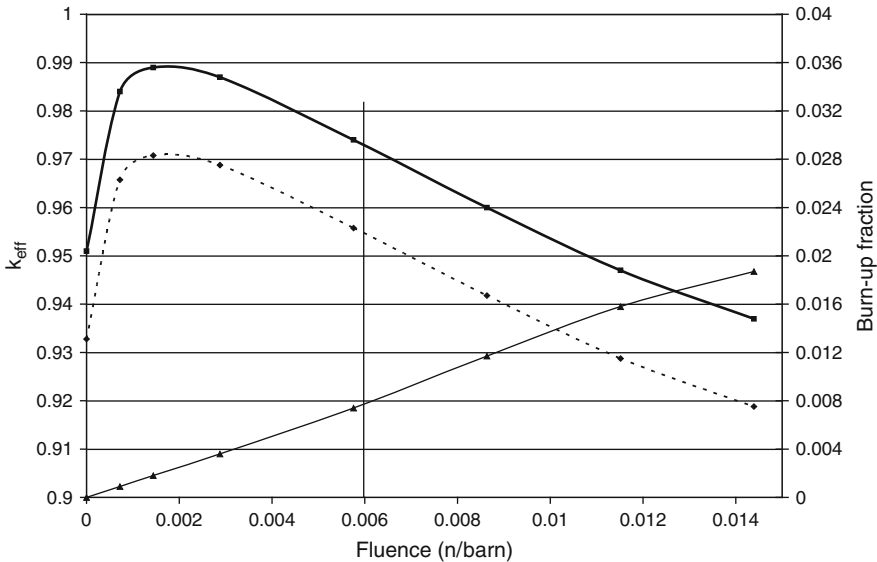
It should be noted that the cross sections used in step 1 could now be used as the starting point values for a completely new calculation at a different fluence. In general, one must expect some change in the cross sections between different burn-up conditions. Steps 1–3, therefore, would be repeated starting with the cross sections derived from the burn-up calculations at 0.009 n/barn to calculate cross sections and burn-up at a different fluence. In general, when a calculation is started in parameter space far from a previous calculation making it necessary to estimate the cross sections, a few iterations are necessary. However, it almost always converges by the third iteration.

7 Corrections for MCNP5 Graphite Absorption

Measurements by the ADNA team (Bowman et al. 2009a) show that the diffusion length for GEM*STAR graphite is 24% larger than is calculated by the $S(\alpha, \beta)$ tables of MCNP5. The measurements also showed that the boron content was lower (< 0.2 ppm) than “reactor grade” graphite (~ 0.6 ppm) providing together a total 30% reduction in graphite absorption from “reactor grade” graphite. Taking account of this correction involves reducing the MCNP5 results for neutron loss in graphite by 24% and redistributing these neutrons to absorption in other nuclides in proportions calculated using MCNP5. The result is a larger absorption in the fuel salt, and therefore a higher k_{eff} . But this method is only practical for pure graphite regions. Another (and much faster) method to account for the new graphite results is by scaling the capture cross section of carbon down by the ratio of the diffusion coefficients, rather than redistributing neutrons. These two methods have been compared and found to be equivalent, although the scaling method allows for a continuous correction, rather than the discreet component correction, otherwise required. This latter method was used to generate  Fig. 7. Nevertheless, to illustrate the first method, calculations were first performed with MCNP5 assuming no boron in the graphite, so the MCNP5 results had to be corrected for the 24% lower neutron loss in diffusion through graphite. The example calculation presented here is somewhat tedious but straightforward (fractions have been normalized to unity).

The leakage fraction of neutrons is 0.0083. The fraction of neutrons lost to carbon absorption in the core of the reactor is found to be 0.0445 and the 24% reduction in loss means that the fraction $0.0445 \times 0.24 = 0.0107$ can be redistributed. The reflector loss by absorption is 0.0120 and so 0.0030 will not be absorbed. However, these neutrons are near the surface and about half of them will leak out. Therefore, the total neutrons to be redistributed will be $0.0107 + 0.0029/2 = 0.0121$. The redistributed loss of neutrons to graphite absorption and leakage is:

Core graphite absorption 0.0445×0.76	0.0338
Reflector absorption 0.0120×0.76	0.0091
Graphite leakage $0.0083 + 0.0014$	0.0097
Total neutrons loss to graphite and leakage	0.0527



■ Figure 7

Burn-up and k_{eff} dependence on fluence for natural uranium for the core-and-blanket geometry. The *dashed curve* is the result of the MCNP5 calculation without the 24% increase in the diffusion length and reduced boron contaminant for graphite. The *solid curve* shows the results of using the improved graphite. The *vertical line* at a fluence of 0.006 n/barn is where one obtains twice the electric energy extracted from mined uranium as a light water reactor (LWR) extracts

Results from MCNP5 of thermal neutron absorption in the fuel are listed in column 2 of ▶ [Table 3](#). The numbers for ^{238}U and ^{240}Pu must be adjusted because resonance and higher kilovolt capture in these nuclides is a significant part of the total absorption. Generally, about 1/3 of the total absorption in weak thermal absorbers is nonthermal so the entries in ▶ [Table 3](#) are 2/3 of the total ^{238}U and ^{240}Pu absorption.

Column 3 of ▶ [Table 3](#) shows the additions to the reaction rates from redistribution of the 0.0121 fraction of neutrons not absorbed in graphite. The sum of column 3 is therefore 0.0121 and the sums of columns 2 and 3 must equal the sums of columns 4 and 5. Corresponding high energy reactions in the core are listed in ▶ [Table 4](#).

Because the blanket was thin compared to the core, corrections were applied to the core and not the blanket. The sum of the fission in the blanket was 0.0442 and the capture was 0.1094. The corrected k_{eff} can be calculated as

$$k_{eff} = [\text{the sum of the product of fissions times neutrons per fission}] / [\text{total absorption}].$$

The numerator is:

$$\begin{aligned} \text{Num.} &= 0.425 \times 0.101226 + 2.88 \times 0.174956 + 2.94 \\ &\quad \times 0.030042 + 2.88 \times 0.00712 + 2.77 \times 0.0442 = 0.9806. \end{aligned}$$

The number of neutrons per fission ν is 2.425 for thermal fission of ^{235}U , 2.88 for ^{239}Pu , and 2.94 for ^{241}Pu . The number 2.77 is the weighted value for fission in the blanket.

■ **Table 3**
Adjustment of thermal neutron absorption in the core

(1) Nuclide	(2) MCNP5	(3) Correction	(4) Capture	(5) Fission
²³⁵ U capture	0.0180	0.000331	0.018331	
²³⁵ U fission	0.0994	0.001826		0.101226
²³⁶ U capture	0.0012	0.000022	0.001222	
²³⁷ Np capture	0.0005	0.000009	0.000509	
²³⁸ U capture (2/3)	0.1958	0.003599	0.199497	
²³⁹ Pu capture	0.0779	0.001431	0.079331	
²³⁹ Pu fission	0.1718	0.003156		0.174956
²⁴⁰ Pu capture (2/3)	0.0333	0.000613	0.033963	
²⁴¹ Pu capture	0.0098	0.000180	0.009980	
²⁴¹ Pu fission	0.0295	0.000542		0.030042
²⁴² Pu capture	0.0022	0.000040	0.002242	
Fission product	0.0088	0.000162	0.008963	
⁷ Li	0.0056	0.000103	0.005703	
¹⁹ F	0.0058	0.000107	0.005907	
Total	0.6597	0.012120	0.365644	0.306224

■ **Table 4**
High energy reactions in the core

Nuclide	Capture	Fission
²³⁸ U capture (1/3)	0.0979	
²³⁸ U fission		0.00706
²⁴⁰ Pu capture (1/3)	0.0167	
²⁴⁰ Pu fission		0.00006
Total	0.1146	0.00712

The denominator is:

$$\begin{aligned} \text{Denom.} = & [0.101226 + 0.174956 + 0.030042 + 0.00712 + 0.0442 + 0.1145 \\ & + 0.3656 + 0.1094 + 0.0527] = 0.99972. \end{aligned}$$

The graphite-absorption-corrected $k_{\text{eff}} = 0.9806/0.9997 = 0.981$ compared to the MCNP5 value of 0.962 for an increase of about 1.9%. If one applies the same correction for a fluence of zero, meaning either very fast flow-through or zero burn-up, we find the same increase of 1.9%. One should note that the ¹³⁵Xe fission product is continuously removed in GEM* STAR, and that the use of ¹⁰B to simulate fission-product absorption was probably too absorptive, so an even higher k_{eff} might be possible.

The calculation of k_{eff} and burn-up described above was performed for fluences up to 0.014 n/barn for a natural uranium feed. Similar calculations using the carbon capture cross section scaling method described earlier were also performed, allowing the boron contamination in the graphite to be included, and the results are shown in [Fig. 7](#). The dashed curve is the MCNP5 calculation and the solid curve is the MCNP5 calculation with improved graphite.

Regarding the burn-up fraction of natural uranium in [Fig. 7](#), one may note that LWR fresh fuel enriched to 4.2% in ^{235}U is obtained by isotopic separations that remove about 0.50% of the 0.72% of the ^{235}U in natural uranium resulting in depleted uranium with 0.22% ^{235}U . Therefore, $1 + [(4.2 - 0.7)/0.5] = 8$ tons of natural uranium is required to produce one ton of uranium enriched to 4.2%. So when an LWR fissions 4% of its fed fuel, it is actually burning only $4\%/8 = 0.5\%$ of the mined uranium.

The peak in the k_{eff} curve is an interesting feature for this equilibrium calculation. A fluence of zero corresponds to such a fast flow-through that no ^{239}Pu or fission products are created. The neutron economy is inferior to a graphite reactor with metallic natural uranium fuel because the fast fission in metal fuel is about four times that in our eutectic molten salt fuel. However, the combination of water cooling, metal fuel, and graphite moderator is a potentially unsafe combination and gas cooling seems not to be compatible with liquid fuel.

Our design goal of $k_{\text{eff}} = 0.99$ at a fluence enabling twice the burn-up of an LWR *without enrichment* seems difficult at first to achieve. However, it is important to note that so far throughout this chapter the simplification has been made that k_{eff} of the reactor by itself is sufficient to describe the reactor response during driven operation. In practice, the reactor has higher neutron multiplication near its center compared to near the walls. Thus, the details of how the neutrons from the target are coupled into the reactor are quite important but are currently proprietary. For completeness, and to illustrate the important impact such refinements can have, [Fig. 8](#) shows the result for a modified GEM* STAR design incorporating a practical central target, where rather than defining a k_{eff} for the system, each proton impinging on the target has all of its interactions and subsequent particles, including fission neutrons, fully tracked. The energy released by fission during this process is compared to the energy of the incoming proton and then accelerator efficiency and thermal to electric conversion efficiency are included to yield the *electrical* multiplication. At a fluence of 0.004 n/barn, the electrical multiplication of a green electrical source is 40 and the burn-up at 0.5% is the same as LWRs for mined uranium. For an electrical multiplication of 10, the uranium resource usage is stretched by 3.5 times without resorting to the complications of breeder technology.

8 GEM* STAR Reactor Parameters

The illustrative parameters described next are for the core-and-blanket configuration shown in [Fig. 6](#) with burn-up of 0.0102, $k_{\text{eff}} = 0.99$, and a fluence of 0.013 n/barn. We continue to use this model for illustration, but the reader should be aware that implementation of a central target as described in the previous section is necessary to achieve the results which follow. Each unit operates at a fission power of 500 MW_t and generates 220 MW_e of electricity when deployed in an array of five units as shown in [Fig. 9](#) using six accelerators. The green energy multiplication for the array of five is 29 and the electricity production is 1.1 GWe. For the deployment of only one unit, the accelerator-produced neutrons are not as efficiently used and the power is 180 MW_e and the multiplication is 23.

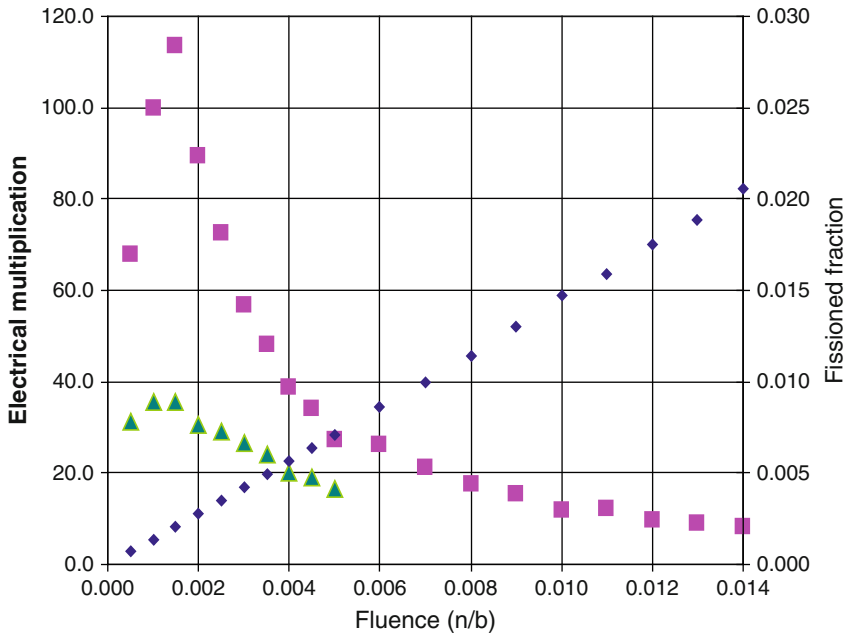


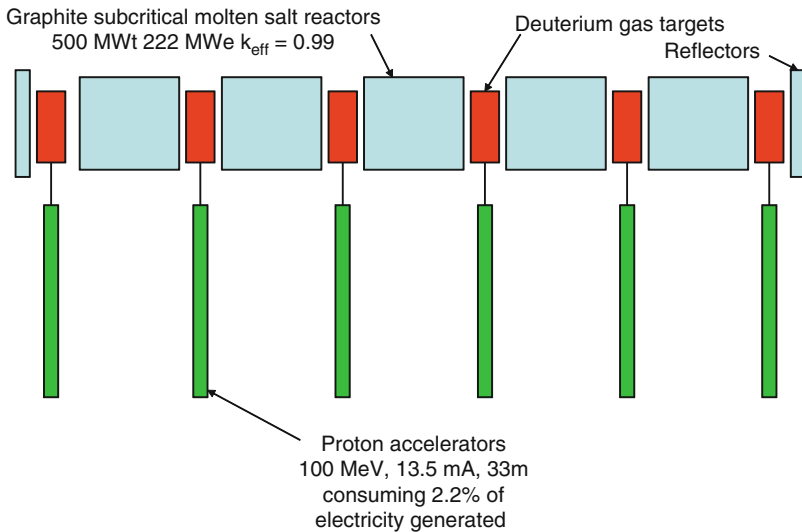
Figure 8

Performance of a GEM*STAR system with a central target burning natural uranium. The *squares* assume, a 35% efficient accelerator, and a thermal to electric conversion efficiency of 44%. The *triangles* are the same using normal MCNP that cannot account for the distorted crystalline structure of graphite. The *diamonds* show the actinide burn-up fraction for operation in equilibrium

Figure 10 shows a view of one GEM*STAR unit as a vertical slice through the center of the cubic reactor core. The density of the graphite is 1.63 g/cm^3 and that of the salt is 3.8 g/cm^3 , so the graphite would float if not constrained by a graphite or Hastelloy cap across the top of the tank that is not shown. The design includes two cooled tanks under the subcritical reactor to collect the outflow. The outflow tube allows the main tank to be pressurized sufficiently with helium to enable salt from the overflow tanks to be pushed out of them through the lid of the reactor and to storage cylinders well away from the reactor. The helium pressure required is about four atmospheres and the containment must be able to contain that pressure. Helium continually flows at lower pressure above the fuel surface to remove volatile fission products such as noble gases and tritium fluoride that are then removed from the helium to enable He recycling. These volatiles are short-lived, and can be readily stored until decay.

Although target details are proprietary, a conceptual system is included for illustration. Two accelerator targets of 4-m length, made of 15-cm thick Be metal tubes containing deuterium gas are shown. High energy neutrons are produced by a proton beam on a stopping length thickness of deuterium gas and these neutrons are multiplied by a factor of two by the beryllium. A 1-m high and 5-m long slot in the graphite reflector is not shown. It enables target neutrons that pass readily through the metal wall to reach the reactor core. A graphite reflector of 50 cm thickness is included on three sides around the target to reflect the neutrons toward the core.

1,100 MWe power plant from five 222 MWe units

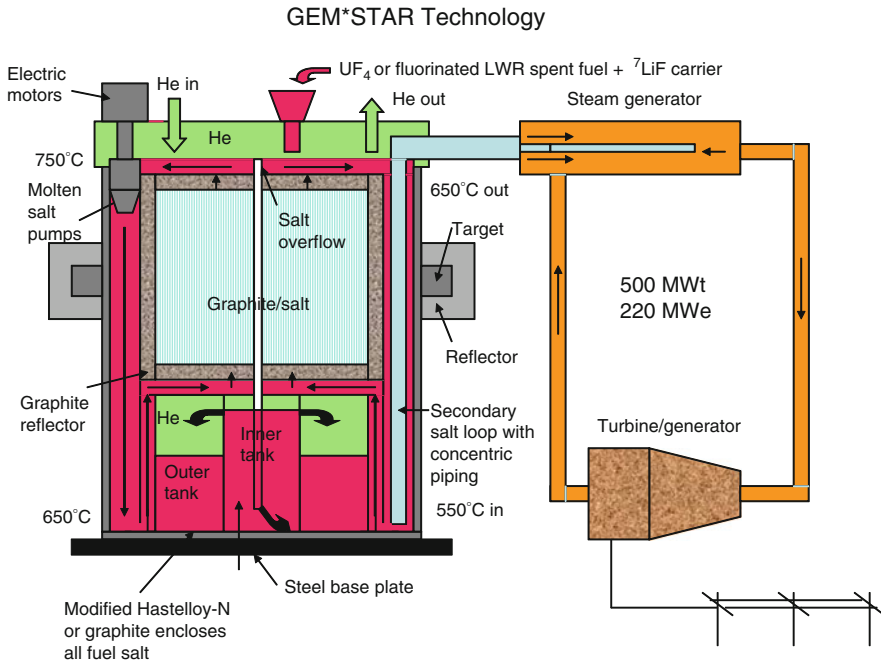


■ Figure 9

Five GEM*STAR units ganged together to produce 1.1 GWe. The 33-m accelerators generate proton beams striking deuterium targets that are expected (Bowman et al. 2009b) to produce neutrons with the same energy cost as a 1-GeV and 1.35 mA proton beam on a lead spallation target or a 0.5 GeV and 1.35 mA proton beam on a uranium spallation target

The core consists of square bars with $15.2 \times 15.2 \text{ cm}^2$ cross section and 503 cm length. They have a hole along the axis with radius 2.30 cm for salt flow. They are arranged in a square 27×27 array and provide a salt/graphite ratio of 0.072. A blanket is included outside of the core consisting of three layers of the same prisms but with holes of radius 5.23 cm. The total volume of the core and blanket together is a 33×33 array. A graphite reflector 50 cm thick is included on all six sides outside of the blanket. The total volume of the core is 86 m^3 . The total volume of salt in the core is 6.1 m^3 giving a salt to graphite volume ratio of 0.072. The volume of fuel in the blanket is 15.6 m^3 with fuel to graphite ratio of 0.37. The fuel in the internal heat exchanger region outside the reflector is 8.9 m^3 and the total fuel volume is 30.6 m^3 . There is a small amount of additional fuel in the plena above the top reflector and below the bottom reflector. The mass of natural uranium in a full load is 76 tons U, or 100 tons of UF_4 , and 4.6 tons of ^7Li .

The actinide isotope fractions in Table 2 enable the calculation of the total inventories in the reactor of 215 kg of ^{235}U and 223 kg of ^{239}Pu . This fissile inventory is at least an order of magnitude lower than the ^{239}Pu in a fast breeder or fast burner reactor of the same power. For a burn-up fraction of 1.2%, the amount fissioned in passing a full volume of 76 tons of actinide through is 912 kg. If the passage time is 4.5 years with fuel burn of 200 kg/year, the fission power is found to be 500 MW_t, which at 44% thermal-to-electric conversion efficiency is 220 MW_e. For a fluence of $0.014 \times 10^{24} \text{ n/cm}^2$, and a total volume flow-through time of 4.5 years, the thermal flux is $1.0 \times 10^{14} \text{ n/cm}^2 \text{ s}$ averaged over all of the fuel with 29% of the fuel in the internal heat exchanger. The lifetime of graphite is usually taken to be a fluence (Weinberg et al. 1970)



■ **Figure 10**

Schematic drawing of a 220 MWe subcritical reactor with dimensions approximately of a 20-ft. cube (see text), which would be located underground. Two targets are present on opposite sides of the reactor. Molten salt fuel is poured into the top and is circulated by pumps down the outside of the reactor, back up to the underside of the reactor, and through the reactor graphite to the top. With each addition of salt an equal salt volume overflows through the tube in the center and down into the inner holding tank. On average an atom of salt spends about 4.5 years in the tank before flowing out. When full, the inner tank overflows into the outer holding tank. Together the two holding tanks can contain all of the salt fuel used over the 40-year life of the reactor. Heat is removed via an internal heat exchanger using a secondary salt in concentric tubes that carry the salt into the reactor at 550 °C and out a 650 °C. The fuel salt is confined everywhere on the outside by modified-Hastelloy-N and otherwise by graphite. Continuously flowing He across the surface of the fuel salt removes noble gases and other volatiles. Overheating of the salt results in expansion that reduces the salt density providing negative feedback and also may result in fail-safe overflow into the storage tanks below. The salt also circulates slowly by thermal convection and air flows upward over the reactor sides enables passive removal of the heat in case of loss of coolant pumping

of 3×10^{22} n/cm² of the flux above 50 keV with the fast fraction being about 30% of the total. According to the ORNL-MSBR design (Weinberg et al. 1970), a lifetime of 4 years is expected for a thermal power density of 22 kw/l. The GEM*STAR average power level is 4.0 kw/l giving a graphite lifetime of about 22 years. Because 29% of the fuel is outside of the core, the average flux actually required is 1.4×10^{14} n/cm² s and the core-blanket graphite lifetime is about 17 years.

The fuel salt does not leave the vessel for heat removal. ● **Figure 10** shows salt being pumped down the four outside walls of the graphite reflector in an 8.9-cm thick channel that is 608 cm wide and 1,200 cm high. Inside this channel 300 concentric tubes carry a lower melting point

secondary salt for heat transfer from the fuel salt. The composition of this salt is $\text{NaBF}_4 : \text{NaF}$ in the mole ratio 92:8 with a eutectic melting point of 385°C . The heated secondary salt then flows outside the reactor vessel to steam generators.

The cooler secondary salt flows down through the inner tube of a concentric pair to the bottom and returns inside the outer sleeve to the top. The wall thickness for both the inner and outer tubes is 3.2 mm. The I.D. of the inner tube is 44 mm. The O.D. of the outer tube is 76 mm. The secondary salt enters the top at a temperature of 550°C , flows at 3.2 m/s down to the bottom where its temperature is about 570°C and flows up at 2.8 m/s reaching 650°C at the top. The primary salt starts at the top at 750°C and exits at 650°C traveling at a velocity of 1.3 m/s. The velocity of salt upward through the tank is about 0.4 m/s and the total circulation time is about 20 s.

In case of a loss-of-coolant accident, the fuel salt will continue to circulate by convection. The heat capacity of the 350 tons of graphite in the core, blanket, and reflector and this natural convection will conduct the heat into the steel wall, which is always cooled by natural air. Fail safe means for interrupting accelerator beam power and for dropping in the on-off rods stop the power production. Naturally convective air cooling flowing up beside the reactor's four metal sides is always present.

The time to reach equilibrium from start-up is estimated to be about two volumes or 9 years although this time can be considerably shortened by appropriate initial starting composition and fuel management during the approach to equilibrium. After equilibrium, if fuel is added each hour, the volume added each time would be about 0.78 l corresponding to a volume fraction of 0.000025. This would roughly correspond to changing the multiplication from $1/(1 - 0.99) = 100$ to $1/(1 - 0.9900230) = 100.25$ and increasing the fission power by 0.25%. The fission power would then decline by that amount over the hour between fuel additions for constant accelerator power.

The accelerator parameters can be calculated from the fission rate at 200 kg of uranium burned per year (producing 220 MW_e) corresponding to 1.6×10^{19} fissions per second. At k_{eff} of 0.99, the fission chains average 100 fissions in length so 1.6×10^{17} fission chains are started per second. If on average 2.6 neutrons are released in fission from ^{235}U and ^{239}Pu and it takes this many to start a fission chain for k_{eff} near 1.00, then the number required from the accelerator is 4.2×10^{17} n/s if all made it inside to the fuel-blanket. However, about 10% will be lost so that the total required is 4.8×10^{17} n/s. A 1-GeV proton beam on a lead target produces about 30 neutrons per proton by spallation, so the number of protons required is 1.6×10^{16} protons per second or 1.35 mA and 1.35 MWb of beam power from each of two accelerators. If the accelerator efficiency for conversion of buss-bar to beam power is 35%, the electric power requirement for one accelerator is 3.9 MW_e . The green energy source for powering the two accelerators would supply the 7.8 MW_e giving a multiplication of 29 for GEM*STAR. The acceleration gradient of a 1-GeV proton linac is probably about 5 MV/m so the accelerator length would be about 200 m.

It might be possible to produce neutrons on a deuterium target (Bowman et al. 2009b) with the same energy efficiency but with a 100-MeV accelerator. In that case, the linac accelerator length would be about 20 m and the proton current for each accelerator would be 15 mA. In the same paper (Bowman et al. 2009b), the advantage of having half the beam from two accelerators each with its own target is discussed. With two accelerators, each 100-MeV accelerator would produce 13.5 mA for a power of 1.35 MWb each. GEM*STAR parameters for the reactor, the heat exchanger, and the accelerator-target are given in [► Tables 5-7](#), respectively. The same neutron input rate could be supplied using uranium targets driven by two 0.5 GeV 1.35 mA proton accelerators. Thus three linac-target options are available probably producing neutrons

■ **Table 5**
Green Energy Multiplier* Subcritical Technology for Alternative Reactors (GEM* STAR) design parameters

Green energy multiplication factor	29
Fission power (MW_t)	500
Thermal to electric conversion efficiency (%)	44.4
Electric power (MW_e)	222
k_{eff}	0.99
Fuel salt melting point ${}^7LiF : 0.5UF_4$ ($^{\circ}C$)	500
Fuel salt maximum operating temperature ($^{\circ}C$)	750
Fuel salt minimum operating temperature ($^{\circ}C$)	650
Fuel flow-through time (years)	4.5
Fuel salt loading temporal spacing (hours)	1.0
Fuel salt loading volume (liters)	0.78
Fission power increase per hourly loading (%)	0.25
Time to equilibrium nat. U burner (years)	9
Time to equilibrium for daughter nat. U burner (years)	0
Side dimension of cubic core and blanket (cm)	502
Thickness of graphite square cylinders (cm)	15.24
Number of cylinders core and blanket (33 \times 33)	1,089
Number of cylinders across the core	27
Volume of core (m^3)	86
Reflector thickness (cm)	50
Volume of blanket (m^3)	42
Reflector volume (m^3)	109
Graphite mass of core, blanket and reflector (T)	350
Radius of core holes (cm)	2.3
Fuel salt volume in core (m^3)	6.1
Radius of blanket holes (cm)	5.23
Fuel salt volume in the blanket (m^3)	15.6
Thickness of salt channel of heat exchanger (cm)	8.9
Height of salt channel of heat exchanger (cm)	1,200
Fuel salt volume in the heat exchanger (m^3)	8.9
Total fuel volume (m^3)	30.6
Total fuel mass (T)	117
Total natural uranium mass (T)	76

■ **Table 5 (continued)**

Total fissioned mass per year (kg)	200
Total ${}^7\text{LiF}$ mass (T)	17
Total ${}^7\text{Li}$ mass (T)	4.6
Isotopic purity of ${}^7\text{Li}$ (%)	99.99
Thickness of isolation layer Hastelloy (mm)	13
Thickness of steel structure vessel (mm)	50
Steel vessel mass (T)	158
Hastelloy bolt spacing, square pattern (cm)	50
Average thermal neutron flux ($\text{n}/\text{cm}^2 \text{ s} \times 10^{14}$)	1.4
Core power density (kW/l)	4.0
Graphite lifetime (years)	17

■ **Table 6**

Internal heat exchanger design parameters

Total heat transfer (MW_t)	500
Melting point of fuel salt (${}^\circ\text{C}$)	500
Number of peripheral molten salt pumps	50
Height of fuel salt transfer layer (cm)	1,200
Fuel salt inlet temperature to transfer layer (${}^\circ\text{C}$)	750
Fuel salt outlet temperature (${}^\circ\text{C}$)	650
Fuel salt down velocity (m/s)	1.3
Number concentric paired tubes for secondary salt	300
Concentric tube pitch (mm)	81.3
Inside down-tube wall thickness (mm)	3.2
ID of inside down tube (mm)	44.5
Outside up-tube wall thickness (mm)	3.2
ID of outside up-tube wall thickness	69.9
Down tube velocity (m/s)	3.2
Up tube velocity (m/s)	2.8
Inlet secondary salt temperature at the top (${}^\circ\text{C}$)	550
Secondary salt temperature at bottom (${}^\circ\text{C}$)	570
Secondary salt temperature at the top (${}^\circ\text{C}$)	650

■ **Table 7**
Accelerator and target parameters for 220 MW_e output

Number of accelerator-target pairs	2
Fraction of neutrons produced that enter the reactor	0.90
Neutrons required per target ($n/s \times 10^{17}$)	2.4
<i>With lead target</i>	
Beam energy (GeV)	1.0
Accelerator current per accelerator (mA)	1.35
Beam power per accelerator (MWb)	1.35
Accelerator power for 35% accelerator efficiency (MW _e)	3.9
Accelerator length (m)	200
<i>Or with uranium target</i>	
Beam energy (GeV)	0.5
Accelerator current per accelerator (mA)	1.35
Beam power per accelerator (MWb)	0.67
Accelerator power for 35% accelerator efficiency (MW _e)	2.0
Accelerator length (m)	100
<i>Or with deuterium target</i>	
Beam energy (MeV)	100
100-MeV-accelerator beam current per target (mA)	13.5
Accelerator beam power one accelerator (MWb)	1.35
Power consumption for one accelerator (MWe)	3.9
Accelerator length (m)	30

at the same rate including 1 GeV and 1.35 mA on a lead spallation target, 0.5 GeV and 1.35 mA on a uranium spallation target, and 0.10 GeV 13.5 mA on a deuterium target.

An appropriate size for a demonstration facility might be 5% of GEM* STAR for a fission power of about 25 MW_t and an electric power of 11 MW_e driven by a single 100 MeV accelerator with a proton current of about 1.5 mA.

9 Burning LWR Spent Fuel

The same core-blanket geometry as was used for natural uranium burning was used to calculate the LWR spent fuel burn-up. The calculation procedure also was the same with the fission product absorption being bundled together as before and being represented again by the equivalent absorption of boron. Of course, the calculation was significantly more complex because there were only ²³⁵U and ²³⁸U as starting nuclides for natural uranium fuel, but for spent fuel there were in addition ²³⁷Np, ^{238,239,240,241,242}Pu, ²⁴¹Am, and ^{244,245}Cm. The starting concentrations

(CURE 1990) were taken for a burn-up of 33,000 MW-days/tons of heavy nuclides that had been out of the LWR for 10 years.

➤ **Table 8** shows the results of the calculation for $k_{\text{eff}} = 0.99$. Columns 1 and 2 give the isotopic composition and fractions of the feed from the LWR spent fuel. If the total actinide fission fraction from the LWR of 0.034 is added to the sum of the second column, the second column adds to one. (The number for the fission product nuclides would of course be twice as large as 0.034.) The row across the top lists the isotopes that flow out of GEM*STAR. The numbers in the rows of the table show the transmuted fractions of the starting isotope in column 1. So numbers across the second row show the results for the ^{235}U feed. There is an entry in the second row for every isotope up to ^{239}Pu . Beyond ^{239}Pu the fractions are too small to record. The bottom row sums each column of the table giving the isotopic composition of the outflow of GEM*STAR at $k_{\text{eff}} = 0.99$. The total of the sums of columns 3–15 across the bottom line is 0.9336. Because the starting fission fraction from the LWR was 0.034, the burn-up by fission in the first GEM*STAR cycle is $1 - 0.9335 + 0.0340 = 0.0324$. The value for k_{eff} from MCNP5, which does not take into account the beneficial effects of distorted crystal structure is 0.962. The correction for the distorted crystalline structure, is 0.028 taking k_{eff} to 0.99.

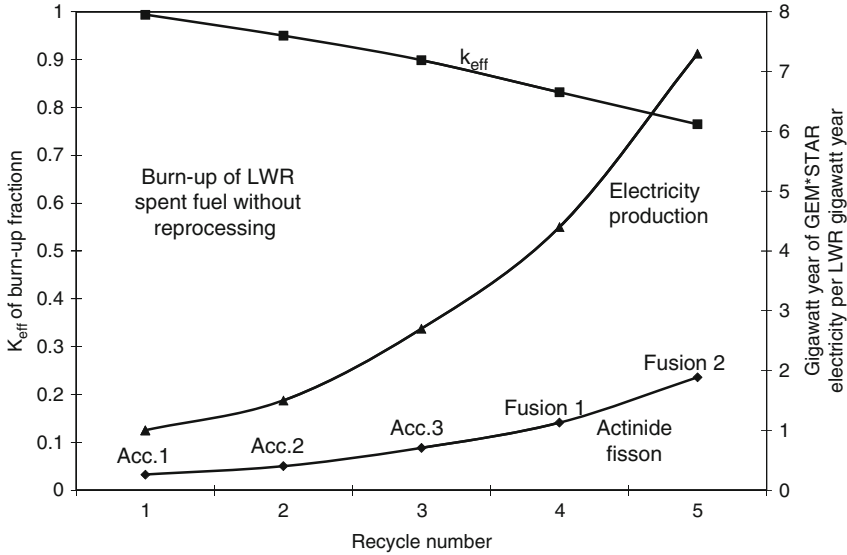
The first burning of LWR spent fuel detailed in ➤ **Table 8** is then followed by a second cycling of the output at $k_{\text{eff}} = 0.95$ and the output of the second cycling is cycled again at $k_{\text{eff}} = 0.90$. The cycling continues with the full series calculated here being for $k_{\text{eff}} = 0.99, 0.95, 0.90, 0.83,$ and 0.76 . The first three cycles would use accelerator neutrons and the last two would use fusion neutron sources. ➤ **Figure 11** shows k_{eff} and the cumulative burn-up fraction for each cycle along with the additional energy in gigawatt-years that would be extracted from the fuel loading from a typical LWR generating 1 GWe-years of energy per year (five modules).

➤ **Table 9** includes more details about the five cycles for burning of the spent fuel from one LWR operating at 1,000 MWe. It begins with starting the LWR waste burning in a GEM*STAR reactor in 2020 at $k_{\text{eff}} = 0.99$ and generating 1 GWe. Because it took 40 years for the LWR to generate its total waste stream, it also takes 40 years for GEM*STAR to make the first pass at $k_{\text{eff}} = 0.99$ generating the same 1 GWe power as the LWR. The second cycle therefore starts in 2060 with a more powerful accelerator referred to in the table as Acc. 2 and $k_{\text{eff}} = 0.95$ where the fission chain averages 20 in length. In this second cycle the *cost per neutron* is the same because the accelerator uses the same technology as Acc. 1, but the system required five times more neutrons so the total neutron cost is a factor of 5 larger. Therefore, whereas the accelerator added about 3% to the final cost of electric power for $k_{\text{eff}} = 0.99$, it will add about 15% for $k_{\text{eff}} = 0.95$. For the third cycle at $k_{\text{eff}} = 0.90$, twice as many neutrons must be generated by Acc. 3 compared with Acc. 2. Accelerator technology advanced beyond that of today is therefore required to *reduce the cost per neutron by two* to keep the cost of electric power the same for Acc. 3 with $k_{\text{eff}} = 0.90$ as with Acc. 2 and $k_{\text{eff}} = 0.95$. Acc. 3 technology is needed in 2100, so reduction of the cost of neutrons by two would be required over the next 90 years.

Achieving the factor of two reduction in cost per neutron for Acc. 3 is probably possible, but today's accelerator technology probably cannot be extended beyond this point. So new accelerator technology would be required to reduce the neutron cost by an additional factor of two by 2140. Alternatively the fourth and fifth cycles would have to use fusion technology reducing the cost per neutron even further in order to keep the relative neutron cost at 5. The fifth and last cycle would begin in 2180 and end about 200 years from now in 2220. At that point the repeated recycle will have reduced the electricity-generated weighted actinide waste per LWR fuel load by a factor of $1/0.068 = 15$. With accelerators alone in the first three cycles, the reduction factor is $1/0.183 = 5.5$.

Table 8
Burn-up of light water reactor (LWR) spent fuel in GEM* STAR at $k_{eff} = 0.99$

(1)	(2)	(3)	(4)	(5)	(6)	(7)	(8)	(9)	(10)	(11)	(12)	(13)	(14)	(15)
LWR	LWR	²³⁵ U	²³⁶ U	²³⁷ Np	²³⁸ Pu	²³⁹ Pu	²⁴⁰ Pu	²⁴¹ Pu	²⁴² Pu	²⁴³ Am	²⁴⁴ Cm	²⁴⁵ Cm	²⁴¹ Am	²³⁸ U
Isotope fraction														
²³⁵ U	0.00737	0.00180	0.000766	0.000057	0.000025	0.000007								
²³⁶ U	0.00380		0.00321	0.000238	0.000104	0.000030	0.000015	0.000006						
²³⁷ Np	0.00040			0.000165	0.000072	0.000021	0.000010	0.000004	0.000005					
²³⁸ Pu	0.000137				0.000042	0.000012	0.000006	0.000002						
²³⁹ Pu	0.00504					0.000655	0.000317	0.000132	0.000146	0.000039	0.000041	0.000002		
²⁴⁰ Pu	0.00232						0.000522	0.000217	0.000241	0.000064	0.000068	0.000003		
²⁴¹ Pu	0.000769							0.000093	0.000103	0.000027	0.000029	0.000001		
²⁴² Pu	0.000471								0.000282	0.000075	0.000080	0.000004		
²⁴³ Am	0.000091									0.000036	0.000038	0.000002		
²⁴⁴ Cm	0.000018										0.000013	0.000001		
²⁴¹ Am	0.000503				0.000124	0.000036	0.000017	0.000008	0.000008	0.000002			0.000095	
²³⁸ U	0.9451					0.003670	0.00177	0.000734	0.000816	0.000216	0.000231	0.000011		0.9161
Sum	0.9660	0.00180	0.00398	0.000460	0.000295	0.00443	0.002660	0.001196	0.001601	0.000459	0.000500	0.000024	0.000095	0.9161
F.p.	0.0340													
	1.0000	Horizontal sum (²³⁵ U + ... + ²⁴⁵ Cm + ²⁴¹ Am + ²³⁸ U) = 0.9336												



■ Figure 11

Five successive burn cycles for LWR spent fuel in GEM*STAR. The *top line* shows k_{eff} for each of the five cycles. The *bottom line* shows the cumulative burn-up fraction for the five cycles. Note that each subsequent cycle consumes a larger fraction of the remaining ^{238}U . The *middle line* shows the cumulative energy extracted from five successive recycles of LWR spent fuel. Note that if the total energy generated from the fresh fuel sent into the LWR is of interest, one must add 1.0 to the right ordinate. In each case, the power to produce the neutrons is assumed to never exceed 15% of the output power (see [Table 9](#))

■ Table 9

LWR fuel repeated cycle summary

Cycle	1	2	3	4	5
k_{eff}	0.99	0.95	0.90	0.83	0.77
Start date	2020	2060	2100	2140	2180
Neutron source	Acc.1	Acc.2	Acc.3	Fusion 1	Fusion 2
End date	2060	2100	2140	2180	2220
Neutron multiplication	100	20	10	6	4
Relative neutron cost	1	5	5	5	5
Energy-weighted LWR waste remnant	0.5	0.324	0.183	0.114	0.068

Because the fission products are not removed by reprocessing, they accumulate in the salt as fluoride compounds. The valence of the fission product atoms averages slightly less than two and there are two product nuclei per fission. The fission of uranium releases four fluorine atoms whereas the capture process on ^{238}U leading to PuF_3 releases one fluorine atom. Overall actinide transmutation in the MSRE experimental reactor at ORNL was found to yield

a slight excess of free fluorine. The free fluorine was not removed but the excess fluorine in the salt was stabilized by using beryllium metal in the salt stream to produce BeF_2 .

The fission product fluoride salts in effect become part of the carrier salt. At the end of the fifth cycle when [Fig. 11](#) shows that 20% of the actinide has been fissioned, the total mole fraction of fission products in the salt has reached about 6.7%. The fission product also is transmuted to some degree while present in the neutron flux. For example, the long lived species ^{99}Tc and ^{129}I from the LWR are reduced by a factor of about three by the end of the five cycles. Of course, these isotopes also are produced in GEM*STAR, so the reduction factor is not as large as for the actinides.

[Fig. 12](#) shows the energy-weighted actinide distribution as the fuel is recycled and the distribution of actinide isotopes cycle by cycle. The sum of the fractions in the back row adds to 1.000 when (off-scale) ^{238}U is added as well as the fission products from the LWR in the amount 0.034. The sum of the isotopes shown in the figure is 0.0209, which can be confirmed by adding all of the isotopes in the second column of [Table 2](#) except ^{238}U . The first pass through with Acc. 1 generated as much energy as that from the LWR, so the total energy is about twice as large and the distribution calculated in [Table 2](#) across the bottom of the table is divided by roughly two. Likewise, as the cycling proceeds through all five cycles, each distribution is divided by the total energy produced up to that point from one original loading of fresh fuel to the LWR. In the fifth cycle the isotope distribution is divided by 7.3 as shown in [Fig. 11](#). It should be noted that when the ^{240}Pu fraction in the front row is multiplied by 7.3 that the fraction of ^{240}Pu is almost as large as found in the output with Acc. 1 and likewise for ^{239}Pu . This is necessarily the case as both isotopes are constantly being replenished by neutron capture on ^{238}U .

The calculation assumes that there is no delay between cycles. If 50 years elapses between cycles, 85% of the ^{244}Cm will have decayed to ^{240}Pu . Then 65% of the ^{240}Pu would undergo fission as ^{241}Pu . In that case, the value of k_{eff} is substantially higher for later cycles than shown in [Fig. 11](#) and the external neutron requirements correspondingly smaller.

It is also instructive to consider the equilibrium distributions of [Fig. 12](#) without the energy production weighting, which is shown in [Fig. 13](#). By the second recycle at $k_{\text{eff}} = 0.95$ and with Acc. 2, almost all of the power originates from ^{238}U . The ^{244}Cm is a large advantage from a proliferation perspective for two reasons. First its 18-year half life for alpha decay results in a large production of neutrons from the $^{19}\text{F}(\alpha, n)^{16}\text{O}$ reaction that strongly inhibits removal and handling of fuel for immediate chemical extraction of weapons-useful plutonium. Second, its decay leads to ^{240}Pu and to an isotopic mix where the ^{239}Pu concentration is about 25% and the delayed neutron fraction from both ^{240}Pu and ^{242}Pu is too large for the Pu to be an interesting weapons-useful material.

10 Other Fuels

The versatility of the molten salt fuels allows a wide variety of fuels for GEM*STAR for various stages of burning or values for k_{eff} .

10.1 Thorium and Depleted Uranium Fuels

As far as the eutectic mixture ${}^7\text{LiF} : 0.5\text{UF}_4$ is concerned, Th can be exchanged almost one for one with U with little influence on the mixture melting point as shown in [Fig. 2](#).

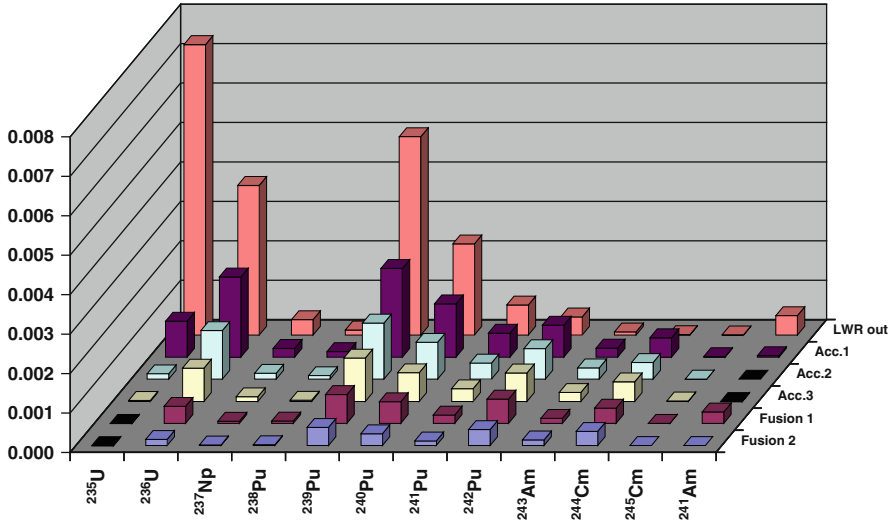


Figure 12

The equilibrium isotropic distribution as the LWR spent fuel is recycled. The back row is the isotropic distribution from an LWR burned to 33,000 MW-days/tons of actinide. The ^{238}U component is not shown because it is off scale for all distributions in the figure, nor is the fissioned fraction of 0.034 shown. When the ^{238}U and the fission fraction are added to the back distribution, the total is 1.00. The second distribution from the back is from the first burn with the accelerator at $k_{\text{eff}} = 0.99$. Because as much electric power is generated from the LWR recycled fuel as was generated from fresh fuel, this distribution is divided by two and so on for the rest of the distributions

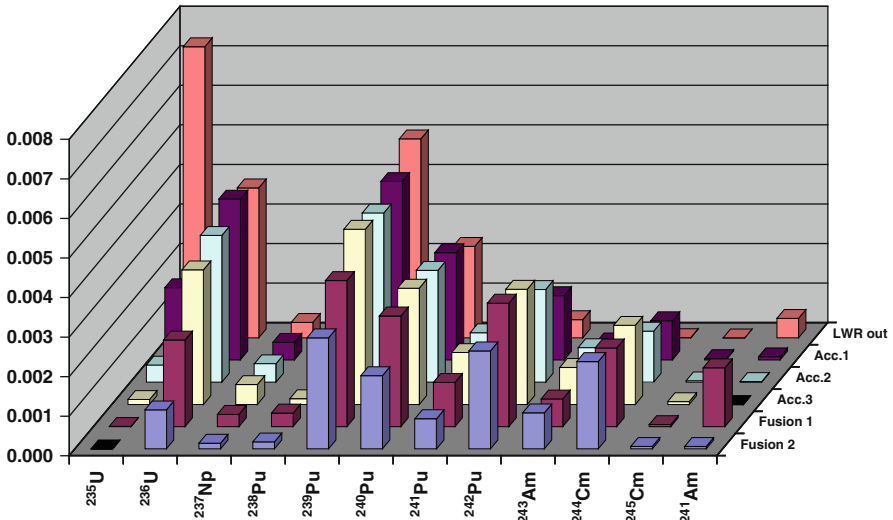
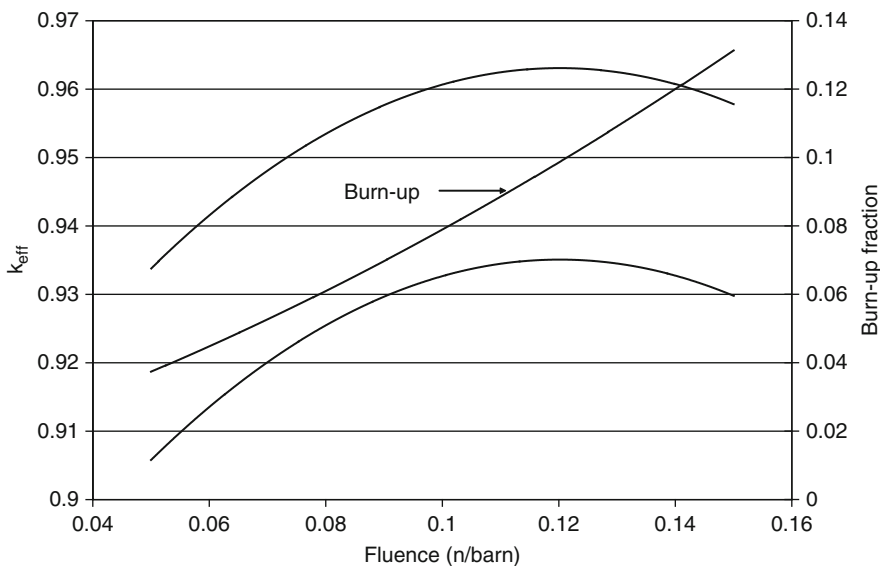


Figure 13

The distributions of [Fig. 12](#) without the energy weighting



■ Figure 14

Burn-up of thorium as function of neutron fluence. The *lower curve* is k_{eff} as calculated from MCNP5 and the *upper curve* is k_{eff} with the graphite correction. The *middle curve* is the burn-up fraction

► Figure 14 shows k_{eff} and burn-up as a function of fluence for a pure thorium fuel. Of course, at start up the fission power is zero, but builds up as ^{233}U grows in. For GEM*STAR's equilibrated continuous flow operation, Th fuel has the disadvantage that k_{eff} never reaches above about 0.963, but the burn-up in the first cycle is large at about 10% for a fluence of $0.12 \times 10^{24} \text{ n/cm}^2$. The reason for the inferior value for k_{eff} compared to natural uranium is obviously the absence of a feed of fissile material using thorium. However, because the ^{233}U capture-to-fission ratio is one-half of that for ^{235}U and one-fourth of that for ^{239}Pu , the burn-up is larger and the ^{235}U produced from multiple ^{233}U neutron capture provides additional fissionable fuel.

Regarding the weapons usefulness of the equilibrium ^{233}U for $k_{\text{eff}} = 0.96$, the $^{234}\text{U}/^{233}\text{U}$ atom ratio is 0.27. While higher enriched ^{233}U might be produced by using smaller fluences such as $0.03 \times 10^{24} \text{ n/cm}^2$, the same constraints against this from the supply of start-up fuel and the inaccessibility of the outflow can be used as explained elsewhere in this paper to avoid production of weapons-useful uranium.

Although calculations have not been done for feeding depleted uranium with ^{235}U present at the 0.20% level, it is expected that optimal performance will be found at $k_{\text{eff}} = 0.96$ with a burn-up of 5%. Because the burn-up for the same amount of fuel at the same k_{eff} is twice as high for thorium as for depleted uranium, thorium might appear to be more attractive fuel than depleted uranium. However, thorium has to be mined and refined to ThF_4 whereas depleted uranium is stored in vast quantities as highly purified almost free UF_6 , which only needs to be converted to UF_4 . As a practical matter the depleted uranium probably would be consumed first.

10.2 Fueling GEM*STAR Over the Long Term

Because uranium and thorium can be exchanged in arbitrary fractions while maintaining a 66.6% mole fraction of ${}^7\text{LiF}$, there is a wide range of options for fueling GEM*STAR. The fueling of stage 1 of GEM*STAR operation is next considered for $k_{\text{eff}} = 0.99$. The obvious initial choices are natural uranium and spent LWR fuel since both burn at $k_{\text{eff}} = 0.99$. Natural uranium would be a good reference fuel because UF_4 is produced on the path to the UF_6 needed for isotopic separation. The fuel feed for GEM*STAR from [Table 5](#) is 76 tons of uranium flowing through in 4.5 years or 17 tons/year with a burn-up fraction of the total uranium of 0.013. The cost of UF_4 is close to that of UF_6 , which was \$150/kg on 11/1/08, which corresponds to 2.9% of the cost of electricity assuming the power is sold at \$0.05/kWh.

The burn-up fraction for (low enriched) LWR spent fuel at $k_{\text{eff}} = 0.99$ is 0.0324 as shown in [Table 8](#). This burn-up fraction is three times higher than that for natural uranium at $k_{\text{eff}} = 0.99$, so the flow rate of spent fuel is 1/3 of that for natural uranium or $17/3 = 5.6$ tons/year. Therefore, the upper limit to what the reactor operator would pay for fluorinated LWR spent fuel is $3 \times \$150/\text{kg}$ or \$450/kg. Presently reactor operators pay \$0.001/kWh into a waste storage fund, which corresponds to about \$350/kg, and this payment in principle absolves the operators of any further responsibility as the spent fuel is owned by the US government. The government has already been paid \$350/kg for the spent fuel and a GEM*STAR reactor operator might be willing to pay the federal government \$450/kg for the fluorinated spent fuel. So if the federal government could perform the fluorination of the spent fuel for \$800/kg, it would break even on the fluorination.

Alternatively if a private organization could do the fluorination at less than \$800/kg, it could turn a profit by being paid \$350/kg by the US government to take it off its hands and selling it at \$450/kg to the reactor operator. Another possibility is that small-scale fluorination technology might be developed enabling fluorination on sites of existing reactors at the rate of one ton per 2 weeks, which is the rate required to keep up with a 1-GWe reactor spent fuel production rate of 26 tons/year. Such an arrangement would eliminate the transport costs for fluorination and offer other advantages as well. Because the spent fuel usage rate for GEM*STAR is only 5.6 tons/year for a production of about 220 MW_e, about five GEM*STAR units would need to be ganged together to match the power of the 1-GWe LWR and the total power from the site would double if an LWR continued to operate on the same site.

It seems likely that stage 1 at $k_{\text{eff}} = 0.99$ would continue until all of the LWR spent fuel was processed. Owing to the advantages of GEM*STAR technology over that of LWRs, spent fuel from LWRs would eventually cease to be generated bringing an end to the use of LWR fuels in step 1. That would not necessarily spell the end of stage 1 operation at $k_{\text{eff}} = 0.99$ as natural uranium is perhaps the fuel of choice for step 1 anyway. Natural uranium would be used at step 1 until its cost owing to scarcity rose to justify moving to stage 2 at $k_{\text{eff}} = 0.95$ with a larger accelerator requiring about 15% of the reactor's generated electricity and with the accelerator capital cost rising to about 15% of the reactor cost. Therefore, if the capital and operating costs are about equal for GEM*STAR at $k_{\text{eff}} = 0.95$, the cost of electric power for stage 2 would rise by 30% to \$0.052/kWh. The switch from stages 1 to 2 might happen when UF_4 costs have risen about four times from \$150/kg to \$750/kg, so that the stage 1 fuel cost percentage has risen from 3.6% to about 15%. However, it should be mentioned that a 50–50 combination

of natural uranium and depleted uranium would exhibit equilibrium $k_{\text{eff}} = 0.97$ and operation with this combination might precede step 2 until the supply of depleted uranium is exhausted.

For stage 2 of GEM*STAR at $k_{\text{eff}} = 0.95$, the thorium and depleted uranium fuels are options in addition to the outflows from the first-cycle-use of natural uranium and LWR spent fuel in stage 1. It should be emphasized that k_{eff} initially for the first loading of pure thorium would be zero, and that k_{eff} for pure depleted uranium would be low also. The value for k_{eff} could be brought up to 0.95 eventually by using only accelerator neutrons, but the power output would be low during this build-up period. However, equilibrium k_{eff} could be reached far quicker by mixing some natural uranium with the first load of thorium or depleted uranium. The multiplication would be boosted by the ^{235}U in the natural uranium and initially there would be no neutron losses to fission products. Because natural uranium would be needed only in the first load, this means of boosting multiplication could be implemented even after the price of natural uranium has become very high.

It should also be mentioned that because the equilibrium k_{eff} is the same for thorium, depleted uranium, stage 1 outflow from natural uranium burning, and reburning of LWR spent fuel, these four fuels for stage 2 could be mixed in arbitrary combinations of two, three, or four of the types as long as the ^7LiF carrier is maintained at the 0.666 mole fraction of the fuel salt. For stages 3–5 any fuel mixture also would be suitable.

Stages 1 and 2 can use today's accelerator technology for electricity production at a cost shown later to be lower than that from new LWRs or coal without CO_2 sequestration, so it is important to estimate how much electricity has been produced at end of stage 2. The IAEA estimates the "reasonably assured uranium reserves" at 36 million tons (Global Uranium Resources, IAEA, June 2005). There is roughly four times as much thorium in the earth's crust as uranium, so the total of the Th and U material is about 180 million tons. Today's LWRs produce 1GW_e -year of electric energy fissioning 3.4% of the 26 tons of low-enriched heavy metal fuel fed per year. With reburning in GEM*STAR through stages 1 and 2, an additional 5% is fissioned for a total of 8.4%. The energy production from the other fuels that contain very little or no ^{235}U is less at about 5% after finishing stages 1 and 2. The reserves of Th and U are much larger than the spent fuel from the LWRs, so 5% burn-up is the useful figure for calculating the total energy recoverable by burning through stage 2.

GEM^*STAR stages 1 and 2 electricity = $(180 \times 10^6 / 26)(0.05 / 0.034) = 10^7 \text{GW}_e$ -year. The world's present nuclear electricity power is roughly 400 GW_e and should increase by 10 if the world is to receive the full benefit of nuclear power. GEM*STAR technology would therefore carry the world's electricity needs at today's prices for 2,500 years *without advances beyond today's accelerator technology without reprocessing, fast reactor technology, or near-term permanent geologic storage*. Advances in accelerators long before the end of that period could be used to reduce the cost of electricity still further. Alternatively accelerator advances reducing the cost of neutrons by two in this period could be used to proceed to stage 3 where the burn-up would be about another 5% extending the fission energy resource from 2,500 to 5,000 years by the end of stage 3 at no increase in electricity cost. Cheaper sources of neutrons from fusion would enable burn-up in stages 4 and 5 and extending the fission resource to 10,000 years without reprocessing.

11 Other Factors Affecting GEM* STAR Success

11.1 Ultimate Ocean Disposal?

GEM* STAR fuel is in the form of fluoride salts that are somewhat water soluble. Data on the solubility of UF_4 are rare with the best coming from a study of the solubility of UF_4 powder mixed with polyethylene in cylinders 5 cm in diameter and 10 cm high (Adams et al. 1997). Different percentages of UF_4 were studied but the maximum density was 90% UF_4 by weight. Extrapolating to a density of 100% the estimate is at least 10 g/l of distilled water, so ultimate remnant waste disposal in the ocean might be an option. Waste disposal in the ocean has not been viable because waste in the form of almost insoluble oxides or metals could lie on the ocean floor a long time before they were finally dissolved and might even be covered by sediment before dissolution. Disposal of waste in the sub-seabed of the ocean has also been considered but rejected because it would lie nearly unprotected for eons. It could be readily retrieved possibly for military purposes, so some international guarding arrangements would have to be established.

Waste dissolution in the ocean water would be an ideal international solution for all nations as all nations share ownership of the oceans. Ships could be built to pull water up from deep ocean depths where the fluoride salt waste on board would be ground into powder and dissolved on board and then pumped back to the same depth. GEM* STAR waste burned through the fifth cycle is still 80% ^{238}U or ^{232}Th . The concentration of natural uranium in the ocean is 0.003 g/tons of seawater. The mass of the world's oceans is 2×10^{20} tons so the mass of uranium in the ocean is 6×10^{11} tons, which may be compared with the earth's "reasonably assured reserves" of uranium of 3.6×10^7 tons. If all the readily available mined uranium were to go into the ocean, its concentration compared to that already dissolved would be only 60 parts in 1,000,000.

Spent fuel is of course radioactive and one needs to estimate the impact of radioactivity on the ocean if it were dissolved into the ocean. The GEM* STAR plan is to recycle the fuel through stage 5 before considering the fuel waste (although because 80% of the ^{238}U and ^{232}Th are still present, the remnant might not be considered waste). The GEM* STAR remnant would then be placed in interim underground storage for 300 years using Hastelloy containers and then dissolved into the ocean if there is no further use for it.

One approach to estimating the risk of the radioactivity in the ocean would be to calculate the ingestion toxicity, which is the volume of pure water required to dilute uniformly dissolved radioactive to drinking water standards. If one does this using the CURE (1990) Report dilution for the waste from stage 5, the result is 1.4×10^9 m³/tons of spent fuel. If all of the 36 million tons of U and Th were burned through stage 5, the radioactivity evenly distributed in sea water would be a factor of about 2,000 below the limit for radioactivity in drinking water.

Another approach is to compare the radioactivity with the radioactivity of uranium and ^{40}K in sea water. If all 36 million tons of uranium and thorium spent fuel at stage 5 were dissolved in sea water after interim storage underground for 300 years, the radioactivity would be about equal to that from the natural uranium dissolved in sea water and would be about 1% of the decay rate of ^{40}K .

To make dissolution on ship practical, the radioactivity concentration of water from the ship would have to be about 100 times higher than the dilution limit and natural mixing processes would have to be relied on to dilute by the additional factor of 100. One ship's capacity would then be about 1,000 tons/year requiring about ten ships to meet the rate of disposing of stage

5 GEM*STAR waste from generating worldwide 10 times the nuclear power we have today. Of course geologic storage beginning in about 500 years remains an option.

11.2 GEM*STAR Comparison with Fast Breeder Reactors

Since 1970, the primary focus of nuclear reactor development has been on FBR. The reason was that nuclear energy was believed to have no long term future owing to the limited abundance of ^{235}U , and many still support this viewpoint. Because the cost of electricity from FBRs is higher than that from the LWRs, one probable implementation strategy would be to continue to generate electricity from LWRs until the cost of the uranium increased to the point that it was economical to implement FBRs.

With GEM*STAR the nuclear energy resource could be doubled, as has been shown above, simply by feeding natural uranium using a modest accelerator with $k_{\text{eff}} = 0.99$ and generating twice the energy from mined uranium as the LWR generates. No reprocessing, enrichment, vast plutonium inventory, fast reactors, or onerous international oversight such as those which were proposed for the GNEP would be necessary. One could argue therefore that instead of focusing nuclear technology development, as for the past 40 years, on addressing the consequences of the limited ^{235}U resource, it would have been better to focus on supplementing the fission neutrons via accelerators.

Looking back, it seems obvious that if there had been no ^{235}U at all in natural uranium, accelerator development would have been pursued with the massive resources that have been spent on enrichment, reprocessing, and fast reactor development to enable burning the ^{238}U as ^{239}Pu . Nuclear electricity probably would be at least as abundant as it is today based on ^{239}Pu and ^{233}U . Nuclear weapons would also be with us, based on accelerator-produced ^{239}Pu with reprocessing being needed only for nuclear weapons. In the later part of the twentieth century, nuclear technologists would have debated the merits of using surplus ^{239}Pu and ^{233}U to move on to FBRs that did not require accelerators, or of continuing the improvement of accelerator and fusion neutron sources.

11.3 Fusion Neutron Sources

With our present understanding of accelerator technology, it seems unlikely that the cost of neutrons from today's accelerators could be reduced by a factor of four to enable stage 4 burning. However, it can be shown (Bowman and Magill 2006) that fusion neutrons must be much cheaper than accelerator neutrons long before a practical fusion reactor can produce electricity competitively priced with fission. The expectation for the ITER magnetic fusion project in Cadarach, France and the NIF project at Livermore, CA is that they will reach physics break-even defined as fusion energy yield matching the laser energy required to confine and heat the plasma. Engineering break-even, which is far more challenging, is to generate and convert fusion energy to the buss-bar power necessary to generate the laser light needed for inertial confinement or the energy required to heat a plasma and confine it by magnetic fields. Yet a practical fusion reactor lies well beyond engineering breakeven. Making neutrons cheaper than accelerators can produce them is a much more practical goal for fusion technology development than an economically competitive fusion power reactor.

It is estimated above that the implementation of GEM* STAR with accelerators would extend the use of nuclear energy for 5,000 years before it became necessary to rely on fusion neutron sources. Of course, if fusion neutrons became cheaper than accelerators at any time during the 5,000-year period, fusion neutron sources would take over from accelerators. This prospect could be moved ahead if the strategic aim for fusion research could switch from the present aim for economically competitive fusion power to producing neutrons cheaper than neutrons from accelerators. Present accelerator neutrons can be produced by spallation at a cost of 33 MeV of proton beam power for a lead target or perhaps 80 MeV of buss-bar power; with a uranium target the costs are lower by a factor of 2–40 MeV of buss-bar power. Fusion neutrons would have to be produced at a cost of 40 MeV of buss-bar power per neutron to be competitive with today's accelerators (after consuming half of the fusion-generated neutrons to produce tritium from ${}^6\text{Li}$) and at 20 MeV per neutron to reach the probable limit of accelerator technology.

Obviously, a practical fusion power plant requires fusion development far beyond that required for a fusion neutron source that is competitive with accelerator technology. It has already been shown here that even if ${}^6\text{Li}$ based fusion power became practical, the fusion energy resource does not exceed that from fission, which is capable of supplying the world's needs for electricity for thousands of years. Perhaps then a more beneficial and practical goal for fusion research than a power plant should be to produce neutrons more cheaply than accelerators. A path to a fusion source of neutrons that is cheaper than accelerators, which could never become a practical fusion reactor, might be quite different technology from the technical path toward an eventual fusion power plant.

12 Nonproliferation Advantages of GEM* STAR

The two channels to nuclear weapon proliferation that concern the world are the production of highly enriched uranium (HEU) and conversion of ${}^{238}\text{U}$ to produce weapons plutonium (W-Pu). As the primary advantage of GEM* STAR is that it can burn natural uranium as fuel and not produce W-Pu in the process, it eliminates the need for LEU for commercial nuclear power. With GEM* STAR's features of higher usage of mined uranium than LWRs and recycle without reprocessing, nuclear can become the world's dominant source of electric power for centuries without enrichment.

As GEM* STAR can also burn spent fuel from today's LWRs without invoking reprocessing and its associated plutonium waste stream, the commercial plutonium (C-Pu) accumulated to date, and that which will be generated before a change-over to GEM* STAR is complete, also can be consumed as fuel in GEM* STAR as a somewhat richer fuel than natural uranium and transformed to a Pu isotopic mixture even more challenging than C-Pu for nuclear weapons use. GEM* STAR therefore cuts off any role in the production of nuclear energy for enrichment and reprocessing and consumes the by-product Pu from LWRs as well.

The remaining option for acquiring nuclear weapons is the misuse of GEM* STAR technology. A key factor in eliminating this prospect is the requirement for very isotopically pure ${}^7\text{Li}$. GEM* STAR can tolerate very little neutron absorption in lithium and still be an economically practical technology today and in the foreseeable future. The burning of the natural uranium at a fluence of 0.007 n/barn, which results in twice the burn-up of mined uranium as in our LWRs, requires ${}^7\text{Li}$ with an isotopic purity of 0.9999. At this level the loss of neutrons to the 0.0001 ${}^6\text{Li}$ contaminant is 1/3 of that lost to fission products. Of course, higher losses could be tolerated

with larger accelerator power with a corresponding higher ultimate cost of electricity that could price GEM* STAR out of the electricity market.

The production of ^7Li at this purity level is not like uranium enrichment, a technology developed long ago and now widely available to nations that want to put in the required resources to duplicate it. Large amounts of ^6Li have been produced in the weapons programs of several nations with a resulting production of ^7Li with ^6Li in the 1% or higher level. In the USA, this was produced by the $\text{LiOH}\cdot\text{H}_2\text{O}$ plus mercury column exchange process. This purification level by a factor of 7.5 is still quite far from the factor of 750 required at a production rates of 1 tons/year per 200 MWe GEM* STAR. With an upper limit for the separation factors of about 1.03 achievable per stage by the column exchange method, 220 stages would be required to reach the 0.9999 purity level.

ADNA Corporation has developed economically practical alternative means to reach the desired purity levels of ^7Li at the production rates required. Of course, the method will be protected as corporate proprietary technology. ADNA's business plan is not to share this technology so as to make ^7Li production a profit center. Of course, it recognizes that unfair pricing of ^7Li would drive the eventual rediscovery and duplication of the method. ADNA however intends to sell ^7LiF to foreign nations for mixing with their own domestic sources of natural UF_4 provided such sales of GEM* STAR units and their required ^7LiF are made with approval of the US government.

Having closed off the primary routes of enrichment and reprocessing for proliferation today by means of GEM* STAR, it is necessary to consider the misuse of GEM* STAR technology by those nations that might purchase these power plants. It is in principle possible to produce W-Pu in GEM* STAR from natural uranium by operating the plants at a lower fluence of 0.001 n/barn instead of the optimum level for electricity production of 0.007 neutrons/barn. In this latter standard mode of operation, the flow through of a full volume of fuel takes 4 years and the fuel outflow of fuel is into tanks under the reactor that are inaccessible and sufficiently large for storage for 40 years of operation.

If the accelerator power were not changed but the fluence lowered to 0.001 n/barn, the fuel flow rate would be seven times higher with resulting production of W-Pu at a substantial rate. GEM* STAR is equipped with a fixed leak rate fixture buried in the most inaccessible part of the reactor. If the fuel feed rate is increased beyond the leak rate, the system will simply overflow and a commode-like fail-safe system will empty the entire loading of reactor fuel into the storage tanks underneath.

The other option is to reduce the feed rate by a factor of seven and reduce the accelerator power by a factor of seven giving the lower fluence of 0.001 n/barn necessary to produce W-Pu. Such an action would require $4 \times 7 = 28$ years for a complete flow-through of one core volume and the fuel in the storage tank would still be inaccessible to a high degree. Such an action also could not be hidden as there are many direct and indirect methods to detect operation at a power level lower by seven than nominal with consequent actions following. For example, the USA could simply forbid any further sales of ^7LiF to the reactor owner.

Finally, there is the possibility of misusing the GEM* STAR accelerator by moving it to another site and using the beam to produce W-Pu by neutron absorption in a subcritical array of natural uranium by means widely known to the nuclear engineering community. The GEM* STAR accelerator structure can be manufactured as a single welded unit that cannot be cut into pieces and reassembled elsewhere. Of course, the owner could tear down the GEM* STAR reactor and target and replace it with a W-Pu-producing assembly, but the radioactivity and the presence of used fuel in and under the facility would significantly complicate such

a measure. The nation probably could copy and duplicate the accelerator elsewhere, but that can be done already today as the GEM*STAR accelerator has no advanced features that are not commonly available knowledge.

The latter examples are extreme measures that might be taken to circumvent GEM*STAR's natural nonproliferation features. ADNA believes that it is probably impossible to devise any nuclear plant that could not be misused or reconstructed to produce W-Pu. However, ADNA's objective is to devise a design that makes the misuse so complicated, expensive, and time consuming that a nation desiring nuclear weapons would instead simply produce HEU using the centrifugal technology that seems to be widespread. Any new nuclear electricity technology that eliminates the need for uranium enrichment and reprocessing of spent fuel, that consumes LWR spent fuel while increasing the ^{240}Pu fraction, and that forces a decision to obtain nuclear weapons down the already existing uranium enrichment path cannot be considered a proliferation-prone technology. No new practical paths to weapons material are opened by GEM*STAR and the major paths existing today are closed.

13 Cost Estimation

Several recent projects involving accelerators approximately the size of those required for GEM*STAR provided cost estimations for the accelerator and also provided other information that enables a cost estimation for the reactor. These enable a cost estimation for GEM*STAR without a "starting from zero" estimation by GEM*STAR advocates.

13.1 GEM*STAR Accelerator Costs

The accelerator transmutation of waste (ATW) project that originated at Los Alamos National Laboratory in the early 1990s evolved into a US Department of Energy program based on an accelerator-driven sodium-cooled fast reactor for fissioning away the plutonium and other higher actinides in LWR spent fuel and for transmuting ^{99}Tc and ^{129}I to stable species. Reprocessing was therefore required to separate out the fission product and uranium destined for geologic storage. Also it was necessary to fabricate the higher actinides, ^{99}Tc and ^{129}I into solid fuel assemblies for insertion and removal from the fast spectrum reactor.

A report on cost for this particular ATW concept was prepared (Smith et al. 1999) by the Pacific Northwest National Laboratory (PNNL), which was considered to be a neutral organization because PNNL was not involved as an originator or advocate of the ATW technology. The report estimated costs separately for the accelerator/beam transport, the transmuter/target/power generator, the reprocessing facility, and the solid fuel fabrication facility. An overall operations cost for the full facility was also estimated. The station included two accelerators with each accelerating 45 MW of beam power, eight 840 MW_t subcritical fast reactors that generated altogether 2,480 MW_e of electricity, and the associated reprocessing plant to chemically separate the actinides and prepare the solid fuel. Eight of these stations were required to burn the higher actinide over a period of 60 years from the roughly 100 LWRs presently operating in the USA for an assumed life of 40 years. The total electric power from the transmuters was then 30% of that from the LWRs that produced the waste.

Another reference for reliable accelerator costing was that for the SNS accelerator at ORNL completed in 2007. Also costs were taken from the 10 MWb CSNS report (Shapiro et al. 2003)

■ **Table 10**

Accelerator costs in 2008 dollars (millions)

(1)	(2)	SNS		PNNL		GEM*STAR
		Actual (3)	Scaled ^a (4)	Estimation (5)	Scaled ^a (6)	Single Acc. ^a (7)
Proton energy	GeV	1.0		1.0		0.5
Average power	MW	1.0		45.0		0.65
Average current	mA	1.0		45.0		1.3
Length	m	186.0		–		93.0
Buss-bar power	MW	3.1		122.0		1.8
Efficiency	%	28.0		37.0		37.0
Capital cost	M\$	113.0	43.0	1413.0	54.0	48.5
Capital cost per MW	M\$	113.0	66.0	31.4	84.0	75.0
Annual operations cost	M\$/year	2.1	0.8	58.0	2.2	1.5
Annual operations cost per MW	M\$/year-MW	2.1	1.0	1.3	3.4	2.2
Annual electricity cost	M\$/year	2.1	1.4	84.0	1.2	1.3
Annual electricity cost per MW	M\$/year	2.1	2.1	1.6	1.8	1.9

^aThe costs in these column are not for one stand-alone accelerator, but the costs are the total costs for six identical accelerators built concurrently for a 1,100 MW_e GEM*STAR system and then divided by six. For a single or a pair of accelerators, the costs would have to be scaled upward using the 0.6 exponential factor as explained in the text. Therefore the capital and operations costs in the seventh column would need to be increased for each of a pair of accelerators by the factor $(6/2)^{0.6} = 1.93$. For the six accelerators required for 1,100 MW_e, the factor is $(6/6)^{0.6} = 1$ and no adjustment is required.

already mentioned. ➤ [Table 10](#) gives the costs in 2008 dollars inflated by the factor 1.3 for the elapsed period from 1999 to 2008 for the PNNL numbers and by the factor 1.03 for the SNS.

The cost estimate for the GEM*STAR accelerators is made assuming that accelerators are constructed in pairs in the same building but with independent power supplies so as to avoid any common-mode failures. Therefore, we estimate the cost of building two accelerators of energy 0.5 GeV and 1.3 mA for a combined beam power of 1.3 MW (using a uranium target).

The estimated costs for the GEM*STAR accelerators based on the costs of other accelerators of other powers must take into account a scaling factor based on power or size. This scaling factor is typically 0.6. Therefore, to derive the capital cost from a single 45 MW accelerator for a set of six accelerators with a total power of 3.9 MW, the factor $(3.9/45)^{0.6} = 0.23$ is applied to the \$1,413 million for the PNNL estimate to find a combined cost for the set of six to be \$326 M. For the cost per accelerator 1/6 of this figure or \$54 M is entered in column six of ➤ [Table 10](#). This is the cost for a power of 0.65 MW, so the cost per megawatt of \$54 M/0.65 MW = \$84 M is entered below in the same column. The same factor of 0.23 also is applied to the operations cost for the set of six and then this number divided by six to obtain the next two entries in the sixth column. There is no economy of scale associated with the power cost so the electric power cost for one accelerator is proportional to the beam power. The factor $0.65/45 = 0.0144$ may be applied to the PNNL estimate of \$84 million to find the annual electric power cost of one GEM*STAR accelerator to be \$1.2 million.

The actual cost from the SNS project must be scaled by the same procedure so that for example the factor $(3.9/1)^{0.6} = 2.26$ gives the total cost for the six accelerators as $\$113 \text{ M} \times 2.26 = \256 million . This number divided by six is then entered in the fourth column.

The cost figures in columns 4 and 6 come out roughly comparable when using the 0.6 scaling factor in spite of starting from accelerators with power different by a factor of 45. The cost figures in columns 4 and 6 are therefore averaged to derive the estimate per accelerator in column 7 *when six are concurrently built*. The cost figures in column 7 must be multiplied by six to find the capital, operating, and electricity costs for an 1,100 MW_e GEM* STAR system. It is important to note that the electricity costs assume a rate of \$0.08/kWh. These costs will be lower if the system is self-powered using GEM* STAR electricity that would otherwise be sold into the grid and higher if a green energy source is used to drive the accelerator with green energy selling at a regulated price that is considerably higher than GEM* STAR electricity.

It should be emphasized that these accelerator costs are derived from a first-of-a-kind actual cost for the SNS and a PNNL estimate. If 100 GEM* STAR units of 1,100 MW_e were constructed so as to burn the spent fuel from the US LWR fleet of 100 reactors as fast as the spent fuel was generated, 600 accelerators would be required. This should be large enough to realize a significantly lower accelerator cost owing to mass production, so the cost estimates from [Table 10](#) are likely to be upper limits.

13.2 GEM* STAR Reactor Costs and Breakeven Electricity Price

The PNNL cost estimates taken from Table F-1 of Smith et al. (1999) for the reactor included the reactor itself along with the beam transport, vertical bending magnets, and a target are given in [Table 11](#) with an inflation factor of 1.31 for the period from 1999 to 2008. The uranium fuel cost is for natural uranium in the form of UF₄ at a December 2008 cost of \$150/kg. From [Table 5](#) the initial inventory is 380 metric tons and the annual use rate is 84 metric tons.

Assuming an on-time of 90% for the system, an interest rate of 7% on the capital, and a 30-year term gives a breakeven electricity sales income of \$390 million/year and a breakeven electricity cost of \$0.043/kWh for a 1,100 MW_e system.

■ Table 11

Capital and operating costs for 1,100 MW_e GEM* STAR

	Capital ^a (\$M)	Operating (\$M)
Six accelerators modules	291	17
Five subcritical reactors modules	2,000	58 ^b
Five turbine-generator modules	700	–
Natural uranium fuel	57	13
Site support	195	34
Total	\$3,243 M	\$122 M

^a“Overnight” construction costs

^bIncludes operating costs for the turbine generators

■ **Table 12**
Capital and operating cost for a 220 MW_e GEM*STAR

	Capital (\$M)	Operating (\$M)
Two accelerators modules	187	5.5
Subcritical reactors module	400	22.4
Turbine-generator module	140	–
Natural uranium fuel	12	2.6
Site support	40	13.1
Total	\$779 M	\$43.6 M

► *Table 12* shows the figures for a 220 MW_e GEM*STAR system. The figures of ► *Table 11* are scaled by the 1.93 factor in the capital column for the pair of accelerators and the site support and in the operating column for the operating reactor and the site support.

For a 7% interest rate, the breakeven electricity cost from the figures in ► *Table 12* is \$0.062/kWh.

If, instead of building two accelerators, the initial 220 MW_e GEM*STAR was built at a site where an accelerator of the required capacity already existed that could supply 0.65 MW of beam power, only one accelerator would need to be built. In that case, using the above figures, the GEM*STAR reactor owner and operator could afford to pay \$13 million per year for beam to the existing accelerator owner and meet the same breakeven cost of \$0.062/kWh for electric power for a 220 MW_e GEM*STAR unit.

The methodology used here in implementing the estimates of the PNNL report was to

1. Assume that the PNNL-costed reactor, and power generation equipment have the same complexity as GEM*STAR.
2. Prorate the PNNL cost to the construction “overnight” of a group of five GEM*STAR systems generating a total of 1,100 MW_e.
3. Add an inflation adjustment by a factor of 1.3 for the interval from the time of the PNNL study in 1999–2008.
4. Use the PNNL report’s NOAK (n-production of a kind) cost figures rather than the first of a kind (FOAK) cost figures.
5. Use an interest rate of 7% for retiring the debt on borrowed construction funds over 30 years and calculate the annual cost of debt retirement.
6. Prorate the PNNL annual operations costs for the relevant components.
7. Determine the break-even price for electricity sales.
8. Consider factors that might reduce or raise the costs estimated for various elements of GEM*STAR.

Perhaps the most uncertain element of this methodology is the assumption that a fast reactor and a graphite reactor of the same power have the same capital cost. The comparisons of the two technologies are much too complex to discuss in detail in this chapter. However, it is useful to mention that the reactor volume to produce the same electric power is half as large for the GEM*STAR reactor as for the fast reactor. Perhaps it is also useful to note that the total raw materials cost for the GEM*STAR system of 1,100 MW_e is about \$15 million compared to

the deduced GEM*STAR reactor cost without power generation of \$2,000 million. Finally, we mention that the GEM*STAR reactor vessel is filled with graphite, molten salt, and an internal heat exchanger and the fast reactor with metallic fuel and liquid sodium. Both reactors use low-vapor-pressure coolants, so neither requires the high pressure reactor vessel needed by an LWR.

14 Summary

The worldwide nuclear power community has spent the past 50 years improving the LWR as an electricity generator, trying to extend the usage of mined fuel, and developing and deploying a closed fuel cycle. While the technology for closing the cycle is available and has been for years, its costs, safety, and proliferation concerns have prevented deployment. As long as uranium is abundant, the once-through LWR seems likely to continue to dominate nuclear power (von Hippel 2007; Bunn et al. 2003) while continuing to be dogged by proliferation and waste disposition concerns. If nuclear power continues on the path of the past, it is unlikely that it will have a chance to live up to its promise until a generation of green energy technology and CO₂ sequestration efforts have been found to be reliable, uneconomic, or both.

This chapter discusses three orphan nuclear technologies that, by themselves, have not been found to lead to new nuclear energy technology competitive with LWRs. When advanced graphite, continuous flow-through molten salt, and supplemental neutrons from accelerators are applied in the optimum arrangement described here, it appears that nuclear electric power will undercut the price of any existing or new green energy technology. It will obviate reprocessing, fast reactors, and near-term geologic storage and eliminate the proliferation concerns that are endemic to them.

GEM*STAR technology is not dependent on a national grid as GEM*STAR reactors can undergo start-up with modest power from intermittent electricity sources, can multiply those sources by thirty or more, and can maintain constant power with less than a 3% voltage drop as their wind and solar power sources turn on and off.

GEM*STAR's UF₄ fuel form, accelerator technology, advanced graphite, and molten salt technologies are not locked up in government security programs or otherwise controlled except perhaps by private sector proprietary protections. Therefore, GEM*STAR technology can be developed in the private sector for deployment as soon as regulatory oversight allows it.

References

- Adams JW, Lageraen PR, Kalb PD, Rutenkroger SP (1997) Feasibility study of dupoly to recycle depleted uranium. Formal Report BNL-52597
- ANL-5800 (1963) Reactor physics constants, 2nd edn. Argonne National Laboratory, Lemont
- Arnold GP, Myers VW, Weber AH (1949) The effect of crystal orientation on the scattering of slow neutrons. *Phys Rev* 75:217
- Bateman H (1927) A modification of Gordon's equation. *Phys Rev* 30:55–60
- Beckurts KH, Wirtz K (1964) Neutron physics. Karlsruhe Nuclear Research Center, Springer, Berlin
- Bowman CD (1998) Accelerator-driven systems for nuclear waste transmutation. *Annu Rev Nucl Part Sci* 48:505–556
- Bowman CD (2000a) Once-through thermal spectrum accelerator-driven light water reactor waste destruction without reprocessing. *Nucl Technol* 132:66–93

- Bowman CD (2000b) Once-through thermal spectrum accelerator-driven light water reactor waste destruction without reprocessing. *Nucl Technol* 132:79–83
- Bowman CD (2001) Apparatus for transmutation of nuclear reactor waste. US Patent US 6,233,298 B1, 15 May 2001
- Bowman CD, Magill J (2006) Potential role for lasers for sustainable fission energy production and transmutation of nuclear waste. In: Schwoerer H, Magill J, Beleites B (eds) *Lasers and nuclei, applications of ultrahigh intensity lasers in nuclear science*. Springer, Berlin, pp 169–189
- Bowman C, Arthur E, Lisowski P, Lawrence G, Jensen R, Anderson J, Blind B, Capiello M, Davidson J, England T, Engle L, Haight R, Hughes H III, Ireland J, Krakowski R, Labauve R, Letellier B, Perry R, Russell G, Staudhammer K, Versamis G, Wilson W (1992) Nuclear energy generation and waste transmutation using an accelerator-driven intense thermal neutron source. *Nucl Inst Meth Phys Res A* 320:336–367
- Bowman CD, Bowman DC, Hill T, Long J, Tonchev AP, Yornow W, Trouw F, Vogel S, Walter RL, Wender S, Yuan V (2008) Measurements of thermal neutron diffraction and inelastic scattering in reactor grade graphite. *Nucl Sci Eng* 159:182–198
- Bowman CD, Bilpuch EG, Bowman DC, Crowell AS, Howell CR, McCabe K, Smith GA, Tonchev AP, Tornow W, Violet V, Vogelaar RB, Walter RL, Yingling J (2009a) Reducing parasitic thermal neutron absorption in graphite reactors by 30%. *Nucl Sci Eng*
- Bowman C, Bowman D, Bilpuch E, Crowell A, Howell C, McCabe K, Smith G, Tonchev A, Tornow W, Vylet V, Walter R (2009b) Neutrons from a proton-driven deuterium target as a possible competitor to spallation for nuclear energy applications. *Nucl Sci Eng* 161: 119–124
- Bunn M, Fetter S, Holdren JP, van der Zwann B (2003) The economics of reprocessing vs. direct disposal of spent nuclear fuel. In: *Project on managing the atom, Belfer Center for Science and International Affairs, Harvard University*. <http://www.ksg.harvard.edu/bcsia/atom>
- CURE: Clean Use of Reactor Energy (1990) Westinghouse Hanford Company Report WHC-EP-0268
- Forsberg CW (2007) Thermal- and fast-spectrum molten salt reactors for actinide burning and fuel production. In: *Global 07, advanced nuclear fuel cycles and systems, American nuclear society meeting, Boise, Idaho, 9–13 Sept 2007*
- Forsberg CW, Peterson PF, Zhao H (2004) An advanced molten salt reactor using high-temperature reactor technology. In: *International congress on advances in nuclear power plants (ICAPP'04), Imbedded international topical meeting, 2004 American nuclear society annual meeting, Pittsburgh, Pennsylvania, 13–16 June 2004*
- Furukawa K, Kato Y, Chigrinov SE (1994) Plutonium (TRU) transmutation and ^{233}U production by single-fluid type accelerator molten-salt breeder (AMSB). In *Accelerator-driven transmutation technology and applications, Las Vegas, 25–29 July 1994*
- Gat U, Dodds HL (1993) The source term and waste optimization of molten salt reactors with reprocessing. In: *GLOBAL '99, Seattle, Washington, 12–17 Sept 1993*
- Gat U, Engel JR, Dodds HL (1992) Molten salt reactors for burning dismantled weapons fuel. *Nucl Technol* 100:390–394
- Glasstone S, Edlund MC (1952) *The elements of nuclear reactor theory*. D. Van Nostrand Company, New York
- von Hippel F (2007) Research report number 3 of the International Panel on Fissile Materials (IPFM), *Managing spent fuel in the U.S.: the illogic of reprocessing*. <http://www.fissilematerials.org>
- Lamarsh JR (1983) *Introduction to nuclear engineering*, 2nd edn. Addison-Wesley, Reading, p 134
- Lawrence in the Cold War (2002) *Center for History of Physics, American Institute of Physics*, chp@aip.org
- Lawrence G et al (1996) Conventional and superconducting RF linac designs for the APT Project. In: *Proceedings of 1996 linear accelerator conference, Geneva, Switzerland*
- Lewis WB (1966) *Atomic energy of Canada Limited Report No. AECL-2600*
- Lide DR (ed) (1991) *Handbook of chemistry and physics*, 72nd edn. CRC Press, Boston
- McLane V, Dunford CL, Rose PF (1988) *Neutron cross sections, volume 2, neutron cross section curves*. National Nuclear Data Center, Brookhaven National Laboratory, Academic, San Diego
- Merle-Lucotte E, Heuer D, Le Brun C, Mathieu L, Brissot R, Liatard E, Meplan O, Nuttin A (2006) Fast thorium molten salt reactors started with plutonium. In: *Proceedings of the international congress on advances in nuclear power plants (ICAPP), Reno*
- Moir RW, Teller E (2005) Thorium-fueled underground power plant based on molten salt technology. *Nucl Technol* 151:334–340
- Mughabghab SF (1984) *Neutron cross sections, volume 1, neutron resonance parameters and thermal cross sections*, pp. 12–16, Part B: Z = 61–100. National Nuclear Data Center, Brookhaven National Laboratory, Academic, New York

- Nightingale RE (1962) Nuclear graphite. Academic, New York
- Peterson PF (1996) Long-term safeguards for plutonium in geologic repositories. *Sci Glob Secur* 6:1–29
- Poulter DR (ed) (1963) The design of gas-cooled graphite-moderated reactors. Oxford University Press, New York
- Report to Congress (2006) Spent nuclear fuel recycling program plan, U.S. Department of Energy, May 2006
- Rosen L (1973) The Clinton P. Anderson Meson Physics Facility (LAMPF). *Proc Natl Acad Sci USA* 70:603–610
- Shapiro S et al (2003) Accelerator based continuous neutron source (ACNS). BNL – Formal Report 71184 (2003); Ruggeiero A, Ludewig H, Shapiro S (2003) Study of a 10-MW continuous spallation neutron source. In: Proceedings of the IEEE 2003 accelerator conference, Portland, Oregon
- Smith R, Shay M, Short S, Ehrman C, Myers T (1999) Estimated cost of an ATW system. Pacific Northwest National Laboratory (PNNL) Report 13018
- Stephenson R (1954) Introduction to nuclear engineering. McGraw-Hill, New York
- US Department of Energy (DOE) (2008) Global Nuclear Energy Partnership (GNEP), Programmatic Environmental Impact Statement (PEIS). <http://www.gnep.energy.gov/peis.html>
- Weinberg AM et al (1970) The status and technology of molten salt reactors – a review of molten salt reactor work at the Oak Ridge National Laboratory. *Nucl Appl Technol* 8:105–219

25 Front End of the Fuel Cycle

Bertrand Barré
INSTN, Chaville, France
bcbarre@wanadoo.fr

1	Description	2896
2	Uranium Exploration and Mining	2897
2.1	The Element Uranium	2897
2.1.1	Uranium Resources	2899
2.1.2	The Oklo Phenomenon	2902
2.2	Uranium Exploration	2904
2.3	Uranium Mining and Milling.....	2905
2.4	Sites Rehabilitation	2906
3	Conversion	2907
4	Uranium Enrichment	2909
4.1	Principle, Cascade, SWU, HEU, LEU.....	2909
4.2	Enrichment Technologies	2912
4.2.1	Gaseous Diffusion	2912
4.2.2	Ultracentrifugation.....	2914
4.2.3	Other Methods	2917
5	Fuel Fabrication	2918
5.1	Elements of Fuel Design.....	2918
5.1.1	Fissile/Fertile Couple	2919
5.1.2	Fuel Material	2919
5.1.3	Cladding Materials.....	2919
5.1.4	Absorber Materials.....	2920
5.2	The LWR Fuel.....	2921
5.2.1	Fuel Pellets Production	2922
5.2.2	Fuel Rods Fabrication.....	2923
5.2.3	Assembly	2923
5.3	MOX Fuel	2923
5.4	Other Fuel	2925
5.4.1	CANDU	2925
5.4.2	FBR.....	2925
5.4.3	HTR	2927
5.5	In-Reactor PWR Fuel Behavior	2928
6	Thorium	2930
7	Plutonium	2931
	References	2933

Abstract: This chapter describes the various industrial steps which constitute the front end of the nuclear fuel cycle, i.e., the complete set of operations needed to produce a functional fuel element ready to be loaded in a nuclear reactor. This chapter also provides data concerning the element uranium, its abundance and its most relevant properties. The exploration, mining, concentration and site rehabilitation processes are then described.

Light water reactors (LWR), which make the vast majority of the nuclear reactors operating today, and those under construction, cannot use “natural” uranium for their fuel: it must be “enriched” in isotope 235 and the enrichment process itself requires the uranium to be “converted” into a gaseous compound.

Once enriched to the required assay, uranium is then fabricated into solid ceramic “pellets,” piled into leaktight metallic “pins.” These pins are then “assembled” to constitute the fresh fuel element.

The chapter also provides additional information on MOX fuel assemblies used to recycle plutonium in LWR, as well as some data on plutonium and thorium.

One shall also find an explanation of the fascinating “Oklo Phenomenon,” which occurred almost 2 billion years ago in some uranium deposits of Gabon, in this chapter.

This chapter is expanded and updated from part of a previous Springer publication (Barré 2005a).

1 Description

In the conventional sense, a fuel is a substance which can be combined with oxygen to produce heat, by combustion. By extension, the nuclear fuel is a substance which can produce heat by fission of its heavy nuclei by neutrons.

Cars do not burn crude oil straight out of the well, and light bulbs are not plugged directly on hydraulic dams. For fissile nuclei to produce heat by undergoing fission in reactor cores, they must follow a “Fuel Cycle,” combining many different industrial steps in a sequence (Barré 2005a; Cochran and Tsoufalnidis 1999; Marshall 1981; Patarin et al. 2002; Wilson et al. 1996). One calls the complete chain of industrial operations leading to the supply of a fuel assembly (or element) to a nuclear plant as the “Front End” of the fuel cycle.

Fuel cycles differ from one reactor type to the other and according to the choice of the fissile/fertile nuclei involved. Let us first describe the most usual fuel cycle, the uranium cycle for light water reactors (LWR) (► Fig. 1). The front end encompasses the following steps:

- Uranium exploration
- Uranium ore mining
- Ore concentration (milling) as “yellowcake,” at the mine mouth
- Shipment of the concentrate
- Conversion to uranium hexafluoride UF_6
- Isotopic enrichment of the uranium
- Fuel fabrication

Between these steps there are, of course, many controls. Each step is, by itself, a complete industrial process which is described in more details hereafter. For reactors using natural uranium and for those recycling plutonium or ^{233}U , the enrichment step is bypassed. The fuel fabrication is the most reactor-specific process.

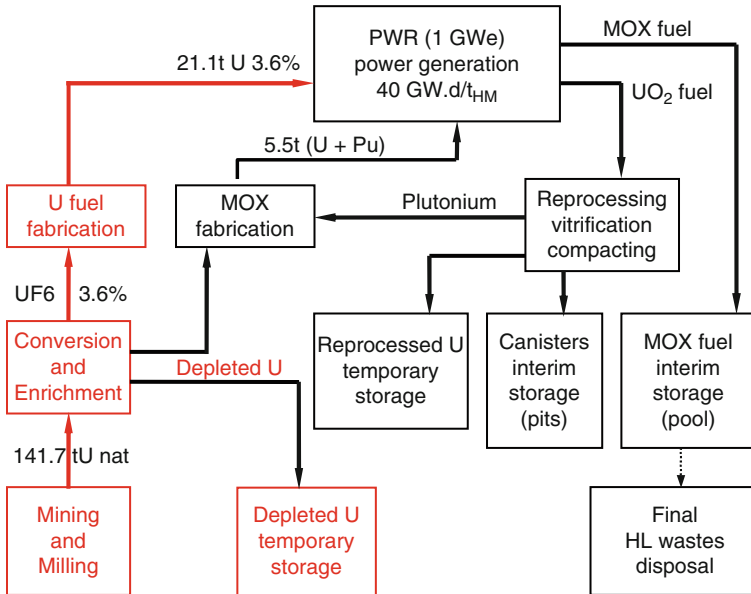


Figure 1

Typical LWR fuel cycle (masses are in metric tons HM per GWe.y). Front end is in red

2 Uranium Exploration and Mining

2.1 The Element Uranium

Uranium and Thorium ores are the raw material and natural resources of nuclear power. They are neither abundant nor very rare metals on the Earth's crust: their abundance is comparable to that of Tin, Tungsten or Molybdenum, of the order of 3 g/tons for uranium, 7 g/tons for thorium.

Discovered in 1789 by Klaproth, uranium, atomic number 92 of the periodic classification of Mendeleev, is the heaviest naturally occurring element on Earth. As a metal, its volumic mass is 19 g/cm^3 , and its melting temperature is $1,133^\circ\text{C}$. It is naturally radioactive and constitutes a mixture of two main isotopes, both radioactive, ^{238}U for 99.28% and ^{235}U for 0.715% (To be precise, there is also 0.006% ^{234}U). Without this tiny fraction of ^{235}U , there would probably be no nuclear power today because ^{238}U has a low probability of being fissioned by neutrons, at least in the energy range of the neutrons released in the fission process, while ^{235}U is easily fissioned by neutrons of any energy.

On the other hand, ^{238}U is very useful because it captures neutrons and then undergoes a series of β decays leading to ^{239}Pu , a fissile isotope of plutonium, analogous to ^{235}U : ^{238}U is "fertile." The specific activity of uranium is 24.4 kBq/g ($0.66 \mu\text{Ci/g}$), half of which is due to ^{238}U and half to ^{234}U , the contribution from ^{235}U being negligible.

Once upon a time... uranium was born in a dying star. It is inside stars that light elements combine, "fuse," to produce heavier elements, liberating energy in the process: hydrogen

■ **Table 1**
²³⁸U decay chain

Nuclide	Decay mode and energy (MeV)			Half-life
	α	β	γ	
²³⁸ U	4.19		0.048	$4.51 \cdot 10^9$ y
²³⁴ Th		0.19	0.03, 1.001	24.1 d
²³⁴ Pa		0.14	0.043	6.75 h
²³⁴ U	4.77		0.053	$2.47 \cdot 10^5$ y
²³⁰ Th	4.69		0.068	$8.0 \cdot 10^4$ y
²²⁶ Ra	4.78		0.186	1,602 y
²²² Rn	5.49			3.82 d
²¹⁸ Po	6.00			3.05 m
²¹⁴ Pb		0.67	0.053	26.8 m
²¹⁴ Bi		1.51	0.61, 1.76	19.7 m
²¹⁴ Po	7.69			$1.64 \cdot 10^{-4}$ s
²¹⁰ Pb		0.015	0.046	22 y
²¹⁰ Bi		1.16		5.01 d
²¹⁰ Po	5.31			138.4 d
²⁰⁶ Pb	Stable			
²³⁵ U	4.46		0.168	$7.04 \cdot 10^8$ y
²³² Th	4.08		0.063	$1.41 \cdot 10^{10}$ y

produces helium, which produces carbon, and so on, until one reaches atomic mass 56, which is the approximate atomic mass of the element iron. The iron nucleus is the most stable of all, with a binding energy of 8.7 MeV per nucleon. To synthesize nuclei heavier than iron, you need to capture neutrons in an extremely high flux, and these endothermic reactions need a lot of added energy: these neutrons and this energy are found during the explosion of supernovae, which, in addition, disperses these heavy elements throughout the interstellar space. The uranium in the Earth's crust was, therefore, born in an old star, during the last cataclysmic seconds of its existence. The dispersed matter must have been used later to form the solar system. In that way, fission energy can be said to be the fossil energy of the stars as coal and oil are the fossil energy of past organic life on Earth.

Uranium is well distributed in the Earth's crust, usually associated with oxygen, and its decay products (► [Table 1](#)). The average content of granite is 4–5 parts of uranium per million (ppm). It is also found in seawater, in huge quantities, perhaps of the order of 4–5 billion tons, but with a very low concentration ~3 parts per billion (ppb). Uranium is only mined from deposits where its concentration exceeds 0.1%, unless it is a by-product of some other mineral production: phosphates, gold, and copper. Some uranium deposits, in veins, are extremely rich: mines in Saskatchewan reach 10% uranium, but most mines exploit ores close to 0.2% U. This is why uranium ores must be concentrated at the mine mouth before transportation.

■ **Table 2**
Usual uranium ores

Mineral	Chemical composition
Uraninite (~pitchblende)	UO ₂
Coffinite	(U ₈ Si ₆ O ₄₀) _{1-x} (OH) _x
Brannerite	(U,Y,Ca,Fe,Th) ₃ Ti ₅ O ₁₆
Betafite	(U,Ca)(NbTaTi) ₃ O ₉ nH ₂ O
Davidite	(Fe,Ce,U)(Ti,Fe) ₃ (O,OH) ₇
Uranothorite	(Th,U)SiO ₄
Uranothorianite	(Th,U)O ₂
Carnotite	K ₂ (UO ₂) ₂ (VO ₄) ₂ 3H ₂ O
Tyuyamunite	Ca(UO ₂) ₂ (VO ₄) ₂ 5–9H ₂ O
Torbernite	Cu(UO ₂) ₂ (PO ₄) ₂ 8–12H ₂ O
Autunite	Ca(UO ₂) ₂ (PO ₄) ₂ 12H ₂ O
Uranophane	Ca(UO ₂) ₂ Si ₂ O ₇ 6H ₂ O

Uranium is a significant constituent of about 100 different minerals, but most minable ores belong to a dozen minerals, listed in ► [Table 2](#). Usually, uranium deposits are classified into four types: vein-type deposits (Canada, Australia), uranium in sandstones (USA, Niger), uranium in conglomerates (South Africa, Canada), and other deposits (like the pegmatites of Namibia, and most phosphates deposits). Most of the deposits formed during the Precambrian era (>600 million years) or during orogenic events such as the Hercynian and Alpine mountain formations in Europe (respectively 300 and 50 million years, respectively) (Valsardieu 1997).

One distinguishes between “primary” minerals, usually black or blackish, formed at some depth inside the crust, where uranium is tetravalent (pitchblende, uraninite, coffinite, and brannerite) and “secondary” minerals, derived from the former by surface oxidation. Secondary minerals are brightly colored, in green, yellow or orange, and uranium is hexavalent.

2.1.1 Uranium Resources

The concept of “resources” or “reserves” must be qualified, because behind any specific figure there are many hypotheses, not always explicit: hypotheses concerning the costs of extraction (the higher the accepted costs, the largest the resources because one can access to lower grade ores), and hypotheses concerning the state of the technologies of exploration, detection, and production. For instance, resources of petroleum have been vastly increased over the last decades by “secondary extraction” technologies.

The “Bible” of uranium resources is the Red Book (OECD 2008) jointly published every second year by OECD/NEA and IAEA. This is a compilation of data supplied by countries that are members of these organizations. The completeness and accuracy of the data vary from

Table 3
NEA-IAEA resources classification (million tons)

Cost of recovery (US\$/kgU)	Identified Resources		Undiscovered Resources	
	Reasonably Assured RAR	Inferred Resources	Prognosticated Resources	Speculative Resources
<40	1.8	1.2		
<80	2.6	1.8	2.0	
<130	3.3	2.1	2.8	4.8
Cost unassigned				7.8

country to country. In addition, with uranium prices extremely low during the last decades (see below), very little was done in terms of exploration by uranium mining companies just able to survive. This means that the figures now available are the results of exploration efforts carried out mostly during the 1970s, and are probably underestimated. Since 2004, uranium spot prices having soared, exploration has resumed worldwide, and the 2008 issue of the Red Book is already more optimistic than the previous one (► [Table 3](#)).

This being said, the Red Book uses a standardized classification to give figures of uranium resources always expressed in *recoverable* metric tons.

If we consider the identified resources recoverable at a cost <130 \$/kgU, the world total figure is quoted around *5.5 million tons U* (it was 4.7 Mt U in the 2006 Red Book). The highest figure for the “ultimate” recoverable resources might be of the order of *16 million tons U*.

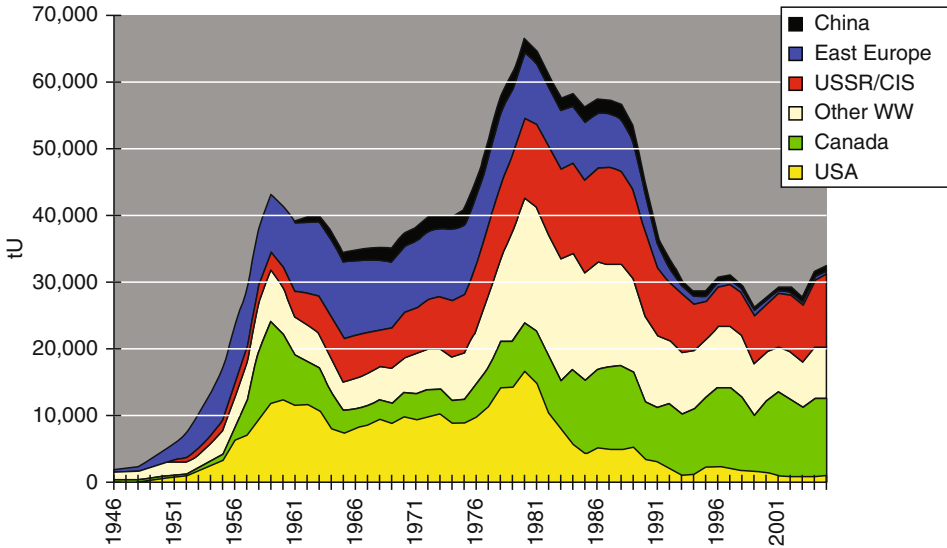
88% of the *identified* resources are in the following 10 States:

Australia	24.1%	Namibia	6.0%
Kazakhstan	17.2%	Brazil	5.9%
Canada	9.2%	Niger	4.8%
South Africa	7.2%	Russian Federation	3.6%
USA	7.2%	Uzbekistan	2.4%

Notably absent are big consumers such as Japan and the European countries – not to mention India and China.

During the 1990s, the world production oscillated between 30,000 and 35,000 tons U per year, but it reached close to 70,000 tons in 1980. Since the origins of the nuclear era, more than *2 million tons U* have been produced. Of these, only 1.15 million tons U has been used in the supply of nuclear fuel for civilian nuclear reactors; 85% of the remaining 850,000 tons in military stockpiles. The history of uranium production (► [Fig. 2](#)) has been rather hectic

- Huge growth from 1946 to 1960, for military purposes
- Slump from 1960 to 1970 when the needs of the emerging nuclear power industry could not match the decrease in the military needs
- Growth – and overproduction – in the 1970s, fuelled by excessive expectations of nuclear power development, and aggravated by the US policy of requiring “feed” delivery by the



■ **Figure 2**
Historical uranium production

utilities 10 years in advance of the delivery of enriched uranium (over which the US government had a monopoly)

- Slow decrease during the 1980s, reflecting the lowered nuclear expectations throughout the world and the numerous cancellations of nuclear projects in the USA
- *Crisis*, since 1990, with production around or below 35,000 tons/y versus a stabilized demand close to 60,000 tons/y (Maillet et al. 1980), and a technical capacity around 45,000 tons/y

“Spot” prices reflect these variations: below 7 \$/lb U_3O_8 in 1972, they jumped above 40 \$/lb in the mid 1970s, to crumble after 1980. They have been meandering around 12 \$/lb from 1995 to 2003. Till 1993, the main reason was overproduction and resale of the inventory of canceled power plants. Since then, the “civilization” of Russian and American military stockpiles, due to the end of the cold war and the reduction of nuclear arsenals, has been adding around 200,000 tons U to the overflowing civilian stockpiles. As a result, many mines have closed, exploration has dramatically slowed down, and many mergers and acquisition have shaken the uranium mining community.

From 1985 to 2000, the number of production sites world-wide has decreased from 102 to 46, and the number of companies involved in uranium mining has shrunk from 38 to 23. But with the expectation of a “nuclear Renaissance,” the trend has been dramatically reversed since 2004. Spot prices even reached 140\$/lb in the summer of 2007 before going down to around 55\$ by the end of 2008.

But this yo-yo behavior has much less impact on nuclear electricity costs than similar volatility had on fossil origin power. As shown in [Table 4](#) below, fuel price volatility as currently observed induces very different generation cost variations according to the technology. For the same factor 3 variation in fuel price, the gas generation cost impact is about twice that of coal. *But, in spite of a factor 8 variation instead of 3, the nuclear generation cost impact remains 4 times less than that of coal, 7 times less than that of gas.*

■ **Table 4**

Impact of fuel prices variations on kWh costs for uranium, gas and coal

	2002 indicative values	2007 indicative ^a	Variation	Cost impact (US\$/MWh)
Uranium volatility US\$/lb U ₃ O ₈	12.5	100	Factor 8	
Resulting fuel cost ^b (US\$/MWh)	4.3	10.1		+5.8
Gas volatility (US\$/MMBtu)	3.5	9.5	Factor 3	
Resulting fuel cost (US\$/MWh)	23.1	62.6		+39.5
Coal volatility (US\$/t)	30	90	Factor 3	
Resulting fuel cost (US\$/MWh)	10.5	31.5		+21

^aIn the higher range

^bIncluding uranium + conversion + enrichment + fuel fabrication

- Assumptions on fuel energy yields
 - Uranium: burnup 60 GWd/t, heat conversion 36%
 - Gas: heat conversion 57%
 - Coal: heat conversion 43%
- Indicative fuel price variations as observed in the past decade
- For comparison, total generation costs are in the range 50–70 US\$/MWh

2.1.2 The Oklo Phenomenon

As we have seen, the half-life of ²³⁸U is 4.51 billion years while ²³⁵U decays by half in “only” 710 million years. Therefore, the relative abundance of ²³⁵U increases if we go back in time: at the creation of the solar system, it was close to 17%, and about 3.58% 2 billion years ago. About 3.5% is the level to which we painfully enrich the uranium today to fuel our LWR... In the 1950s, some authors played with the idea that fission chain reactions could have occurred naturally when the enrichment was so high, but so many conditions would have been required that it seemed far fetched, and there was no evidence left anyway.

In June 1972, at the Pierrelatte enrichment plant devoted to Defense Applications, a routine mass spectrometry analysis of UF₆ feed material exhibited a discrepancy: only 0.7171% of the uranium in the samples ²³⁵U, instead of the magic 0.7202! Even though the discrepancy was small, it was so unusual that the French Atomic Energy commission CEA, operator of the plant,

started a thorough investigation (Barré 2005b). First, it was not an artifact: the anomaly was confirmed on several measurements on other samples. Accidental contamination by depleted uranium from the plant itself was then eliminated and so was the use of reprocessed uranium as there was no ^{236}U in the samples. The investigators then traced the anomaly back through all the stages of uranium processing, from Pierrelatte to Malvesi to Gueugnon where the concentrates exhibited the same low ^{235}U concentrations. These concentrates all came from COMUF which operated two uranium mines in Gabon, at Mounana and Oklo, the mill being located at Mounana. Very soon it appeared that all the anomalous ore came from the northern part of the – very rich – Oklo deposit. In some shipments, the level of ^{235}U was as low as 0.44%. Between 1970 and 1972, in the 700 tons of uranium delivered by the Mounana mill, the deficit of ^{235}U exceeded 200 kg, hardly a trifle!

Oklo uranium was indeed different from natural uranium everywhere else. Why?

“Natural” isotopic separation was excluded: if it had produced depleted uranium, where was the enriched fraction? As soon as August, the hypothesis of very ancient fission chain reactions was formulated, and investigators started to search for fission products (or, rather, the granddaughters of hypothetical fission products). The spectrum of fission products is so distinctive that it constitutes an unmistakable marker that fission reactions have taken place. The presence of such fission products was clearly identified: at some point in the uranium deposit history, it had become a “natural” nuclear reactor. Later on, it was found that there were actually 15 reactor sites in Oklo, and another one in Bangombé, 30 km away from the main deposit. The discovery was duly heralded but many questions remained unanswered. When did the reactor “started”? How long did it “operate”?

It is only around 2.2 billion years ago that the patient work of photosynthesis accomplished by the first algae released enough oxygen in our atmosphere for the surface waters and ground water to oxidize. Only then could the uranium diluted in granite be leached out and concentrated before mineralization in places where oxidoreduction would occur. Rich deposits cannot be older. On the other hand, since 1.5 billion years, ^{235}U abundance has decayed below a level which makes spontaneous fission workable. It took a lot of studies, in geology, chemistry, and reactor physics to narrow the bracket of time to the present estimated value: the reactions must have started 1950 ± 30 million years ago (Naudet 1991).

The deposits were located in very porous sandstone where the ground water concentration may have been as high as 40%, probably due to the partial leaching of the silica (quartz particles) by the hot groundwater, at a time where, the radioactivity of Earth being higher than today, the thermal gradient underground was probably higher too. During the reactors operation, the water temperature rose significantly, accelerating this “desilicification” process and, by difference, increasing the concentration in uranium, therefore compensating for its depletion by fission. As a matter of fact, the concentration of uranium in the reaction zones is extremely high, sometimes above 50%, and the higher the uranium concentration, the lower its ^{235}U content. Furthermore, losing its silica, the surrounding sandstone became clay and thus prevented an excessive migration of groundwater, keeping the uranium in place.

From the fine analysis of the spectrum of fission products, we know that a number of the fissions occurred in plutonium, bred by neutron capture in ^{238}U and now fully decayed to ^{235}U since its half-life is only 24,000 years (By the way, so much for the notion that plutonium is “artificial”). This allowed the physicists to calculate that, varying from one zone to another,

reactions did take place during an enormous period of time ranging from 150,000 to 850,000 years! But if the operating time was immense, the power density in the “core” was only *one millionth* of its value in a commercial reactor today.

By combining geology and temperature considerations, it is now believed that the reactors in the northern part of the deposit operated at a *depth of several thousand meters*, under deltaic and marine sediments. At such depth, the conditions of pressure and temperature were close to those of the pressurized water reactors (PWR) of today (350–400°C, 15–25 MPa), while the southern zones operated at roughly 500 m deep, with conditions resembling more to those of a Boiling Water Reactor (250°C, 5 MPa).

Even though significant alteration occurred in recent times when the tectonic uprising and erosion brought the reactors close to the surface, and especially when the Okolo Néné River gouged the valley, the heavy elements thorium, uranium and plutonium did not move at all, nor did the rare earths fission products, as well as zirconium, ruthenium, palladium, rhodium, and a few others. On the other hand, krypton, xenon, iodine, barium, and strontium have moved, but maybe only after a few million years.

Soon after the discovery, and beyond the pure scientific thrill, the nuclear community was very excited by its implications, notably as a “natural analog” for the geologic disposal of high level radioactive waste (HLW). There, in Oklo, Mother Nature had contained *precisely the same radioactive elements* not for hundreds of thousands, not for millions, but for a couple of billion years, and without engineered barriers or special packaging. But the comparison cannot be pushed too far. Let us say Oklo provides a good presumption, but not a demonstration.

There is no reason to believe that what occurred at least 16 times near Oklo did not happen anywhere else on the Earth, especially in old and rich deposits like that which exist in Australia or Canada... but more than 3 decades after its discovery, Oklo remains unique. It remains unique as a geologic curiosity, and it remains unique as a nuclear detective story.

2.2 Uranium Exploration

In the early days of the Atomic era, uranium prospecting was a pioneer’s job, for lonesome adventurers roaming the deserts of Colorado or Wyoming, with their horses and their Geiger-Müller counter. Today, things are less romantic and more organized, but the basics are the same: detecting the γ rays of some of the decay products of ^{238}U , mostly ^{234}Th , ^{222}Rn and ^{214}Bi , or some gaseous products of spontaneous fission such as ^{85}Kr or ^{135}Xe .

Nowadays, one starts with the geological study of a large area to detect favorable conditions for deposit formation, notably with the help of satellite cartography (since the first ERTS and LANDSAT satellites in the early 1970s).

If a given area looks interesting, the next step is aerial radiometric survey, with planes or helicopters carrying large and sensitive scintillation counters or γ spectrometers, and flying over stripes of land about 1 km wide. This method allows for a rapid identification of the regions having the highest uranium content, and worth further exploring. Radiometric methods, when properly interpreted, will detect uranium ores, but will not give information on the quantity and concentration of the uranium.

If the radiometric measurements are promising enough, geologists go on the spot to perform analysis of ground samples and groundwater, and to drill for logging.

2.3 Uranium Mining and Milling

In order to extract the uranium, access must be gained to the deposit, either by stripping off the sterile rock covering it (as in the case of open-pit mining), or by digging roadways into the sterile rock if the ore lies deeper (as in the case of underground mining), or by in situ leaching (ISL).

Open pit mining is very common for copper, for instance. After removing the topsoil and the overburden with scrapers, the ore is excavated with hydraulic shovels and front loaders, and carried to the mill by trucks traveling on a long helical ramp from the ore bed to ground level. After exploitation, the overburden will be pushed back into the pit and covered by the topsoil for rehabilitation (see below).

Underground mining is commonly used for coal or iron. What is specific to underground uranium mining is the additional hazard caused by the radon gas ^{222}Rn accumulated in the galleries: powerful ventilation must be maintained to keep the radon concentration at an acceptable level and prevent miners' irradiation. Given the cost of underground mining, it is used for relatively high grade ore. Some ores have such a high uranium concentration, in Saskatchewan for instance, that remote mining techniques are used.

ISL, sometimes called solution mining, is a relatively inexpensive way to exploit underground ores in arid and secluded areas where possible underground water pollution is less of a concern: Wyoming, Australia, and Uzbekistan. Several wells are drilled to reach the ore location, then a leaching solution (usually acidic, $\text{pH} \sim 2-3$) is injected in one well and pumped from the surrounding wells (► Fig. 3). A new mine in South Australia, with reserves in excess of 20 million tons U, will produce ~ 1 million tons U per year from 84 wells, with a total manpower under 50 people.

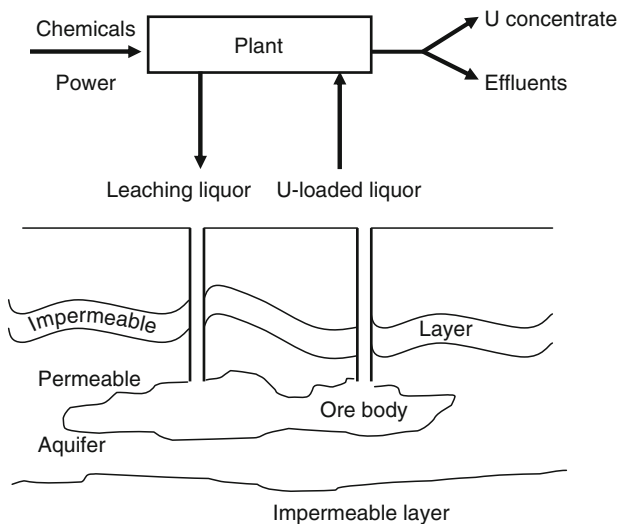
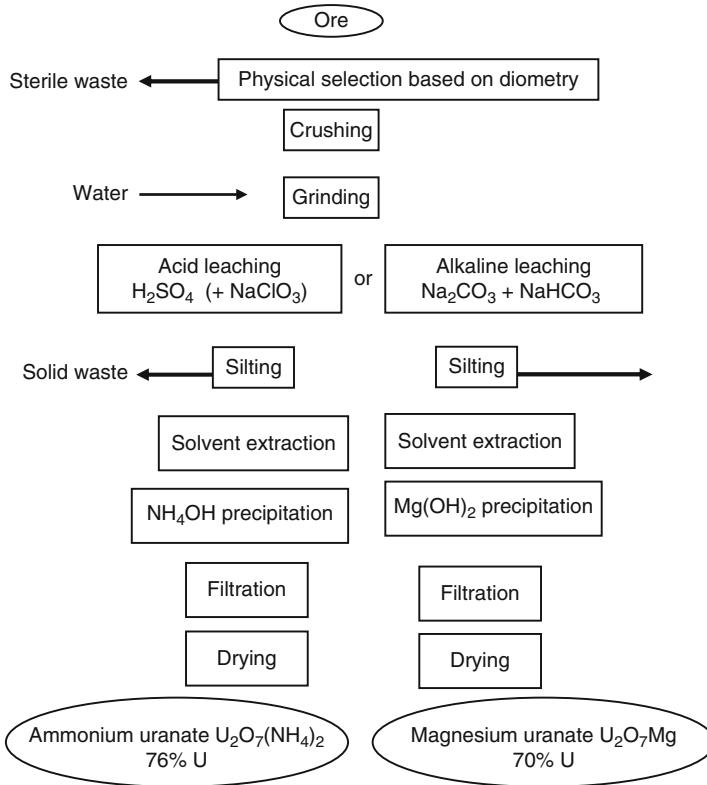


Figure 3
ISL



■ **Figure 4**
Schematic milling processes flow chart

One should mention a fourth method of uranium extraction which bears no resemblance to mining: extraction from seawater is technically possible and has been developed on a laboratory scale, notably in Japan, using either resins (Asahi) or other specific adsorbent (JAERI). It is too early to evaluate the possible costs involved, but they will be much higher than the presently depressed commercial prices. One specific problem is the huge volumes of seawater to handle in the process: most prospective designs consider floating plants anchored in the middle of strong oceanic currents.

After the uranium has been mined, it is concentrated in a mill located close to the mine mouth. ➤ *Figure 4* schematizes the various concentration processes (Rigo and Faron 1995).

2.4 Sites Rehabilitation

At the end of the commercial exploitation, mining operations leave a significant impact on the environment:

- Open pits, and underground galleries
- Leftover buildings and pieces of equipment from the mill

- Excavated materials and *mill tailings*, usually in tailings ponds. Mill tailings, in huge quantities, contain all the radionuclides of the uranium decay family, including radium and radon

Before leaving the site, the operator must therefore “rehabilitate” it at his expenses and subject to strict regulatory rules and close scrutiny. Rehabilitation includes the following operations:

For the mine site itself: filling it with sterile excavated materials, or, alternately, transforming open pits into artificial lakes, and thereafter, remodeling the landscape, tree plantations, etc.

For the mill: complete dismantling of the plant buildings, with the possible exception of some office buildings which can be converted to other uses after cleanup, and storage of uranium contaminated equipment together with the tailings, followed by the monitored cleanup of any contaminated soil.

The most important aspect is the safe disposal of the mill tailings. During operation, they are stored in pits or ponds, and controlled under national regulations. After termination, the operator must assure their durable containment, to safeguard the surrounding environment from radioactive contamination, and prevent exposure of people to unwanted radiation (less than 1 mSv/y for the most exposed group): covering with soil to delay – and therefore limit by decay – radon release, and resist erosion and rain seepage; reinforcement of the levees, water drainage, treatment if need be, and monitoring; suitable plantations.

In addition, there shall remain for a long period of time a regular monitoring of air, water, and food chains in the neighborhood.

3 Conversion

According to its specific process, a uranium mill would deliver concentrates made of:

- Usually uranates (magnesium, sodium or ammonium uranates) such as $Mg_2U_2O_7$, containing up to 65% uranium
- Sometimes oxides, containing up to 80% uranium: black UO_2 , orange UO_3 or yellow U_3O_8

packed in 200 l barrels or 1 m³ containers. Some stringent standards must be met in terms of concentration for some impurities: Boron content, for instance, must be strictly below 0.1%, and preferably <0.005%.

Before fuel fabrication, these concentrates must be transformed either into metallic uranium (MAGNOX metal U fuels, or feed for AVLIS), into pure dioxide UO_2 , or into a gaseous uranium compound necessary for the other enrichment processes. Most usually, the name “conversion” refers to the latter operation (OECD 2006).

The only gaseous uranium compound with a significant vapor pressure at room temperature is *uranium hexafluoride* UF_6 . Fortunately, fluorine has only one stable isotope ¹⁹F, whose atomic mass is much smaller than uranium’s.

At 20°C, the saturation pressure of UF_6 is 80 torr, and it reaches an atmospheric pressure of 760 torr at 55°C: DG and UC plants operate around 50–65°C. The phase diagram of UF_6 is schematized in [► Fig. 5](#).

There are two families of conversion processes, according to whether the purification step takes place at the head end, by solvent extraction, or at the back end of the flowchart, by distillation [► Fig. 6](#).

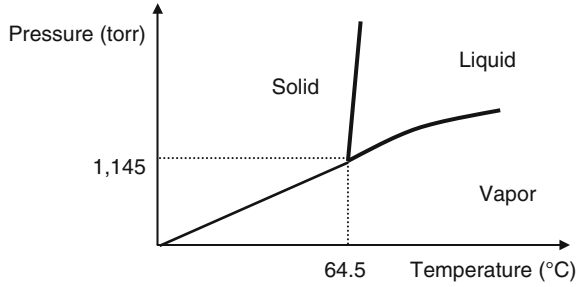


Figure 5
Phase diagram of uranium hexafluoride UF_6

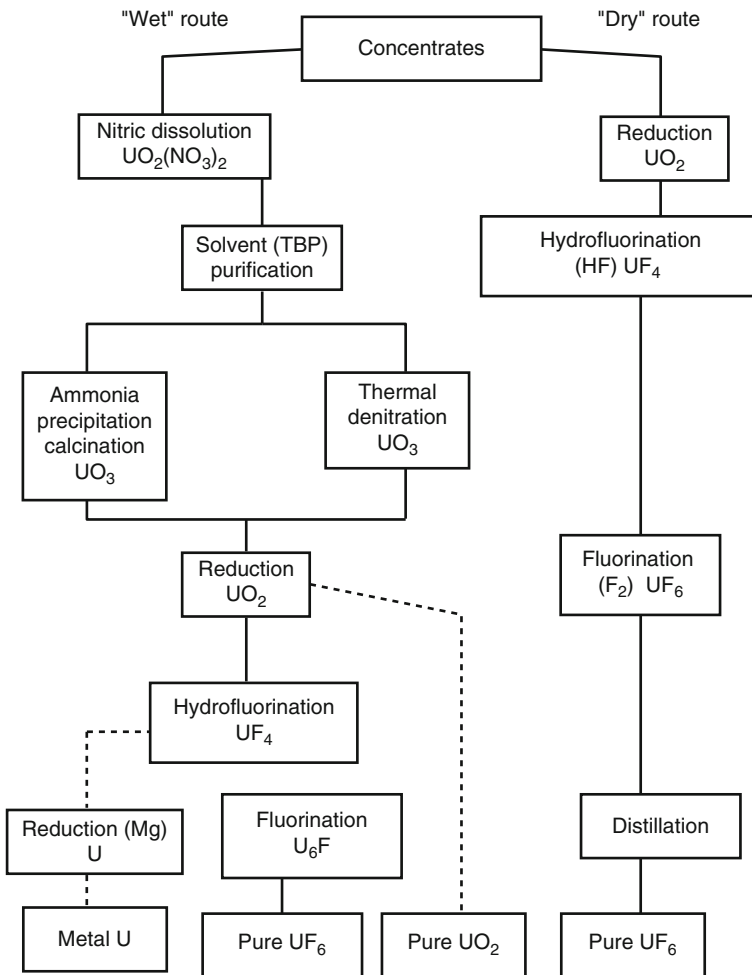


Figure 6
The two conversion routes

The dry route, often used in the USA, is simpler and produces no liquid effluent, but it is only practical if the concentrates are U_3O_8 . COMURHEX, in France has selected the more versatile wet road, where tributylphosphate extraction gives pure (<0.1 ppm total impurities) uranyl nitrate at an early stage in the process. For historical reasons, relating to the early UNGG program, conversion is performed in two separate plants: from concentrates to UF_4 in Malvesi, and final fluorination in Pierrelatte.

At room temperature, UF_6 is a solid (density 4.68 g/cm^3), which facilitates storage and handling. It reacts violently with water and most organic fluids or solids (one cannot use lubricants or rubber seals with it). Both uranium and fluorine being toxic, as well as decomposition product HF, all containers or circuits carrying UF_6 must be leaktight, with metallic seals. UF_6 also corrodes most metals but for aluminum and nickel and some of their alloys.

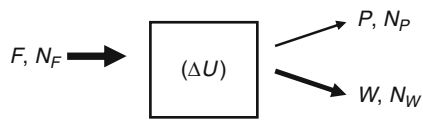
After enrichment, UF_6 is converted back to oxide and the recovered HF is recycled.

4 Uranium Enrichment

Maintaining a chain reaction with natural uranium is not easy because many neutrons are captured by ^{238}U . It is only possible in thermal reactors moderated by graphite or heavy water D_2O . Early British (MAGNOX) and French (UNGG) reactors used graphite as a moderator and were fueled with metallic natural uranium. Canadian reactors CANDU are moderated by D_2O and use the dioxide of natural uranium UO_2 as their fuel. This is because the UK, France and Canada started their nuclear power generation program at a time when enrichment was only mastered by the USA where it had been developed for military purposes during the Manhattan Project.

The capacity to enrich uranium, to increase the isotopic proportion of fissile ^{235}U , allowed for the use of ordinary water H_2O as moderator in the reactors of the nuclear submarines, to be followed by all the LWR, which constitute today more than 85% of the nuclear power plants in the world. But if one needs almost pure ^{235}U to make nuclear weapons, the LWR fuel is enriched only to between 2 and 5% in ^{235}U .

4.1 Principle, Cascade, SWU, HEU, LEU

Enrichment is the partial separation of “feed” natural uranium into its two main isotopes ^{238}U and ^{235}U , to yield a “product” containing a mole fraction N_P of ^{235}U higher than the naturally occurring $N_F = 0.71\%$, leaving a “waste” fraction depleted to $N_W\%$ ^{235}U . An enrichment facility can be considered as a black box with one intake and two exits, each one characterized by a mass flow (F , P or W) and by a concentration in ^{235}U (N_F , N_P or N_W) as shown in  Fig. 7.

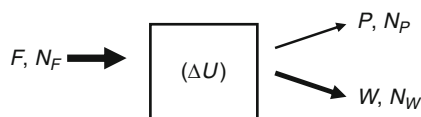


 Figure 7

Enrichment process (schematic)

The equilibrium is described by the following equations:

$$F = P + W \quad \text{mass conservation} \quad (1)$$

$$F \cdot N_F = P \cdot N_P + W \cdot N_W \quad \text{isotopic conservation} \quad (2)$$

$$(\Delta U = P \cdot V(N_P) + W \cdot V(N_W) - F \cdot V(N_F)) \quad \text{value conservation (see below)} \quad (3)$$

Instead of using the mole fraction N , one often uses the abundance ratio $R = N/(1 - N)$; the efficiency of the separation is characterized by the separation factor $\alpha = R_P/R_F$.

Most of the physical properties of a pure element, density, fusion and vaporization temperature, etc. exhibit slight but measurable differences according to its isotopic composition, but very few of these differences can be the basis for isotopic enrichment. The same can be said of the chemical properties. Even for the most efficient methods, α is usually very close to unity, and one must constitute “cascades” by coupling many elementary stages to reach the desired enrichment N_P , as schematized in [▶ Fig. 8](#). In order to minimize the feed supply, the cascade is divided into two sub-cascades: most of the stages are used to enrich the product, while a few are devoted to deplete the tails to reach N_W , an operation known as “stripping.”

The simplest way to constitute a cascade is to feed stage “ n ” with the product of stage ($n - 1$) and the tail of stage ($n + 1$). Of course, not to remix what has been painfully separated, the assay of product $n - 1$ and tail $n + 1$ must be identical: this condition determines the optimum flow in each stage of the cascade, the optimum “shape” schematized in [▶ Fig. 9](#).

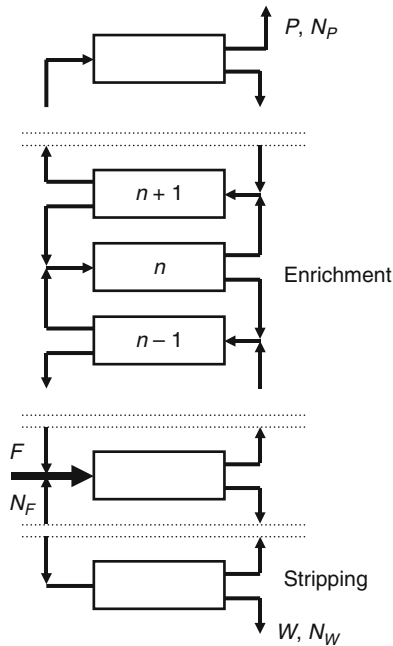


Figure 8
Coupling stages to form a cascade

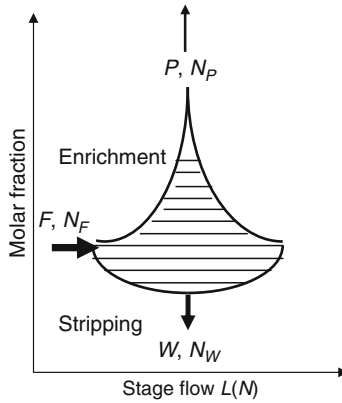


Figure 9
"Profile" of an ideal cascade

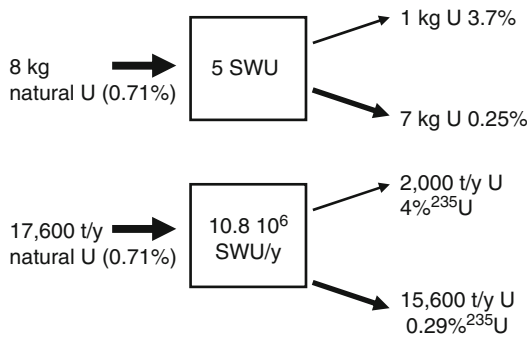


Figure 10
Mass flows in the enrichment process

The choice of N_P is, of course, determined by reactor physics, by the burnup to be reached in the fuel. The choice of N_W results from an economic optimization between the cost of feed uranium and the cost of the enrichment service: the higher the value of N_W , the more feed you need to obtain a given quantity of product. To carry out this optimization, one introduces the concept of "separative work," noted ΔU , which derives from the increase of a "value function" V :

$$V(N) = (2N - 1) \text{Ln} \left(\frac{N}{(1 - N)} \right) \tag{4}$$

$$\Delta U = P \cdot V(N_P) + W \cdot V(N_W) - F \cdot V(N_F) \tag{5}$$

ΔU has the same dimension as F , P and W , and is expressed in *separative work units* (SWU) (Villani et al. 1979). ➤ Figure 10 illustrates typical values of these parameters optimized for the economic conditions of the 1990s (Bottom figures correspond to the EURODIF plant).

3.7% ^{235}U is a typical assay for a PWR fuel capable of reaching 45 GWd/t. From 1% to 5% ^{235}U , one refers to *low enriched uranium* (LEU). Above 20% and up to weapon grade 93%, it is called *highly enriched uranium* (HEU), and subject to very strict safeguards and export restrictions to prevent risks of proliferation of nuclear weapons. The usual enrichment for Research and Irradiation experimental reactors fuel is 19.8%, just below the HEU threshold.

To obtain 1 kg of commercial LEU, one needs typically 5 SWU, while 1 kg of weapon grade HEU requires around 200 SWU. A 1 GWe PWR needs of the order of 100,000 SWU per year.

4.2 Enrichment Technologies

There are many possible classifications of the various uranium enrichment processes, according to the property one wants to emphasize, for instance: statistical processes such as gaseous diffusion (GD) or centrifuge versus selective processes such as AVLIS, reversible processes such as most chemical processes versus irreversible processes such as calutrons, etc. One can also distinguish between established processes and processes under development, or according to the proliferation resistance, which, itself calls for several criteria (ease and time to reach HEU, size and visibility of the facilities, holdup inventory, criticality limitations, need for power, etc.). Of course, for civilian purposes, economics is the key criterion, with its components: plant depreciation, operation and maintenance, and power consumption.

It all started with mass spectrographs, the giant “calutrons” of the early stages of the Manhattan Project: Under a strong magnetic field, ions follow different circular trajectories according to their charge-to-mass ratio. You can therefore completely separate individual uranium ions one by one, but with a very low throughput. This method was soon discarded in favor of more efficient processes. It was considered so obsolete that nobody cared to control this technology that – for this very reason – Iraq chose to revive for its clandestine military program.

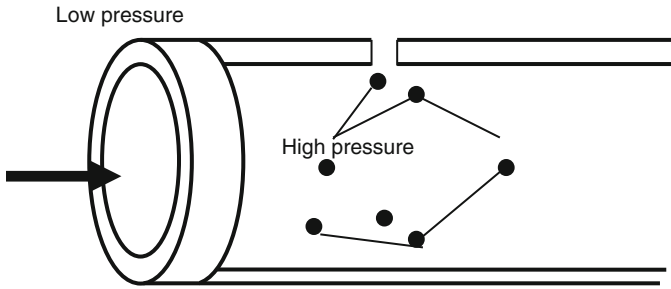
Then GD dominated the market, followed by ultracentrifuge (UC). Some developments were carried out on aerodynamic processes (the German nozzle process and the South African Helicon) and on chemical isotopic separation methods (the French CHEMEX and the Japanese Asahi), and the most recent developments center on laser enrichment.

4.2.1 Gaseous Diffusion

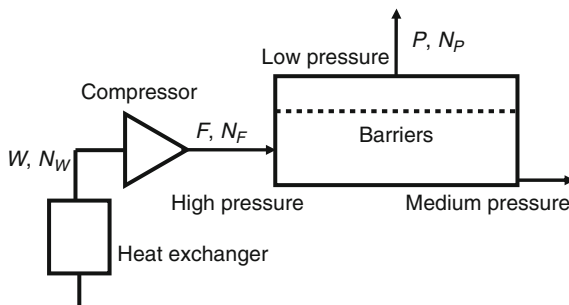
In a vessel containing a mixture of gases in thermal equilibrium with its surroundings, according to Knudsen law, molecules move with an average speed inversely proportional to the square root of their molecular mass:

$$V_i = \left(\frac{8RT}{\pi M_i} \right)^{1/2} \quad (6)$$

As a consequence, in gaseous UF_6 , molecules of $^{235}\text{UF}_6$, mass 349, travel more rapidly than molecules of $^{238}\text{UF}_6$, mass 352, and in a given time interval they impact more often the walls around them. If the walls are porous, $^{235}\text{UF}_6$ molecules are slightly more likely to sneak their way through the pores than $^{238}\text{UF}_6$ molecules, at least if the pore diameter is much smaller than the mean free path of the molecules. If there was a pressure difference between the two faces of



■ Figure 11
GD (elementary process)



■ Figure 12
GD (schematic)

the porous wall, the low pressure side would, therefore, be slightly enriched in $^{235}\text{UF}_6$. Ideally, in pure Knudsen regime, the separation factor across the pore would be proportional to the square root of the ratio of the masses, in our case, $\alpha_0 = 1.0043$. The ideal enrichment factor $\varepsilon_0 = 4.3 \cdot 10^{-3}$, is very small. *In reality, several perturbing factors lower the actual enrichment factor to around $2 \cdot 10^{-3}$.*

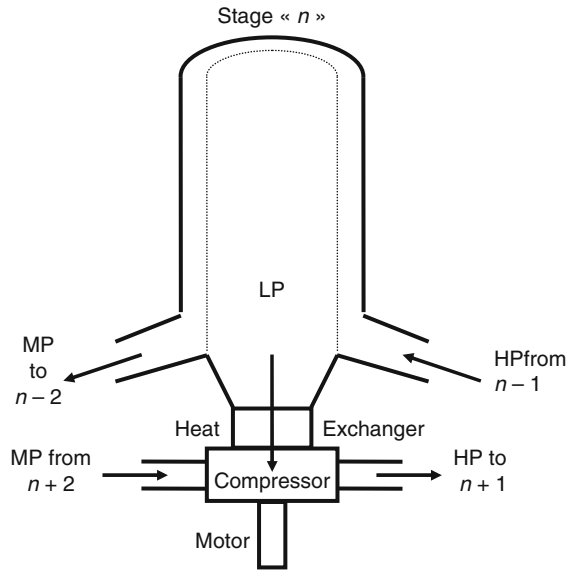
GD, schematized in [► Fig. 11](#), implements this phenomenon to enrich UF_6 by pushing it through a very thin porous “barrier” deposited over a porous support (with larger pores) which can withstand the pressure difference.

The elementary separative stage is constituted of three basic components ([► Fig. 12](#)):

- The “Diffuser,” cylindrical container in which several barriers are set up in parallel, inside their cylindrical support tubes. These barriers define two compartments inside the diffuser, a high pressure compartment inside the barriers and a low pressure compartment outside them
- The compressor which circulates the gas and gives it the right pressure entering the diffuser
- A heat exchanger to remove the calories produced by compression

Of course, one also needs a series of ducts and valves, etc.

In the old US plants, diffusers were horizontal, and barrier supports were made of sintered nickel. In the Tricastin EURODIF plant, the most modern GD plant, diffusers are vertical and



■ Figure 13
EURODIF layout (schematic)

barrier supports are made of ceramic. The actual layout of a EURODIF enrichment stage is shown in ► Figs. 13 and ► 14 shows the actual cascade profile, to be compared with ► Fig. 9: with such a small enrichment factor, one needs as many as 1,400 stages to reach commercial LEU assay (<5%). As a matter of fact, the four huge buildings housing the EURODIF plant contain only a single cascade. It would be quite uneconomical to build 1,400 stages of different sizes, so the cascade is “squared,” using only three diffuser sizes, and adjusting slightly the mass flows.

Being a thermodynamically irreversible process, GD requires a lot of power for the compressors, around 2,400 kWh per SWU: to power its 10.8 million SWU per year, EURODIF needs the full output of three 900 MWe PWR plants located just nearby. On the other hand, it can supply enriched uranium for 100 similar PWR plants. GD plants need a long time to reach equilibrium and have a very significant quantity of uranium “held up” inside the cascade. Furthermore, once a cascade is set up, it is extremely difficult to rearrange it to reach a significantly higher enrichment: a civilian GD plant cannot easily be made to fabricate HEU, and certainly not without a high visibility and a long delay.

4.2.2 Ultracentrifugation

Early works on the gaseous centrifuge method were carried out by Zippe in Germany during World War II. In the 1960s, this process began to appear competitive for large-scale enrichment; it is the process used in Russia and by the Anglo-German-Dutch Company URENCO.

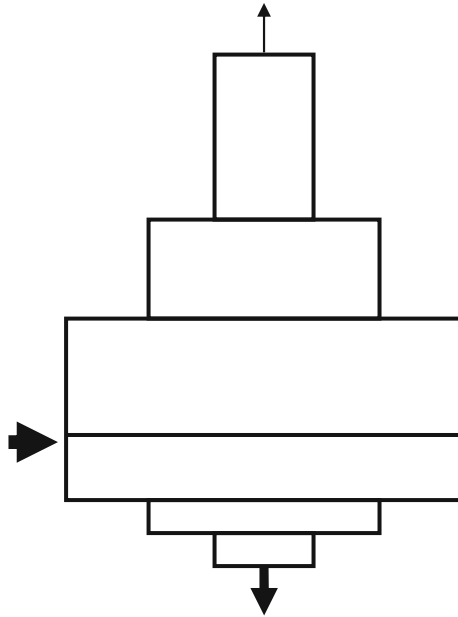


Figure 14
Actual EURODIF "profile"

When a gas rotates, its molecules are subject to a centrifuge force which results in a pressure gradient perpendicular to the rotation axis:

$$P(r) = P(0) \exp\left(\frac{M\omega^2 r^2}{2kT}\right), \quad (7)$$

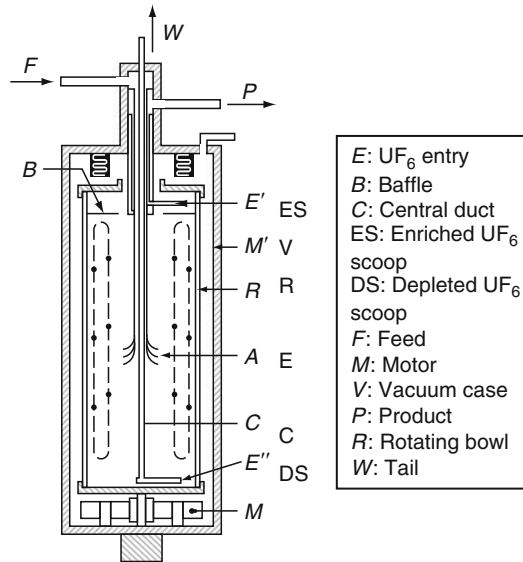
where ω is the angular rotation speed.

Under this pressure gradient, a separation appears, the heavier molecules concentrate at the periphery while the lighter species migrate preferentially toward the center, where the gas density is near zero. Assuming a centrifuge of radius R , the separation factor at a distance r from the axis would be:

$$\alpha_0 = \left(\frac{\exp(M_8 - M_5)\omega^2(R^2 - r^2)}{2kT}\right). \quad (8)$$

With $\omega R = 800$ m/s, $T = 300$ K, and $r = 0.7R$, the separation factor for UF_6 would be equal to 1.23, much larger than the value for gas diffusion – but the mass flow is much smaller.

To improve very significantly the performances of the centrifuge, one creates a vertical countercurrent circulation at the periphery (see Fig. 15), with a thermal gradient for instance: it is somehow equivalent to creating an internal cascade, the upward current being progressively enriched in ^{235}U while the downward current is progressively depleted. With this set-up,



■ **Figure 15**
Centrifuge (schematic)

one shows that the separative capacity of a single rotating bowl, expressed in SWU, can be written as

$$SWU \sim \frac{L \cdot D \cdot (\omega R)^4 \cdot (M_8 - M_5)^2}{T^2}. \quad (9)$$

It is proportional to the length of the bowl, to the diameter of the bowl, to the fourth power of the peripheral speed, and inversely proportional to the square of the temperature.

One should, therefore, use a long bowl and rotate it at the highest possible peripheral speed inside a vacuum case to prevent heating (and contain the fragments of an exploding bowl). But there are constraints: the bowl material must resist the enormous strain of the centrifuge force on its thin wall: it must also withstand the operating temperature and resist UF₆ corrosion. The drum must be extremely well balanced. Reaching the rotational speed is very tricky because one must “pass” a number of critical resonance values. The gas temperature must not go below the solidification point because any plate-out of solid UF₆ would unbalance the rotor and cause it to explode, etc.

The mass flow is so small that one needs a huge number of centrifuges, but as the enrichment factor is significant, one needs a limited number of stages, each constituted by many parallel centrifuges. The most advanced centrifuges, with composite materials and peripheral speeds of more than 700 m/s, are credited with an individual separative power ranging between 30 and 100 SWU/y. From 1977 to 1985, the Americans almost completed a large enrichment plant (8.8 MSWU/y) GCEP, at Portsmouth, which had huge centrifuges, more than 10 m high and believed to have an individual capacity of several hundred SWU/y. No technical reason was given when the project was discontinued, but such “monsters” were probably not reliable enough and, therefore, uneconomical at the time. Nevertheless, this project was restarted a few years ago.

Even with 100 SWU/y/machine, a 5 million SWU/y plant would need 50,000 machines to constitute parallel cascades of less than ten stages. Such a large number of machines require a very high level of reliability.

Since isotopic separation in a centrifuge is a thermodynamically reversible process, it requires a lot less energy than GD, of the order of 50 times less. The cost structure of the SWU is, therefore, very different between the two methods. Those plants can be unobtrusive and could, if unsafeguarded, be used to produce highly enriched weapon-grade uranium.

With the advent of the carbon-carbon composites which allow for very high peripheral speed, UC has become the most competitive process. The technology developed by URENCO is now jointly owned with AREVA, and the new Georges Besse II enrichment plant under construction in France is based on that process. Several new centrifuge enrichment plants should also be built in the USA in the near future.

4.2.3 Other Methods

The AVLIS process (atomic vapor laser isotopic separation, in French SILVA) is based on the selective ionization of the uranium atom by a laser light of convenient wavelength. The electronic spectrum of the uranium atom, with its 92 electrons, comprises many excitation levels, ranging in wavelength from infrared to ultraviolet. Because of the complexity of the interactions between the nucleus and the electrons, some of the excitation levels are not identical for ^{235}U and ^{238}U . The difference in energy is small, but sufficient to be used for isotopic separation.

The ionization energy for the uranium atom is about 6 eV, which cannot be easily provided in one quantum: one reaches the ionization level in three stages, two successive excitations of about 2 eV each, and a final ionization from the most excited level. This kind of energy can be supplied by yellow-orange dye lasers. The separation process would therefore be the following

(► Fig. 16):

A eutectic uranium-iron is melted in a crucible by electron bombardment. The atomic vapor is irradiated by laser rays of the proper wavelengths which ionize the ^{235}U atoms. ^{235}U ions are then deflected by a high-voltage electrical field toward collector plates (which also collect

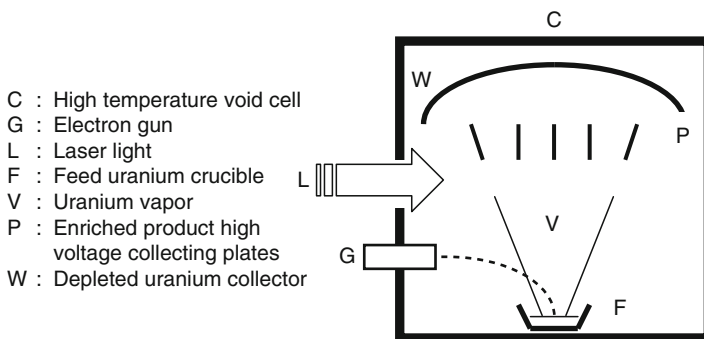


Figure 16
 AVLIS process (schema)

a certain percentage of the vapor). The remaining vapor, depleted in ^{235}U , is condensed on a collecting roof. Taking into account the isotopic dilution on the collecting plates, one should be able to enrich natural uranium to commercial LEU ($\sim 5\%$ ^{235}U) in one single step.

The huge laser power needed is supplied by batteries of high power yellow green lasers (copper vapor lasers or doubled YAG), the wavelength being adjusted by tunable color lasers downstream (Maillet et al. 1980; Schäfer et al. 1990).

The physics of the process has been demonstrated at the laboratory scale, but the technology is very demanding, especially concerning the collector materials. The power requirements, notably for uranium vaporization, are slightly larger than for the centrifuge process, but far smaller than GD. Following the Americans, the French have discontinued the development of AVLIS in 2003 after a demonstration run which produced several kilograms of 3% enriched uranium.

One drawback of AVLIS is that it breaks the UF_6 “chain” from refining to fuel fabrication, introducing a metal technology “link” in-between. This is why a sister technology has been pursued for some time, called MLIS for molecular laser isotopic separation. Infrared lasers would selectively excite $^{235}\text{UF}_6$ molecules in a gaseous mixture of UF_6 and a lighter gas at low temperature ($\sim 100\text{ K}$), and the excited molecules would later be broken into solid UF_5 and fluorine by an ultraviolet laser.

This process as such was not completely demonstrated when abandoned in the mid-1980s. A promising variant to be developed is SILEX, an Australian concept which appears to be based on molecular aggregates and utilizes UF_6 as well as another gas. In 2006, GE Energy (now GE-Hitachi) entered a partnership to develop the SILEX process renamed “Global Laser Enrichment.” In August 2007, GE-Hitachi announced it planned “to complete a test loop program at the end of 2008 which, if successful, would open the way for the first commercial enrichment plant to be constructed.”

5 Fuel Fabrication

5.1 Elements of Fuel Design

With few exceptions – molten salt reactors for instance – the nuclear fuel is fabricated into discrete objects called “elements,” “bundles,” “assemblies” or “subassemblies” (Bailly et al. 1999), where the nuclear materials are inserted inside mechanical, usually metallic, structures. A set of fuel elements constitutes the core of the reactor.

In the reactor, the fuel performs two essential functions: It supplies the heat in the core, and it prevents the radioactive fission products from migrating into the primary coolant circuit (it is the “first barrier” in the safety analysis). It must, therefore, have the capability to sustain for several years the chain reaction in a stable manner while keeping its structural integrity. As a consequence, fuel design must take into account the requirements issued from the core physics and from the coolant chemistry.

Core physics defines the fuel composition, the proper mixture of fissile, and fertile and control materials in order to achieve the required burnup, i.e., the quantity of energy supplied by the fuel during its lifetime, expressed in GWd/t , gigawatt day per metric ton of heavy metal contained in the fuel. Core physics also determines the fuel geometry, taking into account the neutronic and thermal-hydraulic properties of the coolant, as well as the neutronic properties of the structural materials (cladding, other fuel structures as the case may be).

Coolant chemistry dictates some properties of the cladding such as corrosion resistance at operating temperature or above, and even with the fuel material itself, which must not interact chemically with the coolant in case of cladding failure.

Beyond these generic considerations, fuel design and fuel fabrication are very specific for a given reactor type.

5.1.1 Fissile/Fertile Couple

With few exceptions (HEU fuel for some research or space applications reactors), the fuel is a mixture of fissile and fertile nuclides, and the conversion of fertile into fissile during the irradiation makes up partially for the fissile depletion, thus extending the lifetime of the fuel. In a “breeder,” the conversion rate is even higher than the depletion rate.

We have seen that natural uranium itself is a mixture of fissile ^{235}U and fertile ^{238}U , but with a very low concentration in fissile nuclei which severely limits its uses. Any combination, in the proper proportion, of one of the three fissile nuclides ^{233}U , ^{235}U , and plutonium (actually a mixture of ^{239}Pu and ^{241}Pu) with one of the two main fertile nuclides ^{238}U and ^{232}Th can provide the basis for a fuel cycle.

5.1.2 Fuel Material

The simplest fuel material is uranium in the metal form. It is still used in the last gas-cooled MAGNOX power reactors, because only the metal can sustain the chain reaction in a natural uranium/graphite core where the neutron balance is tight, and in some experimental and irradiation reactors. It may also be used as a metallic alloy in fast neutrons reactors. Uranium is a highly reactive metal which oxidizes rapidly in air at room temperature. At temperatures below 600°C , uranium crystallizes in the orthorhombic system (α phase) which is anisotropic: when the metal is formed by rolling or extrusion, the crystals orient themselves along preferred directions which results in dimensional changes when the metal is irradiated (the so-called growth), or thermal cycled.

In most other occurrences, the fuel material is ceramic: it can be uranium carbide or uranium nitride, but most often, by far, it would be uranium dioxide UO_2 . Uranium dioxide has a number of qualities: it is refractory (melting temperature is $2,865^\circ\text{C}$), it is structurally stable and does not interact with high temperature water and oxygen, and it has a very low capture cross section for thermal neutrons. UO_2 density is 10.97 g/cm^3 , and it has a poor thermal conductivity (around $2 \times 10^{-3}\text{ W/m/K}$ at $1,000^\circ\text{C}$).

5.1.3 Cladding Materials

The fuel cladding serves several purposes: it contains the fission products, it protects the fuel against corrosion by the coolant, provides a heat exchange surface with the coolant, and it must do so for extended periods of time (from several weeks to several years) during which it is submitted to irradiation by fast neutrons. In addition, it must have a low neutron absorption cross section not to impair the neutron economy in the core (The cross section, expressed in barns $-1\text{ barn} = 10^{-24}\text{ cm}^2$ – is a measure of the probability for a given reaction to take place when a given nuclide is irradiated with neutrons of a given energy).

■ **Table 5**
Thermal neutrons absorption cross sections

Material	Barns
Beryllium	0.01
Magnesium	0.06
Zirconium	0.18
Aluminum	0.23
Tin	0.63
Niobium	1.1
Iron	2.6
Molybdenum	2.7
Chromium	3.1
Copper	3.8
Nickel	4.6

To provide a good heat transfer, the cladding material must have a good thermal conductivity and a good bonding with the fuel. If such bonding is not possible, an intermediate layer must be introduced: high pressure gas (most often), liquid metal or pyrocarbon in some occurrences. With the exception of the silicon carbide coating of high temperature reactors (HTR) particles (see ▶ [Sect. 5.4](#)), most claddings are made of metals or metallic alloys. ▶ [Table 5](#) gives the thermal neutron cross section values for several metals used as cladding or entering into the composition of cladding alloys.

Beryllium would appear ideal but its mechanical properties, especially under irradiation, are not good. Magnesium alloy MAGNOX is used in namesake reactors but would not withstand a water environment. Aluminum is used in low temperature MTR irradiation reactors but would not resist corrosion at higher water temperatures. Alloyed zirconium is the basic choice for LWR and CANDU fuels. Stainless steel was used in LWR, and is the cladding for sodium cooled FBR (with fast neutrons, absorption in the cladding is negligible).

5.1.4 Absorber Materials

A reactor loaded with fresh fuel is supercritical (This means it has more fissile material in the core than would strictly be necessary to maintain the fission chain reaction going.), if one considers only the reactivity of the fuel: this excess reactivity, which wears out during irradiation, is necessary to compensate for a number of effects for LWR, summarized in ▶ [Table 6](#).

To keep the chain reaction just critical and the power level constant, a combination of neutron absorbers must be introduced in the core, taking into account that most of the above mentioned reactivity effects happen within a few days, only the burnup effect lasting over the complete power cycle.

■ **Table 6**
Reactivity balance (%) in typical LWR

Changes in the core	PWR	BWR
Fuel temperature defect, from cold to hot, full power	1.5	1.5
Moderator effect (same)	2.5	2.0
Equilibrium fission product poisoning	3.5	3.3
Burnup compensation	10.0	6.5
Control margin and xenon–samarium override	1.2	1.0
Shutdown margin	1.0	1.0
Total	19.7	15.3

From (Barré 2005a)

Neutron absorbers, usually referred to as “control poisons,” may be chemical compounds of boron, cadmium, gadolinium, erbium or hafnium. These poisons may be homogeneous in the coolant (soluble boric acid in PWR primary water), homogeneous in the fuel (“burnable” gadolinium oxide in BWR fuel pellets), or heterogeneous in movable “control rods” or fixed burnable absorber rods.

5.2 The LWR Fuel

The fuel assemblies of both families of LWR, PWR, and BWR share a lot of characteristics, which reflect the fact that both use the same material – ordinary water – as coolant as well as moderator:

- The nuclear material is a ceramic made of sintered dioxide of LEU or of mixed uranium and plutonium dioxide, manufactured in cylindrical “pellets.”
- The pellets are inserted inside leaktight metallic “rods” (or “pins”). The rods are pressurized with helium, both for thermal bonding and mechanical resistance.
- The rods are assembled inside a metallic “skeleton” which insures the mechanical stability in the core and during handling and transportation.

Early cladding material was stainless steel, but now cladding is usually made of zirconium-based alloys: zirconium has a low capture cross section (see 📍 [Table 5](#)), a high melting temperature (1,845°C), and a good resistance to corrosion by high temperature water. It is relatively abundant, but must be purified from any trace of hafnium which comes with it, and is a powerful neutron absorber. Alloying materials, varying in proportion from design to design, are used to improve the mechanical properties of zirconium and minimize its growth under irradiation. The various “Zircaloy” alloys use tin (1.2–1.7%), iron, chromium and nickel; niobium is used in advanced cladding materials. Tin improves the mechanical properties, and other additives are used against corrosion.

📍 [Table 7](#) gives typical parameters of PWR and BWR fuel assemblies.

BWR fuel is zoned axially, both in enrichment and in burnable poison, to accommodate for the change in water density between the bottom and the top of the fuel.

■ **Table 7**
Typical LWR fuel assemblies

Characteristics	PWR	BWR
Burnup (GWd/t)	45–60	40–50
Pellet diameter (mm)	8.2	9.5
Pellet length (mm)	13.5	11.5
Cladding material	Zircaloy 4	Zircaloy 2
Pin outer diameter (mm)	9.5	12.3
Cladding thickness (mm)	0.57	0.89
FA length (m)	4.8	4.1
Rod length (m)	4.5	4.5
Number of rods/pins	264	72 (8 tie rods)
Average fuel rating (kW/m)	17.9	15.4
Geometry	17 × 17	9 × 9
Structure	Rods maintained by spacer grids around a skeleton made of guide tubes	4 bundles with spacer grids inside a wrapper tube
Control absorbers	Rods within guide tubes	Cruciform between 4 FA

5.2.1 Fuel Pellets Production

Solid UF₆ is supplied by the enrichment plant to the fabrication plant as a solid stored in steel containers. There, the containers are heated to release gaseous UF₆. From then on, the following operations are performed:

- *Conversion*: UF₆ is heated in an oven with water vapor and hydrogen, to produce UO₂ powder, according to the reaction $UF_6 + 2H_2O + H_2 \rightarrow UO_2 + 6HF$
- *Mixing*: UO₂ is oxidized to U₃O₈ and mixed with a “porogen” material to adjust the final density
- *Precompaction*: the mixture is precompacted, then crushed and made into small granules, which flow easily
- *Pelletization*: the granules and a lubricant (zinc stearate) are pressed into pellets under high pressure
- *Sintering*: the “green” pellets are sintered at 1,700°C in a continuous oven and in a hydrogen atmosphere. In the process, the pellet density increases to ~94% of the theoretical value
- *Grinding*: the pellets are ground to the design diameter and “cupped” at the ends. Each of them is then automatically checked for dimensions, shape, and surface aspect. The finished pellets are finally outgassed in vacuum at high temperature to remove any trace of moisture and organic contaminants

The process described above is the “dry” route. Conversion can also be “wet” through precipitation of ammonium diuranate $(\text{NH}_4)_2 \text{U}_2\text{O}_7$, followed by calcination of the precipitate. Reject pellets are crushed and reintroduced in the precompaction stage.

5.2.2 Fuel Rods Fabrication

Zirconium is delivered as a “sponge,” which is first melted in vacuum in an arc furnace where alloying elements are added, and poured as ingots. Ingots are forged and quenched to preserve the microstructure, then drilled, rolled, and annealed to obtain a long tube of the right diameter and thickness. The tube is 100% controlled for dimensions and internal defects, using ultrasonic transducers. Cut to the design length, the tubes are fitted with a welded bottom plug.

The pellets are introduced inside the tubes up to the proper fuel length and maintained in place by a spring introduced in the upper plenum, designed to provide room for the release of fission gases during fuel irradiation. The top plug is then welded to the tube; this plug has a small hole through which helium is introduced, around 25 bars, before the closure of the hole. The completed fuel rod is then controlled: leaktightness of the welds, length of the pellet column, etc.

5.2.3 Assembly

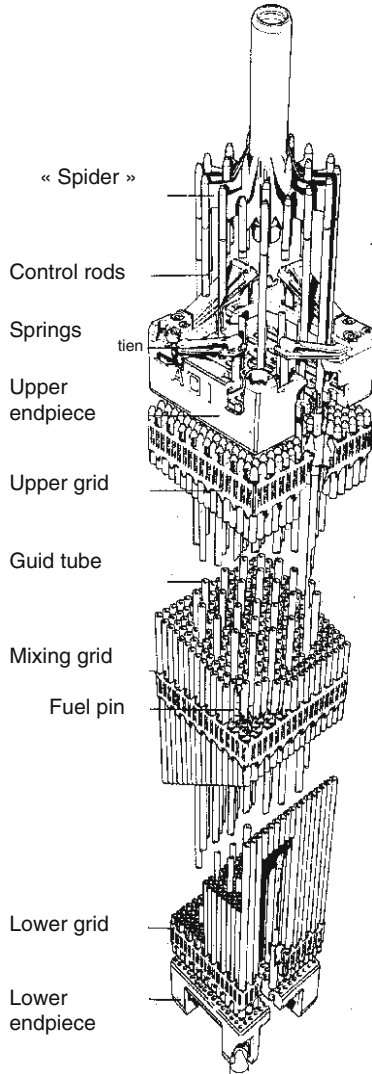
The skeleton is first partially assembled with the inconel bottom end piece, the zircaloy guide tubes (for PWR), and the zircaloy spacer grids. The rods are pulled into place through the grids by a special machine, and the top end piece is fitted. Complete fuel assemblies are then checked for dimensions and rod spacing and stored in vertical position, waiting for transportation to the reactor site. ➤ [Figure 17](#) shows a typical PWR fuel assembly.

5.3 MOX Fuel

Recycle of plutonium (see ➤ Sect. 5.7) in LWR is performed by loading into the core a given percentage of “MOX” fuel assemblies along with the standard LEU fuel assemblies. MOX fuel has identical structures to standard fuel: the only difference is that pellets are made from a mixture of depleted uranium oxide and plutonium oxide $(\text{U,Pu})\text{O}_2$. To protect the operators from the radiotoxicity of plutonium, MOX fabrication must be performed remotely, inside glove boxes.

Because of very large resonances in the neutron absorption cross sections of the plutonium isotopes at low energy (0.3 and 1 eV), the neutron spectrum is “harder” in MOX/water media than in uranium/water. The concentration of plutonium must, therefore, be lowered at the periphery of a MOX assembly to adapt the neutron flux with LEU neighbors and thus avoid power heterogeneity. The average concentration $\text{Pu}/(\text{U}+\text{Pu})$ in a MOX assembly is roughly the double of the ^{235}U enrichment of a LEU assembly in the same batch.

The basic ingredients are UO_2 and PuO_2 , the latter coming from the reprocessing plant after oxalic precipitation of the plutonium nitrate and calcination of the oxalate. Simple mixing of the two powders would not provide enough homogeneity: this is ensured by simultaneous



■ **Figure 17**
17 × 17 PWR fuel assembly

milling at the head-end of the process. After milling, the powder does not flow easily and must be granulated. MELOX, the only industrial size MOX fabrication plant, located in Marcoule (France) and operated by AREVA NC, uses the MIMAS (MICronized MASTer blend) process shown in ► [Fig. 18](#), where a first master mixture of rather high plutonium concentration is later adjusted by mixing additional UO_2 .

Typical recycle scheme would have reloads with 30% MOX assemblies, but it is planned to load 100% MOX reloads in the future Ohma Japanese ABWR plant. The savings in enriched

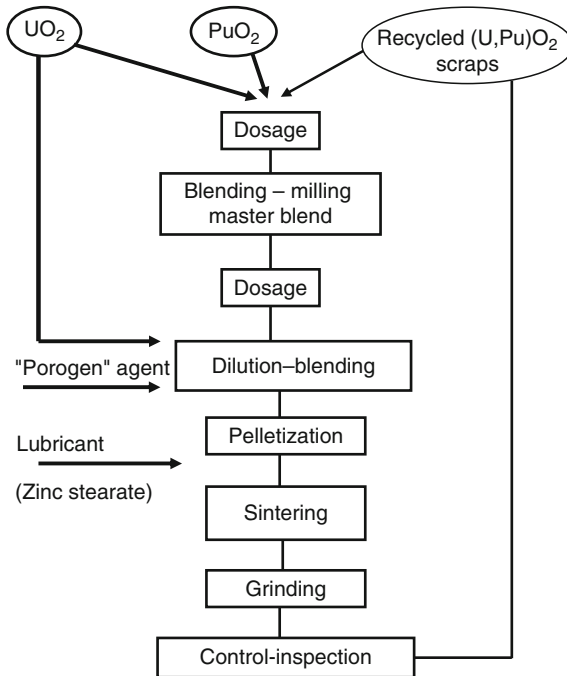


Figure 18
MIMAS blend flowchart

uranium more or less balance the increase in fabrication costs due to the remote operation and maintenance of the plant.

With the end of the cold war, as was already pointed out, significant inventories of weapon grade fissile materials have been released. To “civilize” weapon-plutonium, recycling as MOX is the preferred way, though some of it might be disposed of by mixing ceramic plutonium “pucks” with vitrified HLW.

5.4 Other Fuel

5.4.1 CANDU

As shown in Table 8, CANDU fuel bundles have the same basic components from the same basic materials than LWR fuel assemblies, though they use natural uranium oxide. The fuel bundles, loaded horizontally in the force tubes, are much shorter, and the pellets are thicker.

5.4.2 FBR

When a neutron interacts with a heavy nucleus, it can either fission it, or be captured in a number of different reactions. Very schematically, when the energy of the neutron is higher

■ Table 8
Typical non-LWR fuel assemblies

Characteristics	CANDU	Superphénix
Burnup (GWd/t)	7	> 120
Pellet diameter (mm)	12	7.1
Pellet length (mm)	16	
Cladding material	Zircaloy 4	Austenitic steel
Pin outer diameter (mm)	13	8.5
Cladding thickness (mm)	0.4	0.56
FA length (m)	0.495	5.4
Rod length (m)	0.493	2.7 (1.0 fuel)
Number of rods/pins	37	271
Average fuel rating (kW/m)	57 (peak)	200
Geometry	Circular array	Hexagonal array
Structure	Bundle with spacers	Pins separated by helical spacer wire inside hexagonal wrapper tube
Control absorbers	Metal rods (steel, Cd)	B ₄ C in special subassemblies

(“fast” neutron, rather than “thermal” or “slow”), the total probability of interaction is smaller, but the relative probability of fission is higher. In addition, in the fission process, ²³⁹Pu emits 2.9 neutrons on the average, versus 2.5 for ²³⁵U. This explains why plutonium fuelled fast neutron reactors have a better neutron economy than LEU fuelled thermal reactors such as LWR. So much so that, with a proper core design, fast neutron reactors can breed *more* ²³⁹Pu from ²³⁸U than they burn plutonium: this is called breeding, and those reactors are called breeders, FBR. Breeding allows, with a number of successive recycles, to progressively extract almost all the energy content of uranium, versus less than 1% in LWR. On the other hand, breeders are expensive and will only become competitive when uranium prices are far higher than today. As the total probability of interaction is smaller, *the fissile inventory must be larger*.

In order to keep the neutron fast, the coolant in the core must not slow down the neutrons exiting from the fuel: it cannot be water (ordinary or heavy), it can be a gas or a liquid metal. Only liquid sodium has been used to a significant degree in “liquid metal fast breeders,” LMFBR, like BR2 in the USA, Phénix and Superphénix in France, PFR in the UK, BN 600 in Russia, and Monju in Japan.

The basic LMFBR fuel is a MOX with much higher plutonium concentration (20%). If one wants to breed, the core itself is surrounded by a “blanket” of pure UO₂ fuel. In a LMFBR neutron spectrum, captures in the cladding do not matter much, but the material must be compatible with high temperature molten sodium and resist the irradiation by high fluxes of fast

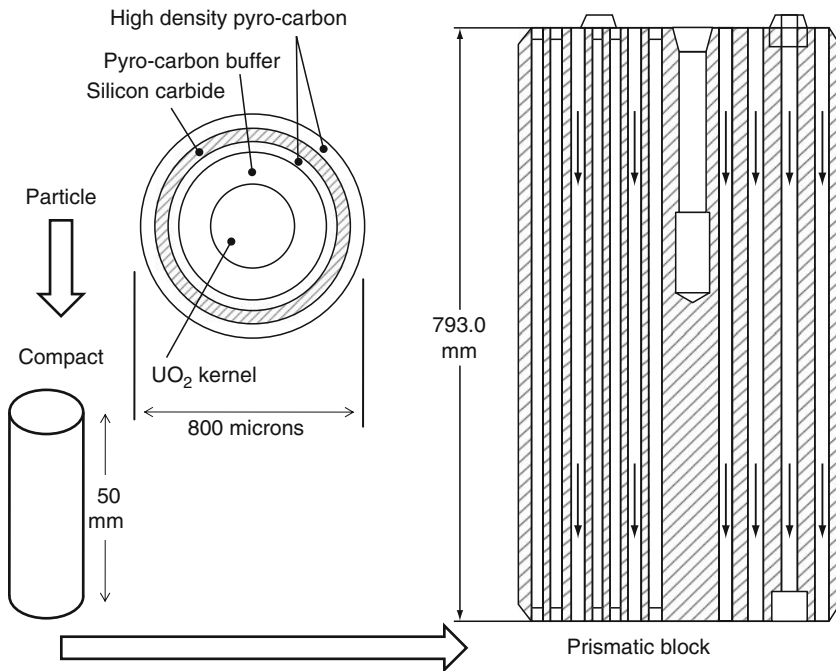
neutrons: the choice is austenitic stainless steel. The pellet fabrication process is slightly different from LWR MOX, in that the pellets are smaller (► [Table 8](#)), and there is no “mother mixture” and no need for grinding.

5.4.3 HTR

HTR, first developed during the 1970s and 1980s in Germany and the USA, may be doing a comeback based on their high thermal efficiency and their very high degree of “intrinsic” safety. These characteristics derive from the use of helium gas as coolant, graphite as moderator, and, above all, a very unusual type of fuel.

The equivalent of a “fuel rod” in other reactors is a tiny ceramic particle of uranium (or plutonium, or thorium) oxide or carbide, the “kernel,” coated with a number of layers, acting together like a cladding. The diameter of a fully coated fuel particle is of the order of 1 mm. There would be around 10 billion such particles in the core of a large reactor!

Those particles are “assembled” in a graphitized matrix, either to form spherical pebbles of 6 cm diameter directly loaded in a heap inside the core cavity of a *Pebble Bed* reactor, or to form cylindrical “compacts” piled up in columns inside the holes drilled in graphite prismatic blocks which act as “fuel assemblies” (see ► [Fig. 19](#)). The whole core is, therefore, entirely refractory: core meltdown is excluded, and it has been shown experimentally that the coating of the particles retains its integrity up to 1,600°C.



■ **Figure 19**
Fuel element of a “prismatic” type HTR

Fertile or fissile kernels are manufactured by powder aggregation or by a sol-gel process, and the layers are deposited around the kernel by pyrolytic cracking of gases in a fluidized bed reactor. From the inside to the outside one finds:

1. A buffer layer of porous carbon to prevent interaction between the hot kernel and the outer layers and to provide space for the gaseous fission products
2. A first layer of dense pyrocarbon
3. A layer of silicon carbide which stops the diffusion of fission products (mainly cesium and strontium outside the coated particle)
4. A second layer of dense pyrocarbon. Together, the two pyrocarbon layers act as a pressure vessel against the gases released during the fission

5.5 In-Reactor PWR Fuel Behavior

While in the reactor, the fuel undergoes a series of transformations interacting with one another, inside the pellets, in the cladding material, and at the interface. The net result of these numerous transformations determines the useful life of a fuel assembly and its “burnup,” which is the quantity of energy the fuel can produce before being “spent” (Marshall 1981).

The first series concerns the neutron physics, the reactivity of the fuel:

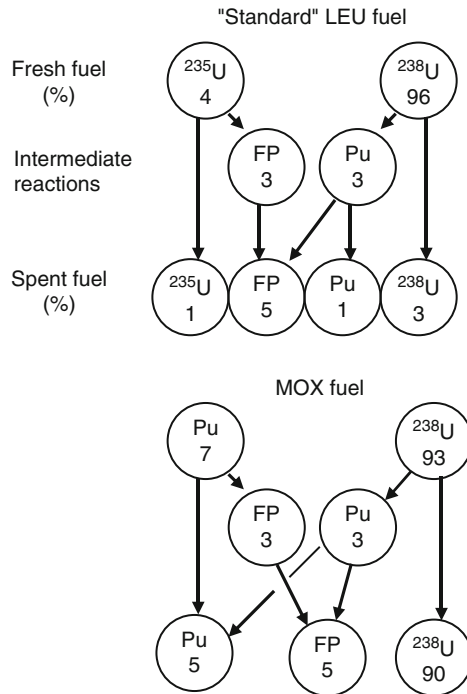
- As irradiation proceeds, the fissile nuclei are progressively consumed, while some of the fertile nuclei are transmuted into fissile nuclei. The balance between these two transformations is usually negative – with the exception of “breeder” reactors – and the fuel gets depleted in fissile nuclei (🔍 *Fig. 20*).
- In parallel, fission generates fission products. Some of those fission products, or their daughter nuclei, capture neutrons efficiently, thus “poisoning” the fuel by impairing the fission reaction.

Consequently, the reactivity of the fuel decreases throughout its lifetime, until it is no longer capable of sustaining the chain reaction (To compensate for this “reactivity swing” in the fuel assemblies, fresh fuel must be – deliberately – poisoned, and those control poisons are progressively removed, or burned in situ, to keep the average reactivity of the whole core constant throughout a cycle of production. As control poisons one uses cadmium alloy rods inserted inside the fuel element, and boric acid diluted in the primary coolant water. In addition, to reach very high burnups, “burnable” poisons, gadolinium or erbium compounds, are incorporated in the fuel pellets).

The “spent” fuel must then be unloaded from the core.

The higher the burnup to be reached, the higher must be the initial concentration in fissile nuclei, i.e., the higher the initial enrichment of LEU fuel or the higher the initial plutonium/uranium ratio in MOX fuel. Conversely, the higher the burnup, the fewer the fuel assemblies to manufacture and to reprocess for a given energy output. The optimum burnup is, therefore, the result of an economic compromise between the costs of enriched uranium supply, fuel fabrication and reprocessing.

But this is not enough: one must demonstrate that, under normal and accidental conditions, the fuel retains its integrity even at its highest burnup. This is where the other transformations above mentioned play a crucial role.



■ **Figure 20**
Schematic physics in PWR fuel assemblies (45 GWd/t_{HM})

The structural integrity of the pellet itself is affected in many ways by the irradiation:

- Most of the energy released by the fission phenomenon appears as kinetic energy communicated to the two fission fragments: their slowing down which produces heat inside the fuel also produces a lot of point defects in the fuel pellet crystallites.
- As a result, the fuel pellets swell, fragmentize, and come in close contact with the cladding.
- Many of the fission products have chemical properties different from those of uranium and plutonium, and alter the stoichiometry of the uranium and plutonium oxides.
- Some of the fission products are gases which either contribute to pellet swelling or permeate outside, increasing the internal pressure of the cladding.
- At high burnups, transmuted plutonium accumulates at the outer "rim" of the pellet, transforming in effect a thin annulus of the pellet into MOX fuel, with a possible loss of cohesion at the interface.

Even more important, the cladding, which constitutes the first safety barrier containing the radioactive elements produced in the fuel, must retain its leaktightness. During its life in the reactor core, the cladding material experiences many "aggressions":

- Corrosion is the first aggression. Even in the absence of irradiation, zirconium reacts actively with oxygen and reduces water to form an oxide, zirconia, ZrO_2 . At low temperature, a thin

coating of impermeable zirconia layer protects the alloys from further oxidation (not unlike aluminum), but at reactor temperatures, above 300°C, the corrosion goes on, together with a secondary hydride formation by the hydrogen released in the water reduction reaction. Under irradiation, this phenomenon is accelerated, and the corrosion rate becomes a limiting factor of lifetime (the zirconia layer is not allowed to exceed 100 microns). Some alloying elements decrease drastically the corrosion rate of zirconium, but their choice remains rather empirical.

- The difference of pressure between the inside of the fuel rod (initially pressurized with helium) and the water of the primary circuit induces a creep which closes the internal gap between the pellet and cladding, sometimes during the second irradiation cycle (A typical PWR fuel assembly stays in the core during four 1-year cycles). From then on, deformations of the pellet, notably during rapid variations of power – the so-called ramps – interact with the cladding and threaten its integrity, a phenomenon known as pellet-cladding interaction (PCI).
- Neutron irradiation itself induces hardening and anisotropic growth of the zirconium. In addition, fission produced iodine may attack the cladding from the inside and induce stress-corrosion, etc. One could add that alteration of the mechanical properties under irradiation also affects spacer grids, especially springs, and guide tubes of the fuel assemblies, therefore, also limiting the fuel lifetime.

All in all, the proper choice of the cladding alloy and its mechanical and thermal treatments is of key importance in the competition between nuclear fuel vendors for optimum burn-up and optimum performance for their utility customers.

6 Thorium

Thorium, element 90 in the periodic classification, is present in nature with only one isotope, ^{232}Th , which is fertile like ^{238}U , giving birth to fissile ^{233}U after a neutron capture and two β^- decays. ^{232}Th is radioactive α , with a half-life of $1.41 \cdot 10^{10}$ years. As thorium has no fissile isotope, it cannot start a fuel cycle on its own. One needs ^{235}U or plutonium to start the thorium cycle (► Fig. 21).

Though it is roughly four times more abundant in the continental crust than uranium, thorium is an essential constituent of only a few minerals: thorite (ThSiO_4), thorianite (ThO_2) and monazite ($\text{Ce,La,Nd,Th} \text{PO}_4$). The beach sands of India, Brazil and Madagascar are rich in monazite, and thorium is sometimes a by-product of uranium mining. As thorium has few applications – thoria is a highly refractory ceramic, and was also used for the luminescent gas lights, but is now abandoned because of its radioactivity – reserves and resources of thorium have not been assessed with the same precision as those of uranium.

There may be two reasons to get interested in thorium:

- On the one hand, ^{233}U is an excellent fissile material which can (barely) allow breeding in a “thermal” reactor (this has been demonstrated in the last experimental core of the Shippingport PWR, dubbed “LWBR.”
- On the other hand, the long term radio-toxicity of the high level waste issued from the $^{232}\text{Th}/^{233}\text{U}$ cycle is significantly lower than from the ^{238}U /plutonium cycle.

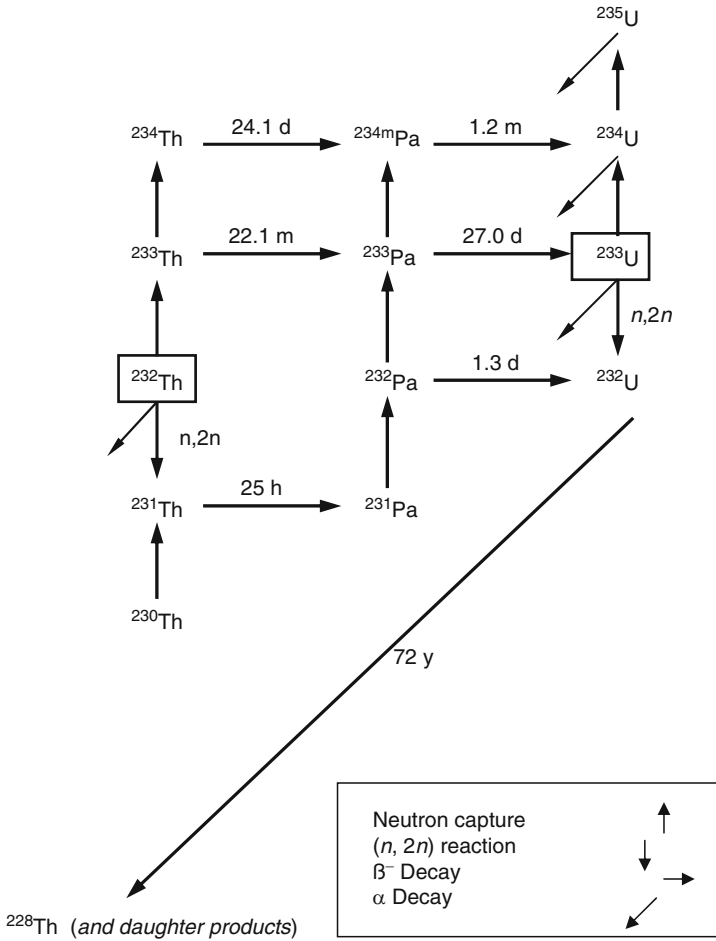
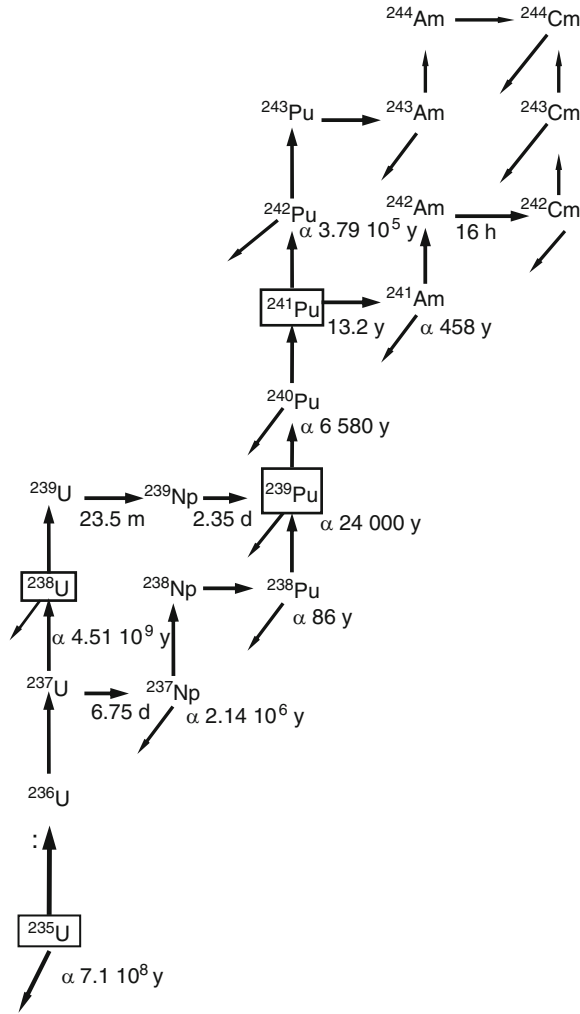


Figure 21
The thorium cycle

The thorium cycle has been used in a number of experimental reactors. India, poor in uranium resources but rich in thorium, is the only country currently developing the thorium cycle but it is considered for use with the molten salt reactor, one of the six “generation 4” concepts.

7 Plutonium

Element 94 of the periodic classification, plutonium exists only as traces in nature, but is produced when uranium fuel is irradiated in reactors, through neutron capture in ^{238}U . Spent fuel elements are, therefore, analogous to “plutonium mines,” from which plutonium is extracted by “reprocessing.”



■ Figure 22
Uranium, plutonium, and minor actinides

■ Table 9
Isotopic composition of discharged plutonium (weight%, PWR fuel, 3 years cooling time) (OECD 1999)

Burnup	²³⁸ Pu	²³⁹ Pu	²⁴⁰ Pu	²⁴¹ Pu	²⁴² Pu	Pu fiss.
33 GWd/t _{HM}	1.7	57.2	22.8	12.2	6.0	69.4
60 GWd/t _{HM}	3.9	49.5	24.8	12.9	8.9	62.4

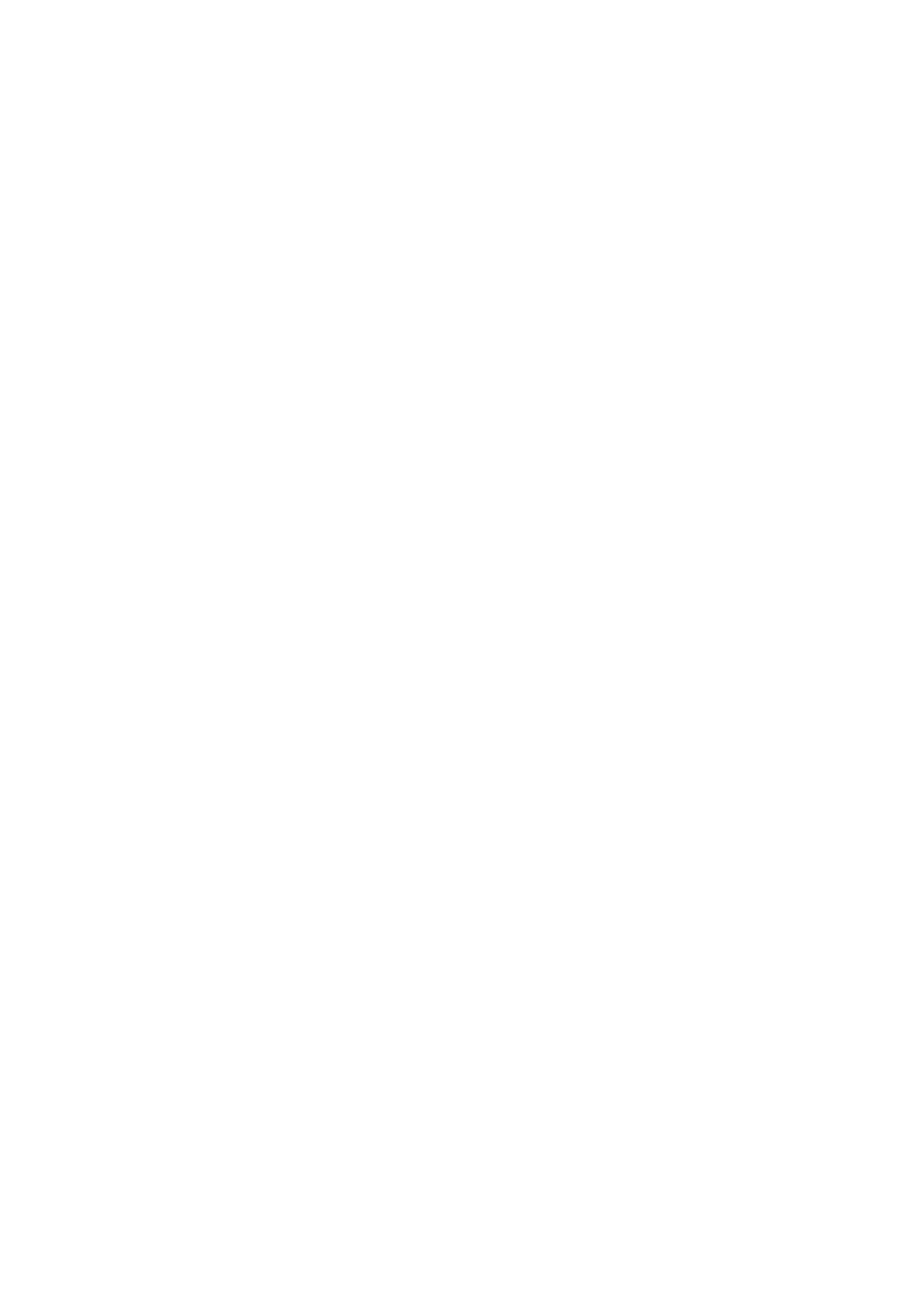
There are five major isotopes of plutonium, ranging in atomic mass from 238 to 242. Neutron capture in ^{238}U produces ^{239}Pu , and further neutron captures produce the higher isotopes, while ^{238}Pu comes from a series of reactions (🔗 Fig. 22). The amount of ^{238}U converted to plutonium increases with the time the fuel stays in the reactor and, similarly, the longer the irradiation time, the greater the proportion of higher plutonium isotopes.

^{239}Pu and ^{241}Pu are fissile isotopes, similar to ^{235}U , while ^{240}Pu can be considered “fertile” like ^{238}U , and ^{242}Pu just captures neutrons to produce higher actinides. Globally, the longer the irradiation time, the less fissile the plutonium (🔗 Table 9).

By comparison, weapon-grade plutonium of low irradiation would be over 90% ^{239}Pu .

References

- Bailly H, Ménessier D, Prunier C (1999) The nuclear fuel of pressurized water reactors and fast reactors – design and behaviour. Intercept Ltd., Bedfordshire, UK
- Barré B (2005a) Nuclear fuel and fuel cycle. In energy technologies. Landolt-Börnstein VIII-3, Springer, Berlin
- Barré B (2005b) Oklo, 2 billion years before fermi! GIFT Geophysical Information for Teachers Workshop, Vienna
- Cochran R, Tsoufalanidis N (1999) The nuclear fuel cycle: analysis and management. ANS, La Grange Parc
- Maillet H et al (1980) Le laser technique et documentation. Lavoisier, Paris
- Marshall W (1981) Nuclear power technology – vol 2: Fuel cycle. Clarendon Press, Oxford
- Naudet R (1991) OKLO: Des réacteurs nucléaires fossiles. Etude physique Eyrolles, Paris
- Nuclear Energy Data (1999) OECD/NEA, Mulineaux, France
- OECD (2008) Uranium, resources, production & demand. OECD/NEA-IAEA, Paris
- Patarin L et al (2002) Le cycle du combustible nucléaire. Collection Génie Atomique EDP-Sciences, Les Ulis, France
- Rigo L, Faron R (1995) Raffinage et conversion des concentrés d'uranium. Techniques de l'Ingénieur B3590:B3590.1-B3590.8
- Schäfer FP et al (1990) Dye lasers topics in applied physics, vol I. Springer, Berlin
- Valsardieu C (1997) Regards sur l'uranium. ESKA
- Villani S et al (1979) Uranium enrichment topics in applied physics, vol 35. Springer, Berlin
- Wilson PD et al (1996) The nuclear fuel cycle – from ore to wastes. Oxford University Press, Oxford



26 Transuranium Elements in the Nuclear Fuel Cycle

Thomas Fanghänel · Jean-Paul Glatz · Rudy J.M. Konings · Vincenzo V. Rondinella · Joe Somers

European Commission, Joint Research Centre, Institute for Transuranium Elements, Karlsruhe, Germany

thomas.fanghaenel@ec.europa.eu

jean-paul.glatz@ec.europa.eu

rudy.konings@ec.europa.eu

1	General Introduction	2937
2	Fundamental Aspects of Transuranium Fuels	2941
2.1	General	2941
2.2	Characteristics of Transuranium Fuel Forms	2941
2.3	Properties of Transuranium Elements and Compounds	2943
3	Transuranium Element Fuel and Target Fabrication	2947
3.1	General Aspects	2947
3.2	Solid Solution Oxide Fuels Fabrication by Wet Routes (Precipitation, Sol-Gel, and Infiltration)	2949
3.3	Powder Metallurgy for the Production of Solid Solution Fuels	2951
3.4	Oxide Fuels with Composite Microstructure	2952
3.5	Minor Actinide Carbide, Nitride, and Metal Fuels	2953
3.5.1	General Considerations	2953
3.5.2	Production of Minor Actinide Nitrides	2955
3.5.3	Production of Minor Actinide Bearing Metal Fuels	2957
4	Irradiation Behavior of Transuranium Fuels	2958
4.1	Mixed Oxide Fuels	2958
4.2	Metal Fuels	2961
4.3	Carbide and Nitride Fuels	2961
4.4	Molten Salt Fuels	2961
4.5	Other Fuel Types	2961
4.6	Summary	2963
5	Reprocessing	2963
5.1	Introduction	2963
5.2	Advanced Aqueous Reprocessing	2965
5.2.1	Fundamental Studies	2966
5.2.2	Process Development	2969
5.3	Pyro-Reprocessing	2971
5.3.1	US Pyrochemistry Projects	2972
5.3.2	European Pyrochemistry Projects	2973

5.3.3	Liquid–Liquid Reductive Extraction in Molten Fluoride/ Liquid Aluminum	2977
5.3.4	Technical Uncertainties of the Pyro-Reprocessing	2979
5.3.5	Head-End Conversion Processes.....	2979
6	<i>Impact of Transuranium Elements on Storage and Waste Disposal Concepts</i>	2982
6.1	General Aspects	2982
6.2	Transuranium Elements and Wasteforms.....	2982
6.2.1	Transuranium Elements in Spent Fuel	2982
6.2.2	Transuranium Elements in Waste Glass.....	2983
6.2.3	Transuranium Elements in Advanced Cycle Waste Forms	2983
6.3	Special Wasteforms for the Immobilization of Transuranium Elements	2984
6.4	Long-Term Behavior of Waste Containing Transuranium Elements.....	2985
6.4.1	Consequences of Alpha-Decay Damage and Helium Build-Up in the Waste Form.....	2986
6.4.2	Corrosion Behavior of the Waste Form in Contact with Water.....	2988
	<i>References</i>	2991

Abstract: Transuranium elements, neptunium, plutonium, americium, and curium, are formed via neutron capture processes of actinides, and are mainly by-products of fuel irradiation during the operation of a nuclear reactor. Their properties significantly impact the nuclear fuel cycle, affecting and often determining requirements and procedures related to handling, storage, reprocessing, and disposal of fuels and high-level waste. It is still debated if, in particular, plutonium is an unwanted waste or, possibly, a resource for the production of energy. A standard universally agreed route for the treatment of transuranium elements is not yet established. This chapter provides an overview of past and ongoing experience and perspectives related to studies on transuranic recovery and incorporation in fuels and targets for advanced nuclear fuel cycles and their disposal as the main component of high-level nuclear waste. In particular, the chapter describes the main properties of transuranium fuels, the specific requirements for their fabrication, their irradiation behavior, and their impact on the back-end of the fuel cycle. For the latter, a major issue is the development of options for reprocessing and separation of transuranium elements from spent fuel to make them available for further treatment. The effects caused by their presence in irradiated fuel and high-level nuclear waste on long-term storage and final disposal are also discussed.

The final destination of transuranium elements is still an open issue. The global context is characterized by a diversified set of options being pursued, which is reflected in this chapter. It is important to have a picture of the knowledge and experience gathered until now through relevant investigation campaigns worldwide. This is necessary to ensure that the renewed interest in nuclear energy as a key component of sustainable development of energy production brings the necessary focus to implement viable, safe, and technologically effective options for the treatment of transuranium elements.

1 General Introduction

The transuranium elements are the chemical elements with an atomic number greater than that of uranium (92). Due to their short half-life compared to the age of the earth, these elements are no longer found in the earth's crust. Neptunium and plutonium found in trace amounts in some uranium ores are thus not of primordial origin but are formed by the capture of neutrons. However, the widespread occurrence of some of the transuranium elements on earth is nowadays mainly related to human activities making use of nuclear reactions: nuclear weapons and nuclear reactors.

The importance of transuranium elements in the fuel cycle of nuclear reactors was recognized rapidly after the discovery of plutonium by Seaborg and McMillan in 1940. ^{239}Pu formed by neutron activation of the uranium (^{238}U) matrix of the nuclear fuel can be used as fuel for nuclear power plants and the concept of breeding plutonium – i.e., producing more fissile material than the fraction fissioned to produce energy – has been the subject of research since the 1950s. Especially in the 1960s and 1970s, when a rapid expansion of civil nuclear power took place and the expectation prevailed that the uranium resources in the world were insufficient to sustain it, fast breeder reactors were developed world-wide and the first prototypes were constructed in the USA, Europe, and USSR.

From the beginning of the development of nuclear power reprocessing of spent nuclear fuel, i.e., recovering of plutonium has been considered an essential part of the fuel cycle. The plutonium thus obtained was intended as startup fuel for fast breeder reactors. In Europe, the primary choice for the fast breeder reactor fuel was mixed uranium–plutonium oxide (MOX) as driver fuel and uranium oxide as fertile blanket, combined with aqueous reprocessing technology

based on plutonium and uranium refining by extraction (PUREX) process. In the USA, the emphasis was originally on metal fuel in combination with pyrochemical reprocessing technology using electrorefining in molten salts (Burkes et al. 2009), but the oxide fuel cycle gained strong interest before the program was stopped in the 1980s. Also dense ceramic fuels such as mixed carbides and mixed nitrides have been the subject of extensive research worldwide.

During irradiation of uranium fuel in a reactor not only plutonium is formed, but also other transuranium elements such as neptunium, americium, and curium. These elements are present in the spent fuel in relatively small quantities compared to plutonium, and for that reason they are often called minor actinides (MA). From the technological point of view, the minor actinides have been considered as uninteresting by-products, though in the past they have found limited applications as high specific power sources for special cases such as smoke detectors, pacemakers, or deep space probes (as an alternative to ^{238}Pu). Therefore, in today's nuclear fuel cycle the minor actinides are destined to final disposal in a geological repository either as vitrified high-level waste (HLW) from the reprocessing of spent fuel, or as part of spent fuel in the case of direct disposal (see ► Sect. 6).

However, the relevant isotopes of americium (^{241}Am , ^{243}Am), curium (^{244}Cm), and, to a lesser extent, neptunium (^{237}Np) are highly active and undergo highly energetic decay. As a result, the radiotoxic inventory of the vitrified waste is relatively high over significant time periods (>10,000 years). This has become one of the key concerns of the general public with respect to nuclear power. It is even more relevant for spent fuel from light water reactors (LWR) that is not reprocessed but disposed of directly, as its radiotoxic inventory is about a factor of 10 higher, because it also contains the plutonium that was produced during reactor irradiation (see ► Fig. 1).

► Figure 2 schematically illustrates the composition of typical irradiated LWR UO_2 . ► Table 1 reports the composition of different types of spent LWR fuel. Typically, ~1% of spent UO_2 fuel is Pu. The content of MA is higher in spent LWR MOX fuel. The use of Pu-based fuel has an impact on the fractions of MA in spent fuel and the waste stream that is destined to final disposal, depending on the type of reactor irradiation (Grouiller et al. 2003).

Since the late 1980s the nuclear research community has been strongly involved in exploring technical solutions to reduce the radiotoxic inventory of the nuclear waste (spent fuel, HLW). The prevailing concept is the further separation of the minor actinides from the spent fuel during reprocessing, generally called *partitioning*, and their destruction by re-irradiation by neutrons, or *transmutation*. The most effective MA destruction process by neutrons is fission, by which the minor actinides are transformed into fission products whose contribution to the radiotoxic inventory becomes very small after about 250 years (► Fig. 1). The technical feasibility of the partitioning and transmutation (P&T) concept is extensively studied (CEA 2004). From the reactor physics point of view, it is clear that the transmutation can be realized best in fast neutron systems, in which the minor actinide nuclides can be fissioned efficiently due to the favorable fission-to-capture ratio for neutrons and the favorable neutron economy. Besides the further development of the fast neutron system, key technological issues remaining to be solved are the establishment of an efficient partitioning scheme for the minor actinides from the spent fuel, and the design of minor actinide fuel that can be introduced in a reactor without adverse effects on the system safety.

These key issues are strongly related to the P&T strategy pursued. In general, one can discriminate between two different concepts:

1. Separation of individual minor actinide elements and their transmutation in dedicated systems optimized to obtain the best overall efficiency. Since the separation of neptunium can

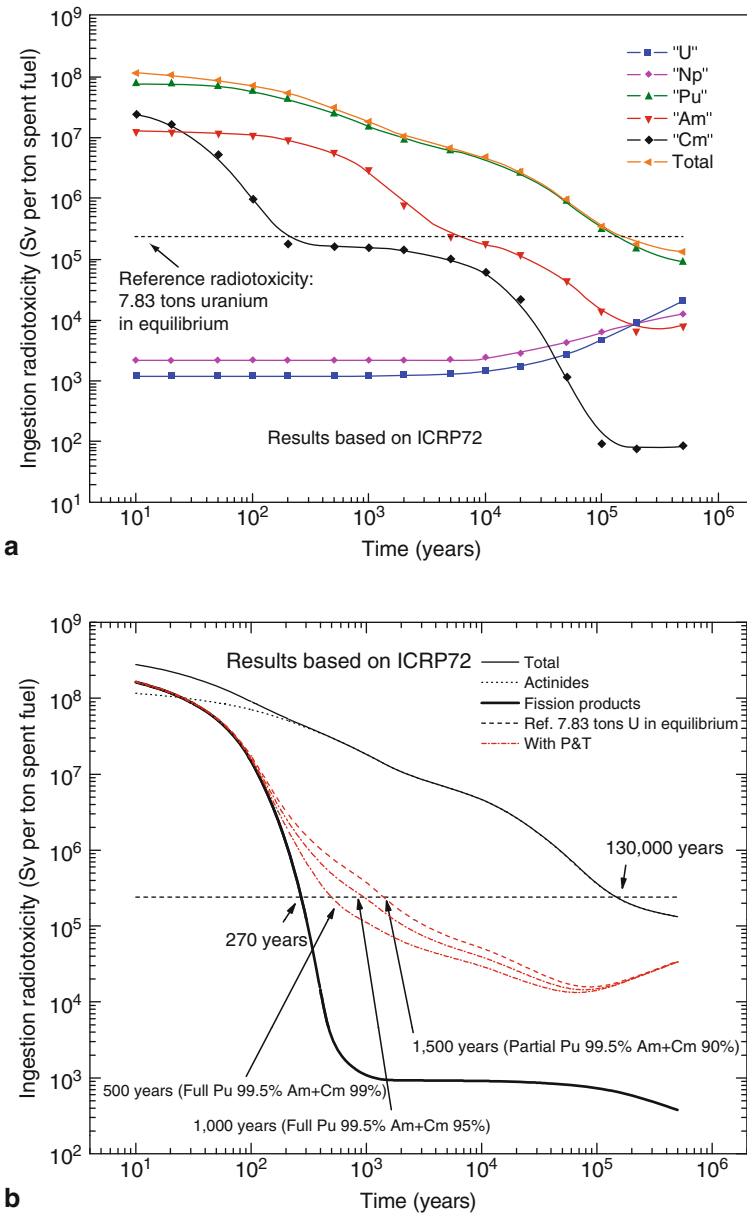


Figure 1

(a) The radiotoxic inventory of the U, Pu, and MA in spent nuclear fuel as a function of storage time. (b) The radiotoxic inventory of spent fuel as a function of storage time separated into the contributions of the actinides and the fission products

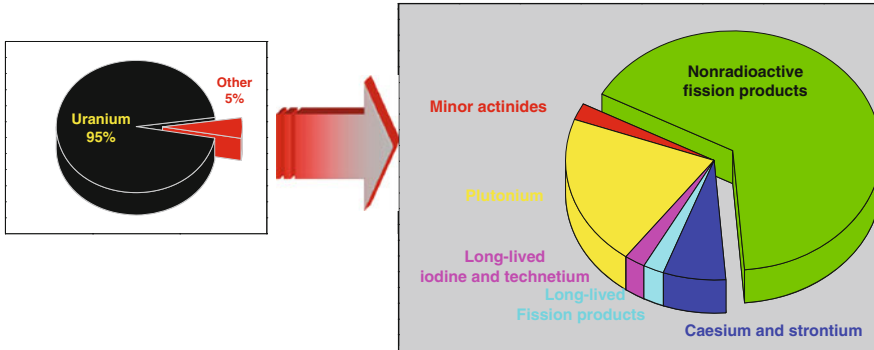


Figure 2
Composition of spent nuclear fuel (UO_2) after 3 years of irradiation in a light water reactor

Table 1

Transuranium elements and fission products (kg) in 1 ton (heavy metal) of spent light water reactor fuel with different initial composition and burnup

TRU	UO_2 35 GWd/tM	UO_2 55 GWd/tM	MOX 50 GWd/tM
Initial fissile content	3.25% ^{235}U	4.7% ^{235}U	4.2% Pu
Pu	9.95	11.60	43.56
Np	0.56	0.90	0.23
Am	0.15	0.30	2.98
Cm	0.05	0.13	1.75
Fission products	35.95	56.37	50.33

Calculations performed using the webKorigen application available at the Nucleonica web portal (<http://www.nucleonica.net>)

be achieved by adjustment of the PUREX process, and its transmutation can be realized by adding it to fast reactor (U, Pu)-based fuel, the research is focused on defining effective solutions for americium and curium. This option must rely on the feasibility of the chemical separation of Am and Cm from the lanthanide fission products as well as from each other. The use of subcritical transmutation devices such as accelerated-driven systems (ADS) in multiple recycling steps or the incorporation of these elements in once-through targets that are subjected to extremely high burn-out levels in a single irradiation, have been proposed in recent years.

- Grouped separation of the minor actinides and their transmutation in fast reactors systems, for example those studied in the Generation IV (Gen IV) International Forum (GIF), in multiple recycling steps. Here the feasibility of the difficult grouped separation must be demonstrated, and the impact of the overall presence of curium (neutron emission and heat production) on the fuel cycle operations (fabrication, handling and transport, and storage) must be assessed.

It is thus clear that the separation technology and fuel technology for minor actinides are critical for the further development of P&T strategies. In this chapter we present the state-of-the-art of these technologies, in view of the two concepts mentioned above.

2 Fundamental Aspects of Transuranium Fuels

2.1 General

The properties of nuclear fuels in general and of transuranium fuels in particular are important for the optimization of the conditions for their fabrication and to predict/assess their performance during irradiation. As discussed in detail in ► Chap. 13, detailed knowledge of the thermodynamic and thermophysical properties of the fuel materials is needed, as well as the stability of the fuels with respect to radiation. For example, the melting temperature and the thermal conductivity together define the margin between the operation temperature and melting point of the fuel, an important criterion for the safety of the fuel. Similarly, knowledge of the evolution of such properties as a function of burnup of the fuel is needed (see next section).

A large knowledge base exists for U and U/Pu-based fuels, but the knowledge of MA bearing fuels is still relatively poor. Some basic data have been generated during the 1950s and 1960s when the science of the actinide elements was explored worldwide but generally not at the high temperatures relevant to nuclear fuels. Transmutation studies have stimulated renewed interest, both by experiments and theoretical calculations, in the properties of MA compounds.

2.2 Characteristics of Transuranium Fuel Forms

Transuranium fuels are characterized by a high concentration of plutonium and minor actinides which have a significant impact on the physical, chemical, and radiation properties of the fuel, affecting the fabrication process, the handling, and the irradiation behavior (Konings and Haas 2002). ► **Table 2** shows the radioactive decay characteristics of various nuclides that must be taken into account. In particular, the γ dose rates of the americium and curium isotopes are orders of magnitude higher than those of uranium or even ^{239}Pu . This means that lead shielding is a prerequisite for safe handling and treatment of any fuel compounds which include MA. In addition, ^{244}Cm presents a very high neutron dose rate due to spontaneous fission, which requires further shielding using materials with high hydrogen density like water or polyethylene. Finally, the power produced by ^{244}Cm is significant and necessitates forced cooling when stored.

Transuranium fuels have by definition a complex composition containing multiple actinide elements. Since the content of fissile isotopes in the reprocessed plutonium and minor actinide products is generally high, a non-fissile matrix is required as support. Two combinations of matrix and fissile phase can be distinguished: solution phases (solid, liquid) or composites (Chauvin et al. 1999).

A solid solution is, in principle, a homogeneous mixture of two or more end member compounds that are distributed randomly/substitutionally on the same crystallographic lattice site, forming a single phase. In a solid solution fuel the fission takes place homogeneously in the fuel, and the effects of radiation are homogeneously distributed in the matrix. The best known example in nuclear technology is the mixed oxide (U, Pu) O_2 in which a substitutional replacement exists in the complete composition range between the end-members UO_2 and PuO_2 . This is not always the case; for example, the solubility of Pu in alpha-uranium metal is only about 5–10%; beyond that two phases with different U/Pu concentrations coexist (Kurata 1999).

■ Table 2

Characteristics of ^{235}U and the main transuranium isotopes

Nuclide	$T_{1/2}$ y	Main decay mode	Spontaneous fission rate ($\text{s}^{-1} \text{g}^{-1}$)	Specific activity (Bqg^{-1})	γ Dose rate ($\text{mSv h}^{-1} \text{g}^{-1}$)	Specific power (Wg^{-1})
^{235}U	7.04×10^8	α	1.6×10^{-6}	8.0×10^4	1.3×10^{-3}	6.0×10^{-8}
^{237}Np	2.1×10^6	α	5.1×10^{-5}	2.61×10^7	–	–
^{238}Pu	87.7	α	1.18×10^3	6.33×10^{11}	–	0.567
^{239}Pu	24100	α	1.0×10^{-2}	2.3×10^9	1.5×10^{-2}	1.93×10^{-3}
^{240}Pu	6564	α	479	8.4×10^{10}	–	7.06×10^{-3}
^{241}Pu	14.3	β^-	9.19×10^{-4}	3.82×10^{12}	–	3.28×10^{-3}
^{242}Pu	3.75×10^5	α	805	1.46×10^8	–	–
^{241}Am	432.7	α	0.505	1.27×10^{11}	312	0.114
^{242m}Am	140	α	62	3.87×10^{11}	12	4.49×10^{-3}
^{243}Am	7370	α	0.27	7.33×10^9	44	6.43×10^{-3}
^{242}Cm	0.45	α	7.47×10^6	1.23×10^{14}	–	122
^{244}Cm	18.1	α	4.0×10^6	3.0×10^{12}	4.9	2.83

The physical properties of the solid solution fuel generally vary gradually between the end-members. For example, the melting temperature of the $\text{UO}_2\text{--PuO}_2$ solid solution varies very regularly, close to the thermodynamic ideal behavior. The thermal conductivity of solid solutions does not follow simple rules. This is due to the fact that the thermal conductivity is strongly dependent on the phonon scattering and hence strongly influenced by substitution or non-stoichiometry of the crystal lattice. The thermal conductivity of the $\text{UO}_2\text{--PuO}_2$ solid solution for low Pu content is somewhat lower than that of UO_2 (Carbajo et al. 2001). However, the thermal conductivity of $(\text{U}_{0.5}\text{Np}_{0.25}\text{Am}_{0.25})\text{O}_{1.93}$ is significantly lower (Schmidt et al. 1986) as shown in ► Fig. 3, but close to that of $(\text{U, Pu})\text{O}_{2-x}$ with similar O/M ratio. Thus the substitution of Am has a much smaller effect than the vacancy formation, which is a consequence of the fact that americium is easily reduced to the trivalent state.

A composite (dispersion) is a mixture of two immiscible phases, the main phase generally serving as the neutronically inert matrix and the dispersed phase containing the fissile material (► Fig. 4). By choosing the right combination of phases, the properties of the composite material can be tailored for the specific conditions expected in-pile (Chauvin et al. 1999). A special form of composite fuel is the high temperature reactor fuel, in which a spherical particle (oxide, carbide, or oxycarbide) is coated with several protective layers (carbon, SiC) and dispersed in graphite. In composite fuels the fission process takes place in the dispersed phase and the effects of the irradiation will be concentrated in and immediately around that phase, giving rise to a much higher, albeit localized extent of radiation damage. The extent of damage to the matrix will depend on the size and volume fraction of the dispersed phase (► Fig. 5).

A liquid solution is a special fuel form mainly relevant for molten salt reactors. In this case, the fissile phase is dissolved in a dilute form in a binary or ternary salt matrix that is liquid at

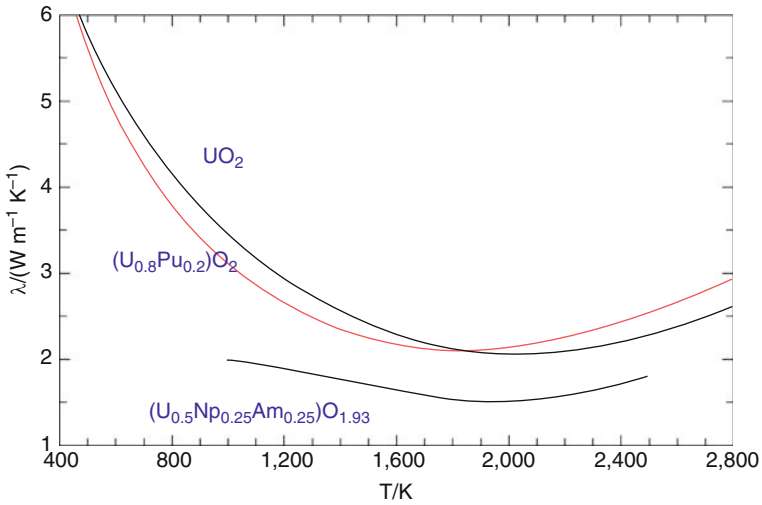


Figure 3 The thermal conductivity, λ , of UO_2 , $(\text{U}_{1-x}\text{Pu}_x)\text{O}_2$ for $0.03 < x < 0.15$, and $(\text{U}_{0.5}\text{Np}_{0.25}\text{Am}_{0.25})\text{O}_{1.93}$

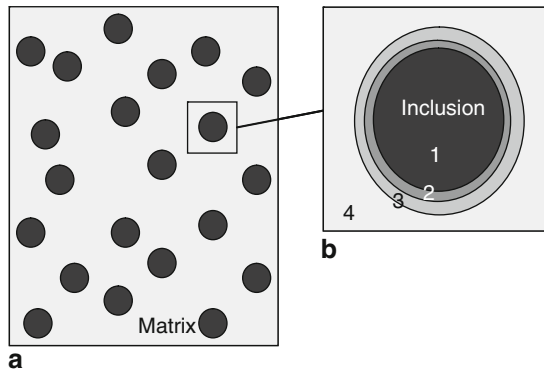


Figure 4 (a) Schematic representation of a composite. (b) Damage regions associated with the actinide particle: (1) actinide particle with very high displacement damage; (2) matrix damaged by recoil of fission products and energetic alpha particles (thickness $\sim 5 \mu\text{m}$); (3) matrix damaged by alpha particles (thickness $\sim 13 \mu\text{m}$); (4) bulk matrix not affected by fission or decay damage (neutrons only)

the operating temperature of the reactor. Since the fuel is liquid – hence no long range order is present – the effects of radiation damage are negligible.

2.3 Properties of Transuranium Elements and Compounds

The unique character of the actinides in the periodic system is due to the fact that their properties change as a function of the filling of the $5f$ electron shell. In the light actinides the

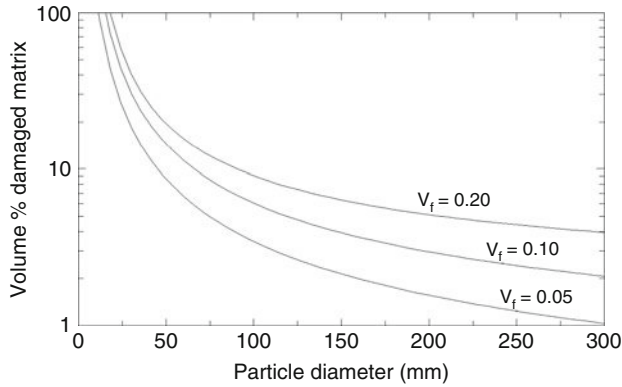


Figure 5
The volume of damaged matrix as a function of particle diameter and volume fraction

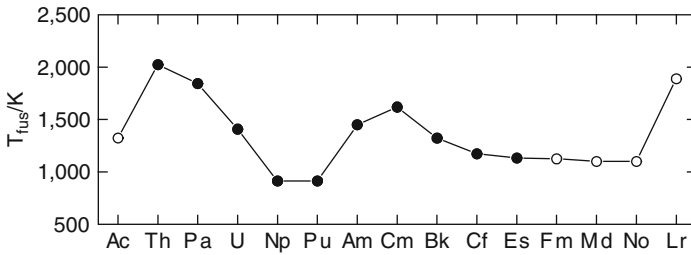
Table 3
The possible stable valence states of the actinides in compounds

	Ac	Th	Pa	U	Np	Pu	Am	Cm	Bk	Cf	Es	Fm	Md	No	Lr
1+															
2+															
3+															
4+															
5+															
6+															
7+															

Black boxes indicate the most stable state (Edelstein et al. 2006)

5*f* electrons participate to the valence band (itinerant), whereas in the heavy actinides the 5*f* electrons are localized in the core, just as in the 4*f* lanthanide series (Edelstein et al. 2006). The transuranium elements, from neptunium to curium, have a special position as they show a gradual change from itinerant to localized electron behaviour. As a result, the physicochemical behavior of the transuranium elements and their compounds show distinct differences that must be taken into account for fuel design and performance applications. For example, whereas plutonium can occur in a wide range of oxidation states (from 3+ to 6+) like the *d*-transition metals, curium is predominantly trivalent, like the lanthanides (Table 3).

The change in physicochemical properties is most pronounced in the actinide metal series. This is strongly reflected in the different metal valence states (Metallic bonds can be considered as a lattice of positively-charged ions (cations) that share delocalized electrons): tetravalent (Th–Pu), trivalent (Ac, Am–Cf, Lr), and divalent (Es–No). Also the change in melting point of the actinide metals is remarkable (Fig. 6), decreasing by about 500 K going from U to Pu (Konings et al. 2006). This has an important technological impact as the melting point of a metal fuel containing large amounts of transuranium elements is significantly lower than that of pure uranium metal fuel, thus reducing the margin to melting during operation in-pile. The vapor



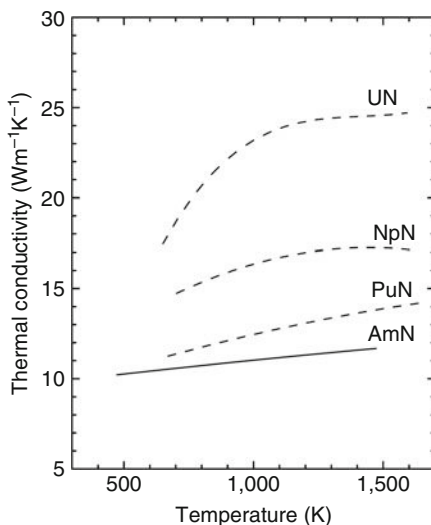
■ **Figure 6**
The melting temperature of the actinide metals

pressure of the light actinide metals increases significantly in the series reaching a maximum at Am, for which the vapor pressure is 0.1 kPa at 1,500 K. Also this has technological implications, because it will complicate the fabrication of metal fuel and may lead to unwanted redistribution during irradiation. Finally, one needs to address the thermal conductivity of the actinide metals. This property is not very well known for the transuranium elements, but the values determined experimentally (Np, Pu) or predicted (Am, Cm) are lower than those of uranium.

The fluorite cubic dioxide (face-centered cubic or fcc) is a stable phase in all light actinide–oxygen binary systems, showing significant ranges of hypostoichiometry for all of the dioxides, whereas hyperstoichiometry only occurs in uranium dioxide. The properties of the actinide dioxides show gradual changes: melting point and chemical stability decrease along the actinide series in a systematic way (Konings et al. 2006). The oxygen potential above AmO_2 is very high (Chikalla and Eyring 1967; Otake et al. 2008), and CmO_2 even decomposes above 700 K (Smith and Peterson 1970). For these elements binary oxides with O/M lower than 2 must be considered, for example, the substoichiometric AnO_{2-x} phase or the sesquioxide An_2O_3 . The mutual solubility of the actinide dioxides is high. UO_2 and PuO_2 form a complete solid solution, and this is very likely the case for the other dioxides. Due to the lower melting points of the transuranium dioxides ($T_{\text{fus}} = 2,386$ K for AmO_2 , $T_{\text{fus}} = 2,478$ K for Am_2O_3 , and $T_{\text{fus}} = 2,543$ K for Cm_2O_3) compared to UO_2 ($T_{\text{fus}} = 3,120$ K), mixed transuranium oxide fuels will have a significantly lower melting point than $(\text{U}, \text{Pu})\text{O}_2$ fuel.

For uranium-free fuels and targets, solid solution fuels with ZrO_2 stabilized in its cubic form by calcium oxide (calcium stabilized zirconia, CSZ) or yttria (YSZ) are considered. These oxides also have the fcc structure and thus can dissolve the actinide oxides. Taking also into account the low thermal conductivity of these actinide-bearing oxide solid solutions, the margin to melting for mixed oxides with high concentrations of minor actinides will be significantly lower than for UO_2 , when operated at the same linear power.

The actinide carbides show complicated phase relations with AnC , AnC_2 , and An_2C_3 as potential stable phases, all showing wide ranges of non-stoichiometry (Holley et al. 1984). The cubic AnC_{1-x} phase is known for $\text{An} = \text{Th}$ to Pu , but with very different lower phase boundary compositions. This phase is in equilibrium with metal. The AnC_2 phase is known for $\text{An} = \text{Th}$, U , and Pu , though in the $\text{U}-\text{C}$ and $\text{Pu}-\text{C}$ systems it is still under debate whether the dicarbide is a high temperature phase or also stable at room temperature. The An_2C_3 is known for $\text{An} = \text{U}$ to Cm , but U_2C_3 is probably a high temperature phase. The monocarbide has been studied as fuel material, but in practice the carbide fuels are a two-phase mixture of the mono- and (as a minor fraction) the sesquicarbide, to avoid metal phase formation during irradiation. This means that the minor actinides likely concentrate in a secondary phase.



■ Figure 7

The thermal conductivity of the actinide nitrides (after Minato et al. 2009)

The melting points of the monocarbides are high (>3,000 K), which, combined with a high thermal conductivity, makes these materials particularly suited as dense fuels for high power applications.

The mononitride is the dominant phase in all An–N phase diagrams and has a rock-salt cubic structure. The relevant properties of the actinide nitrides UN, NpN, and PuN are fairly well established, but those of AmN and CmN are not very well known (Minato et al. 2009). It has been demonstrated that solid solutions exist between all the AnN phases. A systematic decrease of melting point, chemical stability, and the thermal conductivity along the actinide series UN–AmN is observed (see e.g., the thermal conductivity in ► Fig. 7). The thermal conductivity of the nitrides is high and, unlike the metals and oxides, increases with increasing temperature. A major concern is the thermal stability of the nitrides at high temperatures, as they decompose to nitrogen gas and actinide metal, the latter in liquid and gaseous state. Especially for AmN this decomposition is expected to be significant, as was found experimentally for (Pu, Am)N (Ogawa et al. 1995). Also for nitride fuels an inert matrix has been considered and ZrN has been identified as an interesting candidate (Kleykamp 1999).

The pure actinide fluorides (ThF₄, UF₄, PuF₃, AmF₃) and chlorides melt above the operating temperature of a molten salt reactor. For that reason the proposed fuels for molten salt reactors are a mixture of these actinide phases with potential matrix phases that guarantee a low melting temperature of the binary or ternary composition. Originally, the work on the molten salt fuel has focused on LiF–BeF₂ solvent (which is excellently suited for breeding ²³³U from ²³²Th), but this salt shows a relatively low solubility for PuF₃ (Barton 1960; Mailen et al. 1971) as can be deduced from ► Fig. 8. To increase solubility another component such as NaF must be added as matrix component. The binary phase diagrams of the relevant LiF–NaF–BeF₂–PuF₃ systems are well established, with the exception of the BeF₂–PuF₃ system (Beneš and Konings 2009). However, no phase diagrams with other transuranium fluorides are known.

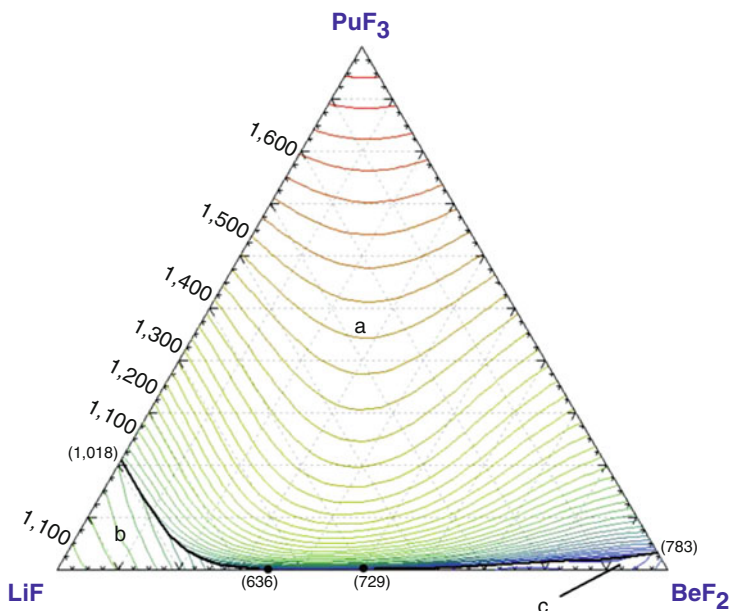


Figure 8

Calculated liquidus projection of the LiF-BeF₂-PuF₃ ternary phase diagram. Isothermals are labeled in K with the interval of 25 K. Primary phase fields: (a) PuF₃; (b) LiF; and (c) BeF₂ (after Beneš and Konings 2009)

3 Transuranium Element Fuel and Target Fabrication

3.1 General Aspects

This section deals with the fabrication of fuels for Gen IV fast reactors and for systems dedicated to transuranium element transmutation, such as the accelerator driven system (ADS). In the former, U-based fertile fuels are the preferred choice, however, other options such as fertile free fuels, often considered for ADS applications, can also be deployed. The fertile free fuel option, also known as inert matrix fuel (IMF), has considered YSZ (e.g., (Zr_{0.85}Y_{0.15})O_{1.925}), magnesium aluminate spinel (MgAl₂O₄), magnesium oxide (MgO), and metallic molybdenum as matrices for the fuel.

The fuel composition and specifications for the Gen IV gas, lead, and sodium fast reactor (GFR, LFR, and SFR) place severe requirements on the fabrication processes. The high-level goals of Gen IV foresee group (U, Pu, Np, Am, and Cm) recycling of the actinides to ensure proliferation resistance in the fuel cycle. In this way, Pu would never be freely accessible for a potential misuse. The main difficulties might not ensue from the liquid to solid conversion itself, rather from the steps required thereafter, wherein the fuel would be brought to the required transuranic content by the introduction of U (depleted, U_{dep}, or natural), transformed in the desired chemical composition (metal, oxide, nitride, or carbide), and formed into the required shape for the irradiation facility being considered.

For the IMF, similar fabrication philosophies apply. By replacing U with YSZ, it is possible to envisage separation schemes involving transuranium elements coextraction and/or separation of Pu and MA streams. Fabrication of YSZ-based fuels and targets can follow similar routes to UO_2 -based fuels, as YSZ just as UO_2 forms a solid solution with Pu and the MA. In addition, the conversion step can also be used to produce actinide oxides in powder or bead form, for blending with a second material, with which no chemical interaction occurs. Such composite fuels permit microstructure tailoring to improve the fuel performance.

This section describes processes used to fabricate experimental fuels in solid solution and composite fuel forms. Thus far, all fabrication of minor actinide bearing fuel has been made on lab scale level, without an industrial implementation.

Handling transuranium elements requires hermetically sealed gloveboxes to prevent the risk of incorporation of highly toxic radioactive materials into the body. The glovebox operating atmosphere should be inert. For oxide fuels, the oxygen to metal (O/M) ratio is an important fuel design parameter and sintered product materials should be maintained in atmospheres with less than 1% O_2 and preferably with less than 100 ppm H_2O . In contrast, the preparation of nitrides and carbides poses more severe atmospheric requirements. Both react readily with O_2 and H_2O , which is detrimental to the quality of the product, and incorporation of oxygen increases with every processing step. A much more severe problem is the pyrophoricity of these materials, being particularly important for carbides in all geometries, but most importantly for finely divided powders with a high surface area. For nitride and carbide fabrication, the O_2 and H_2O contents in the gloveboxes should be maintained below 10 ppm.

The incorporation of the minor actinides in the fuel necessitates additional biological shielding, and concomitant automation of the entire process from conversion to the solid all the way through to assembly loading in the reactor. Lead provides shielding from γ emitters and a combination of water, lead, and cadmium (or boron) provides shielding from neutrons, emanating directly through spontaneous fission (e.g., ^{244}Cm) or by (α, n) reactions with light elements (O, N, or C) either in the fuel or in the aqueous and organic solvents of the processing solutions. While today's MOX plants for pellet production are highly developed with extensive (actually complete) automation, they are so designed that operator intervention can be made via the gloveboxes. Minor actinide presence in the fuel can necessitate the use of hot cells or hybrid facilities, combining glovebox standards with remote operation by telemanipulators (pin and assembly fabrication are not as extensively automated). At least one laboratory scale MA fuel facility has been developed (namely the JRC-ITU Minor Actinide Laboratory), consisting of a chain of seven conventional glove boxes, shielded by 50 cm water and 5 cm lead, for which the limiting masses are 150 g of ^{241}Am and 5 g of ^{244}Cm . Operation is achieved not only by telemanipulators, but also by remote control. Within this concept, operator intervention is possible, when all transuranium elements, including surface pollutants, are removed or stowed in protected zones. Alternative approaches could involve use of fully remotely operated hot cells, without human intervention possibility as was planned for the thorium fuel cycle (Grahmann et al. 1975). Determination of shielding is discussed in detail elsewhere (Magill 2003), and indeed there are commercial software packages available enabling its quantification (<http://www.nucleonica.net>, <http://www.euronuclear.org/e-news/e-news-17/nucleonica.htm>).

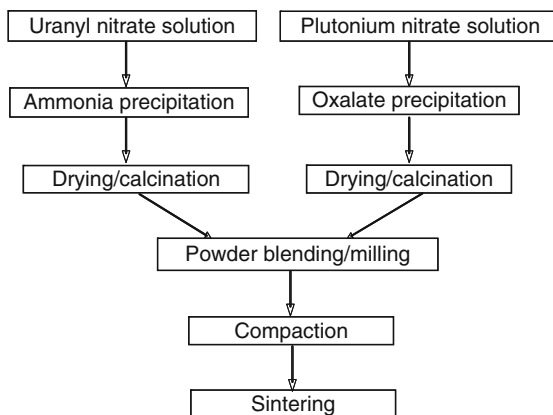
Transposing MOX fuel fabrication philosophy will probably not be satisfactory for another reason, namely dust. Both European commercial fuel fabrication plants (MELOX in France and SMP in the UK) base their fabrication on the use of powder metallurgy methods. While dust is an issue in that it must be collected and reintroduced in the process, it poses no severe insurmountable problem for MOX fuel fabrication. In contrast, however, processes devoid of

dust generation are desirable for minor actinide (MA) fuel production. Nevertheless, such powder metallurgical methods have been used for the production of small quantities of materials for dedicated irradiation tests (Tanaka et al. 2007).

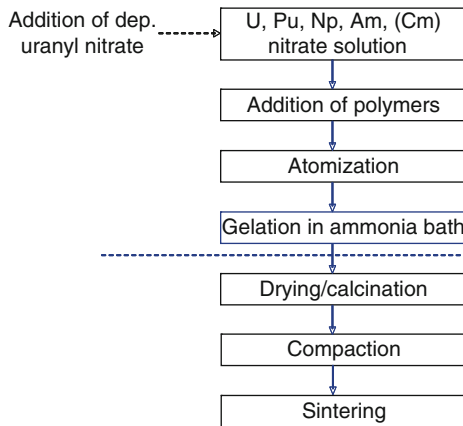
This chapter concentrates on pellet fuel type. There are no specific details given on sphere-pac or VIPAC fuel. In general, they can be based on the procedures described below for pellet type fuel. For sphere-pac, sol-gel and infiltration methods are used to generate spherical particles, which are sintered without compaction into pellets. Different size fractions are loaded into a fuel pin which is then vibrated to generate a fuel column, typically with a smear density of about 82% of the theoretical density (TD). The feed particles for VIPAC fuel is nonspherical and consists of irregular sintered particles, which are loaded in the tube for vibration. Due to their irregular nature higher vibrational amplitudes are required to pack these fuels. Typically, sphere-pac and VIPAC require two or three distinct particle sizes to provide the highest densities. These processes have been used to produce uranium-based fuels containing neptunium (Bart et al. 2007; Bychkov et al. 2002; Mayorshin et al. 2000, 2005).

3.2 Solid Solution Oxide Fuels Fabrication by Wet Routes (Precipitation, Sol-Gel, and Infiltration)

The Gen IV fast reactors (FR) and the ADS should operate in a closed fuel cycle. The actinides must be recovered from the reprocessing unit, where they are in solution form. Conversion to oxide is at the moment the only logical route for aqueous liquid to solid conversion, as there is no available method to produce the nitride or carbide powder directly. Indeed, oxide fuel for fast reactors represents a well developed technology. Former fast reactor fuel production relied on the separation (by the PUREX process) of U and Pu in the reprocessing step, so that the fuel production plant had a feed of UO_2 and PuO_2 as raw materials, from which blends could be made. Following a milling procedure, pellets were compacted and sintered. This dual feed system (see ► Fig. 9) had the advantage that the blend for individual fuel pins or assemblies could easily be manufactured. This is a tried and tested technology for U and Pu oxide recuperation, and is used commercially today for LWR fuel production.



■ Figure 9
Fast reactor mixed uranium-plutonium oxide (MOX) fuel production



■ Figure 10

Sol-gel route for group conversion (homogeneous recycling) of Gen IV fuels

Due to the risk of explosion posed by ammonium nitrate, Pu is generally precipitated by the addition of oxalic acid in solution or solid form (Drain et al. 1999). The Pu oxalate is thermally treated to give the oxide. Recently a co-extraction process (COEX) for all actinides has been developed and the oxalate coprecipitation of U, Pu, and MA solutions tested (Chapelet-Arab et al. 2006; Grandjean et al. 2005, 2006, 2007; Arab-Chapelet et al. 2007, 2008). Reduction of U(VI) in solution to U(IV) is required. The conversion is performed in a vortex reactor typically used for industrial conversion of Pu nitrate solutions. Conversion of the mixed oxalate to the oxide is performed by thermal treatment. Ammonia precipitation offers an alternative route and does not require U(IV) reduction, but care must be taken of the NH_4NO_3 by-product, which possesses an explosion risk when dry.

Consideration must be given to the quality of the powder, in terms of its particle size, when it is generated in the conversion step. Conventional precipitation (oxalate or ammonia) methods result in very fine powders (typically 2–5 μm), which easily become airborne and contaminate the internal surfaces in the gloveboxes. Despite the experience of the past, new solutions to fuel production must be invoked to eliminate fine powders and enable the industrialization of the processes for MA-bearing fuels. One of these was tested in the 1980s (Babelot and Chauvin 1996). MOX fuels with Am, and Np were produced using the sol-gel route (see ► Fig. 10), which at its heart relies on an ammonia precipitation, but maintains the intermediate product not in the form of powder, rather beads with diameters between 20 and 600 μm , depending on the characteristics of the droplet dispersion device. Extension of this process to Cm is possible in principle, but very rigorous cost evaluation and processes to deal with ensuing highly active neutron and alpha-emitting waste need development. This process, or a similar one using hexamethylenetriamine (HMTA) (Kasemeyer et al. 2001), has yet to be applied to Cm fuel production.

A novel process based on minor actinide infiltration has been developed for the production of dust free oxides (see ► Fig. 11) (Fernandez et al. 2002; Somers and Fernandez 2005). In particular, MA-bearing liquid waste streams are essentially eliminated. In a first step, porous beads are manufactured by a sol-gel method to give the oxide in the form of microspheres (20–120 μm in diameter). For YSZ, these beads can be produced in an inactive facility, while for fertile fuels either UO_2 or (U, Pu) O_2 beads can be produced using conventional glovebox

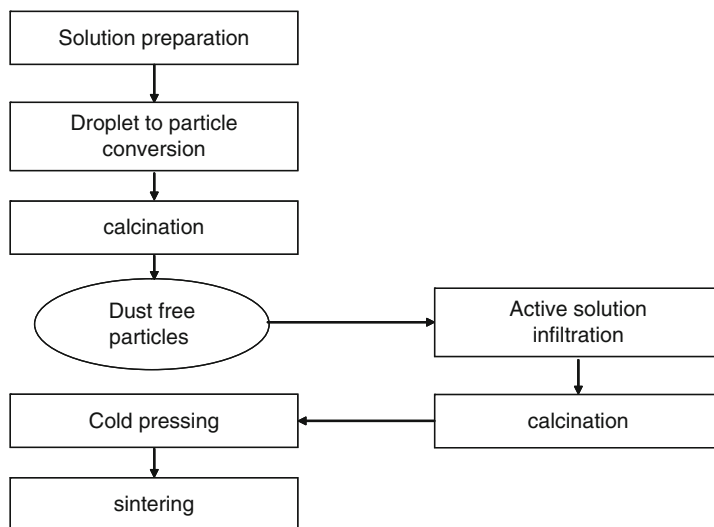


Figure 11
Production of GenIV oxide fuels based on the infiltration of porous beads oxide beads with the minor actinide nitrate solution

technology in use today. The porous microspheres act as a host for the second stream containing minor actinides, which are introduced by simple infiltration of their nitrate solution. Following calcination, the oxide is formed and the only waste is NO_x . At this stage, the material consists of two distinct oxide phases. Due to the excellent sintering properties of the sol-gel microspheres, however, a solid solution is obtained on heating. There are no liquid wastes containing minor actinides, and the conversion results in the difficult to handle minor actinides being securely located in particles that do not generate dust.

This infiltration process has been tested for the production of $(\text{Zr}, \text{Y}, \text{Am})\text{O}_{2-x}$ ($\text{Zr}, \text{Y}, \text{Pu}, \text{Am})\text{O}_{2-x}$ fuel irradiation experiments in the Phénix and HFR Petten reactors (Croixmarie et al. 2003; Fernandez et al. 2006). The precursor beads were $(\text{Zr}, \text{Y})\text{O}_2$ and $(\text{Zr}, \text{Y}, \text{Pu})\text{O}_2$, respectively. The process has yet to be demonstrated for UO_2 -based fuels, where the potential solubility of UO_2 in the nitrate infiltrant solution must be surmounted, though preliminary results show that even this potential drawback can be overcome (Fernandez, Richter, Somers, unpublished).

3.3 Powder Metallurgy for the Production of Solid Solution Fuels


Powder metallurgy is the industrially tried and proven method for the production of UO_2 and MOX fuels for LWR. Its inherent dusty character will pose difficulties for its deployment in MA fuel fabrication plants, and will necessitate technological solutions, possibly requiring full hot cell fuel fabrication facilities.

Recently, powder metallurgy routes have been used to produce $(\text{U}, \text{Pu}, \text{Am})\text{O}_2$ and $(\text{U}, \text{Pu}, \text{Np}, \text{Am})\text{O}_2$ fuels for a series of irradiation tests in the Joyo fast neutron flux reactor (Tanaka et al. 2007). The fabrication was performed in a suite of hot cells, with fully remote operation and maintenance facilities. The precursor actinide oxide powders were weighed and ball milled


to obtain a micronized blend, which was then pressed and sintered. The tests have shown that MOX fuels with 30% Pu and up to 5% Am and Np can be prepared in solid solution form using this route.

3.4 Oxide Fuels with Composite Microstructure

Fuels with two distinct phases have been considered for LWR MOX fuel. The micronized master blend (MIMAS) route has been widely deployed to produce a fuel consisting of Pu rich (ca. 25%) particles distributed in a UO_2 matrix. In contrast, the short binderless route (SBR) provides a fuel with a Pu distribution approaching a solid solution. The heterogeneity (or lack thereof) can be used to tailor the properties of the fuels. Though MA fuel forms based on UO_2 have yet to be investigated, they have been widely tested in programs for MA transmutation in IMF.

Am oxide-bearing fuels have been produced with the MA distributed in fine particles throughout magnesium aluminate spinel (MgAl_2O_4) and MgO matrices. The fabrication of the MgAl_2O_4 -based fuel used a variation of the infiltration process (Richter et al. 1997) shown in  Fig. 11. In this case however, the host material to be infiltrated was in the form of a porous pellet formed by the compaction of spinel granules and subsequent calcination to remove lubricants from the pressing step. This pellet infiltration technique not only eliminates Am-bearing liquid waste streams, just as its bead infiltration counterpart, but also eliminates powder pressing in the fabrication steps involving MA. The resulting product is a composite of fine Am-bearing particles in the spinel matrix. Due to the macroscopic dimensions of the pellet, control of the Am distribution needs extensive testing.

Powder metallurgy has been used for the production of a two phase microdisperse fuel of AmO_2 dispersed in MgO (Croixmarie et al. 2003). The process consists of powder mixing, light compaction (150 MPa), compact pulverization to give particles of 150 μm , renewed mixing, compaction at 250 MPa, and then sintering. The resulting product consisted of Am oxide particles with diameters less than 50 μm dispersed in MgO. A similar procedure has been followed for two MgO-based fuels, but the fissile component was $(\text{Pu}, \text{Am})\text{O}_2$ with 50 and 80% Am, prepared by oxalate precipitation of the corresponding solutions (Jorion et al. 2007).

Damage, due to α recoil and fission product generation, will occur throughout a solid solution fuel. In contrast, composite fuels can be designed to minimize the damage due to fission in the matrix, to a shell typically about 13 μm , surrounding the fissile component. Thus, if the distance between individual fissile particles is large enough, damage in the bulk of the matrix is reduced, and the deterioration of key properties in the matrix during irradiation is limited. The radiation effects in dispersion fuels with very small inclusions will approach that of a solid solution (see  Fig. 5), whereas the effect will be located in a 13 μm region around the inclusions, if they are larger. The maximum size of the inclusion is limited due to the temperature gradient in the host particle and should generally not exceed 300 μm .

An experiment has been performed in the Phénix reactor to investigate this effect (Croixmarie et al. 2003). The production of the fuel followed a hybrid route, integrating advanced wet chemical processing and powder metallurgy. Porous YSZ beads were fabricated by the sol-gel method and sieved to obtain two distinct size fractions (40–60 and 80–100 μm) before infiltration with the Am nitrate solution and subsequent calcination to give the oxide. The final pellet was then obtained by blending the $(\text{Zr}, \text{Y})\text{O}_2$ – AmO_2 beads with MgO, with subsequent compaction, and sintering steps. The fabrication process was successfully

demonstrated, but extreme caution against demixing of the denser actinide phase in the MgO blend was required. A similar procedure has been applied for the production of ceramic-metal (CERMET) fuel pellets for experiments in the high flux reactor (HFR) Petten and Phénix (Fernandez et al. 2006). Wet chemical routes were used to prepare the YSZ–AmO₂ and PuO₂–AmO₂ precursor beads, which were then blended with Mo powder. Due to the higher density of Mo, fewer problems of demixing were encountered.

The uniformity of a composite fuel can be determined by slicing a pellet axially, and polishing its surface. The analysis is achieved by dividing the observed surface into at least nine regions of equal size. The surface occupied by the inclusion in each field, S , is determined, and the average over all fields, S_a , and the standard deviation, σ , is measured. The homogeneity distribution factor, HD, is given by

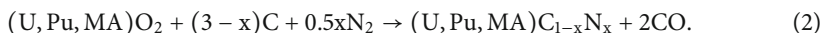
$$HD = \frac{\sigma}{S_a}. \quad (1)$$


Values of HD less than 20 are required in fuel specifications.

3.5 Minor Actinide Carbide, Nitride, and Metal Fuels

3.5.1 General Considerations

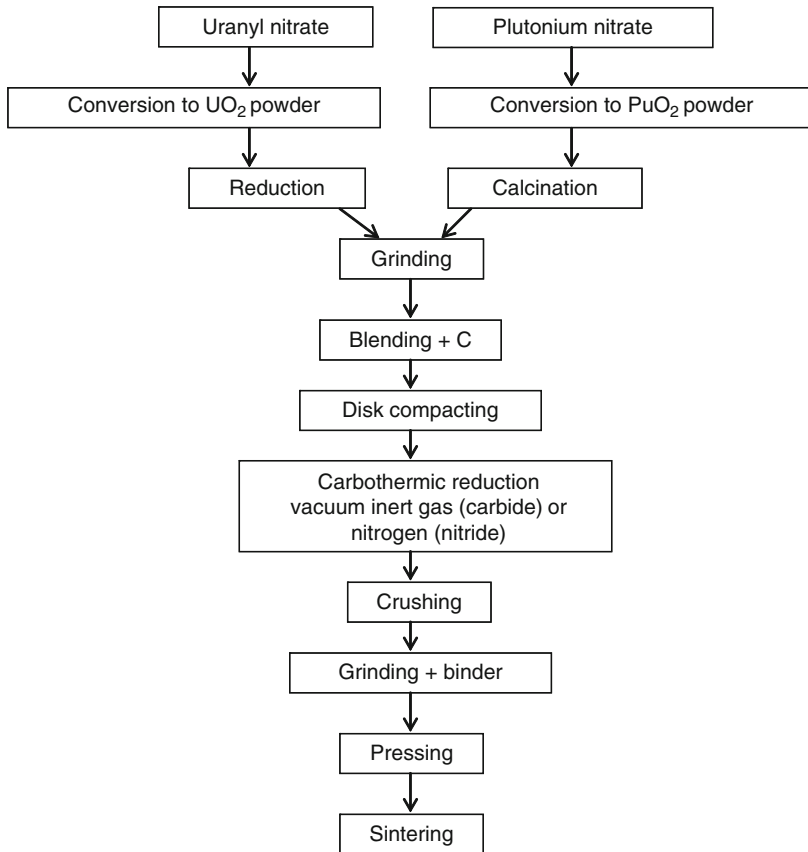
Carbides, carbonitrides, and nitrides can be produced by the general reaction given by



For nitrides, this reaction is performed under flowing nitrogen and requires high temperatures in excess of 1773 K. In the case of the pure carbide, $x = 0$, no nitrogen is used and the powders are heated directly in Ar, or preferably under vacuum. The progress of the reaction can be monitored by the CO in the furnace off gas. This reaction has been widely used for the production of U/Pu mixed metal carbides, nitrides, and carbonitrides and also Zr/Np/Am nitrides for MA incineration tests. An important point is the intimate mixing of the starting materials, usually achieved by co-milling the oxides with carbon. A generalized flow sheet is provided in  Fig. 12.

The production of MA-bearing carbides for fuel testing has not been investigated at all. The production of (U, Pu)C has been studied significantly at a laboratory scale and is complicated by the possibility of sesquicarbide M₂C₃ formation; considerable empirical adjustment of process parameters is needed (Richter et al. 1974, 1978). Manufacturing of carbides under vacuum (10⁻² mbar) gave better results than under Ar. The reaction temperature was 100 K lower, and less N impurity in the product was obtained (Matzke 1986). Nevertheless, Pu losses as high as 10% were observed during manufacturing (Richter et al. 1979; Vollath 1977). This poses a criticality risk in an industrial plant, as Pu is plated out, most likely on the cold surfaces of the furnaces. Increasing the CO partial pressure in the furnace during the carbothermal reduction step from 0.008–0.07 mbar reduces the Pu losses from 7.2–0.2%, respectively (Richter et al. 1979).

The rate or efficiency of the carbothermal reduction for nitride or carbide production depends intrinsically on the homogeneity and fineness of the blend of the U, Pu oxide and carbon powders. Milling times of up to 36 h have been mentioned (Vollath 1977). Poor intimacy in the mixture results in local impurities. If the carbon is locally deficient or in excess, either oxide or carbon impurity persist in the final product. The carbothermal reaction is favored by high surface area powders (>10–15 m² g⁻¹) and small agglomerate sizes (< 15 μm) (Louwrier et al. 1976).



■ Figure 12

Classical carbothermal reduction to produce carbides (or nitrides)

The carbothermal reduction step is often made on compacts, pressed at relatively low pressure to sustain the intimacy of the powder blend. Thereafter, the products have to be crushed in a hammer mill and then ball milled to produce a powder reactive enough to be pressed again to yield a high density pellet upon sintering at temperatures of 1923–2073 K either under Ar or vacuum. A wide range of pellet densities have been reported for the production of carbides. Poorly milled powders from the carbothermal production process yield low density pellets (80% of the theoretical density, TD), whereas highly milled powders can yield pellets in excess of 90% TD. Still higher (>95% TD) densities can be achieved by the addition of Ni as a sintering aid (Horspool et al. 1967; Anselin et al. 1965).

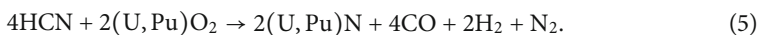
In a novel method to overcome the comminution steps to micronize the product after the carbothermal reduction process, Richter et al. (1985) and Richter (1987) introduced the direct pressing method, which involves the compaction of the uranium oxide, plutonium oxide and carbon blend into pellets for the carbothermal reduction step, which gives a product with a density of about 35–50% of the theoretical density. In contrast to the conventional process, the pellets are put back into the press and compacted again without recourse to an intermediate comminution step. Their density then increases to 65–75% TD which is increased to the target

specifications in the final sintering step. Direct pressing eliminates handling of powders with a high affinity for oxygen and thus the products have lower oxygen content. In addition, dust and consequent pyrophoricity risk is reduced. Finally, the removal of powder milling steps also diminishes impurities.

Excess sesquicarbide MC_{1+x} in the product can be reduced to MC by reaction with H_2 (Harder et al. 1965) i.e.,



This treatment is preferentially performed on the powder derived from carbothermal reduction. However, the presence of M_2C_3 in the fuel is not detrimental and is usually specified at no more than 5–15% M_2C_3 . In the case of nitrides, however, addition of hydrogen induces a parasitic reaction, causing the production of HCN, which also can react with the oxide (Bardelle and Warin 1992).



Specifications for nitrides (and carbides) stipulate low densities (80–85% TD) to limit effects of fuel swelling. In addition, their thermal stability must be guaranteed (i.e., they should not densify in pile). Arai et al. (1992) quotes the use of a pore former, which decreases the pellet density from 95 to 82% of the theoretical density. In this way, pellets with a low open porosity, despite the low density were produced; the stability is caused by 20–30 μm pores derived from the pore formers (Arai et al. 1992, 1988, 1989; Tanaka et al. 2004).

3.5.2 Production of Minor Actinide Nitrides

A large number of actinide nitride compounds (either as single minor actinide nitrides, their mixtures, or mixed compounds with U, Pu, and Zr nitrides) have been produced (Ogawa et al. 1995; Arai and Minato 2005; Minato et al. 2003; Takano et al. 1999, 2001, 2003; Arai and Nakajima 2000; Nakajima et al. 1997; Arai et al. 1997a; Suzuki et al. 1994; Muromura 1982; Okamoto et al. 1993). In all of these studies, the fabrication route was carbothermal reduction of the oxides. In many cases, however, pelletizing was not attempted; rather the samples were used for property determination. The vaporization behavior of the nitrides is a major issue (and even more important for carbides). For the first AmN production from the oxide, the reaction temperatures in the carbothermal reduction step were reduced to 1623 K to alleviate this problem (Voit, private communication). A major part of the effort on nitride fuels has been for the production of fuel for a dual strata actinide transmutation system, in which the minor actinides would be destroyed in a dedicated transmuted facility (e.g., an ADS). Thus the major interest has been incorporation of the minor actinide nitrides in IMF, such as YN or ZrN. Carbothermal reduction of AmO_2 with Y_2O_3 and ZrO_2 have been performed (Minato et al. 2003). In YN, a solid solution obeying Vegard's law was obtained in the range investigated (less than 30 mol% Am). In the (Zr, Am)N system there is an immiscibility gap.

Other laboratories (Voit, private communication) have undertaken programs to produce (Zr, Am, Np)N fuels. Significant Am losses due to vaporization during the fabrication steps were encountered. This was possibly accentuated by the use of a powder blend as the starting material. In subsequent tests, an attempt was made to "solutionize" the starting oxides, by

heating a mixture of them (and carbon) at 1673 K for up to 12 h under Ar, prior to launching the carbothermal reduction step (Voit, private communication). Using this method, low fertile (U, Pu, MA)N and non-fertile (Zr, Pu, MA)N materials have been prepared. The MA contents were significant (Np and Am 10–15 mol%).

A process to produce minor actinide nitrides (see [Fig. 13](#)) based on a modified method of that described in [Fig. 11](#) has been developed elsewhere (Fernandez, Walter, Somers, unpublished). The sol-gel route is used to manufacture the ZrO_2/C or $(U, Pu)O_2/C$ microspheres. These are then infiltrated with an Am nitrate solution and are thermally treated to give $ZrO_2/AmO_2/C$ or $(U, Pu)O_2/AmO_2/C$ microspheres. Due to the small particle size of the AmO_2 infiltrant ($< 2-3 \mu m$) and the high sinter activity of the sol-gel material, a solid solution of the oxide is readily attained at temperatures less than 1473 K. The carbothermal reduction can then be applied, and the resultant nitride powder pressed and sintered to give the product pellets. This process is in the infancy of its development but has been used to fabricate (Zr, Pu)N,

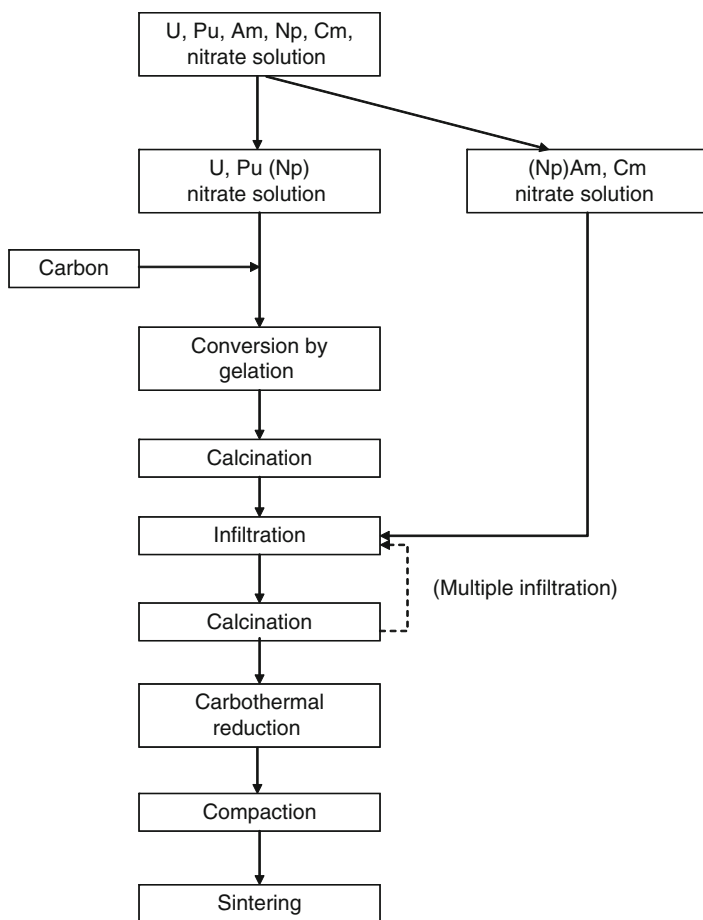



Figure 13

Production of nitrides by a combination of sol-gel, infiltration, and carbothermal reduction

(Zr, Am)N and (U, Pu, Am)N. Pellet densities remain low (70% of the theoretical density), but further process development is possible.

This process bears some similarities with processes used to fabricate (U, Pu)X fuels via aqueous processing routes (Ganguly 1988; Ganguly and Hegde 1997; Prunier et al. 1991, 1992, 1993; Ingold and Ledergerber 1994; Ledergerber et al. 1986). This fabrication method is often known as the sol–gel microsphere pelletization (SGMP) route and was focused on pellets as products. In addition, a variant of this method for the production of sphere-pac fuel was tested in the AC-3 experiment in the fast flux test facility (FFTF) (Adler et al. 1987; Bart et al. 2008). At the heart of both processes is a sol–gel step in which the U and Pu nitrate solutions are mixed in the desired quantity and converted to solid microspheres (400–800 μm) using the internal gelation route (see  Fig. 10). A solution is prepared close to 273 K, with the addition of hexamethylenetetramine (HMTA) and urea, along with carbon as a dispersed powder. The solution is atomized into drops on passing through a vibrating orifice. These drops fall into hot silicon oil, where the HMTA decomposes to produce ammonia, which causes a precipitation of the U, Pu hydroxide. Due to the dual phase system, the particles stay nearly spherical, and have a reasonable strength. Following washing and calcination steps, the microparticles consist of (U, Pu)O₂ and C and are ready for carbothermal reduction, under similar conditions as the powders from the conventional or direct pressing routes.

For the sphere-pac fuels, the nitride or carbide microspheres (with specific size and mass ratios) can be filled directly into fuel pins, and with gentle vibration the fuel pin is fabricated, e.g., for the AC-3 irradiation test in the FFTF reactor (Adler et al. 1987; Latimer et al. 1992). Pressing into pellets requires relatively high pressures (900–1,200 MPa) to give green densities of about 65% TD. Sintering resulted in pellet densities of 81–87% TD. The sol–gel routes have several positive attributes. No dusts are produced, thus reducing the radiotoxicity hazard and pyrophoricity risk. The free flowing spheres facilitate automation and remote operation. Less fabrication steps are required. Excellent homogeneity in U and Pu is achieved, due to the starting solution, and finally the pellets have open porosity for swelling accommodation and fission gas release.

3.5.3 Production of Minor Actinide Bearing Metal Fuels

Metallic fuel has been fabricated extensively for irradiation testing, and the fuel of choice is designated as U–20Pu–10Zr, an alloy with 20% mass Pu and 10% mass Zr. This particular composition was chosen to increase the solidus temperature and widen the range within which desired phases are obtained. Many of the fuels have been fabricated using an injection casting process, whereby a liquid metal alloy is formed and driven (or drawn) into a predefined holder, where, on cooling, it forms a slug. The moulds are often glass or quartz and slug lengths of 300 mm have been obtained (Burkes et al. 2009; Crawford et al. 2007a, b; Hofmann et al. 1997).

There have been few attempts to fabricate metallic fuels with minor actinides. In an early study the casting process was used to manufacture metallic fuel with 2.1 and 1.3% Am and Np, respectively (Keiser et al. 2008; Meyer et al. 2009). Although complete Np retention in the fabrication step could be demonstrated, losses of 60% Am were noted and were attributed to a volatile Am species in the melt. It was also proposed, that these losses could be minimized if high purity Am metal feed stock were available. Otherwise, a dramatic decrease in the processing time is required.

■ **Table 4**
Metallic fuels prepared for the METAPHIX irradiation experiment in the Phénix reactor

U-19Pu-10Zr- (1.2Np-0.6Am-0.2Cm-1.4Nd-0.2 Y-0.2Gd)
U-19Pu-10Zr- (3Np-1.6Am-0.4Cm-3.5Nd-0.5 Y-0.5Ce-0.5Gd)
U-19Pu-10Zr- (3Np-1.6Am-0.4Cm)

Minor actinide bearing metallic fuel was developed for an irradiation experiment (METAPHIX) in parallel elsewhere (Kurata et al. 1997; Ohta et al. 2007a). The fuels in [Table 4](#) were fabricated for irradiation in the Phénix fast reactor using arc melting procedures, which have the advantage that the time in the molten state is relatively short, but throughput is only sufficient for small quantities. U-Pu-Zr and U-Pu-MA-Zr alloys were prepared by arc melting in an argon atmosphere. To improve the homogenization of the alloys, U-Pu or U-Pu-MA alloys were first compounded by arc melting and then molten Zr was added. It proved difficult to prepare homogenized alloys containing highly dispersed rare earth (RE) metals by melting alone, as the miscibility between RE and the U-(Pu-MA)-Zr matrix is low even in the liquid phase. In these cases, powders of U-Pu-Zr and RE were first prepared and then blended mechanically before melting. The four types of alloy prepared were cast into metal fuel rods in yttria moulds that prevented reaction with molten alloys including RE.

Recently, other researchers have used the arc melting procedure to fabricate fertile and non-fertile metallic fuels (MacClean and Hayes 2007; JaECKI et al. 2005; Carmack et al. 2009). The non-fertile fuels have no U present, and are dedicated targets for actinide burning studies. Some of the materials produced are listed in [Table 5](#).

4 Irradiation Behavior of Transuranium Fuels

4.1 Mixed Oxide Fuels

The irradiation experience with transuranium mixed oxide fuels is currently restricted to the SUPERFACT irradiation experiment performed in Phénix (France) during the 1990s (Walker and Nicolaou 1995; Prunier et al. 1997). In this experiment, the irradiation behavior during normal conditions, of minor actinide fuels with four different concentrations was studied and compared with standard Phénix fuel. $(U_{0.55}Np_{0.45})O_2$ and $(U_{0.60}Np_{0.20}Am_{0.20})O_2$ fuels represented the case of heterogeneous transmutation reactor cores, with the minor actinides concentrated in a limited number of high concentration pins or elements; $(U_{0.74}Pu_{0.24}Np_{0.02})O_2$ and $(U_{0.74}Pu_{0.24}Am_{0.02})O_2$ fuels represented the homogeneous transmutation reactor core in which the actinides are added in relatively small quantities to all fuel pins or elements. All fuels were produced by sol-gel technique, resulting in a homogeneous distribution of the minor actinides in the matrix. The linear power was about between 17 and 28 kW/m for high minor actinide content pins, between 38 and 32 kW/m for low minor actinide content pins, and 43 and 37 kW/m for the accompanying standard Phénix pins.

The postirradiation examinations showed good in-pile performance of the SUPERFACT fuels, not very different from the standard MOX fuel of Phénix. The nondestructive

■ Table 5

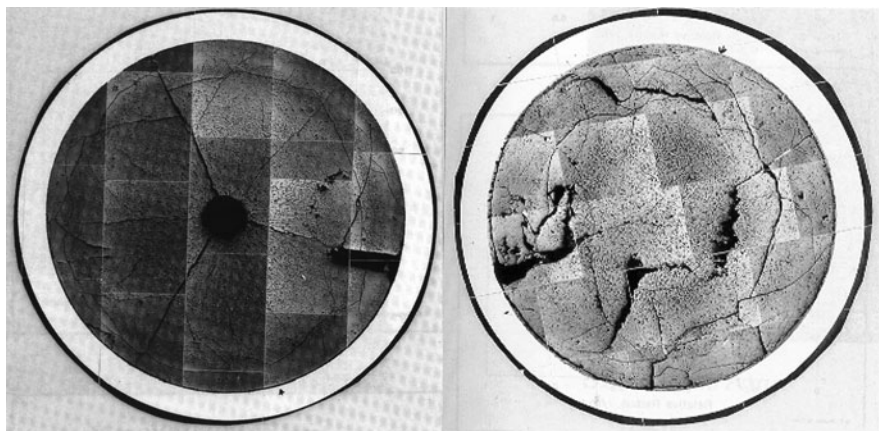
Metallic MA fuels prepared by arc melting for irradiation in the advanced test reactor (ATR) and Phénix reactors

AFC-1B	Pu-10Np-40Zr
	Pu-12Am-40Zr
	Pu-10Am-10Np-40Zr
AFC 1F	U-29Pu-4Am-2Np-30Zr
	U-34Pu-4Am-2Np-20Zr
	U-25Pu-3Am-2Np-40Zr
	U-28Pu-7Am-30Zr
AFC2	U-20Pu-3Am-2Np-15Zr
	U-20Pu-3Am-2Np-1.0RE ^a -15Zr
	U-20Pu-3Am-2Np-1.5RE ^a -15Zr
	U-30Pu-5Am-3Np-1.5RE ^a -20Zr
	U-30Pu-5Am-3Np-1.0RE ^a -20Zr
	U-30Pu-5Am-3Np-20Zr
FUTURIX	U-29Pu-4Am-2Np-50Zr
	Pu-22Am-40Zr

^aRE designates rare earth alloy (6% La, 16% Pr, 25% Ce, 53% Nd)

examinations of the four fuel types did not show any anomaly in their behavior. In particular, no accelerated corrosion was observed. The high concentration of americium in the (U_{0.60}Np_{0.20}Am_{0.20})O₂ fuel led to a significant increase of the fuel column length and to a significant diametrical deformation of the cladding. This is probably due to the beginning of a mechanical interaction between the oxide fuel and the cladding. The fission gas release rates (60–80% of the theoretical yield) were in good agreement with those of standard fuels, even for the fuels with a high concentration of minor actinides. The interpretation of the physicochemical and ceramographic examinations of the fuels led to the following conclusions (Babelot and Chauvin 1999):

- The beginning of a pellet-cladding mechanical interaction was observed for the (U_{0.60}Np_{0.20}Am_{0.20})O₂ pins.
- Cesium was found at the end plugs. Its accumulation was probably due to the particularity of the pins with high Am and Np contents (short fuel column).
- The cesium-profiles for the neptunium-containing fuels showed anomalous behavior of this fission product compared to the other pins.
- The corrosion depth of the cladding was as expected.
- The fuel temperature was probably higher for the americium-containing fuel.
- The fission gas production and release were as predicted for the operating power.
- The Am pins had a higher helium production, mainly due to the activation products with high specific alpha-activity. The released helium contributed to an increase of the internal



■ Figure 14

Ceramographs of the SUPERFACT pellets after irradiation: *left*, $(U_{0.74}Pu_{0.24}Am_{0.02})O_2$, *right*, $(U_{0.60}Np_{0.20}Am_{0.20})O_2$ from Walker and Nicolaou (1995). (©Elsevier BV, reproduced with permission.)

pressure of the pin. In addition, higher porosities and swelling, probably due to the helium still confined in the fuel, were found.

Typical ceramography images of some SUPERFACT fuels at the end of irradiation are shown in ► Fig. 14.

The measured extent of transmutation of americium at the maximal flux level was 31.5% for the fuels with high minor actinide content and 28% for the fuels with low minor actinide content. From neptunium analyses an average extent of transmutation of 30% was determined. The comparison of the measured values with calculations is satisfactory in the case of americium. In the case of neptunium, comparison with the calculations showed less agreement for the fuels with low minor actinide content.

In the TRABANT-1 experiment a sol-gel fuel with composition $(U_{0.55}Pu_{0.40}Np_{0.05})O_2$ was irradiated at a linear power of 52–57 kW/m in the High Flux Reactor (HFR, Netherlands). This fuel reached a burnup of 9.3% and showed a good in-pile performance as derived from the nondestructive analysis (Picard et al. 2000).

Recently, an americium-bearing (5 wt.%) mixed oxide fuel irradiation test was performed in the Joyo reactor (Japan) (Tanaka et al. 2009). The test consisted of a short (10 min at maximum power of 43 kW/m) and a steady state irradiation. The results from the short irradiation have been reported and reveal that within the short period at maximum power a significant restructuring of the fuel occurred. A central void had developed and re-distribution of U, Pu, and Am was detected near the void.

These results clearly indicate the complexity of minor actinide oxide fuels. At low linear power the fuels with low minor actinide content behave well, but at high power (high operating temperature) restructuring starts to play a role leading to significant re-distribution of not only Pu but also Am. This will be even more significant for fuel with high content of americium, in which also a significant helium production will occur due to the complex transmutation scheme for ^{241}Am ► Fig. 15).

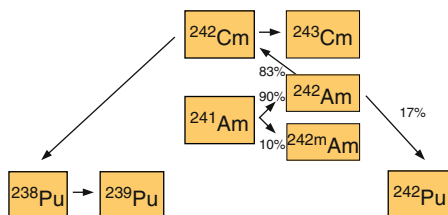


Figure 15
The transmutation scheme of ^{241}Am by thermal neutrons

4.2 Metal Fuels

Although there is a large knowledge on fuel performance of U–Pu–Zr ternary metal fuel (Hofman and Walters 1993), very little is known about the behavior of metal fuel containing minor actinides. Meyer et al. (2009) reported the results of an experimental irradiation of U–Pu–Zr metal fuel pins containing 1.2 wt.% Am and 1.3 wt.% Np and found that the fuel behaved like standard metallic U–Pu–Zr fuel. In the METAPHIX project, fast reactor metal fuels containing minor actinides (MA: Np, Am, Cm) and rare earths (RE) have been irradiated in the fast reactor Phénix. In this experiment four types of sodium-bonded fuel alloys, U–19Pu–10Zr, U–19Pu–10Zr–2MA–2RE, U–19Pu–10Zr–5MA–5RE, and U–19Pu–10Zr–5MA (wt.%), were irradiated up to three different burnup levels, namely ~2.4, ~7, and ~11 at.%. The linear power during the irradiation decreased gradually from 30–32 kW/m (beginning of irradiation) to 25–26 kW/m (end of irradiation). Results of the nondestructive and post-irradiation examinations of the low burnup experiments have been reported (Ohta et al. 2007b; Breton et al. 2007; Ohta et al. 2009), and indicate normal behavior compared to standard fuel.

4.3 Carbide and Nitride Fuels

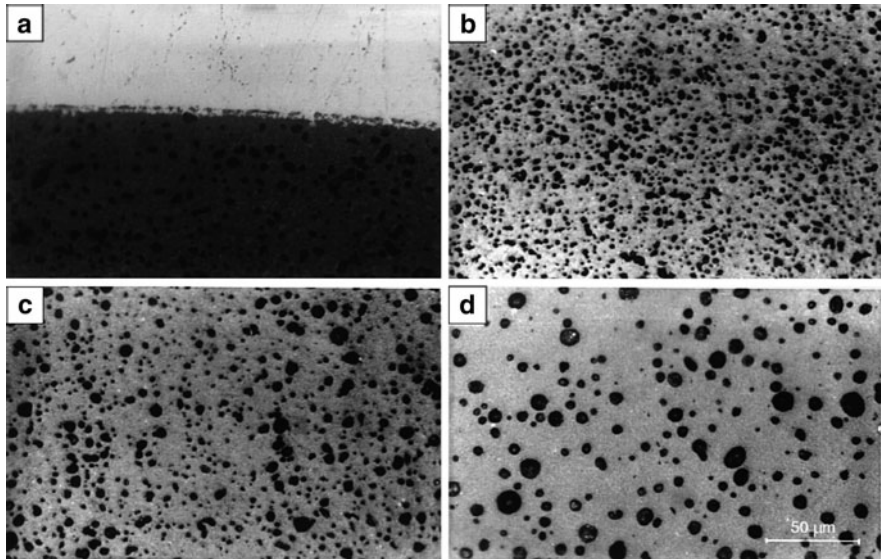
There is no reported irradiation experience with minor actinide containing carbide or nitride fuel. The existing irradiation experiments are all limited to (U, Pu)C and (U, Pu)N.

4.4 Molten Salt Fuels

The operational experience with molten salt fuel is limited to the molten salt reactor experiment (MSRE) at Oak Ridge National Laboratory (ORNL) in the 1960s. The fuel of MSRE was based on the LiF–BeF₂ solvent (0.66:0.34 mole fraction) with 5% ZrF₄ as oxygen getter. During the 4 years of operation, several fissile sources were used, including $^{235}\text{UF}_4$, $^{233}\text{UF}_4$, and $^{239}\text{PuF}_3$.

4.5 Other Fuel Types

Extensive research on various types of dispersion type transmutation targets has been performed by the Experimental Feasibility of Targets for Transmutation (EFTTRA; a collaboration of CEA, FZK, JRC-IE, JRC-ITU, NRG, and EDF) group (Warin et al. 2001). A variety of matrices for dispersion type transmutation targets was studied in irradiation experiments in



■ Figure 16

Ceramographies of the EFTTRA-T4 target showing the porosity at different radial positions from the pellet rim (a) to the pellet center (d) Konings et al. (2000) (©Elsevier BV, reproduced with permission)

the HFR and Phénix. In the EFTTRA-T4 experiment, a $\text{MgAl}_2\text{O}_4\text{-AmO}_2$ target was irradiated in the HFR during 358 full power days, during which 96% of the initial ^{241}Am was transmuted and 28% of the initial americium atoms were fissioned. The irradiation performance of the target was not optimal, however, as swelling up to 18% in volume was observed (Konings et al. 2000; Wiss et al. 2003). The reason for this swelling was revealed by the ceramographic analysis (► Fig. 16), which indicated a porosity increase from 3% in the unirradiated to about 18% in the irradiated pellet. This could be attributed to the accumulation of helium in gas bubbles produced by alpha-decay of ^{242}Cm , a product in the transmutation chain of ^{241}Am (see ► Fig. 15). The MgAl_2O_4 was found to be amorphous by transmission electron microscopic studies, which could be an additional contribution to the swelling. Similar experiments with UO_2 instead of AmO_2 indicated that swelling occurred in these cases also at low operating temperature (Neeft et al. 2003), but not at higher operating temperature (Georgenthum et al. 2001).

No irradiation experience has been reported for zirconia-based targets containing minor actinides, but results have been obtained for Pu-based $(\text{Zr, Y, Er, Pu})\text{O}_2$. Hellwig et al. (2005, 2006) reported results of the irradiation of this material in the Halden reactor. The postirradiation examination showed that:

- The observed fuel temperatures are significantly higher than that of standard UO_2 as could be expected from the significantly lower thermal conductivity of this material.
- A strong densification took place at the beginning of the irradiation.
- The fission gas release is comparable to UO_2 at the same irradiation temperatures.

Further studies with americium-containing targets/fuels will have to prove whether restructuring of the fuel occurs with americium redistribution.

■ Table 6

Summary of the irradiation experiment with minor actinide fuel

Experiment name	Reactor	Fuel type	Materials	Status
FACT		Mixed oxide		Completed
SUPERFACT	Phénix	Mixed oxide	(U, Pu, MA)O ₂ (U, MA)O ₂	Completed
TRABANT-1	HFR	Mixed oxide	(U, Pu, Np)O ₂	Completed
Am-1	Joyo	Mixed oxide	(U, Pu, Am)O ₂	Completed
X501	EBR-II	Metal	(U, Pu, Zr, Np, Am)	Completed
Metaphix	Phénix	Metal	(U, Pu, Zr, Np, Am, Cm)	PIE ongoing
EFTTRA-T4	HFR	Inert matrix	MgAl ₂ O ₄ + AmO ₂	Completed
ECRIX	Phénix	Inert matrix	MgO + AmO ₂	PIE ongoing
CAMIX-COCHIX	Phénix	Inert matrix	MgO + (Zr, Y, Am)O ₂ (Zr, Y, Am)O ₂	PIE to be started
HELIOS	HFR	Inert matrix	Mo + (Pu, Am)O ₂ Mo + (Zr, Am)O ₂	Irradiation ongoing
FUTURIX-FTA	Phénix	Various	Mo + (Pu, Am)O ₂ Mo + (Zr, Pu, Am)O ₂ MgO + (Pu, Am)O ₂ (U, Pu, Zr, Am, Np) (Pu, Am, Zr) (Zr, Pu, Am)N (U, Pu, Np, Am)N	PIE to be started

4.6 Summary

A summary of the irradiation experiments with minor actinides is given in ► [Table 6](#).

5 Reprocessing

5.1 Introduction

Nuclear energy systems of the future, as they are defined by the GIF, should provide sustainable energy generation for the future (<http://www.ne.doe.gov/genIV/neGenIV1.html>). Major objectives are an effective fuel utilization and waste minimization through recycling of all actinides. It is therefore obvious that the corresponding fuel cycles will play a central role in realising these goals.

Partitioning and transmutation (P&T) is being developed since several decades as a radioactive waste management option (Magill et al. 2003), where major parts of the long-lived waste constituents are incinerated for instance in ADS, prior to a direct geological disposal of the

resulting waste. The direct nuclear fuel disposal is the option chosen by countries such as Sweden, Finland, Spain, and the USA, whereas industrial fuel reprocessing has already been used for several decades in France and UK and will soon be implemented in Japan. Germany has adopted a mix of both options. After reprocessing, the HLW raffinate is vitrified and contains all long-lived fission products but also the MA. As discussed above, the major advantage of the P&T option is the reduction of the long-term radiotoxicity in nuclear repositories and thereby an increased public acceptance. In the P&T strategy most of the MA, long-lived fission products ^{99}Tc , ^{129}I , and ^{135}Cs and heat generating fission products ^{90}Sr and ^{137}Cs , are separated in addition to the industrial reprocessing (separation of U and Pu). The separated MA and some long-lived fission products are transmuted in a fast neutron spectrum, either in a fast reactor (FR) or in an ADS.

Over the last couple of decades, considerable scientific and technical effort has been devoted to develop partitioning processes through domestic and international projects: SPIN (France) (Salvatore 1993), OMEGA (Japan) (Mukaiyama et al. 2002), GNEP (AFCI: USA) (<http://www.gnep.gov/>), bilateral cooperations and EURATOM Framework Programs (Madic et al. 2001, 2000, 2004; Madic and Hudson 2004; Adnet et al. 2005).

Two types of processes can be applied to the separation of long-lived radionuclides: hydro-chemical (wet) and pyro-chemical (dry) processes. Both have advantages and disadvantages and should be applied in a complementary way. In a so-called double strata concept e.g., as proposed in the above mentioned OMEGA project, the well established industrial reprocessing of commercial LWR fuel with recycling of U and Pu based on PUREX extraction could be combined in the first stratum with an advanced aqueous partitioning scheme also based on liquid-liquid extraction to separate also the long-lived radionuclides. The MA could be transmuted in the second stratum in an ADS or FR of the new generation reactors systems proposed in the GEN IV roadmap. A large variety of fuels is under investigation in the development projects of these reactor systems (see ► Sects. 3 and ► 4) and this is one of the reasons why pyrochemical techniques could be selected as reprocessing options in the second stratum. Other reasons are:

- Good fuel and target solubility in molten salts, suitability for the treatment of highly refractory materials (e.g., ceramic-based targets). The dry reprocessing technique can be applied as well for the recycling of the homogeneously distributed minor actinides in a fast reactor fuel as in the ADS where the minor actinides are irradiated as oxides, carbides, metals, or in inert matrices with concentrations up to 20%.
- Possibilities to treat materials with minimum cooling time. Due to the higher radiation resistance of the inorganic reactants used in the processes, the reprocessing of short-cooled spent fuel is possible. The doubling time of the bred fissile material decreases because the out-of-pile time of the fuel is reduced. For the spent fuel, cooling times as short as a few months seem possible compared to the present 5 years and longer needed for aqueous reprocessing.
- Integrated irradiation-reprocessing facility. Reprocessing and compact process equipment considerably reduces the number of cost-intensive and complicated transports of nuclear materials.
- Lower criticality hazard due to the absence of water and thus of a neutron moderator in the process.
- Proliferation resistant process. Compared with aqueous methods, dry reprocessing of fuels results in less pure and thus more proliferation resistant fractions of Pu, Np, or Am.

The pyrochemical processes have however also a number of drawbacks:

- Much lower level of technological development compared to aqueous processes.
- Low separation factors compared with hydrochemical processes.
- Aggressive process media (molten salts and liquid metals), high melting points and thus high operation temperatures require very resistant materials.
- In the case of metallic fuels, a highly pure atmosphere and thus a sophisticated technology is required.
- Processes difficult to develop for continuous operation (especially for electrowinning).
- Technological and process wastes need special treatment.

The decision on the partitioning process to be applied should depend on the boundary conditions, such as the type of fuel material to be treated, but aqueous- and pyro-partitioning are not to be seen as options in competition to achieve the partitioning of long-lived MA and fission products from spent nuclear fuel.

In any case, an efficient and selective recovery of the key elements from the spent nuclear waste is absolutely essential for a successful sustainable fuel cycle. This necessitates that Am and Cm can be selectively separated from lanthanide fission products, certainly the most difficult and challenging task in advanced reprocessing of spent nuclear fuel due to the very similar chemical behavior of trivalent elements. There are three major reasons to separate actinides from lanthanides:

- Neutron poisoning: lanthanides (esp. Sm, Gd, Eu) have very high neutron capture cross sections, e.g., >250,000 barn for Gd-157.
- Material burden: in spent LWR fuels, the lanthanide content is up to 50 times that of Am/Cm.
- Segregation during fuel fabrication: upon fabrication, lanthanides tend to form separate phases, which grow under thermal treatment; Am/Cm would also concentrate in these phases.

5.2 Advanced Aqueous Reprocessing

The PUREX process is the industrial hydro-chemical reprocessing technique to separate U and Pu from spent fuel and is based on the dissolution of the fuel in nitric acid. For the separation of MA the process has to be modified/extended using also hydro-chemical extraction techniques (Takanashi et al. 1998).

In the fuel solutions feeding to the first decontamination cycle, Np is present as a mixture of Np (IV), Np (V), and Np (VI). In the standard PUREX process, Np is partially extracted by tri-n-butylphosphate (TBP); this part follows the U stream and is separated in the second U purification cycle and then added to the HLW and vitrified. In the PUREX process adapted for Np recovery, Np is completely oxidized to the oxidation state VI and then co-extracted with U and Pu in the first decontamination cycle. Finally, as in the standard process, Np is recovered through a reducing scrub in the second U cycle. After separation, the Np nitrate, contaminated by β - γ emitters, may be purified by solvent extraction with TBP and finally transformed to oxide by calcination of the oxalate.

Extensive research and development for an extended PUREX process for MA recovery is carried out worldwide; the goal is to synthesize special extractants and to develop the corresponding process schemes required for a selective separation of Am and Cm from high

level liquid waste (HLLW). The process development requires a good basic understanding of the relevant extraction mechanisms.

5.2.1 Fundamental Studies

As aqueous partitioning is based on liquid–liquid extraction from an acidic solution into an organic phase, it is of crucial importance to know about extraction selectivity, thermodynamics, mechanisms, and kinetics. In aqueous MA partitioning schemes, two main routes are possible, see ► Fig. 17. The optimal strategy would be of course a process where MA are selectively directly extracted from the PUREX raffinate, HLLW. However, at present, no extractant could be found capable of selective and efficient separation of the MA at high acidities (>2 M HNO₃) in a highly radioactive solution containing all fission products (FP), among them lanthanide elements (Ln) in a mass excess of 20 times compared to MA. Partitioning of MA involving co-extraction of Ln and a subsequent separation of the two element groups is therefore the only viable option at present.

Extraction mechanisms: One of the major questions to be solved for the extraction of lanthanides (III) and actinides (III) from aqueous nitrate solutions concerns the knowledge of the nature of the extracted species. A dual mechanism of extraction could be envisaged. It would be based on the formation of solvates having the general formula $M(\text{NO}_3)_3\text{L}_n$, (with $M(\text{III}) = \text{Ln}(\text{III})$ or $\text{An}(\text{III})$ and $L =$ organic extractant and could form at low aqueous nitric acid concentrations. For concentrated aqueous nitric acid solutions the formation of ion-pairs,

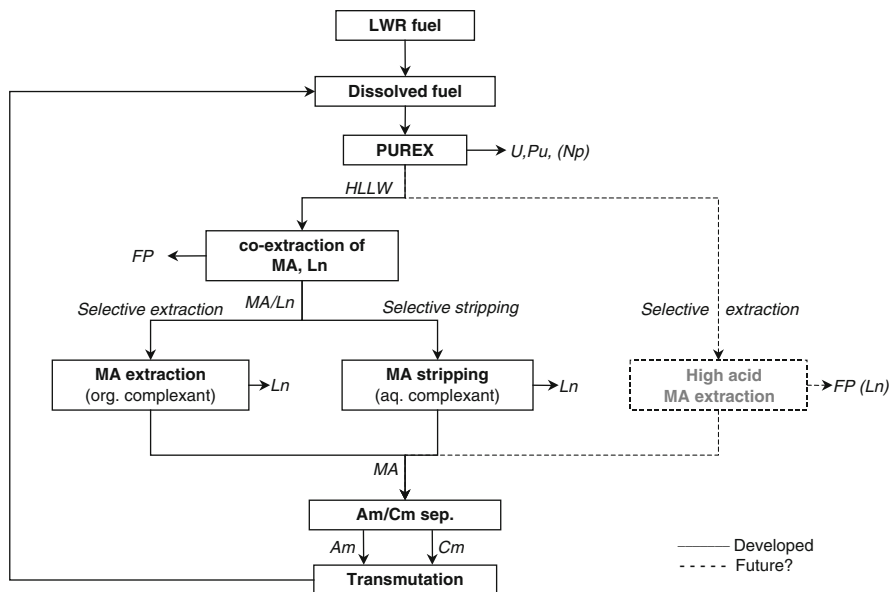
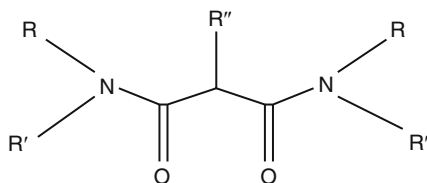


Figure 17


Strategies for the separation of the minor actinides from high level liquid waste (HLLW)



■ **Figure 18**
Structure of the bis-triazinyl-pyridines BTP molecule

with the general formula $[LH^+]_n$, $[M(NO_3)_n^{3+}]_{n-3n}$, as encountered when extracting actinide (VI) or actinide (IV) ions from nitric acid, is being proposed.

Several experiments, involving UV-visible and ^{13}C -NMR spectroscopy and solvent extraction, have been conducted to identify the extracted species. From the data obtained it can be concluded that an ion-pair mechanism involving a protonated ligand is very unlikely.

An extracting molecule which has been extensively studied especially in Europe is the diamide with the general formula: $(R(R')NCO)_2CHR''$ (where R , R' , and R'' are alkyl or oxyalkyl groups, the general structure being given in  Fig. 18. A so-called reference molecule is N,N' -dimethyl- N,N' -dibutyltetradecyl-1,3-malonamide (DMDBDTMA)). A comparison of diamides with different R' groups (butyl, phenyl, and chlorophenyl) in their ability to extract $An(III)$ or $Ln(III)$ from aqueous nitrate media shows that a less basic malonamide has better extraction properties of the $M(III)$ nitrate. If in the central R'' position the alkyl group is replaced by a di-octylhexylethoxy group, the diamide DMDOHEMA exhibits better affinities for $M(III)$ nitrates.

Arrhenius activation energies close to 40 kJ/mol for all $M(III)$ studied, indicate that the extraction is chemically limited at the aqueous/organic interface. For a diffusion limited kinetic regime, this energy is generally close to 20 kJ/mol. The extraction kinetics of $M(III)$ nitrates by DMDBDTMA are much slower than the extraction of $U(VI)$ or $Pu(IV)$ nitrates by TBP (extractant of the PUREX process).

Crystal structures were determined by X-ray absorption spectroscopy and using synchrotron light for a large number of lanthanide – and actinide – diamide complexes. Molecular modeling studies have been conducted to compare calculated structures and X-ray determined crystal structures and to propose structural explanations for experimental differences observed during extraction of $M(III)$ metallic nitrates by several malonamides.

Using the Quanta/CHARM code, the lowest energy conformation calculated for DMDPhMA, DMDCHMA, and BDMDPhMA, were found to be similar to the experimentally determined crystal structures. Also differences between structures of DMDPhMA and BDMDPhMA and that of DMDCHMA were confirmed by calculations. The differences in $M(III)$ extraction efficiency between cyclohexano (DMDCHMA) and phenyl substituted (DMDPhMA and BDMDPhMA) malonamides can be correlated with the difference of the preferred conformations of the malonamide extractants.

Using the Gaussian 94 program, protonation of cyclohexano (DMDCHMA) and phenyl (DMDPhMA) substituted malonamides show that *mono*-protonated malonamide contains an intramolecular hydrogen bond, while the *di*-protonated malonamide does not.

A quantitative structure-activity relationship (QSAR) study related to the extraction of $Nd(III)$ nitrate by a set of 17 malonamides supported the above mentioned improved

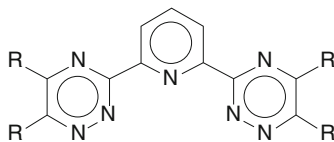


Figure 19
Structure of the bis-triazinyl-pyridines BTP molecule

M(III) nitrate extracting properties in the presence of an oxygen ether atom in the R'' substituent.


Separation of trivalent actinides from lanthanides: To explain the great affinity of actinides for nitrogen-bearing molecules, numerous fundamental studies were carried out using a wide range of experimental methods. Lanthanide/actinide separations often depend on a slightly stronger interaction of the trivalent actinides with ligands containing soft donor bases (S, Cl, or N), or with amine extractants in contact with aqueous solutions containing high concentrations of chloride or thiocyanate. Therefore, the formula, stability, and structure of the complexes containing Ln(III) and An(III) ions were determined both in aqueous solution and in various solvent media. It has been demonstrated that bonds between the nitrogen atoms of these ligands and Ln(III) and An(III) ions include some definite covalent character, which can be explained by the fact that enthalpy is the driving force of these reactions. The covalence observed in bonds with the electron-donor nitrogen atoms of ligands seems higher for An(III) ions than for Ln(III) ions; this could be an indication for the higher affinity of these ligands for An(III). However, sometimes the difference is too small to really explain very high differences in the distribution factor. Those are mainly observed for bis-triazinyl-pyridines BTP molecules (the general structure is shown in [Fig. 19](#)) which have proved to be among the most suitable nitrogen-bearing extractants for developing an An(III) separation process. Their affinity for An(III) ions is more than a hundred times higher than for Ln(III) ions.

Theoretical studies in the fields of quantum chemistry and molecular mechanics have provided greater insight into certain crucial aspects of reactions between these metal ions and nitrogen-bearing ligands ([Fig. 19](#)). In particular, the synergetic extraction mechanism of Ln(III) ions using a mixture of a nitrogen-bearing ligand and a carboxylic acid has been identified by computer calculations. The calculated synergetic complex seems to be consistent with the experimental results (Madic et al. 2002).

First attempts on the theoretical investigation of the actinide-BTP complexes have been conducted by means of quantum chemistry, molecular mechanics, and molecular dynamics (Drew et al. 1998; Guilbaud and Dognon 2000). The structure of Ln(*n*Pr-BTP)₃ crystals has been determined using X-ray diffraction (Drew et al. 2001). It has been confirmed that the complex is composed of three ligands directly bonded to the metal ion. The BTP molecules act as tridentate ligands. They coordinate via the N in the pyridine as well as via the triazinyl N atoms in the 2-position. Cm and Eu complexes with *n*Pr-BTP have been characterized by means of extended X-ray absorption fine-structure spectroscopy (EXAFS), time-resolved laser-induced fluorescence spectroscopy (TRLFS) and quantum-chemical investigations (Gompper et al. 1995). According to the EXAFS study, 9 N atoms are coordinated directly to the metal cations. The coordination structure with three ligands is the same for Cm and Eu (Cm(*n*Pr-BTP)₃ and Eu(*n*Pr-BTP)₃, respectively) and the bond lengths are the same in both complexes. This result

was supported by quantum-chemical calculations. In all calculations, the BTP ligand is nearly planar. This means that the selectivity of $n\text{Pr-BTP}$ for An(III) over Ln(III) is not of structural origin. Besides, there was no evidence for directly coordinated nitrate groups. The results of the TRLFS measurements revealed that the extracted Cm species always contains three ligands, independent on the ligand-to-metal ratio. The fact that $\text{Cm}(n\text{Pr-BTP})_3$ is formed at much lower ligand-to-metal concentration ratios is consistent with $n\text{Pr-BTP}$ high selectivity for An(III) over Ln(III) in solvent extraction.

5.2.2 Process Development

Two alternative approaches based on the scheme shown in  Fig. 17 are described hereafter.

The first approach is based on co-extraction of trivalent MA and lanthanides (Ln) and to separate in a second step MA from Ln (Serrano-Purroy et al. 2005). For the co-extraction, the most important processes are:

- The TALKSPEAK process (USA) (Nash 1993) and DIDPA process (Japan) (Morita et al. 1996) use acidic organophosphorus extractants.
- The TRUEx process (USA) (Arai et al. 1997b) and SETFICS (Japan) (Koma et al. 1998b) are based on the use of CMPO (*n*-octyl-phenyl-di-isobutyl-carbomoylmethyl-phosphine-oxide) as extractant.
- The TRPO process (China) uses a trialkyl phosphine oxide. The hot demonstration of this process using genuine HLLW has been done at JRC-ITU (Glatz et al. 1994).
- The diamide extraction (DIAMEX) process using malonamides as extractant (Nigond et al. 1994) has been developed at CEA (France) and is also the reference process under investigation in the European partitioning projects.

For an efficient recycling scheme, losses of the relevant elements should be as low as possible (0.2% or less); therefore a compromise between extraction and back extraction efficiency has to be made.

The MA/Ln separation can be achieved by the so-called selective actinide extraction process (SANEX). The major options are:

- The BTP (bis-triazinyl-pyridines) developed at the Forschungszentrum Karlsruhe-Institut für Nukleare Entsorgung (FZK-INE, Germany) (Kolarik et al. 1999) or BTBP (bis-triazine-bis-pyridine) are capable of selective extraction of MA at high nitric acid concentration (2 M).
- The TPTZ (tripyridyltriazine) developed at CEA to be used at much lower nitric acid concentrations (Hill et al. 1999).
- Variants of the dithiophosphinic acids (ClPh)₂PSSH in a mixture with TOPO at Forschungszentrum Jülich, Germany (Modolo and Odoj 1999).

Promising results have been obtained on simulated as well as on genuine solutions at lab-scale. Among many extractants tested worldwide, the combination of DIAMEX and BTP (Madic et al. 2000; Geist et al. 2006) appears to be the best combination for an efficient recovery of MA from HLLW or transmutation targets. Diamides do not require feed adjustment, can be easily recycled in the process and do not leave any residue upon incineration. Concerning the separation of MA from Ln, BTP is the most efficient extractant, giving at the same time the highest


separation factor with no feed acidity adjustment required. Separation factors between MA and lanthanides up to 80 are reached in a single stage extraction. These values are considerably improved in a continuous multistage process and an Am/Cm product containing less than 1% of Ln is obtained. However, due to its high sensitivity to hydrolysis and radiolysis, an industrial application of the BTP molecule requires further developments to improve these properties.

The second option is the co-extraction of actinides and lanthanides with DMDOHEMA (DiMethyl-DiOctyl-HexylEthoxy MalonAmide) of DIAMEX followed by selective stripping of the trivalent actinides from the loaded diamide solvent using a mixture of HEDTA (actinide-selective polyamino-carboxylate complexing agent) and citric acid (Miguirditchian et al. 2007).


The scientific feasibility of this process has been demonstrated by the CEA in the ATALANTE facility in Marcoule (Baron et al. 2007). A MA recovery of ~99.9% and less than 0.3 wt.% Ln in the MA fraction was achieved with a flowsheet, where the DIAMEX solvent was supplemented by an acidic extractant, diethylhexylphosphoric acid (HDEHP), to ensure effective extraction at pH > 2.

The Japan Atomic Energy Agency (JAEA) has studied an advanced aqueous process combined with a U crystallization process (Koma et al. 1998a). The main features compared with the conventional PUREX are:

- The purification steps of U and Pu in the conventional PUREX are eliminated, resulting in co-extraction of U/Pu/Np, and simplification of the system. A compact-sized centrifugal type equipment is used to reduce the size of the reprocessing facility.
- Crystallization is used to separate excess U before extraction of U/Pu/Np.
- A combination of the SETFICS process, developed by Japan Nuclear Cycle Development Institute (JNC, now JAEA), and the transuranium extraction process (TRUEX) is applied for the recovery of Am and Cm. The recovery ratio of U/transuranium elements is about 99.7%, and the decontamination factor of the reprocessed product is higher than 100.

As shown in  Fig. 20, another process developed by JAEA, known as the “Four-Group Separation Process”, includes:

- An extraction of all transuranium elements including Np (V) with diisodecylphosphoric acid (DIDPA) at 0.5 M nitric acid.
- A separation of Tc and platinum group metals by precipitation through denitration.
- A separation of Sr and Cs by adsorption with inorganic ion exchangers.
- Selective back-extraction of Am and Cm by 0.05 M diethylenetriaminepentaacetic acid (DTPA).

In  Table 7, the separation efficiency and estimated recovery values obtained in the various processes described above are compared to target values for the recovery of transuranium elements and some key fission products in advanced reprocessing.

The values achieved are quite high and almost satisfy the targeted recovery. The recoveries of Tc and noble metal alloys are around 90–95% which is lower than the targeted recovery. This lower recovery is not so important, as their contribution to the potential radiotoxicity of HLW is not significant.

With respect to aqueous reprocessing, dedicated research facilities are available in France (CEA, Marcoule) and UK (BNFL, Sellafield) where extensive studies are being performed on spent fuel material. Facilities for smaller scale hot-tests are available in other countries and at

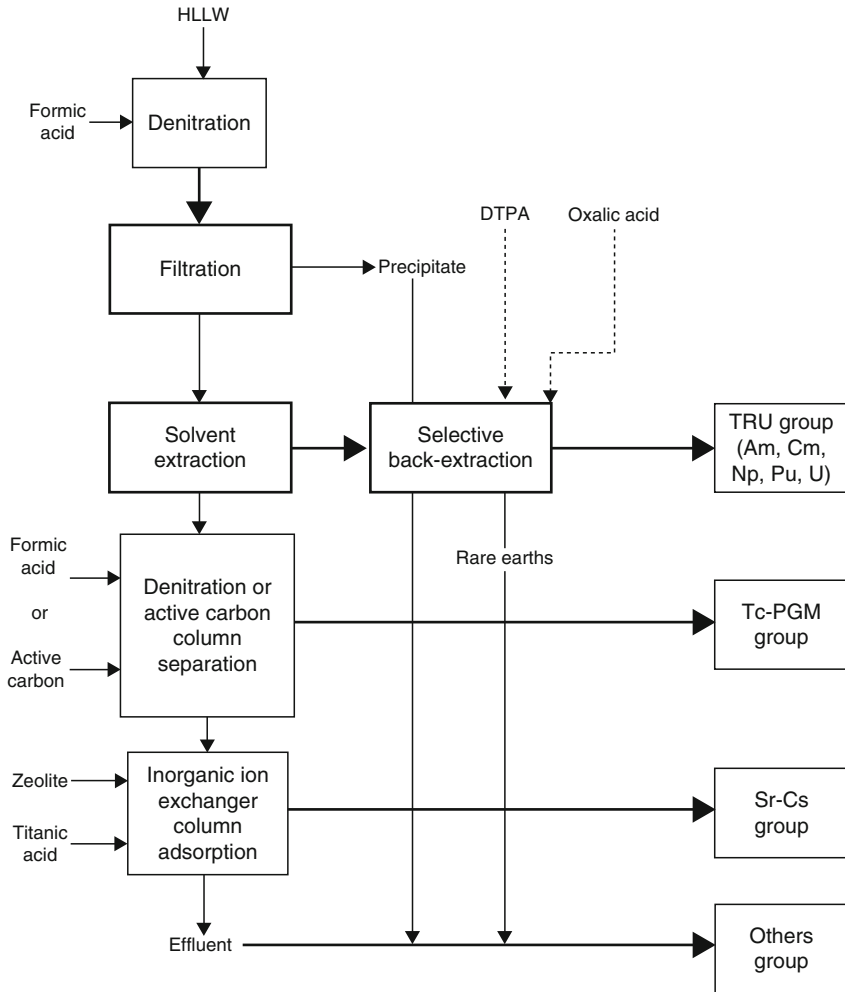


Figure 20 Four group partitioning process (Morita et al. 2004)

the JRC-ITU. In addition, European Universities are strongly involved in this research through the European Commission Framework Programs, especially in the fields of synthesis of new extractants and molecular modeling.

5.3 Pyro-Reprocessing

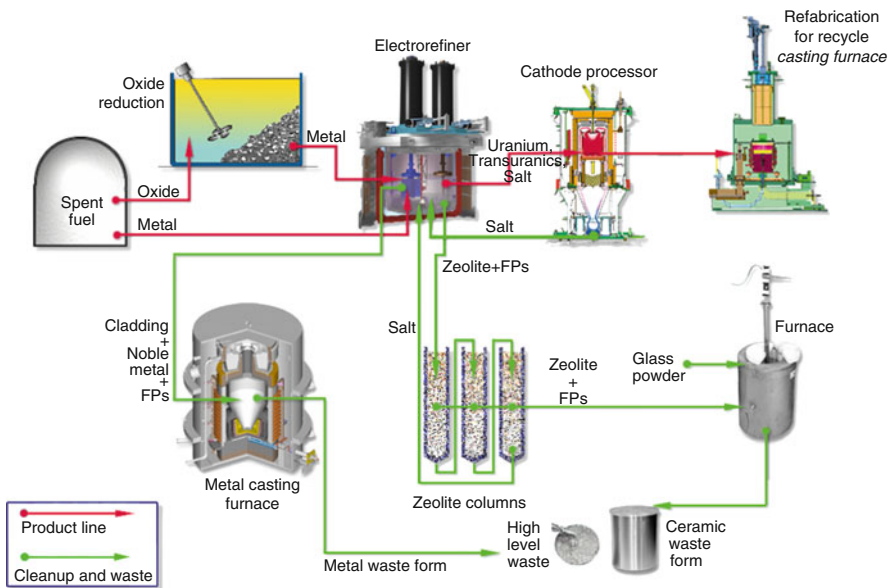
Pyrochemical processes rely on refining techniques at high temperature (500–900°C) depending on the molten salt eutectic used. Typically, chloride systems operate at lower temperature compared to fluoride systems. In nuclear technology the processes are mainly based on electrorefining or on extraction from the molten salt phase into liquid metal.

■ **Table 7**

Target recovery, experimentally obtained separation efficiency and estimated recovery of elements in the four group partitioning process

Elements	Target recovery (%)	Separation efficiency (%)	Estimated recovery (%)	
T ^a	Np	99.5	>99.95	99.85
	Pu	99.9	>99.99	99.85
R	Am	99.99	>99.99	99.97
U	Cm	99.9	>99.99	99.97
Tc	99	~98	~95	
Sr, Cs	99	>99.9	>99.9	

^aTransuranium elements



■ **Figure 21**

Metal and oxide fuel pyroprocess flow sheet (Laidler et al. 1997)

5.3.1 US Pyrochemistry Projects

The electrometallurgical process was applied for the first time as a part of the integral fast reactor (IFR) system. Pyrochemical separation processes for the recovery of uranium and to some extent for plutonium have been investigated since decades (Laidler et al. 1997) and remain the core process in the present EBR-II Spent Fuel Treatment Program. Many of the pyroprocessing systems presently proposed for development are adaptations of this process as depicted in

➤ [Fig. 21.](#)

The fuel is recycled using an electrochemical process that employs molten salts and liquid metals. The molten salt medium for electrorefining is a solution of LiCl–KCl eutectic and dissolved actinide chlorides, such as UCl_3 . The operating temperature is 500°C . With this system, chopped spent fuel is loaded into the electrorefiner in a basket. The fuel is electrochemically dissolved into the system in an operation in which the basket is the anode and another electrode in the salt phase is the cathode. Uranium with small amounts of transuranium elements can be collected on steel electrodes (solid cathodes), and transuranium elements can be co-deposited with uranium in liquid-cadmium cathodes. A liquid-cadmium cathode is a ceramic crucible containing molten cadmium that can be lowered into the salt phase. The cadmium in the crucible is at cathodic potential. The cathode products from electrorefining operations are further processed to distill adhering salt and cadmium and to consolidate the recovered actinides. The recovered actinides are remotely fabricated into new fuel for recycle.

The alkali, alkaline earth, rare earth, and halide fission products are primarily in the salt phase. The elements that distribute into the salt phase are eventually incorporated in a ceramic HLW. More than 90% of the noble metal fission products and fuel alloy material are retained in the chopped cladding segments in the anode baskets. The cladding hull segments and the retained fission products are eventually stabilized into a metal HLW.

Adaptations of this technology exist for the treatment of both oxide and nitride fuels. The flow sheet for the treatment of nitride fuels is similar to that of metal fuel. In this system, the nitride fuels are also fed directly into the electrorefiner. The actinides are dissolved from the fuel cladding and collected electrochemically in liquid cadmium or bismuth cathodes. Nitrogen evolves in the process. It is collected and recycled back into the liquid cathodes so that actinide nitrides are formed, a potentially difficult step. After distillation of the cadmium, the recovered nitrides are sized and then fabricated into new fuel using vibro-packing. This process is being developed in Japan.

5.3.2 European Pyrochemistry Projects

For more than 50 years, pyrometallurgy has been studied as an alternative strategy for reprocessing spent fuel. Until now, two processes have been developed at pilot scale, both in chloride media, the first one starting from and ending with an oxide fuel and the second one starting from and ending with a metallic fuel.

On the basis of these past studies, pyrometallurgy has been considered as the reference route for molten salt reactor fuel treatment, but also as an alternative technology that could be applied to some types of fuels today envisaged for Gen IV systems or ADS in case they would not be compatible with current hydrometallurgical processes.

In the European pyro-reprocessing projects, basic properties of An and some FP in molten salts (chlorides and fluorides) and in liquid metal solvents have been studied. The data allow development of a conceptual design and assessment of reprocessing processes suitable for fuels and targets proposed for advanced fuel cycles. The feasibility of separating U, Pu and MA from FP using pyrometallurgy in a molten chloride or fluoride system was assessed.

Basic data: A very significant investigation was done for thermodynamic data acquisition in molten chloride media, with a comprehensive study of An, Ln, and other important fission products. In comparison to molten chloride salts, studies in molten fluoride are much less

developed. Even if a lot of experiments were carried out in various salts, it seemed difficult to get relevant thermodynamic data. This is mainly due to the lack of a reliable reference electrode.

The studies carried out on liquid metals were at a sufficient level to confirm the choice of aluminum for an electrochemical process in molten chloride as well as for a reductive extraction process in molten fluorides. These results were used to optimize the two reference core processes at a satisfactorily level.

Two efficient processes for the separation of An from Ln have been selected as promising core processes and defined: (1) electrorefining process on solid aluminum cathode in molten chloride, (2) liquid–liquid reductive extraction in liquid aluminum–molten fluoride. Some reference flow sheets have been assessed. Moreover, several new experimental installations for process tests have been constructed.

To be implemented, the whole process must produce the lowest achievable amount of waste, and when a waste is produced, it must be in a convenient form for storage or disposal. In the decontamination of spent chloride salts coming from electrorefining, the complementary techniques of zeolite ion-exchange filtration and phosphate precipitation, have been selected for their potential to clean up the spent salt efficiently. Although some specific matrices for salt confinement were identified (sodalite, pollucite), a lot of work remains to be done in this field.

System studies were performed including: (1) double-strata concept (ADS), (2) IFR and (3) Molten Salt Transmutation Reactor (MSTR). A first step defined the general principles used for the assessment of pyrochemical separation processes, the common methodology for technical and economical comparisons and the selected flow-sheets. During the second step, the work focused on detailed flow-sheeting studies and mass balance calculations and the three options were studied. The major interest of these studies is the validation of the “process approach,” which is deemed very useful for identifying key issues and reorienting R&D programs. Nevertheless, as these flow sheets address different scenarios and fuels it is very difficult to compare them in terms of advantages and drawbacks.


Basic data acquisition: Basic properties of An and some FP in molten salts (chlorides and fluorides) and in liquid metal solvents have been studied (McPheeters et al. 1997; Serp et al. 2004; Caravaca et al. 2007).

Significant work was done in basic data acquisition in molten chloride media, mainly at JRC-ITU with a comprehensive study of actinides (U, Pu, Np, Am, Cm), lanthanides and some other important fission products. Thermochemical properties are derived from the electrochemical measurements and from basic thermodynamic data for instance in the case of Np of NpCl_3 and NpCl_4 in the crystal state (Masset et al. 2005; Konings et al. 2001a). It could be demonstrated, that NpCl_3 has a strong nonideal behavior in molten LiCl–KCl eutectic.

Core processes: Initially three potential chemical routes were identified for a development as core process. The first one based on selective precipitation was rapidly withdrawn due to the poor decontamination factors obtained. The second route is an electrochemical one, which includes electrolysis or electrorefining techniques, either in chloride or in fluoride molten salts. The third one is based on the liquid–liquid reductive extraction from a molten fluoride salt and liquid Al.

In parallel, some studies were carried out on electrolysis in molten fluoride or liquid–liquid reductive extraction using molten chlorides, but in a less extensive way.

Important studies were carried out also in the institutional program of the Nuclear Research Institute Rez (NRI, Czech Republic) on fluoride volatilization.

Electrorefining on solid aluminum cathode in molten chloride media: To comply with the sustainability goals defined for innovative reactor systems, a major objective is the development of a grouped actinide recycling process based on molten salt electrorefining. Special emphasis is given to a selective electrodeposition of actinides with an efficient separation from lanthanide fission products. In contrast to the IFR concept, where U is deposited on a solid stainless steel cathode and transuranium elements on a liquid Cd cathode, the electrorefining processes rely on a co-deposition of all actinides on a solid Al cathode material, because stable actinide alloys are formed. A redissolution of trivalent actinides can thus be avoided in contrast to e.g., W cathodes. Also the redox potentials on solid cathodes show a much larger difference in the reduction potential between actinides and lanthanides. In  Fig. 22 the reduction potentials for U^{3+} , Pu^{3+} , Am^{3+} , La^{3+} , and Nd^{3+} determined by transient electrochemical techniques (mainly cyclic voltammetry and chronopotentiometry) on different materials are shown.

On Bi and Cd, the selectivity of the minor actinide recovery seems to be limited due to the small difference in reduction potentials between actinides and lanthanides.

The choice of the cathode material onto which the actinides are deposited in the electrolysis was essential in this context (Masset et al. 2005b). Solid Al has been selected because of two reasons:

1. Stable actinide deposits (alloys) are formed and are consequently very adherent to the cathode; at the same time a redissolution of the trivalent An by comproportionation with the trivalent actinides in the salt to form divalent An according to: $Am(III) + Am(0) = 3Am(II)$ can be avoided.
2. The difference in the reduction potentials compared to Ln is sufficiently high to avoid their co-deposition.

In these electrolytic processes, the rate of the alloy formation depends on the diffusion of the involved elements in and through the solid alloy phase. Therefore, the maximum amount of actinides that can be collected on a single Al electrode has been investigated in constant current electrorefining experiments in which the cathodic potential was maintained at a suitable level for the separation of An from Ln. With increased charge passed, i.e., with the build-up of a surface layer of An–Al alloy, the applied current is gradually reduced in order to stay above the

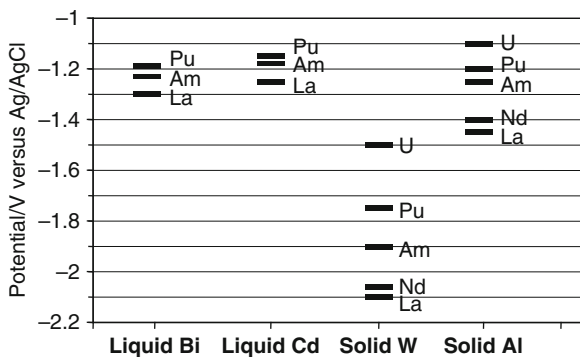
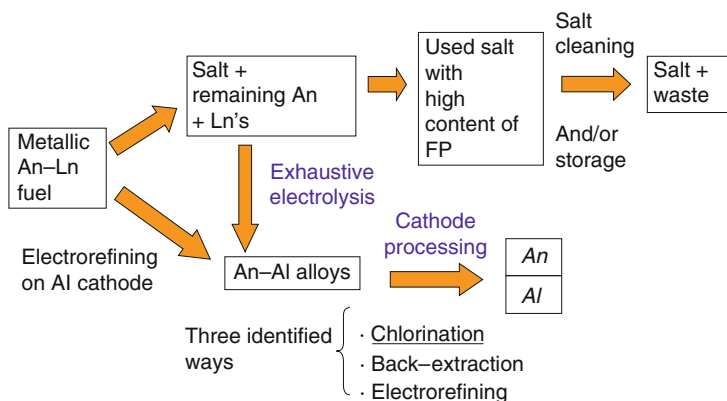


 Figure 22

Reduction potentials of some actinides and lanthanides on different cathode materials



■ Figure 23

Process scheme for molten salt electrorefining of metallic fuels

cathodic potential limit. Based on this information, a process scheme as shown in ► Fig. 23 is proposed.

The electrorefining process is operated in the batch mode. After multiple use of the eutectic salt bath, an exhaustive An electrolysis is required to avoid losses >0.1% to the waste, before the cleaning of the salt bath takes place. It is evident that the Ln content in the electrodeposited An–Al alloy in the exhaustive electrolysis contains more Ln than in the runs where metallic fuel is deposited and must eventually be recycled. For the cathode processing, three options are possible, chlorination, back-extraction and electrorefining. Among those chlorination is the most promising. This step is needed to recycle the An to the fuel fabrication.

Laboratory experiments have shown that 3.72 g of actinides could be deposited in 4.17 g Al, corresponding to 44.6 wt.% An in Al or 68 wt.% of the maximal loading when $AnAl_4$ alloys are formed (Cassayre et al. 2006). A successful demonstration of the Am/Nd separation was carried out using a mixture of 255 mg Am, 281 mg Pu, and 140 mg Nd. Am and Pu were co-deposited in two steps on two Al cathodes of 0.8 g each. The cathodes used were made of Al foam to increase the reaction surface area. The Nd content in the deposit of only about 0.5% proves the feasibility of a selective actinide separation by electrolysis onto Al electrodes.

The results were confirmed further in a multiple run experiment inducing an accumulation of Ln in the salt. These fuels had already been developed in the frame of the IFR concept in the mid 1980s in the USA. The same type of fuel is used for transmutation studies (METAPHIX Project) initiated by Central Research Institute of Electric Power Industry (CRIEPI), Japan in collaboration with JRC-ITU. This fuel containing 2% of Am and lanthanides ($U_{61}Pu_{22}Zr_{10}Am_2Ln_5$) was fabricated at JRC-ITU. The remnants of the fuel fabrication campaign are used for the present studies.

In the pyro-reprocessing, the metallic alloy is anodically dissolved in a LiCl–KCl eutectic (Serp et al. 2004) and the An are collected together onto Al cathodes as alloys, leaving Ln in the salt phase.

To simulate a large-scale pyro-processing by molten salt electrorefining operated as a batch process similar to the industrial Al fabrication process. An experiment of 25 successive runs was carried out. The experiment has also demonstrated the feasibility of a grouped actinide

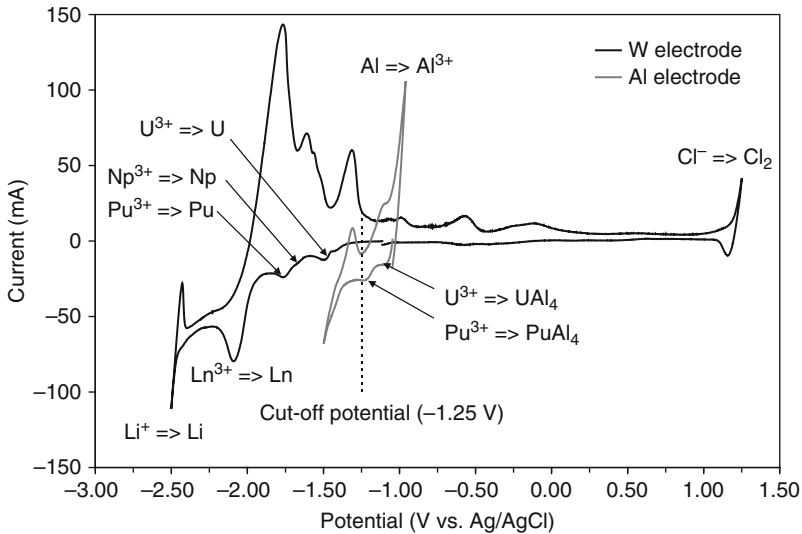


Figure 24

Cyclic voltammogram of $U_{61}Pu_{22}Zr_{10}Am_2Ln_5$ on W and Al wires. Reference electrode: Ag/AgCl-1 wt.%, $v = 100$ mV/s, $T = 450^\circ\text{C}$. Salt composition in wt.%: U-0.29, Np-0.12, Pu-0.28, Am-0.06, Zr < 0.07, and Ln-1.0

recovery from larger amounts of fuel without changing the salt bath. A total amount of more than 5 g of $U_{61}Pu_{22}Zr_{10}Am_2Ln_5$ fuel was treated in this experiment and various process parameters were studied. \blacktriangleright Figure 24 shows the cyclovoltammogram of the alloy on Al and W electrodes.

The goal of this 25-run test was to find optimal conditions for the recovery of Am. The recovery rate of An was difficult to evaluate because new fuel was added in each run. Nevertheless, a stable recovery rate $[m_{An}/(m_{An} + m_{Ln})]$ better than 99.9% was achieved throughout the whole experiment. Uranium, the main constituent of the fuel with a less electronegative electrodeposition potential (see \blacktriangleright Fig. 22) is preferentially deposited in the earlier runs. At the same time the relative Am content in the actinide deposit and the separation from lanthanides (m_{Am}/m_{Ln}) increases despite an increasing content of Ln (not-electro-deposited) in the salt.

The results of this 25-run electrorefining experiment where genuine fuel materials were used and where the salt bath has not been changed, are very promising in view of a large-scale development of pyro-reprocessing in advanced nuclear fuel cycles.

5.3.3 Liquid-Liquid Reductive Extraction in Molten Fluoride/Liquid Aluminum

This process was extensively studied by CEA both as an institutional program and also in European research programs (Lacquement et al. 2005; Conocar et al. 2006). An experimental device and a protocol have been developed to study the distribution of An and Ln in

molten fluoride/liquid metal medium. The results obtained with Pu, Am, Ce, and Sm in the (LiF–AlF₃)/(Al–Cu) medium revealed the potential of the system for separating the actinides from the lanthanides.

With a salt composition corresponding to the basic eutectic (LiF–AlF₃, 85–15 mol%), up to 99% of Pu and Am could be recovered in a single stage, with Ce and Sm separation factors exceeding 1,000. The effect of the AlF₃ concentration in the salt has been investigated. The distribution coefficients decrease as the initial AlF₃ concentration rises. A thermodynamic model of extraction versus fluoroacidity has been developed on the basis of the experimental results for Ce and Sm. The model clearly reveals the difference in solvation between divalent and trivalent Ln in fluoride media.

The results obtained were confirmed by lab-scale experiments under realistic conditions. Two runs have been done at 830°C with LiF–AlF₃ (85–15 mol%) as salt phase: one with the Al–Cu alloy (78–22 mol%) as metallic phase, the other with pure Al. The objective of the second test was to check that the absence of Cu did not penalize the extraction, in terms of both performances and implementation of the process. For each test, the initial concentrations in the salt were the following (wt.%): PuF₃ (11), AmF₃ (0.2), CeF₃ (2.5), SmF₃ (0.5), EuF₃ (0.5), and LaF₃ (0.5). Seventeen grams of salt and metal have been contacted. The results show similar high distribution ratios of Pu and Am in the same order of magnitude than those previously measured at low concentration without Ln (► Table 7).

In the test without Cu, the distribution coefficient of Cm (trace concentration in Am starting material) has been measured for the first time; it is very close to those of other actinides (U, Np, Pu, Am). The distribution coefficients of the Ln are low and allow high separation factors from actinides. The results obtained with Al–Cu and Al are close (see ► Table 8). In these tests the chemical feasibility of the An/Ln group separation by liquid–liquid extraction in molten fluoride with liquid aluminum are assessed. The experimental results compared to those obtained without the presence of Cu in the metallic phase, are summarized in ► Table 8.

The results show that the distribution ratios of Pu and Am have similar high values independent from the presence of Cu in the metallic phase and in all cases there is a high separation

■ Table 8

Mass distribution coefficients and separation factors of actinides and lanthanides with and without Cu in the metallic phase

Al–Cu (78–22% mol)			Al		
M	DM	SAm/M	M	DM	SAm/M
Pu	197 ± 30	0.73 ± 0.21	Pu	273 ± 126	0.78 ± 0.47
Am	144 ± 20	1	Am	213 ± 30	1
Ce	0.142 ± 0.01	1,014 ± 213	Cm	185 ± 31	1.15 ± 0.35
Sm	0.062 ± 0.006	2,323 ± 488	Ce	0.162 ± 0.02	1,315 ± 289
Eu	<0.013	>11,000	Sm	0.044 ± 0.004	4,954 ± 1,139
La	<0.06	>2,400	Eu	<0.03	>7,100
			La	0.03	7,100

efficiency from Ln. Also in this process, the actinide back-extraction from the Al is an important step in view of fuel refabrication. A bibliographic study has identified three possible routes:

- Electrorefining, whose main drawback is its complexity (three steps are necessary)
- Volatilization of the Al matrix by a chlorinating reagent is a simple and efficient method. Nevertheless, high volume of chlorinating gas is necessary and an additional step to convert AlCl_3 into Al should be done in order to recycle Al
- Oxidizing liquid–liquid extraction in molten chloride.

5.3.4 Technical Uncertainties of the Pyro-Reprocessing

The Spent Fuel Treatment Program at ANL demonstrated many parts of the pyroprocess fuel cycle, but for a large scale application there are still key aspects that have yet to be demonstrated on a large scale with radioactive materials. The main outstanding issue is the recovery of transuranium elements. Large-scale equipment has been fabricated for a MA recovery, but with the termination of the IFR program, the equipment and process was never tested beyond the laboratory scale.

The remote fabrication of IFR fuel was not part of the Spent Fuel Treatment Program, but the same technology was used to fabricate cold fuel for the Experimental Breeder Reactor II (EBR-II) and a demonstration of another pyroprocess (melt refining) for recycling EBR-II fuel in the 1960s employed remote fabrication for 34,500 fuel elements (Laidler et al. 1997).

One challenge for a pyro-reprocessing system is selecting the appropriate materials of construction for the high temperature processes. Material improvements are needed in order to lessen the formation of dross streams and increase material recovery and throughput.

The quantity of waste generated from pyro-reprocessing that requires geological disposal appears to be comparable at present to modern commercial aqueous processes. Advancements are being pursued to further reduce the disposal volumes through zeolite ion exchange processes. This technology has not been demonstrated beyond the laboratory scale.

Most of the radioactive work performed to date has been on the pyro-reprocessing cycle for metal fuel. Laboratory work has been performed on the head-end operations for oxide reduction and on the nitride fuel cycle. Demonstrations of these technologies with actual spent fuel have started at a laboratory scale. Additionally for nitride fuels, demonstrating the recycle of nitrogen is critical because ^{15}N is specifically required for the fuel to eliminate the formation of radioactive ^{14}C .

5.3.5 Head-End Conversion Processes

Today all commercial reactors are operated with oxide fuels and advanced reactor systems selected in the GEN IV roadmap rely also on oxides as one of the major fuel options. The pyrometallurgical process based on oxides developed in Russia, Research Institute of Atomic Reactors (RIAR), Dimitrovgrad, does not include MA recycling. Pyro-reprocessing, where all actinides are recycled, is based on metallic materials; therefore, a head-end reduction step for oxides fuels is needed to convert oxides into metals. This conversion can be performed chemically, e.g., by reaction with lithium dissolved in LiCl at 650°C . The recovered metal can directly be subjected to electrorefining and the Li_2O converted back to lithium metal by electrowinning. A more elegant method is the so-called direct electroreduction. In this case, the heat generating

fission products are removed and the fissile materials are recovered as an alloy, which can again be directly reprocessed by electrorefining.

Numerous experiments are carried out today to study this conversion process. The lithium reduction process using lithium metal as a reducing agent is carried out in molten lithium chloride. The reduction of UO_2 (Sakamura et al. 2006) and simulated spent LWR fuel (Sakamura et al. 2008) was studied mainly by CRIEPI in Japan in collaboration with AEA Technology in the UK. The optimized thermodynamic conditions for the reduction of transuranium elements (Iizuka et al. 2006) and the behavior of major fission product elements (Kurata et al. 2004) were determined. Li is converted into Li_2O , and constantly removed during the process from the molten salt bath to prevent the reoxidation of the reduced fuel material. Li is recovered by electrochemical decomposition of the Li_2O and recycled to the process (Herrmann et al. 2007).

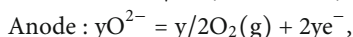
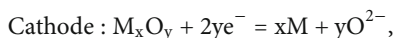
A simulated spent oxide fuel in sintered pellet form, containing the actinides U, Pu, Am, Np, and Cm, and the fission products Ce, Nd, Sm, Ba, Zr, Mo, and Pd, was reduced with Li metal in a molten LiCl bath at 923 K. The pellet remained in its original shape, it became porous and a shiny metallic phase was observed throughout the pellet. The Pu/U ratio did not change during the reduction process. The reduction yield of U and Pu determined by measuring the H_2 formed upon reaction of the reduction product with HBr and using a gas burette was more than 90%. A small fraction of Pu has formed an alloy with Pd. The rare earth elements were found in the gap of the porous U–Pu alloy. As expected from the oxygen potential of Ce, Nd, Sm, and Li, they remained in an oxide form.

Small fractions of the actinide and rare earth elements were leached from the pellet into the molten LiCl bath or were found as precipitate on the crucible bottom. A large part of Am was found in the rare earth oxide phase rather than in the reduced U–Pu alloy. This represents of course a major problem in a grouped actinide recovery. Also the handling of highly reactive Li and problems in developing the corresponding equipment especially for the lithium recovery are major drawbacks of this process.

The electrochemical reduction process is clearly the more reliable technique to convert oxides into metal. The difficult handling of Li metal and recycling through reconversion from Li_2O can be avoided. The oxide ion produced at the cathode is simultaneously consumed at the anode and thus the concentration of oxide ion in the bath can be maintained at a low level. A more complete reduction of the actinide elements can be achieved and the subsequent electrorefining to separate actinides as described in the previous paragraph can be carried out in the same device.

At present, an electrochemical process is being developed mainly in the USA at the Idaho National Laboratory (INL) and, in collaboration with the JRC-ITU, also in Japan at CRIEPI. Both unirradiated and irradiated fuel materials were treated with slightly different concepts.

In the INL process, the oxide fuel is loaded into a permeable stainless steel basket as crushed powder. The basket immersed in a molten LiCl – 1 wt.% Li_2O electrolyte at 650°C is used as cathode and a Pt wire is used as anode. The reduced fuel is retained in the basket. The oxygen ions liberated at the cathode diffuse to the Pt anode, where they are oxidized to oxygen gas. The corresponding reactions are:



where M = metal fuel constituent

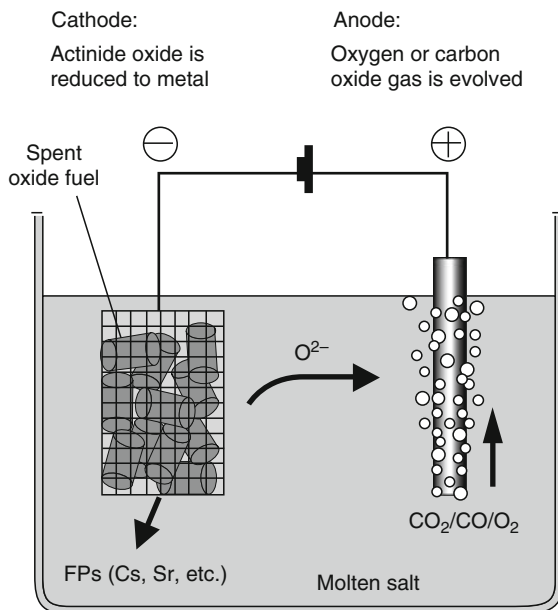
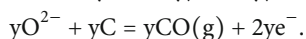
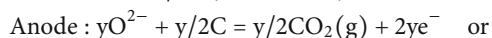
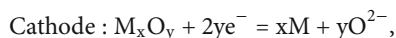


Figure 25
Schematic drawing of the electrochemical oxide to metal conversion process (Sakamura et al. 2006)

The Li_2O present in the salt is reduced to Li together with U and reduces the fuel oxide chemically. Consequently, the INL process is a combined chemical/electrochemical process.

The CRIEPI/JRC-ITU process is schematically shown in [Fig. 25](#).

The fuel is not crushed but loaded as fuel rod segments in a cathode basket, made of Ta. The anode is made of C, the corresponding reactions are:



The molten salt can be either $LiCl$ or $CaCl_2$. In $CaCl_2$, the higher temperature of 1,123 K in comparison to 923 K for $LiCl$ induces a faster diffusion of oxygen ions to the anode. At the same time an increased initial reaction rate leads to the formation of a thin dense metal layer at the fuel surface hindering the diffusion of oxygen ions into the salt.

The INL process scheme was successfully demonstrated using irradiated spent LWR oxide fuel in a hot cell. More than 98% of the U was reduced. Cesium, Ba, and Sr were dissolved in the salt phase, as expected. The rare earth and noble metal fission products remained with U and transuranium elements such as Pu and Np were reduced together with U, however, about 20% of the Am remained as oxide.

The CRIEPI/JRC-ITU process was tested on various MOX compounds. Mixed oxide fuels with a Pu content 5–45% were reduced. It could be shown that U and Pu are efficiently co-reduced, but due to the problems mentioned above, the complete reduction requires very long reaction times. The reduction of irradiated FR fuel particles at JRC-ITU was considerably faster

due to an increased reaction surface and a complete reduction of all fuel constituents including fission products and MA was achieved.

6 Impact of Transuranium Elements on Storage and Waste Disposal Concepts

6.1 General Aspects

The necessity to physically concentrate and isolate from the biosphere radiotoxic nuclides generated during the operation of nuclear power plants is a key safety aspect and a common requirement for existing and future concepts of nuclear fuel cycles. As described in the previous sections of this chapter, the so-called back-end of the fuel cycle encompasses different options, ranging from direct disposal of spent fuel, to reprocessing of U and Pu followed by disposal of vitrified HLW (containing MA and fission products), to reprocessing of U and Pu including partitioning and transmutation of MA (and, in some cases, also of long-lived fission products) followed by disposal of the resulting waste.


With respect to radionuclide isolation, and concerning the spent fuel and/or the end wasteform, two main stages can be defined and are present in all fuel cycle back-end concepts: handling, transport and storage in temporary storage facilities, and final disposal in a geologic repository.

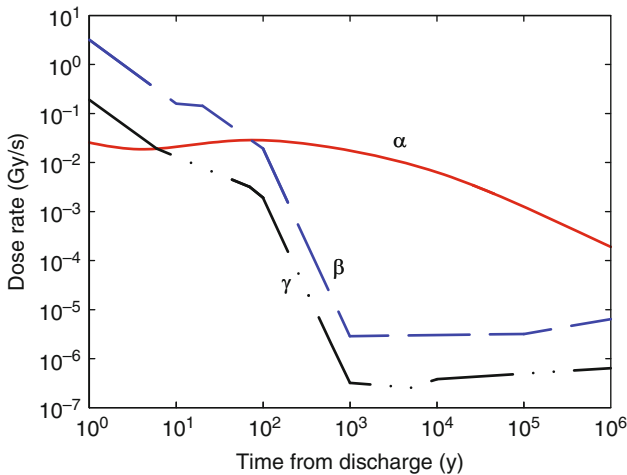
The stability of the wasteform depends on some properties of the waste material, in particular on its composition, chemical state, and radioactivity level. In the case of spent fuel, the irradiation history and conditions (burnup, temperature) determine properties and behavior of the spent fuel rod (fuel + cladding) during storage.

The radioactive decay process is the main factor affecting the property evolution of the wasteform. The radioactive decay heat must be dissipated to maintain the waste package material at a temperature below the safety limit. This, together with criticality safety considerations, ultimately determines the spacing of nuclear waste containers, hence the size of the geological repository sites. Additionally, the accumulation of microstructural damage and of helium, specifically associated with the alpha-decay, may progressively alter the properties of the waste material and ultimately affect its mechanical stability. This may also result in a modification of the corrosion behavior of the waste form in the event of direct contact with groundwater.

6.2 Transuranium Elements and Wasteforms

6.2.1 Transuranium Elements in Spent Fuel

Transuranium elements account for more than 99% of the total alpha-activity of irradiated fuel shortly after discharge, and are responsible for the long-term activity and heat production of spent fuel, as shown in  Fig. 26, which depicts the specific evolution of the contribution due to the alpha-, beta-, and gamma-activity of spent fuel expressed as dose rate as a function of time. Already after a few hundred years, the alpha-activity component dominates the overall activity and dose surrounding spent fuel.



■ Figure 26

Dose rate evolution for spent LWR fuel with a burnup of 60 GWd/tM (Quiñones et al. 2008) (© MRS)

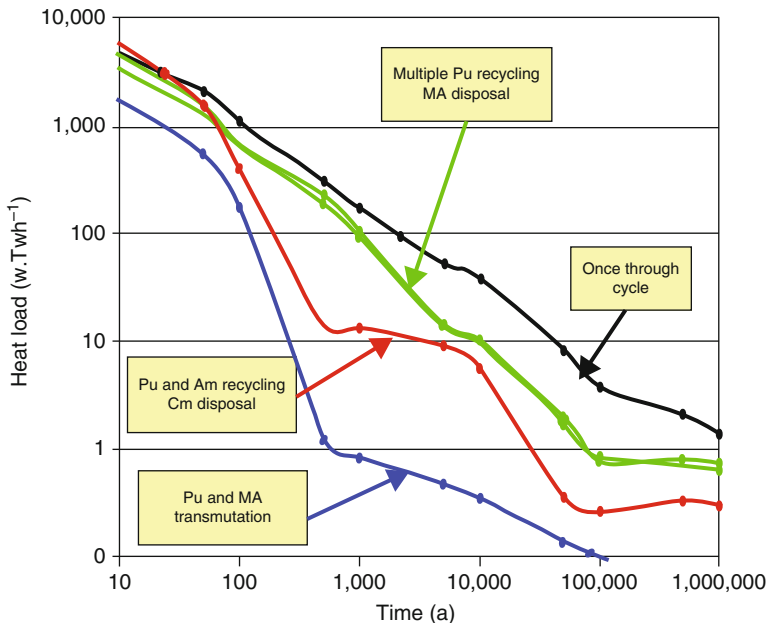
6.2.2 Transuranium Elements in Waste Glass

HLW glass associated with current reprocessing of spent fuel contains all transuranium elements separated from spent fuel with the exception of Pu (Gras et al. 2007). Pu disposition in glass is also considered (Muller et al. 2001). Typically, a loss of U and Pu around 1% is considered to occur in the fraction of these elements recuperated by reprocessing, and is included in the vitrified waste load. The total weight fraction of material separated from spent fuel loaded in today's HLW glass is around 14.4%; the mass of actinide oxides in the glass amounts to ~0.4 wt.%, the rest being constituted by fission products (Gras et al. 2007).

6.2.3 Transuranium Elements in Advanced Cycle Waste Forms

The evolution of the fuel cycle for existing reactors (both LWR and Canada Deuterium Uranium (CANDU) reactors) includes in most concepts an increase in the fuel burnup and/or the use of MOX fuel. The corresponding spent fuel or the reprocessing of this type of fuel will be characterized by a higher content of MA per unit of fuel treated. Therefore, there is a trend in the evolution of current back-end concepts towards achieving and assessing behavior and safety implications of waste form formulations that accommodate different inventories of transuranium elements (NEA (OECD Nuclear Energy Agency) 2008; Gombert et al. 2008).

Advanced fuel cycles for future generations of reactors envisage various waste forms for final disposal, ranging from spent fuel or IMF/target after one irradiation (once-through-then-out, deep-burn concepts), to vitrified waste or ceramic matrices containing the radionuclides separated as waste in reprocessing and/or partitioning stages. The implementation of partitioning and transmutation (P&T) concepts will entail the removal of transuranium elements from the waste stream destined for disposal in a geologic repository. 📌 Figure 27 illustrates the power generated by decay in HLW, including spent fuel and different degrees of recycling of the



■ Figure 27

Power generation as a function of time of different types of high-level waste (HLW) expressed as heat per unit energy produced during reactor operation of the corresponding fuel (Gras et al. 2007) (© Elsevier)

transuranium elements. This diagram highlights the potential gain stemming from the recycling of Cm together with Pu and Am (comparison between red and blue curve). The inclusion of curium in the recycled fuel is currently being debated, as, against the medium-term advantage in terms of reduction of the heat generated in the waste, one has to consider that the handling of Cm requires special measures and thus would cause an increase in the complexity and cost of the facilities and the procedures associated with fabrication of Cm-containing fuel. Moreover, the efficiency of Cm destruction even in fast reactors is quite limited.

6.3 Special Wasteforms for the Immobilization of Transuranium Elements

In the case of recycling of Pu and Minor Actinides, the remaining reference species controlling the long term radiotoxicity of the waste would be long-lived fission products like ^{99}Tc , ^{129}I , ^{135}Cs (with $t_{1/2}(\text{y}) = 2.1 \times 10^5$, 1.6×10^7 , 2×10^6 , respectively). Specific waste forms for these fission products are considered, and are the object of study in various research groups worldwide (Weber et al. 2009).

Crystalline waste forms to immobilize transuranium elements, including Pu from dismantled warheads, are also an object of study. The main compounds proposed for these applications are derived from natural minerals which have contained actinides over geological time-spans.

The main requirements are good resistance against radiation damage and against water corrosion, high loading fraction of transuranium elements, and ease to fabricate and process. Typically, these proposed waste forms are compared to HLW glass in terms of properties, performance, and fabrication routes (Vance 2007; Boyer et al. 1997).



Phosphates like monazite, (RE, An)PO₄, where RE = rare earths and An = actinides, and other phases like rare earth apatite (McCarthy 1977), powellite CaMoO₄, and pollucite CsAlSi₂O₆ have mineral analogs which proved to be durable in nature, and are among the first compounds which were proposed for these applications (Ringwood et al. 1979).

Synroc (synthetic rock) is a multi-phase Ti oxide ceramic where transuranium elements could substitute in zirconolite (CaZrTi₂O₇) and perovskite (CaTiO₃) phases. The synroc formulation would include also hollandite, Ba(Al, Ti)₂Ti₆O₁₆ as suitable host for fission products (Caurant et al. 2006). The initial concept of synroc envisaged a direct coupling to incorporate ~20 wt.% of PUREX reprocessing oxide waste; however, up to 35 wt.% waste loading is considered possible. In addition to its flexibility (additional phases can be added according to the target materials to be immobilized), good leaching resistance characterizes this waste form concept: the corrosion rate of these crystalline phases is up to three orders of magnitude lower than that for waste glass. Single phase zirconolite (Belin et al. 2008) and, to a lesser extent, perovskite, are also studied specifically for immobilization of transuranium elements.

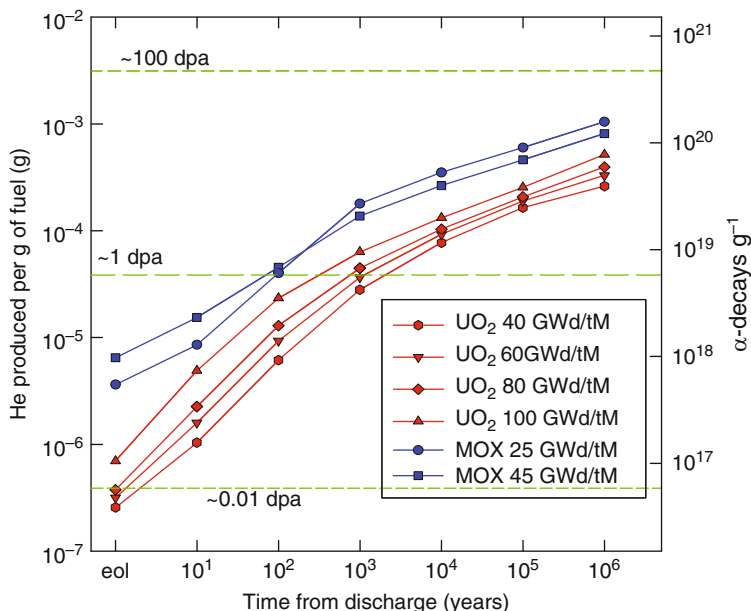
Fluorite-structure materials like cubic ZrO₂, or fluorite-derived structures like pyrochlore, are also considered. Pyrochlores have the general formula A₂B₂O₇, where A and B can be a wide variety of metal cations, with different valences. With respect to the fluorite structure two cation sites and one-eighth of the anions are absent (Sickafus et al. 2000). Both tri- and tetravalent transuranium elements could be incorporated; the matrix would provide good resistance against radiation damage (depending on the host composition) and against corrosion (Lian et al. 2003; Lutique et al. 2003; Strachan et al. 2003). However, by increasing the resistance against amorphization (this can be achieved by replacing Ti with Zr in the B sites), the fabrication process becomes more cumbersome in terms of higher sintering temperature and lower amount of impurities that can be tolerated in the structure.

In some cases, composite materials are under examination, in particular for transmutation in nuclear reactors followed by direct disposal. In these concepts, a refractory compound with high radiation resistance like ZrO₂ is typically hosted in a high thermal conductivity matrix like e.g., a metal (CERamic METal composition, CERMET). The combination allows exploiting the advantages of both host compounds while optimizing the irradiation and postirradiation processes.

6.4 Long-Term Behavior of Waste Containing Transuranium Elements

As shown in  Figs. 26 and  27, if present in the waste form transuranium radionuclides would dominate the long-term radioactivity of HLW. Their presence or absence in the waste will significantly change the time scale during which the radiotoxicity of the waste will exceed the levels of relevant natural geological formations (uranium mines), hence the time limit by which the safe isolation of the waste from the biosphere has to be ensured.

The impact of transuranium elements on the evolution and behavior of the waste form will have physical and chemical aspects.




■ Figure 28

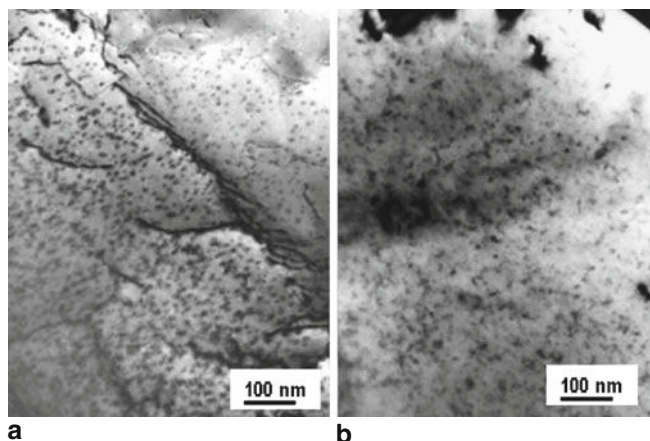
Alpha-decay and helium production as a function of time in spent UO₂ and MOX fuel with different burnup (eol = time of discharge from the reactor; dpa = displacement per atom)

6.4.1 Consequences of Alpha-Decay Damage and Helium Build-Up in the Waste Form

The physical aspects characterizing the long-term solid state evolution of the waste form are related to the specific decay power and the effects associated with the accumulation of alpha-decay damage and He in the material. Alpha-decay damage consists of atomic displacements in the lattice caused by the slowing down of the alpha-particle and the recoil nucleus. The slowing down process occurs by energy transfer (via nuclear and electronic energy loss mechanisms) associated with collision of atoms in the material. The net result of the decay events is the accumulation of microstructural defects and He atoms in the waste material.

It is necessary to assess the waste form behavior under accumulating decay damage conditions to ensure that the required functionality of the material is maintained over the time interval of interest.  Figure 28 shows the evolution of the decay events due to transuranium elements in current LWR spent fuel with different burnup, expressed as He produced and alpha-decays as a function of time (Rondinella et al. 2003).

Formation of point defects, dislocation loops, and, finally, extended defects and small He bubbles are all features observed as a function of accumulated alpha-dose in a (U, Pu)O₂ matrix (Rondinella et al. 2005, 2007; Eyal 1997; Maugeri et al. 2009). Similar microstructural features can be observed also in other crystalline waste forms subjected to alpha-decay damage (Weber et al. 1998; Ewing et al. 2004; Wiss et al. 2007; Wald and Weber 1984). In the case of spent fuel, the defects caused by decay superimpose those from fission damage that occurred during in-pile



■ Figure 29

Transmission electron microscope micrographs showing dislocation loops (appearing as small black dots on the images) caused by alpha-decay damage in the UO_2 matrix: (a) spent fuel, 85 GWd/t, ~ 0.1 displacement per atom (dpa) due to alpha-decay after fuel discharge from reactor; (b) unirradiated (U, Pu) O_2 , ~ 0.2 dpa due to alpha-decay

irradiation. ➤ [Figure 29](#) shows the build-up of dislocation loops in the lattice of unirradiated (U, Pu) O_2 and in spent fuel.

The accumulation of microstructure alterations results in macroscopic property changes. Three extreme consequences, potentially affecting the waste form, are associated with this process:

- Amorphization may cause an increase of the corrosion rate in water by a factor 20–50; this effect may be relevant for crystalline waste forms other than UO_2 (Noe and Fuger 1974).
- Dimensional changes, in particular swelling, may be associated to amorphization and/or to phase transition and hardening in the material: their unwanted consequence consists of interaction/pressurization affecting the mechanical stability of the clad/container that might eventually compromise the integrity of the waste package (Wiss et al. 2007; Weber 1981; Matzke 1982).
- The ultimate consequence of radiation damage and helium accumulation in the waste may be the loss of mechanical integrity. Disaggregation of the waste material would hamper the handling of the waste form during/after intermediate storage prior to disposal, or result in a significant increase of surface area, which, in turn, would produce higher initial mobilization rates of nuclides from the waste upon exposure to water (e.g., in the event of failure of all containment barriers in a final repository).

Sufficient data is available demonstrating that low burnup UO_2 as waste form will not reach the range of conditions that could lead to the above-mentioned extreme consequences. Given the trends toward using higher burnup and transuranium elements-rich fuels/waste forms, the behavior of waste matrices subject to higher specific decay and helium accumulation rate has to be confirmed. Compared to low burnup UO_2 , the use of MOX fuel (see ➤ [Fig. 28](#)) or of

advanced fuels containing MA would increase the specific activity of the material, hence the damage and He accumulated during a given time interval, by several orders of magnitude. For advanced fuel containing MA, in particular, possible implications concerning storage time after fabrication and before reactor irradiation have to be fully evaluated. However, data available from existing high specific activity spent fuels, like SUPERFACT, indicate that no significant degradation of the mechanical stability occurred during more than 20 years of storage, i.e., after accumulating a damage level corresponding to a few dpa. This is due to the fact that the build-up of radiation damage in the material is not linear. Recombination mechanisms, especially significant at relatively high temperature or in materials with a relatively large density of defects, would cause saturation and partial recovery of the defects in the lattice of materials like UO_2 before reaching extreme deterioration of the material properties (Matzke 1982). These observations point to a positive conclusion concerning the long-term behavior of spent uranium dioxide fuel even at high specific activity regimes.

In the case of ceramic matrices for the immobilization of transuranium elements (described in [Sect. 6.3](#)), the most radiation resistant matrices, with behavior similar to UO_2 , appear to be ZrO_2 and ZrO_2 -based compounds. Amorphization, and in some cases, dramatic alteration of the mechanical integrity of the solid phase have been observed in other compounds, depending on host composition and waste loading.

6.4.2 Corrosion Behavior of the Waste Form in Contact with Water

The chemical aspects related to the evolution of the waste form affect its corrosion behavior if exposed to steam and/or groundwater. The likelihood of accidental type of events is minimized by the adoption of rigorous safety procedures during all stages of the fuel cycle; their impact would in any case be limited in time and extension. The contact between HLW and groundwater is an occurrence possible only after a very long time has elapsed since placement of the waste in the final repository. The eventual timeframe of such contact is of the order of 10 or 100,000 years after closure of the geological repository. The corrosion process would then be governed by the chemical conditions in the repository and by the properties of the waste form at the time of the water exposure. The chemistry of the transuranium elements plays an important role in determining the extent of the mobilization and transport of safety relevant radionuclides (Edelstein et al. 2006). [Table 9](#) summarizes chemical properties of transuranium elements relevant for corrosion in aqueous environment. Indicative solubility or, in the case of Pu, apparent concentration ranges are reported, which refer to redox conditions corresponding to different types of geologic repositories. The sorption characteristics are also indicated. High sorption tendency would correspond to significantly lower transport through the geologic media.

If no P&T option is considered, after a few 100 or 1,000 years the radiotoxicity of HLW will be dominated by the transuranium elements contribution, as illustrated by the data in [Fig. 1](#). After 10,000 years, the content, hence the possible role of Am and Cm in the corrosion process will become negligible. Together with long-lived radiotoxic fission products like ^{99}Tc and ^{129}I , transuranium elements Pu and Np will constitute the main sources of hazard. Among these, ^{237}Np is the nuclide with the longest half-life. The content of ^{237}Np in spent fuel will actually increase during the first 10,000 years due to the decay of ^{241}Am . Moreover, Np presents higher solubility and lower tendency to adsorb onto mineral phases compared to Pu, in particular under oxidizing conditions. Pu has a strong tendency to sorption, which in general limits its

■ Table 9

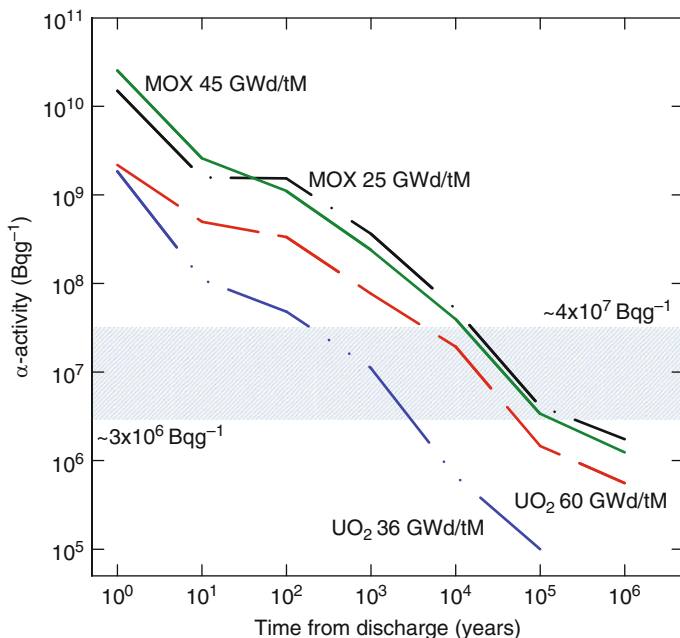
Summary of relevant properties of transuranium elements at near neutral pH

Element	Solubility (mol/l)	Sorption	Oxidation states in aqueous solution	Remarks
Pu	10^{-8} – 10^{-7a} <i>oxidizing</i> $< 10^{-9}$ <i>reducing</i>	High	+3, +4, +5, +6	Redox sensitive, relatively high amounts can be found in the groundwater ^a ; low solubility, high sorption, colloid transport
Np	10^{-6} – 10^{-3} <i>oxidizing</i> $< 10^{-8}$ <i>reducing</i>	Low <i>oxidizing</i> high <i>reducing</i>	+4, +5, +6	Redox sensitive, high solubility under oxidizing conditions, low sorption, colloid transport
Am	10^{-9} – 10^{-3}	High	+3, +5	Oxidation state +3 up to very strong oxidizing conditions
Cm			+3, (+4)	Oxidation state +4 is not stable

^aThe total amount of plutonium that can be measured when analyzing a groundwater solution by spectrometric methods represents an “apparent” concentration. This apparent concentration includes contributions from colloids and sorbed Pu, in excess of actual dissolved plutonium ions

mobility; Pu could, however, be transported mainly through colloid adsorption. Neptunium is often considered the transuranium element of reference for the studies on the long-term safety of the geologic repository (Eckhardt 2000). Both Np and Pu are affected by the presence of complexing species like carbonates and are redox sensitive, i.e., their oxidation state is affected by the redox potential and the pH of the groundwater; the oxidation state, in turn, is a key parameter in determining the mobility behavior of the element. The highest solubilities (and most rapid migration behavior) correspond for Np to the 5+ oxidation state, which would occur under oxidizing conditions. Under reducing conditions the 4+ state is stable and the solubility is significantly lower (see ► Table 9). Similar considerations on the oxidation states can be made also for Pu, although this element presents a more complex behavior, characterized by disproportionation of the 5+ state and the simultaneous presence of different oxidation states (Neck et al. 2007). The solubilities for Pu are generally lower than those for Np.

For most geologic repository concepts, the occurrence of a chemically reducing environment is envisaged as an additional element contributing to minimize the dissolution in water of redox sensitive species present in the waste. In the case of spent LWR fuel, the chemical solubility of the UO₂ matrix will be lower by several orders of magnitude in the absence of oxygen and/or other oxidizing agents. However, an important effect related to the presence and the activity of transuranium elements in the waste is the possible enhancement of dissolution due to the radiolysis of the water molecule caused by alpha-particles and recoil atoms produced in alpha-decay events occurring near the surface of the waste. ◉ Figure 30 shows the evolution of specific alpha-activity as a function of time for different types of spent LWR fuel (Rondinella et al. 2000; Carbol et al. 2005).



■ Figure 30

Specific alpha-activity of irradiated LWR fuel as a function of time. UO₂ and MOX fuel with different burnup levels are represented (Rondinella et al. 2000; Carbol et al. 2005). The shaded area marks the range of alpha-activity below which the dissolution of UO₂ is controlled by chemical solubility rather than radiolytic dissolution-enhancing effects (Rondinella et al. 2004)

The radiolytic process generates an equal number of oxidizing and reducing species, including radicals and molecular species. It has been observed in laboratory simulated experiments that alpha-radiolysis can produce a net enhancement of the dissolution rate of a UO₂ matrix for alpha-activities down to levels in the interval between $\sim 3 \times 10^6$ and $\sim 4 \times 10^7$ Bq/g (shaded area on the diagram in [Fig. 30](#)) (Rondinella et al. 2004), corresponding to spent fuel with an age ranging between one thousand to tens of thousand years (Carbol et al. 2005; Johnson et al. 2005). The enhancement is due to the establishment of oxidizing conditions very near the surface of the waste, almost independent of the nominal redox conditions of the repository. Due to the limited range of alpha-particles in water ($\sim 37 \mu\text{m}$ for a 5 MeV particle), alpha-radiolysis affects only a thin water film surrounding the waste surface.

If radiolysis were the only factor affecting the corrosion behavior of the waste, it would become crucial to ensure (through appropriate design of the containment and isolation barriers enclosing the waste) that no contact with groundwater occurs before a time of the order of some tens of thousand years has elapsed. However, the radiolytic enhancement, caused mainly by the presence of transuranium elements in the waste, is just one of the factors shaping the overall expected behavior of the waste in a repository. If one considers the integral behavior, with all conditions characterizing the repository applied, the dissolution enhancing effect of radiolysis will be offset by other, dissolution-inhibiting agents that will be assuming a governing role in determining the overall interaction process between the waste and the surrounding

environment. Among these beneficial agents the reducing and immobilizing effect on redox sensitive radionuclides due to the presence of relatively large amounts of iron in the vicinity of the waste form will play a major role (Cui et al. 2009a). Additionally, the corrosion reaction of iron with groundwater under anaerobic/anoxic conditions (typical of a chemically reducing geologic repository) will generate hydrogen overpressures. Hydrogen dissolved in groundwater at low temperature (below ~ 370 K) is chemically inert. However, in presence of a suitable catalyst (e.g., the 4d-metallic fission products alloy particles formed in the fuel during irradiation or the UO_2 surface itself) (Cui et al. 2009b), a suppressing effect of the oxidative corrosion is observed that may ultimately block the corrosion of the spent nuclear fuel matrix (Carbol et al. 2009).

References

- Adler HP, Ledergerber G, Stratton RW (1987) Advanced fuel for fast breeder reactors produced by gelation methods. IAEA Technical Committee, Vienna
- Adnet J-M, Miguirditchian M, Hill C (2005) Development of new hydrometallurgical processes for actinide recovery: GANEX concept. In: Proceedings of the Global 2005, Paper no. 119, Tsukuba, Japan
- Anselin F, Calais D, Passefort JC (1965) Survey of uranium-carbon-nickel ternary diagram. In: Report CEA-R2845, France
- Arab-Chapelet B, Grandjean S, Nowogrocki G, Abraham F (2007) Synthesis of new mixed actinides oxalates as precursors of actinides oxide solid solutions. *J Alloys Compd* 387: 444–445
- Arab-Chapelet B, Grandjean S, Nowogrocki G, Abraham F (2008) Synthesis and characterization of mixed An(IV)An(III) oxalates (An(IV) = Th, Np, U or Pu and An(III) = Pu or Am). *J Nucl Mater* 373:259–268
- Arai Y, Nakajima K (2000) Preparation and characterization of PuN pellets containing ZrN and TiN. *J Nucl Mater* 281: 244–247
- Arai Y, Minato K (2005) Fabrication and electrochemical behavior of nitride fuel for future applications. *J Nucl Mater* 344:180–185
- Arai Y, Fukushima S, Shiowaza K, Handa M (1988) Fabrication of uranium-plutonium mixed nitride and thermally stable carbide fuels. In: Proceedings on advanced fuel for fast breeder reactors, IAEA-TECDOC-466, IAEA, Vienna, p 25
- Arai Y, Fukushima S, Shiowaza K, Handa M (1989) Fabrication of (U, Pu)N fuel pellets. *J Nucl Mater* 168:280–289
- Arai Y, Shiowaza K, Ohmichi T (1992) Preparation of uranium-plutonium mixed nitride pellets with high purity. In: Proceedings of the 4th international symposium on advanced nuclear energy research-roles and direction of material science, Ibaraki, Japan, p 167
- Arai Y, Iwai T, Nakajima K, Suzuki Y (1997a) Recent progress of nitride fuel development in JAERI-Fuel property, irradiation behaviour and application to dry processing. In: Proceedings of the Global 1997, Yokohama, Japan, p 664
- Arai K, Yamashita M, Hatta M, Tomiyasu H, Ikeda Y (1997b) Modified TRUEx process for the treatment of high-level liquid waste. *J Nucl Sci Technol* 34(5):521–526
- Babelot JF, Chauvin N (1996) Rapport de synthèse commun CEA/ITU sur l'expérience SUPERFACT 1. In: Note technique SDC/LEMC 96-2028, CEA Cadarache
- Babelot JF, Chauvin N (1999) Report TN-1999-03, Joint Research Centre, Institute for Transuranium Elements, Karlsruhe, Germany
- Bardelle P, Warin D (1992) Mechanism and kinetics of the uranium-plutonium mononitride synthesis. *J Nucl Mater* 188:36–42
- Baron P, Masson M, Rostaing C, Boullis B (2007) Advanced separation processes for sustainable nuclear systems. In: Proceedings of the Global 2007, Boise, Idaho, pp 537–540
- Bart G, Bakker K, Hellwig C, Kihara C, Ozawa T, Wallin H, Shigetome Y (2007) FUJI, an initial sintering comparison test for pelletized-, sphere-pac and vipac-fast breeder reactor mixed oxide fuel. *J Nucl Sci Technol* 44:329
- Bart G, Botta FB, Roth CW, Ledergerber G, Mason RE, Stratton RW (2008) AC-3-irradiation test of sphere-pac and pellet (U,Pu)C fuel in the US fast flux test facility. *J Nucl Mater* 376:47–59
- Barton CJ (1960) Solubility of plutonium trifluoride in fused-alkali fluoride-beryllium fluoride mixtures. *J Phys Chem* 64:306–309

- Belin RC, Valenza PJ, Raison PE, Tillard M (2008) Synthesis and rietveld structure refinement of americium pyrochlore $\text{Am}_2\text{Zr}_2\text{O}_7$. *J Alloys Compd* 448:321–324
- Beneš O, Konings RJM (2009) Thermodynamic evaluation of the (LiF + NaF + BeF₂ + PuF₃) system: An actinide burner fuel. *J Chem Thermodyn* 41:1086–1095
- Boyer L, Carpena J, Lacout JL (1997) Synthesis of phosphate-silicate apatites at atmospheric pressure. *Solid State Ion* 95:121–129
- Breton L, Masson M, Garces E, Desjardins S, Fontaine B, Lacroix B, Martella T, Loubet L, Ohta H, Yokoo T, Ougier M, Glatz JP (2007) METAPHIX-1 non destructive post irradiation examinations in the irradiated elements cell at Phénix. In: Proceedings of the Global 2007, Boise, Idaho, p 1333–1340
- Burkes DE, Fielding RS, Porter DL, Crawford DC, Meyer MK (2009) A US perspective on fast reactor fuel fabrication technology and experience part I: metal fuels and assembly design. *J Nucl Mater* 389:458–469
- Bychkov AV, Skiba OV, Mayorshin AA, Kormilitxyn M, Shishalov OV, Zhemkov I, Kisly V, Babikov LG (2002) Burning of minor actinides in fuel cycle of the fast reactor : DOVITA Programme – Results of the 10 Year Activities. In: Proceedings of the actinide and fission product partitioning and transmutation, 7th international exchange meeting, Jeju, Republic of Korea
- Caravaca C, de Córdoba G, Tomás MJ, Rosado M (2007) Electrochemical behaviour of gadolinium ion in molten LiCl–KCl eutectic. *J Nucl Mater* 360:25–31
- Carbajo JJ, Yoder GL, Popov SG, Ivanov VK (2001) A review of the thermophysical properties of MOX and UO₂ fuels. *J Nucl Mater* 299:181–198
- Carbol P, Cobos-Sabate J, Glatz JP, Ronchi C, Rondinella VV, Wegen DH, Wiss T, Loida A, Metz V, Kienzler B, Spahiu K, Grambow B, Quinones J, Martinez-Esparza A (2005) The effect of dissolved hydrogen on the dissolution of 233U doped UO₂(s), high burnup spent fuel and MOX fuel. Technical report SKB TR-05-09, SKB
- Carbol P, Fors P, Van Winckel S, Spahiu K (2009) Corrosion of irradiated MOX fuel in presence of dissolved H₂. *J Nucl Mater* 392:45–54
- Carmack J, Porter DL, Chang YI, Hayes SL, Meyer MK, Burkes DE, Lee CB, Mizuno T, Delage F, Somers J (2009) Metallic fuels for advanced reactors. *J Nucl Mater* 392:139–150
- Cassayre L, Malmbeck R, Masset P, Rebizant J, Serp J, Soucek P, Glatz J-P (2006) Investigation of electrorefining of metallic alloy fuel onto solid Al cathodes. *J Nucl Mater* 360: 49–57
- Caurant D, Majerus O, Loiseau P, Bardez I, Baffier N, Dussossoy JL (2006) Crystallization of neodymium-rich phases in silicate glasses developed for nuclear waste immobilization. *J Nucl Mater* 354:143–162
- CEA (2004) Les déchets radioactifs à haute activité et à vie longue/Recherches et résultats. Rapport CEA/DEN/DDIN/2004-642
- Chapelet-Arab B, Grandjean S, Nowogrocki G, Abraham F (2006) Synthesis of new mixed actinides as precursors of actinide oxide solid solutions. In: Proceedings of the Pu futures conference, Montrey, California
- Chauvin N, Konings RJM, Matzke HJ (1999) Optimisation of inert matrix fuel concepts for americium transmutation. *J Nucl Mater* 274: 105–111
- Chikalla TD, Eyring L (1967) Dissociation pressures and partial thermodynamic quantities for americium oxides. *J Inorg Nucl Chem* 29:2281–2293
- Conocar O, Douyere N, Glatz J-P, Lacquement J, Malmbeck R, Serp J (2006) Promising pyrochemical actinide/lanthanide separation processes using aluminium. *Nucl Sci Eng* 153: 253–261
- Crawford D, Porter DL, Hayes SL, Meyer MK, Petti DL, Pasamehmetoglu K (2007a) An approach to fuel development and qualification. *J Nucl Mater* 371:232–242
- Crawford D, Porter DL, Hayes SL (2007b) Fuels for sodium-cooled fast reactors: US perspective. *J Nucl Mater* 371:202–231
- Croixmarie Y, Abonneau E, Fernández A, Konings RJM, Desmoulière F, Donnet L (2003) Fabrication of transmutation fuels and targets: the ECRIX and CAMIX-COCHIX experience. *J Nucl Mater* 320:11–17
- Cui D, Ranebo Y, Low J, Rondinella VV, Pan J, Spahiu K (2009a) Immobilization of radionuclides on iron canister material at simulated near-field conditions. In: Hyatt NC, Pickett DA, Rebak RB (eds) Material research society symposium proceedings: scientific basis for nuclear waste management XXXII, Vol 1124, Boston, pp 111–116
- Cui D, Low J, Rondinella VV, Spahiu K (2009b) Hydrogen catalytic effects of nanostructured alloy particles in spent fuel on radionuclide immobilization. *Appl Cat B: Environ* 94: 173–178
- Drain F, Gillet B, Bertolotti G (1999) Oxalate process: the unique way for Plutonium conversion. In: Proceedings of the Global 1999, Jackson Hole, Wyoming

- Drew M, Hudson MJ, Iveson PB, Russell ML, Madic C (1998) Theoretical and experimental structural studies of the extraction of actinides and lanthanides by tridentate nitrogen ligands containing 1,2,4-triazines or 1,2,4-triazoles. In: Proceedings of the 5th OECD/NEA information exchange meeting on actinide and fission product partitioning and transmutation, SCK-CEN, Mol, Belgium, pp 487–489
- Drew MG, Guillaneux D, Hudson MJ, Iveson PB, Russell ML, Madic C (2001) Lanthanide(III) complexes of a highly efficient actinide(III) extracting agent - 2,6-bis(5,6-dipropyl-1,2,4-triazin-3-yl)pyridine. *Inorg Chem Commun* 4:12–15
- Eckhardt RC (2000) Yucca Mountain: look in ten thousand years into the future. *Los Alamos Science* 26:464–489
- Edelstein NM, Fuger J, Morss LR (2006) Summary and comparison of the actinide elements. In: Edelstein NM, Fuger J, Katz JJ, Morss LR (eds) *The chemistry of the actinide and transactinide elements*. Springer, Netherlands
- Ewing RC, Weber WJ, Lian J (2004) Nuclear waste disposal-pyrochlore ($A_2B_2O_7$): nuclear waste form for the immobilization of plutonium and “minor” actinides. *J Appl Phys* 95:5949–5971
- Eyal Y (1997) A radiation annealing model for maintenance of crystallinity in self-damaged actinide dioxides. In: Baker R, Slate S, Benda G (eds) *Radioactive waste management and environmental remediation*. American Society of Mechanical Engineering, New York, pp 303–307
- Fernandez A, Haas D, Konings RJM, Somers J (2002) Transmutation of actinides. *J Am Ceram Soc* 85:694–696
- Fernandez A, Haas D, Hiernaut JP, Konings RJM, Nastren C, Ottmar H, Staicu D, Somers J (2006) Overview of ITU work on inert matrix fuels. In: Proceedings of the 9th international information exchange meeting, Nimes, France, p 99
- Ganguly C (1988) Advanced methods for fabrication of PHWR and LMFBR fuels. BARC Report 1421
- Ganguly C, Hegde PV (1997) Sol-Gel microsphere pelletisation process for fabrication of (U,Pu) O_2 , (U,Pu)C and (U,Pu)N fuel pellets for the prototype fast breeder reactor in India. *J Sol-Gel Sci Technol* 9:285–294
- Geist A, Hill C, Modolo G, Foreman MRSJ, Gompper K, Weigl M, Hudson MJ (2006) 6,6'-Bis(5,5,8,8-tetramethyl-5,6,7,8-tetrahydrobenzo[1,2,4]triazin-3-yl) [2,2']bipyridine, an effective extracting agent for the separation of americium(III) and curium(III) from the lanthanides. *Solv Extr Ion Exch* 24(4):463–483
- Georgenthum V, Brillaud J, Chauvin N, Pelletier M, Planck D (2001) Experimental study and modelling of the thermoelastic behaviour of composite fuel in reactors - emphasis on spinel based composites. *Prog Nucl Energy* 38:317–320
- Glatz J-P, Song C, He X, Bokelund H, Koch L (1994) Partitioning of actinides from HAW in a continuous process by centrifugal extractors. In: Proceedings of the special symposium on emerging technologies in hazardous waste management, Atlanta, Georgia
- Gombert D II, Carter J, Cozzi A, Jones R, Matthern G, Nutt M, Priebe S, Sorenson K (2008) Global nuclear energy partnership integrated waste management strategy. GNEP-WAST-AI-RT-2008-000214, US-DOE
- Gompper K, Geist A, Modolo G, Denecke M, Panak PJ, Weigle M, Fanghänel Th (1995) R&D on partitioning at the German research centers Karlsruhe and Juelich. In: Proceedings of the Global 2005, Paper no. 059, Tsukuba, Japan
- Grahmann U, Tillessen U, Zimmer E (1975) Technical concept for the refabrication of ^{233}U . In: Proceedings of the German atomforum, Nürnberg, Germany, p387
- Grandjean S, Robisson A-C, Dauby J, Picart S, Lecomte M, Masson M, Brossard P (2005) Co-conversion of actinides in the frame of generation IV back-end fuel cycle: first results obtained in the CEA-ATALANTE facility. In: Proceedings of the MS7 – 7th international symposium on molten salts chemistry and technology, Toulouse, France
- Grandjean S, Chapelet-Arab B, Lemonnier S, Robisson A-C, Vigier N (2006) Innovative synthesis methods of mixed actinide compounds: control of the composition homogeneity at a molecular or nanometric scale. In: Sarrao JL, Schwartz AJ, Antonio MR, Burns PC, Haire RG, Nitsche H (eds) *Material research society symposium proceedings: actinides 2005 – basic science, applications and technology*, Vol 893-JJ08-03.1. Warrendale
- Grandjean S, Arab-Chapelet B, Robisson A-C, Picart S, Dancausse JP, Baron P, Brossard P, Warin D (2007) Synthesis of mixed actinide compounds by hydrometallurgical co-conversion methods. In: Proceedings of the Global 2007, Boise, Idaho
- Gras J-M, Quang RD, Masson H, Lieven T, Ferry C, Poinssot C, Debes M, Delbecq J-M (2007) Perspectives on the closed fuel cycle – Implications for high-level waste matrices. *J Nucl Mater* 362:383–394
- Grouiller JP, Pillon S, de Saint Jean C, Varaine F, Leyval L, Vambenepe G, Carlier B (2003) Minor

- actinides transmutation scenario studies with PWRs, FRs and moderated targets. *J Nucl Mater* 320:163–169
- Guilbaud P, Dognon JP (2000) Molecular dynamics simulations of terpyridine, BTP, and their complexes with La³⁺, Eu³⁺ and Lu³⁺. In: Proceedings of the international conference on scientific research on the back-end of the fuel cycle for the 21st century, Atalante 2000, P3-05, Avignon, France
- Harder BR, Read J, Sowden RG (1965) The reduction and sintering of hyperstoichiometric carbides in hydrogen. *J Nucl Mater* 17:203–214
- Hellwig Ch, Pouchon M, Restani E, Ingold F, Bart G (2005) Fabrication and microstructure characterization of inert matrix fuel based on yttria stabilized zirconia. *J Nucl Mater* 340: 163–170
- Hellwig Ch, Streit M, Blair P, Tverberg T, Klaassen FC, Schram RPC, Vettraiño F, Yamashita T (2006) Inert matrix fuel behaviour in test irradiations. *J Nucl Mater* 352:291–299
- Herrmann S, Li S, Simpson M (2007) Electrolytic reduction of spent light water reactor fuel – bench-scale experiment results. *J Nucl Sci Technol* 44(3):361–367
- Hill C, Hérés X, Calor J-N, Guillaneux D, Mauborgne B, Rat B, Rivalier P, Baron P (1999) Trivalent actinides/lanthanides separation using bis-triazinyl-pyridines. In: Proceedings of the Global 1999, Jackson Hole, Wyoming
- Hofman GL, Walters LC (1993) Metallic fast reactor fuels. In: Cahn RW, Haasen P, Kramer EJ (eds) *Nuclear materials, part I, Materials Science and Technology* Vol. 10A, VCH, New York p. 23
- Hofman GL, Walters L, Bauer TH (1997) Metallic fast reactor fuels. *Prog Nucl Energy* 31:83–110
- Holley CE, Rand MH, Storms EK (1984) The chemical thermodynamics of actinide elements and compounds. In: International atomic energy agency the actinide carbides, STI/PUB/424/6, Vienna
- Horspool JM, Rose NF, Finlayson MB (1967) Fabrication of uranium-plutonium monocarbide ceramics. *Proc Br Ceram Soc* 7:23–40
- Iizuka M, Kinoshita K, Koyama T (2005) Modeling of anodic dissolution of U-Pu-Zr ternary alloy in the molten LiCl-KCl electrolyte. *J Phys Chem Solids* 66:427–432
- Iizuka M, Sakamura Y, Inoue T (2006) Electrochemical reduction of (U–40Pu–5Np)O₂ in molten LiCl electrolyte. *J Nucl Mater* 359:102–113
- Ingold F, Ledergerber G (1994) Preparation of transuranium elements fuel and target materials for the transmutation of actinides by gel co-conversion, PSI Annual Report
- Jaecki P, Pillon S, Warin D, Hayes SL, Kennedy R, Pasamehmetoglu HO, Voit SL, Hass D, Fernandez A, Arai Y (2005) Update on the FUTURIX-FTA experiment in Phénix. In: Proceedings of the Global 2005, Tsukuba, Japan, 13 Oct.
- Johnson LH, Poinssot C, Ferry C, Lovera P, Poulesquen A, Miserque F, Corbel C, cavendon JM, Adriambololona Z, Wegen D, Carbol P, Glatz J-P, Cobos-Sabate J, Serrano D, Rondinella VV, Wiss T, Grambow B, Spahiu K, Kelm M, Metz V, Loida A, Kienzler B, Lundstrom T, Christensen H, Jonsson M, de Pablo J, Rovira M, Clarens F, Casas I, Martinez-Esparza A, Gago J, Bruno J, Cera E, Merino J, Gonzalez de la Huebra A, Iglesias E, Quinones J, Cachoir C, Lemmens K, Mayer G, Jegou C (2005) Spent fuel evolution under disposal conditions – synthesis of results from the EU spent fuel stability (SFS) project. Technical Report 04-09, Nagra
- Jorion F, Maillard C, Martin JC, Donnet L, Drin N (2007) The FUTURIX-FTA experiment in Phénix: status of the oxide fuel fabrication. In: Proceedings of the Global 2007, Boise, Idaho, p 1353
- Kasemeyer U, Hellwig Ch, Lee Y-W, Ledergerber G, Sohn DS, Gates GA, Wiesenack W (2001) Irradiation test of inert-matrix fuel in comparison to uranium plutonium mixed oxide fuel at the Halden reactor. *Prog Nucl Energy* 38: 309–312
- Kato T, Inoue T, Iwai T, Arai Y (2006) Separation behaviors of actinides from rare-earths in molten salt electrorefining using saturated liquid cadmium cathode. *J Nucl Mater* 357:105–114
- Keiser D Jr, Kennedy JR, Hilton BA, Hayes SL (2008) The development of metallic nuclear fuels for transmutation applications: materials challenges. *J Miner Metals Mater* 60:29–32
- Kittel JH, Frost BRT, Mustelier JP, Bagley KQ, Crittenden GC, Van Dievoet JJ (1993) History of fast reactor fuel development. *Nucl Mater* 204:1–13
- Kleykamp H (1999) Selection of materials as diluents for burning of plutonium fuels in nuclear reactors. *J Nucl Mater* 275:1–11
- Kolarik Z, Müllich U, Gassner F (1999) Selective extraction of Am(III) over Eu(III) by 2,6-ditriazolyl- and 2,6-ditriazinylpyridines. *Solv Extr Ion Exch* 17(1):23–32
- Koma Y, Watanabe M, Nemoto S, Tanaka Y (1998a) Trivalent f-element intra-group separation by solvent extraction with CMPO-complexant system. *J Nucl Sci Technol* 35:130–136
- Koma Y, Watanabe M, Nemoto S, Tanaka Y (1998b) A counter current experiment for the separation of trivalent actinides and lanthanides by the setfics process. *Solv Extr Ion Exch* 16(6):1357–1367

- Konings RJM, Haas D (2002) Fuels and targets for transmutation. *C R Phys* 3:1013–1022
- Konings RJM, Conrad R, Dassel G, Pijlgroms B, Somers J, Toscano E (2000) The EFTTRA-T4 experiment on americium transmutation. *J Nucl Mater* 282:159–170
- Konings RJM, Malmbeck R, Serp, J (2002) Evaluation of thermochemical and electrochemical data for the pyrochemical partitioning process. *J Nucl Sci Technol*, (Suppl 2), 906–909
- Konings RJM, Morss LR, Fuger J (2006) Thermodynamic properties of actinides. In: Edelstein NM, Fuger J, Katz JJ, Morss LR (eds) *The chemistry of the actinide and transactinide elements*. Springer, Netherlands, pp 2113–2224
- Kurata M (1999) Thermodynamic assessment of the Pu-U, Pu-Zr, and Pu-U-Zr systems. *Calphad* 23:305–337
- Kurata M, Inoue T, Serp J, Ougier M, Glatz J-P (2004) Electro-chemical reduction of MOX in LiCl. *J Nucl Mater* 328:97–102
- Kurata M, Sasahara A, Inoue T, Betti M, Babelot JF, Spirlet JC, Koch L (1997) CRIEPI: fabrication of U-Pu-Zr metallic fuel containing minor actinides. In: *Proceedings of the Global 1997*, Yokohama, Japan, p 1384
- Lacquement J, Bourg S, Boussier H, Conocar O, Laplace A, Lecomte M, Boullis B, Duhamet J, Grandjean A, Brossard P, Warin D (2005) Progress of the R&D program on pyrochemistry at CEA. In: *Proceedings of the Global 2005*, Paper no. 153, Tsukuba, Japan
- Laidler JJ, Battles JE, Miller WE, Ackerman JP, Carls EL (1997) Development of pyroprocessing technology. *Prog Nucl Energy* 31:131–140
- Latimer TW, Chidester KM, Stratton RW, Lederberger G, Ingold F (1992) Design and fuel fabrication process for the AC-3 mixed carbide irradiation test. *Trans Am Nucl Soc* 66: 182–186
- Lederberger G, Adler HP, Ingold F, Stratton RW (1986) Experience in preparing nuclear fuel by the gelation method. In: *ENC'86 Geneva*, Transactions, vol 4, p 225
- Lian J, Chen J, Wang LM, Ewing RC, Farmer JM, Boatner LA, Helean KB (2003) Radiation-induced amorphization of rare-earth titanate pyrochlores. *Phys Rev Condens Matter Mater Phys B* 68:134107
- Louwrier KP, Richter K, Kramer G, Lebrun M (1976) Preparation of a highly reactive plutonium dioxide powder for plutonium-uranium-carbide and nitride fuel. *J Nucl Mater* 61:219–220
- Lutique S, Konings RJM, Rondinella VV, Somers J, Staicu D, Wiss T (2003) Zirconate pyrochlore as a transmutation target: thermal behaviour and radiation resistance against fission fragment impact. *J Nucl Mater* 319:59–64
- MacClean H, Hayes S (2007) Irradiation of metallic and oxide fuels for actinide transmutation in the ATR. In: *Proceedings of the Global 2007*, Boise, Idaho, p 1341
- Madic C, Hudson MJ (2004) European EUROPART integrated project on actinide partitioning. In: *Proceedings of the OECD-NEA: 8th IEM on actinide and fission product partitioning and transmutation*, Las Vegas, Nevada
- Madic C, Hudson MJ, Liljenzin JO, Glatz J-P, Nannicini R, Facchini A, Kolarik Z, Odoj R (2000) New partitioning techniques for minor actinides. European report, EUR 19149
- Madic C, Lecomte M, Testard F, Hudson MJ, Liljenzin JO, Sätmark B, Ferrano M, Facchini A, Geist A, Modolo G, Espartero AG, De Mendoza J (2001) "PARTNEW" A European research program (2000–2002) for partitioning of minor actinides from high level liquid wastes. In: *Proceedings of the Global 2001*, Paris, France
- Madic C, Lecomte M, Baron P, Boullis B (2002) Separation of long-lived radionuclides from high active nuclear waste. *C R Phys* 3:797–811
- Madic C, Testard F, Hudson MJ, Liljenzin JO, Christiansen B, Ferrando M, Facchini A, Geist A, Modolo G, Gonzales-Espartero GA, De Mendoza J (2004) PARTNEW – new solvent extraction processes for minor actinides-final report. CEA-report 6066, France
- Magill J (2003) Nuclides.net – an integrated environment for computations on radionuclides and their radiation. Springer, Berlin
- Magill J, Berthou V, Haas D, Galy J, Schenkel R, Wiese H-W, Heusener G, Tommasi J, Youinou G (2003) Impact limits of partitioning and transmutation scenarios on the radiotoxicity of actinides in radioactive waste. *Nucl Energy* 42(5):263–277
- Mailen JC, Smith FJ, Ferris LM (1971) Solubility of PuF₃ in molten 2 LiF-BeF₂. *J Chem Eng Data* 16:68–69
- Masset P, Bottomley D, Koning RJM, Malmbeck R, Rodrigues A, Serp J, Glatz J-P (2005a) Electrochemistry of uranium in molten LiCl-KCl electric. *J Electrochem Soc* 152(6):1109–1115
- Masset P, Konings RJM, Malmbeck R, Serp J, Glatz J-P (2005b) Thermochemical properties of lanthanides (Ln = La, Nd) and actinides (An = U, Np, Pu, Am) in the molten LiCl-KCl eutectic. *J Nucl Mater* 344:173–179
- Matzke HJ (1982) Radiation damage in crystalline insulators, oxides and ceramic nuclear fuels. *Radiat Eff* 64:3–33
- Matzke HJ (1986) *Science of advanced LMFBR fuels*. Elsevier, North Holland

- Maugeri E, Wiss T, Hiernaut J-P, Desai K, Thiriet C, Rondinella VV, Colle J-Y, Konings RJM (2009) Helium solubility and behaviour in uranium dioxide. *J Nucl Mater* 385:461–466
- Mayorshin AA, Skibbe OV, Tsykanov VA, Kisly A (2000) Russian experience in using UPUO₂ VIBROPAC fuel pins in fast reactors. In: Proceedings of the 8th international conference on the physics of reactor nuclear power (ICONE), Baltimore
- Mayorshin AA, Skibbe OV, Bychkov AV, Kisly A, Shishalov OV, Kormilitsyn MV, Golovchenko YM (2005) RIAR experience in the field of vibropac fuel use in fast reactors. In: Proceedings of the Global 2005 advanced nuclear fuel cycle and systems, Tsukuba, Japan
- McCarthy GJ (1977) High level waste ceramics: materials considerations, process simulation and product characterization. *Nucl Technol* 32:92–105
- McPheeters C, Pierce RD, Mulcahey TP (1997) Application of the pyrochemical process to recycle of actinides from LWR spent fuel. *Prog Nucl Energy* 31:175–186
- Meyer MK, Hayes SL, Carmack WJ, Tsai H (2009) The EBR-II X501 minor actinide burning experiment. *J Nucl Mater* 392:176–183
- Miguirditchian M, Chareyre L, Hérès X, Hill C, Baron P, Masson M (2007) GANEX: adaptation of the DIAMEX-SANEX process for the group actinide separation. In: Proceedings of the Global 2007, Paper no. 81, Boise, Idaho
- Minato K, Akabori M, Takano M, Arai Y, Nakajima K, Itoh A, Ogawa T (2003) Fabrication of nitride fuels for transmutation of minor actinides. *J Nucl Mater* 320:18–24
- Minato K, Takano M, Otobe H, Nishi T, Akabori M, Arai Y (2009) Thermochemical and thermophysical properties of minor actinide compounds. *J Nucl Mater* 389:23–28
- Modolo G, Odoj R (1999) Synergistic selective extraction of actinides(III) over lanthanides from nitric acid using new aromatic diorganylthiophosphinic acids and neutral organophosphorus compounds. *Solv Extr Ion Exch* 17(1): 33–53
- Morita Y, Glatz J-P, Kubota M, Koch L (1996) Actinide partitioning from HLW in a continuous DIDPA extraction process by means of centrifugal extractors. *Solv Extr Ion Exch* 14(3): 385–400
- Morita Y, Yamaguchi I, Fujiwara T, Koizumi H, Tachimori S (2004) A demonstration test of 4-group partitioning process with real high-level liquid waste. In: Proceedings Atalante 2004, Nice, France, 21–25 June, pp 3–7
- Mukaiyama T, Takano H, Ogawa T, Takizuka T, Mizumoto M (2002) Partitioning and transmutation studies at JAERI both under OMEGA program and high-intensity proton accelerator project. *Prog Nucl Energy* 40(3):403–413
- Muller I, Weber WJ, Vance ER, Wicks G, Karraker D (2001) Glass ceramics and composites. In: Hoffman DC (ed) *Advances in plutonium chemistry 1967–2000*, Chap. 10. American Nuclear Society, La Grange, pp 260–297
- Muromura T (1982) Carbothermic synthesis of high purity plutonium nitride from plutonium oxide. *J Nucl Sci Technol* 19:36
- Nakajima K, Arai Y, Suzuki Y (1997) Vaporization behavior of neptunium mononitride. *J Nucl Mater* 247:33–36
- Nash KL (1993) Review of the basic chemistry and recent developments in trivalent f-elements separations. *Solv Extr Ion Exch* 11(4):729–768
- NEA (OECD Nuclear Energy Agency) (2008) *Nuclear Energy Outlook 2008*. OECD Publishing, Issy-les-Moulineaux, France
- Neck V, Altmaier M, Fanghänel Th (2007) Solubility of plutonium hydroxides/hydrous oxides under reducing conditions and in the presence of oxygen. *C R Chim* 10:959–977
- Neeft EAC, Bakker K, Schram RPC, Conrad R, Konings RJM (2003) The EFTTRA-T3 irradiation experiment on inert matrix fuels. *J Nucl Mater* 320:106–116
- Nigond L, Musikas C, Cuillerdier C (1994) Extraction by N,N,N',N'-tetraalkyl-2 alkyl propane-1,3 diamides. I. H₂O, HNO₃ and HClO₄. *Solv Extr Ion Exch* 12(2):261–296
- Noe M, Fuger J (1974) Self-radiation effects on the lattice parameter of ²³⁸PuO₂. *Inorg Nucl Chem Lett* 10:7–19
- Ogawa T, Ohmichi T, Maeda A, Arai Y, Suzuki Y (1995) Vaporization behaviour of (Pu,Am)N. *J Alloys Compd* 224:55–59
- Ohta H, Inoue T, Sakamura Y, Kinoshita K. (2005), Pyroprocessing of light water reactor spent fuels based on an electrochemical reduction technology. *Nuclear Technology* 150(2):153–161
- Ohta H, Yokoo T, Inoue T, Ougier M, Glatz J-P, Fontaine B, Brunon E, Poncet L, Sudreau F, Warin D (2007a) Irradiation test of fast reactor metal fuel containing minor actinides in Phénix reactor. In: Proceedings of the Global 2007, Paper 043, Boise, Idaho
- Ohta H, Yokoo T, Ogata T, Inoue T, Ougier M, Glatz JP, Fontaine B, Breton L (2007b) Irradiation experiment on fast reactor metal fuels containing minor actinides up to 7 at. % burnup. In: Proceedings of the Global 2007, Boise, Idaho, pp 1346–1352

- Ohta H, Ogata T, Papaioannou D, Kurata M, Koyama T, Rondinella VV and Glatz JP (2009) Development of minor actinide-containing metal fuels. Proceedings of the International Conference Fast Reactors and Related Fuel Cycles: Challenges and Opportunities FR09, 7-11 Dec. 2009, Kyoto, Japan, paper 1222
- Okamoto Y, Maeda A, Suzuki Y (1993) Self-irradiation damage in PuN. *J Nucl Mater* 206:94-96
- Otobe H, Akabori M, Minato K (2008) Oxygen potential measurement of americium oxide by electromotive force method. *J Am Ceram Soc* 91(6):1981-1985
- Picard E, Noirot J, Moss RL, Plitz H, Richter K, Rouault J (2000) First in-pile experimental results of high-plutonium-content oxide fuel for plutonium burning in fast reactors. *J Nucl Technol* 129:1-12
- Prunier C, Bardelle P, Pages JP, Richter K, Stratton RW, Ledergerber G (1991) European collaboration on mixed nitride fuel. In: Proceedings of the international conference of fast reactors and related fuels, Kyoto, Japan, p 15.9-1
- Prunier C, Warin D, Stratton R, Ledergerber G (1992) Flow sheet, fabrication and properties comparison of nitride fuel obtained by powder metallurgy and gelation processes. *Trans Am Nucl Soc* 66:187
- Prunier C, Warin D, Bauer M, Ledergerber G, Ingold F, Stratton RW, Adler HP (1993) Application of gel co conversion for transuranium elements (Pu, Np, Am) fuel and target preparation. In: Proceedings of the Global 1993, Washington, p 1273
- Prunier C, Boussard F, Koch L, Coquerelle M (1997) Some specific aspects of homogeneous americium- and neptunium-based fuels transmutation through the outcomes of the superfast experiment in Phénix fast reactor. *J Nucl Technol* 119:141-148
- Quiñones J, Iglesias E, Rodriguez N, Nieto J (2008) Influence of the specific surface area on spent nuclear fuel dissolution rates. In: MRS symposium proceedings 1124, Paper no. 1124-Q02-02, Boston; Grambow B (2006) *Elements* 2: 357-364
- Richter K (1987) Direct pressing: a new method of fabricating MX fuels. In: Vincenzini P (ed) *High tech ceramics*. Elsevier, Amsterdam
- Richter K, Coquerelle M, Gabolde J, Werner P (1974) Preparation of high performance non oxide fuels: first results of fast flux experiments DN1. In: IAEA, fuel and fuel elements for fast reactors, vol 1, Vienna, p 71
- Richter K, Bartscher W, Benedict U, Gueugnon JF, Kutter H, Sari C, Schmidt HE (1978) Report I on swelling in MX type fuels 1973-76. Report EUR 6154 EN
- Richter K, Kramer G, Gueugnon JF (1979) Plutonium depletion by vapour phase transport in carbothermic reduction processes. *Trans Am Nucl Soc* 31:213
- Richter K, Gueugnon J, Kramer G, Sari C, Werner P (1985) Direct pressing: a new method of fabricating MX fuel pellets. *J Nucl Technol* 70(3):401-407
- Richter K, Fernandez A, Somers J (1997) Infiltration of highly radioactive materials: a novel approach to the fabrication of targets for the transmutation and incineration of actinides. *J Nucl Mater* 249:121-127
- Ringwood E, Kesson SE, Ware NG, Hibberson W, Major A (1979) Immobilisation of high level nuclear reactor wastes in SYNROC. *Nature* 278:219-223
- Rondinella VV, Matzke HJ, Cobos J, Wiss T (2000) Leaching behaviour of UO₂ containing a-emitting actinides. *Radiochim Acta* 88: 527-531
- Rondinella VV, Cobos J, Wiss T, Hiernaut J-P (2003) Studies on spent fuel alterations during storage and radiolysis effects on corrosion behaviour using alpha-doped UO₂. In: Proceedings of the ICEM 2003, Paper 4593, Oxford
- Rondinella VV, Cobos J, Wiss T (2004) Leaching behaviour of low activity alpha-doped UO₂. In: MRS symposium proceedings, San Francisco, April 13-16, vol 824, pp 167-173
- Rondinella VV, Cobos J, Wiss T, Staicu D (2005) Studies on spent fuel alterations during storage and effects on corrosion behaviour. In: Proceedings of the ICEM 2005, Paper 1275, Glasgow
- Rondinella VV, Wiss T, Hiernaut J-P (2007) Dose rate effects on the accumulation of radiation damage. In: Proceedings of the ICEM 2007, Paper no. 12755-8, Bruges, Belgium
- Sakamura Y, Kurata M, Inoue T (2006) Electrochemical reduction of UO₂ in molten Ca Cl₂ or LiCl. *J Electrochem Soc* 153:D31-D39
- Sakamura Y, Omori T, Inoue T (2008) Application of electrochemical reduction to produce metal fuel material from actinide oxides. *Nucl Technol* 162:169-178
- Salvatores M (1993) The SPIN program at CEA. In: Proceedings of the Global 1993, Seattle, p 548
- Schmidt HE, Sari C, Richter K, Gerontopoulos P (1986) The thermal conductivity of oxides of uranium, neptunium and americium at elevated temperatures. *J Less-Common Met* 121: 621-630

- Serp J, Konings RJM, Malmbeck R, Rebizant J, Schepler C, Glatz J-P (2004) Electrochemical behaviour of plutonium ion in LiCl - KCl eutectic melts. *J Electroanal Chem* 561:143-148
- Serrano-Purroy D, Baron P, Christiansen B, Malmbeck R, Sorel C, Glatz J-P (2005) Recovery of minor actinides from HLLW using the DIAMEX process. *Radiochim Acta* 93:351-355
- Sickafus E, Minervini L, Grimes RW, Valdez JA, Ishimura M, Li F, McClellan KJ, Hartmann T (2000) Radiation tolerance of complex oxides. *Science* 289:748-751
- Smith PK, Peterson DE (1970) High-temperature evaporation and thermodynamic properties of Cm_2O_3 . *J Chem Phys* 52:4963-4972
- Somers J, Fernandez A (2005) Fabrication routes for yttria-stabilized zirconia suitable for the production for minor actinide transmutation targets. *J Am Ceram Soc* 88:827-832
- Strachan DM, Scheele RD, Kozelisky AE, Sell RL (2003) Effects of self irradiation from ^{238}Pu on candidate ceramics for plutonium immobilization. PNNL-14232, Pacific Northwest National Laboratory, Richland, WA
- Suzuki Y, Arai Y, Okamoto Y, Ohmichi T (1994) Preparation of neptunium mononitride by carbothermic reduction. *J Nucl Sci Technol* 31:677-680
- Takanashi M, Homma S, Koga J, Matsumoto S (1998) Neptunium concentration profiles in the Purex process. *J Alloys Compd* 689:271-273
- Takano M, Itoh A, Akabori M, Ogawa T, Kuikawa S, Ogamoto H (1999) Synthesis of americium mononitride by carbothermic reduction. In: *Proceedings of the Global 1999*, Jackson Hole, Wyoming
- Takano M, Itoh A, Akabori M, Ogawa T, Numata M, Okamoto H (2001) Carbothermic synthesis of $(\text{Cm},\text{Pu})\text{N}$. *J Nucl Mater* 294:24-27
- Takano M, Itoh A, Akabori M, Minato K, Numata M (2003) Study of the stability of AmN and $(\text{ZrAm})\text{N}$. In: *Proceedings of the Global 2003*, New Orleans, p 2285
- Tanaka K, Maeda K, Katsuyama K, Inoue M, Iwai T, Arai Y (2004) Fission gas release and swelling in uranium-plutonium mixed nitride fuels. *J Nucl Mater* 327:77-87
- Tanaka K, Osaka M, Sato I, Miwa S, Koyama S, Ishi Y, Hirotsawa T, Obayashi H, Yoshimochi H (2007) Research and development of americium containing mixed oxide fuel for fast reactors. In: *Proceedings of the Global 2007*, Boise, Idaho p 897
- Tanaka K, Miwa S, Sato I, Hirotsawa T, Obayashi H, Koyama S, Yoshimochi H, Tanaka K (2009) Microstructure and elemental distribution of americium-containing uranium plutonium mixed oxide fuel under a short-term irradiation test in a fast reactor. *J Nucl Mater* 385:407-412
- Vance E (2007) Development of ceramic waste forms for high-level nuclear waste over the last 30 years. In: Dunn D, Poinssot C, Begg B (eds) *MRS symposium proceedings 985*, pp 135-140, Boston, USA, Nov. 27-Dec. 1
- Vollath D (1977) Vorgänge bei der karbothermischen synthese von uran-plutoniumkarbid. *J Nucl Mater* 64:27-36
- Wald JW, Weber WJ (1984) Effects of self-radiation damage in Cm-doped $\text{Gd}_2\text{Ti}_2\text{O}_7$ and $\text{CaTrTi}_2\text{O}_7$. In: Wicks GG, Ross WA (eds) *Advances in ceramics*, vol 8. American Ceramic Society, Columbus, Ohio, pp 71-75
- Walker CT, Nicolau G (1995) Transmutation of neptunium and americium in a fast neutron flux: EPMA results and KORIGEN predictions for the superfast fuels. *J Nucl Mater* 218:129-138
- Warin D, Conrad R, Haas D, Heusener G, Martin P, Konings RJM, Schram RPC, Vambenepe G (2001) 10 YEARS EFTTRA: 1992-2001. In: *Proceedings of the Global 2001*, Paris, France
- Weber WJ (1981) Ingrowth of lattice defects in alpha irradiated UO_2 single crystals. *J Nucl Mater* 98:206-215
- Weber WJ, Ewing RC, Catlow CRA, Diaz de la Rubia T, Hobbs LW, Kinoshita C, Matzke HJ, Motta AT, Nastasi M, Salje EKH, Vance ER, Zinkle SJ (1998) Radiation effects in crystalline ceramics for the immobilization of high-level nuclear waste and plutonium. *J Mater Res* 13:1434-1484
- Weber WJ, Navrotsky A, Stefanovsky S, Vance ER, Vernaz E (2009) Materials science of high-level nuclear waste immobilization. *MRS Bull* 34:46-53
- Wiss T, Konings RJM, Walker CT, Thiele H (2003) Microstructure characterisation of irradiated Am-containing MgAl_2O_4 (EFTTRA-T4). *J Nucl Mater* 320:85-95
- Wiss T, Deschanel X, Hiernaut J-P, Roudil D, Peugeot S, Rondinella VV (2007) Helium release from plutonium and curium-doped zirconolite. *J Nucl Mater* 362: 431-437

27 Decommissioning of Nuclear Plants

Maurizio Cumo

University of Rome, Rome, Italy

maurizio.cumo@uniroma1.it

1	<i>Nuclear Plants Decommissioning Overview</i>	3005
1.1	Definition and Scope of Decommissioning	3005
1.2	Introduction to Some Decommissioning Challenges	3007
1.2.1	Organization and Management	3007
1.2.2	Safety-Related Issues	3008
1.2.3	Decommissioning Funding	3009
1.2.4	Waste Management	3010
1.3	Decommissioning Strategies	3010
1.3.1	Overview	3010
1.3.2	Issues Affecting the Choice of Decommissioning Strategy	3013
1.4	Decommissioning in the World	3015
2	<i>Decommissioning Organization and Management</i>	3026
2.1	Overview	3026
2.2	Issues Affecting Decommissioning Organization and Management	3027
2.2.1	Decommissioning Strategy	3027
2.2.2	Safety Issues	3028
2.2.3	Work Approaches	3028
2.2.4	Impact on Staffing	3029
2.3	Organization and Management in the Various Phases of Decommissioning	3030
2.3.1	The Planning Phase	3030
2.3.2	The Transition Phase	3031
2.3.3	The Active Phases of Decommissioning	3032
2.3.4	The Safe Enclosure Phase	3032
2.3.5	The Post-Dismantling Period	3034
2.3.6	Spent Fuel and Waste Storage	3034
2.4	Management for Active Phases of Decommissioning	3034
2.4.1	Overview	3034
2.4.2	The Decommissioning Management Team	3035
2.4.3	Change Management	3035
2.5	Decommissioning Planning and Licensing	3037
2.5.1	Overview	3037
2.5.2	Decommissioning Planning	3039
2.5.3	Stages of Planning	3039

2.5.4	Content of Decommissioning Plan	3040
2.5.5	Decommissioning Optimization	3041
2.5.6	Project Risk Management	3043
2.5.7	Regulatory Approval	3043
2.5.8	Work Packages and Procedure	3044
2.6	Role of Quality Assurance	3046
2.6.1	Overview	3046
2.6.2	Control of Modifications to the Plant	3046
2.6.3	Radiation Protection and Environmental Safety Control	3046
2.6.4	Control of Outside Contracted Services	3047
2.6.5	Surveillance and Inspections	3047
2.6.6	Information Management	3047
2.6.7	Safety Audits	3049
2.6.8	Management, Assessment and Reporting of Incidents and Events	3049
2.7	Responsibilities and Qualifications	3049
2.7.1	Licensee	3049
2.7.2	Decommissioning Project Manager (DPM)	3050
2.7.3	Technical Support	3051
2.7.4	Decommissioning Operations	3052
2.7.5	Administration Services	3053
2.7.6	Interfaces	3055
3	<i>Plant and Site Characterization</i>	3056
3.1	Initial Plant Characterization	3056
3.1.1	Radioactivity Sources	3056
3.1.2	The Concept and Extent of Characterization	3059
3.1.3	Structure Characterization	3060
3.1.4	System and Equipment Characterization	3061
3.2	Site Characterization	3062
3.2.1	Surface Soil Contamination	3062
3.2.2	The NRC Acceptance Criteria	3062
3.2.3	Subsurface Soil Contamination	3063
3.2.4	Surface Water Contamination	3063
3.2.5	Groundwater Contamination	3064
4	<i>Decontamination Techniques</i>	3064
4.1	Overview	3064
4.1.1	Objectives of Decontamination Techniques	3066
4.1.2	Selection of Decontamination Technologies	3068
4.1.3	Survey of Applied Decontamination Techniques	3069
4.2	Decontamination of Segmented Components	3071
4.2.1	Overview	3071
4.2.2	Chemical Decontamination	3073
4.2.3	Electrochemical Decontamination	3076
4.2.4	Mechanical Decontamination	3078
4.2.5	Decontamination by Melting	3081
4.2.6	Other Decontamination Techniques	3085
4.3	Decontamination of Building Surfaces	3085

4.3.1	Overview	3085
4.3.2	Basic Techniques	3086
4.3.3	Scarifying	3086
4.3.4	Guidelines	3089
4.4	Chemical Decontamination Techniques	3089
4.4.1	Overview	3089
4.4.2	Water/Steam	3090
4.4.3	Strong Mineral Acids	3091
4.4.4	Acid Solutions	3092
4.4.5	Organic/Weak Acids	3093
4.4.6	Alkaline Solutions	3095
4.4.7	Complexing Agents	3095
4.4.8	Oxidizing and Reducing (REDOX) Agents	3096
4.4.9	Organic Solvents	3101
4.4.10	Multiphase Treatment Processes	3101
4.4.11	Selection of Chemical Decontamination Processes	3104
4.5	Mechanical Decontamination Techniques	3105
4.5.1	Overview	3105
4.5.2	Water Flushing	3105
4.5.3	Dusting/Vacuuming/Wiping/Scrubbing	3105
4.5.4	Steam Cleaning	3108
4.5.5	CO ₂ Blasting	3108
4.5.6	Wet-Ice Blasting	3109
4.5.7	Hydroblasting	3110
4.5.8	Ultra-High-Pressure Water	3110
4.5.9	Shot Blasting	3111
4.5.10	Wet Abrasive Cleaning	3111
4.5.11	Grit Blasting	3112
4.5.12	Grinding	3113
4.5.13	Scarifiers	3113
4.5.14	Milling	3115
4.5.15	Drill and Spall	3116
4.5.16	Paving Breaker and Chipping Hammer	3116
4.5.17	Expansive Grout	3116
4.5.18	Asbestos Removal	3117
4.6	Other Decontamination Techniques	3117
4.6.1	Electropolishing	3118
4.6.2	Ultrasonic Cleaning	3120
4.6.3	Vibratory Finishing	3121
5	<i>Cutting and Dismantling Techniques</i>	3122
5.1	Overview	3122
5.2	Thermal Cutting Techniques	3122
5.2.1	Gas Processes	3123
5.2.2	Arc Processes	3127
5.2.3	Plasma-Arc Processes	3133
5.2.4	Laser Cutting	3136

5.2.5	Combined Cutting Processes	3136
5.3	Hydraulic Cutting Techniques	3138
5.3.1	High Pressure Water Jet Cutting	3140
5.3.2	Abrasive Water Jet Cutting	3140
5.4	Mechanical Dismantling Techniques	3141
5.4.1	Grinder	3141
5.4.2	Hacksaw and Guillotine Saw	3143
5.4.3	Shears	3144
5.4.4	Milling Cutters and Orbital Cutters	3144
5.4.5	Knurl Tube Cutter	3145
5.4.6	Diamond Saws and Cables	3146
5.5	Conclusions	3147
6	<i>Remote Control Techniques</i>	3148
6.1	Basis of Remote Operation	3148
6.1.1	Overview	3148
6.1.2	Safety Enhancement	3148
6.1.3	Cost Reduction	3148
6.1.4	Productivity Improvement	3154
6.1.5	Utilization of Facility Resources	3154
6.1.6	Accessibility	3154
6.1.7	Disadvantages of Remote Operation	3154
6.2	Remote Operation Technologies	3155
6.2.1	Overview	3155
6.2.2	Detection Equipment	3155
6.2.3	Segmenting and Demolishing Equipment	3156
6.2.4	Decontamination Equipment	3156
6.2.5	Material-Handling Equipment	3157
6.2.6	Sampling Equipment	3157
6.2.7	Hand-Held Equipment	3157
6.3	Remote-System Configurations	3157
6.3.1	Overview	3157
6.3.2	Control Stations	3158
6.3.3	Communication and Power Links	3159
6.3.4	Support Platforms	3159
6.3.5	Arms	3160
6.3.6	End Effectors and Tools	3161
6.4	Illustrative Experiences with Remote Applications	3162
6.4.1	Detection Equipment	3162
6.4.2	Sampling Equipment	3163
6.4.3	Hand-Held Equipment	3163
6.4.4	Miscellaneous Equipment	3163
7	<i>Spent-Fuel and Waste Management</i>	3164
7.1	Spent-Fuel Interim Storage	3164
7.1.1	Wet Interim Storage	3165
7.1.2	Dry Interim Storage	3167
7.2	Waste Management	3174

7.2.1	Overview	3174
7.2.2	Clearance Levels	3176
7.2.3	Waste-Management Strategy	3178
7.2.4	Waste-Management Arrangements	3179
7.2.5	Treatment and Conditioning of Liquid Wastes	3179
7.2.6	Treatment and Conditioning of Solid Wastes	3181
7.2.7	Treatment and Conditioning of Gaseous and Aerosol Wastes	3181
7.2.8	Packaging and Storing Technologies	3182
7.2.9	Waste Transport	3184
7.2.10	Waste Characterization and Measurement Techniques	3184
7.3	The Waste Management Facility (WMF)	3190
7.3.1	WMF Design Criteria	3190
7.3.2	Description of the Areas and the Equipment	3192
7.3.3	Staff Requirements	3193
8	<i>Safety, Health and Environmental Protection</i>	3194
8.1	Overview	3194
8.2	Safety Culture	3196
8.3	Safety Assessment	3196
8.3.1	Accident Analysis	3196
8.3.2	Human Factors and Organizational Considerations	3198
8.3.3	Emergency Planning	3200
8.4	Environmental Impact Assessment (EIA)	3200
8.4.1	Scoping	3202
8.4.2	Environmental Impact Evaluation	3203
8.4.3	EIA Regulations	3204
8.4.4	Consent Processes for Decommissioning in EU Member States	3205
8.4.5	Consultation and Public Participation	3205
8.4.6	Definition of Preferred Options	3206
8.4.7	Baseline Description	3207
8.4.8	Impact Assessment	3213
8.4.9	Mitigation Measures	3215
8.4.10	Environmental Surveillance Program	3217
9	<i>Decommissioning Cost Evaluation</i>	3218
9.1	Cost Evaluation Methodologies	3218
9.2	Account Presentation	3219
9.3	Responsibilities and Financing	3219
9.4	Standard Criteria for Cost Evaluation	3220
9.5	Cost Evaluations	3220
9.5.1	Overview	3220
9.5.2	Cost-Assessment Methods	3222
9.6	Cost Calculation Model Example	3222
9.6.1	Cost-Breakdown Structure	3223
9.6.2	Mass Analysis	3224
9.6.3	Calculation of Decommissioning Activities	3227
9.7	International Comparisons	3229
9.7.1	Overview	3229

9.7.2	Variations in Cost Estimates	3230
9.7.3	Cost Estimates in the USA	3232
9.7.4	Cost Estimates in Europe.....	3237
10	<i>International Organizations Roles</i>	3241
10.1	UNO-IAEA (United Nations Organization-International Atomic Energy Agency)	3241
10.2	OECD-NEA (Organization for Economic Cooperation and Development)	3243
10.3	EC (European Commission).....	3243
10.4	WANO (World Association of Nuclear Operators)	3244
10.5	WENRA (West European Nuclear Regulator Association)	3244
	<i>References</i>	3244

Abstract: Decommissioning a nuclear plant can be defined as the termination of operations and the withdrawal of the facility from service, followed by its transformation into an out-of-service state without radiological risks and, in some cases, its complete removal from the site. Decommissioning activities shall be carried out in a cost-effective manner assigning top priority to health and safety of the general public and the environment, as well as of the decommissioning workers. This chapter covers all aspects related to the closure of the operating life of nuclear plants and provides a description of all the activities and tools involved in both the decision-making and operative processes of decommissioning.

Nuclear plant decommissioning is a complex, long, and highly specialized activity. In some countries, therefore, it is even called “de-construction” because it is in many respects similar to the construction activity and, in addition, it deals with partly activated and contaminated structures. Activities to perform include technological tools, industrial safety, environmental impact minimization, licensing, safety analysis, structural analysis, etc. Other aspects are short- and long-term planning, calculation of cash flow and financing, waste disposal, and spent fuel strategy.

A lot of technical information is drawn from direct experience of nuclear operators. The widely used references are those from the OECD-NEA, UNO-IAEA, US-NRC, and the European Commission. They cover the results of working groups, special studies, comparisons of technologies, and recommendations.

1 Nuclear Plants Decommissioning Overview

1.1 Definition and Scope of Decommissioning

Decommissioning a nuclear power plant can be defined as the termination of operations and the withdrawal of the facility from service, followed by its transformation into an out-of-service state without radiological risks and, in some cases, its complete removal from the site. Decommissioning activities shall be carried out assigning top priority to health and safety of the general public and the environment, as well as of the decommissioning workers.

Decommissioning is also understood as the actions taken to allow the removal of all regulatory controls on a facility that used radioactive material. These actions include both technical and administrative ones that must be accomplished to show that the facility can be released for unrestricted use or otherwise reused.

They may just consist of performing some decontamination activities and a radiological survey to show that acceptable conditions have been met, or they may include dismantling a system or an entire building.

The operating lifetime of nuclear facilities is determined by economic and safety considerations. Nuclear power plants are normally designed for an operating lifetime of several decades. By appropriate refurbishment, replacement, or upgrading of some equipment, the life of a plant can now be extended to up to 60 or more years. In many cases, it is even very advantageous to extend the operating life of a Nuclear Power Plant (NPP) beyond the amortization period and the initial design life, into the so-called “life extension,” because electrical energy can be produced at a very low cost while matching the required levels of health and safety of the public and the environment. However, ultimately it becomes either technically or economically advantageous to dismantle the facility and, in some cases, to replace it with a new one.

The closure of the operating life of a nuclear installation and the decommissioning sequences should be planned at the design stage, when several design features can be adopted to facilitate dismantling. Also during plant operation several possibilities exist that may facilitate the decommissioning, e.g., better plant configuration control, system, and building radiological status record. In any case decommissioning planning shall start at least some years in advance of the plant closure. The decision of definitive plant closure may be related to:

- Termination of the design life of major components
- Excessive operating costs (e.g., compared with competing energy sources)

Although decommissioning normally occurs at the end of the operating lifetime of the plant, it may also be required for various other reasons:

- The conclusion of a research program that has achieved its goal
- Safety issues that cause an activity using radioactive material to be discontinued
- The initial technology using the radioactive material has become obsolete or uneconomical
- An accident or unplanned event requiring the final decommissioning to be performed
- Changes in government policy that make it unfeasible to continue the operating life

Challenges in the latter cases may be more severe as, in general, all the decommissioning funds might have not been accumulated because the work force had not been adequately planned for a soft phase out and because all preparation and planning activities had not been performed. In addition, especially in case of accidents, some special challenges may be present as, for example, in the cases of major severe accidents such as Chernobyl and Three Mile Island.

Some thousand nuclear facilities worldwide are estimated to require decommissioning over the coming decades. Of these, a thousand facilities are associated with the production of energy and fuel cycle. These include nuclear power plants, reprocessing plants, hot cells, interim storage facilities, enrichment plants, and uranium mill plants. There are approximately 400 other research reactors that require some form of decommissioning. When the number of commercial companies and universities that use radioactive materials is added, the number grows to several thousand. This figure does not include many of the civil and military support complexes associated with former sites for nuclear weapons production or military vessels, such as aircraft carriers and submarines powered by nuclear reactors.

In the context of decommissioning, nuclear installations can be classified as follows:

- Nuclear power plants for electricity production (or, in general, thermal energy production)
- Research, experimental, or isotope production reactors with various thermal powers
- Fuel fabrication plants
- Spent-fuel reprocessing plants
- Experimental laboratories related to the fuel cycle
- Hot cells for activities on activated materials, contaminated materials, or radioisotopes

Among the above mentioned installations, there are also other small installations in the nuclear and even in the nonnuclear field that treat or contain some radioactive materials and that, at the end of their operating life, require some precautions. However, this section does not cover these cases. The experience acquired so far in the first important works of decommissioning constitutes a precious support for designing future reactors.

1.2 Introduction to Some Decommissioning Challenges

1.2.1 Organization and Management

The decommissioning process must be carefully planned and implemented in a safe and economical manner. To set proper decommissioning conditions is a task that should start during the initial design of the facility by including features that facilitate the eventual dismantling and decontamination efforts. This might include, for example, proper material choice to minimize activation, placing hatches in concrete floors and walls to allow for the removal of large pieces of equipment using modular biological shielding or lining a process cell or other areas that might be contaminated during the life of the facility. Decommissioning preparation may continue during the entire life of the plant until conditions allow for the removal of regulatory controls.

Normally, decommissioning operations begin at sites where the operating staff is present. The first strategic choices to accomplish the decommissioning of a facility, which have a substantial effect on the project organization, are the following:

- The first approach is for the licensee to perform the decommissioning with in-house resources supplemented by specialist contractors as needed.
- The second approach is for the licensee to contract with an experienced outside organization to perform the decommissioning activities and then provide general oversight and support services.

There are advantages and disadvantages in each approach.

If the licensee performs the decommissioning activity, there is maximum use of the existing staff, which has a wealth of hands-on experience. Some of the decommissioning activities are similar to maintenance activities for which procedures are already established. An example is the removal and replacement of components as a normal activity during the operation of the plant. The use of existing staff provides continuity of local employment. However, some of the more experienced staff may leave because they see their employment ending when decommissioning is completed and will go to other sites where new jobs or long-term career prospects are available.

A disadvantage of using former staff to perform the decommissioning activity is that such staff may have difficulty in accepting the cultural changes needed as the plant changes from an operational mode to decommissioning mode, e.g., from routine operations to unique tasks requiring more preparation. This causes them to be less motivated than an organization that performs decommissioning activities on a routine basis.

Even in an in-house approach, it is inevitable that at least some contractors are used on-site. This could range from one or two specialist contracts (e.g., plasma cutting) or, at the other extreme, using contracts for selected areas of the site. The extent of contractor usage is dependent on the policy on staff retention, cost, and the availability of suitable contractors.

When an outside contractor is hired to perform the decommissioning activities, the licensee maintains a smaller staff because of its role and responsibility as a supervising organization. The outside contractor takes control of major portions of the facility and ensures that the activities are performed safely and in accordance with the regulatory requirements. These experienced contractors are normally more efficient than the in-house resources during the decontamination and dismantling activities. They have performed these activities on a routine basis and are more familiar with the available technologies that can be used to assist them in their efforts,

such as decontamination of concrete walls and floors. The contractor can also arrange for any subcontractors if needed and this will probably be fewer than if the licensee himself or herself performs the decommissioning activities.

When using contractors the licensee still keeps control of the project. In order to maintain this control, the licensee is required to be in constant contact with the contractor to ensure that all safety and regulatory requirements are met and that the project goals are achieved. It is important that the licensee be familiar with various contracting mechanisms to minimize the risk of cost overruns. Resources and skills needed for the supervising work may be significant. The licensing regime is based on the premise that the licensee is in day-to-day control of the facility, processes, and activities and that its staff manages the operation of the facility. The licensee is an “intelligent customer” for services provided by contractors. This is still necessary during periods of care and maintenance and waste storage. Therefore, the licensee needs to be able to demonstrate that an adequate organization is, and will be, in place to discharge those responsibilities until the facility is finally removed from regulatory control and its period of responsibility has ended.

Project financing may be another challenging issue. The Project Management shall assure that necessary funds are available when necessary. There may be a number of reasons why the funds necessary for decommissioning are not available when the facility is shut down. It may be that the facility was closed prematurely before the total amount of funds was collected. The funds may also be lacking because of poor planning or the lack of a national requirement for prudent financial planning. Another cause may be that political conditions have changed, such as in the case of some of the former Soviet Union countries, and the funds are not available to complete the decommissioning process. No matter what the reason is, the lack of funding can cause substantial delays in the process and can have a significant impact even on safety during the resolution of this problem.

Another issue is maintaining “corporate” knowledge during the operation of the facility and until it is finally released from regulatory control. This could be especially troublesome if a long safe storage period is selected, which might cover a period that would exceed a person’s normal working lifetime. Without the working knowledge of the systems and of accidents or incidents that occurred during the life of the plant, the planning process is made more difficult and unknown or unexpected situations may occur during the decontamination or dismantling activities.

This issue is expanded in [▶ Sect. 2.](#)

1.2.2 Safety-Related Issues


There are some issues related to safety concerns that must be addressed during the development of the decommissioning plan and the planning process. These issues can have a significant effect on the selection of the option that might be chosen. In most cases, failure to resolve these issues leads to placing the facility in a safe storage mode with the deferral of the final decontamination and dismantling activities.

Radiological risks are much lower than during plant operation. This is the case, in particular, with instances where NPP’s decommissioning starts when spent fuel has been removed from the facility and therefore the total radiological inventory has been dramatically reduced to about 1% of the previous one. However, industrial risks may increase due to the decommissioning operation involving chemical and mechanical nonroutine activities, handling of large and heavy pieces, use of protective clothings limiting worker freedom of movement, etc.

Maintaining safety culture in the entire organization and keeping safety as the first priority is another challenge during decommissioning that may appear more an industrial conventional activities than an operation that require high skills and attention to radiological issues.

Another challenge that may also affect the Safety Authority is the capability to properly adapt the regulatory requirements to actual plant conditions and the real associated risks. It is clear that radiological risks tend to zero as the decommissioning process progresses. It is necessary to focus the attention on real risks that may change in nature and dimension.

The lack of a disposal or storage site that would accept the waste generated during the decontamination and dismantling activities may involve both project management and environmental issues. In general, it is not a good practice to generate radioactive waste if there is no national policy on waste management or a facility available to handle and dispose the waste. It is highly recommended that a facility be available for all of the waste streams that will be generated during the decommissioning. However, if an off-site disposal facility is not available, it is reasonable to proceed with the decommissioning, and treat and condition the resulting waste that may be stored temporarily on-site.

All these aspects and other are expanded in  Sect. 8.

1.2.3 Decommissioning Funding

Decommissioning is not producing revenues in general, but it is an activity aimed at solving liabilities and site restoration. Therefore, funding is a key issue to assure a safe, efficient, and economic decommissioning.

Several methods of financing these future decommissioning costs can be used, depending on the circumstances of each utility and the country in which it operates. In several countries, a fund of some type has been established or proposed to ensure the availability of financing.

This is usually done by estimating the cost of decommissioning at the end of the normal plant lifetime and requiring payments, either annually or on a charge per kilowatt-hour basis, to ensure that this sum is in place. This estimate is updated regularly and the charge adjusted accordingly.

The drawback of this system is that the amount estimated would not be in place if the plant were to be shut down before the end of its normal lifetime. To avoid this, a fund could be established at the start of the plant's operation that would cover the cost of decommissioning whenever it is necessary. However, this represents a heavy burden for the utility at the moment when construction and start-up costs are already high, and thus, although it may be imposed by law, this solution is not favored by many utilities.

To assure proper funding (initially and during decommissioning) cost calculations is a very important question.


The cost of decommissioning nuclear power plants is based on the following factors:

- The sequence of decommissioning stages chosen
- The timing of each decommissioning stage
- The decommissioning activities accomplished in each stage

In addition, costs depend on such country-specific and site-specific factors as the type of reactor, waste management and disposal practices, and wage rates. As mentioned previously, a number of other factors influence the choice of decommissioning strategy and therefore the involved costs.

Total decommissioning costs include all costs from the start of decommissioning until the site is released for unrestricted use.

The cost estimates are based on previous decommissioning and decontamination experience, the cost of maintenance, surveillance, and necessary component replacements, and the cost of similar, nonnuclear work.

Cost estimates vary in a wide range even for similar plants in different countries. Calculation assumptions may have also a very significant impact on these differences. The cost of decommissioning therefore may range from 150 to 500 M\$ and more per unit. This subject is expanded in  Sect. 9.

1.2.4 Waste Management

Radioactive wastes are an inevitable legacy of nuclear operations and they must be managed safely. As facilities near the end of their operating lifetimes, tasks associated with their decommissioning assume greater importance.

Governments are sharing experience and information on safety and technological aspects of decommissioning operations required for many types of nuclear facilities. As more facilities are scheduled to go out of service in the coming years, these services and activities can provide valuable support to countries in preparing, planning, and implementing programs for the safe management of radioactive waste associated with decommissioning operations.


The management of the waste generated by dismantling is a component of the complete cost of the operations. Wastes include:

- Nonradioactive wastes (primarily concrete and rubble), which are, a priori, the largest share of total waste.
- Very low-level radioactive waste, more than half of which is scrap. Depending on the nature of this waste, its activity and the relevant regulations, it can be either recycled or stored in packages in a dedicated facility without posing a danger to the public.
- Short-lived or low-medium-level activity waste, which accounts for by far the smallest share. This waste is governed by national regulations that dictate disposal procedures, in either a surface storage or interim storage facility before being sent to a medium-level long-lived waste storage center.
- There are also cases of long lived or intermediate to high level wastes; these may be present in the Gas Graphite NPP's or in the fuel cycle facilities (like reprocessing facilities) where spent fuel has been dissolved.

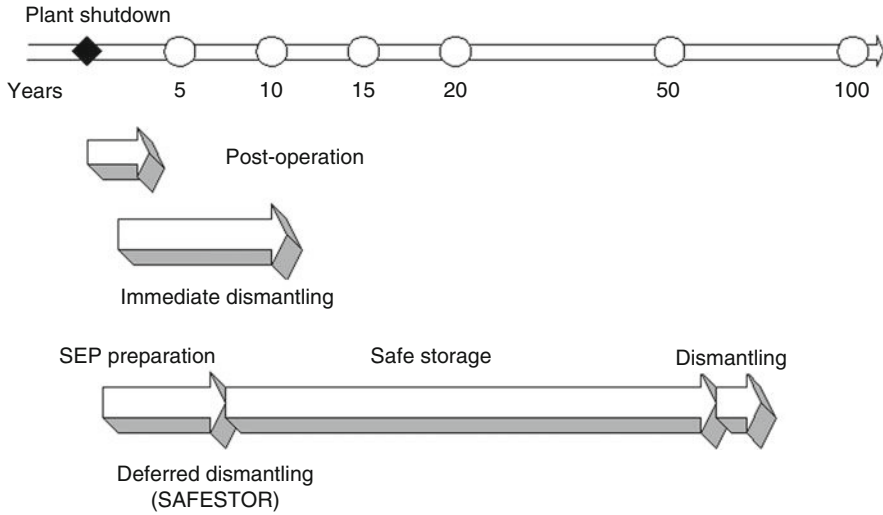
All wastes from dismantling or operations will be sent to a disposal facility. If this is not available, then decommissioning may proceed according to the chosen strategy shipping the waste to a long-term centralized storage center, if available, or may be stored on an interim basis on-site.

1.3 Decommissioning Strategies

1.3.1 Overview

There are three main options used for decommissioning ( Fig. 1):

- Immediate dismantling of the facility
- Safe storage or deferred dismantling of the facility
- Entombment of the facility



■ **Figure 1**
Decommissioning strategies and timescale

Each of these options has advantages and disadvantages.

- The immediate dismantling option (early site release or DECON in the USA) allows the facility to be removed from regulatory control relatively soon after shutdown or termination of regulated activities. Usually, the final dismantling or decontamination activities begin within a few months or years, depending on the facility. The Fort St. Vrain nuclear power plant in the USA is an example where this option has been successfully implemented.
- The safe storage option (Safe Enclosure or SAFSTOR in the USA) postpones the final removal of controls for a longer period, usually on the order of 40–60 years. The facility is placed into a safe storage configuration until the eventual dismantling and decontamination activities occur. This is the case, for example, of the Gas Graphite Reactor of Vandellós 1 in Spain.
- The entombment option (ENTOMB in the USA) entails placing the facility into a condition that allows the remaining radioactive material to remain on-site without the requirement of ever removing it totally. This option usually involves reducing the size of the area where the radioactive material is located and then creating a monolith or other structures that lasts for a period of time, which ensures that the remaining radioactivity is no longer of concern. Most regulators do not prefer this approach as it, in practice, creates a low-level radioactive waste-disposal facility on the site. An example where this option has been implemented is the Hallam nuclear plant in the USA. In general, this option is badly suited for large nuclear power plants because of their size and the amount and type of radioisotopes involved.

Practically, in any option, when operations at a nuclear power plant are terminated, the nuclear fuel, the mobile radioactive materials in the process systems (e.g., process fluids) and the radioactive waste produced during normal operations are removed as soon as the plant ceases

to operate. Certain equipment can also be removed and disposed. It is usual to consider spent fuel removal from the plant as a precondition for the start of decommissioning. All subsequent activities can be grouped according to the goal of reaching some well-defined stage of the decommissioning process.

It is usual to identify three main stages. Each of these stages can be defined by two characteristics: the physical state of the plant and its equipment and the surveillance needed to maintain this physical state:

- Stage 1 decommissioning requires that the spent fuel has already been removed from the reactor and from the plant, draining the liquid systems, disconnecting the operating systems, blocking and sealing the mechanical openings such as valves and plugs, and controlling the atmosphere inside the containment building. The facility is kept under surveillance, access is limited and routine inspections are carried out to ensure that the plant remains in a safe condition.
- Stage 2 decommissioning requires all equipment and buildings that can be easily dismantled to be removed or decontaminated and made available for other uses, leaving only the reactor core structure and its extensive shielding. The containment building and the ventilation system may be modified or removed if they are no longer needed for safety reasons, or they may be decontaminated to allow access for other purposes. Other buildings and equipment that are not radioactive may be converted to serve new purposes as well. Surveillance during Stage 2 is reduced, but it is advisable to continue periodic spot checks of the buildings as well as surveillance of the surrounding environment.
- Stage 3 decommissioning requires that, unless the site, buildings, or equipment are to be reused for other nuclear purposes, all materials with radioactivity levels exceeding those closely equivalent to the natural radiation environment be removed and the site released without restrictions or further surveillance.

In the case of nuclear reactors, about 99% of the radioactivity is associated with the fuel that is removed in Stage 1. Apart from any surface contamination of plant, the remaining radioactivity comes from “activation products” such as steel components that have long been exposed to neutron irradiation. Their atoms are changed into different isotopes such as ^{55}Fe , ^{60}Co , ^{63}Ni , and ^{14}C . The first two are highly radioactive, emitting gamma rays. However, their half-life is such that after 50 years from closedown their radioactivity is much diminished.

These three stages may be carried out by rapidly progressing from one stage to the next or carried out over a prolonged period lasting as long as 100 years or more. Although most countries intend to complete all the three stages, a facility could remain at Stage 1 or 2 for a relatively long period of time, or its decommissioning may proceed directly from Stage 1 to 3.

Although the above definitions are widely used, there are slight differences in the definitions in various countries and in the international organizations.

A licensee may also choose to adopt a combination of the first two choices, in which some portions of the facility are soon dismantled or decontaminated, while other parts of the facility are left in SAFSTOR.

The decision may be based on factors other than radioactive decay, such as the availability of waste disposal sites. To be acceptable, decommissioning must be completed within 60 years. A period beyond that is considered only in accordance with the US Nuclear Regulatory Commission (NRC) regulations.

1.3.2 Issues Affecting the Choice of Decommissioning Strategy

A number of factors must be weighed and balanced when preparing the decommissioning plan for a nuclear power plant. The plan may vary with each facility and these factors must be evaluated on a case-by-case basis.

National Nuclear Strategies

Some questions concerning national strategies and goals for nuclear power development that are relevant to decommissioning are:

- Is there a national policy for the disposal of shutdown nuclear facilities?
- Is this an industry or a government responsibility?
- What is the national radioactive waste management policy?

The answers to these questions may change with time and the decommissioning plan may need to be revised to take into account technical developments, availability of waste disposal sites, changes in health protection requirements, and other factors.

Plant Characteristics

The kind of reactor, the location of the facility, and the total amount of radioactivity it contains are important elements in the selection of a decommissioning strategy. The amount and distribution of the radioactivity are determined by the type of reactor and its operating history. For example, a boiling-water reactor (BWR) circulates steam containing radioactivity in the turbine circuit, whereas in a pressurized water reactor (PWR) the radioactivity is contained in the primary coolant system and does not contaminate the turbine circuit.

The radioactivity produced in nuclear power plants is made up of both short-lived and long-lived radionuclides, but principally of short-lived isotopes which decay in 5–30 years. Thus a significant reduction in radioactivity can be achieved by placing the facility in safe storage for that length of time. This delay reduces the occupational exposure of the decommissioning workers and the amount of waste needing controlled disposal.

Protection of Health, Safety, and the Environment

A primary concern in any decommissioning program is to provide for the health and safety of the workers and to protect the general public and the environment. Public exposure and environmental impacts are expected to be minimal and well within the regulatory limits for operating facilities. Therefore, they are not likely to be significant factors in selecting a decommissioning alternative.

However, protection of the decommissioning workers is an important consideration and a significant effort is made in all nuclear operations to keep the exposure as low as reasonably achievable. A cost-benefit analysis should be carried out to determine the extent to which the delayed dismantlement has a positive effect. Although this depends on the physical state of the power plant, as well as available resources and equipment, it is known that a deferral of Stage 3 for 80–100 years would significantly reduce personnel management and protection costs while raising maintenance and surveillance costs. Delaying decommissioning beyond 100 years would not achieve similar benefits as the decay rate of the radioactive substances is significantly slowed by then. Furthermore, surveillance beyond 100 years is a heavy commitment.

In choosing a decommissioning strategy, a radiological impact assessment should be made to determine:

- Individual and collective doses (i.e., the total dose over a population group exposed to the given source) to workers during the dismantling, including waste handling

- Individual and collective doses to the public throughout the operation, including those generated by waste management, transport and disposal and the residual ones, if any, generated by site use after its release.
- A risk assessment of the probability of a fire or explosion and deterioration of the installation or loss of integrity of the containment barriers leading to the release of radionuclides to the environment

Radioactive Waste Management

As indicated above, decommissioning nuclear power plants require the removal of the fuel prior to completion of Stage 1. Thus the first question is about the availability of reprocessing or storage facilities for this spent fuel. In some cases this might be a determining factor, but usually spent fuel management solutions are planned as part of power plant operations.

Although there is no generally applicable classification of radioactive waste, it is often advisable to refer to low-level, intermediate-level, and high-level waste, depending on their radionuclide content, heat-generation rates, and methods of treatment.

The availability of disposal sites for low- and intermediate-level waste is the most important factor in several countries, which are choosing decommissioning strategies. Most of the waste from nuclear power plant decommissioning is low-level waste, although a small amount of intermediate- and high-level waste is also produced. Low- and intermediate-level decommissioning waste can be disposed in the same repositories that accept the waste continuously produced by the operating facilities. The decommissioning waste volume from a nuclear power plant is of the same order of magnitude as the volume of operation waste produced throughout the normal lifetime of the plant. The volume of decommissioning waste can be substantially reduced using such techniques as surface decontamination, compaction, segmentation, special packaging, incineration, and vitrification.

Future Use of the Site

A nuclear facility site is a valuable resource, particularly for the location of replacement power or processing facilities. Among its advantages are the low seismic activity of the site, proximity to a large supply of water, access to an electrical distribution system, and acceptance by local residents. If the site is to be used for other power generating or nuclear facilities, it does not need to be decommissioned to the same standards as for unrestricted release to the public domain. In sites containing power plants that were constructed at different times, the end of their normal operating life comes at different times, and therefore decommissioning may be limited to Stage 1 until the last unit is shut down. Decommissioning of all units would be more efficient, and maintenance, surveillance, and security could be provided by personnel from the units still in operation, at little or no additional cost.

Development of Decommissioning Technologies

All three stages of decommissioning have been carried out in small tests, training and power demonstration reactors, and supporting fuel cycle facilities. Thus, extended experience has not yet been acquired in decommissioning the major reactor types. Present technology is believed to be adequate for decommissioning to any of the three stages by applying the techniques developed for small plants to the decommissioning of commercial-size power stations. Nevertheless, continued development in some areas to reduce worker exposure, costs, and waste volumes is desirable. Such areas include the development of better equipment and methods for remote dismantlement to reduce worker exposure, the development of better methods to discriminate among radioactivity levels in waste quickly, methods to process wastes rapidly, and techniques

for minimizing waste generation through treatment and volume reduction. New equipment is expected to improve worker protection and reduce costs. Many major decommissioning projects currently in progress or planned increase the available knowledge substantially.




Cost and Availability of Funds

While safety considerations are given priority, the costs of decommissioning can also be a very important factor. At the end of the facility's operations, immediate dismantlement to Stage 3 would obviously be much more costly than to remain at Stage 1. If funds for decommissioning have been set aside while the facility is operating, the immediate cost will be less important than if the decommissioning costs must compete for funds with the owner's other capital needs. In order to prevent this item from becoming a controlling factor, plant owners should plan to have funds set aside to cover the cost of the chosen decommissioning strategy, which in any case would, at most, increase electricity generation costs by only a small percentage.

Social and Other Considerations

Certain social factors should be taken into account when evaluating the decommissioning options. For example, the chosen strategy could affect land values, the aesthetic aspects of the site, and perceived risks associated with the long-term shutdown and delayed dismantlement of a plant on the site. Another consideration, particularly important in areas where employment is scarce, is that immediate dismantlement requires a larger staff and work force than other strategies, resulting in a slower and smoother reduction of the number of job posts.

1.4 Decommissioning in the World

As of 31 December 2007, 119 power reactors, of a total of 557 constructed worldwide, have been shut down and 438 are still in operation. The age of operating reactors ranges from less than 1 year, in the case of new facilities, to up to 41 years.  [Figure 2](#) shows the number of reactors still in operation by age (years from first connection to grid). As of 31 December 2007, 129 (29.5%) of power reactors still in operation are more than 30 years old, 341 reactors (77.8%) are more than 20 years old, and 97 reactors (22.2%) are 20 years old or less. The worldwide distribution of nuclear power reactors definitively shut down as of 31 December 2007 is shown in  [Table 1](#).  [Table 2](#) shows the worldwide distribution of power reactors under decommissioning process. Theoretically, the operational lifetime of power reactors, and hence the needs for decommissioning, can be predicted from the reactor's type or from the operational license issued by the respective regulatory authority.

Over the past 35 years, considerable experience has been gained in decommissioning various types of nuclear facilities. To date, 119 commercial power reactors, as well as over 250 research reactors and a number of fuel cycle facilities, have been retired from operation.

To decommission its retired gas-cooled reactors at the Chinon, Bugey, and St. Laurent nuclear power stations, Electricité de France chose partial dismantling to Stage 2 and postponed Stage 3 dismantling for 50 years. As other reactors continue to operate at those sites, and monitoring and surveillance do not add to the electricity cost. The French are building at Marcoule a recycling plant for steel from dismantled nuclear facilities. This metal contains some activation products, but it can be recycled for other nuclear plants.

Decommissioning has begun at ten UK reactors. For instance, at the Berkeley nuclear power station (2×138 MWe, Magnox reactors), closed for economic reasons in 1989 after 27 years of operation, defueling was completed in 1992. The plant may now be left for 30 years, after which a

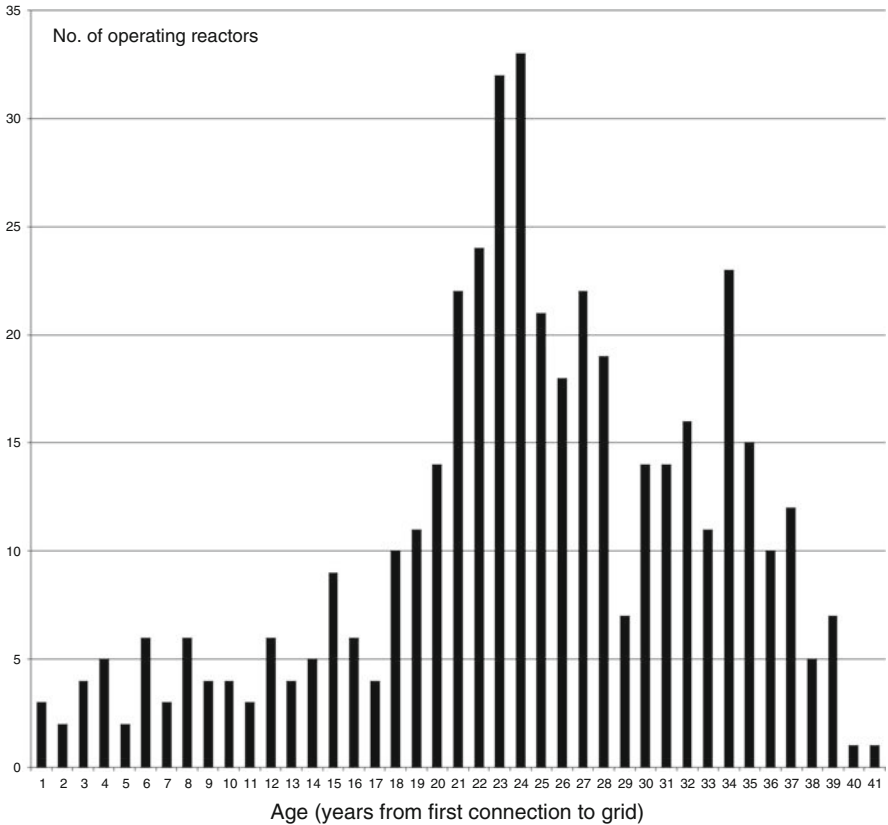


Figure 2
Number of power reactors in operation by age as of 31 December 2007 (IAEA 2008)

containment may be built around the residual buildings for a further storage period of perhaps 100 years.

Japan's Tokai-1 reactor, a UK Magnox design, was decommissioned after 30 years of service in 1998. After 5–10 years storage, the unit will be dismantled and the site released for other uses. Total cost is expected to be about 25 billion yen.

Germany chose more rapid direct dismantling over safe enclosure for the closed Greifswald nuclear power station in former East Germany, where five reactors had been operating. Similarly, the site of the 100-MWe Niederaichbach nuclear power plant in Bavaria was declared fit for unrestricted agricultural use in mid-1995. Following the removal of all nuclear systems, the radiation shield and some activated materials, the remainder of the plant was below accepted limits for radioactivity and the state government approved final demolition and clearance of the site.

The 250-MWe Gundremmingen-A unit was Germany's first commercial nuclear reactor, operated from 1966 to 1977. Its decommissioning work started in 1983, and moved to the more contaminated parts in 1990, using underwater cutting techniques. This project demonstrated that decommissioning can be undertaken safely and economically without long delays, recycling most of the metal.

Table 1
Power reactors permanently shut down in the world as of 31 December 2007

Country	Reactor (IAEA code, name)	Capacity (MW)				Construction start	Grid connection	Shut down
		Type	Thermal	Gross	Net			
Armenia	AM-18 Armenia-1	PWR	1,375	408	376	1969-7	1976-12	1989-2
Belgium	BE-1 BR-3	PWR	41	12	10	1957-11	1962-10	1987-6
Bulgaria	BG-1 Kozloduy-1	PWR	1,375	440	408	1970-4	1974-7	2002-12
	BG-2 Kozloduy-2	PWR	1,375	440	408	1970-4	1975-8	2002-12
	BG-3 Kozloduy-3	PWR	1,375	440	408	1973-10	1980-12	2006-12
	BG-4 Kozloduy-4	PWR	1,375	440	408	1973-10	1982-5	2006-12
Canada	CA-2 Douglas Point	PHWR	704	218	206	1960-2	1967-1	1984-5
	CA-3 Gentilly-1	HWLWR	792	266	250	1966-9	1971-4	1977-6
	CA-1 Rolphton NPD	PHWR	92	25	22	1958-1	1962-6	1987-8
France	FR-9 Bugey-1	GCR	1,954	555	540	1965-12	1972-4	1994-5
	FR-2 Chinon-A1	GCR	300	80	70	1957-2	1963-6	1973-4
	FR-3 Chinon-A2	GCR	800	230	180	1959-8	1965-2	1985-6
	FR-4 Chinon-A3	GCR	1,170	480	360	1961-3	1966-8	1990-6
	FR-5 Chooz-A (Ardennes)	PWR	1,040	320	305	1962-1	1967-4	1991-10
	FR-6 EL-4 (Monts d'Arree)	HWGCR	250	75	70	1962-7	1967-7	1985-7
	FR-1B G-2 (Marcoule)	GCR	260	43	38	1955-3	1959-4	1980-2

Table 1 (continued)

Country	Reactor (IAEA code, name)	Capacity (MW)				Construction start	Grid connection	Shut down
		Type	Thermal	Gross	Net			
Germany	FR-1 G-3 (Marcoule)	GCR	260	43	40	1956-3	1960-4	1984-6
	FR-7 St. Laurent-A1	GCR	1,650	500	480	1963-10	1969-3	1990-4
	FR-8 St. Laurent-A2	GCR	1,475	530	465	1966-1	1971-8	1992-5
	FR-24 Superphenix	FBR	3,000	1,242	1,200	1976-12	1986-1	1998-12
	DE-4 AVR Juelich (AVR)	HTGR	46	15	13	1961-8	1967-12	1988-12
	DE-502 Greifswald-1 (KGR 1)	PWR	1,375	440	408	1970-3	1973-12	1990-2
	DE-503 Greifswald-2 (KGR 2)	PWR	1,375	440	408	1970-3	1974-12	1990-2
	DE-504 Greifswald-3 (KGR 3)	PWR	1,375	440	408	1972-4	1977-10	1990-2
	DE-505 Greifswald-4 (KGR 4)	PWR	1,375	440	408	1972-4	1979-9	1990-7
	DE-506 Greifswald-5 (KGR 5)	PWR	1,375	440	408	1976-12	1989-4	1989-11
	DE-3 Gundremmingen-A (KRB A)	BWR	801	250	237	1962-12	1966-12	1977-1
	DE-7 HDR Grosswelzheim	BWR	100	25	25	1965-1	1969-10	1971-4
	DE-8 KNK II	FBR	58	21	17	1974-9	1978-4	1991-8
	DE-6 Lingen (KWL)	BWR	520	268	183	1964-10	1968-7	1979-1
DE-22 Muelheim-Kaerlich (KMK)	PWR	3,760	1,302	1,219	1975-1	1986-3	1988-9	
DE-2 MZFR	PHWR	200	57	52	1961-12	1966-3	1984-5	

Italy	DE-11 Niederaichbach (KKN)	HWGCR	321	106	100	1966-6	1973-1	1974-7
	DE-5 Obrigheim (KWO)	PWR	1,050	357	340	1965-3	1968-10	2005-5
	DE-501 Rheinsberg (KKR)	PWR	265	70	62	1960-1	1966-5	1990-6
	DE-10 Stade (KKS)	PWR	1,900	672	640	1967-12	1972-1	2003-11
	DE-19 THTR-300	HTGR	750	308	296	1971-5	1985-11	1988-4
	DE-1 Vak Kahl	BWR	60	16	15	1958-7	1961-6	1985-11
	DE-9 Wuergassen (KWW)	BWR	1,912	670	640	1968-1	1971-12	1994-8
	IT-4 Caorso	BWR	2,651	882	860	1970-1	1978-5	1990-7
	IT-3 Enrico Fermi (TRINO)	PWR	870	270	260	1961-7	1964-10	1990-7
	IT-2 Garigliano	BWR	506	160	150	1959-11	1964-1	1982-3
Japan	IT-1 Latina	GCR	660	160	153	1958-11	1963-5	1987-12
	JP-20 Fugen ATR	HWLWR	557	165	148	1972-5	1978-7	2003-3
	JP-1 JPDR	BWR	90	13	12	1960-12	1963-10	1976-3
	JP-2 Tokai-1	GCR	587	166	137	1961-3	1965-11	1998-3
	KZ-10 BN-350	FBR	1,000	90	52	1964-10	1973-7	1999-4
Lithuania	LT-46 Ignalina-1	LWGR	4,800	1,300	1,185	1977-5	1983-12	2004-12
	NL-1 Dodewaard	BWR	183	60	55	1965-5	1968-10	1997-3
Russian Fed.	RU-1 APS-1 Obninsk	LWGR	30	6	5	1951-1	1954-6	2002-4
	RU-3 Belyarsky-1	LWGR	286	108	102	1958-6	1964-4	1983-1
	RU-6 Belyarsky-2	LWGR	530	160	146	1962-1	1967-12	1990-1
	RU-4 Novovoronezh-1	PWR	760	210	197	1957-7	1964-9	1988-2
	RU-8 Novovoronezh-2	PWR	1,320	365	336	1964-6	1969-12	1990-8

Table 1 (continued)

Country	Reactor (IAEA code, name)	Capacity (MW)				Construction start	Grid connection	Shut down
		Type	Thermal	Gross	Net			
Slovak Rep.	SK-1 Bohunice A1	HWGCR	560	143	93	1958-8	1972-12	1977-2
	SK-2 Bohunice-1	PWR	1,375	440	408	1972-4	1978-12	2006-12
Spain	ES-1 Jose Cabrera-1 (ZORITA)	PWR	510	150	141	1964-6	1968-7	2006-4
	ES-3 Vandellos-1	GCR	1,670	500	480	1968-6	1972-5	1990-7
Sweden	SE-1 Agesta	PHWR	80	12	10	1957-12	1964-5	1974-6
	SE-6 Barseback-1	BWR	1,800	615	600	1971-2	1975-5	1999-11
	SE-8 Barseback-2	BWR	1,800	615	615	1973-1	1977-3	2005-5
	GB-3A Berkeley 1	GCR	620	166	138	1957-1	1962-6	1989-3
UK	GB-3B Berkeley 2	GCR	620	166	138	1957-1	1962-6	1988-10
	GB-4A Bradwell 1	GCR	481	146	123	1957-1	1962-7	2002-3
	GB-4B Bradwell 2	GCR	481	146	123	1957-1	1962-7	2002-3
	GB-1A Calder Hall 1	GCR	268	60	50	1953-8	1956-8	2003-3
	GB-1B Calder Hall 2	GCR	268	60	50	1953-8	1957-2	2003-3
	GB-1C Calder Hall 3	GCR	268	60	50	1955-8	1958-3	2003-3
	GB-1D Calder Hall 4	GCR	268	60	50	1955-8	1959-4	2003-3
	GB-2A Chapelcross 1	GCR	260	60	50	1955-10	1959-2	2004-6
GB-2B Chapelcross 2	GCR	260	60	50	1955-10	1959-7	2004-6	
GB-2C Chapelcross 3	GCR	260	60	50	1955-10	1959-11	2004-6	
GB-2D Chapelcross 4	GCR	260	60	50	1955-10	1960-1	2004-6	

	GB-14 Dounreay DFR	FBR	60	15	11	1955-3	1962-10	1977-3
	GB-15 Dounreay PFR	FBR	600	250	234	1966-1	1975-1	1994-3
	GB-9A Dungeness-A1	GCR	840	230	225	1960-7	1965-9	2006-12
	GB-9B Dungeness-A2	GCR	840	230	225	1960-7	1965-11	2006-12
	GB-7A Hinkley Point-A1	GCR	900	267	235	1957-11	1965-2	2000-5
	GB-7B Hinkley Point-A2	GCR	900	267	235	1957-11	1965-3	2000-5
	GB-6A Hunterston-A1	GCR	595	173	300	1957-10	1964-2	1990-3
	GB-6B Hunterston-A2	GCR	595	173	150	1957-10	1964-6	1989-12
	GB-10A Sizewell-A1	GCR	1,010	245	210	1961-4	1966-1	2006-12
	GB-10B Sizewell-A2	GCR	1,010	245	210	1961-4	1966-4	2006-12
	GB-8A Trawsfynydd 1	GCR	850	235	390	1959-7	1965-1	1991-2
	GB-8B Trawsfynydd 2	GCR	850	235	195	1959-7	1965-2	1991-2
	GB-5 Windscale AGR	GCR	120	41	32	1958-11	1963-2	1981-4
	GB-12 Winfrith SGHWR	SGHWR	318	100	92	1963-5	1967-12	1990-9
Ukraine	UA-25 Chernobyl-1	LWGR	3,200	800	740	1970-3	1977-9	1996-11
	UA-26 Chernobyl-2	LWGR	3,200	1,000	925	1973-2	1978-12	1991-10
	UA-42 Chernobyl-3	LWGR	3,200	1,000	925	1976-3	1981-12	2000-12
	UA-43 Chernobyl-4	LWGR	3,200	1,000	925	1979-4	1983-12	1986-4
USA	US-155 Big Rock Point	BWR	240	71	67	1960-5	1962-12	1997-8
	US-014 Bonus	BWR	50	18	17	1960-1	1964-8	1968-6
	US-144 CVTR	PHWR	65	19	17	1960-1	1963-12	1967-1
	US-10 Dresden-1	BWR	700	207	197	1956-5	1960-4	1978-10
	US-011 Elk River	BWR	58	24	22	1959-1	1963-8	1968-2

Table 1 (continued)

Country	Reactor (IAEA code, name)	Capacity (MW)			Construction start	Grid connection	Shut down	
		Type	Thermal	Gross				Net
	US-16 Enrico Fermi-1	FBR	200	65	61	1956-8	1966-8	1972-11
	US-267 Fort St. Vrain	HTGR	842	342	330	1968-9	1976-12	1989-8
	US-018 Ge Vallecitos	BWR	50	24	24	1956-1	1957-10	1963-12
	US-213 Haddam Neck	PWR	1,825	603	560	1964-5	1967-8	1996-12
	US-077 Hallam	X	256	84	75	1959-1	1963-9	1964-9
	US-133 Humboldt Bay	BWR	220	65	63	1960-11	1963-4	1976-7
	US-013 Indian Point-1	PWR	615	277	257	1956-5	1962-9	1974-10
	US-409 Lacrosse	BWR	165	55	48	1963-3	1968-4	1987-4
	US-309 Maine Yankee	PWR	2,630	900	860	1968-10	1972-11	1997-8
	US-245 Millstone-1	BWR	2,011	684	641	1966-5	1970-11	1998-7
	US-130 Pathfinder	BWR		63	59	1959-1	1966-7	1967-10
	US-171 Peach Bottom-1	HTGR	115	42	40	1962-2	1967-1	1974-11
	US-012 Piqua	X	46	12	12	1960-1	1963-7	1966-1
	US-312 Rancho Seco-1	PWR	2,772	917	873	1969-4	1974-10	1989-6
	US-206 San Onofre-1	PWR	1,347	456	436	1964-5	1967-7	1992-11
	US-146 Saxton	PWR	24	3	3	1960-1	1967-3	1972-5
	US-001 Shippingport	PWR	236	68	60	1954-1	1957-12	1982-10
	US-322 Shoreham	BWR	2,436	849	820	1972-11	1986-8	1989-5
	US-320 Three Mile Island-2	PWR	2,772	959	880	1969-11	1978-4	1979-3
	US-344 Trojan	PWR	3,411	1,155	1,095	1970-2	1975-12	1992-11
	US-029 Yankee NPS	PWR	600	180	167	1957-11	1960-11	1991-10
	US-295 Zion-1	PWR	3,250	1,085	1,040	1968-12	1973-6	1998-1
	US-304 Zion-2	PWR	3,250	1,085	1,040	1968-12	1973-12	1998-1

Table 2
Power reactors under decommissioning process in the world as of 31 December 2007

Country	Reactor (IAEA code, name)	Shutdown date	Adopted strategy ^a	Current phase		Decommissioning licensee
				Decommissioning ^b	Fuel management ^c	
Belgium	BE-1 BR-3	1987-6	1	4, 9	4	CEN/SCK
Bulgaria	BG-1 Kozloduy-1	2002-12	2	5		E-00707
	BG-2 Kozloduy-2	2002-12	2	5		E-00613
France	FR-24 Superphenix	1998-12	1	6	3, 6	NERSA
	FR-3 Chinon-A2	1985-6	1	1		EDF
	FR-5 Chooz-A (Ardennes)	1991-10	1	4, 9		SENA
	FR-6 EL-4 (Monts d'Arree)	1985-7	1	9		EDF
	FR-9 Bugey-1	1994-5	1	6		EDF
Germany	DE-10 Stade (KKS)	2003-11	1	3, 4, 6		E.ON
	DE-501 Rheinsberg (KKR)	1990-6	1	3, 9		G 01 KKR
	DE-9 Würgassen (KWW)	1994-8	1	3, 4		E.ON
Italy	IT-1 Latina	1987-12	1	6		SOGIN
	IT-2 Garigliano	1982-3	1	6		SOGIN
	IT-3 Enrico Fermi (TRINO)	1990-7	1	6	3, 7	SOGIN
	IT-4 Caorso	1990-7	1	6	3, 7	SOGIN
Japan	JP-2 Tokai-1	1998-3	3	3, 6, 7		JAPCO
	JP-20 Fugen ATR	2003-3	2	5	2, 5	JAEA
Kazakhstan	KZ-10 BN-350	1999-4	3	1, 5, 6	3, 6	MAEC-KAZ
Lithuania	LT-46 Ignalina-1	2004-12	1	2	1, 2	Planned

Table 2 (continued)

Country	Reactor (IAEA code, name)	Shutdown date	Adopted strategy ^a	Current phase		Decommissioning licensee
				Decommissioning ^b	Fuel management ^c	
Netherlands	NL-1 Dodewaard	1997-3	2	7		BVGKN
Slovakia	SK-1 Bohunice A1	1977-2	3	3, 6		JAVYS
Spain	ES-1 Jose Cabrera-1 (ZORITA)	2006-4	1	3	7	UFG
	ES-3 Vandellos-1	1990-7	3	8		ENRESA
Sweden	SE-1 Agesta	1974-6	2	7		BKAB
	SE-6 Barseback-1	1999-11	5		4	BKAB
	SE-8 Barseback-2	2005-5	5		4	BKAB
USA	US-012 Piqua	1966-1	4	11		CofPiqua
	US-029 Yankee NPS	1991-10	1	4, 6		YAEC
	US-10 Dresden-1	1978-10	2	11		EXELON
	US-133 Humboldt Bay	1976-7	3	3, 4, 6	7	PGE
	US-16 Enrico Fermi-1	1972-11	2	9, 11		DETED
	US-171 Peach Bottom-1	1974-11	2	1		EXELON
	US-206 San Onofre-1	1992-11	3	4, 9, 11		SCE
	US-213 Haddam Neck	1996-12	1	4, 6, 11		CYAPC
	US-245 Millstone-1	1998-7	3		7	DOMIN
	US-295 Zion-1	1998-1	3	1		CommonEd
US-304 Zion-2	1998-1	3	1		COMMED	
US-309 Maine Yankee	1997-8	1	4, 11		MYAPC	

	US-320 Three Mile Island-2	1979-3	2	11	4	GPU
	US-344 Trojan	1992-11	3	11		PORTGE

Source: IAEA (2008)

^a Adopted strategy:

- 1 = Immediate dismantling and removal of all radioactive materials
- 2 = Deferred dismantling, placing all radiological areas into safe enclosure
- 3 = Deferred dismantling, including partial dismantling and placing remaining radiological areas into safe enclosure
- 4 = On-site disposal, involving encapsulation of radioactive materials
- 5 = Other

^{b,c} Current phase:

– For decommissioning:

- 1 = Drawing up the final decommissioning plan
- 2 = Reactor core defueling
- 3 = Waste conditioning on-site (only for decommissioning waste)
- 4 = Waste shipment off site (only for decommissioning waste)
- 5 = Safe enclosure preparation
- 6 = Partial dismantling
- 7 = Active safe enclosure period
- 8 = Passive safe enclosure period
- 9 = Final dismantling
- 10 = Final survey
- 11 = License terminated (end of decommissioning process)

– For fuel management:

- 1 = Transfer to at reactor facility
- 2 = Transfer to away from reactor facility
- 3 = Storage in an on-site facility
- 4 = Storage in an off-site facility
- 5 = Shipment to a reprocessing plant
- 6 = Under water storage
- 7 = Dry storage
- 8 = Encapsulation

Experience in the USA has varied, but 14 power reactors are using the Safstor approach, while 6 are using, or have used, Decon. Procedures are set by the NRC.

For the Trojan plant (1,180 MWe, PWR), Safstor was combined with some dismantling, but the timescale is typical and the task was undertaken by the utility itself. The plant closed in 1993, steam generators were removed, transported, and disposed at Hanford in 1995, and the reactor vessel was removed and transported to the Hanford disposal site in 1999. The buildings are being decontaminated, but demolition is not planned until 2018.

Rancho Seco (913 MWe, PWR), which was closed in 1989, will be in Safstor until 2008, till funds are available for dismantling.

At multiunit nuclear power stations, the choice has been to place the first closed unit into storage until the other ones end their operating lives, so that all can be decommissioned in sequence. This optimizes the use of the staff and the specialized equipment required for cutting and remote operations and achieves cost benefits.

Then, after 14 years of comprehensive cleanup activities, including the removal of fuel, debris, and water from the 1979 accident, Three Mile Island 2 was placed in post-defueling monitored storage (Safstor) until the operating license of Unit 1 expires in 2014, so that both units will be decommissioned together. Safstor was also adopted for San Onofre 1, which was closed in 1992, until licenses for Units 2 and 3 expire in 2013, but after NRC changes, dismantling was brought forward in 1999.

A US Decon project was the 60-MWe Shippingport reactor, which operated commercially from 1957 to 1982. It was used to demonstrate the safe and cost-effective dismantling of a commercial scale nuclear power plant and the early release of the site. Defueling was completed in 2 years, and 5 years later the site was released for use without any restrictions. Because of its size, the pressure vessel could be removed and disposed of intact. For larger units, such components will have to be cut up in many pieces.

Immediate Decon was also the option chosen for Fort St. Vrain, a 330-MWe high temperature gas-cooled reactor which was also closed in 1989. This took place on a fixed-price contract for 195 M\$ (hence costing less than 1 cent/kWh, despite a short operating life) and the project proceeded on schedule to clear the site and relinquish its license in 1997, the first large US power reactor to achieve this.

2 Decommissioning Organization and Management

2.1 Overview

Careful planning and management are essential to ensure that decommissioning is accomplished in a safe and cost-effective manner. Guidance on organizational aspects may lead to better decision making, reductions in time and resources, lower doses to workers, and reduced impact on public health and the environment.

Published information on organizational aspects of decommissioning is scarce in comparison with that on technological aspects. The United Nations Organization-International Atomic Energy Agency (UNO-IAEA) recently published a dedicated report on the experience available globally on organizational aspects of decommissioning. Older IAEA Technical Reports discussed planning and management aspects for decommissioning research reactors and other small nuclear facilities; planning and management were also dealt with as one part of the overall decommissioning project.

The decommissioning of a large nuclear facility is a major project. Thus, best project management and organization practices, tools and techniques, and QA processes are vital. A dedicated waste management strategy is essential for safe and cost-effective decommissioning. Clear lines of communication among all interested parties and responsibilities and accountabilities are of great importance.

A decommissioning project is subject to continuous change, and procedures for the management of changes are essential, starting with a timely plan to deal with the social impact that can occur during plant shutdown.

Clearly stated end states of the decommissioning activities are established. The end states are derived from the objectives of the organization charged with completing the work and are in compliance with the requirements of the regulatory body and other organizations. Further, the agreed upon end states will be readily verifiable, independently measured, and reported in a quantitative way.

The safety of the workforce, public, and environment is paramount throughout the decommissioning project.

Adequate funding provisions are essential prior to implementing the decommissioning process and regular reviews are undertaken to ensure that adequate provisions are in place throughout the decommissioning project.

It is important that the Decommissioning Project Manager (DPM) be identified and the decommissioning team established in time to allow the development and approval of the decommissioning plan. It is important to use a dedicated organization with the necessary responsibilities and qualifications.

Key personnel from the operating facility staff are normally part of the decommissioning management team due to their familiarity with the facility and its systems.

The licensee remains in control and possesses sufficient in-house experience to understand the safety requirements even if use is made of contractors during decommissioning. Assurance is required that contractors provide a service of adequate quality.

The actual organization of the decommissioning team can vary greatly and should be based on the expertise of individual team members, the type of facility, the decommissioning strategy, and government policies. The team composition may also change during the progress of the decommissioning project.

Management of interfaces with organizations external to the decommissioning team is important. This ensures that all interested parties are kept informed of the project's progress and have an opportunity to properly manage their input.

2.2 Issues Affecting Decommissioning Organization and Management

2.2.1 Decommissioning Strategy

Early planning of decommissioning activities provides a sound basis for decommissioning cost estimation and funding provisions. As already discussed, planning for decommissioning begins during the design of the facility and continues during its construction and throughout its operational life. In the case of a facility that is shut down without a decommissioning plan, such a plan should be prepared without undue delay.

There are several important elements (spent fuel management, availability of disposal routes for any radioactive waste generated) influencing the choice of a decommissioning

strategy (immediate dismantling, safe enclosure, and deferred dismantling). But the choice of the strategy for decommissioning is essential to define the timing and sequence of decommissioning activities. A generalized decommissioning strategy can be characterized as follows:

- Carry out a post-operational cleanup and achieve the safe enclosure stage of decommissioning as soon as possible after normal operations have ceased so as to minimize future care and maintenance costs and maximize the use of operational experience
- Dismantle more completely if this is justified by safety, environmental protection, economic or social considerations, or by making maximum use of existing expertise
- Defer dismantling, in other cases, until disposal routes for the radioactive wastes generated are available, or if this reduces substantially the total dose through radioactive decay

For facilities such as nuclear power plants, it may be cost effective to defer dismantling if the site is not required for other reasons or if all nuclear power plants on the site will be dismantled in sequence. Dismantling may be undertaken to allow the reuse of buildings or part of the site, if the space is required, or to reduce surveillance and maintenance costs. For smaller facilities immediate total dismantling may be the best solution. As a general rule for radioactive decay considerations, alpha contaminated facilities should be decontaminated and dismantled soon after closure, whereas facilities involving beta and gamma contaminated or activated materials often benefit from radioactive decay and hence from deferral of the decommissioning work.

The policies of the country and the licensee, with respect to the discounting of future costs, will have a major impact on what project work is judged economic to perform to lower surveillance costs. Considerations influencing decommissioning options are discussed in several IAEA publications.

2.2.2 Safety Issues

The protection of the public, the workforce, and the environment is a major factor in the organization and management of the overall decommissioning project. Compliance with all legal requirements, both national and international, is essential. To achieve appropriate standards of safety during the lifetime of the project, the safety documentation is refined and reviewed as required. In this way, it can be ensured that the safety documentation correctly and accurately reflects the status of the decommissioning project and provides the necessary demonstration and justification that the safety standards are being applied.

By applying the standards, the licensee has access to appropriate health and safety expertise to provide advice, auditing, and peer review of the safety documentation. Results of monitoring and surveillance need to be properly interpreted and recorded, and the licensee must be able to take preventive and remedial action as needed.

2.2.3 Work Approaches

Normally, decommissioning operations begin at sites which already have an operating staff. There are two general approaches that can be followed to accomplish the decommissioning of a facility, both of which have a substantial effect on project organization:

- The licensee performs the decommissioning with in-house resources supplemented by specialist contractors as needed

- The licensee contracts with an experienced outside organization to perform the decommissioning and provides general oversight and support services

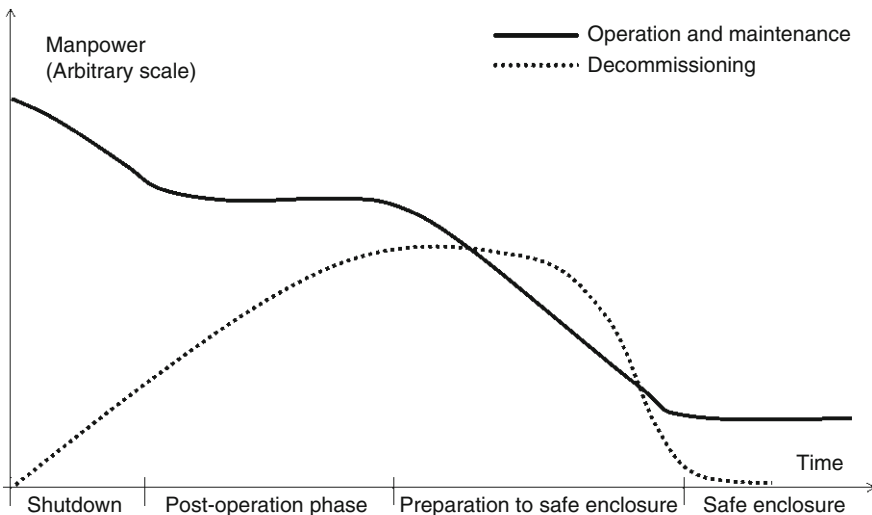
In both cases the licensee must have control of the project. In order to maintain this control efficiently, the licensee is required to be the overall project manager. The licensing regime is based on the premise that the licensee is in day to day control of the facility, processes, and activities and that its staff manages the operation of the facility. Therefore, the licensee needs to be able to demonstrate that an adequate organization is (and will be) in place in order to discharge these responsibilities until the facility is finally removed from regulatory control.

The licensee must weigh all the options carefully and select the option best suited to fulfill its needs, such as cost–benefit, safety, and environmental considerations, as well as social benefits. Multi-attribute analysis is a useful technique to assist the decision making process.

2.2.4 Impact on Staffing

There are inevitable constraints on the approach to staffing for decommissioning. For example, in a reactor plant, staff numbers are likely to be held close to operating plant levels until the fuel has been removed and primary circuit decontamination has been completed. The number of people needed then falls, and the skills needed by the staff becomes somewhat different from those in operation (➤ Fig. 3).

In the USA it is estimated that a single-unit nuclear power plant undergoing early dismantling has a workforce in the range of 100–200 persons. This is approximately one third to one tenth of the number of persons originally employed. During the safe enclosure period the numbers of staff are reduced further to between 20 and 70. For a multiunit power plant site, each unit in safe enclosure would require a staff level of 20 or fewer because common resources are



■ Figure 3
Staff reduction profile during decommissioning

shared. Within the safe enclosure phase for a single-unit facility, staff numbers will increase to 100–200, supplemented by contractor personnel to carry out the remaining dismantling activities. Within these constraints, a range of approaches can be adopted to suit the plant and the social environment in which it is situated. There are a number of basic points to be addressed and important decisions to be made on the following:

- Staff reduction profile
- Use of operating staff to undertake decommissioning project tasks
- Sharing key resources among different plants
- Policies for choosing what work will be put out to contract

The staff reduction profile depends on the work to be done. When such a profile has been established, commitments can be made to staff as to the length of their remaining employment, and progress on staff reduction can be monitored against the planned profile. Maintaining a high number of operational staff necessitates that they undertake decommissioning tasks. This requires training in new skills and reorientation of attitudes towards a project completion outlook.

The use of an outside contractor to perform most of the decommissioning activities may have a negative impact on the local workforce. In order to encourage a job completion attitude, it is helpful if arrangements can be made to guarantee future relocation of staff to other plants, projects, or similar organizations. One way of approaching this would be to form teams of skilled, experienced personnel who could effectively provide services to similar plants as contractors.

It is important to provide appropriate incentives to staff (and contractors) to work effectively and in a manner that completes the decommissioning program safely within the schedule and budget, encouraging staff to seek completion of the work rather than apparently perpetuating their jobs through delay.

Even when using outside contractors, the licensee remains accountable for safety on-site. As such, the licensee is required to have systems in place that guarantees that the contractor personnel are suitably qualified and experienced, and can understand the hazards on the site and are adequately supervised.

2.3 Organization and Management in the Various Phases of Decommissioning

2.3.1 The Planning Phase

In the period well in advance of final shutdown, the decommissioning-oriented organization does not need to be large or employed full-time. The expertise required includes aspects such as decommissioning, waste management, cost estimation, and licensing. Assistance is needed from personnel with detailed knowledge of the plant, technical experts, and planning system specialists. It is also important for this team to learn from experience elsewhere so as to be able to consider the range of options available.

As planning for decommissioning is important but not necessarily urgent, it may tend to be treated as of lower priority than the operational problems. The decommissioning team needs to be protected from such diversions. It will also be appropriate to supplement the core team with

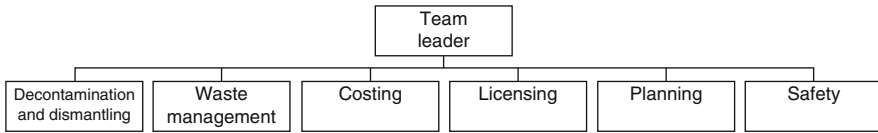


Figure 4
Decommissioning oriented team during plant operation

additional personnel from the licensee's organization, spending limited periods attached to the team to contribute an essential practical element.

The team reports to the senior management, who is not responsible for day to day operations of the plant. A major benefit of the work of the team is establishing accurate decommissioning costs and risks, which could provide important information for allocating and managing the decommissioning fund. The cost of a small organization such as this should be considered an investment in order to achieve a better managed decommissioning project. A simple functional structure could be as depicted in [Fig. 4](#).

Once a decision has been made to decommission a facility, and preferably before operation ends, it is essential to identify and appoint a DPM having the required skills, qualifications and experience, and with the necessary authority. The DPM, in consultation with the management of the operating organization, should set up a decommissioning project management team to perform the necessary project planning. This includes the development of a decommissioning plan, and its approval where necessary, and control of the resources during the physical decontamination and dismantling activities. As decommissioning proceeds, the decommissioning project management team expands to include persons with necessary and adequate qualifications and experience.

2.3.2 The Transition Phase

There are two main transition periods associated with any decommissioning project:

- The transition from an operating facility to the decommissioning period
- The transition from the dismantling period to a post-dismantling period (restricted or unrestricted site release and reuse)

The first transition period takes the facility through a deactivation phase after it has been shut down. During this period, many hazards connected with the operational phase are removed before turning the facility over to the decommissioning team. This includes removal of the spent fuel, draining of systems, and removal of the waste generated during operation. The management structure always reflects the changing circumstances and continuing responsibility of the licensee for the operation, including decommissioning, of the licensed site.

In moving from operation to decommissioning, a cultural change is needed, which is reflected in the appointment of the decommissioning team. [Table 3](#) shows the differences between decommissioning and operational states.

The organization at the commencement of decommissioning will be that which has ended the operational phase of the plant's life. In some cases, a new operator takes over the decommissioning process. Even in these cases, however, most of the operating team is likely to be retained

■ **Table 3**

Differences between decommissioning and operational states

Decommissioning state	Operations state
Temporary design life of structures to assist dismantling	Permanent design of structures for operation
Safety management systems based on decommissioning tasks	Safety management systems on operating nuclear facility
Control based on as-built structures	Control based on drawings
Reduced safety risks but changing situation	Significant safety risks but permanent and routine
Management of changing situation during decommissioning	Management of steady state during operation
Reduced administrative infrastructure	Steady state administration infrastructure
Retraining staff for new activities	Routine training and refresher training
Visible end of employment – refocus their work objective	Permanent employment with routine objectives
New or developing regulations/regulatory requirements	Established and developed regulations for operation

for the initial phases of decommissioning. The operating team needs to evolve to suit the job. Part of the planning is to define how the changes in the organization, staffing, contractor usage, usage of mobile teams, etc., are controlled and when these changes occur, bearing in mind that at least part of the decommissioning project team needs to be in place before operation ends.

During the transition period, plant operations, maintenance, and provision of emergency arrangements are still required and may form a separate part of the organization, which should be derived from the team that operated the facility. This approach may profit from the accumulated experience and help reduce local employment concerns.

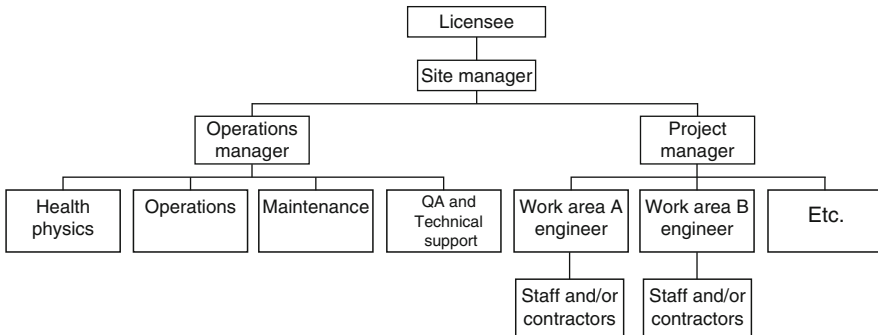
In some cases, this organization may continue into the decommissioning period for some time. A reasonable structure for the site management is depicted in ► [Fig. 5](#).

2.3.3 The Active Phases of Decommissioning

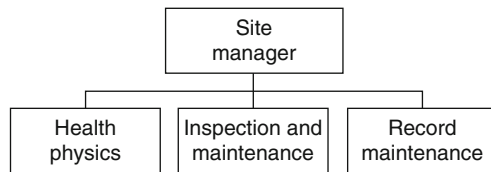
The management and organization during active phases of decommissioning work, either during immediate or deferred dismantling, is discussed in ► [Sect. 2.4](#).

2.3.4 The Safe Enclosure Phase

The safe enclosure phase, if any, is characterized by a plant of relative engineering simplicity requiring minimal operation, inspection, and maintenance and where the hazards are well defined and controlled, preferably in a state of passive storage. A minimal organization is in



■ **Figure 5**
Organization in the transition phase between operation and decommissioning



■ **Figure 6**
Organization in the safe enclosure phase

place during the safe enclosure phase: as it is a phase of stability rather than of change, there are few or even no project staff. It is presumed that sufficient work has been performed to allow relaxation of the need for emergency arrangements of any size. The necessary measure for the physical protection of the facility may also be reduced. Finally, off-site environmental monitoring may also be scaled down.

As a specific example, the Dresden-1 BWR decommissioning project was part of a multi-plant site that was aimed at safe enclosure. This project required seven permanent staff and was supported by 27 persons from other parts of the site organization providing services such as security and emergency planning.

Construction and maintenance organizations would support the project on an as-needed basis.

The size of the safe-enclosure phase organization depends on the level of dismantling and stabilization/immobilization of wastes that has been undertaken. It may even be appropriate to utilize multi-site mobile teams to perform much of the dismantling work. A simple structure is outlined in [Fig. 6](#).

A significant degree of multi-skilling may reduce staff numbers in this organization. Links to a centralized organization would also reduce the number of staff on-site, particularly for a multi-plant site licensee. The role related to record maintenance is very important to the successful completion of decommissioning.

2.3.5 The Post-Dismantling Period

The second important transition phase previously mentioned is from the dismantling period to another state, which might vary depending on the final end point of the decommissioning project. This end point could be either an authorized reuse for other purposes after specified conditions have been met, or the unrestricted release or clearance of the site. Depending on specific circumstances, authorized release of the site may or may not imply the continued presence of a surveillance unit, whereas clearance implies that all organizational units regarding decommissioning will disappear. Until the site release criteria have been met, it remains a nuclear site with associated controls. The persons responsible for record keeping will then transfer relevant records as required by the regulatory body.

Site remediation may be required to meet authorized reuse or clearance criteria. This could involve several activities such as radiological clearance or immobilization, removal of remaining nonradioactive structures, and landscaping.

A final report is prepared and presented to the regulatory authorities before the decommissioning team is dispersed towards other duties and while all relevant data, experience, and knowledge are still readily available. This report demonstrates that the facility and associated areas have been decommissioned to the state specified in the decommissioning plan, or in approved modifications to the plan.

2.3.6 Spent Fuel and Waste Storage

Spent fuel or some decommissioning waste may remain stored on-site in an independent facility after decommissioning. Provisions are made by the licensee to assign personnel with sufficient experience to the responsibility for the long-term care, maintenance, surveillance, and safeguards of such storage arrangements.

2.4 Management for Active Phases of Decommissioning

2.4.1 Overview

Decommissioning planning addresses issues such as worker and environmental protection, preparation of plans, safety assessment, working procedures, time schedules, training, and other technical and administrative aspects. Appropriate additional management, technical, and administrative personnel may need to be recruited and assigned responsibility for one or more functions. It is important to select persons who are technically or professionally qualified and have related practical experience. In particular, persons experienced in coordination, management, and engineering are assigned to the decommissioning project in an early phase, so that they can start effective planning and can successfully accomplish it without undue delays.

For extensive projects such as decommissioning large nuclear facilities, it is helpful to identify important technical, operational, and administrative aspects when defining individual management requirements, even if these aspects may be managed by the same personnel.



2.4.2 The Decommissioning Management Team

The decommissioning team includes staff having all the skills, qualifications, and experience necessary for the decommissioning task, together with a suitable supervisory structure under which it can operate. It is preferable, particularly in the early stages of the project, to include, in the decommissioning team, persons who were involved in the operation of the facility and have knowledge of the plant and its history.

Experienced staffs are preferred, and the team is built up so that all persons are suitably qualified for the tasks they have to perform. Training programs may be established to ensure that the staffs meet the requirements during decommissioning and that records are kept to demonstrate the adequacy of the training. Also, training of the decommissioning team would allow them to perform the decommissioning in accordance with current standards in technology.

The responsibility for managing and implementing the decommissioning project is with the licensee, who appoints a DPM. This is the best way to ensure maximum management commitment, motivation, and understanding of requirements for the program. The DPM would act on behalf of the licensee and would be in charge of the detailed aspects of the planning and management of the decommissioning program.

The DPM selects and recruits a decommissioning management team and assigns specific responsibilities to each group within the organization. The DPM implements the strategy to allocate all or part of the decommissioning program to external organizations. Basic requirements for a decommissioning team are the same, irrespective of who carries out the operations.

Possible functional organizational structures for a decommissioning management team required to successfully implement and complete the decommissioning of a facility are shown in  [Fig. 7](#) (management team where the licensee performs most of the decommissioning tasks using in-house resources) and in  [Fig. 8](#) (management team where the licensee hires an outside organization to perform most of the work and the licensee provides supervision and verification of the activities). In either case, the licensee retains overall responsibility for the project and ensures that all regulatory authority requirements are fulfilled.

Many details on aspects such as workforce requirements, work plans and procedures, selection of speciality contractors, and scheduling for the decommissioning of reference nuclear installations are given in a series of publications by the US NRC.

2.4.3 Change Management

The period between the announcement to shut down a nuclear plant and the start of decommissioning may pose significant challenges to plant management. They need to prepare for new technical and organizational challenges in a climate where there could be pressure to reduce staff numbers. Moreover, increased levels of uncertainty can threaten staff morale and commitment, and the decision to shut down may itself be preceded by periods of rumor and uncertainty. In an industry where security of employment has often been taken for granted, this may be unsettling for plant personnel. The plant management needs to put in place a timely plan to deal with social impact that may occur during plant shutdown.

The move towards decommissioning can thus be regarded as a process of major organizational change. So far, attention has largely focused on the technical aspects of decommissioning,

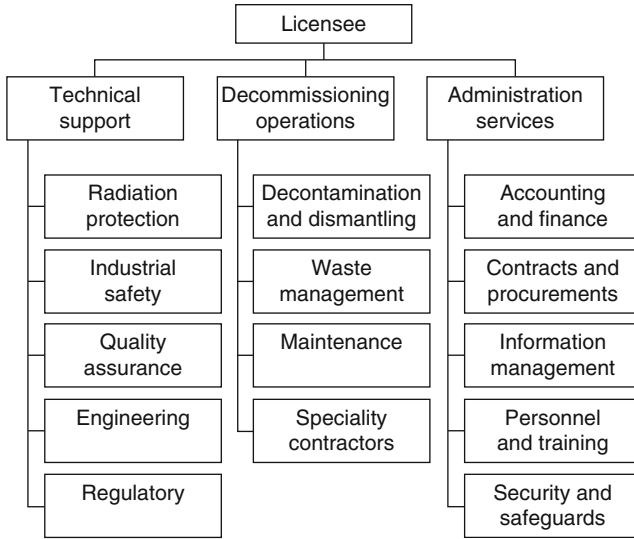


Figure 7
Organization chart: licensee performing decommissioning

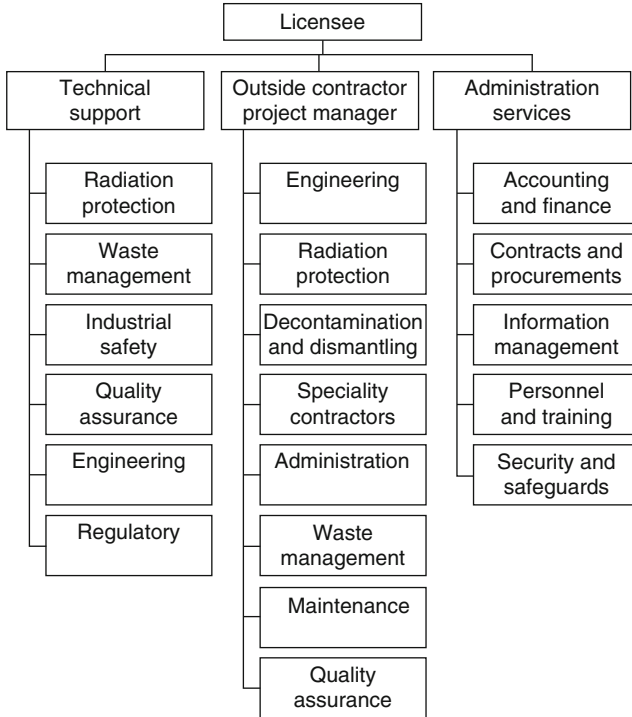


Figure 8
Organization chart: licensee with outside contractor performing decommissioning

with relatively little attention given to organizational and other human factors. Nuclear licensees have embarked on extensive change programs in recent years to reduce fixed costs and to enhance the profitability of their companies. This has involved proposals to achieve significant reductions in personnel. These changes need to be carried out in accordance with rigorous and comprehensive management of change arrangements.

One essential point regards the licensee's considerations as to whether and how any proposed organizational change might impact upon safety. In the context of decommissioning, the organizational challenge is heightened by the changing demands on the workforce. Not all proposed organizational changes have the potential to affect safety. However, where changes involve the loss or redeployment of personnel who have a safety or support role, analysis of the organization's need for the safety function and the way in which it is carried out, both currently and in the future, has to be performed. At all times the licensee's organization remains able to meet projected resource and competence needs.

Decommissioning is often a stage of the plant's life-cycle where large numbers of external contractors are employed. These groups bring specialist skills to bear which were not called for during normal operation. Contractorization may also be viewed by plant management as a way of making up for any shortfalls in staffing levels which have resulted from the premature release of experienced staff (e.g., those who have secured early retirement deals or who have moved to jobs elsewhere which appear to offer a more secure future).

Contractorization can bring benefits, but it is very important that the licensee retains sufficient competent personnel to understand, own, and use the plant safety case, and to act as "intelligent customer" for work by contractors. This is especially important during decommissioning. Older plants may not have a comprehensive set of drawings and procedures, so that many historical aspects of plant design and operation which need to be accessed during decommissioning are vested in individuals rather than in paper work. These persons have to be retained as long as their knowledge and experience can plausibly be required, and it is also preferable that this experience be documented in a form available for use by other personnel.

2.5 Decommissioning Planning and Licensing

2.5.1 Overview

Successful decommissioning depends on careful and organized planning including clear identification of the objectives of the decommissioning process. The end states are derived from the objectives of the organization charged with completing the work and are in compliance with requirements by the regulatory body and other competent authorities. Moreover, the agreed upon end states will readily be verifiable and can be independently measured and reported in a quantitative way.

Once a strategy has been developed, the decommissioning plan is prepared for each nuclear facility. The extent of such plans and their content and degree of detail required may be different, depending on the complexity and hazard potential of the nuclear facility and on regulations. Typical contents of a final decommissioning plan are indicated in [▶ Table 4](#).

Planning to allocate adequate financial resources to ensure the decommissioning of a nuclear facility is made preferably at the early stages of the plant's life-cycle. Especially in the case of deferred decommissioning, where there may be long safe enclosure periods, these

■ **Table 4**

Example of contents of a decommissioning plan

Section	Contents
Introduction	Objectives, scope, goals to be achieved
Facility description	Physical description of the site and the facility and its operational history Radioactive and toxic material inventory
Decommissioning	Objectives, decommissioning alternatives strategy Selection and justification of the preferred option
Project management	Resources Organization and responsibilities Review and monitoring arrangements Training and qualification Reporting and records Risk management
Decommissioning activities	Decontamination and dismantling activities Waste management Maintenance programs
Safety assessment	Dose prediction for tasks, demonstration of ALARA for tasks risk and uncertainty analyses Operating rules and instructions
Environmental impact assessment	Demonstration of compliance with environmental standards and criteria
Quality assurance program	Setting up a QA (quality assurance)/QC (quality control) program Verification of compliance with established QA requirements
Radiation protection and safety program	Radiation monitoring and protection systems Physical security and materials control Emergency arrangements Management of safety Justification of safety for workers, general population and environment
Continued surveillance and maintenance	Development of surveillance and maintenance programs
Final radiation survey	Demonstration of compliance with the cleanup criteria
Costs	Cost estimate Provision of funds

financial provisions are reviewed periodically and adjusted, if necessary, to allow for inflation and other factors such as technological advances, waste disposal costs, and regulatory changes. Responsibility for this review may reside with the licensee, the regulatory body, or other parties depending on the national legal framework.

A radiological characterization and material inventory assessment is carried out for the facility at the early stages of decommissioning planning. This provides support for a number of activities, including waste management, decontamination and decommissioning methodologies, and safety and environmental assessments.

A safety and environmental impact assessment (EIA) forms an integral part of the decommissioning plan. The licensee is responsible for preparing this assessment and submitting it for review by the regulatory body, as required. The safety and EIA should be commensurate with the complexity and the associated hazard potential of decommissioning.

2.5.2 Decommissioning Planning

Planning for decommissioning is an essential prerequisite to ensure that decommissioning activities can be accomplished in a safe, timely, and effective manner. The licensee is responsible for this planning. The regulatory body provides guidance in this respect, and reviews and approves the decommissioning plan before the start of decommissioning activities.

Successful decommissioning depends on careful and organized planning including clear identification of the objectives of the decommissioning process. The end states are derived from the objectives of the organization charged with completing the work and are in compliance with requirements set by the regulatory bodies and other authorities. Moreover, the agreed upon end states will readily be verifiable and can be independently measured and reported in a quantitative way.

When the timing of the final shutdown of a plant is known, the licensee should initiate detailed studies and finalize proposals for decommissioning.

If the selected decommissioning option results in phased decommissioning – with significant periods of time between phases – the higher level of details may only be required for the next immediate phase being executed.

After a general plan has been developed, detailed planning and engineering can begin. As detailed data are made available from the radioactive inventory of the nuclear facility and the site characterization program, decisions on the handling of components, structures, and soil can be made.

Multiple levels of planning documents are usually prepared. A hierarchical work breakdown structure is developed to divide the work into manageable packages, which identify what has to be done and how, and addresses the basic safety considerations of the activity. Another level of documents is constituted by the detailed work procedures.

2.5.3 Stages of Planning

Three stages of planning are envisaged:

- Initial planning
- Ongoing planning
- Final planning

A preliminary plan for decommissioning should be prepared by the licensee before a license application for a new facility is submitted. A generic study showing the feasibility of decommissioning may suffice for this plan. In any event, the plan need not be compiled in detail since many factors in the future can affect it, for example, improvements in technology and changes in regulations and government policy. Environmental aspects of the decommissioning, such as the quantities of wastes and radioactive effluents, should be considered during the initial planning. The plan should also address the costs and the means of financing the decommissioning work. In some countries, the regulatory body requires that the licensee to provide a preliminary cost estimate and assurance of funding.

During the operation of a facility, the preliminary plan should be reviewed in respect of the ease of decommissioning, the environmental impact and, where applicable, cost estimates and financial provisions. All significant system and structural changes should be documented in technical files and kept available for those responsible for the final planning of decommissioning activities. Records of spills or spread of contamination, including details of the radio nuclides involved and their quantities, should be retained.

Regular audits should consider such aspects as operational procedures that may have impacts on decommissioning and operational records and other documentation which is useful for the final decommissioning plan.

When the date and circumstances of the final shutdown of a nuclear facility are known, an application for permission to decommission the facility must be submitted to the regulatory body without undue delay.

In many cases, steps such as the final shutdown, reduction of staff, management of operational wastes, measurements for inventory determination, transport of fissile materials off the site, and decontamination to facilitate decommissioning may be taken under the provisions of the operating license or amendment thereof.

In support of the application to decommission a facility, a decommissioning plan must be submitted for approval and must include a safety assessment and an appropriate level of environmental assessment. If final (Stage 3) decommissioning is deferred, a revised decommissioning plan shall be prepared and submitted for approval before final dismantlement can begin.

Most planning steps are the same for all decommissioning options. The degree of detail required may, however, be different.

2.5.4 Content of Decommissioning Plan

When the timing of the final shutdown of a nuclear facility is known, the licensee should start detailed studies and finalize proposals for decommissioning. Following this, the licensee should submit an application containing the decommissioning plan for review and approval by the regulatory body. The decommissioning plan may require amendments or further refinements as decommissioning proceeds and may require further regulatory involvement.

If the selected decommissioning option results in phased decommissioning – with significant periods of time between phases – the level of detail of the items in [Table 4](#) may only be required for the next immediate phase being executed. As a result of executing an individual phase of the decommissioning, some modification of the planning for subsequent phases may

need to be done. In such cases, subsequent sections of the decommissioning plan may require updating and reviewing.

A decommissioning plan should typically include:

- Choice of the decommissioning strategy, with a description of the steps involved in effecting its completion. Generally, the rationale for the choice of a given strategy should be elaborated, with allowance for such factors as the availability of a waste disposal or storage facility, radiological aspects, and the long term integrity of buildings and structures.
- Description of techniques, tools, and procedures to be used for the decommissioning.
- Time schedule for the decommissioning.
- Analysis of radiological and nonradiological risks for workers.
- Environmental impact analysis, including estimation of maximum individual doses to the public and collective dose commitment from the airborne and liquid releases during decommissioning, as well as from steps such as transport, recycling, reuse, and waste management and residual activity on the site.
- Safety assessment and evaluation of the radiological consequences of postulated accidents during decommissioning.
- Results of surveys, special measurements, and calculations to determine the inventory and distribution of radionuclides in the facility.
- Description of the anticipated inventory (activity, volume, mass, location, physical, and chemical form) of radioactive, toxic, and hazardous material arising from the decommissioning and the manner of disposing of or recovering such material, including means for handling, transporting, and storage.
- Quality assurance program applicable to, including the qualifications of the organization proposing the decommissioning and its contractors.
- Description of the measures incorporated in the procedures and equipment to ensure that the basic principles of radiation protection, health, and safety are followed.
- Description of the methods for ensuring the availability and proper functioning of the systems and structures needed for radiation protection, health, and safety during dismantling. This is particularly important when only some parts of the structure and systems are being dismantled.
- Description of the methods proposed for the final radiometric measurements to ensure compliance with authorized limits for the release of equipment, materials, buildings, and the site.
- Emergency planning during decommissioning.
- Outline and format of the final decommissioning report to the regulatory body at the completion of the planned decommissioning.

2.5.5 Decommissioning Optimization

Consideration should be given at the design stage and subsequent phases of a facility to the various aspects that might optimize the process, with particular attention to:

- Funding
- Minimization of workers' exposure
- Minimization of waste production

Before any decommissioning activities take place, sufficient funds should be available. The owner/operator is responsible for ensuring that a fund for decommissioning is set up.

The cost estimate for decommissioning should include the costs of planning and engineering during the post-operation phase, decontamination, dismantling, and transportation and disposal of the radioactive wastes due to decommissioning. The costs of maintenance, surveillance, and security of the facility should be included if the decommissioning is done in several phases.

It is difficult to set up a decommissioning fund to cover the unplanned premature shutdown of a facility, since the condition of the facility varies considerably depending on the cause of shutdown and the type of facility. However, the financial consequences of such a shutdown may impose a considerable burden on the licensee as a result of obligations to the public (third-party indemnification) and the potential costs of the cleanup which may be required prior to decommissioning. Such funds may be assured through insurance schemes.

Some procedures and practices could aid decommissioning and reduce radiation exposures, as long as this does not reduce overall safety. These considerations may include, among others, an examination and assessment of material composition with the aim of reducing the radioactive inventory, and the provision of easily decontaminable surfaces and an effective system for storing, updating, and accessing records relevant to decommissioning.

Records to be retained should include drawings of structures, descriptions of equipment in areas where radioactive materials are used and the location of possible inaccessible contamination.

If the site is not to be treated for unrestricted release, the plant may be stored in a safe condition for a prolonged period. During this storage period, the facility should be adequately maintained and monitored. Physical security of the facility should be maintained as long as required.

Since some equipment and structures may be removed during this storage period, measures should be taken to prevent releases of radionuclides to clean areas and the environment. This may require periodic checking of some characteristic parameters selected as a result of an assessment of safety. Records should be kept of modifications to the facility to ensure that adequate information is available for conducting final decommissioning.

In support of the plan for deferred decommissioning, the licensee must submit to the regulatory body a description of:

- Maintenance of building and structures, including containment where applicable
- Physical security of the facility
- Systems necessary for keeping the nuclear facility under proper control, including air ventilation and monitoring systems
- Inspection and surveillance plan
- Environmental monitoring program
- Accident analysis
- Emergency planning
- Quality assurance program, including organization and responsibilities


For deferred decommissioning, it may be necessary to ensure that decommissioning funds are secured, and the necessary amounts are updated periodically to cover the cost of inflation during the period of deferment or that other appropriate steps are taken to ensure the availability of funds.

2.5.6 Project Risk Management

Experience has shown that large projects may fail to meet their objectives, in terms of time, cost, and quality. This is a particular concern for projects where there is limited previous experience, the technology has not fully matured and there are risks associated with technical performance. This could be the case for nuclear facility decommissioning and environmental restoration projects which may have uncertainties. Project failure may often be identified as resulting from events which had not been anticipated during project planning, but which might, by hindsight, have been accommodated if identified at the outset.

Accordingly, formal Project Risk Management (PRM) techniques have been developed to address these problems. Such techniques adopt the basic approach of attempting to identify all potential hazards before they materialize and implementing actions to prevent their materialization or to limit their consequences. The process includes commercial and managerial as well as technical risks. A further key role of formal PRM is the allocation of ownership of risk, i.e., the identification of the party who is responsible for a given risk and who bears responsibility for its management. Risk allowance as part of contract negotiation can help prevent disputes later during project implementation, and provide justification for any provision for risk to be made in pricing or program.

Typically, implementation of formal PRM involves the following key steps:

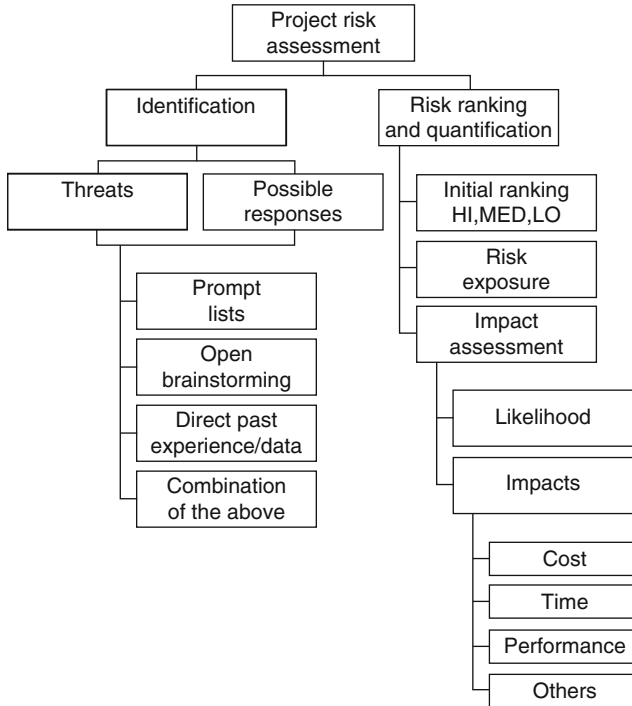
- Development of PRM strategy, to identify the objectives for PRM implementation in the given context and define the requirements for risk assessment, risk analysis, and risk management planning over the project life-cycle
- Risk assessment, a workshop to identify risks to project success and potential consequences (cost and program), as well as to identify possible actions that might be adopted to manage them (the logical process and implementation mechanisms of project risk assessment are described in  Fig. 9)
- Risk analysis, to quantify the overall impact of identified risks on project cost and program and to evaluate the effectiveness of potential responses
- Risk management, to select the preferred responses for addressing the identified risks and to allocate residual risks most appropriately among the parties involved. This is an ongoing process throughout the project.

2.5.7 Regulatory Approval

To ensure compliance with national, regional, and local regulations, standards and laws, it is important that the licensee, before or during the planning stage, identify all relevant legislations likely to be applied in the decommissioning program. If specific requirements for decommissioning have yet to be developed or finalized, decommissioning activities could be undertaken on a case by case basis under existing regulations; for example, the arrangements for carrying out modifications on operational facilities. In such cases, it would be advisable for the licensee to be in regular consultation with the regulatory body throughout the development and implementation of the decommissioning program.

The regulatory body or other competent authorities may review:

- The decommissioning strategy
- The decommissioning plans and programs



■ Figure 9

Summary of elements of project risk assessment and analysis

- The procedures employed during the decommissioning process, in particular clearance of materials/wastes
- The surveillance and inspections
- The safety assessments
- The funding provisions

The timescale for review of the decommissioning tasks by the regulatory authorities should not be underestimated. This can have a significant impact on the whole project time-scales and, consequently, on the costs.

The regulatory body verifies that the final condition of the facility meets the approved objectives established at the beginning of the project.

2.5.8 Work Packages and Procedure

While the decommissioning plan and safety and environmental assessment are being reviewed by regulatory bodies, detailed planning and engineering can begin. As detailed data are made available for the radioactive inventory of the nuclear facility and the site characterization program, decisions on the handling of components, structures, and soil can be made.

Multiple levels of planning documents are usually prepared; an example is described below. A hierarchical work breakdown structure is developed to divide the work into manageable packages, which identify what is to be done and how, and address the basic safety considerations of the activity. Another level of documents is constituted by the detailed work procedures.

The work packages identify the purpose and provide a description of the task, applicable criteria and the activity sequence of events. The criteria include engineering and technical requirements; health, safety, and environmental protection requirements; and reference to applicable standards. Work packages refer to other documents such as the Radiological Health and Safety Manual, Waste Management Manual, Security Plan, Quality Assurance Program, Fire Protection Program, etc.

The detailed work procedures identify the step-by-step instructions for performing each task, the required equipment and associated operating parameters (cutting speeds, gas pressures, power requirements, etc.), safety precautions and disposal methods, as applicable. Detailed work procedures are either general or specific work procedures. General work procedures are used for repetitive activities such as construction of contamination control tents, rigging and lifting, pipe cutting methods, and maintenance of filtered equipment (high-efficiency particulate air (HEPA) vacuum cleaners, ventilation units, liquid filtration systems, etc.). Specific work procedures apply only to unique tasks such as core dismantling activities or asbestos removal, where general work procedures cannot be fully applied.

As the work packages and detailed work procedures are developed, the baseline cost estimate, schedule, and personnel radiological exposure estimates are refined. These can then become the guidelines against which the project performance is measured.

The decommissioning plan identifies and justifies the decommissioning work activities. However, before work commences, work packages are developed for these activities and analyzed in sufficient detail to allow the decommissioning team to execute the work with a clear understanding and without the need for further significant explanation. The packages are arranged into interrelated groups, and a schedule of activities, usually represented by a bar or Gantt chart, is prepared. Formal project management techniques are applied to the creation and management of work packages. A critical path network, i.e., a diagram indicating the sequences and interdependencies of the various work packages may be used. The work packages are planned as soon as possible, because such planning greatly assists in the development of detailed cost estimates and the identification of specialist support and equipment that may be needed. Without this level of planning it is difficult to schedule the decommissioning of a large nuclear facility with any degree of certainty.

Procedures for allocating work packages to the decommissioning team are developed. Work monitoring arrangements are set up so that the project management schedule can be reevaluated when unexpected circumstances arise. The DPM holds periodic formal review meetings with all supervisors and safety staff to assess work done, current status of the facility, and future tasks. Each member of the team should then be aware of what is to be done next in other parts of the program and in other related activities.

From the formal project meeting, progress reports including revised cost estimates are prepared periodically and are presented to the regulatory body, licensee, and other authorities, as required, including the organization providing the funds.

2.6 Role of Quality Assurance

2.6.1 Overview

Any activity having an impact on the health and safety of workers, the public or the environment, or affecting the success of the project, is covered by a quality assurance (QA) program including management and organizational aspects. For such activities, it is necessary to have written procedures, documentation, control guidance on the selective applications of QA procedures, and accurate information and techniques to verify compliance with QA procedures.

A QA program continues to be needed for all activities to be controlled. It is generally adapted from the one used during operation, concentrating on those aspects associated with the management of change. As such, it needs to evolve throughout the decommissioning program. A number of phases can be seen in the program during decommissioning. To give an example, when a reactor is being defueled or the primary circuit is decontaminated, hazards, and activities are not dissimilar to those experienced during operation. During dismantling and demolition the management of change predominates, and the QA program needs to reflect that. At the end of the period of change, the site may go into surveillance with low staff numbers. At this stage, it needs a very simple QA program.

It is important to recognize that the reduction in costs, staff, and administration generally can be achieved by a progressive simplification of the QA program as decommissioning proceeds. This originates ultimately from an adaptation of the safety assessment case, because of lower nuclear hazards as work progresses. This allows a reduction in rules for operating plant systems, maintenance requirements, and their implementing documents. Plant items can be released from service and decommissioned. The overall effect is to reduce the need for staff. The QA program is designed to control this change process so that each step occurs in a coordinated way, and the QA program itself needs to evolve to suit the changing circumstances.

In performing the planning for the decommissioning project, it should be recognized that health and safety are not always affected to the same degree for every facility, and a graded approach to QA can be developed to ensure an adequate level of quality for factors such as maintenance and equipment reliability. Less stringent controls could be utilized for functions not affecting safety, but it must be justified.

The QA program is initiated before the decommissioning activities commence. A summary of the QA program is incorporated in the decommissioning plan and includes, as a minimum, the basic elements to be discussed in the following subsections.

2.6.2 Control of Modifications to the Plant

Procedures for carrying out modifications to the plant may have existed for the operational phase of the facility. These can be utilized, simplified where possible and adapted for the decommissioning phase.

2.6.3 Radiation Protection and Environmental Safety Control

The radiation protection specialist assesses the procedures and instrumentation that are used for various types of radiological and environmental survey to ensure appropriateness.

Decommissioning procedures are reviewed to ensure that the appropriate data for radiological assessments are being used. Criteria for the collection and analysis of radiological samples during the decommissioning process are reviewed by the radiation protection specialist. An independent analysis may be performed to ensure that the results are accurate and reproducible.

2.6.4 Control of Outside Contracted Services

Contractors are used for a wide variety of tasks. A common use is for a self-contained specific project. In such cases the licensee still maintains the capability of defining, monitoring, and supervising the work. However, contractors may also be employed to provide services such as health physics expertise, or maintenance. These contractors need careful management by the licensee to ensure that the licensee retains control of intellectual property and assets remain available to the licensee. If the contractor is replaced, a proper handover is arranged so that the new contractor's staffs are trained to be suitably qualified and experienced when they take over.

The licensee has the responsibility for ensuring that contractors achieve the required quality, although contractors are responsible for the quality of their own work. Once their detailed work plan is approved by the licensee, this assurance is achieved by a program of surveillance and inspections.

2.6.5 Surveillance and Inspections

Procedures of surveillance and inspections are an integral part of quality assurance. In facilities where most of the decommissioning work is carried out by external contractors, surveillance should be documented to show what was inspected, by whom, the results of the surveillance, and the corrective action if there was any nonconformance.

Internal quality audits may be performed to assure that all parts of the program are working properly.

Other inspection activities may include calibration of measuring equipment, verification of characterization, packaging and disposal of radioactive waste, or inspections of quality of materials and equipment purchased. The opportunity exists, during early surveillance and inspection work, to assess the as-built condition of the facility against the existing drawings and documentation. This assessment could be carried out when modifications to the facility are required.

2.6.6 Information Management

An important element to emphasize in the development of a QA program for decommissioning is the collection and retention of records and information relevant to the facility. In the case of deferred dismantling of a facility, the maintenance of accurate and complete information relating to the locations, configurations, quantities, and types of radioactivity and other

hazards remaining at the facility is vital to the successful and safe execution of surveillance and maintenance and of subsequent final decommissioning activities. Furthermore, for clearance, it is important to document that all radioactive materials and other hazards present at the beginning of decommissioning have been accounted for and their ultimate destination has been confirmed. It is also important to have documentary evidence that all cleared waste and materials and the site itself have been properly monitored before being released from regulatory control.

QA verifies the procedures and equipment which will be used to acquire, record, and manage important information related to all aspects of the program and ensures the retrievability of documentation. QA verifies that the records required at the end of decommissioning contain information on all operations described in the plan, including items such as:

- Records of waste or materials origin, processing, characterization, transport arrangements, and destination
- Details of the license, other authorization documents and all criteria and standards used during decommissioning
- Details of the equipment and procedures used
- All recommendations, audit reports, corrective actions, agreements, endorsements, and consents in respect of any stage of the decommissioning program
- All safety assessment documentation
- Any independent reviews prepared in accordance with national requirements
- All references cited in the safety documentation, or a statement as to where the referenced document can be located
- Drawings used during decommissioning activities
- Details of the final radiological survey for release of the site

Some operational records need to be retained during and after the decommissioning period for:

- Legislative requirements
- Aiding further decommissioning activities
- Possible litigation in the future

The characterization of records generally includes the following:

- Requirement for the record (e.g., which legislation)
- Record type (i.e., what is recorded)
- Retention period
- Producer of record
- Responsible holder of record
- Storage medium
- Storage location

The choice of a suitable storage medium is an important consideration. Four media are primarily in use today: paper, microfilm, editable electronic media (magnetic disks/tapes), read-only electronic media (CD-ROM image). 📌 *Table 5* summarizes the advantages and disadvantages of each medium. The solution will probably be a mixture of media to suit the record type, in all cases with adequate backup facilities. In any case, before the original record is destroyed, it is essential to establish the legality of the record keeping medium adopted.

■ **Table 5**
Advantages and disadvantages of record-keeping media

Medium	Advantages	Disadvantages	Costs
Paper	Readily available Storage understood Legally acceptable	Bulky Requires controlled storage conditions	Low
Microfilm	Compact Standard technology Legally acceptable	Awkward to access Requires controlled storage conditions	Medium
Editable electronic	Can be updated Compact	Need to keep hardware and software available Only useful for new records Corruptible Legality unclear	Medium
Read-only electronic	Compact Accessible Easy storage	Need to keep hardware and software available Legality unclear	High

2.6.7 Safety Audits

Periodic safety audits of decommissioning activities are performed and documented to evaluate the effectiveness of worker training, surveillance equipment operability and adequacy, management control, safety controls, compliance with ALARA, the emergency program, documentation systems, and exposure assessments. Audits also review and evaluate the conformance of established specifications and procedure requirements.

To review and track safety audit results, a safety review structure is established to implement an audit program and control the application of radiation protection and environmental safety policies during decommissioning. All necessary procedure requirements are established at the very beginning of the planning stage and should be appropriately documented.

2.6.8 Management, Assessment and Reporting of Incidents and Events

Procedures are in place and agreed with regulatory bodies and other competent authorities for the management, assessment, and reporting of incidents and events. This includes the reporting of incidents under the INES system.

2.7 Responsibilities and Qualifications

2.7.1 Licensee

Depending on the regulatory system, a specific license or authorization, different from the facility operating license, may be required to undertake any decommissioning activity. In some

cases, during the decommissioning period, the facility may be operated by a new licensee separate from the former licensee, but which, nevertheless, satisfies the requirements and is deemed competent to hold a license.

Although the licensee in charge is legally responsible for carrying out the decommissioning activities, including funding, in accordance with the regulatory requirements, the financial liability or funding sources for decommissioning may be held by one or more third parties. This is especially true for government-owned facilities. The licensee then ensures that adequate funds are available and committed before commencing any decommissioning activity.


The licensee is responsible for all decommissioning activities and directs the DPM to ensure the safety and cost effectiveness of the project. The licensee provides the necessary liaison with the regulatory authority and the public, and makes available adequate funds to ensure that decommissioning is completed. The licensee defines the limits of the DPM's delegated powers, which may vary among organizations.

2.7.2 Decommissioning Project Manager (DPM)

The DPM leads the project management group and is directly responsible to the licensee of the facility. This function coordinates and supervises all activities during the whole period of decommissioning or until the desired stage of decommissioning is achieved. The DPM directs the decommissioning team to ensure safety and cost effectiveness of the project. The DPM is responsible for controlling the expenditure of funds and ensures that the decommissioning can be completed within the available budget. The DPM is also responsible for managing staff numbers, skills, and organization to meet the objectives of the decommissioning project.

Typically, the DPM has previous project management experience in a radiological environment. It is preferable if the individual has previous experience in either decommissioning or large-scale maintenance or refurbishment.

Of major importance, during the whole decommissioning period, is for the DPM to monitor, control and evaluate expenditure and activity progress against budgetary estimations and the planned timescale. This involves generation and updating of expenditure profiles and percentage-completed-activity diagrams, together with data on key project milestones, and the extent to which milestones have been achieved or progress has been delayed. This information is essential for the overall management of the project. This enables optimal management of funds or reveals a lack of funding and a need for reevaluation of the further decommissioning activities. Furthermore, the evaluation of the real cost of performed decommissioning activities allow to redefine the cost of work packages, which can be integrated into the cost reevaluation of the resulting decommissioning activities. Finally, achievement of technical and safety milestones are also of particular interest to the regulatory body and the fund manager.

A key function of the DPM is to monitor the progress by meetings, regular reports, performance statistics, post-task and post-project reviews, and by benchmarking performance against similar projects, where available. It is only by monitoring and measuring performance that it is likely that deficiencies are identified and improvements can be obtained. Some suggested key performance indicators (KPI) are detailed in  [Table 6](#).

■ **Table 6**

Some performance indicators in decommissioning activities

Task	Performance indicators
Safety	Accident frequency rate per 100,000 h worked Radiation doses compared to ALARA assessments and legal limits Site reportable events
Project	Project lifetime decommissioning costs (cash and discounted) Waste volume quantities Surveillance costs Site infrastructure costs Estimated cost of subprojects to completion versus sanctioned sums Milestones achieved

2.7.3 Technical Support

The technical support includes staff experienced in technical topics such as radiation protection, industrial safety, quality assurance, and engineering, as discussed in the following section.

Radiation Protection

As part of the decommissioning plan, the radiological protection program is prepared and implemented to ensure the safety of workers and the general public, as well as protection of the environment. Such a program is intended to optimize the working methods according to the ALARA principle. It typically includes on-site, off-site and personal monitoring, record-keeping of dosimetric data and assessment of the results obtained. The involvement of skilled personnel and the use of adequate equipment for dosimetry, personnel protection, radiation and contamination surveys, and clearance measurements for materials/waste are crucial to the safe decommissioning of the facilities.

A radiation protection specialist is responsible for ensuring compliance with radiation work procedures. This person advises or directs the activities of the health physics technicians, who monitor all decommissioning activities and measure and record the radiological information. The radiation protection specialist maintains the occupational exposure records and develops and implements the radiological emergency preparedness plan.

The radiation protection specialist is the advisor to the project personnel on all matters relating to radiation protection. Experience with decommissioning activities is desirable. Including an operational health physics staff from the plant into the team could be of a great advantage, especially in old facilities where operational records may not be up to date.

Industrial Safety

A general industrial safety program must be prepared and implemented to ensure the safety and health of the workers and protection of the environment from nonradiological hazards. This is constructed to comply with all applicable health and safety legislation. Such a program includes approved safety practices, monitoring of worker areas, and identification or specification of the personnel's protective equipment.

An industrial safety specialist is responsible for developing and implementing the industrial safety policy. The specialist advises the project personnel on all industrial safety matters (e.g., fires, toxic substances, noise, dust, etc.) and develops and implements the nonradiological emergency preparedness programs. Consideration is normally given to the provision of medical surveillance for the decommissioning staff.

Quality Assurance

A quality assurance (QA) program is established at the earliest practical time during the decommissioning planning, consistent with the schedule of accomplishing the proposed activities. The program is designed to provide a flexible degree of monitoring of ongoing work, based on a detailed planning, inspection and auditing, and operated with a minimum of personnel involved.

A member of the decommissioning team is assigned the position of QA representative for the project and utilizes the QA department of the organization. To ensure the independence of the QA department, this group has direct access to the licensee, independent of the decommissioning team. The QA representative maintains audit and job records and verifies that established procedures are followed with support from the QA department of the organization. More details on QA during decommissioning are given further on.

Engineering

The engineering group is responsible for the detailed characterization of the facility and its systems and components, including current status and any historical information. The engineering group is also responsible for developing detailed work procedures and specifications for the scheduled tasks. They also identify the need for special equipment and tool and evaluate the technical side of the decommissioning subcontracting. The engineering group helps establish the plans and detailed task schedule, track progress, and identify any potential concerns. It incorporates specific radiological data provided by the radiation protection team. The engineering group and the radiation protection team work closely together, as required, during the decommissioning project.

The required engineering expertise can be drawn from the existing operating facility itself, supplemented by additional specialist resources as necessary. The group typically includes at least a civil engineer, an electrical engineer, and a mechanical engineer.

Regulatory Control

This group provides guidance to the decommissioning team for compliance with regulatory requirements during the decommissioning process. In this way, compliance with license requirements can be demonstrated. For this purpose administrative and technical resources are vital.

2.7.4 Decommissioning Operations

Personnel for the decommissioning operations group are drawn from the plant operations team wherever possible, to obtain maximum benefit from the experience acquired during the operation of the facility. In an organization performing decommissioning in-house, this group provides the workforce that performs most of the decommissioning activities. Typical functions of this group are described in the following sections.

Decontamination and Dismantling

The decontamination and dismantling group is responsible for performing the main actions associated with decommissioning operations in accordance with agreed procedures. This group dismantles or removes components from their design locations and packages the material for further processing. They may decontaminate or segregate components or structures to assist in dose reduction or to meet clearance criteria. This group may perform volume reduction at the removal site if this is more cost effective than having a centralized waste reduction facility operated by the waste management group. This group possesses the necessary skills and trades to carry out these tasks.

Waste Management

The waste management group is responsible for ensuring that requirements and procedures developed for the handling, treatment, conditioning, storage, and transport of the generated waste are met. This group ensures that the waste acceptance criteria are met, in particular, before shipment of the waste to the disposal site. They may be responsible for volume reduction if a centralized waste reduction facility is established, and in developing a waste minimization program. This group, together with the radiation protection and industrial safety groups, characterizes the waste and identifies the various waste streams including verification and compliance with clearance criteria. The waste management group arranges for transport and disposal of the waste and prepares the necessary documentation.

Maintenance

Before decommissioning commences, a routine inspection and maintenance program is implemented for all safety-related systems and components that are required to support the decommissioning activities (e.g., ventilation, fire control, water, filters, radiation monitors, specified pumps, motors, fans). These systems and components have to be maintained throughout the decommissioning project to comply with safety requirements. A special group is responsible for providing inspections of this equipment and keeping records of maintenance performed, defects found, and remedial actions taken. The group may consist of electricians, plumbers, and other specialists familiar with the various support systems.

Specialist Contractors

During decommissioning, specialist contractors may be employed to provide services to the facility's decommissioning team. In the case of large nuclear installations, the list of specialized contractors may include, among others, transport contractors and remotely operated equipment specialists. Use of contractors may increase the overall cost effectiveness of the decommissioning project by improving the efficiency of specialist operations and therefore reducing the need for specialist staff training.

2.7.5 Administration Services

The administrative aspects of the project are the responsibility of the DPM, but expertise may be provided by specialists such as accountants, contract and procurement agents, information managers, personnel and training officers, lawyers, and security personnel. Key aspects of administrative management are described below.

Accounting and Finance

A financial case has to be organized for the selected decommissioning option, which includes a detailed cost estimate and the rate and time-scale of expenditures. The detailed cost estimate would be done as a joint activity between the technical support staff, who define the work packages and resources required, and the administrative staff or external specialist contractor, who have the financial cost estimating expertise. After approval of the estimate, the licensee has to agree on an expenditure budget for the decommissioning program with the organization that is providing the funds. This consists, as a minimum, of a summary of decommissioning activities, the agreed expenditure limit for each activity, and the points of time when funds are required.

For a decommissioning project on a multi-plant site, where other operations are continuing, the licensee may be able to utilize existing accounting services for recording and monitoring expenditures. For a single-plant site it may be appropriate to employ accounting services.

Contracts and Procurement

Contracts and procurement functions are required to assist the DPM in negotiating contracts for speciality contractors, procurement of special installations and equipment, special services, and procurement of consumables. However, it is a responsibility of the DPM to ensure that any contracted work is done in a timely, economic, and safe manner. Before contracts are awarded, the qualifications and experience of the contractor's staff and the quality assurance procedures operated by the contractor are verified. The size of the procurement and contracts group depend on who is going to perform most of the decontamination and dismantling activities, the in-house decommissioning team or the contractor(s).

For decommissioning projects the procurement of large quantities of consumable items, such as the personnel's protective equipment, is a possibly underestimated issue. Because of the quantity and diversity of this equipment, an extra burden may be placed on the contracting organization. The process of resupplying these items is reviewed periodically to ensure continued best value. In addition, the technical support staff ensures that special equipment (e.g., instrumentation, decontamination units, transport containers, and dismantling tools) has been identified in advance and procured in time to suit the planned sequence of decommissioning activities.

Information Management

A system is set up using QA requirements by which the data, operational records and reports are regularly received, registered, controlled, and stored. The regulations may require that all, or some, of these records be kept after decommissioning has been completed. For all decommissioning projects, a technical-data management group is in place; its purpose is to control the large amount of technical data that are generated by the decommissioning team during the decommissioning process. For example, large amounts of technical data may be collected, including survey data which could amount to many thousands of records. Once collected, all these data must be analyzed, retained, and put into a comprehensible and retrievable form.

Personnel and Training

The services of an experienced personnel manager and staff are essential to look after all personnel problems associated with the decommissioning staffing issues which may arise with operational staff after the shutdown of the facility. The principal aspects are likely to be substantial changes in the workforce, involving staff reductions and/or redeployments, and staff counseling related to some uncertainty arising from the closure of the plant or finalization of various stages of the decommissioning program.

It may be difficult to maintain all necessary skills as the workforce changes. This requires a commitment to the retraining of staff, including contractors, in order to meet the different challenges as the work progresses. The nature of the work may push for a reduction in the number of staff originally employed at the plant. Maintaining a site memory, that is, people with immediate personal knowledge of the plant and its history, may require a potentially higher retention of operating phase personnel. Emergency arrangements may also provide a similar pressure for staff retention.

The pressure to reduce costs by reducing staff tends to promote a degree of multi-skilling. Workers who performed only one or two tasks during the operational phase may now be required to perform multiple tasks as part of their normal duties. An example might be that during operations, a pipefitter may have only to cut installed piping. During decommissioning, this person may also be required to remove piping and perform waste minimization and decontamination activities. This may require retraining of this person.

Where operating staff are retrained in certain tasks, this training can be provided under contract from specialists who may go on to supervise the work. In some countries, specialist qualifications are being produced for decommissioning workers.

Finally, it is important to recognize that DPMs may also need retraining, if they are to operate as effective DPMs rather than as operating plant managers. Because of the potential for the decommissioning to be performed over long time periods, refresher courses and retraining are required at established intervals or in view of important activities.

Security and safeguards If spent fuel or other material subject to safeguards (such as plutonium or enriched uranium) remains on the site during decommissioning operations, presence of a security has to be maintained until the material has been removed. Once this material is removed, the safeguard functions can be reduced, but staffs are still retained for general security duties.

2.7.6 Interfaces

The licensee and decommissioning team cannot perform their duties without interfacing with organizations involved or interested in the decommissioning process. This interface may have to go through different parts of the licensee's organization. These organizations provide technical, social, or regulatory input to the decommissioning process. Their involvement can perform a valuable review function and provide constructive input to the decommissioning team. These organizations typically include:

- Regulatory authorities (clearance levels, waste transportation, environmental protection, radiation protection)
- National standards groups, professional societies
- General public (communities, pressure groups, etc.)

A common term used for these organizations is "stakeholders." A stakeholder is a person or group who can affect (or is affected by) an action. Among these, the main subjects are local, regional, and national governments, waste management organizations (nuclear and hazardous), shareholders, international organizations, the nuclear industry, labor unions, customers, and media. It is important that adequate lines of communication with the organizations be established.

As an important interfacing example, licensing-related activities normally continue at a significant level after the decommissioning has been initiated, and staff must have adequate time to continue licensing activities. These activities include possible revisions of the decommissioning plan, safety documents, emergency arrangements, and maintenance and modification procedures.

3 Plant and Site Characterization

3.1 Initial Plant Characterization

3.1.1 Radioactivity Sources

The radioactive inventory in nuclear facilities to be decommissioned can be divided into two categories:

- Radioactivity induced by neutron activation of certain elements in reactor components and adjacent structures
- Radioactive substances deposited on the internal and external surfaces of various systems as contamination. Included in this category are daughter radionuclides which become significant after periods of decay

Some nuclides contained in materials exposed to the neutron flux in nuclear reactors, accelerators, or fusion devices are transformed into radioactive isotopes. The level and type of radionuclides found in neutron irradiated materials depend on:

- The nuclides in the materials
- The duration of the exposure and the intensity of the neutron flux
- The energies of the incident neutrons

The relevant radionuclides composing the induced radioactivity in reactor and accelerator components and adjacent structures are shown in [Table 7](#). In other types of facilities, where neutron flux is minimal or nonexistent, activation products are not a serious concern during decommissioning.

Radioactive contamination of internal surfaces of reactor systems is caused by the deposition from the reactor coolant of neutron activated particles and dissolved elements, and from fission products and actinides released from possible fuel cladding cracks or other fuel failures, which may become very significant in the case of relevant accidents. External surface contamination in nuclear plants is primarily due to leakage and spills from reactor systems, and to maintenance and waste management activities.

Radioactive contamination in other fuel cycle facilities, such as fuel fabrication and reprocessing facilities, glove box lines, and storage basin is due to deposition of radioactive materials from the process stream. This contamination generally consists of uranium, thorium, plutonium, and their daughters in conversion, enrichment, and fabrication plants. Fission product contamination is also present in reprocessing plants.

In facilities not associated with the nuclear fuel cycle the radioactivity arises from radionuclides in the process stream, for example ^{99}Mo in a radiopharmaceutical hot cell facility.

■ Table 7

Major radionuclides identified in nuclear facilities characterization (SOGIN)

Isotope	Half-life (years)	Principal decay mode	Associated γ energy (MeV)	Materials where isotopes can be found
Neutron activation products found in nuclear reactors				
H ³	12.3	β^-	–	C, O, S
C ¹⁴	5,730	β^-	–	G, M, S
Na ²²	2.6	EC, β^+	0.51–1.28	O
Cl ³⁶	3.1×10^8	β^- , EC	–	C
Ar ³⁹	269	β^-	–	C
Ca ⁴¹	1×10^5	EC	–	C
Ca ⁴⁵	0.4	β^-	–	C
V ⁴⁹	0.9	EC	–	S
Mn ⁵⁴	0.9	EC, γ	0.83	A, M, S
Fe ⁵⁵	2.7	EC	–	C, M, O, S
Co ⁵⁷	0.7	EC, γ	0.12–0.14	S
Co ⁶⁰	5.3	β^- , γ	1.2–1.3	C, M, O, S, Z
Ni ⁵⁹	7.5×10^4	EC	–	C, M, O, S, Z
Ni ⁶³	100	β^-	–	C, M, O, S
Zn ⁶⁵	0.7	β^+ , γ , EC	0.51–1.12	A
Zr ⁹³	1.5×10^6	β^-	–	O, Z
Nb ⁹⁴	2×10^4	β^- , γ	0.70–0.87	M, O, S, Z
Mo ⁹³	3.5×10^3	EC, γ^-	0.3	M
Ag ^{108m}	130	EC, γ	0.4–0.6–0.7	M, O, S
Ag ^{110m}	0.7	β^- , γ	0.6–0.9	M, O, S
Ba ¹³³	10.7	EC, γ	0.08–0.36	C
Sm ¹⁵¹	93	β^- , γ	0.02	C
Eu ¹⁵²	13.4	β^- , γ , EC	0.1	C, G
Eu ¹⁵⁴	8.2	β^- , γ	0.1–1.3	C, G
Uranium and transuranic elements found in facilities handling fissile materials				
				Plant type
U ²³²	72	α , γ	0.06–1.3	1
U ²³³	1.6×10^5	α , γ	0.04–1	1
U ²³⁴	2.4×10^5	α , γ	0.05–0.1	1
U ²³⁵	7×10^8	α , γ	0.2	3
U ²³⁷	0.02	α , γ	0.2	2

■ Table 7 (continued)

Isotope	Half-life (years)	Principal decay mode	Associated γ energy (MeV)	Materials where isotopes can be found
Uranium and transuranic elements found in facilities handling fissile materials				
U ²³⁸	4×10^7	β, γ	0.05	2, 3
Np ²³⁷	2.1×10^6	α, γ	0.02–0.08	2, 3
Pu ²³⁸	87.7	α, γ	0.04–1.1	2, 3
Pu ²³⁹	2.4×10^4	α, γ	0.05	2, 3
Pu ²⁴⁰	6,537	α, γ	0.04–0.9	2, 3
Pu ²⁴¹	14.7	α, γ	0.03–0.15	2, 3
Pu ²⁴²	3.8×10^5	α, β^-, γ	0.04	2, 3
Am ²⁴¹	432	α, γ	0.05–0.8	2, 3
Am ²⁴³	7,380	α, γ	0.07–0.6	2, 3
Fission products found in reprocessing plants				
Sr ⁹⁰	29	β^-		
Ru ¹⁰⁶	1	β^-		
Cs ¹³⁴	2	γ	0.8	
Cs ¹³⁷	30	β^-, γ	0.7	
Ce ¹⁴⁴	0.7	β^-, γ	0.1	

C concrete; G graphite; O other; A aluminum; Z Zr alloys; S stainless steel; M mild steel; EC electron capture

These factors play a key role in several aspects of decommissioning process:

- Decommissioning planning
- Schedule and manpower requirements
- Personnel exposure
- Amount and methods of decontamination
- Cost evaluations
- Waste amount calculations

Nuclear Reactors

The radionuclides of concern vary considerably depending upon the type of facility being decommissioned. In the case of a nuclear reactor, the major radionuclides of concern during the first 50–100 years are ⁶⁰Co, which emits high energy gamma rays. Thereafter, other radionuclides such as ⁶³Ni and ¹⁰⁸Ag_m may become predominant.

The dose levels of gamma radiation from activation products such as ⁶⁰Co in the reactor vessel and internal components of the reactor vessel determine the amount of remote operation and shielding that is required. In the longer term, other radionuclides such as ⁶³Ni, ⁵⁹Ni, ¹⁰⁸Ag_m, and ¹⁴C are of greater concern because their long half-lives render them radioactive for hundreds of years.

^{59}Ni has not been of major importance previously because reactors had not been in operation long enough to create significant quantities of this radionuclide. However, a reactor in operation for 40 years may contain significant amounts of ^{59}Ni in certain reactor vessel components. ^{14}C is of concern for graphite moderated reactors.

Of importance, but not well documented, is the radiation resulting from the activation of trace elements to produce radionuclides such as ^{94}Nb that could give rise to significant activity in the very long term. Trace elements may be natural impurities or introduced from scrap metal added to virgin metals during manufacture. For example, niobium is added during the manufacture of steel to improve welding characteristics. When scrap steel is added to the virgin metal melt, diluted niobium remains in trace quantities.

Fission products and actinides may also be present in reactor facilities as a result of fuel failures. If the facility has experienced an accident during its operating lifetime, significantly higher inventories of fission products and actinides may be present.

Radioactive isotopes are also generated by activation in the concrete structures surrounding the reactor. Generally on some tenths of centimeters are involved at a significant level, but this may introduce additional concerns both from radioprotection point of view and from the amount of radioactive wastes that are produced.

Other Nuclear Facilities

In other nuclear fuel cycle facilities, the radionuclides of concern depend on which part of the cycle the facility was used for.

In the case of facilities at the front end of the nuclear fuel cycle, the members of the uranium and thorium decay chains are the most important radionuclides.

For plutonium facilities or those handling highly enriched uranium, actinides such as ^{239}Pu is the main problem. These radionuclides are much more difficult to handle than either fission products or activation products owing to their high specific radiotoxicity and the associated inhalation hazard. However, in reprocessing plants the fission and activation products also contribute significantly to the total potential hazard. For ^{233}U facilities the actinides and the decay product ^{208}Tl (2.6 MeV gamma energy) are the major concerns.

In the case of nonnuclear fuel cycle facilities, the radionuclides of concern depend on the product being used or produced. Examples of nuclides of importance in some plants include: ^{60}Co for gamma irradiation, ^{131}I and ^{51}Cr in radiopharmaceutical facilities, and ^{226}Ra in gypsum residues from the phosphate industry.

In fusion facilities the major radionuclides of concern are activation products similar to those that occur in nuclear reactors.

3.1.2 The Concept and Extent of Characterization

It is necessary to determine whether the description of the current radiological status of the facility is adequate to fully understand the types and levels of radioactive material contamination and the extent of radioactive contamination at the facility. This information is used during the review of the licensee's decommissioning activities, to evaluate the cost estimates for decommissioning, and decommissioning health and safety plans. This information should include summaries of the types and extent of radionuclide contamination in all media at the facility, including buildings, systems and equipment, surface and subsurface soil, and surface and ground water.

A good estimate of the amount and type of radioactivity in a nuclear facility is important because it can directly affect the whole approach to decommissioning including the choice of the time to start decommissioning and the desirability of delay between stages. This information assists the planners in determining factors such as the need for decontamination, shielding or remotely operated equipment, shipping and disposal, and potential radiation exposures to the work force.

The facility inventory should include detailed inventories for individual components and should describe specific radionuclide content, chemical forms, physical forms, and volume distribution. The inventory should be maintained current as decommissioning progresses, and in case of delayed dismantling, the inventory should be projected into the future to demonstrate the required period of confinement of radionuclides.

If the residual radioactivity consists mainly of short-lived radionuclides, a significant reduction in radioactive inventory can be achieved by delaying the dismantlement of the facility. In the opposite case, no major advantage can be achieved by deferring dismantlement.

3.1.3 Structure Characterization

The purpose of the description of the contaminated structures is to evaluate whether the licensee has fully described the types and activity of radioactive material contamination in the structures, as well as the extent of this contamination. This information should be sufficient to allow the evaluation of the potential safety issues associated with remediating the structures, whether the remediation activities and radiation control measures proposed by the licensee are appropriate for the type of radioactive material present in the structure, whether the licensee's waste management practices are appropriate, and whether the licensee's cost estimates are plausible, given the amount of contaminated material that has to be removed or remediated.

Note that, in some instances licensees may choose to dismantle contaminated structures and dispose of the building debris as radioactive waste in lieu of decontaminating the building.

Similarly, licensees may choose to decontaminate portions of buildings to levels appropriate for unrestricted use and dismantle portions of the building to gain access to areas where contamination has migrated, such as floor/wall joints. In these instances, all of the information described below may not necessarily be included in the decommissioning plan. Regulatory staff should discuss these activities with these licensees to ensure that adequate information is provided in the decommissioning plan to allow the staff to perform the evaluations described above, without requiring the licensee to expend substantial resources characterizing the structures.

The information supplied by the licensee should be sufficient to allow the understanding of the types and activity of radioactive material contamination in the structure, as well as the extent of this contamination. The review should verify that the following information is included in the contaminated structures section of the facility decommissioning plan:

- A list or description of all structures at the facility where licensed activities occurred that contain residual radioactive material in excess of site background levels
- A summary of the structures and locations at the facility that the licensee has concluded have not been impacted by licensed operations and the rationale for the exclusion
- A list or description of each room or work area within each of these structures
- A summary of the background levels used during scoping or characterization surveys

- A summary of the locations of contamination (i.e., walls, floors, wall/floor joints, structural steel surfaces, ceilings, etc.) in each room or work area
- A summary of the radionuclides present at each location, the maximum and average radionuclide activities in $\text{dpm}/100\text{ cm}^2$, the chemical form of the radionuclide and, if multiple radionuclides are present, the radionuclide percentages
- The mode of contamination for each surface (i.e., whether the radioactive material is present only on the surface of the material or if it has penetrated the material)
- The maximum and average radiation levels in milli-Sievert per hour (mSv/h) or micro-Sievert per hour ($\mu\text{Sv}/\text{h}$), as appropriate, in each room or work area
- A scale drawing or map of the rooms or work areas showing the locations of radionuclide material contamination and radiation levels. All maps should include compass direction indicators.

3.1.4 System and Equipment Characterization

The purpose of the description of the contaminated systems and equipment at the facility is to evaluate whether the licensee has fully described the types and activity of radioactive material contamination in facility systems or on equipment, as well as the extent of this contamination.

This information should be sufficient to allow the evaluation of the potential safety issues associated with remediating the systems or equipment, whether the remediation activities and radiation control measures proposed by the licensee are appropriate for the type of radioactive material present in the systems or equipment, whether the licensee's waste management practices are appropriate and whether the licensee's cost estimates are plausible, given the amount of contaminated material that has to be removed or remediated.

Note that, in some instances, licensees may choose to remove and dispose (either as radioactive waste or as usable equipment in another radiation area) contaminated systems and/or equipment, in lieu of decontaminating the system or equipment. In these instances, all of the information described below may not necessarily need to be included in the decommissioning plan. Regulatory staff should discuss these activities with licensees to ensure that adequate information is provided in the decommissioning plan to allow the staff to perform the evaluations described above, without requiring the licensee to expend substantial resources characterizing the equipment or system.

The information supplied by the licensee should be sufficient to allow for the understanding of the types and activity of radioactive material contamination present in systems or on equipment, as well as the extent of this contamination. The review should verify that the following information is included in the contaminated systems and equipment section of the facility decommissioning plan:

- A list or description and the location of all systems and equipment at the facility that contain residual radioactive material in excess of site background levels
- A summary of the radionuclides present in each system or on the equipment at each location, the maximum and average radionuclide activities in $\text{dpm}/100\text{ cm}^2$, the chemical form of the radionuclide, and, if multiple radionuclides are present, the radionuclide ratios
- The maximum and average radiation levels in mSv/h, or $\mu\text{Sv}/\text{h}$, as appropriate, on the surface of each piece of equipment

- A summary of the background levels used during scoping or characterization
- A scale drawing, map of the rooms, or work areas showing the locations of the contaminated systems or equipment; all maps should include compass direction indicators.

3.2 Site Characterization

3.2.1 Surface Soil Contamination

If a deep soil contamination did not occur, generally characterization of a 15–30 cm layer of top soil may be considered sufficient at the beginning of the process to identify any necessary soil treatment and at the end of decommissioning to demonstrate that the site may be delicensed. This information is generally sufficient to allow the regulatory staff to evaluate the following:

- The potential safety issues associated with remediating the surface soil
- Whether the remediation activities and radiation control measures proposed by the licensee or person responsible are appropriate for the type of radioactive material present in the surface soil
- Whether the licensee's waste management practices are appropriate
- Whether the licensee's cost estimates are plausible, given the amount of contaminated soil that has to be removed or remediated
- And finally to delicense the site.

3.2.2 The NRC Acceptance Criteria

As an example, the US NRC requirements and guidances are included in the following documents:

- 10 CFR 30.36(g)(4)(i).
- 10 CFR 40.42(g)(4)(i).
- 10 CFR 70.38(g)(4)(i).
- 10 CFR 72.54(g)1.
- “Draft Branch Technical Position on Site Characterization for Decommissioning.”
- NUREG-1575: “Multi-Agency Radiological Survey and Site Investigation Manual.”
- NUREG-1754 – “Technology, Safety and Costs of Decommissioning Reference Non-Fuel Cycle Nuclear Facilities,” Addendum 1.

The information to be supplied by the licensee should be sufficient to allow the NRC to fully understand the types and activity of radioactive material in surface soil, as well as the extent of this contamination. The NRC review should verify that the following information is included in the description of contaminated soil in the facility decommissioning plan:

- A list or description of all locations at the facility where surface soil contains residual radioactive material in excess of site background levels
- A summary of the background levels used during scoping or characterization surveys
- A summary of the radionuclides present at each location, the maximum and average radionuclide activities in pico-Curies per gram (pCi/g), the chemical form of the radionuclide, and, if multiple radionuclides are present, the radionuclide percentages

- The maximum and average radiation levels in mSv/h at each location
- A scale drawing or map of the site showing the locations of radionuclide material contamination in surface soil. All maps should include compass direction indicators.

3.2.3 Subsurface Soil Contamination

The purpose of the review of the description of subsurface soil (i.e., soil below the top 15–30 cm of soil in the soil column) contamination is to determine if the licensee has fully described the types and activity of radioactive material contamination in the subsurface soil, as well as the extent of this contamination. This information should be sufficient to allow the regulatory staff to evaluate the following:

- The potential safety issues associated with remediating the subsurface soil
- Whether the remediation activities and radiation control measures proposed by the licensee are appropriate for the type of radioactive material present in the subsurface soil
- Whether the licensee's waste management practices are appropriate
- Whether the licensee's cost estimates are plausible, given the amount of contaminated soil that has to be removed or remediated

The information supplied by the licensee should be sufficient to allow the NRC to fully understand the types and activity of radioactive material in subsurface soil, as well as the extent of this contamination.

The NRC review should verify that the following information is included in the description of contaminated subsurface soil in the facility decommissioning plan:

- A list or description of all locations at the facility where subsurface soil contains residual radioactive material in excess of site background levels
- A summary of the background levels used during scoping or characterization surveys
- A summary of the radionuclides present at each location, the maximum and average radionuclide activities in pCi/g, the chemical form of the radionuclide, and, if multiple radionuclides are present, the radionuclide ratios
- The depth of the subsurface soil contamination at each location
- A scale drawing or map of the site showing the locations of subsurface soil contamination. All maps should include compass direction indicators.

3.2.4 Surface Water Contamination

The purpose of the review of the description of contaminated surface water is to evaluate whether the licensee has fully described the types and activity of radioactive material present in surface water bodies at the facility, as well as the extent of this contamination. This information should be sufficient to allow the regulatory staff to evaluate potential safety issues associated with remediating the surface water, whether the remediation activities and radiation control measures proposed by the licensee are appropriate for the type of radioactive material present in the surface water, whether the licensee's waste management practices are appropriate and cost estimates are plausible, given the amount of contaminated water that has to be removed or remediated.

The information supplied by the licensee should be sufficient to allow the staff to fully understand the types and activity of radioactive material contamination in surface water at the facility, as well as the extent of this contamination. The staff's review should verify that the following information is included in the description of surface water contamination in the decommissioning plan:

- A list or description and map of all surface water bodies at the facility that contain residual radioactive material in excess of site background levels
- A summary of the background levels used during scoping or characterization surveys
- A summary of the radionuclides present in each surface water body and the maximum and average radionuclide activities in pico-Curies per liter (pCi/l).

3.2.5 Groundwater Contamination

The purpose of the review of the description of contaminated groundwater is to evaluate whether the licensee has fully described the types and activity of radioactive material present in groundwater at the facility, as well as the extent of this contamination. This information should be sufficient to allow the regulatory staff to evaluate potential safety issues associated with remediating the groundwater, whether the remediation activities and radiation control measures proposed by the licensee are appropriate for the type of radioactive material present in the groundwater, whether the licensee's waste management practices are appropriate and whether the licensee's cost estimates are plausible, given the amount of contaminated water that will need to be removed or remediated.

The information supplied by the licensee should be sufficient to allow the staff to fully understand the types and activity of radioactive material contamination in groundwater at the facility, as well as the extent of this contamination. The staff's review should verify that the following information is included in the description of groundwater contamination in the decommissioning plan:

- A summary of the aquifer(s) at the facility that contain residual radioactive material in excess of site background levels
- A summary of the background levels used during scoping or characterization surveys
- A summary of the radionuclides present in each aquifer and the maximum and average radionuclide activities in pCi/l.

4 Decontamination Techniques

4.1 Overview

Decontamination is defined as the removal of contamination from surfaces of facilities or equipment by washing, heating, chemical or electrochemical action, mechanical cleaning, or other techniques. In decommissioning programs, the objectives of decontamination are:

- To reduce radiation exposure
- To salvage equipment and materials

- To reduce the volume of materials requiring storage and disposal in licensed disposal repositories
- To restore the site and facility, or parts thereof, to an unconditional-use situation
- To remove loose radioactive contaminants and fix the remaining contamination in place in preparation for protective storage or permanent disposal work activities
- To reduce the magnitude of the residual radioactive source in a protective storage mode for public health and safety reasons, to reduce the protective storage period or to minimize long-term monitoring and surveillance requirements

Some form of decontamination is required in any decommissioning program, regardless of the form of the end product. As a minimum, the floor, walls, and external structural surfaces within work areas should be cleaned of loose contamination, and simple water rinsing of contaminated systems is performed.

The question of whether to decontaminate piping systems, tanks, and components arises often.

A strong case may be made in favor of leaving adherent contamination within piping as well as components in a dispersed form on the internal metal surfaces rather than concentrating the radioactivity through decontamination. In most cases, decontamination is not sufficiently effective to allow for the unconditional release of the item without further treatment after dismantling. Therefore, savings both in occupational exposure and cost could be achieved by simply removing the contaminated system and its components and only performing certain packaging activities (e.g., welding end caps on pipe sections, using adequate equipment to cut and crimp smaller piping to reduce chances of airborne activity). However, additional cost for the disposal of materials must be weighed in this scenario.

A decontamination program may also require a facility capable of treating secondary waste from decontamination (e.g., processing chemical solutions, aerosols, debris, etc.). The concentrated waste, representing a more significant radiation source, must be solidified and shipped for disposal in licensed disposal facilities unless properly treated in the waste reduction/recycling/reclamation processing alternative.

The optimal waste-reduction configuration must be defined after an economic assessment of treatment versus transportation/disposal costs has been completed. Each of these additional consequences may increase:

- Occupational exposure rates
- The potential for a release
- The uptake of radioactive material

These could conceivably result in even higher doses than those received from removing, packaging, and shipping the contaminated system without extensive decontamination. Resolution of this question depends on specific facts, such as the exposure rate of the gamma-emitting contamination, the contamination level, and the effectiveness of the containing component and piping (wall thickness) in reducing radiation fields in the work area.

The proven and emerging decontamination techniques which may be used to accomplish the goals of decommissioning activities have been discussed by the Technical Advisory Group of the Organization for Economic Cooperation and Development-Nuclear Energy Agency (OECD-NEA), a Cooperative Program on Decommissioning. The work focused on decontamination of both metallic and concrete surfaces for dose reduction as well as for waste decategorization or for conditional or unconditional release of materials.

4.1.1 Objectives of Decontamination Techniques

There are three main reasons for considering the use of decontamination techniques:

- The importance of removing contamination from components or systems to reduce dose levels in the installations; access to the installations could then be made easier so that it becomes possible to use hands-on techniques for dismantling rather than the more expensive use of robots or manipulators
- The aim of minimizing the potential for spreading contamination during decommissioning activities, especially when dealing with systems containing highly radioactive particles and actinides
- It may be possible to reduce the contamination of components or structures to such levels that they may be disposed at a lower, and therefore more economical, waste treatment and disposal category or, indeed, be unconditionally released for recycling or reuse in the conventional industry, or disposed as waste exempt from regulatory concern

Several decontamination techniques have been developed to support maintenance work in nuclear installations. With relative success, the same techniques have also been adopted when decommissioning nuclear installations and components (🔗 [Table 8](#)). Objectives differ among these applications, however.

In maintenance work, the highest degree of decontamination is sought, avoiding any damage to the component so that it may be adequately reused. In contrast, the main aim of decontamination for decommissioning is the removal of as much activity as possible, not only to decategorize waste, but to reach clearance levels so that the material from the system may be reused without radiological restrictions. In many cases, it is necessary to remove all oxides liable to trap contaminants and a thin layer of structural material in order to achieve this aim. The radionuclides indeed tend to concentrate in the intergranular regions, together with other impurities accumulated during the growth of the metal grains. Therefore, much more aggressive decontamination methods are required than those used during the service life of a plant. In this view, technical methods presenting high decontamination factors at high contamination levels do not always allow for achievement of the very low levels required to release the material (e.g., inner surfaces of piping) without restrictions, provided that measurement of these very low levels is feasible.

During decontamination for maintenance, components and systems may not be damaged and the use of very aggressive decontamination methods is not appropriate. In decontamination for decommissioning, however, it is mainly the use of somewhat destructive techniques that make it possible to meet the objectives to release the material at clearance levels.

Another aspect in which techniques for thorough decontamination of materials differ from maintenance or laboratory scale decontamination is the need for industrialization. The large amount of contaminated materials produced during decommissioning procedures and available for decontamination generally do not favor methods or techniques that are labor intensive or difficult to handle, or that present difficulties when automation is envisaged. The latter is also true in the case of decontaminating the full system for maintenance.

Other factors presenting differing influences on the choice of techniques are, for example, secondary-waste production and the possibility of recycling products from decontamination

■ Table 8

Decontamination techniques in decommissioning nuclear installations

Task	Scope	Object	Techniques
Decontamination before dismantling	Reduction of occupational exposure	Pipeline system	Chemical Mechanical
		Pool, tank	Hydro jet Blast Strippable coating, etc.
Decontamination after dismantling	Recycle of contaminated metal Reduction of radioactive waste	Pipes, components	Electropolishing Chemical immersion Blast Ultrasonic wave Gel
Decontamination of building	Unconditional release of building Reduction of radioactive concrete waste	Concrete surface	Mechanical: scabblers Mechanical: shaver Mechanical: drill and spalling Mechanical: steel grit blast Thermal stress: microwave irradiation Thermal stress: flame scarfing

processes. These may be among the parameters for decision-making, for decontamination both for maintenance and decommissioning.

The absolute requirement for effectively obtaining residual contamination levels that prove to be below clearance limits is also a factor of primary influence when making the choices of decontamination techniques to be used. Even if techniques for the decontamination of complex geometries (e.g., pipe bends, small diameter piping) exist, the nonaccessibility of areas may prevent direct radiological measurements being used to show that shifting clearance levels are met.

Presently, the interest of the nuclear industry is moving from decontamination techniques for maintenance to decontamination for decommissioning. Limited data are available from decommissioning on the efficiency of usable techniques to meet the low unconditional-release criteria. In most cases, using available techniques, the clearance levels are only met in an asymptotic way. Not all methods and techniques available present the possibility of decontaminating below the required clearance levels. So, in some cases, decontamination is carried out in different stages, the last step specifically aiming to obtain the required objectives.

When selecting a specific technique for system and/or component decontamination based on these considerations, the following requirements must be considered mainly:

- Safety. The application of the method should not result in increased radiation hazards due to external contamination of workers or even inhalation of radioactive dust and

aerosols formed during its implementation; it should not add other hazards (e.g., chemical, electric, etc.).

- **Efficiency.** The method should be capable of removing radioactivity from a surface to a level which would enable hands-on work instead of robotics, or which would permit recycling/reuse of the material or, at least, a lower waste treatment and disposal category.
- **Cost-effectiveness.** Where possible, equipment should be decontaminated and repaired for reuse; however, the method should not be costly exceeding the costs for waste treatment and disposal of the material, whether including replacement of the equipment or not.
- **Waste minimization.** The method should not give rise to large quantities of secondary waste, the treatment and disposal of which would result in excessive requirements for work and costs, thereby causing additional exposures.
- **Feasibility of industrialization.** Due to the large quantities of contaminated materials involved, methods or techniques should not be labor-intensive, difficult to handle, or difficult to automate.

4.1.2 Selection of Decontamination Technologies

Very early in the process of selecting decontamination technologies for decommissioning, it is important that a cost–benefit analysis be performed to see if it is actually worth decontaminating the component or facility, or to determine whether a mild decontamination at low cost is more advantageous than an aggressive decontamination at a higher cost. This analysis is usually accompanied by extensive experimental work on selected samples from the facility in view of characterization, before the final choice of a decontamination technique is made.

To achieve a good decontamination factor ($DF = \text{contamination after the treatment} / \text{contamination before the treatment}$), a decontamination process must be designed for site-specific application taking into account a wide variety of parameters, some of which are listed below:

- Type of plant and plant process: reactor type, reprocessing plant, etc.
- Operating history of the plant
- Type of material: steel, zircaloy, concrete, etc.
- Type of surface: rough, porous, coated, etc.
- Type of contaminant: oxide, crud, sludge, loose, etc.
- Composition of the contaminant (i.e., activation products, fission products, actinides, etc.), and the specific radionuclides involved
- Ease of access to areas/plant to be decontaminated, external or internal surfaces to be cleaned
- Regulatory requirements and decontamination factors required
- Destination of the components being decontaminated: disposal, reuse, etc.
- Time required for application
- Proven efficiency of the process for the type of contamination in the facility
- Type of component: pipe, tank, pump, valve, etc.

Other factors which are important in selecting the method, but which do not affect the decontamination factor are:


- Availability, cost, and complexity of the decontamination equipment and consumables
- Need and capability of treatment and conditioning of the secondary waste generated
- Potential exposure to hazardous materials and/or chemicals used in the decontamination process
- Occupational and public doses resulting from decontamination (justification of the practice)
- Other safety, environmental and social issues
- Availability of trained staff
- Extent to which the plant needs to be decontaminated to achieve acceptable conditions
- Salvage value of materials which would otherwise be disposed
- Extent to which the facility must be modified to do the decontamination
- Enclosed and ventilated spaces, etc.

In addition, the choice of a process or of a combination of several processes finally depends on several other factors such as:

- The specific nature of the application, the complexity of the system
- The feasibility of industrialization
- The cost–benefit analysis taking into account all aspects of the decontamination operation, i.e., until disposal of remaining radioactive waste

The decision whether to proceed with decontamination and the final process selected depends on the best overall balance of the above factors to minimize the overall impact of the decommissioning activities on workers, the public, and the environment, at acceptable costs.

4.1.3 Survey of Applied Decontamination Techniques

A list of decontamination processes suitable for the purposes of decommissioning is given in  [Table 9](#). For decontamination of metals, the processes are divided into chemical, electrochemical, and physical processes. Moreover, a distinction has been made between the processes used in closed systems (e.g., full-system decontamination of the primary circuit of a reactor or the partial decontamination of closed loops), and the processes used in open tanks (e.g., decontamination of dismantled pieces). For the decontamination of concrete, surface-decontamination processes and demolition processes have been selected.

Some specific characteristics of selected decontamination techniques for segmented components and for building surfaces are discussed in the following sections. In addition, some critical elements of choosing techniques for a practical decontamination problem are mentioned. In addition, practical experience in decontamination has shown that a universal decontamination process does not exist. As such, future users should familiarize themselves with the characteristics of proposed techniques, to make adequate choices based on specific requirements and thorough case studies.

■ Table 9

Overview of decontamination processes for decommissioning

Metal decontamination	Process		Closed systems	Open systems
Chemical processes	Oxidation processes	ODP/SODP	X	
		Cerium/sulfuric acid		X
		Cerium/nitric acid		X
	Oxidation–reduction processes	APCE/NPOX	X	X
		TURCO	X	X
		CORD	X	X
		CAN-DEREM, CAN-DECON		X
		CONAP		X
		AP/NP + LOMI for PWR	X	
		EMMA	X	
	LOMI for BWR		X	
	Phosphoric-acid-based processes			X
	Foams		X	
	Various reagents	HNO ₃		X
		HNO ₃ + HF	X	X
		HNO ₃ /NaF	X	X
HCl		X	X	
DECOHA			X	
Electrochemical processes	Phosphoric acid			X
	Nitric acid			X
	Nitric acid – Electrodeplating			X
	Sodium sulfate – ELDECON proc.			X
	Oxalic acid			X
	Citric acid			X
	Sulfuric acid			X
	Other electrolytes			X
Physical processes	Ultrasonic cleaning			X
	High pressure water			X
	CO ₂ ice blasting			X

■ Table 9 (continued)

Metal decontamination	Process	Closed systems	Open systems
	Ice water		X
	Freon substitutes		X
	Abrasives wet	X	X
	Abrasives dry		X
	Grinding/planing		X
Combined mechanical/chemical processes	Pastes + HP cleaning		
	Foams/gels/HP cleaning		
	Vacuum cleaning (dry/wet)		
Concrete decontamination	Process	Concrete decontamination	Concrete demolition
	Kelly process	X	
	Scabbling	X	
	Sand blasting	X	
	Wet abrasives	X	
	Milling	X	
	Explosives		X
	Microwaves	X	
	Drill/Spalling		X
	Drill/Lime expansion		X
	Jackhammer		X

4.2 Decontamination of Segmented Components

4.2.1 Overview

Simplified overviews of some decontamination techniques in view of their efficiency regarding some selection criteria may be found in the literature. Practical experience indicates that these overviews have to be considered with great care. Small changes in details of application of the selected techniques may have significant impacts on the qualification of influencing parameters.

Chemical decontamination uses concentrated or diluted chemical reagents in contact with the contaminated item, to dissolve the contamination layer covering the base metal and eventually a part of the base metal. In most cases, required decontamination levels may be obtained

by continuing the process as long as necessary, taking care to ensure that tank walls or piping are not penetrated by corrosion.

In mild chemical decontamination processes, dissolution of the contamination layer is envisaged, but the process should be nondestructive to the base metal and is generally used for operating facilities. Aggressive chemical decontamination techniques involving dissolution of the base metal should only be considered in decommissioning programs where reuse of the item will never occur. Chemical flushing is recommended for remote decontamination of intact piping systems.

Chemical decontamination has also proven to be effective in reducing the radioactivity of large surface areas such as drip trays as an alternative to partial or complete removal. They are also suitable for use on complex geometries as well as for a uniform treatment of inner and outer pipe surfaces. These techniques, however, require efficient recycling of reactive chemicals. Insufficient recycling of decontamination products results in very large amounts of secondary waste, which are difficult to treat, and increase costs.

Electrochemical decontamination may be considered in principle to be a chemical decontamination assisted by an electric field. It may be considered the opposite of electroplating since metal layers are removed from a surface rather than added as a coating.

Electrochemical decontamination has been applied by immersion of the contaminated item in an electrolyte bath or by passing a pad over the surface to be decontaminated. The electric current causes the anodic dissolution and removal of metal and oxide layers from the component. The electrolyte is continuously regenerated by recirculation.

These processes may only be applied to conductive surfaces. They are highly effective and give a high decontamination factor. Their use is limited:

- When immersion is used, by the size of the bath
- When a pad is used, by the geometry of the surfaces and the available clearance around the part being treated

This makes the method almost inapplicable for industrial decontamination of complex geometries (e.g., pipes, valves, pumps, etc.). The volume of effluents may be limited. Moreover, handling the parts to be immersed or the pad may lead to additional exposure to workers.

Decontamination by melting presents the particular advantage of homogenizing a number of radionuclides in the ingots and concentrating other radionuclides in the slag and filter dust resulting from the melting process, thus decontaminating the primary material.

Melting may provide an essential step when releasing components with complex geometries, simplifying monitoring procedures for radioactive metal characterization. In addition to the decontamination effects of melting, the problem of inaccessible surfaces is eliminated, and the remaining radioactivity content is homogenized over the total mass of the ingot.

Therefore, melting may be a last step in the decontamination and release of components with complex geometries after they have been decontaminated, for example, by chemical methods which remove radionuclides, such as ^{60}Co . It should be noted that ^{60}Co originating from activation of the base metal remains in the ingot after melting.

Mechanical and manual decontamination are physical techniques. Recently, mechanical decontamination has included washing, swabbing, foaming agents, and latex-peelable coatings. Mechanical techniques may also include wet or dry abrasive blasting, grinding of surfaces,

and removal of concrete by spalling or scarifying. These techniques are most applicable to the decontamination of structural surfaces.

Some of them are also applicable to nonmetallic surfaces, such as plastics.

Abrasive blasting systems, both wet and dry, have been used with success. They employ mechanical methods, derived from conventional industry, that give very high decontamination factors. The longer the operations are continued, the more destructive they are. However, wet abrasive systems produce a mixture of dust and water droplets that might be difficult to treat. Care must be taken not to introduce the contamination into the material surface (hammering effect), jeopardizing the ability to meet clearance levels. These techniques are not appropriate for complicated surfaces where uniform access is not easy.

Innovative decontamination techniques have been proposed in recent years in the framework of radioactive waste management research and development programs. Mostly, these emerging technologies are hybrid technologies comprising one or more of the following methods: chemical, electrochemical, mechanical, laser, or sonic.

4.2.2 Chemical Decontamination

Chemical decontamination is usually carried out by circulating the selected reagents in the system. However, segmented parts may be decontaminated by immersing them in a tank containing the reagent, which is then mainly agitated. Application of specific chemical decontamination depends on many factors, e.g., shape and dimensions of the item to be decontaminated, kind and nature of chemical reagents, type of material and contamination, availability of proper process equipment, etc.

Many chemical reagents and techniques have been developed for the routine decontamination of systems during operation and decommissioning of nuclear facilities. Chemical decontamination processes are basically divided into two groups. Mild chemicals including noncorrosive reagents such as detergents, complexing agents, dilute acids, or alkalis. Aggressive chemicals include concentrated strong acids or alkalis and other corrosive reagents. The dividing line between these two groups of processes is usually at an about 1–10% concentration of the active reagent.

Mild chemical decontamination techniques have generally been used for items where the objective is to remove contamination without attacking the base material. Their advantages are low corrosion rates and low chemical concentrations, which facilitate the treatment of the spent decontamination solutions (secondary waste). Although some low-concentration decontamination techniques have low decontamination factors and require long contact times, they may be made more effective by combining them with processes using noncorrosive oxidizing or reducing agents, and complexing and chelating agents, and applying them in several stages. In many cases, the effectiveness may also be improved by increasing the treatment temperature by 20–90 °C. The selection of redox and chelating agents depends on the composition of the surface corrosion products to be removed.

Aggressive chemical and electrochemical decontamination techniques may involve one or more stages, using different chemical solutions. Intermediate rinses are recommended in order to avoid potential problems with recontamination. The advantages of the process include

short-time application and high decontamination factors (usually from 10 to 100 decrease in activity levels). Its limitations include high chemical concentrations and potential problems for effluent-treatment systems.

A multi-step process (i.e., the application of a strongly oxidizing solution followed by a complexing acid solution) is a common technique for removal of the contaminated oxide layer from metal surfaces, such as stainless steel. The first (alkaline) stage is intended to oxidize the chromium oxides to yield soluble chromate ions. The second (acid) stage is primarily a dissolution reaction for the complexing of dissolved metals.

Alkaline permanganate solutions are the most common reagents for the first stage. At the second stage, a variety of reagents such as ammonium citrate, ammonium citrate followed by ethylenediaminetetraacetic acid (EDTA), oxalic acid, a mixture of citric and oxalic acid, sulfuric acid, etc., have been used successfully for decontamination of stainless steel, carbon steel, inconel, zircaloy cladding, etc. Sulfuric, phosphoric, hydrochloric, and hydrofluoric acids and other reagents have been successfully used separately as individual aggressive decontaminants, generally at concentrations from 2 to 15%. The required decontamination level may necessitate repeating the process a number of times. Care must be taken if the dissolution process might result in unacceptable surface corrosion, e.g., where direct reuse of an item is required. Chemical techniques are generally suitable for use on complex geometries as well for uniform treatment of inner and outer surfaces of equipment, particularly where good contact between the chemical and the surface is provided, (e.g., tank immersion).

Factors considered for in-line chemical decontamination are also valid for the immersion process. However, because the tanks are usually open at the top, a proper ventilation system must be installed, and special care must be taken to avoid contact between the operators and the highly corrosive reagents. It should be noted that chemical reagents at excessively high temperatures might provoke undesirable effects, such as toxic or explosive gases, e.g., hydrogen.

Chemical decontamination requires efficient recycling of reactive chemicals, as insufficient recycling of decontamination products may increase the amount of secondary waste, which may be difficult to treat. It may generate mixed waste, and may result in corrosion and safety problems when misapplied. In addition, it requires both different reagents for different surfaces, and drainage control.

For large jobs, it generally requires constructing a chemical storage and collecting equipment as well as addressing criticality concerns, where applicable. Chemical decontamination is usually not effective on porous surfaces.

In general, knowledge of chemical cleaning methodology is a prerequisite for assessing decontamination technology, as most of the procedures and chemicals used to decontaminate nuclear materials and equipment are also used for cleaning equipment and materials in the chemical processing industry. Both chemical cleaning and decontamination require the same areas of knowledge and experience: chemistry of fouling, corrosion technology, and waste-generation/removal techniques. Furthermore, the same engineering knowledge is required to devise suitable procedures for mixing, pumping, and heating solvents and other chemical-cleaning constituents. Compliance with basic health and safety practices regarding chemical agents is required, in addition to the radiological safety aspects. As a minimum, workers should go through a training program and be equipped with glasses, full-body protective coveralls, impermeable gloves, and foot covers. Additional safety equipment depends on the toxicity of contaminants.

Chemical Reagents

For decommissioning programs, there is a wide range of chemical reagents to choose from, since corrosion of the base metal is of little concern. Certain chemical reagents exhibit a time dependency in the mixing, heating, recirculation, and draining cycle, which affects both the chemical solution stability and the solubility of contained contamination. Each process under consideration should be evaluated for the effect of a loss-of-flow accident and associated cooling of the solvent. Considered factors should include toxic or explosive-gas generation, excessive plate-out, and excessive corrosion.

The selected process must include appropriate emergency procedures, e.g., emergency draining, gas detection, and emergency ventilation.

When the concentration of the contaminants in the solution increases during the decontamination process, the item being cleaned may become re-contaminated. This problem can be minimized by cleaning the least contaminated items first and by cleaning or replacing (recycling if possible) the solution, if the concentration of contaminants exceeds certain levels.

Some multi-step processes are commonly used for removing highly adhesive contamination layers. In many cases, chemical decontamination may be used as a step in a multi-step process (e.g., before electropolishing).

Spent Decontamination Solutions

The selection of the chemical reagent obviously determines the chemical characteristics of the secondary waste arising from the process. Continuous renewing of the solution increases the decontamination effectiveness, but the quantity of spent solution to treat and to dispose of also increases dramatically. In more recent years, the regeneration of chemicals has become a fundamental part in all chemical decontamination processes. Several conventional chemical processes may be used for regenerating the spent solutions, possibly in combination with, for example, ion exchange, evaporation/distillation, and electrodialysis.

The problem of limiting the secondary waste arising from the decontamination process may result in the selection of similar processes, like electropolishing or ultrasound with chemicals, rather than solely chemical decontamination. As stated previously, only a detailed cost-benefit analysis can provide the actual criteria for selecting the best option for a specific decontamination task.

Guidelines

When selecting a suitable chemical decontamination process, in addition to the outlined general considerations and in view of the variety of chemical decontamination processes available, several criteria must be considered in a detailed analysis based on site-specific conditions.

Most criteria are related to the specific features of a nuclear installation, such as:

- Location of the contamination (e.g., inner vs. outer surfaces of closed systems)
- Physical integrity status of the systems
- Materials (e.g., steel, concrete)
- History of operation (to determine the contamination-strata profile)
- Nature of the contamination (e.g., oxide, crud, particulate, sludge)

- Effectiveness of previously used chemical decontamination processes
- Distribution of contamination (e.g., surface, cracks, homogeneous distribution in bulk material)
- Exposure to humans and the environment
- Safety, environmental, and social issues
- Exposure-level-reduction requirements (e.g., recycling vs. disposal)
- Quantity and type of secondary waste from decontamination and conditioning
- Ultimate fate of decontaminated materials
- Time
- Cost

Taking into account the general considerations presented in these sections on chemical decontamination, an overview of the main advantages and disadvantages of this technique is provided in [▶ Table 10](#) for the selection of the most appropriate technique.

4.2.3 Electrochemical Decontamination

Electrochemical decontamination may be considered in principle a chemical decontamination assisted by an electrical field. Electropolishing is a process widely used in nonnuclear industrial applications to produce a smooth polished surface on metals and alloys. It may be considered the opposite of electroplating, as metal layers are removed from a surface rather than added as a coating.

Electrochemical decontamination uses direct electric current, which results in the anodic dissolution and removal of metal and oxide layers from the component. The dissolution may be obtained by immersing the items to be decontaminated in an electrolyte bath as anode, or fitted with anodes.

This method is useful for decontaminating items with easily accessible surfaces.

Current may also be delivered to a submerged component by moving a pad over the surface to be decontaminated, as an efficient method for regular surfaces. The electrolyte is continuously regenerated by recirculation.

For in-tank electropolishing, at least two (stainless steel) tanks are required. One tank contains the electrolyte, electrodes, and parts to be decontaminated. The other tank holds the water used for rinsing the parts after decontamination.

Power supply amperages of up to 2,500 A are common. To control the vapors released from the electrolyte during the electropolishing process, an extraction hood is located alongside the electropolishing tank. Provisions for heating and agitating the electrolyte as well as rinsing the tank are also required.

Electrochemical decontamination processes may only be applied for removing radionuclide contamination from conducting surfaces, such as iron-based alloys (including stainless steel), copper, aluminum, lead, and molybdenum. They are highly effective and give a high decontamination factor.

Important operating parameters for electrochemical decontamination are obviously electrolyte concentration, operating temperature, electrode potential, and current density.

The effectiveness of the decontamination may be limited by the presence of adhering materials on the surface of the items to be decontaminated. Materials such as oil, grease, oxides

■ Table 10

Advantages and disadvantages related to chemical decontamination

Advantages	Disadvantages
<ul style="list-style-type: none"> • Chemical decontamination is relatively simple and similar to classical cleaning in the conventional industry for which a lot of experience exists. It may also be relatively inexpensive where additional equipment is not required • Chemical decontamination is a known practice in many nuclear plants and facilities • With proper selection of chemicals, almost all radionuclides may be removed from contaminated surfaces. Problems of recontamination may be reduced by continuously rinsing the surface with water • With strong mineral acids, a decontamination factor of more than 100 decrease in activity levels may be achieved, and in many cases, the item may be decontaminated up to releasable levels • Chemical decontamination may also remove radioactivity from internal and hidden surfaces. However, in this case, its effectiveness may be low, and measurement at release levels will be a problem • Chemical decontamination involves relatively minor problems of airborne contamination, similar to those of the closed-system approach 	<ul style="list-style-type: none"> • The main disadvantage of chemical decontamination is the generation of secondary liquid waste, resulting in relatively high volumes compared to other processes, such as electropolishing. The treatment and conditioning of this secondary waste requires appropriate processes to be considered when selecting the decontamination option. Moreover, in some cases (e.g., internal and hidden surfaces), the effectiveness of the decontamination may be relatively low • Usually the solution must be heated up to 70 to 90 °C in order to improve the kinetics of the decontamination process • A further disadvantage in obtaining high decontamination factors is that corrosive and toxic reagents may require particular care • Chemical decontamination is scarcely effective on porous surfaces

(rust), and paint or other coatings should be removed before decontamination. The use of electrochemical decontamination is limited:

- When immersion is used, by the size of the bath
- When a pad is used, by the geometry of the surfaces and the available free space around the parts being treated

This makes the method almost inapplicable for industrial decontamination of complex geometries (e.g., small-diameter pipes).

Chemical Reagents

Phosphoric acid is normally used as electrolyte in electropolishing because of its stability, safety and applicability to a variety of alloy systems.

Moreover, the nondrying nature of phosphoric acid helps minimize airborne contamination, and the good complexing characteristics of phosphoric acid for metal ions is a significant factor in minimizing recontamination from the electrolyte.

Other electrolytes, such as nitric acid and sodium sulfate, have been investigated and proposed as alternatives to phosphoric and sulfuric acid. The need for new electrolytes was initially motivated by the incompatibility of phosphoric and sulfuric acids with the existing treatment facilities and the possibility of producing secondary liquid waste which is easier to process or regenerate.

Today, problems associated with the treatment of secondary liquid waste have only partly been resolved.


Secondary-Waste Generation

Electrochemical decontamination by electropolishing causes a steady increase of dissolved iron in the phosphoric acid. If the iron content exceeds 100 g/dm^3 , a precipitation of iron phosphate occurs and ends the efficiency of the decontamination process.

Therefore, the acid has to be exchanged or regenerated periodically. In doing so, the volume of effluents is limited; however, handling the parts to be immersed or the pad, may lead to additional exposure of workers.

Guidelines

When selecting a suitable electrochemical decontamination process, criteria must be considered in a detailed analysis based on site-specific conditions. These are similar to the criteria already mentioned, but taking into account that electrochemical decontamination processes require conducting surfaces.

From the general considerations presented in the foregoing sections on electrochemical decontamination, some main advantages and disadvantages of this technique may be indicated as in  [Table 11](#) to allow selection of the most appropriate technique.

4.2.4 Mechanical Decontamination

Mechanical decontamination methods may be classified as either surface cleaning (e.g., sweeping, wiping, and scrubbing) or surface removal (e.g., grit blasting, scarifying, drilling, and spalling). Mechanical decontamination may be used either as an alternative to chemical decontamination, or simultaneously with chemical decontamination or in sequence with chemical decontamination.

In general, mechanical decontamination methods may be used on any surface and achieve very good results. When these methods are used in combination with chemical methods, even better results may be achieved. Moreover, when dealing with porous surfaces, mechanical methods may be the only choice.

There are two basic disadvantages with the mechanical methods. First, the methods require the surface of the workpiece to be accessible (i.e., the workpiece should generally be free of crevices and corners that the process equipment cannot easily or effectively access). Second, if necessary precautions are not taken, many methods may produce airborne dust. If contamination is a concern, it requires a containment to protect the workers' health and to prevent the spread of contamination.

■ Table 11

Advantages and disadvantages related to electrochemical decontamination

Advantages	Disadvantages
<ul style="list-style-type: none"> • Electropolishing is commercially available. Major equipment is relatively inexpensive and process and processing procedures fairly simple. It is capable of decontaminating to background levels for decommissioning purposes, removing practically all radionuclides covering the surface, including plutonium, uranium, radium, cobalt, strontium, cesium and americium, giving typically decontamination factors of more than 100 in activity levels • Electropolishing may decontaminate flat areas, corners, recessed geometries, tanks, etc., where measurement down to release levels do not cause any problem. It produces a smooth polished surface with a low inherent ability to be recontaminated. The thickness of metal removed during decontamination is generally less than 25 μm • When compared to the volume of liquids required for chemical decontamination, electrolyte volumes for electrode contamination are relatively small 	<ul style="list-style-type: none"> • For the most widely used processes (i.e., in-tank), the item to be decontaminated must be removed from the plant and immersed in the tank with electrolyte. For the in situ process, access or entry for the device into the item to be decontaminated is required. Therefore, the use of electrochemical decontamination is limited by the size of the bath, when immersion is used, and by the geometry of the surfaces and the available free space around the part being treated, when a pad is used. This makes the method less applicable for industrial decontamination of complex geometries (e.g., small diameter pipes) • The treatment of the electrolyte for disposal (if not recyclable) requires neutralization and processing in a treatment system for liquid radioactive waste • Electropolishing does not remove (or removes with difficulty) fuel fines, sludge or any insulating material from the surfaces • Hidden parts as the inside of tubes are treated poorly • Handling of components may lead to additional exposure to workers

As with chemical decontamination, the selection of the most effective technique depends on many variables, such as the contaminants involved, surface material, and cost. The selected treatment may have to be applied several times to meet the established decontamination objective. Because each of these techniques may be modified according to site-specific conditions, the actual effectiveness and implementability of a technique should be explored in site-specific feasibility studies.

Surface-cleaning techniques are used when contamination is limited to near-surface material.

Some techniques may remove thin layers of the surface to eliminate the contamination. However, these techniques differ from surface-removal techniques in that the removal of the

contaminant from the surface is the goal rather than the removal of the surface layer itself. Certain surface-cleaning techniques generate contaminated liquids that need to be collected and treated. Many surface-cleaning techniques may be used for both equipment and building decontamination, and some may be used as a secondary treatment following surface layer removal.

Because these techniques are versatile, it may be advantageous to locate a centralized decontamination facility on-site in which one or more of these techniques are used. Such a facility could then be used to decontaminate components that are dismantled in large pieces, or segmented.

Abrasive-Blasting Decontamination Systems

Wet and dry abrasive-blasting systems, derived from conventional industry, may provide very high decontamination factors. The longer the operations are continued, the more destructive they are. Care must be taken not to introduce contamination into the material surface (hammering effect), so that the ability to meet clearance levels is not jeopardized. Wet abrasive systems also produce a mixture of dust and water droplets that might be difficult to treat.

A wet abrasive-blasting system is a closed-loop, liquid abrasive decontamination technique.

The system uses a combination of water, abrasive media, and compressed air, and is normally applied in a self-contained, watertight, stainless-steel enclosure.

There is no danger of airborne contamination, since a self-contained air ventilation system with absolute filter maintains a negative pressure inside the cabinet. Radioactive waste is mechanically separated from the cleaning media (e.g., by cyclone/centrifuge separation, sieving, etc.). Water may be filtered and recycled, and no soluble or hazardous chemicals are required.

Wet abrasive cleaning is being used in many nuclear facilities to remove smearable and fixed contamination from metal surfaces, such as structural steel, scaffoldings, components, hand tools, and machine parts.

The equipment may be used on close-tolerance parts, such as turbine blades or valves, where the removal of metal is not desired, or it may be adjusted to remove heavy-duty corrosion and paint by varying the amount of air pressure and abrasive media.

The dry abrasive-blasting technique, commonly called sandblasting or abrasive jetting, has been used in nonnuclear industries since the late 1800s. This technique, which uses abrasive materials suspended in a medium that is projected onto the surface being treated, results in a uniform removal of surface contamination. Compressed air or blasting turbines are normally used to carry the abrasive. The removed surface material and abrasive are collected and placed in appropriate containers for treatment and/or disposal. Recirculation of abrasives allows the minimization of secondary waste.

Dry abrasive-blasting is applicable to most surface materials except those that might be shattered by the abrasive, such as glass or plexiglas. Application on aluminum or magnesium should also be avoided due to the risk of dust explosions. It is most effective on flat surfaces, and because the abrasive is sprayed, it is also applicable on hard-to-reach areas. Nonetheless, materials such as oil and grease, or obstructions close to or bolted to components, must be removed before application, and precautions should be taken to stabilize, neutralize, or remove combustible contaminants, because some abrasives may cause some materials to detonate or generate dust explosions.

Static electricity may be generated during the blasting process; therefore, the component being cleaned, or the installation itself, should be grounded. Industrial remotely-operated units are available.

Abrasive Media Used

Depending on the application, a variety of materials may be used as abrasive media:

- Minerals (e.g., magnetite or sand)
- Steel pellets, aluminum oxide
- Glass beads/glass frit, silicon carbide, ceramics
- Plastic pellets
- Natural products (e.g., rice hulls or ground nut shells)
- Carbon dioxide (dry ice, for “cold” oxides, painted surfaces, etc.)

Silica has also been used as an abrasive; however, its use is not recommended since it is moderately toxic as a highly irritating dust and is the chief cause of pulmonary disease.

Prolonged inhalation of dusts containing free silica may result in the development of a disabling pulmonary fibrosis known as silicosis.

Secondary Waste Generation

As indicated previously, abrasives may be applied under either wet or dry conditions. Under dry conditions, dust-control measures are needed for dusts and/or airborne contamination. This problem may be reduced by using filtered vacuum systems in the work area.

When water is used to apply the abrasive, large volumes of waste are produced, including the wastewater, the abrasive, and the removed debris. Proper treatment and disposal of this waste is necessary. Recirculation of abrasives and recycling of the wastewater (treated or not before reuse) allows a significant reduction of the amount of secondary waste.

➤ *Table 12* gives some results on work rates and secondary-waste production during decontamination work carried out with both a dry and a wet abrasive-blasting system on the scale of a pilot project. Water consumption includes washing water to clean components and installation after each decontamination cycle.

Guidelines

When selecting a suitable abrasive decontamination process, again its criteria must be considered in a detailed analysis based on site-specific conditions. These criteria are very similar to the criteria already mentioned, taking into account the specific characteristics of the abrasive-blasting decontamination process.

Some main advantages and disadvantages of dry and wet abrasive blasting are provided in ➤ *Table 13* for the selection of the most appropriate technique.

4.2.5 Decontamination by Melting

During the decommissioning of nuclear plants, large quantities of slightly contaminated metallic scrap are generated. These scraps may also result from maintenance and from the replacement of equipment. Much of this waste consists of bulky equipment (e.g., heat exchangers, moisture separators, steam generators, etc.) that, if disposed in appropriate repositories,

■ Table 12

Some results of dry and wet abrasive blasting decontamination of metals (SOGIN-NIS)

Parameters		Dry abrasive blasting	Wet abrasive blasting
Efficiency		Very high	Lower
Grit consumption		55 g/kg metal	109 g/kg metal
Secondary-waste production	Intervention clothing	5.3%	8.2%
	Grit waste	5.5%	10.9%
	Water consumption	–	6.9 l/kg metal
Decontamination rate	Plates	57.4 kg/h	48.0 kg/h
		2.8 m ² /h	2.3 m ² /h
	Profiles	127.7 kg/h	106.8 kg/h
		1.8 m ² /h	1.3 m ² /h
Grit cost		0.5 euro/kg	2.25 euro/kg

■ Table 13

Advantages and disadvantages of dry and wet abrasive blasting decontamination of metals

Advantages	Disadvantages
<ul style="list-style-type: none"> • Generally, abrasive-blasting techniques have proved effective. In many cases, the equipment is well developed and commercially available. Industrial equipment is also available for remote operation • Several methods remove tightly adherent material, including corrosion layers. Special tools for cleaning the inside of tanks and pipes are also available • The abrasive-blasting technique is effective in a relatively short time 	<ul style="list-style-type: none"> • Abrasive-blasting techniques generally produce a large amount of waste, if recirculation and/or recycling of abrasives and/or water is not available. In some cases, it is difficult to control the amount of base metal removed. In dry abrasive systems, dustcontrol measures are needed to control dust and/or airborne contamination. Wet abrasive systems also produce a mixture of dust and water droplets that might be difficult to treat • Care must be taken not to introduce the contamination into the material surface (hammering effect) in order for the ability to meet clearance levels

would consume considerable volumes of the available space. Moreover, in many cases, this equipment contains valuable material that can be recycled, including pressure-vessel steel, stainless steel, and inconel. By melting slightly contaminated scraps, it is possible to recover much of these valuable metals, while simultaneously sparing valuable space at final disposal facilities. The pieces of equipment considered frequently also have complex geometries, making it extremely difficult, time-consuming, and expensive to determine the exact location and level of radioactivity on the internal surfaces. After melting, however, the radioactivity may be precisely determined from samples of each ingot. Moreover, an ingot may be released for restricted or unrestricted reuse, or stored for decay to appropriate limits.

The melting completely destroys components and, as a decontamination technique, is effective only for contaminants that are volatile or that concentrate in the slag (e.g., plutonium) rather than in the molten metal. The decontamination efficiency varies widely, depending on the considered radioisotope. The radionuclides remaining in the molten material are distributed homogeneously and effectively immobilized, thus, reducing the possibility of the spread of contamination. In some cases, when ingots are found to be so active as to be sent to a final repository, melting would have achieved the maximum volume reduction and thus preserved valuable repository capacity. As an alternative, some ingots with activity levels above unconditional-release limits may be re-melted to make shielding blocks or cold-rolled to fabricate containers for radioactive waste, and thus recycled within the nuclear industry.

A particularly advantageous consequence of melting is its “decontamination” effect on ^{137}Cs , a volatile element that has a half-life of 30 years. During melting, ^{137}Cs accumulates in the dust collected by ventilation filters and is removed. The dominant remaining radionuclide in the ingots (for most reactor scrap) is ^{60}Co . This element has a half-life of only 5.3 years. Other remaining nuclides have even shorter half-lives. Consequently, ingots with reasonably low-activity concentrations may be stored for release in the near future. Moreover, exposure of foundry workers to radiation during the subsequent re-melting of ingots is drastically reduced as a result of the removal of the ^{137}Cs . The secondary waste consists of the slag from segmenting and melting, as well as dust from the ventilation filters. This secondary waste only constitutes between 1 and 4% of the weight of the melted scrap.

Current Melting Practices

Limited quantities of metallic scrap thus far have been released from nuclear facilities for melting at conventional facilities. These releases have been permitted based on each case and the qualifying release limits for radioactivity have varied for different countries. The prevailing practices and conditions at these conventional foundries during the direct melting of contaminated scrap had previously provided the basis for calculating the exposure of workers and the public.

However, within the last 10 years, the melting of contaminated steel in special-purpose plants for recycling has developed as a new industry. Established techniques are being utilized for minimizing the quantity of active metallic waste. A number of plants melt or formerly melted contaminated metals on an industrial scale.

➤ *Table 14* illustrates the accomplishments of some of these facilities. All operate in “controlled” areas using safety precautions, including filtered ventilation and health physics supervision. Moreover, the slag and dust collected in the filters are treated as radioactive waste.

➤ *Table 15* provides some additional details of interest.

At the Studsvik Melting Facility, the ingots are stored, if necessary, to permit them to decay until they may be released for re-melting at commercial foundries. Prior to release, the material is certified by the appropriate radiation protection authorities. After re-melting, the materials may be used without radiological restrictions.

The main advantages from this re-melting strategy are:

- The volatile nuclides like ^{137}Cs have been removed in the first melt. Consequently, dust is no longer a radiological problem in further re-melting processes.
- There is no surface contamination.
- The slag has been removed as radioactive waste.

■ **Table 14**
Operating melting facilities

Facility	Melted scrap (tons)	Recycled/released
CARLA ^a	7,000	6,800 tons recycled in nuclear industry, 50 tons free release
STUDSVIK ^b	1,500	230 tons released, remaining stored for decay (or dis-posal)
INFANTE ^c	3,600	Stored/recycling in nuclear industry
SEG ^d	2,000	Recycling in nuclear industry

^aCARLA Plant, Siempelkamp, Germany (start 1989)

^bSTUDSVIK Melting Facility, Sweden (start 1987)

^cINFANTE Plant, Marcoule, France (start 1992)

^dScientific Ecology Group (SEG) Plant, Oak Ridge, USA (start 1992)

■ **Table 15**
Characteristics of operating melting facilities

Facility	Furnace type	Metal treated	Charge size (tons)	Products	Radiological limitations
INFANTE	Electric arc melting furnace	Carbon steel, stainless steel	12	Ingots, shield blocks, waste containers	Maximum 250 Bq/g for ⁶⁰ Co, other limits for other nuclides
STUDSVIK	Induction for steel, small electric arc for aluminum	Carbon steel, stainless steel, aluminum	3	Ingots	No specified limits
CARLA	Induction	Carbon steel, stainless steel, aluminum, copper, lead (R&D)	3.2	Ingots, shield blocks, waste containers	Maximum 200 Bq/g for beta-gamma nuclides, maximum 100 Bq/g for alpha nuclides, separate limits for uranium
SEG	Induction	Carbon steel, stainless steel, aluminum, (planning to melt copper and titanium)	20	Ingots and shield blocks at present, waste containers and reinforcing steel after 1994	Normally <2 mSv/h, greater dose rates with prior review and approval

Advantages of Melting as a Decontamination Technique

Melting presents the particular advantage of redistributing a number of radionuclides among the ingots, slag, and filter dust resulting from the melting process, thus decontaminating the primary material.

Melting may provide an essential step when releasing components with complex geometries, simplifying monitoring procedures for radioactive metal characterization. In addition to its decontamination effects, the problem of inaccessible surfaces is eliminated and the remaining radioactivity content is homogenized over the total mass of the ingot. So melting may be a last step in the decontamination and release of components with complex geometries, after these pieces have been decontaminated, for example, by chemical methods that remove radionuclides, such as ^{60}Co , that would remain in the ingot after melting.

4.2.6 Other Decontamination Techniques

In special cases, other decontamination techniques (e.g., ultrasonic, laser, high-pressure water jetting or steam spraying, thermal erosion, pastes, gels, foams, etc.) have also been used in decommissioning. Some of them, however, require more or less complex application procedures or still need more development to allow industrial applications.

4.3 Decontamination of Building Surfaces

4.3.1 Overview

When decontaminating building structures, mainly mechanical surface-removal techniques have to be considered. Surface-removal techniques are used when future land-use scenarios include reuse, when it is impractical to demolish the building (e.g., a laboratory within a building), or in view of waste minimization. The techniques considered in the following sections remove various depths of surface contamination (e.g., floors vs. walls), and may be used to reduce the amount of contaminated material for disposal. For example, if a contaminated building is demolished, all the debris is considered contaminated and requires special handling.

However, by first using a surface-removal technique, the volume of contaminant is limited to the removed surface material. The eventual demolition may then be performed conventionally. In this instance, a cost-benefit analysis should be prepared and consider such potential concerns as packaging, shipping, and disposal costs involved when using a surface-removal technique as compared with conventional demolition and disposal.

Before any surface-cleaning or surface-removal activity, surface preparation and safety precautions are required. Surfaces to be treated must be free of obstructions (e.g., piping and supports should be dismantled or segmented), and should be vacuumed to minimize release of airborne contamination during application of the surface-removal technique. Moreover, precautions are needed to prevent explosions when treating an area containing combustibles. In this instance, all combustibles should be neutralized, stabilized, or removed.

Due consideration should be given to industrial hazards associated with the use of these techniques and to unacceptable damage that may be caused.

Finally, contaminated debris (i.e., the removed portion of the surface) must be collected, treated and/or disposed, and any liquids used during the removal process, either as part of the process or as dust control, must be processed/recycled.

In cases in which a contaminant has penetrated the material beyond the surface layer, further treatment may be required.

Most of the surface-removal techniques usually leave an undesirable surface finish. If a smoothly finished surface is required (i.e., if the building is to be reused), a concrete cap or some other surface-smoothing treatment must be applied. Due consideration should also be given to the industrial hazards associated with the use of these techniques and to unacceptable damage that may be caused (i.e., stability of the building).

4.3.2 Basic Techniques

Decontamination processes to be used for contaminated concrete depend greatly on the characteristics of the concrete surface to be cleaned. They may vary from very simple hand-based processes to jackhammer or drilling removal techniques. The former is normally used for cleaning painted or smooth surfaces covered by loose contamination and the latter for decontaminating concrete in which the contamination has penetrated deeply.

Simple processes, such as brushing, washing and scrubbing, and vacuum cleaning, have been widely used, as the need for decontamination/cleaning was first noted in the nuclear industry, and each nuclear facility has, to some extent, a certain practical experience of these kinds of decontamination processes. These processes are generally labor-intensive, but they have the advantage of being versatile. They are often used as a first step (e.g., to vacuum dust and remove loose contamination) before or during dismantling, to prepare items for more aggressive decontamination using stronger processes.

Other, more aggressive techniques are grinding, spalling and drilling, high-pressure water jetting, foam decontamination, the use of strippable coatings, high-frequency microwaves, laser, and induction heating. The use of most of these techniques is limited to specific applications in particular cases. Some of them have disadvantages, such as spreading of contamination or producing a lot of undesirable secondary waste. Other ones are also less suitable for industrial applications. When decontaminating concrete surfaces, mainly mechanical scarifying techniques such as needle scaling, scabbling, or shaving are used.

4.3.3 Scarifying

Scarifiers physically abrade both coated and uncoated concrete and steel surfaces. The scarification process removes the top layers of contaminated surfaces down to the depth of uncontaminated layers. A decade ago, concrete scarifying was considered a radical approach to decontamination owing to poor tool performance and inability to provide a uniform surface profile upon removal of the contaminants. Today's refined scarifiers are not only very reliable tools, but also provide the desired profile for new coating systems, in the event the facility should be released for unconditional use.

Needle Scaling

Needle scalers are usually pneumatically driven and use uniform sets of 2, 3, or 4 mm needles to obtain a desired profile and performance. Needle sets use a reciprocating action to chip contamination from a surface. Most of the tools have specialized shrouding and vacuum attachments to collect removed dust and debris during needle scaling with the result of no detectable concentrations above background levels.

Needle scalers are an excellent tool in tight, hard-to-access areas (e.g., pipe penetrations, etc.), and may also be used for wall and ceiling surface decontamination. This technique is a dry decontamination process and does not introduce water, chemicals, or abrasives into the waste stream.

Only the removed debris is collected for treatment and disposal. Production rates vary, depending on the desired surface profile to be achieved.

Scabbling

Scabbling is a scarification process used to remove layers of concrete surfaces. Scabbling tools typically incorporate several pneumatically operated piston heads striking (i.e., chipping) a concrete surface.

Available scabblers range from one- to three-headed hand-held scabblers to remotely-operated scabblers, with the most common versions incorporating three to seven scabbling pistons mounted on a wheeled chassis.

Scabbling bits have tungsten-carbide cutters, the bits having an operating life of about 100 h under normal use. Both electrically and pneumatically driven machines are available.

Because scabbling may cause a cross-contamination hazard, vacuum attachments, and shrouding configurations have been incorporated, so that scabbling may be done with no detectable increase in airborne exposures.

In practice, floor scabblers may only be moved to within some 5 cm of a wall.

Therefore, other hand-held scabbling tools are needed to remove the last 5 cm of concrete flooring next to a wall, as well as to remove surface concrete on walls and ceilings.

This technique is a dry decontamination method – no water, chemicals, or abrasives are required. The waste stream produced is only the removed debris. Work rates are not easy to predict, due to the variety of concrete composition and characteristics as well as to the different types of bits that may be used.

Scabblers are best suited for removing thin layers (up to 15 or 25 mm thick) of contaminated concrete (including concrete block) and cement. It is recommended for instances where:

- Airborne contamination should be limited or avoided
- The concrete surface is to be reused after decontamination
- Waste minimization is envisaged
- When the demolished material is to be cleaned before disposal

The scabbled surface is generally flat, although coarsely finished, depending on the bit used. This technique is suitable for both large open areas and small areas.

Concrete Shaving

As an alternative for floor scabbling, a floor shaver has been developed. This machine is similar to a normal floor scabbling unit. It has a quick-change diamond-tipped rotary cutting head designed to give smooth-surface finish, easier to measure, and ready for painting. It is capable of cutting through bolts and metal objects, which would have damaged the scabbling head of a traditional scabber. Actual cutting performance results in:

- A three-times higher mean working rate for floor decontamination compared to scabbling
- A 30–45% lower waste production than by scabbling with a comparable decontamination efficiency
- Much less physical load on the operators due to the absence of machine vibration

- End products (concrete dust) that, combined with suitable additives, may be incorporated in a cement matrix

Based on the positive experience with the floor shaver, a remote-controlled diamond wall-shaving system has been developed as a solution for concrete decontamination of larger surfaces.

The machine consists of:

- A remote-controlled hydroelectric power pack for the remote-controlled shaving unit
- Vacuum systems to fix temporarily vacuum pads holding the horizontal and vertical rails of the shaving unit
- A simple xy-frame system containing a guide rail, a vertical rail, and a carriage for the shaving head
- A quick-change diamond-tipped rotary shaving head with a dust-control cover for connection to existing dust-extraction systems

The entire system is built up in sections, which are portable by a single operator. It removes a concrete layer in a controlled and vibration-free manner with the removal depth being controllable between 1 and 15 mm per pass, and producing a smooth-surface finish.

The cutting head is designed to follow the contours of the surface being removed, and depth adjustments may be set manually in increments of 1 mm to minimize waste production. With 300 and 150 mm wide shaving heads, both large areas and awkward corners may be accessed. When the vertical rail is fitted to the wall with the cutting head shaving, the horizontal rail may be disconnected and moved forward, thus ensuring continuous operation.

Production rates vary, depending on the structure and the hardness of the concrete, the depth setting, the cutting speed and the type of diamond used. Heads can be used for shaving up to 2,000 m².

Hydraulic/Pneumatic Hammering

Cutting and decontamination of concrete structures may be carried out with hydraulic or pneumatic hammers, either hands-on or using an electrically-powered, hydraulically-controlled robot.

The latter may be equipped with a hydraulic hammer, an excavator bracket, or other tools, and is well suited for decontaminating floors and walls. A mini electro-hydraulic hammering unit (weighing only 350 kg) is commonly used in areas where contamination has penetrated deeply into the concrete surface, increasing the decontamination possibilities, and reducing significantly the workload for the operators.

Dust Collection

For dustless decontamination of concrete, scabblers, scarifiers and shavers may be integrated into a system of remotely and manually operated scarifying equipment. With these systems, dust, and debris are captured at the cutting-tool surface, which minimizes cross-contamination. For hand scabblers and smaller systems, dust evacuation is carried out using industrial vacuum cleaners (capacities of up to 500 m³/h), and equipped with absolute filtering systems at the outlet.

Larger scabbling or shaving machines are connected to vacuum systems with capacities of up to 2,500 m³/h, or higher. They incorporate a cyclone to evacuate larger concrete particles, a filtering system with cleanable prefilters and absolute filter, and a vacuum pump. The cleanable

■ **Table 16**

Typical work rates obtained with different kinds of scarifying techniques (SOGIN-NIS)

Scarifying technique	Layer thickness removed (mm)	Removal speed (m ² /h machine working time)
Needle scaler	2	0.1
Hand scabblor (1 head)	2	0.6
Floor scabblor (7 heads)	3	4.6
Wall scabblor (3 heads)	3	4.6
Wall scabblor (7 heads)	4	8.4
Floor shaver	1.5	13.6
Wall shaver	1.5	21

filtering system incorporates a fill-seal drum changeout (contamination-free exchange) method that allows the operator to fill, seal, remove, and replace the waste drum under controlled conditions. The unit may accommodate different drum sizes and several scabblers, shavers, and needle scalers at longer distances.

Production Rates

Typical work rates obtained with needle scalers, scabblers, and shavers are indicated in [Table 16](#).

4.3.4 Guidelines

When selecting an appropriate decontamination technique for building surfaces, the general considerations already presented should be taken into account. In any case, the use of techniques that would make contamination penetrate further into the substrate should be avoided. In addition, as general rules:

- For decontaminating painted floors and walls, where it may be proved that contamination has not penetrated into the substrate, simple processes such as brushing, washing, scrubbing, and vacuum cleaning may be used
- For decontaminating concrete surfaces which are not painted and in which the contamination has slightly or more deeply penetrated the substrate, more aggressive techniques (e.g., scabbling, shaving, jackhammering or drilling) must be adopted

4.4 Chemical Decontamination Techniques

4.4.1 Overview

Chemical reagents are widely used in the nuclear industry as decontaminants. The objective of chemical decontamination in the nuclear industry is to remove fixed contamination on surfaces of piping, components, equipment, and facilities.

The advantages of chemical decontamination are that it can be used for inaccessible surfaces, requires less work-hours, can decontaminate process equipment and piping in place, and can usually be performed remotely.

Chemical decontamination also produces few airborne hazards, uses chemical agents that are readily available, produces wastes that can be handled remotely, and generally allows the recycling of the wash liquors after further processing.

The disadvantages of chemical decontamination are that it is not usually effective on porous surfaces, can produce large volumes of waste (although volume may be reduced by a radioactive waste treatment system), may generate mixed waste, and can result in corrosion and safety problems when misapplied.

In addition, it requires different reagents for different surfaces, drainage control; the construction of chemical storage and collecting equipment for large jobs; and addressing criticality concerns, where applicable.

4.4.2 Water/Steam

Water is a universal decontamination agent that acts by dissolving the chemical species or by eroding and flushing loose debris from the surface. It can be used on all nonporous surfaces, and its effectiveness can be enhanced by increasing its temperature, adding a wetting agent and detergent, or using a water jet. Steam is effective partially because of its velocity impinging on the surface, and it can be made more effective with detergents.

Steam can be used on any nonporous surface that can withstand the temperature, but it is most useful on accessible surfaces. Steam generally provides better decontamination factors (DF) than water for flat-coated or polished surfaces. Dry steam has been applied in some cases to uncoated concrete.

Most ionic compounds are soluble in water; therefore, water/steam is the first choice for sluicing bulk salts and solids from tanks. For surfaces with grease or oil, it is not effective unless detergents are added. Water is most effective when the contaminant has been in contact with the surface for only a short time.

Water by itself has little effect in removing longstanding contaminants and those that are chemically bonded to the substrate. It has almost no effect on hard metal oxide and carbonate or silicate scales, and it reacts violently with metallic sodium or potassium. Most transition metal compounds have limited solubility in water, unless the pH is lowered.

The advantages of using water as a decontaminant are that it is cheap, available, nontoxic, noncorrosive, and compatible with most radioactive waste systems. In addition, water/steam requires few support services that are present in the plant. Because of its safe nature, it can be used in large facilities and environmental flushing operations. Remote operations can be accomplished with fire hoses, jets, or steam lances. Most cleaning operations use a water flush before other agents are employed.

The advantage of using steam is that the mass of water is reduced.

The disadvantages of water as a decontaminant are that large volumes are usually required and contaminants can resettle onto other surfaces. In particular, the use of water has the tendency to spread radioactive contamination, which complicates the control of cleanup. If fissile materials are present, criticality concerns become paramount.

4.4.3 Strong Mineral Acids

The strong mineral acids used in decontamination are:

- Hydrochloric acid: HCl
- Nitric acid: HNO₃
- Sulfuric acid: H₂SO₄
- Phosphoric acid: H₃PO₄

These acids can be used by themselves as dilute solutions, in formulation mixtures with acid salts and other compounds, and in combination with each other – such as HNO₃-HCl. Their main purpose is to attack and dissolve metal oxide films and lower the pH of solutions to increase solubility or ion-exchange of metal ions. They can be used on almost all metal surfaces except reactive metals like zinc. The acids work rapidly and very effectively.

All the acids are relatively cheap (except H₃PO₄), and all are commonly available industrial compounds.

The advantages of using the strong acids are that they are relatively cheap, quick, and effective. The disadvantages are that they present safety and handling problems, require neutralization before waste treatment, and are incompatible with many materials. Explosive or poisonous gases can be produced in reactions with some compounds.

Typical examples of the effectiveness of using strong acids for decontamination follow.

Hydrochloric Acid

HCl is one of the first chemical cleaning agents used for utility boilers. It was used in decontaminating the BONUS reactor CrMo steel main steam system and stainless steel purification system in preparation for entombment.

A reagent grade solution (10% by volume) was found to be effective at an operating temperature of 70 °C. One-inch square samples for testing in the United Nuclear Corporation laboratory were cut from sections of piping contaminated with ⁶⁰Co, ⁵⁸Co, and ⁶⁵Zn and small quantities of fission products, including ¹³⁷Cs. Laboratory testing consisted of 30-min cycles in static tests (soaking) of candidate solutions and then 30-min cycles in dynamic tests (stirred) of solutions. The most effective solutions were given a final dynamic test on larger samples from the reactor systems.

Laboratory data indicated HCl decontamination of stainless steel gave repeatable DFs of approximately 10. No inhibitor was used because the systems were not going to be returned to service, and the expected corrosion would not affect the residual radioactivity containment integrity of systems.

Actual system decontamination at BONUS confirmed the laboratory results. Stainless steel CrMo systems were decontaminated with a DF of approximately 10 overall. A brief description of the acid-flushing system is included in the discussion of H₃PO₄.

Nitric Acid

HNO₃ is used for dissolving uranium and its oxides in stainless steel and Inconel systems. A typical solution is 10% by volume at 75 °C. However, it cannot be used on carbon steel because of the high corrosion rate.

HNO₃ is a strong oxidizing agent; users should have knowledge of its compatibility with materials. Use of HNO₃ on incompatible material has resulted in fires and explosions (in closed systems).

HNO_3 is also used at reprocessing plants to dissolve plutonium dioxide, fission products, sludge deposits, and residual contamination from system piping and components.

At the Eurochemic reprocessing facility, potassium permanganate (KMnO_4) was added to the HNO_3 , resulting in the most effective decontaminant of that major decontamination program.

Two similar processes used to decontaminate the cell of the acid recovery evaporator at the Tokai Reprocessing Facility in Japan were general treatment by HNO_3 , followed by a sodium hydroxide (NaOH) rinse, and decontamination of equipment bottoms using a three-stage process (i.e., AP, HNO_3 , and EDTA).

Sulfuric Acid

H_2SO_4 is an oxidizing agent used to a limited extent for removing deposits that do not contain calcium compounds.

This highly corrosive acid is used in dilute form with an inhibitor. The concentrated form has been used for removing organic deposits. H_2SO_4 has not been used extensively as a decontaminating solvent because the DFs are relatively small.

Phosphoric Acid

H_3PO_4 rapidly removes films from and decontaminates carbon steel surfaces. At 60–70 °C inhibited dilute (10%) H_3PO_4 solutions remove 95–99% of the contamination and all visible film in approximately 20 min. In practice, a ferrous phosphate film forms and is deposited on the treated area along with the contamination.

Diluted (15 vol. %) H_3PO_4 was used in decontaminating the BONUS reactor carbon steel and brass piping and components in preparation for entombment. The selection was based on a test program similar to that described for HCl. DFs between 5 and 37 experienced in laboratory tests were generally achieved during actual decontamination flushes. The carbon steel condensate system was passivated using ammonium hydroxide followed by a rust inhibiting rinse.

The use of phosphates is not recommended when the waste end product is glass.

4.4.4 Acid Solutions

Salts of various weak and strong acids can sometimes be used in place of the acids themselves, or as a more effective combination with various acids. The most commonly used salts are

- Sodium bisulphate: NaHSO_4
- Sodium sulfate: Na_2SO_4
- Ferric sulfate: $\text{Fe}_2(\text{SO}_4)_3$
- Ammonium oxalate: $\text{NH}_4\text{C}_2\text{O}_4$
- Ammonium citrate: $(\text{NH}_4)_2\text{HC}_6\text{H}_5\text{O}_7$
- Sodium fluoride: NaF

The salts can be used in combination with acids or acidic solutions to decontaminate metal surfaces. They work in a manner similar to the acid itself by dissolving or complexing the metal oxide surface, but they also provide free sodium and ammonium ions to replace contaminants at ion-exchange sites.

The salts are frequently used in combination with their parent acid and give a better DF than the acid alone. The salts are less corrosive than their parent acid and have fewer material compatibility problems, but are generally corrosive enough to require inhibitors. Their application as single agents is limited, with the exception of NaHSO_4 , which is often used alone for mild decontamination of carbon steel and aluminum.

The advantages of acid salts are that they increase the versatility of acid decontamination, produce less corrosive solutions, and are safer for personnel than the acids.

The disadvantages are that the salt solutions still present some corrosion considerations for both equipment and personnel, have limited application without addition of another acid to lower the pH of solution, and are slower acting than the acids.

4.4.5 Organic/Weak Acids

The use of weak (organic or inorganic) acids for decontamination is now widespread in the nuclear industry for nondecommissioning activities.

The most widely used weak acids include the following (in order of frequency of use):

- Oxalic acid: $\text{C}_2\text{H}_2\text{O}_4$
- Citric acid: $\text{C}_6\text{H}_8\text{O}_6$
- Sulfamic acid: HSO_3NH_2

The weak acids are generally used on metal surfaces and act by dissolving the metal oxide film and sequestering or solubilizing the metal ion. This sequestering or chelating property gives the organic acids a great advantage over the strong mineral acids.

The organic acids, also, are not as corrosive, are less toxic, and have few material compatibility problems. They contain no chloride or fluoride and thus can be used on stainless and high-alloy steels. Stainless steel is usually cleaned with organic acids, usually oxalic and citric. Plastics and other polymeric compounds can also be cleaned with organic acids.

The organic acids are used extensively on all metal surfaces where reuse or nondestructive cleaning is the objective. They may be used with or without inhibitors, depending on the acid and the conditions.

Oxalic, citric, and HSO_3NH_2 are the stronger acids and often are used with inhibitors. The organic acids may be mixed to get the full range of chelating abilities, or they may be matched to the specific surface and contaminant. Oxalic and citric acid mixtures have the greatest general use.

Oxidizing agents are often used with the acids to condition the metal so it may be solubilized. HSO_3NH_2 has the added benefit of being a solid that can be shipped and stored as a dry powder and mixed on-site. All of these organic acids are commercially available.

The advantages of the organic acids are their less corrosive nature, superior safety and handling characteristics, and double role in dissolving oxide films and sequestering the metal contaminant.

Some of the disadvantages are that they are more expensive than some of the strong acids; they react more slowly; although less corrosive than strong acids, they still have some material compatibility and personnel considerations; they can break down at high temperatures; and they require neutralization before treating in a radioactive waste system.

Several examples of the manner in which weak acids have been used are described in the following sections.

Oxalic Acid

Oxalic acid (OX) is effective for removing rust from iron. It is an excellent complexant for niobium (when present) and fission products. Oxalic acid was used at the Savannah River Plant in stainless steel heat exchangers.

The process consisted of filling the system with water, adding a corrosion inhibitor (2.6 g/l ferric sulfate), steam heating to 70 °C, adding oxalic acid to 2 wt. %, and recirculating the mixture. The system was then drained, water-rinsed, and neutralized with 50% potassium hydroxide. The system was drained and rinsed again with water. DFs of 3–20 were achieved. At temperatures of about 90 °C, the oxalic acid reacted with the stainless steel to form a highly insoluble ferrous oxalate film. Subsequent treatment with sulfuric and HNO₃ was necessary to remove the precipitate.

This acid is used as the second step with AP (alkaline permanganate) preconditioning, but because of the precipitate it is not of significant interest.

Problems may occur during evaporation when using oxalic acid because of the formation of crystals.

Oxalate Peroxide

Oxalate peroxide (OPP) is an oxidizing agent consisting of a mixture of oxalic acid and hydrogen peroxide. It is used for the simultaneous dissolution of UO₂ and the defilming and decontamination of metals.

The oxalic acid decontaminates the surface, and the hydrogen peroxide enhances the decontamination and passivates the steel by its oxidative action. However, the peroxide destroys the oxalic acid, preventing reuse of the solvent. The decontamination is fast enough to be effective before the oxalic acid is destroyed.

Hydrogen peroxide acts as a carbon-steel cleaner in concentrations up to 0.2 M H₂O₂ and then as a passivator at concentrations above 1.0 M H₂O₂. In tests at ORNL, carbon and stainless steels heated to about 200 °C and treated with OPP (pH = 4) exhibited DFs of 100–1,000 or more.

Citric Acid

A mixture of citric (0.2 M) and oxalic (0.3 M) acids with a corrosive inhibitor is used as a reducing agent. This process is very effective for decontaminating stainless steel in a two-step process following alkaline permanganate (AP). A typical procedure consists of the following steps:

- Circulate AP for 2 h at 105 °C
- Water-rinse until the (MnO₄)⁻¹ is completely removed and pH is less than 10
- Circulate dilute (10%) mixture for 2 h at room temperature
- Circulate mixture until the conductivity of the rinse water is less than 50 μmho

The citrate ions are added to complex the iron ions and inhibit the formation of any precipitate.

The dilute mixture neutralizes traces of residual NaOH (from AP) and dissolves any MnO₂ (by reduction to Mn⁺²). This dilute rinse may be eliminated for simple systems without dead-legs or crud traps. The process is not very effective unless preceded by the AP flush.

Sulfamic Acid

HSO₃NH₂ with an inhibitor is an effective decontaminant for carbon-steel components, providing good DFs with low corrosion rates. Redeposition or film formation does not occur.

Because it is a less reactive reagent, longer contact times may be necessary than with other reagents. HSO_3NH_2 has not been used extensively in decontaminating reactor carbon-steel systems, but it is acknowledged to be an effective decontaminant.

4.4.6 Alkaline Solutions

Caustic compounds are used for decontamination both by themselves and in solutions with compounds. The primary alkaline salts are:

- Potassium hydroxide: KOH
- Sodium hydroxide: NaOH
- Sodium carbonate: Na_2CO_3
- Trisodium phosphate: Na_3PO_4
- Ammonium carbonate: $(\text{NH}_4)_2\text{CO}_3$

Alkaline salts (i.e., bases) are used to remove grease and oil films, to neutralize acids, as surface passivators, to remove paint and other coatings, as a rust remover for mild steel, as a solvent for species that are soluble at high pH, and as a means of providing the right chemical environment for other agents. As a degreaser, they are normally mixed with detergents, and most commercial detergents contain mild caustic compounds.

The strong bases (KOH, NaOH) are frequently mixed in solutions with oxidizing agents (KMnO_4 and potassium metaperiodate KIO_4) and a reducing agent (NaH_4PO_2), which are not stable in acid solutions. Alkaline permanganate (NaOH and KMnO_4) is a very widely used decontaminating agent for metal surfaces, especially as a first conditioning step for stainless steel. Some important species like iodine are more soluble in alkaline solutions and can be effectively washed from the surface.

The aggressiveness with which these compounds act on paints, coatings, and films and can be controlled by using the strong bases (KOH, NaOH) for harsh attack or the weak bases for milder conditions. The alkaline solution softens the paint so that it can be removed by mechanical means. This process is often preferable to completely dissolving the paint because that may contaminate the surface under it. Alkaline solutions may be used on all nonporous surfaces, except aluminum and magnesium, which react to strong bases.

The advantages of using alkaline solutions are that they are cheap, are easy to store, have fewer material problems than acids, and can be applied in the form of gels for ceilings and walls. The disadvantages include their long reaction time and their destructive effect on aluminum. In addition, the bases are safety hazards: workers can be burned if they come into contact with them.

4.4.7 Complexing Agents

A complexing agent is a chemical species that forms a stable complex with a metal ion in two different manners. Those that are preferential form complexes with certain ions and are called sequestering agents. Chelating agents are complexing agents that bind the metal at two or more locations.

The most common complexing agents used in decontamination are the following:

- EDTA and the monoacid HEDTA
- Organic acids

- Sodium or ammonium salts of the organic acids
- Nitrilotriacetic acid (NTA)

The complexing agents solubilize certain metal ions and prevent their redeposition out of solution. This is most important since metal ions have a strong affinity for bare metal surfaces.

Complexing agents are used with solutions of detergents, acids, or oxidizing agents to dramatically increase the DFs. The ability of the agent to sequester metal ions depends on the specific ion, its oxidation state, and the solution pH.

EDTA works best with most ions, but it is expensive, and its pH range is too high for strong acid solutions used to attack metal oxide layers.

EDTA is most often used with detergent, oxidizing agents, or weak acids, and it is noncorrosive and nontoxic. A very effective decontaminating agent for metal surfaces is a mixture of oxalic and citric acid. The metal ion preferences of the two complement each other, and the organic acids also act to dissolve the oxide film. EDTA is also used with oxalic/citric acid mixtures. When using the organic acids as complexing agents, the precautions described for organic and weak acids should be considered.

The advantages of using complexing agents are that they increase the DF of most decontaminating agents, can perform dual functions (in the case of the organic acids), and are relatively safe and nontoxic.

The disadvantages of EDTA and similar chelating agents are the cost, the limited range of applicability, and the effect on some radioactive waste processes like precipitation and ion exchange. Wastes containing EDTA may present a disposal problem. Site waste management should be consulted before using this chemical.

4.4.8 Oxidizing and Reducing (REDOX) Agents

An oxidizing agent increases the oxidation state of another chemical species, and a reducing agent lowers the oxidation state. A change in oxidation may be beneficial because some oxidation states are more soluble than others. Frequently, these two classes of chemicals are used jointly to maintain a specified oxidation level.

The following oxidizing agents are commonly used in decontamination:

- Potassium permanganate: KMnO_4
- Potassium dichromate: $\text{K}_2\text{Cr}_2\text{O}_7$
- Hydrogen peroxide: H_2O_2

Oxidizing agents find extensive application in decontamination by conditioning metal oxide films, dissolving fission product debris, dissolving various chemical species, and oxidizing the metal surface for either protection or corrosion.

Many metallic and other compounds either break down or are more soluble in higher oxidation states, and base metals must be oxidized to dissolve them. Most metal surfaces can be treated with oxidizing agents, but conditions must be adjusted to avoid excessive corrosion.

Solutions of alkaline permanganate (AP) are used extensively to condition metal oxide films, especially for stainless steel. Because the strong oxy-acids (HNO_3 , H_2SO_4 , and H_3PO_4) are also oxidizing agents, these are usually used alone, but hydrogen peroxide finds application in solutions with the other nonoxidizing acids and salts.

Solutions of organic acids and peroxides frequently get superior DFs to those of strong oxidizing acid, but without some of the corrosion and safety problems.

The advantages of using oxidizing agents are that they complement various acid decontamination solutions, allow less corrosive acids or salts to be used, and perform a unique function in the dissolution of many compounds.

The disadvantages include some metal corrosive action, violent reactions with some compounds, loose activity during storage, and the need to be neutralized before treating in the radioactive waste system.

Reducing agents alone have limited application for decontamination because metals plate-out when reduced, and this is usually undesirable. Under specific conditions, reducing agents could be used to protect a metal surface or reduce higher oxidation states for sequestering agents. Possible reducing agents are sodium hypophosphite (NaHPO_2) and hydrazine (N_2H_2).

Examples of the manner in which this class of chemicals can be used are described in the following sections.

Alkaline Permanganate

Alkaline permanganate (AP) is an oxidizing agent used to oxidize chromium in the corrosion film to Cr_2O_3 , which can subsequently be dissolved in an alkaline solution. It is used as a pre-treatment process in multi-step decontamination programs to expose the remaining corrosion film matrix to subsequent chemical dissolution.

Low Oxidation-State Metal Ion (LOMI)

The low oxidation-state metal ion (LOMI) process was developed by the UK Central Electricity Generating Board (CEGB) in the late 1970s. The process utilizes V^{+2} ions in the form of vanadium picolinate to reduce Fe^{+3} ions in the corrosion product scale to the more soluble Fe^{+2} state, with the V^{+2} ions being oxidized to V^{+3} . The oxidized V^{+3} ions are also formed by the reaction of V^{+2} with oxidizing species formed by the radiolysis of water. Therefore, formic acid is added to the reagent to scavenge these oxidizing radicals.

The LOMI decontamination process is applied in a manner similar to that used for the CAN-Decontamination process. The reactor coolant is first adjusted to neutral pH and a low dissolved-oxygen level and is then brought to a temperature of 80–90 °C. The chemical decontamination solution is then injected, and a side stream of circulation coolant is passed through filter and cation exchange resin columns to regenerate the solution on line.

Decontamination times are very short, typically of the order of 1–3 h. A prior pre-oxidizing AP or nitric acid permanganate (NP) step is required to remove the higher Cr films present on pressurized-water reactor (PWR) components. As with the CAN-Decontamination process, this pre-oxidization step oxidizes the insoluble Cr^{+3} ions to the soluble Cr^{+6} state, and these are dissolved in the subsequent LOMI treatment.

The first formulation of the LOMI reagent typically contained $2\text{--}4 \times 10^{-3}$ M V^{+2} , $1\text{--}2 \times 10^{-3}$ M each of picolinic acid and formate ions in thoroughly deoxygenated water, and sufficient NaOH to adjust the solution pH.

This first formulation generated a relatively large amount of radioactive waste from the ion-exchange process, which had to be disposed. Therefore, a second generation LOMI reagent, containing less formate and NaOH, has recently been introduced, resulting in a 50% reduction in the amount of ion-exchange resin required for waste cleanup.

The advantages of this process are that it has low corrosion without the use of inhibitor and it reacts rapidly. The disadvantages are that the reagent is somewhat expensive and it creates a relatively larger volume of waste.

The LOMI process is the established decontamination process for the Winfrith SGHWR (UK). In 1984, it was used in the decontamination of heat exchangers and recirculation pipe work in the Monticello BWR.

Experience to date indicates that this process is an effective method for routine decontamination of BWR piping and fuel. It can be applied to decontaminate the structural materials of carbon steel, SS304, SS316, SS321, SS410, Inconel 600, Inconel 800, Zircaloy 2, etc.

Electrochemical Low Oxidation-State Metal Ion Exchange (ELOMIX)

Electrochemical LOMI ion exchange (ELOMIX) is a modification of the LOMI process. The primary objective of ELOMIX is to reduce the volume of waste arising from the LOMI decontamination process.

Currently, the resin resulting from the application of the LOMI decontamination process is normally managed by solidification in cement-based matrices for shipment to an appropriate disposal location, but this is not desirable as a long-term solution because of the instability of organic media and the cost of long-term disposal.

The key element of the ELOMIX process is an electrochemical cell consisting of three compartments: anode, cathode, and resin. The following are the principal features of ELOMIX:

- Electrodeposition of metals
- Back-diffusion of nonplating ions
- Continual resin regeneration
- Compatible chemistry and regeneration of the LOMI solution

The concept of ELOMIX has been in development since May 1989. In October 1990, a small pilot-scale ELOMIX cell was operated at Commonwealth Edison's Dresden Unit 2 on a sidestream of actual decontamination solution. This pilot-scale cell operated successfully during three LOMI steps, processing a total of 33 l of decontamination solution through a resin volume of only 0.2 l.

DECOHA Process

The DECOHA process combines important chemical processes – metal dissolution and electrochemical recovery of dissolved metals from a chemical decontamination – into a single “closed loop” process.

Fluoroboric acid (HBF_4) is the heart of the DECOHA process. HBF_4 is a commercially available acid produced when gases are washed during aluminum production.

HBF_4 primary decontamination attribute are its electrolytic properties, which are effective over a wide range of chemical conditions. In general, the acid reacts with a metal to produce the corresponding metal-fluoroborate and hydrogen gas. The HBF_4 reacts similarly with metal oxides-generating water rather than hydrogen gas as a reaction end product.

The effectiveness of these reactions depends in large part upon the solubility of the various metals in HBF_4 .

Experience has confirmed HBF_4 as an extremely powerful solvent for metals. Iron and other important metals exhibit solubilities close to or greater than 200 g/l in 50% HBF_4 , and the pH

of the solution is maintained above 4–5 as a result of the formation of the salt of the acid rather than the formation of the free acid.

Using this process, thin layers of the contaminated metal can be removed from the surface of the contaminated object. Consequently, the level of damage to an object and the corresponding amount of waste produced can be minimized through process control, removing only the depth of metal required to achieve the specific objectives of the decontamination.

The DECOHA process is generally applied at temperatures between 30 and 98 °C. Some metals such as carbon steel, zircaloy, and aluminum may be treated at room temperature. However, the stainless steels and nickel alloys require elevated temperatures to allow realistic application times.

Basically, the speed of the DECOHA process follows a typical dependency on the temperature – for every 10 °C increase in temperature, the reaction requires half as much time to take place.

Typical removal rates range from 3 to 4 μm/h at 80 °C for nickel alloys in 50% solution of HBF₄ to 20–25 mm/h at 21 °C for aluminum in a 5% solution of HBF₄ solution.

Chemical Oxidation Reduction Decontamination (CORD)

In the first step of the chemical oxidation reduction decontamination (CORD) process, permanganic acid is added to the system to oxidate the chromium to the hexavalent state. The decontamination solvent, dicarboxylic acid is added directly without the fluid contents of the system having to be replaced. Permanganic ions are reduced to manganous ions by an equivalent concentration of the decontamination solvent. Dissolved metals may be removed by ion exchange in real-time application or by subsequent evaporation of the solvent.

This procedure is referred to as one cycle and can be applied several times. It may be applied to oxide films. The operating temperature is around 95 °C, and the concentration of chemical does not exceed 3 g/l. An adequate DF is normally achieved after two cycles.

Pressurized Water Reactor Oxidative Decontamination (POD)

The PWR oxidative decontamination (POD) process is applied as follows:

- Apply NP reagents (KMnO₄, at 1.0 g/l and HNO₃ at 0.25 g/l) for 5–24 h, typically 7 h for PWR oxide.
- Apply oxalic (at 1.4 g/l) and HNO₃ (1.5 g/l) for 0.5–1 h to destroy excess permanganate and manganese dioxide.
- Add oxalic (at 0.45 g/l) and citric acids (0.96 g/l) to dissolve the chromium-depleted oxide, and remove dissolved metals in solution using ion exchange.

In the first phase, the permanganate oxidizes chromium in the oxide to bichromate ions as it reduces to manganese dioxide. There is no pH change in this phase.

In the second phase, oxalic and HNO₃ are added to destroy the excess permanganate and manganese dioxide. The primary advantage in using oxalic acid is that it imposes no resin requirements and reacts rapidly.

In the final phase of the process, the chromium-depleted oxide, which can be represented by the formula for hematite or nickel ferrite, is dissolved by the addition of oxalic and citric acids. The former may act as either a chelating or a reduction agent towards Fe⁺³. The dissolved metal ions in all cases are held in solution as complexes of citrate and/or oxalate

The DFs on stainless steel range from 4 to 25, with 5–10 being typical values. On Inconel 600, DFs of approximately 2 were obtained.

Bleaching

The bleach solution is added in generous amounts to the contaminated surface. The surface is scrubbed for 15–60 s, allowed to stand for about 15 min, and then flushed thoroughly with water. The bleach application and wash can be repeated a second time if necessary.

Bleach is most effective against chemical agents and liquid pesticide spills. Bleach has been used on metal, wood, and concrete surfaces, but is most effective on metallic surfaces. Bleach formulations chemically degrade and detoxify many contaminants, especially pesticides. Chemical degradation rates can be affected by other pre- or post-bleach decontamination efforts.

Bleach formulations are normally used in conjunction with other decontamination techniques, most often as a follow-up for detoxifying pesticides on surfaces where a physical procedure did not produce satisfactory results (i.e., did not achieve the cleanup goals).

Solid bleach formulations are generally applied as a slurry, which can result in periodic clogging of application equipment. Depending on their concentration and composition, bleach slurries may cause corrosion of the application equipment and/or the surfaces being treated.

Various types of bleach formulations have been used as decontaminating agents. Traditionally, calcium hypochlorite has been used, although recently sodium-based bleach formulations have had some application.

The various bleaches used include:

- Grades I, II, and III, with >35%, 29–35%, and <29% available chlorine, respectively
- Supertropical bleach (STB), a British formula containing >30% available chlorine
- High test bleach (HTB), which has approximately 42% chlorine content
- Liquid household bleach (sodium hypochlorite and NaOH)

Work is needed to improve the technique for application to porous surfaces and to lessen the corrosive impact of bleach on equipment and building materials.

Detergents and Surfactants

Most commercial detergents involve some formulation of a detergent (sodium laurel sulfate, sodium oleate, alkyl aryl sulfonate) that also acts as a wetting agent or surfactant, a phosphorous or carbonate salt (Na_4PO_4 , Na_2CO_3), a thickening agent (carboxyl methyl cellulose), and other fillers. EDTA or other complexing agents may also be added.

The formulations are numerous and involve foaming or nonfoaming and phosphate or nonphosphate choices. Other surfactants that may be used with the detergent or separately include various sulfonic acid salts, quaternary ammonium salts, and nonionic alcohol, or amine polymers.

Detergents are used in decontamination to remove grease, dirt, and certain organic materials. Surfactants produce similar results by lowering liquid surface tension and providing better contact between the surface and the liquid.

Detergents are effective, mild, all-purpose cleaners for all facility surfaces, equipment, clothes, and glassware. Where applicable, they are preferable to harsher methods. They can be used to increase the effect of water, steam, solvents, and complexing agents. Effectiveness is increased by mechanical agitation. Detergents are not effective on metal corrosion and contamination.

Detergents are cheap, available, safe, and have few material-handling problems. The disadvantages of detergents are their limited effect and possible foaming or ammonia release in a radioactive waste system.

Surfactants are used as wetting agents, detergents, and emulsifiers. They typically consist of long carbon-to-carbon skeletons plus a polar group containing atoms of nitrogen, oxygen, or sulfur. Because the polar group is hydrophilic (water-loving) and the hydrocarbon part is hydrophobic (water-hating), these molecules (or ions) tend to migrate to water-oil interfaces where the polar group is attracted to the water phase and the hydrocarbon residue remains in the oil phase.

4.4.9 Organic Solvents

Solvents are used in decontamination for removing organic materials, grease, wax, oil, and paint from surfaces and for cleaning clothes (dry cleaning). Some typical organic solvents are the following:

- Kerosene
- 1,1,1-Trichloroethane
- Trichloroethylene
- Xylene
- Petroleum ethers
- Alcohols

Dry cleaning of personal protecting equipment (PPE) and rubberized articles have some advantage over detergents in that a much smaller volume of waste is produced. Moreover, dry cleaning in many cases is just as, or more, effective than water cleaning.

In general, the wastes produced include a sludge and a small amount of trichloroethane solvent.

The disadvantages of dry cleaning are that it is limited to certain materials (e.g., plastics must normally be avoided), it gives poor results with wet items or aqueous-soluble stains, and there can be some cross contamination as the solvent is reused.

For other applications, the solvents are used to dissolve certain organic materials from surfaces.

Because of their flammability and their potentially toxic vapors, they are best used on small areas or in contained systems. Some solvents contain chlorine, which is normally avoided in stainless steel systems.

Most radioactive waste systems cannot handle organic solvents. Where other solvents such as alkali or detergents can be used, organic solvents are normally avoided. Conversely, in situations where organic solvents can be properly handled, these solvents are most effective in the decontamination of many RCRA/CERCLA organic constituents.

4.4.10 Multiphase Treatment Processes

Alkaline Permanganate Processing

AP is normally used as the pretreatment in a multi-step process. The AP solution usually includes an inhibitor and a wetting agent to reduce surface tension. Permanganate is also

sometimes used in an acid form as NP for similar applications. Other examples of the manner in which AP is used in multiphase processing are described below.

Alkaline permanganate followed by ammonium citrate. Ammonium citrate (AC) has been successfully used with an AP pretreatment (referred to as APAC) to achieve significant decontamination results. This is a two-step process with intermediate water rinsing. In dilute form, the AC removes residual MnO_2 from the AP solution and neutralizes that solution. In concentrated form, the AC attacks the remaining corrosion film. However, redeposition has been a significant problem with this process.

This process is widely used to decontaminate stainless steel and carbon steel. A dilute APAC process was used to decontaminate the PWR at Shippingport.

A major disadvantage of the APAC procedure, which was discovered during its use at Shippingport, is the necessity of switching from alkaline to acid conditions between stages – a switch that led to a requirement for extensive rinses. An additional problem is that the AP solution degrades ion-exchange resins. Tests on various resins and AP concentrations at Brookhaven National Laboratory (BNL) showed that if the solutions were cooled from their normal operating temperature $> 80^\circ C$ to room temperature, the concentration of AP was reduced sufficiently by being removed in an ion-exchange resin unit. However, at these low concentrations, the reagent was less effective in removing chromium from PWR oxides.

The liquid waste can be deionized using mixed-bed demineralizers, and the resins are disposed as solid waste. The resin volume is of the same order of magnitude as the system volume to be decontaminated. The decontamination solution can be recycled for further use.

Alkaline permanganate ammonium citrate with EDTA. Ethylenediminetetraacetic acid (EDTA) can be added to the ammonium citrate in the APAC process to react with the ion oxides in solution and keep them in solution (referred to as APACE). This inhibits redeposition of the contamination on the treated surface as it permits the oxides to be removed in the waste-processing step via demineralization. Process usage parameters are the same as APAC, with the addition of about 1.0 g/l EDTA.

The liquid waste can be demonized using mixed-bed demineralizers, and the resins are disposed as solid waste.

The resin volume is the same order of magnitude as the system volume to be decontaminated. The decontamination solution can be recycled for further use.

Alkaline permanganate with citric acid. AP with citric acid is a mixture of oxalic acid, citric acid, and an inhibitor. It is an effective decontaminant for stainless steel as the second step after AP pretreatment. The citric acid neutralizes any component of the alkaline solution, dissolves any manganese oxide (MnO_2), and complexes the iron oxides to keep them in solution and retard redeposition.

This process is highly corrosive to carbon steel and 400-series stainless steels. Accordingly, in decontamination, its use is confined to 300-series stainless steels and Inconel.

The liquid waste can be deionized using mixed-bed demineralizers, and the resins are disposed as solid waste. The resin volume is of the same order of magnitude as the system volume to be decontaminated.

Alkaline permanganate with HSO_3NH_2 . This two-step process is similar to the AP with citric acid techniques. AP with $HSO_3NH_2(NH_2SO_3H)$ (APSul) is effective in removing the contaminated film from stainless steel piping without forming a precipitate or causing redeposition.

The liquid waste can be deionized using mixed-bed demineralizers, and the resins are disposed as solid waste. The resin volume is of the same order of magnitude as the system volume to be decontaminated.

Alkaline permanganate with oxalic acid. This two-step process has been successful in removing aged films on high-temperature stainless steel water piping, but it has the disadvantage of causing redeposition in the form of a tenacious oxalate film on the base metal, which has required further treatment with the APACE process.

Foam Decontamination

The cleaning agents use foam such as that produced by detergents and wetting agents as carriers of chemical decontamination agents. They can be applied in a thin layer to a surface in any orientation, even to overhead surfaces. The foam decontamination method can effectively decontaminate metallic walls and parts of complex components. By increasing dwell time, the foam better exploits the capability of the decontamination agent. Surfactants in the foam agent enhance the effect by increasing contact with the surface.

The advantages of this process are that it is effective for large components with complex shapes, it is a good process for internal in situ decontamination to eliminate smearable contamination before dismantlement, and it produces a small final waste volume. In addition, the process is readily applied using remote operations, it is a well-developed and widely used process, it can be operated by recirculation to improve its effectiveness, and it reduces operator exposure to a potential uptake of the acid.

The disadvantages are that it is difficult to obtain a good DF using a one-time application (batch process), difficult to recirculate when it is used to fill large cavities, and it is not appropriate for use on cracked surfaces or where there are deep or convoluted crevices.

This process is well developed and widely used in the nuclear industry. It has been developed at DOE's Savannah River Site (SRS) as a waste minimization tool. Previous experience with foam decontaminants has shown a significant waste reduction of up to 70%, which is higher than that achieved with current decontamination methods. This process has been tested to decontaminate a series of large valves with complex internal configurations. The foam decontamination process also has been applied to contaminated walls at the West Valley Demonstration Project. In this instance, results indicated that decontamination foams achieve better DFs on stainless steel surfaces than on carbon steel or painted concrete.

When using this technique with a closed system for making the foam, extreme caution should be taken. The closed system is pressurized to force a mixture of organic foam makers and decontaminating agent through a chamber where air is added to make the foam and to shoot the foam out through the nozzle.

One experience of this hazard occurred at SRS when a large amount of organic foam maker was added. This resulted in a chemical reaction between the chemical foam maker and the HNO_3 (i.e., decontamination agent) that had a constantly accelerating reaction rate. The volume of gas that was produced was more than the pressure relief setpoint. The system was overpressurized and ruptured. A DOE Class B investigation was conducted. It is worth noting that the equipment was not supplied with a pressure-relief valve and that one was added by the operators before equipment installation and operation.

In general, the collected process waste liquid can be treated by coprecipitation to remove radio-nuclides.

Chemical Gels

Chemical gels are used as carriers of chemical decontamination agents. Gels are sprayed onto a component wall, allowed to work and then scrubbed, wiped, rinsed, or peeled off. An airless compressor can be used for spraying the gel and, with a change in heads, for rinsing.

Typical reagent combinations are a nitric-hydrofluoric-oxalic acid mixture and a nonionic detergent mixed with a carboxymethylcellulose gelling agent, with aluminum nitrate used as a fluoride chelating agent. Steps include scraping and vacuuming solid waste material, using a hot-water rinse as pretreatment, and gel spraying throughout the cell.

The advantages of this process are that it is effective for removing smearable contamination from large components in situ, generates only a small volume of secondary wastes, can be readily applied using remote applications, and can achieve DFs as high as 100.

The disadvantages are that it is a complex that generally requires at least two applications and rinses and requires further treatability studies before the optimum compound composition and operating conditions are adapted to site-specific needs.

Chemical gels have been used to decontaminate cooling carbon dioxide pipes and pipes of ordinary ferritic steel. The following procedure has been used in this project:

- Soda gel spraying (3 M NaOH), 30-min contact time, rinsing
- Acid gel spraying (3 M H₃PO₄, 3 M H₂SO₄, and 16% silica), and rinsing for 30–60 min

The results have indicated that gel spraying is an effective process for beta gamma emitters on ferritic iron steel pipes with simple geometry. It generates a low volume of secondary wastes.

The waste generated from the chemical gel can be collected, neutralized, and treated using precipitation.

4.4.11 Selection of Chemical Decontamination Processes

When selecting a suitable decontamination process, several criteria must be considered in a detailed analysis based on site-specific conditions. Most of the criteria are related to the specific features of the nuclear installation, such as the following:

- Location of the contamination (e.g., inner vs. outer surfaces of closed fluid systems)
- Materials (e.g., steel, concrete)
- History of operation (to determine contamination strata profile)
- Nature of the contamination (e.g., oxide, crud, particulate, sludge)
- Effectiveness of previously used chemical decontamination processes
- Distribution of contamination (e.g., surface, cracks, homogeneous distribution in bulk material)
- Exposure to human health and the environment
- Safety, environmental, and social issues
- Exposure-level reduction requirements (e.g., recycling vs. disposal)
- Quantity and type of secondary waste from decontamination
- Conditioning
- Ultimate placement of decontaminated materials
- Time and cost

4.5 Mechanical Decontamination Techniques

4.5.1 Overview

Mechanical decontamination methods can be classified as either surface cleaning (e.g., sweeping, wiping, scrubbing, etc.) or surface removal (e.g., grit blasting, scarifying, drill, and spall). Mechanical decontamination can be used as an alternative to chemical decontamination, simultaneously with chemical decontamination, or in sequence with chemical decontamination.

Many surface-cleaning techniques can be used for both equipment and building decontamination, and some surface-cleaning techniques can be used as a secondary treatment following surface removal. Because these techniques are so versatile, it may be advantageous to locate a centralized decontamination facility on-site, in which one or more of these techniques may be used. Such a facility could then be used to decontaminate dismantled or segmented components (waste management facility, WMF).

The applications, advantages, and disadvantages of each decontamination technique are presented in  [Table 17](#).

4.5.2 Water Flushing

This technique involves flooding a surface with hot water. The hot water dissolves the contaminants, and the resulting wastewater is pushed to a central collection area. This technique is usually performed after scrubbing, especially on floors. Squeegees can be used to force the wastewater to the collection area. This technique may be used with detergents or other chemicals that enhance the effectiveness of the technique. The volume of the wastewater can be reduced by simply wetting the surface and flushing before drying occurs. The volume of wastewater can also be reduced by using a water treatment system to recycle the flush water.

The water flushing process can be used for areas that are too large for wiping or scrubbing. It is effective on loosely deposited particles (e.g., resins) and readily soluble contaminants, and it can be used as a first step to prepare a surface for a more aggressive decontamination. Obviously, it is not recommended for fixed, nonsoluble contamination.

4.5.3 Dusting/Vacuuming/Wiping/Scrubbing

These techniques refer to the physical removal of dust and particles from buildings and equipment surfaces by common cleaning methods. If dust and particles are contaminated, PPE may be required for workers as a health and safety control.

Vacuuming is performed using a commercial or industrial vacuum equipped with a HEPA filter. If a wet vacuum is used to pick up liquids, however, a replacement filter system has to be used because HEPA filters do not function properly with liquids (i.e., they clog).

Surfaces that cannot be reached with a vacuum can be wiped with a damp cloth or wipe (soaked with water or solvent) to remove dust. If required, the cloth or wipe is disposed as contaminated waste.

Scrubbing is similar to dusting/wiping except that pressure is applied to assist in removing of loosely adhering contamination.

Table 17 Applications, advantages and disadvantages of mechanical decontamination techniques (SOGIN-NIS)

	Flushing with water	Dusting/wiping/scrubbing	Vacuuming	Steam cleaning	CO ₂ blasting	Wet ice blasting	Hydroblasting	Ultra high pressure water	Shot blasting	Wet abrasive cleaning	Grit blasting	Grinding	Scarifier	Milling	Drill and spall	Paving breaker/chipping hammer	Expansive grout	Electropolish	Ultrasonic cleaning	Vibratory finishing
Surface cleaning (C) or surface removal (R)	C	C	C	C	C	C	R	R	R	C	R	R	R	R	R	R	R	C	C	C
Batch (B) or in situ (I)	I	I	I	I	I	I	I	I	I	B	I	I	I	B/I	I	I	I	B	B	B
Application	o	■	■	■	■	o	o	o	o	■	o	o	o	o	o	o	o	■	■	■
o Marginally effective	o	o	o	o	o	o	o	o	o	o	o	o	o	o	o	o	o	o	o	o
■ Highly effective	o	o	o	o	o	o	o	o	o	o	o	o	o	o	o	o	o	o	o	o
Loose particulate contamination	o	o	o	o	o	o	o	o	o	o	o	o	o	o	o	o	o	o	o	o
Bare and painted concrete	o	o	o	o	o	o	o	o	o	o	o	o	o	o	o	o	o	o	o	o
Metal surface	o	o	o	o	o	o	o	o	o	o	o	o	o	o	o	o	o	o	o	o
Components of all size	o	o	o	o	o	o	o	o	o	o	o	o	o	o	o	o	o	o	o	o
Pipe and tank internals	■	o	o	o	o	o	o	o	o	o	o	o	o	o	o	o	o	o	o	o
Embedded material and some oxide surfaces	o	o	o	o	o	o	o	o	o	o	o	o	o	o	o	o	o	o	o	o
Small hand tools	o	o	o	o	o	o	o	o	o	o	o	o	o	o	o	o	o	o	o	o
Special equipment (e.g., motors)	o	o	■	o	o	o	o	o	o	o	o	o	o	o	o	o	o	o	o	o
Soil, ground water and oily wastewater	o	o	o	o	o	o	o	o	o	o	o	o	o	o	o	o	o	o	o	o
Advantages	■	■	■	o	o	o	o	o	o	o	o	o	o	o	o	o	o	o	o	o
o Minor advantages	■	■	■	o	o	o	o	o	o	o	o	o	o	o	o	o	o	o	o	o
■ Major advantages	o	o	o	o	o	o	o	o	o	o	o	o	o	o	o	o	o	o	o	o
Little or no surface damage	■	■	■	o	o	o	o	o	o	o	o	o	o	o	o	o	o	o ^a	o	■

The dusting and vacuuming techniques are applicable to various types of contamination, including lead-based paint chips, PCBs, and asbestos. The techniques are applicable to facility surfaces, although scrubbing should not be used on porous or absorbent materials because loosely deposited materials may be pushed deeper into the surface and should not be used when contaminants are not soluble in water. Wastes are contained in vacuum-cleaner bags, wipe cloths, scrub brushes, or mops, and, depending on the nature of contamination, may need to be containerized or treated before they are disposed. All these techniques are best suited for smooth surfaces.

Several considerations must be addressed before these techniques are applied. The wiping technique can be used to remove dust generated from other operations. Fugitive dusts may be created by the dusting or vacuuming action and spread contamination. It is important to remember that if the source of the contaminated particulate is exterior to the work area, interior vacuuming, or dusting efforts may be ineffective until the external source is controlled. Thermal effects need to be considered when collecting fissile materials (i.e., Pu) while using these techniques.

4.5.4 Steam Cleaning

Steam cleaning physically extracts contaminants from building and equipment surfaces. The steam is applied using hand-held wands or automated systems, and the condensate is collected for treatment. This technique combines the solvent action of water with the kinetic-energy effect of blasting. As a result of the higher temperature, the solvent action is increased and the water volume requirements reduced, compared with hydroblasting.

Steam cleaning is applicable to a wide variety of contaminants and structural materials. This technique is recommended for use on complex shapes and large surfaces to remove surface contamination or to remove contaminated soil particles from earth-moving and drilling equipment. It can be used in conjunction with scrubbing, either as a preliminary step or as part of the scrubbing process.

Although a lesser volume of waste is generated using this technique than in hydroblasting, the installation of sumps and the use of wastewater storage containers may be necessary. As in hydroblasting, existing sumps or water collection systems may be used, but must be checked for leaks to ensure that contamination does not inadvertently migrate to another medium.

4.5.5 CO₂ Blasting

This technique is a variation of grit blasting in which CO₂ pellets are used as the cleaning medium. Small dry-ice pellets are accelerated through a nozzle using compressed air at 3–15 bar. The pellets shatter when they impact the surface, and the resulting kinetic energy causes them to penetrate the base material and shatter it, blasting fragments laterally and releasing the contaminant from the base material. The dry-ice fragments instantly sublime, which adds a lifting force that speeds the removal of the contaminant. Removed debris falls to the ground, and the CO₂ (now gas) returns to the atmosphere. Because the pellets vaporize, they do not pose a collection, treatment, or disposal problem; however, collection of the removed debris is required. Use of CO₂ is advantageous as regards radioactive contamination because it does not become radioactive and because no secondary waste is produced. The airborne contamination

potential is typical of blasting actions. A typical system consists of two major components: a pelletizer that converts liquid CO₂ into dry-ice snow and a cleaning station where the pellets are stored and blasted. The cleaning station is portable and may be used to clean equipment in place, but it may also be used to clean dismantled equipment that has been transported to a centralized cleaning area where the pelletizer is located.

Blasting with CO₂ has proven effective with plastics, ceramics, composites, and stainless steel. Wood and some soft plastics could be damaged, and brittle materials may shatter. Hard coatings that bond very firmly to the base material may not be removed effectively by this technique. Additionally, soft contaminants such as grease and oil tend to splatter and may require specialized application procedures and collection systems. If the object being cleaned is porous, soft contaminants may be pushed into the base material. However, this technique is very effective for hardened, baked-on grease.

Some cooling takes place in the base material, but the amount of cooling seldom exceeds 40 °F. In some applications, cooling makes a small contribution to the cleaning, principally with those contaminants that break up more easily as a result of thermal shock (i.e., those with high moisture content or a high freezing point). The likelihood of damage resulting from cooling is remote, but material analysis should be performed before using this technique on components that may potentially be reused.

In general, CO₂ blasting is best applied in a room or booth that is dedicated to contain the loosened debris and to isolate the noise of blasting, which can range from 75 to 125 dB. In a normal workspace, ventilation is usually sufficient to prevent undue CO₂ build-up; in a confined space, however, ventilation needs to be actively monitored. Because CO₂ is heavier than air, placement of exhaust vents is best at or near ground level. Static electricity may be generated during the blasting process, and, therefore, the component being cleaned should be grounded.

4.5.6 Wet-Ice Blasting

This technique is similar to other decontamination technologies that direct a high-velocity stream of fine particles such as steel pellets, plastic pellets, or glass beads onto a surface to remove contamination. This system employs low-pressure air and wet ice for cleaning and surface preparation. Typical air requirements range between 60 and 250 psig at 280 scfm. Because this system uses water in the form of ice as its medium, no other consumables are required. The contaminated water that is generated by the melting ice particles is the controlling medium for the displaced contamination. The process uses, and therefore generates, a maximum of a few tens of gal/h of water. The water must then be treated for discharge.

When using the wet-ice blasting technique, the ice-blasting cleaning head may be manually moved about on the surfaces being decontaminated. Decontamination efficiency depends on the applicator translation speed, cleaning head distance from the substrate, operating pressure, and geometric complexities of the substrate.

Ice blasting removes coatings and some fixed surface contamination, but will not take off concrete to a significant depth. The waste produced is contaminated water. The amount of water generated depends on the ice blasting rate. For example, a unit recently demonstrated at the ORNL site operated at 11 gal/h.

Because of the low volume of water generated during operation, evaporation, and not recycling, is likely more cost effective. Remote operation requires the adaptation of the ice-blasting and water-collection systems to a robotic control system.

4.5.7 Hydroblasting

In the hydroblasting technique, a high-pressure (several thousand pounds per square inch) water jet is used to remove contaminated debris from surfaces. The debris and water are then collected, treated, and disposed.

Use of the correct lance tip is critical to producing desired results. Configurations range from a jet tip, which produces a narrow stream, to a flat fan shape that produces a flow similar to a point scraper in form. The treated surface may require painting or other refinishing methods if the surface is to be reused. Many manufacturers produce a wide range of hydroblasting systems and high-pressure pumps.

This technique is recommended for surfaces that are inaccessible to scrubbing or that are too large for scrubbing. Hydroblasting can be used on contaminated concrete, brick, metal, and other materials. It is not applicable to wooden or fiberboard materials.

In general, the technique is very effective, completely removing surface contamination. On the average, hydroblasting removes 3/16–3/8 in. of concrete surface at the rate of 40 yd²/h. Hydroblasting may not effectively remove contaminants that have penetrated the surface layer. However, variations such as hot or cold water, abrasives, solvents, surfactants, and various pressures that may increase the effectiveness of decontamination can easily be incorporated into the technique.

Water lances have been successfully used to decontaminate pump internals, valves, cavity walls, spent-fuel pool racks, reactor vessel walls and heads, fuel-handling equipment, feedwater spargers, floor drains, sumps, interior surfaces of pipes, and storage tanks. DFs of up to several hundred have been obtained. Experience at one site indicated that DFs of 2–50 could be achieved using water only and that DFs of 40–50 could be achieved if a cleaning agent, (e.g., Radiac-Wash) is added. Personnel at the site recommend an initial treatment at lower pressures (500 psi) because the lower pressures perform just as well as higher pressures (3,000–5,000 psi).

To decontaminate pipe runs, a variation of the water lance – the pipe mole – is used. In this method, a high-pressure nozzle head is attached to a high-pressure flexible hose and inserted into pipe runs. The nozzle orifices are angled to provide forward thrust of the nozzle so that the hose can be dragged through the pipe.

Hydroblasting has also been used to decontaminate nuclear facilities, remove explosives from projectiles, and decontaminate military vehicles. Hydroblasting also has been employed commercially to clean bridges, buildings, heavy machinery, highways, ships, metal coatings, railroad cars, heat exchanger tubes, reactors, piping, etc.

Given the volume of water generated, installation of sumps and external wastewater storage tanks may be necessary. Existing sumps or water collection systems may be used, although they must be checked for leaks to ensure that contamination does not inadvertently migrate to another medium.

4.5.8 Ultra-High-Pressure Water

In this technique, water is pressurized up to 55,000 psi by an ultra-high-pressure intensifier pump. The water is then forced through a small-diameter nozzle that generates a high-velocity water jet at speeds of up to 3,000 ft./s. The same technique is used in abrasive water-jet cutting, except that for cleaning purposes the nozzle is mounted in a cleaning head.

With the cleaning head attached to a lance, it can be manually moved about the surface being decontaminated. Surface contaminants are first eroded and then removed by the water jet.

Deeper penetration of the surface is possible by adding abrasives to the water jet; however, care should be taken to not damage or cut through the material. The contaminant and wastewater require a processing system in which the contaminant is separated, containerized, and disposed and the wastewater treated and recycled.

Concrete, metallic components, structural steel, and ceramic tile are just a few of the materials that can be decontaminated with ultra high-pressure water. Water jets can remove paint, coatings, and hard-to-remove deposits without damaging the underlying surface. They can also remove galvanized layers from sheet metal.

The decontamination efficiency of the technique is dependent on a number of parameters: water pressure and flow rate, nozzle/cleaning-head configuration, distance of the cleaning head from the surface, and translation speed. These parameters must be evaluated, along with the geometric complexities of the substrate, to achieve optimum results.

Because water jets are omnidirectional and have very little thrust, they are readily adapted to robotics or remote operation. Moreover, the power unit is basically the same as that used for water-jet cutting. Therefore, with minor modifications, the unit can be used for either technique as long as the appropriate nozzle is used (i.e., a cleaning head or a cutting head).

4.5.9 Shot Blasting

Although the shot blasting technique was originally developed and marketed as a surface preparation technique to enhance coating adhesion, it can be used to remove contaminants from floors and walls.

Shot blasting is an airless method that strips, cleans, and etches the surface simultaneously. The technique is virtually dust free, so the potential for airborne contamination is very low. The surface is left dry and free from chemicals, so additional waste treatment is not required.

Portable shot blasting units move along the surface that is being treated as the abrasive is fed into the center of a completely enclosed centrifugal blast wheel. As the wheel spins, the abrasives are hurled from the blades, blasting the surface. The abrasive and removed debris are bounced back to a separation system that recycles the abrasive and sends the contaminants to a dust collector. Larger shot removes more concrete, and the etch depth can be controlled by varying the speed of the unit. Units are available that can remove up to 1/4-in.-thick surface in a single pass. Units are also available for vertical surfaces.

The contaminated debris and contaminated shot must be treated and disposed. The mobile unit must also be decontaminated.

Shot blasting is generally used for concrete surfaces, but it can also be applied to metallic components such as storage tanks. Shot blasting effectively cleans surfaces that have been exposed to acids, caustics, solvents, grease, and oil. It can also remove paint, coatings, and rust.

4.5.10 Wet Abrasive Cleaning

A wet abrasive cleaning system is a closed-loop, liquid abrasive (wet grit blasting) decontamination technique. The system uses a combination of water, abrasive media, and compressed air and is applied in a self-contained, watertight, stainless steel enclosure. There is no danger of airborne contamination because a self-contained HEPA air ventilation system maintains negative

pressure inside the cabinet. The radioactive waste is mechanically separated from the cleaning media, resulting in a very low waste volume. The water can be recycled and filtered, eliminating any access to wastewater drainage.

The system's design is based on field experience and is governed by ALARA concerns. The system uses no soluble or hazardous chemicals, only the abrasive media (e.g., glass beads, aluminum oxide, silicon carbide, and ceramics) and water.

Wet abrasive cleaning is being used by many nuclear facilities to remove smearable and fixed contamination from metal surfaces, such as structural steel, scaffolds, components, hand tools, and machine parts. The equipment can be used on close-tolerance parts such as turbine blades or valves where the removal of metal is not desired, or it can be adjusted to remove heavy-duty corrosion and paint by varying the amount of air pressure and media.

A basic 4 × 4 × 5-ft. or a larger 4 × 8 × 7-ft. system provides enough space to decontaminate small tools or heavy, large-scale parts. If a material cannot be cut down to a smaller size (e.g., long I-beams), it can be fed through small cabinets. Most booths are custom-designed to specific configurations and sizes.

4.5.11 Grit Blasting

The grit blasting technique, commonly called sand blasting and abrasive jetting, has been used since the late 1980s. This technique, which uses abrasive materials suspended in a medium that is projected onto the surface being treated, results in a uniform removal of surface contamination. Compressed air or water, or some combination of both, can be used to carry the abrasive. Removed surface material and the abrasive are collected and placed in appropriate containers for treatment and/or disposal.

Grit blasting is applicable to most surface materials, except those that might be shattered by the abrasive, such as glass, Transite, or Plexiglas. It is most effective on flat surfaces and, because the abrasive is sprayed, it is also applicable on hard-to-reach areas such as ceilings or areas behind equipment. Nonetheless, obstructions close to or bolted to walls must be removed before application, and precautions should be taken to stabilize, neutralize, or remove combustible contaminants because some abrasives can cause some materials to detonate. Static electricity may be generated during the blasting process; therefore, the component being cleaned should be grounded. Remotely operated units are available.

Abrasives may be applied under either wet or dry conditions. Under dry conditions, dust-control measures may be needed to control dusts and/or airborne contamination. This problem can be reduced by using filtered vacuum systems in the work area. When water is used to apply the abrasive, large volumes of waste are produced that include the wastewater, the abrasive, and the removed debris. These wastes must be properly treated and/or disposed. If the wastewater can be recycled, it may or may not need to be treated before it is reused. Depending on the application, the following variety of materials can be used as abrasive media:

- Minerals (e.g., magnetite or sand)
- Steel pellets
- Glass beads/glass frit
- Plastic pellets
- Natural products (e.g., rice hulls or ground nut shells)

Silica has also been used as an abrasive; however, its use is not recommended because silica is moderately toxic as a highly irritating dust and is the chief cause of pulmonary disease. Prolonged inhalation of dusts containing free silica may result in the development of a disabling pulmonary fibrosis known as silicosis.

A grit-blasting system consists of a blast gun, pressure lines, abrasives, and an air compressor. Several grit-blasting equipment manufacturers and contractors are available. Labor cost could be high because this is a relatively slow and labor-intensive technique. Large amounts of abrasive are required, so costs are necessarily dependent on the type of abrasive used.

4.5.12 Grinding

The grinding technique removes thin layers of surface contamination from concrete. In many cases, the contamination is limited to the paint coating or concrete sealer finish. The technique involves abrading the surface that is being treated using coarse-grained abrasives in the form of water-cooled diamond grinding wheels or multiple tungsten-carbide surfacing discs.

Machines to power these abrasives are floor-type grinders whose grinding heads rotate in a circular fashion parallel to the floor.

Water required for cooling is injected into the center of the grinding head, reducing the amount of dust. Supplementary contamination control can be accomplished using HEPA-filtered vacuum systems and wet vacuums attached to or held near the machine. The surface may be moistened before and during grinding to hold down dust.

In general, grinding is recommended for use where thin layers of contamination need to be removed. If the contamination is deep, the grind wheels or discs are quickly worn down, which decreases the overall effectiveness of the technique.

A typical diamond grinding wheel (used on a floor grinder) is capable of removing several thousand square feet of surface per day to an approximate depth of 1/2 in. In smaller areas, the wheel can remove up to 1 in. of surface per day. The machine can be operated by one operator. Floor and hand-held grinding machines have been successfully used at the San Onofre 1 Nuclear Plant to remove surface contamination.

4.5.13 Scarifiers

Scarifiers physically abrade both coated and uncoated concrete and steel surfaces. The scarification process removes the top layers of contaminated surfaces down to the depth of the sound, uncontaminated layers.

Concrete scarification was considered a radical approach to decontamination owing to poor performance of the tools and inability to provide a uniform surface profile upon removal of the contaminants. Today's refined scarifiers are not only very reliable tools, but also provide the desired profile for new coating systems in the event the facility is to be released for unrestricted use.

For steel surfaces, scarifiers can completely remove contaminated coating systems, including mill scale, leaving a surface profile to bare metal. To achieve the desired profile and results for contaminated concrete removal, a scabbling scarification process is implemented; for steel decontamination, a needle scaling scarification process is used.

Scabbling

Scabbling is a scarification process used to remove concrete surface layers. Manufacturers of scabblers typically incorporate several pneumatically operated piston heads to simultaneously strike (i.e., chip) a concrete surface. Today's scabblers range from hand-held scabblers to remotely operated scabblers, with the most common versions incorporating 3–5 scabbling pistons mounted on a wheeled chassis. Because scabbling can cause a cross-contamination hazard, vacuum attachments and shrouding configurations have been incorporated by a few scabbling equipment manufacturers. According to one manufacturer's claim, users can scabble with no detectable increase in airborne exposures above background levels.

One of three types of scabbling bits, which are mounted on the piston heads, can be used: a 6-point anvil bit for surface scabbling, a cross anvil bit for aggressive surface reduction, or a 9-point bit for aggressive removal, leaving a smooth, finished surface profile. All bits have tungsten-carbide cutters from 1 3/4 to 2 1/2 in. in diameter, depending on the manufacturer's configuration. The bits have an operating life of approximately 80 h under normal use.

Before scabbling, combustibles must be stabilized, neutralized, and/or removed. In practice, floor scabblers can only be moved to within 1/2 in. of a wall. Other hand-held scabbling tools are manufactured to remove the last 1/2 in. of concrete flooring next to a wall, as well as surface concrete on walls and ceilings. This technique is a dry decontamination method – no water, chemicals, or abrasives are required. The waste stream produced is only the removed debris.

The approximate removal rates for a scabblers vary, depending on the type of bit that is used. In general, the removal rate for a 6-point anvil bit is 30–40 ft.²/h based on the removal of a 1/6 in.-deep layer. The removal rate for a cross anvil bit varies inversely to the thickness removed: 14–24 ft.²/h for a 1/4-in.-deep layer, 7–12 ft.²/h for a 1/2-in.-deep layer, and 3–6 ft.²/h for a 1-in.-deep layer.

Needle Scaling

Needle scaling is a scarification process used in both concrete and steel surface removal. These tools are usually pneumatically driven and use uniform sets of 2-, 3-, or 4-mm needles to obtain the desired profile and performance. The needle sets use a reciprocating action to chip the contamination from the surface. Some manufacturers have added specialized shrouding and vacuum attachments to collect the removed dust and debris during needle scaling with the result of no detectable concentrations above background levels.

For removing surface contamination from steel surfaces where combustibles were once stored, copper beryllium needle sets can be used to reduce the risk of needle sparking. Needle scalars are an exceptional tool in tight, hard-to-access areas, as well as for wall and ceiling surface decontamination. This technique is a dry decontamination process and does not introduce water, chemicals, or abrasives into the waste stream. Only the removed debris is collected for treatment and disposal.

Production rates vary depending on the desired surface profile to be achieved. Nominal production rates range from 20 to 30 ft.²/h.

Applications

Scabblers are best suited for removing thin layers (up to 1 in. thick) of contaminated concrete (including concrete block) and cement. They are recommended for instances where no

airborne contamination can occur and the concrete surface is to be reused after decontamination, or for instances in which the demolished material is to be cleaned before disposal. The scabbled surface is generally leveled, although coarsely finished, depending on the bit used. If necessary, after release, the surface can be finished with a concrete cap and an epoxy, polymer, or similar finish. This technique is suitable for both large open areas and small areas.

Needle scaling is best suited for removing of surface contamination and coatings from steel surfaces, piping, and conduits. Needle scalers with vacuum attachments and shrouding are ideal for clean room surface removal operations, dustless decontamination operations, and the reduction of containment structures and ventilation schemes. They can also remove surface contamination from concrete surfaces (up to 1/2 in. thick). Needle scaling is generally more versatile than scabbling and is highly effective on concrete walls and ceilings.

A proprietary system integrates scabblers and scarifiers into a family of remotely and manually operated scarification equipment for dustless decontamination of concrete and steel. The system incorporates a high-performance vacuum/waste packaging unit in conjunction with pneumatically operated scabblers and needle scalers to safely remove contaminated material. Dust and debris are captured at the cutting-tool surface, which minimizes cross contamination. The HEPA filtration design incorporates a patented fill-seal drum change-out method that allows the operator to fill, seal, remove, and replace the waste under controlled vacuum conditions. The unit can accommodate 55- and 23-gal drums. It can also simultaneously support several drum sizes, including up to three scabblers/needle scalers from a 100-ft. distance. The remotely operated floor scabber has an on-board vacuum packaging unit. The smaller scabber and needle scaler have vacuum ports that can be attached to the vacuum waste packaging unit. Although the equipment is designed to work as an integrated system, the individual components can also be operated as stand-alone units that can be used with conventional air supplies and vacuum systems.

4.5.14 Milling

There are two milling techniques, one used for shaving metals and one for shaving concrete. Metal milling is the technique by which a machine shaves off a layer of material (up to 1/8 in.) from a surface using rotating cutters. The most commonly used method involves feeding the work piece past stationary cutters that are perpendicular to the cutter's axis. Other types of milling machines (i.e., where the work piece is stationary and the cutter or cutters move) are available. Waste consists of the machined-off chips and any cooling/lubricating fluids (which can be recycled if necessary).

Concrete milling is similar to concrete scabbling or scarifying, except that it may be applied to a much larger surface area. Large, paving-type equipment is generally used to shave the concrete surface. Approximately 2 1/2–10 in. can be removed in this manner.

Because of the set-up time per configuration (1/2–3/4 h), metal milling is most effective when there is a large number of similarly shaped items to be decontaminated. After the equipment is set up and loaded, about 2.5 ft.²/h can be milled. Concrete milling is most effective when used on large, open, horizontal surfaces. Metal milling has been used at the Oak Ridge K-25 site to decontaminate individual metal items.

4.5.15 Drill and Spall

The drill-and-spall technique was developed to remove contaminated concrete surfaces without demolishing the entire structure. All potential obstructions to the drill or spall rig should be removed and combustible sources stabilized, neutralized, or removed. The technique involves drilling 1 to 1 1/2-in.-diameter holes approximately 3 in. deep into which a hydraulically operated spalling tool is inserted. The spalling tool bit is an expandable tube of the same diameter as the hole. A tapered mandrel is hydraulically forced into the hole to spread the fingers and spall off the concrete. The holes are drilled on approximately 12-in. centers so that the spalled area for each hole overlaps the next. The removed concrete is collected, treated, and/or disposed. If the contamination is deeper than that which can be removed in one pass, a second pass may need to be performed.

The drill-and-spall technique is applicable to concrete only (not concrete block) and is recommended for removing surface contamination that penetrates 1–2 in. into the surface. Removal of the near-surface-contamination in this manner decreases the amount of contaminated material that needs to be disposed prior to demolition. This technique is effective for large scale, obstruction-free applications, the only limit being the interior building configuration. The treated surface may require a concrete cap if a smooth surface is desired, because any rebar is exposed and the surface is generally left in an overall rough condition.

A concrete spaller was used at Pacific Northwest Laboratories (PNL) to remove 1 in. of contaminated concrete from the surface of air lock cover blocks. The concrete spaller was first set up and tested on nonradioactive concrete to allow hands-on training of personnel. During these equipment tests, it was found that if the surface was first painted with a latex paint, it acted to keep the spalled aggregates together, somewhat in the same manner as a fixative. A nominal 8-in. spacing between drilled holes was found to be satisfactory. The interface between the push rod and bit was lubricated between each spalling operation rather than every four operations as recommended. This lubrication sequence may have helped prevent wear or galling-type failures. One spalling bit was replaced when the wedge portion broke away from one of the expanding prongs. During operation, workers were required to wear respirators. The spalling rate ranged from 2 to 10 ft.²/h, depending on worker experience.

4.5.16 Paving Breaker and Chipping Hammer

Although paving breakers and chipping hammers are primarily used in demolition activities, they can be used also to remove surface contamination up to 6 in. thick. In this case, surface is left very rough and resurfacing might be required.

4.5.17 Expansive Grout

Although expansive grout is primarily used as a demolition technique, it can also be used as decontamination method to remove a thick layer of contaminated concrete.

4.5.18 Asbestos Removal

There are four methods used to manage the abatement of asbestos contamination in buildings: removal, encapsulation, enclosure, and special operations. Only the first method, removal, permanently eliminates the asbestos from the area or building. The other three methods leave the asbestos in place in some form. For the purposes of decommissioning, removal is the preferred option and therefore is the only one described in detail in this section.

Building materials containing asbestos are removed to prevent the release of asbestos fibers in the air. To maximize worker protection, removal should be performed before any other segmenting or decontaminating activities in the area. Before removing or disturbing materials containing asbestos, the work area is isolated so that all asbestos fibers released by the removal activity will be confined to the work area. Accordingly, temporary partitions are constructed, and all exposed surfaces (other than those being removed) are covered with plastic sheeting. HEPA filtration of the air in the work area is required to minimize the risk of asbestos exposure of removal workers and/or building occupants (if the building remains occupied during removal).

After the work area has been enclosed and plastic sheeting placed over all exposed surfaces, the asbestos-containing material is wetted in place with conditioned water (i.e., water with surfactant added to increase wetting action) or encapsulant. The material is physically removed and placed in sealable bags or containers. When removal is complete, the work area is subjected to thorough cleaning. All surfaces are wet-wiped or mopped. Vacuums equipped with high efficiency filters may be used to vacuum up any visible debris deposited on building floors, ledges, other equipment, etc. Porous surfaces may require sealing with a chemical penetrate to prevent the release of any residual fibers.

To prevent the fibers from becoming airborne or otherwise transported and deposited, equipment and personnel leaving the work area must pass through a partitioned area designated as the decontamination room. In this room equipment is wet-wiped to remove asbestos fibers, and used personal protection equipment is discarded into sealable containers for proper disposal. A portable shower and a change area may be provided for the use of workers exiting the work area. Spent shower water is filtered with a disposable high-efficiency filter.

A visual inspection is conducted following removal of the asbestos-containing materials to detect incomplete work or inadequate cleanup. Following satisfactory visual inspection, the work area remains undisturbed for 24–72 h to allow fibers to settle. Air monitoring is then conducted to measure the level of residual asbestos fibers. Acceptable levels are based on state regulations. When air monitoring results indicate that the work area is adequately decontaminated, the isolation barriers are disassembled, placed in sealable containers, and disposed in regulated landfills.

Potential hazards to personnel include inhalation of asbestos fibers, known to be fibrogenic and carcinogenic; heat stress caused by high temperatures and humidity, minimal or no ventilation, and PPE; and electrical shock from the use of water (for wetting) in proximity to electrical equipment.

4.6 Other Decontamination Techniques

This section presents decontamination techniques in which the primary force is not the result of chemical or mechanical means. These techniques work to decontaminate a surface by inducing a chemical reaction or mechanical action that actually performs the decontamination.

4.6.1 Electropolishing

The electropolishing technique, a cleaning technology developed in the 1950s, has been widely used in the metal-finishing industry. It was not until the 1970s, however, that the nuclear industry recognized its potential for cleaning radiologically contaminated equipment.

Currently, the technology is gaining popularity in the nuclear industry for surface pre-treatment as well as for decontamination operations. The electropolishing technique should be considered for cleaning conductive materials. It has been shown to be particularly effective on conductive materials, reducing contamination to near background levels, and making the free-release option technically obtainable.

Several advantages are associated with electropolishing. Conductive surfaces can be decontaminated to a very low or even nondetectable level for free-release applications. A wide range of contamination and conductive surfaces can be effectively decontaminated (i.e., the technique is versatile).

Relatively complex components and shapes can be decontaminated using the electropolishing technique without disassembly. Fairly large items can be decontaminated without sectioning.

One disadvantage associated with the technique is that nonconductive components cannot be cleaned. Nonconductive coatings (e.g., paint, epoxy) must be removed from conducting components before cleaning can be performed. Exposure levels could be excessive, unless remote techniques are employed when cleaning highly contaminated parts. Components may need to be repeatedly cleaned if excessive amounts of contamination are allowed to build up in the electrolyte.

Description of Technique

Electropolishing is an anodic-dissolution technique. During electropolishing operations, a small, controlled amount of material is stripped from the surface of the object being cleaned. Contamination embedded in the stripped material is carried off into dissolution, resulting in a surface nearly free of contamination. The technique is considered a versatile technique that is equally effective for almost any combination of contamination and conductive surfaces, including corrosion layers.

There are three basic process technologies available: phosphoric-acid-based systems, nitric-acid-based systems, and organic-acid-based systems. Each of these systems is similar in arrangement to plating installations.

Direct current (dc) power is supplied to the system at low voltages. The object being cleaned is connected to the anode (+), and a series of metallic plates is connected to the cathode (-). Both the anode and the cathode are immersed in a chemical bath consisting primarily of one of the three electrolytes listed above. When current is applied, the electrolyte acts as a conductor, allowing metal ions to be removed from the part being treated. While the ions are drawn towards the cathode, the electrolyte maintains the dissolved metals in solution.

Electrolytes

The nature of the electrolyte constitutes the primary difference in each of the following three available systems.

H₃PO₄ Electrolytes

Representative operating conditions for phosphoric-acid-based electropolishing decontamination are as follows:

- Concentrations: 40–80% by volume
- Operating temperature: 40–80 °C
- Electrode potential: 8–12 V dc
- Current densities: 60–270 mA/cm²

The time involved for a typical decontamination ranges from 5 to 30 min, which corresponds to the removal of 0.3–2 mils of surface material at a current density of 160 mA/cm². It is usually necessary to move the anode contacts once during a cycle to decontaminate the area under the contacts.

PNL has demonstrated that phosphoric-acid-based systems are effective on steel, stainless steel, and a number of alloy systems. The electrolyte's hygroscopic nature helps to minimize airborne contamination. Phosphoric acid's good complexing characteristics may be a significant factor in minimizing recontamination from build-up in the electrolyte.

Studies performed at PNL, in cooperation with Rockwell Hanford Operations and United Nuclear Industries, show that components heavily contaminated with plutonium oxide were decontaminated from 1,000,000 dpm/100 cm² to background in less than 10 min.

Phosphoric-acid-based electrolytes are not effective in decontaminating welds. It is believed that metallurgical changes caused by welding make welded areas less soluble than the base materials. It has also been observed that low-current densities produce nonuniform metal removal and that high-current densities produce excessive oxygen evolution.

HNO₃ Electrolytes

Two sets of operating conditions are used in nitric-acid-based systems: high-density current and low-density current. Representative operating parameters for high-density, nitric-acid-based electropolishing decontamination are as follows:

- Electrolyte: HNO₃, 6–12 mole
- Operating temperature: 10–35 °C
- Electrode potential: 5–8 V dc
- Current densities: 400–2,000 mA/cm²

The time for a typical low-density decontamination ranges from 1 to 2 h, which removes 0.3 mils of surface material at a current density of 400 mA/cm².

Because of the low-density current, a basket-style anode can be used, thus eliminating the need to move the anode contacts during the decontamination cycle.

Studies performed at Harwell Laboratories, Oxfordshire, UK, show that low-density current HNO₃ electrolytes could achieve DFs of better than 10⁴ for components contaminated with colloidal plutonium and with PuO₂ in about 2.2–1.7 h, respectively.

Harwell Laboratories have demonstrated that nitric-acid-based systems are effective on steel, stainless steel, and a number of alloy systems. Dissolved substrate levels in the electrolyte of up to 20 g/l have only a minor effect on the recontamination of the object being cleaned.

Nitric-acid-based electrolytes, operated at low-density currents, provide good results on welded surfaces. The systems can generate hydrogen and nitrogen oxide gases, but these gases can be controlled or eliminated by using the proper electrode materials and electrolyte additives.

Organic Acid Electrolytes

Harwell Laboratories have performed research on the relationship between cathode materials and chemical additives and their effect on hydrogen and nitrogen oxide production in

nitric-acid-based electrolyte systems. Representative operating parameters for acetylacetonate-based electropolishing decontamination are as follows:

- Electrolyte: acetylacetonate + KBr + n-propanol
- Operating temperature: 20–40 °C
- Electrode potential: 15–24 V dc
- Current densities: 200 mA/cm²

The time of a typical decontamination ranges from 40 to 100 min, which corresponds to the removal of 1–2 mils of surface material at a current density of 200 mA/cm². It is usually necessary to move the anode contacts once during a cycle to decontaminate the area under the contacts.

There are three major advantages of using an acetylacetonate-based electrolyte:

- Acetylacetonate has good pH stability and can resist changes caused by the formation of hydroxides.
- The organic acid component can be destroyed, resulting in a nonacidic waste.
- The radioactive contents of the electrolyte reach a steady state, governed by the solubility of the acetylacetonate salts. This advantage is a benefit where criticality is a concern and where radiation control is essential. The large salt crystals formed in this process can be removed from the bottom of the electropolishing vessel and isolated in a safe storage condition.

Studies performed at Kraftanlagen Aktiengesellschaft, Heidelberg, Germany, show that an acetylacetonate electrolyte could achieve a DF of 36 for components with generalized contamination consisting largely of ¹³⁷Cs and ⁶⁰Co in about 60 min.

Applications

There are two major divisions in immersion electropolishing equipment:

- Equipment that accommodates total immersion of objects
- Equipment that accommodates partial immersion of objects

Total-immersion The literature reports that several sizes of immersion electropolishing systems have been designed and built. At PNL, a 400-gal system was designed, built, and used for decontamination studies. Mobile electropolishing decontaminating services are available.

Partial-immersion Large equipment can be electropolished in stages by using partial-immersion processes. One such technique makes use of a trough-shaped tank equipped with roller-base supports that provide easy rotation of cylindrical tanks during the polishing process. Some tank interiors can be electropolished using the partial-immersion process. The process involves filling the tank with electrolyte, making the appropriate electrical connections, and setting the power supply to the appropriate current density. After the process is complete, the tank is emptied and the electrodes are removed. The final step is rinsing the tank.

4.6.2 Ultrasonic Cleaning

This technique uses a generator to produce an ultrasonic frequency (above 20 kHz). A transducer then converts this high-frequency energy into low-amplitude mechanical energy (i.e., vibrations) of the same frequency. A vigorous scrubbing action is produced by a cleaning solution and imparted onto the object being cleaned. The scrubbing action is attributed to the

rapid formation and violent collapse of thousands of minute bubbles. The bubbles are created by cavitation, which is caused by the outward and inward movement of the transducer's surface, in the solution.

The most important parameters for ultrasonic cleaning are ultrasonic frequency, power intensity, cleaning-solution viscosity, temperature, and fluid recirculation rate. Additionally, the tank size and the geometry of the object being cleaned in relation to the transducer placement must be evaluated. These parameters must be properly controlled to obtain the best possible decontamination of an object. In addition to cavitation, ultrasonic streaming (induced liquid circulation) contributes to the decontamination of an object.

The cleaning action can be enhanced by heating the solution, performing mechanical stirring, and adding chemicals to the cleaning solution. Additives such as wetting agents and chelating agents can also have a profound effect, although the concentration of chemicals in the bath solution should be approximately 2–5% by weight.

An effective method that may be used for removing radioactive particles from solid surfaces using ultrasonics is the following. First, the parts to be cleaned are sprayed or sonicated with a dilute solution of a high molecular weight fluorocarbon surfactant in an inert perfluorinated liquid to effect particle removal. Second, the parts are then rinsed with the perfluorinated liquid to remove the fluorocarbon surfactant applied in the first step. Third, the residual rinse liquid is evaporated from the parts into an air or nitrogen stream from which it is subsequently recovered.

Objects with loosely deposited and loosely adherent contamination (i.e., not fixed) have been decontaminated successfully using ultrasonics. These objects include metallic hand tools, pump seals and pistons, valves, seal-injection filters and other filters, and control-drive mechanisms. Ultrasonic equipment for small items is commercially available. Ultrasonic equipment for large items can be designed and constructed, although it should be noted that immersion of large items results in less effective decontamination. This technique is not recommended for concrete components, nor should it be used on materials that adsorb ultrasonic energy (e.g., plastics, rubber).

4.6.3 Vibratory Finishing

Objects are placed in a basket filled with abrasive media that is vibrated at a high frequency in a cleaning solution. The vibrating media produces a scouring action that removes contamination as well as tape, paint, and corrosion products from the surfaces of almost any type of item. Commonly used abrasives are triangular ceramic or conical plastic material impregnated with aluminum oxide. Spent abrasives and removed contaminants are carried to a holding tank by the cleaning solution where they are collected and concentrated for disposal. The cleaning solution can be recycled, thus reducing the amount requiring disposal.

This technique is commonly used in manufacturing as a deburring technique. However, it is also applicable for decontaminating such items as hand tools (e.g., hammers, wrenches, screwdrivers, etc.) and large quantities of smaller objects. The size and weight of the objects are obviously limited by the size of the vibratory container. For example, a 4-ft.³ container can handle approximately 300 lb of components, the maximum size of each object being 8–12 in. in diameter. The time required to decontaminate a component is dependent on the component geometry and the amount and type of contaminant. Process times to decontaminate range from 4 to 10 h per batch. Units are commercially available with volumes up to 100 ft.³.

This technique is an effective pretreatment technique for chemical decontamination methods. It removes latex paint, enamel paint, grease, and oil, each of which can limit the effectiveness of chemical decontamination methods. Because an abrasive is used, excessive metal loss may occur as well as curvature of previously sharp corners; however, in decommissioning this is not a problem.

5 Cutting and Dismantling Techniques

5.1 Overview

The dismantling of a nuclear installation requires the cutting and segmenting of equipment and structures with varying sizes, dimensions, and materials.

The conditions under which the cutting operations are carried out depend on the location and space of the working area, on the qualification and experiences of the personnel, on the available tools and technologies as well as on the environmental conditions under which the operations are made: under water, in the air, under radioactive radiation, and under contaminated atmosphere.

There is great diversity in existing cutting tools, which are useful and available under industrial conditions or in the RTD phase, each tool having its own performances, conditions and field of application. The following techniques are available:

- Thermal cutting
- Hydraulic cutting
- Laser cutting
- Mechanical dismantling
- Microwave spalling
- Explosive cutting

When choosing cutting techniques the following factors should be taken into account:

- The technique (tool) should be used in practice, so that experience exists and supply security spare parts and handling are ensured
- The technique (tool) should only generate a minimum of secondary waste, e.g., dust, particles, fumes, aerosols with controlled dispersion, and liquid effluents
- The personnel on-site should be at low risk of contamination, easy to decontaminate
- The technique (tool) has to be compatible with the working-environment

5.2 Thermal Cutting Techniques

In thermal cutting techniques, the solid material is melted and then blown away. Since molten states of material are present, the net amount of force needed is much smaller than for the techniques, which use strain energy. Hence, the use of mechanical force is only a minor part of thermal cutting processes.

It is possible to classify the thermal cutting techniques according to the type of heat source:

- Gas processes
- Arc processes

- Plasma arc processes
- Combined cutting processes (a composition of the above mentioned processes)

The energy density of the heat source increases from the gas flame to the arc and the plasma arc to the laser beam.

5.2.1 Gas Processes

Thermal cutting techniques with gas flames are mainly used for flame-cuttable materials. Most of the process heat is released during the exothermal combustion of the work piece. The residual part is released by burning the heating gas in oxygen. The resulting flame heats the work piece to its ignition temperature and oxygen is then added, in which the work piece is burnt.

Two different kinds of fuel can be used to provide the heating flame:

- Fuel gases, such as hydrocarbon compounds and hydrogen
- Liquid fuels

For safety reasons, only hydrocarbon compounds should be used in nuclear facilities, since hydrogen involves the risk of explosions in connection with possible leaks.

Liquid fuels are more difficult to handle and less effective than hydrocarbons and should only be used for exceptional cases in underwater cutting.

The most important parameters for the selection of fuel gases are the maximum flame temperature, the primary flame efficiency, and the density of the gas in comparison with the density of air (► [Table 18](#)).

Powder Injection Flame Cutting

There are two different types of flame cutting that use additional powder injection:

- (Sand) powder cutting
- Metal-powder fusion cutting

In both cases, a heating flame and an oxygen cutting jet are present as in flame cutting. Different powders are added depending on the material to be cut.

Powder cutting was developed for cutting stainless steel, which cannot be cut by flame. A special sand is added as a powder. Due to its abrasive effect, this sand tears open the oxide skin and thus facilitates the blowing out of the high velocity molten steel. Nowadays, this method has been replaced to a large extent by plasma arc cutting.

In metal-powder fusion cutting, exothermally-burning metal powders are introduced into the oxygen cutting jet. The heat emitted during the oxidation causes the fusion of the work piece.

■ **Table 18**

Hydrocarbon compounds data

Type of fuel	Maximum flame temperature (°C)	Density (kg/m ³)
Acetylene (C ₂ H ₂)	3,150	1.17
Propane (C ₃ H ₈)	2,828	2.02
Methane (CH ₄)	2,786	0.72
Natural gas	Values depend on the composition	

In addition to the oxygen cutting jet, the kinetic energy is significantly increased by means of the developing oxides. In this way, it is easier to blow the molten products out of the kerf.

In most cases, the powder consists of iron or a mixture of iron and aluminum (85% Fe, 15% Al).

Since metal-powder fusion cutting is a pure fusion cutting process, it can be used for cutting stainless steel, non-ferrous metals, cast iron, and concrete. Nowadays, the cutting of concrete is the most important field of application for this technique. The emerging metal oxides convert the viscous slag into a more fluid one. This sort of slag, called lava in case of concrete, can easily be blown out of the kerf.

The latest development is a specially designed flat torch for cutting concrete walls more than 1 m thick. One meter represents the thickest cut that can be achieved with conventional torches, the large size of which normally prevent immersion of the torch into the kerf. Flat torches are smaller than the kerf they produce, and hence the cutting operation becomes a gouging process.

The underwater use does not produce satisfactory results.

Aerosol Emission A series of aerosol measurement tests were carried out during a CEC project carried out by AEA Windscale, UK, and CEA Saclay, France.

Cutting Speed The cutting speed for cutting concrete with metal powder ranges between approximately 15 mm/min for a 300-mm thickness and 5 mm/min for a 1,000-mm thickness. The cutting speed for cutting stainless steel ranges between 200 mm/min for a 10-mm thickness and 170 mm/min for a 30-mm thickness (► [Table 19](#)).

Cut Thickness The thickest cut in concrete by means of conventional torches is about 1,000 mm. This value can be exceeded by using flat torches, which are able to immerse themselves into the kerf. In this case, no limit for the maximal cut thickness exists. The thickest cut in metals should not exceed 500 mm.

Flame Cutting

Flame cutting is performed with an oxy-fuel gas flame and cutting oxygen. The heating flame heats the work piece locally to its ignition temperature. The flame then keeps the work piece at this temperature during the cutting process. In this way, it compensates for heat dissipation by conduction into the work piece and the environment. The cutting-oxygen jet is added after the ignition temperature has been reached. The cutting kerf is formed by the relative motion between the cutting jet and the work piece.

■ **Table 19**

Cut thickness and cutting speed using oxyacetylene torch (SOGIN-NIS)

Guide method	Cut thickness (mm)	Cutting speed (mm/min)
Mechanically guided oxyacetylene torch	10	700
	40	460
	110	250
Manually guided oxyacetylene torch	10	370
	65	115
	110	21

The use of flame cutting is limited to mild steel, titanium, and molybdenum. Stainless steel and the remaining non-ferrous metals are not suitable for flame cutting without additional powder injection. In the field of nuclear facility decommissioning, mainly conventional torches for flame cutting in atmosphere are currently in use.

Underwater Use Firstly, special protection of the heating flame is required so that burning underwater is possible. This can be provided by an additional protection cap or by a concentric water curtain of a conical shape. Under this curtain, combustion gases produce a cavity between nozzle and work piece. Other versions use compressed air instead of water to form the curtain.

Cutting Characteristics The cutting speed mainly depends on the handling technique (manual/mechanical), the type of cutting nozzle, i.e., the design of the cutting oxygen bore, and the applied hydrocarbon. For cut thickness > 100 mm propane is recommended compared to acetylene because of higher cutting speed (see [▶ Table 20](#)).

Cut Thickness In atmosphere, a maximum cut thickness of more than 2,000 mm can be achieved for mild steel. Underwater, the cut thickness obtained with flame cutting range between 3 and 450 mm for mild steel.

Flame Gouging

Flame gouging is a variation of the flame cutting process. The surface of the work piece to be cut is heated to its ignition temperature by means of a heating flame. In this process, the same fuel gases as in flame cutting are used, i.e., acetylene, propane, natural gas, and hydrogen.

Following this, the gouging oxygen is applied, which oxidizes the preheated material and blows it out of the kerf. The oxygen pressure should be 0.5–0.7 MPa. The velocity of the gouging oxygen jet is much slower compared to the velocity of a cutting oxygen jet for flame cutting, i.e., 60–300 m/s in case of gouging and 400–500 m/s in case of cutting.

The slag heats up the work piece in front of the torch. This process supports the effect of the heating flame and renders possible a continuous process with high gouging speeds. When the oxygen jet gets into direct contact with the work piece, without any layer of slag between them, the iron reacts immediately with the oxygen.

Underwater Use The heating flame must be shielded from the surrounding water by shielding gas caps, into which additional oxygen is inserted as a shielding. The tips of these caps must be as acute as possible, so that the required angle between torch and work piece can be achieved.

Compared to flame gouging in atmosphere, the slag cools much quicker, and solidifies directly in front of the heating flame. Because of this, the feed rate of the torch is much slower than that used for flame gouging in atmosphere.

Cutting Characteristics For flame gouging in atmosphere, the maximum feed rate ranges from 500 to 2,000 mm/min. The kerf is 3–10 mm deep and 5–18 mm wide. Deeper kerf can be produced by repeated application of the gouging process. Flame gouging underwater results in a slower gouging speed and a smaller kerf volume.

Oxygen Lance Cutting

Two different types of oxygen lances are available:

- Packed lances
- Powder lances

Table 20
Cutting speed for flame cutting in atmosphere (SOGIN-NIS)

Experiment	1	2	3	4	5	6	7	8	9
Pre-filter (Saclay)	Electrostatic filter								
	Mild steel without powder	Mild steel with powder	Stainless steel with powder	Mild steel without powder	Mild steel without powder	Stainless steel with powder	Mild steel without powder	Mild steel with powder	Stainless steel with powder
Oxypropane cutting									
Cutting time	199	134	97	177	138	201	183	130	114
Upstream aerosol concentration in mg/m ³	0.33	24.1	32.6	0.34	1.9	27.9	0.59	14.3	55.2
Downstream aerosol concentration in mg/m ³	0.011	0.41	6.8	0.24	0.75	9.4	0.012	0.012	<0.009
Mass efficiency in % (according to sampling filters)	96.7	98.3	79.2	–	61	66.1	97.9	99.95	>99.98
Upstream VMD in µm									
DMPs	0.241	0.569	0.564	0.216	0.254	0.579	0.211	0.569	0.639
EAA	0.145	0.191	0.265	0.109	0.163	0.245	0.172	–	–
Downstream VMD in µm									
DMPs	0.227	0.415	0.546	0.290	0.271	0.601	0.320	0.404	0.472
EAA	0.055	0.156	0.187	0.153	0.137	0.277	0.111	–	–
Cutting length in m	17.4	9.15	6.7	12.8	9.75	13.7	13.1	7.3	11
Powder flow in g/min	–	92	96	–	–	82	–	64	109
Increase pressure drop French HEPA filter in daPa	0.5	1.5	21	3	3	7	0	2	3.5
Increase pressure drop WNL main HEPA filter in daPa	0	61	61	11	c2.6	173	23	c43	135
Increase pressure drop WNL loop HEPA filter in daPa	–	–	–	–	1	42	4	5	45

An oxygen lance consists of a tube into which a core wire is inserted. Both tube and wire are made of flame-cuttable mild steel.

The free-end of the oxygen lance is heated to its ignition temperature by means of an external heating flame and then burnt in the pressurized oxygen, which is fed through the lance. The temperature reaches values up to 2,500 °C and the emitted heat melts the metallic work pieces as well as the mineral materials. The molten material is then blown away by the oxygen jet.

In the case of oxygen powder lances, metal powder is blown through a hollow tube by means of compressed air. A mixture of iron and aluminum powder is normally used. Oxygen lance cutting with packed and powder lances is used for cutting high-melting metallic materials and mineral materials such as concrete. Mild steel is burnt in the oxygen jet. Concrete and stainless steel are fused and blown out of the hole by means of the oxygen jet and the combustion gases.

Oxygen lances are usually guided manually. Automation of the process would be difficult to maintain and control, and therefore extremely costly.

In the case of cutting concrete, only a single hole in the work piece is generated instead of a straight kerf. The so-called perforation cut, which consists of a sequence of several holes in a row, represents the first choice for the severance cutting of concrete. The remaining material must be removed mechanically.

Underwater Use The underwater use of oxygen lances is possible. This technique is not widely used underwater for cutting steel less than 40 mm thick. Following the penetration of the lance into the work piece, there is an atmosphere-like condition around the hole, since the intrusion of water into the hole is impeded by the emerging oxygen, the combustion gases, and the slag. For cutting in atmosphere the lance must point upwards, so that the molten metal can drain off. In contrast, for underwater use, the lance must be pointed downwards in order to enable the emerging gas bubbles to rise.

Cut Thickness The thickness of concrete suitable for drilling depends on the cutting position: horizontal approximately 2 m, vertical – top to bottom approximately 1.5 m (► [Table 21](#)).

Aerosol Emission Tests showed that by using aerosol filters, a filtration efficiency of 99.96% was obtained. The service life, however, was not satisfactory. For the cutting of concrete, there was a shift towards bigger particle sizes.

5.2.2 Arc Processes

Oxy-Arc Cutting

The principle of oxy-arc cutting is similar to that of flame cutting but, instead of using a flame, an arc preheats the work piece material. In oxy-arc cutting, the arc is ignited between a hollow

■ **Table 21**
Cutting data for oxygen lance cutting (SOGIN-NIS)

Environment	Material	(Feed rate mm/min)	(O ₂ consumption l/min)	Hole diameter (mm)	Lance consumption ($m_{\text{lance}}/m_{\text{hole}}$)
In atmosphere	Concrete	200	500	45	4.25
	Mild steel	225	550	40	7
Under water	Mild steel	200	400	45	4–6

electrode and the work piece, and heats the latter to its ignition temperature. A cutting oxygen jet is then introduced through the hollow electrode onto the work piece, where it burns the material to be removed and blows the slag out of the kerf. The oxygen jet, therefore, has two functions: first, to establish an exothermic reaction, and second, to form the kerf by blowing the molten slag away. The oxy-arc cutting technique is suited to the cutting of ferritic steel, and with some restrictions is also suitable for fusion cutting of stainless steel, cast iron and non-ferrous metals. The fusion of materials which are not flame cuttable is achieved by means of the arc energy and the combustion heat which is released during the exothermal reaction of the mild steel electrode.

In the case of flame-cuttable materials, the oxygen is required to blow the slag and to oxidize the work piece and the mild-steel pipe electrode.

Underwater Use This cutting technique is mainly used for underwater applications. In contrast to flame cutting underwater, no additional shielding gas is required for oxy-arc cutting. In addition to manual operation, this process can also be automated.

Cut Thickness The most common work-piece thickness is from 5 to 40 mm. If the electrode is moved up and down, so that the kerf is produced in a sawing motion, thicker walls of more than 100 mm can be cut. The quality of the cut obtained, however, is by far inferior than that achieved with continuous feed. For stainless steel, a maximum cut thickness of 10 mm can be achieved with continuous motion. Here, cut thicknesses of over 100 mm are also possible by means of a sawing motion and a lower cutting speed.

Cutting characteristics. Operating speed for underwater cutting of mild steel is shown in **▶ Table 22** (not including the time for electrode replacement).

Consumable Electrode Oxygen Jet Cutting

In this case, an arc burns between the melting wire electrode and the work piece. A wire feed mechanism continuously feeds the cutting wire electrode to the torch. The electrical energy is transmitted from the power source by means of the current contact tip to the electrode. Generally, a mild-steel cutting wire is used, which is connected to the negative pole of a dc power source. The cutting wire diameter for cutting in atmosphere ranges between 1.6 and 2.0 mm.

The short-circuit arc is ignited at the top edge of the work piece when cutting is commenced and then moves down to the bottom edge of the cut. The arc is pressed downward by the magnetic blow-out of the work piece and furthermore by the mechanical pressure exerted by the inner gas jet with a pressure of approx. 0.4 MPa for atmospheric use. The arc then ignites

■ Table 22
Cutting speed for oxy-arc cutting (SOGIN-NIS)

Handling method	Cut thickness (mm)	Cutting speed (mm/min)
Manual handling	9	800
	25	450
	40	350
Mechanized handling	12	950
	40	600
	100	250

again at the top edge of the work piece, thus the process becomes periodical. The oxygen jet blows the wire and work piece material, which are both either molten or burnt, out of the kerf.

In the case of flame cuttable materials, an exothermal combustion process may occur, in which – similar to the oxidation process of the cutting wire – additional heat is released. This technique can also be used for cutting any electrically conductive material, which is not flame-cuttable.

The shape of the torch resembles pistols designed for welding in atmosphere. It usually has two concentric oxygen jets for cutting tasks carried out in atmosphere. The inner jet blows out the molten products and thus forms the kerf. The outer envelopment of shielding gas has a lower flow rate and prevents environmental gases from reaching the inner jet.

Underwater Use The consumable electrode oxygen jet cutting technique has also been developed for underwater applications. The cutting current is higher than for cutting in atmosphere in order to compensate for the heat transfer to the surrounding water. However, the achieved cutting speed is lower. Compared to the consumable electrode water jet cutting technique, the water jet, which is used for blowing the molten material out of the kerf, is substituted by an oxygen jet. In order to prevent the wire from premature oxidation, the mild-steel cutting wire has to be shielded from oxygen.

Cut Thickness The maximum cut thickness for the manual cutting of stainless steel in atmosphere as well as for the automated cutting of mild steel underwater is 90–100 mm (see [▶ Table 23](#)).

Consumable Electrode Water Jet Cutting

The consumable electrode water jet cutting technique is a further development of the consumable electrode oxygen jet cutting technique in atmosphere. It is a pure fusion cutting process, by means of which any metallic, i.e., electrically conductive material, can be cut.

This technique has been used exclusively for automated handling underwater. In contrast to consumable electrode oxygen jet cutting, oxidation of the work piece can be omitted. Substantially higher electric power outputs are required, since greater heat losses occur due to the water jet. The process is much more reliable than consumable electrode oxygen jet cutting, because the cutting wire is not liable to premature oxidation in the torch.

The principal cutting process and the cutting torch resemble those used in mechanical consumable electrode oxygen jet cutting underwater. In both processes, a cutting wire is continuously fed to the torch. The wire feed rate can reach up to 30 m/min. Stainless and mild-steel wires, as well as aluminum wires, are used as consumable electrodes. The best cutting performance can be achieved with mild-steel wire, the best quality of cut with stainless steel wire. The

■ **Table 23**

Cutting speed for consumable electrode oxygen jet cutting (SOGIN-NIS)

Cut thickness (mm)	Cutting speed (mm/min)
30	200
50	95
90	40

water jet, which surrounds the cutting wire, has a pressure of up to 2 MPa and blows the molten products out of the kerf.

An advantage of this technique is the proved possibility of cutting single pipes, tubes or bundles of these. Cutting is achieved by moving the torch and the cutting wire in a slow transverse motion across the work piece. The arc ignites when the wire tangentially touches the pipe. As soon as the pipe's interior is reached, two parallel arcs occur, which cut the front wall and the rear wall when alternated simultaneously.

Cut Thickness The maximum cut thickness is 100 mm for stainless steel and 50 mm for mild steel.

Aerosol Emission Although no shielding gas is used in consumable electrode water jet cutting, hydrogen and oxygen are released during the process, due to the hydrolysis of water. The volume of gas generated is linearly proportional to the cutting current.

The emitted amount of dust ranges from 0.05 to 0.2 g/m, i.e., the emitted amount of dust is smaller than that for plasma arc cutting. A disadvantage is the formation of secondary waste, i.e., the additional wire material.

Cutting Characteristics Cutting speed for consumable electrode water jet cutting is shown in [▶ Table 24](#).

Contact Arc Metal Cutting

Contact-arc metal cutting is a material removing, electrothermal cutting process and belongs to the family of electro discharge processes. The principle is based on the thermal effect of irregularly occurring short-circuit arcs of high current intensity which act on the work piece. All metallic materials can be cut with this method, and, in addition, metallic composite materials, such as clad steel, and matrix composite materials containing nonmetals and minerals, e.g., fiber reinforced metals, can also be cut.

To an extent, reinforced concrete can also be cut. The equipment required for contact arc metal cutting is relatively simple, compared to other thermal cutting techniques, and this makes the process extremely robust and reliable.

The equipment consists of three main parts: the power supply, the electrode with a feed unit, and the flushing fluid supply. By means of a mechanical feed unit, the electrode is continuously moved towards the work piece, until they touch and a short-circuit occurs. The high energy

■ **Table 24**
Cutting speed for consumable electrode water jet cutting (SOGIN-NIS)

Material	Cut thickness (mm)	Cutting speed (mm/min)
Mild steel	10	2,700
	20	1,700
	40	300
Stainless steel	20	1,800
	40	1,000
	60	500
	100	135

density of the developing high-current arc leads to the rapid heating of the work piece. The material melts and evaporates, following a sudden expansion. In this way, the material is blown out of the developing kerf. The arc becomes longer and eventually breaks after having reached a critical voltage. Since the electrode is fed continuously, it touches the work piece again and the cutting process recommences, during the course of which the electrode is immersed into the kerf.

The process is supported by a permanently fed fluid, which in most cases is water, and which flushes the material out of the kerf. Additionally, this fluid functions as a cooling medium, which dissipates the heat of the electrode and thus increases its service life. Using this cutting technique, it is not only possible to cut plate-shaped work pieces, but also to traverse cavities such as those occurring in single pipes or bundles of pipes.

Underwater Use The contact arc metal cutting technique is used both in atmosphere and underwater. Because of the required cooling water and the considerable emission of gases and particles, underwater applications are preferred to atmospheric ones.

Cutting Speed The cutting speed depends on the melting temperature, the specific amount of heat and the latent fusion heat of the material to be cut. For cutting stainless steel and using a 100 kW power source, the maximum cutting speed ranges between 1,000 mm/min (20 mm cut thickness) and 30 mm/min (150 mm). Using two power sources in parallel, the cutting speed ranges between 400 mm/min (50 mm) and 25 mm/min (200 mm).

Cut Thickness The maximum cut thickness depends only on the design and the material of the electrode, since it is consumed during the process: 150 mm (stainless steel) and, with two power sources in parallel, 200 mm.

Aerosol Emission In contact-arc metal cutting underwater, secondary by-products are produced. Since pollution of the water is quite high, water filtration should be considered. Furthermore, aerosols are produced, which reach the atmosphere. In comparison to plasma-arc cutting, the particle concentration is less constant, but is higher if the duration of the cutting process is taken into account. For comparable sheet thickness, the particle concentration is comparable when cutting with contact-arc metal cutting, because the feed rate is essentially slower than in plasma arc cutting.

Electrical Discharge Machining

The basic principle of the electrical discharge machining technique (EDM) is similar to contact arc metal cutting. EDM is in widespread use in the tool manufacturing industry, e.g., for the production of forge tools. With simple modifications, this technique was further developed for the cutting of all electric conductive materials.

Instead of arc erosion as in contact arc metal cutting, EDM uses the spark erosion as its basic mechanism. In comparison to an arc, unsteadily and statistically distributed spark strikes somewhere between the electrode and work piece without generating a plasma column. This is why EDM, in fact, is not really an arc process.

For the initiation of the process, the electrode has to be positioned close to the work piece surface. The gap between the two parts has to be filled with an insulating fluid, i.e., the dielectric. Therefore, the process takes place under immersed conditions, e.g., under water or adequate such fluids as kerosene, less flammable hydrocarbons, alcohol, or glycol. Sometimes,

locally-sealed habitats have to be adapted to enclose the dielectric. This measure enables the dismantling of large structures in atmosphere. For underwater application, similar suction shrouds minimize the spread of contamination as well as the volume of the dielectric.

The cutting performance mainly depends on the cutting conditions in the gap, i.e., the quality of the dielectric, which itself is influenced by the removal of cutting by-products. Therefore, it is necessary to flush the dielectric in the area of the cutting process and, with this, to remove the debris from the gap. Therefore, hollow rod electrodes with internal jetting or thin electrode blades with external jetting, should be preferred.

Cutting Speed For cutting 76 mm stainless steel, a cutting speed of 0.6 mm/min can be achieved with a nonrotating electrode. The cutting speed may further be improved by means of additional motion, e.g., rotating, vibrating, or periodically withdrawing of the electrode.

Cut Thickness Similar to contact-arc metal cutting, the maximum cut thickness depends mainly on the design and the material of the electrodes.

Aerosol Emission The EDM technique produces particles with dimensions ranging from 0.4 to 1 μm . This requires fine mesh filters of up to 1 μm , implying a poor waste density.

Arc-Saw Cutting

The arc saw consists of a circular, toothless saw blade, which cuts any conductive metal. The actual cutting process resembles the contact arc metal cutting process. In contrast to the graphite electrodes of the contact arc metal cutting technique, the saw blade rotates much faster. The residues are not removed from the developing kerf by means of a water jet, but are taken away by the rotary motion of the blade.

Since the arc foot moves continuously, the quick rotation of the blade limits its wear and, furthermore, an even and constant wear over the complete circumference is achieved. The rotation also helps the cooling of the blade and hence increases its lifetime. The depth of cut is limited only by the blade diameter.

Underwater Use The arc-saw cutting technique is suited for applications underwater and in atmosphere. However, underwater cutting is preferred because of the reduced noise level, the effective saw blade cooling resulting in an extended blade life, the shorter arc and narrower kerf, and cutting debris retention in the water. As compared to cutting in atmosphere, the risk of additional arcs occurring at the two sides of the blade is reduced. Because of the restricted kerf size, however, the blade can get jammed when the edges of the cut cool down. The service life of the blade is longer, but the cutting speed is lower.

Cutting Speed The cutting speed decreases significantly with increasing thickness of the work piece from 150–480 mm/min at 80 mm steel to 20–100 mm/min for 250 mm steel.

Cut Thickness Up to now, a maximal cut thickness of 1,000 mm stainless steel was achieved with a 3,000 mm saw blade.

Consumable Electrode Water Jet Gouging

The consumable electrode water jet gouging technique is a further development of the consumable electrode water jet cutting technique. The equipment is similar and the actual erosive process generally corresponds to the basic cutting process.

In contrast to cutting, the torch is positioned at an angle of 30–45° to the work-piece surface. Currently, two possible techniques are available. Both have been developed exclusively for underwater use.

Initial tests on consumable electrode water jet gouging were carried out in Japan. These tests used mild steel with a 6–12 mm stainless steel coating and were carried out underwater.

A second possible application of the consumable electrode water jet gouging technique has been studied in Germany (IW, Hannover) since the late 1980s. Tests were carried out for the removal of material from activated surfaces. With this technique, layers up to 4 mm could be removed with a single operating cycle.

5.2.3 Plasma-Arc Processes

Thermal plasma is a highly heated gas or gaseous mixture which is conductive and consists of ions, electrons and neutral atoms or molecules. Mono-atomic gases such as argon and helium, poly-atomic gases such as nitrogen and hydrogen, and also mixtures of these or air can be used as plasma gases.

The plasma arc is constricted by means of a copper nozzle. The thermal and electric pinch effects are used to attain temperatures which are considerably higher than the temperatures obtained with the open arcs described in the section above. The maximum temperature in the inner plasma arc is approximately 20,000 K or more. There are two groups of plasma-arc processes:

- Those with a transferred arc (the arc strikes between the electrode and the work piece)
- Those with a nontransferred arc (the arc strikes between the electrode and the nozzle)

For practical applications, the transferred arc is used almost exclusively for cutting and eroding any conductive material. The nontransferred arc can cut any material, i.e., also nonconductive materials, but significantly less energy is transmitted to the work piece.

Plasma-Arc Cutting with Single Torch


Conventional plasma-arc cutting with a transferred arc is a pure fusion cutting process by means of which any conductive material can be cut. The plasma arc, with its high energy density, melts or partially evaporates the work piece. The high kinetic energy gas jet blows the molten material out of the kerf.

In cutting processes with direct current, the torch electrode forms the cathode and the work piece forms the anode. The amount of heat which is transferred to the work piece mainly consists of energy from the impacting electrons, the Joule effect and convection.

The following techniques can be grouped according to the plasma gas used:

- Argon-nitrogen-hydrogen technique. For this cutting technique, a mixture of argon, nitrogen and hydrogen is used as a plasma gas. Without an additional shielding gas, this variant is mainly used for cutting in atmosphere.
- Dual-flow technique. The dual-flow technique is a further development of the Ar/N₂/H₂ technique that is especially suited for underwater cutting. Here, the plasma arc is surrounded by a shielding gas, such as carbon dioxide or compressed air. As a result of this measure, the plasma arc is protected against the surrounding water, energy losses are decreased and the quality of cut for mild steel is increased.

- Compressed air technique. In this process, compressed air is used as a plasma gas. This technique is especially suited for cutting mild steel in atmosphere. For underwater use, an additional secondary gas, e.g., compressed air, will decrease energy losses.
- Water-injection-plasma-cutting (WIPC) technique. The special feature of this type of cutting torch is the nozzle, the upper part of which consists of copper. Between these two parts, a concentric water curtain with a low flow rate ($<21/\text{min}$) is sprinkled onto the plasma arc. This leads to a further contraction of the arc and thus to an increase in the energy density and in the temperature. In addition, a swirl ring at the cathode leads to a rotating motion of the plasma gas around the electrode, which stabilizes the plasma arc. For decommissioning purposes, modular cutting torches were developed for the remote-controlled replacement of worn parts by means of manipulators. Thus, those parts with the highest wear rate, i.e., the nozzle and the electrode, can be easily replaced and the torch can be adapted for individual cutting tasks. This also makes it possible to switch between straight and cranked cutting units. Such a unit must be as small as possible, since it is used for cutting confined, complex structures.

Cutting Characteristics The cutting speed and cut thickness which can be obtained mainly depend on the process variants being used (see  [Table 25](#)).

Cut Thickness Maximum cut obtainable in atmosphere is 170 mm deep for stainless steel, 150 mm for mild steel and 80 mm for aluminum. The cut obtainable underwater is 100 mm deep for mild steel and aluminum, and 100 mm for stainless steel.


Aerosol Emission Aerosol emissions can be reduced by a factor of up to 500 if the process is used underwater. For cutting processes in atmosphere, the formation of dust is greater for mild steel than for stainless steel due to the exothermal reaction. For the cutting process underwater, however, higher emission rates are produced for stainless steel sheets with thicknesses up to 60 mm. A greater water depth leads to a further reduction in the number of particles reaching the surface.

Plasma Compass Saw Cutting and Plasma Circular Saw Cutting

The plasma compass saw and the plasma circular saw have been developed for underwater cutting of work pieces with wall thickness of more than 100 mm, which cannot be flame cut. Both techniques are based on similar cutting principles.

The cutting process is based on miniature plasma torches, which are of such a small size that they can be immersed into the kerf.

With both techniques, kerf of any desired depth can be cut by repeated actions of the plasma-arc gouging process.

 **Table 25**
Cutting speed for plasma cutting (SOGIN-NIS)

Cut thickness (mm)	Cutting speed (mm/min)
10	3,500
20	1,800
40	1,100
80	600

This stands in contrast to the conventional plasma-arc cutting process, in which the plasma torch must be positioned outside of the kerf and in which the energy input in the direction of the work-piece thickness, i.e., in the direction of the plasma arc, is limited.

The torches are designed for use with argon as the plasma gas and are equipped with pointed tungsten electrodes. The cooling of the nozzles can be improved by circulating water, which escapes through bore holes in the nozzles. In addition, the water flushes the granulated material out of the kerf.

Plasma Compass Saw

The cutting process is started at the edge of the work piece or from a bore. A kerf is gouged over the whole cut thickness by moving the torch linearly in the direction of the sheet thickness. After turning the nozzle, the process is restarted in order to remove the material adjacent to the kerf. If a sufficiently wide kerf has been produced by repeated application of this process, the torch can be moved in the intended direction of cutting. The result is a discontinuous cutting process in the direction of cutting.

In order to avoid additional arcs, the torch is inserted into a shielding tube made of nonconductive ceramic. The nozzle bore is also inclined with regard to the torch/electrode axis.

Here, the entire torch is moved around its axis by means of an adjustment unit mounted on the head of the torch. Furthermore, oxygen or compressed air exiting from an additional bore directly adjacent to the nozzle bore with a pressure of 1 MPa can be introduced into the plasma arc.

Better erosion results are achieved with this method for both mild and stainless steel.

The rod torch can also be used for cutting pipes and tubes from the inside if they are inaccessible from the outside. The torch is inserted into the pipe, which is then cut while the torch makes a complete turn around its axis.

Cutting Characteristics For cutting thick work pieces, the cutting unit is elevated in the direction of the torch axis with a speed of 80–200 mm/min. With a single operation and the additional input of oxygen or compressed air, kerf depth of approximately 5 mm and kerf widths of approximately 10 mm can be achieved (mild steel as well as stainless steel).

Plasma Circular Saw

The plasma circular saw consists of several single torches which are arranged on the circumference of a circular saw disk. In contrast to plasma compass saw cutting, where the arc burns continuously, in plasma circular saw cutting each torch is ignited just before immersion into the work piece and ceases burning when it leaves the kerf.

Plasma cutting with an immersed torch offers the advantage of cutting single pipes and bundles of pipes, since the arc jumps over from one pipe wall to another.

Since the torches have to be continuously re-ignited, the service life of worn parts is reduced because the arc ignition process represents the highest stress.

Cutting Speed For cutting 300 mm stainless steel, the plasma circular saw reaches a cutting speed of 1.3 mm/min.

Cut Thickness For this technique, the maximum cut thickness only depends on the diameter of the disk. A recent circular saw has a disk diameter of 1,000 mm for maximal cut thickness of 300 mm.

Plasma-Arc Gouging

The plasma torch for gouging resembles the one used for plasma-arc cutting. After being pre-heated, the molten work piece material has to be blown out of the kerf by means of the kinetic energy of the plasma gas.

In principle, this can be achieved with a slanted nozzle orifice or an inclined torch. In the case of a slanted nozzle orifice, the erosive process corresponds to the one described for plasma compass saw cutting.

The obtained erosion rates, however, are relatively small, because the nozzle wear increases due to the highly-energetic plasma arc and because the reduced size leads to a limited cutting performance.

In the case of an inclined torch, the nozzle orifice must be moved as closely as possible to the surface of the work piece. For this reason, the torch tip should have a conical shape. The nozzle diameter can be larger than for plasma cutting, since there is negligible constriction of the arc. The flow rate of the plasma gases should be increased proportionally to the cut depth, so that large amounts of molten material can be blown out.

In the case of plasma-arc gouging flame-cuttable mild steel, additional oxygen can be introduced into the area where the plasma jet leaves the torch. The oxygen then has two functions: it increases the kinetic energy used to blow out the molten products and it initiates the exothermal combustion of the work-piece material, thus generating additional process heat.

Cutting Characteristics In atmosphere, the gouging speed is approximately 1,800 mm/min. At considerably lower speeds, more gas is needed for blowing out the molten products.

5.2.4 Laser Cutting

A more recent technique applied to decommissioning is cutting by CO laser. Some information about the method developed by NUPEC is reported in  [Figs. 10](#) and  [11](#).

5.2.5 Combined Cutting Processes

Combined cutting processes have been developed with the aim of cutting mild-steel work pieces with very thick walls and with stainless steel plating. In this case, the total wall thickness of the work piece to be cut may exceed the maximum cut thickness which can be achieved with single-torch plasma-arc cutting and consumable electrode water jet cutting.

Flame cutting is usually selected for cutting thick flame-cuttable structures. However, in many cases it is difficult to use flame cutting torches exclusively since only the stainless steel liners are accessible for cutting.

The cutting principle of combination cutting processes is as follows: a fusion cutting torch gouges a kerf through the stainless steel liner, followed by a flame cutting torch which cuts the mild-steel walls.

Consumable Electrode Water Jet Gouging/Flame Cutting

This technique has so far been developed for cutting underwater only. The combined cutting process uses the consumable electrode water jet gouging torch as described in the subsequent section.

The maximum gouging speed is approximately 1,000 mm/min, with which kerf depths of 2 mm can be obtained.

The flame cutting torch is an underwater torch with a concentric water curtain. In order to cut mild-steel thicknesses of 300 mm or more, large cutting nozzles can be used at oxygen pressure ranging from 0.8 to 1.2 MPa. The heating flame is a gas mixture of propane and methylacetylene plus the burning oxygen. The overall weight of this system, including an actuator and a supporting plate, is 13 kg.

Cutting Characteristics It is possible to cut mild steel plated with up to 12 mm of stainless steel, with thicknesses up to 450 mm.

Plasma Arc Gouging/Flame Cutting

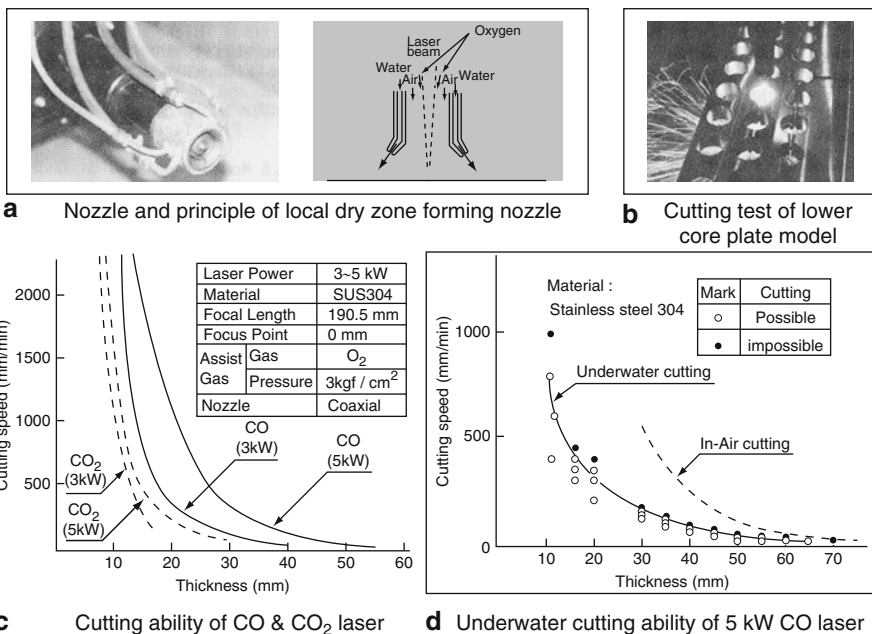
With this technique, the stainless steel cladding is gouged with a plasma-arc cutting torch, so that the following flame cutting torch can cut the uncovered mild steel. This combination cutting process has so far only been tested for atmospheric use. Nevertheless, cutting underwater may be possible, because single torches have already been tested for under-water use.

The arrangement of these two torches differs substantially from that used for consumable electrode water jet gouging/flame cutting. Here, the leading plasma torch produces molten material, the heat of which supports the preheating of the work piece for the flame cutting process. To achieve this, the torches are inclined in the direction of cutting. A commercial Ar/H₂ plasma torch is used for a successful ignition.

A specific characterization of this combined technique reported by NUPEC is shown in

► Fig. 12.

Cutting Characteristics The maximum cut thickness is 610 mm, with the exception of horizontal cutting, where only 310 mm can be achieved.

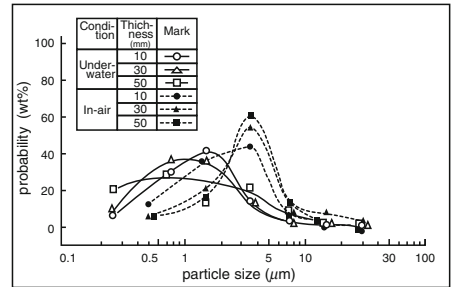


■ Figure 10

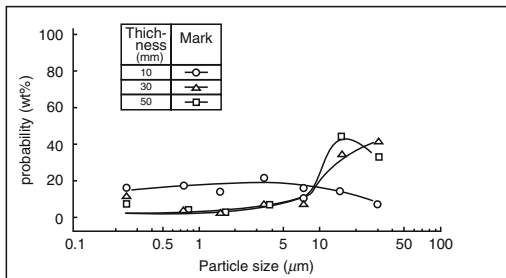
Laser cutting experience developed by NUPEC (Ishigure et al. 1992)

Condition	Thickness (mm)	Cutting speed (mm/min)	Cutting time (min)	H ₂ (%)	O ₂ (%)	N ₂ (%)	CO ₂ (ppm)	CO (ppm)	O ₂ (ppm)	NO _x (ppm)
Under-water	10	500	4.3	0.068	32.5	67.4	0.05	22	3	13
	30	100	7.5	0.064	39.6	60.3	0.04	19	3	10
	50	20	36.5	0.058	48.0	51.9	0.06	16	2	6
In-air	10	500	4.3	0.004	30.8	69.2	0.04	30	3	15
	30	100	4.7	0.004	30.5	69.5	0.04	29	3	11
	50	20	11.5	0.002	30.0	70.0	0.04	15	1	6

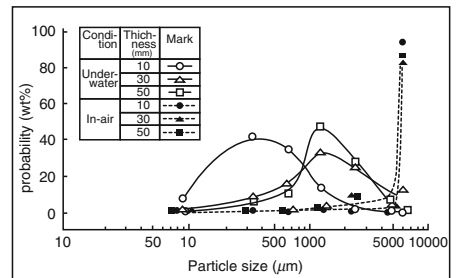
a



b



c



d

Figure 11

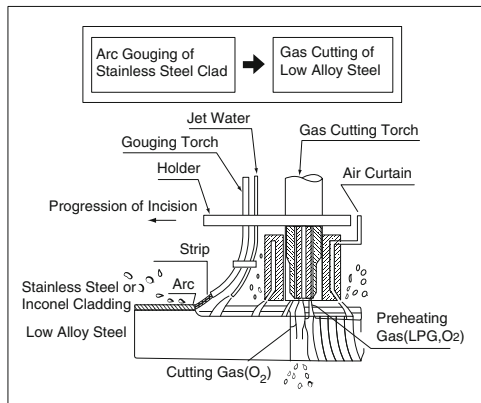
Laser cutting experience developed by NUPEC (Ishigure et al. 1992)

5.3 Hydraulic Cutting Techniques

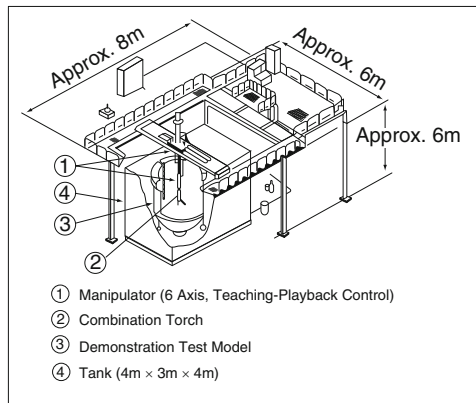
Typical operations that can be carried out by water jets are cleaning, cutting, drilling, milling, marking and excavation. Plain water jets are typically used for nonmetallic and nonceramic materials, while abrasive water jets are used for materials of great hardness, strength or toughness. The main advantages of these water jet processes (with or without abrasives) are the following:

- Cutting can take place in atmosphere as well as underwater.
- Virtually any material can be machined.
- The process neither needs nor generates thermal energy, so that there are no thermal influences which could change the material properties by means of a heat-affected zone.
- Jet reaction forces are lower as compared to mechanical cutting techniques. Thus, manipulation by robots or mullet-axis handling devices is easier and more accurate.
- The jet is a precise noncontacting tool which can cut in all directions (omnidirectional) and does not deform the material during cutting.
- With a jet of a suitable diameter, small kerf widths can be achieved.
- The amounts of dust and aerosols emitted are negligible.

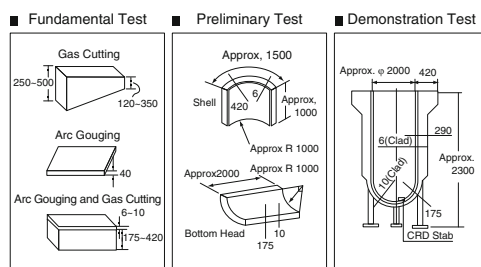
The main principle of both plain water jet and abrasive water jet cutting technology is to use a high-speed stream of water. The essential difference lies in the addition of an abrasive to the water jet. This addition increases the erosive action of the water jet, expanding the range of materials that can be cut. The jet cuts when its loading exceeds the strength of the material.



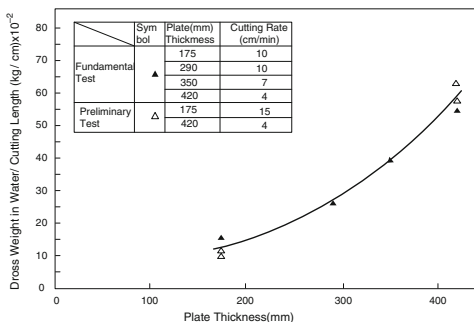
a Combination torch system



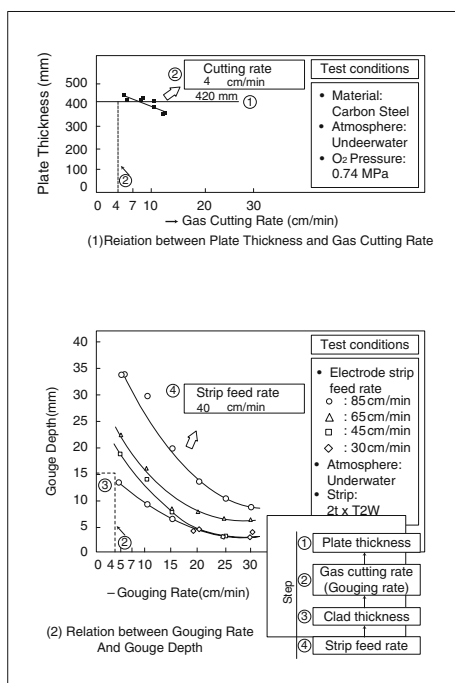
b Test apparatus



c Test models.



e Relation between plate thickness and dross weigh in water



d Step of selecting combination cutting conditions

■ Figure 12

Arc gouging and gas cutting method (G&G method) adopted by NUPEC (Ishigure et al. 1992)

Depending on the properties of the material, the cutting is the result of erosion, shearing, or failure under rapidly changing, localized stress fields. The abrasive water jet has a more powerful compressive strength than the plain water jet.

For cutting purposes, the plain water jet or the abrasive water jet passes through the material and produces a complete cut. A special catcher is needed below the work piece, to receive the

high pressure stream. In the case of abrasive water jet cutting, it is also useful to collect the used abrasives in order to treat them as waste or to reprocess them for further use in cutting processes.

5.3.1 High Pressure Water Jet Cutting

Cutting with plain water jets is based on the erosion effect of high speed water droplets. For manufacturing processes, water jet cutting is used to cut different kinds of nonmetallic materials like plastics, paper, textiles or food. For these applications, high pressures (up to 400 MPa) are used, with small water flow rates.

Plain water jets are widely used for the cutting of concrete. For these jobs, moderate pressures (up to 100 MPa; some designs have been developed for 270 MPa operation) are normally used. In order to reach sufficient cleaning or cutting performances, the water flow rates are much higher than for high pressure water jets (50–100 l/min).

For plain water jets, the treatment of the waste is quite easy. After cutting, the suspended particles in the water (from the jet) and the removed material can be separated by sedimentation or filtration techniques. The water can be reused for cutting purposes: for moderate pressure systems (piston pumps), a simple filtration of particles up to a diameter of some μm is sufficient. When using an intensifier pump, deionization may be necessary.

Underwater Use In general, plain water jets can be used in atmosphere as well as underwater. Nevertheless, the maximum length of the jet underwater is much shorter than in atmosphere, because of the increased friction with the ambient medium.

Cutting Characteristics Both kinds of plain water jets are well established in the manufacturing industry and in civil engineering. They are used to cut nonmetallic materials, to remove debris, paint and surface layers and to clean concrete. The high pressure water jet is not able to machine metallic materials in an economical way: the cutting speed for 1 mm-thick aluminum plates is less than 100 mm/min, for 1 mm steel plates less than 10 mm/min. Much thicker plates are impossible to cut because of the instability of the jets.

5.3.2 Abrasive Water Jet Cutting

The abrasive water jet cutting technique is based on the application of plain water jets for cutting purposes. Abrasive particles are accelerated by the high speed water jet and cause the removal of the material. Instead of an erosion process as in the case of plain water jets, abrasive water jets cut by micro-chipping the material with the sharp-edged particles.

When using the correct abrasive material, which has to be harder than the work-piece material, any material can be cut, metals as well as ceramics, glass and concrete.

With abrasive water jets, severance cutting, as well as gouging, is possible.

To generate abrasive water jets, two different methods are currently available. The abrasive can be added to a plain water jet in a special mixing head (injection jet), or a premixed and pressurized abrasive water suspension can be released into the nozzle to form the abrasive jet (suspension jet). Sharp-edged mineral particles such as silicon sand, corundum or garnet sand are used as abrasives.

The increasing number of cutting applications has helped the abrasive water suspension jet (AWSJ) to become more important, despite the high consumption of water and abrasives.

■ **Table 26**
Cutting speed for abrasive water jet cutting (SOGIN-NIS)

Material	Cut thickness (mm)	Cutting speed (mm/min)	
		Injection jet	Suspension jet
Stainless steel	2	2,000	1,200
	10	350	250
	40	90	70
Concrete	100	30	25
	100	200	200
	300	–	25

Cutting Characteristics Cutting speed values for abrasive jet cutting are shown in ► [Table 26](#).

Aerosol Emission For underwater applications, the quantity of aerosols is reduced by a factor of about 200 as compared to applications in atmosphere. Gouging generates 3–4 times more aerosols than severance cutting, whether the operation takes place in atmosphere or underwater.

For both kinds of jets – suspension jets and injection jets – possible applications for decommissioning nuclear facilities have been investigated. ► [Table 27](#) presents a comparison between cutting parameters for aluminum and stainless steel with suspension and injection jets. The cutting performance for nonreinforced concrete is about six times higher than for steel.

5.4 Mechanical Dismantling Techniques

5.4.1 Grinder

This is an electrically, hydraulically or pneumatically powered disc made of resin-bonded particles of aluminum oxide or silicon carbide. Usually the wheel is reinforced with fiberglass matting for strength.

It cuts through the work piece by grinding the metal away, leaving a clear kerf. Grinding cutters can be used to segment all types of materials (e.g., metals and concrete or reinforced concrete) both in air and underwater.

The maximum thickness of the metallic components that can be cut with this method is limited to 150 mm, but the shape and diameter are not limiting factors. However, grinders used at dismantling sites are not suitable for cutting stainless or mild steel plates thicker than 30 mm.

The abrasive process generates a continuous stream of sparks. Contamination control is a significant problem, since the swarf comes off in very small particles. To limit the spread of contamination, grinders may be fitted with a swarf-containment system.

In most cases the operator would have to work within a contamination control envelope and would have to wear protective clothing and respiratory protection.

Experience in the use of such equipment is widespread both in conventional industry as well as in the nuclear industry.

Some useful information on the use of grinders is the following:

Table 27
Cutting data for injection and suspension jets (SOGIN-NIS)

Material	Abrasive water injection jet						Abrasive water suspension jet			
	Aluminum			Stainless steel			Aluminum		Stainless steel	
	IW	CEA	IW	CEA	IW	IW	Sprint	Sprint	Sprint	
Reference	2,400	2,400	3,000	2,400	3,000	3,000	IW	Sprint	Sprint	
Pressure (bar)	2,400	2,400	3,000	2,400	3,000	3,000	160	690	690	
Water flow rate (l/min)	1.5	12.7	3.9	8.4	3.9	1.6	16.9	38.1	15.8	
Abrasive flow rate (g/min)	480	2,800	1,100	1,320	1,100	600	4,000	4,000	1,700	
Hydraulic jet power (kW)	5.9	50.8	19.5	33.6	19.5	8.0	4.9	43.8	18.3	
Cutting performance (mm ² /min)	3,600	2,300	6,000	1,940	3,300	2,100	2,100	11,400	4,400	
Cutting efficiency ^a (mm ² /kW min)	610	45	308	58	169	263	429	260	137	

^a Cutting efficiency --- cutting performance/hydraulic jet power

- Disc wear increases in proportion to the thickness of the material being cut. For example, a thickness of 30 mm causes nine times as much disc wear as a 10-mm thickness
- For equal thickness of the work piece, disc wear is greater when cutting stainless steel than when cutting mild steel
- The quantity of aerosol produced reduces as the linear speed of the disc increases. This quantity is halved when the speed is increased by 3 and this applies to all types of steel (stainless, mild steel)
- In comparison to the total quantity of secondary emissions, the proportion of dross deposited increases proportionately the thickness being cut.

5.4.2 Hacksaw and Guillotine Saw

These tools are used to cut all types of metal pieces with a hardened reciprocating saw blade. Hundred millimeter is the maximum allowed thickness of metal when the running time is taken in account. The equipment can be used by remote operation, with the necessary adaptations, and it can also be used underwater.

Other characteristics are the following:

- These tools can be used as either portable or stationary units
- Portable power hacksaws weighing less than 10 kg and portable guillotine saws can be clamped with a chain to a pipe
- For both types of portable saw a pneumatic or electric motor may be used
- In general, blade lubrication is not necessary
- The control of the contamination produced by these types of tool is straightforward
- Set-up time for both types of portable saw is relatively short. Moreover, once in place the saws operate without any further action on the part of the operator, thus reducing occupational exposures
- These tools have low operating costs as well as a low initial price
- Reciprocating saws are also available and their use is widespread in both conventional and nuclear activities

Very large stationary hacksaws, weighing up to 5 mg, can be used effectively for large components, since they can cut metal up to 60 cm thick. Cutting speeds of about 100 cm²/min make these machines suitable for segmenting large quantities of material.

The provision of a large stationary hacksaw in decommissioning activities will reduce the costs and exposures associated with handling long sections of pipe, for instance. The decision on whether to use such a stationary facility depends on factors such as the cost of the equipment and labor, the amount of material to be cut, the activity levels on the pieces to be cut and the dose to operators.

Hacksaw The production of aerosols is relatively small compared to other mechanical cutting methods.

The swarf produced represents 99.9% of solid secondary waste. During pipe cutting, part of the swarf may be deposited inside the pipe and must be disposed accordingly. The hacksaw is unsuited to cutting more than 30-mm thick mild steel and is not recommended for cutting stainless steel at all.

Guillotine Saw The principle and characteristics of this saw are similar to those of the hacksaw, the difference being in the method of supporting the blade. Guillotine saws can cut pipes up to

more than 600 mm in diameter. For such large dimensions, the weight and bulk of the machine limit its use on-site.

5.4.3 Shears

Shears consist of a pair of blades arranged so as to exert a slicing force on the material to be cut. Both blades may be mounted on a common axis and operate like a pair of scissors or, alternatively, there may be one fixed blade with another parallel blade which approaches in a perpendicular movement, thus shearing the material to be cut. The latter type is more often used when the material thickness exceeds 1 mm.

Other characteristics are the following:

- Blade wear is not great in parallel-blade shears, where the blades have no direct contact
- Shears are used for cutting sheet steel, pipes, bars and concrete reinforcement bars
- The size of the shears and the power of the hydraulic or pneumatic motor working its jaws determine the cutting capacity
- In the case of a hydraulic motor, the command station can be at a distance from the shears
- Currently available shears can cut steel pipes up to 300 mm in diameter and with 30-mm wall thickness, and steel plates and bars of up to 6 mm thickness or diameter
- Shears are normally portable and can be easily adapted either for remote control or underwater use
- They produce very tiny amounts of dust or smoke

In cutting small-diameter pipes, the crushing effect of the cut closes the end of the tube in the form of two sealed lips. After the two ends of a tube have been cut by shears, the resulting length can be transported without dispersing any of the enclosed contamination into the surroundings. Easy to operate and involving little labor, they are suitable for cutting small-diameter pipes from reprocessing facilities and for use in hot cells.

When cutting highly contaminated materials, it is useful to have removable blades, as this part is generally the most contaminated part of the machine and must therefore be changed or effectively decontaminated.

5.4.4 Milling Cutters and Orbital Cutters

Both these types of tools cut by shaving the metal. The milling cutter consists of a wheel armed with blades which, in rotation, shave off metal particles and trace a continuous kerf in the material, until it is cut through. In orbital cutters a cutting tool is applied tangentially to the circumference of the piece being cut and, in rotating the tool and its holder around the piece, it shaves off the metal.

Such equipment can be used for cutting cylindrical objects, such as pipes, tanks, etc.

The cutting tool may need lubrication (related to cutting speed) and this requires a system for liquid recovery. In most cases, the tool holder is a saddle which moves around the surface of the piece being cut. The interior of the pipe being cut is only exposed on the last pass. The tool holder is guided either by rails or by a system of chains; its movement is achieved using either hydraulic, pneumatic or electric motors.

Of the two machines it is possible to observe that:

- They are widely used in conventional industry
- The initial price and running costs are low

- It is virtually not possible to use them in remote control, owing to their weight
- Large capacity machines are often automatic
- Both machines can work under water

Performances These machines can cut only metallic circular objects whose diameters are between 0.15 and 6 m. The orbital cutter can shave off up to 2 mm per pass in mild steel and can cut a thickness of several centimeters in a number of passes.

A complete cutting operation (setting up, cutting and removal) for a 1,600-mm diameter pipe with a 25-mm wall thickness takes about 1 h. In fact, the actual cutting time is a relatively small part of the total when setting up, removing, retrieval of secondary wastes, cleaning and decontamination are taken into account.

Both of these tools produce practically no aerosols and the resulting shavings are easy to retrieve. As the inside of the pipe or tank is open to the outside air only during the machine's last pass, dispersion of the internal contamination is easier to control.

Large-diameter, thick-walled pipes are particularly suited for cutting by these machines. Their use is made more complex when liquids are required to cool the kerf and it is necessary to recuperate the liquids. These machines are usable on-site, but handling equipment must be available and suitable for their weight and bulk, the larger machines weighing several hundred kilograms.

5.4.5 Knurl Tube Cutter

The knurl tube cutter (rotary disk knife, or cutting wheel, or plumber's pipe cutter) is a circular machine that consists of several wheels which turn whilst pressing against the internal or external surface of the cylindrical piece to be cut. One (or two) of these wheels, called the knurling wheel, has a triangular section and its outside knife edge presses strongly against the metal, penetrating it progressively at each rotation. This causes plastic deformation on each side of the kerf until the tube is finally ruptured. The other wheels, which are normally bearing rollers, have no effect on the cut, except to burr its edges.

Based on traditional plumber's hand tools, powerful, large-capacity machines have now been developed which can be operated by remote control. Rotation is normally powered by an electric motor, while the pressure on the knurl wheel is usually provided hydraulically. These tube cutters can cut a wall thickness of up to 40 mm in stainless steel pipes with an external diameter of 350 mm. Rotational speeds are between 20 and 50 revolutions per minute and the force applied to the knurl wheel is from 1.5 to 5 mg. The cutting takes a few minutes and it is the installation and withdrawal of the equipment that is the time-consuming part of the operation, especially when working inside elbowed pipework.

The use of this procedure enables the machine to be used by remote control and also limits spread of internal contamination, since the tube is ruptured only on the last pass. There is very little secondary waste produced by this method of cutting, as there is no removal of metal, either by abrasion or shaving, only creep by plastic deformation. In addition, no cooling system is needed. Taking account of the need for peripheral equipment (transmission tubes or flexible shafts to power the rotation, electric motor for rotation, hydraulic compressor, etc.) and the time needed for setting up the equipment, interior pipe-cutting tools are seldom used. The exception is where access to the pipe concerned is difficult, either owing to lack of space or to the level of ambient radioactivity.

5.4.6 Diamond Saws and Cables

This technique involves the progressive opening of the desired kerf by scratching diamond particles against the material to be cut. The diamond dust is encrusted or glued on the saw blade or around the cable.

Both these tools are well suited to cut concrete and reinforced concrete and they can also cut steels and alloys of various metals.

One of the problems that may be encountered is kerf clogging. This explains, for example, the difficulties encountered when cutting light alloys where the penetration rate of the blade is so high that the swarf cannot be removed fast enough.

When large cuts are being made, the tools have to be cooled and this is normally done with water. This liquid, injected at the cutting face, prevents the dispersal of dust into the surrounding area. The liquid has to be recuperated and, if there is a risk of contamination, it must be decanted.

Compared to other methods of concrete cutting, diamond cutters produce little or no aerosols or fine unstable particles, and the secondary wastes from cutting are minimal and easily controlled.

The use of diamond saws (circular and cable) is one of the most suitable solutions for making openings in reinforced concrete walls and floors, or for dismantling complete structures, particularly when dispersion of contamination and conservation of the immediate environment are important factors.

Diamond Saws

Only circular saws have been used on nuclear dismantling sites. The largest saw made was developed for cutting concrete biological shields in power reactors and has a diameter of 2.5 m and can cut a 1 m thickness of reinforced concrete. The blade advance of this saw is 180 mm/min, giving a cutting yield of 10 m²/h. The blade has to be changed about once every 200 m², that is about once every 20 h of operation. This tool weighs 2.5 tons, which involves the use of manipulation and guidance equipment which are adapted as necessary to the prevailing conditions in the work zone. Saws of all diameters can be purchased readily and may be portable or operated by remote control.

It is vital that the saw blade be kept aligned in its cutting plane at all times during a cut. Otherwise, the saw blade may become jammed, or break or, less seriously, the kerf may become enlarged, leading to excess production of secondary waste. Diamond saws produce little pollution and are well suited to cutting concrete. They are good for breaching concrete walls, floors and ceilings at competitive costs and with a minimum of harmful effects. Setting them up becomes more difficult when cutting a thickness of more than 30 cm, because the weight and bulk of the machines then require special adaptations to the manipulation and guidance equipment.

Diamond Cables

Diamond cables offer all the advantages of circular saws and enable greater thicknesses to be cut through. One of the disadvantages of using cables is that it is often necessary to bore holes in order to pass the cable in a loop around the piece to be cut. However, an advantage of cables is that the motor driving the loop and its tensioning devices can be placed outside the immediate work area. There are, thus, practically no difficulties which arise from manipulation or lack of space.

The technique of cable cutting is very widespread in conventional industry and is capable of cutting cleanly and precisely with minimal effects on the surroundings, e.g., shocks, vibrations, noise, sparks and dust, and with reduced production of secondary wastes.

5.5 Conclusions

In general, the techniques of thermal cutting are very efficient. They can cut very thick steel, are easy to use and can be carefully employed under water. On the other hand, their use generates gas, fumes and aerosols that require the installation of filtration and ventilation systems, which in turn increase the cost of cutting.

Mechanical means of cutting are particularly adapted to cut small-diameter pipes or thin sheet metals. They generate negligible aerosols. Most of them can be remotely operated, provided that the remote equipment can withstand the forces incurred in the cutting process.

Mechanical cutting under water often poses difficult problems. Many means and cutting tools are already available to meet the needs of nuclear facility decommissioning. It is necessary to compare the different tools used for underwater cutting, on the basis of several criteria such as speed, handling, kerf, and production of secondary wastes.

The main features, which are important for a comparison or judgment with regard to the special requirements of decommissioning tasks, are as follows:

- The cuttable material
- The maximal cut thickness
- The environment (whether applications in air and/or under water are feasible)
- The feasibility of remote controlled operation of the required cutting tools
- The relative cost, including the cost of equipment, consumable costs, and labor costs
- The state of development concerning the decommissioning of nuclear installations

In [Table 28](#) all the above-mentioned thermal and hydraulic cutting techniques are compared; “excellent relative cost” means low cost and “poor relative cost” stands for high cost.

■ **Table 28**

Tool comparison

	Hacksaw	Plasma torch	Grinder	Arc saw	Air saw
Required power	+++	+	+++	+	+
Cutting speed	+	+++	+	++	++
Kerf coefficient	+++	+++	+++	+	+
Wear coefficient	+++	+++	+	+	++
Secondary waste	+++	+++	+++	+	+
Aerosols	+++	+++	+	+	+

Concerning the state of development, “no application” means that currently no information regarding applications of this technique concerning the decommissioning of nuclear facilities is available. ➤ [Table 29](#) shows a comparison of mechanical dismantling tools. ➤ [Table 30](#) shows a comparison of the secondary waste quantities of different cutting techniques.

6 Remote Control Techniques

6.1 Basis of Remote Operation

6.1.1 Overview

In certain situations it is not acceptable for workers to perform a task. For example, when a work area contains a hazardous environment, such as a high radiation field or a mercury-contaminated atmosphere, human presence should be adequately limited to maintain safe operating conditions. For a manually operated system, limiting human presence means limiting operating time and productivity. Therefore, it is often desirable to provide equipment that can be operated from outside the hazardous environment to overcome these limits. This is the primary reason for using remotely operated equipment; some other reasons include further productivity improvement, utilization of facility resources, cost reduction, and access to hard-to-reach work areas.

In decommissioning projects where remote equipment would enter hazardous environments, it is important to remember that the equipment should be kept simple or be tried out under a variety of similar circumstances. This is done to ensure the success of the equipment and to prevent time, effort, and exposure to hazardous environments caused by retrieving and substituting a failed piece of remotely operated equipment.

This section describes the remote technologies that can be used in decommissioning in areas that are inaccessible or are unsafe for occupancy. ➤ [Section 6.1](#) explains why remote technology should be considered in a decommissioning project, and ➤ [Sect. 6.2](#) describes what can be operated remotely. The configurations of remote systems are detailed in ➤ [Sect. 6.3](#), and applications of remote techniques in decommissioning projects are discussed in ➤ [Sect. 6.4](#).

6.1.2 Safety Enhancement

Because the areas of the primary circuit are highly radioactive, workers who enter these fields can receive their legal quarterly dose limit in only a few minutes of work on the equipment, so more workers are required to complete each task. These labor- and exposure-intensive activities adversely affect the goals of reducing worker exposure and lowering operating and maintenance costs. Remote equipment that can tolerate these high radiation fields while performing the required tasks are beneficial to reducing both cost and operator exposure.

6.1.3 Cost Reduction

The use of remotely operated equipment can result in cost reduction as well. The first example of cost reduction is the same as for reduction of personnel exposure. To perform a manual task

Table 29
Comparison of mechanical dismantling tools (SOGIN-NIS)

Cutting technique	Material	Maximum cut thickness	Environment	Remote operation feasibility	Relative cost	State of development
Flame cutting	Mild steel	No limit (>2,000 mm)	Air/uw	+	+	+
Powder injection flame cutting	All metals concrete	ss: 500 mm c: 1,000 mm	Air	o	o	+
Flame gouging	Mild steel	–	Air/uw	o	+	–
Oxygen lance cutting	All metals concrete	c: 2,000 mm	Air/uw	–	+	+
Oxy arc cutting	Mild steel (stainless steel)	ms: 150 mm ss: 12 mm	Air/uw	–	+	No application
Consumable electrode oxygen jet	Mild steel	160 mm	Air/uw	+	+	No application
Consumable electrode water jet cutting	All metals	ms: 50 mm ss: 100 mm	uw	+	o	o
Contact arc metal cutting	All metals	1,000 mm	Air/uw	+	o	+
Electrical discharge machining	All metals	–	Air/uw	o	o	o
Arc saw cutting	All metals	1,000 mm	Air/uw	o	–	+

Table 29 (continued)

Cutting technique	Material	Maximum cut thickness	Environment	Remote operation feasibility	Relative cost	State of development
Consumable electrode water jet gouging	All metals	–	uw	o	o	–
Plasma arc cutting	All metals	ms: 150 mm ss: 170 mm	Air/uw	+	o	+
Plasma compass saw cutting	All metals	–	uw	o	o	–
Plasma circular saw cutting	All metals	ss: 300 mm	uw	o	–	–
Plasma arc gouging	All metals	–	Air/uw	o	o	–
Consumable electrode water jet gouging/flame cutting	Mild steel clad with stainless steel	300 mm ms +8 mm ss	uw	o	o	o
Plasma arc gouging/flame cutting	Mild steel clad with stainless steel	600 mm ms +10 mm ss	Air	o	o	–
Laser beam cutting	All metals concrete	ss: 110 mm al: 25 mm ms: 90 mm	Air/uw	o	–	o
High pressure water jet cutting	All metals	1 mm	Air/uw	+	–	No application
Abrasive water jet cutting	All metals concrete	ss: 100 mm c: 300 mm	Air/uw	+	–	o

uw under water; c concrete; ss stainless steel; ms mild steel; al Aluminum; + excellent; o average; – poor

Table 30
Comparison of secondary waste quantities of different cutting techniques

Reagents and processes	Treatment procedures	Metallic materials					Comments
		Stainless steel	Carbon steel	Cu alloys	Inconel	Al alloys	
AP	Alkaline	Non corrosive	Mildly corrosive				Used as a pre-treatment in multi-step process; AP includes inhibitor and wetting agent, oxides Cr ⁺³ to Cr ⁺⁶
APAC	AP then rinse then ammonium citrate	Non corrosive, removes remaining corrosion film after AP	Highly corrosive; attacks base metals				AC attacks the corrosion film remaining after AP; corrosion to carbon steel; redeposition can be a significant problem
APACE	AP then rinse then ammonium citrate plus EDTA	Non corrosive	Attacks base metals				Addition of EDTA improves the process and prevents redeposition of contamination
AP Citrox	AP then rinse then mixture of citric and oxalic acids	Non corrosive	Non corrosive		Citrox removes corrosion film		Citrox step used to remove remaining residual MnO ₂

Table 30 (continued)

Reagents and processes	Treatment procedures	Metallic materials					Comments
		Stainless steel	Carbon steel	Cu alloys	Inconel	Al alloys	
APSul	AP then rinse then sulfamic acid	Non corrosive	Non corrosive		Non corrosive		Sulfamic acid step prevents formation of precipitates, thus preventing redeposition
APOX	AP then oxalic acid	Non corrosive	Corrosive				Oxalic acid used to remove remaining MnO ₂ corrosive film; potentially forms insoluble precipitate that redeposits and reduces effectiveness
Hydrochloric acid	One step with 100 g/l concentration in water	Corrosive	Corrosive	Non corrosive			Very aggressive process; corrosive to stainless and carbon steels
Oxalic acid	Generally, one step with 100 g/l concentration	Non corrosive		Attacks base metals			Effective for removing rust; reacts with steel to form highly insoluble ferrous oxalate precipitate

Nitric acid	One step with 100 g/l concentration in water	Non corrosive	Attacks base metals	Attacks base metals	Attacks base metals		Non corrosive	Addition of 0.1% hydrofluoric acid improves the DF
Sulfuric acid	One step with 100 g/l concentration in water	Highly corrosive	Highly corrosive					Highly corrosive
Oxalic peroxide	One step with 2 g/l oxalic acid and 5 g/l H ₂ O ₂	Non corrosive	Non corrosive	Non corrosive	Attacks base metals	Non corrosive	Non corrosive	Mainly used to remove uranium, uranium oxide, and plutonium films
Phosphoric acid	One step with 100 g/l H ₃ PO ₄ in water		Corrosive	Non corrosive	Non corrosive			May cause redeposition if left in system too long
Sulfamic acid	One step with 90 g/l sulfamic acid in water		Non corrosive	Non corrosive	Non corrosive		Non corrosive	Not as active as phosphoric acid but redeposition does not occur

in a high radiation field, many workers are required to avoid overdosing. Therefore, there are additional expenses associated with the number of workers employed for the high radiation tasks. In other words, since the remote equipment operating in the high radiation field replaces many human workers, the employment costs of those human workers are saved.

Another aspect of remote operations for cost reduction is accessibility. Remotely operated detection devices can be inserted into piping, and areas in the nuclear facility that are too small for human entry and work. The survey of the pipes may show that the pipes are not contaminated and can remain in the facility after decommissioning. This reduces the cost for removal of potentially contaminated materials as well as reducing the amount of material requiring disposal in a properly designed disposal facility.

6.1.4 Productivity Improvement

Because of the cumbersome nature of some protective clothing, worker efficiency can be greatly reduced. In addition, workers may need to participate in multiple rehearsals to train for a task before it is performed. Thus, the overhead to accomplish a task in an area with a hazard such as a high radiation field is very large. When remotely operated equipment can be used to accomplish the task, fewer workers are required. Even though the operator of a remote system will require training to be able to perform a given task effectively, the overall work-hour requirement is lower.

6.1.5 Utilization of Facility Resources

A facility to be decommissioned often already contains remote equipment. Such equipment can be used again in the decommissioning effort. For instance, remote-operated manipulators such as master-slave manipulators or electromechanical manipulators may be used to aid the decommissioning of the areas in which they are installed. Remotely operated cranes, fuel handling machines, and other equipment can be used in decommissioning as they were used during operation. Such possibilities should be extensively researched, because using the existing equipment reduces the overall cost.

6.1.6 Accessibility

Remote equipment can provide access to work locations that operators cannot physically enter. For example, it is virtually impossible for a human to survey the inside of a 10-in. diameter pipe to validate it for free release, to remove a contaminated component from its perch 25 ft. above a hot cell floor, or to remove abandoned materials from the bottom of a quarry overlain by 50 ft. of water.

6.1.7 Disadvantages of Remote Operation

A major disadvantage of remote operation is the fact that the operator, located at a distance from the work being performed, cannot provide immediate response to the task or its problems. Also,

a worker needs rehearsals with mock-ups of the work area. In most cases, manual operation, no matter how complex, does not require training and rehearsals to prepare for the task. However, for manual operation in a hostile environment, prior training and rehearsals for the task are essential.

6.2 Remote Operation Technologies

6.2.1 Overview

Most of the technologies described could be successfully converted for remote operation. The conversion activity must account for each system function performed by the manual operation and provide for a suitable operator interface at some remote location, with visual and electronic feedback from the work location to that remote location. Other factors to be considered, when preparing remote activities, include tool set-up and change-out, operating clearance for remote equipment, terrain conditions for mobile equipment, and material handling operations. In some cases, basic manual tools can be modified to benefit the remote system. For example, modification may include changing the grip to something an effector can grasp, using remote alignment and pinning methods, and using self-standing bails. Successful remote operation requires the operator to see the area in which the work is being performed and manipulate the equipment well enough to accomplish the required tasks.

The following sections describe the six major categories of remotely operated equipment, including detection, segmenting, decontamination, materials handling, sampling, and hand-held remote equipment.

6.2.2 Detection Equipment

Detection equipment, such as cameras or measuring equipment can be used for surveys and data gathering activities or can be combined with other remote equipment for real-time operator monitoring. It is important to note that, besides real-time monitoring, remote detection equipment can perform the important functions of gathering data for subsequent analysis, data that may not be readily gathered by human observation.

Cameras and Lights

Most remote operations rely on real-time visual feedback to an operator. This information is the main link between the operator and the remote operation being performed. Use of cameras and lights is essential to the success of a remote operation. Signals are transmitted to a receiver and visually displayed on large monitors for the operator's use.

With the use of a stereo camera system, data can be fed to stereo monitors, providing the operator with limited depth perception. A stereo camera system can also permit mapping of the panned areas or creation of a computer model that can be used in self-guided robots or virtual-reality system displays.

For other remote operations, a self-guided robot can be equipped with recording equipment as well as cameras and lights. In this situation, no real-time visual data-are needed; so after

the robot returns from its pre-programmed mission, the tapes are removed and examined in an “off-line” mode.

Other Detectors

Other detection equipment may be required for specialized tasks (e.g., using a radiation detector to determine the most radioactive material in an area so it can be removed first and using an infrared detection system to monitor areas where heat-sensitive materials or equipment are required for decommissioning activities). There are many other techniques that can be used in a remote application.

These applications may include measuring alpha, beta, gamma, or neutron radiation; checking floors for volatile organics and mercury; using infrared cameras to detect heat; using microphones and radios to detect sound; or taking temperature and humidity measurements.

6.2.3 Segmenting and Demolishing Equipment

Almost all of the segmenting equipment (i.e., cutting tools) are applicable for remote use; and many have been converted for remote operations, including circular saws, nibblers, arc saws, plasma arc cutters, reciprocating saws, laser cutters, friction saws, grinders, and rotary hammers. Converting some equipment to remote application is relatively easy.

For example, plasma arc cutters already have remotely operated cutting heads, so extending these to hostile environments is simple. Other cutting tools are designed specifically for manual operation, so special fixtures, equipment, or custom-designed tools are required for remote operation.

Heavy equipment, which is usually used for handling materials, is now being converted for remote operation.

Some remotely operated heavy equipment is exclusively used for segmenting. An example is remotely operated backhoes with a ram implement attachment, which are used for breaking concrete.

Other remote equipment that falls into this category includes nut running tools and impact wrenches. These are standard tools that have long been used with remote systems and can be applied to decommissioning activities where applicable.

6.2.4 Decontamination Equipment

Some of the decontamination techniques are suitable for remote operation, including processes such as scabbling, vacuuming, steam cleaning, and spraying. However, some techniques may be more difficult to adapt to remote use.

For example, a remotely positioned, vacuum bell, in situ cleaning device can be used to apply electropolishing electrolyte or other surface cleaning chemicals, but the system may have to be coupled to a bridge-mounted, remote-operated manipulator if the task is to decontaminate cladding in a hot cell.

Although the adaptation is made more difficult by situational complexities, it is still feasible.

As required tasks become increasingly complex, the functions to be combined become more numerous, inputs to the remote system increase, and remote operations become more difficult and sometimes impossible.

6.2.5 Material-Handling Equipment

Lifting, packaging, and removing materials generated in the decommissioning effort are some of the most important parts of the operation. Most facilities have an established material-handling system, and if it is still functional at the time of decommissioning, operating costs and potential procurement delays can be reduced. It also minimizes frustration at the end of the project, when it comes time to survey clean subcontractor equipment. Where facility-based material-handling equipment is not available or usable, equipment should be carefully selected to minimize recontamination of clean areas.

Materials that are generated during decommissioning can be lifted using grapples, clamshells, or specially designed tools mounted on a remote manipulator. In general, the lifting capacity of a remote manipulator is limited. Another limiting factor is the physical clearance available in the material-handling corridor. Existing operating systems that can aid in handling operations include automatic guided vehicles, palletizing robots, cranes, hoists, elevators, and conveyors.

6.2.6 Sampling Equipment

Mobile robots can be designed to take air samples, water samples, and soil/debris samples. Some robots also have drilling capabilities, so they can bore through concrete walls and extract samples from inside a structure. This technology has been best applied in disaster management, when the situation renders process knowledge useless and alters structural configurations by scattering debris and blocking normal passageways.

6.2.7 Hand-Held Equipment

Hand-held remote equipment usually takes advantage of the distance rule in limiting radiation doses to operators. This class of equipment is utilized when dose rate limits to operators are exceeded in contact situations, but where dose rates are manageable. Examples include long-reach extensions to power wrenches and long-reach hand-triggered grapples. Using a long-reach power wrench, an operator can, for example, reach down into a vault and loosen remote bolts associated with a dismantlement task. A long-reach hand-triggered grapple might be used to remove hot elements from a mist eliminator or to retrieve equipment that has fallen into an inaccessible location.

6.3 Remote-System Configurations

6.3.1 Overview

Remote systems can be designed and procured in a number of useful configurations. However, already existing facility-based remote handling equipment may be useful in decommissioning. This is particularly true when equipment was specifically designed to be used in hostile environments. If this equipment is still functional, its use in the decommissioning project may be appropriate, efficient, and cost-effective.

Most existing remotely operated cranes or other existing moving equipment can also be useful in the decommissioning. All existing remote equipment should be carefully considered in decommissioning planning to maximize its use because of the potential project benefits.

Newly installed equipment for remote operations could be used in the hostile environments. This equipment could be designed specifically for the project, or produced commercially for a wide variety of similar work.

Newly installed remotely operated equipment can cut or otherwise disassemble the material being removed and lift and transport it to an area for removal and packaging by other equipment. Such equipment can be designed to be easily decontaminated.

Mobile remotely operated units can move about a facility and perform decommissioning tasks where necessary, and then transport the removed material to a staging area for further processing or packaging for disposal. These units do not have to be custom-designed, because a large number of mobile remote systems are now being built for use in hazardous environments.

Remotely operated equipment consists of five units:

- Control station, which controls all movements and actions of the remote equipment
- Communication and power link, through which control signals and power are transferred to the remote equipment
- Supporting platform, from which the arm is mounted and all work is managed
- Arm of the remote equipment, which provides orientation and fine positioning of the tools
- Operating tool at the end of the arm, which performs the actual work involved, such as cutting

These five units are described in the following sections.

6.3.2 Control Stations

The control station monitors and directs all actions associated with the remote equipment, including manipulating the operating tool. The control station is located in a nonhostile environment from which either radio or hard-wired signals are transmitted to the support platform, arm, and operating tool. In addition to the operating controls, the control station may provide displays of the work area provided by cameras and detectors mounted on the support platform. Some systems do not provide displays. For example, automated data-gathering systems record optical data for off-line playback.

Teleoperator Control Stations

A teleoperator control station is where an operator takes real-time control decisions. These decisions may be directed towards manipulating or navigating the system. Very few of the operations are directed by automated support functions. Currently, two types of teleoperator control stations are most common: traditional control stations and advanced control stations. Virtual-reality systems are quickly evolving in the research sector, however, and are expected to be useful for this kind of work.

The traditional control station was developed in the 1940s and 1950s at the time teleoperator manipulators were being developed. The system consists of two master-slave manipulators positioned in front of a viewing window. Operations are restricted by the reach of the manipulators and the field of view provided by the window.

In advanced control stations, the operations are even more isolated than those in the traditional control station, because operators are seated in front of a control console. Feedback is received through monitors for visual display of computer-generated graphics for data display. Controls include power switches and joysticks for control of the operating tool. The operator makes operational decisions, but the computer may aid in controlling the remote operations. Operations are restricted by camera coverage, length of cable and length of manipulator mast.

Virtual-reality control stations currently provide information to the operator using computer animation. This technology is rapidly developing. Other researchers are using helmet-mounted optical displays to enhance further the virtual-reality effect.

Teleoperator Managed Stations

Teleoperator managed stations are very similar to advanced control stations, except that the computer controls most of the operations of the robot, and the operator monitors the progress and only intervenes at critical points to perform specialized tasks, make navigational corrections, or recover the system from unexpected encounters.

Automated Stations

Automated control stations are used in situations where all functions are known and unexpected or unanticipated interference is very unlikely. All the functions are computer-controlled, and operator adjustments require reprogramming. This type of system has limited applications in decommissioning programs.

6.3.3 Communication and Power Links

Communication links may be of two types: radio-controlled or hard-wired. For multi-terrain robots, radio control makes sense, because hard-wired communication links limit the distance the robot can travel and may affect its overall performance, and unexpected field conditions may result in the robot becoming trapped by its own hard-wired umbilical.

When remote equipment travels a prescribed path only, hard-wire technology makes sense. These systems include cranes, hoists, bridge-mounted manipulators, and some inspection robots. Stationary systems like master-slave manipulators, wall- and pedestal-mounted electromechanical manipulators, and industrial robots are inherently hard-wired. The hard wiring can be one of several different methods or even a combination of methods. These methods include bus bar, festoon, umbilical, and flat cable systems.

The only control system that does not require a communication link is the automated station. The automated station can have all control functions located onboard. However, if the environment in which the robot operates is sufficiently hazardous, it may be wise to locate the controller in a safe environment and to establish a communication link to the robot.

Typically, radio-control units use onboard batteries, engines, or fuel cells as a power source. Hard-wired control systems usually use a hard-wire technology to provide power to the remote.

6.3.4 Support Platforms

The support platform is the base from which all remote activities are carried out. The platform includes all auxiliaries and housekeeping equipment required to keep the remote operation

functioning in a hazardous environment. Among the items required on the platform are the hardware (to transmit power from the source to the tool), monitoring devices (to control movements of the tool), and any onboard equipment for movement. There are two classes of support platforms: stationary and mobile.

Stationary platforms cannot move and must be placed in position by other equipment. Examples of this kind of remote equipment are platforms for cutting up a single component, from small tanks to large reactor internals. The platforms typically have the tools extending in only one direction from the platform, either completely above or completely below the platform.

Unlike stationary platforms, most of the equipment installed on a mobile platform is dedicated to performing the navigation and movement of the platform. Under the direction of the operator, the mobile platform moves from the vicinity of the control station into the hostile environment to perform the decommissioning task.

6.3.5 Arms

The arms of a remote system provide positioning and orientation of the end effector or tool in relationship to the work. Three different classes of arms include existing equipment, robots, and specially systems.

Existing Equipment

Existing equipment sometimes includes remotely operated cranes, master-slave manipulators, and electromechanical manipulators. They would only be used in facilities where this equipment is available and in operational order. Given the selection of current robotic and mobile equipment, there is very little reason to install this type of fixed equipment for a decommissioning project.

Robots

A robot can be defined as a re-programable, multifunctional manipulator designed to move materials, parts, tools, or specialized devices through variable program motions. Emphasis is placed on the reprogramable and program portions of the above definition. These types of robots pertinent to decommissioning include the following:

- Automated or flexible manufacturing robots: these “industrial” robots are employed in a wide range of manufacturing processes, including assembly and inspection, material handling, welding, and material painting
- Remote-exploration robots: this type of robot is designed to survive in environments that humans cannot tolerate (remote-exploration robots to examine tank interiors, cooling tower basins, larger service piping, and sewers)
- Hazardous material handling robots: robots of this type have been employed to remove bombs and handle hazardous materials and are similar to the other two, but usually incorporate a cargo hold in their configuration, which may be armored or have a criticality-safe geometry

The geometrical configuration of robot arms usually falls into one of the following categories:

- Cartesian (rectangular)
- Cylindrical
- Spherical (polar)
- Revolute (articulated)
- Tensor-arm (snakelike)

The cartesian-geometry arm consists of three linear motions that correspond to the cartesian coordinate system designation: X, Y, and Z. This geometry can provide extremely accurate motions, provide easy joint motion controls, and possess good obstacle-avoidance characteristics.

These robot arms require large structural frameworks and a large floor space in which to operate. They are usually more mechanically complex than other systems, because of the linear sliding motion of the joints.

The cylindrical-geometry arm consists of two linear motions and a rotary-type motion. The two-linear-axis design makes the mechanical system less complex than in the cartesian-geometry configuration. The arm has good joint motion control and collision-free movement. It is less accurate compared to the cartesian geometry, yet requires a large support structure.

The spherical-geometry arm consists of two rotary motions and a single sliding (telescopic) motion.

This geometry provides the lightest-weight construction and minimizes structural complexity. It also provides short joint travel for each motion.

However, the system has limited ability to avoid collisions with workplace obstacles. Because of the two rotary motions, position errors can be comparatively large, and the arm can have counterbalance problems created by large and variable torque on the second and third joints.

The revolute geometry arm is a humanoid-type arm with redundant degrees of freedom. The arm has the flexibility to reach over or under workplace objects, but has limited obstacle-avoidance ability. It also usually has poor resolution and accuracy relative to positioning and can have counterbalance problems. This geometry has a high moment of inertia and is subject to gravity effects. Dynamic instability can be a problem.

The tensor-arm can take any shape in three-dimensional space. It is constructed from many sub-elements that can move with respect to their adjacent elements.

Speciality Systems

Remote speciality systems form a separate class of remote equipment. Typically, these systems are designed to perform one task, like removing fuel pin assemblies from the reactor core or closing a 50 tons shield door. Material-handling speciality systems are usually amenable for use in a decommissioning effort. When these systems are available, their use should be considered in the overall decommissioning plan.

6.3.6 End Effectors and Tools

The objective of the remote operation is to perform some decommissioning task. This task is ultimately accomplished by the tool that is attached to the remote unit. Almost any tool identified in this book can be incorporated into the remote unit. Specifically, all demolition tools

and mechanical decontamination tools, most chemical decontamination tools, and some waste treatment techniques can be incorporated into the remote equipment.

In addition to the tools that have been previously described, manipulator systems can be designed with end effectors (grippers). Some systems allow these effectors to be “changed out” during the operation, to provide flexibility of use in the system.

6.4 Illustrative Experiences with Remote Applications

The following sections present examples of remote applications to decommissioning projects. The examples cover detection equipment, segmenting equipment, decontamination equipment, material-handling equipment, sampling equipment, hand-held equipment, and miscellaneous equipment.

6.4.1 Detection Equipment

Five projects that use remote detection equipment under circumstances that prohibit human entry are described in the following paragraphs. These projects are at the Idaho National Engineering Laboratory (INEL), SRS, French nuclear program, Nine Mile Point Nuclear Station, and Shoreham Nuclear Power Station.

INEL High-Level Waste Tank Farm Project The new high-level waste tank farm at INEL, which currently is under design, includes provisions for remote operations, including robotic inspection of the tanks’ interiors and exteriors.

The primary method of inspection is visual to detect slow seepage in the tanks. If seepage is detected during the visual inspection, additional inspections are performed remotely using an ultrasonic transducer.

Remote Radioactive Waste Drum Inspection (SRS) SRS is committed to reducing potential personnel exposure to radiation in its programs. Currently, large numbers of drums containing dry radioactively contaminated waste are stored at various sites awaiting final processing. These drums must be inspected as part of routine site operations and in compliance with federal regulations. An autonomous mobile robot is being developed to perform remote surveillance and inspection of these drums. The robot will be self-guided through narrow storage aisles and will record the visual image of each viewable drum for subsequent off-line analysis and filing.

Robotic Devices for Pipe Inspection Electricité de France has designed and developed remote devices that allow televisual inspection of the insides of water and steam lines. One of the systems developed is a small tracked vehicle, equipped with an onboard television camera, floodlights, and an umbilical data link and power system. The second system developed is a push-pull system that provides repair services to sections of the lines requiring maintenance.

Mobile Surveillance System The Surveyor Mobile Surveillance System, a remotely operated vehicle at Niagara Mohawk Power Corporation’s Nine Mile Point Nuclear Power Station, measures radiation, temperature, and relative humidity. It also provides optical inspection capabilities.

Shoreham nuclear power station termination survey The Shoreham Nuclear Power Station contains more than 8,000 ft. of embedded pipe ranging in diameter from 1 to 12 in. Some of the runs were in excess of 60 ft. in length.

The pipe was believed to meet the release criteria. A technique was developed to survey the lines in place to demonstrate compliance with the release criteria, rather than trying to cut the lines out of the concrete.

Two fixtures were made, one for lines with inside diameters of 3 in. or more and the other for 1.5- and 2-in. lines. The larger fixture consisted of six GM “pancake” probes and a television camera mounted onto a carriage to facilitate in-line transport. The detector for the smaller probe was a thin-end window GM tube. The television inspection and radiation measurements were done separately for the smaller lines, because doing them simultaneously was found to cause delays. The detector packages were pulled into and out of the lines by cable, since both ends of each piece of embedded pipe were made accessible. For the longer pipes the detector package was inserted once from each end, to enable it to measure the full embedded length.

6.4.2 Sampling Equipment

At the containment structure Sarcophagus at the fourth unit of the Chernobyl Nuclear Power Station, pairs of robots are used to gather sampling data. The first robot, equipped with a video camera, observes the motion of the second, which carries the main equipment. The first robot remains stationary until the second robot travels a certain distance, and at this time, the observation robot proceeds further. The robots continue in this way to the intended destination, while they are continuously observed and controlled by an operator. The second robot drills boreholes and collects samples under concrete and rubble up to 600 mm deep. This robot is equipped with a special electromechanical system that includes a drill bit, bore extensions, a servo mechanism for rotational or impact drilling, a bore extension feed mechanism with automatic drill pressure support, and a special plastic tube designed to accept and store core samples.

6.4.3 Hand-Held Equipment

Chernobyl’s Sarcophagus was completed in November 1986. An isolation and recovery program was commissioned a year later, and its emphasis was on locating and characterizing the site’s fuel. Bore holes were established to accommodate special inspection periscopes, photographic and video cameras, thermography equipment, and neutron and gamma detectors. These hand-held systems are of primary importance to cleanup at the Chernobyl plant.

6.4.4 Miscellaneous Equipment

The Shippingport Station Decommissioning Project provided access to the walls and superstructure of the Fuel Handling Building using a cherry-picker mounted on a bridge crane. The fuel handling canal occupied the main portion of the center of the building; and there was scarcely room to walk between the canal and the walls, so erecting scaffolding would have been difficult and time consuming. The fuel handling equipment was removed from the bridge and

a cherry-picker installed. In this configuration, workers were able to reach the entire inner surface of the building for the full length of the canal. Although the system was not entirely remotely operated, it provided an example of the variety of applications possible. Remotely operated systems, whether entirely or partially remote, help equipment to become more flexible for difficult tasks.

7 Spent-Fuel and Waste Management

7.1 Spent-Fuel Interim Storage

Depending on a number of conditions and considerations, two options are available for spent-fuel management: reprocessing and direct disposal; a third option (partitioning and transmutation, P&T) is today in an early R&D stage, and could be available in the future. A flow chart describing the two available strategies is shown in [▶ Fig. 13](#).

The disposal of spent fuel requires a first period of interim storage in the plant pool, a second period in interim dry storage and finally disposal in an adequate container.

Dry storage facilities were initially conceived as single-purpose facilities: buffer short-time (10–20 years) storage before transporting the spent fuel to reprocessing or final storage or interim centralized storage. Storage systems were not initially also qualified for transport off-site and, therefore, the spent fuel had to be transferred into transport casks at the time of off-site delivery.

Afterwards it became evident that it would be advantageous to avoid spent-fuel transfer from a storage system into a transport system at the time of its off-site delivery. This is because the transfer operation is always a complex operation, because there might not be enough space in the plant pool, or because the pool does not exist at all, since the plant has to undergo a decommissioning operation. Generally metallic casks are well suited for the double function (storage and transport), since they are mainly transport casks with additional design provisions

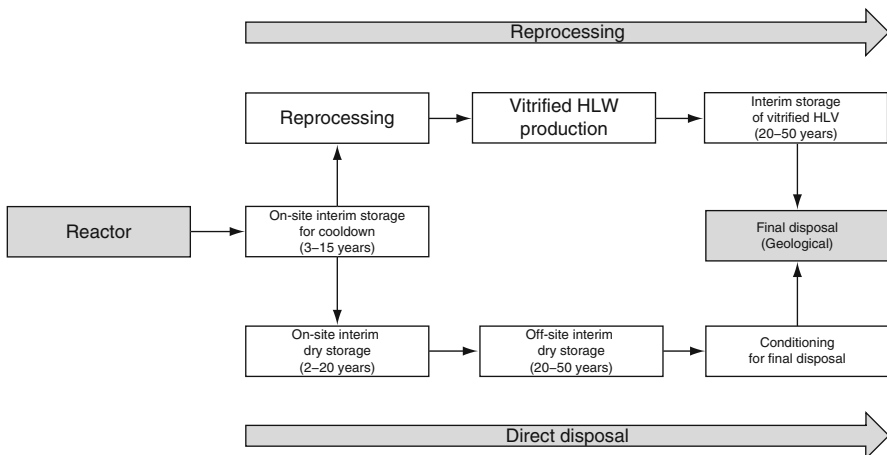


Figure 13
Spent fuel management alternative strategies

to enable them to remain in long-term storage. However, some other technologies have also developed special systems to allow off-site transport without transferring the spent fuel.

Recently in the USA, multipurpose systems have also been proposed, i.e., containers that would be qualified for on-site storage, transport, and final geological disposal. The qualification, of course, would require knowledge of the technical requirements of geological disposal and the acceptability of final disposal without spent-fuel conditioning. For these reasons, in Europe there is, at the moment, no container which is intended to be multipurpose.

At the same time, on-site storage periods became longer and longer, since both interim storage facilities and disposal sites were either not available or delayed (e.g., the case of the Yucca Mountain site for final disposal and the German case of Gorleben). Also for these reasons, the licenses have been requested for longer periods, up to 50 years. Moreover, there are research programs to check the limiting storage time for these systems, identifying the expected degradation in the storage components and in the spent fuel itself for up to 100 and even 300 years. The first results show that there are no strong indications of degradation for any components. It is therefore expected that in the future licensing for these systems can be extended.

7.1.1 Wet Interim Storage

For a long time, this was the only way to store the spent fuel of power reactors after their defueling. Each nuclear power plant with LWRs has a pool with different sizing criteria, but with at least enough space to store in adequate racks the spent fuel produced in 10 years of operation plus a full core in case of the need to completely defuel the reactor.

The water of the pool has both the function of removing the decay heat through cooling systems and of beta-gamma and neutron shielding. The shielding function requires a minimum depth of several meters.

In many cases, the need of spent fuel storing exceeds the former design values. This may happen mainly in relation to the difficulties experienced in most countries in sending the fuel to reprocessing or to a final disposal site. This need generally does not apply to a decommissioning phase, because at the time of the final shutdown, it is needed only to defuel an entire core and the lodgments in the racks that will always be available for an entire core. In addition, at an early stage of decommissioning, it is necessary to remove the spent fuel from the pool to proceed with dismantlement.

However, if an extension of wet storage capacity is needed, several alternatives are available, including:

- Recovery of spent-fuel pool capacity by removal of non-fuel items
- Re-racking (i.e., increasing the fuel-assembly density, with added poisons, in the racks)
- Rod consolidation
- Trans-shipping of spent fuel to another existing pool with free space available
- Construction of an additional spent-fuel storage pool

Pool Re-Racking

Subcriticality was originally maintained for LWR spent fuel (without credit to burnup) by spacing it in the storage racks or baskets. However, with the need to store greater quantities of fuel, higher storage density has been achieved by the introduction of neutron-absorbing materials in storage racks and baskets such as borated stainless steel or Boraflex. Re-racking has been often

considered the first choice and the least-cost alternative for expansion of at-reactor spent-fuel storage capacity. Some utilities have done so several times.

Adoption of neutron-absorbing materials increases rack costs and must be considered with care, taking account of existing operating experience. For example, some applications of Boraflex in existing racks have caused severe problems due to the contraction of such material under heavy irradiation and some consequential concerns have arisen about the maintenance of subcriticality calculated safety margins.

Long and very long wet storage is not really an issue for fuel and fuel cladding. Some zircaloy clad fuel has been wet-stored satisfactorily for over 40 years. In this case, care should be taken to maintain the required quality of the pool water.

Spent-Fuel Consolidation

Rod consolidation involves the disassembly of the intact fuel assembly (FA) by removing the fuel rods from the assembly hardware (shrouds, grids, etc.) and reconfiguring them in a metal storage container. Fuel-rod volume reduction of up to a factor of 2 has been achieved placing the rods from two FAs into a container not larger than a single assembly. After the fuel rods are removed, the non-fuel bearing components (i.e., end fittings and spacers) can be compacted and placed in a separate container. In the latter case, a volume reduction ratio of 6:1 can be accomplished.

Spent-fuel consolidation demonstration programs have been conducted in the US (Oconee, Main Yankee, West Valley, Battelle Columbus, Millstone 2, and Prairie Island), but no utility has yet proceeded with rod consolidation on a full-scale basis. Reasons for the lack of interest include:

- Need for license amendment to address criticality issues
- Seismic and structural analysis for the increased loads associated with storing consolidated fuel
- Thermal hydraulic analysis to demonstrate the capacity of the pool cooling system to provide adequate coolant flow to remove decay heat from the consolidated fuel canisters
- Increase of release of corrosion products (crud) during the consolidation operations, with consequent spent-fuel pool visibility problems and increase in duty and cost of pool water clean-up system
- Possible increase in worker exposure due to crud and failed fuel fission product release

Independent Wet Storage Pool

Independent, or away-from-reactor (AFR), pools are basically similar to at-reactor (AR) pools. They receive fuel from AR pools in either wet or dry transport canisters and store it in stationary racks or movable baskets.

A wet storage facility may have the following features:

- Cask reception, decontamination, unloading, maintenance, and dispatch
- Underwater spent-fuel storage (pool)
- Auxiliary services (radiation monitoring, water cooling and purification, solid radioactive waste handling, ventilation power supply, etc.)

Usually this solution is reasonable for large quantities of spent fuel (usually for many reactors) and in a situation where an intensive nuclear program is underway and will be maintained for

a long time. In addition, also in relation to the high operational costs, it is considered a rather short-term buffer system for more long-term solutions and/or for reprocessing. For example, there are AFR pools in all reprocessing plants.

7.1.2 Dry Interim Storage

Since the 1980s, the technologies of dry storing spent fuel, after an initial cool-down in a pool, have been gradually introduced for several applications.

This overview focuses on solutions already licensed and operated for storing spent nuclear fuel in an inert, dry environment. The feasibility of dry storage has been essentially demonstrated for all types of spent fuel. All types of storage concepts (metal casks, modular vaults, concrete casks, concrete silos and concrete canister-based storage systems) have exhibited good performances. The most significant concepts are outlined below.

Dry storage facilities can be AFR or at-reactor AR. Dry storage alternatives include:

- Metal casks
- Concrete casks
- Vaults
- Concrete modules

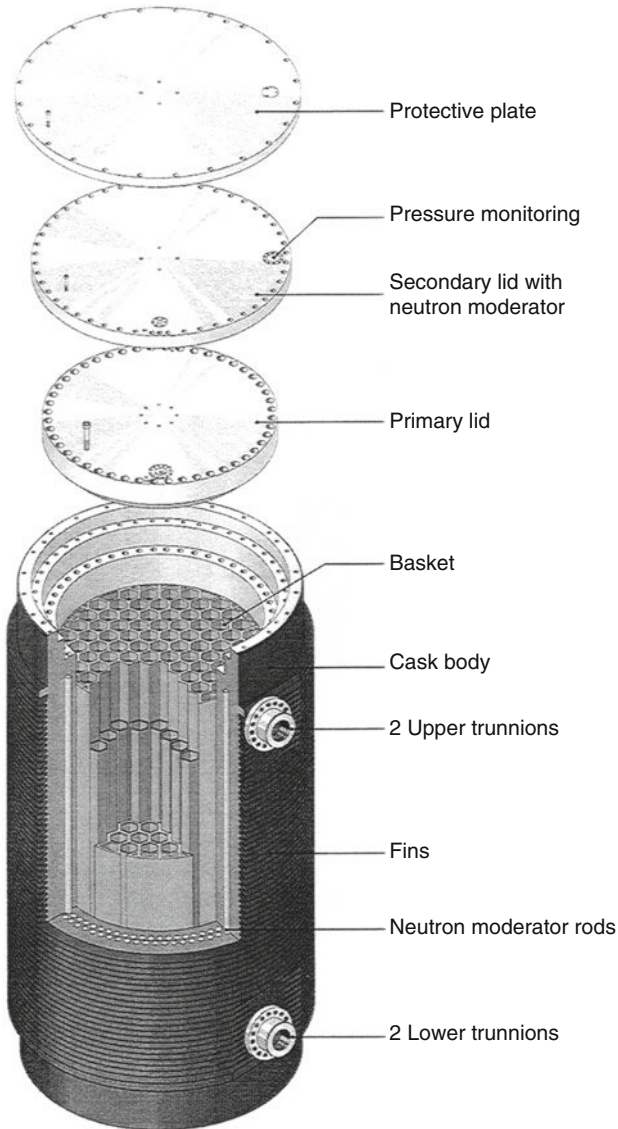
Metal Casks

Metal casks are massive containers used in the transport, storage and eventual disposal of spent fuel. The structural material for the metal casks may be forged steel, nodular cast iron, or a steel/lead sandwich structure. They are fitted with an internal basket or sealed metal canister, which provides structural strength and also assures subcriticality. Metal casks may have a single or a double lid, generally bolted. In any case, they have a double seal and the volume between the seals is monitored for leaks.

Metal casks are usually transferred directly from the fuel loading area to the storage site. Some metal casks are licensed for both storage and off-site transportation. Fuel is loaded vertically into the casks, which are usually stored in a vertical position. As an example, in [Fig. 14](#) and [Table 31](#) the main characteristics of the metal cask CASTOR 440/84 supplied by GNB are given.

In general, metal casks are expensive components. However, they provide the maximum flexibility, since, if they are licensed also for transport, they can be moved off-site without any further direct handling of the fuel and without leaving structures to be decommissioned. For limited quantities of fuel (e.g., up to 500 tons HM) they may also be economically advantageous. Another advantage is that they are highly modular and the supply may be adapted temporarily to the need. In the total cost, expenses for a storage building should be included.

Metal casks are used in a number of countries such as Germany, the USA, the Czech Republic, Switzerland, Spain and Italy. In Europe, most of the casks are licensed for both storage and transport. They are protected from all design accidents (air crash included), and can be stored indoors or outdoors. In the USA, casks are usually stored on a concrete pad in the open air. In most countries they are hosted in a dedicated building. A typical layout of these buildings is presented in [Fig. 15](#). Major functions of these buildings are to contribute to shielding and to enhance air circulation.



■ Figure 14
CASTOR 440/84 type metal cask (GNB)

Vaults

A vault (► Fig. 16) is an above- or below-ground reinforced concrete building containing arrays of storage cavities suitable for containment of a number of fuel units. Shielding is provided by the exterior structure. Heat removal is normally accomplished by forced or natural convection of air or gas over the exterior of the fuel-containing units or storage cavities, and subsequently exhausting this air directly to the outside atmosphere, or dissipating the heat via a secondary heat-removal system.

■ **Table 31**
CASTOR™-440/84 metal cask parameters

Max heat output	21 kW
Max enrichment	3.65%
Max burnup	42 GWd/tU
Typical cooling time	60 months
Cask length	4.080 mm
Cask diameter	2.660 mm
Wall thickness	370 mm
Cask body material	Ductile cast iron
Lid material	Stainless steel
Mass of transport configuration	131 tons

Typical features of the vaults are their modularity, which facilitates incremental capacity extension, separate shielding and containment functions, capability for containment monitoring, and a vertical fuel loading methodology.

Spent fuel is received (either dry or wet) at a vault facility using transfer or transportation casks. Spent fuel is removed from the cask, prepared for storage if needed, and placed in a metal storage tube (single fuel element) or a storage cylinder (single or multi-element canister) which is housed within a concrete storage cavity in the vault structure. The storage tubes or storage cylinders are sealed and may be backfilled with an inert gas to improve heat transfer from the fuel and prevent oxidation of spent fuel while in storage. They are usually fitted with connections to a continuous or periodic monitoring system.

In vaults using metal storage tubes, fuel assemblies are dried, as necessary, and transferred one by one directly into their storage locations. Typical components of this type of storage facility are the vault modules, the fuel handling machine operating in the charge hall, the cask receiving area and the auxiliary facilities (areas for plant control, maintenance, services, offices, etc.).

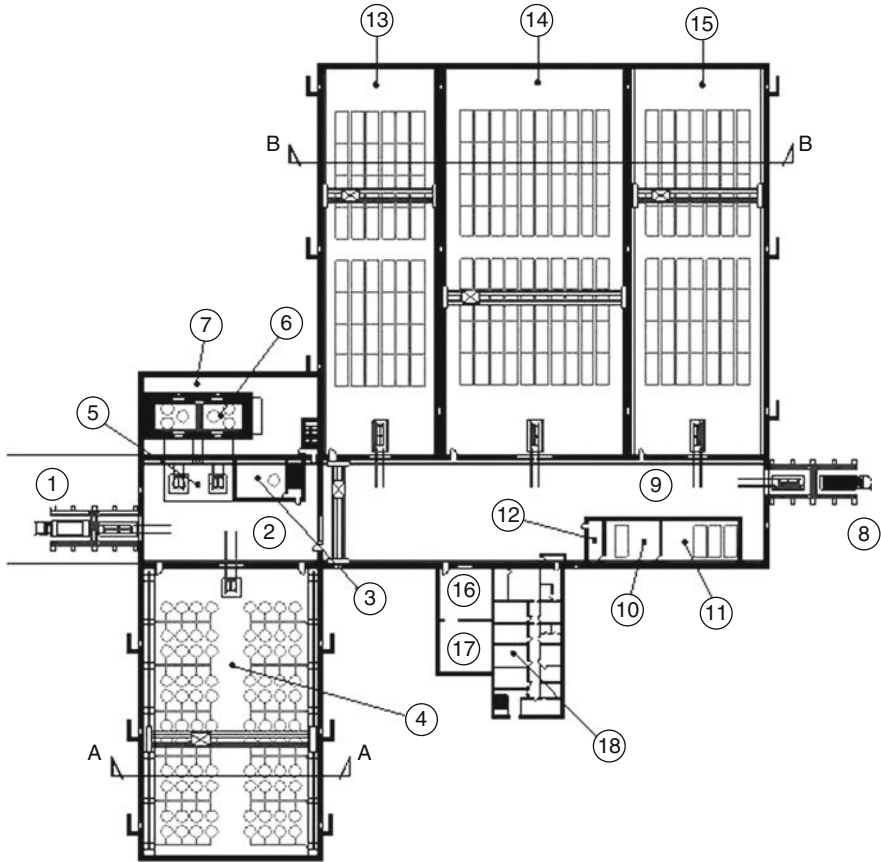
Single tube vaults are in place at Paks NPP in Hungary and at Wylfa NPP in the UK.

Storage-cylinder vaults receive the fuel already sealed in containers. They are used at Gentilly-2 in Canada (CANSTORE application of the MACSTORE system), the CASCAD facility in France, and Fort St. Vrain in the USA.

Generally, vault facilities are more advantageous for large inventories of spent fuel, since they require a number of auxiliary systems. They also need some efforts to be considered for decommissioning. One advantage is that they can be built in modules (all expenses for auxiliary systems are, however, upfront), and that the facility is completely independent of NPP facilities, since it can also provide necessary equipment for off-site transportation of the fuel in transport casks.

Concrete Casks

Concrete casks are movable structures with one storage cavity. They are used in the storage and, in some cases, transport of spent fuel. Structural strength and radiological shielding are provided by reinforced concrete or high-density concrete.



Spent fuel and vitrified waste section:

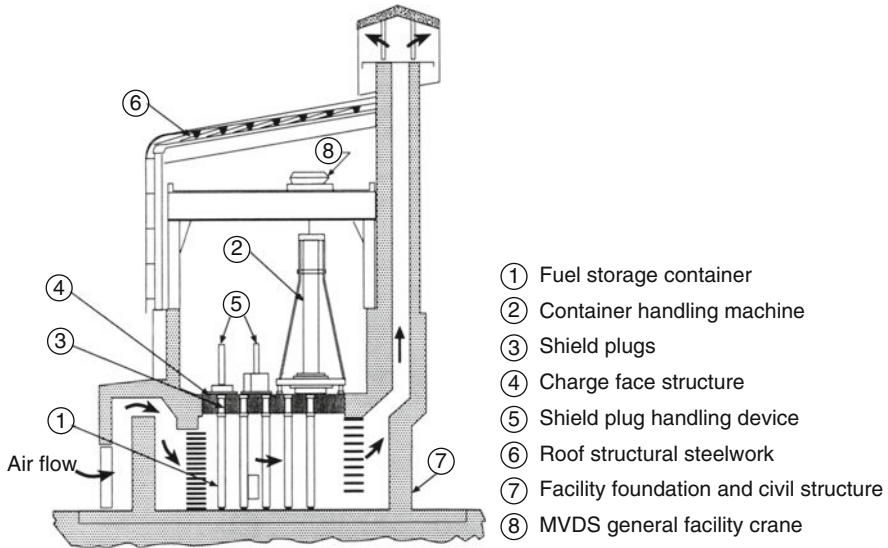
1. Loading and unloading zone
2. Reception zone
3. Testing and preparation zone
4. Storage hall
5. Hot cell input zone
6. Hot cell
7. Hot cell control hatch

Other radioactive waste section:

8. Loading and unloading zone
9. Reception zone
10. Testing zone
11. Out-of-standard storage hall
12. Laboratory
13. Storage hall no. 1
14. Storage hall no. 2
15. Storage hall no. 3
16. Workshop
17. Warehouse
18. Housing and offices

■ Figure 15

Combined waste and cask storage building (SOGIN-SRS)



■ **Figure 16**
Typical vault facility (NRC)

Concrete cask systems generally use sealed metal canisters housed inside the concrete storage cask to contain spent fuel. The metal canister may be cooled by natural convection of environment air and use a double-lid closure system.

Sealed metal canisters may be contained in an on-site transfer cask for loading spent fuel from the fuel loading station and for transfer to the concrete storage cask. Spent fuel may be loaded directly into a concrete cask in the fuel loading station and the concrete cask may be transferred directly to the storage site. Some sealed metal canisters may be licensed for transportation as part of an off-site transportation package.

Alternatively, concrete cask systems may use a metal liner in the cask cavity to contain spent fuel and a single lid closure system. Heat transfer may take place solely by conduction through the concrete structure.

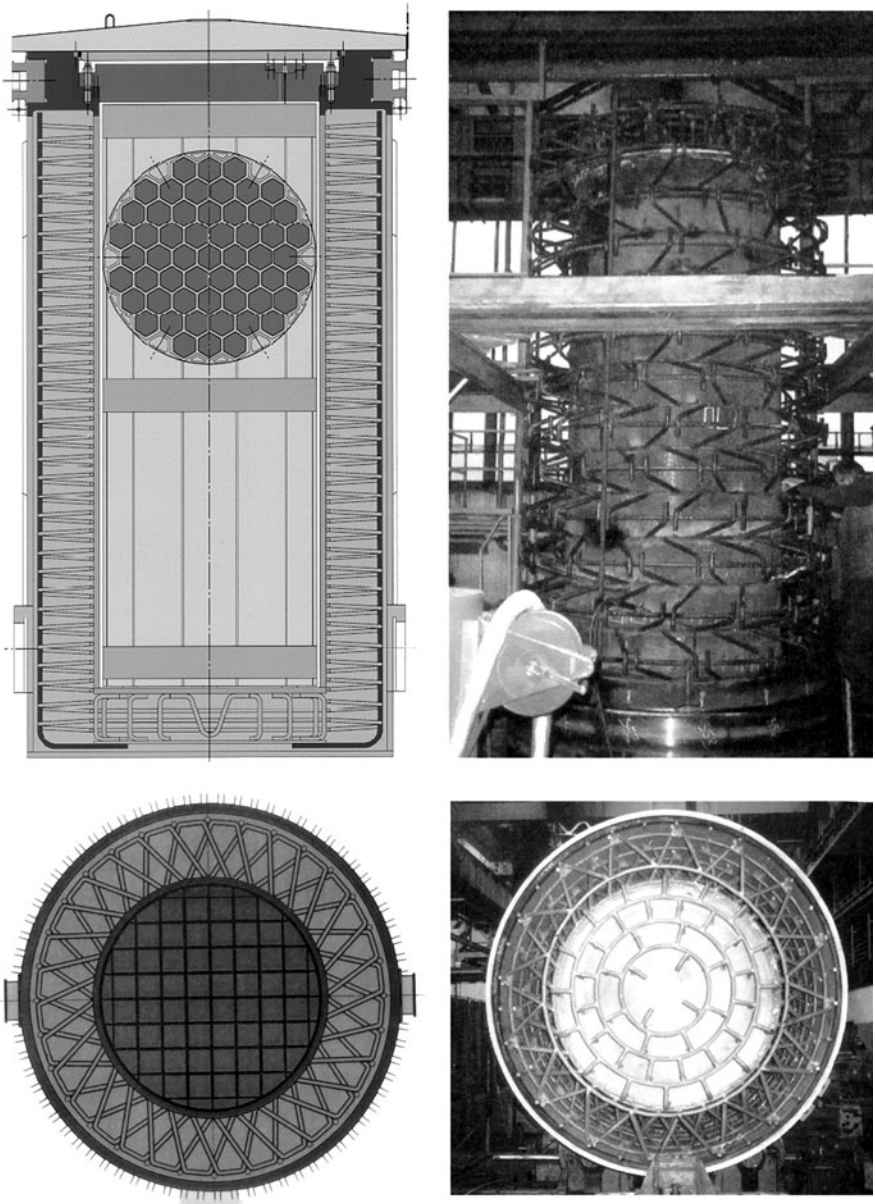
Concrete casks that rely on conductive heat transfer have more thermal limitations than those using natural convection air passages.

Fuel is loaded vertically into the concrete casks and the concrete cask systems are stored in a vertical orientation.

Concrete casks use single or double lid systems, are welded closed and tested for fuel tightness. Concrete cask systems may, or may not be monitored for fuel tightness.

Examples of vertical concrete casks include the Sierra Nuclear VSC cask and Ontario Hydro's Pickering concrete dry storage container, which is also designed for off-site transport.

GNB developed CONSTOR casks (● *Fig. 17*) for VVER and RBMK fuel, which are made of a material sandwich. It consists of an outer steel shell, a reinforced heavy concrete layer and an



■ Figure 17
Conceptual schemes and construction phases of a CONSTOR 440/54 concrete cask (GNB)

inner steel shell (40 mm/340 mm/40 mm). The aggregates for concrete are 40% barite and 60% steel balls. Inside the concrete, steel reinforcement is arranged to improve the strength and heat removal properties. The lid system is designed as a multi-barrier system. The bolted primary lid performs strength and shielding functions. The sealing plate and the secondary lid are welded to the forged steel ring after loading and servicing the cask.

The CONSTOR can contain 54 fuel assemblies because the allowable heat input is reduced and may be licensed also for transport. Since it can be manufactured by conventional methods with conventional materials, its cost is significantly lower than that of the CASTOR metal casks. The CONSTOR version for VVER 440 fuel requires 7 years of cooling time, at an average burnup of 42 GWd/tons of HM and a maximum enrichment of 3.8%. The total mass of the loaded cask is 95 tons.

Concrete Silos

Silo systems are monolithic or modular concrete reinforced structures. The concrete provides shielding, while containment is provided by either an integral inner metal vessel (liner), which can be sealed after fuel loading, or by a separate sealed metal canister. In silos, spent fuel may be stored in vertical or horizontal orientation. Fuel loading into silos always takes place at the storage site.

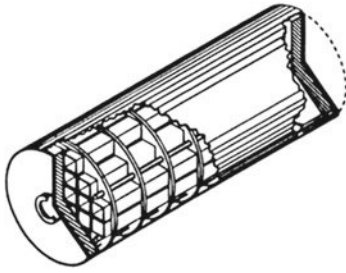
A typical example of a silo system is AECL's concrete canister, which is built on-site, using regular reinforced concrete, and is fitted with an inner steel liner. Spent fuel is transferred in increments in sealed baskets, using a shielded transfer cask, and loaded vertically. Once loading operations are complete, a closure shield plug is placed and welded to the inner liner, to provide additional containment.

NUHOMS Modular System

The NUHOMS (NUteck HOrizontal Modular Storage) is a family of dry storage facilities which are basically formed by a concrete structure into which metallic welded canisters are placed in horizontal position (► [Fig. 18](#)).

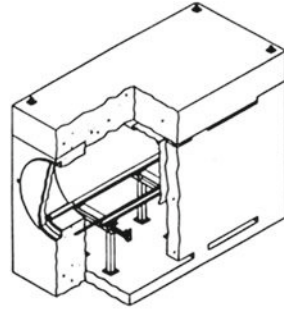
NUHOMS have been developed under the name of various companies (Nuteck, Pacific Nuclear, Vectra Technologies Inc.). Outside the USA, fabrication and commercial license have been granted to FRAMATOME. In 1998, Transnucleaire (a company 100% owned by the French COGEMA) purchased the NUHOMS system and created Transnuclear West, taking over all Vectra assets. So far, the NUHOMS system has been adopted only in the USA and in Armenia at the Medsamor plant. The main designs are known as NUHOMS-7P, NUHOMS-24P, and the standardized NUHOMS-24P/52B (where P stands for PWR fuel, B stands for BWR fuel, and the associated number stands for the quantity of fuel assemblies that can be stored in a single canister). Recently the Multi Purpose Canister (MPC) 187 has been approved by NRC, both for storage and for transport with the addition of an overpack.

The principal components of the NUHOMS are a stainless steel dry shielded canister (DSC) with an internal fuel basket, a concrete horizontal storage module (HSM) that protects the DSC and provides radiological shielding (overpack), a compatible transfer cask (TC) used to transfer the DSC from the spent fuel pool to the HSM, and a hydraulic ram system (HRS) used to insert the DSC into the HSM and TC (see ► [Table 32](#)).



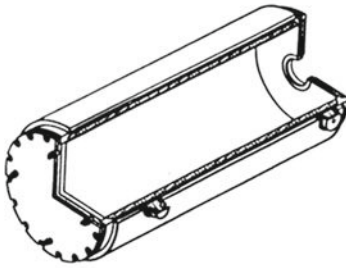
Canister

Provides containment and structural support for the fuel assemblies



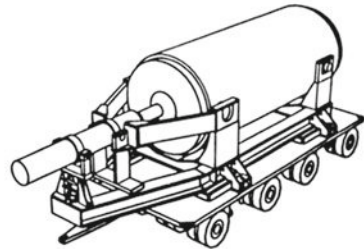
Storage module

Provides shielding, physical protection and cooling for the canister during long term storage



Transfer cask

Provides shielding and physical protection for the canister during transfer from the plant to the dry storage facility



Transporter

Transfers the cask and the canister from the plant to the dry storage facility

■ Figure 18

Main components of the NUHOMS system

7.2 Waste Management

7.2.1 Overview

Waste management in decommissioning activities concerns the treatment, conditioning, handling, storage, transport and disposal of the primary and consequential waste streams.

The wastes arising from decommissioning operations fall into categories that are defined principally by the methods employed to prepare the wastes for disposal.

Liquid waste encompasses contaminated liquids, usually dilute acidic or alkaline solutions, and materials bearing significant quantities of liquids such as sludges, ion-exchange media, and concentrates from evaporators and membrane separators.

Dry solid waste encompasses those wastes that do not contain any unbounded liquids, and includes both combustibles and noncombustibles. There may also be some gaseous effluents deriving from decommissioning, such as tritium and other aerosols.

The salient consideration in all waste management processes is that the applicable safety and radiological protection regulations must be complied with. The secondary objectives are to minimize the volume of material requiring disposal, to minimize the mobility of the radionuclides

■ Table 32

Design parameters for NUHOMS™ storage systems

	Site specific licenses		Standardized NUHOMS™	
	NUHOMS™ 7P	NUHOMS™ 24P	NUHOMS™ 24P	NUHOMS™ 52B
Initial enrichment ²³⁵ U	3.5	4	4	4
Burnup (MWd/tons HM)	35,000	40,000	40,000	35,000
FA per DSC	7 PWR	24 PWR	24 PWR	52 BWR
DSC length (m)	4.6	4.7	4.7	4.7
DSC diameter (m)	0.9	1.7	1.7	1.7
DSC shell thickness (cm)	1.3	1.6	1.6	1.6
HSM length (m)	5.9	6.1	6.1	6.1
HSM height (m)	3.7	4.6	4.6	4.6
HSM width (m)	1.7	2.7	2.7	2.7
HSM concrete walls and roof thickness (cm)	106	91	91	91
HSM concrete interior walls thickness (cm)	61	61	61	61
Transfer cask length (m)	4.60	4.75	4.75	4.75
Transfer cask diameter (m)	0.95	1.7	1.7	1.7

contained in the wastes, and to segregate the wastes by the type of radioactivity contained (alpha-bearing, non-alpha-bearing, low-, intermediate-, or high-activity-level). The purpose of minimizing waste volume and mobility and segregating wastes is to achieve an optimum combination of safety and economic disposal.

The likely sources of and the types of treatment and conditioning appropriate for liquid, solid, and gaseous radioactive wastes resulting from decommissioning are discussed in the following subsections. Also discussed are the factors involved in the selection of appropriate packaging, the methods of transport available, the factors involved in the selection of the proper disposal facility for the various waste types, and the possible release of decontaminated materials.

The wastes related to plant decommissioning derive only from the structures of the plant, which are irradiated or contaminated.

For irradiated materials, such as the reactor vessel, only a decrease of the natural radioactivity and appropriate shielding can reduce the irradiation. This explains the option of deferred decommissioning, by which the worker dose is reduced. Contaminated materials are first decontaminated before being dismantled.

These two solutions are recalled to highlight that the main goal of those responsible for plant decommissioning is to reduce as much as possible the impact on workers, the public at large, and the environment.

Another selection criterion for wastes related to nuclear plant decommissioning is to consider low- and intermediate-level waste and very-low-level waste.

For the first category, the final disposal process is similar to that of operational waste, for which disposal sites usually exist as they are built first. The capacity of the disposal site has, of course, to take into account this additional quantity of waste. There exists also another option, which is to dispose of these wastes on-site temporarily or definitively, for example in one of the not dismantled controlled buildings. This depends on the decommissioning strategy adopted according to the country-specific strategies and plant-specific conditions.

For the second category of waste, the very low-level waste (VLLW), the problem to be solved is related to the large volume, even after decontamination. The volume of such waste is a function of the clearance of such waste. Clearance is “the removal of material from a system of regulatory control provided that the radiological impact of these sources after removal from the system is sufficiently low as not to warrant any further control.” The definition of this clearance will of course have an important impact on the quantities of waste to be stored as VLLW or that can be considered as conventional waste.

Two main policies exist for this definition. One uses a criterion linked to the activity level to be considered as a threshold, while the other uses a criterion linked to the origin of the waste: a controlled-area structure or building of the plant. There are, of course, pros and cons for each solution and finally the decision rests with the country’s authority in the framework of its policy. But the impact is twofold: the amount of waste to be stored, which depends on the country’s policy, but also the released material, which may travel from one country to another and may pose a problem of harmonization of the clearance levels.

But in both cases the technologies necessary for processing the waste from dismantling are the same as those used during plant operation life. They vary from waste minimization at source, by means of optimized management, to concentration, sorting, packaging and finally, at specific waste-processing plants, nitrification, bitumization, polymerization, cementation, incineration, etc.

All these technologies are designed for safe conditioning of the waste in order to reduce to negligible values the risk of dispersion and radiation. The only real major difference between operation waste and dismantling waste is the quantity. This means that adequate large repository sites have to be made available, in one or more decades, to store these large amounts.

From the country-specific situations, the following overview of existing or planned repositories can be summarized. In all industrial countries, solutions exist at least for interim storage of all categories of waste (low level, intermediate level, high level, short lived and long lived). Final disposal is mainly under investigation and experimentation, with various lead times (years or decades).

There is no open, unanswered scientific question, which would cast doubt on the demonstration and implementation of disposal concepts. Thanks to the intermediate storage solutions, there is no critical urgency to speed up these final disposal solutions. But, from a public acceptance point of view, it would nevertheless be advisable to start the demonstration and implementation of radioactive waste disposal in underground repositories as soon as possible. This would be of paramount importance in confidence-building for society and would jointly provide the possibility for scientific and technical developments.

7.2.2 Clearance Levels

The concept of clearance is defined by the IAEA as the removal of radioactive materials or radioactive objects within authorized practices from any further regulatory control applied for

radiation protection purposes. Conceptually, clearance is closely linked to exemption, which means the determination by a regulatory body that a source or practice needs not to be subject to some or all aspects of regulatory control, on the basis that the exposure (including potential exposure) due to the source or practice is too small to warrant the application of those aspects. However, clearance can be seen as the process of relinquishing regulatory control, while exemption is the process of deciding that no regulatory control is necessary from the outset.

Clearance is based on the concept of triviality of exposure, generally taken to mean:

- The radiation risks to individuals caused by the practice or source be sufficiently low as to be considered trivial
- The collective radiological impact of the practice or source be sufficiently low as not to warrant regulatory control under the prevailing circumstances
- The practices and sources be inherently safe, with no appreciable likelihood of scenarios that could lead to doses above dose limit. In quantitative terms, this is generally related to the stipulation that the effective dose expected to be incurred by any member of the public due to cleared materials is of the order of 10 μ Sv or less in a year

It is implicit in the concept of clearance that materials, once cleared, are subjected to no further regulatory restriction or control. Consequently, cleared waste may be treated as normal waste; and materials cleared for reuse or recycling may be sold or transferred to any other party and used for any purpose without being considered to be radioactive.

This, however, does not preclude the concept of clearance for a specific purpose, often referred to as “conditional clearance,” i.e., the case where a certain condition has to be fulfilled before the act of clearance has been completed. Examples for “conditional clearance” are clearance of metal scrap for melting only (i.e., not for direct reuse), clearance of buildings for demolition only (i.e., not for reuse), or clearance of material for disposal on conventional landfill sites. After this condition has been fulfilled, the material is also subject to no further regulatory restriction or control.

Clearance levels that have been calculated with the radiological models presented in [▶ Sect. 3.2](#) are summarized in [▶ Table 33](#) for a set of radionuclides. These radionuclides are relevant in reactor and fuel cycle facilities and represent various groups of nuclides, such as weak beta emitters (^3H , ^{14}C , ^{63}Ni), strong beta/gamma emitters as activation and fission products (^{60}Co , ^{137}Cs), strong beta emitters (^{90}Sr), and alpha emitters of different origins (^{235}U , ^{241}Am , ^{239}Pu).

The first two rows of [▶ Table 33](#) relate to unconditional clearance from the two recommendations RP 122 part I of the European Commission (2000b) and RS-G-1.7 of the IAEA (2004j). Both documents contain a set of rounded clearance levels that are based on different scenarios and assumptions, but resulting in quite similar values. RS-G-1.7 has a slightly more conservative tendency, as these values are not merely meant as unconditional clearance levels, as is pointed out in the following: “The Safety Guide includes specific values of activity concentration for both radionuclides of natural origin and those of artificial origin that may be used for bulk amounts of material for the purpose of applying exclusion or exemption. It also elaborates on the possible application of these values to clearance.”

The third row in [▶ Table 33](#) provides the clearance levels from RP 89 (European Commission 1998a) for metal scrap for melting. In comparison with the values from RP 122/I, they are generally the same or larger, indicating that a smaller, and, therefore, less restrictive set of scenarios has been used.

■ **Table 33**

Clearance levels for some radionuclides

Purpose	³ H	¹⁴ C	⁶³ Ni	⁶⁰ Co	¹³⁷ Cs	⁹⁰ Sr	²³⁵ U	²⁴¹ Am	²³⁹ Pu	Unit
Unconditional clearance, RP 122/I	100	10	100	0.1	1	1	1	0.1	0.1	Bq/g
Unconditional clearance, RS-G-1.7	100	1	100	0.1	0.1	1	–	0.1	0.1	Bq/g
Metal scrap for recycling or reuse, RP 89	1,000	100	10,000	1	1	10	1	1	1	Bq/g
Building rubble, RP 113	100	10	1,000	0.1	1	1	1	0.1	0.1	Bq/g
Buildings for reuse, RP 113	10,000	1,000	10,000	1	1	100	1	1	0.1	Bq/cm ²
Buildings for demolition only, RP 113	10,000	10,000	100,000	1	10	100	10	1	1	Bq/cm ²

Recommendations European Commission RP 122 part I and IAEA RS-G-1.7

Similar observations apply to clearance levels for building rubble, shown in the fourth row in ► [Table 33](#). These values are closer to those of unconditional clearance, as they also apply to large quantities and therefore need to be more conservative in nature.

The last two rows in ► [Table 33](#) provide clearance levels for buildings from RP 113 (European Commission 2000b). As they are expressed in Bq/cm², no direct comparison with the other sets of values is possible or meaningful. It can be observed, however, that the values for clearance of buildings for demolition only (i.e., where any reuse would not be permitted) are generally higher or equal to those for clearance without restrictions (i.e., for reuse or demolition).

7.2.3 Waste-Management Strategy

The waste management strategy should ensure that the generation, conditioning, and disposal of wastes from the decommissioning process is conducted in a manner consistent with the project, waste minimization and the acceptance criteria. This strategy is based on national and regional waste management regulations and also takes into account government policy. It generally includes items such as

- An estimate of the sources and types of waste, their physical and chemical characteristics, and the volume of each waste category, including the rate at which waste is generated
- Criteria for the restricted/unrestricted reuse or recycling of equipment or materials from decommissioning
- Criteria for segregating waste into various categories
- The plans and procedures for handling, treating, conditioning, storing, and disposing of each category of radioactive, nonradioactive and hazardous wastes from decommissioning
- Procedures for monitoring and recording radioactivity, including the monitoring of cleared wastes before unrestricted release, as well as taking and analyzing samples
- Requirements for packaging and package design for transport and disposal

- Identification of adequate storage and disposal routes and sites (in some cases the waste streams may not have readily available routes for conditioning, treatment, storage, and/or disposal or reuse)
- A safety assessment of the waste-management strategy

The waste-management strategy considers aspects such as the possible reuse and minimization of waste, including secondary waste, through the use of waste-minimization and volume-reduction techniques. Techniques that may be employed include, among others, decontamination, size reduction, process optimization and volume reduction, e.g., evaporation of liquids or compaction of solids. It is expected that several different waste streams will be generated during the course of decommissioning; these may need to be considered based on each case in the development, modification, and application of appropriate waste-management techniques.

The waste-management strategy addresses how the applicable waste acceptance criteria for disposal will be met. If wastes from restricted areas are to be disposed by landfill or similar methods, the means of demonstrating that the release criteria are met have to be specified and documented. If some wastes are to be released for unrestricted use, special monitoring and analysis procedures capable of measuring the very low levels of radioactivity that are specified for unrestricted release are of concern. For this purpose, an area with low background radiation may be required, so that the necessary measurements can be made and/or extensive sampling and counting in the laboratory can be performed.

7.2.4 Waste-Management Arrangements

Decommissioning operations, which produce radioactive wastes can only be initiated when well-defined waste-management arrangements have been made. In some situations, the final disposal of waste will be transferred to an organization different from the facility licensee.

The conditioning, packaging, and recording arrangements are formally agreed with the repository organization before the recovery and conditioning of any waste is commenced.

In addition, many facilities generate both radioactive and other hazardous wastes. The development of a plan for hazardous material characterization provides an important insight into the impact of these materials on treatment, conditioning, packaging, storage, and final disposal.

The procedures, processes, and systems to be used for handling, treatment, conditioning, storage, and disposal of radioactive wastes are defined.

If radioactive wastes are to be temporarily stored on-site, the quantities of wastes, expected length of storage, location of storage areas, radiation levels at access points, and manner in which control is maintained are defined.

The methods of managing radioactive wastes from decommissioning are, in general, similar to those used in other parts of the nuclear industry during operation, maintenance, and refurbishment of facilities. However, the huge volumes and characterization of the waste streams may require some modifications to the methods used.

In  *Fig. 19* the conceptual decommissioning waste routes are presented.

7.2.5 Treatment and Conditioning of Liquid Wastes

Liquid wastes that consist of large volumes of dilute solutions containing dissolved and/or finely divided contaminated material are usually treated to extract the contaminated material from

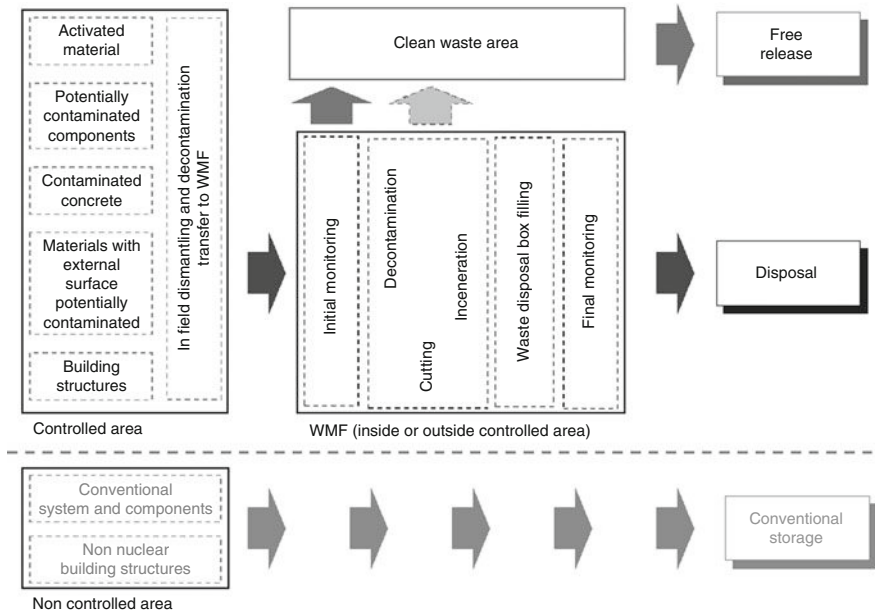


Figure 19
Decommissioning waste routes

the carrier solution, thus reducing the volume of material requiring further conditioning and disposal at a radioactive disposal facility.

The usual techniques for decontamination of liquid wastes are ion-exchange, filtration, membrane separation, and chemical treatment and evaporation. These techniques are used singly or in series combination, depending upon the characteristics of the solution being treated. The purified liquids resulting from these processes are usually decontaminated sufficiently so that discharge to the environment is possible after monitoring to ensure compliance with regulations.

Certain liquids used in some decontamination processes, such as phosphoric acid in electropolishing and organic solvents in surface cleaning, may require special treatment because of their specific chemistry.

The concentrated radioactive residues contained in the ion-exchange media, filters, or concentrator bottom liquids require conditioning to immobilize them. The immobilization required is accomplished by mixing the radioactive residues with a matrix material and subsequently solidifying the mixture within a suitable container. Matrix materials that have been and are being used include cement, bitumen, a variety of polymers (such as polystyrene, polyesters, epoxies, and urea-formaldehyde), glasses, and ceramics.

The choice of treatment and conditioning processes for a particular project will depend upon the following factors:

- Radiological and general safety considerations
- Technical requirements of the liquor streams
- Waste transport and disposal alternatives
- Economic considerations

The availability of appropriate liquid-waste treatment and conditioning processes at the facility may also be an important consideration in the selection of decontamination techniques for use on a specific project.

7.2.6 Treatment and Conditioning of Solid Wastes

Solid wastes arising from decommissioning operations consist principally of contaminated and activated structural materials and system components, including concrete, reinforcement and structural steels, graphite, stainless and carbon steels, and a miscellaneous assortment of other metals, rubber, plastics, and paper and other fibrous materials.

The principal objectives in the treatment and conditioning of solid wastes are:

- To minimize the waste volume in ways compatible with minimizing the mobility of the radioactive materials contained and the radiation dose associated with waste processing and handling
- To segregate the waste into groups according to the types of radioactive contaminants present to facilitate emplacement in the appropriate disposal facility
- To process and package the wastes in containers suitable for transport from the site and for disposal in the appropriate disposal facility
- To accomplish these actions in an economical manner

Treatment and conditioning of materials that are not combustible or compactable is generally limited to segmentation to facilitate packaging in standard types of disposal containers and to grouting within the containers when appropriate.

Treatment of combustible and compactable materials is usually accomplished using mechanical compaction and/or incineration. Compaction may be performed as the first step, followed by incineration, or it may be the only step, with the materials compacted within the shipping container. Numerous compacting devices are commercially available for compressing compactable wastes within steel drums or similar containers. Incineration of combustible wastes results in a concentrated waste form which requires further conditioning by immobilization in solidifying matrices, similar to those used with liquid waste concentrates.

Because of the radiological detriment aspects and, therefore, the higher cost of disposal of alpha-bearing waste (perhaps ten times more costly than beta-gamma waste), for certain waste sources there may be an incentive to segregate waste streams during the processing and packaging phase.

7.2.7 Treatment and Conditioning of Gaseous and Aerosol Wastes

Small quantities of tritiated water vapor are the most likely gaseous radioactive wastes to result from decommissioning operations. If necessary, removal of the tritiated water vapor from the ventilation air can be accomplished using selected adsorber material that is contacted by the air streams.

Aerosols containing finely divided radioactive materials are likely to result from the various cutting methods used during decommissioning. Similarly, some of the cutting methods will produce large volumes of potentially toxic smoke and fumes. In all cases, the use of contamination-control envelopes coupled with appropriate filters in the ventilation streams should be adequate to collect and retain the particulate material.

Treatment of the resulting solid wastes (adsorbers and filters) is accomplished as described in the previous subsection.

7.2.8 Packaging and Storing Technologies

The selection of the waste-disposal boxes to be used for off-site transport and disposal should take into account:

- Existing regulations
- Technical requirements
- Infrastructure aspects
- Radiological conditions
- Economical aspects

Technical requirements can be derived from the Authority or Agency that operates the final national repository. If no explicit indication on the type of repository has been provided by the competent authorities, the only requirements to be met are those included in the international standards and code of practices such as, for example, IAEA documentation.

Based on the experience acquired from the repositories currently operated worldwide, including their acceptance criteria, the following assumptions may be considered for cost estimating purposes:

- Low- and intermediate-level waste produced during the safe enclosure phase (SEP) preparation phase and releasable as nonradioactive waste during the subsequent SEP phase, is packaged in 20-ft. containers without any filling or conditioning material.
- LLW produced during the SEP preparation phase and not free releasable during the subsequent SEP phase, will be packaged in one of the standard waste disposal boxes listed in [▶ Table 34](#). Packaged wastes are then stored on-site in dedicated buildings or inside plant buildings, until the national repository is available. To store waste inside the plant, some removal of equipment is necessary.
- Low- and intermediate-level waste produced during the site release phase is placed in one of the waste-disposal boxes listed in [▶ Table 35](#), and disposed.
- Already packed low- and intermediate-level waste is transported in 20-ft. containers (about 50 200-l drums per container). The drums qualify as an industrial package.
- Medium- and high-contaminated materials are conditioned and packed in 200- or 400-l drums. The drums qualify as an industrial package.
- Highly contaminated or activated material is packed in 200-l drums, which can be used with shielded overpacks or in shielded cast iron casks (for instance, German MOSAIK cast iron casks).

It should be noted, however, that the final decision on the proper packaging concept could be made only when the situation concerning the final repository is definitively assessed.

The waste drums, whose levels of radioactive contamination at the end of a 40-year SEP are expected to have decayed to levels satisfying the criteria for unrestricted use, will not be transported to the final repository, even if available.

It has been assumed that 4-m boxes will be used for the packaging of all LLW as well as of the ILW graphite. The filled box will be finally consigned for disposal as LLW or ILW, depending on the activity and therefore the origin of the contents.

■ Table 34

Waste disposal boxes to be used during safe enclosure phase (SEP) preparation phase

Container type	Closure	Contained waste	Waste treatment (example)
220 l metallic drum	Beaded with clamping-ring lid closure	Compacted DAW's	Baling
320 l metallic drum	Beaded with clamping-ring lid closure	Supercompacted DAW's	Supercompaction
220 l metallic drum	Welded with circumferential hoops and clamping ring lid closure	Conditioned ashes, liquids, resins, and sludge	Cementation
400 l metallic drum	Welded with clamping ring lid closure and internal mixer	Conditioned liquids, resins, and sludge	Cementation

■ Table 35

Waste disposal boxes to be used during the site release phase

Container type	Dimension	Wall thickness	Contained waste (example)
Steel plate container	1.7 m × 1.7 m × 1.6 m	4 mm steel	Dismantled components
Cast iron cylindrical cask	1.06 m diameter, 1.5 m high	160 mm cast iron, <80 mm lead	Activated components from reactor area
Cast iron cylindrical cask	1.06 m diameter, 1.5 m high	160 mm lead	Concentrates from liquid waste
200 l metallic drum	0.6 m diameter, 0.9 m high	1.5 mm	Metallic and concrete waste from small parts
400 l metallic drum	0.75 m diameter, 1.1 m high	1.5 mm	Metallic and concrete waste from small parts

The maximum gross weight of the box is limited to 65 tons. The box has provision for shielding, but this is not expected to be required, as the wastes do not exhibit high gamma dose rates. It has therefore been assumed that all waste using these boxes will be packaged without shielding.

The 3-m³ box is used for all ILW, except graphite. This box is unshielded and requires a shielded steel overpack for transportation. The design has been approved for transport and disposal in the UK. Each box is identified by a machine-readable identity plate which, when used in conjunction with the documentation prepared during waste processing and box filling and with repository details, allows a total record of the box, its contents, and repository location.

Re-usable concrete overpacks can be used for shielding these boxes during temporary storage.

The 3-m³ boxes are transported to the repository in a reusable steel shielded transport container. These are steel boxes with a hinged and/or removable lid. The small boxes have wheels, a 3-m³ socket and pin for linking together and can be moved on a pallet truck with lifting points for transfer via a crane. The boxes have provision for shielding if required. Two sizes are employed, a small box 1.05 × 1.2 × 0.9 m high (volume = 1.134 m³) and a large box 2 × 1.2 × 0.9 m high (volume = 2.268 m³). The boxes provide containment of active and potentially active materials during transfer. These boxes are re-usable.

7.2.9 Waste Transport

Transport of the conditioned and packaged wastes from the packaging facility to the disposal site is performed using conventional means via highways, railways or waterways. The mode of transport utilized is influenced by the type of transport access and handling equipment available at the packaging site and at the selected disposal site, and by the physical size of the packaged unit. Very large components can be transported intact most effectively by barge or ship.

For large-scale decommissioning projects, e.g., a nuclear power reactor, the logistic problems of moving many thousands of cubic meters of waste are likely to be significant and the total impact on existing systems should be assessed.

The sizes and weights permitted in shipments are governed by regulations issued by the appropriate national and local regulatory agencies. Protection of the public from harmful radiation is governed by the appropriate national regulations, which are based upon international recommendations.

7.2.10 Waste Characterization and Measurement Techniques

Estimation of the radiological inventory in a facility is required to define the operational decommissioning plan and estimate costs and radiological risks associated with the plan.

Once the decommissioning program is under way, wastes must be monitored and characterized for regulatory, safety, and waste disposal considerations. The objective of this characterization is to ensure that the wastes are handled and disposed in a safe and economic manner. Therefore, the characterization program should be able to:

- Segregate wastes into active and inactive (exempt from regulatory control) streams quickly and accurately, so that inactive materials and equipment can be released for unrestricted use or for conventional disposal
- Determine the radiological characteristics (major radionuclides present, quantities and chemical form of each radionuclide) for communication to the authorities responsible for waste disposal sites
- Characterize the site for final release

Characterization Methods

The methods and equipment used to characterize the radioactive wastes, which arise from decommissioning will vary considerably, depending upon the type and complexity of the facility and the radionuclide mix in the plant.

The simplest type of decommissioning waste arises from facilities containing only one type of radionuclide, for example a ^{60}Co processing plant. Similarly, decommissioning wastes arising from plants that processed materials with a fixed ratio of alpha, beta, and gamma activity would be relatively easy to characterize. Such plants could include:

- Certain fuel fabrication facilities
- Mining/milling buildings
- Spent fuel storage facilities

Also some types of components can be included in this type of wastes, such as pressure vessels and pressure tubes, which have been decontaminated, as well as concrete from biological shields, since the ratio of radionuclides should not vary even though the concentrations may change. In all the above cases, the quantity and quality of activity in unit packages of waste arising from the decommissioning of the facilities could be determined by gross gamma measurement and a suitable modeling protocol.

The waste streams arising from the decommissioning of reactors, reprocessing plants and fuel fabrication plants would be the most difficult to characterize, especially if the locations in the plant where the waste streams arise are not well defined. Complications arise because of the possible presence of streams having separated plutonium or variable mixes of alpha, beta, and gamma activity.

In the following sections, a review is made of the possible methods of measuring the activity in the waste, the instruments currently available and the means of establishing a waste characterization program.

Gross Gamma Measurement

The easiest and least expensive characterization of radioactive waste comes from measuring the gamma and X-ray intensity external to the package. This type of characterization requires that the waste arising from facilities have fixed ratios of alpha and beta to gamma activity, which can be predetermined by laboratory measurements. However, in many cases these ratios are not constant (particularly for alpha radiation) and other methods are required.

Measurements of total radiation fields due to gamma and X-rays from waste containers can provide an acceptable estimate of the activity if the relationship between activity content and radiation field has been well established. Because the characteristics of the bulk of the waste are measured, this method is more suitable than sample spectrum analysis for the examination of heterogeneous low-level wastes, but is not as indicative of activity content as bulk spectrum analysis. As with bulk spectrum analysis, the need for taking a sample is eliminated and the measurement time is short; so large volumes of waste can be processed relatively quickly.

A gross gamma reading alone will not indicate the nature and quantity of each of the major isotopes in a given waste package, unless a previous detailed analysis of the waste stream was done to derive isotope concentrations comparable with total gamma readings. Such relationships lose their validity if the ratios of radionuclides in the waste deviate from those of the initial quantification analysis.

The accuracy of this method, then, is dependent upon factors such as container geometry, relative isotope mixture, distribution of activity in the package, background radiation and actual measurement procedure (probe distance, measurement points, instrumentation used, etc.). The successful use of total gamma measurement as a waste characterization tool requires that all of these factors remain constant or be accounted for.

Gamma Spectrum Analysis

The most detailed analysis of the gamma emitting radionuclides can be obtained using gamma spectroscopy. This approach is required if the ratio of gamma emitters in the waste changes (e.g., if there are large variations in the ratio of ^{60}Co to ^{137}Cs).

In assaying wastes using gamma spectra, it is neither necessary nor desirable to measure all the gamma emitting radionuclides, and selection criteria must be established. In general, isotopes with half-lives of less than 1 year can be disregarded since they have little bearing on the potential detriment to people during most decommissioning operations and in waste disposal. The selection of the remaining radionuclides to be measured depends on the waste stream.

Accurate characterization requires that a small representative sample taken from the material stream or package be characterized. The spectrum of gamma radiation from the sample is measured and from it the constituents and their activities are deduced. Assuming that the sample is representative of the stream, the total activity per unit weight of the stream can be calculated.

To be effective, such analysis generally requires the use of sophisticated equipment such as Ge detectors and multi-channel analyzers. The necessity of qualified personnel and a suitable laboratory environment makes this method time-consuming and further increases the cost.

Although gamma spectroscopy gives an accurate determination of activity for gamma-emitting isotopes, this method cannot detect the presence of non-gamma emitters. The overall accuracy of this technique, when applied under decommissioning conditions, is further limited by the small sample size analyzed. The composition of low-level wastes, which constitute the major portion of total wastes, is known to vary considerably. Therefore, a small sample does not necessarily give a true indication of the radionuclide content of a package or component, unless supplemented by multiple sampling.

Gamma spectrum analysis based on measurements of the external radiation from a waste package or component is also possible. This method is generally much less accurate than the specific sampling method, but does benefit from the fact that the entire bulk of the waste is assayed. Its use requires that final results be corrected for factors such as the effects of package geometry, package shielding, and self-shielding of wastes. The capital investment in energy-sensitive, high-resolution gamma detectors, multichannel analyzers, and other analytical control hardware remains the same as that for sample analysis.

Energy-Sensitive Detectors

To some extent, the combined advantages of the spectrum analysis and gross gamma measurement systems can be achieved through measurement with an energy-sensitive detector and a single-channel analyzer. Gamma rays of one or more energies are externally counted at various positions on the waste container. Given the proper pre-established relationships, the activity content can then be derived. For example, if ^{60}Co and ^{137}Cs are known to be the major isotopes present, two counts would be taken on the waste, one with the single-channel analyzer set for 1.35 MeV (for ^{60}Co), the other with the analyzer set for 0.6–0.7 MeV (for ^{137}Cs). This procedure has the advantage of a bulk field count combined with the accuracy afforded by being able to count and integrate the photons from one or more specific isotopes in the waste. Measurement procedures and activity derivation factors must still be developed to account for the effects of package geometries, self-shielding and the presence of non-gamma-emitting isotopes. The major advantage of this method over externally measured full spectrum analysis is in the lower cost of equipment.

The methods described lend themselves to high-volume/production-scale automation. Such adaptation, however, requires that all influencing factors such as package characteristics, presence of non-gamma emitters and self-shielding be accounted for in the control analysis logic.

Instrumentation

Accurate characterization of radioactive waste requires that the detector be suited to the energy levels of the radiation emitted and that the resolution and accuracy of the detector be sufficient to meet the needs of the characterization program.

A wide variety of instruments have been developed for measuring the radiation emitted from waste material. Three general categories of instruments have been used to measure this radioactivity:

- Gas-filled detectors
- Scintillation detectors or phosphor detectors
- Solid-state detectors

In general, the energy emitted during the interaction of the radiation with the material in the instrument is converted into an electrical pulse that can be recorded. The total radioactivity can be measured by summing the pulses over a fixed interval of time or by converting them to a pulse rate. In spectrum analyses, the pulses are sorted out by energy level and the number of pulses at each level is stored separately using a pulse height analyzer.

Gas Filled Detectors

One widely used type of gas-filled detector is the Geiger-Muller (GM) detector, which consists of a sealed tube containing the counting gas, anode, cathode, and a secondary gas to quench the discharge and prevent secondary discharges.

The counter is inexpensive, trouble-free, and generally used to measure gross gamma or beta/gamma. Certain designs can be used to detect alpha, beta, and gamma radiation. The detectors can measure alpha above 3.5 MeV, beta above 35 keV, and gamma above 6 keV.

Since GM detectors are incapable of resolution, they cannot be used for spectrum analysis. However, such instruments can be used effectively to measure the quantity of radiation in waste having fixed ratios of alpha and/or beta to gamma radiation, provided that:

- Samples of the waste have been well characterized in the laboratory as to radionuclide mix and content
- The ratio of radionuclides in the stream does not change
- The operators are well trained and use the instruments in a consistent manner
- The total weight of material is known

The method is quite susceptible to error since it is subject to possible changes in the radionuclide mix, at least in some plants, and to operator inconsistency.

Another type of gas-filled detector that has been widely used is the gas-flow proportional detector. This type of detector can be made with a thin window, which increases the detection capability for alpha particles. A third type of gas-filled detector, the ionization chamber, can be made in a variety of shapes and sizes. It is extremely rugged and can operate over a wide range of temperature and gamma radiation levels.

Scintillation Detectors

A zinc sulfide scintillator may be used during decommissioning as an alpha survey meter. Plastic scintillators have been used as beta detectors and have a 100% efficiency for particles as low as 60 keV which pass through the protective foil window. The plastic is rugged and large detector sizes are possible; however, resolution for gamma rays is poorer than for sodium iodide (NaI).

Sodium iodide is the best scintillation detector material for high energy gamma detection and overall gamma ray resolution. The best resolution achievable is about 7% (for 662 keV ^{137}Cs gamma). NaI detectors are widely used in gamma spectrometers where portability and counting efficiency are the key parameters.

NaI detectors could best be used to segregate active/inactive waste since their detection ability and resolution are sufficient to define wastes above and below a minimum radiation level. Detailed characterization of active wastes is best left to the higher-resolution solid-state detectors.

Solid-State Detectors

These detectors are essentially solid-state ionization chambers, but with a higher efficiency owing to a solid, rather than a gas, detection medium. They are operated at liquid-nitrogen temperatures to reduce thermal noise.

The decision on which type of solid state detector to adopt for a particular program will depend on items such as which radioisotopes are to be quantified, which measurement method is to be implemented (gross gamma, gross alpha, single-channel analysis, multichannel analysis), throughput, degree of automation and cost. While the range and resolution of the instruments are prime considerations, the electronics (i.e., preamplifiers, amplifiers, analyzers, etc.) required with each of the different types must also be carefully evaluated since they affect both the cost and the flexibility of the final instrumentation set-up.

For decommissioning activities, completely portable high-resolution germanium diode spectrometer systems have been developed. These instruments are capable of measuring gamma and X-rays, and to detect transuranics (TRUs), activation products and fission products at very low levels. The data acquisition is accomplished using a multi-channel analyzer and a digital recording system for subsequent computer reduction and analysis.

Special Alpha Techniques

Wastes contaminated with TRU nuclides – for example, ^{239}Pu , ^{241}Pu and ^{241}Am – are difficult to detect, especially in the presence of certain fission products. The selection criteria for the measurement of TRU are not as clear-cut as for activation and fission products, especially if the waste is in packages. The only radiation that can be measured unequivocally from TRU wastes in the presence of other radionuclides which usually occur are the neutrons emitted spontaneously from the waste (passive) or those emitted following interrogation of the waste with pulsed neutron or photon sources (active).

Passive neutron techniques can be used to measure many of the TRU nuclides in low- or high-gamma-activity wastes. Such techniques are being developed for the verification of the TRU content of waste packages.

Waste Characterization Program

The essential steps of a waste characterization and verification program for a decommissioning project consist of:

- a) Conducting extensive sampling and laboratory analyses

- b) Dividing the intact facility into waste streams which are likely to have similar radionuclide mixes
- c) Obtaining suitable criteria which would permit inactive waste to be segregated from active waste and permit the active waste to be classified according to disposal facility
- d) Obtaining or developing instruments and equipment which would allow the waste to be segregated as in c) as quick, economical, and accurate as possible
- e) Developing a well-trained monitoring crew

The monitoring personnel should understand the equipment and criteria used for segregating the waste and should supervise and give directions to a team of operators who actually do the work.

The data required to divide the intact facility into discrete waste streams with similar radionuclide mixes could be obtained from the radiological inventory estimates and sampling procedures initially done in the facility to be decommissioned. The volumes of these streams can be calculated from the construction drawings. Depending on the type of facility, the radionuclides present and the thoroughness of the initial survey, samples of the waste streams from the dismantling may or may not have to be analyzed in detail to identify all the important radionuclides present using spectrographic and possibly chemical analyses. This type of confirmation would not be required for plants with fixed mixes of radionuclides, for example a natural-uranium-fed fabrication plant, but would be required for more complex plants such as reprocessing plants.

Once the streams have been defined, the type of instrumentation and sampling protocol required to verify the activity can be determined. Depending on the waste stream, monitors for gross gamma, beta and possibly alpha may be required as well as equipment for doing spectrum analyses on some or all of the waste. Depending on the form of the waste and the part of the plant or site being monitored, the physical design of the monitor could vary from hand-held types to a more advanced production-line monitoring assembly.

While for small samples the most accurate method of characterizing the radioactivity in waste is gamma spectrum analysis, this is not practical for large volumes of solid waste. For waste streams that require spectrum analysis, economies in time and labor can be achieved by combining several techniques. For example, in a specific waste stream having reasonably fixed mixes of gamma radionuclides, but variations in activity levels, the total activity content can be estimated fairly well using gross gamma measurements on most of the waste and spectrum analysis on selected samples from the wastes containing the highest activity levels.

Sources suspected of containing significant quantities of radioisotopes which are difficult to measure with gamma detection equipment, for example, weak or non-gamma emitters, would require further analysis to develop effective scaling factors to relate gamma levels to the content of the other radionuclides. Further analysis, enhanced by chemical separation of the relevant isotopes and combined with an isotope-behavior analysis, would yield relatively constant relationships between the hard-to-detect radioisotopes and those that can be readily measured. Scaling factors can be established from these relationships. Subsequent surveys of wastes being removed from specific source areas or systems can then be accomplished with more practical gamma measurement techniques. The concentrations of detectable isotopes would be used, with the scaling factors, to derive the concentrations of non-gamma isotopes.


Once specific waste streams are characterized in this manner, regular assaying of the waste packages by external gamma measurement, either with a multichannel or single-channel

analyzer, will be sufficient to ensure compliance with safety and regulatory criteria. The initial source characterization would show which radioisotopes are present and, hence the specific gamma energy regions to be surveyed if single-channel analysis is used. Periodic laboratory analysis of wastes would still be required to confirm the validity of the scaling factors and the assumed radioisotope mix. The frequency of both the regular waste surveys and the periodic confirmatory analysis should be high during the initial periods of waste generation and can be permitted to drop off as confidence in the methods grows.

The degree of reliability of these mixed survey methods, and the resultant time and cost savings, depend primarily on the consistency of the waste streams. This requires that the waste be sorted into streams as homogeneous as possible. The ability to effectively define general sources in such an economical manner varies from facility to facility. Any difficulty in establishing a suitable definitive source-base characterization can be compensated for by adopting more conservative scaling factors and/or more precise gamma measurement procedures. The latter applies to single-channel analysis and would be achieved by regularly surveying beyond the energy regions indicated by the detailed source-base analyses. Such a measure would result in more operator time being required, while the use of conservative scaling factors would ultimately result in less efficient use of disposal space.

In the special case of fissile material facilities, the requirements for criticality control may necessitate measurement of all the waste streams from selected areas.

7.3 The Waste Management Facility (WMF)

The removal from a nuclear plant of activated or contaminated materials, particularly during its decommissioning, requires a number of operations and precautions. Most of these operations are usually performed inside a special area, adequately confined and equipped, called a WMF. In  [Fig. 20](#) a simplified flow diagram is shown for a typical WMF.

7.3.1 WMF Design Criteria

The main design criteria for WMF are similar to the general radioprotection criteria, which could be summarized as follows:

- Minimizing the operational collective dose to the workers
- Confining contamination as much as possible to where it is generated
- Minimizing environmental impact by minimizing liquid and gaseous releases
- Minimizing risks to the environment and to the workers associated with accidents
- Radiologically classify all operational areas
- Preparing detailed procedures for operations in the radiologically affected areas
- Minimizing radioactive wastes generated during operation of the facility

A typical classification of a WMF identifies four levels:

- Clean areas where any ambient contamination can be excluded
- Clean areas where a limited contamination may occasionally be present
- Areas where only surface contamination may be expected

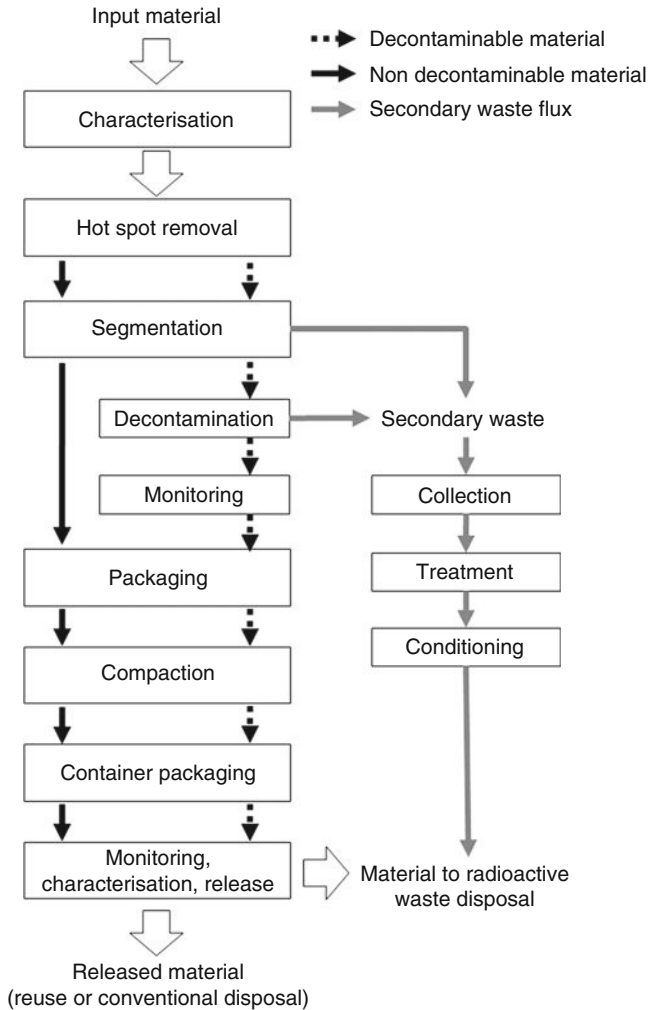


Figure 20
Typical waste management facility (WMF) material flow diagram

- Highly contaminated areas, where access is controlled and only personnel properly equipped with protection devices, including filtered masks, may be allowed

Minimization should be applied to primary wastes (those directly created by the dismantled materials), secondary wastes (those produced by the conditioning processes inside the WMF) and tertiary wastes (those consisting of equipment brought in from outside).

In addition, the WMF layout should optimize the logistics associated with material paths. These paths, called “waste routes,” can be grouped into four families:

- Entering-material waste routes
- Nondecontaminable-material (typically activated materials) waste routes

- Decontaminable-material waste routes
- Released-material waste routes

7.3.2 Description of the Areas and the Equipment

Specific WMF equipment may vary widely from one plant to the other and also from one NPP type to others. However, in general terms the following functional areas can be identified:

- Component segmentation (production of spools of predetermined size)
- Chemical or mechanical decontamination
- Volume reduction (compaction)
- Immobilization by grouting
- Monitoring, characterization and release
- Interim storage areas (“buffers”)

Segmentation

The main equipment of the segmentation area is that necessary to reduce large components into spools to be decontaminated that are compatible with the decontamination pools. This equipment is supplemented by static and dynamic confinement systems, usually associated ventilation systems for dust and smokes.

In this area, removal of hot spots (contamination concentration spots, such as piping elbows, drains, or highly oxidized areas) can be considered. This removal has the objective of facilitating subsequent decontamination and reducing secondary waste production.

Decontamination

Toward this area are forwarded the spools to be decontaminated for further release. This stream generally does not include small components, whose decontamination is complex and/or too expensive, and which are more advantageously directed to compaction and inclusion in waste barrels.

Typical equipment of the decontamination area consists of:

- Pool for pickling treatment
- Washing station with high-pressure pump
- Pools for acid treatment
- Pools for electric-chemical treatment

A dynamic containment is also foreseen for this area, in addition to a system of collection, filtering and treatment of liquid effluents.

The decontamination techniques of systems and components can be divided in two groups:

- “On-line” decontamination processes
- “Off-line” decontamination processes

“On-line” processes pertain to systems and components where they are installed, before dismantling. These processes, obviously, are performed outside the WMF. “Off-line” processes provide for the prior dismantling of systems and components to be treated and their transportation to instrumented areas for decontamination.

Volume Reduction

In this area waste volumes are reduced by filling standard drums with waste and then compacting them with a hydraulic press. This treatment is particularly advantageous for waste products that because of their size and shape would not allow a high filling factor of the containers.

Immobilization by Grouting

In this area, wastes may be immobilized by adding grout, or fluid cement, in standard containers compatible with the specifications of the final disposal site. The Safety Authority may provide special specifications, identifying two cases:

- Immobilization of the contamination only during handling and transport
- Full waste conditioning by inclusion

The grouting process must be qualified by the Safety Authority, and the cement should also be fully qualified and characterized in its composition to obtain the required performance of the final product (after maturation) in terms of mechanical resistance, leaching, etc.

Monitoring, Characterization and Release

In this area, the automatic volumetric contamination control equipment operates together with other equipment for surface contamination measurements.

In this area all data related to a specific waste package are prepared (as an ID of the package) and a Certificate for Disposal is issued, which, with the help of a database, will assure traceability of the package and its content at all times.

If contamination levels are below a threshold (generally between of 0.1 and 1 Bq/g) the material can be released as conventional waste. In particular, metallic wastes (the great majority in terms of weight and volume) can be recycled as metallic scraps in this case.

In many cases, this area is not fully integrated with the WMF, since the formed should be clean, not contaminated by proximity to contaminated areas and used only for controls and administrative operations.

Interim Storage Areas (Buffers)

It is difficult to control all waste routes and the material flow rate in a manner compatible with the processes occurring in each area, which are usually of the batch type. This creates the need for an interim storage area at the entrance and at the exit of the areas indicated above.

7.3.3 Staff Requirements

A typical WMF staff includes:

- One operator for spool acceptance from dismantling operations and their storage in buffer areas
- One or two operators for segmenting operations
- One or two operators for decontamination activities
- One operator for spool handling inside the WMF
- One specialist for preliminary and final monitoring
- One operator for waste-route management and treatment of each single spool

8 Safety, Health and Environmental Protection

8.1 Overview


There is a general feeling that decommissioning is an activity involving limited risks, compared to NPP operation, and in particular risks involving the general public. This is technically confirmed by licensing analysis and evaluations, where, once the spent fuel has been removed from the plant, the radioactivity inventory available to be released to the environment is very limited.

Decommissioning activities performed so far in the world have also confirmed the first assumptions and no specific issue has been identified in this field to justify a completely new approach. Commercial interest in international harmonization, which could drive an in-depth assessment about the bases of this approach, is weak at the moment.

However, there are several reasons why a discussion in an international framework about the safety case for decommissioning (and, in particular, about accident assessment) may be considered necessary and important, and why it may show some specific and peculiar aspects.

- Risk for workers could increase. The need for safety approach optimization, considering both radiological accidents and conventional industrial accidents, will be developed later. However, it is common experience from practical decommissioning work as well as feedback experience from annual outages and major refurbishment work at the power plants. Not only is it during these periods that most of the collective dose is absorbed, but many accidents also occur when people are testing or changing the systems of a plant. Handling of hazardous material (alkaline metal coolants, lead, asbestos, mercury, beryllium, etc.) requires special attention and the industrial safety issues are also of prime concern (high pressure, corrosive liquids, lasers, electrical hazards, falls, vibrations from jackhammers and scabblers).
- Regulations and technical guides are usually at an early stage in the development process. This is true in most countries. This is an additional reason why the approach to accident assessment in decommissioning is considered at a case-by-case level and, as a consequence, significant differences exist among different situations. Clearance levels for decommissioning material and rules for site release are still lacking.
- Peculiar issues exist. Accident assessment in decommissioning may be challenging, since a reference plant configuration practically does not exist and an accurate review of the decommissioning stages and activities should be considered in order to assure that the analysis is conservative and all-enveloping. Additional peculiarities are, as mentioned above, the combination of radiological and industrial risks and uncertainties about the quantification of releases.
- Harmonization advantages. A national and international harmonization process could imply a positive outcome in terms of the predictability of licensing processes, better public acceptance, reliable scheduling, and cost reductions.
- In some cases, the safety systems do not provide the same level of redundancy and protection as during plant operation.

- During the decommissioning process, the plant undergoes a number of mechanical and chemical stresses.
- Progressive dismantlement of systems and structures that may be degraded and not in a design configuration.
- Large quantities of liquid waste produced.
- Liquid pathways may become more important than in operation.
- Unusual source term may be present, which during plant operation may have been well confined inside systems and materials.

In  [Table 36](#) are summarized major differences in the approach between operation and decommissioning phases.

 **Table 36**

Major differences between operation and decommissioning phases

	Operation	Decommissioning
Hazard profile	Stable Well-characterized Radiological hazards dominant Potential for significant off-site effects	Frequently changing Often not well-characterized Industrial safety issues more significant Lower potential for off-site effects due to removal of inventory
Work planning	Frequently performing routine Focused on operation and maintenance Relatively short tasks	Task- or job-oriented New, first-of-a-kind tasks Work planning for workplace safety critical
Hazard analysis	Operation-oriented Generally stable focus on off-site consequences	Dynamic Mainly task-oriented Changeable Focus on-site
Workforce experience	Familiar with facility operation and routine work according to approved design	New mission Limited experience Subcontractors may not have process knowledge of facility operations Knowledge may need to be maintained for long periods
Contract management	Licensee managed and operated	More short-term subcontractor involvement, high level of Dependence on contractors performance Need for strong project management

8.2 Safety Culture

The issue of keeping an adequate level of safety culture during decommissioning has been brought to the attention of the safety authorities and decommissioning implementers in the last years.

The concept of safety culture became popular in the nuclear field after the Chernobyl accident in 1986, but in particular after the issue of the IAEA Report INSAG-4, where the group of safety experts assisting IAEA placed the basis for the application of the concept to nuclear activities.

Safety culture is not only knowledge and competence, it is mainly composed of a set and a mix of attitudes and explicit and implicit behaviors of individuals and of organizations as a whole. The concept would need a longer discussion, but here we would like to stress the key element related to decommissioning.

Loss of experienced personnel, unjustified sense of safety about radiological risks, the activities of a number of contractors not specialized to work in a nuclear environment, organizations more project oriented than safety oriented, lack of indication from the top of the organizations that safety is still a priority and other specific conditions may be cause of sharp reduction in safety levels and in an increased level of risks.

A number of initiatives help the organizations to keep and continuously improve the safety levels and the attitudes of all the personnel. Among the initiatives that may contribute to the above goal, the following is listed:

- Continuous indication by the top managers that safety is a Company priority
- Periodic review of the safety culture levels by means of KPI
- Periodic interview of the personnel by dedicated and experienced team
- Training program for all contractor personnel
- Review of operation experience and of specific incidents or near misses.

8.3 Safety Assessment

Experts involved in the safety analysis of operating plants might consider the same approach and rules (such as defense in depth, the single failure, the safety classification of equipment, prevention vs. mitigation, pervasive roles of quality assurance and safety culture), but it would be common sense to adapt these safety cornerstones to the real safety significance of decommissioning activities.

8.3.1 Accident Analysis

A number of data and assumptions are relevant to accident analysis. In several cases, the database and the assumptions used for operational safety analysis are not relevant or not applicable. Examples are:

- Source term for radiation fields and release calculations
- Statistical data on human errors and specific job conditions
- Computer codes for release and consequence calculations

- Approach to structural analysis for intermediate plant structural configuration
- Approach to fire protection
- Acceptance criteria in terms of plant damage and mechanical stresses

Once the list of accidents to be considered is complete, they must be classified in terms of expected frequency or probability, in order to associate appropriate acceptance criteria and their grouping in accidents of similar cause/evolution/effect, in order to be able to identify the most representative and consequently reduce the number of calculations to be performed.

An example of event grouping is presented in [Table 37](#). Events are grouped according to the type of challenge and activities involved.

Table 37
Some events to be considered in accident analysis

Events caused by the decommissioning activities	Decontamination activities	Leaks of pressurized fluids during decontamination activities (...)
	Dismantling activities	Metal components and piping cutting Concrete removal (...)
	Material handling	Drop of a contaminated component Drop of a concrete chunk Drop of a contaminated filter or of containers with radioactivity (...)
Loss of supporting systems	Loss of off-site power supply	Loss of ventilation and filtration lines (...)
	Loss of service water	Sudden interruption of decontamination, cutting and dismantling equipment (...)
	Loss of compressed air	Loss of dismantling equipment and loss of pneumatically operated valves (...)
Fires and explosions	Fires	Fire in the radioactive waste storage facility (...)
	Explosions	Explosion of a gas bottle used in the operations (...)

■ Table 37 (continued)

External events	Earthquakes	Integrity of structures and of systems and components during partial dismantling: generally the plant has been designed and verified for earthquakes according to regulations. In general, there is no reason to increase the seismic level during decommissioning. The only concern is the resistance of partially dismantled structures and the possible consequential release of radioactivity in the environment (...)
	Flooding	Internal flooding caused by water body exondation (...)
	Wind and tornados	(...)
	Volcanic activity	(...)
	Lightnings	(...)
	Toxic chemical releases	(...)
	Aircraft crashes	(...)
	Gas cloud explosions	(...)
	(...)	(...)

Some of the above events might not be applicable and some may fall below the credibility threshold. However, it could be of interest to fill out a comprehensive list of events, from which in each specific case one could identify those to be considered. It is estimated, for example, that at the beginning of dismantling activities there will be various potentially toxic or hazardous chemical products stored at the plant, such as those indicated in [▶ Table 38](#).

It is also of interest not to spend unnecessary resources on events of small probability and with small consequences, which could be difficult to quantify exactly. Therefore, experience and engineering judgment are of utmost importance in the selection process.

8.3.2 Human Factors and Organizational Considerations

The period before and after termination of operation could be one of stress and insecurity. Confidence in the management can deteriorate and motivation can decrease, a state of affairs, which

■ Table 38

Potentially toxic or hazardous chemical products stored in a nuclear power plant (SOGIN)

Substance	Estimated inventory (kg)
Acetylene	70
Carbon dioxide	12,000
Butane	70
Propane	110
Freons	500
Hydrogen	100
Nitrogen	10,000
Chlorine	200
Paints, varnishes and enamels	1,000
Solvents	1,000
Boric acid	500
Hydrazine	200
Ethanol	50
Acetone	300
Trichloroethylene	200
Gasoil	100,000
Lubricating oils	10,000
Ammonium	500
Sodium hypochlorite	10,000
Calcium hydroxide	10,000
Sulfuric acid	20,000
Halon	300

can affect safety and the decommissioning work. The process of decreasing the staff and the development of a decommissioning organization should be separated. Experience has shown that a special organization for re-education and job finding could be helpful.

The persons who will carry out the decommissioning activities should be given the possibility to develop their knowledge and improve their competence. Instead of detailed central planning, it is better to work in a participative way and to have staff involved in the preparations of the decommissioning work from the beginning.

An open question is how to consider human factors in accident assessment, i.e., what type of mistakes might be made, how many, for how long and their probability.

Unlike plant supervisors and plant operators, in decommissioning personnel with less education and shorter experience in the plant may be utilized, probably increasing the risk

of radiological and conventional accidents. This is also the experience with operating plant maintenance work.

8.3.3 Emergency Planning

Related to accident assessment is the question of the importance of one of the mitigation features available, i.e., the emergency plan.

The role (if any) of an emergency plan in decommissioning is a subject for discussion. In some countries, there is confidence in the fact that, after the spent fuel has been removed from the site, there is no need for a special emergency preparedness plan. Six months after a reactor has closed the content of iodine-131 in the fuel is so low so that iodine prophylaxis is no longer justified. But, for reasons of public confidence and psychology, a strategy for the downsizing of the emergency plan should be carefully planned and each step should be well thought-out.

Information to the public about the activities at the site is needed at all stages in the decommissioning process.


The IAEA report Preparedness and Response for a Nuclear or Radiological Emergency, Draft Safety Requirements No. GS-R-2, DS43 addresses this issue. In this report five different categories of nuclear or radiation threat are identified.

- Installations for which events that can give rise to severe deterministic health effects off-site are postulated or have occurred in similar installations, including very low probability events.
- Installations for which events that can give rise to off-site doses warranting urgent protective actions consistent with international standards are postulated or have occurred in similar installations. This category (as opposed to category I threats) has no credible events postulated that could give rise to off-site doses resulting in severe deterministic health effects.
- Installations for which events that could give rise to doses on-site resulting in severe deterministic health effects are postulated or have occurred within similar installations. This category (as opposed to category II threats) has no credible events postulated for which urgent off-site protective actions are warranted.
- Minimum level of threat assumed for all countries and jurisdictions. This category includes events involving: facilities for which events could give rise to doses warranting urgent actions consistent with international standards on-site, but for which no credible events are postulated that could result in severe deterministic effect; mobile practices using dangerous sources; medical misadministration; transportation; and other events that could occur virtually anywhere (the public finding a source resulting in exposure and contamination, loss or theft of or damage to a dangerous source, reentry of a satellite, and illicit trafficking) that may warrant emergency intervention.
- Areas that could be contaminated to levels necessitating food restrictions consistent with international standards as a result of events at installations in threat categories I or II, including installations in nearby countries.

8.4 Environmental Impact Assessment (EIA)

The role of EIA as a tool for pollution prevention and minimization has gained wide acceptance since the late 1960s. EIA definition generally incorporates the following key principles:

- EIA identifies and assesses a project's likely significant environmental effects to inform decision-making
- EIA allows consideration of the environment early in the decision-making process on a proposed project
- EIA enables proposals to be modified, in light of potential impacts, in order to eliminate or mitigate them

The EIA process outlined in this guidance document is shown in  Fig. 21. This process can be divided into various phases, which are described in the following sections.

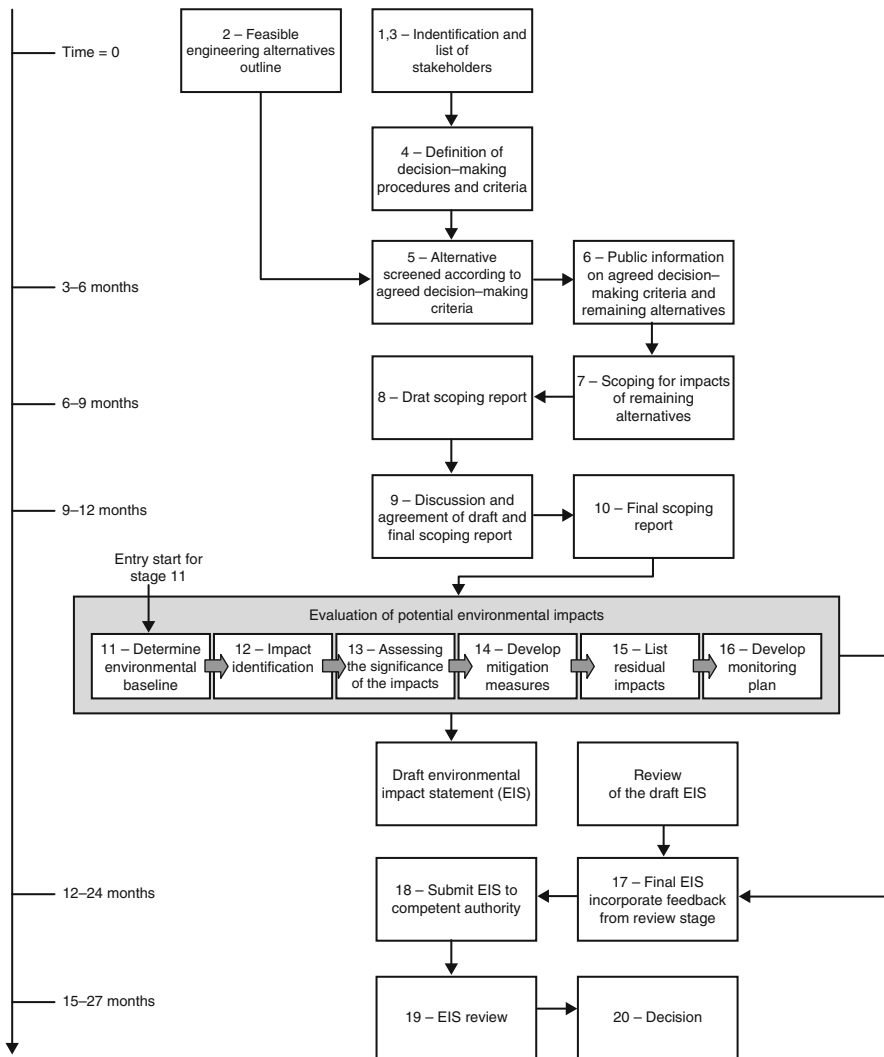


 Figure 21

Block diagram of environmental impact assessment (EIA) process (EU 2001)

8.4.1 Scoping

The scoping stage is the phase when, among other things, the terms of reference (ToR) for the EIA are defined.

At this stage, stakeholders (including competent authorities and the developer) should have an opportunity to express their opinions and concerns over the proposed decommissioning project, integrating them into the definition of the ToR. The decision-making procedures and criteria should be described at this stage and feasible alternative(s) selected.

In spite of not being formally required by the EIA Directive, the introduction of a formal scoping stage with stakeholder involvement has gained wide support for its advantages and is generally considered to represent best practice. Formal scoping ensures that stakeholders learn of the proposed development at an early stage, that key concerns are reflected in the ToR, and that resource use is optimized in further stages by focusing on the (previously agreed) fundamental elements for evaluation. In addition, it has been found (EC 1996b) that one of the principal causes of significant costs and time delays in the decision-making process is the lack of a proper scoping exercise and the subsequent failure to undertake systematic studies, resulting in need for supplementary information.

Scoping corresponds to Steps 1–10 of the proposed process. The technically feasible alternatives to be subjected to EIA are selected in this phase, firstly by rejecting alternatives that do not meet agreed decision-making criteria.

These criteria are likely to include considerations such as unacceptable environmental risks or excessive cost. Reducing the number of alternatives in this way makes the scoping phase more efficient in terms of the use of resources.

- Steps 1, 3: Identification and list of stakeholders. The input of stakeholders is vital to the success of the scoping stage and thereby to the entire EIA process, thus it is important to start by identifying all stakeholders and listing them in a single document. The list of stakeholders should include all contact details and be made publicly available.
- Step 2: Outline of feasible engineering alternatives. At the start of the process, and in parallel with the identification of stakeholders, an initial outline of feasible alternatives should be prepared. These alternatives are later screened, based on agreed criteria, to obtain a list of the alternative(s) to be assessed in more detail.
- Step 4: Definition of decision-making procedures and criteria. This is the core of the scoping stage. The agreed decision-making procedures and criteria are used throughout the EIA process and thus the widest support from stakeholders should be sought. Public participation plays a key role in integrating the public's concerns in the EIA and in the decision-making process in general. Another aspect to be considered at this point is the definition of the project baseline, specifying the existing situation against which comparisons of potential environmental impacts should be made.

It is expected that Steps 1–4 would take from 3 to 6 months to be completed. The amount of time required depends to a large extent on the degree of support for the decommissioning project. If there are disagreements between stakeholders, repeated meetings may be necessary before reaching an agreement on the scope.

- Step 5: Alternatives screened according to agreed decision-making criteria. A first screening of the proposed (technically feasible) alternatives should be undertaken as part of the public

participation procedure at this stage. The aim of this step is to concentrate resources on the investigation of realistic decommissioning options.

- Step 6: Public information on agreed decision-making criteria and remaining alternatives. The public should be informed about the results of this first part of the scoping stage, i.e., the decision-making procedures and criteria, as well as the alternatives selected for further examination.
- Step 7: Scoping for impacts of remaining alternatives. The remaining alternatives must then be scoped for impacts, in order to select the final alternative(s) for the remainder of the EIA process. This ensures that only alternatives that are technically feasible, socially acceptable and with potentially low environmental impacts are subjected to a detailed assessment.
- Step 8: Draft scoping report. A draft scoping report is produced at this stage, establishing the scope of the EIA for the decommissioning project. This document is made publicly available. The process, including the rejection of alternatives not meeting decision-making criteria (Step 5) through to the production of the draft scoping report (Step 8), is expected to take approximately 3–6 months.
- Steps 9, 10: Discussion and agreement of draft and final scoping reports. As scoping is the key to efficient EIA, helping to focus all resources on the significant issues of concern, all stakeholders must have the opportunity to discuss the draft scoping report, and outstanding issues or inaccuracies are pointed out at this stage (Step 9). The public review of the draft scoping report should take place according to the guidance on public participation provided in [▶ Sect. 3](#) and is expected to last approximately 3 months. A final scoping report (Step 10) is then produced and made publicly available. This report incorporates all the changes to the draft report agreed at the stakeholder meeting, and this document then forms the basis of the EIA to be undertaken.

8.4.2 Environmental Impact Evaluation

Once the scope for the EIA has been defined, the developer may proceed with it. In order to make an assessment of the potential environmental impacts and define ways to mitigate or eliminate them, as well as how to ensure their proper monitoring, a series of steps needs to be undertaken.

- Step 11: Determination of the environmental baseline. In order to predict the potential environmental impacts of the proposed project, the initial environmental conditions must be known. Environmental damage varies according to the initial conditions: for example, a given level of emissions may be more damaging in ecologically-sensitive zones or may surpass the ecosystem's tolerance level if the area is already polluted; tall structures may be tolerable in industrial areas but not within a site of outstanding natural beauty. The definition of the baseline conditions (e.g., meteorological conditions, geological formations, and groundwater flow direction) also provides data necessary to make impact predictions.

Because the same baseline conditions apply to all of the options, this step can be started before the full scope of the EIA has been agreed. There may be some unnecessary expenditure incurred, but this would be small compared to the wider project ones and are likely to be more than offset by the benefits of completing this stage early in the process.

- Step 12: Impact identification. Potential environmental impacts are identified at this stage, based on parameters related to the degree of physical and social-economic impact, as well as according to the public's perceptions and values. For each alternative being evaluated, a separate analysis needs to be carried out to determine the likelihood of environmental impacts.
- Step 13: Assessment of the significance of impacts. This step considers the implications of the impacts identified previously and assesses their significance. Significance can be gauged relative to environmental standards or against public perception for some more subjective impacts. Therefore, frequent dialogue with stakeholders throughout the Environmental Impact Evaluation can be very helpful.
- Step 14: Development of mitigation measures. One aim of EIA is to remove or reduce to acceptable levels all the impacts that may occur. The identification of possible mitigation measures must have the agreement of the developer, if they are to be included in the EIS.
- Step 15: Listing of residual impacts. Mitigation can rarely remove all the identified impacts and a clear statement has to be made about the impacts, which would still occur even after the implementation of the mitigation measures.
- Step 16: Development of monitoring plan. In recognition of the fact that the evaluation of impacts is subject to uncertainties, it is appropriate to develop a monitoring plan, which would be able to check that the residual impacts identified are the only ones which occur. This would ensure that no unexpected impacts arise and that the proposed mitigation measures are working adequately. If unexpected impacts do arise, these would provide an opportunity to take remedial actions. The study to evaluate the impacts of the alternatives under investigation (Steps 11–16) is expected to last up to 12 months. This timing depends on the information that is already available and that must be specifically collected (e.g., local meteorological and ecological data). The developer may have ongoing communication with stakeholders during this phase, in order to ensure that their concerns are being properly addressed and that local and expert knowledge has been used effectively.

8.4.3 EIA Regulations

The requirements of the EIA Directives and of the relevant guidance on EIA methodology provided by the European Commission are reviewed. Although the existing guidance is necessarily of a general nature, the advice given (e.g., advice on the assessment of indirect and cumulative impacts, European Commission 1999a) has been taken into account in developing the guidelines.

The report also examines the potential implications of two UNO Conventions, the Espoo Convention on EIA in a transboundary context (adopted in 1997) and the Aarhus Convention on access to information, public participation in decision making and access to justice in environmental matters.

The provisions of the Espoo Convention were largely taken into account in the 1997 EIA Directive, the main difference being that the Directive refers only to Member States, whereas the Convention has no such limitation.

Some modifications of the EIA Directive will be required when the Aarhus Convention comes into force, which will be when it receives its 16th ratification. The European Union is already a signatory, together with all of the Member States and most of the Applicant Countries participating in this study. The Aarhus Convention stipulates that public participation should

occur early in the EIA process, but at present the Directive requires only that the concerned public be given an opportunity to express an opinion before development consent is granted. In general, the Directive presently allows Member States more discretion than will be allowed by the Aarhus Convention on the issues about which views should be sought and on the timing of such public involvement.

8.4.4 Consent Processes for Decommissioning in EU Member States

Although a permit must be obtained before decommissioning can begin, there is some diversity of views about what operations signal the start of decommissioning. In particular, the removal of spent fuel (defueling) is a normal part of reactor operations as well as part of decommissioning operations. Since the decision to shut down a reactor permanently may be made on quite short notice – perhaps for economic or technical reasons, or prompted by a major outage – some countries (such as the UK, Spain, Sweden, and Germany) regulate the final defueling under the existing procedures for reactor operation. This avoids the need to keep spent fuel on-site if a decommissioning plan has not yet been fully developed and consent obtained.

There is general acceptance in all the countries that the EIA should include the selection of the strategy for decommissioning, i.e., the process of choosing between different possible decommissioning strategies. There is also a general acceptance that the process should address a wide range of impacts, including social impacts, land use and transport considerations, and both radiological and nonradiological impacts. All countries agree that the report should consider impact minimization.

The roles of the competent authority for decommissioning and for the EIA vary between countries, in accordance with the differences in national legislation already noted. There are different mechanisms for ensuring that all technological, safety and environmental aspects are covered, and that the permit is only granted with the consent of all the relevant authorities.

8.4.5 Consultation and Public Participation

There is a range of approaches being taken in all the countries to the question of what the EIA process comprises. A key distinction is the extent to which there is a formal scoping procedure to establish the issues that should be addressed by the EIA, including consideration of alternatives.

The definition of a public participation strategy for the EIA of proposals to decommission a NPP will depend on various factors, including the stage of the EIA in question and the specific context in which the EIA takes place.

An important aspect of undertaking an EIA for a nuclear decommissioning project is that the decision to undertake the project has been taken.

Therefore the focus of the assessment would normally be on how and when, rather than if, the project should be carried out. The comparison and selection of alternative decommissioning strategies will form the basis of the assessment. Another key feature of nuclear decommissioning projects is their high public profile: there is likely to be broader public support for the project if information on alternative decommissioning strategies is available and the public is consulted on them.

The responsibility for facilitating public participation depends on the stage of the EIA process and the country-specific legislation. Thus, some countries may require the developer to

organize the participation, including any mandatory public meetings or inquiries, whilst in other countries it may be the responsibility of the competent authority. These guidelines do not specify who should be responsible for defining the public participation strategy throughout the EIA process, but are applicable to whichever party holds such responsibilities. However, some opportunities for participation are more appropriate for the developer to organize, such as the ongoing consultations during the impact evaluation studies and the EIS preparation stage. Other roles are equally appropriate for the competent authorities, such as preparation of the ToR (scoping).

There are certain key issues in the definition of a public participation strategy which are common to all stages of the EIA process; guidance on these is defined first. Following this, guidance is provided on public participation for each stage of the EIA process.

8.4.6 Definition of Preferred Options

Once the decision to terminate the operation of a nuclear power plant has been made, preparation for the decommissioning phase begins. The end of the operational phase of a nuclear plant is characterized by the complete removal of the fuel from the reactor core and by the conditioning of operating wastes.

The central element of NPP decommissioning is made up of the activities of dismantling, decontamination and restoration. One result of these activities is the production of wastes of various types, including radioactive wastes. The dismantling option, and the particular methods and techniques selected for any particular project, is partly determined by the possibilities for management of these wastes.

The dismantling alternatives analyzed will imply the possible achievement of one of the three levels of decommissioning described by the UNO-IAEA (1983a):

- No action, implying maintenance of the shutdown situation.
- Long-term or “safe” storage, which entails modifying the installation to establish a structure that safely contains the radioactive material for a prolonged period. This allows radioactive decay to reduce the quantity of radionuclides in the former NPP, with a view to the eventual dismantling and unconditional release of the site. This period may cover from 10 to up to 100 years or more, depending upon the detailed decommissioning strategy adopted and the availability of radioactive waste storage or disposal facilities.
- Immediate dismantling, consisting of the dismantling of the facility in the short term, leaving the site free for unconditional use after a short waiting period (3–10 years), during which it is subject to surveillance.

The components to be analyzed in choosing the preferred alternative are summarized below:

- Requirements of the regulatory bodies
- Characteristics of the installation, including design, operation, and the radiological inventory existing after the definitive shutdown
- Evaluation of the radiological and nonradiological risks
- Physical status of the installation and its evolution; this analysis should include a study of the integrity of the buildings, structures, and systems
- Alternatives for management of the radioactive wastes (including spent fuel)
- Environmental impact of the decommissioning options

- Availability of funds for carrying out the various decommissioning alternatives
- Availability of qualified personnel and suitable techniques for dismantling tasks (including decontamination and waste volume reduction techniques)
- Experience of similar projects
- The possible end land-use for the installation site

As well as providing a tool for assessing impacts and for developing mitigation measures, the EIA process will also result in the development of information needed in due course to facilitate monitoring the environmental situation as the project proceeds.

In the particular context of the emission of effluents that contain radioactivity, the ongoing objective is to demonstrate that these emissions remain within the requirements of the applicable nuclear or radiological protection standards. The radiological impacts of emissions are assessed as individual and collective doses both for the workers engaged in the project and for the general public.

8.4.7 Baseline Description

The description of the environmental baseline must be as complete as possible about the environment as it exists prior to performance of the decommissioning project, so that it can serve as a basis for assessment of the project's potential impacts. The interaction between the environmental factors defined by the baseline description and the actions occurring as a result of the decommissioning project is described as well.

As regards the scope and depth of the baseline description, and for economic reasons, the greatest use possible should be made of existing information, ensuring that it is accurate. The competent authorities and organizations in the affected area should be consulted to obtain the maximum amount of existing data, thereby reducing the overall costs. The scoping exercise carried out as part of the EIA has identified those environmental factors that need the most attention at this stage and for the impact prediction stage which comes later. The main environmental factors that would be expected to be included in any baseline description are outlined below.

Impact Factors Relating to the Natural Environment

Air. The quality of the air should be characterized in terms of the pollutants known to have potentially harmful effects on either human beings or the environment, particularly concentrating on those which may be released from the installation. A study should be made of the potential sources and quantities of emissions. The meteorological characteristics of the region should be investigated including temperature, rainfall, humidity, wind speed and direction and climate classification. This information is used to assess the capacity for contaminant dispersion in the atmosphere and may be a factor in the design of structures, for example if waste stores are to be built.

Water. The hydrology and hydrogeology of the land and the quality of surface water and groundwater should be characterized in relation to both human activity and the environment in general. In this respect, any alteration in water quantity, quality, spatial location and availability will have a major repercussion on both mankind and on plant and animal communities. Furthermore, water may act as a receiver of contaminants and information on the pollutant capacity and response should be collected, taking account of the likely use of the water. Information on the ecological value of the water should be included, as should economic

factors and other issues such as the role of the NPP in controlling water flow, including possible flood risks.

Land and Soil Factors to be investigated include land use (in terms of physical, chemical and biological parameters), soil type and quality, terrain morphology, erosion potential, ecological risk, and agricultural capacity. The contamination status of the soil should be clarified before the dismantling tasks begin. The soil studies should focus on the soils on the site and in the adjacent areas, which may be affected by release and dispersion of effluents.

Flora and Fauna The baseline description should include a study of the plant and animal species existing in the area surrounding the plant site, as well as of their habitats and distribution. Rare and protected species should be identified along with analysis of the nature of the habitats and ecosystems in the area. Studies should be carried out at appropriate times during the year to ensure that flowering plants are properly identified and that migratory species, present only for short time periods, are also considered.

The Landscape An assessment must be made of the quality of the landscape. This includes both objective and subjective assessment criteria in areas such as:

- Visibility, including the extent of the domain from which the installation is visible
- The quality of the landscape, characterized by its morphology, vegetation, plant formations, lithology, and presence of large bodies of water
- Human presence, including the nature and extent of man-made structures and other influences (e.g., agriculture) on the landscape

Noise and Vibrations The background noise level prior to dismantling should be ascertained, either from existing monitoring reports or through direct measurement. This information is critical in the determination of noise impacts which might require mitigation or compensation to be paid.

Of equal importance to noise, in terms of future predictions, are vibration levels expected to be associated with decommissioning works. It is necessary to investigate buildings and other structures likely to be at risk, to determine their likely resilience to vibration damage.

Identification of Potential Impacts

This work must be carried out in a structured manner, in order to ensure that all actions having the potential to cause an impact are identified and considered. Various methodologies allowing such actions to be identified are listed.

The actions relating to the decommissioning of a NPP that might cause impacts are defined on the basis of the project activities.

Each of these activities is made up of a set of actions that may potentially have an impact on the environment. The actions, or their scope, will vary depending on each dismantling alternative, this being deduced from the data specific to the projects to be assessed.

Included below is a generic list of the main actions to be considered. As indicated above, these actions should be identified in the EIA and their alternatives considered:

- Modification of the level of occupation or manpower
- Modification of the industrial site
- Modification of industrial buildings
- Modification of property limits
- Demolition of buildings
- Construction of new buildings

- Landfill and earth movements
- Siting and drainage
- Recycling of waste materials
- Transport of materials
- Handling of hazardous materials (radioactive and toxic)
- Work in monitored and controlled zones
- Treatment of liquid and gaseous effluents (radioactive and nonradioactive)
- Use of rubble tips or tips for inert solid wastes on or off site
- Storage or disposal of radioactive wastes
- Risks of dismantling (potential accidents and actions)
- Fires of various types (involving radioactive and/or toxic materials)
- Releases and leakage of contaminating liquids and gases
- Maintenance failures (e.g., leading to dropping of loads)
- Personnel accidents (e.g., falling from heights and impact by falling objects)
- Structural failures due to the action of external agents (e.g., earthquakes, flooding and sabotage)

The environmental factors that might be affected by impacts belong to the physical, chemical and biological media or to the social-economic media. The description of the environmental baseline to be included in the study characterizes these factors in the situation prior to decommissioning, so that the subsequent impact can be assessed.

In the following, a list is presented of environmental factors that may be affected by a decommissioning project, with a brief description of the impacts. It is important to emphasize the fact that this list may serve as a guide when applying the guidelines to a specific project. The EIA should develop a specific list drawn up from the environmental baseline of the particular installation being studied.

Air The dismantling works include the demolition of buildings, crushing of rubble, disassembly of plant and machinery, and movement of vehicles and machinery. All these activities lead to the emission of radioactive and nonradioactive gases, particulates, and aerosols, and affect the quality of the air.

Alterations to the local or regional climate would not be expected, since the dismantling activities will not lead to the release of significant quantities of material or energy that might result in such impacts. Consequently, the environmental factor that may primarily be affected is the air quality.

Land and Soil The importance of the factors included in this category varies considerably depending on the dismantling alternative selected. Any parts of the site to be released for unconditional use must be decontaminated, and the buildings demolished if no further use is foreseen for them. The rubble and wastes generated may be stored on-site or removed from it. If materials are stored on-site, the project has to include a design for safe storage facilities. The potential modifications of the land will be caused by the refilling of gaps, leveling operations, the compacting and re-profiling of the terrain and, in certain cases, the removal of underground structures. The deposition on the surface of the soil of contaminated particles emitted during the dismantling operations might affect soil quality, although the contaminated areas would be strictly localized and would normally be within the site boundary. In view of the above, the main environmental elements likely to be affected are natural materials used for construction, soil replacement, compacting and settling, and the topography.

Water The environmental factors vary depending on the hydrological and hydro-geological characteristics of the site. Consideration should be given to the possible contamination of surface water and groundwater as a result of releases and to contamination by leaches. Among the positive effects associated with decommissioning, common to all the alternatives analyzed, special mention might be made of the elimination of thermal contamination caused by the need to dissipate the surplus thermal energy arising during plant operation. The inclusion of such a benefit in the EIA is dependent upon the definition of the project baseline. The removal of artificial surfaces (occupied by buildings and roads) modify surface water runoff, the drainage of the plot and infiltration to the groundwater. Consequently, the aquatic environmental factors that might be affected are fundamentally water quality, water resources, the hydrological regime, aquifers and marine contamination.

Flora The effects on flora are due fundamentally to the emission of particles during the work with the potential to cause indirect effects by their deposit on land and leaf surfaces. The environmental factors that may be affected include species diversity, positive or negative effects on rare or endangered species, productivity, stability, and plant communities.

Fauna Effects on the habitats and/or behavior of certain species may arise as a result of increased noise levels and also changes in flora (e.g., food plants), as noted above.

Factors which may be affected include diversity, positive or negative effects on rare or endangered species (including fecundity), the stability of the ecosystem, food chains, and animal communities.

Landscape The landscape should be considered an integral part of natural resources. The scope of the modifications of this environmental factor varies considerably from one dismantling alternative to the next. In general, the demolition of buildings and structures decreases the visual impact associated with a NPP.

Noise and Vibrations Nuclear power plants are large structures, made of reinforced materials. There will necessarily be a lot of noise associated with dismantling works, and the transport from the site of dismantled materials will lead to heavy traffic noise and associated vibrations.

Land Use The factors encompassed depend heavily on the specific project and on the dismantling alternatives, as a result of which no general patterns can be established. All of the alternatives analyzed imply a total removal or partial reduction in classified land on-site (land which will be subject to restrictions on use). As a result, the net effect is of restoration of land for other uses.

This affects leisure and recreation, the development of tourism, the availability of land for industrial, commercial or residential development, changes in the use of industrial land, surplus areas, and rights of way.

Cultural Factors The factors included depend on the site location. The factors considered may include cultural heritage and archeological remains.

Infrastructures Factors which may be considered under this heading include transport and communications networks and services, water supply, electricity supply, commercial and industrial equipment, and sewerage.

Generally, the dismantling activities cause an increase in vehicle traffic, which may be more or less significant, depending on the geographical location of the plant, the dismantling

alternative selected and the specific project. Dismantling activities do not require additional public services, such as sewers, etc., since the number of dismantling personnel is expected to be somewhat fewer than those previously involved in plant operation. As regards water supply, electricity supply and sanitary networks, the subsequent use of the site affects the permanence, or otherwise, of the installations.

Human Factors In general, consideration may be given to the following factors under this heading: the quality of life, nuisance, health and safety, well-being, and lifestyle. As regards health and safety, the decommissioning project implies certain activities that give rise to radiation exposure of the workers and to a series of other occupational risks. The project and its associated documentation will have to identify such risks and will need to identify methods to prevent or minimize risks. The most important of these risks are associated with the following:

- Exposure to ionizing radiation
- Exposure to toxic products (e.g., aerosols containing lead, asbestos)
- Exposure to high concentrations of dust
- Falls, contact with electricity and other risks typical of construction work
- Exposure to high noise levels

Risks to the public should be established and documented, though these are considerably lower than those existing during the operational phase of the plant.

Population and the Economy In general, consideration may be given to the following factors under this heading: levels of employment, population density, migratory movements, population centers, economic benefits, the appearance of auxiliary industries, investment and expenses, the local, provincial and national economies, and energy consumption. In some cases, a significant social-economic effect may result from the ending of plant operations, which may result in lower employment, a reduction in revenue from taxes in the area and problems associated with a downturn in the industries supplying the installation. The number of workers at the installation is smaller than during the operational phase, although for some options there may be a short-term increase in employment associated with construction activities.

Impact Identification Matrix

A commonly used methodology for identifying of the impacts of a project on the environment consists of drawing up an identification matrix. This relates the project actions that might cause impacts on the components of the physical, chemical, biological, and social-economic environments affected. When there is an interaction, the intersection box of the matrix is marked with a symbol and the interaction is subsequently analyzed.

These matrices make it possible only to identify impacts, after which it is necessary to evaluate each cell marked in the matrix. Care should be taken to ensure that additional approaches are used in order to identify indirect and cumulative impacts, such as, network approaches.

► *Table 39* shows an example of a matrix applied to the decommissioning of a nuclear power plant, with consideration given to the options of “long-term storage” or “immediate dismantling.” These are more illustrative than the “no action” option because of their greater complexity. The intersection symbols used are only illustrative in this example; they must be identified for each particular project. This matrix should be used as a starting point in future studies and should not be regarded as a definitive indicator of likely impacts.

8.4.8 Impact Assessment

This phase includes evaluation of the effects that the project has on the environment. The qualitative evaluation of impact requires the application of assessment criteria similar to those previously indicated. For each factor, an assessment of the impact is obtained on the basis of the indicated classification. For the quantitative assessment of impacts, comparisons can be made with detailed impact indicators, where they are sufficiently well developed.

Impact Indicators

As more environmental research is carried out, environmental indicators begin to play a more important role in the assessment of impacts. Impact indicators constitute a particularly useful tool when they reflect the value of a parameter that measures an impact whose limits are regulated, or when there are guideline values. For this reason, the use of indicators is recommended for those impacts that may be quantified by means of internationally agreed methodologies.

The impacts obtained in this way can be easily transformed into qualitative values.

Specific indicators can be developed for each particular project. As an example, some of the indicators, which can be used for certain factors previously indicated, are given below:

- Air: concentrations of radioactivity in the air, concentration of dust particles in the air, effluent flow, level of acoustic intensity or pressure, and affected population (human, animal, and plant).
- Land and soils: concentration of contaminants in the soil, contaminated surface, volume affected, and surface to be restored.
- Water: concentrations of contaminants in surface waters, volume of releases, water consumption, priority routes for infiltration, and changes in temperature gradient.
- Flora: number and identity of species (especially protected species that might be damaged), areas in danger of contamination and areas with increased potential for fires.
- Fauna: number and identity of species, especially protected species that might be affected, and migration routes.
- Landscape: visual quality, changes in and/or destruction of existing structures, volume of earth movements, type and location of embankments, and cleared areas.
- Noise and vibration: noise levels adjacent to inhabited properties, location of inhabited properties, location of susceptible (to vibration damage) structures, etc.
- Land use: surface area of site to be reclassified for free use, following decommissioning.
- Infrastructure: energy supply, changes in the transport network, and levels of use.
- Human factors: doses due to levels of radiation in the area and from radioactive effluents; areas with high levels of noise and inputs of atmospheric contaminants, etc.
- Population and economy: changes in local revenue from taxes and special levies.
- Level of employment, population required to change the activity performed to date, etc.

The following sections describe major issues regarding the assessment of impacts for a nuclear power plant decommissioning project.

Radiological Impacts

The radiological impacts of the different dismantling alternatives result in different doses occurring, at different times, to different groups of people. The doses are due to changes in the

installation, as a result both of the activities involved in decontamination and dismantling themselves and of the duration of each phase.

The health effects, expressed in terms of radiation dose, correspond firstly to the normal execution of the different alternatives, and secondly to the effects of possible accidents for each alternative considered.

In assessing the radiological safety of dismantling, consideration needs to be given to three important routes of exposure: inhalation, ingestion, and external irradiation from radioactive materials. The most important route of exposure for the workers involved in dismantling is probably the external irradiation. The ingestion and inhalation routes must be minimized through application of the protection techniques normally used in these activities (surveillance and control of radiological conditions, filtration, containment, use of confined areas with controlled ventilation, and protective clothing and breathing apparatus).

Inhalation is likely to be the dominant route of exposure for the public, since external irradiation due to radioactive materials deposited on surfaces and ingestion should both be minimized as exposure routes during dismantling.

In the transport of radioactive materials, application of the IAEA Transport Regulations (IAEA 1996d), as enacted in the particular country, will ensure that inhalation and ingestion are eliminated as routes of exposure for the public and workers in normal transport operations, leaving external irradiation as the dominant route.

Noise and Vibrations

Another important and significant indicator for a nuclear power plant decommissioning project is the noise level. It is important to determine the characteristics of the noise produced: a continuous noise is one whose level is constant with time or has only minor variations; intermittent noise varies continually over time.

It should be determined whether during the dismantling work the operation of fixed or moving machinery and the performance of activities will cause noise levels in excess of the permissible limits for those affected, the human population and biological communities in the natural protected spaces located close to the plant.

The environment receiving the impact and its characteristics has been defined in the Environmental Inventory; as a result, the study focuses on the potential sources of noise.

The main machinery that causes an increase in noise levels during a dismantling project is constituted by concrete crushers, cranes, pneumatic drills, compressors, diggers, bulldozers, dumpers, concreting plant, radial cutting machines, concrete mixers, ventilation and suction equipment, demolition hammers, electrical generators, conveyor belts, vibrating rollers, and motor-driven levelers.

In addition to the machinery, consideration should be given to the noise caused by the activities themselves, especially those relating to the transport, handling, and treatment of waste materials.

Account should be taken of the possibility of multiple noise sources emitting simultaneously. Some of the activities on-site that create noise are also likely to cause vibrations which may lead to off-site noise.

Of particular importance for vibration are heavy goods vehicles, and their routes should be carefully planned and controlled.

Air Quality

The dismantling activities cause an increase in the concentration of dust particles both in the atmosphere and on the surrounding land as a result of their deposition. The main activities that produce dust are those relating to the demolition of structures, walls, and floors and to rubble-handling work (e.g., transport and refilling).

The concentrations will be determined taking the following into account: the quantity and nature of the material, the size of the particles produced, the meteorological conditions of the area (mainly the distribution of wind frequencies and intensities), the EIA radius, and the duration of the work.

Mathematical models can be used to calculate the factors of dispersion and deposition. These factors, along with the rate of emission, give rise to the concentrations of particles in the air and deposition on the surrounding land.

Land Use

Land use is strongly conditioned by the possibility of storing off site the radioactive and nonradioactive wastes produced during operation and during the dismantling tasks themselves.

The alternatives of “Immediate Dismantling” and “Long-Term Storage” imply a total or partial reduction of the land area that will continue to be subject to restrictions on use, consequently leading to partial restoration of the site.

Results of Assessment

The results of the assessment are discussed not only in terms of comparison of the predicted impacts with the impact indicators, but also with the significance of the impacts.

If environmental indices have been calculated for groups of impacts or for the total impact, these will be discussed in the light of the weighting factors used and also, if information is available, in the light of sensitivity testing of alternative weighting schemes.

8.4.9 Mitigation Measures

An important step in the EIA process is the definition of measures to be applied to prevent, mitigate or correct the environmental impact of the decommissioning project.

Identification of Mitigation Measures

Each dismantling alternative implies the implementation of a series of measures on the negative effects of the project, the scope and duration of which depend on both the project itself and on the characteristics of the site and the installation to be decommissioned.

These measures may be preventive, if they remove the impact by modifying the project activity causing it, or mitigatory, if they cancel, attenuate, or modify the impact once it has been caused. Listed below is a generic set of measures designed to correct possible negative impacts. These are applicable to the alternatives analyzed, although the scope and duration will differ, depending on the dismantling project:

- Minimization of exposure to radiation (the ALARA principle) and to contaminants through the effective implementation of the programs required by the radiological protection and occupational safety standards in force, which will have to be sufficiently rigorous and detailed, and through the use of remote handling and/or robot-based techniques

- Minimization of atmospheric emissions of contaminants by means of the best and most cost-effective techniques available. These techniques should include the use of emission-capturing systems, high-efficiency filters, dust-emission control systems such as moving covers, confined enclosures, spraying with coagulant and fixing solutions, and the careful planning of operations for the handling, and transfer of dust-producing materials
- Minimization of releases to surface waters and of concentrations of contaminants through the recycling and re-use of waste waters, the conditioning of solid radioactive wastes and/or their treatment using the best and most economic techniques available
- Control of leachates in collecting areas and rubble tips
- On-line control and tracking of the production and location of waste materials, associated with methods promoting their recycling or reuse
- Control of landfills and clearing of areas
- Safe arrangement of the main areas used for the handling and storage of radioactive, toxic and other waste materials. Those areas, in which the quantities of materials and the risk are highest, will need to incorporate construction characteristics and equipment preventing flooding, leakage, spillage and uncontrolled or inadvertent releases, and to achieve confinement and control if such events were to occur. The design of such areas should include measures preventing uncontrolled access and consideration of the risk of fires
- Minimization of the extent of land required for the storage of radioactive wastes and installations during the latency period. This requires the intensive use of waste-production minimization techniques such as the following:
 - Detailed identification and characterization of materials prior to dismantling
 - Classification at the point of origin, elimination of intermediate stages, and decontamination prior to dismantling
 - Minimum secondary waste treatment
 - Prevention of cross-contamination and recontamination through the control of contaminated materials and of transport vehicles
 - Reduction of the number of potential sources of risk, preventing the dispersion of storage facilities and intermediate collecting areas, and consequently reducing transport operations
 - Reuse of materials from demolition and excavation operations for refilling and topographic restoration activities
- Application of a flexible fire protection system. Flexibility is an essential element, given the changing nature of the situation of the plant during dismantling
- General use of silencers on vehicles and machinery, and minimization or elimination of blasting operations
- Adequate personnel training, for all levels and areas of the organization
- Truck-washing station to prevent problems of mud on the roads
- Periodic overhaul of obligatory safety elements, e.g., fire extinguishers and alarms
- Maintenance of hygienic conditions in the toilets for the operation personnel and other users, as well as in the cafeteria and canteen areas if they exist
- Modification of buildings (e.g., size, shape, and color) to minimize the visual impact
- Restoration of the natural morphology and replanting with native species if the site is not to be re-used
- Measures to promote employment, including use of the available operation personnel and promotion of sub-contracting in areas around the plant


- Adherence to strict working hours and transport routes for movement of materials off-site and on-site

Although these measures, and others that might be specified for a particular project, are usually incorporated into the project, it is necessary for them to be defined to a degree of detail sufficient to demonstrate not only that attempts have been made to carry them out, but also that further improvements would not be justified.

Final Impact

Once the preventive and mitigative measures have been defined, the impact generated by the project may be re-assessed.

8.4.10 Environmental Surveillance Program

The general objective of the Environmental Surveillance Program is to establish a system that guarantees compliance with environmental, health and safety standards and ensures implementation of the prevention and mitigation measures contained in the EIS. As such, reference will be made to the monitoring plan developed as part of the EIA (see step 16 of  Fig. 21). This control should be accomplished in such a way as to allow:

- Determination of real effects
- Direct tracking of work
- Monitoring of compliance with the environmental protection prescriptions (mitigation measures)
- Provision of data for the preparation or calibration of models predicting the existing and/or residual contamination

In a decommissioning project, the radioactive inventory will have been considerably reduced when compared with the plant's former operational phase. The parameters to be controlled will be:

- Concentrations of contaminants in the air, including gases and particles of dust, at the site itself (work areas), at its boundaries and in the closest inhabited areas, as well as at other points where the highest concentrations have been forecast
- Noise and vibration levels
- Control of possible leaches from waste-storage areas (if appropriate)
- Levels of contamination in water, soils and sediments
- Levels of contamination in the flora and fauna of the areas closest to the site
- Phenomena of settling and erosion of landfills and embankments
- Efficiency of replanting operations, where applicable
- Surveillance of the use of authorized tips
- Surveillance of the cleanliness of roadsides
- Other surveillance operations required by the standards governing fires at industrial establishments and by civil protection standards

In order to control these parameters, it will be necessary to define the measuring points and the frequency and methodologies used for such measurements, as well as the values that are to be expected, in order to be able to detect differences between the actual situation and that predicted by the EIA.

The environmental surveillance program should include a chronological flowchart indicating the frequency of the tracking work to be performed and the effectiveness of that work. The environmental surveillance program will involve the following phases:

- Installation of a surveillance network
- Data acquisition, storage and classification
- Analysis of the information acquired and of the causes of deviations from the expected levels

Finally, periodic reports are required indicating: the levels of impact generated by the project, the effectiveness of the mitigation measures, the degree of accuracy of the EIS forecasts and the required modifications: enhancement of the environmental protection system and adaptive changes in the surveillance plan itself.

9 Decommissioning Cost Evaluation

9.1 Cost Evaluation Methodologies

The methods of evaluating and presenting decommissioning costs differ from one country to another and even from one operator to another within the same country. In all countries, total expenditures are estimated based either on costs resulting from the experience in similar situations or on particulars related to each installation. For example, the cost of dismantling a power plant is generally estimated at 15–20% of the initial cost of construction. Dismantling represents less than 1% of the production cost of each kWh in actualized figures, or 2–3% without discounting.

According to current accounting standards, two methods are used by companies to evaluate expenses which will occur in the future, but for which a precise date cannot be attributed:

- The method of current value consists of evaluating future expenses by their present cost. The result is corrected every year for inflation and is revised periodically for technical and legal changes. In this way, the value of future expenses does not depend on when the expenditure is made. This is the method generally used in France and Germany.
- The method of net present value consists of calculating the current value by discounting future costs. This method is used in Belgium, the United Kingdom, Italy, and Sweden.

When choosing the method of calculation, the various companies are largely influenced by the legal requirements and accounting practices used in their respective countries, as well as by contractual considerations:

- The net-present-value method is very sensitive to the precise calendar of the forecast expenditures and to the real yield (above inflation) expected in the long run of accumulated capital.
- The current-value method accelerates the making of the necessary provisions, which are made gradually during the operation of the installations, according to their estimated duration and pace of activity (economic and technical). The net-present-value method provides an annuity to cover future costs by comparing the difference with the previous year's calculations.

9.2 Account Presentation

Regarding the account presentation, in some countries (Germany, Belgium, France, the United Kingdom, and Switzerland) assessments must normally show the provisions necessary to cover future costs. Costs must be justified to controlling bodies such as boards of directors, independent inspectors, and official authorities. Consequently, the estimated total cost is checked at the time of the audit of the responsible entities. This system is the most widespread.

On the other hand, in countries where responsibilities for the end of cycle and dismantling have been transferred to agencies funded by taxpayers, these costs no longer appear in the producers' financial statements, but in those of the agencies. A wide variety of situations exists, covering both these cases and all situations in between.

Once future costs are recognized in the accounts of the organizations that will have to bear these charges, it is then appropriate to secure the availability of the necessary funds at the appropriate time. The operator either pays into an external fund controlled by the competent authorities or makes provisions in his accounts whether associated or not with a mechanism of internal funds managed inside the company.

9.3 Responsibilities and Financing

An organization ensuring the availability of funds is usually created by governments, which can take responsibility for final waste storage and/or dismantling (in Belgium and France, in particular, the government created public establishments responsible for the storage of waste). Based on the final usage of sites, the government is often directly involved in dismantling the installations and managing the waste.

In most European countries, the government is not responsible technically or financially for dismantling operations except when managing historical waste. Operators in Germany, Belgium, France, the United Kingdom, Sweden, and Switzerland take responsibility for both activities.

In certain countries, like Germany, Belgium, Sweden, and Switzerland, laws stipulate operator financing. In other countries, where the companies involved have been privatized, part of the future charges is subject to special agreements (e.g., USEC in the USA, Magnox Electric/BNFL in the United Kingdom).

The various existing practices concerning technical responsibility and financing have been analyzed by the NEA of the OECD and split into four categories:

- Control of funds and responsibility in a centralized account, with operations and their financing transferred to a central governmental organization; examples are ENRESA (Spain), ONDRAF/NIRAS (Belgium).
- Control of centralized funds accompanied by decentralized responsibilities. The companies remain responsible for operations and financing (e.g., Sweden and Finland).
- Decentralization of responsibility for operations with legal or contractual guarantee mechanisms (e.g., USA and Canada for the mining industry).
- Complete decentralization of technical and financial responsibilities, with companies remaining responsible for operations and their financing. This category includes the most situations in the Netherlands, Switzerland, the United Kingdom, and France, with various degrees of control of the financial responsibilities.

It is often the case that in the same country, the solutions adopted for dismantling and the management of waste differ.

9.4 Standard Criteria for Cost Evaluation

Decommissioning projects for various types of nuclear facilities have also demonstrated that decommissioning costs may show relatively large variations. Studies attempting to understand the reasons for these differences have been somewhat hampered by the fact that different types of costing methods are used, with different data requirements. Although some uncertainty is inevitable in any costing method, an understanding of the costing methods used in particular projects is useful to avoid key uncertainties. Difficulties of understanding can be encountered and invalid conclusions drawn in making cost comparisons without regard to the context in which the various cost estimates were made.

The basis of the cost estimates for decommissioning projects derives from the world-wide experience acquired either in decommissioning projects or in maintenance and repair work at operating nuclear facilities where conditions are similar to some extent. This experience was utilized in the past either directly as an analogue for estimating the costs of similar tasks in decommissioning projects or indirectly for the assessment of unit costs for basic decontamination and dismantling activities.

Different costing methods have different data requirements, however, and consequently their reliability depends on the extent to which the various data are available and applicable to the specific case being considered. Regardless of the assessment method, some uncertainty is inevitable in all estimates of future costs, and no costing method is generally superior to others in this respect. However, analysis of the costing method may be useful in order to locate the key uncertainties in each specific estimate. It has been shown, indeed, that there is a potential for making errors, and that difficulties can be encountered in performing quick international cost comparisons. Numbers taken at face value, without regard to their context, are easily misunderstood and misinterpreted. This is due, among other things, to the fact that no standardized listing of cost items has been established specifically for decommissioning projects. Such a standardization would not only be useful for making cost comparisons more straightforward and meaningful, but would also provide a good tool for cost-effective project management.

The European Commission (EC), the IAEA, and the OECD-NEA agreed to start a coordinated action in order to produce a standardized listing of cost items and related cost-item definitions for decommissioning projects. Such a standardized list, as described previously, would facilitate communication, promote uniformity and avoid inconsistency or contradiction in the results or conclusions of cost evaluations for decommissioning projects carried out for specific purposes by different groups. The resulting list represents a uniform and more complete approach to decommissioning costs, and is hoped that the standardized list will be widely accepted and used.

9.5 Cost Evaluations

9.5.1 Overview

The total cost of decommissioning is dependent on the sequence and timing of the various stages of the program. Deferment of a stage tends to reduce its cost, because of decreasing radioactivity, but this may be offset by increased storage and surveillance costs.

The cost of decommissioning nuclear power plants is based on the following factors:

- The sequence of decommissioning stages chosen
- The timing of each decommissioning stage
- The decommissioning activities accomplished in each stage

In addition, costs depend on such country- and site-specific factors as the type of reactor, waste management and disposal practices, and labor costs.

Total decommissioning costs include all costs from the start of decommissioning until the site is released for unrestricted use. It is assumed that each facility will eventually be decommissioned to Stage 3, because some radioactivity will continue to exceed the limits for unrestricted access to the site for a much longer period than provided for in Stage 2. Hence, the total cost will either be that of an immediate Stage 3 decommissioning or that of a delayed Stage 3 plus the intermediate stages.

The cost estimates are based on previous decommissioning and decontamination experience, on the cost of maintenance, surveillance and component replacements, and on the cost of similar nonnuclear work. They are also based on a minimum storage period of 30 years after Stage 1, to allow for significant decay of radioactivity, and a period of 100 years after Stage 2, to allow worker access, generally without the need for shielding or remote operations. Estimates have been made by several European countries as well as Japan, Canada, and the United States.

Several methods of financing the decommissioning costs can be used, depending on the circumstances of each utility and the country in which it operates. In several countries, a fund of some type has been established or proposed to assure the availability of financing. This is usually done by estimating the cost of decommissioning at the end of the normal plant lifetime and requiring payments, either annually or on a charge per kilowatt-hour basis, to ensure that this sum is in place. This estimate is updated regularly and the charge adjusted accordingly.

The drawback to this system is that the amount estimated would not be in place if the plant were to be shut down before the end of its normal lifetime. To avoid this, a fund could be established at the start of the plant's operation which would cover the cost of decommissioning whenever it became necessary. However, this represents a heavy burden for the utility as construction and start-up costs are already high, and thus, although it may be imposed by law, this solution is not favored by many utilities.

The total cost of decommissioning is dependent on the sequence and timing of the various stages of the program. Deferment of a stage tends to reduce its cost, due to decreasing radioactivity, but this may be offset by increased storage and surveillance costs.

Financing methods vary from country to country. Among the most common ones are:

- External sinking fund (Nuclear Power Levy): This is built up over the years from a percentage of the electricity rates charged to consumers. Proceeds are placed in a trust fund outside the utility's control. This is the main US system, where sufficient funds are set aside during the reactor's operating lifetime to cover the cost of decommissioning.
- Prepayment, where money is deposited in a separate account to cover decommissioning costs even before the plant begins operation. This may be done in a number of ways, but the funds cannot be withdrawn other than for decommissioning purposes.
- Surety fund, letter of credit, or insurance purchased by the utility to guarantee that decommissioning costs will be covered even if the utility defaults.

In the USA, utilities are collecting 0.1–0.2 cents/kWh to fund decommissioning. They must then report regularly to the NRC on the status of their decommissioning funds.

9.5.2 Cost-Assessment Methods

Various methodologies are available for the calculation of decommissioning costs. The methodologies present different level of reliability and precision and are used according to the different objectives of the evaluations.

The major reasons that usually lead to the need of a cost evaluation are the following:

- To provide an input for the decommissioning funding during plant operational life
- To compare costs associated with different strategies for the decision-making process
- To prepare long-term budgeting and cash flow
- To provide a tool for project control

According to the above objectives, the methods include:

- Scaling up or down similar plant evaluations or experiences according to plant power, total plant activity, waste masses, or other criteria
- Simple calculations based on unit costs for a number of overall parameters like mass of activated metals, mass of contaminated concrete and mass of contaminated metals. This method can also be used for a generic power plant (not site-specific)
- Detailed site-specific calculations based on a very detailed bottom-up approach, separating each elementary work package

In the last case, a detailed database and a computer code treating a large amount of information are needed. The procedure for the calculation is generally the following:

Input data:

- Mass, activation and contamination analysis
- Strategy
- Organizational structure, work organization and personnel costs
- Boundary conditions (e.g., laws, standards and regulations, clearance levels, waste-disposal costs)
- Decommissioning technologies
- Operational practices and personnel performances

Output data:

- Actualized costs
- Overnight costs
- Cash flow
- Time schedule of the activities and their logical structure
- Manpower
- Waste characteristics and streams
- Worker doses

9.6 Cost Calculation Model Example


The procedure for the collection of the needed input data and evaluation of the specific plant data covers the following working tasks:

- Cost structure: definition of a list of all necessary decommissioning activities.

- Mass analysis: calculation of the decommissioning masses, radioactive waste, and radioactive reusable material based on the existing inventory of the plant.
- Calculation of the decommissioning activities: estimation of the cost, personnel capacity, and expected radiation exposure for every decommissioning activity.
- Elaboration of a time schedule: definition of the sequence of the decommissioning activities.

The key elements of the STILLKO 2 cost estimating process are described in the following sections.

9.6.1 Cost-Breakdown Structure

The cost breakdown structure (CBS) includes all decommissioning activities that are necessary for the successful completion of the decommissioning project, beginning with the licensing procedure up to green field status at the end. The CBS is organized into different levels in a hierarchical structure.  *Figure 22* shows this organization.

On the first level, the division of a decommissioning project is effected according to decommissioning phases, which are separated according to time and necessary permits.

On the second level, the decommissioning phases are divided into the following cost categories:

- Project management and project administration
- Planning and licensing
- Plant operation and security
- Plant technical activities for safe enclosure
- Preparations for dismantling

Phases	Subdivide the decommissioning effort into independent sections which usually require separate licenses. Operation (Ph 1A), SEP preparation (Ph 1B), SEP (Ph 2), Site release (Ph 3), Site restoration (Ph 4).
Cost categories	Subdivide the phases into sections which are important for the planning and implementation General planning and licensing, dismantling, decontamination, waste management, project management and administration, plant operation and security, etc.
Areas	Allocate cost categories to building areas. Plant, controlled area, ER, EA, ET and AT, support building for SEP, storage facilities, safe enclosure area, conventional area.
Tasks	Subdivide the cost categories within the areas into sections which allow a time and personnel oriented planning. About 200 tasks conditioning of primary waste, packaging of primary waste, release measurements, etc.
Activities	Subdivide the tasks into sections which allow a clear cost calculation. Ex: work permission, preparation of working area, restoration and cleaning of working area, etc.

 **Figure 22**

Decommissioning cost breakdown structure (CBS) organization

- Dismantling activated and contaminated components
- Decontamination
- Conventional dismantling
- Waste management
- Radiological and conventional worker protection

These cost categories have been created according to functional points of view and represent the volume of the decommissioning activities. The cost categories may occur in every decommissioning phase, with suitable contents of the cost categories regarding the respective decommissioning phase.

The third level is used to allocate the decommissioning activities to the buildings and areas on-site.

Using this level in the cost structure, it is possible to assign the work directly to the place where it arises, but also to determine the sequence of the activities and their schedule in relation to the building.

On the fourth level, individual tasks are defined that allow room-by-room or system-by-system planning regarding the situation on-site.

The execution of the tasks may be done at the same in different buildings, building levels or rooms.

On the fifth, the lowest level, the decommissioning tasks are divided into decommissioning activities. These activities are formed in such a way that each of them can be individually calculated. The bases of the calculation are illustrated in the following sections.

9.6.2 Mass Analysis

The components that are to be dismantled during decommissioning are partially activated by neutron radiation and partially contaminated through their contact with radioactive media. Taking into account technical and economical aspects, these components will be safely recovered as residuals or, if this is not possible for technical or economical reasons, properly disposed as radioactive waste.

The masses arising with such decommissioning are divided into three groups, according to their origin:

- Primary masses are all equipment, components and buildings of the controlled area as well as of the nonnuclear part of the plant existing in the nuclear power plant at the beginning of the decommissioning work and which have to be removed
- Secondary masses are articles of consumption which are necessary for the dismantling, crushing and treatment of the existing primary masses
- Tertiary masses, or additional masses, are tools and equipment which are necessary for the execution of the decommissioning work and which are placed in the controlled area

For each of these mass types a plan will be made out concerning how and at what time they occur, which possibilities are available for their treatment, or how to pack the radioactive wastes.

Primary Masses

Knowledge of the primary masses, including the pertinent radioactivity inventory, the geometry of the parts and the place of the installation, is a fundamental condition for the calculation of the costs.

As the decommissioning of radioactive waste and the unrestricted use of residuals also include external costs, the handling and whereabouts of the primary masses are to be defined in order to calculate the costs. These definitions are called “Mass Distribution.”

► *Figure 23* shows the different possible ways of handling and disposal.

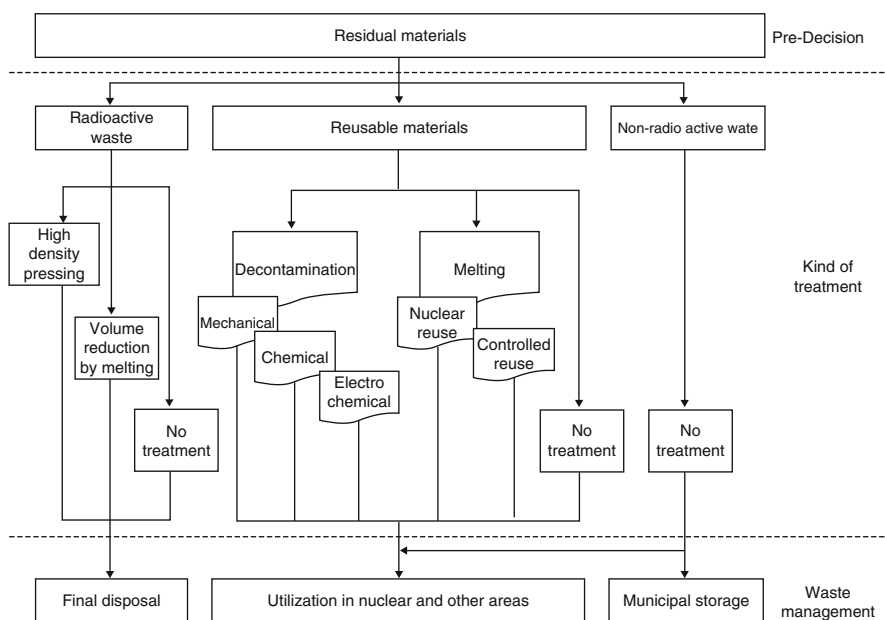
It is supposed that the prefixed result aimed at for each method of treatment will be achieved. After having executed all steps of sorting, attributing and calculating, it reveals which masses have to be treated with which method, which masses have to be disposed as radioactive waste, and which masses can be unrestrictedly used.

Secondary Masses

The determination of the arising secondary masses is important for the calculation of the costs for two reasons:

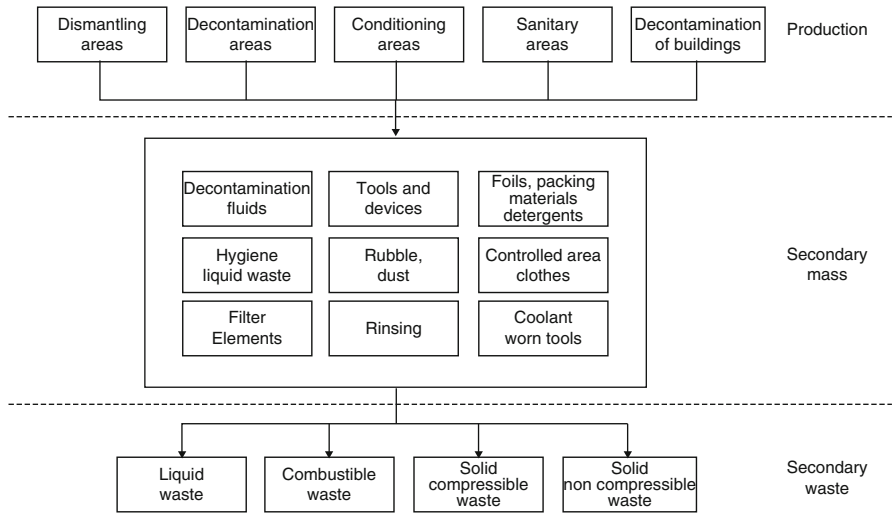
- In general, the activity inventory of the secondary masses is very high, as, for example, contamination is extensively removed from the primary masses during the decontamination process and concentrated on a possibly small secondary mass
- During chemical and/or electro-chemical decontamination, aggressive media are produced, which demand quite costly reprocessing

In the course of the decommissioning work, the secondary masses will be treated and reprocessed on-site to the greatest possible extent, so that a form will be achieved that can be disposed. The secondary masses cannot be recycled and have to be added 100% to the radioactive wastes. In the following, we will therefore talk about secondary waste. ► *Figure 24* shows the basic interrelations in the production of secondary waste.



■ **Figure 23**

Mass distribution model for primary and additional waste



■ **Figure 24**

Secondary mass and secondary waste

The main sources of secondary waste are dismantling and the activities for treatment of primary masses, especially the decontamination process. During decommissioning the following types of secondary wastes are produced:

- Solid, combustible secondary wastes. The most frequent ones are:
 - Work clothes worn in the controlled area
 - Cleaning wool
 - Paper

These waste materials are collected in plastic bags, pressed, packed into containers, and transported to an external incineration plant. The ashes are disposed as radioactive waste.

- Solid, noncombustible secondary wastes:
 - Contaminated tools or tool accessories
 - All kinds of plastic foils, adhesive tapes, etc.
 - Jointing material, chips and slags resulting from the dismantling of the components
 - Contaminated shielding material
 - Concrete rubble produced during the decontamination of building surfaces by removal of the surface layers

The noncombustible secondary waste is treated like contaminated components. Part of these secondary wastes can be pressed by high pressure to reduce the volume to be disposed.

- Filter materials

When dismantling contaminated or active parts by means of thermal separation methods, an additional exhaust system will be provided directly at the separation line in order to keep the exposure to aerosol of the air in the building to a minimum. The exhausted air will be cleaned by means of mobile filtering units. By doing so, filter media, including dusts separated from the air, are produced. The filter waste will be packed into barrels and disposed as radioactive waste.

Liquid secondary wastes are produced in the following areas:

- During the decontamination. In order to pre-decontaminate, an oxidic method will be employed, for example, for removing the oxide films and cleaning surfaces
- For chemical decontamination, an acid mixture consisting of HNO₃ and hydrofluoric acid will be used
- After treatment with the acids, the parts will be rinsed with water
- During the mechanical decontamination of metallic parts by means of high pressure water or steam jet appliances, which may contain abrasive additives, radioactive liquid waste polluted with suspended solids is produced
- During the decontamination of building surfaces, radioactive liquid waste polluted with suspended solids is produced
- In the hygiene area, i.e., in the hot-laundry area and decontamination of personnel, low-radioactive liquid waste polluted with suspended solids is produced

In order to estimate the quantities of secondary waste arising in these areas, it is necessary to execute different model assumption experiments. In detail, the needed quantities of the different acids and decontamination solutions have to be found out. On the basis of a calculation model, which takes into account the quantity of the parts to be decontaminated, the assumed thickness to be removed as well as the time available for the decontamination, the size and equipment of the decontamination area is determined. In this calculation model, the consumption of decontamination solutions resulting from the production of iron salts and the washing out losses, is also taken into consideration.

The liquids will be prepared for disposal by performing the following procedures and/or combinations of procedures:

- Neutralization
- Precipitation
- Evaporation
- Centrifugation
- Immobilization of the concentrates

Tertiary Masses

The dismantling and treatment of the primary masses as well as the reprocessing of the secondary masses demand the employment of equipment and tools, which will be especially installed for the decommissioning of the controlled area. After having served their purpose, the tertiary masses will be treated like primary masses. If possible, they will also be decontaminated and unrestrictedly used.

9.6.3 Calculation of Decommissioning Activities

Decommissioning Cost

For each activity of the cost structure, the following decisions have to be made and/or the related quantities estimated:

- Employable technology
- Necessary tools and equipment
- Other articles of consumption

- Required manpower, amount of labor, and duration of an activity
- Expected personnel radiation exposure

After determination of these data, it is possible to calculate the costs of each activity. The following types of costs are distinguished:

- Personnel costs as the product of the resulting amount of labor and payroll costs
- Costs for facilities, machines, special tools, and devices (expenses or rent)
- Costs for articles of consumption such as saw blades, drilling devices, clothes for the controlled area, acids for the decontamination and others
- Fees for the license and the disposal of radioactive wastes
- External costs for all activities which may not be carried out on the decommissioning site, for example incineration or super-compaction of radioactive wastes, melting for unrestricted use, etc.
- All other costs, e.g., insurance

Employable Technology

The technology and procedures employed for decommissioning are selected according to the following criteria:

- Radiation exposure of working personnel (ALARA)
- Production of secondary waste
- Safety
- Economic efficiency

The selection depends on the respective state of technology. The most important and especially required techniques for decommissioning are the following:

- Dismantling and size-reduction techniques
- Decontamination techniques
- Techniques for the safe and harmless recovery of residuals
- Techniques for radioactive waste disposal
- Measuring techniques for radiological protection

Necessary Tools and Equipment

During the decommissioning of a nuclear power plant a large number of marketable equipment will be employed. After recognizing the necessity of a certain device in an activity, it will be selected and the costs will be calculated.

Furthermore, special equipment and tools will also come into use during decommissioning. In the last few years, various research projects have been carried out in order to develop such special equipment. Many of them have passed their test phase and are ready for use. The selection of such special equipment is based on previous decommissioning experiences as well as on research results that are taken into consideration and analyzed. If necessary, special devices will be developed for single cases and the respective costs are considered as well.

Other Articles of Consumption

Other articles of consumption are, for example:

- Cutting gases
- Coolants

- Clothes for the controlled area
- Cover foils, one-way packages, adhesive tapes
- Decontamination agents

What aids are necessary and in what quantity depends on the technology employed and from the masses to be dismantled or treated.

Required Manpower and Duration

The execution of decommissioning requires qualified personnel who are accustomed to work in the controlled area. The personnel organization will be structured in a way that all requirements of decommissioning are met. The number of personnel required for each activity will be estimated. The criteria and boundary conditions for these estimates are the following:

- Amount of labor to be expected
- Room conditions
- Local radiation levels
- Use capability of tools and devices
- Already available equipment, e.g., lifting devices

The number and qualifications of the personnel are determined. The duration of one activity results then from the following formulations:

- The duration will be estimated
- The duration of an activity is a function of other activities
- The amount of labor is calculated using specific cost values (e.g., man-h/kg) in connection with the masses and other ratings regarding the plant

If the number of personnel is established at the same time, it is then possible to find out the duration of an activity.

The product of the duration and the personnel in the amount of labor.

Expected Personnel Radiation Exposure

The decommissioning activities will be carried out according to applicable radiological protection regulations, so that radiation exposure is as low as possible (ALARA principle). Determining the radiation exposure to be expected prior to carrying out the measure is an important criterion.

For this reason, the decommissioning plan includes a calculation model for the determination of the collective dose which is based on the activities as defined in the cost structure. An average dose rate will be assigned to every activity. Multiplying by the amount of labor, gives the overall activity dose (man-Sievert).

9.7 International Comparisons

9.7.1 Overview

Decommissioning cost evaluation comparisons carried out at the international level have always shown a large spread in relation to a number of factors, i.e., the specific conditions of the plant,

the national regulatory framework and local social-economic factors. Among the first, staff organization, on-site infrastructure, plant radiological characterization and the duration of the entire project can be mentioned as examples. Among other boundary conditions, the availability of a national waste disposal site with fixed prices and criteria for package acceptance and standards for unconditional release of radioactive materials with associated demonstration procedures are the most important.

In particular, it should be noted that most cost evaluations have been ordered by utilities from specialized companies with the main objective of assuring the adequacy of the decommissioning funding accumulation scheme during plant operation.

More recently, with many NPPs decommissioned, in decommissioning or close to decommissioning, and with the privatization process also involving the need for clear accounting of future decommissioning costs at the time of selling shares, cost evaluations became more important and subject to closer scrutiny by various organizations.

Various companies have specialized in decommissioning cost evaluations. Two important examples are TLG Services Inc. in the US and NIS in Europe, the latter recently extending its interest from the German to the entire European market. Other companies are in the market with increasing expertise but in the following we focus on the studies performed by the above companies, which are the most important in the international field.

9.7.2 Variations in Cost Estimates

Cost estimates are more and more based on the accumulated world-wide decommissioning experience. They are internationally evaluated as being 15% of the total investment, but from one country to another there may be differences due to national licensing policies, requirements and practices.

The factors affecting decommissioning costs can be grouped into the following categories:

- Scope of calculation
- Decommissioning timing
- Technical factors
- Waste-management system
- Administrative factors (labor costs and legal systems)
- Financial factors

The scope of the calculation turns out to be the single most important factor. The smallest scope considered comprises only the radioactive parts, while the largest scope includes some spent-fuel management. Normally the scope should include all the activities needed from the cessation of power production in the reactor until all the radioactive material has been removed off-site as radioactive waste and the site has been released for other use. The cost of the spent-fuel management should not be included. The differences in costs due to differences in scope could be a factor of two or more.

The timing of decommissioning, i.e., immediate compared to delayed decommissioning, will also have a great influence, particularly if undercounted costs are used. The costs of surveillance during the dormancy period will be important. The result could be quite different if discounted costs are used.

The most important technical factor is of course the type and size of the reactor, but this was not considered specifically in the study. On the basis of the literature, however, it can be

concluded that the cost of decommissioning a gas-cooled reactor would normally be larger than for a light-water reactor of similar electricity output.

During decommissioning, a large volume of radioactive waste has to be managed. The cost of decommissioning will therefore be affected in different ways by the specific waste-management system in the country. The influence will be both direct (e.g., fees for transport and disposal) and indirect (e.g., optimum cutting sizes, need of waste treatment and decontamination). In the study it was shown that this single factor could account for differences of more than 30% of the total decommissioning costs.

Decommissioning will be quite labor-intensive and thus the cost of labor in different countries will have a substantial effect. In the study a difference of up to 30% of the total cost was been found.

Finally, when comparing different cost calculations, caution is recommended with regard to the presentation of decommissioning costs from the financial point of view. Factors such as currency exchange rates, year of cost levelization, and the financing system considered should be kept in mind. The factor which could greatly change the global cost figures is, however, whether discounted or undiscounted costs are used. In cases where decommissioning extends over many decades, even a moderately low discounting rate makes the present value of the total cost substantially smaller than the basic undiscounted costs. Discounted cost 30 years ahead will, for instance, be only 25% (at a 5% discount rate) of the undercounted costs. Discounted cost estimates are useful for financing considerations and for comparison of different decommissioning strategies for the same facility, but for understanding the differences between estimates for different plants, undiscounted cost estimates are more appropriate.

In conclusion, the study shows that great care must be exercised when comparing different decommissioning cost estimates, as the boundary conditions may vary substantially. Only some of the different boundary conditions reflect real differences, while others reflect differences in scope and planning. It is thus not possible to define a universally applicable decommissioning cost.

Cost estimates are usually established by the company responsible for the plant operation, but they are reviewed and approved independently by regulators or ministries. This means that there is a regular adaptation of the amount of the fund and the national energy policy. Should this policy lead to an early shut-down of the plant (with respect to its economical life time), the fund would have to be reassessed accordingly.

The resulting funds are either set aside in a special fund in the company accounts or managed by an organization in charge of radioactive-waste management or by specific government funds.

In any case, the distribution of responsibilities is usually clearly defined in the national regulation establishing the national policy (responsibility for plant decommissioning, cost establishment and review, collection and management of the necessary funds). It is important to link responsibility for decommissioning activities and management of the provision funds, to make sure that the latter will be available in due time. The availability of funds is also dependant upon long-term economic stability.

It is unfair for decommissioning funds to be taxed differently from other types of provision funds (pension funds, etc.) because it would mean an increase of the money to be collected in order to make sure that the necessary amount is available in due time and thus indirect taxation of the customer. In addition, this special taxation would be an additional penalization of nuclear energy, which is the only electricity-production source whose costs include external costs.

It may nevertheless happen that a NPP is shut down before its useful life-time is over, before enough funds for its decommissioning have been set aside. This happened, for instance, in Italy where all NPPs were shut down by a political decision. Funds necessary for decommissioning, considering the adopted strategy and local conditions, shall be provided both by the owner of the plant (on the basis of the set-aside fund) and by the “electricity system,” on the basis of a limited charge per kWh.

9.7.3 Cost Estimates in the USA

In the USA in recent years, discussions have been held on the most appropriate methodologies and principles to be used in decommissioning cost evaluations. The most important issues are presented below to provide a proper perspective on various available estimations.

As discussed before, one of the reasons to assess decommissioning costs even well before final plant shutdown is to demonstrate to the authorities (in the US system to the NRC) the adequacy of the funds accumulated. The NRC has defined a minimum value, i.e., a lower threshold for the funds to be accumulated, respectively for BWR and PWR plants. However, as far as the NRC is concerned, these funds should cover only activities necessary for site release from any radiological restraints (license termination) and not for the remaining dismantlement activities to return the site to “green field” regardless of the Decon or Safstor strategy to be adopted. On these bases, the NRC adopts simplified methodologies, average plant features and conditions without considering project duration. In the last revision of their evaluation, in 1999, the NRC defined this lower threshold as 290 M\$ for a generic PWR and 370 M\$ for a generic BWR.

On the other hand, the Nuclear Energy Institute (NEI), on the basis of independent analyses, has proved that the above thresholds are underestimated because the methodology is not adequate the cost of the final disposal of the radioactive waste is not properly taken into account. In addition, the NEI is trying to include in US legislation the requirement to also include in the total cost evaluation the costs associated with the final plant dismantling, i.e., with the dismantlement of the noncontaminated buildings as well as the decontaminated buildings and structures, as already required in some US states.

In 1999, TLG Services Inc. (USA) presented a decommissioning cost assessment for 30 BWRs and 60 PWRs carried out between 1990 and 1997 (see [▶ Tables 40](#) and [▶ 41](#)). Costs are evaluated for DECON strategy and include spent fuel disposal, radioactive waste disposal, final site restoration and contingencies associated with the uncertainties of the process. In the tables costs associated with the site radiological release (or license termination) are identified, since they are the basis of the NRC evaluation, as discussed above. As usually accepted internationally, costs associated with spent fuel disposal are not included in the total costs. All costs are presented in 1998 dollars. It can be easily verified that costs associated with license termination present a wide spread, but they are above the minimum NRC thresholds.

A separate source of data is provided by the official assessments that each US NRC licensee has to present, i.e.:

- Post Shutdown Decommissioning Activity Report (PSDAR), to be presented to the NRC within 2 years from the final shutdown and before initiating any significant decommissioning activity.
- License termination plan (LTP), to be presented 2 years before receiving the License Termination Approval.

Table 40
Decommissioning cost evaluation for boiling-water reactors (BWRs) (TLG, 1998)

Plants	Net MWe	Base year	On-site High Level Waste storage costs – MS-1998	Site restoration cost [2] MS-1998	License termination decommissioning cost MS-1998	Total contingency (%)	Total decommissioning cost incl. site rest MS-1998
<i>Boiling water reactors</i>							
Brunswick 1	767	1993	n/a	49,512	318,357	21.24	367,869
Brunswick 2	754	1993	n/a	64,363	281,664	20.99	346,027
Clinton Power Station	930	1996	144,097	n/a	457,228	19.99	457,228
Cooper	764	1996	–	n/a	522,629	20.75	522,629
Dresden 1	207	1996	n/a	91,005	348,048	10.46	439,053
Dresden 2	772	1996	n/a	51,264	336,610	24.79	387,874
Dresden 3	773	1996	n/a	51,580	520,393	21.28	571,974
Duane Arnold	538	1993	n/a	n/a	406,004	16.02	406,004
Grand gulf	1,142	1993	18,123	88,762	411,931	21.39	500,693
Hatch 1	741	1997	n/a	n/a	382,916		382,916
Hatch 2	761	1997	n/a	n/a	466,109		466,109
LaSalle County 1	1,036	1996	n/a	84,590	312,514	24.12	397,104
LaSalle County 2	1,036	1996	n/a	36,600	427,521	23.51	464,121
Limerick 1	1,055	1995	30,425	35,881	360,729	22.61	396,610
Limerick 2	1,055	1995	n/a	56,596	483,484	21.70	540,081
Millstone 1	660	1997	–	n/a	505,850		505,850
Monticello	536	1996		14,453	298,040	22.07	312,493

Table 40 (continued)

Plants	Net MWe	Base year	On-site High Level Waste storage costs – MS-1998	Site restoration cost [2] MS-1998	License termination decommissioning cost MS-1998	Total contingency (%)	Total decommissioning cost incl. site rest MS-1998
Oyster Creek	610	1995	–	n/a	545,532	17.47	545,532
Perry	1,205	1993	n/a	73,354	567,779	16.71	641,134
Quad CMES1	769	1996		29,024	325,968	25.60	354,993
Quad CMES 2	769	1996		89,692	458,799	21.80	548,490
River Bend	936	1996	122,971	95,970	242,956	19.64	338,926
Susquehanna 1	1,032	1993	–	29,097	418,271	18.37	447,367
Susquehanna 2	1,038	1993	–	27,024	525,781	17.75	552,805
Vermont Yankee	504	1993		22,151	376,988	18.55	399,139

Table 41
Decommissioning cost evaluation for pressurized water reactors (PWRs) (TLG, 1998)

Plants	Net MWe	Base year	On-site storage of HLW cost [1] MS-1998	Site restoration cost [2] MS-1998	License termination decommissioning cost MS-1998	Total contingency (%)	Total decommissioning cost incl. site rest MS-1998
<i>Pressurized water reactors</i>							
Beaver Valley 2	833	1992	n/a	103,557	244,987	19.17	348,544
Connecticut Yankee	590	1992	n/a	124,179	290,062	16.23	414,241
Crystal River 3	821	1994	n/a	55,833	419,471	17.00	475,304
Davis Besse	877	1993	n/a	80,609	361,559	17.15	442,168
Farley 1	814	1993		43,427	308,546	19.41	351,973
Farley 2	824	1993		33,165	335,506	19.65	368,672
Harris	860	1993	n/a	38,405	394,382	19.10	432,787
Kewaunee	503	1992	76,104	43,915	338,346	15.35	382,261
Maine Yankee	840	1993	n/a	12,931	391,169	15.92	404,100
North Anna 1	911	1990	n/a	277,886	64,338	25.00	342,224
North Anna 2	909	1990	n/a	283,545	65,648	25.00	349,194
Oconee 1	846	1994		92,964	131,968	22.08	224,932
Oconee 2	846	1994		49,106	198,650	22.83	247,757
Oconee 3	846	1994	50,565	57,800	220,064	20.89	277,864

Table 41 (continued)


Plants	Net MWe	Base year	On-site storage of HLW cost [1] MS-1998	Site restoration cost [2] MS-1998	License termination decommissioning cost MS-1998	Total contingency (%)	Total decommissioning cost incl. site rest MS-1998
Prarie Island 1	503	1996	n/a	90,100	131,977	23.02	222,077
Prarie Island 2	500	1996			288,569	21.78	288,569
Robinson	683	1993	n/a	56,745	272,209	19.57	328,954
St. Lucie 2	839	1994	n/a	4,000	302,800	17.61	306,800
Surry 1	781	1990	n/a	223,717	61,273	25.00	284,989
Surry 2	781	1990	n/a	280,556	76,840	25.00	357,396
Three Mile Island 1	786	1995	n/a	19,680	528,257	17.16	547,936
Trojan	1,095	1993	5,360	n/a	364,563	13.18	364,563
Turkey Point 3	666	1994	10,023	36,906	255,425	17.95	292,332
Turkey Point 4	666	1994	8,383	38,422	316,884	17.67	355,306
V.C. Summer	885	1990	n/a	n/a	338,039	25.00	338,039

These documents are not currently available for all US plants. However, as an example, the license termination cost for Haddam Neck (PWR, 590 MWe) PSDAR (1997) is 344.4 M\$ (1996 currency). The corresponding value calculated in 1992 is 290 M\$ (1998 currency) and, finally, the LTP value is 410 M\$ (2000 currency). Adjusting all values to 2000 values the above values are:

- 1992 : 352 M\$
- 1997 : 405 M\$
- 2000 : 410 M\$

This shows that, calculating costs on the same bases, there is a cost increase trend due to increased costs of waste disposal and for activities not well evaluated in the past, such as, for example, the cost of the final site characterization.


It is worth mentioning that the cost associated with the final site restoration, as evaluated in the most recent study, is 19.3 M\$ (2000 currency).

SOGIN (Italy) performed in 2006 a study on decommissioning costs taking into account all available information. The result for USA plants (under decommissioning or operating) is shown in  [Table 42](#).

9.7.4 Cost Estimates in Europe

In addition to the OECD-NEA study mentioned above, and mainly based on related to European data, the organization of European electrical utilities (UNIPED) has published in recent years studies on how local boundary conditions may influence decommissioning costs. The most complete study was carried out for UNIPED by the NIS (Nuklear Ingenieur Gesellschaft, Germany) in 1997 (Comparison of European decommissioning costs, June 1997). The study covers 12 countries (10 European countries plus Canada and South Africa), whose utilities contributed with data, assumptions (including unitary costs) and methodologies. The exercise was to apply different assumptions and approaches to a single NPP, Biblis-A (PWR, Germany). The methodology used by the NIS was the same as used in Germany by the company for the periodic re-evaluation of decommissioning funds adequacy.

In this way, all differences could be traced to assumptions and boundary conditions. The result is that spreads as large as a factor of 6 were identified between the lowest cost and highest cost. One of the major factors in these differences was the different items included in the cost evaluations in different countries, such as the cost for spent fuel disposal. Once the items included were standardized the spread factor was reduced to two.

In  [Table 43](#) all details discussed above are presented except for contingencies. It should be emphasized that the purpose of the exercise was not to calculate the real decommissioning cost for the plant, but only, to identify the source of the cost spread.

The following data were not provided by some participants in the exercise, and, therefore, standard Germany data were used by the NIS:

- Some parameters of the group “Operation on-site, Project management” were not provided by Canada and France
- Some parameters of the group “Waste treatment, container” were not provided by the Netherlands and South Africa
- No parameters of group E were provided by Italy

■ Table 42

Decommissioning cost evaluation in the USA (SOGIN, 2006)

Unit	Type	Capacity (MWe)	Overall cost (2004 currency) (M€)	Mean cost (2004 currency) (M€/MWe)
Plants under decommissioning				
Big Rock Point	BWR	67	290	4.32
Maine Yankee	PWR	860	618	0.72
Connecticut Yankee	PWR	580	478	0.82
Rancho Seco	PWR	920	465	0.51
Yankee Rowe	PWR	185	432	2.33
SONGS 1	PWR	450	527	1.17
Operating plants				
Vermont Yankee	BWR	510	514	1.01
Fermi 2	BWR	1,100	734	0.67
Monticello	BWR	590	581	0.98
Oyster Creek	BWR	600	553	0.92
Palo Verde 1	PWR	1,240	502	0.40
Palo Verde 2	PWR	1,240	532	0.43
Palo Verde 3	PWR	1,240	565	0.46
Turkey Point 3	PWR	693	443	0.64
Turkey Point 4	PWR	693	443	0.64
St. Lucie 1	PWR	840	530	0.63
St. Lucie 2	PWR	840	530	0.63
Seabrook	PWR	1,160	533	0.46
Callaway	PWR	1,140	464	0.41
Wolf Creek	PWR	1,170	422	0.36
Prairie Island 1	PWR	525	484	0.92
Prairie Island 2	PWR	525	484	0.92
Kewaunee	PWR	543	485	0.89
Millstone 2	PWR	870	426	0.49
Millstone 3	PWR	1,140	454	0.40

Table 43 (continued)

Cost group	Working package	Belgium	Canada	France	Germany	Hungary	Italy	Netherlands	South Africa	Spain	Sweden	Switzerland	UK
	Measurements at building surfaces	4.7	4.9	5.0	5.5	5.5	4.8	5.3	5.7	5.1	5.9	5.6	3.7
D	Operation on-site, project management	112.4	89.2	126.3	125.3	89.7	57.9	119.4	40.2	69.7	36.6	98.3	48.3
	Radiological and worker protection	57.6	51.6	57.8	69.5	69.5	50.3	62.6	35.0	51.6	28.4	71.7	35.7
E	Decontamination	40.2	43.6	29.4	38.4	38.4	22.9	34.1	23.7	34.4	20.1	41.3	17.2
	Waste treatment, container	81.2	38.2	60.3	98.5	37.3	92.7	98.6	96.3	25.6	14.3	27.6	22.2
	Waste disposal, transport	40.5	9.0	56.3	98.9	46.1	98.9	46.7	3.8	28.5	10.0	21.7	49.7
F	Demolition of buildings, site recovery (nuclear part)	42.3	34.9	30.2	42.3	33.2	27.7	38.2	42.3	15.9	34.3	30.9	21.1
	Demolition of buildings, site recovery (conventional part)	67.0	37.8	35.4	ndc	35.8	32.5	60.7	ndc	18.9	40.1	36.2	21.9
		548.0	403.1	497.7	601.1	458.8	465.6	561.7	340.0	323.0	272.7	457.9	292.8

"Cost group" comparison in various countries for the Biblis-A NPP (currency: million DM) (NISUNIPED 1997)

It can be noted that, while the costs associated with the dismantling activities are very similar and differences can be easily explained by the different unitary labor costs, for the activities of Planning, Licensing and Project Management, the range is a factor of 3 and for waste disposal the range extends to a factor of 10, not including the extreme case of South Africa.

The available data on decommissioning costs for gas-graphite reactors cannot be easily compared. It is worth mentioning that in the UK the strategy adopted is a very long Safstore, which will extend for a period longer than 100 years.

Some information has been provided by ENRESA (the Spanish company in charge of decommissioning activities) for the Vandellós 1 plant, whose total costs have been estimated in the range of 300 million euros.

In the already mentioned study performed in 2006 by SOGIN (Italy), the decommissioning costs for European plants (under decommissioning or operating) are evaluated as shown in

► [Table 44](#).

■ **Table 44**

Decommissioning cost evaluation in Europe (SOGIN, 2006)

Country	Unit	Type	Capacity (MWe)	Overall cost (2004 currency) (M€)	Mean cost (2004 currency) (M€/MWe)
Switzerland	Leibstadt	BWR	1,145	445	0.39
	Muhleberg	BWR	355	230	0.65
	Beznau 1	PWR	365	168	0.46
	Beznau 2	PWR	365	168	0.46
	Gosgen	PWR	970	307	0.32
Germany	Reference plant	BWR	800	463	0.58
	Reference plant	PWR	1,200	398	0.33
	MZFR	HWPR	57	190	3.33
France	Brennilis	GCHWR	70	423	6.05
	Superphénix	LMFBR	1,200	1.060	0.88
	900 series	PWR	900	262	0.29
	1300 series	PWR	1,300	378	0.29
	1400 series	PWR	1,400	407	0.29
United Kingdom	Sizwell A	GCR	2 × 210	1.650	3.9
Italy	Caorso	BWR	860	485	0.56
	Garigliano	BWR	160	292	1.82
	Trino	PWR	270	293	1.09
	Latina	GCR	210	770	3.66

10 International Organizations Roles

Major international organizations are dealing with decommissioning in various roles and aiming at different goals. In the following section a brief review is presented, leaving to those interested the possibility to access to their web sites, where very often valuable documentation is downloadable for free.

10.1 UNO-IAEA (United Nations Organization-International Atomic Energy Agency)

The IAEA was created in 1957 in response to the deep fears and expectations resulting from the discovery of nuclear energy. Its fortunes are uniquely geared to this controversial technology that can be used either as a weapon or as a practical and useful tool.

The IAEA is the world's center of cooperation in the nuclear field. It was set up as the world's "Atoms for Peace" organization in 1957 within the United Nations family. The Agency works with its Member States and multiple partners worldwide to promote safe, secure and peaceful nuclear technologies. The IAEA Secretariat is headquartered at the Vienna International Centre in Vienna, Austria.

Decommissioning technology issues are dealt with the Division of nuclear fuel cycle and waste technology and in the waste technology section (WTS). The IAEA's WTS covers a broad spectrum of activities from radioactive waste characterization and conditioning to disposal, decommissioning and site remediation. The work covers the planning, technologies and approaches needed for the safe and efficient management of different types of radioactive waste, including waste from nuclear power plants, nuclear fuel cycle facilities, nonpower nuclear activities, decommissioning, and environmental remediation.

IAEA Decommissioning Activities include development of Safety Standards and supporting documents. Subjects include:

- Decommissioning of all types of facilities
- Release of the sites from regulatory control
- Release of material from regulatory control
- Safety assessment
- Management of contaminated material

The IAEA also publishes safety-related documents for each thematic or facility-specific area. These publications, commonly referred to as supporting documents, are designed to complement the Safety Standards.

A selected list of IAEA publications on the theme of decommissioning is presented in the References section.

10.2 OECD-NEA (Organization for Economic Cooperation and Development)

The NEA is a specialized agency within the OECD, an intergovernmental organization of industrialized countries, based in Paris, France.

The mission of the NEA is to assist its Member countries in maintaining and further developing, through international co-operation, the scientific, technological and legal bases required for the safe, environmentally friendly and economical use of nuclear energy for peaceful purposes. To achieve this, the NEA works as: a forum for sharing information and experience and promoting international co-operation; a center of excellence which helps Member countries to pool and maintain their technical expertise; a vehicle for facilitating policy analyses and developing consensus based on its technical work.

The NEA Secretariat serves seven specialized standing technical committees under the leadership of the Steering Committee for Nuclear Energy – the governing body of the NEA – which reports directly to the OECD Council.

The standing technical committees, representing each of the seven major areas of the Agency's program, are comprised of Member country experts who are both contributors to the program of work and beneficiaries of its results.

One of the committees is the Radioactive Waste Management Committee, within which there are two major groups dealing with decommissioning:

- The Working Party on Decommissioning and Dismantling (WPDD)
- The Cooperative Project on Decommissioning (CPD)

A list of major publications is reported in the section on References.

10.3 EC (European Commission)

Since 1979, the European Commission's DG Research has conducted four successive 5-year research and development programs on the decommissioning of nuclear installations performed under cost-sharing contracts with organizations within the European Union. The main objective of these programs was, and still is, to establish a scientific and technological basis for the safe, socially acceptable and economically affordable decommissioning of obsolete nuclear installations.

These programs were carried out by public organizations, research institutes and private companies in the Member States under shared-cost contracts and concerted actions. The main objectives of these activities were to strengthen the scientific and technical knowledge in this field, with a particular view to enhance safety and environmental protection aspects, minimizing the occupational exposures and dismantling costs as well as the radioactive waste arisings.

Within the EC program, *two databases* on decommissioning have been created:

1. EC DB TOOL for collecting technical performance data
2. EC DB COST for collecting data on waste arising, doses, etc.

Both are now being merged into one database, EC DB NET, which will be available on the internet (so far only, in first instance, for members of the project group).

The interest from the IAEA and the OECD/NEA and EC in the development of a common understanding of the decommissioning process led to the creation of a list of *Standardized Decommissioning Cost Item Definitions* (INCOSIT), another project under FP-4, to ease a world-wide comparability and transferability of data on decommissioning.

European Commission also proposes Directives, recommendations and laws of the European Union dealing directly and indirectly to the issues of decommissioning.

10.4 WANO (World Association of Nuclear Operators)

The World Association of Nuclear Operators (WANO) is an organization created to improve safety at every nuclear power plant in the world.

Part of the mission is to exchange operating experience and improve the safety culture. In these areas attention is given also to decommissioning activities.

10.5 WENRA (West European Nuclear Regulator Association)

West European Nuclear Regulator Association (WENRA) is a nongovernmental organization comprised of the Heads and senior staff members of Nuclear Regulatory Authorities of European countries with nuclear power plants.

The main objectives of WENRA are to develop a common approach to nuclear safety, to provide an independent capability to examine nuclear safety in applicant countries and to be a network of chief nuclear safety regulators in Europe exchanging experience and discussing significant safety issues.

In January 2009 the following publications are related to decommissioning:

- WGWD – Waste and Spent Fuel Storage Safety Reference Levels Report (version 1.0, working document)
- WGWD – Decommissioning Safety Reference Levels Report (version 1.0, working document)
- WENRA Reactor Safety Reference Levels January 2007

References

UNO-IAEA Documents

- UNO-IAEA (1970) Standardisation of radioactive waste categories. Technical report series no. 101. IAEA, Vienna
- UNO-IAEA (1975) International atomic energy agency, decommissioning of nuclear facilities, TECDOC-179. IAEA, Vienna
- UNO-IAEA (1983a) Decommissioning of nuclear facilities: decontamination, disassembly and waste management, technical reports series no. 230, IAEA Vienna
- UNO-IAEA (1986a) Methodology and technology of decommissioning nuclear facilities. Technical reports series no. 267. IAEA, Vienna
- UNO-IAEA (1986b) Safety in decommissioning of research reactors. Safety series no. 74. IAEA, Vienna
- UNO-IAEA (1988) Principles for the exemption of radiation sources and practices from regulatory control, co-sponsored by IAEA and OECD/NEA. Safety series no. 89. IAEA, Vienna
- UNO-IAEA (1990) Regulatory process for the decommissioning of nuclear facilities. Safety series no. 105. IAEA, Vienna
- UNO-IAEA (1992a) Concepts for the conditioning of spent nuclear fuel for final waste disposal. Technical reports series no. 345. IAEA, Vienna
- UNO-IAEA (1992b) Application of exemption principles to the recycle and reuse of materials from nuclear facilities, SS-111-P-1.1. IAEA, Vienna
- UNO-IAEA (1992c) INES – the international nuclear event scale, user's manual, revised and extended edition. IAEA, Vienna
- UNO-IAEA (1993a) Planning and management for the decommissioning of research reactors. Technical reports series no. 351. IAEA, Vienna
- UNO-IAEA (1993b) National policies and regulations for decommissioning nuclear facilities, TECDOC-7 14. IAEA, Vienna
- UNO-IAEA (1993c) Radioactive waste management glossary. IAEA, Vienna
- UNO-IAEA (1994) Establishing a national system for radioactive waste management, 1995. Safety

- series no. 111-S. UNO-IAEA, safety series no. 116 – design of spent fuel facilities. IAEA, Vienna
- UNO-IAEA (1995a) Summary record of the consultants meeting of 26–29 June 1995 on radioactive waste management and decommissioning costs, CT2506. IAEA, Vienna
- UNO-IAEA (1995b) Safe enclosure of shut down nuclear installations, TECDOC-375. IAEA, Vienna
- UNO-IAEA (1995c) Safety assessment of near surface radioactive waste disposal facilities: model inter-comparison using single hypothetical date. First report of NSARS-IAEA-TECDOC-846. IAEA, Vienna
- UNO-IAEA (1995d) The principles of radioactive waste management. Safety series no. 111-F. IAEA, Vienna
- UNO-IAEA (1996a) Quality assurance for safety in nuclear power plants and other nuclear installations. Code and safety guides Q1-Q14. Safety series no. 50-C/SG-Q, safety guide Q-14, Quality assurance in decommissioning. IAEA, Vienna
- UNO-IAEA (1996b) International basic safety standards for protection against ionizing radiation and for the safety of radiation sources. Jointly sponsored by FAO, IAEA, ILO, OECD/NEA, PAHO, WHO, Safety series no. 115. IAEA, Vienna
- UNO-IAEA (1996c) The IAEA program on biosphere modelling and assessment methods. Themes for a new co-ordinated research program on environmental model testing and improvement, BIOMASS/G/WDOI. IAEA, Vienna
- UNO-IAEA (1996d) Regulations for the safe transport of radioactive material. Safety standards series no. ST-1. IAEA, Vienna
- UNO-IAEA (1997a) Safety assessment for near surface disposal. Safety series no. 111-G. IAEA, Vienna
- UNO-IAEA (1997b) Near surface disposal of radioactive waste. Safety series no. 111-S. IAEA, Vienna
- UNO-IAEA (1997c) The international program for improving long term safety assessment methodology for near surface radioactive waste disposal facilities: objective, content and work program. IAEA, Vienna
- UNO-IAEA (1998a) Approaches relating to decommissioning of nuclear facilities: peer discussions on regulatory practices. IAEA, Vienna
- UNO-IAEA (1998b) Decommissioning of nuclear facilities other than reactors. IAEA, Vienna
- UNO-IAEA (1998c) Factors for formulating strategies for environmental restoration. IAEA, Vienna
- UNO-IAEA (1998d) Radiological characterization of shut down nuclear reactors for decommissioning purposes. IAEA, Vienna
- UNO-IAEA (1998e) Technologies for gas cooled reactor decommissioning, fuel storage and waste disposal: proceedings of a technical committee meeting held in Juelich, Germany, 8–10 September 1997. IAEA, Vienna
- UNO-IAEA (1998f) Nuclear power reactors in the world: reference data series no. 2, April 1998 edition. IAEA, Vienna
- UNO-IAEA (1998g) Factors relevant to the recycling or reuse of components arising from the decommissioning and refurbishment of nuclear facilities. Technical reports no. 293. IAEA, Vienna
- UNO-IAEA (1999a) Decommissioning of medical, industrial and research facilities: safety guide. IAEA, Vienna
- UNO-IAEA (1999b) Decommissioning of nuclear power plants and research reactors. IAEA, Vienna
- UNO-IAEA (1999c) On-site disposal as a decommissioning strategy. IAEA, Vienna
- UNO-IAEA (1999d) Review of selected cost drivers for decisions on continued operation of older nuclear reactors: safety upgrades, lifetime extension, decommissioning. IAEA, Vienna
- UNO-IAEA (1999e) Classification of radioactive waste. Safety series no. III-G. IAEA, Vienna
- UNO-IAEA (1999f) State of the art technology for decontamination and dismantling of nuclear facilities. IAEA, Vienna
- UNO-IAEA (1999g) Derivation of default acceptance criteria for disposal of radioactive waste to near surface facilities. Working document, version 3. IAEA, Vienna
- UNO-IAEA (1999h) Maintenance of records for radioactive disposal, TECDOC-1097. IAEA, Vienna
- UNO-IAEA (1999i) Derivation of quantitative acceptance criteria for disposal of radioactive waste to near surface facilities: development and implementation of an approach. Working material, draft safety report – version 3. IAEA, Vienna
- UNO-IAEA (1999j) Decommissioning of nuclear power plants and research reactors. Safety standards series no. WS-G-2.i. IAEA, Vienna
- UNO-IAEA, Gonzales AJ (1999) Restoration of environment with radioactive residues international symposium, Arlington, VA, 29 November–3 December 1999
- UNO-IAEA (2000a) Organization and management for decommissioning of large nuclear facilities. IAEA, Vienna
- UNO-IAEA (2000b) Predisposal management of radioactive waste, including decommissioning: safety requirements. IAEA, Vienna
- UNO-IAEA (2000c) The decommissioning of WWER type nuclear power plants: final report

- of an IAEA regional technical co-operation project. IAEA, Vienna
- UNO-IAEA (2000d) Organisation and management for decommissioning of large nuclear facilities. Technical report series no. 399. IAEA, Vienna
- UNO-IAEA (2001a) Decommissioning of nuclear fuel cycle facilities: safety guide. IAEA, Vienna
- UNO-IAEA (2001b) Methods for the minimization of radioactive waste from decontamination and decommissioning of nuclear facilities. IAEA, Vienna
- UNO-IAEA (2002a) Decommissioning techniques for research reactors: final report of a coordinated research project 1997–2001. IAEA, Vienna
- UNO-IAEA (2002b) International conference on safe decommissioning for nuclear activities: assuring the safe termination of practices involving radioactive materials, Berlin, Germany, 14–18 October 2002. IAEA, Vienna
- UNO-IAEA (2002c) Decommissioning costs of WWER-440 nuclear power plants: interim report: data collection and preliminary evaluations. IAEA, Vienna
- UNO-IAEA (2002d) Safe and effective nuclear power plant life cycle management towards decommissioning. IAEA, Vienna
- UNO-IAEA (2002e) Safe enclosure of nuclear facilities during deferred dismantling. IAEA, Vienna
- UNO-IAEA (2002f) Record keeping for the decommissioning of nuclear facilities: guidelines and experience. IAEA, Vienna
- UNO-IAEA (2003a) Bundesamet fuer Strahlenschutz (Germany). In: Proceedings of the international conference on safe decommissioning for nuclear activities held in Berlin, 14–18 October 2002. IAEA, Vienna
- UNO-IAEA (2003b) Decommissioning of small medical, industrial and research facilities. IAEA, Vienna
- UNO-IAEA (2004a) Gestion des dechets radioactifs avant stockage definitif, y compris le declassement: prescriptions. IAEA, Vienna
- UNO-IAEA (2004b) Planning, managing and organizing the decommissioning of nuclear facilities: lessons learned. IAEA, Vienna
- UNO-IAEA (2004c) Status of the decommissioning of nuclear facilities around the world. IAEA, Vienna
- UNO-IAEA (2004d) Operational and decommissioning experience with fast reactors: proceedings of a technical meeting held in Cadarache, France, 11–15 March 2002. IAEA, Vienna
- UNO-IAEA (2004e) Safety considerations in the transition from operation to decommissioning of nuclear facilities. IAEA, Vienna
- UNO-IAEA (2004f) Transition from operation to decommissioning of nuclear installations. IAEA, Vienna
- UNO-IAEA (2004g) Declassement des installations du cycle du combustible: guide de surete. IAEA, Vienna
- UNO-IAEA (2004h) Declassement des centrales nucleaires et des reacteurs de recherche: guide de surete. IAEA, Vienna
- UNO-IAEA (2004i) Declassement des installations medicales industrielles et de recherche: guide de surete. IAEA, Vienna
- UNO-IAEA (2004j) Application of the concepts of exclusion, exemption and clearance. IAEA, Vienna
- UNO-IAEA (2005a) Standard format and content for safety related decommissioning documents. IAEA, Vienna
- UNO-IAEA (2005b) Selection of decommissioning strategies: issues and factors – report by an expert group. IAEA, Vienna
- UNO-IAEA (2005c) Comision Chilena de Energia Nuclear. In: Proceedings of the international conference on research reactor utilization, safety, decommissioning, fuel and waste management, Santiago, Chile, 10–14 November 2003. IAEA, Vienna
- UNO-IAEA (2005d) Financial aspects of decommissioning: report by an expert group. IAEA, Vienna
- UNO-IAEA (2005e) Dismantling of contaminated stacks at nuclear facilities. IAEA, Vienna
- UNO-IAEA (2006a) Release of sites from regulatory control on termination of practices: safety guide. IAEA, Vienna
- UNO-IAEA (2006b) Decommissioning of facilities using radioactive material: safety requirements. IAEA, Vienna
- UNO-IAEA (2006c) Characterization, treatment and conditioning of radioactive graphite from decommissioning of nuclear reactors. IAEA, Vienna
- UNO-IAEA (2006d) Decommissioning of research reactors: evolution, state of the art, open issues. IAEA, Vienna
- UNO-IAEA (2006e) Management of problematic waste and material generated during the decommissioning of nuclear facilities. IAEA, Vienna
- UNO-IAEA (2006f) Decommissioning of underground structures, systems and components. IAEA, Vienna
- UNO-IAEA (2006g) Redevelopment of nuclear facilities after decommissioning. IAEA, Vienna
- UNO-IAEA, OECD-NEA, European Commission (2007) Proceedings of the international conference on lessons learned from the

decommissioning of nuclear facilities and the safe termination of nuclear activities, Athens, Greece, 11–15 December 2006. IAEA, Vienna

- UNO-IAEA (2008a) Decommissioning of research reactors and other small facilities by making optimal use of available resources. IAEA, Vienna
- UNO-IAEA (2008b) Long term preservation of information for decommissioning projects. IAEA, Vienna
- UNO-IAEA (2008c) Managing low radioactivity material from the decommissioning of nuclear facilities. IAEA, Vienna
- UNO-IAEA (2008d) Managing the socioeconomic impact of the decommissioning of nuclear facilities. IAEA, Vienna
- UNO-IAEA Decommissioning of nuclear power plants and research reactors. Safety guide no. WS-G-2.1. IAEA, Vienna
- UNO-IAEA Safety assessment for spent fuel storage facilities. Safety series no. 118. Safety practice

OECD-NEA Documents

- OECD-NEA (1984) Storage with surveillance versus immediate decommissioning for nuclear reactors. In: Proceedings of an NEA workshop, Paris, 22–24 October 1984
- OECD-NEA (1986) Decommissioning of nuclear facilities: feasibility, needs and costs. Report by an NEA expert group. OECD, Paris
- OECD-NEA (1987) Shallow land disposal of radioactive waste: reference levels for the acceptance of long-lived radionuclides – report of a nuclear energy agency group. OECD, Paris
- OECD-NEA (1991a) Co-operative program for the exchange of scientific and technical information concerning nuclear installation decommissioning projects. Report from the task group on decommissioning costs. CPD/DOC(91), Paris
- OECD-NEA (1991b) Decommissioning of nuclear facilities – an analysis of the variability of decommissioning cost estimate. OECD, Paris
- OECD-NEA (1992) International co-operation on decommissioning. Achievements of the NEA co-operative program 1985–1990. OECD, Paris
- OECD-NEA (1996a) The NEA co-operation program on decommissioning: the first ten years 1985–1995. OECD-NEA, Paris
- OECD-NEA (1996b) Recycling and reuse of scrap metal. OECD-NEA, Paris
- OECD-NEA (1996c) Future financial liabilities of nuclear activities. OECD, Paris
- OECD-NEA (1999a) Co-operative programme for exchange of scientific and technical information concerning nuclear installations decommissioning projects. Decontamination techniques used in decommissioning activities. OECD-NEA, Paris
- OECD-NEA (1999b) Co-operative program for exchange of scientific and technical information concerning nuclear installations decommissioning projects. OECD-NEA, Paris
- OECD-NEA (1999c) Decontamination techniques used in decommissioning activities – a report by the NEA task group on decontamination. OECD-NEA, Paris
- OECD-NEA, European Commission, UNO-IAEA (1999d) A proposed standardized list of items for costing purposes in the decommissioning of nuclear installations: interim technical document. OECD-NEA, Paris
- OECD-NEA, Committee on Nuclear Regulatory Activities, Working Group on Inspection Practices (WGIP) (2000a) Regulatory practices for decommissioning of nuclear facilities with special regard of regulatory inspection practices. OECD-NEA, Paris
- OECD-NEA, Committee on the Safety of Nuclear Installations (CSNI) (2000b) Report on the CSNI workshop on nuclear power plant transition from operation into decommissioning: human factors and organisation considerations, May 17–18, 1999, Rome, Italy. OECD-NEA, Paris
- OECD-NEA (2002) The decommissioning and dismantling of nuclear facilities: status, approaches, challenges. OECD-NEA, Paris
- OECD-NEA (2003a) The regulatory challenges of decommissioning nuclear reactors. OECD-NEA, Paris
- OECD-NEA (2003b) Decommissioning nuclear power plants: policies, strategies and costs. OECD-NEA, Paris
- OECD-NEA (2004a) Strategy selection for the decommissioning of nuclear facilities: seminar proceedings, Tarragona, Spain, 1–4 September 2003. OECD-NEA, Paris
- OECD-NEA (2004b) Decommissioning of nuclear power facilities. It can and has been done. OECD-NEA, Paris
- OECD-NEA (2005a) Achieving the goals of the decommissioning safety case: a status report prepared on behalf of the WPDD by its task group on the decommissioning safety case. OECD-NEA, Paris
- OECD-NEA, UNO-IAEA, EU, SOGIN (2005b) Safe, efficient and cost-effective decommissioning. NEA international workshop, Rome, 6–10 September 2004. SOGIN, Rome
- OECD-NEA (2006a) The NEA co-operative programme on decommissioning a decade of progress. OECD-NEA, Paris

- OECD-NEA (2006b) Releasing the sites of nuclear installations: a status report. OECD-NEA, Paris
- OECD-NEA (2006c) Selecting strategies for the decommissioning of nuclear facilities: a status report. OECD-NEA, Paris
- OECD-NEA (2006d) Liberation des sites des installations nucléaires: rapport de synthèse. OECD-NEA, Paris
- OECD-NEA (2006e) Decommissioning funding: ethics, implementation, uncertainties: a status report. OECD-NEA, Paris
- OECD-NEA (2006f) Choisir des stratégies de démantèlement des installations nucléaires: rapport de synthèse. OECD-NEA, Paris
- OECD-NEA (2007) Stakeholder involvement in decommissioning nuclear facilities: international lessons learned. OECD-NEA, Paris
- OECD-NEA (2008a) Release of radioactive materials and buildings from regulatory control a status report
- OECD-NEA (2008b) Regulating the decommissioning of nuclear facilities relevant issues and emerging practices. OECD-NEA, Paris
- OECD-NEA (2008c) Regulating the decommissioning of nuclear facilities [electronic resource]: relevant issues and emerging practices. OECD-NEA, Paris
- EU Documents**
- EU (1984) Framework research action program 1984–1987 on the decommissioning of nuclear power plant. European scientific and technical strategy. In: Proceeding of a European conference, Luxembourg, 22–24 May 1984
- EU, Commissions of the European Union (1988a) Radiological protection criteria for the recycling of materials from the dismantling of nuclear installations. Radiation protection recommendation no. 43. Office for Official Publications of the European Communities, Luxembourg
- EU (1988b) Radiological protection criteria for the recycling of materials from the dismantling of nuclear installations, radiation protection recommendation no. 43. EU, Luxembourg
- EU, European Commission (1989a) Recommended radiological protection criterium for the recycling of metals from the dismantling of nuclear installations
- EU, European Commission (1989b) Communication and fourth report of the commission, Situation and perspectives of radioactive waste management in the European Union, COM, p 799
- EU (1991) Inventory of information for the identification of guiding principles in the decommissioning of nuclear installations. Report EUR-13642. CEC, Brussels
- EU (1996a) Laying down basic safety standards for the protection of the health of the workers and the general public against the danger arising from ionising radiation. Council directive 96/29 EURATOM of 13 May 96, Luxembourg, Official journal no. L159, 29 June 1996
- EU, European Commission (1996b) Application of procedures and disposal criteria developed for nuclear waste packages to cases involving chemical toxicity. European commission report, EUR 16745 EN. EU, Luxembourg
- EU, European Commission (1998a) Radioactive waste categories. Current position in the UE member states and in the Baltic and Central European countries. EU, Luxembourg
- EU, Commission of the European Communities, Directorate-General for Science, Research and Development, Guglhoer P (1998b) High resolution in situ gamma spectrometer for use on contaminated reactor building structures and outdoor grounds under decommissioning: final report. Office for Official Publications of the European Communities, Luxembourg
- EU, Commission of the European Communities, Directorate-General for Science, Research and Development, Steiner H (1998c) Pilot dismantling of the KRB a boiling water reactor: final report. Office for Official Publications of the European Communities, Luxembourg
- EU, Commission of the European Communities, Directorate-General for Science, Research and Development, Davies MW (1998d) A review of the situation of decommissioning of nuclear installations in Europe: final report. Office for Official Publications of the European Communities, Luxembourg
- EU (1998e) Nuclear fission safety program. Progress report 1997, EUR 18322/2
- EU, European Commission (1999a) Assessment of the consequences of the presence of toxic elements in some common radioactive waste stream. European Commission report, EUR 18211 EN. European Commission, Luxembourg
- EU, European Commission (1999b) Recommendation 15 September 1999 about the classification of solid radioactive waste. GUCE L 265/37
- EU, UNO-IAEA, OECD-NEA (1999c) A proposed standardised list of items for costing purposes in the decommissioning of nuclear installations. Technical document. OECD-NEA, Paris

- EU, Commission of the European Communities, Directorate-General for Environment, Nuclear Safety, and Civil Protection (1999d) 1st European ALARA network workshop on ALARA and decommissioning. Office for Official Publications of the European Communities, Luxembourg
- EU, European Commission, DG XI/C.2 (1999e) Decommissioning of nuclear installations in the European Union – supporting document for the preparation of an EC Communication on the subject of decommissioning nuclear installations in the EU, EUR 18.860. European Commission, Luxembourg
- EU, Commission of the European Communities, Directorate-General for Environment, Mobbs SF, Harvey MP (2000a) Methodology and models used to calculate individual and collective doses from the recycling of metals from the dismantling of nuclear installations: final report. Office for Official Publications of the European Communities, Luxembourg
- EU, Commission of the European Communities, Directorate-General for Environment, Deckert A et al (2000b) Definition of clearance levels for the release of radioactively contaminated buildings and building rubble: final report. Office for Official Publications of the European Communities, Luxembourg
- EU, Commission of the European Communities, Directorate-General for Research (2000c) Euradwaste 1999: radioactive waste management strategies and issues. In: Davies C (ed) Fifth European commission conference on radioactive waste management and disposal and decommissioning, Luxembourg, 15 to 18 November 1999. Office for Official Publications of the European Communities, Luxembourg
- EU, Commission of the European Communities (2000d) Recommended radiological protection criteria for the clearance of buildings and building rubble from the dismantling of nuclear installations: recommendations of the group of experts set up under the terms of Article 31 of the Euratom Treaty. Office for Official Publications of the European Communities, Luxembourg
- EU (2000e) Management of occupational radiological and non radiological risks. EAN workshop, Antwerp, November 20–22
- EU, Commission of the European Communities (2001) Study on the current regulatory status in the EU member states and applicant countries concerning EIA for decommissioning of nuclear installations
- EU Recommendation EURATOM n. 829/99. Application of art. 37 of EURATOM treaty and modification of recomm. 16.11, 1960; 82/181; 91/4

US-NRC Documents

- US NRC (1974) Termination of operating licenses for nuclear reactor. Regulatory guide 1.86
- US-NRC (1984) Technology, safety and costs of decommissioning: a reference independent spent fuel storage installation. Report NUREG/CR-22 10. US-NRC, Washington, DC
- US NRC (1988) General requirements for decommissioning nuclear facilities, Amending 10CFR 30, 40, 50, 51, 70 & 72, effective July 27, 1988. Federal Register, vol 53, no. 123, June 27, 1988, pp 24018–24056
- US NRC (1993) Revised analyses of decommissioning for the reference pressurized water reactor power station, NUREG/CR-5884. NRC, Washington, DC
- US-NRC (1995) Revised analyses of decommissioning for the reference pressurized water reactor power station. Report NUREG/CR-5884, vols 1 and 2. US-NRC, Washington, DC
- US NRC (1996a) Revised analyses of decommissioning for the reference boiling water reactor power station, NUREG/CR-6174. NRC, Washington, DC
- US NRC (1996b) Decommissioning of nuclear power reactors, Amending 10 CFR Parts 2, 50, and 51, effective August 28, 1996. Federal Register, vol 61, no. 146, July 29, 1996, pp 39278–39304
- US NRC (1997) Radiological criteria for license termination, Amending 10 CFR Parts 20, 30, 40, 50, 51, 70 and 72, effective August 20, 1997. Federal Register, vol 62, no. 139, July 21, 1997, pp 39058–39095
- US NRC, Office of Nuclear Regulatory Research (1998a) Division of engineering technology. In: Proceedings of the workshop on review of dose modeling methods for demonstration of compliance with the radiological criteria for license termination: held at NRC headquarters auditorium, Rockville, MD, November 13–14, 1997. US NRC, Washington, DC
- US-NRC (1998b) Staff responses to frequently asked questions concerning decommissioning of nuclear power reactors. Report NUREG1628 (draft). US-NRC, Washington, DC
- US NRC (1999) Risk informed and performance based regulation. Announcement no. 019. March 11
- US NRC (2000) Office of nuclear material safety and safeguards, Division of waste management,

NMSS decommissioning standard review plan. US NRC, Washington, DC

US NRC (2002) Consolidated NMSS decommissioning guidance: final report. US NRC Office of Nuclear Material Safety and Safeguards, Washington, DC

US-NRC, Office of Nuclear Material Safety and Safeguards (2004) Status of decommissioning program: 2004 annual report: final report. US-NRC, Washington, DC

Further Reading

Other Organizations

AEA (1954) The atomic energy act of 1954, as amended. Public Law No. 83-703, 68 Stat. 919, Section 274

American Nuclear Society (ANS) (1999) ANS executive conference nuclear power plant decommissioning and spent fuel, Traverse City, MI, June 27-30, 1999, Attendance report. ANS, La Grange Park, IL

American Nuclear Society (ANS) (1999) Oak Ridge/Knoxville Section. Second topical meeting on decommissioning, decontamination & reutilization of commercial and government facilities, September 12-16, 1999, Knoxville, TN. ANS, La Grange Park, IL

American Nuclear Society (ANS) (2005) ANS topical meeting on decommissioning, decontamination & reutilization: the transition to closure and legacy management, Denver, Colorado, August 7-11, 2005. ANS, La Grange Park, IL

American Nuclear Society (ANS) (2007) ANS topical meeting on decommissioning, Decontamination & reutilization: (DD&R 2007), September 16-19, 2007, Chattanooga, TN. ANS, La Grange Park, IL

American Society of Mechanical Engineers (ASME) (2004) Environmental engineering division. In: Taboas A, Moghissi AA, LaGuardia TS et al (eds) The decommissioning handbook. ASME, New York, NY

Canadian Nuclear Society (2005) Waste management, decommissioning and environmental restoration for Canada's nuclear activities. Hotel Crowne Plaza Hotel, Ottawa, Ontario, May 8-11, 2005 = Gestion des dechets, declassement et restauration environnementale pour les activites nucleaires au Canada: pratiques actuelles et besoins futurs. Canadian Nuclear Society, Ottawa, ON

Energy Agency of Lithuania (2000) Decommissioning of Unit 1 of INPP - donors conference,

20-21 June, Vilnius, Lithuania. Energy Agency of Lithuania, Vilnius

ENRESA (2000) Dismantling of the Vandellos I nuclear power plant: report on activities (1998-1999). ENRESA, Madrid

ENRESA (2006) Universitat Rovira i Virgili de Tarragona, Centro Tecnologico Mestral, Informe final: impacto economico del desmantelamiento de la central nuclear Vandellos I. Enresa, Madrid

Health Physics Society (HPS) (2002) Decommissioning and environmental restoration. In: Proceedings of the 35th health physics society midyear topical meeting, February 17-20, 2002, Orlando, FL. Health Physics Society, McLean, VA

Health Physics Society, Slobodien MJ (1999) Decommissioning and restoration of nuclear facilities: Health Physics Society 1999 Summer School. Medical Physics Publications, Madison, Wisconsin

NEI 98-01 (1998) Industry spent fuel storage handbook, May 1998

ORNL/M-5003 (1998) The radioactive materials packaging handbook - design, operations and maintenance

SKB, Svensk Karnbranslehantering AB (1986) Technology and costs for decommissioning the swedish nuclear plants. SKB Technical Report 86-16, Stockholm, May 1986

Sweden Statens Kaernkraft Inspektion (SKI), Varley G (2002) Agesta-BR3 decommissioning cost comparison and benchmarking analysis. SKI, Stockholm

Sweden Statens Kaernkraft Inspektion (SKI), Varley G, Rusch C (2001) R2/RO-WTR decommissioning cost comparison and benchmarking analysis. Statens kaernkraftinspektion (SKI), Stockholm

UK Department of Trade and Industry (2002) Managing the nuclear legacy: a strategy for action. Presented to parliament by the secretary of state for trade and industry by command of her majesty. Stationery Office, London

UK House of Commons, Business, Enterprise and Regulatory Reform Committee (2008) Funding the nuclear decommissioning authority: fourth report of session 2007-08. Stationery Office, London

UK National Audit Office (2008) Taking forward decommissioning: the nuclear decommissioning authority. Stationery Office, London

UNIPED (1998) Cost estimates for decommissioning nuclear reactors - why do they differ so much?. UNIPED/Nuclear Waste and Decommissioning, Paris

- US Institute of Peace, Albright DA, Brannan P (2007) Disabling DPRK nuclear facilities. US Institute of Peace, Washington, DC
- US National Institute of Standards and Technology, Snyder KA (2003) Condition assessment of concrete nuclear structures considered for entombment. US Department of Commerce, Technology Administration, National Institute of Standards and Technology, Gaithersburg, MD
- US-DOE (2000) Decommissioning handbook, January 2000 (DOE P450.4, Safety Management System Policy)
- Other Documents**
- Anderson HF, Bantz PD, Luthy DF (1996) Safe shutdown of defense program facilities at the Mound Plant, Miamisburg, OH, Nuclear Engineering (ICONE-4 International conference, New Orleans, 1996), vol 5. ASME, New York, NY, pp 119–126
- Andrews PJ, McAndrew M, Barents MS (1995) Stage I decommissioning of the steam generating heavy water reactor, current achievements. Nuclear decommissioning (Proceedings of international conference, London, 1995)
- Baranski SC, Lankford DM (1985) Addressing decommissioning and associated radiological issues: a community outreach program. NEA Newsletter, Fall 1985
- Bayliss C, Langley K (2003) Nuclear decommissioning, waste management, and environmental site remediation. Elsevier, Amsterdam
- Bayliss CR, Langley KF (2003) Nuclear decommissioning, waste management, and environmental site remediation. Butterworth-Heinemann, Amsterdam
- Bragg K (1985) Decommissioning large power reactors: strategie. NEA Newsletter, Fall 1985
- Brown M (1998) Fostering community participation in decommissioning. Radwaste Magazine, September 1998
- Card R (1998) Rocky flats – transitioning from nuclear operations to deconstruction. Paper presented at X-Change'97, The Global D&D Marketplace, Miami, FL, December 1997. Hemispheric Centre for Environmental Technology, Miami
- Codd G, Clements D (1998) People issues on a major nuclear decommissioning project. In: Proceedings of the WM'98, international conference on waste management, Tucson, 1–5 March 1998. Waste Management Symposia Inc., Tucson
- Cumo M, Tripputi I, Spezia U (2002) Nuclear plant decommissioning, 1st edn. Università di Roma La Sapienza, SOGIN
- Cumo M, Tripputi I, Spezia U (2004) Nuclear plant decommissioning, 2nd edn. Università di Roma La Sapienza, SOGIN
- Delaney EG (US-DOE) (1986) The methodology and technology of decommissioning. Scientific Afternoon, IAEA General Conference
- Dragolici F et al (2003) Technical aspects regarding the management of radioactive waste from decommissioning of nuclear facilities, WM Symposia Inc., Tucson, AZ
- Essmann I (1991) Planning structure for normal decommissioning procedures. Kerntechnik 56:358–361
- Feraday MA (1985) Building on experience: an international perspective. IAEA Bulletin, Winter 1985
- Granados B et al (1995) An overview of ALARA considerations during Yankee atomic's component removal project. In: Proceedings of the third international workshop on the implementation of ALARA at nuclear power plants, Hauppauge, Long Island, NY, Report NUREG/CP143, March 1995
- Heider KJ, Mellor RA (1995) Timely component removal at Yankee, 1994 decommissioning conference, Captiva, Island, FL, October 1994. TLG Services Inc., Bridgewater, CT, Mechanical Engineering Publications Ltd. for IMechE, London
- Hoopes J, Corsi J (1998) Stakeholders can help: improving D&D policy decisions at Rocky Flats. Decommissioning and decontamination and nuclear and hazardous waste management (Proceedings of SPECTRUM'98 international conference, Denver, 1998). ANS, La Grange Park, IL, pp 1501–1505
- IBC Global Conferences, Energy and Safety Division (1999) 6th international conference & exhibition on decommissioning of nuclear facilities: 15/16 June 1999. London Marriott Hotel, IBC Global Conference Limited, London
- IBC Global Conferences, Energy and Safety Division (2007) IBC's 23rd annual residential summer school on decommissioning and radioactive waste management. Christ's College, Cambridge, IBC Global Conferences, London
- IBC Global Conferences, Safety and Nuclear Division (2004) Decommissioning experience. The London Marriott Hotel, Grosvenor Square, IBC Global Conferences, London
- IBC Global Conferences, Safety and Nuclear Division (2004) Decommissioning of nuclear facilities. The London Marriott Hotel, Grosvenor Square, IBC Global Conference, London
- IBC Global Conferences, Safety and Nuclear Division (2006) Decommissioning of nuclear facilities: taking experience forward, 20th–22nd

- November 2006. Millennium Gloucester Kensington, London
- Ishigure K et al (1992) Development of decommissioning technology for commercial nuclear power plants in Japan, Decommissioning Policies for Nuclear Facilities (Proc. OECD/NEA Int. Sem. Paris, 1991), OECD, Paris 77-86
- Lackey MB, Kelly ML (1996) The Trojan large component removal project. Nuclear engineering (ICONE-4 international conference, New Orleans, 1996), vol 5. ASME, New York, NY, pp 89-94
- Liederman JM (1986) An overview of past, present and future activities relevant to decommissioning including unplanned events. Scientific Afternoon, IAEA General Conference
- Lischinsky J, Vigliani AA (1993) Planning and management in decommissioning. In: Paper presented at the health physics society annual meeting, July 1993, Atlanta, GA
- Lundby JE (1994) Decommissioning of a uranium reprocessing pilot plant. Final report of the Nordic nuclear safety research project KAN-I.2, Temanord 1994:594, May 1994
- Luykx F (CEC) (1986) Safety and regulatory aspects of decommissioning. Scientific Afternoon, IAEA General Conference
- Mellor RA, Heider KJ (1992) Technical aspects of premature shutdown, 1992 decommissioning Conference, Captiva, Island, FL, October 1992. TLG Services Inc., Bridgewater, CT
- Nelson RL (1998) UKAEA's approach to the management of nuclear liabilities. Nuclear Decom'98 (International conference, London, 1998). Professional Engineering Publishing Ltd., London, pp 305-316
- Rahman A (2008) Decommissioning and radioactive waste management. CRC Press, Boca Raton, FL
- Rahman A (2008) Decommissioning and radioactive waste management. Whittles Publishing, Dunbeath
- Ralph RO, Dresden I (1996) Decommissioning activities. Nuclear engineering (ICONE4, International conference, New Orleans, 1996), vol 5. ASME, New York, NY, pp 127-130
- Riitscher D, Leushacke DE (1998) Waste management and decommissioning of VVER reactors in Germany. ASME, Baltimore
- Rimando RV et al (1997) Decommissioning a Savannah River Site tritium facility. Report DOE/SR-5000-508. Washington, DC
- Schultz JW (1994) Overcoming the grief of plant closure. Nucl Eng Int 22-23
- Taboas AL, Moghissi AA, La Guardia T (2004) The decommissioning handbook. ASME, New York, NY
- Thexton HE (1986) The cost and financing of the decommissioning of nuclear power plants. NEA, Scientific Afternoon, IAEA General Conference
- Thomson P, Perry J (1992) Engineering construction risks: a guide to project risk analysis and risk management. Thomas Telford, London
- Tothill SJ, Tuck MD (1998) Integrating radiochemical and conventional land remediation with site development. Nuclear Decom'98 (International conference, London, 1998). Professional Engineering Publishing Ltd., London, pp 219-228
- Wilkinson RH (1998) Why and when to use turnkey remediation. Decommissioning and decontamination and nuclear and hazardous waste management (Proceedings of SPECTRUM'98 international conference, Denver, 1998). ANS, La Grange Park, IL, pp 1421-1425

28 The Scientific Basis of Nuclear Waste Management

Bernard Bonin

Commissariat à l'Energie Atomique, France

Nuclear Energy Directorate, CEA Saclay, Gif-sur-Yvette Cedex,
France

Bernard.Bonin@cea.fr

1	<i>Generalities on Waste</i>	3257
1.1	Origin, Nature, Volume, and Flux of Waste	3258
1.1.1	Waste Classification	3261
1.1.2	Volume and Flux of Waste	3261
1.1.3	Which Radionuclides in the Spent Fuel?	3261
1.1.4	Fission Products Are Radioactive	3266
1.1.5	Formation of Transuranic Isotopes in the Reactor Core	3268
1.1.6	Radioactive Decay	3270
1.1.7	What Kind of Radioactive Emission Do We Expect from the Nuclear Waste?	3272
1.1.8	Penetration of Ionizing Radiations into Matter	3273
1.1.9	The Radioactive Half-Life of the Main Radionuclides Found in Nuclear Waste	3273
1.1.10	Radioactive Waste: How Dangerous Is It?	3276
1.2	Management Options: An Overview	3276
1.2.1	Dispersion or Concentration?	3276
1.2.2	Waste, Effluents, Decontamination, and Conditioning: A Systemic Vision	3276
1.2.3	Reprocessing or Not Reprocessing?	3277
1.2.4	World Situation for Waste Management	3279
1.2.5	The Institutions In Charge of Waste Management in the World	3280
1.2.6	The Waste Management Process	3280
1.2.7	Uranium Mine Tailing Management	3281
1.2.8	Management of Low and Intermediate Level, Short-Lived Waste (LIL-SL)	3282
1.2.9	Interim Storage of Spent Fuel	3283
1.2.10	High Activity Waste from Reprocessing is Vitrified	3284
1.2.11	Options for the Management of Long-Lived Nuclear Waste	3285
1.2.12	Waste Management and Radioprotection	3287
1.2.13	From Radioactivity to Radiotoxicity	3288
1.2.14	Ingestion Dose Factors	3288
1.2.15	The Long-Term Radiotoxicity of Spent Fuel	3289

1.2.16	Deep Geological Disposal: The Multibarrier Concept	3291
2	<i>Waste Conditioning</i>	3291
2.1	Conditioning of LL and IL Waste in Cement-Based Matrices	3295
2.1.1	Elaboration of Cement-Based Materials	3296
2.1.2	Waste Conditioning in Cement-Based Materials	3297
2.1.3	Long-Term Behavior of Cement-Based Materials	3298
2.1.4	R&D on Cement-Based Materials for Waste Conditioning	3301
2.1.5	Waste Container Manufacturing	3301
2.2	Conditioning of HL-LL Waste in Glass	3302
2.2.1	Vitrification of Solutions of Fission Products	3302
2.2.2	Requirements for the Glass Material	3304
2.2.3	Physicochemistry of Glass	3304
2.2.4	Glass Composition	3305
2.2.5	Incorporation of Radionuclides in Glass: Where Is the Limit?	3306
2.2.6	Glass Fabrication: The Hot Crucible Vitrification Process	3308
2.2.7	The Vitrified Waste Package	3309
2.2.8	Cold Crucible Vitrification	3310
2.2.9	Long-Term Behavior of Glass	3311
2.2.10	Long-Term Behavior of Glass in Contact with Water	3311
2.2.11	Phenomenology of Glass Alteration by Water	3311
2.2.12	Glass Alteration by Water Depends Greatly on Temperature	3315
2.2.13	Toward a Model of Glass Alteration	3315
2.2.14	The Residual Alteration Regime of Glass	3316
2.2.15	Long-Term Behavior of Glass: The Effect of Self-Irradiation	3318
2.3	Other Conditionings for Waste	3320
2.3.1	Bituminization of Low- or Intermediate-Level Waste	3320
2.3.2	Bitumen Manufacturing	3321
2.3.3	Bitumen Package Evolution Under Self-Irradiation	3322
2.3.4	Bitumen Alteration by Water	3323
2.3.5	Conditioning of Fuel Claddings and End Caps	3323
2.3.6	The Long-Term Behavior of the Compacted Metallic Waste Package	3324
2.3.7	Melting: A Possible Future Conditioning for Metallic Waste	3325
2.3.8	Specific Conditioning for Minor Actinides and Fission Products	3325
2.4	Conditioning of Spent Fuel	3326
2.4.1	Can Spent Fuel Be a Conditioning Matrix?	3326
2.4.2	Spent Fuel Evolution After Unloading	3327
2.4.3	Packaging Spent Fuel	3328
2.4.4	Choice of the Container Material	3330
2.4.5	Corrosion Rates of Low-Alloyed Steels	3331
2.4.6	Post-Irradiation State of the Spent Fuel	3332
2.4.7	Fuel Evolution in a Closed System	3334
2.4.8	Spent Fuel in a Water-Saturated Repository	3335
2.4.9	Conclusion on the Storage and Direct Disposal of Spent Fuel	3336
3	<i>Waste Storage and Disposal</i>	3337
3.1	Interim Storage of Long-Lived Waste and Spent Fuel	3337

3.1.1	Storage: A Temporary Solution for Waste Management	3337
3.1.2	An Important Stake of Interim Storage: Reduce the Cost of the Disposal ..	3338
3.1.3	The Objects To Be Stored	3338
3.1.4	The Storage Facilities for Long-Lived Waste	3340
3.1.5	Duration of the Interim Storage	3345
3.2	Geological Disposal	3346
3.2.1	The General Principles of Deep Geological Disposal	3346
3.2.2	The Technical Principles of Deep Geological Disposal	3346
3.2.3	The Multibarrier Concept	3347
3.2.4	Repository Lifetime	3347
3.2.5	Repository Architecture	3348
3.2.6	Cost of an HL LL Waste Repository	3352
3.2.7	The Foreseen Evolution of a Repository	3353
3.2.8	Geodynamic Evolution of a Deep Geological Repository	3354
3.2.9	The Criteria for the Choice of a Suitable Location for a Deep Geological Repository	3355
3.2.10	Choice of the Host Rock for the Waste Disposal	3356
3.2.11	Hydrogeology	3357
3.2.12	Calculation of Water Flow in a Permeable Porous Medium	3358
3.2.13	Radionuclide Migration	3359
3.2.14	Kinematic Dispersion	3361
3.2.15	The Tracer Equation	3361
3.2.16	Characteristic Migration Time Through a Geological Barrier	3363
3.2.17	Sorption of a Non-Perfect Tracer	3365
3.2.18	Migration of a Sorbing Tracer	3367
3.2.19	Migration of Actinides	3369
3.2.20	Radionuclide Speciation and Solubility Limits	3370
3.2.21	Porewater Chemistry	3372
3.2.22	How to Evaluate the Transport of RN Underground	3374
3.2.23	Validation of the Models of RN Transport Underground	3375
3.2.24	Thermo-Hydro Mechano-Chemical Effects in the Near-Field of a Geological Repository	3377
3.2.25	Thermal Behavior of High-Activity Waste	3377
3.2.26	Chemical Phenomena in the Near-Field	3380
3.2.27	Mechanical Behavior of a Repository	3381
3.2.28	Mechanical Effects Due to the Excavation of the Galleries	3382
3.2.29	Hydraulic Effects	3383
3.2.30	Hydro-Mechanical Effects in the Near-Field	3384
3.2.31	Hydro-Chemical Couplings in the Near-Field	3384
3.2.32	Gas Production and Release in an Underground Repository: An Example of H-M-C Coupling	3386
3.2.33	Underground Laboratories	3387
3.2.34	Natural Analogues Can Help Validate the Models of Long-Term Behavior of a Repository: The Example of Oklo	3388
3.3	Safety of Waste Disposal Facilities	3389
3.3.1	How to Evaluate the Radiological Impact of a Deep Geological Repository?	3390

3.3.2	Evaluation of the Order of Magnitude of the Activity at the Exutory for a Simplified Repository	3394
3.3.3	The Source-Term	3394
3.3.4	Transit Time from the Repository to the Exutory	3395
3.3.5	Transfer Through the Geosphere.....	3396
3.3.6	Activity at the Exutory.....	3397
3.3.7	Evaluation of the Order of Magnitude of the Dose to Man	3400
4	<i>Conclusions</i>	3402
4.1	Waste: The Achilles' Heel of the Nuclear Industry?.....	3402
4.2	Technical Solutions and Political Advances for Waste Management.....	3402
4.3	The Main Principles of Nuclear Waste Management	3402
4.4	Recycling: The First Link of the Waste Management Chain.....	3402
4.5	Transmute, Recycle: Where Is the Limit?	3403
4.6	Waste Conditioning: The Essential Second Link in the Chain of Waste Management	3403
4.7	What To Do with the Final Waste?.....	3404
4.8	Interim Storage, A Temporary Solution That Gives Flexibility to the Management of Waste.....	3404
4.9	Underground Disposal, The Last Link of the Chain: A Final Place for the Final Waste	3405
4.10	Underground Disposal: A Simple and Robust Concept	3405
4.11	Let Us Behave Responsibly, Let Us Try To Be Sensible.....	3406
5	<i>Glossary</i>	3407
	<i>References</i>	3416

Abstract: Waste is produced at every stage of the nuclear fuel cycle. While large volumes of short-lived radioactive waste are already handled by the nuclear industry in surface storage facilities, the management mode of high-activity, long-lived waste has not been decided in detail and is still under study in all nuclear countries. Scientific knowledge is in progress, technical solutions are emerging, in a context where science and technology interact strongly with social and economical issues.

With a closed fuel cycle, waste management from its production to its final destination looks like a chain whose links are treatment recycling, conditioning, storage, and disposal of the final waste. With the open cycle option, the first link is absent.

This chapter provides the concepts and data that form the scientific basis of nuclear waste management.

➤ **Section 1** deals with the origin, nature, volume, and flux of nuclear waste, and describes the management options.

➤ **Section 2** deals with waste conditioning, with special emphasis on two important conditioning matrices: cement-like materials and glass. The elaboration and long-term behavior of these matrices are treated successively. In many countries, spent fuel is considered as waste, and must be conditioned as such. A special section is devoted to this issue.

➤ **Section 3** deals with waste storage and disposal. Interim storage of long-lived waste is already an industrial reality, and the design and properties of the corresponding installations are described. The final disposal of ultimate waste in deep geological repositories is more prospective, but the main concepts are described, with emphasis on the mechanisms, models, and orders of magnitude of the main physical and chemical phenomena that come into play in the long-term evolution of these installations. Finally, a short description of the methodology used to evaluate the safety of these installations is given. A simplified example of application of this methodology is given to evaluate the order of magnitude of the radiological impact of geological disposal of long-lived waste.

1 Generalities on Waste

In the world, 16% of the electricity is generated by nuclear power plants. The properties of radioactivity are also used in many other applications: in chemistry, biology (study of cells), geology, archaeology (dating), agriculture, and medicine (diagnosis and treatment of cancers). It also has many uses in industry, for example, food preservation, the inspection of welds in metallurgy, the sterilization of medical equipment, or the detection of fire.

All these activities produce waste, some of which are radioactive.

Radioactive waste is material that cannot be reused or reprocessed. Its radioactive nature makes it potentially dangerous for health. It must therefore be specifically managed.

The purpose of this chapter is to provide a general background on the scientific basis of radioactive waste management. The aim is to display the scientific disciplines involved, and to

show how they are used and put together to manage nuclear waste. We shall concentrate on the methods and principles, on the main physical and chemical processes at play, and on the orders of magnitude.

Definitions

The notions that seem intuitive are often quite difficult to define precisely, and such is the case for nuclear waste. In order to avoid any misunderstanding, we propose the following set of definitions, inspired from French law:

A *radioactive substance* is a substance containing natural or artificial radionuclides in a concentration such that it justifies some radioprotection action or control.

Radioactive matter is a radioactive substance for which an ulterior use is foreseen or envisaged, eventually after some processing.

A nuclear fuel is regarded as spent fuel when it has been irradiated in a nuclear reactor and withdrawn definitively.

Radioactive waste is a radioactive substance for which no ulterior use is foreseen or envisaged.

Ultimate radioactive waste is radioactive waste, which cannot be processed under present technical and economic conditions, either to extract its valuable part, or to reduce its dangerous or polluting character.

The legislator has introduced much flexibility in these definitions, to take into account a variable technical and economic context. The important thing is that the notion of waste is less a matter of nature than a matter of destination foreseen or envisaged.

Although the nuclear waste management policy of the nuclear states in the world differs widely, the above definitions seem to apply rather generally.

Nuclear energy is a very concentrated form of energy. Consequently, the volume of nuclear waste generated by the production of a given amount of nuclear energy is very small as compared to that generated by the production of the same amount of energy from fossil fuels. To give an order of magnitude, the typical mass of waste produced yearly per person in an average western country is:

Domestic waste	2,200kg
Industrial waste	800kg(100 kg of high toxicity)

If this country used exclusively nuclear energy to produce its electricity, the yearly production of nuclear waste would be 1kg (10 g of high activity), excluding the uranium mine tailings (uranium is usually much diluted in the ore [grades range from 0.1% to 10%], therefore, uranium mining produces much waste in volume) (🔗 [Table 1](#)).

1.1 Origin, Nature, Volume, and Flux of Waste

In order to understand the origin of nuclear waste, a possible approach is to follow the nuclear fuel cycle step by step.

At the front-end of the fuel cycle, waste is produced during the mining operations. After chemical extraction of the uranium from crushed ore, the tailings still contain the daughter nuclides of uranium, and especially radium. These mine tailings can be considered as waste. Its

Table 1
Origin, nature, volume of nuclear waste

Waste	Origin	Nature	Radioactive half-life	Volume	Activity	Management
Mine tailings	Uranium mines	After chemical extraction of the uranium from crushed ore, the tailings still contain the daughter nuclides of uranium, and especially radium	A few thousand years	50 million cubic meters of mine tailings have been produced in France	Very low (a few ten thousand Becquerel per kilogram)	In situ storage. The mine tailings are covered by a layer of sterile rock and soil to prevent their dispersion, to screen the gamma radiation and to limit radon exhalation
Very low level waste (VLL)	VLA waste comes mainly from dismantled nuclear facilities	Steels, and concrete rubble containing activation products	Variable	The dismantling of the present French nuclear fleet (58 reactors) will produce 80 million tons of VLA waste	Very low (a few ten thousands Becquerel per kilogram)	Sort them, decontaminate whenever possible, then store in surface facilities (such a storage already exists in France in Morvilliers)
Low level short-lived waste (LL-SL)	Operation of nuclear plants	Gloves, boots, filters immobilized in concrete	Short (10–100 years) After 300 years, all the radioactivities will be disappeared	The production of 1 GW electricity during 1 year with a typical LWR generates 120 m ³ of short-lived low activity waste	Low (smaller than 3.710 ⁸ Bq/kg)	Surface storage of the concrete blocks in dedicated surface installations. The waste is stored above the water table, covered with an impermeable clay layer and a few meters of soil. Two such storage facilities already exist in France in La Hague and Soullaines

Table 1 (continued)

Waste	Origin	Nature	Radioactive half-life	Volume	Activity	Management
Intermediate level long-lived waste (IL-LL)	Fuel reprocessing	Processing residues and fuel claddings immobilized in concrete	Long (up to million years)	The production of 1 GW electricity during 1 year with a typical LWR generates 5 m ³ of long-lived medium activity waste	Medium (smaller than 3.7·10 ¹¹ Bq/kg) This waste does not generate heat	Probably underground disposal (The WIPP facility is already in operation in USA; disposal is not yet decided in other countries)
High level long-lived waste (HL-LL)	This waste comes from spent fuel	Glass blocks (if the spent fuel is processed); spent fuel assemblies (if no processing)	Long (up to a million years)	The production of 1 GW electricity during 1 year with a typical LWR generates 2.5 m ³ of long-lived high-activity glass (if processing); or 40 m ³ of spent fuel (if no processing)	High (of the order of 10 ¹³ Bq/kg)	No decision yet about what to do with this category of waste. Technical solutions already exist or are under study for the separation, transmutation conditioning of HLA waste, and for its storage or underground disposal In the mean time, these wasteforms are stored in interim storage facilities (pools, or dry storage surface facilities)

activity is very low, indeed less radioactive than the original ore (a few ten thousand Becquerel per kilogram), but its volume is very large, in the order of $100,000 \text{ m}^3$ to produce the uranium necessary to fuel a 1 GW light water power plant during 1 year.

The main waste stream comes from the back-end of the fuel cycle: the spent fuel itself can be considered as waste if no ulterior use is foreseen; if the spent fuel is reprocessed, process waste is produced, for example, the solution of fission products and minor actinides, which will be vitrified, or structure waste of the fuel assemblies, which will be compacted. This waste type is usually of intermediate or high-level activity; the corresponding volume is relatively small: the production of 1 GW electricity during 1 year with a typical LWR generates 5 m^3 of long-lived medium activity waste and 2.5 m^3 of long-lived high-activity glass (if processing) or 40 m^3 of spent fuel (if no processing).

Technological waste is produced in small amounts during the operations of conversion, enrichment, and fuel fabrication at the front-end of the fuel cycle as well as at the back-end. It consists mainly of solid waste (gloves ion exchange resins, or waste from the dismantling of installations) and liquid waste (decontamination effluents, used solvents, and scintillating liquids used for analysis). Even though the activity is much smaller for technological waste as for processing waste, the volume of technological waste can be relatively large: the production of 1 GW electricity during 1 year with a typical LWR generates 120 m^3 of short-lived low-activity technological waste.

Another waste stream comes from the dismantling of nuclear installations. It consists of steels, and concrete rubble containing activation products. The dismantling of the present French nuclear fleet (58 reactors) will produce 80 million tons of very low-level waste.

The radioactive content of nuclear waste is a specific feature, which imposes special precautions for its management.

1.1.1 Waste Classification

Usually, radioactive waste is classified on the basis of two criteria: its activity and the period of the radionuclides it contains (► [Figs. 1](#) and ► [2](#)).

Note the apparent contradiction between high activity and long life. In fact, another factor comes into play: the high-level (HL) waste is highly concentrated!

This HL waste represents a very small volume (► [Figs. 3](#) and ► [4](#)), but its high activity and heat generation prevent us from assembling it in a small-size disposal facility.

1.1.2 Volume and Flux of Waste

1.1.3 Which Radionuclides in the Spent Fuel?

There are two main categories of radionuclides in the spent fuel:

- *Actinides* (U, Pu, Am, Np, Cm). Pu, Cm, and Am are produced by successive neutron capture on uranium and plutonium in the core of the reactor. These nuclei have a high-specific activity and contribute to heat generation in the waste.

		Short life (SL) Period < 30 years	Long life (LL) Period > 30 years
< A few 10^5 Bq/kg	Very low level (VLL)	VLL	
< A few 10^8 Bq/kg ($\beta\gamma$) < A few 10^6 Bq/kg (α)	Low level (LL)	LIL-SL	LL-LL
< A few 10^{11} Bq/kg ($\beta\gamma$)	Intermediate level (IL)		IL-LL
10^{13} Bq/kg ($\beta\gamma$) 10^{11} Bq/kg (α)	High level (HL)	HL	

Figure 1

Waste classification. The radioactivity limits given here are only indicative. They may vary from country to country

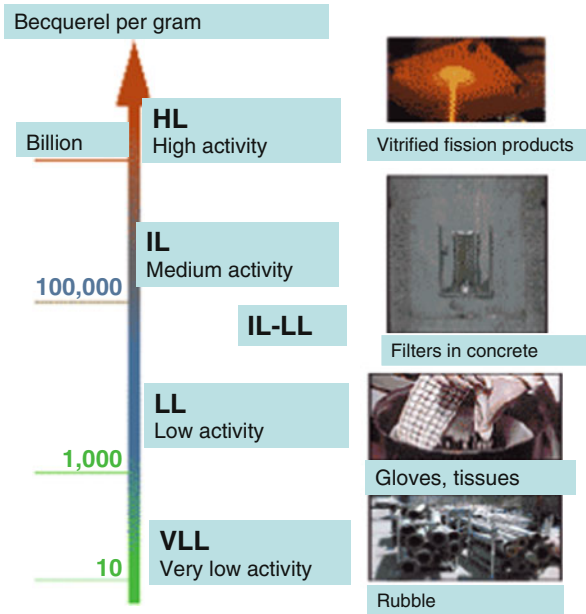


Figure 2

Waste nature and classification

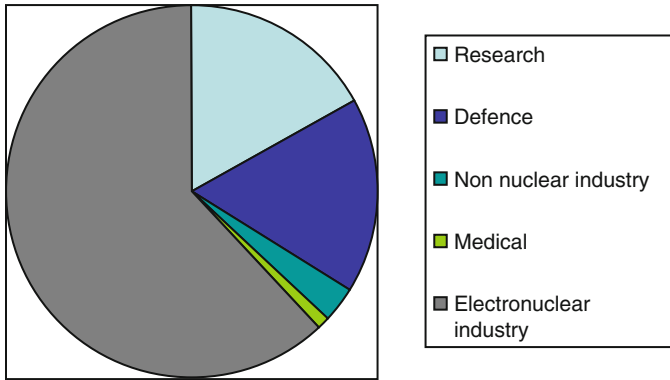


Figure 3 Origin of radioactive waste in France per sector and by volume (Source: National inventory of recoverable materials and radioactive waste 2009)

Volume and flux of waste

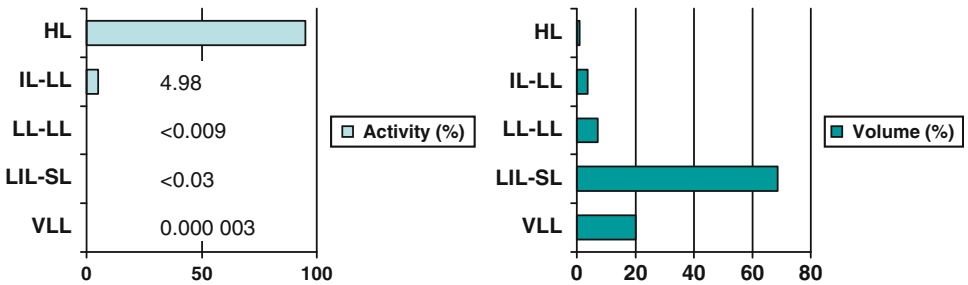
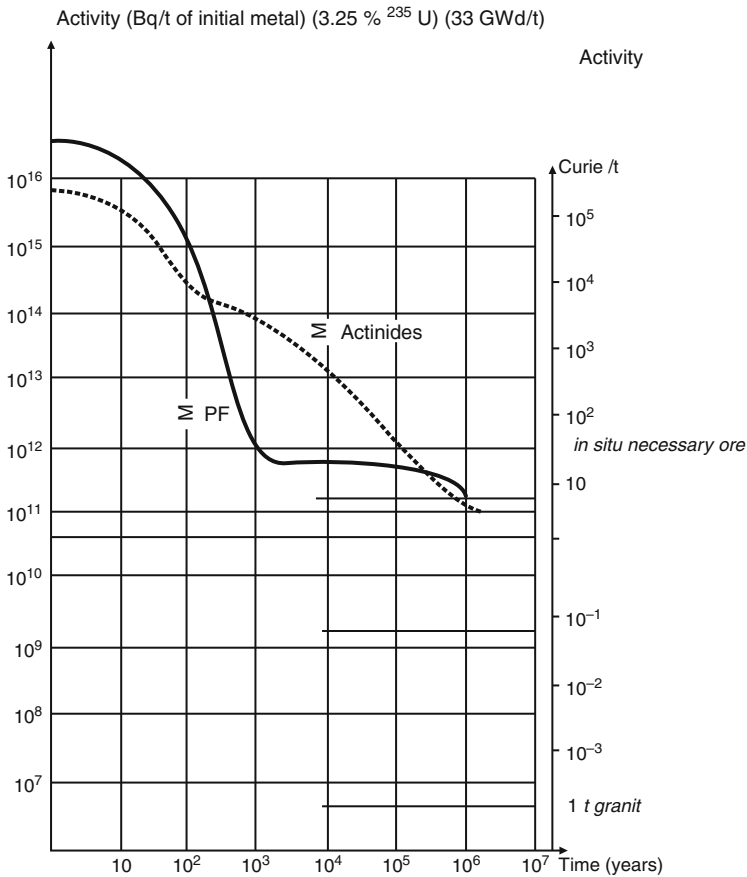


Figure 4 Volume and level of radioactivity, by type of radioactive waste. Typical distribution of the volume and level of radioactivity by type of radioactive waste: the example of France (France’s National Inventory 2009). Note the inversion in the diagram: the high-activity waste concentrates most of the activity under a very small volume, whereas most of the volume is in the low-activity waste

- *Fission products* (e.g., Cs, Sr, Tc, I) are medium mass nuclei produced by the scission of fissile nuclei (^{235}U , ^{239}Pu) during the fission. In the spent fuel, one finds short-lived FPs ^{137}Cs , ^{90}Sr , ^{90}Y (about 30 years) and long-lived FPs, ^{99}Tc , ^{135}Cs , ^{129}I (about 1 million years).



■ Figure 5

The activity of spent fuel, expressed in Bq/t of heavy metal, in the case of an LWR fuel, irradiated with a burnup of 33 GWd/t, after 3 years cooling time

In the structure materials used in the reactor core, one also finds *activation products* (e.g., ^{14}C , ^{36}Cl , ^{60}Co , ^{93}Zr , ^{63}Ni), which result from nuclear reactions (neutron capture). This category is much less important in terms of activity) (● Figs. 5–7).

Fission products are the unavoidable ashes of the fission process. The quantity of fission products is directly proportional to the amount of energy produced in the reactor. It does not depend much on the nuclei, which undergo fission (uranium or plutonium). It is also almost independent of the energy of the neutrons, which cause the fission in the reactor (fission induced by fast neutrons tends to be more symmetrical than fission induced by slow neutrons, but the difference is small). Therefore, fission products will be present in same amounts in the spent fuel of nuclear fission reactors, whatever the kind of reactor or the type of fuel used.

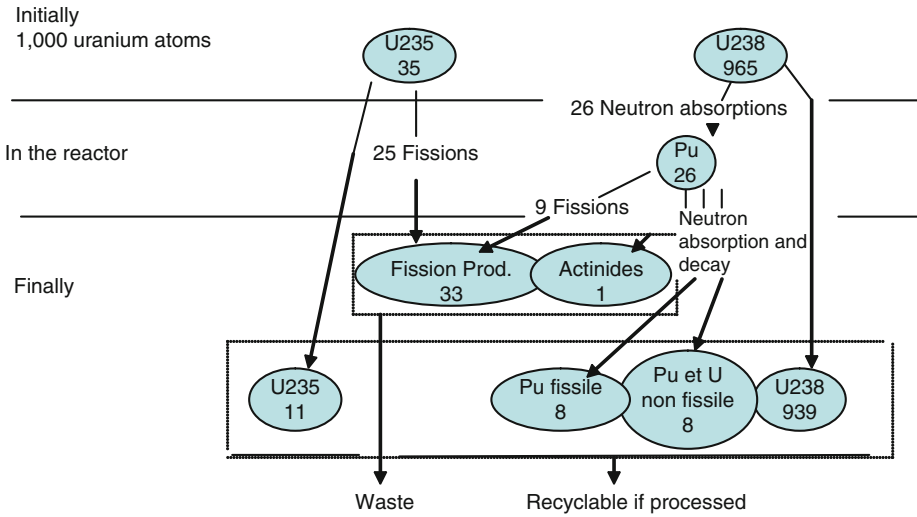


Figure 6

Transformation of the nuclear fuel during its stay in a light water reactor. The fuel of the light water reactors, which constitutes the major part of the world nuclear fleet, is enriched uranium, with an enrichment ratio of the order of 3–5%. This diagram follows the fate of 1,000 uranium atoms (965 fertile atoms of U238 and 35 fissile atoms of U235) present in the initial nuclear fuel. A fuel rod stays about 4 years in the reactor. At the exit, the spent nuclear fuel still contains 939 atoms of U238 and 11 atoms of U235, plus fission products, plutonium isotopes, and a small quantity of heavier nuclides, the “minor actinides”

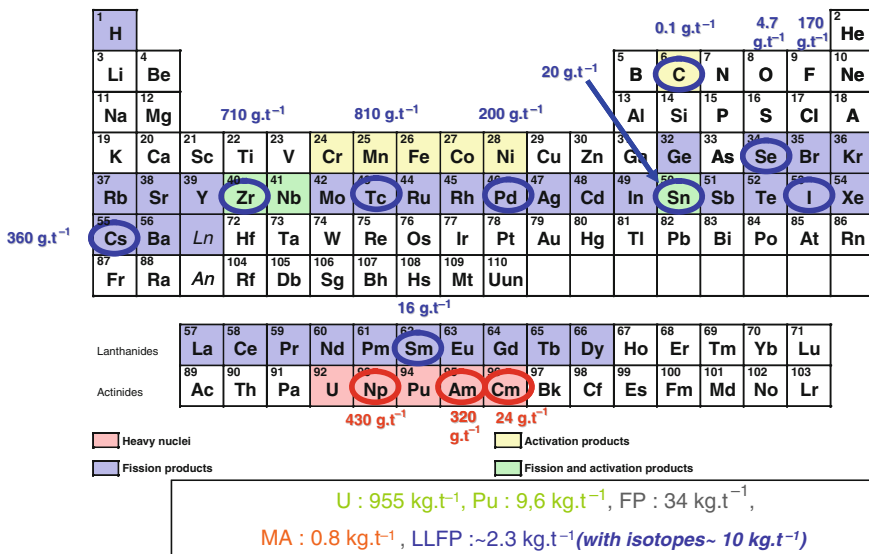


Figure 7

The main long-lived radionuclides produced in the spent fuel (in the case of an UOX LWR fuel, with 3.5% enrichment in U235 and irradiated with a burnup of 33 Gwd/t)

1.1.4 Fission Products Are Radioactive

Fissile nuclei are heavy nuclei, with a large ratio of neutrons versus protons. Fission fragments inherit this ratio. Consequently, they are too neutron-rich to be stable (on [Fig. 8](#), the dashed line is the bottom of the stability valley). Most of the fission products are radioactive, and tend to turn into more stable nuclei by getting rid of this neutron excess. Their radioactive period can go from a microsecond to a million years. They are the true ashes of nuclear combustion.

The fission process does not give the same pair of fission products every time. Fission is a stochastic phenomenon characterized by a probability distribution for the mass of the fission products. Fission is most often asymmetric, producing a light fragment (around mass 90) and a heavy fragment (around mass 140).

This bimodal distribution of the fission fragments is illustrated in [Fig. 8](#).

[Figure 9](#) shows what happens when a ^{235}U nucleus undergoes fission to give, for example, the fission products ^{90}Br and ^{143}Xe . One has in fact two cascades of radioactive decay. The radionuclides upstream in the cascades are in general so unstable (and thus short-lived) that they decay in situ, and are never seen in the waste. The fission products, which are present in the waste, have at least a few months (or even years) of half life ([Fig. 10](#)).

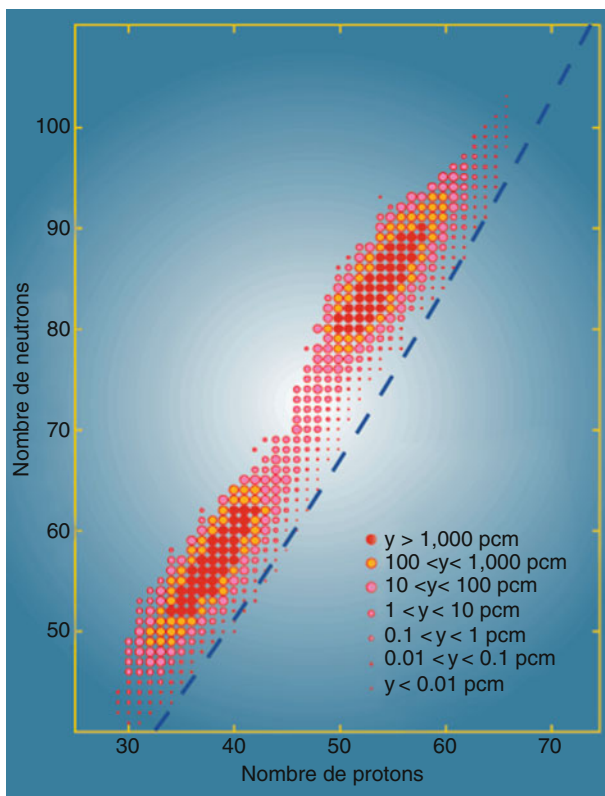


Figure 8

The Z-N diagram of fission products

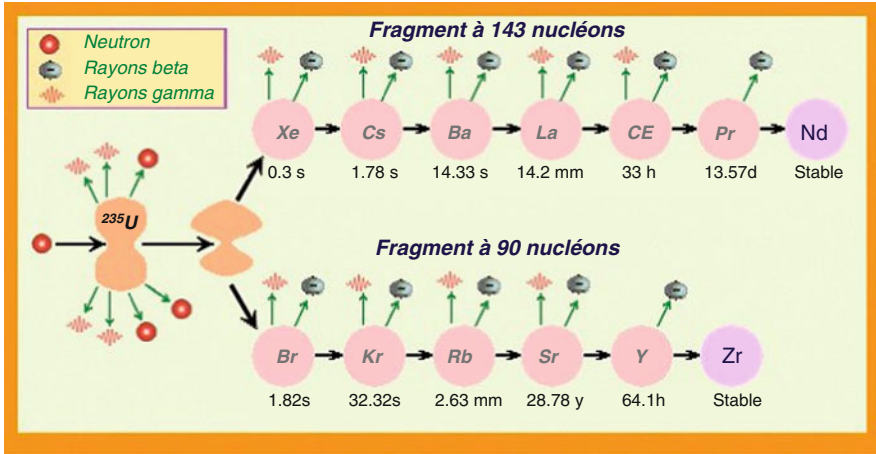


Figure 9
 An example of a decay chain of fission products

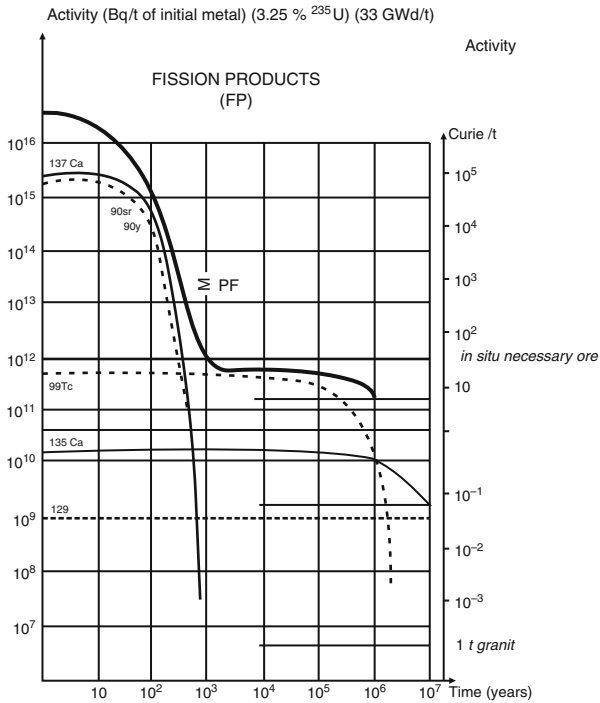


Figure 10
 The activity of fission products in spent fuel, as a function of time

Two types of fission products are found in the waste:

1. ‘Short-lived’ ones ($T < 30$ years), for example, ^{137}Cs , ^{90}Sr (very short-lived FP also exist, but they generally decay before their exit from the reactor, e.g., ^{131}I).
2. ‘Long-lived’ ones ($T > 1$ million years), for example, ^{99}Tc , ^{135}Cs , ^{129}I .

1.1.5 Formation of Transuranic Isotopes in the Reactor Core

The isotopes heavier than uranium are formed in the reactor core by successive neutron captures on uranium nuclei, followed by radioactive alpha and beta decay (\odot Fig. 11).

The longer the irradiation, the higher the minor actinide content of the spent fuel (\odot Table 2).

One should note that for a given amount of energy produced, the quantity of minor actinides produced depends on the fuel burnup. The higher the burnup, the higher the amount of minor actinides produced. This is especially true for the heaviest actinides, which are produced by successive neutron captures on lighter actinides in the reactor core. This self-promoted production of minor actinides is an undesirable feature of light water reactors.

The inventory of actinides evolves with time in a complicated manner, because some actinides are produced by the decay of others (e.g., ^{241}Am gives ^{237}Np). This explains why the activity of ^{237}Np increases with time during the first 1,000 years (\odot Fig. 12).

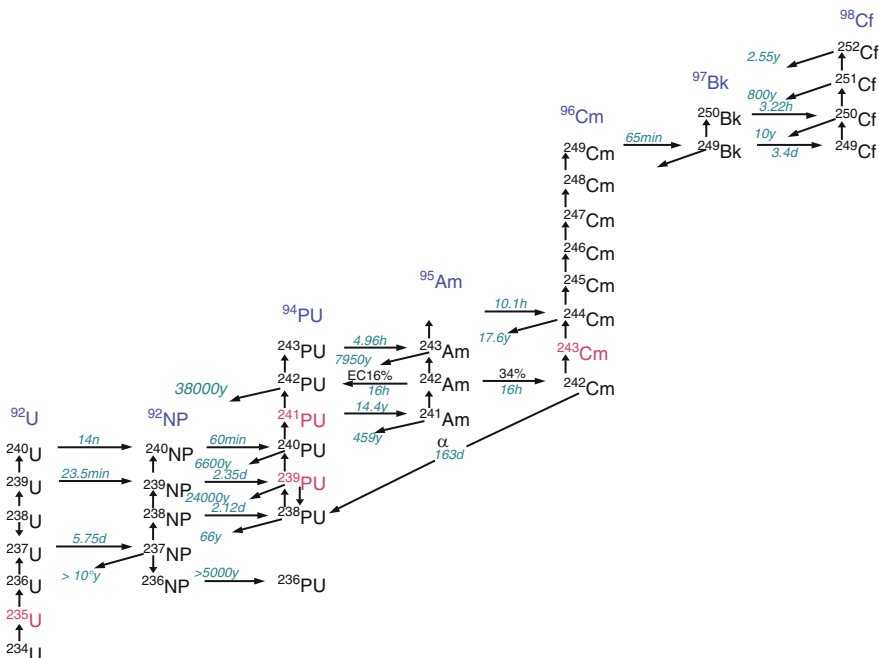


Figure 11
Transuranic element formation

Table 2
Actinide formation in UOX fuel in LWRs as a function of the burnup

Burnup (GWd/t)	Initial enricht. (%)	Pu quality (%)	Np 237	Am 241	Am 243	Cm 244	Cm 245
42	3.70	66	1.81	0.58	0.49	0.14	0.01
55	4.50	63	1.70	0.47	0.56	0.22	0.02
65	4.95	60	1.90	0.48	0.71	0.34	0.03

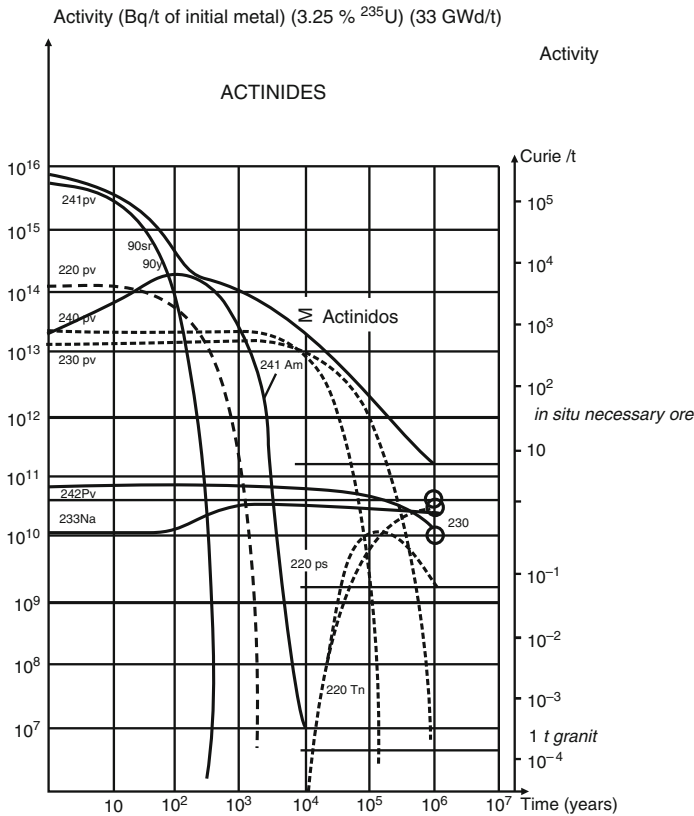


Figure 12
The activity of the actinides contained in spent fuel, as a function of time

1.1.6 Radioactive Decay

The radioactive decay of a nucleus is a purely random event governed by the laws of quantum mechanics. However, the decay probability per unit time is determined, and is a characteristic of the radionuclide considered. The random character of the decay results in an exponential decrease of the population of radioactive nuclei with time.

$$N = N_0 \cdot \exp(-\lambda t) \quad \lambda = \text{radioactive decay constant}$$

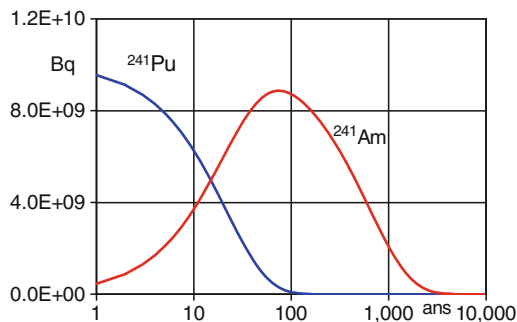
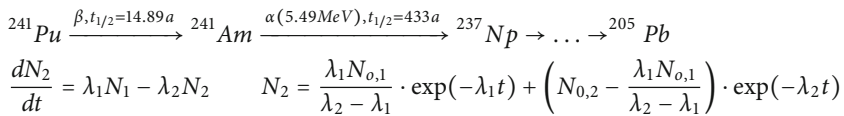
$$t = \text{time}$$

$$N_0, N = \text{initial and final number of radioactive nuclei}$$

$$A = \lambda \cdot NA = \text{activity}$$

The half-life of the radionuclide is defined as the time needed for its population to decrease by a factor 2: $T_{1/2} = \ln 2 / \lambda$.

If the daughter nucleus itself is radioactive, we have a chain of radioactive parents and daughters (► Figs. 13 and ► 14), and the population of radionuclides obey more complicated laws.



■ Figure 13

An example of radioactive filiation, of relevance for waste management: Am 241 is the daughter nucleus of Pu 241, which decays mainly via beta-radioactivity

4N+1 Disintegration chain

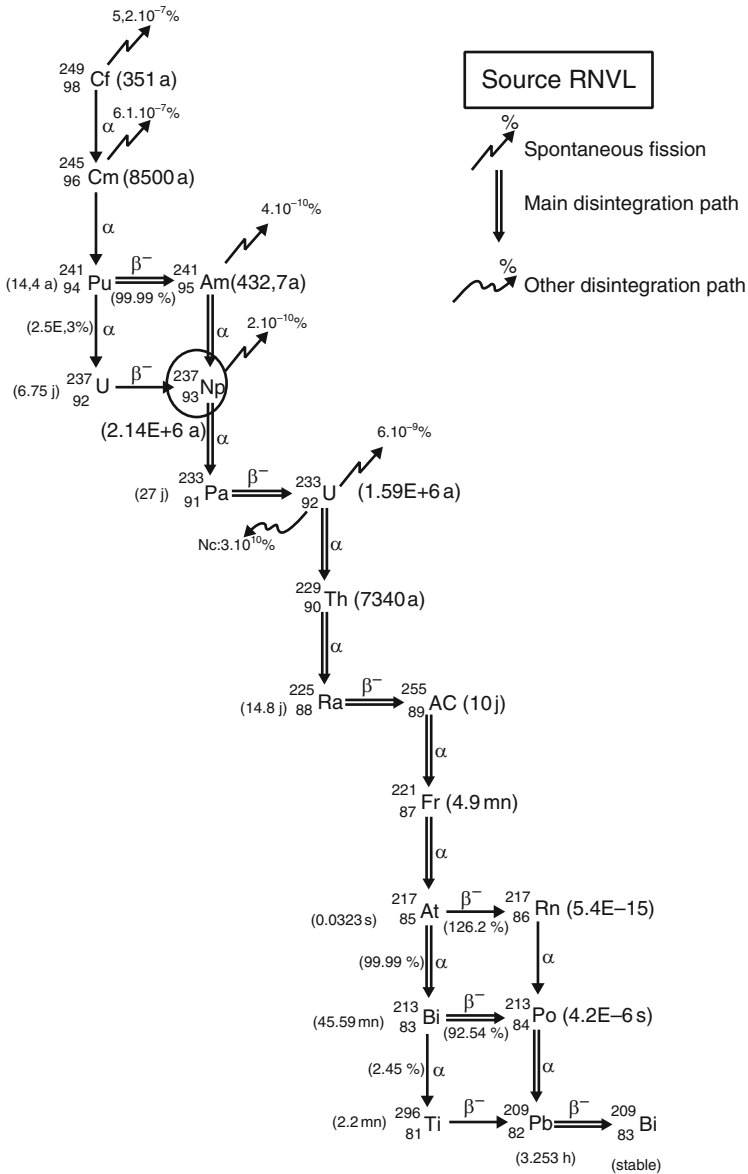


Figure 14

A disintegration chain. For heavy nuclei, four disintegration chains exist: labeled 4N, 4N + 1, 4N + 2, 4N + 3

1.1.7 What Kind of Radioactive Emission Do We Expect from the Nuclear Waste?

The types of radioactivity are different for nuclei placed differently with respect to the stability valley (🔍 *Fig. 15*). All decay modes tend to bring the daughter nucleus closer to the bottom of the valley. For example, nuclei with an excess of neutrons decay mainly via a beta-radioactivity process, which transforms one of their neutrons into a proton. This is the case of fission products.

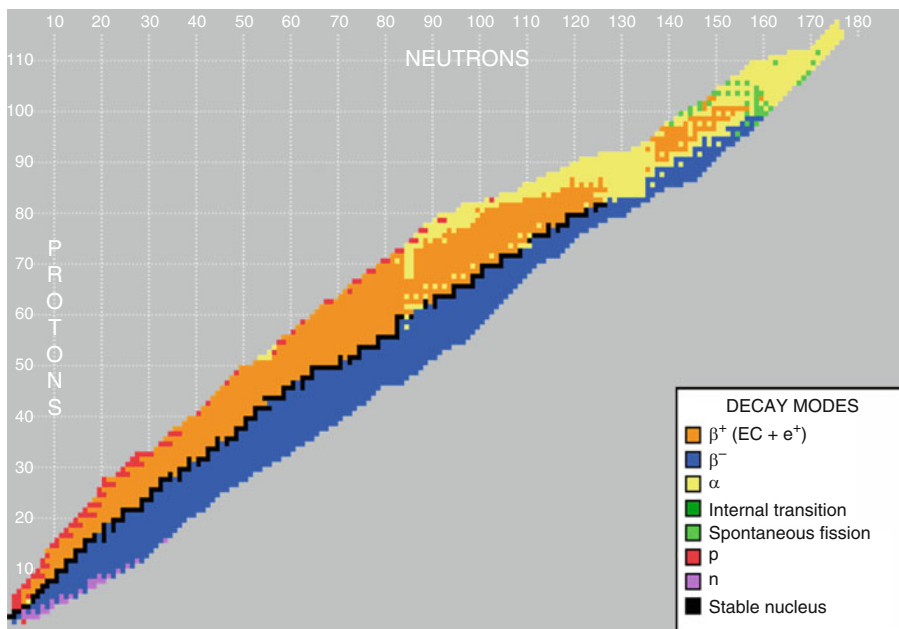
Another example is that of very heavy nuclei which get rid of their excess weight by alpha-radioactivity, with the departure of four nucleons at the same time. This is the case of actinides, which are mainly alpha emitters.

Of course, this particle emission generally leaves the daughter nucleus in an excited state. The return to the fundamental state implies the emission of gamma photons.

It is important to note the order of magnitude of the energy taken away by these radioactive decays:

An alpha particle takes away roughly 5 MeV

Beta and gamma particles take away a fraction of MeV.



🔍 **Figure 15**
Radioactive decay modes

1.1.8 Penetration of Ionizing Radiations into Matter

When dealing with nuclear waste management, it is also important to know *how ionizing radiations penetrate into matter* (🔗 [Table 3](#)).

■ **Table 3**

The typical range of ionizing radiations emitted by radioactive substances

	α (5 MeV)	β (1 MeV)	γ (1 MeV)
Air 1.293 mg/cm ³	3.6 cm	3 m	90 m
Water 1 g/cm ³	36 μ m	4.3 mm	10 cm
Pb 11.34 g/cm ³	15 μ m	3 mm	9 mm

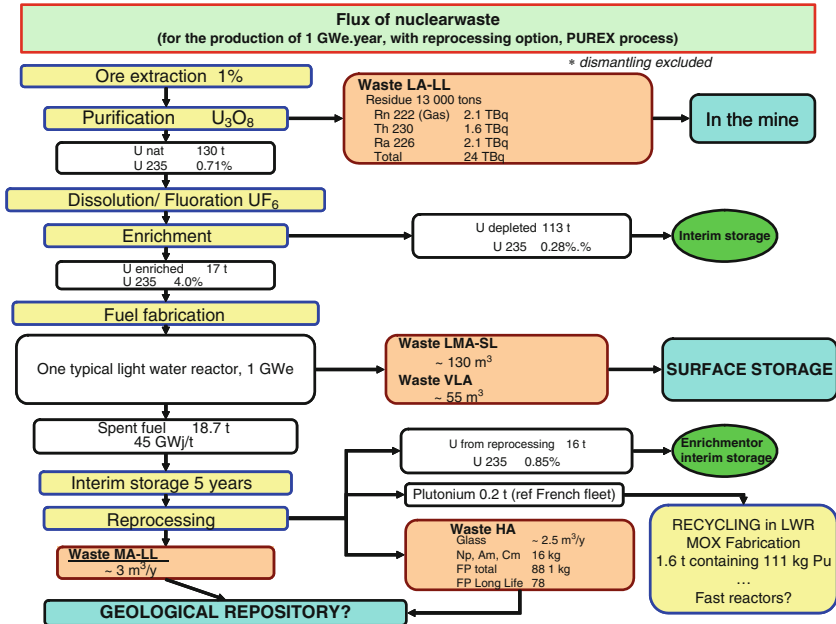
Alpha particles have a very short range, of the order of 1 μ m, in solid matter. They therefore dissipate much energy into a very small volume. In the ceramic of spent fuel or in vitrified waste, the alpha emitters will dissipate their energy in the matrix itself; almost no alpha particles will come out of the waste. The waste will generate heat, will possibly degrade with time, but will not represent a significant danger of external irradiation for the operator.

Beta particles are electrons with a range of a few millimeters in condensed matter. This range is of the same order of magnitude as the diameter of a fuel rod, and is not much smaller than the size of a vitrified glass package. One therefore expects that part of the energy of the decay will be dissipated in the matrix, and part of it will be radiated outside (with some danger of irradiation for the operator).

Gamma photons have a larger range in condensed matter, on the order of 1 dm to 1 m depending on their energy and on the atomic weight of the matter traversed. They contribute marginally to the power dissipation in the waste, but are very effective to make the waste irradiating and therefore dangerous for the operators.

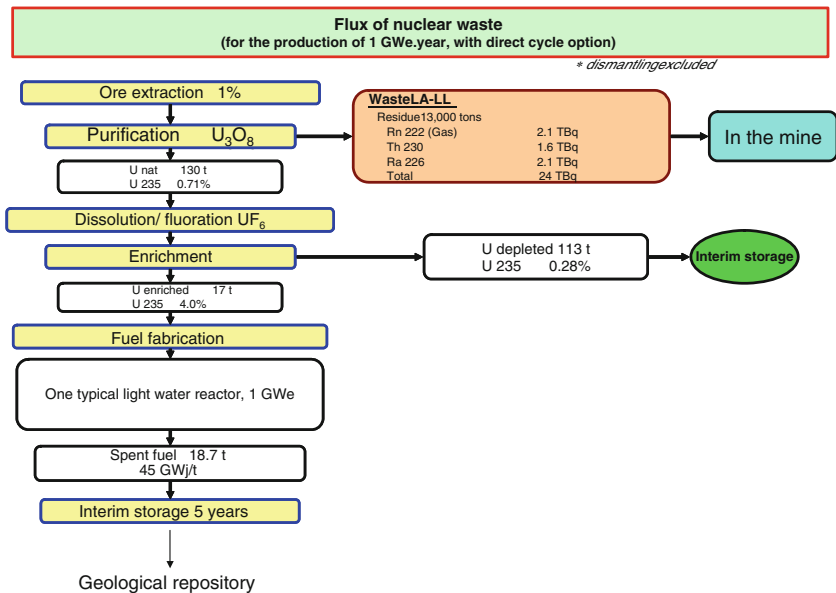
1.1.9 The Radioactive Half-Life of the Main Radionuclides Found in Nuclear Waste

Spent fuel contains a cocktail of short-lived and long-lived radionuclides. Each category brings specific problems: short-lived RNs generate heat and make spent fuel highly irradiating; long-lived RNs do not pose acute problems, but their presence obliges us to care about the spent fuel – or waste generated from spent fuel – for very long periods of time (🔗 [Figs. 16](#) and 🔗 [17](#); 🔗 [Table 4](#)).



■ Figure 16

The waste flux produced by a typical light water reactor producing 1 GWe.year (closed cycle option, i.e., the spent fuel is reprocessed)



■ Figure 17

The waste flux produced by a typical light water reactor producing 1 GWe.year (open cycle option, i.e., the spent fuel is not reprocessed)

Table 4
The half-life of some radionuclides relevant for waste management

Fission products	T1/2
¹²⁹ I	1.5 e7 years
¹³⁵ Cs	2.0 e6 years
⁹⁹ Tc	2.1 e5 years
⁷⁹ Se	1.1 e6 years
¹³⁴ Cs	754 days
⁹⁰ Sr	28.8 years
¹³⁷ Cs	30 years
¹²⁶ Sn	1. e5 years
¹⁵⁴ Eu	8.59 years
¹⁰⁶ Ru	373 days
¹⁴⁴ Ce	285 days
Actinides	T1/2
²³³ U	1.6 e5 years
²³⁵ U	703 million years
²³⁸ U	4.5 e9 years
²³⁷ Np	2.1 million years
²³⁸ Pu	87 years
²³⁹ Pu	24,110 years
²⁴¹ Pu	14.3 years
²⁴¹ Am	432 years
²⁴³ Am	7,370 years
²⁴⁴ Cm	18 years
²⁴⁵ Cm	8,500 years
²⁴⁶ Cm	4,730 years
Activation products	T1/2
¹⁴ C	5,730 years
³⁶ Cl	3.0 e5 years
⁶⁰ Co	1,925 days
⁹³ Zr	1.53 e6 years
⁶³ Ni	100 years

Source: Tuli

1.1.10 Radioactive Waste: How Dangerous Is It?

The danger of radioactive waste depends on how it is managed! Despite its small volume, high-activity waste is very radioactive.

For example, an HL glass package from spent fuel reprocessing (400 kg glass) has an activity of 16,000 TBq after 6 years, and the dose rate is 500 Gy/h at contact and 80 Gy/h at 1 m distance. This is several $\times 10$ times the lethal dose in 1 h. These values are divided by 10 after 100 years. The same orders of magnitude also hold for a 500 kg spent fuel assembly.

As a consequence, a very tight confinement of HLA waste is compulsory, and the packages must be handled with caution.

1.2 Management Options: An Overview

1.2.1 Dispersion or Concentration?

From the beginning of the nuclear industry, the choice has been made to concentrate the radionuclides in the waste, for three main reasons:

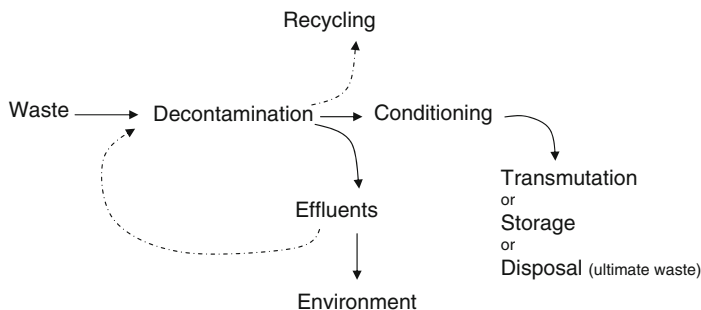
- An environmental reason: the travel of radionuclides in the biosphere is poorly known and difficult to control. It is thus difficult to prove that there is no risk of reconcentration of some radionuclides in some specific compartments of the biosphere. Such events have already occurred with chemicals dumped in the sea: heavy metals tend to concentrate at the end of the trophic chain, with very detrimental consequences for the local populations.
- An industrial reason: processing the spent fuel already implies concentration.
- An image reason: very low levels of radioactivity are easily detectable in the environment.

For these reasons, the concentrated waste is then isolated from the environment by means of several barriers, both complementary and redundant (multibarrier concept).

This philosophy, concentrate and isolate, is applied to all radionuclides, with a few notable exceptions: Tritium, Chlorine 36, Krypton 85, and Iodine 129. Iodine is volatile and soluble, two characteristics that make it very difficult to confine. The iodine present in spent fuel is released during the operations of processing of the spent fuel. A small part of it is sent to the atmosphere, the major part is sent to the sea, where it is rapidly diluted. For example, at the La Hague processing plant, 1 km away from the release point, the radioactivity level due to Iodine 129 is already very small compared to the natural radioactivity of seawater, but this activity can be detected even in the North Sea.

1.2.2 Waste, Effluents, Decontamination, and Conditioning: A Systemic Vision

Radioactive waste is a radioactive substance for which no ulterior use is foreseen. Ultimate radioactive waste is the waste, which cannot be treated to extract any reusable fraction, or to reduce its polluting or dangerous character in the present technical or economic situation (➤ Fig. 18).



■ **Figure 18**
Waste, effluents, decontamination, and conditioning: a systemic vision

An effluent is the liquid or gaseous residue of a chemical treatment. In some cases, these residues are dispersed in the environment; another option widely used in the nuclear industry is to separate their toxic fraction (decontamination) and to put this fraction under a stable form (conditioning).

The reusable fraction can optionally be recycled.

Conditioning (of radioactive waste) is the ensemble of operations aiming at putting radioactive waste under a stable form, which will permit its ulterior safe management, e.g., transmutation, storage, or disposal.

1.2.3 Reprocessing or Not Reprocessing?

A chapter on waste management cannot avoid the question of spent fuel reprocessing, because the choice to reprocess or not has a strong influence on the nuclear waste management (► [Table 5](#)).

The principle of reprocessing is to separate chemically U and Pu from the fission products, in order to:

1. Reuse valuable materials (U et Pu)
2. Optimize the final waste management by reducing the quantities (mass, volume, radiotoxicity) and by confining it in suitable long-lasting materials

The process commonly in use today is the PUREX process (► [Figs. 19–21](#)). Several variants of PUREX can be envisaged to extract U and Pu separately or together. Several complements to the PUREX process can also be envisaged to extract the minor actinides from the fission products. These variants or complements are not yet implemented at the industrial scale.

The processing operations result in a partitioning of the radionuclides, but their total amount remains the same as the initial one (no transformation).

The choice to reprocess or not is a matter of industrial strategy, guided by many criteria, including economy and politics. A complete discussion on the pros and cons of reprocessing is outside the scope of this chapter. We shall restrict ourselves to the waste management point of view.

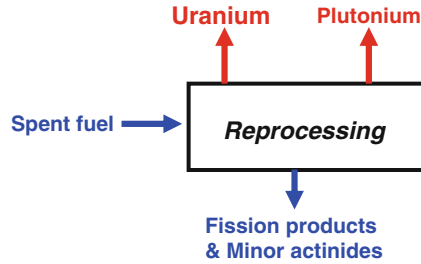


Figure 19
The principle of the PUREX processing process

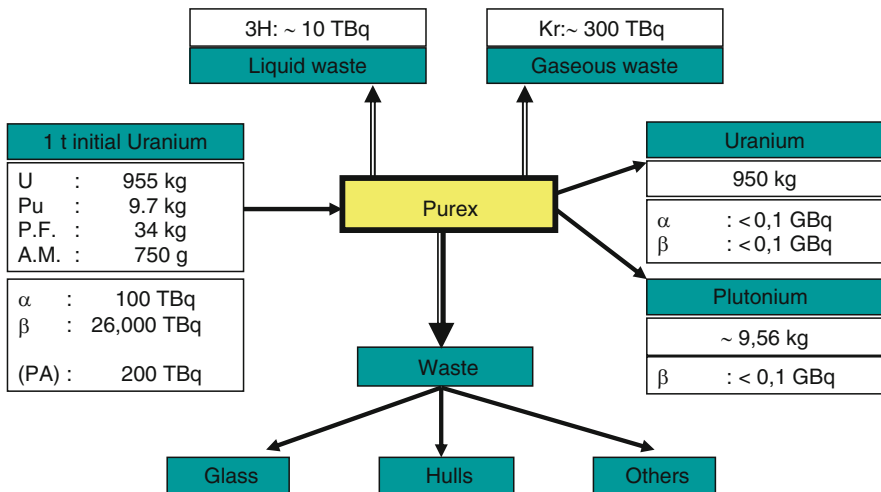


Figure 20
The mass and activity flow of the PUREX process, for 1 t of initial uranium irradiated with a burnup of 45 GWd/t

The advantages are:

- A volume reduction of the waste, which is put under a compact, stable, and durable form (vitrification). The waste from reprocessing is thus easier to manage (handling, storage, disposal) than the spent fuel.
- A reduction of the potential radiotoxicity of waste, by removal of the plutonium it contains.

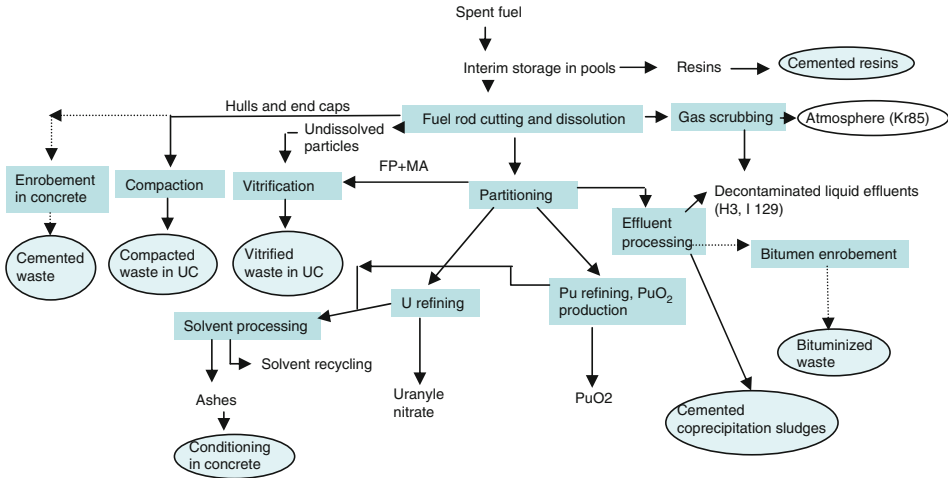


Figure 21
Overall scheme of the waste streams from reprocessing

The drawbacks are:

- The use of heavy technology, with safety concerns during the processing operations
- The need to transport very active nuclear material to and from the processing plant
- The production of effluents with a significant radioactive content

1.2.4 World Situation for Waste Management

About 15 countries are involved in nuclear waste management, including the USA, Canada, Japan, France, Finland, Sweden, Germany, Belgium, Spain, Switzerland, UK, Korea, China, and India.

In those countries, many storage facilities are in operation for short-lived waste. Three repositories are in activity for IL LL waste (East Germany, Sweden, USA). High-Level waste is stored in interim storage facilities.

No repositories are in operation for high-level long-lived waste (but there is a general consensus among experts about their feasibility). Decision to build has been taken in Finland and Sweden.

There is no international consensus on spent fuel processing.

Waste management remains a national issue: even though it might make sense from a technical point of view to group the waste from different countries, such a decision would raise such ethical and political problems that no move in this direction can be envisaged in the near- or mid-term future.

1.2.5 The Institutions In Charge of Waste Management in the World

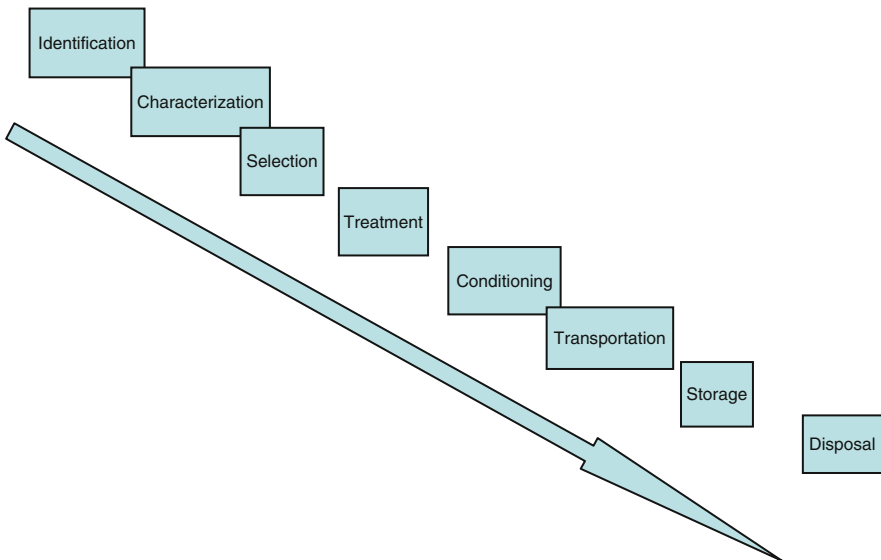
■ Table 5

Main organizations in charge of waste management in the world

Country	Name	Status	Waste managed
USA	OCWRM (US-DOE)	PO	HL and SF
Germany	BfS	PO	LL, IL, HL
	DBE	50% PO, 50% UT	
Belgium	Ondraf/NIRAS	PO	LL, IL, HL
France	ANDRA	PO	VLL, LL, IL, HL
Spain	ENRESA	PO	VLL, LL, IL, HL
Japan	Numo	PO	IL, HL
Switzerland	Nagra/Cedra	UT	LL, IL, HL
Sweden	SKB	UT + PO	LL, IL, HL (SF)
Finland	POSIVA	UT	HL (SF)
Canada	SGDN/NWMO	UT	HL
UK	NDA	PO	LL, IL, HL

PO: public organization, UT: utility, VLL: very low level waste, LL: low level waste, IL: intermediate level waste, HL: high level waste, SF: spent fuel

1.2.6 The Waste Management Process



■ Figure 22

Waste management process

Waste management features the following successive operations: identification, characterization, selection, treatment, conditioning, transportation, storage, and disposal (🔍 Fig. 22).

The ensemble of these operations is specifically adapted to the nature of each category of waste.

1.2.7 Uranium Mine Tailing Management

During the extraction operations, the uranium ore is crushed down to a granulometry of the order of a fraction of a millimeter, and exposed to the action of an acid (generally sulfuric), more seldom of an alkali, depending on the nature of the minerals. This treatment extracts 90–98% of the uranium from the ore, but leaves in the tails all the daughter atoms from the uranium decay chains, including radium. The mine tailings, which are the true waste of the mining operations, thus contain 80% of the initial radioactivity. These tailings are gamma emitters. Since they also contain Radium 226, they are also able to emit its daughter, Radon 222. This atom can eventually exit in gaseous form from the mineral grains, all the more easily if the grains are smaller. It is necessary to protect the public and the workers both from the gamma emissions and from the radon exhalations. The quantities of mine tailings are such that these tailings cannot be stored elsewhere, but in the mine itself. The tailings are used to backfill the excavations in the mine, a form of storage, which enables one to monitor their evolution. After the closure of the mine, the residues are covered by a layer of sterile rocks a few meters thick, in order to shield the gamma emissions and to prevent the exit of radon to the open air (🔍 Fig. 23). This method is effective because ^{222}Rn (period 3.8 days) atoms have no time to diffuse out of this layer.

However, the mine tailings have been perturbed by the chemical attack, and may undergo mineralogical transformations, with subsequent release of radium and residual uranium in the water, which percolates through the residues. These waters are therefore drained and chemically treated to get rid of their radium before their release in the hydrographic network. The control is maintained as long as the radium content of the water remains significant.

Another option to manage the uranium mine tailings is to keep them under water. The water shields the environment from the gamma radiation emitted by the tails, and prevents the release



🔍 Figure 23

The uranium mine of Puydelage (France) during its exploitation and after its closure

of radon in the atmosphere. This management mode is convenient in lake regions, and has been used, for example, in Canada. Here again, the radioactive content of the water is monitored.

1.2.8 Management of Low and Intermediate Level, Short-Lived Waste (LIL-SL)

This type of waste is mostly conditioned in concrete or metallic drums:

Metallic drums for the least noxious waste (gloves, masks, clothes, etc.)

Concrete shells for medium radioactive waste

Concrete casings, containing compact metallic drums or nuclear plant filters

Metallic casings for the most bulky waste (tubes, scraps, etc.)

The management principle for this type of waste is to leave the waste stored for two or three centuries (more than ten times the period of the longest-lived radionuclides contained in the waste), a time sufficient for all radionuclides to decay.


The conditioned waste is piled up in watertight cells. The voids are filled with gravel or mortar, the cells are closed by a concrete cover and coated with a watertight polymer. Later on, the storage is covered by a watertight blanket, plus a few meters of soil. After 300 years, the radioactivity will have almost completely decayed.

Several installations for the storage of LIL-SL waste exist in the world, shared almost equally between underground storage-disposal facilities and surface storage installations.


Geological storage facilities at medium depth (100 m) exist in Sweden and in Finland.

A geological disposal in sedimentary host rock is in operation in the ancient iron mine site of Konrad (Germany). In 2007, this site obtained the authorization to store all types of non-exothermic waste, short-lived or long-lived.

In Canada, the utility OPG is preparing the project of deep geological disposal (DGR) LIL-SL waste in the site of Kincardine (Ontario).

Surface installations are also working in France (Centre de l'Aube), in Spain (El Cabril,  Fig. 24), in the UK (Drigg), and in Japan (Rokkasho-Mura).



 Figure 24

Example of LIL-SL waste storage facilities: the Spanish site of El Cabril has a capacity of 76,000 m³ (LIL-SL waste) and 130,000 m³ (VLL waste) (photographs ENRESA)

In Switzerland, as in other countries where the search for storage sites has triggered much local opposition, a unique storage facility for all types of waste is being sought.

1.2.9 Interim Storage of Spent Fuel

An assembly of spent fuel is made of fuel rods (tubes of zirconium alloys containing the UO_2 or $\text{UO}_2\text{-PuO}_2$ pellets). These rods are 4–5 m long, closed at both ends, and bound together in a square lattice by grids and spacers, which maintain a specified distance between them. A device at the top of the assembly permits the handling of this bundle (► Fig. 25).

After their unloading from the reactor core, the bundles of spent fuel can be stored, most often in pools (► Fig. 26), but also possibly in dry casks. This storage leaves some time for the fuel to cool down by decay of its short-lived radionuclide content. After a few years of cooling,

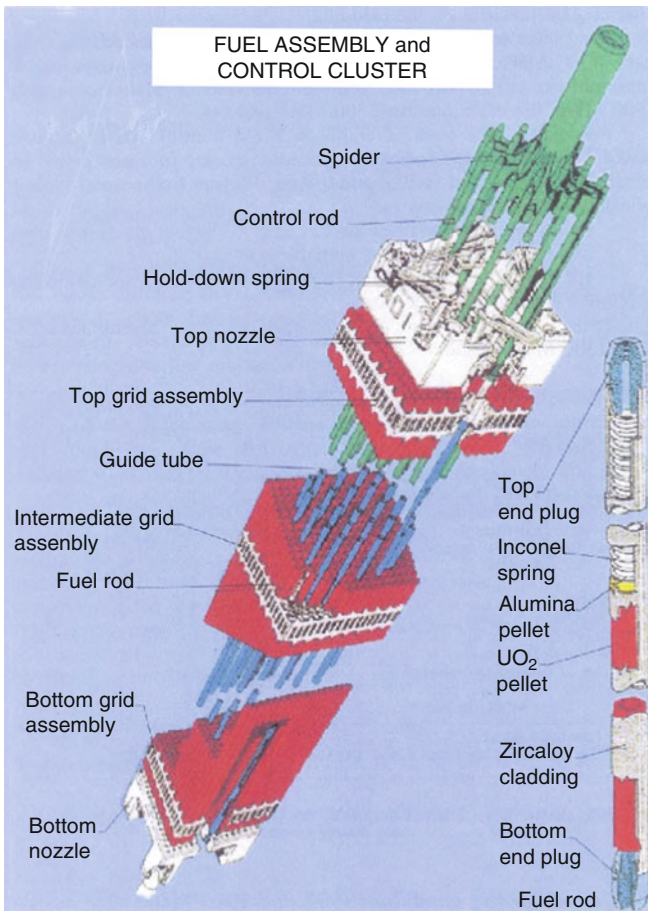
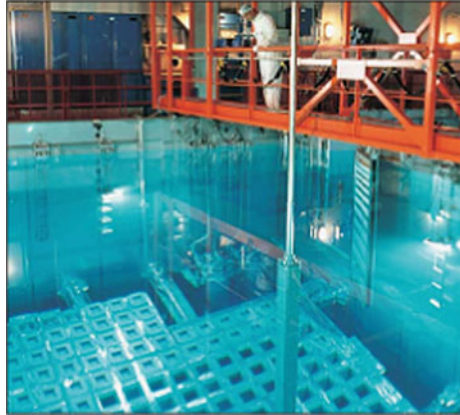


Figure 25
A PWR fuel bundle



■ Figure 26

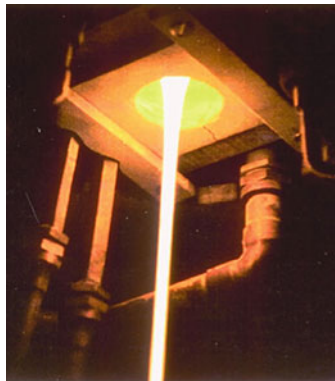
A pool for the interim storage of spent fuel

the spent fuel can then be reprocessed (closed fuel cycle option) or considered as final waste (open fuel cycle option) (See ▶ Sect. 3.1).

1.2.10 High Activity Waste from Reprocessing is Vitrified

The idea is to cast the waste into a very stable form, able to confine the radionuclides (▶ Figs. 27 and ▶ 28).

The vitrified waste is stored in ventilated wells, close to the processing unit (▶ Fig. 29). This storage is (by definition) temporary.



■ Figure 27

Glass casting of high-activity waste from reprocessing



■ Figure 28
An example of vitrified waste package



■ Figure 29
The EEV-SE facility for the interim storage of vitrified HL waste

1.2.11 Options for the Management of Long-Lived Nuclear Waste

Partitioning and Transmutation

The main purpose of partitioning and transmutation is to minimize the waste quantity and toxicity (🔍 [Fig. 30](#)).

The general idea of partitioning is to separate transmutable radionuclides from others and to separate long-life radionuclides from others in order to manage these categories of waste separately. The general idea of transmutation is to transform the long-lived radionuclides into inactive or short-lived isotopes.

There are good prospects to transmute actinides in Fast Reactors. This could permit a big gain on waste radiotoxicity and residual power (this last parameter dictates the size and cost of a repository). But before transmuting actinides, one needs to separate, and to store them.

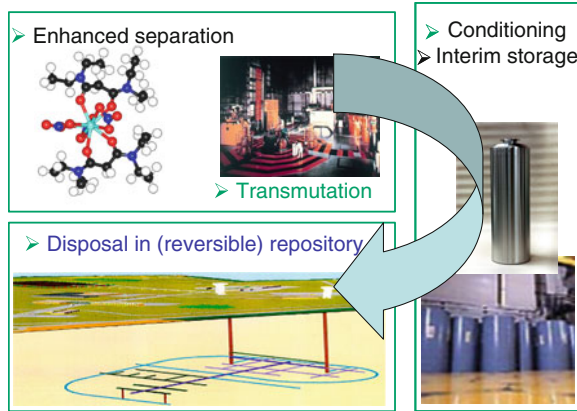


Figure 30
Options for the management of long-lived nuclear waste

Thanks to considerable progress in hydrometallurgy, selective extraction methods have been developed. Nowadays, separation between Fission Products (^{129}I , ^{99}Tc , and ^{135}Cs) and Minor Actinides (Np, Am, Cm) (more than 95%) has been proven feasible at the laboratory scale and will not pose big problems at the industrial scale because the new processes are merely adaptations and variants of the PUREX process.

Separation of Minor Actinides would permit one to avoid their incorporation in vitrified waste, with a considerable gain in radiotoxicity and thermal load of the glass. This option will become interesting if (and when) minor actinides can be transmuted efficiently.

Transmutation of Fission Products is very difficult because these nuclei require one neutron per transmutation, or even more than that, because the result of this transmutation is often another radioactive nucleus.

Transmutation of Minor Actinides is technically feasible, especially in a fast neutron reactor, because these nuclei are fissile in fast neutron spectrum. Their fission produces additional neutrons and energy. However, the timescale for the transmutation is quite slow, of the order of 10–100 years.

Conditioning

Waste conditioning consists in putting the waste under a stable and safe form, with packages, which can be handled.

It has been shown that glass and cementitious materials are satisfactory conditioning matrices for long-life waste (see [Sect. 2](#)).

Interim Storage

The main idea behind interim waste storage is to give time for the waste to cool down and time to decide on an appropriate waste posttreatment.

Interim storage is temporary by definition. It implies the possibility of a secure and safe recovery of waste from a facility able to protect the waste durably.

Interim storage appears as an option, which gives some flexibility to the nuclear waste management: it acts as a buffer for the waste stream, between production and disposal. An important parameter is the *duration* of the interim storage.

Long-term interim storage (>100 years) in surface or subsurface has been proven to be feasible technically (see [Sect. 3.1](#)).

Deep Geological Disposal

The main idea of deep geological disposal is to get rid of the waste definitively, without leaving the burden of our waste to future generations (note the apparent contradiction with the interim storage philosophy).

This solution could be the ultimate one, for ultimate waste. The geological medium ensures a stable long-lasting barrier.

A *reversible* disposal gives the possibility to retrieve the waste after some time. The idea of reversibility bridges the gap between storage and disposal. All degrees of reversibility are possible. The reversibility option is still under study. If chosen, this option will hamper somewhat the safety of the repository, and increase its cost. To what extent?

Interim storage and disposal facilities do not differ only in their philosophy: they are objects of two different natures. While disposal facilities are designed to be safe without any surveillance or maintenance, interim storage facilities require both. Secondly, there is no return of experiment on the operation of nuclear waste repositories, whereas interim storage facilities are already an industrial reality. Thirdly, the lifetime of the interim storage facility is of the order of a century, i.e., a duration familiar to engineers who build bridges or other artifacts, whereas the lifetime of a repository is so long that it challenges the human imagination. Lastly, the radiological impact of an interim storage is designed to be zero for the public (no leaks) during its entire lifetime, whereas such a goal is inaccessible for a repository. However, the radiological impact for the workers in the storage facility will be nonzero, and the hazards, which might affect the storage facility are nonnegligible. Consequently, the duration of the interim storage must be decided, taking into account these factors, and weighing them against the industrial advantages of this option.

Thanks to the studies in underground laboratories, the technical feasibility of a reversible geological disposal has been established (see [Sect. 3.2](#)).

These options for the management of long-lived nuclear waste are complementary, not antagonistic. They are listed here in an order that could be chronological. The deep geological disposal is at the end of the sequence.

1.2.12 Waste Management and Radioprotection

The units of radioactivity

Quantity	Units	Definitions
Activity	Becquerel (Bq)	Measure of the number of disintegrations per unit time within a radioactive source. 1 Bq = 1 disintegration/s
Absorbed dose	Gray (Gy)	Measure of the energy received per mass unit of irradiated matter. 1 Gy = 1 J/kg
Equivalent dose	Sievert (Sv)	Measure of the biological damage on irradiated living tissues. 1 Sv corresponds to 1 Gy (in the special case of gamma irradiation, on the whole body); ponderation factors are introduced to take into account the nature of the radiation and the vulnerability of the different organs

1.2.13 From Radioactivity to Radiotoxicity

One defines the radiotoxicity of a given quantity of a radioactive substance as the dose that would be received by someone who would ingest this quantity.

$$\text{Radiotoxicity} = \sum X_i^* \text{DF}_i,$$

where X_i is the activity of radionuclide i in the substance, and DF_i is a dose factor associated to radionuclide i . The sum runs over all radionuclides contained in the substance.

Each radionuclide has a characteristic “dose factor” DF (expressed in Sv/Bq), which characterizes its intrinsic radiotoxicity. This dose factor depends on the type and energy of the radioactivity emitted by the RN, on its biological period (i.e., the time during which it stays in the organism) and on the organs in which it tends to concentrate.

Radiotoxicity is merely an indicator of the danger induced by the waste, used to compare different waste management options.

1.2.14 Ingestion Dose Factors

Relationship Between Radioactive Dose and Effect

The effect of low doses (<10 mSv/year, i.e., the domain of interest for waste management) is poorly known. In the absence of scientific evidence, the radioprotectionists assume a proportionality between the dose and the effect. This assumption facilitates the evaluation of danger, and the establishment of radioprotection rules (► [Fig. 31](#); ► [Table 6](#)).

■ **Table 6**

The ingestion dose factors of some radionuclides of interest for waste management

	<i>FD (Sv/Bq)</i>
Tritiated water	1.8×10^{-11}
^{14}C	5.8×10^{-10}
^{40}K	6.2×10^{-9}
^{90}Sr	2.7×10^{-9} à 2.8×10^{-8}
^{99}Tc	7.8×10^{-10}
^{129}I	1.1×10^{-7}
^{131}I	2.2×10^{-8}
^{135}Cs	2.0×10^{-9}
^{226}Ra	2.8×10^{-7}
^{232}Th	9.2×10^{-8} à 2.2×10^{-7}
^{238}U	2.6×10^{-9} à 4.4×10^{-8}
^{237}Np	1.1×10^{-7}
^{241}Am	2.0×10^{-7}

Source: ICRP report 72

10 Sv	Lethal dose (whole body)
100 mSv	Lowest dose with carcinogen effect detected
20 mSv	Worker's maxi permitted dose (year)
2 mSv	Natural irradiation average level
1 mSv	Public maxi permitted dose (year)

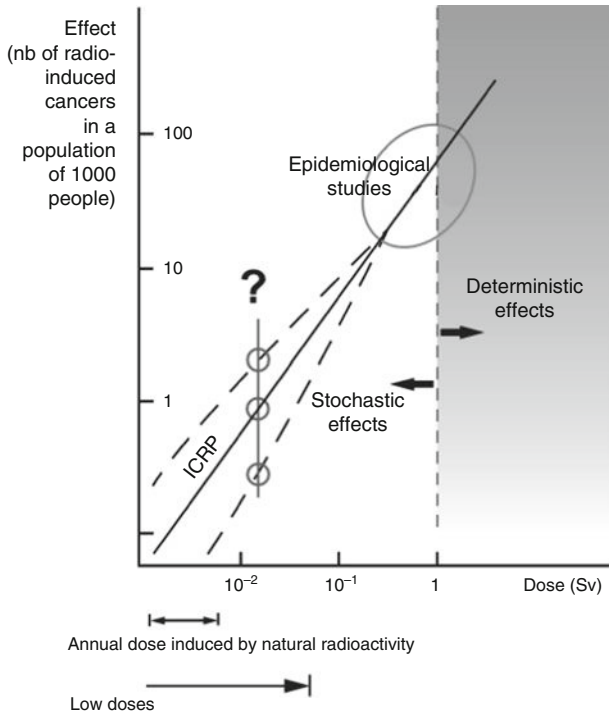


Figure 31
The dose–effect relationship

1.2.15 The Long-Term Radiotoxicity of Spent Fuel

For a short time after the fuel discharge, the radiotoxicity of spent fuel is shared about equally between actinides and fission products; after a few decades, actinides (and especially plutonium) dominate. Plutonium is the main contributor to the long-term radiotoxicity of the waste (🔍 Fig. 32).

The radiotoxicity of waste decreases with time. The rule of thumb generally adopted for the management of LLW is to confine the waste long enough for its radiotoxicity to decrease below the level of the initial uranium in mined ore (🔍 Fig. 33).

If spent fuel is considered as waste, one then has to confine it during several hundred thousand years.

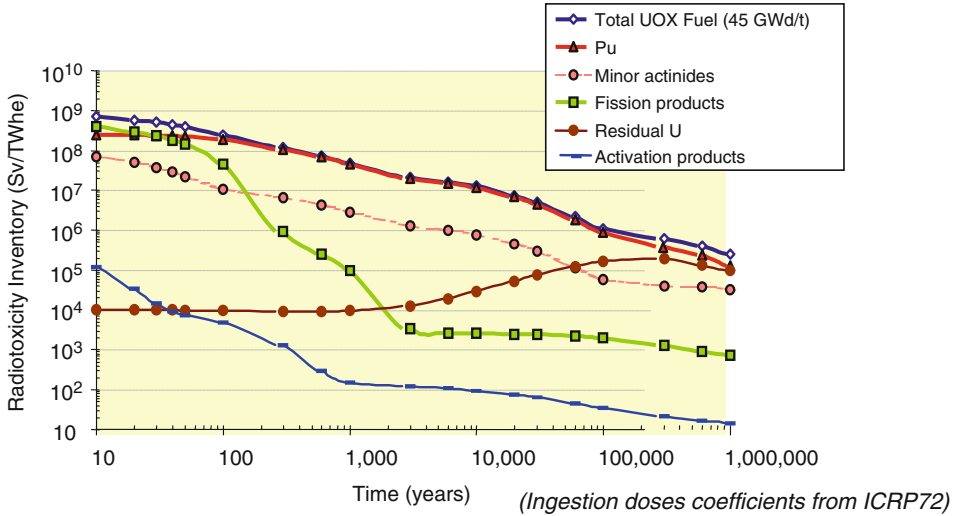


Figure 32
The radiotoxicity of spent fuel

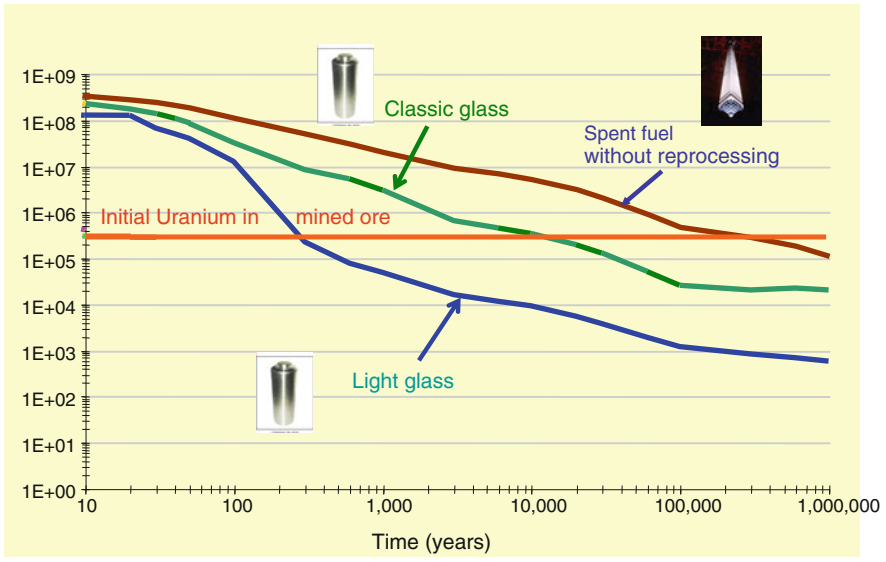


Figure 33
Comparison of the radiotoxicity of spent fuel and of HL waste from reprocessing

Reprocessing brings a drastic reduction of the radiotoxicity of the waste, as well as a reduction of the needed confinement time.

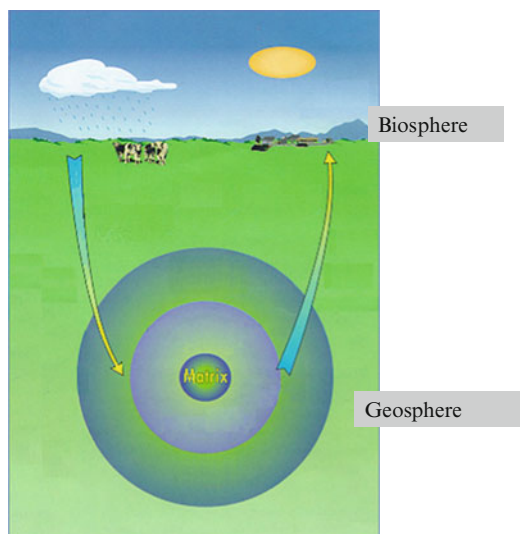
A removal of the actinides from the glass would permit another reduction of both toxicity and confinement time, which could be cut down to a few centuries.

1.2.16 Deep Geological Disposal: The Multibarrier Concept

The principle of a deep geological disposal is to interpose several barriers (🔍 Fig. 34), i.e., confinement matrix (glass, concrete), engineered barrier (overpack, clay layer), and geological barrier (host rock) between waste and biosphere, in order to prevent and delay the radionuclide migration. The delay must be long enough for the radioactive decay to take place.

The curves of the radiotoxicity versus time (▶ Fig. 33) give the timescale needed for this delay. They are of the order of several 100,000 years for spent fuel, several 10,000 years for “classical” glass, and several 100 years for “light” glass.

The challenge is to predict the evolution of the repository over the next 100,000 years. No direct demonstration is possible. One can only try to convince (oneself and others) by means of modeling and partial experiments.



■ Figure 34

The multibarrier concept applied to the deep geological disposal of nuclear waste

2 Waste Conditioning

Waste conditioning ensures the confinement of the radioactivity on the long range, based on the timescale of the storage or disposal. The usual methodology of waste conditioning involves several steps:

Treatment of the waste: this step covers two major goals.

Putting the waste under a form compatible with the confinement matrix and reducing the waste volume through methods (decontamination, incineration of organic waste, compacting, etc.) designed to produce the smallest possible quantity of secondary waste.

Packaging: this step consists of incorporating the waste in an adapted confinement matrix, then in a container. Conditioned waste is under the form of a “package.”

Characterization of the package: this step involves determination of the quantity, the nature, and the location of the radioactivity contained in the package, in order to forward it toward the most adapted exutory (and to check that the regulatory requirements are complied with).

The aim is to demonstrate the quality of the radioactivity confinement on a timescale related to the type of exutory considered for the waste: some 10–100 years for storage and up to several hundred thousand years for geological disposal. This constitutes the stake of studies on the long-term behavior of packages.

Nowadays, this methodology has been widely tried. In the first place, a research should be carried out on the laboratory scale (under inactive conditions, but also in the presence of actual radio-elements) for a detailed description of the waste alteration phenomena, which could lead to a dispersal of radioactivity in the environment. Alteration can be endogenous to the package (waste radioactivity effects on the confinement matrix, or chemical reactions between the waste and the matrix), possibly leading to a modification in the package confinement properties (swelling, fissuring, etc.), or exogenous, and linked to the environment. It may occur when different engineered barriers have been soaked through by the water of the site. Alteration phenomena can also be linked to the interaction between the package and the environment; for instance, when the package alteration products or the radiolysis modify the properties of the water of the site (heat production, increase of the pH in presence of cement, increase of the oxidizing nature of the water by radiolysis, etc.).

These phenomena are then modeled, taking into account the safety margins. One then obtains an operational model, which will constitute a basis for the safety demonstration. With that aim, this model must be evaluated and its conservative character must be ascertained. This can be achieved quantitatively by means of a set of laboratory tests, or using geological or archeological analogues of the waste under study.

We recall that if the reprocessing option has been chosen:

- The solution of fission products and minor actinides is vitrified.
- Fuel cladding and end caps are rinsed and compacted or cemented.
- Sludges are bituminized or cemented.

In the following, we describe these conditioning processes, together with the long-term behavior of these different matrices, cement, glass, and bitumen. In countries, which have chosen the open fuel cycle option, spent fuel is considered as waste. The end of the chapter is devoted to the conditioning of spent fuel.

Decontamination is an important part of the waste treatment process. Decontamination of raw waste aims at extracting from the waste some of its radioactive content, which will then be isolated from the initial waste and conditioned into an ad hoc form.

Decontamination operations are carried out daily in the nuclear industry on solid, liquid, and gaseous waste. Eventually, the residual radioactivity level of the initial waste becomes sufficiently low to downgrade the waste or even to transform it into reusable material. In the case of solid waste, decontaminating small equipment (pumps, valves, or waste packages) can allow the equipment to be reused. Larger equipment items (hot cells, fission product storage tanks, pipes, steam generators, etc.) are decontaminated for maintenance or dismantling. The difficulty of

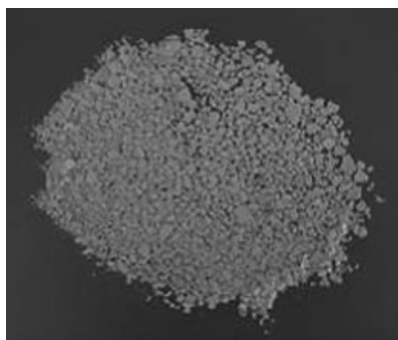
decontaminating a solid generally results from the chemical form in which the contamination is fixed:

- In layers adhering to the substrate such as fat, grease, and extraction solvents (e.g., the tributyl-phosphate used in the PUREX process),
- In oxide layers that trap radionuclides,
- In inorganic precipitates that may or may not adhere to the bottom of vessels,
- In the material bulk, radionuclides can migrate into the solid, for example, tritium in metals, or cesium in porous concrete.

Carefully identifying the physicochemical form of the contamination ensures that the most suitable decontamination processes can be implemented. Each process must minimize the quantity of waste produced and must be designed or developed with attention to a range of parameters: the nature of the contamination and its accessibility, the temperature and humidity, the nature of the contaminated material, etc. For this reason, there is no universal process. A suitable process must be specified for each decontamination operation.

Research carried out on decontamination techniques has led to efficient processes to decontaminate solids with high efficiency, in replacement of conventional acid–base rinsing operations that generate large quantities of liquid effluents:

- Dryable gels, sprayed or brushed onto the surface to be decontaminated (▶ Fig. 35). After drying, these gels produce a small quantity (typically $250 \text{ g} \cdot \text{m}^{-2}$) of solid residue in the form of flakes containing the radioactivity transferred from the decontaminated surface, and suitable for vacuum recovery. This decontamination technique eliminates the need for rinsing and thus produces no liquid effluent requiring subsequent treatment.
- Tensio-active foams (▶ Fig. 36). The aqueous foams considered for decontaminating components or structures in nuclear facilities consist of air bubbles dispersed in water containing one or more foaming surfactants and one or more chemical decontaminating agents (acids, bases, oxidizing or reducing agents). This technique is an attractive alternative to liquid phase processes, because it diminishes the quantity of chemical reagents used and the volume of liquid effluents generated.
- Decontamination by laser or super-critical fluids, which produce no effluent.



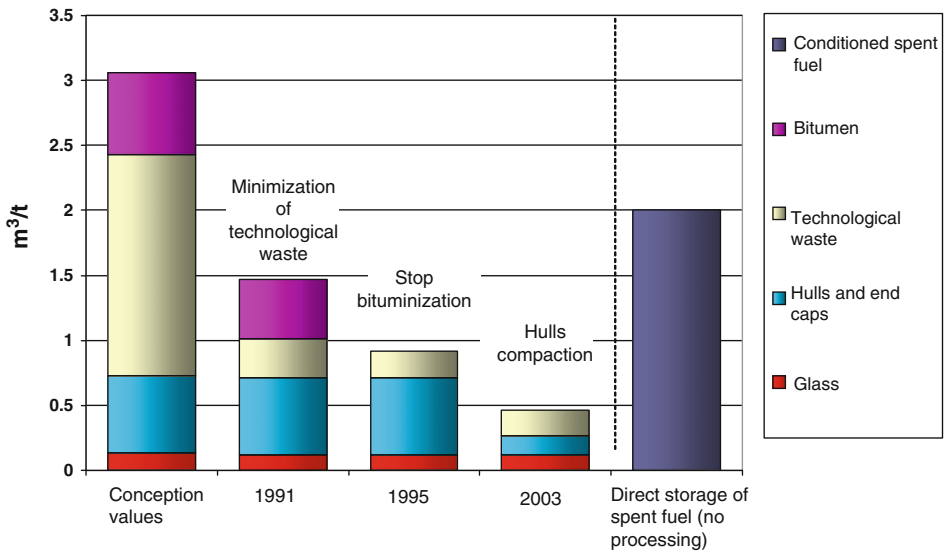
■ Figure 35
Decontamination by dryable gel



■ Figure 36

Decontamination of a tank contaminated by adhering deposits by a tensioactive foam

Volume of the waste conditioned in the UP3 processing unit in La Hague (long-life waste for one ton of initial uranium)



■ Figure 37

The volume of conditioned waste has steadily decreased, thanks to the producer's efforts. It is shown here that the processing of spent fuel also permits a reduction of the volume of the waste, by a factor larger than 4 as compared to the original spent fuel.

The first two methods (gels and foams) reached a development level permitting their use on an industrial scale.

Continuous improvement of the waste treatment and conditioning results in a large reduction of the waste volume over the last 20 years (► Fig. 37).

2.1 Conditioning of LL and IL Waste in Cement-Based Matrices

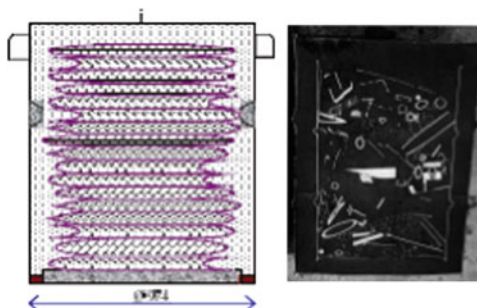
Cement-based materials are widely used in radioactive waste conditioning: grouts for waste embedding, mortars for immobilization operations, and concretes for container manufacturing on disposal sites.

Cementitious matrices are used to encapsulate waste such as:

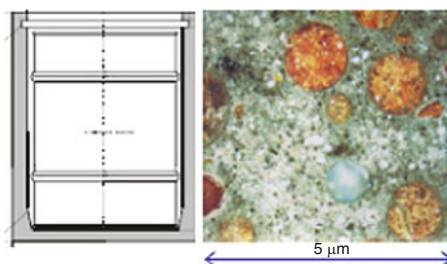
- Sludges of co-precipitation
- Evaporation concentrates of effluents
- Fuel cladding (<1995 in France)
- Ion exchange resins
- Technological waste (small materials, compacted drums, etc.)

The advantages of such a conditioning are as follows:

- Cementitious materials are versatile; they are able to confine a number of physicochemical waste forms, and to immobilize a high number of radionuclides owing to the interstitial solution basicity.
- Cementitious materials are cheap and readily available.
- Implementation is simple (cold process); liquid effluents can be directly incorporated into the concrete mixes.
- They have interesting mechanical properties (compressive strength).
- This conditioning permits handling and confinement by embedding (➤ Fig. 38) or homogeneous mixing (➤ Fig. 39).



■ Figure 38
Embedding of heterogeneous metallic waste



■ Figure 39
Cementation of ion exchange resins

The main drawback is linked to the fact that the incorporation rate is small, hence large volumes of waste are produced.

2.1.1 Elaboration of Cement-Based Materials

Cements are mixtures of calcium, silicon, and aluminum oxides under powder form, which react chemically with water to produce a solid made of hydroxides (mainly calcium hydroxide called portlandite and hydrated calcium silicates, under the generic acronym of C-S-H) (► [Table 7](#)).

Cement-based materials (grout, mortar, concrete) result from the setting of a mixture of anhydrous cement, aggregates of various sizes, and water (► [Fig. 40](#)).

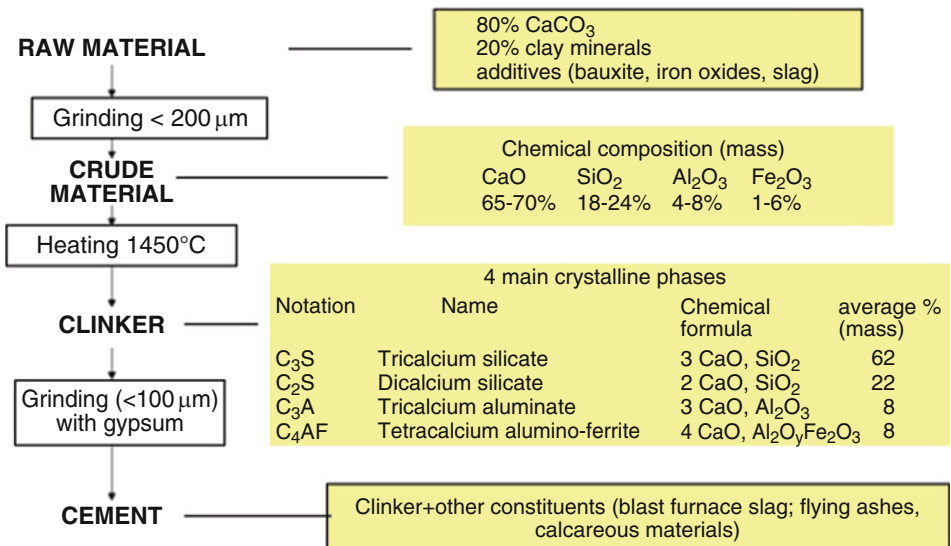
Hydration reactions start as soon as cement and water come into contact. Mechanical features change very rapidly in the hours following the setting, then this evolution goes on more and more slowly for several months.

Hardened cement paste is a heterogeneous material, which consists of a porous solid, a liquid phase and, generally, a gaseous phase present in the pores. The solid is formed with hydrated minerals and possibly residual anhydrous cement.

The interstitial pore solution is very basic (pH around 13.5) and its composition varies with the material age.

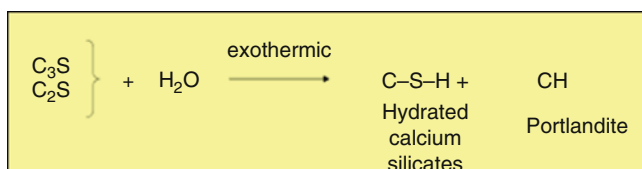
C-S-H minerals have a stoichiometry close to $C_{1.5}-S-H_{2.5}$ (calcium to silicon ratio about 1.7). They are responsible for the mechanical properties of the material.

The CH mineral, $Ca(OH)_2$, called portlandite plays a role in the material durability. It makes big crystals which are soluble in water ($s = 1.6 \text{ g/L}$ at 25°C). This dissolution has two important consequences: an increase of the porosity of the material; and a very basic porewater (pH



■ **Figure 40**
Manufacturing of cement

increases up to 13.5 during hydration). This high pH contributes to the passivation of the steel reinforcement in concrete.



Basic reaction of hydration in cements



■ Table 7

Composition of the cements most widely used in the area of nuclear waste conditioning and disposal. CEM I Portland cements are those used conventionally in the building industry. CEM III and CEM V cements differ from the CEM I Portland cement by the addition of large quantities of blast-furnace slag and pozzolanic materials

Composition of standardized cements								
Main types	Notation		Composition (wt %)					
			Clinker	Blast-furnace slag	Pozzolans			Secondary constituents
					Natural	Natural calcinated	Silica-containing fly ash*	
CEM I	Portland cement	CEM I	95–100	–	–	–	–	0–5
CEM III	Blast-furnace cement	CEM III/A	35–64	35–65	–	–	–	0–5
		CEM III/B	20–34	66–80	–	–	–	0–5
		CEM III/C	5–19	81–95	–	–	–	0–5
CEM V	Composite cement	CEM V/A	40–64	18–30		18–30		0–5
		CEM V/B	20–38	31–50		31–50		0–5

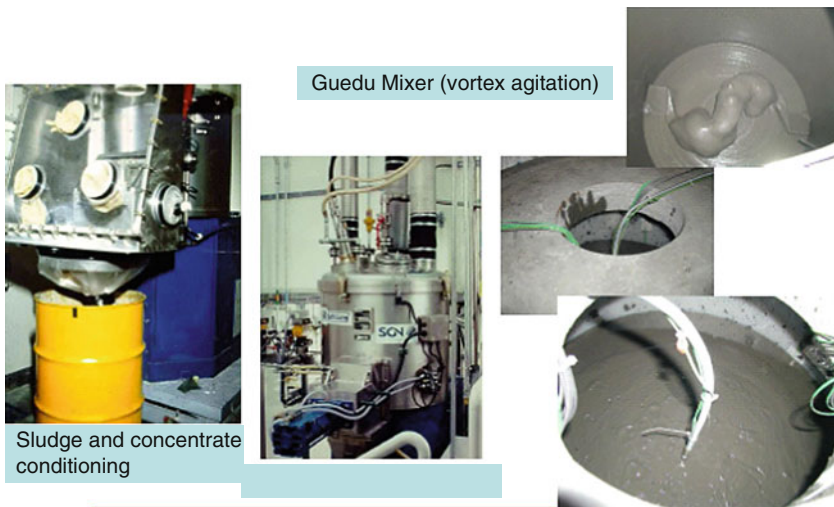
2.1.2 Waste Conditioning in Cement-Based Materials

One should distinguish between the following:

- Embedding of solid waste in a cementitious matrix (e.g., fuel claddings) (➤ Fig. 41)
- Homogeneous mixing, for which the waste is incorporated in liquid form into the cement matrix (e.g., sludges of co-precipitation, evaporation concentrates of effluents) (➤ Fig. 42).



■ Figure 41
Industrial implementation of waste cementation (embedding of solid waste)



■ Figure 42
Industrial implementation of waste cementation (case of a homogeneous mixing)

2.1.3 Long-Term Behavior of Cement-Based Materials

The long-term behavior of cementitious materials in water-saturated media is rather well understood. The main mechanism is first the leaching of alkalis (Na, K) and then the dissolution of portlandite (which releases calcium ions), and the diffusion of these calcium ions in the cement porewater (➤ Fig. 43). This mechanism predicts an altered zone with a thickness growing roughly like the square root of time, a fact well confirmed by experiment.

The Ca flux in the altered zone is

$$\vec{j} = -D_e \cdot \text{grad}(c),$$

where c is the concentration of calcium ions in the porewater and D_e is the effective diffusion coefficient of calcium ions in the porous cement.

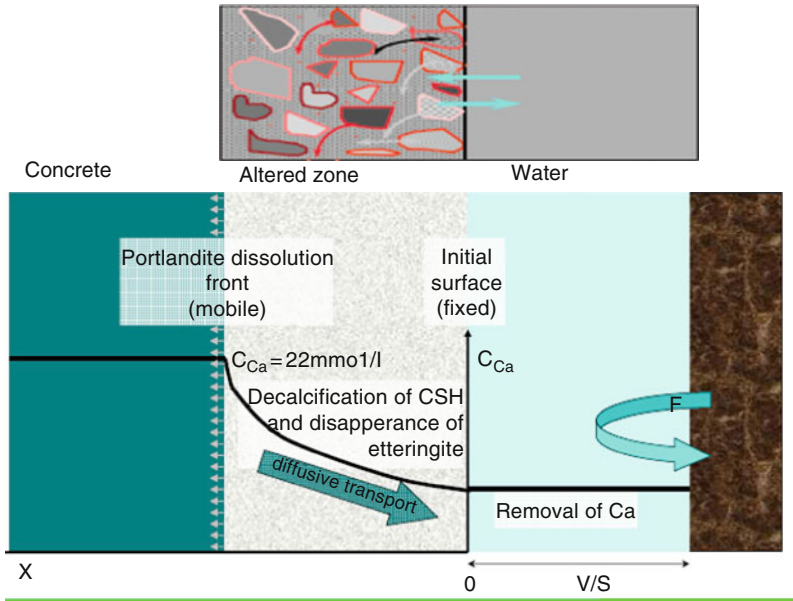


Figure 43
Schematic representation of the mechanism of cement-based material alteration by water

The progression of the alteration front obeys the differential equation:

$$\frac{de}{dt} = \frac{|j|}{X},$$

where X is the molar concentration of soluble portlandite in the cement and e the thickness of the already altered zone at time t .

The concentration of calcium ions in the porewater of the unaltered cement is assumed to be limited to c_{sat} , solubility of the portlandite. The concentration gradient is approximated as uniform throughout the altered zone:

$$grad(c) = -c_{sat}/e.$$

This leads to a differential equation for the evolution of the thickness of the altered zone:

$$\frac{de}{dt} = \left(\frac{D_e \cdot c_{sat}}{X} \right) \cdot \frac{1}{e}.$$

This equation is easily solved:

$$e(t) = (2 \cdot D_e \cdot c_{sat} \cdot t/X)^{1/2}.$$

The thickness of the altered zone increases as the square root of time.

Orders of magnitude for the parameters are:

$8,000 \text{ mol} \cdot \text{m}^{-3}$ of soluble portlandite in the cement paste (20% of portlandite)

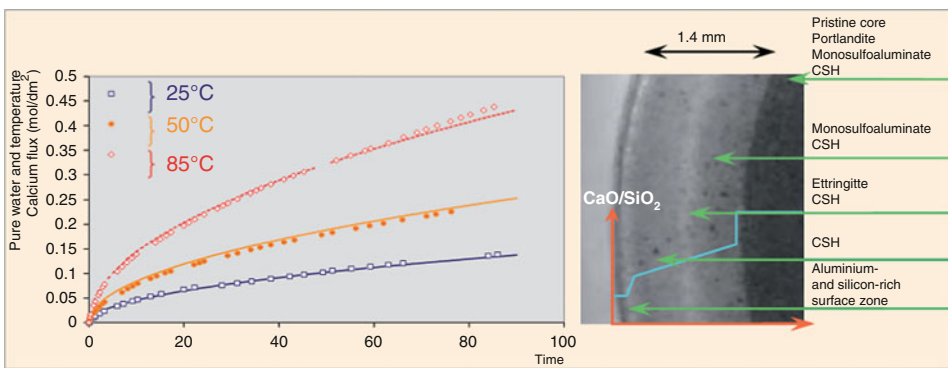
Effective diffusion coefficient of Ca^{2+} ions in the cement = $10^{-11} \text{ m}^2 \cdot \text{s}^{-1}$

Solubility limit of portlandite in the interstitial medium = $22 \text{ mol} \cdot \text{m}^{-3}$ (at 25°C)

These figures give an altered thickness of 2 mm in 200 days, in rough agreement with the experiment (► Fig. 44).

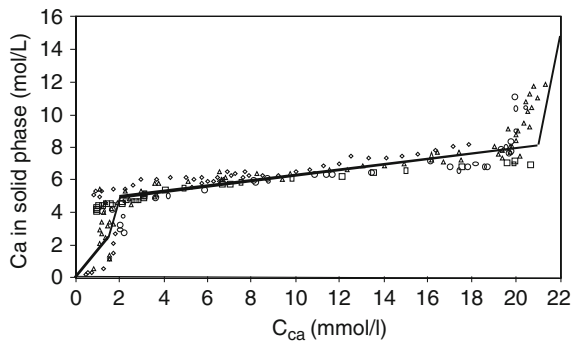
This very rough modeling, displayed here only to give orders of magnitude, neglected the fact that the dissolution of portlandite modifies the porosity of the material, and the diffusion coefficient of calcium ions in the porewater.

In fact, the equilibrium between calcium-rich phases ($\text{Ca}(\text{OH})_2$, C-S-H) and in-solution calcium concentration leads to a more complicated, but well-established relationship between calcium concentration in the solid phase and that in the solution (► Fig. 45).



■ Figure 44

Experimental quantification and modeling of leached species (Ca^{2+}), along with the visualization of the associated solid phases during chemical degradation tests on CEM I-type cement pastes in pure water



■ Figure 45

Calcium equilibrium between the solid phase and the interstitial porewater solution of a Portland cement-based material (Compiled from Berner 1992)

Porosity evolution is directly linked with the mineralogical evolution of the system, which later on allows the diffusion coefficient of the material to be traced according to the material degradation state. The application of this model is fully validated on CEM I pastes and concretes (Bejaoui et al. 2006).

The validation of models of cement alteration can be done by means of leaching experiments on samples, with circulating water (with or without a controlled composition).

2.1.4 R&D on Cement-Based Materials for Waste Conditioning

The incorporation of waste in the Cement-Based matrices can perturb the formation of the minerals, which constitute the cement (chemical perturbation), and reduce the mechanical resistance of the material (physical perturbation). In order to reduce the consequences of these perturbations, the waste may require a pretreatment (precipitation in the case of effluents, pyrolysis in the case of organic resins). This causes a limitation of the waste concentration in the cement, and research is going on to determine reasonable limits to the incorporation rate.

Phosphated or borated waste is not easily conditioned in cement, and research is going on to find cement formulations compatible with these components.


Phosphate ions are found in evaporation concentrates from the facilities of treatment of liquid effluents. These ions are known to delay or prevent the hardening of the cement matrix, and to degrade its mechanical properties (with a pessimism around a concentration of the order of 30 g/L (Bernard et al. 2005)). The mechanism involves the adsorption of phosphate ions on the C_3S phase, thereby inhibiting its hydration. A possible solution to this problem would be the addition of small amounts of hydroxyapatite to the cement, to help the precipitation of phosphate ions.

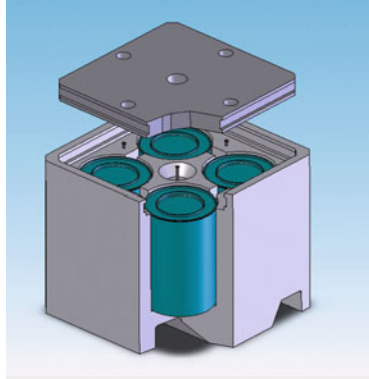
Borate or zinc ions also prevent the hardening of the Portland cement paste. Sulfo-aluminous cements are less inhibited, and offer interesting perspectives for waste containing these two ions.

Radiolysis is another topic of interest for the R&D on cemented nuclear waste. Cementitious materials contain water in their pores, and this water is irradiated by the radionuclides enclosed in the cemented package. Under these radiolytic conditions, water can decompose and form dihydrogen. This dihydrogen itself can cause an increase in pore pressure, and thus threaten the integrity of the matrix. Recent results show that the main parameter, which determines the kinetics of hydrogen production is the dose rate, and that with the dose rate expected from a medium activity waste package ($< 510^{-2}$ Gy/s), the pore pressure will remain well below the resistance limit of the material (Bouniol 2004).

Atmospheric carbonation and degradation of steel-reinforced concrete is another subject of active research. However, this material is mainly used in civil engineering rather than in waste management, and the mechanisms of its degradation are therefore outside the scope of this chapter.

2.1.5 Waste Container Manufacturing

Cementitious materials are used not only for confinement of waste by embedding or homogeneous mixing, but also for the waste container elaboration.  *Figure 46* shows the example of a standardized concrete package, designed to facilitate the handling and storage of intermediate-level long-lived waste.



■ **Figure 46**
Sketch of an IL LL waste package concept involving a concrete container

Several types of waste can be accommodated in this universal concrete container:

- Activated metal waste
- Bituminized sludge
- Cemented technological waste
- Cemented hulls and nozzles
- Compacted structural and technological waste

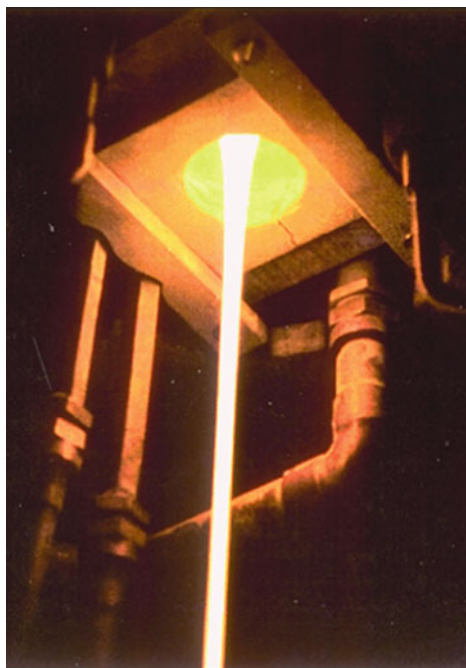
2.2 Conditioning of HL-LL Waste in Glass

2.2.1 Vitrification of Solutions of Fission Products

After being preconcentrated so as to reduce their volume, fission product solutions are stored in stainless steel tanks where they are constantly stirred and cooled. Their activity, related to spent fuel burnup, may reach $4 \cdot 10^{13}$ Bq/L and the power released is significant (up to 7 W/L). These nitric solutions (1–2 N) feature high physicochemical complexity. Their chemical composition generally includes:

- Corrosion products (Fe, Ni, Cr)
- Additive products (Al, Na, etc.)
- Solvent degradation products (P)
- Elements issued from clad materials (Al, Mg, Zr, etc.)

There is also a broad range of radioactive elements, fission products, and actinides, ranging from germanium ($Z = 32$) to californium ($Z = 96$). Contrary to what is suggested by the word “solution,” usually reserved for homogeneous liquids, “solutions of fission products” also prove physically complex as they contain flocculates and precipitates (zirconium phosphates and molybdates) as well as small metallic particles (undissolved platinoids such as ruthenium,



■ **Figure 47**
Vitrification of a solution of fission products

palladium, rhodium, or intermetallics, e.g., with molybdenum), and particles resulting from fuel clad shearing (zirconium, for LWR fuels) (► *Figs. 47* and ► *48*).

The conditioning of solutions of fission products is aimed at:

- Turning waste from the liquid to solid state
- Reducing the volume to be stored and, then, disposed off
- Getting a material that complies with the safety requirements peculiar to storage and disposal

Glass was selected by the world's community as the confinement material for solutions of fission products, due to the flexibility of its disordered structure that enables glass to confine many chemical elements. It must be emphasized that the aim is not a mere embedding, but an atomic-scale confinement, since radionuclides are intimately incorporated in glass structure.

Glass is an interesting material for the confinement of radionuclides, because it is endowed with satisfactory properties of thermal stability, chemical durability, quasi-insolubility in water, and resistance to self-irradiation.

Glass resists very well to irradiation (little swelling, no recrystallization observed, no degradation of the glass mechanical properties). Thanks to the flexibility of the lattice, broken bonds reform easily a few picoseconds after the ionizing radiation.

Glass incorporates well the He that will be produced by the alpha disintegrations.



■ Figure 48
Vitrified waste package (CSD-V)

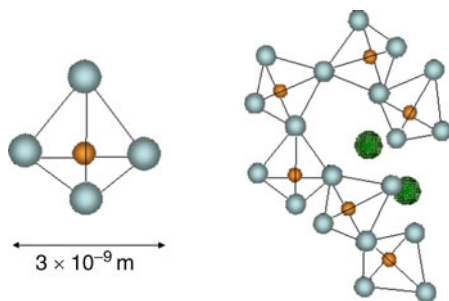
2.2.2 Requirements for the Glass Material

- Glass must be able to incorporate the various elements from the fission product solution to be vitrified (15% in mass).
- Glass must be homogeneous.
- Crystallization must be avoided.
- Elaboration must be easy (radioactive ambiance): the melting temperature must not be too high to limit volatility, the viscosity must be small to allow glass pouring, and the melted glass must not be too corrosive for the crucible.
- Large chunks of glass must solidify without too much fracturing.
- Glass must withstand irradiation and alteration by water.

2.2.3 Physicochemistry of Glass

Glass is solid like a crystal, and disordered at the atomic scale, like a liquid.

Upon cooling below the melting point, most liquids crystallize, but glass has a continuously increasing viscosity (this viscosity is higher than 10^{13} Poise below the glass transition temperature, $T_g = 520^\circ\text{C}$ for borosilicated glass). It is thermodynamically metastable, and could



■ **Figure 49**

Glass structure: a silica tetrahedron (left), and a chain of tetrahedra with lattice modifiers (right)

recrystallize, yet this process can be very slow (we know of geological glass which is 100 million years old).

Glass melt and glass properties depend upon the atomic ordering of the elements.

The cohesion of the oxide glass skeleton is ensured by the ionic-covalent chemical bonds, which are formed by the glass network formers (Si, B, Al) in combination with oxygen atoms. One oxygen atom bound with two network formers is said to be “bridging,” whereas one oxygen atom bound with a single network former is said to be “non-bridging.” These bonds are oriented and take part in the formation of tetrahedra SiO_4 , BO_4 , AlO_4 , and of triangles BO_3 . Silicon tetrahedra and Boron triangles are connected by one oxygen summit. These elementary structures form chains and rings of different sizes, thus contributing to the solidity of the edifice (► Fig. 49). These covalent bonds coexist with bonds with a more ionic character, formed between the alkaline or alkaline-earth metals (Na, Ca) and the oxygen atoms.

The Na and Ca elements may play two distinctive roles within the glass network. They may either behave as charge-compensators near a locally negative-charged BO_4^- or AlO_4^- -type group, or they may behave as “modifying” elements, forming a X-O-Na or X-O-Ca bond (with X being a network former).

The progressive addition of network modifiers to silica, SiO_2 , leads to network depolymerization by the formation of non-bridging oxygen atoms.

Modifying elements contribute to reduce the melting temperature and viscosity, and increase molten glass reactivity, which makes its fabrication easier. Their presence makes the glass structure flexible, and permits the incorporation of radionuclides in the glass structure.

2.2.4 Glass Composition

The glass composition generally chosen for the conditioning of the fission product solutions from the reprocessing of LWR spent fuel is a borosilicated glass, because of several interesting properties:

- Its lower temperature of elaboration compared to silica
- Its very low tendency to crystallization
- Its very good resistance to water alteration
- In addition, boron helps digest the calcinate during glass elaboration and lowers the equilibrium pH after leaching

The good performance of nuclear borosilicate (a temperature melting not too high *and* a good chemical durability) comes from the right balance between boron and the intermediate elements (Al, Fe, Zr) on one side and the alkali elements on the other side, allowing a high polymerization rate as most of alkali are found as charge compensators rather than forming non-bridging oxygen links.

Typical French “R7T7” glass incorporates up to 18.5% (mass) of fission product oxides and 0.9% of actinide oxides (🔍 [Table 8](#)).

■ **Table 8**

Typical composition of borosilicated glass for the conditioning of HL waste

Chemical composition range of R7T7 glasses produced in the AREVA - La Hague plant workshops			
Oxides	Specified interval for the industry (wt%)		Average composition of industrial glasses (wt%)
	min	max	
SiO ₂	42.4	51.7	45.6
B ₂ O ₃	12.4	16.5	14.1
Al ₂ O ₃	3.6	6.6	4.7
Na ₂ O	8.1	11.0	9.9
CaO	3.5	4.8	4.0
Fe ₂ O ₃		<4.5	1.1
NiO		<0.5	0.1
Cr ₂ O ₃		<0.6	0.1
P ₂ O ₅		<1.0	0.2
Li ₂ O	1.6	2.4	2.0
ZnO	2.2	2.8	2.5
Oxides (PF + Zr + actinides)	7.5	18.5	17.0
Fines suspension			
Actinide oxides			0.6
SiO ₂ + B ₂ O ₃ + Al ₂ O ₃	>60		64.4

2.2.5 Incorporation of Radionuclides in Glass: Where Is the Limit?

In order to minimize the number of glass packages produced per ton of spent fuel, one tries to produce glass with a high load of fission products and minor actinides. The increase of fuel burnup results in a higher content of radionuclides in the spent fuel. This is also an incentive to increase the radionuclide load in the glass.

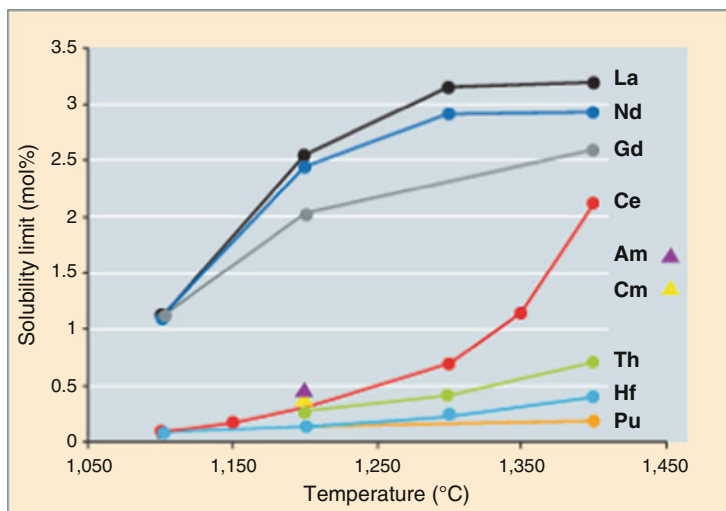
However, one should keep in mind that the dimensions (and cost) of a geological repository are determined mainly by the total heat load of the waste, and are not changed by reducing the number of glass packages and increasing the RN concentration in the glass at the same time.

Moreover, the RN load is limited by the need to make homogeneous glass. The temperature of elaboration of the glass plays an essential role. In most vitrification processes, this temperature is around 1,150°C.

Phenomena to be avoided are:

- Crystallization. For example, chromium tends to form chromites (spinel) with Ni, Fe, Zn beyond a concentration of 1% in mass. Aluminum and cerium oxide crystallites dissolve slowly in the glass melt if their concentration is larger than 10% and 1%, respectively
- Phase separation. The oxides, MoO₃ and P₂O₅, lead to a phase separation (one silicated, the other molybdc or phosphatic) if their concentration is beyond 2–3% in mass
- Settling of platinoïds at the bottom of the crucible. Platinoid fission products do not incorporate well into the glass matrix. They tend to coalesce into metallic particles, or as droplets of low melting point alloys (typically 700°C) that can settle at the bottom of the melter.
- Foaming, for instance, by oxygen bubble formation due to some change in redox state.

Some of these problems would be alleviated by the redox control or by an elevation of the glass elaboration temperature (► Fig. 50), but limitations arise from the corrosion of the melting pot. Cold crucible vitrification will make it possible to overcome this.




■ Figure 50

Solubility limit of various elements versus temperature in borosilicate glasses manufactured under standardized conditions. The results reported for Americium and Curium stand for the highest content incorporated without reaching their limit of solubility

2.2.6 Glass Fabrication: The Hot Crucible Vitrification Process

Two techniques of hot crucible are used in the world:

The melter can be metallic (lifetime of the melter = 5,000 h) and heated inductively (France [La Hague], UK [Sellafield];  Fig. 51). It is fed with calcinated waste and glass frit.

The melter can also be made of ceramic (liquid-fed ceramic melter) (lifetime 6 years), the glass is heated by Joule effect. It is fed directly by the liquid solution; the steps of water evaporation and calcination take place at the surface of the molten glass (USA, Savannah, West Valley), Japan (Tokai Mura, Rokkasho Mura), Russia (Mayak).

With the hot crucible technique, the melt temperature is limited to 1,150°C approximately, due to corrosion of the metallic melter. In the case of high-level borosilicate nuclear glasses, made through a reaction between FPs calcinate and glass frit, the series of steps is the following:

- The glass frit (centimetric flakes, a few millimeters thick) is turned discontinuously from the elastic solid state to the viscous liquid state, beyond the glass transition region around 510°C.
- The viscous frit impregnates the calcinate fragments, which consist of FPs nitrate- and oxide-type complex compounds. The calcinate is a highly refractory product, as it is rich in rare-earth oxides, Zr and Al. Crystals such as rare-earth silicates and cerium oxides, as well as chromites (mixed oxides of Fe, Zn, and Cr) are formed as a result of localized supersaturations. This results in the formation of a heterogeneous product.
- The following step – helped by the stirring of the mixture – dilutes the crystallized aggregates, which are then dissolved. The final glass becomes homogeneous in chemical composition. In this final step, only insoluble particles of noble metals remain, the size of which is about 10–100 μm.

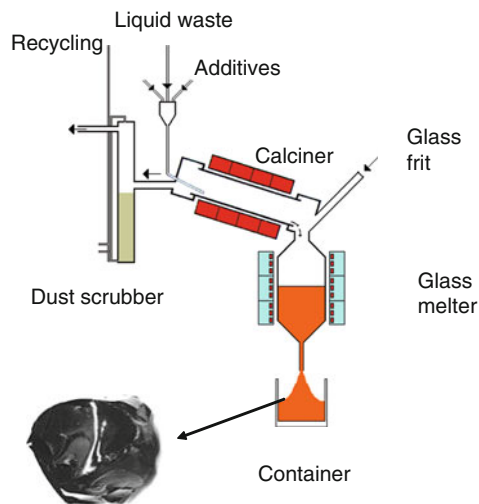
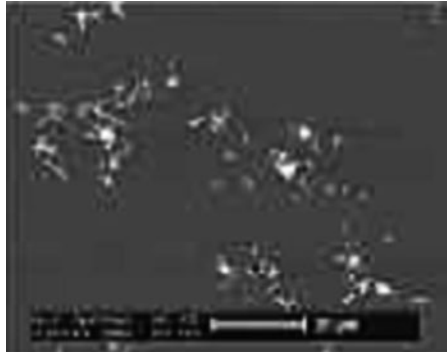


 Figure 51

An inductive metallic melter for the waste vitrification (hot crucible)



■ **Figure 52**
RuO₂ crystals in the glass matrix

Platinoïds do not incorporate readily in glasses. Depending on redox conditions, they form oxide crystals (e.g., RuO₂) in the glass matrix (► [Fig. 52](#)), or metallic particles, e.g., Rh, Pd-Te metallic particles. These particles can segregate to form undesired phases at the bottom of the crucible.

In order to control the redox potential of the glass during its elaboration, one adds iron and cerium in the glass frit (Pinet et al. [2005](#)).

2.2.7 The Vitrified Waste Package

The “R7T7” waste package (► [Fig. 48](#)) is given here as an example of vitrified waste package. The envelope is 5-mm thick stainless steel and contains 150 L of glass (diameter 40 cm, height 1.3 m).

Composition contains 12–18% (in weight) of fission products. Each package is made of two castings, 200 kg each.

13,000 CSDV glass canisters have been produced as of September 2007 in La Hague, confining a total radioactivity of 2.10^8 TBq beta gamma.

One glass package (400 kg) corresponds to the treatment of 1.3 t of spent fuel. It contains 95–99% of the radioactivity of the spent fuel.

Radioactivity of this glass package: 5,800 Ci ($2.1 \cdot 10^{14}$ Bq) alpha; 400,000 Ci ($1.5 \cdot 10^{16}$ Bq) beta gamma; dose 500 Gy/h (contact).

One ton of glass corresponds roughly to 1 TWhe of energy produced.

Power of a glass package due to the radioactivity (processing of UOX fuel) is 2.5 kW (after conditioning), 1 kW (10 years later), and 0.4 kW (50 years later). This power must be evacuated in the glass package storage facilities. The size of the package has been chosen such that, with a convective air cooling, $T < 500^\circ\text{C}$ at the center of the package (i.e., below the glass transition temperature).

2.2.8 Cold Crucible Vitrification

The vitrification processes currently in industrial operation in the world (ceramic furnace or metallic pot) display limitations as regards the following features:

- The lifetime (about 5,000 h) of metallic pots, which stand as a source of secondary waste
- The capacity of metallic pots (about 25 kg/h in the case of R7T7 glass), which requires several parallel treatment lines
- Dismantling difficulties for end-of-life metallic or ceramic furnaces, as they account for a big volume of technological waste
- A composition range limited to glasses with a glassmaking temperature of 1,150°C

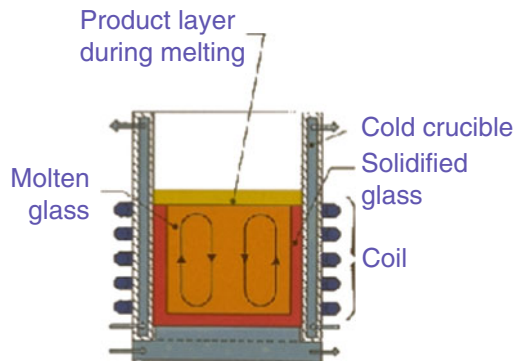
A new melting technology has been developed in order to cope with all these limitations. It is based upon the use of a cooled metallic crucible coupled with direct induction heating in glass.

The cold crucible technique consists in inductively heating the glass itself (► Fig. 53). The crucible is protected by a solidified glass layer, and does not undergo corrosion. The temperature of elaboration of the glass can be increased, with subsequent benefits on all the items listed above.

Cold crucible technology makes it possible to reach high temperatures without corrosion of the crucible. This opens the possibility to vitrify many types of waste, for example, the solutions from the processing of high burnup fuel with a high fission product content. Vitrification of the solutions from the processing of the fuel from research reactors or graphite-gas reactors is also possible with this technology.

The absence of contact between molten glass and the crucible extends considerably the crucible lifetime.

The cold crucible technology already replaced the hot crucible in one of the six vitrification lines of the La Hague processing plant.

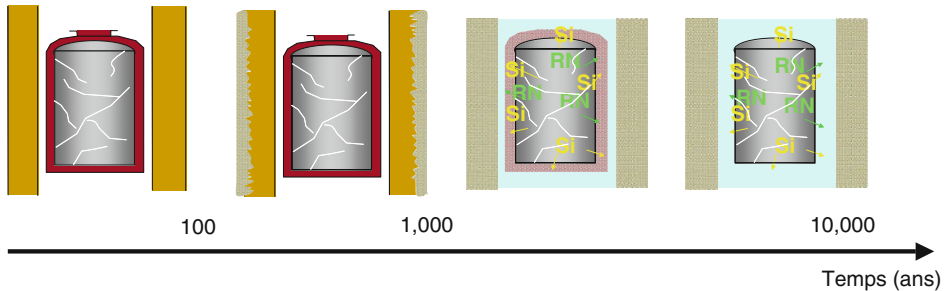


■ Figure 53

The cold crucible for high-temperature vitrification

2.2.9 Long-Term Behavior of Glass

Glass alteration by water, autoirradiation, and fracturation must be studied because these phenomena may cause the release and migration of radionuclides from the glass matrix (🔍 Fig. 54).



■ Figure 54

The sequence of alteration of a vitrified waste package. In the case of a deep geological disposal for vitrified waste packages, underground water will come into contact with glass sooner or later, after corroding the containers and overcontainers. Glass matrix alteration by water is the chief factor likely to lead to the radionuclide release into the natural environment

2.2.10 Long-Term Behavior of Glass in Contact with Water

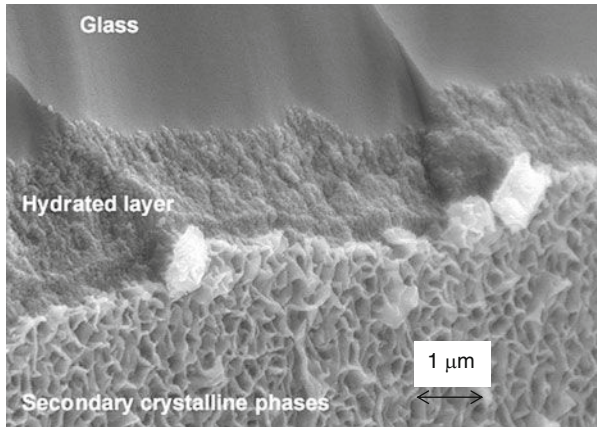
When the underground water reaches the glass package after the loss of the tightness of the envelopes, a slow dissolution of the components of the glass then occurs (🔍 Fig. 54). Its rate depends on the glass composition and on its degree of fragmentation, which determines the reactive surface area between glass and water. Other parameters also come into play, e.g., temperature and ion content of the water. These parameters determine the dissolution-precipitation phenomena in the vicinity of the glass. The leaching of the glass can cause the release of its radioactive content.

2.2.11 Phenomenology of Glass Alteration by Water

When a silicated glass is exposed to water, after a quick period of alkali and water interdiffusion, one observes the dissolution of silica in water. The initial kinetics of this dissolution is quite rapid at high temperature (typically a few $\text{g} \cdot \text{m}^{-2} \cdot \text{day}^{-1}$ at 100°C , pH 7, i.e., $1 \mu\text{m day}^{-1}$, and 1 nm day^{-1} at 20°C), but a significant slowdown occurs after some time if the water renewal is small.

One also observes the formation of an amorphous layer of hydrated silica (🔍 Fig. 55). Its thickness depends on the experimental conditions, and especially on the modalities of the water circulation around the glass sample.

One also often observes the precipitation of newly formed crystals (phyllosilicates) onto the outer surface of the hydrated layer.



■ Figure 55

Scanning electron microscope view of a borosilicated glass sample altered at 150°C for 4 months in pure water. One can distinguish from *top to bottom*: the unaltered glass, the hydrated layer, and the secondary phases, which precipitated from the solution

If the water flow is slow enough, the mass flow of dissolved silica is independent of the glass surface area, and is simply proportional to the water flow and to the solubility limit of amorphous silica (60 mg/L at pH 8 and 90°C). This dissolved silica comes probably from the dissolution of the hydrated layer itself.

The release rate of tracers contained in the glass (e.g., Li, B) is initially high, and decreases slowly with time (► Fig. 56). However, this tracer release never goes to zero for very long times, even in the absence of water renewal and in water already saturated with silica. The residual alteration rate becomes a constant, which can be as low as 10^4 times smaller than the initial alteration rate. This rate depends on the pH of the water and the glass composition.

Isotopic tracer experiments suggest that the hydrated layer forms at the internal interface (between the layer and the pristine glass) by transformation of oxide glass into a hydrated oxide layer.

In the alteration regimes of borosilicated glasses, one can distinguish (◄ Fig. 57):

The initial rate, limited by the hydrolysis of the silicated 1 μm lattice.

The rate drop, associated with the formation of a dense and passivating layer within the hydrated layer. This zone is built by ion exchange reactions, hydrolysis reactions, and in situ recondensation of a fraction of the hydrolyzed silica. At the same time, this layer gets dissolved on its external interface, as long as the solution does not become saturated. This layer acts as a diffusive barrier for water, and for the hydrolyzed species from glass.

The residual rate regime corresponds to a dynamic equilibrium between formation (at the internal interface) and dissolution (at the external interface) of the hydrated layer. When this dynamic equilibrium is reached, the hydrated layer thickness becomes constant, as well as the glass alteration rate. Water renewal and precipitation of secondary phases like phyllosilicates can withdraw silica from the solution. By acting as silica sinks, these two mechanisms are the motors by which the glass alteration goes on in this “residual” regime.

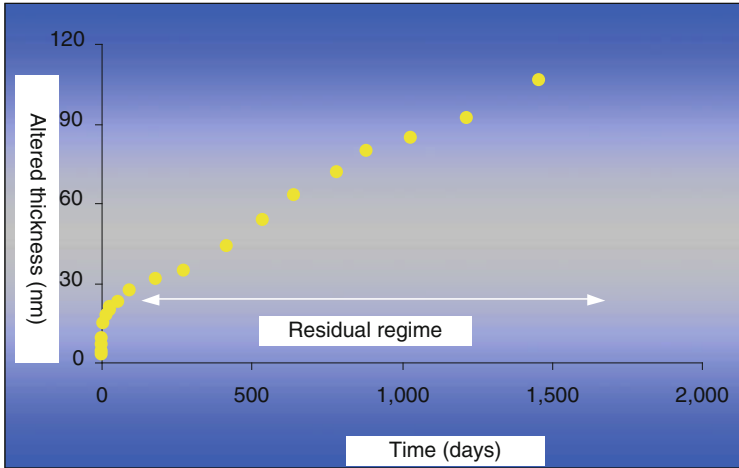


Figure 56
 Kinetics of glass alteration by water. Evolution of the thickness of R7 T7 altered glass at 90°C. In the conditions of the experiment (large glass surface area, small quantity of water, the residual regime (where the alteration rate is constant) is rapidly reached. Note the order of magnitude of the residual alteration rate: $0.03 \mu\text{m year}^{-1}$, or 3 cm in 1 million years at 90°C (After Gin et coll, 2003)

Phenomenology of glass alteration by water

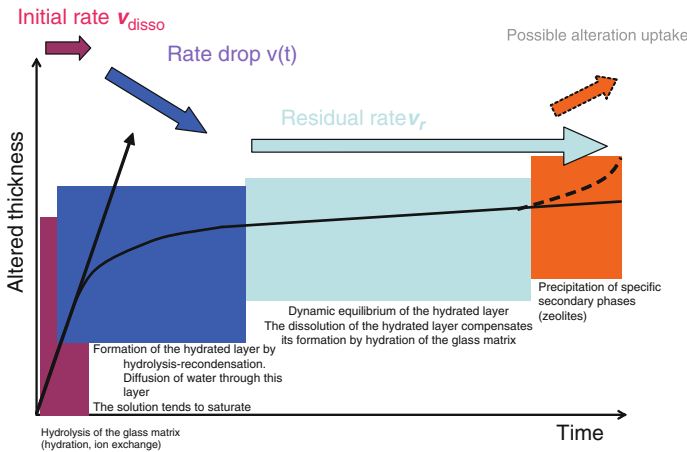
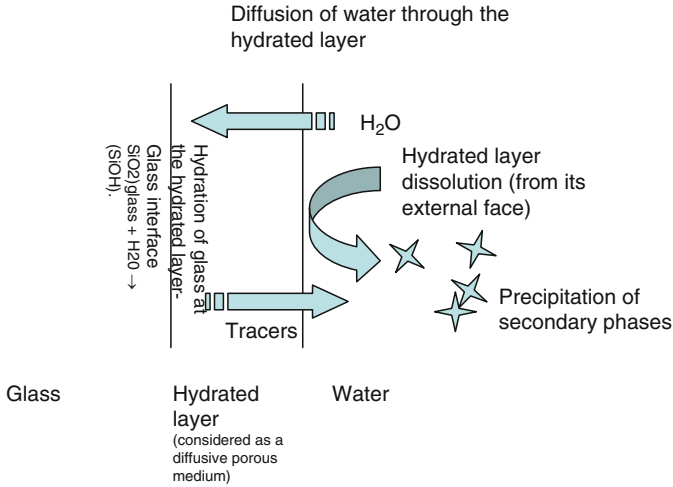
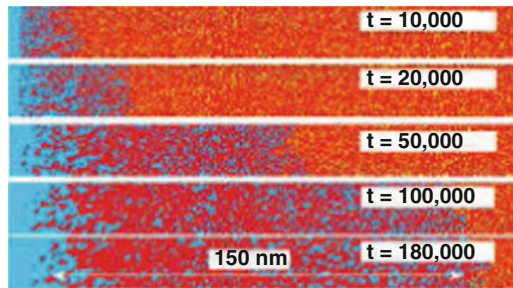


Figure 57
 Phenomenology of glass alteration by water

A possible alteration uptake can eventually occur in special cases, when the composition of the porewater surrounding the glass permits the precipitation of zeolitic secondary phases. Conditions for this to occur are met only in very basic waters, which are not likely met in geological media, except possibly in the vicinity of concrete artifacts (Vernaz 2002).



■ **Figure 58**
Mechanism of glass alteration by water



■ **Figure 59**
Simulation of the alteration of glass by Monte-Carlo method. Bond-breaking and bond-forming probabilities are treated as free parameters. Water appears in blue, Si in red, Zr in black, and B in black. The porosity of the hydrated layer evolves with time. In soft alteration conditions, this porosity tends to close, thus enhancing the protective properties of this layer (Cailleteau et al., 2008)

The four mechanisms at play during the alteration of glass by water are (↻ [Figs. 58](#) and ↻ [59](#)):

- The building of a hydrated layer by hydration of the pristine glass at the interface between this pristine glass and the hydrated layer
- The destruction of this hydrated layer by dissolution at its external interface
- The diffusive transport of water through the hydrated layer
- The precipitation of secondary phases in the water surrounding the glass

2.2.12 Glass Alteration by Water Depends Greatly on Temperature

The activation energy of the reaction of glass hydration is of the order of 73 J/mol. This means that the glass alteration rate increases by a factor 30 when the glass temperatures increase from 25°C (rest temperature of the geological medium) to 90°C (maximum temperature of the host rock at the peak of the waste thermal crisis). This increase is not a major concern for the disposal of vitrified waste because the thermal crisis is supposed to occur before the water comes into contact with the glass.

On the other hand, this temperature dependence is used to accelerate the glass alteration in laboratory experiments.

2.2.13 Toward a Model of Glass Alteration

We describe in the following a typical model of glass alteration. The GRAAL model incorporates the known phenomenology in a form as simple as possible (Frugier et al. 2008, 2009).

Please keep in mind that it is not the only possible model. This is a domain where research is open.

Hypotheses

The hydrated layer is soluble; it is the dissolution of this layer, which provides the silica present in the water. Hydrated layer dissolution goes on if water is renewed.

The hydration reaction, which transforms the glass (oxide) into a hydrated oxide, is initially rapid, but becomes limited by the transport of water through the hydrated layer.

The hydrated layer plays the role of a diffusive barrier for the water, which goes from the solution to the reactive glass interface.

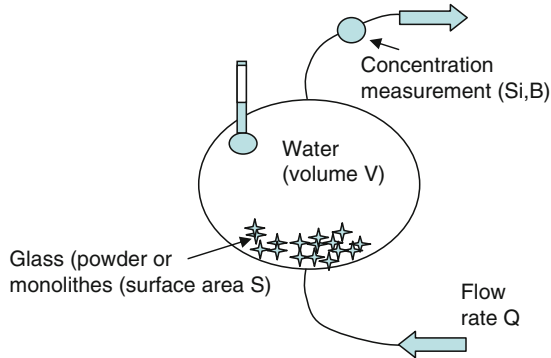
The hypotheses listed above can be easily transcribed into equations:

- One equation for the dissolution of the hydrated layer (assuming, for example, a first-order kinetics)
- One equation for the glass hydration (assuming a first-order kinetics)
- One equation for the transport of water through the hydrated layer (assuming a diffusive transport and uniform water concentration gradient across the hydrated layer)
- One equation for the precipitation of secondary phases (assuming a zeroth- or first-order kinetics).

In the simple case of a glass sample placed in a recipient where the concentrations can be considered uniform everywhere in the solution, these equations close the system, which can then be readily solved.

In the more complicated case of a glass sample embedded in a porous environment (for instance, clay), the concentration in dissolved silica cannot be considered uniform in the porous medium, and one must add another equation for the transport of solute in the medium to close the system.

Such a model reproduces all phases of glass alteration, including the transient ones at the beginning of alteration, and the residual regime, where the hydrated layer reaches a dynamic



■ Figure 60

A typical laboratory experiment for the study of glass alteration

equilibrium between its building by glass hydration at the internal interface and its dissolution at the external interface.

Parameter values can be extracted from independent experiments. We give here a few orders of magnitude:

- $C_{\text{sat}} = \text{hydrated layer solubility} = 2 \text{ mol} \cdot \text{m}^{-3}$
- $D = \text{diffusion constant of water in the hydrated layer} = 5.10^{-21} \text{ m}^2 \cdot \text{s}^{-1}$
- $V_{\text{hydr}} = \text{kinetic constant of glass hydration} = 10^{-11} \text{ m} \cdot \text{s}^{-1}$
- $V_{\text{disso}} = \text{kinetic constant of hydrated layer dissolution} = 10^{-12} \text{ m} \cdot \text{s}^{-1}$
- $V_{\text{pr}} = \text{kinetic constant of secondary phase precipitation} = 10^{-15} \text{ m} \cdot \text{s}^{-1}$.

The laboratory experiments on glass alteration are usually performed by putting glass (often in a divided form to increase the glass surface area) in a recipient where water is controlled in temperature, and renewed with a determined flow rate (● Fig. 60). The concentration in glass constituents and tracers (Si, B) in the water are then measured at the exit of the recipient. The total amount of altered glass can then be deduced from these concentration measurements.

2.2.14 The Residual Alteration Regime of Glass

The residual alteration regime of glass is of special importance for the safety of a glass repository, because the glass will spend most of its time in this regime. The residual alteration regime is reached when the hydrated layer reaches its equilibrium thickness. From that moment onwards, the layer growth by glass hydration at the hydrated layer–glass interface compensates the hydrated layer dissolution at the hydrated layer–water interface. The residual alteration rate then equals the hydrated layer dissolution rate. This rate depends on the modalities of water renewal in the vicinity of the altering surface. The important parameter, which describes this water renewal is the ratio Q/S (water flow rate/glass surface area).

If the water renewal is very fast (case of a piece of glass in a stream of running water), the alteration rate V is limited by the kinetics of dissolution of the hydrated layer, and the residual rate is simply equal to the kinetic constant of this dissolution V_{disso} .

If the water renewal is very slow, the water in the glass vicinity has enough time to become saturated in dissolved silica, and the residual alteration rate depends on the rate of secondary phase precipitation kinetics V_{pr} .

It should be noted that precipitation of secondary phases removes silicium from the solution and is equivalent to an effective renewal of the water. The model thus predicts the existence of a residual alteration even in the case of perfectly static water.

This residual alteration rate of glass depends strongly (three orders of magnitude) on the glass environment: surrounding minerals and modalities of water renewal.

Altogether, the model reproduces reasonably well the laboratory experimental data on the residual alteration rate of glass, for various values of the rate of water renewal (🔗 Fig. 61).

Laboratory experiments are unable to demonstrate the confinement properties of a glass matrix on a million-year timescale. The longest laboratory experiment on glass alteration has lasted for 25 years only. But Nature did the experiment for us with *natural analogues*, both geological and archaeological (🔗 Fig. 62).

The study of *glass natural analogues* permits to:

- Validate the long-term model predictions, and confirm the orders of magnitude of the alteration rates
- Stress the importance of environmental parameters (glass in a clay environment does not alter at the same rate as a glass in seawater, because the clay environment limits the renewal of water around the glass, inhibits the transport of silica, and favors the precipitation of newly formed phases).

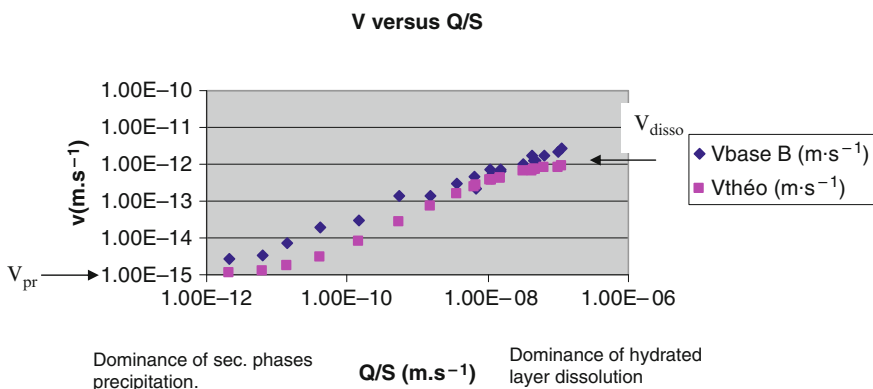
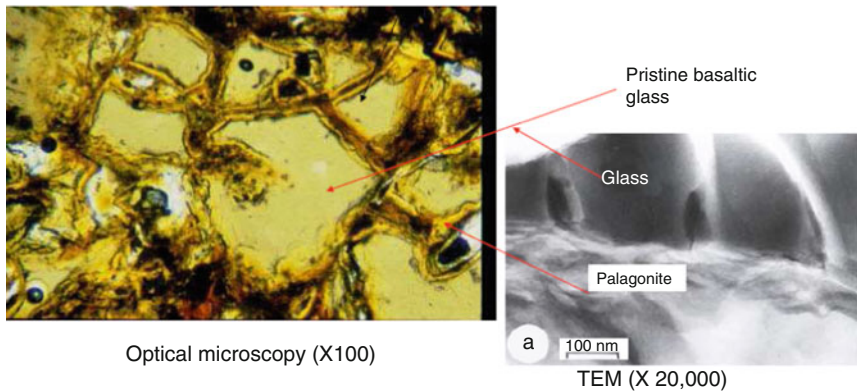


Figure 61
 The residual alteration rate as a function of the water renewal rate. Comparison between the experimental results and the GRAAL alteration model



■ Figure 62

A natural analogue of glass alteration: Iceland hyaloclastite (basalt, 90,000 years)

2.2.15 Long-Term Behavior of Glass: The Effect of Self-Irradiation

During its lifetime, the nuclear glass will undergo self-irradiation (► Table 9): Alpha disintegrations cause atomic displacement and ionization. It is mainly the recoil nuclei from these alpha disintegrations, which cause the atomic displacements.

Beta gamma irradiation causes only ionization.

During the lifetime of a high-activity glass in a repository, one atom out of three will have been displaced once, due to radioactive decays in the glass. One needs to know whether this self-irradiation modifies the glass structure and hampers the long-term durability of the glass matrix.

The typical kinetic energy of a recoil nucleus due to alpha decay is 70 keV. Its range in the glass is of the order of 30 nm. The maximum temperature of the heat wave is about 1,200 K, and the typical cooling time is 12 ps. The number of displaced atoms is about 2,000. Most broken bonds are restored within a few picoseconds (► Fig. 63). Glass is a self-repairing material.

For research purposes, one can accelerate irradiation damage in glass by doping the glass with actinides. For example, a glass doped with a few percent ^{244}Cm undergoes the same number of alpha disintegrations in a few years as an industrial glass during its whole life.

The question as to whether the glass alteration rate can be altered by self-irradiation has been investigated. No significant influence of the self-irradiation on the glass initial dissolution rate is observed for the fluences encountered in high-activity, long-life waste.

A slight modification of the glass density is observed, but a little swelling has stabilized at a level below 1% after a cumulative dose of $2 \cdot 10^{18}$ alpha disintegrations per gram.

The glass mechanical properties are also modified by irradiation: fracture toughness is increased and then stabilizes at the same cumulative dose.

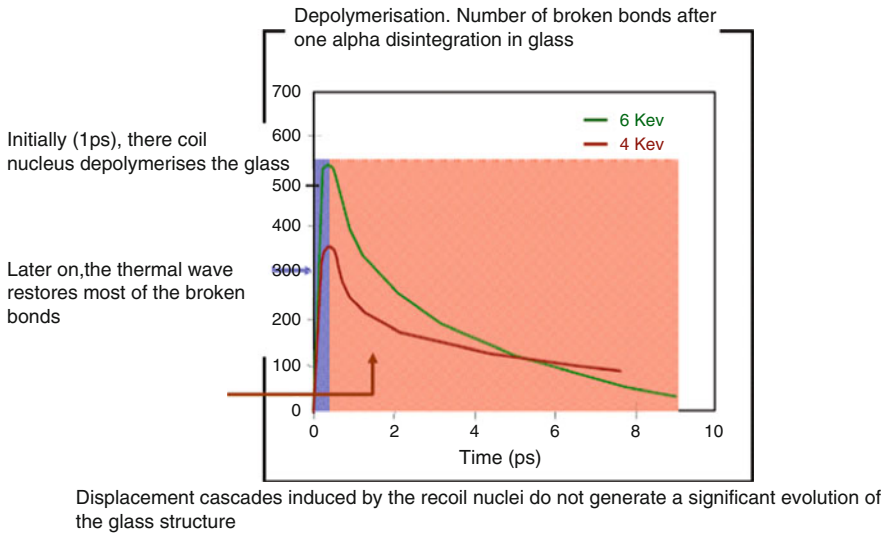
Molecular dynamics enable one to understand why the glass properties get stabilized beyond a cumulated dose of $2 \cdot 10^{18}$ alpha disintegrations per gram: beyond this limit, the number of broken bonds no longer increases.

Table 9

Characteristics of the various radiation sources in nuclear glass

Radiation sources	Path in the glass	Energy deposited (Gy)		Number of atomic displacements prevent	Number of disintegrations per gram of glass over 10 ⁴ years	Number of atomic displacements per gram of glass over 10 ⁴ years
		over 10 ⁴ years	over 10 ⁴ years			
α Disintegration Helium ion (4–6 Mev)	~20 μ m	~3.10 ⁹	~10 ⁹	~200	~3.10 ¹⁸	~6.10 ²⁰
Recoil Nucleus (0,1 Mev)	~30 nm	~6.10 ⁷	~3.10 ⁸	~2.000		~6.10 ²¹
β Disintegration	1 mm	~3.10 ⁹	~4.10 ⁹	~1	7.10 ¹⁹	7.10 ¹⁹
γ Transition	qqs cm	~2.10 ⁹	~2.10 ⁹	~1	~2.10 ¹⁹	~2.10 ¹⁹
Reactions (α , n)	1 m	~2.10 ²	~9.10 ³	200 à 2,000	3.10 ¹²	6.10 ¹⁴ à 6.10 ¹⁵
Spontaneous and induced fissions	FP : 10 μ m	~2.10 ⁴	~4.10 ⁴	10 ⁵	10 ¹¹ à 10 ¹²	10 ¹⁶ à 10 ¹⁷
	Neutron : 1 m			200 à 2,000		2.10 ¹³ à 10 ¹⁶

Characteristics of various sources in nuclear glasses (the number of disintegrations per gram refers to the R777 glass used for vitrifying solution from the treatment of PWR spent fuels a 33GW d/t bump)



■ Figure 63

Structural evolution of glass under irradiation (Peuget et al., 2006)

2.3 Other Conditionings for Waste

2.3.1 Bituminization of Low- or Intermediate-Level Waste

Bituminization is used for embedding co-precipitation sludges arising from either effluent insolubilization treatments or evaporation concentrates issued from spent fuel chemical treatment.

Co-precipitation consists in adding reagents to effluents so as to form various strongly insoluble salts. Radionuclides are carried over in the solid phases according to different mechanisms, which ensure effluent decontamination up to the levels prescribed by release standards. Co-precipitation treatments may vary according to the treatment station considered. Co-precipitation sludges typically contain barium sulphate, nickel, and potassium ferrocyanide, as well as different hydroxides, for example, iron hydroxide. This sludge also contains variable contents in soluble salts, which mostly are sodium sulfate and sodium nitrate. This wet sludge may then be cemented (see above) or bituminized.

Although bituminization is to be replaced more and more by cementation, the amount of bitumen drums already produced in the world justifies that a section of this chapter should be devoted to this process.

The bituminization process, commonly used to condition the sludges resulting from the treatment of liquid effluents by chemical precipitation, is a well-known process, which benefits from a wide experience backup. As a conditioning matrix, its advantages and drawbacks are as follows:

Advantages:

- Bitumen is cheap and readily available.
- It is insoluble in water.
- It is chemically inert with respect to the environment.

Drawbacks:

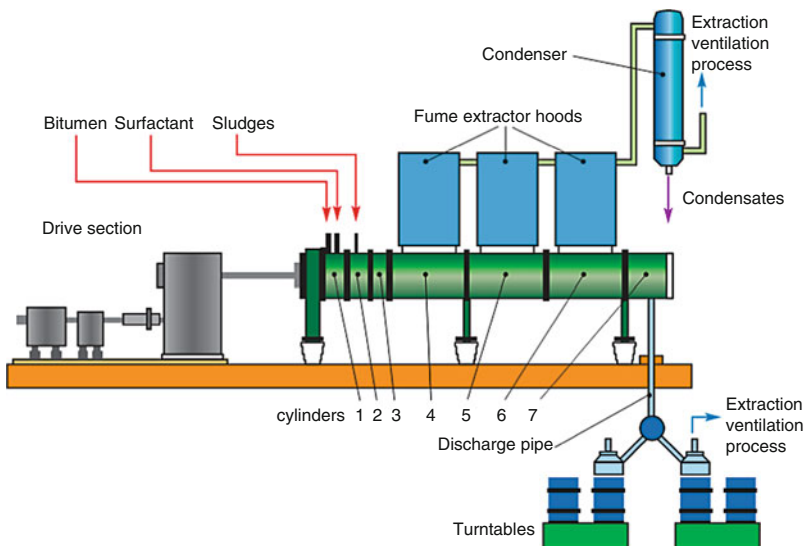
- Large volumes are needed (e.g., 36,000 m³ were produced in France).
- Exothermic reactions during the mixing create risks of fire.
- Long-term behavior is poorly mastered (radiolysis, gas generation, swelling).

2.3.2 Bitumen Manufacturing

The embedding process consists in hot mixing of sludge waste to bitumen in an extruder (➤ Fig. 64). The resulting mixture is dehydrated and poured into a steel drum (about 222 L) where it can cool down. Hot extruding ensures sludge dehydration, waste homogeneous dispersion, and radionuclide immobilization within the bitumen matrix. The waste incorporation rate into bitumen is typically 40 wt%. From a chemical viewpoint, the embedded waste mostly consists of salts insoluble in water (barium sulfate, ferrocyanides, cobalt sulfide), and soluble salts (sodium nitrate, sodium sulfate). The use of soft bitumen from straight distillation of crude oils allows the embedding process to be implemented with moderate temperatures ranging between 130°C and 180°C in the extruder, thereby limiting fire risks.

The waste packages thus produced are of low or intermediate level and, for some of them, long-lived.

Once they have cooled down, packages are stored on the production sites and periodically monitored pending their transfer to the disposal site. An important concern in bituminization is related to thermal behavior control in the short term, that is, in the hours following the pouring so as to take fire risks into account. The studies carried out on the control over fire risk led to the determination of a safe operating domain. This simulation relies on the kinetic parameters of the



■ **Figure 64**
Schematic of the industrial-scale process of bituminization in an extruder



■ **Figure 65**
A drum of bituminized waste

exothermic reactions taking place inside the enrobed drum. These parameters are determined by micro-calorimetric measurements prior to embedding.

The typical bitumen drum issued from the conditioning of co-precipitation sludges or effluent concentrates has the following characteristics (● [Fig. 65](#)):

- *Volume* 0.23 m^3
- *Typical activity* 1.6 TBq (beta gamma), 0.03 TBq (alpha)
- *Ratio bitumen/dry precipitate* = 1.5
- *Dose rate at 1 m* = 0.1 Gy/h

Once the bituminized package has been manufactured, its good behavior has to be ensured in the long term. The two phenomena to be considered are the radiolysis caused by the package self-irradiation and the leaching induced by a possible package contact with water.

2.3.3 Bitumen Package Evolution Under Self-Irradiation

Bitumen is a continuum of organic compounds of molar masses between 400 and 4,000 g/mol, most of which are unsaturated and polycyclic. This organic composition endows bitumen with the property of emitting radiolytic gases, essentially hydrogen, under self-irradiation. These gases are issued from the cleavage of the existing C–H bonds.

According to the activity incorporated, about 1–10 L of radiolytic gases per year are generated by a drum on the production line. The gas source term falls to less than 1 L after 1,000 years owing to decay. The volume of accumulated gas over 1,000 years is about 1 m^3 per drum.

The gases generated in the whole volume of the embedded waste are first dissolved in the matrix up to saturation (about 1% in volume). Beyond this step, hydrogen forms gas bubbles,

the growth of which may lead to the swelling of the embedded waste. A swelling rate of about 1 cm/year could be observed in some packages.

In some cases (e.g., packages manufactured with no apical vacuum), swelling evolution can cause the embedded waste to overflow out of its container, or even induce the pressurization of the container if the overflow is halted (e.g., by a lid).

This swelling does not impair bitumen confinement properties with respect to radioactivity, but requires a suitable package management during the storage period and the reversibility period of the geological disposal phase.

The swelling of bitumen can be controlled by three main ways:

- Limiting the incorporated activity
- Limiting the drum filling
- Trapping the radiolytic hydrogen by means of salts added to the bitumen (cobalt sulfur)

2.3.4 Bitumen Alteration by Water

Although pure bitumen is not very permeable to water and dissolved species, the initial presence of salts favors water uptake through diffusion and osmosis. On contact with water within the embedded waste, the most soluble salts are dissolved locally. Formation of saline solution bags results in porosity developing, which facilitates the dissolved species diffusion back to the outer leachant. The kinetics that characterize water uptake and the release of the most soluble salts comply with square-root laws for time, specific of a diffusion mechanism. These kinetics are chiefly controlled, first, by the contents and solubilities of the various embedded saline species, and, secondly, by the leaching solution. It is noteworthy that water uptake is about 100 times faster than the release of the most soluble salts, due to the low values of effective diffusion coefficients, of the order of $10^{-15} \text{ m}^2 \text{ s}^{-1}$ for solubilized salts. This difference results in the swelling of the embedded waste, due to the porous area maturation and the leaching front progress. Regarding the latter, it proceeds at a rate of the order of $\text{mm} \cdot \text{yr}^{-1/2}$.

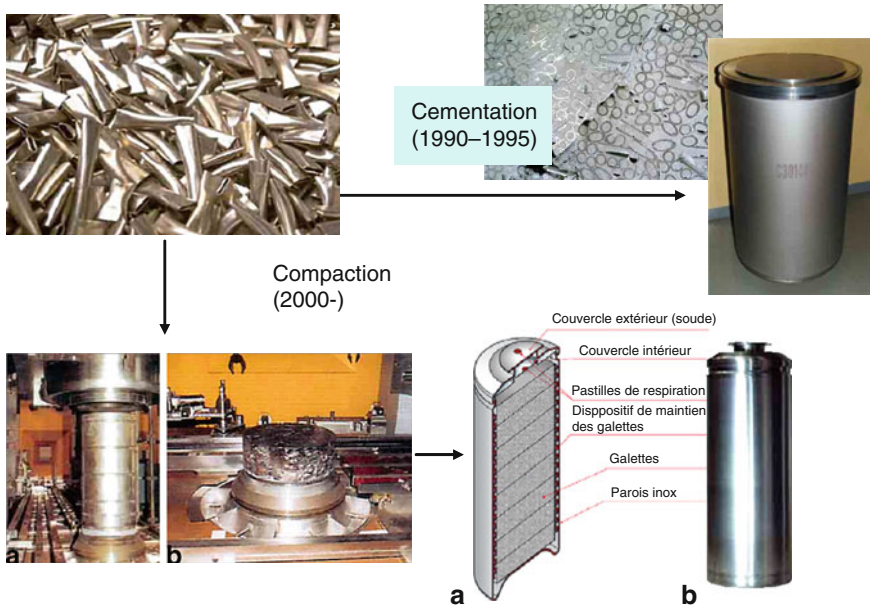
Globally, bitumen is a good confinement matrix: the rate of release of radionuclides, controlled by the diffusion, is slow and altogether compatible with the requirement of a disposal facility. The return of experiment acquired from industry shows that the risk of fire can be mastered if the chemical reactivity of the sludge is correctly analyzed and taken into account.

Similarly, the swelling of bitumen can be managed by limiting the activity in the package, by imposing a void space in the upper part of the drum, and by adding cobalt salts.

However, bituminization is increasingly replaced by cementation as a conditioning matrix.

2.3.5 Conditioning of Fuel Claddings and End Caps

After the dissolution of the spent Fuel in the processing facility, one obtains metallic residues: the undissolved end caps and grids of the fuel assembly (made of stainless steel), and pieces of the zircaloy fuel cladding. Despite a thorough rinsing, this waste contains activation products (distributed in the entire volume of the metal), 0.2% of the total inventory of fission products, and 0.03% of the actinides from the spent fuel (located close to the surface of the metal). It is thus classified as intermediate level activity, long-lived waste. In the 1990s, hulls and end caps were conditioned in concrete. The cement package weighs about 4 t, its activity is of the



■ Figure 66
Conditioning of fuel claddings and end caps

order of 50 TBq beta-gamma, and 0.1 TBq alpha. This gives a dose rate of 10 Gy/h at the package surface.

In the 2000s, this process of cementation of hulls has been replaced by a process of compaction, thereby enabling a volume reduction of a factor 5. The waste is introduced in a metallic case and compressed hydraulically up to a density of 65% of the metal density. The obtained “cakes” are piled up in a stainless steel container (► Fig. 66). The obtained package (CSD-C) has no confinement matrix. Each container contains five to ten compacted cakes. For standardization purposes, these containers have the same external geometry as the standard container of vitrified waste (CSD-V).

2.3.6 The Long-Term Behavior of the Compacted Metallic Waste Package

The CSDC package is essentially heterogeneous. Its confinement properties depend on the durability of the materials, which contain the radionuclides (metal, oxide, hydride). For 300 years, the package is expected to remain leak tight. Later on, the RN release occurs, at a rate, which depends on their location within the metal. Fission products and minor actinides (located close to the metal surface) are expected to be released soon after water reaches the waste. Activation products (distributed in the entire volume of the metal) will be released at the rate of the metal corrosion. Typical confinement durations are of the order of 10,000 years for zircaloy; 100,000 years for stainless steel, and 1,000 years for nickel-base alloys.

2.3.7 Melting: A Possible Future Conditioning for Metallic Waste

Research is being carried out on melting the metallic waste. The process would enable one to reduce further the waste volume, to decontaminate the ingot by transferring the alpha emitters, Cs and Sr in a slag, which would then be separated from the ingot and vitrified. The remaining radioactive nuclei would be distributed within the bulk of the ingot. The alloy composition and reduced surface of the ingot would make it able to withstand corrosion.

2.3.8 Specific Conditioning for Minor Actinides and Fission Products

Tailored Ceramics for the Confinement of Specific Radionuclides

Today, vitrification constitutes “the” reference solution for conditioning high-level waste from reprocessing. Yet, conditioning some radionuclides within a glass matrix may prove to be difficult owing to low solubility in the glassy lattice or to high volatility during high-temperature manufacturing.

Although they do not display the chemical flexibility of a glassy matrix (i.e., the capacity to integrate into the structure a number of elements), ceramics can be optimized for the radionuclide considered, thereby presenting the best confining properties.







Example of ceramics displaying good RN confinement properties: zirconolite, hollandite, apatite (➤ [Table 10](#)).

- Zirconolite could confine minor actinides
- Hollandite could confine cesium
- Apatites $M_{10}(PO_4)_6X_2$ could confine iodine

These ceramics are cited here only for the sake of completeness, because they will probably never be used for the confinement of radionuclides on the industrial scale. Their good resistance to lixiviation does not compensate for the drawbacks associated to their use: production of secondary waste, and complexity of a chemical separation of each radioelement.

■ **Table 10**

Main characteristics and fabrication processes for the ceramic matrices developed for the conditioning of long-lived radionuclides (From Clefs CEA n°53, 2006)

Radionuclide	Matrix	Radionuclide loading factor (wt%)	Fabrication process	Chemical durability (g/m ² .d)	Behavior under self-irradiation
Iodine (I)	Iodoapatite (composite matrix) $Pb_{10}(VO_4)_4O(PO_4)_12I_2$	7	 Sintering under load (580°C-25 MPa)	$V_f(I): 10^{-4}$ at 90°C (confined environment)	-
Cesium (Cs)	Hollandite $Ba_1Cs_{0.26}(Fe_{0.02}Al_{1.46})Ti_{5.72}O_{16}$	5	 Natural sintering (1,250°C)	$V_f(Cs): 10^{-5}$ at 90°C (confined environment)	Point defects with no effects on structure
Actinides (An)	Britholite $Ca_{10-x}An_x(PO_4)_5(SiO_4)F_2$	10	 Natural sintering (1,475°C)	$< 10^{-6}$ (confined environment)	Slight damage (external irradiation)
	Monazite-brabantite $La_{1-3x}An_xCa_xTh_xPO_4$	10	 Natural sintering (1,450°C)	Ongoing investigations	No amorphization (natural analogs)
	TPD $Th_{4-x}An_x(PO_4)_2P_2O_7$	10	 Natural sintering (1,250°C)	10^{-6} at 90°C -pH 7 (confined environment)	Ongoing investigations
	Zirconolite $(Ca_{1-x}An_x^{3+})Zr(Ti_{2-x}Al_x)O_7$	10	 Natural sintering (1,450°C)	$< 10^{-6}$ (confined environment) cessation of alteration	Amorphization of the structure with no loss of confinement

Synroc (a polycrystalline material based on titanates, and developed by ANSTO (Australia)) is also a possible challenger for the confinement of fission products, but its implementation is complex, and has never been made on an industrial scale.

2.4 Conditioning of Spent Fuel

2.4.1 Can Spent Fuel Be a Conditioning Matrix?

At the reactor output, the spent fuel can be considered in two radically different ways, depending on the strategy followed on fuel cycle:

Should the “closed cycle” be selected, the spent fuel will be in remission; it will have to undergo storage (by definition, temporary), awaiting its treatment.

Should the “open cycle” be chosen, the spent fuel will be considered as waste. It will then have to undergo not only storage, but also disposal (final, by definition, accompanied, however, by a reversibility option) in a geological repository.

Whatever the selected option, the spent fuel will have to undergo a storage period, ranging from 5 years (minimum time to allow the fuel to “cool down” before treatment processes) to 100 years. Even with the “closed cycle” option, the storage time can be as long as a century; for instance, for the spent MOX fuels, the preferred option is to store the assemblies and to wait for future fast neutron reactors, capable of efficiently recycling their plutonium.

This storage can be carried out under water or in dry conditions, but, in any case, the spent fuel sheath will have to play its part and prevent the dispersion of radionuclides produced during the time the fuel stayed in the reactor. Under dry storage conditions, this raises the question of *dry corrosion* and of the mechanical behavior of the spent fuel rod under the pressure generated by the gas produced by the radioactive disintegration of actinides within the fuel. Under dry storage, the spent fuel is locked within a container, which protects it, allows its handling, and plays the role of a confinement barrier. The degradation modes of this container must also be studied.

Under water storage, the temperature reached by the fuel is lower. Thermomechanical problems liable to affect the spent fuel are less critical. However, attention should be paid to radiolysis, as well as to *aqueous corrosion* problems.

With the “open cycle” option, the spent fuel, encased in its container, will have to ensure the retention of radionuclides during an even longer time period.

Hundred of thousands of years will be necessary to allow the radioactive decay to bring back the spent fuel radioactivity to the level of that of the initial uranium ore. It will be probably impossible to avoid direct contact of the fuel ceramic with underground water, as the metallic casings wrapping the latter will not be able to withstand corrosion over such long time periods. The problem to study in that case is that of the leaching of the ceramic. Contrary to glasses, which have an amorphous microstructure, the fuel ceramic is polycrystalline.

It is also fragmented, due to the temperature gradients within the reactor. When contact occurs with underground water, some of the radionuclides located at the interfaces and at the grain boundaries will be freed very rapidly. This “*instant release*” fraction is also subject to detailed studies, as it determines the “source term” of deep storage carried out on used fuels.

Definition of the fuel burnup

- $\text{FISSION YIELD } (Tf) = \text{fissioned atoms/fissionable atoms}$

fissionable = fissile + fertile (= "heavy atoms")

- $\text{BURNUP } (BU) = \text{extracted energy per ton of irradiated initial heavy metal}$
(M(G)Watt.day per ton)
- Standard UOX LWR spent fuel:
 - Tf ~ 3–6%
 - BU ~ 30–60 GWd/t
- 1 fission: ~200 Mev

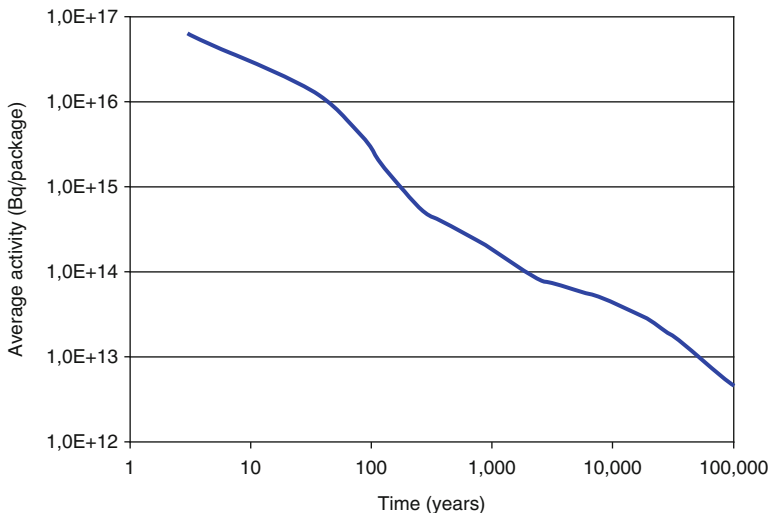
$$BU \text{ (GWd/t)} = 9.6 \text{ Tf}(\%)$$

The burnup is defined as the energy extracted per ton of irradiated initial heavy metal in the nuclear fuel. It indicates how many nuclei have undergone fission within the fuel. It depends on the neutronic flux and on the staying time of the fuel element within the reactor.

If the spent fuel is to be considered as a waste, the burnup is an important indicator of the physicochemical state of the fuel element: in particular, it tells how much fission products will be found in it.

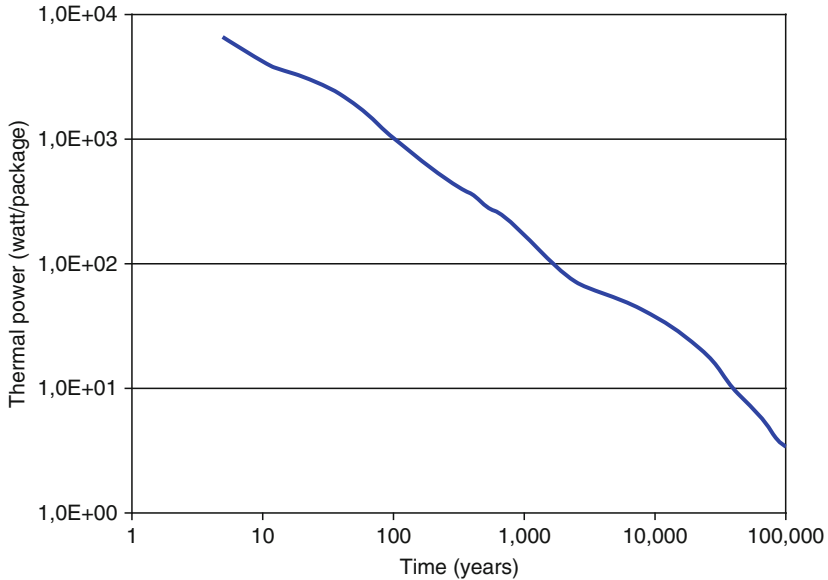
2.4.2 Spent Fuel Evolution After Unloading

An important characteristic of the spent fuel is its large residual power (several kW per assembly after 10 years storage) (► Figs. 67 and ► 68). This residual power is larger than for glass



■ Figure 67

Radioactivity of spent fuel versus time. Case of a package of 4 PWR assemblies, for a burnup of 45 GWd/t (ANDRA and Dossier 2005, argile)



■ Figure 68

Residual power of spent fuel versus time. Case of a package of 4 PWR assemblies, for a burnup of 45 GWd/t) (ANDRA, Dossier 2005, argile)

packages coming from the processing of the same amount of fuel, because plutonium is present in the spent fuel whereas it has been removed from the glass.

2.4.3 Packaging Spent Fuel

The packaging of spent fuel has to be seen in the context of the whole disposal system and has different functions, which are determined by the time for interim storage, considerations of transport and emplacement, and the duration of containment.

A package is necessary for storing assemblies of spent fuel, because the irradiated fuel pellet is not a containment matrix: it degrades over the very long term through auto-irradiation. Moreover, the integrity of the cladding cannot be easily demonstrated.

Two confinement barriers are recommended: a case and a container (🔗 Figs. 69 and 🔗 70). It must ensure functions of confinement, taking into account the mechanical and thermal constraints, and avoiding any risk of criticality. It must permit both spent fuel transportation (optionally), long-term interim storage, and spent fuel retrieval.

Canisters are usually made from stainless steel and contain an array of storage sleeves to hold the bundles of spent fuel. Canisters are filled with an inert gas such as helium and sealed by welding.

In Europe, a typical cask design for dry storage of spent fuel is the German CASTOR concept. CASTOR casks provide an overpack for the medium-term storage and transport of heat-generating waste.

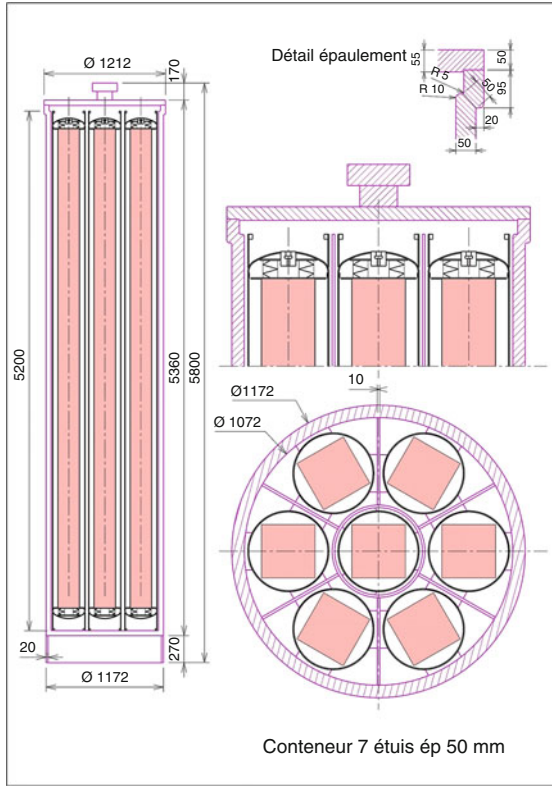


Figure 69
An example of packaging of spent fuel



Figure 70
An example of spent fuel packaging: the SKB Swedish concept, with a thick-walled copper canister (photo SKB) (Papp 1998a)



■ Figure 71

Examples of packages for spent fuel, intended both for transportation and for dry storage

Another type of spent fuel dry storage package is BNFL's TranStor system, which is extensively used in the United States (*ref. IAEA, 2000. Multi-purpose Container Technologies for Spent Fuel Management. IAEA, Vienna. Report no. IAEA-TECDOC-1192*).

In this design, the casks are made of concrete with a thick internal steel liner for enhanced shielding and strength. The cask is designed to provide radiological shielding and to create a natural air circulation path for cooling of the canister. TranStor casks can be stored in the open air on a reinforced concrete pad without building cover. Such open-air storage is implemented at several sites in the United States (📍 *Fig. 71*).

2.4.4 Choice of the Container Material

Availability, cost, and industrial feasibility factors have led to a limited choice of **candidate materials for containers**. These materials can be classified into two main categories:

- Consumable materials, like low-alloyed steels. Given the order of magnitude of their corrosion rate in a reducing environment (a few $\mu\text{m}\cdot\text{year}^{-1}$), these materials must be used in thick foils to last a long time. These materials are cheap. They also have the advantage of undergoing generalised corrosion, easier to foresee and control than localised corrosion. Conversely, the drawback is the production of hydrogen by the corrosion reaction.
- Non-consumable materials, either thermodynamically or kinetically stable. These expensive materials (copper, stainless steels, nickel or titanium alloys) are much more durable, but are potentially sensitive to localised corrosion.

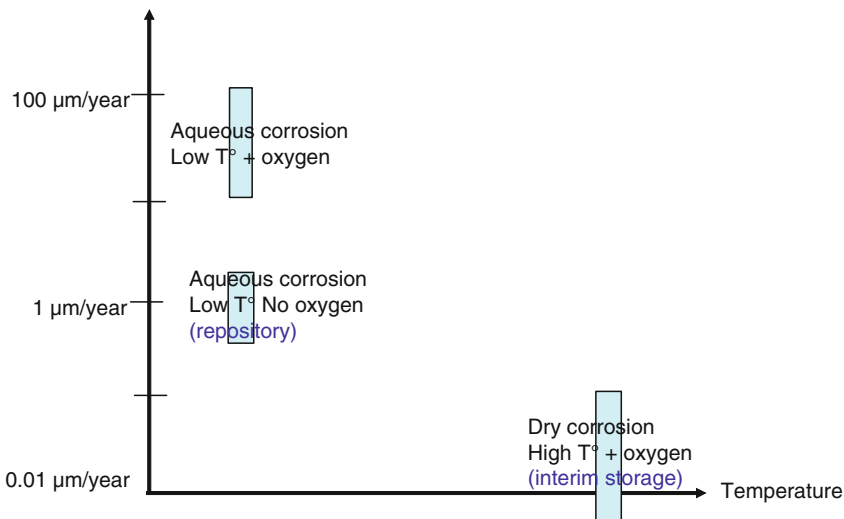
2.4.5 Corrosion Rates of Low-Alloyed Steels

Dry corrosion of low-alloyed steels is much slower than aqueous corrosion (🔗 Fig. 72). The storage facility must therefore be designed so as to avoid aqueous corrosion. Another reason to avoid water in interim storage is that corrosion rates could be affected by water radiolysis. Irradiation of water molecules close to the radioactive waste surface creates free radicals that are very reactive.

Archaeological analogues can help understand the corrosion of metals on a long timescale. The corrosion rates of low-alloyed steel evaluated on analogues spans over three orders of magnitude, depending on the material and surrounding environment. The average value is on the order of $1 \mu\text{m}/\text{year}$ (B. Kursten et al. Eurocorr, Nice, Sept. 2004.)

Note that the picture of a constant corrosion rate may be oversimplified. The corrosion of metals in an underground environment does not proceed generally at a constant rate. Indeed, an equilibrium between the metal and the environment establishes itself. Progression of the corrosion then slows down and can even stop completely if the environment is stable.

Recent results indicate that the aqueous corrosion rate of low-alloyed steels is enhanced in presence of argillaceous minerals. The influence of clay minerals on the pH and eH of the water is one possible explanation. Sorption of iron ions onto clay minerals or precipitation of iron-containing minerals on the clay mineral surfaces can also remove iron from the solution, and explain the acceleration of corrosion in presence of dispersed clay minerals. This acceleration effect can be counterbalanced by the fact that clay layers act as barriers for the transport of water and chemical species, and can thus limit the availability of reagents in the vicinity of the metallic surface. All these effects combine in a complicated manner. Research is going on to understand the influence of the clay environment on the corrosion resistance of steel overpacks.



■ Figure 72
Orders of magnitude for the corrosion rate of unalloyed steel

This problem of the influence of the surrounding mineral environment on the alteration rate is quite general: it is also encountered in the case of glass alteration.

2.4.6 Post-Irradiation State of the Spent Fuel

Irradiated Clad State

During in-reactor irradiation, the microstructure of clad and structure materials is altered on account of both irradiation (alteration of the dislocation structure) and corrosion (oxidation and hydride formation). In-reactor irradiation thus results in a strong hardening of materials.

The thickness of the oxidized layer depends upon the axial temperature profile during irradiation and the type of alloy used. Internal oxidation remains superficial, affecting only the first 10 μm . Outer oxidation of clads is deeper: its depth reaches a maximum level in the hotter area, and generally remains lower than 100 μm in the clad alloy Zircaloy-4 (it is reduced to 25 μm after six irradiation cycles with more advanced zirconium alloys).

On the other hand, clad oxidation by water releases hydrogen, part of which is absorbed into the metal. This hydrogen forms hydride plates, which make the clad more fragile.

Besides, following the fission gas release in the free volumes of the rod, the pellet swelling and the clad creep under the coolant external pressure during in-reactor irradiation; the rod internal pressure after irradiation is higher than the filling pressure. For UOX fuel rods clad with Zircaloy-4, it is 40 bars on the average (after cooling) for an initial helium pressure of 26 bars and a burnup of 60 GWd/t. In the same conditions, it is slightly higher for a MOX fuel (50 bars).

It is this very clad, with enhanced fragility and high stresses following in-reactor irradiation, which will have to contain radioactivity in spent fuel under storage conditions. This implies that the weaknesses mentioned above will have to be taken into account in the design of containers and storage facilities.

Post-Irradiation Physical State of Spent Fuel Pellet

The developing of a high radial temperature gradient in the pellet during its in-reactor irradiation induces considerable mechanical constraints, which lead to the pellet cracking. Whatever the burnup reached, the spent fuel pellet after in-reactor irradiation may be seen as cut into 15 fragments or so on the average (► [Figs. 73](#) and ► [74](#)).

The macroscopic swelling observed during the irradiation results from fission products formation, irradiation defects, and emerging fission gas bubbles in UO_2 grains.

In-reactor irradiation strongly alters the microstructure of the fuel pellet, especially in the two following zones:

- The grain boundaries in which metallic precipitates as well as fission gas bubbles accumulate (► [Fig. 75](#)). Even if the grain boundaries withstand high constraint levels, they are made more fragile by in-reactor irradiation. For the burnups and irradiation temperatures considered herein, post-irradiation fractographies of spent fuel pellets evidence chiefly intergranular ruptures, save in the central zone of the pellet, whereas they are of the transgranular type in the unirradiated fuel.



Figure 73
Radial macrograph of a spent fuel pellet

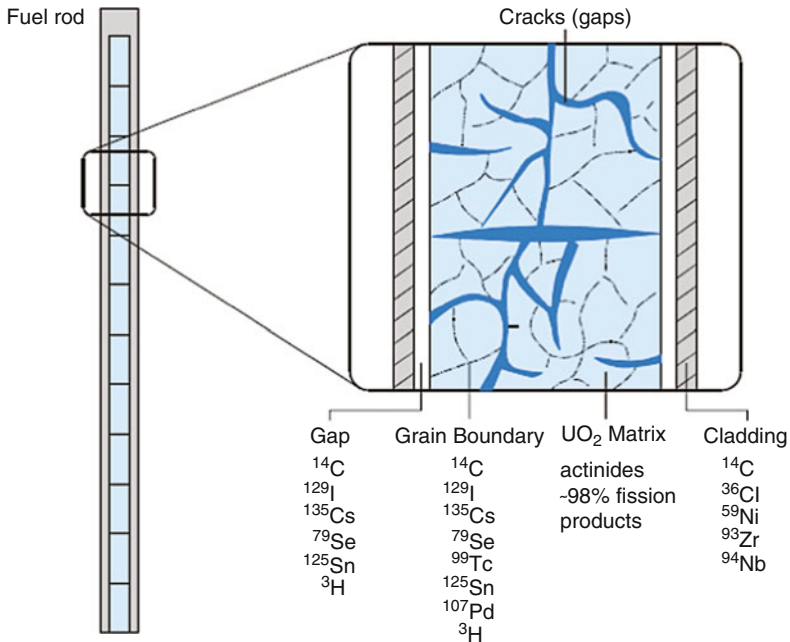
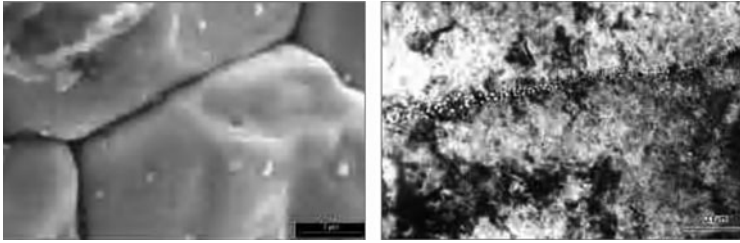


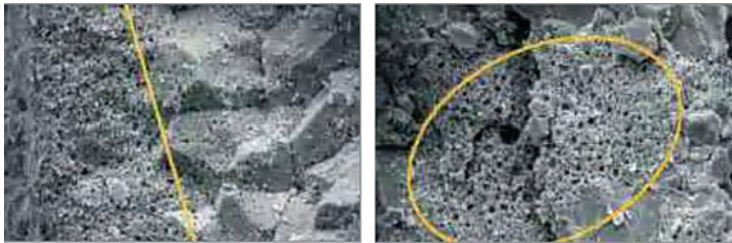
Figure 74
Schematic representation of the nature and location of the main radionuclides in a UO₂ fuel with a low burnup (no rim formation) (From IAEA 1991)

- The restructured zones in the peripheral part of the pellet (rim), in UOX fuels where burnup is higher than 40 GWd/t and in big Pu-rich aggregates (of size >10 μm) located in the outer zone of the MOX fuel pellet. These restructured zones are characterized by a porosity of micrometric size of about 10% (closed after in-pile irradiation) and small-sized grains (0.1–0.2 μm) (► Fig. 76).



■ Figure 75

SEM (*left*) and TEM (*right*) microphotographs of the ceramic after irradiation. They show a buildup of metallic precipitates (*left*) and of gas bubbles on grain boundaries (*right*)



■ Figure 76

Microphotographs of restructured zones on the pellet circumference in an UOX fuel (*left*) and in a MOX fuel plutonium agglomerate (*right*)

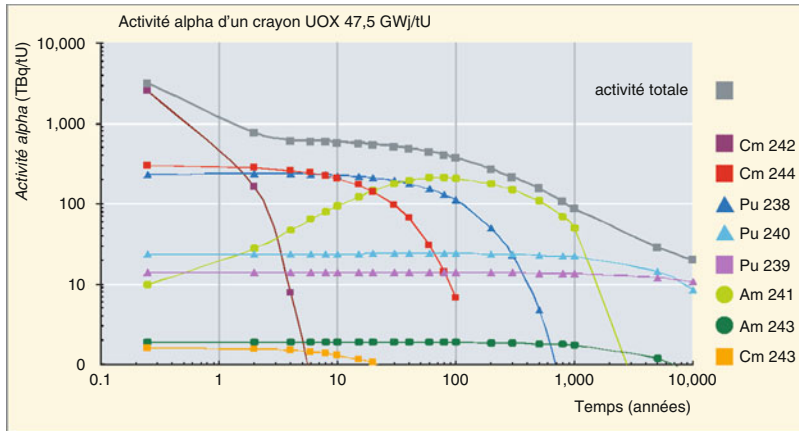
2.4.7 Fuel Evolution in a Closed System

Radionuclide radioactive decay is the origin of the physicochemical phenomena, which characterize the long-term intrinsic evolution of spent fuel.

Helium generation through *alpha* decay of actinides raises an important issue for the long-term behavior of spent fuel. ▶ [Figure 77](#) shows the residual alpha activity on a timescale of 10,000 years for an irradiated uranium dioxide fuel with a burnup of 47.5 GWd/t. Helium concentration will reach 0.7 at.% per heavy metal atom over 10,000 years. For a MOX fuel with the same discharge burnup, it would reach 4%. If helium is released to the free volumes of the fuel rod, this would entail a significant increase of internal pressure in the rod, and, consequently, of the clad tangential constraint.

Reversely, if helium is retained in the fuel pellet, it will precipitate as nanometric-sized bubbles, or pile up at the grain boundaries (trapping in preexisting fission gas bubbles) in the event of reduced mobility in the crystalline network. The helium atoms have been shown to be much more mobile in the grain boundaries than in the crystal itself (Martin et al. 2006; Roudil et al. 2004).

The production of helium in spent fuel can cause potential damage in the ceramic *via* bubble formation, formation of fissures, and decohesion of the grains. This grain decohesion itself is a matter of concern because some radionuclides localized on the surface of grains can be released



■ **Figure 77**
Evolution of the alpha activity of an irradiated UOX fuel versus time

during this process. However, the helium amount formed within 10,000 years in UOX fuels is not sufficient to alter the initial microstructure of the spent fuel pellet (Bonin 2009).

Under incidental conditions in a dry storage facility, the irradiated fuel runs the risk of being in contact with air or an oxidizing gaseous atmosphere. UO_2 conversion into U_3O_8 , a pulverulent oxide with a density much lower than that of UO_2 , constitutes a major risk of fuel rod degradation under storage conditions.

2.4.8 Spent Fuel in a Water-Saturated Repository

Part of the activity is released instantly, as soon as water comes in contact with the ceramic.

The Instant Released Fraction (IRF) depends on the degree of decohesion of the matrix (decohesion induced by irradiation in the reactor, and by self-irradiation and He production thereafter). This Instant Released Fraction can be as high as 10% of the RN inventory (► [Table 11](#)). It usually dominates the radiological impact of a spent fuel disposal facility (SPA Benchmark).

After the instant release, the UO_2 matrix undergoes leaching. The rate of lixiviation (and the rate of RN release) depends on the redox potential of the surrounding environment: the release is fast in oxidizing conditions, and slow in reducing conditions.

Although uranium oxide solubility is very small (typically 10^9 mol/L) under the reducing conditions usually encountered in a repository site, this solubility can increase significantly because of the water radiolysis induced by the long-lasting alpha irradiation field. Radiolysis can create oxidizing radicals close to the UO_2 -water interface. The kinetics of leaching then depends on the alpha dose rate, and on the modalities of transport of the species around the fuel.

■ Table 11

Instant release fraction estimates (% of total inventory) for various radionuclides for PWR UOX fuel, best estimates values, with pessimistic estimate values in brackets (Research program on the long-term evolution of the spent fuel [PRECCI] project 2008; Johnson et al. 2005; Ferry 2008)

BURNUP (GWd/tU)	41	48	60	75
RN	IRF	IRF	IRF	IRF
fission gas	1(2)	2(4)	4(8)	8(16)
¹⁴ C	10	10	10	10
³⁶ Cl	5	10	16	26
⁹⁰ Sr	1(2)	1(3)	1(5)	1(9)
⁹⁹ Tc, ¹⁰⁷ Pd	0.1(1)	0.1(3)	0.1(5)	0.1(9)
¹²⁹ I	1(3)	2(4)	4(8)	8(16)
¹³⁵ Cs, ¹³⁷ Cs	1(2)	2(4)	4(8)	8(16)

2.4.9 Conclusion on the Storage and Direct Disposal of Spent Fuel

The above section demonstrates that the spent fuel *is not* a confinement matrix.

At the reactor output, the fuel rod is indeed still tight, but its state does not permit one to guarantee a long-term confinement of the radionuclides.

The ceramic matrix has been damaged through irradiation and thermal stress; the rod is under pressure due to an accumulation of gaseous fission products and helium inside it; the cladding has been weakened through irradiation; it has been corroded inside by fission gas, and outside by the pressurized water from the reactor.

In spite of this, the studies on the corrosion kinetics under storing conditions indicate that the spent fuel will be able to confine the radionuclides *under storing conditions*, that is to say, protected from external aggressions, and during a limited time period.

Storage under dry conditions is more favorable than storage under water for a long-term preservation of the spent fuel, as the corrosion phenomena, which endanger the integrity of the cladding are slower, provided, however, that the latter storage be well conceived and maintains the fuel under acceptable temperature and hygrometric conditions.

However, *under disposal conditions*, the corrosion of metal envelopes and of the cladding will make its way in the long term, with the risk of putting the ceramic in contact with underground water. This situation is absolutely to be avoided, as the instant release fraction (a few percent) of the radioactive inventory would be released, with consequences that would not be acceptable for the safety of the disposal.

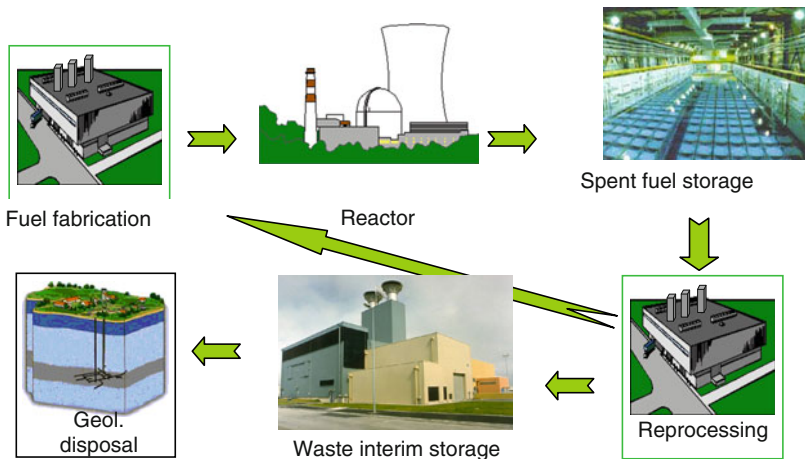
The countries that have chosen the final disposal of spent fuel (Sweden, Finland, the USA) are facing this problem. In order to solve it, all of them make the disposal safety rely on sophisticated engineered barriers, which will ensure long-term confinement of radionuclides.

3 Waste Storage and Disposal

3.1 Interim Storage of Long-Lived Waste and Spent Fuel

Today, long-lived waste is mostly stored in industrial facilities, exploited by utilities, with the prospect of retrieving it later and giving it a more definitive destination.

In any industrial process, storage plays the role of a buffer between two steps of the process (► Fig. 78). In the case of nuclear waste, storage provides some flexibility in the management of spent fuel, between its production and processing, giving some time for the spent fuel or the waste to cool down by radioactive decay, and allowing the possibility to wait for the availability of the geological disposal of the final waste.



► Figure 78

The position of waste or spent fuel storage in the back-end of the fuel cycle

In countries that reprocess spent fuel, it is stored before reprocessing; vitrified waste is also stored before its geological disposal.

3.1.1 Storage: A Temporary Solution for Waste Management

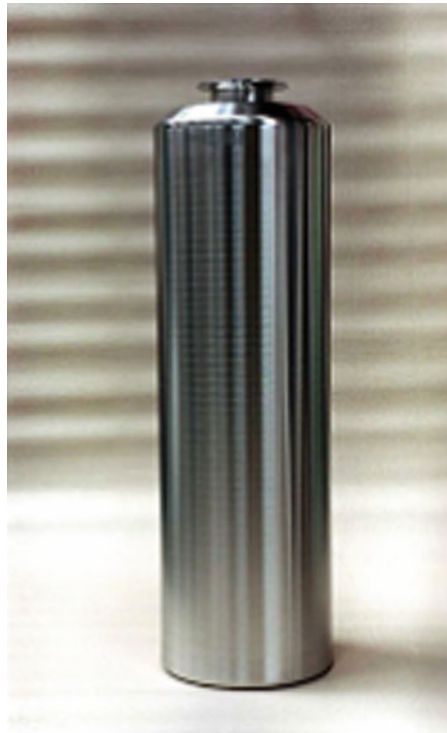
A storage period of a few years is necessary before the reprocessing of spent fuel, in order to let the short-lived radionuclides decay and make the spent fuel less irradiating. Another period of storage is also needed after the processing, in order to reduce the thermal power of the vitrified waste.

3.1.2 An Important Stake of Interim Storage: Reduce the Cost of the Disposal

The dimension (and cost) of a geological disposal facility of high-activity waste is roughly proportional to the thermal power produced by the waste. Indeed, the thermal conductivity of the host rock is generally so poor that the heat generated by the waste is not easily evacuated. In order to avoid an excessive heating of the waste and of the surrounding host rock, the waste packages must be spaced in the disposal in such a way that the average power is less than a few tens of watts/m^2 (see [Sect. 3.2](#)). The surface area needed for the geological disposal of high-activity waste decreases considerably with cooling time (typically a factor 2 for a 40-year cooling time). This could be an incentive for the facilities to postpone the disposal of the waste.

3.1.3 The Objects To Be Stored

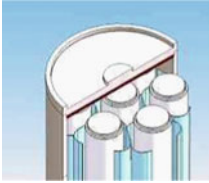
Before its storage, waste is conditioned in the form of packages designed to confine the radioactivity, and facilitate its handling. These packages are, for example, 400 kg glass canisters for the high-activity waste from the reprocessing of spent fuel ([Fig. 79](#)) or the spent fuel bundles



■ Figure 79

An example of high-activity waste package produced by the La Hague reprocessing plant (France)

Container for 7 UOX fuel bundles



Container for 4 MOX fuel bundles



Container for 6 CSDV glass packages

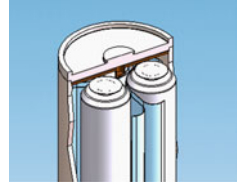


Figure 80

An example of container for the storage of spent fuel or glass packages



Claddings enrobed in concrete



Compacted claddings



Bituminized sludges



Technological waste enrobed in concrete

Figure 81

Examples of conditioning of intermediate-level long-lived waste

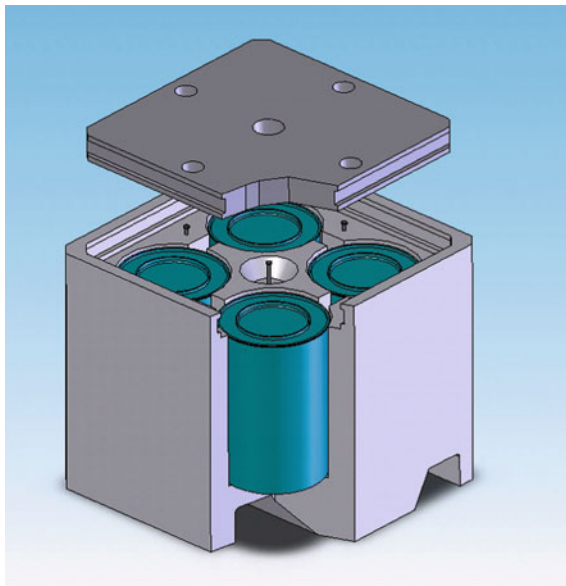


Figure 82

Example of universal container for intermediate-level long-lived waste. This container is able to accommodate all types of conditioned waste shown in Fig. 81, and can be used for intermediate storage as well as for disposal

themselves, gathered by groups in sheaths (🔍 Fig. 80). These packages are the objects that are to be stored.

In the case of intermediate-level waste, the form in which the waste can be conditioned is more diverse (🔍 Fig. 81), but the outer envelope of the package is generally made of concrete, and an effort is made to standardize the packages in order to facilitate the waste management (🔍 Fig. 82).

3.1.4 The Storage Facilities for Long-Lived Waste

The storage of spent fuel or of vitrified waste is already a mature industrial process. The storage facility is generally a surface installation consisting of a building or massive structures securing the protection of the packages. The conception of the storage facility makes possible the retrieval of the package, and warrants the safe confinement of the radioactive materials. There are two main types of storage facilities: pools (🔍 Figs. 83 and 🔍 84) and dry storage facilities (🔍 Figs. 85–87). Both types require some monitoring and maintenance to perform their function in accordance with the objectives generally ascribed to these installations by the Safety Authorities.

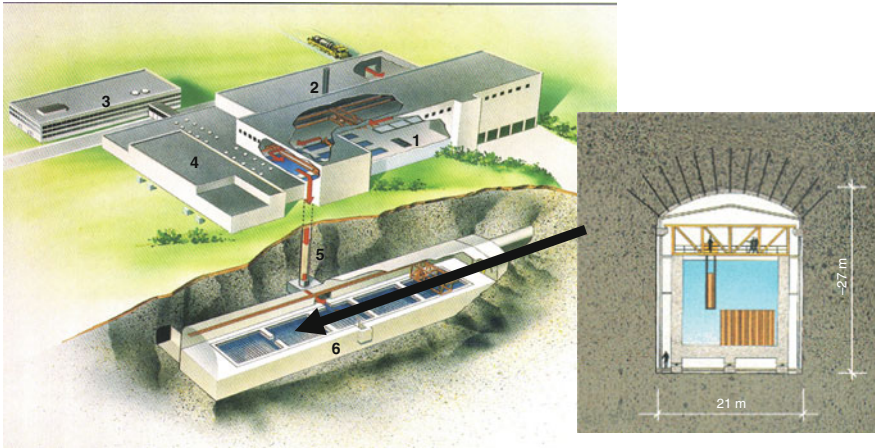
While the wet storage is used only for spent fuel (which is waste only if no reprocessing is envisaged), dry storage is used for both spent fuel and glass.

In pool storage facilities, the water of the pool cools the spent fuel and shields the operators from the radiation. The presence of water must be permanent; its chemical composition must be monitored and adjusted, if necessary, to avoid corrosion phenomena and subsequent radioactive leaks from the fuel.



■ Figure 83

Pool for the interim storage of spent fuel at the La Hague reprocessing plant (France) Dimensions: L: 50 m; l: 16 m, P: 9 (about 7,200 m³ water) Storage capacity: 730 baskets, each bearing 9 PWR assemblies or 16 BWR assemblies (~4,000 t, ~ 200 reactor.years)



■ Figure 84

An example of pool storage of spent fuel at CLAB (Sweden) 1. Receipt building; 2. Auxiliary systems building; 3. Offices; 4. Electric installation building; 5. Lift for the fuel; 6. Storage cave

Dry storage is generally preferred when long duration storage is envisaged (several decades).

In *dry storage* facilities, the radiation from spent fuel must be shielded, and the residual power produced by the waste must be evacuated to avoid an excessive heating of the waste. This is accomplished by organizing the circulation of air around the waste. Dry storage facilities come into three main categories: vault storage, cask storage, and silo storage.

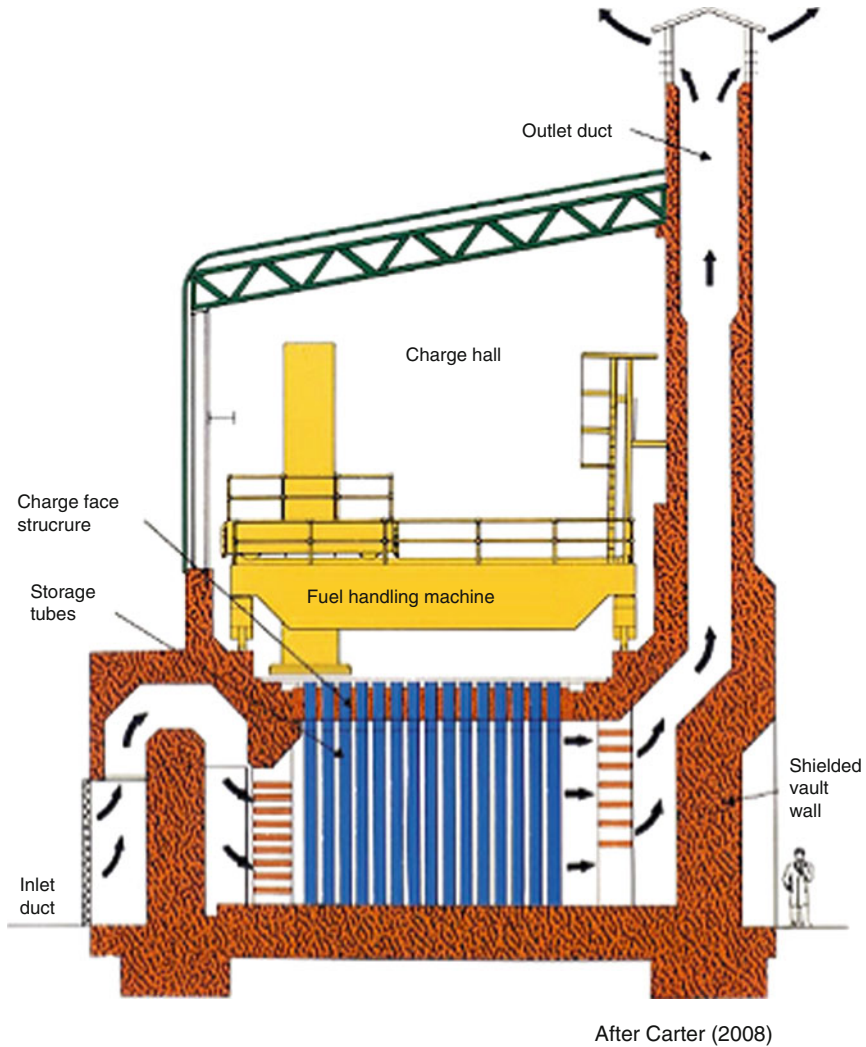
Vault storage consists of a concrete structure containing storage wells or pits. The spent fuel can be bare or containerized. The fuel is stored in tubes and heat is removed by convection of air across the external surface of the well (🕒 Fig. 85).

In some vault systems, fuel is removed from the transport cask and moved without any container to its storage tube. In others, the fuel stays in the container in which it arrives, which is then placed in a transfer cask and moved by crane to its storage cylinder.

The radiological impact of spent fuel is minimized by shielding from the concrete structure. Criticality control is ensured by the geometry of the vault well array.

Examples are:

- Wylfa (UK) facility, for the storage of spent Magnox fuel.
- CASCAD facility (France) for the storage of research reactors and naval propulsion reactor spent fuels, and UNGG fuels from early French gas-cooled reactors. The fuel is stored in helium-filled canisters in vertical wells.
- Paks MVDS (Hungary) facility, for the storage of VVER 440 uranium dioxide fuel. The fuel assemblies are stored bare in carbon steel storage tubes filled with nitrogen.
- Idaho spent fuel facility, for the storage of Peach Bottom (graphite clad), TRIGA (Al and steel clad) and Shippingport (Zircaloy clad) fuels. The fuel is packaged into welded canisters at the facility, filled with inert gas and placed in sealed storage tubes.
- Chalk River (Canada) facility, for the storage of legacy Al clad uranium metal fuels.



■ Figure 85

Typical design of a vault for the interim storage of spent fuel

Cask storage consists of a moveable concrete or metal structure, which provides containment and shielding (Fig. 86). The casks do not require any building and can be stored in the open air. Heat is removed from the spent fuel by convection or conduction. Casks can be designed and licensed for both storage and transportation.

Examples are:

- The German CASTOR concept is a dual-purpose device (transport and storage) for PWR or BWR spent fuel. It consists of borated stainless steel baskets placed underwater into a cast iron cask, then drained and vacuum dried. CASTOR casks are stored in Gorleben,

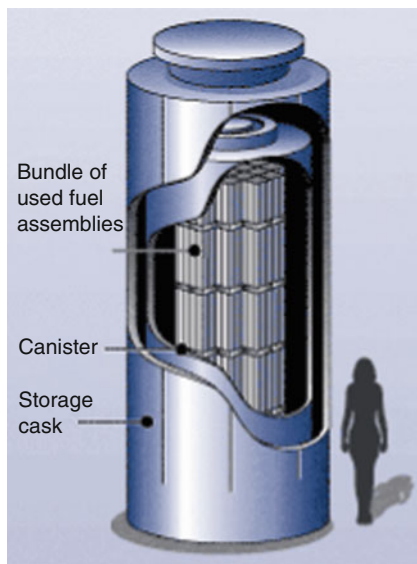


Figure 86

Typical design of a cask for the storage of spent fuel (After NRC, <http://www.nrc.gov/waste/spent-fuel-storage.html>)

Ahaus (Germany) and Dukovany (Czech Republic). The Belgian Transnuclear concept is very similar, and is implemented in Doel (Belgium).

- MACSTOR concrete casks (Canada), for the storage of CANDU spent fuel. The fuel is cooled for 6 years, and then transferred to galvanized carbon steel canisters. Each MACSTOR module holds 20 CANDU canisters (alternatively two LWR canisters). Casks are stored in the open air.

Silo storage consists of monolithic or modular immovable structure, providing containment and shielding for canisters loaded into reinforced concrete modular storage modules.

An example is the NUHOMS Silo Storage designed for PWR and BWR spent fuel (► *Figs. 87* and ► *88*). The NUHOMS silo system incorporates neutron-absorbing panels for criticality control.

The facilities for the interim storage of vitrified waste are very similar to the vault concept for spent fuel. They feature the same precautions for the residual heat removal by convective air cooling.

Examples of interim stores for vitrified HLW include the French EEV-SE facility (► *Fig. 89*), BNFL's Vitrified Product Store, Japanese Nuclear Fuel's vitrified waste storage building, and COVRA's HABOG store in the Netherlands which opened in 2003.

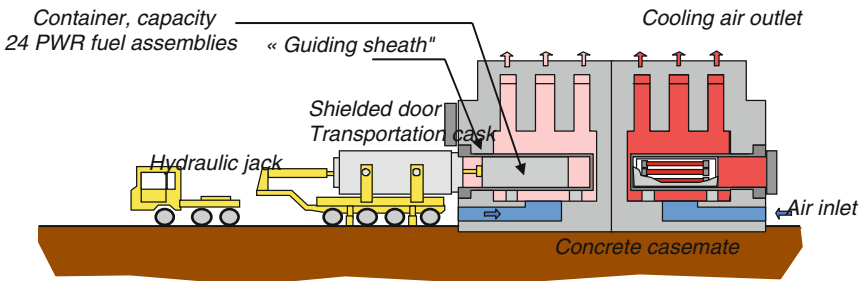
The intermediate-level waste storage facilities do not request precautions to cool the waste, which can be put in nonventilated wells or cells (► *Fig. 90*).

All these storage facilities (wet or dry) work presently without any special difficulty, and their foreseen lifetime is of the order of several decades.



■ Figure 87

An example of dry spent fuel storage facility using the American container NUHOMS



■ Figure 88

The scheme of a dry spent fuel storage facility using the American silo concept NUHOMS



■ Figure 89

The La Hague EEV-SE vault facility for the dry storage of vitrified waste. The glass packages are stored vertically in ventilated wells plugged at the level of the floor, under each circle on the *right* photograph. The thick concrete floor shields the operators from the radiation. Ventilation chimneys can be seen on the *left* photograph



■ Figure 90

An example of long-lived, intermediate-level waste storage: the compacted hulls storage facility ECC, at the La Hague plant (France)

Studies for longer-term storage have shown that the factors liable to limit the lifetime of these installations are the durability of structures made of concrete, and the corrosion of metals. However, the main weakness of the concept of long-term waste storage does not lie in technical issues. There remains the risk that the society may fail to maintain or may even forget the existence of these installations, which require continuous surveillance and maintenance. Another risk lies in the fact that long-term waste storage installations preserve the possibility of accessing the waste at any time, and are therefore vulnerable to malevolent or accidental human intrusions.

3.1.5 Duration of the Interim Storage


A nuclear waste interim storage facility looks very much like other facilities intended for the storage of other materials or goods, and the timescales that come into play are comparable. In normal exploitation, a nuclear waste storage facility has no radiological impact on the environment, since it is designed to confine totally the radioactivity it contains. The present return of experiment on these installations confirms these forecasts. However, even though nuclear waste storage facilities have never given rise to severe accidents, at least in the Western world, this does not mean that the risk is zero. These facilities are designed to make possible the retrieval of the waste, and are thus easily accessible. Their situation on the surface or subsurface implies some sort of surveillance in order to avoid unwanted human intrusions. As a result, the scenarios where everything does not go as scheduled can lead to a radiological impact on man and the environment. So far, these altered scenarios have been studied case by case, and are specific to each installation. They are characterized both by a low probability of occurrence, and by rather

severe consequences. The severity of the consequences is due to the fact that there is no geological barrier to slow down and dilute escaping radionuclides. That is why it remains advisable to limit the duration of the interim storage as much as reasonably possible. Who can guarantee that social structures will remain stable enough to ensure the safety of a storage facility over secular timescales?

On the other hand, a long-duration interim storage (longer than a century) would offer an appreciable flexibility in the nuclear waste management, giving time to make good decisions, to wait for the development of fourth-generation nuclear systems, and to take full benefit of the radioactive decay.

Ethics, economy, and technique will necessarily be involved in the decision on the duration of the interim storage of nuclear waste. The choice will be a compromise!

3.2 Geological Disposal

Deep geological disposal is at the end of the sequence of the waste management process (see  Fig. 30). This solution could be the ultimate one, for waste which has been adequately separated, conditioned, and cooled down.

3.2.1 The General Principles of Deep Geological Disposal

The main idea of a deep geological repository is the *definitive* disposal of the waste. The main argument is “do not leave the burden of our waste to future generations.”

A *reversible* disposal facility gives the possibility to retrieve the waste. Reversibility bridges the gap between the interim storage and the geological disposal concepts.

All degrees of reversibility are possible. A deep geological storage that could be gradually converted into a repository leaves time for debate, and for complementary solutions to emerge. And if one finally decides to leave the waste underground, there is not much to do to implement the decision! The reversibility option has many advantages. However, it raises some questions, such as: What is the additional cost for reversibility? Does it hamper safety by adding constraints to the conception of the disposal facility? Does this option increase the danger of proliferation, by making radioactive and fissile material accessible?

A particular challenge is posed by deep geological disposal; given the timescales of a repository, no direct demonstration of its safety is possible. One can only try to convince (oneself and others) by means of modeling, and (partial) validations.

3.2.2 The Technical Principles of Deep Geological Disposal

- Isolate the radioactive waste from man, by means of multiple barriers protecting the waste package (protect the waste from geological and human accidents, secure an environment favorable to the canister durability), and delaying radionuclide migration long enough for radioactive decay to take place.
- Secure a significant dilution at the exutories for the residual amount of radionuclides, which have managed to travel to the biosphere in spite of the abovementioned precautions.

3.2.3 The Multibarrier Concept

In order to isolate waste from man, the repository concept interposes several barriers between the two:

1. The matrix (glass, concrete, etc.). Its solid form and highly insoluble character prevents the release of radionuclides.
2. The engineered barrier (overpack, clay layer) protects the matrix, and delays the release of radionuclides.
3. The geological barrier (host rock) delays the release, and dilutes the radionuclides.

Although the multibarrier concept can be found in all designs of radioactive waste repositories (► *Figs. 91* and ► *92*), details can differ from site to site, depending on the nature of the waste to be disposed of, and on the nature of the host rock. For example, in the case of spent fuel disposed of in a granitic host rock, the backfilling with clay material is an important part of the concept. In the case of vitrified waste in a clay host rock, the engineered barrier does not necessarily feature any backfilling.

3.2.4 Repository Lifetime

The diagram of the total activity of spent fuel (actinides + fission products) shows that the initial activity is dominated by fission products during the first 200 years. Later on, the actinides activity dominates (► *Fig. 5* in ► *Sect. 1*).

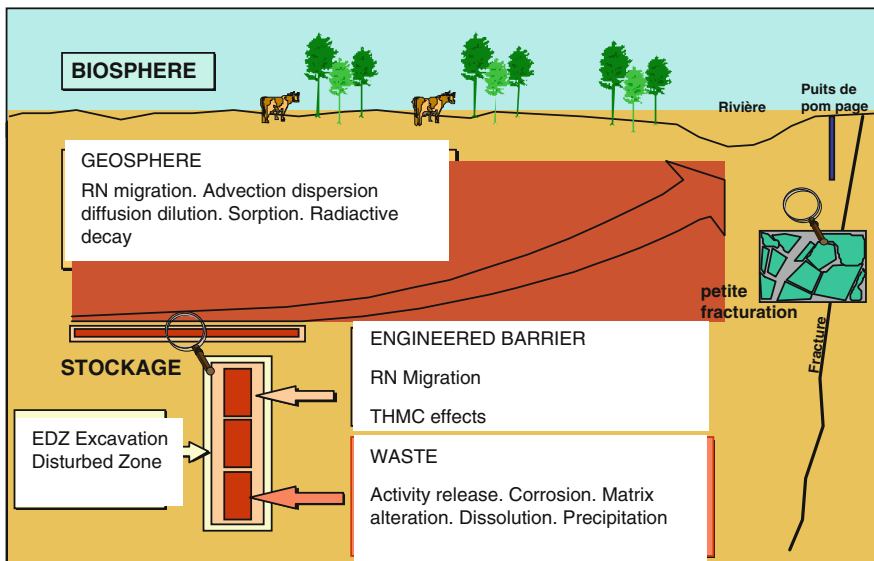


Figure 91

Illustration of the technical principles of deep geological waste disposal, with the main phenomena at play

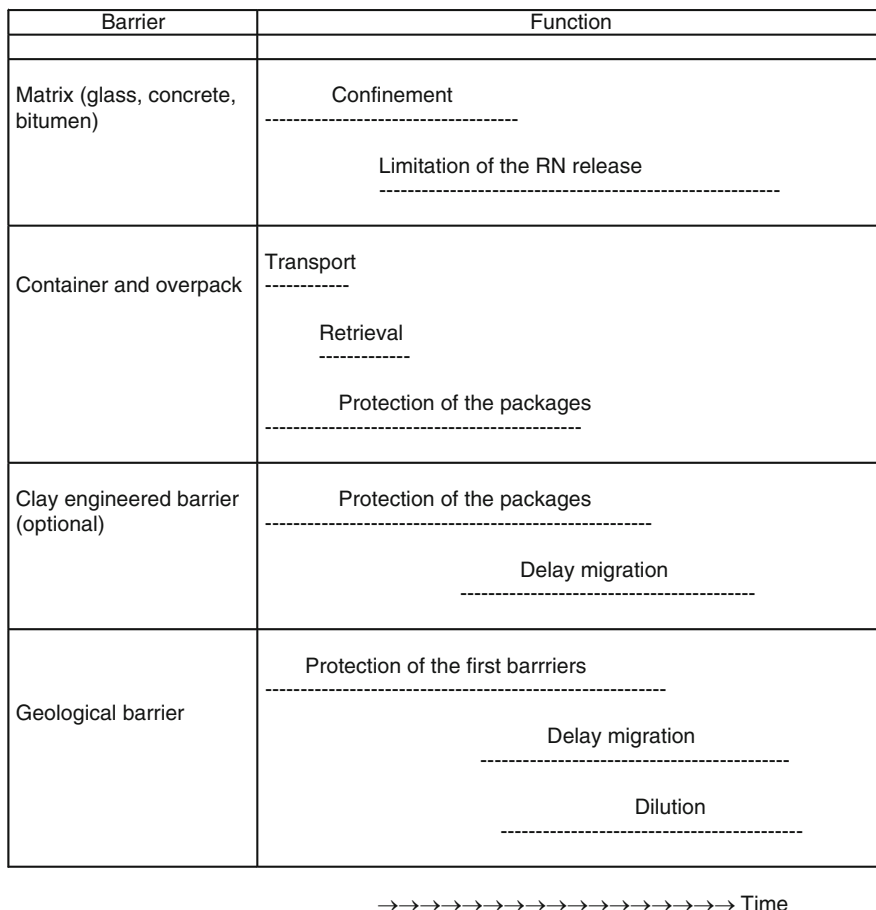


Figure 92
Functional analysis of the barriers in a deep geological disposal facility. All the barriers in a repository contribute to the safety, but they do not have the same role, and they come into play at different times

The diagram of the waste radiotoxicity as a function of time (► *Figs. 32* and ► *93*) gives the order of magnitude of the time during which the repository must be able to confine its radioactive content: 10,000 years for vitrified waste from reprocessing, and more than 100,000 years for spent fuel.

3.2.5 Repository Architecture

Details of the architecture are not completely defined yet, since no repository of high level, long-lived (HL LL) waste is in operation. They depend on the geological medium, but all the envisaged concepts share similar features.

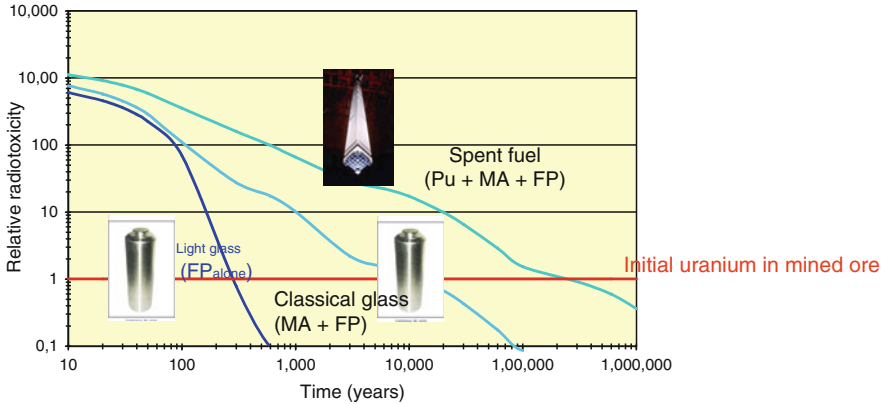


Figure 93

The radiotoxicity of waste as a function of time. This picture gives the characteristic time needed for waste confinement in the various fuel cycle options. It is the time taken by the waste radiotoxicity to decrease the level of the initial uranium in mined ore. The spent fuel radiotoxicity is dominated by Pu and more generally by actinides. The needed confinement time in the repository is reduced by Pu recycling, and would be reduced further by minor actinides recycling. The cost and size of the repository would also be considerably reduced

The depth of the repository will be typically a few hundred meters, a compromise between safety (which depends on the thickness of the geological barrier), cost, and technical feasibility.

Dimensions of a High-Level Repository

There is one major difference between storage and disposal facilities of high-activity waste. In a storage facility, the heat generated by the waste can be removed by air convection. In a disposal facility, the heat must be removed by conduction through the host rock. This heat removal mechanism is much less efficient than convection, and that is why the power density in a repository has to be so small, in order to avoid excessive heating of the packages and of the surrounding host rock.

The dimensions of the repository are imposed by the thermal load of the radioactive inventory.

At its closure, a typical repository containing the HL LL waste generated by 50 years of exploitation of a 60 GW LWR fleet will produce a power P_0 of the order of 10 MW.

In order to minimize the heating of both the packages and the host rock, the heat-generating waste must be spread out as much as possible within the host rock. This constraint imposes a planar geometry for the repository, which can thus be assimilated to a heating plane of surface area A , embedded in a host rock with thermal conductivity λ and specific heat $\rho \cdot C_p$.

The temperature of the heating plane increases at the beginning of the repository life because of the heat generation, and decreases later on because of the decrease of the power generated by the decaying waste. Assuming that the power generated by the waste decreases with time, like $\exp(-\beta t)$, with $\beta = 0.024 \text{ year}^{-1}$, the maximum temperature reached by the heating plane is then:

$$T_{\max} \approx \frac{0.315 P_0/A}{\sqrt{\beta \cdot \lambda \cdot \rho \cdot C_p}} \tag{1}$$

This maximum temperature is reached at time $1/\beta$, that is, 40 years after the closure of the repository. In order to limit this maximum temperature to less than 100°C (beyond this temperature, the host rock might undergo mineralogical transformations), the power density P_0/A must be smaller than $10\text{ W}\cdot\text{m}^{-2}$, and this imposes a surface area of the order of a square kilometer for the repository. Equation (1) shows that the maximum temperature depends on the thermal properties of the host rock via the product $\lambda \cdot \rho \cdot C_p$. This product depends on the nature of the host rock (slightly larger for salt and granite, slightly smaller for clay, see [► Tables 12](#) and [► 13](#)), but the difference is not considerable, so the above conclusions about the size of the repository are valid for all repositories, at least for the order of magnitude.

Because they are comparable in depth, surface area, gallery length, and excavation technology, a geological repository of nuclear waste looks very much like a mine.

The HL waste is placed on a plane to put as much distance as possible between the heat-generating waste packages, and minimize the heating ([► Fig. 94](#)).

In order to make the general management and the handling easier, repository designs generally feature a separation of the waste categories in distinct zones.

The waste packages are accommodated in elementary cavities (alveoles) dug into the rock ([► Fig. 95](#)). These alveoles are grouped in ensembles or modules interconnected by galleries.

■ **Table 12**

Types of waste packages that could be disposed off in a geological repository

Waste	Matrix	Container
FP AND MA	Glass	Stainless steel
Sludges, concentrates	Bitumen	Carbon steel
		Stainless steel
Hulls and end caps	Cement	Stainless steel
Technological waste	Cement	Fiber-reinforced concrete
		Stainless steel
Spent fuel		Carbon steel
		Stainless steel

■ **Table 13**

Criteria and characteristics of host rocks suitable for waste disposal

	Impermeability	Chemical stability	Mechanical properties	Thermal properties
Granite (S, CH ?, Fine)	No (fractures)	Not bad	Excellent	Good
Salt (D, USA)	Yes	Good	Creep	Good
Clay (F, B, J, E ?)	Yes	Good	Mediocre	Mediocre

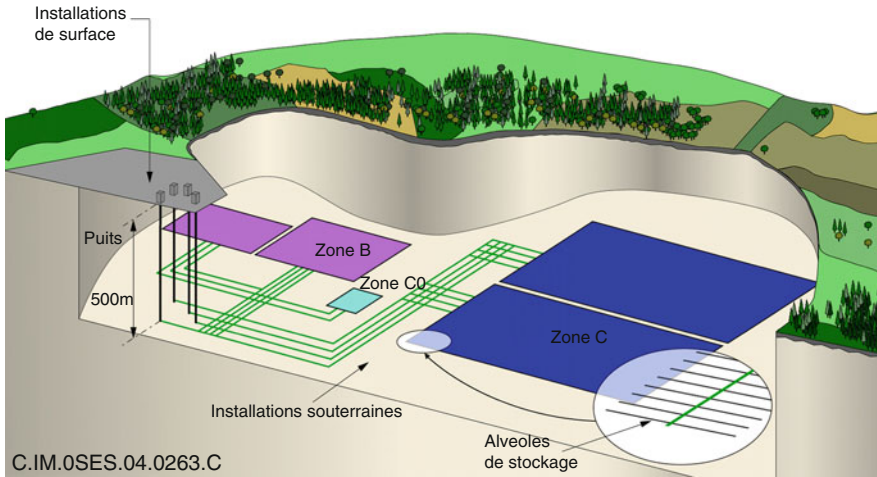


Figure 94
 Architecture of a repository (kilometric scale) (here, French concept, ANDRA and Dossier Argile 2005, http://www.andra.fr/interne.php?id_article=934&id_rubrique=160)

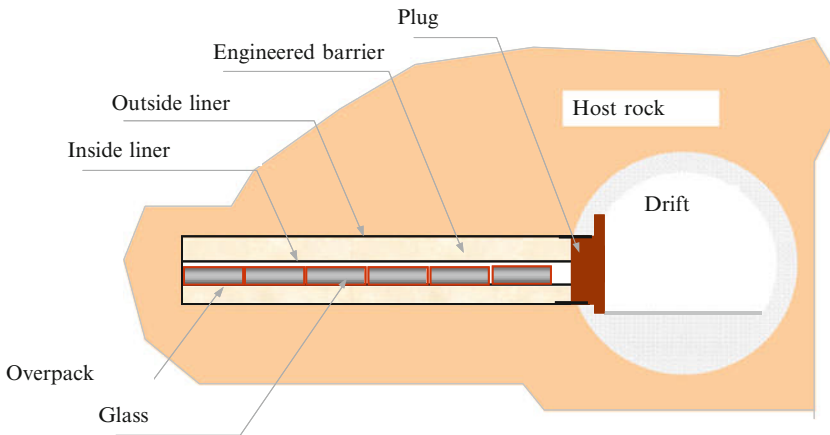
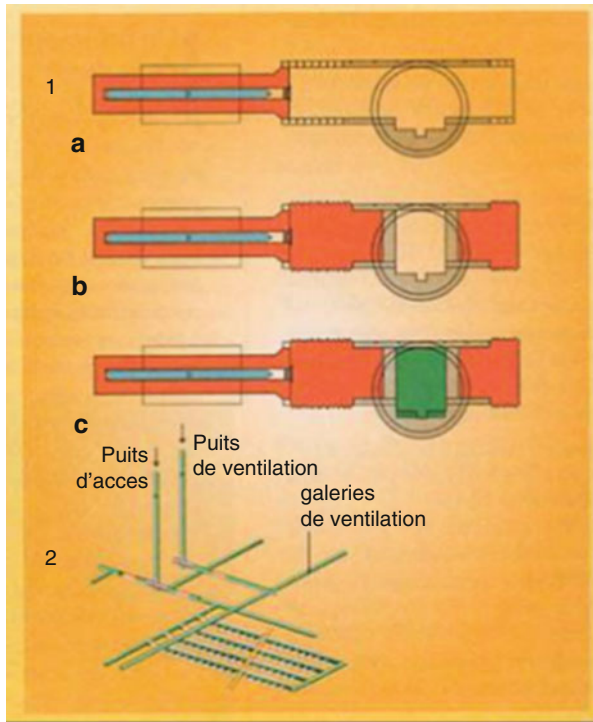


Figure 95
 Typical design of a repository of vitrified waste at the decametric scale (ANDRA, http://www.andra.fr/interne.php?id_article=934&id_rubrique=160) Note the overpack of the waste package. In this example, the overpack is made of thick (several cm) low-alloyed steel. Note that in this design, there is a liner separating the overpack and the host rock. This liner is intended to ensure the reversibility by avoiding an early collapse of the gallery under the lithostatic pressure

These horizontal access ways are connected to the surface by vertical shafts. The surface installations feature the support facilities, for example, the installations for waste characterization and conditioning.



■ Figure 96

Closure of a repository unit. Four steps of closure, in chronological order, and with a decreasing degree of reversibility: 1a: The tunnel plug is in place. At this stage, the installation is like an interim storage 1b: The unit is closed 1c: The handling drift is closed 2: All shafts and drifts are closed

As long as the drift is not backfilled, the waste canisters can be easily retrieved (reversibility) (► Fig. 96).

For medium-activity waste, the architecture of the repository can be more compact, because there is no heat generation.

3.2.6 Cost of an HL LL Waste Repository

According to ANDRA, the cost of a repository able to host the waste corresponding to 40 years of production of a 60 GWe nuclear fleet with closed cycle option would be of the order of 15 G€ (dossier ANDRA synthèse argile 2005). In this total, the investment cost is about 40%, the exploitation cost is 40%, and miscellaneous costs (taxes, overheads, insurance, and study costs) amount to 20%. The cost of the disposal facility depends largely on its size, hence the powerful incentive to design a compact facility.

Another example is that of the American repository of Yucca Mountain, envisaged for the disposal of spent fuel, which has a surface area of 6 km², with a honeycomb network of galleries 100 km long. Its capacity would be 70,000 t for a cost of 15 G\$ (Nuclear Waste, National Academy Press, 1996).

Utilities already pay provisions (under the form of dedicated assets) to prepare for this big investment. So, the money will be there on time, but the delayed nature of the investment is another incentive to postpone the decision of the disposal.

Far-field, near-field. Some terminology.

One usually distinguishes two zones in the geological barrier:

The near-field is the zone of the geosphere perturbed directly and rapidly by the repository.

The perturbations can be thermal, mechanical (decompression, cracks), hydraulic (desaturation etc.), and chemical (oxidation). They generate high gradients (stress, pressure, temperature, and concentration).

In the near-field, the system is well characterized (we know what the repository contains!), but its description is difficult because the phenomena, which take place in the near-field are complicated and coupled together.

The near-field encompasses the engineered barrier and a part of the geological barrier: EDZ, “Excavation Disturbed Zone”).

The far-field is the zone of the geosphere not perturbed directly by the repository, extending up to the biosphere.

The gradients are small, the thermo-hydro-mechanico-chemical couplings are weak.

The phenomena are simpler to describe phenomenologically, but the geological medium is generally ill-characterized and heterogeneous.

The far-field encompasses the geological barrier minus the EDZ.

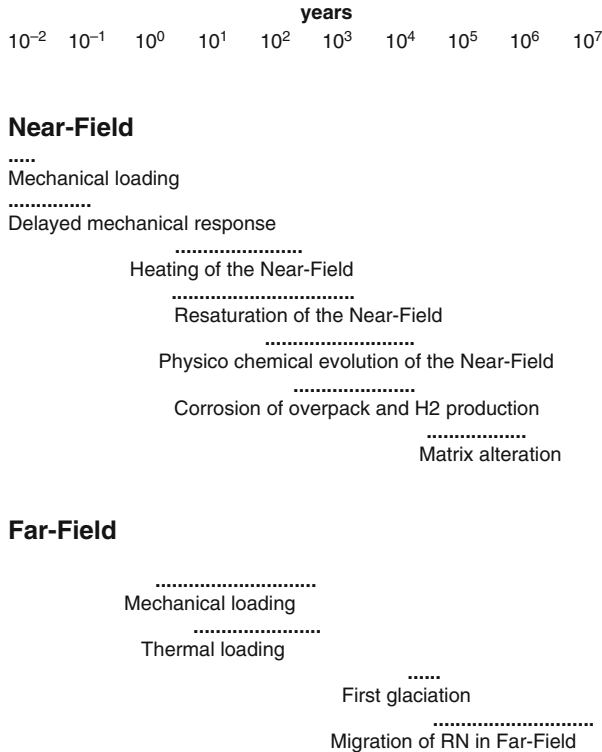
3.2.7 The Foreseen Evolution of a Repository

The First One Thousand Years

The likely evolution of the repository is described in the following “normal” scenario (🔍 Fig. 97). High-level waste packages will heat up the surrounding rock, until it reaches a temperature of about 100°C or so during the first 100 years, at the start of their time in disposal. The rock will then slowly cool down in step with the radioactivity decay rate. The clay barriers will become saturated at the same time. Rocks a few hundred meters below the surface will become resaturated with water because they are generally below the water table. It is also during the first millennium that the underground structures will settle, possibly opening fissures in nearby rock. This settlement, compounded by the corrosion of secondary metal canisters will make it harder – but not impossible – to recover the packages at a later date.

10,000 Years On and More

Much later (at least 10,000 years and no doubt much later) the glass packages and uranium oxide will have started to dissolve through the action of the underground water, causing the few released radionuclides to disperse. These will then slowly begin to migrate through the bedrock. The water will percolate through host rock pores and fissures before reaching a groundwater reservoir to migrate horizontally, finally ending up in a river. Very impermeable host rock will greatly slow down this migration while a “slow” aquifer and a distant outlet should lengthen the journey time even more. Calculations indicate that in low permeability geological formations, millions of years could elapse before any water would flow back to the outlet.



■ **Figure 97**

The foreseen evolution of a deep geological repository

Millions of Years On

A few radionuclides will surface their activity level diminished by radioactive decay: “*delay means decay*”!

At the end of its evolution, deep disposal will indeed have some radiological impact on the environment, as the quantity of radionuclides reaching the biosphere is not nil. But research carried out so far suggests that compared with natural radioactivity flows, a properly designed engineered barrier, combined with a well-chosen geological barrier will delay the return of the radionuclides to the biosphere to such an extent that the releases will be minute.

3.2.8 Geodynamic Evolution of a Deep Geological Repository

The above prediction of the evolution of a repository could be overturned by a volcanic eruption or a major earthquake, but the timescale of these internal geodynamic events is much larger than the lifetime of a repository. Time constants for the creation of new faults or new mountains are of the order of 10 million years. The local stress field can thus be considered constant during the next million years, except in the vicinity of active faults. Consequently, no creation of new faults across the repository is expected before several 10 million years, provided the repository is located in a tectonically inactive region. No extension of the existing faults across the repository is expected either, provided the repository is located far enough (more than a few kilometers

since the order of magnitude of the earth crust is typically a centimeter per year) from the nearest fault. If precaution has been taken to avoid well-known seismically active areas and to place the disposal far enough away from active faults, it is extremely unlikely that any new fault will cross the facility during its lifetime.

However, strong earthquakes are expected during the lifetime of the disposal. But their consequences should be fairly limited, if only seismic movement is weaker down in the depths than it is on the surface.

Erosion is potentially capable of exposing the disposal during its lifetime, but the risk is minimized by choosing sites on plains, where the erosion rate is smaller than 0.1 mm/year. Finally, glaciations will no doubt occur. They could slow down underground water circulation if the repository is located below the permafrost, thus increasing the efficiency of the geological barrier.

Geodynamic events liable to affect the evolution of a deep geological repository

Internal geodynamics

Tectonic phenomena

Volcanism

External geodynamics

Climatic phenomena

Effect of glaciations

Ice cap

Permafrost depth and morphology

Glacial erosion

Evolution of the sea level

Evolution aquifers (permeability, grad h)

Chemical and thermal phenomena

Chemical alteration of rocks

Erosion

Miscellaneous

Meteorites

3.2.9 The Criteria for the Choice of a Suitable Location for a Deep Geological Repository

- **Hydrogeology**
 - Low permeability
 - Small hydraulic gradients
- **Site stability**
 - No active fault, no volcanism close to the site
 - Limited consequences of glaciations

- **Chemistry**
 - Good sorption capacities of the host rock
 - Chemical stability, buffering capabilities
- **Thermal and mechanical properties**
 - Excavations must be technically feasible
 - Good heat diffusivity
- **Minimal depth**
 - Protection against erosion, earthquakes, and human intrusions
- **No natural resources underground**

3.2.10 Choice of the Host Rock for the Waste Disposal

Granite is considered as a potential host rock by North European Countries (Sweden LSR Aspö, Finland) and Switzerland (LSR Grimsel).

It is a very hard rock, a favorable factor for civil engineering. It is a well-characterized medium with a well-known water chemistry and a very low porosity ($\sim 1\%$ if not less on the local scale), a factor, which simplifies the geochemical behavior of the medium.

Its good thermal conduction properties reduce to some extent the surface area needed for the repository.

However, in granite, large-scale fractures are frequently found. These fractures could represent fast transfer pathways for radionuclides, thus hampering the confinement properties of the geological barrier.

Salt is considered as a rock suitable for hosting a repository by the USA (WIPP) and Germany (Gorleben).

Salt is the host rock of the sole operating repository: the Waste Isolation Pilot Plant (New Mexico) for military IL LL waste. Its advantages are a high thermal conductivity, low water content, and a good plasticity. Cracks in salt are self-healing.

On the other hand, salt is a natural resource, potentially exploitable by future generations, with an associated risk of a human intrusion. Salt is a medium, which can be very aggressive chemically. The corrosion phenomena must thus be under control. The complexity of the chemistry of brines (salt concentration can be as high as 5 M!) is also an important drawback of salt.

Clay rocks are studied by France (LSR Bure), Switzerland (LSR Mt Terri), Japan, and Belgium (LSR Mol).

Clays are specially interesting for geological repositories, because they can be used as engineered barriers *and* as host rocks.

Water motion in clays is very slow because of the very low permeability (in soft clays, fractures can be self-healing). Solute motion is even slower, thanks to the strong sorption capacity of clays and to their nanofiltration capabilities. Moreover, clay waters are alkaline and reducing, two factors that promote the speciation of metallic radionuclides under the form of low-solubility compounds. Clays can also protect the waste forms due to their good chemical stability, combined with their strong ability to buffer chemical perturbations.

Plastic mechanical properties (provided the clay content of the rock is sufficient) give clayey rocks interesting sealing capabilities. However, these mechanical characteristics can also be viewed as a drawback, because they entail the necessity for an important gallery-supporting structure. In addition, the clay rocks have a bad thermal conductivity, and a strong variability.

Volcanic formations are studied exclusively by the USA on the site of Yucca Mountain. This geological medium is very specific at least in one respect: it is an unsaturated medium.

3.2.11 Hydrogeology

Hydrogeology is the study of water travel underground. Water will be the vector for the travel of radionuclides released by a waste repository. This justifies an overview on hydrogeology, to describe the main mechanisms and the order of magnitude. Hydrogeology can be divided into two parts: the study of the water motion (hydrogeology proper) and migration of solutes. Hydrogeology considers the underground medium as a porous medium, characterized by its porosity and permeability (► [Figs. 98](#) and ► [99](#), ► [Table 14](#)).

Hydrogeology: the important quantities and laws

ω Porosity (proportion of the porous medium left unoccupied by minerals).

K ($\text{m} \cdot \text{s}^{-1}$) Permeability.

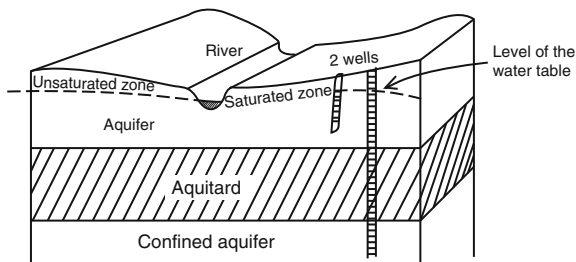
$h(\text{m})$ Hydraulic potential, that is, the pore pressure expressed in water height units, and corrected from altitude: $h \equiv P(z)/(\rho_w \cdot g) - z$.

U ($\text{m} \cdot \text{s}^{-1}$) Darcy's velocity, that is, the water flow rate through a unit surface area of the porous medium. Darcy's velocity, permeability, and hydraulic potential are related, but the Darcy's law: $U = -K \cdot \text{grad}(h)$, which says how the water moves underground under the influence of pressure gradients.

U^* ($\text{m} \cdot \text{s}^{-1}$) Microscopic velocity, average water velocity of a water molecule. $U^* = U/\omega$.

Aquifer: Underground medium containing much water, and permeable enough to allow the circulation of this water.

Aquitard: Underground medium with little permeability.



■ **Figure 98**

Aquifers and aquitards in a typical sedimentary basin

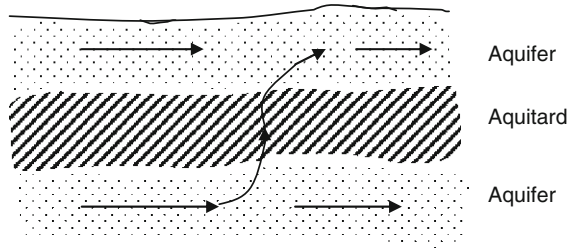


Figure 99

The travel of water underground is generally vertical in aquitards and horizontal in aquifers

Table 14

Orders of magnitude for the permeability, porosity, and water velocity in aquifers and aquitards

	Permeability $K (m \cdot s^{-1})$	Porosity ω	Typical hydraulic gradient Grad h	Microscopic water velocity $U^* (m \cdot s^{-1})$
Aquitard	10^{-11}	$2 \cdot 10^{-1}$	1	$5 \cdot 10^{-11}$ (1.5 mm/year)
Aquifer	10^{-6}	$3 \cdot 10^{-1}$	10^{-3}	$3 \cdot 10^{-9}$ (10 mm/year)

The repository is placed in an aquitard, where the motion of water is very slow (► Fig. 98).

In general, the place of the repository will be below the water table. This means that in the surroundings of the repository, the host rock will be water-saturated.

The only exception is the site of Yucca Mountain (USA), located in a desert where the water table is very low, below the place foreseen for the repository.

3.2.12 Calculation of Water Flow in a Permeable Porous Medium

In the far field, one is interested mainly in determining the direction and velocity of the underground water fluxes. One assumes generally permanent flow regime. The rock is described as a porous permeable medium with imposed hydraulic potential. In those conditions, the problem would be mathematically very simple in the case of a homogeneous medium, with the same permeability everywhere. Unfortunately, the rock is, in general, very heterogeneous, and even fractured. The permeability of an equivalent homogeneous porous medium is then determined by means of homogenization techniques, which request good statistical information on the medium heterogeneities to determine the representative elementary volume (REV). In very heterogeneous media, for example, fractured media with a wide hierarchy of fracture sizes, homogenization over an REV may be illegitimate. In this case, large fractures must be taken into account explicitly, one by one.

3.2.13 Radionuclide Migration

Hydrogeology addresses the motion of water in the geosphere. It will be seen below that the migration of radionuclides is more complicated than transport under the sole influence of water *advection*, because of physicochemical effects like *diffusion and dispersion* (► Fig. 100). In addition to these three phenomena, chemical interactions between the solute and the porous skeleton must be taken into account.

Three main phenomena cause the migration of solutes in a porous media: molecular *diffusion*, kinematic *dispersion* and *advection*.

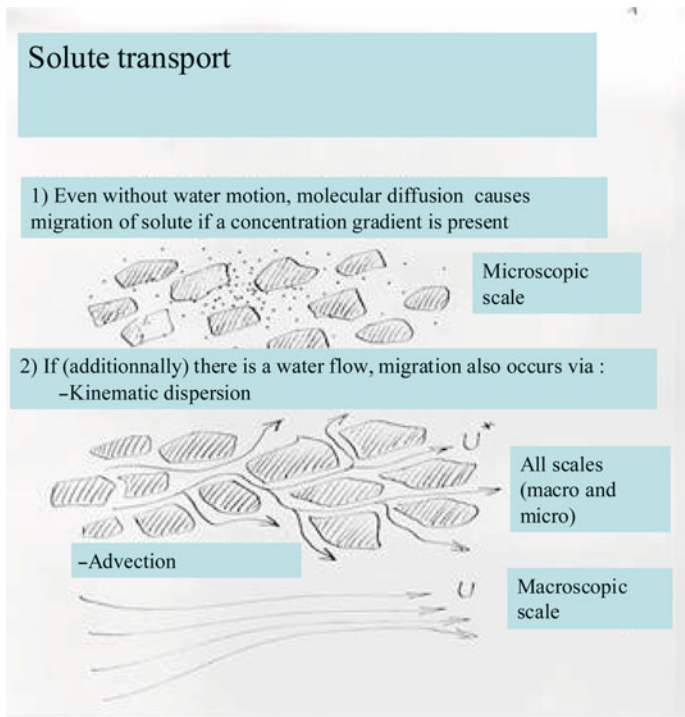
Advection is a very simple transport mechanism: the solute follows the water in its travel. The advective flux of solute is equal to

$$\mathbf{j} = \mathbf{c} \cdot \mathbf{U},$$

where c is the solute concentration and U is the Darcy velocity.

Diffusion occurs whenever a population of microscopic objects (atoms, molecules, electrons, ions, neutrons, etc.) collides with obstacles in the medium.

Diffusion is governed by the Fick's law, which relates the solute flux j to the solute concentration c :



■ Figure 100

The three main phenomena that cause the migration of solutes in a porous media are molecular *diffusion*, kinematic *dispersion*, and *advection*

3.2.14 Kinematic Dispersion

The flow in a porous medium is broken by the solid objects that constitute the skeleton of the medium. These dispersing objects can be of any size. They can be microscopic clay minerals, grains of sand, or rock blocks delimited by fractures.

The motion of a water molecule in this network resembles a random walk, and can be described by an effective tensor diffusion coefficient D_{kin} , which depends on the speed of the flow and on the size of the dispersing objects. If the dispersing medium is isotropic, the tensor D_{kin} reduces to a scalar:

$$D_{kin} = \alpha \cdot |U|.$$

The quantity α is the *dispersivity* of the medium. It is equal to the size of the largest dispersing objects in the geological medium. The dispersivity can be measured via tracer experiments. If the medium is heterogeneous and contains several scales of heterogeneity with a hierarchy in size, alpha will depend on the scale of the experiment.

➤ *Table 15* gives orders of magnitude for the dispersivity and kinematic dispersion of geological media:

Generally, in aquifers, alpha and U are large: the kinematic dispersion dominates over the molecular diffusion. The opposite is true in aquitards.

The phenomenon of kinematic dispersion is important to describe the dilution of tracers or pollutants in an aquifer.

■ **Table 15**
Typical dispersion in geological media

Media	Dispersivity (m)	Typical Darcy velocity (m · s ⁻¹)	Kinematic dispersion (m ² · s ⁻¹)
Sand	1 · e-3	1 · e-6	1 · e-9
Granite(fractured)1	1 · e-6	1 · e-6 (dominant)	
Clay	1 · e-8	1 · e-12	1 · e-20 (negligible)

3.2.15 The Tracer Equation

The contributions of solute flux due to molecular diffusion, kinematic dispersion, and advection must be added to obtain the total solute flux.

$$\vec{j} = \underset{\substack{\uparrow \\ \text{Solute} \\ \text{flux}}}{-D_{mol}} \cdot \underset{\substack{\uparrow \\ \text{Molecular} \\ \text{diffusion}}}{grad} \vec{c} - \overline{\overline{D}}_{Kin} \cdot \underset{\substack{\uparrow \\ \text{Kinematic} \\ \text{dispersion}}}{grad} \vec{c} + c \cdot \underset{\substack{\uparrow \\ \text{Advection}}}{\vec{U}}$$

The conservation law applied to the solute writes:

$$\frac{\partial c}{\partial t} = -\frac{1}{\omega} div(\vec{j}) - \lambda \cdot c$$

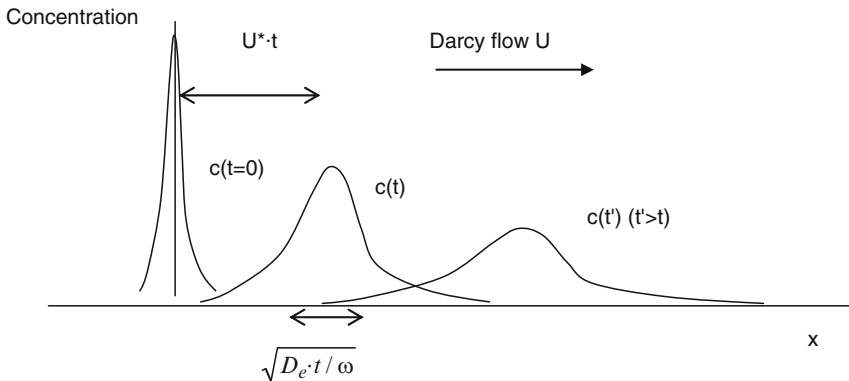
The term $\lambda \cdot c$ has been added to describe the case of a radioactive solute, which decays with a radioactive constant λ .

In the case of an isotropic medium, the concentration of radioactive solute obeys the equation:

$$\frac{\partial c}{\partial t} = \frac{1}{\omega} \left(D_e \cdot \Delta c - \vec{U} \cdot \text{grad}(c) \right) - \lambda \cdot c. \tag{2}$$

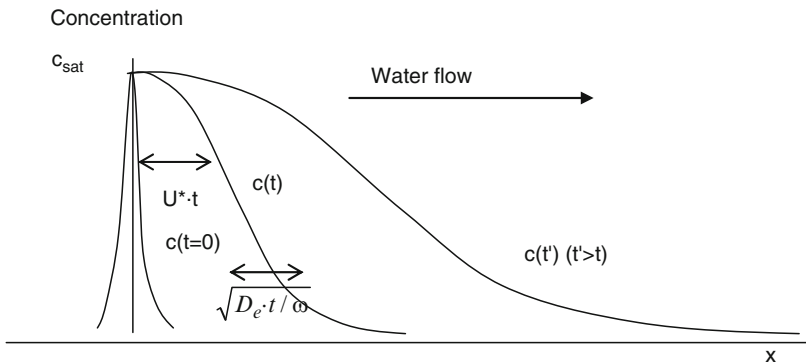
The equation above is the master equation, which describes the migration of the solute. It tells how the concentration field evolves in space and time.

This equation looks like a diffusion equation, with an added term associated to convection.



■ Figure 101

Solution of the one-dimension tracer equation in the special case of an instant and local release of a limited quantity of tracer. The plume shifts downstream by advection, with velocity U^* . It also spreads by diffusion, and its width increases as the square root of time



■ Figure 102

Solution of the one-dimensional tracer equation in the special case of a permanent and local release of tracer, limited by a saturation concentration. The plume keeps a constant concentration in the vicinity of the source. It extends downstream by advection with velocity U^* , and spreads by diffusion. The width of the concentration front is $\text{sqrt}(D \cdot t / \omega)$

Examples of solutions of the tracer equation in particularly simple cases are given below (Figs. 101–103)

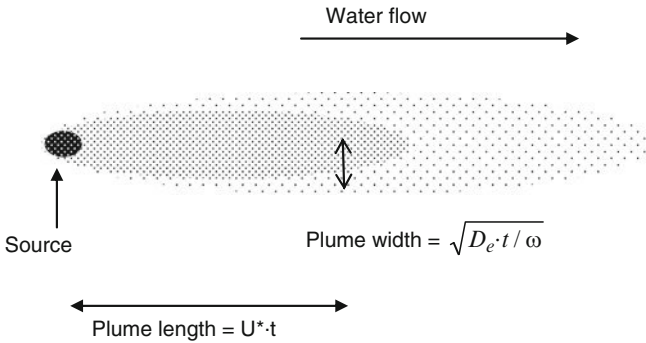


Figure 103

Solution of the two-dimensional tracer equation in the special case of a permanent and local release of tracer, limited by a saturation concentration. In 2D, the flow has a cylindrical symmetry with respect to the axis defined by the water flow. The picture here is a cut of the plume across a plane containing the source and this axis

3.2.16 Characteristic Migration Time Through a Geological Barrier

We give here the order of magnitude of the migration time of a perfect tracer (no chemical interaction with the porous medium) through a geological barrier made of a homogeneous clay layer. We consider two extreme cases (Figs. 104 and 105):

1. Pure advection, under a typical hydraulic gradient of 1 m/m
2. Pure molecular diffusion (no hydraulic gradient)

The advective migration time is $\tau_{adv} = \frac{X \cdot \omega}{K \cdot |gradh|}$.

The diffusive migration time is $\tau_{diff} = \frac{X^2 \cdot \omega}{D_e}$.

With the transport characteristics of a typical clay layer (Table 16), $\tau_{adv} = 70,000$ years, and $\tau_{diff} = 6$ million years. These long travel times are favorable to the safety of repositories. It can be seen from this example that the advective migration time is shorter than the diffusive migration time. This dominance of advection over diffusion is general in the case of solute transport through hectometric geological barriers.

The Péclet number is a convenient indicator of the dominant transport mode. It is defined as the ratio between the diffusive and advective characteristic times through a barrier of thickness X:

$$Pe = \frac{\tau_{diff}}{\tau_{adv}} = \frac{X \cdot U}{D_e}$$

If the Péclet number is smaller than 1, that is, if the diffusion time is smaller than the advection time, diffusion dominates over advection. If $Pe > 1$, advection dominates over diffusion

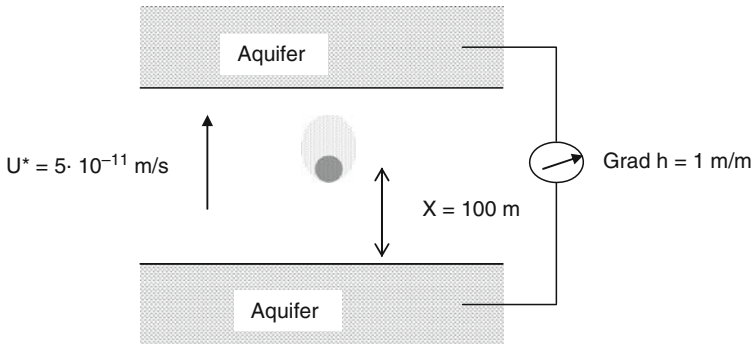


Figure 104
Advective migration

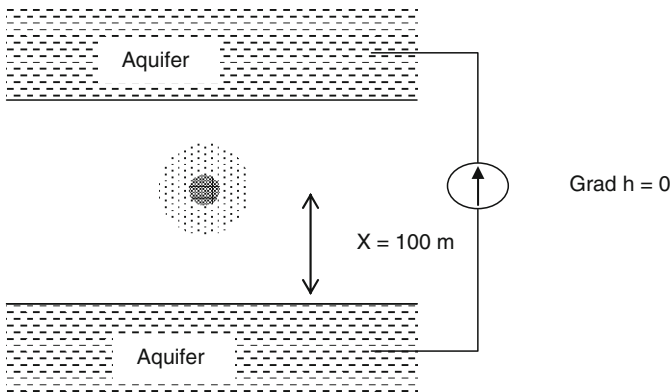


Figure 105
Diffusive migration

Table 16

Typical transport properties of a clay layer usable for hosting a repository

Permeability K ($\text{m}\cdot\text{s}^{-1}$)	10^{-11}
Porosity ω	0.2
Effective diffusion constant De ($\text{m}^2\cdot\text{s}^{-1}$)	10^{-11} (kinematic dispersion is negligible compared to molecular diffusion)
Hydraulic gradient grad (h) (m/m)	1
Layer thickness X (m)	100

For more detailed data, see, for example, Distinguin and Lavanchy (2007)

(Fig. 106). For values of Péclet numbers of the order of unity, both phenomena come into play. Advective transport generally dominates over diffusive transport for large space scales. This is generally the case for transport of solutes from a geological repository.

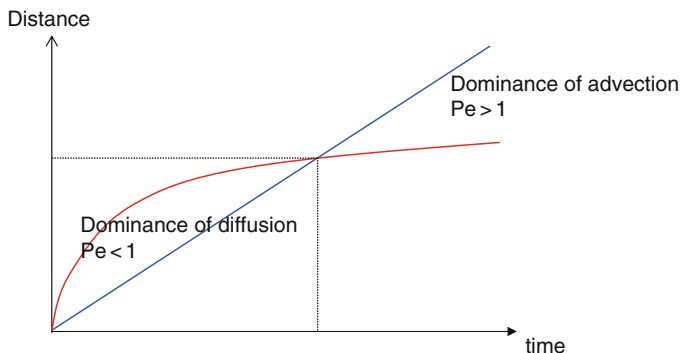


Figure 106 The average travel distance of a tracer as a function of time, in the case of diffusion (red) and advection (blue)

3.2.17 Sorption of a Non-Perfect Tracer

We consider here the case of a non-perfect tracer, that is, a tracer which is able to be sorbed onto the mineral surface of the porous medium (► Fig. 107).

We consider here the case of a species A, which can exist both in solution and sorbed on the free surface of the porous medium. We introduce two concentrations: c is the concentration of species A in solution, and γ is the concentration of this species in sorbed form. Concentration c is expressed in $\text{kg} \cdot \text{m}^{-3}$, and γ in $\text{kg} \cdot \text{kg}^{-1}$.

One observes an equilibrium between the sorbed ions and the ions in the solution.

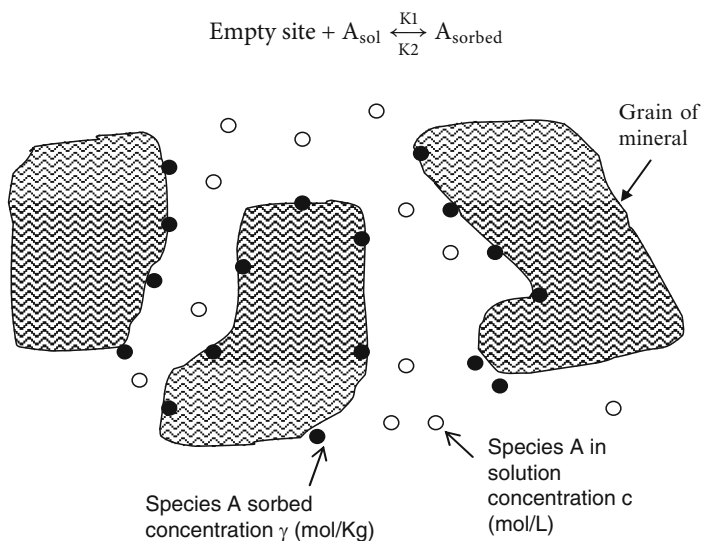


Figure 107 Sorption in a porous medium

■ **Table 17**
Values of Kd for caesium

Phase solide	CEC (méq/100g)	BET (m ² /g)	pH	Kd (mL/g)
Montmorillonite	87	722	8.7	1,120
Vermiculite	77	313	8.2	58,767
Biotite	15	69	8.2	61,000
Illite	14	165	5.9	12,947
Kaolinite	5	31	6.8	909
Albite	1.5	8	7.8	519
Microcline	1.2	5	7.8	319
Chlorite	5	24	8–9	~ 5
Goethite	11	39	2–11	0
Hematite	0.05	1.8	8–9	6
Quartz	0.02	2.8	8–9	1
Calcite	0.02	2.9	8–9	1
Pyrite	0.15	7.0	8–9	3
Cements	--	--	10–13	10–100

Note: Note the very high value and large variability of Kd coefficients for different clay minerals
Source: Poinssot et al. (1999)

For a dilute solution, the law of mass action

$$\rho \cdot \gamma = \frac{K_1}{K_2} \cdot c$$

predicts a linear relationship between the number of ions in solution and the number of sorbed ions. The proportionality constant is denoted Kd(m³/kg).

Exact definition is

$$Kd \equiv \frac{\gamma}{c} = \frac{1}{\rho} \cdot \frac{K_1}{K_2}$$

This distribution coefficient Kd, that is, the ratio γ/c , can be measured in experiments where a known quantity of solute is put in contact during a long time with a known quantity of mineral. After reaching the sorption equilibrium, the quantity of species A remaining in solution is measured by titration. The distribution coefficient of caesium is given in ► [Table 17](#).

Note that the distribution coefficient Kd is constant (independent of Cs concentration) only for small values of the Cs concentration. For values higher than about 10⁻⁵ mol/L, the saturation of the sorption sites comes into play. Other factors, like the presence of chloride or carbonate ions influence the sorption equilibria and modify the Kd value. The distribution coefficient of different chemical species on bentonite is shown in ► [Fig. 108](#).

Several types of sorption sites can coexist in the same mineral, with different equilibrium constants. Their successive saturation gives several plateaux in the sorption isotherm (► [Table 18](#)).

The Kd model has many shortcomings, and its validity is limited by strong hypotheses:

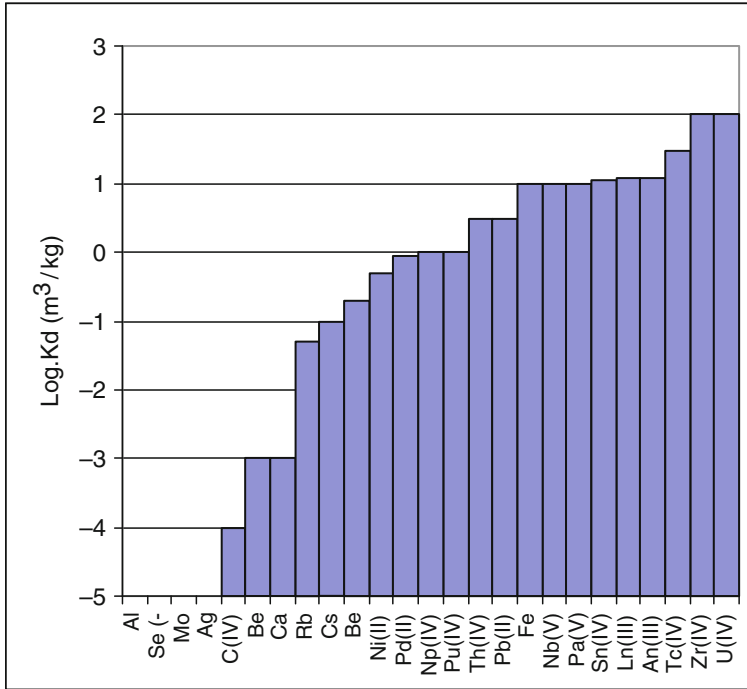


Figure 108

Classical distribution coefficient at neutral pH for different radionuclides on a smectite-rich material used for bentonite engineered barrier, MX80

- The number of sorption sites is supposed to be large compared to the number of ions.
- The kinetic aspects of the sorption reaction are neglected (hypothesis of a reversible reaction, in thermodynamic equilibrium).

Consequently, the distribution coefficient K_d is not universal. It depends on the cation, the mineral, and the water composition (existence of concurrent ions, in particular H^+). Even on a pure mineral phase, several types of sorption sites can coexist, with various K_d values. Furthermore, in general, a natural rock is composed of many minerals.

Despite its shortcomings, the K_d model will probably remain in wide use, because of its convenience, which comes from a very simple property: the migration of a linearly sorbing tracer is the same as the one for a nonsorbing tracer, except for one thing: *it is retarded by a constant factor*. This retardation factor depends on the sorbing capability of the medium for the migrating chemical species.

For a more detailed treatment of sorption onto minerals, see Limousin et al. (2007) and Beaucaire et al. (2008).

3.2.18 Migration of a Sorbing Tracer

We consider here the case of a species A which can both sorb on the free surface of the porous medium and migrate through this medium. Here, we no longer assume that equilibrium is

■ Table 18

Value of the transport parameters of some radionuclides in the Callovo-Oxfordian claystone

	Horizontal permeability $K_h = 5.10^{-13}$ m/s				
	Vertical permeability $K_v = 5.10^{-14}$ m/s				
	Period (years)	$\omega_{\text{Diffusion}}$ (-)	De (m ² /s)	R (-)	C_{sat} (mol/m ³)
¹⁰ Be	1,600,000	0.18	$2.5.10^{-10}$	31,900	10^{-2}
¹⁰ Be (delta T > 20)	1,600,000	0.18	$2.5.10^{-10}$	3,200	10^{-2}
¹⁴ C	5,730	0.05	5.10^{-12}	5.6	2.3
³⁶ Cl	302,000	0.05	5.10^{-12}	1	Soluble
⁴¹ Ca	103,000	0.18	$2.5.10^{-10}$	16	2.3
⁴¹ Ca (delta T > 20)	103,000	0.18	$2.5.10^{-10}$	2.5	2.3
⁵⁹ Ni	75,000	0.18	$2.5.10^{-10}$	2,050	5.10^{-2}
⁷⁹ Se	65,000	0.05	5.10^{-12}	1	5.10^{-7}
⁹³ Zr	1,530,000	0.18	$2.5.10^{-10}$	12,800	2.10^{-5}
⁹³ Mo	3,500	0.05	5.10^{-12}	139	1.10^{-5}
⁹³ mNb	16.4	0.05	5.10^{-12}	53,400	2.10^{-4}
⁹⁴ Nb	20,300	0.05	5.10^{-12}	53,400	2.10^{-4}
⁹⁹ Tc	213,000	0.18	$2.5.10^{-10}$	128,000	4.10^{-6}
¹⁰⁷ Pd	6,500,000	0.18	$2.5.10^{-10}$	8,950	4.10^{-4}
¹²⁶ Sn	100,000	0.18	$2.5.10^{-10}$	179,000	1.10^{-5}
¹²⁹ I	15,700,000	0.05	5.10^{-12}	1	Soluble
¹⁶⁶ mHo	1,200	0.18	$2.5.10^{-10}$	639,000	1.10^{-4}
¹³⁵ Cs	2,300,000	0.18	$2.5.10^{-10}$	Langmuir*	Soluble
			* Langmuir : $K_d = 1.8462.10^{-7} / (4.7552.10^{-7} + C_{\text{eq}})$		
			Ceq : solute concentration (mol/L)		

Source: ANDRA (2005), dossier argile

reached everywhere in the porous medium, and we allow the migration of the solute, by the mechanisms (diffusion, dispersion, advection) described above.

The concentration of species A in solution and in sorbed form depends on space and time: $c = c(x, t)$ and $\gamma = \gamma(x, t)$. In order to determine the evolution of the concentration field in space and time, one must take into account both solute transport and the kinetics of the sorption reaction.

$$\begin{aligned} dc/dt &= TT + KT \\ d(\rho \cdot \gamma)/dt &= -KT \end{aligned}$$

where TT is the transport term of the tracer equation (2), and KT is the kinetic term:

$$KT = K_2 \cdot \rho \cdot \gamma - K_1 \cdot c.$$

In the case of a sorbing tracer, the equations for chemistry and transport are thus coupled.

If the chemical reaction is locally at equilibrium, one can write a relationship between the time derivative of concentrations in solution and in sorbed form (weak formulation of the law of mass action):

$$d(\rho \cdot \gamma)/dt = (K_1/K_2) \cdot dc/dt.$$

The ratio between these two quantities is the distribution coefficient K_d introduced previously. With this assumption, the equation of the evolution of the solute concentration becomes

$$dc/dt \cdot (1 + K_1/K_2) = TT.$$

This equation is formally identical to the transport equation for a non-sorbing tracer

$$dc/dt = TT,$$

with an important difference: the migration is R times slower, where R is a retardation factor given by

$$R = 1 + \rho^* K_d.$$

The exit time of a solute tracer across a barrier can be calculated:

$$\tau_{solute} = R \cdot \tau_{water},$$

where τ_{water} is the migration time of a water molecule (or of a non-sorbing tracer), as given by the tracer equation (2) (► Table 19).

Note that the porosity of clay is not accessible in the same way for all radionuclides: the clay minerals are negatively charged, and repel the anions. This **anionic exclusion** effect reduces the porosity accessible to anions (► Fig. 109).

For the same reason (electrostatic repulsion), anions are generally not sorbed on the porous skeleton: the retardation factor of anions (Cl, Se, I) is unity.

Typical values for the transport parameters of some radionuclides in claystones are given in ► Table 18.

The understanding and microscopical description of ion sorption phenomena onto rock minerals is an important challenge for geochemists.

3.2.19 Migration of Actinides

Laboratory experiments (Dossier ANDRA 2005) suggest that the actinides are very efficiently sorbed on many minerals present underground (especially clay minerals), and are therefore almost immobile in underground environment (total immobility would correspond to an infinite retardation factor R).

Indeed the *retardation factor* of actinides can be very large (of the order of 1,000) (see ► Table 19). For the Callovo-Oxfordian clay, precise values of retardation factors can be found in ANDRA and Dossier (2005), dossier argile.

■ **Table 19**
Transport of actinides in clay environment

	Callovo-Oxfordien					
	$K_h = 5 \cdot 10^{-13} \text{m/s}$ $\rho = 2,300 \text{ kg/m}^3$					
	$K_v = 5 \cdot 10^{-14} \text{m/s}$ $\omega_{\text{Diffusion}} = 0.09$					
	Period (years)	$\omega_{\text{Diffusion}}$ (-)	De (m^2/s)	Kd (m^3/kg)	R (-)	C_{sat} (mol/m^3)
^{244}Cm	18.1	0.18	$2.5 \cdot 10^{-10}$	50	638,900	4.10^{-4}
^{240}Pu	6,560	0.18	$2.5 \cdot 10^{-10}$	0.9	11,500	2.10^{-4}
^{236}U	23,400,000	0.18	$2.5 \cdot 10^{-10}$	8	102,200	7.10^{-4}
^{232}Th	1,410,000,0000	0.18	$2.5 \cdot 10^{-10}$	8	102,200	6.10^{-4}
^{245}Cm	8,500	0.18	$2.5 \cdot 10^{-10}$	50	638,900	4.10^{-4}
^{241}Pu	14.4	0.18	$2.5 \cdot 10^{-10}$	0.9	11,500	2.10^{-4}
^{241}Am	433	0.18	$2.5 \cdot 10^{-10}$	50	638,900	4.10^{-4}
^{237}Np	2,140,000	0.18	$2.5 \cdot 10^{-10}$	0.9	11,500	4.10^{-4}
^{233}U	159,000	0.18	$2.5 \cdot 10^{-10}$	8	102,200	7.10^{-4}
^{229}Th	7,340	0.18	$2.5 \cdot 10^{-10}$	8	102,200	6.10^{-4}
^{246}Cm	4,730	0.18	$2.5 \cdot 10^{-10}$	50	638,900	4.10^{-4}
^{242}Pu	374,000	0.18	$2.5 \cdot 10^{-10}$	0.9	11,500	2.10^{-4}
^{238}U	4,470,000,000	0.18	$2.5 \cdot 10^{-10}$	8	102,200	7.10^{-4}
^{234}U	246,000	0.18	$2.5 \cdot 10^{-10}$	8	102,200	7.10^{-4}
^{230}Th	75,400	0.18	$2.5 \cdot 10^{-10}$	8	102,200	6.10^{-4}
^{226}Ra	1,600	0.18	$2.5 \cdot 10^{-10}$	1	12,800	1.10^{-4}
^{210}Pb	22.3	0.18	$2.5 \cdot 10^{-10}$	0.16	2,050	4.10^{-4}
^{243}Am	7,370	0.18	$2.5 \cdot 10^{-10}$	50	638,900	4.10^{-4}
^{239}Pu	24,100	0.18	$2.5 \cdot 10^{-10}$	0.9	11,500	2.10^{-4}
^{235}U	704,000,000	0.18	$2.5 \cdot 10^{-10}$	8	102,200	7.10^{-4}
^{235}Pa	32,800	0.18	$2.5 \cdot 10^{-10}$	1	12,800	1.10^{-4}
^{227}Ac	21.8	0.18	$2.5 \cdot 10^{-10}$	50	638,900	4.10^{-4}

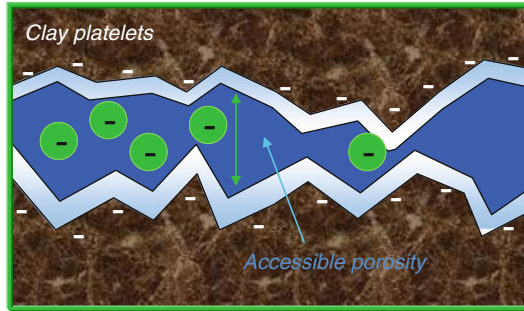
Source: ANDRA (2005), dossier argile. See also Hu et al. (2008)

3.2.20 Radionuclide Speciation and Solubility Limits

We have seen above that the solute concentration was limited by *sorption*.

We see here that it can also be limited by *solubility limits*, which depend on the speciation of the considered element in the geological environment.

► *Figures 110* and ► *111* show the example of the speciation and solubility of neptunium. In oxidizing conditions, Np can be in soluble form (ionic). In reducing conditions, Np is



■ Figure 109

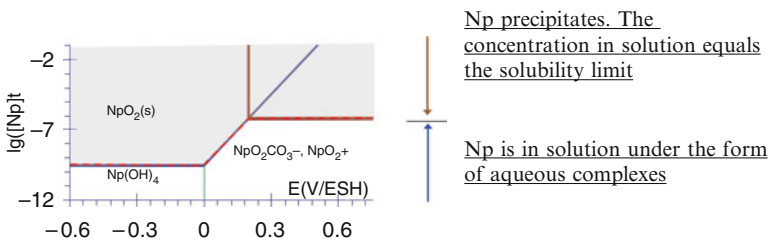
Origin of anionic exclusion within clay-rich rocks. Due to the presence of negatively charged surfaces, anions have only access to a restricted part of the porosity, here the darker blue part (Descostes et al. 2008)

Existence of a maximal concentration in solution, depending on the physico-chemical conditions

Extremely low solubility limits for actinides

Strong limitation of the actinide amounts able to migrate

The example of Np speciation as a function of the redoxpotential



■ Figure 110

The example of Np speciation and solubility as a function of the redox potential in underground environment (From Vitorge and Poinssot 2005)

in solid form (oxide or hydroxide). This behavior is qualitatively the same for most metallic atoms.

Solubility of a species depends on the ionic content of the water. In principle, one should give a solubility product taking into account all the ions playing a role in the dissolution process. In practice, we give in [Table 20](#) a solubility domain for a typical water composition found underground (pH = 8, reducing conditions).

As a rule of thumb, the actinides present underground with the oxidation degree III and IV are immobile, whereas those with the oxidation degrees V and VI are more mobile ([Table 20](#), [Fig. 112](#)).

In the reducing conditions typical of underground environments, most actinides are immobile.

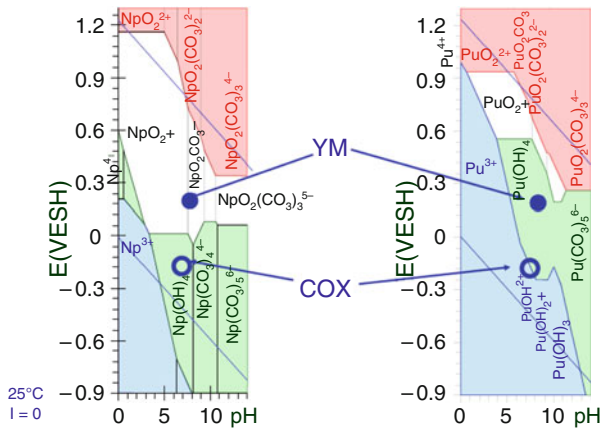


Figure 111

Pourbaix diagram of neptunium describing the dominant aqueous species as a function of pH and redox potential (E measured by comparison to hydrogen saturated electrodes) (Vitorge et al.). The red, white, green, and blue fields correspond to the respective stability fields of hexavalent, pentavalent, tetravalent, and trivalent Np. The open circle describes the chemical conditions measured in the French underground research laboratory (Meuse/Haute-Marne), whereas the open circle corresponds to the chemical conditions measured at Yucca Mountain. The dominant Np aqueous species is different in both cases, thus explaining the difference of Np mobility in these two underground environments (Lemire et al. 2001)

However, actinide migration has indeed been observed in some cases, for example, on the Nevada test site and in Mayak. This migration has been ascribed to actinide-bearing colloids (Kersting 1999; Ewing et al., 2006). The possibility of actinide migration via colloids is still an active field of investigation.

3.2.21 Porewater Chemistry

In order to determine the radionuclide speciation, one must know the ionic content of the water.

The composition of the porewater is determined by rock-water equilibria:

- Reactions of dissolution-precipitation: $A_nB \leftrightarrow nA^- + B^{n+}$, governed by a solubility product $K_s = (A^-)^n \cdot (B^{n+})$
- Interfacial ion-exchange reactions, for example, $\text{Mineral-Na} + C^+ \leftrightarrow \text{Mineral-C} + Na^+$

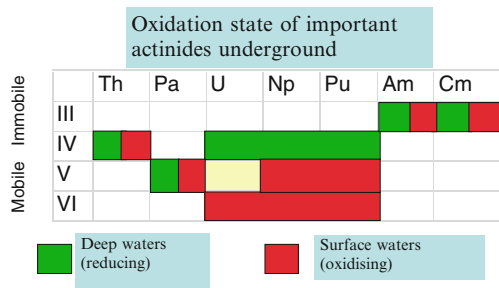
Many minerals come into play in these equilibria. In order to determine the groundwater composition, one must know the mineralogical composition of the rocks with which it is equilibrated. Even minerals present in small quantities in the rock can play an important role in determining (buffering) the water composition.

➤ Table 21 gives the composition of the Callovo-Oxfordian claystone. ➤ Table 22 gives the composition of the corresponding porewater.

■ Table 20

The dominant radionuclide speciation and solubility in underground waters (pH = 8, reducing conditions)

Radionuclide	Solubility limit (mol/L) min. value	Solubility limit (mol/L) ref. value	Solubility limit (mol/L) max value
Sélénium (-II) (sulfure)	1.10^{-10}	1.10^{-9}	1.10^{-8}
Zirconium (oxyhydroxyde)	2.10^{-12}	2.10^{-11}	2.10^{-10}
Palladium (oxyhydroxyde ?)	$1,5.10^{-7}$	$1,5.10^{-6}$	$1,5.10^{-5}$
Technétium (IV) (oxyhydroxyde)	2.10^{-9}	2.10^{-8}	2.10^{-7}
Etain (IV) (oxyhydroxyde)	1.10^{-10}	1.10^{-9}	1.10^{-8}
Neptunium (IV) (oxyhydroxyde)	2.10^{-11}	2.10^{-9}	2.10^{-7}
Uranium (IV) (oxyhydroxyde)	1.10^{-11}	1.10^{-9}	1.10^{-7}
Thorium (oxyhydroxyde)	2.10^{-12}	2.10^{-10}	2.10^{-8}
Américium (III) (oxyhydroxyde)	2.10^{-10}	2.10^{-8}	2.10^{-6}
Plutonium (IV) (oxyhydroxyde)	2.10^{-10}	2.10^{-8}	2.10^{-6}
Curium (III) (oxyhydroxyde)	2.10^{-10}	2.10^{-8}	2.10^{-6}
Protactinium (V) (oxyhydroxyde)	3.10^{-8}	3.10^{-7}	3.10^{-6}
Radium (II) coprécipité	1.10^{-14}	1.10^{-13}	1.10^{-12}
Niobium (V) (oxyhydroxyde)	1.10^{-9}	1.10^{-8}	1.10^{-7}
Nickel (II) (sulfure)	1.10^{-10}	1.10^{-9}	1.10^{-8}
Iode (-I)		Soluble	
Carbone (carbonates)		Soluble	
Césium (soluble) coprécipité	Soluble 1.10^{-8}	Soluble 1.10^{-7}	Soluble 1.10^{-6}



■ Figure 112

Oxidation state of important actinides underground

■ Table 21

The mineralogical composition of the Callovo-Oxfordian claystone

Composition minéralogique des argillites du COX (% pondéral)	
Muscovite	12.5
Illite	22.5
Montmorillonite-Ca	15
Daphnite (chlorite Fe)	1.5
Kaolinite	0.5
Quartz	25
Calcite	17
Dolomite	3
Feldspath-K	2
Pyrite	1

■ Table 22

The composition of the porewater of the Callovo Oxfordian claystone. Its reducing and slightly alkaline character is characteristic of clay environments

Parameter	Best estimate	Conservative
Eh (mV)	-156	-180
pH	7.0	7.3
Ionic strength (mol/l)	0.12	0.09
Alkalinity (mol/l)	$2.5 \cdot 10^{-3}$	$1.4 \cdot 10^{-3}$
Cl (mol/l)	$3.0 \cdot 10^{-2}$	$1.5 \cdot 10^{-2}$
S(VI) (mol/l)	$3.4 \cdot 10^{-2}$	$3.1 \cdot 10^{-2}$
Na (mol/l)	$3.2 \cdot 10^{-2}$	$2.6 \cdot 10^{-2}$
K (mol/l)	$7.1 \cdot 10^{-3}$	$6.2 \cdot 10^{-3}$
Ca (mol/l)	$1.5 \cdot 10^{-2}$	$1.1 \cdot 10^{-2}$
Mg (mol/l)	$1.4 \cdot 10^{-2}$	$1.1 \cdot 10^{-2}$
Fe (mol/l)	$3.3 \cdot 10^{-4}$	$7.1 \cdot 10^{-5}$
Si(aq) (mol/l)	$9.4 \cdot 10^{-5}$	$9.4 \cdot 10^{-5}$

Source: Motellier et al. (2003), Leroy et al. (2007)

3.2.22 How to Evaluate the Transport of RN Underground

The four steps of modeling of the transport of radionuclides underground are the following (➤ Fig. 113):

1. Rock-water equilibrium determines the *porewater composition*.
2. The characteristics of porewater (ion content, and more specifically pH, eH, $p\text{CO}_2$) determine the *radionuclide speciation*.

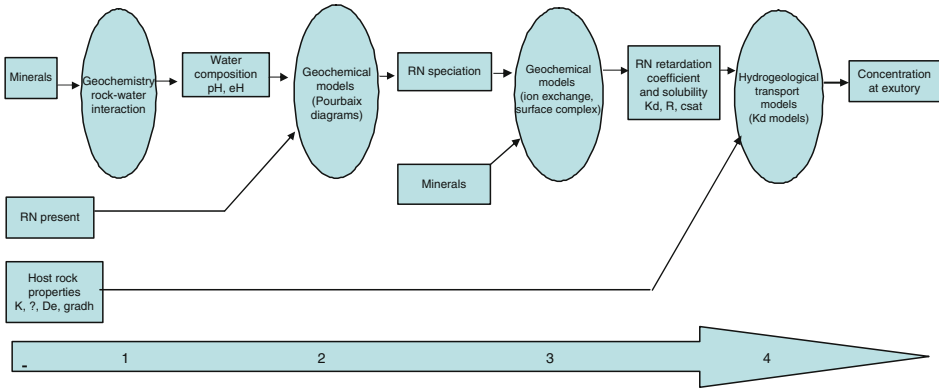


Figure 113

The four steps of modeling of the transport of radionuclides underground

3. The speciation of RN determines the *solubility* and *sorption* properties of these radionuclides.
4. Solubility and sorption properties determine the way RNs are *transported* underground.

The three first steps pertain to geochemical modeling with one single generic formalism: the law of mass action.

3.2.23 Validation of the Models of RN Transport Underground

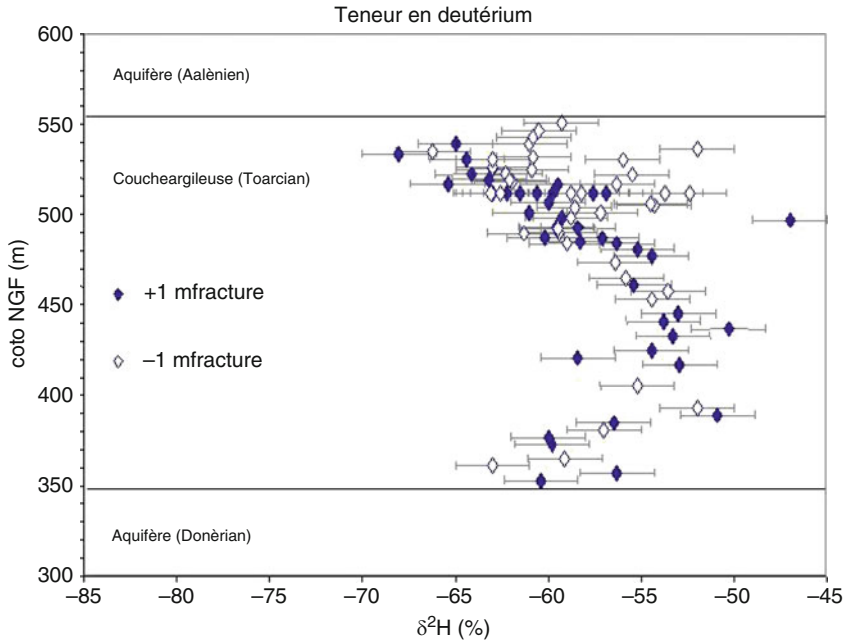
Tracer experiments investigate the migration of radionuclides in the host rock by injecting a cocktail of tracers in a borehole. The rock around the injection point is then analyzed after some time (typically 1 year) to determine the migration distance of the various chemicals in the cocktail.

In clays, this migration distance in 1 year is very small (typically centimeters for non-sorbing tracers, depending on the modalities of the experiment, that is, pure diffusion or advection under the influence of an imposed pressure gradient). Given the reduced time and distance scales involved, these experiments cannot provide direct clues of the efficiency of the geological barrier. Natural analogues give evidence for tracer migration on larger time and length scales (Fig. 114). Generally, tracer experiments permit us to validate migration models, and participate in building the confidence in the safety of deep geological repositories.

The travel of nonreactive species through a geological barrier is already very slow. Reactive tracers are R times slower ($R = 10, 100, 1,000$ depending on the considered species, cf. Kd model). It is difficult to do human scale experiments to check this.

However, *natural tracers* enable us to study the migration of chemical species in the geosphere on large time and space scales. The principle is to measure the present distribution of some chemical or isotopic species in the geological medium. In order to reconstruct their migration during past eras, the source term must be known.

An example of useful natural tracers is the chloride ion and stable isotopes of water.



■ Figure 114

An example of natural tracer in the claystone of Tournemire (Aveyron): the analysis of the deuterium in the clay porewater shows that the migration of water through the argillaceous layer is very slow. Despite the very ancient age of the clay layer (Toarcian, 180 million years), the initial composition of the water (initially, seawater) has been partially preserved at the center of the layer. Close to the upper and lower aquifers, the isotopic composition of the porewater becomes equal to the composition of rainwater. The deuterium concentration profile has been measured along a vertical borehole across the horizontal layer. The profile is smooth for samples measured far from tectonic fractures (full points) and more irregular for samples measured close to the fractures (empty points). This suggests that fractures played a role in the migration of the tracer. (Source: Y. Moreau Le Golvan, IPSN). The shape of the deuterium profile in the unfractured region permits us to deduce a diffusion constant in the claystone, which matches the measurements made on samples ($10^{-12} \text{m}^2 \cdot \text{s}^{-1}$)

All the knowledge gained on RN migration will be applied to modeling of the *radionuclide travel* through the geosphere.

The radionuclides will be released slowly by the package through the near-field (altered package, engineered barrier), and will start their travel through the host rock, if they have not yet decayed. In all cases, they will be trace elements in the geological system, and will therefore obey the chemical conditions dictated by the major chemical constituents of the geological environment.

The rate of release of the radionuclides depends on the phenomena taking place in the near-field.

3.2.24 Thermo-Hydro Mechano-Chemical Effects in the Near-Field of a Geological Repository

In the near-field, one has to take into account simultaneously four types of effects:

1. Thermal (the waste generates heat)
2. Hydraulic (desaturation-resaturation of the host rock)
3. Mechanical (decompression due to the excavation; dilation; shrinkage/swelling)
4. Chemical (oxidation and other chemical perturbations of the host rock due to its exposure to air and to foreign elements)

It will be shown that THMC phenomena are *coupled*.

3.2.25 Thermal Behavior of High-Activity Waste

As has been seen in the section devoted to the architecture of the repository, a careful modeling of the thermal behavior of high-activity waste in a geological repository is important to avoid uncontrolled heating of the waste and of the surrounding rock. We give here the data necessary to perform such calculations (► Figs. 115 and ► 116, ► Table 23).

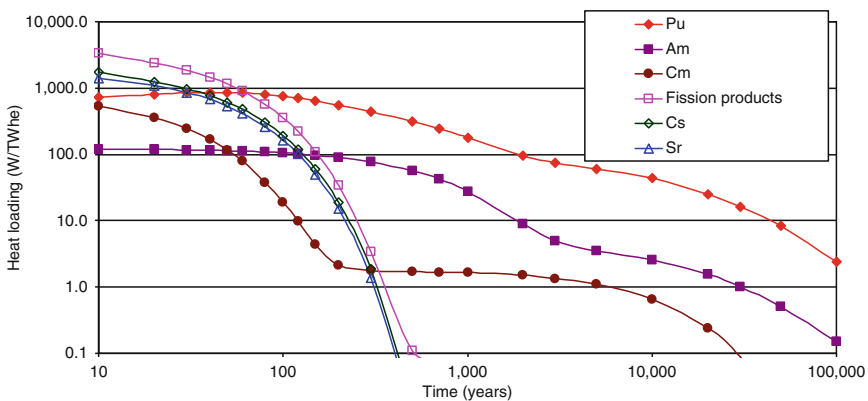


Figure 115

Heat emission contributors in spent fuel (UOX, 45 GWd/t, 4 years cooled). For short times, the residual power of spent fuel is dominated by short-lived fission products. For $t > 100$ years, actinides dominate

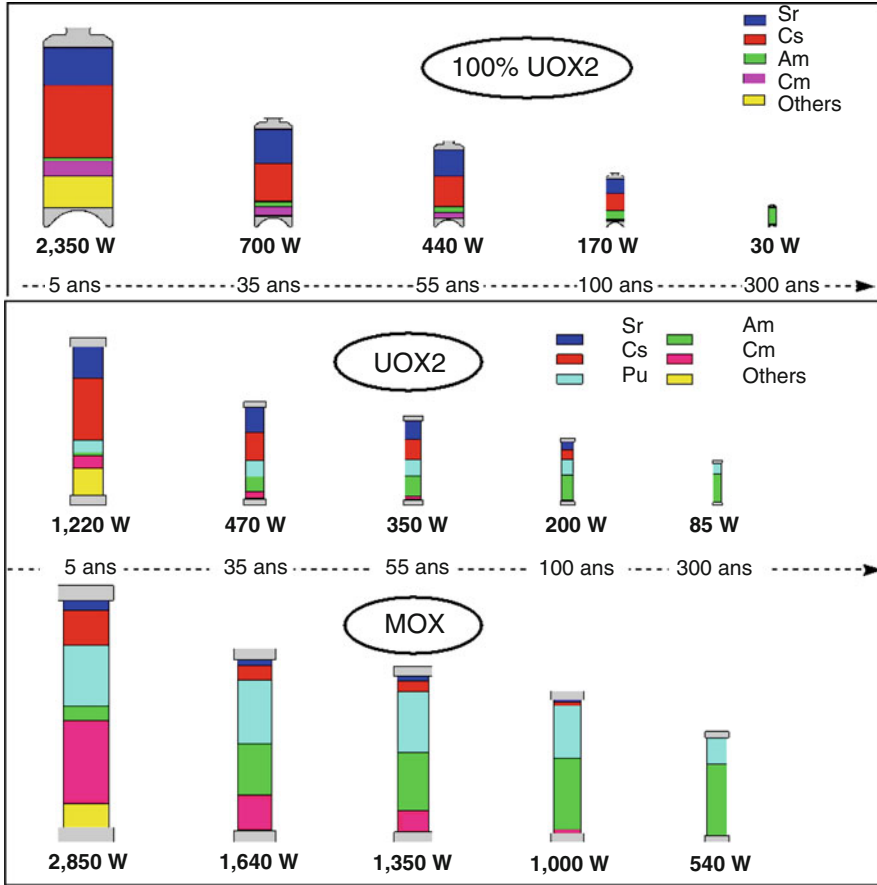


Figure 116
Thermal dissipation of spent fuel

Table 23
The thermal characteristics of some rocks

	Specific heat $\rho \cdot Cp$ ($J \cdot m^{-3} \cdot K^{-1}$)	Thermal conductivity λ ($W \cdot m^{-1} \cdot K^{-1}$)
Clay	2,040×940	1.5
Granite	2,700×800	2.5
Salt	2,150×850	5.2

The Heat Source-Term

A few years after its discharge from the reactor, the spent fuel generates a residual power of the order of 1 kW/t. It is approximately proportional to the burnup.

MOX fuels generate more heat than UOX fuels, and the decrease of the thermal power with time is slower.

The thermal power generated by glass after reprocessing of spent fuel is of the same order of magnitude, because most of the radionuclides, which contribute to the heat generation in the spent fuel are also in the glass, and because 1 t of spent fuel gives 0.5 t of glass.

The heat equation has the same form as the tracer equation discussed above:

$$\frac{\partial T}{\partial t} = D_{th} \cdot \Delta T + \frac{Q}{C}$$

where Q is the heat source-term, and D_{th} is the thermal diffusivity of the host rock.

$D_{th} = \lambda / (\rho \cdot C_p)$, with

ρ = material density

C_p = heat capacity

λ = thermal conductivity

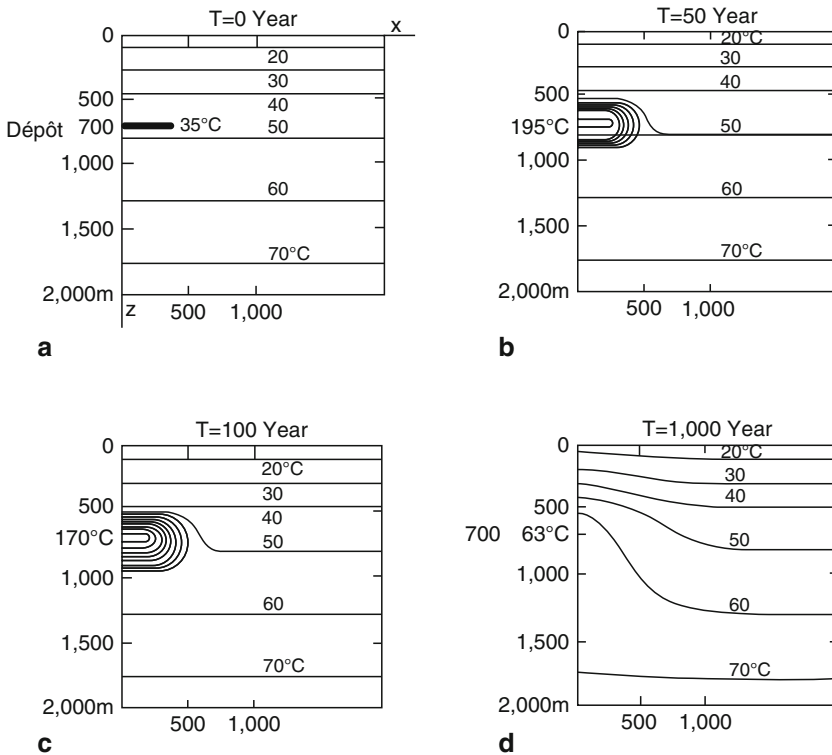


Figure 117

Thermal evolution of a repository at the kilometer scale (From Habib, La vie des Sciences)

The solutions of the heat equation have the same general form as the ones for the tracer equation. In particular, the typical size of the zone heated by a source after time t is $(D_{th} \cdot t)^{1/2}$. Rocks have a small thermal diffusivity D_{th} , of the order of $10^{-6} \text{ m}^2 \cdot \text{s}^{-1}$. Consequently, the size of the heated zone is small, even after very long heating times (this size is typically decametric after one century). This is rather bad news for a repository: it means that the heat generated by the waste will remain confined in a small space, and that the increase of temperature will be large, unless the heat-generating waste is widely spread within the host rock.

The evolution of the temperature in the repository is found by solving the heat equation. The temperature increases at first, because of the power dissipated by the waste. Later on, the temperature decreases back to the initial temperature, because the power dissipated by the waste decreases by depletion of its radioactive content.

► *Figure 117* gives an example of the temperature field as a function of time in the host rock around a repository.

Such thermal calculations must be made at the kilometer scale to check that the macroscopic waste distribution in the repository is not too dense. They must also be made at the scale of an alveole to check that the detailed geometry of the galleries or alveoles does not create hot spots liable to damage the host rock. Thermal calculations must also be made at the scale of the package, taking into account eventual air gaps, to make sure that the temperature at the interior of the package will not exceed a prescribed security value (e.g., the glass vitreous transition temperature in the case of vitrified waste).

3.2.26 Chemical Phenomena in the Near-Field

Chemical phenomena in the near-field are of various natures: *redox front propagation*, *dissolution-precipitation* with formation of new mineral phases, *corrosion*, etc. These complicated phenomena occur under radiation, mechanical stress, and thermal gradient. Fortunately, thanks to the very limited transport properties of the geological barrier, they are slow and affect a restricted zone in space.

Redox Front Propagation

The underground environment is often reducing. The excavation of the galleries of the disposal facility exposes the host rock to oxidizing conditions. Slow chemical reactions can then take place, with subsequent modification of the mineralogical composition of the host rock.

For example, clay rocks frequently contain pyrite (FeS). When exposed to humid air, this mineral is readily oxidized, producing sulfuric acid, with a drastic decrease of the pH of the porewater. Another example is that when put in contact with a host rock, a cemented material generates an alkaline perturbation, which propagates in the porous medium, with a remineralization of the perturbed zone (dissolution of the smectites and precipitation of CSH phases).

Dissolution–Precipitation

The exposure of the host rock to atmosphere during the excavation of the gallery has other consequences: the modification of the water chemistry due to redox front propagation combines with the modification of the water circulation to create conditions where the rock minerals can eventually dissolve and reprecipitate (e.g., in cracks) under the form of new mineral phases,

with subsequent modification of the porosity, permeability and diffusion constant of the host rock. For example, the carbonatation of concrete (either atmospheric or aqueous) results in the dissolution of portlandite and precipitation of calcite.

Corrosion

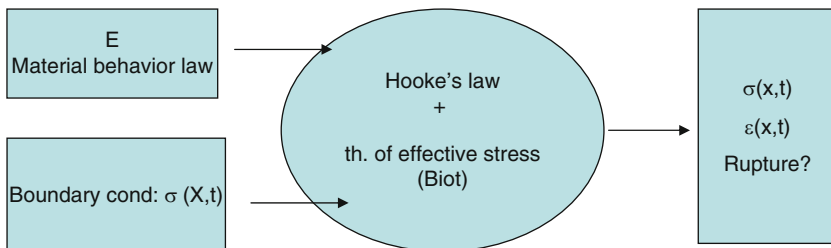
The metal of the containers and overpack are usually unstable thermodynamically in underground conditions (a possible exception is copper). A reaction of oxidation of the metal can then take place, which must be controlled, because its rate determines the lifetime of the containers, and therefore the contact time between the water and the waste. The products of this corrosion (oxides and hydroxides) accumulate in the near-field. They can locally modify the porosity of the medium and the solute transport.

Ideally, all these interlinked phenomena should be taken into account when describing the evolution of the near-field. The presence of radiation (which induces water radiolysis and the formation of reactive radicals), mechanical stress (which influences the dissolution-precipitation phenomena and the corrosion process), and thermal gradients (which influence the migration of solutes) complicate the picture even further. Fortunately, the rate of the chemical reactions in play is necessarily small, because it is limited by the transport of water and reactants in the host rock. Since the transport is slow, the spatial extension of the perturbation is quite small, typically tens of centimeters after a century.

3.2.27 Mechanical Behavior of a Repository

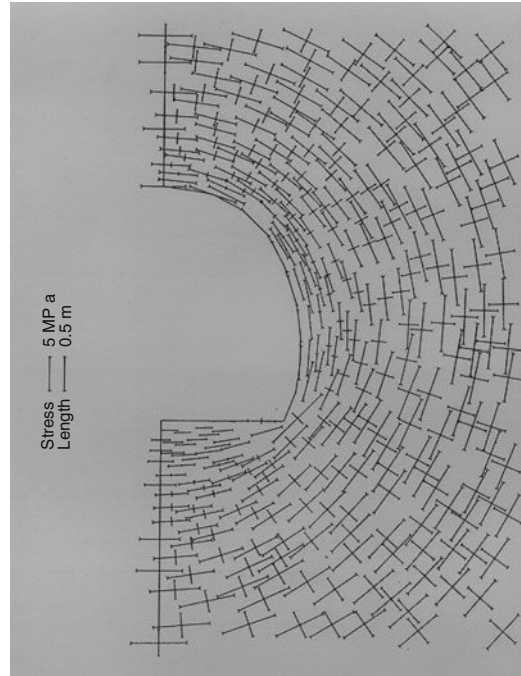
The excavation of a gallery underground causes a perturbation of the stress field in the host rock (► Figs. 118 and ► 119, ► Table 24).

In claystone, stress due to excavation can cause fracturing of the rock in the near-field, or modification of the existing fractures and local modification of the rock permeability.



■ Figure 118

Schematics of the inputs and outputs of a mechanical calculation applied to the near-field of a geological repository. The mechanical characteristics of the geological medium (Young's modulus, or more generally, material behavior laws) are known. The geometry of the excavation imposes the boundary conditions for the stress tensor at the tunnel surface. Application of the Hooke's law and/or the theory of effective stress gives the stress tensor field and strain field as a function of space and time. The stress field can then be compared to the resistance limit of the host rock to determine if fractures are to be expected



■ Figure 119
The principal components of the stress tensor in the vicinity of a tunnel

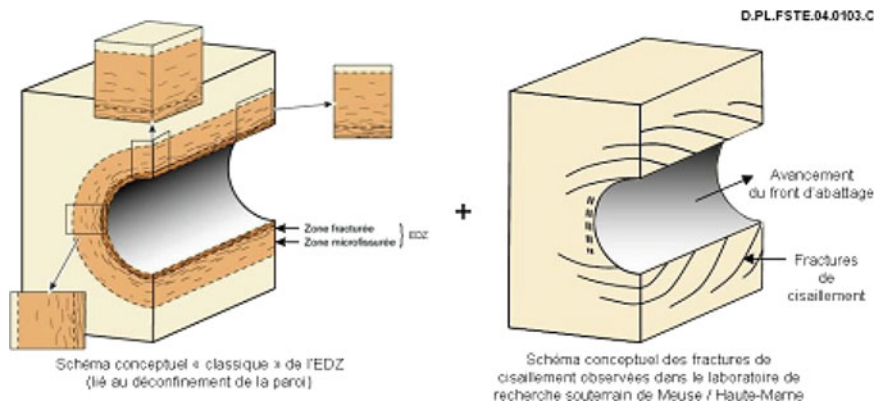
■ Table 24
Mechanical properties of geological barriers

	MOL (plastic clay)	Tournemire (claystone)	Granite
Young's modulus E (GPa)	0.1–0.3	8–30	50–90
Poisson coeff.	0.25–0.40	0.15–0.25	0.18–0.27
Rc (MPa)	0.09–0.25	18–33	140–265
Rupture deviator	1.9–2.0	80–120	405
	$(\sigma_1 - \sigma_3)_{\max}$ (MPa)	$(\sigma_3 = 30 \text{ MPa})$	$(\sigma_3 = 3 \text{ MPa})$
Shear modulus G (GPa)	0.06–0.08	4–12	26–32

Note: Note that the above figures are only indicative. The mechanical properties of rocks are highly variable!

3.2.28 Mechanical Effects Due to the Excavation of the Galleries

The stress field in underground rocks is made of two terms: a vertical compression component due to the weight of the above lying rocks; and a horizontal component due to tectonics. This last component is very much site dependent. If a tunnel is excavated at a depth $h = 500 \text{ m}$ in a rock with negligible tectonic stress, the stress deviator in the vicinity of the tunnel will vary by $\rho \cdot g \cdot h = 10 \text{ MPa}$ due to the excavation (order of magnitude for a repository with a depth



■ **Figure 120**
Conceptual scheme of the Excavation Disturbed Zone (EDZ), and shape of the shear-stress fractures induced by the excavation (From ANDRA)

of 500 m). This figure is smaller than the rupture deviator of a hard rock like granite. Such a rock can be drilled without reinforcing the excavation by struts (borehole ovalisation has been observed in granite in locations with strong tectonic stress). However, 10 MPa is the order of magnitude of the rupture deviator in clay rocks. One therefore expects fracturing of the rock in the tunnel vicinity, and the creation of an Excavation Disturbed Zone (EDZ). Far from the tunnel, one finds again the lithostatic stress field (➤ Fig. 119).

Note that the fractured zone around the tunnel is created initially during the excavation (the cracks are perfectly audible!). When the cracks propagate, the stress field relaxes and extends outwards. The extension is initially rapid, and slows down with time. Ultimately, the perturbation of the stress field stops expanding when the stress deviator becomes smaller than the rupture deviator everywhere in the rock. When this happens, the extension of the fractured zone is of the order of the tunnel diameter (➤ Fig. 120).

Coupled thermal and mechanical effects are expected in the near-field of a repository of high-activity waste. Thermo-mechanical coupling occurs via dilation.

The stress deviator due to dilation is of the order of $E \cdot \alpha \cdot \Delta T$

with $E \equiv$ bulk modulus of the rock

$\alpha \equiv$ rock dilation constant

$\Delta T \equiv$ the temperature difference

This deviator amounts to a few tens of MPa, a value comparable to the rupture deviator in claystone, but smaller than the rupture deviator in granite.

In claystone, the dilation due to heating by the waste can thus cause a fracturation of the rock in the near-field, or a modification of the existing fractures and local modification of the rock permeability.

3.2.29 Hydraulic Effects

Hydraulic effects are expected in the near-field. They are induced by the excavation of galleries in an initially saturated host rock. This excavation can *desaturate* the rock in its vicinity, due to

evaporation of the porewater in the ventilated tunnel. After repository closure, the host rock will become *resaturated*. These phenomena of saturation-desaturation represent an important perturbation of the water circulation underground, because they generate hydraulic gradients considerably larger than the naturally preexisting gradients. They are governed by the permeability (via Darcy's law) and by the capillary behavior of the porous medium.

In a desaturated porous medium, the difference between the pressure in the liquid and the pressure in the vapor is given by the Jurin's law:

$$P_c = \frac{4.(E/A)}{a},$$

where a is the pore size, and E/A is the wetting energy per surface area ($E/A = 0.8 \text{ J.m}^{-2}$ for hydrophilic surfaces).

In finely divided media like clay, the capillary pressure P_c can reach very large values, in the order of 100 MPa. It can be interpreted as a hydraulic potential $h_c = P_c/(\rho.g)$, with the same meaning as in hydrogeology. It is this potential, which is imposed at an interface between the porous medium and the atmosphere.

The kinetics of the resaturation in a porous medium is governed by the Washburn equation, describing the motion of the front, which separates the saturated zone from the desaturated zone: neglecting poroelastic effects, evaporation, and gravity, in the very simple case of a one-dimensional porous medium with one end in free water, it takes a time

$$t = \frac{e^2}{2.K.h_c}$$

to resaturate a thickness e , where K and h_c are the permeability and capillary potential of the medium.

Desaturation-restoration phenomena in clays are quite slow. To give an order of magnitude, the resaturation time of a clay barrier with 1 m thickness is about 10 years.

3.2.30 Hydro-Mechanical Effects in the Near-Field

In a desaturated porous medium, the remaining fluid is under tension. This tension is transmitted to the porous skeleton and can cause shrinkage and even cracking of the material (cf. drying clay). Conversely, the resaturation of porous media causes a swelling. This swelling is exploited to ensure sealing in engineered barriers. The order of magnitude of the shrinkage/swelling due to desaturation/resaturation is $\Delta l/l \approx P_c/E$, where P_c is the capillary pressure of the material and E the Young's modulus of its porous skeleton.

3.2.31 Hydro-Chemical Couplings in the Near-Field

Hydro-chemical couplings in the near-field of a repository are of various natures: *dissolution-precipitation* phenomena, *corrosion*, and *osmosis* are only a few examples.

Dissolution-precipitation phenomena in the near-field host rock (mediated by water circulation) can be triggered by the local imbalance induced by the excavation (hydraulic perturbation)

or by the presence of the waste (chemical perturbation). Dissolution-precipitation might cause modifications of the permeability of the rock, with a subsequent modification of the water circulation itself. For example, fracture filling by precipitation of calcite in calcite-rich claystone has been observed in the Tournemire site.

Another example of hydro-chemical coupling is that of clays which can behave as osmotic membranes.

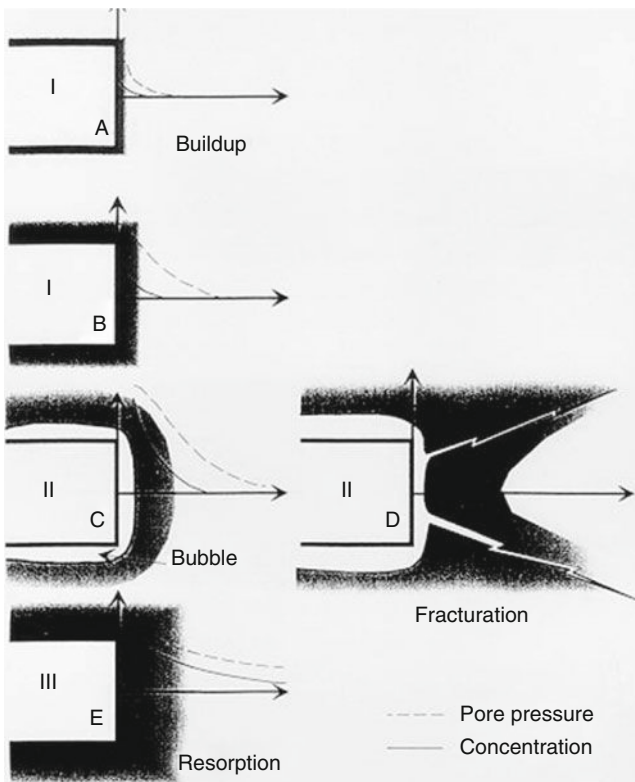
The osmotic pressure of an ideal solution can be evaluated via the kinetic theory, and obeys a law similar to the one for perfect gases:

$$p = (n/V) \cdot R \cdot T$$

↑

nb of solute moles per cubic meter of solution.

Osmosis can generate nonnegligible overpressures and hydraulic gradients in an heterogeneous rock. For a freshwater-seawater interface 100 m wide, the hydraulic gradient is about $h = 1.2 \text{ m/m}$, that is, the same order of magnitude as the gradients naturally found in aquitards.

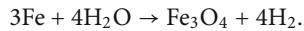


■ Figure 121

Gas production and release in the vicinity of a canister in underground repository

3.2.32 Gas Production and Release in an Underground Repository: An Example of H–M–C Coupling

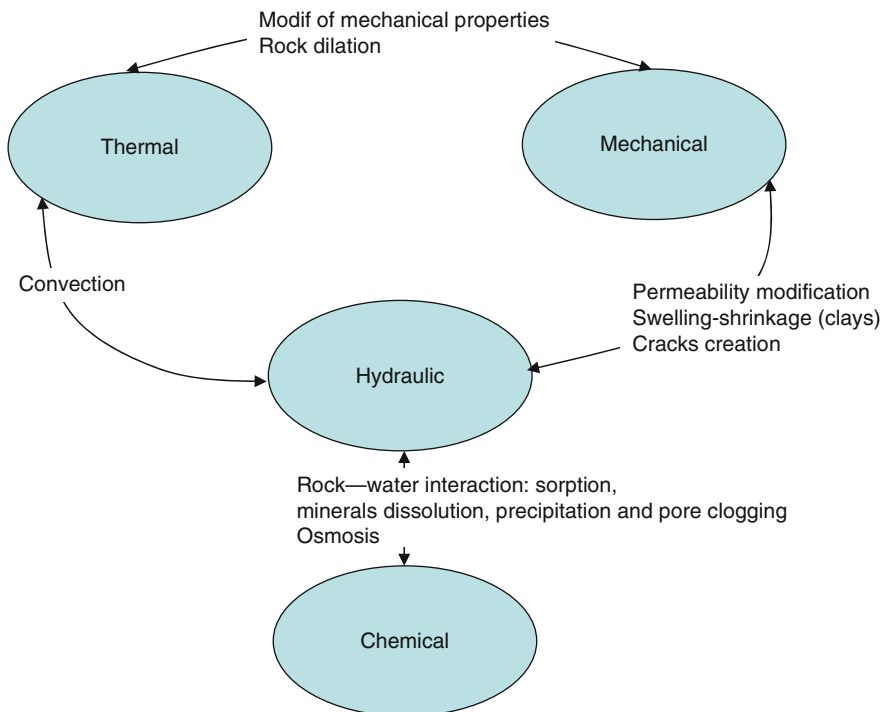
The radiolysis of water and the corrosion of steel canisters by water can generate significant amounts of hydrogen. After closure, anoxic corrosion of steel produces hydrogen via the reaction



In repository conditions, the corrosion rate of carbon steels is of the order of 0.2–2 μm/year (Neff 2003)

If the barrier is very impermeable, this hydrogen can cause pressure buildup and fracturation of the barrier (► Fig. 121). The quantitative evaluation of the consequences of this hydrogen release is the subject of active research.

As shown by the above examples, *thermal, mechanical, hydraulic, and chemical effects are intricately coupled*, and must be treated together. The main couplings are summarized in ► Fig. 122.



■ Figure 122
THMC couplings in the near-field

3.2.33 Underground Laboratories

All major nuclear countries are conducting a research program on waste deep geological disposal (🔍 [Table 25](#)). Studies in URLs are motivated by industrial feasibility assessments, and, more important, by safety assessments of the repository.

There are three categories of objectives:

Mechanism understanding

Model validation

Data acquisition

Site characterization

Development of techniques

Techniques of characterization

Excavation and sealing techniques

■ **Table 25**

The main underground research laboratories in the world

Country	Site	Rock nature	Institute
USA	Yucca Mountain (Nevada)	Tuff	DOE
	WIPP (New Mexico)	Salt	DOE
Canada	URL (Manitoba)	Granite	AECL
Japan	Kamaishi	Granite	PNC
	Tono	Granite	PNC
Germany	Asse	Salt	GSF
	Gorleben	Salt	DBE
	Konrad	Calcic clay	BFS
Belgium	Mol	Clay	SCK/CEN and ONDRAF/NIRAS
Finland	Olkiluoto	Tonalite	POSIVA
France	Bure	Clay	ANDRA
	Tournemire	Clay	IRSN
UK	Sellafield	Volcanic	NIREX
Sweden	Stripa	Granite	SKB
	Aspö	Granite	SKB
Switzerland	Grimsel	Granite	CEDRA
	Mt Terri	Clay	NAGRA

The geologic waste disposal poses several difficult scientific problems:

- The evolution of the repository over very large scales of space and time
- The reactivity of materials (glass matrix, steel container, engineered barriers of concrete, or clay)
- THMC couplings in the near-field

These open problems do not mean that the geological disposal concept is not mastered (by nature, it will never be completely mastered!). But they justify the continuation of research in underground laboratories. The main research topics are summarized in [Table 26](#):

■ **Table 26**

The main research topics in underground laboratories

Barrier	Function	Research topic
Matrix (glass,	<ul style="list-style-type: none"> • Confinement • Limitation of RN release 	1. Matrix degradation, lixiviation
Container and	<ul style="list-style-type: none"> • Transport • Retrieval • Protection of packages 	2. Corrosion 3. Interaction steel-clay and
Engineered barrier	<ul style="list-style-type: none"> • Protection of packages • Delay migration 	4. Coupled THMC phenomena 5. Sealings
Geological barrier	<ul style="list-style-type: none"> • Protection of the first • Delay migration • Dilution 	6. EDZ 7. Preferential pathways, heterogeneities, 8. RN speciation, solubility, sorption 9. Characterization of the deep geological medium 10. Seismic behavior, geospectroscopic
Biosphere		11. Interaction of RN with man and environment

3.2.34 Natural Analogues Can Help Validate the Models of Long-Term Behavior of a Repository: The Example of Oklo

The “Oklo phenomenon” was discovered in Pierrelatte in 1972. Routine measurements of the isotopic composition of uranium ore samples from this mine in Gabon showed a depletion in ^{235}U . The enquiry concluded that the anomaly was due to fission chain reactions. Divergence of “natural reactors” took place in 15 sites in the vein, shortly after its formation, 2 GY ago.

Nuclear reaction started in very rich parts of the deposit (grade 10%). The presence of water (playing the role of neutron moderator) was necessary to reach the criticality.

Pressure and temperature in the reactors were close to those encountered in the present PWRs. Even the isotope composition of the fuel was similar (3.7%)! However, the neutron flux was considerably smaller, and the nuclear reactions lasted much longer (20,000–350,000 years).

From the knowledge of the age of the event, and the depletion in ^{235}U , one could calculate the quantity of fission products, which formed during the active life of the reactors. Soon after the discovery of Oklo, the scientific community realized that the site was an interesting natural analogue of a waste repository. The study of the site confirms the efficiency of the geological barrier for radionuclide confinement (e.g., the uranium remained trapped in the vein for 2 billion years!). The extraordinary confinement power of some minerals like apatites was also discovered in Oklo. Unfortunately, all results are not as clear. Since 2 GY, most radionuclides formed by the nuclear reactions have decayed, and it is difficult to disentangle the migration properties of these radionuclides from the ones of their daughters, which have in general very different chemical properties. The numerous hydrogeochemical changes the site has undergone since 2 GY also complicates the migration pattern (Pourcelot et al. 1999; Gurban et al. 2003; Gauthier-Lafaye 2002).

Chain nuclear reaction occurred spontaneously on the Earth during the only possible time window: before 2 GY, vegetal life had not produced enough free oxygen in the atmosphere to allow the development of a geochemistry of uranium based on redox, and the concentration of uranium deposits rich enough to become critical. After 1.7 GY, the depletion of ^{235}U in the natural uranium due to radioactive decay forbade criticality. The possibility of underground chain reaction is a consequence of the emergence of life, much like the present nuclear industry, which is a consequence of the presence of man!

3.3 Safety of Waste Disposal Facilities

Waste disposal in a deep geological repository will have a nonzero radiological impact for the public, even if the installation evolves as foreseen according to the reference scenario.

The main purpose of this section is to evaluate the order of magnitude of this impact, and, more generally, to explain how a safety evaluation of a geological repository can be made.

In order to make the performance assessment of a geological repository, one needs to estimate the radiological impact of the installation.

The method to estimate this impact is as follows:

1. Define scenarios for the evolution of the installation. A scenario is a chronological sequence of elementary phenomena (Features, Events, and Processes, FEPs). Several scenarios can be envisaged: the “normal evolution” scenario is the most probable one; altered scenarios describe abnormal evolutions of the repository, leading to a degradation of its performance (human intrusion, for instance, the digging of a well close to the repository; failure of one or several barriers, for example, defective sealings, or containments).
2. Model the travel of the radionuclides from waste to man. This travel can be divided in two parts: from the waste to the biosphere, through the geosphere; and through the biosphere to man. The first step evaluates an activity flow from the repository to the exutury (this activity flow is expressed in Bq/year). The second step evaluates the dose rate to the population for the various scenarios (the dose rate is expressed in mSv/year). This last step requires the definition of a biosphere, a reference population, and a critical group.

In all cases, the dose received by the most exposed part of the population should not exceed a predefined limit. In most countries, the upper limit for this radiological impact should be smaller than a fraction of the radiological impact due to natural radioactivity, i.e., ~ 1 mSv/year.

3.3.1 How to Evaluate the Radiological Impact of a Deep Geological Repository?

The three main indicators for the impact of a radioactive waste repository are the *activity* (in Bq/m^3) and *activity flux* (in Bq/s) at the exutory, and the *collective dose* (in Sv) to the population.

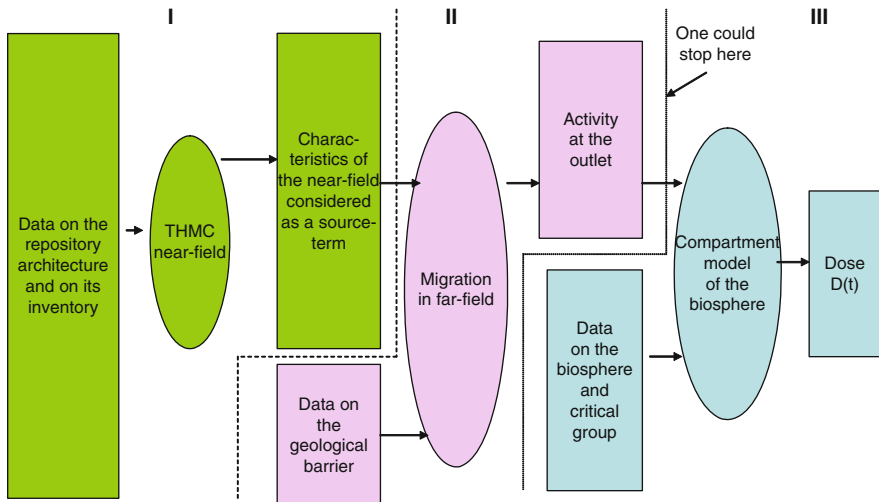
We have reviewed and modeled the elementary phenomena.

Now we arrange them together to evaluate successively

- The source-term
- The activity flux at the exutory, deduced from the source-term characteristics and from a transfer function
- The exposure of the population

► **Figure 123** shows the general scheme to articulate the models together to evaluate the impact of a geological repository.

- Data on the repository and on its content enable us to calculate the characteristics of the near-field, seen as a *source-term* (step I).
- One lets the radionuclides migrate from this source-term to calculate the *activity at the exutory*. This calculation requires the knowledge of the characteristics of the geological barrier (step II).
- From the activity at the exutory, one can then calculate a *dose* as a function of time. This calculation requires the definition of a biosphere and of a critical population (step III).



■ **Figure 123**

General view of the impact evaluation of a geological repository. The ellipses represent models; the rectangles represent the input or output data used or produced by the models

Step III is probably the most difficult part of the evaluation: the dose calculation is uncertain, dose factors are poorly known, and the definition of the biosphere and critical group can raise many discussions. Fortunately, two important indicators of the impact of the repository (the activity [in Bq/m³] and activity flux [in Bq/s] at the exutory) do not require the passage through this step.

Step I: Evaluation of the source-term

In the near-field, thermal, hydro, mechanical, and chemical effects are intricately coupled. Modeling the evolution of this near-field is difficult. Fortunately, the release rate of radionuclides in the near-field will be limited by the physicochemical phenomena described in ▶ Sect. 3.2: residual alteration rates of the confinement matrixes, or solubility limits of the RN themselves. With this remark in mind, one can attempt to model the near-field as a *maximum source-term*, even if we do not know in detail what happens in this zone. Altogether, we need to evaluate the properties of this source-term (geometry, concentration at the boundaries, duration of the activity) (▶ Fig. 124).

Step II: Migration of RN in the far-field

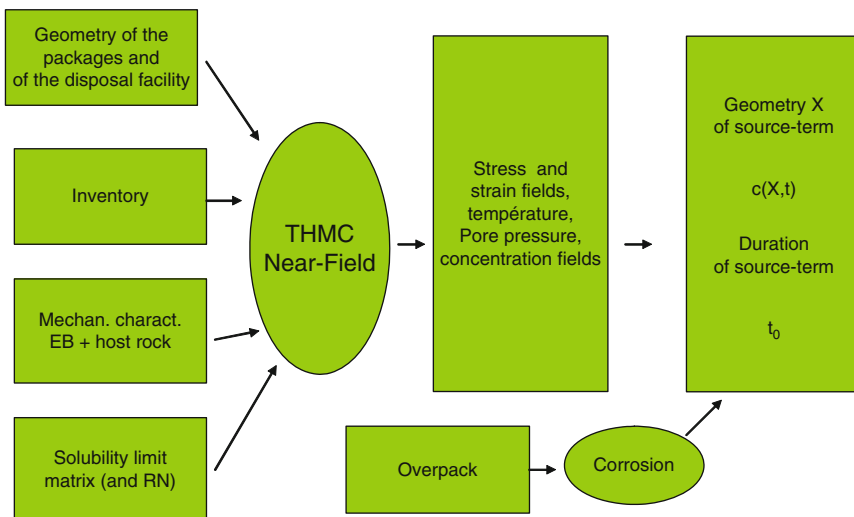
The geological barrier is represented by a few porous permeable, homogenized domains, whose characteristics are supposed to remain constant in time.

The transport of radionuclides is described by a linear sorption model (Kd) (▶ Fig. 125).

Step III: From the exutory to man

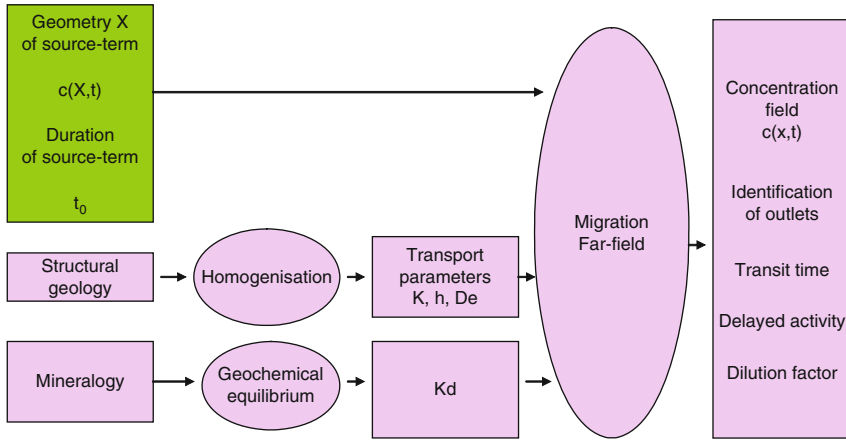
The evaluation of a dose to man requires the modeling of the travel of the radionuclides through the biosphere. This is the subject of radioecology (▶ Fig. 126).

The biosphere is modeled as several compartments, which can exchange radioactivity (usually, one assumes that the transfer coefficients between compartments depend linearly on the



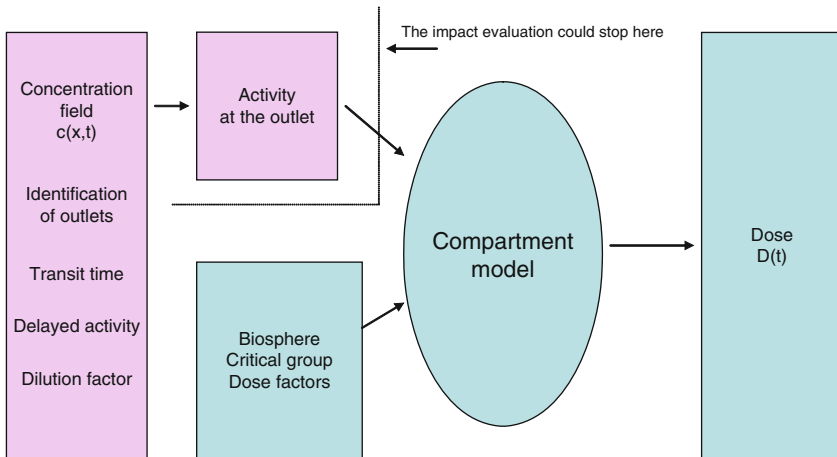
■ Figure 124

The impact evaluation of a geological repository (detail of step I, evaluation of the characteristics of the source-term)



■ Figure 125

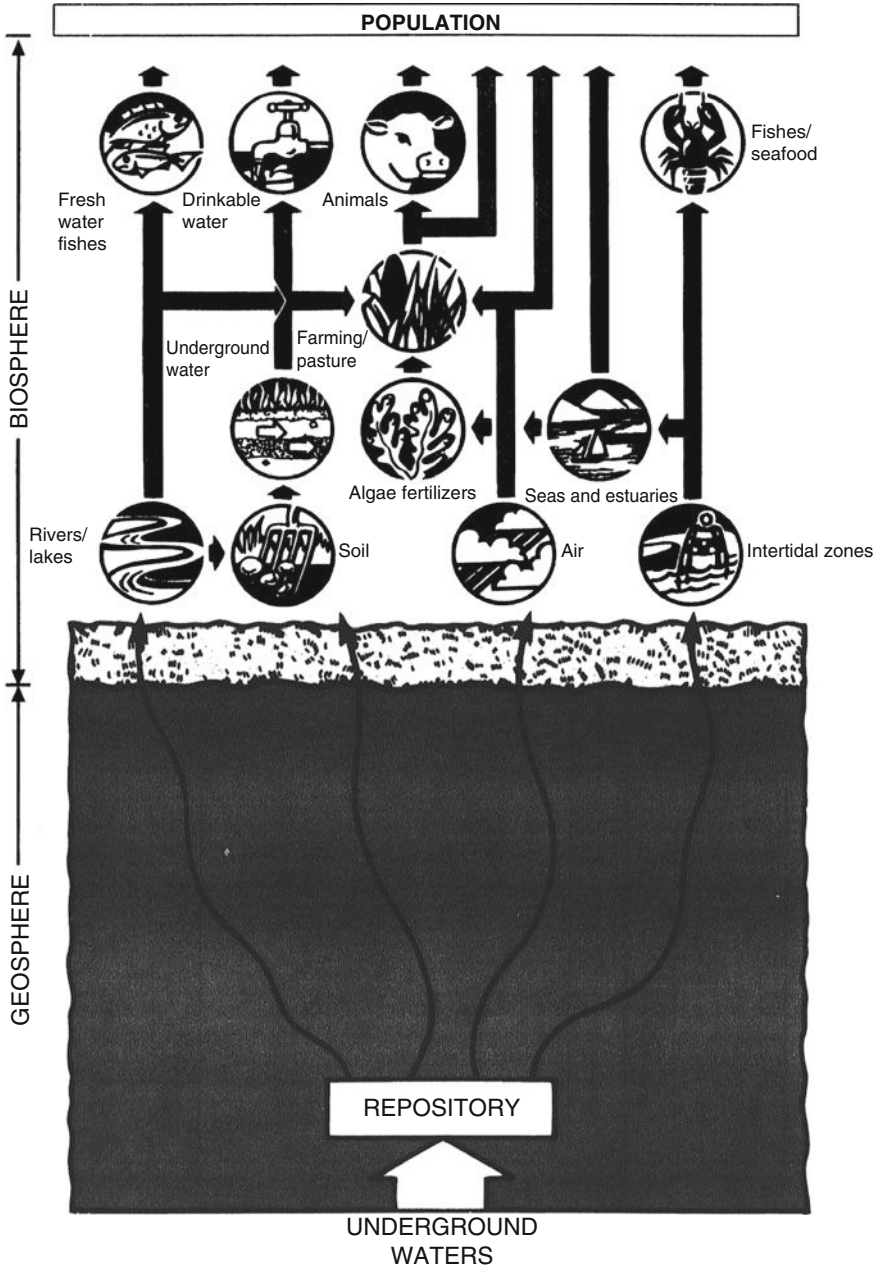
The impact evaluation of a geological repository (detail of step II) far-field. From the source-term to the exutry



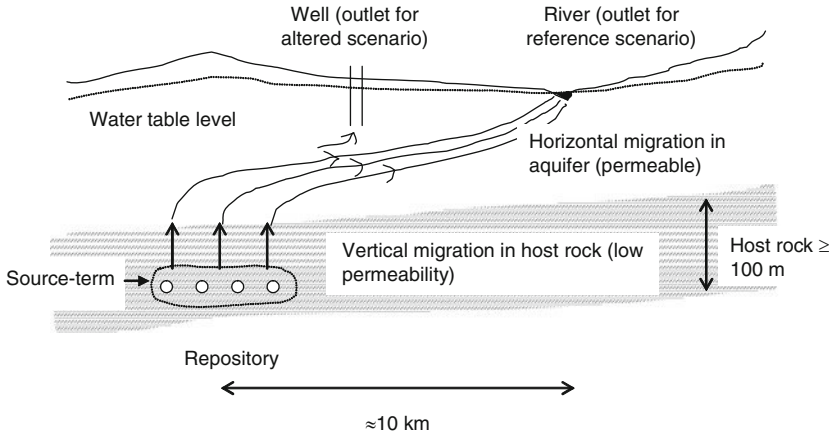
■ Figure 126

The impact evaluation of a geological repository (detail of step III) from the exutry to man

radionuclide concentration). Compartments include rivers, lakes, air, soil, sea, and various kinds of plants and animals. The top compartment is the population, and, more precisely, the critical group, which is the part of the population liable to receive the highest dose (► Fig. 127).



■ **Figure 127**
 An example of compartment model describing the transfer of radionuclides from the geosphere to man, through the biosphere



■ Figure 128

Schematics of the repository and the migration path of the radionuclides from the repository to the exutury

3.3.2 Evaluation of the Order of Magnitude of the Activity at the Exutury for a Simplified Repository

In order to show the methodology of the evaluation, we propose to evaluate the activity at the exutury for a very simplified repository of vitrified waste. This exercise requires the modeling of the travel of the radionuclides from the repository to the exutury. As a prerequisite, this exercise requires the knowledge of the radionuclide inventory in the repository, the knowledge of the long-term behavior of glass, and the knowledge of the site hydrogeology and geochemistry. All these elements have been addressed previously in ► Sect. 3.2; now is the time to link them together.

Schematically, the travel of radionuclides from repository to exutury can be divided into two parts (► Fig. 128):

1. The travel through the host rock (in an aquitard): very slow, over a short distance (typically the thickness of the aquitard layer, i.e., about 100 m). In the present exercise, we shall assume that the radionuclides migrate vertically upwards.
2. The travel from the aquitard to the exutury (in an aquifer): faster, but over a large horizontal distance (typically the distance between the repository and the nearest river, i.e., about 10 km).

3.3.3 The Source-Term

In this example, for the sake of simplicity, we neglect the possible precipitation of all radionuclides (including actinides) in the geological medium. This hypothesis is conservative.

We assume that the glass alteration is a constant, equal to the residual alteration rate V_r (the notation is the same as the one used in ► Sect. 2.2 “glass long-term behavior”). In the residual

alteration regime, there is a congruent release of all RNs from the glass (same proportion of RN in the source-term as in the matrix).

With these assumptions, the source-term takes a very simple form: for each radionuclide i , it is defined by an activity flux at its boundary, expressed in Bq/s, and given by the expression:

$$\phi^i = V_r \cdot S \cdot A_{matrix}^i,$$

where S is the total surface area of glass, which undergoes alteration, and A_{matrix}^i is the activity of radionuclide i in one unit volume of glass.

The activity of the matrix is conveniently expressed as a function of the activity of radionuclide i in the waste generated by the production of a given amount of nuclear power.

Therefore, we pose

$$S \cdot A_{matrix}^i = W \cdot \sigma \cdot A_{specific}^i,$$

where σ is the specific surface area of the glass matrix (in m^2/m^3 , taking into account its degree of fragmentation), W is the total nuclear power whose production generated the waste (in TWhe), and $A_{specific}^i$ is the specific activity of radionuclide i generated per unit generated power (in Bq/TWhe).

The activity flux of the source-term is therefore

$$\phi^i = V_r \cdot W \cdot \sigma \cdot A_{specific}^i.$$

The RN flux described by this constant source-term will then migrate through the geosphere.

The release of radionuclides from the matrix lasts as long as the glass alteration goes on. The alteration time is thus given by

$$\tau_{alteration} = X/V_r,$$

where X is the typical size of the glass blocks, taking into account the degree of fragmentation of the package. Assuming a more or less regular shape for the glass blocks, X is related to σ , the specific surface area of the glass by $X = 6/\sigma$.

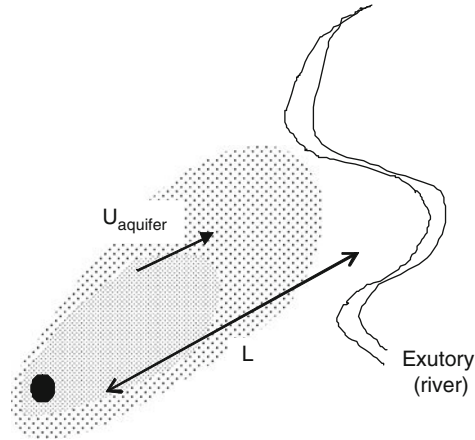
With realistic values for σ (250/m) and for V_r (10^{-15} m/s), we get $\tau_{alteration} = 1$ million years. The source-term thus produces radionuclides at a constant rate ϕ during the time $\tau_{alteration}$, of the order of 1 million years.

3.3.4 Transit Time from the Repository to the Exutory

In order to evaluate the transfer time from the repository to the exutory, we assume that the transport of radionuclides through the geosphere is mainly advective (► Fig. 129). The dominance of advection over diffusion has been justified earlier for large space scales (cf. ► Sect. 3.2 on the transit times through a barrier in diffusive and advective regimes). This dominance holds for both parts of the RN travel: through the aquitard and through the aquifer.

The transit time of the radionuclides from the repository to the exutory is the sum of the transit time through the engineered barrier and aquitard and the transit time through the aquifer. These two components can readily be evaluated using Darcy's law applied to these two different geological media.

$$\tau_{aquitard \text{ or } aquifer} = \left(\frac{X \cdot \omega}{K \cdot \text{grad}(h)} \right)_{aquitard \text{ or } aquifer}.$$



■ **Figure 129**
Radionuclide travel through the geosphere

With typical values for the transport parameters $X, \omega, K, grad(h)$ in aquitards and aquifers (cf. ▶ [Tables 14](#) and ▶ [16](#)), one gets the following orders of magnitude for the transit time of a perfect tracer through the geosphere.

The above evaluation of the order of magnitude of this transit time is robust: even though the actual pathway of the water may be very different from the one sketched here, the journey will always entail crossing at least one aquitard and one aquifer. Moreover, since the transit times through aquitard and aquifer have the same order of magnitude, a failure of one of these two barriers would not modify drastically the total transit time through the geosphere (▶ [Table 27](#)).

■ **Table 27**

Order of magnitude of the transfer time of a perfect tracer from the source-term to the exutory

Transport through engineered barrier and aquitard	$\tau_{aquitard}$	$\approx 70,000$ years (cf. ▶ Sect. 3.1)
Transport aquifer \rightarrow river	$\tau_{aquifer}$	$\approx 100,000$ years
Total	τ	≥ 0.1 million years

For sorbed radionuclides, the transit time is $R^i \cdot \tau$, where R^i is the retardation factor associated with radionuclide i .

3.3.5 Transfer Through the Geosphere

Here again, we assume that advection is the dominant transport mode through the geosphere.

The radionuclide travel through the geosphere can be represented as a transfer function in a pipe through which water and radionuclides flow from the source to the exutory (▶ [Fig. 130](#)). This pipe is somewhat abstract:

The water flux is not conserved along the pipe.

The activity per unit water volume is not conserved along the pipe.

But the activity flux ϕ (product of the water flux by the activity per unit volume) is conserved (or, more precisely, would be conserved if radioactive decay did not take place).

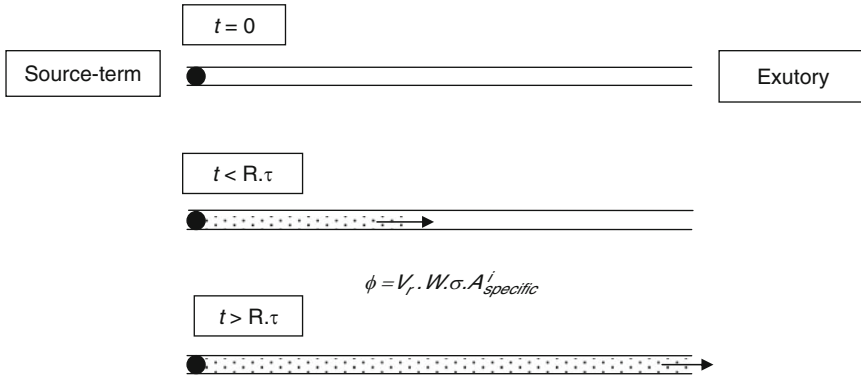


Figure 130 The transfer through the geosphere is modeled as a travel in a “pipe,” in which the activity flux Φ is conserved

This prescription of conservation of the activity flux along the pipe is valid only if no accumulation of RN occurs in the geosphere. This is consistent with the previously stated assumptions: no RN precipitation; and diffusion is neglected.

With this prescription, the activity flux transferred at the exutory for each radionuclide i is given by the following transfer function:

$$\begin{aligned} \phi_{exutory}^i(t) &= 0 \quad (t < R^i \cdot \tau) \\ \phi_{exutory}^i(t) &= \phi_{source-term}^i(t - R^i \cdot \tau) \quad (R^i \cdot \tau < t < \tau_{alteration}) \\ \phi_{exutory}^i(t) &= 0 \quad (t > \tau_{alteration}) \end{aligned}$$

3.3.6 Activity at the Exutory

The activity at the exutory (expressed in Bq per unit volume of water) is simply deduced from the activity flux at the exutory, by

$$A_{exut}^i = \phi_{exut}^i / Q, \text{ where } Q \text{ is the flow rate of the exutory.}$$

Therefore,

$$A_{exut}^i(t) = \left(\frac{V_r \cdot W \cdot \sigma}{Q} \right) * A_{specific}^i(t - R^i \cdot \tau) \quad (R^i \cdot \tau < t < \tau_{alteration}).$$

Because of the *delay*, the activity at the exutory is zero for early times. The first radionuclides arrive at exutory around time $t = R^i \cdot \tau$, where R^i is the retardation factor of radionuclide i due to sorption.

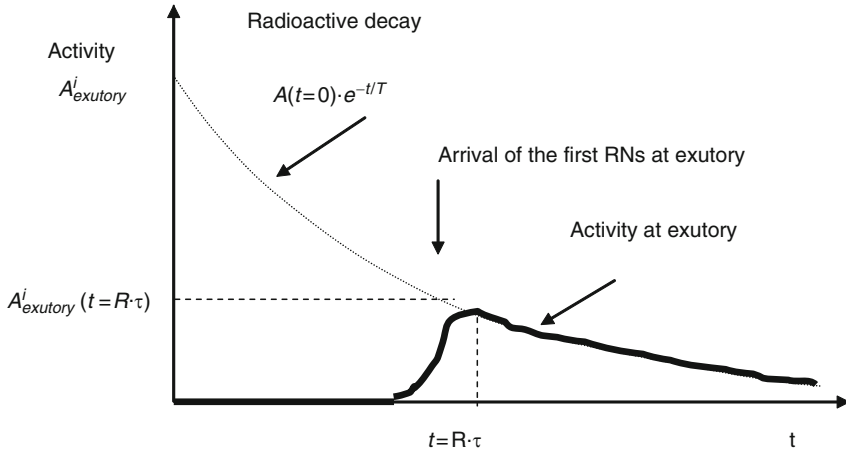


Figure 131
The activity at exutory

Because of the *decay*, the maximum activity at the exutory is smaller than the one we would have had for a non-radioactive tracer, by a factor $\exp(-R^i \cdot \tau / T_{1/2}^i)$ (👉 Fig. 131).

We define the “delayed activity” as the specific activity of radionuclide *i* in the matrix at time $R^i \cdot \tau$:

$$\text{Delayed activity} \equiv A_{\text{specific}}^i(R^i \cdot \tau).$$

For each radionuclide, the delayed activity can be read on a diagram like the one shown in 👉 Fig. 132. It is the activity, which remains after time $R^i \cdot \tau$ (circles on the diagram), where $R^i \cdot \tau$ is the duration of the travel of the considered radionuclide through the geosphere.

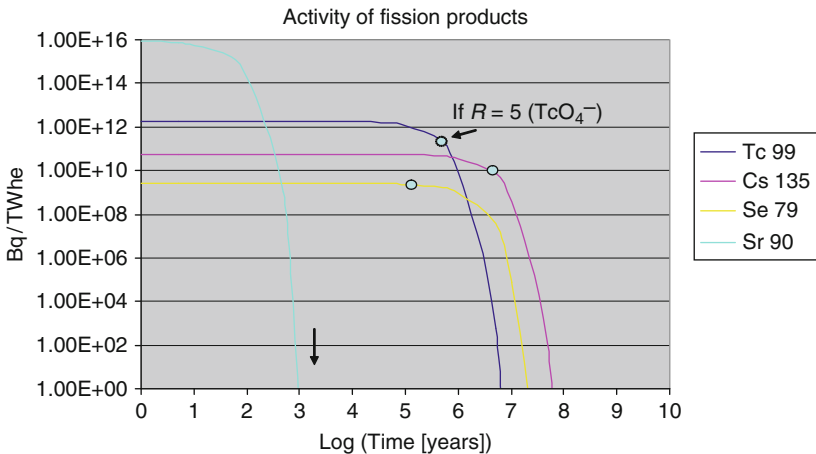


Figure 132
The delayed activity of fission products

Here, a value of $\tau = 0.1$ million years has been assumed. A retardation factor of 5 has been assumed for Tc, 30 for Cs, 1 for Se, and 30 for Sr.

The delayed activity of ^{90}Sr (a fission product with a period of only 28 years) is zero. Only long-lived radionuclides can have a significant delayed activity.

Three important long-lived fission products (^{99}Tc , ^{135}Cs , ^{79}Se) found in glasses have been represented on the diagram. The highest delayed activity is the one of ^{99}Tc , but this result is valid only under the hypothesis of migration in oxidizing conditions, where the Tc is under the form of pertechnetate ion. In the reducing conditions, which will prevail in a repository, the retardation factor of Tc is of the order of 100,000, and the delayed activity of Tc drops to zero. Thus remain only ^{135}Cs and ^{79}Se , the two “winners” of the radionuclide survival race through the several barriers of the repository (► [Table 28](#)).

Table 28
The delayed activity of some important radionuclides

	Retardation factor R	Initial activity $A_m(t=0)$ (Bq/TWhe)	Delayed activity $A_m(t=R \cdot \tau)$ for $\tau = 0.1$ MA (Bq/TWhe)	Remarks
^{135}Cs	30	5.510^{10}	10^{10}	
^{99}Tc	5	1.810^{12}	2.10^{11}	$R = 5$ if ion TCO_4^-
	$> 10^5$		0	$R > 10^5$ if other chemical forms
^{79}Se	1	2.510^9	2.510^9	
^{242}Pu	$> 10^4$	2.10^{11}	0	
^{237}Np	$> 10^4$	2.610^{10}	0	No actinides will come out of the repository
^{229}Th	$> 10^5$	0	0	

Laboratory experiments (Dossier ANDRA and Dossier 2005) suggest that the actinides are very efficiently adsorbed on many minerals present underground (especially clay minerals), and are therefore almost immobile in an underground environment (this would correspond to an infinite retardation factor R). Here, we have taken the retardation factors given by ANDRA in ANDRA and Dossier (2005), Dossier argile. This retardation is more than enough to “kill” the actinides; radioactive decay occurs before the actinides make it through the geological barrier.

The maximum activity arriving at the exutory is given by

$$A_{exut\ max}^i = \left(\frac{V_r \cdot W \cdot \sigma}{Q} \right) * A_{specific}^i(t = R \cdot \tau). \tag{3}$$

For each radionuclide, this maximum activity occurs a time $t = R \cdot \tau$. This depends on the retardation factor of the considered radionuclide, that is, 0.1 million years for ^{79}Se and 3 million years for ^{135}Cs .

This activity is maximum because for earlier times, the radionuclides have not yet reached the exutory; and for later times, the radioactive decay reduces the activity.

With realistic figures for V_r , W , σ , Q and $A_{specific}^i$,

$V_r = 10^{-15}$ m/s, corresponding to the order of magnitude of the secondary phases precipitation rate in a clay environment (Frugier et al. 2009)

$\sigma = 250$ /m (taking into account the degree of fracturation of glass in R7T7 packages)

$Q = 4$ m³/s, order of magnitude of the volumic flow rate of the nearest river flowing closer than 10 km away from the repository, in a hydrographic network typical of temperate climate

$$A_{specific}^{(R,\tau)} = 10^{10} \text{ Bq/TWhe for Caesium 135, we obtain :}$$

$$A_{exut \max}^{Cs135} = 6.10^{-4} \text{ Bq} \cdot \text{m}^{-3} / \text{TWhe}$$

For a typical repository containing the vitrified waste corresponding to 50 years of activity of a fleet of 60 GW light water reactors ($W = 2.10^4$ TWhe), the maximum caesium 135 activity at the exutory will be of the order of 10 Bq/m³.

One can compare this “added” activity to the activity of a natural mineral water, which can be as high as 10,000 Bq/m³.

Equation (3) clearly shows the important factors, which determine the activity at the exutory:

- As expected, the activity at the exutory is proportional to the RN inventory in the repository.
- The residual alteration rate of glass is of prime importance because the activity at the exutory is proportional to $V_{residual}$.
- The degree of fracturation of the glass is also very important, for the same reason.
- The characteristics of the geological barrier (permeability, hydraulic gradients) are also important because they determine, together with the retardation factor R , the travel time of the radionuclides, and, subsequently, the delayed activity of the RN.

Additionally, the equation also shows the unimportant factors: the activity at the exutory, as given by (3), is quite insensitive to the details of the travel of the radionuclides in the geosphere: the only significant quantity is the total travel time through the geosphere.

It is also quite insensitive to the coupled THMC phenomena taking place in the near-field: the only significant outcome of these phenomena is the value of the residual alteration rate V_r .

3.3.7 Evaluation of the Order of Magnitude of the Dose to Man

The radiological impact of the repository can now be evaluated. Continuing in the same line of extreme simplicity of the above exercise, we assume here that the main contributor of the dose to man is drinking water, and we neglect all other contributions coming from other compartments of the biosphere; with a consumption of 1 m³/year, and a caesium 135 ingestion dose factor of 2.10^{-9} Sv/Bq (cf. ➤ Table 6 in ➤ Sect. 1, ICRP 72), the maximum annual impact of caesium 135 will be

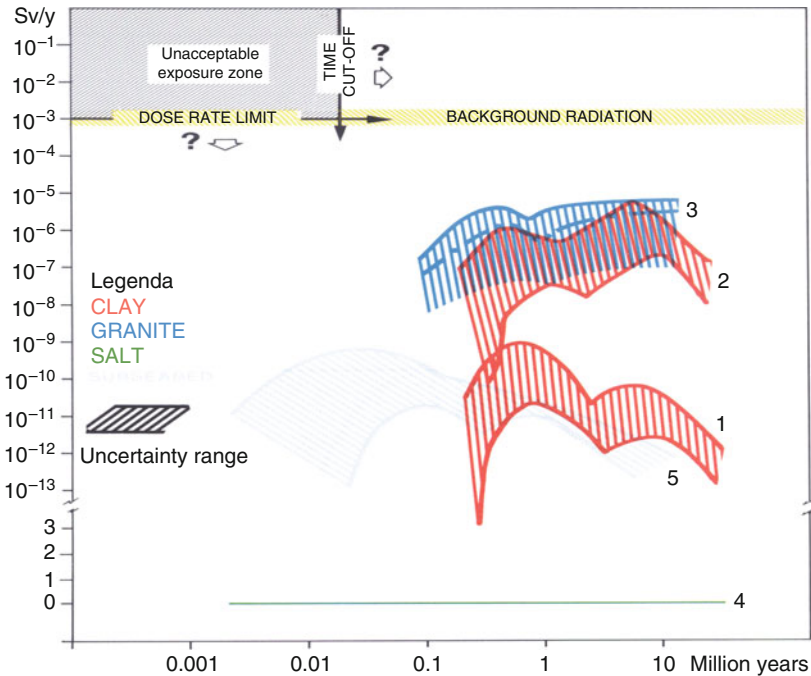


Figure 133 Result of the international exercise PAGIS “Performance Assessment of Geological Isolation Systems,” evaluation of the radiological impact of a deep geological repository of vitrified HALL waste. The impact depends on the nature of the host rock, and on the studied scenario, but in all cases, this impact is small (microsieverts/year for worst cases, i.e., 1,000 times less than the total dose induced by natural radioactivity), local, and delayed (migration is so slow that nothing arrives at the exutory before 100,000 years)

$Dose = A_{exut}^{Cs135} \cdot W \cdot Consumption \cdot DF^{Cs135} = 2 \cdot 10^{-8}$ Sv/year in the case of the above repository, containing the waste production from 50 years of exploitation of a 60 GW light water reactor fleet. . . . For a drinker 3 million years from now!

The small exercise proposed above gives orders of magnitude of released activities and timescales, but it is by no means sufficient to evaluate the radiological impact of a repository. More detailed simulations have been made using meshed codes, in the frame of national research programs. International benchmarks have also been performed to compare the modeling tools, and their results (PAGIS, EVEREST, SPA) (Fig. 133).

The impact of *altered scenarios* can be much higher than the one of the *reference scenario*; and other radionuclides, with shorter lifetime, can come into play. In granite, the impact of these altered scenarios can be higher than the natural dose. In clay, the situation is more favorable. Even for the altered scenarios, the impact is well below the dose induced by the natural background radiation, and below the legal limits.

Altogether, thanks to the efficiency and redundancy of its multiple barriers, a geological repository of radioactive waste is a robust concept. The radiological impact of deep geological disposal should remain small, local, and postponed.

4 Conclusions

4.1 Waste: The Achilles' Heel of the Nuclear Industry?

The nuclear waste issue is often presented by the media and seen by the public as an unsolved problem that hampers the future of nuclear energy. However, the nuclear industry took care of this problem very early on and has developed proven technical solutions.

4.2 Technical Solutions and Political Advances for Waste Management

While large volumes of short-lived radioactive wastes are already handled by the nuclear industry in surface storage facilities, the management mode of high-activity, long-lived waste has not been decided in detail and is still under study in all nuclear countries. Scientific knowledge is in progress, technical solutions are emerging, in a context where science and technique interact strongly with social and economical issues. Many advances have been made during the last 20 years in fields as varied as partitioning, transmutation, waste conditioning, storage, and underground disposal.

4.3 The Main Principles of Nuclear Waste Management

The following principles pertaining to domestic waste management also apply to nuclear waste: reducing the dangers induced by waste, decreasing its volume, partitioning the waste into homogeneous categories, and recycling.

With a closed fuel cycle, waste management from its production to its final destination looks like a chain whose links are treatment recycling, conditioning, storage, and disposal of the final waste. With the open cycle option, the first link is absent.

4.4 Recycling: The First Link of the Waste Management Chain

The first option is thus to close the fuel cycle. This option has a very important influence on the nature of the waste produced, as well as on its ulterior management.

The alternative options (direct storage of spent fuel or specific conditioning of separated actinides) have been studied throughout the world. These options may have distinct advantages for the nuclear industry considered as a whole, but as far as waste management is concerned, the closed fuel cycle is clearly more favorable, because it offers the possibility of considerably reducing the radiotoxic inventory, and putting the waste into a stable and safe form. Recently, the validity of this option has been further reinforced by the rise of the price of natural uranium, which provides a powerful incentive to save on fissile matter.

In the long run, the probable development of fourth-generation nuclear systems will make the closed fuel cycle compulsory. With these new systems, one can hope to reduce further the waste toxicity by transmuting actinides.

Indeed, the nature of the final nuclear waste (by definition non-recyclable) depends on the nuclear technology at hand; final waste 30 years from now may well be different from the present

final waste. For example, it may be possible to further reduce the radiotoxicity of vitrified waste by eliminating some radionuclides (e.g., minor actinides) from the inventory. The exclusion of these radionuclides from the waste would also reduce the exothermicity of the waste, with a subsequent simplification of the waste management. This objective of a cleaner and cooler waste is the main stake for the research on partitioning and transmutation. However, in order to gain a substantial benefit in terms of radiotoxicity, one needs to transmute the separated radionuclides. The technology is already at hand for recycling plutonium, but research is still needed to make the recycling of other radionuclides viable on the industrial scale.

4.5 Transmute, Recycle: Where Is the Limit?

It is already clear that fission products are not readily transmutable, neither with the present nuclear reactors, nor with the fast reactors envisaged for the future. Whatever the nuclear system, fission products will therefore remain present in the final nuclear waste. The issue of actinides is less certain, since the future of these radionuclides depends on the nuclear reactors available, as well as on the policy of fuel cycle chosen. With the present reactors, plutonium can be recycled under a MOX form, but minor actinides tend to accumulate in the waste. Fast reactors might offer the possibility of transmuting these radionuclides, but this transmutation will remain slow and difficult. Moreover, putting minor actinides in the fuel complicates both fuel fabrication and reactor operation, and one can doubt that those responsible for the facilities will be very enthusiastic about taking on this burden. The actinides are very insoluble and immobile in geological media, and could go in an underground repository without compromising its safety. The only important stake for the transmutation of actinides is the relief of the waste thermal loading and toxicity, with the associated reduction of the size and cost of the repository.

The first two links of the waste management chain, fuel processing and waste conditioning, work well together, and are already implemented in some countries (e.g., France, at the La Hague facility, or Japan at Rokkasho-Mura). Once conditioned under the form of a package, one still has the problem of deciding what to do with the package. Thanks to their chemical and mechanical stability, the present conditioning forms (concrete, metallic compacted waste, glass) are well adapted to storage, eventually followed by an underground disposal for long-lived waste. These links of the waste management chain are coherent, and this coherence will be kept with the development of fourth-generation nuclear systems, since future reactors will call for a closed fuel cycle with processes of treatment of the spent fuel that will complete rather than replace the existing process.

4.6 Waste Conditioning: The Essential Second Link in the Chain of Waste Management

The industrial processes for the conditioning of nuclear waste are already ripe and operating. Basic research has permitted a good understanding of the physicochemical mechanisms at play during both the fabrication and the aging of the conditioning matrices, glass, concrete, or bitumen. The safety study of waste management relies on this scientific knowledge of the long-term behavior of the confinement matrices.

Suitable conditioning forms have been developed for all types of wastes.

Solutions of fission products and minor actinides, which possess by far the highest radiotoxicity, are vitrified in facilities, which work on the industrial scale. The quality of the glass obtained is well established. For instance, the R7T7 glass developed for the confinement of fission products from the processing of light water spent fuel has become a world reference. There are probably more scientific articles on this glass than on any other industrial glass.

Structure waste from the spent fuel bundles is compacted and introduced in steel canisters identical to the ones used for glass casting. The radiological impact of this waste form in a geological repository would probably be very small.

Technological waste associated with the exploitation of nuclear facilities is conditioned in concrete. Most of these wastes are short-lived, low or medium activities. In many countries, including France, this waste is already stored in dedicated surface or subsurface facilities. A wide spectrum of concrete formulae has been developed to fit the diversity of the waste to be conditioned, solid or liquid. These concrete packages are well characterized, and a sufficient knowledge of their alteration mechanisms enables one to guarantee their confinement properties.

4.7 What To Do with the Final Waste?

Radioactivity possesses two important characteristics, which might somewhat mitigate the fear it inspires: it is easy to detect, even at very low levels. A unique disintegration can be detected, whereas billions and billions of molecules must be present to detect chemicals. Once detected, it is relatively easy to protect oneself from the radioactivity, by combining shielding, distance, limitation of the exposure time, and radioactive decay.

The problem of the final nuclear waste then boils down to confining the radionuclides in an isolated, shielded installation, during a time long enough for radioactive decay to operate. This is the idea behind both storage and underground disposal facilities.

4.8 Interim Storage, A Temporary Solution That Gives Flexibility to the Management of Waste

Whatever the fate envisaged for the spent fuel, this spent fuel must, at first, be stored temporarily. Countries that have chosen the open fuel cycle option must store the spent fuel before its disposal; the ones which have opted for the closed fuel cycle option must store it a few years, in order to let it cool before its processing. The vitrified final waste is then stored temporarily. In all cases, storing is a temporary solution, which provides flexibility for the management of waste, because it permits one to let the waste cool down, thereby decreasing its thermal load in the ulterior disposal facility, and the cost of the installation. However, the safety of storage facilities is less well assured than that of an underground disposal facility, because these installations demand active maintenance, and are more vulnerable to human intrusions. Even if economical arguments plead in favor of a long-term interim storage, public policy would be well advised to limit the duration of this storage to a reasonable maximum.

4.9 Underground Disposal, The Last Link of the Chain: A Final Place for the Final Waste

Last but not the least, one has to find a final place for the final waste. The deep geological underground disposal seems to be the only long-term solution, which does not require a continuous control by the society. A general consensus has been reached on this issue, under the aegis of the International Agency for Atomic Energy (IAEA) and of the Nuclear Energy Agency of OECD. No alternative solution has appeared.

Disposal in a geological repository will always be a rare and expensive resource; hence there is a need for reducing the volume and the thermal power of the waste as much as possible. These two parameters largely determine the repository capacity, and therefore, its duration of exploitation and its cost. The processing of spent fuel is already a major step toward this reduction, since it involves the removal of the uranium (which represents 90% of the mass of the spent fuel) and the removal of the plutonium (which represents the major contribution to the total waste radiotoxicity). The American Advanced Fuel Cycle Initiative (AFCI) is exemplary in this respect. After more than 20 years of efforts leading to the project of disposal of spent fuel in the Yucca Mountain repository, the US Department of Energy is reconsidering the optimization of its use, and the nature of the objects that will be disposed of.

4.10 Underground Disposal: A Simple and Robust Concept

The safety of the underground disposal relies on its capacity to confine radionuclides within an underground facility, until radioactive decay has brought their radiotoxicity down to an acceptable level. The safety demonstration of such an installation will rely *in fine* on the confidence that the installation will behave as foreseen. Studies have thus been made to better understand the evolution of the waste packages in an underground situation, and the migration of radionuclides through the man-made and geological barriers that isolate them from the biosphere. Removing from the waste the long-lived radionuclides, which contribute most to its long-term radiotoxicity, could significantly shorten the duration over which the waste will remain dangerous. This could also reduce the scientific uncertainties associated with long timescales. This option will only be open if and when one is able to separate and transmute minor actinides.

The concept of underground disposal is flexible. Initially designed with the idea of definitively and irreversibly getting rid of the waste, the underground disposal concept imposed itself in all nuclear countries, with a major evolution in its philosophy: the idea of reversibility (which means being able to retrieve the waste from the repository after some time) seems to have become a prerequisite for public acceptance of these installations. It contributes to modifying the image of underground repositories, without changing their general conception too much.

Thanks to the efficiency and the redundancy of its barriers, underground disposal is also a robust concept. The radiological impact of a deep geological waste disposal evolving should normally remain very small, local and delayed. However, the altered evolution scenarios, which are by definition unpredictable (especially those associated with human intrusions) can have a larger impact.

Strictly speaking, the safety of a deep geological repository cannot be *demonstrated*, because the very long timescales make direct experiments inaccessible. Therefore, the objective must be

more modest: showing by means of partial experiments that the main physical and chemical phenomena at play are understood and mastered, and therefore validating the main pieces of the modeling of repository evolution.

All national and international studies show that the impact of a repository on man and on the environment will remain negligible, even in the very long term. In order to convince, it will be necessary to build confidence with convergent indications showing that all the possible events liable to affect the repository have been envisaged and are found to be within acceptable limits... in short, that the repository conception is well mastered.

This confidence is already there among most of the specialists, but not in the public. And, as long as public opinion doubts, the politicians will tend to postpone their decisions. The example of Finland and Sweden, two countries that decided democratically to build geological repositories for nuclear waste, shows that it is possible to overcome this obstacle.

So, even if the majority of the public still thinks the opposite, one can conclude: "We know what to do about nuclear waste!"

4.11 Let Us Behave Responsibly, Let Us Try To Be Sensible

We have inherited nuclear waste from our predecessors, and we produce some waste ourselves. We cannot transmit this burden to our children. That is why we must put all our efforts into minimizing final waste, and disposing off this waste in the best safety conditions, with the technologies available today. The technologies exist, but their implementation requires a political decision. Contrary to a view widespread within the public, much progress has been made toward technically and socially acceptable nuclear waste repositories. Most of the experts agree, but the public and the political circles are still reluctant, and must be convinced by a faultless process of confidence building. In any case, one thing appears very clear to the author: it would be an irresponsible attitude to store this waste for a long time, awaiting a hypothetical scientific advance. Science also has its limits!

As shown above, even if one considers only the scientific and technical aspects, waste management is a very pluridisciplinary problem. Knowledge in reactor physics is needed, because the nature of the waste produced depends on the reactors used; knowledge in chemistry, to determine which radionuclides are left in the waste after the processing of the fuel; in physico-chemistry and material science to understand waste conditioning and the long-term behavior of waste; in engineering to master the thermal and aerodynamic phenomena at play in the storage installations; in mining engineering to design the underground repository; in earth sciences to understand and predict the long-term evolution of these installations; in radioprotection to evaluate the impact of all the processes and installations on man and environment. The global view on all these subjects is shared by very few people. Nonetheless, a global vision is necessary to keep research and industry focused on the main priorities, to keep the common sense. This common sense is already under stress when it comes to choosing the right options for the management of nuclear waste; even more so when one must give its right importance to the problem of nuclear waste, in the hierarchy of the problems caused by industrial development.

A nuclear renaissance seems inevitable at present: this makes the issue of nuclear waste management even more important. This problem is not only a technical one, it has also economic

and social implications. If this document has given to the reader the technical elements enabling him to forge for himself not only an engineer's vision, but also a citizen's opinion on nuclear waste management, it will have reached its aim.

5 Glossary

Actinides	The rare earth element group with atomic numbers 89–103, corresponding to electron subshells 5f and 6d. Actinides have very close chemical properties.
Activation (radioactivation)	Action tending to make certain nuclides * radioactive when bombarded by neutrons * or other particles, particularly within reactor structural materials.
Activity	1. For a radioactive substance: the number of spontaneous nuclear transitions per unit time within a radionuclide or mixture of radionuclides. It is expressed in becquerels * (Bq). A becquerel is equivalent to one disintegration per second. 2. In a chemical reaction: the chemical activity of a species corresponds to the active concentration of this species. Electrostatic interactions between the various species within a solution reduce their reactivity potential. Therefore, the concentration term must be corrected with a coefficient lower than one unit, the so-called activity coefficient. Substituting activity for chemical species concentration allows the mass-action law to be applied.
Advection	The movement or transfer of a substance, heat, etc. by the motion of the fluid medium (e.g., air or water) in which it is present.
Alpha	See Radioactivity .
Alpha particle (or <i>alpha radiation, alpha ray</i>)	A positively charged particle made up of two neutrons and two protons. It is the least penetrating of the three forms of radiation most commonly encountered.
Amorphous	Of a solid with a disordered crystalline structure.
Assembly	See Fuel assembly .
Barrier (confinement)	See Confinement barrier .
Becquerel (Bq)	A unit of radioactive decay equal to one disintegration per second. 37 billion becquerels are equal to 1 curie (Ci). 30,000 disintegrations per second occur in a household smoke detector. As the becquerel is a very small unit, large multiples are often used: mega-, giga-, or terabecquerel (MBq, GBq, and TBq, respectively).

Beta particle (or beta radiation, beta ray)	An electron (or a positively charged particle with a mass equal to that of an electron) emitted from a radionuclide. It means less damage than the same dose of <i>alpha</i> radiation, but has a higher penetrating power. A <i>beta</i> radiation may be stopped by a thin sheet of metal or plastic.
Biosphere	Ecosystem encompassing all living organisms and their environment (soils, water, atmosphere).
Burn-up (or burn-up, burn-up fraction, burn-up rate)	Strictly speaking, it corresponds to the percentage of heavy atoms (uranium and plutonium) that have undergone fission * over a given time interval (referred to as the " burn-up fraction "). It is commonly used to determine the thermal energy produced in a reactor per unit mass of fissile * material, between fuel loading and unloading operations, expressed in megawatt.days per ton (MWd/t). (see also Specific burn-up *). The discharge burn-up * is the value for which a fuel assembly must be effectively unloaded (i.e., after several irradiation cycles).
Capture	The capture of a neutron by a nucleus. The capture is said to be "radiative" if it is immediately followed by emission of gamma radiation. It is said to be "fertile" if it induces the generation of a fissile nucleus.
Cask	A vessel for the transport and/or storage of spent fuel and other radioactive materials. The cask serves several functions. It provides chemical, mechanical, thermal, and radiological protection, and dissipates decay heat during handling, transport, and storage.
Clad (or cladding)	The envelope surrounding the fuel material, intended to ensure its insulation and mechanical resistance within the reactor core.
Cleanup (radioactive)	All the operations intended to reduce radioactivity in a facility or at a site, especially by decontamination or equipment removal.
Conditioning (of radioactive waste)	All the successive operations to be performed to bring radioactive waste to a stable, safe form suitable for its future management, whatever it may be: storage *, transmutation *, or disposal *. In particular, these operations may include compaction, embedding *, vitrification *, and enclosing in containers (packaging).
Confinement barrier (or containment barrier)	A device able to prevent or limit dissemination of radioactive materials.

Containment barrier	See Confinement barrier .
Contamination (radioactive)	See Radioactive contamination .
Critical group	A group of members of the public, which is reasonably homogeneous with respect to its exposure for a given radiation source and given exposure pathway and is typical of individuals receiving the highest effective dose or equivalent dose (as applicable) by the given exposure pathway from the given source.
Criticality	A configuration characteristic of a mass of material containing fissile elements, and possibly other elements, with a composition, proportions, and a geometry such that a fission chain reaction * can be maintained within it.
Decay (radioactive)	The transformation of a radionuclide into different nuclides by spontaneous emission of <i>alpha</i> , <i>beta</i> , or <i>gamma</i> radiation, or by electron capture. The final product is a nucleus of lower energy and higher stability. Each decay process has a well-defined radioactive half-life.
Decontamination (radioactive)	See Radioactive decontamination .
Deep geological disposal (of radioactive waste)	See Disposal (of radioactive waste)*.
Delayed activity	The specific activity of a given radionuclide in its original confinement matrix after a time equal to its transit time between the repository and the exutory .
Direct disposal	The act of sending spent fuel to a disposal facility without going through the steps of treatment and recycling.
Discharge burn-up	See Burn-up *.
Disposal (of radioactive waste)	The action of radioactive waste emplacement in a facility specifically laid out to confine it in a potentially permanent way. The disposal facility in which waste is placed without intent to retrieve it is called repository . Retrieval would still be possible, however, in the case of a reversible disposal (see also Storage *). Deep geological disposal of radioactive waste is the disposal of such waste in an underground facility specifically laid out for this purpose. The underground disposal facility is referred to as a deep repository or a geological repository.
Distribution coefficient, Kd	The ratio of the amount of substance sorbed on a unit mass of dry solid to the concentration of the substance in a solution in contact with the solid, assuming equilibrium conditions.

Dose	A general term for the amount of energy from radiation that is absorbed in a specific mass.
Effluents	The residues of a chemical treatment under liquid or gaseous form. In some cases these unwanted residues are released to the environment. Another option widely practised in the nuclear industry is separating the toxic fraction and condition it into a tailored matrix so that the remainder may be released with no significant harm to the environment. Radioactive waste discharges to the environment are subject to authorization and control.
Embedding (or immobilization US, immobilization UK, encapsulation) (of radioactive waste)	The immobilization of radioactive waste through fixation within a material in order to obtain a solid, compact, and stable product, which is physically indispersible.
Encapsulation (of radioactive waste)	See Embedding (of radioactive waste)
Exutory	The compartment of the biosphere, which firstly receives the radionuclides released by a waste repository . In the scenario describing the normal evolution of the repository, the exutory is generally a nearby river.
Fast neutron reactor (or fast reactors)	Referred to in French as “RNR” (standing for <i>Réacteurs à Neutrons Rapides</i>).
FEP (Features, Events, Processes)	Elementary phenomena in the evolution of a waste storage or disposal facility.
Fertile	Refers to a material the nuclei of which yield fissile * nuclei when they absorb neutrons. This is the case with uranium-238, which yields plutonium-239. Otherwise, the material is said to be sterile.
Fissile	Refers to a nucleus capable of undergoing fission * through neutron * absorption. Strictly speaking, it is not the so-called fissile nucleus that undergoes fission, but rather the compound nucleus formed after neutron capture.
Fission	The splitting of a heavy nucleus into two fragments of approximately equivalent masses. This transformation, a special case of radioactive decay in some heavy nuclei, releases a large amount of energy and is accompanied with neutron and <i>gamma</i> radiation emission. The fission of the so-called fissile heavy nuclei can be induced by a collision with a neutron.
Fission products (FPs)	Nuclides * generated either directly through nuclear fission, or indirectly through the disintegration of fission fragments.

Fly ash	The pulverulent residues resulting from combustion. They fall into two categories: calcium fly ash arising from the incineration of some lignites recovered in thermal power plant scrubbers, and coal fly ash arising from pulverized coal combustion, which mostly contain silica and alumina in a glassy form. Fly ash may be used as additives in concretes.
FPs	See Fission products .
Fuel	The constituent material of a nuclear reactor core, which contains the fissile * nuclides maintaining the chain reaction * in the core.
Fuel assembly	In the core of a water reactor, fuel rods are gathered together in clusters of suitable rigidity, which are set in place with a definite position in the reactor core. The so-called assembly is the whole of this structure, grouping 100 to a few hundred rods, which is loaded into the reactor as a single unit.
Fuel cycle	The industrial operations which fissile * materials are subjected to. The cycle includes ore mining, fissile material concentration, enrichment, fabrication of fuel elements, fuel use in reactors, spent fuel treatment, waste conditioning, and the disposal of the resulting radioactive waste *.
Fuel pellet	See Pellet (fuel) .
Fugacity (for a gaseous substance)	An expression of chemical activity * (see acceptance 2). The fugacity of a gas equals its partial pressure weighed by its activity coefficient. This is also the pressure that the real gas would have if behaving as an ideal gas.
Gamma radiation (or <i>gamma rays</i>)	High-energy, short-wavelength, electromagnetic radiation emitted from atomic nuclei. It can be stopped by a sufficient layer of lead, concrete, or other materials.
Geological repository	See Disposal (of radioactive waste)*.
Geosphere	Those parts of the lithosphere not considered to be part of the biosphere . In radioactive waste management, usually used to distinguish the subsoil and rock from the soil that is part of the biosphere. See also biosphere.
Half-life	The time it takes for half the initial number of radioactive * atoms in a radioactive nuclide sample to disappear by spontaneous decay.
Immobilization (or immobilization UK) (of radioactive waste)	See Embedding (of radioactive waste).

Instant release fraction	Refers to the radionuclide fraction likely to be released very rapidly from a waste on contact with water.
Inventory (of radionuclides)	See Radionuclide inventory .
Ionizing radiation (or ionizing radiation UK)	Radiation capable of producing ions when it passes through matter.
Isotopes	The different forms of atoms of the same chemical element, the nuclei of which have an identical number of protons, but a different number of neutrons (i.e., the same atomic number, but different atomic masses). Uranium-238 and uranium-235 are uranium isotopes. Isotopes may be stable (i.e., not decay spontaneously) or unstable (i.e., decay spontaneously emitting ionizing radiation).
Leaching	The contacting of a solid body with a liquid with the purpose of extracting some elements. By extension, refers to any experiment focusing on the alteration of a solid in a liquid.
Major actinides	Heavy nuclei of uranium and plutonium occurring or formed in nuclear fuel.
Minor actinides	Heavy nuclei formed in a reactor through successive neutron captures from the fuel nuclei. These isotopes * mainly are neptunium (237), americium (241, 243), and curium (243, 244, 245).
Mixed OXide fuel	See MOX .
MOX (<i>mixed oxides</i>) (or Mixed OXide fuel)	A nuclear fuel containing Mixed OXides of (natural or depleted) uranium and plutonium.
Nuclear waste	An unusable residue arising from nuclear energy utilization.
Package (spent fuel)	Conditioned spent fuel in a form suitable for transport, storage and/or disposal.
Package (waste)	The product of conditioning that includes the waste form and any container(s) and internal barriers (e.g., absorbing materials and liners), prepared in accordance with the requirements for handling, transport, storage, and/or disposal.
Partitioning	See Separation .
Pellet (fuel)	A small cylinder made up of ceramic consisting of uranium, plutonium, or other actinides, which is used as nuclear fuel and stacked within a clad * to make up a fuel rod .
Potential radiotoxicity (of a certain quantity of radionuclides, e.g., in waste)	Radionuclide inventory multiplied by ingestion dose factor, indicating the potential harmfulness of a given quantity of radionuclides under accident conditions.

PWR	<i>Pressurized Water Reactor.</i>
Pyrochemistry	High-temperature chemistry (several hundred degree Celsius). Pyrochemistry does not involve water or organic molecules, only liquid metals and molten salts.
Radioactive cleanup	See Cleanup (radioactive) .
Radioactive contamination	The undesirable presence of a radioactive substance on the surface of or within a medium.
Radioactive decontamination.	Partial or total removal of radioactive contamination through methods that allow contaminating materials to be recovered in a controlled way.
Radioactive half-life	See Half-life (radioactive) .
Radioactive waste	Any radioactive substance for which no subsequent use is planned or contemplated. Ultimate radioactive waste is the radioactive waste, which can no longer be treated under current technical and economic conditions, especially through extracting their valuable content or reducing their polluting or hazardous character.
Radioactive waste disposal	See Disposal (of radioactive waste).
Radioactivity	The property of some isotopes with an unstable nucleus to spontaneously emit <i>alpha</i> and <i>beta</i> particles or <i>gamma</i> radiation. This term more generally designates the emission of radiation accompanying the decay * of an unstable element.
Radiolysis	The breakdown of molecules by ionizing radiation.
Radiolytic species	Products arising from water radiolysis * by ionizing radiation. They fall into two categories: radical species (e_{aq}^- , $\bullet OH$. . .) and molecular species (H_2 , O_2 , H_2O_2 . . .). Radiolytic yields associated with the generation of the various species depend upon the radiation type through linear energy transfer.
Radionuclide	An unstable nuclide * of an element, which spontaneously decays emitting radiation.
Radionuclide inventory	Quantities of fission products and actinides contained in irradiated fuel, generally expressed in Bq/gIHM (Becquerels per gram of initial heavy metal) or g/tIHM (grams per ton of initial heavy metal). These quantities and the associated isotopic spectra depend on various parameters, such as fuel type and irradiation conditions (burn-up, etc.). Average inventories are calculated at a given date using computer codes. Reversely,

	distribution of radionuclide inventories, which depends on irradiation conditions and fuel thermal behavior, requires the implementation of characterization tools (electron microscope).
Radiotoxicity (potential)	See Potential radiotoxicity .
Recycling (or recycle)	Reuse in a reactor of nuclear materials derived from spent fuel treatment *.
Repository	See Disposal (of radioactive waste).
Reprocessing	See Treatment (of spent fuel).
Rheology	The study of the deformation and flow of materials. It includes the study of viscosity, elasticity, and plasticity.
Rim effect (or rim)	See Rim zone .
Rim zone	The restructuring of a zone on the very edge of the pellet as a result of irradiation and thermal gradient.
Rod	A small-diameter tube closed at both ends, making up the core of a nuclear reactor and containing fissile, fertile, or absorbing material. When containing fissile material, the rod is a fuel element.
Scenario	Chronological sequence of elementary phenomena (FEPs) in the evolution of a waste storage or disposal facility.
Separation	A chemical process among treatment * operations through which the various constituent elements of spent fuel are separated. The PUREX process isolates uranium and plutonium. Other more advanced chemical processes (DIAMEX, SANEX, GANEX) are currently being studied to separate actinides from lanthanides, or actinides from one another (which is referred to as partitioning).
SF	See Spent fuel .
Sorbed	See Sorption .
Sorption	The light, reversible fixation of an atom or a molecule onto a solid surface.
Source term	The nature and quantity of radioactive products released or likely to be released from a nuclear facility or a package of radioactive materials. In particular, the “source term” used in computational models can help evaluate the consequences of an accidental radioactive release into the environment.

Specific burn-up (or specific burn-up, burn-up rate, burn-up)	The total amount of energy released per unit mass in a nuclear fuel. Generally expressed in megawatt × day per ton (MWd/t).
Spent fuel (or spent nuclear fuel, SF)	The fuel assemblies definitively removed from a nuclear reactor after a period of useful energy output. They are also referred to as “irradiated fuel.”
Spent fuel treatment	See Treatment (of spent fuel).
Spent nuclear fuel	See Spent fuel .
Storage (of radioactive materials or waste)	The action of placing radioactive materials or waste temporarily in a surface or subsurface specially designed facility, pending their retrieval. The facility in which waste is placed with the intention of further retrieval is referred to as a storage facility (see also Disposal).
Transmutation	The transformation of one nuclide into another through a nuclear reaction. Transmutation considered in relation to radioactive waste management aims at converting a long-lived nuclide into a shorter-lived or stable nuclide.
Treatment (of spent fuel) (or reprocessing, spent fuel treatment)	An operation that consists in separating valuable materials in spent fuel from the remainder, which can be then considered as waste and conditioned accordingly.
UOX	The standard fuel used in light-water reactors, composed of uranium oxide enriched with uranium-235.
Uranium	The heaviest natural element with an atomic number of 92.
Vitrification	An operation, which consists in incorporating radioactive wastes into a glass melt to ensure their conditioning in a stable form as packages likely to be stored or disposed off.
Waste (nuclear)	See Nuclear waste .
Waste (radioactive)	See Radioactive waste .
Waste immobilization (or waste immobilization UK)	See Embedding (of waste).

Acknowledgments

Acknowledgments to L. Strudel, C. Poinssot, P. Vitorge, J. Cabrera, C. Gallé, E. Vernaz, L. Martin-Deidier

References

- ANDRA, Dossier Argile 2005, ISBN 2-951 0108-8-5, http://www.andra.fr/interne.php3?id_article=934&id_rubrique=160
- Atkins M, Damidot D, Glasser FP (1994) Performance of cementitious systems in the repository. *Mater Res Soc Symp Proc* 333:315–326
- Beaucaire C, Tertre E, Coreau N, Juery A, Legrand S (2008) A multi-site ion exchange model to predict contaminants sorption in sediments. *Geochim Cosmochim Acta* 72:A62
- Bejaoui S, Bary B, Nitsche S, Chaudanson D, Blanc C (2006) Experimental and modelling studies of the link between microstructure and effective diffusivity of cement pastes. *Revue Européenne de Genie Civil* 10–9:1073–1106
- Bennett DG, Higgs JJW, Wickham SM (2001) Review of waste immobilisation matrices. Galsco Sciences Limited Report to United Kingdom Nirex Limited (0126–1, Version 1)
- Bernard P et al (2005) Hydration process and rheological properties of cement pastes modified by orthophosphate addition. *J Eur Ceram Soc* 25(11):1877
- Berner UA (1992) Evolution of pore water chemistry during degradation of cement in a radioactive waste repository environment. *Waste Manage* 12:201–219
- Bouniol P (2004) Etat des connaissances sur la radiolyse de l'eau dans les colis de déchets cimentés et son approche par simulation. CEA-R report n° 6069
- Brown P, Curti E, Grambow B (2005) Chemical thermodynamics of zirconium, chemical thermodynamics series Volume 8, OECD Publication Prediction of long-term corrosion behaviour in nuclear waste systems, Eurocorr workshop, Nice 2004
- Cailleteau C, Angeli F, Devreux F, Gin S, Jestin J, Jollivet P, Spalla O (2008) Insight into silicate glass aqueous alteration mechanisms. *Nat Mater* 7:978–983
- Blondiaux G, Fillet C (2006) The promise of specific conditioning. Clefs CEA n°53
- CEA Report CEA-R 6026 (2003) Database on long-lived radionuclides
- David D Analogues archéologiques et corrosion, doc ANDRA, collection sciences et techniques, ISSN 1629-7237 (2003), http://www.andra.fr/publication/produit/192_analogues.pdf
- de Marsily G (1981) Quantitative hydrogeology. Academic, New York
- Descostes M, Blin V, Bazer-Bachi F, Meier P, Grenut B, Radwan J, Schlegel ML, Buschaert S, Coelho D, Tevissen E (2008) Diffusion of anionic species in Callovo-Oxfordian argillites and Oxfordian limestones (Meuse/Haute-Marne, France). *Appl Geochem* 23:655–677
- Distinguin M, Lavanchy JM (2007) Determination of hydraulic properties of the Callovo-Oxfordian argillite at the Bure site: synthesis of the results obtained in deep boreholes using several in situ investigation techniques. *Phys Chem Earth* 32:379–392
- Dossier ANDRA synthèse argile (2005) ISBN 2-951 0108-8-5
- Ewing R et al (27 October 2006) Colloid transport of plutonium in the far-field of the Mayak Production Association, Russia. *Science* 314(5799):638–641
- Ferry C, Piron J-P, Poulesquen A, Poinssot C (2008) Radionuclides release from the spent fuel under disposal conditions: re-evaluation of the instant release fraction, basis for nuclear waste management. In: W.E. Lee, J.W. Roberts, N.C. Hyatt, R.W. Grimes (eds). *Mater Res Symp* 1107:447–454
- France's National Inventory (2009) <http://www.andra.fr>, book AND 0001013 ISSN 1629-5730
- Frugier P, Gin S, Minet Y, Chave T, Bonin B, Godon N, Lartigue JE, Jollivet P, Ayrat A, De Windt L, Santarini G (2008) SON68 nuclear glass dissolution kinetics: current state of knowledge and basis of the new GRAAL Model. *J Nucl Mater* 380:8–21
- Frugier P, Chave T, Gin S, Lartigue JE (2009) Application of the GRAAL model to leaching experiments with SON68 nuclear glass in initially pure water. *J Nucl Mater* 392:552–567
- Gallé C, Peycelon H, Le Bescop P, Bejaoui S, L'Hostis V, Bary B, Bouniol P, Richet C Concrete long-term behaviour in the context of nuclear waste management: experimental and modelling research strategy. *Journal de Physique IV (France)* 136:25–38
- Gauthier-Lafaye F (2002) 2 billion year old natural analogs for nuclear waste disposal: the natural nuclear fission reactors in Gabon (Africa). *CR Phys* 3:839–849
- Geckeis H, Rabung T (2008) Actinide geochemistry: from the molecular level to the real system. *J Cont Hydrol* 102:187–195
- Geological Disposal of Radioactive Waste Safety Requirements IAEA Safety Standards Series No. WS-R-4 (2006) ISSN 1020-525X

- Glasser FP (1997) Fundamental aspects of cement solidification and stabilisation. *J Hazard Mater* 52:151-170
- Glasser FP (2002) Characterization of the barrier performance of cements. *Materials Research Society Symposium Proceedings* 713, JJ9.1.1-JJ9.1.12
- Glasser FP, Atkins M (December 1994) Cements in radioactive waste disposal. *MRS Bulletin*, pp 33-37
- Grenthe I, Fuger J, Konings R, Lemire R, Muller A, Nguyen-Trung C, Wanner H (1992) Chemical thermodynamics of uranium, chemical thermodynamics series Volume 1. Elsevier, North-Holland, Amsterdam
- Gurban I, Laaksoharju M, Made B, Ledoux E (2003) Uranium transport around the reactor zone at Bangombe and Okelobondo (Oklo): examples of hydrogeological and geochemical model integration and data evaluation. *J Cont Hydrol* 61: 247-264
- Gwinner B, Sercombe J, Tiffreau C, Simondi-teisseire B, Felines I, Adenot F (2006) Modelling of bituminized radioactive waste leaching. Part II: experimental validation. *J Nucl Mater* 349: 107-118
- Handbook of Parameter Values for the Prediction of Radionuclide Transfer in Terrestrial and Freshwater Environments (2010) IAEA Technical Reports Series No. 472
- Horseman ST, Higgs JJW, Alexander J, Harrington JF (1996) Water, gas and solute movement through argillaceous media. Nuclear Energy Agency, OECD publication, 290pp
- Hu Q, Zavarin M, Rose T (2008) Effect of reducing groundwater on the retardation of redox-sensitive radionuclides. *Geochem Trans*, 9:12, doi:10.1186/1467-4866-9-12
- IAEA, Policies and strategies for radwaste management (2009) ISBN 978-92-0-103909-5 Nuclear Energy Series No. NW-G-1.1
- IAEA Categorizing operational radioactive wastes (2007) ISSN 1011-4289 TECDOC Series No. 1538
- IAEA (1991) IAEA Technical Report Series n°320, Evaluation of spent fuel as a final waste form, ISBN 92-0-1-125091-6
- IAEA (1993) IAEA Technical Report Series n°352, Bituminization processes to condition radioactive wastes, ISBN 92-0-100793-0
- IAEA (International Atomic Energy Agency) (1998) Interim storage of radioactive waste packages. IAEA Technical Reports Series No. 390, ISBN 92-0-103698-1, Vienna, Austria
- IAEA (1999) Survey of wet and dry spent fuel storage. Report no. IAEA-TECDOC-1100, IAEA, Vienna, ISSN 1011-4289
- IAEA (2000) Multi-purpose container technologies for spent fuel management. Report no. IAEA-TECDOC-1192, IAEA, Vienna, ISSN 1011-4289
- IAEA, Technical report series n° 435 (2004) Implications of Partitioning and Transmutation in Radioactive Waste Management, ISBN 92-0-115104-7
- ICRP (1996) Age-dependent doses to members of the public from intake of radionuclides Part 5 Complication of ingestion and inhalation dose coefficients 72, ISBN 0 08042737 5
- Johnson ER, Saverot PM (1997) Monograph on spent nuclear fuel storage technologies. Institute of Nuclear Materials Management, Deerfield
- Interim storage of spent nuclear fuel: a safe, flexible, and cost-effective near-term approach to spent fuel management (2001) A Joint Report from the Harvard University Project on Managing the Atom and the University of Tokyo Project on Sociotechnics of Nuclear Energy, June 2001
- Johnson LH, Ferry C, Poinssot C, Lovera P (2005) Spent fuel radionuclide source term model for assessing spent fuel performance in geological disposal. Part I - assessment of the instant release fraction. *J Nucl Mater* 346:56-65
- Kersting AB et al. (7 January 1999) Migration of plutonium in groundwater at the Nevada Test site. *Nature* 397:56-59
- Lemire R, Fuger J, Nitsche H, Potter P, Rand M, Rydberg J, Spahiu K, Sullivan J, Ullman W, Vitorge P, Wanner H (2001) Chemical thermodynamics of neptunium and plutonium. Chemical thermodynamics series volume 4, OECD Publication
- Leroy P, Revil A, Altmann S, Tournassat C (2007) Modelling the composition of the pore water in a clay-rock geological formation (Callovo-Oxfordian, France). *Geochim Cosmochim Acta* 71(5):1087-1097
- Limousin G, Gaudet JP, Charlet L, Szenknect S, Barthès V, Krimissa M (2007) Sorption isotherms: a review on physical bases, modelling and measurement. *Appl Geochem* 22: 249-275
- Lutze W, Ewing R (1988) Radioactive wasteform for the future. North Holland, New York, 778pp, ISBN 978-0-44487104-6
- MacQuarrie KM, Mayer K (2005) Reactive transport modelling in fractured rock: a state-of-the-science review. *Earth-Sci Rev* 72:189-227
- Mainguy M, Tognazzi C, Torrenti J-M, Adenot F (2000) Modelling of leaching in pure cement paste and mortar. *Cement Concrete Res* 30: 83-90

- Martin G et al (2006) A quantitative μ NRA study of helium intergranular and volume diffusion in sintered UO₂. NIMB 249:509–512
- Miller W, Alexander R, Chapman R, McKinley I, Smellie J (1994) Natural analogue studies in the geological disposal of radioactive wastes. Studies in environmental science 57, Elsevier, Amsterdam
- Moreau Le Golvan Y, Study of fluid flow and transport properties using natural and artificial tracers at the Tournemire claystone site (France). Intl conf on tracers and modelling in hydrogeology (TRAM 2000) IPSN
- Motellier S, Ly J, Gorgeon L, Charles Y, Hainos D, Meier P, Page J (2003) Modelling of the ion-exchange properties and indirect determination of the interstitial water composition of an argillaceous rock. Application to the Callovo-Oxfordian low-water-content formation. Appl Geochem 18:1517–1530
- Mukhopadhyay S, Sonnenthal EL, Spycher N (2009) Modelling of coupled heat transfer and reactive transport processes in porous media: application to seepage studies at Yucca Mountain, Nevada. J Porous Media 12:725–748
- Neff D Contribution of archaeological analogs to the estimation of average corrosion rates and long-term corrosion mechanisms of low-carbon steel in soil. PhD thesis, FRNC-TH-5814 (2003)
- NRC, <http://www.nrc.gov/waste/spent-fuel-storage.html>
- (1996) Nuclear Wastes: technologies for separation and transmutation, National Academy Press, Washington, DC, ISBN 0309052262
- Ojovan MI, Lee WE (2005) An introduction to nuclear waste immobilisation. Elsevier, Amsterdam, 315 pp
- PAGIS: Performance Assessment of Geological Isolation Systems (1990) ISBN 92-64-0334-3
- The EVEREST project: Sensitivity analysis of ecological disposal systems, Reliability Engineering and System Safety, vol 57, n^o, p 79–90 (1997)
- Papp R (1998a) Technische und geologische Barrieren bei der Endlagerung (in German), ATW 43, Jg 1998a, Heft 4, April, pp 252–255
- Petit JC (1992) Natural analogues for the design and performance assessment of radioactive waste forms: a review. J Geochem Explor 46:1–33
- Peugot S, Cachia J-N, Jégou C, Deschanel X, Roudil D, Broudic V, Delaye J-M, Bart J-M (2006) Irradiation stability of R7T7-type borosilicate glass. J Nucl Mater 354:1–13
- Peycelon H, Adenot F, Le Bescop P, Richet C, Blanc V (2001) Long-term behaviour of concrete: development of operational model to predict the evolution of its containment performance. Application to Cemented Waste Packages. Global 2001 Conference, Paris, France, September 9–13, 2001
- Pinet O, Grandjean A, Schuller S, Blisson T (2005) “Procédé de confinement d’une matière par vitrification, French patent EN 05/52218
- Poinssot C, Baeyens B, Bradbury M (1999) Experimental and modelling studies of caesium sorption on illite. Geochim Cosmochim Acta 63:3217–3227
- Poinssot C, Ferry C, Lovera P, Jégou C, Gras J-M (2005b) Spent fuel radionuclide source term model for assessing spent fuel performance in geological disposal. Part II: matrix alteration model and global performance. J Nucl Mater 346:66–77
- Policies and Strategies for Radioactive Waste Management, IAEA Nuclear Energy series NW-G-1.1 (2009) ISBN 978-92-0-103909-5
- Posiva Oy (1999) The final disposal facility for spent nuclear fuel: environmental assessment report, General Summary
- Pourcelot L, Gauthier-Lafaye F (1999) Hydrothermal and supergene clays of the Oklo natural reactors: conditions of radionuclide release, migration and retention. Chem Geol 157:155–174
- Principles of Radioactive Waste Management Safety Fundamentals IAEA Safety Series No. III-F, Metcalf P.E., ISBN 92-0-103595-0
- Report of the CEA working group (2003) CEA report 6026
- Research program on the long-term evolution of the spent fuel [PRECCI project, 2008, CEA report]
- Ribet I, Crovisier JL, Curti E, Del Nero M, Grambow B, Lemmens K, Lukscheiter B, Schwyn B (2004) Long-term behaviour of glass: improving the glass source term and substantiating the basic hypotheses. GLASTAB Final report. European Commission
- Rotenberg B, Marry V, Dufrêche JF, Giffaut E, Turq P (2007) A multiscale approach to ion diffusion in clays: Building a two-state diffusion–reaction scheme from microscopic dynamics. J Colloid Interface Sci 309:289–295
- Roudil D, Deschanel X, Trocellier P, Jégou Ch, Peugeot S, Bart J-M (2004) Helium thermal diffusion in a uranium dioxide matrix. J Nucl Mater 325:148–158
- Safety Indicators for the Safety Assessment of Radioactive Waste Disposal IAEA TECDOC Series No. 1372, ISBN 92-0-108703-9
- Savage D (ed.) (1995) The scientific and regulatory basis for the geological disposal of radioactive waste. Wiley, West Sussex

- Schindler PW, Stumm W (1987) The surface chemistry of oxides, hydroxides and oxide minerals. In: Stumm W (ed.) Aquatic surface chemistry. Wiley-Interscience, New York
- Sercombe J, Gwinner B, Tiffreau C, Simondi-teisseire B, Adenot F (2006) Modelling of bituminized radioactive waste leaching. Part I: constitutive equations. *J Nucl Mater* 349:96–106
- Silva R, Bidoglio G, Rand MH, Robouch P, Wanner H, Puigdomenech I (1995) Chemical thermodynamics of americium, chemical thermodynamics series Volume 2, Elsevier, Amsterdam
- Baudin P. et al. Major results and lessons learned for performance assessments of spent fuel geological disposal: the SPA project. Eurosafe 2000 (2001) <http://www.eurosafe-forum.org>
- Stumm W, Morgan JJ (1996) Aquatic chemistry. Wiley Interscience, New York, 1022pp
- Taylor HFW (1997) Cement chemistry. Academic, London
- IAEA Tech. Report Series 435, Implications of partitioning and transmutation in radioactive waste management (2004) ISBN 92-0-115104-7
- Tuli JK (ed) (2000) Nuclear Wallet Cards, Brookhaven National Laboratory, Upton, New York
- United States Department of Energy (2002) Environmental impact statement for a geologic repository for the disposal of spent nuclear fuel and high-level radioactive waste at Yucca Mountain, Nye County, Nevada
- Van Iseghem P, Aertsens M, Gin S, Deneele D, Grambow B, McGrail P, Strachan D, Wicks G (2007) A critical evaluation of the dissolution mechanisms of high-level waste glasses in conditions of relevance for geological disposal (GLAMOR). In: SCK.CEN, CEA, Subatech, PNNL, SRNL (eds) EUR 23097 ed., pp 1–164
- Vernaz E (2002) Role of neoformed phases on the mechanisms controlling the resumption of SON68 glass alteration in alkaline media. *CR Phys* 3:813
- Wickham SM (2003) Literature review of approaches to long-term storage of radioactive waste and materials. Galson Sciences Ltd., Oakham. GSL Report no. 0331-1



29 Proliferation Resistance and Safeguards

Scott F. DeMuth

Los Alamos National Laboratory, Los Alamos, NM, USA
scott.demuth44@comcast.net

Principal Authors

Robert Bari

Brookhaven National Laboratory, Upton, NY, USA
bari@bnl.gov

Charles Bathke

Los Alamos National Laboratory, Los Alamos, NM, USA
bathke@lanl.gov

Brian Boyer

Los Alamos National Laboratory, Los Alamos, NM, USA
bboyer@lanl.gov

Thomas Burr

Los Alamos National Laboratory, Los Alamos, NM, USA
tburr@lanl.gov

Michael Ehinger

Oak Ridge National Laboratory, Oak Ridge, TN, USA
ehingermh@ornl.gov

Magnus Hedberg

Institute for Transuranium Elements, Karlsruhe, Germany
Magnus.HEDBERG@ec.europa.eu

John Howell

Department of Mechanical Engineering,
Systems and Control
University of Glasgow, UK
j.howell@mech.gla.ac.uk

Klaus Luetzenkirchen

Institute for Transuranium Elements, Karlsruhe, Germany
Klaus-Richard.luetzenkirchen@ec.europa.eu

Klaus Mayer

Institute for Transuranium Elements, Karlsruhe, Germany
Klaus.mayer@ec.europa.eu

Mark Schanfein

Idaho National Laboratory, Idaho Falls USA
Mark.Schanfein@inl.gov

Rebecca Stevens

Los Alamos National Laboratory, Los Alamos, NM, USA
rstevens@lanl.gov

Richard Wallace

Los Alamos National Laboratory, Los Alamos, NM, USA
rwallace@lanl.gov

Maria Wallenius

Institute for Transuranium Elements, Karlsruhe, Germany
Maria-S.Wallenius@ec.europa.eu

1	<i>Proliferation Resistance</i>	3425
1.1	Material Attractiveness	3426
1.1.1	Figure of Merit	3426
1.1.2	Meaning of FOM Values	3427
1.1.3	Comparison of Various Reprocessing Schemes	3427
1.1.4	Conclusions	3434
1.2	Nonproliferation Impact Assessments	3434
1.2.1	Methodology	3435
1.2.2	Technical Factors and Metrics	3438
1.2.3	Policy Factors and Grading	3449
1.2.4	PR&PP Example	3450
2	<i>Safeguards</i>	3453
2.1	Domestic Safeguards: Implementing a State System of Accounting and Control (SSAC)	3454
2.1.1	Primary Features of an SSAC	3454
2.2	IAEA Inspection Regime	3456
2.2.1	Timeliness Goals	3459
2.2.2	Quantity Goals	3460
2.2.3	Deterrence by Risk of Early Detection	3461
2.2.4	Frequency of Inspection to Fulfill Technical Objectives of Safeguards	3461
2.2.5	IAEA Nuclear Facility Categories	3461
2.2.6	Keystones of Bookkeeping, Material Accountancy, and Containment and Surveillance	3463
2.2.7	Strengthened Safeguards	3465
2.3	Safeguards Design	3466
2.3.1	Safeguards Requirements	3466
2.3.2	Safeguards by Design	3468
2.4	Unattended Monitoring	3470
2.4.1	Background	3471
2.4.2	Definition of an Unattended Monitoring System (UMS)	3471
2.4.3	Why Does the IAEA Use UMS?	3472
2.4.4	Benefits of UMS	3472
2.4.5	Key to Maintaining a Balanced Approach in IAEA Safeguards	3473
2.4.6	Major Cost Drivers in the Department of Safeguards	3473

2.4.7	Primary Goals of UMS	3474
2.4.8	Method of Obtaining Primary Goals	3474
2.4.9	Conclusion	3492
2.5	Process Monitoring	3492
2.5.1	Key Elements.....	3494
2.5.2	Role of Models and Simulation	3496
2.5.3	Strategy for Reprocessing Plants	3497
2.5.4	Operational Evaluation Systems.....	3498
2.6	Environmental Sampling	3501
2.6.1	Basic Principles of Environmental Sampling	3502
2.6.2	Sampling Methods	3503
2.6.3	Bulk Measurements of Dust Samples	3504
2.6.4	Particle Measurements of Dust Samples	3505
2.7	Forensics	3507
2.7.1	Methodology.....	3507
2.7.2	Characteristic Parameters in Nuclear Forensic Investigations	3509
2.7.3	Data Interpretation and Attribution	3515
2.7.4	Conclusions	3517
2.8	Statistics for Accountancy.....	3518
2.8.1	Background	3518
2.8.2	Measurement Error Models.....	3520
2.8.3	Propagation of Variance	3521
2.8.4	Sequential or Trend Testing.....	3522
2.8.5	ID Test	3524
2.8.6	SITMUF Test.....	3524
2.8.7	Verifying Declarations	3525
2.8.8	Other Purposes of the PI	3526
2.8.9	Sampling.....	3527
2.8.10	Difficulties with ID Evaluation	3527
2.8.11	Solution Monitoring	3528
2.8.12	Conclusions	3529
2.9	Accountancy for Abrupt Diversion	3529
	References	3534
	Website	3538

Abstract: The Nuclear Nonproliferation Treaty (NNPT or NPT) is the primary cornerstone of international efforts to prevent the proliferation of nuclear weapons. Currently, 189 countries are party to the treaty, with only four sovereign states abstaining: India, Israel, Pakistan, and North Korea. The treaty is broadly interpreted as having three pillars: (1) nonproliferation, (2) disarmament, and (3) the right to the peaceful use of nuclear technology.

Five countries are recognized by the NPT as nuclear weapon states (NWSs): the United States (US), the Soviet Union (obligations and rights now assumed by Russia), France, the United Kingdom, and the People's Republic of China. These five nations are also the five permanent members of the United Nations (UN) Security Council. In accordance with the NPT, the NWSs agree to not transfer nuclear weapons to a nonnuclear weapons state (NNWS) or assist NNWSs in acquiring nuclear weapons. Additionally, the NNWSs party to the NPT agree not to receive or manufacture nuclear weapons. NNWSs also agree to accept safeguards monitoring by the International Atomic Energy Agency (IAEA) to verify that they are not diverting material derived from the peaceful use of nuclear technology to weapons.

The NPT's preamble also contains language affirming the desire of all signatories to halt the production of nuclear weapons worldwide and to develop an additional treaty related to complete nuclear disarmament and liquidation, including their delivery vehicles. However, the NPT wording does not strictly require all signatories to actually conclude a disarmament treaty, but rather to negotiate in good faith. Some NNWSs belonging to the Non-Aligned Movement (an international organization of states considering themselves not formally aligned with or against any major power block) have interpreted the NPT as requiring the NWSs to disarm themselves and argue that these states have failed to meet their obligations.

The Strategic Arms Reduction Treaty (START) between the United States (U.S.) and Soviet Union is considered by many to be the largest and most complex arms control treaty in history. The treaty was signed on 31 July 1991, but entry-into-force was delayed until 5 December 1994 due to the collapse of the Soviet Union. By way of the Lisbon Protocol to the START treaty signed 23 May 1992, Russia, Belarus, Kazakhstan, and Ukraine became Parties to the treaty as legal successors to the Soviet Union. Upon initiation of the START II negotiations, the original START was renamed to START I. START II was signed by the U.S. and Russian presidents on 3 January 1993, banning the use of multiple independently targetable reentry vehicles (MIRVs) on intercontinental ballistic missiles (ICBMs). Russian ratification of START II was contingent on preservation of the Antiballistic Missile (ABM) treaty. START II was never entered-into-force because the U.S. withdrew from the ABM treaty 13 June 2002 in order to pursue a missile defense system, whereupon Russia withdrew from START II one day later. As a result of START I, there has been a significant reduction in the number of deployed warheads for both the U.S. and Soviet Union.

Under the May 2002 Strategic Offensive Reductions Treaty (SORT), both the U.S. and Russia pledged to reduce the number of deployed strategic nuclear weapons to between 1700 and 2200 by the year 2012. SORT is different from START in that it limits actual warheads, whereas START I limits warheads only through their means of delivery (ICBMs, SLBMs, and Heavy Bombers). Experts have estimated that by the year 2009, the U.S. and Russia arsenals for strategic nuclear weapons ranged from 2200 to 3000 each. The U.S. and Russian presidents signed a preliminary agreement on 6 July 2009 to further reduce the number of active nuclear weapons to between 1,500 and 1,675 from 2,200. In accordance with the agreement, the new caps on nuclear arsenals will need to be fully implemented by 2012.

Although the START and SORT treaties have been the backbone of joint US and Russia efforts toward nuclear disarmament, the treaties have not addressed the discontinuation

of weapons-grade fissile material production and disposition of excess weapons-grade materials. The 1993 UN Assembly resolution 48/75L called for negotiations leading to a verifiable treaty banning the production of fissile materials for nuclear weapons. Additional UN activities have followed the initial resolution; however, a final treaty has not yet been completed. The current situation is that the US, France, and the United Kingdom have ceased production. In 1997, the US and Russia signed the Plutonium Production Reactor Agreement (PPRA) to cease production of plutonium for weapons production, which included provisions for monitoring. Although Russia still operates nuclear reactors used previously for production of weapons material, to generate heat and electricity, they do not process the spent fuel. Plans are in place to decommission the Russian production reactors. Unsubstantiated reports indicate that China also has instituted a moratorium on production. Both India and Pakistan apparently are still producing weapons-grade material, and Israel's position is unclear.

Throughout the Cold War, the US and the Soviet Union produced ~100 and 150 metric tons (MT) of weapons-grade plutonium, respectively. In September 2000, the US and Russia each formally agreed to transform 34 MT of excess military plutonium into a more proliferation-resistant form over the course of 20 years. Current plans for both countries are to irradiate all 34 MT of its plutonium in nuclear power reactors. Plutonium disposition programs in both countries are still in the early stages. The start-up costs of plutonium disposition are extremely high. Currently, Russia favors irradiation in a new generation of fast reactors yet to be developed, and the US favors irradiation in their existing commercial light-water-reactor (LWR) fleet. Additionally, a joint program was developed by the US and Russia to disposition excess highly enriched uranium (HEU). Excess HEU is currently being dispositioned by way of the joint HEU downblend program. The HEU downblend program includes 500 MT of HEU from Russia (of the 1,000–1,500 MT of HEU produced by the USSR during the Cold War), whereas ~175 MT of HEU from the US (from 500 to 750 MT of HEU produced during the Cold War) has been declared excess. The HEU is downblended with natural uranium to produce low enriched uranium (LEU) for commercial power reactor fuel. Over 300 MT of HEU from Russia and tens of MT from the US have already been downblended.

1 Proliferation Resistance

Proliferation resistance refers to the ability to hinder the theft or diversion of weapons, weapon components, special nuclear materials (SNMs), or alternate nuclear materials (ANMs). With regard to nuclear power, or more generally the nuclear fuel cycle, theft or diversion of SNM is the primary concern. This section focuses only on the nuclear fuel cycle. A long standing debate among global participants involved with the nuclear fuel cycle has been material attractiveness of the various SNMs and in some cases ANMs. This ranges from differences between weapons-grade plutonium and reactor-grade plutonium, to the consideration of actinides such as americium and neptunium. The debate over weapons-grade versus reactor-grade plutonium is related to the distribution of its isotopes, and their effect on the construction and deployment of a nuclear weapon. One aspect of this debate is centered on the question of how much intrinsic heating is sufficient to thwart the construction and deployment of a weapon. The advocates of plutonium denaturing claim that 6–12% ^{238}Pu content provides a sufficient heat deterrent (see Saito et al. 2008 and references therein), whereas others, including the authors, assert that $\geq 80\%$ ^{238}Pu is required to eliminate any risk. The amount of ^{238}Pu required ultimately is dependent upon an assessment of the technical ability of the proliferator.

Conservatively speaking, entry into the “nuclear club” is more dependent upon the fact that the device will produce nuclear yield, than it is on the amount of nuclear yield that is produced. The point at which the nuclear explosive energy exceeds the conventional explosive energy, is the point at which there is a credible nuclear threat. At this point, the weapon is referred to as a threshold nuclear device. Consequently, the authors have focused on nuclear devices that are capable of a threshold yield. The factors that are relevant to building a threshold device are bare critical mass, internal heat generation, and radiation dose rate. Neutron background rate is another aspect of material attractiveness that is relevant to optimizing the nuclear yield, but it is not relevant to whether there is a credible nuclear threat.

A long standing objective for those involved with proliferation assessments has been the development of a methodology for quantifying proliferation risk. This becomes particularly complex recognizing that one may want to assess an individual component of a nuclear fuel cycle, or compare entire fuel cycles. Comparison of aqueous reprocessing versus electrochemical reprocessing is an example of individual components. An example of comparing entire fuel cycles is the open fuel cycle based on light-water reactors (LWRs) with an underground repository for spent fuel, compared with a closed mixed oxide (MOX) fuel cycle based on LWRs with an underground repository for high level waste (HLW). Recently, interest has centered on quantifying the reduced proliferation risk for a closed transmutation fuel cycle, where the minor actinides americium, neptunium, and curium are considered for reburning in fast reactors (FRs).

1.1 Material Attractiveness

This section introduces the concept of “material attractiveness” for potential use in threshold nuclear weapons by proliferators. A figure of merit (FOM) is given for calculating material attractiveness. The FOM is then applied to a comparison of the “material attractiveness” of intermediate and end products associated with the UREX, COEX, ^{238}Pu spiking, and PYROX reprocessing schemes. The results of the comparison are expressed in terms chosen for consistency with those normally used for nuclear materials (Bathke et al. 2008a, b; Bathke et al. 2009a, b). These results illustrate the inverse relationship between material attractiveness and proliferation resistance, and can be used to inform policy makers about some of the issues related to reprocessing.

1.1.1 Figure of Merit

The metric used for evaluating the attractiveness of SNM or ANM for use in a threshold nuclear device is the FOM shown in (1) (Ebbinghaus et al. 2006a, b):

$$\text{FOM} = 1 - \log_{10}(x), \quad (1)$$

where x is given by:

$$x = M \left[\frac{1}{800} + \frac{h}{4,500} \right] + \left[\frac{D}{500} \right]^{\frac{1}{\log_{10} 2}},$$

M is the bare critical mass of the metal in kg, h is the heat content in W/kg, and D is the dose rate at 20% of M evaluated at $1 - m$ from the surface in rad/h.

The FOM applies to pure elements (e.g., U, Np, Pu, Am, etc.) and to actinide metal mixtures. It also conservatively bounds impure metal mixtures such as mixtures of actinides and lanthanides. How the FOM is to be applied depends upon the capability of the adversary and the time available to the adversary. In one extreme, one must assume that the adversary has sufficient capability and time to purify the material. In this case, it is only valid to apply the FOM to pure elements (e.g., Pu, U, Np, Am, etc.). In the other extreme, it is possible that the adversary has limited technical ability or limited time, and the best for the adversary is an actinide or impure metal mixture. In this case, it is appropriate to apply the FOM to the actinide metal or the impure metal mixture. The authors have calculated both extremes as shown in the following figures.

1.1.2 Meaning of FOM Values

An absolute scale to judge numeric values of the FOM is given in [Table 1](#), which casts the FOM in terms of the utility of SNM for use in threshold nuclear device. Materials with high utility require greater safeguarding than low utility.

In Bathke et al. (2008a, b) and Bathke et al. (2009a, b), the FOM was mapped into the US Department of Energy (DOE) attractiveness levels (Nuclear Material Control and Accountability, the US Department of Energy manual DOE M 470.4-6, see [Table 2](#)). The DOE requires more stringent material control and accountability for higher attractiveness levels. Such a mapping is not strictly applicable, because the DOE attractiveness levels are determined by both quantity and quality of the SNM. Nevertheless, a meaningful correlation still exists between the FOM, utility, and the attractiveness levels. From a safeguards perspective, SNM of high (H) utility ($FOM > 2$) is comparable in quality to material with an attractiveness level of B. Similarly, SNM of moderate (M), low (L), and offscale (O) utility are comparable to material with the Attractiveness levels of C, D, and E, respectively. To avoid confusion for those dealing with SNM that must be safeguarded according to US DOE regulations, the FOM henceforth is only described in terms of its utility. From a safeguards and security perspective, the products of an ideal reprocessing scheme would have utility L or O (i.e., $FOM < 1$).

1.1.3 Comparison of Various Reprocessing Schemes

The reprocessing schemes analyzed to date and reported herein are: UREX, COEX, ^{238}Pu spiking, and PYROX. The source of material for all the reprocessing schemes analyzed herein

Table 1
Mapping of the figure of merit (FOM) into utility

FOM for metals	Utility	Designation on plots
> 2	High	H
1–2	Moderate	M
0–1	Low	L
< 0	Off scale	O

■ **Table 2**

US Department of Energy (DOE) attractiveness levels

Attractiveness level	Description
B	Pure products
C	High-grade materials
D	Low-grade materials
E	All other materials

is spent uranium oxide from pressurized water reactors (PWRs) and boiling water reactors (BWRs). Such spent fuel is typically characterized by its burnup, expressed in MW d/kg of initial heavy metal. The average burnup of spent fuel in the United States historically has ranged from ~15 MW d/kg for BWRs and from ~25 MW d/kg for PWRs (Spent Nuclear Fuel Discharges from US Reactors 1994) to present day values of 45–50 MW d/kg. For this analysis, the isotopic composition of spent fuel was generated with ORIGEN2.2 (Ludwig and Croff 2002) for burnups ranging from 7.5 to 90 MW d/kg. Calculations of the required ^{235}U enrichment for the fuel charge, and the spent fuel compositions, are in good agreement with similar published results (AFCF Development of LWR Fuel Source Terms and Non-Fuel Bearing Component Elemental Weights for 4-Corners Study 2007; Neeb 1997; Hill et al. 2002; Pellaud 2002; Stillman et al. 2004; Xu et al. 2005; Secker et al. 2005). Also varied was the spent fuel age at the time of reprocessing relative to the time of discharge and the time after reprocessing.

The UREX process is a suite of alternate reprocessing schemes based on similar chemistry. A list of the possible UREX products that contain transuranic elements and their associated process version is given in ▶ Table 3. The FOM results for the non-uranium-bearing products listed in ▶ Table 3 are shown in ▶ Fig. 1. The products with the highest FOM are Pu and Pu + Np, which have the same FOM value. The FOM for both Pu and Pu + Np decreases significantly with increasing burn-up, because the concentrations of ^{239}Pu and ^{241}Pu (i.e., the isotopes with relatively high fission cross sections) decrease and the concentration of ^{238}Pu , which is an intense heat source, increases with increasing burn-up. The age of the spent fuel at the time of reprocessing has only a minor effect on the FOM (i.e., the FOM increases slightly with increasing age). Heat is the primary proliferation barrier for Pu and Pu + Np.

The next highest FOM value belongs to TRU (i.e., the transuranic elements). The FOM of TRU decreases significantly with increasing burn-up, because the concentration of highly fissile isotopes (e.g., ^{239}Pu and ^{241}Pu) decreases with increasing burn-up. However, the FOM for TRU increases significantly with increasing spent-fuel age, because ^{242}Cm and ^{244}Cm , which are intense heating sources, quickly decay away (their half lives are 163 days and 18 years, respectively).

In contrast, the FOM of Am increases with increasing burn-up, because of the build up of ^{243}Am relative to ^{241}Am as the burn-up increases and because ^{243}Am produces less heat relative to ^{241}Am . The FOM of Am decreases with increasing spent-fuel age, because of the build up of ^{241}Am relative to ^{243}Am with increasing age due to the beta decay of ^{241}Pu to ^{241}Am .

The FOM of Cm also increases with increasing burn-up, because of the build up of ^{244}Cm relative to ^{242}Cm , where ^{244}Cm produces less heat relative to ^{242}Cm . As with TRU, the FOM of Cm increases significantly with increasing spent-fuel age. Although Cm has a significant

■ **Table 3**
List of UREX products and associated processes

Product	Process(es)
Pu + Np	UREX + 2, UREX + 3, UREX + 4
Pu + Np + U	UREX + 2a, UREX + 3a, UREX + 4a
TRU	UREX + 1A
TRU + U	UREX + 1B
TRU + Ln	UREX + 1
Am	UREX + 4, UREX + 4A
Cm	UREX + 4, UREX + 4A
Am + Cm	UREX + 3, UREX + 3A
Am + Cm + Ln	UREX + 2, UREX + 2A

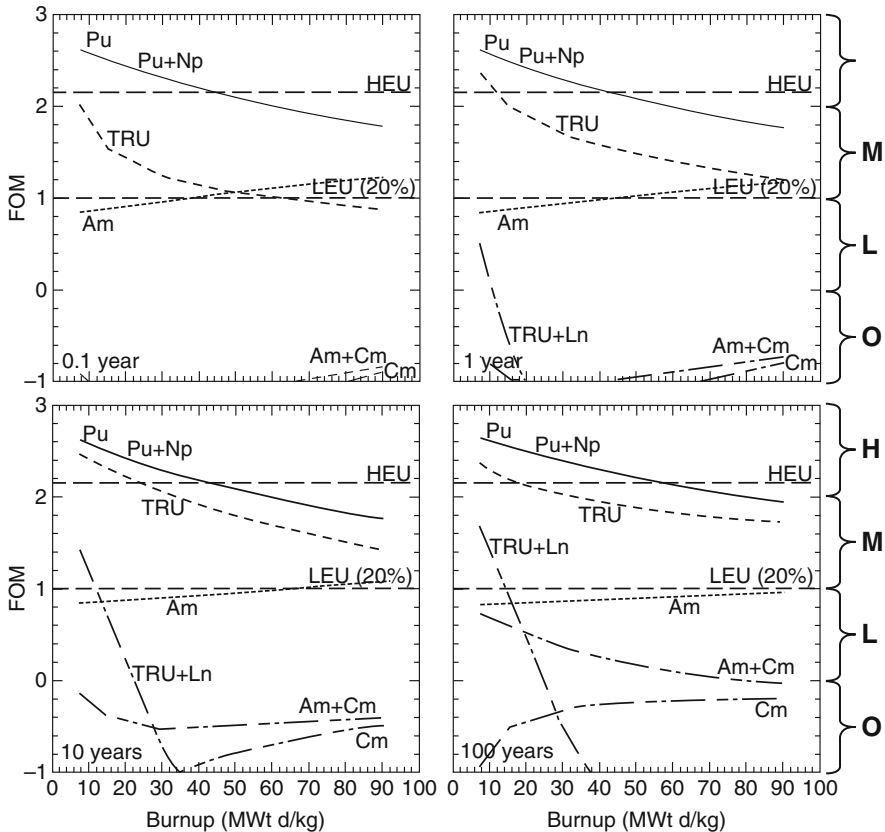
neutron dose, the FOM is dominated by its heating. Interestingly, the Am + Cm mixture has a maximum utility of low, independent of burnup, and age.

The retention of the lanthanides (Ln) with TRU or with Am + Cm, greatly reduces the FOM (the FOM of Am + Cm + Ln is very low), because the lanthanides provide an intense photon dose and, more importantly, an intense heat source. The FOM of TRU + Ln decreases with increasing burn-up, because of the relative buildup of lanthanides. The FOM of TRU + Ln increases with increasing spent-fuel age, because the lanthanides have half lives that are of the order of 100 years. Although the addition of the lanthanides ameliorates the safeguards and security issues, it would pose huge problems for any subsequent fuel fabrication using these materials.

The effect of diluting Pu and TRU with spent uranium is shown in ► Fig. 2. The FOM is reduced with the addition of spent uranium. However, significant quantities of uranium are required to attain a low utility. For example, >80% U is required for Pu, and ≥75% U is required for TRU, both obtained from 10-year old spent fuel burned to 45 MWt d/kg. It should be noted that this study focuses only on the utility of uranium mixtures and does not consider any subsequent reprocessing by an adversary.

The effect that the period of time after reprocessing has on the FOM of Pu is shown in ► Fig. 3. Increasing the post-reprocessing time decreases the FOM of Pu, because of the buildup of ^{241}Am from the beta decay of ^{241}Pu and the resulting increase in heating. As the age before reprocessing of Pu increases, there is less ^{238}Pu which is the dominant heat source in Pu. Consequently, as the spent fuel age increases, the effect of the period of time after reprocessing decreases.

The effect that the period of time after reprocessing has on the FOM of TRU is shown in ► Fig. 4. The behavior of TRU is dominated by the concentration of ^{242}Cm and ^{244}Cm , which are intense heating sources that quickly dissipate (their half lives are 163 days and 18 years, respectively). Then, for TRU taken from relatively fresh spent fuel, increasing the post-reprocessing time significantly increases the FOM. As the age of the spent fuel from which the TRU is taken increases, the change in the FOM with increasing post-reprocessing time decreases.



■ Figure 1

Figure of merit (FOM) of non-uranium bearing UREX products versus burn-up for various spent-fuel ages at time of reprocessing (lower left corner). The letters H, M, L, and O refer to the utility of the material (► Table 1)

The effects of “denaturing” the plutonium isotopic vector are shown in ► Fig. 5 (Kessler 2007; Saito et al. 2008). The plutonium in spent fuel has up to 8% ^{238}Pu , depending on the burn-up. Adding additional ^{238}Pu does reduce the utility of the plutonium. However, 80% ^{238}Pu is required to reduce the plutonium to low utility. A source for that much ^{238}Pu has not yet been identified.

There are two PYROX products: U with trace (~100 ppm) amounts of TRU and a U + TRU mixture that is 1/3-U with small amounts (12,500 ppm) of the rare earth fission products (Bathke et al. 2008a, b; Bathke et al. 2009a, b). The U product is effectively void of ^{235}U , and is innocuous. The PYROX U + TRU mixture is similar to the UREX + 1B product shown on the right of ► Fig. 2, and can be of moderate to high utility depending on the age and burn-up of the source material. However, there are locations in the flow-sheet where the TRU is diluted with only a ~5% mixture of active metal and rare earth (i.e., lanthanides) fission products, and may have higher utility than the end product. Consequently, this section examines TRU with various concentrations of U and various concentrations of fission products, where the fission products

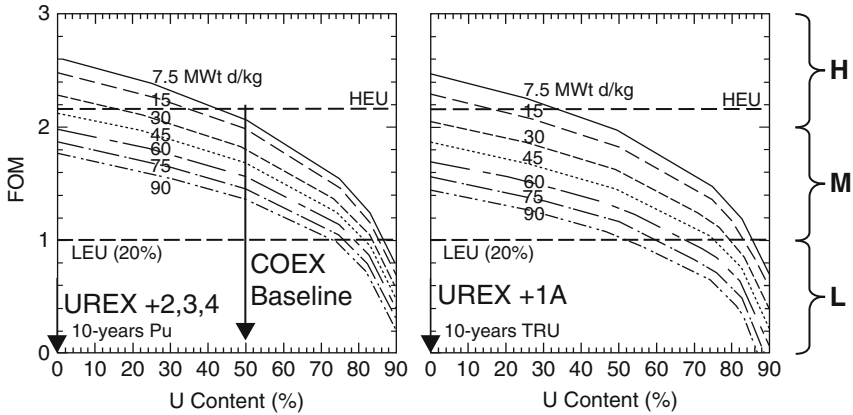


Figure 2 FOM of Pu (left) and transuranic elements (right) versus spent uranium concentration for various burn-ups

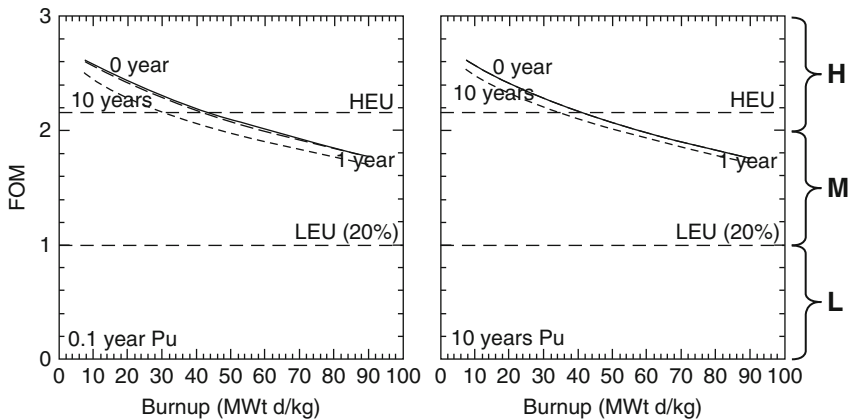
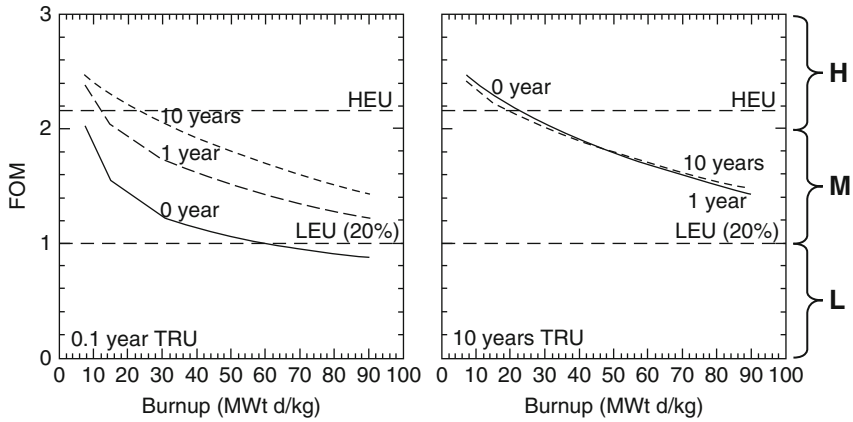


Figure 3 FOM of Pu versus burn-up for various spent fuel ages (lower left corner of each plot) and range of times after reprocessing (alongside of curves)

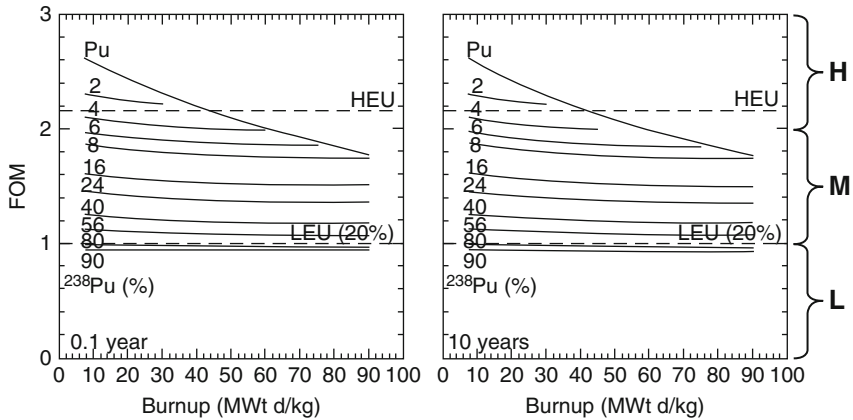
are either the active metal and rare earth fission products that represent the contaminants at an intermediate step in the flow-sheet, or just the rare earth fission products that are the only contaminants in the end product.

The FOM for a range of mixtures of U, TRU, and fission products is shown in Fig. 6. The addition of increasing quantities of fission products relative to TRU monotonically reduces the FOM, as seen in the two plots on the right-hand side of Fig. 6. However, the FOM reduction is accelerated significantly once sufficient fission products have been added to make the heating term dominant in (1). The effect of adding U relative to TRU upon the FOM is shown in the upper left plot of Fig. 6 and depends on which term in (1) is dominant. At low fission-product concentrations relative to TRU, the bare-critical-mass term is dominant, and the addition of



■ Figure 4

FOM of TRU versus burn-up for various spent fuel ages (lower left corner of each plot) and range of times after reprocessing (alongside of curves)



■ Figure 5

FOM of Pu versus burn-up for various concentrations (%) of added ^{238}Pu

increasing quantities of U decreases the FOM. At high fission-product concentrations relative to TRU, the heating term is dominant, and the addition of increasing quantities of U increases the FOM, because these additions reduce the amount of heating. Further additions of U in this regime eventually reduce the importance of the heating term and establish the bare-critical-mass term as the dominant term. Then, further additions of U decrease the FOM. Note that the combined active metal and rare earth fission products afford a significantly greater deterrent than just the rare earth fission products.

For a nominal reactor discharge that has been burned to 45 MWt d/kg and then cooled for 10 years before reprocessing, the TRU from that discharge would require $\geq 75\%$ -U to qualify as low utility material for $M_{\text{FP}}/M_{\text{TRU}} = 0$, where M_{FP} is the mass of the fission products and M_{TRU}

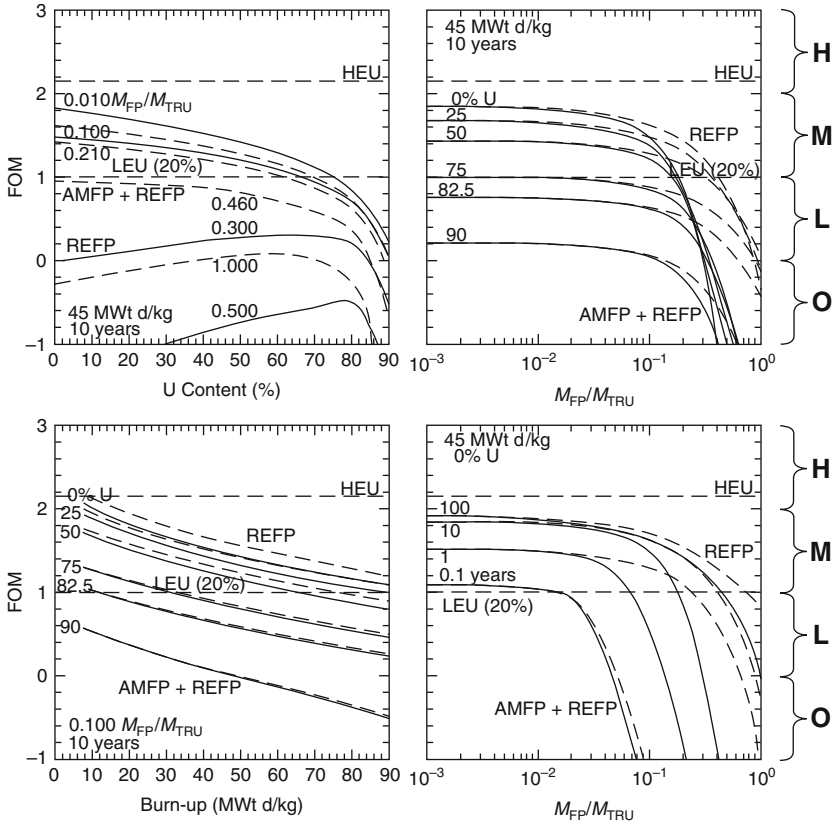


Figure 6
 FOM of PYROX material versus uranium concentration (%), ratio of fission-product mass to TRU mass, and burn-up for various mass ratios, uranium concentrations, and spent fuel ages. The fission products are either all of the active metals and rare earths (solid lines) or just the rare earths (dashed lines)

is the mass of the TRU. If both active metal and rare earth fission products are retained, then that same TRU would require $M_{FP}/M_{TRU} > 0.15$ to qualify as low utility material for 0%-U. If, however, just the rare earth fission products are retained, then that same TRU would require $M_{FP}/M_{TRU} > 0.4$ to qualify as low utility material for 0%-U. Similarly, an infinite number of combinations of U and M_{FP}/M_{TRU} can be used to achieve low utility. For example, 65%-U and $M_{FP}/M_{TRU} = 0.1$ is also low utility with active metal and rare earth fission products, whereas 70%-U and $M_{FP}/M_{TRU} = 0.1$ is low utility with rare earth fission products. It should be noted that the value of M_{FP}/M_{TRU} in spent fuel ranges from ~ 1.0 for 15-MWt d/kg spent fuel to 3.0 for 90-MWt d/kg spent fuel for active metal and rare earth fission products, and from $\sim 2/3$ for 15-MWt d/kg spent fuel to ~ 2.0 for 90-MWt d/kg spent fuel for rare earth fission products.

1.1.4 Conclusions

The FOM of Pu + Np is the highest of the UREX products. The FOM of TRU, which is a UREX + 1A product, is dependent upon spent-fuel age and burn-up. Because the FOM of TRU increases significantly with spent-fuel age, spent fuel should be reprocessed as soon as is practical. Furthermore, reprocessed TRU should be burned as soon as is practical, because the FOM of TRU increases significantly with increasing post-reprocessing time. For 10-year, 45-MWt d/kg UREX + 1A material (i.e., TRU), a U content > 75% is required to reduce the FOM to L.

The Pu + Np product has the same FOM as Pu product; coextracting Np with Pu does not reduce its utility. Conversely, extracting only Pu leaves attractive Np in the waste stream and ultimately in a repository. Both the Np-laden waste stream and repository have to be safeguarded (spent fuel requires safeguarding as well). For 10-year, 45-MWt d/kg COEX material (i.e., Pu), a U content \geq 82% is required to reduce the FOM to L. The FOM of Pu (and Pu + Np) is not significantly affected by changing the postirradiation time or by changing the post-reprocessing time.

The FOM of Pu denatured with ^{238}Pu concentration < 80% is still at least a utility of M. On the basis of the FOM formula used in this study, there is not enough ^{238}Pu (nor Np for breeding ^{238}Pu) to reduce the FOM to L.

The PYROX (or any pyro-processing product) is potentially of moderate to high utility. The PYROX product shares many properties with TRU. Its FOM is also dependent upon spent-fuel age and burn-up. It can also be made low utility with a U content > 75%. The PYROX product differs from TRU in that it can also be made low utility with $M_{\text{FP}}/M_{\text{TRU}} > 0.15$ for 0%-U and active metal and rare earth fission products or with $M_{\text{FP}}/M_{\text{TRU}} > 0.4$ for 0%-U and rare earth fission products.

There is a safeguards and security benefit with respect to diluting the reprocessing end products with lanthanides, and/or reprocessed, natural, or depleted U. *However, there is no single measure that fully eliminates the proliferation risk. None of the proposed flow-sheets examined to date justify reducing international safeguards or physical security protection levels. All of the reprocessing products evaluated to date need to be rigorously safeguarded and provide the highest levels of physical protection.*

1.2 Nonproliferation Impact Assessments

A generic nuclear fuel cycle (GNFC) is used here to demonstrate the methodology of a Nonproliferation Impact Assessment (NPIA). This methodology is partly based on the proliferation resistance and physical protection (PR&PP) approach (Evaluation Methodology for Proliferation Resistance and Physical Protection of Generation IV Nuclear Energy Systems 2006) that was developed as part of the Generation IV International Forum (GIF) (www.gen-4.org/Technology/horizontal/PRPPEM.pdf). The NPIA assessment consists of a short list of technical and policy factors. To the extent possible, each factor is graded (or rated) for each alternative to or within the GNFC. Where appropriate, the factors that are expected to be important in the subsequent assessments, the GNFC technology, or sites, are listed. The grading is expressed in qualitative terms, with each grade supported by specific technical and policy evaluations as described in the following subsections.

A clear definition of proliferation resistance, as relates to nuclear power generation, is needed to establish a firm foundation for the analysis and assessment to be performed in the

NPIA. The definition given below has been agreed to by the GIF, and agrees with the definition established at the international workshop sponsored by the IAEA in Como, Italy, in 2002 (Proliferation Resistance Fundamentals for Future Nuclear Energy Systems 2002). For comparison and distinction, the PR&PP definition of physical protection is also given.

Proliferation resistance is a characteristic of a Nuclear Energy System (NES) that impedes the diversion or undeclared production of nuclear material or misuse of technology by the host state seeking to acquire nuclear weapons or other nuclear explosive devices. The GNFC is regarded here to be the facilities that comprise it, their safeguards, physical security, the fuel supply and take-back services among its participants, and the corresponding transportation of nuclear materials or sensitive technology. Thus, the GIF definition of proliferation resistance applies to the GNFC. Notably, although the PR&PP definitions provide a foundation for evaluating the relative PR&PP risks of the GNFC, other factors can influence the nonproliferation impact of the GNFC. For example, the nuclear fuel cycle decisions of various countries need to be considered with regard to the benefits and challenges for the GNFC.

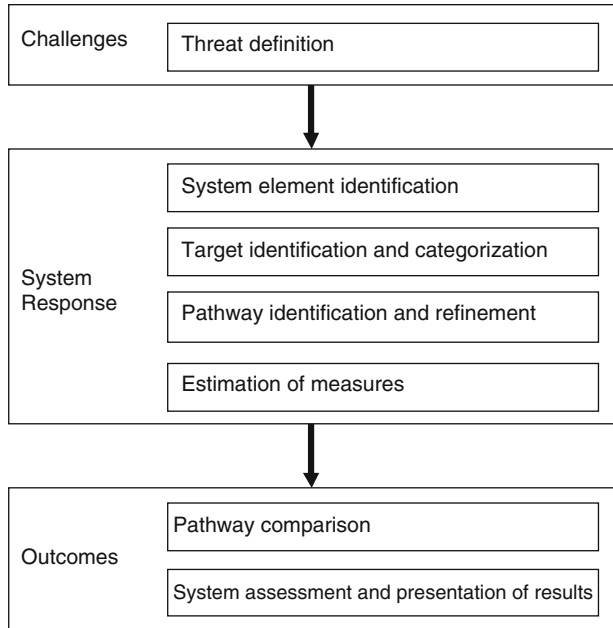
Physical protection is a characteristic of an NES that impedes the theft of materials suitable for nuclear explosives or radiation dispersal devices (RDDs), and the sabotage of facilities and transportation by subnational entities and other nonhost state adversaries. Although PP is discussed here for completeness and to distinguish it from PR, it is not evaluated for the GNFC in this NPIA.

1.2.1 Methodology

The PR&PP methodology is based on defining a set of challenges, analyzing the system response to these challenges, and finally assessing the outcomes. The challenges to the GNFC are the threats posed by potential proliferant states and by subnational adversaries. The technical and institutional characteristics of the NES are used to evaluate the response of the system and determine its resistance to proliferation threats and robustness against sabotage and terrorism threats. The outcomes of the system response are expressed in terms of PR&PP measures. The evaluation methodology accounts for both the intrinsic and extrinsic protective features of the GNFC system. Intrinsic features include the physical and engineered aspects of the GNFC system; extrinsic features include the institutional aspects such as safeguards and external barriers.

➤ *Figure 7* provides an outline of the methodological approach. The first step is threat definition. For both PR and PP, the threat definition describes the challenges that the system may face and includes characteristics of both the actor and the actor's strategy. For PR, the actor is the host state within the GNFC system, and the threat definition includes both the proliferation objectives, and the capabilities and strategies of the host state. For PP threats, the actor is a subnational group or other nonhost state adversary. The characteristics of the PP actors are defined by their objective, which may be either theft or sabotage, and their capabilities and strategies.

Challenges to the GNFC are defined in terms of a standard reference threat set (RTS), which covers the anticipated range of actors, capabilities, and strategies. System response to a given threat is evaluated independent of the probability that the system is actually challenged by the threat. In other words, PR&PP evaluations are contingent on the challenge occurring.



■ **Figure 7**

Detailed framework for the proliferation resistance and physical protection (PR&PP) evaluation methodology

For PR, the threats include

- Concealed diversion of declared materials
- Concealed misuse of declared facilities
- Overt misuse of facilities or diversion of declared materials
- Clandestine dedicated facilities

For PP, the threats include

- Radiological sabotage
- Material theft
- Information theft

After the threats have been sufficiently detailed for evaluation, the system response is performed and consists of four components:

System Element Identification

The GNFC system decomposes into smaller elements or subsystems at a level amenable to further analysis. The elements can comprise a facility (in the systems engineering sense), part of a facility, a collection of facilities, or a transportation system within the identified the GNFC subsystem where acquisition (diversion) or processing could take place.

Target Identification and Categorization

Target identification is conducted by systematically examining the GNFC system for the role that materials, equipment, and processes in each element could play in each of the strategies identified in the threat definition. PR targets are nuclear material, equipment, and processes to be protected from threats of diversion and misuse. PP targets are nuclear material, equipment, or information to be protected from threats of theft and sabotage. Targets are categorized to create representative or bounding sets for further analysis.

Pathway Identification and Refinement

Pathways are potential sequences of events and actions followed by the actor to achieve objectives. For each target, individual pathways are divided into segments through a systematic process and analyzed at a high level. Segments are then connected into full pathways and analyzed in detail. The selection of appropriate pathways will depend on the scenarios themselves, the state of design information, the quality and applicability of available information, and expert input.

Estimation of Measures

The results of the system response are expressed in terms of PR&PP measures. Measures are the high-level characteristics of a pathway that affect the likely decisions and actions of an actor, and, therefore, are used to evaluate the actor's likely behavior and the outcomes. For each measure, the results for each pathway segment are aggregated as appropriate to compare pathways and assess the system, so that significant pathways can be identified and highlighted for further assessment and decision making.

For PR, the measures are:

- *Proliferation technical difficulty* (TD): The inherent difficulty, arising from the need for technical sophistication and materials handling capabilities, required to overcome the multiple barriers to proliferation.
- *Proliferation cost* (PC): The economic and staffing investment required to overcome the multiple technical barriers to proliferation, including the use of existing or new facilities.
- *Proliferation time* (PT): The minimum time required to overcome the multiple barriers to proliferation (i.e., the total time planned by the host state for the project).
- *Fissile material type* (MT): A categorization of material based on the degree to which its characteristics affect its utility for use in nuclear explosives (material attractiveness).
- *Detection probability* (DP): The cumulative probability of detecting a proliferation segment or pathway.
- *Detection resource efficiency* (DE): The efficiency in the use of staffing, equipment, and funding to apply international safeguards to the NES.

For PP, the measures are:

- *Probability of adversary success* (PAS): The probability that an adversary will successfully complete the actions described by a pathway and generate a consequence.
- *Consequences*: The effects resulting from the successful completion of the adversary's action described by a pathway.

- *Physical protection resources*: The staffing, capabilities, and costs required to provide PP, such as background screening, detection, interruption, and neutralization, and the sensitivity of these resources to changes in the threat sophistication and capability.

The final steps in PR&PP evaluations are to integrate the findings of the analysis and to interpret the results. Evaluation results include best estimates for numerical and linguistic descriptors that characterize the results, distributions reflecting the uncertainty associated with those estimates, and appropriate displays to communicate uncertainties.

1.2.2 Technical Factors and Metrics

As noted previously, two categories of factors and metrics are essential to the NPIA: technical factors and policy factors. The former are derived from the PR&PP methodology, whereas the latter capture the broader suite of policy, legal, and institutional approaches used to secure non-proliferation objectives. This section elaborates on the technical aspects, and policy aspects are discussed later sections.

The link between technical factors, and PR&PP measures and their underlying metrics can be summarized by the following:

1. The measures are the fundamental constituents of proliferation resistance.
2. The metrics are the scales or units in which they are expressed.
3. The technical factors are higher-level expressions of proliferation resistance that are more readily usable by the decision maker. They are supported by the measures.

Three high-level technical factors are evaluated in this NPIA:

T1: Avoiding proliferator success

T2: Facilitating cost-effective international monitoring

T3: Resulting in less-attractive material types and forms

These technical factors are informed by the PR&PP measures using the association of

➤ [Table 4](#).

Grading Structure for Technical Factors

A grading structure has been proposed for the three technical factors:

- Immediate and substantial impact
- Delayed but substantial impact
- Significantly delayed and/or minimal impact

Other grading approaches exist as well, but undefined notions of high, medium, and low are not useful because of their vagueness. The example “grades” shown here provide a qualitative notion of time and scale of possible consequence.

Proliferation Resistance Measures

For an evaluation of proliferation resistance to host state threats, after measures have been estimated for pathways, the pathways are compared and ranked according to significance. To facilitate pathway comparison, quantitative metrics are applied to the TD, PC, PT, MT, and

■ **Table 4**

Technical factors and associated proliferation resistance and physical protection (PR&PP) measures

Technical factors	Associated PR&PP measures
Avoiding proliferator success (T1)	Technical difficulty (PR)
	Proliferation cost (PR)
	Proliferation time (PR)
	Detection probability (PR)
	Probability of adversary success (PP)
	Consequences (PP)
Facilitating cost-effective international monitoring (T2)	Detection resource efficiency (PR)
	Detection probability (PR)
	Physical protection resources (PP)
Resulting in less-attractive material types and forms (T3)	Material type (PR)
	Consequences (PP)

DP measures to relate them to linguistic values, from very low to very high, based on decision making by a proliferant state. Likewise, for the DE measure, a quantitative metric is applied to reflect the magnitude of required resources, relative to the resources that the IAEA commonly applies to safeguard facilities. The analyst may select other quantitative metrics appropriate for comparing pathways for the specific threat being considered. As a starting point, the analyst may choose to apply the approximate, representative metrics given in ▶ [Table 5 \(continued\)](#). These metrics are presented as an example. The evaluation of measures is not prescriptive and is generally tailored to the specific questions being addressed.

In ▶ [Table 5 \(continued\)](#), the PP measures have also been included for completeness. However, explicit example metrics are not shown in this report. These metrics would be tailored to the purposes and needs of a national assessment and would be associated with the specific threats to be addressed. A brief discussion of the PP measure is given at the end of this section.

Each of the PR measures and corresponding metrics is discussed in greater detail in the following section.

Proliferation Technical Difficulty (TD) Measure

The TD measure is estimated using a metric scale as shown in the example given in ▶ [Table 5 \(continued\)](#). Technical difficulties arise from inherent characteristics of the pathway that create a potential for failure from technical problems. When scaled to reflect the state's capability, the TD measure assists in distinguishing pathways that a proliferant state would judge to have a higher risk of technical problems, and to have the potential to greatly increase the time and resources to complete a pathway, or to result in the failure to complete a pathway.

An estimation of TD uses expert judgment to identify the sources of intrinsic difficulty in completing a pathway segment, such as difficulty from criticality hazards, radiation, a lack

■ Table 5

Example quantitative metrics and scales for PR measures

Measures and metrics	Metric scales bins (median)	Proliferation resistance
Proliferation resistance measures determined by intrinsic features		
Proliferation technical difficulty (TD): Example metric: probability of pathway failure from inherent technical difficulty considering threat capabilities	0–5% (2%)	Very low
	5–25% (10%)	Low
	25–75% (50%)	Medium
	75–95% (90%)	High
	95–100% (98%)	Very high
Proliferation cost (PC): Example metric: fraction of national resources for military capabilities	0–5% (2%)	Very low
	5–25% (10%)	Low
	25–75% (50%)	Medium
	75–100% (90%)	High
	>100% (>100%)	Very high
Proliferation time (PT): Example metric: total time to complete pathway	0–3 months (2 months)	Very low
	3 months to 1 year (8 months)	Low
	1–10 year (5 year)	Medium
	10–30 year (20 year)	High
	>30 year (>30 year)	Very high
Fissile material type (MT): Example metric: dimensionless ranked categories (HEU, WG-Pu, RG-Pu, DB-Pu, LEU); interpolation based on material attributes	HEU	Very low
	WG-Pu	Low
	RG-Pu	Medium
	DB-Pu	High
	LEU	Very high
Proliferation resistance measures determined by extrinsic measures and intrinsic features		
Detection probability (DP): Example metric: cumulative detection probability	a	Very low
	b	Low
	c	Medium
	d	High
	e	Very high
Detection resource efficiency (DE): Example metric: GW(e) years of capacity supported (or other normalization variable) per person days of inspection (PDI) (or inspection \$)	<0.01 (0.005 GWyr/PDI)	Very low
	0.01–0.04 (0.02 GWyr/PDI)	Low
	0.04–0.1 (0.07 GWyr/PDI)	Medium
	0.1–0.3 (0.2 GWyr/PDI)	High
	>0.3 (1.0 GWyr/PDI)	Very high

■ Table 5 (continued)

Measures and metrics	Metric scales bins (median)	Proliferation resistance
Probability of adversary success (for PP)		Very low
		Low
		Medium
		High
		Very high
Consequences (for PP)		Very low
		Low
		Medium
		High
		Very high
Physical protection resources (for PP)		Very low
		Low
		Medium
		High
		Very high

Notes: HEU high-enriched uranium, nominally 95% ^{235}U ; WG-Pu weapons-grade plutonium, nominally 94% fissile Pu isotopes; RG-Pu reactor-grade plutonium, nominally 70% fissile Pu isotopes; DB-Pu deep burn plutonium, nominally 43% fissile Pu isotopes; LEU low-enriched plutonium, nominally 5% ^{235}U

^aSignificantly lower cumulative detection probability than the IAEA detection probability and timeliness goal for depleted, natural, and LEU uranium

^bFifty percent in 1 year (this equates to IAEA detection probability and timeliness goal for one significant quantity of depleted, natural, and LEU uranium)

^cTwenty percent in 3 months, 50% in 1 year (this equates to IAEA detection probability and timeliness goal for one significant quantity of spent fuel/irradiated material)

^dFifty percent in 1 month, 90% in 1 year (this equates to IAEA detection probability and timeliness goal for one significant quantity HEU/separated Pu)

^eSignificantly greater cumulative detection probability than the IAEA detection probability and timeliness goal for HEU/separated Pu

of design information, a lack of access, or the inability to fabricate or produce equipment or materials covered by export controls. An estimation of TD for a complete pathway uses the combined sources of difficulty for all segments.

The metric scale for the TD measure reflects the probability that a pathway will end in failure, and thus depends on the resources and capabilities available to a proliferant state. Thus, for example, the TD of an external segment to construct and operate a concealed centrifuge enrichment plant may become lower if a state has an operating commercial enrichment capability, or can access expert guidance. However, the TD for manufacturing specific components for centrifuges, such as frequency invertors, may remain high if a state does not have a domestic commercial capability to manufacture these components. Most of the nuclear components that have high TD to manufacture are monitored by international export controls and by national intelligence services. The evaluation of the DP measure may include the potential for export controls to detect the acquisition of such equipment.

■ **Table 6**

Summary of characteristics for the proliferation technical difficulty (TD) measure

Characteristic	Description
Definition	Inherent difficulty of the segment
Typical attributes to be considered for estimation	Criticality hazards Radioactivity levels Availability of open information Access to specialized export-controlled components or materials
Example metric	Probability of pathway failure from inherent technical difficulty considering threat capabilities
Segments-to-pathway aggregation method	Calculation of the probability of pathway failure on the basis of the segments involved

■ **Table 7**

Summary of characteristics for the proliferation cost (PC) measure

Characteristic	Description
Definition	Total cost of segment
Typical attributes to be considered for estimation	Minimum cost for setting up the minimum needed infrastructure to complete the segment Cost from misuse of civilian infrastructure/personnel
Example metric	Fraction of national resources for military capabilities
Segments-to-pathway aggregation method	Sum of segment estimates. Can be normalized to national resources for military capabilities

The use of probabilistic methods can facilitate aggregation of the TD measure associated with each segment in a pathway. Examples based on Markov models are contained in Yue et al. (2005). ➤ [Table 6](#) summarizes key characteristics of the TD measure.

Proliferation Cost (PC) Measure

The PC measure is estimated in dollars and can be scaled with the total resources available to a proliferant state for military expenditures, which may be on the order of \$2 billion per year for a reactor state or \$20 billion per year for a fuel cycle state. ➤ [Table 7](#) provides an index for scaling the value of PC from low (<10%) to very high (>100%). This measure expresses the economic and staffing investment required to overcome the multiple barriers that impede completion of the action associated with the segment.

■ **Table 8**

Summary of characteristics for the proliferation time (PT) measure

Characteristic	Description
Definition	Total time required to complete segment
Typical attributes to be considered for estimation	Maximum diversion or production rate Storage duration Extent of required equipment modifications
Example metric	Total time to complete pathway (e.g., months, years)
Segments-to-pathway aggregation method	Appropriate aggregation of parallel and serial activities

The PC measure is aggregated over a pathway by summing the value of the measure for each segment in the pathway. In many cases, this measure is dominated by one segment. Notably, this measure does not include the cost of the declared Generation IV NES, but does include the cost of modifications made to that system to complete the segment. These modifications may include process modifications, as well as modifications intended to defeat safeguard verification activities. ➤ [Table 7](#) summarizes key characteristics of the PC measure.

Proliferation Time (PT) Measure

The PT measure is estimated in units of time, as shown in ➤ [Table 8](#), and ranges from very low (<3 months) to very high (>30 years). The proliferation time is the minimum time required to overcome the multiple barriers that impede completion of the action associated with the acquisition and processing segments. Typically, PT is measured from the time that the proliferant state initiates its first detectable activity (e.g., its first action to divert material or misuse a declared facility). However, the analyst may select other initiation times, such as the time when the proliferant state's planning starts if the analyst judges this to be important in affecting the state's preferences between pathways. The analyst should state explicitly the basis used for selecting an initiation time and use it consistently. Typically, PT is estimated at the end of the processing segment and does not include the weapon fabrication time.

For example, abrupt diversion of spent fuel from a storage facility might require <1 month. Extraction of plutonium from irradiated targets might require 3–12 months, assuming that the extraction facility (whether clandestine or obtained through misuse of a declared facility) is already available. In making these estimates, the analyst must clearly state assumptions. These assumptions include what preparations the proliferant state has completed before initiating the action associated with the segment (e.g., an assumption that the proliferant state constructed and commissioned a clandestine plutonium extraction facility before initiating this segment).

For a pathway, the PT measure is aggregated by summing serial activities and taking into account parallel activities. Parallel and serial activities depend on the details of each pathway. ➤ [Table 8](#) summarizes key characteristics of the PT measure.

■ **Table 9**

Summary of characteristics for the fissile material type (MT) measure

Characteristic	Description
Definition	Characteristics of metal for weapons fabrication
Typical attributes to be considered for estimation	Spontaneous neutron emission rate Heat generation rate Gamma radiation activity Bare-sphere critical mass
Example metric	Dimensionless ranked categories (HEU, WG-Pu, RG-Pu, DB-Pu, LEU); interpolation based on material attributes
Segments-to-pathway aggregation method	Not applicable

Fissile Material Type (MT) Measure

The MT measure ranks types of fissile material produced by the processing segment based on their utility for use in fabrication of a nuclear explosive, and the relative preference of a proliferant state. As such, the MT measure is only estimated for pathways; it is not estimated for segments. However, it is of interest to report MT at the end of major stages. For example, as an intermediate result, an analyst may want to know the various possible MTs emerging from the acquisition stage.

The PR methodology applies an approximate ranking (🔍 [Table 9](#)) of nuclear material types. This ranking reflects relative PR based on the preferences of a proliferant state in attempting to acquire its first few weapons. The basic range is as follows:

- Very low PR – HEU
- Low PR – weapons-grade plutonium (WG-Pu)
- Medium PR – reactor-grade plutonium (RG-Pu)
- High PR – “deep-burn” plutonium (DB-Pu)
- Very high PR – LEU

The very low PR ranking for HEU results primarily from the extremely low spontaneous neutron emission rate as compared with all plutonium compositions.


For plutonium, a very wide range of isotopic compositions can be generated, depending on the conditions of reactor operation and recycle of spent fuel. The basis for categorizing the attractiveness of different plutonium compositions is complex. Here the MT PR ranking for plutonium compositions is based on the study of the US National Research Council on the spent-fuel standard (The Spent-Fuel Standard for Disposition of Excess Weapon Plutonium: Application to Current DOE Options [2000](#)):

If it is assumed that proliferators in all categories will ultimately be capable of obtaining reasonably pure plutonium metal... then the main intrinsic barriers in this category are those associated with deviation of the plutonium’s isotopic composition from “weapons grade.” ...

In the case of... a proliferant state we rate the barrier (from reactor-grade plutonium) as “moderate” in importance: such a state would probably prefer to avoid if possible the burdens posed by isotopic deviations for design, fabrication, and maintenance of nuclear weapons, but it would also probably

have the capabilities to cope with the burdens in ways that achieved a level of weapon performance adequate for the proliferant state's initial purposes.

When plutonium is recycled, it is possible to further degrade the isotopic composition. For the MT measure, such degraded plutonium is listed as DB-Pu, which would have high concentrations of ^{238}Pu and thus high heat generation rates. A proliferant state would be expected to expend great effort to identify proliferation pathways that would result in acquiring material with a lower MT PR ranking; thus, the MT PR ranking of DB-Pu is listed as high. A more detailed discussion regarding the level of preference that a proliferant state would display between materials of higher and lower MT ranking is contained in Appendix D of the PR&PP methodology report (Evaluation Methodology for Proliferation Resistance and Physical Protection of Generation IV Nuclear Energy Systems 2006).

In many cases, the simple MT ranking, along with the qualitative discussion of MT provided above and in Appendix D.4 of the PR&PP methodology report (Evaluation Methodology for Proliferation Resistance and Physical Protection of Generation IV Nuclear Energy Systems 2006), is sufficient to allow pathways to be compared and ranked.  Table 9 summarizes key characteristics of the MT measure.

Detection Probability (DP) Measure

The DP measure expresses the probability that action described by a pathway segment is detected. DP results from measurements that (1) detect anomalies generated during the execution of pathway segments and (2) are performed to assess that anomalies originate from actions in actual pathway segments rather than legitimate, inadvertent sources. DP is generally expressed as a cumulative probability function. However, if a defined safeguards approach is not available, DP can be expressed only by a very wide uncertainty band.

In addition, a variety of concealment strategies may affect the DP. The effects of a concealment strategy are determined by analyzing pathways that include the strategy, not by assigning an arbitrary DP uncertainty for assumed effects of concealment methods.

Safeguards involve continuously evolving technology. Many system attributes can affect both the optimal approach for the application of safeguards and the effectiveness of that approach in providing high DP. The following paragraph assumes a robust IAEA safeguards regime with the attendant technologies that would promote the ability to safeguard facilities and operations.

To detect *internal material diversion segments*, measurements may be combined to detect the material transfer, and the resulting change in material inventory detection error arises from three sources: (1) instrument measurement uncertainty; (2) the possibility that a measured anomaly has a legitimate origin, such as inadvertent hold up of material, inadvertent operator destruction of a seal, or inadvertent delay of an inspection due to legitimate safety or access restrictions; and (3) uncertainty that the actual facility configuration is the same as that assumed in the design of the safeguards system where, for example, an undeclared penetration may exist in or be added to a facility.

To detect *internal facility misuse segments*, measurements to detect misuse must be tailored to detect anomalies that the action of a segment would generate. Uncertainties in detection of misuse have similar origins to those listed previously for internal material diversion segments.

To detect *external segments*, methods include the use of tools, such as commercial satellite photography and environmental sampling, as well as the use of various types of information that may be supplied by third-party sources. These sources include information from national export

control programs, which monitor and detect purchases or transfers of sensitive or dual purpose equipment and technologies, and information gathered by national technical means. External segments that use equipment diverted from declared facilities, such as frequency invertors in enrichment plants, could also be detected by monitoring the inventory of this equipment in declared facilities. Although the IAEA does not currently have goals for detection of clandestine activities and facilities, the IAEA uses information obtained from a variety of sources, including nonsafeguards databases, open sources, and third parties.

A potentially significant tool for enhancing the detection of external segments is the additional protocol (AP). In NPT countries, this tool enables programs to develop more transparent nuclear capabilities, including enrichment and reprocessing, (and also subject to verification). It would create a broader IAEA toolkit, including location-specific environmental sampling, to verify the declarations. AP, for example, would be a principal means of verifying that a user states that had agreed to forego development of enrichment, in exchange for fuel assurances, was in fact in compliance with such an undertaking and that there was no evidence of activities that might be inconsistent with this. AP is thus relevant to both internal segments – misuse of a declared facility – and external segments.

Under modern integrated safeguards, safeguards detection resources such as the frequency of inspections are increased progressively as anomalies are detected. These resources provide a higher cumulative confidence of detection with lower detection resources. Likewise, safeguards approaches that provide multiple and diverse measurements capable of detecting the actions described by a pathway segment increase the DP.

For internal pathway segments, the reference metric scale for the DP measure, shown in [▶ Table 10](#), is based on a comparison with the applicable IAEA safeguards detection goals contained in the IAEA Safeguards Criteria. A “medium” DP meets the IAEA safeguards detection goals for spent fuel and irradiated materials. A “high” DP meets IAEA goals for HEU and separated plutonium, and a “low” DP meets IAEA goals for depleted uranium, natural uranium, and LEU.

For external pathway segments, DP may have large uncertainty unless the segment generates obvious visual, thermal, or other signatures. If detection uncertainty is large, it may be useful to provide decision makers with a qualitative, general description of the methods available to detect the external segment, particularly if the actual DP cannot be readily evaluated and presented on a metric scale such as that of [▶ Table 10](#). [▶ Table 10](#) summarizes key characteristics of the DP measure.

Detection Resource Efficiency (DE) Measure

The DE measure is estimated for each pathway segment by summing estimates of the manpower (e.g., person days of inspection (PDI)) or the cost (in US dollars) required to implement the detection methods for the segment. Safeguards resources are then aggregated for all segments of a pathway, using logical assumptions (e.g., a single instrument may provide detection capabilities for multiple segments). Estimates of time or cost will necessarily be based on currently accepted safeguards approaches, but anticipated changes to safeguards approaches and safeguards technology (e.g., increased use of remote monitoring) should be considered that could occur over the multi-decade life cycle for most nuclear facilities. The DE measure is normalized by a variable, such as the energy production supported by the system element, and is presented as the ratio of that normalization variable divided by the inspection time or cost (e.g., in units of gigawatt years per PDI). [▶ Table 11](#) summarizes key characteristics of the DE measure.

■ **Table 10**
Summary of characteristics for the detection probability (DP) measure

Characteristic	Description
Definition	Cumulative probability and confidence level for detection of a pathway segment
Typical attributes to be considered for estimation	<p>Attributes important to design information verification</p> <p>Transparency of layout</p> <p>Possibility to use 3D scenario reconstruction models</p> <p>Possibility to have visual access to equipment while operational</p> <p>Comprehensiveness of facility documentation and data</p> <p>Attributes important to nuclear material accounting</p> <p>Uniqueness of material signature</p> <p>Hardness of radiation signature</p> <p>Possibility of applying passive measurement methods</p> <p>Item/bulk</p> <p>Throughput rate</p> <p>Batch/continuous process</p> <p>Nuclear material heat generation rate</p> <p>Attributes important to containment and surveillance</p> <p>Operational practice</p> <p>Extent of automation</p> <p>Standardization of items in transfer</p> <p>Possibility to apply visual monitoring</p> <p>Number of possible transfer routes for items in transit</p>
Example metric	Cumulative detection probability
Segments-to-pathway aggregation method	<p>Calculate the probability of pathway detection on the basis of the segments involved (e.g., the probability of pathway detection will be $P(d) = 1 - P(nd)$, where the probability of pathway nondetection, $P(nd) = \prod(1 - P_i(d))$, with $P_i(d)$ being the probability of detection of the ith segment, under the hypothesis of the independence of detection events)</p>

Physical Protection (PP) Measures

The three PP factors are considered differently.

- **Probability of adversary success (PAS):** The probability that an adversary will successfully complete the actions described by a pathway and generate a consequence. This measure assesses the probability that an adversary will successfully complete the actions described by a pathway and generates a consequence. If the actions required to complete the pathway are within the resources and capability of the adversary, then the PAS depends on the capability of the physical protection system (PPS) to detect the actions, delay the adversary, and neutralize the adversary before the actions can be completed. The PAS measure is commonly used in the design and analysis of PPSs, and various tools are available to quantitatively

■ **Table 11**
Summary of characteristics for the detection resource efficiency (DE) measure

Characteristic	Description
Definition	Total inspector time or cost of safeguarding the segment
Typical attributes to be considered for estimation	See Table 2.10 of Evaluation Methodology for Proliferation Resistance and Physical Protection of Generation IV Nuclear Energy Systems (2006)
Example metric	GW(e) years of capacity supported (or other normalization variable) per PDI (or inspection \$)
Segments-to-pathway aggregation method	Aggregation to total inspection time or safeguards cost, normalized to an appropriate scale, such as nuclear energy production supported (GW(e) year)

evaluate the measure. For some pathways, the PAS may be controlled by a small number of segments, such as the physical difficulty in obtaining access to safety equipment in attempting to sabotage passively safe nuclear reactors and the difficulty of removing and processing spent-fuel assemblies in attempting to steal plutonium.

- **Consequences (C):** The effects resulting from the successful completion of the adversary's action described by a pathway. Consequences are defined as the effects resulting from the successful completion of the adversary's intended action described by a pathway. This measure reflects both the attractiveness to the adversary and the relative importance of a pathway in generating adverse effects. Theft consequences can be expressed in terms of the quantity and quality of the material removed. Sabotage consequences can be measured by the number of physical quantities, acute fatalities, latent fatalities, quantities of material per unit area, etc. Perhaps the most meaningful measurement of sabotage consequences at the coarse pathway level is whether a release is contained, kept to the plant site, or released offsite.
- **Physical protection resources (PPR):** The staffing, capabilities, and costs required to provide PP, such as background screening, detection, interruption, and neutralization, and the sensitivity of these resources to changes in the threat sophistication and capability. This measure reflects the resources devoted to provide extrinsic features, for instance a PPS to detect, delay, and neutralize an adversary. At the lowest end, in system elements that provide very long intrinsic delay times, this measure may involve the cost of alarm systems and offsite police response. At the high end, this measure may involve extensive investments in maintaining large, armed security forces and in detection, delay, and response systems. The PPR measure quantifies the staff, capabilities, and costs (both infrastructure and operation) required to provide a level of PP for a given NES. As with the DE measure for PR, the PPR measure for a given pathway is evaluated for each pathway segment and then aggregated appropriately, noting that some PPS elements can provide responses to multiple segments. PPR for targets can be evaluated by aggregating resources for all pathways associated with the target. Likewise, PPR for a system element can be evaluated by aggregating the resources required for all targets in the system element. The PPR measure can also be expressed as a cost per unit of energy (TWh) produced.

The three measures for PP are consistent with those commonly used by national programs to make efficient investments to protect critical infrastructure and key assets. PP is a national

responsibility and thus involves national policies. The goal is to allocate resources optimally to limit risk to a uniform level across both nuclear and nonnuclear critical infrastructure and key assets. Quantitative analysis for PAS, C, and PPR will also be required to support licensing and deployment decisions for new nuclear infrastructure.

1.2.3 Policy Factors and Grading

In addition to “technical factors” that are supported by the PR&PP metrics and measures, the final GNEP NPIA should evaluate alternative actions against notable nonproliferation “policy factors.” The purpose of this additional aspect of the approach is to capture any high-level US nonproliferation policy value. It is difficult to evaluate fully the nonproliferation merit of the GNEP “architecture” as a technology transfer restraining mechanism, when measuring purely against technical factors that do not consider the broader suite of policy, legal, and institutional approaches used to secure nonproliferation objectives.

The following draft policy factors are proposed for use in the NPIA analysis.

1. This factor would allow policy effect analysis for GNEP approaches, products, and facilities that contribute to restraint in the spread of sensitive fuel cycle technology beyond existing technology holding states. This President-of-the-US (POTUS)-level policy factor was put forward in the National Defense University speech by President George Bush in February 2004.

2. Minimizes and avoids accumulation of stocks of separated weapons useable material.

This factor would allow policy-effect analysis for GNEP approaches, products, and facilities that contribute to minimization and avoidance of accumulation of separated stocks. This POTUS-level policy factor was put forward in National Security Presidential Directive 17 (NSPD-17) (President George Bush, December 2002) and other documents.

3. Enhances US tangible nonproliferation policy and legal influence on the structure of the international fuel cycle.

This factor would allow policy-effect analysis for GNEP approaches, products, and facilities that contribute to tangible enhancement of US influence, for example, through the system of legal obligations set forth in bilateral peaceful nuclear cooperation agreements. The word “tangible” is used to indicate that the effect should be as direct as practicable through policy, regulatory, or legal mechanisms. Indirect effects are also meaningful (setting an “example”), but of much lesser value generally. For example, the “no domestic reprocessing policy” of the US was an indirect policy approach. Some argue that this approach formed the basis for a policy of global restraint that largely retarded development of reprocessing technology worldwide, whereas others argue that fuel cycle economics have been largely responsible for the current situation rather than the policy. By way of comparison, the general decline of US nuclear manufacturing capability is having a direct and long-term impact on the ability of the US to influence the future international fuel cycle through an accelerating loss of nuclear trade obligations on technology and material – a direct effect.

4. Strengthens nuclear nonproliferation and nuclear security by encouraging the adoption and implementation of sound nonproliferation infrastructures.

This factor would allow policy effect analysis for GNEP approaches that lead to the adoption by others, for example, of additional protocols; the IAEA Convention on Physical Protection of Nuclear Materials (CPPNM) and its amendment; export controls, and

implementation of the UN Security Council Resolution 1540 (UNSCR/1540). It could look at capacity building efforts to help others put in place the appropriate legal and regulatory frameworks and develop and deploy the human resources needed. This factor speaks both to the issue of reducing the risk of terrorism worldwide and of promoting nonproliferation practices.

Proposed Grading Structure

The policy analysis should cast logical arguments as to how GNEP approaches, products, and facilities participate and enable US nonproliferation policy objectives. The analysis should be as brief, straightforward, and understandable as possible as to educated lay persons. The following set of “grades” is suggested to be applied to the above policy factors:

Meets US Nonproliferation Policy Objectives This grade is given if the vast majority of reasoned arguments supports the conclusion. The main points for should be laid out in a bulletized list.


May Create US Nonproliferation Policy Uncertainty This grade is given if significant reasoned arguments can be made for and against. The main points for and against should be laid out in bulletized pro and con lists.

Raises US Nonproliferation Policy Concerns This grade is given if the vast majority of reasoned argument supports the conclusion. The main points against should be laid out in a bulleted list.

1.2.4 PR&PP Example

A Markovian model is used as an example for detailed pathway analysis to quantify the measures of proliferation resistance for an advanced light water reactor (ALWR). This example can serve as a baseline for comparison of Generation IV concepts (Generation IV International Forum, www.gen-4.org). The scenarios evaluated include reactor misuse and diversion at both front-end and back-end of the ALWR once-through fuel cycle. The full set of analyses and results are too extensive to present here. Rather, to provide a sense of the methodology, the case of material diversion is illustrated here. For additional detail see Aigner et al. (2002).

The goal of diversion is to accumulate a significant quantity (SQ) of either HEU or reactor grade plutonium. In this study, obtaining one SQ of material is defined as a successful diversion. Generally, diversion may occur before the fuel assemblies are loaded into the reactor, which corresponds to the front-end of the fuel cycle, and after the fuel assemblies are taken out of the reactor, which corresponds to the storage and reprocessing of spent fuel (the back-end). It should be noted that diversion while the fuel is in an operating ALWR is almost impossible. For reactors, in general, diversion is possible during the refueling process. Thus, the reactor is also included in this diversion scenario study.

The diversion along the path leading to fuel fabrication, the front-end, will first be considered. A standard fuel fabrication process is shown in  Fig. 8. Here the goal of the proliferator is to obtain HEU. After mining and milling, the so-called “yellowcake” of about 0.7% enrichment is obtained and converted chemically UF_6 . This material needs to be enriched to about 4% either through gaseous diffusion or gaseous centrifuge facilities before regular fuel assemblies, the fresh fuel, can be fabricated for a light water nuclear reactor. It is assumed that the proliferator may possess the necessary clandestine facilities to produce the desired weapons grade

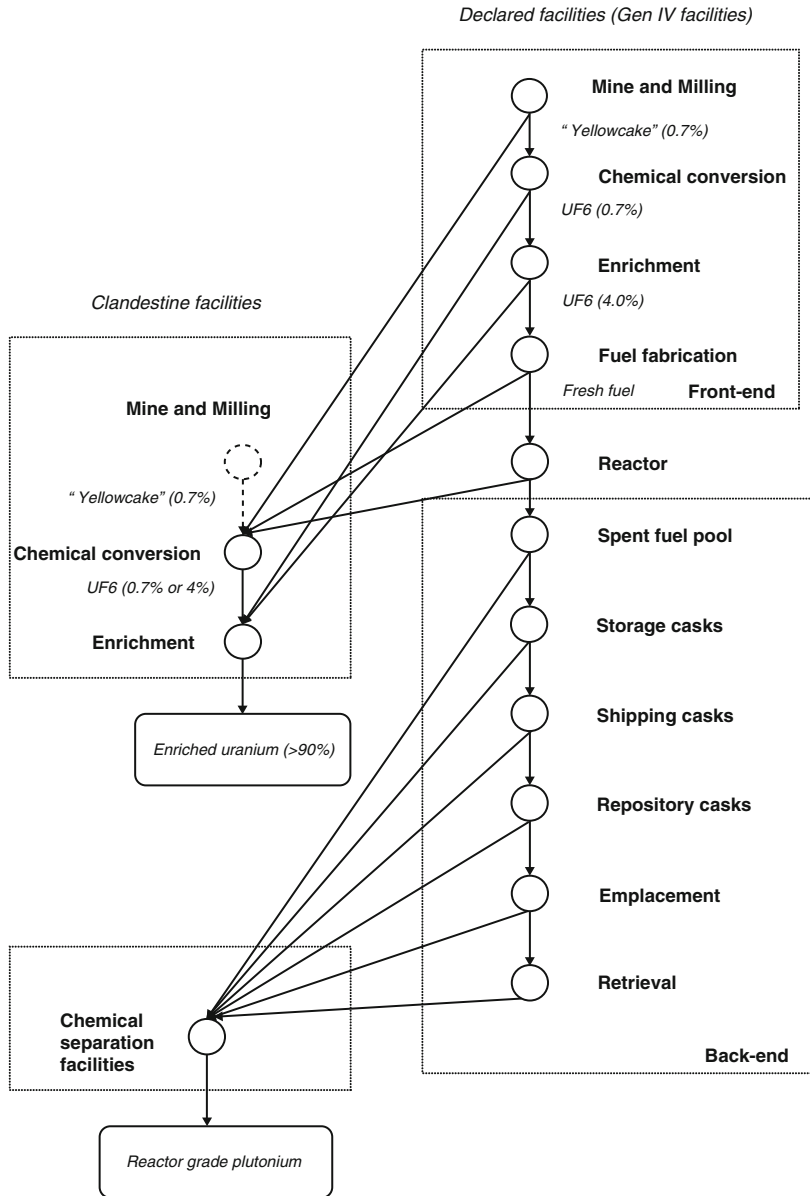


Figure 8
Diversion scenarios

materials. Therefore, all the material may be attractive to the proliferator despite the different levels of enrichment along this path. To avoid the mixed scenario of diversion and misuse (this will be considered in the future), clandestine facilities are solely used to obtain the enriched uranium material of weapons grade, i.e., once the material is diverted it will not be returned to

the declared facilities for further processing. In the front-end diversion, the clandestine facilities are used for chemical conversion and for enrichment as shown in [▶ Fig. 8](#).

The path of diversion at the back-end is also shown in [▶ Fig. 8](#). Spent fuel may contain enough reactor grade plutonium to fabricate nuclear weapons after proper processing. After the spent fuel is unloaded from the core of the reactor, it needs to be cooled down inside the spent fuel pool, then stored onsite, shipped, and emplaced within different casks or containers. Diversion may occur at various stages of this process. Furthermore, retrieval of emplaced fuel could also happen although the spent fuel is intended to be emplaced permanently.

The parameters for the Markov model are determined from the point of the view of the proliferator. The materials flow through the NES continuously, i.e., the material may be diverted from all or some of the facilities of the system at any moment. In the diversion goal, which is to obtain I-SQ HEU or reactor grade plutonium, the transition time periods between declared and clandestine facilities are determined based on the amount of the material the NES can process and by the diversion rates at different facilities. The detection time periods are determined by the periods of inspection, verification, and confirmation of the diversion activities.

The cumulative probability of detection with time for each stage of diversion in the front-end of the fuel cycle is shown in [▶ Fig. 9](#). Similar results can be shown for the back-end of the fuel cycle.

The aim of this study is to investigate the Markov approach as a design tool to be used by Generation IV designers at an early stage of the design process. It is a fast running software tool

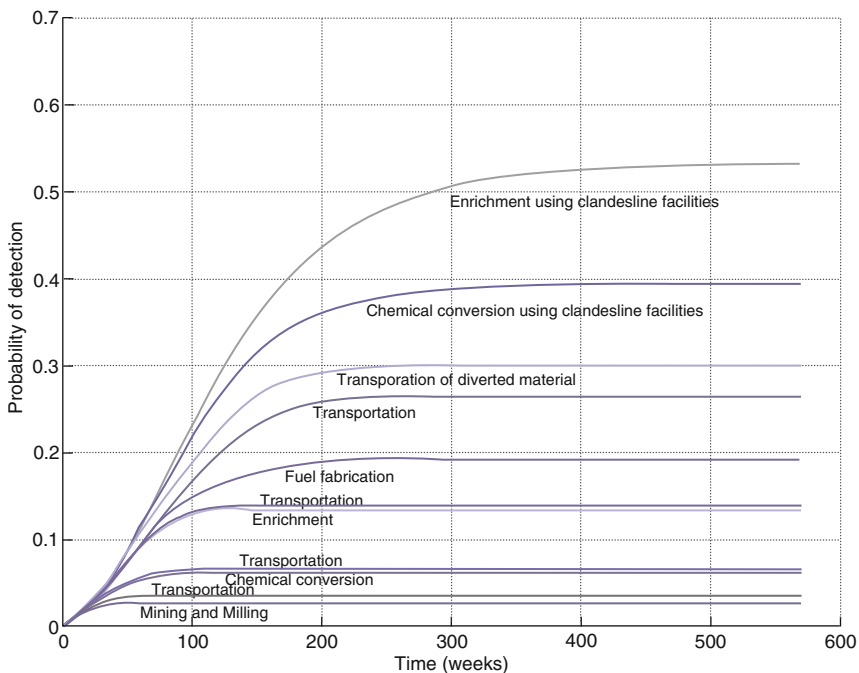


Figure 9
Detection probability for front-end diversion

that can be used to quickly explore “what if” scenarios and to perform design trade-offs. It fully allows the time-dependent nature of the proliferation process to be explored and displayed. The model can incorporate both declared and undeclared facilities and operations into a uniform framework. Further, if an additional protocol is in place, then detection rates for the clandestine facilities and operations can be incorporated. The possibility of technical failure by the proliferators due to the technical difficulty of key step on the path to proliferation is readily modeled in the Markov approach. Material quality is determined as an input to the proliferator’s scenario and strategy, i.e., the proliferator decides, before acting on which type of material to go after in the overall scenario. If successful, it is not a surprise to the proliferator that she/he obtained the material that was the objective of the act of proliferation.

Future work is guided by the needs of the Generation IV program and the proliferation resistance methodology in particular. The near term emphasis will be on further exploration of an example sodium fast reactor system and on consideration of recycle scenarios whereby reprocessing is part of the fuel cycle. It would be worthwhile to incorporate more data on safeguards approach, particularly where realistic alternative can be explored. A more comprehensive exploration of alternative scenarios should be explored, especially to investigate how to identify dominant scenarios and pathways.

2 Safeguards

Safeguards are measures taken to reduce proliferation risk. The terms or expressions (1) safeguards and (2) material control and accountability (MC&A) are often used interchangeably. Frequently, their definition depends on whether the audience is domestic or international. Material protection, control, and accounting (MPC&A) can be considered MC&A with the addition of physical security.

The governing agencies that regulate safeguards are both domestic and international. In 1953, the United States President Dwight Eisenhower suggested the creation of an international organization to develop and control atomic energy, in his “Atoms for Peace” speech before the UN General Assembly. The IAEA was established to promote the peaceful use of atomic energy while safeguarding against its use for military purposes. The IAEA reports directly to the UN General Assembly and Security Council; however, it was formed independently by way of its own international treaty, the IAEA Statute. The relationship between the IAEA and UN is described in INFCIRC/11, 30 October 1959. For the European Union, the IAEA has delegated selected responsibilities to Euratom (INFCIRC/263, October 1978).

Domestic agencies typically defend against the subnational threat (or theft), and the IAEA defends against the state threat (i.e., diversion). As such, it is the plant operator’s responsibility to satisfy the domestic and international safeguards requirements. However, domestic requirements are typically verified by auditing operations; whereas, international requirements are verified by independent and authenticated measurements and monitoring.

In addition to the IAEA Statute that is concerned with the peaceful use of atomic energy, bilateral agreements such as the United States and Russia MPC&A program have been established to enhance the safeguards of military facilities (<http://library.lanl.gov/cgi-bin/getfile?00326622.pdf>). While safeguards measures are often similar whether for civilian or military purposes, the focus of this chapter is civilian nuclear energy.

2.1 Domestic Safeguards: Implementing a State System of Accounting and Control (SSAC)

The application of safeguards is the responsibility of any state that possesses nuclear materials, and the control of their use should be a priority for the security interests of the state. A state therefore is obligated to establish an infrastructure for domestic safeguards for its own domestic purposes, to ensure the protection and accountability of its nuclear assets. However, this infrastructure is also required of all states with a comprehensive safeguards agreement (CSA) in place with the IAEA. The requirements of a CSA are that “The state shall establish and maintain a system of accounting for and control of all nuclear material subject to safeguards under the Agreement” (INFCIRC/153, para 7). The mandate for accounting and control of all nuclear materials subject to safeguards is commonly referred to as a State System for Accounting and Control (SSAC) of nuclear materials.

In the “Guidelines for States’ Systems of Accounting for and Control of Nuclear Materials,” the IAEA is quick to point out that a system of accounting for and control of nuclear material may have dual objectives:

- (a) A national objective, to account for and control nuclear material in the state and to contribute to the detection of possible losses, or unauthorized use or removal of nuclear material.
- (b) An international objective, to provide the essential basis for the application of IAEA safeguards pursuant to the provisions of an Agreement between the state and the IAEA (IAEA Safeguards Criteria, INF/2, 2004, p. 2).

A state’s SSAC may be entrusted with the execution of both international safeguards and domestic safeguards duties because in many states, the objectives of these two distinct interests coincide to a large degree. The elements of an IAEA-mandated SSAC and a domestic safeguards program share many features that are summarized in [▶ Table 12](#).

2.1.1 Primary Features of an SSAC

The term “State System for Accounting and Control” suggests first that the state has the ultimate authority for nuclear material, and second that the requirements for discharging its duties can be generally grouped into two categories: the duty of controlling the use of nuclear materials and the duty of maintaining an accountability system that tracks their use. Although a state takes the final responsibility for nuclear material in its possession, it is likely to authorize entities within the state to own and use these materials. Thus, a primary feature of an SSAC is the legal structure in which a state authorizes nuclear activities and those laws and norms that govern their use. The oversight of these activities is a second feature of an SSAC – the regulatory body in charge of establishing guidelines for the control and accounting of material and for ensuring compliance with these guidelines is commonly considered the primary element of an SSAC. However, a third important element is the facilities themselves that have direct responsibility for material accounting and control. It is at this level that accounting data are generated, which become the basis of national accounting reports submitted to the IAEA, and it is the facilities that must ensure the materials in their possession are controlled.

Table 12
Features of international and domestic safeguards objectives

SSAC functional area	International safeguards objectives	Additional domestic safeguards objectives
National policy	Ensure adherence to safeguards agreements (INF/CIRC 66 or 153, 540)	Ensure adherence to all treaties and agreements governing nuclear use to which the state is a party
National authority	Demonstrate compliance with IAEA requirements; bolster international	Ensure that nuclear materials in the state are within control of the state Demonstrate compliance with national requirements, which will be determined based on state determination of threat Bolster confidence that nuclear materials are safe from insider and outsider attack or sabotage through establishing requirements for all facilities that operate with nuclear material and ensuring compliance with these requirements through effective oversight
Facility safeguards organization	Provide data for required reports and verification visits	Meet operating requirements, operational costs, production schedules, profit demands, etc., as determined by facility owner
	Perform activities in accordance with safeguards requirements	Comply with all national regulations; demonstrate compliance
	Cooperate with IAEA verification activities	Ensure safeguards provide minimum detection, as prescribed by state

These three elements of an SSAC – legislative, regulatory, and facility – each have a role in addressing the specific aspects of accounting and control that comprise an effective safeguards system for nuclear materials. These aspects include practices such as establishing the starting point, terminating and exempting accounting and control, categorizing nuclear material, delineating material balance areas (MBAs), the capacity to generate records and reports from facility data, definition of material flows, performing physical inventory taking (PIT), analyzing shipper/receiver differences, evaluating the material balance closing, performing measurements within a regimented measurement control system, making use of containment and surveillance systems, and properly documenting material transfers, particularly international transfers. These aspects comprise the basis of effective accounting and control.

Taken together – the organizational elements of an SSAC and the functional aspects of their duties – the need for a system becomes clear. To carry out the necessary requirements of safeguards, the impetus from the state must exist to adhere to international treaties and promulgate legislation within the government to enforce adherence to the treaty obligations. Next, a state-designated authority must establish requirements for nuclear material accounting and control within the state and have the authority to ensure compliance through inspections and audits of facilities with nuclear material holdings. This authority must also be responsible for maintaining an information system that collects accounting and control information for the state as a whole. This system may be used for both domestic and international safeguards purposes. Finally, the operators at facilities where nuclear material is used are responsible for incorporating all safeguards elements mandated by the state authority into their operations to ensure that material is properly accounted for and controlled. The records of these practices must be provided to the state authority and demonstrated through periodic audits. The interaction of these three levels becomes the system in which nuclear safeguards practices are mandated, implemented, and verified.

► **Table 13** summarizes the requirements at each level of an SSAC. This table summarizes the requirements found in the IAEA “Guidelines for States’ Systems of Accounting for and Control of Nuclear Materials” (IAEA/SG/INF/2). Further elaboration of the specific elements of the system can also be found in the IAEA safeguards glossary (www-pub.iaea.org/MTCD/publications/PDF/nvs-3-cd/PDF/NVS3_prn.pdf). With these elements in place, a state can have an effective international system of accounting for and control of nuclear material.

2.2 IAEA Inspection Regime

IAEA defines in the model CSA (IAEA, INFCIRC/153, p. 1)

...the objective of safeguards is the *timely detection of diversion of significant quantities of nuclear material* from peaceful nuclear activities to the manufacture of nuclear weapons or of other nuclear explosive devices or for purposes unknown, and *deterrence of such diversion by the risk of early detection*.

The italics are inserted to emphasize the essential technical metrics of safeguards.

1. Timeliness
2. Significant quantities of nuclear material
3. Deterrence by risk of early detection

Table 13

Requirements at each level of an State System of Accounting and Control (SSAC)

Elements required in the design of the SSAC	Element description	Specific requirements
Legal structure	National legislation is required to ensure that domestic practices meet international safeguards requirements. An oversight agency should be granted authority to set requirements and ensure compliance. Provisions for enforcement should also be stipulated	Conditions for possession and use of nuclear materials Facility requirements Conditions for international transfer of nuclear material
SSAC information system	Information on nuclear material control and accounting should be collected by the National Authority	
Accounting and control requirements	Accounting and control requirements should be established by the National Authority and adhered to by all facilities possessing nuclear materials	Starting point, termination, and exemption of accounting and control
		Material categorization
		Material balance areas
		Measurement and measurement control systems
		Defined nuclear material flows
		Physical inventory taking
		Shipper/receiver difference
		Material balance closing
		Containment and surveillance
		International transfers of nuclear material
Ensure compliance with requirements	The National Authority is responsible for ensuring that facilities possessing nuclear material meet IAEA and any additional domestic requirements. Compliance will be verified by the IAEA through periodic inspections	

The IAEA provides guidelines for timeliness and significant quantities of nuclear material. The timeliness guidelines are based on open-source estimates of the conversion time for various types of nuclear material into a weapons-usable form. The significant quantities of nuclear material are amounts estimated to be needed to create one weapon. These material amounts include production losses and the level of skills possessed by first-time weapons designers and builders. This section shows how the IAEA has built its safeguards system to fulfill this technical aim of safeguards, by defining the concepts of timeliness of detection, significant quantities of nuclear material, and deterrence by risk of early detection. Thus, the principles behind the IAEA Safeguards Criteria are based on defining a set of guidelines using the concepts of significant quantities and timeliness allow inspectors to fulfill the technical aims of safeguards for the suite of facilities that the IAEA must inspect. Safeguards inspectors and their management use these criteria and established IAEA practices for a facility to lay out an inspection schedule for a material balance period (MBP), which is approximately one calendar year and no more than 14 months long, and is the period between two IAEA physical inventory verification (PIV) inspections.

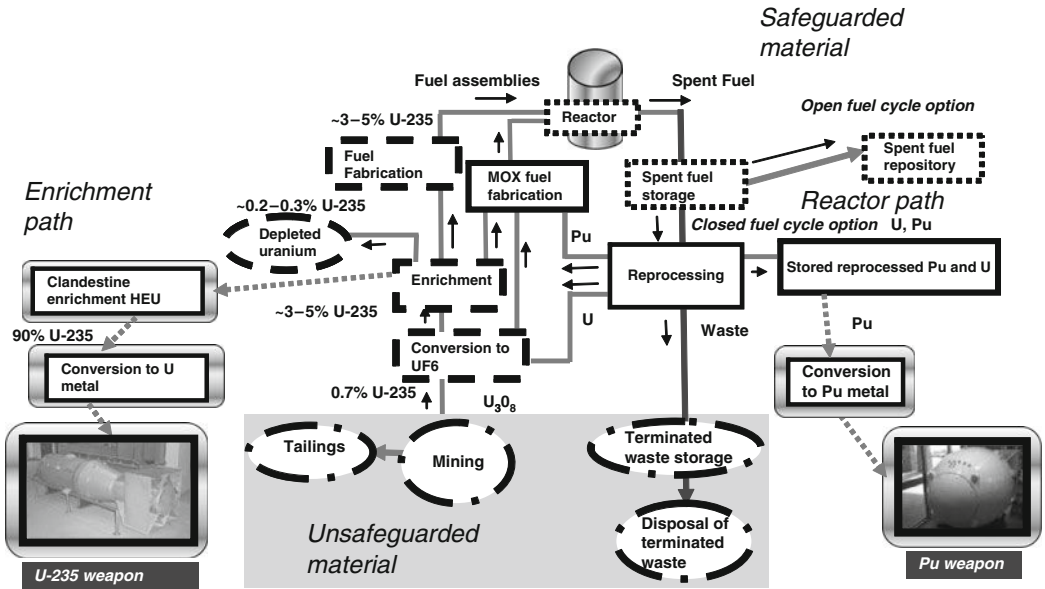
The types and amounts of nuclear materials and their physical forms determine the quantity goals and timeliness goals for a facility. This section provides the driving philosophies behind the material accountancy regime of IAEA safeguards. Verification of material accountancy in traditional safeguards is a keystone of IAEA safeguards, and even with the implementation of INFCIRC/540 additional protocols, and the move to more investigative safeguards as part of the Strengthened Safeguards System (SSS) (Hooper 1997), material accountancy will remain the keystone of the safeguards system. Thus, traditional comprehensive safeguards must be understood as a first step in comprehending the challenges the IAEA safeguards system faces. This section also shows the significance and relevance of the SSS.

The first step in understanding IAEA safeguards is to take a broad overview of the nuclear fuel cycle to understand the proliferation pathways available to a state intent on obtaining a nuclear weapon. ► *Figure 10* shows a nuclear fuel cycle with reprocessing.

The difficulty of obtaining HEU or plutonium has helped keep the number of declared nuclear weapons states to five and the nondeclared nuclear weapons states to under a half-dozen. The HEU path requires an infrastructure capable of enriching natural uranium to HEU, and the production and handling of HEU metal. As shown by the industrial scale efforts of the five nuclear weapons states, this is not a trivial technical or industrial endeavor. The plutonium path requires reactors to produce plutonium from uranium, a reprocessing facility to separate plutonium from the uranium and fission products, and a conversion facility to be capable of making plutonium metal and shaping it into weapons-usable forms. Thus, the key nuclear fuel cycle technology in the HEU path is the enrichment facility. In the plutonium path, the key technology is the reprocessing facility. Both facilities provide unirradiated direct use material, which provides highly attractive material.

The next step in understanding IAEA safeguards is to define what the Agency (i.e., IAEA) sees as nuclear material, as defined in IAEA, Statute of the IAEA, Article XX, 1957:

1. The term “special fissionable material” means plutonium-239; uranium-233; uranium enriched in the isotopes 235 or 233; any material containing one or more of the foregoing; and such other fissionable material as the Board of Governors shall from time to time determine; but the term “special fissionable material” does not include source material.
2. The term “uranium enriched in the isotopes 235 or 233” means uranium containing the isotopes 235 or 233 or both in an amount such that the abundance ratio of the sum of these



Dashed line represents indirect-use material
 Dotted line represents irradiated direct-use material
 Solid line represents unirradiated direct-use material
 Gradient shaded background represents diverted nuclear material
 Dashed plus dotted line represents waste or material not in safeguards

Figure 10
 The closed nuclear fuel cycle with highly enriched uranium (HEU) and plutonium weapons paths

isotopes to the isotope 238 is greater than the ratio of the isotope 235 to the isotope 238 occurring in nature.

3. The term “source material” means uranium containing the mixture of isotopes occurring in nature; uranium depleted in the isotope 235; thorium; any of the foregoing in the form of metal, alloy, chemical compound, or concentrate; any other material containing one or more of the foregoing in such concentration as the Board of Governors shall from time to time determine; and such other material as the Board of Governors shall from time to time determine.

The IAEA also defines a threshold between LEU and HEU as follows: HEU is uranium enriched greater than or equal to 20% of ²³⁵U. Thus, LEU is any uranium enriched in ²³⁵U beyond natural but <20% of ²³⁵U. Natural uranium (NU) is uranium with 0.711% ²³⁵U, and depleted uranium (DU) is uranium depleted in ²³⁵U to below 0.711% ²³⁵U.

2.2.1 Timeliness Goals

The timeliness criteria for thorium, uranium, and plutonium in a nuclear facility originate from estimates of the conversion time for uranium into a weapon, as shown in [Table 14](#). The

■ **Table 14**

Estimated material conversion times for finished uranium and plutonium metal components

Beginning material form	Conversion time
HEU or plutonium metal	Order of days (7–10)
HEU, plutonium, or other pure uranium compounds MOX or other unirradiated pure mixtures containing plutonium and uranium ($^{235}\text{U} \geq 20\%$) HEU or plutonium in scrap or other miscellaneous impure compounds	Order of months (1–3)
HEU or plutonium in irradiated fuel	Order of months (1–3)
Uranium containing $<20\%$ ^{235}U Thorium	Order of months (3–12)

■ **Table 15**

Timeliness goals for thorium, uranium, and plutonium

Material	Timeliness goal
Unirradiated direct use material: plutonium, ^{233}U , or HEU	1 month
Irradiated direct use material: plutonium, ^{233}U , or HEU	3 months
Indirect use material: LEU, NU, DU, thorium	1 year

■ **Table 16**

Quantity goals for uranium in GCEPS

Material	Quantity goal
Pu ($<80\%$ ^{238}Pu)	8 kg Pu
^{233}U	8 kg ^{233}U
HEU, $\geq 20\%$ ^{235}U	25 kg ^{235}U in uranium
LEU, $<20\%$ ^{235}U	75 kg ^{235}U in uranium
NU	10 tons NU (= 71.1 kg ^{235}U in uranium)
DU	20 tons depleted uranium ($\sim 40\text{--}60$ kg ^{235}U in uranium)
Thorium	20 tons thorium

timeliness goals for thorium, uranium, and plutonium are given in [▶ Table 15](#). The timeliness goals assume that a state have clandestine facilities that can process diverted material. Thus, timeliness and conversion time are roughly equivalent.

2.2.2 Quantity Goals

The quantity criteria for uranium, thorium, and plutonium in a nuclear facility arose from estimates of the material needed to produce a weapon, as shown in [▶ Table 16](#). These estimates are seen as reasonable for a first-time weapon designer and include material production losses.

■ **Table 17**
Probability of detection goal bands

Probability of detection	Goal (%)
Random high	90
Random medium	50
Random low	20
Random low–low	10

2.2.3 Deterrence by Risk of Early Detection

Once the definition of the timeliness and quantity goals for the material is set, the level of measures needed to safeguard the material can be judged by providing probabilities of detection, with higher probability and certainty of detection for more strategic materials. ➤ [Table 17](#) outlines the level of probability of detection the IAEA uses. Thus, in general for unirradiated direct use material, a random high-detection probability is desired for a 90% probability of detection. For indirect use material, a random medium probability of detection of 50% is deemed sufficient to detect the diversion of LEU or NU.

2.2.4 Frequency of Inspection to Fulfill Technical Objectives of Safeguards

When the above-defined goals are used for timeliness, quantity, and probability of detection, an inspection regime can be defined to provide coverage for verifying enough material in a satisfactory statistical manner to ensure that the detection goals can be met. In general, an annual PIV is required for all facilities except those with extremely small amounts of material. The IAEA requires interim inspections for timeliness for facilities having material with timeliness of <1 year. Thus, a facility with irradiated direct-use material, such as spent fuel in the core of a reactor, needs inspections every 3 months for timeliness. A facility with unirradiated direct use material, such as HEU fresh fuel for a research reactor, or separated plutonium in a reprocessing plant, or MOX fuel fabrication plant, requires 1 month timeliness inspections. It should be noted that inspection frequency is not determined just by the type of material at a facility, or the amount at any moment in time. If a production facility such as a conversion, fuel fabrication, or enrichment plant has indirect use material with a timeliness of 1 year, it could still require more frequent inspection. If the amount of material received in-site, processed, and shipped off-site during the year is such that an annual inspection does not give a representative random sample of the total material yearly throughput, then interim inspections are needed to verify that enough material throughput occurs to statistically satisfy inspection goals.

2.2.5 IAEA Nuclear Facility Categories

The IAEA attempts to define nuclear facilities by functional categories. A current estimate of the number of each type of facility that is under IAEA safeguards is given in ➤ [Table 18](#) (IAEA

■ Table 18

Facilities under safeguards

Facility type (defined by IAEA Safeguards Criteria)	Approximate number of facilities under IAEA safeguards worldwide
LWRs	180
On-load reactors (OLRs)	20
Other types of reactors	10
Research reactors and critical assemblies (RRCAs)	170
Natural and low enriched uranium conversion and fabrication plants	50
Fabrication plants handling direct-use material (MOX or HEU)	5
Reprocessing plants	10
Enrichment plants	20
Storage facilities	80
Other facilities (~60 other facilities under SGs)	60
Locations outside facilities (LOFs)	60–70

Annual Report 2006). The Agency classifies the facilities into two basic categories of item or bulk-handling facilities. The item facilities have nuclear material that is contained in an “item” form such as fuel rods and fuel pins, while bulk handling facilities have nuclear material that is contained in a “bulk” form such as UF_6 in cylinders, UO_2 powder, or reprocessed plutonium stored in containers. Item facilities have the advantage to the inspector of having the nuclear material being in an integral physical form that will not change. Bulk handling facilities have the disadvantage of having nuclear material being in gas, liquid, or powder forms that is altered chemically or isotopically.

In a bulk handling facility, the inspector will encounter material stored in containers where an uncertainty of the measurement regarding just how much material is present will always exist for both the operator and the inspector. The operator will always have, over the course of a material balance period (as stated above to be approximately 1 year), some material unaccounted for (MUF). MUF is calculated for a MBA over a material balance period (MBP) using the material balance equation, commonly written as:

$$MUF = (PB + X - Y) - PE, \quad (2)$$

where

- PB = the beginning physical inventory
- X = the sum of increases to inventory
- Y = the sum of decreases from inventory
- PE = the ending physical inventory

Because book inventory is the algebraic sum of PB, X and Y, MUF can be described as the difference between the book inventory and the physical inventory. (The equivalent term in US

domestic safeguards, for both the US Nuclear Regulatory Commission (NRC) and the DOE, is inventory difference (ID), as described in 10CFR 74.4 and DOE Manual 470.4-6.) For item MBAs, MUF should be zero, and a nonzero MUF is an indication of a problem (e.g., accounting mistakes), which should be investigated. For bulk-handling MBAs, a nonzero MUF is expected because of measurement uncertainty and the nature of processing bulk materials. The operator's measurement uncertainties associated with each of the four material balance components are combined with the material quantities to determine the uncertainty of the material balance (IAEA Safeguards Glossary 2001, p. 55).

Thus, the operators of large enrichment plants and large reprocessing plants, with their large throughputs of material, find it statistically difficult to obtain an MUF that is smaller than a significant quantity of nuclear material using the best measurement techniques. Verification of the large amounts of material moving through these facilities is a major challenge for the IAEA and its inspectors.

2.2.6 Keystones of Bookkeeping, Material Accountancy, and Containment and Surveillance

The verification regime of the IAEA can be seen as analogous to an audit of a major corporation by a large accounting firm. For the IAEA, the goal is to be able to not only ensure that the bookkeeping of material accountancy records is in order, but to verify the material using a battery of physical tests and measures. The Agency then uses containment and surveillance techniques to maintain "continuity of knowledge" (CoK) of the verified material.

Material accountancy is seen as a safeguards measure of fundamental importance. The Agency breaks down the accountancy verification methods available to the inspectors in an alphabetical system as follows:

- A Identification
- B Weighing
- C Volume determination
- D Sampling and analysis
- E Variables by non destructive assay (NDA) (bias defects)
- F Variables by NDA in attribute mode (partial defects)
- G Criticality check for verification
- H Attribute test by NDA (gross defects)
- M Facility specific method for in-process inventory verification

Other methods include the following:

- I Item counting
- K Spent fuel inventory check for verification (only for multiple layer spent fuel stores)
- T Tag check
- Z Other

Thus, the inspector can use Method A, combined with Methods I and T, to verify material in containers or fuel elements by checking serial numbers, counting the items, and checking tags on items. An example of this technique is counting fuel items in an LWR reactor core and verifying the serial numbers through the use of an underwater TV camera.

An inspector can use Method B to weigh a container holding nuclear material, or an LWR or research reactor fuel assembly, to obtain the mass of nuclear material.

An inspector can use Method C to get a volume determination of nuclear material in a liquid form in a reprocessing facility, to ensure the operator's declaration of material in process or in process tanks.

An inspector can use Method D to get a destructive assay (DA) sample on the order of grams to be able to perform very accurate laboratory analysis that allows for the measure the isotopics of plutonium or uranium on the order of 0.1% uncertainty. The IAEA routinely performs DAs at reprocessing and enrichment facilities.

Methods E, F, and H are NDA bias, partial, and gross defect tests of material verification, respectively. The concept of defect, as defined by the IAEA, is a difference between the declared amount of nuclear material and the material actually present (IAEA Safeguards Glossary 2001, p. 78). The IAEA defines the three levels of defect testing as the following:

- (a) Gross defect refers to an item or a batch that has been falsified to the maximum extent possible so that all or most of the declared material is missing.
- (b) Partial defect refers to an item or a batch that has been falsified to such an extent that some fraction of the declared amount of material is actually present.
- (c) Bias defect refers to an item or a batch that has been slightly falsified so that only a small fraction of the declared amount of material is missing.

For these three NDA and one DA techniques described above, [Table 19](#) describes the desired uncertainties for safeguards measurements where total (relative) measurement uncertainty is defined as:

$$\delta_i = (\delta_O^2 + \delta_I^2)^{1/2}.$$

The subscripts O and I designate operator and inspector measurements, respectively. Thus, any systems used to meet gross, partial, or bias defect tests should have these recommended measurement uncertainties.

In addition, Methods I, K, T, and Z can be facility-specific methods (e.g., the method for in-process inventory verification in the case of near real-time accountancy and item counting that can be specified for use as verification methods (IAEA Safeguards Glossary 2001, p. 55).

Other methods are also part of the containment and surveillance (C/S) realm that is a huge part of the IAEA safeguards effort in maintaining CoK. CoK is common phrase in IAEA safeguards that reflects the use of the following methods:

- S Stratum under surveillance
- V Seal verification
- X Monitors

C/S allows the IAEA to have confidence that a verified nuclear material item has not been diverted or tampered with. [Figure 11](#) shows the difference between containment and surveillance.

Containment, as shown here, attempts to provide a means to show if a nuclear asset has been tampered with. A seal, such as an Agency metal seal, is not a lock. The seal is a tamper indicating device (TID) if broken, tampered with, or counterfeited that provides evidence to the tampering. Surveillance, as shown here, allows access to a nuclear asset but should be able

Table 19
Operator/inspector measurement system recommended error limits

Method codes	Interpretation	Relative error ranges	Detectable defect size
H	Quantitative through NDA (verification in the attribute mode using the least accurate method)	$0.0625 < \delta_i \leq 0.125$	Gross
	Qualitative through NDA (e.g., Cerenkov, bundle counter)	Error cannot be assigned	Gross
F	Quantitative through NDA (verification in the attribute mode using a more accurate method)	$0.010 < \delta_i \leq 0.0625$	Partial
E	Quantitative through NDA (verification in the variables mode using the most accurate method) e.g., K-edge densitometer	$\delta_i \leq 0.01$	Bias
D	Quantitative through DA (verification in the variables mode using the most accurate method)	$\delta_i \leq 0.01$	Bias

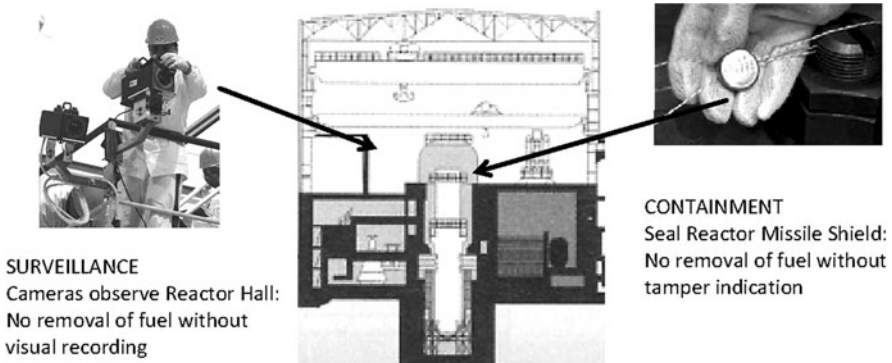


Figure 11
Containment and surveillance examples options at VVER-440 reactor

to determine if an asset has been diverted or tampered with by the images. Method X, using monitors such as radiation detectors, can be seen as surveillance attempting to use radiation signatures to discern if an asset is moving through a strategic point as declared or is a diversion.

2.2.7 Strengthened Safeguards

The SSS evolved after the first Gulf War and the discovery of the Iraqi clandestine nuclear program. The SSS has the following objectives, as defined by the IAEA board of governors (BOG) in March 1995: “The safeguards system should be designed to provide credible assurances that

there has been no diversion of declared nuclear material, and that there is no undeclared nuclear material and activities.” Thus, the SSS conclusions should be able to determine that the





1. State’s nuclear material declarations are correct
2. State’s nuclear material declarations are complete

This goes beyond the traditional safeguards that focused on goal #1 and had for 20 years a tacit assumption of completeness for goal #2. With the SSS, goal #2 was seen to be reached by additional information from a state and analysis of open sources. The codification of how to gain more access to a state, and codify the information to reach goal #2, was reached in the AP. The AP gives the IAEA more information from the state, and increased access to verify the completeness of a state’s declaration. Thus, the IAEA has an increased ability to provide credible assurances that no declared nuclear material has been diverted, and that no nuclear material or activities are undeclared.

2.3 Safeguards Design

Safeguards design is essentially two tier, the first being instrument and/or equipment level and the second systems level. Like all design efforts, safeguards design is dictated by requirements. Unlike process design requirements that are based on the desired product, safeguards design requirements are usually dictated by the regulating and/or governing agencies based on the need for control of nuclear materials.

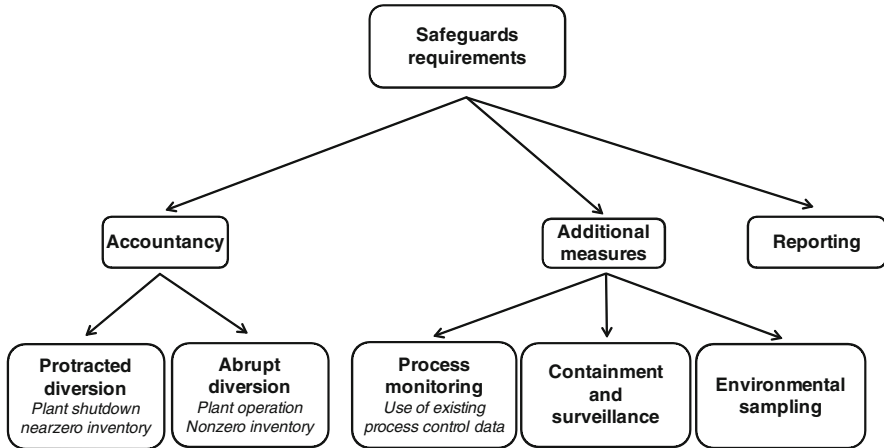
2.3.1 Safeguards Requirements

High-level safeguards requirements, whether domestic or international, can be generalized as shown in  Fig. 12. In addition to that shown in  Fig. 12, additional protocol (AP) can be considered a supplementary requirement imposed by the IAEA for those countries that are signatories. While safeguards terminology is often inconsistent between governing agencies, the concepts represented by the high-level requirements of  Fig. 12 are not. Requirements not shown in  Fig. 12 do exist, but those that are shown dictate a significant portion of the safeguards design.

Accountancy

Primary accountancy is usually based on destructive assay (DA) rather than nondestructive assay (NDA), due to the smaller measurement error. DA requires the collection of samples and transfer to an analytical laboratory; whereas, NDA can be conducted in-place often without collecting a sample. NDA is used principally for verification in conjunction with DA, by the IAEA. NDA may also be used for criticality control by the operator, but this is not a safeguards activity. NDA techniques are thoroughly described in the Passive Nondestructive Assay (PANDA) manual (<http://www.lanl.gov/orgs/n/nl/panda/index.shtml>). A discussion of both NDA and DA can be found in Ottmar 2010.

Abrupt Diversion This represents the theft or diversion of material during a short period of time. As such, its timely detection is paramount. Inventories used to detect abrupt diversion are



■ **Figure 12**
Example safeguards requirements

usually performed during plant operation due to their short interval. Both domestic and international agencies have a quantitative requirement or goal for abrupt diversion measurement performance, often referred to as the (1) standard deviation for MUF ($\sigma\text{-MUF}$ or σ_{MUF}), (2) standard deviation in the inventory difference ($\sigma\text{-ID}$ or σ_{ID}), or standard error in the inventory difference (SEID).

Protracted Diversion This represents the theft or diversion of material during a long period of time. Inventories used to detect protracted diversion are often performed during annual plant shutdown and cleanout.

Additional Measures

While the contribution of additional measures to safeguards justifies their use in and of themselves, they are often supplemental when accountancy requirements or goals cannot be completely satisfied.

Process Monitoring Process monitoring as part of additional measures refers to the use of the operator's process control data. This data is often limited due to its proprietary nature, and for the most part cannot be authenticated. It can include, tank levels, tank transfers, temperatures, and non-SNM chemical compositions such as acid.

Containment and Surveillance Containment and surveillance refer to the tracking of objects and personnel. For example, this can be by way of cameras, or more quantitatively with bar codes on individual items.

Environmental Sampling Environmental sampling as part of traditional safeguards is concerned with sampling to determine if operations have been conducted as declared. For example, surface swipes within a LEU enrichment facility are analyzed to determine if HEU is present. With the additional protocol, similar sampling may be extended to search for clandestine facilities.

Additional Protocol

As of October 2008, 127 states and other parties had received Board Approval for additional protocols (APs) to their IAEA Safeguards Agreements, for the Agency's application of strengthened safeguards. These APs are described in "Model Protocol Additional to the Agreement(s) between state(s) and the IAEA for the Application of Safeguards," INFCIRC/540 (Corrected) (IAEA 1972). AP grants the IAEA complementary inspection authority beyond that given by the traditional safeguards agreements. The AP expands inspection authority particularly in the area of undeclared activities, for which the IAEA is given expanded rights of access to information and sites. Implementation of the AP allows IAEA collection of environmental samples at locations beyond declared locations when deemed necessary by the Agency.

2.3.2 Safeguards by Design

Safeguards by Design (SBD) is defined as the incorporation of safeguards design early in the design phase of a new nuclear facility in order to avoid the need to redesign the process and/or facility at a later date, or retrofit the completed facility. The safeguards design itself should be based on best practices, lessons learned, and advanced concepts. Integration of the safeguards design with process and facility design will allow design trade-offs that maximize safeguards effectiveness based on overall capital and operating cost.

In its most simple form, SBD implies safeguards requirements of the governing agencies are considered early in the overall design effort. More specifically, the sequencing of safeguards design activities are dictated by high-level requirements of the facility owner. ➤ [Table 20](#) provides a high-level example of sequencing the facility and process design with the safeguards design (DeMuth et al. 2009).

Conceptual Design

Primary Objective: Initial Capital Cost Estimate The initial capital cost estimate is primarily dictated by the amount of steel and concrete required for construction. As such, the necessary design features developed for conceptual design are those that significantly affect the facility foot print (area). Conceptual design is usually conducted by way of Trade-Studies that are used to analyze alternatives.

1. Determine regulatory and product requirements.
2. Determine the category and attractiveness of nuclear material. This impacts the physical protection, and material control and accountancy requirements. Document functional requirements based on nuclear material categories and attractiveness, where the functional requirements define the purpose of relevant systems and components.
3. Determine MBAs and outline on process flow sheets.
4. Plan for accountancy of nuclear material by destructive analysis and verification by nondestructive analysis measurements. Identify equipment and instruments that meet measurement requirement needs. Select key measurement points (KMPs).
 - (a) DA accountancy is important during conceptual design because it dictates the sample locations and consequent number of samples. The number of samples is then directly related to the size of analytical laboratory.
 - (b) NDA monitoring is important during conceptual design because instrumentation is typically colocated with production equipment in process cells. Process cells require

■ **Table 20**
Safeguards by design (SBD) example activities

Design phase	Process and facility design activities	Safeguards design activity
Conceptual	Define requirements Process design Equipment list Plant layout Initial capital cost estimate Conceptual design report	Define goals/requirements Determination of SNM attractiveness and category MBA designation Identify SNM measurements (DA & NDA) Laboratory layout (domestic and international) Personnel access control Identify technology development needs Prepare a conceptual safeguards design report
Preliminary	I&C design Piping design Utilities/infrastructure Begin equipment design Operating labor Initial estimate of overall economics Preliminary design report	Prepare process monitoring plan SNM containment and surveillance Estimate accountancy performance (sigma-MUF) Identify accountancy monitoring (IAEA) Develop data authentication and protection Update the conceptual safeguards design report for the preliminary safeguards design report
Final	Complete equipment design Detailed design report Regulatory approval	Detailed instrument and equipment design Reporting and data integration Requirements validation Final overall design with integrated safeguards Update the preliminary safeguards design report for the final safeguards design report

more concrete and steel than the remainder of the facility. Accurate sizing of the process cells is required for an accurate initial cost estimate.

5. Determine DA measurement throughput for both domestic (SSAC) and international (IAEA) needs, and size laboratories for each. Additionally, determine office space needs for IAEA inspectors.
6. Identify personnel access control concepts.
7. Identify long-lead time technology development needs.
8. Write and issue a Conceptual Safeguards Design Report.

Preliminary Design

Primary Objective: Performance Baseline A primary objective for preliminary design is preparation of the performance baseline, an event-driven schedule with defined accomplishment criteria for each event leading to facility operation. The performance baseline results from a near-complete, although not necessarily detailed design. Since the safeguards conceptual design is focused on those aspects that affect facility capital cost, preliminary design should be used to complete the full safeguards design with enough detail to create the performance baseline.

1. The process monitoring plan can be completed during this design phase following completion of the process and facility I&C design. The process monitoring design makes use of the process and facility I&C design, and must therefore await its completion.
2. Containment and surveillance features are prepared during this phase. This affects safety and security, and allows for more efficient material processing if designed well.
3. The accountancy performance is estimated following completion of the process and facility I&C design. The accountancy performance is characterized by way of the sigma-ID. This is the cumulative measurement error for the inventory difference at one standard deviation. This design is primarily dependent on DA.
4. The accountancy monitoring/verification design is prepared following completion of the process and facility I&C design. This design is primarily dependent on NDA, which is adequate for validation of accountancy DA, in most cases. Redundant but independent DA samples are required for limited verification.
5. Incorporate data authentication and protection into the preliminary design. This dictates wiring and security issues.
6. Update the conceptual design and issue the preliminary design, which should address all safeguard and security issues.

Final Design

Primary Objectives: Regulatory Approval and Construction Readiness Regulatory and customer approval is a primary objective for the final design. Paramount in gaining regulatory approval is validation that the safeguards design meets regulatory requirements. Another primary objective for final design is readiness for construction. Readiness for construction implies all aspects of the design must be fully complete.

1. Detailed instrumentation and equipment design is conducted during this phase.
2. Review reporting and data integration systems.
3. Update with any recent technology advances. This is dependent on the completed safeguards system design.
4. Validate that safeguards requirements are fully met as required for regulatory approval.
5. Update safeguards design if needed based on requirements validation.
6. Update the preliminary design documents for the final safeguards design report.

2.4 Unattended Monitoring

The IAEA relies heavily on the use of Unattended Monitoring Systems (UMS) to provide continuous monitoring at declared nuclear facilities around the world as part of its treaty-based mandate to ensure that nuclear material in these facilities is not being diverted from peaceful uses. Currently, over 100 UMS exist worldwide, with an average of ten new systems installed per year. The primary overall goal for these systems is to never lose safeguards-significant data under even the most challenging infrastructure and operational environments. The stringent data loss goal demand that these systems have high reliability through fault tolerant designs for both hardware and software and the success of these systems, has led to a growing reliance on UMS. Also of concern is the more practical operational side of the hardware and software used by the IAEA in multiple platforms, the interplay among worldwide vendors, the flexibility for upgrades and enhancements, the ease of implementation and configuration, and the training aspects. This

section introduces the current UMS as deployed by the IAEA, as well as the goals, benefits, challenges, and financial drivers. For any organization meeting new challenges in a rapidly evolving technology environment, it must be remembered that these technologies are always in flux as the next generation is designed, tested, and implemented. Nevertheless, the basic principles do not change.

2.4.1 Background

The concept of UMS is new neither in concept nor in implementation. The first example is the use of film cameras to monitor spent-fuel ponds in reactors. In the 1970s, the IAEA relied on twin Minolta film cameras for this monitoring effort. The cameras had a fixed interval of 20 min based on the operational time for moving a spent fuel cask, and required regular film cassette changes. The effort to review these images was quite problematic. Black and white images of a spent fuel pond with very little activity and no way to advance rapidly to images of interest challenged the most astute viewer to maintain attention through the entire review process.

With the advent of integrated circuitry and computers, this field has seen a revolution in capability. One of the first implementations of a modern distributed UMS took place at the Darlington CANDU reactor in Canada in the late 1980s. A Los Alamos National Laboratory (LANL)-developed system was installed to monitor the discharge of spent fuel from this online reactor. Even today this system continues to operate with high reliability. The only recent upgrade was made to the computer data collection system because the old PCs were obsolete, thus making them difficult to repair or support new devices such as data storage.

2.4.2 Definition of an Unattended Monitoring System (UMS)

An UMS comprises a single or multiple set of sensors designed to maintain CoK about the content and location of all nuclear material of interest in a facility 24 hours a day and 365 days a year. The concept of CoK can take many forms, from simply tracking spent fuel bundles or assemblies to performing a quantitative analysis on cans of MOX fuel. The intent is that the system can provide the necessary assurance for the IAEA to draw rapid, comprehensive, and definitive conclusions that nuclear material is not being diverted from peaceful use. This intent directly relates to two specific IAEA criteria and two scenarios: goal quantity and conversion times; and abrupt and protracted diversion.

As an example, the IAEA considers 8 kg of plutonium and 25 kg of HEU to be goal quantities that indicate quantities of interest to a diverter and, therefore, detection goals for the IAEA safeguards system. Conversion times are the estimated times for a diverter to convert these quantities into a nuclear weapon. These conversion times are based on the form of the material. The two high-level diversion scenarios consider the complete diversion of a goal quantity in a short time (abrupt) versus a series of small diversions that lead to a goal quantity over a long time (protracted). Taken in combination, all of these factors lead to the basis for the detection sensitivity of the IAEA safeguards system and the periods in which definitive safeguards conclusions must be drawn. The IAEA defines the word “remotely” (see item 4 below) as data going from a computer server in a monitored facility to some remote location. This transfer could go to an inspector data review room, an IAEA field office (such as Toronto or Tokyo), or the headquarters in Vienna.

Basically, a UMS

1. Is a system that automatically monitors the flow of nuclear materials 24 hours a day, 365 days a year, without the need for human interaction
2. May use a variety of sensors, such as radiation, pressure, temperature, flow, vibration, optical, and electromagnetic fields to collect qualitative or quantitative data
3. Is permanently installed in a nuclear facility
4. Is computer-based for data retrieval either on site or remotely
5. Has all of its components in tamper-indicating enclosures

Regarding 5, the IAEA must be able to independently verify its conclusions regarding the nuclear material in a facility. At the same time, the IAEA must consider that every state is a potential adversary. As such, there is always the potential threat that a state might try to alter the data being collected by the IAEA. The IAEA takes several steps to prevent an adversary from succeeding and to ensure that the data is authentic. One step is to design all enclosures so that the IAEA can detect tampering. The IAEA cannot prevent tampering; it can only detect it. Specific examples of tamper-indicating enclosures are presented in this document.

2.4.3 Why Does the IAEA Use UMS?

Before UMS was used, the routine inspection approach was periodic, relying on inspectors to visit nuclear facilities at a specified frequency, perform specific activities, and draw timely conclusions based on the data collected. This approach had many problems. Because it was periodic, the information collected at a facility by an inspector was no longer current once the inspector finished. This approach also meant that a significant effort could be required to reestablish this information across the inventory during the next inspection. Requiring a physical presence to carry out inspections also meant that the operator had to support every inspector's visit with personnel resources and interrupt activities to allow an inspector access. This process placed a heavy burden on both the IAEA and the facility operator. Some facilities, such as reprocessing, on-load reactors, and hot cells, precluded inspector presence because of health and safety concerns. Even in the case where inspectors could have complete access, it was not economically feasible for a facility that operated continuously, or for the IAEA, to provide around-the-clock safeguards using inspectors and the facilities' support staff. In fact, it was the design of fully automated facilities that actually drove the advancement into modern unattended safeguards as the only rational solution to the problem.

2.4.4 Benefits of UMS

1. Provides the highest level of safeguards assurance through continuous monitoring of activities in nuclear facilities
2. Minimizes the impact on the facility operator by allowing uninterrupted facility operation
3. Minimizes the impact on the IAEA by reducing inspector visits and inspection resources (including the high cost of worldwide travel)
4. Reduces radiation exposure to personnel and can operate in radiation areas too dangerous for humans

2.4.5 Key to Maintaining a Balanced Approach in IAEA Safeguards

The process of applying international safeguards to the entire fuel cycle encompasses the balanced nature of the approach and, particularly, the negotiations between the facility operator and the IAEA. The IAEA must be able to draw independent conclusions to fulfill its mission as a neutral arbiter of compliance with the Nonproliferation Treaty (NPT). Although it is true that certain principles must be maintained, such as independent verification, it does not imply that the means of gaining information to reach this verification cannot be flexible.

This balanced approach is possible because of the foresight of those who wrote the key provisions of Information Circular (INFCIRC)/153 as follows:

INFCIRC/153 – The structure and content of agreements between the agency and states in connection with the NPT

- PART I, Para 4, The Agreement should provide that safeguards shall be implemented in a manner designed:
 - To avoid hampering the economic and technological development of the state . . . in the field of peaceful nuclear activities, including international exchange of nuclear materials
 - To avoid undue interference in the state's peaceful nuclear activities, and in particular in the operation of facilities
 - To be consistent with prudent management practices required for the economic and safe conduct of nuclear activities

This instruction to the IAEA stressed the need to be expeditious in implementing safeguards. It also gave the state and the facility operator, who has the deepest knowledge of the facility, the right to negotiate efficient safeguards, while the IAEA maintained its right to independent verification. Any state can learn from this example in its own domestic compliance policies.

2.4.6 Major Cost Drivers in the Department of Safeguards

One of the primary selling points for UMS is cost-effective safeguards, which would include not only cost-effective safeguards at facilities, but also a reduced burden on IAEA resources. A 2004 financial plan shows the following average breakdown of costs in the department:

- Staff = 68%
- Other direct costs = 13%
- Travel = 10%
- Laboratory = 5%
- Shared costs = 3%

With the exception of travel, very little can be done to reduce the costs in these areas. If technology could be used to replace some portion of an inspector's effort without sacrificing independent verification, it is logical that the travel required for the scheduled periodic worldwide inspections could be dramatically reduced. The intent of the current push is to spread the use of UMS to appropriate facilities around the world as fast as possible.

Worldwide Deployment of UMS

The push to deploy UMS started in the late 1980s and has rapidly advanced, along with technological leaps in the capability and reliability of hardware, firmware, and software. From 2000 to

2004, the IAEA installed an average of ten new systems per year. In August 2004, statistics on these systems were as follows:

- 90 Systems installed (~115 in 2005)
 - 79 Radiation-based
 - 5 Thermohydraulic-based
 - 6 Process monitoring-based
- 44 Facilities
- 22 Countries
 - SGOA, 30 systems (SE Asia)
 - SGOB, 40 systems (North and South America, Africa, India, Pakistan, Iran)
 - SGOA, 20 systems (Europe, Kazakhstan, Ukraine)

The abbreviations SGOA, SGOB, and SGOA indicate the Department of Safeguards Operations Division that has specific geographical areas defined to implement their safeguards mission. The increase of nearly 25 systems in a little over 1 year primarily reflects the UMS installations in the Japanese Rokkasho Reprocessing Facility. For the IAEA to draw timely safeguards conclusions, this complex, high-throughput facility represents the greatest challenge to date. In 2004, 18 UMS were planned to allow the IAEA to draw independent verification.

2.4.7 Primary Goals of UMS

The commitment to implement UMS around the world is a daunting task. The consequences of failure are both technical (the need to reestablish the knowledge of content and location of the nuclear material at a facility and the complexity and cost in doing so) and political (the state impacted by a UMS failure will rightfully complain to the IAEA about the additional costs it will face because of a failure of IAEA equipment). These consequences, in turn, can raise questions about the IAEA's competence in accomplishing its mission (it should be noted that some installed systems are "joint use" by the state Inspectorate and the IAEA and therefore are jointly specified – the state often has equal responsibility and also often funds the development and installation). Therefore, the UMS unit established two primary goals in order of priority: no loss of safeguards-significant data and assurance that the data is authentic.

The key in the first goal is "safeguards significant." It is not possible to ensure that all components work all the time. Instead, the emphasis is on providing fault-tolerant systems that can continue to meet the needs of the IAEA in maintaining knowledge of the nuclear material in a facility in spite of some equipment failures. Therefore, by using systems that are designed to be robust and reliable while eliminating or minimizing single points of failure through redundancy, components can fail without jeopardizing the IAEA's mission.

Authentication of data is a tremendous challenge. Because the IAEA must assume that every state could be a potential adversary, it goes to great lengths to protect its data from the point of origin in the sensor through data analysis. Nevertheless, data authentication is of secondary importance to data loss. Authentication must not jeopardize the reliability of the data collection scheme.

2.4.8 Method of Obtaining Primary Goals

Considering the primary goal, "No loss of safeguards significant data," some key approaches include the use of high reliability and/or redundant critical components and/or reduced reliance

on low reliability components. High reliability components can be a great challenge in the UMS area primarily due to the low unit volume for some key components. Specialty components such as the data generators are only made by small vendors, so reliability is always tested to assure performance. The current design philosophy at the IAEA strives to use as many high-volume, commercial, off-the-shelf (COTS) products as possible, which helps not only with reliability but also with costs. Fortunately, many high-reliability components are available commercially, including sensors, batteries, cables, software, air conditioners, uninterruptible power supplies, industrial PCs and servers, operating software, connectors, encryption and wireless hardware and software, and cabinets.

Using independent redundant components to monitor the same event is another primary design approach to prevent the loss of data. Defense in depth by layering both the sensor and data collection systems is another fault-tolerant approach. Some approaches include the use of signal splitters. The sensor could be a gas-filled tube for neutron detection, which has demonstrated reliability over many decades (unlike the data generator, which may not be so reliable), and has its signal split and sent to two different data generators. Therefore, a single sensor can be used in conjunction with two data generators (radiation data generators can support multiple sensors) to ensure robust data collection.

The use of an uninterruptible power supply (UPS) to ensure uninterrupted data collection even after a loss of supply is a clear application to UMS. It is even more crucial considering that the infrastructure in many countries around the world is such that loss of power of varying duration is a routine event. It is the practice of the IAEA to negotiate with the facility to obtain Class 2 power from the facility (Class 1 supports the facility's safety system. Because of its importance, nothing else is added that might risk its integrity). This system is their backup power, and obtaining power for IAEA systems from it helps ensure reliability for the IAEA system. Besides a main UPS deployed in an electronics rack, the same defense in depth is applied where other critical components, such as data generators, have battery backup internally.

Using multilayer security is the second goal, and it reflects all the activities that the IAEA performs to secure its data. These activities include mechanical approaches, such as secured housings that hold sensors and all other associated equipment used to collect data, such as electronics cabinets, cabling, and junction boxes. The activities also include electronic approaches, such as authentication and encryption.

The primary objective for any UMS is to collect safeguards information reliably without an inspector's presence, on a continuous basis, and to

- Verify flow and inventory of nuclear materials
- Minimize intrusiveness on the operator
- Reduce IAEA and operator manpower requirements
- Decrease radiation exposure to the IAEA inspector and facility operator
- Standardize hardware and software for the IAEA to minimize maintenance and training

When beginning the design of a UMS, the following design considerations are investigated for each application:

- Cost benefit: A cost benefit analysis is made, comparing inspector days in the field with and without a UMS.
- Reliability and stability: Have the UMS components demonstrated a reliability of at least 150 months mean time between failures (MTBF) for the requested application? Can the components stably perform within the available infrastructure?

- Meet operation's user requirements: Can the UMS meet the performance and functionality required by the operation division that will use the data from the UMS?
- Operator-provided equipment: Is there operator equipment that could be used jointly by the IAEA and the operator while maintaining the independent verification capability required by the IAEA?
- Authentication requirements: Can the UMS be secured to assure the IAEA that the data is authentic?
- Early involvement of the agency in the planning stages: allows integration of facility-specific safeguards features into final plant designs, attaining the most cost-effective design before the facility is constructed, and thus avoiding the high cost and restrictions associated with facility retrofits.

Authentication

Authentication is defined as all measures taken to ensure that the safeguards measurement systems collect and provide authentic data. This broader category also includes encryption. For the classical application of electronic authentication and encryption on cryptographic modules, the IAEA follows FIPS-140 (Federal Information Processing Standard-140). This standard specifies the security requirements for a cryptographic module used within a security system protecting sensitive information in computer and telecommunication systems. Because of the nature of its work, the IAEA must monitor activities by leaving its equipment in facilities in states that are potential adversaries; this action represents a great challenge for UMS authentication.

Some examples of the steps taken by the IAEA to ensure that its data are authentic include the following security methods:

- Software controlled: IAEA software is not accessible by states, nor are systems shipped with hard drives in them. These actions eliminate opportunities for a state to examine the software during the process of shipment, customs clearance, and receipt at a facility.
- Tamper-indicating enclosures: Includes all external housings and shipping containers.
- Containment/surveillance (C/S) on detector head and electronics: Containment devices, such as seals and surveillance, as with optical sensors, can be used to protect any enclosure (seals at any time and surveillance during operation).
- Visual inspection of components and cables: Because the IAEA cannot prevent tampering, it is critical that inspections identify potential tampering. Currently, this identification is limited to visual techniques; however, many other techniques are applicable.
- Efficiency check with normalization source: It is common practice to use an IAEA source that is stored at a facility under IAEA seal to check the operational response of equipment that the IAEA will use for any measurements.
- Supervision of maintenance: In cases where the IAEA must use local companies to perform maintenance or repair on IAEA equipment, all such work is done under the supervision of the IAEA.
- Cross-correlation with other SG measures: As difficult as authentication can be for the IAEA, the use of multiple sensors on time correlated activities increases the difficulty for an adversary to compromise such a system.
- Use of unique data signature on all digital data: The IAEA maintains a cryptographic standard for all digital data and communications. Currently, this standard requires 128-bit encryption algorithms.

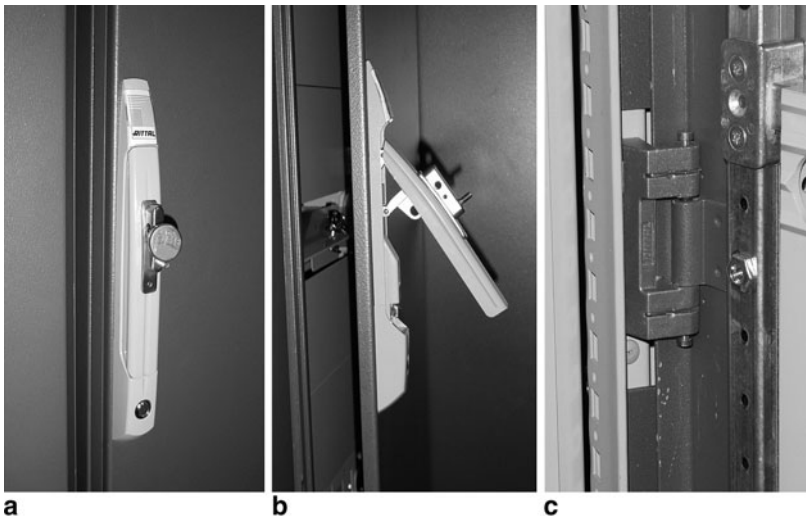
- Encrypted data transmission between cabinets and for remote monitoring: Data encryption is used both on site and off site for all data (special consideration for each state is also given for off-site data, as appropriate).
- Uninterrupted power supplies (UPS): Maintaining power is not only key for uninterrupted data collection, but for data protection as well. A layered approach is used.

Tamper-Indicating Features

Tamper-indicating features address all detection mechanisms, both electrical and mechanical. Although not separately categorized, various design features are used to minimize or eliminate access points by an adversary. At the most basic hardware level, the IAEA uses simple mechanical approaches to eliminate easy tamper routes. Consider the standard 19-in. Rittal industrial rack and enclosure that are used to house IAEA instrumentation. ➤ [Figure 13a–c](#) shows details of this enclosure.

➤ [Figure 13a](#) shows the application of an IAEA tamper-indicating metal seal that is applied to the locking mechanism for the cabinet. ➤ [Figure 13b](#) shows the locking mechanism in the open configuration; this mechanism moves full-length door pins so that the edges of the door cannot be pried open. ➤ [Figure 13c](#) shows the use of internal hinges (because external hinge pins are readily removed). The standard UN blue used on all IAEA equipment is applied using a powder process to make touchup of tampering more challenging.

The concept of “protected enclosure” reaches out to sensors, as well. ➤ [Figure 14](#) shows a picture of the entrance gate monitor used to measure fresh MOX fuel prior to entry into the reactor core. The application of the standard IAEA metal seal to detect attempts to access the upper portion of the neutron tube electronics can be seen. This neutron collar uses coincidence counting to assay the plutonium content of each assembly. ➤ [Figure 15](#) shows the IAEA tamper-indicating conduit used to protect unauthenticated signal cabling that connects



■ **Figure 13**
Cabinet close-ups



■ Figure 14
Entrance gate monitor (ENGM) detector



■ Figure 15
Tamper-indicating conduit

sensors to the electronic equipment in the IAEA instrument enclosures. This attempt to protect the cabling is problematic. Some facilities can have kilometers of cabling, including many portions that must go through wall penetrations that cannot be accessed. The addition of this stainless-steel bellows-type conduit is expensive and must be visually inspected periodically by an inspector to detect tampering. This requirement is very impractical because some areas cannot be accessed due to operational and radiation constraints, let alone the task of examining the conduit in a thorough-enough manner to actually detect tampering. This area clearly needs to apply new technical means to either authenticate all cabling or detect electronic tampering.



■ **Figure 16**
AP-10

Security Solution: Virtual Private Network (VPN)

The Virtual Private Network (VPN) transmits data both between cabinets and remotely from a facility through various available mediums such as internet, satellite, public switched telephone network (PSTN), and digital subscriber line (DSL).

One device that has been used at the IAEA is made by NetScreen. Specifically, models 5XP and 5XT have been installed. These products meet the FIPS 140 Level 2 standards used by the IAEA. They are small and relatively inexpensive, at less than US \$1,000 each. Expert installation is not required, and they can be used for wire or wireless applications.

Wireless Solution

A particularly costly activity in any nuclear facility is the installation of cabling. Installing tamper-indicating conduit further increases this cost. In addition, the IAEA often must install monitoring equipment on movable platforms. Taking a wireless transmission approach is quite attractive for these reasons. The IAEA recently installed a wireless system using the Alvarion AP-10 indoor wireless hub (~US \$1,000 and shown in ▶ [Fig. 16](#)) and the SA-10 station adaptor (~US \$500 and shown in ▶ [Fig. 17](#)) for the end-user computer. This system operates on 10BASE-T Ethernet using RJ-45 connectors with data rates up to 3 Mbps and a range up to 150 m (500 ft.).

Software Standards The IAEA has gone through a learning process in terms of the software it uses in UMS. Of particular note is that, in the past, the IAEA accepted custom software from each developer for both collection and review functions. This technique significantly complicated training, upgrades, field support, installation, and debugging. As a result, the IAEA has now defined single standards for collect-and-review software. However, this transition is an ongoing process because the IAEA does not have the resources for a major program to upgrade all systems to these new standards. On average, it takes at least 2-years for any worldwide software upgrades to be completed. This approach is based solely on the standard 2-year maintenance replacement cycle required for all batteries.



■ **Figure 17**
SA-10

It should also be pointed out that there are always unique one-of-a-kind systems that do not warrant the time and effort to migrate such unique limited-use systems to the standard software platform. Collect Software is the automated software application used by the IAEA in a local cabinet's computer system to collect data from sensors at the facility being monitored. This technique could be a large distributed sensor system or one that is very small (on the order of just a few sensors). The primary function is the polling of data from data generators. A data generator is the first electronic device that receives the sensors' input and, if required, digitizes the signal.

The IAEA's current data collection standard is called multi-instrument collect (MIC). MIC was designed by LANL under the auspices of the US Support Program. This application has the following functions:

- Data collection (can support ~40 data generators)
- Startup service (automatically starts up during the PC's start-up routine)
- File transfer service (can provide automatic file transfer to an archive)
- Delete files (can automatically clear data storage space as desired)
- Binary files to text (can convert error code to readable text)
- Debug tool (a self-diagnostic tool to discover/resolve problems)
- Tracker (transmission of state of health)
- File copy routine (can provide automatic copies of data as desired)
- Display instrument messages (allows user to view messages from polled instruments)

Review Software is used by IAEA inspectors to analyze and draw conclusions on the data collected at a facility. In general, this software is used in an attended mode. That is, it takes an inspector to use this software for the analysis effort. It is also important to note that, in general, the IAEA does not perform real-time data analysis; the IAEA's inspection methodology is based on drawing timely, but periodic, conclusions based on the type of nuclear material, its form, its quantity, and the estimated time for conversion into a weapon.

The IAEA's current data collection standard is called Integrated Review Software (IRS). IRS was designed by LANL for the Rokkasho Spent Fuel Storage Facility and was funded by the Japanese Nuclear Material Control Center (NMCC) (Abhold et al. 1998). It was further developed to integrate INCC for the Japanese Plutonium Fuel Production Facility (PFPP), with funding provided by the Japan Nuclear Fuel Cycle (JNC) Development Institute. Further enhancements have been made under the auspices of US Support Program because this software has been rolled out worldwide. This application has the following functions:

- Allows for review of data outside of active area. Inspectors are encouraged to minimize their time in a radiation area. Therefore, the IRS software is usually on a PC in an office area controlled by the IAEA.
- Provides event screening by threshold settings. A sort on events detected by a sensor can be screened first using threshold settings to eliminate events that are not of safeguards significance.
- Provides graphical display. This plots the sensors' events against time for a visual display.
- Provides data analysis. This capability uses algorithms to assess events.
- Provides campaign management. This capability allows for data partition in line with the operator's declaration of activities.
- Marks assays by time correlation. This capability allows for specific selection of an event based on time.
- Transfers marked data to software for analysis. This capability allows the use of more sophisticated analysis algorithms in other modules to assess the events.

This modular piece of software allows for any vendor to add capability to its suite of analysis tools. The current suite of review tools includes

- RAD: radiation review (graphical plot of radiation signals against time)
- DVR: digital video review (display of video images against time)
- PR: position review (display of global positioning system (GPS) data on a two-dimensional map)
- ISO: plutonium isotopic review (quantitative analysis of isotopic composition)
- OP: operator review (operator's declaration of events/activities)
- IR: integrated review (comparison engine that uses defined limits to match the operator's declaration against the IAEA data)

An example of IR in association with the RAD, INCC, and OP modules is shown in  Fig. 18.

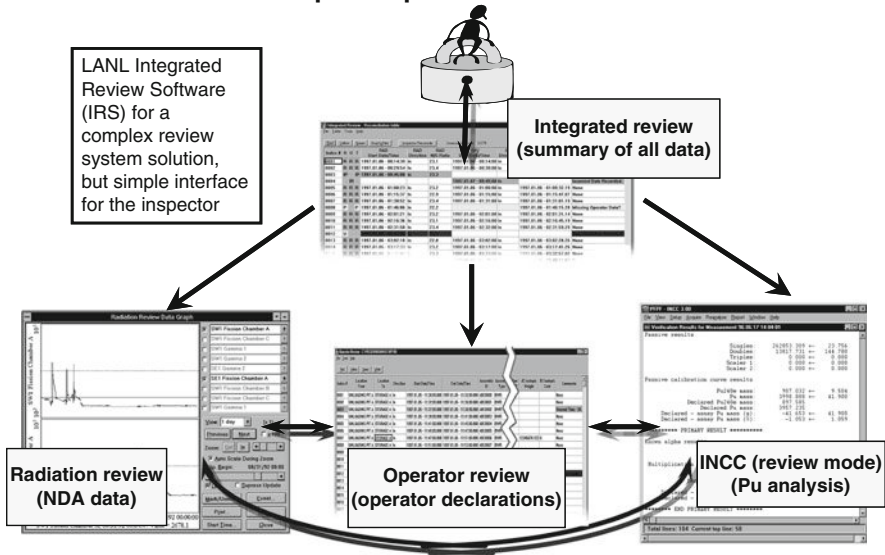
Hardware Standards

A similar learning process has occurred with hardware. Originally, entire UMS cabinets were designed by vendors. However, it quickly became clear that these specialty vendors needed to focus only on safeguards-unique hardware, whereas the remaining components would be COTS units. This approach would give the IAEA the best combination of dedicated devices and cost-effective commercial components, providing maximum flexibility by using a building block approach to UMS.

System Components

Computers One of the least reliable components used in a UMS is the computer. A standard model is impossible to maintain because the technology changes so rapidly that having two PCs

IAEA assistance: inspector point of view



■ Figure 18
Integrated Review Software (IRS)

with the same name and model number may not mean that the internal components remain the same; therefore, reliability always remains an issue. The IAEA has used configurations to ensure higher reliability. This method is based on the following basic approaches: minimize or eliminate moving parts (by using passive cooling and solid state drives), use redundant components “redundant array of independent disks” (RAID, multiple independent cooling fans, or a fail-over box that starts up a second PC), and use an independent watchdog that can restart a PC.

A fault-tolerant system should be able to run without a “collect” PC. One of the approaches used by the IAEA is the LANL-designed intelligent local operating node (ILON). This device can maintain certain critical functions that allow a distributed sensor network to continue to collect data without the collect PC. In addition, these instruments collect data even during total failure of both the collect computer and the IILON. However, certain critical functions, such as triggering, can be disabled without the IILON. This particular device is undergoing an upgrade to meet the IAEA’s Ethernet standards and to use strong authentication. It has the following characteristics and functions:

- Open topology and cabling: This approach allows maximum versatility for facility upgrades that require additional monitoring sensors that were not planned at the time of installation due to a new facility capability or new IAEA requirements. The newly upgraded IILON is Ethernet compatible.
- Instrument or collect function.
- Time synchronization: This approach can keep all of the data generators on the same clock setting.

- **Triggering (direct and indirect):** This critical function allows sensors to be combined to obtain the highest level of safeguards assurance. One example is a radiation sensor triggering a camera.
- **Authentication:** The current ILON has weak 32-bit wrapper authentication; the upgrade brings this to 128-bit authentication.
- **Watchdog:** If a data generator fails to check into the ILON, it can send a hard reset command.
- **Functions independent of collect computer:** It operates at the same independent level as a data generator using batteries as necessary.
- **Narrow bandwidth:** The current ILON has a limited bandwidth of 78 kb/s because it was not intended for digital images; the upgrade brings this speed up to 100 MB/s.

Surveillance Data Generator The Digital Camera Module 14 (DCM-14) was designed by Dr. Neumann GmbH under the auspices of the German Support Program. The module is commonly combined with a charge-coupled device (CCD) camera. The DCM-14 also has a rotating buffer memory for up to eight images. This capability plays a key role when triggering is used for safeguards applications. The camera is set at a regular “heartbeat,” where an image is taken at a designated frequency. As an untriggered image, this new image is placed in the rotating buffer as the new #1 image, and the previous images rotate through the buffer, with the last image, old #8, being deleted. When a trigger takes place, such as from a radiation sensor, the DCM-14 dumps the rotating buffer to the permanent data storage as permanent images. It then goes into a triggered mode with the subsequent post-trigger images at some set interval that will also be dumped to permanent data storage. In this way, a complete cycle of images is available to fully define the triggering event.

The DCM-14 has the following capabilities:

- Digital image
- Scene change detection
- Image compression
- Image/data authentication
- Image/data encryption (triple DES algorithm)
- Power management (minimization mode when on battery power)
- Battery backup (~2–3 days, depending on image frequency)
- External triggers
- On-board 100-day data storage (in removable flash cards)
- State of health

The module can store up to 100 days of images, which allows a safeguards inspector on a 90-day inspection cycle to recover all images, if the collect computer has failed, by removing the flash cards. The internal battery is another fault-tolerant approach because the main cabinet has a “smart” UPS that extends the maximum life to the data generator by shutting down the collect computer; the UPS batteries are dedicated to the data generators. If the UPS’s life is exceeded, the data generators’ internal batteries further extend the life of the module. All of these layers of power are intended to carry the IAEA systems through the majority of power outages without a loss of data.

Radiation Data Generators These data generators follow the same functionality as that seen with the surveillance generator; the difference is the capability to support radiation sensors and transmit triggers. The two primary radiation data generators are the LANL designed MiniGRAND

(miniature gamma-ray and neutron detector) developed under the auspices of the US Support Program, and the BOT Engineering-designed standalone autonomous data acquisition module (ADAM) developed under the auspices of the Canadian Support Program. Both radiation data generators are undergoing upgrades.

The MiniGRAND supports three pulse channels and two current channels, allowing a broad assortment of radiation sensors to be attached. The Standalone ADAM data generator supports eight pulse channels; however, an adaptor is under development to allow current-based sensors, as well.

Dedicated Simple Systems

VXI-Based Flow Monitor (VIFM) In contrast to the modular units mentioned previously, the IAEA has had a complete UMS developed by a single vendor. One example is the VXI-based flow monitor (VIFM), which was designed in the last decade by BOT Engineering, under the auspices of the Canadian Support Program, specifically to monitor spent-fuel bundles from CANDU reactors. The primary specification established by the IAEA required the use of the industrial VXI architecture, whereas the manufacturer was free to design the rest of the system. This unit is used to monitor core discharges from the reactor face (core discharge monitor-CDM), and bundles (bundle counter-BC) as they are moved into the spent fuel pond. It has proven to be very reliable, using paired ADAM data generators, which provide full data generator backup, and up to eight SOLGEL batteries, which provide up to 90 days of operation without power supply. The main problem with the unit is the custom design of nearly all components, including the collect computer. Upgrades have been costly and lengthy. This experience helped the IAEA focus on using COTS where it is most logical.

The VIFM is a qualitative system that can count items but cannot assay nuclear material quantities. ➤ *Figure 19* shows a typical spectrum from the CDM sensors for a CANDU 600. In this display, we show counts along the ordinate axis (traditional y -axis) and time along the abscissa axis (traditional x -axis). The neutron signal is represented in white and the gamma in black. An algorithm is applied that can count bundle movements using this peak structure. The algorithm is designed to detect off-normal responses. To understand the radiation profile shown in ➤ *Fig. 19*, a short review of CANDU reactor operations is in order. This reactor uses natural uranium for fuel and heavy water for the moderation necessary to sustain a nuclear reaction. The fuel channels are aligned horizontally in the reactor. In this on-load power reactor (the category of power reactors that can be refueled during operation), approximately 15–23 bundles per full power day are replaced on a daily basis to refuel the reactor. Each spent fuel bundle is tracked because it will contain plutonium once the fission process has occurred. Therefore, the CDM detectors are located only on the reactor face from which spent fuel will be removed. Thus, the IAEA must be able to conclusively count and maintain surveillance on the nearly 3,000 spent bundles removed from the reactor each year.

The process of removing and replacing fuel bundles follows a specific sequence. Two fuel-handling machines are aligned on the same fuel channel from opposite faces of the reactor. One fuel-handling machine has four pairs of fresh fuel bundles (total: eight) loaded in its rotating cylinders (much as the barrel on a revolver-type handgun) for insertion into the reactor. The other fuel-handling machine is empty and is ready to receive the spent fuel bundles that are removed. When the neutron (white) spectrum of ➤ *Fig. 19* is considered, the first peak represents the removal of the channel plug from the reactor face where the spent fuel is removed. The second peak represents the removal of the radiation shield plug, now allowing direct access

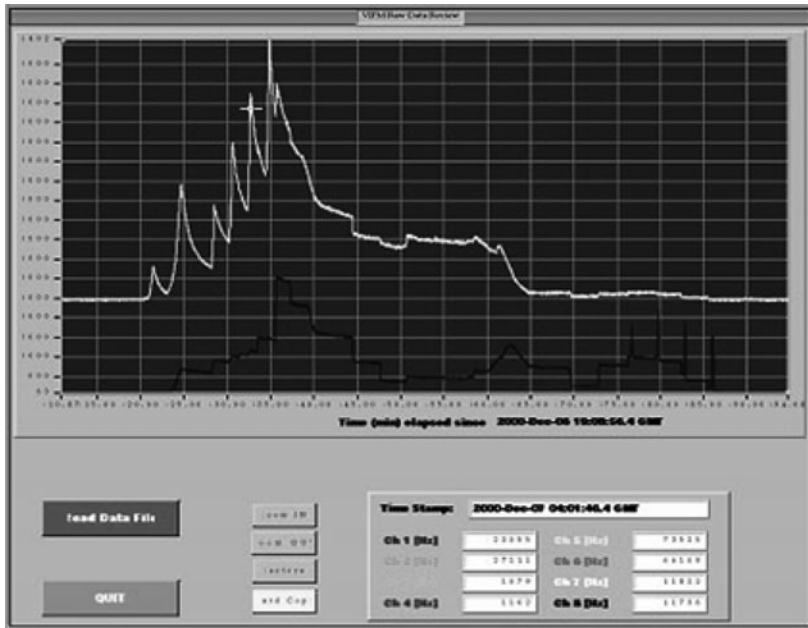


Figure 19
Core discharge monitor (CDM)

to the fuel. The next four peaks represent the removal of four pairs of spent fuel bundles, representing eight bundles from the reactor.

Figure 20 represents the bundle counter. This counter uses three solid-state gamma ray detectors located above the tray mechanism that transfers the spent fuel bundles from the reactor hall to the spent fuel storage pond. The response from these three detectors is represented by the sequential response graphs. A fourth sensor is located at a point where it can detect the transfer of the two bundles into the spent fuel pond and is indicated by the last trace. The first three sensors are used to verify the transfer of the two bundles from the reactor core face onto the transfer tray. These sensors are located longitudinally along the axis of the tray transfer mechanism, with the first two sensors above the final resting position of the second bundle and the third above the final resting position of the first bundle. The forward location of the first two sensors allows them to view the spacing between the two bundles, which is evident by the dip in response on the graphs of the peaks (see Fig. 20).

The response from the third sensor that is located toward the rear of the transfer tray shows only the first bundle; therefore, this sensor never sees this gap, as evidenced by the lack of a response dip. The specific locations of these three sensors were chosen to detect all possible scenarios of diverting bundles from the tray.

The VIFM system, as is true for most UMS, uses counting algorithms to aid the inspector in drawing conclusions from the data collected by these automated systems. In the normal first screen display, the total counts of bundles from the CDM and BC systems are displayed. Under conditions of normal operation, the two bundle counts must match. In this case, the inspector can consider his or her inspection of the data as complete, and looking at the detailed response would be unnecessary, as shown in Figs. 19 and 20. A mismatch in count would

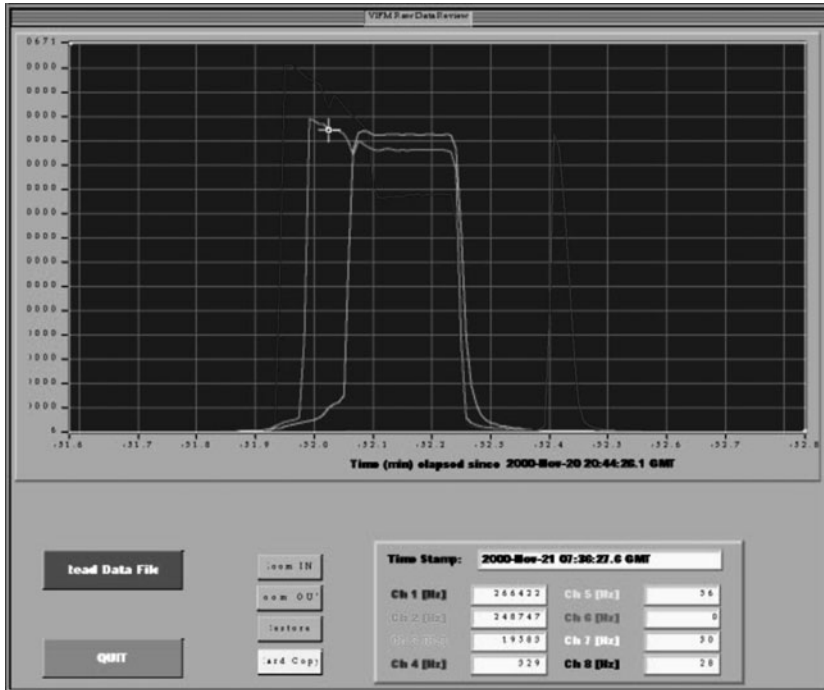


Figure 20
Bundle counter

indicate an anomalous condition. It would then be up to the inspector to determine the cause of this discrepancy. Under a condition that requires detailed investigation, the inspector can then “drill down” to a lower-level screen in the software to see the response peaks for each event. A mismatch would not immediately cause the inspector to suspect potential diversion. In fact, discrepancies are not that uncommon because problems may occur during operations at a facility. As part of the operator’s obligation to the IAEA, an operator declaration of activities for the period covered by the inspection is made. In this declaration, the IAEA inspector would most likely find mention of some difficulties during operations that may be detected by the UMS.

Advanced Thermohydraulic Power Monitor (ATPM) Although the majority of UMS use radiation sensors for safeguards on nuclear facilities, the IAEA deploys a wide range of sensors. One nonradiation sensor system is the ATPM. This system was designed specifically to meet the safeguards challenges associated with plutonium production in research reactor fuel. Unlike commercial power reactors that operate at full power in a fixed-core configuration for extended periods of time as part of a state’s base power grid, research reactors typically operate for short (2–3-week) periods at varying power levels and can have the flexibility to change the core configuration. In addition, spent fuel is routinely replaced in commercial power reactors on a routine basis (typically every 12–14 months in LWRs and daily in on-load reactors such as the CANDU), allowing for direct monitoring and measurement. Because of the periodic nature of operation in research reactors, a single core loading of fuel lasts for many years.

The challenge to the IAEA is how to determine plutonium production in the fuel in the core accurately throughout the lifetime of a research reactor. Because the IAEA has access to the detailed design of each facility (through the design information verification process), knowledge of power can be used to calculate plutonium production in the core of the reactor. This methodology is the basis for the ATPM approach.

➤ *Figure 21* shows a schematic representation of the ATPM system design. The data collection side of the system is located in the radioactive cold portion of the facility. On the “Hot Area” portion of the schematic, two redundant sets of sensors are mounted on the hot and cold sides of the primary core cooling loop. Each set contains a resistive-type temperature sensor (T) and an ultrasonic flow monitor (F). The output from these sensors provides a velocity measurement on the cooling loop’s water and the temperature drop as heat is removed from the loop. The data from these sensors, in combination with the required reactor design information, are used to calculate reactor power output. This calculation is plotted against the unit’s internal clock. In addition to being used as a direct comparison with the operator’s declaration on reactor operations, this information can be used with predictive reactor operation codes, such as ORIGEN, to calculate plutonium production.

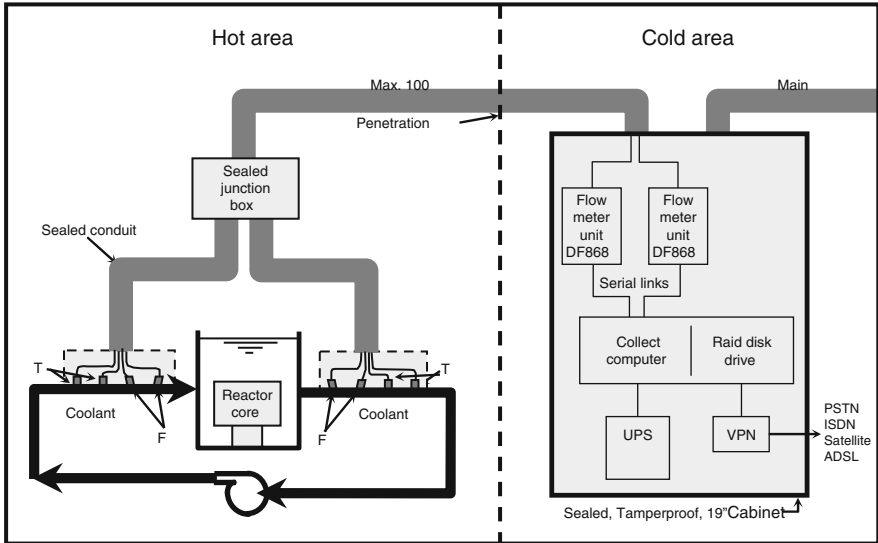
➤ *Figure 22* shows an IAEA engineer installing an ultrasonic flow sensor on the primary core cooling pipe. The long frame that is strapped onto this cooling pipe (the IAEA makes every attempt to apply its sensors in a manner that minimizes interference in operations and safety) is used to secure the ultrasonic sensors at the required angle for this specific pipe diameter. The engineer has one sensor in his hand and is securing it on the frame. A matching sensor is installed at the far end of the frame (not visible in this image). Note the two threaded rods that are mounted perpendicular to the frame and extend away from the cooling pipe. The first is located immediately adjacent to the engineer’s left hand. The second is in the center of the frame. A third rod is on the other end, not visible in this picture. This photo shows the difficult work environment often faced by the UMS staff.

➤ *Figure 23* shows the tamper-indicating cover applied to the sensor frame shown in

➤ *Fig. 23*. Nuts have been tightened on the threaded rods securing the cover. Tamper-indicating wire has been pulled through the holes in each threaded rod and tied off at the center rod, awaiting the application of a metal seal by the IAEA inspector.

➤ *Figure 24* shows the primary computer screen display when an inspector or UMS staff member opens the sealed cabinet door. In the lower left-hand corner, note the power versus time display that indicates that the system is functioning. Above that display are current read-outs from the sensors and the power calculation. At the upper right is a state-of-health button with the following legend: green (current status) = all sensors are functioning; yellow = loss of one sensor, conclusions can still be drawn using the backup sensor; red = loss of both sensors, conclusions are in jeopardy. The remaining buttons serve many functions for the inspector, such as viewing the graphs for each sensor, data for specific periods, and data downloads. Other buttons are used for UMS staff to set up the system, make diagnostic checks, and fulfill other requirements.

Dedicated Complex Systems The previous systems were defined as “simple” systems solely from the perspective of the nuclear material they were designed to safeguard. Both the VIFM and the ATPM were designed to provide safeguards on an item facility. In an item facility, all nuclear materials are permanently sealed within a container that has no access point and structurally never changes during the entire time at the facility. Nuclear fuel contained in fuel rods that are mounted in assemblies fits this definition. In a bulk facility, material can be accessed directly



■ Figure 21
Advanced thermohydraulic power monitor (ATPM) system diagram



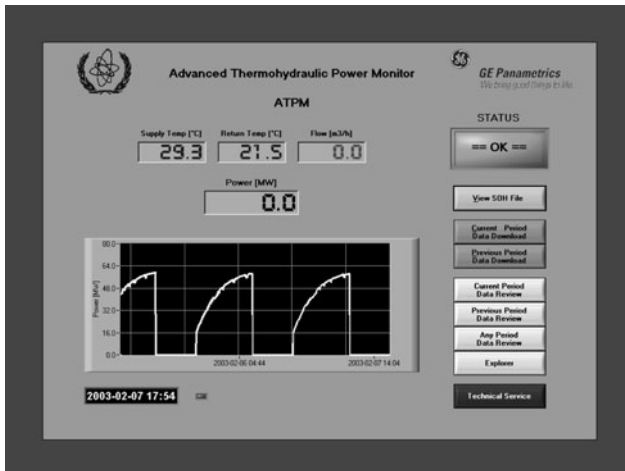
■ Figure 22
Flow sensor installation

and could change form. Examples include gases, powders, solutions, and metals. Many of these forms are found in enrichment, reprocessing, and fuel fabrication facilities. Access to bulk materials present a much greater safeguards challenge for the IAEA as small portions of material can be diverted.

One of the greatest facility challenges is safeguarding a reprocessing facility. The plutonium–uranium reduction extraction (PUREX) process is one example. At this facility, nuclear material



■ Figure 23
Tamper cover installed



■ Figure 24
ATPM main screen

progresses through the following different forms: feed material (spent fuel, which contains irradiated nuclear material with actinides and fission products); processed material (input liquids, separated liquids, undissolved solids, and low-level and high-level liquid and solid wastes); and product material (separated oxides and MOXs). High radiation levels dictate that most of these activities be controlled remotely. Good safety and business practices demand that such facilities be fully automated. This is the case at the Japanese Rokkasho Reprocessing Plant (RRP).

► Figure 25 shows a picture of the Improved Plutonium Canister Assay System (iPCAS). This dedicated quantitative system is fully integrated into the operational flow of the facility. It

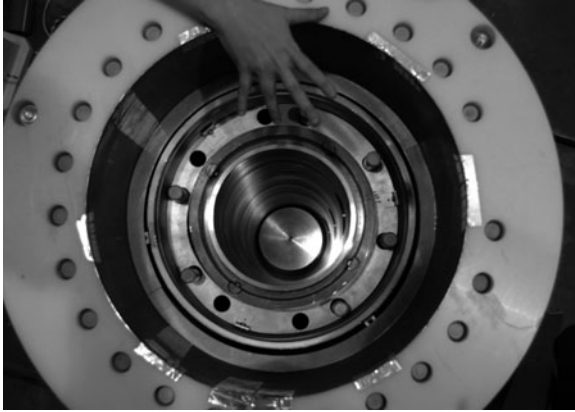


■ **Figure 25**
Improved Plutonium Canister Assay System (iPCAS) side view

is owned by the Japanese safeguards authority and used by the IAEA. It was designed by LANL and represents 1 of 10 systems from LANL that are deployed throughout the flow stream at the RRP. iPCAS was designed to measure precisely three cans totaling 36 kg (18 kg of plutonium and 18 kg of uranium) (Abhold and Baker 2000) of MOX product ($(\text{Pu}/\text{U})\text{O}_2$) from the reprocessing activities that provides the feed material for a fuel fabrication facility currently under construction.

One unique aspect of this neutron coincidence and gamma isotopic counting system is the use of unmoderated ^3He tubes to correct for moisture content. The inner unmoderated and outer moderated (high-density polypropylene polyethylene) neutron tubes can be seen in ▶ [Fig. 26](#), which shows a top view into the iPCAS counter. ▶ [Figure 27](#) shows the three gamma spectroscopy units and the associated electro-coolers for the intrinsic germanium detectors, the location of which can be seen in ▶ [Fig. 25](#). This spacing along the vertical axis of the iPCAS allows each gamma detector to view one can and determine the isotopics. Combining the isotopic measurement with the neutron measurement allows for an accurate quantitative determination of plutonium in each can.

Pre-Field Installation Testing With the primary focus on reliability, the UMS Unit spends considerable time assembling and testing complete field-configured systems at the IAEA in Vienna, in the Safeguards Equipment Support Facility (SESF). Although not always possible, the goal is to test all systems for 90 days before installation in the field to ensure that all infant mortality and configuration issues have been addressed. The testing protocols include the full range



■ Figure 26
iPCAS top view



■ Figure 27
Isotopic system

of expected field conditions, with one exception: testing of the sensors to matching radiation fields. It is not practical to create duplicate radiation environments nor required because radiation sensors are very robust and reliable. Testing with smaller sources either at the SESF or at the IAEA's Seibersdorf Analytical Laboratory, where stronger sources are available, is sufficient to guarantee performance in the field. The IAEA's experience has been that these sensors, if defective, are defective upon delivery. Therefore, these simple tests are sufficient to ensure reliable performance.

To test these units fully without the actual radiation field present, the IAEA UMS Unit has developed a dedicated signal generator that can duplicate the exact response peak, allowing full testing of the counting algorithms in these instruments. The importance of the focus on laboratory testing of these generators before they are installed in the field becomes clear when considering that the cost of travel alone averages approximately US \$5,000 per trip. Whether simple or complex problems surface in the field, repair trips are expensive. Because of the distances traveled and the unique nature of the equipment, even simple trips require that a technician or engineer carry sufficient replacement parts and tools to deal with all contingencies; this excess baggage adds considerably to the expense of traveling.

2.4.9 Conclusion

Over the last two decades, the IAEA has successfully developed and deployed UMS, automating what was once a periodic inspection effort by inspectors. The success of these systems is based on effective design methodologies that emphasize reliability through fault-tolerant designs, by taking a component building block approach to ensure maximum flexibility in meeting the needs at the diverse and complex facilities that comprise the nuclear fuel cycle. This approach has been accomplished in a cost-effective manner that benefits both the IAEA and the facility operator. As the use of nuclear power continues to expand across the world, UMS are leading a revolution in safeguards capability so that the IAEA can continue to meet its treaty-based obligations, which ensure the peaceful use of nuclear technologies.

2.5 Process Monitoring

The main goal of nuclear materials accounting (NMA) is to confirm within measurement error uncertainty the quantity of SNM in all declared locations. Because the absolute value of measurement error uncertainty increases as throughput increases, in spite of monumental and successful efforts to improve the uncertainty of measurements over the years, modern large scale facilities are unlikely to meet the quantitative safeguards goals by NMA alone. NMA involves material balance (MB) closures, which require estimates of SNM inventories throughout the facility. Traditionally, these inventories were estimated after extensive shutdown and cleanout measures to move material into measurable locations. The procedures to accomplish these inventories are time consuming and are conducted only on an annual basis, during what has become known as "physical inventory taking" (PIT), where, in international safeguards, "physical inventory verification" (PIV) is conducted.

In international safeguards, an annual PIT is not sufficient, partly because the IAEA's timeliness goal for detection of the removal of a goal quantity is 30 days. Since the 1980s, the concept of near-real-time accounting (NRTA) has been pursued, where an "in-process inventory" or

Interim Inventory taking is implemented to measure and/or estimate the facility inventory without shutdown and flush-out. The verification of this inventory by the international safeguards regime has become known as the interim inventory verification (IIV). Typically, IIVs have been conducted on a 30-day basis to meet the timeliness goals of international safeguards. But the large throughputs of modern facilities and propagated uncertainties of measurement make even the relatively short 30-day detection goal difficult to meet. Therefore, modern applications in large facilities are moving to shorter intervals, making the same in-process inventories and referring to the procedures as special inventory verifications (SIVs). Particularly when SIVs include partial SNM assays such as bulk volume combined with SNM concentration estimates to estimate SNM amounts rather than direct measurement of SNM, the distinction between SIVs and some forms of process monitoring (PM) becomes blurred.

PM has become a tool of international safeguards. It provides additional assurances of proper facility operations and increases confidence in IIV procedures. For example, PM helps guarantee continuity of information on process solutions as they move through the plant, helping to ensure that materials are not moved to clandestine locations.

The same constraints exist in process facilities in the United States. Within the DOE complex, the local implementation of DOE rules have typically required monthly PIV's in bulk handling facilities. Under these conditions, the facilities lose a large percentage of operating time during a month. In addition, in drawing safeguards conclusions, such monthly PIV's do not reflect normal operating conditions of the facility and so are arguably less effective than more frequent accounting. Therefore, there has been a push to implement PM even if it includes a combination of full measurements, partial measurements, and estimates of the SNM. Although quantitative metrics are lacking, many believe that the combination of PM and less frequent PIV's is highly effective (Burr et al. 2003a, b). The reduced frequency of PIV's is an added bonus for the facility.

Regulated by the NRC, US domestic industry requirements have been established for timely (depends on facility category) detection of a loss of a "formula quantity" (5 kg HEU and 2 kg Pu). NRC regulations specifically mention "process monitoring" as a method to meet the requirements, but leave its specification to the facility operator. Those facilities operating under these rules have also implemented PM.

PM can be defined in terms of measures to ensure "timely information on the location and movement of nuclear materials." That same definition on timely information also applies to measures for process control and can also be applied to meet the requirements of safety and criticality control. Therefore, there is an overlap of instrumentation needed to meet the goals of all three important plant functions. In all three cases there may be measures and evaluations that do not make use of traditional MBs and NMA but instead evaluate related process measurements.

In the modern safeguards applications NMA is rarely meant to be the only safeguards component. PM can increase safeguards effectiveness of NMA when viewed as a tool to enhance the accuracy of NRTA, either by indirect or direct support of inventory measurements, or when viewed as a type of data consistency monitoring (DCM). Used for DCM, PM can provide assurance that the facility is operating as declared and that IIV procedures are appropriate for the conditions. In PM, bulk volumes, masses, and temperatures are tracked. In circumstances where samples are analyzed or on-line assays are available, SNM quantities can be estimated on the basis of mixing and transfer calculations to support NRTA. In other PM examples, mass quantities might be computed using gross neutron counting and/or gross weight and confirmatory attribute measurements.

As an aside, concerning jargon, which is often important for the IAEA because operators are hesitant to release certain kinds of data, the catch-all term “data consistency monitoring” might be preferred to “process monitoring” for two reasons. First, plant operators have reserved the latter to encompass information that might be proprietary. Second, the term “monitoring” is also applied to safeguards-specific surveillance systems such as certain cameras, TIDs, and radiation detectors. DCM would in that case refer to the acquisition and evaluation of any type of safeguards-relevant data, including traditional NMA data. We, instead, continue to use the term PM as described in the previous paragraph, with DCM being one type of PM to be discussed here.

Operation as declared, and procedures supporting various NMA activities, when viewed in the continuous evaluation of PM, can generate typical “reference signatures.” The term “reference signature” describes, for example, the sub-events in a tank’s operational cycle such as filling, homogenizing, sampling, and shipping. In other plant components it can describe signals from related and connected equipment.

The definition of PM must include some mention of the difference between domestic and international applications. Domestic applications are directed at the detection of loss or unauthorized removal of material at the sub-national level. Therefore, the regulatory bodies require implementation at the facility level, typically by an organizational unit that is independent of the organization responsible for control and processing of the materials. Typically, the national regulatory organization approves the procedures within the licensing process and only monitors that the facility operating plan is properly implemented. On the international level, the concern is for diversion at the national level, where the facility operator and the national regulatory organization are in collusion for the diversion. Therefore, the authority cannot be sure of the accuracy of the data reported. Thus the accuracy of data supplied must be guaranteed through verification and authentication measures that guarantee the accuracy.

2.5.1 Key Elements

There are four key elements in any process monitoring system: sensors, data acquisition, data storage, and evaluation. These elements are not unique to safeguards. The minimum data set necessary for process monitoring is difficult to define because it is defined by the scope application itself. The earliest efforts were limited by the instrument technology itself and the extent of computer technology available. The earliest efforts preceded concerns such as technology and export control, and concerns over propriety information. They were very ambitious in the scope, but limited in technology. More recent efforts have been implemented with technology that makes large amounts of information available, but depending on the safeguards end users, whether they are facility personnel or regulatory agencies, there has developed a reluctance to provide information to support very robust applications. But if process monitoring is to grow in applications for safeguards purposes, particularly for international safeguards, a careful evaluation of what is needed and can be supplied is necessary.

Sensors and Data

Sensors Safeguards inspectors might install their own sensors, or, more likely, share those used by the operators. Pressure and temperature sensors are commonly used. The case for installation of more sophisticated sensors has to be accepted by the operators. In recent times, this has led to rather limited success for international inspectors because of proprietary concerns.



■ Figure 28
Rack of six modern pneumacator instruments

Data Acquisition Modern data acquisition equipment can collect data at rates far in excess of what is required. It is therefore possible to collect data at one rate, while exporting at a slower rate. For instance data collected every 0.1s can be filtered with every tenth point output (i.e., at a rate of 1/s). Its standard deviation can be estimated and “state-of-health” tests can be applied. A major issue is the design of this so-called “pre-processing” stage. ➤ [Figure 28](#) shows a rack of six modern pneumacator instruments.

Data Storage and the Estimation of Indirect Measurements

Each sensor outputs one or more variables every time period, so that at the end of say, every day, one could imagine all the data would be stored in a 2D table with each variable in a separate column and each time instance in a separate row. So called Real-Time Databases or Data Historians

are available commercially to handle such data. They gather, store, archive, and process operational data from sensors and control systems. They also provide tools needed to manipulate and distribute the data, turning it into meaningful information that can be processed.

Mass, volume, and other variables might be estimated from each time instance of the raw data. These estimates are then accommodated in extra fields (i.e., columns) that can be added to the real-time database. Mass/volume estimation is based on calibration equations obtained, empirically, for each vessel. A certain amount of uncertainty is associated with these estimates and this uncertainty might “drift” with time (De Ridder et al. 2004; Binner et al. 2008). Key vessels are regularly recalibrated because of this. However, other vessels are likely to be monitored, so there is a possibility that re-verification might become an issue (Howell 2009).

Evaluation

Large, modern, industrial complexes have extensive, state-of-the-art digital control systems (DCSs) that enable operators to observe the performance of their plants. The primary role for DCS data is to inform the operators in real-time. This is achieved largely through displays of trends and schematics. Most of the information is processed visually, and far less is processed quantitatively. Although major software vendors do provide products to evaluate data, quantitatively, commercial pressures tend to mean that these products are necessarily targeted for relatively wide application areas, like the petrochemicals industries. There are considerable costs in developing and maintaining custom software during the lifetime of a plant, and hence the incentives to purchase tried, broadly-applicable and well-supported software are clear.

Materials balance issues are not special to reprocessing plants. Similar tasks for data reconciliation or gross error detection are performed in other chemical industries (Rosenberg et al. 1987), and commercial software is available to support these activities. However, the focus is on steady state mass balances based on flow meter measurements. Nuclear facilities operate very differently. In particular, they can have a rather unique blend of batch and continuous operations. Therefore, custom developed software is the only option.

2.5.2 Role of Models and Simulation

There are at least two roles for modeling and simulation in process monitoring: models are sometimes an integral part of the detection, isolation, and diagnostic tools (Howell 1994; Howell and Scothern 1995, 2000; Scothern and Howell 1997; Garcia and Yoo 2005); simulations are often used to assess the performance of these tools (Burr and Wangen 1996; Howell and Scothern 1998; Burr et al. 2003a, b). Clearly the former cannot be tested with their own models, although in practice these models are usually simplified for reasons of both computational necessity and for ease of reasoning (Howell 1994). One of the most extensive reprocessing plant simulations developed for safeguards purposes was FACSIM (Li 1996). A product storage area simulation of Howell and Scothern (1995) was also quite extensive, in that it modeled thermodynamic effects. Although these simulations are less detailed than those used for design purposes, they are somewhat different in that they are dynamic (i.e., they model variations with time). They can, however, exploit the more detailed models primarily by extracting reduced models (Cobb et al. 1980; Walford et al. 1983).

Experience has shown that results obtained from simulation-based performance evaluations have to be viewed with considerable caution. There are at least three reasons for this: the physical

models are rarely comprehensive resulting in so-called “systematic errors”; models of operational activities are rarely comprehensive, so that the data tends to look more sanitized than it should be; data acquisition effects are rarely incorporated. For instance, Binner et al. (2008) describe the types of systematic errors that still plague tank volume measurement. Simulation-based performance evaluations are therefore more likely to be appropriate for comparisons rather than for making any absolute conclusions.

2.5.3 Strategy for Reprocessing Plants

The RRP is the first, and to date the only facility where safeguards process monitoring was considered for implementation early in the overall design phase (Johnson et al. 1997; Ehinger et al. 2004; Johnson 2005). And it is the first facility where it was considered for areas other than just the solution processing area. All applications prior to the RRP were limited to what can be considered to be “solution monitoring,” where the data collected and evaluated was limited to process vessels in the main process line. In the case of the RRP, process monitoring was included in the design and it included data from cameras and radiation sensors monitoring movement of items and packages from the receipt of the spent fuel, through the pool storage area and mechanical processing. Specialized equipment was designed and installed to monitor the movement of materials through the MOX conversion area and the packages of MOX powder through to the product storage area. And the data from specialized NDA equipment was included for quantitative measurements at key locations.

The complete list of systems deployed at RRP for IAEA use is as follows:

- Integrated Spent Fuel Verification System (ISVS)
- Integrated Head-end Verification System (IHVS)
- Solution Measurement and Monitoring System (SMMS)
- Independent Jug Passage Detectors (IJPD)
- Automatic Sample Authentication System (ASAS)
- Waste Crate Assay System (WCAS A&B)
- Waste Drum Assay System (WDAS)
- Vitrified Canister Assay System (VCAS)
- Plutonium Inventory Measurement System (PIMS)
- Temporary Canister Verification System (TCVS)
- Improved Plutonium Canister Assay System (iPCAS)
- Directional Canister Passage Detector (DCPD)
- Uranium Bottle Verification System (UBVS)
- Uranium Storage C/S System (USCS)

From the above list, the SMMS represents the extension of the previous solution monitoring efforts. There was an extensive dialog between the IAEA, facility operator JNFL, and the Japanese regulatory authority to select the vessels and associated instruments that would be made available. There was also consideration of proprietary information on the part of the operator and their agreement with the plant designer, in this case COGEMA, that influenced the decisions.

The SMMS had to meet the needs of process monitoring as well as verification at flow key measurement points (FKMPs) and inventory key measurement points (IKMPs). In the end, the

deciding factor was to select all vessels that potentially contained more than one gram of plutonium based on vessel capacity and expected concentration. In one sense this was adequate since it included all tank-like vessels in the main process line, from the dissolver to the plutonium conversion facility. The final decisions allowed for monitoring of tank to tank transfers of solutions in the process that contain 98% of the plutonium in the facility under normal operations. But it excluded measurements of some processing equipment within important solvent extraction and concentrator systems.

The RRP represents a significant step forward in application of process monitoring over previous applications in the monitoring, beyond the solution processing area of the facility. But in the solution monitoring area, the application was again limited to level, density and temperature measurements, and evaluation of solution transfers between vessels. There were a few additional sensors, principally gross neutron detectors deployed along the pulsed columns of the solvent extraction systems that were also included. These were included on the basis of their value in estimation of column inventory for NRTA. The deployment of these sensors and the algorithms for calculation were based on a research project conducted by the Japanese.

The RRP system extends the concepts of process monitoring to areas where items and product packages are handled. Much of this was driven by the need to verify measurements at FKMPs. Additional equipment was also added to track movement of materials.

From the above list, the ISVS consists of a camera, and pairs of gross neutron and gross gamma monitors positioned at the point where spent fuel assemblies unloaded from shipping casks, move into the spent fuel storage pool. The pairs of detectors are spaced so that the timing of the signals between the sensors provides direction of movement, to verify receipt of fuel.

The integrated head end verification also combines gross neutron sensors with cameras. Comparison of the timing of signals again provides information of movement of spent fuel assemblies from the pool through the head end to the shear. And the cameras supplement the information. A second set of detectors associated with the system monitors movement of hulls containers.

The IJPD, with software for analysis of the signals, and the Automated Sample Authentication system, track sample bottles from the laboratory to the sampling stations and return.

The PIMMS is a complex system to measure the inventory of plutonium at a number of locations in the conversion process. Sequential measurements can track material as it moves through the process. The DCPDs combine neutron detectors and cameras to track the movement of filled MOX storage containers from the process, to the measurement station (IPCAS) and on to storage.

2.5.4 Operational Evaluation Systems

Currently, a number of evaluation systems are either fully operational, undergoing field trials, or in the process of commissioning. Here we attempt to deal with them in terms of their roots.

IAEA TAMES Root

Tank Monitoring and Evaluation Systems (TAMES) have been implemented at Tokai (TRP) in Japan. Safeguards at the TRP evolved after the Tokai Advanced Safeguards Experiments (TASTEX) of the late 1970s. One of the recommendations following TASTEX was to implement Process Monitoring in future facilities, and it was this recommendation that spurred related

developments at the US Barnwell plant, and later the US Integrated Engineering Test (IET) facility at Oak Ridge National Laboratory.

A rudimentary process monitoring system was implemented in the IET and in the plutonium nitrate storage area in Tokai which became operational by the early 1980s. But Tokai was an older generation facility with typically pneumatic measurement equipment. The solution monitoring installation for the IAEA included dedicated differential pressure measurement. However, the equipment was expensive, and consequently the installation included a pneumatic multiplexer to allow a single device to step through the measurements. Only level measurements were available in the three original product tanks, while density and temperature signals were also available in the four newer product tanks. The use of pneumatic multiplexers meant that simultaneous measurements of all vessels were not available, as had been done at Barnwell and the IET. Interpretation of data had to consider time delays between related measurements. A similar system was eventually implemented at the plutonium conversion demonstration facility (PCDF) in Japan. This facility received plutonium product solutions from the TRP and was based on a 50/50 mixture of uranium and plutonium. These installations were limited to level, density, and temperature measurements only, and they used the pneumatic scanner which precluded collection of time correlated data from all vessels.

Currently, TAMES-PCDF and TAMES-TRP are the only solution monitoring systems that are premised on mass balance data. TAMES-PCDF (Sirajov and Wang 2008) evaluates data pertaining to four tanks placed in series, which link a facility where concentrated plutonium nitrate solution is stored, to a MOX conversion plant. There are two input streams, the first contains plutonium nitrate and the second contains uranium nitrate, and one output stream used to fill small dishes, batch-wise for processing. The volume, density, and temperature of the solution, contained in each tank, are monitored. The quantity and assay of the plutonium nitrate solution input to the first tank is known. The uranium nitrate solution is input directly into the third tank. All transfers are carried out as batches. The evaluation draws on temperature measurements to confirm that a particular batch input to the third tank contains plutonium, as opposed to uranium. Knowledge of the plutonium concentration enables the evaluation system to propagate plutonium concentrations forwards from input to output. Density estimates derived from concentrations thus propagated can then be compared with densities measured.

This evaluation system has probably the most sophisticated preprocessing algorithms of any of the systems, mainly because of the complexities involved in filling the small dishes. In addition, the system is able to verify that “Operation is as Declared” by looking at more than just internal flows. To do this, it seeks to detect then explain all features that are observable in the data.

Euratom’s System 7 Root

Euratom installed System 7 in La Hague during the early 1990s. At that time, it was the only system to be actively used to monitor solutions in a large commercial reprocessing plant. This system has since formed the basis for Ispra’s (EU Joint Research Center) DAI software and also for the IAEA’s SMES at RRP. Although the later products are clearly not identical, they have evolved from the same root and still have many of the same attributes, so the original specification (Dekens et al. 1995) is still of key importance here. At that time, System 7’s main published objectives were as follows:

Euratom:A. To produce a log of safeguards related events for each measurement point

Euratom:B. To verify the plant inventory accessible to measurements in a timely manner

- Euratom:C. To verify in a near-real-time the flows at KMPs and other strategic plant locations
- Euratom:D. To analyze the plant parameters and to identify safeguards related events
- Euratom:E. To evaluate the equipment cycle characteristics and to establish their conformity with expected equipment behavior
- Euratom:F. To perform a flow consistency check and a flow follow-up at strategic locations of the reprocessing plant
- Euratom:G. To identify the non standard plant operations, which might give rise to safeguards related concerns

There is considerable overlap with the IAEA objectives. It appears that the system mainly sought to verify operations at the KMPs. Presumably the original intention was to monitor the bulk contents for inventory taking purposes only. The system focused on accountancy tanks and their adjacent feed/receipt tanks. In particular, the system sought to eliminate the recognized diversion scenario, in which the input accountancy tank (the IAT) is filled at the same time that it is emptied enabling more solution to be processed than “declared.” Another important system feature was that evaluations were based on reference signatures. This was hardly surprising, because operation of the IAT was largely automatic, so that its measurement histories repeated themselves cyclically and looked something like that shown in Fig. 29. This tightly prescribed operation could be represented by a reference signature.

The system has since been extended to analyze data from facilities, which handle “dry” materials like powder (Janssens-Maenhout and Dechamp 2004).

PIMMS

The FissTrack[®]: PIMS provides a full-time unattended monitoring function for the Co-Denitration Facility at THORP in the UK, ensuring CoK of in-process materials and providing assurances that the plant process is operating as declared.

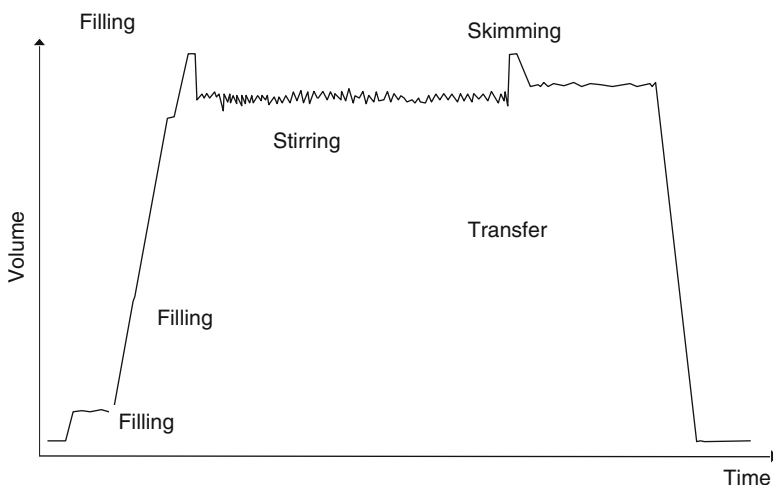


Figure 29
Measurement histories

The PIMS is a distributed total neutron counting system jointly used by JNFL, IAEA, and JSGO to meet a number of requirements. The sharing of such instrumentation and data reduces the costs associated with such safeguards equipment to both the operator and the safeguards authorities. The system is based on total neutron counting techniques to determine the overall count rate at each neutron detector and mathematically deconvolutes the responses from each detector to determine the number of neutrons emitted from each plant item (vessels, glove-boxes, etc.), using a knowledge of the response of each detector to each plant area determined during commissioning.

The calculated neutron emission is then converted into an equivalent mass of plutonium using known or declared material characteristics (plutonium and uranium isotopic composition, chemical compositions, etc.). This enables a determination of the distribution of material throughout the plant to be made. A vulnerability assessment of the techniques and system design has been performed on behalf of the IAEA with the system design reviewed to address specific areas of concern.

The ability to monitor the whole of the processing plant simultaneously and the rapid update time of the system (approximately 30 s) permits near real-time tracking of process material to be performed.

2.6 Environmental Sampling

The use of trace analysis of uranium and plutonium for safeguards purposes was first developed within national safeguards programs. In the United States, a large program was developed that included many US national laboratories and private companies that specialized in forensic analysis. Other countries and international organizations, such as the UK, France, Russia, and the European Commission developed similar methods within its safeguards work.

The IAEA started a development program called “93 + 2” in the mid-1990s that included an evaluation of environmental samples as part of the IAEA’s international safeguards work (Hooper 1997; Kuhn 1995; Kuhn et al. 2001). This environmental sampling started as a complement to traditional safeguards and was driven mainly by a need for better verification of the correctness and completeness in state declarations of nuclear material handling. The use of environmental sampling, together with the implementation of the additional protocol that gives the IAEA more access for this sampling, has enhanced the IAEA’s ability to verify the declarations made.

In the startup of the IAEA environmental program, field trials were made on different types of samples taken around nuclear facilities from vegetation, soil, sediments, water, dust, etc. Tests were also made collecting larger amounts of dust in air samplers in an attempt to cover wider areas. Later, the sampling focused more on dust samples collected on cotton swipes taken in the nuclear facilities or at locations suspected of clandestine nuclear material handling. A special case is the use of cellulose swipes that were developed for sampling small amounts of materials on the surfaces inside hot cells. A closer sampling at the facilities under verification significantly improves the possibility to detect materials and also increases the relevance of the sample results.

The IAEA has established a capacity for analyzing environmental dust samples at its own laboratories in Seibersdorf, Austria. However, these facilities cannot manage the full amount of samples collected by IAEA inspectors around facilities. A network of analytical laboratories (NWL) in IAEA member states makes the main bulk of sample analysis in support to the

IAEA's safeguards efforts. These laboratories are situated in many countries, including the USA, UK, France, Russia, Finland, Japan, Australia, and the European Commission. In addition, new countries adding laboratories to the NWAL include South Korea, Brazil and China.

Apart from the IAEA's work, environmental sampling is also carried out by national and international safeguards organizations, like the European Commission's work within the Euratom treaty and the Argentinean–Brazilian collaboration within the safeguards organization ABACC.

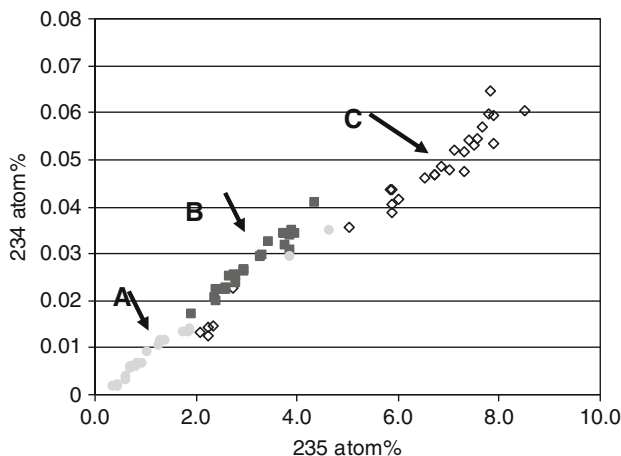
2.6.1 Basic Principles of Environmental Sampling

In most handling or processing of nuclear material there is a small but detectable release of fine particulate material or aerosols containing uranium and/or plutonium materials. The released particles are highly mobile and can be found in many locations at a nuclear facility. These particles are representative of the original material, and their composition provides specific information about the source. The fact that it is difficult to clean up and remove the released particles is what makes environmental sampling so efficient. Samples taken at a facility that has been operated over a long period provide an insight into the entire history of the operation.

The analysis of the samples can be treated either as a bulk sample, where the average plutonium and uranium isotopic and elemental concentration are determined, or an isotopic analysis on individual particles. The bulk measurements have the main advantage of being able to detect and analyze very small amounts of plutonium mixed with a larger amount of matrix materials (Vogt et al. 2001). Bulk can also detect small amounts of nonnatural uranium isotopes such as ^{233}U and ^{236}U . However, the bulk measurements have a fundamental limitation in the uranium measurements, as there is a background component of natural uranium from the swipe material and from the dust matrix. In addition, there is a small background component from the chemical separation work. However, the background problem is less of a limitation on samples richer in materials.

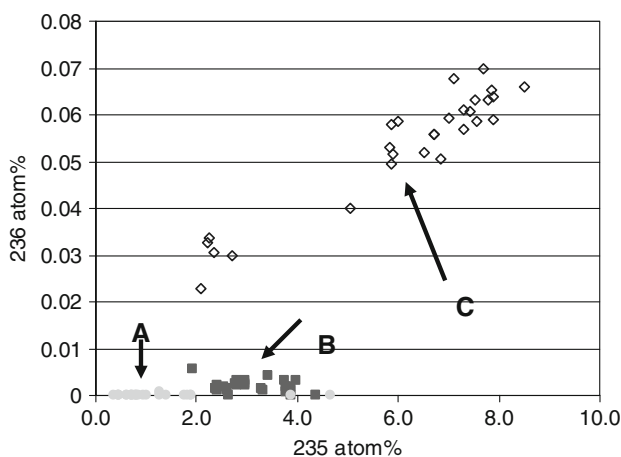
The individual particle analysis does not have the background problems of the bulk measurements and can give precise isotopic information on individual particles. In addition, particle analysis can be used to map relationships in isotopic ratios on populations of particles specific to a nuclear activity. An example is irradiated nuclear fuel, where there is a rapid increase of ^{236}U and ^{240}Pu and a decrease of ^{234}U with increased burn-up (decreased ^{235}U abundance) (Fischer and Wiese 1983). The consistency from the isotopic measurements can be compared with declared irradiation that can be modeled with the ^{236}U , ^{240}Pu , ^{234}U versus ^{235}U abundance. Another typical application for particle analysis is samples taken from enrichment plants (Bush et al. 2001). The particles isotopic signature is typically plotted with the ^{234}U versus ^{235}U , and ^{236}U versus ^{235}U . The $^{234}\text{U}/^{235}\text{U}$ and the $^{236}\text{U}/^{235}\text{U}$ relationship are dependent on the layout of the enrichment facility and on the feed material used.

► **Figures 30 and 31** show an example of materials produced in three different enrichment plants (A, B, and C), with the plotted $^{234}\text{U}/^{235}\text{U}$ and $^{236}\text{U}/^{235}\text{U}$ relationship. As shown in ► **Fig. 1**, the observed $^{234}\text{U}/^{235}\text{U}$ ratio shows that small variations typically stay within a range of 0.005–0.012. As shown in ► **Fig. 2**, the $^{236}\text{U}/^{235}\text{U}$ changes significantly for the three different facilities, depending on the feed material used. Facilities A and B have little or no ^{236}U in the feed material; however, facility B does exhibit a ^{236}U background possibly from prior feed that did contain ^{236}U .



■ Figure 30

The relationship of ^{234}U versus ^{235}U in three samples (A, B, and C) from different facilities



■ Figure 31

The relationship of ^{236}U versus ^{235}U for the same samples as in [Fig. 3](#)

2.6.2 Sampling Methods

The main sampling methods used today are sampling in hot cells using specially designed cellulose swipes that can be handled with the hot-cell manipulators or the more common cotton swipes for sampling dust at nuclear facilities. [Figure 32](#) shows a typical sample kit for dust sampling using cotton swipes. The kit contains a set of swipes, gloves, labels, a report form with instructions, and zip bags for the swipes used in the sampling.



■ **Figure 32**
Sample kit for dust sampling using cotton swipes

The sampling locations differ for the type of facility that is inspected. Typical sampling locations can be tube connections for UF_6 at enrichment facilities or ventilation ducts, changing rooms, etc.

2.6.3 Bulk Measurements of Dust Samples

For the bulk method, it is common to dissolve the swipe together with the sample material and to make a chemical separation to obtain pure fractions of the elements of interest, mainly uranium and plutonium. Dissolution can be performed directly on the swipe or after ashing the swipe in a furnace. Dissolution is made using an oxidizing acid such as nitric acid. Separation of the elements normally is made using traditional methods of ion exchange resins.

To determine the assay of uranium and plutonium, a spike is added for isotope dilution mass spectrometry (IDMS) measurements. Typically, high-purity ^{233}U spikes are used for uranium and ^{244}Pu or ^{242}Pu spikes are used for plutonium. Commonly, one spiked fraction and one unspiked fraction are prepared for the uranium which improves the isotopic measurements of the isotopes. The plutonium fraction is often so small that only a spiked fraction is prepared. The isotopic measurements are typically made by either thermal ionization mass spectrometry (TIMS) or multi collector-inductive coupled mass spectrometry (MC-ICPMS).

2.6.4 Particle Measurements of Dust Samples

The particle analysis can be split into two tasks. The first task is to find the particles of interest in a matrix of other materials. This task is followed by precise and accurate analysis of the individual particles. High demands are set on the analysis techniques to obtain reliable information and not to overlook any undeclared activities. Both tasks are a challenge. To find a single man-made uranium particle in a matrix of hundreds of millions of other particles is a typical “needle-in-the-haystack” problem. To perform isotopic analysis of both the major and minor isotopes on particles, often not having more than sub-pg amounts of material, is also a challenge. The precision of the isotopic analysis is limited mainly by counting statistics because of the very small amounts of materials at hand. Two methods are routinely used: fission track/TIMS (FT/TIMS) and magnetic sector secondary ion mass spectrometry (SIMS).

FT/TIMS

FT/TIMS is a two-step method. The location of the particle is made by using polycarbonate fission track detectors, followed by the precise and accurate isotopic measurements using TIMS. The particles are removed from the swipe either by ultrasonification of the swipe in a suspension (typically heptane), or by ashing the swipe in a furnace (Baude et al. 2001; Lee et al. 2007). The material is then mixed with flexible collodium and spread out and dried on a set of polycarbonate plates and placed in a capsule to prepare it for irradiation. After neutron radiation of the plates, the collodium film containing the particles is removed and the polycarbonate plates are treated in a bath of sodium hydroxide for chemical etching to visualize the star-shaped damages (fission tracks) caused by the induced fission in uranium or plutonium particles. The collodium film containing the sample material is then replaced on the plates so that the location of the uranium and plutonium particles in the film can be determined. At the location of the particles, a small piece of the collodium film is removed from under a microscope and placed on a rhenium filament to prepare it for the final TIMS analysis.

The fission-track method has been proven to be very effective for finding single particles in a large amount of other material. The TIMS measurements are very reliable and can provide highly precise and accurate measurements on both uranium and plutonium particles. TIMS analysis does not have any significant baseline or background problem, and it does not have the SIMS hydride interference problem of $^{235}\text{U}^1\text{H}$ overlapping the ^{236}U . The main limitation is that the method is both costly and very time consuming because it involves many processing steps; it requires the availability of a suitable neutron source, and requires each particle to be loaded on individual filaments for the TIMS analysis. Another common limitation compared to SIMS is lower ion yields in the TIMS measurements.

Secondary Ion Mass Spectrometry (SIMS)

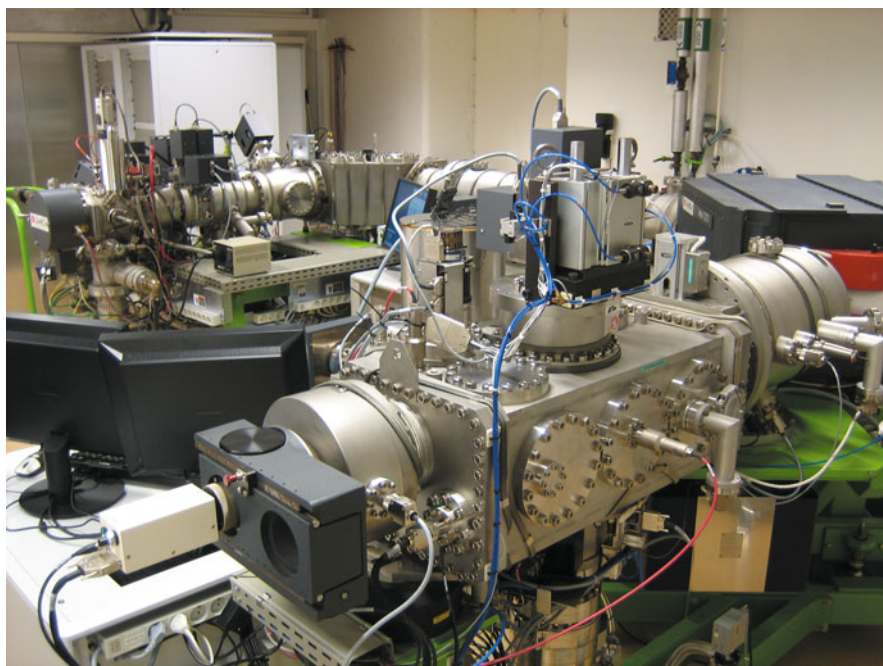
The SIMS technique combines the search of particles and the final measurement within one instrument (Tamborini et al. 1998). Before the samples are measured, the particles must be removed from the swipe and placed on a substrate, typically pyrolytical graphite planchets. The particles and their dispersion on the sample planchet can be removed by the ultrasonification of pieces or of the entire sample swipe, thus releasing the particle into a suspension. The suspension is deposited and dried on a sample planchet. An alternative method is to use the vacuum impactor technique, which pulls particles from the sample swipe with a vacuum suction and sprays them directly on a sample planchet (Esaka et al. 2004).

One of the fundamental strengths of the SIMS is its ability to perform automatic particle screening measurements very quickly in isotopic imaging mode on deposits containing millions of particles, to find those of interest (Simons et al. 1998; Nittler and Alexander 2003). These measurements provide the exact particle location and a first estimate of the enrichment. The final isotopic measurement on an individual particle is made with a focused primary microbeam.

Compared with FT/TIMS, the SIMS technique is fast and requires smaller laboratory facilities and fewer staff resources for a given sample throughput. The technique can also provide the enrichment distribution of thousands of uranium particles from the screening measurements.

A main limitation to the SIMS measurements, which to date have been performed almost solely using small-geometry SIMS (SG-SIMS) instruments (typically the Cameca F-series), is the presence of isobaric background interferences that can significantly reduce the accuracy of the isotopic measurements. It has been demonstrated that background problems in SG-SIMS measurements can be reduced, or in some cases even eliminated, by improving the sample preparation. Improving sample preparation can be effective for some samples, but are problematic if the uranium particle itself includes interfering elements (Esaka et al. 2007).

An alternative to SG-SIMS is provided by large-geometry SIMS (LG-SIMS) instruments, which were developed in response to a demand in geosciences and cosmochemistry, for high mass resolution at a high transmission (see ► Fig. 33). As with the SG-SIMS, these instruments are based on a double focusing mass spectrometer, but with the implementation of a large-radius magnetic sector and improved secondary ion optics. It has been demonstrated that these



► Figure 33

Large geometry secondary ion mass spectrometry (LG-SIMS) (Cameca 1280) at the Nordic NORDSIM Laboratory

instruments have a superior quality of the isotopic measurements, and allow for faster screening measurements without any noticeable drawback compared with SG-SIMS instruments (Ranebo et al. 2009). Due to the availability of multi ion counting systems for the LG-SIMS, there is also an improvement in the detection efficiency.

2.7 Forensics

Since the beginning of the 1990s, more than 1,000 cases of illicit trafficking involving radioactive or nuclear material have been recorded in the IAEA illicit trafficking database. Most of the reported seizures refer to radioactive sources, such as ^{137}Cs , ^{192}Ir , ^{60}Co , and ^{90}Sr , which pose a radiological hazard due to their high activity. The seized samples of nuclear material were generally of higher mass, yet of lower activity as compared with medical or industrial radionuclide sources. However, the radiotoxicity of the alpha-emitting nuclides typically encountered in nuclear material is significantly higher than that of beta or gamma emitters usually applied in medical sources. As such, nuclear materials represent a considerable hazard if the material is handled in an inappropriate way and particularly if considered in a terrorist context. The use of nuclear material in a radiological dispersal device therefore is a matter of serious concern.

The reported seizures of nuclear material prove that, despite the strict control of national or international safeguard authorities, nuclear material can be diverted or stolen. These seizures lead to the conclusion that the implementation of treaties, agreements, or conventions on safeguards and physical protection has not been fully achieved, or that they suffer from gaps. Closing these gaps and improving the control of nuclear material at the sites where theft or diversion occurred are therefore of prime importance; however, this requires the identification of the origin of the seized nuclear material.

As a result of illicit trafficking, nuclear material has become a part of the forensic investigations and a new discipline, nuclear forensic science, was developed. The nuclear forensics methodology developed for the nuclear security area also may be applied to source attribution in a much broader range of applications:

- In *proliferation* issues the investigation of particles of HEU found in Iran provided insights into Iran's clandestine nuclear program. The comparison of the uranium isotopic pattern with material obtained from Pakistan showed that the scenario was consistent with the available evidence (Bokhari 2005).
- The measurement of chemical impurities is increasingly applied in *nuclear safeguards*. Particularly, samples of uranium are analyzed to establish relations between different samples and to check consistency of the impurity pattern with the declared processes.
- Also, *environmental samples* can be subject to nuclear forensic investigations. As demonstrated by Ray et al. (2002), particles found on the seabed and occasionally on the beaches of Dounreay could be attributed to the materials testing reactor at Dounreay.

2.7.1 Methodology

Nuclear forensic investigations must be considered as part of a comprehensive set of measures for detection, interception, categorization, and characterization of illicitly trafficked nuclear

material. As mentioned previously, nuclear forensic analysis may result in important conclusions on the origin of the material and thus provide the most essential contribution to the prevention of future diversions from the same source. Therefore, it is crucial to ensure the integrity and authenticity of the collected evidence throughout the entire process. This requires a close collaboration between the various actors on the scene: law enforcement, radioprotection services, forensics experts, and nuclear measurement experts. The International Technical Working Group (ITWG) on combating nuclear smuggling has developed a model action plan (MAP) for handling cases of seized nuclear material (Fig. 34). This action plan lays out the elements that are needed in the instance that illicit nuclear material is uncovered (e.g., incident response, crime scene analysis, collection of evidence, transportation to a nuclear facility, subsequent laboratory analysis, and then development of the case) (Janssens et al. 2001; IAEA Nuclear Security Series No. 6, 2007; Smith et al. 2008). The MAP clearly needs to be adapted to the regulatory, logistical, and technical specifics in each country. Many states have implemented the concept of the MAP and have developed a dedicated handbook summarizing the responsibilities and processes relevant in response to illicit trafficking of nuclear material.

For each seized sample, a specific analytical strategy must be developed, considering the particular conditions of the seizure, the very nature of the material and of its packing, and other evidence. The analytical strategy is based on a step-by-step approach, where experimental

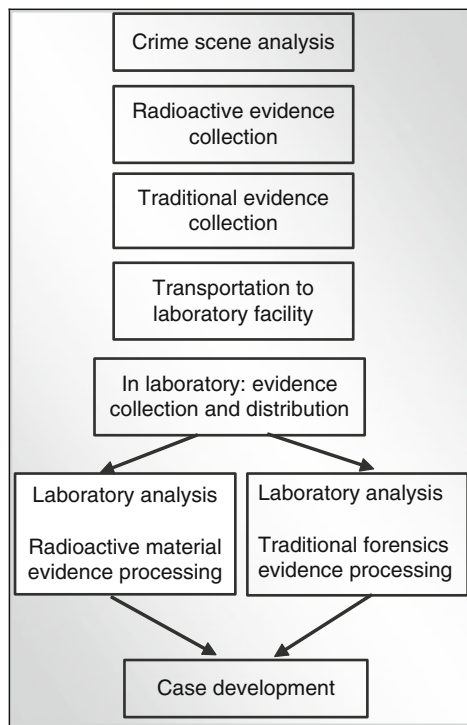


Figure 34

The model action plan (MAP) as developed by the nuclear smuggling International Technical Working Group (ITWG) provides guidance on incident response


results are compared with information on nuclear material of known origin contained in a relational database if available. Based on the actual findings, the next step is defined and performed. Beyond the actual analytical work in the laboratory, the actions to be taken at the incident site (place of seizure of the material), the legal and law enforcement aspects, and the question of data interpretation must be considered. The complexity of these issues, and the fact that illicit trafficking of nuclear material is a border-crossing problem, call for international collaboration and coordinated measures.

2.7.2 Characteristic Parameters in Nuclear Forensic Investigations

Nuclear forensics is a methodology that reveals information inherent to nuclear material. Nuclear material has either been subjected to technological processing or is entirely of anthropogenic origin. Consequently, nuclear material carries “toolmarks” or “fingerprints” of the process to which it was subjected. Uranium fuels are examples of the first category, whereas plutonium belongs to the second category. Both elements contain fissile isotopes, substantiating the broad interest in the history, origin, and intended use of these materials.

Nuclear forensic investigations start after material has been seized and categorized as “nuclear material.” These investigations are performed to answer specific questions on the nature of the material and its origin, such as the intended use, the mode of production, the plant and production batch, the last legal owner, and the smuggling route. The investigations may comprise conventional forensic tests applied to radioactive material, the morphology of the material, the structure of the material components, the composition of traces in the material and its packing, and the isotopic composition of the nuclear material itself and of minor constituents. Consequently, a suite of analytical techniques, specifically adapted to the needs of radioactive material, is required. Most of the analytical techniques used are normally applied for accountancy and safeguards measurements or for the characterization of nuclear fuel. However, specific measurement protocols may apply (Mayer et al. 2005; Tandon et al. 2008).

Controlling the radiological hazard is of paramount importance at all stages of the investigation. Furthermore, attention should be given to preserving classical forensic evidence. In the nuclear analytical laboratory, the material is first subjected to visual inspection which may reveal useful information on the material itself (e.g., physical form, geometry, and primary packing) and provides the starting point for further analysis. This process may be complemented by imaging techniques: specifically, optical microscopy for examination of the sample at high magnification.

If the analyzed material contains fuel pellets, their dimensions (height, diameter, and the size of a possible central hole) and mass are measured. These so-called macroscopic parameters, together with the ^{235}U enrichment are characteristic and often reveal the reactor type for which the pellets are intended. Other characteristic parameters are shown in  [Table 21](#) and are discussed in more detail in the following section.

Isotopic Patterns of Uranium and Plutonium

The isotopic composition of uranium and plutonium allows us to draw conclusions on the reactor type in which the material has been irradiated, as well as on the intended use of material. Depending on the enrichment of the main isotope (i.e., ^{235}U or ^{239}Pu), the material can be categorized as weapons grade, reactor grade, or fuel grade (Smith et al. 2008). In the case of

■ **Table 21**

Parameters of interest for nuclear forensic analysis

Parameter	Elements of interest	Information
Major elements	Uranium and plutonium	Intended use, production reactor (plutonium)
Minor/trace elements	Metallic impurities, gadolinium, oxygen, lead, thorium, etc.	Age, geolocation (uranium), production process, reactor type
Macrostructure	Pellet dimensions	Intended use/reactor type
Microstructure	Particle size and form grain size	Production process

plutonium, its isotopic composition may also reveal the reactor type, using the so-called isotope correlation technique. The isotope correlation technique was used in safeguards in 1970s for two reasons: to verify the consistency of the isotopic analyses performed at the reprocessing plants and to deduce the amount of specific isotopes by measuring other isotopes and using established correlations.

The isotope correlation shown in [Fig. 35](#) is based on the following principle: The neutron capture cross-sections of the individual plutonium isotopes vary as a function of neutron energy. As a consequence, the buildup of plutonium isotopes is different in reactors with different neutron energy spectra. In addition, the initial enrichment of ^{235}U varies in different reactors. These two parameters then are reflected in the isotopic composition of plutonium (Wallenius et al. 2000). To demonstrate the feasibility of the correlation, a sample seized in the context of a criminal investigation has been added in [Fig. 35](#). The sample seems to originate from an LWR having initial ^{235}U enrichment close to 3.5%, which was later confirmed (Wallenius et al. 2007) ([Fig. 35](#)).

The minor isotopes of uranium, ^{234}U and ^{236}U , carry information about the irradiation history, enrichment process, and geological origin of the material. First, the presence of small amounts of ^{236}U indicates a contamination with recycled uranium, which thus points at reprocessing activities. Second, different enrichment processes may result in slight differences in the ^{234}U abundance. Last, variations in ^{236}U as well as in ^{234}U abundances have been recorded in natural uranium, which may help to locate the mine that is the source of the uranium (Richter et al. 1999; Keegan et al. 2008). The isotope abundances of ^{234}U and ^{236}U may also help to verify coherence between different samples and consistency with declared operations.

Minor Constituents and Trace Elements

Uranium and plutonium materials contain variable amounts of minor constituents from different “origins.” These materials arise from processes such as production, companion elements in uranium ores, and radioactive decay.

Age Determination of nuclear materials uses the radioactive decay of these elements. If a complete separation of the daughter products is assumed during the production process (e.g., during chemical purification of the material), the “age” of the material (i.e., the time that has elapsed between the last chemical treatment of the material and today) can be determined by quantifying the amounts of parent and daughter nuclides. Age determination of plutonium classically is

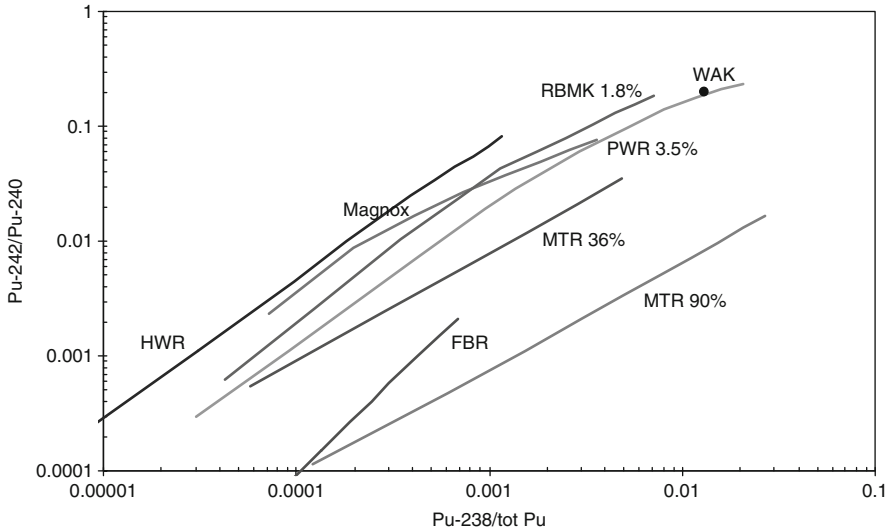


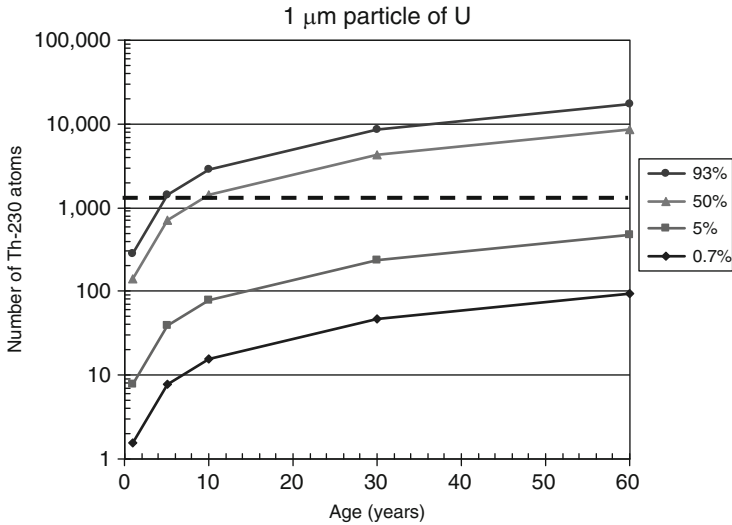
Figure 35

Plutonium isotope correlation for different types of reactors. “WAK” denotes seized material, which can be attributed to an light-water-reactor (LWR)

being performed by gamma spectrometry using the $^{241}\text{Pu}/^{241}\text{Am}$ parent/daughter ratio. However, in a few cases it has been noticed that the americium separation has not been complete, and thus the age from this parent/daughter may give a wrong answer. Using the uranium daughters of ^{238}Pu , ^{239}Pu , and ^{240}Pu offers a consistency check because these three parent/daughter relations should result in the same age, provided that the separation of uranium was complete during processing of the material (Wallenius et al. 2000; Nygren et al. 2007). Residual amounts of uranium isotopes lead to biased results in the plutonium age determination. The degree of the bias is dependent on the plutonium composition (weapons-grade or reactor-grade), as well as on the parent/daughter relationship (Mayer et al. 2001).

Age determination of uranium is more complicated because (1) uranium has only two possible candidates of parent/daughter ratios, namely $^{234}\text{U}/^{230}\text{Th}$ and $^{235}\text{U}/^{231}\text{Pa}$, and (2) the half-lives of uranium parent isotopes are much longer compared with the plutonium parents. Therefore, only tiny amounts of daughter nuclides grow in with time (Morgenstern et al. 2002; Wallenius et al. 2002a; Varga and Suranyi 2007).

Another interesting aspect in the age determination, especially in the safeguards context, is the question of the age of particles. Age determination of plutonium particles has been demonstrated (Wallenius et al. 2002). Age determination of uranium particles proves to be much more challenging, as already stated. Even if the ^{234}U is the lower abundant isotope in uranium materials, due to the 1,000-fold-shorter half-life, the parent daughter ratio $^{234}\text{U}/^{230}\text{Th}$ is more favorable for the age determination of uranium as compared with the $^{235}\text{U}/^{231}\text{Pa}$ ratio. The particles of interest in swipe samples from enrichment plants typically are only $1\ \mu\text{m}$ in diameter. Based on this assumption, we can calculate the detection limit for the age determination as a function of the age of the particles and the ^{235}U enrichment. If we assume further a detection efficiency of 0.5% and a dark noise of 2 cpm with 3 min measurement time in the secondary ion



■ Figure 36

The number of ^{230}Th atoms contained in a uranium oxide particle (with an assumed number of 10^{10} atoms of uranium per particle) depends on the age of the particle and on the ^{235}U enrichment. The detection limit of a typical SIMS instrument is marked with a fragmentary line and is about 1,500 atoms of ^{230}Th

mass spectrometer, we see from ► Fig. 36 that age determination can be successfully performed only for “old” particles of HEU.

Metallic Impurities Metallic impurities are present in nuclear material samples at varying concentration levels. In starting materials (e.g., uranium ore), the impurities may have the character of accompanying elements and are present in relatively high concentrations. In intermediate products (e.g., yellow cake), the concentration of most of the chemical impurities has been drastically reduced. After this reduction, toward the final product, a further decrease of impurities is minute if at all. ► Figure 37 shows metallic impurities in natural uranium compounds of different origins. Five samples from the same origin can be recognized clearly through their identical pattern of metallic impurities (Wallenius et al. 2002b; Keegan et al. 2008).

Although metallic impurities can be used for identifying coherences between samples or batches of material, the systematics behind the impurity patterns are not well understood because the metallic impurities may be carried into the material at different stages of the process. For example, the concentration of some impurities may vary as a function of exposure time to the container material or the storage tank as they are leached from the surface of the walls. In sample analysis, the concentration of such elements appears to be fluctuating randomly.

The drawback of using impurities is that cross-contamination (e.g., from environment) must be prevented. In addition, the level of impurities within a production plant may vary with time, thus requiring continuous input from the production plants, as well as updating of the database. In general, the use of common elements as indicators should be avoided. Another solution to this dilemma could be to look at ratios of chemical elements instead of looking at

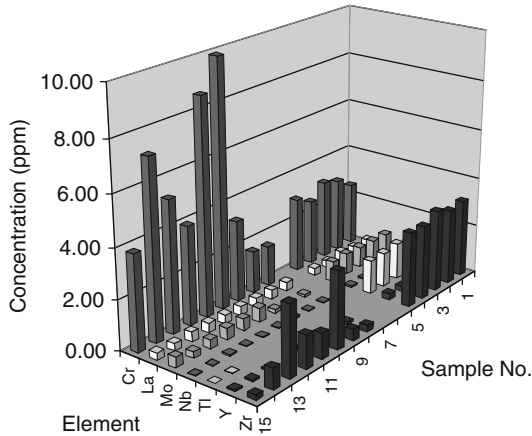


Figure 37

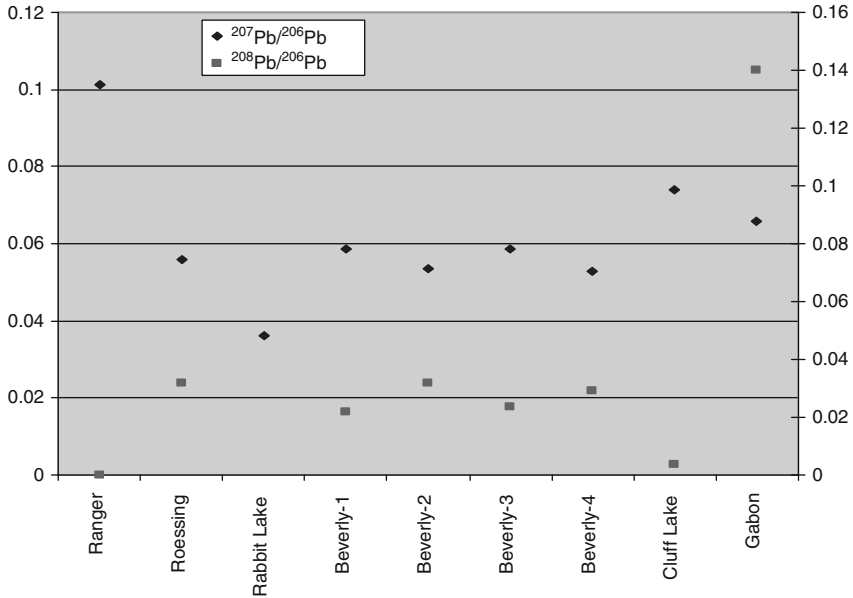
Selected metallic impurities in intermediate natural uranium products. Samples 1–5 are apparently of the same origin

the absolute concentrations of impurities. Although the absolute concentration of the impurities may change, the ratio of certain elements will vary only within narrow limits. This variation applies in particular for elements of similar chemical behavior (e.g., the rare earth elements) (Wallenius et al. 2002; Keegan et al. 2008).

Stable Isotopes In the field of food science and geochemistry, the analysis of stable isotopes (e.g., ^1H , ^2H , ^{12}C , ^{13}C , ^{16}O , and ^{18}O) has been successfully applied for a few decades. The principle of the use of stable isotopes is very straightforward: The stable isotope compositions of elements, which are part of a substance, are a function of the origin and history of that substance. That is, two substances that are chemically the same may have different stable isotope compositions if either their origin and/or history differ. This methodology was also introduced recently to nuclear forensics.

The application of oxygen isotope ratio measurements for geo-location purposes was demonstrated several years ago (Pajo et al. 2000). A correlation between the geographic location of the production site of uranium oxide samples and the variation in the $n(^{18}\text{O})/n(^{16}\text{O})$ ratio could be established. Moreover, it could be shown that the method is also applicable to individual particles (i.e., the oxygen isotope ratios established by “bulk” measurements using TIMS could be reproduced on individual particles using SIMS) (Pajo et al. 2001). This type of information certainly does not identify a specific plant, but it provides a parameter for attributing the material to a region. This parameter can be used, for instance, to distinguish between imported and domestic materials.

Another parameter that has been widely used in geochemistry and in environmental sciences is the isotopic composition of lead. Lead isotopes may be primordial (natural lead), or they may be produced through the decay of uranium isotopes. The small variations in the isotopic composition of natural lead have been used to locate the origin of some fuel additives (mainly consisting of tetra-ethyl lead). The adaptation of this methodology for nuclear safeguards and nuclear forensics purposes has been studied (Svedkauskaite-LeGore et al. 2007; Keegan et al.



■ Figure 38

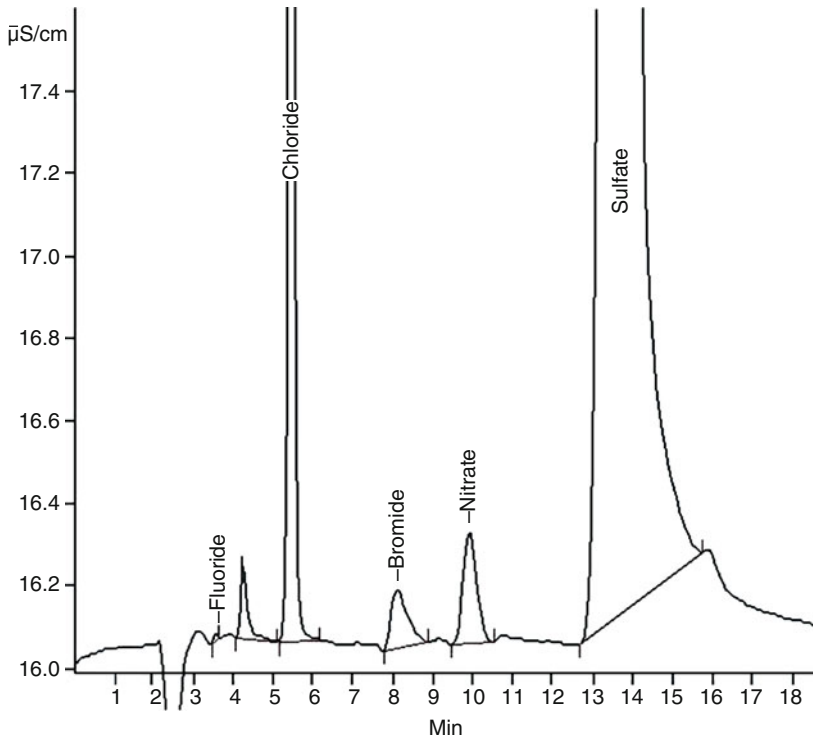
Lead isotope ratios observed in yellow cake samples from different mines, adapted from Svedkauskaite-LeGore et al. (2007). Combined uncertainties, U_c (with $k = 2$) on the ratios $n(^{207}\text{Pb})/n(^{206}\text{Pb})$ and $n(^{208}\text{Pb})/n(^{206}\text{Pb})$ are between 0.0002 and 0.00008, and are thus too small to be visualized on the graph

2008). It could be shown that the lead isotopic composition of yellow cake provides useful information to distinguish between natural uranium materials of different origins (see 🔍 Fig. 38). Because lead is omnipresent in our environment, special care must be taken when performing the chemical separation of the lead from the uranium samples in order not to introduce any natural lead from dust particles or chemical reagents and thus bias the results.

Anionic Impurities Aqueous processing of nuclear material is encountered at many stages in the nuclear fuel cycle. In these processes, mineral acids are frequently used. They leave anionic impurities (e.g., Cl^- , F^- , SO_4^{2-} , and NO_3^-) in the material behind, together with those anions that were initially present in the starting material. It has been demonstrated that, depending on the type of ore from which the uranium was extracted and the type of process applied as well as the associated chemical reagents used, the isotopic patterns generated in the yellow cake are significantly different (Badaut et al. 2006). These patterns provide additional information for distinguishing materials from different origins, or if appropriate reference data are available, for relating a given material to a specific facility. For data evaluation, the pattern of anionic species is more informative than the actual concentration values (see 🔍 Figs. 39 and 🔍 40).

Microstructure

The microstructural properties of nuclear materials are another important parameter. The particle and grain size distributions and the surface structure of the particles are material characteristics that reflect the production process of the material. Therefore, these data allow the



■ Figure 39

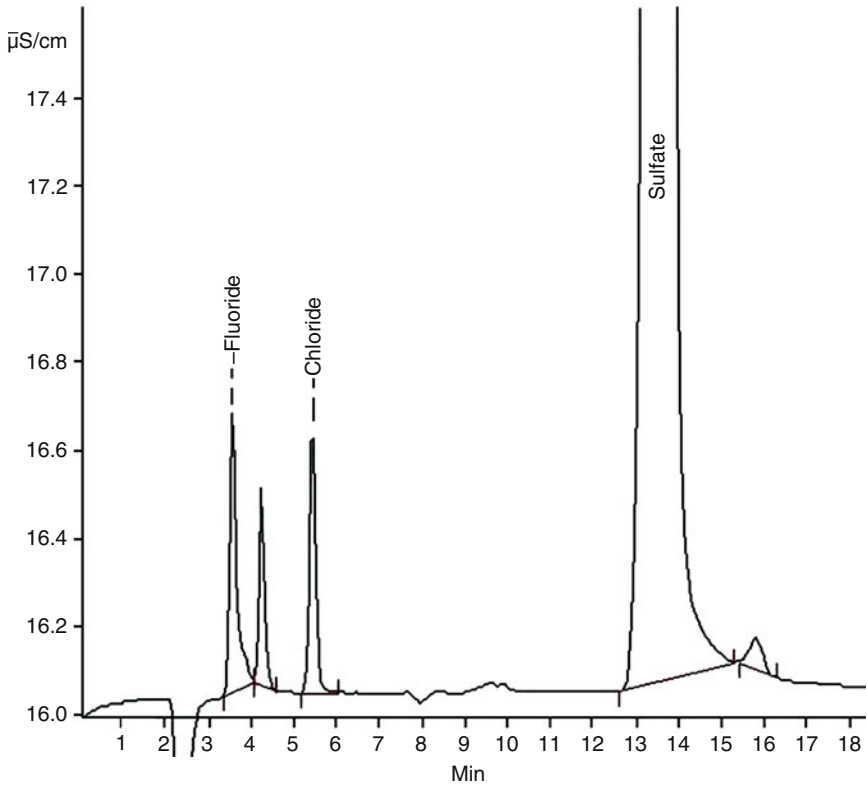
Anionic impurities determined in yellow cake samples from a German mine by ion chromatography

direct comparison of samples, enabling conclusions on coherence between samples. For example, ► Fig. 41 shows a comparison of four UF_4 samples. The particles are shaped and sized very differently; thus, they can be distinguished clearly from each other, indicating different origins of the four samples in question.

2.7.3 Data Interpretation and Attribution

The main challenges in nuclear forensics are the identification of characteristic parameters and the availability of reference information. Based on the reliable measurements of well-chosen parameters, clues on the origin of the material can be obtained. Information obtained by nuclear forensic analyses from an unknown nuclear material can basically be divided into two groups: endogenic and exogenic. Endogenic information is to be understood as being self-explaining, and only some model calculations might be required to help data interpretation. The isotopic compositions of uranium and plutonium and the age are good examples of endogenic information. These compositions provide immediately important features regarding the material (in this case, about its intended use and production date, and additionally for plutonium, the reactor type where the material was produced).

In contrast, exogenic information must be compared with data from known samples. The availability of “reference information” or comparison samples is essential for the interpretation



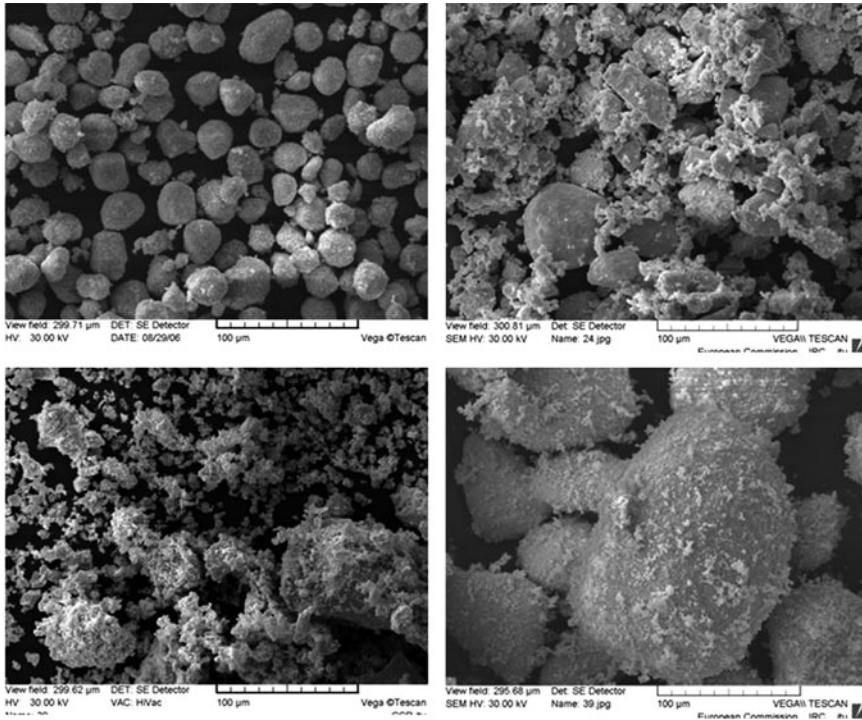
■ Figure 40

Anionic impurities determined in yellow cake samples from a Gabonese mine by ion chromatography

of data such as chemical impurities or the isotopic composition of minor constituents. This type of information includes all geolocation and production parameters (i.e., impurities, lead isotopic composition, $^{18}\text{O}/^{16}\text{O}$ ratio, and microstructure). Known data can be either compiled and systematized in form of a relational database, where data (e.g., from fuel manufacturers) is collected, or it can be a collection of analytical results of known samples (Dolgov et al. 1997, 1999; Schubert et al. 1998).

A major challenge in data interpretation is the accessibility of reference data. Measured data on reactor-grade nuclear material, which is essentially produced for power reactors, are available with the fuel manufacturers. Note that certain data (e.g., chemical impurities) might be commercially sensitive, and therefore their accessibility might be limited. Detailed information on weapons-grade material (HEU and low burn-up plutonium) is clearly subject to confidentiality for national security reasons, and data are not shared.

Source attribution is generally done by comparing measurement results to data contained in a database applying the “exclusion principle.” The results of the first measurements on the unknown material (e.g., pellet dimensions and isotopic composition) are used for a query. All nonmatching records (database entries from known materials) are rejected, and the matching records are compared with each other to identify parameters to be analyzed next. Thus,



■ Figure 41
Comparison of the microstructure of four different UF_4 samples

the database query also serves for analytical guidance, streamlining the laboratory work and rendering the measurement effort more efficient. Based on the subsequent measurement data, another query is performed in the database, and further records are rejected. This process then results in records where all search parameters match within the stated tolerances. Ideally, the search results point to a single production location.

2.7.4 Conclusions

Nuclear forensics is highly relevant in the areas of nonproliferation and of nuclear security, and it is also increasingly used for investigative nuclear safeguards and environmental studies. Forensics provides support (e.g., to law enforcement authorities) in combating illicit trafficking and dealing with criminal environmental issues. Characteristic parameters of nuclear material, such as isotopic composition, chemical impurities, age of the material, and microstructure, provide clues to the origin and the intended use of the material. A wide variety of analytical techniques, specifically adapted for measuring nuclear material from various scientific disciplines, is used for the investigations. The availability of up-to-date references on nuclear material is essential to identify the origin or to exclude certain origins. Continued development activities and strengthened international cooperation is the key to perfecting nuclear forensics. Nuclear

forensics provides sustainability in combating illicit trafficking of nuclear material and thus in preventing nuclear terrorism.

2.8 Statistics for Accountancy

In the context of international nuclear nonproliferation agreements and domestic safeguards requirements, declared facilities that process and/or store SNM are required to perform periodic NMA measurements. In traditional safeguards, a key function of periodic NMA measurements is to confirm the presence of SNM in accountability vessels to within relatively small measurement error. Containment and surveillance (C/S) are used as a complementary measure to confirm the absence of undeclared flows that could divert SNM for possible illicit use. NMA, C/S, and related topics involve statistical methods that are described here.

International safeguards face several issues that are distinct from domestic safeguards. In the IAEA context, the entire facility could be involved in a diversion plan; therefore, for example, safeguards components such as gates, vaults, and guards are irrelevant. In domestic safeguards, no credible basis for concern exists that the entire facility might attempt a diversion; therefore, these same components are highly relevant. The commensurate distinctions between IAEA and domestic safeguards do not concern us here; however, for example, the IAEA's need to monitor for possible data falsification and the role of C/S in reducing required verification measurements lead to statistical issues that are described.


2.8.1 Background

The inventory difference (ID) for SNM at time t is defined as,

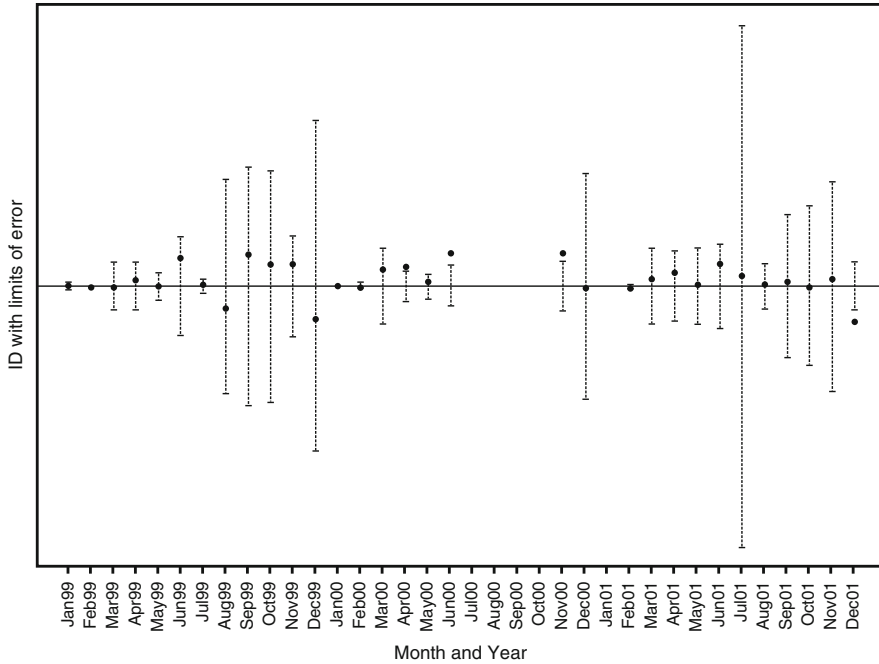
$$ID_t = BI_t + R_t - EI_t - S_t, \quad (3)$$

where BI is the beginning physical inventory, R is the receipts, EI is the ending physical inventory, and S the shipments, and all terms include measurement error. Equation (3) is similar to (2).

If we know all terms in (3), and the measurement uncertainty associated with each measurement system, we apply statistical rules involving the variance of a sum (propagation of variance, or POV) to estimate the measurement error standard deviation of the ID, or σ_{ID} . Note that (3) is a sum of many terms, some of which have negative signs.

An example ID sequence is plotted in  Fig. 42. The alarm limits are at $0 \pm 2\hat{\sigma}_{ID}$ (where $\hat{\sigma}_{ID}$ is the estimate of σ_{ID}). A good estimate of σ_{ID} is usually all that is required for statistical evaluation of an ID because of the central limit effect, whereby sums of approximately 10 or more random variables (all measurement errors are random at some stage, even the so-called “systematic” errors) will have approximately a Gaussian distribution. If no material loss is assumed, the ID has an approximate $N(0, \sigma_{ID})$ distribution (denoted $ID \sim N(0, \sigma_{ID})$), where $N(\mu, \sigma)$ is the normal distribution with mean μ and standard deviation σ . Therefore, to test for SNM loss, the ID can be compared to $k\hat{\sigma}_{ID}$, where k is 2–3, depending on the desired false alarm probability.

NMA to confirm declared facility operation involves periodically comparing the latest ID to a predefined goal. To check for abrupt loss, the null hypothesis, $H_0: ID_{true} = 0$, is tested versus the alternative $H_A: ID_{true} > ISQ$, where SQ is the significant quantity of interest, such as



■ **Figure 42**
Data for process status

8-kg of plutonium (IAEA SQ). To check for trends in a sequence of IDs, which could indicate small protracted loss, the n -by- n measurement error covariance matrix Σ_{ID} is used (see [▶ Sect. 2.8.5](#)).

The magnitude of σ_{ID} determines what SNM loss L would lead to an alarm with high probability. For example, if testing is performed only for SNM loss (not gain) with a false alarm probability of $\alpha = 0.05$, the alarm probability $1 - \beta$ is 0.95 for $L = 3.3\sigma_{ID}$ (and $1 - \beta > 0.95$ if $L > 3.3\sigma_{ID}$). Usually the safeguards goals include a goal that $1 - \beta$ is at least 0.95 if $L \geq SQ$, which is accomplished if and only if $\sigma_{ID} \leq SQ/3.3$. If $\sigma_{ID} > SQ/3.3$, then either measurement errors should be reduced to achieve $\sigma_{ID} \leq SQ/3.3$ (if feasible) or additional measures such as enhanced C/S are required.

Statistical science includes methods to summarize and describe large data sets, and methods to infer population parameters using samples. Such inference is inductive reasoning using probability models to describe how population data are generated and is sometimes referred to as “the inverse problem.” That is, given observations (data) from a population, the goal is to infer various properties of the population(s).

Statistical hypothesis testing receives considerable attention in NMA, partly because of the appeal of quantified, objective testing. Speed and Culpin (1986) focused on NMA, but NMA is only one component of safeguards. C/S is another key component. In addition, in all cases, IAEA must “trust, but verify” by making random confirmatory (qualitative and/or quantitative) measurements of the operator’s declared measurements; consequently, the IAEA’s measurement

error is even larger than the operator's measurement error, making the quantified portions of the safeguards conclusions even less capable.

The most important statistical concept involved in evaluating ID sequences is variability. Measured values (e.g., inventory differences and shipper-receiver differences) are often compared with their nominal values, and decisions must be made whether they are within the estimated variability due to measurement error (Jaech 1973; Bowen and Bennett 1988; Venables and Ripley 1999) (🔍 Fig. 42).

2.8.2 Measurement Error Models

All assay measurements involve multiple errors that can have different relative contributions in different contexts. Therefore, measurement error modeling is a complex topic that is briefly discussed here to describe some of the models that are commonly used in NMA.

The terms “random” and “systematic” errors are qualitative terms until we specify a particular measurement system and associated error model. Generally, random errors are unique to each measurement, whereas a systematic error affects two or more measurements (Neuilly 1999; Aigner et al. 2002; Burr et al. 2003a, b). Sometimes the term “long-term systematic error” is contrasted to “short-term systematic error” (“long-term” implying that all measurements in the campaign share a common systematic error and “short-term” implying that two or more measurements in the time period share that error, but not all do).

An example error model is,

$$M = T(1 + S_{\text{item}} + S_{\text{inst}} + R), \quad (4)$$

where M is the measured mass, T is the true mass, S_{item} is the item-specific systematic error (bias), S_{inst} is the measurement-instrument-specific systematic error (bias), and R is the random error. All errors are random at some stage, which we denote as $S_{\text{inst}} \sim N(0, \sigma_{S_{\text{inst}}})$, for example, and $N(\mu, \sigma)$ is the normal distribution with mean μ and standard deviation σ .

It is often assumed that a new S_{inst} is generated if and only if the instrument is recalibrated, leading to new estimates of calibration parameters. Therefore, $\sigma_{S_{\text{inst}}}$ can be estimated by using calibration data and commensurate results for uncertainties in estimated parameters or by using measurement control (MC) data on standards. Replicate measurements on the same item allow us to estimate the standard deviation σ_R of R . It is always challenging to estimate $\sigma_{S_{\text{inst}}}$. In fact, because S_{item} varies from item to item, we would model it as random error, at least for the purposes of POV for ID evaluation. However, items having the same characteristics tend to have similar biases, so it is preferred to model S_{item} as being random within a class of items.

To some extent, how well the relevant properties of the standards match those of the items has always been an issue. This issue is becoming increasingly important in the United States. DOE complex because of the need to measure scrap, waste, and residues, which can have highly variable material composition. Often S_{item} can be included with R . The implication is that either S_{item} is negligible compared with R or auxiliary methods must be included to measure selected items as part of the MC program and thereby have data to support per-item estimates of systematic error. For example, we might be characterizing a nondestructive (NDA) neutron assay method using (4), but with $S_{\text{item}} + R$ redefined to be R .

If we use a “gold standard” assay method (with negligible S_{item}) such as calorimetry to occasionally remeasure an item, we can redefine σ_R appropriately, and use such item remeasurements to estimate σ_R . Some facilities maintain a remeasurement database that provides selected data for this purpose. As an important aside, it is necessary to separately estimate σ_S and σ_R to estimate $\sigma_{S_{\text{inst}}}$. After estimating $\sigma_{S_{\text{inst}}}$, it is usually acceptable to replace σ_R with

$$\sigma_{R_{\text{effective}}} = \sqrt{\sigma_R^2 + \sigma_S^2}.$$

In addition to remeasurement results, calibration data are useful for developing measurement error models by applying the results of statistical function fitting (such as regression and least squares fitting of response to predictors). Assay methods are often calibrated on items having accurately known SNM amounts; however, the material form of the calibration items might not match the form of test items in all respects, such as density, impurity effects, and source distribution. Therefore, statistical issues are often involved in designing experiments to assess the impact of mismatch between calibration standards and test items and to develop assay methods that measure and correct for mismatches.

2.8.3 Propagation of Variance

A common way to estimate the variance of a sum of measurements is to apply (2) and assume that two measurements have nonzero covariance if and only if they are in the same measurement group and made during the same calibration period. Other models such as additive error models are available (Taylor and Kuyatt 1994). The variance of a sum of two measured items using (4) (with $S_{\text{item}} + R$ redefined to be R) can be written as (Taylor and Kuyatt 1994)

$$\sigma_{M_1+M_2}^2 = \text{var}(T_1(1 + S_1 + R_1) + T_2(1 + S_2 + R_2)).$$

Because $S_1 = S_1$ during the same calibration period, it follows that

$$\sigma_{M_1+M_2}^2 = (T_1 + T_2)^2 \sigma_S^2 + (T_1^2 + T_2^2) \sigma_R^2. \quad (5)$$

Equation (5) follows either by applying the statistical principle that the variance of a sum of random variables is the sum of all variances plus the sum of all covariances, or by substituting the measurement error model (5) into the $M_1 + M_2$ expression and carefully interpreting terms as just shown. It is then straightforward to derive a useful formula for a given strata with SNM total T as shown by,

$$\sigma_T^2 = T^2 (\sigma_R^2/n + \sigma_S^2), \quad (6)$$

where $\sigma_R^2 (\sigma_S^2)$ is the sum of all random (systematic) error variances and n is the number of items in the strata. Or, more correctly,

$$\sigma_T^2 = T^2 (\sigma_R^2/n + \sigma_S^2) + (n-1)(S_T)^2 (\sigma_R)^2, \quad (7)$$

where

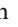

$$S_T^2 = \sum_{i=1}^n (T_i - \bar{T})^2 / (n-1).$$

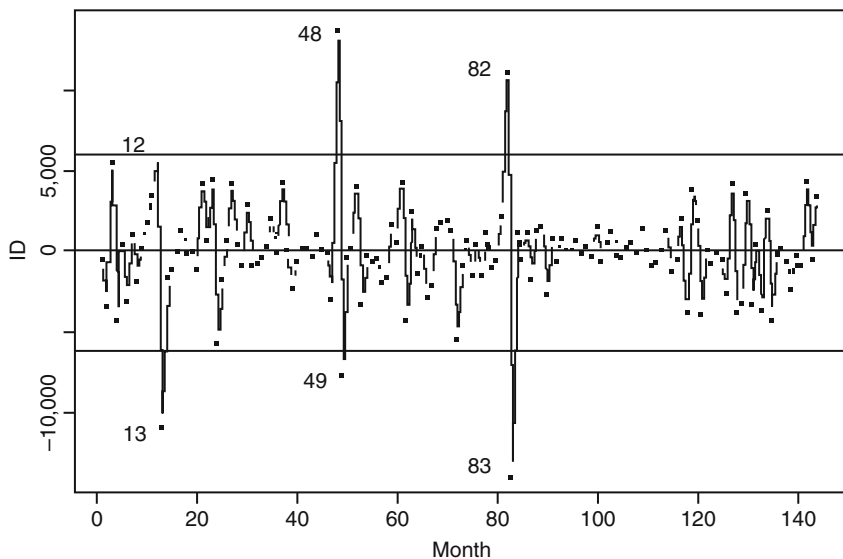
Equation (7) differs from (6) only in the term $\sigma_R^2 = \sum_{i=1}^n (T_i - \bar{T})^2$, which is assumed to be zero in (6) “stream-average” assumption. Also, if there are recalibrations of all measurements on the same schedule (unlikely, but used for illustration here), with a total of n_{cal} recalibrations, then (6) is modified as,


$$\sigma_T^2 = T^2 (\sigma_R^2/n + \sigma_S^2/n_{\text{cal}}), \quad (8)$$

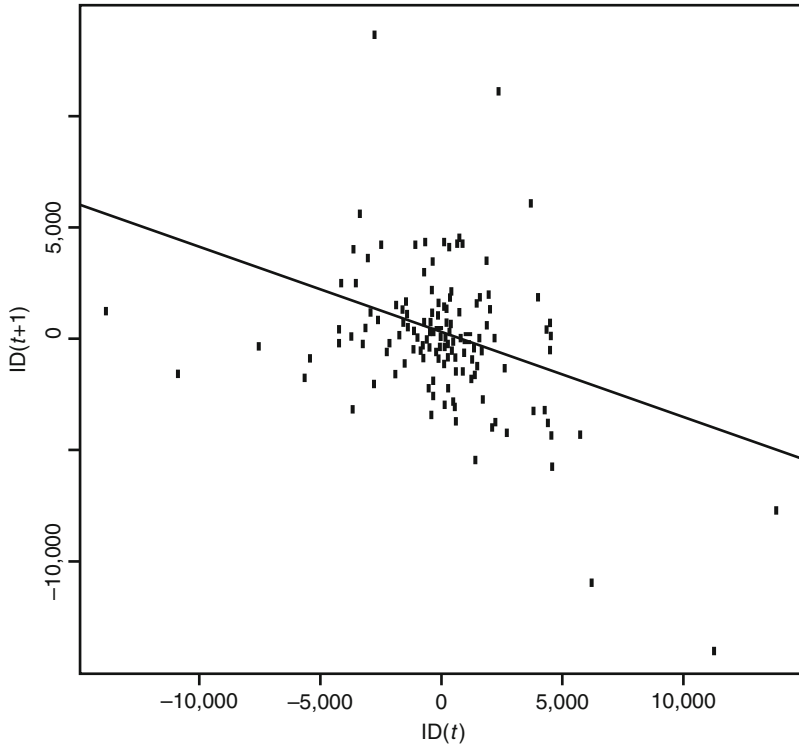
where again we use the stream average assumption. Generally, instruments will be recalibrated on different schedules, so no simple formulas are available. However, it is often useful to bind the correct solution by assuming two extreme cases: recalibrate each instrument after each measurement (effectively converting all errors to random errors) or never recalibrate. In the simplest case, we apply (6) to each strata. Sometimes we must also allow for nonzero covariance among terms in BI, EI, and R and among terms in EI and S or R and S (Burr et al. 1997).

2.8.4 Sequential or Trend Testing

In  Fig. 43, apparent losses on periods 12, 48, and 82 are followed by apparent gains in successive periods. Even if the three pairs of large values are removed, a large negative correlation remains between successive IDs  Fig. 44). This is consistent with a gaseous diffusion facility where large SNM (uranium, in this case) inventories are present, where a large inventory loss (or gain) for period “1” is followed by a large inventory gain (or loss) for period “2,” if there are no actual losses. Therefore, the inventory measurement error is a large contributor to σ_{ID} and leads to negative serial correlation.



 Figure 43
Monthly IDs



■ Figure 44

Same as  Fig. 43 except monthly IDs are plotted as $ID(t + 1)$ versus $ID(t)$

A typical performance measure for the NMA system of a declared facility is the magnitude of σ_{ID} . Note that because throughput usually increases for longer balance periods, a facility often can use more frequent balance closures (such as weekly rather than monthly) to reduce σ_{ID} . However, this will not improve the detection of protracted loss, and because facilities must monitor for abrupt and protracted loss, either sequential testing or at least monitoring IDs for trends is often used (Burr et al. 2003a, b).

Sequential tests include those for abrupt and protracted loss, and the best sequential test depends on the exact loss scenario. Therefore, in practice it is common to use a sequential test that performs well (although perhaps not as well as the best test for the given scenario) for a wide range of scenarios.

A large abrupt loss leads to a single large ID, and a large protracted loss leads to multiple large IDs. First, it is assumed that the random vector of IDs observed through the n th period $x = \{x_1, x_2, \dots, x_n\}$ is approximately normally distributed with mean μ_n and $n \times n$ covariance matrix Σ_{ID} . If no material loss occurs, then $\mu_n = 0$. The covariance matrix, Σ_{ID} , contains the variances of each ID along the diagonal, and the off-diagonal entries are the covariances.

We are concerned with tests for the null hypothesis $NH: \mu_n = 0$ versus an alternative hypothesis: $AH: \mu \neq 0$ with $\sum_{i=1}^n \mu_i > 0$.

The best test (the most power to detect loss for a given false alarm rate, in the sense of the Neyman Pearson lemma), depends on the exact form of the alternative hypothesis. We cannot

assume to know the exact form of the alternative hypothesis, or a test would be unnecessary (Avenhaus and Jaech 1981). Therefore, many tests have been proposed, with each test designed to do well for certain forms of the alternative hypothesis. Many tests are assembled to study their performance over a range of loss scenarios and covariance matrices. In practice, a facility would implement one or a few of these tests, depending on individual circumstances. If the false-alarm probability for any one test is denoted α , then α is the probability that the test alarms one or more times during the n balance periods when the null hypothesis of zero loss is true.

2.8.5 ID Test

The ID test is the same as a one-at-a-time Shewhart test, except that a serial correlation exists among successive IDs (Avenhaus and Jaech, 1981; Burr et al. 1995).

This test alarms if $x_i \geq h_i \sqrt{\sigma_i}$ for at least one i in $1, 2, \dots, n$, where $h = \{h_1, h_2, \dots, h_n\}$ is selected so that,

$$P(x_i \geq h_i \sqrt{\sigma_i}) \leq \alpha \quad \text{for at least one } i \text{ in } 1, 2, \dots, n.$$

Many methods can be used to select h . One method is to fix $h_i = h$ for all i and select this threshold via simulation. Analytical methods are also available but are complicated to compute because Σ_{ID} is not a diagonal matrix in general. Until Σ_{ID} is known, which in practice does not occur until the entire MUF (MUF is another name for the ID) sequence is observed, it is impossible to determine h to achieve the overall false-alarm rate of α .

2.8.6 SITMUF Test

The SITMUF test is the standardized, independently transformed MUF test (Picard 1987; Burr et al. 1995). This test is based on the unique linear transform of x to y that preserves the time ordering implied in x , and with the components of the transformed y being independent, approximately normally distributed random variables with variance 1.

To transform the original MUF sequence x to an independent sequence $y = \{y_1, y_2, \dots, y_n\}$, a well-known linear algebra method (Cholesky decomposition) is used. We assume that the measurement error covariance matrix of x , Σ , is estimated using variance propagation of all key measurements.

It is helpful to consider the y sequence as arising from calculating $y_t = x_t - E(x_t | x_{t-1}, \dots, x_1)$, where $E(x_t | x_{t-1}, \dots, x_1)$ is the expected (i.e., average) value of x_t given all previous x values, and then standardizing so that the variance, $\sigma_{y_t}^2 = 1$ for all balance periods t . The transformed vector, y , has mean μ_y that depends on the mean μ_n of x . Under the NH, $\mu_y = \mathbf{0}$. Under the AH, $\mu_y \neq \mathbf{0}$. The test alarms if $y_i \geq h_i$ for at least one i in $1, 2, \dots, n$, where $h = \{h_1, h_2, \dots, h_n\}$ is selected so that $P(y_i \geq h_i \text{ for at least one } i \text{ in } 1, 2, \dots, n) \leq \alpha$ for at least one i in $1, 2, \dots, n$ when $\mu_n = \mathbf{0}$.

Because the y_i are mutually independent, we have $h = z(1 - \alpha)^{1/n}$, where $h = z(1 - \alpha)^{1/n}$ is the $(1 - \alpha)$ quantile of the standard normal distribution. To explicitly show the time-order interpretation of the transformed vector, y , the transformation of the component x_i to y_i is written as $y_t = (x_t - E(x_t | x_{t-1}, \dots, x_1)) / \bar{\sigma}_i = (x_t - \sigma_{i-1}^T \Sigma_{i-1}^{-1} x_{i-1}) / \bar{\sigma}_i$, where $\bar{\sigma}_i = \sigma_i$, and where

we decompose Σ_i as

$$\Sigma_i = \begin{pmatrix} \Sigma_{i-1} \sigma_{i-1} \\ \sigma_{i-1}^T \sigma_{i,i} \end{pmatrix}.$$

These two expressions for y_t arise from a standard result for the multivariate normal distribution. The $\mathbf{y} = \{y_1, y_2, \dots, y_n\}$ sequence is referred to as the standard innovation sequence or the MUF residuals, and testing for loss in this sequence is the same as testing for loss in a sequence of independent normal random variables having mean zero and variance 1. However, because of the transformation from \mathbf{x} to \mathbf{y} , any true loss will also be transformed.

Picard (1987) has shown that a numerically stable and convenient way to calculate the SITMUF sequence from the MUF sequence is to apply the Cholesky decomposition of Σ as follows. For $\Sigma = \mathbf{C}\mathbf{C}^T$, where $\mathbf{C} = c_{ij}$ is the lower-triangular Cholesky factor, it can be shown that $\mathbf{y} = \mathbf{C}^{-1}\mathbf{x}$. The Cholesky decomposition is available in many standard linear algebra libraries, such as LinPack.

Other common tests in safeguards that consider more than one period at a time include cumulative MUF (CUMUF) and GEMUF (a likelihood ratio that is equivalent to the Mahalanobis distance from $\mathbf{0}$ at each time period).

Page's Test Applied to the SITMUF Sequence

An effective sequential test that is often used in nuclear safeguards and elsewhere is Page's test applied to the SITMUF sequence, y (Picard 1987; Burr et al. 1995). Picard (1987) examined other sequential tests and found that Page's test applied to the SITMUF sequence is competitive for a wide range of diversion scenarios. Other safeguards studies also evaluated sequential tests for safeguards and for anomaly detection in time series, such as a sequence of MUF values (Speed and Culpin 1986).

Page's test can be applied to any sequence, but its properties (e.g., average run length) are most easily studied if the sequence is independent. It is therefore common to apply Page's test to the SITMUF sequence. Page's test is similar to the CUMUF test but restarts the sum at 0 if the sum is negative. The motive for this restart mechanism is to achieve a compromise between the MUF statistic and the CUMUF statistic. Page's statistic applied to the SITMUF sequence, y , is defined as,

$$P_i(\mathbf{y}) = \text{maximum}(P_{i-1}(\mathbf{y}) + y_i - k, 0).$$

The test alarms if $P_i(\mathbf{y}) \geq h_i$ for some $i = 1, 2, \dots, n$, where the h_i are selected to give the desired false-alarm probability, α . The parameter k is a control parameter intended to give the user some control over the size loss that the test is well suited to detect. Generally, smaller values of k are best for detecting small protracted losses, and larger values of k are best for detecting abrupt losses. If we specify that we want good detection probability for a loss of 1σ , then $k = \sigma/2$ should be chosen. Because the y sequence is standardized to zero mean and variance is equal to 1, we choose $k = 1/2$.

2.8.7 Verifying Declarations

Verification measurements of items that are randomly selected from various strata (usually available inventory) at the time of physical inventory (PI) are compared to their book values. In

a processing area that measures each input “batch” and each output “batch,” there could be snapshots in time when the in-process batch is difficult to measure. Assume that we have input items that will change material form while in process, possibly distributing some SNM in glove boxes, pipes, furnaces, uncalibrated tanks, etc. In situations with non-negligible amounts of SNM in difficult-to-measure forms (“holdup”), “data-driven” rules could determine when a process area cleanout is required during PI.

“Data-driven” rules to determine when a process cleanout and PI are required include (1) σ_{CID} increases to its allowed upper limit (currently 2% of cumulative throughput since the previous cleanout); (2) the ID exceeds two or three times σ_{CID} ; (3) the ID exceeds (by a negotiated amount) what can be expected to be recovered from process cleanout; and (4) it has been more than a negotiated time (e.g., 5 years) since the previous cleanout.

Generally, facilities fall into two groups: (1) facilities that rely on activities during PI to get material into measurable form and (2) facilities that evaluate IDs in NRTA. Those of Type 1 probably need to continue to do periodic PIs and the associated verification or confirmation measurements of statistical samples of items in various strata. The LANL Plutonium Facility is of Type 2, provided in some cases that we assume that material control is adequate to allow certain shortcuts in assay methods. For example, the input material to one process is plutonium metal. This metal is weighed, and the weight is multiplied by a historical plutonium purity factor to estimate the plutonium mass. Strictly speaking, this is not a safeguards measurement because the plutonium is not directly measured (but a gross attribute gamma measurement is used to confirm the presence of plutonium). If a credible substitution scenario exists that material control procedures failed to detect, the input would be overestimated. Fortunately, the plutonium in the final product is assayed, so there is a loss detection capability. We believe it is acceptable to treat the input plutonium measurement as though it were a true plutonium assay, compare it with the assay of the plutonium output, and track the ID of each batch as well as the CID. And generally, many facilities could be granted certain shortcuts in assay methods, provided that material control procedures were adequate. When feasible, it is clearly preferred to have complete assay methods for all SNM streams.

In summary, for facilities that do batch tracking or some type of NRTA, it is possible to argue that the PI is required only when a “data-driven” rule as described comes into effect (Burr et al. 2001).

2.8.8 Other Purposes of the PI

Because it is desirable to reduce the PI frequency when feasible, it is important to recognize all of the purposes of the PI under current DOE practices. The purposes of the PI are as follows: for some facilities, the PI is the mechanism that allows IDs to be computed; and for all facilities, the PI provides a convenient time for auditors to ensure that the accounting system captures the true picture of SNM in the facility (the audit role to detect data falsification).

Suppose we measure all inputs and outputs for the MBA and do not rely on the PI to compute IDs. How will auditors know that the accounting system captures the true picture of SNM in the facility? In the case of international safeguards as performed by the IAEA, the effort to detect or deter data falsification is substantial because the IAEA must protect against the entire facility or state falsifying data. Generally, the threat of widespread data falsification is thought to be less in the context of domestic safeguards. Nevertheless, the MC&A approaches (such as the “difference statistic” D , which measures the average difference between operator

and inspector measurements) that have been in use for many years by the IAEA do provide a logical framework for evaluating verification measurements.

This chapter focuses on domestic safeguards; therefore, verifying facility declarations is not typically as high a priority as it is in international safeguards. Nevertheless, modern domestic safeguards approaches recognize that if IDs are evaluated frequently, the real goal of the PI is not to check for loss but to audit the facility's accounting records for accuracy. Therefore, verification measurements to verify book values of SNM items are required in domestic safeguards, much in the same way that the IAEA's difference statistic is used in international safeguards.

The IAEA's difference statistic D for a given stratum (e.g., inputs) is defined as the average difference between operator (o) and inspector (i) measurements for n items, multiplied by the number of items in the strata, N . That is,

$$D = N \sum_{i=1}^n (o_i - i_i) / n.$$

The IAEA's estimate of the ID is the operator's ID minus D . For example, consider a simple case with one input (x_1) and one output (x_2) measurement by the operator that are both verified by the IAEA (y_1 and y_2 , respectively). Then $ID - D = (x_1 - x_2) - \{(x_1 - y_1) + (x_2 - y_2)\} = (y_1 - y_2)$, which is the IAEA's ID. Usually, the IAEA or the domestic safeguards auditor verifies a small random sample from some or all strata (inputs, outputs, and inventory). In the case of the IAEA, the average difference in each strata is multiplied by Picard (1988) provides variance calculations (and the IAEA maintains several technical manuals regarding D) for several situations to estimate σ_D^2 and $\sigma_{ID-D}^2 = \sigma_D^2 - \sigma_{ID}^2$ (not obvious but true).

2.8.9 Sampling

Statistical sampling is used in several ways in safeguards. One of the most commonly used is attributes sampling, in which each measured item is either acceptable or not acceptable. Typically, in attributes sampling, a random sample n containers of SNM from a population of N containers is selected, and the population, N , is unacceptable if one of more defects is found in a sample of size n . This process is called "zero-acceptance" sampling, which refers to the fact that the only "acceptable" number of defects in the sample is zero.

The usual zero-acceptance sampling procedure is to specify the minimal detectable percent defective (p) and the detection probability ($1 - \beta$) (confidence level), then calculate sample size n and randomly select n items. Perform attributes tests on each selected item. The required sample size is approximated by: $n = N(1 - \beta/pN) = N(1 - \beta/D)$, where $D = pN =$ the minimal number of detectable defects.

Often, container tags and seals in a C/S program can reduce the required number of samples (Olinger et al. 2002). Properly sealed items can either be simply omitted from the list of possible items to measure, or inspection of the tag and seal constitutes a "measurement."

2.8.10 Difficulties with ID Evaluation

Issues that complicate ID evaluation include (1) the impact of holdup on σ_{ID} ; (2) serial correlation in successive IDs; (3) poorly characterized measurement quality leading to poor estimates

of σ_{ID} , and (4) time delays in measurement results. Issue 2 was addressed in the section on sequential testing. Issue 3 can be addressed by using a measurement control program that is designed to reflect accurately how measurements are actually performed. An example of Issue 4 is destructive analysis (DA) elsewhere, destructive assay of grab samples required to assay plutonium. Often, many days are required for DA lab results, so the ID cannot be computed in a timely manner, perhaps not until many days after a balance period closure. Typically, estimated values based on previous or target concentration values are allowed, but note that this introduces vulnerability unless plutonium presence is at least confirmed using rapid, low-accuracy confirmatory measurements. Generally, real facilities face processing challenges, and the impact of safeguards to operations needs to be as minor as possible. Ideally, safeguards measures are not viewed as pure overhead but can add value by forcing the operator thoroughly to understand and control the process.

We now consider Issue 1 by evaluating the impact of changing material holdup (poorly measured or unmeasured inventory) on ID evaluation. Changing holdup from period to period leads to larger-than-POV-based estimates of σ_{ID} .

Let $\Delta H = \text{Holdup}_i - \text{Holdup}_{i+1}$ be the change in holdup from balance period i to $i + 1$. The key point is that if holdup is changing (ΔH is nonzero), then instead of estimating the true loss, the ID estimates ΔH . Note that because of measurement error, the IDs vary randomly around ΔH . This error adds uncertainty to the ID equation that must be considered but is often difficult to quantify. Fortunately, NDA measurements are often very effective at estimating changes in holdup and sometimes effective in estimating holdup itself; thus, NDA measurements play a key role in holdup and ID evaluation.

2.8.11 Solution Monitoring

Solution monitoring (SM) is a form of process monitoring (see [Sect. 2.5](#)) that can be considered to provide a C/S capability. Experience to date has shown that SM is a challenging but useful safeguards measure that contributes to both NMA and C/S. Part of the challenge involves choosing effective evaluations of SM data that avoid data indigestion, enable anomaly detection and/or resolution, and do not burden the operator or the inspector with too many investigations.

Potential benefits of SM include improved abrupt loss detection while controlling for multiple tests, anomaly resolution, measurement error model validation, and data authentication. Data authentication results from the many internal consistency checks that arise when relating level, density, and temperature readings; these checks make it very difficult to alter data without being detected.

SM is the nearly continuous monitoring of solutions in all key process tanks. Typically, the level (L) and density (D) of the solution in a tank is obtained by measuring the differences in pressures that are required to bubble air through dip tubes located at various points in the tank. Temperature (T) is obtained via thermocouples. The (L, D, T) data are collected frequently, perhaps every few seconds or even less. At this stage, the data can be analyzed to check their validity, filtered, and perhaps compressed before they are uploaded to some form of real-time database. Various data storage and/or change-detection rules determine how frequently these measurements are archived (Miller and Howell 1999). The various time histories are then combined with tank calibrations to estimate their associated volume and mass histories. All of these histories can then be evaluated by so-called solution monitoring evaluation systems.

Burr et al. (1997) considered the effect of analyzing frequent IDs over small MBAs (individual tanks in this case) and concluded that in the worst-case protracted diversion scenario, less-frequent IDs over a single MBA, actually lead to higher detection probability. The proof used the Neyman Pearson lemma from classical statistics and assumed that the diversion was optimally (from the diverter's view) allocated. This worst-case loss vector is proportional to the sum of the rows of the variance-covariance matrix Σ_{ID} .

SM involves tanks and frequent balance closures (each transfer and wait mode in the example that follows). If the worst-case diversion occurred, it is straightforward to prove that the optimal strategy is to compare the total input to tank 1 with the total output from tank 15. This would be classical ID accounting, not SM as we have defined it. However, frequent balance closures around each transfer and wait mode will have very high detection probability against abrupt loss and nearly as high of a detection probability against the worst-case loss as an annual ID comparing tank 1 input with tank 15 output.

SM cannot improve protracted loss detection against this worst-case loss vector; however, it dramatically improves loss detection against other protracted loss vectors and against any abrupt loss (Burr et al. 2003a, b).

In addition, the bias corrections that become available via SM data could possibly reduce the volume measurement error, thereby leading to improved loss detection against even the worst-case loss vector. Shipments and receipts between tanks will have many paired comparisons; each of these should agree with the propagated total measurement error, or the error models must be refined.

Any statistically detectable diversion would have to be concealed by replacing the lost mass with a proper density solution. The adversary would have to work hard to conceal the diversion (and would probably be discovered at the time that plutonium was measured offline because of out-of-specification chemical species). The same type of calculations would apply if we use an in-tank plutonium concentration measurement, in which case the adversary would have no way to conceal a statistically detectable diversion.

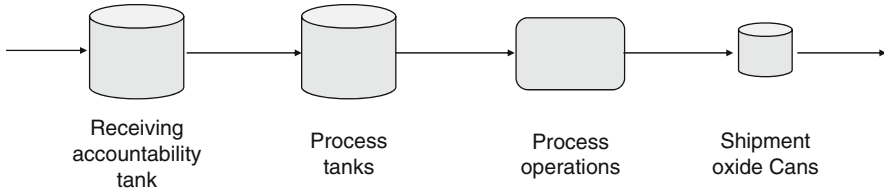
2.8.12 Conclusions

This overview of statistical methods for nonproliferation at declared facilities included (1) POV of algebraic combinations such as products and sums of random variables, such as $\text{mass(uranium)} = \Sigma (\text{volume} \times \text{concentration})$; (2) measurement error modeling; (3) sequential testing to support NRTA; (4) specialty topics such as holdup and NDA of heterogeneous material; and (5) other specialty topics such as process and solution monitoring.

At declared facilities, the key statistical concept is variability and the main tool for ID evaluation is σ_{ID} . Statistical methods are used to estimate measurement uncertainties of individual assay methods and to combine these via the ID equation to estimate σ_{ID} . A numerical example is given in [▶ Sect. 2.9](#). In the broader nonproliferation context, monitoring for undeclared activities involves many statistical issues.

2.9 Accountancy for Abrupt Diversion

An example is given of validating a safeguards design for detection of abrupt diversion, based on a simplified PUREX-type MBA as shown in [▶ Fig. 45](#). The objective here is to solve



■ **Figure 45**
Example reprocessing material balance area (MBA)

for the inventory period at which the σ_{ID} equals the IAEA goal for the interim inventory. Greater inventory periods will then exceed the IAEA goal. A simplified statistical approach is used.

Sigma for the inventory difference (σ_{ID}), or in other words the overall measurement error at one standard deviation, is derived from the material balance of (9) to obtain (10), where t_0 is beginning time for the inventory period and t_{inv} the end.

$$M_{\text{inventory difference}} = M_{\text{receipts}} + (M_{\text{process}, t_0} - M_{\text{process}, t_{inv}}) - M_{\text{shipped}}, \quad (9)$$

$$\sigma_{ID}^2 = \sigma_{\text{receipts}}^2 + \sigma_{\text{process}, t_0}^2 + \sigma_{\text{process}, t_{inv}}^2 + \sigma_{\text{shipped}}^2. \quad (10)$$

If an approximation is made that the mass of each receipt measurement is equal, the mass of each shipment measurement is equal, and the mass of similar process measurements is equal, then (11) and (12) can be used to represent random (σ_r) and systematic errors (σ_s). As shown in (11) and (12), “ M ” represents the total mass measured during the inventory period, “ n ” the number of measurements made during the inventory period, and “ ε ” the percent or fractional measurement error at one standard deviation.

$$\sigma_r^2 = \sum_{i=1}^{n_r} \left(\frac{M}{n_r} \varepsilon_{r,i} \right)^2,$$

$$\varepsilon_1 = \varepsilon_2 = \dots = \varepsilon_n,$$

$$\sigma_r^2 = \frac{1}{n_r} (M \varepsilon_r)^2, \quad (11)$$

$$\sigma_s = \sum_{i=1}^{n_s} \frac{M}{n_s} \varepsilon_{s,i},$$

$$\sigma_s = M \varepsilon_s. \quad (12)$$

If it is also assumed that the mass of process holdup at the beginning of the inventory period t_0 is approximately equal to the end of the inventory period t_{inv} , then (10) through (12) can be combined to yield (13). This approximation represents steady-state operation. As shown in (13), “ x ” represents the fraction of process holdup in tanks, $(1 - x)$ the fraction in “other” process

equipment, such as solvent extraction equipment, precipitation equipment, etc.

$$M_{\text{process}, t_0} \approx M_{\text{process}, t_{\text{inv}}},$$

$$\begin{aligned} \sigma_{\text{ID}}^2 = & M_{\text{receipts}}^2 \left(\frac{\varepsilon_{r,\text{receipts}}^2}{n_{r,\text{receipts}}} + \varepsilon_{s,\text{receipts}}^2 \right) \\ & + 2M_{\text{process}}^2 \left[x^2 \left(\frac{\varepsilon_{r,\text{process,tanks}}^2}{n_{r,\text{process,tanks}}} \right) + (1-x)^2 \left(\frac{\varepsilon_{r,\text{process,other}}^2}{n_{r,\text{process,other}}} \right) + \varepsilon_{s,\text{process}}^2 \right] \\ & + M_{\text{shipped}}^2 \left(\frac{\varepsilon_{r,\text{shipped}}^2}{n_{r,\text{shipped}}} + \varepsilon_{s,\text{shipped}}^2 \right). \end{aligned} \quad (13)$$

If it is further assumed that the mass of receipts is approximately equal to that of shipments, then (13) can be further simplified as (14). Once again, this approximation represents steady-state operation.

$$M_{\text{receipts}} \approx M_{\text{shipped}},$$

$$\begin{aligned} \sigma_{\text{ID}}^2 = & M_{\text{receipts}}^2 \left[\left(\frac{\varepsilon_{r,\text{receipt}}^2}{n_{r,\text{receipt}}} + \varepsilon_{s,\text{receipt}}^2 \right) \right] + \left(\frac{\varepsilon_{r,\text{shipped}}^2}{n_{r,\text{shipped}}} + \varepsilon_{s,\text{shipped}}^2 \right) \\ & + 2M_{\text{process}}^2 \left[x^2 \left(\frac{\varepsilon_{r,\text{process,tanks}}^2}{n_{r,\text{process,tanks}}} \right) + (1-x)^2 \left(\frac{\varepsilon_{r,\text{process,other}}^2}{n_{r,\text{process,other}}} \right) + \varepsilon_{s,\text{process}}^2 \right]. \end{aligned} \quad (14)$$

Receipts, process and product measurements each consist of a bulk and concentration measurement. In the case of the tanks, bulk measurement consists of tank volume. In the case of oxides, bulk measurement consists of mass.

$$\sigma_{\text{measurement}}^2 = \sigma_{\text{bulk}}^2 + \sigma_{\text{concentration}}^2,$$

$$\sigma_b = \sigma_{\text{bulk}},$$

$$\sigma_c = \sigma_{\text{concentration}}.$$

Covariance applies to systematic errors for which they approximately cancel when the same or a similar instrument is used. An example of this is concentration measurement for receipts and shipments. The oxide is dissolved and then the plutonium concentration is determined with an instrument similar to that used for the receipt inventory tank. This also applies to the beginning and end process holdup measurements.

$$\sigma_{s,\text{receipts},c} = 0,$$

$$\sigma_{s,\text{receipts},c} = 0,$$

$$\sigma_{s,\text{process}} = 0.$$

Equation (15) reflects the incorporation of bulk and concentration measurement error, plus the elimination of systematic error for receipt and shipment concentration, and the elimination of

systematic error for all process holdup measurements.

$$\begin{aligned} \sigma_{ID}^2 = & M_{\text{receipts}}^2 \left[\left(\frac{1}{n_{r,\text{receipts}}} \right) (\varepsilon_{r,\text{receipts},b}^2 + \varepsilon_{r,\text{receipts},c}^2) + \varepsilon_{s,\text{receipts},b}^2 \right] \\ & + M_{\text{receipts}}^2 \left[\left(\frac{1}{n_{r,\text{shipped}}} \right) (\varepsilon_{r,\text{shipped},b}^2 + \varepsilon_{r,\text{shipped},c}^2) + \varepsilon_{s,\text{shipped},b}^2 \right] \\ & + 2M_{\text{process}}^2 \left[x^2 \left(\frac{\varepsilon_{r,\text{process,tanks}}^2}{n_{r,\text{process,tanks}}} \right) + (1-x)^2 \left(\frac{\varepsilon_{r,\text{process,other}}^2}{n_{r,\text{process,other}}} \right) \right]. \end{aligned} \quad (15)$$

As previously mentioned, the objective for this example is to solve for the inventory period at which the σ_{ID} equals the IAEA goal for interim inventory. For this reasons, the number of measurements are expressed in terms of the inventory period, t_{inv} .

$$\begin{aligned} n_{r,\text{receipts}} &= \left(\frac{M_{\text{receipts},1 \text{ year}}}{t_{1 \text{ year}}} \right) \left(\frac{t_{\text{inv}}}{M_{\text{receipts},\text{inv}}} \right), \\ n_{r,\text{shipped}} &= \left(\frac{M_{\text{shipped},1 \text{ year}}}{t_{1 \text{ year}}} \right) \left(\frac{t_{\text{inv}}}{M_{\text{shipped},\text{inv}}} \right) \approx \left(\frac{M_{\text{receipts},1 \text{ year}}}{t_{1 \text{ year}}} \right) \left(\frac{t_{\text{inv}}}{M_{\text{shipped},\text{inv}}} \right), \\ M_{\text{receipts}} &= \left(\frac{M_{\text{receipts},1 \text{ year}}}{t_{1 \text{ year}}} \right) t_{\text{inv}}. \end{aligned}$$

Based on an 800-MTHM/year reprocessing facility (1% plutonium in spent fuel), operation of 250-days/year, with a process holdup equal to 10% of the annual throughput, (16) is produced from (15). The number of receipt measurements is based on 55 kg-Pu/measurement (inventory tank), and that for shipment is based on 5 kg-Pu/measurement (product can). The number of tanks within the process is assumed to be eight of equal inventory, and unique pieces of process equipment are six of equal inventory. These numbers are oversimplifications for the sake of example.

$$M_{\text{receipts},1 \text{ year}} \approx M_{\text{shipped},1 \text{ year}} \approx \left(\frac{0.01 \text{ MT-Pu}}{\text{MTHM}} \right) \left(\frac{1,000 \text{ kg}}{\text{MT}} \right) \left(\frac{800 \text{ MTHM}}{\text{year}} \right),$$

$$t_{1 \text{ year}} = 250 \text{ days/year},$$

$$M_{\text{receipts},\text{inv}} \approx 55 \text{ kg Pu},$$

$$M_{\text{shipped},\text{inv}} \approx 5 \text{ kg Pu},$$

$$n_{r,\text{process,tanks}} = 4,$$

$$n_{r,\text{process,other}} = 3,$$

$$M_{\text{process}} = 0.1(M_{\text{receipts},1 \text{ year}}),$$

$$x = 0.9,$$

$$n_{r,\text{receipts}} = \frac{8,000 \text{ kg-Pu/year}}{250 \text{ day/year}} \left(\frac{t_{\text{inv}}}{55 \text{ kg Pu}} \right) = \left(\frac{800}{1,375} \right) t_{\text{inv}},$$

$$\begin{aligned}
 n_{r,\text{shipped}} &= \left(\frac{8,000 \text{ kg-Pu/year}}{250 \text{ day/year}} \right) \left(\frac{t_{\text{inv}}}{5 \text{ kg Pu}} \right) = \left(\frac{800}{125} \right) t_{\text{inv}}, \\
 M_{\text{receipts}} &= \left(\frac{M_{\text{receipts,1 year}}}{t_{1\text{year}}} \right) t_{\text{inv}} = \left(\frac{8,000 \text{ kg-Pu/year}}{250 \text{ day/year}} \right) t_{\text{inv}} = 32t_{\text{inv}}, \\
 M_{\text{process}} &= 0.1(M_{\text{receipts,1 year}}) = 800 \text{ kg-Pu/year}, \\
 \sigma_{\text{ID}}^2 &= (32t_{\text{inv}})^2 \left\{ \left[\frac{1,375}{800} \left(\frac{1}{t_{\text{inv}}} \right) \right] (\varepsilon_{r,\text{receipts},b}^2 + \varepsilon_{r,\text{receipts},c}^2) + \varepsilon_{s,\text{receipts},b}^2 \right\} \\
 &+ (32t_{\text{inv}})^2 \left\{ \left[\frac{125}{800} \left(\frac{1}{t_{\text{inv}}} \right) \right] (\varepsilon_{r,\text{shipped},b}^2 + \varepsilon_{r,\text{shipped},c}^2) + \varepsilon_{s,\text{shipped},b}^2 \right\} \\
 &+ 2(800 \text{ kg Pu})^2 \left[(0.9)^2 \left(\frac{\varepsilon_{r,\text{process,tanks}}^2}{8} \right) + (1 - 0.9)^2 \left(\frac{\varepsilon_{r,\text{processed,other}}^2}{6} \right) \right]. \quad (16)
 \end{aligned}$$

Rearranging (16) to solve for t_{inv} yields,

$$\begin{aligned}
 1,024 (\varepsilon_{s,\text{receipts},b}^2 + \varepsilon_{s,\text{shipped},b}^2) t_{\text{inv}}^2 &+ [1,760 (\varepsilon_{r,\text{receipts},b}^2 + \varepsilon_{r,\text{receipts},c}^2)] t_{\text{inv}} \\
 &+ [160 (\varepsilon_{r,\text{shipped},b}^2 + \varepsilon_{r,\text{shipped},c}^2)] t_{\text{inv}} + 129,600 (\varepsilon_{r,\text{process,tanks}}^2) \\
 &+ 2,133 (\varepsilon_{r,\text{process,other}}^2) - \sigma_{\text{ID}}^2 = 0. \quad (17)
 \end{aligned}$$

And finally, the following typical measurement errors (fractional standard deviation) have been approximated for existing PUREX reprocessing facilities. The measurement errors for process equipment are chosen only for the example, and may not represent actual operations.

$$\begin{aligned}
 \varepsilon_{r,\text{receipts},b} &= 0.003, \\
 \varepsilon_{r,\text{receipts},c} &= 0.003, \\
 \varepsilon_{s,\text{receipts},b} &= 0.003, \\
 \varepsilon_{r,\text{shipped},b} &= 0.0005, \\
 \varepsilon_{r,\text{shipped},c} &= 0.002, \\
 \varepsilon_{s,\text{shipped},b} &= 0.0005, \\
 \varepsilon_{r,\text{process,tank}}^2 &= \varepsilon_{r,\text{process,tank},b}^2 + \varepsilon_{r,\text{process,tank},c}^2 = (1.5\varepsilon_{r,\text{receipts},b})^2 + \varepsilon_{r,\text{receipts},c}^2 = 0.000029, \\
 \varepsilon_{r,\text{process,other}}^2 &= \varepsilon_{r,\text{process,tank},b}^2 + \varepsilon_{r,\text{process,tank},c}^2 = (0.01)^2 + (0.01)^2 = 0.0002.
 \end{aligned}$$

The IAEA goal for interim inventory requires that $3.3 \sigma_{\text{ID}}$ is less than or equal to a significant quantity of SNM (8 kg Pu). The 3.3 factor represents high confidence of detection, and the goal can then be rewritten as:

$$3.3\sigma_{\text{ID}} \leq 8 \text{ kg Pu}. \quad (18)$$

Equation (17) is a quadratic in t_{inv} where the solution is given by (19). There are two roots to the equation, -15 and 12, with 12-days being the “real” solution. Therefore, for this example, to satisfy the IAEA goal, the interim inventory period must be 12-days or less.

$$t_{\text{inv}} = \frac{-b \pm \sqrt{b^2 - 4ac}}{2a} = \frac{-0.032 \pm \sqrt{0.0639}}{0.019} = (-15 \text{ and } 12). \quad (19)$$

Acknowledgments

Special thanks are owed to James Doyle, Kevin Hase, and Lisa Rothrock of Los Alamos National Laboratory for advice related to content and editing of this chapter.

References

- Abhold ME, Baker MC (2000) Design of the improved plutonium canister assay system, LA-UR-00-5383, Naples, FL, October 2000
- Abhold ME, Buck SE, Yokota Y et al. (1998) Integrated monitoring and reviewing systems for the Rokkasho spent fuel receipt and storage facility. In: Proceedings of the 39th INMM, July 1998
- AFCF Development of LWR Fuel Source Terms and Non-Fuel Bearing Component Elemental Weights for 4-Corners Study (2007) Washington Group International, WP-25-001, Rev 1, October 2007
- Aigner H, Binner R, Kuhn, E (2002) International target values 2000 for measurement uncertainties in safeguarding nuclear materials. ESARDA Bull 31:39–68
- Avenhaus R, Jaech J (1981) On subdividing material balances in time and/or space. *J Inst Nucl Mater Manage* 10(3):24–33
- Badaut V, Wallenius M, Mayer K (2006) Investigating the applicability of anions as indicators for verification of consistency of declarations (IAEA-CN-148/174P). In: Addressing Verification Challenges – International Safeguards Symposium, Vienna, Austria, 16–20 October 2006
- Bathke CG et al (2008a) An assessment of the proliferation resistance of materials in advanced nuclear fuel cycles. In: Eighth international conference on facility operations-safeguards interface, Portland Oregon, April 2008
- Bathke CG et al (2008b) Further assessments of the attractiveness of materials in advanced nuclear fuel cycles from a safeguards perspective. In: Tenth information exchange meeting on actinide and fission product partitioning and transmutation, Mito, Japan, October 2008
- Bathke CG et al (2009a) An assessment of the attractiveness of material associated with a MOX fuel cycle from a safeguards perspective. In: Proceedings of INMM 50th Annual Meeting, Tucson, AZ
- Bathke CG et al (2009b) The attractiveness of materials in advanced fuel cycles for various proliferation and theft scenarios. In: Proceedings of Global 2009, Paris, FR.
- Baude S, Chiappini R (2001) Isotopic measurements on micrometric particles: the French experience to detect fissile material – international safeguards symposium, Vienna, Austria, 29 October – 2 November 2001. IAEA-SM-367/10/05
- Binner R, Howell J, Janssens-Maenhout G, Sellinschegg WD, Zhao K (2008) Practical issues relating to tank volume determination. *Ind Eng Chem Res* 47:1533–1545
- Bokhari F (2005) Pakistan may hand over nuclear centrifuges. *Financial Times*, 25 March 2005; and Centrifuge parts sent to IAEA, Dawn (Karachi), 27 May 2005
- Bowen W, Bennett C (1988) Statistical methods for nuclear materials management. US Nuclear Regulatory Commission, NUREG/CR-4604
- Burr T, Coulter C, Hakkila E, Kadokura H, Ai I, Fujimaki K (1995) Statistical methods for detecting loss of materials using near-real time accounting data. In: Proceedings of the 36th INMM meeting, Naples, FL
- Burr T, Coulter A, Prommel J (1997) VPSim: variance propagation by simulation, LA-13382-MS. In: Proceedings issue, 38th INMM
- Burr T, Strittmatter R, Scott B, Murdock C, Schanfein M (2001) Evaluation of a continuous physical inventory approach for the Los Alamos plutonium facility, LAUR01-3542. In: Nuclear material management proceedings
- Burr T, Hemphill G, Longmire V, Smith M (2003a) The impact of combining nuclear material categories on uncertainty. *Nucl Inst Meth Phys Res A* 505:707–717
- Burr TL, Coulter CA, Howell J, Wangen L (2003b) Solution monitoring: quantitative and qualitative benefits to nuclear safeguards. *Nucl Sci Technol* 40(4):256–263
- Burr T, Sampson T, Vo D (2005) Statistical evaluation of FRAM γ -ray isotopic analysis data. *Appl Radiat Isot* 62:931–940
- Burr T, Wangen L (1996) Development and evaluation of methods for safeguards use of solution monitoring data, L19-13185-MS (ISPO-389)
- Bush W, af Ekenstam G, Janov J, Kuhn E, Ryjinski M (2001) IAEA experience with environmental sampling at centrifuge enrichment plants in the European Union – international safeguards

- symposium, Vienna, Austria, 29 October – 2 November 2001. IAEA-SM-367/10/04
- Cobb DD, Beyerlein AL, Burkhart LE (1980) In-process inventory estimation for pulsed columns and mixer-settlers. ESARDA Mtg. Edinburgh
- Cobb DD et al (1981) Demonstration of near-real-time accounting: the AGNS 1980 miniruns. JNMM 10(1):34–43
- Dekens JP, Goerten J, Lahogue Y, Wagner G (1995) An integrated safeguards system for large reprocessing plants. In: Fifth international conference on facility operations-safeguards interface, Jackson Hole, WY
- DeMuth SD, Scherer C, Bean R, Therios I, Duran F (2009) Safeguards by design (SBD): safeguards requirements and success criteria. Los Alamos National Laboratory, LA-UR-09-06481, September 2009
- De Ridder P, Binner R, Richet S, Peter N (2004) Tank calibration data evaluation. In: Proceedings of the 44th annual meeting of the INMM
- Dolgov J, Bibilashvili Y, Chorokhov N, Koch L, Schenkel R, Schubert A (1997) Case studies with a relational database system for identification of nuclear material of unknown origin. In: Russian international conference on nuclear material protection, control and accounting, Obninsk, Russia
- Dolgov J, Bibilashvili Y, Chorokhov N, Schubert A, Janssen G, Mayer K, Koch L (1999). In: Proceedings of the 21st ESARDA symposium, Sevilla, Spain, Report EUR 18963 EN
- Ebbinghaues et al (2006a) Proliferation resistance and the attractiveness of nuclear materials: application to the UREX + 1A process flow sheet. Lawrence Livermore National Laboratory, COPJ-2006-0232, 28 March 2006
- Ebbinghaues et al (2006b) Proliferation resistance and the attractiveness of nuclear materials: application to the UREX + 1A process flow sheet. Lawrence Livermore National Laboratory, slides, 30 March 2006
- Ehinger M, Chesnay B, Creusot C, Damico J, Johnson S, Wuester J, Masuda S, Kajii M (2004) Solution monitoring applications for the Rokkasho reprocessing plant. In: Seventh international conference on facility operations-safeguards interface, Charleston, SC
- Esaka F, Watanabe K, Fukuyama H, Onodera T, Esaka K T, Magara M, Sakurai S, Usuda S (2004) Efficient Isotope Ratio Analysis of Uranium Particles in Swipe Samples by Total-Reflection X-ray Fluorescence Spectrometry and Secondary Ion Mass Spectrometry. *Journal of Nuclear Science and Tech.*, Vol. 41, No. 11, p. 1027–1032 (November 2004)
- Esaka F, Esaka KT, Lee CG, Magara M, Sakurai S, Usuda S, Watanabe K (2007) Particle isolation for analysis of uranium minor isotopes in individual particles by secondary ion mass spectrometry *Talanta* 71:1011–1015
- Evaluation Methodology for Proliferation Resistance and Physical Protection of Generation IV Nuclear Energy Systems (2006) Revision 5, Generation IV International Forum Report GIF/PRPPWG/2006/005, November 30. <http://www.gen-4.org/Technology/horizontal/PRPPEM.pdf>
- Fischer U, Wiese HW (1983) Improved and consistent determination of the nuclear inventory of spent PWR fuel on the basis of cell-burnup methods using korigen. KFK-3014, January 1983
- Frigo AA, Wahlquist DR, Willit JL (2003) A conceptual advanced pyroprocess recycle facility. In: Proceedings of the global 2003, American Nuclear Society, New Orleans, LA
- Garcia HE, Yoo TS (2005) Model-based detection of routing events in discrete flow networks. *Automatica* 41:583–594
- Hill RN et al (2002) Multiple tier fuel cycle studies for waste transmutation. In: Proceedings of ICONE 10, Arlington, VA, 14 April 2002
- Hooper R (1997) The system of strengthened safeguards. *IAEA Bull* 39(4):26–29
- Howell J (1994) Model-based fault detection in information poor plants. *Automatica* 30(6):929–943
- Howell J (2009) Towards the re-verification of process tank calibrations. *Trans Inst Measure Control* 31(2), 117–128
- Howell J, Miller E (2001) Evaluation of process information to obtain additional safeguards assurances in reprocessing plants. DTI SRDP-R279
- Howell J, Scothern SJ (1995) Physical-model-based anomaly resolution. In: Fifth international ANS topical conference on facility operations-safeguards interface, Jackson Hole, WY
- Howell J, Scothern SJ (2000) An explicit model-based diagnostic approach in plutonium nitrate tank storage facility. *Control Eng Pract* 8(6): 645–656
- Howell J, Scothern SJ (1998), Assessing Solution Monitoring System Performance Using Simulated Data, UK Department of Trade & Industry report, SRDP-R261.
- IAEA (1972) INFCIRC/153 (Corrected), The structure and content of agreements between the agency and states required in connection with the treaty on the non-proliferation of nuclear weapons, June 1972
- IAEA (1997) INFCIRC/540 (Corrected), Model protocol additional to the agreement(s) between state(s) and the international atomic energy

- agency for the application of safeguards, September 1997
- IAEA Safeguards Glossary (2001) IAEA Safeguards Glossary, 55, 2001 edition
- IAEA (2006) IAEA Annual Report, 2006
- IAEA Nuclear Security Series No. 6 (2007) Combating Illicit trafficking in nuclear and other radioactive materials
- Jaech J (1973) Statistical methods in nuclear materials control. US Atomic Energy Commission, Washington, DC
- Janssens W, Daures P, Mayer K, Cromboom O, Schubert A, Koch L (2001) Assisting Eastern European countries in the setting up a national response to nuclear smuggling (IAEA-CN-86/11). In: Proceedings of the International Conference on Measures to Prevent, Intercept and Respond to Illicit Uses of Nuclear Material and Radioactive Sources, Stockholm, Sweden, 7–11 May 2001
- Janssens-Maenhout G, Dechamp L (2004) Process monitoring appropriate for near-real-time accountancy. JNMM 32(3):10–16
- Johnson SJ (2005) Development of an IAEA safeguards system for RRP. NMCC News
- Johnson S, Avelin-Zadeh R, Pearsall C et al (1997) Development of the safeguards approach for the Rokkasho reprocessing plant. In: IAEA symposium on international safeguards, Vienna
- Keegan E, Richter S, Kelly I, Wong W, Gadd P, Kühn H, Alonso-Munoz A (2008) The provenance of Australian uranium ore concentrates by elemental and isotopic analysis. Appl Geochem 23:765–777
- Kessler G (2007) Plutonium denaturing by ^{238}Pu . Nucl Sci Eng 155:53–72
- Kuhn E (1995) Environmental monitoring for safeguards applications. In: 36th INMM annual meeting proceedings, Palm Desert, CA
- Kuhn E, Fischer D, Ryjinski M (2001) Environmental sampling for IAEA safeguards: a five year review – international safeguards symposium, Vienna, Austria, 29 October – 2 November 2001. IAEA-SM-367/10/01
- Li TK (1996) Near-real-time accounting as a safeguards measure at the rokkasho reprocessing plant. Los Alamos National Laboratory, Los Alamos, NM, NIS-5-96-1
- Lee CG, Iguchi K, Inagawa J, Suzuki D, Esaka F, Magara M, Sakurai S, Watanabe K, Usuda S. (2007) Development in fission track-thermal ionization mass spectrometry for particle analysis of safeguards environmental samples. Journal of Radioanalytical and Nuclear Chemistry, 272, 299–302
- Ludwig SB, Croff AG (2002) ORIGEN2 V2.2 isotope generation and depletion code. Oak Ridge National Laboratory Report CCC-371
- Marks JC (1990) Reactor-grade plutonium's explosive properties. Nuclear Control Institute, August 1990
- Mayer K, Morgenstern A, Wallenius M, Tamborini G, Apostolidis C (2001) Development of analytical methodologies in response to recent challenges. In: Proceedings of the 42nd INMM annual meeting, Indian Wells, CA, 15–19 July 2001
- Mayer K, Wallenius M, Ray I (2005) Nuclear forensics – a methodology providing clues on the origin of illicitly trafficked nuclear materials. Analyst 130: 433–441
- Miller EC, Howell J (1999) Tank measurement data compression for solution monitoring. J Inst Nucl Mater Manage 27(3):25–32
- Morgenstern A, Apostolidis C, Mayer K (2002) Age determination of highly enriched uranium: Separation and analysis of ^{231}Pa . Anal Chem 74:5513–5516
- National Academy Press (2000) Office of International Affairs, The spent-fuel standard for disposition of excess weapon plutonium: application to current DOE options. Washington, DC. <http://www.nap.edu/books/0309073200/html/>
- National Research Council, Office of International Affairs (2000) The spent-fuel standard for disposition of excess weapon plutonium: application to current DOE options, Washington, DC
- Neeb KH (1997) The Radiochemistry of Nuclear Power Plants with Light Water Reactors, Walter de Gruyter, Berlin
- Neuilly M (1999) Modeling and estimation of measurement errors. Lavoisier, Paris
- Nittler LR, Alexander CMO (2003) Automated isotopic measurements of micron-sized dust: application to meteoritic presolar silicon carbide. Geochim Cosmochim Acta 67:4961–4980
- Nuclear Material Control and Accountability (2006) U.S. Department of Energy manual DOE M 470.4-6 Chg 1, August 14
- Nygren U, Ramebäck H, Nilsson C (2007) Age determination of plutonium using inductively coupled plasma mass spectrometry. J Radioanal Nucl Chem 272(1):45–51
- Olinger O, Burr T, Dawson P, Kwei L, Longmire V (2002) Realizing benefits from technology for inventory monitoring. In: Nuclear material management proceedings, Orlando, FL
- Ottmar H (2010) The chemistry of the actinide and transactinide elements, 3rd ed, vol 6, chap 37. In: Morss LR, Edelstein NM, Fuger J (eds) Springer, Dordrecht <http://www.clickindia.com/detail.php?id=3645967>

- Pajo L, Mayer K, Koch L (2000) Application of thermal ionisation mass spectrometry for oxygen isotope ratio measurements in uranium oxide. In: 6th Finnish-Russian Radiochemistry Symposium, Helsinki, Finland, 7–8 November 2000
- Pajo L, Tamborini G, Rasmussen G, Mayer K, Koch L (2001) A novel isotope analysis of oxygen in uranium oxides: Comparison of secondary ion mass spectrometry, glow discharge mass spectrometry and thermal ionization mass spectrometry. *Spectrochim Acta Part B* 56:541–549
- Pellaud B (2002) Proliferation aspects of plutonium recycling. *J Nucl Mater Manage* XXXI(1), pp 30–38
- Picard R (1987) Sequential analysis of materials balances. *J Nucl Mater Manage* 15(2):38–42
- Picard R (1988) Note on the MUF-D statistic. In: ANS topical conference, proceedings third international conference on facility operations-safeguards interface. American Nuclear Society, La Grange Park, IL, pp 414–423
- Proliferation Resistance Fundamentals for Future Nuclear Energy Systems (2002) IAEA, STR-332, December 2002
- Ranebo Y, Hedberg PML, Whitehouse MJ, Ingeneri K, Littman S (2009) Improved isotopic SIMS measurements of uranium particles for nuclear safeguard purposes. *J. Anal. At. Spectrom.*, 2009, 24, 277–287
- Ray ILF, Wiss T, Thiele H (2002) Recent developments and case studies in nuclear forensic science (IAEA-CN-98/2/05). In: International Conference on Advances in Destructive and Non-Destructive Analysis for Environmental Monitoring and Nuclear Forensics, Karlsruhe, Germany, 21–23 October 2002
- Richter S, Alonso A, de Bolle W, Wellum R, Taylor PDP (1999) Isotopic “fingerprints” for natural uranium ore samples. *Int J Mass Spectrom* 193:9–14
- Rosenberg J, Mah RSH, Iordache C (1987) Evaluation of schemes for detecting and identifying gross errors in process data. *Ind Eng Chem Res* 26(3):555–564
- Saito M, Artisyuk V, Takibayev A, Ismailov K, Sagara H (2008) Development of methodology for plutonium categorization (II) – improvement of evaluation function “attractiveness.” *Trans Amer Nucl Soc* 97, pp 669
- Schubert A, Janssen G, Koch L, Peerani P, Bibilashvili Y, Chorokhov N, Dolgov J (1998) A software package for nuclear analysis guidance by a relational database: In: Proceedings of the ANS International Conference on the Physics of Nuclear Science and Technology, New York, 5–8 October 1998
- Scothern S, Howell J (1997) A physical-model-based diagnostic aid for safeguarding nuclear material in a liquor storage facility. *JNMM* 25(4):20–29
- Scothern SJ, Howell J (1998) An automatic diagnostic aid generator. DTI SRDP-R262
- Secker JR et al (2005) Optimum discharge burnup and cycle length for PWRs. *Nucl Tech* 151:109–119
- Simons DS, Gillen G, Zeissler CJ, Fleming RH, McNitt PJ (1998) Automated SIMS for determining Isotopic Distributions in Particle Populations – Secondary ion mass spectrometry SIMS XI. In: Gillen G, Lareau R, Bennet J, Stevie F (eds) Wiley, New York, pp 59–62
- Sirajov B, Wang X (2008) Tank monitoring evaluation system for PCDF. In: Eighth international NAS/INMM conference on facility operations-safeguards interface, Portland, OR
- Smith DK, Kristo MJ, Niemeyer S, Dudder GB (2008) Documentation of a model action plan to deter illicit trafficking. *J Radioanal Nucl Chem* 276(2):415–419
- Speed TP, Culpin D (1986) The role of statistics in nuclear materials accounting: issues and problems, with discussions. *J Roy Stat Soc A* 149 (Part 4):281–313
- Spent Nuclear Fuel Discharges from U.S. Reactors (1994) Energy information administration, SR/CNEAF/96-01, February, 1996
- Stillman JA, Bauer TH, Hill RN, Wigeland RA (2004) Follow-up analysis for the ANTT review. Argonne Report ANL-AFCI-132, September 2004
- Svedkauskaite-LeGore J, Mayer K, Millet S, Nicholl A, Rasmussen G, Baltrunas D (2007) Investigation of the isotopic composition of lead and of trace elements concentrations in natural uranium minerals as a signature in nuclear forensics. *Radiochim Acta* 95:601–605
- Tamborini G, Betti M, Forcina V, Hiernaut T, Giovannone B, Koch L (1998) Application of secondary ion mass spectrometry to the identification of single particles of uranium and their isotopic measurement. *Spectrochimica Acta Part B* 53, (1998) 1289–1302
- Tandon L et al (2008) Nuclear, chemical, and physical characterization of nuclear materials. *J Radioanal Nucl Chem* 276(2):467–473
- Taylor B, Kuyatt C (1994) Guidelines for evaluating and expressing the uncertainty of NIST measurement results. NIST Technical Note 1297
- Varga Z, Surányi G (2007) Production date determination of uranium-oxide materials by inductively coupled plasma mass spectrometry. *Anal Chim Acta* 599:16–23

- Venables W, Ripley B (1999) *Modern applied statistics with splus*, 3rd edn. Springer, New York
- Vogt S, Zahradnik P, Klose D, Swietly H, Bulk (2001) Analysis of environmental swipe samples – international safeguards symposium, Vienna, Austria, 29 October – 2 November 2001. IAEA-SM-IAEA-SM-367/10/06
- Walford FJ, Mills AL, Waterman MJ, Boler SA (1983) Variations in the plutonium inventory of solvent extraction contactors, ESARDA Mtg. Versailles
- Wallenius M, Mayer K (2000) Age determination of plutonium material in nuclear forensics by thermal ionisation mass spectrometry. *Fresenius J Anal Chem* 366:234–238
- Wallenius M, Peerani P, Koch L (2000) Origin determination of plutonium material in nuclear forensics. *J Radioanal Nucl Chem* 246:317–332
- Wallenius M, Tamborini G, Koch L (2001) The “age” of plutonium particles. *Radiochim Acta* 89:55–58
- Wallenius M, Morgenstern A, Apostolidis C, Mayer K (2002a) Determination of the age of highly enriched uranium. *Anal Bioanal Chem* 374:379–384
- Wallenius M, Mayer K, Tamborini G, Nicholl A (2002b) Investigation of correlations in some chemical impurities and isotope ratios for nuclear forensic purposes (IAEA-CN-98/3/05). In: *International Conference on Advances in Destructive and Non-Destructive Analysis for Environmental Monitoring and Nuclear Forensics*, Karlsruhe, Germany, 21–23 October 2002
- Wallenius M et al (2007) Nuclear forensic investigations with a focus on plutonium. *J Alloys Compd* 444–445: 57–62
- Xu Z, Kazimi MS, Driscoll MJ (2005) Impact of high burnup on spent fuel characteristics. *Nucl Sci Eng* 151:261–273
- Yue M, Cheng L, Papazoglou I, Azarm M, Bari R (2005) Calculations of proliferation resistance for generation III nuclear energy systems, *Proceedings of Global 2005*, Tsukubo, Japan, 9–13 October 2005

Websites

www.gen-4.org

www.iaea.org/NewsCenter/Features/RadSources/

[PDF/fact_figures2006.pdf](#)

Index

A

- Aarhus Convention, 3204, 3205
- Abrasive-blasting systems, 3080, 3081
- Abrasive water-jet cutting, 3110, 3138, 3140–3141
- Absolute error (of a measuring instrument), 1938
- Absolute filter, 3080, 3088
- Absolutely constant elementary error, 1930, 1938
- Absolutely constant errors, 1930
- Absolute measurement error, 1927, 1929
- Absorbed dose, 1339–1343, 1345–1347, 1350–1352, 1361, 1369, 1381–1383, 1385, 1431–1433, 1435, 1437
- Absorber control cross, 2068
- Absorber follower, 2270
- Absorber of variable strength, 1683, 1691–1696, 1716
- Absorbers, 545, 546, 548, 549, 627, 2920–2922, 2926
- Absorbing states, 1973
- Absorption cross section, 952–954, 959–961, 966, 972, 989, 990, 1014, 1016, 1019, 1061, 1152, 1162, 1171–1173, 1196, 1197, 1201, 1202, 1210, 1216, 1220
- Absorption resonances, 506, 516
- Accelerated-driven systems (ADS), 1632, 1636, 1653–1658, 1733, 2947, 2949, 2955, 2963, 2964, 2973, 2974
- Accelerators, 4, 6, 11–13, 19, 21, 24, 25, 27–31, 35, 37, 46, 47, 51
 - cost, 2888–2890
 - requirements, 2872
 - targets, 2869, 2872, 2875
- Acceptable risk, 1441
- Acceptance criteria, 3053, 3062–3063, 3178, 3179, 3182, 3197
- Accident analysis, 3042, 3196–3198
- Accountancy, 3458, 3463–3470, 3500, 3509, 3518–3533
- Accounting and finance, 3036, 3054
- Acid gel spraying, 3104
- Acid mixture, 3074, 3093, 3104, 3227
- A-conjugate, 648
- Acoustic modes, 216–218
- Actinide-BTP, 2968
- Actinide carbides, 2945, 2953–2958
- Actinide fluorides, 2946
- Actinides, 2938–2941, 2944–2951, 2953–2970, 2973–2980, 2983–2985, 3059, 3261, 3268, 3269, 3285, 3286, 3306, 3325–3326, 3370–3373, 3399, 3402–3405
- Actinides, major, 3412
- Activated structural materials, 3181
- Activation
 - detectors, 2073, 2135
 - library, 169
 - neutrons, 1327
 - products, 1336, 3012, 3015, 3056–3059, 3068, 3188, 3259, 3261, 3264, 3275, 3323, 3324
 - radioactivation, 3259, 3261, 3264, 3275, 3315, 3323, 3324, 3407
- Acute radiation syndrome, 1430
- Adaptive mesh refinement (AMR), 2043
- Added mass, 1816, 1833, 1840, 1844, 1845, 1852, 1860
 - velocity fluctuation, 1827–1829
- Additional protocol (AP), 3446, 3449, 3453, 3458, 3466–3468, 3501
- Addition theorem, 466, 758, 764
- Adiabatic approximation, 1676–1677, 1682, 1685, 1687
- Adjoint, 1632, 1633, 1641, 1675, 1682, 1723, 1733, 1917, 1954–1994, 2023, 2024, 2027, 2029, 2047
 - angular flux, 485, 493–495, 498, 499
 - boundary conditions, 1961–1963, 1968
 - cross sections, 234
 - flux, 765, 766, 771, 863, 937, 1223, 1225, 1228
 - functions, 1689–1690, 1956, 1962, 1970, 1971, 1976, 1977, 1987, 2023
 - models, 1917
 - multiplication factor, 1225
 - operator, 486, 487, 490, 494, 499
 - problem, 765, 766
 - sensitivity system, 1956–1958, 1962, 1963, 1970, 1976, 1977, 2024
 - transport equation, 430, 485, 490–494, 496–499, 540
- Adjoint sensitivity analysis procedure (ASAP), 1923, 1955–1958, 1960–1963, 1967–1983, 2023, 2047
- Adjunctons, 493, 498
- Admixed moderator, 989, 991
- Advanced boiling water reactor (ABWR), 2057, 2068, 2070
- Advanced fuel performance capability (AFPC), 1511, 1513
- Advanced light water reactor (ALWR), 2188, 2193, 2246
- Advanced power reactor 1400 (APR1400), 2187, 2188, 2201–2230, 2246, 2247
- Advanced recycle reactors (ARR), 1283, 1285–1286, 1309, 1310

- Advanced Simulation and Computing Initiative (ASCI), 1500
- Advection, 3359, 3361–3363, 3365, 3368, 3375, 3395, 3396, 3407
- Advection upstream splitting method (AUSM), 1815, 1816, 1867, 1872, 1875, 1880, 1882, 1884, 1889
- Advisory Committee on Reactor Safeguards, 1760
- AEGIS, 922, 928, 934, 958, 1138, 1152
- Aerosol emission, 3124, 3127, 3130–3132, 3134, 3141
- Aerosols, 3065, 3068, 3122, 3124, 3126, 3127, 3131, 3138, 3141, 3143, 3145–3147, 3174, 3181–3182, 3209, 3211, 3226
- AETNA, 1223
- Ag, 964, 1068
- Age approximation, 507, 512–514, 517, 518
- Age-diffusion equation, 273
- Agency, 3457, 3458, 3462–3464, 3468, 3473, 3476
- Age theory, 266, 272–274
- Age theory for a pulse, 274
- Aggregate, 1396, 1398, 1427
- AIC, 548, 549
- AIC absorber, 2061, 2067, 2082
- Airborne contamination, 3077, 3080–3082, 3085, 3087, 3108, 3111, 3112, 3115, 3119
- Air streams, 3181
- Air ventilation system, 3111
- Al-alloys, 549
- ALARA concept, 2200
- Albedo, 780, 790, 794, 811, 820, 837, 855, 858, 865–867, 869, 1359, 1379, 1400–1407, 1412, 1413, 1417, 1418, 1420–1423
- approximations, 1403–1407
 - boundary condition, 762, 785, 793, 819, 833, 865, 867, 876, 877, 879–881, 883–885, 894
 - concept, 1400, 1412, 1422
- Alcohols, 3101
- Algebraic collapsing acceleration, 853–858
- Alkaline permanganate (AP), 3074, 3092, 3094–3097, 3101–3103, 3151, 3152
- Alloy 690, 2190, 2194
- Alpha-decay damage, 2962, 2982, 2986–2988
- Alpha emission, 1323
- Alpha particle (or alpha radiation, alpha ray), 3272, 3273, 3407, 3408
- Alpha-uranium metal, 2941, 2944
- Alternating direction implicit (ADI), 887
- ²⁴¹Am, 2961
- ²⁴³Am, 2961
- Ambient dose equivalent, 1348, 1352, 1404–1406
- Amdahl's Law, 1476–1477
- American National Standard Nuclear Safety Criteria
- condition I occurrences, 1756
 - condition II occurrences, 1756
 - condition III occurrences, 1756, 1757
 - condition IV occurrences, 1756, 1757
 - design requirements, 1755–1757
 - general design criteria, 1755, 1756
- American Nuclear Society, 1769, 1771, 1783
- American Physical Society, 1767–1768
- Americium, 2938, 2941, 2942, 2959, 2960, 2962
- Ammonium carbonate ((NH₄)₂CO₃), 3095
- Ammonium citrate ((NH₄)₂HC₆H₅O₇), 3074, 3092, 3102, 3151
- Ammonium oxalate (NH₄C₂O₄), 3092
- Amorphization, 563–566, 579–581, 619, 620
- Amorphous, 3311, 3312, 3326, 3407
- Amplified source method (ASM), 2145, 2147–2152
- Amplitude factor, 1680–1682
- Amplitude function, 1680
- AMPX code, 386
- Analytical solution for 2 bands, 403–405
- Analytical solutions, 2043
- Analytic nodal method (ANM), 887, 889, 890, 892–894
- AnC, 2945
- AnC₂, 2945
- An₂C₃, 2945
- AnC_{1-x}, 2945
- Angular current, 754, 755
- Angular dependence, 971, 1036
- Angular derivative, 479
- Angular-direction coordinate system, 772, 774, 777
- Angular distribution, 204, 220, 238–241, 250, 252, 253, 275, 286, 292–294, 296, 300–302, 376–381, 383–387
- Angular fluence, 1320, 1392, 1413, 1414
- Angular flux, 440–445, 453, 457–461, 466–469, 471–473, 476–481, 484–486, 493–495, 498, 499, 504, 506, 524, 530, 535–538, 753, 759, 761–763, 776–778, 792, 796–799
- Angular neutron density, 440–444
- Angular redistribution, 774, 775, 777, 825, 831, 835
- Anharmonicity, 194
- Anisotropic, 557, 562, 574, 579, 613, 627
- scattering, 930, 932, 934, 952, 953, 958, 959, 968, 1034, 1117, 1160
 - sources, 461, 478
- Anisotropy in inelastic scattering, 212, 229, 242
- Annular core, 2732, 2733
- Annular tank, 2259
- ANOVA-like decompositions, 1953
- ANSI/ANS-51.1-1983, 1756
- ANSI N18.2-1973 criteria, 1755, 1756, 1758
- Anthropomorphic phantoms, 1339, 1343, 1349–1352, 1400, 1424
- Anticipated operating occurrence (AOO), 1754, 1758, 1782, 1784
- Anti-correlated, 2033, 2034
- APOLLO, 922, 934, 945, 1035
- APOLLO-2 code, 2064, 2067, 2068, 2088, 2101, 2102
- a posteriori estimation*, 1927, 1934, 1957
- a posteriori probability*, 1996

- Approximated area, 1132, 1133, 1137, 1138
a priori estimation, 1927
a priori probability, 1918, 1996
 Aqueous reprocessing, 2937, 2964–2971
 Arc saw, 3132, 3147, 3149, 3156
 Arnold and Dannels model, 1065, 1066
 Asbestos, 3045, 3108, 3117, 3194, 3211
 Askew cylinderization, 812
 As low as reasonably achievable (ALARA), 3013, 3038, 3049, 3051, 3112, 3215, 3228, 3229
 Assembly, 2896, 2918, 2921–2930, 2948, 2949, 3260, 3261, 3276, 3283, 3323, 3326–3328, 3340, 3341, 3407, 3408, 3411, 3415
 Assembly discontinuity factors, 941
 Assimilation, 1913–2048
 Associated Legendre function, 467, 697–698
 –asymptotic series, 699
 –recursion relations, 700
 –spherical functions integral indices
 –addition theorems, 702
 –first kind, 701
 –first and second kind, 698–699, 702
 –hypergeometric functions, 702
 –Legendre polynomial, 702
 –sectoral harmonics, 701
 –tesseral harmonics, 701
 Asymptotic approximation, 2015
 Asymptotic synthetic acceleration (ASA), 853
 ATLAS, 2225, 2227, 2228
 Atomic Energy Commission, 1743–1744, 1751, 1755, 1760–1763, 1767
 Atomic volume, 551, 552, 562
 Atomization, 2950
 Atoms of nuclide, 288
 At-reactor (AR), 3166, 3167
 Attenuation, 1336, 1338, 1353–1378
 Attenuation factor, 1353, 1359, 1362, 1372–1375, 1381, 1382, 1394, 1416
 Auger electrons, 1328, 1337, 1424
 Augmented adjoint opera, 1967
 Augmented nonlinear large-scale systems, 1915
 Augmented systems, 1964–1971
 AUSM⁺ scheme, 1877
 AUSM⁺-up scheme, 1878
 Austenitic SS
 –Burgers vectors, 598
 –IASCC, 599, 600
 –radiation induced segregation (RIS), 600–601
 –segregation, 598, 600–601
 –yield strength, 598, 601
 Authentication, 3469, 3470, 3474–3477, 3482, 3483, 3494, 3497, 3528
 Automated control stations, 3159
 Automatic guided vehicles, 3157
 Automatic power controller (APC), 2280, 2310
 Auxiliary building, 2256, 2263, 2295
 Auxiliary feed water system (AFWS), 2199, 2215, 2219, 2220
 Average chord length, 993–998, 1053–1056
 Average cosine, 204, 238, 273
 Average cross sections, 36, 44, 72–74
 Average shear stress τ , 2592
 Away-from-reactor (AFR), 3166, 3167
 Axial, 2361, 2363, 2371, 2470–2474, 2487, 2504, 2508, 2517, 2519, 2521, 2523–2526, 2530, 2549, 2564, 2572, 2574, 2589–2593, 2595–2600, 2673–2675
 –buckling, 235
 –clad and wrapper expansion, 2534, 2535
 –compression σ_a , 2592
 –expansion, 2487, 2530, 2680, 2681
 Azimuthal angle, 432, 433, 437, 458, 465, 468, 473, 477, 933, 1083, 1095–1097, 1108–1112, 1114–1116, 1121, 1125–1130, 1134, 1135, 1137, 1138, 1145, 1146, 1153, 1154, 1156
 Azimuthal symmetry, 468
- ## B
- Back-end fuel cycle, 2982
 Background cross section, 255–257, 260, 924–927, 955–958, 961, 964–968, 973–975, 979, 981–983, 986, 988–991, 1005, 1012–1020, 1023, 1024, 1026–1029, 1035, 1037–1040, 1042, 1043, 1046–1049, 1051, 1057, 1059, 1063, 1065, 1068
 Background levels, 3060–3064, 3079, 3086, 3114, 3118
 Backup pressure, 2747
 Backward Euler method, 535, 2019
 Backward transport equation, 493
 Baer–Nunziato model, 1816, 1842, 1844
 Banach space, 666
 Band cross sections, 967, 975
 Band parameters solution, 402–408
 Band probability, 967, 975, 1041, 1043
 Bandwidth, 1465, 1471–1472, 1478
 Bare critical mass, 3426, 3431, 3432
 Barnwell, 3499
 Barrier, 2736, 2793, 2904, 2913, 2914, 2918, 2929, 3276, 3291, 3292, 3326, 3331, 3338, 3346, 3353–3356, 3363–3365, 3367, 3369, 3375, 3376, 3380, 3386, 3388–3391, 3395, 3396, 3399–3403
 Barrier (confinement). *See* Confinement barrier
 Base cross section, 924, 1026, 1208, 1214, 1216, 1218, 1219
 Basis elements, 1970
 Bateman equation, 1244–1247, 1309
 Bateman method, 1178, 1183, 1186–1187, 1198, 1199
 Bayesian approach, 94
 Bayesian inference, 1924
 Bayesian interpretation, 719
 Bayes' theorem, 714, 718, 720, 722, 733, 1995–1997, 2046
 B₄C absorber, 2061, 2067, 2068, 2114
 Beam-mode, 1704, 1705, 1707, 1708

- Becquerel (Bq), 3259, 3261, 3287, 3407, 3413
- BeF₂-PuF₃ system, 2946
- Bell factor, 257, 998-1001, 1005, 1011, 1018, 1019
- Benchmark blowdown experiment ICI, 2017, 2021, 2025
- Benchmarks, 146, 149, 1917, 1918, 2044
 - fast, 120, 122, 147-151, 157
 - identifier, 148, 149
 - thermal, 125, 148, 151-156
- Bending stress σ_b , 2591, 2592, 2594
- B₀ equations, 255
- Berger form, 1365
- Bernoulli
 - numbers, 687
 - polynomials, 686, 687
 - trials, 1997
- Bessel coefficients, 689
- Bernoulli distribution, 733
- Bernoulli trials, 733, 734
- Bernoulli's polynomials, 686
- Bessel functions
 - addition theorems and related series, 697
 - asymptotic expansions, large order, 694-695
 - asymptotic expansions, large variable, 694
 - general order
 - first and second, 688
 - second kind, 688
 - third kind, 688
 - integer order, 690
 - first kind, 689
 - modified
 - first kind, 689
 - third kind, 689
 - spherical, 690
 - Wronskians, 691
 - zeros
 - first kind, 691-692
 - second kind, 692
 - third kind, 692
- Bessel functions, spherical, 61, 62
- Bessel's inequality, 649
- Basset's function, 689
- Best-estimate, 1913-2048
 - adjusted (calibrated) values, 1924
 - codes, 1963, 2043
 - predicted mean values, 2046
 - predicted parameters, 2034
 - upper, 2039
 - values, 1924, 1926, 2036, 2037
- Best values, 1994, 1999, 2001
- Beta_{eff}, 2058, 2065, 2083, 2124, 2146, 2151, 2177, 2178
- Beta energy, 939
- Beta function, 684-685
- Beta particle (or beta radiation, beta ray), 3273, 3408, 3413
- Beyond design basis accidents (BDBA), 1755, 1784
- B₁ heterogeneous streaming, 862
- BHS transport approximation, 229
- Biasing parameters, 534, 538, 539
- Bi-CGSTAB, 858
- Bickley functions, 806, 807, 848, 852
- Bickley-Naylor function, 1083, 1094, 1095
- Big Picture, 282
- Bilinear form
 - concomitant, 1961, 1967, 1968
 - quadratic form, 658
 - second-degree multivariate polynomial, 658
- Binomial likelihood function, 1997
- Biosphere, 3276, 3291, 3347, 3353, 3354, 3388-3393, 3400, 3405, 3408, 3410, 3411
- Birnbaum importance, 1795
- BISO, 2724, 2729
- Bis-triazinyl-pyridines (BTP), 2967-2970
- Black body, 1079
- Black boundary collision probability, 1085, 1087, 1089
- Black box, 1916
- Black limit, 996, 1005, 1014, 1015, 1018, 1020, 1022
- Blackness of a cell, 1021
- Blackness of region, 1053, 1054
- Blowdown pump, 2277
- BNL-325 report, 89
- Boilers, 2712, 2715
- Boiling water reactors (BWR), 1631, 1632, 1666, 1670, 1671, 1689-1691, 1695, 1699-1702, 1704, 1708-1723, 1732, 1733
- Boltzmann, 1491, 1493
 - constant, 247
 - equation, 753-774, 776, 778, 821, 825, 827, 829, 833, 836
 - transport equation, 227, 254, 928, 931, 970, 971, 975, 1029, 1071, 1093, 1104, 1231, 1232
- Bondarenko, 924
 - method, 256, 258, 264
 - model, self-shielding, 360
 - type cross section library, 1026
- Bonnet, 2256, 2259, 2261
- BONUS, 3021, 3091, 3092
- Boolean algebra, 1995
- Boraflex, 3165, 3166
- Boric acid, 2262, 2284, 2299, 2314, 2315
- Boron (B), 546, 548, 549, 577, 586-588, 627, 1384, 1424, 1428, 2948
 - coefficient, 1220-1221
 - rods, 2299
- Boronized steel, 2270
- Bottom grid, 2266, 2299
- Bottom nozzle, 2207, 2211, 2269-2271, 2299
- Boundary
 - condition, 66-68, 410-411, 762-763, 779-781, 785-787, 790, 794, 796, 801, 811, 812, 819, 820,

- 855, 864–869, 871–873, 875, 877, 879, 880, 883–885, 1078, 1079, 1085–1089, 1120–1121, 1135
 - effects, 1369–1370
 - functional, 487, 489, 491
 - sources, 444–445, 452, 453, 456, 460, 484, 485
 - Bragg edges, 200, 201, 203, 204, 220, 237
 - Bramblett–Czirr plate measurements, 415–416
 - Branching ratio, 940, 968, 1170
 - Breeding (conversion) ratio, 1247–1249
 - Briet–Wigner, 329
 - formalism, 87, 89, 90
 - multi level approximation, 70–71
 - resonance, 39, 42, 43
 - shape, 39
 - single level approximation, 70
 - Bremsstrahlung, 1322, 1323, 1327, 1330, 1336–1338, 1341, 1342, 1345, 1360, 1363
 - Broad-beam attenuation, 1372–1376
 - $\psi\chi$ Broadening, 247–248
 - BROADR, 955
 - BROND-2.2 library, 134, 135, 168
 - Brownian motion, 1825
 - Brute-force method, 1955
 - Bubble expansion rate, 1830
 - Bubbling chutes, 2262
 - Buckling, 859, 866–868, 889, 890, 2065, 2082, 2118, 2124, 2142, 2159, 2164–2165
 - Buffer zone, 929, 1070, 1087–1091, 1101
 - Building structures, 3085
 - Buildup factors, 1353, 1359–1373, 1379, 1386, 1388, 1395, 1396, 1411, 1429
 - Bulk spectrum analysis, 3185
 - Bundle counter (BC), 3465, 3484–3486
 - Burgers vectors, 571, 578, 579, 591, 598, 619, 621, 622
 - Burnable, 2921, 2928
 - absorber, 919, 962, 964, 968, 1068, 1100, 1158, 1163, 1164, 1197, 1201, 1202, 1556–1557, 2252, 2299, 2300, 2320
 - poison, 1161, 1163, 1176, 1247, 1249–1251, 1254, 1258, 1265, 1266, 1270, 1271, 1276, 1277, 1279, 1280, 1284, 1285, 1291–1294, 1297, 1298, 1301, 1304, 1306, 2068, 2082, 2100, 2105, 2108
 - poison nuclides, 1164, 1168
 - Burn-up (or burn-up fraction, burn-up rate), 1243–1251, 1253, 1256–1267, 1272, 1273, 1276, 1278, 1284–1286, 1297, 1306–1309, 2918, 2920–2922, 2928–2930, 3264, 3265, 3268, 3278, 3310, 3327, 3328, 3332–3334, 3409, 3413, 3415
 - calculation, 918, 922, 939–940, 952, 1059, 1068, 1161–1208
 - chain, 923, 962, 964, 968, 969, 1161, 1163–1170, 1179–1182, 1186–1188, 1190, 1195, 1199, 1231, 1232
 - equation, 1161, 1170–1174, 1176–1178, 1180, 1181, 1184–1186, 1195, 1198, 1199, 1206
 - matrix, 1161, 1173, 1174, 1178, 1180–1183, 1185, 1188–1190
 - related data, 961, 962, 968–969
 - time, 1171, 1174–1177, 1196, 1197, 1206
 - Butyl, 2967
 - BWR instability, 1670, 1691, 1713, 1715–1719, 1732
- ## C
- Cable cutting, 3147
 - CACTUS, 934
 - Cadmium (Cd), 2948, 2973
 - Cadmium measurements, 2108, 2109
 - Calandria, 2231, 2232, 2234, 2236, 2237, 2242
 - Calcium oxide, 2945
 - Calculation of phase diagrams (CALPHAD), 1503
 - Calutrons, 2912
 - Cancer risks, 1435–1439
 - CANDU, 2187, 2188, 2230–2247
 - CANSTORE, 3169
 - Capacity factor, 2187, 2226, 2227, 2230
 - Capture, 1633, 1634, 3264, 3268, 3408–3410, 3412
 - cross section, 952, 967, 981, 982, 984, 986, 987, 1040, 1049, 1172, 1173, 2135, 2175
 - effect, 2529–2530
 - gamma photons, 1322, 1324, 1327, 1332–1334, 1378, 1389, 1394–1396, 1399
 - Carbides, 2938, 2942, 2945, 2947–2949, 2953–2958, 2961
 - Carbon-carbon composites, 2917
 - Carbonitrides, 2953
 - Carbothermal reduction, 2953–2957
 - Carbuncle phenomenon, 1879–1880
 - Carlvikns two-term rational approximation, 1001, 1005, 1022, 1058
 - 3-D Cartesian geometry, 465–467, 473
 - CASCAD, 3169
 - Case matrix, 919, 1207–1222
 - Cash flow, 3005, 3222
 - CASMO, 922, 928, 944, 949, 1020
 - CASMO-5, 928
 - CASTOR, 3167–3169, 3173
 - Catching chambers, 2260, 2262
 - CATHARE, 1818, 1844, 1845, 1859, 1860
 - Cauchy distribution, 739
 - Cauchy sequence, 665, 666
 - Cauchy–Schwarz inequality, 647, 727
 - Cavity flooding system (CFS), 222
 - CCCC, 959
 - CCCP, 932–934, 1152
 - Cell homogenization, 234
 - Cell numbers, 1138–1140
 - Cell types, 1138, 1141–1145, 1147
 - CENDL-2 library, 168
 - Central limit theorem, 533, 1932, 1934, 2000
 - Central tube, 2269, 2272, 2280, 2299
 - Centroid, 1112, 1129

- Ceramic metal (CERMET)
 –composition, 2953, 2985
 –fuel pellets, 2953
- Ceramics
 –antite, 577
 –charge defect, 577
 –fuel, 576, 577
 –nuclear reaction control, 577
 –silicon carbide, 577
- Certificate for Disposal, 3193
- Cesium, 2959, 2981
 10 CFR 20, 1756, 1757
 10 CFR 50, 1749–1752, 1757, 1758
 10 CFR 52, 1757
 10 CFR 100, 1757
- CFX, 1859
- Chain reaction, 430
- Channel, 574, 599, 601, 612, 622
 –radius, 245, 246
 –spin, 248, 250
- Chapman–Jouguet detonation, 1878
- Chapman–Kolmogorov equations, 1633
- Characteristics-based flux splitting, 1867–1871
- Characteristics-based matching (CBM) method, 1866
- Characteristics equation, 934, 1106, 1116–1125, 1133–1134, 1140
- Characteristic speed, 1861, 1863, 1864
- Characteristic X rays, 1336–1338
- Charged particle equilibrium, 1341, 1345
- Chebyshev
 –acceleration, 537
 –polynomials, 1961
- Chebyshev or-norm, 647
- Chebyshev polynomials normalized, 705
- Chebyshev polynomials $T_n(x)$ and $U_n(x)$
 –of first kind, 709
 –generating functions, 709
 –recursion formulas, 710
 –of second kind, 709
 –special cases, 710
- Chebyshev's theorem, 729, 730
- Checker-board loading pattern, 1269, 1270
- Chemical and volume control, 2252, 2276–2277, 2306
- Chemical gels, 3104
- Chemical oxidation reduction decontamination (CORD), 3070, 3099
 χ^2 of the calibration, 2015, 2047
 χ^2 -distribution, 2015
 χ^2 per degree of freedom, 2015, 2037
- Chipping hammers, 3106, 3116
- Chlorophenyl, 2967
- Choppers, 4, 46
- Chord average model, 1065, 1066
- Chord distribution function, 995, 1009
- Chromium-molybdenum steel, 2264, 2270
- Chromosome abnormalities, 1434, 1435
- Circulation loop, 2251, 2254, 2263, 2264, 2273, 2283, 2284, 2286, 2295, 2306, 2314, 2317
- Citric acid ($C_6H_8O_6$), 3070, 3093, 3094, 3096, 3099, 3102
- Clad/cladding, 549, 556–558, 565, 569, 575, 577, 599, 602, 603, 610, 612, 614, 615, 617, 621, 625, 626, 631, 2714, 2717–2720, 2918–2922, 2926–2930, 3260, 3292, 3295, 3297, 3302, 3303, 3323–3324, 3328, 3332–3334, 3336, 3341, 3408, 3412
- Cleanup (radioactive), 3408, 3413
- Clearance limits, 3067, (AU: Found only as clearance limits)
 ^{244}Cm , 2938, 2941, 2948
- CM-lab Jacobian, 244
- Coarse grain parallel computing, 1464–1465, 1482
- Coarse mesh, 1124, 1125, 1140, 1141, 1155–1157
 –finite difference, 1156–1158
 –rebalance (CMR), 1124, 1125, 1148, 1155–1156
- Coated fuel particle, 2927
- CO_2 blasting, 3106–3109
- Code scaling and applicability uncertainty (CSAU), 2043
- Code verification, 282, 318
- Co-extraction of MA, Ln, 2969
- Co-extraction process (COEX), 2950
- Coherent elastic scattering, 192, 200–202, 204
- Coherent scattering, 192–193, 200, 220, 1345, 1360, 1362, 1363
- Collision density, 273
- Collision probability (CP), 794–820, 929, 930, 932–934, 991–993, 999, 1007–1010, 1012–1017, 1019–1021, 1032, 1047–1049, 1051, 1053, 1054, 1070, 1071, 1075–1085, 1087–1089, 1091, 1092, 1094, 1152
 –matrix, 236
 –methods, 191, 235–236
 –normalization condition, 992, 1007, 1015, 1042, 1044, 1048
- Column matrix, 650
- Column vector, 645, 679, 737
- Combined licenses (COLs), 1757
- Combined measurement, 1928, 1939
- Combining modes, 199
- Communication graph, 1465
- Compaction, 2949, 2950, 2952, 2954, 2956, 3014, 3179, 3181, 3183, 3191, 3192, 3228
- Competitive width, 262, 263, 265
- Complete orthonormal set, 649
- Completion theorem, 648
- Component/coordinate, 645
- Compaction, 2949, 2950, 2952, 2954, 2956, 3014, 3179, 3181, 3183, 3191, 3192, 3228
- Competitive width, 262, 263, 265
- Complete orthonormal set, 649
- Completion theorem, 648
- Component/coordinate, 645
- Compound nucleus, 35–39, 42, 45, 47, 53–55, 57–60, 70–73, 89, 98–99, 103, 104, 119, 159, 1332
- Compound nucleus reactions, 37, 39, 58
- Compressed-air, 3080, 3108, 3111, 3112, 3125, 3127, 3133–3135, 3197

- Compressible fluid, 1825, 1826, 1828, 1830, 1832, 1862
- Compressible particle, 1826, 1830–1832, 1836–1838, 1841
- Compton interactions, 547
- Computational fluid dynamics (CFD), 1484, 1491–1499
- Computational solutions, 2044
- Computer size and power, 282
- Concrete, 1361–1363, 1373–1376, 1385, 1396–1400, 1404–1407, 1418, 1427, 3067–3069, 3071, 3073, 3086–3090, 3109–3111, 3113–3116, 3124, 3127, 3140, 3141, 3146, 3163, 3167, 3169, 3171–3173, 3175, 3214, 3222, 3226
- Concrete spaller, 3116
- Condensation scheme, 928–932, 935, 1069–1104, 1116, 1138, 1160, 1232
- Condenser, 2254, 2278, 2309
- Conditionally constant elementary error (of a measurement), 1939
- Conditionally constant errors, 1930–1931, 1934
- Conditioning (of radioactive waste), 3276, 3277, 3295, 3408
- Confinement barrier (or containment barrier), 3326, 3328, 3407–3409
- Congenital abnormalities, 1434, 1435
- Conservation equation, 445, 449
- Conservation laws, 1816, 1819, 1859, 1862, 1874, 1880
- Conserved variables, 1862, 1872
- Consistency indicator, 1924, 1925
- Consistent-P approximation, 229
- Constant interpolation, 305, 307
- Constant reaction rate, 331, 342, 344
- Constant systematic error, 1933
- Constitutive laws, 1834–1836, 1838
- CONSTOR, 3171–3173
- Constrained minimization problem, 2007
- Consumable electrode, 3128–3130, 3132–3133, 3136–3137, 3149–3150
- Contact-arc metal cutting, 3130–3132
- Containment barrier. *See* Confinement barrier
- Containment filtered vent system (CFVS), 2201
- Contaminated area, 2263
- Contamination (radioactive). *See* Radioactive contamination
- Continuous cumulative angular, 300
- Continuous energy, 297–303, 333, 394, 395, 417, 420
- Continuous-energy problem, 500, 502, 505
- Continuous slowing down, 272, 274, 513, 517
- Continuum inelastic scattering, 241
- Control blade cells, meshing, 1144
- Contours of constant best-estimate uncertainties, high-dimensional parameter-space, 2047
- Control blade coefficient, 1215
- Control blade history coefficient, 1208, 1215
- Control cell core, 1272, 1273, 1275–1277, 1301, 1302
- Control element drive mechanism (CEDM), 2194–2195
- Control experiment, 1942
- Control rod, 548–549, 579, 632, 1641, 1666, 1670, 1671, 1673, 1674, 1684, 1695–1699, 2251, 2252, 2254, 2255, 2291, 2298, 2299, 2301, 2723, 2725, 2734, 2735
- Control rod clusters, 2301
- Control Rod Programming (CRP), 1271–1275, 1282, 1284, 1294, 1297, 1300, 1302, 1303, 1309
- Control valves, 2278, 2308
- Conventional core, 1272–1275, 1301, 1302
- Convergence, 1916, 1922, 1941, 1958, 1970, 1984, 1987, 1990–1992, 1994, 2013, 2048
- angular flux, 1121–1122
 - criterion, 1097, 1098
 - multiplication factor, 1122–1123
 - scalar flux, 1089, 1097, 1122, 1123
- Conveyors, 3157, 3214
- Coolant, 86, 101, 128, 2712–2714, 2716–2720, 2722, 2724, 2725, 2729, 2734, 2735, 2745–2747
- cleaning, 2276
 - flow, 1699, 1703, 1704
- Cooling calculation, 1200–1201
- Cooperative Project on Decommissioning (CPD), 3243
- Core barrel, 2257, 2265–2268, 2270, 2289, 2290, 2297, 2298, 2734
- bottom, 2257, 2266–2268
 - vibrations, 1691, 1704–1708
- Core damage frequency (CDF), 2199
- Core neutron power, 2280
- Core ratings, 2712, 2713
- Core simulation, 1307–1309
- CORRAL code, 1766
- Correction factors, 924, 926, 927, 991, 1100, 1101
- Correlated distribution, 376, 377, 383–386
- Correlated energy-angle distributions, 293
- Correlated systematic, 1933
- Correlated/uncorrelated, 292, 376, 377
- Correlation ratio-based methods, 1940, 1941, 1951
- Correlations common errors, 1933
- Corrosion products, 2712
- Cosine angular distribution, 1021
- Cost breakdown structure (CBS), 3223–3224
- Cost estimation, 3010, 3027, 3030, 3038, 3040, 3042, 3045, 3054, 3059–3064, 3182, 3184, 3220, 3221, 3223, 3230–3241
- Cost values, 3229
- Counter-current, 2915
- Coupled sets, 234
- Coupling calculation, 928, 930–932, 1069, 1070, 1091–1102, 1123, 1156
- Courant–Friedrichs–Lax (CFL) condition, 1859, 1870, 1879, 1889

- Covariance, 1919, 1922, 1935, 1936, 1974, 2000, 2004, 2009, 2013, 2036–2040, 2042, 2046, 2048, 3519, 3521–3524, 3529, 3531
 –actinides, 140–143
 –data, 86, 134, 135, 137, 143, 145, 171, 178
 –fast neutrons, 137–145
 –library, 141–146
 –matrix, 1923, 1925, 1932, 1937, 1999–2002, 2006, 2008, 2009, 2012, 2015, 2029, 2032, 2047
 –methodology, 135–139
 –resonances, 119, 136–137, 140–142, 144, 171, 172
- CPM, 922
- CRC Handbook of Nuclear Reactors Calculations, 282
- Credit burn up, 2100–2102, 2104, 2106, 2109, 2141
- Criticality, 452, 455, 497, 499, 524–526, 531, 2712, 2716, 2722, 2724, 2725, 2730, 2735, 2739, 3328, 3341, 3343, 3411
 –axial compressive stress σ_{a-cr} , 2592, 2593
 –bending stress σ_{b-cr} , 2592, 2952
 –eigenvalue, 452
 –group, 3389, 3391, 3392, 3409
 –shear stress τ_{cr} , 2592
 –testing, 146–148, 156–157
- Cross-contamination, 3087, 3088, 3101, 3107, 3114, 3216
- Cross section, 545, 546, 548–552, 554–556, 602, 605, 616, 626, 631, 2919–2921, 2923
 –(n,2n), 952–953, 960, 961, 967
 –(n,3n), 952, 953, 960
 –flux dependence, 358–359, 399
 –laboratories, 6–35
 –library, 922–924, 926–928, 930, 931, 936, 941–969, 1004, 1023, 1024, 1026, 1051, 1069, 1070, 1091, 1098, 1102, 1103, 1161, 1165, 1225, 1226
 –measurements, 3–74
 –processing, 954–961, 1026–1027
 –processing code, 955, 1026
 –references, 3, 5, 6, 12, 28, 52, 54, 59
- Cross Section Evaluation Working Group (CSEWG), 140, 170, 176, 179
- Crowdion, crystals, 552
- Crystallographic structure factor, 200, 201
- Crystallographic texture, 557, 579, 618, 619, 621, 627, 628
- CSIRS compilation, 213, 214, 216, 217
- Cultural factors, 3210, 3212
- Cumulative angular distribution, 300
- Cumulative probability density function, 1039
- Cumulative yield, 1168
- Curium, 2937, 2938, 2940, 2941, 2944, 2984
- Curved OAT, 1942
- Curvilinear geometries, 465, 479
- Curvilinear variables, 474
- Cut thickness, 3124, 3125, 3127–3132, 3134–3137, 3141, 3147, 3149, 3150
- Cutting speed, 3045, 3088, 3124–3126, 3128–3132, 3134, 3135, 3140, 3141, 3143, 3144, 3147
- Cycle energy, 1250, 1254–1260, 1264–1266, 1268, 1291, 1292, 1295
- Cycle energy production, 1263, 1265, 1266, 1270, 1271, 1297
- Cyclic tracking, 841, 1145–1152, 1158
- Cycling scheme table, 1258–1262, 1264, 1292
- Cyclohexano, 2967
- Cylindrical coordinates, 1076, 1133
- Cylindrical geometry, 1001, 1076, 1080–1086, 1125–1134, 1137
- Cylindrical symmetry, 477, 485
- Cylindrical variables, 473
- Cylindrical vessel, 2018
- ## D
- Dancoff correction/factor, 234, 235, 257, 926, 1008–1020, 1022, 1023, 1025, 1035, 1037, 1049, 1053, 1057–1059, 1063, 1742–1744, 1751, 1758, 1760, 1770, 1772, 1775, 1776, 1783, 1784, 1806, 2199–2200, 2216, 2242–2244
 –coolant accident, loss, 1745
 –deterministic safety analysis, 1747
 –engineered safety features, 1746, 1748
 –epistemic uncertainty, 1747
 –multiple barriers, 1747
 –physical barriers, 1746–1748
 –quality assurance, 1746, 1747
 –reactor coolant system, 1745, 1747
 –reactor protection system, 1748
 –safety assessment, 1747
- Data adjustment, 1917, 1963, 2011, 2046
- Data assimilation, 1913–2048
- Data consistency, 2003, 2013–2017
- Data library, 86, 124, 146, 166, 168, 170, 175, 181
- Data parallel, 1458, 1462–1463, 1472, 1483, 1487
- Data processing codes, 283, 287
- Data validation, 179
- Darboux–Christoffel formula, 704
- DCHAIN, 1187
- DDREF, 1437, 1438
- Deactivation phase, 3031
- Dead band, 1928, 1939
- Deaerator, 2306–2308
- Debris-filter, 2207, 2211
- de Broglie wave length, 35, 39, 61
- Debye–Waller coefficient, 196, 200
- Decay, 288, 289, 940, 953, 1119, 1161, 1162, 1168, 1170–1173, 1176, 1181, 1182, 1186, 1200, 1201, 1216, 1224, 3266–3268, 3270–3273, 3281–3283, 3322, 3350, 3362, 3376, 3410–3413
 –constant, 288, 940, 966, 968, 1173, 1181, 1224
 –data, 86, 162, 165–167, 169, 171, 173, 176, 179

- heat, 165–167, 2730, 2731, 2745
- radioactive, 283, 3266, 3268, 3270–3272, 3291, 3318, 3326, 3334, 3337, 3346, 3353, 3354, 3389, 3397, 3399, 3400, 3404, 3405, 3407, 3409
- Decay ratio (DR), 1711–1723
- Decision theory, 1997, 2001–2002, 2006, 2046
- DECOHA, 3070, 3098–3099
- Decommissioning costs, 3009, 3015, 3027, 3031, 3051, 3218–3241, 3243
- Decommissioning Project Manager (DPM), 3027, 3031, 3035, 3045, 3050–3051, 3053–3055
- DECON, 3011, 3026, 3070, 3232
- Decontamination, 3005, 3007–3011, 3014, 3029, 3031, 3038, 3039, 3042, 3053–3055, 3058, 3060, 3064–3122, 3145, 3155, 3156, 3162, 3166, 3176, 3180, 3181, 3192, 3193, 3197, 3206, 3207, 3214, 3220, 3221, 3223–3229, 3239, 3240, 3261, 3276–3277, 3291–3294, 3320, 3408, 3409, 3413
 - factor, 3066, 3068, 3069, 3072–3074, 3076, 3077, 3079, 3080, 3090
 - radioactive (*see* Radioactive decontamination)
- Deductive statistics, 1994
- Deep dose equivalent index, 1347–1348, 1352, 1399
- Deep geological disposal (of radioactive waste). *See* Disposal (of radioactive waste)
- Defense-in-depth (DID), 1742–1744, 1748, 1751, 1758, 1760, 1770, 1772, 1775, 1776, 1783, 1784, 1806, 2199–2200, 2216, 2242–2244
 - coolant accident, loss, 1745
 - deterministic safety analysis, 1747
 - emergency core cooling system, 1745
 - engineered safety features, 1746, 1748
 - epistemic uncertainty, 1747
 - multiple barriers, 1747
 - physical barriers, 1746–1748
 - quality assurance, 1746, 1747
 - reactor coolant system, 1745, 1747
 - reactor protection system, 1748
 - safety assessment, 1747
- Degree of belief, 1916, 1924, 1945, 1995, 1996
- Delayed activity, 3398–3400, 3409
- Delayed fission source, 230
- Delayed neutron, 107, 116, 119, 122–125, 157, 166, 172, 1322, 1327, 1636, 1645, 1655, 1657, 1674, 1691, 1717, 2745, 2746
 - fission spectrum, 438, 1223, 1225
 - fraction, 438, 937, 966, 1224, 1225
 - testing, 157
- DeMoivre–Laplace theorem, 736
- Density functional theory (DFT), 567, 1502
- Dependency graph, 1465
- Depletion chains, 922, 923, 932
- Depressurization, 2017, 2018
- Design basis earthquake (DBE), 2200, 2228
- Design calculation, 1303–1304
- Design of experiments, 1942–1945
- Design points, 1941, 1942
- Destructive assay (DA), 3464–3466, 3468–3470, 3528
- Detail balance, 194, 195, 199, 237, 299
- Detection equipment, 3155–3156, 3162–3163, 3189
- Detergent, 3073, 3090, 3095, 3096, 3100–3101, 3103–3105, 3107
- Deterministic, 464, 485, 532–540
 - effects, 1431–1433
 - methods, 1923, 1941, 1955
 - solution, 772
- Diagnostic X-ray, 1429
- Diagonally dominant, 658
- Diagonal matrix, 649, 650, 652, 654, 656, 658, 661, 663, 674, 726, 728, 738, 742
- Diagonal transport approximation, 229
- Diamide DMDOHEMA, 2967
- Diamide extraction (DIAMEX), 2969, 2970
- Diamond, 3087, 3088, 3113, 3146
 - differencing scheme, 782, 828, 831, 835, 837, 838, 840, 846
 - saws, 3146–3147
- Diethylhexylphosphoric acid (HDEHP), 2970
- Differential angular distributions, 300
- Differential cross section, 288
- Differential formulation, 793, 875
- Differential scattering cross section, 437, 466, 504, 507, 509
- Diffuser, 2913, 2914
- Diffusion, 297, 298, 326, 327, 340–342, 394, 395
 - ballistic, 560
 - coefficient, 560, 562, 565, 604, 607, 609, 930, 936, 1156–1158, 1211, 1222, 1224, 1226
 - creep, 562
 - equation, 518–523, 537, 839, 859–894, 930, 1156–1158, 1211, 1674
 - phase transformation, 562–565
 - singularity, 208
 - theory, 1091, 1092, 1389–1391, 1670–1679, 1683–1690
 - thermal diffusion, 560, 562, 565
 - type spectrum, 195
- Diffusion-synthetic acceleration (DSA), 537, 839, 840
- Diffusive translational modes, 192, 205
- Digital technology, 1759
- Dimethyl-dioctyl-hexylethoxy malonamide (DMDOHEMA), 2967, 2970
- N,N'-Dimethyl-N,N'-dibutyltetradecyl-1,3-malonamide (DMDBTDMA), 2967
- Dini expansion, 693
- Di-octylhexylethoxy, 2967
- Dirac delta function, 329, 376, 377, 383, 384, 398, 402, 1997, 1998

- Direct containment heating (DCH), 2200, 2205, 2222
 Direct cycle, 2731, 2732, 2739, 2744, 2746
 Direct disposal, 3336, 3409
 Direct effect term, 1960, 1961, 1969
 Direct integration, 369–373
 Directional derivative, 481
 Directional diffusion coefficients, 862
 Directional dose equivalent, 1348
 Direction cosines, 432, 756, 758, 772–774, 776, 777, 779, 783, 789, 806, 821–823, 827, 836, 847
 Direct measurements, 1933–1935, 1939
 Direct numerical simulation (DNS), 1479, 1491–1499
 Direct reactions, 39, 58, 97–98, 101
 "Direct" sub-group approach, 1036
 Direct sum, 648
 Direct-use material, 3458, 3460–3462
 Direct vessel injection (DVI), 2205, 2223, 2225, 2247
 Dirichlet problem generalized, 672
 Discharge burnup. *See* Burn-up (or burn-up fraction, burn-up rate)
 Discrete dislocation dynamics (DDD), 1479, 1480, 1503
 Discrete inelastic scattering, 240, 241
 Discrete ordinates, 534, 535, 991, 1032, 1070, 1075, 1091, 1093
 Discrete ordinates method, 226–235, 782, 792, 821–840
 Discrete oscillators, 195, 196, 199, 200, 205, 207, 208
 Discrimination threshold, 1928
 Dislocation channeling, 612
 Dislocation dynamics (DD), 1503
 Dislocation loops, 551, 557, 559, 562–563, 568, 571, 578, 579, 598, 607, 611, 619–622, 627, 2986, 2987
 Dislocation network, 560, 562, 563, 598, 603, 608, 611
 Dispersed phase stress, 1820, 1822
 Disperse media, 1819
 Displacement
 –cascade, 545, 551–553
 –cross section, 550, 555, 556
 –energy, 550, 552, 555, 560, 578, 627
 production (DPA), 289–291
 Dissipation rate, 1833–1837, 1842, 1856, 1857
 Dissipative model, 1832–1839
 Distant energies, 342, 343
 Distributed computing, 1464, 1482, 1488
 Distributed control system (DCS), 2198, 2215–2217
 Distributed memory, 1453, 1455, 1456, 1458, 1459, 1462, 1463, 1472, 1474, 1475
 Distribution, 1631–1633, 1635–1640, 1642, 1648, 1650, 1654, 1655, 1657, 1659–1661, 1666, 1667, 1677, 1704, 1728, 1731, 1732
 –coefficient, K_d , 3366, 3367, 3369, 3409
 –functions, 1317, 1320
 DIT, 922
 Dithiophosphinic acids, 2969
 Divalent, 2944, 2975, 2978
 Diven factor, 2177, 2178
 Divergence theorem, 443, 446, 491
 Divertor, 546, 631
 DMDCHMA, 2967
 DMDPhMA, 2967
 Domain decomposition, 1468, 1481, 1487, 1488, 1490, 1491
 DOORS, 1340, 1429
 Doppler
 –broadening, 13, 40, 43, 248, 253, 275, 276, 291, 298, 299, 303, 311, 319–352, 361, 371, 1039, 1040, 1065
 –calculation, 2533
 –coefficient, 1066, 1214
 –constant, 2514, 2532, 2535
 –effect, 955, 975
 –width, 283, 337–339, 348
 Dose, 3276, 3287–3290, 3301, 3309, 3318, 3322, 3324, 3335, 3389–3392, 3400–3401, 3408–3410, 3412
 –conversion coefficient, 1339, 1340, 1345–1348, 1351–1354, 1379, 1398, 1402
 –conversion factor, 1347–1348, 1352, 1395, 1398–1400, 1403, 1414
 –and dose rate correction factor, 1437
 –equivalent, 1342–1344, 1347–1348, 1350–1352, 1361, 1371, 1397–1399, 1402, 1435, 1441, 1442
 Dose-response relationships, 1441
 Dosimetry, 556, 1316, 1340–1344, 1346–1353, 1409, 2072, 2083, 2129, 2178
 Double-ended guillotine break, 1749, 2251, 2254, 2285
 Double-envelope containment, 2291
 Double heterogeneity effect, 1050
 Double-strata concept, 2964, 2974
 Doubling time, 2101, 2127, 2141–2144, 2156
 Dp_1 acceleration, 853
 DRAGON, 934
 Drill and spall, 3071, 3106–3107, 3116
 Drilling, 3078, 3086, 3089, 3108, 3127, 3138, 3157, 3163, 3228
 Drying/calcination, 2949, 2950
 Dry shielded canister (DSC), 3173, 3175
 Dry storage, 3164, 3167
 Dry storage for spent CANDU fuel, 2245
 DTF format, 231, 959
 Dual discretization, 875, 894
 Dual-time depletion method, 1206
 Ductile-brittle transition temperature (DBTT), 574, 589–596, 615
 Ductility, 563, 569, 573–575, 594, 598, 599, 611, 612, 618, 622, 626
 Dumbbell, 551–552
 Dust explosions, 3080
 Dynamic effects, 1752
 Dynamics of interface, 1842–1843

E

- EBR-II, 2963, 2972, 2979
- EDA code, 101, 128, 129
- Effect bound to leakages, 2529
- Effective cross section, 944, 970–971, 973, 974, 981, 986, 988–991, 998, 1002–1005, 1013, 1019, 1022, 1023, 1026–1029, 1032, 1035–1038, 1040, 1042, 1043, 1046, 1047, 1049–1051, 1057, 1059–1063, 1065, 1067–1069, 1164, 1170
- Effective delayed neutron fraction, 937, 966, 1224, 1225
- Effective dose equivalent, 1349, 1350, 1352, 1353, 1407, 1442
- Effective energy release, 1226
- Effective heat conductivity, 1835
- Effective microscopic cross sections, 967, 981, 982, 987, 1049, 1176, 1198
- Effective multiplication factor, 763, 859–861, 863, 874, 893
- Effective scattering radius, 925
- Effective temperature, 198, 199, 211, 1065–1066
- Effective viscosity, 1835, 1843
- Effective width, 198
- Effluents, 3261, 3276–3277, 3279, 3293, 3295, 3297, 3301, 3320, 3322, 3410
- Egelstaff, 195, 198
- Eigenfunction, 452, 455, 485, 525, 526, 531, 532, 539
- Eigenfunctions for a slab, 272
- Eigenmode, 1713, 1717
- Eigenproblem, 765, 771, 863, 867
- Eigensolutions, 765
- Eigenspectrum, 863, 867
- Eigenvalues, 765, 766, 799, 828, 859–861, 863, 867, 888, 1677, 1713
- and eigenfunctions, 271–272
 - and eigenvectors
 - algebraic multiplicity, 659, 660
 - characteristic equation, 659, 660
 - characteristic polynomial, 659
 - characteristic roots, 659
 - characteristic values, 659, 670
 - characteristic vectors, 659
 - diagonalizable, 660
 - distinct eigenvalues, 659, 660
 - linearly independent, 660
 - multiple eigenvalues, 660
 - nondiagonalizable, 660
 - nonsemi-simple, 660
 - null space, 659
 - secular equation, 659
 - semi-simple, 660
 - spectral radius, 659
 - spectrum of A, 659
- Eigenvalue temporal, 272
- Einstein oscillator, 216, 219
- Elastic down scatter, 241–243
- Elastic interaction, 545, 546, 548, 550, 555, 604, 613
- Elastic neutron scattering, 508
- Electrical discharge machining technique, 3131–3132, 3149
- Electrical resistivity, 560
- Electric generators, 2279
- Electrochemical LOMI ion exchange (ELOMIX), 3098
- Electrodialysis, 3075
- Electron capture, 1337
- 5*f* electron shell, 2943
- Electronic structure (ES), 1500–1503, 1505, 1507, 1512
- Electropolishing, 3067, 3075–3079, 3118–3120, 3156
- Electrorefining, 2938, 2971, 2973–2977, 2979, 2980
- Elementary effect, 1943
- Elementary error (of a measurement), 1930, 1939
- Embarrassingly parallel, 1471, 1484, 1486
- Embedded atom method, 1502
- Embedding (of radioactive waste), 3295, 3410, 3411
- Emergency boron injection system, 2315
- Emergency core cooling system (ECCS), 1745, 2264, 2283, 2284, 2314
- Emergency diesel generators (EDGs), 2198, 2202, 2204, 2218
- Emergency feedwater system, 2316
- Emergency gas removal system, 2285, 2316, 2318
- Emergency power supply system, 2312, 2317
- Emergency programme, 3049
- EMPIRE code, 99, 104, 119, 130, 132, 143, 144
- Encapsulation (of radioactive waste). *See* Embedding (of radioactive waste)
- End effectors, 3160
- grippers, 3162
- ENDF/B format, 284–286, 304, 310–313, 315–318, 331, 369
- ENDF/B pre-processing codes, 283
- ENDF/B-VII, 191, 202, 205, 213, 214, 216, 220, 221, 223, 237–240, 245, 247, 249, 250, 252–254, 268, 269, 275
- ENDF/B-VII.0 library, 86–89, 93, 97, 98, 101, 104–109, 111, 112, 116, 117, 119, 121, 122, 124–126, 128–132, 134, 135, 139, 140, 144–169, 176–179, 181
- ENDF fission-product data, 1165, 1168
- ENDF format, 191, 195, 230, 245, 252, 262, 263
- ENDF-6 format, 86, 97, 122, 136, 146, 169–176, 178, 180
- Endothermic reactions, 1325
- Energetic self-shielding effect, 972, 974
- Energy absorption coefficient, 1345
- Energy collapsing, 971, 1069
- Energy condensation, 768–770, 969, 1069–1103, 1116
- Energy-dependent diffusion equation, 521, 522
- Energy-dependent Watt spectrum, 382
- Energy deposition rate, 284

- Energy distributions, 286, 290, 292, 294, 301–302, 357, 376, 377, 381–383
 Energy exchange, 192
 Energy groups, 453, 461, 500–502, 505, 506, 536, 768, 794, 796, 800, 820, 841, 859–861, 863, 865, 866, 871, 872, 875, 890, 894
 Energy group structure, 920, 922, 926–928, 930–932, 935, 936, 938, 940–952, 957, 974, 975, 989, 1023, 1030, 1036, 1038–1040, 1049, 1067, 1069, 1070, 1091, 1102, 1103, 1159, 1223–1229, 1231
 Energy imparted, 1340–1342
 Energy loss in elastic scattering, 200, 979, 980, 1030
 Energy release per fission, 954, 966, 1226
 Energy Reorganization Act, 1761
 Energy self shielding, 226
 Energy transfer coefficient, 1345
 Engineered safety feature actuation system (ESFAS), 2280, 2310, 2317
 Enhanced neutron current method, 1009, 1013, 1014, 1018–1020
 ENRESA, 3024, 3219, 3241
 Enthalpy rise (radial) peaking factor, 1267
 ENTOMB, 3011
 Entombment, 3010, 3011, 3091, 3092
 Entropy balance, 1823, 1838
 Entropy fix, 1870
 Environmental factors, 3207, 3209, 3210, 3212
 Environmental impact assessment (EIA), 3038, 3039, 3200–3218
 Environmental indicators, 3213
 Environmental sampling, 3445, 3446, 3467, 3468, 3501–3507
 Environmental surveillance, 3217–3218
 EOLE, 2057–2064, 2067, 2071–2073, 2077, 2079–2084, 2104, 2127–2128, 2135, 2138, 2142, 2161, 2162, 2169, 2176
 Epistemic uncertainties, 1916, 1941, 1945
 Epithermal, 507, 508
 EPRICELL, 1028
 Equal angles, 1111–1113, 1116, 1127, 1152
 Equally probable angular bins, 300
 Equal weights, 1111–1113, 1116, 1129, 1130, 1152
 Equilibrium emission, 241
 Equilibrium solution, 1183
 Equivalence theory, 261, 973–976, 992, 997–998, 1006, 1009, 1010, 1012–1014, 1019, 1020, 1023–1026, 1034–1037, 1047, 1051, 1053, 1065, 1067, 1069
 Equivalence theory, lattice system, 1011–1012, 1020
 Equivalent homogeneous system, 993, 996–998, 1008, 1025, 1037, 1090, 1098, 1123
 ERC assembly, 2257, 2266–2268, 2270–2272
 ERC (emergency reactor control) drives, 2257, 2266, 2270
 Errors, 1916, 1917, 1926–1938, 1949, 1950, 1955, 1957, 1994, 1999–2006, 2010, 2013, 2015, 2043, 2045–2048
 –measurement error, 1939, 1940
 –measurement, pairs, 1933
 –single measurements, 1932
 –standards, detector calibration, 1933
 Escape cross section, 256, 257, 925, 926, 973, 974, 997–999, 1006, 1013, 1018, 1024, 1064
 Escape probability, 797, 812, 973, 993–1006, 1008–1011, 1014, 1016, 1020, 1023, 1025, 1034, 1036, 1037, 1047, 1051–1054, 1058
 ESPROSE-3D, 1859
 Ethylenediaminetetraacetic acid (EDTA), 3074, 3092, 3095, 3096, 3100, 3102, 3151
 Euclidian or 2-norm, 647
 Euler equation, 875, 878, 883, 1862, 1867
 Euler method, 1178–1180, 1183, 1199, 2019
 European Commission (EC), 3177, 3204, 3220, 3243
 European Facility for Industrial Transmutation (EFIT), core design, 2814–2815
 European lead-cooled system (ELSY), core design, 2804–2807
 Evaluated data library, 86, 130, 146, 168
 Evaluated nuclear database, 3, 59
 Evaluated Nuclear Data File (ENDF), 191, 212, 220, 245, 265, 923, 925, 942, 955, 957, 960, 962, 1024, 1165
 Evaporation spectrum, 381
 Evolution equations
 –internal energy, 1824
 –total energy, 1825
 Excess reactivity, 2299, 2920
 Exchanges at interface, 1834, 1835
 Ex-core detector, 1705–1707
 EXFOR library, 3, 131, 181
 Exhaust system, 3226
 Existence, uniqueness, and non-negativity of transport solutions, 455
 Exothermic reactions, 1325
 Expansive grout, 3106–3107, 3116
 EXPOKIT, 1195
 Exponential attenuation, 1354, 1372, 1381, 1389
 Exponential function, 801, 802, 846
 Exponential integral, 1077, 1080, 1083
 External envelope, 2291, 2294, 2295, 2316
 External region, 58, 60–63, 65–68
 External sinking fund, 3221
 External source, 1073, 1087, 1114, 1118, 1119
 Exutory, 3292, 3347, 3375, 3389–3392, 3394–3401, 3409, 3410
 Ex-vessel cooling (EVC), 2222
- F**
 Face-centered cubic, 2945
 Factorial design (FD), 1942, 1944
 Factorial geometry, 1138
 Failure (or hazard) rate, 1973
 False-alarm, 3524, 3525

- False convergence, 308, 313, 316
 Fast burn-up reactor, 2123
 Fast flux test facility (FFTF), 2957
 Fast neutron fluence, 554
 Fast neutron reactor (or fast reactors), 3272, 3285, 3326, 3403, 3410
 Fast neutrons, 87–89, 97–101, 106–119, 124, 130, 132, 137–145, 168
 Fast reactor fuel assembly, 1049, 1050
 Fast region, 239, 241
 Faucet problem, 1817, 1889–1891
 Feature sensitivity analysis, 1958, 1984
 Features, Events, and Processes (FEPs), 3389, 3410, 3414
 Feed fuel, 1243, 1261, 1263, 1264, 1266, 1268, 1270, 1271, 1294, 1295, 1297, 1298, 1302, 1308
 Feedstock, 2741, 2748
 Feedwater loss, 2285
 Feedwater pumps (FWPs), 2278, 2285, 2307, 2308, 2316
 Fermi age, 273, 274, 1389, 1391–1393
 Ferric sulphate ($\text{Fe}_2(\text{SO}_4)_3$), 3092, 3094
 Fertile, 3265, 3327, 3408, 3410, 3414
 –blanket, 2937
 –nuclide, 1162
 Fick law, 862–866
 Figure of merit (FOM), 1485, 1486, 3426–3434
 File format, 962
 Filtration, 1338, 1373, 3115, 3117, 3127, 3131, 3140, 3147, 3180, 3197, 3214
 Final-time value problem, 2024
 Fine grain parallel computing, 1465–1466, 1476, 1491
 Fine mesh, 928, 931–935, 1069, 1070, 1091, 1102–1161, 1224, 1227, 1229, 1232
 Finite-difference method, 535, 781, 782, 788, 790, 859, 863, 875–880, 887, 894
 Finite-element method (FEM), 535, 859, 863, 883–887, 894
 Fire protection, 1752, 1785, 1797–1802, 1805–1807
 First-flight reflection probability, 1021
 First-order numerical solution, 781
 First-order reliability methods (FORM), 1940, 1941
 First-order sensitivity index, 1953, 1954
 Fissile nuclides, 1162–1164, 1170–1172, 1199
 Fission, 87, 92–94, 107, 121, 122, 124, 125, 1633–1636, 1641, 1649–1653, 1656, 1660, 1663, 1664, 1692, 1703, 1723, 1733, 3261, 3263–3268, 3272, 3275, 3277, 3286, 3289, 3292, 3302–3307, 3323–3327, 3332, 3334, 3336, 3348, 3377, 3388, 3389, 3398, 3399, 3403, 3404, 3408–3411
 –barrier, 102, 104, 106, 118, 119
 –chambers, 2127, 2130–2134, 2160–2161
 –chi, 262
 –cross section, 942, 952, 960, 966, 967, 1088, 1173, 1200, 1227, 1229
 –energy, 126–128, 153
 –evaluation, 101–106, 108, 120, 122, 123, 131, 132, 134, 135, 157
 –gas production, 2959
 –gas retention, 2746
 –neutrons, 933, 943, 954, 960, 976, 1118, 1119, 1322, 1323, 1325, 1326, 1336, 1380–1383, 1385, 1405
 –process, 1631, 1659, 1660, 1667
 –product gamma photons, 1328–1332
 –product gamma rays, 1328–1332
 –product yield, 1165–1170
 –source, 445, 451, 452, 479, 506, 508, 1029, 1033, 1098, 1117–1118, 1122, 1123, 1322–1323
 –source iteration, 230
 –spectrum, 109, 112, 115, 116, 120, 153, 929, 936, 941, 953–954, 956, 960–961, 967, 976, 1070, 1088, 1118, 1223, 1225
 –yield, 86, 162–163, 171, 176, 177, 179, 180, 940, 1168, 1229
 Fission products (FPs), 93, 122–124, 131–135, 177, 577, 588, 602, 625–626, 631, 923, 946, 953, 958, 962, 978, 1031, 1168, 1190, 1252–1254, 1329–1332, 1334, 2101, 2720, 2736, 2743, 2903, 2904, 2928–2930, 2938, 2964–2966, 2973–2975, 2980–2985, 3056, 3059, 3266–3268, 3286, 3302–3304, 3324–3326
 Fissions per initial metal atom (FIMA), 557
 Fitting method, 1041–1043
 Fitt's problem, 1817, 1889, 1891–1892, 1894–1896, 1900
 Flame cutting, 3124–3125, 3136–3137, 3149
 Flame gouging, 3125, 3149
 Flat flux approximation, 1078, 1108, 1116, 1124
 Flat leakage approximation, 890
 Flight path, 438, 458–460, 479
 Floor shaver, 3087–3089
 Flora and fauna, 3208, 3210, 3212, 3213, 3217
 Flow, 1316, 1319–1322, 1361, 1398, 1401, 1402, 1413, 1414, 1417, 1418, 1422, 1423
 –pattern, 1818
 –rate, 2277, 2284, 2285, 2315
 –regime, 1818
 –velocity, 1699–1704
 Fluence rate, 442, 1318
 FLUENT, 1859
 Fluid cement, 3193
 Fluidic device (FD), 2219, 2220, 2223, 2225, 2247
 Fluid-induced stress, 1829, 1833
 Fluorescence, 1338, 1360, 1362, 1363
 Fluorescent radiation, 1337
 Fluoroboric acid (HBF_4), 3098, 3099
 Flurig scheme, 899, 906, 908
 Flux, 1318, 1346, 1388, 1390, 1397
 –calculator, 191, 257–261
 –factorization, 1675–1677
 –independent neutron source, 288
 –initialization, 1090, 1117

- per unit lethargy, 222, 231–233
- volume weighted, 940, 1088, 1090, 1098, 1099, 1123, 1159, 1225
- Flux difference splitting (FDS) method, 1867, 1869, 1876, 1878, 1880
- Flux vector splitting (FVS) method, 1867, 1878, 1880
- Fly ash, 3411
- Flynn's classification, 1452, 1453
- FOM. *See* Figure of merit
- Force constant model, 202, 216
- Forced cooling, 2941
- Forensics, 3501, 3507–3518
- Formal accuracy, 1916
- Formal adjoint, 1961, 1967
- Formation energy, 551, 562, 567, 627
- Form factors, 940, 941
- Forward eigenfunction, 525
- Forward sensitivity analysis procedure (FSAP), 1956, 1960, 1966, 1967, 2023
- Forward sensitivity equations (FSE), 1960, 1966, 1967
- Forward sensitivity system, 1963, 1975, 1976, 2022
- Forward transport equation, 485, 490, 493, 495, 496, 499
- Forward variational tangent model, 1960
- Foundation plate, 2294
- Fourier amplitude sensitivity test (FAST), 1940, 1941, 1951
- Fourier coefficients, 666, 668
- Fourier expansion
 - Fourier coefficients, 649, 748, 1961, 1969
 - spectral expansion of z , 649
- Fourier-Bessel expansion, 693
- Fourier series, 666–668
- Fourier transform, 722
- Fourier transforms
 - angular frequency, 746
 - continuous time, 746
 - convolution theorem, 747
 - discrete convolution theorem, 747
 - discrete time, 747
 - Fourier series, 747–748
 - inverse transform, 746
 - least squares property, 748
 - linearity, 747
 - norm, 747, 748
 - orthogonal system, 747, 748
 - orthonormal system, 747, 748
 - rotational frequency, 746
 - shifting property, 747
 - spectral representation, 746
 - stretching property, 747
 - time reversal property, 747
- Fourth-order Runge-Kutta method, 940, 1179, 1180, 1183, 1190
- FPs. *See* Fission products
- Fractile, 2015
- Fractional factorial design (FFD), 1942, 1944
- Fréchet derivative, 677
- Fréchet differential, 676–678
- Fréchet partial differential, 677
- Fréchet variations, 675–678
- Fredholm alternative theorem, 674–675
- Free atom cross section, 204, 209
- Free defects, 553
- Free flight kernel, 484, 485
- Free gas, 191, 192, 195, 196, 205, 210, 211, 217, 234
- Free OAT, 1942
- Frenkel pair, 551–553, 560, 578, 600
- Frequency distribution, 193, 205, 214–218
- Friction wear, 2719
- Fuel, 3260–3265, 3267–3269, 3273, 3274, 3276–3280, 3283, 3289–3291, 3303, 3305, 3306, 3309, 3310, 3320, 3323–3324, 3326–3379, 3402–3409, 3411–3415
 - batch, 1258, 1262
 - burn-up, 556
 - burn-up fractions, 2882
 - channels, 2231–2233, 2242
 - cycle, 2896–2933, 2937–2991, 3258, 3261, 3284, 3292, 3411
 - element, 1523–1527, 2712, 2714, 2716–2721, 2723, 2724, 2730, 2732, 2735, 2736
 - expansion, 2530, 2532, 2533, 2535
 - irradiation, 2951, 2960
 - lump, 993–995, 997, 998, 1001, 1005, 1006, 1010–1011, 1014–1016, 1020–1022, 1025, 1036, 1037, 1039, 1047, 1051, 1053, 1067
 - LWR spent fuel, 2486, 2843, 2858, 2875–2880, 2882, 2883, 2888
 - natural uranium, 2843, 2846, 2875, 2886, 2890, 2891
 - pellet, 569, 625 (*see also* Pellet, fuel)
 - region, 1258–1263, 1268, 1270
 - reserves, 2883
 - rod, 1526, 2251, 2253, 2268–2273, 2288, 2298–2300, 2320
 - sodium, clad or wrapper calculation, 2533
 - thorium and depleted uranium, 2883
- Fuel assembly (FA), 1244, 1250, 1258–1267, 1271, 1273, 1275, 1277–1279, 1281, 1282, 1284, 1293, 1294, 1297, 1298, 1301, 1302, 2255, 2266–2268, 2270–2272, 2288, 2297–2299, 3165, 3166, 3175, 3261, 3323
- Fuel-coolant interaction, 2712
- Fuel performance capability (FPC), 1509, 1510, 1513
- Fuel temperature coefficient, 1066, 1214, 1215, 1220
- Fuel-to-fuel, and moderator-to-fuel collision probabilities, 991
- Fugacity (for a gaseous substance), 3411
- Full-core calculation, 763, 778, 859–861, 883
- Fully shielded condition, 964, 1046

Functional analysis

- adjoint operators, 673
 - adjoint matrices, 673
 - bi-orthogonal, 673
 - dual, 672, 674
 - Hermitian, 673, 674
 - normal, 673, 674
 - orthonormal basis, 672, 673
 - positive definite, 673, 674
 - positive semidefinite, 673, 674
 - unitary, 672–674
 - adjoint unbounded linear operator
 - formal adjoint operator, 675
 - self-adjoint, 675
 - bilinear form, 671–672
 - chain rule, 676, 677
 - complete, 665, 666
 - conjugate indices, 664
 - continuous at point, 664, 668
 - derivatives, 675–678
 - differential operator, 670
 - differentials, 675–678
 - directional continuity, 676
 - directional derivative, 676, 679
 - F-derivative, 678, 680
 - F-differential, 678
 - first derivative
 - matrix-valued function, scalar, 680
 - matrix-valued function, trace, 680–681
 - scalar-valued function, matrix, 680
 - first variations, 680
- Dirichlet problem generalized, 672
- formal adjoint, 670–671
 - formally self-adjoint, 670
 - formal ordinary differential operator, 670
 - formal partial differential operator L , 670
 - G-derivative, 678
 - G-differential, 678
 - gradient, 678–679
 - Hessian, 678–679
 - inner product, 666
 - Jacobian, 679
 - joint continuity, 664
 - multi-index, 670
 - normed vector space, 664–666
 - vector, norm, 664
 - operator, function, functional
 - bijective, 668–670
 - bounded on, 669
 - characteristic functions, 670
 - characteristic space, 670
 - characteristic value, 670
 - continuous spectrum, 670
 - eigenfunctions, 670
 - eigenspace, 670
 - eigenvalue, 670
 - identity operator, 669
 - injective, 668–670
 - is injective but not surjective, 669
 - not injective, 669
 - null space, 669
 - operator from \mathfrak{c} , 668, 669
 - point spectrum, 670
 - residual spectrum, 670
 - resolvent set, 670
 - spectrum, 670
 - surjective, 668, 669
 - unbounded, 669, 670
 - optimization
 - absolute, 681
 - constrained minimization, 681
 - global minimum, 681
 - local minimum, 681
 - necessary condition, 681
 - relative, 681
 - strict global minimum, 681
 - strict local minimum, 681
 - sufficient condition, 681
 - unconstrained minimization, 681
 - orthonormal basis
 - nondegenerate, 666
 - orthogonal coordinate, 667
 - orthogonalization, 666, 667
 - orthogonal matrix, 667
 - unitary, 666, 667
 - unitary matrix, 667
 - partial differential equation, 670
 - principal part, 670
 - second variation, 680
 - separate continuity, 664
 - sequence space, 664, 666
 - sup norm, 665, 668
 - total, 677
 - totally, 677
 - uniformly continuous, 664, 665
 - vector space, bounded continuous complex valued functions, 665
 - weak derivative, 671
- Functional decomposition, 1468–1470
- Function of presence, 1820, 1839
- Fundamental mode, 272, 452, 494, 497
- equation, 936, 937, 1090, 1099, 1124, 1225
 - rebalancing, 1090, 1098–1099, 1123
 - shape, 232, 235, 269, 271, 272
- Fundamental solution, 765, 863, 867, 868
- Fusion neutrons, 1327–1328
- Fusion reactors, 546, 549, 573, 605
- blanket, 420, 629–631
 - first wall, 629, 630
 - tritium breeding, 631
- Fussell–Vesely, 1795
- Fussell–Vesely importance, 1774

G

- Gadolinia-bearing fuel, 954, 1013, 1067, 1176, 1201–1207
- Gadolinium depletion, asymmetry effect, 1204–1205
- Gaerttner LINAC Laboratory, 6, 8–11
- Gamma, 3259, 3272, 3273, 3281, 3287, 3309, 3318, 3322, 3324, 3408–3411, 3413
- cross section library, 969, 1231
 - cross sections, 938, 953–954, 957, 969
 - detectors, 3163, 3186
 - energy, 938, 939, 969
 - energy deposition, 937–939, 1227
 - function, 682–683
 - asymptotic expansions, 684
 - Legendre’s formula, 683
 - ionisation chambers, 2104, 2133–2134
 - measurement, 3185, 3189, 3190
 - radiation (or gamma rays), 3259, 3281, 3408–3411, 3413
 - ray sources, 1321, 1328–1336, 1364, 1370
 - spectroscopy, 3186
 - spectrum analysis, 3186, 3189
 - transport calculation, 937–939, 954, 957, 969
- Gaseous radioactive wastes, 3175, 3181
- Gas-filled detectors, 3187
- Gas flames, 3123, 3124
- GASKET, 196
- Gas pressure, 2018, 2021, 2025–2029, 2032–2034, 2037–2040, 2042
- Gas temperature, 2018, 2021, 2027, 2028, 2030, 2033, 2038–2041
- Gâteaux derivative, 676
- Gâteaux-derivatives, 2005, 2022, 2023
- Gâteaux differentiable, 677
- Gâteaux differential, 676, 677
- Gâteaux-differential, 1956, 1957, 1960, 1966, 1983, 1984, 1987
- Gâteaux partial differential, 677
- Gâteaux variation, 676
- Gauss multiplication formula, 683
- Gauss’ theorem, 1861, 1862
- Gaussian approximation, 193
- Gaussian elimination, 1089
- Gaussian prior distribution, 2046
- Gaussian quadratures, 1089, 1113, 1116
- Gaussian white noise, 746
- Gauss–Legendre quadrature, 821, 824, 826, 827, 833, 887, 899
- Gauss–Lobatto quadrature, 887
- Gauss–Seidel scheme, 1098
- Gd₂O₃ burnable absorber, 2252
- Gegenbauer polynomials
 - recursion formulas, 708
 - special cases, 708–709
 - summation theorem, 708
- Gegenbauer polynomials normalized, 705
- Geiger-Muller (GM) detector, 3187
- Gelation, 2957
- GELINA, 6, 7, 13, 15–17
- GEM*STAR, 2843–2892
 - accelerator parameters, 2872
 - burnup calculations, 2859–2865
 - core geometry, 2866, 2875
 - costs, 2839, 2845–2847, 2851, 2856–2859, 2870, 2876, 2882, 2883, 2885–2892
 - fuels, 2688, 2843–2849, 2851, 2852, 2855–2859, 2863, 2864, 2866, 2868–2870, 2872–2884, 2886–2888, 2890–2892
 - cycle, 2844, 2859, 2892
 - equilibration, 2857, 2872, 2880, 2881
 - graphite corrections, 2881
 - k_{eff} calculation, 2859, 2863, 2865, 2868, 2876
 - multiplier(energy), 2843
 - performance, 2843, 2844, 2848, 2852–2854, 2856, 2858–2865, 2868, 2869, 2881
 - proliferation issues, 2845
 - reactor parameters, 2868–2875
 - system integration, 2856–2858
- GENEPI, 2123
- General design criteria, 1749, 1755, 1756
 - engineering judgment, 1751
- Generalized feedback shift register (GFSR), 1485
- Generalized geometry, 1138, 1156
- Generalized sub-group cross sections, 1039
- Generalized zeta and Riemann’s zeta functions
 - asymptotic expansion, 687
- Generation III, 2252, 2253, 2255, 2272, 2313
- Generation III working assembly, 2273
- Generation IV, 2712, 2737, 2738, 2744, 2747
- Generation IV (Gen IV) International Forum (GIF), 2940, 2963
- Generic geometric and design features, 2380–2584
- Genetic algorithms (GAs), 1286, 1287, 1289, 1290, 1292, 1297–1300
- Genetic effects, 1431, 1434–1435, 1441
- Genetic risks, 1434, 1435
- Geological repository. *See* Disposal (of radioactive waste)
- Geometric attenuation, 1355
- Geometric phantoms, 1339, 1343, 1347–1348
- Geometric progression, 1365–1367, 1429
- Geosphere, 3353, 3359, 3376, 3389, 3393, 3395–3398, 3400, 3411
- GH MLBW method, 249
- Gibbs relation, 1824, 1855
- Glass box testing, 1916
- Global adjoint sensitivity analysis procedure (GASAP), 1958
- Global nuclear energy partnership (GNEP), 2844, 2885

- Global OAT, 1940, 1943, 1944
 Global sensitivity analysis, 1955
 Glovebox, 2948, 2950
 GMRES(m), 840, 858
 GM tube, 3163
 GNASH code, 100, 108, 116, 130
 Godunov method, 1862–1867, 1875
 Goldstein's work on intermediate resonances, 395
 Government Performance and Results Act, 1772
 Grammian matrix, 659
 Granularity, 1476
 Graphical processor unit (GPU), 1452, 1454, 1456
 Graphite, 191, 200–206, 220, 237, 261, 266, 268–270, 274, 546, 626–629
 - anisotropy, 2853, 2856
 - form factor, 202
 - moderation, 2850, 2851
 - new measurements, 2854, 2856, 2865
 - sleeves, 2718
 - temperature dependence, 2854
- Grapples, 3157
 Green's function, 461, 485, 489, 497–499, 1632, 1639, 1669, 1679, 1683–1691, 1695, 1698, 1699
 - Green's functions, 485, 498, 499
- Grid calculation, 2533
 Grid expansion, 2530–2533, 2535
 Grinding technique, 3071, 3072, 3086, 3106–3107, 3113, 3141
 Grinding + binder, 2954
 Grit blasting, 3078, 3105–3108, 3111–3113
 Groundwater, 3064, 3203, 3207, 3210
 Group collapse, 234
 Group cross sections, 255
 Grouped separation, minor actinides, 2940
 Group fluxes, 501–503, 505
 Group ordering, 231
 GROUPR module, 956–957
 Group screening designs, 1944
 Group theory, 1994–2001
 Group-to-group source, 506
 GTsN-195M reactor coolant pumps, 2251
 GUARDIAN, 2190, 2206
 Guide channel, 2299
 Guillotine saw, 3143–3144
 Gypsum wallboard, 1429
- H**
- H-1, 234, 238, 239, 242
 H-2, 238, 239, 242
 Haar measure, 1998
 Habit planes, 562
 Hafnium absorber, 2064, 2068
 Half-life (radioactive), 2937, 2988, 3259–3260, 3266, 3270, 3273–3275, 3409, 3411, 3413
 Half-value thickness, 1354, 1376
 Hamilton–Cayley theorem, 659
 Hammering effect, 3073, 3080, 3082
 Hankel functions, 688
 Hausdorff moments problem, 406
 Hausert–Feshbach model, 73, 88–89, 98–100, 119
 Hazardous materials, 3041, 3069, 3160, 3179, 3194, 3209
 Head-end conversion, 2979–2982
 Health physics, 1322, 1430–1441, 3047, 3051, 3083
 Heat exchanger, 2716–2719, 2744
 Heat transfer, 1557–1563, 1572, 1585, 1586, 1600
 Heat transfer function H, 2566
 Heat transport
 - cladding, 1559
 - cladding to pellet, 1560
 - coolant, 1558–1559
 - fuel pellet, 1561–1563
 - gap conductance, 1561
- Heavy ions, 548, 551, 555, 563, 583
 Heavy nuclides, 942, 946, 954, 955, 957, 965, 972, 986, 1030, 1031, 1050, 1068, 1164–1166, 1173, 1176, 1190
 Heavy reflector, 2073–2075, 2084
 Heavy water, 191, 212, 214–217, 237, 238, 267, 269, 274, 275
 Heavy water cooled reactor, 2231, 2232
 Heavy water moderated, 2231, 2232, 2234
 Heavy water reactors (HWR), 1247, 1283, 1284, 1306, 1309, 1310
 HELIOS, 922, 928, 932, 1035, 1152
 HELIOS-2, 934
 - Helium bubbles, 549, 605, 606, 610
 - production, 2959, 2960, 2986
- Hankel functions, first and second, 688
 Hereditary effects, 1430
 Hereditary illness, 1350, 1430, 1433–1435, 1441
 Hermitian matrix, 650, 673, 674
 Hermite polynomials, normalized, 705
 Hermite polynomials, 667, 705, 710, 712
 - asymptotic representation, 711
 - generating function, 711
 - inequalities, 711
 - recursion formulas, 711
 - special cases, 711
- Heterogeneous fuel arrangement, 226
 Heterogeneous isolated system, 991–997
 Heterogeneous systems, 991–1025, 1032–1034, 1037, 1047
 Heterogenous media, 1369–1372, 1385
 HEU downblend, 3425
 Hexagonal geometry, 2251
 Hexagonal grid, 2253, 2268
 Hexamethylenetetramine, 2959
 Hexamethylenetriamine, 2952
 Hafnium (Hf), 1068
 H-factor, 863

- High burn up, 2082, 2102
- High burnup structure
 –characteristics, 1582–1584
 –modelling of, 1586–1589
- High-efficiency particulate air (HEPA) vacuum cleaners, 3045, 3105
- High flux reactor (HFR) Petten, 2951, 2953
- High-level waste (HLW), 2937, 2938, 2964, 2965, 2970, 2973, 2982–2985, 2988, 3010, 3014, 3162, 3233, 3234
- Highly enriched uranium (HEU), 2724, 2727
- High performance computing, 1452–1514
- High-pressure emergency cooling system, 2284, 2302, 2314
- High pressure melt ejection (HPME), 2200
- Hilbert spaces, 1958, 1959, 1961, 1967, 1970
 –complete with respect to the norm, 666
 –orthonormal, 666
- Hindered rotations, 192, 205
- Histogram smoothing, 244
- Historical boron concentration, 1218–1220
- Historical moderator temperature, 1218–1220
- Historical void, 1208–1212, 1214, 1216, 1219
- Hölder or-norm, 647, 662
- Hölder vector norm, 662
- Homogeneity distribution factor, HD, 2953
- Homogeneous fuel arrangement, 226
- Homogeneous system, 973, 975–991, 993, 996–998, 1006, 1008, 1013, 1029–1032, 1034, 1037, 1043, 1047, 1090, 1098, 1123, 1225, 1633, 1667, 1671, 1673, 1674, 1683
- Homogenous function, 1871
- Horizontal storage module (HSM), 3173, 3175
- Horizontal type steam generators, 2251, 2253
- HPC. *See* High performance computing
- HST42-5 critical assembly, 222
- Human factors, 1754, 1768, 3037, 3198–3200, 3211–3213
- Human factors engineering (HFE), 2198, 2217–2218
- Human–machine interfaces, 1759, 1783
- Hybrid, 499, 532, 533, 538–540, 1455, 1456, 1458, 1463, 1502, 1512
 –approach for dispersed mixture, 1839–1840
 –(symmetry-breaking) model, 1821–1823
- Hydraulic cutting techniques
 –abrasive water jet, 3138–3141, 3150
 –high pressure water jets, 3140, 3150
 –water jet, 142, 3138, 3139
- Hydroblasting, 3106–3108, 3110
- Hydrocarbons, 3101, 3123, 3125, 3131
- Hydrochemical, 2965
- Hydrochloric acid (HCl), 3070, 3091, 3092, 3152
- Hydrogen igniters, 2201, 2240, 2243
- Hydrogen peroxide (H₂O₂), 3094, 3096
- Hydrotests, 2276
- Hyperbolicity, 1829, 1843–1845, 1847–1850, 1852, 1853, 1859–1861, 1869, 1889, 1891, 1892, 1894, 1896, 1898
- Hyperbolic system, 1845, 1858, 1860
- Hyperstoichiometry, 2945
- Hypostoichiometry, 2945
- I**
- I&C safety system, 2310, 2311
- Idaho National Engineering Laboratory (INEL), 3162
- Identification matrix, 3211
- IDX, 1028
- Ill-posedness, 1816, 1843, 1859
- Immediate dismantling, 3010, 3011, 3027, 3206, 3211, 3215
- Immiscibility gap, 2955
- Immobilization (of radioactive waste). *See* Embedding (of radioactive waste)
- Implicit Continuous-Fluid Eulerian (ICE), 1817, 1859
- Importance function, 485, 494–497, 499, 539, 765
- Importance sampling, 1940, 1941, 1946–1948
- Improved Plutonium Canister Assay System (iPCAS), 3489–3491, 3497
- Inaccuracy (of a measurement), 1939
- Incineration, 3014, 3176, 3181, 3226, 3228
- Incoherent scattering, 192–193
 –cross section, 194
 –elastic, 200, 219, 220
- Incoming current, 755, 832, 833, 855, 865, 866
- Incomplete information, 1994, 1998, 2001, 2003
- Inconsistent-P approximation, 229
- In-containment refueling water storage tank (IRWST), 2202, 2203, 2210, 2219, 2220, 2222, 2225, 2226, 2247
- Incore instrumentation detectors (ICID), 2298
- In-core nuclear fuel management, 1254, 1266–1286, 1291, 1293–1303, 1309–1310
- Independent measurements, 1933
- Independent yields, 1168
- Indices of performance, 1955
- Indirect effect term, 1960, 1961
- Indirect measurements, 1928, 1935–1939
- Indirect-use material, 3459–3461
- Indium (In), 546, 548, 549, 1068
- Inductive inference, 1994
- Industrial safety, 3005, 3051–3052, 3194, 3195
- Inelastic competition, 262
- Inelastic interaction, 547–549
- Inelastic neutron scattering, 1334–1336, 1378
- Inelastic scattering, 1322, 1335, 1378, 1393, 1394, 1428
- Inert matrix fuel (IMF), 2947, 2948, 2952, 2955, 2983
- Infiltration methods, 2949
- Infinite dilution, 256, 257, 964, 965, 967, 1038, 1062
- Infinite lattice, 223, 225, 234, 235
- Infinitely dilute, 924, 1229

- Infinite multiplication factor, 1073, 1091, 1119, 1227, 1229
- Infinite spectrum, 1086, 1229
- Inflection point, 342
- Inflow transport approximation, 229
- Information entropy, 1998
- Information theory, 1931, 1998, 2046
- Initial flux guess, 1117, 1123
- Initial-value problem, 2024
- Injection casting, 2957
- Injection jet, 3140–3142
- Inner iterations, 1089, 1097–1098, 1101, 1122, 1124, 1125, 1150, 1156
- Inner product, 486, 487, 490, 491, 494, 496
- additive, 646
 - commutative, 646
 - homogeneous, 646
 - positive definite, 646
- In situ leaching, 2905
- Inspection periscopes, 3163
- Instantaneous void, 1208–1210, 1214, 1216
- Instant Released Fraction (IRF), 3326, 3335, 3336, 3412
- Institute for Electrical and Electronics Engineers, 1769
- Instrumental measurement errors, 1929
- Instrumentation and control (I&C) systems, 2215–2216, 2252, 2280, 2281, 2309–2311
- Integral data, 1924, 1998, 1999
- Integral experiments, 2057, 2058
- Integral equation for the scalar flux, 484–485
- Integral fast reactor (IFR), 2972, 2974–2976, 2979
- Integral fuel burnable absorber (IFBA) pellets, 1158
- Integral transport equation, 235, 479–485
- Integrated absorptions, 1196, 1230
- Integrated current, 755
- Integrated Engineering Test (IET), 3499
- Integrated fissions, 1230
- Integrated flux, 753–755, 759, 794, 796, 798
- Integrated head assembly (IHA), 2194, 2208, 2210
- Integrated in-scattering, 1230
- Integrated neutron leakage, 1230
- Integrated neutron production, 1230
- Integrated out-scattering, 1230
- Integro-differential equation, 430, 431, 449, 485
- Interaction cross section, 545, 548, 552
- Interface-indicator function, 1860
- Interfacial pressure, 1816, 1840, 1844, 1845, 1860
- Interference effect, 926–927, 976, 1061, 1062, 1065, 1176
- Interim inventory verification (IIV), 3493
- Intermediate heat exchanger (IHX), 2744
- Intermediate resonance (IR) approximation, 260, 983–991. *See also* Narrow resonance (NR) approximation
- Intermediate resonances, 357–358
- Intermediate rod, 2257, 2270
- Intermediate scattering function, 193
- Intermolecular coherence, 214, 237
- Internal conversion, 1337
- Internal diameter, 2018, 2027
- Internal envelope, 2294
- Internal neutron source, 444, 461, 506
- Internal region, 59, 60, 65, 66
- International Atomic Energy Agency (IAEA), 1746, 1786, 3005, 3016–3026, 3028, 3176–3178, 3182, 3200, 3220, 3242, 3243, 3435, 3439, 3441, 3445, 3449, 3453–3466, 3468–3484, 3486–3488, 3490, 3492, 3494, 3497–3502, 3507, 3508, 3518, 3519, 3526, 3527
- goal, 3446, 3530, 3532, 3533
 - report INSAG-4, 3196
 - safety standards, 1744
 - transport regulations, 3214
- International Criticality System Benchmark Experiment Program (ICSBEP), 221
- International nuclear event scale (INES), 3049
- International Space Station, 1762
- Inter-phase energy exchange, 1828, 1832
- Interphase force, 1819, 1821, 1822, 1826, 1840
- Interpolation error, 306, 311
- Interpolation of self-shielding factor table, 1027–1029
- Intrinsic error, 1930, 1939
- Invariance, change of evidence, 1997
- Inventory (of radionuclides). *See* Radionuclide inventory
- Inventory difference (ID), 3463, 3467, 3470, 3518, 3520, 3523, 3524, 3526–3530
- In-vessel retention (IVR), 2222, 2247
- Ion-exchange, 3075, 3091, 3092, 3096–3099, 3102, 3174, 3180
- Ionizing radiation, 3273, 3303, 3412, 3413
- IREN, 6, 7, 19–21
- IR parameter, 966, 986, 988–991, 1025
- Irradiation creep, 545, 547, 557, 562, 574–576, 612–614, 619, 621, 628
- bias, 574, 575, 614
 - climb and glide, 575, 621
 - climb velocity, 575
 - creep rate, 574–576, 613, 614
- Irradiation damage, 545–559, 570, 576–561, 628–630, 633
- Irradiation embrittlement, 573, 574, 589, 591–595, 631
- Irradiation hardening, 549, 572, 589, 590, 611–612
- Irregularly inherited traits, 1434, 1435
- IRWST sparger, 2225, 2226
- Isoshield, 1340
- Isotopes, 3265, 3268–3269, 3285, 3375, 3389, 3412, 3413

- Iterated fractional factorial design (IFFD), 1944, 1945
- Iterative methods, 536, 538
- J**
- J values, 248
- Jacket, 2252, 2255, 2268–2272, 2298
- Jacket-free fuel assemblies, 2255
- Jackhammer, 3071, 3086, 3089, 3194
- Jacobi polynomials normalized, 705
- Jacobian matrix, 1868, 1869, 1889
- Japanese evaluated nuclear data library (JENDL), 942, 955, 1049
- JEFF, 942, 955
- JEFF-3.1 library, 86, 92, 111, 125, 135, 149, 157, 158, 164, 166–169, 179, 181
- Jeffreys' prior, 1997
- JENDL-3.3 library, 86, 107, 108, 125, 134, 135, 145, 157, 158, 168, 177, 179–181
- JNDC nuclear data library of fission products, 1168
- Joyo fast neutron flux reactor, 2951
- JRC-IRMM, 7, 13, 15–16
- Jules Horowitz reactor, 2057, 2069, 2077–2079, 2104
- K**
- k_{∞} , 224, 234
- KACHINA, 1859
- KALMAN code, 136, 137
- k -effective (k_{eff}), 147, 157, 2058, 2076, 2080, 2082, 2149, 2159, 2178
- for fission, 230, 231
- for production, 222, 230
- k -eigenvalue, 1677
- Kelvin fluid impulse, 1827, 1828, 1831, 1847
- Kernel broadening, 247, 249, 330–333
- Kernels safety graded, 2736
- Kerosene, 3101, 3131
- Key measurement points (KMPs), 3468, 3500
- Key performance indicators (KPI), 3050, 3196
- K-FIX, 1859
- Kinetic approximations, 1632, 1675–1677, 1682, 1685, 1733
- Kinetic energy, 939, 954, 957
- Kinetic energy, balance, 1824, 1825
- Kinetic energy released in materials (KERMA), 127, 289, 291, 1339–1342, 1345–1347, 1352, 1361, 1363, 1365–1368, 1373, 1374
- Kinetic measurement, 2127
- Kinetic Monte Carlo (KMC) method, 1479, 1502
- Kinetics equations, 557
- Kinetic theory model, 1820–1821
- Knurl tube cutter, 3145
- Kolmogorov's expansion, 1633, 1953, 1972–1977
- Korean Utility Requirement Document (KURD), 2219, 2221, 2222, 2246, 22188
- Kori unit 1, 2187
- Kronecker symbol, 673
- Krylov methods, 537
- Krylov subspace method, 662, 1178, 1188–1190, 1195, 1199
- Kudankulam NPP, 2252, 2255
- Kurtosis, 1935, 1936
- Kyoto University Research Reactor Institute (KURRI), 6, 7, 21–24
- L**
- Lagrange's method
- Lagrange multipliers, 682
- Lagrangian functional, 682
- Lagrange multipliers, 1985–1989, 1999, 2000, 2007
- Lagrangian FEM, 881, 883–887
- Laguerre polynomials normalized, 705
- Laguerre polynomials
- asymptotic behaviour, 713
- recursion formulas, 711
- special cases, 712
- LANCER01, 932
- LANCER02, 922, 928, 929, 931, 934, 1069, 1138, 1150, 1223
- Land and soil, 3208, 3209, 3212, 3213
- Land use, 3085, 3205, 3207, 3208, 3210, 3212, 3213, 3215
- Langevin technique, 1631, 1668
- LANSCE, 6, 7, 11–13
- Lanthanide fission products, 2940, 2965, 2975
- Lanthanide series, 2944
- Laplace equation, 867
- Laplace operator, 867, 868, 874
- Large-scale discontinuity (LSD), 1818, 1819
- Laser, 3073, 3085, 3086, 3123, 3136, 3194
- Laser cutting, 3122, 3136–3138, 3156
- Latin hypercube sampling, 1940, 1941, 1946–1948, 1952
- Lattice
- calculation, 768, 772, 786, 811, 841, 859, 862
- physics, 1293, 1304
- physics code, 918–928, 931, 932, 934, 935, 940–943, 952, 953, 955–964, 969–971, 975, 990, 991, 1012, 1014, 1020, 1029, 1035, 1051, 1052, 1057, 1059, 1065, 1070, 1087, 1102–1105, 1139, 1142, 1152, 1155, 1175, 1176, 1180, 1198, 1203, 1204, 1207, 1210–1214, 1216, 1221, 1226, 1229
- system, 1005–1012, 1014–1016, 1018–1023, 1057
- LBRF. *See* Line-beam response function
- Leaching, 3298, 3301, 3305, 3311, 3322, 3323, 3326, 3335, 3412
- Lead, 1338, 1360–1363, 1365, 1367, 1368, 1371, 1373, 1375, 1384, 1388, 1389, 1404, 1405, 1418, 1428–1433, 1437

- compressibility, 2784
 - critical constants, 2785
 - density, 2784
 - electric resistivity, 2785
 - heat capacity, 2785
 - vaporisation heat, 2783
 - melting, latent heat, 2783
 - melting point, 2783
 - normal boiling point, 2783
 - saturation vapour pressure, 2784
 - sound velocity, 2784
 - surface tension, 2784
 - thermal conductivity, 2785
 - thermal diffusivity, 2785–2786
 - thermal expansion, 2784–2786
 - viscosity, 2785
 - volume change at melting, 2783
- Lead slowing-down spectrometer, 8, 11–13, 23, 267
- Least square fitting, 1020, 1043, 1189
- Legendre, 953, 1113, 1116, 1152, 1153
 - angular flux moment, 519
 - moment, flux, 354, 358–360, 375, 377
 - polynomial, 466, 504, 518, 519, 756, 757, 759, 764, 773, 779, 780, 789, 790
 - quadrature set, 1152
- Legendre polynomials normalized, 704
- Legendre polynomials, 667, 705
 - generating function, 706
 - inequalities, 706
 - integrals, 707–708
 - recurrence relations, 706
 - summations and series, 707
- LEOPARD, 921
- LET. *See* Linear energy transfer
- Lethal dose, 1432, 1433
- Level-symmetric quadratures, 822–824
- Levine factors, 257
- Library
 - access, 181
 - ENDF/B-VII.0, 86–89, 93, 97, 98, 101, 104–109, 111, 112, 116, 117, 119, 121, 122, 124–126, 128–132, 134, 135, 139, 140, 144–169, 176–179, 181
 - JEFF-3.1, 86, 92, 111, 125, 135, 149, 157, 158, 164, 166–169, 179, 181
 - JENDL-3.3, 86, 107, 108, 125, 134, 135, 145, 157, 158, 168, 177, 179–181
- License termination plan (LTP), 3232, 3237
- Licensing process, 2043
- Life extension, 3005
- Life-time extension, 2288
- LiF–NaF–BeF₂–PuF₃, 2946
- Light nuclei, 87, 88, 97, 101, 128–129, 145
- Light water reactor (LWR)
 - fission gas behaviour, 1572–1573
 - atomic diffusion, 1573–1574
 - bubble migration, 1576
 - grain boundary diffusion, 1575–1576
 - resolution, 1575
 - trapping, 1575
 - fuel
 - fabrication, 1618
 - pellet-cladding mechanical interaction, 1589–1591
 - pellet-coolant interaction, 1596–1598
 - stress corrosion cracking, 1591–1596
 - thermal conductivity, 1529–1534, 1541–1542
 - heat transfer, 1557–1563
 - lattice, 1275–1283, 1307
 - loss-of-coolant accidents
 - high burnup, 1604–1608
 - safety criteria, 1600–1604
 - mechanical behaviour, 1563–1572
 - elastic strain, 1564
 - nuclide evolution, 1552
 - reactivity-initiated accidents, 1608–1617
 - safety criteria, 1610–1617
- Lindeberg condition, 741
- Linear Boltzmann equation, 430–464
- Linear characteristic (LC) scheme, 846
- Linear combination, 651, 655, 660, 661, 682, 688, 748
 - linearly dependent, 648
 - linearly independent, 648
- Linear energy transfer (LET), 1342–1343, 1351, 1431–1435, 1438, 1439
- Linear function, 1936, 1969
- Linear interaction coefficient, 1354, 1416
- Linearized Boltzmann equation, 283, 284, 287, 288
- Linearized burnup chains, 1186, 1187
- Linearly anisotropic flux approximation, 759
- Linearly interpolable data, 286, 300, 307, 309–313, 317, 318, 331–336, 340, 361–365, 369, 373, 378, 382, 383, 386, 387
- Linear operator, 485, 486
- Linear power, 2945, 2958, 2960, 2961
- Linear surface characteristic (LSC) scheme, 846
- Linear systems, 1956–1963
- Linear system solution
 - consistent system, 660
 - determined, 660
 - full rank, 660
 - homogeneous system, 660
 - inconsistent, 660
 - non-homogeneous system, 660
 - over-determined, 660
 - rank deficient, 660
 - under-determined, 660
- Linear transformation technique, 650, 653, 663, 723, 738, 871, 872, 888, 892, 893
- Linear vector space
 - associative, 645
 - boundary point, 646
 - closed under addition, 645

- commutative, 645
 - distributivity, 645
 - finite dimensional, 646
 - finite-dimensional vector space, dimension n , 646
 - infinite dimensional, 646, 664
 - interior point, 646
 - interior S° of S , 646
 - neighborhood, 646
 - open, 646
 - sequence space, 646, 664
 - square summable, 646
 - Line-beam response function (LBRF), 1359, 1407–1410, 1412
 - Line equation, 1148, 1150
 - Line integral, 483
 - Line source, 1356–1359, 1368–1369
 - Liquid, 192, 193, 195, 198, 199, 205, 208, 214, 220
 - filtration systems, 3045
 - radioactive waste collection, 2295
 - secondary wastes, 3077, 3078, 3227
 - wastes, 3077, 3078, 3102, 3103, 3174, 3179–3181, 3183, 3195, 3227
 - Liquid-liquid reductive extraction, 2974, 2977–2979
 - Lithium, 1384, 1424, 1428–1429
 - Livoltant acceleration, 840
 - Load balancing, 1475–1476, 1486, 1496
 - Load factor, 2724
 - Load follow, 1252, 1253, 1269
 - Local importance function transform, 539
 - Localizing systems, 1692–1699, 2316–2317
 - Local parameters, 859
 - Local sensitivity analysis, 1955–1658, 1960–1963, 1983, 1984, 1989
 - Location parameter, 1997, 1998
 - London's Imperial College, 2017
 - Los Alamos National Laboratory (LANL), 2850, 2851, 2854
 - Loss function, 2001, 2002, 2006
 - Loss of coolant accident (LOCA), 1745, 1748, 1750, 1760–1762, 1764, 1766–1769, 2195, 2201, 2202, 2220, 2223, 2225, 2234, 2236, 2239–2241, 2283, 2294, 2314, 2315, 2317
 - Low enriched, 2712, 2719, 2722, 2733, 2736
 - Lower grid, 2269
 - Lower triangular matrix, 650, 656, 726
 - Lower uncertainty bands, 2039
 - Low oxidation-state metal ion (LOMI), 3070, 3097–3098
 - Low-pressure emergency cooling system, 2314, 2315
 - LWRWIMS, 921, 922
- M**
- MA-bearing carbides, 2953
 - MacFarlane–Boicourt method (84), NJOY code, 385
 - Mach number, 1815–1817, 1829, 1844, 1845, 1847–1854, 1859, 1874, 1875, 1889, 1891, 1893, 1899
 - Mach split function, 1872, 1874, 1876
 - Macro-band, 1151–1152, 1160
 - Macroscopic cross section, 436, 443, 462, 463, 1354, 1390
 - MACSTORE, 3169
 - MA extraction, 2966, 2969
 - Magnesium aluminate spinel (MgAl_2O_4), 2947, 2952, 2962
 - Magnesium oxide (MgO), 2947, 2952, 2953, 2963
 - Magnetic bearings, 2732
 - Main control room (MCR), 2198–2199, 2204, 2216–2218, 2242, 2243, 2280–2281, 2311
 - Main feedwater system, 2252, 2278, 2307–2308
 - Main gate valve (MGV), 2256, 2264, 2265, 2286
 - Main steam header (MSH), 2277, 2284, 2307
 - Main steam isolation valves (MSIVs), 2195
 - Main steam line system, 2252, 2277, 2307
 - Main steam supply system (MSSS), 2212
 - Makeup deaerator, 2306
 - Malonamides, 2967, 2969
 - Manhattan or 1-norm, 647
 - Man machine interface (MMI), 2198, 2217
 - Man-machine system, 2280
 - Markov model, 3442, 3450, 3452, 3453
 - Markov chains, 1957, 1972, 1974, 1976
 - Marshak boundary condition, 521, 522, 780, 787, 790
 - Martensite, 574
 - Mass distribution, 3225
 - Mass distribution coefficients, 2978
 - Mass exchange, 1820, 1824, 1830, 1833–1838, 1854, 1855
 - Mass flow rate, 2032–2034
 - Mass inventory, 2031–2034, 2040
 - Mass matrix, 791, 886
 - Mass scaling, 214
 - Master equation, 1631, 1633, 1634, 1636–1640, 1648, 1659, 1660, 1667
 - MA stripping, 2966
 - MASURCA, 2057, 2058, 2088, 2095, 2099, 2106, 2109–2111, 2113–2126, 2176
 - Material attenuation, 1338, 1355, 1356, 1388
 - Material attractiveness, 3426–3434, 3437
 - Material balance area (MBA), 3456, 3457, 3462, 3463, 3468, 3469, 3526, 3529, 3530
 - Material balance period (MBP), 3462
 - Material control and accountability (MC&A), 3427, 3453, 3457, 3526
 - Material ordering, 231
 - Material protection, control and accounting (MPC&A), 3453
 - Materials, 1316, 1323–1327, 1332, 1335–1338, 1340–1343, 1345, 1346, 1355, 1356, 1358, 1365,

- 1368–1370, 1373, 1375–1378, 1382–1389, 1391, 1394–1396, 1403, 1405, 1416, 1418, 1420, 1424–1430
 –characterization, 1424
 –regions, 928, 931, 938, 939, 1069, 1091, 1102, 1107, 1109, 1113, 1124, 1138–1140, 1148, 1154, 1223, 1227
- Material sciences, 1452, 1478, 1483, 1499–1513
- Material testing reactor (MTR), 2057, 2084, 2085, 2178
- Material unaccounted for (MUF), 3462, 3463, 3467, 3469, 3524, 3525
- Mathematical adjoint, 765, 863
- Mathematical optimization, 1284, 1286–1303, 1310
- Matrix decomposition method, 1178, 1183–1187, 1199
- Matrix exponential method, 1178, 1181–1183, 1188, 1189, 1245
- Matrix-matrix product
 –commuting, 651
 –inner product, 651
 –outer product, 651
 –permutable, 651
 –scalar times a vector, 651
- MATXS, 957–961, 967, 968, 1026
- MATXSR, 957
- Maximum entropy principle, 1999–2001, 2006, 2046
- Maximum flowrate, 2277
- Maximum fraction of average power ratio to the limiting value (MAPRAT), 1267
- Maximum fraction of limiting critical power ratio (MFLCPR), 1267
- Maximum fraction of limiting power density (MFLPD), 1267
- Maxwell–Boltzmann energy distribution, 36, 191, 192, 197
- Maxwell–Boltzmann flux shape, 194
- Maxwell gas model, 323
- MBANISN (MultiBand ANISN), a variant of ANISN, 399
- McMillan method, 2937
- MCNP, 220–223, 231, 232, 234, 237, 238, 242, 253, 264, 266, 268, 957, 962, 1340, 1406, 1407, 1409, 1418, 1429
- MCNP5, neutron transport issues, 2853
- MC²-2 quadrature scheme, 263
- Mean chord length, 257, 925, 1129
- Mean-free-path, 226, 236–238, 255, 269, 438, 439, 454, 456, 457, 484, 536, 537, 1354, 1356, 1358, 1361–1364, 1369, 1370, 1373, 1377, 1388, 1395, 1400, 1412, 1416, 1418
- Mean number of secondary neutrons, 454
- Mean pressure, 1822–1824, 1840
- Mean value, 1924, 1936, 1965, 1974, 2000–2002, 2004, 2015, 2046, 2048
- Measurable quantity, 1926, 1927, 1929
- Measurement, accuracy, 1939
- Measurement equation, 1935
- Measuring instrument, 1919, 1926–1930, 1933, 1934, 1938–1940
- Measuring standard, 1939
- Mellin convolution, 722
- Mellin transform, 722
- MELOX, 2948
- Meltdown, 2718, 2729
- Membrane separation, 3180
- Mesh-centered finite-difference, 875, 878–880, 887, 894
- Mesh-corner-finite differences, 875–878, 880, 887
- Mesh subdivisions, 1124, 1125, 1138–1145, 1147, 1150
- Mesoscale, 1500, 1503, 1505, 1512
- Message passing, 1458, 1459, 1461, 1463, 1472
- Message passing interface (MPI), 1459, 1461, 1463, 1472, 1477
- Metal fuels, 2938, 2944, 2945, 2953–2958, 2961, 2973, 2979, 2980
- Metallic bonds, 2944
- Metallic composite materials, 3130
- Metallic fuel, 2957, 2958, 2965, 2973, 2976
- Metallic shield materials, 1428
- Method of characteristics (MoC), 840–858, 932, 934–938, 953, 991, 1014, 1018, 1032, 1075, 1091, 1104–1108, 1113, 1114, 1121, 1123, 1126, 1133, 1138, 1140, 1141, 1143, 1145, 1152, 1154–1160, 1225, 1491
- Method of collision probabilities, 929, 932, 934, 1012–1014, 1017, 1020, 1032, 1047, 1070, 1071, 1075–1085, 1094, 1152
- Method of propagation of errors, 1936, 1957, 2005
- Methodological errors, 1929
- MF-ICE/MAC, 1859
- Micro-reversibility principle, 767, 770
- Microscale conservation equations, 1820
- Microscopic cross sections, 288, 924, 926, 928, 938, 964, 971, 972, 979, 1171, 1172, 1176, 1177, 1197, 1198, 1223, 1228
- Microscopic data, 86, 87, 155
- Microshield, 1340
- MIDAS facility, 2223, 2224
- Milling technique, 3071, 3106–3107, 3116, 3138, 3144–3145, 3185
- Milling cutter, 3144–3145
- Mill tailings, 2907
- MIMD. *See* Multiple Instruction, Multiple Data streams
- MINERVE, 2057, 2058, 2077, 2084–2096, 2098–2106, 2108, 2109, 2118, 2127–2130, 2135–2139, 2141, 2144, 2154, 2156, 2159, 2161, 2162, 2176
- Minkowski inequality, 647, 664
- Minor actinides (MA), 106, 119–120, 145, 2938–2941, 2945, 2948–2966, 2969, 2970, 2975, 2979, 2982–2984, 2988, 3261, 3265, 3268, 3277, 3286, 3292, 3306, 3324–3326, 3349, 3403–3405, 3412
- MINX (34), 286, 385
- MINX's successor NJOY (33), 286

- Mitigation measures, 3204, 3207, 3215–3218
- Mixed-dual variational formulation, 887
- Mixed oxide fuel. *See* Mixed oxides (MOX)
- Mixed oxides (MOX), 3326, 3332–3334, 3379, 3403, 3412
- Mixed uranium-plutonium oxide (MOX), 2937, 2938, 2940, 2948–2952, 2958, 2981, 2983, 2986, 2987, 2990
- MMIS, 2215–2218
- Mobile equipment, 3155, 3160
- MoC. *See* Method of characteristics
- Mock-ups, 2057–2084, 2109, 2113, 2126–2142, 2147, 2159, 2161, 2162, 2169, 2175, 3155
- Model
- calibration, 1913–2048
 - extrapolation, 1917, 2002, 2003, 2045, 2047
 - qualification, 2044
 - validation, 1916, 2003, 2043–2048
 - verification, 1916, 1917, 2029, 2043, 2044
- MODER, 955
- Moderator system, 2234–2236, 2238
- Moderator temperature coefficient (MTC), 1163, 1214–1215, 1220, 1666, 1711, 1723–1731, 1733
- Modified embedded atom method (MEAM), 1502
- Modified source multiplication method, 2081, 2145, 2149–2150
- Moisture-separator reheater (MSR), 2252, 2279–2280
- Molecular aggregates, 2918
- Molecular dynamics (MD), 552, 553, 568, 573, 1479, 1502
- computations, 552–554, 568, 573
 - interatomic potential, 554, 568
- Molten chloride, 2973–2975, 2979
- Molten lithium chloride, 2980
- Molten salt electrorefining, 2975, 2976
- Molten salt fuel, 2946, 2961
- Molten salt reactor experiment (MSRE), 2847–2850, 2878
- Molten salt reactors, 2942, 2946, 2961, 2973
- Molten salt transmutation reactor (MSTR), 2974
- Molybdenum, 2947
- Moment method, 1041, 1043–1046, 1049, 1067
- Moment of a cross section, 1043, 1044, 1046
- Moment theorems, 194, 195
- Momentum exchange, 192
- Monazite (RE, An) PO₄, 2985
- Monoacid HEDTA, 3095
- Monoenergetic, 452–454, 456, 464, 465, 478, 496, 497, 506, 515
- fast neutron facilities, 24–35
 - neutron transport equation, 452–454
- Monotonicity preserving, 1861, 1867
- Monte Carlo (MC), 485, 499, 532–534, 538–540, 569, 570, 1316, 1340, 1377, 1404, 1408, 1412, 1418, 1421, 1429, 1479, 1481, 1482, 1484–1488, 1502
- Monte Carlo method functional, 539
- codes, 297–298, 300, 420
- discrete ordinates, 297
 - method, 221–226, 235, 241, 272, 275, 276, 771, 772
- Moore–Penrose generalized inverse, 654–655, 660
- range space, 654, 655
- MOSAIC, 3182
- MOx, 2060, 2061, 2063–2068, 2070, 2080–2082, 2090–2092, 2100, 2102, 2104, 2123, 2142, 2144, 2152, 2161, 2165, 2171
- MPI. *See* Message passing interface
- MPMD. *See* Multiple program multiple data
- MUFT, 920
- Multiband equations, 397–399
- Multiband method, 286, 299, 303, 395, 396, 399, 406, 409–412, 414, 417, 421
- Multiband parameters, 399–402, 405, 410, 415, 421
- Multi-channel analysers, 3186, 3188–3190
- Multicore architecture, 1466
- Multigroup, 286, 287, 290, 297, 298, 302–303, 333, 354–356, 359–373, 388, 390, 393–406, 408–410, 414–416, 418, 420, 431, 453, 461, 462, 478, 501, 503, 504, 506, 523, 535, 536, 538
- approximation, 430, 462, 500, 502, 503, 505–507
 - cross sections, 502, 504–507, 535, 538, 539, 923, 955–959, 971, 973, 1023, 1026, 1039, 1043, 1047
 - discretization, 768–772
 - fission source, 227
 - flux, 769, 799
 - vs. Monte Carlo, 235, 241, 272
 - transport equations, 501–505
- Multilayer perceptrons, 1953
- Multilevel Breit–tWigner, 245, 247–249
- Multilevel energy representation, 768
- Multi-objective optimization, 1290, 1297, 1298, 1300
- Multiphase flows, general formulation, 1823–1825
- Multiple determination coefficient, 1949
- Multiple direct measurements, 1933, 1934
- Multiple instruction, multiple data streams (MIMD), 1453–1456
- Multiple measurements, 1928, 1930, 1934
- Multiple program multiple data (MPMD), 1463–1464, 1484
- Multiplication constant, 1632
- Multiplying system, 1119–1120, 1632, 1636
- Multi-scale Simulation Code-SIM (MuSiC-SIM), 1817, 1888
- MVP-BURN, 1164–1170, 1182, 1187, 1190, 1198
- ## N
- Nanoscale, 1500, 1501, 1512
- Narrow resonance, 313, 318, 319, 356, 978
- Narrow resonance (NR) approximation, 255, 257, 258, 264, 924, 926, 956, 975, 977–986, 992, 997,

- 998, 1007, 1014, 1016, 1019, 1023, 1024, 1028, 1033, 1034, 1038, 1041, 1046, 1047, 1051, 1052, 1059, 1061, 1063–1064
- Narrow resonance infinite mass (NRIM)
approximation, 981
- NASA PSA Procedures Guide, 1785, 1788
- National Aeronautics and Space Administration, 1762
- National Nuclear Data Center, 213, 214
- Natural materials, 1425–1426
- Natural nuclear reactor, 2903
- Navier–Stokes equations, 1494, 1495
- Near-real-time accounting (NRTA), 3492, 3493, 3498, 3526, 3529
- Needle scaling, 3086–3087, 3089, 3113–3115
- Negative definite, 658, 661
- Negative semi-definite, 658
- Neptunium, 2937, 2938, 2944, 2949, 2959, 2960, 2989
- Net current, 224, 225
- Net neutron in-current, 1231
- Net particle flow, 1319
- Net positive suction head (NPSH), 2196
- Neumann's function, 688
- Neutron, 3–74, 545–559, 563, 567, 568, 572, 573, 576, 577, 579, 580, 582, 584, 587, 592, 593, 595, 598, 600, 602–605, 607, 609, 610, 612, 614, 616, 619, 621, 622, 626, 627, 629–631
–absorption, 2843, 2852–2854, 2856, 2860, 2866, 2867, 2886, 2887
–accelerator sources, 2845–2847, 2858, 2868, 2876, 2883, 2885, 2886, 2892
–activation, 3056, 3057
–albedos, 1402, 1403, 1405–1407, 1412, 1420
–attenuation, 1396, 1426, 1428–1429
–capture, 89, 90, 98, 113–115, 132, 133, 141, 158, 161, 162, 169, 2965
–cross sections, 3–74
–current, 507
–current method, 1008, 1009, 1013–1017
–data for actinides, 86, 106–128
–density distribution, 52–54, 58
–diffusion equation, 862, 863, 874–894
–dose, 546, 610
–economy
 –control rods, 2858
 –fission products, 2687, 2851, 2852, 2863, 2883
 –graphite (*see* Graphite)
–fluctuations, 1631–1633, 1664, 1666, 1731, 1733
–flux, 284, 288, 289, 326, 352, 353, 355, 395, 399, 765, 799, 805, 859, 862–864, 867–869, 874, 875, 877, 878, 880, 883, 1664–1667, 1669, 1674, 1718, 1722, 1723, 1726, 1729
 –distribution, 53
 –harmonics, 863
–fusion sources, 2886
 –induced photon production, 290, 293–295
 –moderators, 238
 –multiplicity, 104, 121–123
–noise, 1631–1640, 1665–1668, 1670, 1678–1696, 1698–1704, 1711, 1716–1720, 1722, 1724, 1725, 1729–1731
–noise simulator, 1690, 1691, 1695, 1716, 1717, 1719, 1731
–poisoning, 2965
–scattering, 86, 90, 91, 162–165, 169, 173, 177, 179
–shielding, 1378–1400, 1412, 1425, 1427–1429
–slowing down, 939, 944, 956, 983, 991–997, 1005–1012, 1014, 1023, 1024, 1032, 1033, 1047, 1061, 1069, 1119
–sources, 1322–1328, 1353, 1385, 1387, 1388, 1390
–spectrum, 502, 506, 507, 512, 513, 517, 547, 602, 2923, 2926
–speed, 288, 326
–standards, 107, 179
–streaming, 1420–1423
–transport, 427–540
–velocity, 1228
- Neutronic current, 860
- Neutronics, 1478, 1481–1483, 1489, 1490, 1511
- Neutron noise simulator, 1690, 1691, 1695, 1716, 1717, 1719, 1731
- Neutron's-eye-view, 435
- Neutron time of flight method, 6, 7, 13, 16, 51–53
- Neutron transport equation limitations, 462–464
- Nikolaev and Phillipov for neutrons, 394
- Nikolaev's, "all the way" method, 410
- Nil ductility reference temperature (RTNDT), 2206
- NIS, 3082, 3089, 3106, 3124, 3126–3130, 3134, 3141, 3142, 3149, 3230, 3237
- Nitric acid (HNO₃), 3070, 3078, 3091–3092, 3094, 3096, 3097, 3099, 3103, 3118–3120, 3153
- Nitric acid electrolytes, 3078, 3119, 3120
- Nitride fuels, 2961, 2979
- Nitrides, 2946–2949, 2953–2958, 2961, 2973, 2979
- Nitrilotriacetic acid (NTA), 3096
- Nitrogen, 2018, 2021, 2024, 2030, 2031
- Nitrogen benchmark blowdown experiment, 2018
- NJOY, 196, 202, 205, 220, 234, 250, 252, 253, 257, 260, 264, 923, 924, 926, 942, 955–959, 961, 964, 965, 989, 990, 1026, 1032, 1063, 1232
- NJOY processing code, 126–128, 147, 163, 170, 178
- Nodal balance equation, 890, 892, 893
- Nodal collocation method, 880
- Nodal infinite multiplication factor, 1227
- Noise and vibrations, 3147, 3208, 3210, 3212–3214, 3217
- Noise source, 1631, 1665–1671, 1687–1689, 1691–1711, 1716, 1718, 1719, 1721, 1725, 1732, 1733
- Nominal parameter values, 1923, 1935, 1955, 1959, 1965, 1971, 1984, 1987, 2005, 2006, 2022, 2024, 2025

- Nominal values, 1923, 1935, 1936, 1942, 1959, 1962, 1966, 1974, 1983, 1987, 1988, 1991, 1994, 2001–2002, 2004, 2007, 2008, 2013–2016, 2029, 2048
- Non-coincident group boundaries, 390–393
- Non-condensable gases, 2262
- Nondestructive assay, 3463–3466, 3468–3470, 3497, 3520, 3528, 3529
- Non-integer moments, 1046
- Nonlinear functional, 1956, 1970
- Nonproliferation Impact Assessment (NPIA), 3434–3453
- Nordheim equation, 2143
- Norm
- direction cosines, 647
 - distance between two vectors, 647
 - energy norm, 647
 - equivalent, 647
 - finite-dimensional Euclidean space, 647
 - floating point operations (FLOP), 647
 - homogeneous, 647
 - normed vector space, 647, 664–666
 - parallelogram identity, 647
 - positive definite, 647
 - triangle inequality, 647, 662, 664
 - unit vector, 647
- Normal distribution, 1918, 1919, 1931, 1934, 2001, 2015, 2016
- Normalization condition, 197
- Normal operating conditions, 1939
- Novovoronezh NPP, 2251
- ²³⁷Np, 2938, 2988
- NPP-92 design, 2252, 2255
- nPr-BTP, 2968, 2969
- NR. *See* Narrow resonance
- NRIM approximation, 260
- N-reactor, 1761
- N-streaming, 1295
- N-terms rational approximations, 1000–1002, 1019, 1020, 1027, 1052, 1054, 1057
- n_TOF CERN, 6, 7, 16–19
- Nubar, 121–122, 124, 125, 144, 174
- Nuclear data evaluation, 83–181
- Nuclear data files, 941, 942, 954–956, 960, 1165
- Nuclear data library, 86, 131, 134, 167–181
- Nuclear data processing, 178
- Nuclear data processing codes, 282, 285–287, 311
- Nuclear Energy Agency (NEA), 3005, 3065, 3219, 3220, 3237, 3242–3243
- Nuclear Energy Institute (NEI), 1780, 3232
- Nuclear energy systems, 2737, 2738
- Nuclear fission related problems, 283
- Nuclear fuel management, 1254–1309
- Nuclear heating, 126–128
- Nuclear Island (NI), 2201, 2202
- Nuclear Management and Resources Council, 1780
- Nuclear material, 1631, 1659–1664
- Nuclear model codes, advances, 282
- Nuclear Nonproliferation Treaty, 3424
- Nuclear plants, 1758–1759
- Nuclear propulsion, 2712, 2737
- Nuclear reaction model, 87–89, 97, 112, 130, 137
- Nuclear reactor kinetics, 450
- Nuclear Regulatory Commission (NRC), 1761, 1768–1774, 1777–1781, 3005, 3012, 3026, 3035, 3062–3063, 3171, 3173, 3221, 3232
- Nuclear waste, 3257–3415
- Nuclide identifiers, 962–964, 968
- Null/zero matrix, 649, 650
- Null/zero vector, 645, 648
- Number albedo, 1401
- Number field, 645, 649
- Numerical algorithm verification (NAV), 1916, 2043
- Numerical error estimation, 1916
- NUPEC, 3136–3139
- NUREG, 3062
- NUREG-0800, 1757, 1758
- NUREG-1150, 1771
- Nusselt correlation, 2027
- Nuteck horizontal modular storage (NUHOMS), 3173–3175
- Nu-value and fission spectrum, 960–961
- O**
- Oblique beams, 1372–1373
- Occupancy factor, 1375
- Occupational risks, 1441
- Off-line, 2011
- decontamination, 3192
 - with foresight, 2011
- One-at-a-time (OAT), 1940, 1942–1944
- One-over-E, 767
- One-speed approximation, 492, 499
- One-speed transport equation, 430, 452, 453, 500–507
- One-speed primal functional, 880, 881
- Onion-skin effect, 1067, 1202–1204
- "On-line" decontamination, 3192
- On-load refueling, 2714
- OpenMP, 1460, 1461, 1463, 1466, 1477, 1491
- Operating basis earthquake (OBE), 2286, 2318
- Operating cycle, 1255, 1256, 1309
- Operating experience, 1744, 1747, 1754, 1760, 1771, 1785, 1808
- Operating lifetime, 3005, 3006, 3010, 3059, 3221
- Operation and Maintenance (O&M) costs, 1773
- Operational reliability, 2277
- Operational waste, 3176
- Operation monitoring (OM), 2311
- Operations on matrices
- addition(summation), 649–651, 663
 - inner product, 651
 - matrix-vector product, 651

- scalar multiplication, 650, 651
 - sum/difference, 651, 662
 - Optical depth, 454
 - Optical distance, 484, 1074, 1081, 1094, 1095
 - Optical model, 87, 97–100, 104, 119, 130, 134
 - Optical modes, 216
 - Optical reciprocity relationship, 1078, 1080
 - Optimized polar quadratures, 848, 850, 851
 - Optimized power reactor 1000 (OPR1000), 2187–2201
 - Orbital cutters, 3144–3145
 - ORELA, 6, 7, 12–15
 - Organic acid electrolytes, 3120
 - Organic solvents, 3101, 3180
 - ORIGEN2, 1165, 1177, 1181, 1183, 1187
 - ORNL, 2845–2847, 2849–2852, 2856, 2857, 2871, 2878, 2888
 - Orthogonal complement, 648, 673
 - Orthogonality, 647
 - mutually orthogonal, 648
 - orthonormal set, 648
 - two vectors, 647
 - Orthogonal matrix, 654, 655, 658, 659, 661, 667
 - Orthogonal polynomials, 667
 - recursion formula, 704
 - system of orthogonal polynomials, 704–705
 - weight function, 704
 - Orthonormal basis, 1961, 1969, 1970
 - Oscillation technique, 2087, 2088, 2104, 2105, 2136–2141, 2145, 2154
 - Oscillator energies, 207
 - Osher–Chakravarthy TVD method, 1886
 - Outer iterations, 1089, 1090, 1098, 1122, 1123
 - Outer product, 646, 647, 651, 653, 654, 661, 663
 - Outgoing current, 755, 832, 833
 - Out-of-core nuclear fuel management, 1254–1266, 1291–1293
 - Out-of-service state, 3005
 - Over the top method (OTM), 2228–2230, 2233
 - Oxalic acid ($C_2H_2O_4$), 3070, 3074, 3093, 3094, 3099, 3102–3104, 3151–3153
 - Oxide fuels, 2938, 2945, 2948–2953, 2958–2960, 2972, 2973, 2979–2981
 - Oxy-arc cutting, 3127–3128, 3149
 - oxygen jet cutting, 3128–3129, 3149
 - Oxygen lances, 3125, 3127, 3149
- P**
- Ψ Function
 - asymptotic expansion, 686
 - gamma function, logarithmic derivative, 685
 - Package, 3273, 3276, 3285, 3286, 3292, 3301, 3302, 3304, 3307, 3311, 3321–3324, 3328, 3338–3341, 3344, 3346, 3349–3353, 3376, 3380, 3388, 3395, 3400, 3403–3405, 3408, 3414, 3415
 - spent fuel, 3306, 3309, 3327, 3328, 3330, 3412
 - waste, 3285, 3292, 3301, 3302, 3304, 3309, 3311, 3321, 3324, 3338, 3346, 3350–3353, 3405, 3412
 - Padé approximation, 1044, 1045, 1178, 1187–1188, 1190
 - Paired OAT, 1942
 - Pair of distinct trials, 1932
 - Palletizing robots, 3157
 - PANACEA, 1223
 - PARAGON, 932
 - Parallel programming, 1452, 1458, 1459, 1462, 1463, 1466, 1468, 1474–1478
 - Parameter importance ranking table (PIRT), 2044, 2045
 - Parameter variations, 1942, 1956–1958, 1960, 1962, 1963, 1966, 1967, 1974–1976, 1983, 1988, 1989, 2024, 2029
 - Parseval’s equality, 668
 - Parseval’s identity, 649, 668
 - Parseval’s theorem, 747
 - Particle, 282–285, 288–290, 297, 298, 304, 319, 321, 322, 331, 384, 411, 2712, 2720, 2721, 2723, 2724, 2729, 2733, 2734, 2736, 2737, 2743, 2746, 2903, 2920, 2927, 2928
 - balance absorption, 231
 - conservation, 753, 776, 777, 833
 - deformation, 1825, 1841–1843
 - flux, 753, 772, 821, 840, 883
 - pressure, 1829, 1832
 - stress, 1821, 1822, 1827, 1828
 - stresslet, 1839, 1840
 - velocity fluctuations, 1829, 1833
 - PARTISN, 1340, 1429
 - Partition function, 1999
 - Partitioning and transmutation (P&T), 2938, 2940, 2963, 2964, 2982, 2983, 3164
 - Passive autocatalytic recombiners (PARs), 2201, 2222
 - Passive emergency core cooling system, 2282, 2314
 - Passive nondestructive assay (PANDA), 3466
 - Path length density, 442
 - Paving breakers, 3106–3107, 3116
 - Peak check technique, 2165–2167
 - Peierls’ equation, 485
 - Pellet, 2921–2923, 2925–2930, 3283, 3332–3334, 3414
 - fuel, 2949, 2953, 3332–3335, 3411, 3412
 - infiltration technique, 2952
 - Pellet-cladding interaction (PCI), 2930
 - Penalty function, 1288, 1289, 1300
 - Periodic boundaries, 461, 479
 - Periodic boundary conditions, 762, 796, 801, 1120
 - Periodic errors, 1934
 - Perkins and Giles (95), CLYDE code, 386
 - Permissible doses, 1375, 1440
 - Permutation matrix, 652, 658–659
 - Personal errors, 1929, 1933
 - Personnel organization, 3229
 - Perturbation theory, 766

- Petroleum ethers, 3101
- PGV-1000 horizontal steam generators, 2251, 2276
- Phase diagrams
- ab-initio, 567, 568
 - amorphous transformation, 566, 567, 580
 - ballistic mixing, 563, 566
 - clustering, 558-560, 562-563, 569, 571, 582
 - disorder, 566
 - equilibrium phase diagrams, 565
- Phase field (PF), 1503, 1505, 1506
- Phase-indicator function, 1860
- Phase shifts, 246, 251, 252
- Phase space, 753, 760
- Phase space density, 440
- Phasic stress, 1826, 1845, 1846, 1860
- Phénix reactor, 2952, 2958, 2959, 2961
- PHOENICS, 1859
- PHOENIX, 922, 1020
- Phonon, 192, 205, 207
- density of states, 202
 - dispersion curves, 202
 - expansion, 196-197, 200, 202, 203
- Phosphoric acid (H_3PO_4), 3070, 3077, 3078, 3091, 3092, 3096, 3104, 3118, 3119, 3153, 3180
- Phosphoric acid electrolytes, 3119
- Photon, 546-548
- attenuation, 1359-1378, 1394, 1396, 1415
- and electrons, 582-589
- Photon neutron production, 1323, 1324
- Physical inventory verification (PIV), 3458, 3461, 3492, 3493
- Physical protection, 2739
- Physical quantities, 1926, 1934, 1939, 1994
- Physical security, 3038, 3042
- Pilot operated safety relief valves (POS RVs), 2205, 2210, 2220, 2225, 2247
- Planar symmetry, 460, 467
- Plane sources, 1362-1369, 1414, 1416, 1417, 1421, 1422
- Plasma-arc, 3123, 3156
- cutting, 3131, 3133-3137
 - cutting torch, 3137
 - gouging, 3134, 3136, 3137, 3150
- Plasma circular saw, 3134-3135, 3150
- Plasma compass saw, 3134-3136, 3150
- Plate glass, 1429
- Plenum, 2923
- Plexiglas, 3080, 3112
- PLUS7, 2190, 2206, 2209, 2211, 2212, 2246
- Plutonium, 2937, 2938, 2941, 2944, 2949, 2954, 2972, 2989
- commercial-Pu, 2844, 2886
 - denaturing, 3425
 - disposition, 3425
 - weapons-Pu, 2844, 2851, 2886-2888
- Plutonium and uranium refining by extraction (PUREX), 2729, 2938, 2940, 2949, 2964-2967, 2970, 2985
- Plutonium Inventory Measurement System (PIMS), 3497, 3500-3501
- P_n method, 778-794, 862
- Pohang neutron facility (PNF), 6, 7, 20-21
- Point defects (PD), 545, 551, 554, 557-559, 577-579, 582, 621
- Point-Kernel, 1340, 1353-1354, 1362, 1365-1370, 1381
- Point-kinetic approximation, 1679
- Point kinetics equations, 431, 485, 524, 527-531
- Point model, 1633, 1641
- Point reactor approximation, 1676-1677
- Point-to-point, 1472
- Poisson distribution, 735-737, 1631, 1636
- Polar angle, 432, 433, 465, 1080, 1094, 1095, 1108, 1109, 1111-1116, 1121, 1134, 1137, 1145, 1150-1154, 1156
- Polar directions of motion, 1076, 1080, 1111, 1112, 1152
- Polar integration, 1076
- Population and the economy, 3211-3213
- Population density, 753
- Porter-Thomas distribution, 94-96
- Position and time correlation function, 193
- Positive definite, 646-648, 658, 659, 661, 662, 673, 674, 681, 682, 727, 728, 737, 738
- Positive semi-definite, 658, 659, 673, 674
- Positivity preserving, 1867, 1879
- Posterior distribution, 1996
- Post-irradiation examination (PIE), 1165, 1177, 1509
- Post Shutdown Decommissioning Activity Report (PSDAR), 3232, 3237
- Postulated accident, 1748, 1749, 1752, 1758, 1782
- Potassium dichromate ($K_2Cr_2O_7$), 3096
- Potassium hydroxide (KOH), 3094, 3095
- Potassium permanganate ($KMnO_4$), 3092, 3095, 3096
- Potential scattering cross sections, 925, 958, 966, 977, 988, 989, 992, 997, 1016, 1018, 1019, 1027, 1049, 1057
- Powder cutting, 3123
- Powder injection flame cutting, 3123-3124, 3149
- Powder metallurgy, 2948, 2951-2952
- Power factor, 765
- Power governor (PG), 2280
- Power normalization, 1161, 1175, 1176, 1199-1200
- Power operated relief valves (PORVs), 2205
- Power peaking, 1266-1271, 1276, 1278-1281, 1297, 1300, 1304, 1309
- Power reactor, 1631-1711, 1715, 1726, 1731, 1732
- Power reactor noise, 1631-1711
- PRA policy statement, 1772-1773
- Prandtl's relation, 1877
- Precursor densities, 431, 444, 445, 449-451, 455, 462, 464, 524
- Predictive best-estimate parameters, 2007

- Predictive estimation (PE), 1917, 2002, 2003, 2036, 2043, 2045, 2046
- Predictor-corrector method, 1195–1198, 1205
- Preequilibrium emission, 241
- Preequilibrium model, 100–101
- PREPRO, 283, 286, 319
- Pressure, 2021, 2029
 - head, max, 2277
 - relief tower, 2260, 2262–2263
 - tube, 2231, 2232, 2237, 2242
 - vessel, 546, 556, 557, 565, 573, 574, 589–598, 632, 634
- Pressurized heavy water reactor (PHWR), 2187, 2230, 2236, 2238, 2245
- Pressurized water reactor (PWR), 549, 557, 573, 587, 591–593, 598, 599, 607, 625, 632, 1631, 1697–1699, 1701, 1703, 1704, 1706, 1707, 1727–1729, 1731, 3283, 3319, 3327, 3328, 3336, 3340, 3342, 3343, 3389
- Pressurizer, 2252, 2263, 2273–2275, 2277, 2283, 2285, 2295, 2296, 2302–2304, 2315, 2316
- Prestressed concrete, 2715–2717, 2725
- Price-Anderson Act, 1760
- Primal discretization, 875
- Primal–dual agreement, 875
- Primary circuit, 2252, 2254, 2263–2277, 2282–2285, 2295–2306, 2314, 2316, 2318
- Primary knocked-on atom (pka), 551–554, 568, 627
- Primary masses, 3224–3225, 3227
- Primary standard, 1939
- Primitive variables, 1848, 1862, 1879, 1887
- Principal axis, 756
- Principal/main diagonal, 649, 652, 727
- Prior probability distribution, 1924, 2003
- Probabilistic risk assessment (PRA), 1762, 1772–1773, 1784
- Probabilistic safety assessment (PSA), 1784–1808, 2199
 - acceptance criteria, 1783, 1784
 - accident sequence precursor (ASP) program, 1769
 - anticipated transients without scram, 1769
 - common cause failures, 1764, 1767, 1770, 1785, 1786, 1790–1793, 1795, 1800, 1803, 1808
 - conditional containment failure probability, 1771, 1784
 - core damage frequency, 1771, 1775, 1776
 - data analysis, 1792, 1800
 - dependent failure analysis, 1791, 1792
 - design basis events, 1782, 1783
 - dynamic analyses, 1808
 - dynamic methodologies, 1808
 - dynamic process system reliability and safety analysis, 1808
 - emergency operating procedures, 1783
 - engineered safety features, 1764
 - event tree, 1762–1765, 1781, 1789–1794, 1799, 1800, 1808
 - expert judgment, 1792, 1800, 1804
 - failure data, 1764
 - failure modes and effects analysis, 1788
 - fault trees, 1763–1765, 1767, 1781, 1790–1793, 1799, 1800
 - fault trees and event trees, 1763–1765, 1781
 - frequency-consequence (F-C) curve, 1784
 - human–machine interface, 1783
 - individual plant examination, external events, 1771–1772
 - initiating events, 1763–1764, 1766, 1773, 1778, 1784, 1785, 1787–1796, 1798–1799, 1804
 - inspections, tests, analyses, and acceptance criteria, 1783
 - interim reliability evaluation program, 1769
 - large early release frequency, 1770, 1771, 1775, 1776, 1784
 - licensee event reports, 1769
 - logic modeling, 1790–1791, 1799–1802
 - loss of fluid tests, 1762–1764
 - maintenance rule
 - 10 CFR 50.65, 1779
 - non-safety-related SSCs, 1779, 1780
 - safety-related, 1779, 1780
 - master logic diagrams, 1790, 1799
 - minimal cut-sets, 1793, 1797, 1806
 - reactor operators, 1783
 - Regulatory Guide 1.174, 1773, 1774
 - release categories, 1766–1767
 - risk achievement worth, 1774
 - risk informed regulation, 1772, 1774–1777, 1781
 - requests for additional information, 1774
 - risk reduction worth, 1774, 1795
 - safe design, 1782–1784
 - safety analysis reports, 1781, 1782
 - safety goals
 - core damage frequency, 1770
 - large release frequency, 1770
 - quantitative health objectives, 1770
- sensitivity analysis, 1765, 1794–1795, 1797
- sodium-cooled fast reactor, 1782
- software reliability, 1791
- technical specifications
 - allowed outage times, 1781
 - consolidated line item improvements process, 1781
 - limiting conditions for operation, 1781
 - risk-informed technical specifications, 1781
 - safety evaluation report, 1781
 - standard technical specifications, 1781
 - surveillance requirements, 1781
- three mile island accident, 1768–1769
- uncertainty analysis, 1764–1765, 1772, 1793–1794, 1804

- WASH-740, 1760, 1767
- WASH-1400, 1760, 1762-1768, 1808
- Probability, 288-290, 294, 299, 301, 302, 320, 352, 374, 377, 395, 400-402, 408-411, 1631-1635, 1637-1639, 1646, 1647, 1650, 1651, 1657, 1659-1661, 1664, 1667, 1732, 1916, 1919, 1931-1933, 1946-1948, 1974, 1994-1997, 2001, 2002, 2017
 - density function, 1038, 1039, 1043
 - distribution, 288, 316
 - distribution for total, 264, 265
 - table(s), 241, 264, 265
 - table approach, 956, 1035, 1038-1041, 1047, 1067
- Probability theory
 - A.Kolmogorov, 714, 716
 - axiom I (existence), 716
 - axiom II (additivity), 716
 - axiom III (normalization), 716
 - beta distribution, 739, 740
 - binomial and multinomial distributions, 733-734
 - central limit theorem, 737, 738, 740-741
 - chi-square (χ^2)-distribution, 738, 740
 - conditional probability, 714, 717-720, 743
 - continuous uniform distribution, 732-733
 - degenerate distribution, 732
 - discrete uniform distribution, 732
 - expectations and moments
 - central moments, 724, 725
 - crude moments, 724
 - mean values, 724
 - mixed central moments, 724
 - moment of order, 724
 - moments about origin, 724
 - moments about the mean, 724
 - raw, 724, 725
 - standard deviation, 724
 - variance, 724
 - zeroth-order moment, 724
 - exponential distribution, 735, 739, 740
 - F-distribution, 740
 - few-parameter distribution and Pearson's equation, 740
 - finite random variables, 718
 - gamma distribution, 739, 740
 - Gaussian distribution, 735-738, 745
 - geometric distribution, 734
 - infinite discrete random variables, 718
 - log-normal distribution, 738-739
 - multivariate normal distribution, 737-738
 - multivariate probability distributions
 - conditional probability, 721
 - marginal probability density, 721
 - probability density function, 721, 722
 - negative binomial (Pascal) distribution, 734
 - non-denumerable random variables, 718
 - parameter, 715, 725-727, 732, 733, 735-737, 739, 740
 - population, 715
 - random variable, 718, 720-735, 737-741
 - statistically independent, 718
 - student's t-distribution, 739
 - subjective, 718-720
 - subjective inductive reasoning, 716
 - three axioms, 714, 716
 - variance, standard deviation, covariance and correlation
 - central limit theorem, 726
 - conditional covariance, 728
 - conditional density, 728
 - conditional expectation, 727
 - conditional mean, 728
 - correlation coefficients, 726-727
 - correlations, 726-729
 - covariances, 726-729, 732
 - degeneracy, 728
 - errors, 725-727, 729
 - fractional error matrix, 729
 - fully anti-correlated, 728
 - fully-correlated, 728
 - kurtosis, 729
 - law of iterated expectations, 728
 - leptokurtic, 729
 - mesokurtic, 729, 736
 - minimum variance theorem, 725
 - moment generating function (MGF), 730, 731
 - nondegenerate, 728
 - platykurtic, 729, 736
 - relative covariance matrix, 729
 - scaling, 726, 731
 - skewness, 729
 - translation theorem, 726, 731
 - waiting time, 734
- Processing of nuclear data, 178
- Process monitoring, 3467, 3469, 3470, 3474, 3492-3501, 3528
- Production, 2712, 2714, 2716, 2730, 2739-2744
 - bias, 554
 - cross section, 952, 954, 967, 976, 1151, 1211
- Product quadrature, 826, 829
- Product rules, 1995
- Programmable logic controller (PLC), 2215
- Progressing errors, 1934
- Project control, 3222
- "Projected" PC (PPC) methods, 1206
- Projected ratio, 1076, 1077
- Projected track segment, 1134
- Projection pursuit algorithms, 1953
- Project management, 3008, 3009, 3027, 3031, 3038, 3045, 3050, 3195, 3220, 3223, 3237, 3240, 3241
- Project risk management (PRM), 3043

- Prompt fission, 1323, 1324, 1328–1329
 –gamma photons, 1328–1329
 –spectrum, 438
- Prompt neutron fission spectrum, 1225
- Prompt neutrons, 2746
- Propagation of errors, 1935–1938, 1957, 2005
- Propagation of moments, 1935, 1936, 1938, 2004, 2013, 2047
- Proper orthogonal decomposition, 2047
- Protective clothing, 3008, 3141, 3154, 3214
- Protective tube unit (PTU), 2257, 2266, 2267, 2289, 2290, 2297, 2298
- PSA applications guide, 1773–1774
- PSA quality, 1774, 1783
- Pseudo-elastic peak, 198
- Pseudo fission products, 1164, 1165, 1170
- Pseudo-transport equation, 1836
- Pseudo-turbulent
 –kinetic energy, 1816, 1825, 1827, 1828, 1830–1832, 1836, 1839, 1841, 1846, 1847
 –velocity fluctuation, 1815, 1819, 1860
- ²³⁹Pu evaluation, 115–118
- PUFF processing code, 178
- Pulsated neutron generator, 2058
- Pumping power, 2712, 2713, 2745
- Purely random errors, 1930, 1931
- Purely scattering medium, 414
- PWR oxidative decontamination (POD), 3099–3100
- Pyrocarbon, 2720, 2724, 2729, 2920, 2928
- Pyrochemical, 2938
 –processes, 2965, 2971
 –separation, 2972, 2974
- Pyrochemistry, 2972–2977, 3413
- Pyrochlores, 2985
- Pyrometallurgy, 2973
- Pyrophoricity, 2948, 2955, 2957
- Pyro-reprocessing, 2971, 2973, 2976, 2977, 2979
- Q**
- QAD, 1340, 1429
- Quadratically interpolable, 300
- Quadratic-leakage approximation, 890
- Quadratic loss, 2002, 2006, 2046
- Quadrature ball, 1109, 1110
- Quadrature set, 1040, 1075, 1105, 1108–1114, 1116, 1126, 1127, 1150, 1152–1155
- Quality assurance (QA), 1744, 1745, 1747, 1749, 1752, 1753, 1774, 1783, 3027, 3038, 3041, 3042, 3045–3049, 3051, 3052, 3054, 3196
- Quantity Criterion, Quality control criterion, 1751–1752
- Quality factor, 1343, 1344, 1350–1353, 1379, 1435
- Quantity Criterion, Quantitative model
 extrapolation, 2003, 3460
- Quantum mechanical (QM), 1502, 1503
- Quantum Monte Carlo (QMC), 1502
- Quasi-conservative form, 1880–1882
- Quasi-random errors, 1930, 1931
- Q value, 1324–1326, 1343
- R**
- Radial clad and wrapper expansion, 2534
- Radial expansion, 2504, 2530, 2531
- Radiation field, 1316–1339, 1341, 1343, 1346–1348, 1354, 1408
- Radiation hardening
 –channels, 573
 –dislocations, 571–573
 –ductility, 571, 573
 –strain hardening, 571, 572
 –yield strength, 570, 571
- Radiation induced conductivity, 581–583
- Radiation induced electrical degradation, 581
- Radiation output factor, 1373
- Radiation Protection Standards, 1439–1441
- Radiation Safety Information Computational Center (RSICC), 1330, 1375, 1409, 1412, 1429
- Radiation streaming, 1400, 1412–1423
- Radiation weighting factors, 1343, 1344, 1351
- Radiation yield, 1338
- Radiative capture, 1332, 1335
- Radioactive cleanup, 3408, 3413
- Radioactive contamination, 3409, 3413
- Radioactive decay, 3266, 3270–3272, 3291, 3318, 3326, 3334, 3337, 3346, 3354, 3389, 3397, 3399, 3400, 3404, 3405, 3407, 3410
- Radioactive decay constant, 438
- Radioactive decontamination, 3409, 3413
- Radioactive dust, 3067
- Radioactive half-life. *See* Half-life (radioactive)
- Radioactive inventory, 3039, 3042, 3044, 3056, 3060, 3217
- Radioactive waste, 3257, 3258, 3261, 3263, 3276, 3277, 3282, 3295, 3331, 3346, 3347, 3390, 3401, 3402, 3408–3411, 3413–3415
 –disposal, 3347, 3413
 –storage, 2263, 2291, 2295
- Radiological emergency, 3051, 3052, 3200
- Radiological impact assessment, 3013, 3207, 3213–3214
- Radiological inventory, 3008, 3184, 3189
- Radiological protection, 3051, 3174, 3207, 3215, 3228
- Radiolysis, 2718, 2970, 2989, 2990, 3292, 3301, 3321, 3322, 3326, 3331, 3335, 3381, 3386, 3413
 –boron, 587, 588
 –BWR, 586–588, 599
 –free radicals, 584, 585
 –generation rates, 584
 –hydrogen water chemistry, 588
 –linear density of energy deposition rate (LET), 584, 585

- PWR, 587
- spurs, 584, 585
- Radiolytic species, 3413
- Radiometric, 1316, 1318, 1319, 1340, 2904
- Radiometric measurements, 3041
- Radionuclide inventory, 3394, 3400, 3412–3414
- Radionuclides, 3261, 3263–3266, 3270, 3273–3277, 3282–3285, 3288, 3293, 3301, 3303, 3305–3307, 3311, 3320, 3321, 3323–3326, 3354, 3359–3360, 3367–3369, 3371–3377, 3379, 3389–3401, 3403–3410
- Radiotoxicity, 2739, 3278, 3285, 3286, 3288–3291, 3348, 3349, 3403, 3405, 3412, 3414
- Radiotoxicity potential, 3278, 3412, 3414
- Radiotoxicity (potential). *See* Potential radiotoxicity
- Random error, 1928–1931, 1933, 1934, 1939
 - measurement, 1939
 - and "systematic" errors, 3497, 3518, 3520–3522, 3530–3532
- Random sampling, stratified importance sampling, 1947
- Range and null space matrix
 - column space, 655
 - elementary functions of a matrix, 657
 - image space, 655
 - kernel of A, 655
 - nullity of A, 655
 - null space of A, 655
 - partitioned, or blocked, matrix, 655–657
 - quasi-diagonal, 656
 - range, 655
 - reflexivity, 657
 - row space, 655
 - Schur formula, 657
 - similar, 657
 - symmetry, 657
 - transitivity, 657
 - upper (lower) quasi-triangular, 656
- Rankine–Hugoniot (RH)
 - conditions, 1865, 1870, 1876
 - relations, 1864
- Rank of matrix
 - column (row) rank, 653
 - linearly independent columns(rows), 653
- Rank-one perturbation, 654
- Rank transformation, 1948, 1950, 1951
- Rate of disappearance/build-up of materials, 284
- Raviart–Thomas finite-element, 887, 894
- Ray effects, 535, 838
- Rayleigh coefficient
 - generalized eigenvalue, 662
 - generalized eigenvector, 662
- Rayleigh–Lamb equation, 1830–1832, 1837, 1841
- Rayleigh ratio, 766
- Rayleigh–Ritz method, 880
- Ray tracing, 933, 1032, 1086, 1096, 1097, 1114–1116, 1133, 1138, 1139, 1141–1152, 1160
- RBE. *See* Relative biological effectiveness
- Reaction channel, 67
- Reaction cross section, 288, 371
- Reaction rate distributions, 2058, 2102, 2120
- (α, n) Reactions, 1325–1327
- Reaction yield, 41
- Reactivity, 452, 525–527, 531, 1631–1634, 1641–1659, 1680–1682, 1713–1717, 1723–1731, 2058, 2060, 2062, 2067–2069, 2076–2078, 2081–2083, 2101–2103, 2106–2108, 2114, 2120, 2126, 2137, 2140–2159, 2745–2747
 - control systems, 2734
 - measurement methods, 1632
 - peak, 1213
 - swing, 2928
- Reactor, 3, 4, 6, 13, 31, 36, 43, 46, 47, 2251–2320
 - breeder reactors, 2843, 2844, 2847–2849, 2856, 2885
 - building, 2252, 2256–2263, 2290, 2291, 2294
 - coolant systems, 2252, 2254, 2263, 2295–2297, 2315
 - core, 2252, 2253, 2257, 2266–2272, 2288, 2298–2301, 2314, 2315
 - database, 859
 - dosimetry, 168, 169, 175
 - (in)homogeneous, 2854, 2856
 - internals, 2266, 2269, 2286
 - k_{eff} , 2865, 2868, 2882
 - molten salt, 2580, 2847, 2849, 2851, 2852
 - physics, 1452, 1479, 1483, 1501
 - power limitation system, 2208, 2280, 2310
 - vessel, 2253, 2257, 2259, 2260, 2263–2266, 2275, 2280, 2282, 2284–2286, 2297–2298, 2313, 2314, 2317
 - Reactor and unit power control system, 2310
 - Reactor coolant pump (RCP), 2190, 2203, 2207, 2210, 2251, 2256, 2263, 2264, 2273, 2281, 2286, 2295, 2296, 2302, 2303, 2306
 - Reactor design safety, 1769, 1783
 - defense-in-depth, 1743
 - Manhattan Project, 1742
 - Reactor pressure vessel
 - Charpy, 591, 592, 594–596
 - depletion, 593, 601
 - dislocation pinning, 591
 - ductile brittle transition temperature, 589–596
 - embrittlement, 589–598
 - glide, 591
 - master curve, 594, 596–598
 - non destructive examination, 595
 - obstacles, 591
 - plastic strain, 591, 594
 - segregation, 590
 - stress intensity factor, 594

- surveillance program, 589, 595, 597
- tempering heat treatment, 590
- Reactor oversight process, 1777
 - crosscutting issues, 1778
 - human performance, 1778
 - International Nuclear Safety Advisory Group, 1779
 - performance indicators, 1778
 - problem identification and resolution, 1778
 - safety-conscious work environment, 1778
 - safety culture, 1778, 1779
 - significance determination process, 1778
- Reactor safety study, 1760, 1762–1769
- Reactor Safety Study Methodology Application Program, 1769
- Reactor trip system, 2252, 2280, 2297, 2310, 2311, 2317
 - emergency protection, 2280
 - reactor scram, 2310
- Reactor V-230, 2257, 2259, 2260, 2264–2267, 2274, 2283, 2285, 2291, 2295
- Reactor vessel internals (RVI), 2190, 2193, 2206
- Real row vector, 645
- Rebalance method, 537
- Receptor characterization, 1424
- Reciprocal lattice, 201
- Reciprocity relationship, 494, 497, 498
- Reciprocity theorem, 256, 992–993, 1007, 1048
- Recombination volume, 552, 557, 562
- RECONR, 955
- Recoverable energy, 765, 859, 863
- Recriticality, 2745, 2746
- Rectangular duct, 1415, 1418–1420, 1423
- Rectangular matrix, 649–651, 655, 656, 663
- Recuperator, 2735
- Recurrent states, 1973
- Recursive procedure, 196
- Recycling (or recycle), 3326, 3349, 3402–3403, 3409, 3414
- Red-black iteration scheme, 1101, 1102, 1156
- Red Book, 2899, 2900
- Reduced covariances, 2046
- Reduced neutron width, 263
- Reduced-order modeling, 1962, 1970, 2047
- Reduced singular value decomposition (SVD)
 - left/right singular vectors, 663
 - rank-one matrix, 663
 - singular values, 663
- Reduced uncertainties, 1924, 2003, 2007, 2034, 2047
- Reduction potentials, 2975
- Reflected angles, 1135, 1136
- Reflective boundary conditions, 932, 941, 1079, 1120–1121, 1135
- Reflector, 2728
- Regeneration system, 2278, 2295, 2309
- Region averaged flux, 1230
- Region integrated flux, 1230
- Regularly inherited traits, 1434
- Regulatory authorities, 3015, 3034, 3035, 3044, 3050, 3055, 3244
- Regulatory Guide 1.206, 1749, 1757, 1758, 1773–1775, 1780
- Reich–Moore, 245, 249–252
 - approximation, 71–72
 - formalism, 88, 93, 142
- RELAP5, 1818, 1844, 1845, 1859, 1860
- Relative biological effectiveness (RBE), 1340, 1342, 1343
- Relative error, 1927, 1931, 1939
- Relative frequency, 1931–1933, 1995
- Relative measurement error, 1927
- Relaxation volume, 551, 552
- Reliability algorithms, 1940, 1941
- Reliability/availability, 1972, 1973, 1977, 1979, 1980, 1999, 2046
- Relief tank, 2260, 2262, 2263, 2275, 2316
- Remediation activities, 3060, 3062–3064
- Removal coefficient, 1381–1383, 1386, 1387, 1389, 1393, 1420
- Removal cross section, 862, 881, 893, 936, 937, 1030, 1090, 1157, 1211, 1228, 1229, 1382–1387
- Removal-diffusion, 1387, 1392–1394
- Repeatability, measurement, 1939
- Reproducibility, measurement, 1929, 1939
- Resolution, instrument, 1928
- Resolved and unresolved resonance energy ranges, 976
- Resolved resonance region, 239, 241, 242, 245
- Resolved resonances, 87, 88, 92–95, 97, 110, 139, 142, 143, 161, 172
- Resonance
 - calculation, 927, 943, 944, 956, 967, 969–977, 979, 989, 995, 1000, 1004, 1013, 1023–1025, 1034–1036, 1047, 1051, 1052, 1059, 1061–1063, 1065–1069, 1231, 1232
 - cross section, 39, 42–43, 70
 - energies, 299, 316, 317, 339, 350
 - escape probability, 516
 - integral, 92, 110, 111, 136, 137, 144, 161–162, 181, 254, 260, 1004–1005, 1027–1029
 - interference factor, 926, 927, 1062, 1064, 1065
 - interference factor (RIF) table, 1062–1063
 - overlap effect, 946, 977, 1023, 1034, 1061–1065
 - parameters, 282, 286, 291, 303, 304, 312, 313, 316, 317, 320, 330, 335, 336, 340, 369, 373
 - reconstruction, 253
 - scattering, 948, 1023
 - shift factors, 246, 247, 251, 252
 - structure, 38, 44, 49
- Response, 1916, 1917, 1923–1926, 1928, 1935–1946, 1948–1952, 1954–1994, 2003–2017, 2021, 2022, 2024, 2027, 2029, 2032–2040, 2042, 2044–2048

- covariance, 2008, 2009, 2032, 2037
 - function cross sections, 231
 - matrix, 931, 1092, 1093, 1097–1099, 1101, 1102
 - Restart file, 1214, 1231
 - R' groups, 2967
 - Rheology, 3414
 - Riemann problem, 1817, 1862–1867, 1875, 1879, 1889, 1891, 1892, 1900–1908
 - Riesz representation theorem, 674
 - Rim effect (or rim). *See* Rim zone
 - Rim zone, 3414
 - Ring-forged shells, 2190
 - Ring of fire low leakage loading pattern, 1271
 - RIPL library, 89, 98, 99, 102, 131, 145
 - Risk ranking importance analysis
 - risk achievement worth, 1795
 - Risk-related dose limits, 1440–1441
 - R-matrix
 - approximations, 69–72
 - formalism, 43, 57–72
 - theory, 87, 88, 92, 101, 129, 136
 - Rod bowing effect, 2064, 2065
 - Rod consolidation, 3165, 3166
 - Rod substitution effect, 2065
 - Roe's approximate Riemann solver, 1870
 - Roe's average states, 1870, 1871
 - Rokkasho, 3474, 3481, 3489
 - Rotary hammers, 3156
 - Rotationally invariant, 436, 466
 - Rotational modes, 192, 208, 209
 - Routes of exposure, 3214
 - Rowlandns model, 1065
 - Row matrix, 650
 - RP V-392, 2252, 2255
 - RP V-428, 2252, 2255, 2299, 2302, 2310, 2318
 - Runge–Kutta method, 1178–1180, 1183, 1188–1190, 1195, 1199, 1886
 - r - z geometry, 231
- S**
- Saddle-point method, 2046
 - Safe enclosure phase (SEP), 3030, 3032–3033, 3182, 3183
 - Safeguards by design (SBD), 3468–3470
 - Safe shutdown earthquake (SSE), 2195, 2220, 2228
 - Safe storage, 3008, 3010, 3011, 3013, 3120, 3206, 3209, 3244
 - Safety
 - analysis, 1917, 2043, 2046, 3005, 3196
 - assurance, 1762, 1783
 - accident scenarios, 1744, 1745, 1747, 1755, 1759
 - design basis accidents, 1745
 - deterministic analysis, 1744, 1745, 1759
 - probabilistic safety analysis, 1745
 - three mile island (TMI) accident, 1745
 - culture, 3009, 3196, 3244
 - features, 1742, 1743, 1745, 1746, 1748, 1756, 1758–1759
 - functions, 1748, 1749, 1751–1753, 1759, 1789
 - injection systems (SISs), 2202, 2204, 2219, 2221, 2225, 2247
 - rods, 2060, 2073, 2074, 2079, 2087, 2113–2115
 - Safety, Levels 1–4, 2313
 - Safety depressurization system (SDS), 2193, 2199, 2205, 2210, 2242, 2243
 - SAFSTOR, 3011, 3012, 3026, 3232
 - Salt, molten
 - eutectics, 2868
 - MSRE, 2847–2850, 2878
 - SAMMY code, 87–89, 92, 97, 106, 110–112, 118, 130, 135, 136, 139, 143
 - Sample correlation coefficient, 1949
 - Sampling-based methods, 1940, 1941, 1945, 1948, 1951
 - Sampling-based uncertainty and sensitivity analysis, 1941, 1945, 1946, 1949
 - Sandwich formula, 2032, 2033
 - Sandwich rule, 1923, 1937
 - Savannah River Site (SRS), 3103, 3162, 3170
 - Scabbling, 3071, 3086–3089, 3113–3115, 3156
 - Scalar flux, 484–485, 489, 495, 499, 507, 525
 - Scalar multiplication of a vector, 645, 646
 - Scalar neutron flux, 289
 - Scalar product, 486
 - Scale parameter, 1997
 - Scarification, 3086, 3087, 3113–3115
 - Scattering, 430, 431, 436, 437, 446, 448, 453, 454, 456, 457, 460, 461, 464, 479, 484, 492, 493, 499, 500, 503, 504, 507–511, 513–519, 533, 539, 550
 - cross section, 925, 938, 942, 953, 961, 969, 976–980, 985, 986, 988, 997, 1007, 1016, 1018, 1019, 1023, 1024, 1057, 1071, 1073, 1104, 1117
 - function, 193, 214
 - integral, 465–467, 475, 477, 478, 514, 518
 - kernel, 930, 1117, 1118, 1228
 - length, 91, 92, 129, 193
 - matrix, 952, 953, 961, 964, 966, 968, 971, 1161
 - radius, 245, 246
 - source, 445, 451, 506, 536, 537, 1089, 1098, 1105, 1116, 1117
 - source iterative scheme, 838, 839
 - Schofield, 195, 198
 - Scintillation detector, 3187, 3188
 - Scintillation detectors or phosphor detectors, 3187
 - Scoping report, 3203
 - Screening design methods, 1940–1945
 - SCT cross section, 211
 - Secondary circuit, 2252, 2276, 2277, 2314, 2316
 - Secondary masses, 3224–3227
 - Secondary neutron distributions, 286, 292–293, 298
 - Secondary structure, 263, 275

- Secondary waste, 3065, 3066, 3068, 3069,
 3072–3078, 3080–3083, 3086, 3104, 3108, 3122,
 3130, 3143, 3145–3148, 3151, 3179, 3191, 3192, 3216,
 3225–3228
- Second-order reliability methods (SORM), 1940,
 1941
- Second-order Runge–Kutta method, 1179, 1180, 1183
- Second-order sensitivity index, 1954
- Security Council, 3450, 3453
- Segmenting equipment, 3156
- Segregation, 560, 565, 574, 590,
 –grain boundaries, 551, 564, 569, 570, 579, 590,
 596, 598–601, 603, 608, 612, 621, 623, 624
 –inverse Kirkendall effect, 564, 601
 –radiation induced segregation, 563, 564,
 600–601
- Seismic design, 2286, 2318
- Seismic impact classification (MSK), 2318
- Selective actinide extraction process (SANEX), 2969
- Self-collision factor, 845, 846, 849–851, 858
- Self shielded cross sections, 231, 234, 257, 260, 264,
 265
- Self-shielding factors, 354, 358, 360, 361, 369, 370,
 394, 399, 400, 402, 403, 952, 991, 1026–1029, 1051
- Sensitivity
 –instrument, 1928
 –measuring instrument, 1940
 –vector, 1937
- Separation factor, 2910, 2913, 2915, 2965, 2970, 2978
- Separative work units (SWU), 2909–2912, 2914,
 2916, 2917
- Separator-superheater (SSH), 2278, 2308, 2309
- Sequential bifurcation (SB), 1940, 1944
- Sequential design, 1944
- Service water system, 2317
- Severe accidents, 2282, 2285–2286, 2317–2318
- SG super-emergency feedwater system (EFPW),
 2285
- Shallow dose equivalent index, 1348
- Shape function, 1675–1677, 1679, 1680, 1682, 1685,
 1722
- Shared memory, 1453, 1455, 1458–1463, 1465, 1466,
 1474, 1475, 1491
- Shared memory multiprocessors (SMP), 1455, 1463,
 1478
- Sharp interface method (SIM), 1866, 1888
- Shell-mode, 1704–1708
- SHEM 281 groups, 946–949
- Sherman–Morrison formula, 654
- Sherman–Morrison–Woodbury, 2010
- Shielded cross section, 1026
- Shield heterogeneities, 1376–1378
- Shielding design, 1316, 1322, 1362, 1364, 1370, 1372,
 1375, 1388, 1389, 1421, 1424–1430
- Shielding standards, 1425, 1430
- Shielding testing, 159–161
- Shield optimization, 1424
- Shock fix, 1879
- Shock tube problem, 1817, 1864, 1889, 1892–1893,
 1896, 1897
- Shooting method, 828, 833, 837
- Short Collision Time approximation, 197–198, 211
- Short-lived/low-medium-level activity waste, 3010
- Shot blasting, 3106–3107, 3111
- Shutdown cooling coefficient, 1216–1218
- Shutdown earthquake (SSE), 2195, 2220, 2228, 2251,
 2254, 2318
- Shutdown system no.1, 2239
- Shutdown system no.2, 2239
- SIGAR method, 330, 331, 335, 336
- SIGMA1 method, 332, 333, 335, 340, 342, 344
- Sigma-ID, 3467, 3470
- Sigma-MUF, 3467, 3469
- Sigma retrieval, 92, 163
- Silo, 3167, 3173
- SIMPLE, 1817, 1859
- Simplified P_n equation, 778, 792, 860, 862
- Simplified spherical harmonic, 523
- Simplified transmission probabilities, 931, 1092,
 1094
- SIMULATE-3, 1208, 1223
- Simulated annealing (SA) selection, 1288, 1290
- Single-channel analyser, 3186, 3188–3190
- Single direct measurement, 1933
- Single-envelope containment, 2291
- Single failure criterion
 –code of federal regulations, 1749
 –structure, system and component, 1748
- Single indirect measurements, 1935
- Single instruction, multiple data streams (SIMD),
 1452–1456
- Single-level Breit–Wigner (SBLW) resonance,
 245–247, 249, 250, 252, 262–264, 275, 317, 330,
 339, 343, 349
- Single measurements, 1928, 1932
- Single program multiple data (SPMD), 1463
- Singular/nonsingular matrix
 –inverse matrix, 654
 –nonsingular, 653–654, 657, 663, 738
 –singular, 653–654, 663
- Sink strength, 559
- Sintering, 2951, 2952, 2954, 2955, 2957, 2985
- SIPA, 575, 612–614, 621
- Size effect, 2731
- Skew–Hermitian matrix, 650
- Skewness, 1935, 1936
- Skew-symmetric matrix, 650
- Skold approximation, 214
- Skyshine analyses, 1359, 1410, 1412
- Slab and cylinder phantoms, 1348
- Slab geometry, 254
- Slant incidence, 1398

- Slowing down, 939, 943–945, 948, 952, 956, 957, 966, 972, 975–979, 981–984, 986, 988, 991–997, 1005–1012, 1014, 1018, 1023, 1024, 1026, 1030–1033, 1037, 1043, 1047, 1052, 1061, 1069, 1119, 1154, 2714
 –density, 273
 –time, 268, 269
- Small secure transportable autonomous reactor (SSTAR), core design, 2760
- Smoothness of the angular flux, 431, 457–460
- SMP. *See* Shared memory multiprocessors
- S_N method, 227, 233, 236, 275, 821
- Sobolev space, 880
- Sobolev spaces, 671
- Sobol's method, 1940, 1941, 1951, 1953
- Soda gel spraying, 3104
- Sodium (Na), 557, 602, 603, 615
- Sodium bisulphate (NaHSO_4), 3092, 3093
- Sodium carbonate (Na_2CO_3), 3095, 3100
- Sodium expansion, 2529–2530, 2532, 2534, 2670
- Sodium fluoride (NaF), 3070, 3092
- Sodium hydroxide (NaOH), 3092, 3094, 3095, 3097, 3100, 3104
- Sodium sulphate (Na_2SO_4), 3070, 3078, 3092
- SOFOCATE, 920
- Software quality assurance (SQA), 1916, 2043, 2045
- Software resources, 1429
- SOGIN, 3023, 3057, 3082, 3089, 3106, 3124, 3126–3130, 3134, 3141, 3142, 3149–3150, 3170, 3199, 3237, 3238, 3241
- Sol-gel, 2949–2952, 2956–2958, 2960
- Solid angle, 433, 434, 440, 753, 755–758, 762, 772, 776, 794, 821, 823, 825, 826, 1317, 1320, 1401, 1402, 1414, 1415
- Solid solution, 2941, 2942, 2945, 2946, 2948–2952, 2955, 2956
- Solid-state detectors, 3187, 3188
- Solid-state ionization chambers, 3188
- Solid-type spectrum, 195, 198
- Solid wastes, 3102–3104, 3174, 3181, 3182, 3189, 3209
- Soluble boron efficiency, 2058
- Solvability condition, 528
- Somatic effects, 1430, 1431, 1434
- Sorbed, 3365–3369, 3396, 3409, 3416. *See also* Sorption
- Source characterization, 1322, 1424
- Source-detector problems, 538, 539
- Source isolation method, 846
- Source iteration, 457, 536, 537
- (α, n) Sources, 1326, 1327
- Space-dependent Dancoff method (SDDM), 1051–1060, 1067, 1069
- Space-dependent self-shielding effect, 1039, 1047, 1051, 1067
- Spacer grid, 2269, 2273, 2298, 2299
- Space-time behavior, 266–274
- Spacing between tracks, 1131
- Spallation source, 2122
- Spatial averaging (homogenization), 971
- Spatial eigenvalues, 271, 272
- Spatially dependent, 288, 353, 355, 405
- Spatial self-shielding effect, 226, 236, 972, 974, 1025, 1036, 1066, 1067
- Special geometries, 453, 464–479
- Specific burnup (or specific burn-up, burn-up rate, burn-up), 3408, 3415
- Spectral calculations, 1070–1092, 1094, 1099, 1100, 1158, 1160
- Spectral distribution, 1320
- Spectral effect, 2529
- Spectral indexes, 2058, 2065, 2080, 2083, 2099, 2102, 2105, 2127, 2130, 2142, 2160, 2168–2172
- Spectrometry gamma, 2068, 2072, 2083, 2103, 2127–2129, 2159–2164
- Spectrum of excitations, 193
- Specular reflection, 762, 779, 780, 855
- Spent fuel (or spent nuclear fuel, SF), 2719, 2736, 2931, 3006, 3008, 3012, 3014, 3027, 3034, 3055, 3164–3194, 3205, 3206, 3230, 3232, 3244, 3258, 3261, 3263–3265, 3267–3269, 3276–3280, 3283–3284, 3289–3292, 3294, 3309, 3320, 3323, 3326–3344, 3347–3350, 3377–3379, 3402–3405
- Spent fuel pool, 1201
- Spent fuel treatment. *See* Treatment (of spent fuel)
- Spent nuclear fuel. *See* Spent fuel
- Sphere-pac, 2949, 2957
- Spherical-geometry transport equation, 465, 473, 478, 479
- Spherical harmonics
 –functions, 465, 466, 471, 518
 –method, 778–794
- Spherical phantoms, 1348
- Spherical symmetry, 471, 472
- Spin effects, 192, 214
- Spinel, 579
- Split function
 –pressure split function, 1873, 1876
- Spontaneous fission, 1323, 1325, 1330, 2941, 2942, 2948
- Sqrt(E) shape, 244
- Square matrix
 –determinant
 –cofactor, 652, 653
 –leading, 652
 –minor, 652
 –principal minor, 652
 –properties of determinants, 652–653
 –norm
 –condition number, 662, 663
 –ill-conditioned, 663
 –matrix-Hölder norm, 662
 –maximum column sum matrix norm, 662

- maximum row sum matrix norm, 662
 - spectral norm, 662
- power
 - index of nilpotence, 652
 - in matrix, 652
 - nilpotent, 652
 - polynomial, 652
- Square pincell, 814, 815, 820, 847, 849, 900–906
- Stability indicator, 1711, 1713–1714
- Stacking fault tetrahedra, 554, 562, 568
- Stainless steel, 549, 556, 563, 564, 588, 598–615, 619, 634, 635, 2253, 2263, 2266, 2270, 2279, 2282, 2283, 2295
- Stakeholders, 3055, 3202–3204
- Stammlers method, 1020–1023, 1025, 1057, 1059
- Standard deviation, 533, 534, 1919, 1935, 2029, 2031, 2032
- Standard OAT, 1942
- Standard review plan, 1749, 1757, 1758
- Standard unit vectors
 - standard basis, 648
 - standard unit vector, 648
- STAR Codes, 1343
- State system for accounting and control (SSAC), 3454–3457, 3469
- Static and dynamic multiplication factor, 284
- Static flux, 1667, 1676, 1684, 1685
- Static structure factor, 214, 215, 274
- Stationary point, 875, 880–883
- Stationary random sequence and white noise
 - stationary white noise, 746
 - time series, 746
 - weakly (or second-order) stationary, 746
- Statistical averaging, 1820
- Statistical estimation
 - best linear unbiased estimator (BLUE), 742, 743
 - confidence interval, 744, 745
 - consistent, 741, 742, 744, 745
 - efficient estimator, 742
 - estimation rule, 742, 744
 - estimator, 742–745
 - generalized least-squares method, 744
 - interval estimation, 744
 - likelihood function, 743, 744
 - maximum likelihood estimator (MLE), 743, 744
 - mean-squared error, 742
 - null hypothesis, 746
 - point estimator, 742, 744
 - power, test, 746
 - sample central moment statistic of order k , 743
 - sample mean, 742–745
 - sample moment of order k , 742–743
 - sampling process, 742, 743, 745
 - significance level, 745
 - statistical hypothesis, 745–746
 - sufficient estimator, 742
 - test of hypothesis, 746
 - type I error, 746
 - type II error, 746
 - unbiased, 741–744
 - uniformly most powerful tests., 746
- Statistical mechanics, 753
- Statistical methods, 28, 36, 1923, 1930, 1934, 1940–1954, 2004
- Steady state Boltzmann equation, 928, 1071, 1104
- Steady-state problems, 432, 451, 455, 456
- Steam cleaning, 3106, 3108, 3156
- Steam generator, 2251–2254, 2256, 2258, 2263, 2276–2278, 2285, 2286, 2295, 2296, 2304–2308, 2320
- Steam generator PGV-4, 2276, 2306
- Steel drums, 3181
- Steel/sodium reflector, 2121, 2122
- Steger and Warming's method, 1871
- Step-characteristic, 844, 846, 850, 854
- Stepwise regression analysis, 1950
- Stewart for photons, 394
- Stieltjes–Hilbert moments problem, 406
- Stiffness matrix, 886, 887
- Stochastic effects, 1350, 1430, 1431, 1441, 1442
- Stochastic effects in neutron transport, 463
- Stochastic uncertainties, 1916
- Stoker–Weiss method, 1051–1060, 1067, 1069
- Stopping power, 1337, 1342
- Storage, 2736, 3259, 3260, 3277–3278, 3281–3287, 3291, 3292, 3301, 3303, 3309, 3323, 3326–3328, 3330–3332, 3335–3380, 3402–3404, 3406, 3408–3410, 3412, 3414, 3415
 - facilities, 3010, 3041, 3164, 3166, 3167, 3169, 3173, 3185, 3197, 3209
 - of radioactive materials/waste, 3277, 3340, 3408, 3415
- Straight ducts, 1414–1416, 1420–1421
- Strategic Arms Reduction Treaty (START), 3424
- Strategic Offensive Reductions Treaty (SORT), 3424
- Stratified media, 1370–1372
- Streaming, 431, 434, 445, 481, 484, 490, 491, 499, 535
 - operator, 760, 772–778
 - tracks, 934, 935, 1080, 1094, 1095
- Stress corrosion cracks (SCCs), 549, 588, 598–600, 625, 626, 631, 632, 2196, 2205, 2213
- Stretch out, 1254, 1257–1259, 1284, 1291
- Strictly diagonally dominant, 658
- Strict OAT, 1942
- Structural materials, 128–131, 145, 179, 180
- Structural mechanics, 1478, 1483
- Sub-assemblies, 2918, 2926
- Subcritical, 452, 455, 493, 494, 525, 531, 1119
 - state, 1632
 - systems, 2118, 2176
- Sub-group
 - cross section, 1028, 1035–1046, 1067

- method, 943, 956, 967, 973–976, 1035–1047, 1049–1051, 1067–1069
 - parameters, 1036, 1039–1044, 1046, 1047, 1050, 1067
 - structure, 1036
 - Subjective probability, 1995
 - Subjective uncertainties, 1916, 1945, 1948
 - Subjective (epistemic) uncertainties, 1941
 - Sub-meshing, 874
 - Subspace, 649, 654, 655, 662, 666, 668–670, 673, 675, 730
 - subspace, R^n , 648
 - trivial subspace, 648
 - Sub-step method, 1198–1200
 - Suction pressure, 2277, 2278
 - Sulfamic acid (HSO_3NH_2), 3093–3095, 3102, 3152, 3153
 - Sulfuric acid (H_2SO_4), 3070, 3074, 3078, 3091, 3092, 3096, 3104, 3153, 3199
 - Sum/addition of vectors, 645
 - Sum rules, 194–195
 - Superconvergent, 875, 887
 - Super (sub) diagonals, 649
 - SUPERFACT, 2958, 2960, 2963, 2988
 - SUPERFACT irradiation experiment, 2958
 - Superposition principle, 499, 1356, 1358–1359
 - Support platform, 3158–3160
 - Surety fund, 3221
 - Surface-cleaning, 3078–3080, 3085, 3105, 3106, 3156, 3180
 - Surface currents, 931, 932, 941, 1079, 1080, 1092, 1093, 1098, 1158
 - Surface decontamination, 3014, 3069, 3087, 3114
 - Surface removal, 3078, 3079, 3085, 3086, 3105, 3106, 3114, 3115
 - Surface water, 3063–3064, 3207, 3210, 3213, 3216
 - Surrogate reactions, 53–57
 - Surveillance, 3447, 3456, 3457, 3463–3465, 3467, 3469, 3470, 3476, 3483, 3484, 3494, 3518
 - Suspension jet, 3140–3142
 - s-wave neutron scattering, 436
 - Sweeping, 440, 536
 - Swelling, 549, 560, 569, 580, 588, 602, 612–615, 623, 627, 632
 - annihilation, 604, 605
 - cold work, 603, 606, 608, 609
 - nucleation, 559, 574, 604–607, 610, 611, 630
 - vacancy, 557, 559, 563, 575, 579, 604–606
 - Symmetric and positive (negative) definite matrix, 647, 648
 - hyper-ellipsoid, 661
 - Symmetric matrix, 647, 648, 650, 654, 655, 658, 659, 662, 663, 679, 726
 - orthogonal projection matrices, 661
 - rank-one outer-product, 661
 - spectral decomposition, 661
 - Symmetric scattering law, 195
 - Symmetry/reflecting boundary conditions, 460, 479, 518, 521
 - Synroc, 2985
 - Synthetic acceleration, 838–840, 853, 857
 - Systematic error, 1916, 1929–1934, 1940, 2001
 - Systematic fractional replicate design (SFRD), 1940, 1943, 1944
 - System code, 1818, 1819, 1844–1845, 1859
 - System response, 1916, 1924, 1935, 1943, 1955, 1956, 1959, 1960, 1965, 1970, 1974, 1979, 1983, 1985, 2044, 2045
 - Systems without feedback, 1962
- ## T
- TALKSPEAK process, 2969
 - Tamper indicating device (TID), 3464, 3494
 - Tangent linear model (TLM), 1966–1967
 - Tank fluence, 2072
 - Tank in tank, 2215, 2263
 - Target atom, 550–552
 - Target-at-rest cross section, 210, 234, 253
 - Taylor form, 1365, 1369
 - Taylor-series expansion, 680, 681, 1936, 2004
 - Taylor series second order, 680
 - Taylor's expansions, 802, 807, 875, 876, 878
 - Tchebyshev (Chebyshev) polynomials, 667
 - Technical Specification Task Force, 1781
 - Telem manipulators, 2948
 - Teleoperator control station, 3158–3159
 - Teleoperator managed stations, 3159
 - Televisual inspection, 3162
 - Temperature accelerated dynamics (TAD), 1502
 - Temperature coefficient, 2058, 2063, 2067, 2068, 2080, 2082, 2142, 2144, 2147, 2153–2154
 - TEMPO and psi-chi methods, 339, 340, 347
 - Tendons, 2725
 - Tensor-arm, 3161
 - Tenth-value thickness, 1354
 - Terms of reference (ToR), 3202, 3206
 - Tertiary masses, 3224, 3227
 - TGBLA, 922
 - Thermal activation, 557, 570, 615
 - Thermal alpha, 254
 - Thermal conductivity, 2941–2943, 2945, 2946, 2962, 2985
 - Thermal constants, 90, 121, 171, 253, 254
 - Thermal cross section, 46
 - Thermal energy, 86, 87, 89–92, 110, 125, 139, 163
 - Thermal eta, 254
 - Thermal expansion, 560, 569, 625, 627, 628
 - Thermal flux, 1673, 1689
 - Thermal g-factors, 253, 254
 - Thermal insulation, 2256, 2259–2261, 2286
 - Thermalization, 1378, 1389, 1390, 1392, 1394, 1396, 1412, 1428

- neutrons, 943
- size, 236–238
- time, 269
- Thermal KI, 253, 254
- Thermal output, 177, 1175, 1176
- Thermal scattering, 91, 129, 163, 171, 177–179
- Thermal values, 89, 124, 137, 161–162, 181
- Thermochemical, 2741, 2743
- Thermo-chemical methods (TCM), 1503, 1505, 1512
- Thermography, 3163
- Thermoluminescence technique, 2070
- THERMOS, 228, 236, 920, 921
- THERMR, 955–956
- ²³²Th evaluation, 118–119, 143
- Thick-target bremsstrahlung, 1338
- Three mile island (TMI) nuclear power reactor, 1768
- Threshold energy, 1325, 1327, 1336, 1388
- Tianwan NPP, 2252, 2255, 2290, 2307, 2313, 2318
- Time-independent problems, 2013
- Timeliness criteria, 3459
- Time-of-flight laboratories, 6–24
- Time-resolved laser-induced fluorescence spectroscopy (TRLFS), 2968, 2969
- Tissue weight factor, 1350, 1351
- TLG, 3230, 3232–3236
- Tokai, 3498, 3499
- Tokai Reprocessing Facility, 3092
- Tolerable doses, 1440
- Tones method, 1047–1051, 1067, 1069
- Top head unit, 2257, 2267
- Top nozzle, 2269, 2270, 2273, 2299
- Torch, 3124, 3125, 3128–3130, 3133–3137, 3147
- Total absorption, 353
- Total cross section, 9, 13, 15, 39–41, 43–47, 50, 64, 65, 70, 927, 930, 952, 966, 991–993, 1005–1007, 1010, 1013, 1016, 1019–1021, 1042
- Total effective dose equivalent (TEDE), 1757, 1758
- Total (or scalar) flux, 929–931, 935, 941, 971, 1072–1074, 1077–1080, 1089, 1090, 1092, 1093, 1097–1099, 1102, 1113, 1114, 1116, 1122–1125, 1134
- Total interaction coefficient, 1345, 1355, 1357, 1362
- Total loss of feed-water (TLOFW), 2199, 2210, 2211, 2220
- Totally absorbing, infinite medium, 353
- Total macroscopic cross section, 288, 436
- Total peaking factor, 1267
- Total phasic energy, 1825
- Total scattering, 353
- Total source for a non-multiplying system, 1119
- Total variation diminish (TVD) condition, 1879
- TRABANT-1 experiment, 2960, 2963
- TRAC, 1859
- Trace, matrix, 680
- Track adjustments, 1132–1133
- Tracking file, 796, 820, 900
- Tracking operator, 847, 900
- Track separations, 1135, 1154
- Transfer cask (TC), 3171, 3173, 3175
- Transfer function, 1646, 1665, 1666, 1668–1670, 1679–1681, 1687, 1690–1692, 1694, 1697, 1698, 1726, 1727
- Transfer matrix, 303, 375, 376, 381, 388, 390, 392, 393, 408–410
- Transient states, 1973
- Transition probabilities, 1633, 1667
- Transition rate matrix, 1972, 1974, 1977, 1980
- Translational modes, 192, 205, 208
- Translational spectrum, 195
- Transmission probability (TP), 797, 812, 816, 819, 905, 931, 932, 1021, 1053, 1091–1094, 1096, 1103
- Transmutation, 1163, 1164, 1172, 1249, 2739, 2938, 2940, 2941, 2947, 2952, 2955, 2958, 2960–2963, 2966, 2969, 2974, 2976, 2982, 2983, 2985, 3260, 3277, 3285–3287, 3402, 3403, 3408, 3415
- Transport approximations, 228
- Transport-corrected cross sections, 930, 932, 934, 953, 1073, 1105, 1108, 1117, 1160
- Transport cross section, 521, 930, 953, 1105, 1226
- Transport equation, 753, 760–763, 765–768, 770–772, 778, 794, 796, 821, 823, 839–841, 853, 857, 859, 860, 862, 900, 1484, 1488, 1491, 1509
 - characteristic, 760–761, 840, 841
 - interfacial energy, 1842
 - pseudo-turbulent energy, 1833
 - total energy, 1832, 1856
 - volume fraction, 1816, 1830, 1832, 1833, 1839, 1841–1842, 1844, 1857
- Transport matrix, 1075, 1083, 1084, 1087
- Transport table, 231, 232
- Transpose of matrix, 650, 672, 674, 679
- Transuranic (TRU) nuclides, 3188
- Transuranium elements, 2937–2991
- Transverse integration, 889
- Transverse-leakage, 889, 890, 893
- TRANSX code, 234, 235
- Treatment (of spent fuel) (or reprocessing, spent fuel treatment), 3326, 3403, 3409, 3414, 3415
- Trial functions, 785, 883–885
- Triangular grid, 2251, 2253, 2268, 2269
- Tributylphosphate, 2909
- 1,1,1-Trichloroethane, 3101
- Trichloroethylene, 3101
- Tridiagonal structure, 877
- Trio_U, 1495–1498
- TRIPOLI-4^Z, 1484, 1485
- TRIPOLI4 code, 1486, 2072, 2075, 2076, 2088
- Tripyridyltriazine (TPTZ), 2969
- TRISO, 2724, 2725, 2729, 2736, 2743
- Trisodium phosphate (Na₃PO₄), 3095
- TRPO process, 2969
- True area, 1131, 1137, 1138, 1141, 1144

- True value, 1927, 1929, 1930, 1932, 1933, 1935, 1939, 1940, 1972, 1974, 1994, 2001, 2002
- TRUOX process, 2969, 2970
- Turbine, 2252, 2278, 2279, 2307–2310
 –building, 2263, 2291, 2295
 –generators, 2263, 2273, 2277, 2281, 2312
 –hall, 2256, 2263
- Turbine Island (TI), 2201–2202, 2205
- Two-fluid model, 1819–1820
- Two-group theory, 1632, 1670, 1671, 1673–1675, 1678, 1682, 1685–1690, 1695, 1699
- Two-level computational scheme, 859
- Two-phase momentum balance, 1822, 1840
- Two-step, 2034, 2047
- U**
- (U,Gd)O₂
 –heat capacity, 1534–1536
 –melting temperature, 1536–1537
 –thermal conductivity, 1529–1537
 –thermal expansion, 1527–1528
- (U,Pu)O₂
 –heat capacity, 1534–1536
 –melting temperature, 1536–1537
 –thermal conductivity, 1529–1537
 –thermal expansion, 1527–1528
- (U_{0.5}Np_{0.25}Am_{0.25})O_{1.93}, 2942
- ²³³U evaluation, 119–120
- ²³⁵U evaluation, 106–110
- ²³⁸U conversation rates, 2058, 2103
- ²³⁸U evaluation, 110–115, 156
- UK Central Electricity Generating Board, 3097
- Ultra-fine energy group calculation, 943, 967, 973, 974, 1032, 1034, 1043, 1063, 1064, 1067, 1069
- Ultra-fine group method, 976, 1029–1036, 1061
- Ultra-high-pressure, 3106–3107, 3110–3111
- Ultrasonic cleaning, 3070, 3106–3107, 3120–3121
- Unattended monitoring, 3470–3492, 3500
- Uncertainty assessment method (UAM), 2043
- Uncertainty of measurement, 1940
- Unconditional release, 3065, 3067, 3083, 3206, 3230
- Uncorrelated, 1921, 1937, 1947, 1954, 2009, 2029, 2032, 2034
 –distributions, 301, 376–378
 –parameters, central moments, 1938
 –reactions, 292
 –statistics, 1932, 1933
- UNPEDE, 3237
- Unit cell, 794, 795, 800, 801, 806, 811, 812, 859
- United Nations (UN), 3425, 3450, 3453, 3477
- Unit (identity) matrix, 650, 654, 659, 738
- Unit power control, 2280, 2310
- Unresolved range penetrabilities, 263
- Unresolved range self shielding, 263–265
- Unresolved resonance, 44, 49–51, 87, 88, 95–98, 106–107, 110–111, 119, 130, 140, 142, 168, 172
 –ladders, 264
 –region, 239, 241, 262–266, 275, 286, 291, 299, 304, 316–317, 350, 369, 372, 373, 394, 395
- UNRESR, 956
- Unrestricted release, 3014, 3034, 3042, 3178, 3179
- ²³⁵U nubar, 121, 124, 125
- UO₂
 –heat capacity, 1534–1536
 –melting temperature, 1536–1537
 –thermal conductivity, 1529–1537
 –thermal expansion, 1527–1528
- UO₂–GdO₃ absorber, 2061, 2067
- UO₂–PuO₂ solid solution, 2942
- UOX, 2063, 2064, 2067, 2082, 2101, 2102, 2107, 2169, 3265, 3269, 3309, 3327, 3332–3336, 3377, 3379, 3415
- (U, Pu)O_{2-x}, 2942
- Upper grid, 2269
- Upper guide structure (UGS), 2190, 2193, 2206, 2208, 2229
- Upper triangular matrix, 650, 656, 726
- Up-scattering, 920, 944, 945, 1030, 1033, 1090, 1099, 1124, 1154
- Upwinding, 1861, 1865, 1867, 1871, 1874, 1875, 1877
- Uranium dioxide, 2919
- Uranium molybdenum aluminium fuel, 2103
- Uranium oxide, 2937, 2945, 2954
- V**
- V-412, 2252, 2255
- V-428, 2252, 2255, 2291, 2295, 2298, 2299, 2301, 2302, 2304, 2308, 2310, 2311, 2313, 2317, 2318
- Vacuum, 1121, 1226
 –bell, 3156
 –boundary, 444, 451, 457, 495, 524, 525, 527
 –boundary condition, 763, 780, 787, 790, 812, 828, 833, 837, 897, 1078, 1083, 1120
 –cleaners, 3045, 3108
- Vacuum-relief system, 2254, 2260, 2262, 2286
- Validation, 86, 107, 112, 119, 146–162, 179, 1916–1918, 2027, 2029, 2043–2048
 –domain, 1917, 2002, 2003, 2045, 2047, 2048
 –domain estimation, 1917, 2003, 2045
 –experiments, 2044, 2045
 –tier hierarchy, 2044
- Vanadium, 630
- Vapor pressure, 2945
- Variance-based correlation ratio, 1952
- Variance-based first-order sensitivity indices, 1952, 1953
- Variance-based methods, 1940, 1941, 1951–1954
- Variational coefficients, 883–885
- Variational formulation, 875, 878, 880–884, 887
- Vector architectures, 1456–1458
- Vector difference, 645
- Vector processor, 1456, 1457

Vector projection, 649, 666
 –orthogonal projection of z onto S , 649
 –unit vector, 649
 Ventilation units, 3012, 3042, 3045, 3074, 3080, 3111, 3147, 3192
 Very high temperature gas-cooled reactors (VHTR), 1283–1285, 1309
 Very high temperature reactor, 1782
 Very low-level radioactive waste, 3010
 Very low level waste (VLLW), 3010, 3175, 3176
 Vessel bottom, 2260, 2286
 Vibrating absorber, 1684, 1691–1693, 1696
 Vibrational modes, 192, 195, 199, 209, 212
 Vibratory finishing, 3106–3107, 3121–3122
 Villarino–Stamm’ler normalization, 819, 820
 VIPAC fuel, 2949
 Vitrified HLW, 2938, 2964, 2982
 Void coefficient, 1214, 2065
 Void history, 1209
 Volume average model, 1065
 Volume integral, 446, 483
 V-213 reactor design, 2251, 2252, 2254, 2259, 2260, 2263, 2264, 2266, 2267, 2273, 2275, 2277, 2280, 2281, 2283, 2285, 2288
 V-230 reactor design, 2251, 2254, 2259, 2260, 2263–2267, 2273, 2281, 2283, 2285
 V-320 reactor plant, 2251, 2254, 2289, 2291, 2295, 2302, 2306–2308, 2311
 V-428 RP reactor, 2290
 VVER-440, 2251–2254, 2256–2288, 2313, 2320
 VVER-1000 reactor, 2289–2319

W

Wall thickness, 2018, 2024
 Waste, 2843, 2845, 2846, 2850, 2857, 2858, 2878, 2882, 2885, 2886, 2888, 2892
 –characterization, 3184–3190, 3222, 3242
 –equilibrium isotopes, 2880
 –geologic storage, 2844, 2851, 2856
 –management, 3038, 3053, 3174, 3224, 3230
 –ocean disposal, 2884
 –per MWe produced, 2876
 –routes, 3179, 3180, 3191–3193
 –Yucca Mtn, 2844
 Waste (nuclear). *See* Nuclear waste
 Waste (radioactive). *See* Radioactive waste
 Waste immobilization. *See* Embedding (of radioactive waste)
 Waste management facility (WMF), 3105, 3190–3193
 Waste technology section (WTS), 3242
 Water, 191, 192, 205, 207–217, 223–225, 3013, 3014, 3026, 3053, 3059, 3064, 3065, 3080–3082, 3085–3087, 3097–3106, 3108–3114, 3122–3125, 3127–3147, 3152–3154, 3207–3208, 3210–3212
 –flushing, 3105
 –purification systems, 2295

Water-cooled reactors, 1749
 water jet cutting, 3129–3130, 3136, 3149
 water jet gouging, 3132–3133, 3136–3137, 3150
 Water-injection-plasma-cutting (WIPC), 3134
 Watt approximation, 1324
 Wave number, 1860
 Weak formulation, 881
 Weak solution, 1861
 Weapon-grade, 2714, 2731, 2732, 2917, 2933
 Weighted residual approach, 875, 883
 Weight, heavy metal, 1174–1176
 Westcott factor, 89, 92, 121
 West European Nuclear Regulator Association (WENRA), 3244
 Wet abrasive cleaning, 3080, 3106–3107, 3111–3112
 Wet-ice blasting, 3106–3107, 3109
 Wet routes, 2949–2951
 White boundary collision probability, 1087
 White boundary conditions, 762, 787, 790, 811, 812, 819, 820, 832, 833, 855, 1032, 1070, 1085–1089
 White limit, 996
 Wide resonance (WR) approximation, 260, 980–986, 1023, 1024, 1034
 Wide resonance infinite (mass) absorber (WRIA) approximation, 980
 Width fluctuation, 89, 99, 100
 Wigner approximation, 430, 431, 507, 513–518
 Wigner cylinderization, 812
 Wigner effect, 628–629, 2714
 Wigner rational, 925, 996–1000, 1005, 1009, 1011, 1019
 Wigner rational approximation, 256, 257
 Wigner–Seitz approximation, 786, 787, 811
 Wigner’s rational approximation
 WIMS, 921, 922, 934, 944, 945, 957, 959, 962, 1005, 1020, 1028, 1035
 WIMS 69 groups, 922, 944–946, 957
 WIMS group structure, 191, 228, 259–262
 Within-group transport equation, 505–506
 Wolsong 1, 2231, 2232, 2235, 2245, 2246
 Woodbury’s extension, 654
 Work breakdown structure, 3039, 3045
 Working assembly, 2257, 2267–2270, 2272, 2273, 2280
 Working Party on Decommissioning and Dismantling (WPDD), 3243
 Work packages, 3044–3045, 3050, 3054, 3222
 World Association of Nuclear Operators, 1753, 3244

X

Xenon effect, 2714
 Xe oscillation, 1200
 XMAS 172 groups, 945–947, 957, 982–990, 1028, 1039, 1061
 X-ray absorption fine-structure spectroscopy (EXAFS), 2967, 2968

X-ray attenuation factors, 1375
X-ray beams, 1338, 1373–1375
X-ray machines, 1338–1339, 1359, 1375
X-ray sources, 1336–1339, 1372, 1373, 1376
Xylene, 3101

Y

Yield strength, 569–571, 574, 589–592, 596, 598, 601, 611, 612, 616, 618, 621, 622, 625
Yonggwang (YGN) 3&4, 2187, 2200, 2230–2232
Yttria (YSZ), 2945, 2958

Z

Zero-flux boundary condition, 763, 864, 867, 868, 873, 879, 883–885
Zero matrix, 649, 650
Zero-phonon term, 198, 200
Zero power noise, 1631, 1632, 1668, 1674
Zircaloy, 1068, 1537

- composition, 1537–1538
- elastic constants, 1543
- emissivity, 1542
- high temperature corrosion, 1549–1551
- hydriding, 1593
- irradiation-induced creep, 1544–1545

- irradiation-induced growth, 1543–1544
- irradiation-induced hardening, 1544
- nodular corrosion, 1545
- oxidation, 1547
- shadow corrosion, 1546, 1548
- specific heat capacity, 1542
- thermal conductivity, 1541–1542
- thermal expansion, 1541

Zirconium (Zr), 554, 555, 557–559, 565–567, 601, 602, 607, 629

- alloys, 545, 546, 556, 588, 616–619, 621, 622, 625, 631
- amorphization, 619, 620
- cladding thickness, 621
- corrosion, 616, 617, 622–625
- growth, 617, 619–621, 624
- pellet cladding interaction (PCI), 625–626
- precipitate, 617, 619, 620, 624, 625
- stress corrosion cracking (SCC), 625–626, 631, 632
- Zircaloy, 616–622, 625, 626

Zirconium hydride, 191, 216
Zirconium–niobium, 2251, 2253
Zirlo alloy, 2207